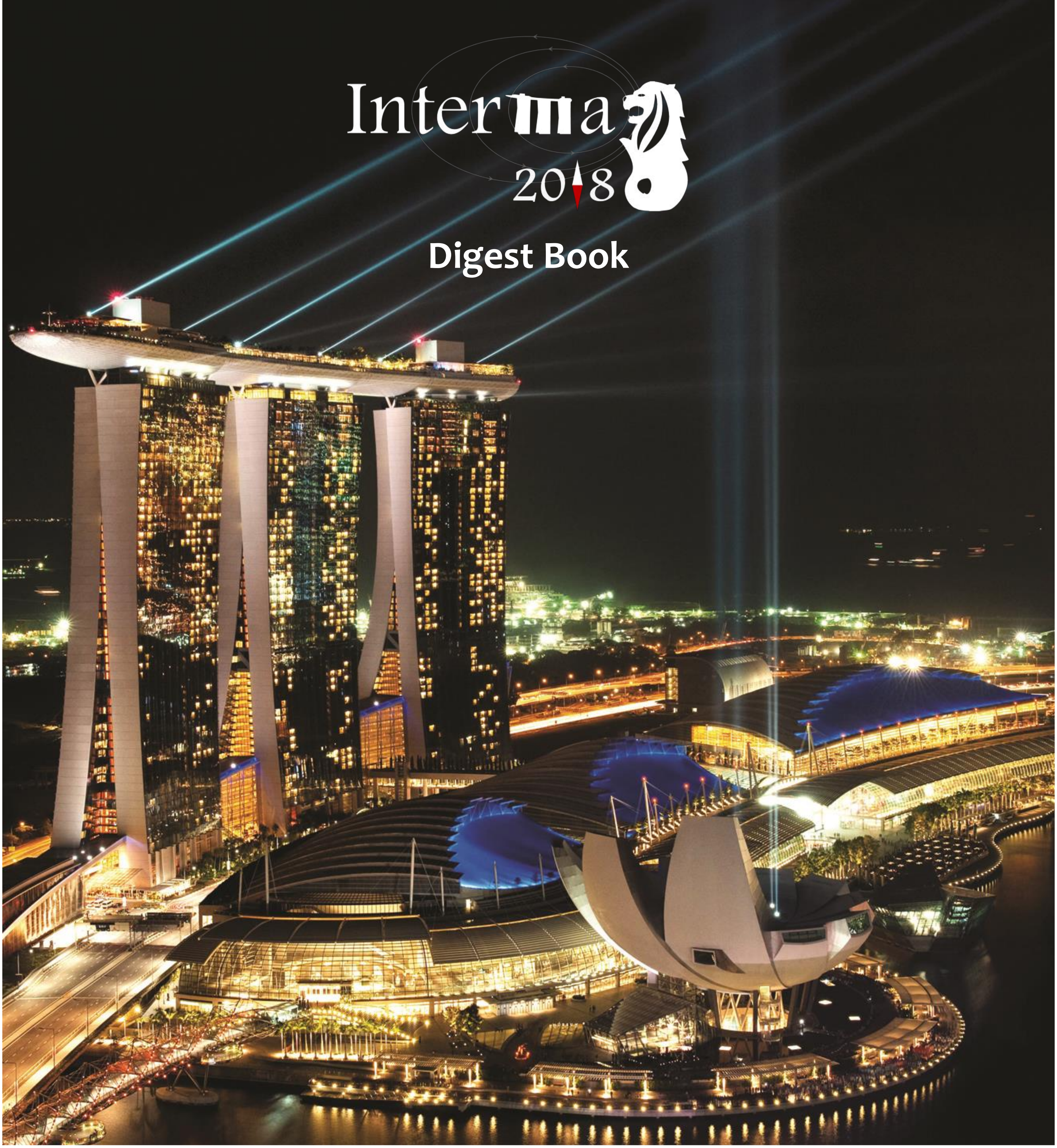

23-27 April 2018, Marina Bay Sands Convention Centre

www.intermag2018.com

Supported by
SINGAPORE EXHIBITION & CONVENTION BUREAU

NANYANG TECHNOLOGICAL UNIVERSITY SINGAPORE

IEEE MAGNETICS

Held in
SG
Singapore
Passion Made Possible

Session TU

TUTORIAL ON ANTIFERROMAGNETIC SPINTRONICS

Atsufumi Hirohata, Chair
University of York, York, United Kingdom

INVITED PAPERS

3:30

TU-01. Characterisation of Antiferromagnets.

K. O'Grady[1] and G. Vallejo-Fernandez[1]
1. University of York, York, United Kingdom

The characterisation of antiferromagnets (AFs) for almost all applications is very challenging because intrinsically an AF gives little or no signal. Above the Néel temperature (TN) AF materials exhibit paramagnetic behaviour in a similar manner to a ferromagnet above its Curie point. This does allow for the determination of the Néel temperature but reveals little about the behaviour of the material once the AF order is established. Historically the structure of AFs was determined using techniques such as neutron scattering [1, 2] and more recently some studies have been undertaken using X-ray techniques such as XMCD [3]. However such techniques and particularly neutron scattering require large samples with dimensions of the order of millimetres. For all technological applications AF materials are used in thin film form and hence such techniques are not available for use due to the very long counting times that would be required. A second problem with AF materials is that their behaviour has not been well established until recently. For example Néel predicted the existence of AF domains but there are very few reports of their observation [4, 5]. Their behaviour is not well understood because conventional domain theory is based around the existence of magnetostatic energy in a conventional ferromagnet which is not present in an AF. Other critical factors associated with the structure of thin films are also poorly understood. Principal amongst these is that in polycrystalline films a granular structure will exist but the question then arises as to at what critical grain size will single domain behaviour be observed? In single crystal or large grain thin films where presumably AF domains will form, what is the nature and consequence of domain wall pinning? In this tutorial lecture the fundamental nature of antiferromagnets will be discussed addressing metals, alloys and oxides. However the focus will be on those materials which have, or are most likely to find application in spintronic devices. Techniques that allow the behaviour of AF thin films at least to be inferred will also be discussed. These are principally associated with the measurement of exchange bias systems where a ferromagnetic layer is used as an indicator of the structure of an underlying AF. However in exchange bias systems it is also the case that the exchange field from the ferromagnet causes a reaction and possibly a change of order in the AF. This concept is the basis of the so-called York Protocols which allow for the measurement of the behaviour of granular, generally sputtered, AF films. The underlying York Model of Exchange Bias developed in 2008 will then be discussed in detail as it allows for the full characterisation of granular films and in particular the determination of the anisotropy constant of AFs. This model has been used by all the major manufacturers of hard drive read heads to design improved AF layers in their stacks. For the case of large grain or single crystal thin films a brief review of complex large scale computer models of possible domain structures will be presented with the emphasis placed on a simple strong domain wall pinning model which has been found to replicate qualitatively the observed behaviour in such structures. Finally the effect of reduced dimensions on the behaviour of AFs will be presented as it is well established that small lithographically defined structures containing AF layers behave quite differently to bulk films.

1. Shull, C.G. and J.S. Smart, Physical review, 1949. 76(8): p. 1256. 2. Shull, C.G., W.A. Strauser, and E.O. Wollan, Physical Review, 1951. 83(2): p. 333-345. 3. Priolkar, K.R., et al., Physical Review B, 2013. 87(14): p. 144412. 4. Chien, C.L., et al., Physical Review B, 2003. 68(1): p. 014418. 5. Scholl, A., et al., Science, 2000. 287(5455): p. 1014-1016.

4:15

TU-02. Making the Invisible Visible: Probing Antiferromagnetic Order in Novel Materials.

E. Arenholz[1,2]
1. Advanced Light Source, Lawrence Berkeley National Laboratory, Berkeley, CA, United States; 2. Material Sciences and Enegineering, University of California, Berkeley, CA, United States

In antiferromagnetic materials, the exchange interaction aligns adjacent atomic magnetic moments antiparallel to each other. As a result, antiferromagnets have no net spontaneous magnetization and their response to external magnetic fields is weak. Can we still determine their atomic magnetic moments and spin axis relative to the crystal lattice? Can we explore their nanoscale magnetic heterogeneity (domains, domain walls) and use this knowledge to develop new antiferromagnetic materials? Can we make the invisible antiferromagnetic spin order visible? Yes, we can! The absorption of polarized X-rays allows us to probe antiferromagnetic order with element-specificity, nanometer spatial resolution and ultrafast time resolution. Moreover, the magnetic moment of neutrons interacting with the periodic spin arrangement in antiferromagnets gives rise to neutron diffraction patterns that reflect the antiferromagnetic spin order, analogous to how X-ray diffraction is used as a fingerprint of atomic order in crystalline materials. In this talk, these sophisticated and powerful X-ray and neutron techniques which are accessible to every researcher (!) through collaborative research facilities, will be discussed in detail. The goal is that at the end of this talk, all researchers in the audience will be able to develop their research idea into an experimental plan in the exciting field of antiferromagnetic spintronics, which they could then propose and execute at a collaborative research facility.

5:00

TU-03. Antiferromagnetic Devices.

T. Jungwirth[1,2]
1. Institute of Physics, Academy of Sciences of the Czech Republic, Praha, Czechia; 2. School of Physics and Astronomy, University of Nottingham, Nottingham, United Kingdom

Louis Néel pointed out in his Nobel lecture that while abundant and interesting from theoretical viewpoint, antiferromagnets did not seem to have any applications. Indeed, the alternating directions of magnetic moments on individual atoms and the resulting zero net magnetization make antiferromagnetic order hard to control by tools common in ferromagnets. Strong coupling would be achieved if the externally generated field had a sign alternating on the length-scale of a lattice constant at which moments alternate in antiferromagnets. However, generating such a field has been regarded unfeasible, hindering the research and applications of these abundant magnetic materials. We will discuss recent prediction and experimental confirmation that relativistic quantum mechanics can provide a staggered current induced field whose sign alternates within the magnetic unit cell of the antiferromagnet [1,2]. We demonstrate that this staggered spin-orbit field facilitates a reversible switching of an antiferromagnet CuMnAs deposited at low temperature on a structurally compatible Si or GaP substrate. Electrical readout is facilitated by anisotropic magnetoresistance. The complete write/store/read functionality has been realized in a USB demonstrator memory device with a multi-level bit-cell characteristics which enhances the storage capacity and allows to integrate memory with logic/neuromorphic functionality within a bit cell [3]. The absence of dipolar fields in the zero net moment antiferromagnets makes the memory invisible to magnetic probes and robust against external magnetic field perturbations. Moreover, antiferromagnets have ultra-fast, THz spin dynamics which allowed to demonstrate switching by pulse lengths scaled down to a picosecond [4].

[1] P. Wadley et al. Science 351, 587 (2016); C. Marrows (Editorial), Science 351, 558 (2016). [2] T. Jungwirth et al., Nature Nanotech. 11, 231 (2016); Editorial, Nature Nanotech. 11, 231 (2016). [3] K. Olejník et al., Nature Commun. 8, 15434 (2017). [4] K. Olejník et al., Science Adv. in press, arXiv:1711.08444.

TUESDAY MORNING, 24 APRIL 2018 ORCHID I, 9:00 TO 12:00

Session AA
SYMPOSIUM ON COMPENSATED SPINTRONICS

Michael Coey, Chair
Trinity College Dublin, Dublin, Ireland

INVITED PAPERS

9:00

AA-01. Compensated ferromagnetic Heusler compounds for antiferromagnetic spintronics.

C. Felser[1], G. Fecher[1], R. Stinshoff[1], A. Nayak[1] and M. Coey[2]
1. Solid State Chemistry, Max Planck Institute for Chemical Physics of Solids, Dresden, Germany; 2. Physics, Trinity College Dublin, Dublin, Ireland

Heusler compounds are a remarkable class of materials with more than 1,000 members and a wide range of extraordinary multifunctionalities including half-metallic high-temperature ferri- and ferromagnets, multiferroic shape memory alloys, and tunable topological insulators with a high potential for spintronics, energy technologies and magnetocaloric applications. Half Heusler and Heusler compounds can be designed antiferromagnetic, ferri- and ferromagnetic properties. Antiferromagnetic and compensated ferrimagnetic properties are interesting in the context of antiferromagnetic spintronics. Simple rules allows for a rational design of Heusler compounds [1]. Mn-rich Heusler compounds are a source for compensated ferrimagnets ranging from metals via bad metals to semiconductors [2-4]. Some of the cubic compensated ferrimagnets can be designed by simple electron counting rules [5-7] As stated by the famous Slater-Pauling rule, L21 Heusler compounds with 24 valence electrons never exhibit any spin magnetic moment. In the case of strongly localized magnetic moments at one of the atoms (here, Mn), they will exhibit a fully compensated half-metallic ferromagnetic state instead, in particular, when symmetry does not allow for antiferromagnetic order. With the aid of magnetic and anomalous Hall effect measurements, it is experimentally demonstrated that Mn1.5V0.5FeAl absolutely follows such a scenario. A small residual magnetization that arises owing to a slight mismatch of the magnetic moment in the different sublattices results in temperature dependence of the magnetic compensation, confirmed by observation of magnetic reversal and sign change of the anomalous Hall effect [6,7]. Tetragonal Heusler compounds with large magneto crystalline anisotropy can be easily designed by positioning the Fermi energy at the van Hove singularity in one of the spin channels. Because of the ferrimagnetic arrangement of the sublattice artificial antiferromagnets: compensated ferrimagnets, can be even easier designed in the hard magnetic tetragonal Mn2YZ Heusler compounds [8]. In the vicinity of the compensation composition in Mn–Pt–Ga, a giant exchange bias (EB) of more than 3 T and a large coercivity are found The large exchange anisotropy originates from the exchange interaction between the compensated host and the ferrimagnetic clusters that arise from intrinsic anti-site disorder. Our design approach is also demonstrated on a second material with a magnetic transition above room temperature, Mn–Fe–Ga, exemplifying the universality of the concept and the feasibility of room-temperature applications [8]. The compensation point in cubic as well as tetragonal Heusler compounds is confirmed by observation of magnetic reversal and sign change of the anomalous Hall effect.

[1] Tanja Graf, Stuart S. P. Parkin, and Claudia Felser, Progress in Solid State Chemistry 39 (2011) 1-50 [2] Jürgen Winterlik, et. al., Adv. Mat. 24 6283 (2012). [3] A. K. Nayak, M. Nicklas, C. Shekhar, Y. Skourski, J. Winterlik, and C. Felser, Phys. Rev. Lett. 110 127204 (2013) [4] S. Ouardi, G. H. Fecher, J. Kübler, and C. Felser, Phys. Rev. Lett. 110 100401 (2013) [5] S. Wurmehl, G. H. Fecher, H. C. Kandpal, and C. Felser, J.Phys. Cond. Matter. 18 (2006) 6171. [6] R. Stinshoff, A. K. Nayak, G. H Fecher, B. Balke, S. Ouardi, Y. Skourski, T. Nakamura, C. Felser, Physical Review B 95 (Rapid) (2017) 060410(R) [7] Rolf Stinshoff, Gerhard H. Fecher, Stanislav Chadov, Ajaya K. Nayak, Benjamin Balke, Siham Ouardi, Tetsuya Nakamura, and Claudia Felser, AIP Advances 7 (2017) 105009 [8] A. K. Nayak, et al., Nature Mat. 14 679 (2015).

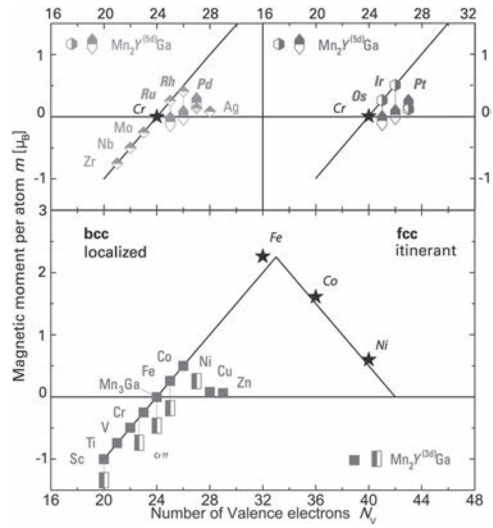

Fig. 1. Slater Pauling Rule for cubic Mn2-Heusler compounds

9:30

AA-02. New functionality in half-metallic Mn_2Ru_xGa close to compensation.

Y. Lau[1,2]
1. Department of Physics, The Univeristy of Tokyo, Tokyo, Japan;
2. National Institute for Materials Science (NIMS), Tsukuba, Japan

Compensated half-metallic ferrimagnets (CFHMs) have a spin gap at the Fermi level and an electron occupancy that ensures compensation of two inequivalent antiparallel chemical sublattices at a specific composition and temperature, T_{comp}. The prototypical CFHM is Mn_2Ru_xGa (MRG), which we have investigated intensively ever since discovering it [1]. MRG crystallises in the cubic space group No. 216 with -43m point symmetry and Mn in 4*a* and 4*c* positions. MRG can exhibit perpendicular magnetic anisotropy (PMA) because of substrate-induced biaxial strain, and the point symmetry is then reduced to -4m2, with no inversion centre. The conduction electrons originate from predominantly one of the two Mn sublattices, giving rise to high spin polarization, large spontaneous Hall effect [2] and finite tunnel magnetoresistance [3] at T_{comp}, where the magnetisation is strictly zero, and the coercivity diverges. A strong Kerr signal that arises from the spin-polarised conduction band allows optical detection of resonance modes in sub-terahertz range and also offers a unique opportunity to study quasi-antiferromagnetic domains, domain walls and their motion using standard magneto-optical imaging techniques. The effective magnetic coupling of the MRG 4*c* sublattice moment to a perpendicularly-magnetized CoFeB layer via a thin Hf spacer leads to a robust pinned layer structure that exploits the high coercivity of MRG near the compensation [4]. This stack provides an alternative to the current synthetic antiferromagnetic multilayers but with a much simpler structure. Using the harmonic Hall technique [5,6], we have found evidence of current-induced spin-orbit effective fields at room temperature in MRG films. Systematic investigation of films of different Ru concentrations (hence with T_{comp} below or above room temperature) and of devices patterned along different crystallographic axes reveals several interesting features. First, the direction of the spin-orbit effective fields reverses upon reversing the current polarity *and* the MRG magnetization direction. The symmetry of the observed spin-orbit effective fields differs from that reported in single-layer MBE-grown NiMnSb [7], for which magnetization-independent terms are dominant. Second, the longitudinal effective field (parallel to the applied current) more than an order of magnitude greater than the transverse effective field, suggesting a dominant role of the diagonal terms in the response tensor. Third, the magnitude of the effective fields per unit current density reaches ~ 5 $mT/10^{10}$ A/m^2 near the compensation, nearly an order of magnitude higher than the values reported in conventional heavy metal/ferromagnet bilayers. The origin of spin-orbit effective fields in CFHMs, and potential generalization to other classes of magnetic materials will be discussed.

[1] Kurt et al., Physical Review Letters 112, 027201 (2014) [2] Thiyagarajah et al., Applied Physics Letters 106, 122402 (2015) [3] Borisov et al., Applied Physics Letters 108, 192407 (2016) [4] Borisov et al., Applied Physics Letters 111, 102403 (2017) [5] Kim et al., Nature Materials 12, 240 (2013) [6] Garello et al., Nature Nanotechnology 8, 587 (2013) [7] Ciccarelli et al., Nature Physics 12, 855 (2016)

10:00

AA-03. Ultrafast spin dynamics in antiferromagnets.

O. Gomonay[1], T. Jungwirth[2] and J. Sinova[1,2]
1. Institute of physics, Johannes Gutenberg University, Mainz, Germany;
2. Institute of Physics ASCR, Praha, Czechia

Antiferromagnets are promising materials for spintronics because they show fast magnetic dynamics, low susceptibility to magnetic fields, and produce no stray fields. In addition, the antiferromagnetic dynamics can be efficiently manipulated by spin and charge currents. Here we discuss spin and/or charge current induced dynamics of the antiferromagnetic textures (domain walls, skyrmions) and nanoparticles. We consider and analyse four types of torques which (spin) current can generate in an antiferromagnet with two magnetic sublattices. These torques can be classified as the staggered/nonstaggered (S/NS) according to the effective spin accumulation at the magnetic sublattices and the field-like/antidamping-like (FL/ADL) according to the produced energy dissipation (Fig.1). The NS-FL torque is similar to the torque created by the magnetic field. The recently predicted [1] Néel spin orbit torque gives an example of the S-FL torque, while the spin transfer and antidamping Néel spin orbit torques [2,3] represent the NS-ADL case. The S-FL and NS-ADL torques can efficiently move the antiferromagnetic domain walls [4,5]. The symmetry matching between these torques and staggered magnetization provides high mobility compared to other torques. Due to the absence of the Walker breakdown, the velocity of the domain wall motion can reach 30 km/s at the reasonable values of currents. The NS-ADL is sensitive to the structure of the domain wall and pushes all the domain walls in the same direction, which is suitable for the race-track memory. On the contrary, the S-FL torque splits degeneracy of the domains, pushes the domain walls toward the unfavourable domain and thus is suitable for switching. Moreover, this torque is the only physical field which allows to distinguish domains with the opposite orientation of the Néel vector and to manipulate 180^0 domain walls in antiferromagnets. The dynamics of the Néel vector induced by the S-FL and NS-ADL torques is assisted by large internal torques of the exchange origin which allow to achieve an ultrafast (compared to ferromagnets) magnetic dynamics. In particular, NS-ADL torque induced by dc spin current induces stable autooscillations of the Néel vector with THz frequency. This paves a way to the antiferromagnetic-based devices fitting THz gap, e.g. emmiters and detectors of THz radiation, which couples to the magnetic dynamics via Néel spin orbit (S-FL) torque [6]. The S-ADL torque, whose effect up to our knowledge was not yet discussed in the literature, can induce fast and reliable 180^0 switching of the Néel vector, similar to the spin transfer torque in the ferromagnets. In contrast to NS-ADL which always competes with the internal damping and thus supports precession rather than switching of the Néel vector, the S-ADL torque can either compensate or enhance the internal damping depending on the geometry. The time-dependent S-ADL torque can also induce oscillations with THz frequency. However, the dynamics induced by this torque is not assisted by the internal exchange torques and thus is less efficient than S-FL and NS-ADL torques. From the symmetry point of view, the S-ADL torque can also compensate the Bloch damping which controls relative orientation of the magnetic sublattices and their length. Thus, this torque can play an important role in the vicinity of the Néel point. We also discuss the effects which different torques produce on an antiferromagnetic skyrmion. The field-like torques (both S-FL and NS-FL) influence the skyrmion stability. They allow to control uniaxial (via S-FL) and unidirectional (via NS-FL) anisotropy of the Néel vector. The NS-ADL torque creates a force which can induce linear motion of a skyrmion [7]. To summarise, (spin) current induced dynamics of antiferromagnets is much richer compared to ferromagnetic materials due to the variety of torques and magnetic degrees of freedom. By tuning and combining different types of torques is it possible to induce switching, precession, domain wall motion and other nontrivial dynamical regimes which give antiferromagnetic-based deivces new functionalities.

[1] Wadley, P., Howells, B., Elezny, J., Andrews, C., Hills, V., Campion, R. P., … Jungwirth, T. (2016). *Science*, *351*, 587. [2] Gomonay, H. V, & Loktev, V. M. (2010). *Phys. Revi. B*, *81*., 144427. [3] Zelezný, J., Gao, H., Výborný, K., Zemen, J., Mašek, J., Manchon, A., … Jungwirth, T. (2014). *Phys. Rev. Lett.*, *113*, 157201. [4] Gomonay, O., Jungwirth, T., & Sinova, J. (2016). *Phys. Revi. Lett. 117*, 17202. [5] Shiino, T., Oh, S.-H., Haney, P. M., Lee, S.-W., Go, G., Park, B.-G., & Lee, K.-J. (2016). *Phys. Rev. Lett.*, *117*(8), 87203. [6] Gomonay, O. Jungwirth, T., & Sinova, J. (2017). arxiv:1712.02686 [7] Velkov, H., Gomonay, O., Beens, M., Schwiete, G., Brataas, A., Sinova, J., & Duine, R. A. (2016). *New Journal of Physics*, *18*, 75016.

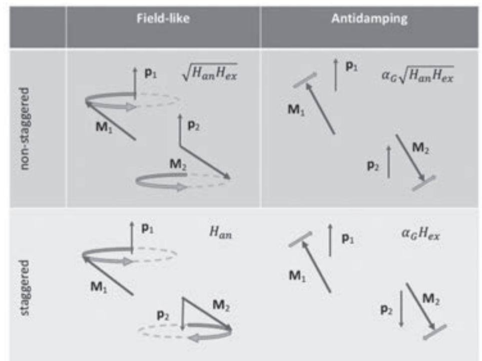

Fig. 1. Classification of torques in antiferromagnets according to the symmetry of spin accumulation (p_1, p_2)and their action of sublattice magnetizations (M_1, M_2)

10:30

AA-04. Electrical detection of reversed antiferromagnetic states switched by unidirectional current pulses.

J. Godinho[1,2], H. Reichlova[1], D. Kriegner[1,2], K. Olejnik[1], Z. Soban[1], V. Novak[1], R. Otxoa[3], P. Roy[3], T. Jungwirth[1,4] and *J. Wunderlich*[3,1]
1. Institute of Physics ASCR, Prague, Czechia; 2. Faculty of Mathematics and Physics, Charles University, Prague, Czechia; 3. Hitachi Cambridge Laboratory, Hitachi Europe LTD, Cambridge, United Kingdom; 4. School of Physics and Astronomy, University of Nottingham, Nottingham, United Kingdom

Ferromagnetic storage of binary information in hard disk drives (HDD) and magnetic random access memories (MRAMs) is based on uniaxial switching between two stable, energetically equivalent magnetic states of reversed magnetisation which are separated by a high anisotropy energy barrier in order to guarantee thermal stability. The electrical switching of the ferromagnetic bits is realised by current induced spin-transfer torques or by spin-orbit torques whereby giant or tunnelling magnetoresistance (GMR, TMR) effects are used for reading out the two collinear states. [1] In antiferromagents (AFs) such as CuMnAs or Mn_2Au, where the constituent magnetic sub-lattices form inversion partners, efficient and fast current induced switching between orthogonal Néel vector states was recently proposed [2-3] and experimentally realised [3-8]. In those experiments, the anisotropic magnetoresistance (AMR) was used to identify the biaxial switching between non-collinear magnetic states. However, reversible biaxial switching requires a complex (at least) four-terminal device architecture since writing currents have to be applied along two different axes. Moreover, the AF system needs to exhibit biaxial magnetic anisotropy to prevent relaxation between the non-collinear states. Uniaxial switching in AFs is in principle more favorable than biaxial switchinbg. Writing can be realised by simply changing the current polarity and only uniaxial magnetic anisotropy is required to ensure stable switching between collinear states. Theoretically, uniaxial switching driven by the current induced staggered Néel ordered spin-orbit field has been proposed by propagation of 180° antiferromagnetic domain walls [9] and by coherent spin rotation of the Néel ordered state. [10] Distinguishing between reversed antiferromagnetic states by electric measurements is not straightforward since macroscopic charge-currents in AFs are unpolarised. Nevertheless, antiferromagnetic GMR or TMR like spin-valves have been proposed which are based on subtle spin-coherent quantum interference phenomena that rely on perfectly epitaxial commensurate multilayers, and it is the relative orientation of the local spins on the last atomic planes of the two antiferromagnets facing each other across the non-magnetic spacer that determines the readout resistance signal. [11] The difficulty in observing these spin-valve effects experimentally and the even-in-magnetic moment dependency of the AMR has cast doubts on the ability to detect by practical means uniaxial switching in antiferromagnets. [12]. In my talk I will show that it is possible to separate macroscopic states of reversed Néel vectors by combining the even under Néel vector reversal AMR effect with the odd under Néel vector reversal staggered field like spin-orbit torque. The later appears in antiferromagnets where the crystal lattice lacks local inversion symmetry and where the antiferromagnetic sublattices form space-inversion partners [2,3]. Using this methode, reversible and stable uniaxial switching at room temperature in antiferromagenic CuMnAs, triggered by writing current pulses of opposite polarity will be shown. We detected the uniaxial switching by means of a homodyne detection method where an alternating probe current periodically perturbs the AF coupled moments by the staggered spin-orbit field so that a 2nd harmonics signal appears due to the periodically changing AMR. Since the 2nd harmonics signal changes sign under Néel vector reversal we can identify nonvolatile uniaxial switching between states of opposite Néel vectors. The reversed states show no decay over days. In contrast, we detected in the same devices by conventional AMR measurements biaxial switched states with relatively short retention times of 10′s of minutes.

[1] C. Chappert, et al., Nature Materials 6, 813 (2007). [2] J. Zelezny, et al., Phys. Rev. Lett. 113, 157201 (2014). [3] T. Jungwirth, et al., Nature Nanotechnology 11, 3, 231 (2016). [4] P. Wadley, et al., Science 351, 6273, 587 (2016). [5] K. Olejnik, et al., Nat. Comm. 8, 15434 (2017). [6] S. Yu. Bodnar, et al., arXiv:1706.02482 (2017). [7] K. Olejnik, et al., arXiv:1711.08444 (2017). [8] P. Wadley, et al., arXiv:1711.05146 (2017). [9] O. Gomonay, et al., Phys. Rev. Lett. 117, 017202 (2016). [10] P. E. Roy, Phys. Rev. B 94, 014439 (2016). [11] A. Nez, et al., Phys. Rev. B 73, 214426 (2006). [12] A. MacDonald, Phil. Trans. R. Soc. A 369, 30983114 (2011).

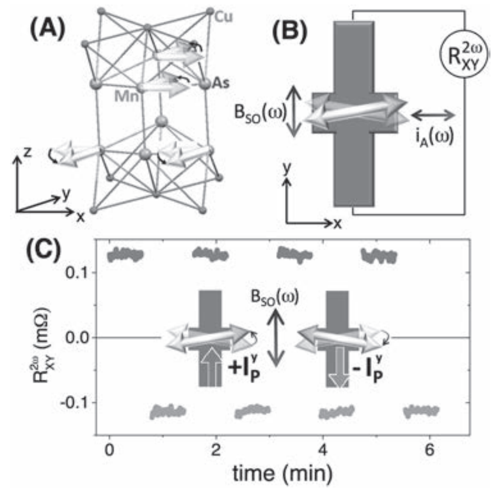

Fig. 1. (A) The antiferromagnet lattice of CuMnAs with local inversion-asymmetry: the magnetic sub-lattices (Mn atoms with yellow and blue arrows) form inversion partners. A charge current applied along x-direction generates non-equilibrium spin-polarizations along y (Mn with blue arrows) and -y (Mn with yellow arrows). The corresponding staggered effective SO field rotates the moments as indicated by the black arrows.

Fig. 2. (B) Basic idea of the experiment to discriminate between reversed antiferromagnetic states: An alternating probe current $i_{A}(\omega)$ periodically tilts the AF coupled moments and a 2nd harmonics signal $R_{XY}^{2\omega}$ appears due to the mixing of the periodically changing anisotropic magnetoresistance with the alternating current.

Fig. 3. (C) $R_{XY}^{2\omega}$ signals of opposite polarity after indevidual current pulses I_P^Y (red) and $-I_P^Y$ (orange) have been applied.

11:00

AA-05. Spin Current Generation, Detection, and Transport with Antiferromagnets.

Z. Wei[1,2], M. Jungfleisch[1,3], W. Jiang[1,4], H. Saglam[1,5], F. Freimuth[6], J. Sklenar[1,7], J. Pearson[1], J. Ketterson[7], Y. Mokrousov[6] and *A. Hoffmann*[1]
1. Materials Science Division, Argonne National Laboratory, Lemont, IL, United States; 2. Department of Physics, Oakland University, Rochester, MI, United States; 3. Physics Department, University of Delaware, Newark, DE, United States; 4. State Key Laboratory of Low-Dimensional Quantum Physics, and Department of Physics, Tsinghua University, Beijing, China; 5. Department of Physics, Illinois Institute of Technology, Chicago, IL, United States; 6. Peter Grünberg Institut and Instiute for Advanced Simulation, Forschungszentrum Jülich, Jülich, Germany; 7. Department of Physics and Astronomy, Northwestern University, Evanston, IL, United States

Harnessing spin currents is a promising pathways towards low-power electronics [1]. Towards this end, it recently has been recognized that antiferromagnetic materials can play a more active role beyond their traditional use for providing a reference magnetization direction via exchange bias. Namely, antiferromagnets may be conduits for spin currents, as well as, actively enable spin current generation and detection. With respect to the later, we demonstrated spin current generation both via spin Hall effects in conducting antiferromagnets and spin Seebeck effects in insulating antiferromagnets. Using CuAu-I-type metallic antiferromagnets (PtMn, IrMn, PdMn, and FeMn) we showed by using spin pumping that these alloys have significant spin Hall effects, which in the case of PtMn become comparable to the ubiquitously used Pt [2]. The spin Hall angles increase for the alloys with heavier element; a behavior that is well reproduced by first-principle calculations of the spin Hall conductivities based on intrinsic spin Hall effects. Furthermore, the calculations suggest pronounced anisotropies of the spin Hall conductivities, which we tested using spin transfer torque ferromagnetic resonance measurements using epitaxially grown antiferromagnetic films [3]. We observe that indeed the spin Hall conductivity is maximized for different growth orientations (a-axis for PtMn and PdMn, and c-axis for IrMn) in accordance with the first principle calculations. In addition using spin pumping measurements with permalloy/FeMn/W trilayers, we observe that there are two distinct mechanism for transporting a spin current in the metallic antiferromagnet, which we associate with electronic and magnonic spin transport, respectively [4]. This work was supported by the U.S. DOE, Office of Science, Materials Sciences and Engineering Division and DFG.

1. A. Hoffmann and S. D. Bader, Phys. Rev. Appl. 4, 047001 (2015). 2. W. Zhang, *et al.*, Phys. Rev. Lett. 113, 196602 (2014). 3. W. Zhang, *et al.*, Phys. Rev. B 92, 144405 (2015). 4. H. Saglam, *et al.*, Phys. Rev. B 94, 140412(R) (2016).

11:30

AA-06. Spin Transport in Speromagnets: Disordered Spintronic Materials with Antiferromagnetic Correlations.

B.L. Zink[1]
1. Physics & Astronomy, University of Denver, Denver, CO, United States

Recent efforts in spintronics research have shown that first ferromagnetic (FM), and now antiferromagnetic (AF) insulators support spin transport. This is particularly exciting since the lack of charge transport in these magnetically ordered insulating materials removes the scattering and dissipation that leads to heat losses that currently limit silicon nanoelectronics. These systems are crystalline or otherwise structurally ordered in addition to their magnetic order, and spin transport effects are usually interpreted in terms of collective excitations such as magnons. Some of the most promising materials, such as the ferrimagnetic insulator yytrium iron garnet (YIG), are also quite complicated crystals. This presents challenges in integrating these materials in silicon or other nanoelectronics elements for potential future use as spintronic memory or logic elements. We have recently added a dramatic twist to the study of spin transport in insulators, as we have demonstrated long-distance spin transport in disordered magnetic insulators. This talk describes our work that follows on recent electrical generation and detection of spin transport through the crystalline ferrimagnetic insulator yttrium iron garnet (YIG). These non-local transport experiments use charge currents to excite spin dynamics in the YIG via the spin Hall effect (SHE), and subsequently detect a spin current some distance away using the inverse spin Hall effect (ISHE). As shown schematically in Fig. 1, we have carried out similar experiments on amorphous YIG (*a*-YIG), a material showing no long- or medium-range order (either structural or magnetic). *a*-YIG, sometimes historically classified as a speromagnet, where spins are fixed in random directions due to the randomness of the magnetic anisotropy, typically shows a spin freezing near 50 K, and above this temperature follows the Curie-Weiss law with parameters suggesting very strong antiferromagnetic correlations in an essentially paramagnetic state. Our results, as shown in Fig. 2, show surprisingly long length-scale spin transport with easily measurable signals even for distances greater than 100 microns at temperatures near and above 300 K [1]. Experiments performed on a-YIG supported both on a bulk substrate and on suspended Si-N membrane thermal platforms show that spin injection and transport does not require thermal gradients, but the presence of in-plane thermal gradients enhances spin transport and reveals a large non-equilibrium spin thermal conductance. Among other intriguing aspects of this unexpected spin transport, we clarify that the effects are large not in the low-temperature spin-glass state, but at higher temperatures where only antiferromagnetic spin correlations are present. We will also show similar effects in a second disordered magnetic material, present data directly comparing use of Pt strips that cause spin transport via the SHE and Cu strips that show no spin transport as expected, and argue that the role of correlations is a more general feature that could dominate even in spin transport through more structurally ordered systems. This work is supported by the US National Science Foundation (DMR-1709646 and EECS-1610904).

1. D. Wesenberg, T. Liu, D. Balzar, M. Wu and B. L. Zink, Nature Physics, v. 13, 987 (2017) DOI:10.1038/NPHYS4175

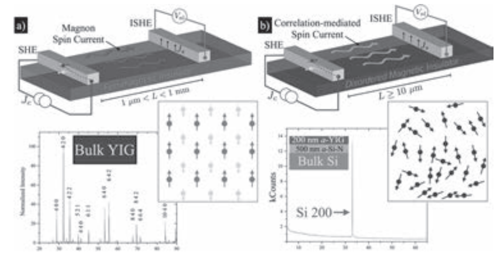

Fig. 1. a) Schematic view of the SHE-driven non-local transport experiment in a crystalline ferrimagnet such as YIG (with typical XRD data for bulk polycrystalline YIG).
b) Schematic view of the SHE-driven non-local transport in amorphous YIG, with a similar XRD scan showing no evidence of peaks other than in the supporting Si substrate.

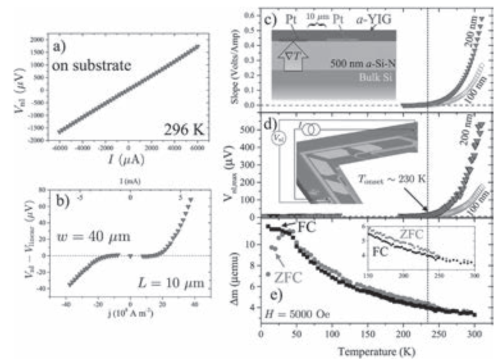

Fig. 2. Non-local spin transport in amorphous YIG supported on a Si-N coated Si substrate. Here thermal gradients are minimal. a) The non-local voltage, V_{nl} vs applied current near room temperature (without *a*-YIG there is essentially zero voltage measured in this experiment). b) After subtracting the linear term determined for currents lower than 2 mA, a non-linear component of the signal is clearly visible. c-e) The temperature dependence of both the linear (slope) and nonlinear components of this voltage shows a turn-on in temperature only above all observed spin-freezing in the *a*-YIG, so that spin tranpsort occurs in the AF-correlated paramagnetic state.

TUESDAY MORNING, 24 APRIL 2018 ORCHID III, 9:00 TO 12:00

Session AB
RARE EARTH TRANSITION METAL BORIDES I

Weibin Cui, Co-Chair
Northeastern University, Shenyang, China
Jinbo Yang, Co-Chair
Peking University, Beijing, China

CONTRIBUTED PAPERS

9:00

AB-01. Electronic states and magnetic properties around the grain boundary in Nd-Fe-B sintered magnets studied by first-principles calculations.

Y. Tatetsu[1] and Y. Gohda[1]
1. Department of Materials Science and Engineering, Tokyo Institute of Technology, Yokohama, Japan

Nd-Fe-B sintered magnets, known as the strongest magnets, are used in various kinds of applications, for example, vehicles, turbines, etc., since they have the largest $(BH)_{max}$ among permanent magnets. However, the mechanism of the thermal instability in the coercivity of Nd-Fe-B magnets is not clear because there are numerous unknown factors that reduce the coercivity. These unknown factors are strongly related to the complicated grain boundary structures in Nd-Fe-B magnets. In general, understanding of grain boundaries in materials is very important from the aspect of controlling physical properties, and this can be also applicable to Nd-Fe-B magnets. In fact, several experimental studies have been clarifying important relationships between the coercivity and the grain boundaries which are constructed by $Nd_2Fe_{14}B$ main grains and subphases [1]. There are some experimental approaches to improve the coercivity of Nd-Fe-B magnets by adding a small number of elements, for example, Cu, Ga, etc., instead of Dy which is expensive, but even so it is mostly used in commercial magnets to keep high coercivity at high temperatures [1-4]. According to atom prove measurements, added Cu covers the $Nd_2Fe_{14}B$ main grains, and this might be one of the reasons for the coercivity improvement. Despite these efforts, what reduces the coercivity of Nd-Fe-B magnets is still unclear. This is because it is hard to observe and understand the nanoscale physics around grain boundaries only from experiments. First-principles electronic-structure calculations, based on density functional theory, are a powerful tool to investigate nanoscale physics in not only bulk systems but also grain-boundary systems, and can be applicable to analyze the atomic position and electronic states. We performed first-principles calculations for Cu-added Nd-Fe-B magnets [1-3] by using the OpenMX code [5] within density functional theory in order to understand the magnetic properties, especially the magnetic anisotropy around the interface which is strongly related to the coercivity [6, 7]. In addition, we analyzed where added Cu atoms should exist around the grain boundary by comparing the formation energies of five model systems labeled I~V. As a subphase, we chose $NdO_{0.25}$ which has been confirmed the presence around the triple junction in Nd-Fe-B magnets in experiments. The cutoff energy is 500 Ry and a k-point mesh is $3 \times 3 \times 2$. From our analysis, Cu prefers being around the interface (II and III in figure 1) to being the inner region of subphases and the main phase (IV and V). Furthermore, Fe at the interface of the $Nd_2Fe_{14}B$ main phase can be replaced by Cu because the formation energy is lower in the system (III) with Cu at Fe sites than the system (I) without Cu. This replacement improves the magnetic anisotropy of Nd atoms at the interface. Interestingly, the anisotropy improvement in Nd near Cu is about 40% from the non-Cu-doped system. Because the magnetic interaction between the 5d electrons in Nd and valence electrons in added Cu is weak. As a result, the 5d electrons tend to spread in the [001] direction, and the large total-angular momentum of 4f electrons in Nd is toward the [001] direction. This is one of the reasons for the coercivity improvement. The coercivity in Ga-doped Nd-Fe-B magnets is enhanced about 80 % recovering from the non-Ga-doped sintered magnets after annealing processes. From experimental analyses, Ga is the key to the wettability improvement of the Nd-rich phase [4], and the coercivity increases due to $Nd_6Fe_{13}Ga$ present at triple junctions. In order to examine the reason why the coercivity is improved by $Nd_6Fe_{13}Ga$, we performed first-principles calculations for $Nd_2Fe_{14}B/Nd_6Fe_{13}Ga$ grain-boundary model structures. Practically, large-scale simulations are necessary for understanding the coercivity improvement in Nd-Fe-B magnets from nanoscale. For example, figure 2 shows a large-scale $Nd_2Fe_{14}B/Nd_6Fe_{13}Ga$ grain-boundary-model system containing about 3000 atoms in a unit cell, in which the lattice mismatch between the $Nd_2Fe_{14}B$ main phase and $Nd_6Fe_{13}Ga$ subphase is less than 0.5 %. In this study, however, we chose smaller unit cells to seek the termination layer of $Nd_6Fe_{13}Ga$ at the interstitial regions of Nd-Fe-B magnets for large grain-boundary model systems. All atomic positions and cell parameters were optimized. After the structural optimization, the atomic positions of the inner region of the main phase and subphase are barely changed. On the other hand, the interface structures are complicated. In the $Nd_2Fe_{14}B$ surface system, K_1 of Nd at the surface shows strong in-plane anisotropy that can cause the coercivity decrease of Nd-Fe-B magnets [8]. In our grain-boundary model systems, K_1 of Nd is improved compared with that of the surface system thanks to $Nd_6Fe_{13}Ga$ present at the interface. This is due to Nd 5d electrons distributing in the longitudinal direction around interstitial regions, which improves K_1 of Nd. In conclusion, Ga doping works effectively in terms of improving K_1 of Nd at the interface.

[1] H. Sepehri-Amin *et al*., Acta Mater. 60, 819 (2012). [2] H. Sepehri-Amin *et al*., Acta Mater. 61, 6622 (2013). [3] C. D. Fuerst and E. G. Brewer, App. Phys. Lett. 56, 2252 (1990). [4] T.T. Sasaki *et al*., Scripta Mater. 113, 218 (2016). [5] http://www.openmx-square.org. [6] Y. Tatetsu, S. Tsuneyuki, and Y. Gohda, Phys. Rev. Appl. 6, 064029 (2016). [7] Y. Gohda, Y. Tatetsu, and S. Tsuneyuki, Mater. Trans., in press. [8] C. Mitsumata, H. Tsuchiura, and A. Sakuma, Appl. Phys. Express 4, 113002 (2011).

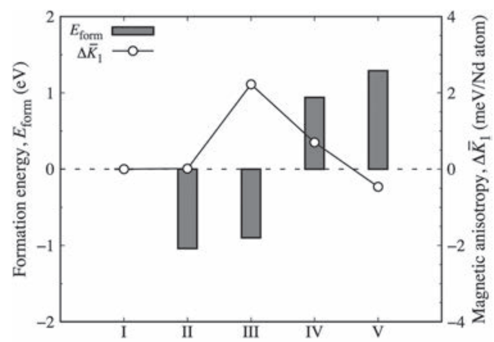

Fig. 1. The formation energies and the magnetic-anisotropy improvement of Nd at the interface in Cu-doped Nd-Fe-B magnets.

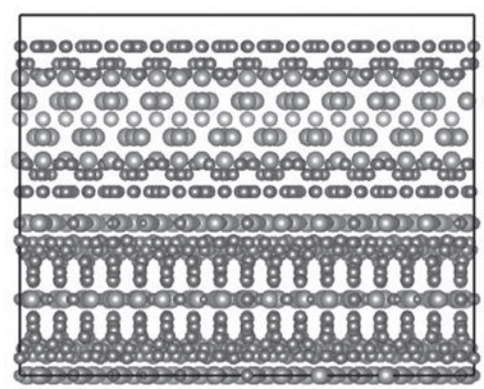

Fig. 2. $Nd_2Fe_{14}B/Nd_6Fe_{13}Ga$ Grain-boundary model structure.

9:15

AB-02. A novel approach of substitution of Ce for Nd in preparing $R_2Fe_{14}B$ nanocrystalline magnets with high coercivity.

L. Zha[1], Z. Liu[1], G. Tian[1], K. Li[1], M. Xue[1], Z. Shao[1], H. Zhao[1], Y. Zhang[1], W. Yang[1], Y. Lai[1], G. Qiao[1], X. Li[1], L.S. Ding[1], S. Liu[1], H. Du[1], C. Wang[1], J. Han[1], Y. Yang[1] and J. Yang[1,2]
1. State Key Laboratory for Mesoscopic Physics, School of Physics, Beijing, China; 2. Collaborative Innovation Center of Quantum Matter, Beijing, China

A novel approach of substitution of Ce for Nd in preparing $R_2Fe_{14}B$ nanocrystalline magnets with high coercivity Liang Zha[1]; Zhou Liu[1]; Guang Tian[1]; Kun Li[1]; Mingzhu Xue[1]; Zhuyin Shao[1];Hui Zhao[1]; Yinfeng Zhang[1]; Wenyun Yang[1]; Youfang Lai[1]; Guanyi Qiao[1]; Xin Li[1]; Shilei Ding[1]; Shunquan Liu[1]; Honglin Du[1]; Changsheng Wang[1]; Jinzhi Han[1]; Yingchang Yang[1]; Jinbo Yang[1,2,3] [1] State Key Laboratory for Mesoscopic Physics, School of Physics, Peking University, Beijing 100871, P. R. China. [2] Collaborative Innovation Center of Quantum Matter, Beijing, 100871, P.R. China [3] Beijing Key Laboratory for Magnetoeletric Materials and Devices,Beijing 100871, P. R. China ABSTRACT The Ce substituted $(Nd_{1-x}Ce_x)_{12.2}Fe_{81.6}B_{6.2}$ ribbons were prepared by annealing amorphous ribbons from melt spinning. It was found that all annealed ribbons consist of α-Fe, Nd(Ce)-rich phases, and $R_2Fe_{14}B$ phase. The coercivity of the $Nd_{12.2}Fe_{81.6}B_{6.2}$ ribbons with multiphase can reach a value of about 11.34 kOe, and the coercivity decreases slightly with the increasing of the Ce content. The coercivity still shows a value of 7.46 kOe when the Ce substitution of Nd was over 60% (x= 0.6). The Mr/Ms ratios of the ribbon are above 75% with the Ce content increasing from 0.2 to 0.6. It is expected that these results could provide a novel approach for preparing high coercivity Ce-substituted Nd-Fe-B materials. Key word: Nd–Fe–B alloy; Ce substitution; Coercivity INTRODUCTION The substitution for Nd by abundant rare earth element such as Ce is a practical approach for the comprehensive utilization of rare earth resources in permanent magnets, which can not only reduce costs but also provide a feasible way for integrated and effective utilization of rare earth resource [1,2,3]. The coercivity mechanism has been systematically studied for developing Ce-containing Nd-Fe-B permanent magnetic materials. Researchers[4,5,6,7] have found that the microstructure and grain boundary as well as the composition may play a pivotal role in the magnetic properties and coercivity mechanisms. Yang et al. found that the coercivity increased when 20% Nd was replaced by Ce in $(Nd_{1-x}Ce_x)_{14}Fe_{79.5}B_{6.5}$ melt-spun ribbons, and pointed out that scattering lattice parameters is the direct reason for the abnormal increase [8]. Shen et al. obtained $Nd_{12}Fe_{82}B_6$ ribbon with a coercivity of 10.93 kOe by melt spinning directly [9]. While M. Grigoras et al. made a comparison between the magnetic properties and microstructure of $Ce_{10+x}Fe_{78-x}B_6$ (x = 0, 2, 4, 6) nanocrystalline ribbons, prepared directly by melt spinning from the melt, and the ones obtained after annealing of amorphous precursors, whose corresponding coercivities are 4.7kOe ($Ce_{14}Fe_{80}B_6$) and 6.21kOe ($Ce_{16}Fe_{78}B_6$), respectively. It was found that the best preparation method was annealing the amorphous strip appropriately [10]. Obviously, the coercivity mechanisms of Ce-containing permanent alloys depend both on compositions and preparation processes. Consequently, it is significant to design proper composition and structure, optimize processing, and analyze the mechanisms in depth for this kind of magnet. Therefore, in this work, the $(Nd_{1-x}Ce_x)_{12.2}Fe_{81.6}B_{6.2}$ ribbon with the main phase of $Re_2Fe_{14}B$ was obtained by melt spinning following by annealing appropriately. The relationship between coercivity and Ce content was studied. Fig.1 XRD patterns of the $(Nd_{0.8}Ce_{0.2})_{12.2}Fe_{81.6}B_{6.2}$ (A) Crystallized ribbons, (B) Amorphous ribbons and (C) Raw material Fig.1 shows the XRD patterns of the $(Nd_{0.8}Ce_{0.2})_{12.2}Fe_{81.6}B_{6.2}$ alloy prior to and after annealing at 700 ° C for 15 min. As is evidently shown in Fig.1, the as-spun $(Nd_{0.8}Ce_{0.2})_{12.2}Fe_{81.6}B_{6.2}$ ribbon exhibits features of an amorphous structure, of which magnetic softness expectedly provides further verification. The x-ray diffraction of the tetragonal $Nd_2Fe_{14}B$, Nd-rich phase and α-Fe emerge after annealing compared with raw material. Fig.2 Hysteresis loop of samples of $(Nd_{1-x}Ce_x)_{12.2}Fe_{81.6}B_{6.2}$ (Ce=0.0, 0.2, 0.4, 0.6) Figure 2 shows the room temperature hysteresis loop of the ribbons annealed at 700 ° C for 15 minutes. It is interest to note that the coercivity of the $Nd_{12.2}Fe_{81.6}B_{6.2}$ ribbons can reach a value of about 11.34 kOe under the multiphases condition, and the coercivity decreases slightly with the increasing of the Ce content. The $(Nd_{1-x}Ce_x)_{12.2}Fe_{81.6}B_{6.2}$ shows a coercivity value of 7.46 kOe for x=0.6, which is abnormally high for the Ce-substituted magnets[9]. The Mr/Ms ratios of the ribbon are all above 75% with the Ce content increasing from 0.2 to 0.6. It can be seen from the inset that at x = 0, there was a small kink on the hysteresis loop, further suggesting that $Re_2Fe_{14}B$ coexists with α-Fe. As the Ce atomic percentage increases, the coercivity decreases on account of the introduction of Ce decreasing the magnetocrystalline anisotropy, which is consisted with the conclusion of Shen et al. [9]. However, the squareness of the loop does not deteriorate significantly with the increase of Ce. The double annealing process that maintains high coercivity at high Ce substitution provides a practical approach to comprehensive utilization of rare earth resources.

References 1. M. Sagawa, S. Fujimura, N. Togawa, H. Yamamoto, and Y. Matsuura, J. Appl. Phys. 55 (1984), 2083. 2. Yang Y.C, Zhang X.D, Kong L.S, Pan Q. and Ge S.L., Appl. Phys. Lett. 58(1991), 2042. 3. J.J. Croat, J.F. Herbst, R.W. Lee, F.E. Pinkerton, Appl. Phys. Lett., 44 (1984), pp. 148-149. 4. X.C. Wang, M.G. Zhu, W. Li, L.Y. Zheng, D.L. Zhao, X. Du, A. Du, Electron. Mater. Lett., 11 (2015), pp. 109-112. 5. M. Zhang, Z.B. Li, B.G. Shen, F.X. Hu, J.R. Sun, J. Alloys Compd., 651 (2015), pp. 144-148. 6. M. Hussain, J. Liu, L.Z. Zhao, X.C. Zhong, G.Q. Zhang, Z.W. Liu, J. Magn. Magn. Mater., 399 (2016), pp. 26-31. 7. Q. Z. Jiang, Z. C. Zhong, J. Mater. Sci. Technol.,33(2017), pp.1087-1096. 8. M. N. Yang, H. Wang, Y. F. Hu, L. Y. M. Yang,A. Maclennan, B. Yang, J. Alloys Compd., 710(2017), pp.519-527. 9. Li Z.B., Shen B.G., Zhang M, J. Alloys Compd., 628(2015), pp.325-328. 10. M. Grigoras, M. Lostun, G. Stoian, D. D. Herea, H. Chiriac, N. Lupu, J. Magn. Magn. Mater.,432(2017), pp.119-123.

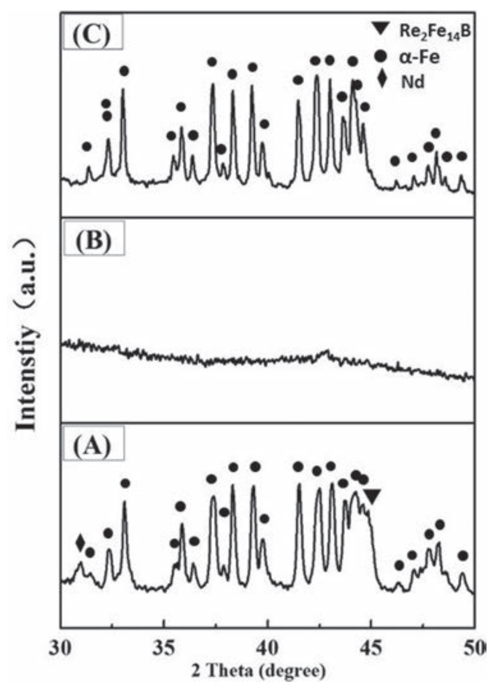

Fig. 1. XRD patterns of the $(Nd_{0.8}Ce_{0.2})_{12.2}Fe_{81.6}B_{6.2}$ (A) Crystallized ribbons, (B) Amorphous ribbons and (C) Raw material

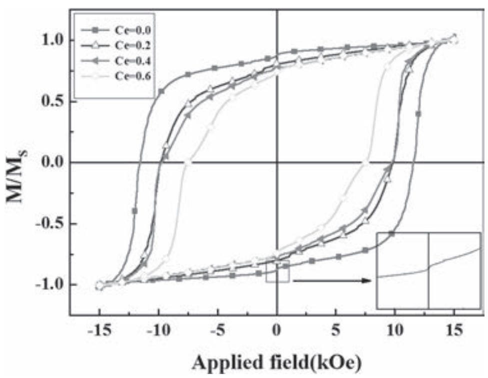

Fig. 2. Hysteresis loop of samples of $(Nd_{1-x}Ce_x)_{12.2}Fe_{81.6}B_{6.2}$ (Ce=0.0, 0.2, 0.4, 0.6)

9:30

AB-03. Magnetic performance change of multi-main-phase Nd-Ce-Fe-B magnets by diffusing (Nd, Pr)H_x.

W. Zhang[1], T. Ma[1], B. Peng[1] and M. Yan[1]
1. School of Materials Science and Engineering, Zhejiang University, Hangzhou, China

Grain boundary diffusion process (GBDP) is effective to enhance coercivity of the single-main-phase (SMP) $RE_2Fe_{14}B$ (RE, rare earth) magnets through forming magnetic hardening shells surrounding the hard grain cores. Here GBDP was applied to the multi-main-phase (MMP) (Nd, Pr)$_{22.3}$Ce$_{8.24}$Fe$_{bal}$ M$_{1.0}$B$_{1.0}$ (wt.%) magnets prepared by sintering the mixture of Ce-free and Ce-containing 2:14:1 powders, which have shown superior magnetic properties, especially coercivity, to the SMP ones at the same average composition. The remanence of the (Nd, Pr)H_x diffused magnets increases gradually with the increase of diffusion temperature from 480 to 880 °C, the coercivity however slightly decreases. The highest $(BH)_{max}$ of 350.1 kJ/m^3 is achieved when diffusing at 680 °C, which is 9.2 % higher than 320.7 kJ/m^3 for the as-prepared magnet. The remanence increment is due to the diffusion of Nd/Pr into the 2:14:1 phase grains, enlarging the intrinsic saturation magnetic polarization. The slight coercivity reduction is due to the gradual homogenization of RE distribution within the 2:14:1 grains of the undiffused parts, i.e. approaching the ‘‘close to equilibrium (or SMP)’’ state, which offsets the positive contributions from the enrichment of Nd/Pr in the Ce-rich 2:14:1 phase and the formation of continuous RE-rich intergranular phase. These findings suggest that the GBDP effect on coercivity of the MMP Nd-Ce-Fe-B magnets is distinctly different from the SMP ones, which suggests that the chemical heterogeneity should be carefully controlled to improve the magnetic performance of such high cost-performance permanent magnets.

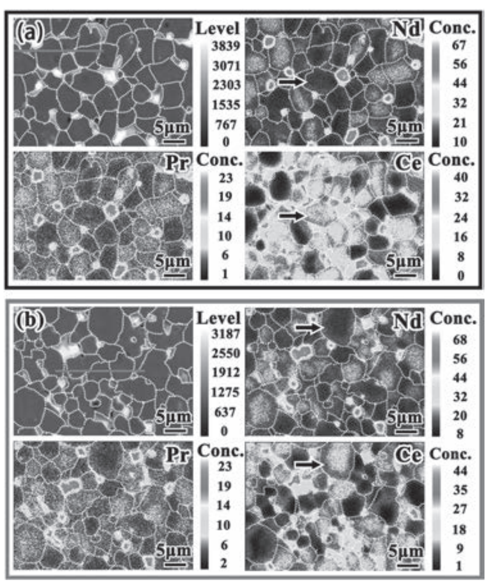

Fig. 1. Back-scattered SEM and EPMA images of the center part for the virgin magnet (a) and the one processed at 680 °C (b).

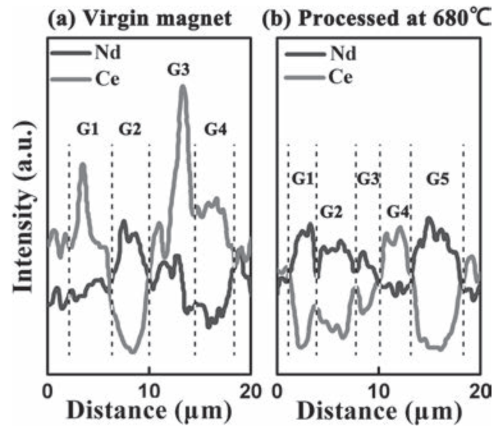

Fig. 2. Elemental distributions within the Ce-lean and the Ce-rich 2:14:1 grains (the lines drawn in Fig. 6) for the virgin magnet (a) and the one processed at 680 °C (b).

9:45

AB-04. Coercivity enhancement of multi-main-phase Ce-Fe-B magnets by spark plasma sintered technique and dual alloy method.

Q. Jiang[1], W. Lei[1], S. Rehman[1], Q. Zeng[1], L. He[1], X. Hu[1], L. Zhang[1], M. Zhong[1], S. Ma[1], W. Cui[2] and Z. Zhong[1]
1. Jiangxi University of Science and Technology, Ganzhou, China;
2. Northeast University, Shenyang, China

NdFeB-based permanent magnets have been widely applied in various fields. The critical rare earth (RE) elements, such as Pr, Nd, Dy or Tb, have been overused by large amount of consuming RE for making RE-Fe-B magnets. As the most abundant rare earth element on earth and the byproduct of Nd and Pr extraction processes, Cerium (Ce), however, is overstock. The development of the Ce-based magnets is a feasibly economic way for using the rare earth resources effectively. In this paper, we have investigated the Ce-Fe-B magnets prepared by spark plasma sintered (SPSed) technique and so called dual alloy method with different ratio of alloys of Ce-Fe-B and Pr-Nd-Fe-B. As expected, the remanent magnetization J_r, coercivity H_{ci} and maximum energy product $(BH)_{max}$ of SPSed magnets increase obviously with increasing weight percentage of Pr-Nd-Fe-B alloy. The magnetic properties of J_r = 0.71 T, H_{ci} = 915 kA/m, $(BH)_{max}$ = 72 kJ/m^3 are obtained for the SPSed magnets with 20 wt.% of the Ce-Fe-B alloy. The temperature coefficients of remanence (α) and coercivity (β) of the magnets are better off from -0.46 %/K, -0.60 %/K to -0.23 %/K, -0.53 %/K in the temperature range of 300-400 K. Fig.1 shows a typical M-T curve and dM/dT for the Ce-containing magnets with Pr-Nd-Fe-B alloy produced by dual alloy method. Three Curie temperatures are exhibited in dual-alloy magnets. The existence of three Curie temperatures may indicate three types of hard magnetic main phases with different compositions. The first Curie temperature T_{c1} = 441 K is close to that of the Pr-Nd-Fe-B-free magnet. It is the Curie temperature of Ce-Fe-B-based main phase. The third Curie temperature T_{c3} = 580 K is that of the Pr-Nd-Fe-B-based main phase. The second Curie temperature T_{c2} = 493 K is between T_{c1} and T_{c3}. It appears to be the Curie temperature of Pr-Nd-Ce-Fe-B magnetic phase. In addition, with increasing Pr-Nd-Fe-B content, there is no obvious change for T_{c1} and T_{c3}, but T_{c2} increases from 493 K to 516 K depending on the content of Pr-Nd-Fe-B alloy. It was confirmed that Ce tends to get into grain boundary while Nd is more likely to get into main phase[1]. The changing Curie temperature may result from the main phase grains with different Ce concentrations. Element diffusion and immigration lead to form a new magnetic phase and therefore T_{c2} appears. Thus, a nano-crystalline multi-main-phase Ce-containing sintered magnet was fabricated by SPS technique. Fig. 2 gives a BSE image and corresponding EDX elemental mappings of Ce-based magnet with 20% Pr-Nd-Fe-B alloy addition. The Ce mapping exhibits non-uniform contrasts in different areas. For example, area 1 and area 2 marked in BSE image are Ce-lean while area 3 and area 4 marked in BSE image are Ce-rich. The results of elemental weight percentage analysis shows that the ratio of Ce/(Ce+Nd+Pr) is almost equal to 1 for area 3 and area 4. The ratio of Ce/(Ce+Nd+Pr), however, is about 0.52-0.55 for area 1 and area 2. Therefore, Pr-Nd-Ce-Fe-B main phase is formed because of element diffusion and immigration. According to the weight percentage of Ce, Pr, Nd in the compositions, the theoretical Curie temperature of Pr-Nd-Ce-Fe-B phase is calculated to be in the range of 503-507 K, being closer to the measured Curie temperature T_{c2}. The EDX result demonstrates the inhomogeneous distribution of Ce, which consists with the M-T result. The present research may offer potential references on further research and development for the practical applications of this type high abundant rare earth permanent magnetic material. This work was supported by the National Natural Science Foundation of China (Grant Nos. 51564037 and 51661011), Innovation Fund Designated for Graduate Students of Jiangxi Province (Grant No. YC2016-B078), Outstanding Doctoral Dissertation Project Fund of Jiangxi University of Science and Technology (Grant No. YB2017006), Qing Jiang Scholar and the Start-up Fund of Jiangxi University of Science and Technology (Grant No. 3208600001).

[1] Z. Li, W.Q. Liu, S.S. Zha, Y.Q. Li, Y.Q. Wang, D.T. Zhang, M. Yue, J.X. Zhang, X.L. Huang, J. Magn. Magn. Mater. 393 (2015) 551-554.

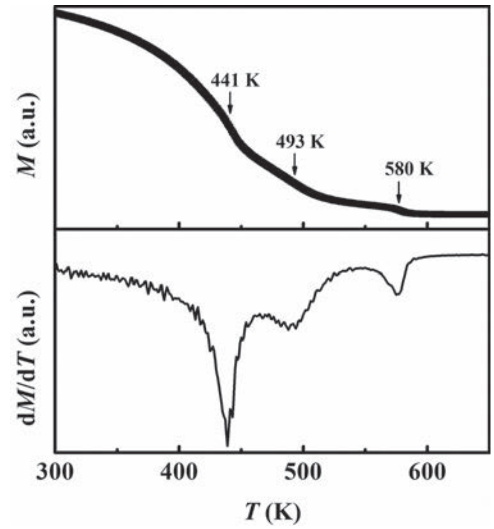

Fig. 1. Typical M-T curve and dM/dT for the dual alloy Ce-containing magnets.

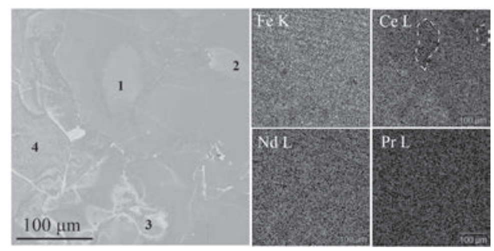

Fig. 2. BSE SEM image and corresponding EDX elemental mappings of Ce-based magnet with 20% PrNdFeB alloy addition

10:00

AB-05. Nd-Fe-B films with perpendicular magnetic anisotropy and extremely large room temperature coercivity.

C. Ma[1], S. Wang[1], A. Morisako[1], S. Piramanayagam[2] and X. Liu[1]
1. Faculty of Engineering, Shinshu University, Nagano, Japan; 2. School of Physical and Mathematical Sciences, Nanyang Technological University, Singapore, Singapore

Nd-Fe-B thin films have potential applications in high sensitive magnetic sensors and high density magnetic recording media due to its large magneto-crystalline anisotropy and high saturation magnetization[1-3]. They are also being investigated for energy harvesting. For all those applications, controlling the magnetic anisotropy to prepare films with perpendicular magnetic anisotropy are important[4]. In this digest, we present a novel process to prepare Nd-Fe-B thin films with perpendicular magnetic anisotropy. Substitution of various elements such as Tb, Dy and Sm were carried out. Of particular interest is that a 1 at% addition of Tb, Dy, or Sm can strongly enhance the perpendicular magnetic anisotropy of the Nd-Fe-B films. Films with additions of Tb show coercivity larger than 30 kOe. A clear correlation between perpendicular magnetic anisotropy of annealed state and the domain formation in the as-deposited state were noticed[5,6]. In this experiment, Nd-Fe-B films were deposited by a facing targets sputtering system. The films were deposited onto thermally oxidized silicon wafer. The substrate temperature was ranging from 100 ^{o}C to 400 ^{o}C. It was confirmed by X-ray diffractometry (XRD) that all the deposited films are amorphous. The films were then subjected to a flash annealing process. Crystallized, magnetically hard films were obtained by annealing the samples at 650 ^{o}C for 5 minutes[7,8]. All the as-deposited amorphous films showed soft magnetic properties with coercivities less than 100 Oe in both perpendicular and in-plane direction. Fig. 1 shows magnetic force microscopy (MFM) images of as-deposited films without Tb addition (a) and with 1 at% Tb addition (b). We could not find any particular domain configuration in films deposited without Tb addition. However, well defined stripe domains with period of around 110 nm were present in the as-deposited films with Tb addition. The stripes were found to be aligned in the same direction as the stray magnetic field direction of facing targets sputtering system. Well aligned stripe domains are originating from the induced in-plane anisotropy field and perpendicular magnetic field as indicated by micromagnetic simulations. Further investigation of the perpendicular magnetic anisotropy from the saturation magnetization and domain period showed that the films have perpendicular magnetic anisotropy of around 5.0×10^{4} J/m^{3}. Films became magnetically hard and crystallized after annealing at 650 ^{o}C. Fig. 2 shows hysteresis loops of films deposited without Tb addition (a) and with Tb addition (b). According to Fig. 2 (a). films deposited without Tb addition show almost identical perpendicular and in-plane hysteresis loops. However, as shown in Fig. 2(b), films deposited with addition of Tb show excellent perpendicular magnetic anisotropy with large perpendicular remanence but very low in-plane remanence. It should be noted that the films have very large coercivity that a maximum applied field of 24 kOe could not even reverse the magnetization. Films show almost zero coercivity at in-plane direction further confirms the excellent perpendicular magnetic anisotropy. XRD results shows c-axis normal to the film plane crystallographic properties for films with Tb addition, which further confirmed the perpendicular magnetic properties in those films. Our results show clear magnetic correlations between as-deposited amorphous films and annealed crystallized films. Our research provides a simple way to evaluate crystallographic and magnetic properties of Nd-Fe-B films even without annealing the films. Addition of Tb, Dy, and Sm were found can enhance the perpendicular magnetic anisotropy in the Nd-Fe-B films.

1. Sagawa M;Hirosawa S; Ymamoto H;Fujimura S; Matsuura Y:JAPANESE JOURNAL OF APPLIED PHYSICS, VOL. 26, No.6, JUNE.1987, pp. 785-800 2. Yamasawa, K; Liu, XX; Morisako, A: JOURNAL OF APPLIED PHYSICS, 99, 08N302 (2006) 3. Liu, X; Okumoto, T; Matsumoto, A; Morisako, A:JOURNAL OF APPLIED PHYSICS, 97(10) 2005(May) 4. Liu, XX; Ishida, G; Morisako, A: JOURNAL OF APPLIED PHYSICS, 109, 07A725 (2011) 5. Shima, T; Sato, K; Mishina, Y; Ohtsuki, T; Iwama, H: JOURNAL OF THE JAPAN INSTITUTE OF METALS, 76, 52-58 (2012) 6. Hono, K; Ohkubo, T; Sepehri-Amin, H: JOURNAL OF THE JAPAN INSTITUTE OF METALS, 76, 2-11 (2012) 7. Morisako, A; Liu, XX: JOURNAL OF MAGNETISM AND MAGNETIC MATERIALS, 304, 46-50 (2006) 8. Okumoto, T; Yamasawa, K; Liu, X; Matsumoto, A; Morisako, A: IEEE TRANSACTIONS ON MAGNETICS, 10, 3139-3141 (2005)

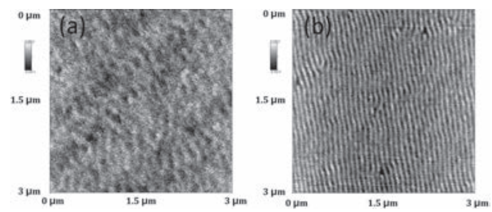

Fig. 1. MFM images as-deposited films without Tb addition (a) and with 1 at% Tb addition (b).

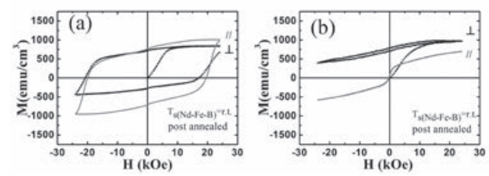

Fig. 2. Films deposited without Tb addition (a) and with Tb addition (b).

10:15

AB-06. Development of non-rare earth grain boundary diffusion process for Nd-Fe-B permanent magnets.

Z. Liu[1], Q. Zhou[1], H. Zeng[1], H. Yu[1], X. Zhong[1] and X. Che[1]
1. School of Materials Science and Engineering, South China University of Technology, Guangzhou, China

Nd-Fe-B based rare earth permanent magnets are essential for a variety of devices. The performances of the magnetic materials are directly related to their microstructure. Recent researches have shown that the magnetic properties are very much dependent on the grain boundary structure. As a result, grain boundary diffusion (GBD) process has become an effective approach for improving the coercivity and reducing the heavy RE content of Nd-Fe-B magnets since the beginning of this century. In this paper, the development of GBD process has been introduced. Aiming to continuously reduce the material cost, GBD process has undergone three stages, as shown in Fig.1. In the early stage, heavy rare earth elements Dy or Tb and their compounds like Dy_2O_3, Dy-H, Dy-F were employed as the diffusion media. The magnetic properties, especially coercivity, of sintered NdFeB magnets and melt spun Nd-Fe-B powders were significantly enhanced. In the second stage, eutectic compounds RE-TM (RE=Nd, Pr, etc.; TM=Cu, Ni, etc.) were used for GBD. These compounds do not contain expensive rare earth elements Dy and Tb, and thus further reduced the material cost. The coercivities of both sintered magnets and hot deformed magnets have been greatly improved. Recently, we reported the enhancements of the magnetic properties and corrosion resistance of Nd-Fe-B magnets by a non-RE compound diffusion process[1], which can be regarded as the third stage of GBD. The details of non-RE GBD process and our very recent work will be presented in this paper. For the details, metal oxides were firstly employed as the diffusion media. The Tb, Dy-free sintered Nd-Fe-B magnets were coated with an oxide layer by magnetron sputtering, followed by solid diffusion heat treatment. With the successful diffusion of oxide into the magnet, the coercivity of the magnets has increased significantly and the maximum energy product was also enhanced without a significant decrease in remanence. The underlying mechanisms for these enhancements have been analyzed. The microstructural investigations show that the oxide entered mainly into the intergranular regions and modified the composition and structure of the grain boundary phase. The intergranular oxide phases observed in the oxide diffused magnet also contribute to the improved temperature stability and corrosion resistance of the magnet. Two types of oxides including MgO and ZnO have been discussed in this paper and both are effective in improving the coercivity of sintered Nd-Fe-B magnet. One example is shown in Fig.2. Our further studies indicate that not only oxides but also the low melting point alloys can work as the grain boundary diffusion medium for improving the coercivity of RE-lean Nd-Fe-B magnets. This novel GBD approach may overcome the limitations of conventional grain boundary diffusion, which requires heavy rare earth or rare earth compound, and has significance in further minimizing the use of rare earth resources.

[1] Q. Zhou, Z.W. Liu, X.C. Zhong, G.Q. Zhang, Properties improvement and structural optimization of sintered NdFeB magnets by non-rare earth compound grain boundary diffusion, *Materials and Design*, 86 (2015) 114-120

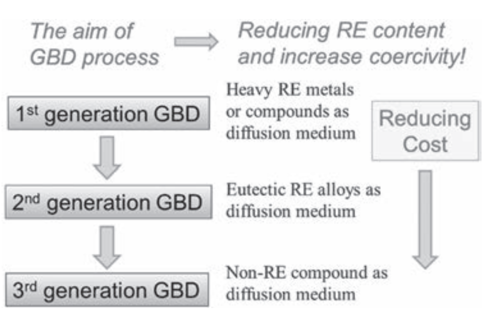

Fig. 1. The development of grain boundary diffusion process for Nd-Fe-B magnets

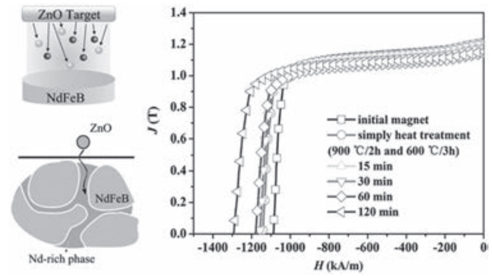

Fig. 2. Non-rare earth grain boundary diffusion process and the enhancement of coercivity

10:30

AB-07. Low spin reorientation transition temperature, high coercivity, $Nd_2(Fe,Co,Cr)_{14}B$ based hard magnetic nanoparticles.

V. Chaudhary[1], Y. Zhong[1], H. Parmar[1], X. Tan[1] and R.V. Ramanujan[1]
1. Nanyang Technological University, Singapore, Singapore

Abstract: We have synthesized high coercivity $Nd_2Fe_{10.5}Co_2Cr_{1.5}B$ magnetic nanoparticles through a green and low cost mechanochemical method. The coercivity (H_C) of isolated $Nd_2(Fe_{10.5}Co_2Cr_{1.5})B$ nanoparticles and nanoparticles embedded in a CaO matrix was found to be 11.3 kOe and 9 kOe, respectively. The thermal coefficient of remanence (α (*Mr*)) and coercivity (β (H_C)) of these nanoparticles after removal of CaO, measured from room temperature to 400 K, was found to be -0.0015 and -0.0065, respectively. These nanoparticles exhibit the spin reorientation transition temperature (T_{SR}) of ~ 89 K, which is ~46 K less than that of bulk $Nd_2Fe_{14}B$ magnets, hence, more attractive for cryogenic applications. *Introduction:* NdFeB magnets are the strongest permanent magnets and are extensively used in energy generation and conversion systems. The magnetic properties can be tuned by modifying their microstructure or grain boundaries. Sintering, melt spinning, alloying, infiltration and diffusion based techniques are commonly used for this purpose. Nanostructuring of NdFeB materials is of high current interest[1-4]. Hence, we synthesized Cr alloyed NdFeCoB hard magnetic nanoparticles using green and cost effective mechanochemical processing. The process involves grinding of starting oxide materials to nanoscale powders, unlike the processes of elemental melting or production from solutions at high temperatures. Corrosion is a limitation of current NdFeB magnets, our Cr alloyed NdFeCoB magnets exhibit better corrosion resistance compared to alloys without Cr. *Experimental details:* $Nd_2Fe_{10.5}Co_2Cr_{1.5}B$ nanoparticles were prepared through processing a mixture of Nd_2O_3 (99.9 %, Alfa Aesar), Fe_2O_3 (99.9 %, Sigma Aldrich), CoO (99.9%, Alfa Aesar), B_2O_3 (99.9%, Alfa Aesar) and Cr_2O_3 (99.9 %, Sigma Aldrich) powders and Ca granules (99.9%, Sigma Aldrich) using a mechanochemical process. The content of each precursor first selected to produce $Nd_2Fe_{10.5}Co_2Cr_{1.5}B$. Excess amount of Nd_2O_3 and Ca granules was then added to compensate potential loss and ensure full reduction during processing, respectively. All precursors were milled using a Fritch Pulverisette-7 planetary ball mill at 500 rpm for 6 h under Ar. The milled powder samples were collected in a glove box filled with Ar. These nanoparticles were cold pressed, and heat treated in a vacuum furnace (~10^{-5} torr) at 850 °C for 90 min. NH_4Cl/methanol solution was used to remove the by-product, i.e., CaO. For structural, compositional, morphology and magnetic property measurements, several characterization techniques, e.g., XRD, SEM, EDX, TEM, PPMS were used. *Results and discussion:* Figure 1a shows the room temperature M–H hysteresis curves of mechanochemically processed $Nd_2(Fe_{10.5}Co_2Cr_{1.5})B$ nanoparticles before and after removal of CaO from the samples. The room temperature coercivity (H_C) decreases from 11.4 kOe to 9 kOe, while remanent magnetization (*Mr*) increases from 7.3 emu/g to 38.3 emu/g after removal CaO from the samples. The decrease in H_C is attributed to diffusion of hydrogen in the tetragonal structure of $Nd_2(Fe_{10.5}Co_2Cr_{1.5})B$ during CaO removal by NH_4Cl/methanol or the percolation effect due to strong particle-particle interactions when particles are not in the CaO matrix. Figure 1(b) shows the temperature dependent demagnetization curve for $Nd_2(Fe_{10.5}Co_2Cr_{1.5})B$ nanoparticles in the temperature range from 150 K to 400 K. Fig 2 shows the change of H_C and *Mr* with temperature, these values are a maximum at 150 K. H_C and *Mr* are lower at low temperatures due to spin reorientation arising from the interplay between the magneto-crystalline anisotropies of the different magnetically ordered sub-lattices. The easy axis of magnetization changes at the spin reorientation temperature (T_{SR}). The T_{SR} for bulk/single crystal Nd-Fe-B magnet is 135 K. The T_{SR} was determined by the derivative of the magnetization versus temperature (*dM/dT*) curve for our Cr alloyed Nd-Fe-Co-B nanoparticles at low applied field of 100 Oe, which was found to be 89 K. We have measured the thermal coefficient of remanence (α) and coercivity (β) in different temperature windows e.g., from 300 K to 400 K (α= -0.0015, β= -0.0065), from 150 K to 400 K (α= -0.0024, β= -0.0080) and from 250 K to 350 K (α= -0.0012, β= -0.0041). The thermal stability of our nanoparticles up to 350 K is comparable to those of commercial NdFeB magnets. *Conclusion:* We present the structural and magnetic properties of low cost, high performance and heavy rare earth free $Nd_2(Fe_{10.5}Co_2Cr_{1.5})B$ nanoparticles synthesized by a mechanochemical process which uses low cost oxide powders. Low spin reorientation transition temperature and high coercivity values of our Nd-Fe-Co-Cr-B magnets make them useful for low temperature corrosive environments.

[1] Y. Zhong, V. Chaudhary, X. Tan, H. Parmar, R.V. Ramanujan, *Nanoscale*, 2017, 9, 18651. [2] X. Tan, H. Parmar, Y. Zhong, V. Chaudhary, R.V. Ramanujan, *IEEE Magnetics Letters*, 2017, 8, 5508805. [3] H. Parmar, T. Xiao, V. Chaudhary, Y. Zhong, R.V. Ramanujan, *Nanoscale*, 2017, *9,* 13956. [4] M. Yue, X. Zhang, J.P. Liu, *Nanoscale*, 2017, *9,* 3674.

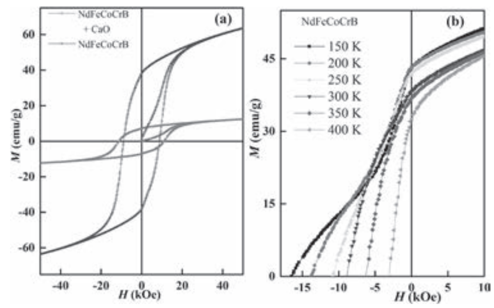

Fig. 1. (a) Room temperature *M-H* hysteresis loops of $Nd_2(Fe_{10.5}Co_2Cr_{1.5})B$ nanoparticles before (grey curve) and after removal of CaO (blue curve) (b) Demagnetization curves of *M-H* hysteresis loops at temperatures ranging from 150 K to 400 K for $Nd_2(Fe_{10.5}Co_2Cr_{1.5})B$ nanoparticles after removal of CaO

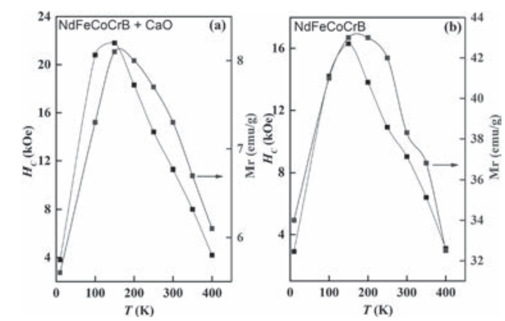

Fig. 2. Coercivity (H_C) (left axis, black square) and remanent magnetization (M_r) (right axis, blue square) versus temperature from 10 K to 400 K for (a) $Nd_2Fe_{10.5}Co_2Cr_{1.5}B$ nanoparticles embedded in a CaO matrix (b) isolated $Nd_2Fe_{10.5}Co_2Cr_{1.5}B$ nanoparticles

10:45

AB-08. Effect of impurities on magnetic properties in Nd-Fe-B particles synthesized by reduction-diffusion process.

D. Kim[1,2], V. Galkin[1,2] and K. Haider[1,2]
1. Korea Institute of Materials Science, Changwon, The Republic of Korea; 2. DMR CRC, Korea Institute of Geoscience and Mineral Resources, Daejeon, The Republic of Korea

Abstract: A novel route to prepare Nd-Fe-B magnetic particles by utilizing both spray drying and reduction-diffusion (R-D) processes was investigated in this study. Precursors were prepared by spray drying method using the aqueous solutions containing Nd salt, Fe salt and boric acid with stoichiometric ratios. Nd-Fe-B particles with the uniform size of 1 micrometer were obtained by R-D with reducing agent of CaH_2 followed by additional washing with wet ball milling. Especially, these two step washing process contributed to the excellent magnetic properties with high remanence and coercivity. $Nd_2Fe_{14}B$ particles were synthesized after washing and vacuum drying with the maximum energy product above 20.0 MGOe. Experimental methods: In order to prepare $Nd_2Fe_{14}B$ powders, $NdCl_3{\cdot}6H_2O$, $FeCl_3{\cdot}6H_2O$ and H_3BO_3 were weighted considering stoichiometry of compositions and dissolved in deionized (DI) water. Spray drying was performed under the condition of hot air of 250 ^oC, and feed rate of aqueous solution of 20 ml/min. Subsequently, the spray dried powders were desalted at 800 ^oC for 2 hours in air, followed by ball milling for 2 hours. The powders after ball milling were mixed with CaH_2 and then they were compressed into compacts. R-D of the compacts was carried out at 1000 ^oC for 3 hours in Argon (Ar) atmosphere. For the effective washing, the compacts were pulverized to coarse powders and the powders were washed with DI water and wet ball milling. Results and Discussion: After R-D process, $Nd_2Fe_{14}B$ clusters were embedded in CaO matrix uniformly, and bright contrasts in SEM images identified as Nd-rich phase appeared in the clusters. The corresponding EDX spectra showed atomic ratio of Fe/Nd was 4.89 that is close to the Fe/Nd ratio of 5.1 for the nominal constituent $Nd_{15}Fe_{77.5}B_{7.5}$. The atomic ratio of Ca/O approaches to 1, implying that the $Nd_2Fe_{14}B$ phase has not been oxidized. After one-step of washing, just the matrix CaO was removed, but the oxygen content was as high as 3.12 wt%. After two-step washing including wet ball milling, no obviously different contrast was observed and the atomic ratio of Fe/Nd was increased to 5.3 which meant the process lost the part of Nd-rich phase. Compared to the one-step washed powders, the weight of oxygen was increased from 3.12% to 4.37%. TEM image showed well dispersed magnetic phase of $Nd_2Fe_{14}B$ with particle size below 1 micrometer and displayed a shape of bacilliform, and the insert is the SADP pattern of the nanocrystalline $Nd_2Fe_{14}B$. HRTEM image showed an assembly of $Nd_2Fe_{14}B$ particles. It can be seen that the nanoscale domains adopt different structural orientations. The lattice fringes within each crystal domain have an interfringe nanocrystalline $Nd_2Fe_{14}B$ spacing of 3.14Å, which is close to the interplane distance of 3.11Å between the (220) planes in tetragonal structure of $Nd_2Fe_{14}B$. From M-H demagnetization curves at room temperature, magnetic properties for the powders after R-D were coercivity value of 10.6 kOe, but low remanence (Mr) and saturation magnetization (Ms). The coercivity of powders after two-step washing proposed in this work was decreased to 5.1 kOe, while Mr increased drastically. A (BH)max value as high as 22.1 MGOe was obtained. Conclusion: $Nd_2Fe_{14}B$ particles from the precursors obtained by spray drying were successfully synthesized. A high coercivity of 10.6 kOe of the Nd-Fe-B particles was attained before washing, which is attributed to isolation of nonmagnetic phase CaO and Nd-rich phase between $Nd_2Fe_{14}B$ particles. Finally, the particles with high (BH)max more than 20 MGOe by the control of washing step in R-D process were obtained. It was revealed that the ratio of CaH_2/the oxide powders and efficient washing system were important factors affecting magnetic property of final products.

1. M. Sagawa, S. Fujimura, M. Togawa, H. Yamamoto, Y. Matsuura, *Journal of Applied Physics*, vol. 55, p. 2083, 1984. 2. J.J. Croat, J.F. Herbst, R.W. Lee, F. E. Pinkerton, *Journal of Applied Physics*, vol. 55, p. 2078, 1984. 3. E. Burzo, *Reports on Progress in Physics*, vol. 61, p. 1099, 1998. 4. R.E. Cech, *Journal of Metals*, vol. 26, p. 32, 1974. 5. S. Ram, J.C. Joubert, *Journal of Applied Physics*, vol. 72, p. 1164, 1992. 6. J.H. Lin, S.F. Liu, Q.M. Cheng, X.L. Qian, L.Q. Tang, M.Z. Su, *Journal of Alloys and Compounds*, vol. 249, p. 237, 1997. 7. C.W. Km, Y.H. Km, H.G. Cha, Y.S. Kang, *Physica Scripta*, vol. T129, p. 321, 2007. 8. P.K. Deheri, V. Swaminathan, S.D. Bhame, Z.W. Liu and R.V. Ramanujan, *Chem. Mater*. vol. 22, p. 6509, 2010. 9. V. Swaminathan, P.K. Deheri, S.D. Bhame and R.V. Ramanujan, *Nanoscale*, vol. 5, p. 2718, 2013. 10. C. Chen, D. Kim, C. Choi, *Journal of Magnetism and Magnetic Materials*, vol. 355, p. 180, 2014. 11. H.X. Ma, C.W. Kim, D.S. Kim, J.H. Jeong, I.H. Kima and Y.S. Kang, *Nanoscale*, vol. 7, p. 8016, 2015

11:00

AB-09. Coercivity enhancement of hot-pressed magnet prepared by HDDR Nd–Fe–B powders using Pr-Cu eutectic alloys diffusion.

T. Song[1], X. Tang[1], W. Yin[1], R. Chen[1] and A. Yan[1]
1. Ningbo Institute of Industrial Technology, Chinese Academy of Sciences, Ningbo, China

Hydrogenation-disproportionation-desorption-recombination (HDDR) has been developed as a well-known method synthesizing $R_2Fe_{14}B$ (R=Nd, Pr) magnetic powders with ultrafine-grained microstructure [1]. The $Nd_2Fe_{14}B$ phase disproportionates into neodymium hydride, Ferro boron, iron during a heat treatment in hydrogen up to temperatures higher than 650 °C. During evacuation of system, hydrogen desorbs and the dispropertionated mixture of Nd, Fe_2B, and Fe recombines forming submicrom grains of $Nd_2Fe_{14}B$ with an average grain size of about 0.3 μm. It may be a promising way preparing R-Fe-B powders with high coercivity and remanence [2-3]. However, the coercivity of the magnets prepared by HDDR powders are far below the expected value [4]. Grain boundary diffusion of Nd–Cu or Pr–Cu alloy was employed to enhance the coercivity of HDDR ternary Nd–Fe–B powders recently. Therefore, the grain boundary diffusion process, an effective method to prepare magnets with high coercivity [5], is also applied in this study. The ingot with the nominal composition of $Nd_{30}Co_{5.28}Al_{0.6}Zr_{0.14}Ga_{0.54}Fe_{bal.}B_{1.05}$ (wt. %) crushed into powders and followed by Hydrogenation-disproportionation process. The low melting-point $Pr_{82}Cu_{18}$ (wt. %) melt-spun powders was mixed with the Hydrogenation-Disproportionation powders and followed by Desorption-Recombination was defined as S1. The low melting-point $Pr_{82}Cu_{18}$ (wt. %) melt-spun powders was mixed with the HDDR powders was defined as S2. The powders was hot pressed at 750 °C. Demagnetization curves of hot-pressed magnets with Pr-Cu eutectic alloys addition as shown in Fig.1. Compared to the reference sample, the coercivity of S2 is improved drastically to 15.2 kOe, however, the coercivity of S1 was decreased to 10.6 kOe. L-TEM Fresnel images of S2 observed in zero magnetic field was shown in Fig. 2a-c. There are no obvious lines at just-focus state (Fig. 2a). However, when the sample is investigated at under-focus and over-focus states, dark and white lines can be observed (Fig. 2b and c). Moreover, the dark line at under-focus state turns into the white line at over-focus state while the white line at under-focus state turns into the dark line at over-focus state. It is clear that the magnetic domains are continuous across the grain boundary. The continuous magnetic domain walls suggest short-range exchange coupling between adjacent grains. Note that the magnetic domains are interrupted by the thick grain boundary phases indicating the magnetic decoupling of the adjacent grains. The present work further reveals that magnetic isolation between adjacent grains is essential to obtain a higher coercivity. The present work further reveals that magnetic isolation between adjacent grains is essential to obtain a higher coercivity. In addition, we strongly believe that the diffusion process will be also beneficial for preparation of hot-deformed HDDR magnets due to the existence of R-rich phases in adjacent grains.

[1] T. Takeshita, K. Morimoto, J.Appl.Phys.79 (1996) 5040-5044 [2] O. Gutfleisch, K. Khlopkov, A. Teresiak, K. H.Muller, G. Drazic, C. Mishima, Y.Honkura, IEEE. Trans. Magn. 39 (2003) 2926-2931. [3] Y. Honkura, C. Mishima, N. Hamada, G. Drazic, O. Gutfleisch, J. Magn. Magn. Mater. 290–291(2005)1282. [4]S. Sugimoto, H. Nakamura, K. Kato, D.Book, T.Kagotani, M. Okada, M.Homma, J. Alloys. Compd. 293–295 (1999) 862-867. [5] H. Sepehri-Amin, T. Ohkubo, T. Nishiuchi, S. Hirosawa, and K. Hono, Scripta Mater., 63 (2010) 1124–1127.

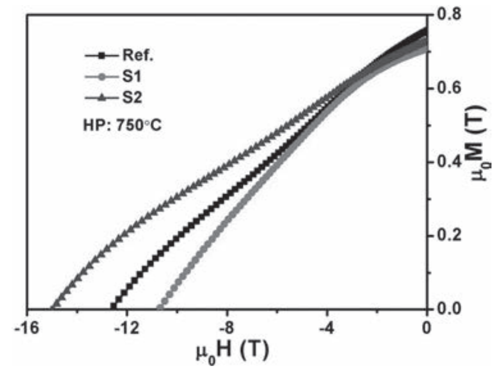

Fig. 1. Demagnetization curves of hot-pressed magnets with Pr-Cu eutectic alloys addition

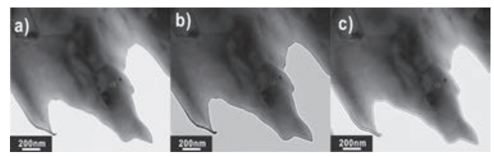

Fig. 2. L-TEM Fresnel images of S1 observed at (a) just-focus, (b) under-focus and (c) over-focus states in the zero applied magnetic field

11:15

AB-10. Corrosion of Co,Al-alloyed NdFeB magnetic nanostructures processed by microwave synthesis.

H. Parmar[1], X. Tan[1], Y. Zhong[1], V. Chaudhary[1], D. Peng[1], Y. Huang[1] and R.V. Ramanujan[1]
1. Nanyang Technological University, Singapore, Singapore

Abstract NdFeB based alloys were synthesized by microwave combustion followed by reduction diffusion process. The corrosion resistance were improved in nanostructured Co-NdFeB alloyed by minimal substitution of Al and Nd, which is comparable to sintered NdFeB magnets. The corrosion potential and current density of Al and Nd substitution of Fe improved corrosion resistance to -0.87V, -0.74V and 329 μA/cm^2, 144 μA/cm^2 respectively, and Ni-plating of appropriate thickness provided a high degree of protection against corrosion. Introduction Sintered NdFeB (neodymium–iron–boron) permanent magnets exhibit excellent magnetic properties[1]. Magnets been used for many extreme applications in various fields like electrical machines, electronics, acoustics, communications, automation, magnetic resonance imaging and biomedical applications. The low corrosion resistance of these magnets in humid environments has limited its wide applications [2]. Alloy additions and surface metal coatings[3-5] have been used to improve the corrosion resistance. The aim of the present paper is to study the effect of Al and Nd content in nanostructured NdFeB alloys on corrosion and to determine the influence of thickness of electroplated nickel coatings on improving the corrosion resistance of Co,Al-NdFeB magnets. Experiments Three alloy compositions, i.e., $Nd_{15}Fe_{62}Co_{15}B_8$, $Nd_{15}Fe_{59}Co_{15}Al_3B_8$ and $Nd_{20}Fe_{54}Co_{15}Al_3B_8$ named as a ND15, ND15Al3 and ND20Al3 respectively were prepared by microwave combustion followed by reduction diffusion process. The synthesis process was described earlier[6]. Cold pressed bulk sample was used for further corrosion and coating experiments. Corrosion study of the bulk sample was performed by measuring its electrochemical polarization curve in 3.5wt% NaCl solution at room temperature (25 ± 1 °C). A typical 3 electrode potentiostatic system from AUTOLAB PGSTAT 302N was used, with the sample as a working electrode, a platinum foil : counter electrode and an Ag/AgCl : reference electrode in the electrochemical cell. An external electric potential was applied between the reference electrode and the working electrode, current flow between these 2 electrodes are continuously monitored. A current vs. potential curve or a potentiostatic curve was then observed to analyse corrosion behaviour. Ni electroplating of 2μm and 10μm was conducted for ND15Al3 and ND20Al3 compositions. Results and Discussion $Nd_{15}Fe_{62}Co_{15}B_8$ composition considered as a parent samples and 3% of Fe was replaced Al to form the 2nd composition $Nd_{15}Fe_{59}Co_{15}Al_3B_8$ and 5% Fe was replaced by Nd in the 2nd composition to form the 3rd composition $Nd_{20}Fe_{54}Co_{15}Al_3B_8$. XRD pattern of ND15Al3 and ND20Al3 composition before corrosion study and after corrosion study (Fig 1(a) & (b). ND 15Al3 and ND20Al3 samples XRD pattern confirms the tetragonal phase formation. However, ND20Al3 samples consist of two phases one was Nd-rich phase marked by asterisk and the other was $Nd_2(FeCoAl)_{14}B$ tetragonal phase. The coercivity was increased for the ND20Al3 sample (Fig 1(d)), while the saturation magnetization and remanence magnetization decreased due to Fe replacement by Nd. The polarization curves for ND15, ND15Al3 and ND20Al3 are shown in figure 1(c). The replacement of Fe by 3% Al has improved corrosion resistance. The corrosion potential (Ecorr) and current density (Jcorr) observed for ND15 and ND15Al3 were -1.02V, 557 μA/cm^2 and -0.94V to 848 μA/cm^{2}respectively. When Fe was replaced by Nd for ND20Al3 composition, Nd-rich phase appeared which improved Ecorr. The Ecorr and Jcorr for ND20Al3 composition were -0.82 V and 349 μA/cm^2. The observed Ecorr for ND20Al3 composition was better than commercial sintered magnet[5]. The detailed study of ND15Al3 and ND20Al3 corroded samples were carried out by XRD and SEM EDS. All peaks of ND15Al3 samples were broadened after corrosion, while for ND20Al3 samples the Nd-rich phase peaks disappeared, which indicates that the Nd-rich phase actively dissolves[7](Fig 1(a) & (b). SEM and EDS results supported the XRD results. The corrosion study indicates the improvement in corrosion resistance of ND15Al3 and ND20Al3 sample compared to ND15 samples, hence Ni-plating was carried out for both these compositions. 2μm thickness Ni-plating was done by electroplating process for both compositions, while 10μm thickness plating was also performed for ND20Al3 composition. After Ni-plating corrosion resistance improved for both the compositions, Ecorr and Jcorr for ND15Al3 and ND20Al3 compositions were -0.87V, -0.74V and 329 μA/cm^2, 144 μA/cm^2 respectively. Further increase in Ni-plating to 10μm improved corrosion potential and current density to -0.66V and 45 μA/cm^2 for ND20 compositions. Conclusion $Nd_2(FeCo)_{14}B$ corrosion resistance was improved by substituting 3% Al and further improved by replacing Fe by 5% Nd. Fe replacement by Nd leads to a multiphase system. A Nd-rich phase dissolves and protects the tetragonal phase from corrosion. Ni-plating on both Al and Nd substituted substrate improved protection. Moreover, 10μm thickness of Ni-plating on Nd substituted composition has the best corrosion potential of -0.66V and current density of 45μA/cm^2.

1. O. Gutfleisch, M. A. Willard, E. Brück, C. H. Chen, S. G. Sankar and J. P. Liu, *Advanced Materials*, 2011, 23, 821-842. 2. Z.-n. Yang, C. Wang, Y. Zhang and Y. Xie, *Transactions of Nonferrous Metals Society of China*, 2015, 25, 832-837. 3. H. Chen, Q. Wang, H. Dong, L. Xi, X. Lin, F. Pan and Z. Ma, *Materials Research*, 2015, 18, 1089-1096. 4. L. Song, Y. Wang, W. Lin and Q. Liu, *Surface and Coatings Technology*, 2008, 202, 5146-5150. 5. D. J. Blackwood, B. Balakrisnan, Y. Z. Huang and C. K. Tan, *Journal of Magnetism and Magnetic Materials*, 2001, 223, 103-111. 6. H. Parmar, T. Xiao, V. Chaudhary, Y. Zhong and R. V. Ramanujan, *Nanoscale*, 2017, 9, 13956-13966. 7. A. A. El-Moneim and A. Gebert, *Journal of Applied Electrochemistry*, 2003, 33, 795-805.

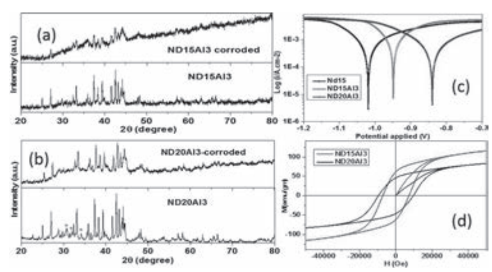

Fig. 1. XRD pattern of ND15Al3(a) and ND20Al3 (b) composition before and after corrosion study (C) Polarization curve for ND15, ND15Al3 and ND20Al3 composition (d) M-H hysteresis loop for ND15Al3 and ND20Al3

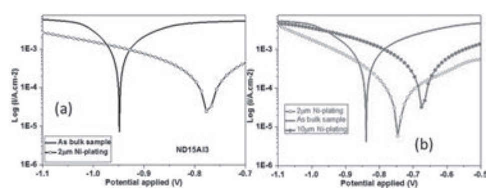

Fig. 2. (a) ND15Al3 polarization curve before and after Ni-plating of 2μm (b) ND20Al3 polarization curve before and after 2μm and 10 μm Ni-plating

11:30

AB-11. Mechanism for the enhancement of magnetic properties of Nd-Fe-B, after the addition of Pr, Dy and Tb.

K. Haider[1,2], V. Galkin[1,2], Y. Kang[3] and D. Kim[1,2]
1. Development of Mineral Resources, Korea Institute of Geoscience and Mineral Resources, Daejeon, The Republic of Korea; 2. Powder & Ceramics Division, Korea Institute of Materials Science, Changwon, The Republic of Korea; 3. Department of Chemistry, Sogang University, Seoul, The Republic of Korea

Abstract: Magnetic properties of Nd-Fe-B can be enhanced with the substitution of RE (RE = Pr, Tb, and Dy). Magnetic particles of $Nd_{13.5}RE_{4.5}Fe_{77.5}B_{7.5}$ were prepared by co-precipitation followed by reduction diffusion. After substitution, Pr is ferromagnetic but Tb and Dy are anti-ferromagnetic to the Fe in the Nd-Fe-B crystal lattice. The magnetic moment was increased after substitution of Pr into Nd-Fe-B, but decreased after substitution of Tb and Dy. The calculated magnetic moment for Nd-Fe-B, Nd-Pr-Fe-B, Nd-Tb-Fe-B and Nd-Dy-Fe-B were 25.50, 26.32, 21.03, and 21.01 μB, respectively. Pr substitution decreases the magneto crystalline energy, while Tb and Dy substitution increases it. Enhancement in the anisotropy energy increased the domain wall width and consequently, the coercivity was increased. Introduction: Improvement of the magnetic properties of Nd-Fe-B has been an important goal of researchers. Significant improvement in the properties of Nd-Fe-B magnets has been observed when Ce, La, Pr, Dy, and Tb were substituted for Nd [1-2]. Dy and Tb are thought to be the best choices to increase coercivity; however, Gd is very useful for increasing the thermal stability of Nd-Fe-B. Higher coercivity can also be achieved by reducing grain size, and many researchers are trying to improve the magnetic properties by refining the microstructure [3-5]. Not only coercivity, but also remanence can be improved by substitution with RE [6]. Experimental Process: Chloride compounds of Nd, Fe, and RE (where RE = Pr, Tb and Dy) were dissolved in DI water and then 3.5 M NaOH solution was added drop-by-drop to raise the pH of the solution to 13 to convert the metal chlorides to metal hydroxide. These hydroxides were washed twice with DI water and ethanol, and dried overnight at 80 °C. Product obtained was annealed at 700 °C for 30 minutes to convert all hydroxides to oxides while air was flowing in the furnace. Mixture of oxides obtained was mixed with boric acid and CaH_2 in a glove box and then pressed into pellet form. The pellet was reduced in a tube furnace by heating at 1000 °C for 3 h. The product was washed with water again and again to remove CaO completely, then washed twice with acetone and stored in inert environment. Structure analysis: XRD patterns confirmed the formation of RE-Fe-B, although patterns have a few Nd peaks. The presence of this Nd was further confirmed by SEM and TEM analysis. The shape of the particles produced was irregular and size ranged from 0.6 to 10 μm. The particles produced were single crystals, however some particles fused during the reductive annealing at 1000 °C. SEM and TEM confirmed the homogenous distribution of Nd, RE, and Fe in all the Nd-RE-Fe-B particles produced. Magnetic properties analysis: Magnetic properties on atomic level originate from the coupling of the unpaired electrons in the valance shell of the atoms. Properties enhance/decreases further, after the exchange coupling between these atoms in the crystal lattice. In Nd-Fe-B, coupling of Nd, and Fe decides the total magnetic moment of the crystal. If an atom substitutes Nd in Nd-Fe-B, it can be ferromagnetic or antiferromagnetic to the neighboring Fe atoms. In Nd-Fe-B lattice, Nd is ferromagnetic to the Fe, and when Pr is substituted for Nd it is also ferromagnetic to the Fe. Pr substitution should increase the total magnetic moment, and this was also found in our experiment. When Tb and Dy replace Nd, they are antiferromagnetic to the Fe. This anti-ferromagnetic coupling reduces the overall magnetic moment of a RE-Fe-B crystal. The products below are arranged in descending order of magnetic moment. Nd-Pr-Fe-B > Nd-Fe-B > Nd-Tb-Fe-B > Nd-Dy-Fe-B The experimental values of the magnetic moment for Nd-Fe-B, Nd-Pr-Fe-B, Nd-Tb-Fe-B, and Nd-Dy-Fe-B from our experiment were 25.50, 26.32, 21.03, and 21.01 μB, respectively. Magnetic moment is inversely proportional to the anisotropic energy. The magneto crystalline anisotropy energy was increased from 0.2284 MJ/m^3 to 0.3910 and 0.3924 MJ/m^3 after the substitution of Tb and Dy respectively in Nd-Fe-B. However, the magneto crystalline anisotropy energy decreased to 0.2050 MJ/m^3 after the substitution of Pr. Below, our products are arranged in ascending order of anisotropic energy. Nd-Pr-Fe-B < Nd-Fe-B < Nd-Tb-Fe-B < Nd-Dy-Fe-B Domain wall energy is directly proportional to the magneto crystalline energy, hence substitution of Tb and Dy increases the domain wall energy that ultimately increases the domain wall width and coercivity.[7] Nd-Fe-B at 4.7 kOe and Nd-Pr-Fe-B around 4.0 kOe were demagnetized. Coercivity for Nd-Tb-Fe-B and Nd-Dy-Fe-B was around 9.6 kOe.

References: [1] Sagawa M, Hirosawa S, Tokuhara K. J. Appl. Phys., 1987, 61(8): 3559. [2] Micski A, Uhrenius B. J. Appl. Phys., 1994, 75: 62. [3] R. Ramesh, K. Srikrishna, J. Appl. Phys. 64 (1988) 6406. [4] R. Ramesh, G. Thomas, B.M. Ma, J. Appl. Phys. 64 (1988) 6416. [5] P. Nothnagel, K.H. Muller, D. Eckert, A. Handstein, J. Magn. Magn. Mater. 101 (1991) 379. [6] K.D. Durst, H. Kronmüller, J. Magn. Magn. Mater. 68 (1987) 63. [7] M. V. Fischetti, S.E. Laux J. Appl. Phys., Vol. 89, No. 2, 15 January 2001.

11:45

AB-12. Magnetic Properties of NdFeB Alloys Obtained by Gas Atomization Technique.

G. Sarriegui[1,2], *J.M. Martín*[1,2], M. Ipatov[3], A.P. Zhukov[4,5] and J. Gonzalez[5]
1. Materials and Manufacturing, CEIT-IK4, San Sebastián, Spain; 2. Tecnun (University of Navarra), San Sebastián, Spain; 3. SgiKER (Magnetic Measurements), University of the Basque Country, San Sebastián, Spain; 4. IKERBASQUE Foundation, Bilbao, Spain; 5. Department Materials Physics, Faculty of Chemistry, University of the Basque Country, San Sebastián, Spain

Since Sagawa reported in [1] on the excellent hard magnetic properties of NdFeB permanent magnets, the utilization of anisotropic sintered NdFeB magnets in large motor and generator applications has grown spectacularly. Such hard magnetic material consists of a major tetragonal intermetallic compound ($Nd_2Fe_{14}B$), with excellent intrinsic hard magnetic properties, and a minor Nd-rich phase. Obviously, the magnetic behavior depends strongly on the microstructure of the magnet material, which in turn is determined by the production process. Microstructural factors affecting the hard magnetic character include the mean and the standard deviation of the grain size distribution, the orientation degree of the grains, the distribution of the Nd-rich phase, and the presence of a residual amount of other secondary phases (e.g. α-Fe, $NdFe_4B_4$, and other borides). All kind of defects in the microstructure, especially soft magnetic phases, can easily deteriorate the hard magnetic properties. It has been reported a slope change in the curve of magnetization as a function of temperature at around 150 K due to a spin reorientation transition (SRT) [2]. Such effect has been carefully analyzed for sintered magnets, since it is essential for the design of sensors, magnetic apparatus or magnetomechanical devices for cryogenic applications [3]. Alternative production routes of NdFeB magnets result in new microstructures whose impact on magnetic properties has to be carefully studied. Inert gas atomization is one of the novel processes under evaluation to produce NdFeB powders [4]. This technique consists on breaking a liquid metal stream into droplets by means of a high velocity inert gas flow. These droplets become spherical particles after solidification. The small size of the droplets, typically in the microns range, and the high velocity of the gas enable a fast heat transfer between both, resulting in high cooling rates and fine microstructures. Using this technique, we have produced several NdFeB alloys. After splitting the as-atomized powders in different size fractions by sieving, their microstructure and magnetic properties have been studied. In this work, we report the magnetic properties as a function of temperature, between 1.8 and 400 K, and of particle size. Fig. 1 shows the characteristic microstructure of a single gas atomized NdFeB particle, whose main constituents are $Nd_2Fe_{14}B$ grains of a few microns in size. The Inverse Pole Figure (IPF) demonstrates the random crystallographic texture of the material. The cooling rate of gas atomized particles increases when the particle size is reduced. As a result, larger particles exhibit higher microsegregation and, hence, the precipitation of soft magnetic α-Fe phase. On the other hand, smaller particles display finer microstructures. As for the coercive field, it was observed that it increases significantly when the particle size is reduced, reflecting a higher difficulty for reverse domain nucleation (less surface defects, finer grain size, lower volume fraction of secondary soft magnetic phases, etc.). Fig. 2 shows the temperature dependency of the saturation magnetization, $M_s(T)$. The anomaly, i.e. a slope change of the $M_s(T)$ curve, observed around 150 K could be ascribed to the spin-reorentation transition (SRT) mentioned before, which has been reported to occur in the same temperature range when the magnetic field is applied parallel and perpendicularly to the sample direction [2]. In contrast with the measurements performed in single crystals and anisotropic sintered magnets, isotropic gas atomized powders exhibit an increment of saturation magnetization below the split tilt temperature of the SRT. This work has received funding from the European Union's Horizon 2020 research and innovation programme under grant agreement No 720838 (NEOHIRE project).

[1] M. Sagawa, S. Fujimura, N. Togawa, H. Yamamoto, and Y. Matsuura, "New material for permanent magnets on a base of Nd and Fe (invited)," *J. Appl. Phys.*, vol. 55, no. 6, pp. 2083–2087, Mar. 1984. [2] M. Foldeaki, L. Koszegi, and R. A. Dunlap, "Structure sensitivity of magnetization processes at the spin-reorientation transition in Nd 2 Fe 14 B," *J. Appl. Phys.*, vol. 69, no. 8, pp. 5562–5564, Apr. 1991. [3] E. Diez-Jimenez *et al.*, "Magnetic and morphological characterization of Nd2Fe14B magnets with different quality grades at low temperature 5–300 K," *J. Magn. Magn. Mater.*, vol. 451, pp. 549–553, Apr. 2018. [4] W. Tang *et al.*, "Magnetic properties and microstructure of gas atomized MRE2 (Fe,Co) 14 B powder with ZrC addition (MRE=Nd+Y+Dy)," *J. Appl. Phys.*, vol. 105, no. 7, 2009.

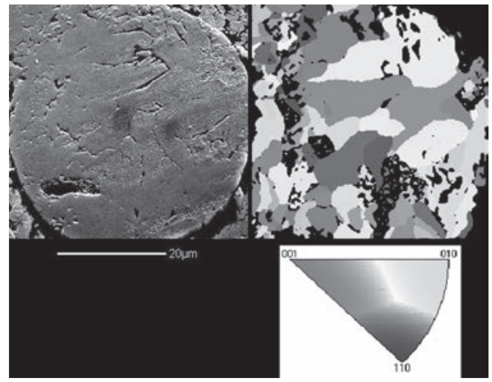

Fig. 1. Secondary electrons micrograph (left) and IPF image (right) of a particle with composition 27.3Nd-71.4Fe-1.01B.

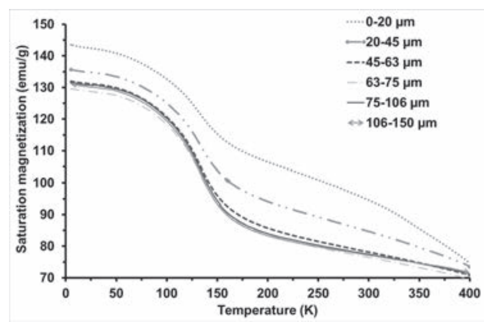

Fig. 2. Thermomagnetic analysis curves of gas atomized powders with composition 27.3Nd-71.4Fe-1.01B for different particle size fractions. Applied magnetic field is 5000 Oe.

TUESDAY MORNING, 24 APRIL 2018 ORCHID IV, 9:00 TO 12:00

Session AC
MICROSCOPY, IMAGING AND CHARACTERIZATION I

Xiaoyan Zhong, Chair
Tsinghua University, Beijing, China

INVITED PAPER

9:00

AC-01. Quantitative magnetic measurement by electron magnetic chiral dichroism with high spatial resolution in the transmission electron microscope. ***(Invited)***

J. Zhu[1] and D. Song[1]
1. Tsinghua University, Beijing, China

Electron magnetic chiral dichroism (EMCD) is a newly developed technique that allows the local spin and orbital magnetic moment of materials to be quantitatively measured with close-to-atomic spatial resolution, element specificity, spin specificity and site specificity in the transmission electron microscope (TEM). In the talk, three parts will be involved: (1) a general way for quantitative EMCD measurement of magnetic parameters [1-3]; (2) high spatial resolution EMCD for magnetic measurement down to 1 nm or even atomic-plane scale [4-5]; (3) three-dimensional magnetic measurement by EMCD [6]. In the first part, a general way to experimentally achieve the quantitative measurement of magnetic parameters are presented, assisted with our theoretical simulations of dynamical diffraction effects. We will use three typical cases to demonstrate the procedure and results of quantitative EMCD technique, namely spinel $NiFe_2O_4$, garnet $Y_3Fe_5O_{12}$ (YIG) and perovskite $La_{0.7}Sr_{0.3}MnO_3$, which are with different crystallographic, magnetic structures and specific applications. The basic and intrinsic magnetic parameters, spin and orbital magnetic moment with element specificity, spin specificity and site specificity, are resolved as shown in Table 1 (take the example of YIG), many of which can not be obtained by other magnetic characterization techniques. These comprehensive information might provide a deep insight of their intrinsic magnetic properties. In the second part, we develop the method of high spatial resolution EMCD to get the magnetic information at nanometer scale. By combining the converged beam electron diffraction with EMCD technique, the magnetic measurement with ~ 1nm spatial resolution is applied the $Y_3Fe_5O_{12}$-Pt interface,which is a typical system to study the transport efficiency of pure spin current. Along with the analysis of atomic structure, electron structure and chemical composition by some other advanced techniques in the TEM, the origin of disorder layer at the interface is revealed and the decreased efficiency of spin current transport is attributed to the deteriorated magnetic properties. Our results provide the knowledge to control and manipulate the interfacial structure and properties in order to obtain higher spin transport efficiency. Also, recently we have proposed a new approach to probe local magnetic information with atomic-plane-scale spatial resolution by combining EMCD with chromatic-aberration-corrected transmission electron microscopy. At last, in-plane EMCD technique is developed, as the traditional EMCD technique has been restricted to measurements of magnetic signal in the electron beam direction. We introduce an approach that allows both in-plane and out-of-plane magnetic signals to be measured using EMCD in the Lorentz TEM, taking the example of Co nanoplate. Therefore, three-dimensional magnetic measurement by EMCD is possible. Meanwhile, the magnetic signals can be detected by applying the out-of-plane magnetic field, achieving the in-situ study of magnetic behaviors.

[1] Wang Z Q, Zhong X Y, Yu R, Cheng Z Y and Zhu J 2013 *Nat. Commun.* **4** 1395 [2] Song D, Li G, Cai J and Zhu J 2016 *Sci. Rep.* **6** 18489 [3] Li G, Song D, Li Z P and Zhu J 2016 *Appl. Phys. Lett.* **108** 242414 [4] Song D, Ma L, Zhou S and Zhu J 2015 *Appl. Phys. Lett.* **107** 042401 [5] Wang Z C, Tavabi A, Jin L, Rusz J, Tyutyunnikov D, Jiang H, Moritomo Y, Mayer J, Dunin-Borkowski R, Yu R, Zhu J and Zhong X Y 2018 *Nat. Mater.* doi.org/10.1038/s41563-017-0010-4 [6] Song D, Tavabi A H, Li Z-A, Kovács A, Rusz J, Huang W, Richter G, Dunin-Borkowski R E and Zhu J 2017 *Nat. Commun.* **8** 15348

Table 1 Magnetic parameters of YIG

Magnetic parameters	EMCD (present work)	XMCD	Neutron diffraction	First principle calculation	Macro measurement (SQUID, present work)
m_L/m_S (oct)	0.06±0.02				
m_L/m_S (tet)	0.08±0.02				
m_L (oct)	0.28±0.03				
m_L (tet)	0.31±0.03				
m_S (oct)	4.5±0.2				
m_S (tet)	3.9±0.2				
M_{oct}	4.8±0.2			4.12[34]	
M_{tet}	4.2±0.3			4.20[34]	
M_{total}(unit cell)	3.0±0.7		3.1[33]	4.36[34]	3.3

Note: m_L/m_S refers to the ratio of orbital and spin magnetic moment (m_L is the orbital magnetic moment and m_S is the spin magnetic moment). M_{oct} and M_{tet} are the total atomic magnetic moments (including the orbital and spin magnetic moment) of oct and tet Fe in the units of μ_B per atom. M_{total} is the total magnetic moments for $Y_3Fe_5O_{12}$ in a unit cell.

Table 2 magnetic moment of Fe at YIG/Pt interface

Position / $M \times K$ (μ_B)[a]	Bulk	~3 nm distance from interface	~2 nm distance from interface
With disorder layer	1.43±0.10 (5 μ_B)	1.04±0.11 (3.6 μ_B)	0.76±0.10 (2.7 μ_B)
Without disorder layer	1.57±0.15 (5 μ_B)	-	1.55±0.12 (4.9 μ_B)

[a]Note: *M* is the magnetic moment of Fe element; *K* is the dynamical coefficient as shown in equation (1). The magnetic value in the brackets is normalized with magnetic moment Fe^{3+} in YIG bulk, which is estimated to be 5 μ_B according to Hund laws.

CONTRIBUTED PAPERS

9:30

AC-02. Stable skyrmion states at room temperature confined in corrals of artificial surface pits fabricated by a focused electron beam.

T. Matsumoto[1], Y. So[2], Y. Kohno[3], Y. Ikuhara[1,4] and N. Shibata[1,4]
1. The University of Tokyo, Tokyo, Japan; 2. Akita University, Akita, Japan; 3. JEOL, Ltd., Tokyo, Japan; 4. Japan Fine Ceramic Center, Nagoya, Japan

Stable confinement of elemental magnetic nanostructures, such as a single magnetic domain, is fundamental in modern magnetic recording technology [1]. It is well known that various magnetic textures can be stabilized by geometrical confinement using artificial nanostructures. The magnetic skyrmion [2,3], novel spin texture promising for future memory devices because of its topological protection and dimensions at the nanometer lengthscale, is no exception. So far, skyrmion confinement techniques using large-scale boundaries with limited geometries such as isolated disks and stripes prepared by conventional microfabrication techniques have been used. Here we demonstrate an alternative technique confining skyrmions to artificial nanostructures (corrals) built from surface pits fabricated by a focused electron beam. Using aberration-corrected differential phase contrast scanning transmission electron microscopy (DPC STEM) [4-6], we directly visualize stable skyrmion states confined at a room temperature to corrals made of artificial surface pits on a thin plate of bulk β-Mn-type chiral magnet $Co_8Zn_8Mn_4$ (Curie temperature; Tc ~300 K) [7,8]. DPC STEM images (Figure 1) clearly demonstrate a stable single skyrmion state located at the center of a 800 nm equilateral triangular corral at a room temperature (295 K) under the perpendicular magnetic field of 59.9 mT. Under the residual field of the objective lens (~20 mT), the single-skyrmion state turned into a triple-skyrmion state. The transition from the single-skyrmion state to the triple-skyrmion state occurred in a very narrow range of perpendicular magnetic field (40.0±1.0 mT). Intriguingly, a two skyrmion state was not evident during the transition. Moreover, no helical magnetic state was observed inside the triangular corral under the residual field of objective lens. On the other hand, a single-skyrmion state becomes unstable under an increasing magnetic field and vanishes above 77 mT. To understand the present results, it is important to characterize the nature of the defects fabricated by a focused electron beam. By using plan-view TEM/STEM and STEM energy dispersive X-ray (EDX) analysis techniques, we confirmed that the linear surface defects are built of a sequence of separated tiny surface pits with no preferential sputtering of specific atomic species. Their diameters and the separation depend on the conditions of fabrication, such as probe size and exposure time, and also on the thickness of the thin plate at the irradiated region, but their typical diameter is 5 nm and they are typically separated by 10 nm as shown in Figure 2a. To characterize the nature of the defects more in detail, we observed cross-sectional views of the surface pits. It should be noted, however, the thin plate specimen shown here is not exactly the same as the one used to demonstrate the stable skyrmion states as shown in Figure 1. We usually use standard ion thinning method to prepare thin plate specimens to observe skyrmions in order to minimize surface damage and ensure surface quality, but it is extremely difficult to prepare a cross-sectional specimen from such a thin plate by the ion thinning method. We therefore fabricated the cross-sectional specimen by using a focused ion beam (FIB) technique. We fabricated four linear surface pits (indicated as A–D in the plan-view in Figure 2b). The linear surface pits indicated as A were fabricated using the same beam condition used when we created the 800 nm triangular corral as shown in Figure 1. We confirmed that the defect on the top (beam entrance) crystalline surface (indicated by A) is actually a pit with a diameter and depth of 5 nm, while the defect on the bottom (beam exit) damage layer (indicated by A') is larger than that on the top surface (Figure 2c,d). After all, it proved that the defects are a pair of surface defects, one on the top surface of the thin plate and the other on the bottom surface of the thin plate. In conclusion, we have demonstrated stable skyrmion states at a room temperature in a thin plate of $Co_8Zn_8Mn_4$ confined to artificial corrals built from the periodic array of top and bottom surface pits fabricated by a focused electron beam. Artificial control of skyrmion states with the present technique [9] should be a powerful way to realize future non-volatile memory devices using skyrmions.

[1] H. J. Richter, J. Phys. D 40, R149–R177 (2007) [2] T. H. R. Skyrme, Nucl. Phys. 31, 556-569 (1962) [3] X. Z. Yu et al., Nature 465, 901-904 (2010) [4] N. Shibata et al., Nat. Commun. 8,15631 (2017) [5] T. Matsumoto et al., Sci. Adv. 2 e1501280 (2016) [6] T. Matsumoto et al., Sci. Rep. 6 35880 (2016) [7] K. Karube et al., Nat. Mater. 15, 1237-1243 (2016). [8] D. Morikawa et al., Nano Lett. 17, 1637-1641 (2017) [9] T. Matsumoto et al., submitted. [10] This work was supported by the Japan Science and Technology Agency SENTAN.

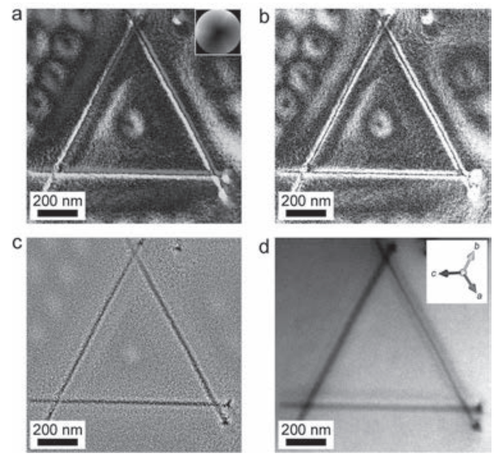

Fig. 1. Stable skyrmion states at a room temperature (295 K) in an 800 nm equilateral triangular corral of linear surface defects fabricated by scanning a focused electron beam under perpendicular magnetic field of 59.9 mT. (a) In-plane magnetic field vector map, (b) field intensity, (c) magnetic helicity image, and (d) ADF image.

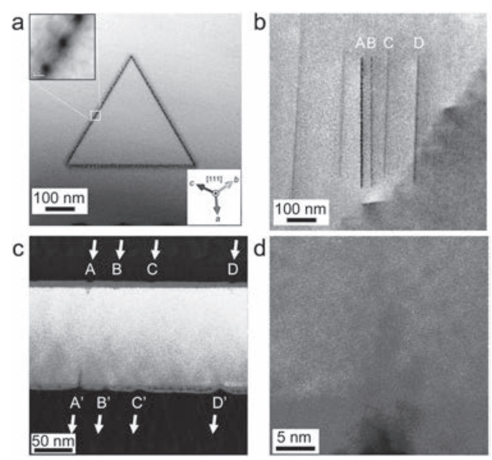

Fig. 2. (a) Plan-view STEM images of a 440 nm equilateral triangular corral of linear surface defects fabricated by scanning a focused electron beam. (b) A plan-view STEM image of linear defects (A-D) fabricated with several different experimental conditions. (c) A false-color cross-sectional STEM image of the defects. Arrows indicate directions of a focused electron beam. (d) An enlarged image of the defect designated as A' in (c).

9:45

AC-03. Tuning Magnetic Domains with Ion-beam Irradiation in Co/Pd Multilayer.

A. Talapatra[1], A. Chelvane[2], C. Günther[3,4], S. Eisebitt[4,3], T. Shibayama[5] and J. Mohanty[1]
1. Physics, Indian Institute of Technology Hyderabad, Hyderabad, India;
2. Defence Metallurgical Research Laboratory, Hyderabad, India;
3. Technical University Berlin, Berlin, Germany; 4. Max Born Institute, Berlin, Germany; 5. Hokkaido University, Sapporo, Japan

Thin film structures exhibiting perpendicular magnetic anisotropy (PMA) are of technological importance and promising candidates for spintronic nano-devices in the context of ultrahigh density magnetic storage, fast memory applications and nano-sensors. At favourable atomic ordering, ultra-thin alloys of Co with Pd or Pt and sandwiches display PMA. In Co based multilayer (ML) systems, the effective anisotropy originates from the interplay between the interface and volume contribution of anisotropy. Comparable values of these two anisotropies help the system to break into multiple domains. The characteristic features of magnetic domains in such systems can be controlled by the growth condition [1], thickness of the constituent layers as well as with external stimuli *viz.,* magnetic field, heat-treatment [2], laser [3] and ion-beam irradiation [4]. Ion-beam irradiation is a viable technique to tune magnetic properties, associated with locally induced structural imperfection or intermixing, relevant in the context of magnetic ML [5]. The irradiation energy and fluence can be separately adjusted to control the depth and the lateral extent of the damaged region, which leads to the modification of magnetic properties. The ions lose energy during their passage through the material, which is either spent in displacing target atoms by elastic collision (nuclear stopping) or exciting the atoms by inelastic collisions (electronic stopping) [6]. In this study, we are going to show the modification of magnetic domains in Co/Pd ML by ion-beam irradiation. There are a variety of studies of ion-beam modifications in magnetic ML either in the context of patterning [7] or depth resolved structural modifications [8]. The focus in this work will be on the modification of nano-scale magnetic domains and their modelling along with the investigation of integral magnetic properties and structural changes. ML films with the composition (Si (substrate) / Ta (30) / Pd (30) / [Co (3) / Pd (8)] $_{50}$ / Pd (12) Å) have been deposited by ultra-high vacuum DC magnetron sputtering with Ar pressure of 2×10^{-3} mbar. The ion-beam irradiation was performed with Ar^+ ions having three different energies of 50, 100 and 150 keV along with six different fluences ranging from 10^{14} to 10^{16} ions/cm^2. Simultaneous atomic and magnetic force microscopy (AFM/MFM) was carried out for the pristine and irradiated films to observe the topography and magnetic domains. Magnetization measurement has been performed with vibrating sample magnetometer (VSM) with applied field along in-plane (IP) and out-of-plane (OOP) direction of the film surface. Cross-sectional transmission electron microscopy (XTEM) was carried out for selected samples employing high voltage (1250 kV) electron microscopy. The pristine ML film displays a nano-scale maze-like domain pattern in as-deposited condition as shown in Fig. 1(a). The two opposite contrasts designate the presence of oppositely magnetized domains with high magnetic phase difference. The average dimension of the domains turned out to be 464 (±12) nm, estimated from the power spectral density curve associated with the 2D Fourier transform of the domain image. The hysteresis loop in Fig. 1(b) clearly shows the predominant OOP magnetization of the film with a square hysteresis loop. The coercivity along the OOP and IP direction is estimated to be 880 (±5) and 440 (±5) kG respectively. The OOP saturation field is around 5 kG, whereas the IP loop cannot be brought up to saturation within the limited field of the VSM. Figure 1(c) displays the overall cross-section view of the film. The high resolution TEM image of the selected area clearly depicts the presence of ultra-thin layer stacking for the pristine film (Fig. 1(d)). However, the selected area electron diffraction pattern in Fig. 1(e) shows the polycrystalline nature of the film, in agreement with similarly prepared ML systems. Ion beam irradiation was performed at three different energies *viz.,* 50, 100 and 150 keV of Ar^+ ions. Calculation shows that the ions completely penetrate the ML and stop on average deep inside the Si substrate. The fluence was varied by varying the time of irradiation. The magnetic domains (before exposing to external magnetic field) of the irradiated samples have been shown in Fig. 2(a) and (b) for ion energies 50 and 100 keV respectively for the fluences of 10^{14}, $10^{15}$and 10^{16} ions/cm^2. Irradiation with the lowest energy and fluence shows the presence of periodic domain structure with alternating contrast. The average domain size decreases to 117 (±7) nm and the periodic domain pattern no longer exists at higher fluences. The reduced domain size and contrast with increasing ion energy and fluence designates the decrease in PMA. The feather-like domains with cross-tie domain walls are observed in MFM images with fluences $>10^{14}$ ions/cm^2 according to Fig. 2(a). For 100 keV ion energy, the MFM image is largely influenced by topographic features with higher roughness. Magnetization measurements also support the spin re-orientation from OOP to IP of the film surface with increasing ion-energy and fluence.

[1] M. S. Pierce, J. E. Davies, J. J. Turner, K. Chesnel, E. E. Fullerton, J. Nam, R. Hailstone, S. D. Kevan, J. B. Kortright, K. Liu, L. B. Sorensen, B. R. York and O. Hellwig, *Phys. Rev. B* 87, 184428 (2013). [2] A. Talapatra, J. Arout Chelvane and J. Mohanty, *J. Magn. Magn. Mater.* 448, 360 (2018). [3] A. Talapatra and J. Mohanty, *J. Magn. Magn. Mater.* 418, 224 (2016). [4] E. Knystautas, *Engineering Thin Films and Nanostructures with Ion Beams*, CRC Press, 2005, Chapter 3. [5] A. Ehresmann, O. Hellwig, O. Buhl, N. D. Müglich, T. Weis and D. Engel, *J. Appl. Phys.* 112, 063901 (2012). [6] D. K. Avasthi, *Current Science* 78, 1297 (2000). [7] S. Streit-Nierobisch, D. Stickler, C. Gutt, L.-M. Stadler, H. Stillrich, C. Menk, R. Frömter, C. Tieg, O. Leupold, H. P. Oepen and G. Grübel, *J. Appl. Phys.*106, 083909 (2009). [8] T Som, S Ghosh, M Mäder, R Grötzschel, S Roy, D Paramanik and A Gupta, *New J. Phys.* 9, 164 (2007).

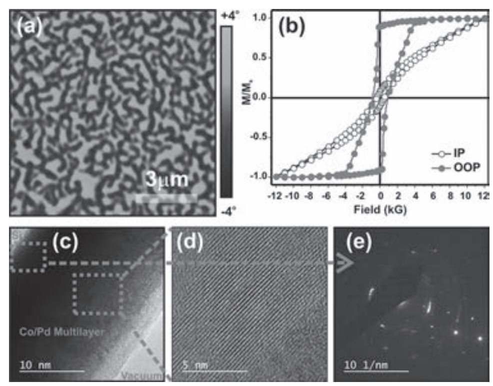

Fig. 1. (a) Magnetic domains, (b) hysteresis loops, (c) XTEM image with selected area (d) high resolution image and (e) electron diffraction pattern for pristine Co/Pd ML.

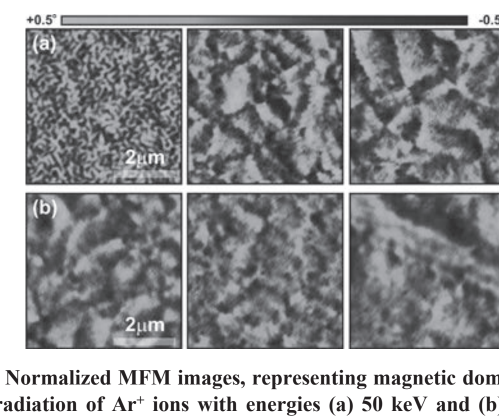

Fig. 2. Normalized MFM images, representing magnetic domains after the irradiation of Ar^+ ions with energies (a) 50 keV and (b) 100 keV having variable fluences, 10^{14}, 10^{15} and 10^{16} ions/cm^2 from left to right.

10:00

AC-04. Directly observed dynamics of distorted vortex cores including asymmetric Bloch walls utilizing soft X-ray microscopy.

M. Im[1], H. Han[2], M. Jung[3], P. Fischer[1], J. Hong[3] and K. Lee[2]
1. LBNL, Berkeley, CA, United States; 2. UNIST, Ulsan, The Republic of Korea; 3. Daegu Gyeongbuk Institute of Science & Technology (DGIST), DAEGU, The Republic of Korea

Spin structures including domain walls and magnetic vortices have attracted enormous interests not only due to their fascinating topological textures but also their potentials in a wealth of technological applications such as high efficient storage and memory devices. In the research of those spin structures, synchrotron-based microscopes have been playing key roles by direct imaging of static and dynamic behaviors of spin structures and therefore providing a powerful insight into the underlying physics of nanospin phenomena and an essential knowledge for their applications in advanced nanotechnologies [1, 2]. In our work, we employed a full-field soft X-ray microscope (XM-1) at Advanced Light Source (ALS) to directly observe non-trivially distorted vortex cores consisting of asymmetric Bloch walls and their dynamics. Fig. 1 shows the deformed vortex core observed in an asymmetric permalloy (Py, $Ni_{80}Fe_{20}$) disk with a height of h = 100 nm, a diameter of D = 500 nm, and an asymmetric ratio of $r = 0.3D$ (a) together with simulated vortex core and the out-of-plane (OOP) magnetic component (m_z) larger than 0.7 (b). The distorted vortex core was found to be vortex cores placing non-coaxially on top and bottom surface of the disk, which are connected by an asymmetric Bloch wall creating flux closer domain. Such core structure is significantly distinguished from common circular vortex cores characterized by a single vortex core (polarity, p) aligned on both surfaces of a magnetic element pointing either up or down and a circular in-plane domain (circularity, c) rotating either clockwise or counter-clockwise [3,4]. Interestingly, the nontrivially shaped vortex core shows an abnormal dynamic behavior. Unlike the traditional gyrotropic motions of circular vortex cores, sloshing motion was observed in the distorted core although micromagnetic simulations demonstrated that vortex cores on top and bottom surfaces still have gyrotropic motions. The unique dynamic motion of the deformed vortex core is likely due to the asymmetric Bloch wall restricting the motions of vortex cores on surfaces [5]. This research was also supported by Leading Foreign Research Institute Recruitment Program through NRF (2012K1A4A3053565) and by the DGIST R&D program of the Ministry of Science, ICT and future Planning (17-BT-02. Work at the ALS was supported by the U.S. Department of Energy (DE-AC02-05CH11231).

[1] M.-Y. Im *et al.*, *Nat. Commun*. 5, 5620 (2014). [2] M.-Y. Im *et al.*, NPG Asia Materials 9, e348 (2017). [3] T. Shinjo, *et al.*, *Science* 289, 930-932 (2000). [4] M.-Y. Im *et al*., *Nat. Commun. 3*, 1978 (2012). [5] M.-Y. Im *et al.*, submitted (2018).

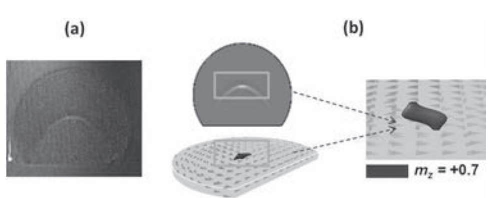

Fig. 1. Magnetic image for the vortex core observed in an asymmetric shaped Py disk where the white contrast indicates the out-of-plane (OOP) magnetization pointing up (a) and simulated vortex core (b). The OOP magnetic components (m_z) larger than 0.7 were extracted.

10:15

AC-05. Calibrated MFM: electrostatic compensation of μ-coils.

C. Barton[1], R. Puttock[1,2], H. Corte-León[1], M. Gerken[3], A. Manzin[5], V. Neu[4], H. Schumacher[3] and O. Kazakova[1]

1. Quantum Science, National Physical Laboratory, Teddington, United Kingdom; 2. Physics department, Royal Holloway, Egham, United Kingdom; 3. Physikalisch-Technische Bundesanstalt, Braunschweig, Germany; 4. IFW Dresden, Dresden, Germany; 5. INRIM, Torino, Italy

Magnetic force microscopy (MFM) is used to detect and visualise the stray magnetic fields that emanate from the surface of magnetic materials [1]. With typical resolution limits of ≈30 nm MFM can be used to image the magnetisation configuration of a vast range of materials and magnetic phenomena in a laboratory-based environment. Typically, MFM is used only in a qualitative capacity to gain physical insight into the morphology of magnetic domains, however, there are established calibration methods that can be employed to make quantitative measurements. These involve precise determination of the probes magnetic properties and subsequent contribution to the measured image. Two such methods include image deconvolution in the frequency domain, the so called real space tip transfer (RSTTF) approach [2], and probe calibration using current carrying microstructures, which are used to generate a well-defined field profile [3,4]. In this work we explore the use of current-carrying coils of micro-metric, in particular, we focus on the crucial role of electrostatic compensation on the measured values of the effective monopole and dipole contributions of the magnetic probe. In order to generate the measurable MFM signal with an appropriate signal-to-noise ratio, a current of a reasonable magnitude should be driven through the coil. Hence, the potential difference becomes non-negligible and appreciable parasitic electrostatic fields can arise. The gradients of the electrostatic force are superimposed with those originating from magnetic interactions, making accurate quantitative analysis impossible. It is therefore of extreme importance to measure the magnitude of these electrostatic force gradients and develop an effective way of their full compensation. The electrical compensation is achieved through the application of an a.c. signal between the probe and sample, which introduces an additional force observed as side bands to the fundamental mode of the cantilever. An additional lock-in is used to measure these bands and a feedback loop is employed to keep the magnitude of these side bands to zero by applying a d.c. voltage equivalent to the error signal. This signal is then applied during the second lifted pass where the MFM response is recorded. The experimental setup displaying the typical coil topography and the electrical ground configurations is shown in Fig. 1a. The effect of electrostatic compensation switched off and on is shown in Fig. 1b and c, respectively. Without the use of compensation, there is a clear electrostatic influence on the measured MFM signal, which is mainly observed at the coil edges as well as charging effects on the surrounding SiO_2 substrate. Conversely, the addition of electrostatic compensations is shown to significantly reduce these parasitic effects (Fig. 1c phase). The electrostatic nulling signal (i.e. the d.c. voltage required to reduce the measured scanning Kelvin probe microscopy (SKPM) signal to zero) is shown in Fig. 1c SKPM. Finally, average line profiles of the MFM signals with/without electrostatic compensation are presented in Fig. 1d. Even qualitatively these line profiles vary significantly, which dramatically impacts on quantitative solutions, making the measurements taken without compensation not trustworthy. Finally, we investigate the effects of electrostatic compensation on calibrated measurements and compare the extracted magnetic properties of an MFM probe. This work builds upon the existing framework [3,4] where current carrying coils are used in generating known magnetic fields for calibrated MFM measurements. We extend the robustness and accuracy of this technique to include considerations of the effect of the electrostatic field. Furthermore, we use the combined MFM-SKPM method to eliminate unwanted artifacts. This is of high importance for research areas where nanoscale quantification of the stray magnetic field is required. One emerging example is the quantitative measurement of the field emanating from magnetic skyrmions, which can be used to gain insight to the local spin structure. This will provide a better understanding of fundamental properties of these novel nanostructures, paving the way for future technologies [5].

[1] E. Meyer, *et al.*, *Scanning probe microscopy (Springer)*, 97 (2004). [2] P.J.A. van Schendel *et al.*, *J. Appl. Phys*, 88, 435 (2000). [3] J. Lahou, *et al.*, *J. Appl. Phys*, 86, 3410(1999). [4] Th. Kebe and A. Carl, *J. Appl. Phys*, 95, 775 (2004). [5] M. Baćani, *et al,* arXiv:1609.01615v1 [cond-mat.mtrl-sci], (2016).

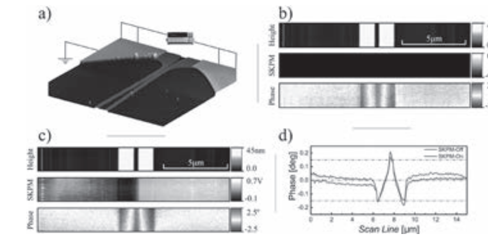

Fig. 1. Calibrated MFM: a) μm-coil topography with the contact pads and electrical configuration including the grounding scheme used in this work; b) MFM scan (bottom) without electrostatic compensation; c) MFM scan (bottom) with electrostatic compensation demonstrating reduced contrast in the region of the the coil and also the charged substrate around the coil. The sub figures in (b-c) are topography, SKPM and phase signals respectively; d) an example of the extracted average line profiles taken from the MFM data with/without any electrostatic compensation.

INVITED PAPER

10:30

AC-06. Off-axis electron holography for the quantitative study of magnetic properties of nanostructures: from the single nanomagnet to the complex device.

C. Gatel[1], B. Warot-Fonrose[1], M. Casanove[1], A. Masseboeuf[1], N. Biziere[1], F.B. Bonilla[2], L. Lacroix[2], A. Meffre[2] and T. Blon[2]
1. CEMES, CNRS, University of Toulouse, Toulouse, France;
2. Laboratoire de Physique et Chimie des Nano-objets - INSA, Toulouse, France

Electromagnetic properties are one of the keys for understanding and mastering nano systems used in many applications, as in medical treatment, optics, microelectronic or data storage. Various methods exist to map magnetic fields. Some are based on near field microscopy, like magnetic force microscopy, other on X-ray set-ups, like photoemission electron microscopy. Electron holography (EH), a powerful transmission electron microscopy method, is another appropriate tool which combines high sensitivity with a high spatial resolution. EH allow the quantitative measurement of both internal and external fields in individual nano-objects instead of assemblies of nanoobjects. This interferometric method can also be used for performing in situ/in operando experiments. We thus developed and applied EH on very different systems, from the single nanoparticles to the thin layer and the complex magnetic device, for studying their magnetic properties. In this presentation, we will present our investigations on a single Fe nanocube and an FeRh thin layer. - Nanomagnets recently attracted considerable interest due to their possible application as building blocks for hard drive disks and permanent magnets or as nanobiological vectors for drug delivery and hyperthermia. Despite theoretical studies, the size-dependence of spin arrangements in single nanomagnets has not yet been evidenced experimentally due to sensitivity limitations of the investigation tools. The single domain limit, corresponding to the critical nanomagnet size separating vortex/single domain configurations, has never been observed although it will dictate the optimized size for applications. In such small nano-objects, micromagnetic simulations show that the magnetic internal structure changes from single domain (SD) to vortex states as the cube size increases (Fig. 1). Some years ago, we reported symmetrical vortices, i.e. vortex of <001> axis, in isolated 30 nm single crystal Fe cubes with a 14 nm vortex core size [2]. Next, we showed that vortices can also be stabilized in the presence of dipolar interactions thanks to holes in the cubes inducing a pinning of the vortex core [3]. Here we will present the spin configuration phase diagram in size-controlled single Fe nanocubes combining EH experiments and micromagnetic simulations [4]. High sensitivity imaging explicitly reveals how three different spin arrangements can be stabilized within a 3 nm window, evidencing the key importance of nanometric size control of magnetic nanoparticles. Moreover, it gives a deeper understanding of the single domain limit, which is more complex than expected with the appearance of a previously unreported <111> vortex state. Such a measurement opens the door to fine magnetic control of nano-objects. - In situ heating/cooling EH has been used to quantitatively map the magnetization of a cross-sectional FeRh thin film through its magnetic transition [5]. This alloy presents a remarkable and unusual magnetic transition from a low temperature antiferromagnetic state (AFM) to a high temperature ferromagnetic state (FM) close to 370K accompanied by a 1% volume expansion.[6-8] The transition is obtained for a narrow composition range 0.48<x<0.56 in the B2-ordered a' crystal phase of Fe1-xRhx. These remarkable features make FeRh particularly well suited for advanced magnetic devices for instance in heatassisted or even electrically –assisted magnetic recording [9-10] and magnetic random access memories based on AFM spintronics [11], or for magnetocaloric materials [12]. Further developments of reliable devices including thin FeRh films or others materials presenting a magnetic transition require a full control of the magnetic state within the film, a perfect knowledge of the mechanisms involved in the transition and a deep understanding of the influence of interfaces and low dimensionality. However, the mechanisms involved in the transition are still under debate. EH experiments provide a direct observation of an inhomogeneous spatial distribution of the transition temperature along the growth direction. Most interestingly, a regular spacing of the ferromagnetic domains nucleated upon monitoring of the transition is also evidenced. Beyond these findings on the fundamental transition mechanisms, EH also brings insights for in operando analysis of magnetic devices and a very promising approach to investigate the mechanisms of phase transitions in various magnetic systems (as MnAs [13]) at all pertinent scales.

[1] L.-M. Lacroix et al, J. Am. Chem. Soc. 131, 549 (2009) [2] E. Snoeck et al, Nano Lett 8, 4293 (2008) [3] L.-M. Lacroix et al, Nano Lett. 12, 3245 (2012) [4] C. Gatel et al, Nano Letters 15, 6952-6957 (2015) [5] C. Gatel, et al, Nature Communications 8, 15703 (2017) [6] M. Fallot, M. Ann. Phys. 10, 291–332 (1938) [7] F. de Bergevin et al., Compt Rend 252, 1347 (1961). [8] M.R. Ibarra et al., Phys. Rev. B 50, 4196–4199 (1994). [9] J.-U. Thiele, S. Maat, and E.E. Fullerton, Appl. Phys. Lett. 82, 2859 (2003). [10] R.O. Cherifi et al., Nat. Mater. 13, 345 (2014). [11] X. Marti et al., Nat. Mater. 13, 367 (2014). [12] Y. Liu et al., Nat. Commun. 7, 11614 (2016). [13] C. Gatel et al., Nano Letters 17, pp 2460-2466 (2017)

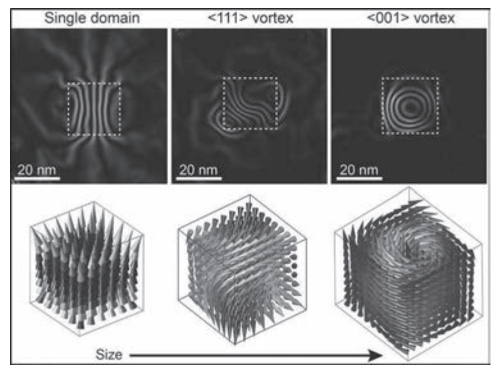

Fig. 1. Three different stable spin arrangements as a function of size of a single Fe nanocube. Top images: magnetic maps extracted for holograms for different nanocubes. Bottom images: corresponding 3D micromagnetic simulations.

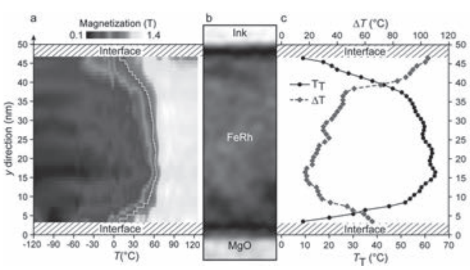

Fig. 2. Evolution of the AFM/FM transition in the FeRh layer depth. (a) Map of the magnetization as a function the temperature and the position in the layer depth. The color scale corresponds to the magnitude of the magnetization and the transition temperature is displayed by the white profile corresponding to magnetization of 0.75 T. (b) Amplitude image of the part of the FeRh layer used for the calculation. (c) Profiles of the transition temperature TT and the transition width DT as a function of the position within the FeRh layer.

CONTRIBUTED PAPERS

11:00

AC-07. Atomic-plane resolved magnetic circular dichroism by transmitted electrons.

Z. Wang[1] and X. Zhong[1]
1. School of Materials Science and Technology, Tsinghua University, Beijing, China

Zechao Wang[1], Amir H. Tavabi[2], Lei Jin[2], Ján Rusz[3], Dmitry Tyutyunnikov[3], Hanbo Jiang[1], Yutaka Moritomo[4], Joachim Mayer[2,5], Rafal E Dunin-Borkowski[2], Rong Yu[1], Jing Zhu[1] and Xiaoyan Zhong[1,*] [1]National Center for Electron Microscopy in Beijing, Key Laboratory of Advanced Materials (MOE), The State Key Laboratory of New Ceramics and Fine Processing, School of Materials Science and Engineering, Tsinghua University, Beijing 100084, P.R. China [2]Ernst Ruska-Centre for Microscopy and Spectroscopy with Electrons and Peter Grünberg Institute, Forschungszentrum Jülich GmbH, 52425 Jülich, Germany [3]Department of Physics and Astronomy, Uppsala University, P.O. Box 516, 75120 Uppsala, Sweden [4]Graduate School of Pure & Applied Science and Faculty of Pure & Applied Science, University of Tsukuba, Tennodai 1-1-1, Tsukuba, Ibaraki 305-7571, Japan [5]Central Facility for Electron Microscopy, RWTH Aachen University, 52074 Aachen, Germany In order to obtain a fundamental understanding of the interplay between charge, spin, orbital and lattice degrees of freedom in magnetic materials and to predict and control their physical properties, experimental techniques are required that are capable of accessing local magnetic information with atomic-scale spatial resolution. Our study demonstrates a breakthrough in the ability to provide direct real-space insight into atomic-plane resolved magnetic circular dichroism in materials. This information is important on a fundamental level in physics, materials science and nanotechnology, as well as for applications such as new designs of energy-efficient spintronic devices. Our approach combines the latest developments in chromatic aberration corrected electron microscopy with electron energy-loss magnetic chiral dichroism(EMCD). We study the double perovskite Sr_2FeMoO_6 and quantitatively measure the ratio of orbital to spin magnetic moment atomic plane by atomic plane.[2,3] The spatial resolution of atomic-plane resolved EMCD method goes beyond that of any currently available technique, including XMCD and neutron diffraction. It is applicable to studies of spin configurations, atomic structure and chemical bonding at different magnetically coupled interfaces, including magnetic spring effects at interfaces between hard and soft magnets, magnetoelectric coupling between ferromagnetic and ferroelectric materials and exchange bias between antiferromagnetic and ferromagnetic materials.

1.Schattschneider, P. *et al.* Detection of magnetic circular dichroism using a transmission electron microscope. *Nature* 441, 486–488 (2006). 2.Zechao Wang. *et.al*. Effects of dynamic diffraction conditions on magnetic parameter determination in a double perovskite Sr_2FeMoO_6 using electron energy-loss magnetic chiral dichroism. *Ultramicroscopy* 176, 212-217 (2017). 3.Zechao Wang. *et.al*. Atomic scale imaging of magnetic circular dichroism by achromatic electron microscopy. *Nature Materials*. (2018) In press

11:15

AC-08. Effect of annealing on the structural and magnetic properties of CoMnSi investigated by X-ray diffraction and X-ray absorption fine structure measurements.

R. Kou[2,1], J. Gao[2], Y. Ren[1], S. Heald[1], B. Fisher[1] and *C. Sun*[1]
1. Argonne National Laboratory, Argonne, IL, United States; 2. Key Laboratory of Electromagnetic Processing of Materials (Ministry of Education), Northeastern University, Shenyang, China

The CoMnSi compound has aroused much interest because it shows a metamagnetic transition and useful magnetic properties [1–5]. Annealing was often used to improve its properties. However, the underlying mechanism is not well understood. In this work, we investigated the effect of annealing on the structure and magnetic properties of an as-cast sample of CoMnSi. As shown in Fig. 1, the annealing increases magnetic moments at ferromagnetic state but decreases magnetic moments at antiferromagnetic state. As a result, the annealing brings about a doubling of the maximum magnetic entropy change. Synchrotron radiation X-ray diffraction revealed that the annealing does not change the crystal structure but brings about different changes of two nearest Mn-Mn distances. As displayed in Fig. 2, the X-ray absorption near edge structure (XANES) experiments unveiled that the local environment around the Mn atoms are changed slightly by annealing but that the local environment around the Co atoms are changed significantly. When compared with the as-cast sample, the intensity corresponding to the electronic transition from 1s to 3d of the annealed sample reduces, while the intensity corresponding to the electronic transition from 1s to 4p increases. The Fourier transforms analysis of the extended X-ray absorption fine structure (EXAFS) showed that the Co-Si bond length of the annealed sample is shorter than that of the as-cast sample, but he Co-Mn bond length of the annealed sample is same as that of the as-cast sample. Such observations suggested that the annealing promotes the p-d hybridization between Co and Si atoms, causing a sharper metamagnetic transition.

List of References: [1] K. G. Sandeman, R. Daou, S. Özcan, J. H. Durrell, N. D. Mathur, D. J. Fray, Phys. Rev. B, 74, 224436 (2006). [2] Q. Zhang, W. F. Li, N. K. Sun, J. Du, Y. B. Li, D. Li, Y. Q. Zhang, Z. D. Zhang, J. Phys. D: Appl. Phys., 41, 125001 (2008). [3] A. Barcza, Z. Gercsi, K. S. Knight, K. G. Sandeman, Phys. Rev. Lett., 104, 247202 (2010). [4] Y. Y. Gong, D. H. Wang, Q. Q. Cao, Y. W. Du, T. Zhi, B. C. Zhao, J. M. Dai, Y. P. Sun, H. B. Zhou, Q. Y. Lu, J. Liu, Acta Mater., 98, 113–118 (2005). [5] H. Binczycka, A. Szytula, J. Todorovic, T. Zaleski, A. Zieba, Phys. Stat. Sol. A, 35, K69–K72 (1976).

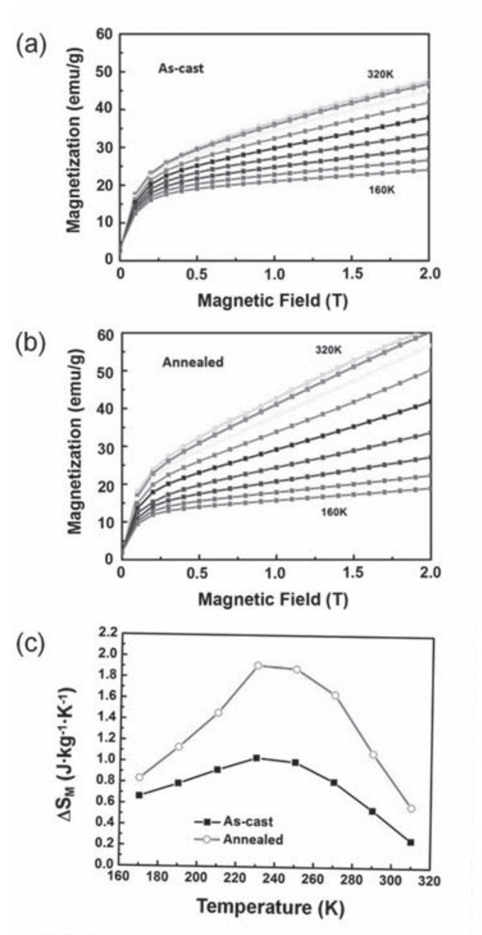

Fig. 1. Isothermal magnetization of (a) as-cast and (b) annealed samples of CoMnSi as well as (c) their magnetic entropy changes for a field change from H = 0 T to 2.00 T. The isothermal magnetization was measured at temperature intervals of 20 K.

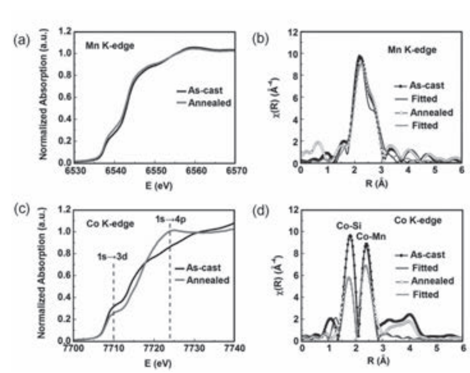

Fig. 2. (a) XANES spectra of the Mn K-edge and (b) the Fourier transforms and fittings of the Mn K-edge EXAFS. (c) XANES spectra of the Co K-edge and (d) the Fourier transforms and fittings of the Co K-edge EXAFS.

11:30

AC-09. Spatially resolved investigation of all optical magnetization switching in TbFe alloys.

M. Mawass[1], A. Arora[1,5], O. Sandig[3], C. Luo[2], A.A. Ünal[1,4], F. Radu[1], S. Valencia[1] and F. Kronast[1]
1. Department Materials for Green Spintronics, Helmholtz-Zentrum Berlin für Materialien und Energie, Berlin, Germany; 2. Department of Physics, University of Regensburg, Regensburg, Germany; 3. Institut für Experimentalphysik, Freie Universität Berlin, Berlin, Germany; 4. Max Born Institute for Nonlinear Optics and Short Pulse Spectroscopy, Berlin, Germany; 5. Institut für Physik und Astronomie, Universität Potsdam, Potsdam, Germany

High storage density magnetic devices rely on the precise, reliable and ultrafast switching times of the magnetic states. Optical control of magnetization using femtosecond laser without applying any external magnetic field offers the advantage of switching magnetic states at ultrashort time scales, which has attracted a significant attention. Recently, it has been reported and demonstrated the, *so-called*, all-optical helicity-dependent switching (AO-HDS) in which a circularly polarized femtosecond laser pulse switches the magnetization of a ferromagnetic thin film as function of laser helicity [1]. Afterward, in more recent studies, it has been reported that AO-HDS is a general phenomenon existing in magnetic materials ranging from rare earth – transition metals ferrimagnetic (e.g. alloys, multilayers and hetero-structures system) to even ferromagnetic thin films. Among numerous studies in the literature which are discussing the microscopic origin of AO-HDS in ferromagnets or ferrimagnetic alloys, the most renowned concepts are momentum transfer via Inverse Faraday Effect (IFE) [1-3] and the concept of preferential thermal demagnetization for one magnetization direction by heating close to Tc (Curie temperature) in the presence of magnetic circular dichroism (MCD)[4-6]. In this study, we investigate all-optical magnetic switching using a stationary femtosecond laser spot (3–5 μm) in TbFe alloys via photoemission electron microscopy (PEEM) and x-ray magnetic circular dichroism (XMCD) with a spatial resolution of approximately 30 nm. We spatially characterize the effect of laser heating and local temperature profile created across the laser spot on AO-HDS in TbFe thin films. We find that AO-HDS occurs only in a 'ring' shaped region surrounding the thermally demagnetized region formed by the laser spot and the formation of switched domains relies further on thermally induced domain wall motion. Our temperature dependent measurements highlight the importance of attaining Tc, local temperature and temperature gradients for helicity-dependent switching. In addition, by investigating a series of samples with different Tb concentrations and film thicknesses, we demonstrate that the switching direction for a given laser helicity, inverts at a threshold film thickness [7]. We show that our results can be explained in the presence of one orientation MCD. Magnetic domains are heated preferentially and consequently, demagnetized in the region close to Tc, leading to an asymmetrical response with respect to the incoming laser helicity. These new findings shed light on a robust and reliable switching process, which paves the way for further understanding of the AO-HDS and its microscopic origin.

[1] Stanciu, C. D. *et al.* All-optical magnetic recording with circularly polarized light. *Phys. Rev. Lett.* 99, 1–4 (2007). [2] Kimel, A. V. *et al.* Ultrafast non-thermal control of magnetization by instantaneous photomagnetic pulses. *Nature* 435, 655–657 (2005). [3] Kirilyuk, A. *et al.* Ultrafast optical manipulation of magnetic order. *Rev. Mod. Phys.* 82, 2731–2784 (2010). [4] Cornelissen, T. D., Córdoba, R. & Koopmans, B. Microscopic model for all optical switching in ferromagnets. *Appl. Phys. Lett.* 108 (2016). [5] Khorsand, A. R. et al. Role of magnetic circular dichroism in all-optical magnetic recording. *Phys. Rev. Lett.* 108, 1–5 (2012). [6] Ellis, M. O. A., Fullerton, E. E. & Chantrell, R. W. All-optical switching in granular ferromagnets caused by magnetic circular dichroism. *Sci. Rep.* 6, 30522 (2016). [7] Arora, A. *et al.* Spatially resolved investigation of all optical magnetization switching in TbFe alloys *Sci. Rep.* 7: 9456 (2016).

11:45

AC-10. A Magnetic Field Camera for Real-Time Subsurface Imaging Applications.

A.B. Suksmono[1,2], D. Danudirdjo[1], R.P. Prastio[1], A.D. Setiawan[3] and D. Rahmawati[1]
1. School of Electrical Engineering and Informatics, Institut Teknologi Bandung, Bandung, Indonesia; 2. ITB Research Center on ICT (PPTIK-ITB), Institut Teknologi Bandung, Bandung, Indonesia; 3. School of Electrical Engineering, Telkom University, Bandung, Indonesia

We have constructed an imaging device that can show spatio-temporal distribution of magnetic field in real-time. The device employs 16 units of AMR (anisotropic magneto resistance) 3-axis magnetometers, which are arranged into a 4×4 size sensor-array. All of the magnetic field values measured by the array are collected by a microcontroller, which then preprocess and send the data to a smartphone or a PC using a USB or wireless (bluetooth) channel. An interpolation and display software in the smartphone/PC have also been built to present the field as a larger video on a screen; hence, the device serves as a magnetic field camera. In the experiments, we show that the magnetic-field distorted by objects buried under a surface can be imaged by the proposed device; therefore, we can use it for a real-time subsurface imaging or NDT (non-destructive testing) applications. Camera is an image capturing device. A distinctive feature of a camera is that the entire image (or sequence of images/video) are captured simultaneously, instead of elements-by-elements or pixel-by-pixel. In the latter case, the device will be called a scanner. In the digital camera, usually the captured image is displayed instantly; therefore, we refer the generic name "camera" to refer to a device capable to capture and display the image instantly. Previously, we have constructed a magnetic imaging system utilizing the built-in magnetometer of a smart-phone [1]. To obtain an image representing the distribution of magnetic field intensity, one has to scan the area of interest and then run a reconstruction program to obtain the field values. Therefore, this device is categorized as a (magnetic field) scanner, which will be referred as B-Scanner. The "B" in the names follows the notation of magnetic flux density, which is denoted as B. In this paper, we present a design and realization of a magnetic field camera or the B-Camera. The B-Camera has the capability to capture and display magnetic field distribution of a region instantly. Instead of sequential scanning of a gridded area done in the B-Scanner, we employ an array of magnetometers that measure the field values on a regular grid of the area simultaneously. Then, a reconstruction software will interpolate entire values of in the domain and display the result on the screen instantly. Block diagram and implementation of the device is displayed in Fig.1. The magnetic field camera (MFC) blocks consist of sensor-array part, display, and communication between sensor and the display. In principle, the camera works like the magnetic field scanner, unless the sensors position are fixed at regular grid points/array. The MFC (Magnetic Field Camera) is divided into the following functional blocks: (a) sensor array and multiplexer, (b) microcontroller, (c) communication-1: sensor-array side, (d) communication-2: smartphone side, and (e) computing/interpolator and display. Fig.2 shows the block diagram of the camera and the obtained results. In (a), a coin (made of nickel) is located at the center of the camera array. The display unit, which in this case is a smartphone, shows magnetic field distribution as an image. From the menu, a user can select either the x, y, z, components of the field or its magnitude. The (b) part of the figure shows the image of field distribution when the coin is located at the corner of the array. Both of (a) and (b) consistently shows the magnetic field distribution at the correct place, considering that the user will direct the array downward when performing the imaging.

[1] A. B. Suksmono, D. Danudirdjo, A. D. Setiawan, and D. Rahmawati, "Magnetic subsurface imaging systems in a smartphone based on the built-in magnetometer," IEEE Trans. on Magnetics, Vol.53, No.11, Nov. 2017. [2] M. Volk, S. Whitlock, C. H. Wolff, B. V. Hall, and A. I. Sidorov, "Scanning magnetoresistance microscopy of atom chips," Rev. Sci. Instruments, 79, 023702, 2008.

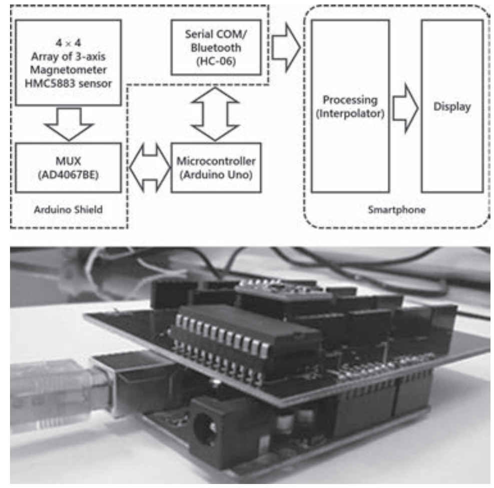

Fig. 1. Block diagram and realization of the magnetic field camera.

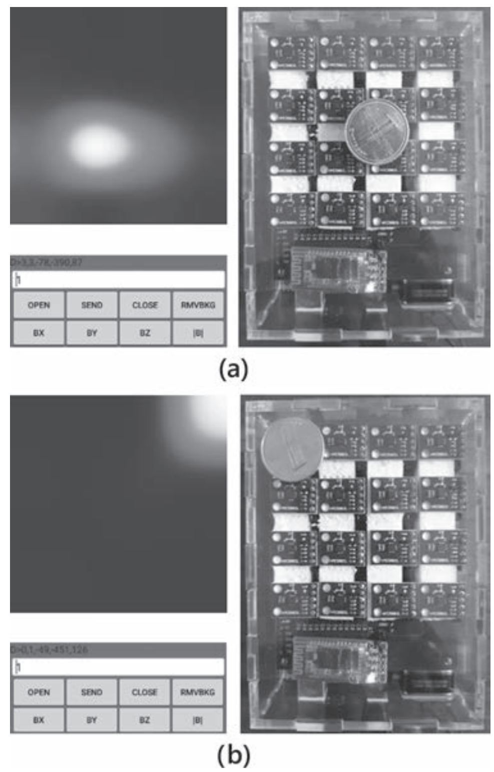

Fig. 2. Magneto-photographs of a coin and its corresponding position at the sensor array. The array is designed to be used downward, so that the left-right position of the image is inverted. The object is a coin (Rp.1000,-), which is made of ferromagnetic material.

TUESDAY MORNING, 24 APRIL 2018

PEONY IV, 9:00 TO 12:00

Session AD
SPIN-ORBITRONICS I

Wanjun Jiang, Chair
Tsinghua University, Beijing, China

CONTRIBUTED PAPERS

9:00

AD-01. Modulated spin orbit torque in a Pt/Co/Pt/YIG multilayer by nonequilibrium proximity effect.

Q. Liu[1], K. Meng[1], X. Xu[1], J. Miao[1], Y. Wu[1], J. Chen[1] and Y. Jiang[1]
1. School of Materials Science and Engineering, University of Science and Technology Beijing, Beijing, China

K. K. Meng*,Y. Jiang* *kkmeng@ustb.edu.cn *yjiang@ustb.edu.cn Spin orbit coupling (SOC) has attracted considerable attention as it is central to the rich phenomena observed in heavy metal (HM)/ferromagnetic metal (FM) heterostructures, such as spin orbit torque (SOT), spin Hall magnetoresistance (SMR), spin Seebeck effect and magnetic skyrmions[1-2]. Especially, the charge current passing through the HM film with strong SOC produces transveral pure spin current due to the spin Hall effect (SHE), which exerts torques on the magnetization of the FM film, and the sign and magnitude of SOT are essentially determined by the spin Hall angle (SHA) of HM. According to the physical origin, enhancing the effective SHA and spin accumulation at HM/FM interfaces has been the central method for improving the switching efficiency in SOT-active devices. Because SHA is hard to be intrinsically controlled, many extrinsic ways to control it have been proposed. Qiu et al.[3] utilized the large spin absorption at Ru/FM interface to decrease the spin memory loss and effectively enhance SHA. In our study, we will modulate the spin accumulation and the efficiency of SOT by nonequilibrium proximity effect *[accepted by Appl. Phys. Lett.]*. According to the geometric relation between the flow of electrons and accumulated spins in the multilayers of Pt/Co/Pt/SiO_2 and Pt/Co/Pt/YIG illustrated in Figure 1(a) and (b), respectively. The charge current J_e applied in the Pt layer is converted into spin current J_s due to SHE, which travels perpendicular to the film plane with the spin polarization parallel to the plane. A part of the spin current at Pt/Co/Pt/YIG multilayers, compared with Pt/Co/Pt/SiO_2 multilayers, will be absorbed by the magnetization M of YIG through spin transfer torque when J_e is parallel to M. In this case, we expect that the reduction of J_s^{back} in Pt/Co/Pt/YIG will enhance the SHA of Pt closing to YIG. According to the magnetic field H dependence of the out-of-plane magnetization M and the anomalous hall resistance R_H at room temperature for the two multilayers shown in Fig. 1 (c) and (d), which indicating that the saturation magnetizations M_s and the coercivities H_c are almost the same in the two multilayers, however, the critical switching current in Pt/Co/Pt/YIG is only half of that in Pt/Co/Pt/SiO_2 as shown in Fig. 2(a) and (b), indicating the enhancement of effective SHA in the former structure. To quantitatively determine the strength of the spin orbit effective fields in the two samples, the non-adiabatic harmonic Hall voltage measurements with sweeping magnetic field parallel or perpendicular to the current direction were carried out at room temperature. The harmonic measurements by applying a sinusoidal AC current with the amplitude of 10×10^6A/cm^2 at 300 K are taken as an example as shown in Fig. 2 (c), in which the results were measured with the out-of-plane magnetization component $M_Z > 0$ and $M_Z < 0$ respectively. According to the calculated H_D values plotted with respect to the applied current in Fig. 2 (d), the SHA in Pt/Co/Pt/SiO_2 is calculated to be 0.049 while the value is 0.071 in Pt/Co/Pt/YIG. The harmonic measurements demonstrated that the effective SHA has been enhanced in Pt/Co/Pt/YIG/GGG. In conclusion, we have studied the SOT-induced magnetization switching in the two multilayers of Pt/Co/Pt/SiO_2 and Pt/Co/Pt/YIG. The critical current in Pt/Co/Pt/YIG is effectively reduced compared to that in Pt/Co/Pt/SiO_2. We propose that the nonequilibrium proximity effect at the Pt/YIG interface suppresses the spin current reflection and enhances the effective spin accumulation at the Co/Pt interface. The harmonic measurements demonstrated that the effective SHA has been enhanced in Pt/Co/Pt/YIG/GGG. Our method provides an efficient way to modulate SOT.

[1] A. Soumyanarayanan, N. Reyren, A. Fert, and C. Panagopoulos, Nature 539, 509 (2016). [2] K. K. Meng, J. Miao, X. G. Xu, Y. Wu, X. P. Zhao, J. H. Zhao, and Y. Jiang, Phys. Rev. B. 94, 214413 (2016). [3] X. P. Qiu, W. Legrand, P. He, Y. Wu, J. W. Yu, R. Ramaswamy, A. Manchon, and H. Yang, Phys. Rev. Lett. 117, 217206 (2016). [4] Q. B. Liu, K. K. Meng, Y. Z. Cai, X. H. Qian, Y. C. Wu, S. Q. Zheng, Y. Jiang, accepted by Appl. Phys. Lett.

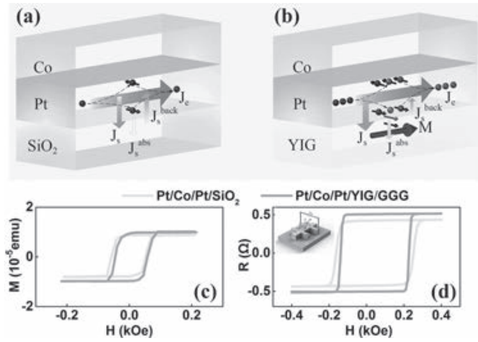

Fig. 1. (a) and (b) Illustrations of the geometric relation between the flow of electrons, accumulated spins and magnetization in Pt/Co/Pt/SiO_2 and Pt/Co/Pt/YIG. Field dependence of the anomalous hall resistance (c) and the out-of-plane magnetization (d) in the two multilayers. The inset Schematic measurement setup along with the definition of the coordinate system.

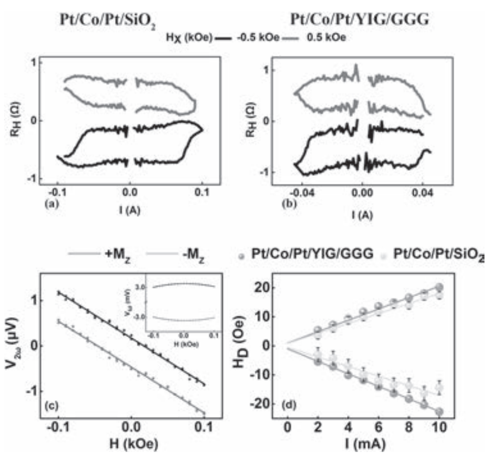

Fig. 2. The R_H-I curves in Pt/Co/Pt/SiO_2 (a) and Pt/Co/Pt/YIG (b) with H_x=500 Oe and -500 Oe.(c) The second $V_{2\omega}$ harmonic Hall voltages plotted against the small in-plane external fields. Inset:the first V_ω harmonic Hall voltages plotted against the small in-plane external fields. (d) Current-induced effective field H_D versus applied AC current for Pt/Co/Pt/SiO_2 and Pt/Co/Pt/YIG.

9:15

AD-02. Spin orbit torque and topological Hall effect in MnX(X=Ga or Al)/heavy metal bilayers.

K. Meng[1], J. Zhao[2] and Y. Jiang[1]
1. University of Science and Technology of China, Beijing, China;
2. Institute of Semiconductors Chinese Academy of Sciences, Beijing, China

Spin Hall effect (SHE) that converts charge currents into spin currents in a heavy metal (HM) with strong spin-orbit coupling (SOC) has attracted much interest due to its practical use in technological applications. When a HM comes in contact with a ferromagnet, the spin currents that diffuse into the FM will modify the spin dependent transport properties such as anomalous Hall effect (AHE). On the other hand, the spin currents will also exert torque on the magnetization, which is similar to spin transfer torque. The investigation and clarification of these intriguing issues are of fundamental importance for better understanding the underlying physics. In HM/FM heterostructures with perpendicular magnetic anisotropy (PMA), the generated pure spin current can also exert torques on the magnetization, which is referred as to spin orbit torques (SOT). On the other hand, spin accumulation can take place at the FM/HM interface via the Rashba effect, which has also generated significant effective torques and caused current-induced domain nucleation and fast domain wall motion. Both mechanisms can result in the exertion of dampinglike torques and fieldlike torques on the FM, which can be characterized by equivalent dampinglike effective field H_D and fieldlike effective field H_F respectively. It should be noted that, quite generally, the SOT induced magnetization switching has been mostly investigated in HM/FM multilayers with the interfacial induced PMA, in which the HM layer modifies the interfacial orbital angular momentum of the FM layer and enhances its SOC. From a practical viewpoint, however, the interfacial PMA is not thermally stable in nanoscale magnetic devices. Recently, we have systematically investigated the SOT in MnGa/HM and MnAl/HM films with intrinsic PMA, which seems to be ideal for the current induced magnetization switching[1-4]. However, the switching current density (~10^7 A/cm^2) in MnX/HM bilayers as shown FIG. 1 is similar with those in interface induced PMA multilayers, which is unsatisfactory for practical low-power spintronic devices. In the magnetic systems that lack inversion symmetry (whether due to underlying crystal structure or interfaces), SOC can combine with the exchange interaction to generate an anisotropic exchange interaction that favors a chiral arrangement of the magnetization. This is known as the Dzyaloshinskii-Moriya interaction (DMI), which has a form $D_{12}\bullet(S_1\times S_2)$. The vector D_{12} depends on the details of electron wave functions and lies parallel or perpendicular to the line connecting the two spins, depending on the symmetry. Contrary to the Heisenberg exchange interaction, which leads to collinear alignment of lattice spins, the form of DMI is therefore very often to cant the spins by a small angle. If DMI is sufficiently strong enough to compete with the Heisenberg exchange interaction and the magnetic anisotropy, it can stabilize long-range non-collinear spin textures. Therefore, if the presence of strong SOC introduces a strong interfacial DMI in the MnX/HM films, the non-collinear spin textures such as Néel-type skyrmion could be driven and a much smaller switching current density (~10^2 A/cm^2) should be realized. On the other hand, when a conduction electron passes through a non-collinear magnetic structure, the spin of the conduction electron adiabatically couples to the local spin and experience a fictitious magnetic field (Berry curvature) in real space, which deflects the conduction electrons perpendicular to the current direction. Therefore, it will cause an additional contribution to the observed Hall signals that has been termed topological Hall effect (THE) as shown in FIG. 2. THE can be described by the same theoretical scheme as the intrinsic AHE, which has been clarified to be a Berry phase in momentum space. In the presence of a non-collinear magnetic structure, the total Hall resistivity can usually be expressed as the sum of various contributions: $\rho_H=R_0H+\rho_A+\rho_T$, where is the normal Hall coefficient, the anomalous Hall resistivity, and the topological Hall resistivity[5]. Based on our previous works of SOT, the results will open the route to engineer non-collinear spin textures for SOT devices, in which a much smaller switching current density is expected if the chiral DW, such as Néel-type skyrmion, can be confirmed.

[1] K. K. Meng, J. Miao, X. G. Xu, J. X. Xiao, J. H. Zhao and Y. Jiang, Physical Review B 93, 060406(R) (2016). [2] K. K. Meng, J. Miao, X. G. Xu, Y. Wu, X. P. Zhao, J. H. Zhao and Y. Jiang, Appl. Phys. Lett. 110, 142401 (2017). [3] K. K. Meng, J. Miao, X. G. Xu, Y. Wu, X. P. Zhao, J. H. Zhao and Y. Jiang, Physical Review B 94, 214413 (2016). [4] K. K. Meng, J. Miao, X. G. Xu, Y. Wu, J. X. Xiao, J. H. Zhao and Y. Jiang, Scientific Reports. 6, 38375 (2016). [5] K. K. Meng *et al* submitted to Physical Review B.

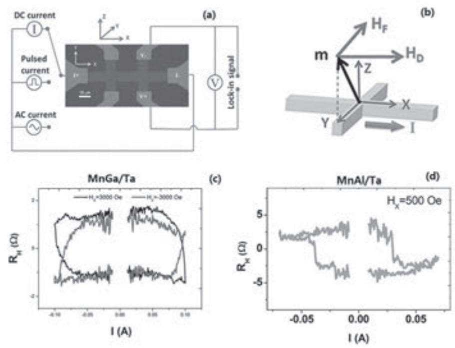

Fig. 1. (a) The SEM image of a patterned Hall bar and the schematic measurement setup along with the definition of the coordinate system. (b) The corresponding field-like effective field H_F and damping-like effective field $H_D$when the magnetization is tilted perpendicular to the current direction. R_H-I curves of MnGa/Ta (e) and MnAl/Ta (f) bilayers.

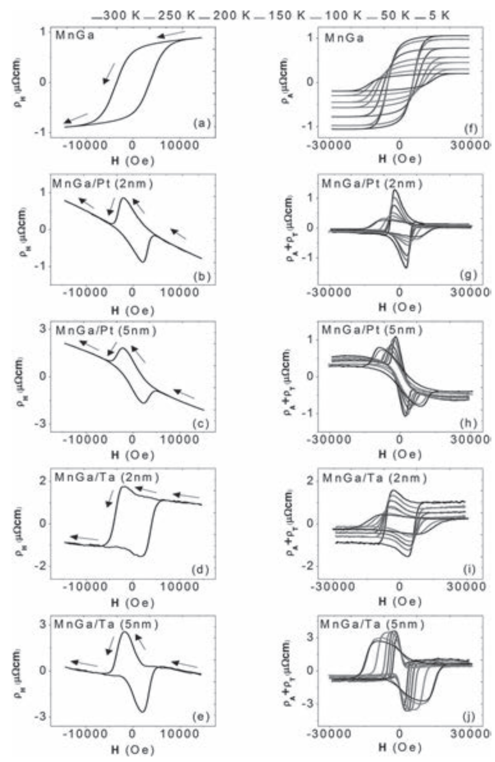

Fig. 2. (a)-(e) Total Hall resistivities in the single MnGa, MnGa/Pt (*t*) and MnGa/Ta (*t*) (*t* =2, 5 nm) films at 300 K. The arrows denote the change tendency of hall resistivity when the magnetic field is applied from positive to negative. (f)-(j) ($\rho_A+\rho_T$)*vs H* for the single MnGa, MnGa/Pt (*t*) and MnGa/Ta (*t*) (*t* =2, 5nm) films in the temperature range from 5 to 300 K.

9:30

AD-03. Strong suppression of spin Hall effects induced by spin fluctuations.

H. Taniguchi[1*], T. Arakawa[1,2], T. Taniguchi[1], Y. Niimi[1,2] and K. Kobayashi[1,2]
1. Graduate School of Science, Osaka University, Toyonaka, Japan;
2. Center for Spintronics Research Network, Osaka University, Toyonaka, Japan

Spin current, flow of spin angular momentum, is at the heart of spintronics. Since it is closely related to device application, the effective generation and detection of spin current have been intensively studied so far in this field. Spin Hall effect (SHE) and its inverse (ISHE) are typical phenomena to generate and detect the spin current. Recently, it has been revealed that the SHE and ISHE are affected by spin fluctuations in magnetic systems such as weak ferromagnetic metals near Curie temperatures [1] and spin-glass metals [2]. The latter is well-known as one of the magnetic ordering states with complex spin structures. It appears when magnetic impurities are randomly distributed in a nonmagnetic noble metal. The interaction between the localized magnetic moments is mediated by conduction electron spins, which is referred to as the Ruderman-Kittel-Kasuya-Yosida (RKKY) interaction. Depending on the distance between the two magnetic impurities, the exchange coupling is either ferromagnetic or antiferromagnetic. As a result of the RKKY interaction, spin glasses exhibit a cusp anomaly in the magnetic susceptibility as a function of temperature T. It is commonly believed that most of the magnetic moments are randomly frozen below the cusp temperature, so-called spin glass temperature T_g. However, according to recent SHE measurements in CuMn spin-glass metals [2], the SHE signal started to decrease at a temperature labeled as T^*, which is 4 times higher temperature than T_g. This result indicates that the spin current can detect magnetic fluctuations of the localized moments in a much more sensitive manner compared to the conventional magnetic susceptibility measurements. On the other hand, in order to deeply understand the relation between the spin current and magnetic fluctuations, further experiments are highly desirable. Here we have performed SHE measurements in $Cu_{99.5-x}Mn_xBi_{0.5}$ alloys with much higher Mn concentrations (x = 4.2, 10.6) than the previous work [2]. With increasing the Mn concentration x, T_g monotonically increases. This enables us to investigate the effect of spin fluctuations on the SHE in spin glasses at much lower temperatures than T_g. A small concentration of Bi (0.5%) has been added to induce large SHEs in CuMn spin-glass metals [2, 3]. The inset of Fig. 1 shows a typical spin Hall device used in the present work. The device is based on the lateral spin valve with a strong spin orbit material in the middle, which allows us to induce a spin current in the Cu channel and to inject it into the CuMnBi wire [4]. The measured ISHE resistance ΔR_{ISHE} (the detected Hall voltage divided by the injection current illustrated in the inset of Fig. 1) for different Mn concentrations $Cu_{99.5-x}Mn_xBi_{0.5}$ (x = 1.5, 4.2, 10.6) is plotted as a function of temperature T in Fig. 1. With decreasing T, ΔR_{ISHE} increases because the spin diffusion length of the Cu channel becomes longer with T. For $T < T^*$, however, ΔR_{ISHE} starts to decrease and becomes almost zero for higher concentrations (x = 4.2 and 10.6) at low temperatures. Such a large suppression of ISHE has never been seen for lower Mn concentrations [2]. The result shown in Fig. 1 can be explained by the following scenario: at high enough temperatures, the Mn moments fluctuate with high frequencies and the conduction electron spins cannot follow this fast motion. Thus, the ISHE signal is simply determined by skew scattering at the Bi impurity sites [2,3]. With decreasing T, the fluctuation of the Mn moments is getting slower. The conduction electron spins can feel the fluctuation and the directions of conduction electron spins are randomized. Since the Mn moments are randomly frozen for $T < T_g$, the directions of conduction electron spins become completely random and thus the ISHE signal disappears well below T_g. The relations of T_g and T^* with the Mn concentration x are summarized in Fig. 2. For all the investigated x region, T^* is always a few higher than T_g. From the present SHE measurements, we are able to shine a new light on the spin fluctuation regime ($T_g < T < T^*$, indicated by blue shade in Fig. 2) where conduction electron spins are affected by the motions (or interaction) of localized magnetic moments, which has never been detected with other experimental methods.

[1] D. H. Wei *et al*., Nat. Commun. 3, 1058 (2012). [2] Y. Niimi *et al*,. Phys. Rev. Lett. 115, 196602 (2015). [3] Y. Niimi et al., Phys. Rev. Lett. 109, 156602 (2012). [4] Y. Niimi and Y. Otani, Rep. Prog. Phys. 78, 124501 (2015).

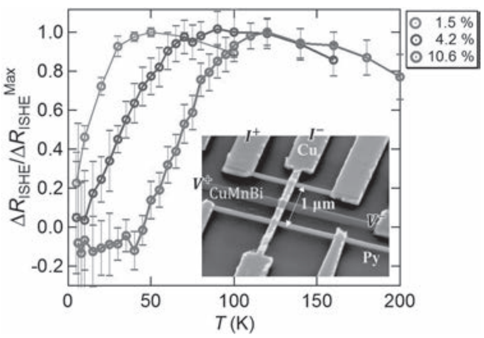

Fig. 1. The temperature dependence of ISHE in $Cu_{99.5-x}Mn_xBi_{0.5}$(x = 1.5, 4.2, 10.6). Each ISHE signal is normalized by the maximum value. T^* and T_g are indicated in the figure. The inset is a SEM image of a spin Hall device with CuMnBi. The device consists of two ferromagnetic permalloy ($Ni_{81}Fe_{19}$; Py) wires and CuMnBi middle wire bridged by a Cu channel.

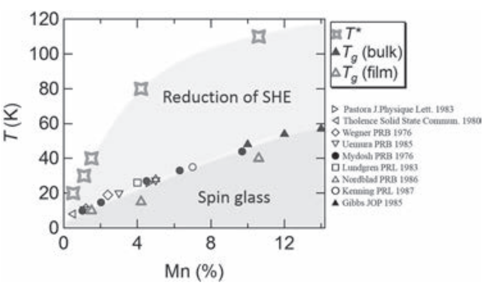

Fig. 2. Relations of T_g and T^* with the Mn concentration x for CuMn spin glass. T_g of thin films and bulk are indicated by the red triangle and the black symbol, respectively. T^* is shown with the open star.

9:45

AD-04. Symmetry and magnitude of intrinsic spin-orbit torques in the half-Heusler alloy PtMnSb.

J. Mendil[1], J. Krieft[2], P. Dao[1], C. Avci[5], M.H. Aguirre[3], K. Rott[2], J. Schmalhorst[2], F. Freimuth[4], G. Reiss[2], T. Kuschel[2] and P. Gambardella[1]
1. Department of Materials, ETH Zurich, Zurich, Switzerland; 2. Center for Spinelectronic Materials and Devices, Department of Physics, Bielefeld University, Bielefeld, Germany; 3. Instituto de Nanociencia de Aragón & Laboratorio de Microscopías Avanzadas, Dpto. de Física de Materia Condensada, Universidad de Zaragoza, Zaragoza, Spain; 4. Peter Grünberg Institut and Institute for Advanced Simulation, Forschungszentrum Julich and JARA, Julich, Germany; 5. Massachusetts Institute of Technology, Materials Science and Engineering, Cambridge, MA, United States

Magnetization manipulation by spin-orbit torques (SOTs) has advanced to an active research field over the past few years. Most work so far has focused on material systems with conventional ferromagnets deposited on heavy metal layers where the space inversion symmetry is broken at the interface [1-4]. However, space inversion symmetry is intrinsically broken in non-centrosymmetric crystals and thereby could give rise to SOTs even in single-layer materials [5,6]. Moreover, materials with inversion-asymmetric point groups promise a variety of novel SOT symmetries [6] compared to the well-known field-like and damping-like SOTs. While novel SOT symmetries have been reported for bilayer systems [7] or ferromagnetic semiconductors [8,9], their investigation in metallic ferromagnetic materials with inversion-asymmetry has only been recently addressed in NiMnSb [5]. Here, we present the first observation of intrinsic SOTs in single layers of PtMnSb, which is a magnetic half-Heusler alloy. For this, we prepared PtMnSb single crystal thin films by co-sputter deposition on MgO(111) substrates [10]. It crystallizes in the C1b crystal structure as schematically shown in Fig. 1. Similar to NiMnSb, its inversion asymmetry allows for a local spin-polarization upon current-injection that persists even when integrating over the whole unit cell. To perform electrical transport measurements, the full sheet samples were patterned into Hall bar structures with dimensions 80x10 um by means of electron beam lithography. Magnetotransport measurements were carried out using the Harmonic Hall resistance technique [1] where the first harmonic Hall resistance gives access to the magnetoresistance characteristics due to the equilibrium orientation of magnetization and the second harmonic Hall resistance carries information about any current-induced effects such as current-induced effective fields. In our study, we simultaneously record the first and second harmonic Hall resistance while rotating the externally applied magnetic field in the sample plane (xy angle scans) and subsequently apply different external magnetic fields in the range from 50 to 2000 mT. From the first harmonic Hall resistance, we deduce magnetic anisotropy parameters such as an effective demagnetization field and fourfold in-plane anisotropy. The latter was found in the crystallographically similar material (Ga,Mn)As [11]. We perform macrospin simulations for xy angle scans to quantify the anisotropy in our system by fitting it to our data. We find a dominating in-plane fourfold anisotropy with corresponding anisotropy fields in the range of few mT and a less dominant uniaxial anisotropy that is one order of magnitude smaller. This information is used to evaluate the second harmonic Hall resistance where all effective fields have to be taken into account to correctly interpret the lineshape of the second harmonic Hall resistance. An example data set for the second harmonic Hall resistance is shown in Fig. 2 obtained for a 10 nm thick single layer PtMnSb Hall bar. Here a current density of $5x10^6$ A/cm^2 is applied. One can clearly see that its amplitude within a xy angle scan decreases when increasing the field as indicated by the black arrow. This behavior is characteristic for current-induced effective fields that are more and more suppressed when increasing the external field. We can assign the effective fields to SOTs that are linked to the crystal structure. Using crystallographic symmetry arguments, we can separate the observed the SOTs in odd and even components with respect to magnetization inversion. For both the even and odd SOTs, we reveal corresponding effective fields that scale up to the 2nd and 3rd power of the magnetization components and have a distinct symmetry compared to the well-known field-like and damping-like SOTs reported in ferromagnetic/heavy metal bilayers. Finally, we characterize the SOTs as a function of PtMnSb thickness and discuss the possibility of using PtMnSb for magnetic switching applications.

[1] K. Garello et al., Nat. Nanotech. 8, 587 (2013) [2] C. O. Avci, K. Garello., J. Mendil et al., Appl. Phys. Lett. 107, 192405 (2015) [3] L. Neumann et al., Appl. Phys. Lett. 109, 142405 (2016) [4] L. Liu et al., Science 336, 555 (2012) [5] C. Ciccarelli et al., Nat. Phys. 12, 855 (2016) [6] J. Zelezny et al., Phys. Rev. B 95, 014403 (2017) [7] MacNeill et al., Nat. Phys. 12, 3933 (2016) [8] Chernyshov et al., Nat. Phys. 5, 1362 (2009) [9] Kurebayashi et al., Nat. Nanotech. 9, 211 (2014) [10] J. Krieft, J. Mendil et al., Phys. Status Solidi (Rapid Res. Lett.) 11, 1600439 (2017) [11] W. Limmer et al., Phys. Rev. B 77, 205210 (2008)

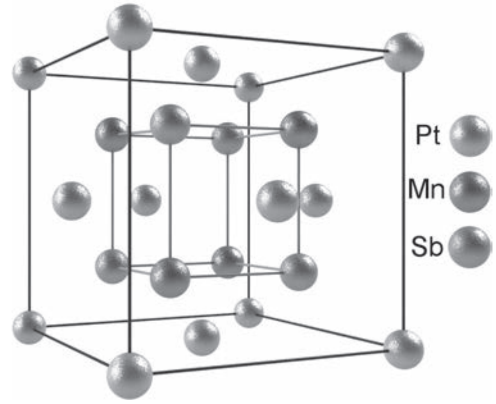

Fig. 1. PtMnSb is a half Heusler compound and crystallizes in the C1b crystal structure that is schemetically shown in the drawing above. Its unit cell is inversion-asymmetric allowing for non-zero spin-polarization when sending a current through the material.

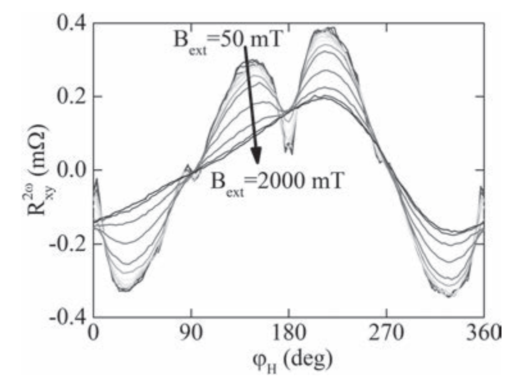

Fig. 2. Exemplary measurement of the second harmonic Hall resistance ($R_{xy}^{2\omega}$) of a 10 nm thick single layer Hall bar of PtMnSb in an xy angle scan where the magnetization orientation is controlled in the sample plane by rotating the azimuthal angle of the external magnetic field (ϕ_H). The magnitude and lineshape changes as a function of the magnitude of the externally applied field. This is used to extract several SOTs that go beyond the well-known field-like and damping-like SOTs.

INVITED PAPER

10:00

AD-05. Anomalous Hall effect in fully compensated half-metallic Mn_2Ru_xGa thin films.

C. Fowley[1], K. Rode[2], Y. Lau[2], N. Thiyagarajah[2], D. Betto[2], K. Borisov[2], G. Atcheson[2], E. Kampert[1], Z. Wang[1], Y. Yuan[1], S. Zhou[1], J. Lindner[1], P.S. Stamenov[2], M. Coey[2] and A. Deac[1]
1. Helmholtz-Zentrum Dresden-Rossendorf, Dresden, Germany; 2. School of Physics, AMBER and CRANN, Trinity College Dublin, Dublin, Ireland

Films with ultra-high magnetic anisotropy fields hold great promise for future telecommunications as they possess magnetic resonance frequencies in the THz range [1-3]. In the context of spin-transfer driven nano-oscillators (STNOs), which work on the principle of angular momentum transfer from a spin-polarised current to a small magnetic element [4,5], stabilising auto-oscillations, certain Heusler alloys represent a suitable choice for achieving communication beyond 5G [6]. The recently discovered half-metallic compensated ferrimagnet, Mn_2Ru_xGa, is such a Heusler alloy. It has been shown experimentally [7] and confirmed by DFT calculations [8] to possess a spin-gap at the Fermi level. Here, the transport properties of MRG are investigated in applied magnetic fields up to 58 T and analysed in the context of a molecular field model to determine the anisotropy and exchange energies. Large out-of-plane magnetic anisotropy is observed, with a Hall resistivity of 5 μOhm.cm, shown in figure 1 (a). Between 135 K and 165 K the coercivity is larger than 6.5 T and the sign of ρ_{xy} reverses. The change in sign indicates a reversal of the spin-polarisation with respect to the applied magnetic field, consistent with reaching the compensation temperature, T_{comp} ≈ 155 K. Hall loops obtained in pulsed magnetic fields, shown in figure 1 (b), follow the same trend as that in figure 1 (a) and at 150 K the coercivity is in excess of 9 T. At fields larger than the coercivity, MRG also exhibits a temperature dependent spin-flop transition, μ_0H_{sf}, where the antiferromagnetic alignment of the two Mn sub-lattices is broken. The temperature dependence of μ_0H_c, figure 1 (c), shows a clear divergence around T_{comp} indicated by the shaded region. This behaviour is expected: as the net magnetisation vanishes, the magnetic anisotropy field will tend to infinity and with it the coercivity. The temperature dependence of μ_0H_{sf} is also plotted in figure 1 (c). Temperature dependent scans of ρ_{xy} in zero applied field across T_{comp} show that, despite having a vanishing net magnetic moment, the Hall resistivity is finite and does not change sign (figure 1 (d)). In normal ferromagnets and non-half-metallic ferrimagnets, the anomalous Hall effect is proportional to the component of the net magnetisation along the surface normal, z [9]. In MRG, the Hall signal is due to the magnetic moment on the Mn 4c sub-lattice only. The Mn 4a sub-lattice states form the spin-gap. Unlike rare-earth - transition-metal alloys, such as TbFe and GdCo [10], the only magnetic element in MRG is Mn, and therefore the retention of ρ_{xy} over T_{comp} is not due to differing contributions to the Hall signal from the two magnetic sub-lattices. Molecular field modelling [11] is used to determine the intra and inter-lattice exchange constants from the Curie temperature and the compensation temperature, reproduced in figure 2 (a). Figure 2 (b) shows clearly that the Hall conductivity, σ_{xy}, follows the magnetisation of the 4c sub-lattice and not the net magnetisation. The response of the net magnetisation can be obtained by subtracting the value of the Hall conductivity at the compensation temperature, $\sigma_{xy\text{-}comp}$, from the raw data, $\sigma_{xy}(T)$. $\sigma_{xy}(T) - \sigma_{xy\text{-}comp}$ follows the net magnetisation from the molecular field model (Figure 2 (b)). From the field dependent data in high magnetic fields, we calculate the sub-lattice anisotropy energy, K_{4c}, from the spin-flop field $H_{sf} = (2\, H_{k\text{-}4c}\, H^{i}_{4c})^{1/2}$ where $H_{k\text{-}4c}$ is the 4c sub-lattice anisotropy field and H^{i}_{4c} is the molecular field on the 4c sub-lattice. A comparison of the z-component of the Mn 4c sub-lattice from the model and the experimental data, as a function of both the in-plane, μ_0H_x, and out-of-plane field μ_0H_z at 220 K, is shown in figure 2 (c). Despite slight discrepancies, the molecular field model reproduces the experimental data. Furthermore, knowing the molecular field experienced by the Mn 4c sub-lattice, $\mu_0H^{i}_{4c}$, and the sub-lattice anisotropy energy, K_{4c}, magnetic resonance frequencies of 0.700 THz and 0.145 THz are predicted. As such, MRG behaves magnetically as an antiferromagnet and electrically as a fully spin-polarised ferromagnet. It is also capable of operating in the THz regime. The immediate technological relevance is that any spin-transfer torque effects will also be dominated by the properties of the 4c sub-lattice. Part of this work was carried out under the EU Project TRANSPIRE - DLV-737038. We acknowledge the support of the HLD at HZDR, a member of the European Magnetic Field Laboratory (EMFL).

[1] Mizukami, S., et al. Physical Review Letters 106, (2011) [2] Awari, N., et al., Applied Physics Letters 109, (2016) [3] Mizukami, S., et al., Journal of Applied Physics 120, (2016) [4] Slonzewski, J. Journal of Magnetism and Magnetic Materials 159, L1 (1996) [5] Berger, L. Physical Review B 54, 9353 (1996) [6] Dhillon, S., et al., Journal of Physics D: Applied Physics 50, 043001 (2017) [7] Kurt, H., et al., Physical Review Letters 112, 027201 (2014) [8] Zic, M., et al., Physical Review B 93, 140202 (2016) [9] Nagaosa, N., et al., Reviews of Modern Physics 82, 1539 (2010) [10] McGuire, T. et al., Journal of Applied Physics 48, 2965 (1977) [11] Smart, J., Effective Field Theories of Magnetism. Studies in Physics and Chemistry, p216. Saunders, (1966)

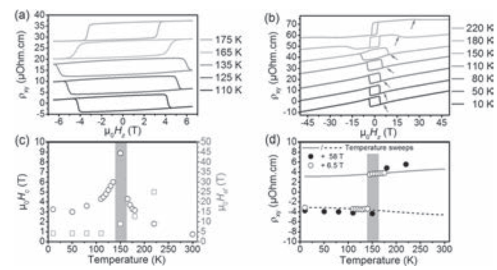

Fig. 1. (a) AHE loops up to 6.5 T for $Mn_2Ru_{0.61}Ga$ around the compensation temperature 155 K. (b) AHE loops up to 58 T, the spin-flop transition is indicated by the grey arrows. The linear slope is due to the ordinary Hall effect. (c) μ_0H_c (black open circles) and μ_0H_{sf} (red open squares) as a function of temperature. The divergence of the coercivity is consistent with M_{net} = 0 at T_{comp}. (d) Zero applied field temperature dependence of the remanent Hall resistivity when saturated at 10 K in negative (green line) and positive (blue-dashed) applied field. The black open (closed) circles record the remanent Hall resistivity after the application of +6.5 T (+58 T). The grey box in (c) and (d) indicate T_{comp}.

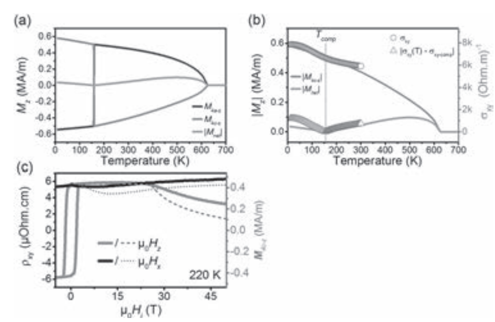

Fig. 2. (a) Temperature dependence of $M_{4a\text{-}z}$ and $M_{4c\text{-}z}$ and $|M_{net}|$, the compensation temperature is 155 K. (b) The Hall conductivity, σ_{xy}, $|\sigma_{xy} - \sigma_{xy\text{-}comp}|$, $|M_{4c\text{-}z}|$, and $|M_{net}|$ as a function of temperature. (c) Comparison of the experimental data and the model at 220 K for in-plane (μ_0H_x) and out-of-plane (μ_0H_z) applied fields.

CONTRIBUTED PAPERS

10:30

AD-06. A Comparative Study on Spin-Orbit Torque Efficiencies from W/ferromagntic and W/ferrimagnetic Heterostructures.

T. Wang[1], C. Pai[1], H. Yen[1], T. Chen[1] and C. Wu[1]
1. Material Science and Engineering, National Taiwan University, New Taipei City, Taiwan

It has been shown that W in its resistive form possesses the largest spin-Hall ratio among all heavy transition metals, which makes it a good candidate for generating efficient dampinglike spin-orbit torque (DL-SOT) acting upon adjacent ferromagnetic or ferrimagnetic (FM) layer. Here we provide a systematic study on the spin transport properties of W/FM magnetic heterostructures with the FM layer being ferromagnetic $Co_{20}Fe_{60}B_{20}$ or ferrimagnetic $Co_{63}Tb_{37}$ with perpendicular magnetic anisotropy. The DL-SOT efficiency $|\xi_{DL}|$, which is characterized by a current-induced hysteresis loop shift method, is found to be correlated to the microstructure of W buffer layer in both $W/Co_{20}Fe_{60}B_{20}$ and $W/Co_{63}Tb_{37}$ systems. Maximum values of $|\xi_{DL}|\approx0.144$ and $|\xi_{DL}|\approx0.1$ are achieved when the W layer is partially amorphous in the $W/Co_{20}Fe_{60}B_{20}$ and $W/Co_{63}Tb_{37}$ heterostructures, respectively. Our results suggest that the spin Hall effect from resistive phase of W can be utilized to effectively control both ferromagnetic and ferrimagnetic layers through a DL-SOT mechanism.

[1] M. I. Dyakonov and V. I. Perel, Physics Letters A 35, 459 (1971). [2] J. E. Hirsch, Physical Review Letters 83, 1834 (1999). [3] S. F. Zhang, Physical Review Letters 85, 393 (2000). [4] L. Q. Liu, T. Moriyama, D. C. Ralph, and R. A. Buhrman, Physical Review Letters 106, 036601 (2011). [5] L. Q. Liu, C.-F. Pai, Y. Li, H. W. Tseng, D. C. Ralph, and R. A. Buhrman, Science 336, 555 (2012). [6] C.-F. Pai, L. Q. Liu, Y. Li, H. W. Tseng, D. C. Ralph, and R. A. Buhrman, Applied Physics Letters 101, 122404 (2012). [7] I. M. Miron, K. Garello, G. Gaudin, P. J. Zermatten, M. V., Costache, Stéphane Auffret, Sebastien Bandiera, Bernard Rodmacq, Alain Schuhl, and P. Gambardella, Nature 476, 189 (2011). [8] K. S. Ryu, L. Thomas, S. H. Yang, and S. Parkin, Nature Nanotechnology 8, 527 (2013). [9] S. Emori, U. Bauer, S. M. Ahn, E. Martinez, and G. S. D. Beach, Nature Materials 12, 611 (2013). [10] V. E. Demidov, S. Urazhdin, H. Ulrichs, V. Tiberkevich, A. Slavin, D. Baither, G. Schmitz, and S. O. Demokritov, Nature Materials 11, 1028 (2012). [11] L. Q. Liu, C.-F. Pai, D. C. Ralph, and R. A. Buhrman, Physical Review Letters 109, 186602 (2012). [12] C. F. Pai, Y. X. Ou, L. H. Vilela-Leao, D. C. Ralph, and R. A. Buhrman, Physical Review B 92, 064426 (2015). [13] W. Zhang, W. Han, X. Jiang, S.-H. Yang, and S. S. P. Parkin, Nature Physics 11, 496 (2015). [14] A. Brataas, Y. V. Nazarov, and G. E. W. Bauer, Physical Review Letters 84, 2481 (2000). [15] K. Xia, P. J. Kelly, G. E. W. Bauer, A. Brataas, and I. Turek, Physical Review B 65, 220401 (2002). [16] J. C. Slonczewski, Journal of Magnetism and Magnetic Materials 159, L1 (1996). [17] J. Sinova, S. O. Valenzuela, J. Wunderlich, C. H. Back, and T. Jungwirth, Reviews of Modern Physics 87, 1213 (2015). [18] Q. Hao and G. Xiao, Physical Review Applied 3, 034009 (2015). [19] Q. Hao, W. Chen, and G. Xiao, Applied Physics Letters 106, 182403 (2015). [20] C.-F. Pai, M. H. Nguyen, C. Belvin, L. H. Vilela-Leao, D. C. Ralph, and R. A. Buhrman, Applied Physics Letters 104, 082407 (2014). [21] H. L. Wang, C. H. Du, Y. Pu, R. Adur, P. C. Hammel, and F. Y. Yang, Physical Review Letters 112, 197201 (2014). [22] J. Liu, T. Ohkubo, S. Mitani, K. Hono, and M. Hayashi, Applied Physics Letters 107, 232408 (2015). [23] S. Cho, S. H. C. Baek, K. D. Lee, Y. Jo, and B. G. Park, Scientific Reports 5, 14668 (2015). [24] J. Kim, P. Sheng, S. Takahashi, S. Mitani, and M. Hayashi, Physical Review Letters 116, 097201 (2016). [25] O. M. J. van't Erve, A. T. Hanbicki, K. M. McCreary, C. H. Li, and B. T. Jonker, Appl. Phys. Lett. 104, 172402 (2014). [26] S. Mondal, S. Choudhury, N. Jha, A. Ganguly, J. Sinha, and A. Barman, Phys. Rev. B 96, 054414 (2017). [27] C. F. Pai, M. Mann, A. J. Tan, and G. S. D. Beach, Physical Review B 93, 144409 (2016). [28] D. D. Djayaprawira, K. Tsunekawa, M. Nagai, H. Maehara, S. Yamagata, N. Watanabe, S. Yuasa, Y. Suzuki, and K. Ando, Appl. Phys. Lett. 86, 092502 (2005). [29] S. Ikeda, K. Miura, H. Yamamoto, K. Mizunuma, H. D. Gan, M. Endo, S. Kanai, J. Hayakawa, F. Matsukura, and H. Ohno, Nature Materials 9, 721 (2010). [30] M. Cubukcu, O. Boulle, M. Drouard, K. Garello, C. O. Avci, I. M. Miron, J. Langer, B. Ocker, P. Gambardella, and G. Gaudin, Applied Physics Letters 104, 042406 (2014). [31] J. Finley and L. Liu, Physical Review Applied 6, 054001 (2016). [32] K. Ueda, M. Mann, P. W. P. de Brouwer, D. Bono, and G. S. D. Beach, Phys. Rev. B 96, 064410 (2017). [33] R. Mishra, J. W. Yu, X. P. Qiu, M. Motapothula, T. Venkatesan, and H. Yang, Phys. Rev. Lett. 118, 167201 (2017). [34] Y. X. Ou, D. C. Ralph, and R. A. Buhrman, Appl. Phys. Lett. 110, 192403 (2017). [35] P. Hansen, C. Clausen, G. Much, M. Rosenkranz, and K. Witter, J Appl Phys 66, 756 (1989). [36] K. Ueda, M. Mann, C.-F. Pai, A.-J. Tan, and G. S. D. Beach, Applied Physics Letters 109, 232403 (2016). [37] S. Yuasa, Y. Suzuki, T. Katayama, and K. Ando, Appl. Phys. Lett. 87, 242503 (2005). [38] T. Miyajima, T. Ibusuki, S. Umehara, M. Sato, S. Eguchi, M. Tsukada, and Y. Kataoka, Appl. Phys. Lett. 94, 122501 (2009). [39] O. J. Lee, L. Q. Liu, C. F. Pai, Y. Li, H. W. Tseng, P. G. Gowtham, J. P. Park, D. C. Ralph, and R. A. Buhrman, Physical Review B 89, 024418 (2014). [40] S. Emori, E. Martinez, K. J. Lee, H. W. Lee, U. Bauer, S. M. Ahn, P. Agrawal, D. C. Bono, and G. S. D. Beach, Physical Review B 90, 184427 (2014). [41] A. Thiaville, S. Rohart, E. Jue, V. Cros, and A. Fert, Europhys. Lett. 100, 57002 (2012). [42] J. H. Han, A. Richardella, S. A. Siddiqui, J. Finley, N. Samarth, and L. Q. Liu, Phys. Rev. Lett. 119, 077702 (2017).

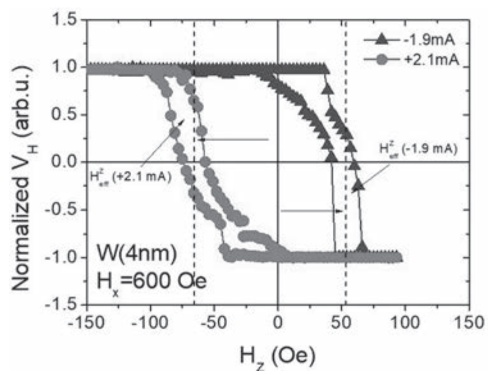

Fig. 1. Representative shifted Hall voltage loops from a W(4)/Co-Fe-B(1.4) sample with different DC currents DC I and an in-plane bias field H_x = 600 Oe.

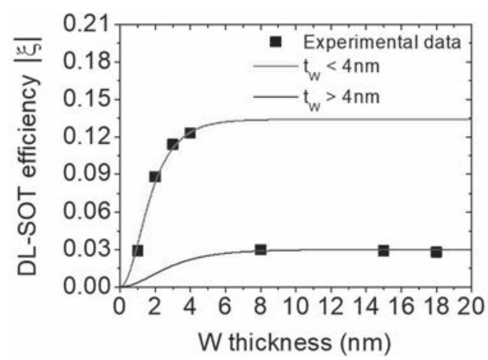

Fig. 2. The magnitude of DL-SOT efficiency $|\xi_{DL}|$ of W/CoFeB magnetic heterostructures as functions of W thickness (t_w).

10:45

AD-07. All-Optical Measurements of Spin Hall Angles in Tungsten and Tantalum.

S. Mondal[1], S. Choudhury[1], J. Sinha[1] and A. Barman[1]
1. S. N. Bose National Centre for Basic Sciences, Kolkata, India

The quest to find an energy efficient alternative to charge-current based magnetic memory devices has led the scientific community to exploit spin current driven phenomena. The generation and manipulation of pure current is a hot topic and spin Hall effect (SHE) is one of the most efficient means to achieve this. Various methods have been developed to determine the conversion efficiency from charge current to spin current, the so-called spin Hall angle (SHA) but there remain large discrepancies between the values of SHA determined by those methods even for a well studied heavy metal (HM), Pt. Recently we developed a novel all-optical method to determine the SHA in HM and demonstrated a large value of about 0.11 in Pt [1]. Here, we have extended this method to determine the SHA for two important HMs, namely, Tungsten (W) and Tantalum (Ta) [1, 2]. In this method, the spin current (J_s) generated by the change current in a HM layer exerts a damping-like spin torque in an adjacent ferromagnetic (FM) layer in HM/FM/Oxide heterostructure. Using an all-optical time resolved magneto optical Kerr effect (TR-MOKE) technique, we measure the modulation of Gilbert damping (MOD) of the FM layer (see fig.1 (a)). Here, we first investigate the thickness (t) dependence of SHA in tungsten (W) in sputter deposited Substrate/W(t)/CoFeB(3nm)/SiO_2(2nm) heterostructures (t = 2, 3, 4, 5, 6, 7 nm) by applying charge current through chromium/gold contact electrodes. The ultrafast magnetization dynamics is measured in polar Kerr geometry using pump pulse (λ = 400 nm, pulsewidth = 100 fs, spot diameter ~ 800 nm) with 10 mJ/cm^2 fluence and probe pulse (λ = 800 nm, pulsewidth = 80 fs, spot diameter ~1μm) with 2 mJ/cm^2 fluence. The time dependent magneto-optical Kerr rotation was measured in presence of a constant bias field and with varying charge current. We observe a linear variation of effective damping (up to ±15%) with applied charge current density (J_c) from which the SHA is derived [2]. A nonmonotonic variation of SHA with W layer thickness is observed which shows sudden reduction to a very low value for t < 3 nm and t > 5 nm. SHA attains maximum value of 0.40 ± 0.04 at t = 3 nm as shown in fig. 1 (b), which is one of the highest reported values to date. A transition from β-phase to α-phase of W and the corresponding change in resistivity is found to be responsible for the variation of SHA [3] with thickness for 3 nm ≤ t ≤ 7 nm, while for t = 2 nm the W layer is below its spin diffusion length, which may cause backflow of the spin current to the W layer and underestimation of MOD and SHA. Next, we have performed a comparative study between the SHA of W and Ta by varying the thickness of Ta (t = 3 nm to 20 nm). Within β phase of Ta, SHA is found to be almost constant around 0.13 ± 0.03, which is much lower than the highest SHA observed in W [4]. Simultaneously, we observe substantial redshift in the precessioanl frequency with J_c for all the heterostructures which is attributed to the contribution from Joule heating and field-like torque [1, 2]. Our findings can promote heavy metal based magnetic heterostructures to be suitable candidate for future spintronics devices. At the same time, the study of modulation of damping in CoFeB layer having important for development of MTJ-based magnetic switching devices. We acknowledge the financial assistance from the Department of Science and Technology Government of India (Grant No. SR/NM/NS-09/2011) and S. N. Bose National Centre for Basic Sciences (Project No. SNB/AB/12-13/96). S.M. acknowledges DST under the INSPIRE scheme and S.C. acknowledges support from the S. N. Bose National Centre for Basic Sciences.

1. A. Ganguly *et al.*, Appl. Phys. Lett., 105, 112409 (2014). 2. S. Mondal *et al.*, Phys. Rev. B, 96, 054414 (2017). 3. C. F. Pai *et al.*, Appl. Phys. Lett., 101, 122404 (2012). 4. L. Liu *et al.*, Science, 336, 555 (2012).

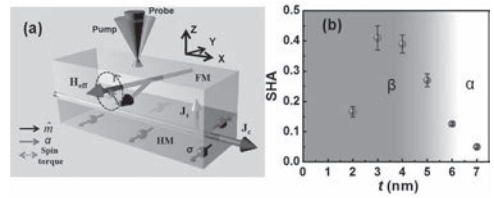

Fig. 1. (a) Schematic of sample and illustration of experimental geometry. (b) Variation of SHA with W layer thickness across the phase transition regime.

11:00

AD-08. Demonstration of unidirectional spin Hall magnetoresistance by using naturally oxidized Cu.

G. Okano[1] and Y. Nozaki[1,2]
1. Department of Physics, Keio University, Yokohama, Japan; 2. Center for Spintronics Research Network, Keio University, Yokohama, Japan

Bilayer systems consisting of a ferromagnet (FM) and a heavy metal (HM) have been widely used to investigate a variety of spin-dependent transport phenomena. Recently, the unidirectional spin Hall magnetoresistance (USMR) was reported in NiFe/Pt and Co/Pt bilayer systems [1,2]. As schematically shown in Fig. 1, the USMR shows a unidirectional change in the electrical resistance with respect to an angle θ between an electrical current and a magnetization of FM, although a uniaxial variation was observed in the ordinary SMR. In the ordinary SMR, both the spin Hall effect (SHE) and the inverse spin Hall effect (ISHE) in HM are essential. When an electric current is applied to the FM/HM bilayer, a spin accumulation appears at the interface between FM and HM which produces a spin current (SC) in the bilayer. It is noted that, as schematically shown in Fig. 1(a), the amount of the backflow of the SC depends on a relative orientation of spin angular momentum of the SC with respect to the magnetization of FM which leads to the uniaxial change in electrical resistance. On the contrary, it is theoretically suggested that the USMR is attributable to a spin polarization dependence of both an electron mobility and a density of electrons in the FM [3]. The latter can be modulated by a spin accumulation and causes the change of the electrical resistance of the FM. Thus, unlike the ordinary SMR [4], the ISHE in HM does not contribute to the USMR. In this study, we demonstrated the USMR without using HMs, such as Pt, Ta or W, which is significant to verify that the mechanism of USMR is totally different from the ordinary SMR. Recently, it was experimentally reported that a naturally oxidized Cu can generate a SC similarly to HMs with large SOI [5]. Hence, the SC generated by the naturally oxidized Cu enables us to exclude not only the effect of the ISHE but also other effects owing to large SOI of HMs. Figure 2(a) shows the experimental setup with the SEM image of the sample. Four bilayers were prepared, Sample 1: Pt(10)/NiFe(5)/Sub., Sample 2: NiFe(5)/Pt(10)/Sub., Sample 3: Cu(10)/NiFe(5)/Sub. and Sample 4: NiFe(5)/Cu(10)/Sub. (All thicknesses are in nm.) All bilayers were patterned into 8 μm wide and 20 μm long rectangles. On each bilayer, electrodes with 8 terminals composed of Au(20)/Ti(3) were fabricated to measure 1st and 2nd harmonic components of the resistances (R^{1f} and R^{2f}) of the bilayers, which enables us to evaluate the AMR and USMR, respectively. It is also noted that a coplanar waveguide (CPW) composed of Au(100)/Ti(3) was deposited on the rectangle with insulating SiO_2(120) to demonstrate the spin pumping (SP) and successive ISHE detection. A continuous alternating current with a frequency of 137 Hz was applied to the bilayers and both R^{1f} and R^{2f} were measured using a lock-in amplifier. An external magnetic field in the range from 300 to −300 mT was applied along θ direction from the long axis of the rectangle. It is noted that the values of R^{2f}/R^{1f} were averaged in the field range from –300 to –200 mT for the evaluation of the USMR. Figure 2(b) shows the θ dependence of the USMR. The USMR in Sample 1 and 2 show sinθ dependence although the sign of USMR is opposite because SCs with opposite spin polarization were injected into the NiFe layer. The signs and amplitudes of the USMR (approximately 0.3×10^{-5}) were similar to those reported previously [1]. In Sample 4, the USMR signal was not observed similarly reported for Co/Cu/Sub. in Ref. [2]. Namely, the USMR does not appear when the nonmagnetic metal adjacent to FM has weak SOI. In Sample 3 which also consist of NiFe and Cu with weak SOI but the stacking order is different from Sample 4, the USMR shows clear sinθ dependence and the sign is always positive. The result is similar to Ref.[5] which shows that SCs generated in a naturally oxidized Cu has same polarization with those generated in Pt. The electric current J dependence of the USMR was also measured as shown in Fig. 2(c) and the absolute values of the USMR linearly increase with J in all samples except Sample 4. It is noted that Figs. 2(b) and 2(c) which show that the amount of the USMR is proportional to $J\sin\theta$ are the clear evidences that the USMR appears in Cu(10)/NiFe(5)/Sub. Furthermore, from the spin pumping and successive ISHE experiment, we also confirmed that the naturally oxidized Cu in Sample 3 does not convert SCs into charge currents. Namely the ISHE does not occur in the naturally oxidized Cu. The result suggests that the SC generation in the naturally oxidized Cu is not attributed to the SHE. In summary, we have demonstrated that, unlike the ordinary SMR, the USMR does not require SHE nor ISHE because Cu/NiFe/Sub. bilayer which does not consist of a strong SOI material shows the clear USMR although further experiment must be required to clarify the physical origin for the SC generation in the naturally oxidized Cu.

[1] C. O. Avic, K. Garello, A. Ghosh, M. Gabureac, S. F. Alvarado, and P. Gambardella, Nat. Phys. 3356 (2015) [2] C. O. Avci, K. Garello, J. Mendil, A. Ghosh, N. Blasakis, M. Gabureac, M. Trassin, M. Fiebig, and P. Gambardella, Appl. Phys. Lett. 107, 192405 (2015). [3] S. S. L. Zhang and G. Vignale, Phys. Rev. B 94, 140411 (2016) [4] H. Nakayama, M. Althammer, Y. T. Chen, K. Uchida, Y. Kajiwara, D. Kikuchi, T. Ohtani, S. Geprägs, M. Opel, S. Takahashi, R. Gross, G. E. W. Bauer, S. T. B. Goennenwein, and E. Saitoh, Phys. Rev. Lett. 110, 206601 (2013). [5] H. An, Y. Kageyama, Y. Kanno, N. Enishi, and K. Ando, Nat. Commun. 13069 (2016)

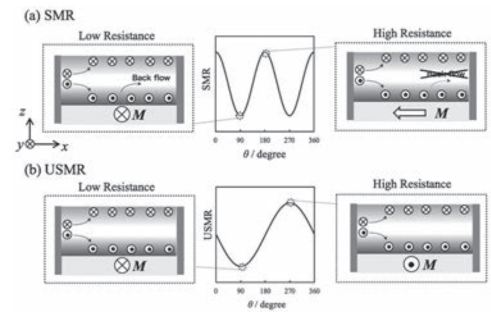

Fig. 1. Schematic illustrations of (a) ordinary SMR and (b) USMR.

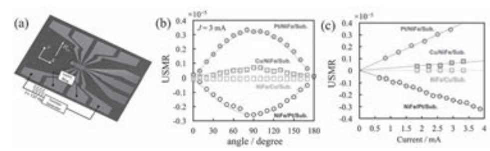

Fig. 2. (a) Scanning electron micrograph of sample and experimental setup. (b) θ and (c) J dependences of USMR.

11:15

AD-09. Dzyaloshinskii-Moriya interaction and spin-orbit torques for controlling skyrmions in Co-based trilayers.

J. Hanke[1,2], F. Freimuth[2], S. Bluegel[2] and Y. Mokrousov[2]
1. Institut fur Physik, Johannes Gutenberg University, Mainz, Germany;
2. Peter Grunberg Institut and Institute for Advanced Simulation, Forschungszentrum Julich, Juelich, Germany

Originating from the interplay of spin-orbit coupling and broken spatial inversion symmetry, the antisymmetric exchange interaction, also known as Dzyaloshinskii-Moriya interaction (DMI), attracts ever-growing attention as it mediates the formation of fascinating chiral spin textures that are perceived to be of great technological relevance, *e.g.*, for future memory devices. Recently, the interfacial DMI was shown to be tunable in magnetic heterostructures of Co sandwiched between different heavy transition metals such as Pt and Ir, heralding bright prospects for the observation of small magnetic skyrmions at room temperature [1-3]. In this context, the phenomenon of current-induced spin-orbit torques (SOTs) can be envisaged to provide a particularly efficient means for controlling and manipulating the dynamical properties of such chiral nano-scale objects. Remarkably, electrically driven switching of the magnetization due to SOTs in inversion-asymmetric crystals has been demonstrated in single ferromagnetic layers [4] and even in antiferromagnets [5]. In *ab initio* calculations of the electronic structure, the antisymmetric exchange interaction stabilizing chiral skyrmions is typically obtained either from demanding computational frameworks associated with non-collinear spin spirals, or by adopting restrictive approximations for the magnitude of the spin-orbit interaction. In sharp contrast, we present here an advanced Wannier interpolation scheme [6] that enables us to evaluate the DMI in its efficient Berry phase theory [7] based on the ferromagnetic state including the full spin-orbit interaction self-consistently. Applying this technique to the ferromagnetic trilayers $Ir_{\delta}Pt_{1-\delta}$/Co/Pt and $Au_{\gamma}Pt_{1-\gamma}$/Co/Pt, we correlate the microscopic origin of the DMI and the intimately related SOTs with the first-principles electronic structure [6]. Strikingly, we find that the DMI changes sign when we tune the composition ratio in the heterostructures, which promotes the corresponding systems as promising candidates for detailed experimental studies of the antisymmetric exchange interaction. While the DMI is nearly isotropic with respect to the orientation of the ferromagnetic Co moments, the current-induced antidamping torques in clean Ir/Co/Pt reveal a particularly pronounced dependence on the magnetization direction according to our density functional theory calculations. Finally, we elucidate how the obtained anisotropy of fieldlike and antidamping SOTs imprints on the general control and manipulation of the dynamical properties of chiral nano-scale skyrmions in Co-based trilayers. We gratefully acknowledge funding from the German Research Foundation (DFG) under Grant No. MO 1731/5-1 as well as from the EU Horizon 2020 research and innovation programme under grant agreement number 665095 (FET-Open project MAGicSky).

[1] Hrabec, A. et al. Phys. Rev. B 90, 020402 (2014). [2] Moreau-Luchaire, C. et al. Nat. Nanotechnol. 11, 444-448 (2016). [3] Yang, H. et al., Phys. Rev. Lett. 115, 267210 (2015). [4] Miron, I. M. et al. Nature 476, 189-193 (2011). [5] Wadley, P. et al. Science 351, 587-590 (2016). [6] Hanke, J.-P. *et al.* arXiv:1711.02657 (accepted in J. Phys. Soc. Jpn.). [7] Freimuth, F. *et al.* J. Phys. Condens. Matter 26, 104202 (2014).

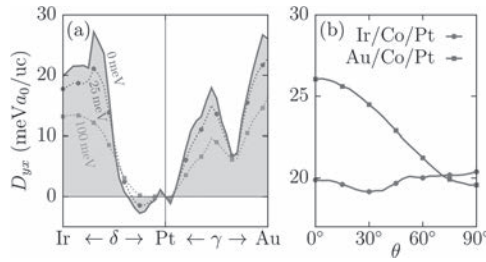

Fig. 1. Dzyaloshinskii-Moriya interaction (DMI) in the Co-based trilayers $Ir_{\delta}Pt_{1-\delta}$/Co/Pt and $Au_{\gamma}Pt_{1-\gamma}$/Co/Pt. (a) If the overlayer composition varies from Ir over Pt to Au, the DMI as characterized by the spiralization D_{yx} reveals a complex behavior with characteristic sign changes. In addition to the solid line indicating the clean limit, we show as dotted lines results for the disordered case modeled by a constant broadening of the energy bands by 25 meV and 100 meV, respectively. (b) Dependence of the DMI on the magnetization direction m=(sinθ, 0, cosθ) in Ir/Co/Pt and Au/Co/Pt, where the z-axis is perpendicular to the film plane. The spiralization is given in units of meVa_0/uc, where a_0 is Bohr's radius and "uc" refers to the in-plane unit cell.

11:30

AD-10. Spin-orbit effective fields in CoTb single layer.

L. Liu[1], J. Deng[1], J. Yu[1], C. Zhou[1] and J. Chen[1]
1. Materials Science and Engineering, National University of Singapore, Singapore

Recently current-induced spin-orbit torque (SOT) has been widely investigated in nonmagnet /ferromagnet (NM/FM) bilayer structures in order to achieve lower power consumption in scalable memory devices. The SOT exerted on the FM layer was considered to arise from the spin Hall effect (SHE) in the NM and/or the Rashba effect at the interfaces. For the former case, the critical switching current density (J_c) increases with increasing thickness (t_{FM}) of the FM layer, while for the later case, an ultra-thin FM layer is necessary to maintain the structure inversion asymmetry (SIA). SOT was also studied in magnetic single layers[1, 2] where there is non-centrosymmetric space group (bulk inversion asymmetry, BIA) or non-centrosymmetric site point group (local structure inversion asymmetry) in their crystal structure[3]. Because the SOT induced effective fields are uniformly distributed in magnetic layer, the switching current density is assumed to be independent of the thickness. More importantly, because the carrier spins are exchange coupled to the local magnetic moments which produces a direct SOT without involving any spin transfer, the SOT efficiency should be higher than that in the NM/FM bilayer structures. Until now, the observed SOT in single magnetic layer is focusing on magnetic semiconductors[1] or antiferromagnetic metals[2] with in-plane magnetic anisotropy. The SOT in magnetic single layer with perpendicular anisotropy has not been observed. In our study, we grow 20 nm CoTb thin films with bulk perpendicular magnetic anisotropy (PMA) and observe very large spin-orbit effecitve fields from Harmonic Hall measurement. Since there is no extra heavy metal layer to act as spin Hall source and the thickness of CoTb single layer is thick enough to eliminate the Rashba effect from the interfaces, we suggest these effective fields originate from the bulk especially from Tb, which is evidenced by recent report that rare-earth thin films can generate spin Hall torque[5]. The spin torque efficencies 100 Oe/(10^7 A/cm^2) and 140 Oe/ (10^7 A/cm^2) for 20 nm $Co_{89}Tb_{11}$ and 20 nm $Co_{81}Tb_{19}$ single layers are serveral time larger than that of NM/FM bilyer structures. In order to verify our observation, we develope a “pulsed AHE“ technique to esitimate the out-of-plane (OOP) effective field (H_z) of 20 nm $Co_{89}Tb_{11}$ thin film. By measuring the anomalous Hall effect under different in-plane electrical current pulse with certain pulse widths, we eliminate the Joule heating and obtain the spin torque efficiency of OOP effective filed (H_z/J_e) to be 105 Oe/(10^7 A/cm^2), which is close to in-plane spin torque efficiency calculated from Harmonics Hall measurement. The large spin orbit torque observed in CoTb single layer may open a way to explore the rich spin orbit physics in metallic alloy with bulk PMA. The direct coupling between the carrier spin and local magnetic moments in CoTb alloy may makes it possible to manupinate the magenetization by electrical current. Although the mechnism is still unclear, its potential in appliation is promising.

1. Chernyshov A, Overby M, Liu X, Furdyna JK, Lyanda-Geller Y, Rokhinson LP. Evidence for reversible control of magnetization in a ferromagnetic material by means of spin-orbit magnetic field. *Nat Phys* 2009, 5(9): 656-659. 2. Wadley P, Howells B, Zelezny J, Andrews C, Hills V, Campion RP, et al. Electrical switching of an antiferromagnet. *Science* 2016, 351(6273): 587. 3. Zhang X, Liu Q, Luo J-W, Freeman AJ, Zunger A. Hidden spin polarization in inversion-symmetric bulk crystals. *Nat Phys* 2014, 10(5): 387-393. 4. Reynolds N, Jadaun P, Heron JT, Jermain CL, Gibbons J, Collette R, et al. Spin Hall torques generated by rare-earth thin films. *Physical Review B* 2017, 95(6): 064412.

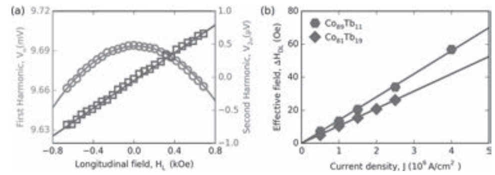

Fig. 1. Harmonic Hall measurement to characterize effecitve magnetic fields induced by SOT. (a) First and second harmonic signals for a 20 nm $Co_{89}Tb_{11}$ alloy film. (b) Calculated effective fields at different current densities for $Co_{89}Tb_{11}$ and $Co_{81}Tb_{19}$ films.

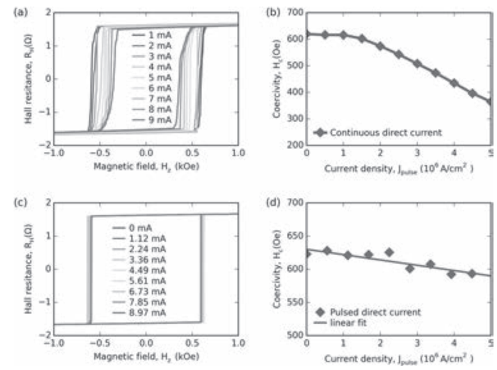

Fig. 2. Pulsed AHE measurement of out of plane effective field. (a) R_H-H_Z loops of 20 nm $Co_{89}Tb_{11}$ film for different continous electrical current. Each Hall resistance value is measured with nano-volt meter. (b) Coercive field H_c as a function of current density for the continous current method. (c) R_H-H_Z loops of 20 nm $Co_{89}Tb_{11}$ film for different electrical current pulses with 200 ns pulse width. Each Hall resistance value is measured with lock-in, 6 seconds after the applying of current pulse, to ensure a equilibrium magnetic state. (d) Coercive field H_c as a function of current density for the pulsed current method.

11:45

AD-11. Chiral magnetization switching induced by spin orbit torque in Pt/Co/Ta structure.

S. Li[1] and W. Lew[1]
1. School of Physics and Physical Science, Nanyang Technological University, Singapore, Singapore

Spin-orbit torque (SOT) has attracted extensive attention as an efficient method of controlling the magnetization of multilayered magnetic structures[1]. To realize SOT-induced magnetization switching in the structure with perpendicular magnetic anisotropy (PMA), an external in-plane magnetic field is required to break the symmetry along the current direction[2]. The chiral magnetization switching behavior as a result of opposite applied field direction when the applied field is sufficiently large has been widely reported[2-5]. However, the SOT switching behavior under a small applied field is remained unclear. In this work, we investigated the SOT-induced magnetization switching behaviors in Pt/Co/Ta structure under the influence of external magnetic fields. The structure consisting of a thin Co layer sandwiched by Pt and Ta has an enhanced SOT, due to the opposite sign of spin Hall angle in Pt and Ta[6]. The characterized effective fields were found to be ~ 162 Oe per 10^{11} A/m^2 for the damping-like term and ~ 108 Oe per 10^{11} A/m^2 for the field-like term. SOT-induced magnetization switching was detected by measuring the Hall resistance using a sweeping DC current with a fixed longitudinal field H_x. The measurements were performed with up and down initial magnetized states under both positive and negative H_x, respectively. For each configuration, the measurement was repeated using different current sweeping directions, from -10 mA to +10 mA to -10 mA and from +10 mA to -10 mA to +10 mA. It is found that SOT-induced switching can be achieved under a field $H_x \geq 500$ Oe. The switching behaviors are influenced by all the directions of the field, the initial magnetization and the current sweeping when $H_x = 500$ Oe. When $H_x > 1$ kOe, the switching behavior is only dependent on the field direction. Figure 1 shows the experimental results under $H_x = \pm 500$ Oe. For $H_x = +500$ Oe, the down initial magnetization and current sweeping from +10 mA to -10 mA to +10 mA configuration result in different switching behavior. For $H_x = -500$ Oe, a different switching behavior happened in the configuration of up initial magnetization and current sweeping from +10 mA to -10 mA to +10 mA. When the applied H_x increased to 1 kOe, the same switching behaviors were obtained for $H_x = +1$ kOe and $H_x = -1$ kOe, respectively. As shown in Fig. 2, the opposite switching loops were obtained due to the direction of the applied fields.

1. Katine, J. A., Albert, F. J., Buhrman, R. A., Myers, E. B. & Ralph, D. C. Current-driven magnetization reversal and spin-wave excitations in Co /Cu /Co pillars. *Phys. Rev. Lett.* 84, 3149 (2000). 2. Liu, L. Q., Lee, O. J., Gudmundsen, T. J., Ralph, D. C. & Buhrman, R. A. Current-Induced Switching of Perpendicularly Magnetized Magnetic Layers Using Spin Torque from the Spin Hall Effect. *Phys. Rev. Lett.* 109, 096602 (2012). 3. Liu, L.Q., Pai, C.-F., Li, Y., Tseng, H. W., Ralph, D. C. & Buhrman R. A. Spin-Torque Switching with the Giant Spin Hall Effect of Tantalum. *Science* 336, 555 (2012). 4. Cao, J. W., *et. al*., Spin-orbit torque induced magnetization switching in Ta/$Co_{20}Fe_{60}B_{20}$/MgO structures under small in-plane magnetic fields. *Appl. Phys. Lett.* 108, 172404 (2016). 5. Zhang, C., Fukami, S., Sato, H., Matsukura, F. & Ohno, H. Spin-orbit torque induced magnetization switching in nano-scale Ta/CoFeB/MgO. *Appl. Phys. Lett.* 107, 012401 (2015); 6. Woo, S., Mann, M., Tan, A. J., Caretta, L., Beach & G. S. D. Enhanced spin-orbit torques in Pt/Co/Ta heterostructures. Appl. Phys. Lett. 105, 212404 (2014).

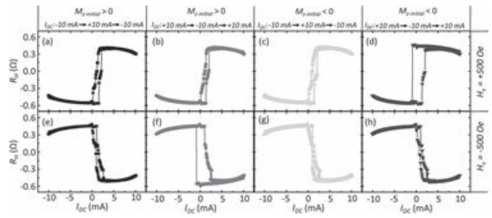

Fig. 1. The Hall resistance versus DC current at different configurations.

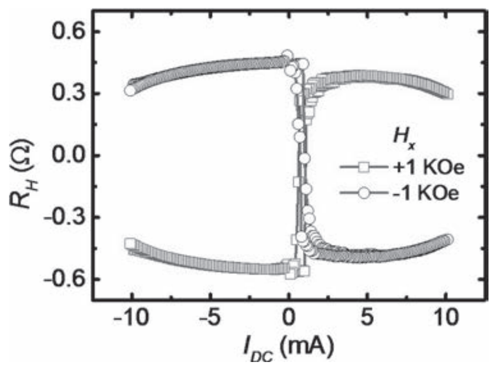

Fig. 2. The measured chiral SOT switching under a longitudinal fields of ±1 kOe.

TUESDAY MORNING, 24 APRIL 2018 ROSELLE II, 9:00 TO 12:00

Session AE
SKYRMIONS, VORTICES & MAGNETISATION DYNAMICS

Teruo Ono, Chair
Kyoto University, Uji, Japan

CONTRIBUTED PAPERS

9:00

AE-01. Modulation of chaotic nanocontact vortex oscillators.

J. Létang[1*], T. Devolder[1], S. Petit-Watelot[2], K. Bouzehouane[3], V. Cros[3] and J. Kim[1]
1. Centre de Nanosciences et de Nanotechnologies, CNRS, Université Paris-Sud, Université Paris-Saclay, Orsay, France; 2. Institut Jean Lamour, CNRS, Université de Lorraine, Vandoeuvre Lés Nancy, France; 3. Unité Mixte de Physique, CNRS, Thales, Université Paris-Sud, Université Paris-Saclay, Palaiseau, France

Spin-torque nano-oscillators (STNO) have strong potential for applications such as rf communications, microwave generation, field sensing, and neuro-inspired computing. An important aspect involves phase-locking [1] and modulation [2] due to external signals, which have been studied extensively in vortex-based systems. However, the role of vortex core reversal [3] in this context has remained largely ignored. Indeed, in nanocontact-based systems, core reversal can give rise to more complex states such as chaos [4]. Because of the sensitivity to initial conditions, chaos is potentially useful for information processing as a large number of patterns can be generated rapidly [5]. We have conducted experiments to probe how nanocontact vortex oscillators can be modulated in the chaotic state by an external signal. Such states are obtained by sweeping the applied dc electrical current or magnetic field, where transitions between different oscillation regimes can be seen as jumps in the central frequency and changes in the number of modulation sidebands, as shown in Figure 1. These different regimes correspond to how the periodicity of the vortex core reversal relates to the frequency of core gyration around the nanocontact [4]; a commensurate phase appears when the reversal rate is an integer fraction of the gyration frequency, while a chaotic state appears when this ratio is irrational. An example of the effect of external modulation is shown in Figure 2, where the power spectral density exhibits rich features due to the modulation between the external source frequency, gyration frequency, and core reversal frequency. We can explain these features with first- or second-order modulation between the three frequencies. Phase-locking is also visible between the external source frequency and internal vortex modes. We explored the phase-locking properties in both the commensurate and chaotic regimes, where chaos appears to impede phase-locking while a more standard behavior is seen in the commensurate phase. We have also conducted micromagnetics simulations with the MuMax code [5], where most of the salient features are reproduced. We also explored larger coupling strengths between the external signal and the NCVO, where different fractional regimes can be identified in Arnold tongue diagrams [6]. This allows us to quantify the role of the coupling strength on synchronization and transitions to chaos. This work was partially supported by the Agence Nationale de la Recherche (France) under Contract No. ANR-17-CE24-0008 (CHIPMuNCS).

[1] W. H. Rippard et al. *Physics Review Letters* 95, 067203 (2005) [2] M. R. Pufall et al. *Applied Physics Letters* 86, 082506 (2005) [3] B. Van Waeyenberge et al. *Nature* 444, 461-464 (2006) [4] S. Petit-Watelot et al. *Nature Physics* 8, 682-687 (2012) [5] M. Sciamanna and K. A. Shore, Nat. Photon. 9, 151 (2015) [6] A. Vansteenkiste et al. *AIP Advances* 4, 107133 (2014) [7] A. Pikovsky et al. Synchronization: *A universal concept in nonlinear science*, Cambridge University Press

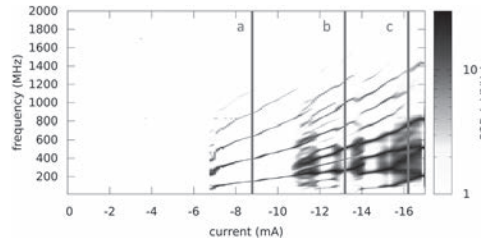

Fig. 1. Frequency vs current map of the power spectral density. On this figure is given the natural output power of the vortex according to the sent DC current. Different dynamical regimes are observed. No oscillations are observed below 6.8 mA. (a) Steady state gyration, where harmonics indicate elliptical trajectories. (b) Commensurate state, where periodic core reversal modulates the vortex gyration. (c) Chaotic state, where gyration and core reversal frequencies are incommensurate.

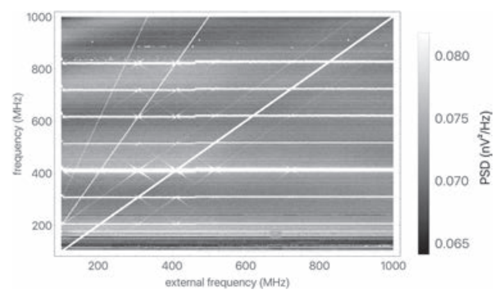

Fig. 2. Power spectral density map as a function of external frequency for an NCVO in the commensurate state. Phase-locking occurs when the external frequency is equal to gyration frequency, 3:4 and 4:3 synchronization orders. Phase-locking between core reversal and external frequencies are also visible. Crossing frequencies near synchronization regions are due to modulation between external, gyration, and core reversal frequencies. Amplitudes are qualitatively higher if signals involve gyration or external frequencies, close to a synchronization region, and for increasing external frequency sweeps.

9:15

AE-02. Magnetic vortex dynamics and frequency tunability in Cr-implanted permalloy disks.

L. Ramasubramanian[1,2], A. Kakay[1], C. Fowley[1], O. Yildirim[3], P. Matthes[4], R. Böttger[1], J. Lindner[1], J. Fassbender[5], S. Gemming[1,2], S.E. Schulz[2,4] and A. Deac[1]

1. Institute of Ion Beam Physics and Materials Research, Helmholtz-Zentrum Dresden-Rossendorf, Dresden, Germany; 2. TU Chemnitz, Chemnitz, Germany; 3. Empa-Swiss Federal Laboratories for Materials Science and Technology, Dübendorf, Switzerland; 4. Fraunhofer Institute for Electronic Nano Systems, Chemnitz, Germany; 5. Institute for Physics of Solids, TU Dresden, Dresden, Germany

The fundamental oscillation mode of magnetic vortices in thin-film elements has recently been proposed for designing spin-torque-driven nano-oscillators [1]. Commercial applications require tuning of the output frequency by external parameters, such as applied fields or spin-polarised currents. However, the tunability of vortex-based devices is limited, since the gyrotropic frequency is specific to the individual sample design. Indeed, the fundamental frequency is known to be determined by the saturation magnetisation,M_s, as well as the geometrical confinement of the magnetisation, i.e. the diameter and height of the magnetic disk [2, 3]. Micromagnetic simulations [4] have shown that if regions with different saturation magnetisation can be induced in a magnetic disk, multiple precession frequencies can be generated. We show that ion implantation [5] is a novel route to fabricate such devices. Permalloy (Py) disks of various diameters and thicknesses were prepared using electron beam lithography followed by electron beam evaporation. Individual disks were contacted by gold leads to study the interaction of spin-polarized current with the magnetic vortex. The presence of a vortex is verified by magneto optic Kerr effect (MOKE), X-ray magnetic circular dichroism (XMCD) and magnetotransport measurements. The magnetic field dependence of the vortex position can be tuned by the disk size as shown by XMCD (Figure 1 (a)). Higher magnetic stability due to larger annihilation fields can be achieved by smaller disk diameters, whereas larger field sensitivity is present in larger disks (Figure 1 (b)). Magnetotransport measurements on electrically contacted disks show the presence of anisotropic magnetoresistance (AMR) in different disks with varying thickness (Figure 1 (c)). Using a conventional lock-in technique, the resonance frequencies are measured for disks with different radii as shown in Figure 2 (a), with the inset showing the scanning electron microscope image of an electrically contacted disk. In order to modify the magnetisation within a single disk and to achieve two different oscillation frequencies, we implant chromium in different regions of the disk (inner and outer). Cr-implantation leads to a decrease in the Curie temperature and thus a reduction in the magnetic moment [6]. The reduction of M_s as a function of Cr fluence was optimised on extended Py films using a vibrating sample magnetometer – superconducting quantum interference device (VSM-SQUID), see figure 2 (b). A clear drop in M_s with increasing the chromium ion fluence is observed. Concentric donut-like structures were then implanted with Cr and the modification of dynamics as a function of magnetic field was investigated. An example of Cr-implantation in a 3 μm radius disk at 30 keV with a fluence of $1.2 * 10^{16}$ ions/ cm^2 is shown in Figure 2 (c). The vortex core is shifted between the two different magnetisation regions by applying an external in-plane field. The vortex nucleates in the irradiated region at – 2.281 mT, leading to a resonance frequency of 30.2 MHz (shown in orange in Figure 2 (c)). Further increasing the external field pushes the vortex core to the non-irradiated region where the resonance frequency is 42.3 MHz (shown in green), corresponding to a field of + 1.597 mT. The results show that ion implantation is a novel way to obtain multiple frequencies from a single disk. Acknowledgements: This work is supported by the Helmholtz Young Investigator Initiative Grant No. VH-N6-1048. Support of the Nanofabrication Facilities of Rossendorf at the Ion Beam Centre is gratefully acknowledged (Dr. Artur Erbe, Mr. Bernd Scheumann). We thank Dr. Shengqiang Zhou for the assistance with VSM measurements.

[1] V. S. Pribiag, et al., Nat. Phys., 3:498 (2007). [2] V. Sluka, et al., Nat. Commun., 6:6409 (2015). [3] S. Gliga, Forschungszentrum Jülich GmbH, 978-3-89336-660-6 (2009). [4] A. Kákay, unpublished. [5] J. Fassbender, et al., Phys. Rev. B 73, 184410 (2006). [6] R. M. Bozorth, Ferromagnetism, IEEE Press, 978-0-7803-1032-2 (1978).

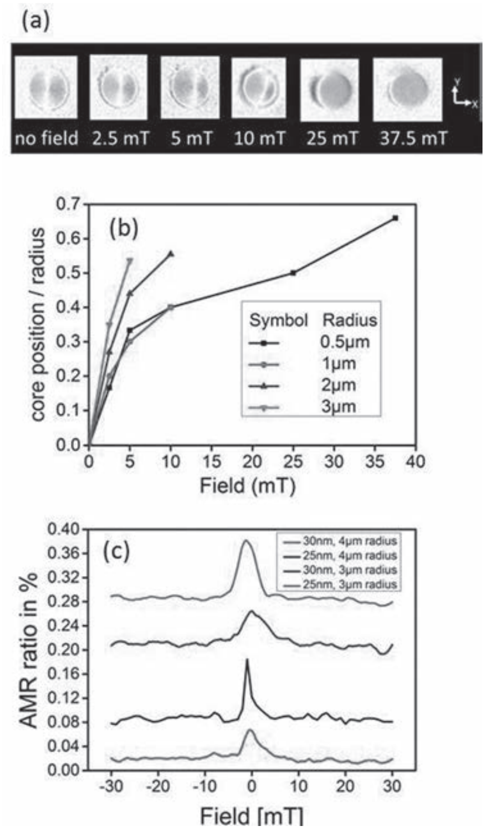

Fig. 1. (a) XMCD images showing the in-plane magnetisation direction with field applied in the Y direction for a 1 μm radius, 30 nm thick permalloy disk, (b) Normalised core position as a function of magnetic field for 30 nm thick permalloy disks derived from the XMCD experiment and (c) AMR ratio (change in resistance) versus applied magnetic field for different disks (curves are shifted vertically for clarity).

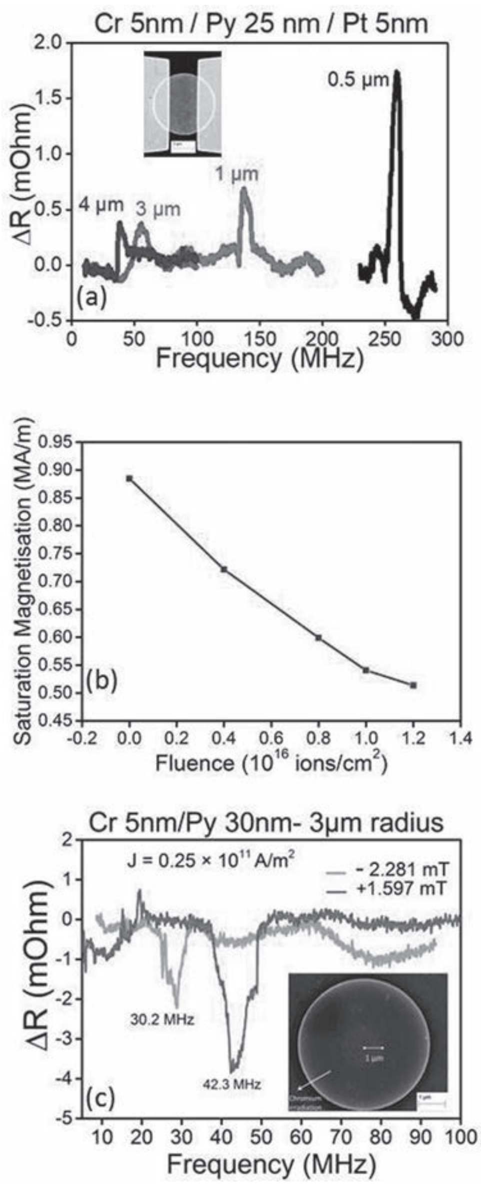

Fig. 2. (a) Electrically detected dynamics on disks with different radii (inset: SEM of electrically contacted disk), (b) Saturation magnetisation measured using VSM-SQUID on extended films of permalloy implanted with chromium ions at different fluence, (c) Modified dynamics from a 3 µm radius disk (30 nm permalloy) with chromium implanted in the outside region with a fluence of 1.2 * 10^{16} ions/ cm^2 (inset: SEM of the disk).

INVITED PAPERS

9:30

AE-03. Stability and manipulation of magnetic skyrmions.

G. Finocchio[1]
1. University of Messina, Messina, Italy

Magnetic skyrmions are topological protected solitons with a chirality that can be stabilized by the Dzyaloshinskii-Moriya interaction (DMI). Understanding the physical properties of magnetic skyrmions is important for fundamental research with the aim to develop new spintronic device paradigms where both logic and memory can be integrated at the same level or for unconventional computing. We have recently studied different mechanism of stabilization of skyrmions in confined devices, one of them needs a large DMI to introduce in the energy landscape an energetic minimum associated with a metastable skyrmion state and one that gives a skyrmion state which size depends on a trade off among magnetostatic, exchange and DMI energies. Here, we firstly show a universal model based on the micromagnetic formalism combining a proper ansatz and scaling relationships and a specific Q-d phase space (quality factor Q vs. reduced DMI d) that can be used to study skyrmion stability as a function of magnetic field and temperature. We consider ultrathin, circular ferromagnetic magnetic dots. Our results show that magnetic skyrmions with a small radius—compared to the dot radius—are always metastable, while large radius skyrmions form a stable ground state. The change of energy profile determines the weak (strong) size dependence of the metastable (stable) skyrmion as a function of temperature and/or field. We also show as this fundamental results can be used for specific application. Fig. 1 shows a racetrack memory device where the skyrmions in the track are metastable and therefore small—giving a high storage density. The skyrmions are detected under a magnetic tunnel junction (green square) with a polarized layer with a magnetization pointing along the out-of-plane direction which generates a dipolar field parallel to the skyrmion core magnetization. This field can modify the stability properties of the skyrmion in the region below the contact, moving it through the Q-d phase space. By shifting the skyrmions across the line of stability, their radius will expand significantly making it much easier to detect from the tunnel magnetoresistance signal. After leaving the detection regions, the skyrmions will return to their small size in the metastable region. The spin-Hall effect(SHE)-driven skyrmion motion is characterized by an in-plane angle, i.e. the skyrmion Hall angle (SHA)[1]. Finally, we micromagnetically report, for the first time, the SHE-driven dynamics of a breathing skyrmion. In particular, we can excite the breathing mode by applying an ac perpendicular-polarized current and we can control the SHA by an in-plane external field Hy. Our results show that the SHA depends on the SHE current only under the simultaneous presence of Hy and breathing mode[2]. Our achievements can be important for understanding the origin of the SHA current dependence when the field-like torque comes from the SHE and the breathing mode is due to temperature and/or disordered parameters[3]. These results can open a path toward the design of optimal materials for skyrmion based devices. Acknowledges The author thanks R. Tomasello, K. Y. Guslienko, A. Giordano, O. Fesenko, J. Baker, S. Chiappini, R. Zivieri, V. Puliafito, B. Azzerboni and M. Carpentieri for the support in the activities of this research.

[1] G. Chen, Nat. Phys. 13, 112 (2017). [2] G. Finocchio et al., Appl.Phys. Lett. 107, 262401 (2015). [3] J.-V. Kim and M.-W. Yoo, Appl. Phys. Lett. 110, 132404 (2017).

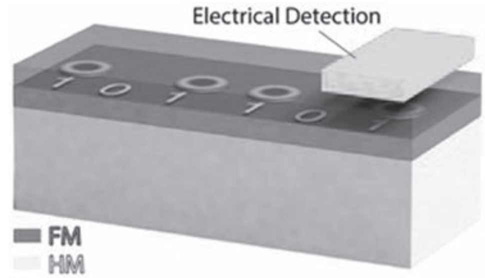

Fig. 1. Sketch of a racetrack memory device where the skyrmions (bit '1') are electrically detected below an MTJ (green square).

10:00

AE-04. Entropy-limited topological protection of skyrmions.

J. Wild[1], T. Meier[1], S. Pöllath[1], M. Kronseder[1], A. Bauer[2], A. Chacon[2], M. Halder[2], M. Schowalter[3], A. Rosenauer[3], J. Zweck[1], J. Müller[4], A. Rosch[4], C. Pfleiderer[2] and *C. Back*[1,2]
1. Universität Regensburg, Regensburg, Germany; 2. Technical University of Munich, Munich, Germany; 3. University of Bremen, Bremen, Germany; 4. University of Cologne, Köln, Germany

Chiral magnets may host skyrmion lattices, that can be equivalently described as a superposition of plane waves or lattice of particle-like topological defects. In the skyrmion hosting crystal $Fe_{0.5}Co_{0.5}Si$ we use Lorentz transmission electron microscopy (L-TEM) to investigate the energetics associated with the topological decay of magnetic skyrmions far from equilibrium. We record Field-Cooled (FC) and Zero-Field-Cooled (ZFC) phase diagrams of thinned $Fe_{0.5}Co_{0.5}Si$ single crystals using cryo L-TEM. Measurements are performed using thin $Fe_{0.5}Co_{0.5}Si$ platelets with a thickness of d =250 nm. The [110]-direction is aligned parallel to the sample normal and to the externally applied magnetic field direction. Phase diagrams are established by taking series of images as a function of magnetic field and temperature. An example phase diagram and the measurement protocol for the decay into the helical phase in zero magnetic field is shown in Fig. 1 with exemplary L-TEM images and corresponding Fourier transform data. When lowering the temperature through the skyrmion pocket for the FC case a metastable skyrmion phase extending to temperatures much below the skyrmion pocket can be achieved. Note that at low temperatures a novel skyrmion cluster phase in a conical background is found. From the metastable phase we investigate the decay time of the skyrmion lattice when increasing or decreasing the externally applied magnetic field. We observe that the life time of the skyrmions depends exponentially on temperature. The prefactor of the Arrhenius law describing the skyrmion decay changes by about 30 orders of magnitude for small changes of magnetic field reflecting a substantial reduction of the life time of skyrmions by entropic effects and thus an extreme case of enthalpy-entropy compensation. Such compensation effects, being well-known across many different scientific disciplines, affect topological transitions and thus topological protection on an unprecedented level [1].

[1] "Entropy-limited topological protection of skyrmions", J. Wild, T.N.G. Meier, S. Pöllath, M. Kronseder, A. Bauer, A. Chacon, M. Halder, M. Schowalter, A. Rosenauer, J. Zweck, J. Müller, A. Rosch, C. Pfleiderer, C.H. Back, Science Advances 3, e1701704 (2017).

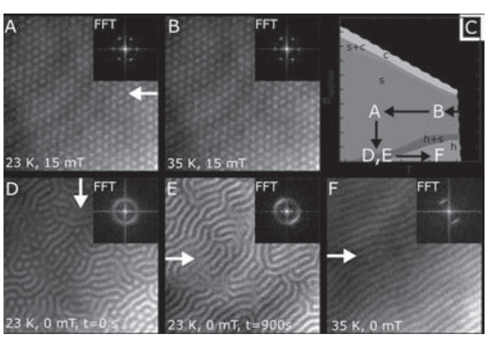

Fig. 1. Metastable phase diagram and measurements protocol with example images and Fourier transforms at positions indicated in the phase diagram.

CONTRIBUTED PAPERS

10:30

AE-05. Tunable geometrical frustration in magnonic vortex crystals.

C. Behncke[1,2], C.F. Adolff[1,2], S. Wintz[3], M. Hänze[4,5], B. Schulte[5], M. Weigand[6], S. Finizio[3], J. Raabe[3] and G. Meier[2,5]
1. Institute of Applied Physics, University of Hamburg, Hamburg, Germany; 2. The Hamburg Centre for Ultrafast Imaging, Hamburg, Germany; 3. Paul Scherrer Institut, Villigen, Switzerland; 4. Max Planck Institute for Solid State Research, Stuttgart, Germany; 5. Max Planck Institute for the Structure and Dynamics of Matter, Hamburg, Germany; 6. Max Planck Institute for Intelligent Systems, Stuttgart, Germany

Frustration is of great general interest as it gives rise to new physical phenomena, such as magnetic monopoles [1]. Frustration arises when competing interactions cannot be all satisfied at the same time [2]. We combine this research field with magnetic vortices that can be described as magnonic crystals when arranged periodically. Geometrical frustration is observed in vortex crystals that are positioned analogous to the nanoislands in artificial spin ice. The crystal properties of magnonic vortex crystals can be manipulated dynamically on the timescale of milliseconds [3]. In contrast to artificial spin ice systems, the frustration in the vortex crystals can be tuned and turned on and off at will [4]. The magnetic vortex state forms in ferromagnetic nanodisks of suitable geometry and features an in-plane curling magnetization with an out-of-plane component in the center region, the vortex core [5]. The vortex is described by two state parameters: the polarization of the core pointing either up or down and the circularity, the sense of the in-plane magnetization curling either clockwise or counter-clockwise. We study two-dimensional magnonic vortex crystals that are arranged analogous to the nanoislands in artificial kagome spin-ice (see Fig. 1(a)). Scanning transmission x-ray microscopy (STXM) measurements at the MAXYMUS microscope of the BESSY II synchrotron in Berlin, Germany and at the PolLux endstation at the SLS in Villigen, Switzerland are used to observe the vortex core motions temporally and spatially resolved. Artificial spin ice systems consist of nanoislands that are in a single domain state. The spins in the junctions of the nanoislands follow the so called ice-rule [6]. In the hexagonal kagome spin ice, a junction consists of three nanoislands. The ice rules are obeyed if all spins do not point towards or away from the junction. Since the overall spin has always a finite value, the system is frustrated. In our system, two vortices with alternating polarization are analogous to one nanoislands (Fig. 1 (b)). Thus, the hexagons consist of twelve vortices. The vortices in the pairs are in close proximity and are strongly coupled. Vortices in triple junctions at the connections of the hexagons are weaker coupled. If each vortex in the triple junction prefers an alternating polarization with each neighbor, frustration arises. For the comparison with a nanoisland in artificial spin ice, a vortex pair with alternating polarization is represented by a blue arrow pointing from a polarization of p=-1 (black dots in Fig. 1) to the vortex with a polarization of p=+1 (white dots in Fig. 1). The eight possible configurations of arrows in a junction are shown in Fig. 1(b). If the ice rule is obeyed, two arrows point into the center and one points out of it, or vice-versa. If all three arrows point in or out of the center, the ice rule is broken. An adiabatically decreasing high frequency magnetic field is used to tune the polarization configuration in the crystal. Depending on the frequency of this state formation signal, different ground states can be tuned [7]. In Fig. 2 the polarization patterns determined by the STXM measurements are shown for the whole vortex crystal. For a state formation frequency of 234 MHz (Fig. 2(a)) the strongly coupled vortex pairs always have alternating polarizations. In this situation, a vortex pair can be compared to a nanoisland of artificial spin ice systems with a certain alignment of the magnetization. The ice rule violations are marked in orange in Fig. 2(a). As in spin ice systems there is no long-range order perceptible. That means that even though a highly symmetric state might be the lowest-energy state, it is not necessarily adjusted to the crystal. The data suggest that the vortices favor an alternating polarization configuration with each of their neighbors during the state formation with a frequency of 234 MHz. As this is not possible for three vortices in a triple junction, the polarization state formation process is frustrated. It is also possible to tune a non-frustrated polarization state to the system. For a state formation frequency of 261 MHz (Fig. 2(b)) an almost complete homogeneous polarization configuration is tuned. The strongly coupled vortex pairs always have equal polarizations. There are few defects that occur at the weaker coupled triple junctions. Compared to the frustrated state a long-range order is observed. It is thus possible to change the polarization configuration from a frustrated state to a non-frustrated state and vice-versa. In the present experiments, the frustration is turned on and off within milliseconds but this can be accelerated to the nanosecond regime. This allows future studies to compare the frustrated and the non-frustrated state of an otherwise identical system to gain deeper insight into the geometrical frustration itself.

[1] E. Mengotti, L. J. Heyderman, A. F. Rodríguez, F. Nolting, R. V. Hügli, and H.-B. Braun. Real-space observation of emergent magnetic monopoles and associated Dirac strings in artificial kagome spin ice. *Nat. Phys.* 7, 68 (2011). [2] R. F. Wang, C. Nisoli, R. S. Freitas, J. Li, W. McConville, B. J. Cooley, M. S. Lund, N. Samarth, C. Leighton, V. H. Crespi, and P. Schiffer. Artificial 'spin ice' in a geometrically frustrated lattice of nanoscale ferromagnetic islands. *Nature* 439, 303 (2006). [3] C. Behncke, M. Hänze, C. F. Adolff, M. Weigand, and G. Meier. Band structure engineering of two-dimensional magnonic vortex crystals. *Phys. Rev. B* 91, 224417 (2015). [4] C. Behncke, C. F. Adolff, S. Wintz, M. Hänze, B. Schulte, M. Weigand, S. Finizio, J. Raabe, G. Meier. Tunable geometrical frustration in magnonic vortex crystals. *Sci. Rep.*, in press (2018). [5] T. Shinjo, T. Okuno, R. Hassdorf, K. Shigeto, and T. Ono. Magnetic Vortex Core Observation in Circular Dots of Permalloy. *Science* 289, 930 (2000). [6] P. W. Anderson. Ordering and Antiferromagnetism in Ferrites. *Phys. Rev.* 102, 1008 (1956). [7] C. F. Adolff, M. Hänze, A. Vogel, M. Weigand, M. Martens, and G. Meier. Self-organized state formation in magnonic vortex crystals. *Phys. Rev. B* 88, 224425 (2013).

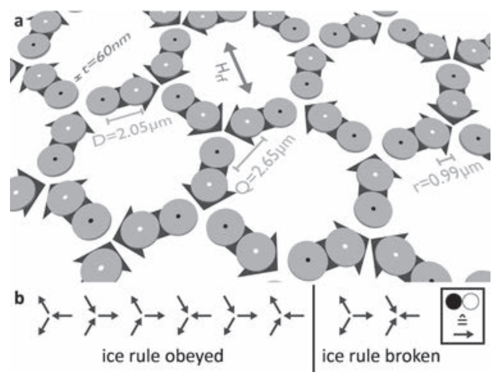

Fig. 1. (a) Schematic representation of the investigated vortex system. The black and white dots represent the polarization of the vortices. The blue arrows illustrate the analogy of two vortices with alternating polarizations to a nanoisland in artificial spin ice systems. (b) Possible configurations of six vortices in a junction depicted by blue arrows.

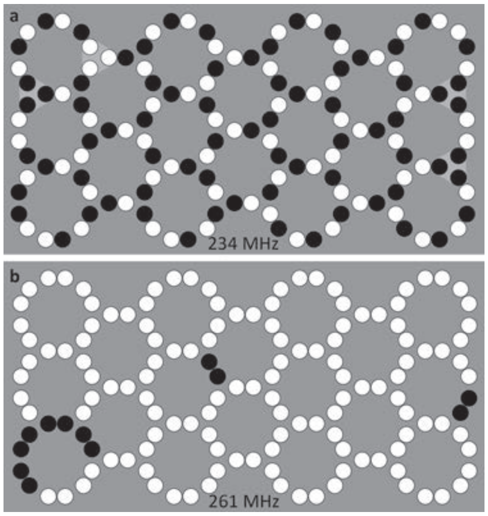

Fig. 2. Polarization patterns of the vortex crystal after state formation with a frequency of (a) 234 MHz and (b) 261 MHz. In (a) an alternating polarization of neighboring vortices is favored. Exceptions of the ice rules are highlighted in orange. In (b) homogeneous polarizations of neighboring vortices are favored.

10:45

AE-06. Static and dynamic behavior of Interlayer exchange coupled $Ni_{80}Fe_{20}$/Ru Continuous Films and Nanowires.

L. Xiong[1] and A. Adeyeye[1]
1. National University of Singapore, Singapore

INTRODUCTION Spin valve structures where two ferromagnetic (FM) thin film layers are separated by a non-magnetic (NM) spacer layer have attracted tremendous interest due to their potential applications in giant magnetoresistance (GMR)[1] based read sensors[2] and magnetic random access memory (MRAM)[3]. The magnetization of the FM layers in such a trilayer structure are coupled to each other by the interlayer exchange coupling[4] (IEC), which is strongly dependent on the thickness and material of the spacer. As the thickness of the spacer layer is varied, the IEC oscillates in sign and magnitude, known as the Ruderman-Kittel-Kasuya-Yosida (RKKY)[5] interaction, leading to either FM or antiferromagnetic (AFM) ordering of the magnetic layers. Varied coupling types and strength lead to significantly different magnetization reversal processes and dynamic responses when the structure is subjected to a microwave power excitation. It provides an interesting way to engineer the spin wave propagation and thus the ferromagnetic resonance (FMR). However, most of the works reported in the literature only focus on the trilayer structures, with little work reported on the IEC for more complex heterostructures. In this work, we explore both the static and dynamic behaviors of complex heterostructures. EXPERIMENTAL AND SIMULATION DETAILS The multilayer Ni80Fe20(Py)/Ru NWs with fixed width W = 180 nm and period P = 400 nm were fabricated over an area of 4x4 mm^2 on top of a silicon substrate for direct comparison. Corresponding continuous films (CFs) were deposited on silicon substrates at the same time. The structures are Py(10 nm)/Ru(t_{Ru})/Py(20 nm) and Py(10 nm)/Ru(t_{Ru1})/Py(10 nm)/Ru(t_{Ru2})/Py(10 nm) as shown in Fig. 1(a). The t_{Ru} is in the range of 0 to 1.5 nm and the t_{Ru1} (and t_{Ru2}) is 1 or 1.4 nm. Typical scanning electron microscope (SEM) image of the NWs is shown in Fig. 1(b). The thickness t of the wires is varied in the range from 5 to 70 nm. The collective magnetization reversal processes of the arrays were characterized at room temperature using vibrating sample magnetometer (VSM) by sweeping the magnetic field along the easy axis of the NWs. The dynamic behaviors of the NWS were investigated using broadband ferromagnetic resonance spectroscopy (FMR). In order to understand the dynamic response of the wires, micromagnetic simulations were performed using the LLG micromagnetic simulator, which computes the equilibrium magnetization distribution of the NWs based on the Landau-Lifshitz-Gilbert (LLG) equation. The resonant mode profiles were extracted using spatially and frequency-resolved Fast-Fourier-Transform (FFT) imaging method. In all the simulations, periodic boundary condition was used to mimic the wire arrays. RESULTS AND DISCUSSION In conclusion, we have investigated the static and dynamic behavior of engineered interlayer exchange coupled Py/Ru with two coupling interfaces. We demonstrate a robust control of the coupling mechanism by varying the thickness of Ru. We found that the AFM strength affects both the static and dynamic behaviors of the FM layers. We observed a strong AFM coupling when the Ru thickness is 1 nm and negligible AFM coupling when Ru thickness is 1.4 nm. By fitting the simulated hysteresis loops with the experimental results, we find that the bilinear coupling parameter J1 dominated over a negligible biquadratic J2. For $t_{Ru1} = t_{Ru2}$ = 1 nm, the extracted exchange constants are J1 = -0.2 erg/cm2 and J2 = 0. For $t_{Ru1} = t_{Ru2}$ = 1.4 nm, the extracted exchange constants are J1 = -0.02 erg/cm^2 and J2 = 0. In addition, multiple resonant modes were found for five-layer NWs at remanence due to different IEC as shown in Fig. 2(b). The resonant frequencies can be explained by the Kittel's equation: $\omega_0 = \gamma\ ([H_{app}+(N_z-N_x)4\pi M_x]\times[H_{app}+(N_y-N_x)4\pi M_x])^{1/2}$ (1) In addition, we ran simulations for further understanding of the dynamic responses.[6] There is a good qualitative agreement between the experiments and the micromagnetic simulations.

[1] P. A. Grünberg, "*Exchange anisotropy, interlayer exchange coupling and GMR in research and application*", Sens. Actuators A: Phys. 91, 153 (2001). [2] J.-G. Zhu, " *New heights for hard disk drives*", Mater. Today 6, 22 (2003). [3] B. N. Engel et al., " *A 4-Mb toggle MRAM based on a novel bit and switching method*", IEEE Trans. Magn. 41, 132 (2005). [4] M. D. Stiles, " *Interlayer exchange coupling*", J. Mag. Mag. Mat. 200, 322 (1999). [5] Y. Yafet, " *Ruderman-Kittel-Kasuya-Yosida range function of a one-dimensional free-electron gas*", Phys. Rev. B 36, 3948 (1987). [6] L. L. Xiong, and A. O. Adeyeye, "*Static and dynamic behavior of interlayer exchange coupled Ni80Fe20 /Ru continuous films and nanowires*", J. Phys. D: Appl. Phys. 51 025004 (2018).

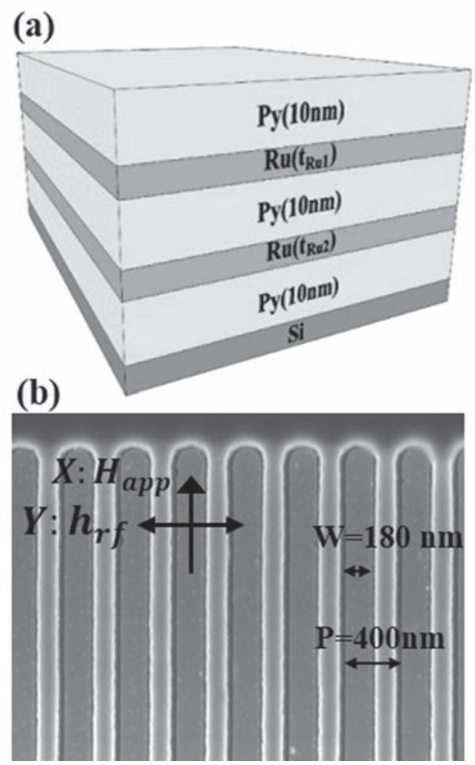

Fig. 1. (a) Sketch of five-layer structure with Py(10 nm)/Ru(t_{Ru1})/ Py(10 nm)/Ru(t_{Ru2})/Py(10 nm). (b) Typical SEM images for multilayer NWs.

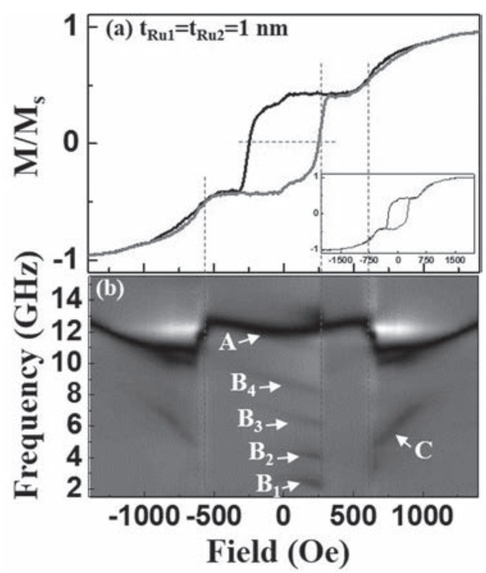

Fig. 2. (a) Experimental hysteresis loops and (b) corresponding 2D FMR spectra of the five-layer structure with $t_{Ru1} = t_{Ru2}$ = 1 nm. (The insets in (a) show the corresponding M-H loops in a field range of ± 2kOe.

INVITED PAPER

11:00

AE-07. Three-dimensional localized spin textures in chiral magnets.

H. Du[1,2] and M. Tian[1,2]
1. High Magnetic Field Laboratory of Chinese Academy of Sciences, Hefei, China; 2. Collaborative Innovation Center of Advanced Microstructures, Nanjing University, Nanjing, China

The emergence of a topologically nontrivial vortex-like magnetic structure, the magnetic skyrmion, has launched new concepts for memory devices. Extensive studies have theoretically demonstrated the ability to encode information bits by using a chain of skyrmions in confined geometries. So far it is generally assumed that skyrmion is two-dimensional (2D) localized magnetic structure. In this talk, we report experimental evidence of three-dimensional (3D) skyrmions in confined helimagnets. The 3D skyrmion will give rise lots of novel phenomena that can not be observed in 2D one. Moreover, we report the discovery of another 3D localized spin texture, termed as magnetic bobber, in chiral magnets.

[1] Du, H. F., *et al.*, *Nature Communications.*, 6, 8506 (2015) [2] Zhao X. B., and Du H. F., *et al.*, *PNAS*, 113, 4918 (2016) [3] Wang. C., and Du H. F., *et al.*, *Nano Letters* (2017) [4] Jin. C. M., and Du H. F., *et al.*, *Nature Communications.*, (2017)

CONTRIBUTED PAPERS

11:30

AE-08. Development of the New Measurement Techinque for Spin Dynamics of Magnetic Thin Films.

Y. Endo[1,2], O. Mori[3], S. Yabukami[4], R. Utsumi[3] and Y. Shimada[3]
1. Department of Electrical Engineering, Graduate School of Engineering, Tohoku University, Sendai, Japan; 2. Center for Spintronics Research Network, Tohoku University, Sendai, Japan; 3. Toei Scientific Industrial Co Ltd., Sendai, Japan; 4. Faculty of Engineering, Tohoku Gakuin University, Sendai, Japan

I. INTRODUCTION The spin dynamics in magnetic thin films have attracted much attention from both fundamental and application viewpoints. The dynamics are described using the phenomenological Landau-Lifshitz-Gilbert (LLG) equation consisting of both the precession torque of the magnetization and the damping torque. Especially, a Gilbert damping constant (α), which describes the strength of damping torque, is one of the dominant parameter to predict the dynamics. Until now, we reported the correlation between α and the saturation magnetostriction (λ_s) for Ni-Fe and Ni-Fe-M films[1]-[3] and found different behaviors of α depending on positive or negative values of λ_s. To investigate this correlation in more detail, these parameters must be estimated simultaneously for each film using a same measurement instrument. Herein, we proposed a new measurement technique, which employs a microstripe line probe to detect ferromagnetic resonance (FMR) spectra for a magnetic thin film either with tensile stress or stress free, which enables simultaneous evaluation of α and λ_s II. EXPERIMENTAL PROCEDURES In our proposed FMR measurement technique, a substrate such as a glass, a quartz, a Si and so on is bent with a certain curvature radius giving uniaxial tensile stress to the magnetic thin film on the substrate. The FMR frequency shifts to either lower or higher side by the uniaxial anisotropy derived from magneto-elastic effect. This frequency shift reflects the strength of λ_s of the films, that is, the relation between the FMR frequency and λ_s is expressed as $(f_{r\sigma}^2 - f_{r0}^2)/ f_{r0}^2 = (3\lambda_s t_{sub} E_f/2rM_s)/(H_{kf} + H_{ex})$, (1) where $f_{r\sigma}$, f_{r0}, t_{sub}, E_f, r, M_s H_{kf}, and H_{ex} are FMR frequencies under tensile stress and in stress free state, a substrate thickness, Young's modulus, curvature radius determined by position censor, saturation magnetization, other kind of uniaxial anisotropy field such as induced anisotropy, and the external magnetic field, respectively. Therefore, the difference of FMR frequency ($f_{r\sigma}$, f_{r0}) between the stress improved state and tensile free stress is carefully measured at each external magnetic field (H_{ex}) and λ_s is calculated with the curvature radius (r). Furthermore, the damping constants (α) of these films were evaluated from FMR spectrum with stress free. These measurements were performed at room temperature. The film to be measured is 10-nm Ni_xFe_{100-x} fabricated by DC magnetron sputtering onto glass substrates. The Ni composition (x) of Ni_xFe_{100-x} films varied from 66.6 to 90.7. The composition of the film was determined by energy dispersive x-ray spectroscopy (EDX). III. RESULTS AND DISCUSSION Figure 1 shows FMR spectrum in Ni_xFe_{100-x} films with and without stress and. In case of $Ni_{90.7}Fe_{9.3}$ (Fig. 1(a)), each FMR frequency with tensile stress ($f_{r\sigma}$) shifts to lower frequency side because of uniaxial magnetostrictive anisotropy. The frequency difference ($\Delta f_r = f_{r\sigma} - f_{r0}$) in external magnetic field (H_{ex}) increases from -716 to -383 MHz as H_{ex} increases. As can be seen in Fig. 2(a), λ_s was evaluated by fitting to the $|(f_{r\sigma}^2 - f_{r0}^2)/ f_{r0}^2|$ vs. H_{ex} plot using eq. (1) and was approximately -8.95 ppm. This value agrees well with that measured by the optical cantilever method (-16.0 ppm). α was evaluated from half width of the FMR spectra without tensile stress, which keeps constant for H_{ex} > 150 Oe and is approximately 0.0190. In case of $Ni_{75.5}Fe_{24.5}$ (Fig. 1(b)), every $f_{r\sigma}$ shifts to higher frequency. Δf_r in H_{ex} decreases from +484 to +181 MHz as H_{ex} increases. As shown in Fig. 2(b), λ_s was determined by fitting to the $|(f_{r\sigma}^2 - f_{r0}^2)/ f_{r0}^2|$ vs. H_{ex} plot using eq. (1), that is, approximately +3.22 ppm and is in good agreement with that measured by the optical cantilever method (+7.34 ppm). α is maintained constant for H_{ex} > 50 Oe and is approximately 0.00725. Therefore, these results demonstrate that our proposed measurement technique can determine both α and λ_s simultaneously for individual sample with high reliability allowing more precise evaluation of spin dynamics. ACKNOWLEDGEMENT This work was supported in part by JSPS KAKENHI Grant Number JP26289082, JP17H03226 and JP17F17070. This work was supported in part by CIES collaborative research from CIES, Tohoku University. This work was also supported in part by the Murata Science Foundation and ASRC in Japan.

[1] Y. Endo et al., J. Appl. Phys. 109, 07D336 (2011). [2] Y. Endo et al., IEEE Trans. Magn. 47, 3324 (2011). [3] Y. Endo et al., IEEE Trans. Magn. 48, 3390 (2012).

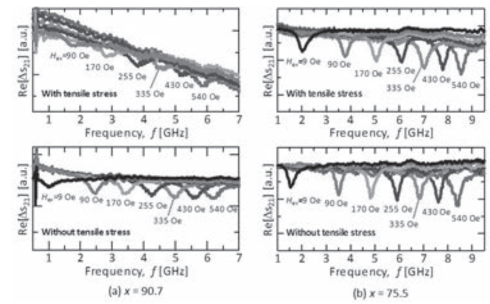

Fig. 1. FMR spectrum with and without tensile stress for 10-nm thick Ni_xFe_{100-x} films with various Ni compositions (x) ((a) x = 90.7, (b) x = 75.5).

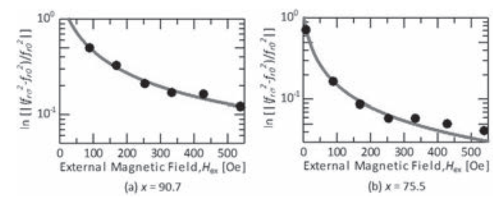

Fig. 2. Relationship between $|(f_\sigma^2 - f_{r0}^2)/ f_{r0}^2|$ and H_{ex} for 10-nm thick Ni_xFe_{100-x} films with various Ni compositions (x) ((a) x = 90.7, (b) x = 75.5). Black marks and the red line represent data points and the fitting line by eq. (1), respectively.

11:45

AE-09. Effects of Anisotropic Dipolar Interaction on Spin-Wave Dynamics in $Ni_{80}Fe_{20}$ Nanodot Arrays with Honeycomb and Octagonal Lattice Symmetries.

S. Mondal[1], S. Barman[2], S. Choudhury[1], Y. Otani[3] and A. Barman[1]
1. S. N. Bose National Centre for Basic Sciences, Kolkata, India; 2. Institute of Engineering and Management, Kolkata, India; 3. Institute for Solid State Physics, University of Tokyo, Kashiwa, Japan

Investigations of ultrafast magnetization dynamics of two-dimensional nanodot arrays are significant for their potential applications in high density magnetic storage, memory, logic device, magnonic crystal, spin torque nano-oscillator and sensors. The spin-wave (SW) dynamics of such arrays strongly depend upon the shape and size of the nanodots as well as the lattice arrangements due to the modulation of the internal magnetic field as well as the inter-element interaction field. The collective magnetization dynamics of nanodot arrays arranged in square lattice symmetry has been studied in detail but the same in lower symmetry lattices have not been investigated in detail. Here, we have done a comparative study of collective magnetization dynamics in nanodot arrays arranged in octagonal and honeycomb lattice symmetry. Cylindrical $Ni_{80}Fe_{20}$ (Py) nanodots having diameter (*d*) of 100 nm and thickness (*t*) of 20 nm are fabricated in 10×10 μm^2 arrays on top of self-oxidized Si (100) substrate by a combination of e-beam lithography and e-beam evaporation. The collective dynamics in the above two lattice symmetry is studied by varying inter-dot separations (*S*) from 30 to 300 nm, by using an all optical time resolved magneto optical Kerr effect microscope (TR-MOKE) [1]. In this two-color pump-probe technique, the probe beam (λ = 800 nm, pulse width ≈ 80 fs, spot size ≈ 800nm) is exploited to detect the time varying polar Kerr signal of the sample while pump beam (λ = 400 nm, pulse width ≈ 100 fs, spot size ≈ 1 μm) excites the magnetization dynamics in presence of a bias field (fig.1(a)). The collective magnetization of the array undergoes a number of transitions between various weakly collective regimes with increasing inter-dot separation [2]. The rich band of SW spectra gradually converge to only two distinct self-standing modes corresponding to centre and edge mode of a single nanodot, for both the lattices. The SW modes show high stability with the bias magnetic field. Micromagnetic simulations qualitatively reproduce the experimental observations. Interestingly, we have observed a splitting of the centre mode in case of octagonal lattice (mode 1 and 2 for *S* = 75 nm) as a consequence of the anisotropic dipolar field between the nanodot pairs coupled horizontally and vertically, which is not found in the honeycomb lattice (fig. 1 (b), (c)). With increasing separation these two modes merge together to form the centre mode of an individual dot at $S \geq 150$ nm. Our findings will show that the usage of nanodot lattices with complex basis structures will provide more control parameters which can be advantageous for the designing of high density magnetic recording media, spin-wave filter and logic devices. The authors gratefully acknowledge the financial supports from the Department of Science and Technology, Government of India under Grant No. SR/NM/NS-09/2011(G) and S. N. Bose National Centre for Basic Sciences, India (Grant No. SNB/AB/12-13/96). S.M. acknowledges DST under the INSPIRE scheme and S.C. acknowledges support from the S. N. Bose National Centre for Basic Sciences.

1. A. Barman and A. Haldar, Solid State Physics, vol. 65, p. 1-108 (2014). 2. S. Mondal *et al*,. RSC Advances 6, 110393 (2016).

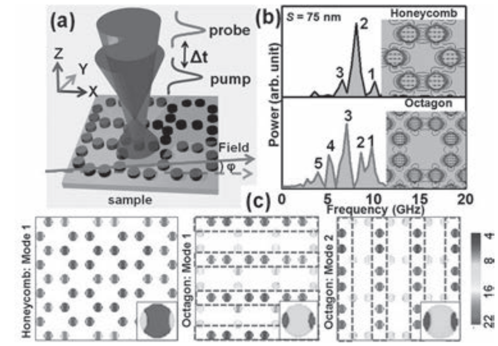

Fig. 1. (a) Experimental geometry and (b) spin-wave spectra of Py dots arranged in honeycomb and octagonal lattices with *S* = 75 nm. Mode numbers are mentioned in numerical figure. The magnetostatic field distributions are shown at the insets. (c) Simulated power maps of different spin wave modes at *S* = 75 nm. Color map for the power distribution is shown at the right hand side of the images. Phase of individual dot is also shown at the inset.

Session AF

MAGNETIC RECORDING: COMPONENTS AND ARCHITECTURE

Ganping Ju, Chair

Seagate, Cupertino, CA, United States

INVITED PAPER

9:00

AF-01. Comparison between Interlaced, Shingled, and Conventional Heat Assisted Magnetic Recording. ***(Invited)***

S. Hernandez[1], S.D. Granz[1], Z. Liu[1], P. Krivosik[2], P. Huang[3], G. Ju[3], T. Rausch[1] and E. Gage[1]
1. Seagate Research Group, Seagate Technology, Shakopee, MN, United States; 2. Recording Head Operations, Seagate Technology, Bloomington, MN, United States; 3. Recording Media Operations, Seagate Technology, Fremont, CA, United States

Recent advances in Heat Assisted Magnetic Recording (HAMR)[1][2] have solidified this technology's future as the leading candidate for hard disk drive products in the years to come. Most demonstrations have so far focused on Conventional Magnetic Recording (CMR), where tracks can be written and over-written at any time with no intentional overlap. Achieving high track pitch capability (TPIC) will require coupling HAMR with more advanced recording schemes. Shingled Magnetic Recording (SMR) [3] involves writing tracks sequentially on the disk, with overlap on one of the sides only. In Interlaced Magnetic Recording (IMR) [4] tracks are written in an "interlaced fashion". First, the bottom tracks are written at a large track width then top tracks are subsequently written at narrow track width between two bottom tracks. The final track pitch will be roughly half of the distance between the bottom tracks. The signal to noise ratio (SNR) is preserved at high areal density using this scheme: bottom tracks are written at a high laser power with wide track width thereby minimizing curvature, and top tracks are written at lower laser power with narrow track width but are not subject to adjacent track interference effects. Although both SMR and IMR require re-writing entire sections of tracks (or bands) to overwrite a single track, they enable much higher track pitch than possible with CMR. In addition to novel writing schemes, read-back can be engineered to increase areal density. Multi-Sensor Magnetic Recording (MSMR) [5] uses two or more readers to read-back the same track. By combining different signals from readers at different cross-track positions more of the signal can be resolved, therefore improving SNR compared to a single reader configuration. This work aims to compare HAMR combined with the technologies described above (CMR, CMR + MSMR, SMR, SMR + MSMR, IMR, IMR + MSMR) through spin-stand experiments and micromagnetic modeling. Table 1 lists the areal density capability (ADC) estimates for all of the recording technologies, obtained from a spin-stand. The ADC quoted is estimated using the ASTC Areal Density Metric [6], which is scaled for channel density. Spin-stand measurements were captured at a writer current of 55 mA, active clearance of 1 nm, radius of 23 mm, skew of 0 and 5400 RPM. MSMR signal processing was performed by reading back the same track with the same reader at different cross-track positions. The signals are combined for two and three reader configurations as described in [5], in order to find the optimal combination of readback signals. As expected, significant areal density gains are observed in SMR and IMR over CMR, for all MSMR configurations. SMR offers the best TPIC of all technologies, but no linear density entitlement. In fact, linear density is lower with a single reader configuration than CMR. This is likely due to adjacent track interference effects caused by the shingling. However, using multiple readers more of the SMR signal can be preserved, thereby enabling an increase in linear density. The TPIC of IMR is reduced compared to SMR, since it is limited by how closely you can place the top tracks without incurring an SNR penalty. Ultimately, the areal density is higher, given that the wide bottom tracks can have much higher linear density than CMR and SMR. Figure 1 shows (a) transition SNR and (b) BER as a function of the number of readers for a CMR configuration at 600 KTPI and 2100 KFCI, obtained using a micromagnetic recording model. HAMR magnetization dynamics are simulated using the renormalized Landau Lifshitz Gilbert equation [7]. Magnetic writer and near field transducer (NFT) designs are consistent with those used in the experiment. Transition SNR is calculated using the ensemble waveform analysis described in [8] and BER is estimated using a pattern dependent Viterbi detector [9]. Three tracks are written on fifty different media sections in order to obtain the proper statistics. The center track is a 31 bit pseudo random sequence, which remains the same for all 50 media sections. The side tracks are random and uncorrelated for all fifty writes. The maximum temperature of the thermal profile is chosen such that the width of an isolated track is the same as the intended track pitch. The effect of multiple read-backs is included using the method described in [5]. Results show that transition SNR increases and BER decreases for MSMR configurations compared to single-reader read-back. The gain in SNR when going from two reader MSMR to three-reader MSMR which is consistent with the minimal increase in areal density from CMR + 2 reader MSMR to CMR + 3 reader MSMR shown in Table 1. Given that the model replicates the effects observed at spin-stand for CMR with single, two and three reader configurations, SMR and IMR will be simulated and compared to experiment. The ultimate ADC entitlement of IMR and SMR will be modeled and optimal recording conditions and writer/NFT characteristics for each of these schemes will be quantified.

[1] A.Wu et al. "HAMR Areal Density Demonstration of 1+Tbpsi on Spinstand", IEEE Trans. Magn., vol. 49, 2013, pp.779 -782 [2] G. Ju et al., "High Density Heat-Assisted Magnetic Recording Media and Advanced Characterization—Progress and Challenges," in IEEE Transactions on Magnetics, vol. 51, no. 11, pp. 1-9, Nov. 2015. doi: 10.1109/TMAG.2015.2439690 [3] R. Wood et al. "Feasability of Magnetic Recording at 20 Terabits per square inch on Conventional Media" [4] S. Granz et al. "Heat Assisted Interlaced Magnetic Recording", IEEE Trans Magn. [5] C. Rea et al. "Heat Assisted Recording: Advances in Recording Integration", IEE Trans Magn. [6] S. Granz et al., "Definition of an Areal Density Metric for Magnetic Recording Systems" IEEE Trans. Magn. Vol. 53, Issue: 2, Feb. 2017. [7] R.H. Victora, P. Huang, "Simulation of Heat Assisted Magnetic Recording Using Renormalized Media Cells", IEEE Trans Magn. 49, 751-757 (2013) [8] S. Hernandez, Pu-Ling Lu, P. Krivosik, P.W. Huang, W.R. Eppler, T. Rausch, E. Gage, "Using Ensemble Waveform Analysis to Compare Heat Assisted Magnetic Recording Characteristics of Modeled and Measured Signals" IEEE Trans Magn. 52, 3000406 (2016) [9] A. Kavcic and J.M.F. Moura, "The Viterbi Algorithm and Markov Noise Memory", IEEE Trans. On Inf. Theory. Vol 46, no 1 (2000)

Recording Scheme	Linear Density (KFCI)	Track Density (KTPI)	ADC (TBPSI)*
CMR	2200	608	1.17
CMR + 2 reader MSMR	2302	608	1.23
CMR + 3 reader MSMR	2329	608	1.25
SMR	2095	842	1.55
SMR + 2 reader MSMR	2185	842	1.62
SMR + 3 reader MSMR	2236	842	1.66
IMR	2301	789	1.60
IMR + 2 reader MSMR	2399	789	1.67
IMR + 3 reader MSMR	2432	789	1.69

Table 1: Linear density, track density and ADC estimates obtained from spin-stand measurements for HAMR technologies including single reader readback, and MSMR readback in two and three reader configurations. Note: ADC = KBPI x KTPI, where KBPI = 0.88 x KFCI (meaning that it is scaled by the channel code rate) [6].

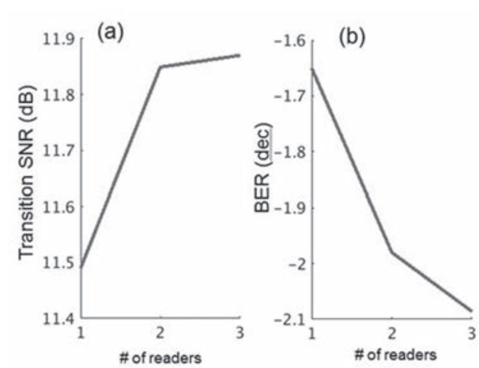

Fig. 1. Transition SNR and BER as a function of number of readers for CMR at 600 KTPI and 2100 KFCI.

CONTRIBUTED PAPERS

9:30

AF-02. Reader noise due to thermally driven asymmetric oscillations.

A. Stankiewicz[1], T. Pipathanapoompron[2,4], K. Subramanian[3] and A. Kaewrawang[4]
1. Seagate Technology, Bloomington, MN, United States; 2. Seagate Technology, Korat, Thailand; 3. Seagate Technology, Shakopee, MN, United States; 4. Department of Electrical Engineering, Khon Kaen University, Khon Kaen, Thailand

It has been shown that random excitations of a nonlinear asymmetric oscillator produce low frequency noise [1]. Such effects have been predicted to exist in magnetoresistive sensors [2], where precession asymmetry is introduced by anisotropy energy (either shape or crystalline). This effect has been used to explain the M-shape profiles of magnetic noise vs the external field [3]. In this work we provide direct experimental evidence of asymmetric ferromagnetic resonance in actual devices, and their contribution to low frequency noise. Typical magnetoresistive (tunneling) readers are comprised of ferromagnetic free, reference and pinned layers (FL, RL, PL, respectively), which are stabilized with interlayer interactions and bias magnetic fields. External fields (e.g. due to magnetic media) cause magnetization rotations in the FL, resulting in resistance changes. At finite temperature, the magnetization fluctuates around the energy minimum, resulting in output noise. In nanostructures, these oscillations may be quite large (10-20 deg), and go beyond the range of the harmonic approximation. However, the resonant frequency is large (~5 GHz), and the resulting noise in the operational band (<2 GHz) remains small, until the excitations become asymmetric around the equilibrium [2], resulting in 1/f-like noise. In this experiment, the quasi-static reader output signal has been probed in the time domain using an ISI FMR tester and an external oscilloscope. The system analog bandwidth was 18 GHz, and waveforms were collected at a sampling rate of 80 GSa/s. Fig. 1a shows a small section of a reader noise waveform, in which oscillation asymmetry is evident. Fig 1b represents the corresponding power spectral density (PSD) distribution, with a strong 1/f tail in the low frequency (LF) range. In order to prove that LF noise is a result of the observed oscillation asymmetry, the signal has been decomposed into LF (<2 GHz) and high frequency (HF, >2 GHz) components. Such operations can be done by either empirical mode decomposition (EMD), or by zero-phase-shift numerical filters. The HF portion was then used to produce the instantaneous amplitude waveform, using a simple envelope algorithm (the Hilbert transform may be used as well). A two-dimensional histogram of the LF noise and HF instantaneous amplitude is shown in Fig. 2. The strong correlation (~0.9) observed in Fig. 2 is direct proof that the LF noise is caused by random thermal excitations of the asymmetric magnetic precession in the FL. Another indicator of asymmetric oscillations is a shift of the equilibrium state signal, which can be attributed to very low instantaneous amplitudes. While this study was focused on the presence of low frequency noise in asymmetric magnetic readers, it is fully expected to be manifest in many other systems, possibly explaining the widespread presence of 1/f noise.

[1] A.Stankiewicz, to be published. [2] T.Pipathanapoompron, A.Stankiewicz, A.Grier, K.Subramanian, A.Kaewrawang, "1/f thermally excited noise in asymmetric oscillators", *Dig. Intermag 2018*, Singapore, Apr 2018. [3] A. Stankiewicz, "Low frequency thermal noise in magneto-resistive sensors," *Dig. 8th Joint European Magnetic Symposia (JEMS)*, Glasgow (UK), Aug 2016.

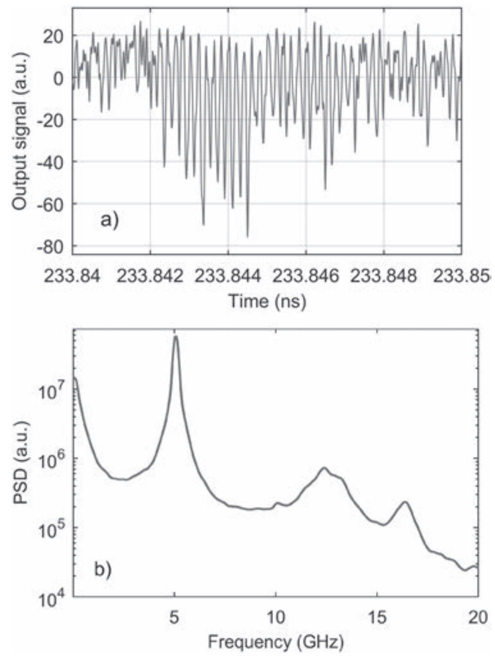

Fig. 1. Oscillation asymmetry is visible in time-domain data (a). Power spectrum density reveals a prominent FL resonance peak (at ~5 GHz), along with other resonance lines at high frequencies (>10 GHz), and strong 1/f-like noise below 2 GHz (b).

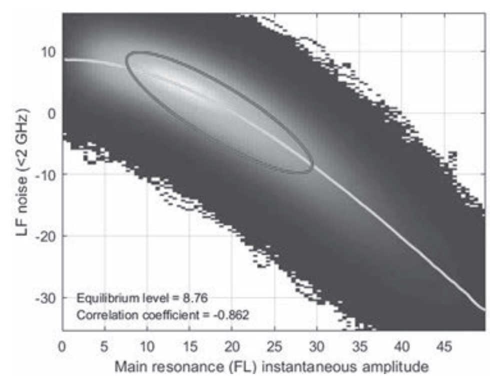

Fig. 2. 2-D histogram of filtered LF noise and FL resonance instantaneous amplitude. Strong correlation (red ellipse) and shift of the low equilibrium signal confirm oscillation asymmetry to be a source of LF noise, while regression nonlinearity (green line) reveals oscillation nonlinearity.

9:45

AF-03. Probe-based Spin Torque Transfer Device for Writing Hard Disks.

J. Hong[2], O. Lee[3], K. Dong[4], S. Khizroev[5], L. You[2] and J. Bokor[1]
1. University of California, Berkeley, Berkeley, CA, United States; 2. Huazhong University of Science & Technology, Wuhan, China; 3. Korea Institute of Science and Technology, Seoul, The Republic of Korea; 4. China University of Geosciences, Wuhan, China; 5. Florida International University, Miami, FL, United States

In magnetic hard disk technology, continued scaling of bit density requires higher coercivity and anisotropy media in order to maintain data retention time. This creates a major challenge for scaling the electromagnet-based write head, which is currently being addressed by heat-assisted magnetic recording (HAMR) technology. In this work, we investigate the use of spin transfer torque point contacts induced by spin-polarized current injected from a nanoscale probe tip across a very narrow gap into magnetic media to change magnetization direction. We present our recent experiment using a functional nanoprobe to substitute the disk writer structure. State-of-the-art He-ion focused ion beam (FIB) trimming was used to develop a nanoscale magnetic structure on top of a tip as shown in Fig 1(A). The standard Ta(5nm)/CoFeB(1nm)/MgO(0.9nm) on tip side and another Ta(5nm)/CoFeB(1nm)/MgO(0.9nm) stack on media side were deposited via sputter deposition and milled. The IV characteristics are shown in Fig 1(B) and show magnetization switching of the media through MTJ-type probing. The magnetization change of practical medial structures which consist of sub-10-nm L1(0) ordered FePt structures was observed using the fixed layer of the tip as shown in Fig 1(C). This result suggests a completely new approach for hard disk writing and could pave the way to the field of magnetic recording with ultra-small, ultra-high density, and ultra-fast data rate further.

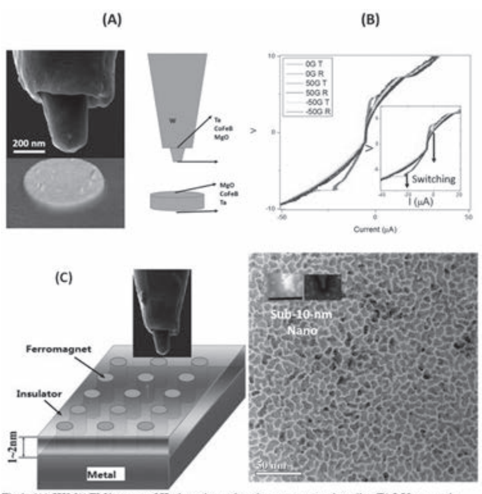

Fig 1. (A) HIM/AFM images of He-ion trimmed probe structure and media. (B) I-V curve via sweeping voltage by changing magnetic field. (C) Sub-10-nm FePt media structure. Bright and dark colors indicate two distinctive magnetization switching. The scale bar is 5 nm.

10:00

AF-04. Large magnetoresistive outputs in Heusler alloy-based CPP-GMR sensors using with AgInZnO spacers.

T. Nakatani[1], T. Sasaki[1], Y. Sakuraba[1] and K. Hono[1]
1. Research Center for Magnetic and Sprintronic Materials, National Institute for Materials Science (NIMS), Tsukuba, Japan

Non-magnetic nanolayer / conductive oxide-hybrid spacer structures for current-perpendicular-to-plane giant magnetoresistance (CPP-GMR) sensors such as Cu/ZnO [1], Ag/InZnO (IZO) [2] and Cu/AlMgO [3] are critical to realize large magnetresistive (MR) outputs at the resistance-area product (*RA*) of 0.05-0.2 Ω μm^2, which cannot be realized by either conventional all-metallic CPP-GMR or tunnel magnetoresistance devices. MR ratio ($\Delta R/R$) = 26% at RA = 0.1 Ω μm^2 has been reported using practical polycrystalline CPP-GMR spin-valves with the Ag/InZnO spacer and $Co_2(Mn_{0.6}Fe_{0.4})$Ge (CMFG) Heusler alloy ferromagnetic layers. [2] It should be noted that $\Delta R/R$ = 20% at RA = 0.1 Ω μm^2 has been predicted to be the minimum requirement of the MR output for the read sensor applicable to the 2 Tbit/in^2 areal recording density. [4] However, to ensure the process margins for the actual read sensor manufacturing, a realization of higher $\Delta R/R$ is strongly required. In this work, we systematically studied the MR properties of polycrystalline spin-valve (SV) and pseudo spin-valve (PSV) devices using AgSn/IZO-bilayer spacer. Also, we developed a new AgInZnO (AIZO) single-layer spacer which realized $\Delta R/R$ = 50% at RA = 0.08 Ω μm^2. Polycrystalline SV films with Ta(2) / Ru(2) / $Ir_{20}Mn_{80}$(6) / CoFe(3) / Ru(0.8) / CoFe(0.6) / CoFeBTa(0.8) / CMFG(2.5) / CoFe(0.4) / $Ag_{90}Sn_{10}$(0.4) / IZO(1.4-1.85) / CoFe(0.4) / CMFG(4) / CoFe(1) / Ru(8) (thickness in nm) structure was deposited by magnetron sputtering and annealed at 280 °C for 3 h. [5] The CPP-GMR devices showed *RA* values ranging from 0.05 Ω μm^2 to 0.2 Ω μm^2 and $\Delta R/R$ ranging from 20% to 30% depending on the IZO thickness. *RA* was larger for a thicker IZO layer. The maximum $\Delta R/R$ of ~30% at RA ~0.1 Ω μm^2 was obtained with a AgSn(0.4)/IZO(1.7) spacer. For comparison, SV devices with a AgSn(3.5 nm) conventional metal spacer showed $\Delta R/R$ of 13% at RA = 0.045 Ω μm^2. The output voltage (ΔV) *vs*. bias current density (J_{bias}) was tested for linearized *R*-*H* transfer curves under an application of a constant bias magnetic field of 80 mT perpendicular to the pinning direction (utilization ~33%), which simulates the actual read sensor operation (inset of Fig. 2(a)). The maximum ΔV (ΔV_{max}) of the sensor with the AgSn(0.4)/IZO(1.7) spacer (RA = 0.11 Ω μm^2, $\Delta R/R$ = 32%) was ~6 mV, whereas ΔV_{max} of the conventional all-metallic sensor with a AgSn(3.5) spacer was only 1.1 mV. PSV devices with a Ta(2) / Ru(2) / CoFe(0.5) / CoFeBTa(1.5) / CMFG(5) / CoFe(0.4) / spacer / CoFe(0.4) / CMFG(5) / CoFeBTa(1.5) / Ru(8) cap stacking structure annealed at 280 °C were also studied for so-called *scissors read sensors*. As shown in Fig. 1, the PSV devices showed larger $\Delta R/R$ at given *RA* values than the SV devices due to the thicker CMFG magnetic layers in the PSV films and the absence of the synthetic antiferromagnet pinned layer structure in PSVs. The PSV devices with the AgSn(0.4)/IZO(t_{IZO}) spacers showed $\Delta R/R$ ~ 33% at RA ~ 0.06 Ω μm^2 for t_{IZO} = 1.3 nm and $\Delta R/R$ ~ 38% at RA ~ 0.11 Ω μm^2 for t_{IZO} = 1.6 nm as shown in Fig. 1. Higher $\Delta R/R$ were obtained using a AgInZnO (AIZO) single-layer spacer. The AIZO films were co-sputtered from Ag and IZO. The PSV device with a 1.2 nm-thick AIZO spacer with a nominal Ag concentration of ~30 at. % showed $\Delta R/R$ up to 50% at RA ~ 0.08 Ω μm^2, which is higher by ~15% than that of the AgSn/IZO spacer at the same *RA* value (Fig. 1). The ΔV *vs*. J_{bias} of the PSV devices were tested by applying an external magnetic field (*H*) parallel to the minor axis of the ~60 nm×~120 nm elliptical shaped device, by which the magnetizations of the two free layers of PSV rotate gradually as the magnitude of *H* is increased due to the magnetic shape anisotropy of the device pillar. Fig. 2(b) shows ΔV (= ΔR × bias current)-*H* of a PSV device with RA = 0.08 Ω μm^2 and $\Delta R/R$ = 45%. ΔV_{max} was 18 mV at J_{bias} = 9.6×10^6 A/cm^2, which is much larger than that with a conventional AgSn spacer (RA = 0.03 Ω μm^2 and $\Delta R/R$ = 18%) of 3 mV. It should be noted that the PSV device shows a wide linear response range in -20 mT ≤ $\mu_0 H$ ≤ -80 mT with a large ΔV of 15mV as shown in Fig. 2(b). At J_{bias} = 1.3×10^8 A/cm^2, the magnetization of the CMFG-based ferromagnetic layers are destabilized by spin transfer torque in the high resistance state near the anti-parallel magnetization configuration, however, the linear response range is still stable. We will discuss the electric properties and the microstructure of the AIZO films and the CPP-GMR devices.

[1] Shimazawa *et al*. IEEE Trans. Magn. 46, 1487 (2010). [2] Nakatani *et al*. Appl. Phys. Express 8, 093003 (2015). [3] Iwasaki *et al*. Joint MMM-Intermag 2016, EH-01. [4] Takagishi *et al*. IEEE Trans. Magn. 46, 2086 (2010). [5] Nakatani *et al*. IEEE Trans. Magn. (2018) DOI: 10.1109/TMAG.2017.2753221

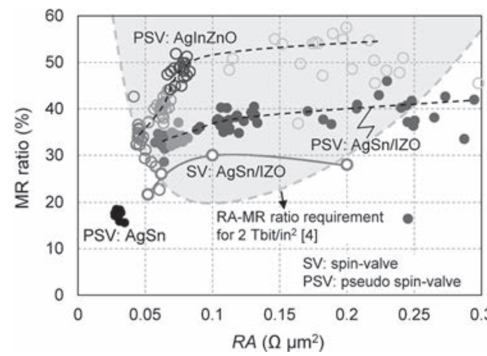

Fig. 1. *RA* and MR ratio of the CPP-GMR devices with AgSn/IZO and AgInZnO spacers.

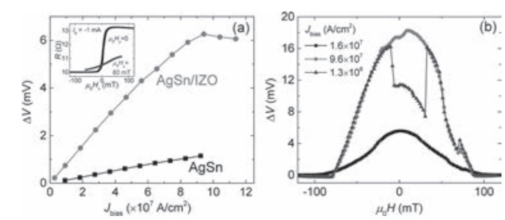

Fig. 2. (a) Output voltage *vs*. bias current density of spin-valves with AgSn spacer ($\Delta R/R$ = 13%, RA = 0.045 Ω μm^2) and AgSn(0.4)/IZO(1.7) spacer ($\Delta R/R$ = 32%, RA = 0.11 Ω μm^2). (b) Output voltage-external magnetic field curves of the pseudo spin-valves with AIZO spacer ($\Delta R/R$ = 45%, RA = 0.08 Ω μm^2) under various bias current densities.

10:15

AF-05. Tailoring epitaxially grown exchange spring Fe/L10-FePt multilayers as perpendicular recording media.

A. Syed Mohd[1], S. Pütter[1], S. Mattauch[1] and T. Brückel[1,2]
1. Jülich Centre for Neutron Science (JCNS) at MLZ, Forschungszentrum Jülich GmbH, Garching, Germany; 2. Jülich Centre for Neutron Science JCNS and Peter Grünberg Institut, JCNS-2, PGI-4: Scattering Methods, Forschungszentrum Jülich GmbH, Jülich, Germany

High density storage in the hard disk drive (HDD) is realized using magnetic nanostructures which have perpendicular magnetic anisotropy (PMA) and is often termed as perpendicular recording media (PRM). $L1_0$-FePt films are very promising candidates for the PRM because of their large PMA [1]. In the HDD industry, $L1_0$-FePt films are replacing conventional CoCrPt films and extending the superparamagnetic limit. Hence they improve the thermal stability [2, 3]. Superparamagnetism is a phenomenon in which the magnetization direction may flip due to thermal activation without the application of an external magnetic field. This appears when the volume (V) of the magnetic particle is reduced in such a way that $K_uV \gg k_BT$ where K_u is magnetic anisotropy constant, k_B is Boltzmann constant and T is ambient temperature. But the problem with $L1_0$-FePt films is their hard ferromagnetic behavior which limits the writing process in the PRM due to the high switching field. One way to solve this issue is to combine a soft ferromagnet e.g. Fe with $L1_0$-FePt films to form an exchange spring magnet [4, 5]. In exchange spring magnet it is expected that the exchange coupling across the interface will reduce the coercivity as compared to hard ferromagnet alone. Further, exchange spring magnet Fe/$L1_0$-FePt has additional advantage that the increased out of plane saturation magnetisation will make the signal strong enough to be detected easily. However, previous studies have shown that the magnetic moments in Fe layers below ~ 2 nm remains collinear with respect to $L1_0$-FePt and there is insignificant change in the coercivity [6]. On one hand, for a Fe layer thickness above ~ 2 nm coercivity decreases with increasing thickness but on the other hand PMA decreases [7, 8]. In order to create a possible balance between the coercivity and the PMA, we have optimized the epitaxial growth of Fe/$L1_0$-FePt multilayers (MLs) which will have an addition interaction i.e. interlayer exchange coupling. The growth of thin ML is challenging because at room temperature (RT) the FePt film has an A1 (fcc) structure which is a soft ferromagnet with low magnetic anisotropy and undergoes to $L1_0$ (fct) structure only at high temperature [9]. However, high temperature growth of Fe/$L1_0$-FePt ML has the risk of interdiffusion at the interface so there is a strong demand of optimization. It is important to note that once the FePt film is in $L1_0$ structure, it remains in this phase even at RT.

[1] Y. K. Takashahi et al., Phys. Rev. Appl. 5, 014006 (2016). [2] D. Goll et al., phys. status solidi (a) 210, 1261 (2013). [3] S. Piramanayagam et al., J. Magn. Magn, Mater. 321, 485 (2009). [4] E. F. Kneller et al., IEEE Trans. Magn. 27, 3588 (1991). [5] D. Suess et al., Appl. Phys. Lett. 87, 012504 (2005). [6] N. de Sousa et al., Phys. Rev. B 82, 104433 (2010). [7] G. Varvaro et al., New J. Phys. 14, 073008 (2012). [8] D. A. Gilbert et al., Sci. Rep. 6, 32842 (2016) [9] O. Gutfleisch et al., Adv. Eng. Mater. 7, 208 (2005)

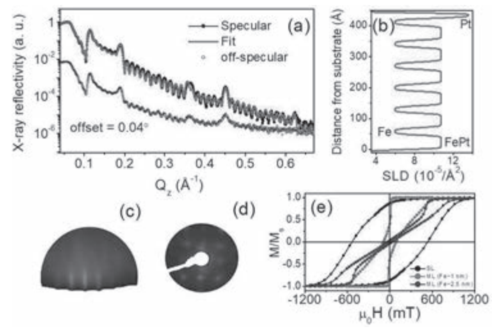

Fig. 1. shows specular x-ray reflectivity (a) of Pt capped [Fe(2.35 nm)/ $L1_0$-FePt(4.7 nm)] $_6$ ML where 3rd and 6th order Bragg peaks are missing due to 1:2 thickness ratio of Fe and $L1_0$-FePt layers. Pronounced Kiessig's oscillation in off-specular reflectivity indicates that there is a minimal intermixing at the interface. Figure (b) shows the scattering length density (SLD) profile obtained from the fitting of specular reflectivity. In-situ RHEED (c) and LEED (d) confirms the epitaxial growth of the ML. Figure (e) shows the comparison of the out-of-plane hysteresis loops obtained for single layer (SL) of $L1_0$-FePt and the MLs with nominal structure of Fe(x)/$L1_0$-FePt (4. 5 nm) where x=1 and 2.5 nm.

INVITED PAPER

10:30

AF-06. Data Temperature and Future Data Storage Architecture.

K. Gao[2,1]
1. Energy Systems, Argonne National Laboratory, Argonne, IL, United States; 2. International Business and Technology Service, North Oaks, MN, United States

There has been tremendous technological development over the past two decades in the magnetic data storage industry, with current products at an areal density of more than 1Tb/in^2 using shingled magnetic recording (SMR) and only until recently, the areal density capability (ADC) of hard disk drive (HDD) has been slowing down [1-3]. Over the past few decades, along with adoption of PC, small form factor HDDs became the new industry standard. There are a number of technologies that were invented/discovered, demonstrated and adopted as HDD industry standard over the past three decades, including: 1) GMR and TMR based read head technologies [4-6], implemented in 1997 and 2005 respectively; significantly improved the playback signal amplitude and the signal to noise ratio (SNR); 2) Transition from longitudinal magnetic recording (LMR) to perpendicular magnetic recording (PMR), where from a recording media perspective, leads to a higher media coercivity (Hc) and a reduced switching field distribution (SFD), which in PMR, are primarily due to media anisotropy and grain size distributions [7-9]. Media design combine coupled granular continuous (CGC) structure and the vertically exchanged coupled gradient anisotropy or exchange spring/composite structure helped to achieve this goal, which enables a steady improvement of the media SNR [10-13]; 3) PMR write head with a tapered write pole, as well as later added tapered wrap around shielded, enables early introduction and rapid adoption of PMR product, provide sufficient large write field and field gradient to allow high coercivity media to be utilized with a small grain size and a high SNR [7, 14-15]; 4) Introduction of heater to enable a further reduction of recording head to media spacing (HMS) in the read and write operations [16]. This approach primarily enables a down-scaling of HMS, which drives dynamic flying height to be less than 2nm; 5) The contact detection sensor (CDS), placed at the air bearing surface (ABS) of the recording head provide real time feedback on the HMS value for a given head and media interface, which helps to reduce the number of head media contact during read/write operations, and therefore significantly improves HDD's life spans [17]. Recently, the ADC of HDD has slowed down, even when including new technologies such as heat assisted magnetic recording (HAMR), the demonstrated ADC gain is around 15%/year [3]. Therefore, beyond component technology, drive systems and write architectures were optimized to further improve HDD capacity, despite most are "one time change", with success, such as 1) Shingled Magnetic Recording (SMR) as a write architecture to extend the ADC of HDD, has been demonstrated and implemented. Although due to excessive latency, SMR has slowly gained markets, mostly in the data archive systems, nevertheless, it is an approach enable further improvement of drive capacity. 2) Helium filled drive, an approach does not increase ADC, but increase HDD drive volumetric capacity due to reduction of disk to disk spacing, has been implemented, mainly for cloud based data centers with large capacities. 3) Interlaced Magnetic Recording (IMR) or Blocked Magnetic Recording (BMR), which further optimize write configurations for different tracks to improve ADC with reduced latency penalty as compare to SMR [19-21]. Recent study shown using IMR in HAMR, 30%$^+$ ADC gain can be achieved as compared to conventional random access recording condition, consistent with theoretical predictions [20, 22]. The BMR modeled results also shown ADC gain in addition to SMR [21]. Here the impact of write architecture will be reviewed and potential ADC gain in each approach are given. From data storage perspective, the write architecture change may incur data rate, and more precisely, the random accessed read and write operation frequency penalty. Over the past 10 years, due to wide adoption of mobile and social network, large amount of data are migrated to the Cloud. In the meantime, 3D NAND based solid state drive (SSD) starts to take over part of the HDD markets [23]. This type of technology evolution and transition cannot be explained using ADC or drive capacity comparison between different technologies. A STANDARD "*Data Temperature*" for all digital data stored, based on the frequency of the data being accessed is given, where the archived data, personal user data, work place storage and the most searched data at a given time can be represented as freezing, room temperature, hot data and boiling data respectively [24]. Different data storage technologies and their evolutions can be illustrated together using data temperature definition, to identify what will be future technologies for data storage. It is desired to have different technologies to store data with different *Data Temperature*, in reality, most data stored in a given device has much lower *Data Temperature* than the device average *Data Temperature* capability. As the size of the digital universe increases, the amount of cold data increased rapidly. This leads to new opportunity for data archive storage technology. In addition to the write architecture, new HDD based data storage architecture is proposed. Based on the detailed analysis, a solution for low cost data archive system well below current HDD system is given. Based on the detailed analysis, the proposed data storage solution has the potential to replace existing HDD, Tape and Blu-ray based storage for cloud based data centers.

[1] Information Storage Industry Consortium (INSIC) Tape and HDD Technology Roadmap 2012-22 & 2015-25. [2] ASTC/ASRC Technology Roadmap [3] K. Z. Gao, Write Architectures and Their Impact on Hard Disk Drive Capacity, Intermag, 2017 DE03. [4] Binasch G, Grünberg P, Saurenbach F and Zinn W (1989), "Enhanced magnetoresistance in layered magnetic structures with antiferromagnetic interlayer exchange", Physical Review B, Rapid Communications, Vol. 39, No. 7, p. 4828, March 1, 1989. [5] Grünberg P, "Magnetic Field Sensor With Ferromagnetic Thin Layers Having Magnetically Antiparallel Polarized Components", US4949039 Aug. 14, 1990. Grunberg P, (2008), "Nobel Lecture: From Spin Waves to Giant Magnetoresistance and Beyond", Review of Modern Physics, Vol. 80, p.1531, Dec. 17 2008, DOI: 10.1103/RevModPhys.80.1531 [6] Baibich M N, Broto J M, Fert A, Nguyen Van Dau F, Petroff F, Eitenne P, Creuzet G, Friederich A and Chazelas J, "Giant Magnetoresistance of (001) Fe/(001) Cr Magnetic Superlattices", Phys. Rev. Lett., Vol. 61, No. 21, p.2472, Nov. 21, 1988. [7] Gao K Z, Bertram HN, "Magnetic Recording Configuration for densities beyond 1Tb/in2 and data rates beyond 1Gb/s", IEEE Trans. Magn. Vol. 38, Is. 6, p 3675-83, 2002 [8] Gao K Z and Bertram HN, "Transition jitter estimates in tiled and conventional perpendicular recording media at 1Tb/in2", IEEE Trans. Magn. Vol. 39, Is 2, p. 704-9, March 2003 [9] Gao K Z, Fernandez-de-Castro J, and Bertram H N, "Micromagnetic Study of the Switching Fields in Poly-Crystalline Magnetic Thin Film Media", IEEE Trans. Magn., 41, No. 6, Nov. 2005. [10] Y. Sonobe ; H. Muraoka ; K. Miura ; Y. Nakamura ; K. Takano ; A. Moser ; H. Do ; B.K. Yen ; Y. Ikeda ; N. Supper ; W. Weresin, "Thermally stable CGC perpendicular recording media with Pt-rich CoPtCr and thin Pt layers", IEEE Trans. Magn. Vol. 38, Is. 5, p. 2006-2011, Dec. 2002. [11] Suess D., etc. "Exchange spring media for perpendicular recording", Appl. Phys. Lett., Vol 87, Is. 1, 012504, (2005) [12] Victora R and Xiao S, "Composite media for perpendicular magnetic recording", IEEE Trans. Magn., Vol. 41, Is 2, p. 537-42, Feb. 2005. [13] Li S, Gao K Z, Zhu W, Wang L, Wang X "Perpendicular magnetic recording media with magnetic anisotropy/coercivity gradient and local exchange coupling", US patents 7846564, 8048545, 8501330, 8962164, 9848074, 2005-2017 [14] Mallary M, "One terabit per square inch perpendicular recording conceptual design", IEEE Trans. Magn., vol. 38, no. 4, pp. 1719-1724, Jul. 2002. [15] Lijie Guan, Hung Liang Hu, Yaw Shing Tang, "Perpendicular write head with tapered main pole", US 7777987, 7777988, 2004. [16] Mayer D, Kupinski P, Liu J, "Slider with temperature responsive transducer positioning", US patent 5991113, Apr. 1997. [17] Roy M, Gao K Z, Jin I, etc. "Magnetic recording device including a thermal proximity sensor", US patent 7589928, Mar. 2007. [18] Wood R, Williams M, Kavcic A, Miles J, "The Feasibility of Magnetic Recording at 10 Terabits Per Square Inch on Conventional Media", IEEE Trans. Magn. Vol. 45, Is. 2, p.917-23, Feb. 2009 [19] Krichevsky A., Heat Assisted Magnetic Recording with interlaced High-Power heated and Low Power Heated tracks, US9099103, Oct. 2014 [20] Gao K Z etc. Write management for interlaced magnetic recording devices, US 9,508,362. Prioritized random access for magnetic recording, 9,601,154. Enhanced capacity recording,

9,607,631. Interlaced magnetic recording super parity, 9,633,675, Nov 2014. [21] Gao K Z, Magnetic Recording Architecture/Blocked Magnetic Recording, US Patent Application 15,294,231 and 62,240,598, 2015. [22] Granz S, etc. Heat Assisted Interlaced Magnetic Recording, TMRC 2017, D3 [23] L. Mearian, Flash memory's density surpasses hard drives for first time, Feb. 2016, Computer World [24] K. Z. Gao, Temperature of Data, News and Views, International Business and Technology Service 2016

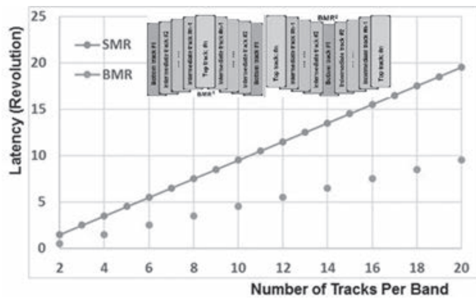

Fig. 1. Illustration of BMR write architecture and its latency penalty vs. SMR

CONTRIBUTED PAPERS

11:00

AF-07. CoPt capped FePtC based ECC media for HAMR.

T. Dutta[1,2], S. Piramanayagam[3], M. Saifullah[2], C.S. Bhatia[1] and H. Yang[1]
1. Electrical and Computer Engineering, National University of Singapore, Singapore; 2. Institute of Material Research and Engineering, Singapore, Singapore; 3. School of Physical and Mathematical Sciences, Nanyang Technological University, Singapore, Singapore

$L1_0$ FePtC granular media is extensively researched as potential future magnetic recording media and is set to be used with Heat assisted magnetic recording (HAMR) to enable recording at write fields within the range of current day recording heads [1, 2]. The current media designs suffer from SFD issues during high temperature writing. FePtC based media structures with a capping layer can alleviate the switching field distribution (SFD) requirements of HAMR. Consequently, it can reduce the noise originating from the writing process. In accordance to this we investigated a CoPt/FePtC exchange coupled composite (ECC) structure, where FePtC serves as the storage layer and CoPt (with higher Curie temperature, T_c) as the capping layer. CoPt remains ferromagnetic at near T_c of FePtC. A stack structures of $L1_0$ CoPt (t_{CoPt})/$L1_0$ FePtC (10 nm)/MgO (3 nm)/CrRu (25 nm)/Glass were fabricated by sputter deposition. The CoPt layer thickness (t_{CoPt}) was varied from 2 to 6 nm. The $L1_0$ FePtC and $L1_0$ CoPt layers were deposited at nominal temperatures of 600 °C and 640 °C, respectively. An uncapped sample (without any CoPt capping) was also prepared under similar conditions for reference. Switching field (H_s) and SFD was extracted from the out-of-plane hysteresis loops for each sample. SFD was calculated as $SFD=(H_s\text{-}H_n)/H_c$, where H_n is the nucleation field and H_c is the coercive field, extracted from the out-of-plane loops. Both H_s and SFD decreased steadily with an increase in the CoPt thickness. In fact, for the t_{CoPt} = 6 nm sample, H_s and SFD decreased by 23.11% and 26.03%, respectively, as compared to that of the uncapped granular sample. For such capped media design it is important that the capping layer remains ferromagnetic at temperature near T_c of $L1_0$ FePtC ($T_{c,FePtC}$ < 700K). Out-of-plane hysteresis loops of the samples were measured at high temperatures of 250, 300, 350 and 400 °C as presented in Fig. 1. It was observed that 400 °C is well above the Curie temperature of FePtC but lower than that of CoPt. Two additional samples were also prepared with 4 nm and 6 nm $L1_0$ FePt capping layer on $L1_0$ FePtC granular layer. The H_c, Hs, and H_k for all the samples at 250 °C were lower than that at room temperature and continued to decrease with a further increase in temperature. At 300 °C the uncapped FePtC sample turned paramagnetic while all other samples exhibited reduced ferromagnetism. On increasing the temperature beyond 350 °C, the sample with 4 nm $L1_0$ FePt capped sample also turned paramagnetic. However, the all the CoPt capped media and the 6 nm FePt capped media remained ferromagnetic. Although the 6 nm FePt capped sample remains ferromagnetic at 400 °C, the magnetization was much lower compared to the CoPt capped samples. Clearly, the CoPt capping layer remains ferromagnetic at 350 °C and 400 °C, although the uncapped FePtC granular media becomes paramagnetic at those temperatures. During the actual recording process using HAMR, the target grains are heated to T_c of the media, at which they become paramagnetic. Subsequently, during the cooling process, the presence of the $L1_0$ CoPt capping layer (which remains ferromagnetic near T_c of $L1_0$ FePtC) will facilitate a counter exchange energy to minimize the stray field from the adjacent grains. Therefore, the magnetization in the target grains would no longer be affected by the stray field during the recording process. Thus, we have demonstrated that $L1_0$ CoPt capping for $L1_0$ FePtC granular media can lead to lower switching fields, and improved switching field distribution during the high temperature writing process. The presence of ferromagnetic exchange coupling from $L1_0$ CoPt capping layer makes $L1_0$ CoPt/$L1_0$ FePtC media best suited for future HAMR technology.

1] D. Weller, G. Parker, O. Mosendz, E. Champion, B. Stipe, X. Wang, T. Klemmer, G. Ju, and A. Ajan, "A HAMR Media Technology Roadmap to an Areal Density of 4 Tb/in^2," *IEEE Transactions on Magnetics,* vol. 50, no. 1, pp. 1-8, 2014. [2] S. D. Granz, and M. H. Kryder, "Granular L10 FePt (001) thin films for Heat Assisted Magnetic Recording," *Journal of Magnetism and Magnetic Materials,* vol. 324, no. 3, pp. 287-294, 2012.

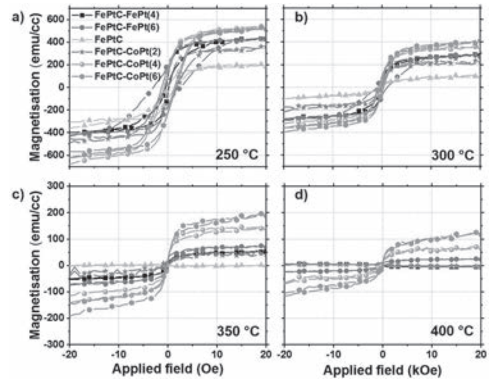

Fig. 1. Out-of-plane hysteresis loops of uncapped, CoPt capped and FePt capped samples at temperatures of 250, 300, 350, and 400 °C.

11:15

AF-08. Order-disorder Temperature of MnGa Thin Films on Glass Substrate.

C. Huang[1], Y. Chen[2], S. Wang[1] and A. Sun[2]
1. Institute of Materials Science and Engineering, National Taipei University of Technology, Taipei, Taiwan; 2. Chemical Engineering and Materials Science, Yuan Ze University, Taoyuan, Taiwan

Introduction MnGa with $L1_0$ phase was firstly discovered by Tsuboya and Sugihara in 1965 [1]. $L1_0$-MnGa has attracted much attention due to its large coercivity (H_c) [2], high magneto-crystalline anisotropy ($K_u \sim 10^7$ erg cm^{-3}), high perpendicular magnetic anisotropy (PMA) [3], and Pt element free, which massively reduces the cost during the materials preparation. Thus, it is regarded as the promising candidates to replace $L1_0$-CoPt and $L1_0$-FePt thin films for next generation of hard magnetic phase film applications, such as magnetic sensor, magnetic recording media, spintronic devices, etc. However, the amount of related reports were much fewer than those of the $L1_0$-CoPt or $L1_0$-FePt cases, so that people seem not clearly to realize what the magnetic material is. Thus, in the presented work, MnGa alloy thin films with different thicknesses (t) were directly sputtered on an amorphous glass substrate at varied substrate temperature (T_s). The results demonstrated that high H_c MnGa thin film could be prepared on glass substrate if the film had sufficient growth volume. The coercivity mechanism and the effects of t and T_s on magnetic properties and microstructure of MnGa thin film will be discussed in full article. Experiment In this study, MnGa magnetic alloy thin films with different t were deposited on an amorphous glass substrate at varied T_s by an ultrahigh vacuum magnetron sputter system, where t and T_s were 10-200 nm and RT(room temperature)-600 °C, respectively. The working Argon pressure was set to 5 mTorr during sputtering. The thickness of the film was cheched by an Atomic Force Microscope (AFM). The phase and magnetic domain structures were characterized by a X-ray diffractometer (XRD) and a Magnetic Force Microscope (MFM). The magnetic properties were carried out with the vibration sample magnetometer (VSM). Mircostructure of the films were investigated by a Transmission Electron Microscope (TEM) with a accelerating voltage of 200 keV. Results and Disscussion Figure 1 shows XRD diffraction patterns of MnGa films with different T_s. The thickness of films is kept at 200 nm. In Fig. 1, the film shows poor crystallization at T_s = RT. When T_s is 300 °C, Mn_8Ga_5(330) and Mn(101) peaks are presented clearly. The diffraction peaks of $L1_0$ MnGa (111), (200), (220), and (202) peals can be observed as T_s increases to 350 °C. The intensity of $L1_0$-diffraction peaks would be further increased with increasing the T_s, indicating that the crystallinity of $L1_0$-type MnGa thin films are enhanced when T_s is increased. Therefore, phase transformation MnGa thin films from amorphous to $L1_0$ phase needs thermal energy during heat treatment process. Figure 2(a)-(d) show the magnetic hysteresis loops of MnGa thin films with t = 200 nm at varied T_s, where T_s are 300, 400, 500 and 600 °C, respectively. Of course, Fig.2(a) presents that the film shows poor magnetic properties at T_s = 300 °C due to Mn_8Ga_5(330) and Mn(101) are poor magnetic phases. However, H_c is largely enhanced and clear hysteresis loops are observed when T_s is further increased, as shown in Fig.2(b)-(d). The higher H_c is about 7.1 kOe which is obtained at T_s = 600 °C. Nevertheless, the presented results are sufficient to demonstrate that the order-disorder temperature of MnGa thin film is between 300 to 350 °C. The is also a strong evidence that $L1_0$ MnGa thin film with high H_c can be prepared at low processing temperature, an outstanding advantage in hard magnetic film application. Conclusion MnGa films with high H_c have been deposited on glass substrate. MnGa films show poor magnetic properties with $T_s \leq 300$ °C, because the films presented nonmagnetic phases. MnGa thin films start to transfer into $L1_0$ phase at T_s = 350 °C, and exhibit hard magnetic properties with large coercivity. The the order-disorder temperature of MnGa thin film is thus confirmed between 300 to 350 °C. The detail mechanism would be discussed in the manuscript.

[1] M. Hasegawa and I. Tsuboya, "Magnetic Properties of η Phase in Mn-Ga System", *Journal of the Physical Society of Japan*, vol. 20, no. 3, pp. 464-464, 1965. [2] K. Minakuchi, R. Umetsu, K. Ishida and R. Kainuma, "Phase equilibria in the Mn-rich portion of Mn–Ga binary system", *Journal of Alloys and Compounds*, vol. 537, pp. 332-337, 2012. [3] L. Zhu, S. Nie, K. Meng, D. Pan, J. Zhao and H. Zheng, "Multifunctional L10-Mn1.5Ga Films with Ultrahigh Coercivity, Giant Perpendicular Magnetocrystalline Anisotropy and Large Magnetic Energy Product", *Advanced Materials*, vol. 24, no. 33, pp. 4547-4551, 2012.

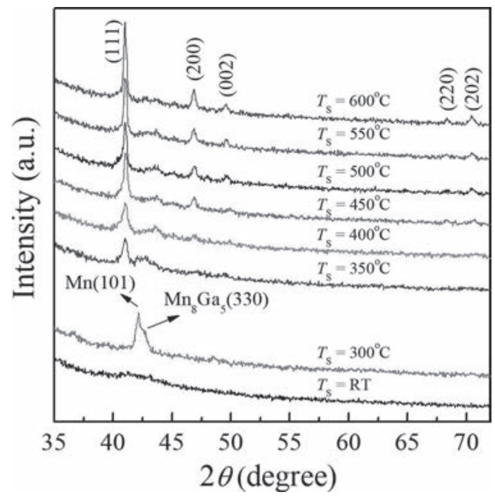

Fig. 1. XRD pattens of MnGa films with different T_s.

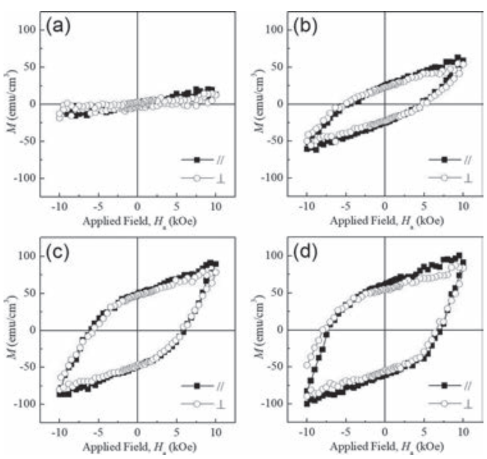

Fig. 2. In-of-plane (//) and out-of-plane (⊥) hysteresis loops of MnGa thin films with different T_s. T_s = (a) 300 °C, (b) 400 °C, (C) 500 °C, and (d) 600 °C.

11:30

AF-09. Controlling Size Distribution of FePt Nuclei by Tuning Sputtering Conditions.

B. Zhou[1,2], B. Varaprasad[1,3], E. Zhang[1,2], D. Laughlin[1,2] and J. Zhu[1,3]
1. Data Storage Systems Center, Carnegie Mellon University, Pittsburgh, PA, United States; 2. Materials Science and Engineering, Carnegie Mellon University, Pittsburgh, PA, United States; 3. Electrical and Computer Engineering, Carnegie Mellon University, Pittsburgh, PA, United States

FePt-C granular film structure has been considered as the most promising candidate for heat-assisted magnetic recording (HAMR) media since its first successful demonstration of well-isolated FePt grains with ~ 6 nm thickness and a size distribution ($\sigma \approx 2.3$ nm) in 2008. [1] However, the FePt-C based media still have some vital issues hindering its practical application and to reach uniform grain size distribution without losing number density of grains is one of them. Wide grain size distribution causes grain-to-grain variation in chemical ordering (S), curie temperature (T_c), anisotropy field (H_k), affecting the recording performance of HAMR. We believe that one of the reasons causing the wide distribution in grain size of granular FePt-C based media is the size non-uniformity of FePt nuclei in nucleation stage. Therefore, it is crucial to obtain a uniform FePt nuclei in order to narrow the grain size distribution in granular FePt films. In our previous works, we demonstrated the strategy of utilizing templated layer in order to control the grain size distribution.[2][3] In this work, we explore the possibility of modifying the kinetic energy and thus the mean free path of ad-atoms FePt-C by varying the sputtering conditions in order to reach more uniform nucleation. All films were sputtered on thermally grown a-SiO_2 substrates using an AJA Orion-8 system with base pressure better than torr. All substrates are cleaned by acetone, IPA, DI water and dry etching by O_2 plasma. The film stack is Si | SiO_2 | MgO (9nm) | FePt + 35 vol.%C (1.5nm). Media layer was kept constant at 1.5 nm for all samples, since the nucleation stage of FePt-C grains is the main focus in this study. MgO was sputtered at 10mTorr with at room temperature with deposition rate of 0.57 nm/min. FePt alloy target and carbon target were co-sputtered at substrate temperature of 650°C with different deposition pressure (5 – 20mTorr) in order to modify the kinetic energy of FePt and C when it arrives at MgO surface so that to examine the effect of deposition pressure on FePt grain nucleation. The film microstructures were examined by in-plane transmission electron microscope (TEM). Fig.1 (a) and (b) shows the plane-view TEM images of FePt-C films deposited at 5 and 20 mTorr, respectively. Note that in the case of 5 mTorr, there are significant amount of small size nuclei relative to that of majority nuclei, typically with diameter < 1.5nm, whereas in the case of 20 mTorr, the small nuclei are rarely observed. This observation is confirmed by the grain size distribution histogram, shown in Fig. 1 (c) and (d), for both cases. Multiple number of plane-view TEM images, taken from different regions of each sample, are used for calculating the statistical distribution with total number of grains counted exceeding 500. For FePt-C film deposited at 5 mTorr, the bimodal distribution shows one peak in between 0.5-1.0 nm and the other in between 2.5-3.0 nm. The mean grain size is 2.2 nm. The smaller grain size peak is actually quite significant, counted as 30% of the total number of grains. Experimental evidences show that with continued film growth, this bimodal distribution would continue with both peaks moving to larger sizes. The bimodal grain size distribution have been reported in several other previous studies, all at slightly different grain size [4] and we tend to believe they all arises from the bimodal distribution at nucleation stage. At the high deposition pressure, 20mTorr, the grain size distribution only shows a single peak located in between 2.0-2.5 nm. The total number density of FePt grains and packing fraction listed in table 1 are similar for both cases. It clearly shows that by tuning the deposition pressure of FePt-C in the nucleation stage, more uniform FePt nuclei can be obtained without scarifying the number density of FePt nuclei.

[1] A. Perumal, Y.K. Takahashi and K. Hono, "$L1_0$ FePt-C nanogranular perpendicular anisotropy films with narrow size distribution", *Appl. Phys. Express*. 1, 101301 (2008). [2] V. Sundar, B. Zhou, Y. Liu, J. Zhu, D. Laughlin and J. Zhu, "Fabrication of templates for achieving one-to-one grain matching in HAMR media", *Intermag conference* (2015) [3] B.D.S.Ch.S. Varaprasad, B. Zhou, T. Mo, "MgO-C interlayer for grain size control in FePt-C media for heat assisted magnetic recording", AIP Advances, 7, 056503 (2017) [4] Y. Zhang, J. Wan, V. Skumryev, S. Stoyanov, Y. Huang, G. C. Hadjipanayis, and D. Weller "Microstructural characterization of L10 FePt/MgO nanoparticles with perpendicular anisotropy", App. Phy. Letters, 85, 5343 (2004)

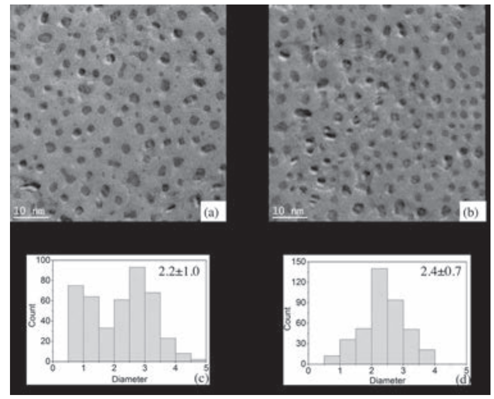

Fig. 1. Plane-view microstructure of films Si | SiO_2 | | MgO (9nm) | FePt + 35 vol.%C (1.5nm) with FePt + C layer sputtered at (a) 5 mTorr and (b) 20 mTorr; (c) and (d) are grain size distribution histograms for 5 mTorr and 20 mTorr, repectively.

Deposition Pressure (mTorr)	Number density of FePt grain (T grians/in²)	Packing fraction	Mean grain size (nm)
5	85.2	0.256	2.2±1.0
20	84.0	0.267	2.4±0.7

Table 1. Number density of FePt grains, packing fraction and grain size as a function of deposition pressure.

11:45

AF-10. Influence of Stress and Strain on the $L1_0$-ordered Phase Formation in FePt Thin film.

M. Futamoto[1], T. Shimizu[1], M. Nakamura[1] and M. Ohtake[1]
1. EECE, Chuo University, Shinjuku, Japan

Introduction FePt thin films with $L1_0$-ordered structure have been investigated for magnetic recording media application. The film involves phase transformation from disordered fcc ($A1$, $c/a = 1$) to $L1_0$-ordered phase with tetragonal structure ($c/a = 0.97$). For applications, the easy magnetization axis (*c*-axis) must to be controlled to be perpendicular with respect to the substrate surface while achieving a high ordering degree. Previous studies have shown that *c*-axis orientation and ordering degree of FePt crystal depend on various factors including substrate material, processing condition, film thickness, etc., where the stress distribution in FePt material is interpreted to have influenced on the resulting film structure[1-3]. The stress/strain in FePt material varies depending on the film morphology and the stacking structure[4]. In the present study, structure analysis using a high-resolution TEM is carried out for $L1_0$-FePt thin films with different film morphology or stacking structure, where the average thickness of 10 nm and the final processing temperature of 600 °C are employed. The effect of stress/strain in FePt material on the ordered phase formation has been investigated. Experimental procedure FePt films of 10 nm thickness were prepared on MgO(001) substrates using an UHV RF magnetron sputtering system, by direct deposition at 600 °C (sample A), by a two step-process consisting of low temperature (200 °C) deposition followed by annealing at 600 °C without (sample B) and with 2-nm-thick MgO cap-layer (sample C) [4,5]. The film structures were observed by AFM, XRD, and TEM. The magnetic properties were measured by using a VSM. Results and discussion Figure 1 compares the film morphology and the magnetic property of samples A, B, and C. The volume fraction of $L1_0$-(001) crystal with the c-axis perpendicular and the ordering degree determined by XRD are also shown in the lower part of this figure. Although the final processing temperature is same at 600 °C, the highest perpendicular anisotropy is observed for the sample C, while the sample A is showing even an in-plane magnetic anisotropy. The magnetic property is influenced by the volume fraction and the ordering degree, both of which apparently strongly affected by $L1_0$-ordering through atomic diffusion under an influence of stress/strain within the FePt thin films. The lateral tension stress is presumably in the sample order of C > B > A, where a lateral tension caused by lattice mismatch with MgO material (-9 %) is provided from both the substrate and the cap-layer sides for the sample C, from only the substrate side for the sample B, and a curved surface profile of isolated FePt crystal in the sample A is apparently reducing the lateral tension from the surface-side. Figure 2 shows the atomic structure analysis around the FePt/MgO interfaces for the sample C. Although the lattice misfit is nearly relieved by introduction of misfit dislocations, there still remains a lateral tension strain in the FePt material, which has possibly promoted formation of $L1_0$(001) crystal. A relation between the strain/stress and formation of $L1_0$-phase will be discussed at the conference.

[1] J. S. Kim, Y. H. Koo, and B. J. Lee, J. Appl. Phys., 99, 053906 (2006). [2] K. F. Dong, H. H. Li, and J. S. Chen, J. Appl. Phys., 113, 233904 (2013). [3] S. Wicht, S. H. Wee, O. Hellwig, V. Mehta, S. Jain, D. Weller, and B. Rellinghaus, J. Appl. Phys., 119, 115301 (2016). [4] M. Futamoto. M. Nakamura, M. Ohtake, N. Inaba, and T. Shimotsu, AIP Adv., 6, 085302 (2016). [5] M. Ohtake, M. Nakamura, M. Futamoto, F. Kirino, and N. Inaba, AIP Adv., 7, 056320 (2017).

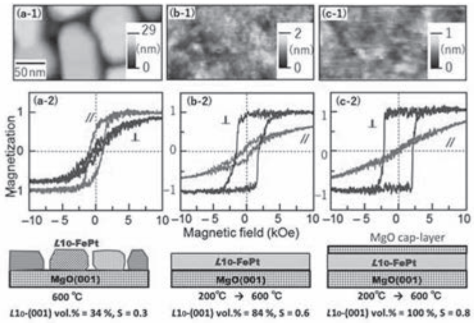

Fig. 1. Surface structure (AFM), magnetic property (VSM), and cross-sectional structure (schematic illustration) for the samples of A, B, and C.

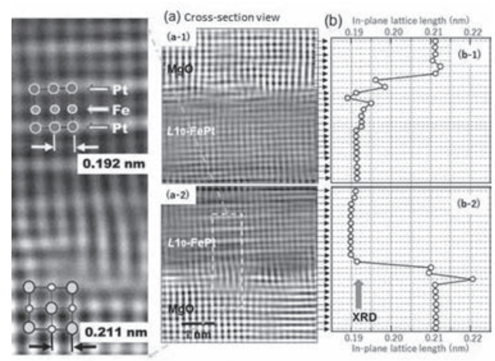

Fig. 2. High-resolution TEM analysis for the sample C.

TUESDAY MORNING, 24 APRIL 2018

PEONY III, 9:00 TO 12:00

Session AG
ELECTRICAL MACHINES AND CONTROL I

Jiadan Wei, Co-Chair
Nanjing University of Aeronautics and Astronautics, Nanjing, China
Andrew Knight, Co-Chair
University of Calgary, Calgary, AB, Canada

CONTRIBUTED PAPERS

9:00

AG-01. Design of a Novel Variable-stiffness Permanent Magnetic Mechanism for Flexible Robots.

M. Zhang[1], L. Fang[2] and F. Sun[3]
1. School of Mechanical Engineering and Automation, Northeastern University, Shenyang, China; 2. Faculty of Robot Science and Engineering, Northeastern University, Shenyang, China; 3. School of Mechanical Engineering, Shenyang University of Technology, Shenyang, China

ABSTRACT: This paper describes the design, modeling, and analysis of a novel variable-stiffness mechanism for wire-driven flexible robot joint. Compared with the mechanical device, it can effectively increase the range of variable-stiffness, without increasing the wire-tension. Then improve the energy efficiency, safety and lightweight of the robot joint. Based on Ampere' molecular current hypothesis, through estimating the induced magnetic field and magnetic force in the system, the variable-stiffness mechanism force and stiffness models are obtained. It is verified by the FEM simulation and experiment. The variation regulation of the magnetic force and stiffness between permanent magnets is consistent with that of magnetic field. Therefore, the variable-stiffness law of the permanent magnet mechanism can through the design of the magnetic field of the air-gap. 1. Introduction Variable-stiffness robot joint is a kind of flexible joint with adjustable stiffness, which can greatly improve the safety and environmental adaptability, has become the future robot joint development. Wire-driven variable-stiffness joints are usually connected with nonlinear elastic components on both sides of the joint, that can buffer the collision, absorbing energy. This form is closest to the position and stiffness control of human skeletal muscle. Scholars have done a lot of research on these components, such as the add-on nonlinear spring unit [1], compact nonlinear spring unit using natural rubber latex [2]. The variable-stiffness ability of the above elastic components are directly related to the wire-tension. Due to the limit of motor torque, the range of variable-stiffness is not wide. In this paper, we propose a variable-stiffness mechanism for robot joint which can realize more wide stiffness range without increasing wire-tension. 2. Structure and principle The permanent magnet mechanism consists of permanent magnetic spring and wire-driven system as shown in Fig.1-(a~b). One pair of magnet rings arranged in coaxial direction and same permanent poles are opposite. Moveable magnet ring just can slide in axial direction due to the limit of slideway that can form a permanent spring. The magnetic force and stiffness increase nonlinearly with decreasing air-gap. The wire-driven system is composed of a movable pulley and two fixed pulleys, that arranged in isosceles triangle. When we apply some force to the wire, the movable pulley is pulled up, the air-gap z_0 decreases, the wire angle α increases. The relationship between the wire-tension T and magnet force F is $T=F/2\cos\alpha$. The increasing of wire length and the wire-tension (stiffness) are nonlinear. The nonlinear combined effect of the permanent magnet spring and the wire-driven system makes more wide variable-stiffness range than pulley systems with linear springs [1-2], therefore, the motor power and volume can reduce. The variation range and slope of tension and stiffness curves can change through optimization the structural parameters. 3. Model and theoretical analysis The nonlinear force and stiffness characteristics of permanent magnet mechanism are mainly caused by the air-gap magnetic field between permanent magnets. The magnetic flux density of the air-gap determines the changing law of magnetic force and stiffness. The magnetic flux density model is established, as shown in Fig.1-(c). Due to the symmetry, the magnetic components along the x-axis and along the y-axis between the permanent magnet rings offset each other, the magnetic force is only in the z-direction. According to Ampere' molecular current hypothesis, the magnetic force between permanent magnets is obtained. Based on model mechanics, as shown Fig.1-(b), the wire tension T and stiffness K are obtained. 4. FEM model and experimental measurement In order to show the magnetic field distribution and verify the correctness of the mathematical model, the FEM model was build, FEM results were as shown in Fig.1-(d). Experimental prototype was built as shown in Fig.2-(b). Calculation, simulation and experimental values are basically the same. The nonlinear laws of magnetic flux density and force with axial air-gap z_0 are basically the same, as shown in Fig.2-(a,c). Therefore, the law of the magnet force and stiffness can change through the design of the magnetic field of the air-gap. The variable-stiffness range of permanent magnet mechanism is much wider than mechanical ones when the wire-tensions are the same, as shown in Fig.2-(d). 5. Conclusion This paper describes a novel variable-stiffness mechanism used for wire-driven flexible robot joint. Compared with the traditional mechanical ones, it can effectively increase the range of variable-stiffness without increasing the wire-tension. The variation regulation of the magnetic force and stiffness between permanent magnets can change through the design of the magnetic field of the air-gap. The method described in this paper for calculating the air-gap magnetic flux density is very close to the FEM simulation and experimental measurement value. Based on this, the calculation of the force and stiffness between permanent magnets is closer to the true value.

[1] Osada M, Ito N, et al. Realization of flexible motion by musculoskeletal humanoid "Kojiro" with add-on nonlinear spring units[C]// IEEE/RAS International Conference on Humanoid Robots. Piscataway, USA: IEEE, 2010: 174-179. [2] Nakanishi Y, Ito N, et al. Design of powerful and flexible musculoskeletal arm by using nonlinear spring unit and electromagnetic clutch opening mechanism[C] // IEEE/RAS International Conference on Humanoid Robots. Piscataway, USA: IEEE, 2011: 377-382. [3] Myung Wook Hyun, Jeonghoon Yoo, Seoung Tack Hwang, et al. Optimal Design of a Variable Stiffness Joint Using Permanent Magnets[J]. IEEE Transactions on Magnetics, 2007, 43(6): 2710-2712.

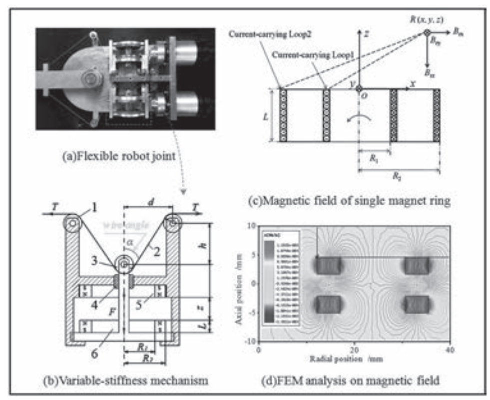

Fig. 1. Schematic of variable-stiffness mechanism
1.Fixed roller 2.Wire 3.Movable roller 4.Sliding bear 5.Fixed permanent magnet ring 6.Movable permanent ring

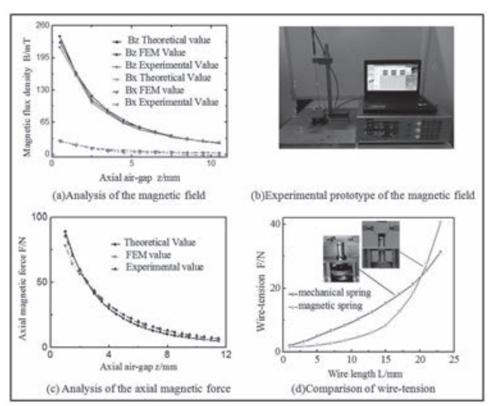

Fig. 2. Nonlinear characteristics of variable-stiffness mechanism
1.Measuring head 2. Permanent magnet ring 3.2 DOF stage 4.Ruler 5.Gaussmeter 6.PC

9:15

AG-02. Two-Converters Based Synchronous Operation and Control of a Brushless Doubly-Fed Reluctance Machine.

R. Rebeiro[1] and *A. Knight*[1]
1. Electrical Engineering, University of Calgary, Calgary, AB, Canada

I. Introduction The Brushless Doubly Fed Reluctance Machine (BDFRM) has promising prospect as a commercial machine, since it's a low cost, low maintenance machine. It does not require brushes, slip rings, rotor circuit or magnets. Having a robust winding-free ducted rotor, it can also work with a simpler control technique than a doubly fed induction generator (DFIG). Therefore, BDFRM can be very useful for applications like wind turbine system and electric vehicle. Apart from research on BDFRM [1-9], recent research efforts also address the analysis of other similar machines [10-13], and their comparisons with BDFRM [14-16]. However, topics like control and operation of prototype machines have remained largely unexplored. This paper focuses on this side of BDFRM research. An analytical magnetic design process is carried out, and a prototype machine is built based on the proposed optimum design. Subsequently, two-converters based control approach and real-time synchronous operation are investigated. II. BDFRM Analysis for Synchronous Operation Two sets of 3-phase windings with different numbers of magnetic poles are wound on the stator. The magnetic pole numbers of the windings chosen for this BDFRM are 8 and 4. Control of power flow between the windings and the rotor shaft occurs through the salient rotor design, which modulates the magnetic coupling between the windings. Coupling between the windings occurs under the following constraints [9]: $2p_r = p_8+p_4$ and $p_r\omega_m = \omega_8+\omega_4$; where p_8, p_4 and p_r are the 1st winding, 2nd winding and rotor pole numbers respectively; ω_8 and ω_4 are the 1st and 2nd winding electrical angular supply frequencies, and ω_m is the rotor mechanical speed in rad/s. The desired number of rotor poles is 6 according to the first equation. For synchronous operation, ω_4 is set to zero such that the 4-pole winding acts as the field circuit of a conventional synchronous machine. A ducted rotor pattern has been followed in this design following the example of [8]. Structural FEA has been carried out on several variations to find out the optimized ducted rotor. Detailed machine design and mathematical analysis can be presented in full paper. The *q-d* axes currents in the arbitrary rotating reference frame of angular frequency ω_8 can be expressed as, $i_{q8}=I_8cos(\theta_{8\text{-}0})$, $i_{d8}=-I_8sin(\theta_{8\text{-}0})$, $i_{q4}=I_4cos(\omega_8t+\theta_{8\text{-}0})$, $i_{d4}=I_4sin(\omega_8t+\theta_{8\text{-}0})$ where I_8, I_4 are the two windings peak currents and $\theta_{8\text{-}0}$ is the relative phase of 8-pole winding current with respect to the arbitrary reference frame at $t=0$. From these equations, corresponding *q-d* axes flux linkages can be deduced as, $\lambda_{q8}=L_8I_8cos(\theta_{8\text{-}0})+L_{84}I_4cos(\theta_{8\text{-}0}+\theta_{r\text{-}0})$, $\lambda_{d8}=-L_8I_8sin(\theta_{8\text{-}0})-L_{84}I_4sin(\theta_{8\text{-}0}+\theta_{r\text{-}0})$, $\lambda_{q4}=L_4I_4cos(\omega_8t+\theta_{8\text{-}0})+L_{84}I_8cos(\omega_8t+\theta_{8\text{-}0}-\theta_{r\text{-}0})$, $\lambda_{d4}=L_4I_4sin(\omega_8t+\theta_{8\text{-}0})+L_{84}I_8sin(\omega_8t+\theta_{8\text{-}0}-\theta_{r\text{-}0})$ where $\theta_{r\text{-}0}$ is the rotor initial position. It can be observed from these equations that the *q-d* axes 8-pole winding flux linkages are constant dc quantities in its reference frame while the 4-pole winding flux linkages act as ac variables in the opposite reference frame. III. Control Approach The block diagram of the field oriented control scheme is shown in Fig. 1. The diagram has two almost identical halves; the top half is showing the control blocks for the 8-pole winding and the bottom half is associated with the 4-pole winding. The 3-phase currents for both windings i_{abc8} and i_{abc4} are measured by two sets of current sensors, and they are fed to the respective Clarke transformation modules. The outputs of these projections are the stationary two-axes current components $i_{\alpha\beta 8}$ and $i_{\alpha\beta 4}$. These current components are the inputs for the Park transformation modules which yield i_{qd8} and i_{qd4} currents in the respective *q-d* rotating reference frames. These *q-d* axes actual current components are subsequently compared with the corresponding flux component references (i_{d8}^* & i_{d4}^*) and torque component references (i_{q8}^* & i_{q4}^*). Reference i_{q8}^* is the output of the speed PI controller. The current errors are fed as the inputs to the four current PI controllers. The outputs of the current controllers are v_{qd8} and v_{qd4} which are applied to the inverse Park transformation modules. The outputs of these modules are $v_{\alpha\beta 8}$ and $v_{\alpha\beta 4}$ which are the components of the stator vector voltage in the (α, β) stationary orthogonal reference frame. These are the inputs for the SVPWM modules. The SVPWM modules generate the gating signals to drive the two power converters which supply power to the two stator windings. Electrical angle calculations (θ_{8e} and θ_{4e}) required for the Park transformations are carried out from the following relations: $\omega_e=p_r.\omega_m$, $\omega_{8e}=x.\omega_e$, $\theta_{8e}=\int\omega_{8e}\,dt$, $\theta_{4e}=\theta_e\text{-}\theta_{8e}$. Here, x defines the ratio of the 8-pole winding frequency to the total applied frequency. For synchronous operation, x is set to 1 as the total frequency is applied on the 8-pole winding. IV. Experimental Data The BDFRM drive is implemented by using the PwrCon system from Denkinetic Pty Ltd. which is a DSP based system. A permanent magnet synchronous machine is used as the load machine. In this test, the BDFRM drive is operated as a synchronous machine at different speed levels with a fixed dc field (4-pole winding) current to yield optimum torque output. The experimental torque and output power responses are plotted in Fig. 2. V. Conclusion This work discusses the analysis and control approach for a two-converters based synchronous operation of a prototype BDFRM. The motor drive is also tested in real-time.

[1] L. Xu, F. Liang, and T. Lipo, "Transient model of a doubly excited reluctance motor," *IEEE Transactions on Energy Conversion*, vol. 6, pp. 126-133, March 1991. [2] R. Betz and M. Jovanovic, "Theoretical analysis of control properties for the brushless doubly fed reluctance machine," *IEEE Transactions on Energy Conversion*, vol. 17, pp. 332–339, Sep. 2002. [3] Y. Liao, L. Xu, and L. Zhen, "Design of a doubly fed reluctance motor for adjustable-speed drives," *IEEE Transactions on Industry Appl*ications, vol. 32, pp. 1195–1203, Sep./Oct. 1996. [4] R. E. Betz and M. G. Jovanovic, "The brushless doubly fed reluctance machine and the synchronous reluctance machine – a comparison," *IEEE Transactions on Industry Applications*, vol. 36, no. 4, pp. 1103 - 1110, Jul./Aug. 2000. [5] M. F. Hsieh, Y. H. Chang, and D. G. Dorrell, "Design and Analysis of Brushless Doubly Fed Reluctance Machine for Renewable Energy Applications," in *IEEE Transactions on Magnetics*, vol. 52, no. 7, pp. 1-5, July 2016. [6] S. Khaliq, S. Atiq, T. A. Lipo, and B. I. Kwon, "Rotor Pole Optimization of Novel Axial-Flux Brushless Doubly Fed Reluctance Machine for Torque Enhancement," in *IEEE Transactions on Magnetics*, vol. 52, no. 7, pp. 1-4, July 2016. [7] D. G. Dorrell, A. M. Knight, W. K. Song, and R. E. Betz, "Saturation and Ducting Effects in a Brushless Doubly-Fed Reluctance Machine," in *IEEE Transactions on Magnetics*, vol. 49, no. 7, pp. 3933-3936, July 2013. [8] A. M. Knight, R. E. Betz, and D. G. Dorrell, "Design and Analysis of Brushless Doubly Fed Reluctance Machines," *IEEE Transactions on Industry Applications*, vol. 49, no. 1, Jan./Feb. 2013, pp. 50-58. [9] R. E. Betz and M. G. Jovanovic, "Introduction to the space vector modelling of the brushless doubly fed reluctance machine," *Electric Power Components and Systems*, vol. 31, Aug. 2003. [10] T. D. Strous, X. Wang, H. Polinder, and J. Ferreira, "Evaluating Harmonic Distortions in Brushless Doubly Fed Induction Machines," in *IEEE Transactions on Magnetics*, vol. 53, no. 1, pp. 1-10, Jan. 2017. [11] T. D. Strous, X. Wang, H. Polinder, and J. Ferreira, "Brushless Doubly Fed Induction Machines: Magnetic Field Analysis," in *IEEE Transactions on Magnetics*, vol. 52, no. 11, pp. 1-10, Nov. 2016. [12] X. Wei, M. Cheng, W. Wang, P. Han, and R. Luo, "Direct Voltage Control of Dual-Stator Brushless Doubly Fed Induction Generator for Stand-Alone Wind Energy Conversion Systems," in *IEEE Transactions on Magnetics*, vol. 52, no. 7, pp. 1-4, July 2016. [13] J. Chen and W. Zhang, "Harmonics in Brushless Doubly Fed Induction Generator for Torque Ripple Analysis and Modeling," in *IEEE Transactions on Magnetics*, vol. 50, no. 11, pp. 1-4, Nov. 2014. [14] M. F. Hsieh, I. H. Lin and D. Dorrell, "Magnetic Circuit Modeling of Brushless Doubly-Fed Machines with Induction and Reluctance Rotors," in *IEEE Transactions on Magnetics*, vol. 49, no. 5, pp. 2359-2362, May 2013. [15] M. F. Hsieh, I. H. Lin, Y. C. Hsu, and R. A. McMahon, "Design of Brushless Doubly-Fed Machines Based on Magnetic Circuit Modeling," in *IEEE Transactions on Magnetics*, vol. 48, no. 11, pp. 3017-3020, Nov. 2012. [16] Y. Wang, S. L. Ho, W. N. Fu, and J. X. Shen, "A Novel Brushless Doubly Fed Generator for Wind Power Generation," in *IEEE Transactions on Magnetics*, vol. 48, no. 11, pp. 4172-4175, Nov. 2012.m

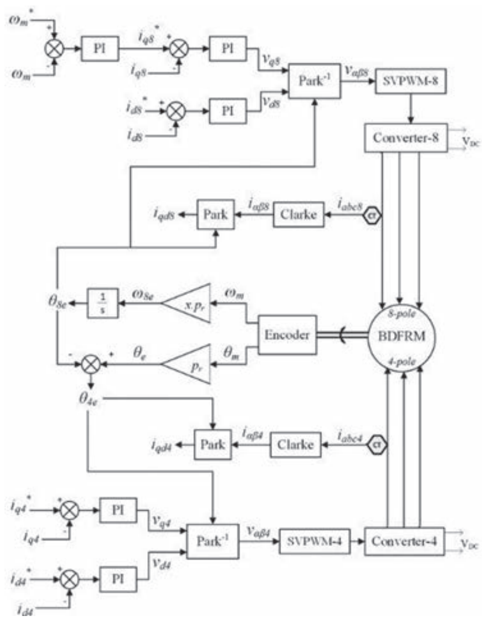

Fig. 1. Block diagram of control approach.

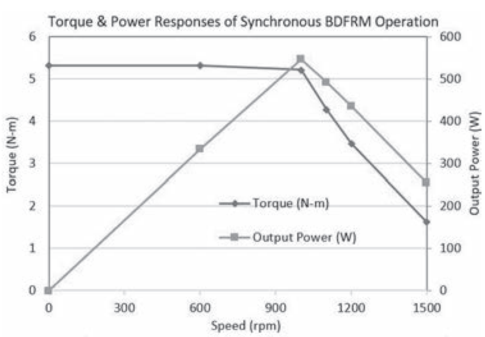

Fig. 2. BDFRM torque and power responses in synchronous operation.

9:30

AG-03. A Novel Two-Phase Excitation Switched Reluctance Motor with Symetrical Winding Distribution.

Y. Zhu[1], C. Yang[1] and Y. Zhang[1]
1. Tianjin University of Sicence and Technology, Tianjin, China

Abstract Two-phase simultaneous excitation mode of the switched reluctance motor (SRM) has been shown to effectively improve the average torque output of electric vehicles compared to traditional single-phase excitation mode. But the torque ripple of the two-phase excitation SRM with traditional winding distribution increases because of the inconsistent electromagnetic field. In order to reduce the torque ripple, a two-phase excitation 8/6 SRM with novel winding distribution is proposed in this paper. The torques generated by various magnetic circuits are analyzed and obtained to verify the torque increase. Finally, a prototype of the novel SRM is manufactured and an experiment for measuring the SRM electromagnetic characteristics is designed based on the novel mode, and the comparison results show that the proposed excitation mode is effective. I.INTRODUCTION Most SRMs applied in industries are operated in single-phase excitation mode. Another excitation way of the SRM is the two-phase excitation mode in which the windings of two phases are energized simultaneously and excited regularly. Compared with single-phase excitation mode, two-phase mode has some advantages, including torque ripple reduction, torque density improvement and efficiency raise [1-5]. However, for further analysis, the two-phase simultaneous exciting magnetic field of the four-phase 8/6 SRM with traditional winding structure is inconsistent, which can result in asymmetrical torque output and increased torque ripple. II.Novel SRM with Symmetrical Winding Distribution In order to avoid the inconsistent magnetic field distribution of the two-phase simultaneous excitation mode to reduce the torque ripple of the SRM, a novel winding distribution leading to consistent magnetic field is proposed in this paper based on the two-phase simultaneous excitation mode. The novel winding distributions of all phases are shown in Fig.1 b). It can be seen that the distribution of the four phases is the same, which is different than the traditional winding as shown in Fig.1 a). The adjacent exciting stators' magnetic poles near the rotor are N and S respectively when two phases of the proposed SRM are simultaneously excited by current i_{AD}. Take phase A and D for example, the current i_{AD} successively flows through phase A and D from the connection terminal of phase A to that of phase D. Thus, AD is energized by power U, in which the negative and positive poles are connected to terminal of phase D and phase A respectively. As a result, the magnetic field distribution of the motor is short magnetic circuits(SMC) when phase AD is excited. Furthermore, the magnetic paths of AB, CB, and CD are the same as AD and all the field distributions are SMC in one working cycle of the motor. However, for the two-phase SRM with traditional winding shown in Fig.1 a), it should be noted that magnetic circuits of CD, CB, and AB are also SMC, which is completely different from AD defined as the LMC. Therefore, it can be confirmed that the novel winding distribution will avoid the torque ripple caused by the inconsistent and variable magnetic fields. III.Comparisons and Verification Fig. 2 is the transient analysis results when the SRM drive system works under speed closed-loop and current chopping control mode. Fig.2 a) is the current waveforms with speed of 750 r/min and load torque of 17 Nm,where the blue, green, red and light blue curve represent phase CD, CB, AB and AD. Fig.2 b) is the total torque waveforms of the SRMs with two winding distributions, which are respectively traditional and proposed distributions. Compared to the SRM with traditional winding which has three SMC and one LMC within a cycle, the proposed SRM has absolute four SMC. It can be seen from Fig. 2 b) that, for the SRM with traditional winding distribution (TSRM), the torque waveforms will change and decrease obviously when phase AD is energized in one cycle due to the variation of magnetic circuits, which will lead to a reduction of the average torque. And a periodic vibration will be occurred as shown in the red curve, which will directly cause more torque ripple. However, the output torque of the SRM with proposed winding distribution (NSRM) shown in the blue curve can keep steady and smooth. The generated torques of each two-phase are uniform and the average torque increases approximate 11.3% in one cycle and 22.3% during exciting phase AD period, compared to the SRM with traditional winding. IV.Conclusions In this paper, electromagnetic field for the single-phase and the two-phase excitation mode were analysed respectively with the traditional winding distribution of the 8/6 SRM. And an inconsistent flux field distribution was found when the 8/6 SRM with traditional winding works in the two-phase excitation mode, which can result in additional torque ripple. In order to reduce the ripple caused by the inconsistent electromagnetic field, a novel winding distribution for the 8/6 SRM which works in the two-phase simultaneous excitation mode was proposed. The prototype of the novel mode SRM was developed and manufactured. The analysis and experimental results have demonstrated that the proposed SRM can improve the torque performance of the two-phase excitation mode. V.Acknowledgments This research was financially supported by the NSFC (51505332, 51405341) and TRPAFAT (15JCQNJC06900).

[1] A. Jin-Woo, O. Seok-Gyu, M. Jae-Won, and H. Young-Moon, "A three-phase switched reluctance motor with two-phase excitation," *IEEE Trans. Ind. Appl*., vol.35, no.5, pp. 1067 - 1075, 1999. [2] Shoujun Song, Zekun Xia, Zhihui Zhang, Weiguo Liu, "Control Performance Analysis and Improvement of a Modular Power Converter for Three-Phase SRM With Y-Connected Windings and Neutral Line," *IEEE Trans. Ind. Eletron*., vol.63, no.10, pp.6020-6030, 2016. [3] A. M. Michaelides, C. Pollock, "Modelling and Design of Switched Reluctance Motors with Two Phases Simultaneously excited," *IEE Proc. –Electr. Power Appl*., vol.143, no.5, pp. 361-370, 1996. [4] Amit K J, Ned M. Dynamic Modeling, Experimental Characterization, and Verification for SRM Operation with Simultaneous Two-Phase Excitation. *IEEE Trans. Ind. Eletron*., vol.53, no.4, pp. 1238-1249, 2006. [5] G. J. Li, J. Ojeda, E. Hoang, M. Lecrivain, and M. Gabsi, "Comparative studies between classical and mutually coupled switched reluctance motors using thermal-electromagnetic analysis for driving cycles," *IEEE Trans. Magn*., vol.47, no.4, pp. 839 - 847, 2011.

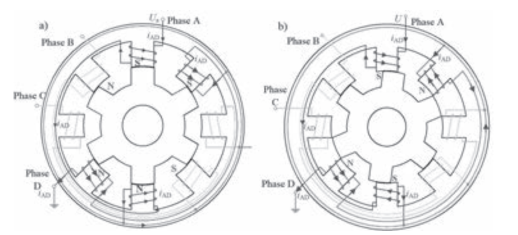

Fig. 1. Winding distribution and magnetic circuits based on two-phase excitation mode. a) Traditional SRM, b) Proposed SRM

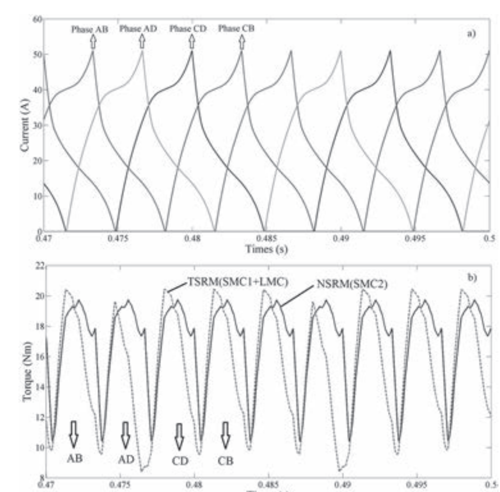

Fig. 2. Transient analysis results of two-phase excitation. a) Current, b) Torque

9:45

AG-04. Rotor Design Optimization of a new Flux Assisted consequent Pole Spoke type Permanent Magnet Torque Motor for low speed applications.

M. Onsal[1], Y. Demir[1] and M. Aydin[1,2]
1. R&D, MDS Motor Ltd., Kocaeli, Turkey; 2. Mechatronics Engr., Kocaeli University, Kocaeli, Turkey

I. INTRODUCTION Permanent magnet (PM) motors are frequently used for special applications over decades. Direct drive PM motors with high torque capability without any gear system have some benefits over high speed motors. In this study, a new spoke-type PM synchronous torque motor with consequent pole rotor (CPR) and flux assisted magnets is proposed for low-speed high-torque direct-drive applications with reduced permanent magnet volume compared to conventional surface PM motors. The new rotor structure is composed of two different rectangular magnets: The large rectangular magnets are used consecutively in the spoke-type rotor and the others are small magnets located below each rotor segments. The small magnets are used to assist the flux which are produced by spoke-type magnets. The motor performance of the proposed motor is compared with a conventional SPM motor which has the same OD and slot-pole combinations. The newly proposed PM motor with CPR and flux assisted magnets offers lesser amount of magnet than surface permanent magnet (SPM) rotor and wider torque-speed range in constant power region as compared to SPM synchronous motor. In addition, especially in constant power region, magnet and iron losses of the CPR motor are lower than that of SPM motor. II. DESIGN AND FINITE ELEMENT MODELING OF CONSEQUENT POLE TORQUE MOTOR The preliminary motor design is carried out considering the design criteria summarized in Fig. 1(a). The DC bus voltage value of the CPR torque motor is 24V. Winding layout and MMF distribution of the motor are respectively shown in Fig. 1(b) and Fig. 1(c). As seen from the both figures, motor has a conventional concentrated winding distribution. After completing the preliminary design process, magnet and airgap optimizations are performed using 2D finite element analysis (FEA) to obtain optimum rotor design. 2D FEA model and flux density levels of the final design are respectively shown in Fig. 2(a) and Fig. 2(b). Cogging torque variation for CPR torque motor is given in Fig. 2(c). As seen from the figure, the cogging torque value is only 0.025% of the average torque. Fig. 2(d) shows the back-electromotive force (EMF) voltage waveform of CPR torque motor. As seen from the figure, line back EMF waveform is almost sinusoidal with a THD level of 0.1%. On-load analyses of the motors are also performed. Torque output of the both motors is almost the same with very low ripple. The proposed CPR torque motor has 39.1 Nm average torque with 0.57% ripple while the conventional SPM torque motor has 40.46Nm average torque with 0.54% torque ripple. As the magnet weights are compared, it is seen that the proposed CPR motor, has 0.6345kg magnets while the SPM motor has 0.691kg magnets. Considering the average output ratio to magnet weight, CPR motor has roughly %5.4 more torque-to-weight ratio compared to conventional SPM synchronous motor. Flux weakening capability of the proposed CPR motor is determined using 2D-FEA tools and compared with that of SPM torque motor. Torque-speed curve of CPR torque motor and comparison with SPM motor are illustrated in Fig. 2(f). As seen from the figure, CPR motor has much more continuous power range than SPM motor. Additionally, iron loss levels of both motor are shown in Fig. 2(g). Structural FEA is also carried out to determine stress level of the rotor bridges. Von-Misses stress result on rotor is given in Fig. 2(h). Lastly, the design was completed and a prototype was produced to verify the FEA results. One piece of rotor lamination which are cut during manufacture process of motor and final shape of CPR torque motor are respectively given in Fig. 2(i) and Fig. 3(j). More detailed information and test results will be given in the final version of the paper. III. CONCLUSION In this paper, a new flux assisted consequent pole spoke type PM synchronous torque motor is proposed, analyzed and designed. Initial design, detailed magnetic and structural finite element modelling and torque quality investigation are all carried out to validate the proposed motor for high-torque, low-speed application. The motor offers wider constant power region than conventional SPM motor which is has same outer dimensions and same stator. The main benefits of the proposed motor are lower magnet cost, higher torque-to-weight ratio with comparable torque density and high-speed capability as opposed to conventional SPM synchronous torque motors. Detailed test data, comparison with the FEA results will also be presented in the final paper. ACKNOWLEDGMENT This work was supported within R&D Grant Programme by The Scientific and Technological Research Council of Turkey and Kocaeli University.

1. Castellini L., Carmignano M., D'Andrea M. and Villani M., "Brushless PM Actuator for Metal Bending Machine, "*39th Annual Conference of the IEEE Industrial Electronics Society (IECON)*, Vienna, Austria, 2013, pp. 2644-2649. 2. X. Ge, Z. Zhu, J. Li and J. Chen, "Analysis of Spoke-Type IPM Machine by Step-Staggered Rotor with Alternate Airspace-Barriers," *IEEE Magnetics Conference (INTERMAG)*, Beijing, China, 2015, pp. 1-1. 3. S. U. Chung, J. W. Kim, Y. D. Chun, B. C. Woo and D. K. Hong, "Fractional Slot Concentrated Winding PMSM With Consequent Pole Rotor for a Low-Speed Direct Drive: Reduction of Rare Earth Permanent Magnet," *IEEE Transactions on Energy Conversion*, vol. 30, no. 1, pp. 103-109, March 2015. 4. Nerg J., Rilla M., Ruuskanen V., Pyrhönen J.and Ruotsalainen S., "Direct-Driven Interior Magnet Permanent-Magnet Synchronous Motors for a Full Electric Sports Car," *IEEE Transactions on Industrial Electronics*, vol. 61, no. 8, pp. 4286-4294, Aug. 2014. 5. J. Shi, F. Chai, X. Li and S. Cheng, "Study of The Number of Slots/Pole Combinations for Low Speed High Torque Permanent Magnet Synchronous Motors," International Conference on Electrical Machines and Systems, Beijing, 2011, pp. 1-3. 6. Wrobel R. and Mellor P. H., "Design Considerations of a Direct Drive Brushless Machine with Concentrated Windings," *IEEE Transactions on Energy Conversion*, vol. 23, no. 1, pp. 1-8, March 2008.

Terminal Voltage	24V	# of Slot	36
Rated Torque	~40Nm	# of Poles	32
Rated Speed	~85rpm	# of Phases	3

a) Design specifications of the torque motor with CPR

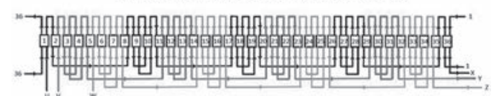

b) Winding layout of CPR torque motor

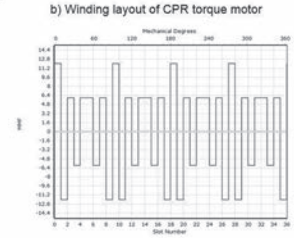

c) Distribution of the winding MMF

Fig. 1. Design specifications and preliminary design outputs

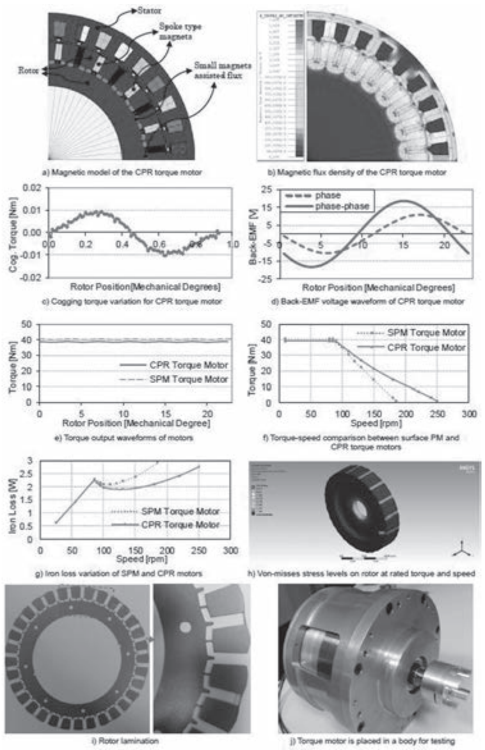

Fig. 2. 2D FEA results of the proposed motor topology and CPR torque motor prototype

10:00

AG-05. Manufacturing Condition and Variations of Soft Magnetic Composite Cores for Application in PM Motors Based on Taguchi Method.

G. Lei[1], Y. Guo[1] and *J. Zhu*[1]
1. University of Technology Sydney, Sydney, NSW, Australia

Soft magnetic composite (SMC) material has been investigated for the development of cores for permanent magnet (PM) motors in recent years. Compared with the cores made of traditional silicon steel sheet, there are several special properties of SMC cores, including (1) the isotropic performance in electromagnetic and thermal properties due to the powder nature of SMC, making it ideal for the PM motors with 3D flux path, such as transverse flux machine (TFM) and claw pole motor (CPM); (2) the lower eddy current loss and magnetic permeability because of the isolation coat of the particles, (3) the easier manufacturing ability of stator/rotor cores by using molding technology [1]-[3]. On the other hand, there are two main challenges for the manufacturing and application of SMC cores in PM motors. First, heat treatment is a crucial process in the manufacturing of SMC cores. There are several control parameters in this step such as the burn-off and curing temperatures and times. They will determine the core loss and magnetic permeability of the manufactured SMC cores. Therefore, optimal manufacturing factors should be investigated to obtain the best magnetic properties of the cores. Second, there are some manufacturing variations of the SMC cores like core densities and dimension, which will lead variations of the motor performances, such as output power and efficiency. Thus, the quality of the manufactured SMC cores will affect the quality of the SMC motors. To gain the best performances and good quality of the SMC cores and motors, manufacturing uncertainty analysis should be investigated for both SMC cores and motors. This work will consider these two challenges by using the Taguchi method. The Taguchi method is a robust design method with consideration of manufacturing variations and other noise factors in the manufacturing and usage of a product like motor. It is a structured approach for determining the best combination of inputs to produce a product or service, based on the orthogonal design technology and quality loss functions (or S/N ratio). It is one of the most powerful methods available to reduce product cost, improve quality, and simultaneously reduce development interval [4]-[6]. In this work, this method will first be used for the determination of the best parameters for the heat treatment of SMC cores, and some manufacturing variations will be discussed. Then, to decrease the effects of manufacturing variations of SMC cores on the motor performances, this method will be investigated again to find out the best dimension of a 3D TFM to increase the manufacturing quality of the motor. 1. Determination of the best heat treatment parameters of SMC cores Fig. 1 illustrates several manufacturing facilities and samples for a 3D TFM with SMC cores. The hydraulic compact machine (Fig.1(c)) uses the die tools (Figs.1(a) &(b)) to compact the SMC powders to produce the raw SMC core (Fig.1(e)), then the high-temperature furnace will cook the raw core with a controlled heat treatment plan as shown in Fig. 1(g) to obtain a cooked core (Fig.1(f)). As shown in Fig.1(g), there are five main parameters for the heat treatment of the SMC cores. They are Te1, Te2, Te3, Ti1 and Ti2. Te1 is the initial temperature of the furnace. The basic effect of temperature Te2 is to ensure the mechanical strength of the compacted SMC core. The effect of temperature Te3 is to eliminate the stress and improve the magnetic performance. Ti1 and Ti2 are the cooking times. To determine the best parameters of them, an orthogonal design is adopted with three levels for each factor. Table 1 lists the details of the orthogonal array. As shown, there are 18 experiments. For each experiment, the relative permeability and the core loss are measured for the cooked core. The measured results are shown in the table as well. Based on the analysis of Taguchi method, it is found that the best levels for those five heat treatment parameters are [200 °C, 480 °C, 60 mins, 500 °C, and 30 mins]. The obtained relative permeability is 267 and core loss is 4.48 W/kg. 2. Determination of the best dimension of a SMC motor Based on the experimental results, it is found that there are some manufacturing variations for the cooked SMC cores. The most important one is the relative permeability, which will affect the electromagnetic analysis and performances of the designed motor. However, it is hard to decrease these variations in the core manufacturing step (high cost will be required to upgrade the equipment like the high-temperature furnace). Therefore, the dimension of the motor is optimized to decrease the sensitivity of these variations by using the Taguchi method. In the implementation, seven parameters including PM dimension and air gap are selected as the control parameters and the relative permeability is regarded as noise factor. With a similar analysis to the heat treatment part, an optimal design is obtained. This design can increase the motor reliability from around 76% to 98% by using the proposed method. In conclusion, Taguchi method benefits the manufacturing of good quality SMC cores and PM-SMC motors.

[1] G. Lei, J. G. Zhu, and Y. G. Guo, Multidisciplinary Design Optimization Methods for Electrical Machines and Drive Systems, Springer-Verlag Berlin Heidelberg, ISBN: 978-3-662-49269-7, 2016. [2] G. Lei, J. Zhu, Y. Guo, C. Liu and B. Ma, “A review of design optimization methods for electrical machines”, Energies, vol. 10, no. 12, Art. ID 1962, pp. 1-31, Dec. 2017. [3] C. Liu, G. Lei, T. Wang, Y. Guo, Y. Wang and J. Zhu, “Comparative study of small electrical machines with soft magnetic composite cores,” IEEE Trans. Ind. Electron., vol. 64, no. 2, pp. 1049-1060, Feb. 2017. [4] C. C. Hwang, L. Y. Lyu, C. T. Liu, P. L. Li, “Optimal design of an SPM motor using genetic algorithms and Taguchi method,” IEEE Trans. Magn., vol. 44, pp. 4325–4328, 2008. [5] M. Ashabani, Y. A. Mohamed, J. Milimonfared, “Optimum design of tubular permanent-magnet motors for thrust characteristics improvement by combined Taguchi-neural network approach,” IEEE Trans. Magn., vol. 46, pp. 4092–4100, 2010. [6] S. I. Kim, et al., “Optimization for reduction of torque ripple in interior permanent magnet motor by using the Taguchi method,” IEEE Trans. Magn., vol. 41, pp. 1796–1799, 2005.

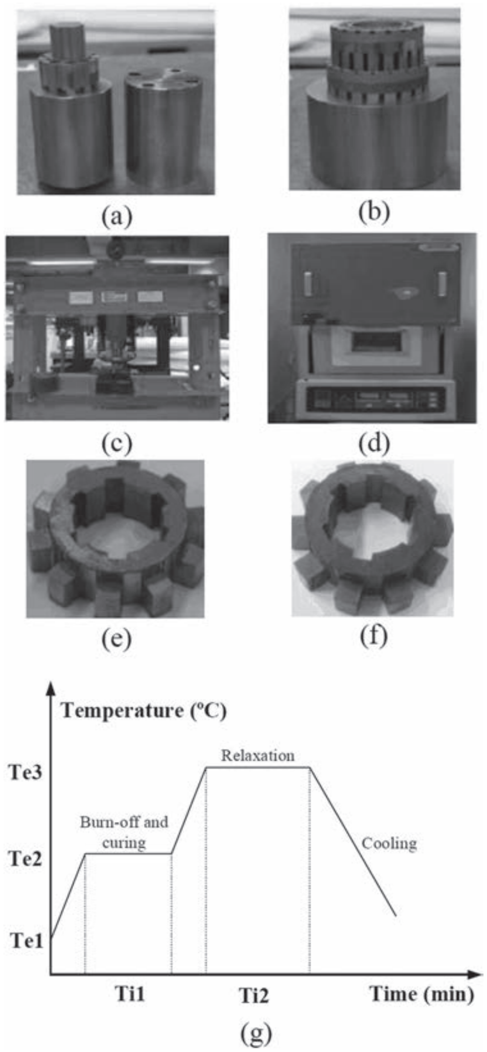

Fig. 1. Manufacturing facilities and SMC cores for the proposed 3D TFM, (a) die tools for compaction of rotor core, (b) die tools for compaction of stator cores, (c) hydraulic compact machine, (d) high-temperature furnace, (e) rotor core before heat treatment, (f) rotor core after heat treatment, (g) heat treatment plan.

No.	X1. Te1 (°C)	X2. Te2 (°C)	X3. Ti1 (min.)	X4.Te3 (°C)	X5. Ti2 (min.)	μ_r	Core loss (W/kg)
1	25	420	30	500	10	210.73	10.87
2	25	450	60	550	30	239.76	14.73
3	25	480	90	600	50	192.1	66.21
4	100	420	30	550	30	243.34	67.48
5	100	450	60	600	50	197.12	70.42
6	100	480	90	500	10	261.68	7.56
7	200	420	60	500	50	249.63	5.71
8	200	450	90	550	10	265.92	14.57
9	200	480	30	600	30	206.15	67.48
10	25	420	90	600	30	222.22	48.72
11	25	450	30	500	50	273.33	7.42
12	25	480	60	550	10	274.41	15.13
13	100	420	60	600	10	202.56	83.4
14	100	450	90	500	30	226.28	5.94
15	100	480	30	550	50	250.75	14.9
16	200	420	90	550	50	271.49	13.59
17	200	450	30	600	10	183.11	74.4
18	200	480	60	500	30	267.1	4.48

Table 1. Orthogonal array and experimental results for heat treatment

10:15

AG-06. Design of Cryogenic Permanent Magnet Synchronous Motor for Submerged Liquefied Natural Gas Pump.

C. Guo[1], S. Huang[1], J. Wang[1] and *Y. Feng*[1]
1. College of Electrical & Information Engineering, Hunan University, Changsha, China

Abstract—Cryogenic motors, as the key component of submerged liquefied natural gas (LNG) pumps, have gradually attracted the attention of researchers with the vigorous development of LNG industry. This paper presents the design of cryogenic permanent magnet synchronous motor (C-PMSM) submerged in LNG pump. In cryogenic environment of –161 °C, the magnetic and electric characteristics of PMSM differ greatly from the operating conditions at room temperature. So, in order to obtain the operating characteristics corresponded with theory and design of the motor are discussed. Finite element method (FEM) is adopted to establish models and to carry out the multi-field coupling simulation. A prototype is fabricated and built, in order to validate the theory. I.Introduction Because of its cleanliness, innocuity and many other advantages, the LNG have been widely accepted. Submerged pumps with simple structures and safety operation, are used in many aspects of the LNG industrial chain, such as pipeline transportation, tank filling, vehicle fueling etc.. The motor is sealed in the pump chamber and soaked in the LNG fuels under a very low temperature of -161°C. It is obvious that the conventional motors may not meet the operating requirements well in the cryogenic environment. Therefore, cryogenic motors have been investigated in recent years. For example, in [1], it present the design of cryogenic induction motor submerged in LNG for operating LNG spray pump, and the result of designed motor was fabricated and torque performance measured agreed well with design goals. However, the measured efficiency of the motor is only 88.8% at a rated speed of 3920 rpm. In [2] investigated a radial flux super-high speed PMSM, which operates to drive a two-stage cryocooler in the temperature of 77K, the operation efficiency was as high as 90%. However, the experiment was only carried out in water cooling test. In combination with practical application, excessive heat may cause a lot of LNG gasification and affect the operation efficiency of the pump system. Therefore, this paper the theory and design method of C-PMSM for submerged LNG pump are discussed, A prototype a rated power of 18.5kW at a rated speed of 6000 rpm has been fabricated and tested to verify the design methodology. II.theory and design of the C-PMSM In order to detect the magnetic and electric characteristics at cryogenic environment, the Sm2Co17 permanent magnet (PM) was tested after soaking in liquid nitrogen (-196°C) for one hour, the magnetic remanence (B_r) of PM is a little higher than at room temperature, and the resistivity ratio (ρ_{Cu}) of copper at room temperature and cryogneic temperature can be averaged by multiple measurements with three-arm bridge, and the specific value are shown in Fig.1 (a), the decrease of the increase of PM remanence [3] and winding resistance [4] will be changed which directly affect the operation characteristics of the motor, the magnetic properties of silicon steel are not sensitive to temperature changes known from the previous studies, similar to the results introduced in [5]. The cryogenic (CT) method suggests the redesign process that the stator slot area determined by conventional method can be reduced by the same ratio of the decreasing rate for ρ_{Cu} with temperature, also the PM volume can be reduced by the same ratio of the increasing rate for PM B_r with temperature. Fig. 1 (b) shows the shape and dimensions of stator and PMs for the CT design. The proposed submerged C-PMSM is soaked in -161°C, so the stress field should also be taken in consideration to ensure that there is no locking, crack or abnormal gap in the motor components caused by different degree of shrinkage or expansion. A coupled simulation model of electromagnetic-fluid-thermal-stress field will be analyzed in detail in the full paper. III.Experimental Study In consideration of the cost and safety, liquid nitrogen is used as the experimental medium instead of LNG, the prototype is enclosed in the pump and submerged in liquid nitrogen (-196°C), as shown in Fig. 2 (a). When C-PMSM is no loaded, the pump bypass channel opened, at this time both the readings of export pressure gauge and flow meter are zero; When it is loaded, the controller is adjusted to provide a frequency of 400Hz, when the outlet pressure gauge reading reaches 2MPa, the flow meter reading is greater than 20m^3/h, and temperature gauge in stable condition, it is determined that the load at this time is rated. The comparison between the simulation results and experimental data is shown in Fig. 2 (b), because of the physical difference between the two liquids, current tested is about 1.6 times. IV.Conclusion In this paper, an 18.5kW C-PMSM for submerged LNG pumps is designed with consideration of the low temperature influence on material properties. In cryogenic environment, the the magnetic, electric characteristics and key dimensions of stator and PM would differ greatly from the operating conditions at room temperature, Therefore, CT design method is proposed to redesign the slot area and PM volume as well as the whole motor volume by conventional design. Designed C-PMSM for cryogenic environment was fabricated, and measured results agreed well with design goals.

[1] H. M. Kim, K. W. Lee, D. G. Kim *et al.,* "Design of Cryogenic Induction Motor Submerged in Liquefied Natural Gas," *IEEE Trans. Magn.,* DOI 10.1109/TMAG.2017.2751099. vol. 6, no. 5, pp. 357–359, Sep. 2012. [2] L. Zheng1, T. X. Wu1, D. Acharya *et al., "*Design of a Super-High Speed Permanent Magnet Synchronous Motor for Cryogenic Applications" *IEEE Int. Conf. on Electric Machines and Drives*, United States, Sep. 874-881, 2005. [3] L Dlugiewicz, J Kolowrotkiewicz, W Szelag *etal.,* "Permanent magnet synchronous motor to drive propellant pump." *IEEE Int. Sym. on Power Electronics, Electrical Drives, Automation and Motion*. Sorrento, Italy, Jan. 822-826. 2012 [4] M. Baranski and W. Szelag, "Finite-element analysis of transient electromagnetic-thermal phenomena in a squirrel-cage motor working at cryogenic temperature," *IET Sci., Meas. Technol.*, vol. 6, no. 5, pp. 357–359, Sep. 2012. [5] D. Miyagi; D. B. Otome, M. Nakano, "Measurement of magnetic properties of nonoriented electrical steel sheet at liquid nitrogen temperature using single sheet tester." *IEEE Trans. Magn.*, vol. 46, no. 2, pp. 314–317, Feb. 2010.

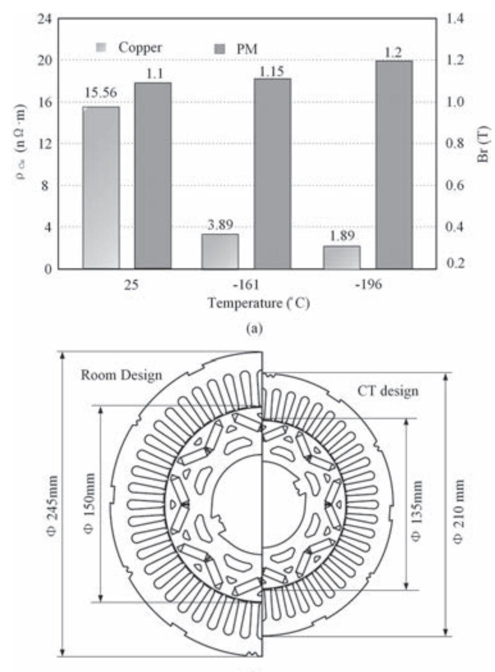

Fig. 1. Design differences at rooml and cryogenic temperature between (a) B_r and ρ_{Cu} characteristics, and (b) key dimensions of stator and PM.

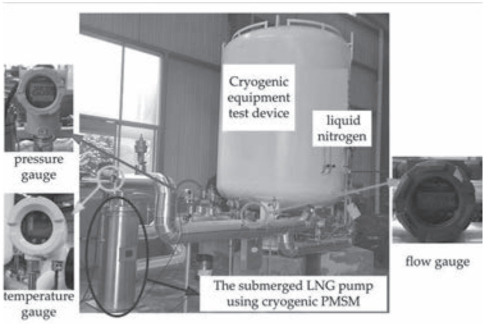

(a)

Parameter	Simulation in LNG(-161°C)	Experimental in liquid nitrogen (-196°C)
Input voltage U (V)	408	412.3
Line voltage fundamental wave U_N(V)	371.3	374.8
Input current I_N(A)	37	59.5
efficiency η (%)	91	92.2
Speed ω (rad/s)	630	—
Torque T_N(N.m)	29.4	—
Pump output flow L (m^3/h)	—	20.4
Pump discharge pressure P (MPa)	—	2.05

(b)

Fig. 2. (a) Measured device in Liquid nitrogen and (b) simulation and experiment results of the C-PMSM.

10:30

AG-07. Study on Optimal Current Allocation Strategy for Doubly Salient Electromagnetic Machine based on Particle Swarm Optimization.

A. Wang[1], Z. Chen[1], H. Li[1] and C. Zhang[1]
1. Department of Electrical Engineering, Nanjing University of Aeronautics and Astronautics, Nanjing, China

I. Introduction The magnetic field of doubly salient electromagnetic machine (DSEM) can be controlled by the field current, and it can be used in flux-weakening control of motor and voltage control of generator [1]. However, due to the existence of field windings, the efficiency of DSEM is lower. And the efficiency optimization control is needed. The research focuses on two aspects: based on loss model and on-line searching technology [2-3]. Based on asymmetric current control, this paper builds the loss model of a four-phase DSEM, defines the torque constraint and improves efficiency by particle swarm optimization (PSO). In the end, validity is confirmed by simulation and experiment. II. Asymmetric Current Control The output torque (eq.1) of DSEM can be expressed as the sum of reluctance torque T_r and mutual torque T_m. In eq.1, i_p is the armature current, i_f is the field current, L_{pp} is the self-inductance of phase winding, L_{pf} is the mutual inductance between phase and field winding. Because the field current does not change, it is necessary to inject the positive current into the armature winding when the inductance is rising and the negative current in the opposite situation to make mutual torque positive. In the method of asymmetric current control, the positive and negative current are controlled by the H-bridge topology respectively, so that the effective control can be realized. III. Optimal Current Allocation Strategy Eq.1 shows that the output torque of DSEM is mainly linked to the field current, the armature current and the rate of change of mutual inductance with respect to angle. The rate is determined in the motor design, therefore the essence of controlling torque is the control of the field current and the armature current. The optimal current allocation strategy proposed in this paper is to reasonably allocate the above currents when the inductance of armature windings is ignored, i.e., armature current is constant within the conduction interval. The idea is to find the minimum value of the copper loss function *f(ij)* under the condition of nonlinear torque constraint *g(ij,T)*. In eq.2&3, the relationship expression $T_{input}(W'_f)$ between the torque and the magnetic co-energy can be obtained by using Matlab. The torque and magnetic co-energy of different current combinations are fitted to get it. Magnetic co-energy (W'_f shown in eq.4) is positively correlated with the output torque. To solve it, the relationship between the flux and the current is needed. Two boundary magnetization curves are selected and fitted by first-order and piecewise fitting [4]. Considering the conservation of the field and armature ampere turns, W'_f is gotten by integral. The problem is a single-objective optimization problem with constraints. PSO shown in Fig.2 uses penalty function to satisfy constraints and competition to solve the border issue. Population size is 40 and learning factors are 2 [5]. Linearly decreasing inertia weight is used in inertia factor [6]. III. Verification The optimized and non-optimized current combinations (i_f, i_p, i_n) of ideal torque 0-40Nm are chosen to compare the efficiency. The rated power is 1kW and rated speed is 240 rpm. According to P=TΩ, the torque under the rated condition is about 40Nm. Due to it, the maximal torque in the simulation is 40 Nm and the step size is 5. The losses in the model include copper loss (p_{cu}), core loss (p_{fe}) and mechanical loss (p_m). The input power (P_{in}) is the sum of losses and electromagnetic power (P_e). Efficiency (η) is the ratio of P_e to P_{in}. Computational formulas are shown in eq.5. Core loss is gotten by the finite element analysis. The result is shown in Fig.3&4. In order to verify the feasibility of the algorithm in practical situation, the H-Bridge topology is built to excite the armature windings and standard angle control (Fig.5) is used. Due to the phase inductors, the phase current has a certain rise and fall time, and the current in the conductive interval is fluctuating, the phase current cannot keep the maximum. As shown in Fig.6&7, the torque is lower than ideal one. To mend the error, correction factor will be introduced into $T_{input}(W'_f)$ in the strategy. Related test platform is being built. IV. Conclusion Based on PSO and asymmetric current control, the optimal current allocation strategy can suppress copper loss significantly and improve efficiency. Some key issues remained to be solved: finding other control modes to improve the output torque and reducing core loss. Acknowledgement This work was supported by the State Key Program of National Natural Science Foundation of China under Grant No.51737006.

[1]W. Y. Jia, L. Xiao, and D. M. Zhu, "A mini-ripple control method for doubly salient electromagnetic motor control system," *2017 IEEE Applied Power Electronics Conference and Exposition (APEC)*, pp. 1886-1890, March 2017. [2]R. Mbayed, G. Salloum, L. Vido, E. Monmasson and M. Gabsi, "Hybrid excitation synchronous motor control in electric vehicle with copper and iron losses minimization," IECON 2012 - 38th Annual Conference on IEEE Industrial Electronics Society, pp. 4886-4891, Oct. 2012. [3]X. F. Liu, X. Peng, M. F. Li, and Y. X. Song, "Efficiency Optimization Control (Considering Core Loss) of Induction Motor based on Loss Model Method," Explosion-Proof Electric Machine., vol. 50, no. 1, pp. 10-26, January 2015. [4]Z. H. Zhang, "Fitting of the magnetization curve," Mcromotors Servo Technique, no. 4, pp. 27-34, April 1983. [5] X. Y. Chang, R. J. Li. "Experimental Analysis of Acceleration Coefficient in Particle Swarm Optimization Algorithm" [J]. Computer Engineering, 2010, 36(04):183-186. [6]Eberhart R C, Shi Y. Tracking and optimizing dynamic systems with particle swarms[C]// Evolutionary Computation, 2001. Proceedings of the 2001 Congress on. IEEE, 2002:94-100 vol. 1.

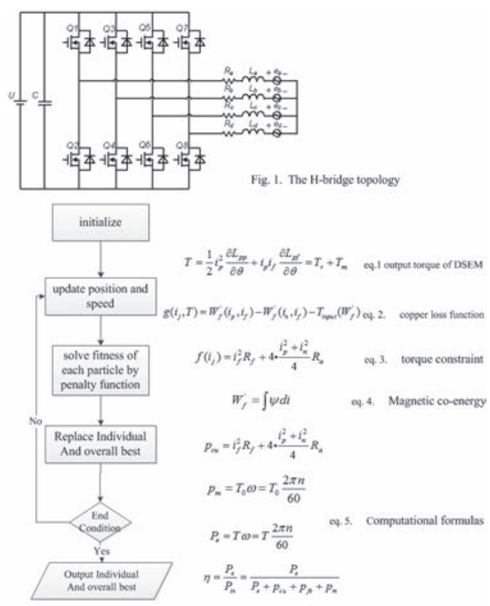

Fig. 1. The H-bridge topology
Fig.2. Flow chart of PSO

Fig.1/2+eq.1-5

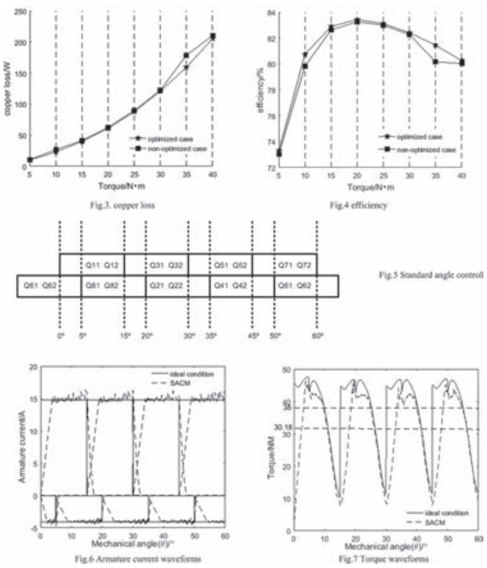

Fig.3. copper loss

Fig.4 efficiency

Fig.5 Standard angle controll

Fig.6 Armature current waveforms

Fig.7 Torque waveforms

Fig.3-7

10:45

AG-08. A Novel Coupled Auto-transformer and Magnetic Control Soft Starter for Super Large Capacity High Voltage Motor.

J. Yuan[1], *C. Wang*[1], Y. Zhu[1], H. Zhou[1], L. Wei[1,2], C. Tian[1], Y. Gao[3], K. Muramatsu[3] and B. Chen[1]
1. Electrical and Engineering, Wuhan University, Wuhan, China; 2. Department of Electrical Engineering, Graduate School of Engineering, Kyoto University, Kyoto, Japan; 3. Department of Electrical and Electronic Engineering, Saga University, Saga, Japan

I. Introduction The start current can reach up to as high as 4-7 times of the motor's rated current when high voltage motors start directly. For super large capacity motors (voltage above 6 kV, power above 10000 kW), the direct start current could reach 5000 Ampere or more[1]. Such large start current will not only have a huge impact on the motor itself but also cause a sudden decline of the grid voltage[2]-[3]. In order to resolve this issue, a novel coupled auto-transformer and magnetic control (CATMC) soft starter method was proposed in this paper. The new structure of CATMC soft starter combines the two functions of the auto-transformer and the magnetic control reactor (MCR) through ingenious electric and magnetic circuit design. Hence the start current is reduced in two ways and the structure becomes more compact and flexible. II. Basic Principle Fig.1 (a) shows the configuration of the CATMC soft starter studied in this digest. The device consists of eight windings. The two DC excitation windings and two AC windings are included in the upper and lower sections respectively. The two AC windings are connected in parallel and then connected in series. AC power supply is connected between AX and aX link to AC load. The two DC excitation windings are inversely connected in series, and then connected to the DC excitation source. The upper and lower DC magnetic fluxes regulate the excitation reactance of the high and low voltage side windings respectively. Utilizing the saturation characteristic of the iron core magnetic material, DC excitation is injected into the excitation winding to change its magnetic saturation, thereby changing the equivalent permeability and changing the reactance value and the reactance capacity smoothly. Fig.1 (b) shows the magnetic circuit for iron core of single phase CATMC soft starter. The magnetic circuit decomposition approach proposed in literature[4] is used to analyze the magnetic circuit model and obtain the winding voltage equations: U_1-U_2=$i_{11}R_{11}$+$N_1(d\Phi_5/dt+d\Phi_{11}/dt)$ (1) U_1-U_2=$i_{21}R_{21}+N_1(d\Phi_7/dt+d\Phi_{21}/dt)$ (2) $U_{d1}=i_{10}R_{12}+i_{10}R_{22}+N_{10}(d\Phi_5/dt+d\Phi_{12}/dt)-N_{10}(d\Phi_7/_{\mathrm{dt}}+d\Phi_{22}/dt)$ (3) $U_2=i_{12}R_{13}+N_2(d\Phi_6/dt+d\Phi_{13}/dt)$ (4) $U_2=i_{22}R_{23}+N_2(d\Phi_8/dt+d\Phi_{23}/dt)$ (5) $U_{d2}=i_{20}R_{14}+i_{20}R_{24}+N_{20}(d\Phi_6/dt+d\Phi_{14}/dt)-N_{20}(d\Phi_8/dt+d\Phi_{24}/dt)$ (6) By applying the Kirchhoff's first law of magnetic path, the node equations are shown as follows: $\Phi_1=\Phi_4+\Phi_6$ (7) $\Phi_8=\Phi_4+\Phi_2$ (8) $\Phi_5=\Phi_0+\Phi_6$ (9) $\Phi_8=\Phi_0+\Phi_7$ (10) $\Phi_5=\Phi_1+\Phi_3$ (11) $\Phi_2=\Phi_3+\Phi_7$ (12) By applying the Kirchhoff's second law of magnetic path, the loop equations are shown as follows: $H_1l_1+H_5l_5+H_6l_6=N_1i_{11}+N_{10}i_{10}+N_2i_{12}+N_{20}i_{20}$ (13) $H_2l_2+H_7l_7+H_8l_8=N_1i_{21}-N_{10}i_{10}+N_2i_{22}-N_{20}i_{20}$ (14) $H_0l_0+H_3l_3+H_5l_5-H_7l_7=N_1i_{11}-N_1i_{21}+2N_{10}i_{10}$ (15) $H_0l_0+H_4l_4-H_6l_6+H_8l_8=-N_2i_{12}+N_2i_{22}-2N_{20}i_{20}$ (16) $H_0l_0=H_3l_3+H_4l_4$ (17) In addition, each magnetic circuit also satisfies the corresponding magnetization curve: $\Phi_k=f_k(H_k)$, k=0,1,…8. Assume that: $i_{11}=i'_{11}+i''_{11}$ (18) $i_{12}=i'_{12}+i''_{12}$ (19) $i_{21}=i'_{21}+i''_{21}$ (20) $i_{22}=i'_{22}+i''_{22}$ (21) And it satisfies the following constraints: $H_5l_5=N_1i'_{11}+N_{10}i_{10}$ (22) $H_6l_6=N_2i'_{12}+N_{20}i_{20}$ (23) $H_7l_7=N_1i'_{21}-N_{10}i_{10}$ (24) $H_8l_8=N_2i'_{22}-N_{20}i_{20}$ (25) The magnetic potential drop expressions for the remaining magnetic paths are obtained: $H_0l_0=1/3(N_1i''_{11}-N_2i''_{12}-N_1i''_{21}+N_2i''_{22})$ (26) $H_1l_1=N_1i''_{11}+N_2i''_{12}$ (27) $H_2l_2=N_1i'_{21}+N_2i''_{22}$ (28) $H_3l_3=2/3N_1i''_{11}+1/3N_2i''_{12}-2/3N_1i''_{21}-1/3N_2i''_{22}$(29) $H_4l_4=-1/3N_1i''_{11}-2/3N_2i''_{12}+1/3N_1i''_{21}+2/3N_2i''_{22}$ (30) According to the winding voltage equations (1)~(6) and the magnetic potential drop expressions (22)~(30), the nine-segment magnetic path model of CATMC soft starter is constructed as shown in Fig.1 (c). In Fig.1 (c), the magnetic circuit is represented by the double winding saturation transformer model. T0~T8 respectively represent the middle transverse iron core, the left paraxial column and the left upper and lower yoke, the right paraxial column and the right upper and lower yoke, the middle upper yoke, the middle lower yoke, the left upper center column, the lower left center column, the right upper center column and the right lower center column magnetic circuits. III. Simulation and Experimental Results To validate the effectiveness of CATMC soft starter, 18MW/10kV model is established in ANSOFT. Fig.2 (a) shows the flux density distribution of CATMC soft starter and motor. Simulation results of stator current for direct start and CATMC soft start are shown in Fig.2 (b). It can be seen that, the start current can be reduced to about 2570 A (2.5 times of the rated current) from 4680 A (4.5 times of the rated current) when starting directly. The soft starter based on CATMC for super large capacity high voltage motor has been designed successfully. The 18MW/10kV motor is selected as the experimental object, whose rated current is 1039A. The start curve is shown in Fig.2 (c). According to actual measured data, the start current is 2210 A. IV. Conclusion From the simulation and experimental results, we know that the start current can be restricted within 2.5 times of the rated current, which is very favorable to reduce harm to the power grid and the motor. Therefore, the CATMC method exhibits a promising alternative for popularization and real application in motor soft start.Contrast analysis with traditional soft start methods will be carried out soon.More details will be analyzed in full paper.

[1] W. Huang, Y. Yuan, Y. Chang, "A Novel Soft Start Method Based on Autotransformer and Magnetic Control," *International Conference on Industrial Technology*, pp. 2108-2113, March 2016.[2] S.-K. Kim and T.-K. Kim, "A Novel Hybrid Sequential Start Control System for Large Inductive Loads," *Jouranl of Electeical Engineering & Technology*, vol. 10, no. 1, pp. 388-394, January 2015.[3] M. Falahi, K. Butler-Purry, and M. Ehsani, "Induction Motor Starting in Islanded Microgrids," *IEEE Transactions on Smart Grid*, vol. 4, no.3, pp. 1323-1331, September 2013.[4] X. Wang, Z. Deng, K. Yu, et al. "Steady-state Characteristics of Extra-high Voltage Magnetically Controlled Shunt Reactor," *Proceedings of the CSEE*, vol. 28, no. 33, pp. 104-109, November 2008.

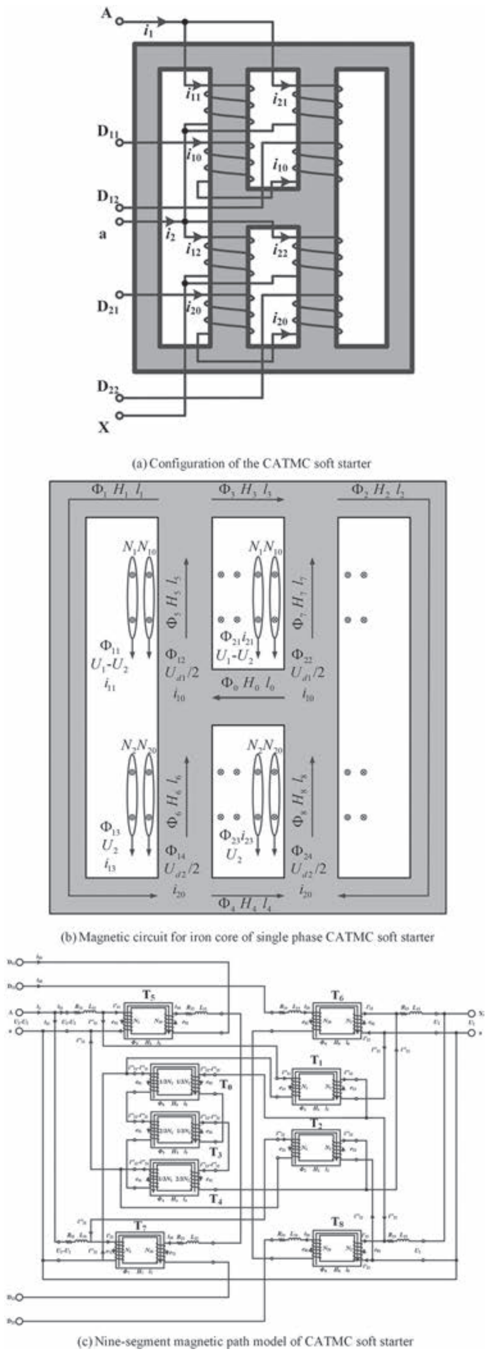

(a) Configuration of the CATMC soft starter

(b) Magnetic circuit for iron core of single phase CATMC soft starter

(c) Nine-segment magnetic path model of CATMC soft starter

Fig. 1. Theoretical analysis of CATMC soft starter

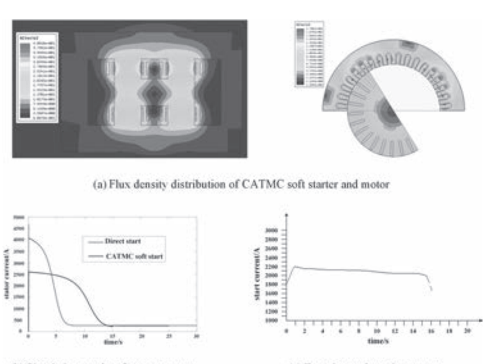

(a) Flux density distribution of CATMC soft starter and motor

(b) Simulation results of stator current

(c) Experimental starting current

Fig. 2. Simulation and experimental results

11:00

AG-09. A novel vector control strategy for six-phase induction motor with low torque ripples and harmonic currents.

H. Heidari[1], *A. Taheri*[1] and M. Holakooie[1]
1. University of Zanjan, Zanjan, The Islamic Republic of Iran

Abstract: In this brief, a new vector control strategy is proposed to efficient control of six-phase induction motor (SPIM). In order to reduce torque ripples represented in switching table-based direct torque control (ST-DTC), a new set of inputs is provided for switching table (ST). These inputs are based on the decoupled current components in synchronous reference frame. Indeed, using both field-oriented control (FOC) and direct torque control (DTC) concepts, precise inputs are used for ST to achieve better steady-state torque responses. Considering duty cycle control strategy, the loss subspace components are eliminated through a suitable set of virtual voltage vectors. Each virtual vectors are based on a combination of a large and a medium voltage vectors to make the volt-sec outcome near to zero. The proposed strategy not only notably reduces the torque ripples, but also suppresses low frequency current harmonics. I. Introduction With emergence of power electronic devices and adjustable-speed drives, the usage of multiphase machines has been widely developed in some industrial applications such as electrical trackers, renewable-energy generation, aerospace applications, and electric ship propulsions. The key needs to apply these machines are reliability, fault tolerance capability, higher motive power and current, lower torque pulsation, and lower DC-link voltage requirement [1], [2]. Direct torque control (DTC) strategy is a simple, powerful and effective scheme for adjustable-speed drives of SPIM, providing high performance torque and stator flux control. However, it suffers from some serious drawbacks, especially for multi-phase machines, including high torque ripples and low-frequency current harmonics which can degrade the performance of the drive system [3]. A great deal of efforts have been done to amend high torque ripples of DTC, which mostly include modification of hysteresis controller [4],[5] switching table [6],[7], replacing the hysteresis controller with another regulators, such as proportional-integral (PI) regulator, to provide PWM-based DTC [8], [9]. A global minimum torque ripple using modified switching pattern are proposed in [10]. In [11], torque ripples have been reduced by applying active and zero vectors in each sampling period using a predictive DTC. On the other hand, for reduction of harmonic currents, elimination of z_1-z_2 subspace components, using duty cycle concept in DTC are proposed in [12], [1] and [5] for six-phase induction motor, five-phase induction motor, and six-phase permanent magnet motor, respectively. Simultaneous reduction of torque ripple and low-order harmonic currents is a is still a challenging research task. II. Proposed method for the SPIM drive The block diagram of the proposed scheme is shown in Fig. 1. In order to decrease the torque ripples in the SPIM, a new approach is made by improving the ST's inputs. Using FOC framework [13], since the inputs of ST in classical ST-DTC are the errors between set and actual values of T_e and Ψ_s, it is a good idea to use the errors between the set and actual values of i_{ds} and i_{qs}, instead. In this case the steady-state torque ripple is considerably reduced because of adding an inner control loop to the drive system. According the sign of $\Delta i_{qs\ \mathrm{and}}$ Δi_{ds} and also flux position, propoer voltage vector is selected and applied during each sampling period. The digital output signals of the hysteresis controllers are described as Δi_{qs}=1 if $|i_{qs}|\leq|i_{qs}{}^*|$-|hysteresis band| Δi_{qs}=0 if $|i_{qs}|=|i_{qs}{}^*|$ (1) Δi_{qs}=-1 if $|i_{qs}|>|i_{qs}{}^*|$+|hysteresis band| Analogically, for the changes required for the d-axis of the stator current, Δid_s is described as Δi_{ds}=1 if $|i_{ds}|\leq|i_{ds}{}^*|$-|hysteresis band| Δi_{ds}=0 if $|i_{ds}|>|i_{ds}{}^*|$+|hysteresis band| (2) To reach low THD in the phase current of the SPIM, the proposed vector control scheme is synthesized with duty cycle control strategy. The ST applies two voltage vectors in each sampling period in order to eliminate z_1-z_2 subspace components. In comparison to the conventional DTC, the switching frequency of the proposed scheme is increased. In contrary, both harmonic currents and torque ripples are reduced. Moreover, the proposed scheme has fast dynamic, similar to the conventional DTC, and do not need any PWM modulator, which produces complexity and time delay. III. Experimental setup The performance of the proposed method is validated by the experimental tests. The experimental setup contains the SPIM and its coupled load, the main processor, two three-phase VSIs, current and voltage transducers, shaft encoder and single phase bridge rectifier. The processor used in the driver is eZDSP F2812. The motor speed is measured by an Autonics incremental shaft encoder coupled mechanically to the SPIM with resolution of 2500 P/R. The LEM LTS6np current transducers are implemented to measure all the currents. The dc-link voltage is also measured using LV 25-p voltage transducer. The selected experimental results are shown in Fig. 2. These tests confirm the good tracking capability of the proposed method. The proposed method provides significant reduction of torque ripples, stator flux ripples, and harmonic currents in comparision with the conventional DTC method while maintaining the simplicity and also the fast dynamics of the drive system.

[1] Levi, E., Bojoi, R., Profumo, F., Toliyat, H. A., & Williamson, S. (2007). Multiphase induction motor drives–a technology status review. *IET Electric Power Applications*, *1*(4), 489-516. [2] Levi, E. (2016). Advances in converter control and innovative exploitation of additional degrees of freedom for multiphase machines. *IEEE Transactions on Industrial Electronics*, *63*(1), 433-448. [3] Zheng, Libo, et al. "A novel direct torque control scheme for a sensorless five-phase induction motor drive." IEEE Transactions on Industrial Electronics 58.2 (2011): 503-513. [4] Ambrozic, Vanja, Giuseppe S. Buja, and Roberto Menis. "Band-constrained technique for direct torque control of induction motor." IEEE Transactions on industrial Electronics 51.4 (2004): 776-784. [5] Ren, Yuan, and Zi-Qiang Zhu. "Enhancement of steady-state performance in direct-torque-controlled dual three-phase permanent-magnet synchronous machine drives with modified switching table." IEEE Transactions on Industrial Electronics 62.6 (2015): 3338-3350. [6] Taheri, Asghar, Abdolreza Rahmati, and Shahriyar Kaboli. "Comparison of efficiency for different switching tables in six-phase induction motor DTC drive." Journal of Power Electronics 12.1 (2012): 128-135. [7] Singh, Bhoopendra, Shailendra Jain, and Sanjeet Dwivedi. "Torque ripple reduction technique with improved flux response for a direct torque control induction motor drive." IET Power Electronics 6.2 (2013): 326-342. [8] Lai, Yen-Shin, and Jian-Ho Chen. "A new approach to direct torque control of induction motor drives for constant inverter switching frequency and torque ripple reduction." IEEE Transactions on Energy Conversion 16.3 (2001): 220-227. [9] Ammar, Abdelkarim, Amor Bourek, and Abdelhamid Benakcha. "Nonlinear SVM-DTC for induction motor drive using input-output feedback linearization and high order sliding mode control." ISA transactions 67 (2017): 428-442. [10] Shyu, Kuo-Kai, et al. "Global minimum torque ripple design for direct torque control of induction motor drives." IEEE Transactions on Industrial Electronics 57.9 (2010): 3148-3156. [11] Abad, Gonzalo, Miguel Ángel Rodríguez, and Javier Poza. "Two-level VSC based predictive direct torque control of the doubly fed induction machine with reduced torque and flux ripples at low constant switching frequency." IEEE Transactions on Power Electronics 23.3 (2008): 1050-1061. [12] A. Taheri, "Harmonic reduction of direct torque control of six-phase induction motor", ISA Transactions 63 (2016) 299-314. [13] Holakooie, M. H., Taheri, A., & Sharifian, M. B. B. (2015). MRAS based speed estimator for sensorless vector control of a linear induction motor with improved adaptation mechanisms. Journal of Power Electronics, 15(5), 1274-1285.

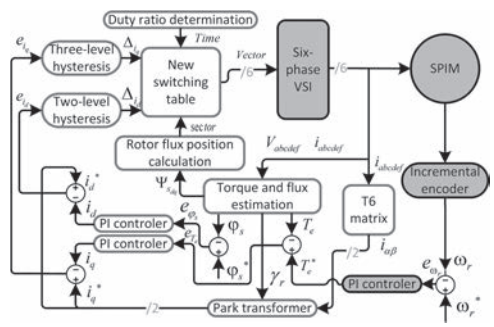

Fig. 1. The block diagram of the proposed control scheme

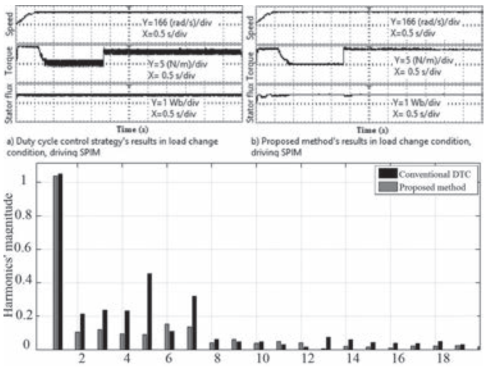

Fig. 2. The selected Experimental results

11:15

AG-10. A Novel Dual-Sided PM Variable Flux Memory Machine.

H. Yang[1], H. Lin[1], Z. Zhu[2], S. Lyu[1] and K. Wang[1]
1. School of Electrical Engineering, Southeast University, Nanjing, China; 2. Department of Electronic and Electrical Engineering, The University of Sheffield, Sheffield, United Kingdom

I. INTRODUCTION Memory machine (MM) was regarded as a promising candidate for wide-speed-range applications [1]-[6]. Since the low coercive force (LCF) PM is employed in MM, the air-gap flux can be flexibly adjusted by changing the magnetization state (MS) of PM with a temporary current pulses. The speed range can be subsequently extended with high efficiency maintained. According to the magnetizing current pattern, MMs can be generally categorized into AC- [1]-[3] and DC-magnetized [4]-[6] types. The former MM normally employs vector-control algorithm to apply *d*-axis current pulse in stator windings to vary the magnetization level of LCF PMs, while the latter one adopts auxiliary DC magnetizing coils to facilitate the magnetization control. Besides, the rotor-PM topologies of MMs have structures similar to conventional interior PM machines, which shows comparable torque density with those conventional surface-mounted PM machines [3]. Nonetheless, LCF magnets on the rotor generally suffer from to armature reaction demagnetization effect, and the integration of armature and magnetizing functions in the stator winding results in complicated online FW control. On the other hand, the stator-PM MMs have the advantages of easy online magnetization control, and a simple and robust salient rotor as well as easy thermal management can be obtained. Nevertheless, the fact that two kinds of PMs, i.e., NdFeB and LCF PMs, as well as two sets of windings are located on stator leads to excessively crowded stator space and low torque density. Therefore, this paper attempts to propose a novel dual-sided PM memory machine (DSPM-MM) by combing the distinct advantages of "high torque density" of rotor-PM MM and "simple online PM flux control" of stator-PM MM. In the proposed design, the consequent-pole NdFeB PMs are placed in the rotor, while LCF PMs are mounted between the adjacent stator teeth to enable flexible air-gap flux adjustment. The machine topology and operating principle are introduced and addressed, respectively. Then, the electromagnetic performance is analyzed, which confirms the feasibility of the proposed design. II. MACHINE TOPOLOGY AND OPERATING PRINCIPLE Fig. 1 (a) shows the topology of the proposed DSPM-MM with 6-stator-slot/7-rotor-pole configuration, which is characterized by a combination of two single-sided machines having two kinds of magnets on rotating and stationary sides, respectively. For the rotor, the alternate arrangement of homopolar NdFeB PMs and iron poles forms a consequent-pole configuration. For the stator, the LCF PMs are alternately buried in air space between adjacent stator tooth poles, and the DC magnetizing coils are wound on the LCF magnets. The NdFeB PMs serve as a dominant contributor for air-gap flux, while the LCF PMs work as a flux adjustor by applying the current pulse in the magnetizing coils. The flux regulation principles for the flux-enhanced and flux-weakened operations are illustrated in Figs. 1(b) and (c), respectively. The air-gap flux can be flexibly varied as the LCF PMs are either remagnetized or demagnetized in same or opposite direction with the NdFeB PMs, i.e., the flux-enhanced and flux-weakened states. For low-speed region, NdFeB and LCF PMs are with identical magnetization direction, the torque density can be subsequently improved. On the other hand, for high-speed region, the LCF PMs are reversely demagnetized to short-circuit and weaken the NdFeB PM fields, and hence the constant-power operating range (CPSR) can be effectively extended within the limitation of inverter power rating. The major advantages of the developed machine, which combines the distinct synergies of the conventional rare-earth magnet machine and stator-PM MM, which can be summarized as follows: 1) The merits of high torque density in conventional rotor-PM machine and easy magnetization control in stator-PM MM can be well synthesized; 2) The wide speed range and high efficiency at CPSR can be realized due to excellent flux adjusting capability and negligible excitation copper loss in the proposed DSPM-MM. 3) The ferromagnetic stator and rotor iron poles provide an effective circulating path for the armature fields as well as the magnetizing fields. That is to say, the parallel PMs and armature reaction fields can prevent the LCF PMs from accidental armature demagnetization. III. ELECTROMAGNETIC PERFORMANCE Fig. 2 (a) shows the open-circuit field distributions of the proposed machine under different MSs of LCF PMs. It can be observed that the machine shows fairly good flux adjusting capability. The corresponding radial air-gap flux density and phase back-EMF waveforms at 1500 r/min are shown in Figs. 2(b) and (c), respectively. The fact that the machine exhibits basically sinusoidal EMFs regardless of MS indicates that the proposed machine is suitable for brushless AC operation. Furthermore, the efficiency maps subject to different MSs are plotted in Fig. 2(d). The results confirm that the proposed machine can achieve high efficiency within a wide range of speeds and loads by choosing appropriate MSs under different operating regions. The detailed design considerations and experimental results will be given in the full paper.

REFERENCES [1] V. Ostovic, "Memory motors," *IEEE Ind. Appl. Mag*., vol. 9, no. 1, pp. 52-61, Jan./Feb. 2003. [2] K. Sakai, K. Yuki, Y. Hashiba, N. Takahashi, and K. Yasui, "Principle of the variable-magnetic-force memory motor," in *Proc. Int. Conf. on Electr. Mach. Syst.*, Tokyo, Japan, 2009, pp. 1-6. [3] N. Limsuwan, T. Kato, K. Akatsu, and R. Lorenz, "Design and evaluation of a variable-flux flux-intensifying interior permanent magnet machine," *IEEE Trans. Ind. Appl.*, vol. 50, no. 2, pp. 1015-1024, Mar./Apr. 2014. [4] C. Yu and K. T. Chau, "Design, analysis, and control of DC-excited memory motors," *IEEE Trans. Energy Convers.*, vol. 26, no. 2, pp. 479-489, Jun. 2011. [5] H. Yang, H. Y. Lin, Z. Q. Zhu, D. Wang, S. Fang, and Y. Huang, "A variable-mode stator consequent pole memory machine," *AIP Adcances*, vol. 8, no. 5, Article no: 056612, May. 2018. [6] H. Yang, Z. Q. Zhu, H. Lin, S. Fang, and Y. Huang, "Comparative study of novel variable-flux memory machines having stator permanent magnet topologies," *IEEE Trans. Magn*., vol. 51, no. 11, Article. 8114104, Nov. 2015

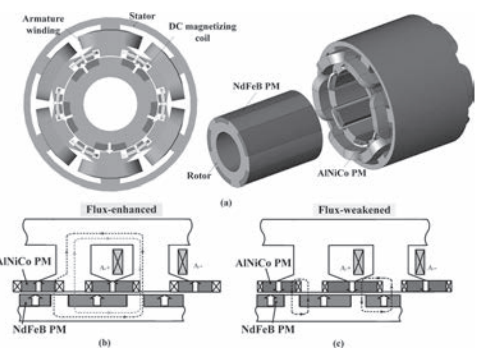

Fig. 1. Topology and operating principles of the proposed DSPM-MM. (a) Structure. (b) Flux-enhanced state. (c) Flux-weakened state.

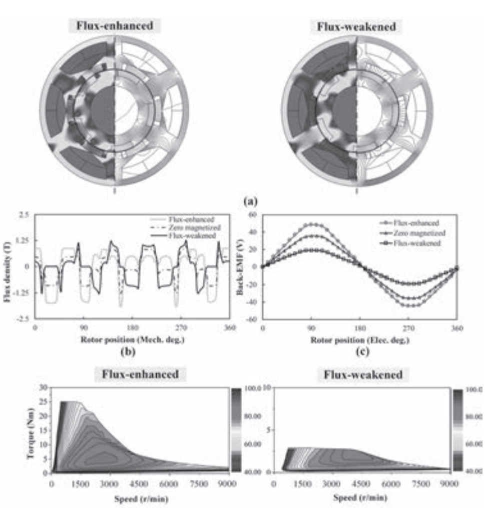

Fig. 2. Electromagnetic characteristics. (a) Open-circuit field distributions. (b) Open-circuit air-gap flux density distributions. (c) Back-EMF, 1500r/min. (d) Efficiency maps under different magnetization states.

11:30

AG-11. Analysis of Torque Characteristics of A Parallel Hybrid Excitation Machine Drives with Sinusoidal and Rectangular Current Excitations.

Y. Wu[1], L. Sun[1], Z. Zhang[1], Z. Miao[1] and C. Liu[1]
1. Nanjing University of Aeronautics and Astronautics, Nanjing, China

I. Introduction A new paralleled hybrid excitation machine (PHEM), consisting of axial paralleled permanent magnet machine (PMM) part and doubly salient excitation machine (DSEM) part, has the advantages of simple structure and independent flux path [1]. The synthetic phase inductance and back electromotive force (EMF) performances of the PHEM are different from the separated PMM and DSEM. Therefore, the optimized control schemes for the PMM and DSEM are not suitable for the PHEM [2]. In this paper, the torque characteristics of the PHEM drives with sinusoidal and rectangular current excitations are comparatively analyzed. II. Configuration and Control Scheme The 3D model of the PHEM is presented in Fig.1. It consists of two separated parts and a flux barrier gap sandwiched between them. The left part is 12/8-pole DSEM, while the right part is 24-slot/16-pole spoke-type PMM. The two rotors are installed in the same shaft and the two stators share one set of armature winding. The field source consists of non-overlapping concentrated windings allocated on the stator of DSEM and permanent magnets (PMs) mounted interior in the rotor of PMM. The independent flux paths of two parts present the merit of stable operation point of PMs with an attractive flux regulation capability. The driving strategies are commonly classified as either brushless AC (BLAC) drives, or brushless DC (BLDC) drives based on the waveforms of back-EMF. Fig.2 shows the back-EMF waveforms at open circuit and corresponding ideal current waveform. The back-EMF of PHEM is the sum of PMM and DSEM, which can be regulated by the field current. In BLAC drives (Fig.2 (a)), the phase current waveforms are sinusoidal, whereas in BLDC drives (Fig.2 (b)) the phase current waveforms are rectangular. Back EMFs of PHEM (I_f =5A n=1600rpm) and PMM are neither sinusoidal nor trapezoidal. Both sinusoidal and rectangular current excitations can be adopted in PHEM. III. Comparative Study of BLAC and BLDC Drives The sinusoidal and rectangular current excitations are used in two driving strategies and the current rms values are equal. Fig.3 shows the relationship between the torque and armature current when the field current is 5A. The BLAC drives exhibit greater torque density at the same armature current. Fig.4 shows the torque versus current angle with different armature current. In BLAC drives, when the armature current is relatively small, the current angle at the maximum torque per amp (MTPA) point is small. The dashed line shows the MPTA trajectory. An increase in the armature current causes an increase of the reluctance torque and thus the current angle becomes larger. In BLDC drives, the torque characteristics are similar to BLAC drives, except for the smaller current angles on the MPTA trajectory. When the armature current is larger than 100A, the current angles on the MPTA trajectory in BLDC drives are smaller. Fig.5 shows the torque ripple versus current angle for different armature current. In BLAC drives (Fig.5 (a)), the torque ripple decreases first and then increases with an increase in the armature current at a constant current angle. Due to the flux path saturation and the severe q-axis armature reaction, overload condition will cause a large torque ripple. In BLDC drives, the overall torque ripple are larger than the BLAC drives. The torque ripple becomes larger as the armature current increases. This is because the higher armature current is, the higher commutation torque ripple will be. IV. Experimental Verification A prototype PHEM has been designed and developed as shown in Fig.6. The line voltage of PHEM versus field current at open-circuit is shown in Fig.7. The excellent flux regulation capability can be realized. In detail, Fig.8 shows the back EMF of PMM and PHEM at 1600rpm under open-circuit condition. Fig.9 and Fig.10 show the torque versus armature current under the sinusoidal current excitations and rectangular current excitation, respectively. Fig.11 shows the torque versus current angle. It can be seen that the simulations agree well with the experiments. V. Conclusion In this paper, the torque characteristics of PHEM are comparatively analyzed in different current excitations. It shows that in BLAC drives, the PHEM exhibits a larger torque density with a lower torque ripple. A prototype PHEM has been designed and developed. Experiments shows the PHEM has an excellent flux regulation capability.

[1] W. Geng, Z. Zhang, K. Jiang, and Y. Yan, "A new parallel hybrid excitation machine: Permanent-magnet/variable-reluctance machine with bidirectional field-regulation capability," *IEEE Trans. Ind. Electron.*, vol. 62, no. 3, pp. 1372–1381, Mar. 2015. [2] Z. Q. Zhu and D. Howe, "Electrical machines and drives for electric, hybrid, and fuel cell vehicles," *IEEE Proc*., vol. 95, no. 4, pp. 746–765, Apr. 2007.

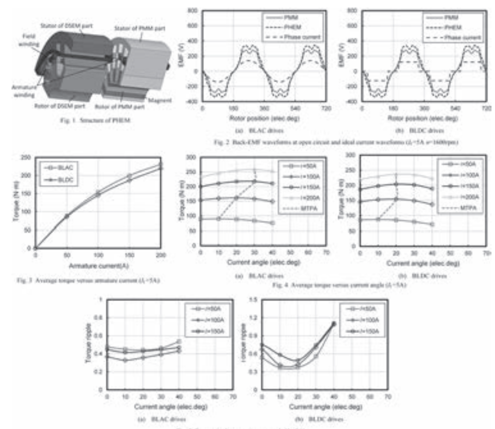

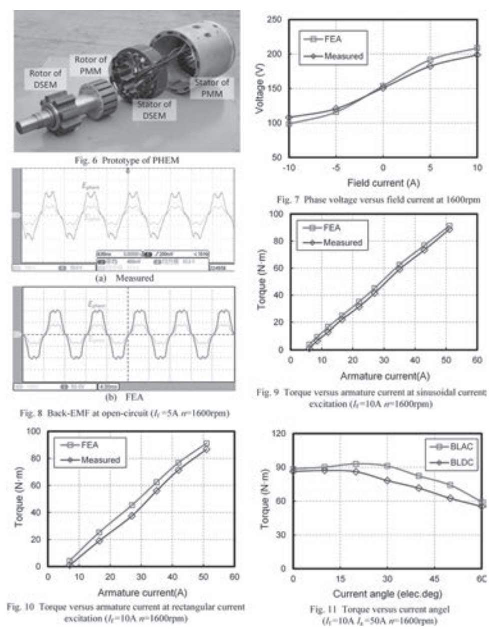

11:45

AG-12. Improved Analytical Eddy Current Loss Modelling Considering Carrier Harmonics towards Maximum Efficiency Control of PMSM- Drive Systems.

A. Balamurali[1], C. Lai[1], H. Dhulipati[1], V. Loukanov[2] and N. C. Kar[1]
1. University of Windsor, Windsor, ON, Canada; 2. D&V Electronics Ltd., Woodbridge, ON, Canada

I. Introduction Efficiency improvement of permanent magnet synchronous motor (PMSM) drive systems through control techniques has been of vital interest in the literature [1]-[4], [6]. The understanding of loss sources, accurate calculation of various losses and motor parameters are important during motor drive control development towards increased efficiency [1] - [3]. The pulse-width modulated (PWM) inverter generates time harmonics that leads to increased stator harmonic core losses and magnet eddy current losses, especially at higher speeds [2], [5]. In conventional loss minimization procedures for PMSM, core loss computations generally ignore the harmonic components and consider no-load conditions and fundamental air-gap flux density (B_g) [3]. In some of the methods, harmonic loss models were considered but in a simplified manner [4]. In order to fully exert the advantages of maximum efficiency control techniques to improve PMSM drive system efficiency, accurate loss models that include controllable fundamental and harmonic losses and non-linearities in the motor parameters should be considered. In [1], investigations were performed towards system level loss reduction using hybrid model of motor- drive system. It was seen that current angle, γ can be used as a control variable to reduce total motor and motor-drive system losses. In order to achieve improved efficiency, this paper proposes novel loss models to accurately calculate the total losses to be used towards the calculation of optimal γ. The effect of carrier order time harmonics in copper and core losses are considered in addition to improving core loss calculation by including armature reaction effects due to loading. II. Fundamental and Harmonic Loss Models in PMSM In this paper, improved loss models for PMSM have been developed considering fundamental and harmonic copper and core losses to be used towards efficiency improvement control. The results of the loss models can be used for offline loss minimization approach using look-up table (LUT) or can be solved online using terminal measurements. The source of harmonic losses is the voltage harmonics from inverter. The voltage harmonic spectrum from a sine- PWM modulated (SPWM) inverter is used to derive the current harmonics for the 4.25 kW test interior PMSM (IPM). The derived current harmonics are used to calculate harmonic copper losses. A magnetic circuit model (MCM) given in Fig 1(a) has been used to derive the flux density considering current harmonics using magnetomotive force in the airgap [5]. This paper extends the work in [5] by developing a novel, accurate loss model for core losses incorporating PWM time harmonics. The stator teeth and yoke flux densities are derived from the resultant on-load air-gap flux density. The flux density is calculated using a Fourier decomposition of the time series waveform derived from the MCM which includes fundamental and harmonic components. This method improves existing core loss calculation methods by predicting the flux densities during loaded condition. The space harmonics have been neglected intentionally in the MCM as the source of harmonic core loss is considered to be eddy currents from PWM carrier harmonics [2]. The comparison of air-gap flux density calculated using the developed model with that from finite element analysis (FEA) follow closely as shown in Fig 1 (b). The total losses in the motor is calculated as the summation of fundamental copper and core losses and harmonic copper and core losses and used further in the search for optimal efficiency. Sample results for total motor losses and core loss variation with γ are given in Figs. 1 (c) and 1 (d) for 575 rpm. The relationship between core loss and γ can be used to obtain an optimal point different from conventional maximum torque per ampere (MTPA) technique that consider only copper losses, leading to improved efficiency [6]. III. Validation of Loss Models and Implementation in Maximum Efficiency Control The loss values from the developed method have been compared with 2-D FEA co-simulation model as well as experimental loss segregation results for same operating conditions. Fig 2 (a) shows the harmonic loss comparison with FEA and Fig 2 (b) shows total electrical loss comparison with experimental results. The experimental loss values were measured using a power analyzer to measure the three- phase input power to motor and a torque sensor at the shaft between test IPM and dynamometer for output power. The results have been applied towards the loss minimization search for optimal current vector in *dq*-axis for varying operating conditions. The derived optimal values have been used to create a LUT for varying loads and speeds. The control diagram for current control implementation is given in Fig 2 (c). The results of the maximum efficiency control utilizing the developed model and conventional loss model considering no-load core losses and neglecting harmonic losses are compared in Fig 2 (d). IV. Conclusions It is concluded that the consideration of harmonic losses changes the optimal point for maximum efficiency and the efficiency can be improved, especially at higher speeds. The full paper will include detailed derivations of the analytical loss model, application of maximum efficiency control and further experimental validations conducted on the test IPM.

1. A. Balamurali, G. Feng, C. Lai, V. Loukanov and N. C. Kar, “Investigation into variation of permanent magnet synchronous motor-drive losses for system level efficiency improvement,” *proc. of IECON*, pp. 2014-2019, 2017. 2. K. Yamazaki, and S. Watari, “Loss analysis of permanent-magnet motor considering carrier harmonics of PWM inverter using combination of 2-D and 3-D finite-element method”, *IEEE Trans. Magn*., vol. 41, no. 5, pp. 1980-1983, 2005. 3. C. Cavallaro et al., “Efficiency enhancement of permanent-magnet synchronous motor drives by online loss minimization approaches”, *IEEE Trans. Ind. Electron*., vol. 52, no. 4, pp. 1153-1160, 2005. 4. X. Ding, G. Liu, M. Du, H. Guo, C. Duan and H. Qian, “Efficiency Improvement of Overall PMSM-Inverter System Based on Artificial Bee Colony Algorithm Under Full Power Range,” *IEEE Trans. Magn*, vol. 52, no. 7, pp. 1-4, 2016. 5. A. Balamurali, C. Lai, A. Mollaeian, V. Loukanov and N. C. Kar, “Analytical Investigation Into Magnet Eddy Current Losses in Interior Permanent Magnet Motor Using Modified Winding Function Theory Accounting for Pulsewidth Modulation Harmonics,” *IEEE Trans. Magn*, vol. 52, no. 7, pp. 1-5, 2016. 6. R. Ni, D. Xu, G. Wang, L. Ding, G. Zhang, L. Qu, “Maximum efficiency per ampere control of permanent-magnet synchronous machines”, *IEEE Trans. Ind. Electron*., vol. 62, no. 4, pp. 2135-2143, 2015.

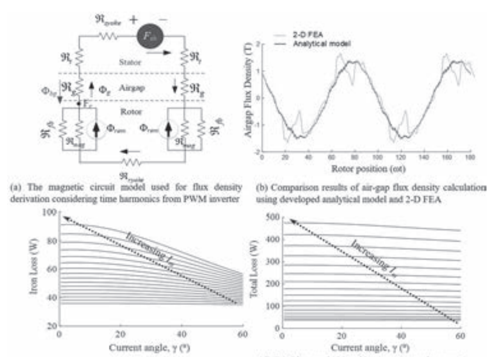

(a) The magnetic circuit model used for flux density derivation considering time harmonics from PWM inverter
(b) Comparison results of air-gap flux density calculation using developed analytical model and 2-D FEA
(c) Core loss variation with respect to peak current and current angle at 575 rpm in test IPM
(d) Total loss variation with respect to peak current and current angle at 575 rpm in test IPM

Fig. 1. Developed magnetic circuit model and sample results for loss calculations at 575 rpm in test IPM

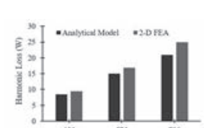

(a) Total harmonic loss (core and copper) comparisons of developed model with 2-D FEA co-simulation results at varying speeds

Speed (rpm)	Total electrical losses (W)	
Model	Developed analytical model	Experimental loss segregation
450	88	92.1
575	108.2	115
700	158.4	165

(b) Comparison of total electrical losses using developed loss model and experiments at half-rated current and varying speeds

Speed (rpm)	Efficiency (%)	
	Conventional	Developed loss model
200	78.9	78.93
325	81	81.16
450	84.4	84.68
575	86.9	87.59
700	81.5	82.3

(d) Comparison of efficiency using developed and conventional loss models at half-rated Current and varying speeds in Test IPM

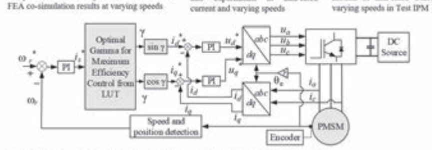

(c) Control diagram for implementation of maximum efficiency control of laboratory IPM

Fig. 2 Sample results for comparison of loss calculations and control implementation methodology

Session AH

SENSORS: FUNDAMENTAL DEVELOPMENTS AND MATERIALS I

James Deak, Chair
MultiDimension Technology Co., Ltd, Zhangjiagang, China

INVITED PAPER

9:00

AH-01. Integrated NEMS Magnetoelectric Sensors and Antennas.

N. Sun[1]
1. ECE, Northeastern University, Boston, MA, United States

The coexistence of electric polarization and magnetization in multiferroic materials provides great opportunities for realizing magnetoelectric coupling, including electric field control of magnetism, or vice versa, through a strain mediated magnetoelectric coupling in layered magnetic/ferroelectric multiferroic heterostructures [1-9]. Strong magnetoelectric coupling has been the enabling factor for different multiferroic devices, which however has been elusive, particularly at RF/microwave frequencies. In this presentation, I will cover the most recent progress on new integrated magnetoelectric materials, magnetoelectric NEMS (nanoelectromechanical system) based sensors and antennas. Specifically, we will introduce magnetoelectric multiferroic materials, and their applications in different devices, including: (1) novel ultra-compact RF NEMS acoustic magnetoelectric antennas immune from ground plane effect with $< l_0/100$ in size, self-biased operation and potentially 1~2% voltage tunable operation frequency; and (2) ultra-sensitive RF NEMS magnetoelectric magnetometers with ultra-low noise of $\sim 1 pT/Hz^{1/2}$ at 10 Hz for DC and AC magnetic fields sensing. These novel magnetoelectric devices show great promise for applications in compact, lightweight and power efficient sensors and sensing systems, ultra-compact antennas and for radars, communication systems, biomedical devices, IoT, etc.

1. N.X. Sun and G. Srinivasan, *SPIN*, 02, 1240004 (2012); 2. J. Lou, et al., *Advanced Materials*, 21, 4711 (2009); 3. J. Lou, et al. *Appl. Phys. Lett*. 94, 112508 (2009); 4. M. Liu, et al. *Advanced Functional Materials*, 21, 2593 (2011); 5. T. Nan, et al. *Scientific Reports*, 3, 1985 (2013); 6. M. Liu, et al. *Advanced Materials*, 25, 1435 (2013); 7. M. Liu, et al. *Advanced Functional Materials*, 19, 1826 (2009); 8. Ziyao Zhou, et al. *Nature Communications*, 6, 6082 (2015). 9. T. Nan, et al. *Nature Comm*. 8, 296 (2017).

CONTRIBUTED PAPERS

9:30

AH-02. Giant photo-Hall effect in metals.

A. Ruotolo[1,2] and D. Li[1,2]
1. City University of Hong Kong, Kowloon, Hong Kong; 2. City University Shenzhen Research Institute, Shenzhen, China

The Hall-effect in semiconductors has been used for more than one century to measure the intensity of magnetic fields. While Hall sensors have been replaced by magnetoresistive sensors in digital systems, they still retain two features which make them preferable to the latter in analog applications: they are intrinsically linear because they do not make use of magnetic materials and their sensitivity is directly proportional to the bias current J through the charge velocity v. Yet, the latter of these features is more theoretical than practical. Commercial Hall sensors are engineered to work at a specific, and very low, bias current because Joule heating severely compromises their linearity. The Hall effect exists in metals, where the low resistance to electrical current would make Joule heating be negligible. Yet, so would be the transverse voltage. We engineered a system in which the Hall effect in a metal is greatly enhanced and Joule heating suppressed [1]. The device recovers tunable sensitivity, without compromising linearity, by replacing current bias with light bias. Our system consists of an extended metal/semiconductor junction, where the metal is highly transparent to light and forms a Schottky interface with the semiconductor (see figure 1). Light reaching the interface is the driving force to diffuse carriers across the bilayer. A magnetic field applied in the junction plane exerts a magnetic force on the carriers diffusing in the metal, which accumulate on opposite sides, according to their sign. This charge accumulation can be detected as an open-circuit voltage transverse to the metal. The voltage is proportional to the field strength, as well as to light intensity. At equilibrium, the net current is zero and no Joule heating is produces, regardless light intensity. In order to demonstrate this effect, we deposited three metallic films, platinum (Pt), gold (Au) and aluminum (Al) with thickness t = 3 nm on 1 × 1 cm^2 un-doped (100) silicon (Si) dice. These metals were chosen because they have progressively lower work-functions (Φ_{Pt} = 5.9 eV, Φ_{Au} = 5.5 eV and Φ_{al} = 4.20 eV)[6]. A Si dye and a sample consisting of Pt with the same thickness deposited on insulating sapphire, α-Al_2O_3 were used as references. The magnetic field was generated by using an electromagnet. The voltage was measured by connecting the midpoints of two opposite edges of the metallic film to a voltmeter. a controlled light source consisting of a bulb lamp and a manual shutter were employed. The bulb lamp emitted unpolarized light with a spectrum that covers all and only the visible range from 450 nm (violet) to 750 nm (red). One can see from Figure 1 that no voltage appears when a Si dye is used, which excludes that the effect is due to photo-Hall effect in the semiconductor [2]. Similarly, no signal was detected on a Pt/sapphire chip, which excludes that the voltage is due to excitation of electrons in the Pt. One can also see that the effect diminishes with decreasing work-function, which suggests that the establishment of a Schottky barrier is a necessary condition for the effect to exist and that light is absorbed in the space-charge layer of the junction. The experiment was repeated by using optical polarizers. The voltage signal was found to be insensitive to light polarization, which excludes any contribution from optical-Hall effect or photo voltaic-Hall effect [3]. For Pt and Au, the effect was found to be strongly linear with both magnetic field strength and light intensity. Similarly the voltage increased linearly with light intensity for fixed values of magnetic field. The current-voltage (I_S /V_S) characteristics across the metal/Si interfaces were measured by placing the electric contact on the Si as close as possible to the edge of the metal. As expected, the I_S / V_S was found to be Schottky-like, strongly dependent on the light and independent on the magnetic field. The experimental evidences lead us to draw the following scenario. Metals with high work-functions form a Schottky contact with the semiconductor. A space-charge region arises in the semiconductor, near the interface. If the light penetration depth through the metal is longer than the film thickness, photons can be absorbed and charge can overcome the Schottky barrier, hence be injected into the metal. More specifically, once an electron-hole is photo-generated in the Si, the hole crosses the space-charge region to recombine with an electron in the metal and an electron crosses the space charge region to replace the recombined electron. In the Hall configuration of figure 1, no net current flows and the effect is strictly confined near the interface. Yet, electrons and holes *diffusing* across the space charge region are accelerated by the high built-in electric field and acquire a substantial velocity. The force $F = qv \times B$ exerted by the magnetic field is large because so is v. This is what makes the effect *giant*. The magnetic field bends the trajectory of the charge and an imbalance of charge appears at the edges of the metal. The voltage is detected in open-circuit conditions and no bias current across the junction. Therefore, no Joule heating is produced. The system shown here can reach the same sensitivity of a standard Hall-sensor but has a linearity-error that is independent on sensitivity because no Joule heating is produced.

[1] D. Li and A. Ruotolo, under review (2017). [2] W. Bludau et al., Solid State Commun. 18, 861-863 (1976). [3] T. Oka, et al., Phys. Rev. B 79, 081406 (2009).

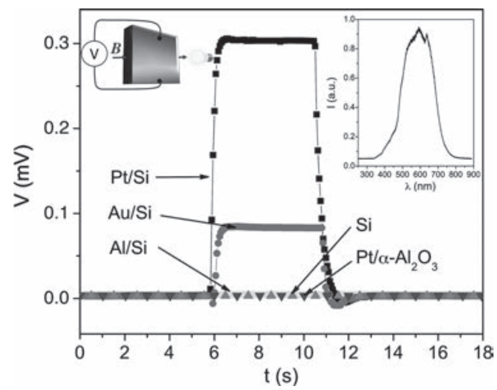

Fig. 1. Voltage *vs* time elicited when exposing the samples to a controlled light source with intensity *I* = 1 W and *B* = 0.5 T. The upper right inset shows the spectrum of the light.

9:45

AH-03. Magneto-optical magnetic field sensor based on magnetoplasmonic crystal.

N. Gusev[1,3], *A. Kalish*[1,4], V. Belotelov[1,4], G.A. Knyazev[1,4], P. Kapralov[1,3], P. Vetoshko[1,2] and A. Zvezdin[1,3]
1. Russian Quantum Center, Moscow, Russian Federation; 2. Kotelnikov Institute of Radioengineering and Electronics Russian Academy of Sciences, Moscow, Russian Federation; 3. Prokhorov General Physics Institute Russian Academy of Sciences, Moscow, Russian Federation; 4. Faculty of Physics, Lomonosov Moscow State University, Moscow, Russian Federation

Magneto-optical magnetic field sensors are devices that use magneto-optical effects, in particular the Faraday effect, to record magnetic fields by magneto-optical reading of the magnetization state of a sensitive medium under the influence of an external field. In some cases optical fiber is used as a sensitive element [1]; in others, a magneto-optical material [2], including iron garnet [3-4], is used as a sensitive element. The simplest way to increase the sensitivity of the magneto-optical method with respect to the magnetic field is a multi-pass method, i.e.stretching the optical path of light within the magnetic medium, which should lead to an accumulation of the Faraday effect. However, due to high losses on long optical trajectories, this approach does not allow achieving threshold sensitivity of more than 10 $\mu T/Hz^{1/2}$. In [4], the sensitivity level of 100 pT is demonstrated by using a waveguide iron garnet microstructure with homogeneous magnetization and oscillating (along the direction of light propagation) pump field. Nevertheless, the size of the sensitive element in the experiment is a few millimeters, that leads to a low spatial resolution. The present work is devoted to the development of a magneto-optical magnetic field sensor using the advantages of magnetomodulation method with high-quality monocrystalline low magnetic dissipative iron garnet films [5] and the advantages of the method of resonant amplification of magneto-optical effects with the help of a magnetoplasmonic crystal [6]. The sensor consists of a ferrimagnetic dielectric film with a diffractive metal grating deposited on its surface, in which plasmon eigenmodes are excited, leading to a tenfold enhancement of the magneto-optical effects. For optical detection of the magnetization state of a sensitive element is proposed to use the newly discovered longitudinal magnetophotonic intensity effect (LMPIE), which consists in changing the intensity of light reflected or transmitted through a magnetic film with a plasmon grid, when the film magnetization is reversed in the direction lying in the plane of the film perpendicular to the lattice slits. This effect is sensitive to the planar component of the magnetization, and, unlike other intensity magneto-optical effects, is maximal at normal incidence, which makes one possible to realize a magneto-optical reading circuit with magnetization reversal of the sample by uniform rotation of the magnetization and to read the signal by an ordinary photodetector. In this case, the LMPIE arises at the frequency of the second harmonic, with respect to the frequency of the external rotating plume, and the signal corresponding to the measured feild arises at the frequency of the third harmonic. In a series of experiments with test magnetic fields, the sensitivity for gratings with different periods and films with different thicknesses and compositions has a maximum sensitivity of 4 nT in a band from 1 to 60 kHz.

1. Rogers, A. J. “Optical fiber current measurement.” *Optical Fiber Sensor Technology*. Springer, Dordrecht, 1995. 421-439. 2. Gorchakov, V. K., V. V. Kutsaenko, and V. T. Potapov. “Electro-optical and magneto-optical effects in bismuth silicate crystals and optical polarization sensors using such crystals.” *Int. J. Optoelectron.* 5.3 (1990): 235-250. 3. Svantesson, Kjell, H. Sohlstrom, and Ulf Holm. “Magneto-optical garnet materials in fibre optic sensor systems for magnetic field sensing.” *SPIE Proc*. Vol. 1274. 1990. 4. Doriath, G., R. Gaudry, and P. Hartemann. “A sensitive and compact magnetometer using Faraday effect in YIG waveguide.” *Journal of Applied Physics* 53.11 (1982): 8263-8265. 5. Vetoshko, P. M., Zvezdin, A. K., Skidanov, V. A., Syvorotka, I. I., Syvorotka, I. M., & Belotelov, V. I. The effect of the disk magnetic element profile on the saturation field and noise of a magneto-modulation magnetic field sensor. *Technical Physics Letters* 41.5 (2015): 458-461. 6. Belotelov, V. I., et al. “Plasmon-mediated magneto-optical transparency.” *Nature communications* 4 (2013).

10:00

AH-04. Phase Transitions in Spin-Crossover Thin Films Probed by Graphene Transport Measurements.

J. Dugay[1], M. Aarts[2], M. Giménez-Marqués[1], T. Kozlova[2], h. Zandbergen[2], E. Coronado[1] and H. van der zant[2]
1. Molecular Materials, Institute of Molecular Science (ICMol), Paterna, Spain; 2. Department of Quantum Nanoscience, Delft University of Technology, Delft, Netherlands

Future multifunctional hybrid devices might combine switchable molecules and 2D material-based devices. Spin-crossover compounds are of particular interest in this context since they exhibit bistability and memory effects at room temperature while responding to numerous external stimuli. Atomically thin 2D materials such as graphene attract a lot of attention for their fascinating electrical, optical, and mechanical properties, but also for their reliability for room-temperature operations. In this work [1], we demonstrate a new concept to detect, in a noninvasive way, the spin-state switching of a thin film containing nanoparticles made of the SCO compound $[Fe(Htrz_2)(trz)](BF_4)$ and for a chemical alloy $[Fe(Htrz)_{2.95}(NH_2trz)_{0.05}](ClO_4)_2$ nanoparticle system. The method consists of measuring the electric properties of graphene in a four-probe field-effect configuration, while covered with a monolayer of switchable nanoparticles. The coupling between the spin-state dependent physical properties and the scattering in the graphene layer is ascribed to a changing contribution of remote interfacial phonon scattering. Using model calculations, we showed that the charge carrier-nanoparticle coupling changes due to the spin-state dependence of the dielectric constant. As the contact printing method yields a homogeneous coverage of a thin film with single nanoparticle thickness, this graphene field-effect sensor device is already able to probe small volumes of ca. 2000 μm^3 in the experimental setup presented here, while exhibiting a clear spin-change dependence in the graphene resistance. In the near future, this method should pave the way for the investigation of even smaller amounts of spin crossover materials using optimized graphene nanosensor platforms.

J. Dugay, M. Aarts, M. Giménez-Marqués, T. Kozlova, H. W. Zandbergen, E. Coronado, and H. S. J. van der Zant, *Nano Lett.* 17, 186–193 (2017).

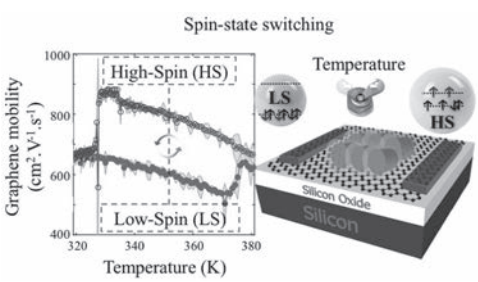

Fig. 1. (Left) Hole mobility versus temperature for the heating and cooling modes. Shaded error bars represent experimental errors in determining the field-effect mobility. (Right) Schematic of the device employed in this work made of CVD graphene on top of a silicon−silicon oxide substrate where a bistable SCO nanoparticle thin film prepared by μ-contact printing is decorating graphene.

10:15

AH-05. Custom-designed GMR- and TMR-sensor functionalities via oblique-incidence deposition.

S. Willing[1,2], K. Schlage[2], L. Bocklage[2,3], G. Meier[4,3] and R. Roehlsberger[2,3]
1. PIER Helmholtz Graduate School, Hamburg, Germany; 2. Deutsches Elektronen-Synchrotron (DESY), Hamburg, Germany; 3. The Hamburg Centre for Ultrafast Imaging, Hamburg, Germany; 4. Max-Planck Institute for the Structure and Dynamics of Matter, Hamburg, Germany

Magnetic field sensors are extensively used in today's information technology, automotive control, and industrial process management because of their ability to provide accurate data without physical contact. A variety of sensor types exists, however, magnetoresistance sensors have the benefit of being small, low-cost, and easy to produce. By using oblique-incidence deposition (OID) [1], we overcome one of the major challenges in these sensors: the control of the easy axis and the coercive field of one or both magnetic layers. In practice, often one of the two magnetic layers is pinned, meaning magnetically fixed via coupling to an antiferromagnet [2] while the other magnetic layer is free and can follow an external magnetic field. Alternatively, the relative orientation of the two magnetic layers' easy axes can be defined to be antiparallel by choosing specific spacer thicknesses to maximize the Ruderman-Kittel-Kasuya-Yoshida (RKKY) interaction [3]. Both of these techniques to engineer a magnetoresistive sensor are widely used, however, they lack flexibility and only allow for a few selected sensor characteristics. By oblique-incidence deposition of magnetic layers, an additional and tunable shape anisotropy is induced that enables full control over the coercivity and preferred magnetic orientation of each individual layer without the limitations of interlayer exchange or exchange-biased pinning. With this technique, the coercive field of a magnetic material is no longer a material constant but a function of the incidence angle during deposition. The coercive field of iron, for example, can then be tuned from 0.5 mT to almost 40 mT by increasing the polar deposition angle from 0° to over 80°. Although interlayer coupling between the magnetic films is still available, it is no longer necessary, making it possible to orient adjacent layers' easy axes in arbitrary angles instead of only antiparallel. In a magnetoresistive sensor system, tunable switching fields and arbitrarily crossed easy axes now allow for a versatile and individual tailoring of the single layers' properties to adapt the functionality to the needs of an application [4]. In the angular GMR measurements shown in Fig. 1, the magnetic field is rotated at constant field strength. In all four cases, the layer sequence is Co/Cu/Co with identical thicknesses, only the deposition angles are varied. The resulting functionalities change from sinusoidal to various peaked periodicities. Figure 2A demonstrates how different polar deposition angles lead to a step-like GMR characteristic in a field sweep. The magnetic field strength, at which the sensor has a plateau in the GMR curve is adjustable, which makes this system valuable for a variety of applications. In Fig. 2B the azimuthal deposition angle is altered, which leads to canted easy axes. This enables new functionalities, e.g., the linear GMR signal can be used to detect the absolute field strength within an adjustable working range (0-100 mT). Both figures clearly demonstrate the potential of sensor tuning via OID. Presently, we are taking the next steps towards actual industrial application of OID. The sensors have been optimized regarding temperature stability and performance, which remains unaffected by the preparation method. First experiments with TMR systems yield very promising results even with ultra-thin MgO barriers. Furthermore, OID can be combined with industry-compatible fabrication and microstructuring, see Fig. 2C. The additional surface shape anisotropy induced via OID is stronger than the shape anisotropy resulting from the aspect ratio of structured magnetic elements in circuits. Thus, the electrical resistance can be adjusted by sensor stripes of the required geometry without altering their magnetic properties. Oblique-incidence deposition is an alternative or complementary way to tailor the properties of magnetoresistive sensors. It enables a large variety of new functionalities and, thus, solves the main disadvantage of exchange-coupled systems. As the coercivity and orientation of the magnetic materials can be tuned and no interlayer coupling is needed, the technique provides an easy accessible handle to tune each layer's properties. Simply by changing the polar and azimuthal deposition angle, a custom-made sensor can be created to match the needs of an application. In addition, OID can be combined with industry-compatible microstructuring to yield desired base resistances and sensor sizes. It is valuable for all magnetoresistive systems, especially GMR and TMR sensors, and beyond that to create more complex multilayers.

[1] K. Schlage, L. Bocklage, D. Erb, J. Comfort, H.-C.Wille, R. Röhlsberger, Spin-Structured Multilayers: A New Class of Materials for Precision Spintronics, *Adv. Funct. Mater.* 26, 7423 (2016). [2] R. Coehoorn, Multilayers and Giant Magnetoresistance (Ed: U. Hartmann), Springer Series in Surface Science, Vol. 37,Springer, Berlin 2000. [3] M.D. Stiles, Interlayer exchange coupling, *J. Magn. Magn. Mater*. 200, 322 (1999). [4] K. Schlage, D. Erb, R. Röhlsberger, H.-C. Wille, D. Schumacher, L. Bocklage, European Patent EP 2 846 334 A1, (2015).

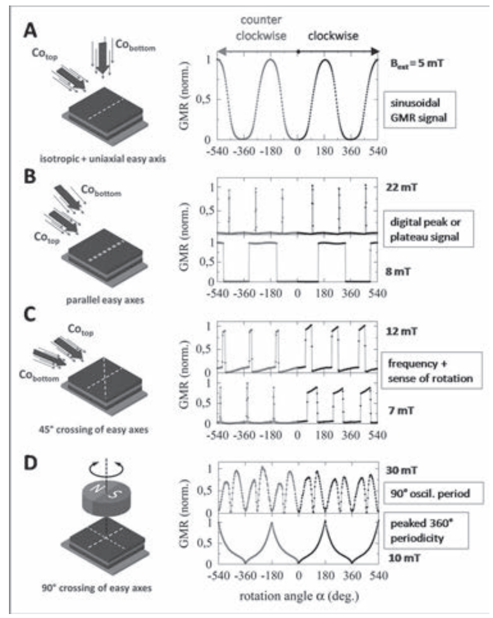

Fig. 1. GMR multilayer tuning for sensing of rotary fields. OID is used to imprint various new functionalities into a Co/Cu/Co trilayer structure.

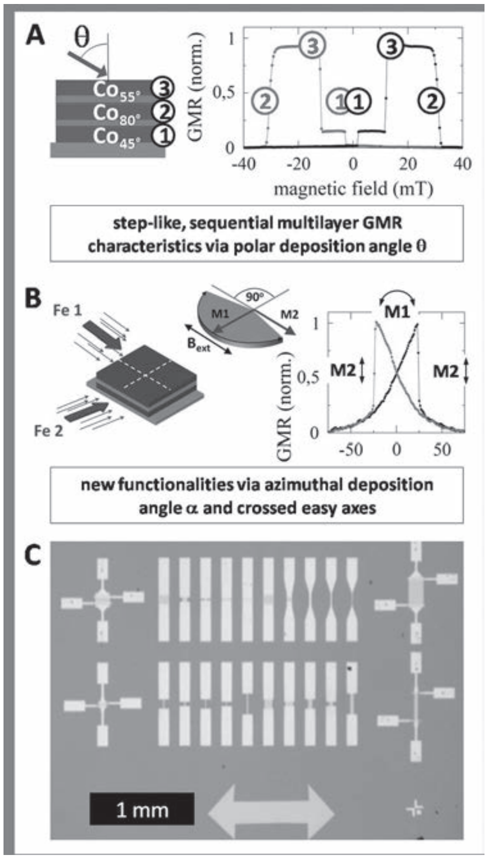

Fig. 2. Characterization of GMR sensors. (A) Multilayers with different polar deposition angles display step-like switching. (B) Crossing of easy axes leads to a linear GMR dependency. (C) Microstructured sensors and contacts.

10:30

AH-06. Magnetic tunnel junctions with perpendicular synthetic antiferromagnetic CoPt pinned layers for magnetic sensors with wide dynamic range.

T. Ogasawara[1], M. Oogane[1], M. Tsunoda[2] and Y. Ando[1]

1. Department of Applied Physics, Tohoku University, Sendai, Japan; 2. Department of Electronic Engineering, Tohoku University, Sendai, Japan

Introduction Magnetic tunnel junctions (MTJs) based magnetic sensors have been actively investigated for detection of a quite small magnetic field such as a bio-magnetic field. Moreover, it is possible to apply them to magnetic sensors with wide dynamic range, for example, magnetic sensors for current monitoring in electric vehicles require wide dynamic range above 1 kOe. In order to obtain wide dynamic range, large switching field of pinned layers of MTJs is required. One of the most promising materials to increase the switching field is perpendicular synthetic antiferromagnetic (p-SAF) pinned layer. Yakushiji et al., have demonstrated extremely large switching field of ca. 10 kOe in $[Co/Pt]_x/Ru/[Co/Pt]_x$ p-SAF structure [1]. In addition, MTJ-based magnetic sensors with $[Co/Pd]_x/Ru/[Co/Pd]_y$ p -SAF pinned layer showed a wide dynamic range of 2.5 kOe [2]. In this work, we investigated nonlinearity, which is one of the most important properties for current monitoring, for MTJ sensor devices with p-SAF pinned layers. Especially, we focused on the relationship between the nonlinearity and dispersion of magnetic anisotropy in CoFeB free layers. Experimental method Films were deposited on thermally oxidized Si(001) substrates using DC/RF magnetron sputtering ($P_{base} < 1\times10^{-6}$ Pa) at room temperature. Films of the MTJs with structure of Si/SiO_2-sub/Ta(3nm)/ Ru(10)/Pt(2)/$[Co(0.28)/Pt(0.16)]_9$/Co(0.28)/Ru(0.4)/Co(0.28)/$[Pt(0.16)/Co(0.28)]_5$/Co(0.28)/Ta(0.2)/$Co_{40}Fe_{40}B_{20}$(1.0)/MgO(2)/$Co_{20}Fe_{60}B_{20}$(t_{CoFeB} = 1.5 – 2.0)/Ta(5)/Ru(8) were fabricated into circular devices with 100 mm diameters. After the micro-fabrication, MTJ devices were annealed at T_a = 300 - 400°C for 1 hour without applying magnetic field. The magnetoresistance curves were measured by dc four-probe method. The films with structure of Si/SiO_2-sub/Ta(3)/MgO(2)/$Co_{20}Fe_{60}B_{20}$(t_{CoFeB} = 1.45 – 1.70)/Ta(5) were also prepared and annealed at 300°C to investigate their magnetic properties which were measured at room temperature by vibrating sample magnetometer (VSM) and ferromagnetic resonance (FMR). Results Fig. 1 shows conductance curves for MTJ sensor devices with various thicknesses of $Co_{20}Fe_{60}B_{20}$ free layers after annealing at T_a = 300°C. All of the MTJ sensor devices showed a linear conductance response within H = ±1 kOe. The jump of conductance curves at H = ±4.8 kOe corresponds to the switching field of the p-SAF pinned layer. In contrast, magnetic anisotropy field (H_k) of $Co_{20}Fe_{60}B_{20}$ free layers was 1.8, 2.3 and 2.9 kOe for the t_{CoFeB} = 1.50, 1.55 and 1.60 nm respectively. The sensitivity which is defined as the slope of conductance curves increased with decreasing CoFeB thickness due to the decrease of H_k. The highest sensitivity evaluated in the range of H = ±1 kOe was 0.055 %/Oe for t_{CoFeB} = 1.50 nm. This sensitivity is much higher than reported value of 0.0053 %/Oe [2] thanks to both high TMR ratio and low H_k in $Co_{20}Fe_{60}B_{20}$ free layers because of large interfacial perpendicular anisotropy at MgO barrier interface. The nonlinearity defined as $(G_{meas.}-G_{fit.})/(G_{meas.max}-G_{meas.min})\times100$ (% FS) was also investigated. According to Stoner-Wohlfarth [3] and Slonczewski models [4], a conductance curve is expressed as $G_0(1+P^2H/H_k)$ and should linearly respond against external magnetic field H, where G_0 is the conductance at H=0 and P is tunneling spin polarization. Fig. 2 shows the $Co_{20}Fe_{60}B_{20}$ thickness dependence of nonlinearity in the MTJ sensor devices. The nonlinearity decreased with increasing $Co_{20}Fe_{60}B_{20}$ thickness. In order to investigate the mechanism of nonlinearity, dispersion of magnetic anisotropy (ΔH_{keff}) was measured by FMR in Si/SiO_2-sub/Ta(3)/MgO(2)/$Co_{20}Fe_{60}B_{20}$(t_{CoFeB} = 1.45 - 1.80)/Ta(5) films. As shown in Fig. 2, the magnitude of $\Delta H_{keff}/H_{keff}$ decreased with increasing $Co_{20}Fe_{60}B_{20}$ thickness, similarly to the nonlinearity. These results indicate that the dispersion of magnetic anisotropy in $Co_{20}Fe_{60}B_{20}$ free layer is the main origin of nonlinearity in the MTJ sensor devices. Summary We investigated the performance of MTJ sensor devices with wide dynamic range using p-SAF pinned layers. The sensitivity was improved by optimizing the thickness of $Co_{20}Fe_{60}B_{20}$ free layers and achieved a high sensitivity of 0.055 %/Oe for t_{CoFeB} = 1.50 nm. This is the highest sensitivity in the MTJ-based magnetic sensors with a wide dynamic range above 1 kOe. Conversely, the nonlinearity increased with decreasing thickness of $Co_{20}Fe_{60}B_{20}$ free layers due to the increase of magnetic anisotropy dispersion. We found that the reduction of magnetic anisotropy dispersion is needed in order to achieve both high sensitivity and nonlinearity in the MTJ sensor devices.

[1] K. Yakushiji, et al., Appl. Phys. Express 8, 083003 (2015). [2] T. Nakano, et al., Appl. Phys. Lett. 110, 012401 (2017). [3] E. C. Stoner and E. P. Wohlfarth, Philos. Trans. R. Soc. A, 240, 599 (1948). [4] J. C. Slonczewski, Phys. Rev. B, 39, 6995 (1989).

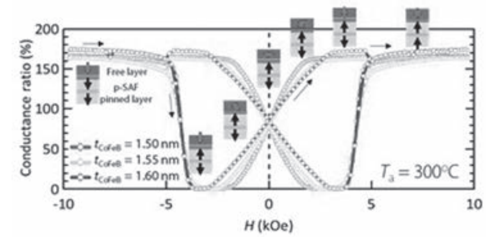

Fig. 1. Conductance curves for the MTJ devices with t_{CoFeB} = 1.50, 1.55 and 1.60 nm using p-SAF pinned layers.

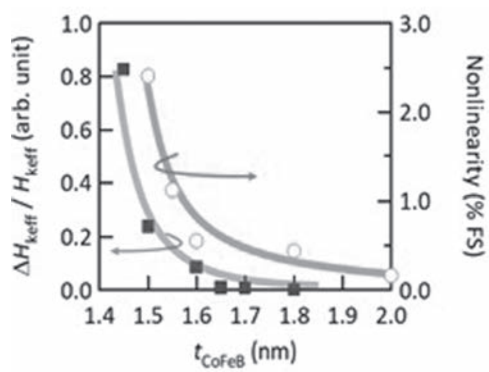

Fig. 2. Free layer $Co_{20}Fe_{60}B_{20}$ thickness dependence of the nonlinearity (circle marks) and magnetic anisotropy dispersion ($\Delta H_{keff}/H_{keff}$, square marks) in the MTJ devices with p-SAF pinned layers.

10:45

AH-07. Magnetic Sensor Using Spin-orbit Torque Effective Field as Transverse Bias.

Y. Xu[1], Y. Yang[1], Z. Luo[1] and Y. Wu[1]
1. Electrical and Computer Engineering, National University of Singapore, Singapore

I. INTRODUCTION Magnetic biasing is commonly used to enhance the linearity, sensitivity and dynamic range of magnetic sensors[1-4]. For anisotropic magnetoresistance (AMR) sensor, the two most commonly used biasing schemes are soft-adjacent layer (SAL) biasing and barber pole biasing, as shown schematically in Fig.1a and b. The SAL biasing (Fig. 1a) normally requires a soft magnetic layer, or SAL, layered with the sensing layer via an insulating spacer. When the thickness and magnetization of both the sensing and SAL layers are optimized, the angle between the current and magnetization of the sensing layer can be readily set to be 45^o by adjusting the sensing current. While the SAL scheme was successfully implemented in AMR sensors, it requires dedicated process work to optimize the structure and, moreover, it also suffers the drawback of non-uniformity in the biasing field, particularly at the edges. On the other hand, in the case of barber pole biasing, instead of changing the magnetization direction, the local current is directed away from the easy axis direction by patterned conducting strips deposited directly atop the sensing layer (Fig.1b). The strips are aligned at an angle of 45^o from the easy axis direction of the sensing element, leading to a linear response to transverse field. It is apparent that the barber pole design also suffers from requirement of additional process steps and current shunting by the conducting strips. To simplify the biasing structure and at the same time provide a uniform bias across the active area of the sensor, we have recently introduced a biasing technique based on spin-orbit torque[5] (SOT) effective field (see Fig.1c). The SOT, present in ferromagnet (FM) / heavy metal (HM) heterostructures, has been widely studied as a promising mechanism for switching the magnetization of ultrathin FM layers. It is commonly accepted that both damping-like (DL) and field-like (FL) SOTs are present in FM/HM bilayers. The FL effective field, which in-plane and perpendicular to the current (Fig.1d), forms naturally as a transverse bias. As demonstrated in our recent work, the use of SOT biasing greatly simplifies the sensor structure and, in fact, what one needs is only a FM/HM bilayer. A byproduct of this is that the sensor can also be made semi-transparent. Here we present a systematic study of SOT-biased AMR and spin Hall magnetoresistance (SMR) sensors by focusing on how the dimension of the sensor would affect its dynamic range, linearity, sensitivity and power consumption. II. RESULTS AND DISCUSSION In order to evaluate the field sensing performance of SOT biased sensors with different dimensions, we fabricated full Wheatstone bridge sensors with ellipsoidal shape in NiFe(1.8)/Pt(2) bilayers. The long to short axis ratio is fixed at $a/b = 4$, with a = 800, 400 and 200 μm, respectively. Fig.2a shows the scanning electron micrograph of the four sensor elements with a = 800 μm, which are connected to form a Wheatstone full bridge. When a current source is connected to the top and bottom terminals of the bridge sensor as depicted in the Fig. 2a, the magnetization of the sensor elements, 1 and 4, are rotated to the direction opposite to that of the sensor elements, 2 and 3, with respect to the easy axis, leading to a linear response to the external field which is detected as a voltage signal from the other two terminals of the bridge. Fig. 2b and 2c (symbols) summarized the simulated and experimental power consumption, sensitivity, and dynamic range of sensors with different dimensions. By changing the long and short axis length (a and b), the shape anisotropy of the sensor can be changed accordingly; this leads to tunable bias current density, power consumption, sensitivity and dynamic range. The solid curves in Fig.2b and 2c are simulation results based on a macro-spin model, using parameters extracted experimentally. From the calculation results, we can observe, by reducing a from 1000 μm to 100 μm, the power consumption decreases significantly from 2.06 mW to 0.05 mW, the sensitivity decreases from 243.2 to 157.0 mΩ/Oe and the dynamic range increases from 0.83 to 1.28 Oe. These changes are attributed to the increased shape anisotropy and reduced current as the dimension decreases. The agreement between experimental and simulated results shows clearly that it is possible to tune the sensor's power consumption, sensitivity and dynamic range via adjusting the dimensions. Potential applications of the AMR/SMR sensors will be discussed.

1. A. V. Silva, D. C. Leitao, J. Valadeiro, J. Amaral, P. P. Freitas, and S. Cardoso, The European Physical Journal Applied Physics 72, 10601 (2015). 2. S. Tumanski, Thin film magnetoresistive sensors (CRC Press, 2001). 3. J. C. Mallinson, Magneto-resistive heads : fundamentals and applications (Academic Press, San Diego, 1996). 4. Y. H. Wu, in Encyclopedia of Nanoscience and Nanotechnology; Vol. 7, edited by H. S. Nalwa (American Scientific Publishers, Stevenson Ranch, 2003), p. 493. 5. Y. Yang, Y. Xu, H. Xie, B. Xu, and Y. Wu, Appl. Phys. Lett. 111, 032402 (2017).

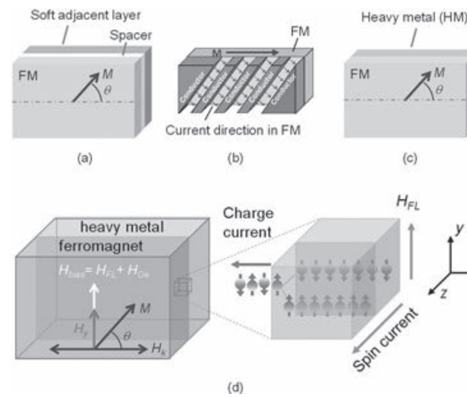

Fig. 1. Different types of transverse bias schemes for AMR sensors: (a) soft-adjacent layer biasing, (b) barber-pole biasing, and (c) spin-orbit torque biasing. (d) illustration of field-like effect field (H_{FL}) functioning as a transverse bias together with the Oersted field (H_{Oe}) generated by the current in the heavy metal layer.

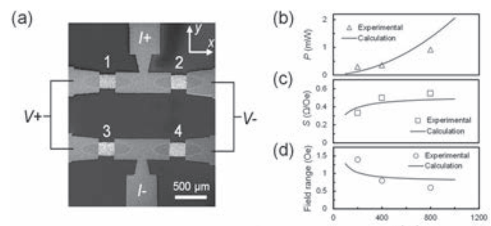

Fig. 2. (a) SEM image and schematic of the SOT biased Wheatstone bridge sensor. Scale bar: 500 μm. (b-d) Dependence of power consumption (b), sensitivity (c), and dynamic range (d) on the long axis length *a* (symbols: experiment; solid curve: simulation).

11:00

AH-08. Co/Pd Multilayer Structure for Hydrogen Sensing.

J. Liang[1], K. Chang[1], K. Chen[1] and Y. Tseng[1]
1. Materials Science & Engineering, National Chiao Tung Universoty, Hsin-chu, Taiwan

This paper reports on a magnetic device with a Co/Pd multilayer structure for use in the detection of H_2. In a magneto-optical, transport and gas-detection system, the proposed device presented sharp, reproducible H_2-dependent magnetic/electrical properties. The electrical signal-to-noise ratio of the device can be restored ~ 50% by exposing it to a magnetic field of 1000 Oe, even when the sensitivity of the device dropped at low H_2 pressure (0.7 KPa). This demonstrates the applicability of the device for use as a low-pressure H_2 detector. Arduino prototyping platform was adopted to test the modularization of Co/Pd with a Hall bar structure, through which the device displayed a read-out signal (R_{Hall}) exceling traditional resistivity-type (R_{xx}) structure by a factor of ten. By varying the Co/Pd interface number we were able to vary the H_2-detetcing sensitivity as a result of the change of magnetic anisotropy. Operando x-ray spectroscopy and in-situ Kerr microscope were used to explore the underlying mechanism. It revealed that the changes in H_2-induced magnetism arose from a Co-Pd charge transfer effect coupled to magnetic domain reversal.

J. Y. Liang at al., Appl. Phys. Lett. 111, 023503 (2017)

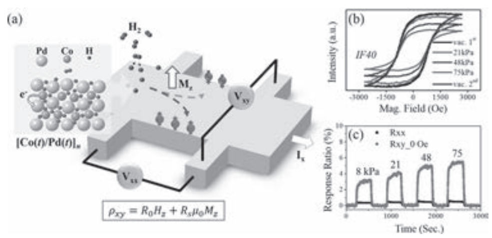

Fig. 1. Schematic illustration of the anomalous Hall effect measurement of the proposed device upon H_2 exposure. Inset of (a) illustrates the Co-Pd charge transfer effect at atomic scale. The Hall resistivity measured in the proposed device is given by (: Hall resistivity; : normal Hall coefficient; : magnetic field; : anomalous Hall coefficient; magnetic permeability; : magnetization). (b) H_2-pressure dependent hysteresis loops of the device. Vac 1st and Vac 2nd refer to the initial vacuum state, and the later vacuum state upon removal of H_2, respectively. (c) Comparison of R_{xx} and R_{xy} by calculating the response ratio $|(R-R_0)/R_0|$ under various hydrogen pressures.

11:15

AH-09. Enhanced annealing stability of exchange biased pinned layer in magnetic tunnel junctions using a thin Ta/Ru/Ta/Ru underlayer for analog sensor applications.

K. Okamoto[1], Y. Fuji[1], Y. Higashi[1], S. Kaji[1], T. Nagata[1], S. Baba[1], A. Yuzawa[1] and M. Hara[1]
1. Corporate Reserch & Development Center, Toshiba Corporation, Saiwai-ku,Kawasaki, Japan

MgO-based magnetic tunnel junctions (MTJs) are a key component technology for spintronic devices such as hard drive heads and magnetic random access memory (MRAM). Moreover, there is a great deal of interest in utilizing MTJs in analog sensor applications such as magnetic field sensors [1], current sensors, and angle sensors because of the large tunneling magnetoresistance (TMR) effect of MTJs. In a new analog sensor application of MTJs, it has been reported that MTJs can also serve as a strain sensor by using a magnetostrictive sensing layer [2]. These MTJ strain sensors can be applied to various kinds of physical sensors by combination with micro-electro-mechanical-system (MEMS) technology, and we have recently reported a novel MEMS microphone utilizing MTJ strain sensors [3]. As seen from the above, the range of possibilities for analog sensor application using MTJs have greatly expanded, and there is strong demand for further improvements in the signal-to-noise ratio (SNR) of MTJ elements. To obtain high SNR in analog sensors, it is important to have not only a high TMR ratio, but also low 1/f noise. Annealing is effective for improving the TMR ratio because it enhances the crystallinity of the MgO barrier layer, and it has also been reported that annealing is effective for decreasing MgO barrier noise [4]. Thus, a higher annealing temperature is preferable in order to enhance these effects. However, in the case of MTJs with an exchange biased pinned layer, which is generally used in analog sensor applications, excessively high-temperature annealing causes degradation of the exchange bias field (H_{ex}). This degradation decreases the effective TMR ratio and increases the magnetic 1/f noise coming from pinned layer [5], thus creating an obstacle to the adoption of high-temperature annealing. In this study, we aimed to improve the annealing stability of the exchange biased pinned layer in MgO-MTJ for analog sensor applications. We therefore focused on enhancing the crystallinity of the anti-ferromagnetic IrMn layer and investigated the effect of an underlayer structure on the crystallinity of the IrMn layer and annealing stability of the exchange biased pinned layer. We fabricated MTJs consisting of underlayer/IrMn7/CoFe2.5/Ru0.9/CoFeB3/MgO1.8/CoFeB4/Cu1/Ta2/Ru20 (layer thicknesses shown in nanometers). We prepared two kinds of underlayer structures: a generic Ta1/Ru2 underlayer (TR-UL); and an improved Ta1/Ru2/Ta2/Ru2 underlayer (TRTR-UL). Fig. 1 (a) and (b) show the R-H curves for the MTJ with TR-UL (TR-MTJ) and MTJ with TRTR-UL (TRTR-MTJ) annealed at 380 °C. As can be seen in Fig. 1, the TRTR-MTJ exhibits a larger H_{ex} and larger TMR ratio compared with those of TR-MTJ, We also evaluated the noise level of these MTJs, with the Hooge parameter α estimated by fitting the frequency dependence of the noise level measured at 200 Oe. The estimated α values for both MTJs are shown in Fig. 1(a) and (b). The value of α at 200 Oe for TRTR-MTJ is lower than that for TR-MTJ. Therefore, the magnetic 1/f noise is clearly improved by using TRTR-UL thanks to the high annealing stability of the exchange bias field. To clarify the microstructure of both MTJs, cross-sectional high-resolution transmission electron microscopy (HRTEM) and electron energy-loss spectroscopy (EELS) were performed. Insets of Fig. 1(a) and (b) show the HRTEM and EELS results for TR-MTJ and TRTR-MTJ annealed at 420 °C, solid lines in the figure show the EELS intensity of Mn. These results confirmed that the Mn diffusion is quite different between TR-MTJ and TRTR-MTJ. For TR-MTJ, Mn diffused from the IrMn layer to the pinned layer, whereas for TRTR-MTJ, there is almost no Mn diffusion from the IrMn layer to the neighboring layer. To investigate why TR-MTJ and TRTR-MTJ exhibited different Mn diffusion, the crystallinity of IrMn for both MTJs was analyzed by X-ray diffraction measurement. As a result, the crystallinity of IrMn on TRTR-UL was found to be clearly improved compared with that on TR-UL. Furthermore, we investigated the detailed structure of TR-UL and TRTR-UL. TEM measurement and fast Fourier transform measurement (FFTM) analysis were used to confirm the detailed d spacing of each layer in TRTR-UL (Fig. 2). From Fig. 2, it was successfully confirmed that the first Ta layer and second Ta layer in TRTR-UL have different d-spacing. The second Ta layer deposited on Ru layer has the d-spacing corresponding to the (110) textured α-Ta structure and highly crystallinity, whereas the first Ta layer does not have the component of (110) textured α-Ta structure. These results indicate that Ta-on-Ru structure is responsible for the high crystallinity of IrMn layer disposed on TRTR-UL, resulting in the high annealing stability thanks to small Mn diffusion. Therefore, Ta/Ru/Ta/Ru structure is promising as an underlayer for realizing a high SNR in MTJ analog sensor applications.

[1] P. P. Freitas, R. Ferreira, S. Cardoso, and F. Cardoso, J. Phys.: Condens. Matter 19, 165221 (2007). [2] M. Lohndorf, T. Duenas, M. Tewes, and E. Quandt, Appl. Phys. Lett. 81, 313 (2002). [3] Y. Fuji, M. Hara, Y. Higashi, S. Kaji, K. Masunishi, T. Nagata, A. Yuzawa, K. Otsu, K. Okamoto, S. Baba, T. Ono, A. Hori, and H. Fukuzawa, Digest on Transducers 2017 conference, pp. 63-66. [4] G. Q. Yu, Z. Diao, J. F. Feng, H. Kurt, X. F. Han, and J. M. D. Coey, Appl. Phys. Lett. 98, 112504 (2011). [5] Ryan Stearrett, W.G. Wang, L.R. Shah, J.Q. Xiao, and E.R. Nowak, Appl. Phys. Lett. 97,243502 (2010).

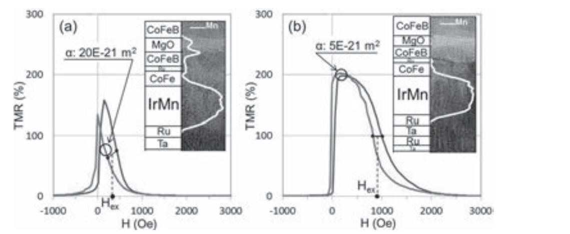

Fig. 1. R-H curves of MTJs using (a) Ta1/Ru2 underlayer and (b) Ta1/Ru2/Ta2/Ru2 underlayer. Both MTJs were annealed at 380 °C. Values of a shown in Fig. 1 are the Hooge parameter estimated for 1/f noise measured at 200 Oe. Insets show the EELS depth profiles of Mn in each MTJ annealed at 420 °C.

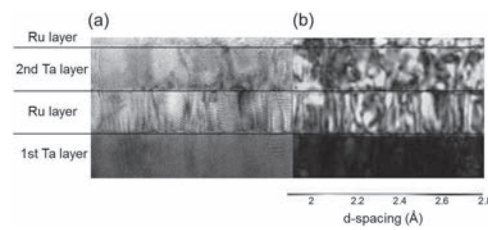

Fig. 2. (a) TEM image and (b) FFTM analysis result for Ta20/Ru20/Ta20/Ru2 stacks. *d*-spacing map perpendicular to the plane obtained by FFT. The color scale is shown below Fig. 2 (b).

11:30

AH-10. Modification of Ce valence states by Y/Dy co-doping of CeO_2 nano-particles for effective Electrical and Sensing properties.

C. Madhusudan[1,2]

1. Department of Physics, Osmania University, Hyderbad, India; 2. S.R.R Govt. Arts & Science College, Karimnagar, India

Abstract Improved electrochemical and sensing properties of CeO_2 nanoparticles were obtained by co-doping with Y^{3+} and Dy^{3+} to attain Ce^{4+}/Ce^{3+} valence states with the associated generation of oxygen vacancies. $Ce_{0.8}Y_{0.20-x}Dy_xO_{2-\delta}$ (x=0.00,0.10,0.20) nanoparticles were synthesized by sol-gel auto combustion method, calcined at 800^0C for 2hr in air and innovatively sintered by means of microwave heating at 1300^0C for 30min. The phase identification, structural and morphological analysis were characterized by XRD, SEM, TEM and Raman Spectroscopy. The ionic conductivity was analyzed by Impedance Spectroscopy. The gas sensing properties were tested at room temperature. Intense F_{2g} Raman band at 460cm^{-1} from Raman spectra in concurrence with XRD diffractograms revealed that the investigated samples exhibited the cubic fluorite structure of CeO_2. SEM and TEM results ascertained the nano level microstructure. The shift in XRD peak ascertained that the dopants were dissolved into the host lattice, and the subsequent creation of oxygen vacancies, due to the change in valence state from Ce^{4+} to Ce^{3+}. The generation of oxygen vacancies and the resultant enhancement in ionic conductivity was validated by the results of Raman specta and Impedance analysis. Because of special microstructure, the obtained sample showed excellent gas sensing properties towards the ethanol at room temperature. High response, fast response-recovery time and excellent selectivity to ethanol gas, suggested the promising gas sensing application of the sample $Ce_{0.8}Y_{0.10}Dy_{0.10}O_{2-\delta}$. 1. Introduction In the recent past, Cerium oxide or Ceria (CeO_2) has been extensively studied due to its potential applications in devices such as a catalyst, gas sensor, magnetic semiconductors and electrolytes in Intermediate Temperature Solid Oxide Fuel Cells (ITSOFCs) [1-3]. In principle, when Ce^{4+} cationic sub-lattice gets partially substituted with a trivalent Rare earth (RE) ion, oxygen vacancies are created in anionic sub-lattice in order to compensate the effective negative charge produced by the substituent cations. In the nano regime, easily accessible oxidation states from Ce^{3+} to Ce^{4+} gives ceria advantageous properties by the creation of oxygen ion vacancies and Ce^{3+} defects and hence the materials become good ionic conductors for a variety of applications mentioned [4]. Many researchers found that ceria doped with two or more cations (co-doping) showed improved electrical, magnetic and sensing properties than the best singly doped ceria. Co-doping aims to obtain an average or effective cation radius that is very close to that of Ce^{4+}, hence the average strain introduced by the dopant cations is minimized [5-7]. Ethanol is one of the most commonly and widely used alcohols and has many applications in food, medicine, chemical industries and beverages. Ethanol is volatile and flammable, and a long time exposure to it can cause central nerous disorders. Thus, its detection is important in many aspects [15-17]. the present work, investigates the possibility of improving the sensing and electrochemical properties of Y and Dy co-doped ceria $Ce_{0.8}Y_{0.20-x}Dy_xO_{2-\delta}$ (CYDO) nanoparticles synthesized via sol-gel auto combustion route and innovatively sintered by means of microwave heating [8-9]. 2. Results and discussion: Powder XRD patterns of the as-grown samples confirmed the dissolution of the dopants into the host lattice due to conversion of Ce^{4+} to Ce^{3+} and the subsequent creation of oxygen vacancies without any significant change in the lattice structure of host [10-11]. SEM and TEM results confirmed the nano-level dense microstructure with negligible porosity. Raman spectra of the samples consisted of a less predominant broad band at and around 570 cm^{-1} along with the characteristic F_{2g} peak of pure ceria at 460 cm^{-1}, which confirms the creation of oxygen vacancies [12]. The relative number of oxygen vacancies was found to be highest for the sample $Ce_{0.8}Y_{0.10}Dy_{0.10}O_{2-\delta}$. Impedance data collected for the obtained samples showed high ionic conductivity of 7.5 mS cm^{-1} at 500°C for $Ce_{0.8}Y_{0.10}Dy_{0.10}O_{2-\delta}$ with a low activation energy of 0.90 eV. These results can be attributed for high concentration of oxygen vacancies [13-14]. The gas sensing properties of $Ce_{0.8}Y_{0.10}Dy_{0.10}O_{2-\delta}$ nanoparticles were investigated by testing their gas response towards ammonia, acetone, methanol and ethanol with 1000 ppm concentrations at room temperature (R.T.). The response studies confirm that CYDO sensor show high response to ethanol (72%) compared to ammonia (6%), acetone (2%) and methanol (53%). So CYDO sensor can be treated as ethanol sensor and further gas sensing properties were studied. The gas sensing response of CYDO sensor was tested towards ethanol gas for different concentrations at R.T. It is clearly demonstrated that the response of the sensor increased with increase in concentration of ethanol gas. A sensor with fast response and recovery are needed to real-time usage in practical applications. For 1000 ppm ethanol gas, response time found to be 32 s and recovery time is 29s for $Ce_{0.8}Y_{0.10}Dy_{0.10}O_{2-\delta}$, as shown in Fig 1. 3. Conclusions The sensor developed in the present work has higher response and exhibited excellent gas sensing abilities toward ethanol gas. Results reported are promising and encouraging for application as a sensor in ethanol monitoring in breath analyzers and other fields. Also with nano regime microstructure and good oxide ion conductivity, it can also be used as electrolyte in ITSOFCs.

[1] John A. Kilner and Monica Burriel. Materials for Intermediate-Temperature Solid-Oxide Fuel Cells. Annu. Rev. Mater. Res., 44, 365-393, 2014. [2] Daniel J. L. Brett, Alan Atkinson, Nigel P. Brandon and Stephen J. Skinner, "Intermediate temperature solid oxide fuel cells. Chemical Society Reviews", 2008. DOI: 10.1039/b612060c [3] M. J. D. Rushton & A. Chroneos. "Impact of uniaxial strain and doping on oxygen diffusion in CeO_2. SCIENTIFIC REPORTS", 4: 6068. DOI: 10.1038/srep06068 [4] RSC Adv., 5, 103465-103473, 2015. DOI: 10.1039/C5RA15336K [5] Van Herle J, Senevirante D, McEvoy AJ, "Lanthanide co-doping of solid electrolytes: AC conductivity behavior",J Eur Ceramic Soc., vol19, pp.837-841,1999. [6] [7] Nandini Jaiswal, Shail Upadhyay, Devendra Kumar, Om Parkash, "Sm^{3+} and Sr^{2+} co-doped ceria prepared by citrateenitrate auto-combustion method", International journal of Hydrogen energy, 39, 543-551, 2014. [8] A. Wain-Martin, A. Moran-Ruiz, K. Vidal, A. Larranga, M.A. Laguna-Bercero, M.I. Arriortua, "Scalable synthetic method for SOFC compounds", Solid State Ionics vol. 313, pp.52-57, 2017. 9] C.K. Ng, S. Ramesh, C.Y. Tan, Andanastuti Muchtar, Mahendra Rao Somalu, "Microwave sintering of ceria-doped scandia stabilized zirconia as electrolyte for solid oxide fuel cell", international journal of hydrogen energy, 41, 14184 -14190, 2016 [10] RD. Shannon, "Revised Effective Ionic Radii and Systematic Studies of Interatomie Distances in Halides and Chaleogenides", Acta Cryst, A32,751, 1976. [11] Dae-Joon Kim, "= ". 1989. [12] R. C. Maher, V. Duboviks, G. J. Offer, M. Kishimoto, N. P. Brandon, L. F. Cohen. "FUEL CELLS 13, No. 4, 455–469,. [13] Kasarapu Venkataramana, K. Ravindranath, Chittimadula Madhuri, Ch Madhusudan, N. Pavan Kumar, C. Vishnuvardhan Reddy, "Low temperature microwave sintering of yttrium and samarium co-doped ceria solid electrolytes for IT-SOFCs", Ionics (2017). DOI: 10.1007/s11581-017-2293-5 [14] Ramesh S., V.PrashanthKumar, P. Kistaiah,C. Vishnuvardhan Reddy, "Preparation, characterization and thermo electrical properties of co-doped $Ce_{0.8-x}Sm_{0.2}Ca_xO_{2-d}$ materials", Solid State Ionics, 181, 86, 2010. [15] Sunghoon Park, HyunsungKo, SoyeonAn, WanInLee, SangminLee, Chongmu Lee, "Synthesis and ethanol sensing properties of CuO nanorods coated withIn_2O_3", Ceramics International, 39, 5255–5262, 2013 [16] Dongmin An, Ning Mao, Guozhi Deng, Yunling Zou, Yan Li, Tong Wei, Xiaoxue Lian, "Ethanol gas-sensing characteristic of Zn_2SnO_4 nanospheres", Ceramics International. DOI: 10.1016/j.ceramint.2015.10.161 [17] A. Mirzaei, K. Janghorban, B. Hashemi, M. Bonyani, S. G. Leonardi, G. Neri, "Highly stable and selective ethanol sensor based on α-Fe_2O_3 nanoparticles prepared by Pechini sol-gel method", Ceramics International. DOI:10.1016/j.ceramint.2015.12.176

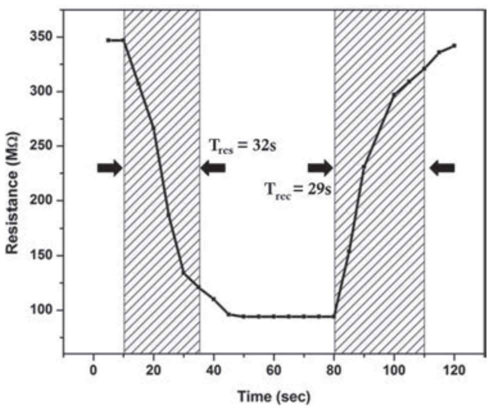

Fig. 1. Response & Recovery times of CYDO sensor

11:45

AH-11. Dural Field Frequency Mixing in Piezoelectric/Piezomagnetic Laminates at Acoustic Resonance.

P. Li[1], L. Bian[2], Y. Wen[1], X. Ji[1], T. Han[1] and Y. Wang[1]
1. Instrument Science and Engineering, Shanghai Jiaotong University, Shanghai, China; 2. Mechanical Engineering, Nanjing Technology University, Nanjing, China

Piezoelectric/piezomagnetic laminates can exhibit strong magnetoelectric (ME) coupling mediated by the strain, which may be produced either by magnetic field or electric field. A class of magnetic sensors are straightforward derived from piezoelectric/piezomagnetic laminates and their sensing output are the direct ME voltage, i.e. the electric response in piezoelectric layer produced by the magnetic-field-induced stain. Because of the nature of piezoelectric output, only a dynamic electric response is detectable. Hence, in this way ME composite laminates can only be exploited as dynamic magnetic sensors. To realize DC magnetic sensors, composite laminates have to be AC excited to oscillate and the sensed static magnetic field modulate the acoustic oscillation in terms of the dependences of ME coupling parameters on magnetic field.[1][2]Usually it is applying an AC magnetic field on a piezoelectric/piezomagnetic laminate to make it oscillating. In actual, an AC magnetic field used for excitation is produced by a coil. This configuration makes complicated the constitution of a practical device and loses the advantage of device simplicity from ME heterostructure. It is generally accepted that manipulating magnetism using pure electric fields instead of magnetic fields or large currents in multiferroic heterostructure is a goal for low-power spintronics. Both the constituents of a composite ME laminate have nonlinear properties. The nonlinearity in piezomagnetic material seems more noticeable as there is obvious saturation in magnetization. In most composite ME applications, usually it is desirable to avoid the saturated magnetostriction by biasing composites with appropriate DC magnetic fields. However, the nonlinearity may be beneficial to specific applications. Researchers have reported the resulting nonlinear ME effects, including frequency doubling of the voltage response at either low frequencies or resonance,[3] frequency mixing of the voltage response for magnetic fields with different frequencies applied to ME composites.[4]These nonlinear behaviors derive from the action of the nonlinearity on identical field-the magnetic field. In this work, we study the frequency mixing of electric field and magnetic field in piezoelectric/piezomagnetic laminates to retain strong ME effect and larger ME response even for a DC/low frequency magnetic field. This way, magnetic sensors with high sensitivity and enhanced resolution can be realized simply by electrically exciting ME composite laminates to oscillate around or at acoustic resonance. We design the composite with two electric terminals: one used for electric field (voltage) excitation, another for the strain-induced voltage output. To realize this, a piezoelectric/piezomagnetic heterostructure is made by sandwiching a piezomagnetic layer into two piezoelectric layers as shown in Figure1. Either piezoelectric layer can be used as input or output port. The laminate is magnetically biased at the nonlinear range and electrically excited to oscillate at its acoustic resonance. In the fabricated sandwiched ME laminate, the longitudinal resonant frequency of the laminate is about 231.5 kHz. We let the sandwiched laminate be excited by an AC voltage at the longitudinal frequency 231.5 kHz (f0) with an amplitude respectively of Vp-p=2.5 V and 3.5 V. To evaluate the dual field frequency mixing performance, an AC magnetic field of 0.5Oe at 1 kH(fH) is applied superposed with a DC biased field. Checking the electric output from another piezoelectric layer, we can see that due to the nonlinearity, the output contains frequency-mixing components, which are at the either sides of the exciting frequency: 230.5 kHz (f0-fH, left) and 232.5 kHz (f0+fH,right). The magnitudes of the frequency-mixing components vs. DC fields are recorded in Figure 2. At the optimal DC field, the ME voltage coefficients for the left modulated components are about 300mVOe^{-1} and 240 mVOe^{-1} respectively with electric voltage excitation of 3.0 Vp-p and 2.5 Vp-p and that for the right modulated components are about 250mVOe^{-1} and 170 mVOe^{-1}. These coefficients are almost the same as the resonant ME voltage coefficient. From the results, we conclude that through the nonlinearity a piezoelectric/piezomagnetic composite laminate can respond DC and low frequency magnetic fields at the maximum ME gain (the resonant ME coefficient). Principally in this scheme the piezoelectric/piezomagnetic composite can respond magnetic fields from zero to the resonance frequency by controlling the E-H mixing frequency in the pass band with electrically exciting frequency and share the high ME gain at mechanical resonance. Such features makes the sandwiched piezoelectric/piezomagnetic composite laminate greatly available for magnetic sensors required to sense both static and dynamic magnetic field in a rather wide frequency band.

[1]L. Bian, Y. Wen, P. Li, Sens. Actuators, A, 2015, 236, 338; [2]L. Chen, P. Li, Y. Wen, D. Wang, J. Alloys Compd. 2011, 509, 4811. [3]A. Rose, D. Huang, D. R. Smith, Appl. Phys. Lett. 2012, 101, 051103; [4] M. Li, Y. Wang, Y. Shen, J. Gao, J. Li, D. Viehland, J. APPL. PHYS. 2013, 114, 144501

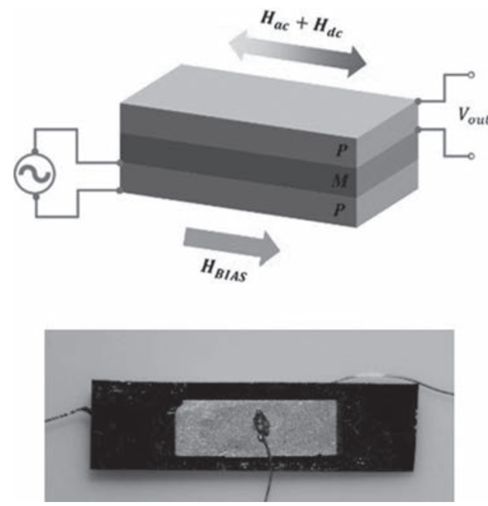

Fig. 1. Schematic of sandwiched piezoelectric/piezomagnetic laminate and the prototype

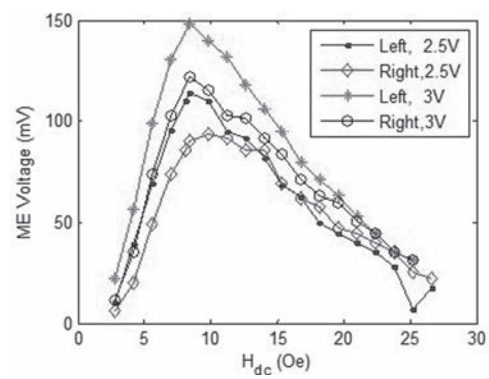

Fig. 2. Magnitudes of the frequency mixing components vs. DC magnetic field

TUESDAY MORNING, 24 APRIL 2018 ORCHID II, 9:00 TO 12:00

Session AI
EMERGING AND INTERDISCIPLINARY APPLICATIONS I

Albrecht Jander, Chair
Oregon State University, Corvallis, OR, United States

INVITED PAPER

9:00

AI-01. Highly and tunable spin-to-charge conversion in 2D electron gas at $LaAlO_3/SrTiO_3$ interfaces.

J. Rojas-Sánchez[1], E. Lesne[2], Y. Fu[3], S. Oyarzun[3], D. Vaz[2], E. Jacquet[2], J. George[2], L. Vila[3], S. Petit-Watelot[1], A. Barthélémy[2], H. Jaffres[2], M. Bibes[2] and A. Fert[2]

1. Institut Jean Lamour - CNRS - Univ. Lorraine, Nancy, France; 2. Unité Mixte de Physique, CNRS, Thales, Univ. Paris-Sud, Université Paris-Saclay, Palaiseau, France; 3. Spintec, Institut Nanosciences et Cryogenie, Univ. Grenoble Alpes, CEA, CNRS, Grenoble, France

Eldelstein [1] was the first to realize that in a Rashba two-dimensional electron system [2], the flow of a charge current is accompanied by a non-zero spin accumulation coming from uncompensated spin-textured Fermi surfaces. The opposite effect, spin-to-charge conversion through inverse Edelstein effect or IEE (also known as spin galvanic effect [3]), was recently demonstrated and its efficiency quantified at Ag/Bi(111) interfaces [4]. Here, we make use of such interface-driven spin–orbit coupling mechanism—the Rashba effect—in the oxide two-dimensional electron system (2DES) $LaAlO_3/SrTiO_3$ [5] to achieve spin-to-charge conversion with unprecedented efficiency [6]. Through spin pumping at 7 K, we inject a spin current from a NiFe film into the oxide 2DES and detect the resulting charge current, which can be strongly modulated by a gate voltage. We highlight the importance of a long scattering time to achieve efficient spin-to-charge interconversion. Thus we can explain why the IEE efficient at LAO/STO interface is much higher than metallic Ag/Bi Rashba interface or than topological insulator alpha-Sn capped with Ag [7].

[1] V. M. Edelstein, Solid State Commun. 73, 233 (1990) [2] Y. A. Bychkov & E. I. Rashba, J. Phys. C 17, 6039 (1984) [3] S. D. Ganichev et al. Nature 417, 153 (2002) [4] J. C. Rojas-Sánchez et al., Nat. Commun. 4, 2944 (2013) [5] A. Ohtomo and H. Y. Hwang, Nature 427, 423 (2004) [6] E. Lesne, J.-C. Rojas-Sánchez et al. Nat. Materials 15, 1261–1266 (2016) [7] J.-C. Rojas-Sánchez et al. Phys. Rev. Lett. 116, 096602 (2016). ArXiv 1509.02973 (2015) [8] J.-C. Rojas-Sánchez et al. Phys. Rev. Lett. 112, 106602 (2014)

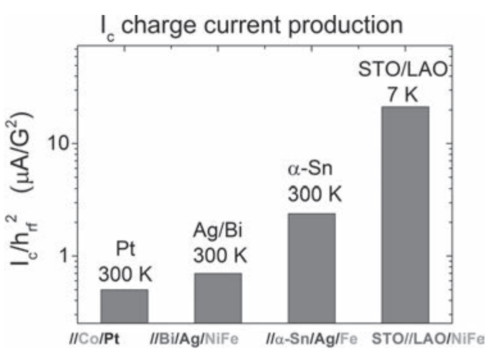

Fig. 1. Comparison of the normalized Ic charge current production by spin pumping-ferromagnetic resonance performed in the very same setup (X-band cylindrical cavity). It is displayed the results for Pt [8], Ag/Bi [4], α-Sn [7] at 300 K and STO/LAO [6] at 7 K. The charge current production is normalized by the square of the microwave field strength h_{rf}^2. All the samples measured have the same width of 0.4 mm.

CONTRIBUTED PAPERS

9:30

AI-02. An Electromagnetic Field Reduction Method for Inductive Power Transfer in Transportation System.

J. Kim[1], K. Kim[1] and S. Ahn[1]
1. The Cho Chun Shik Graduate School for Green Transportation, Korea Advanced Institute of Science and Technology (KAIST), Daejeon, The Republic of Korea

1. Introduction Currently, inductive power transfer (IPT) applications to transportations are being researched for safe and convenient power transmission [1,2]. However, the IPT system for transportations require to use high electrical power. This means that high density of magnetic field would be generated during IPT system operation and some magnetic fields would be a leakage magnetic field. These leakage magnetic fields influence negative effects to human body or other electrical device. Therefore, an leakage field reduction method for high power IPT system is necessary. In this paper, an adaptive active shield system is proposed that can eliminate leakage magnetic field generated from source and pickup coil by using one shield coil. Canceling magnetic field strength is controlled by measuring source current of IPT system for effective magnetic field reduction. 2. Proposed adaptive active shielding method The active shielding methods are already used for reducing leakage magnetic field but precedent researches require two shield coils [3]. In addition, canceling magnetic field strength is controlled by adjusting coil turns so efficient canceling magnetic field generation is limited. Fig. 1(a) shows the conceptual diagram of proposed active shield system using one coil. In order to achieve leakage magnetic field reduction, 1)radius and array, and 2) magnetic field strength and phase should be considered. *A. Shield coil radius selection* Biot-savart law can estimate the magnetic field strength over the distance as (A.1) [4]. r is the radius of the coil, x is the specific position from the center of the coil, u_0 is the permeability of free space, and R=root(r^2+x^2). In the case of rectangular coil, magnetic field strength will be decreased as $1/r^2$, and magnetic field strength will be a half when x and r are same. This means that decreases of magnetic field strength will be different in accordance with coil radius. In order to maintain the powering magnetic field, compensation region can be employed by tuning coil radius of active shield. The magnetic field strength is increased in the area between active shield coil and the source and pickup coil in accordance with magnetic vector directions. Consequently, shield coil radius could be determined as (A.2) when source and pickup coil are identical. r_{TX}, r_{TX}, and r_{SH} are radius of the source, pickup, and active shield coil respectively. *B. Strength and phase of canceling magnetic field* Fig. 1(b) is an equivalent circuit model of IPT system with active shielding system. When l_1 and l_2 are width and height of coil, magnetic flux B can be calculated as (B.1). If the parameters related to pickup system such as inductance L_{RX}, capacitance C_{RX}, and resistance R_{RX} are determined, induced voltage V_{RX} and current I_{RX} of pickup system can be calculated by (B.2.) and (B.3). M is the mutual inductance between source and pickup coil. This means that magnetic flux can be calculated not only B_{TX} generated from source but also B_{RX} generated from pickup coil by only measuring source current. $B_T(x)$ is the total magnetic field at specific position at x, and it is determined by subtracting leakage magnetic field $B_{LK}(x)$ and $B_{SH}(x)$. Therefore, current of active shielding system can be controlled for minimizing leakage magnetic field by measuring source current. In order to achieve effective magnetic cancelation, phase of canceling magnetic field should be tuned. Shielding performance is maximized when achieving 180 degree of phase difference with the leakage magnetic field. Phase of leakage magnetic field can be estimated by calculating current of source and pickup current with the magnetic flux R_{TX} and B_{RX}. Phase of canceling magnetic field for leakage magnetic field can be controlled as (B.5). 3. Simulation For the EM simulation setup of the proposed active shielding system, current of source and pickup coil was set as 500A and 392A respectively with 60 kHz of operating frequency. In order to measure the total magnetic field, two observation points were set. In order to measure the total magnetic field in the vicinity of IPT system for human influences, 1.5m of vertical observation points at the side of train body has set [5]. In addition, 10m of horizontal observation points at 1.5m of height from source coil has set for measuring total magnetic field at far distance [6]. Fig. 2(a) shows the simulation results for magnetic flux at the vicinity of IPT system. The case that is applied active shield has shown 3.1uT, 1.2uT, and 0.6uT for the distance of 0.5m, 1m, and 1.5m respectively. The reduction rate at each point is 53%, 64%, and 73% respectively. Fig. 2(b) shows the simulation result of total magnetic field at the far distance from IPT system. The case that is applied active shield was 95.7, 87.6, 80.2, 73.1, and 66dBuA/m respectively. For the all observation points, about 20dB A/m of magnetic field strength has decreased. Although total magnetic field at the close and far distance were reduced, powering magnetic field between source and pickup modules were hardly reduced. 4. Conclusion In this paper, an active shield system for reducing leakage magnetic field generated from IPT system has been proposed. A proposed method has advantages that uses only one coil and provides efficient magnetic cancelation through adaptive shielding current control. A proposed method has shown the performance that electromagnetic fields at the closed and far distance were effectively reduced without powering magnetic field loss between source and pickup coil.

[1] J. Kim, B. Lee, J. Lee, S. Lee, C. Park, S. Jung, K. Pyo, and J. Beck, "Development of 1-MW Inductive Power Transfer System for a high-speed Train," *IEEE Trans. Ind. Electron*., vol. 62, pp. 6242-6250, Oct. 2015. [2] J. Sallan, J. L. Villa, A. Llombart, and J. F. Sanz, "Optimal Design of ICPT Systems Applied to Electric Vehicle Battery Charge," *IEEE Trans. Ind. Electron*., vol. 56, pp. 2140-2149, Jun. 2009. [3] Choi et al., "Generalized Active EMF Cancel Methods for Wireless Electric Vehicle," *IEEE Trans. Power Electron*., vol. 29, no. 11, pp. 5770-5783, Dec. 2014. [4] S. Ramo, J. R. Whinnery, T. V. Duzer, "Fields and Waves in Communication Electronics, 3rd Ed, 1994. [5] IEC 62110, "Electric and magnetic field levels generated by AC power systems. Measurement procedures with regard to public exposure," 2009. [6] IEC 62236-2, "Railway applications - Electromagnetic compatibility - Part 2: Emission of the whole railway system to the outside world," 2008.

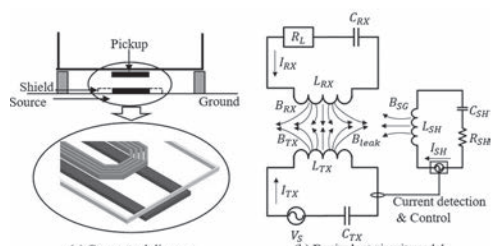

(a) Conceptual diagram (b) Equivalent circuit model

$$B(x) = \frac{\mu_0}{4\pi}\frac{Ir^2}{\left(r^2+R^2\right)^{3/2}} \quad \text{(A.1)}$$

$$r_{SH} = \sqrt{r_{TX}^2 + r_{RX}^2} \quad \text{(A.2)}$$

$$B = \frac{\mu_0\sqrt{l_1^2+l_2^2}}{2\pi l_1 l_2} I \quad \text{(B.1)}$$

$$V_{RX} = -j\omega M I_{TX} \quad \text{(B.2)}$$

$$I_{RX} = \frac{V_{RX}}{\left(j\omega L_{RX} + 1/j\omega C_{RX}\right) + R_L} \quad \text{(B.3)}$$

$$B_{LK} = \sqrt{B_{TX}^2(x) + B_{RX}^2(x)} \quad \text{(B.4)}$$

$$\phi_{SH} = 180 + \frac{\left(\left|\phi_{TX} - \phi_{RX}\right|\right) - 90^\circ}{2} + \tan^{-1}\left(\frac{B_{RX}}{B_{TX}}\right) \quad \text{(B.5)}$$

(c) Equations

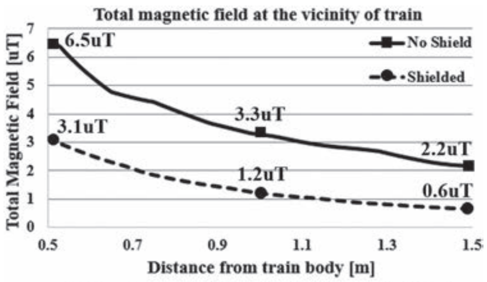

(a) Total magnetic field at the vicinity of train (1.5m)

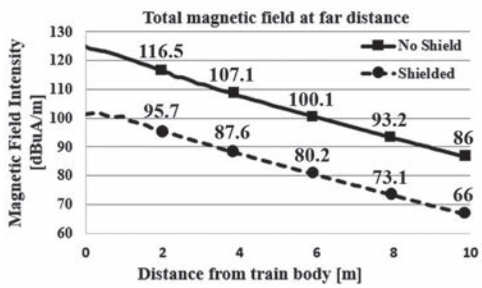

(b) Magnetic field intensity at far distance (10m)

9:45

AI-03. Optimal Design of Quadrature-Shaped Pickup for Omnidirectional Wireless Power Transfer.

Z. Zhang[1], B. Zhang[1], R. Tong[1], W. Ai[1], *S. Chang*[1] and J. Wang[1]
1. School of Electrical and Information Engineering, Tianjin University, Tianjin, China

INTRODUCTION Omnidirectional wireless power transfer (WPT) technology is a brand-new way of energy supply which is able to transfer power to the pickup unit wherever it locates around the transmitter. One of the most important purposes of such a system is to ensure the pickup unit can obtain enough energy evenly at all directions in 3-dimensional space around the transmitter [1]. However, there exists some special positions where the received power decreases to a lower level, such as the position as Fig.1 (a) depicts. Taking the current limit of transmitting coils into consideration and avoiding the input excitation beyond the restriction, this paper proposes a quadrature-shaped pickup which can effectively enhance the ability of capturing power at specific positions instead of just increasing the input. The optimized load power and transmission efficiency are able to be achieved according to different requirements by adjusting the key size variable. PROPOSED QUADRATURE-SHAPED PICKUP The widely-accepted omnidirectional WPT system consists of an orthogonal transmitting unit and a single coil as the pickup as depicted in Fig.1 (a). Besides, the load power of such a position where the pickup coil is vertical to one or two of transmitting coils will reach an extremely low level compared to other positions. Thus, the quadrature-shaped pickup is designed to improve the obtained power which is composed of three vertical coils connected with compensation capacitor and the load in series, as shown in Fig.1(b). The two crossed coils that have the same number of turns *N* are wound closely around a magnetic core called PC40 at the center. The width *a* of the cross-shaped core is a key variable which determines the turns *N* as each millimeter can be wound around one turn of the wire and also affects the performance of the system. By selecting appropriate value of width *a*, either maximum load power or maximum efficiency at specific positions is able to be achieved. VERIFICICATION The simulation is carried out to validate the enhancement of the proposed pickup and analyze how the width *a* affects the load power and efficiency of the system by JMAG. Moreover, the experimental prototype is also built up with a 7W bulb as the load to verify the feasibility of the proposed pickup for omnidirectional WPT as shown in Fig.1(c). The transmission distance is 100mm and the operation frequency is 100kHz both in simulated and experimental verifications. When the transmitting coils are all fed with current of 3A without phase difference, as depicted in Fig2. (a) and (b), the maximum magnetic flux density value reaches around 1.9mT and 5.5mT respectively when utilizing the conventional pickup and the proposed pickup, which reveals that the proposed pickup has the ability to obtain more power than the conventional one under the same condition. In order to optimize the design, the relationship between the width *a* and the load power, as well as efficiency, is also studied as shown in Fig.2 (c), and it represents that the conventional pickup is applied in the system when the value of *a* equals to zero. The result demonstrates that the load power increases from 6W to 54W while the efficiency drops from 83% to 64% as width *a* gets larger, which means that the width *a* can be designed at different values according to the different requirements of the load. Fig.2 (d) and Fig.2 (e) are the waveforms of the experiment using the conventional and proposed pickup, respectively, which are both tested at the position as shown in Fig.1 (a). V_{L1}, V_{L2}, and V_{L3} are the inductance voltage of three transmitting coils, and V_R represents the voltage of the load. Without varying the input, the RMS of load voltage is around 8V when adopting the proposed pickup, while it drops to 3V when using the conventional one. The comparative result illustrates that the proposed pickup can effectively improve the load power with the same input and position. The simulated and experimental results can verify the feasibility of the proposed pickup for the power improvement of omnidirectional WPT system. Furthermore, the optimal design of the quadrature-shaped pickup can be achieved depending on the different demands of load power and efficiency. CONCLUSION This paper proposed a quadrature-shaped pickup which can effectively enhance the transmitted power without varying the excitation for specific positions where the receiving power is weak. By adjusting value of the width *a*, the optimal design can be achieved to satisfy various application demands, such as high load power and high efficiency. The experimental results well agree with the simulated analysis, which validates that the proposed quadrature-shaped can effectively improve the performance of the omnidirectional WPT system without changing the input through the proposed optimal design. Besides, the detailed parameters, theoretical analysis, simulated results, and experimental waveforms will be presented in the full manuscript.

[1] D. Lin, C. Zhang, and S. Y. R. Hui, “Mathematic analysis of omnidirectional wireless power transfer—Part-II three-dimensional systems,” *IEEE Transactions on Power Electronics*, vol. 32, no. 1, pp. 613-624, January 2017.

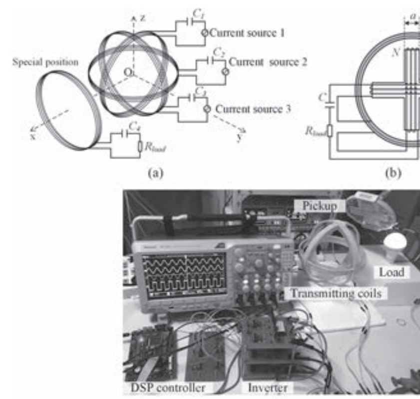

Fig. 1. 3-D omnidirectional WPT system: (a) schematic; (b) proposed quadrature-shaped pickup; (c) experimental prototype.

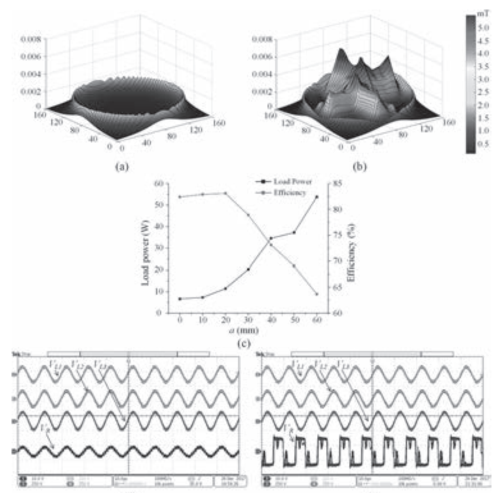

Fig. 2. Verifications: (a) 3-D distribution of magnetic flux density of conventional pickup; (b) 3-D distribution of magnetic flux density of proposed pickup; (c) power and efficiency of the system varying with *a*; (d) measured results using conventional pickup (Ch1: 10.0V/div, Ch2: 250V/div, Ch3: 250V/div, Ch4: 250V/div); (e) measured results using proposed pickup (Ch1: 10.0V/div, Ch2: 250V/div, Ch3: 250V/div, Ch4: 250V/div).

10:00

AI-04. A 3D-Printing Magnetic Forward Method for Objects in Motion.

Y. Sui[1] and K. Liu[1]
1. Jilin University, Changchun, China

I.Introduction Magnetic forward methods are of great importance in many areas such as geophysical exploration, electric machine, and have been investigated by a lot of scholars [1-3]. Many commercial or open-source software like Comsol Multiphysics and Ansoft Maxwell reliant on the finite element analysis can be used to calculate the magnetic fields generated by the 3D objects, but they require tremendous computational time and large numerical resources, especially for objects in motion [3-5]. Take COMSOL Multiphysics and Ansoft Maxwell for example. When simulating the complicated movements of 3D objects with COMSOL Multiphysics, the arbitrary Langrangian-Eulerian (ALE) moving mesh has been often used to trace their movements [4]. If the mesh displacement becomes large, the mesh elements will have a bad quality or even become inverted, so remeshing has to be used [6]. For the similar situation, Ansoft Maxwell does not have an adaptive mesh solution and requires significant mesh operations to help the transient solver [7]. The magnetic field of a static 3D object could be derived by dividing the object into an array of magnetic dipoles, calculating the field of each dipole, and then summing the effects of all dipoles [1]. Therefore, we proposed a 3D-printing magnetic forward method for objects in motion. The core idea is to design and create the virtual 3D objects with 3D printing technology, and replace the magnetic materials emitted from nozzles of a 3D printer with a collection of magnetic dipoles. Then superpose the effects of all dipoles, and the magnetic forward of static 3D objects is accomplished. In view of the fact that each component in a rigid body has the same laws of motion while the body moving and rotating in three-dimensional space, coordinate transformations can be used to implement the six-degrees-of-freedom (6DoF) motions of 3D objects. Similarly, the magnetic fields generated by objects in motion are calculated by summing the effects of all dipoles. The advantages of the proposed 3D-pringting magnetic forward method could be summarized as follows: (1) It is simple and easy to implement. The computational accuracy can be improved regardless of whether the user is a sophisticated expert or not. (2) It has strong practicability. The computational accuracy and the amount of time and memory consumed by the forward method are independent of the mode and complexity of motion. (3) It is perhaps the simplest method to obtain multiple-order magnetic gradient tensors of magnetic objects because of the analytical tensor expressions of a magnetic dipole. (4) The forward process for multiple magnetic objects in motion is consistent with that for a single object, so it has powerful expansibility. The proposed method could be used in many applications such as the magnetic test for a scientific spacecraft, the analysis of magnetic interference on instruments with high precision. II.The process of the 3D-printing magnetic forward method The steps of the 3D-pringting magnetic forward method are listed below: (1) Models of 3D magnetic objects may be obtained via a computer-aided design (CAD) package, medicine imaging techniques or a 3D scanner. Then the 3D magnetic models are exported in STL format, which is an interface in rapid prototyping system. (2) Import the STL file into Slic3r, which is a 3D slicing engine for 3D printers. Slic3r converts the model into a series of thin layers, and then produces a G-code file (a numerical control programming language used in computer-aided manufacturing). The height of layers and the filling density can be changed according to different discrete accuracy. (3) Parse the G-code file to gain printing positions of the nozzle of a 3D printer and other useful information. Simulate the extrusion process of the nozzle by interpolating new printing positions within the moving path. (4) Set each point as a magnetic dipole, then the magnetic materials emitted from nozzles of a 3D printer are replaced with a collection of magnetic dipoles. With regard to the magnetic objects whose components have various magnetic properties or positions, we can output the corresponding STL files for each component or use multiple extruders setting in the Slic3r to accomplish the modeling. (5) Use coordinate transformations to implement the 6DoF motions of 3D objects. The magnet fields generated by 3D objects in motion are derived by calculating the fields of each magnetic dipole and summing the effects of all dipoles. III. Application of magnetic test of satellites Rotating the spacecraft about the vertical axis and the horizontal axis of a swivel table is a practical and proven method in magnetic test [8-10]. As the representatives of soft and hard materials respectively, we rotated three magnetorquers and three momentum wheels which have been widely utilized in attitude control of satellites [11-13]. The satellite was simulated as a 400 mm×400 mm×400 mm cube. The radial permanent magnetic bearings has the axial magnetic moment of 2 Am^2. Bearings are simulated by two inner loops in the momentum wheel. Set three momentum wheels along yaw, pitch and roll axis, respectively. The magnetorquer has the magnetic moment of 1.3 Am^2. Six components are shown in Figure 1. Set the observation point along the yaw axis with distance of 600 mm from the center of the satellite and the results are illustrated in Figure 2.

(1) R. J. Blakely, "Potential theory in gravity and magnetic applications," pp. 182-209, 1996. (2) M. N. Nabighian, V. J. S. Grauch, R. O. Hansen, T. R LaFehr, Y. Li, J. W. Peirce, J. D. Phillips, and M. E. Ruder, "The historical development of the magnetic method in exploration," *GEOPHYSICS*, vol. 70, no. 6, pp. 33-61, Nov-Dec. 2005. (3) M. Yilmaz, "Limitations/capabilities of electric machine technologies and modeling approaches for electric motor design and analysis in plug-in electric vehicle applications," *Renewable and Sustainable Energy Reviews*, vol. 52, pp. 80-99, 2015. (4) W. Choi, S. H. Lee, C. T. Kin and S. Jun, "A finite element method based flow and heat transfer model of continuous flow microwave and ohmic combination heating for particulate foods," *Journal of Food Engineering,* vol. 149, pp. 159-170, 2015. (5) M. Dal, P. L. Masson and M. Carin, "A model comparison to predict heat transfer during spot GTA welding," *International Journal of Thermal Sciences*, vol. 75, pp. 54-64, 2014. (6) COMSOL AB 2008, "COMSOL Multiphysics User's Guide," (7) "Ansoft Maxwell v.11 User Guide," 2006. (8) R. Moskowitz and R. Lynch, "Magnetostatic measurement of spacecraft magnetic dipole moment," *IEEE Transactions on Aerospace*, vol. 2, no. 2, Apr. 1964. (9) W. Eichhorn, "A new method for determining the magnetic dipole moment of a spacecraft from near-field date," 1969. (10) State Administration for Science, Technology and Industry for National Defence(SASTIND), "Environment test methods for spacecraft unit- Part 4: Magnetic test," Jan. 2016. (11) F. Yin, H. Lühr, J. Rauberg, I. Michaelis and H. T. Cai, "Characterization of CHAMP magnetic data anomalies: magnetic contamination and measurement timing," *Measurement Science and Technology*, 2013. (12) T. Inamori, K. Otsuki, Y. Sugawara, P. Saisutjarit and S. Nakasuka, "Three-axis attitude control by two-step rotations using only magnetic torquers in a low Earth orbit near the magnetic equator," *Acta Astronautica*, vol. 128, pp. 696-706, 2016. (13) K. Sathyan, H. Y. Hsu, S. H. Lee and K. Gopinath, "Long-term lubrication of momentum wheels used in spacecrafts-An overview," *Tribology International*, vol. 43, no. 1, pp. 259-267, 2010.

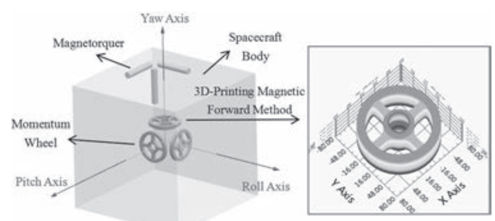

Fig. 1. Rotation of the satellite with three magnetorquers and momentum wheels for magnetic test.

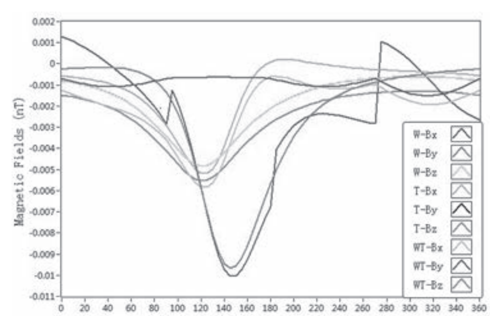

Fig. 2. Results of rotating the satellite. W: momentum wheel, T: magnetorquer, WT: conbined.

10:15

AI-05. Fabrication technology of low-propagation-loss plasmonic waveguide containing a ferromagnetic metal.

V. Zayets[1], H. Saito[1] and S. Yuasa[1]
1. Spintronics Center, National Institute of Advanced Industrial Science and Technology (AIST), Tsukuba, Japan

The optical isolator is an important element of optical networks. It protects optical elements from an unwanted back reflection. The integration of optical elements into Photonic Integrated Circuits (PIC) is an important task, because it reduces the cost and improves the performance of high speed optical data processing circuits of the optical networks. Figure 1 (a) shows the proposed design of the plasmonic isolator[1,2]. It consists of a Si nanowire waveguide, a part of which (about 2-16 mm) is etched out, and a ferromagnetic metal is deposited in the gap. The ferromagnetic metal is not transparent and the direct light propagation from the input Si waveguide to the output Si waveguide is blocked by the Co. However, a surface plasmon is excited at the Co / TiO_2 / SiO_2 interface. As a result, light reaches the output fiber. The Co is a magneto-optical material. When its magnetization is perpendicular to the light propagation direction and is in the film plane, its optical constants are different for two opposite light propagation directions. The plasmonic waveguide is optimized so that a plasmon is excited only in one direction, but a plasmon can not be excited in the opposite direction. Therefore, light can pass from input to output only in forward direction, but light is blocked in the opposite direction. A device, which is transparent only in one direction, is called the optical isolator. Figure 1(b) shows a top view of a Co / TiO_2 / SiO_2 plasmonic waveguides of different lengths integrated with a Si nanowire waveguides. Figure 1(c) shows the fiber-to-fiber transmission as function of wavelength for different lengths of the Co / TiO_2 / SiO_2 bridge-type plasmonic waveguide integrated with a Si nanowire waveguide. The measured propagation loss is 0.7 dB/mm and the measured coupling loss between plasmonic and Si nanowire waveguides is 4 dB per a facet. A metal is an essential material of a plasmonic waveguide. Any metal significantly absorbs light. Therefore, some optical loss is unavoidable in a plasmonic waveguide. In case if this loss is too large, all light is absorbed in plasmonic waveguide. Even if such plasmonic waveguide might have a unique property, it has no any practical use. Therefore, any practical plasmonic waveguide should have a reasonably-low propagation loss. It is known[3] that the propagation loss of the surface plasmons in a structure made of a ferromagnetic metal like Fe, Co or Ni is at least an order of magnitude larger than that of plasmons in structure made of Au, Ag and Cu, which are the conventional metals for the plasmonic devices. We have found that the in-plane and out-plane optical confinement are critically important in order to fabricate a low-optical loss plasmonic waveguide. When both the in-plane and out-plane optical confinement are well optimized, the propagation loss of a plasmon in ferromagnetic metal becomes even smaller (See Fig.1(c)) than the propagation loss in a conventional plasmonic waveguide, which is made of Au or Ag or Cu. The out-of-plane confinement is important because it minimizes the loss due to the absorption of light in the bulk of a metal. Since a metal absorbs light, the less light is inside of the metal and the more light is inside of the dielectric, the smaller propagation loss is. In a double-dielectric or multi-dielectric plasmonic structure, the thickness of one dielectric can be optimized so that the amount of light in the metal becomes smaller and the amount of light in the dielectric becomes larger. Additionally, in such structure a substantial enhancement of MO effect is observed[1,2,4,5]. The in-plane confinement is critically important because it minimizes the loss due to the scattering at a side edge of a plasmonic waveguide. Often a metal stripe is used for in-plane confinement of a plasmon (Fig.2 (a)). In this case a surface plasmon propagates just under the metallic stripe. Even though the fabrication of a stripe-type plasmonic waveguide is very simple, the propagation loss of a plasmon in such structure is very high. We have studied 3 types of in-plane confinement for a surface plasmon: groove-type[6], wedge-type and bridge-type (Fig. 2 (b)-(d)). All these types of the in-plane confinement are effective for the reduction of the propagation loss of a plasmon. The reduction is at least in 10 times comparing to the stripe confinement. The reason of the reduction of the propagation loss is that light is removed from the place of the metal edge. This work was partially supported by a Grant-in-Aid for Scientific Research (No. 16H04346) from JSPS.

[1] V. Zayets, H. Saito, S. Yuasa, and K. Ando, *J. Appl. Phys.* 111, 023103 (2012). [2] V. Zayets, H. Saito, K. Ando, and S. Yuasa, *Materials* 5, 857 (2012). [3] G. Armelles, A. Cebollada, A. García-Martín, and M. U. González, *Adv. Optical Mater.* 1, 10 (2013). [4] T. Kaihara, H. Shimizu, A. Cebollada, and G. Armelles, *Appl. Phys. Lett.* 109, 111102 (2016). [5] T. Kaihara, T. Ando, H. Shimizu, V. Zayets, H. Saito, K. Ando, and S. Yuasa, *Optics Express* 23, 11537 (2015). [6] A. I. Ignatov, A.M. Merzlikin, A.V. Baryshev, A.V. Zablotskiy, and A.A. Kuzin, *Optics Comm.* 359, 353 (2016).

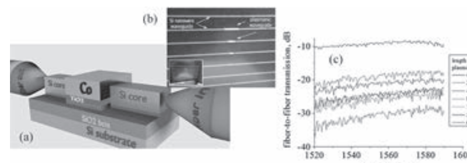

Fig. 1. (a) Integration of a Co/TiO_2/SiO_2 plasmonic waveguide with a Si nanowire waveguide. From input fiber (at right), light is coupled into a Si nanowire waveguide (green) and into a plasmonic waveguide. Next, light is coupled again in a Si nanowire waveguide and finally into the output fiber (at left); (b) Top view from an optical microscope of Si nanowire waveguide integrated with plasmonic waveguides; (c) Fiber-to-fiber transmission as function of wavelength for different lengths of Co/TiO_2/SiO_2 plasmonic waveguide integrated with Si nanowire waveguide. Black line shows the case of waveguide without plasmonic part.

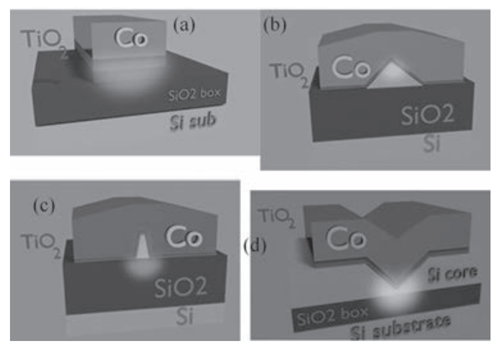

Fig. 2. Lateral optical confinement of a plasmon. (a) wedge-type (b) bridge-type; (c) grove-type; (d) metal stripe. The distribution of optical field is shown in yellow color. The propagation direction of a plasmon is perpendicularly to the page. Top and bottom Si is shown in green color.

10:30

AI-06. Area Efficient Multi Level Cell SOT-MRAM with Shared Diode for High Density Memories Applications.

K.A. Ahmed[1,2], L. Fei[1], S.Y. Lua[1] and C. Heng[2]
1. NVM, Data Storage Institute, Singapore, Singapore; 2. ECE, National University of Singapore, Singapore

Spin-orbit torque magnetic random access memory (SOT-MRAM) is considered as one of the most promising technologies to replace or co-exist with the current leaky CMOS charge based memories such as SRAM and DRAM, thanks to SOT-MRAM's non-volatility, high energy efficiency, endurance and reliability. However, conventional SOT-MRAM bit-cell [1] requires two access transistors to fully separate the selected bit from the non-selected bits, which limits the density of SOT-MRAM. Hence, in this work, we propose a diode based multilevel cell (MLC) SOT-MRAM with only one access transistor per 2-bits, which will at least double the density compared to various designs in the literature. Our proposed cell, shown in Fig. 1(a), employs a shared diode between two in-parallel MTJs to eliminate the need for a read transistor. The diode is oxide based, thus, it can be 3D stacked over the MTJs and does not consume any additional silicon area. The employed diode is unidirectional, where it conducts current only under forward bias. In SOT programming, the read transistor only needs to supply a relatively small unidirectional read current (10's of μA) during the read operation. Hence, the proposed shared diode can satisfy the requirements to replace the read transistor in conventional SOT-MRAM. The two MTJs are connected in-parallel and have different low (R_P) and high (R_{AP}) electrical resistances. Four different states could thus result based on their equivalent resistance. The four resistance states can thus be mapped into four different 2-bit configurations, i.e. '00', '01', '10' and '11'. The two MTJs are placed in-contact to a common heavy metal (HM) electrode that allows accessing the two MTJs (i.e. 2 bits) using only single transistor. The bias conditions for the different signals during read/write operations in our proposed cell are shown in Fig. 1(b). During the write operation, all the RWL signals are pulled low to ensure that the diodes in all cells are reverse biased and no leakage current would flow across the cells. In addition, the WWL of the row comprising the targeted cell is set high to activate the cell's write access transistor. To write a '0' ('1') on either of the MTJs, the BL and SL of the column comprising the targeted cell are asserted high (low) and low (high), respectively. This permits the write current (I_{write}) to flow through the HM electrode in the essential direction, as indicated in Fig. 1(a). It should be pointed out that to permit writing the two MTJs per cell with different data, the two SOT-MTJs are designed to have different critical currents (I_c). Hence, they require different switching time for the same supplied I_{write}. Writing the two MTJs with identical data ('00'or '11') is done simultaneously by passing I_{write} with one longer pulse width that follows the SOT-MTJ with longer switching time requirement, under spin charge conservation assumption. To program the 2nd bit differently, i.e. '01'or'10', I_{write} with shorter pulse width is sent subsequently. Due to the larger I_c of 1st bit, the 2nd write pulse would not vary the bit-content of 1st bit. SOT-MTJs with distinct I_c can be realized by either employing MTJs with different free layer thicknesses (t_{fl}) or using different widths of the HM (W_{HM}) below each MTJ, as both t_{fl} and W_{HM} have a direct impact on the SOT-MTJ's I_c. During the read operation, the WWL signals are pulled low to deactivate all the write transistors, allowing the read current to flow through the targeted MTJs by activating its corresponding RWL. Thereafter, the SL of the column comprising the targeted cell is set to ground, while its row RWL is connected to the sense amplifier to forward-bias the diode. Depending on combined resistance states of the two MTJs, four different currents level could be sensed by the amplifier, which can then be mapped into the corresponding 2-bit stored data. The proposed cell operation is validated in a 2×2 array as shown in Fig. 1(c). The simulations are performed using a Verilog-A model of a SOT-MTJ and a diode with a 32-nm CMOS technology library. As demonstrated in Table I, our proposed cell offers at least 50% smaller 1-bit effective area compared to other designs with nearly similar energy consumption. Furthermore, the in-parallel combination of the two MTJs results in lower overall equivalent resistance, which permits reducing the read voltage compared to design in [2] that uses a diode with single MTJ stack. In addition, an improvement of at least 30% in a figure-of-merit defined as energy area product is obtained compared to various designs.

[1] Y. Kim, X. Y. Fong, K. W. Kwon, M. C. Chen, and K. Roy, "Multilevel Spin-Orbit Torque MRAMs," *IEEE Transactions on Electron* vol. 62, pp. 561-568, Feb. 2015. [2] Y. Seo, K. W. Kwon, and K. Roy, "Area-Efficient SOT-MRAM With a Schottky Diode," *IEEE Electron Device Letters,* vol. 37, pp. 982-985, Jun. 2016.

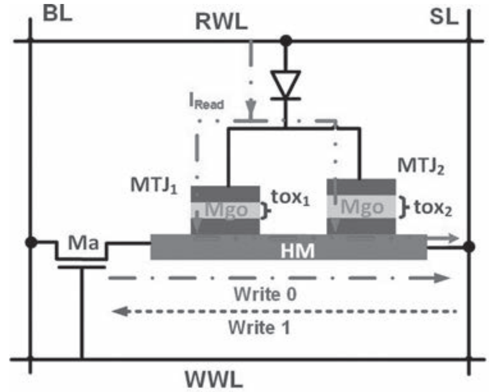

(a)

	Read	Write '0'/'1' to MTJ_1	Write '0'/'1' to MTJ_2
WWL	0	V_{DD}	V_{DD}
RWL	V_{Read}	0	0
BL	0	$V_{WR1}/0$	$V_{WR2}/0$
SL	0	$0/V_{WR1}$	$0/V_{WR2}$

(b)

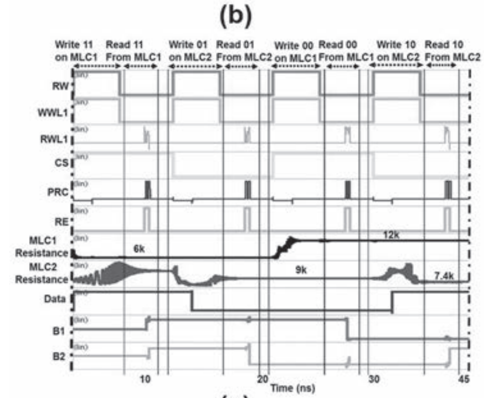

(c)

Fig. 1. (a) Proposed shared diode 1diode, 1 transistor and 2 MTJs (1D1T2R) MLC SOT-MRAM. (b) Bias conditions in Read/write modes. (c) Simulated waveform of the proposed 1D1T2R MLC SOT-MRAM. The waveform shows the successful write and read for the various data in a 2x2 memory array.

		SLC SOT (2-bit)	P- MLC [2]	1D1T-SOT (2-bit) [1]	This Work
Energy per 2-bit (pJ)	Write [a]	1.4	1.4	1.4	1.4
	Write Leakage	0	0.051	0	0.05
	Read	0.0184	0.031	0.033	0.048
Total Energy/2-bit		1.42	1.482	1.43	1.5
Delay per 2-bit (ns)	Write [a]	7	6.5	7	6.5
	Read	0.23	0.43	0.23	0.43
Read Voltage (V)		1	0.9	1.8	1.4
Area per 1 bit (F^2)		69	34.5	34.5	17.25
FOM (Er*Ew*A)		1.5X	1.3X	1.33X	1

a. Energy and delay are the average of writing the various data ‘00’, ‘01’, ‘10’, ‘11’.

Fig. 2. Comparison of Different MRAM cells.

10:45

AI-07. Rowhammer for Spin Torque based Memory: Problem or not?

S. Agarwal[1], H. Dixit[3], D. Datta[1], M. Tran[2], D. Houssameddine[2], D. Shum[2] and F. Benistant[2]
1. GLOBALFOUNDRIES Engineering Pvt. Ltd, Bangalore, India;
2. GLOBALFOUNDRIES Singapore Pte. Ltd, Singapore, Singapore;
3. GLOBALFOUNDRIES, 400 Stone Break Rd Extension, Malta, NY, United States

Rowhammer is a known security vulnerability in recent Dynamic Random Access Memory (DRAM) devices, where repeated access to an array of memory can flip the bits in the adjacent row owing to the charge leakage/capacitive coupling. Several studies have documented the Rowhammer effect [1,2] and Google's project zero demonstrates two working examples of a security exploit [3]. Furthermore, many published scenarios highlight that scaled DRAM below 32nm [1] is exposed to potential hacking attacks because of the Rowhammer problem [3], owing to reduced spacings in DRAM bits. Thus, it is only natural to test any new upcoming technology for a similar problem. Though the working mechanisms of DRAM and spin transfer torque magnetic random access memory (STT-RAM) are drastically different, whether the STT-RAM is also potentially vulnerable to an analogous Rowhammer effect or not is not documented or discussed in literature. While the mechanism of failure is high enough charge leakage in DRAM, the corresponding mechanism in STT-RAM may be the lowering of the thermal barrier because of the dipolar magnetic field exerted by adjacent selected bits. The lowering of the thermal barrier in turn can increase the probability of an erroneous bit flip. To ascertain whether the effect is substantial, nearest (A bit) and next nearest neighbour bits (B bit) adjacent to an unselected bit (O bit) are simulated as shown in Fig 1. The bit diameter is 55nm and the center to center bit spacing is 200 nm. The magnetic field at the O bit is simulated, when all the A and B bits have been assumed to have the magnetization pointing in the same direction. While this configuration does not necessarily conform to the conventional idea of selecting an adjacent row of bits or even both the adjacent rows (double sided hammering), it provides a scenario where the most favorable conditions for an erroneous bit flip can be evaluated in STT-RAM. Three magnetic layers are assumed in each bit separated by appropriate non-magnetic regions corresponding to the STT-RAM stack. The top most layer corresponds to the Free layer (FL) and can be flipped while the others are held fixed. While calculating the magnetic field at the O bit, the middle layer is assumed to have a magnetization opposite to the topmost and bottom layers. The other configuration in which the topmost layers is flipped and is parallel to the middle layer is known to give a smaller magnetic field. A magnetostatic calculation is done to determine the magnetic field at the site of the FL layer of the O bit. The average of the field over the entire volume of the O bit is evaluated as a function of bit spacing using magnetostatic calculations as shown in Fig 2. For the largest bit spacing of 200 nm the simulated field is only around 7 Oe while for a 100nm bit spacing it increases to 60 Oe. The analytical calculation assumes each magnetic layer in each bit to be a point. The vector sum of all of these at the location of the O bit is shown here. The discrepancy between the simulated and the analytical results increases as the bit spacing decreases. This is because of the assumption that each layer is assumed to be a point. To assess the impact of these fields, the string method is used to evaluate the energy barrier between two magnetic states corresponding to 0 or 1 stored on the O bit. Inset of Fig 2 shows that for a field of 7 Oe the change in energy barrier is less than 1 kT which is not large enough to cause an appreciable change in the bit error rate. For example based on Eqn 18 of [4] the bit error rate will only double for a 1 kT change in energy barrier assuming a retention time of 10 years and a relaxation time of 1 ns. Even for a bit spacing of 150 nm the increase in the BER will be less than an order of magnitude. However for a smaller bit spacing of 100 nm the BER can go up by 3 orders of magnitude. Therefore, as it stands rowhammer effect in STT-RAM does not appear to be appreciable at the 200 nm bit spacing. However at lower bit spacings the effect might become prominent and would require additional design rules to circumvent. As in the case of DRAM different techniques might have to be adopted to mitigate the problem.

[1] K. S. Bains, J. B. Halbert, C. P. Mozak, T. Z. Schoenborn, and Z. Greenfield, "Row hammer refresh command," US20140006703 A1. [2] Y. Kim et al., "Flipping bits in memory without accessing them: An experimental study of DRAM disturbance errors," in 2014 ACM/IEEE 41st International Symposium on Computer Architecture (ISCA), 2014, pp. 361–372. [3] "Exploiting the DRAM rowhammer bug to gain kernel privileges." [Online]. Available: https://googleprojectzero.blogspot.com/2015/03/exploiting-dram-rowhammer-bug-to-gain.html. [Accessed: 14-Nov-2017]. [4] D. Apalkov, B. Dieny, and J. M. Slaughter, "Magnetoresistive Random Access Memory," Proceedings of the IEEE, vol. 104, no. 10, pp. 1796–1830, Oct. 2016.

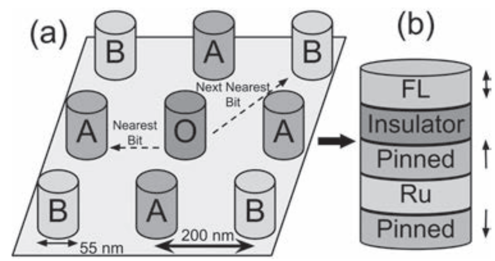

Fig. 1. (a) Schematic depicting the rowhammer configuration used to simulate the magnetic field at the unselected O bit. Both the nearest neighbour (A bits) and the next nearest neighbour (B bits) are assumed to have the Free Layer of the STT-RAM stack pointing in the same direction so as to maximize the magnetic field experienced at the central O bit. The centre to centre bit spacing is 200 nm while the diameter of a bit is 55nm. (b) The individual layers in the MRAM stack have been indicated where the FL and the two pinned layers are magnetic while the Insulator and Ru layers are not magnetic. The direction of magnetization is indicated with arrows.

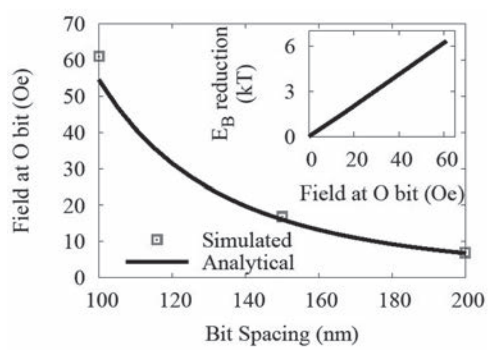

Fig. 2. Simulated and analytical fields observed at the unselected O bit are shown as a function of bit spacing. Simulated fields are computed using magnetostatic calculations. Analytical results are arrived at assuming each layer of the STT-RAM stack to be a point with a given magnetization. The inset shows how much the thermal energy barrier of the FL layer reduces as the magnetic field experienced by it from the surrounding bits is increased.

11:00

AI-08. Artificial neural network based on spin-wave coupled spin torque oscillators.

H. Arai[1,2] and H. Imamura[1]
1. Spintronics RC, National Institute of Advanced Industrial Science and Technology (AIST), Tsukuba, Ibaraki, Japan; 2. JST-PRESTO, Kawaguchi, Saitama, Japan

Artificial neural networks (ANNs) are the key technology for machine learning involving deep learning, which can be applied in the fields such as object detection and recognition. Artificial neurons are constructed on the model focusing on biological behaviors of a neuron in brain. The integrate-and-fire model reproduces simple spiking behavior caused by external stimulations, and develops integrated circuits based on simple electronic devices [1]. The oscillation model is other neural model using periodic spiking behaviors of the biological neuron. In order to obtain highly integrated oscillators as processing units for ANNs, the size of the oscillator should desirably be of a nano-order scale. The important property required for artificial neurons in ANNs is to show nonlinear relation between input and output signals. The relation is called as activation function. The typical activation function in deep learning is the sigmoid function [2]. If a processing unit provides a sigmoid-like nonlinear relation between input-output signals, one can easily utilize the framework of computation of ANNs. In this study, we propose an ANN based on spin-wave coupled spin torque oscillators (STOs), providing sigmoid function-like input-output relation. We also perform a task-solving demonstration to recognize handwriting digits using ANN. Figure 1(a) shows a schematic illustration of an STO unit we propose, which is a laterally-long magnetic resistant device with double point contacts. The dc current induces the dynamics of the magnetization underneath the point contacts, m^L and m^R. The dynamics propagates spin waves between both point contacts which couples the dynamics of m^L and m^R. We propose in the following, the operation method of STO-based ANN processing unit. The STO receives an oscillating magnetic field (H_{ac}) as an input signal. The output signal from the STO is ac current, which produces the Oersted field (H_{Oe}) which is applied to the next STO unit. In order to yield the sigmoid-like input-output (H_{ac}-H_{Oe}) relation, we utilize out-of-phase oscillation for H_{ac}=0. By applying H_{ac} field to the out-of-phase oscillation state, the phase difference between m^L and m^R is varied. This result indicates the control of output ac signal from the STO unit, or H_{Oe} via H_{ac}. The out-of-phase oscillation appears by taking the Dzyaloshinskii-Moriya interaction (DMI) [3] on the free layer of the STO, as shown below. The magnetization dynamics is obtained by solving Landau-Lifshitz-Gilbert equation with the DMI being incorporated. We used micromagnetic numerical simulator, mumax3 [4]. The shape of a free layer is assumed as 2 nm wide, 40 nm long, and 1nm thick, with an one-dimensional magnetization chain. The effective field is the sum of exchange field and DMI, designated as A and D, respectively. The positive current is defined as the electrons flowing from the free layer to the reference layer. The magnetization of the reference layer (p) is fixed to the positive x-direction. Figure 1(b) shows the time development of the magnetization x-components of the contacts, m_x^L and m_x^R, with A=7 pJ/m, and D=0.8 mJ/m^2. As mentioned above, the out-of-phase oscillation is obtained where output signal from the STO is small. The oscillation frequency is about 4 GHz. Next, the oscillating magnetic field (H_{ac}) with 4 GHz frequency is applied to the free layer along y-direction. The phase difference is varied between m_x^L and m_x^R, which accordingly leads to obtaining output signal from the STO, m_x^{out}, as plotted in Fig. 1(c). The m_x^{out} is calculated by summing up m'^L_x and m'^R_x, where m'_x corresponds to an oscillating component obtained through a bias tee (BT) shown in Fig. 1(a). The phase difference depends on the intensity of H_{ac}. The amplitude of m_x^{out} after reaching a stable oscillation is plotted as a function of H_{ac} in Fig. 1(d). The curve looks similar to a shifted sigmoid function. We assumed H_{Oe}=c m_x^{out}, where c is constant, and found that the best performance was obtained for the following recognition task when c=90 Oe. We performed typical recognition task for ANN, using the handwriting digits recognition for MNIST database [5]. Figure 2 shows the structure of ANN with three layers. The first layer is the input layer with 784 nodes, receiving signals from normalized gray-scaled pictures with 28 pixels each side. The second (hidden) layer has 50 nodes. The last layer is the output layer with 10 nodes, corresponding to numbers from 0 to 9 digits. The back propagation is used for the learning algorithm. After learning, STO-based ANN with the activation function shown in Fig. 1(d), provides recognition accuracy of 75% on average.

[1] P. A. Merolla, et al., Science 345, 668 (2014) [2] Y. LeCun, et al., Nature 521, 436 (2015) [3] I. E. Dzyaloshinskii, J. Phys. Chem. Sol. 4, 241 (1958); T. Moriya, Phys. Rev. 120, 91 (1960) [4] A. Vansteentiste, et al. AIP Advances, 4, 107133 (2014) [5] http://yann.lecun.com/exdb/mnist

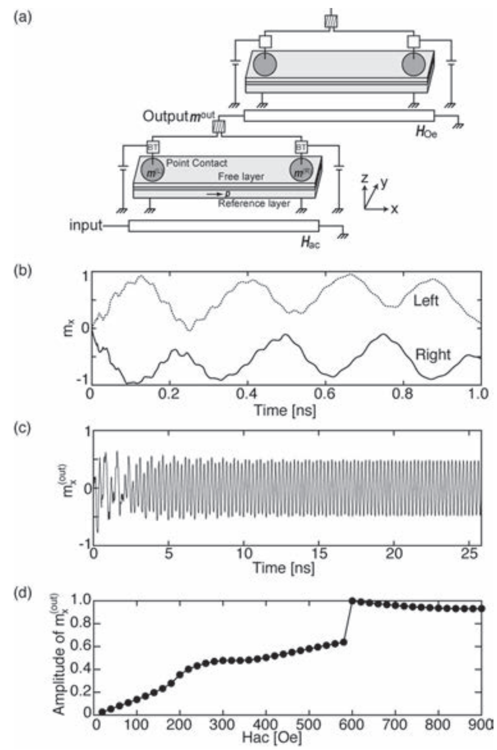

Fig. 1. (a) Schematic illustration of the spin-wave coupled spin torque oscillator with double point contacts. The dc current is applied through each point contact, and external oscillating magnetic field H_{ac} is also applied. The output signal (m^{out}) obtained through a bias tee (BT) produces an Oersted field H_{Oe} which is applied to the next unit. (b) Time development of m_x under left and right point contacts for H_{ac}=0. (c) Time development of m_x^{out} for H_{ac}=300 Oe. (d) Hac dependence of the amplitude of m_x^{out} averaged for t=40-50 nsec.

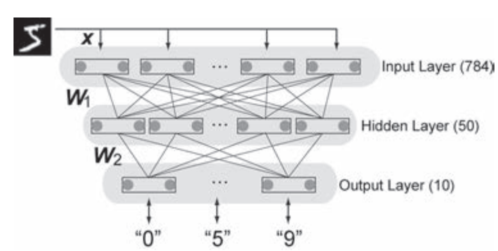

Fig. 2. Schematic illustration of artificial neural network for handwriting digit recognition task. Figures in brackets indicate the numbers of processing unit. Each processing unit has an activation function *f*. The output signal from each layer is multiplied by the weight *W*. Then total amount of the signals are fed to the next layer.

11:15

AI-09. Spin-Hall effects and unconventional Anomalous Hall Effects in transition-metal based metallic spintronic multilayers for THz Emission.

H. Jaffres[1], T. Dang[1], Q. Barbedienne[1], H. Nong[2], J. Tignon[2], N. Reyren[1], J. George[1], S. Collin[1], L. Vila[3], L. Divay[4], P. Bortolotti[4] and S. Dhillon[2]
1. Unité Mixte de Physique CNRS-Thales, Palaiseau, France;
2. Laboratoire Pierre Aigrain, ENS, Equipe THZ & Infrarouge, PARIS, France; 3. INAC/SP2M, CEA-Université Grenoble-Alpes, Grenoble, France; 4. Thales Research & Technology, Palaiseau, France

It was recently reported that THz emission can be realized in heterostructures composed of ferromagnetic (FM) and non-FM metal films *via* dynamical spin-to charge conversion originating from interfacial spin-orbit coupling or inverted spin-Hall effect (ISHE). Those phenomena are generally investigated through time-dependent spectroscopy (TDS) [1-3]. In that mind, we will present our last lattest results of THz emission provided by optimized grownth bilayers composed of a high-spin orbit material (Pt, Au :W) in contact with a thin ferromagnetic layer Co/Pt, NiFe/Au:W, NiFe/Au:Ta (Fig.1). Those bilayers state-to-the art bilayers model systems are also used in experiments combining RF-spin pumping and spin-to-charge conversion by ISHE [4-5]. Here These kind of experiments consist in exciting magnetization and spin-currents within the FM layer via femtosecond laser excitation and measuring, in the picosecond timescale, the relaxation of the correlated oscillating spin and charge currents or dipoles responsible for THz dipolar emission. According to the resutl results presented in Fig. 1, we see acn observe that the amplitude of TDS of our Co/Pt sample has the oder compete with the standard electro-optic (EO) delivered from ZnTe crystals, as known as « traditional conventional » material for THz [2-3]. It is very point because For potential applications, the main advantages of the THz spintronic emitters THz emitter based on magnetic hetrostructures are low-cost and the controle of the polarization of the emitted THz wave being easily tuned with an external magnetic field. In comparaison with Co/Pt systems, In NiFe/Au:Ta and NiFe/Au:W bilayers, the provide a smaller signalsignals is very small even though the spin Hall angles for Au:Ta and Au:W are larger than for Pt [6]. This is mainly due to their smaller spin-mixing conductance in comparaison with the optimized Co/Pt one. To understand this point, we will discuss the role of the generalized spin-mixing conductance on the spin-transport properties and spin-orbit torques involved in the time-dependent diffusion and relaxation phenomena. In Fig.2, we demonstrate that the THz signals strongly depend on the spin Hall angle of non-FM metal, spin diffusion length, and spin-mixing conductance. In the structures with large spin-mixing conductance and spin length diffusion, *e.g.,* Co/Pt, the THz signal is comparable to ZnTe signal. It should be a rapid method to know the characteristic of spintronics samples. Moreover, in order to study the SHE spin-current profiles in those $[Co,Ni]_N$/Pt and $[Co,Ni]_N$/Au:W multilayers, we have studied in the static regime, their the unconventional Anomalous Hall effect (AHE) properties showing up a characteristic AHE spin-inversion from Pt to Au:W samples by proximity effect. We analyze our results in the series of samples: the exact conductivity profile across the multilayers via the 'extended' Camley-Barnas approach [7] and the spin current profile generated by SHE. The values of spin Hall angles in layers are found: -0.2 for Pt (enhanced compared to CIP geometry), 0.01 for CoNi, and 0.1 for Au:W (resistivity). In $[Co,Ni]_N$/Pt sample, we show that the transverse current changes from negative (N<20) to positive (N>20) values.

[1] T. J. Huisman et al., Nat.Nano 11, 455–458 (2016) [2] T. Seifert et al., Nat.Photo 10, 483-488 (2016) [3] D. Yang et al., Adv.Opt.Mat. 4, 1944-1949 (2016) [4] J.C Rojas-Sanchez et al., PRL. 112, 106602 (2014) [5] P. Laczowski et al, APL 104, 142403 (2014) [6]P. Laczowski et al, Phys. Rev. B 96, 140405(R) (2017) [7] R. E. Camley et al., Phys. Rev. Lett. 63, 664 (1989); J. Barnas et al., Phys. Rev. B 42, 8110 (1990)

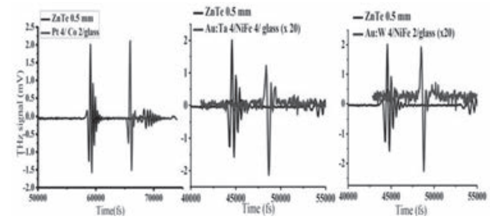

Fig. 1. Time-Dependent Spectroscopy (TDS) of bilayer (blue curve) and ZnTe crystal (black curve): Co/Pt (left), NiFe/Au:Ta (middle), NiFe:Au:W (right).

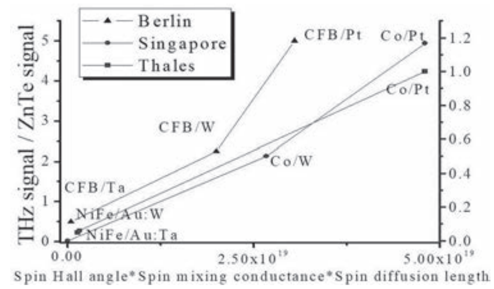

Fig. 2. THz signals vs. spin Hall angle, spin diffusion length, spin mixing conductance performed in our group (blue, square), Singapore group (blue, round), Berlin group (black) and in different structures.

11:30

AI-10. Investigation of intrinsic large anomalous Nernst effect in Co-based Heusler compounds for novel energy harvesting applications.

Y. Sakuraba[1,2], K. Hyodo[3], S. Mitani[1] and A. Sakuma[3]
1. National Institute for Materials Science (NIMS), Tsukuba, Japan; 2. JST-PRESTO, Saitama, Japan; 3. Tohoku University, Sendai, Japan

Introduction: Developing energy harvesting technologies is an urgent task for coming IoT to supply electric energy (μW-mW level) to the numerous sensors network independently. Thermoelectric power generation (TEG) is one of the important technologies to obtain electricity from various types of heat surrounding us, i.e. environmental heat, exhaust heat, body heat etc. In previous studies, it was proposed that there are many advantages to use anomalous Nernst effect (ANE) in magnetic materials for novel thermoelectric applications in comparison with conventional TEG using Seebeck effect.[1-4]. Because ANE generates the electric field to the outer product direction between magnetization and temperature gradient, we can expect to realize different types of TEG having high flexibility, cost-effectiveness, and expandability to large area heat source. However, because the reported anomalous Nernst coefficient S_{ANE} that determines the thermopower of ANE is less than 1-2 μV/K, it is necessary to explore magnetic materials showing one order of larger thermopower of ANE (few tenth μV/K) for realizing practical applications for energy harvest.[3] From the linear response expression of the electric field under temperature gradient, anomalous Nernst coefficient S_{ANE} can be expressed by the following equation, using diagonal and off-diagonal parts of resistivity tensor and Peltier tensor, suggesting that materials having the large Seebeck effect(α_{xx}), electric resistivity(ρ_{xx}) and anomalous Hall effect (AHE) (ρ_{xy}) are promising to obtain large S_{ANE}. It has been recently reported that antiferromagnetic material Mn_3Sn shows large anomalous Nernst effect because of its predicted large anomalous Hall effect due to significantly large Berry curvature[5], which is the result indicating the importance of large intrinsic anomalous Hall effect for large S_{ANE}. On the other hand, large intrinsic AHE has been also predicted in ferromagnetic Co-based Heusler compounds such as Co_2MnAl[6,7]. However, ANE in these compounds has not been ever systematically investigated. Because Fermi level of Co_2YZ Heusler can be controlled by changing Z element having different valence electron number, this group of materials is interesting to understand how Fermi level position affect the response of ANE. Therefore, in this study, we systematically investigated AHE, ANE, and Seebeck effect in $Co_2MnAl_{1-x}Si_x$ epitaxial thin films to observe large intrinsic ANE and also investigate the Fermi level position dependence of ANE. Experimental procedure : 30nm-thick $Co_2MnAl_{1-x}Si_x$ (CMAS) epitaxial thin films were deposited by a UHV magnetron sputtering system on (001)-oriented MgO single crystalline substrate at ambient temperature and then annealed at 500-700°C. CMAS films having a different composition ratio of Al:Si, x = 0 to 1, were prepared. ANE were characterized by giving the temperature gradient to in-plane direction and applying magnetic field to out-of-plane direction of the films (shown in the inset of Fig.1). Given temperature gradient ∇T was evaluated by IR camera with black body coating strictly. Experimental result : The structural analysis using XRD confirmed all CMAS films have epitaxial single phase. Monotonic increase of lattice constant was also observed with increasing Si composition ratio x. Figure 1 shows perpendicular magnetic field dependence of ANE signals normalized by temperature gradient ∇T and the sample width in the CMAS films annealed at 600°C. Interestingly, although Co_2MnAl shows the largest AHE as theoretically predicted[6], we found the largest ANE signal ever reported 4.2μV/K in $Co_2MnAl_{0.63}Si_{0.37}$. The systematical analysis by measuring AHE, ANE and Seebeck effect confirmed that large ANE in $Co_2MnAl_{0.63}Si_{0.37}$ originates from both large intrinsic AHE (not only large ρ_{xy} but also large α_{xy}) and large Seebeck effect. By increasing annealing temperature over 600°C, we found further enhancement of S_{ANE} in $Co_2MnAl_{0.63}Si_{0.37}$ film up to 6.2 μV/K at 650°C together with the improvement of $L2_1$ atomic ordering.(Fig.2) Our first principle calculations for the off-diagonal part of electric and Peltier tensors (σ_{xy} and α_{xy}) qualitatively well explained the enhancement of ANE from disordered B2 structure to ordered $L2_1$ structure in experiment. This result suggests a possibility to realize giant ANE due to intrinsic large Berry curvature, which opens up a way for realizing practical thermoelectric energy harvesting applications using magnetic materials.

[1] Y. Sakuraba et al., APEX 6, 033003 (2013) [2] K. Hasegawa, et al., APL 106, 252405 (2015). [3] Y. Sakuraba, Scripta Materialia 111, 29-32 (2016) [4] Y. Sakuraba and K. Takanashi, Parity 2014, 6 [5]M. Ikhlas, et al., Nature Physics, 13, 1085-1090 (2017). [6] J-C. Tung, and G.-Y. Guo, New. J. Phys. 15, 033014 (2013). [7] J. Kubler and C. Felser, Phys. Rev. B 85, 012405 (2012).

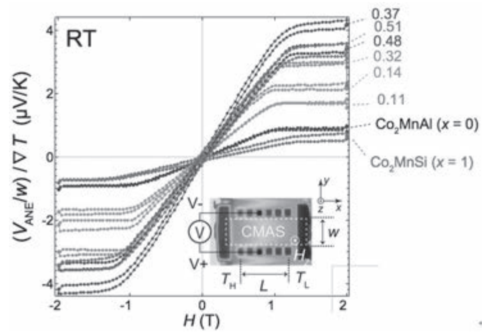

Fig. 1. ANE signal normalized by sample width and given temperature gradient in fabricated CMAS thin films

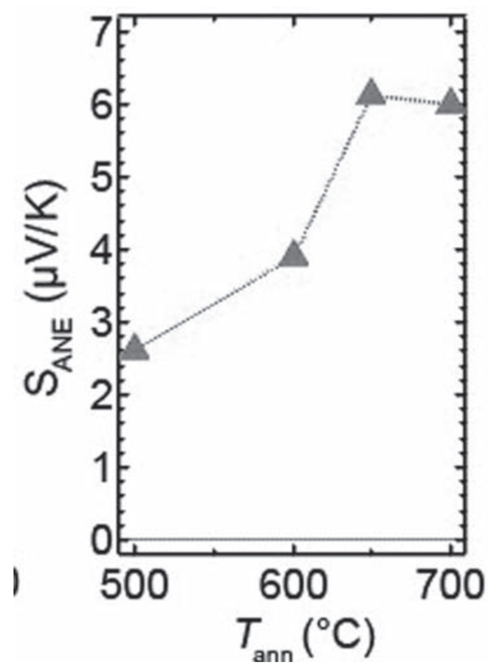

Fig. 2. Annealing temperature dependence of S_{ANE} in $Co_2MnAl_{0.63}Si_{0.37}$ thin film

11:45

AI-11. Mutually synchronized 2D spin Hall nano-oscillator arrays.

M. Zahedinejad[1*], A.A. Awad[1], S. Muralidhar[1], M. Dvornik[1] and J. Åkerman[1]
1. Physics, University of Gothenburg, Gothenburg, Sweden

Abstract Mutual synchronization of spin current driven nano-oscillators can both increase their output power and reduce their linewidth and is therefore a critical mechanism to reach sufficient microwave signal quality for actual applications. Here, we, for the first time, demonstrate two-dimensional *N* x *N* SHNO arrays (*N* = 2 – 10) of Pt/Hf/NiFe nano-constrictions, and observe robust mutual synchronization for *N* = 2 – 8 and partial synchronization in the larger arrays. Our results indicate that each nano-constriction interacts with its neighbors via both dipolar and exchange coupling. For the smaller arrays, the net coupling is strong enough to have robust mutual synchronization for nano-constrictions separated by up to 300 nm (pitch). However, to achieve robust synchronization in the larger arrays, the pitch size must be reduced to increase the coupling strength. Our results also indicate that neighboring nano-constrictions synchronize with a net relative phase shift, such that the initial rapid improvement of power and linewidth with increasing *N*, levels off for larger N and even deteriorates for of the largest arrays. Spin Hall nano oscillators (SHNOs) operate via the injection of a pure spin current into a ferromagnetic (FM) layer by passing a direct current through a non-magnetic (NM) heavy metal layer (e.g. Pt, W, Ta). The spin current exerts a torque on the local magnetization of the FM and can fully compensate the intrinsic damping to sustain a steady state precession of the magnetization around the local effective magnetic field. Some of us recently demonstrated robust mutual synchronization of chains of up to nine Pt/NiFe SHNOs [1]. Such chains can resemble the human brain where neurons interact with neighboring neurons through synaptic couplings resulting in a synchronization of their action potential activity. Synchronized networks have also been proposed for non-Boolean computing approaches such as bio-inspired neuromorphic computing with coupled oscillators [2-3] in which the synchronization frequency, the integrated output power, and/or the phase can be considered as the computation output. In this digest, we demonstrate 2D arrays of SHNOs fabricated in $Ni_{80}Fe_{20}$(30)/Hf(5)/Pt50) tri-layers (numbers in parenthesis indicate thickness in Å). Figure 1 shows a schematic of a typical device and a scanning electron microscopy (SEM) image of a 8 x 8 SHNOs array. An external magnetic field (H) was applied during the microwave measurements with an out of plane (OOP) angle θ and an in-plane (IP) angle ϕ as shown in Fig.1. The nano-constriction width was varied from *w* = 80 to 120 nm while the pitch size (*p*) in both the *x* and the *y* directions was set to 140, 200 and 300nm, to modify the dipolar and exchange coupling. Fig.2 shows auto-oscillation measurements for 2 x 2 and 4 x 4 SHNOs array (*w* = 300 nm and *p* = 300 nm). As can be seen, the oscillators within the array synchronize with increasing current and the integrated power increases while the linewidth decreases. However, for larger arrays with the same *w* and *p*, we could not observe complete synchronization (not shown). By reducing both the nano-constriction width and array pitch to *w* = 80 nm and *p* = 140 nm we are able to increase the nearest neighbor coupling in the arrays and demonstrate complete synchronization in arrays as large as 8 x 8 (Fig.2 (c)). It is however quite interesting that these large fully synchronized arrays do not demonstrate the same beneficial improvement in their power and linewidth as smaller arrays. We believe this is a result of a non-zero relative phase shift between neighboring nano-constrictions. While the total cumulative phase shift can remain small within the smaller arrays, it will eventually grow important as *N* increases, potentially leading to non-constructive addition of the individual nano-constriction signals. To benefit from very large fully synchronized SHNO arrays it will hence be important to reduce the relative phase shift between neighboring nano-constrictions. Our demonstrated SHNO array architecture imitates artificial neural networks in which neurons (individual construction within the array) communicate with neighboring neurons via synaptic connections. We believe that the synaptic coupling can be tailored through both the dipolar coupling and the direct exchange interactions between the array elements in the 2D SHNO arrays, where both can be tunable by the applied current, and the magnitude and angle of the applied field.

[1] Awad, A. A., et al. "Long-range mutual synchronization of spin Hall nano-Oscillators." *Nature Physics* (2016). [2] Torrejon, Jacob, et al. "Neuromorphic computing with nanoscale spintronic oscillators." *Nature* 547.7664 (2017): 428. [3] Yogendra, et. al. "Energy efficient computation using injection locked bias-field free spin-hall nano-oscillator array with shared heavy metal." *2017 IEEE/ACM International Symposium on Nanoscale Architectures (NANOARCH)*. IEEE, 2017.

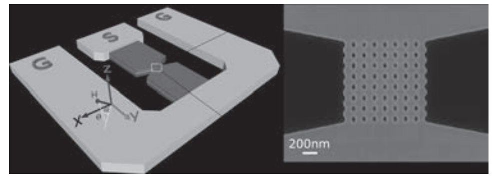

Fig. 1. Schematic of a typical SHNO (left) and an SEM image of the fabricated 8 x 8 SHNOs array (right).

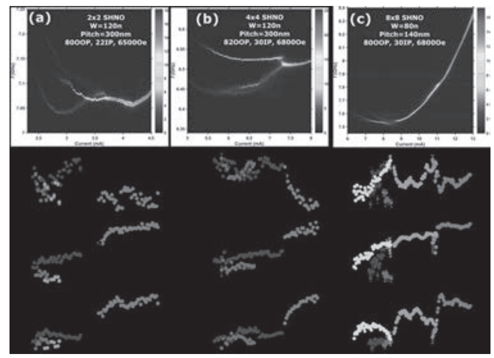

Fig. 2. Auto-oscillation measurement of arrays of different sizes for (a) 2x2, (b) 4x4 and (c) 8x8.

Session AP
BIO-IMAGING AND BIO-DETECTION II
(Poster Session)

Neil Telling, Co-Chair
Keele University, Stoke-on-Trent, United Kingdom
Alfredo García-Arribas, Co-Chair
Universidad del País Vasco, UPV/EHU, Leioa, Spain

AP-01. Histamine Magnetic Test for Wine.

M. Rivas[1], A. Moyano[1,3], M. Salvador[1,4], J.C. Martínez-García[1], M. Fernández[2] and M.C. Blanco-López[3]

1. Physics Department, University of Oviedo, Gijón, Spain; 2. Dairy Research Institute of Asturias, CSIC, Villaviciosa, Spain; 3. Physical and Analytical Chemistry Department, University of Oviedo, Oviedo, Spain; 4. Institute of Structure of Matter, National Research Council, Rome, Italy

Histamine is a biogenic amine produced by microorganisms during the fermentation process of several food products such as fish, meat, cheese, vegetables, chocolate, beer, or wine. These amines are produced by bacteria during amino acids decarboxylation. The ingestion of high levels of histamine may cause serious toxicological problems on humans. In addition, 1% of the population is intolerant to it, displaying gastrointestinal symptoms, rhinitis or urticaria. For these reasons, it is important to set up a rapid method for the detection and quantification of histamine in food where fermentation takes place. Analytical techniques for its determination include liquid chromatography, enzymatic methods and ELISA immunoassays [1, 2]. These are efficient but expensive to be used at large scale, requiring centralized facilities and qualified analysts. An inexpensive quantification method that can be used by untrained individuals in non-laboratory environments would be very useful for industrial or personal usage. This work aims to develop a rapid, cheap, and simple test for the detection and quantification of histamine in wine. Competitive lateral flow immunoassays (CLFI) have been developed by using magnetic (iron oxide) and non-magnetic (gold) nanoparticles as labels. The CLFI signal read out is performed by a magnetic sensor sensitive to superparamagnetic particles [3,4] in the first case, and a commercial optical strip reader (ESE-Quant LR3 lateral flow system, QIAGEN) that quantifies the colour intensity of the gold line by reflectance measurements in the second one. Figure 1 schematises the design of the CLFI: the sample to be analysed flows by capillary along a nitrocellulose membrane across which two lines of bioreagents have been previously deposited. One of them is the test line on which a dense band of BSA-histamine complexes has been immobilised. The other one is the control line, composed by anti-IgG antibodies. At the beginning of the strip (left in the figure) there is a sample pad to absorb the sample and transfer it to the paper; at the right end there is a wicking pad with the role of drawing the sample off and prevent the backflow. The sample to be analysed is mixed with a monoclonal anti-histamine antibody in a test tube. The assay is as follows: 1. The sample is mixed with a fixed and known concentration of a monoclonal anti-histamine antibody. Binding of the histamine to those antibodies occurs. If the sample has no histamine (blank), the antibodies remain free. If the analyte concentration is high, all of them are bound. 2. The sample pad is introduced in the liquid sample (or a sample aliquot is deposited on it). The fluid flows along the strip and crosses the test line. At that point, only the anti-histamine circulating antibodies which are free (not bounded to histamine in the sample) attach to the immobilised complexes. In the blank sample, all of them are free. The larger the concentration of histamine in the sample, the smaller the fraction of retained antibodies. 3. To develop the assay the strip is immersed in a solution of protein G conjugated to the nanoparticles. This protein has a strong affinity for the Fc fragments of antibodies. Therefore, it specifically binds to the antibodies that had been captured in the test line. The labels reveal a signal (either coloured or magnetic) whose intensity is inversely proportional to the concentration of histamine in the sample. 4. The surplus of protein G-nanoparticle conjugates proceeds along the strip until it is trapped in the control line. This serves as verification of the correct performance of the test. Histamine was determined in the concentration range 10^{-6} to 10^{-1} mg/mL. The tests were applied to histamine detection in wine, and results were validated by comparison with those obtained by a liquid chromatography method. This concentration range is suitable for control of histamine in foods, and particularly in wine.

[1] Önal, A., *A review: Current analytical methods for the determination of biogenic amines in foods*. Food Chemistry, vol. 103(4), pp. 1475 - 1486, 2007. [2] Mahmoudi, R. and Mardani K., *Histamines and foods: a review on importance, detection and controlling in foods*. Malaysian Journal of Science, vol. 34(1), pp. 103-107, 2015. [3] Lago-Cachón, D. et al., *Cu impedance-based detection of superparamagnetic nanoparticles*. Nanotechnology, 24 (2013). 245501. [4] Lago-Cachón, D. et al., *Scanning Magneto-Inductive Sensor for Quantitative Assay of Prostate-Specific Antigen*. IEEE Magnetics Letters, vol. 8, pp. 1-5, 2017.

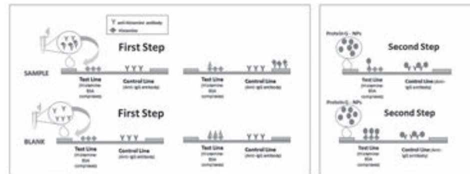

Fig. 1. Scheme of the competitive lateral flow immunoassay for histamine. On the left, the first step represents the result of running the sample; on the right, the developing step with the dilution of the conjugate nanoparticle@Protein G. On top, the result of running a sample containing histamine; at the bottom, the scheme of a blank sample.

AP-02. Microstructure engineering of polymer-based magnetic composites for microfluidic devices.

D. Le Roy[1], M. Samir[2], V. Dupuis[1] and A. Deman[2]
1. Institut Lumière Matière, Villeurbanne, France; 2. Institut des Nanotechnologies de Lyon, Villeurbanne, France

Magnetophoresis, which refers to the motion of an object in a magnetic field gradient, permits to address numerous biomedical applications when implemented in microfluidic devices [1-3]. The implementation of micrometer-sized soft magnetic structures is particularly beneficial in this context as it permits (i) to create large magnetic field gradients, and (ii) to modulate or even cancel the magnetic forces in order to release the trapped objects on demand. In order to achieve high concentration of magnetic flux, the soft magnetic material should combine a large magnetization and preferentially a high effective magnetic susceptibility χ_{eff}, to operate at relatively low magnetic fields, while maintaining no hysteresis loss. To overcome the technological challenges owing to heterogeneous integration of metallic material with polymers such as PolyDiMethylSiloxane (PDMS), as well as limitations related to pure metals micropatterning using time consuming, costly and complex UV-LIGA process, the approach of polymer-based composites is promising [4-6]. Here we focus on I-PDMS composites, made of the widespread PDMS polymer as a matrix and carbonyl iron particles as magnetic loads. PDMS properties are preserved such as soft-lithography micropatterning and O_2 surface activation for plasma bonding with glass and PDMS. Mass fractions of carbonyl iron particles as high as 83 wt% were achieved, which leads to saturation magnetization in the excess of 600 kA/m, which is comparable to benchmark soft magnetic metallic alloys such as Mumetal or Permalloy. In addition, the relatively easy microstructure engineering enables ones to tune magnetic properties. We recently reported on the effect of applying a magnetic field during the polymer reticulation in order to self-order particles in the polymer matrix [7]. High aspect ratio particle-agglomerates create a uniaxial magnetic anisotropy over the whole range of investigated compositions. Such composites can be exploited in different ways in microsystems: (i) at high concentration as a cost effective alternative to purely metallic micro-patterns or (ii) at low concentration, as arrays of individual magnetic flux micrometer sized concentrators. In highly concentrated I-PDMS the particles form ramificated chains oriented along the flux lines. It gives rise to 20% increase in the susceptibility as compared to composites with isotropic particle distribution. To study the impact on the generated magnetophoretic force, we developed a microfluidic channels with a wall made of I-PDMS. For one batch of devices we implemented isotropic I-PDMS and for the second batch anisotropic I-PDMS (see Fig. 1a). Microbeads flowing in the channel were submitted to different forces: magnetophoretic forces, fluidic drag force, gravitational force, and buoyancy forces. The motion of a magnetic bead in a laminar flow can be then described by the balance of forces. To measure the magnetophoretic force experienced by the beads for each batch of devices we used the following protocol. The channel was first filled up with beads. By stopping the flow rate, the initial position of the beads in the channel was defined. An external magnetic field was applied. The superparamagnetic beads were then attracted toward the I-PDMS composite wall of the channel. Fig. 1b displays a stacking of video frames revealing microbeads trajectories. From beads velocities measurements, we could map the magnetophoretic force in the channel. Fig. 1c shows the deduced force at different distances from the composite wall. At a distance of 150 µm from the microconcentrator, we measured a force reaching 60 pN using the anisotropic I-PDMS, a force twice as large as the one measured using isotropic composite. Based on the measured variation of the magnetophoretic force and on finite element simulations, we highlighted that the benefit of using anisotropic composite does not only rely on the global susceptibility increase, but also on local magnetic field gradients originating from its fine periodic microstructure [8]. In contrast, at low particle concentrations (1 and 5 wt%), the obtained microstructure is made of well-defined and isolated chains, as revealed by X-Ray Tomography (see Fig 2a). We observed two types of organizations: chain-like agglomerates and isolated clusters of particles concentrated at the bottom surface of the composite membrane. This leads to two populations of micrometer sized traps with average diameter of 1.5 and 6.7 µm, larger ones mostly corresponds to particle chains. We integrated 1 wt% and 5 wt% I-PDMS membranes in microfluidic systems and studied their magnetic trapping performances. Micrometer trap enabled to isolate magnetic beads and to organize them on large surfaces. Fig. 2b reports microscopic images of microfluidic channel integrating a trapping membrane (1 wt%), before and after beads injection at 250 µL/h. We tested the persistence of trapping when increasing the flow rate. Using 5 wt% composite, 50 % of beads remain trapped at 2 mL/h. We have also shown that these dense arrays of traps permit to create a monolayer of beads, with a density of 1200 beads/mm^2, 89 % of large traps being occupied. This original array of magnetic flux concentrator is promising as the implementation is quite simple while it permits to address biological characterization that require the controlled immobilization of a target population, such as drug assays.

[1] Tekin HC and Gijs MAM (2013) Ultrasensitive protein detection: a case for microfluidic magnetic bead-based assays. Lab Chip DOI: 10.1039/c3lc50477h. [2] Plouffe BD, Murthy SK, Lewis LH (2015) Fundamentals and application of magnetic particles in cell isolation and enrichment: a review. Rep. Prog. Phys. 78 016601. [3] Zhu Y, Kekalo K, Dong CN, Huang YY, Schubitidze F, Griwold KE, Baker I and Zhang JXJ (2016) Magnetic-Nanoparticle-Based Immunoassays-on-Chip: Materials Synthesis, Surface Functionalization, and Cancer Cell Screening. Adv. Funct. Mater. 26 22, pp. 3953-3972. [4] Faivre M, Gelszinnis R, Degouttes J, Terrier N, Rivière C, Ferrigno R, Deman AL (2014) Magnetophoretic manipulation in microsystem using carbonyl ironpolydimethylsiloxane microstructures. Biomicrofluidics 8, 054103. [5] Zhou R, Wang C (2016) Microfluidic separation of magnetic particles with soft magnetic microstructures. Microfluid. Nanofluid. 20:48 [6] Royet D, Hériveaux Y, Marchalot J, Scorreti R, Dias A, Dempsey N M, Bonfilm M, Simonet P, Frenea-Robin M (2016) Using injection molding and reversible bonding for easy fabrication of magnetic cell trapping and sorting devices. J. Magn. Magn. Mater. http://dx.doi.org/10.1016/j.jmmm.2016.10.102 [7] Le Roy D, Dhungana D, Ourry L, Faivre M, Ferrigno R, Tamion A, Dupuis V, Deman AL (2016) Anisotropic ferromagnetic polymer: A first step for their implementation in microfluidic systems. AIP Advances 6, 056604. [8] Deman AL, Mekkaoui S, Dhungana D, Chateaux JF, Tamion A, Degouttes, J, Dupuis V, Le Roy D (2017) Anisotropic composite polymer for high magnetic force in microfluidic systems, Microflu. Nanoflu. accepted.

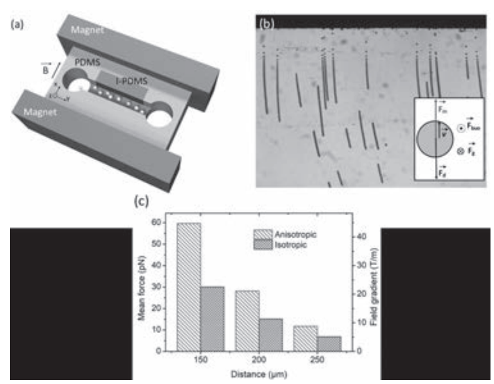

Fig. 1.

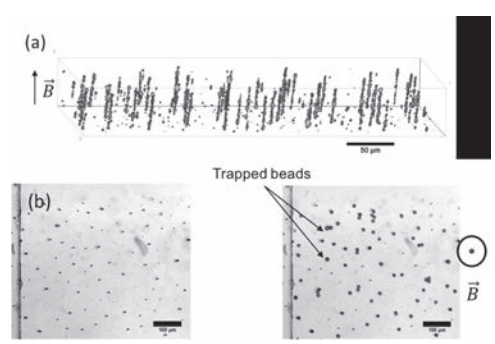

Fig. 2.

AP-03. Temperature dependence of transverse relaxivity of the nanoparticle contrast agents for MRI: different magnetic cores and coatings.

O. Kaman[1], V. Herynek[2], P. Veverka[1], L. Kubickova[1], M. Pashchenko[1,3], J. Kulickova[1] and Z. Jirak[1]
1. Institute of Physics, Czech Academy of Sciences, Praha, Czechia;
2. Institute for Clinical and Experimental Medicine, Praha, Czechia;
3. Faculty of Mathematics and Physics, Charles University, Praha, Czechia

The transverse relaxivity r_2 of contrast agents for MRI describes their efficiency to shorten transverse relaxation times T_2 of ^{1}H nuclear spins of nearby water molecules, and thus the contrast media with high r_2, typically magnetic nanoparticles, are used as so-called negative contrast agents for T_2-weighted images. The role of magnetic particles consists in creating of inhomogeneities in the applied magnetic field, which leads to a loss of phase coherence of precessing ^{1}H spins. The magnitude of this effect is treated by theoretical models (see, e.g. [1]) that take into account both the fundamental properties of magnetic particles and self-diffusion of water, suggesting several distinct regimes of relaxation. In the present contribution, several distinct types of magnetic particles are prepared, and temperature dependences of the transverse relaxivity are analysed and compared with the theory. Four types of magnetic nanoparticles were synthesized, namely $La_{0.65}Sr_{0.35}MnO_3$ (LSMO) and $La_{0.80}Na_{0.20}MnO_3$ (LNMO) manganites with perovskite lattice (R-3c) and $Mn_{0.61}Zn_{0.42}Fe_{1.97}O_3$ (MZFO) and $Co_{0.44}Zn_{0.70}Fe_{1.86}O_4$ (CZFO) ferrites with spinel structure (Fd-3m). The manganites were prepared by a sol-gel process followed by thermal treatment and mechanical processing (for LSMO see [2]). Ferrite particles were synthesized under hydrothermal conditions (for MZFO see [3]). All four materials were coated with silica (denoted by @ silica) by using tetraethoxysilane. In addition, two other surface modifications were employed for MZFO particles. Titania-coated nanoparticles (MZFO@TiO_2) were achieved by a procedure similar to encapsulation into silica but titanium tetrabutoxide was used as a precursor. Further, citrate-stabilized nanoparticles (MZFO@cit) were obtained by chemisorption of citric acid and subsequent ionization by ammonia. XRD measurements of bare particles evidenced single-phase character of all products. The Rietveld analysis of peak broadening provided the mean crystallite size of 23-31 nm for manganite nanoparticles, and 11 nm for both the ferrite samples. TEM study confirmed typical core-shell structure of silica-coated particles and uniform thickness of the shell with the mean of ≈15-20 nm. The magnetic cores of silica-coated particles were formed by small clusters of crystallites, the mean core size was ≈50 nm for manganites and 26-31 nm for ferrites (i.e. several crystallites were present in an average magnetic core). The image analysis of MZFO@TiO_2 was not straightforward but TEM analysis evidenced larger particles. And DLS measurements provided comparable data (z-average hydrodynamic size 1.8 × larger for MZFO@TiO_2 than for MZFO@ silica). Magnetic behaviour was analysed based on hysteresis loops at 5 K and 300 K (see Fig. 1), ZFC-FC susceptibility studies and temperature scans of magnetization at 0.5 T (see Fig. 2). Shortly, the manganite systems showed ferromagnetic ground state with magnetic moments of spontaneous ordering of 2.28 μ_B and 1.63 μ_B per f.u. at 5 K and Curie temperatures T_C of 352 K and 309 K for LSMO and LNMO, respectively. The ferrimagnetic arrangement of MZFO and CZFO was characterized by 4.55 μ_B and 2.64 μ_B at 5 K and T_C of ≈425 K and 345 K, respectively. Aqueous suspensions of coated samples with concentrations determined by chemical analysis were subjected to relaxometric study at 0.5 T (Fig. 1b). The relaxivities of silica-coated particles correlated well with the magnetization of cores at a given temperature (see magnetization data at 300 K in Fig 1a), and high relaxivites were observed especially for particles based on MZFO and LSMO. The role of different relaxation regimes was analysed based on the temperature dependences $r_2(t)$, normalized using the values of r_2(6°C). The data were compared with similarly normalized dependences of certain quantities, namely the self-diffusion coefficient of water $D(H_2O)$ according to [4], the magnetization M of bare particles at 0.5 T, and the expression $M^2/D(H_2O)$ (Fig. 2). The last quantity describes the temperature dependence of r_2 in the motional averaging regime (MAR), whereas the temperature dependence in static dephasing limit (SDL) is shaped only by $M(t)$ [1]. Generally, the observed dependences were found within the limits given by MAR and SDL. The behaviour of silica-coated ferrite samples was closer to MAR, whereas CZFO@TiO_2, containing larger clusters, seemingly approached SDL. The LNMO@silica exhibited the most pronounced dependence of $r_2(t)$ due to a rather sharp FM-PM transition. Nevertheless, more thorough analysis revealed considerable limits of the traditional model and indicated a possible role of thermally activated processes related to chemical exchange of ^{1}H.

[1] Carroll, M. R. J., Woodward, R. C., House, M. J., Teoh, W. Y., Amal, R., Hanley, T. L., and St Pierre, T. G., 2010. Experimental validation of proton transverse relaxivity models for superparamagnetic nanoparticle MRI contrast agents. *Nanotechnology*, 21(3): art. no. 035103. [2] Veverka, P., Kaman, O., Kacenka, M., Herynek, V., Veverka, M., Santava, E., Lukes, I., and Jirak, Z., 2015. Magnetic $La_{1-x}Sr_xMnO_3$ nanoparticles as contrast agents for MRI: The parameters affecting ^{1}H transverse relaxation. *Journal of Nanoparticle Research*, 17(1): art. no. 33. [3] Kaman, O., Kulickova, J., Marysko, M., Veverka, P., Herynek, V., Havelek, R., Kralovec, K., Kubaniova, D., Kohout, J., Dvorak, P., and Jirak, Z., 2017. Mn-Zn Ferrite Nanoparticles with Silica and Titania Coatings: Synthesis, Transverse Relaxivity and Cytotoxicity. *IEEE Transactions on Magnetics*, 53(11): 1-8. [4] Holz, M., Heil, S. R., and Sacco, A., 2000. Temperature-dependent self-diffusion coefficients of water and six selected molecular liquids for calibration in accurate ^{1}H NMR PFG measurements. *Physical Chemistry Chemical Physics*, 2(20): 4740-4742.

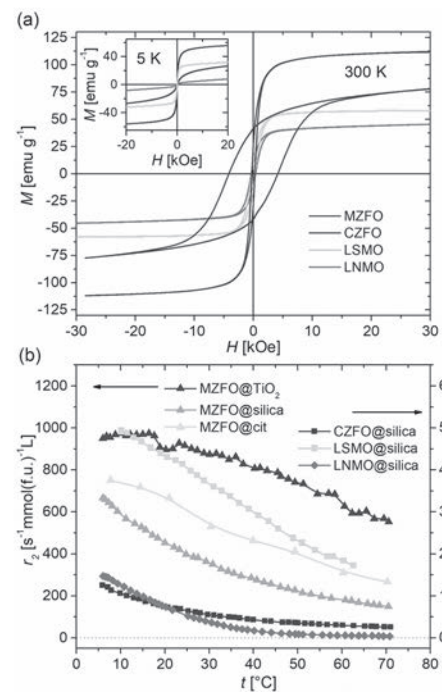

Fig. 1. Hysteresis loops for bare magnetic particles at 300 K (a) and 5 K (inset) and temperature dependence of transverse relaxivity for coated particles (b).

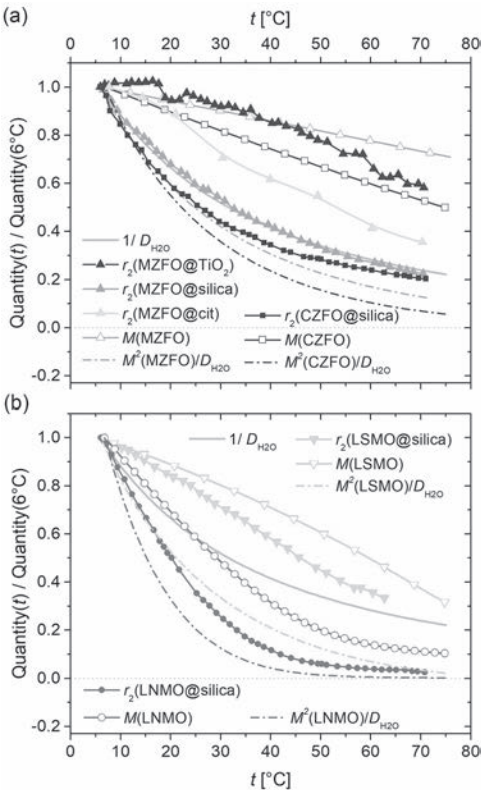

Fig. 2. Analysis of the temperature dependence of r_2 for silica-coated manganite particles (a) and for ferrite particles with different coatings (b). The relaxivities are compared with the inverse value of the self-diffusion coefficient of water, 1/*D*(H_2O), and magnetization of the bare particles at 0.5 T, *M*. All the quantities are normalized using their values at *t* = 6 °C.

AP-04. A Novel 1H/ 3He Dual-Tuned Transmit Coil at Ultra-low Field MRI Designed by Using Electromagnetic Field and Radio Frequency Circuit Co-Simulation Method.

Y. Dou[1,2], Y. Li[2], J. Xu[1], Q. Chen[2], L. Wang[1], X. Zhang[3], N. Li[2], C. Luo[2] and F. Du[2]

1. School of Electrical Engineering and Automation, Hefei University of Technology, Hefei, China; 2. Shenzhen Institutes of Advanced Technology, Chinese Academy of Sciences, Shenzhen, China; 3. Department of Radiology and Biomedical Imaging, University of California San Francisco, San Francisco, DC, United States

Abstract: In the development of noble gas MRI in humans, the traditional single-tuned transmit coil does not suitable for imaging acquisitions. This paper presents a novel radio frequency(RF) coil design method for applications of 1H/3He MRI system at the ultra-low field of 0.06mT.For the complex model of the dual-tuned 1H/3He coil, the traditional Electromagnetic(EM) simulation is not applicable due to its long computing time, the EM field and radio frequency (RF) circuit co-simulation method thus is implemented to accelerate the analysis, which results in an effective evaluation. The simulation results show that the proposed model has the potential for imaging of lung with 1H/3He MRI system at the ultra-low field. 1 Introduction : MRI as a non-invasive imaging method plays an important role in medical imaging for diagnosis of various diseases. Conventional clinical MRI is mainly based on proton imaging, which shows limited MRI signals in lung imaging due to its specific tissue structures. With the development of the noble gases polarized technique, some gases such as 3He and 129Xe can be applied in MRI and fMRI for diagnosis of lung disease at low field[1-2]. In the conventional MRI system, the transmit coil is usually designed with single frequency for proton imaging[3-5].Currently, the development of dual- tuned transmit coils are mainly for 1H/31P/19F/13C nucleus[6-7].The 1H/3He dual-tuned coil at low field for MRI imaging of different organs has not been intensively studied. For the construction of RF coils in MRI, the traditional electromagnetic(EM) simulation is usually implemented with advanced numerical algorithms such as the boundary-element method (BEM)and finite-element method(FEM) to get the distributions of magnetic field and the component values in the circuit of the coils[8-11].However, the simulation speed is really slow for the complex coils with multiple ports. In order to reduce the simulation time, the EM field method and RF circuit co-simulation method is applied[12-13]. To implement noble gas 3He lung MRI on a permanent magnet open MRI system at 0.06mT, a novel 1H/3He dual-tuned quadrature transmit coil has been designed and simulated by EM field method and RF circuit co-simulation method. The performance of the proposed coil was evaluated in the aspects of the homogeneity of the transmit magnetic field and the Specific Absorption Rate(SAR) of energy in human body[14]. 2 Materials and methods : The coil system consists of four butterfly-shaped elements[7].The coils 1,3 excite 3He(coils 2,4 excite 1H). The working frequency is 1.94 MHz for 3He(2.5548 MHz for 1H)corresponding to 0.06 mT.Fig.1(a) shows the structure of coil (d1=80 mm, d2=220 mm,l1=490 mm,l2=830 mm). The distance between each two coils is 20 mm(coils 1,2;coils 3,4), and 420 mm for the opposite coils(coils 1,3;coils 2,4)(See Fig.1(b)(c)). All coil elements are made of copper with thickness of 0.1 mm. A cubic phantom(400×770×300 mm^3)was selected to simulate human body, it was placed in the center region. The co-simulation approach was conducted by using the commercial CST(Computer Simulation Technology Darmstadt, Germany) software. In the simulation, the boundaries of RF coil model were set to "open". The distance between phantom and background was 500 mm, the bandwidth was 1~50MHz, and the total number of mesh cells was 6438700.Each coil had an independent tuning/matching/detuning circuit. The Lamour frequency of 1H and 3He at the ultra-low field of 0.06mT was tuned by adjusting capacitors C1,C2. The input impedance of coils was matched to 50 Ω through the matching capacitor Cm. The ports were excited with Gaussian pulses. The coils were tuned by changing the capacitance in RF circuit and combining the individual EM field based on the tuned data of the external ports in order to obtain the EM field. The B_1+ is denoted as transmit magnetic field was calculated as: B_1+=u(Hx+ iHy)/2; The homogeneity of B1+ field was calculated as: $B_1{}^+{}_{homogeneity}=(B_1{}^+{}_{max}- B_1{}^+{}_{min})/(2B_1{}^+{}_{mean})$; The transmit efficiency in ROI was calculated by: Transmit Efficiency=$B_1{}^+{}_{mean}$/Total SAR; 3 Result After decoupling, both S11 and S22 reached −30dB or higher, S13 and S24 also measured about−30dB.According to B1+ field distribution and the part of thoracic cavity located in body, the ROI was selected as cuboid area (See Figure 2). At the same scale, the B1+ field is strongest when signal source of the coils 1 and 3(the coils 2,4) have the same phase. With the increasing of phase difference, the field strength is gradually weak, but the $B_1{}^+{}_{homogeneity}$ in the ROI is basically unchangeable(See Fig.2). As phase difference is increasing, the transmission efficiency is increasing for 3He, while it is decreasing for 1H. 4.Conclusion In this paper, EM field and RF circuit co-simulation method was applied in designing of a novel 3He/1H dual-tuned quadrature transmit coil for noble gas 3He lung MRI applications at ultra-low Fields. Simulation work has been conducted to validate the proposed coil design. The results showed that phase delay of both 3He and 1H is chosen as 90° to ensure a high strength of B1+ field, a great field homogeneity and a relatively large transmission efficiency. The homogeneity in the ROI was well under various phase delays, which shows the applicable of the dual-tuned transmit coil.

Reference: [1] Zhou X, Sun XP, Mazzanti M, et al. MRI of stroke using hyperpolarized (129)Xe. NMR in Biomedicine [J]., vol.24,no.2) pp.: 170-175,2011 [2] Tsai L L, Mair R W, Rosen M S, et al. An Open-Access, Very-Low-Field MRI System for Posture-Dependent 3 He Human Lung Imaging[J]. J Magn Reson., vol.193,pp:274–285,2008. [3] H.Siebold. "Design optimization of main, gradient and RF field coils for MR imaging", IEEE Trans.Magn.,vol.26, no.2, pp.841-846, Mar.1990 [4] M.Fujita, M.Higuchi, H.Tsuboi, H.Tanaka, T.Misaki. "Design of the RF antenna for MRI". IEEE Trans. Magn,VOL.26,NO.2,pp.901-904,Mar.1990 [5]D.A.Molyneaw, A.H.Qureshi. "Quadrature coil system for simulation reception", IEEE Trans. Magn, vol.29, no.6,pp.2470 -2472,Nov.1993. [6] L.Hu, F.D.Hockett, J.Chen, L.Zhang, S.D.Caruthers, G.M.Lanza, "A generalized strategy for designing 19F/1H dual-frequency MRI coil for small animal imaging at 4.7 Tesla", J.Magn. Reson. Imag., vol.34, no.1, pp.245–252, 2011. [7] Hockett F, Wallace K, Schmieder A, et al. "Simultaneous dual frequency and open coil imaging of arthritic rabbit knee at 3T". IEEE Trans Med Imaging; vol.30, pp.22–27. 2010 [8] J.Chi, F.Liu, L.Xia, T.Shao, and S.Crozier, "An improved cylindrical FDTD algorithm and its application to field-tissue interaction study in MRI", IEEE Trans. Magn., vol.47, no.2, pp.466–470, Feb.2011. [9] Yilong Lu, Jianling Ying, Tat-Kee Tan, K. Arichandran., "Electromagnetic and Thermal Simulations of 3-D Human Head Model under RF Radiation by Using the FDTD and FD Approaches", IEEE Trans. Magn,wol.32, no.3,pp.1653–1656, May 1984 RF. [10]C. C. Scanchez, R. Bowtell, H. Power, P. Glover, L. Marin, A. A.Becker, and A. Jones, "Forward electric field calculation using BEM for time-varying magnetic field gradients and motion in strong static fields," Eng. Anal. Bound. Elem., vol. 33, pp. 1074–1088, 2009. [11]Guofa Shou, Ling Xia et al. "MRI Coil Design Using Boundary-Element Method With Regularization Technique: A Numerical Calculation Study". IEEE Trans. Magn.,,vol.46,no. 4, pp.1052-1059,Apr. 2010 [12] M. Kozlov and R. Turner, "Fast MRI coil analysis based on 3-D electromagnetic and RF circuit co-simulation", J. Magn. Reson., vol.200, no.1, pp.147–152, 2009. [13] Nan Li, Shengping Liu, Xiaoqing Hu et al, "Electromagnetic Field and Radio Frequency Circuit Co-Simulation for Magnetic Resonance Imaging Dual-Tuned Radio Frequency Coils". IEEE Trans.Magn., pp.1-4.Oct.2017 [14] Junghwan Kim, Narayan Krishnamurthy, Tales Santini, et al. "Experimental and numerical analysis of B1+ field and SAR with a new transmit array design for 7T breast MRI", J Magn Reson., vol.269, pp.55–64, 2016

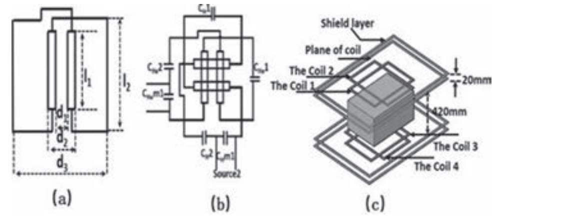

Fig. 1. (a)The structure of butterfly-shaped element;(b)The structure of adjacent coils(the coil 1,2;the coil 3,4);(c)The simulation model of the coil system and saline phantom(the blue cube)

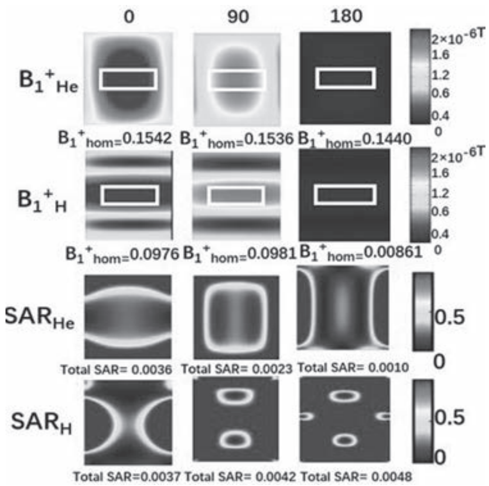

Fig. 2. The distribution of B1+ field and SAR about 1H/3He transmit coil when the phase difference of each port is 0°,90°,180°

AP-05. Peak to Peak Voltage Detector Type MI Gradiometer for Real Time Alpha Rhythm Measurement.

J. Ma[1] and T. Uchiyama[1]
1. Graduate School of Engineering, Nagoya University, Nagoya, Japan

1. Introduction As the source of all our thoughts, emotions and behaviors, the brain activities play a very important role in our life. The brain activities have attracted considerable attentions in medical & healthcare area, and engineering application. Some disease and injuries can be diagnosed by analyzing the brain activities, such as tumors, epilepsy, and neural damage [1]. Magnetoencephalogram (MEG) is a non-invasive technique for mapping and evaluating the functional activity of brain. According to the previous studies, the MEG has been demonstrated to have better spatial resolution than EEG, as the skull and scalp are not very good conductors, magnetic field change is less distorted than voltage change. On the other hand, the magnetic field produced by neurons of brain is extremely weak. It is commonly measured by Superconducting Quantum Interference Devices (SQUIDs) which is the most reliable sensitive magnetometer for MEG measurement. However, the SQUIDs are still threatened by the need of cryogenic cooling liquids and a shielding room. The high-cost and large-scale of SQUIDs result in pressure to develop some miniature, low-cost, and highly sensitive magnetic sensor systems for MEG measurement [2, 3]. As one of the spontaneous neural oscillations in the frequency range of 8-13 Hz, the alpha rhythm is generally associated with relaxed wakefulness, drowsiness period and REM sleep stage, whose amplitude is stronger when one is relaxed but alert. Meanwhile alpha rhythm can be identified at a maximum amplitude when the eyes are close, over the occipital region [2, 4]. In this study, we have developed a peak to peak voltage detector type MI gradiometer (shortened: Pk-pk VD-type MI gradiometer) for real time MEG measurement. Meanwhile, we have demonstrated the real time alpha rhythm measurement, with simultaneous measurement of EEG. 2. Pk-pk VD-type MI gradiometer For measuring extremely weak magnetic field such as a bio-magnetic field, we have to cancel the background uniform noises such as geomagnetic field. We have developed the Pk-pk VD-type MI gradiometer based on the pk-pk VD-type MI magnetometer reported recently [5]. The new MI gradiometer is composed of a pair of MI elements: a sensing element and a reference element with distance between elements of 3 cm. we have achieved a high sensitivity of 1.4×10^{7} V/T with good linearity and a low noise level of 2 $pT/Hz^{1/2}$ in 1-100 Hz range, 3. Alpha rhythm measurement In this study, MEG measurements of spontaneous brain activity (Alpha rhythm) are carried out on a female subject (aged 24), by using the Pk-pk VD-type MI gradiometer. We set up the Pk-pk VD-type MI gradiometer system in a shielded room, with the simultaneous measurement of EEG. We study the visual alpha rhythm, which presents in the 8-12 Hz range. The subject lies on a comfy bed in a state of relaxed wakefulness, in a shielded room. The sensor head is placed 5 mm apart from the scalp of the subject, on the occipital region, at the point between O1 and O2 of the international 10-20 system. We record the MEG and EEG signals from 44 s to 60 s, by the Pk-pk VD-type MI gradiometer and EEG device, with a 7-15 Hz bandpass filter. The subject lies with eyes open during the first 8 s of the recording (44s-52s). Then, the subject is instructed to close her eyes for the remaining 8 s of the recording (52s-60s). As illustrated in Fig. 1, the time-frequency analysis is applied to both raw recordings (MEG and EEG recordings). The time-frequency spectrograms of EEG recording and un-averaged Pk-pk VD-type MI gradiometer recording are shown in Fig. 1(a) and (b). Of note is that both the Fig. 1(a) and Fig. 1(b) show a marked enhancement of alpha rhythm between first 8 s and remaining 8 s. As expected, the alpha rhythm signals simultaneously measured by EEG and MI sensor are significantly attenuated when the subject opens eyes, and intensified with eyes close. As shown in Fig.1 (b), the MEG signal of alpha rhythm for this subject has main frequency components at 10-11 Hz with a maximum amplitude of approximately 25 $pT/Hz^{1/2}$. For further demonstrating alpha rhythm measurement by MI sensor, we investigate the spectral density of alpha rhythm signals simultaneously measured by EEG and MI sensor in eyes opening and closing. As illustrated in Fig. 2(a) and (b), the spectral density of both MEG and EEG alpha rhythm recording significantly decrease with the subject's eyes open, in 8-12 Hz range. Furthermore, the Fig. 2(c) illustrates the sum power spectrum level of MI sensor recording with the subject's eyes open and close. According to the results shown in Fig.1 & 2, the considerable enhancement of alpha rhythm in the 52-60 s range further evidences the signals recorded are emanating from spontaneous brain activity. In this paper, we have developed a Pk-pk VD-type MI gradiometer for real time alpha rhythm measurement. We have achieved a clear sensitivity for spontaneous brain activity with SNR of about 8.

[1] Aydin. Ü, Vorwerk. J, Dümpelmann. M, Küpper. P, Kugel. H, Heers. M, Wellmer. J, Kellinghaus. C, Haueisen. J, Rampp. S, Stefan. H, Wolters. CH, "Combined EEG/MEG can outperform single modality EEG or MEG source reconstruction in presurgical epilepsy diagnosis.", PloS ONE. doi:10.1371/journal.pone.0118753 [2] M I Faley, J Dammers, Y V Maslennikov, J F Schneiderman, D Winkler, V P Koshelets, N J Shah and R E Dunin-Borkowski, "High-Tc SQUID biomagnetometers", Supercond. Sci. Technol. 30 (2017) 083001 (21pp) [3] K. Wang, C. Cai, M. Yamamoto, and T. Uchiyama, "Real-time brain activity measurement and signal processing system using highly sensitive MI sensor", AIP ADVANCES 7, 056635 (2017). [4] C. Ciulla, T. Takeda, and H. Endo, "MEG Characterization of Spontaneous Alpha Rhythm in the Human Brain", Brain Topography, Volume 11, Number 3,1999. [5] J. Ma, and T. Uchiyama, "High Performance Single Element MI Magnetometer with Peak to Peak Voltage Detector by Synchronized Switching", IEEE TRANSACTIONS ON MAGNETICS, VOL. 53, NO. 11, NOVEMBER 2017.

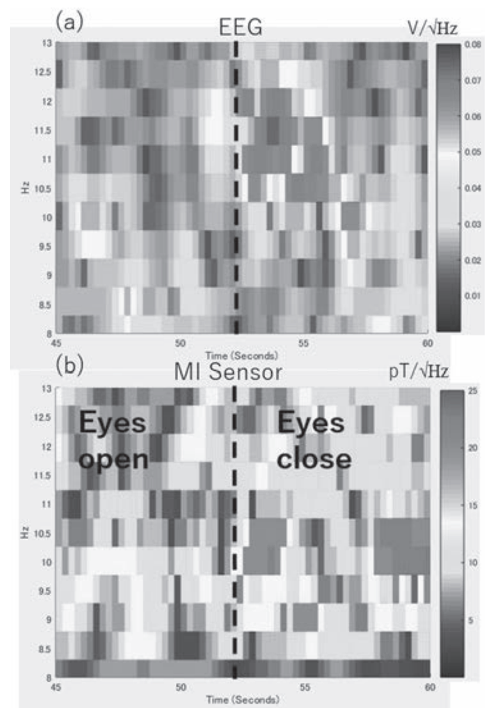

Fig. 1. Time-frequency spectrograms of simultaneously measured ECG and MCG alpha rhythm signals. During first 8 s (44-52 s), the subject lies with open eyes. Then, the subject is instructed to close her eyes for the remaining 8 s (52-60 s). (a) EEG. (b) MEG measured by MI sensor.

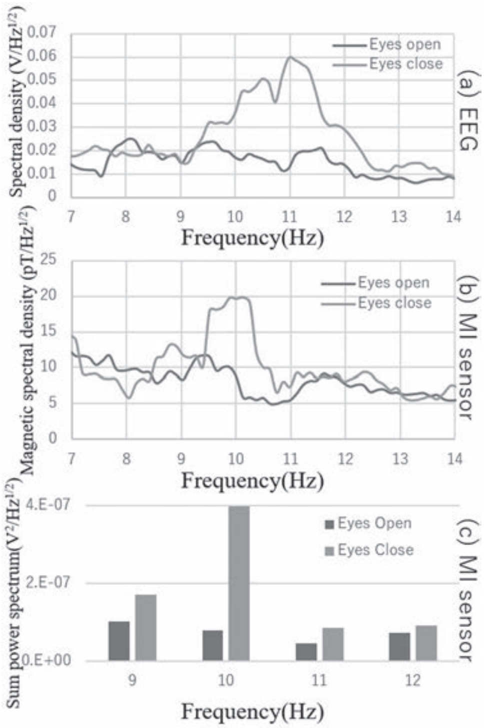

Fig. 2. Comparison of the spectral density of alpha rhythm signals simultaneously measured by EEG and MI sensor between eyes opening and closing. (a) EEG. (b) measured by MI sensor. (c) the sum power spectrum level of MI sensor recording.

AP-06. A Theoritical and Simulational Study on the Chemical Shift Effects on the Magnetic Susceptibility of Iron at Ultra-Short Echo Times.

X. Lu[1], J. Zhu[1], Z. Wang[1], S. Wei[1], H. Wang[1] and W. Yang[1]
1. Institute of Electrical Engineering, Chinese Academy of Science, Beijing, China

1. Introduction Magnetic Resonance Imaging(MRI) has been proven to be important for in vivo quantitative characterization of iron deposition, either endogenous or exogenous(Iron Nanoparticles, IONPs). Iron has endogenous paramagnetic characteristics, and causes shortened T1, T2, and T2* relaxation times as well as phase and susceptibility changes by affecting the magnetic environment of water protons [1-2]. Among all the quantitative MRI methods, quantitative susceptibility mapping (QSM) has gained increased interest as iron is paramagnetic, leading to a linear increase in susceptibility with iron concentration. 2017, it has been shown that the iron could be quantified by both QSM and R2* to a range as high as 22 mM by using ultra-short TE(UTE) technics[3]. However, for in vivo study environment, as fat is an essential contents exists everywhere in human body, the chemical shift effects caused by fat will cause severe streaking artifacts in the QSM results and make the quantification failure[4].The H protons of fat, are nestled within long-chain triglycerides and covered by electron clouds. These clouds partially shield the fat protons from the full effects of an externally applied magnetic field. It is still unknown how much the fat will effects the MRI phase signals with UTE acquisitions, as at a very short TE, the chemical shift effects caused phase shift could not be very obvious. In this study, simulation study was performed to evaluate the chemical shift effect on the quantification of the magnetic susceptibility with UTE sequences based on a fat combined susceptibility-phase change model. 2. Method and Results To study the magnetic susceptibility changes that comes from fat, a relationship between the chemical shift from fat and the frequency changes caused from the background magnetic susceptibility(x) is established as shown in Equ 1. $S_{fat}(t) = m((1\text{-}ff)+ff^{*}\sum\alpha_n exp(\text{-}i2\pi f_n t))exp(\text{-}t/t_2{}^{*})exp(\text{-}i\gamma\delta Bt)$, $\delta B = conv(\chi,D)$ *(1)* Where, $t_2{}^{*}$ is the transverse relaxation time and χ is the magnetic susceptibility of the irons. The phase change of the MRI signal is come from the background field change δB, which is the convolution between the susceptibility χ and magnetic dipole D. For MRI signals with fat, a multi-peak fat model were used in this study by adding a frequency shift with different fat comports, as shown in equ 1, ff means fat fraction. A numerical phantom for simulation was designed. For each study, six spheres in a ring have different magnetic susceptibility (2, 4,6,8,10,12 ppm) but the same fat fraction. By changing different fat fraction and then the QSM performance are different as shown in fig 1, where fat fraction are 0, 0.1,0.2,0.3,0.4,0.5,0.6,0.8 correspondingly. Signal were obtained at a ultra-short TE combination(TE1= 0.032ms, dTE = 0.1ms). As can be seen in fig 1, the streaking artifacts become more severe when the fat fraction increases even at UTE. Fig 2 shows the phase of different fat fraction when acquisition time is 0.332 ms. For the first row images, the phase differences between different fat fraction is not obvious, but for the second row, where all the phases are subtracted by the first one that without fat(ff=0), it could be easily observed that the phase increases when the fat fraction increases. 3. Discussion and Conclusion In this study, simulation studies were performed to verify the chemical shift effects on the UTE QSM. Several factors were considered, such as the TE times, fat fractions, etc. It could be concluded from the simulation results that the streaking artifacts becomes more and more severe when the fat fraction becomes greater, even when TEs are very short. Furthermore, the streaking artifacts should be the phase difference caused by the chemical shift of fat. This study issued a huge challenge for the quantification of high concentrated iron with QSM especially for irons that is adjected to fat. Because at the very short echo times(<0.5ms), the fat effects cannot be easily removed by traditional method, such as IDEAL, which has requirement on the TE interleaves(>0.8 ms). In the future studies, we will take efforts to find ways to eliminate the chemical shift problems when using UTE. *Acknowledgement* This work is supported by National Natural Science Fundation(NSFC 51607169).

[1] Thorek DLJ, Chen AK, Czupryna J, Tsourkas A. Superparamagnetic iron oxide nanoparticle probes for molecular imaging. Annals of Biomedical Engineering 2006;34:23–38. [2] Chertok B, Moffat BA, David AE, Yu F, Bergemann C, Ross BD, Yang VC. Iron oxide nanoparticles as a drug delivery vehicle for MRI monitored magnetic targeting of brain tumors. Biomaterials 2008;29:487–496. [3] Lu X, Dimov A, He Q, et al. Ultrashort Echo Time Quantitative Susceptibility Mapping (UTE-QSM): Limitations in Quantifying High Iron Concentration. Proc. Intl. Soc. Mag. Reson. Med. 25, 2017. [4] Dimov A V., Liu T, Spincemaille P, Ecanow JS, Tan H, Edelman RR, Wang Y. Joint estimation of chemical shift and quantitative susceptibility mapping (chemical QSM). Magnetic Resonance in Medicine 2015;73:2100–2110.

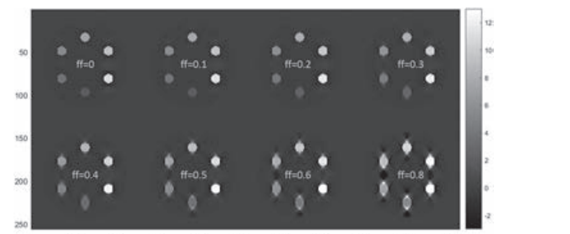

Fig. 1. The QSM results for different fat fraction (0,0.1,0.2,0.3,0.4,0.5,0.6,0.8) of different susceptibility (2,4,6,8,10,12 ppm) at ultra-short echo times (0.032,0.132,0.232,0.332, 0.432, 0.532 ms).

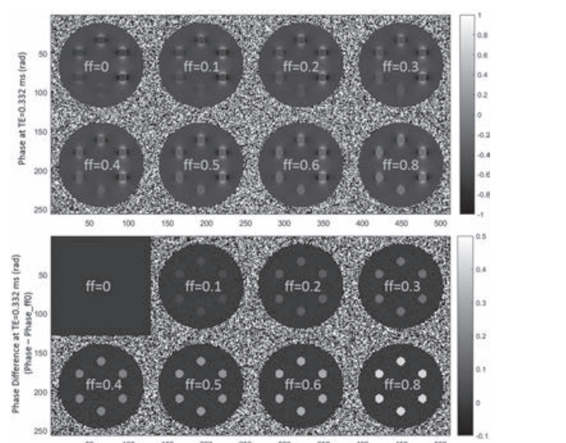

Fig. 2. At echo time of 0.332ms, the phase of different fat fraction with different susceptibility. The first row shows the original phase, while the second row shows the phases subtracted by the first phantom with 0 fat fraction.

AP-07. Magnetic-Fluorescent Fe_3O_4@Chitosan-Graphene Quantum Dots Nanocomposites for Dual-Modal nanoprobes of Fluorescence and Magnetic Resonance Imaging.

Y. Li[1], K. Wang[1], X. Xu[1] and Y. Jiang[1]
1. University of Science and Technology Beijing, Beijing, China

The recent development of nanoprobes with multiple functionalities has attracted considerable interests for various biomedical applications.[1] The Fe_3O_4 Nanoparticles (NPs) are superparamagnetic and usually used as magnetic resonance imaging (MRI) contrast agents. The graphene quantum dots (GQDs), a new zero dimensional graphene nanomaterial, exhibit tunable photoluminescence property, excellent stability and biocompatibility. If the Fe_3O_4 NPs and GQDs can combine together, the composites are expected to be dual-modal nanoprobes of fluorescence and MRI. In this work, we study on the Fe_3O_4@chitosan-graphene quantum dots (Fe_3O_4@CS-GQDs) NPs which are demonstrated to be a fluorescence and MRI contrast agent. The Fe_3O_4 NPs were fabricated by hydrothermal synthesis and had an average diameter of 9 nm. Next, the Fe_3O_4 NPs were dispersed in chitosan solution to obtain the Fe_3O_4@CS NPs. Then, the Fe_3O_4@CS-GQDs NPs were synthesized by crosslinking between carboxyl groups of GQDs and amine groups of Fe_3O_4@CS.[2] The magnetic property and fluorescence of Fe_3O_4@CS-GQDs NPs were characterized by vibrating sample magnetometer measurements and photoluminescence (PL) spectroscopy. As shown in Figure 1a, the magnetization hysteresis loop shows a near zero coercivity, indicating the superparamagnetic property of Fe_3O_4@CS-GQDs NPs. The PL spectrum of Fe_3O_4@CS-GQDs NPs shown in Figure 1b exhibits a emission peak at 434 nm, which is under the excitation of ultraviolet 350nm. These results show that the Fe_3O_4@CS-GQDs NPs have both fluorescent emission and superparamagnetic properties. The T_2-weighted MRI of Fe_3O_4@CS-GQDs NPs were taken on a 3 T clinic MRI scanner. As shown in Figure 2a, the T_2 signal intensity decreased significantly with increasing Fe concentration, which indicates the Fe_3O_4@CS-GQDs NPs to be a promising contrast agents for MRI applications. To investigate the biocompatibility of the nanoprobes, the cytotoxicity of Fe_3O_4@CS NPs and Fe_3O_4@CS-GQDs NPs on Hela cells were studied with an MTT assay. According to Figure 2b, the viability of Hela cells is higher than 80% after 48 h of incubation with 50 μg/mL Fe_3O_4@CS NPs and Fe_3O_4@CS-GQDs NPs. Therefore, the Fe_3O_4@CS-GQDs NPs were demonstrated to be a potential dual-modal MRI contrast agent and fluorescence probes with high biocompatibility.

[1] Xia B, Li J, Shi J, et al. Biodegradable and Magnetic-Fluorescent Porous Silicon @ Iron Oxide Nanocomposites for Fluorescence/Magnetic Resonance Bimodal Imaging of Tumor in Vivo. ACS Biomaterials Science & Engineering, 2017, 3(10): 2579-2587. [2] Wang Y H, Yu C M, Pan Z Q, et al. A gold electrode modified with hemoglobin and the chitosan@Fe_3O_4 nanocomposite particles for direct electrochemistry of hydrogen peroxide. Microchimica Acta, 2013, 180(7-8): 659-667.

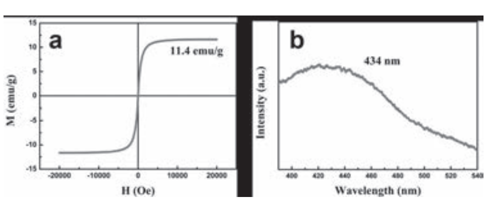

Fig. 1. (a) Magnetization curve of the Fe_3O_4@CS-GQDs NPs. (b) PL spectra of Fe_3O_4@CS-GQDs NPs under excitation of 350 nm.

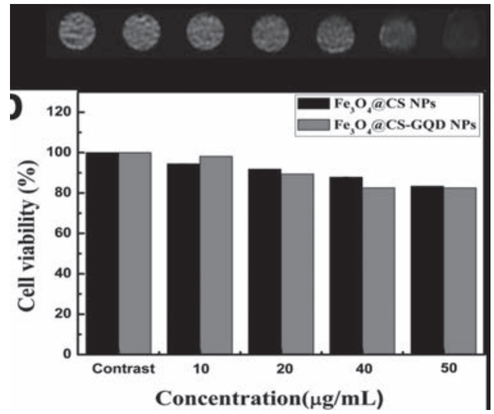

Fig. 2. (a) T_2-weighted MR images of Fe_3O_4@CS-GQDs NPs at the increase concentrations of Fe at 3 T. (b) Cell viability of Hela cells after treatment with different concentrations Fe_3O_4@CS NPs and Fe_3O_4@CS-GQDs NPs after 48h.

AP-08. Asymmetric Gradiometer System for Magnetocardiograms Measuring Without Magnetic Shielding.

Q. Wang[1], J. Du[2,1] and *T. Song*[1]

1. Department of Bioelectromagnetism, Institute of Electrical Engineering, Chinese Academy of Sciences, Beijing, China; 2. University of Chinese academy of sciences, Beijing, China

Abstract In this paper, an asymmetric gradiometer system is designed to measure the magnetocardiograms without magnetic shielding environment. The gradiometer mainly included three-dimensional second-order gradient coils, and a three-dimensional SQUID magnetometer, which can configurate a 4-channel magnetocardiography measurement system. The asymmetric second-order gradient coil can be used to eliminate different gradient magnetic noise in the environment. The design of a 3D gradient coil can not only measure magnetic field information in the Z direction but also the X-Y direction. The 3D SQUID magnetometer can be used to compensate the additional noise caused by the area and parallel error because of the process of winding gradient coil. The measurement system contained nine low-temperature dc SQUID sensors and can measure the human magnetocardiograms signal without shielding. I. INTRODUCTION The magnetocardiograms which is only about 10^{-12} Tesla is much weaker than environmental magnetic field[1]. So how to curb environmental noise is a key technology problem in magnetocardiograms measuring. The mainly method is to build a high performance magnetic shielding room which can reduce the environmental field value into an acceptable range[2]. On the one hand, such magnetic shielding room is expensive, about $1 million or so. On the other hand, the shielding chamber limits the mobility of the magnetograph. Therefore, this method greatly restricts the development of magnetocardiograph[3]. So, it is very important to carry out the magnetocardiograms measurement technology without shielding environment magnetic. At present, the main method is to manually winding the hardware gradiometer on the coil rack with high machining accuracy, or using SQUID magnetometer and digital signal processing technology to build software gradiometer[4]. However, the manually winding gradiometer must generate area and parallel errors which increase the additional environmental noise. Therefore, it is necessary to combine the triaxial magnetometer measuring environmental noise to compensate the analysis and eliminate the errors[5]. Finally, the magnetocardiograms measuring is realized in the environmental magnetic field. II. DESIGN OF THE GRADIOMETER SYSTEM If the environmental magnetic field is homogeneity, such as the geomagnetic field or the far radio-frequency field, it can be eliminated by a first-order gradiometer. But the electromagnetic environment of the laboratory is relatively complex, and there are a lot of first-order gradient fields[6]. It is necessary to use the second-order gradient to suppress both of the uniform and first-order fields. On the other hand, the Z direction measurement of the magnetocardiograms that are perpendicular to the chest does not reflect all the information of the heart activity, sometimes we have to separate multiple sources overlapping time when cardiac tissues are active[7]. Therefore, a 3D second-order gradient coil is designed in this paper. By measuring the magnetic field information in the X-Y direction, it can help to locate the overlap sources of the heart in Z direction. The coil is shown in figure 1 with a size of 29mm x 29mm x 58mm. The dotted line arrow in the Z axis points to is the asymmetric second-order gradient coils we designed. By trial and error, the optimal baseline proportionis adjusted at 50%, 62.5%, 75% or 87.5% to better eliminate different gradient environmental magnetic fields and improve system sensitivity. Let's suppose that the magnetic field at the bottom of the gradient coil is T(x,y,z). The bottom half of the baseline is the length of the Δz and the upper half of the baseline is 58-Δz, so the gradient value T_g of the asymmetric gradient coils in the Z direction is, $T_g= T(x,y,z)-2T(x,y,z+\Delta z)+T(x,y,z+58)$. (1) Where the Δz can chose 29mm, 36.25mm, 43.5mm and 50.75mm. In order to improve the detection efficiency, three 2th-order gradient coils are also made, and the 4-channel magnetocardiography system is realized. All parts of the gradiometer system are shown in figure 2. The bottom layer is the four gradient coils which are winding on the polyimide coil rack by 200μm diameter titanium superconducting wires. In the middle layer is cryogenic SQUID sensors, the top layer is a 3D SQUID magnetometer. All of the sensors were made by Supracon AG, GERMANY. Suppose the output of the 3D magnetometer are B_x,B_y and B_z, and the gradiometer output in the Z direction is T_z. We can get that, $T_g=T_z-\alpha B_x-\beta B_y-\gamma B_z$ (2) Through the theoretical calibration value T_g and the actual measured value T_z, the regulation coefficient α,β and γ can be obtained. By formula (2), we can calculate the ideal magnetic signal, and finally get the magnetocardiograms. III. CONCLUSION The gradiometer system designed in this paper has the following characteristics. a. 3D gradiometer design can isolate multiple source overlaps in Z direction. b. Asymmetric second-order gradient coil design can more accurately suppress the environmental magnetic field gradient. c. By using the 3D SQUID magnetometer, it can be compensated the additional noise caused by the area and parallel error because of the process of winding gradient coil. ACKNOWLEDGMENT This work was supported by the National Science & Technology Support Program of the Ministry of Science and Technology of China (2015BAI01B07).

[1] C. S. Kang et al., "Measurement of MCG in unshielded environment using a second-order SQUID gradiometer," IEEE Trans. Magn., vol. 45, no. 6,pp. 2882–2885, 2009. [2] J. Vrba, "SQUID gradiometers in real environment," in SQUID Sensors: Fundamentals, Fabrication and Applications, H. Weinstock, Ed. Dordrecht: Kluwer, pp. 117–178,1966. [3] R. Stolz, V. Zakosarenko, et al., "Integrated SQUID-Gradiometer System for Magneto-Cardiography Without Magnetic Shielding,"IEEE Trans. Appl. Supercond., VOL. 13, NO. 2, 2003. [4] K. Yang, H. Chen, et al., "Weakly Damped SQUID Gradiometer With Low Crosstalk for Magnetocardiography Measurement," IEEE Trans. Appl. Supercond., VOL. 26, NO. 8, 2016. [5] X. Y. Kong, et al., "Multi-channel magnetocardiography system based on low-Tc SQUIDs in an unshielded environment," Phys. Procedia, vol. 36, pp. 286–292, 2012. [6] H. Li et al., "Baseline optimization of SQUID gradiometer for magnetocardiography,"Chin. Phys. B, vol. 24, no. 2, 2015. [7] M. Liu, Y. Uchikawa, "Discussion of Estimating Multiple Sources Based on Three-Dimensional Magnetocardiograms Measurement, " Procedia Environmental Sciences, Vol. 8, pp.408-414, 2011.

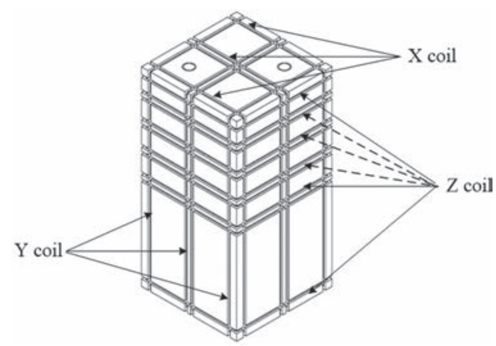

Fig. 1. Diagram of the 3D second-order gradient coil

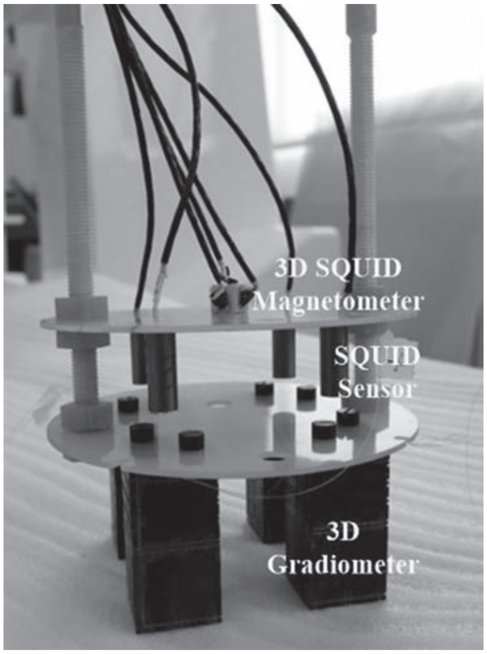

Fig. 2. Photo of the Gradiometer System

AP-09. Demonstration of low-field unilateral nuclear magnetic resonance (NMR) for future medical diagnostics.

N. Prabhu Gaunkar[1], S. Utsuzawa[2], M. Mina[1], Y. Song[2] and D.C. Jiles[1]
1. Department of Electrical and Computer Engineering, Iowa State University, Ames, IA, United States; 2. NMR Fluids Division, Schlumberber-Doll Research, Boston, MA, United States

Nuclear magnetic resonance (NMR) measurements in low-fields (0.01-0.1 T) brings the challenge of low signal to noise ratio caused due to fewer spin transitions [1,2]. Despite this challenge, earlier NMR measurements have been performed in the Earth's magnetic field [3], using stray fields [4] and using unilateral magnet geometries [5,6]. In this work, an alternative method of low-field unilateral NMR measurements will be demonstrated. Experimental measurements using a ring magnet, as a unilateral field source and a pulsed field excitation system [7] will be presented. As in conventional NMR instruments, uniform bias fields are first used to pre-align the spins within the sample and pulsed fields are then used to initiate the conditions of magnetic resonance. The pre-alignment field dictates the precession frequency of the magnetic spins [2] and a spatially larger region can be detected with ease if all the magnetic moments in the region are precessing at the required resonant frequency. In this work, finite element simulations were used to initially estimate the pre-alignment magnetic field in the vicinity of a cylindrical ring magnet. A small region of uniform magnetic field forms away from the magnet surface. This region, commonly termed as the "saddle point", was found to be located at a distance equal to the inner radius of the ring magnet. Saddle points will occur at locations where the field is maximal in one direction and minimal in another. For cylindrical ring magnets, the saddle point occurs when the field is maximum in the z direction and minimal in the r (radial) direction (Figure 1, saddle point is the peak), thus, at a point exterior to the magnet. All test samples can be placed at this location. On identification of the saddle point, different simulations were then performed to verify the effect of varying the magnet geometry such as the height, inner and outer radii on the saddle point's location. The simulation results show that the inner radius greatly affected the location of the saddle point (Figure 2). The outer radius contributed to an increased magnetic flux density at the saddle point. In our experiment, an outer radius of 0.5-1 inch was selected to achieve increased portability of the designed system. Finally, it was found that beyond a certain height, the improvement in static flux density at the saddle point was minimal. The static flux density at the saddle point was further used to obtain an estimate of the NMR voltage signal based on the precession frequency of protons (H). The estimated NMR voltage is directly proportional to the square of the static field strength and the coil sensitivity that depends on the pulsed field strength [8]. Therefore, an efficient combination of the two interacting fields is required to achieve the highest NMR voltage at the saddle point. Through this work, a systematic analysis and development towards designing portable NMR systems based for examining localized targets will be achieved. Incorporating the estimations from the simulation results, NMR measurement results and design considerations for the magnet and the coil will be presented.

1. Levitt, Malcolm H. "Spin dynamics: basics of NMR." (2008). 2. Keeler, James. *Understanding NMR spectroscopy*. John Wiley & Sons, 2011. 3. Fridjonsson, Einar Orn, Sarah A. Creber, Johannes S. Vrouwenvelder, and Michael L. Johns. "Magnetic resonance signal moment determination using the Earth's magnetic field." *Journal of Magnetic Resonance* 252 (2015): 145-150. 4. Casabianca, Leah B., Yifat Sarda, Elad Bergman, Uri Nevo, and Lucio Frydman. "Single-Sided Stray-Field NMR Profiling Using Chirped Radiofrequency Pulses." *Applied Magnetic Resonance* 46, no. 8 (2015): 909-919. 5. Utsuzawa, Shin, and Eiichi Fukushima. "Unilateral NMR with a barrel magnet." *Journal of Magnetic Resonance* 282 (2017): 104-113. 6. Eidmann, G., R. Savelsberg, P. Blümler, and B. Blümich. "The NMR MOUSE, a mobile universal surface explorer." *Journal of Magnetic Resonance, Series A* 122, no. 1 (1996): 104-109. 7. Prabhu Gaunkar, Neelam, Jayaprakash Selvaraj, Leif Bauer, Mani Mina, Robert J. Weber, and David Jiles. "Design and experimental implementation of a low frequency pulsed magnetic field generator." *IEEE Transactions on Magnetics* 53, no. 11(2017). 8. Hürlimann, M. D., and D. D. Griffin. "Spin dynamics of Carr–Purcell–Meiboom–Gill-like sequences in grossly inhomogeneous B 0 and B 1 fields and application to NMR well logging." *Journal of Magnetic Resonance* 143, no. 1 (2000): 120-135.

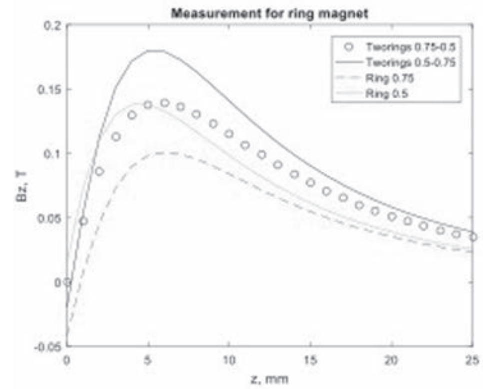

Fig. 1. Depiction of saddle point for a combination of two cylindrical ring magnets with different inner radii (Magnet dimensions: Inner radius varies, Outer Diameter: 1 inch, Height: 0.5 inch).

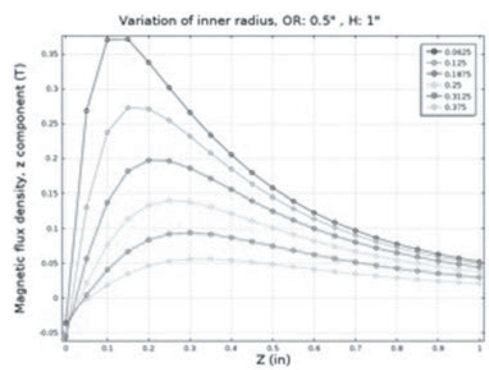

Fig. 2. Simulation results for relationship between the inner radius and location of saddle point

AP-10. Noise reduction in magnetocardiograph based on time-shift PCA just using measurement data.

M. Iwai[1] and K. Kobayashi[1]
1. Science and engineering, Iwate University, Morioka, Japan

Background Magnetocardiograms (MCGs) have become increasingly relevant for clinical research, due to its potential to detect early stages of heart disease. However, it is difficult to assess heart activity precisely without some form of noise reduction, because MCG measurements are extremely small compared to environmental magnetic noise. One of solutions that can suppress the noise is the use of a digital signal processing (DSP) method. The finite impulse response (FIR) filter is a well-known method in reducing noise via DSP. However, FIR filters have various issues such as distorted waveforms, generation of phase differences, and reduced signal peaks. Hence, a noise reduction method using a time-shift principal component analysis (PCA) [1], [2], [3] is considered. This method reduces noise by subtracting reconstructed noise by reference data from measurement data. This method has to need reference sensor, so this method cannot use without reference sensor system. We propose a new time-shift PCA method without reference sensor in order to apply the time-shift PCA without reference sensor systems. *Methods* The proposed method has same basic process as the conventional time-shift PCA [1]. Difference from the conventional method is adding the process to reconstruct reference data from measurement data. The method to reconstruct reference data can be summarized as follows. First, apply PCA to measurement data. Second, sort the principal components according to the ordering provided by kurtosis order. Third, select the principal components with lower values of kurtosis (Selected number is arbitrarily). Fourth, apply inverse PCA to selected principal components for reconstructing reference data. The reason why we use kurtosis order in this method is that the principal components represent the noise have low values of kurtosis [4]. After this process, we apply the conventional time-shift PCA by using reconstructed reference data. *Simulation* Simulations were carried out in this study with considering time-shift point and that noise reduction accuracy. In this simulation has used the simulation data that were mixed with the MCG signal data and the noise data with signal-to-noise ratios (SNRs) of 0 dB, -10 dB and -20 dB [4]. In this simulation, the reference data was reconstructed from measurement data, and then we assumed that reference sensors are at the four corners in measurement positions and we evaluated the noise reduction accuracy with correlation coefficient between the MCG signal data and the signal processed data. *Simulation Results* The noise reduction accuracy at each time-shift points is shown in Fig. 1. The leftmost data shows correlation coefficients between the MCG signal data and the simulation data at each SNR (0 dB, -10 dB and -20dB). And the waveform of the simulation data, the MCG signal data and the signal processed data at -20 dB simulation are shown in Fig. 2. Fig. 2 (a) shows waveform of the simulation data with -20dB SNR, Fig. 2 (b) shows that of the MCG signal data and Fig. 2 (c) shows that of the signal processed data. As shown in Fig.1, improvement of the noise reduction accuracy were seen in all sift points. Among them, best shift point was 1 (0.002 [s]) at all SNRs. Machine time was 0.18 s in this case. In addition, improvements of correlation coefficient were 0.49, 0.68, 0.49 and improvements of SNR were 31.29 dB, 40.37 dB, 40.83 dB at each SNR. *Summary* We proposed a new time-shift PCA method without reference sensor. We carried out the simulation with considering time-shift point and that noise reduction accuracy. As a result of simulation, we found that the method can reduce the noise about 40 [dB] and that best shift point that has the highest noise reduction accuracy is 1.

[1] Alain de Cheveigne, Jonathan Z. Simon, "Denoising based on time-shift PCA", Journal of Neuroscience Methods, vol. 165, pp. 297-305, 2007. [2] Alain de Cheveigne, Jonathan Z. Simon, "Sensor noise suppression", Journal of Neuroscience Methods, vol. 168, pp. 195-202, 2008. [3] Alain de Cheveigne, Jonathan Z. Simon, "Time-shift denoising source separation", Journal of Neuroscience Methods, vol. 189, pp. 113-120, 2010. [4] M. Iwai, K. Kobayashi, "DIMENSIONAL CONTRACTION BY PRINCIPAL COMPONENT ANALYSIS AS PREPROCESSING FOR INDEPENDENT COMPONENT ANALYSIS AT MCG", Biomedical Engineering Letters, August 2017, vol. 7, no. 3, pp. 221–227.

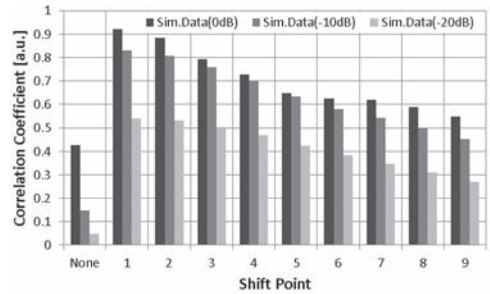

Fig. 1. Correlation coefficients when change shift point.

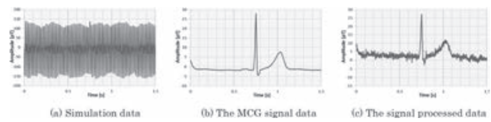

Fig. 2. Wave forms at -20dB simulation data.

AP-11. Quantitative component selection method using attractor analysis for noise reduction by ICA of magnetocardiogram.

K. Kobayashi[1] and M. Iwai[1]
1. Faculty of Science and Engineering, Iwate University, Morioka, Iwate, Japan

Introduction Magnetocardiogram (MCG) is a noninvasive technique that detects the magnetic field generated by the electrical activity in the heart. Recently, MCG has been attracting a lot of attention in relation to the early detection of heart diseases [1]. As MCG is a multichannel measurement technique and as the signals are not affected by the shape of the lungs and torso, it has high potential for clinical applications [2]. On the other hand, MCG is very weak signal less than 100 pT, and then signal-to-noise ratio (SNR) is very low. Many noise reduction methods are proposed for biomagnetic measurements, particularly independent component analysis (ICA) for separating the signal and noise. However, ICA has the problem that is to distinguish signal or noise components from separated components. In many cases, these is decided by personal qualitative evaluations (knowledge and sense). We have studied a method of environmental magnetic noise reduction using ICA for MCGs. The purpose of this study is to establish quantitative component selection method of the cardiac magnetic field component and the noise component separated by ICA. Therefore, we proposed the method to use attractor analysis and the multiple coefficient of determination. Method Fig.1 shows examples of attractor analysis. Attractor analysis is a kind of chaos analysis, it is a method to express periodic features of waveforms by using time and amplitude, and is effective for discriminating independent signals. As shown in Fig. 1 (a) right side, measurement signal x(t+1) is plotted on the x-axis and measurement signal x(t) is plotted on the y-axis. Then discrimination between the cardiac magnetic field component and the noise component is performed by utilizing the property that each component has a different waveform. In order to quantitative component selection of the signal and the noise, the multiple coefficient of determination is used. The multiple coefficient of determination is calculated as the correlation coefficient with the waveform after the attractor analysis and the regression line from the least squares method in the waveform after attractor analysis. The multiple coefficients of determination for the components shown in Fig. 1 became about 0.9 for the cardiac magnetic field component in (b), about 0.6 for the sine wave in (c), about 0.001 for random noise in (d). It is found that the magnetocardiogram component is a high multiple coefficient of determination and the noise component is a low multiple coefficient of determination. Simulation studies Simulation studies were performed using MCG. The MCG data was measured with a 64-channel (8 x 8) SQUID magnetometer in a magnetically shielded room (MSR) [3]. To reduce noise, the data were averaged 150 times. The averaged data represent here the ideal signal data. Noise data was also measured with the same SQUID magnetometer while applying environmental magnetic noise with a coil in the MSR. For the simulations, the ideal signal data and noise data were mixed with the SNRs of 0 and −10 dB. Fig.2 shows the example waveform of 0dB simulation data, ideal signal data, and after noise reduction data. It is found that the noise is eliminated in 0 dB simulation data, and the waveforms of the magnetocardiogram are restored. The correlation coefficient of after noise reduction data and ideal signals data is 0.97. And the correlation coefficient of -10 dB simulation data is 0.88. Conclusion We proposed the noise reduction method by ICA using attractor analysis and the multiple coefficient of determination as quantitative component selection. The simulation data with SNRs of 0 dB and -10 dB were examined and evaluated. As the result, high noise reduction accuracies were obtained.

[1] J. S. W. Kwong, B. Leithäuser, J.-W. Park, C.-M. Yu, “Diagnostic value of magnetocardiography in coronary artery disease and cardiac arrhythmias: A review of clinical data,” *Int. J. Cardiol.*, vol. 167, pp. 1835-1842, 2013. [2] K. Nakai et al., “Construction of a three dimensional outline of the heart and conduction pathway by means of a 64-channel magnetocardiogram in patients with atrial flutter and fibrillation,” *Int. J. Cardiovasc. Imaging*, vol. 21, pp. 555-561, 2005. [3] M. Iwai, K. Kobayashi, M. Yoshizawa, Y. Uchikawa and F. Bui, “Automatic component selection for noise reduction in magnetocardiograph based on independent component analysis,”, *J. Magn. Soc. Jpn.*, vol. 41, pp.41-45, 2017.

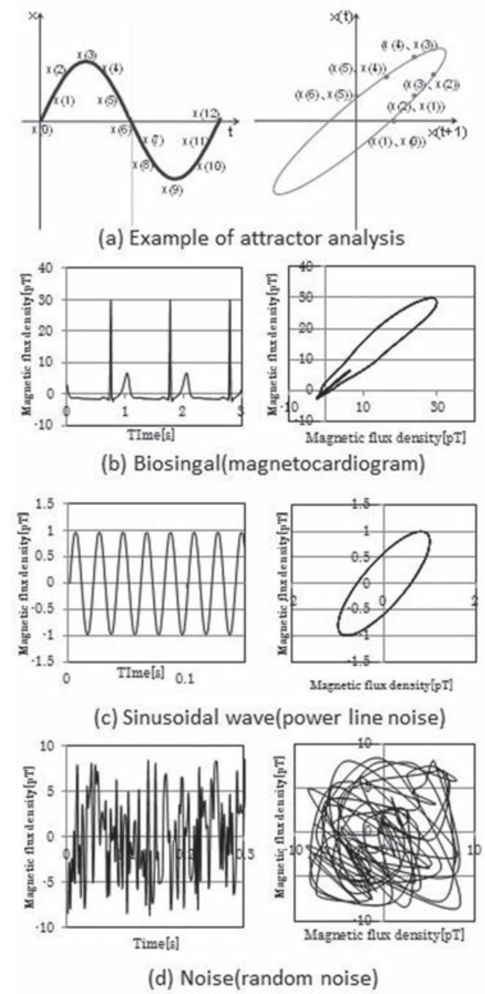

Fig. 1. Example of attractor analysis and each component. The multiple coefficients of determination of (b), (c), (d) are 0.9, 0.6, 0.001 respectively.

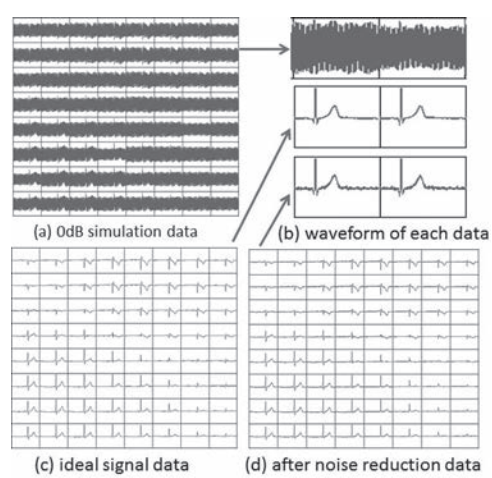

Fig. 2. Waveform of 0dB simulation data, ideal signal data, and after noise reduction data.

AP-12. Electromagnetic Field and Radio Frequency Circuit Co-simulation Approach for Strongly Coupled Coil Array in Magnetic Resonance Imaging.

N. Li[2,1], S. Liu[2], F. Du[2,1], Q. Chen[1], C. Luo[1], Y. Dou[1], X. Zhang[3,4] and Y. Li[1]

1. Shenzhen Institutes of Advanced Technology, Chinese Academy of Sciences, Shenzhen, China; 2. Department of Biomedical Engineering, Chongqing University of Technology, Chongqing, China; 3. Department of Radiology and Biomedical Imaging, University of California, San Francisco, CA, United States; 4. UCSF/UC Berkeley Joint Graduate Group in Bioengineering, San Francisco, CA, United States

Abstract : The theoretical analysis of co-simulation in the conditions of strongly coupled RF coils is proposed in this paper. The proposed co-simulation method is evaluated through the comparison with the conventional simulation methods in terms of the efficency, electromagnetic field (EM) and specific absorption rate (SAR) of a 2-channel strongly coupled coil array. The results demonstrate the proposed co-simulation method saves approximately 94.5% of total simulation time for strongly coupled coil arrays while the EM field and SAR variation is less than 4%. *Index Terms*—magnetic resonance imaging, numerical analysis, radio frequency coil. Introduction: In magnetic resonance imaging (MRI), the performance of radio frequency (RF) coil arrays is critical, determining the imaging quality and safety [1]. Coupling between coil elements is a common cause of performance degradation and must be sufficiantly reduced in design of multi-channel RF coil arrays to maintain the array performance [2]. The EM field simulation is the main tool to analyze the coupling condition and optimize the decoupling method [3]. The conventional EM field simulation methods are often time-consuming, sometimes even not practical because of the unacceptibly long computing time. In previous studies, fast MRI coil analysis based on 3-D electromagnetic and RF circuit Co-simulation has been uesd to improve coil performance [4]. However, current analysis is based on the assumption that the interaction between ports can be negligible [5] and there is no theoretical analysis of strong coupled condition. In this paper, an extended theoretical analysis of strongly coupled coil arrays is proposed. Through the numerical study of a 2-channel strongly copuled coil array model, the efficency, the scattering parameter, electromagnetic field (EM) and specific absorption rate (SAR) [6] are compared using the propsoed co-simulation method and the conventional simulation methods. Theory: The power of incident wave and reflected wave is deduced of a 2-port network model as shown in Fig. 1. The power of incident wave and reflected wave of each port are a_1^1, b_1^1, a_1^2, b_1^2, i=1,2,respectively. The input power of the 2-port network $x_{circuit}(w) = [a_1^1, b_1^1, a_1^2, b_1^2]$, S^1, S^2 of sub-network represent the tuning and matching circuit [5]. $_S{}^{coi}$ represents the scattering matrix of coils. While coupling is not neglectable, the non-diagonal elements in the matrix $_S{}^{coi}$ will become non-zero numbers. H^i_{field} (ω) signifies the transfer function of field distribution. Since $a_2^1= b_1^{coil}$, $b_2^1= a_1^{coil}$ and $a_2^2= b_2^{coil}$, $b_2^2= a_2^{coil}$, the interaction between different ports is redefined as shown in Fig. 1 (1)-(3), The EM field distribution Y(w) based on the above equations, in strongly coupled coil array is expressed as shown in Fig. 1(3). Method: As an example, a 2-channel phased array coil which was comprised of two square coils, each with dimensions 80×80 mm^2 and 5 mm in conductor width. The adjacent distance was only 4 mm so the coupling between the two coils was very strong with S_{12}=S_{21}=-4.8dB. Commercial software (Computer Simulation Technology, Darmstadt, Germany) was used to validate the co-simulation method in the strongly coupled case. A cubic phantom measuring 300×300×200 mm^3 was placed 10 mm above the RF coil model. The material property of the phantom was set as conductivity = 0.6 S/m, relative permittivity εr = 78 and relative permeability μr = 0.99. The two simulation methods are modeled as shown in Fig. 2. (a). The red and blue components in Fig. 2(a) denote ports and lumped elements, respectively. In the proposed simulation, all the lumped elements were replaced by ports with 50 W. The linear equation system solver accuracy was set to -40 dB.The boundary condition of the RF coils were set to open and the bandwidth was set to 50 MHz ~ 200 MHz. The mesh cells of the two simulations were all 7126140. The coils was resonant by adjusting the capacitance without any decoupling and the coupling condition was evaluated by analyzing the S parameters. It was compared with the conventional simulation by analyzing the results of simulation time, the EM field, SAR and time of simulation [2]. Results : S-parameters of the strongly coupled coil array are obtained and agree well in both methods with S_{12}=S_{21}=-4.8dB. The EM field and SAR distribution of the YZ plane in the phantom is compared as shown in Fig. 2(a)-(d). The field distribution data for the two simulation procedures was below 4%. The total simulation time of the conventional simulation methods and the proposed co-simulation methods is 729 hous and 40.7hous, respectively. A total of 27 iterations for both methods are required to optimized S parameters and the proposed co-simulation method saves about 94.5% of total simulation time. Conclusion : A systematical theoretical analysis of EM and RF circuit co-simulation approach for strongly coupled coil arrays in MRI applications was proposed in this paper. Through the simulation study of a 2-channel coil array model, the co-simulation method demonstrates the advantages of high efficiency and accuracy over the conventional EM simulation method.

[1] P. B .Roemer, W. A .Edelstein, C. E .Hayes, S.P.Souza and O.M.Mueller. "The NMR phased array," *Magn. Reson. Med.*, vol.16, no.2, pp.192-225, 1990. [2] Y. Li, Z. Xie, and Y. Pang, D. Vigneron and X. Zhang, "ICE Decoupling Technique for RF Coil Array Designs," *Medical*, vol.38,no.7, pp.4086-4093, 2011. [3]Y. Guo, and X. Jiang, "Simulations of the Tent Artifacts in Magnetic Resonance Imaging," *IEEE Trans. Magn*., vol. 48, no. 2, pp. 659-662, 2012. [4] M. Kozlov and R. Turner, "Fast MRI Coil Analysis Based on 3-D Electromagnetic and RF circuit Co-simulation," J. Magn. Reson. vol.200, no.1, pp.147-152, 2009. [5]N. Li, S.Liu, X. Hu, C. Luo, X. Zhang, Y. Li. "Electromagnetic Field and Radio Frequency Circuit Co-simulation for Magnetic Resonance Imaging Dual-tuned Radio Frequency Coils,". *IEEE Trans. Magn*. DOI: 10.1109/TMAG.2017.2758518. pp.1-4,2017 [6] A. Amjad, R. Kamondetdacha, A. V. Kildishev, S. M. Park and J. A. Nyenhuis, "Power Deposition Inside a Phantom for Testing of MRI Heating," *IEEE Trans. Magn*., vol.41, no.10, pp. 4185-4187, 2005.

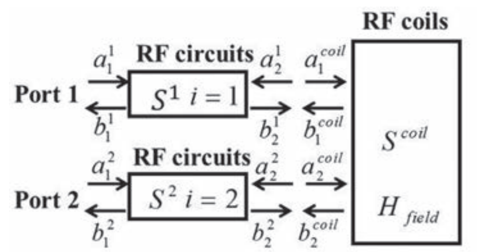

$$(1)\quad \begin{bmatrix} a_2^2 \\ b_2^2 \end{bmatrix} = \begin{bmatrix} S^1 & A_{12} \\ A_{21} & S^2 \end{bmatrix} \cdot \begin{bmatrix} a_1^1 \\ b_1^1 \end{bmatrix}$$

$$(2)\quad A_{21} = A_{12} = \left[S^2\right] \cdot \begin{bmatrix} 0 & 1 \\ 1 & 0 \end{bmatrix} \cdot \left[S^{coil}\right] \cdot \begin{bmatrix} 0 & 1 \\ 1 & 0 \end{bmatrix} \cdot \left[S^1\right]$$

$$(3)\quad Y^i(\omega) = H^i_{field}(\omega) \cdot \begin{bmatrix} 0 & 1 & 0 & 0 \\ 1 & 0 & 0 & 0 \\ 0 & 0 & 0 & 1 \\ 0 & 0 & 1 & 0 \end{bmatrix} \cdot \begin{bmatrix} S^1 & A_{12} \\ A_{21} & S^2 \end{bmatrix} \cdot \begin{bmatrix} a_1^1 \\ b_1^1 \\ a_1^2 \\ b_1^2 \end{bmatrix}$$

Fig. 1. Wave parameters and the interaction between ports of 2-port

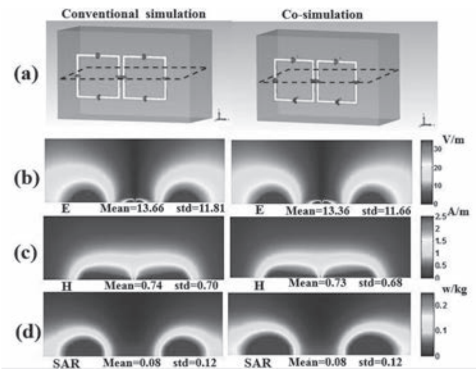

Fig. 2. The data of conventional simulation (left) and co-simulation (right) in water phantom. The "E" and "H" represent the electric field and the magnetic field, respectively. "STD" represents the standard deviation. (a) The RF coil models for EM field simulation. (b) The electric field distribution. (c) The magnetic field distribution. (d)The SAR distribution.

AP-13. Improving Tip Position Estimation Accuracy of Gastric Tube by Compensating Geomagnetic Field with Offset Coils.

T. Sasayama[1], Y. Gotoh[2] and K. Enpuku[1]
1. Kyushu University, Fukuoka, Japan; 2. Oita University, Oita, Japan

Introduction Naso- or oro-gastric tubes are used for patients who have difficulty swallowing, to deliver nutrients or medicines to the stomach. To observe whether the tube is inserted into the stomach correctly, we have proposed a method that estimates the position of the permanent magnet attached to the tip of the tube using several magnetic sensors placed outside the patient's body [1], [2]. The mean of the tip position estimation error is less than 10 mm when the distance between the sensor plane and the permanent magnet is 150 mm [2]. However, if the system is used on pregnant or fat patients, the system needs to perform accurately even for distances greater than 150 mm. To achieve the requirement mentioned above, the sensitivity of the magnetic sensors should be enhanced. Although high-sensitivity magnetoimpedance (MI) and magnetoresistance (MR) sensors can detect signals of the order of nT, the performance is only achieved in a magnetically shielded room due to the limitation of the measurement range and the existence of the geomagnetic field; this creates a problem for the system's practical use in hospitals. Therefore, we propose a method to compensate the geomagnetic field using offset coils. *Methods* Figure 1 shows the proposed system. Four three-axis MR sensors (HMC2003, Honeywell International Inc.) were used for detecting magnetic flux. The MR sensors have offset coils, and the current through the coils was generated by an operational amplifier (OPA350, Texas Instruments Inc.). The output voltage of the amplifier was set using a D/A converter with a 16-bit resolution (DAC8532, Texas Instruments Inc.). The output voltages of the MR sensors were measured using an A/D converter with 32-bit resolution (ADS1262, Texas Instruments Inc.). First, the geomagnetic fields were recorded using these MR sensors. Then, the current through the coil was adjusted so that the signals from these MR sensors were zero. The permanent magnet was finally arranged, and the magnetic fields generated by the permanent magnet were recorded. The magnetic moment, m, and the position, r, of the permanent magnet were estimated using N magnetic sensors and the following equation: minimize $||b(r, m) - b_{meas}||^2$, (1) where $b(r, m) = [b_1(r, m), \ldots, b_N(r, m)]^T$ is the magnetic flux density and $b_{meas} = [b_{meas,1}(r, m), \ldots, b_{meas,N}(r, m)]^T$ is the measured magnetic flux density. $b_k(r, m)$ can be calculated using the following equation: $b_k(r, m) = m_0/4\pi \times \{3(m \bullet r_k')r'/\|r_k'\|^5 - m/\|r_k'\|^3\} \bullet u_k$, (2) where $r_k' = r - r_k$, r is the position vector of the permanent magnet, r_k is the position vector of the kth magnetic sensor, u_k is the direction vector of the sensitive direction of the kth magnetic sensor, and m_0 is the permeability of a vacuum. The nonlinear least squares expression in (1) was solved using the trust-region method provided in the Intel Math Kernel Library. *Results* Figure 2 shows the values of the tip position estimation error when the distance z between the sensor plane and the permanent magnet is 130, 150, 170, and 190 mm respectively. Figure 2 (a) and 2 (b) show the estimation error without and with the geomagnetic field compensation, respectively. As shown, the estimation error with geomagnetic field compensation is less than that without compensation. This indicates that the compensation using offset coil improves the estimation accuracy. The mean of the tip position estimation error in Fig. 2(b) is less than 10 mm even when z = 190 mm, thus meeting the requirement in the real clinical application for pregnant or fat patients.

[1] T. Sasayama, Y. Gotoh, and K. Enpuku, "Application of minimum variance beamformer for estimation of tip position of a nasogastric tube," IEEE Trans. Magn., vol. 50, no. 11, 5101404, 2014. [2] T. Sasayama, Y. Gotoh, and K. Enpuku, "A Gastric Tube Monitoring System for Clinical Applications," IEEE Trans. Magn., vol. 53, no. 11, 8109104, 2017.

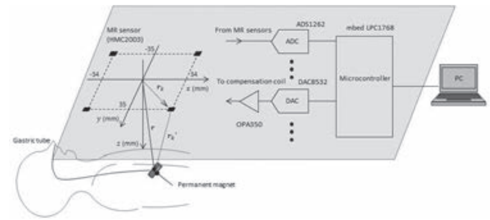

Fig. 1. The proposed position estimation system of the gastric tube with compensation of the geomagnetic field.

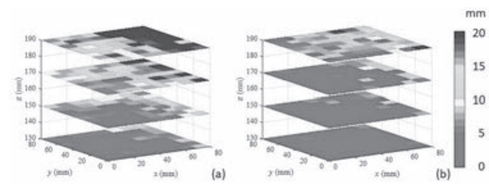

Fig. 2. Tip position estimation error distribution (a) without and (b) with compensation.

AP-14. Effect of Gd_5Si_4 ferromagnetic nanoparticle sizes on T_1, T_2 and T_2* relaxation in MRI.

S. Hunagund[1], J. Rosenberg[2], S.M. Harstad[1], A.A. El-Gendy[3], S. Gupta[4], V. Pecharsky[5,4] and R.L. Hadimani[1]

1. Department of Mechanical and Nuclear Engineering, Virginia Commonwealth University, Richmond, VA, United States; 2. The National High Magnetic Field Laboratory, Florida State University, Tallahassee, FL, United States; 3. Dept. of Physics, University of Texas at El Paso, El Paso, TX, United States; 4. Iowa State University, Ames Laboratory, US Department of Energy, Ames, IA, United States; 5. Dept. of Material Science and Engineering, Iowa State University, Ames, IA, United States

Until now most contrast agents (CA) that are used in Magnetic Resonance Imaging (MRI) studies have been paramagnetic. However, ferromagnetic CAs are potentially more sensitive as T_2 CAs than T_1 paramagnetic compounds due to their large magnetic moments. Previous study has shown that ferromagnetic gadolinium silicide (Gd_5Si_4) nanoparticles (NP) could be useful as potential T_2 CA for MRI with significantly reduced echo time (TE) compared to Superparamagnetic Iron Oxide Nanopartilces (SPION) which are currently the most widely used T_2 CA [1]. Furthermore, the need for better MRI images without the need of upgrading to the higher magnetic field strength can be achieved using better CA such as Gd_5Si_4 NP. The quality of the image contrast in MRI is improved by shortening T_1 and T_2 relaxation times at the site or close proximity to the CA. The efficiency of a T_1 CA is defined by its relaxivity, r_1, which is field and temperature dependent. While, T_2 agents are defined by their relaxivity, r_2, which is dependent on both the saturation magnetization (Ms) value and the effective radius of the NPs [1, 2]. In this study, effect of Gd_5Si_4 NP of varying sizes and with different concentrations are investigated on T_1, T_2 and T_2* (effective/observed T_2) relaxations times. Gd_5Si_4 was synthesized by arc-melting of the stoichiometric mixture of gadolinium and silicon under Ar atmosphere and then the Gd_5Si_4 NPs were prepared by high energy ball milling of the crushed ingot. The synthesis process is described in detail elsewhere [3,4]. Ferromagnetic Gd_5Si_4 is extracted with NdFeB grade N52 permanent magnets placed below the beaker containing the ball milled powder in ethyl alcohol before size separating the NPs through time sedimentation process that provided three fractions (named S1, S2 and S3) with average sizes of 586 nm, 287 nm and 135 nm respectively as analyzed from SEM images (Fig. 1). XRD analysis on pre-separated sample show that Gd_5Si_4 is the major phase while GdSi and Gd_5Si_3 is the minor phases present in all fractions (Fig. 1). Magnetic properties measured in VSM reveal that the Curie temperature (Tc) decreases for Gd_5Si_4 phase from 312 K for S1 to 304 K for S2 and is undetectable in S3. Another Tc observed at 105 K can be attributed to Gd_5Si_3 phase. The M-H curves at 300 K exhibits ferromagnetic behavior descending to paramagnetic as we move from S1 to S3 fraction (Fig. 1). Prior to MRI measurements, NPs are diluted in solution with low-temperature 2% agarose with the following dilutions - 1:20, 1:200, 1:2000 and 1:20000. The high dilution factors were chosen based on solution MRI with lower dilution factors (data not shown) that exhibited extremely strong contrast at 21.1 T and unquantifiable results. Each nanoparticle layer was separated with a 1% agarose layer. MR images were acquired on the 21.1 T (900 MHz) magnet at the National High Magnetic Field Laboratory (NHMFL) in Tallahassee, FL. The magnet is equipped with Bruker Avance III console and Paravision 6.0.1 (Bruker, Ettlingen Germany). For all acquisition a 10-mm birdcage coil was used. Measurements were performed to quantify T_1, T_2 and T_2* relaxation times for each sample and dilution. For T_1 measurements, a turbo spin echo (TSE) sequence was used with two rare factors. The echo time (TE) was 8.8 ms and ten incrementing (12000 - 26 ms) repetition times (TR) were used. T_2 relaxation were acquired with a multi slice multi echo (MSME) sequence using a TR=5000 ms and 20 incrementing echo time (7.5 – 150 ms). For T_2*, a 2D gradient echo (GRE) sequence were used with TR=5000ms and eight incrementing TE (1.5 – 28.5 ms). Common acquisition parameters for T_1 and T_2 sequences were 2 averages, matrix = 110x200, FOV = 1.1x 2.0 cm resulting in a 100x100 mm in plane resolution using a 1-mm slice while the 2D T_2* sequence were acquired with 2 averages and a matrix of 100x55 resulting in a 200x200 mm in-plane resolution. Magnitude images were analyzed in Paravision using region-of-interest (ROIs) to cover each agarose layer as well as spacing layers. The average signal intensities were extracted and analyzed in Matlab using the Levenberg-Marquardt algorithm. For T_1 a three-parameter exponential growth function were used while for T_2 and T_2* a three-parameter exponential decay function were employed. The results shown in Table 1 indicate higher concentrations of NPs shortens the T_2 and T_2* relaxation times and the contrast disappears rapidly with any higher dilutions. Fraction S2 at 1/20 dilution show notable shortened T_1 and T_2 relaxation times compared to the other two fractions. Although S1 has more Gd_5Si_4 phase volume fraction and larger average particle size compared to S2, further investigation is needed inorder to establish the cause in shortened relaxation times compared to S1 fraction. *Acknowledgements* Synthesis and materials processing at the Ames Lab was supported by DOE (contract No. DE-AC02-07CH11358). Work at VCU was partially funded by NSF, Award Number: 1610967. Part of this work was performed at the NHMFL which is supported by the State of Florida and the NSF cooperative agreement No. DMR-1157490.

[1] El-Gendy, A. A. et al. "*Ferromagnetic Gd5Si4 Nanoparticles as T2 Contrast Agents for Magnetic Resonance Imaging*". IEEE Magnetics Letters 8, 1–4 (2017). [2] De León-Rodríguez, L. M. et al (2015). *"Basic MR relaxation mechanisms and contrast agent design."* Journal of Magnetic Resonance Imaging, 42(3), pp.545-565. [3] Harstad S.M. *et al.*, *"Enhancement of β-phase in PVDF films embedded with ferromagnetic Gd5Si4 nanoparticles for piezoelectric energy harvesting," AIP Adv.*, vol. 7, no. 5, (2017). [4] Hunagund, S. G., et al. "*Investigating phase transition temperatures of size separated gadolinium silicide magnetic nanoparticles*". AIP Advances, (In Press).

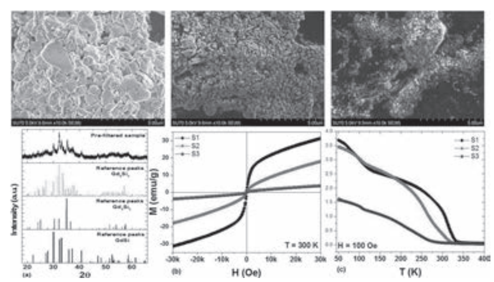

Fig. 1. ***(Top row)*** **SEM images of fractions S1 - S3.** ***(Bottom row)*** **(a) XRD patterns obtained from fractions. Reference peaks of Gd_5Si_4, Gd_5Si_3 and GdSi matches with the patterns. (b) M-H curve for all fractions. (c) M-T curve for all fractions.**

S1 Dilution in agarose	T1 (ms)	T2 (ms)	T2* (ms)
1/20	2436.0	38.7	5.2
1/200	2442.2	59.5	22.7
1/2000	2706.2	67.5	45.8
1/20000	2768.6	70.2	54.8
1/200000	2685.6	68.0	46.8
Agarose	2630.2	67.7	46.5

S2 Dilution in agarose	T1 (ms)	T2 (ms)	T2* (ms)
1/20	1365.9	18.4	1.3
1/200	1562.5	52.9	24.3
1/2000	1673.9	56.3	53.9
1/20000	1777.1	58.6	44.6
Agarose	1811.4	66.5	54.1

S3 Dilution in agarose	T1 (ms)	T2 (ms)	T2* (ms)
1/20	2438.6	63.4	34.1
1/200	2681.6	63.4	34.1
1/2000	2785.3	63.2	45.1
1/20000	2726.5	67.9	48.8
Agarose	2640.0	75.8	51.8

Table. 1 - T_1, T_2 and T_2* relaxation times of S1, S2 and S3 fractions at different concentrations.

Session AQ
HIGH FREQUENCY MAGNETIC MATERIALS AND DEVICES I
(Poster Session)

Zhongming Zeng, Chair
Suzhou Institute of Nano-tech and Nano-bionics,CAS, Suzhou, China

AQ-01. Analysis and Optimization of a New Structure for Wireless Charging System of Electric Vehicles.

Z. Li[1] and *J. Yi*[1]
1. College of Traffic Engineering, Hunan University of Technology, Zhuzhou, China

INTRODUCTION Magnetic resonant wireless power transfer (WPT) is an emerging technology that may create new applications for wireless power charging[1]. However, the output voltage fluctuations and reduced efficiency resulting from lateral are main obstructing factors for promoting this technology. In this paper, a new WPT topology for electric vehicles is proposed. The mathematical model of the proposed topology with lateral misalignments is built based on equivalent circuit method. A method of optimizing coil parameter is proposed, the sum of mutual inductance between each receiving coil and the transmission coil is nearly constant with lateral misalignments. The output voltage can be kept constant and the high efficiency can be obtained by using the proposed method. The WPT system via magnetic resonance coupling is designed. Simulation and experimental results validating the proposed method are given. PROPOSED STRUCTURE AND MODEL The proposed structure is composed of a transmission resonance coil (labeled as Tx_1), four receiving resonance coils (labeled as Rx_1, Rx_2, Rx_3, and Rx_4), the power source, four full-bridge rectifiers, and load resistor, as shown in Fig.1. The power source via the compensation capacitor C_1 is connected in series with the transmission coil Tx_1. The power is transferred from the transmitter to the receiver using magnetic fields. The output voltage of each receiving resonance coil is converter to DC by full-bridge rectifier. Then the output voltage of each full-bridge rectifier is connected in series. The output voltage of load is equal to the sum of the voltage of each full-bridge rectifier. SIMULATION AND EXPERIMENTAL VERIFICATON To validate the proposed method, the prototype model of the system has been built, as shown in Fig. 1(a) and Fig. 1(c). It is composed of two transmission resonant coils, four receiving resonant coils, H-bridge inverter, four full-bridge rectifiers, and the load. The transmission resonant coil is placed on the below. The receiver resonant coils are placed on the top. Two transmission resonant coils are labeled as Tx_1 and Tx_2. The parameters of Tx_1 are optimized according to the proposed method; whereas the parameters of Tx_2 are not optimized. The diameter of Tx_1 is 45cm with a pitch of 0cm for approximately 17 turns. The diameter of Tx_2 is 28cm with a pitch of 0cm for approximately 11 turns. The diameter of each receiving resonant coil is 15cm with a pitch of 0cm for approximately 9 turns according to the proposed method. All coils are made from 300-strand AWG 38Litz-wire. The ferrite plate material is PC95 from TDK. H-bridge inverter is used at the transmitter side to provide AC excitation. Four full-bridges rectifiers are used at the receiver side to convert AC to DC. An impedance analyzer TH2829 is used to extract the parameters in (1) and (2). The original resonant frequency is set to be 85.0kHz. The transmission distance is 14cm. The unload quality factors of Tx_1, Tx_2, Rx_1, Rx_2, Rx_3, Rx_4 are 160, 150, 405, 397, 397, and 390, respectively. Owing to the symmetry of coils, the lateral misalignments are only analyzed to the right (Δ is the misalignments). Fig. 2(a) shows the calculated and measured mutual inductances between transmitter and Rx_1 versus misalignments for different transmission coils. It can be seen that the mutual inductance between Tx_1 and Rx_1 is changed from 7.8μH to 3.45μH as the misalignment is varied from 0cm to 20cm; whereas the mutual inductance between Tx_2 and Rx_1 is changed from 5.05μH to 0.15μH as the misalignment is varied from 0cm to 20cm. Fig. 2(b) shows the sum of the measured mutual inductances M_{12}, M_{13}, M_{14}, and M_{15}. It can be seen that the sum of mutual inductance is nearly constant at 24μH when Tx_1 is used; whereas the sum of mutual inductance is changed from 14.0μH to 10.3μH as the misalignment is varied from 0cm to 10cm. This is because the increments of M_{12} and M_{14} (compare with mutual inductance with Δ=0) are the same as the decrements of M_{13} and M_{15} when Tx_1 is used; whereas the increments of M_{12} and M_{14} are smaller than the decrements of M_{13} and M_{15} when Tx_2 is used. CONCLUSIONS In this paper, the topology of cascaded a transmission coil to four receiving coils is proposed. The mathematical model of the proposed topology with lateral misalignments is built based on equivalent circuit method. The expressions of the output voltage and the efficiency are then derived by solving the system equivalent equations. The output voltage of the load resistor is only dependent on the mutual inductance between the transmitter and receiver when the parameters of each coil and the load are given. A method of optimizing parameter is proposed in order to optimize the mutual inductance between the transmitter and receiver. The mutual inductance between the transmitter and receiver can be kept 24.0μH, the output voltage is ranged from 26.1V to 27.9V, and the transmission efficiency is nearly equal to 90.0% as the misalignment is varied from 0cm to 10cm. The advantage of the proposed topology is that the efficiency is high and the output voltage is nearly constant. Therefore, the proposed method allows for an efficient and robust WPT system for charging of EVs.

[1] C. C. Mi, G. Buja, S. Y. Choi*, et al.*, Modern Advances in Wireless Power Transfer Systems for Roadway Powered Electric Vehicles[J] IEEE Transactions on Industrial Electronics, 2016, 63(10): 6533-6545.

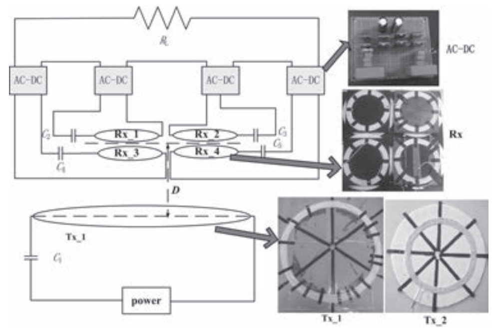

Fig. 1. Structure of the proposed topology.

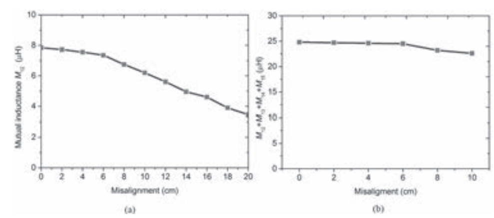

Fig. 2. Measured and calculated results, (a) Mutual inductance M_{12} versus misalignments for different transmission coils. (b)the sum of mutual inductance versus misalignments for different transmission coils.

AQ-02. Influence of the phase structure on the acoustic and optical mode ferromagnetic resonance of FeNi stripe domain films.

D. Cao[1], L. Pan[2], Y. Song[1], X. Cheng[2], H. Feng[2], C. Zhao[2], Q. Li[1], J. Xu[1], S. Li[1], Q. Liu[2] and J. Wang[2]
1. College of Physics, Qingdao University, Qingdao, China; 2. Lanzhou Univercity, Lanzhou, China

The investigation of magnetization dynamics in magnetic film is currently attracting significant attention [1]. This interest is driven by the requirement for understanding the physics and application of magnetic microwave devices. There has been an increasing research for the soft magnetic film with ultra high ferromagnetic resonance (FMR) frequencies in recent years [2], and the films in these results are mainly resonated based on the traditional FMR, which belongs to the acoustic mode. In the acoustic mode, the magnetizations of films show the in-plane uniform precession, and the resonance frequency of the film is determined by the in-plane anisotropy field, which can be included by the preparation methods [3]. However, the results of the optic mode FMR are rarely investigated. This is due to the low permeability of optic mode FMR, and it only observes in some particular structure films. The two observable FMR modes have mainly discovered in two kinds of magnetic thin films: exchange-coupling-biased multilayer films [4] and thin films with stripe domains [5]. This attributes to the moments of the optical mode for two systems precess an out-of-phase when compared with those of the acoustic mode [6, 7]. Significantly, FeNi film will arise from both the in-plane and out-of-plane magnetizations when the film thickness is above a critical film thickness, and an array of oscillating “up and down” magnetic domains forms, which are known as the stripe domain [7]. FeNi stripe domain structure film has been widely studied for its dynamic microwave magnetic properties [8-10], and the magnetic spectra exhibit multiple resonance modes, which are interpreted in terms of the magnetization configuration of stripe domains [8, 9]. In this work, FeNi films with different phases structure were prepared by electrodeposition method, the phase structures of films were controlled by the composition of the film. We focused the discussion on the influence of the phase structure on the acoustic and optical mode FMR of FeNi stripe domain films. The results indicated that the domain structures of films were changed by the phase structure of film, which depended on the composition of the film. The acoustic and optical mode FMR of films shows the similar laws in FeNi alloys but not in the pure Fe and Ni films. In addition, the magnetization dynamics of FeNi stripe domain films are further disscussed.

[1] I. Lemesh, F. Büttner, and G. S. D. Beach, “Accurate model of the stripe domain phase of perpendicularly magnetized multilayers,” *Phys. Rev. B,* vol. 95, no. 17, pp. 174423, 2017. [2] Derang Cao, Xiaohong Cheng, Lining Pan, Hongmei Feng, Chenbo Zhao, Zengtai Zhu, Qiang Li, Jie Xu, Shandong Li, Qingfang Liu, and Jianbo Wang, “Tuning high frequency magnetic properties and damping of FeGa, FeGaN and FeGaB thin films,” *AIP Adv.,* vol. 7, no. 11, pp. 115009, 2017. [3] Derang Cao, Zengtai Zhu, Hongmei Feng, Lining Pan, Xiaohong Cheng, Zhenkun Wang, Jianbo Wang, and Qingfang Liu, “Applied magnetic field angle dependence of the static and dynamic magnetic properties in FeCo films during the deposition,” *J. Magn. Magn. Mater.,* vol. 416, pp. 208-212, 2016. [4] S. Li, Q. Li, J. Xu, S. Yan, G.-X. Miao, S. Kang, Y. Dai, J. Jiao, and Y. Lü, “Tunable Optical Mode Ferromagnetic Resonance in FeCoB/Ru/FeCoB Synthetic Antiferromagnetic Trilayers under Uniaxial Magnetic Anisotropy,” *Adv. Funct. Mater.,* vol. 26, no. 21, pp. 3738-3744, 2016. [5] E. F. Silva, M. A. Corrêa, R. D. D. Pace, C. C. P. Cid, P. R. Kern, M. Carara, C. Chesman, O. A. Santos, R. L. Rodríguez-Suárez, A. Azevedo, S. M. Rezende, and F. Bohn, “Thickness dependence of the magnetic anisotropy and dynamic magnetic response of ferromagnetic NiFe films,” *J. Phys. D: Appl. Phys.,* vol. 50, no. 18, pp. 185001, 2017. [6] Y. Chen, X. Fan, Y. Zhou, Y. Xie, J. Wu, T. Wang, S. T. Chui, and J. Q. Xiao, “Designing and Tuning Magnetic Resonance with Exchange Interaction,” *Adv. Mater.,* vol. 27, no. 8, pp. 1351-1355, 2015. [7] C. Derang, P. Lining, C. Xiaohong, W. Zhenkun, F. Hongmei, Z. Zengtai, X. Jie, L. Qiang, L. Shandong, W. Jianbo, and L. Qingfang, “Thickness-dependent on the static magnetic properties and dynamic anisotropy of FeNi films with stripe domain structures,” *J. Phys. D: Appl. Phys.,* vol. 51, no. 2, pp. 025001, 2018. [8] J. Ben Youssef, N. Vukadinovic, D. Billet, and M. Labrune, “Thickness-dependent magnetic excitations in Permalloy films with nonuniform magnetization,” *Phys. Rev. B,* vol. 69, no. 17, pp. 174402, 2004. [9] W. Tee Soh, N. N. Phuoc, C. Tan, and C. Ong, “Magnetization dynamics in permalloy films with stripe domains,” *J. Appl. Phys.,* vol. 114, no. 5, pp. 053908, 2013. [10] A. V. Svalov, I. R. Aseguinolaza, A. Garcia-Arribas, I. Orue, J. M. Barandiaran, J. Alonso, M. L. Fernandez-Gubieda, and G. V. Kurlyandskaya, “Structure and Magnetic Properties of Thin Permalloy Films Near the “Transcritical” State,” *IEEE Trans. Magn.,* vol. 46, no. 2, pp. 333-336, 2010.

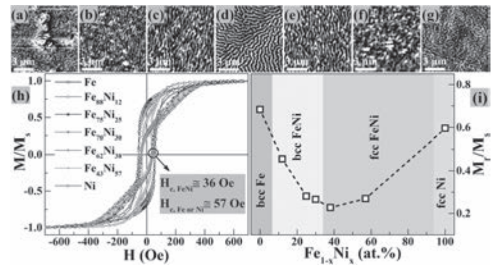

Fig. 1. (a-g) MFM images of the films as a function of film composition. (h) Hysteresis loop of the films with different film compositions. (i) Film compositions or phase structures dependence of the normalized remanent magnetization of the films.

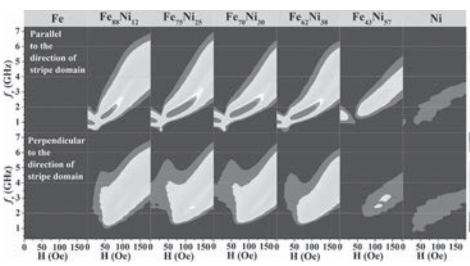

Fig. 2. Two-dimensional plot of the imaginary permeability as a function of both in-plane magnetic field and frequency for the films with different film compositions.

AQ-03. Indirect Permeability Measurements using a 'Strip-coil' for $Co_{0.6}Zn_{0.4}Fe_{1.7}Mn_{0.3}O_4$.

U. Chaudhuri[1], M. Kumari[1] and R. Mahendiran[1]
1. Physics, National University of Singapore, Singapore

Cobalt ferrite ($CoFe_2O_4$, CFO) is a well-known room temperature ferromagnet insulator with high magnetic anisotropy and large coercivity. It is reported in literature that an optimal substitution of Fe by Mn and Co by Zn in CFO ($Co_{0.6}Zn_{0.4}Fe_{1.7}Mn_{0.3}O_4$,CZFMO), reduces both anisotropy and coercive field along with a significant improvement in the resistivity [1]. A sample with low anisotropy, large resistivity and low eddy current losses can be an ideal candidate for high frequency devices. Keeping this in mind, we choose CZFMO to measure frequency dependence of electrical impedance, i.e., magneto-impedance (MI) in this work. Previous methods to measure MI involve passing a high frequency current through the sample and probing the permeability up to a skin depth $\delta(=\sqrt{((2\rho)/(2\pi f\mu_o\mu_r))})$ from the sample surface[2, 3]. The skin depth defines the region where electromagnetic waves propagate, perpendicular to the surface of the sample and depends on resistivity (ρ), relative permeability of the material (μ_r), AC frequency (f) and permeability in vacuum (μ_o). For insulating samples like CZFMO, we are unable to pass a current through the sample and hence indirect methods are needed to measure permeability. An indirect method using a strip-coil is used to measure MI using a single port impedance analyzer E4199A which directly measures the impedance of the coil surrounding the sample using RF-VI technique. Conventional test devices provided by impedance analyzer manufacturers use toroidal samples. However, in our setup we are not constrained to use any particular dimension or shape. This method has been altered from an experiment done on thin films [4] to incorporate bulk materials. Our sample was in the shape of a cylinder which homogenously filled a cylindrical strip-coil. An alternating current flowed through the strip-coil and an RF magnetic field was generated inside it along its axial direction. Using ohm's law, we write impedance (Z) as $Z= V_\Phi/I = -(d\Phi/dt)/I$ … (1) where Φ is the magnetic flux passing through the strip-coil given by $\Phi = \mu_o\mu_r H\bullet A$. Here, H is the magnetic field inside the strip-coil and A is the cross-sectional area of the strip-coil. On solving Eq.1 we get Z in terms of its real (Resistance 'R') and imaginary (Reactance 'X') components. Mathematically, $R=K(\omega\mu_o\mu_r'')$ and $X=K(\omega\mu_o\mu_r')$, where K is a constant depending on the geometry of the strip-coil. Since a sample contributes to the flux passing through the strip-coil the impedance of the strip-coil is affected by the material inserted in it. Thus variations in MI arises due to the changes in permeability of the sample. MI measurements were taken with the DC magnetic field (H_{DC}) perpendicular to the high frequency AC magnetic field (h_{rf}). In Fig. 1 we report $(\Delta R/R_0)\%=(\Delta\mu''/\mu_0'')\%$ and $(\Delta X/X_0)\%=(\Delta\mu'/\mu_0')\%$ for CZFMO from 500MHz to 2200MHz. Large resistivity of CZFMO ensures that most of the h_{rf} passes through the bulk of the sample and not just the surface, thus probing the bulk permeability of the sample. In Fig. 1(c) we show the presence of FMR signatures in our MI experiment as theoretically explained by Yelon et al.[5] The maximum percentage change observed at 2.2 GHz was ~108% for $\Delta\mu''/\mu_0''$ and ~2639% for $\Delta\mu'/\mu_0'$ on applying a DC magnetic field of ~1888 Oe and ~2943 Oe respectively (Fig.1.(c)). Such large changes in sub-tesla fields can be implemented for sensor applications and magnetic microwave devices.

1. Gupta, A., et al., *Improved magnetoelectric coupling in Mn and Zn doped CoFe 2 O 4–PbZr 0.52 Ti 0.48 O 3 particulate composite.* Applied Physics Letters, 2011. 98(11): p. 112901. 2. Kumar, P., K. Rubi, and R. Mahendiran, *Room temperature giant magnetoimpedance in polycrystalline La0. 75Ba0. 25MnO3.* AIP Advances, 2016. 6(5): p. 055913. 3. Ciureanu, P., L. Melo, and A. Yelon, *Circumferential and longitudinal 1GHz permeabilities in Co-rich melt-extracted amorphous wires.* Journal of magnetism and magnetic materials, 2002. 242: p. 224-228. 4. Korenivski, V., et al., *A method to measure the complex permeability of thin films at ultra-high frequencies.* IEEE Transactions on Magnetics, 1996. 32(5): p. 4905-4907. 5. Yelon, A., et al., *Calculations of giant magnetoimpedance and of ferromagnetic resonance response are rigorously equivalent.* Applied physics letters, 1996. 69(20): p. 3084-3085.

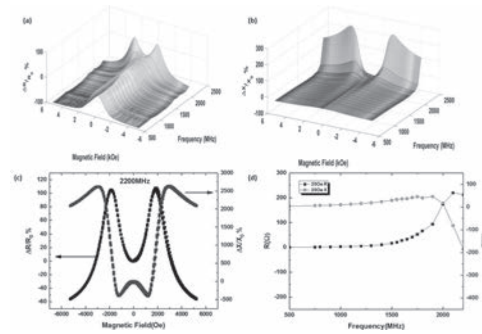

Fig. 1. (a)Variations of $(\Delta R/R_0)\%$ with magnetic field is shown which is equivalent to $(\Delta\mu''/\mu_0'')\%$ and (b) $(\Delta X/X_0)\%$ is shown which is equivalent to $(\Delta\mu'/\mu_0')\%$ from 500MHz to 2100MHz. (c)Percentage changes with magnetic field for $\Delta R/R_0$ and $\Delta X/X_0$ measured at 2200MHz. The peak in $(\Delta R/R_0)\%$ corresponds to the point of inflection in $(\Delta X/X_0)\%$. (d) Keeping H_{DC} field at 20Oe we show the R and X as measured by the impedance analyzer.

AQ-04. Microwave absorption properties of polymeric ferrite core-shell nanocomposites.

K. Song[1], K. Seo[1] and *J. Jung*[1]
1. Chemistry, Gangneung-Wonju National University, Gangneung city, The Republic of Korea

The need for protecting human or devices from a new kind of pollution known as electromagnetic interference(EMI) is becoming a world attention in the development of the efficient shielding methods to reduce EMI. An ideal EM wave absorber is necessary to have light weight, thin thickness, high EM wave absorption, broad width, tunable absorption frequency, and multi functionality. To date, considerable efforts have been made to design various materials to reach the ideal targets. In this study, we report a simple surface modification process that induces the ferromagnetic ferrite spheres and hexagonal plates to be functionalized with conducting polyaniline(PANI) for improved electromagnetic interference shielding materials. The aim of this study is to find out the effect of morphology on the electromagnetic properties, and also, effectiveness of EMI shielding of the nanocomposite with different weight ratios between ferromagnetic and polyaniline. The ferromagnetic nanomaterials were prepared in hydrothermal method with the formation of polyaniline coating and core ferromagnetic ferrite nanocomposite. The X-ray diffraction patterns and FE-SEM images confirmed the spherical core/shell of Fe_3O_4@PANI nanocomposite and the plate core/shell of $BaFe_{12}O_{19}$@PANI nanocomposite. The electromagnetic interference shielding effectiveness and EMI shielding mechanisms of core/shell nanocomposites with different morphology and different thickness in the 1-18 Hz range were studied. The microwave absorption property of the composites strongly depends on the intrinsic properties of core ferrite morphology in the polyaniline matrix and with the increasing of the thickness, the effective electromagnetic absorbing frequency band was shifted to the lower frequency.

[1] M. sharma, M.P. Singh, C. Srivastava, G. Madras, S. Bose, ACS Appl. Mater. Interfaces 6(2014) 2151-21160 [2] S. Das, G.C. Nayak, S.K. Sahu, P.C. Routray, A.K. Roy, H. Baskey, J.Magn. Magn. Mater. 377(2015)111-116

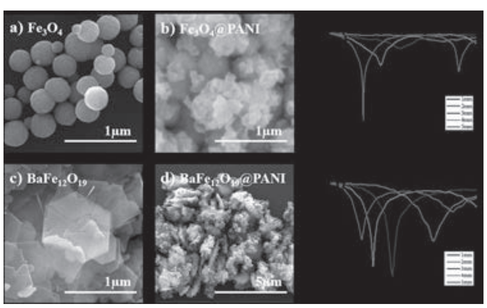

Fig. 1. SEM images of Fe3O4(a) Fe_3O_4@PANI(b) $BaFe_{12}O_{19}$(c) $BaFe_{12}O_{19}$@PANI(d), and the reflection losses in different thickness of the Fe_3O_4@PANI(e) $BaFe_{12}O_{19}$@PANI(f)

AQ-05. High frequency magnetic loss in nanogranular FeCoTiO films with different history of induced uniaxial anisotropy.

Y. He[1], Y. Wang[1], Z. Zhong[1], H. Zhang[1] and *F. Bai*[1]
1. University of Electronic Science and Technology, State Key Laboratory of Electronic Thin Films and Integrated Devices, Chengdu, China

Soft magnetic films have attracted considerable attentions for high frequency applications, such as on-chip power inductors, transformers and voltage regulaters. Loss control is the most critical tasks for these applications.[1] The high frequency loss of magnetic thin films typically includes hysteresis loss, eddy current loss, and ferromagnetic resonance (FMR) damping loss. Nanogranular FeCo-X-O (N) (X denotes Si, Hf, Zr, Ti, Zn etc.) have higher resistivity and saturation magnetization than those of permalloy or amorphous alloys. Meanwhile, the critical thickness can be 500 nm or above due to the suppressed growth of columnar structures by insulating layers.[2] All these make the nanogranular films very attractive for on-chip passive devices. So far, nanogranular films are mainly grown by sputtering. The in-plane uniaxial anisotropy (H_k) required for hard-axis exited inductors and transformers can be induced through in-situ magnetic biasing field (H_{bias}) during growth or oblique sputtering, both of which are widely adopted in the fabrication of CMOS compatible magnetic devices.[4] However, the research about high frequency magnetic loss related to these two processes is still scarce. We here report our efforts to reducing the effective damping factor of nanogranular FeCoTiO films. Fig. 1(a-c) show the imaginary part of the permeability spectra of FeCoTiO films deposited at different oblique angles (β) upon applying magnetic field along the easy axis (called low-field FMR). It can be seen that the FMR frequency (f_r) increases from 3 GHz to 5 GHz upon increasing β from 17° to 32° at zero field. Therefore, the working frequency of nanogranular films can be simply tuned by adjusting β angle. Fig. 1(d) shows that full width at half maximum (Δf) of the imaginary permeability spectra. The lowest Δf about 0.76 GHz was obtained in the film with β of 17°, corresponding to a low α_{eff} of 0.013. Further increasing β angle cause significant structural inhomogeneities and larger α_{eff}. Fig.2(a-c) show the permeability spectra of FeCoTiO films deposited with in-situ H_{bias} of 15, 70 and 115 Oe, respectively. Regardless of the magnitude of H_{bias}, it is found that H_k varies in a small range between 70 Oe and 80 Oe. Our results clearly reveal that the rearrangement of Fe-Fe(Co) atom pairs almost fully completed at an external field as small as 15 Oe during sputtering. According to the two magnon theory, the extrinsic α_{eff} is generally related to the magnetic inhomogenieties.[4] The low field FMR results in Fig. 2 indicate that (i) further increasing biasing field cannot fully suppress magnetic inhomogenieties, which is true for even for H_{bias} up to 900 Oe (not shown); and (ii) Δf decreases with the increase of the external field and the minimal Δf is 0.55 at an external field of 200 Oe, as shown in Fig.2 (d). Finally, we calculated the high frequency loss μ''/μ' of FeCoTiO films. The two sets of data are from the film deposited under in-situ H_{bias} of 115 Oe and the film by oblique sputtering at β=17°. The μ''/μ' of oblique sputtered FeCoTiO film dominantly comes from FMR damping above 1.6 GHz, below which only hysteresis loss can be observed. However, for the FeCoTiO film deposited under H_{bias} of 115 Oe, the FMR damping can be observed down to 200 MHz due to a large α_{eff} of 0.026. Furthermore, the overall high frequency loss of oblique sputtered FeCoTiO film is much smaller than that of the FeCoTiO film deposited under in-situ Hbias, although the coercivity along the hard axis (H_{ch}) of the former (11 Oe) is much larger than the latter, 3 Oe. The large H_{ch} of oblique sputtered FeCoTiO films may come from the pinning effect of columnar structures. On the other hand, such columnar structure also brings the advantages of well aligned magnetic moments and reduced magnetic inhomogeneities in the FeCoTiO film.

1. D. S. Gardner, G. Schrom, F. Paillet, et al. Review of on-chip inductor structures with magnetic films, IEEE Tran. Magn., 45, 4760-4766, 2009. 2. Z.W. Liu, C.K. Ong, Microstructure and thickness dependent magnetic properties of nanogranular Co-Zn-O thin films for microwave applications, J. Alloys Compd. 509, 10075, 2011 3. C. Ó. Mathúna, N. N. Wang, S. Kulkani and S. Roy, Review of integrated magnetics for power supply on chip (PwrSoC). IEEE Trans. Power Electron., 27, 4799-4816, 2012. 4. Seemann K, Leiste H, Kovàcs A. Damping and ferromagnetic resonance linewidth broadening in nanocrystalline soft ferromagnetic Fe–Co–Hf–N films[J]. Journal of Magnetism & Magnetic Materials, 2008, 320(13):1952-1957.

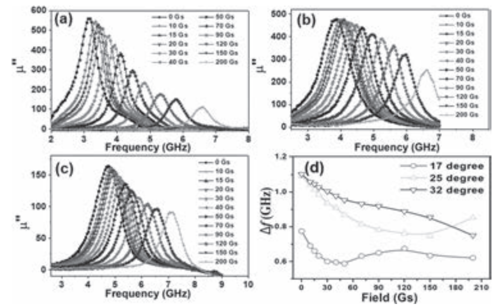

Fig. 1. Permeability spectra of FeCoTiO films deposited at different oblique angles upon applying magnetic field along the easy axis, (a) 17°, (b) 25° and (c) 32°. (d) field dependent Δf of the imaginary permeability spectra.

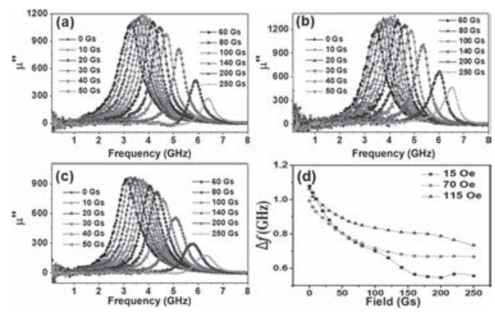

Fig. 2. Permeability spectra of FeCoTiO films deposited with different in-situ H_{bias} upon applying magnetic field along the easy axis, (a) 15 Oe, (b) 70 Oe and (c) 115 Oe. (d) field dependent Δf of the imaginary permeability spectra.

AQ-06. Foldover effect in spin-wave optoelectronic active ring resonators.

V. Vitko[1], A. Nikitin[1], A.B. Ustinov[1] and B.A. Kalinikos[1]
1. Saint-Petersburg Electrotechnical University "LETI", Saint Petersburg, Russian Federation

Active ring resonators (ARRs) in the form of a feedback loop consisting of a spin-wave delay line and microwave amplifier are widely used for investigation of nonlinear dynamics in driven damped systems (see, e.g. [1-5]). Recently, generation of spectrally pure and low noise microwave (MW) signal was observed using optoelectronic feedback loops with optical delay lines [6-8]. An advantage of such schemes is due to attain an ultrahigh Q-factor, which is defined by the length of optical fiber [9]. It is physically clear that a connection in the closed-loop of a ferrite waveguide and a high-Q optical storage element opens new opportunities to investigate nonlinear effects. The aim of this work is to study the foldover effect that appears due to the spin-wave nonlinearity enhanced by the high-Q optical element in a combined spin-wave/optical ARR. The considered ARR scheme consists of a spin-wave delay line, a microwave attenuator, a microwave amplifier, an electro-optic modulator, an optical fiber, and a microwave photodetector, as it is shown in Fig. 1. In this scheme, the light from the external laser is introduced into the modulator, closing the circuit to the ring. Note that this ring, like an optoelectronic oscillator [9], may start up into MW self-generation in case a microwave amplification compensates for losses. In the regime preceding the self-generation, the amplitude of the signal circulating in the high-Q ring increases significantly at the resonant frequencies, and exceeds the nonlinear phenomena threshold, which is determined by the nonlinear properties of the spin waves. It manifests itself as a resonant frequency shift and foldover effect. The important feature of the investigated ARR in comparison with a typical spin-wave ARR is much higher Q-factor. It means that the optical delay line affects the nonlinear wave properties of the spin-wave ARR. Hence, the "hybrid nature" of the proposed ARR proves itself. To investigate the foldover effect in the spin-wave ARR with high-Q optical element the experiments were carried out. The spin-wave delay line consisted of an yttrium-iron garnet 5-μm thick film and two microstrip transducers separated by 4 mm. The YIG film was magnetized perpendicularly to its surface by a magnetic field of 2630 Oe. The optical part of the ARR consisted of the commercially available elements: a laser giving optical radiation of 1.55 μm, a 10-GHz electro-optical Mach–Zehnder modulator, a single mode fiber with length of 100 m, and a 10-GHz photodetector. It was found out that an increase in the amplifier gain resulted in a nonlinear upper-shift by 110 kHz of all resonant frequencies. Note that for a bigger nonlinear frequency shift the foldover instability occurred. In order to illustrate a development of foldover effect the resonant peak shapes measured for -9 dB and -1 dB below the self-oscillation threshold are shown in Fig. 2 by solid blue line and solid red line, respectively. To better understand the physics underlying the foldover effect in the ARR, a theoretical model was developed as follows. First, a nonlinear dispersion relation for the carrier spin waves was derived from the linear dispersion relation taking into account the dependence of the static magnetization on the amplitude of circulating signal. This amplitude was determined as the product of the amplitude of the input signal and the transmission coefficient of the investigated ARR. Then, the wave-number as a function of frequency was numerically calculated from the nonlinear dispersion relation. Its substitution into the linear transmission coefficient resulted in the nonlinear transmission characteristic (NTC) of the ARR. The obtained NTC was used for a comparison with the experimental results (see Fig. 2). One can see that the theoretical and experimental results have a good agreement. In conclusion, the theoretical model of the resonance spectra for the spin-wave optoelectronic ARR was developed taking into account both the dispersion and nonlinear properties of the ferrite film. Results of the numerical simulation have a good agreement with the transmission characteristic measured in the experiment. The developed theory gives a possibility to investigate the foldover effect evolving due to the nonlinear spin-wave properties of the ferromagnetic film included in the ARR containing the high-Q optical elements. The work was supported by the Ministry of Education and Science of Russian Federation (agreement 14.575.21.0157, unique identifier RFMEFI57517X0157).

[1] B. A. Kalinikos, N. G. Kovshikov, and C. E. Patton, "Decay free microwave magnetic envelope soliton pulse trains in yttrium iron garnet thin films," Phys. Rev. Lett., 1997, Vol. 78, pp. 2827 – 2830. [2] V. E. Demidov and N. G. Kovshikov, "Mappings leading to randomization of an envelope of high-intensity spin waves," Tech. Phys. Lett., 1998, Vol. 24, Iss. 8, pp. 647-649. [3] S. O. Demokritov, A. A. Serga, V. E. Demidov, B. Hillebrands, M. P. Kostylev, and B. A. Kalinikos, "Experimental observation of symmetry-breaking nonlinear modes in an active ring," Nature, 2003, Vol. 426, Iss. 6963, pp. 159-162. [4] M. Wu, B. A. Kalinikos, L. D. Carr, and C. E. Patton, "Observation of Spin-Wave Soliton Fractals in Magnetic Film Active Feedback Rings," Phys. Rev. Lett., 2006, Vol. 96, Iss. 18, p. 187202. [5] A. B. Ustinov, V. E. Demidov, A. V. Kondrashov, B. A. Kalinikos, and S. O. Demokritov, "Observation of the chaotic spin-wave soliton trains in magnetic films," Phys. Rev. Lett., 2011, Vol. 106, Iss. 1, p. 017201. [6] J. M. Soto-Crespo, M. Grapinet, P. Grelu, and N. Akhmediev, "Bifurcations and multiple-period soliton pulsations in a passively mode-locked fiber laser," Phys. Rev. E, 2004, Vol. 70, Iss. 6, p. 066612. [7] L. M. Zhao, D. Y. Tang, and B. Zhao, "Period-doubling and quadrupling of bound solitons in a passively mode-locked fiber laser," Opt. Comm., 2005, Vol. 252, Iss. 1, pp. 167-172. [8] F. Li, X. Feng, H. Zheng, C. Lu, H. Y. Tam, J. N. Kutz, and P. K. A. Wai, "Multiwavelength lasers with homogeneous gain and intensity-dependent loss," Opt. Comm., 2011, Vol. 284, Iss. 9, pp. 2327-2336. [9] X. S. Yao, L. Maleki, "Optoelectronic microwave oscillator," JOSA B, 1996, Vol. 13, Iss. 8, pp. 1725-1735.

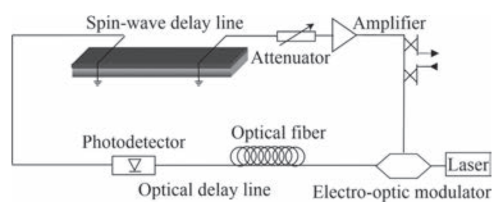

Fig. 1. Diagram of spin-wave optoelectronic ARR arrangement

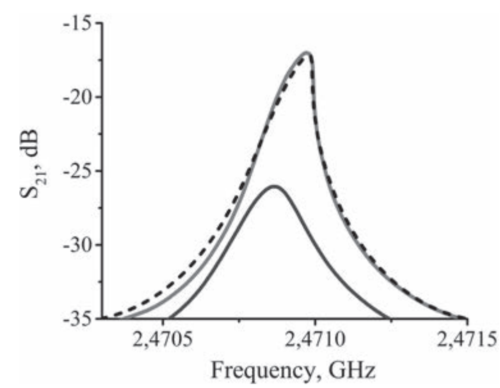

Fig. 2. Comparison of the experimental (solid lines) and numerically simulated (dashed lines) nonlinear transmission characteristics

AQ-07. Effect of annealing on the structural and FMR properties of epitaxial YIG thin films grown by RF magnetron sputtering.

B. Bhoi[1], N. Venkataramani[2], R. Aiyar[1], *S. Prasad*[3] and M. Kostylev[4]
1. Center for Research in Nanotechnology and Science, Indian Institute of Technology Bombay, Mumbai, India; 2. Metallurgical Engineering & Materials Science (MEMS), Indian Institute of Technology Bombay, Mumbai, India; 3. Dept of Physics, Indian Institute of Technology Bombay, Mumbai, India; 4. Physics, The University of Western Australia (M013), Perth, WA, Australia

Yttrium iron garnet (YIG) or $Y_3Fe_5O_{12}$ has continued to attract attention over the years due to its low microwave loss, essential for microwave device technology [1]. Apart from microwave application, recently the nanometer (nm) thick YIG films have been used to realize spin transfer torque devices, magnetic logic devices, and frequency tunable metamaterials [2]. This has enhanced the interest in the study of physical properties of YIG thin films. The fabrication of epitaxial YIG films in micrometer thick range on Gadolinium Gallium Garnet ($Gd_3Ga_5O_{12}$ or GGG) substrates has been commonly done by liquid phase epitaxy (LPE). However, Pulsed laser deposition (PLD) and RF sputtering are known to be better suited techniques to deposit nm thick epitaxial YIG films on GGG and polycrystalline YIG films (on substrates other than GGG) [3-4]. Recently large amount of work has been reported on PLD deposited YIG thin films that are grown on different substrates [3-4]. One curious finding has been that whenever YIG films were grown on GGG substrate, effective saturation magnetization ($4\pi M_{eff}$) larger than bulk has been observed when studied using Ferromagnetic resonance (FMR). where $4\pi M_{eff} = 4\pi M_S - H_U$. Here $4\pi M_S$ is the bulk saturation magnetization and H_U is uniaxial anisotropy field. In our previous study, we performed a systematic structural, magnetic and microwave studies on PLD deposited YIG/GGG films and established that the high $4\pi M_{eff}$ value is due to the presence of negative H_U arising from the compressive stresses present in the film. The presence of this stress in YIG film was confirmed by multiple {*hkl*} stress measurements with grazing incidence X-ray diffraction performed at different depth of penetration on the YIG film. The question then arose whether this effect is only seen in YIG/GGG films deposited by PLD technique or can also be observed in thin films grown by other techniques. RF sputtering is a technique widely used for industrial application due to uniform and large area deposition. Hence, to cheek the above hypothesis of stress induced anisotropy, we further extended our study to YIG thin films deposited on GGG substrate by RF sputtering. In the present work, we report the growth and microwave studies at different frequency of ~250 nm thick YIG film deposited on GGG (111) substrates by RF magnetron sputtering. (Edward Z400) at room temperature. The YIG film is deposited at an RF power of 100 W and in an argon atmosphere of 1.6×10^{-2} mbar. The chamber was evacuated to 5×10^{-6} mbar prior to film deposition using a turbo molecular pump. The target to substrate distance was maintained at 4 cm. After the deposition, the thin films were *ex-situ* annealed in air at 700 ^{o}C for different time intervals (2, 4, 6 and 10 hours). X-ray diffraction (XRD) shows that as-grown layer is amorphous and pure YIG phase is formed with preferred (111) orientation after annealing. We observe ~ 0.4% increased lattice parameter (*a*) for 2h annealed YIG films (12.429 Å) over the YIG bulk (12.376 Å) and this difference in '*a*' is reduced with the increase in annealing time (*a*=12.410 Å for 10h annealed film). The microwave properties have been investigated using a field-modulated broadband FMR in the frequency range 2-18 GHz. The magnetic field (*H*) was applied normal to the film plane. Fig. 1(a) shows the measured FMR fields as a function of frequency for YIG/GGG films annealed for different times. The $4\pi M_{eff}$ for each film has been estimated by fitting experimental data to Kittel formula for perpendicular position [3]. Similar to our previous results on PLD deposited YIG/GGG films, all the rf sputtered annealed YIG films here show $4\pi M_{eff}$ value larger than the SQUID measured $4\pi M_S$ value (~ 1780 G). Hence the higher value of $4\pi M_{eff}$ observed in the rf sputtered case can also be explained by considering the presence of negative H_U. The $4\pi M_{eff}$ value also found to decrease with the increase in annealing time. This indicates the presence of negative H_U decreases with the increase in annealing time due to stress relaxation. These values are, however, much smaller than those observed for PLD films, where we observed $H_U = -830$ Oe. Another interesting result obtained from the present study pertains to the FMR line width (ΔH) as a function of annealing temperature. Fig. 1(b) represents variation of ΔH as a function of annealing time and is plotted for frequencies 6 GHz and 18 GHz. It is seen that, the 10h annealed film shows a minimum ΔH value, lying between 30 Oe to 54 Oe over a wide frequency range (2-18 GHz). Compared to the 2h films, the FMR ΔH was reduced by ~50 % upon annealing for 10h. Although the FMR linewidth and coercively (H_C) of rf sputtered films (H_C=18 Oe, ΔH = 30 Oe) are nearly six times larger than that of PLD deposited YIG films (H_C=3 Oe, ΔH = 5 Oe), they are still much smaller than some of the results reported in recent years [5-6]. From the present investigations it is evident that the annealing helps in YIG phase formation as well as in reducing the stress, resulting a decrease in the FMR line width. Following a detailed analysis, a correlation between the microstructure and microwave properties has been established.

1. A. Goldman, Modern Ferrite Technology (Springer US, 2006). 2. A. V. Chumak, V. I. Vasyuchka, A. A. Serga, and B. Hillebrands, Nat. Phys. 11,453 (2015). 3. B. Bhoi, Ph.D Thesis, Centre for Research in Nanotechnology and Science, IIT Bombay 2016. 4. B. Bhoi, *et al*, "Observation of large easy plane anisotropy in pulsed laser deposited Yttrium iron garnet thin films," Appl. Phys. Lett. (*Submitted*). 5. Rong Ma, M. Liu, J. Wang, H. Wang, J Alloys Compd. 708, 213e219 (2017). 6. G. Wang, et al, Appl. Phys. Lett. 109,162405 (2016).

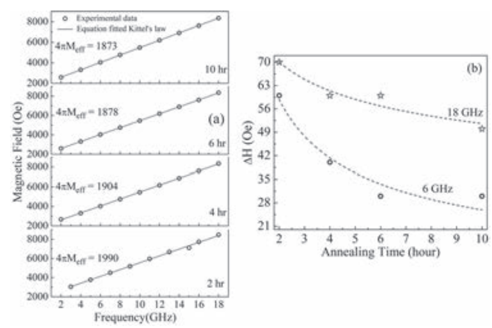

Fig. 1. (a) Frequency vs H_r for a field applied to perpendicular to film surface. (b) ΔH as a function of annealing time measured at 6 GHz and 18 GHz.

AQ-08. Design of an implantable antenna operating at ISM band using magneto-dielectric material.

Z. Luan[1], L. Liu[2], W. Zong[2], Z. Jin[2], D. Cao[1], H. Lin[3], N. Sun[3] and *S. Li*[1]
1. Physics, Qingdao University, Qingdao, China; 2. Electronics and information, Qingdao University, Qingdao, China; 3. Northeastern University, Boston, MA, United States

In recent years, wireless capsule endoscope has attracted much attention in the test and diagnosis digestive disorders. The implantable antenna is an important component of a capsule endoscope to transmit medical image from inner body to outside body. The popularly used frequency bans in medical devices are Medical Implant Communication Service (MICS) band (403-405 MHz) and Industrial Scientific Medical (ISM) bands (433.05-434.79 MHz, 869.7-870 MHz, and 902-928 MHz) [1]-[2]. An implantable antenna is required with small size. To obtain antenna miniaturization, traditional techniques mainly focus on geometry design using folded or spiral shape [3]-[5]. In this paper, we proposed a novel flexible implantable antenna operating at ISM bands of 869.7-870 MHz and 902-928 MHz. The antenna is of a coplanar waveguide (CPW) fed antenna printed on a 20 µm thick Kapton polyimide substrate. Figure 1(a) shows the configuration of the CPW antenna. A magneto-dielectric sheet with 0.5 mm thickness is placed at the bottom layer of the antenna to tune the antenna bandwidth covering ISM bands. Figure 1(b) shows the side view of the arrangement of the antenna with magneto-dielectric sheet. The relative dielectric constant of Kapton polyimide is 3. The magneto-dielectric sheet has relative permittivity εr=13, relative permeability μr=20.7, dielectric loss tangent $\tan\delta\varepsilon$=0.17, and magnetic loss tangent $\tan\delta\mu$=0.12. The antenna was simulated and optimized by using Ansys High Frequency Structure Simulator (HFSS). To simulate the antenna inside a human body, a single-layered body phantom with box shape of 110 mm×110 mm×50mm was used as shown in Figure 1(c). The dielectric constant of human phantom is adopted of skin with εr=45.2 and σ=0.61 s/m. The antenna is fabricated and measured inside chopped meat. Figure 1(d) shows photograph of fabricated antenna. Figure 2 shows simulated and measured |S11| of the proposed antenna. The simulated -10 dB bandwidth of the proposed antenna with magneto-dielectric sheet is 1013-1063.6 MHz, the bandwidth is 930-1310 MHz for the antenna without magneto-dielectric sheet. The measured bandwidth of the antenna with magneto-dielectric sheet is 835.9-995.4 MHz(-15dB), and the bandwidth is 840-1035.6 MHz for the antenna without magneto-dielectric sheet. There is some disagreement between measurement and simulation which is caused by the difference between simulation model of body phantom and chopped meat used in measurement. The measurement and simulation both show that the adoption of magneto-dielectric sheet results in frequency bands shifting to the left The measured bandwidths of the antenna with magneto-dielectric sheet cover ISM bands of 869.7-870 MHz and 902~928 MHz.

[1] S Bakogianni, and S Koulouridis. "Design of a novel miniature implantable rectenna for in-body medical devices power support," European Conference on Antennas and Propagation., 2016. [2] S M Islam, K P Esselle, and D Bull, et al. "A miniaturized implantable PIFA antenna for indoor wireless telemetry," IEEE Conferences. pp. 526-530, 2012. [3] S. Bakogianni, and S. Koulouridis, "An Implantable Planar Dipole Antenna for Wireless MedRadio-Band Biotelemetry Devices," IEEE Antennas and Wireless Propagation Letters, vol.15, pp. 234-237, Jun. 2015. [4] H. Li., and Y.X. Guo, "A Miniature-Implantable Antenna for MedRadio-Band and Biomedical Telemetry," IEEE Antennas and Wireless Propagation Letters, vol.14, pp.1176-1179, 2015. [5] Z. Duan, Y.X. Guo, M. Je, and D.L. Kwong,: "Design and in vitro test of a differentially fed dual-band antenna for implantable operating at MICS and ISM bands," IEEE Trans. Antennas Propag, vol. 62, pp. 2430-2439, 2014.

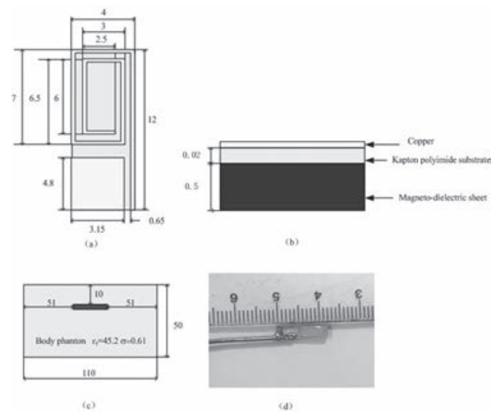

Fig. 1. Proposed antenna (unit: mm). (a) Top view of the antenna configuration. (b) Side view of the proposed antenna configuration. (c) Side View of antenna in body phantom. (d) Top view of the fabricated antenna.

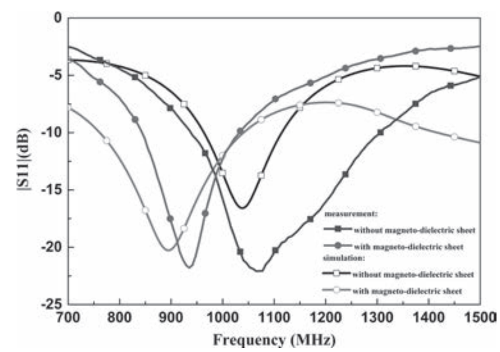

Fig. 2. |S11| of the proposed antenna.

AQ-09. Electromagnetic Noise Suppression Composite Sheet Made of Hexagonal Ferrite Particles.

M. Sato[1], R. Sai[1], Y. Miyazawa[1], A. Takahashi[1] and *M. Yamaguchi*[1,2]
1. New Industry Creation Hachery Center, Tohoku University, Sendai, Japan; 2. Department of Electrical Engineering, Tohoku Unviersity, Sendai, Japan

Introduction - In the early stage 5th generation mobile phone system, it is expected to use high frequencies up to the SHF band (3 to 30 GHz) [1]. Therefore new noise countermeasure material is necessary in this band [2]. In this paper, we studied M-type, Y-type and Z-type hexagonal ferrite fine particles in composite form with epoxy resin, to find candidate for this application through SEM observation, XRD, DC hysteresis loop, high frequency complex permeability, and conduction noise suppression effect on micro stripline(MSL). *Preparation and properties of fine particles* - While Sr and Ba hexagonal ferrite materials are known as permanent magnet materials, they are also useful as high frequency materials whose ferromagnetic resonance (FMR) frequency exceeds 20 GHz, which corresponds to the center frequency of noise suppression exceeds 20 GHz. Firstly we followed a known direction to reduce magneto-crystalline anisotropy by a 1 – 2 at% substitution of Fe^{3+} ions by a combination of metal ions such as Co^{2+} and Ti^{4+}. Table I shows list of test particles; Z-type $Ba_3Zn_{2-X}Co_xFe_{24}O_{41}$(x = 1.25), Y- type $Ba_2Zn_2Fe_{12}O_{22}$, and M- type $SrCo_xTi_xFe_{2-x}O_{19}$ (x = 1.4) [3]. The fired polycrystalline material was pulverized to obtain fine particles. The XRD pattern showed that the crystal structure is mainly composed of hexagonal crystals since the relative intensity and diffraction angle of the main diffraction peak agree with the values of the JCPDS database. *Fabrication and properties of composite sheet* - The fine particles were mixed with the epoxy resin at a volume ratio of about 50%. This mixed solution was dropped onto a polymer sheet and screen-printed with a metal squeegee to a certain thickness, then a composite sheet was obtained. On the premise of mounting the composite in the gap between the interposer substrate and the IC chip, the coating thickness was chosen as 50 ± 5 um in total. The Y-type fine particles were almost flat in planar state even after grinding and the Z-type and M-type fine particles were close to spherical and randomly oriented, according to the SEM observation. The coercive force obtained from the DC magnetization curve is 8 to 9 Oe in a composite sheet of Y-type and Z-type fine particles (hereinafter referred to as Y-type sheet, etc.), which is smaller by one order of magnitude than the M-type sheet (90 Oe). Correspondingly, the maximum value of the relative imaginary part permeability was the maximum of 1.8 for the Y-type sheet, and it was 0.9 for the Z-type sheet, and 0.3 for the M-type sheet. As shown in Fig. 1, measured input loss ratio [4] $P_{loss}/P_{in}=1-(|s_{11}|^2+|s_{21}|^2)$ with a network analyzer (Agilent Technologies, Model N5244A) became the larger as the relative imaginary part magnetic permeability became higher. The measured P_{loss}/P_{in} was as high as 0.21 at 6 GHz, which should correspond to more than 5 dB conduction noise suppression. This research was supported in part by the R&D program of the Radio Use, Ministry of Internal Affairs and Communications, and the Cooperative Research Project Program of the RIEC (H27-B05) Tohoku University.

[1] 3GPP, Release 14: TR 38.913 - Study on Scenarios and Requirements for Next Generation Access Technologies, 2016. [2] M. Yamaguchi, et al, IEICE Transactions on Communications (Japanese Edition), DOI:10.14923/transcomj.2017PEI0001, 2017 [3] S. Thompson, et al, Journal of Magnetism and Magnetic Materials, Vol. 292, pp. 100–107, Nov. 2005. [4] S. Yoshida et al, EMC '03, Istanbul, Turkey, DOI: 10.1109/ICSMC2.2003.1429071, May 2003.

Composite sheet Name	Hexaferrite particle Composition	Particle Size [μm]	Composite Sheet Thickness [μm]	Ms [emu/g]	Hc [Oe]
Z	$Ba_3Zn_{2-X}Co_XFe_{24}O_{41}$ (X=1.25)	0.6	50	51	9
Y	$Ba_2Zn_2Fe_{12}O_{22}$	3.2	55	38	8
M	$SrCo_XTi_XFe_{12-2X}O_{19}$ (X=1.4)	0.3	46	37	90

Table I List of Test samples

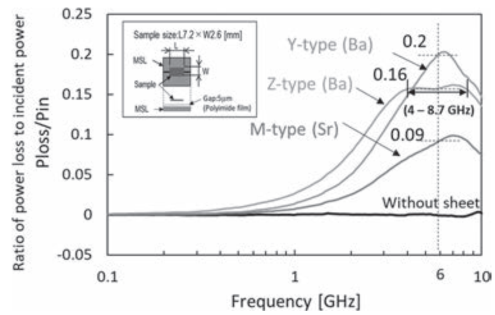

Fig. 1. Measured Loss/Input ratio, P_{loss}/P_{in}

AQ-10. Enhancement of Phase-Shifting Nonreciprocity in Metamaterial Lines Loaded with Comb-Shaped Stubs Supporting Slow Wave Propagation of Edge Guided Modes.

T. Ueda[1], K. Okamoto[1], J. Yamauchi[1] and T. Itoh[2]
1. Electrical Engineering and Electronics, Kyoto Institute of Technology, Kyoto, Japan; 2. Electrical Engineering Department, University of California, Los Angeles, Los Angeles, CA, United States

Nonreciprocal metamaterials have been investigated to discover new electromagnetic phenomena and to invent state-of-the-art functional circuits and antennas [1],[2]. By using nonreciprocal metamaterials, we can have unidirectional wavenumber vectors along the wave-guiding structures regardless of the propagation directions. Transmission-line resonators based on such noneciprocal metamaterials show unique characteristics in that the resonance frequency is independent of the resonators' size and that the field profiles have uniform magnitude and linearly-varying phase distribution, referred to as pseudo-traveling-wave resonators [3]. In addition, phase gradient of the fields along the resonators can be arbitrarily varied by changing the nonreciprocity of the lines under the resonant condition, which is implemented to highly-efficient beam scanning leaky wave antennas [4], and to polarization-switchable circularly polarized antennas. However, most of phase-shifting nonreciprocal metamaterials have resulted in relatively small magnitude of nonreciprocity even with considerably large applied dc magnetic field with the help of strong permanent magnets or huge size of electromagnets, which limit the availability and applications to beam steering antennas for practical use. In order to make the steering beam angle wider for antenna applications or to reduce the magnitude of the dc magnetic field, enhanced nonreciprocity is essential. Recently, the phase-shifting nonreciprocity for the normally magnetized ferrite-based metamaterials was analytically formulated showing that this phenomenon is described by a product of two factors; the one corresponds to off-diagonal component in Polder permeability tensor determining gyro-magnetic characteristics. Another factor is the geometrical asymmetry which is realized by periodically and asymmetrically inserting stubs into the normally magnetized ferrite rod-embedded microstrip lines at the center [5], [6]. So far, shunt stubs periodically inserted in previous metamaterials were constructed on the non-magnetic dielectric substrates to avoid the influence of dc magnetic field on the stub performance. However, capacitive stubs constructed on the dielectric substrate suffer from the coupling between adjacent stubs and cause degradation of enhanced phase-shifting nonreciprocity. In this paper, we propose a new enhancement technique for the phase-shifting nonreciprocity in metamaterial lines loaded with comb-shaped periodic open stubs constructed on the normally magnetized ferrite substrate at one side of strip edges, as shown in Fig 1. In the configuration, the edge guided mode [7] is excited that caused zigzag propagation along each stub. This mechanism corresponds to longer distance for one propagation direction. This situation is realized by reducing the coupling between adjacent stubs. At the other side of strip edges, inductive stubs are periodically inserted to realize negative effective permittivity and to reduce the propagation distance in the opposite direction of propagation. Combination of capacitive and inductive stub insertion results in enhanced nonreciprocity. Polycrystalline Yttrium Iron Garnet was employed as the ferrite material. The configuration parameters for the prototype circuit are as follows; thicknesses of the ferrite and dielectric substrates are both 0.8 mm, dielectric constants of ferrite and dielectric substrates are 15 and 2.6, respectively. The width of the center strip is 2 mm. The length and width of capacitive stubs are 2 mm and 0.8 mm, respectively. The unit cell length is 1.9 mm. In Fig. 2, the simulated and measured phase shifting nonreciprocity $\Delta\beta$ are extracted from the S-parameters for five unit cells and plotted as a function of the operating frequency and externally applied dc magnetic fields. It is found from Fig. 2 that experimental results agree well with numerical simulation results. It is noted that the beam sweep of ±15 degrees in the present configuration corresponds to the nonreciprocity for the external dc magnetic field of ±26 mT only which is about a quarter compared to the typical value of 100 mT required for previous nonreciprocal metamaterials. Thus, reduction of the applied dc magnetic field required for the nonreciprocity will open up realization of tunable nonreciprocity of metamaterials and beam steering antennas for practical use.

[1] T. Ueda, K. Horikawa, M. Akiyama, and M. Tsutsumi, "Nonreciprocal phase-shift composite right/left handed transmission lines and their application to leaky wave antennas," IEEE Trans. Antennas Propag., vol. 57, no. 7, pp. 1995-2005, July 2009. [2] T. Ueda and M. Akiyama, "Nonreciprocal phase-shift composite right/left handed transmission lines using ferrite-rod-embedded substrate." IEEE Trans. on Magnetics, vol. 45, no. 10, pp. 4203-4206, Oct. 2009 [3] T. Ueda and H. Kishimoto, "Pseudo-traveling wave resonator based on nonreciprocal phase-shift composite right/left handed transmission lines," in 2010 IEEE MTT-S Int. Microw. Sym. Dig., pp. 41-44, May 23-28, 2010 [4] T. Ueda, S. Yamamoto, Y. Kado, T. Itoh, "Pseudo-traveling wave resonator with magnetically tunable phase gradient of fields and its applications to beam steering antennas," IEEE Trans. Microw. Theory Tech., vol. 60, no. 10, pp. 3043-3054, Oct. 2012. [5] A. Porokhnyuk, T. Ueda, Y. Kado, T. Itoh, "Mode analysis of phase-constant nonreciprocity in ferrite-embedded CRLH metamaterials", IEICE Trans. on Electron., vol. E96-C, no. 10, pp. 1263-1272, Oct. 2013. [6] J. Yamamuchi, T. Ueda, Y. Kubo, T. Itoh, "Enhancement of phase-shifting nonreciprocity in microstrip-line-based metamaterials by using a combination of their curvatures and asymmetrical insertion of stubs," IEEE Trans. on Microw. Theory Tech., vol. 65, no. 12, pp. 5123-5132, Dec. 2017. [7] M. E. Hines, "Reciprocal and nonreciprocal modes of propagation in ferrite strip line and microstrip devices," IEEE Trans. Microw. Theory Tech., vol. 19, no. 5, pp. 442–451, May 1971.

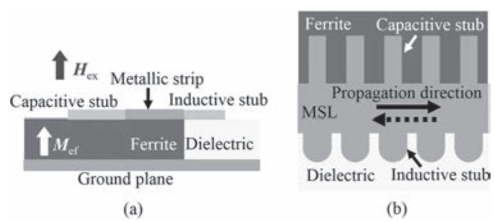

Fig. 1. Geometry of the proposed nonreciprocal metamaterial line. (a) Cross section. (b) Top view.

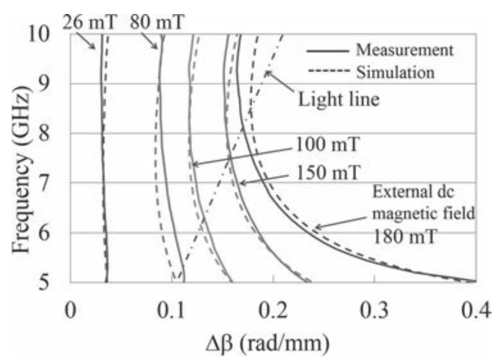

Fig. 2. Simulated and measured phase shifting nonreciprocity as a function of the externally applied dc magnetic field.

AQ-11. Synthesis and Microwave Absorbing Property of $SrZn_xFe_{(2-x)}Fe_{16}O_{27}$ ($0.0 \le x \le 1.0$).

J. You[1], S. Choi[1], S. Lee[1] and S. Yoo[1]
1. Material science and engineering, Seoul National University, Seoul, The Republic of Korea

Strontium W-type hexaferrite ($SrFe_{18}O_{27}$, SrW) is a ferromagnetic material possessing high saturation magnetization (M_s) about 80 emu/g and high anisotropy field (H_a) about 19 kOe [1]. Due to its cost-effectiveness and suitable magnetic properties, W-type hexaferrite has attracted attention for permanent magnet application and microwave application especially for microwave absorber in the large frequency range of 8–40 GHz [2,3]. In this report, we tried to prepare Zn-substituted SrW bulk samples with the compositions of $SrZn_xFe_{(2-x)}Fe_{16}O_{27}$ ($SrZn_xFe_{(2-x)}W$) where x value was $0.0 \le x \le 2.0$ for the first time in a reduced oxygen atmosphere, and identify the effect of Zn^{2+} substitution on their magnetic properties. Furthermore, microwave absorbing properties of $SrZn_xFe_{(2-x)}W$ with varying x were investigated in the frequency range of 1-18 GHz. For these purposes, the samples with different x values were annealed at the temperature region of 1125–1350°C for 2 h in the PO_2 of 10^{-3} atm. As a result, single phase of $SrZn_xFe_{(2-x)}W$ could be obtained for x values of 0.0, 0.5, and 1.0. It was found that cell volumes of the samples increased with increasing x until $x = 1.25$ due to the larger ionic radius of Zn^{2+} than Fe^{2+}, and then remained constant with further increased x. Static magnetic property measured by vibrating sample magnetometer revealed that anisotropy field value of the samples decreased with increasing x from 0.0 to 1.0, and decreased from $x = 1.0$ to 2.0. In contrast, saturation magnetization value increased with increasing x value. And also, the complex permeability and permittivity values for the $SrZn_xFe_{(2-x)}W$-epoxy resin composites with ferrite filling ratios of 30, 50, 70, 90 vol% were measured by vector network analyzer. The measurement revealed that real permeability value increased and ferromagnetic resonance frequency decreased with increasing x value which is attributable to increase in saturation magnetization and decrease in anisotropy field. The reflection loss values were calculated based on the obtained complex permeability and permittivity values. It was found that the reflection loss values larger than -20 dB (90% absorption) could be obtained with absorber thickness less than 1.5mm. Detailed properties of $SrZn_xFe_{(2-x)}W$ will be presented for a discussion.

[1] J. Smit, H. Wijn, Ferrites, Philips Technical Library, Eindhoven, 1959. [2] U. Ozgur, Y. Alivov, H. Morkoc, Microwave ferrites, part 1: fundamental properties, J. Mater. Sci Mater. El. 20 (2009) 789e834. [3] V.G. Harris, Modern microwave ferrites, IEEE Trans. Magn. 48 (2012) 1075e1104.

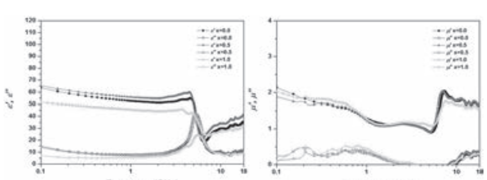

Fig. 1. The complex permittivity and permeability spectra at the frequency range of 1-18 GHz of the $SrZn_xFe_{(2-x)}W$ composites with ferrite filling ratio of 90vol%

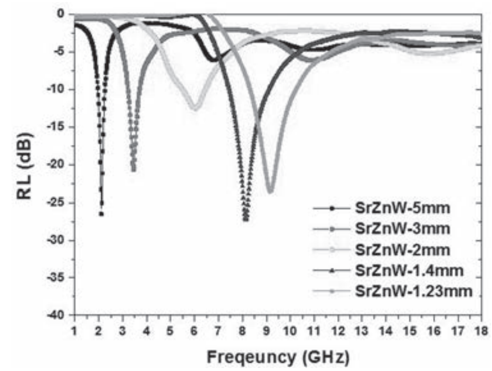

Fig. 2. The reflection loss spectra at the frequency range of 1-18 GHz of the $SrZn_xFe_{(2-x)}W$ ($x = 1.0$) composites with ferrite filling ratio of 90vol%

AQ-12. Transport, magneto-optical and micromagnetic characterization of domain-wall resonance (DWR) in giant magnetoimpedance strain and magnetic field sensors.

G. Büttel[1] and U. Hartmann[1]
1. Institute of Experimental Physics, University of Saarland, Saabrücken, Germany

Recently, very high strain-gauge factors have been determined on micromachined thin-film and multilayer giant magnetoimpedance sensors [1]. The observed domains walls and different magnetization reversal mechanisms are complex and difficult to predict in advance in such sensors, but strongly determine the high-frequency transport characteristics and are critical for strain and magnetic field sensitivity in the low-field regime. In this contribution we report on observed domain walls emerging during sweeping of the external field. Domains were imaged and distinguished by longitudinal magneto-optical widefield Kerr and magnetic force microscopy. The main goal of this study was to obtain a match with micromagnetic simulations carried out by the MUMAX framework. While typically a double peak GMI response has been reported in mm-sized NiFe multilayer thin-film and ribbon GMI sensors with a Cu core layer and surrounding NiFe layers [2], we show that in microstructured and -machined multilayers a well-pronounced fourfold peak behavior can occur. Measurements were performed by a VNA in distinct frequency regimes below the FMR frequency of the Kittel mode. Similar multi-peak effects were also reported for GMI thin-film sensors with CoNbZr in the low-MHz regime, but no explanation could be found so far [3]. The DWR depends on the actual structure of the multilayer system, on materials, post-deposition annealing processes, ac current amplitude and domain-wall types and density. The implications of DWR in GMI sensors may be dis-/advantageous in future GMI sensor applications for magnetic field/particle or strain detection. Therefore, a thorough understanding and prediction of such processes by micromagnetic simulations is very helpful. A careful/thorough set-up of the exciting-field geometries has to be defined in the simulations to understand and verify the more or less pronounced occurrence of DWR in the MHz regime for different multilayer designs. The Oersted field that is generated by the ac current in the Cu core layer has antiparallel orientations in the surrounding bottom and top NiFe layers. For a single layer system, the dipolar coupling between the top and bottom layers adjacent to the Cu core leads to an antiparallel orientation of domain walls and opposing oscillations of the Oersted field and of vortices and anti-vortices in the single layers (Fig. 1). For a double layer system, experimentally and in micromagnetic simulations, the amount of vortex structures is strongly reduced and the DWR peaks in the GMI curve are less pronounced (Fig. 2). This can be qualitatively understood by a very weak antiparallel dipolar coupling of bottom and top double layers and by the antiparallel coupling of the single NiFe layers in each surrounding double layer. This leads to a damping of strong oscillations/DWR as the Oersted field is parallel and antiparallel to the single layers below and on top of the Cu core. In addition, the domain walls of the individual layers of the double-layer system are much stronger coupled by dipolar interactions. Both aspects can be experimentally verified by an identical shape of MOKE-recorded hysteresis curves from the top of the double layer and VSM hysteresis curves of the whole multilayer stack. By applying tensile strain to such double layer GMI sensors, the field regime exhibiting DWR increases as well as the number of domain wall annihilations/nucleations in the low-field regime before the magnetization rotates towards the saturated state. This further proves that a high density of domain walls in microscaled GMI sensors strongly influences or dominates the change of permeability and impedance in the skin-effect regime far below the FMR frequency regime. This may lead to fundamental scaling limits for GMI sensors or it may stimulate new design and materials concepts, when a rotation of magnetization in the low-field regime cannot be established. In conclusion, we show that micromagnetic simulations, not presented so far for GMI devices, are a powerful tool for the prediction of DWR in relatively large GMI devices with odd and even numbers of NiFe layers and alternating changes of dipolar coupling and occurring domain walls. Thereby, optimal strain and field sensitivities can further be explored and optimized for future smaller GMI sensors.

[1] G. Buettel et al., Appl. Phys. Lett. 111, 232401 (2017) [2] A. Garcia-Arribas et al., J. Magn. Magn. Mater. 400, 321 (2016) [3] H. Kikuchi et al., J. Magn. Magn. Mater. 420, 269 (2016)

Fig. 1. Longitudinal Kerr-microscopy image of a single system (400µm x 40µm) at 4 Oe. For zero field no vortices/anti-vortices occur in the films and no DWR in the corresponding GMI curves. The density of the vortices strongly depends on the thickness of the Cu core layer

Fig. 2. Longitudinal Kerr-microscopy image for two double (NiFe/Ti/NiFe) layers (400µm x 20µm) surrounding the Cu Core layer at an external field of 4 Oe. Due to the large size and soft magnetic properties of NiFe only a qualitative match (shape, density) to the micromagnetic simulations can be reached. Vortices/anti-vortices do not occur in the double layer system as well as flux closure domains parallel to the longitudinal axis of the GMI structures in comparison to single layers.

AQ-13. New Measurement Method of Broadband Permittivity and Permeability of Non-Solid Materials in Small Quantity.

K. Miura[1], Y. Odagiri[1], T. Umesaka[1], D. Suzue[1] and H. Osada[1]
1. Faculty of Science and Engineering, Iwate University, Morioka, Japan

Evaluation of permittivity (ε) and permeability (μ) of magnetic/dielectric material in microwave band becomes more important with the rapid expansion of microwave technologies. Transmission/reflection line method is well known as a simultaneous measurement method of ε and μ in the band. However in this method material under test (MUT) is limited to solid state. On the other hand, for measuring liquid material open ended coaxial probe method was proposed. The method is disadvantageous in terms of requiring deciliter volumes of MUT for approximating a semi-space filled by MUT. We propose a new measurement method with the aim of simultaneous measuring both of permittivity and permeability of not only solid material but also a small amount of liquid, powder, and gel state material. A plastic toroidal case was utilized to encapsulate non-solid state MUT and whole the case was evaluated by coaxial line method. In this study the cases were modeled using Acrylic 3-D printer (Stratasys, Objet 260 Connex). An example of the plastic case with a cap fabricated is shown in Fig. 1. Outer and inner diameter (7.00 and 3.00 mm) of the case was designed to fit to a coaxial sample holder (KEAD Inc., CSH2-APC7). The length of the case including a cap thickness measured by digital vernier caliper was 5.00 mm. In the same way, thickness of wall, bottom, and cap was 0.45, 0.50, and 0.50 mm, respectively. Accordingly the volume of MUT required for the case was about 70 microliters. The specimen which MUT was encapsulated was inserted to the coaxial sample holder and complex scattering (*S*) parameters from 1-10 GHz were taken using a vector network analyzer (Hewlett-Packard, HP 8720D). *S*-parameters whose reference planes were both upper and lower surface of the specimen were obtained by shifting reference planes of the measured *S*-parameters. After that we obtained *S*-parameters of MUT in numerical calculations mentioned below in order to take away unwanted plastic case portions. The specimen can be divided into three coaxial portions: Inner cylindrical wall, outer cylindrical wall, and middle core including MUT between their walls. From the viewpoint of electric circuit it corresponds to a series connection of the three two-port networks. Impedance (*Z*) parameters of the middle core were obtained using the relationship: *Z*-matrix of the specimen equals to the sum of their three *Z*-matrices. *Z*-matrix of the specimen was obtained by converting *S*-matrix of it by a reference impedance. *Z*-matrix of outer and inner wall was obtained from ε and μ measured in advance using solid specimens of the plastic material and outer and inner diameters of their cylindrical walls. *Z*-matrix of the middle core was converted *S*-matrix again. The middle slender core can be divided into three coaxial portions: a part of cap, a part of bottom, and MUT. The core corresponds to a cascaded connection of the three two-port networks. Transfer (*T*) parameters of MUT were obtained using the relationship: *T*-matrix of the core equals to the product of their three *T*-matrices. *T*-matrix of the core was obtained by converting *S*-matrix of it. *T*-matrix of a part of bottom and cap was obtained from ε and μ of the plastic material used and bottom and cap thickness. Finally ε and μ of MUT were calculated from *S*-parameters of it using Nicolson-Ross-Wier algorithm [1, 2]. In this study, the air at the volume was measured as MUT in order to confirm a validity of the proposed method. The dependences of real and imaginary part of relative permittivity of air obtained by this method on frequency were shown in Fig. 2(a) and Fig. 2(b). Although the both values had a margin of error of plus or minus 10% a constant and nearly ideal relative permittivity of air was confirmed in the band measured from these figures. This result indicates that the proposed method is effective for measuring non-solid materials.

[1] A. M. Nicolson, et al., IEEE Trans. On Instrumentation and Measurement, Vol. IM-19, No. 4, 1970. [2] W. Wier, Proceedings of the IEEE, Vol. 62, No. 1, 1974.

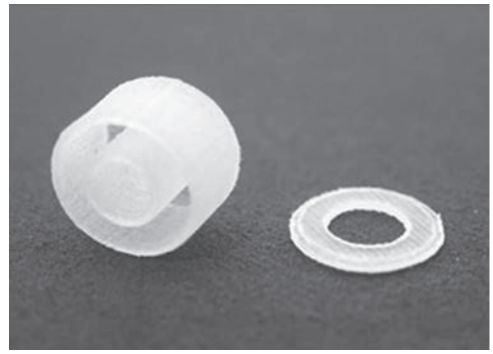

Fig. 1. A plastic toroidal case with a cap fabricated using 3-D printer.

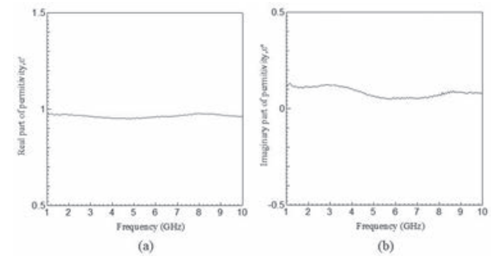

Fig. 2. Dependence of (a) real part and (b) imaginary part of relative permittivity of air on frequency by the proposed method.

AQ-14. Comparative Analysis of Core Loss Calculation Methods for Magnetic Materials Under Nonsinusoidal Excitations.

Y. Li[1], S. Yue[1] and Q. Yang[2]

1. Hebei University of Technology, Tianjin, China; 2. Electrical Engineering, Tianjin Polytechnic University, Tianjin, China

I. Introduction Magnetic components in power electronic devices usually suffer from nonsinusoidal excitations. In this paper, a brief description about the existing core loss calculation methods for nonsinusoidal excitations is given. Then calculation formulas of aforementioned methods for two typical excitation waveforms, that is square and rectangular with variable duty cycle, are derived and analyzed. Core loss of nanocrystalline FT-3KS, under both sinusoidal excitations and above two nonsinusoidal excitations, are measured on an established test setup. The experimental results are then compared with the calculated values from derived formulas. It is found that the waveform coefficient Steinmetz equation (WcSE) is more applicable for the case of relatively small harmonic content of *H*, while the improved generalized Steinmetz equation (IGSE) has relatively good precision when the harmonic content is large. The results can provide reference for core loss prediction. II. Core Loss Calculation A. Brief Review of Existing Methods Traditionally, core loss for sinusoidal excitations can be divided into hysteresis model method, core loss separation method and Steinmetz equation (SE) method. In recent years, many other core loss calculation approaches based on SE have been developed for non-sinusoidal excitations, including the modified Steinmetz equation (MSE)[2], the generalized Steinmetz equation (GSE)[3], the improved generalized Steinmetz equation (IGSE)[4] and waveform coefficient Steinmetz equation (WcSE)[5]. In this paper, we only discuss SE, MSE, IGSE and WcSE for IGSE is considered as an improved version of GSE. B. Calculation Formulas for Typical Waveforms In this part, the calculation formulas are derived by applying MSE, GSE, IGSE and WcSE to square and rectangular waveform excitations, which will be presented in the full paper. It can be seen from these formulas how the core loss is affected by the waveform duty cycle *D*. III. Experimental Verification and Discussions A. Core Loss Measurement Both sinusoidal excitations and two nonsinusoidal excitations with variable *D* [0.05-0.95] are built to conduct the experiments, as shown in Fig. 1. The *B-H* loop measurement method is selected to calculate core loss for the copper loss is excluded. Fig. 2 (a) and Fig. 2 (b) illustrate the exciting voltage and current waveforms of square excitations and rectangular excitations at 10kHz when *D* is 0.3 (up), 0.5(middle), 0.7(bottom), respectively. B. Results Comparision and Discussion Fig. 2 (c) and Fig 2 (e) present the comparision results of loss prediction through SE, MSE, IGSE, WcSE and the corresponding percentage errors under square excitations with variable *D*, at 10 kHz and 0.8T. For square excitations, it is clear that the WcSE exhibits better accuracy (>92%) in predicting core loss than SE, MSE and IGSE for a duty cycle range of about[0.4-0.6]. However, the accuracy decreases rapidly with the duty cycle out of this range, where the IGSE shows relatively good prediction instead. Similarly, Fig. 2 (d) and Fig 2 (f) indicate the comparision results of loss prediction and the corresponding percentage errors under rectangular excitations with variable *D*, at 10 kHz and 0.8T. In this case, the IGSE demonstrates satisfactory precision (>90%) over the whole range of duty cycle, although the WcSE is more accurate in the range of [0.6-0.95]. Actually, the above phenomena can be summarized as: the WcSE is more suitable for the case of relatively small harmonic content of exciting current (namely *H*), while the IGSE, due to the consideration of major and minor hysteresis loops resulting from harmonics, can maintains a relatively good accuracy where the harmonic content counts. For square excitations, the harmonic currents are gradually increasing with *D* approaching 1 or 0 from 0.5. For rectangular excitations, it has the same effect as the previous one when *D* approaches 0 from 1. More details about the discussion will be presented in the full paper. IV. Conclusions In this paper, the calculation formulas for square and rectangular excitations are derived based on the existing methods. Core loss of nanocrystalline FT-3KS, under both sinusoidal excitations and above two nonsinusoidal excitations, are measured on an established test setup. The experimental results are then compared with the calculated values from derived formulas. It is found that the waveform coefficient Steinmetz equation (WcSE) is more applicable for the case of relatively small harmonic content of *H*, while the improved generalized Steinmetz equation (IGSE) has higher precision when the harmonic content is relatively large. The results can provide reference for core loss prediction.

[1] I. Villar, U. Viscarret, I. Etxeberria-Otadui, and A. Rufer, "Global Loss Evaluation Methods for Nonsinusoidally Fed Medium- Frequency Power Transformers," IEEE Transactions on Industrial Electronics, vol.56, no. 10, pp. 4132-4140, 2009. [2] J. Reinert, A. Brockmeyer, and R. W. A. A. De Doncker, "Accurate calculation of losses in ferro- and ferrimagnetic materials based on the modified Steinmetz equation," Industry Applications Conference, 1999. Thirty-Fourth Ias Meeting. Conference Record of the IEEE Xplore, vol. 3, pp. 2087-2092, 2001. [3] J. Li, Abdallah T, and Sullivan C R, "Improved calculation of core loss with nonsinusoidal waveforms"[C]// Industry Applications Conference, 2001. Thirty-Sixth Ias Meeting. Conference Record of the. IEEE, vol. 4, pp. 2203-2210, 2001. [4] K. Venkatachalam, C. R. Sullivan, T. Abdallah, and H. Tacca, "Accurate prediction of ferrite core loss with nonsinusoidal waveforms using only Steinmetz parameters"[C]// Computers in Power Electronics, 2002. Proceedings. 2002 IEEE Workshop on. IEEE, pp. 36-41, 2002. [5] W. Shen, F. Wang, D. Boroyevich, and C.W. Tipton, "Loss Characterization and Calculation of Nanocrystalline Cores for High-Frequency Magnetics Applications," IEEE Transactions on Power Electronics, vol. 23, no. 1, pp. 475-484, 2008.

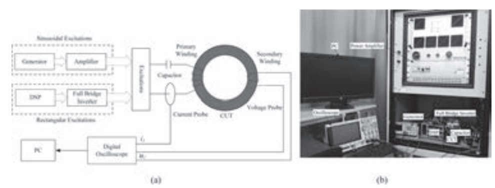

Fig. 1. (a) Schematic diagram of the test setup (b) Prototype of the test setup

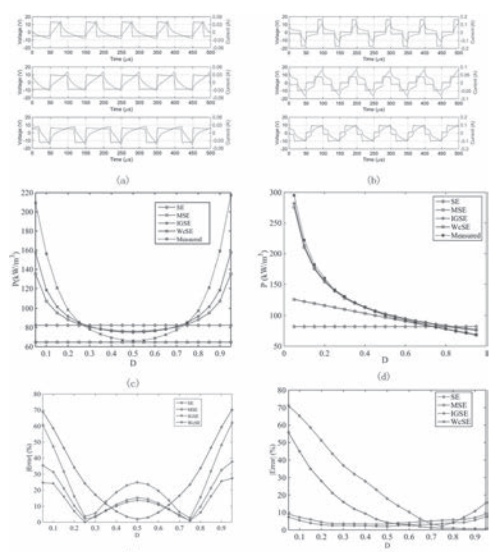

Fig. 2. (a) Voltage and current waveforms of square excitations at 10kHz when *D is* 0.3 (up), 0.5(middle) and 0.7(bottom). (b) Voltage and current waveforms of rectangular excitations at 10kHz when *D* is 0.3 (up), 0.5(middle) and 0.7(bottom). (c) Core loss comparison of measurement and calculation under square excitations with *D* [0.05-0.95], at 10 kHz and 0.8T. (d) Core loss comparison of measurement and calculation under rectangular excitations with *D* [0.05-0.95], at 10 kHz and 0.8T. (e) Absolute values of error between measured and calculated from SE, MSE, IGSE and WcSE under square excitations with *D* [0.05-0.95], at 10 kHz and 0.8T. (f) Absolute values of error between measured and calculated from SE, MSE, IGSE and WcSE under rectangular excitations with *D* [0.05-0.95], at 10 kHz and 0.8T.

AQ-15. Design and Analysis of a Novel High Frequency 2-D Magnetization Structure with Ultra-Thin Silicon Steel Sheet.

Y. Li[1], Y. Dou[1], C. Zhang[1], A. Li[1] and J. Zhu[2]
1. Hebei University of Technology, Tianjin, China; 2. Electrical engineering, University of Technology, Sydney, Sydney, NSW, Australia

I. Introduction The measurement of high frequency magnetic properties is very important, not only in the application of emerging power electronics and special motors, but also in traditional motors and transformers, because the existence of higher harmonics will cause large additional losses. Whereas, the Epstein frame can only measure the 1-D magnetic properties, and the high frequency magnetic properties are measured with ring sample method. In addition to these, numerous engineering-oriented testing electromagnetic analysis methods and devices have been proposed in [2]- [4]. In order to solve these problems, the high frequency magnetic properties of silicon steel sheets should be measured, or the ultra-thin silicon steel and nanocrystalline that can generate high-frequency magnetic field are used as cores to measure the2-D high-frequency magnetic properties. To magnetize the sample to saturation, ultra-thin silicon steel is chosen as the material of magnetization circuit instead of nanocrystalline, because the saturated magnetic density of the device can be higher if the sample is saturated. Ultra-thin silicon steel is gradually applied to electromagnetic equipment for its excellent magnetic characteristics, which is of great significance in accurate magnetic properties measurement in high frequency. By using this material, a novel high frequency 2-D magnetization structure with multi-layer excitation winding and composite sensing box is proposed. In order to measure vector *B* and *H* of the nanocrystalline or ultra-thin silicon steel sheet samples in high frequency, a feedback control method based on LabVIEW is applied, which can effectively diminish the adverse effects of harmonics and obtain more uniform magnetic fields. II. novel 2-d magnetization structure A. Modeling of the 2-D Magnetization Structure The novel 2-D magnetization structure consists of four "C-type" cores, magnetic material specimen and four multi-layer exciting windings, which are wound around the orthogonal core poles, as shown in Fig. 1(a). In order to magnetize the specimen to saturation in high frequency, a high-grain-oriented ultra-thin (0.05mm) silicon steel is applied in the excitation core, which can increase the excitation field and reduce the core loss, comparing with the common silicon steels. The testing specimen is placed in the center of the 2-D tester and jointed by four core poles. As illustrated in Fig. 1(b), the four "C-type" cores are almost the same shape except for the core pole part. They can be classified into two types according to the different core pole shapes. The multi-layer excitation winding is composed of three layers with different turns, which can be connected in series or parallel to satisfy variable exciting frequency range, flexibly. B. B-H Composite Sensing Structure The *B-H* composite sensing structure combines one piece of testing specimen, two fixing frames, two guarding pieces, two sets of *B-H* composite sensor, as shown in Fig. 2(a). The *B-H* composite sensor is fixed in the fixing frame as shown in Fig.2 (b), which consists of two crossed *H*-sensing coils and *B* needle probes, that is B_x, B_y, H_x, H_y. *H* sensing coils are wrapped around the epoxy resin board with 80 turns to test the magnetic field strength in both directions. According to the theory that the strength of magnetic field along the tangential direction is continuous at the boundary of the different media, the *H*-sensing coils can detect the magnetic field strength *H* on the specimen surface. Therefore, the air gap between the *H*-sensing coils and the testing specimen should be as smaller as possible. The magnetic flux density *B* can be detected by four needle probes placed on the four corners of the epoxy resin board. The magnetic material specimen needs to be magnetized by a strong and homogenous field. To acquire a uniform field, two guarding pieces, which are the same material and with the same grain oriented direction as the specimen, are attached on every surface of the specimen. Fig.2 (c) exhibits the distinctive comparison of the magnetic flux density distribution with and without guarding pieces. By comparing the simulation results in the diagram, it can be concluded that the adoption of guarding pieces obviously improves the uniformity of the field on the specimen surface, improving the measurement precision significantly. III. 2-d Magnetic Properties Measurement Systerm The existing 2-D magnetic properties measurement system mainly consists of 2-D magnetic properties tester, *B-H* composite sensing structure, NI PXIe-6368, differential amplifier circuit and two power amplifiers, which are used to amplify the excitation signal. In order to get an ideal magnetization loci within the specimen, the feedback control method based on LabVIEW is used, which greatly diminishes the adverse effects of harmonics and increase the accuracy of the measurement. Excitation of different frequencies are given to the tester, thus a series of well controlled circular *B* loci and corresponding experimental *H* loci are obtained at 50 Hz, 500Hz, and 1kHz for ultra-thin silicon steel sheet. The detailed measurement and analysis will be presented in the full paper.

[1] Yongjian Li, Qingxin Yang, JianguoZhu, "Design and Analysis of a Novel 3-D Magnetization Structure for Laminated Silicon Steel," *IEEE Transaction on Magnetics*, vol. 50, no. 2, pp. 389-392, Feb. 2014. [2] Brix W, Hempel K, Schulte F, "Improved method for the investigation of the rotational magnetization process in electrical steel sheets," *IEEE Transactions on Magnetics*, vol. 20, no. 5, pp. 1708-1710, 1984. [3] Hasenzagl A, Weiser B, Pfützner H. "Novel 3-phase excited single sheet tester for rotational magnetization," *Journal of Magnetism and Magnetic Materials*, vol. 160, no. 7, pp. 180-182, 1996. [4] De la Barriere O, Appino C, Fiorillo F, et al. "Extended frequency analysis of magnetic losses under rotating induction in soft magnetic composites," *Journal of Applied Physics*, vol. 111, no.7, pp. 2137, 2012

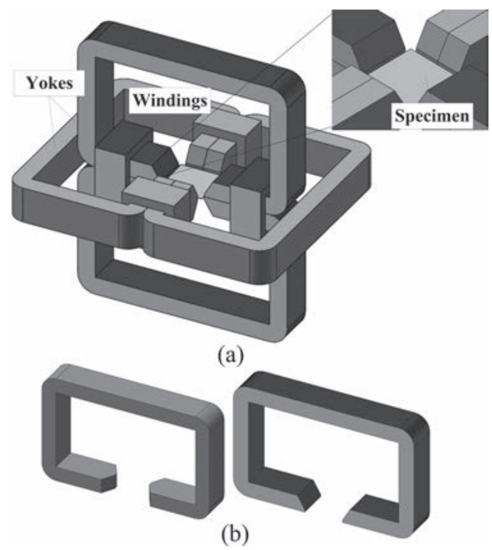

Fig. 1. Novel 2-D magnetization structure. (a) 2-D magnetic properties magnetization structure. (b) Two types of laminated "C-type" cores.

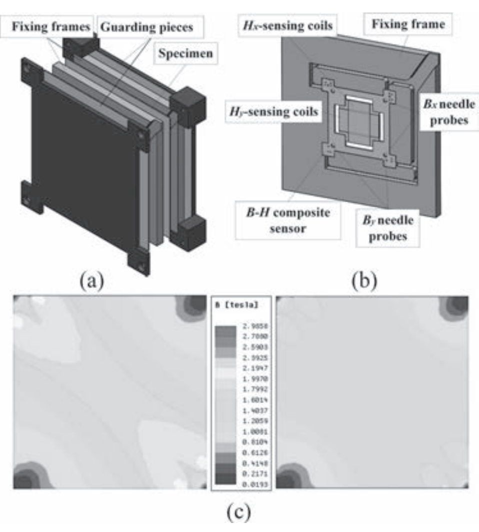

Fig. 2. (a) *B-H* composite sensing box. (b) Fixing frame with *B-H* composite sensor. (c) Magnetic flux density of the specimen without and with guarding pieces.

AQ-16. High-frequency magnetic and dielectric properties of CaO-SiO_2 codoped NiZnCo spinel ferrites.

Z. Zheng[1], Y. Li[1], T. Liu[1], Q. Xiang[1] and Q. Feng[1]
1. School of Information Science and Technology, Southwest Jiaotong University, Chengdu, China

Nowadays, as the rapid development of electronic and communication technology, the various devices are developing towards miniaturization and lightweight, especially the devices with small size and high performance are ever increasingly demanded. A challenge in this process is that the reduced size of device often produces performance degradation due to the fact that the performance of many devices is dependent on their size. In recent years, magneto-dielectric ferrite materials have received considerable attention and show unique advantage for miniaturized and high-performance radio frequency (RF) and microwave devices since ferrites have concomitant medium to high permeability and permittivity. Such as in antenna applications, by employing a ferrite substrate, antenna's dimensions can be largely reduced while larger impedance bandwidth is also expected to be achieved. In this paper, a serious of NiZnCo ferrites with the simultaneous additions of CaO and SiO_2 are synthesized, and the magnetic and dielectric properties of the samples are investigated over a wide frequency range of 10 MHz-1 GHz. The crystal phase, densification and microstructure of the NiZnCo samples were analyzed in detail to correlate with the variations of the magnetic and dielectric properties. NiZnCo spinel ferrites with nominal composition $Ni_{0.5}Zn_{0.3}Co_{0.2}Fe_2O_4 + x$ (CaO, SiO_2) (where x = 0, 0.3, and 0.6 wt% and the molar ratio between CaO and SiO_2 is 1:1) were prepared by solid-state reaction method. For the present experiment, the second time ball-milling was prolonged to 24 h and the samples were sintered at 1100 °C for 3 h in an air atmosphere. The phase compositions of the sintering samples were determined by X-ray diffraction (XRD) using Cu Kα radiation at room temperature. The XRD results indicate that all the samples show the formation of cubic spinel structure. The microstructures of the samples were examined by scanning electron microscope (SEM) and an energy-dispersive spectrum analyzer (EDS). The effects of CaO-SiO_2 additions on the magnetic and dielectric properties of NiZnCo ferrite were systematically investigated. The complex permeability and permittivity spectra, as well as magnetic and dielectric losses of the samples were measured in 10 MHz-1 GHz (here using E4991 impedance analyzer). Fig. 1(a) shows the measured real permeability μ' with CaO-SiO_2 content from 0 to 0.6 wt%. It is observed that the permeability increases gradually with CaO-SiO_2 addition. With x varying from 0 to 0.6 wt%, μ' increases from ~7.0 to ~7.3 at 10MHz. The permeability ε', however, exhibits obvious decrease with x, as illustrated in Fig. 1(b). For the undoped NiZnCo ferrite, ε' is around 10.5 over the studied frequency range. With 0.3 wt% CaO-SiO_2 addition, ε' decreases to ~10.0, and when x is up to 0.6 wt%, ε' decreases to ~9.5. These variations in magnetic and dielectric properties were proved to be closely related to the changed microstructure and densification. Additionally, the losses of the samples are found to be closely dependent on CaO-SiO_2 addition content. Fig. 2 presents the variations of dielectric loss tan δ_ε with CaO-SiO_2 content at 100 MHz and 300 MHz, respectively, and there are similar variations at the two frequencies. At 300 MHz, tan δ_ε is about 1.9×10^{-3} for the samples with x=0 and 0.3 wt%, and for the sample with x= 0.6 wt%, tan δ_ε is reduced to 1.5×10^{-3}. For the doped NiZnCo ferrites, the decreased dielectric loss is attributed to the combined effect of the high-resistance CaO and SiO_2. The above observations indicate that a certain amount of codoping of CaO and SiO_2 can modify both the magnetic and dielectric properties of NiZnCo ferrite, with opposite effects on the permeability and permittivity. This point could be helpful to balance the impedance matching of ferrite materials to free space environment ($Z = Z_0 (\mu'/\varepsilon')^{1/2}$, where Z_0 is impedance of free space) for realizing miniaturized and high-performance RF and microwave devices.

[1] H. Mosallaei and K. Sarabandi, IEEE Trans. Antennas Propag. 52, 1558 (2004). [2] V. G. Harris, IEEE Trans. Magn., 48, 1075, (2012). [3] Z. Zheng, Q. Feng, Q. Xiang, Z. Di, and V. G. Harris, J. Appl. Phys. 121, 063901, (2017). [4] L. B. Kong, Z. W. Li, G. Q. Lin, and Y. B. Gan, J. Amer. Ceram. Soc. 90, 2104 (2007) [5] Z. Zheng, H. Zhang, J. Xiao, and F. Bai, IEEE Trans. Magn. 49, 4214 (2013). [6] J. Mattei, E. Guen, and A. Chevalier, J. Appl. Phys. 117, 084904 (2015). [7] M. L. S. Teo, L. B. Kong, Z. W. Li, G. Q. Lin, Y. B. Gan, J. Alloys Compd. 459 (2008) 567-575. [8] H. Su, X. Tang, H. Zhang, Y. Jing, F. Bai, and Z. Zhong, J. Appl. Phys. 113, 17B301 (2013).

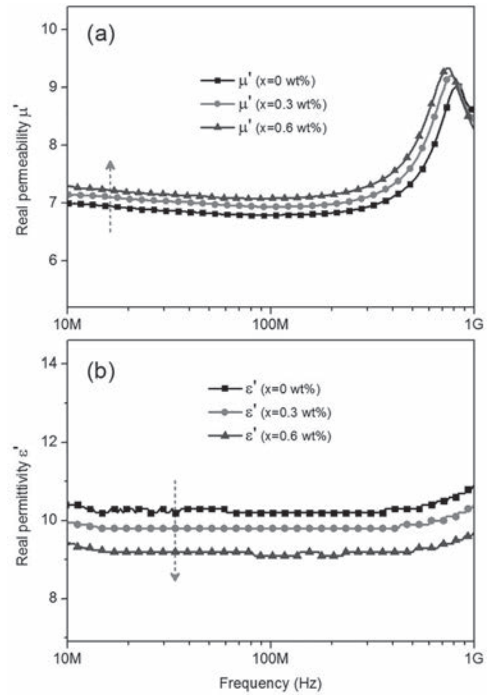

Fig. 1. Frequency dependences of (a) real permeability μ' and (b) real permittivity ε' for the NiZnCo samples with various CaO-SiO_2 additions over a frequency range of 10 MHz-1 GHz.

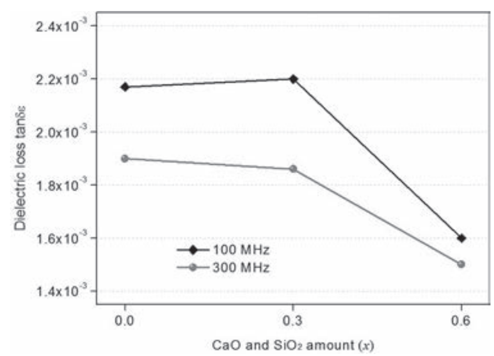

Fig. 2. The dielectric loss tan δ_ε at 100 MHz and 300 MHz, respectively, for the NiZnCo samples with various CaO-SiO_2 additions.

TUESDAY MORNING, 24 APRIL 2018 SIMPOR/ROSELLE BALLROOM, 8:30 TO 11:30

Session AR
MAGNETO-ELECTRONIC DEVICES
(Poster Session)

Yumeng Yang, Chair
National University of Singapore, Singapore

AR-01. Radiation Hardening Techniques for SOT-MRAM Peripheral Circuitry.

B. Wang[1,2], Z. Wang[1], C. Hu[2], Y. Zhao[2], Y. Zhang[1] and W. Zhao[1]
1. Beihang University, Beijing, China; 2. Beijing Micoelectronics Technology Institute, Beijing, China

Magnetic RAM (MRAM) is experimentally proved intrinsically immune to radiation effects including heavy-ion irradiation and total ion does [1-3] as the data is represented by the spin instead of charges. It is considered as a promising candidate for aerospace and avionic electronics. However, its CMOS peripheral read/write circuits are much more vulnerable to radiation-induced single event upset (SEU) and multi-bit upset (MBU), also called soft errors [4]. Therefore radiation hardening techniques are required to correct soft errors induced by irradiation. Currently, existing radiation hardening techniques are focused on sensing amplifiers of spin transfer torque (STT)-MRAM rather than write circuits since the write pulse is longer than the radiation-induced current pulse. However, for spin orbit torque (SOT)-MRAM, the magnetization switching time (<1ns) is comparable to the width of radiation-induced pulse. Therefore write circuits for SOT-MRAM is seriously required to harden since it may be disturbed by irradiation to switch the storage state of magnetic torque junction (MTJ), which called non-volatile SEU (NVSEU) [5]. Although radiation hardening techniques of sensing amplifiers have been proposed, such as C-element and XOR logic gate [6], they cannot correct MBU induced by charge sharing especially with the decreasing process dimension. In this work, we first proposed a novel hardening peripheral CMOS read/write circuitry for SOT-MRAM shown in Fig. 1. By using a physics-based SOT-MTJ compact model and a 65nm CMOS design kit, hybrid simulations are performed to validate the radiation tolerance of the novel peripheral read/write circuitry. For write circuits, sensitive nodes are A and B shown in Fig. 1(a). Unprotected write circuits may be disturbed by NVSEU to induce incorrect magnetization switching. For hardening write circuits, wherever radiation-induced particles strike, the struck node can be recovered within hundreds of picoseconds through added redundant nodes and feedback connections. Meanwhile the incorrect magnetization state is corrected, as verified by the simulation results of Fig. 2(a). For hardening read circuits shown in Fig. 1(b) [7], sensitive nodes may be Q, Qb, S0 and S1 depending on the stored data. For example, during the clock rising edge of reading "0", sensitive nodes are node Q, S0 and S1. Meanwhile Qb is a stable high voltage node since it is connected to PMOS transistors (when PMOS is struck, a positive transient pulse is generated [8]). Every sensitive node is immune to SEU as the following reasons: i) When node Q is turned "1" by a struck particle, S0 and S1 as cross-coupled connections retain initial states. Q is discharged through PM16 to recover. ii) When node S0 is turned "0" by a struck particle, S1 stays floating state with "0" and Qb stays throughout high voltage as the driving ability of PM12 is stronger than PM15. iii) Similarly, S1 is corrected through the similar path to S0 since the hardening read circuits are symmetrical. In addition, if nodes S0 and S1 are simultaneously struck to induce MBU, the proposed hardening read circuits also can be recovered, as shown in Fig. 2(b). Although the proposed read circuits are vulnerable to MBU for the rest multi-sensitive nodes (i.e. S0-Q and S1-Q), the solution is that using physically apart approach [9] to expand the space between sensitive nodes (the layout is omitted). More importantly, the proposed hardening read circuits effectively reduce the hardware area compared to those of the previous works [5-6]. The circuitry reliability is also validated by a Monte-Carlo statistical analysis tool taking into account process variations. This spintronic/CMOS circuitry can be reliably integrated into aerospace and avionics electronics in hostile environments.

[1] D. Kobayashi et al., "Influence of heavy ion irradiation on perpendicular-anisotropy CoFeB-MgO magnetic tunnel junctions," *IEEE Trans. Nucl. Sci.*, vol. 61, no. 4, pp. 1711-1715, Aug. 2014. [2] H. Hughes et al., "Radiation studies of spin-transfer torque materials and devices," *IEEE Trans. Nucl. Sci.*, vol. 59, no. 6, pp. 3027–3033, Dec. 2012. [3] F. Ren et al., "Radiation tolerance of magnetic tunnel junctions with MgO tunnel barriers," *IEEE Trans. Nucl. Sci.*, vol. 59, no. 6, pp. 3034–3038, Dec. 2012. [4] J. D. Black et al., "Physics of multiple-node charge collection and impacts on single-event characterization and soft error rate prediction," *IEEE Trans. Nucl. Sci.*, vol. 60, no. 3, Jun. 2013. [5] W. Kang et al., "A radiation hardened hybrid spintronic/CMOS nonvolatile unit using magnetic tunnel junction," *J. Phys. D: Appl. Phys.*, vol. 47, no. 40, 2014. [6] Y. Lakys, W. Zhao, J. O. Klein, and C. Chappert, "Hardening techniques for MRAM-based nonvolatile latches and logic," *IEEE Trans. Nucl. Sci.*, vol. 59, pp. 1136-1141, 2012. [7] W. Zhao et al., "High speed, high stability and low power sensing amplifier for MTJ/CMOS hybrid logic circuits" *IEEE Trans. Magn.*, vol. 45, pp. 3784-3787, Oct. 2009. [8] J. Guo, L. Xiao and Z. Mao, "Novel low-power and highly reliable radiation hardened memory cell for 65 nm CMOS technology," *IEEE Trans. Circuits Syst.* vol. 61, pp. 1994–2001, 2014. [9] O. A. Amusan et al., "Charge collection and charge sharing in a 130nm CMOS technology," *IEEE Trans. Nucl. Sci.*, vol. 53, no. 6, pp. 3253–3258, Dec. 2006.

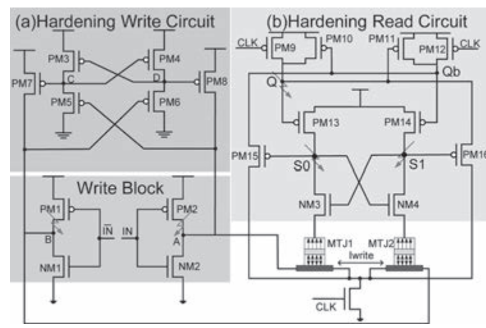

Fig. 1. Schematic of the proposed radiation hardening peripheral circuitry for SOT-MRAM cell whose storage element is a pair of MTJs to maintain opposite magnetization direction (parallel and antiparallel). (a) Hardening write circuits, which include six PMOS transistors (PM3-PM8) and feedback connections to perform the hardening construction. (b) Hardening read circuits, which utilize a pair of cross-coupled connections (i.e. NM3-NM4). Nodes Q and Qb are driven by two PMOS transistors. Nodes S0 and S1 are driven by a NMOS and a PMOS transistor. Meanwhile, their gates are connected to two different nodes. For reading "0", outputs Q and Qb are "0" and "1" (i.e. MTJ1 and MTJ2 are in low and high resistance states, respectively).

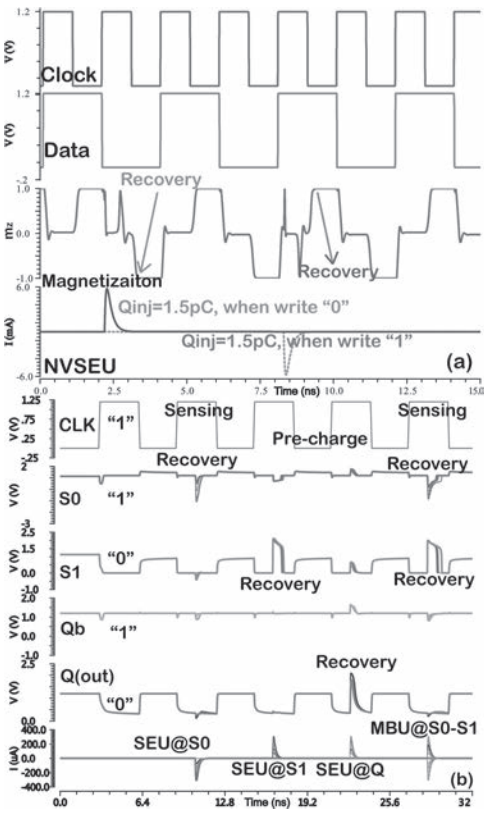

Fig. 2. (a) Transient simulation waveforms of the hardening write unit when Q_{inj} is 1.5 pC. The magnetization state can be recovered in several hundred picoseconds no matter write "1" or write "0". (b) Transient simulation waveforms when Q_{inj} varies from 20 fC to 100 fC. Struck nodes are S0, S1, Q and S0-S1 respectively, and output Q can be correctly accessed without soft errors.

AR-02. Magnetization uniformity and threshold current of out-of-plane precession in spin-torque oscillator with synthetic ferrimagnet free layer under perpendicular magnetic field: Micromagnetic simulation study.

T. Kanao[1], T. Nagasawa[1], H. Suto[1] and K. Mizushima[1]
1. Corporate Research & Development Center, Toshiba Corporation, Kawasaki, Japan

A spin-torque oscillator (STO) is a microwave oscillator based on a magnetoresistive (MR) element [1,2], and has been investigated for applications such as information storages, communications, and computing units. For these applications, large output signal and stable oscillation are necessary. So far, it has been reported that the large output signal can be obtained by out-of-plane precession (OPP) of free layer in an STO based on a magnetic tunnel junction (MTJ) and having an in-plane pinned layer [3-6]. This is because in OPP change of angle between the magnetizations of free and pinned layers is large and the relative angle change is converted into the output signal through the large MR effect of the MTJ. To further improve the output power and the stability of the OPP, we have recently fabricated an STO based on an in-plane MTJ with a synthetic ferrimagnet (SyF) free layer (SyF-STO). We have chosen the SyF free layer because improvement of the output power and the stability has been reported for in-plane oscillation [7-9]. We have investigated whether the OPP is possible in the SyF-STO. As a result, by the OPP of the free layer we have obtained large output power of the order of 1 μW in perpendicular field [10]. (In Ref. [10] we reported the maximum output power of 3.7 μW. This value includes an error in estimation, and the correct value is 0.93 μW.) In this study, to clarify the reason for the large output power obtained in the SyF-STO, we compare the SyF-STO with an STO with a single free layer (SFL-STO) by micromagnetic simulation. Figure 1 shows schematics of these STOs. The SyF-STO has two free layers which are antiferromagnetically coupled (AFC) by the interlayer coupling. The pinned layers are also AFC. An external field H_z and a current I are applied in the perpendicular direction. The spin-transfer torque acts on the free layer 2 and the pinned layer 1. To the bottom pinned layer, a -x-direction magnetic field is applied, modeling an exchange bias field. In the simulation, we use the parameters corresponding to the sample in the experiment. The parameters for the SFL-STO are the same as the SyF-STO except that the SFL-STO has a single free layer. Figure 2(a) shows oscillation powers of each STO as a function of H_z for I=8.5 mA, which are obtained from the y-components of the spatially-averaged magnetizations. The oscillation power is estimated by time average of square of the y-component of normalized magnetization. For H_z≥5 kOe, both STOs exhibit the large oscillation powers due to the OPP. In the SyF-STO, the magnetizations of the two free layers are synchronized and their in-plane components are in opposite directions. The oscillation power is larger for the SyF-STO. In the parameter range of the OPP, the oscillation frequencies of both STOs show essentially the same dependence on H_z, that is, the oscillation frequencies increase, showing a step. By investigating the waveforms of the magnetizations, we find that this step originates from coupled magnetization oscillation of the free and pinned layers due to magnetic dipolar field and the spin-transfer torque. This dependence of the oscillation freqeuncy on H_z well reproduces that observed in the experiment [10]. Such steps of oscillation frequency have been reported for SFL-STOs with OPP [1-3,7,11]. To clarify the reason of the difference of the oscillation power, we compare amplitudes of the spatially-averaged magnetizations of the free layers. Figure 2(b) shows time averages of the amplitudes. Since the magnetization is normalized, the amplitude is closer to 1 when the magnetization is spatially uniform. It is found that the amplitude for the SyF-STO is kept near 0.9 for the OPP, while that for the SFL-STO decreases to about 0.75 at around H_z=5 kOe. This difference means that the free layer magnetization of the SyF-STO is uniform compared with the SFL-STO. Inset in Fig. 2(b) shows magnetization configurations of the free layers of the SyF- and SFL- STOs for H_z=5 kOe. The y-component is shown by the color scale at a moment when the in-plane components of the spatially-averaged magnetizations are in the x-direction. In the SyF-STO, although local fluctuations can be seen, their magnitudes are relatively small. On the other hand, in the SFL-STO, the free layer is divided into two regions in which the in-plane components of the magnetizations are almost in opposite directions. This non-uniform magnetization pattern reduces stray field outside the free layer, and stabilizes magnetic field distribution. From this result we think that the almost uniform magnetization precession in the SyF-STO is because the SyF free layer reduces the stray field and thus the magnetic field distribution can be stabilized even by the uniform magnetizations. The uniform OPP of free layer magnetizations leads to the larger output power, which is a possible explanation for the large output power observed in the experiment [10]. Finally, in Fig. 2(c) we compare threshold current for the OPP, and find that the threshold current is smaller for the SyF free layer. It can be thought that this lower threshold current enables the OPP by a bias voltage lower than a voltage at which the dielectric breakdown of the MTJ occurs.

[1] W. H. Rippard et al., Phys. Rev. Lett. 92, 027201 (2004). [2] S. I. Kiselev et al., Phys. Rev. Lett. 93, 036601 (2004). [3] T. Wada et al., Phys. Rev. B 81, 104410 (2010). [4] H. Kubota et al., Appl. Phys. Express 6, 103003 (2013). [5] H. Maehara et al., Appl. Phys. Express 7, 023003 (2014). [6] B. Wang et al., Appl. Phys. Lett. 108, 253502 (2016). [7] D. Gusakova et al., Phys. Rev. B 79, 104406 (2009). [8] D. Houssameddine et al., Appl. Phys. Lett. 96, 072511 (2010). [9] T. Nagasawa et al., Appl. Phys. Lett. 105, 182406 (2014). [10] T. Nagasawa et al., 62nd MMM Conference, CC-04 (2017). [11] T. Seki et al., Appl. Phys. Lett. 105, 092406 (2014).

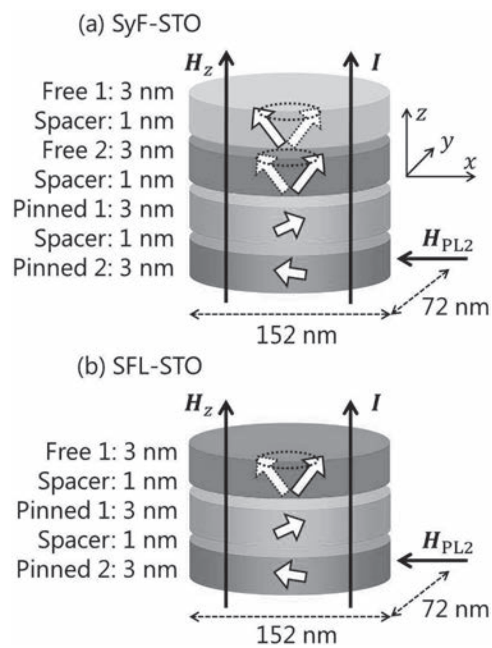

Fig. 1. Schematics of (a) SyF-STO and (b) SFL-STO.

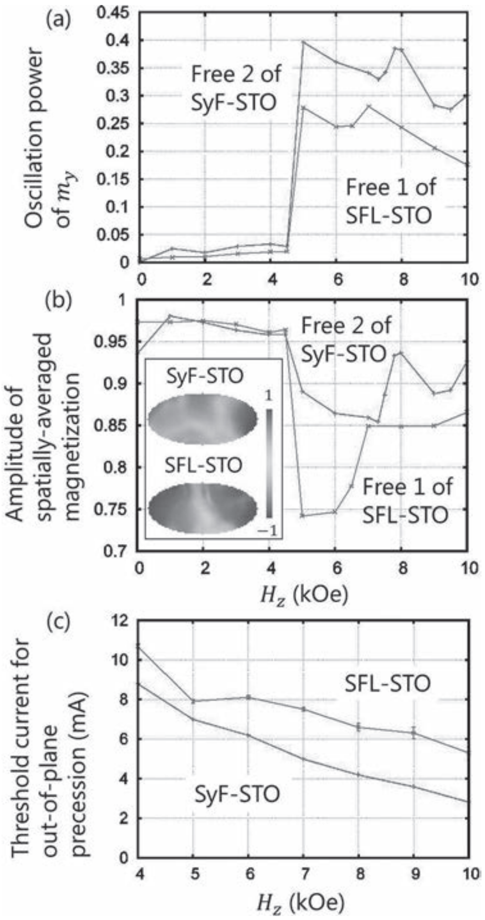

Fig. 2. (a) Oscillation powers of SyF-STO and SFL-STO as a function of H_z for I=8.5 mA, obtained from y-components of magnetizations. (b) Amplitudes of spatially-averaged magnetizations. Inset shows configurations of y-component magnetizations for H_z=5 kOe. (c) Threshold current for OPP.

AR-03. Fabrication of $L1_0$-MnAl thin films with high perpendicular magnetic anisotropy for STT-MRAM.

M. Parvin[1], M. Kubota[1], M. Oogane[1], M. Tsunoda[2] and Y. Ando[1]
1. Applied Physics, Graduate School of Engineering, Tohoku University, Sendai-shi, Japan; 2. Electronic Engineering, Tohoku University, Sendai, Japan

Magnetic tunnel junctions with perpendicularly magnetized ferromagnetic materials (*p*-MTJs) have great potential to realize the ultra-high-density STT–MRAM. The switching current density (J_{co}) in STT-MRAM is directly related to saturation magnetization (M_s) and Gilbert damping constant (α) of the ferromagnetic free layer of MTJs [1]. In order to achieve high thermal stability and low switching current density in *p*-MTJs, ferromagnetic materials with large perpendicular magnetic anisotropy energy (K_u), small M_s and low α are required. Here, we focus on a $L1_0$-MnAl alloy, which exhibits small M_s and high K_u[2,3]. In our previous works, we obtained large K_u in $L1_0$-MnAl films prepared at high substrate temperature [4]. However, high-substrate-temperature can cause increasing roughness of the films and atomic diffusion between the MnAl films and their buffer layers. In this work, we systematically investigated substrate and annealing temperature dependences of structural and magnetic properties in the MnAl thin films. The film stacking structure was MgO(001)-sub./CrRu(40)/MnAl(50)/Ta(5) (in nm). All the films were prepared by a magnetron sputtering system. The Mn-Al alloy target composition was $Mn_{46}Al_{54}$.The substrate temperature (T_s) during deposition was varied from 200^{0}C to 400^{0}C and the post-annealing temperature (T_a) was varied from 200^{0}C to 500^{0}C. The crystal structure of MnAl(50nm) films was investigated by an X-ray diffraction (XRD). The magnetic properties and surface morphology of the films were measured by superconductive quantum interference device (SQUID), vibrating sample magnetometer (VSM), and atomic force microscope (AFM). We confirmed that CrRu buffer layers had good structural property and very smooth surface morphology after annealing at 650^{o}C. Fig. 1showsXRD patterns of the films at T_s =250^{o}C with different annealing temperature. In the XRD patterns,(001) and (002) peaks of $L1_0$-MnAl were observed. This result indicates that both $L1_0$-ordered and (001)-oriented MnAl films were successfully fabricated. The peak intensity of $L1_0$-MnAl was improved with increasing both substrate and annealing temperature. However, surface roughness drastically increased above T_s = 300^{o}C. The annealing temperature dependence of magnetic properties was systematically investigated in MnAl films with T_s = 250^{o}C. A very high K_u was obtained at T_a = 350^{o}C as shown in *M-H* curve in Fig. 2.We finally obtained a $L1_0$-ordered MnAl film with high K_u of 13.0 Merg/cc, relatively low M_s of 497 emu/cc and small roughness (R_a)of 0.3 nm in the condition of T_s = 250^{o}C and T_a =350^{o}C. The optimized MnAl film will be greatly useful to realize the high-density STT-MRAM. This work was part of a research and development project for ICT key technology to realize future societies.

[1] J. C. Slonczewski, J. Magn. Magn.Mater.159, L1 (1996) [2] A. Sakuma, J. Phys. Soc. Jpn., 63, 1422 (1994). [3] J. H. Park*et al.*, J. Appl. Phys., 107, 09A731 (2010). [4] M.Oogane and K. Watanabe *et al.*, Jpn. J. App. Phys., 56, 0802A2(2017)

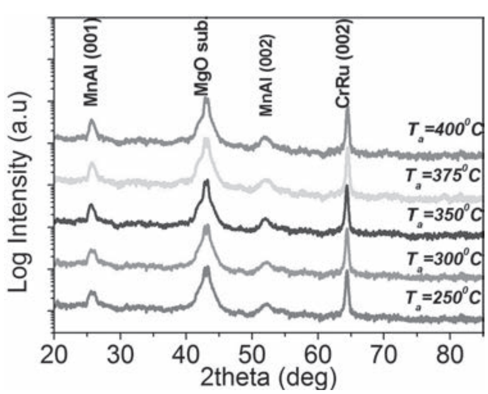

Fig. 1. XRD patterns for MnAl(50nm) films on T_s = 250^{0}C and various T_a

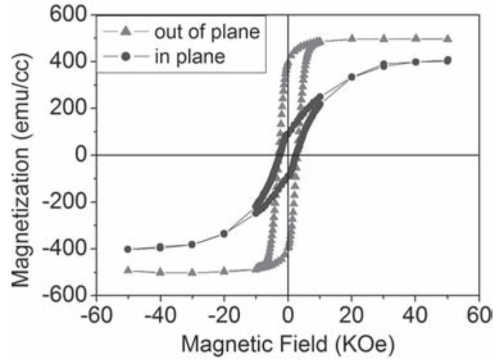

Fig. 2. The *M-H* curve for MnAl(50nm) films on T_s = 250^{0}C and T_a =350^{0}C

AR-04. Hybrid memory layer with low Curie temperature CoPd/Pd multilayer for high-density magnetic random access memory cells.

W. Zhao[1], T. Kimura[1], T. Kato[1], D. Oshima[3], Y. Sonobe[2], Y. Kawato[2] and S. Iwata[3]
1. Department of Electronics, Nagoya University, Nagoya, Japan; 2. Samsung R&D Institute Japan, Yokohama, Japan; 3. Institute of Materials and Systems for Sustainability, Nagoya University, Nagoya, Japan

Introduction Spin transfer torque (STT) switching is considered as a promising writing scheme to realize a Gbit-class magnetic random access memory (MRAM). To create a high density MRAM with more than 10 Gbit capacity, further improvements of the memory cells with high thermal stability Δ and low switching current density J_{sw} are required. We have designed bi-multilayers (MLs) stack with high Curie temperature (T_C) Co/Pd and low T_C CoPd/Pd MLs for the memory layer to achieve efficient spin transfer torque (STT) switching [1, 2]. Previously, we have reported that the switching of only the high T_C Co/Pd MLs at 170°C promoted the full switching of bi-MLs hybrid stack due to the exchange coupling between high and low T_C MLs [1]. In this work, we fabricated a tri-MLs hybrid stack with Co/Pd, CoPd/Pd, and Co/Pt MLs, since the tri-MLs stack is calculated to be more efficient than bi-MLs stack, and we report temperature dependence of the hysteresis of the tri-MLs and STT switching of the memory layer with low T_C CoPd/Pd. Experimental method The tri-MLs hybrid stacks were fabricated by magnetron sputtering on thermally oxidized silicon substrates. The stack is substrate / Ta (10 nm) / Pt (5nm) / [Pt (1.2 nm) / Co (0.4 nm)]$_6$ ML / [Pd (1.2 nm) / $Co_{48}Pd_{52}$ (0.3 nm)]$_3$ ML / [Pd (1.2 nm) / Co (0.4 nm)]$_3$ ML / SiN (5 nm). The intermediate Pd/CoPd ML exhibits low T_C of ~ 130°C, and we also fabricated the sample replacing the low T_C Pd/CoPd by Pd (4.5 nm) as a control sample. We refer to the former stack as stack A and the latter stack B. Hysteresis loops were checked by magneto-optical Kerr spectrum measurement system at various sample temperatures. Experimental result Figure 1 (a) shows hysteresis loop of stack A at room temperature. The loop exhibits square shape indicating that the magnetizations of tri-MLs switch simultaneously due to the exchange coupling through intermediate CoPd/Pd MLs. On the other hand, at 172°C, the loop exhibited two-step feature suggesting the Co/Pd and Co/Pt MLs switch independently as shown in Fig. 1 (b). The H_c of Co/Pd and Co/Pt MLs were estimated to be 0.42 kOe and 1.8 kOe, respectively. The H_c of the two MLs were similar to those of sample B with intermediate Pt 4.5 nm layer (not shown in the figure). Figure 2 shows temperature dependence of Kerr rotation and coercivities of the two MLs in the stack A estimated from the hysteresis shown in Fig. 1 (a) and (b). The Kerr rotation gradually decreased with increasing the temperature. The single step hysteresis, indicating the two MLs switch simultaneously, was observed up to 120°C, and then the two-step feature with different H_c of Co/Pd and Co/Pt MLs was obvious above 130°C, which is consistent with T_C of the intermediate CoPd/Pd ML. The H_c of Co/Pd (Co/Pt) ML decreased (increased) with increasing the temperature, which may indicate the gradual decrease of the exchange coupling through the CoPd/Pd ML by elevating the temperature. In the presentation, STT switching of the bi-MLs stack with CoPd/Pd and Co/Pd MLs is also discussed.

[1] X. Dong et al., Annual Conference on Magnetism and Magnetic Materials 2016, FT-03 (2016). [2] K. Machida et al., IEEE Trans. Magn., 53, 2002205 (2017).

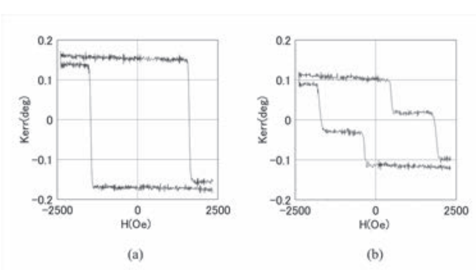

Fig. 1. (a) Kerr hysteresis loops of stack A, [Pt/Co] / [Pd/CoPd] / [Pd/Co], measured at (a) 25.8°C and (b) 172.3°C. Kerr hysteresis was measured at the wavelength of 400 nm.

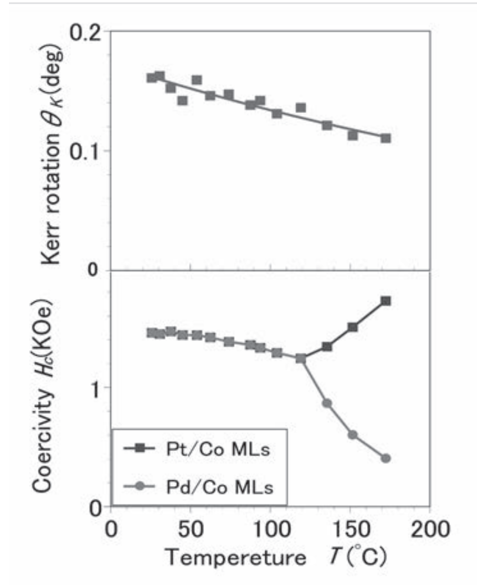

Fig. 2. Temperature dependences of Kerr rotation and coercivities of Pt/Co and Pd/Co MLs in the stack A.

AR-05. Magnetic Properties of Mn-based Heusler alloy films with Ru doping.

L. Ren[1], Y. Zheng[1], Y. Liu[1] and K. Teo[1]
1. Department of Electrical & Computer Engineering, National University of Singapore, Singapore

Recently Mn-based Heusler alloys have attracted considerable attention for the potential spintronic applications due to their high spin polarization, low damping constant, high magnetic anisotropy, and low magnetization [1-3]. Especially the tetragonal Mn-based Heusler alloys like Mn_3Ga, Mn_3Ge, Mn_2RhSn have been found to be possible candidates for spin transfer-torque applications [4, 5]. It is noted that most of the previous investigations are focused on Mn-based heusler alloys composed of 3*d* transition metal elements like Cu, Co, Fe, and Ni. But there are few reports about Mn-based Heusler alloys composed of 4*d* and 5*d* elements [6]. Here we report a series of Mn-based Heusler alloy films with Ru doping grown on MgO substrate with Cr buffer layer using co-sputtering method from Ru and a series of Mn_xGe (x = 2, 2.2, 2.4, 2.5) targets. All the films were deposited at room temperature and then *in-situ* annealed at 700 *K* for 1h. Finally, a 2 nm Ta cap layer was deposited at room temperature in order to prevent oxidation. X-ray diffraction measurements were carried out using *Singapore Synchrotron Light Source* (*SSLS*). The results indicate that all the films with the thickness of 35 nm exhibit ordered $L2_1$ structure and that the epitaxial relationship is $Mn_{3-x}Ru_xGe$ [110]//Cr [110]//MgO [100]. The magnetizations of the films were measured at room temperature using VSM in a magnetic field of up to ±2 T along [100], [110], and [001] directions of the film. The measurement results of the 35 nm $Mn_{2.2}Ru_{0.8}Ge$ film are shown in Fig. 1, which indicates that the direction perpendicular to the film is a magnetic hard axis. Moreover, the magnetization shows very sharp switching at 25 Oe with applied filed along [110] direction of the film, and the residual magnetization almost equals the saturation magnetization value 135 emu/cc. Besides, the magnetization along [100] direction is a hard magnetic axis compared to the [110] direction one. For further comparison, we selected the easy axis *M-H* loop measurements of all the films with different Ru concentration as shown in Fig.2. The results indicate that both residual magnetization (M_r) and saturation magnetization (M_S) increase with Ru concentration increasing, while the coercivity (H_C) becomes smaller. Considering of the different valence electrons number (N_v) between Ru (N_v=8) and Mn (N_v=7), the fact that the Ru substitution of Mn can alternate the total magnetic moment and ferrimagnetic magnetic structures of the $Mn_{3-x}Ru_xGe$ Heusler alloys. Our attempts provide alternative candidates for the Heusler alloys-based spintronic applications.

Reference [1] L Wollmann, A K Nayak, S S P Parkin, and C Felser, *Annual Review of Materials Research* 47 1-28 (2017) [2] V Alijani, J Winterlik, GH Fecher, and C Felser, *Appl. Phys. Lett.* 99, 222510 (2011) [3] J Winterlik, S Chadov, A Gupta, V Aligani, Y Gasi, K Filsinger, B Balke, G H Fecher, C A Jenkins, F Casper, J Kubler, GD Liu, L Gao, S S P Parkin, C Felser, *Adv. Mater.* 24, 6283-6287 (2012) [4] B Balke, GH Fecher, J Winterlik, C Felser, *Appl. Phys. Lett.* 90, 152504 (2007) [5] J Jeong, Y Ferrante, S V Faleev, M G Samant, C Felser, S S P Parkin, *Nat. Commun.* 7, 10276 (2016) [6] H Kurt, P Stamenov, M Venkatesan, Y C Lau, E Fonda, J M Coey, *Phys. Rev. Lett.*, 112, 027201 (2014)

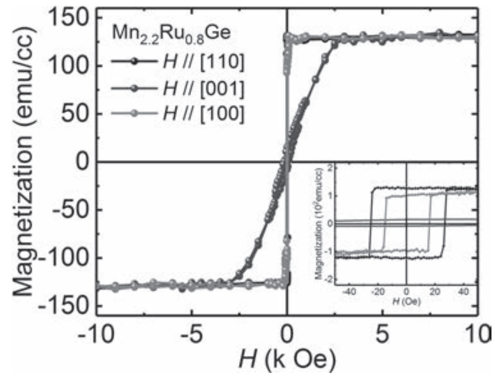

Fig. 1. Magnetization dependence on the applied magnetic field at room temperature with *H* along [100], [110], and [001] directions of the $Mn_{2.2}Ru_{0.8}Ge$ film. The inset shows the *M-H* loops in the range of -50 Oe to 50 Oe.

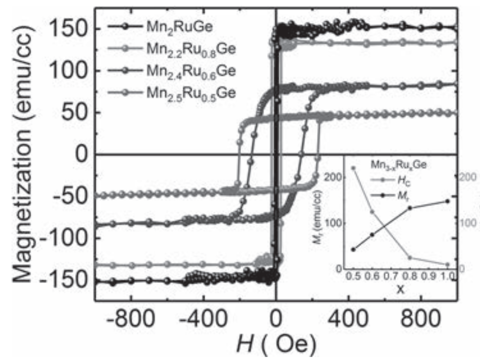

Fig. 2. *M-H* loops of the $Mn_{3-x}Ru_xGe$ films (35 nm) measured at room temperature with *H* along [110] direction (easy magnetic axis) of the films. The inset shows the coercivity H_C (red ball, right axis) and residual magnetization M_r (black ball, left axis) dependence of the Ru doping concentration (x).

AR-06. Reducing the switching current with a Dzyaloshinskii-Moriya interaction in nanomagnets with perpendicular anisotropy.

S. Takamatsu[1], K. Yamada[2] and Y. Nakatani[1]
1. University of Electro-Communications, Chofu, Japan; 2. Gifu University, Gifu, Japan

Reducing the switching current keeping the thermal stability in nanomagnets with perpendicular anisotropy are key factors in the development of STT-MRAM, which is expected to be a next generation nonvolatile memory[1][2]. In this paper, we investigated the effect of the Dzyaroshinskii-Moriya interaction (DMI) on the switching current and the thermal stability in nanomagnets[3][4]. It is expected that the magnetization structure and the swiching mechanism of nanomagnets will be changed by DMI, therefore not only the swiching current but also the thermal stability will be changed. We investigated the conditions to reduce the switching current keeping the thermal stability by DMI using micromagnetic simulations. In the simulation, a circular disk with 30 nm of the diameter and 2 nm of the thickness was used as the recording layer of STT-MRAM. The disk was discretized by 1.875×1.875 ×2 nm^3 of the calculation cells. The material parameters used in the simulation were a saturation magnetization M_s = 600 emu/cm^3, a gyromagnetic ratio γ = 17.6 Mrad/s/Oe, an exchange stiffness constant A = 1.0 μerg/cm, the Gilbert damping constant α = 0.1~0.001, and the DMI constant D = 0.0~1.0 erg/cm^2 [5]. The thermal stability factor (Δ) changes by the perpendicular anisotropy constant (K_u) and the DMI. We investigated the condition to keep the thermal stability factor of Δ = 60 [6] by simulations (Fig. 1). The pulse width (t_p) of the spin current was varied for 0.1~10 ns. Figures 2 (a) - (c) show the effect of the Gilbert damping constant, pulse width, and DMI on the switching current density. The switching current decreased with increasing DMI for t_p =0.1,1,10 ns and α=0.001 (Fig.2(a)), t_p =0.1,1 ns and α=0.01 (Fig.2(b)), and t_p = 0.1 ns and α = 0.1 (Fig. 2 (c)). The switching current was decreased 60% in maximum. In the short pulse case (t_p = 0.1 ns), the reduction rate of the switching current does not change by the Gilbert damping constant. However in a long pulse, the switching current increasese as the Gilbert damping constant is increased (Figs. 2 (b), (c)). The results are explained as follows. In the previous study, an empirical equation of the switching current was derived (Eq. 1) [6]; $I_{sw} = 2eM_sV / \mu_B gP\ (\alpha\gamma 2K_u / M_s + C_1 / t_p)$ (1) where, $C_1 = [\ln\{(1-\cos\theta_{crit}) / (1+\cos\theta_{crit})\} - \ln\{(1-\cos\theta_{init}) / (1+\cos\theta_{init})\}]/2$, θ_{init} is the initial magnetization angle with respect to the easy magnetization axis, and θ_{crit} is the critical angle ($\theta_{crit} = \pi - \theta_{init}$). Therefore, C_1 changes by θ_{init}. The right side of Eq. 1 has two terms. In order to keep the thermal stability as described above, it is necessary to increase K_u, therefore the first term increases as D is increased. However, the initial magnetization angle (θ_{init}) increases with increasing D, and then C_1 is decreased, therefore, the second term decreases. The first term is small when α = 0.001, the switching current is determined mainly by the second term, therefore, the switching current decreases as DMI is increased (Fig. 2(a)). On the other hand, when α is large and t_p is long, the second term decreases, therefore, the switching current increases as DMI is increased (Figs. 2 (b), (c)).

[1] M. Hosomi *et al.*, International Electron Devices Meeting (IEDM), 2005, pp. 459-462. [2] E. Chen *et al.*, IEEE Transactions on Magnetic, 46, no. 6, pp. 1873-1878 (2010). [3] T. Moriya, Phys. Rev. 120, 91 (1960). [4] I. E. Dzialoshinskii, Sov. Phys. 5, 1259 (1957). [5] S.Rohart and A.Thiaville, Phys. Rev. B, 88, 184422 (2013). [6] K.Yamada *et al.*, Appl. Phys. Lett. 106, 042402 (2015).

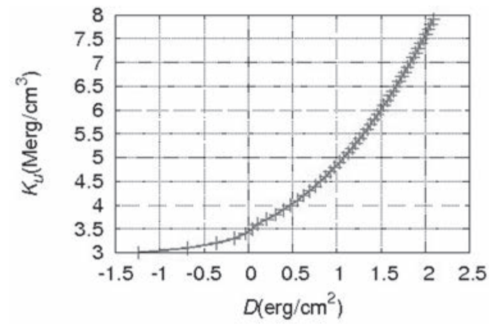

Fig. 1. Relation of the DMI and the anisotropy constant K_u to keep the thermal stability factor Δ = 60.

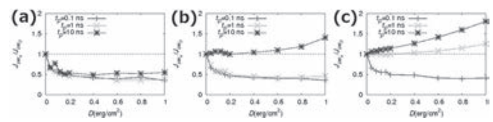

Fig. 2. Changes of the switching current by the Gilbert damping constant, DMI, and the pulse width. The vertical axis shows the switching current normalized by the switching current at D = 0 (J_{swx} / J_{sw0}). (a) α=0.001 (b) α=0.01 (c) α=0.1

AR-07. Effect of the damping constant on switching time distribution in the magnetic tunnel junction.

J. Moon[1], T. Lee[2] and C. You[3]
1. Department of Materials Science and Engineering, Korea University, Seoul, The Republic of Korea; 2. New Memory Device and Process Integration Group, SK hynix, Icheon, The Republic of Korea; 3. Department of Emerging Materials Science, Daegu Gyeongbuk Institute of Science and Technology, Daegu, The Republic of Korea

Magnetization dynamics are strongly influenced by damping process, which describes energy dissipation of magnetization. For spin-transfer torque magnetic random-access memory (STT-MRAM), it is very crucial to know an exact value of the damping constant because the critical current density of STT-MRAM is proportional to the damping constant. In the determination of the damping constant, a ferromagnetic resonance (FMR) spectroscopy which provides information on the magnetic damping through study of the linewidth of the microwave absorption peak (full-width half-maximum, FWHM) is widely used [1,2]. However, FMR technique requires un-patterned ferromagnetic thin films, so that FMR technique is hard to apply to the nano-sized patterned MTJ cell, which is practically important. In this paper, we report the effect of the damping constant on the FWHM of switching time distribution in case of nano-size patterned MTJ by solving Fokker-Planck equation (FPE). Proposed method relies on the recent experiments of the time evolution of the device conductance change in sub-ns STT switching event in perpendicular MTJ [3]. One derived a FPE for the probability distribution of the angle as a function of time in case of MTJ [4]. With a limit of the large energy barrier where the thermal stability factor is larger than 60, the approximated analytic expression of FWHM of switching distribution, δ, in reduced time scale (reduced by $\alpha\gamma H_k/(1+a^2)$) can be obtained as below $\delta=\{W(0,-1/2e)-W(-1,-1/2e)\}/2v$, ... (eq. 1) where W(k,x) is the kth branch of the Lambert W-function and $v = H_{app}/H_k -1$, and H_{app} is the applied field and H_k is effective anisotropy field. Figure shows the difference between the exact solution and approximated solution assuming a larger energy barrier (eq.(1)). The difference between exact and approximated solution is quite large (~5% with low current v=0.5) in case of small thermal stability factor. However, in case of a high thermal stability factor larger than 60, the difference becomes smaller than 1% at v=0.5. It shows that the approximated equation is valid when assuming a high thermal stability factor (Δ>60 is easily achieved in STT-MRAM). To conclude, we find that δ is a function of damping constant and derive its approximated solution in the limit of high energy barrier. This analytic solution shows a good agreement with full numerical results. Practically, the thermal stability factor required for MRAM cell is higher than 60 so that the reliable value of damping constant can be extracted by measuring δ and analyzing it with the proposed approximated solution. We believe our work is helpful to estimate the damping constant in the device level.

[1] R. Urban *et al.*, Phys. Rev. Lett. 87, 217204 (2001). [2] B. Heinrich *et al.*, Phys. Rev. Lett. 90, 187601 (2003). [3] T. Devolder *et al.*, Phys. Rev. B 93, 224432 (2016). [4] W. H. Butler *et al.*, IEEE Trans. Magn., 48, pp 4684-4700 (2012).

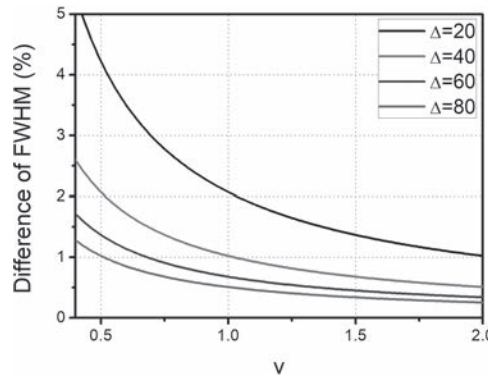

Fig. 1. Difference of full-width half-maximum (FWHM) between exact solution and approximated solution (eq.(1)) as a function of v with varying thermal stability factor. With the limit of high-energy barrier, the error between exact solution and approximated solution becomes smaller.

AR-08. Proposal of an ultra-fast all spin logic device based on RE-TM ferrimagnetic material.

Z. Zheng[1,2], Y. Zhang[1,2], Z. Zhang[1,2], J. Nan[1,2], K. Zhang[1,2], J. Klein[3], D. Ravelosona[3], Y. Zhang[1,2] and W. Zhao[1,2]
1. Fert Beijing Institute, Beihang University, Beijing, China; 2. School of Electrical and Information Engineering, Beihang University, Beijing, China; 3. Center for Nanoscience and Nanotechnology, University of Paris-Sud, Orsay, France

Power consumption of logic operations has become the key bottleneck hindering the miniaturization of ICs. All Spin Logic Device (ASLD) using pure spin current, instead of charge current, is considered as a promising candidate for building future ultra-low power computing systems [1]. A typical ASLD based on ferromagnetic (FM) material is illustrated in figure 1a. Applying a voltage to the FM injector, a spin accumulation can be generated in non-magnetic (NM) channel. This spin accumulation can propagate spin angular momentum by spin diffusion, and switch the FM detector via Spin Transfer Torque (STT) effect [1,2]. Exclusive of lower power consumption, higher computing speed is another significant requirement for future logic device [1,3]. Recently, researchers have observed ultra-fast magnetic dynamics in ferrimagnetic (FI) alloys composed by rare-earth (RE) metal and transition metal (TM) [4-6]. Different from FM materials, the magnetic properties of RE-TM alloys in figure 1b are controlled conjointly by RE and TM sublattices [4]. Considering the different magnetizations and gyromagnetic ratios, the value of total angular momentum for RE-TM alloy can be calculated as the difference between angular momenta of RE element and TM element. In fact, this angular momentum can be controlled by adjusting the concentration of RE metal [4] or the temperature[5-6]. When the total angular momentum tends to vanish, FI alloys will arrive at an angular momentum compensated point (AMCP), where antiferromagnetic-like properties appear [4]. It has been demonstrated that laser or Spin Orbit Torque (SOT) effect assisted by external magnetic field can activate this mechanism [4-5,7]. However, neither of these activating methods suits ASLD, since laser and external magnetic field will largely increase the power consumption and harm the integrability. We hence propose an alternative ASLD structure based on RE-TM FI material to realize ultra-fast speed. $Co_{1-x}Tb_x$ FI alloy is used to replace the FM layer in the proposed ASLD (figure 1b). Moreover, spin torque induced by SOT effect is applied to FI layer, driving the magnetization of $Co_{1-x}Tb_x$ to precess at an extremely high frequency [5]. Here we apply a reasonable condition x = 0.165, which is close to the value for experimentally proved AMCP, to implement the following analyses. As shown in figure 2a, the lowest energy state for precession under the sole impact of SOT is a circle in x-z plane, indicating that the precession caused by SOT effect doesn't have a certain destination. In this occasion, magnetization switching in FI alloys is inaccessible. To break the precession balance, we introduce a spin current propagated from the injector which can exert STT effect on FI detector. Under the co-effect of these two external forces, the distribution of energy states changes, and the magnetization of FI detector can stabilize at the unique lowest energy state point shown in figure 2b. In order to describe the magnetic dynamics of FI layer, we use the typical Landau-Lifshitz-Gilbert (LLG) equation which contains effective magnetic field term, damping term, SOT term and STT term [8-9]. Figure 2c shows the switching process of $Co_{0.835}Tb_{0.165}$ layer. SOT current drives the initial magnetization to precess, while STT current prefers to stabilize the magnetization at the lowest energy state. Also, magnetizations for Co and Tb sublattices stay opposite during the switching. This process takes 2.4 ps, about 2 orders lower than the FM detector (0.2ns shown in figure 2d), which means a much quicker computing speed. Our work contributes to improve the performance of ASLD, and it is also a further step to explore the application of ferrimagnetic material in future potential spintronics devices.

[1] B. Behin-Aein, D. Datta, S, Salahuddin, et al, Proposal for an all-spin logic device with built-in memory, *Nature nanotechnology*, vol. 5, no. 4, pp. 266-270 (2010). [2] S. Manipatruni, D. E. Nikonov, I. A. Young, Material targets for scaling all-spin logic, *Physical Review Applied*, vol. 5, no. 1, pp. 014002 (2016). [3] J. Kim, A. Paul, P. A. Crowell, et al, Spin-based computing: Device concepts, current status, and a case study on a high-performance microprocessor, *Proceedings of the IEEE*, vol. 103, no. 1, pp. 106-130 (2015). [4] K. Ueda, M. Mann, P. W. P. de Brouwer, et al, Temperature dependence of spin-orbit torques across the magnetic compensation point in a ferrimagnetic TbCo alloy film, *Physical Review B*, vol. 96, no.6, pp. 064410 (2017). [5] J. Finley, L. Liu, Spin-orbit-torque efficiency in compensated ferrimagnetic cobalt-terbium alloys, *Physical Review Applied*, vol. 6, no. 5, pp. 054001 (2010). [6] K. J. Kim, S. K. Kim, Y. Hirata, et al, Fast domain wall motion in the vicinity of the angular momentum compensation temperature of ferrimagnets, *Nature materials*, vol. 16, no. 12, pp. 1187 (2017). [7] A. Kirilyuk, A. V. Kimel, T. Rasing, Laser-induced magnetization dynamics and reversal in ferrimagnetic alloys, *Reports on progress in physics*, vol. 76, no. 2, pp. 026501 (2017). [8] C. E. Graves, A. H. Reid, T. Wang, et al, Nanoscale spin reversal by non-local angular momentum transfer following ultrafast laser excitation in ferrimagnetic GdFeCo, *Nature materials*, vol. 12, no. 4, pp. 293-298 (2013). [9] R. F. L. Evans, T. A. Ostler, R. W. Chantrell, et al, Ultrafast thermally induced magnetic switching in synthetic ferrimagnets, *Applied Physics Letters*, vol. 104, no. 8, pp. 082410 (2014).

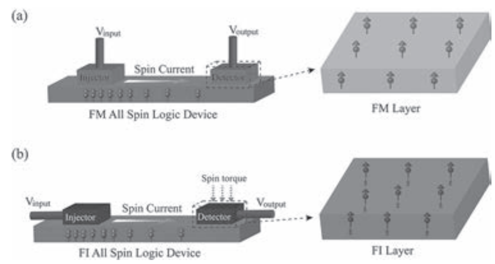

Fig. 1. (a) Schematic of a typical ASLD based on FM material. In FM material, angular momenta of all the lattices align one certain direction. (b) Schematic of the proposed ASLD based on FI material. In FI material, angular momenta of Co and Tb sublattices always stay opposite.

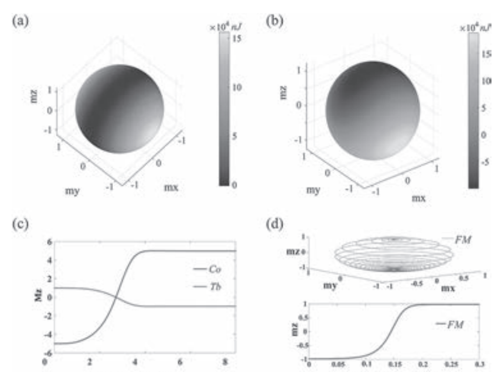

Fig. 2. (a) Distribution of energy states for CoTb under the sole impact of SOT. The lowest energy state is a circle in x-z plane. (b) Distribution of energy states for CoTb under the co-effect of SOT and STT. The lowest energy state is a certain point. (c) Switching process for $Co_{0.835}Tb_{0.165}$ layer in proposed ASLD. (d) Switching process for FM layer in traditional ASLD.

AR-09. Evaluation of ultrahigh-speed magnetic memories using field-free spin orbit torque.

Z. Wang[1], L. Chang[1], X. Lin[1], J. Yang[1], Y. Zhang[1] and W. Zhao[1]
1. Beihang University, Beijing, China

Spin orbit torque (SOT) is a promising technology of magnetization switching thanks to the high-speed, low power and separate read/write paths [1-2]. In particular, sub-nanosecond switching delay qualifies the SOT device as a candidate for the non-volatile cache memory. Generally, such an ultrafast switching is achieved by enhancing the initial spin torque in specific device geometries (e.g. a perpendicular magnetization with an in-plane-polarized spin current). However, in most cases an additional magnetic field is required to achieve the deterministic switching by breaking the structure symmetry. The use of magnetic field hinders the application of the SOT in non-volatile memories. Therefore recently field-free SOT mechanisms have been proposed based on various technologies such as the wedge-shaped asymmetric structure [3], tilted anisotropy [4], spin-Hall-assisted spin transfer torque (SHA-STT) [5-6], and antiferromagnet/ferromagnet exchange bias [7-8]. Nevertheless, some of them employ the special fabrication processes or device structures, which are difficult to be applied to the design and evaluation of the non-volatile memories or circuits. In this work, we focus on two emerging mechanisms of field-free SOT switching, which use the general device structure and thus show good compatibility with the existing non-volatile designs [9-10]. The first mechanism is shown in Fig. 1(a)-(b), where an in-plane magnetic tunnel junction (MTJ) is deposited above a heavy-metal with a cant angle between the easy-axis and charge current. The breaking of structure symmetry enables bipolar deterministic switching. The second one occurs in the conventional three-terminal SOT-MTJ with a perpendicular easy-axis, where it is demonstrated that an appropriate field-like torque can induce the deterministic switching. But this switching is non-bipolar and thus a read operation is needed before the data writing. Here, we evaluate the performance of above two switching schemes in the field of magnetic memories to show their application potential. First, we program two Verilog-A models of the three-terminal SOT-MTJs switched by the above-mentioned schemes. Combined with a CMOS 28 nm design kit, a magnetic random access memory based on two-transistor-one-MTJ bit-cell is designed (see Fig. 1(a)). Transient simulation is performed to validate the feasibility of our models (see Fig. 1(c) for the simulation results of the first switching mechanism). Then, the results of access transistor size and the write energy under a switching time of 500 ps are shown in Fig. 2, where the thermal stability barrier is fixed by adjusting the anisotropy constant at various MTJ sizes. For the first switching mechanism, the performance is strongly dependent on the cant angle of the easy-axis. Clearly an optimal cant angle is found around 45°. In the case of smaller cant angle, the performance degradation is attributed to the competition among SOT, anisotropy field and damping torque. For a cant angle larger than 45°, the easy-axis is close to the polarization direction of the spin injection and thus the incubation delay becomes dominant. Until the cant angle is up to 90°, the spin torque reduces to the conventional STT so that a huge access transistor is needed to provide the adequate current for the ultrafast switching. Finally, the results of the second switching mechanism show insignificant variation and more excellent performance than the first switching mechanism, partly due to the high efficiency of field-like torque-induced magnetization precession. Another reason is that, as the switching is non-bipolar, a unidirectional current can achieve the switching and thus the source degeneration of the access transistor is avoided. Nevertheless, the non-bipolar switching requires a read-before-write operation and leads to a circuit overhead. Therefore a trade-off needs to be taken into account for the performance comparison of these two switching mechanisms.

[1] L. Liu et al. Science, 336,555 (2012). [2] I. M. Miron et al. Nature, 476, 189 (2011). [3] G. Yu et al. Nature Nanotechnol. 9, 548 (2014). [4] L. You et al. PNAS, 112 (33), 10310 (2015). [5] A. Van den Brink et al. Appl. Phys. Lett. 104 (1), 012403 (2014). [6] Z. Wang et al. J Phys. D : Appl. Phys. 48 (6), 065001 (2015). [7] S. Fukami et al. Nature Mater. 15, 535 (2016). [8] Y. W. Oh et al. Nature Nanotechnol. 11, 878 (2016). [9] S. Fukami et al. Nature Nanotechnol. 11, 621 (2016). [10] W. Legrand et al. Phys. Rev. Appl. 3, 064012 (2015).

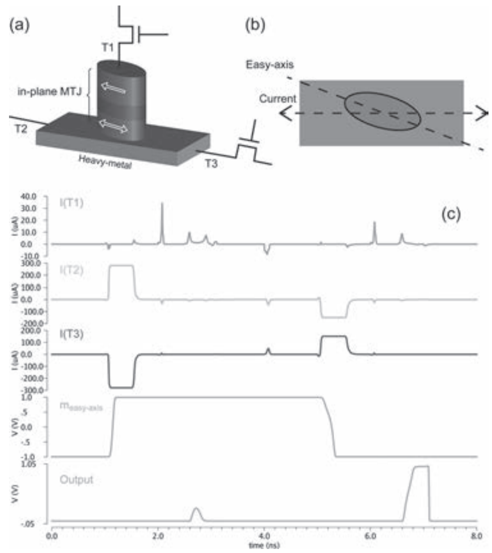

Fig. 1. (a) Two-transistor-one-MTJ (2T1J) bit-cell for the design of SOT-based magnetic memory. (b) Top view of the three-terminal SOT-MTJ based on the first switching mechanism, where the canted easy-axis can be seen. (c) Transient simulation results of the magnetic memory constructed with the above-mentioned 2T1J bit-cell.

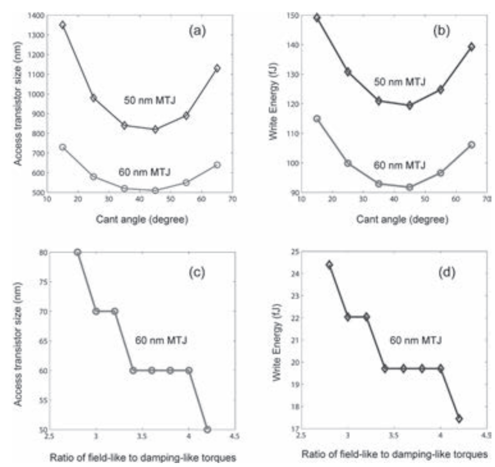

Fig. 2. Performance results of the first (a)-(b) and second (c)-(d) switching mechanisms. In (a) and (b), the width of the heavy-metal is equal to the length of the MTJ long-axis to ensure the sufficient range of the cant angle. The same aspect ratio is used for both the heavy-metal and MTJ.

AR-10. Observation of local spin signals at room temperature in germanium lateral devices.

M. Tsukahara[1], M. Yamada[1], T. Naito[1], Y. Fujita[1], S. Yamada[1,2], K. Sawano[3] and K. Hamaya[1,2]
1. Graduate School of Engineering Science, Osaka University, Toyonaka, Japan; 2. Center for Spintronics Research Network, Osaka University, Toyonaka, Japan; 3. Advanced Research Laboratories, Tokyo City University, Todoroki, Japan

For realizing CMOS-compatible spintronic devices, electrical spin injection and detection in Si[1] and Ge[2] have been explored. In particular, Ge is expected to be a next-generation channel material for CMOS transistors because the electron and hole mobility are twice and four times as large as those in Si. As evidence for spin transport in semiconductors, four-terminal nonlocal magnetoresistance measurements with Hanle-effect curves have been utilized [3-5]. Recently, we reported evident room-temperature spin transport in *n*-type Ge (*n*-Ge) by using four-terminal nonlocal magnetoresistance measurements [6], meaning the demonstration of pure spin current transport. For Ge-based device structures with nonvolatile memory effect [7], the observation of two-terminal local magnetoresistance effect is also important. However, there is no report on the local spin signals at room temperature in *n*-Ge. In this study, we show evident two-terminal local spin signals at room temperature in lateral spin valves (LSVs) with *n*-Ge spin transport channel. Using LSVs with low resistance-area product (*RA*) ferromagnetic Heusler-alloy/Ge Schottky-tunnel contacts, we can detect hysteretic resistance changes depending on the magnetization states between the spin injector and detector. The condition for observing the local spin signals in our LSVs is within a framework of the theory by A. Fert and H. Jaffrès [8]. We fabricated LSVs [Fig. 1(a)] with the *n*-Ge spin transport channel (~ 10^{19} cm^{-3}) and the ferromagnetic Heusler-alloy contacts, Co_2FeAl (CFA). The detailed fabrication processes of LSVs and the growth procedure of the spin transport channels and CFA/*n*-Ge contacts are shown elsewhere [6,9]. To adjust the *RA* values to 100 - 300 Ωμm^2 in the spin-injector and spin-detector contacts, we tuned the concentration of the δ-doped P atoms [10] near the CFA/*n*-Ge interface. The sizes of the spin injector and detector were 0.4 × 5.0 μm^2 and 1.0 × 5.0 μm^2, respectively, and the edge-to-edge distance (*d*) between the contacts was ~0.35 μm, as shown in Fig. 1(a). To confirm reliable spin transport in *n*-Ge, we firstly measured four-terminal nonlocal magnetoresistance, ΔR_{NL} (= ΔV_{NL} / *I*), and its Hanle-effect curves at 150 K, as shown in Figs. 1(b) and 1(c), respectively. These nonlocal signals represent the generation, manipulation, and detection of pure spin currents in *n*-Ge. Using the same device, we recorded a two-terminal local spin signal at 150 K, as displayed in Fig. 2(a). Evident positive ΔR_L (= ΔV_L / *I*) changes ($|\Delta R_L|$) at 150 K with hysteretic nature can also be observed. The value of $|\Delta R_L|$ is nearly twice as large as that of $|\Delta R_{NL}|$ at 150 K, consistent with the one-dimensional spin diffusion model [11,12]. These features are largely different from the previous works on Si-based LSVs with MgO tunnel-barrier contacts [13,14]. Figure 2(b) shows a local spin signal measured at room temperature, together with a minor-loop data, in the same LSV. Even at room temperature, a clear hysteretic magnetoresistance curve and a clear minor-loop meaning that the anti-parallel magnetization state between two ferromagnetic contacts is stable can be seen. By comparing $|\Delta R_{NL}|$ with $|\Delta R_L|$ at room temperature, we can also confirm $|\Delta R_L|/|\Delta R_{NL}|$ ~ 2 [11,12]. This is the first experimental demonstration of the two-terminal local magnetoresistance at room temperature in *n*-Ge based devices. However, the ratio of the magnetoresistance (*MR*) is still small (~0.001 %). According to a standard theory based on the one-dimensional spin drift-diffusion model by A. Fert and H. Jaffrès [8], r_b^* ~r_N is an ideal condition for observing a larger *MR* ratio in ferromagnet/semiconductor/ferromagnet structures with tunnel barriers, where r_b^* indicates *RA* in this study and r_N is the spin resistance of the *n*-Ge layer (~8.4 Ωμm^2). Although it is generally difficult for MgO tunnel barriers to reduce the *RA* value down to less than ~ 1000 Ωμm^2 [13,14], we now obtain the *RA* value of ~100 Ωμm^2 by using δ-doping techniques, leading to r_b^*/ r_N ~10. This condition is within a framework of the theory by A. Fert and H. Jaffrès [8]. To further enhance the *MR* ratio, we should reduce the value of *RA* down to ~10 Ωμm^2 in CFA/*n*-Ge contacts. This study will open a way for developing Ge spintronic applications with low power consumption. This work was partly supported by Grant-in-Aid for Scientific Research (A) (No. 16H02333) and (S) (No. 17H06120) from the Japan Society for the Promotion of Science (JSPS), and a Grant-in-Aid for Scientific Research on Innovative Areas 'Nano Spin Conversion Science' (No. 26103003) from the Ministry of Education, Culture, Sports, Science and Technology (MEXT). M.Y. acknowledges Scholarships from Toyota Physical and Chemical Research Institute Foundation. Y.F. acknowledges JSPS Research Fellowships for Young Scientists.

[1] I. Appelbaum *et al*., Nature (London) 447, 295 (2007). [2] Y. Zhou *et al*., Phys. Rev. B 84, 125323 (2011). [3] M. Johnson and R. H. Silsbee, Phys. Rev. Lett. 55, 1790 (1985). [4] F. J. Jedema *et al*., Nature 416, 713 (2002). [5] X. Lou *et al*., Nat. Phys. 3, 197 (2007). [6] M. Yamada *et al*., Appl. Phys. Express 10, 093001 (2017). [7] M. Kawano *et al*., Phys. Rev. Mater. 1, 034604 (2017). [8] A. Fert and H. Jaffrès, Phys. Rev. B 64, 184420 (2001); A. Fert, *et al*., IEEE Trans. Electron Devices 54, 921 (2007). [9] Y. Fujita *et al*., Phys. Rev. Appl. 8, 014007 (2017). [10] M. Yamada *et al*., Mat. Sci. Semicon. Proc. 70, 83 (2017). [11] F. J. Jedema *et al*., Phys. Rev. B 67, 085319 (2003). [12] T. Kimura and Y. Otani, J. Phys. Condens. Matter. 19, 165216 (2007). [13] T. Sasaki *et al*., Appl. Phys. Lett. 98, 262503 (2011). [14] Y. Saito *et al*., J. Appl. Phys. 115, 17C514 (2014).

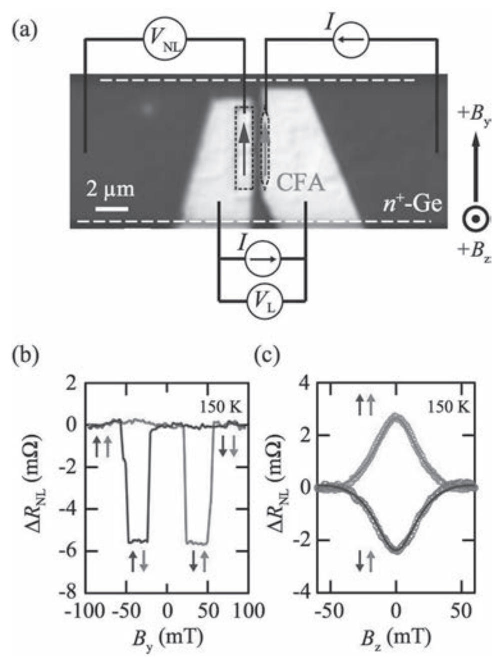

Fig. 1. (a) Optical micrograph of a lateral four-terminal and two-terminal spin-valve device with Co_2FeAl/*n*-Ge Schottky tunnel contacts. (b) Four-terminal nonlocal magnetoresistance curve, and, (c) nonlocal Hanle effect curves of the CFA/*n*-Ge LSV for the parallel and antiparallel magnetization configuration at 150 K at *I* = -1.0 mA.

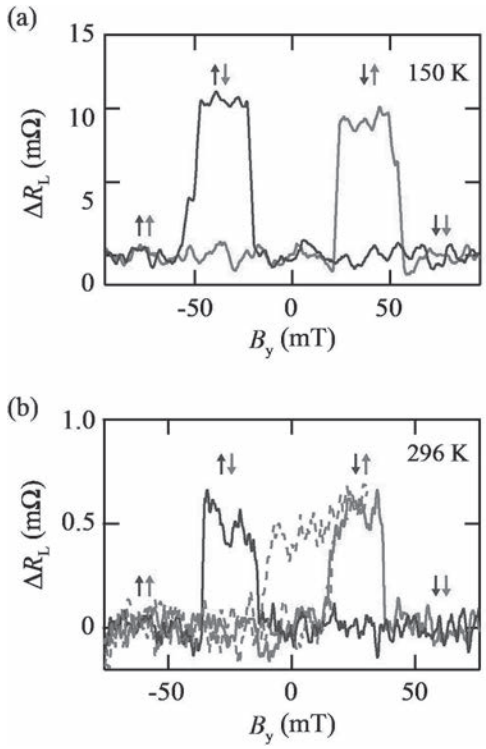

Fig. 2. (a), (b) Two-terminal local magnetoresistance at 150 K and 296 K, respectively. The gray dash curve in (b) is a minor-loop meaning that the anti-parallel magnetization state is stable.

AR-11. Proposal for Multi-gate Spin Field Effect Transistor (Spin-FET).

G. Wang[1], Z. Wang[2,3], J. Klein[1] and W. Zhao[3,2]

1. Centre de Nanosciences et de Nanotechnologies, Université Paris Saclay, Orsay, France; 2. Spintronics Interdisciplinary Center, Beihang University, Beijing, China; 3. Fert Beijing Institute, Beihang University, Beijing, China

Spin field effect transistor (spin-FET) is one of the fundamental spin-based devices which promises to replace the conventional CMOS device thanks to the advantage of ultra-low power consumption. The interesting scheme of spin-FET proposed by Datta and Das is using a gate voltage to control the spin modulation which can realize the switching and logical output [1]. Plenty of efforts on realizing the spin-FET have been done by a number of groups both theoretically and experimentally [2]-[5]. The basic mechanism of spin-FET is using two ferromagnetic (FM) electrodes for spin injection and detection, a gate voltage control for modulating the spin current flowing through the two-dimensional electron gas (2DEG) formed in the semiconductor channel. The injected spin current can be controlled by a Rashba effect-induced effective magnetic field. An applied gate voltage can generate an electric field to modulate the Rashba effect and therefore the spin current. Spin detection is realized by measuring the relative orientation between the spin polarization of the arriving electrons and the magnetization of the FM electrode at the drain. In this work, we proposed a new structure called multi-gate spin-FET, which uses two gates to control the spin current in one 2DEG channel. The structure is shown in Fig. 1 (a). Two gates are set serially on the channel in order that the injected spin current can be modulated by the two gates successively. The spin injection and detection can be modeled based on Datta-Das theory [1]. The dependence of the spin precession angle on the gate voltage is calculated as $\Delta\theta=2m^*\alpha(V_g)L/h^2$, where $\Delta\theta$ is the spin precession angle, m* is the effective mass, α (Vg) is the Rashba effect coefficient which is a function of the gate voltage Vg, L is the channel length and h is the reduced Planck constant. More details about the electrical models can be found in our previous work [6]. The expression of α (Vg) is strongly dependent on the material of the semiconductor channel. For a two-gate spin-FET, the spin precession angle can be calculated as $\Delta\theta=\Delta\theta_1+\Delta\theta_2=2m^*[\alpha(V_{g1})L_1+\alpha(V_{g2})L_2]/h^2$. Thus the final spin precession angle is decided by both gate voltage modulation and the channel length. Unlike the conventional CMOS transistors cascading, the multi-gate spin-FET can generate different outputs using the same input (gate voltage) but with different channel lengths. We set the gate voltage to 0 V as logic input “0” and 1.4 V as logic input “1”. Fig. 1 (b) shows the different outputs with different kinds of channel length settings. For a single channel, if we set the length to 86 nm, the output will be “0” (“1”) when the input is “1” (“0”) as shown in Figure 1 (b). Under this setting, the function of the spin-FET is the same as a P-type CMOS transistor. For the 82 nm channel, the output is “0” (“1”) when the input is “0” (“1”) which acts as an N-type CMOS transistor. Also, we can get a fixed output “1” regardless of the logic inputs. Fig. 1 (c) shows the output with the various combinations of inputs and channel lengths, here we fix the length of the first channel to 82 nm. The results of output voltage indicate that the multi-gate spin-FET can form a NAND logic gate when the second channel length is 82 nm. Also, an XNOR logic gate can be obtained if the second channel length is set to 78 nm. Furthermore, other different kinds of logic gates can be implemented with only one multi-gate spin-FET device by varying channel lengths. In these simulations, we fix the injection current to 1 mA and assume that the resistance between the drain and the source is 1.4 KΩ. The BiTeX (X=I, Br, and Cl) material is used for the semiconductor channel which experimentally shows a very large Rashba effect coefficient (α~3.8eÅ) [7]. Thus the period phase shift can be definitely obtained in a short channel. Following the above results, a plenty of logic circuits can be designed with the multi-gate spin FETs. In Figure 2 (a), a compact 2-bit full adder is designed using both multi-gate spin-FETs and single-gate spin-FETs. Two multi-gate spin-FETs are configured to XNOR logic gates and three multi-gate spin-FETs function as NAND logic gates. The single-gate spin-FETs are set to P-type CMOS function. The transient simulation results shown in Fig. 2 (b) validates the function of the 2-bit full adder. Only 7 semiconductor channels are used, which is much more compact than the conventional CMOS full adder. Thus the multi-gate spin-FETs provides an approach to achieving the area-efficient and low power logic computing.

[1] S. Datta and B. Das, “Electronic analog of the electro-optic modulator,” Appl. Phys. Lett., vol. 56, no. 7, pp. 665–667, 1990. [2] J. H. Kim, J. Bae, B.-C. Min, H. Kim, J. Chang, and H. C. Koo, “All-electric spin transistor using perpendicular spins,” J. Magn. Magn. Mater., vol. 403, pp. 77–80, Apr. 2016. [3] A. S. Sheremet, O. V Kibis, A. V Kavokin, and I. A. Shelykh, “Datta-and-Das spin transistor controlled by a high-frequency electromagnetic field,” vol. 165307, pp. 1–5, 2016. [4] T. Nie et al., “Enhancing electric-field control of ferromagnetism through nanoscale engineering of high-Tc MnxGe1−x nanomesh,” Nat. Commun., vol. 7, p. 12866, Oct. 2016. [5] L.-T. Chang et al., “Electrical detection of spin transport in Si two-dimensional electron gas systems,” Nanotechnology, vol. 27, no. 36, p. 365701, Sep. 2016. [6] G. Wang, Z. Wang, J. Klein, and W. Zhao, “Modeling for Spin-FET and Design of Spin-FET-Based Logic Gates,” IEEE Trans. Magn., vol. 53, no. 11, pp. 1–6, Nov. 2017. [7] T. Wang and H. Jeng, “Wide-range ideal 2D Rashba electron gas with large spin splitting in Bi2Se3/MoTe2 heterostructure,” npj Comput. Mater., vol. 3, no. 1, p. 5, Dec. 2017.

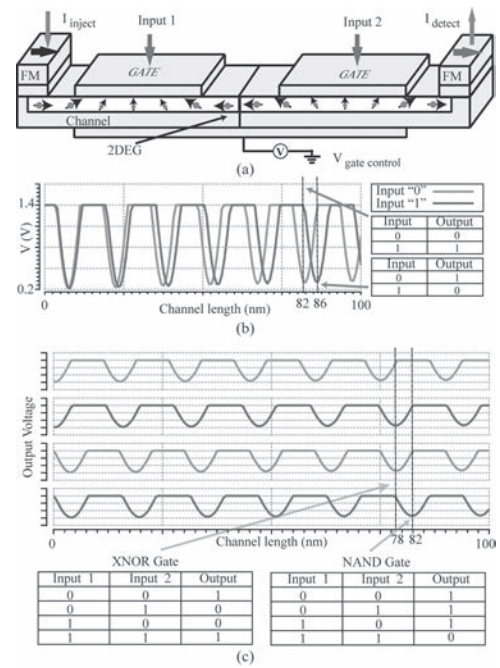

Fig. 1. (a) Schematic structure of multi-gate spin-FET. (b) By varying the lengths of the first channel, we can get different outputs at the end of the first channel. (c) Different kinds of logic gates can be implemented with only one multi-gate spin-FET device by changing channel lengths. An XNOR logic gate is obtained when the first and second channels are respectively set to 82 nm and 78 nm. When both the channels are set to 82 nm, we can get a NAND logic gate.

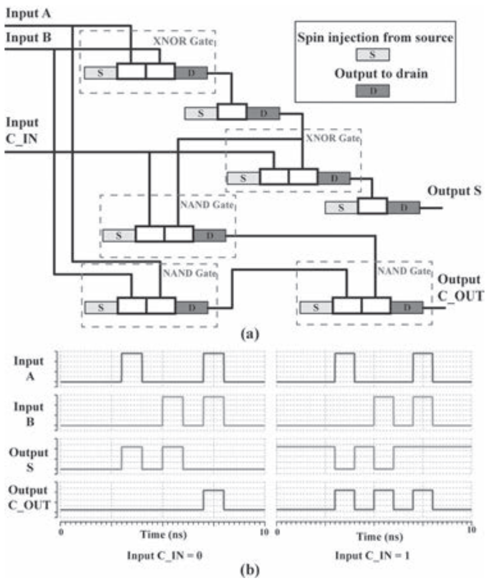

Fig. 2. (a) A 2-bit full adder constructed by multi-gate spin-FETs. (b) Transient simulation of the proposed full adder.

AR-12. Estimating the spin relaxation time of platinum by second harmonic electrical transport measurement.

C. Fang[1], *C. Wan*[1], A. Hoffmann[2], B. Tao[1], H. Wu[1] and X. Han[1]
1. State Key Lab of Magnetism, Institute of Physics, Beijing, China;
2. Materials Science Division, Argonne National Laboratory, Lemont, IL, United States

The application potential of spin-orbit-torques in magnetic random access memory attract great attention and research interest in spin-orbit coupling in heavy metals like Platinum. Thus the spin relaxation time, as a crucial parameter to investigate spin relaxation mechanism in the heavy metals, requires accurate and effective estimation. However, the traditional ways such as electron spin resonance (ESR) or time-resolved optical technique developed by Elezzabi *et al*. fail for thin films of heavy metals with short. So the spin injection and detection as a well-developed electrical transport method, is important candidate to estimate the. Although working reliably in Au or Cu, four-terminal non-local spin valves is not able to be adopted in the systems with ultrashort spin diffusion length. A traditional three-terminal method is also widely utilized to estimating of semiconductors and light metals. Its reliability, however, has recently been challenged by some experiments in which tunneling anisotropic magnetoresistance (MR) or spin blockage MR rather than the MR induced by spin injection and subsequent Hanle effect is more appropriate to explain the data. traditional dc three-terminal method seems not reliable in ferromagnetic metal/tunnel barrier/nonmagnetic metal systems in which the tunnel barrier resistances are at least several orders of magnitude larger than the spin-injection-induced additional resistance. In our work, the spin-injection-induced magnetoresistance of which the magnitude is comparable with other MR phenomena originating from the tunnel barrier is observable at room temperature as well as low temperatures in the second harmonic signals (Figure 1 and 2). Three-terminal and second harmonic method are combined in our measurement in Pt and Ta systems. Furthermore, we could estimate of heavy metals through fitting the signal with Lorentz function. The of Pt about 3.8 ps at room temperature. This experimental approach make it possible to directly acquire of heavy metals with electrical method.

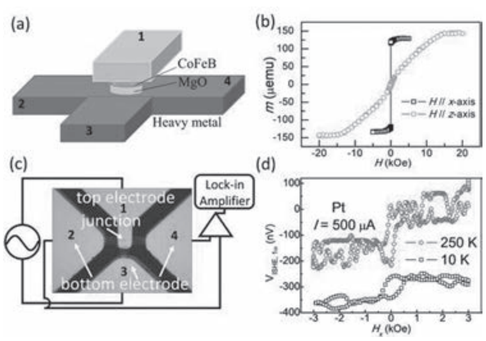

Fig. 1. (a) The junction schematic. (b) First harmonic measurement. (c) The magnetic hysteresis loop of unpattern Pt/MgO/CoFeB film. (d) The ISHE voltage.

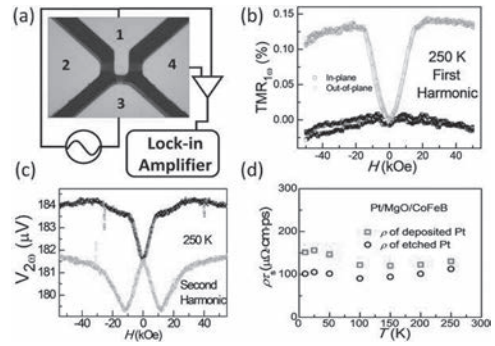

Fig. 2. (a) TMR measurement setup (b) First Harmonic measurement of TMR. (c) Second harmonic voltage of 3-terminal method. (d) Temperature dependence of spin relaxation time.

AR-13. Spin Dice Based on Orthogonal Spin Transfer Devices.

X. Li[1] and L. You[1]
1. School of Optical and Electronics Information, Huazhong University of Science and Technology, WuHan, China

With the advent of the era of big data, data information to bring convenience to lives at the same time, the problem of information security has become increasingly prominent. True random number generator (TRNG) based on physical entropy sources such as thermal fluctuations acts a crucial role in cryptography and information security applications. [1-4] Multi-junctional magnetic tunneling junction (MTJ) Spin dice based on orthogonal spin transfer devices, a new type of random number generator (RNG) is proposed. Orthogonal spin-transfer devices use a spin-polarizing layer magnetized perpendicularly to a free layer, to push free layer with perpendicular anisotropy in metastable (high energy) state, when current or power is on. Thermal noise is the key source to bias the magnet off its metastable state. Once the power is off, the anisotropy field and demagnetization field relax the free layer magnetization from metastable state to one of the two stable states, produces a true random bit whose value is determined solely by thermal noise in magnetization switching. There are two tunneling layers put among three ferro-magnetic layers, as depicted in Fig. 1(a). In-plane anisotropy is owned by layer_1 and layer_2, out-of-plane anisotropy is owned by layer_3. Here layer_3 is considered as spin polarizing layer, while layer_2 and layer_1 is assumed as free layer and reference layer, respectively. A reference magnetic layer is used to read out the magnetic state of free layer. In the initial state, all of the three layers' magnetization are stay in its anisotropy direction. In 1st stage, writing current, mainly carried the polarize direction same as magnetization of layer_3, keeps the magnetization of aimed layer_2 in metastable state, therefore the magnetization of layer_2 lies perpendicular to the plane upwards or downwards according to the current direction. In 2nd stage, writing current is turned off, uniaxial magnetic anisotropy energy relaxes the magnetization to one of the stable states, that is to say, thermal noise tilts the magnetization to be parallel to the plane, in +x direction or -x direction, a true random bit is determined. And in 3rd stage, reading current, which is not large enough to switch the magnetization of layer_2, is applied on the proposed spin dice to read the random bit generated in 2nd stage. The macro-spin simulations are performed to evaluate our spin dice device performance. The saturation magnetization (Ms), exchange constant (A), magnetic anisotropy constant (Ku) and Gilbert damping factor (α), for aimed layer_2 are 1.34 MA/m, 30×10^{-12} J/m, 670 KJ/m^3 and 0.014, respectively, spin polarization (p) for layer_1 and layer_3 are 0.3 and 0.7, respectively. Environment temperature (T) is 300 K. Writing current density is 1.85×10^7 J/cm^2, and reading current density is 2×10^6 J/cm^2. In writing process and reading process, spin polarized current both from layer_1 and layer_3 give a spin torque to layer_2 in the magnetization procession. With properly spin polarization set, the polarization value could hardly have any influence on the generating process of RNs. Limited by time and sever, only 10000 RNs were generated and evaluated. Among these 10000 RNs, 4990 processions have a final state of +x direction saturation magnetization in aimed layer_2. We also evaluated the quality of the RNs by using the statistical test suite NIST SP-80018 [5], the RN sequence only failed a few tests due to the small data size, the high passing test numbers promising the proposed spin dice a high quality TRNG. The multi-junctional spin-dice promises low energy-consumption, non-volatility,high scalability, easy operation, stable writing process and reading process. With the simulation results provided, we argue that the proposed spin dice can overcome the earlier described problems [2] such as scalability and high-quality randomness. We argue that the proposed multi-junctional spin dice is a true random number generator and a promising candidate for a scalable truly random number generator suitable for encrypting.

[1] W. H. Choi, Y. Lv, J. Kim, A. Deshpande, G. Kang, J-P. Wang, C. H. Kim. "A magnetic tunnel junction based true random number generator with conditional perturb and real-time output probability tracking," Electron Devices Meeting, IEEE International. pp. 12.5.1–12.5.4, Dec. 2014. DOI: 10.1109/IEDM.2014.7047039 [2] A. Fukushima, T. Seki, K. Yakushiji, H. Kubota, H. Imamura, S. Yuasa, K. Ando. "Spin dice: A scalable truly random number generator based on spintronics," Appl. Phys. Exp., vol. 7, no. 8, pp. 083001, Jul. 2014. DOI: 10.7567/APEX.7.083001 [3] S. Srinivasan, S. Mathew, R. Ramanarayanan, F. Sheikh, M. Anders, H. Kaul, V. Erraguntla, R. Krishnamurthy, G. Taylor. "2.4 GHz 7 mW all-digital PVTvariation tolerant true random number generator in 45 nm CMOS," VLSI Circuits (VLSIC), IEEE Symposium pp. 203–204, Jun. 2010. DOI: 10.1109/VLSIC.2010.5560296. [4] S. Yuasa, A. Fukushima, K. Yakushiji, T. Nozaki, M. Konoto, H. Maehara, H. Kubota, T. Taniguchi, H. Arai, H. Imamura, K. Ando, Y. Shiota, F. Bonell, Y. Suzuki, N. Shimomura, E. Kitagawa, J. Ito, S. Fujita, K. Abe, K. Nomura, H. Noguchi, H. Yoda H. "Future prospects of MRAM technologies," Electron Devices Meeting (IEDM), IEEE International, pp. 3.1.1–3.1.4, Dec. 2013. DOI: 10.1109/IEDM.2013.6724549. [5] National Institute of Standards and Technology, Special Publication 800-22 rev.1a, April 2010. NIST Statistical Test Suite version 2.1 was used for the evaluation. Available at http://csrc.nist.gov/.

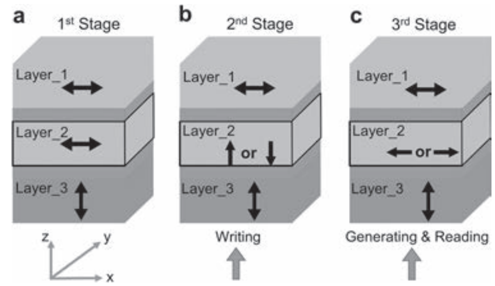

Fig. 1. (a) Initial state of the proposed spin dice. (b) State of 2nd stage. With writing current applied on the spin dice, the magnetization of layer_2 lies perpendicular to the plane, upwards or downwards, according to the current direction. (c) State of 3rd stage. When writing current is turned off, magnetization of layer_2 switches to its anisotropy direction. A random bit is generated and it can be read through layer_1 and layer_2.

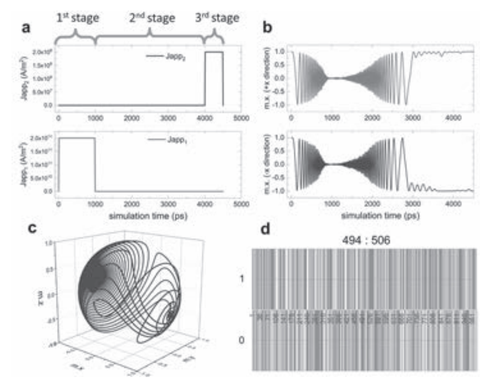

Fig. 2. (a) Magnitude of writing current and reading current varied with time in three stages. (b) Variation of m_x in layer_2 in 3 stages, random numbers generating. Final state of m_x in +x direction is corresponding to 1, while final state of m_x in -x direction is corresponding to 0. (c) Magnetization procession of layer_2. (d) Arbitrarily 1000 random numbers' distribution.

AR-14. Magnetization behaviors of magnetic tunnel junctions driven by the spin-orbit torque.

T. Wu[1]
1. Graduate School of Materials Science, National Yunlin University of Science and Technology, Douliu, Taiwan

Recently perpendicular magnetic tunnel junctions (pMTJs) attract much interest because of higher thermal stability and smaller writing currents for applications in magnetoresistive random access memory (MRAM). In order to have high magnetoresistance (MR) ratio, the thickness of barrier layer in pMTJ is usually less than 2 nm, which restricts the maximum writing current. To overcome this issue, the spin-Hall effect (SHE) has been shown to be a promising solution to replace the conventional spin-transfer torque (STT) writing scheme. The in-plane polarized spin current produced by SHE can reverse the free-layer magnetization through STT; however, for pMTJs, additional mechanisms such as applied field or exchange-bias coupling are required to switch out-of-plane magnetization. Until now, most of studies focus on the reversal behaviors of single perpendicular-anisotropy layer and only few reports are about full pMTJ stacks. In this study we report the experimental results of magnetization reversal of pMTJ by SHE. The pMTJ stacks consisting of Ta(5)/$Co_{40}Fe_{40}B_{20}$(1.2)/MgO(2)/$Co_{20}Fe_{60}B_{20}$(2.3)/Ta(5)/Ru(5) were deposited on SiOx substrate. The numbers in parentheses are layer thicknesses in nm units The $Co_{40}Fe_{40}B_{20}$ layer serves as the free layer, while $Co_{20}Fe_{60}B_{20}$ is used as the fixed layer. The film was annealed at 200 and 300 ^{o}C for one hour, respectively, and then patterned into devices of various sizes for resistance measurements. The R-H and R-I measurement results are depicted in Fig.1. The lateral dimension of the device is 900x1200 nm2. From Fig. 1(a) one can see that both the free and fixed layer magnetizations switched in a single step at clearly seperated switching fields, and the MR ratio is 31%. Oppositely, at current below 0.1 mA under 30 Oe applied field, a fast falling of the resistance can be observed as shown in Fig. 1(b) with MR ratio 180%. The nonlinear R-I curves indicate that the magnetization of the fixed layer rotated even at very small current.

AR-15. Recognizing and memorizing patterns with delayed feed-back spin-torque nano-oscillators.

M. Riou[4], J. Torrejon[4], F. Abreu Araujo[4], G. Khalsa[1], M. Stiles[1], S. Tsunegi[2], K. Yakushiji[2], A. Fukushima[2], H. Kubota[2], S. Yuasa[2], D. Querlioz[3], V. Cros[4] and J. Grollier[4]
1. National Institute of Standards and Technology, Gaithersburg, MD, United States; 2. National Institute of Advanced Industrial Science and Technology (AIST), Tsukuba, Japan; 3. Centre de nanosciences et nanotechnologies, Université Paris-Sud, Orsay, France; 4. Unité Mixte de Physique CNRS/Thales, Palaiseau, France

For many recognition and classification tasks, the brain processes information with much less power than any computer. Therefore, developing neuromorphic chips opens the path to reducing dramatically the energy consumption of data processing. Biological neurons can be seen as interconnected non-linear oscillators which generate a collective chain-reaction response to an excitation. Memory in biological neural network is part due to the intrinsic behavior of each neuron and part due to the recurrences that occur in the network. Recently we have shown experimentally that a nanoscale spin torque oscillator can be used to achieve spoken-digit recognition thanks to its non-linearity and reliability[1]. Among the different strategies for brain-inspired computing with spin torque oscillators[1, 2], we leveraged the transient dynamics of a single oscillator to mimic the chain-reaction response of a whole neural network. The oscillator plays one by one the role of each neuron: the temporal chain reaction replaces the spatial chain reaction of a biological neural network. This reservoir computing with a single node[3] did only use the oscillator intrinsic memory which is insufficient when longer term memory is needed. Optical delayed feedback systems have shown their efficiency at dealing with memory tasks such as chaotic series prediction[3], but they suffer from a scalability limitation. Here we show experimentally that a delayed feedback loop added to a spintronic oscillator can create memory and improve recognition in cases where memory is critical. The spin torque oscillators that we use are magnetic tunnel junctions with a vortex magnetization configuration in the FeB free layer. Due to a high TMR ratio (130%), the emitted power of such oscillators is of the order of the microwatt. These oscillators also have a very low linewidth[4]. The preprocessed input is created by an arbitrary waveform generator (figure 1) and is injected to the oscillator as a varying voltage. A delay feedback loop made of an electronic delay line of 4300ns and an amplifier is added so that the oscillator is fed by the input signal and its own past response. It creates a longer term memory than the ~200ns intrinsic memory of the oscillator induced by its relaxation. The operating point is tuned by changing the dc current and the magnetic field. The response of the oscillator is sent through a diode that extracts its amplitude and recorded with an oscilloscope. The classification is achieved by reconstructing an output signal which is a linear combination of points from the recorded response. To investigate the effect of delayed feedback on pattern recognition performances, we perform the piecewise classification of sine and square[3] waveforms. 160 preprocessed periods of sine and square are sent in random order to the system (figure 2a). A clear effect of the feedback loop is observed in the oscillator response which varies even when the input voltage is zero because of its own past emission (figure 2b). The feedback allows improving the classification for many different operating points (figure 2c and 2d). Error reduction is up to a factor of 11. In this talk we will highlight that some patterns cannot be classified without remembering the previous input patterns and that all the errors without feedback are concentrated on these cases. We demonstrate that feedback brings memory of previous states without deteriorating the signal and achieves a nearly perfect separation of the inputs. Thanks to the memory it brought, clear benefic effects of a delay feedback loop on classification are shown. This work opens the path to identifying patterns in complex data sequences such as chaotic series. *This work was supported by ERC grant bioSPINspired 682955*

[1]J. Torrejon, M. Riou *et al*, *Nature* 547, 428-431 (2017) [2]M. Romera *et al, ArXiv* :1711.02704 (2017) [3]L. Appeltant *et al, Nat Commun*. 2, 468 (2011); Y. Paquot *et al*, *Sci. Reports* 2, 287 (2012) [4]S. Tsunegi *et al, APEX*, vol 7, 3 (2014)

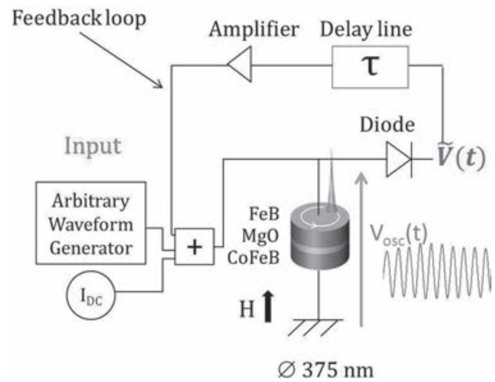

Fig. 1. The input is created by an arbitrary waveform generator. The current and the magnetic field set the operating point. The diode allows measuring the envelope of the signal which simplifies the reconstruction of the output. The envelope of the oscillator response is delayed and injected with the input.

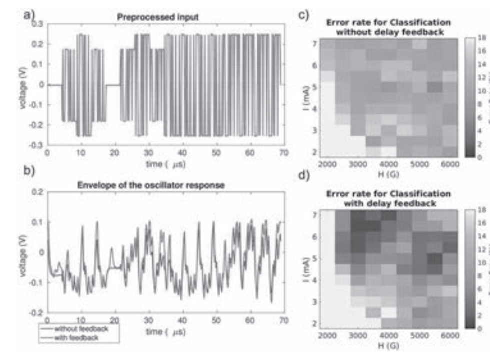

Fig. 2. a) Preprocessed input created by the arbitrary waveform generator. The input corresponds to a sine and a square pattern. The goal is to recognize these two patterns piecewise. b) Envelope of the oscillator response for I=6.5mA and H=3000G. The response in presence of feedback is in red and without feedback in blue. The delay line is 4300ns. Clear effect of the feedback is observed at 20 microseconds, because even without input there is a peak in the oscillator response due to emission 4300 ns before. c) Error rate for pattern recognition without feedback. d) Error rate for pattern recognition with feedback. One can notice an improve of the error in comparison with c) (for instance at 6.5mA and 3000G error is reduced by a factor of 11)

TUESDAY MORNING, 24 APRIL 2018 SIMPOR/ROSELLE BALLROOM, 8:30 TO 11:30

Session AS
NANOPARTICLES AND NANOSTRUCTURED ARRAYS
(Poster Session)

Joachim Gräfe, Co-Chair
Max Planck Institute for Intelligent Systems, Stuttgart, Germany
Valeria Rodionova, Co-Chair
Immanuel Kant Baltic Federal University, Kaliningrad, Russian Federation

AS-01. Domain structure and magnetic properties of magnetostatically coupled epitaxial Co nanostripe arrays with induced anisotropy.

A. Kozlov[1], A. Kolesnickov[1], E. Pustovalov[1], A.S. Samardak[1] and L. Chebotkevich[1]
1. School of Natural Sciences, Far Eastern Federal University, Vladivostok, Russian Federation

Magnetostatic interaction in the arrays of magnetic nanostripes plays an important role in the switching processes and significantly affects the critical fields, spin dynamics, magnetotransport properties and orientation of effective magnetic anisotropy [1]. Shape anisotropy in such arrays leads to the closure of the magnetic flux at the poles of adjacent nanostrips. If in the system of magnetic coupled nanostrips to induce the magnetic anisotropy oriented across the nanostrip long axis, this will change the micromagnetic configuration of each nanostrip in the array due to the appearance of the laminar domain structure formed by domains with an antiparallel orientation of the magnetization [2]. In this work we investigate the switching processes in 800-2000-nm wide Co nanostrip arrays with mutually perpendicular anisotropies (shape anisotropy and steps-induced anisotropy). We study the field-dependent behavior of spin vortices in Neel domain walls of the laminar domain structure of the magnetostatically coupled epitaxial nanostrip arrays. The dependence of the critical fields on the width and number of nanostripes in the array is established and the mechanisms of the magnetization reversal processes were investigated. The nanostripe arrays were produced by focused ion beam etching of the 15 nm Co films deposited by molecular beam epitaxy on the vicinal Si(111) surface. Magnetic properties were investigated by magneto-optical Kerr effect, magnetic force and Kerr microscopies. Micromagnetic simulations were performed with OOMMF software. Experimental MFM-image and micromagnetic simulation (fig.1.) of domain structure of four 800-nm wide nanostripes with 80 nm distance, is showed that magnetostatic interaction between nanostripes favors the magnetization orientation leading to a closure of the magnetic flux. The magnetization process starts from the shift of vortices along the domain walls. The direction of the movement depends on the vortex chirality. The displacement of the Neel domain walls starts only after the vortices achieve the nanostrip edges in magnetic field value is more then 50 Oe. Moreover in this work we established the dependence of the magnetization switching field on the number of nanostrips in an array and on their width was clearly observed when the H_c value had the same order as the dipolar interaction field between nanostrips. We revealed rather complex mechanisms of magnetization reversal depending on direction of the applied magnetic field. If the field applied along the long side of nanostrips, then domains with vortex walls nucleated. With the increasing field, vortices moved along the domain walls and finally transformed them into 90° Neel walls. Only after this, domains started to grow and completely reversed the magnetization at the higher fields. If the magnetic field was aligned along the easy axis of magnetization, then magnetization reversal mode was represented by the vortex domain nucleation and propagation without movement of vortices in domain walls. We found that magnetization reversal mechanisms are driven by the effective magnetic anisotropy and dipolar coupling between nanostrips, but they are independent on the width of nanostrips. This work was supported by the RFBR (grant 16-02-01015 A), by the Russian Ministry of Education and Science under the state task (3.5178.2017/8.9), by Act 211 of the Government of the Russian Federation (contract 02.A03.21.0011), by the Grant program of the Russian President (MK-2643.2017.2)

[1] A.G. Kozlov, M.E. Stebliy, A.V. Ognev, A.S. Samardak, A.V. Davydenko, L.A. Chebotkevich, *J. Magn. Magn. Mater.*, 422 (2017) 452-457 [2] A.G. Kozlov, E.V. Pustovalov, A.G.Kolesnikov, L.A. Chebotkevich, A.S. Samardak, *J. Magn. Magn. Mater.* (2017) doi:10.1016/j.jmmm.2017.11.093

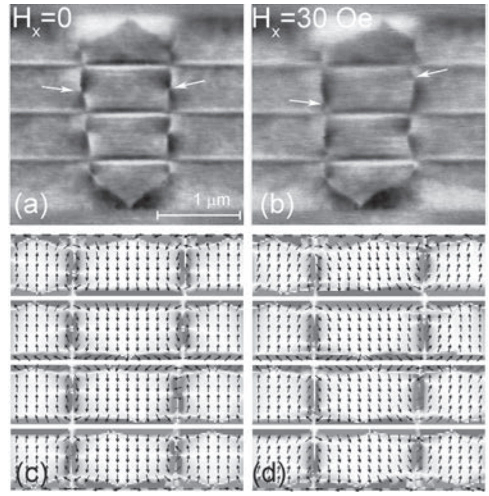

Fig. 1. Domain structure (a,b) and micromagnetic simulation(c,d) images of the epitaxial 800-nm wide nanostripes array. White arrows are shown vortices displacement along domain wall in magnetic field.

AS-02. Exchange bias in Co/CoO core-shell nanowires: roles of antiferromagnetic grain size distribution and interfacial spin glass.

X. Wen[1], K. Gandha[3], P. Liu[2] and *J. Yang*[1]

1. Physics, Peking University, Beijing, China; 2. Physics, University of Texas at Arlington, Arlington, TX, United States; 3. Ames Laboratory, US Department of Energy, Ames, IA, United States

ABSTRACT Exchange bias effect in aligned Co/CoO core-shell nanowires with high aspect ratio was studied. Large exchange bias fields of about 2.2 kOe and 1.0 kOe in easy axis and hard axis, respectively, were obtained after field cooling. We demonstrate that both antiferromagnetic grains and the interfacial spin glass make strong contribution to the observed exchange bias, which is demonstrated with both the cooling field dependence of the exchange bias field and the training effect at different temperatures. The difference in the thermal activation temperature for these two magnetic states leads to a bimodal distribution of the blocking temperature which, in combination with the interplay between the fluctuating spin ordered antiferromagnetic grains and the demagnetizing field of Co core, is likely to explain the anomalous drop of coercivity at the temperature in range from 200 to 110 K. INTRODUCTION The Co/CoO composites have been fairly intensively studied, which is motivated by the exchange bias effect (EB). This effect has a significant impact on the technological applications of data storage products, spintronic devices, permanent magnets, and many other devices. After the discovery of this effect in Co/CoO particles, EB effect has been found in a large number of heterogeneous structures such as layer structures, core-shell structured nanoparticles, and FM nanoparticles embedded in an AFM matrix compounds. Nevertheless, to date, both experimental and theoretical investigations of the EB effects have been mainly focused on the layered structures and core-shell structured nanoparticles with well-defined FM/AFM interfaces. Meanwhile, core-shell nanowire with high aspect ratio has also attracted a lot of research activities due to its unique features. In this paper, we have investigated the temperature dependence of EB effect and the training effect in quasi one-dimensional Co/CoO core-shell nanowires. This study underlines the importance of the AFM grain size distribution and spin glass fluctuation in the exchange-bias mechanism. METHODOLOGY Cobalt nanowires with high aspect ratio (diameter to length d/l = 1:10) have been synthesized via a solvothermal chemical process, which has been described in ref. Then the Co nanowires are naturally oxidized in air forming a core-shell structure. After few weeks the system reaches a stable magnetic state via a passivation mechanism. The nanowires were dispersed in epoxy and oriented by using an external magnetic field of 15 kOe before the epoxy completely curing. The solidified epoxy was shaped as a rod along the orientation of magnetic field. All the magnetic hysteresis loops were measured by superconducting quantum interference device (SQUID) magnetometer. RESULTS AND DISCUSSION Fig. 1 is the HRTEM images of Co/CoO nanowires and the cross section of orientated Co/CoO nanowires dispersed in epoxy. It can be seen from Fig. 1(a) that the nanowire is about 200 nm long with a 9 nm thick Co core surrounded by a CoO shell of 4nm thick. Fig.1(b) is the high-resolution transmission electron microscope (HRTEM) image of the cross section of the orientated nanowires, where the Co core and CoO shell are identified with two circles. Fig. 2 (a)-(b) indicate a strong disordered spin state at the interface with competitive FM and AFM exchange interactions. To get a further exploration the interfacial spin glass, the relationship between H_E and cooling field was studied. The sample was firstly to various temperatures of 5 K, 60 K and 100 K under various cooling fields H_{FC}. Then, a hysteresis loop was measured after each FC. As shown in FIG. 2 (f), the H_{FC} dependence of H_E varies with temperature.

[1] W. H. Meiklejohn and C. P. Bean, Phys. Rev. 1956, 102, 1413. [2] J. Nogues and I. K. Schuller, J. Magn. Magn. Mater. 1999, 192, 203. [3] R. Wu, J. Z. Wei, X. L. Peng, J. B. Fu, S. Q. Liu, Y. Zhang, Y. H. Xia, C.S. Wang, Y. C. Yang, and J. B. Yang, Appl. Phys. Lett. 2014, 104, 182403. [4] H. L. Liu, S. Brems, Y. J. Zeng, K. Temst, A. Vantomme, and C. Van Haesendonck, Phys. Rev. B.2014, 90, 214402 (2014). [5] J. Hong, T. Leo, D. J. Smith, and A. E. Berkowitz, Phys. Rev. Lett. 2006, 96,117204. [6] Gandha K, Elkins K, Poudyal N, Liu X and Ping Liu J 2014 Sci. Rep. 4 5345 [7] D. Gallant and S. Simard, Corros. Sci. 47, 1810 _2005_][S. Gangopadhyay, G. C. Hadjipanayis, C. M. Sorensen, and K. J. Klabunde, J. Appl. Phys. 73, 6964 _1993

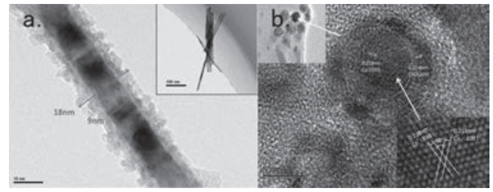

Fig. 1. HRTEM images of (a) Co/CoO nanowires and (b) the cross section of orientated Co/CoO nanowires dispersed in epoxy.

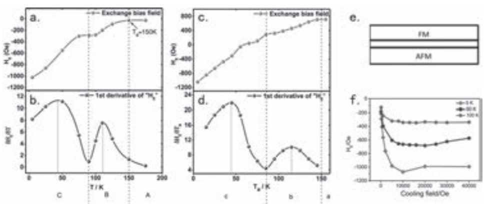

Fig. 2. Temperature dependence of (a) and (b), cooling from 310 K to 5 K under 30 kOe. Annealing temperature dependence of (c) and (d), positive cooling field is +30 kOe while the annealing cooling field is -30 kOe,where TM = 5. (e) A simple illurstration of the structure of exchange bias system. (f) Dependence of HE on the cooling field at 5 K, 60 K and 100 K.

AS-03. Synthesis and magnetic investigation of $CoCr_2O_4$/Ni hybrid core-shell nanowires.

W. Li[1], C. Wang[3], X. Zhang[1], M. Irfan[1], U. Khan[1], Y. Liu[2] and *X. Han*[1]
1. State Key Lab of Magnetism, Institute of Physics, Beijing, China; 2. Tongji University, Shanghai, China; 3. Tongji University, Shanghai, China

Recently, one-dimensional magnetic nanostructures have been intensively investigated for its widely use in high density magnetic recording media, drug delivery, transistor as well as spintronic devices. Meanwhile, the combination of two different materials in one hybrid nanowires (NWs) and nanotubes (NTs) may provide a novel way to control electric polarization by magnetic field or use an electric field to regulate magnetization state. Besides, by adjusting the proportion of two materials, this new entity may exhibit superior properties and conquer the short comings of its individual component. It is known that the template assisted electro-deposition method is simple and economical in synthesizing magnetic NWs and NTs, and most importantly it is easily combined with other technologies. In this work we first fabricated $CoCr_2O_4$ nanotube by dipping the AAO template in a sol–gel solution. Subsequently, filling Ni nanowires inside $CoCr_2O_4$ nanotube using electro-deposition to form core-shell $CoCr_2O_4$/Ni hybrid nanowires. The morphology and magnetic properties of $CoCr_2O_4$ nanotubes and hybrid $CoCr_2O_4$/Ni nanowires at different temperature were investigated. An enhanced coercivity and saturation field were observed for $CoCr_2O_4$/Ni core-shell NWs compared to single-phase Ni NWs. Then, we also conducted micromagnetic simulation to explore the magnetization reversal process of the hybrid nanowires. Results showed that there exsits a strong coupling between the shell and core layers during the magnetization reversal process. We believed that this new structure may have potential use in future high density magnetic recording medium and varies multifunctional devices.

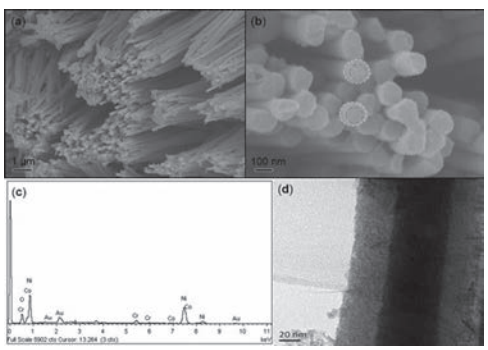

Fig. 1. (a) and (b) SEM images of $CoCr_2O_4$/Ni in different magnification, (c) is the corresponding EDS spectrum, (d) TEM image of single CoCr2O4/Ni core-shell NW.

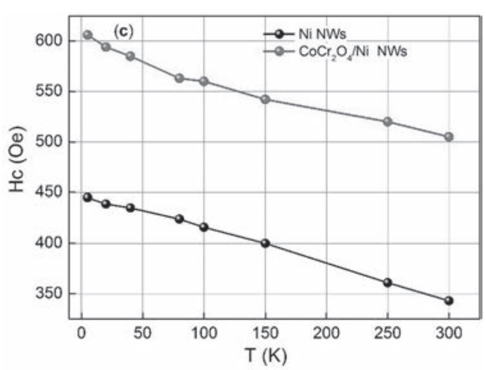

Fig. 2. Temperature dependence of coercivity for $CoCr_2O_4$/Ni and single phase Ni NW arrays.

AS-04. Magneto-thermodynamic properties and anomalous magnetic phase transition in FeRh nano-wires.

K. Matsumoto[1], M. Kimata[2], K. Kondou[3], R.C. Temple[4], C.H. Marrows[4] and Y. Otani[1,3]
1. Iustitute for Solid State Physics, The University of Tokyo, Kashiwa, Japan; 2. Institute for Material Research, Tohoku University, Sendai, Japan; 3. Center for Emergent Matter Science, RIKEN, Wako, Japan; 4. School of Physics and Astronomy, University of Leeds, Leeds, United Kingdom

The FeRh alloy with B2-order shows a first-order phase transition from an antiferromagnetic (AFM) to a ferromagnetic (FM) phase with rising temperature at around 370 K.[1] The AFM to FM transition temperature is suppressed under the application of external magnetic field because of the reduction of the free energy of the FM phase.[2] This transition temperature suppression by an external field enables the derivation of some thermodynamic parameters from magnetization measurements,[3] which gives consistent results with thermal measurements.[4, 5] From these reports, it is known that both a bulk specimen and a thin film of FeRh exhibit similar transition temperatures and entropy changes. Recently, a discontinuous and asymmetric resistance change around the AFM – FM phase transition was reported in submicron wires of FeRh.[6] This anomalous behavior was said to be due to a suppression of the nucleation process of antiferromagnetic domains during the cooling process, which is also expected to make a significant difference to the thermal properties. However, it is difficult to conduct thermal or magnetization measurements on such small volume samples. Here, we report resistivity measurements of submicron wires of FeRh as a function of temperature and external magnetic field. As the resistance change in a submicron specimen reflects local magnetic states, entropy change and energy loss due to temperature hysteresis were estimated from electrical transport measurements. Epitaxial films of B2-ordered Pd-doped FeRh alloys were prepared by DC magnetron sputtering from an $Fe_{47}Rh_{50}Pd_3$ alloy target with a thickness of 60 nm on top of MgO (001) substrates. According to the elemental substitution effect by a Pd doping,[7] the phase transition temperature of FeRhPd films was decreased to 290 K. Submicron wires were fabricated by electron beam lithography and Ar ion milling. Cu electrodes were deposited on top of the wires for 4-terminal resistance measurements. An external in-plane magnetic field was applied parallel to the current. The resistance of a 270-nm-wide wire as a function of both temperature and in-plane magnetic field are shown in Fig. 1, with an inset of a SEM image of the wire. Asymmetric temperature and magnetic field hysteresis loops are observed, being consistent with the previously reported behavior.[6] We derived an entropy change in AFM and FM phases, ΔS, from these transport measurements. The largest resistance change during the transition from FM to AFM phase occurred at 0 T and 256.6 K in a temperature-driven measurement, and at 240.0 K and 1.50 T in a field-driven measurement. A latent heat exported during the transition from high-temperature to low-temperature phase is $T\Delta S$. The sum of the latent heat and Zeeman energy term $H\Delta M$ represents a total exported energy during temperature- or field-driven phase transition. ΔM is a change in magnetization between FM and AFM phases, here we use a value of 1.6 T from magnetometry on an unpatterned film sample shown in Fig. 2. We obtained an entropy change ΔS = 115 mJ cm^{-3} K^{-1}, which is comparable to reported values for a bulk specimen[4] (138 mJ cm^{-3} K^{-1}) and a thin film[3] (140 mJ cm^{-3} K^{-1}). We also compared the energy loss during the temperature loop in a submicron wire with that in a thin film. The energy loss Q' is a sum of latent heat around a temperature hysteresis loop. As we have derived ΔS for this specimen, Q' can be determined from M-T plot: $Q' = \oint S(T)\, dT = (\Delta S/\Delta M) \oint M(T)\, dT$. The temperature hysteresis loop of the magnetization of the film before patterning is shown in Fig. 2 with red symbols. From the calculation of the M-T hysteresis area, we obtained 2.56 J cm^{-3} of energy loss in the unpatterned film. Though it is difficult to measure the magnetization of a sample with a tiny volume, estimation of FM volume ratio in a submicron wire is possible from electrical transport measurements as shown in Fig. 2 with black symbols. Q' in our submicron wire was 3.28 J cm^{-3}, which was 28% larger than that in a film. Because both were calculated on the identical film before and after patterning, this increase was surely due to size effect of the specimen. In conclusion, we performed electrical transport measurements on submicron wires of Pd-doped FeRh alloys. As the resistance on a submicron specimen reflects local magnetic states, entropy change ΔS and hysteresis energy loss Q' were estimated from electrical measurements. We also found a change in Q' before and after shaping into wires, which exhibited an increase by 28% on a submicron structure. This discrepancy is mainly contributed by an abrupt change during the transition from FM to AFM phase probably due to a suppression of AFM domain nucleation. We achieved a quantitative evaluation of an influence of domain nucleation process in submicron wires by simple electrical measurements.

[1] J. S. Kouvel and C. C. Hartelius, *J. Appl. Phys*. 33, 1343 (1962). [2] N. V. Baranov and E. A. Baranove, *J. Alloys Compd.* 219, 139 (1995). [3] S. Maat, J. U. Thiele and E. E. Fullerton, *Phys. Rev. B* 72, 214432 (2005). [4] J. S. Kouvel, *J. Appl. Phys.* 37, 1257 (1966). [5] M. P. Annaorazov, S. A. Nikitin, A. L. Tyurin, K. A. Asatryan and A. Kh. Dovtetov, *J. Appl. Phys.* 79, 1689 (1996). [6] V. Uhlír, J. A. Arregi and E. E. Fullerton, *Nat. Comms.* 7, 13113 (2016). [7] R. Barua, F. Jimenez-Villacorta and L. H. Lewis, *Appl. Phys. Lett.* 103, 102407 (2013).

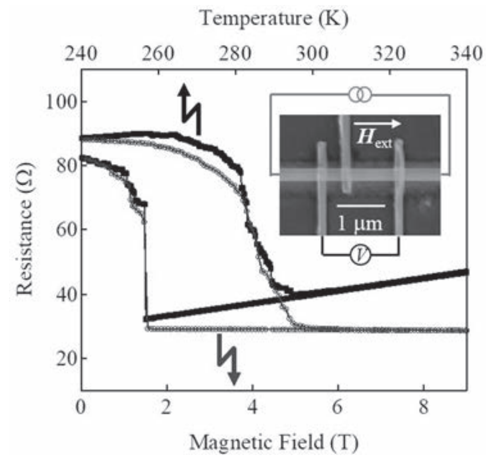

Fig. 1. Resistance measurements on a submicron wire of FeRhPd/MgO (001) as a function of temperature (black, closed square symbols) and in-plane magnetic field (blue, open circle symbols). The temperature-driven hysteresis loop was measured without applying a magnetic field and the field-driven one was done at a constant temperature of 240.0 K. The inset shows a SEM image of the wire.

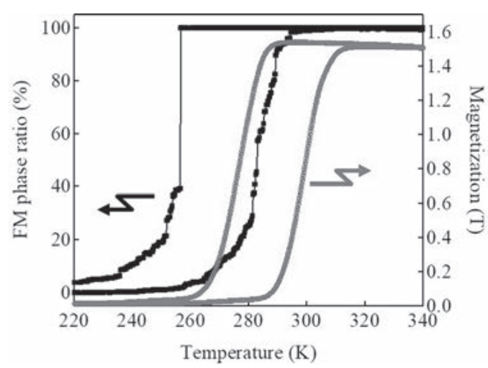

Fig. 2. Ferromagnetic (FM) phase volume ratio (black, closed square symbols) of a submicron wire of FeRhPd/MgO (001) and magnetization (red, open circle symbols) of an unpatterned film are shown. The FM volume ratio was calculated from the resistance measurement.

AS-05. Atomic pair ordering and strain relaxation in thermally and vacuum Annealed NiCu nanowires prepared in Al_2O_3 nanoporous templates.

N. Ahmad[1] and q. abbas[1]
1. Physics, International Islamic University, Islamabd, Pakistan

The magnetic nanowires have been widely investigated to understand their physical and magnetic properties and their applications in magnetic nanodevices [1] nanosensors [2], recording media [3], and microwave circulator [4]. The NiCu nanowires are used in spintronics and microwave absorption devices. Transition metals and their alloys have been fabricated by electrochemical deposition into anodic alumina oxide (AAO) template nanopores which is very low cost and versatile technique to synthesize magnetic nanowires and nanotubes having tunable length and diameter with high aspect ratio [5, 6]. A low cost and direct method to synthesize Ni nanowires such as AC electrochemical deposition in AAO (anodized aluminium oxide) templates are used. AAO templates are preferred over the polycarbonate membrane due to regular pore structure, high density and wide area [7]. Recently nickel cobalt (Ni-Co) nanowires have been fabricated in square shape by electrochemical method and the planar Hall Effect is observed in detail. Also the anisotropic magneto resistance (AMR) is measured. Cobalt nanowires with uniform and regular arranged patterned have been prepared by electro deposition method having diameter 80nm and the length 40nm at different pH values [8]. Nickel (Ni)-Copper (Cu) alloy nanowires with diameter about 65 nm and aspect ratio about 180 were synthesized in highly porous Al_2O_3 templates via AC electrodeposition method. The as-deposited nanowires were simple annealed and vacuum annealed at 300, 400, and 500. Annealing of alloy caused homogenization in alloy nanowires which give degenerate the magnetic properties. The elemental composition of nanowires was checked through energy dispersive X-ray spectroscopy and found 75:25 ratio between Ni and Cu respectively. Structural and magnetic properties of as-deposited, simple and vacuum annealed nanowires were studied by X-ray diffraction and vibrating sample magnetometer. Result revealed that nanowires have stable face center cubic phase with polycrystalline nature and it was not affected after annealing but only improved the structure parameters. Magnetic properties were studied along two different axis of nanowires and results shows that nanowires have easy magnetization axis along to long-axis wire due to higher aspect ratio. Furthermore, Coercivity and remanence ratio of $Ni_{75}Cu_{25}$ nanowires were improved after annealing but effects were more prominent in vacuum annealing due to atomic pair ordering and strain relaxations.

[1] B. Yang, B. Aksak, Q. Lin, M. Sitti, "Complaint and low-cost humidity nanosensors using nanoporous polymer membranes" Sensors and Actuators B: Chemical 114 (2006) 254. [2] M. Almasi Kashi, A. Ramazania, H. Abbasian, A. khayyatiana. "Capacitive humidity sensors based on large diameter porous alumina prepared by high current anodization" Sensors and Actuators 174 (2012) 69 [3] G. H. Yue, X. Wang, L.S. Wang, P. Chang, R.T. Wen, Y.Z. Chen, D.L. Peng, Structure and magnetic properties of $Fe_{1-X}Co_X$ nanowires in self-assembled arrays. Electrochemica Acta54 (2009) 6543. [4] M. Darques, J. De. La, T. Medina, L. Piraux, L. Cagnon, L. Huynen, Microwave circulator based on ferromagnetic nanowires in an alumina template, Nanotechnology 21 (2010) 145208. Fabrication and magnetic properties of ultrathin Fe nanowire arrays. Appl. Phys. Lett. 83 (2003) 3341 [6] D.H. Qin, L. Cao, Q.Y. Sun, Y. Huang, H.L. Li, Fine magnetic properties obtained in FeCo alloy nanowire arrays, Chem. Phys. Lett. 358 484-488 (2002) [7] S.Khalid, "Tailoring of magnetic easy axis of nickel nanowires by varying diameter" Surface Review and Letters, Vol.23, No. 4 (2016) 1650024 [8] N. Zafar, S. Shamaila, R. Sharif, H. Wali, S. Naseem, S. Riaz, M. Khaleeq-ur-Rahman, Effect of PH on the crystallographic structure and magnetic properties of electrodeposited cobalt nanowires, Journal of magnetism and magnetic materials 377 (2015) 215-219 [9] M Jergel, I Cheshko, Y Halahovets, P Siffalovi, I Mat'ko, R Senderak, S Protsenko, E Majkova and S Luby Annealing behaviour of structural and magnetic properties of evaporated Co thin films J. Phys. D:Appl. Phys. 42 (2009)135406 [10] Narayan Poudyal, Girija S Chaubey, Vikas Nandwana, Chuan-bing Rong, Kazuaki Yano and J Ping Liu "Synthesis of Fe Pt nanorods and nanowires by a facile method" Nanotechnology 19 (2008) 355601

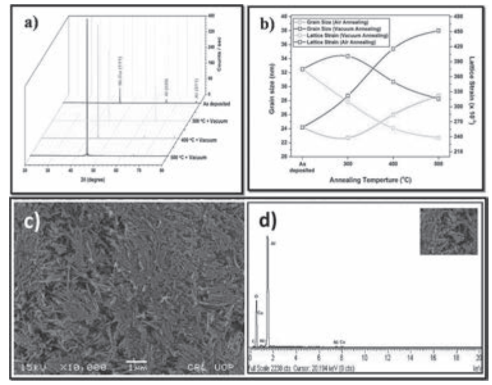

Fig. 1. (a) XRD of all NiCu nanowires (b) Change of grain size and lattice strain with annealing temperature (c) SEM images of NiCu nanowires (d)EDX analysis of nanowires

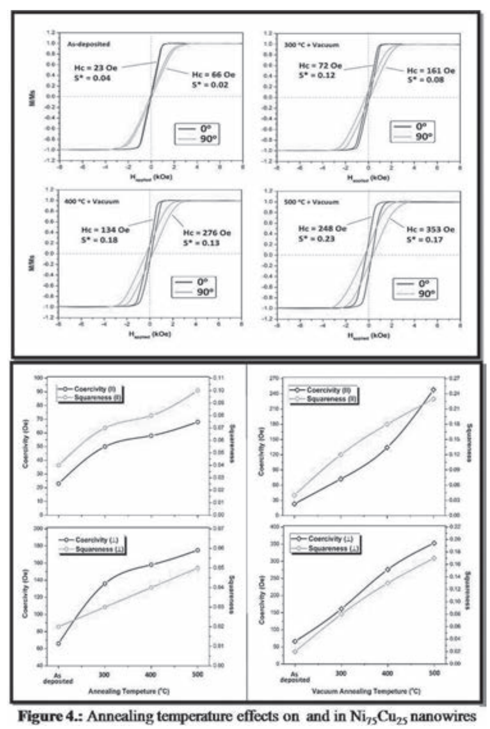

Fig. 2. Change of magnetic properties with thermal annealing and vacuum annealing

AS-06. Controlled growth of Fe_3O_4 nanopillars and their magnetic properties.

M. Guan[1], G. Dong[1], Z. Zhou[1] and M. Liu[1]
1. Xi'an Jiaotong University, Xi'an, China

Single-crystal Fe_3O_4 nanopillars were deposited on $SrTiO_3$ substrate using pulsed laser deposition. The nanopillars were shaped by using an AAO template as the mask. The dimension of the nanopillars can be modified by choosing the different AAO template. The XRD results shown an single crystal behavior of the nanopillars. The magnetic properties of the nanopillars was recorded using Vabriating Sample Magneticmeter(VSM) and electric paramagnetic resonance(ESR), both shown ferromagnetic behavior of the nanopillar. Our result provide an new choice to deposit Fe_3O_4 nanopillars.

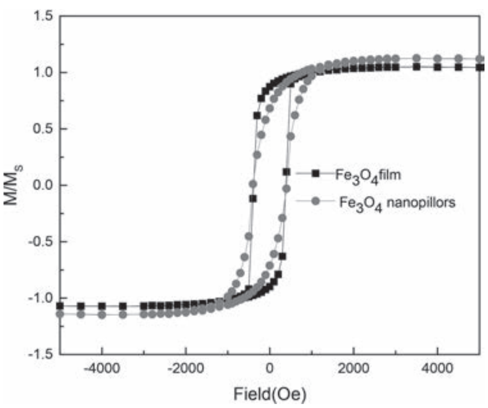

Fig. 1. The M-H loop of the Fe_3O_4 nanopillar (red) and Fe_3O_4 film (black)

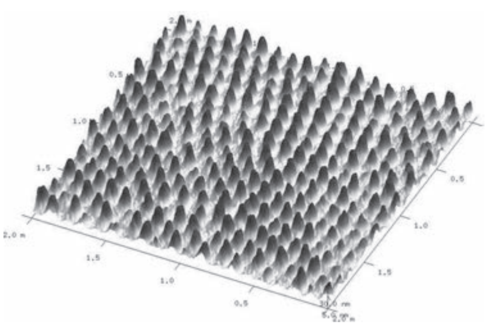

Fig. 2. Surface morphology of the Fe_3O_4 nanopillors

AS-07. Effect of size on multiferroic $SmMn_2O_5$ nanorods.

T. Hsu[1], C. Yang[1], C. Yang[1], Y. Tung[1], C. Kao[1], W. Wu[1] and K. Lin[2]
1. Physics, Chung Yuan Christian University, Taoyuan City, Taiwan;
2. Department of Chemical Engineering and Material Science, Yuan Ze University, Zhongli, Taiwan

Three sizes $SmMn_2O_5$ multiferroic nanorods are fabricated by the hydrothermal method. The HRTEM images show the diameters ($<L_C>$) × axial of three samples are 58(17) nm×25(6) nm, 92(21) nm×32(8) nm, and 126(25) nm×52(13) nm. Figure 1(a) displayed an antiferromagnetic (AFM) peak at around 6K, which was correlative with Sm magnetic ordering and independent of $<L_C>$. A small AFM peak appeared at 26 K, 28 K, and 30 K in $<L_C>$ = 58 nm, 92 nm, and 126 nm sample, respectively. It is correlated with the Mn magnetic ordering and shifts to higher temperature with the $<L_C>$. All samples show a hysteresis loop at 2 K. The coercivity decreased as the size increasing to $<L_C>$ = 126 nm. The temperature profile of Raman spectra exhibited a red-shift of A_g+B_{1g} mode (680 cm^{-1}) only appears in the $<L_C>$ = 126 nm sample. This observation implied the interaction between the Mn ions via Mn-O bond is more sensitive to temperature in large SmMn2O5 nanorods. These results reveal the structure and magnetic properties are influenced by the size. The critical dimension is between the $<L_C>$ = 92 nm and 126 nm.

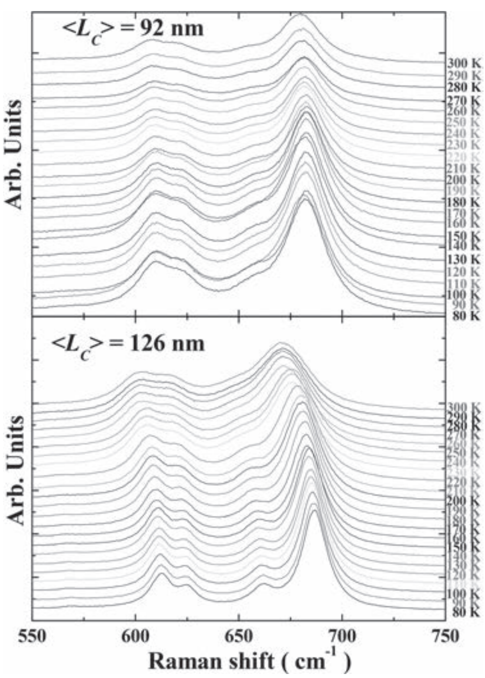

Fig. 2. Raman spectra of $<L_C>$ = (a) 92 nm and (b) 126 nm samples at various temperatures.

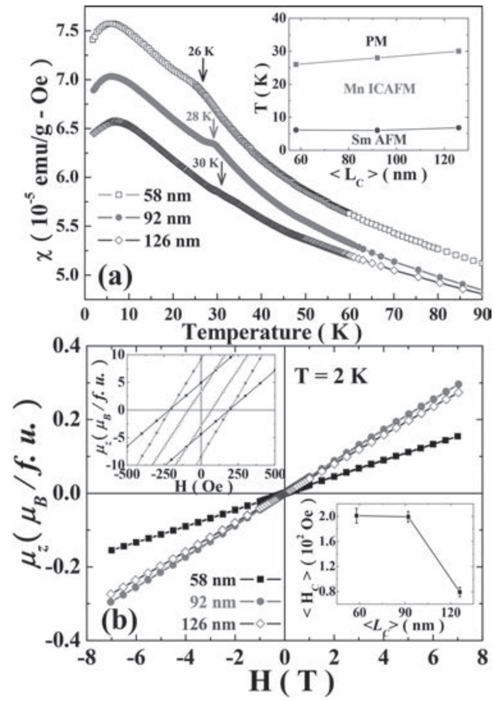

Fig. 1. (a) Zero-field cooling curves of magnetic susceptibility of nanorods with $<L_C>$ = 58 nm, 92 nm, and 126 nm (b) Hysteresis loop of nanorods with $<L_C>$ = 58 nm, 92 nm, and 126 nm.

AS-08. Fabrication of high-density metal alloy nanodots by a facile block copolymer inclusion method.

T. Maity[1], T. Ghoshal[2] and S. Roy[1]
1. Tyndall National Institute, Cork, Ireland; 2. University College Cork, Cork, Ireland

We report the fabrication of ultra-high density ordered arrays of magnetic metal alloy nanodots by a simple and cost-effective facile block copolymer inclusion method. Spectroscopic, microscopic and structural characterisations show that the nanodots have uniform size, shape and their placement mimics in the large area i.e. wafer scale. The size of the nanodots varies between 10 nm to 35 nm and can be controlled by the fabrication process. The magnetic nanodots show good thermal stability and strong adherence to the substrate surface, making them useful for high density memory and other nanomagnetic device applications. [1,2] To fabricate such precise patterned magnetic nanostructures for device applications, lithographic approaches by electron beam, optical interference, X-rays or nanoimprint are being employed but are limited by cost and speed. Self-assembly techniques such as di-block copolymer (DBCPs) microphase separation can be used as an alternative and cost-effective technique. [3, 4, 5] Ordered patterns of magnetic nanodots have been fabricated by using DBCP micellar films and selective chemical co-ordination of metal precursors to one polymer blocks. Using the techniques reported here, we are able to generate different magnetic nanodots array of both alloy and oxides with controllable size and separation over wafer-scale areas. At first step hexagonal array of the oxide nanodots (A_XO_Y) are fabricated. After that, the oxide nanodots are reduced to metal nanodots where the oxygen is removed. The size of the nanodots can be varied by process modification. In Figure 1 the scanning electron microscopy (SEM) image and atomic force microscopic (AFM) image of Ni nanodots have been shown. Detail characterisations have been done to investigate the magnetic properties of such nanodots of different sizes (10 – 35nm) and composition (Ni, Fe, NiFe, etc). The magnetic properties of such nanodots depend on the size of the nanodots. The nanodots diameter size above ~20 nm shows ferromagnetic behaviour throughout the temperature range (2 – 300 K) whereas nanodots with diameter size below ~20 nm show superparamagnetic behaviour at room temperature with a blocking temperature (T_B) below room temperature. In figure 2.a the zero-field-cooled, field cooled and remanence (ZFC, FC and REM) magnetization (M) versus temperature (T) measurements of 25 nm Ni nanodots array are plotted which shows the ferromagnetic behaviour of the nanodots array throughout the temperature range. The inset figure shows M vs T measurement for superparamagnetic Ni nanodots with size ~20 nm and blocking temperature (T_B) at ~150 K. In Figure 2.b the hysteresis loops measured at 300K and 2K are shown. The dipole-dipole interaction between the well-ordered hexagonal arrays influence the overall magnetic properties of the nanodots which can lead to increase of blocking temperature (T_B). By the reported cost effective block copolymer inclusion method it's possible to deposit ultra-high density nanodots array of different metals/metal-alloys which can be used for next-generation nano-scale magnetic devices like high-density memory.

1. D. X. Chen, J. A. Brug, R. B. Goldfarb; IEEE Trans. Magn., 27 (4), 3601–3619 (1991) 2. J. Cui, J. L. Hockel, P. K. Nordeen, D. M. Pisani, C. Y. Liang, G. P. Carman, C. S. Lynch; Appl. Phys. Lett. 103, 23. (2013) 3. Tandra Ghoshal, Tuhin Maity, Jeffrey F. Godsell, Saibal Roy, Michael A. Morris; Adv. Mater. 24, 2390–2397 (2012) 4. Tandra Ghoshal, Tuhin Maity, Ramsankar Senthamaraikannan, Matthew T Shaw, Patrick Carolan, Justin D Holmes, Saibal Roy, Michael A Morris; Scientific Reports, 3 (2013) 5. Shivaraman Ramaswamy, Ganesh K. Rajan, C. Gopalakrishnan, and M. Ponnavaikko; Journal of Applied Physics 107, 09A331 (2010)

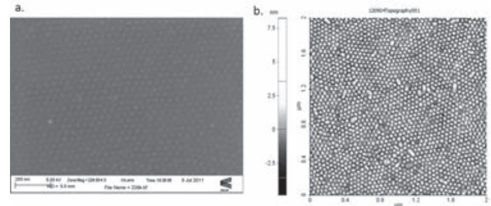

Fig. 1. SEM (a) and AFM (b) topographical image of 25 nm Ni nanodots array. The figures show the well separated hexagonal array of Ni nanodots.

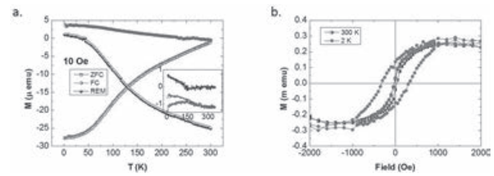

Fig. 2. (a) The zero-field cooled (ZFC), field-cooled (FC) and remanent magnetization (REM) versus temperature (T) plot for hexagonal array of Ni nanodots of 25 nm diameter. The inset figure shows M vs T measurement for nanodots diameter size below ~20 nm where the blocking temperature (T_B) is ~150 K. Figure b shows the hysteresis loops measured at both room temperature (300 K) and very low temperature (2K) for 25 nm nanodots.

AS-09. One–Pot Synthesis and Surface Modification of Lauric-Acid-Capped CoFe2O4 Nanoparticles.

Y. Teng[1] and P. Pong[1]
1. Electrical and Electronical Engneering, The University of Hong Kong, Hong Kong, Hong Kong

Ferromagnetic cobalt ferrite (CoFe2O4) nanoparticles (NPs) have attracted enormous attention because they has large coercivity values due to the high intrinsic magnetocrystalline anisotropy and can translate into a higher heat dissipation than other ferrite nanoparticle with similar size [1], and thus they can be used to induce magnetic hyperthermia for various application [2-3]. Several synthesis methods of cobalt ferrite nanoparticles have been reported previously. However, the reported methods involved multiple-step syntheses which is more sophisticated and time-consuming to obtain the desired resulting nanoparticles. Therefore producing nanoparticles with an efficient and facile route is still challenging. In this work, a facile one-pot method was developed for the synthesis of lauric-acid-capped CoFe2O4 nanoparticles (cobalt ferrite nanoparticles) with promising stability and uniformity, and the nanoparticles were further transferred into aqueous phase through surface modification using surfactants including CTAB and SDS. These water-soluble cobalt ferrite nanoparticles can be directly functionalized with target biomolecules to be applied in aqueous environment for biosensing, protein separation and drug delivery [4-5]. Experimental The monodisperse lauric-acid-capped CoFe2O4 nanoparticles were synthesized via one-pot reaction of Fe(acac)3 and Co(acac)2, and 1,2-tetradecanediol in benzyl ether mixed with lauric acid and a small amount of oleic acid [6]. The as-synthesized nanoparticles were transferred to water using CTAB and SDS following the protocol previously developed in [7]. Furthermore, the performance of water-soluble lauric-acid-capped CoFe2O4 nanoparticles for drug loading was conducted. The morphology and structure of CoFe2O4 nanoparticles were analyzed by transmission electron microscopy (TEM) and selected area electron diffraction (SAED). The elemental analyses of the as-synthesized nanoparticle powders were performed using energy dispersity X-ray spectroscopy (EDX) while X-ray powder diffraction patterns of the particle assemblies were collected by X-ray diffractometer (XRD). The CoFe2O4 nanoparticles were characterized by the presence of various functional groups by Fourier transform infrared spectrometer (FTIR). The ultraviolet visible spectroscopy (UV-Vis) characterized the optical property of CoFe2O4 nanoparticles. The magnetic properties of CoFe2O4 nanoparticles were investigated using vibrating sample magnetometer (VSM). Results and discussion The resulting CoFe2O4 nanoparticles were nearly spherical with particle size of 15.3 ± 1.7 nm as shown in Figure 1(a), and they can be slightly dissolved in water due to the use of lauric acid as the surfactant (solubility in water = 55 mg/L at 20 °C). The CTAB and SDS modified CoFe2O4 nanoparticles are presented in Figure 1(c) and 1(d). The SDS modified CoFe2O4 nanoparticles exhibit better uniformity and stability without coalesce and agglomeration,indicating that surface modification using SDS is a more effective strategy for phase transfer of CoFe2O4 nanoparticles. FTIR shows characteristic bands (in the range of 900–1600 cm-1) for the SDS surfactant, and the absorption band nearly 1600 cm-1 confirmed that the surfactant were successfully modified on CoFe2O4 nanoparticles. Magnetic hysteresis loops of both pure and SDS modified CoFe2O4 nanoparticles at room temperature are shown in Figure 2(b). The coercivity of the CoFe2O4 is around 185 Oe, which is much larger than that of Fe2O3 nanoparticles. This indicates that the incorporation of the Co cation in the Fe-O matrix greatly increases the magnetic anisotropy of the CoFe2O4 materials. The magnetic properties of the SDS modified CoFe2O4 nanoparticles also present superparamagnetic properties. The saturation magnetization (Ms) of the SDS modified CoFe2O4 nanoparticles is 33.6 emu/g, which is smaller than that of the pure CoFe2O4 nanoparticles (72 emu/g). The dispersion behavior of the lauric-acid-capped CoFe2O4 nanoparticles was investigated by observing the stability of nanoparticles suspension in aqueous medium as shown in Figure 2(c). The sample was dispersed in water and the stability of the suspension sustained even after 48h. The stable suspension of the CoFe2O4 nanoparticles indicates the existence of the hydrogen bond between the aqueous solution and lauric acid layer. The aqueous solubility of the lauric-acid-capped CoFe2O4 nanoparticles makes it an ideal candidate for various in-vivo biomedical applications like cancer treatment [8]. Conclusion In summary, the study reported a facile one-pot heat-up method to synthesize the monodisperse ferrite spinel lauric-acid-capped CoFe2O4 nanoparticles. The lauric-acid-capped CoFe2O4 nanoparticles with particle size of 15.3 ± 1.7 nm were successfully obtained. The phase transfer of lauric-acid-capped CoFe2O4 nanoparticles through further surface modification in water with CTAB and SDS were achieved. The water soluble lauric-acid-capped CoFe2O4 nanoparticles can be utilized as promising candidate in cell sorting and labeling applications and as MRI contrast agent in aqueous solution.

References [1] Carrey, J.; Mehdaoui, B.; Respaud, M. Simple Models for Dynamic Hysteresis Loop Calculations of Magnetic Single-Domain Nanoparticles: Application to Magnetic Hyperthermia Optimization. J. Appl. Phys. 2011, 109, 083921. [2] Hafeli, U.; Schutt, W.; Teller, J.; Zborowski, M. Scientific and Clinical Applications of Magnetic Carriers. Plenum Press: New York, 1997. [3] Oswald, P.; Clement, O.; Chambon, C.; Schouman-Claeys, E.; Frija, G. Liver positive enhancement after injection of superparamagnetic nanoparticles: respective role of circulating and uptaken particles. Magn. Reson. Imaging 1997, 15, 1025. [4] Hergt, R.; Andra, W.; d'Ambly, C. G.; Hilger, I.; Kaiser, W. A.; Richter, U.; Schmidt, H.-G. Physical limits of hyperthermia using magnetite fine particles. IEEE Trans. Mag. 1998, 34, 3745. [5] Kim, D. K.; Zhang, Y.; Kehr, J.; Klason, T.; Bjelke, B.; Muhammed. M. Characterization and MRI study of surfactant—coated superparamagnetic nanoparticles ad—ministered into the rat brain. J. Magn. Magn. Mater. 2001, 225, 256. [6] Sun, S.; Zeng, H. Size-controlled synthesis of magnetite nanoparticles, J. Am. Chem. Soc. 2002, 124, 8204. [7] Mitra, S.; Das, S.; Mandal, K.; Chaudhuri, S. Synthesis of a α-Fe2O3 nanocrystal in its different morphological attributes: growth mechanism, optical and magnetic properties. Nanotechnology 2007, 18, 275608. [8] Yang, H.; Ogawa, T.; Hasegawa, D.; Takahashi, M. Synthesis and Magnetic Properties of Monodisperse Magnetite Nanocubes. J. Appl. Phys. 2008, 103,07D526.

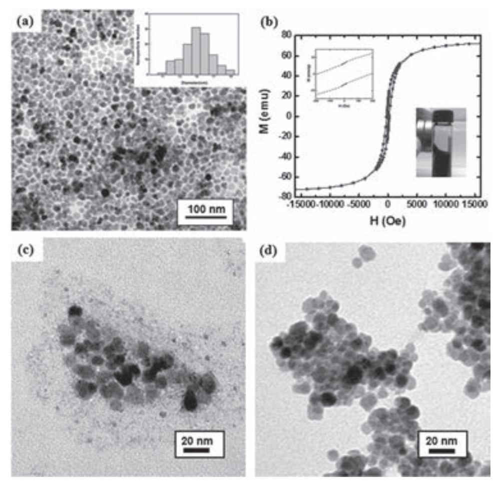

Fig. 1. TEM image(a) and M-H loops (b) of CoFe2O4 nanoparticles; TEM images of CTAB modified (c) and SDS modified CoFe2O4 nanoparticles (d). Inset in (a) is the histogram of particles size.

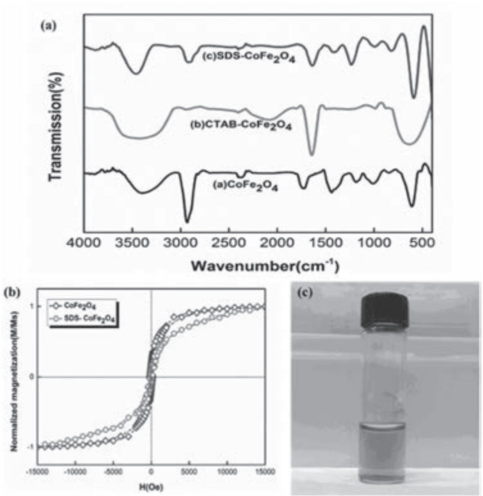

Fig. 2. (a)FTIR of synthesized (black); CTAB modified (red) and SDS modified CoFe2O4 nanoparticles (blue). (b) M–H loops of synthesized (blue) and SDS modified (red) CoFe2O4 nanoparticles. (c) Synthesized lauric-acid-capped CoFe2O4 nanoparticles as stable aqueous solution.

AS-10. Enhanced photocatalytic degradation of tri-chlorophenol by Fe_3O_4@TiO_2@Au photocatalyst under visible-light.

K. Song[1], k. Choi[2], B. Park[3] and J. Jung[1]

1. Chemistry, Gangneung-Wonju National University, Gangneung city, The Republic of Korea; 2. 1Institute of Biomaterials, Kwangwoon University, Seoul, The Republic of Korea; 3. Department of Electrical & Biological Physics, Kwangwoon University, Seoul, The Republic of Korea

Over the last century, rapid modernization and quick industrialization have cause to increased discharge of noxious pollutants into rivers and the sea. Also, the population growth has led to increased use of chemical fertilizers and pesticides for surplus production. Among them, chlorophenols are widely used as biocides and pesticides. Specifically, 4-chlorophenol has been used as a disinfectant at home, in hospital and farms [1], as well as an antiseptic in root canal treatment [2]. Most of the chlorophenols released into the environment go into water, and can cause severe effects on the liver and the immune system of human body. Furthermore, chlorophenols (such as 2, 4, 6-trichlorophenol) are possibly carcinogenic. Therefore, it is of utmost importance to mineralize the chlorophenols in water to harmless products. Therefore, an efficient and ecofriendly treatment for removal of phenolic compounds from water system has become an urgent demand. Removal technologies of phenolic contaminants in the fluid streams were classified in two types as separation (such as distillation extraction, adsorption, membranes-related processes) and destructive ones (such as supercritical, wet air, thermal and catalytic oxidations) [3, 4]. Advanced oxidation processes (AOPs) [5], such as heterogeneous photocatalysis [6] and Fenton-like oxidation [7], were categorized to the destructive type and reported that can effectively remove CPs [8]. Titanium dioxide (TiO_2) is the most popular photocatalyst due to its highly stable chemical structure, relatively low cost, lack of toxicity, and photo-generation of highly oxidizing holes [9]. In this study, a facile and efficient approach for the fabrication of Fe_3O_4@TiO_2@Au particles with a good core–shell structure has been demonstrated. The synthetic protocol involves the coating of successive layers of TiO_2 nanoparticles on to a magnetic core using a sol-gel method at low temperature. To further improve the visible light responsiveness and the dispersibility of the catalysts, noble Au nanoparticles were deposited on the surface of the Fe_3O_4@TiO_2 particles through a chemical anchoring route. The Fe_3O_4@TiO_2@Au photocatalyst exhibited high photocatalytic activity in the degradation of 2, 4, 6-trichlorophenol under UV-VIS light. Also, the Fe_3O_4@TiO_2@Au photocatalyst showed an effective photocatalytic activity under only visible light.

[1] W. H. O, Environmental Health Criteria 93. Chlorophenols other than pentachlorophenol, *World Health Organization Geneva*, Switzerland, 1989. [2] B. F. Gurney, D. P. Lautenschlager, Nearly non-toxic parachlorphenol antiseptics, J. *Dent. Assoc. S. Afr,* vol. 37, 815–818, 1982. [3] G. Busca, S. Berardinelli, C. Resini, L. Arrighi, Technologies for the removal of phenol from fluid stream a short review of recent developments, *J. Hazard. Mater*, vol. 160, 265-288, 2008. [4] Y. Tu, Y. Xiong, S. Tian, L. Kong, C. Descormea, Catalytic wet air oxidation of 2-chlorophenol over sewagesludge derived carbon based catalysts, *J. Hazard. Mater*, vol. 276, 88-96, 2014. [5] R. Andreozzi, V. Caprio, A. Insola, R. Marotta, Advanced oxidation processes (AOP) for water purification and recovery, *Catal. Today,* vol. 53, 51–59, 1999. [6] S. Ahmed, M.G. Rasul, R. Brown, M.A. Hashib, Influence of parameters on the heterogeneous photocatalytic degradation of pesticides and phenolic contaminants in wastewater: a short review, *J. Environ. Manage*, vol. 92, 311–330, 2011. [7] H. H. Huang, M. C. Lu, J. N. Chen, Catalytic decomposition of hydrogen peroxide and 2 chlorophenol with iron oxides, *Water Res*, vol. 35, 2291–2299, 2001. [8] M. Peratitus, V. Garciamolina, M. A. Banos, J. Gimenez, S. Esplugas, Degradation of chlorophenols by means of advanced oxidation processes a general review, *Appl. Catal. B Environ*, vol. 47,219–256, 2004. [9] A. Fujishima, T. N. Rao, D. A. Tryk, Titanium dioxide photocatalysis, *J. Photochem. Photobiol. C*, vol. 1,1–21, 2000.

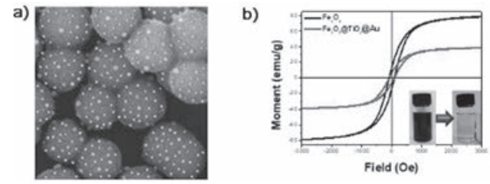

Fig. 1. FE-SEM images of Fe_3O_4@TiO_2@Au photocatalysts and their magnetic hysteresis loops

AS-11. Solvothermal Synthesis of Uniform Water-Soluble Fe_3O_4 Nanoparticles.

S. Lee[1], Y. Chen[1] and A. Sun[1]
1. Chemical Engineering and Materials Science, Yuan Ze University, Taoyuan, Taiwan

Biomaterials are becoming increasingly important in biomedical practice, particularly as the population ages. Iron oxides magnetic nanoparticles such as magnetite (Fe_3O_4) and maghemite (γ-Fe_2O_3) have attracted much attention due to the superparamagnetic properties, biocompatibility and low toxicity which are promising candidates in application in biomaterials to the synthetic scaffolds, drug carriers, sensing media, etc. In addition, the size, dispersity and magnetic property of the magnetic nanoparticles are significance in biomedical applications [1]. Different methods of synthesizing magnetite nanoparticles were developed to address the above conditions [2, 3]. However, the hydrophobic or polydisperse are still found in products and really require cumbersome post-synthesis size selection procedures, which are not suitable for biomedical applications. In order to obtain uniform particle size, hydrophilic surface and aqueous dispersibility, the solvothermal method was proposed in this study. The anionic polyelectrolyte poly(4-styrenesulfonic acid-co-maleic acid) sodium salt (PSSMA) was used as a stabilizer to synthesis of electrostatic stabilization magnetite nanoparticles since it can strongly coordinate to iron cation to form linear polymeric molecules further restrain grain growth and the containing carboxyl groups can modify particle surface to be hydrophilic [4]. Typically, anhydrous ferric chloride, anhydrous sodium acetate, PSSMA, L-Ascorbic acid and appropriate amount of deionized water was thoroughly dissolved in ethylene glycol into a Erlenmeyer flask. After addition of sodium hydroxide which was placed in an oven and heated to 190°C for 10 h. The products were separated by magnetic separation and then washed with deionized water and ethanol for several times. Finally, the obtained products were dried in a vacuum oven. Results pointed out that the magnetic nanoparticles with excellent water dispersity and uniform size by modified solvothermal method. The amount of coated polymer, PSSMA, can strongly influence the particles size and size distribution. X-ray Diffraction (XRD) data showed diffraction peaks at $2\theta = 30.2°$, 35.5°, 43.2°, 53.6°, 57.2° and 62.7°, which can be indexed to (220), (311), (400), (422), (511) and (440) planes of Fe_3O_4 in a cubic phase, respectively. Vibration Sample Magnetometer results showed the nanoparticles are superparamagnetic magnetite. Dynamic Light Scattering results showed tunable particle size with narrow size distribution. Furthermore, the uniform size distributions with diameter about 120 nm were obtained in Transmission Electron Microscope (TEM) images. High Resolution-TEM confirmed the good crystallinity and clear lattice images with *d*-spacing about 2.54 Å, which can be indexed to (311) plane of cubic magnetite. The detail mechanism to affect particle size and dispersion will be discussed in full manuscript.

[1] L. Reddy, J. Arias, J. Nicolas and P. Couvreur, "Magnetic Nanoparticles: Design and Characterization, Toxicity and Biocompatibility, Pharmaceutical and Biomedical Applications," *Chemical Reviews*, vol. 112, no. 11, pp. 5818-5878, 2012. [2] J. Liang, L. Li, M. Luo, L. Wang and R. Yang, "Synthesis of Monodisperse Magnetite Nanocrystals via Partially Reduced Precipitation Method," *Materials and Manufacturing Processes*, vol. 25, no. 9, pp. 915-918, 2010. [3] X. Yang, Y. Shang, Y. Li, J. Zhai, N. Foster, Y. Li, D. Zou and Y. Pu, "Synthesis of Monodisperse Iron Oxide Nanoparticles without Surfactants," *Journal of Nanomaterials*, vol. 2014, pp. 1-5, 2014. [4] L. Cai, M. Wang, Y. Hu, D. Qian and M. Chen, "Synthesis and mechanistic study of stable water-soluble noble metal nanostructures," *Nanotechnology*, vol. 22, no. 28, p. 285601, 2011.

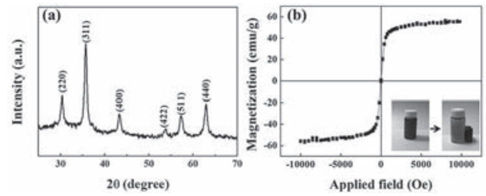

Fig. 1. (a) XRD patterns and (b) hysteresis loop of Fe_3O_4 nanoparticles synthesized by solvothermal method.

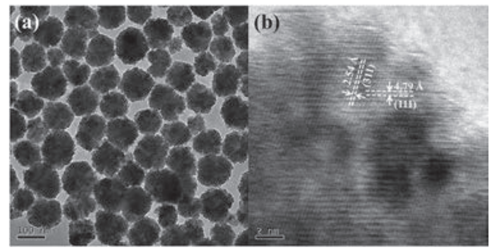

Fig. 2. TEM images for Fe_3O_4 nanoparticles synthesized by solvothermal method with the addition of PSSMA: (a) overall view and (b) high-resolution image.

AS-12. Synthesis of Triangular Shaped Single Crystalline Magnetite Nanoparticles and Their Magnetorheological Response.

D. Bae[1], W. Han[1], C. Gao[1], Y. Dong[1] and *H. Choi*[1]
1. Dept. of Polymer Science and Engineering, Inha University, Incheon, The Republic of Korea

I. INTRODUCTION As one of the most interesting magneto-responsive smart materials, magnetorheological (MR) fluids, micron or sub-micron sized soft-magnetic particles suspended in a nonmagnetic liquid of hydrocarbon or silicone oil, have drawn a huge attentions recently, due to their rapid, continuous and reversible phase change from a liquid-like to solid-like state within milliseconds [1]. This phenomenon occurs by forming chain structures following the magnetic field direction, induced by attractive magnetic dipole interactions among the adjacent magnetic particles, while showing a Newtonian fluid-like behavior of random dispersion of the particles under zero magnetic field. This chain-like structure formation intensifies rheological properties of the MR fluids such as yield stress, shear viscosity, shear stress, and dynamic modulus [2]. Based on these advantages of controlling their rheological and mechanical characteristics, MR fluids have been widely investigated in their industrial applications such as engine mount, vehicle shock absorber and polishing devices, with some commercialization. As for typical materials to form MR fluids, carbonyl ion (CI) particles have been widely accepted with their suitable particle size and high saturation magnetization [3]. In spite of these advantages, CI particles often show dispersion stability problem because of their high density, limiting their engineering applications [4]. Thus, numerous methods were introduced to overcome these problems [5]. Instead of progressing complicated methods of modifying CI characteristics, iron oxide (Fe_3O_4) particles with enough magnetic properties as well as low density, have been also adopted, along with their improved anti-corrosion characteristics owing to the oxidation state. In this study, triangular Fe_3O_4 based MR fluid is expected to provide stronger chain structure than spherical Fe_3O_4 particles because the contact angle of triangular Fe_3O_4 is larger than that of spherical Fe_3O_4 [6], being stacked well due to the prism structure. II. EXPERIMENT Following the synthetic process reported [7], iron chloride hexahydrate ($FeCl_36H_20$) (1g) was liquefied in ethylene glycol (25ml), being stirred for 30 min with a magnetic bar to form a clear solution, and then both 1,3-propanedimaine (10ml) and CH_3COONa (3g) were added. The solution was mixed for 30 min and put into a stainless-steel autoclave. It was then heated at 200 degC and maintained for 12h. The black Fe_3O_4 particles were washed with ethanol and water for several times, following their drying process in an oven at 55 degC for 10h. The synthesized Fe_3O_4 particles were dispersed in silicone oil with 7 vol% particle concentration. The morphology of the synthesized particles was checked by using transmission electron microscopy (TEM) (CM200, Philips, U.S.A), and the rheological behavior of Fe_3O_4 based MR fluid was measured using a rotational rheometer (Physic MCR 300, Anton Paar, Germany) which possesses an external magneto-cell (MRD 180, Anton Paar, Germany). III. RESULT AND DISCUSSION Figure 1 shows TEM image of size and surface morphology of the triangular shaped Fe_3O_4 nanoparticles fabricated, in which most of the Fe_3O_4 particles has triangular and flat morphology with some particle size distribution. As for their MR performance, Fig. 2 represents flow curves of shear stress of triangular Fe_3O_4-based MR fluid as a function of shear rate ranging from 0.01 to 30 (1/s) for various magnetic field strengths. From the controlled shear rate test, the measurement points were set from initial values of 10s to final values of 2s in a log-log scale. Under the zero magnetic field, the shear stress linearly increases with increasing the shear rate, following a Newtonian fluid-like behavior of a typical dilute suspension. However, under applied magnetic fields, the MR fluid shows a sharp increase of its shear stress with applying magnetic field strengths and the shear stresses represent a plateau area over the entire shear rate range, also showing distinctive solid-like behaviors with a yield stress. This phenomenon occurred owing to the formation of a fibril-like structure of magnetized triangular Fe_3O_4 nanoparticles. Because the MR fluid showed characteristics of non-Newtonian fluid possessing yield stress, the Cho-Choi-Jhon equation with six-parameters was adopted in order to fit the flow curves given in Fig. 2, as can be seen from the solid lines. Furthermore, along with their typical MR characteristics, triangular Fe_3O_4 based MR fluid demonstrated higher MR performance compared to spherical Fe_3O_4 [6] for potential engineering application, because of high stacking ability and surface contact angle of the triangular Fe_3O_4 nanoparticles. Furthermore, the dynamic yield stress obtained from Fig. 2 was further analysed as a function of applied magnetic field strength with a power-law correlation along with various dynamic moduli results which will be beneficial to its engineering application [8].

1) S. G. Sherman, N. M. Wereley, "Effect of particle size distribution on chain structures in magnetorheological fluids", *IEEE Trans. Magn.* 49, 3430-3433 (2013). 2) H. Chiriac, G. Stoian, "Influence of the particles size and size distribution on the magnetorheological fluids properties", *IEEE Trans. Magn.* 45, 4049–4051 (2009). 3) M. Mrlik, M. Ilcikova, M. Sedlacik, J. Mosnacek, P. Peer, P. Filip, "Cholesteryl-coated carbonyl iron particles with improved anti-corrosion stability and their viscoelastic behavior under magnetic field", *Colloid Polym. Sci.* 292, 2137–2143 (2014). 4) F. F. Fang, H. J. Choi, "Noncovalent self-assembly of carbon nanotube wrapped carbonyl iron particles and their magnetorheology", *J. Appl. Phys.*, 103, art. No. 07A301 (2008). 5) M. Mrlik, M. Ilcikovac, V. Pavlineka, J. Mosnacekc, P. Peerd, P. Filipd, "Improved thermooxidation and sedimentation stability of covalently-coated carbonyl iron particles with cholesteryl groups and their influence on magnetorheology", *J. Colloid Interf. Sci.* 396, 146-151 (2013). 6) H. S. Chae, S. H. Piao, H. J. Choi, "Fabrication of spherical Fe_3O_4 particles with a solvothermal method and their magnetorheological characteristics", *J. Ind. Eng. Chem.*, 29, 129-133 (2015). 7) X. Y. Li, Z. J. Si, Y. Q. Lei, J. K. Tang, S. Wang, S. Q. Su, S. Y. Song, L. J. Zhao, H. J. Zhang, "Direct hydrothermal synthesis of single-crystalline triangular Fe3O4 nanoprisms", *CrystEngComm*, 12, 2060-2063 (2010). 8) H. S. Chae, S. D. Kim, S. H. Piao, H. J. Choi, "Core-shell structured $Fe_3O_4@SiO_2$ nanoparticles fabricated by sol–gel method and their magnetorheology", *Colloid Polym. Sci.* 294, 647-655 (2016).

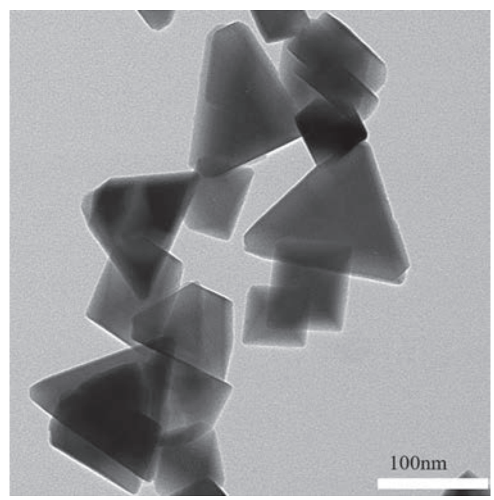

Fig. 1. TEM image of crystalline triangular Fe_3O_4 nanoparticles

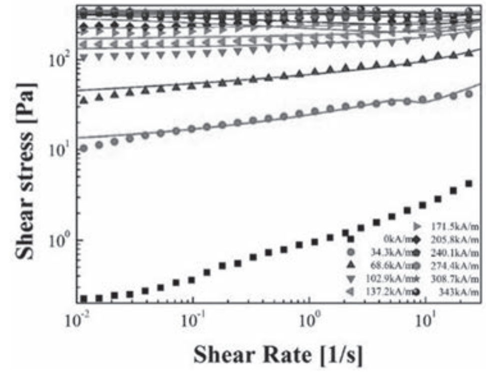

Fig. 2. Shear stress data of triangular Fe_3O_4 nanoparticle based MR fluid under different magnetic field strengths

AS-13. Structure and magnetic properties of MnBi nanoparticles prepared by laser ablation and arc discharge method.

X. Wang[1], H. Qian[2], *P. Si*[1], Y. Yang[2], C. Choi[2], J. Park[2], X. Wang[1], H. Ge[1], K. Shinde[2] and K. Chung[2]
1. China Jiliang University, Hangzhou, China; 2. Korea Institute of Materials Science, Changwon, The Republic of Korea

MnBi has attracted renewed research interests as hard magnetic materials due to its large magnetocrystalline anisotropy and unusual positive temperature coefficient of coercivity. To produce coercivity in MnBi, it is crucial to reduce the dimensions of the MnBi powders, which are usually prepared by ball milling and the size of the powders is in micrometers [1, 2]. MnBi nanoparticles with reduced size in the range 100-300 nm were fabricated from a mixture of Bi_2O_3 and Mn in the presence of Ca as reducing element by a mechanochemical process [3]. MnBi ribbons/powders with further reduced grain size of 20-30 nanometers were prepared by melt spinning method [4] The arc discharge method and the laser ablation method have been widely used for the synthesis of nanoparticles. However, no reports of these methods on the synthesis of MnBi powders could be found. In this work, the MnBi spherical nanoparticles with size around 100 nm or less were prepared by arc discharge method, as shown in Figure 1. The MnBi powders prepared by laser ablation method show a wide size distribution in the range of several tens of nanometers to several micrometers. The composition of the MnBi powders is different from that of the original alloys due to varied evaporation rate of Mn and Bi at high temperatures during arc discharge and laser heating. The samples were annealed at varied temperatures for varied time intervals, after which the structure and magnetic properties of the samples were studied systematically. Fig. 2 shows the magnetic hysteresis loops of the MnBi nanoparticles prepared by laser ablation and heated at different temperature for varied time intervals. The coercivity of the MnBi powders reached up to 0.8 T after annealing at 423 K for half hour and was reduced to 0.3 T when the annealed at 538 K. With increasing annealing time, the coercivity of the powders was further reduced. We ascribed the reduced coercivity of MnBi to the grain growth with annealing temperature and time. However, the saturation magnetization increases with increasing annealing temperature and time due to the formation of MnBi phase. This work was supported by NSFC (Nos. 51671177, 11074227) and the Future Materials Discovery Program through the NRF funded by the Ministry of Science, ICT and Future Planning (2016M3D1A1027835).

[1] B. Li, Y. Ma, B. Shao, et al., Physica B: Cond. Matter 530 (2018) 322-326. [2] K. Kanari, C. Sarafidis, M. Gjoka, D. Niarchos, O. Kalogirou, J Magn. Magn. Mater. 426(2017)691-697 [3] N. V. R. Rao, A. M. Gabay, X. Hu, G. C. Hadjipanayis, J. Alloys Compd. 586 (2014) 349-352 [4] J. B. Yang, Y. B. Yang, X. G. Chen, et al., Appl. Phys. Lett. 99 (2011) 082505

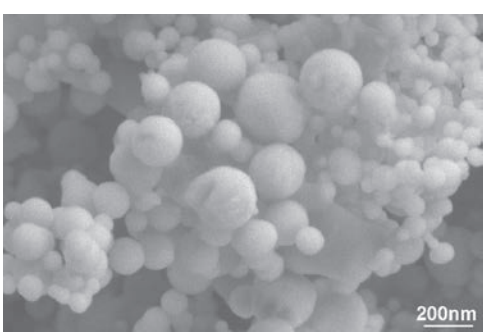

Fig. 1. SEM images of the MnBi nanoparticles prepared by arc discharge method

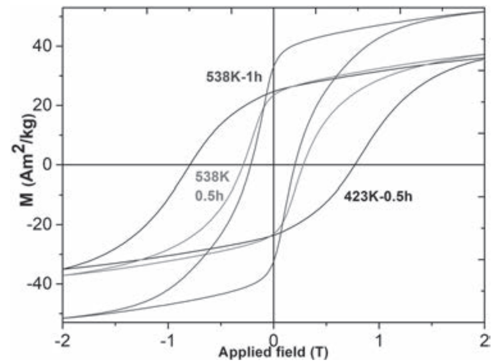

Fig. 2. M-H curves of the MnBi powders prepared by laser ablation and subsequent annealing.

AS-14. Organization and magnetic properties of FePt nanoparticles deposited on graphene/Ir moiré pattern.

F. Tournus[1], P. Capiod[1], L. Bardotti[1], A. Tamion[1], O. Boisron[1], C. Albin[1], V. Dupuis[1], G. Renaud[2] and P. Ohresser[3]

1. Institut Lumière Matière, Université Lyon 1 & CNRS, Villeurbanne, France; 2. CEA-INAC, Grenoble, France; 3. Synchrotron SOLEIL, Gif sur Yvette, France

The FePt alloy, when chemically ordered in the $L1_0$ phase, is among the magnetic materials displaying the highest magnetic anisotropy constant (K around 7 MJ/m^3). Therefore it is a perfect candidate for ultra-high density magnetic storage applications, provided nanoparticles can be prepared in such a high anisotropy phase [1]. Another requirement for applications, as well as for fundamental studies, is to organize the magnetic nanoparticles in a 2D array. In parallel to investigations on chemically synthesized systems, a great effort is devoted to the bottom-up elaboration of nanomagnet arrays following a physical route. In this context, one widely used path consists in using template surfaces with specific sites regularly distributed. Such a 2D lattice can be obtained with the moiré phenomenon, which appears when two crystalline structures of slightly different cell parameters are stacked. Thus, a graphene layer epitaxially grown on a Ir(111) surface displays a 2D spatial modulation corresponding to a hexagonal lattice of 2.5 nm cell parameter [2]. For the first time, we have characterized the organization and the magnetic properties of FePt nanoparticles on such a moiré pattern. We will first describe the formation of size-selected (typically from 2 nm to 4 nm) FePt nanoparticles by Low Energy Cluster Beam Deposition (LECBD) and the preparation of FePt/graphene/Ir(111) samples. We will discuss the organization of such particles on specific sites of the moiré lattice, as determined by grazing incidence x-ray scattering measurements (GISAXS technique) (figure 1) and x-ray diffraction performed at the European Synchrotron Radiation Facility (ESRF) [3]. The deposited nanoparticles are sensitive to the moiré pattern and we find that the resulting organization can be preserved up to temperatures around 700°C. Finally, we will report a clear evolution of the magnetic properties of the FePt nanoparticles induced by annealing (phase modification, anisotropy modification, interface effects between FePt and the graphene...), while the particles keep their individuality (no layer formation is observed). This is put into evidence by X-ray Magnetic Circular Dichroism (XMCD) measurements on the DEIMOS beamline at SOLEIL Synchrotron (figure 2). The magnetic properties will also be compared to those of FePt diluted in an amorphous carbon matrix [4].

[1] P. Andreazza, V. Pierron-Bohnes, F. Tournus, C. Andreazza-Vignolle, and V. Dupuis, Surface Science Reports 70, 188 (2015). [2] A. T. N'Diaye, J. Coraux, T. N. Plasa, C. Busse, and T. Michely, New Journal of Physics10, 043033 (2008). [3] S. Linas, F. Jean, T. Zhou, C. Albin, G. Renaud, L. Bardotti, and F. Tournus, Scientific Reports 5, 13053 (2015). [4] V. Dupuis, G. Khadra, S. Linas, A. Hillion, L. Gragnaniello, A. Tamion, J. Tuaillon-Combes, L. Bardotti, F. Tournus, E. Otero, P. Ohresser, A. Rogalev, F. Wilhelm, Journal of Magnetism and Magnetic Materials 383, 73 (2015).

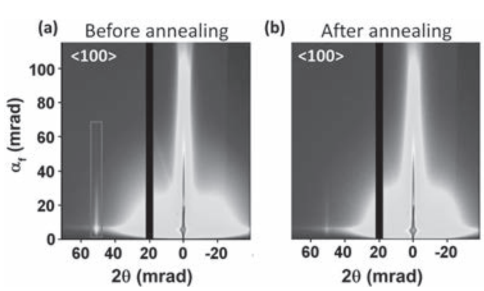

Fig. 1. GISAXS intensities, along the <100> direction of the moiré lattice, before (a) and after (b) annealing at 700°C. The presence of the correlation peak (red frame on left) in those directions reflects the hexagonal organization of the FePt nanoparticles on the graphene/Ir moiré lattice.

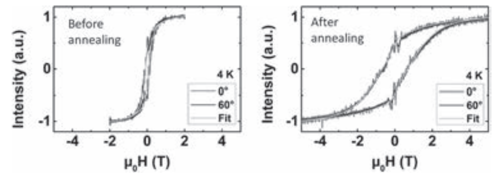

Fig. 2. Low temperature (4 K) hysteresis loop, deduced from XMCD measurements (at Fe L_3 edge) at different indicence angles (normal incidence, i.e. 0°, and 60°) for FePt nanoparticles before (left) and after (right) annealing. The hysteresis loops display an isotropic behavior and can be fitted to infer the magnetic anisotropy value in each case: a huge increase is observe (reflected by the coercivity increase) upon annealing, which is the signature of $L1_0$ chemical ordering of the particles.

AS-15. Research on Eddy Current Testing of Functional Polymer Composite Material.

Z. Cai[2] and *C. Liu*[1]

1. Province-Ministry Joint Key Laboratory of Electromagnetic Field and Electrical Apparatus Reliability, Hebei University of Technology, Tianjin, China; 2. East China Jiaotong University, Nanchang, China

1. Introduction Eddy current testing method can be used to realize the noncontact measurements for mechanical quantities, material testing and flaw detection which made of conductive material (e.g., metallic material, carbon fiber reinforced polymer material and so on)[1-2]. Therefore, electromagnetic nondestructive method have rarely used in functional applications, such as electro-magnetic interference shielding and absorbing material. Nowadays, the coating of shielding and absorbing material is widely used by specific conductive material which made of polymer composite material mixed with conductive particles. The insulating matrix of polymer composite material is separated by nanoscale conductive filler particles. Recently, the experimental results on the lift-off effect show that the induced voltage of the coil with alternating current changes regularly with the variations in the distance between the coil and the composite object. This phenomenon indicates that there exists an eddy current composed of the tunnelling current and the conduction current in the composite object. The results indicate that eddy current testing method has the potential to apply specific conductive polymer composite non-destructive testing. 2. Mechanism analysis To realize the damage of specific conductive polymer composite based on eddy current effect, we fabricate a composite specimen. Nanoscale Fe/FeSiB is used as conductive phase, Nylon is used as insulating matrix. After several hours of mixing, the polymer material composed of Fe/FeSiB and Nylon is fabricated. Nylon is separated by nanoscale conductive filler particles. As the conductivity of nanoscale conductive filler particles is far more than that of nylon, the adjacent Fe/FeSiB can be considered as electrodes. According to the classic conclusions on the conductivity of the composite [3], if the distance between the adjacent conductive filler particles is small enough, the tunneling effect occurs. Fig. 1 shows the schematic of the process that the electrons pass through the potential barrier. Based on the previous research on the tunneling effect of the polymer composite material, the tunneling current density J can be given by the function of the distance between the adjacent particles D and the height of potential barrier λ. 3. Results Fig. 2 shows the relation between the excitation frequency and the impedance of the composite spiral element when the lift-off is zero. The induced voltage amplitude of 1MHz excitation decreases observably with the lift-off increased, while under the other frequencies excitation (low-frequency stage), the induced voltage amplitude almost consistent no matter whether the lift-off is zero or infinite. The behavior "eddy current phenomenon" is caused by the specific electromagnetic effect of "insulating" polymer composite material. 4. Conclusions The experiment results indicate that high frequency eddy current effect is existed if polymer composite material mixed with conductive particles approaches the spiral eddy sensor carried with alternating current. The impedance amplitude and angle of the composite element decrease with the increasing of the testing frequency. Therefore, the impedance of the eddy sensor can be used to find the superficial defect of the composite material. The finite element analysis results show that the concentration and the size of conductive particles which have the monotonous influence of equivalent capacitance. Therefore, the eddy sensor has the potential for the nondestructive testing of stealth structure with high frequency. The future works can be summarized as follows. To extend the application scope, the superficial defect characteristics of the composite material should be studied quantitatively. To make the higher sensitivity of the eddy testing, the key technologies (i.e. the optimization of eddy sensor, etc.) should be developed to improve the impedance change effects, such as environment dependent degradation of the composite material.

[1] L.S. Rosado, F.A. Cardoso, S. Cardoso, P.M. Ramos, P.P. Freitas and M. Piedade, Eddy currents testing probe with magneto-resistive sensors and differential measurement, *Sens. Actuat. A: Phys*., 212(2014), 58-67. [2] H. Wang, W. Li and Z. Feng, Noncontact Thickness Measurement of Metal Films Using Eddy-Current Sensors Immune to Distance variation. *IEEE Trans. Instrum. Measur*., 64(2015), 2557-2564. [3] J. C. Fisher and I. Giaever, Tunneling through thin insulating layers, *J. Appl. Phys*.,32(1961), 172-1771.

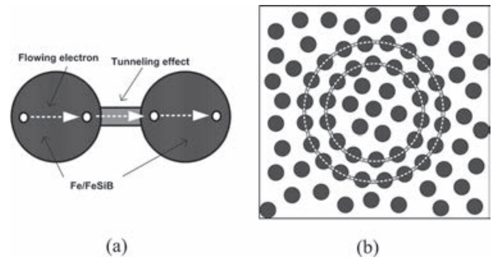

Fig. 1. Schematic for the mechanism of the current formation (a) Tunneling effect(b) Eddy current of polymer composite object

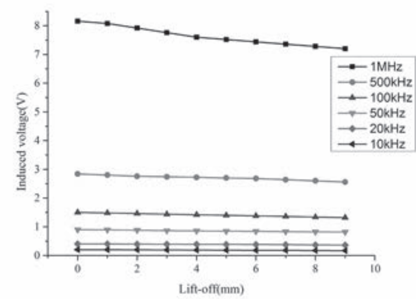

Fig. 2. Schematic for the polymer composite material of lift-off effect.

TUESDAY MORNING, 24 APRIL 2018 SIMPOR/ROSELLE BALLROOM, 8:30 TO 11:30

Session AT
PERMANENT MAGNET AND RELUCTANCE MACHINES I
(Poster Session)

Hui Yang, Co-Chair
Southeast University, Nanjing, China
TW Ching, Co-Chair
University of Macau, Macau, China

AT-01. Optimal Design of Asymmetric Step-Sloping Notches for Reduce the Cogging Torque of Single Phase BLDC Motor.

D. Kim[1,2], *Y. Park*[1,2], J. So[1,2] and y. You[3]
1. Electrical Control Engineering, Sunchon National University, Suncheon, The Republic of Korea; 2. Greenenergy Laboratory, Sunchon National University, Suncheon, The Republic of Korea; 3. Honam University, Gwangju, The Republic of Korea

I. Introduction In the case of BLDC (Brushless Direct Current) motors, cogging torque is produced with motors containing permanent magnets. A shape design for reducing the cogging torque, which is a cause of vibration noise, is essential [1][2]. Many methods have been suggested to reduce the cogging torque. The most prevalent is the use of the ease of application and the use of relatively inexpensive changes in the rotor and stator shape during construction [3]. The application of a notch is also one of the methods using the shape changes of the rotor and stator, and a method for applying the notch position and size as variables has been reported [4][5]. In this study, two different notches were applied to the stator tooth to reduce the cogging torque. The two sloping notches were used a diagonal line of different angles at different asymmetric locations. The optimal experiment planning, LHS, was used to locate the optimal location and radius and sloping angles, and the creegging model and optimization technique, as well as genetic algorithms, were used to approximate the model. The objective function was the cogging torque, and the constraints were set to make the torque and efficiency higher than a certain value. The validity of this paper was verified by comparing characteristics through finite element analysis. The accuracy of the 3D method was verified by comparing the results of the cogging torque experiment and 3D analysis of the conventional model with the conventional asymmetric notch, and then with the characteristics of the sloping notch model using the existing model, the sloping notch model. II. Single-Phase BLDC motor A single-phase BLDC motor is generally arranged in a region where the torque is zero because a rotor position may fail to perform an initial start-up operation, thereby solving the problem by configuring the shape of the stator asymmetrically. On the other hand, an asymmetric stator shape affects the cogging torque. Moreover, because the cogging torque causes vibration noise, the shape design for reducing the cogging torque is essential [4][5]. Cogging torque means a non-uniform torque of a stator inevitably generated in an electric motor using a permanent magnet, and a torque in the radial direction, in which the magnetic energy of the electric motor is minimum, i.e., a state in which the electric motor moves to an equilibrium state. These cogging torques are the cause of noise and vibration. Therefore, it is essential to consider the cogging torque for a motor that requires precision. The cogging torque is determined by B_{nNL} and G_{nNL}, and the application of the appropriate notch changes the effective slot number, so that the value of changes and the cogging torque can be reduced. On the other hand, when the asymmetric air-gap is applied, the relative permeance function of the air-gap is not constant but asymmetric. In this paper, the position, radius and sloping angle of notch (a) and notch (b) were designed asymmetrically, as shown in Fig. 1. The notch was designed by applying the optimization technique to determine the optimal position, radius, and sloping degree. III. Stator Shape Optimal Design for Cogging Torque Reduction To minimize the cogging torque reduction, an optimized design analysis was used to apply a sloping notch to the stator teeth. The position angle, radius, and sloping angle of each notch (a) and notch (b) were set as variables. The torque and efficiency are important characteristics affecting the performance. So these seted Constraints condition. LHS was used to extract the samples. The creegging model and genetic algorithm were applied to model the approximation and optimal design method. ● Objective function - Reduce the cogging torque ● Constraints - Efficiency ≥75[%] (5), Torque ≥295[Nm] ● Design variables - 0 ≤ X1 (Notch (a) deg) ≤ 20[°], 0 ≤ X2 (Notch (a) Size) ≤ 3[mm], -20[°] ≤ X3 (Notch (a) Sloping deg) ≤ 20[°] - 0 ≤ X4 (Notch (b) deg) ≤ 20[°], 0 ≤ X5 (Notch (b) Size) ≤ 3[mm], -12[°] ≤ X6 (Notch (b) Sloping deg) ≤ 12[°] IV. Stator design optimization result Fig. 2 compares the cogging torque of the initial and proposed models through finite element analysis. In the case of the basic model, the cogging torque was reduced by 39.2 [%] from the basic model while maintaining the efficiency and torque of the initial model at 65.5 [mNm]. Compared to the finite element analysis results, the error rate was less than 1.3 [%], which is consistent with the finite element analysis results. V. Conclusion This study examined the stator shape of a single phase BLDC motor with the aim of reducing the cogging torque. An asymmetric sloping notch was applied to reduce the cogging torque in a single phase BLDC motor with an asymmetric air gap. To minimize the cogging torque within the limited conditions, the position, radius, and sloping angle of the notch were determined by an optimization method using a genetic algorithm. The cogging torque of the proposed model using the sloping notch was found to be 40.3 [mNm], which was 38.5% lower than that of the basic model (65.6 [mNm]).

[1] Mohammed Fazil, K. R. Rajagopal, "A Novel Air-Gap Profile of Single-Phase Permanent-Magnet Brushless DC Motor for Starting Torque Improvement and Cogging Torque Reduction", IEEE TRANSACTIONS ON MAGNETICS, Vol. 46, No. 11, pp.3928-3932, 2010 [2] Dae-Won Chung, Yong-Min You, "Cogging Torque Reduction in Permanent-Magnet Brushless Generators for Small Wind Turbines", Journal of Magnetics, Vol. 20, No. 2, pp. 176-185, 2015 [3] S. Bentouati, Z. Q. Zhu, D. Howe, "Influence of Design Parameters on the Starting Torque of a Single-Phase PM Brushless DC Motor", IEEE TRANSACTIONS ON MAGNETICS, Vol. 36, No. 5, pp. 3533-3536, 2000 [4] Young-Un Park, Ji-Young So, Dong-hwa Chung, Yong-Min Yoo, Ju-Hee Cho, Kang-Soon Ahn, Dae-Kyong Kim, "Optimal Design of Stator Shape for Cogging Torque Reduction of Single-phase BLDC Motor", The Transactions of the Korean Institute of Electrical Engineers, Vol. 62, No. 11, pp. 1528-1534, 2013 [5] Young-Un Park, Ju-Hee Cho, and Dae-kyong Kim, "Cogging Torque Reduction of Single-Phase Brushless DC Motor With a Tapered Air-Gap Using Optimizing Notch Size and Position", IEEE TRANSACTIONS ON INDUSTRY APPLICATIONS, Vol. 51, No. 6, pp. 4455- 4463, 2015

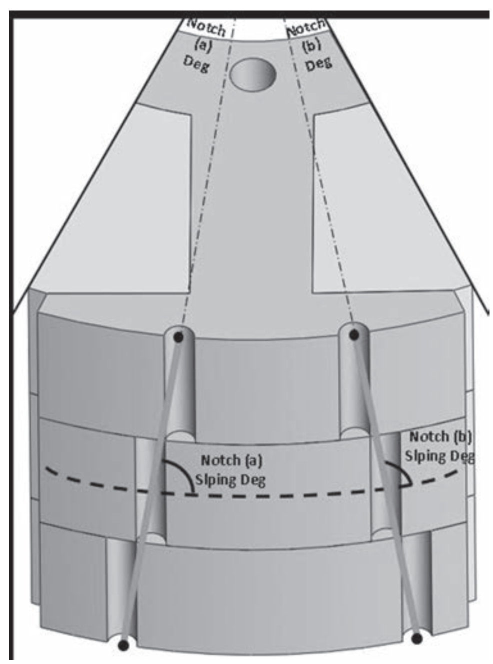

Fig. 1. Sloping Notch Model

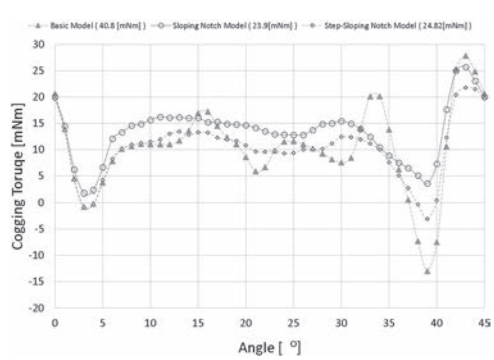

Fig. 2. Cogging torque comparison

AT-02. Comparison of Electromagnetic Characteristics of Linear Oscillating Actuator according to Magnetic Flux Path.

C. Kim[1], G. Jang[1], S. Seo[1], J. Ahn[3,1], S. Jeong[2] and J. Choi[1]
1. electrical engineering, Chungnam National University, Daejeon, The Republic of Korea; 2. R&D, LG Electronics, Seoul, The Republic of Korea; 3. R&D, MAGNETAR, Deajeon, The Republic of Korea

INTRODUCTION A linear oscillating actuator (LOA) is a machine that performs linear reciprocating motion within specific strokes at a specific frequency. With advantages such as high transmission efficiency, simple structure, and low noise, LOA is more suitable for electro-medical machines, electric hammers, linear pumps, refrigeration compressors, and other similar fields, than the traditional way by using rotatory motor and crankshaft [1]. The LOA can be classified as longitudinal flux LOA (LFLOA) and transverse flux LOA (TFLOA) according to the flux path. In the LFLOA, the direction of the current flow and the direction of the moving part are vertical, while the direction of the current flow in the TFLOA is parallel to the direction of the moving part. It is generally known that the transverse flux structure used in a machine can simultaneously increase power density and efficiency [2]. However, there is no research on the output power and efficiency in relation to the flux path in the two types of LOA of the same volume yet. Therefore, this study compares the electromagnetic characteristics of the LFLOA and TFLOA. For comparison, the axis and radius lengths of the two types of LOA are set equal. Next, both moving parts of LFLOA and TFLOA consist of permanent magnets. The moving-magnet-type LOA can lighten the moving part, produce a desired stroke through the length of the permanent magnet, and has a higher power density than the moving-iron-core type. Finally, the volume of the moving magnet is set the same. Under the above conditions, the optimal design of LFLOA and TFLOA is carried out. Finally, electromagnetic characteristics, such as magnetic flux density, force, and efficiency at a specific frequency, are compared. Fig.1. (a) shows two-dimensional (2D) and three-dimensional (3D) analysis models of the LFLOA. The LFLOA consists of an inner core, outer core, coil, and permanent magnet. Because the outer core consists of two shoes, one or three-pole permanent magnets are used to construct a magnetic circuit [3]. In this LFLOA model, the three-pole magnets are used to increase the magnetic flux density. As can be seen from the 3D analysis model, the magnetic flux in the LFLOA flows in the axial direction, and this type of LOA is radially laminated to reduce core loss. Fig.1. (b) also shows the 2D and 3D analysis model of the TFLOA. The TFLOA consists of the inner core, outer core, coil, permanent magnet, and a non-ferromagnetic material. To create the magnetic circuit in the TFLOA, the non-ferromagnetic material is inserted between the outer cores and the moving permanent magnets of the four poles are connected in reverse. In this type of LOA, the magnetic flux flows radially, and the outer core is stacked axially to reduce core loss. Fig.2. (a) shows the magnetic flux density distribution and flux flow in LFLOA and TFLOA. In the TFLOA, it can be seen that the flow of magnetic flux in the upper core is opposite to that in the bottom core. Fig.2. (b) shows the magnetic flux density at the air gap in the LFLOA and TFLOA. Fig.2. (c) shows the force characteristics of LFLOA and TFLOA in terms of the current. Under the same condition, the LFLOA is more dominant in the force characteristics. More detailed discussions and analysis results will be presented in the final paper. Acknowledgment This work was supported by the Basic Research Laboratory (BRL) of the National Research Foundation (NRF-2017R1A4A1015744) funded by the Korean government.

REFERENCES [1] Yuqiu Zhang, Qinfen Lu, Minghu Yu, and Yunyue Ye, “A Novel Transverse-Flux Moving Magnet Linear Oscillatory Actuator,” *IEEE Trans., Magn.*, vol. 48, no. 5, May, 2012. [2] Qian Wnag, Jiming Zou, and Mei Zhao, “Analysis and Computer-Aided Simulation of Cogging Force Characteristic of a Linear Electromagnetic Launcher with Tubular Transverse Flux Machine,” *IEEE. Trans. Magn*., vol. 39, no. 1, Jan., 2011. [3] Z. Q. Zhu, X. Chen, D. Howe, and S. Iwasaki, “Electromagnetic Modeling of a Novel Linear Oscillating Actuator,” *IEEE Trans. Magn.*, vol. 44, no. 11, Nov., 2008.

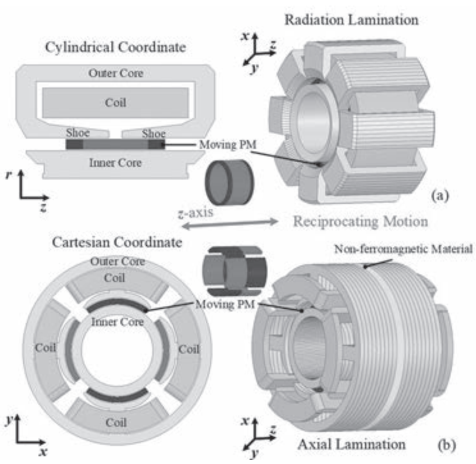

Fig. 1. (a) Analysis model of LFLOA, (b) analysis model of TFLOA.

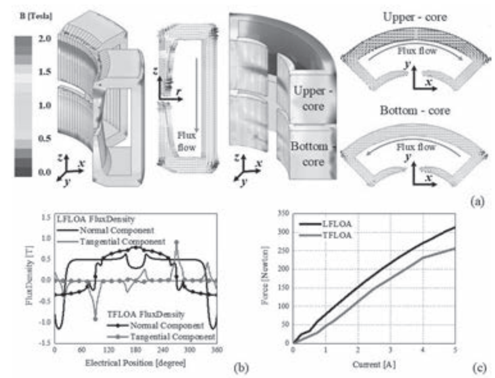

Fig. 2. Analysis results: (a) magnetic flux density distribution and flux flow of LFLOA and TFLOA, (b) comparison of magnetic flux density between LFLOA and TFLOA, (c) force characteristics of LFLOA and TFLOA in terms of current

AT-03. Analysis of Flux Reversal Permanent Magnet Machines with Different Consequent-Pole PM Topologies.

H. Li[1] and *Z. Zhu*[1]
1. Electronic and Electrical Engineering, University of Sheffield, Sheffield, United Kingdom

Abstract—This paper comprehensively studies electromagnetic performance of flux reversal permanent magnet (FRPM) machines with different consequent-pole PM (CPM) topologies. Several possible CPM topologies are firstly introduced and classified by different numbers of PM pieces and PM locations on stator teeth. Then, the magnetic flux distribution and torque performance of each CPM topology are analyzed and compared by both analytical and finite element (FE) analyses, from which the CPM topology with the highest torque density is identified. 1. Introduction FRPM machines [1, 2] have advantages of robust rotor structure and easy heat management of PMs, making them promising in low-speed and high-torque applications. However, the large equivalent air-gap length resulted from surface-mounted PM (SPM) topology limits the field modulation effect of rotor teeth, thus impairing the torque performance. In [3], one kind of CPM topology is proposed to replace the SPM topology, which is beneficial to improve the armature field and the resulted torque, as well as to reduce the PM volume, as shown in Fig. 1(a). For each stator tooth, one PM piece together with the adjacent ferromagnetic piece make the magnitude and direction of flux through the coil vary with the relative rotor position. Moreover, the magnetization directions of PMs are identical for all the stator teeth, but the PM locations are different for two adjacent stator teeth. Therefore, the CPM topology can be designated as N/Fe-Fe/N. In this paper, three new CPM topologies are proposed, as shown in Fig. 1(b)-(d), which are designated as N/Fe-N/Fe, N/Fe/N/Fe-Fe/N/Fe/N, and N/Fe/N/Fe-N/Fe/N/Fe, respectively. Similar to N/Fe-Fe/N, each stator tooth of N/Fe-N/Fe has one PM piece and one ferromagnetic piece. However, the PM locations of all the stator teeth are identical. Both N/Fe/N/Fe-Fe/N/Fe/N and N/Fe/N/Fe-N/Fe/N/Fe have two PM pieces and two ferromagnetic pieces on each stator tooth, and the PM locations of two adjacent stator teeth are different for the former, while they are exactly the same for the latter. Considering the fact that different CPM topologies largely influence the PM field in air-gap and associated winding connections, the torque performance of different CPM topologies is quite different. Therefore, the comparison of various CPM topologies will be the main focus of this paper as it is of great significance for the design of FRPM machines aiming at high torque density. 2. Torque Comparison of Various CPM-FRPM Machines Four 14-pole-rotor FRPM machines with different CPM topologies are globally optimized under the same stator outer diameter (90mm), stack length (25mm) and copper loss (20W), and their torque results are compared in Fig. 2. It should be noted that for Type1 and Type2, the stator slot number N_s=12; for Type3 and Type4, N_s=6. As can be seen, the average torques of the CPM-FRPM machines are largely affected by CPM topologies, which can be illustrated from the following two aspects: 1) The CPM topologies with identical PM locations on two adjacent stator teeth are more likely to produce higher torque than those with different PM locations, e.g. Type2 has 13% higher torque than Type1, Type4 has 34% higher torque than Type3; 2) The CPM topologies with two PM pieces on each stator tooth produce higher torque than those with one PM piece, e.g. Type3 has 34% higher torque than Type1, Type4 has 60% higher torque than Type2. The influence of PM location and number of PM pieces can be attributed to the different working harmonics of air-gap field in different CPM topologies. In terms of PM location, it influences the order (pole-pair number $p_{m,k}$) of the PM field harmonics, for Type1 and Type3, $p_{m,k}=|mN_s/2+kN_r|$; for Type2 and Type4, $p_{m,k}=|mN_s+kN_r|$, where m is the order of Fourier series of PM magnetomotive force (MMF) and m=1,2,3…, k=0,±1,±2…, is the order of the permeance harmonics produced by salient rotor teeth, and N_r is the rotor pole number. As for the number of PM pieces on each stator tooth, although it has no influence on the order of the field harmonics, it largely influences the magnitude of each harmonic. Taking Type2 and Type4 for example, for Type2, the N_sth harmonic is of the largest magnitude whereas the $2N_s$th harmonic has the largest magnitude in Type4. The detailed analysis and comparison of working harmonics in different CPM topologies will be given in full paper, and the optimal number of PM pieces will also be discussed. 3. Conclusion In this paper, various FRPM machines with different CPM topologies are analyzed and compared. It is found that the torque performance of the CPM machine is largely related to the CPM topology. In full paper, for each CPM topology, the detailed analysis of working harmonics, key design parameters and performance comparison against the SPM counterpart will be given. In addition, two prototypes with different CPM topologies are being manufactured, of which the test results will be provided.

1] R. P. Deodhar, S. Andersson, I. Boldea, and T. J. E. Miller, "The flux-reversal machine: A new brushless doubly-salient permanent-magnet machine," *IEEE Trans. Ind. Appl.*, vol. 33, no. 4, pp. 925–934, 1997. [2] C. Wang, S. A. Nasar, and I. Boldea, "Three-phase flux reversal machine (FRM)," *Proc. IEE. Elec. Power Appl.*, vol. 146, no. 2, pp. 139–146, Mar. 1999. [3] Y. Gao, R. Qu, D. Li, J. Li, and G. Zhou, "Consequent-pole flux-reversal permanent-magnet machine for electric vehicle propulsion," *IEEE Trans. Appl. Supercond.*, vol. 26, no. 4, 2016.

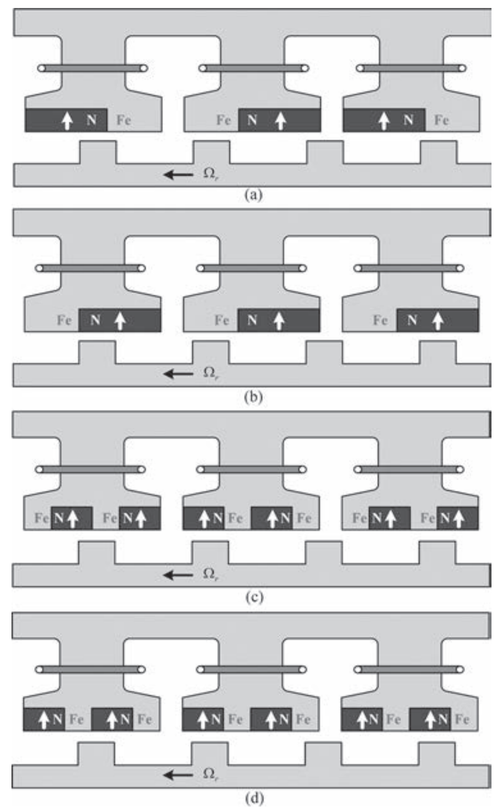

Fig. 1. Various CPM-FRPM machines. (a) Type1: N/Fe-Fe/N. (b) Type2: N/Fe-N/Fe. (c) Type3: N/Fe/N/Fe-Fe/N/Fe/N. (d) Type4: N/Fe/N/Fe-N/Fe/N/Fe.

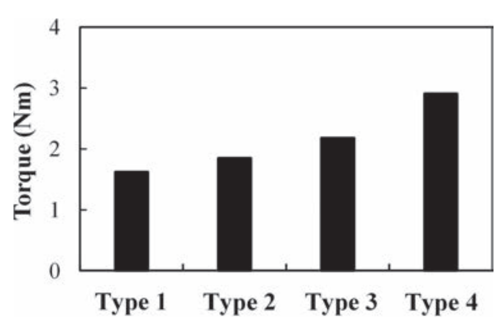

Fig. 2. Torque comparison of different CPM-FRPM machines.

AT-04. Influence of Aluminum Die-Cast Rotor Porosity on the Efficiency of Induction Machines.

J. Yun[2,1] and S. Lee[1]
1. Korea University, Seoul, The Republic of Korea; 2. Hyundai Electric Co., LTD, Yongin, The Republic of Korea

I. Introduction With the increasing demand for energy efficiency, the international legislative actions are enforcing motor manufacturers to produce motors that meet the mandated efficiency ratings [1]-[2]. This makes it crucial to predict the motor efficiency with high accuracy in the design stage. Porosity in aluminum die cast rotors is inevitably introduced during the die casting process and causes the rotor fill factor (FF) to vary from motor to motor for a given design. This causes non-negligible variance in motor performance considering that rotor losses account for up to 20% of induction machine losses. However, the influence of porosity distribution in rotor bars and end rings is not properly considered in existing publications [3]-[5]. This makes it difficult for motor designers to predict the performance of motors accurately to guarantee that they meet the specified efficiency. In this paper, a method based on a combined 2 and 3 dimensional finite element analysis (2D/3D FEA) that takes the porosity level and distribution into account is proposed for accurate prediction of motor performance. The proposed method is verified through FEA and experimental testing. II. Proposed method It is important for the motor designer to use suitable analysis tools to meet mandatory motor efficiency regulations. The equivalent circuit model most commonly used for optimizing the design does not provide sufficient accuracy because the influence of non-ideal factors are not taken into account. Although FEA is well suited for precise prediction of motor performance, 2D FEA is not capable of accounting for the effect of the rotor end region, and the limitation of 3D FEA is the excessive computation time. The main concept of the proposed method is to perform a half single slot pitch 3D FEA shown in Fig. 1(a) for precise calculation of rotor end ring resistance and leakage reactance, R_{ring} and X_{ring}, and then perform a 2D FEA of the slot portion with the end ring parameters obtained. The FF and porosity distribution in die-cast rotors were accounted for in the 2D and 3D FE models based on the X-ray scans shown in [6]. It was assumed that porosity is concentrated in the center of the bars in the slot portion, and distributed in the radial center of the end rings close to the rotor core, as shown in Figs. 1(b),(d). The proposed method was compared to the conventional method that assumes uniform distribution of porosity. FEA and experimental testing were performed on a 440 V, 8 P, 15 kW induction motor to analyze and verify the proposed method. The temperature of the stator winding and rotor end ring were obtained using a thermocouple installed on the end winding surface and a thermal tape in end ring. The no-load and load tests were performed according to IEC 60034-2-1 [7] for calculating the full-load efficiency. The influence of FF and porosity distribution on motor performance was investigated by performing FEA and experimental testing on rotors with 67% and 93% FF. The end ring parameters for the proposed method were calculated using the half axial length, single slot pitch rotor 3D FE model shown in Fig. 1(b). The transient solution is obtained with the pre-determined values of R_{ring} and X_{ring}, and the 2D FE 1/8 model shown in Figs. 1(c),(d). For the rotor with 93% FF, the rotor conductor losses obtained assuming uniform porosity distribution in the bar and end ring is lower (by 2.5%, 1.9%) than that of the test results and proposed method. As a result, the error in the efficiency estimate with proposed method is noticeably lower by -0.01%, when compared to conventional method (+0.30%). This indicates that the proposed method can predict the performance with improved accuracy. For the rotor with 67% FF, the error in the efficiency were +0.78%, and -0.08% for conventional and proposed methods, respectively. This shows that the values with conventional method have a tendency to overestimate the values of motor efficiency significantly. This can be attributed to the influence of porosity distribution on the rotor loss not being taken into account, which leads to lower rotor loss estimates. Test results show that the rotor loss for the 67% FF rotor is 75% larger than that of the 93% FF rotor. The increased ohmic loss in the rotor cage has a significant impact on the temperature rise of rotor bars from 87°C to 117°C, and also causes the temperature in the stator winding to increase from 84°C to 97°C. The full-load efficiency obtained with experimental testing is 91.81% and 90.15% for rotors with 93% and 67% rotor FF, respectively. This shows that porosity has significant impact on efficiency of die-cast rotors to a degree where it can fail to meet efficiency classes. The relationship between FF and motor performance was investigated by performing the calculations with the proposed method for varying FF levels between 67% and 100% as shown in Fig. 2. There is a 2.04% decrease in motor efficiency as the rotor FF is decreased from 100% to 67%. The following can be concluded from the FE and test results: - Rotor FF and porosity distribution have a significant influence on motor efficiency - The proposed method can provide reliable prediction of motor efficiency

[1] Rotating Electrical Machines-Part 30-1: Efficiency Classes of Line Operated AC Motors (IE code), IEC60034-30-1, 1st Ed, 2014. [2] A.T. De Almeida, F.J.T.E. Ferreira, A.Q. Duarte, "Technical and Economical Considerations on Super High-Efficiency 3 Phase Motors," *IEEE Trans. on Ind. Appl.*, vol. 50, no. 2, pp. 1274-1285, Mar. 2014. [3] J. Steffan, K.R. Rither, "A numerical verification of the Clausius-Mossotti relation," *IEEE Trans. on Magn.*, vol. 26, no. 2, pp. 528-531, Mar. 1990. [4] K. S. Lee, S. H. Lee, J. H. Park, J. M. Kim and J. Y. Choi, "Experimental and Analytical Study of Single-Phase Squirrel-Cage Induction Motor Considering End-Ring Porosity Rate," *IEEE Trans. on Magn.*, vol. 53, no. 11, pp. 1-4, Nov. 2017. [5] H. C. Liu and J. Lee, "Optimum Design of a IE4 Line-Start Synchronous Reluctance Motor Considering Manufacturing Process Loss Effect," *IEEE Trans. on Ind. Electron.*, Early Access Article. [6] J. Yun, S.B. Lee, M. Jeong, S. B. Lee, "Influence of Die-Cast Rotor Fill Factor on the Starting Performance of Induction Machines," *IEEE Trans. on Magn.*, Early Access Article. [7] Rotating Electrical Machines-Part 2–1: Standard Methods for Determining Losses and Efficiency from Tests (Excluding Machines for Traction Vehicles), IEC60034-2-1, 2nd Ed., 2014.

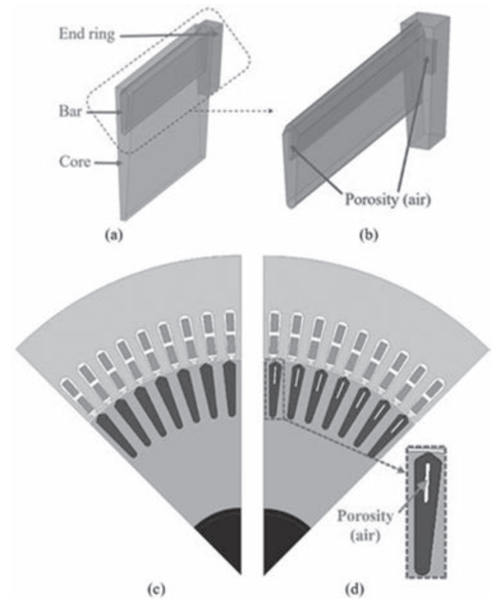

Fig. 1. (a) Half axial length, single slot pitch 3D FEA model, and (b) bar and end ring model with FF and porosity distribution considered; 2D FEA model for (c) conventional method (d) proposed method with FF and porosity distribution taken in to account

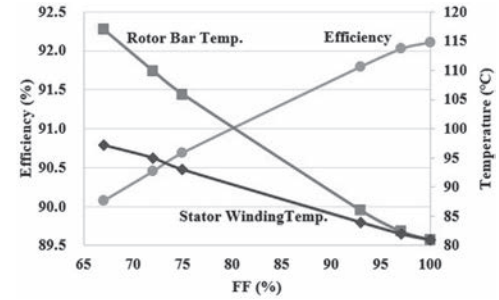

Fig. 2. Estimates of stator winding and rotor bar temperature, and efficiency with proposed method as a function of FF

AT-05. Influence of Cooling Air Flow Velocity on Temperature Rise and Output Power for Permanent Magnet Servo Motor.

G. Zhao[1], X. Gao[1], Y. Wang[1] and B. Bai[1]
1. Shenyang University of Technology, Shenyang, China

I.INTRODUCTION Power density is a very important index for permanent magnet servo motor. The motor is asked to output more power and more torque in a finite volume, as a result the problem of the higher motor temperature rise is becoming more and more prominent with the increase of power density. So more researchers pay more attention in the heat dissipation of the motor, more heat dissipation methods are adopted to reduce the temperature rise and the influence of the internal flow field of the motor on the temperature rise is studied [1][2]. The flow field and temperature field of the motor are analyzed by the flow-heat coupling in [3][4], but the quantitative relation between the velocity of the cooling air and the temperature of the motor is not involved. Because the air flow velocity can influence the heat dissipation coefficient and the heat dissipation capability, in this pater the Finite Element Method (FEM) is used to analyze the flow-heat of the permanent magnet servo motor and the flow field and temperature field in the motor are analyzed. Then the influence of the flow velocity of the cooling air on the temperature of the motor is studied and the best flow range is found. Finally the experiment is carried out to verify the validity of the simulation and summarize the influence of cooling air velocity on motor temperature. II. GEOMETRY MODEL In this paper, a three-dimensional calculation model is established and the corresponding boundary condition is applied to the finite element analysis based on an 8-pole 36-slot surface mounted permanent magnet servo motor. For calculation convenience the motor model is simplified properly, as shown in Fig.1. III. ANALYSIS AND EXPERIMENT Applying the rated rotational speed to the rotor and simulating the internal air flow field, temperature distribution of the motor is figured out, as shown in Fig. 2. Fig 2(a) shows the distribution of fluid velocity inside the motor and Fig. 2(b) shows the steady-state temperature distribution cloud picture. According to Fig.2 the winding end temperature is the highest, the reason is that the convection heat dissipation coefficient of the winding end is less than the heat conduction for this kind of fully-closed motor. The convection heat dissipation coefficient of the motor is proportional to the velocity of the fluid velocity. So the velocity of the cooling air can affect the motor temperature rise. The relationship between the motor temperature and the cooling air velocity is obtained through calculating the steady motor temperature in different cooling air velocity by FEM, as shown in Fig.3. According to Fig.3 the motor temperature gets lower for higher cooling air velocity. But the changing trend is not linear, the motor temperature decreases rapidly even if a relative slow velocity of the cooling air exerts to the motor, the tendency of the motor temperature reduction get gently when the cooling air velocity boosts. The cooling effect does not improve much when the cooling air velocity goes beyond 3m/s. In order to verify the validity of the method, a series of experiments are done on the permanent magnet servo motor, as shown in Fig.4. The experimental data at different cooling air velocities are shown in table 1. By comparing the experimental data, It can be seen that the motor winding end temperature decreases remarkably by 40 degree centigrade when the cooling air velocity is 3m/s and the FEM analysis agree with the experimental data well. Now that the motor temperature can be reduced remarkably because of the exertion of the cooling air, the motor output capacity must be enhanced and the power density can be boosted. So another experiment and analysis have been done. The output power is increased from 630W to 780W at the same air flow velocity 3m/s, the tested and calculation results are shown in table 2. When the motor works in the overload torque 5Nm, its temperature is also within the reasonable temperature rise requirements, and the motor output power increases by about 24%, but the temperature increases by about 14% merely. Therefore, the motor capacity is improved by improving the velocity of cooling air. IV.CONCLUSIONS This paper investigates the effect of cooling air flow velocity on the temperature and output capacity of permanent magnet servo motor. The fluid field and the temperature distribution are analyzed by FEM in different cooling air velocity and the experiments are carried out to verify the validity of the FEM analysis. Increasing the velocity of the cooling air can decrease the motor temperature and enhance the motor power density. More details will be given in full paper.

[1] W. M. Tong, J. Y. Sun, and S. N. WU, "Effect of Rotor Structure on Rotor Dissipation for Totally-Enclosed High-Speed Permanent Magnet Motor", Transactions of China Electrical Society, Vol.32, No. 22, Nov. 2017. [2] F. G. Zhang, G. H. Du, and T. Y. Wang, "Integrated Design of 1.12MW High Speed PM Machine Based on Multi-Physics Fields, " Transactions of China Electrical Society, Vol.30, No. 12, Jun, 2015. [3] Y. P. Lu, J. N. Zhu, and M. P. Feng, "Numerical Calculation and Analysis of Flow Field for a New Type of Vertical Squirrel Cage Motor", Proceedings of the CSEE, Vol.37, No.19, Oct.5, 2017. [4] Y. J. Zhang, J. J. Ruan, and T. Huang, "Calculation of Temperature Rise in Air-cooled Induction Motors through 3-D Coupled Electromagnetic Fluid-Dynamical and Thermal Finite-Element Analysis", IEEE Transaction on Magnetics, Vol. 48, No. 2, February 2012.

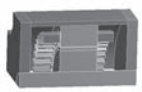

Fig.1. Geometrical model of the motor

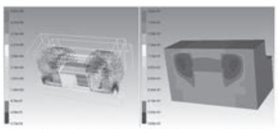

(a) Distribution of fluid velocity (b) Steady-state temperature distribution
Fig.2. Results of Finite Element Analysis

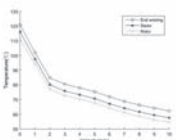

Fig.3. Temperature of motor varies with the velocity of cooling air

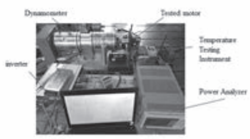

Fig.4 Temperature rise test for the prototype

Table 1 The comparison of simulation and experiment results

Velocity(m/s)	Winding Temperature (℃)	
	FEM	Experiment
0	121	118
1	102	98
2	84.8	82
3	80.5	78

Table 2 Motor performance under different loads

Output power	630W(4Nm)	780W(5Nm)
Temperature(℃)	78	89

AT-06. The Method for Reducing Intrinsic Shaft Voltage by Suitable Selection of Pole-arc Coefficient in Fractional Slot Permanent Magnet Synchronous Machines.

B. Peng[1], X. Wang[1] and W. Zhao[1]
1. Shandong University, Jinan, China

1. Introduction Fractional slot Permanent magnet synchronous machines (FSPMSMs) are widely used in electric vehicles, industrial automation, wind power, and other fields[1]. However, the bearing damage and premature failure occur frequently due to the shaft voltage. Actually, with certain pole and slot number combinations will generate a net dissymmetry flux to induce intrinsic shaft voltage, even without rotor eccentricity, inter-turn short circuit or other faults. When the shaft voltage exceeds a threshold, the bearing oil film breakdown will induce a large bearing current and corrode bearing. In order to reduce the maintenance cost, plenty of researches have been concentrated on the shaft voltage and bearing current mitigation technologies[2]. In [3], ceramic bearings were used to avoid the electric corrosion of shaft voltage, but it has the disadvantage of low mechanical strength. In [4], a conductive ring microfibers was proposed to provide a low impedance path to ground for bearing currents, yet it needs to be replaced frequently due to wear. In order to solve these disadvantages and suppress the intrinsic shaft voltage in FSPMSMs without additional devices, this paper proposes a novel mitigation method based on suitable selection of pole-arc coefficient by analytical analysis. Then, the optimal pole-arc coefficient is verified and corrected by finite element analysis(FEA). 2. Principle of intrinsic shaft voltage in FSPMSMs In general, the flux under per pole is divided into two equal fluxes as clockwise flux Φ_L and anti-clockwise flux Φ_Y in stator yoke after across the air gap. However, when the motor magnetic circuit is imbalance, the Φ_L is not equal to the Φ_Y, a net dissymmetry flux as (Φ_Y-Φ_L) will be yielded as shown in Fig. 1. And the superposition of the net dissymmetry flux under each pole pairs can be equivalent to a shaft encircling flux which can link with shaft and induce shaft voltage. 3. Determination of the optimal pole-arc coefficient by analytical analysis In the following analytical analysis, the permeability of the rotor yoke and stator core are assumed as infinite. On the based of orthogonality of trigonometric functions, when the slot number N_s and pole number p satisfies the relationship as $p(2n\text{-}1)=kN_s$ (like 8-pole/9-slot, 6-pole/9-slot), there would exist a net dissymmetry flux which can be expressed as: $B_{nk}=\sum\lambda_k F_{2n\text{-}1}\cos[(2n\text{-}1)\omega_e t]$(1) where ω_e is the electrical angular velocity. λ_k is the kth order harmonic of the stator slotting effect coefficient; $F_{2n\text{-}1}$ is the $(2n\text{-}1)$th order harmonic of magnetic-motive-force (MMF) of permanent magnet (PM) (n, k=1,2,3…). $F_{2n\text{-}1}$ can be expressed as: $F_{2n\text{-}1}=4/[(2n\text{-}1)\pi]h_m\sin[(2n\text{-}1)\alpha_p\pi/2]$(2) where h_m and α_p are the thickness and pole-arc coefficient of PM respectively. The intrinsic shaft voltage which is induced by B_{nk} can be defined as: $V_s=\sum V_{s\_2n\text{-}1}=\sum(1\text{-}2n)\omega_e\lambda_k F_{2n\text{-}1}S_L\sin[(2n\text{-}1)\omega_e t]$(3) Meanwhile, the of $V_{s\_2n\text{-}1}$ is $(2n\text{-}1)=kN_s/p$ times to stator current frequency f. Based of (3), suppressing $F_{2n\text{-}1}$ can reduce the value of V_s. And for costs saving, it prefers adjusting pole-arc coefficient to changing the magnet shape for reducing $F_{2n\text{-}1}$. Hence, if the pole-arc coefficient meets the values as: $\alpha_{py}=2m/(2n\text{-}1)$ (4) where m=1,2,3…$(n\text{-}1)$, the amplitude of $F_{2n\text{-}1}$ and $V_{s\_2n\text{-}1}$ will reduce to 0 due to $\sin[(2n\text{-}1)\alpha_p\pi/2]=0$. For 6-pole/9-slot FSPMSMs, V_{s_3} is the fundamental component of shaft voltage whose amplitude is much larger than subharmonic V_{s_3}. From (3) and (4), it owns a maximum value as V_{s_3m} when α_p=1, and reaches the minimum as 0 when α_p=0.67 or 0.33. Considering the influence of pole-arc coefficient on other performances in motor[5], 0.67 is deemed to the optimal pole-arc coefficients in this machine which achieves maximum suppression of shaft voltage. 4. Correct of the Optimal Pole-arc Coefficient by FEA By FEA, the shaft voltage in 6-pole 9-slot FSPMSMs with different pole-arc coefficients are calculated under open circuit and 1000 r/min rated speed, hence the fundamental frequency of shaft voltage is 150Hz from (3). The region is set as (0.6, 1) to find the optimal pole-arc coefficient by the method of bisection. As a result, the amplitudes of fundamental shaft voltage in 6-pole/9-slot FSPMSMs with different α_p are shown in Fig.2. It is obvious that 0.63 is the more optimal α_p since its amplitude of V_{s_3} can be approximated at 0. Although it does not reach the minimum value, the amplitude of V_{s_3} in the machine with α_p=0.67 is much lower than the one with α_p=1, whilst the error between the optimal values calculated by analytical analysis and FEM is little. 8-pole/12-slot and 8-pole/9-slot FSPMSMs are also analyzed to increase the persuasiveness in the full paper. 5. Conclusion The method of suitable selected pole-arc coefficient has been proved to suppress the intrinsic shaft voltage effectively. In addition, to ensure precision and save time, a superposition method should be adopted to determine the optimal pole-arc coefficient, where the optimal value was firstly calculated by analytical analysis, then was corrected constantly by FEA to reach an exact value.

[1] Ayman M. EL-Refaie. "Fractional-slot concentrated-windings synchronous permanent magnet machines: Opportunities and challenges," *IEEE Transaction Indusrial Electronics*, vol. 57, no. 1, pp.107–121, Sep, 2009. [2] T. Plazenet, T. Boileau, B. N. Mobarakeh. "An overview of shaft voltages and bearing currents in rotating machines," *IEEE Industry Applications Society Annual Meeting.*, Portland, 2016: 1-8. [3] A. Muetze, A. Binder. "Practical rules for assessment of inverter-induced bearing currents in inverter-fed AC motors up to 500 kW," *IEEE Transactions on Industrial Electronics*, vol.50, no.3, pp. 1614-1622, June 2007. [4] A. Muetze, H. W. Oh. "Current-carrying characteristics of conductive microfiber rings for high frequencies and current amplitudes," *IEEE Transactions on Power Electronics*, vol.25, no.8, pp.2082-2092, Aug.2010. [5] Yubo Yang, Xiuhe Wang, Rong Zhang, et al. "The optimization of pole arc coefficient to reduce cogging torque in surface-mounted permanent magnet motors," *IEEE Transaction on magnetics*, vol. 42, no.4, pp. 1135-1138, April, 2006.

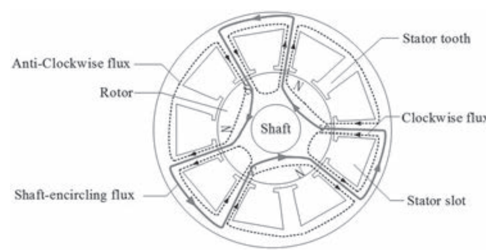

Fig. 1. Magnet circuit in 6-pole/9-slot FSPMSMs.

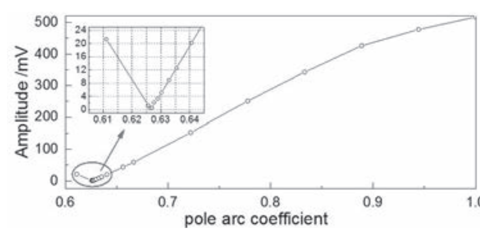

Fig. 2. The amplitude of fundamental shaft voltage with different α_p in 6-pole/9-slot FSPMSMs.

AT-07. Comparison of Rotor Eddy Current Losses in Fractional-Slot Concentrated-Winding IPM machines with Different Rotor Topology.

L. Cong[1,2], X. Li[1] and *L. Wu*[2]

1. College of Electrical Engineering, Guangxi University, Nanning, China; 2. School of Automation and Electrical Engineering, Linyi University, Linyi, China

I. Introduction Interior permanent magnet (IPM) machines have been widely used in many applications, such as electric vehicle, servo drive, and so on, due to its high torque density [1]. By using fractional-slot concentrated-winding (FSCW),the IPM machines have short end windings and less copper loss, and can further improve torque density under same cooling capacity. However, the IPM machines with FSCW have rich harmonics of magnetomotive force (MMF) and the higher rotor eddy current losses [2]. This paper will compare the rotor eddy current losses in FSCW IPM machines with different rotor topology and discuss rotor topology's influence on the harmonics of the armature field. II. Topology and Specification of FEA Models Figs. 1 & 2 show 12-slot 10-pole and 9-slot 10-pole IPM machine's FEA models with different rotor topology. The specification of IPM machine's FEA models is listed in Table I. To compare rotor eddy current losses reasonably, the stator outer/inner diameter, stator yoke, air gap, stack length, size of each magnet, slot opening width and electric loading of all IPM machines are set same value, respectively. III. FEA Results of Torque and Eddy Current Losses In this section, the MMF harmonics and rotor eddy current losses of IPM machines are detailed analyzed by the theoretical and FEA method. The main harmonics of the MMF in 12-slot/10-pole and 9-slot/10-pole IPM machines are listed in Table II & III, respectively. In the Table, the slip [%] is defined as the slip of the rotor speed relative to the rotation speed of MMF's harmonics and the MMF [%] is defined as percentage of the harmonics magnitude to working harmonics [3]. Fig. 3 shows the FEA results of the electromagnetic torque and rotor eddy current losses in 12-slot/10-pole IPM machines under the maximum of torque/current control. It can be seen the torque of the IPM machine with I type, V type and spoke rotor type are 8.61 Nm, 8.75 Nm and 9.44 Nm, respectively. The IPM machine with spoke rotor type has the highest torque due to its parallel connection magnetic circuit type and small magnetic resistance per pole. The rotor eddy current losses of I type, V type and spoke rotor type IPM machines are 12 W, 7.6 W and 8.6 W respectively. The rotor eddy current losses in the 12-slot/10-pole IPM machines are mainly caused by the 1st and 7th order harmonics of MMF. The pole-shoes in I type IPM machine is very small, the armature field by 1st and 7th order MMF harmonics can easily penetrate each magnet and produced the higher eddy current losses. The V type and spoke type IPM machines have larger pole-shoes, the armature field by 7th order MMF harmonics partly penetrate pole-shoes only and don't produced PM eddy current losses, so, the rotor eddy current losses in V type and spoke type IPM machines are less than I type machine. According to the Table II, the 7th order harmonics of MMF is a dominant component, the each pole armature field of which will penetrate 2 piece magnets in V type IPM machine and the 1 piece in spoke type IPM machine, therefore the armature field by 7th order harmonics of MMF in V type IPM machine is less than that in spoke type machine. Due to the 7th order harmonics of MMF be dominant component, the rotor eddy current losses in V type IPM machine is less than that in spoke type IPM machine in spite of the 1st MMF harmonic be significant reduced by its specific rotor topology. Fig. 4 shows the FEA results of the electromagnetic torque and rotor eddy current losses in 9-slot/10-pole IPM machines under the maximum of torque/current control. It can be seen the torque of the IPM machine with I type, V type and spoke rotor type are 8.81 Nm, 9.03 Nm and 9.74 Nm, respectively. The reason of the highest torque in IPM machine with spoke rotor type is analyzed above. The rotor eddy current losses of I type, V type and spoke rotor type IPM machines are 35.2 W, 25.2 W and 37 W respectively. According to the Table III, the 4th order harmonics of MMF is a dominant component, and which will produce the longer wave-length armature field of each pole. The each pole armature field by 4th order harmonics of MMF can penetrate 2 piece magnets in I type IPM machine, 2 to 4 piece magnets in V type IPM and 1 to 2 piece magnet in spoke type IPM machine, therefore the armature field by 4th order MMF harmonic is least in V type IPM machine and is largest in spoke type machine. As a result, the eddy current loss in V type IPM machine is least. Compared to I type IPM machine, the spoke type IPM machine has the highest eddy current losses due to its largest dominant armature field, although which has less 1st order harmonic armature field and other higher armature fields are mainly penetrate pole-shoes only. IV. Conclusion This paper is detailed analysis the armature field by MMF and eddy current losses in FSCW IPM machines with different rotor topology. Under the same electric loading, the FEA results reveal that the V type IPM machine has the least eddy current losses both in 12-slot/10-pole and 9-slot/10-pole combination machines. The spoke type IPM machine has less eddy current loss than I type IPM machine in 12-slot/10-pole combination and has larger eddy current loss than I type IPM machine in 9-slot/10-slot combination.

[1] A. M. EL-Refaie, "Fractional-slot concentrated-windings synchronous permanent magnet machines: opportunities and challenges," *IEEE Trans. Ind. Electron.*, vol.57, no.1, pp. 107-121, Jan. 2010 [2] K. Atallah, D. Howe, P. H. Mellor, and D. A. Stone, "Rotor loss in permanent-magnet brushless AC machines," *IEEE Trans. Ind. Appl.*, vol. 36, no. 6, pp. 1612–1618, Nov./Dec. 2000. [3] L. Wu, R. Qu, and D. Li, "Reduction of rotor eddy-current losses for surface PM machines with fractional slot concentrated windings and retaining sleeve," *IEEE Trans. Magn.*, vol.50, no.11, pp. 1-4, Nov. 2014.

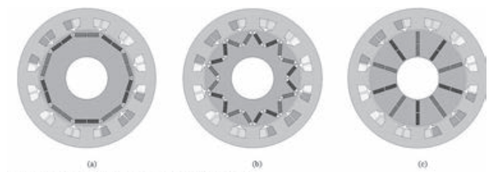

Fig. 1. 12-slot/10-pole IPM machines. (a) I Type. (b) V Type. (c) Spoke Type

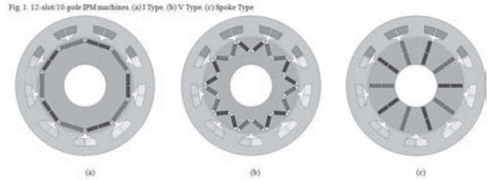

Fig. 2. 9-slot/10-pole IPM machines. (a) I Type. (b) V Type. (c) Spoke Type

TABLE I SPECIFICATION OF IPM MACHINE'S FEA MODELS

Item, unit	12 slot/10-pole	9-slot/10-pole
Stator outer diameter, mm	122	
Stator inner diameter, mm	85	
Stator yoke length, mm	8	
Tooth width, mm	12	15
Slot opening width, mm	2.5	
Tooth tip, mm	1	
Air gap length, mm	0.8	
Stack length, mm	50	
Each magnet thickness, mm	3	
Each magnet width, mm	10	
Bridge, mm	1	
Magnet residual flux density, T	1.2	
Winding Type	FSCW/Double Layer	
Electric loading, A/cm	287.6	
Steel	50WW470	
Speed, rpm	6000	

TABLE II HARMONICS OF 12-SLLOT/10-POLE MACHINE

Harmonics	Slip [%]	MMF [%]
1	120	35.9
5	0	100
7	240	71.4

TABLE III HARMONICS OF 9-SLLOT/10-POLE MACHINE

Harmonics	Slip [%]	MMF [%]
1	120	32.1
2	50	40
4	180	125
5	0	100
7	137	10.6

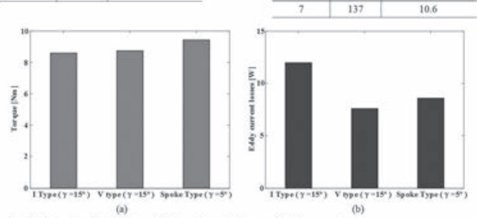

Fig 3. FEA results of 12 slot/10-pole IPM machines. (a) Torque. (b) Eddy current losses

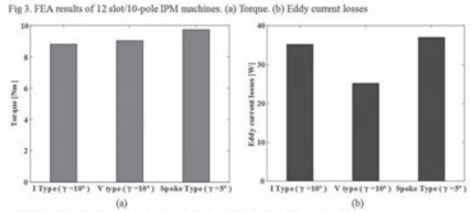

Fig 4. FEA results of 9 slot/10-pole IPM machines. (a) Torque. (b) Eddy current losses

AT-08. Design and Analysis of A Mechanical Flux-varying PM Machine with Auto-rotary PMs.

X. Liu[1], Z. Zhang[1], H. Xu[1], J. Xiao[1] and Z. Liu[1]
1. School of Electrical Engineering and Automation, Jiangxi University of Science and Technology, Ganzhou, China

I. Introduction Due to the constant magnetic field of the permanent magnet(PM) machine, its terminal voltage cannot be maintained constant as a generator[1], and the constant power area is narrow and the adjustable speed range is also limit as a motor[2]. In order to overcome these shortcomings, a new type of mechanical flux-varying PM machine with auto-rotary PMs (MFVPMM) is proposed in this paper. The operation principles of this machine presented are analyzed, and its flux weakening ability is studied by FEA. II. Text A. Machine topology Fig.1 shows the topology structure of MFVPMM which includes stator winding, stator core, PM, rotor core. The armature winding adopts single layer distributed short pitch winding. The material of PM adopts N36Z_20, which magnetic induction coercive force is -920000 A/m. The material of rotor core and stator core adopts M19_29G. There is a slot on the cylindrical PM, which can connect with mechanical flux-adjusting device. Fig.2 shows the mechanical device, which clearly shows its parts and their mechanical relations. Disc have sliding chutes and connecting rod slots, which can make sliding block rectilinear moving and gear auto-rotating respectively. The sliding block connects with the disc by the spring. The surface of disc and sliding block is set to the ideal state, which means ignoring the friction between them. The sliding block is the driven source of mechanical flux-adjusting device and makes full use of centrifugal force to drive the gear. There exists some distance between initial sliding block and gear, which ensures no flux weaken under basic speed. *B. Operation principle* Fig.3 shows the operation principle of ARPMMFVPMM, the PM flux linkage of machine, Ψ_f, is supplied by the PMs in one pole, which is the result of vector synthesis. When the PMs rotates an angle, such as 30°, the composite PM flux linkage is √3/2 than basic, which achieves the effect of *d*-axis demagnetization. Fig.4 shows the principle of mechanical flux weakening. When the machine operates under basic speed, the magnetizing direction of PMs is radial. The PMs will rotates with an angle automatically when the motor operates above basic speed, and its magnetizing direction is varied. As a result, the air-gap flux density can be changed correspondingly. C. FEA model And Results Fig. 5 (a) shows the FEA structure, the structure of machine is axisymmetric and centrosymmetric, and its pole is 8. Fig.5 (b) gives its FEA mesh model with 141127 nodes and 101494 elements. Fig.6 shows the flux density distribution in the MFVPMM. By comparing the same color map and color of flux density contour, the flux is weakened evidently by the proposed mechanical device. Fig.7 and Fig.8 shows the flux linkage and the induced EMF when the machine operates at different speed(the basic speed is 750rpm), which shows that the flux and EMF of MFVPMM can be reduced with the proposed Mechanical device. The analysis results shows that an excellent field control ability has obtained for the proposed MFVPMM with the simple structure. III. Conclusions A new type of auto-rotary PMs mechanical flux-varying PM machine is proposed in this paper. The magnetic flux distribution, winding flux linkage and EMF, flux weakening ability are analyzed by 2D FEM. The results show that a good field control ability without any additional loss is obtained for the ARPMMFVPMM. Therefore, the ARPMMFVPMM can be widely applied in the fields of constant power driven and constant voltage generation.

[1] B. Massimo, B. Nicolachi and M. Freddy, "Permanent-magnet Optimization in Permanent-magnet-assisted Synchronous Reluctance Motor for a Wide Constant-power Speed Range," IEEE Transactions on Industrial Electronics, vol. 59, no. 6, pp. 2495-2502, Jun. 2012. [2] Z. Q. Zhu, M. M. J. Al-Ani and X. Liu, "A mechanical flux weakening method for switched flux permanent magnet machines," IEEE Transactions on Energy Conversion, vol. 30, no. 2, pp. 806-815, June.2015.

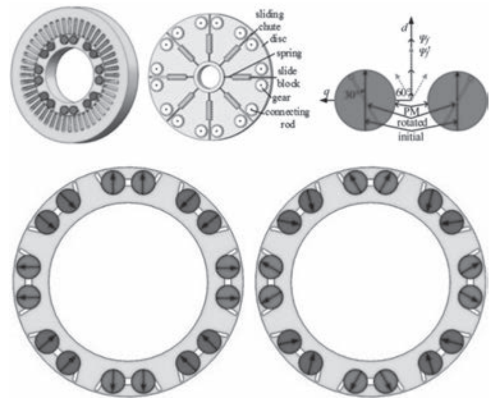

Fig. 1. Topology Structure of ARPMMFVPMM
Fig. 2. Mechanical flux-adjusting device
Fig. 3. The operation principle of ARPMMFVPMM
Fig. 4. The magnetization direction schematic diagram of PMs (a) Under basic speed (b) Above basic speed

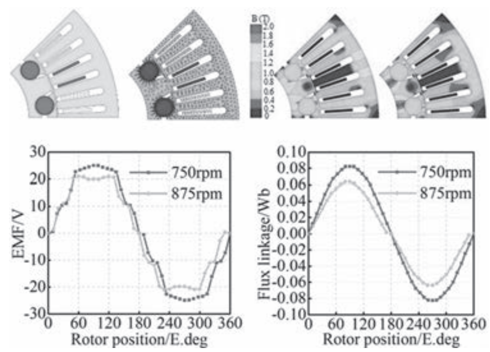

Fig. 5. FEA model of ARPMMFVPMM (a) FEA structure model (b) FEA mesh model
Fig. 6. Magnetic flux in ARPMMFVPMM (a) Under basic speed (b) Above basic speed
Fig. 7. The flux linkage of ARPMMFVPMM
Fig. 8. The induced EMF of ARPMMFVPMM

AT-09. Development of Variable Stress Applying System for Shrink Fitting of Stator Housing in IPM Motor.

J. Kitao[1], J. Aizawa[1], M. Nakano[1], M. Yamada[1] and A. Daikoku[1]
1. Mitsubishi Electric Corp., Hyogo, Japan

High efficiency electrical machines such as rotating machines and transformers are expected to be realized for solving the environmental problem. It is well known that the iron loss of stator core for rotating machines increases by a mechanical stress caused by the shrink fitting of the stator housing. In order to clarify the influence of the mechanical stress to the characteristics of rotating machines, several papers [1]–[6] describe the simulation technic such as the combined analysis of a mecahnical stress and an electromagnetic field. In this paper, we develops the variable applying stress system with the hydraulic unit to clarify the influence of the shrink fitting to the motor characteristics. Fig. 1 shows the schematic of the variable applying stress system. We designed these system following three requirement. (a) The circumferential compressive stress of the stator core caused by these system is more than 100 MPa. (b) These system can adjusts the circumferential compressive stress of the stator core at an interval of 1 MPa. (c) These system uniformly applies the circumferential compressive stress of the stator core in the axial and circumferential direction. In order to realize the concept of these three points, these system is adopted the hydraulic mechanism. When the hydraulic unit applies the oil pressure to the oil room, the pressure bulk head is deformed by the oil pressure and consequently the circumferential compressive stress is generated in the stator core. These system can adjusts the circumferential compressive stress of the stator core by the oil pressure of the hydraulic unit. The circumferential compressive stress, which is measured by eight biaxial strain gages installed on the surface of the back-iron for the stator core, is changed linearly with respect to the applied oil pressure by the hydraulic unit, and the maximum circumferential compressive stress is generated more than 100 MPa under the oil pressure 15 MPa. Fig. 2 shows the measurement results of the iron loss in no-load with respect to the applied oil pressure by the hydraulic unit. The load motor rotates the test motor, which is adopted the interior permanent magnet motor with concentrated winding, at a constant rotating speed. Then, the loss of the test motor with the unmagnetized and magnetized permanent magnet rotor in no-load is measured by the torque detector. The iron loss of the test motor is calculated by a difference between the loss of the test motor with the magnetized permanent magnet rotor ant it with the unmagnetized permanent magnet rotor, which is included only the mechanical loss without the iron loss. As the applied oil pressure increases, the iron loss is gradually increased and the iron loss under the circumferential compressive stress of 100 MPa (applied oil pressure 15 MPa) in the stator core is increased by 2 times compared with the non-stress. As explained above, the proposed system can measures the iron loss of the actual motor under mechanical stress with various operating point. The more measurement results will be included in the full paper. ACKNOWLEDGMENTS This paper is based on results obtained from the Future Pioneering Program "Development of magnetic material technology for high-efficiency motors" commissioned by the New Energy and Industrial Technology Development Organization (NEDO).

[1] K. Fujisaki and S. Satoh, "Numerical calculation of electrical fields in silicon steel under mechanical stress," *IEEE Trans. Magn.*, vol. 40, no. 4, pp. 1820–1825, 2004. [2] A. Daikoku, M. Nakano, S. Yamaguchi, Y. Tani, Y. Toide, H. Arita, T. Yoshioka, and C. Fujino, "An Accurate Magnetic Field Analysis for Estimating Motor Characteristics Taking Account of Stress Distribution in the Magnetic Core," *IEEE Trans. IAS,* vol. 42, no. 3, pp. 668-674, 2006. [3] K. Fujisaki, R. Hirayama, T. Kawachi, S. Satou, and C. Kaido, "Motor Core Iron Loss Analysis Evaluating Shrink Fitting and Stamping by Finite-Element Method," *IEEE Trans. Magn.*, vol. 43, no. 5, pp. 1950-1954, 2007. [4] L. Daniel and O. Hubert, "An equivalent stress for the influence of multiaxial stress on the magnetic behavior," *J. Appl. Phys.*, vol. 105, no. 7, pp. 07A313-1–07A313-3, 2009. [5] D. Miyagi, N. Maeda, Y. Ozeki, K. Miki, and N. Takahashi, "Estimation of iron loss in motor core with shrink fitting using FEM analysis," *IEEE Trans. Magn.*, vol. 45, no. 3, pp. 1704–1707, 2009. [6] K. Yamazaki and W. Fukushima, "Loss Analysis of Induction Motors by Considering Shrink Fitting of Stator Housings," *IEEE Trans. Magn.*, vol. 51, no. 3, #8182004, 2015.

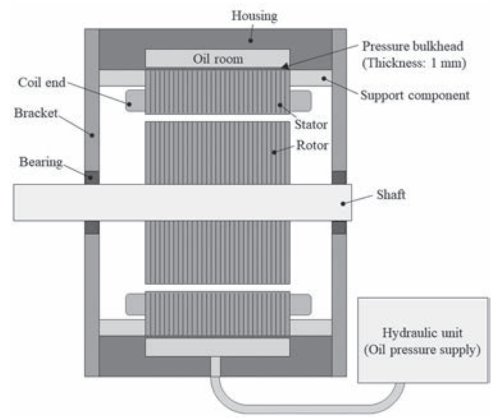

Fig. 1. Variable applying stress system with the hydraulic unit.

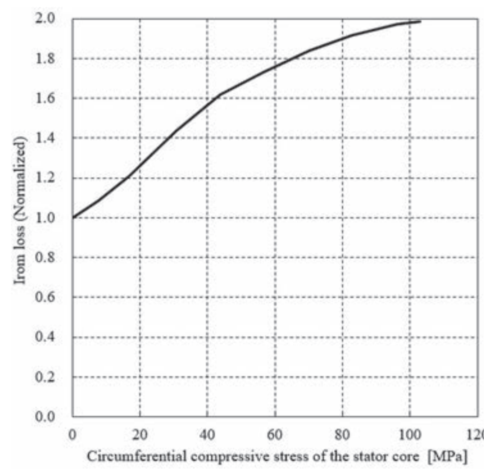

Fig. 2. Measurement results of the iron loss in no-load.

AT-10. Study on structure aimed at low vibration of 16-pole 18-slot IPM motor for Mild-HEV.

Y. Hirai[1]
1. Motor Drive Laboratory, Tokyo City University, Tokyo, Japan

I. INTRODUCTION The efficient construction method of mild hybrid is to minimize the mechanical loss by directly connecting the engine and the assist motor. The shape of the motor to be directly connected to the engine output shaft has a flat structure with a diameter of 250 to 300 mm and an axial length of 60 to 90 mm, and various multipolar PM motors have been proposed in order to obtain high output and high power generation. As a slot pole combination, it is known that a combination of 8-9 is good, but it was said to be impractical due to the problem of magnetic imbalance due to eccentricity. For large diameter motors, it is possible to combine 16-18 times, which is considered an effective combination. In this paper, we propose an IPM motor with 16 - 18 - combination for mild hybrid considering performance and low vibration during startup and power generation. The usefulness of 16 poles and 18 slots combination and the cogging torque torque ripple reduction structure were clarified by finite element analysis. II. SLOT COMBINATION STUDY OF MOTOR The principle of the cogging torque generation, the slot combination is a significant impact. Therefore it is possible to reduce by changing the combination of the number of poles and the number of slots. Therefore, we focused on the 8-pole 9 slot. This combination is the exciting side is a magnetic unbalance the pole. Therefore vibration during rotation is increased when the shaft is displaced. However, by the doubling of the ratio of the pole and the slot (16-pole 18-slot), it is possible to reduce the influence of these problems. In addition, it is possible to further reduce the cogging torque and torque ripple. Using SPMSM model were cogging torque analysis of 4 patterns of "16-pole 18-slot" and "8-pole 12-slot", "12-pole 18-slot", "20-pole 24-slot". The results are shown in Fig. 1 (a). Fig. 1 (a), 16 poles 18 slots, it is possible to most cogging torque is reduced has been confirmed. Thus, creating the IPM motor model at 16 poles and 18 slots. Fig. 1 (b) shows the created IPMSM model. In addition, it indicates the motor specifications in Table I. III. IMPROVEMENT OF THE COGGING TORQUE AND TORQUE RIPPLE As a method of optimizing the torque waveform, a method of providing a cutout or the like in the rotor / stator opposing part is known, but this method generates an order component due to the notch shape in addition to the basic order, This may cause noise and vibration. In this magnetic circuit, the gaps between the rotor-stator as shown in Fig. 2 (a), employing a rotor shape gradually expanding toward the switching portion of the stator core. Thus, to mitigate the steep magnetic flux change in the air gap and reduce the cogging torque and torque ripple without placing a new order components. Fig. 2 (b) shows the model after applying the shape. Fig. 2 (c), (d) shows the cogging torque before and after application of the shape and the torque ripple improvement effect at 200 Arms energization, Table II shows the average torque and torque ripple rate values. By changing the curvature, the cogging torque 1/7 times reduced, the average torque 5Nm improved, torque ripple it was confirmed that the reduced about 6%. IV. CONCLUSION Characteristics of 16 pole 18 slot IPM motor directly connected to the engine output shaft were analyzed and compared with other multipolar motors. It was confirmed that the reduction of cogging torque and torque ripple without increasing order components by changing the curvature of the stator and the rotor. The proposed motor is currently prototyping and the results will be presented on the conference.

[1] I.Uquhant, D.Tanaka, R.Owen, Z.Q.Zhu, J.B Wang, D.A Stone, "Mechanically actuated variable flux IPMSM for EV and HEV applications" EVS27 Barcelona, Spain, Novenber 17-20, 2013 [2]Masahiro Aoyama, Kazukiyo Nakajima, Toshihiko Noguchi, "Proposal and Preliminary Experimental Verification of Electrically Reversal Magnetic Pole Type Variable Magnetic Flux PM Motor" IEEJ Transactions on Industry Applications Vol.137 No.9 pp.725–736 [3]B. Aslan, E. Semail, J. Korecki, J. Legranger, "Slot/pole Combinations Choice for Concentrated Multiphase Machines dedicated to Mild-Hybrid Applications" IECON 2011, 7-10 Nov. 2011 [4]Zhou Yafu, Chang Cheng, "Study on the Powertrain for ISG Mild Hybrid Electric Vehicle" IEEE Vehicle Power and Propulsion Conference (VPPC), September 3-5, 2008, Harbin, China

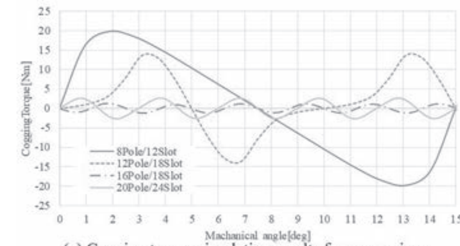

(a) Cogging torque simulation results for comparison

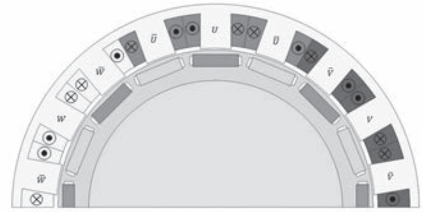

(b) The created 16-pole 18-slot IPM model

Table I Specifications of the created motor

Stetor	Diameter	266	[mm]
	Back yoke thickness	6	[mm]
	Teeth width	20	[mm]
Rotor	Diameter	206	[mm]
	Airgap length	2	[mm]
Stack length	40		[mm]
Output	18		[kW]
Maximum torque	160		[Nm]
Maximum speed	6000		[rpm]
Power-supply voltage	DC48		[V]
Maximum phase current	400		[A]
Coil	Coil Turn	32/teeth	[Turn]
	Wire diameter	φ2.0	[mm]
	Coil resistance / 1slot	0.033	[Ω]
Magnet	Width	30	[mm]
	Thickness	8	[mm]
Pole	16		
Slot	18		

Fig. 1 16 pole 18 slot IPM motor model and parameters, Cogging torque waveform comparison

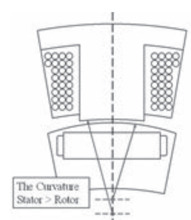

(a) Change of curvature of stator and rotor

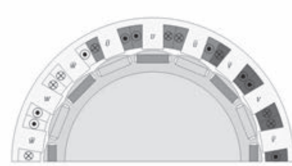

(b) Curvature change adaptation model

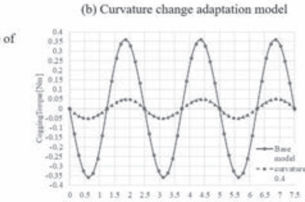

(c) Comparison of cogging torque waveform

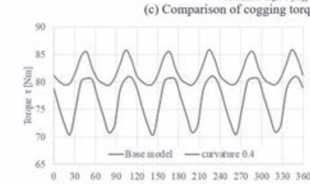

(d) Torque waveform at 200Arms energization

Table II Average torque and torque ripple rate

	Base model	curvature 0.4
Average Torque[Nm]	76.51	81.90
Torque ripple ratio[%]	13.79	7.89

Fig.2 Comparison of characteristics of curved model and base model

AT-11. Torque Improvement in Partitioned Stator Wound Field Switched Flux Machine By Using Assisted Ferrites.

Z. Wu[1] and Z. Zhu[1]
1. Electronic and Electrical Engineering, The University of Sheffield, Sheffield, United Kingdom

Wound field (WF) synchronous machines without rare-earth permanent magnet (PM) have been attractive recently due to lower cost than PM machines [1]. The wound-rotor synchronous machines suffer from brushes and slip rings which are essential for DC field excitation [2]. However, they can be eliminated in the wound-stator synchronous machines in which both DC winding and AC windings are placed in the stator, e.g. the WF switched flux (WFSF) machine [3], [4]. Due to the magnetic gearing effect in the stator-excitation machines [5], [6], the partitioned stator WFSF (PS-WFSF) machine having separated DC and AC windings in two stators and hence a higher total slot area and >19% larger torque is proposed and analyzed in [7], e.g. the 12/10-stator/rotor-pole PS-WFSF machine shown in Fig. 1(a). In this paper, to further improve the torque density of the 12/10-stator/rotor-pole PS-WFSF machine shown in Fig. 1(a), short-circuited ferrites are introduced to reduce the inner stator tooth saturation and improve the air-gap field density. The developed 12/10-stator/rotor-pole PS-WFSF machine with assisted ferrites can be obtained as shown in Fig. 1(b). They have similar machine topologies, i.e. two stators wound by AC windings and DC winding, respectively, and a sandwiched rotor consists of several modulation iron pieces. The only difference is that the short-circuited ferrites are introduced in the proposed topology. As shown in Fig. 1(c), flux density B_1 can be produced in both the inner stator tooth and the inner air-gap due to the WF magnetomotive force (MMF). However, an opposite flux density B_2 can be generated in the short-circuited magnetic circuit for the ferrite MMF, as shown in Fig. 1(d), whilst the corresponding inner air-gap flux density is B_3. Due to the opposite directions of B_1 and B_2, as shown in Fig. 1(e), the inner stator saturation and hence the iron loss will be decreased with a reduced flux density B_1'-B_2', where $B_1' > B_1$ and $B_2' > B_1$. Moreover, as shown in Fig. 1(e), the inner air-gap flux density can be improved from B_1 in the machine without ferrite to $B_1' + B_3'$ in the machine with ferrite, where $B_3' < B_3$. Therefore, both the open-circuit phase flux-linkage and the average electromagnetic torque can be improved in the proposed PS-WFSF machine with assisted ferrites. This can be evidenced by the 2D FE predicted results shown in Fig. 1(f) and Fig. 1(g). As shown in Fig. 1(f), the fundamental phase flux-linkage when the AC coil number of turn is N_{ac}=1 can be improved by 2.33%, from 0.272mWb to 0.278mWb. However, since the on-load inner stator tooth saturation in the PS-WFSF machine without ferrite is stronger than the open-circuit one due to armature reaction, the average electromagnetic torque can be more effectively improved by 3.76%, from 1.47Nm to 1.53Nm, when both the DC winding copper loss p_{cuf} and the AC windings copper loss p_{cua} are 30W and the machines operate at BLAC mode under zero d-axis current control, i.e. i_d=0, due to negligible reluctance torque [7]. Moreover, as shown Fig. 1(h), a higher total copper loss and hence a stronger saturation in the machine without ferrite will result in more effective torque improvement in the its counterpart with ferrites. Both the proposed 12/10-pole PS-WFSF machine with assisted ferrites and its counterpart without ferrite are built and tested to validate the FE predicted results. The machine components are shown from Fig. 2(a) to Fig. 2(d), i.e. Fig. 2(a) for the shared outer stator, Fig. 2(b) for the shared cup rotor, Fig. 2(c) for the inner stator with ferrites and Fig. 2(d) for the inner stator without ferrite. The comparison between the measured and 2D FE predicted phase-back-EMFs is given in Fig. 2(e) and Fig. 2(f), respectively. It can be observed that the 2D FE predicted results agree well with the measured results in both machines. The comprehensive comparison including loss and efficiency between the proposed topology with ferrites and its counterpart without ferrite will be given in the full paper, together with the investigation of the average torque separation by DC winding and ferrites by using frozen permeability.

[1] I. Boldea, L. N. Tutelea, L. Parsa, and D. Dorrell, "Automotive electric propulsion systems with reduced or no permanent magnets: an overview," *IEEE Trans. Ind. Electron.*, vol. 61, no. 10, pp. 5696-5711, Oct. 2014. [2] M. L. Bash, and S. D. Pekarek, "Modeling of salient-pole wound-rotor synchronous machines for population-based design," *IEEE Trans. Energy Convers.*, vol. 26, no. 2, pp. 381-392, Jun. 2011. [3] J. T. Chen, Z. Q. Zhu, S. Iwasaki, and R. Deodhar, "Low cost flux-switching brushless AC machines," *Proc. Conf. Veh. Pow. Prop.*, Lille, France, 2010, pp. 1-6. [4] Y. Tang, J. J. H. Paulides, T. E. Motoasca, and E. A. Lomonova, "Flux switching machine with DC excitation," IEEE Trans. Magn., vol. 48, no. 11, pp. 3583-3586, Nov. 2012. [5] Z. Z. Wu, and Z. Q. Zhu, "Analysis of air-gap field modulation and magnetic gearing effects in switched flux permanent magnet machines," *IEEE Trans. on Magn.*, vol. 51, no. 5, May 2015, Art. ID 8105012. [6] K. Atallah, and D. Howe, "A novel high-performance magnetic gear," *IEEE Trans. Magn.*, vol. 37, no. 4, pp. 2844-2846, Jul. 2001. [7] Z. Q. Zhu, Z. Z. Wu, D. J. Evans, and W. Q. Chu, "A wound field switched flux machine with field and armature windings separately wound in double stators," *IEEE Trans. Energy Convers*, vol. 30, no. 2, pp. 772-783, Jun. 2015.

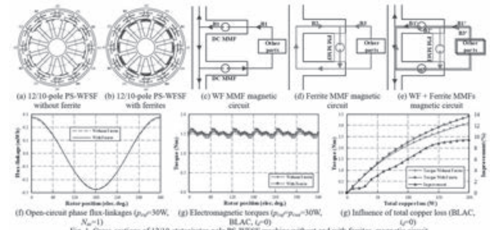

Fig. 1. Cross-sections of 12/10-stator/rotor-pole PS-WFSF machine without and with ferrites, magnetic circuit, open-circuit phase flux-linkages and electromagnetic torques.

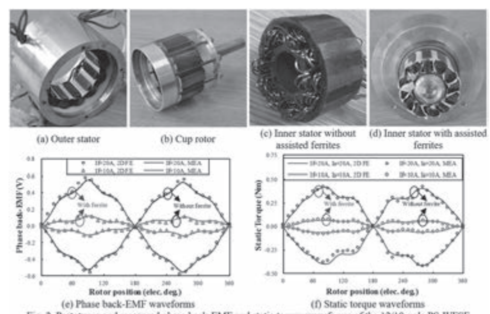

Fig. 2. Prototypes and measured phase back-EMF and static torque waveforms of the 12/10-pole PS-WFSF machines without and with assisted ferrites.

AT-12. Rotor Shape Optimization for Improving Torque Performance of PM-Assisted Wound Field Synchronous Machine.

W. Chai[1], B. Kwon[1] and T.A. Lipo[2]
1. Hanyang University, ANSAN, The Republic of Korea; 2. University of Wisconsin–Madison, Madison, WI, United States

I. INTRODUCTION Wound field synchronous machines (WFSMs) utilize rotor windings to generate flux without magnet. However, the current in field winding causes much copper loss, thereby the efficiency is decreased and temperature rise is increased. With the development of the permanent magnets (PMs), the permanent magnet synchronous machines (PMSMs) have been widely used in many industry applications instead of the WRSMs. But its development is restricted by the high cost of PMs and the limited supply of the rare earth magnets [1]. And another problem is that once the magnet is magnetized, it is difficult to achieve flux weakening control [2]. Furthermore, the danger of the demagnetization should be considered when PMSMs design. To overcome these problems, many kinds of hybrid excited machines have been developed. Inserting PMs into rotor's slot opening, there are two kinds of assist effects: one is the reduction of the magnetic saturation, and the other is the direct flux linkage increase of the armature windings from the permanent magnets. And the total assisted effects are ensured for wide load condition [3]. The demagnetization analysis of the assisted-PM is evaluated due to sudden three-phase short circuits in [4]. Meanwhile, it can be benefit for the motor's reluctance torque and affect the operation range. In paper [5], the optimized single flux barrier is introduced in the WRSMs. It is an effective and simple method to improve the motor's reluctance torque and widen the operating region. In this paper, PM was introduced in a WRSM with a single flux barrier configuration for high quality wide load condition and wide operating range, then the rotor shape of PM-Assisted Wound Field Synchronous Machine (PMa-WFSM-B) was optimized for improving torque characteristic and decreasing torque ripple under constant permanent magnet (PM) volume and motor size. The optimization method mainly includes Kriging method and genetic algorithm (GA). Then, JMAG-Designer is used as the tool of 2-D finite-element analysis to confirm the validity. II. MODELING, OPTIMIZATION AND DISCUSSION Fig.1 shows the rotor topologies of the investigated models, which stator has six slots with three-phase concentrated windings. The normal single flux barrier in the basic model was chosen to stop the magnetic field line in q-axis and increase the reluctance torque. NdFeB is assisted in the slot opening as the proposed model to decrease pole magnetic saturation and increase the direct flux linkage of the armature winding. And it is considered that the torque performance can be improved by optimizing the rotor shape. There are five design variables selected as shown in Fig.2: *h* is the width of the assisted-PM, whereas the length of the assisted-PM *w* is automatically changed in order to keep the volume of assisted-PM as a constant, *m* and *l* are the main parameters to define the rotor slot area and the magnetic flux path of the Assisted-PM. *d* is the width of single flux barrier that can keep the new motor with a wider operating range. *x* is the offset distance between the rotor pole center and flux barrier center which can adjust the magnetic unbalance of the two pieces in each rotor pole. Because the assisted-PM changes the across-sectional area of the FWs, in order to maintain the slot filling ratio, the number of turns is proportionately changed. The stator is fixed during the whole optimal process of the motor. To further improve the torque performance, the optimization using the Kriging Method and Genetic Algorithm (GA), is then applied to the proposed model. Fig.3 (a), (b), (c) give the torque performances of three investigated machines, in which the point value is the torque values of each components when the total torque gets the maximum. The main specifications and FEM analysis results of the three investigated models are listed in the Table I. It is clarified that the torque is improved by 37.6% and the torque ripple is decreased by 18.8% without decrease efficiency, increase PM volume and motor size, compared with that the conventional machine. More detailed results and analysis will be presented in the full paper.

[1] D. G. Dorrell, "Are wound-rotor synchronous motors suitable for use in high efficiency torque-dense automotive drives?," in IECON 2012-38th Annual Conference on IEEE Industrial Electronics Society, 2012, pp. 4880-4885. [2] M. Tursini, E. Chiricozzi, and R. Petrella, "Feedforward flux-weakening control of surface-mounted permanent-magnet synchronous motors accounting for resistive voltage drop," IEEE Transactions on industrial electronics, vol. 57, no. 1, pp. 440-448, 2010. [3] K. Yamazaki, K. Nishioka, K. Shima, T. Fukami, and K. Shirai, "Estimation of assist effects by additional permanent magnets in salient-pole synchronous generators," IEEE Transactions on Industrial Electronics, vol. 59, no. 6, pp. 2515-2523, 2012. [4] T. Hosoi, H. Watanabe, K. Shima, T. Fukami, R. Hanaoka, and S. Takata, "Demagnetization analysis of additional permanent magnets in salient-pole synchronous machines with damper bars under sudden short circuits," IEEE Transactions on Industrial Electronics, vol. 59, no. 6, pp. 2448-2456, 2012. [5] W. Chai, W. Zhao, and B.-i. Kwon, "Optimal Design of Wound Field Synchronous Reluctance Machines to Improve Torque by Increasing the Saliency Ratio," IEEE Transactions on Magnetics, vol.53, no.11, Article Squence Number: 8206604, 2017.

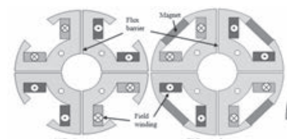

(a) Basic rotor (b) Proposed rotor
Fig.1 Rotor topologies of the investigated model

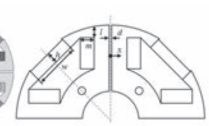
Fig. 2. Design variables

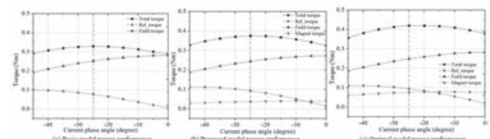
(a) Basic model torque performance (b) Proposed model torque performance (c) Optimal model torque performance
Fig. 3. The magnetic pole structures and torque performances of three investigated models

Table I Specifications and FEM analysis results

Item	Unit	Basic model	Proposed model	Optimal model
Slots/Poles	-	6/4		
Stator outer diameter	mm	88		
Airgap length	mm	0.5		
Axial length	mm	52		
Rotor flux barrier width (d)	mm	0.700	0.700	0.934
Magnet volume	mm^3	0	3*12*52	5.6*6.4*52
Offset distance of flux barrier (x)	mm	0	0	0.003
Rotor pole width	mm	4	4	4.003
		4	4	3.997
Torque	Nm	0.329	0.375	0.420
Reluctance torque	Nm	0.082	0.093	0.095
Torque ripple	%	52.5	44.7	29.0
Efficiency	%	87.4	87.5	87.6

AT-13. Torque Ripple Improvement for Ferrite-Assisted Synchronous Reluctance Motor by Using Asymmetric Flux-barrier Arrangement.

M. Xu[1], G. Liu[1] and W. Zhao[1]
1. Jinagsu university, Zhenjiang, China

Introduction Ferrite-assisted synchronous reluctance motors (FASRM) provide high torque density and a wide range operation speeds for many applications, ranging from electric vehicle and electric home appliance [1]. Moreover, the ferrite magnet has received increased attention, following the increase of the price of rare earth magnet. However, the main drawback of the FASRM is the high torque ripple which will lead to serious vibration and acoustic noises [2]. Therefore, it is greatly significant to research the torque ripple suppression strategy for FASRMs, thus improving the smoothness of the torque [3]. This paper introduces a low torque ripple FASRM with asymmetrical flux barrier, which can reduce the torque ripple effectively. Novel Topology Fig. 1 shows the structure of the proposed FASRM. This motor has 48 slots and 8 poles, with two flux barriers per poles. The detailed configuration of the asymmetrical flux barrier is shown in Fig. 2. There are two kinds of flux barriers with different opening angle, and the changing of the angle based on the original flux barriers B_1. The opening angle of flux barriers B_2 is enlarged θ based on original flux barriers B_1. In this way, a shift of the torque waveform phase can be achieved, and the torque amplitudes offset each other. In addition, the amount and location of ferrite magnets have not changed, and reduce the torque ripple effectively without sacrificing the average torque. Results The proposed method is evaluated by a theoretical analysis and finite-element method (FEM). Fig. 3 shows the no-load field distribution and on-load flux density of the proposed FASRM. It can be seen that the magnetic fields are symmetrical distributions, and the asymmetrical flux barriers will not affect the electromagnetic performance of the proposed FASRM. Fig. 4 shows the reluctance torque waveforms and harmonics. As adopted the asymmetric flux barrier arrangement, a shift of the torque waveform phase can be achieved, and the torque amplitudes offset each other. It can be seen that the reluctance torque ripple is reduced from 85% to 24%, approximately. Fig. 5 shows total torques waveform and their harmonics. It can be seen that the total torque ripple is reduced to 14%, and the 6th and 12th harmonics have been successfully eliminated.

[1] T. A. Huynh and M. F. Hsieh, "Comparative study of PM-assisted SynRM and IPMSM on constant power speed range for EV applications," *IEEE Trans. Magn*., vol. 53, no. 11, p. 8211006, Nov. 2017. [2] H. Liu, I. Kim, Y. Jun Oh, S. Go, "Design of permanent magnet-assisted synchronous reluctance motor for maximized Back-EMF and torque ripple reduction" *IEEE Trans. Magn*., vol. 53, no. 6, p. 8202604, Jun. 2017. [3] M. Ferrari, N. Bianchi, and E. Fornasiero, "Analysis of rotor saturation in synchronous reluctance and PM-Assisted reluctance motors," *IEEE Trans. Ind. Appl*., vol. 51, no. 1, pp. 169-177, Feb. 2015.

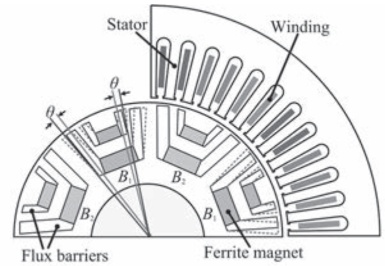

Fig. 1. Configuration of proposed FASRM with asymmetrical flux barrier.

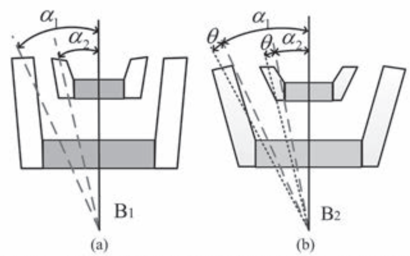

Fig. 2. Detailed configuration of the asymmetrical flux barrier.

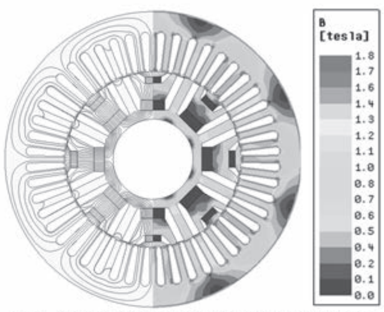

Fig. 3. No-load field distribution and on-load flux density.

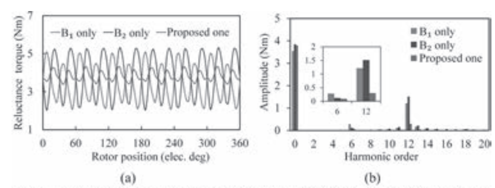

Fig. 4. Comparison of reluctance torque in both FASRMs. (a) Reluctance torque. (b) Reluctance torque harmonic order.

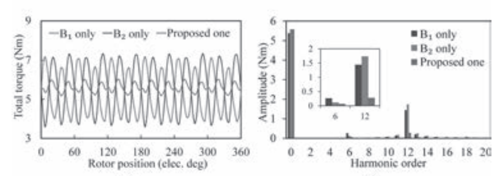

Fig. 5. Comparison of total torque in both FASRMs. (a) Total torque. (b) Total torque harmonic order.

AT-14. Influence of Magnetic Saturation and Rotor Eccentricity on Back-EMF of Novel Hybrid-excited Stator Slot Opening Permanent Magnet Machine.

M. Zheng[1], *Z. Zhu*[1], S. Cai[1], H. Li[1] and Y. Liu[1]
1. Department of Electronic and Electrical Engineering, University of Sheffield, Sheffield, United Kingdom

Abstract—This paper introduces a novel hybrid-excited stator slot opening permanent magnet (PM) machine (HSSPMM). The operation principle of the machine is investigated and the effects of magnetic saturation due to PMs and rotor eccentricity are analyzed by finite element method (FEM). It shows that different from the conventional PM machines, the open-circuit back-EMF in this novel HSSPMM should be zero but may become non-zero if significant magnetic saturation exists, and further, the rotor eccentricity has a detrimental effect on the waveforms, amplitudes and symmetries of 3-phases back-EMFs, as confirmed by FEA and tests. I. Introduction The idea of locating PMs in the stator slot opening area comes from [1, 2] which places PMs between adjacent stator teeth on switched reluctance machine to enhance the torque. The conventional hybrid-excited stator slot opening PM machine (HSSPMM) can be modified by adding PMs between adjacent stator teeth in variable flux reluctance machine (VFRM) [3]. The PMs are used to reduce the magnetic saturation produced by current excitation and enhance the torque density. Moreover, the HSSPMM maintains good flux regulation capability as the VFRM due to DC excitation. In this paper, a novel HSSPMM is developed by placing PMs in the slot opening area of the stator slots for field windings of a DC-excited switched flux machine (DC-SFM) [4]. The novel HSSPMM has a coil span of one slot pitch for field windings (F1) while a coil spans over three slot pitches for the armature windings (A3), as shown in Fig. 1(a). The stator DC-SFM can be easily magnetically saturated due to both armature and DC excitations. However, the magnetic saturation can be reduced since the PM flux direction is opposite to that produced by current excitation, and meanwhile, the torque of the HSSPMM can be increased. The operation principle of the F1A3 HSSPMM is similar to that of the conventional HSSPMM. When the machine has no current excitation, the PM flux will be shunted in the stator, and the PM flux can be pushed to the rotor via air-gap by the flux produced by current excitation. The PM volume, stator outer radius, stack length, air-gap length, and copper loss of the F1A3 HSSPMM are fixed during optimization and same as the conventional HSSPMM. The F1A3 HSSPMM is also prototyped, as shown in Fig. 1(b), and is tested with focus on the open-circuit back-EMFs to validate the finite element analysis (FEA) predictions. II. Open-circuit Magnetic Saturation and Rotor Eccentricity analysis Based on the machine operation principle, the F1A3 HSSPMM should have negligible open-circuit back-EMF since the PM flux is shunted in the stator. However, the machine with the stator and rotor material of laminated steel (non-linear material) is found to have a large amplitude of the back-EMF waveforms, while the back-EMF is negligible for that of linear material as shown in Fig. 2. The large PM flux leakage caused by stator magnetic saturation results in the significant back-EMF, which is validated by the measured results. Moreover, the waveforms and amplitudes of 3-phase back-EMFs are different, and further, those of each coils in the same phase are different as well. In addition, the back-EMF waveforms are asymmetric, indicating the prototype machine might have the issue of rotor eccentricity. Based on the measured results, 2D FEA is applied to determine the rough position of the rotor, and the FEA predicted and measured back-EMF waveforms are shown in Fig. 2. The amplitudes of measured back-EMFs for coils B1 and C1 are almost twice larger than those of B2 and C2, respectively, as shown in Fig. 2(c) and Fig. 2(d). Thus, the rotor of the prototype machine exhibits static eccentric towards the center of B1 and C1 of almost 50%. Since the measured back-EMF of coil A1 is slightly larger than that of coil A2, as shown in Fig. 2(b), the rotor eccentricity is found to be further 6% towards coil A1 which is selected according to the amplitude difference. The predicted and measured waveforms are of a good agreement but not perfectly the same since the exact eccentric position of the rotor is not sure and even 3D rotor eccentricity may exist which is quite different from the previous 2D FEA predicted rotor eccentricity. Moreover, the rotor shaft may also be slightly dynamically eccentric. III. Conclusion In this paper, a novel HSSPMM is proposed and the operation principle of the machine is introduced. It is found that the open-circuit back-EMFs of the machine are large, indicating the stator is severely magnetically saturated and large PM leakage flux exists. The prototype machine test results verified the existence of stator magnetic saturation. The predicted and measured open-circuit back-EMF waveforms show the prototype machine has rotor eccentricity and the eccentric rotor position is determined according to the measured amplitudes of coil EMFs. Good agreements exist between the 2D-FE predicted and measured results of open-circuit back-EMFs.

[1] K. Nakamura, K. Murota, and O. Ichinokura, "Characteristics of a novel switched reluctance motor having permanent magnets between the stator pole-tips," *European Power Electronics and Appl. Conf.*, 2-5 Sept. 2007. [2] P. Andrada, B. Blanqué, E. Martínez, M. Torrent, "New hybrid reluctance motor drive," *Int. Conf. On Elec. Mach. (ICEM)*, 2012. [3] I. A. A. Afinowi, Z. Q. Zhu, Y. Guan, J. C. Mipo, and P. Farah, "Hybrid-excited doubly salient synchronous machine with permanent magnets between adjacent salient stator poles," *IEEE Trans. on Magn.*, vol. 51, no. 10, 2015. [4] Y. J. Zhou and Z. Q. Zhu, "Comparison of wound-field switched-flux machines," *IEEE Trans. on Ind. Appl.*, vol.50, no. 5, pp. 3314-3324, 2014.

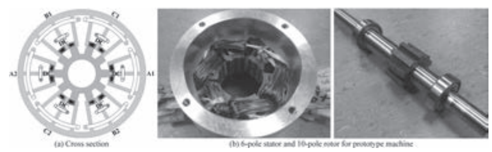

Fig. 1. Cross-section and prototype machine of F1A3 HSSPMM.

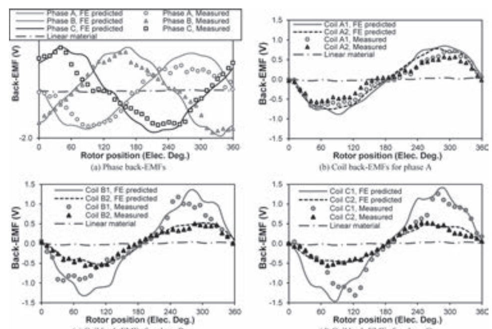

Fig. 2. Comparison of measured and FEA predicted back-EMF waveforms for non-linear material stator and rotor with the rotor shaft eccentricity of 50% towards to the centre between coils B1 and C1, and 6% towards the centre of coil A1, 400rpm.

AT-15. Design and Analysis of Variable Flux Memory Motor with Series-Parallel Structure Considering Permanent Magnet Load-Line.

J. Song[1], Y. Kim[2] and S. Jung[1]

1. Department of Electronic, Electrical and Computer Engineering, Sungkyunkwan University, Suwon-si, The Republic of Korea; 2. Department of Electrical Engineering, Chosun University, Gwangju, The Republic of Korea

1. Introduction In order to achieve high efficiency over wide-speed operation, variable flux memory motor (VFMM) has been proposed. This new class of motor can control the magnetization state by applying direct-axis (d-axis) current pulses [1]. When designing VFMM, it is important to study nonlinear magnetization characteristics considering the electrical constraints, since the PM magnetization strength must be controlled only with limited current fed by inverter [2], [3]. Especially, in the process of re-magnetization, the magnetic circuit becomes highly saturated, so that large current is requisite. Meanwhile, the PM magnetization characteristics of VFMM are highly correlated with how PMs are arranged in the rotor. Therefore, it is important for designers to select proper structure topologies at initial design stage, in order to design a VFMM with outstanding magnetization performance while satisfying the current limit conditions of the inverter. According to conventional studies, VFMMs can be classified into series and parallel magnetic circuits according to how the PMs within rotor are arranged [4]. It is known that series type VFMM is superior to parallel type in terms of magnetization performance [5]. However, re-magnetizing current larger than demagnetizing current is still considered to be a drawback of series type VFMM with ferrite PM only. In this paper, we propose a VFMM with novel series-parallel structure, of which magnetization characteristic is superior to both series and parallel type VFMMs. We investigated PM load-lines via finite element analysis (FEA) to identify the magnetization characteristics for three types of VFMMs, which are series type, parallel type, and proposed model, respectively. We confirmed that the proposed model is suitable for VFMM by analyzing and comparing shapes and behaviors of the PM load-lines under no-load and loaded conditions. 2. Magnetic characteristics of the proposed model Prior to deriving PM load-line, we investigated the PM operating point under no-load condition. Generally, it is known that the PM operating point of general PM motor is positioned on the second quadrant of B-H characteristic curve under no-load state, which is because the PM motor has air-gap on the magnetic circuit. However, due to structural characteristics of the proposed model, in which the magnetic field generated by PMs arranged in parallel is applied to PMs arranged in series in forward direction, the no-load operating points of the PMs arranged in series are on the first quadrant. On the other hand, the operating points of the parallel PMs in the proposed model are on the second quadrant as of general PM motor. Accordingly, the external magnetic field for re-magnetizing the series PMs is less than the parallel PMs. In consideration of these magnetic characteristics of each PM, we employed two types of PMs for the proposed VFMM, which are low-coercivity (variable magnetized PM) and high-coercivity PMs (constant magnetized PM). The series PMs are low-coercivity and parallel PMs are high-coercivity materials, respectively. 3. Analysis of magnetization characteristics based on PM load-line For the comparison of series type, parallel type, and the proposed model, we derived the PM load-lines which are essential factors to examine magnetization characteristics of VFMMs. Theoretically, the PM operating point is the intersection point of PM load-line and B-H characteristic curve of the PM. Hence, the PM load-line can be inversely derived by connecting the calculated PM operating points in accordance with different values of remanence flux density, which have regular interval [5]. To consider magnetic saturation, the PM load-line is derived via nonlinear FEA in this study. Fig. 1 shows the PM load-lines under no-load condition, where the curved lines with triangular, circular, and rectangular symbols are the PM load-lines of series, parallel type, and the proposed VFMM, respectively. It can be observed that the PM operating points of the series and parallel type VFMMs (A and B in Fig. 1) are located on the second quadrant. On the contrary, the PM operating point of the series PM in the proposed model (C in Fig. 1) is on the first quadrant, as mentioned above. In the process of re-magnetization, the main magnetic circuit of VFMM is highly saturated, while it is relatively free of saturation in demagnetization process. For this reason, it is necessary to identify magnetization characteristics, so that it has been studied with the shifted PM load-lines owing to positive d-axis current input (Ni_d=4kAT) as shown in Fig. 2. Here, N denotes the number of armature turns and i_d denotes d-axis input current. It should be noted that the shifted operating point of the proposed model (C' in Fig. 2) is positioned above the point M in Fig. 2, which means the variable magnetized PM becomes fully re-magnetized. However, the PMs of series and parallel type VFMMs are not fully magnetized yet, under identical d-axis current condition (Ni_d=4kAT), because the shifted PM operating points (A' and B' in Fig. 2) are under the point M. The supplementary computation results, which are not represented in Fig. 2, indicate that 15kAT and 50kAT of Ni_d are requisite to fully magnetize the PMs of series and parallel type VFMMs, respectively, which are 3.75 and 12.5 times larger Ni_d compared to that of proposed model.

[1] V. Ostovic, "Memory motors," IEEE Trans. Ind. Appl., vol. 9, no. 1, pp. 52-61, Jan./Feb. 2003. [2] N. Limsuwan, T. Kato, K. Akatsu, and R. D. Lorenz, "Design and Evaluation of a Variable-Flux Flux-Intensifying Interior Permanent-Magnet Machine," IEEE Trans. Ind. Appl., vol. 50, no. 2, pp. 1015-1024, Mar./Apr. 2014. [3] J. Jang, M. Humza, and B. Kim, "Design of a Variable-Flux Permanent-Magnet Synchronous Motor for Adjustable-Speed Operation," IEEE Trans. Ind. Appl., vol. 52, no. 4, pp. 2996-3004, Jul./Aug. 2016. [4] S. Maekawa, K. Yuki, M. Matsushita, I. Nitta, Y. Hasegawa, T. Shiga, T. Hosoito, K. Nagai, and H. Kubota, "Study of the Magnetization Method Suitable for Fractional-Slot Concentrated-Winding Variable Magnetomotive-Force Memory Motor," IEEE Trans. Power Electron., vol. 29, no. 9, pp.4877-4887, Sep. 2014. [5] J. Song, J. H. Lee, D. Kim, Y. Kim, and S. Jung, "Analysis and Modeling of Permanent Magnet Variable Flux Memory Motors Using Magnetic Equivalent Circuit Method," IEEE Tran. Magn., vol. 53, no. 11, 8208905, Nov. 2017.

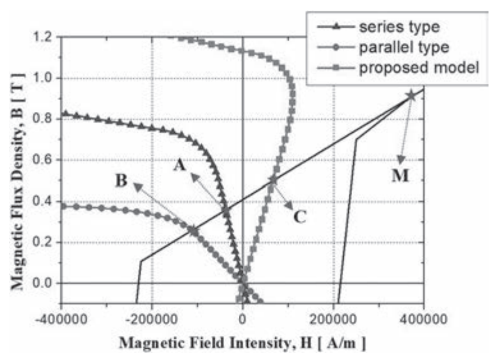

Fig. 1. PM load-lines under no-load condition

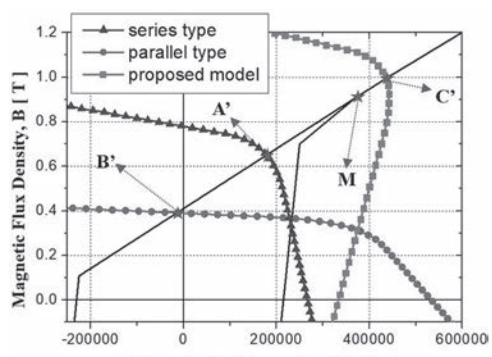

Fig. 2. PM load-lines under positive d-axis current condition

AT-16. Design and Verification of 80kW Traction Motor for EV.

H. Kim[1], K. Jung[2] and J. Moon[1]
1. Rotating Machinery Center, Korea Testing Certification, Gunpo-si, The Republic of Korea; 2. Automotive Engineering, Hanyang University, Seoul, The Republic of Korea

I. Motor Specification and Initial Design The 80kW traction motor which is designed in this thesis is an interior permanent magnet synchronous motor. Table 1 indicates the design specification of the 80kW traction motor. In order to increase the saliency ratio, distributed winding was decided and in order to increase the winding factor, full pitch was decided. The driving method is sinusoidal wave driving with space vector(SV) PWM applied. The TRV and SR have to be decided first for the initial design [1,2]. In this paper, the traction motor which is applied to Nissan LEAF which has the same output power was referenced. Figure 1 demonstrates the magnetic reluctance curve following the stator tooth width. In the magnetic reluctance curve, the minimum point is small so the stator tooth width was determined. When the magnetic reluctance is the minimum, the no-load back EMF and torque density become the maximum. In traction motor for EV, improving the torque density is one of the important objectives. If the torque density of the motor is improved, the motor volume and the weight can be reduced [3]. If the motor weight is reduced, it can enhance the fuel efficiency of the electric vehicle. Therefore, in this paper, the shape of the rotor was changed just like Figure 2 with regards to the initial model. Figure 2 (a) is the initial model. It is a shape of which the motor dimension calculated previously has been applied. If the cross section area of the permanent magnet is increased, the air-gap flux density is increased and finally, torque density improves. In the case of (b) model, the cross section area of the permanent magnet is enhanced, increasing the torque density. In the traction motor for EV, the input current is big so the reluctance torque can be increased by enhancing the saliency ratio. If the reluctance torque is enhanced, the torque density is improved. If the thickness of the permanent magnet is increased, the saliency ratio is increased. However, the amount of usage of permanent magnet also increases simultaneously. In order to increase the saliency ratio without increasing the usage amount of the permanent magnet, the permanent magnet was allocated with 2-layer just like Figure 2 (c). Figure 2 (c) is a structure with a bridge added in order to disperse the stress in the magnetic rib. The bridge was inserted between the permanent magnet of the lower part and a flux barrier was inserted between the magnetic ribs to add the bridge. Figure 2 (c) is a structure that has 3 more bridges when compared to (a) and (b) model and by doing so, (c) model can disperse the stress of rotor core when compared to (a) and (b) model. Figure 3 demonstrates the 2D-FEA stress analysis with regards to the 3 types of model in Figure 2. It can be seen that the stress of magnetic rib in (a), (b) model has exceed the yield strength(410MPa). However, in (c) model, the yield strength is not exceeded. *II. Optimum Design and Characteristic Analysis* In order to reduce the input current and torque ripple and the induced voltage in the high speed operation, optimum design was conducted. As it can be seen in Figure 4, the objective functions are input current, torque ripple and induced voltage. Figure 5 demonstrates the optimum model. With regards to optimum model, motor parameter such as d, q-axis inductance and no-load phase back EMF, core loss resistance and others are calculated and by applying equivalent circuit of IPMSM, the characteristic analysis was conducted. Figure 6 (a) demonstrates the torque curve, line to line voltage curve and others in maximum power condition. If the no-load phase back IMF is not selected appropriately and in case it is designed bigger in the initial design, the field weakening current increase in high speed area and the copper loss increases. Figure 6 (b) demonstrates the efficiency map. *III. Experimental Verification* The Load test was conducted with regards to the motor that was fabricated. Through the load test of the fabricated motor, the current and the inductance per current angle were measured and the characteristics of efficiency, input current line to line voltage and others were measured following the torque and speed. Figure 7 demonstrates the experiment composition for the load test. The d, q-axis inductance was measured following the current and the current angle. Through no-load test, the winding resistance and no-load back EMF were measured and through the load test, the input current, line to line voltage and power factor were measured. The measured value was applied to the vector diagram to calculate d, q-axis inductance. Such method used to calculate the inductance ignores the core loss which could lead to deviation. Figure 8 compares the test result and the analysis result with regards to d, q-axis inductance. Figure 9 demonstrates the test result and the analysis result of the efficiency. As it can be seen in the figure, the efficiency map exhibits similar patterns from each other. In the base rpm, Maximum torque sector, the test result and the analysis result with regards to efficiency have deviation of approximately 2%. Figure 10 demonstrates by comparing the test result and analysis result of line to line voltage. The measured line to line voltage is the effective value of fundamental components. It can be seen that the deviation of test result and analysis result of line to line voltage is not big.

[1] Surong Huang, Jim Luo, Franco Leonardi, Thomas A. Lipo "Comparison of Power Density for Axial Flux Machines Based on General Purpose Sizing Equations," *IEEE Transactions on Energy Conversion*, Vol. 14, No. 2, June 1999 [2] V.B.Honsinger, "Sizing Equations for Electrical Machinery," *IEEE Transactions on Energy Conversion*, Vol. EC-2, No. 1, March 1987 [3] T. Finken and K. Hameyer, "Design of Electric Motors for Hybridand Electric- Vehicle Applications," 12th International Conference on Electrical Machines and Systems, ICEMS 2009, Tokyo, Japan, 2009.

Table 1

List	Value	Note
Number of pole and slots	8/48	-
DC link voltage [V_{dc}]	360	-
Maximum torque [Nm]	280	2700rpm
Maximum speed [rpm]	10000	-
Winding method	Distributed winding	full pitch
Driving method	Sinusoidal wave	SV PWM

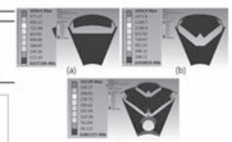

Fig. 3. Result of rotor stress analysis of the respective model

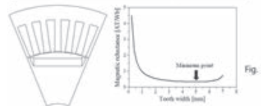

Fig. 1. Determining tooth width by using magnetic reluctance

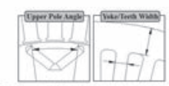

Fig. 4. Optimum design using response surface methodology

Fig. 2. Changing the rotor shape for torque density improvement and stress reduction

Fig. 5. Result of optimum design

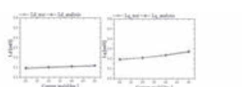

Fig. 8. Test result of inductance(400Arms)

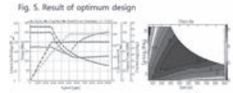

Fig. 6. Characteristics curve (max. power) and Efficiency map

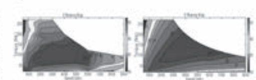

Fig. 9. Test result of efficiency

Fig. 7. Experiment composition

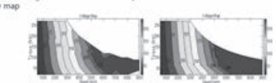

Fig. 10. Test result of line to line voltage

TUESDAY MORNING, 24 APRIL 2018 SIMPOR/ROSELLE BALLROOM, 8:30 TO 11:30

Session AU
PERMANENT MAGNET AND RELUCTANCE MACHINES II
(Poster Session)

Daohan Wang, Co-Chair
Shandong University, Shandong, China
Hongmei Li, Co-Chair
Hefei University of Technology, Hefei, China

AU-01. Design of slit-like flux barriers to improve space harmonic distribution in a slit stator motor.

Y. Yokoi[1], R. Hashizume[1] and T. Higuchi[1]
1. Nagasaki University, Nagasaki, Japan

1. Introduction Space harmonic distribution of magnetic flux density across the air gap governs torque and iron loss in electrical machines. Fractional-slot concentrated winding (FSCW) configurations generate several dominant space harmonics. One of them produces the drive torque. The others increase undesirable effects such as iron loss in cores and eddy-current loss in magnets and do not contribute to the torque production. In the design of FSCW machines, the space harmonic distribution is improved with many design methods [1-4]. A slit stator motor (SSM) has been proposed to improve the space harmonic distribution for 12-slot 10-pole motors [5]. In general, the fundamental, 5th, and 7th space harmonics generate as dominant space harmonics in conventional 12-slot 10-pole motors. The 5th space harmonic produce the drive torque. The other space harmonics increase losses. For this reason, the space harmonic distribution can be improved by increasing the 5th space harmonic and decreasing the fundamental and 7th space harmonics. In the SSM, the stator has slit-like flux barriers that are located at the center of alternate teeth to separate the stator core. The stator winding coils are wound around the slit teeth to arrange single-layer windings. This stator design, which is called slit stator, improve the space harmonic distribution. Hence, the slit stator increases the 5th space harmonic and decreases the fundamental and 7th space harmonics. As the result, the SSM achieves more torque production and high efficiency than a conventional stator motor (CSM). In the SSM, the width of the slit-like flux barriers determines the space harmonic distribution and the motor performance. The effect of slits to barrier magnetic flux across the slits is enhanced with the increase of the slit width. However, the stator teeth width and/or the slot area decreases as the slit width increases. In addition, the flux density drops at the air gap faced by the slits. This influences the space harmonic distribution. Therefore, the design of SSMs requires the dependence of the space harmonic distribution on the slit width. In this digest, the slit-like flux barriers are designed to improve the space harmonic distribution of the air-gap flux density in the SSM. The influence of the slit width on the space harmonic distribution is investigated through a finite element method (FEM) analysis. The improved space harmonic distribution is verified experimentally. 2. Structure and Performance This section briefly describes the structure and the performance of a SSM. Fig. 1 shows the cross section of the SSM. The motor configures a 12-slot 10-pole permanent magnet motor with single-layer windings. Slit-like flux barriers are located at the center of the wound teeth in the stator. The dimensions of the SSM and a CSM are presented in Table 1. The width of teeth with slits is greater than that of teeth without slits by the slit width. All the teeth have the identical width of iron core not to enhance magnetic saturation at the slit teeth. The width of the yoke in the SSM can be less than that in the CSM. In the SSM, the width of the yoke is set at half of the teeth width because the magnetic flux across the slits should be suppressed. Table 2 presents the performance of the SSM and the CSM. The SSM requires smaller current than the CSM to produce the identical torque. The losses in cores and magnets are decreased by the slit arrangement. The enhanced performance is due to the space harmonic distribution improved in the SSM. 3. Numerical and Experimental Space Harmonic Distribution The slit width is determined to improve the space harmonic distribution of the air-gap flux density in the SSM. The influence of the slit width on the dominant space harmonics is investigated at a fed current of 10 A through an FEM analysis, as shown in Fig. 2. The 5th space harmonic is maximized at a slit width of 2.3 mm. The fundamental and 7th harmonics are decreased with the increase of the slit width. These results clarify that the slit arrangement can increase the 5th space harmonic and decrease the fundamental and 7th space harmonics. For the slit width that is greater than 2.3 mm, the 5th space harmonic decreases gradually in comparison with the other harmonics. For this reason, the slit width can be greater than 2.3 mm to improve the space harmonic distribution. However, the slit width is restricted because an increase of the slit width decreases the area of slots. Here, it is noted that the yoke width of the slit stator can be decreased from that of the conventional stator. The decreased yoke width contributes to the increase of the slot area. In SSM, the slit width is determined at 2.5 mm not to decrease the slot area from that in the CSM. The improved air-gap flux density distribution is verified through the FEM analysis and an experiment performed with a prototype. In the prototype, the gap corresponding to each slit is maintained at 2.5 mm by inserting a nonmagnetic material plate. Both ends of each slit have a gap of 1.5 mm to support the plate. Fig. 3 shows the air-gap flux density distribution at a current of 10 A. The numerical and experimental results are consistent with each other. The harmonic components in the distribution are shown in Fig. 4. It is numerically and experimentally confirmed that the slit stator increases the 5th harmonic and decreases the fundamental and 7th harmonics. The slight difference between the numerical and experimental results is caused by the difference in the shape at the ends of slits.

[1] L. Alberti and N. Bianchi, "Theory and design of fractional-slot multilayer windings," *IEEE Trans. Ind. Appl.*, vol. 49, no. 2 pp. 841-849, Mar./Apr. 2013. [2] D. Ishak, Z. Q. Zhu, and D. Howe, "Permanent-magnet brushless machines with unequal tooth widths and similar slot and pole numbers," *IEEE Trans. Ind. Appl.*, vol. 41, no. 2, pp. 584-590, Mar./Apr. 2005. [3] G. Dajaku, W. Xie, and D. Gerling, "Reduction of low space harmonics for the fractional slot concentrated windings using a novel stator design," *IEEE Trans. Magn.*, vol. 50, no. 5, 8201012, May 2014. [4] G. J. Li, Z. Q. Zhu, M. Foster, and D. Stone, "Comparative studies of modular and unequal tooth PM machines either with or without tooth tips," IEEE Trans. Magn., vol. 50, no. 7, 8101610, Jul. 2014. [5] Y. Yokoi and T. Higuchi, "Design analysis of slit stator motors," *Proc. ICEMS*, 2016.

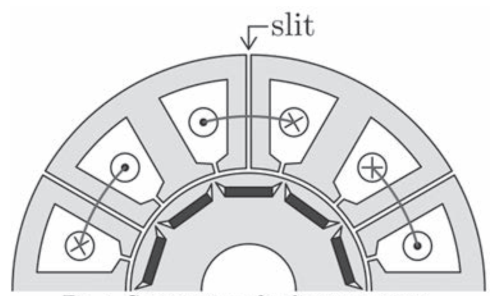

Fig. 1 Cross section of a slit stator motor.

Table 1 Dimesions of the analyzed motors.

	SSM	CSM
Stator core length	50 mm	50 mm
Stator outer diameter	160 mm	160 mm
Rotor outer diameter	88 mm	88 mm
Air gap length	1 mm	1 mm
Stator tooth width	15.5 mm	15.5 mm
Stator slit tooth width	18 mm	—
Slit width	2.5 mm	—
Stator yoke width	7.8 mm	10.0 mm
Number of turns per coils	80	80

Table 2 Performance of the analyzed motors.

	SSM	CSM
Current	15.9 A	17.4 A
Current phase	24°	21°
Rotational speed	1,500 $\min^{-1}$	1,500 $\min^{-1}$
Output torque	10.0 Nm	10.0 Nm
Output power	1.57 kW	1.57 kW
Loss in cores	67.5 W	83.7 W
Loss in magnets	1.4 W	3.1 W
Loss in windings	75.8 W	90.8 W
Efficiency	91.6 %	89.8 %

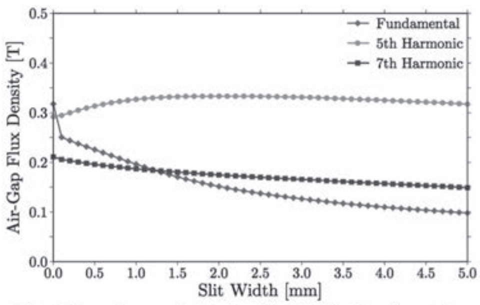

Fig. 2 Space harmonics for the slit width in the air-gap flux density distribution.

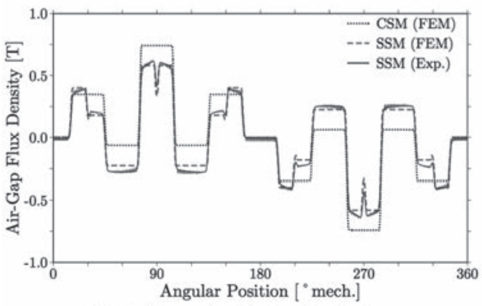

Fig. 3 Air-gap flux density distribution.

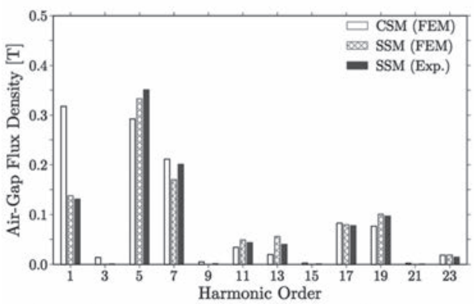

Fig. 4 Harmonic components in the air-gap flux density distribution.

AU-02. A New Modular Flux-Concentrated Doubly Salient Machine with PMs in Both Stator Yoke and Slot Openings.

Q. Wang[1] and S. Niu[1]
1. Department of Electrical Engineering, The Hong Kong Polytechnic University, Hung Hom, Hong Kong

Abstract: This paper proposes a new modular flux-concentrated doubly salient machine(MFCDSM), in which the PMs are employed in both the stator yoke and the slot openings. The magnetic flux excited by the PMs in the stator yoke will be pushed by the PMs in the slot openings to pass through the air-gap and link the rotor, hence the leakage flux is reduced consequently. Meanwhile, the PMs in the stator yoke can act as magnetic reluctance, so the magnetic flux excited by the PMs in the slot openings will also pass through the air-gap and link the rotor, not short-circuited by the salient stator poles. Therefore, the magnetic flux excited by the PMs in both the stator yoke and the slot openings can be concentrated to the air-gap and link the rotor, and the torque capability of the proposed machine can be improved. With slot PMs, the electromagnetic torque of the proposed machine can be increased with 62%. Modular design of the stator can be achieved, which can simplify the manufacturing. Finite element method coupled with an improved Tabu search algorithm, namely FEM-ITS coupled method, is used to optimal design the proposed MFCDSM machine. Its electromagnetic performances are studied in detail using FEM. *Index Terms*—Doubly salient, flux-concentrated, modular design, optimal design, Tabu search. I. Introduction Doubly-salient machines have been extensively researched due to their robust rotor structure, high reliability and easy cooling with most of the heating sources located on the stator [1-3]. In order to achieve high torque density, doubly salient permanent magnet machines(DSPMM) have been investigated for many decades [4]. In this paper, a new modular flux-concentrated doubly salient machine(MFCDSM) is proposed, in which the PMs are employed on both the stator yoke and the slot openings. High torque density can be achieved because the PM flux can be concentrated to pass through the air-gap and link the rotor, so the leakage flux can be reduced. With the merits of modular stator design, the manufacturing cost of the proposed machine can be reduced. Finite element method coupled with an Tabu search algorithm [5], which is referred as FEM-TS coupled method, is used to optimize the design of this proposed machine. The electromagnetic performances are investigated in detail using FEM. II. Machine Configuration Fig. 1 shows the configuration of the proposed MFCDSM and its stator module. The stator consists of T-shaped modular segments, between which are mounted with PMs. The armature windings are concentric wound on the stator teeth. Each stator module consists of one stator tooth and one tooth-wound coil, the total number of stator modules is equal to the number of stator teeth. PMs are employed on both the stator yoke and the slot openings, and the adjacent PMs are magnetized in opposite direction, so the PM flux can be concentrated to the air-gap and link with the rotor. The rotor is simply made up of salient poles, which is mechanically robust. Various combinations of the stator slot number and rotor pole number can be used in the MFCDSM. In the proposed design in this paper, the stator slot number and rotor pole number is 12 and 11, respectively. The stator and rotor pole numbers are differed by one, which can result in sinusoidal back-EMF and reduce the torque ripple [6]. III. Design Optimization and Torque Characteristics A. Multi-Objective Optimization Before investigating the electromagnetic performances, the proposed MFCDSM is optimally designed using FEM-TS coupled method. Three objectives are investigated, which include the average output torque, the torque ripple ratio, and the efficiency. During the optimization process, the proposed machine is applied with a fixed current density 8A/mm^2 and rotates at rated speed 818rpm. Fig. 2(a) shows the optimization results of the efficiency and the average output torque, it can be observed that the efficiency is positive correlated with the average output torque, which means the proposed machine can work with high efficiency when designed with large output torque. The relationship between the torque ripple ratio and the average output torque is given in Fig. 2(b). One can find that there is no clear relationship between the torque ripple and average torque. The torque ripple ratio varies almost randomly during the optimization process. B. Single-Objective Optimization After the multi-objective optimization, the proposed machine is optimized through single-objective optimization. The objective is to achieve the largest output torque when applied with a fixed current density 8A/mm^2, and the constraint is the torque ripple ratio should lower than 12%. The average output torque versus iterative number is shown in Fig. 2(c), one can see that the optimization can converge within 20 iterations, which shows the effectiveness of the optimization method. C. Torque Characteristics Fig. 2(d) shows the torque angle waveforms of the proposed MFCDSM when the current density is 8A/mm^2. The electromagnetic torque generated by the slot PMs and yoke PMs are calculated separately. The total electromagnetic torque of the proposed machine is 20.4Nm, in which 7.8Nm is generated by the slot PMs and 12.6Nm is generated by the yoke PMs. Therefore, with the PMs in the slot openings, the electromagnetic torque of the proposed machine can be increased with 62%.

[1] X. Zhu, M. Cheng, W. Zhao, C. Liu, and K. T. Chau, "A transient cosimulation approach to performance analysis of hybrid excited doubly salient machine considering indirect field-circuit coupling," *IEEE Trans. Magn.,* vol. 43, pp. 2558-2560, 2007. [2] Q. Wang and S. Niu, "Overview of flux-controllable machines: Electrically excited machines, hybrid excited machines and memory machines," *Renewable and Sustainable Energy Reviews,* vol. 68, pp. 475-491, 2017. [3] X. Zhu, L. Quan, D. Chen, M. Cheng, Z. Wang, and W. Li, "Design and analysis of a new flux memory doubly salient motor capable of online flux control," *IEEE Trans. Magn.,* vol. 47, pp. 3220-3223, 2011. [4] Y. Liao, F. Liang, and T. A. Lipo, "A novel permanent magnet motor with doubly salient structure," *IEEE Trans. Ind. Appl.,* vol. 31, pp. 1069-1078, 1995. [5] S. L. Ho, S. Yang, G. Ni, and H. C. Wong, "An improved Tabu search for the global optimizations of electromagnetic devices," *IEEE Trans. Magn.,* vol. 37, pp. 3570-3574, 2001. [6] D. Wu, J. T. Shi, Z. Zhu, and X. Liu, "Electromagnetic performance of novel synchronous machines with permanent magnets in stator yoke," *IEEE Trans. Magn.,* vol. 50, pp. 1-9, 2014.

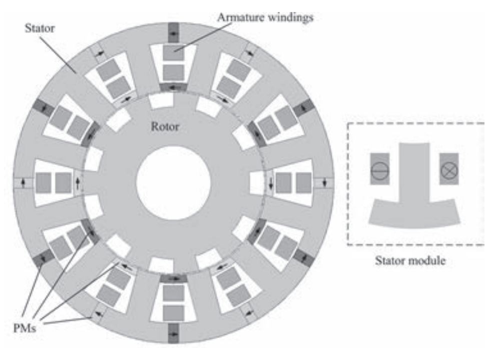

Fig. 1.Configuration of the proposed MFCDSM and its stator module.

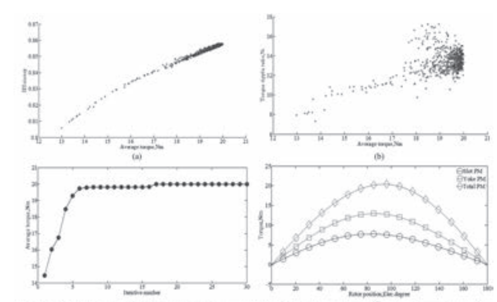

Fig. 2. (a) The relationship between efficiency and average torque. (b) The relationship between torque ripple ratio and average torque. (c) The average torque at different iterative number. (d) Torque angle waveforms.

AU-03. Rotor Structure for Reducing Demagnetization of Magnet and Torque Ripple in a PMa-synRM with Ferrite Permanent Magnet.

Y. Kong[1], M. Lin[1], G. Yang[1] and K. Liu[1]
1. Engineering Research Center for Motion Control of MOE, Southeast University, Nanjing, China

Abstract—A rotor structure of permanent magnet assisted synchronous reluctance motor (PMa-synRM) with ferrite permanent magnet is presented in this paper, in which the irreversible demagnetization of magnet and torque ripple are reduced. The bypass-rib is proposed and added to the flux barrier of the rotor. The path for the demagnetizing field of armature windings are provided and the torque ripple can also be reduced by the bypass-rib. Based on the 2-D finite element analysis (FEA), the location and dimensions of the bypass-rib are investigated and improved. A PMa-synRM with the proposed rotor structure is designed and compared with the PMa-synRM with a conventional rotor. A prototype of the PMa-synRM is manufactured and tested to validate the FEA results. I.Introduction The magnetless machines and non-rare-earth machines are attracting more and more attention in recent years due to the high and dramatic rise price of rare-earth [1]. The PMa-synRM with ferrite permanent magnet is a good alternative machine to replace the machine using rare-earth permanent magnet. But the coercivity of the ferrite permanent magnet is weaker than that of the rare-earth permanent magnet. The operating point of the ferrite permanent magnet will pass over the knee point of the demagnetization curve under the large magnetomotive force of the armature reaction which lead to the irreversibly demagnetization [2]. Another drawback of the PMa-synRM is the large torque ripple [3]. Many research works have been done to solve these problems [4-8]. The tapered flux barrier is used to improve the antidemagnetization ability [4]. While the saliency ratio is decreased due to the decrease of the barrier thickness which leads to the output torque capacity reduction. The antidemagnetization ability can be obviously improved by using more permanent magnet to increase the thickness along the magnetization direction [5]. But this will make the costs increased. The asymmetrical flux barrier design was proposed to reduce torque ripple [6-7]. However, the asymmetrical structures increase the complexity of the initial design. This paper proposes a rotor structure to reduce the irreversible demagnetization of magnet and torque ripple without discounting the output torque. The complexity of the design is not increased owing to the symmetrical structure. The influences of the bypass-rib on the saliency ratio, no-load back electromotive force and antidemagnetization ability of the PMa-synRM are investigated in section II. In section III, the performances of the machine, especially the antidemagnetization ability, are analyzed and compared to that with the same design dimensions but without the bypass-rib structure. A prototype is manufactured and tested. Experiments results will be shown in the full paper. II.Rotor Design Fig.1 illustrates the topology and parameters of the bypass-rib. The bypass-rib structure is composed of two unconnected ribs and the permanent magnet is located in the flux barrier between the two bypass-ribs. The influences of the parameters on the saliency ratio, no-load back electromotive force and antidemagnetization ability are investigated which will be shown in the full paper. A PMa-synRM with the proposed rotor structure is designed and compared with a PMa-synRM with a conventional rotor. A series of demagnetization currents is applied to the PMa-synRMs from small to large. Fig.2 shows the demagnetization characteristics of the two PMa-synRMs. Most of the magnets in the conventional rotor structure are irreversibly demagnetized when the applied current is 15A while the irreversibly demagnetization rate in the proposed rotor is less than 10%. Experiments results based on the prototype will be shown in the full paper. III. Conclusions To improve the antidemagnetization ability of the PMa-synRM, the bypass-rib structure is proposed and added to the flux barrier of the rotor. The main parameters of the bypass-rib are studied based on the 2-D FEA. The saliency ratio and the antidemagnetization ability is mainly influenced by the length and width of the bypass-rib respectively. A PMa-synRM with the bypass-rib is designed and compared to a PMa-synRM with conventional rotor. A prototype is manufactured and tested. The results demonstrate that the PMa-synRM with the bypass-rib has almost the same output torque and much higher antidemagnetization ability and lower torque ripple than that of the PMa-synRM with conventional rotor structure.

[1] N. Bianchi, E. Fornasiero, M. Ferrari and M. Castiello, “Experimental Comparison of PM-Assisted Synchronous Reluctance Motors,” in IEEE Transactions on Industry Applications, vol. 52, no. 1, pp. 163-171, Jan.-Feb. 2016. [2] S. Ooi, S. Morimoto, M. Sanada and Y. Inoue, “Performance Evaluation of a High-Power-Density PMASynRM With Ferrite Magnets,” in IEEE Transactions on Industry Applications, vol. 49, no. 3, pp. 1308-1315, May-June 2013. [3] A. Fratta, G. P. Troglia, A. Vagati and F. Villata, “Evaluation of torque ripple in high performance synchronous reluctance machines,” Conference Record of the 1993 IEEE Industry Applications Conference Twenty-Eighth IAS Annual Meeting, Toronto, Ont., 1993, pp. 163-170 vol.1. [4] M. Sanada, Y. Inoue and S. Morimoto, “Rotor structure for reducing demagnetization of magnet in a PMASynRM with ferrite permanent magnet and its characteristics,” 2011 IEEE Energy Conversion Congress and Exposition, Phoenix, AZ, 2011, pp. 4189-4194. [5] H. Huang, Y. S. Hu, Y. Xiao and H. Lyu, “Research of Parameters and Antidemagnetization of Rare-Earth-Less Permanent Magnet-Assisted Synchronous Reluctance Motor,” in IEEE Transactions on Magnetics, vol. 51, no. 11, pp. 1-4, Nov. 2015. [6] N. Bianchi, S. Bolognani, D. Bon and M. Dai Pre, “Rotor Flux-Barrier Design for Torque Ripple Reduction in Synchronous Reluctance and PM-Assisted Synchronous Reluctance Motors,” in IEEE Transactions on Industry Applications, vol. 45, no. 3, pp. 921-928, May-june 2009. [7] M. Sanada, K. Hiramoto, S. Morimoto and Y. Takeda, “Torque ripple improvement for synchronous reluctance motor using an asymmetric flux barrier arrangement,” in IEEE Transactions on Industry Applications, vol. 40, no. 4, pp. 1076-1082, July-Aug. 2004.

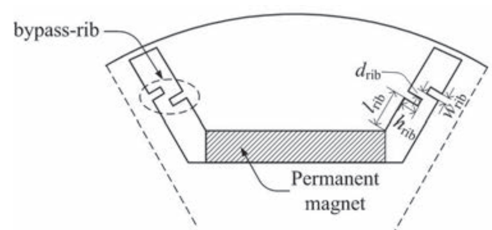

Fig. 1. the topology and parameters of the bypass-rib.

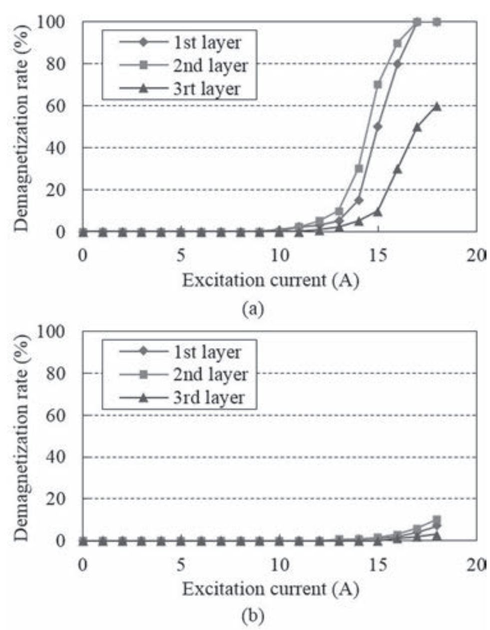

Fig. 2. Demagnetization rate characteristics. (a) Conventional rotor structure. (b) Proposed rotor structure.

AU-04. Electromagnetic Performance Analysis of Hybrid Excited Segmental Rotor Flux Switching Machine.

Y. Yang[1], J. Chen[1], B. Yan[1], X. Wang[1] and C. Zhu[1]
1. Shandong University, Jinan, China

I. INTRODUCTION Due to high torque density, simple rotor structure and good heat dissipation, the electrically and permanent magnet (PM) excited segmental rotor flux switching machines (SRFSMs) have attracted much attentions in recent years [1-2]. The machine topology [3], analysis method [4], and torque ripple reduction method [5] are studied in the literatures. In order to reduce the excitation loss of electrically excited SRFSM and increase the magnetic field regulation capacity of PM excited SRFSM, the new hybrid excited SRFSM is proposed and the analytical subdomain model is derived to calculate the magnetic field and electromagnetic performance. The magnetic field regulation capacity is verified with the results of finite element method (FEM) and prototype machine experiment. II. THE WORKING PRINCIPLE The hybrid excited SRFSM is shown in Fig. 1(a), and three N-pole PMs are replaced by three field windings F1-F3. The exciting magnetic flux will alternately go through the two adjacent stator teeth due to the segmental rotor core, so the flux paths of the two adjacent PM and field winding are parallel. Because the flux path of field winding doesn't include any PM, the magnetic field can be easily regulated by the field current due to the small reluctance, and the PMs have no risk of demagnetization. As shown in Fig. 1(b), the coil flux linkage is the summation of those produced by the adjacent PM and field winding independently. For the model, the flux linkages produced by the PM and field winding have nearly the same phase angles for the positive field current, so the total flux linkage is increased with the field current. For the negative field current, the phase difference between the two flux linkages becomes 180 electrical degrees, so the total flux linkage will be decreased with the increment of field current. By changing the value and direction of the field current, the flux linkage is also easily regulated. III. THE ANALYTICAL MODEL In order to study the magnetic field and electromagnetic performance, the analytical subdomain model is derived for the hybrid excited SRFSM. The inner part of rotor iron core (dotted portion in Fig. 1(a)) is to fix the rotor laminations to the rotor support, and has little effect on the magnetic field, so it is ignored in the analytical model. The rotor support is usually made of non-magnetic stainless steel, and is divided into two subdomains, i.e. the shaft and "rotor slot". The whole solving domain is divided into six subdomains, including the shaft, rotor slot, air gap, PM, stator slot opening and stator slot. The governing equations and general solutions of all the subdomains are obtained, and the equations including the integration constants are derived according to the boundary conditions, i.e. the magnetic vector potential and tangential magnetic field intensity should be continuous, respectively at the boundary between the adjacent subdomains. All the equations are transformed into matrix forms, and solved by the math software Matlab. With the magnetic vector potential, the magnetic field and electromagnetic performance including the flux linkage, back-EMF, cogging torque, electromagnetic torque and PM loss are calculated, and the regulation capacity of magnetic field is also analyzed. IV. THE RESULTS AND VALIDATIONS In order to verify the analytical model and performance of the hybrid excited SRFSM, one prototype machine with 12-stator-slot and 7-rotor-segment is designed and produced as shown in Fig. 2(a). In order to reduce the eddy current loss, every PM pole is consisted of three segments along the axial direction. The air gap flux densities with field current densities of 9A/mm^2, 0, and -9A/mm^2 are shown in Fig. 2(b). It can be found that the radial flux density is greatly increased corresponding to the flux path of field winding with the increment of field current density. The back-EMFs with different field current densities are calculated by the analytical model and compared with the experiment results. As shown in Fig. 2(c), when the field current density increases from -9A/mm^2 to 9A/mm^2, the back-EMF regulation ratio (defined by $(E_{pm}-E_{he})/E_{pm}$, where E_{pm} and E_{he} are the back-EMFs produced by the PMs and by the hybrid excitation) changes from -50% to 77%. In order to evaluate the torque capacity, the static torque is tested and the three-phase currents are set as $I_a=-I_b=0.866I_{amp}=17.32$A and $I_c=0$, where I_{amp} is the amplitude of phase current. It can be found that the torque can be easily regulated by the field current for the hybrid excited SRFSM.

[1]Zulu A., Mecrow B.C., and Armstrong M., 'A wound-field three-phase flux-switching synchronous motor with all excitation sources on the stator', IEEE Transactions on Industry Applications, 2010, 46(6), pp. 2363–2371. [2]Zulu A., Mecrow B. C., and Armstrong M., "Permanent-magnet flux-switching synchronous motor employing a segmental rotor," *IEEE Transactions on Industry Applications*, vol. 48, no. 6, pp. 2259-2267, 2012. [3]Zulu A., Mecrow B. C., and Armstrong M., "Topologies for wound field three-phase segmented-rotor flux-switching machines," in *Int. Conf. Power Electronics, Machines and Drives*, Brighton, UK, 2010, pp. 1-6. [4]Zulu A., Mecrow B. C., and Armstrong M., "Investigation of the dq-equivalent model for performance prediction of flux-switching synchronous motors with segmented rotors," *IEEE Transactions on Industrial Electronics*, vol. 59, no. 6, pp. 2393-2402, 2012. [5]Abdollahi S. E., and Vaez-Zadeh S., "Reducing cogging torque in flux switching motors with segmented rotor," *IEEE Transactions on Magnetics*, vol. 49, no. 10, pp. 5304-5309, 2013.

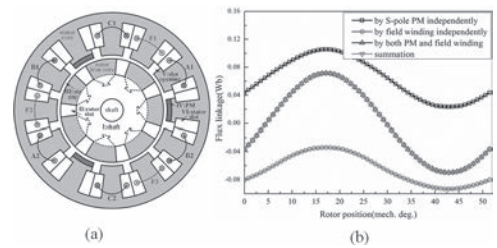

Fig. 1. (a) The configuration of hybrid excited SRFSM, and (b) coil flux linkage is the summation of those produced by the PM and field winding independently

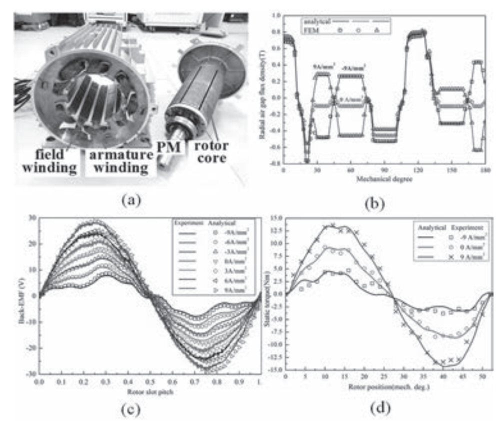

Fig. 2. (a) The prototype machine, (b) radial air gap flux density with different field current densities, (c) back-EMFs with different field current densities, and (d) static torques with different field densities

AU-05. Performance Analysis of Suspension Force and Torque in an IBPMSM with V-shape PMs for Flywheel Batteries.

B. Su[1], *X. Sun*[1], G. Lei[2], Z. Yang[1], J. Zhu[2], Y. Guo[2] and K. Diao[1]
1. Automotive Engineering Research Institute, Jiangsu University, Zhenjiang, China; 2. School of Electrical, Mechanical and Mechatronic Systems, University of Technology, Sydney, Sydney, NSW, Australia

Abstract:Due to the advantages such as high energy density, high power density, high cyclic-life, and environmentally friendly, flywheel have the potential to solve the problem of energy storage. In this paper, the interior bearingless permanent magnet synchronous motors (IBPMSMs) with V-shape permanent magnets (PMs) used for flywheel batteries of electric vehicles (EVs) is researched in detail. Especially, the influence of geometrical parameters of V-shape PMs on suspension force is investigated. Furthermore, the corresponding static electronic magnetic characteristics including inductances, electromagnetic torque is also studied. The finite-element method (FEM) is employed to evaluate the theoretical analysis. 1 *Introduction* Comparing with the traditional vehicles, electric vehicles (EVs) have advantages including low emissions, high energy conversion efficiency and multiple sources, and they are considered as an important way to deal with environment deterioration and energy shortage. As one of key technique of EVs, the power battery technique is extremely important. Comparing with conventional chemical battery, flywheel battery has relative advantages such as maintenance free, high energy density, high power density, rapid charge and discharge, high cyclic-life and environmentally friendly. The bearingless permanent magnet synchronous machine [1,2] (BPMSM) with the advantages of high efficiency, high power density, high power factor and friction-free is favourable for the flywheel battery [3,4]. In this paper, the structure and feature of proposed bearingless motor is introduced firstly in first part. Then the influence of V-shape PMs geometrical parameters on suspension force will be investigated. Furthermore, the electromagnetic performance, such as torques and inductances are analysed in following section. *Structure and features:* Fig. 1 illustrates the proposed IBPMSM with V-shape PMs. From the front view, it can be seen that the proposed motor has a similar structure with permanent magnet synchronous machine (PMSM), but the difference is the stator houses the torque winding and the suspension winding which fulfilled P_S=P_T±1 ω_S=ω_T (1) where P_T is the pole-pair number of the torque winding, ω_T is the current frequency of torque winding, P_S is the pole-pair number of the torque winding, and ω_S is the current frequency of suspension winding. The suspension force generation can be seen form[5]. 2 *Influence of PM Geometrical Parameters on Suspension Force* When the rotor is not eccentric, the suspension force F_p can be given as F_P=(F_x^2+F_y^2)^½(2) where F_x and F_y are suspension forces along x- and y-axes, respectively, and they can be written as F_x=$k_\alpha I_S I_{PM}$cos(θ_M-θ_S) F_y=$k_\alpha I_S I_{PMsin}$(θ_M-θ_S)(3) where I_S is suspension winding current, I_{PM} is the equivalent current of PM, θ_M and θ_S are the initial angle of torque winding current and initial angle of suspension winding current, respectively. In this part, the influences of two geometrical parameters (angle between two PMs *A* and number of segments *N*) on performances of suspension force and torque are investigated. It is not so easy to determine the angle between two PMs since there is currently no definite rule to choosing it, and it is usually determined according to the experiments. In this paper, keeping the length and width of magnetic bridge as a constant, and changing the angle between two PMs of one pole. Then the performance of suspension force and electromagnetic torque are obtained by using finite-element method (FEM). Fig. 2(a) shows the suspension force with different *A*. It can be seen that the angle between two PMs has a little influence on the amplitude of suspension. The suspension forces of the proposed IBPMSM with different *N* are shown in Fig 2(b), in which the segment gaps of PM is 0.5mm and the volume of PMs is fixed. It can be seen from Fig. 2(b) that the *N* has a significant influence on amplitude of suspension force. The large fluctuation of the suspension force occurs when *N* is equal to 5, and the suspension force is biggest when *N* is equal to 3. 3 *Electrical magnetic characteristic* Considering rotor strength and complex of process, two geometrical parameters are set *A*=20 and *N*=3. In this part, the corresponding results of torque characteristic and the inductance characteristic are calculated by using the FEM. The inductance is one of the important technical parameters for the proposed motor, and it will have an important effect on radial suspension forces and output power. In order to control motor easily, the two phase rotating reference frame d-q axis is widely used. According three phase inductance, the d-axis inductance L_d and q-axis L_q can be calculated $L(d,q,0)=C_{3/2}L(a,b,c)C^{\mathrm{T}}_{3/2}$(4) According to the simulation result, it can be found that the proposed motor has a large diffidence in d-q axis inductance, which can provide more reluctance torque. 4 *Conclusion* An IBPMSM with V-shape PMs used for EVs flywheel battery is proposed in this paper. The influences of two geometrical parameters on performances of suspension force and torque are investigated The performance are sensitive to those geometrical parameters The angle between two PMs influences the stability of suspension force, and the number of segments influences the amplitude of suspension force. Furthermore, according to electrical magnetic characteristic, the proposed motor can also provide large reluctance torque and low cogging torque.

1 X. Sun, L. Chen and Z. Yang.: 'Overview of Bearingless Permanent-Magnet Synchronous Motors,' *IEEE Transactions on Industrial Electronics*, 2013, 60, pp. 5528-5538 2 X. Sun, L. Chen, Z. Yang and H. Zhu.: 'Analysis of inductance characteristics for a bearingless permanent magnet synchronous motor,' *Electrical Engineering*, 2013, 95, (3), pp. 277-286 3 Y. Yuan, Y. Sun and Y. Huang.: 'Design and analysis of bearingless flywheel motor specially for flywheel energy storage', *Electronics Letters*, 2016, 52, (1), pp. 66–68 4 Y Yuan, Y Sun and Y Huang.: 'Accurate mathematical model of bearingless flywheel motor based on Maxwell tensor method', *Electronics Letters*, 2016, 52, (11), pp. 950–952 5 X Sun and H. Zhu.: 'study on Static Electromagnetic Characteristics of a Bearingless Permanent Magnet Synchronous Motor," *Advanced Science Letters*, 2011, 4, 1-9

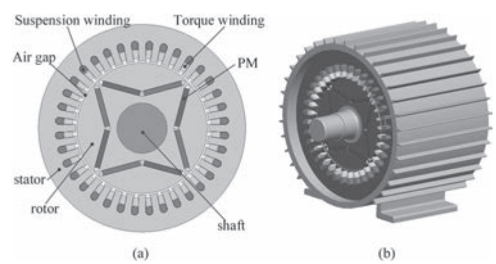

Fig. 1. Proposed bearingless machine. a Front view. b Side view.

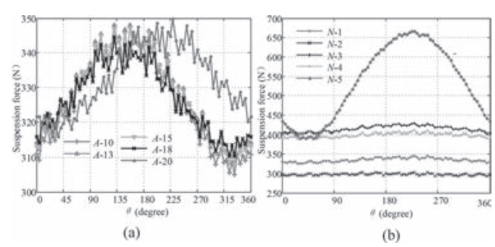

Fig. 2. Suspension force with different geometrical parameters. a Angle-A. b Number of segments-N.

AU-06. Characteristic analysis of a consequent-pole motor with vernier structure using ferrite magnets.

M. Choi[2], *B. Han*[1] and B. Kim[1]
1. Electrical, Electronic and Control Engineering, kunsan National university, South Korea, Gunsan, The Republic of Korea; 2. Electrical System R&D Team Assistant Research Engineer, Jeonbuk Institute of Automotive convergence Technology, South Korea, Gunsan, Jeollabuk-do, Korea (the Democratic People's Republic of)

Introduction Recently, the research on permanent magnet vernier machine (PMVM) is increasing due to its features of high power density and efficiency for low speed application. The machine utilizes slot harmonics of air gap permeance to develop the modulation flux, so it is beneficial to use of thin magnets in a surface permanent magnet(SPM) structure because it causes effective air gap shorter, resulting in the increment of slot harmonic of the stator permeance. Therefore, considering the demagnetization and torque density, it is hard to avoid using expensive Nd-magnets [1]-[4]. Meanwhile, a consequent pole machine has the advantage of being able to achieve nearly same levels of air gap flux density, although it reduce the used magnet quantity by half as compared to conventional machine [5]-[7]. If the consequent-pole structure is applied to a surface PMVM, the decrement of average air gap length is expected due to removal of half area of PM, resulting in increment of the air gap permeance harmonics as well. Consequently, even though thick ferrite magnet is used for the vernier motor, this motor is expected to resolve the problem of the average air gap length greatly and to get the higher vernier effect and demagnetization characteristics. In this paper, the characteristics of a consequent-pole motor with vernier structure using ferrite magnet analyzed and the characteristics are compared with those of general SPM and vernier machines by using finite element(FE) simulations in order to verify the advantages of proposed structure. Proposed Idea To get the vernier effects, common relation of Z_r-Z_s=-p is used, where Z_r is the number of rotor pole pairs, Z_s is the number of stator slots, p is the number of winding pole pairs. The vernier structure can be converted into consequence pole structure by replacing the S pole of magnet with iron core, which will reduce the average air gap length. Fig.1 shows general structure of a PM vernier machine and the proposed structure of the consequent pole vernier motor. The both prototypes given in Fig.1 are able to create vernier effect and the induced voltage can be expressed by (1) [1]. $E=N_{ph}D_il_c\omega_m(B_{g0}+(6q-1)B_{g1})\cos\{Z_r\theta\}$ (1), where N_{ph} is the number of turns in a phase, D_i is the inner diameter of stator core, l_c stack length of core, ω_m is the motor rotation speed, q is the number of stator slots/pole/phase. In addition, the expressions of B_{g0} and B_{g1} are given by (2) and (3). $B_{go} = B_{go.peak}\mu_0(1\text{-}1.6\beta(o/td))\cos\{Z_r(\theta\text{-}\theta_m)\}$ (2) $B_{g1} = B_{go.peak}\mu_0\pi\beta(0.39/(0.39\text{-}(o/td)^2))\sin\{1.6\pi(o/td)\}\cos\{\{Z_r\text{-}Z_s\}\theta\text{-}Z_r\theta_m)\}$ (3), where F_{1m} is the fundamental component of the MMF through magnet and can be obtained by using the magnetic equivalents circuit of the vernier and the proposed structures. Especially, the peak flux densities of (2) for both motors are given by (4) and (5), where g_a represents the air gap length, g_m represents the thickness of the magnets, A_m and A_g are the magnet and air gap area per pole respectively, and β is a non-linear function determined by the slot opening width and effective air gap length [5]. $B_{go.p.ver} = g_mA_mB_r/(\mu_0(g_mA_g+\mu_rg_aA_m))$ (4) $B_{go.p.prop} = g_mA_mB_r/(\mu_0(g_mA_g+2\mu_rg_aA_m))$ (5) The relation (4) and (5) shows that even if the number of magnets are reduced half but the main flux density B_{g0} of both motors are similar when g_m is quite larger than g_a. However, B_{g1} of the proposed vernier motor is greater than B_{g1} because the effective air gap length of the proposed structure is quite smaller, causing increases of the coefficient β. Therefore, when the machine has thicker g_m, it is possible to get the higher induced voltage due to the relationship (B_{g0}+(6q-1)B_{g1}. Therefore, the use of thick ferrite magnets can provide advantageous characteristics. Verification through FE simulations Three different prototypes of conventional, vernier and consequent pole type vernier motors with same geometric specifications are used for the FE analysis to verify the characteristics and are shown in Fig 2 (a), (b), and (c). In addition, fast fourier transform analysis is conducted to distinguish B_{g0} and B_{g1} from air gap flux density. Ferrite magnets with a thickness of 6mm is used for the analysis structures. The Fig 2 (f) shows that the magnitude of the fundamental component of Back EMF waveform given in Fig 2 (d), and it is proportional to the total combined composition of the air gap flux densities (B_{g0}+5B_{g1}, since q=1). As B_{g1} increases due to the reduction of the effective air gap length, the vernier effect is increased. Generally, the power density of a vernier motor is approximately two times that of conventional machines, but for the use of ferrite magnets, large thickness is required which reduces the advantage of the vernier effect, making the power density less than two times. On the other hands, the proposed structure has half number of magnets, but the power density is increased approximately 2.5 times. The use of ferrite magnets in proposed structure has shown an advantage in reducing the number of magnets and increasing the power density. Full paper further discusses detail analytical analysis of motor, the design limitations by considering demagnetization characteristics and reluctance effects.

[1] Byungtaek Kim, and Thomas A. Lipo, "Operation and Design Principles of a PM Vernier Motor," IEEE Trans.Mage., vol. 50, no. 6, pp. 3656 – 3663, Nov - Dec 2014 [2] H. Kakihata, Y. Katoka, and M. Takayma, "Design of surface permanent magnet-type Vernier motor," in Proc. 15th Int. Conf. Elect. Mach. Syst., 2012, pp. 1–6. [3] D. Li and R. Qu, "Sinusoidal back-EMF of Vernier permanent magnet machines," in Proc. 15th Int. Conf. Elect. Mach. Syst., 2012, pp. 1–6. [4] K. Okada, N. Niguchi, and K. Hirata, "Analysis of a Vernier motor with concentrated windings," IEEE Trans. Magn., vol. 49, no. 5, pp. 2241– 2244, May 2013. [5] Shi-Uk Chung, Ji-Won Kim, Byung-Chul Woo, Do-Kwan Hong, Ji-Young Lee, and Dae-Hyun Koo, "A Novel Design of Modular Three-Phase Permanent Magnet Vernier Machine With Consequent Pole Rotor," IEEE Trans. Magn., vol. 47 no. 10, pp. 4215 – 4218, Oct 2011 [6] Jun Amemiya, Akira Chiba, David G. Dorrell, and Tadashi Fukao, "Basic characteristics of a consequent-pole-type bearingless motor," IEEE Trans. Magn. Vol. 41 no. 1, pp. 82 – 89, Jan 2005 [7] D.G. Dorrell, J. Amemiya, A. Chiba, and T. Takenaga "Analytical modelling of a consequent-pole bearingless permanent magnet motor," in Power Electronics and Drive Systems, 2003. PEDS 2003. The Fifth International Conference on, 17-20 Nov. 2003

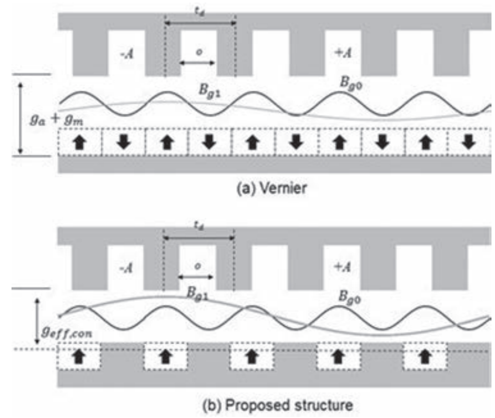

Fig. 1. Conceptual structure of a consequent pole vernier motor

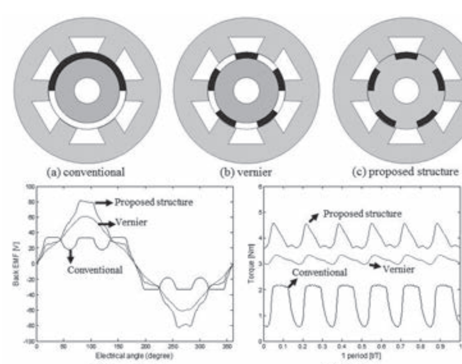

Motor type	B_{g0} [T]	B_{g1} [T]	$B_{g0}+5B_{g1}$ [T]	Back EMF [V]	Torque(0°) [Nm]	Torque(Max) [Nm]
Conventional	0.322	-	0.322	35.041	1.771	-
Vernier	0.311	0.052	0.570	53.875	2.746	-
Proposed structure	0.259	0.085	0.684	65.564	3.656	4.424

(f) FFT analysis results

Fig. 2. Prototypes and characteristics Comparison

AU-07. Static Characteristics of Hybrid Excitation Machine with Parallel Magnetic Path.

J. Zhang[1], Z. Xu[1], Y. Jiang[1] and W. Hua[1]
1. School of Electrical Engineering, Southeast University, Nanjing, China

Introduction: Electrical machine is the key component of power conversion systems where permanent magnet (PM) machine is popular due to its high efficiency and high power density. However, the airgap field of the PM machine could not be regulated and then it is not qualified in some applications, such as wide variable speed operation with high efficiency in whole speed range. According to the limitation of flux regulation for the PM machine, hybrid excited electrical machines are put forward and studied by many researches in recent decades, which combine both advantages of the PM machines and electrical excitation machines[1-4]. There are mainly two different hybrid excitation machines according to the relationship of PM and electrical excitation path, namely serial and parallel magnetic path. In the serial magnetic path, the PM is located and serial connected with the electrical magnetic circuit which has larger resistance of the magnetic circuit due to the PM has similar magnetic permenance as the air space, and then large excitation force is needed for flux regulation of the airgap field. An effective way to decrease the excitation force of the hybrid electrical winding, is adoption of parallel magnetic path, where the PM and electrical excitation in the magnetic circuit is paralleled. However, additional airgap has to be adopted in the hybrid excitation machine to avoid short-circuit of the PM flux. The introduction of additional airgap will lead to larger magnetic resistance for the electrical excitation and leakage flux of PM going through. *Topology*: This paper firstly proposes a new hybrid excitation machine with parallel magnetic path however without additional airgap and PM leakage flux. This machine has a novel compound structure with two salient-pole parts side by side, as shown in Fig. 1(a). Between two salient-pole parts, there is a PM ring with axis direction magnetization. It is shown in Fig. 1(a) that there are two serial airgaps in the PM flux path and both of them are the working airgap. Then the utilization of the PM is quite high since no leakage PM flux will be existed. The cross-section of the right salient-pole part with 12/8 stator rotor pole combination is shown in Fig. 1(b), where the PM flux will be in same direction for the stator teeth with armature windings. Three excitation windings are set on the stator teeth in which the flux direction and strength are determined by the current in the excitation windings. If the flux direction is shown as Fig. 1(b) then the magnetic strengthening is realized. Obviously the flux of excitation windings is not passed through the PM and then parallel magnetic path is achieved. It is inevitable the direction of PM flux in left and right airgap is different due to the side by side structure. So, if the rotor teeth of two sides are aligned shown as Fig. 1(a), the separate armature windings have to be used in the stator and it is not good since more terminal winding and accommodation space are required. Then the power density and efficiency will be low due to larger volume and winding resistance. However the rotor teeth in left and right side might be not aligned to avoid the PM flux cancellation and it is easy to produce due to the simple rotor structure. By shifting the rotor teeth in different side in a mechanical angle to make phase angle deviation of the flux in the stator, the armature windings in the side-by-side stator teeth may be combined into one due to the symmetrical structure. In this case the winding resistance is lowered and the power density is improved also. In order to verify the operation theory and obtain the static characteristics of this machine, 3D finite element analysis (FEA) tool is used for modeling of this machine. *Simulation Results*: By using 3D FEA, simulation results are obtained shown as Fig. 2. Fig. 2(a) shows the simulation results of different shifted angle for rotor tooth, where the excitation current and load current are zero. The no-load PM flux is varied according to the tooth shifted angle greatly. As mentioned before, the aligned rotor tooth will lead to reversal PM flux in two airgap fields and the total flux will be near zero if one combined armature winding is used. It shows the 22.5 degree is quite good for the tooth shifted angle and in this case the PM flux is positive added for right and left part. In Fig. 2(b) it shows the no-load PM flux under different PM thickness in axis direction while the rotor tooth shifted 22.5 degree with combined windings. The flux linkage is quite similar when the PM thickness is larger than 7.5mm. The flux linkage is related to the power density. However, larger PM thickness means consumptions of more rare-earth magnet and less iron at the situation of constant total stack length(75mm include PM). In this case, it is better the PM thickness is small at same flux linkage. So the optimized PM thickness is 10mm under the design parameters of this paper (outer dia. Φ128mm). The simulation results of co-action of excitation winding and PM are shown in Fig. 2(c). It shows very good magnetic field weakening and strengthening when the excitation winding is put into action. More details of machine design and characteristic analysis will be given in the full paper.

1. Shakal A, Liao Y, Lipo T. A. A permanent magnet AC machine structure with true field weakening capability. Electric Machines and Power Systems, 1996, 24(4): 497-509. 2. Chan C C, Zhang R, Chau K T, Jiang J Z. A novel permanent magnet hybrid motor for electric vehicles, Proceedings of China International Conference on Electric Machines, Hangzhou, China, 1995:1-6. 3. Hua W, Cheng M, Zhang G. A Novel Hybrid Excitation Flux-Switching Motor for Hybrid Vehicles. IEEE Transactions on Magnetics, 2009, 45(10): 4728-4732. 4. Wang Y, Deng Z, Wang X. A Parallel Hybrid Excitation Flux-Switching Generator DC Power System Based on Direct Torque Linear Control. IEEE Transactions on Energy Conversion, 2012, 27(2): 308-318.

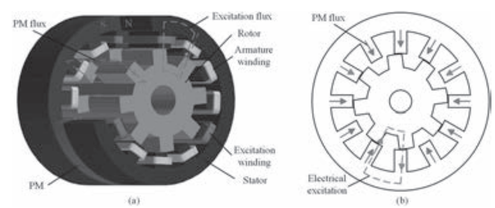

Fig. 1. Machine topology. (a) 3D view with aligned rotor teeth; (b) cross-section and flux path.

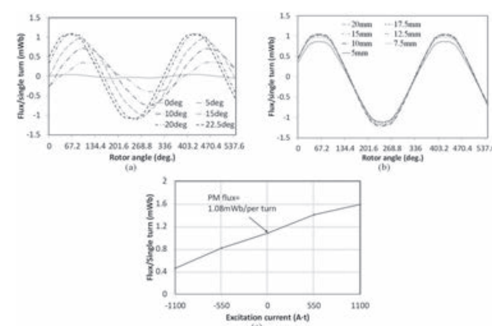

Fig. 2. Simulation results. (a) Rotor tooth shifting; (b) PM thickness; (c) Flux regulation at no-load.

AU-08. A Double-Rotor Consequent-Pole Vernier Permanent-Magnet Machine with Toroidal-Winding Arrangement for Hybrid Electric Vehicles.

C. Lee[1]
1. Research Laboratory of Electronics, Massachusetts Institute of Technology, Cambridge, MA, United States

I. INTRODUCTION Due to the increasing concerns on energy utilization and environmental protection, the development of hybrid electric vehicles (HEVs) has been accelerating recently [1]. As one of key components in HEV systems, the electric machines have to offer several key features, including high efficiency, high power density, high controllability, wide-speed range, maintenance-free and fault-tolerability [2]. Since the permanent-magnet (PM) machines can fulfil most of the goals, this machine type has become the mainstream in the past few decades [3]. In particular, the Vernier permanent-magnet (VPM) machine, which utilizes the magnetic gearing effect to boost up the torque density, has been accepted as a very promising candidate for direct-drive HEV applications [4]. The VPM machine generally adopts the inner-rotor (IR) topology, such that its armature windings have to be installed with the distribution arrangement [5]. This conventional design suffers from two major disadvantages, namely the wastage of the inner machine space and larger end-winding length. To improve the situation, the outer-rotor VPM (OR-VPM) machine that adopts the toroidal-winding arrangement has been developed [6]. Upon the installation of the toroidal-winding arrangement, shorter end-winding length and better fill winding factor can be achieved. However, similar as the conventional IR-VPM design, the OR-VPM machine still suffers from the poor utilization of the inner space. The purpose of this paper is to artfully incorporate the concepts of double-rotor and consequent-pole into the VPM machine, and hence forming the proposed double-rotor consequent-pole VPM (DR-CPVPM) machine, purposely for HEV applications. With the implementation of the double-rotor structure, the toroidal-winding arrangement can be fully utilized to power up both rotors simultaneously. In the meantime, the consequent-pole topology can improve the PM utilization and hence further boosting up the power and torque densities. To illustrate the effectiveness of the proposed design, the proposed DR-CPVPM machine will be purposely compared with the well-known Prius HEV counterpart. II. MACHINE DESIGN The structures of the conventional IR-VPM machine and the proposed DR-CPVPM machine are shown in Fig. 1(a), and Fig. 1(b), respectively. Unlike the conventional IR-VPM machine that consists of only one rotor, the proposed DR-CPVPM machine instead utilize its inner space to accommodate the additional rotor. For simplicity, the pole arrangement of the outer- and inner-segments are purposely set equal. Since the proposed DR-CPVPM machine is derived from the IR-VPM machine, its design equations such as the pole arrangement can be extended from that of the profound ancestors. As mentioned, the traditional IR-VPM machine installs the armature winding with the distribution arrangement, such that it suffers from poor winding fill factor and larger end-winding length. On the other hand, the proposed DR-CPVPM machine instead artfully adopts the toroidal-winding arrangement, such that the armature winding can power up the two rotors simultaneously. Upon the employment of the toroidal-winding arrangement, better winding fill factor and shorter end-winding length can be achieved. Consequently, higher power and torque densities can be produced. To further improve the machine performance, unlike the conventional IR-VPM machine that equips with the alternating PM arrangement, the proposed DR-CPVPM machine instead employs the concept of consequent-pole for PM installation. With the consequent-pole arrangement, the leakage PM flux can be minimized. Consequently, even with a lower PM consumption, the proposed machine can still generate a larger PM flux-linkage. As a result, the proposed DR-CPVPM machine can potentially achieve a better cost-effectiveness than its counterparts. III. MACHINE PERFORMANCE ANALYSIS The no-load electromotive forces (EMFs) of the proposed DR-CPVPM machine at base speed of 500 rpm are shown in Fig. 2(a). It can be shown the two machine segments can produce the EMFs with same pattern, i.e., same polarity and same phase angle. Consequently, the feasibility of the toroidal-winding arrangement is verified. In the meantime, the results show the proposed machine can generate a very sinusoidal-like EMF waveforms, from both its outer- and inner-segments. With the bipolar brushless AC (BLAC) conduction algorithm, it can be expected that the proposed machine can produce a resultant torque with very little pulsation, which is highly desirable for HEV applications. The output torque waveforms of the conventional IR-VPM machine and the proposed DR-CPVPM machine are shown in Fig. 2(b). It can be found that the average torque of the IR-VPM machine and the proposed DR-CPVPM machine are 241.5 Nm and 376.3 Nm, respectively. In the meantime, their corresponding torque ripples are about 10.2 % and 12.3 %, respectively. As a result, with the double-rotor and consequent-pole structures, the proposed machine can achieve 56 % larger torque than its conventional counterpart, upon a comparable torque ripple value. All these values are very attractive for modern HEV applications [2]. The detail machine designs and comparisons based on the requirement of HEV applications will be included in the full paper.

[1] A. Emadi, Y. J. Lee, and K. Rajashekara, "Power electronics and motor drives in electric, hybrid electric, and plug-in hybrid electric vehicles," *IEEE Trans. Ind. Electron*., vol. 55, no. 6, pp. 2237–2245, Jun. 2008. [2] R. Cao, C. Mi, and M. Cheng, "Quantitative comparison of flux-switching permanent-magnet motors with interior permanent magnet motor for EV, HEV, and PHEV applications," *IEEE Trans. Magn.*, vol. 48, no. 8, pp. 2374–2384, Aug. 2012. [3] C. H. T. Lee, J. L. Kirtley, and M. Angle, "A partitioned-stator flux-switching permanent-magnet machine with mechanical flux adjusters for hybrid electric vehicles," *IEEE Trans. Magn.*, vol. 53, no. 11, p. 3000807, Nov. 2017. [4] B. Kim, and A. Lipo, "Operation and design principles of a PM Vernier motor," *IEEE Trans. Ind. Appl*., vol. 50, no. 6, pp. 3656–3663, Nov./Dec. 2014. [5] D. Li, R. Qu, J. Li, L. Xiao, L. Wu, and W. Xu, "Analysis of torque capability and quality in Vernier permanent-magnet machines," *IEEE Trans. Ind. Appl*., vol. 52, no. 1, pp. 125–135, Jan./Feb. 2016. [6] D. Li, R. Qu, J. Li, and W. Xu, "Consequent-pole toroidal-winding outer-rotor Vernier permanent-magnet machines," *IEEE Trans. Ind. Appl*., vol. 51, no. 6, pp. 4470–4481, Nov./Dec. 2015.

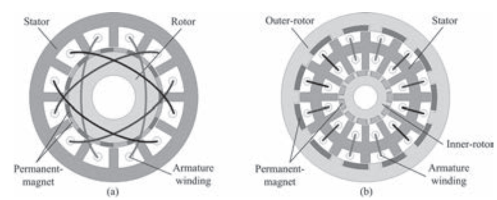

Fig. 1. Machine structures: (a) Conventional IR-VPM. (b) Proposed DR-CPVPM.

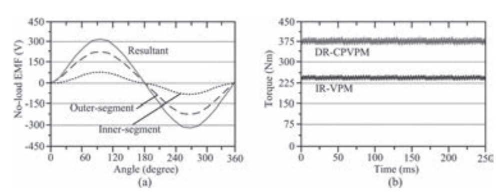

Fig. 2. Machine performances: (a) No-load EMFs of DR-CPVPM. (b) Steady torques.

AU-09. Efficiency-Enhanced Variable Flux Reluctance Machine with Reduced Excitation Coils for Electric Vehicles.

X. Zhao[1] and S. Niu[1]
1. Electrical Engineering, The Hong Kong Polytechnic University, Kowloon, Hong Kong

Abstract: Due to a limited source of rare-earth PMs, developing high-performance non-PM electrical machine is an important research topic for electrical vehicles. DC-excited variable flux reluctance machine is a promising candidate. However, conventional design of such machine suffers from large excitation copper loss and reduced efficiency, due to an identical distribution of excitation components at stator side. This paper aims to propose an efficiency-enhanced variable flux reluctance machine. The key is to reconstruct effective magnetic circuit with halved excitation coils, thus to reduce excitation copper loss while keeping the power density not sacrificed. A comparative study is performed between the proposed topology and existing counterparts, which reveals that, with the same machine size, slot factor and excitation copper loss, the proposed design provides higher power density and higher efficiency. Moreover, the proposed topology can also eliminate the mutual inductance. Therefore, this new design is a more competitive non-PM solution for electric vehicle propulsion. I.Introduction Due to the lack of rare-earth permanent magnet (PM) source, developing high-performance electrical machines with no PMs or reduced PMs is still an important research field for some industrial applications such as electric vehicles. Switching reluctance machine (SRM) is a promising solution, but it has severe torque ripple. Compared with SRM, DC-excited variable flux reluctance machine (VFRM) owns an excitation flux which is similar to traditional synchronous machine [1]. Therefore, it can obtain a smooth torque performance if driven by sinusoidal current. However, one of the most significant drawbacks in VFRM is its energy consumption in the DC field terminal, which leads to increased copper loss and reduced efficiency. This paper aims to propose a new VFRM with improved efficiency while maintains the same excitation ability compared with existing topology. With halved field coils, the copper loss in field terminal can be almost cut down and an efficiency-significantly-enhanced non-PM machine can be provided for electrical vehicle propulsion. II. Machine structure and magnetic circuit analysis. The machine structures of the existing and proposed design are shown in Fig. 1(a) and Fig. 1(b), respectively. One can see, both DC field coils and armature coils are located at stator side, with the rotor only consisting of iron materials, which makes VFRM a robust and cost-effective solution for EVs. Compared with existing design, the proposed topology cuts off the number of field coils and rearranges the armature coils as well, aiming to achieve a comparable performance with reduced excitation copper loss. The effective DC magnetic circuits of two designs are denoted and compared in Fig. 1 by yellow dash lines. One can see, the fundamental DC magnetic circuit of existing design starts from a wounded stator tooth, shunting into two adjacent teeth and coming back from the rotor part. Obviously, the effective magnetic circuit generated by each DC coil are coupled together. However, for the proposed design, the effective DC loop encircles only one DC component and there is no cross linking between different excitation coils. Hence, in the proposed topology, a modular magnetic circuit is actually built with halved excitation coils. III.performance comparison By using the finite element analysis, a comparative study is performed to verify the advantages of the proposed topology. For a fair comparison, FE models for two machines share the same outer dimension, axial length and air gap length. Besides a common design optimization is performed for two machines, considering the influence of structure parameters are different when the effective magnetic circuit is reconstructed. When the armature copper loss is fixed at 60W, the output torque curves for two designs with different excitation copper loss are presented in Fig. 2(a). With the same excitation loss, the proposed machine can achieve a higher output torque than the existing topology, which verifies that the proposed design owns a comparable excitation ability with halved DC coils. An improved efficiency can be aslo derived out from Fig. 2(a). Further, the inductance characteristic for two designs is also plotted in Fig. 2(b). Benefiting from a modular DC magnetic circuit as discussed in Part A above, the proposed machine has a negligible mutual inductance, compared with existing design, giving a fault-tolerance potential for high-reliability EV drives. IV.Conclusion This paper proposes an efficiency-enhanced variable flux reluctance machine. The key is by reconstructing effective magnetic circuit with halved excitation coils, aiming to reduce excitation copper loss while keeping the power density not sacrificed. By using finite element analysis, a comparative study is performed between the proposed design and existing counterpart, which reveals that with excitation copper loss, the proposed design provides higher power density and higher efficiency. Moreover, the proposed topology also eliminates the mutual inductance. Therefore, this new topology is more competitive non-PM machine for electric vehicles.

[1] X. Liu and Z.Q. Zhu, "Comparative study of novel variable flux reluctance machines with doubly fed doubly salient machines", *IEEE Trans. Magn.*, vol. 49, no. 7, pp. 3838-3841, 2013.

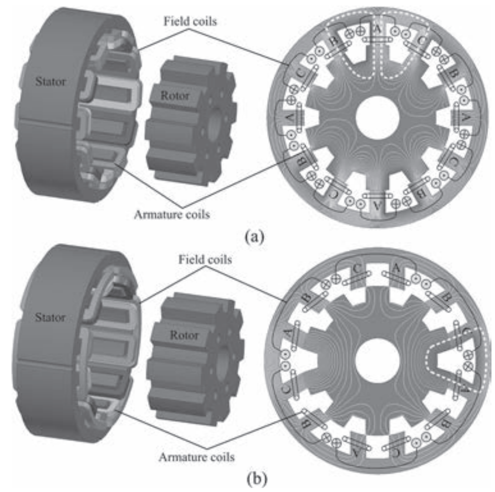

Fig. 1. DC-excited VFRM. (a) Existing topology. (b) Proposed topology.

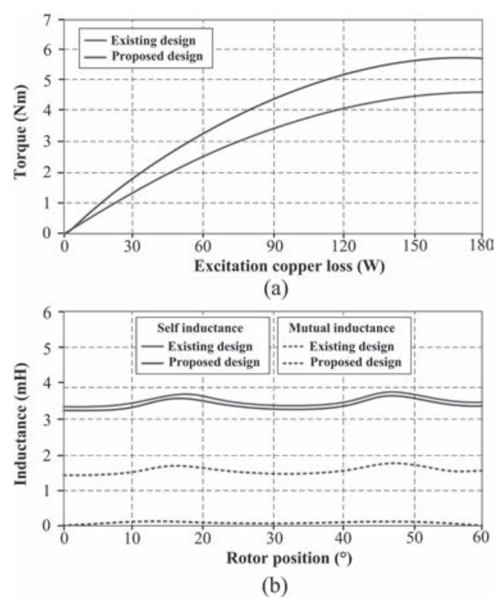

Fig. 2. (a) Output torque versus different excitation copper loss with armature copper loss fixed at 60W. (b) Inductance characteristics.

AU-10. Parametric Optimization of Flux Focusing Type Double Stator and Single Rotor Axial Flux Permanent Magnet Motor.

Q. Syed[1] and I. Hahn[1]
1. Electrical Drives and Machines, University of Erlangen-Nürnberg, Erlangen, Germany

Recently, great interest is developing towards axial flux permanent magnet motor (AFPM) for direct-driven in-wheel applications, due to their inherent multipolar disc-type structure and small axial length. Three-disc AFPMs have a high torque density because they effectively utilize the intermediate disc and are compact enough to be easily mounted in the wheel. Mechanical problems are also reduced because an intermediate disc is equally attracted in axial direction by its both sides. The slotted double stator and single rotor (DSSR) AFPM has more power and torque density and less cost, weight, volume, inertia and cooling problems in comparison to the single stator and double rotor (SSDR) AFPM topologies [1]. The flux focusing type slotted DSSR AFPM consumes a less amount of the permanent magnets (PMs) and has more torque density compared to the surface mounted permanent magnet (SPM) type slotted DSSR AFPM [2]. Therefore, in this paper flux focusing type DSSR AFPM is further investigated for parametric optimization. Initial dimensions of the flux focusing type DSSR AFPM are selected using the basic analytical modelling. A 3D finite element analysis (FEA) is utilized for its detailed characteristic analysis. The flux focusing type DSSR AFPM has 24 number of poles and 36 number of stator slots on each stator disc. Although it has a less winding factor (0.866), which decreases the output electromagnetic torque, it has a less total harmonic distortion (THD), zero fundamental or 1st harmonic, which reduces the losses, especially core losses. Due to the symmetry and its high periodicity of 12, 1/24th of each geometrical model of the flux focusing type DSSR AFPM is analysed using a 3D FEA, which decreases the computation time. The design of experiments (DoE) method is used for the parametric optimization of the flux focusing type DSSR AFPM. Although it is time-consuming due to the 3D FEA, it is suitable for the electromagnetic optimization of motor [3]. Initially, the full factorial design (FFD) is applied to analyse the effect of different design variables on the performance of the flux focusing type DSSR AFPM. With the help of the FFD, the significant design parameters can be identified easily. The FFD is very time-consuming, therefore, only the minimum, maximum and mean values of each design variable are considered, which limits the DoE. To extend the DoE and also to reduce the computation time compared to the FFD, the Latin hypercube sampling method (LHS) is used for the detailed characteristic analysis of the flux focusing type DSSR AFPM. The objective is to get best motor performance, such as high electromagnetic torque and back EMF and low torque ripple, cogging torque and total harmonic distortion (THD). The flux focussing type DSSR AFPM has constant outer radius length, current density, airgap, and stator yoke height. The design variables of the flux focussing type DSSR AFPM are shown in Fig. 1, where "*A*" is the ratio of the stator slot width and the slot pitch, "*B*" is the height of the stator slot, "*C*" is the ratio of the PM width and the pole pitch, "*D*" is the height of the PM, "*E*" is the ratio of the slot opening width and the slot pitch, "*F*" is the height of stator tooth tip, and "*G*" is the rotor's inner to outer radius ratio. Fig. 2, represents the output torque characteristics of the flux focusing type DSSR AFPM. Initially, a number of one hundred experiments were carried out for the LHS. The experiment "X" has the highest electromagnetic torque, however, it does not have the lowest torque ripple. Similarly, experiment "Y" has the lowest torque ripple but does not have the highest electromagnetic torque. Experiment "Z" has almost same torque ripple, as that of "Y" but has a higher electromagnetic torque. Therefore, the optimal solution is in between "X" and "Z". Interpolation between both geometrical models will provide an optimal solution of the flux focusing type DSSR AFPM. In the full manuscript, a detailed parametric optimization of the flux focusing type DSSR AFPM will be presented, based on the DoE method coupled with the 3D FEA. The effect of each design variable on the output characteristics, as determined by the analytical modelling and realized by the FFD will be presented and discussed. Along with the FFD, optimal design and a meta-parametric analysis of the flux focusing type DSSR AFPM will be carried out using the LHS.

[1] M. Aydin, M. K. Guven. "Comparing Various PM Synchronous Generators: A Feasible Solution for High-Power, Off-Highway, Series Hybrid, Electric Traction Applications", IEEE Vehicular Technology Magazine, vol. 9, no. 1, 2014. [2] Q. A. S. Syed, I. Hahn, "Comparative Analysis of Surface Mounted and Flux Focusing Type Axial Flux Permannent Magnet Motor", IET International Conf. on Power Electronics, Machines and Drives, 2016. [3] F. Gillon, P. Brochet, "Shape optimization of a permanent magnet motor using the experimental design method", *IEEE Trans. Magn.*, vol. 35, pp. 1278-1281, May 1999.

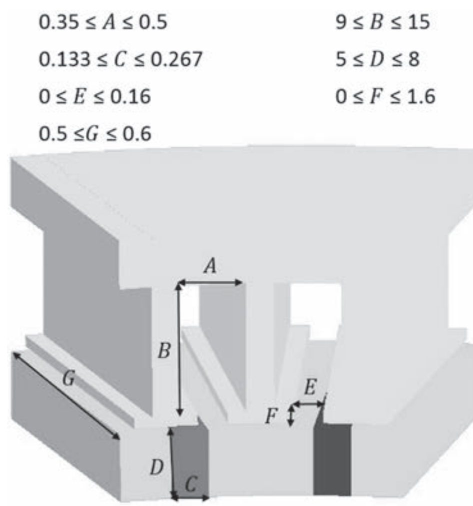

Fig. 1. Design variables of the flux focusing type DSSR AFPM

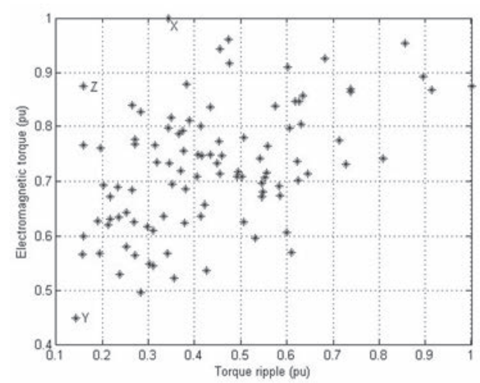

Fig. 2. Distribution of torque characteristics of the flux focusing type DSSR AFPM

AU-11. Comparative Assessments of Flux-switching PM Motor Drives for EV Applications.

C. Liu[1], *C. Hwang*[2], Y. Chao[2], H. Chang[3] and C. Hong[4]

1. Electrical Engineering, National Sun Yat-sen University, Kaohsiung, Taiwan; 2. Electrical Engineering, Feng Chia University, Taichung, Taiwan; 3. Automatic Control Engineering, Feng Chia University, Taichung City, Taiwan; 4. Ph.D. Program in ECE., Feng Chia University, Taichung, Taiwan

Introduction: Recently, many flux-switching permanent magnet machine (FSPMM) topologies and their electromagnetic designs, winding layouts, and performance characteristics are broadly investigated [1]-[3]. For the potential applications onto a micro-sized vehicle with front and rear drives, with the desired continuous torque output of 35.5 Nm at a rated speed level of 1350 rpm, a comparative assessment of three different flux-switching permanent magnet motor topologies will be performed from the results calculated by detailed finite element method (FEM). The three FSPMMs that can meet their specific operational requirements will all be optimized based on their own features. The hardware constructions and the related experimental measurements will be supplied to validate the design adequacies. Model of the Proposed Motors: Fig. 1 illustrates the three proposed FSPMM topologies, they are respectively the conventional FSPMM with all poles wound (type A), the multi-tooth (type B), and the C-core (type C) FSPMMs. They have the same stator outer diameter of 140 mm, air gap length of 0.5 mm, rotor outer diameter of 91 mm, and stack length of 135 mm. The Results: For a fair comparison, the valid stator slot (S) and rotor pole (P) combinations for each topology with the same dimensions and operation conditions are designed and analyzed using FEM, and the one among each topology that has the best electromagnetic performance is selected. Then a design sensitivity analysis and the genetic algorithm are used to optimize the torque ripple whereas the desired torque for each selected topology being fixed. From the comparison results as provided in Table I, some of the key observations and features of these three FSPMMs can be summarized: 1) The conventional FSPMM (12S/13P of type A) is not a good candidate for use in EV applications among the three types as far as the usage of PM material is concerned. 2) The multi-tooth core FSPMM (6S/19P of type B) has a minimum usage of PM and copper materials, and hence a low manufacturing costs can be accomplished. However, design optimization must be performed to further increase the machine efficiency. 3) The C-core FSPMM (6S/13P of type C) has the highest average torque and efficiency. However, the two values are very close to the other two types. Also it will exhibit the largest value of torque ripple. Therefore, design modifications must be performed to further reduce the torque ripple for practical implementations.

[1] Z. Q. Zhu, J. T. Chen, Y. Pang, D. Howe, S. Iwasaki, and R. Deodhar, "Analysis of a novel multi-tooth flux-switching PM brushless AC machine for high torque direct-drive applications," *IEEE Trans. Magn*., vol. 44, no. 11, pp. 4313-431, Nov. 2008. [2] J. T. Chen, Z. Q. Zhu, S. Iwasaki, R. Deodhar, "A novel E-core flux-switching PM brushless AC machine for direct-drive applications," *IEEE Trans. Ind. Appl*., vol. 47, no. 3, pp. 1273-1282, Jun. 2011. [3] Z. Q. Zhu and J. T. Chen, "Advanced flux-switching permanent magnet brushless machines," *IEEE Trans. Magn.*, vol. 46, no. 6, pp. 1447–1453, Jun. 2010.

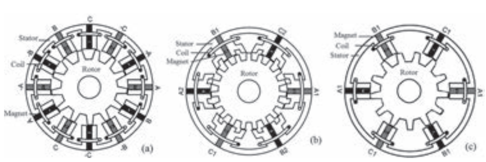

Fig. 1. Cross section of motors. (a) Type A 12S/13P, (b) Type B 6S/19P, and (c) Type C 6S/13P.

Parameter	Type A	Type B	Type C
Average torque (Nm)	36.26	37.22	37.75
Torque ripple (%)	1.41	1.64	4.3
Output power (W)	5216.15	5261.87	5336.79
Power density (W/cm^3)	2.46	2.532	2.57
Copper loss (W)	92.68	79.984	105.377
Iron loss (W)	201.6	311.85	173
Efficiency (%)	94.36	92.665	94.88
Magnet volume (mm^3)	220527	88024	103498
Copper weight (kg)	1.237	1.166	1.544

TABLE I Comparisons of Performance

AU-12. Analysis and improvement of a variable flux hybrid-permanent-magnet synchronous machine.

Y. Hu[1,2], *B. Chen*[1,2], B. Zhou[1], Y. Xiao[1] and M. Wang[1]
1. Gree Electric Appliances Inc. of Zhuhai, Zhuhai, China; 2. State Key Laboratory of Air-Conditioning Equipment and System Energy Conservation, Zhuhai, China

Abstract—A variable flux hybrid-permanent-magnet synchronous machine (VFHPMSM) is propose in this paper, which is equipped with aluminum-nickel-cobalt (AlNiCo) PMs and neodymium-iron-boron (NdFeB) PMs. A prototype of VFHPMSM is built, and the experimental results are in good correlation with the FEA simulation. The simulation and experimental results show that VFHPMSM has a good flux adjusting ability and efficiency. *Index Terms*—hybrid-permanent-magnet, flux adjusting ability, finite element analysis (FEA), re- and demagnetization; I. INTRODUCTION Along with the development of rare earth permanent magnet materials, the permanent magnet synchronous motor is used in many applications, such as electric vehicles, industrial drive, domestic appliance and power generation. However, due to the constant of PM magnetic field, the motor flux is always difficulty to adjusting. And with the vigorous development of electric vehicles, a high-performance permanent magnet synchronous is urgent demanded. In this paper, a variable flux hybrid-permanent-magnet synchronous machine (VFHPMSM) is presented and a prototype is built. The operation principle of VFHPMSM is analyzed and the re- and demagnetization characteristics analysis is studied based on finite element analysis (FEA). II. TOPOLOGY AND OPERATION PRINCIPLE *Machine Topology* Fig.1 shows the topology of VFHPMSM, which is designed at 4-pole 24-slot. The rotor adopts with hybrid-permanent-magnet in each pole, and PMs are arranged in W-shape. The AlNiCo PMs mount on the middle of the pole, and NdFeB PMs arranged with V-shape in the side of AlNiCo PMs. *Operation Principle* The flux weakening principle of VFHPMSM is illustrated in Fig.2. According to the magnetization state of AlNiCo PMs, two typical states are defined: flux-enhanced (AlNiCo PMs identically magnetized with NdFeB PMs) and flux-weakened (AlNiCo PMs oppositely magnetized with NdFeB PMs). The magnetization state of AlNiCo PMs can be regulated by an impulse current in the stator coils. III. ELECTROMAGNETIC PERFORMANCE OF VFHPMSM *Magnetic Field Distributions* The magnetic field distributions of 1/4 motor model under different demagnetizing current *I* are shows in Fig.3. By applied the demagnetizing current of d-axis, the magnetic field distributions and magnetization state of AlNiCo PMs are changed. *Flux-Adjusting performance* The FEA predicted flux linkage and back EMF waveforms of the VFHPMSM at 1560 rpm under different magnetization state of AlNiCo PMs are compared in Fig.4 and Fig. 5. It is found that the amplitudes of the flux linkage and back EMF waveforms will decrease as the demagnetizing current increases. The weakening rate may increase with the demagnetizing current and it can be 51% when the demagnetizing current *I* reach 35A. As shown in the Fig.5, the changes of EMF are the same tendencies with flux linkage, and the waveforms had a distortion. The reason for this is that the air-gap magnetic density with the center of the pole is small or even negative when AlNiCo PMs demagnetization. *Efficiency Characteristics* The FEA predicted efficiency of VFHPMSM and general IPM at 1500 rpm are compared in Fig.6. It is found that the efficiency of VFHPMSM is improved with constant magnet IPM. IV. EXPERIMENTAL VERIFICATION The rotor lamination and photographs of the VFHPMSM are shows in Fig.7 and Fig.8. Fig.9 shows the machine testing setup. The test bench includes a voltage source inverter, a control board, VFHPMSM, load machine, Oscilloscope and a test cabinet. V. CONCLUSION A variable flux hybrid-permanent-magnet synchronous machine has been presented, which shows a wide range of flux-adjusting, and the flux linkage is varied obviously at different demagnetizing current. Furthermore, the results of FEA and experiments of VFHPMSM prove that the machine can change the flux of permanent magnet, and realized that the motor operate in wide speed areas with high performance.

N. Limsuwan, T. Kato, K Akatsu and R. D. Lorenz. "Design and Evaluation of a Variable-Flux Flux-Intensifying Interior Permanent-magnet Machine," *IEEE Trans. Ind. Appl*., vol.50, no.2, pp. 1015-1024, Mar. 2014. K. C. Kim, "A novel magnetic flux weakening method of permanent magnet synchronous motor for electric vehicles," *IEEE Trans. Magn*., vol.48, no.11, pp. 4042-4045, Nov. 2012. S. Maekawa, K. Yuki, M. Matsushita, I. Nitta, Y. Hasegawa, T. Shiga, T. Hosoito, K. Nagai and H. Kubota, "Study of the Magnetization Method Suitable for Fractional-Slot Concentrated-Winding Variable Magnetomotive-Force Memory Motor," *IEEE Trans. Power Electron.*, vol. 29, no. 9, pp. 4877-4887, Sep. 2014.

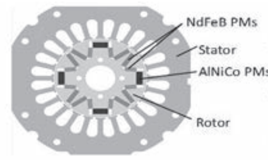

Fig.1 Cross-section of VFHPMSM

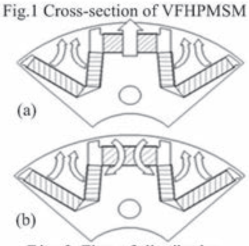

Fig.2 Flux of distribution of rotor. (a) flux-enhanced, (b) flux-weakened

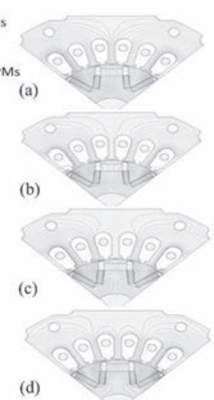

Fig. 3 Flux distributions of machine under no-load. (a)*I*=0, (b) *I*=10A, (c)*I*=20, (d)*I*=35A

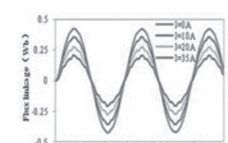

Fig. 4 Line-line flux linkage waveform

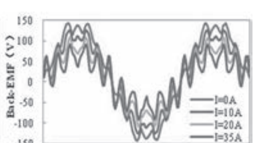

Fig. 5 Line-line back-EMF waveform

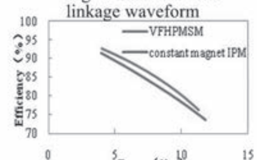

Fig. 6 Efficiency improvement of the VFHPMSM

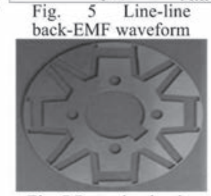

Fig. 7 Rotor lamination

Fig. 8 VFHPMSM machine

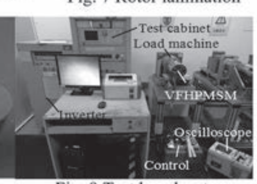

Fig. 9 Test bench setup

AU-13. A Simplified Rotor-Shape Optimization Method for IPM Motor to Torque Ripple Reduction.

G. Yu[1], J. Li[1], Y. Xu[1], J. Zou[1], L. Xiao[1] and H. Lan[1]
1. Harbin Institute of Technology, Harbin, China

I. INTRODUCTION Permanent magnet synchronous motors (PMSMs) have risen steadily in various industrial and domestic applications owing to their superior performance such as high power density and efficiency. According to the different winding type, PMSMs can be generally divided into distributed winding (DW) and fractional slot concentrated winding (FSCW) motors [1]. Compared with DW, FSCW motor own low cogging torque, compact structure, and convenient fabrication. However, FSCW contains abundant stator MMF harmonics, which results in a great deal of rotor eddy current loss. In consideration of heat dissipation difficultly within the rotor, a higher temperature rise of rotor can result in permanent magnets demagnetization and motor itself breakdown. Nationwide studies of the effects of pole-slot combination on stator MMF harmonics indicate that PMSMs with 1/2 slots per phase per pole are preferred due to a less MMF harmonics than others in order to lower rotor loss. Meanwhile, if interior permanent magnet (IPM) structure is selected for rotor, a better flux-weakening ability can be achieved [2-4]. However, a larger cogging torque and back EMF harmonics of IPM motors with 1/2 slots per phase per pole than the other FSCW motors results in greater torque ripple, which can further brings vibration and acoustic noise problem. When the motor load is small, cogging torque is the dominant source from all the components of torque ripple. The interaction of a few back EMF harmonics and input current generate torque ripple even if the injected current can be controlled as ideal sinusoidal wave. This paper investigates the rotor-shape optimization method for IPM motors with 16 poles/24 slots (1/2 slots per phase per pole) in detail to improve both cogging torque and back EMF wave, and finally achieve the purpose of optimizing torque ripple. Different from the previous contributions, a simplified rotor-shape optimization method for IPM motor is proposed by the combination both shape function optimization of rotor surface and PM shaping technology, which can effectively decrease the optimization parameters of rotor to improve the optimization efficiency. II. BACK EMF AND COGGING TORQUE ANALYSYS A.MMF harmonics and Back EMF analysis Based on the principle of winding function, the winding factor is analyzed for a unit motor with 2 poles/3 slots. It can be revealed that the winding factor of 5th and 7th order harmonic is 0.866 as equal to the fundamental order. Meanwhile, the notable 5th and 7th EMF harmonics are induced. Worthy of mention is that the MMF harmonics of 2 poles/3 slots are an integral multiple of the number of pole pairs. For motors with q less than1/2, excepting the MMF harmonics with an integral multiple of the pole pair number of the motor, the motor also contains rich non-integer multiple space harmonics called sub-harmonics, which is a significant characteristic of FSCW. B.Cogging torque analysis Based on the visual displacement approach, cogging toque order is the LCM of slot number and pole number. According to the orthogonality of trigonometric function, only when the indexes of two factors are identical to each other, the integral results are not zero. For the motor with 1/2 slot per phase per pole, the basic order of cogging torque is 6, so the 6th and 12th order can be as cogging torque dominant components. III.ROTOR-SHAPE OPTIMIZATION METHOD A. Optimization method A simplified rotor-shape optimization method for IPM motor is proposed by the combination both shape function optimization of rotor surface and PM shaping technology. For reducing the number of parameters and improving optimization efficiency, an modified inverse cosine function as the optimization function for rotor surface, at the same time, the PM shaping technology is employed to further improving the cogging torque and back EMF wave,and suppressing the torque ripple. The related structure and optimization parameters are illustrated in Fig. 1. During the optimization process, the stator is assumed to a slotless solid without regard for the slot effects. B.Optimization results The optimization results are summarized in Table I, and cogging torque for the IPM motors is shown in Fig. 3. Such results can indicate that the optimized machine owns the lowest cogging torque, agrees well with that the flux density analysis aforementioned. IV.EXPERIMENT VERIFICATION A prototype machine as the results of optimization is manufactured shown in Fig. 3, in which (a) shows the modified inverse cosine shape for rotor core and corner-cut permanent magnet poles. Back EMF waveforms @320rpm of measure and FEA are compared in Fig. 4. It can be found that the test result agrees with the simulation very well. The *THD* of the test EMF waveform is only 1.76%, conforming to the value of 1.8% in Table I. It is clear that the optimized rotor reduces the EMF harmonics obviously. More experiment will be listed in this Section. V. CONCLUSION 1) The 3rd, 5th and 7th harmonics of airgap flux density are the main cause of the cogging torque, among which the 3rd harmonic is the dominant for IPM motor with 1/2 slots per phase per pole. 2) The simplified optimization method can effectively improve the both back EMF and cogging torque problems, and further reduce torque ripple of IPM motor with 1/2 slots per phase per pole. The *THD* of no-load EMF is 1.76%, and the cogging torque is 0.687% relative to the rating torque.

[1].Bianchini C,Immovilli F,Lorenzani E,et al. Review of Design Solutions for Internal Permanent-Magnet Machines Cogging Torque Reduction[J]. IEEE Transactions on Magnetics,2012,48(10): 2685-2693. [2].Barcaro M,Bianchi N,Magnussen F. Permanent-Magnet Optimization in Permanent-Magnet-Assisted Synchronous Reluctance Motor for a Wide Constant-Power Speed Range[J]. IEEE Transactions on Industrial Electronics,2012,59(6): 495-2502. [3].Dutta R,Rahman M F,Chong L. Winding Inductances of an Interior Permanent Magnet (IPM) Machine With Fractional Slot Concentrated Winding[J]. IEEE Transactions on Magnetics,2012,48(12): 4842-4849. [4].Bianchi N,Fornasiero E. Impact of MMF Space Harmonic on Rotor Losses in Fractional-Slot Permanent-Magnet Machines[J]. IEEE Transactions on Energy Conversion,2009,24(2): 323-328.

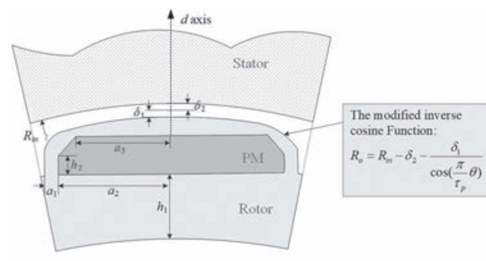

Fig.1 The related structure and optimization parameters (the optimization parameters of rotor: δ_1, δ_2; the optimization parameters of PM: a_3, h_2)

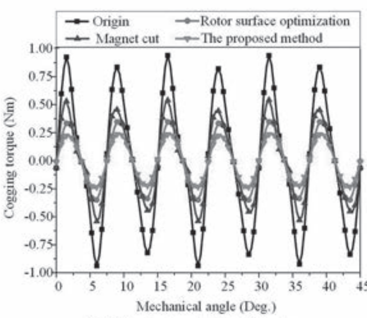

Fig. 2 Cogging torque for the IPM motors

Table I Back EMF comparison results of IPM motor with 16 poles/24 slots

EMF	Original	Surface	Magnet cut	Optimization
E_1 (V)	6.97	6.54	6.69	6.94
E_3 (V)	0	0	0	0
E_5 (V)	0.57	0.31	0.11	0.11
E_7 (V)	0.05	0.0466	0.074	0.062

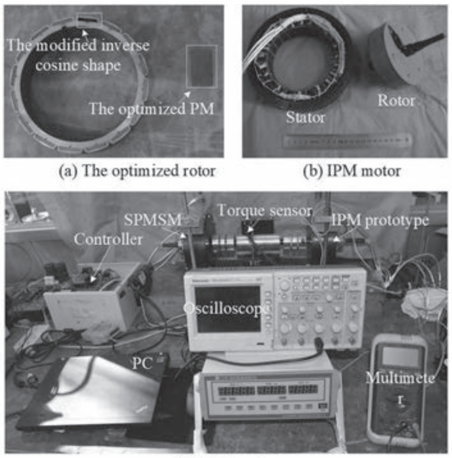

(a) The optimized rotor (b) IPM motor

(c) Test bench

Fig. 3 The Prototype machine and test bench

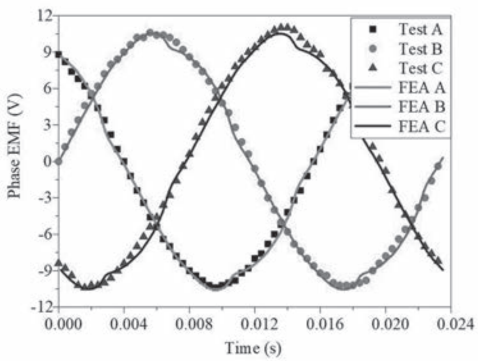

Fig. 4 Test result of no-load back EMF of for the IPM prototype

AU-14. Design for an Six-Phase Synchronous Reluctance Motor Mounted with Centrifugal Compressor Using Multiobjective Optimization Methods.

C. Lin[1] and C. Hwang[2]
1. Electrical Engineering, National United University, Miaoli, Taiwan;
2. Department of Electrical Engineering, Feng Chia University, Taichung, Taiwan

This paper describes a two-step design using optimization method for a six-phase synchronous reluctance motor mounted with a centrifugal compressor to achieve minimum cost, lower torque ripple, maximum efficiency and higher power factor. In the first-step optimization, the multiobjective design of adopted altered bee colony optimization (BCO) and Taguchi method combined with finite element analysis (FEA) are used for optimizing the barrier shape and layer number in the rotor to reduce torque ripple and raise power factor. In the second-step optimization, the adopted multiobject design method can be emplyed for optimizing the geometry of stator to achieve minimum cost and maximum efficiency. Experimental results show that these techniques can not only improve the efficiency and power factor but also reduce the material cost and torque ripple. The multiphase machine offers numerous advantages over the conventional three-phase motor drives such as increased torque per ampere for the same volume machine, reduction of the stator current per phase, improvement of torque density and increase of the fault tolerance [1-2]. Some of the most suitable applications are electric, hybrid electric vehicles [3] and ship propulsion [4]. An multiobjective optimization design of a six-phase synchronous reluctance motor applied in a centrifugal compressor provides an important role in helping the consumption systems. The factors of design optimization in the six-phase synchronous reluctance motor are minimizing material cost, minimizing torque ripple, maximizing efficiency, and maximizing power factor. One of the popular design methods of the electromagnetic devices is the use of finite-element analysis (FEA) coupled with optimization algorithms. However, the classical optimization algorithms, such as deterministic and stochastic methods, seem to be not very efficient by using the FEA because it needs longer computing time. Therefore, a multiobjective optimization design of a six-phase synchronous reluctance motor used in both the altered bee colony optimization (BCO) [5], [6] and the Taguchi method [7], [8] with FEA [9], [10] in practical methodology is applied in a centrifugal compressor system. In this paper, the motor is rated at a power of 3kW, rotating at 1800r/min. The initial design of the motor consists of a stator having 36 slots that carry two-layer windings, as shown in Fig. 1 and Table I. The losses of the motor include iron loss in the stator, copper loss in the winding, eddy current loss in the rotor, and rotational losses due to friction and wind resistance. The iron and copper losses were the dominant contributor in a centrifugal compressor. The finite-element method with the measurement that combined the BCO and the Taguchi method is a very efficient and effective approach in the robust design of a high-performance motor. This paper presents the optimization design of a six-phase synchronous reluctance motor using two-stage optimization processes, which mainly depends on the stator and rotor regions between cost and efficiency. The stator region is applied to reduce the use of the iron and the winding to minimize cost and maxmimize efficiency in the first stage, while the rotor parameters are kept unchanged. An optimization design based on the altered BCO and the Taguchi method with FEA is employed to further enhance the machine performance. The Taguchi method can optimize the machine parameter of performance characteristics in electrical discharge machining. The experimental results are then converted into a signal-to-noise (S/N) ratio. The S/N ratio can be used to measure the deviation of the show characteristics from the desired values. In the second-stage optimization, the objectives are the maximization of power factor and minimization of toque ripple. while the stator parameters are kept unchanged. An optimization design based on the altered BCO and the Taguchi method with FEA is employed to further enhance the machine performance. In summary, it is seen that the two-stage optimization can reduce both cost and torque ripple, and further increase efficiency and power factor from the experimental values. Finally, the photo view of a six-phase synchronous reluctance motor is shown Fig. 2. The views of stator, rotor and winding combination in the six-phase synchronous reluctance motor mounted with a centrifugal compressor is shown in Fig. 2(a)–(b). This paper has presented an optimization design using the altered BCO and Taguchi method with FEA for tacking multiobjective optimization problems on a six-phase synchronous reluctance motor mounted with a centrifugal compressor compressor. The results of this paper confirm the effectiveness of the proposed technique for obtaining lower cost and better performance characteristics. This technique can be applied to solve multiobjective optimization problems of any electromagnetic devices.

[1] T. Wang, F. Fang, X. Wu, and X. Jiang, "Novel filter for stator harmonic currents reduction in six-step converter fed multiphase induction motor drives," *IEEE Trans. Power Electron.*, vol. 28, no. 1, pp. 498–506, Jan. 2013. [2] H. Zhao, J. Zhang, X. Wang, Q. Wang, X. Liu, and Y. Luo, "A design method for cage induction motors with non-skewed rotor bars," *IEEE Trans. Magn.*, vol. 50, no. 2, Feb. 2014, Art. no. 7019004. [3] J. I. Leon, O. Lopez, L. G. Franquelo, J. Doval-Gandoy, S. Vazquez, J. Alvarez, F. D. Freijedo, "Multilevel multiphase feedforward spacevector modulation technique", *IEEE Trans. Industrial Electron.*, vol. 57, no. 6,pp. 2066–2075, 2010. [4] J. M. Apsley, A. Gonzalez-Villasenor, M. Barnes, A. C. Smith, S. Williamson, J. D. Schuddebeurs, P. J. Norman, C. D. Booth, G. M. Burt, and J. R. McDonald, "Propulsion drive models for full electric marine propulsion systems", *IEEE Trans. Industry Applications*, vol. 45, no. 2, pp. 676–684, 2009. [5] C. C. Hwang, C. M. Chang, and C. T. Liu, "A fuzzy-based Taguchi method for multiobjective design of PM motors," *IEEE Trans. Magn.*, vol. 49, no. 5, pp. 2153–2156, May 2013. [6] C. H. Lin and C. C. Hwang, "Multiobjective optimization design for a six-phase copper rotor induction motor mounted with a Scroll compressor," *IEEE Trans. Magn.*, vol. 52, no. 7, Jul. 2016. Art. no. 9401604. [7] D. Karaboga and B. Basturk, "On the performance of artificial bee colony (ABC) algorithm," *Applied Soft Computing*, Vol. 8, No. 1, pp. 687-697, Jan. 2008. [8] C. H. Lin, "Modelling and control of six-phase induction motor servo-driven continuously variable transmission system using blend modified recurrent Gegenbauer orthogonal polynomial neural network control system and amended artificial bee colony optimization," *Int. J. Numer. Model.*, vol. 29, pp. 915–942, 2016. [9] K. Yamazaki, A. Suzuki, M. Ohto, T. Takakura, and S. Nakagawa, "Equivalent circuit modeling of induction motors considering stray load loss and harmonic torques using finite element method," *IEEE Trans. Magn.*, vol. 47, no. 5, pp. 986–989, May 2011. [10] J. Ahn, D. Lee, G.-J. Park, Y.-J. Kim, J. Kim, and S.-Y. Jung, "Numerical design compatibility of induction motor with respect to voltage and current sources," *IEEE Trans. Magn.*, vol. 50, no. 2, Feb. 2014, Art. no. 7019104.

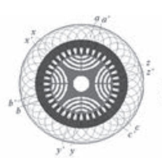

Fig. 1. Cross sectional view of stator, rotor and stator windings in the six-phase synchronous motor.

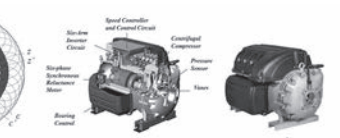

Fig. 2. Photo view of six-phase synchronous motor mounted with centrifugal compressor (a) cross sectional view (b) packing view.

Table I
Initial design of motor specifications

Parameter	Value
Rotor outer diameter [mm]	37.5
Stator outer diameter [mm]	72.5
Air gap length [mm]	0.5
Stack length [mm]	46
Layer number of barrier rotor	4
Stator slot number	36
Pole number	4
Steel material	50CS600

AU-15. Design and investigation of a V-shaped Permanent Magnet Vernier Motor with enhanced Flux-Modulated effect and Low Torque Ripple.

Y. Chen[1] and *L. Quan*[1]
1. Electrical Engineering, School of Electrical and Information Engineering,Jiangsu University, Zhenjiang, China

I. Introduction Vernier permanent magnet (VPM) machines have attracted more and more interest and attention, which have been considered as one of promising candidates for direct-drive applications, such as electric vehicles (EVs) and wind power generation [1]. As one of the new type of flux-modulated machines, the VPM machine not only has a relatively simple geometry structure of only single PM rotor and one modulating stator, but also possesses abundant harmonic contents in the air-gap magnetic field to realize the flux-modulated effect. Based on such concept of the flux modulation, many various VPM machine topologies are proposed and studied in recent years. Generally, the competitive torque characteristic can be achieved in existing studies, such as the surface-mounted VPM machine and spoke type VPM machine [2], [3]. However, because of the inevitable internal and external flux leakages in above mentioned VPM machines, the PM utilization and torque ripple of them will be affected to some extent. In addition, from existing studies, the utilization of fundamental and high-order harmonics in air-gap magnetic field are usually taken into consideration, while the low-order harmonics with high amplitude are neglected. It is worth noting that the effective utilization of low-order harmonics will more effectively enhance the machine toque capability, which offers a new path for further improving the torque density of the VPM machine. Hence, how to design a high torque density VPM machine with high performances is becoming a hot issue and research orientation in motor filed. In this paper, based on the design concept of flux modulation, a V-shaped permanent magnet vernier (V-PMV) motor is proposed, where the effective working harmonic are fully utilized. And by utilizing the unique V-shaped PM topology in rotor, the flux leakage phenomenon can be avoid effectively. It provides the possibility for the proposed motor achieving low torque ripple, high torque density and high efficiency. II. Motor Topology and Features To extensively explore the performance advantages of the V-PMV motor, the flux-concentrating VPM (FC-VPM) machine of [3] is selected purposely and designed with the same size for fair comparative analysis. The specific motor structures of the proposed V-PMV motor and FC-VPM motor are respectively shown in Fig. 1 (a) and (b). From the figures, the main differences between the two motors are the different PM topologies in rotor and different stator tooth designs. To the former, the spoke-type PM topology of the FC-VPM motor will bring up an external flux leakage, while the V-shaped one can artfully solve such problem. It contributes to improving the machine torque characteristics to large extent. For the latter, the V-PMV motor uses the split-slot design, which aims at changing the flux-modulated form for obtaining an enhanced flux-modulated effect and reducing the torque ripple. Fig. 1 (c) and (d) depicts the no-load flux distributions of the two motors. It can be found that, as expected, the external flux leakage is avoided in the proposed V-PMV motor. At the same time, the maximum flux density of stator teeth in the proposed motor is under 1.8T, while the local flux density of that in FC-VPM motor is exceeded 1.8T. It indicates that the proposed V-PMV motor has a relatively low magnetic saturation in operation. III. Results For obtaining optimal machine performances of the V-PMV motor, the influences of some key design parameters on output torque are investigated, such as slope angle of PMs s_v and slot width h_{slot}, as illustrated in Fig. 2 (a) and (b). After the parameter designs, the no-load air-gap flux density curves of the V-PMV motor and FC-VPM motor are calculated and compared in Fig. 2 (c). It can be seen that the peak value of the air-gap flux density in the V-PMV motor is 1.7T, while that of the FC-VPM motor reaches 1.9T. It agrees with the results from Fig. 1 (c) and (d). The corresponding harmonic spectrum analysis of air-gap flux density is given in Fig. 2 (b). Obviously, under the same volume of PM, the amplitude of the fundamental and high-order harmonic of the V-PMV motor are higher than the FC-VPM motor, and the low-order harmonic with high amplitude is also utilized in the V-PMV motor. It means that the PM utilization is improved effectively by an enhanced flux-modulated effect in the V-PMV motor. In addition, the no-load back-EMF and steady torque of the two motors are also compared in Fig. 2 (e) and (f). It can be seen from Fig. 2 (e) that the V-PMV motor possesses a symmetrical and sinusoidal back-EMF waveform, where its amplitude is larger than that of the FC-VPM motor. Then the comparison of the torque performances is presented in Fig. 2 (f). It can be observed that the average torque of the V-PMV machine is 102.9 Nm, which is about 24.4% bigger than that of the FC-VPM motor. Meanwhile, the torque ripple of the proposed design is only about 35.2% of the FC-VPM motor, achieving the small value of 0.012. In conclusion, the above study results reveal that the proposed V-PMV machine can offer a high PM utilization and low torque ripple. More detailed theoretical analysis and experimental results will be given in full paper.

[1] H. Wang, S. Fang, H. Yang, H. Lin, D. Wang, Y. Li and C. Jiu, "A novel consequent-pole hybrid excited Vernier machine," *IEEE Trans. Magn.*, vol. 53, no. 11, article number: 8112304, Nov. 2017. [2] D. Jang and J. Chang, "Effects of Flux Modulation Poles on the Radial Magnetic Forces in Surface-Mounted Permanent-Magnet Vernier Machines," *IEEE Trans. Magn.*, vol. 53, no. 6, article number: 8202704, June. 2017. [3] X. Li, K. T. Chau, and M. Cheng, "Comparative analysis and experimental verification of an effective permanent-magnet vernier machine," *IEEE Trans. Magn*., vol. 51, no. 7, article number: 8203009, July. 2015.

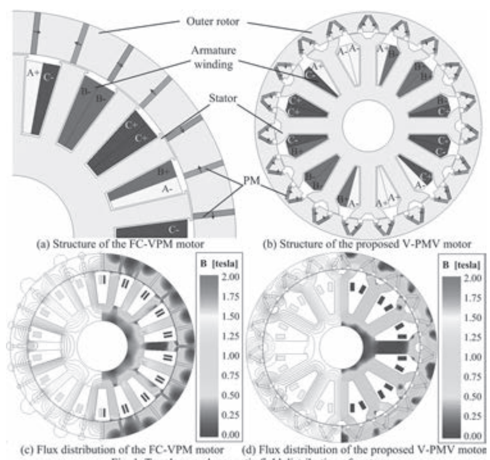

Fig. 1. Topology and magnetic field distribution of motors.

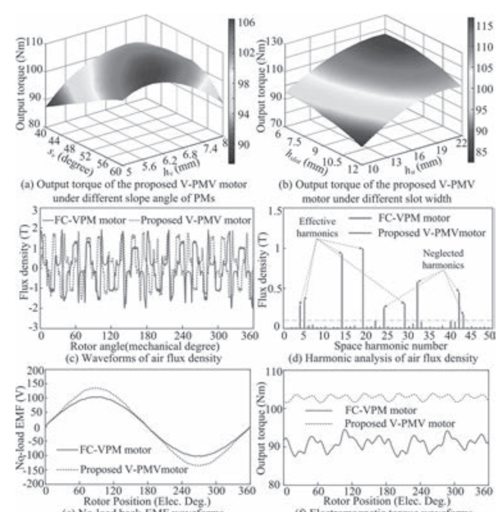

Fig. 2. Partial electromagnetic performances of motors.

AU-16. A Novel Wide Speed Range Permanent Magnetic Machine Based on Mechanical Flux Weakening Control.

Y. Mao[1] and *S. Niu*[1]
1. Electrical Engineering, The Hong Kong Polytechnic University, Hong Kong, Hong Kong

I. Introduction Permanent magnetic machine which has many advantages such as high power density, lower friction loss and fast dynamic response becomes very attractive in EVs propulsion [1-2]. For the purpose of entirely replace fuel cars by EVs, there are many things that to be improved. One of the most important issue is to increase EV's speed limit. If the machine need to run in a high speed level, two approaches can extend the maximum speed under constant power. One is to increase the drive's output voltage, another one is to carry out flux weakening controls to reduce the back emf. Since the drive's output voltage is limited by the DC source, usually the flux weakening control is adopted. But for the permanent magnetic machine, flux weakening control is very difficult because that permanent magnet provide constant flux distribution intrinsically. Nevertheless, many researches have been done to achieve flux weakening solution in PM machine. In [3] a hybrid-excited dual-PM machine for electric vehicle propulsion is proposed. In this design both ac current and dc current are employed where the ac component is used to produce the rotating armature field, and the dc bias current is used for the flux regulation. But in these designs, there exist the risk of demagnetizing the PM material irreversibly. More than that, the flux weakening effect is achieved at the expense of cutting down the torque density. To solve these problems, a novel wide speed range PM machine based on mechanical flux weakening control is proposed. In this machine, the flux weakening effect is achieved by adjusting the rotation angle of the inner rotor mechanically. To control the inner rotor, an extra machine can be employed and connected to the inner rotor. The electromagnetic characteristics of this machine are also analyzed. II.Configuration and Working Principle of The Proposed Machine The topology of this machine is shown in Fig. 1. The machine is composed one stator, where two armature winding are housed in, a common machine rotor, and an inner rotor for mechanical control. Wherein the Winding I interacts with the inner and outer rotor simultaneously due to flux modulation effect. Winding II interacts with the outer rotor only. When turning the inner rotor for a small angle, the initial phase of the back EMF of the Winding I is changed with its amplitude stays constant. The initial phase and amplitude of the back EMF of the second winding both remains unchanged. So after series connection of the two winding, the magnitude of the back EMF can be changed. By rotating the inner rotor little by little, the complex back EMF of two winding can change from 0 to the maximum value. Thus according to the speed requirement, it can be adjusted to realize the wide speed range control. The rotors of this machine have consequent-pole PM array which is constituted by radially outwardly directed magnetized permanent magnet segments and ferromagnetic segments. Wherein the number of the permanent magnets of the inner rotor $N1$, the number of the permanent magnets of the outer rotor $N2$, and the number of armature magnetic pole pairs of the Winding I $P1$ satisfy the equation:$N1 = N2\text{-}P1$.The number of the permanent magnets of the outer rotor $N2$ and the number of the armature magnetic fields of the Winding II $P2$ satisfy the equation:$N2 = P2$. The invention also discloses several methods for controlling the rotation of the inner rotor by applying the extra motor or by adding the inner stator. The invention provides a continuous and smoothed speed control for the hybrid electric vehicle and the wind power generation device. Fig. 2 shows some scheme of the complex machine. In Fig. 2 (a), an inner stator is employed. The inner stator winding can interact with the inner rotor so as to give electric control of the rotation of inner rotor. In Fig. 2 (b), the inner rotor may be stretched in the axial direction by a certain length with the axial lengths of the outer rotor and the outer stator stayed unchanged. The outer rotor is sleeved on the inner rotor and the outer stator is sleeved on the outer rotor. The inner stator is coaxial with the outer rotor and the outer stator and arranged side by side. The inner stator is sleeved on the inner rotor (elongated axial length portion). In Fig. 2 (c), the motor adopts a coaxial disc type structure. III.Performance Analysis The back EMF waveform of the machine is calculated based on finite element method. Fig. 3 shows the waveform of both winding, and the sum of the value are also depicted in the same figure. It can be seen that by rotating the inner rotor step by step, the back emf of the sum of Winding I and Winding II is changed. The back EMF spans from 10V to 40V. IV.Conclusion This paper proposed a wide speed range PM machine based on mechanical flux weakening control. The conventional field-weakening method for permanent magnet motors is by adding field windings which may cause demagnetization of the PM and add more loss. This invention neither involves any field windings nor a very complicated structure. More than that, this machine has a wider speed control range than traditional field excitation machine.

[1]Y. Gao, R. Qu, D. Li, J. Li, and G. Zhou, "Consequent-pole flux-reversal permanent-magnet machine for electric vehicle propulsion," *IEEE Trans. Appl. Supercond.*, vol. 26, no. 4, Jun. 2016, Art no. 5200105. [2]K. T. Chau, C. C. Chan, and C. Liu, "Overview of permanent-magnet brushless drives for electric and hybrid electric vehicles," *IEEE Trans.Ind. Electron.*, vol. 55, no. 6, pp. 2246–2257, Jun. 2008. [3]Qingsong Wang, Shuangxia Niu, and Xiang Luo, "A Novel Hybrid Dual-PM Machine Excited by AC With DC Bias for Electric Vehicle Propulsion," *IEEE Trans.Ind. Electron.*, vol. 64, no. 9, pp. 6908-6919, Sep. 2017.

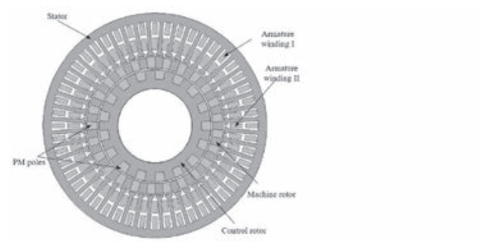

Fig. 1

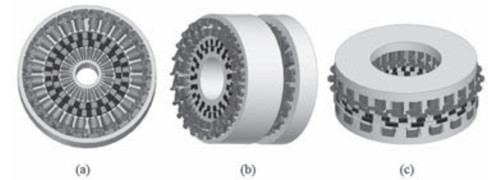

Fig. 2

Fig. 1. Topology of the wide speed range PM machine based on mechanical flux weakening control.

Fig. 2. Schematic diagram of the wide speed range machine with controlling device of (a) an extra inner stator (b) an extra coaxial machine (c) an extra coaxial machine in disc type.

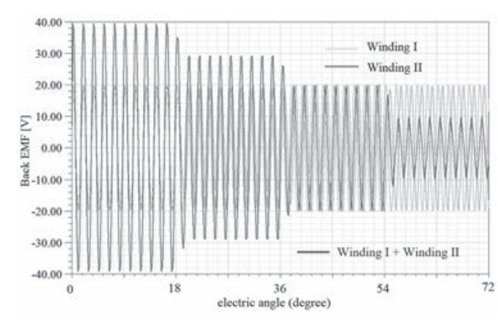

Fig. 3. Schematic diagram of the back EMF waveform of the machine.

TUESDAY MORNING, 24 APRIL 2018 SIMPOR/ROSELLE BALLROOM, 8:30 TO 11:30

Session AV
SOFT MAGNETIC MATERIALS I
(Poster Session)

Nobuyoshi Imaoka, Co-Chair
Advanced Industrial Science and Technology, Nagoya, Japan
Shinpei Yamamoto, Co-Chair
Advanced Industrial Science and Technology, Nagoya, Japan

AV-01. CoFe–Based Amorphous Microwires for GMI Sensor Applications.

P. Sarkar[1,2], F. Yuan[3], M. Lai[2], J. Jeng[4] and C. Lu[1]
1. Department of Mechanical Engineering, National Taipei University of Technology, Taipei, Taiwan; 2. iSentek Inc, Taipei, Taiwan; 3. iSentek Inc., New Taipei City, Taiwan; 4. Department of Mechanical Engineering, National Kaohsiung University of Applied Sciences, Kaohsiung, Taiwan

Magnetic sensors and transducers play an essential role in modern technologies involving self-monitoring and control. They are widely used in fields including Non-Destructive Testing and Evaluations and Bio-magnetic inspections etc. A wide range of magnetic sensors, such as fluxgate sensors, induction sensors, Hall Effect sensors, Giant magneto-resistive (GMR) sensors and superconducting quantum interference device (SQUID) gradiometers are available. Recently, the area of sensor development traversed a new milestone with the introduction of Giant magneto-impedance (GMI) based sensors. It has attracted considerable scientific and technological interest especially because of its ultra-high sensitivity allowing high precision magnetic field sensing and as an additional tool to investigate soft magnetic materials properties of other materials, e.g. ferritic steel. Amorphous materials with tunable shapes and magnetic properties can be designed for a wide range of applications. In this regard, amorphous alloys are studied in different forms including thin films [1], ribbons [2], wires [3], powders [4] and recently in the form of rods [5]. The characteristics which make the amorphous alloy superior magnetic materials compared to their crystalline counterpart are: (i) high magnetic permeability due to the negligible magnetocrystalline anisotropy which is closely related to the small coercive force, (ii) high electrical resistivity that reduces the eddy current losses and (iii) low magnetic noise owing to the absence of grain boundaries. Moreover, excellent corrosion resistance makes it a perfect candidate for uses in tough environments. In the present work, investigation has been carried out on the development of amorphous metallic materials in the form of microwires having diameter of around 100 micrometer for GMI magnetic sensing applications. The wires are fabricated through rapid solidification route using in-rotating water quenching technique. The objective of the work is to optimize CoFe-based amorphous microwires for GMI sensing applications. Alloy compositions $(Co_{94}Fe_6)_{72.75}Si_{12.25}B_{15}Cr_0$, $(Co_{94}Fe_6)_{72.75}Si_{12.25}B_{12.75}Cr_{2.25}$, $(Co_{94}Fe_6)_{72.75}Si_{12.25}B_{11.25}Cr_{3.75}$, $(Co_{94}Fe_6)_{72.75}Si_{12.25}B_{10}Cr_5$ having nearly zero-magnetostrictive microwires were designed to develop highly magnetic sensitive wires. The alloy was prepared from pure materials by vacuum arc melting technique. The developed wires have diameter of 110 μm. The Curie (730K) and crystallization temperature (762K) were measured via standard measuring units while amorphous nature of as-quenched materials was confirmed through X-ray diffraction and Differential Scanning Calorimetry observations. The GMI property of as-quenched and annealed wire was investigated using an automated computer-controlled GMI measurement system with conventional four-probe technique. The GMI profile was measured for different driving frequency (0.5-10MHz) at driving current amplitude 3 mA. The GMI studies have been performed with variation of driving frequency at a fixed driving current of 3 mA. The maximum GMI ratio was observed at 5 MHz about 125% with Cr=0 sample with single peak structure (Fig-1 Inset). The GMI ratio has increased with the content of Cr. A maximum GMI ratio of about 430% was achieved in the wire with Cr = 2.25 with double-peak structure (Fig-1). The coercivity also reduced from 0.687 A/m to 0.389 A/m. Post annealing were found to further enhance the GMI ratio. The annealing temperatures 650K, 750K, and 800K were selected based on the Curie temperature of the material 730K: below T_C the wires remains amorphous only strain relaxation or recovery takes place, nano-crystallization occurs in wires annealed at temperature around T_C. The maximum GMI ratio for the wire with Cr = 2.25 at 5 MHz enhanced from 430% to about 650% when annealed at 750K for 5-minutes. In terms of GMI ratio, the sensitivity of 9.47% per A/m has been obtained in as-cast condition which improved to 14.5% per A/m for annealed sample. The sensitivity of around 802 V/T has been achieved as the maximum with the optimized frequency of 5 MHz and driving current amplitude of 3 mA. The Noise level of the microwires measured around 10 nT/√Hz at 1Hz. Features of high GMI ratio, high operating frequency, high sensitivity and low noise of the developed microwires highlight the potential of the presented wires for magnetic field sensor with ultra-high sensitivity.

[1] Cahn R.W., in Rapidly Solidified Alloys: Processes, Structures, Properties, Applications, ed. H.H. Liebermann, Marcel Dekker Inc, New York, Ch.1, (1993), pp.1. [2] Shingu P.H. and Ishihara K.N., in Rapidly Solidified Alloys: Processes, Structures, Properties, Applications, ed. H.H. Liebermann, Marcel Dekker Inc., New York, Chap.4, (1993), pp.103. [3] Masumoto T., Inoue A. and Hagiwara M., US Patent No. 4523626, (1985). [4] Schwartz R.B., in Rapidly Solidified Alloys: Processes, Structures, Properties, Applications, ed. H.H. Liebermann, Marcel Dekker Inc., New York, Chap.7, (1993), pp.157. [5] Konovalov I. I., Komissrov V.A., Maslov A.A., Orlo V.K., J. Non-Cryst. Sol., 205-207, (1996), pp. 536.

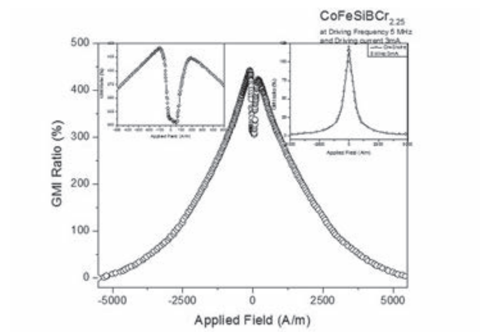

Fig-1: GMI ratio of $(Co_{94}Fe_6)_{72.75}Si_{12.25}B_{15}Cr_0$ with single -peak structure (Inset-2) and $(Co_{94}Fe_6)_{72.75}Si_{12.25}B_{12.75}Cr_{2.25}$ microwires with double-peak structure (Inset-1) at optimized frequency of 5 MHz and driving current amplitude 3 mA

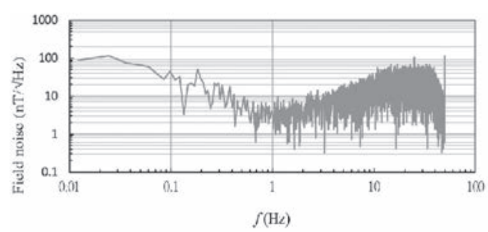

Fig-2: Noise structure of $(Co_{94}Fe_6)_{72.75}Si_{12.25}B_{12.75}Cr_{2.25}$ microwire at driving frequency of 5 MHz and driving current amplitude 3 mA

AV-02. Stress Induced Domain Wall Motion in FeCo microwires for Energy Harvesting.

S. Bhatti[1], C. Ma[2], X. Liu[2] and S. Piramanayagam[1]
1. School of Physical and Mathematical Science, Nanyang Technological University, Singapore, Singapore; 2. Department of Electrical and Computer Engineering, Shinshu University, Nagano, Japan

In spintronics, the motion of domain walls is usually governed by applying external polarized currents [1] or magnetic fields [2]. Such domain wall motion is used mainly for logic or memory applications [3]. Domain wall motion can also be used for energy harvesting by converting stress into changes in magnetization and thus into electrical voltage. In the energy harvesting investigations reported so far, domain wall motion by stress is accomplished only in multiferroic structures, where stress was induced by providing an electrical energy to the ferroelectric layers [4]. A peculiar method exhibiting mechanical stress regulated motion of domain walls in a pure magnetic structure has been proposed by us. This approach relies on the deposition of magnetostrictive FeCo with induced magnetic anisotropy on a polyimide flexible thin film. The use of flexible substrates with low Young's modulus and the special magnetic stack enabled us to achieve significant magnetization rotation or domain wall motion. The changes in the magnetization angle or the domain wall motion induced voltage in the pickup coils. In order to induce the efficiency of such devices, an increase in thickness is speculated to give a higher induced voltage in the pickup coils. However, at the same time, it warrants a detailed study, as increasing thickness could lead to circular magnetization and contrarily, a reduced flux. Therefore, we have carried out a detailed study on the effect of thickness of FeCo microwires on the extent of change in magnetic properties under applied stress. For the experiment, microwires of the type CoNi/FeCo/CoNi with different thicknesses were deposited by facing targets sputtering (FTS). Using FTS, an anisotropy was induced in transverse direction to the length of the microwires. We also deposited microwires of FeCo with different thicknesses varying as 30, 40, 50 and 60 nm to measure the effect of thickness in the extent of change of magnetic properties. We pasted the samples to concave or convex curved surfaces with the radii of curvature of 16 mm and 18 mm to measure the effect of stress under different compressive and tensile stresses, respectively. Bitter Patterns technique using Kerr microscope was used to observe the domain wall motion in the microwires. To understand the effect on the magnetic properties of the microwires with different thicknesses under applied stress, a custom made micro-MOKE was used. Figure 1 (a) shows the bitter patterns of the 30 nm thick as deposited FeCo microwires and Fig 1 (b) shows the microwires with applied stress. Under small stress, rotation of domain walls was observed, whereas application of large stress resulted in diminishing of domain walls, as can be seen from fig. 1(b). Figure 1 (c) to (e) show the hysteresis loops of 30 nm thick microwires, measured using the micro-MOKE. Alteration of axial magnetization anisotropy was noticed under applied stress, changing easy axis to hard axis and vice-versa, as shown in fig. 1. From the micro-MOKE results, it can be inferred that the motion of domain walls under applied stress results due to the stress induced shifting of the easy axis. To understand the effect of the varying thicknesses of FeCo on M_rt (product of the magnetic remanence and thickness), we measured the hysteresis loop of as deposited samples. We observed an increase in the M_rt value (as expected) and coercivity at larger thickness of the sample. Then we measured the effect in the coercivity of FeCo microwires with different thicknesses under same stress values. It can be seen from the fig. 2 that the change in the coercivity of FeCo microwires increases as the thickness of the FeCo increases. Moreover, the effect of applied stress induced to the microwires increases as the thickness of the deposited FeCo increases, which can be calculated by the Stoney's formula[5]. We speculate this enhancement in the induced stress is the reason behind the increase in coercivity change with thickness. Such enhancement in the magnetic properties is speculated to give rise to a higher induced voltage in the pickup coils. The results of this experiment open the gateway to stress controlled motion of domain wall, which in future, can be used for energy harvesting.

1. Grollier, J., et al., *Spin-polarized current induced switching in Co/Cu/Co pillars*. Applied Physics Letters, 2001. 78(23): p. 3663-3665. 2. Kimura, T., et al., *Magnetic control of ferroelectric polarization.* nature, 2003. 426(6962): p. 55-58. 3. Bhatti, S., et al., *Spintronics based random access memory: a review.* Materials Today, 2017. 4. Lahtinen, T.H., K.J. Franke, and S. Van Dijken, *Electric-field control of magnetic domain wall motion and local magnetization reversal.* Scientific reports, 2012. 2: p. 258. 5. Schwarzer, N. and F. Richter, *On the determination of film stress from substrate bending: STONEYs formula and its limits.* 2006.

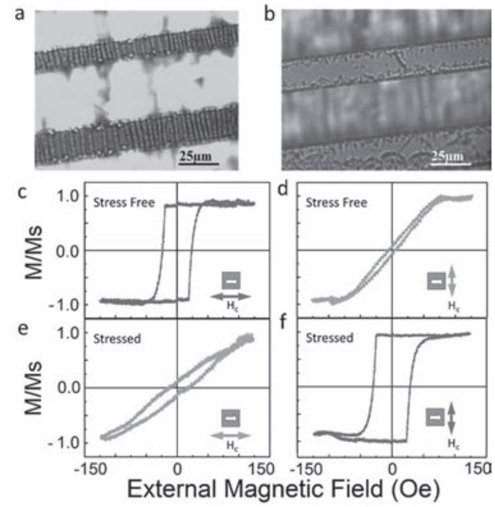

Fig. 1. Bitter patterns of CoFe nanowires of (a) as-deposited with induced transversal magnetic anisotropy; (b) with applied compressive stress. (c) – (f) Hysteresis Loops of FeCo before and after applying stress. (c) and (e) show the easy axis before and after applying stress; (d) and (f) show the hard axis before and after applying stress. Conversion of axial magnetization anisotropy under applied stress has been observed.

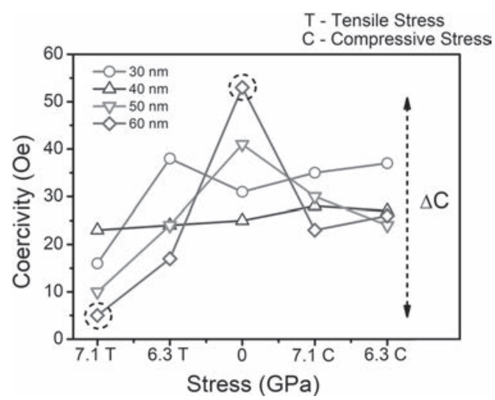

Fig. 2. Effect of microwire thickness on the change in the magnetic properties under externally applied stress (where ΔC shows the change in coercivity).

AV-03. Magnetic Property of Amorphous Magnetic Thin Ribbon and its Laminated Bulk under the Tensile and Compressive Stress.

T. Mizuta[1], Y. Tani[1] and K. Fujiwara[2]
1. Mitsubishi Electric Corporation, Amagasaki, Japan; 2. Doshisha University, Kyotanabe, Japan

In the context of energy conservation, it is required to enhance the efficiency of electrical motor in recent years. The magnetic property is closely related to the efficiency of the electrical motor, thus it is necessary to clarify the magnetic property for the design of energy-efficient motor. It's known that the magnetic property deteriorates under distortion and residential stress by punching, press fitting and lamination process. Therefore, there is a large difference between the efficiency of design and that of actual measurement. To reflect the influence of distortion and residential stress, there are several reports of measuring magnetic properties of Fe-Si steel sheet under stress condition[1]-[2] and of estimating motor characteristics taking account of stress distribution[3]. On the other hand, amorphous magnetic materials have been attracting a lot of attention as a core of motor because of its high permeability and low iron loss. There are some reports of applying amorphous magnetic thin ribbon to motor core[4]-[5]. Although it is more sensitive to distortion and residential stress because of its high magnetostriction, magnetic property of single amorphous thin ribbon is not measured under tensile and compressive stress without loading any unnecessary stress. There is the report of measuring magnetic property of amorphous alloy under stress[6]. However, bending stress is not taken into account. In this paper, we develop the measurement device with stress loading mechanism for magnetic thin ribbon and laminated bulk. We measured magnetic property of amorphous thin ribbon and laminated bulk under up to 40MPa tensile and compressive stress. The increase of iron loss by compressive stress and lamination is discussed. Fig.1 shows the measuring device with stress loading mechanism for magnetic thin ribbon. The size of specimen is W30mm×t0.025mm×L220mm. Specimen is set on the holder which is grooved as much as thickness of magnetic thin ribbon and pressured by surface pressure load mechanism(surface pressure load mechanism 1) through the holder to prevent the specimen from buckling during measurement. There is another surface pressure load mechanism(surface pressure load mechanism 2) that pressure the specimen through the york. The direction of loading stress is the same with the direction of magnetization. The loading stress is controlled to the command value by feedback regulation. We also develop the measuring device with stress loading mechanism for the laminated bulk. The size of specimen is W10mm×t10mm×L100mm. The specimen is laminated of which around 400 pieces of magnetic thin ribbons are stacked and glued. The only tensile stress can be applied by the measuring device for the laminated bulk. We measured the magnetic properties of amorphous thin ribbon and its laminated bulk under stress by our developed measuring devices. Fig.2 shows the iron loss results of the thin ribbon and laminated bulk at 0.5T and 50Hz. The plus stress means tensile stress and the minus stress means compressive stress. The iron loss of thin ribbon increases with the compressive stress and decreases with the tensile stress. Comparing the iron loss of thin ribbon and laminated bulk at no stress, the iron loss of laminated bulk is twice larger than that of thin ribbon. It is inferred that approximately 10MPa compressive stress is caused by gluing and it deteriorates the magnetic property of laminated bulk. The iron loss increase ratio of laminated bulk under the compressive stress is larger than that of thin ribbon. More detailed results will be presented in the conference.
ACKNOWLEDGMENTS This paper is based on results obtained from the Future Pioneering Program "Development of magnetic material technology for high-efficiency motors" commissioned by the New Energy and Industrial Technology Development Organization(NEDO).

[1] D.Miyagi, K.Miki, M.Nakano, and N.Takahashi, "Influence of compressive stress on magnetic properties of laminated electrical steel sheets," *IEEE Trans.Magn.,vol.46,no.2,pp.318-321,Feb.2010* [2] Y.Oda, H.Toda, N.Shiga, S.Kasai, and T.Hiratani, "Effect of Si content on iron loss of electrical steel sheet under compressive stress," *IEEE Trans. Magn.,vol.50,no.4,April.2014* [3] A.Daikoku, M.Nakano, S.Yamaguchi, Y.Tani, Y.Toide, H.Arita, T.Yoshida, and C.Fujino, "An accurate magnetic field analysis for estimating motor characteristics taking account of stress distribution in the magnetic core," *IEEE Trans.Indus.,vol.42,no.3,pp.668-674,May-June.2006* [4] Z.Wang, R.Masaki, S.Morinaga, Y.Enomoto, H.Itabashi, M.Ito, and S.Tanigawa, "Development of an axial gap motor with amorphous metal cores," *IEEE Trans.Indus.,vol.47,no.3,pp.1293-1299,May-June.2011* [5] S.Okamoto, N.Denis, Y.Kato, M.Ieki, and K.Fujisaki, "Core loss reduction of an interior permanent-magnet synchronous motor using amorphous stator core," *IEEE Trans.Indus.,vol.52,no.3,pp.2261-2268,May-June.2016* [6] H.Hase, and M.Wakayama, "The stress-magnetic properties of amorphous magnetic alloy," *IEEE Trans.Magn.in Japan,vol.5,no.8,pp.697-703,Aug.1990*

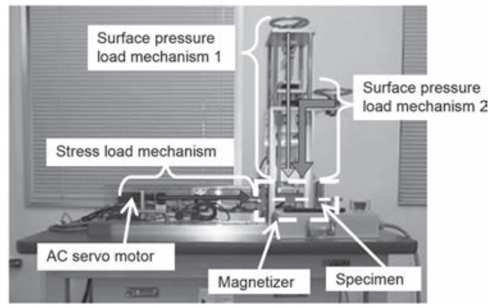

Fig. 1. Measuring device for magnetic thin ribbon

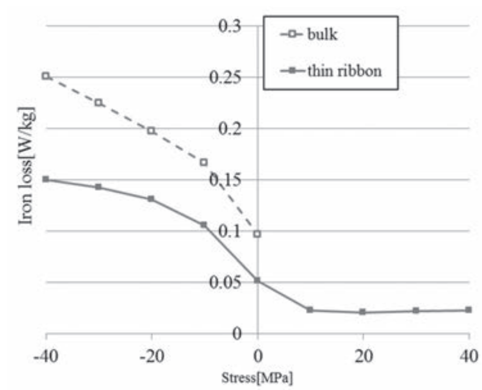

Fig. 2. Iron loss property comparison between thin ribbon and laminated bulk(B=0.5T 50Hz)

AV-04. Fabrication and evaluation of composite magnetic core using iron-based amorphous alloy powder with different particle-size distribution.

N. Yabu[1], K. Sugimura[1], Y. Inagaki[1], D. Ueda[1], M. Sonehara[1] and T. Sato[1]
1. Faculty of Engineering, Shinshu University, Nagano, Japan

Application of silicon carbide (SiC) and gallium nitride (GaN) based power devices with lower on-resistance and higher switching frequency, compared to the silicon(Si)-based power devices to DC-DC converter, enables to realize a compact, lightweight and high efficient switching converter at a switching frequency beyond 1 MHz [1], [2]. To realize such a DC-DC converter, magnetic components with small core loss are strongly required. We developed a composite magnetic core consisting of 2.56 μm-diameter iron-based amorphous alloy (Fe-AMO) powder and epoxy–resin, which had low core loss at MHz band [3]. In addition, we proposed the method of forming the surface-oxidization layer for Fe-AMO powder to decrease the eddy current overlapped between adjacent Fe-AMO powders in the composite magnetic core [3]. The fabricated 91.5 wt.%-AMO (2.56 μm-diameter)/epoxy composite magnetic core exhibited low core loss at MHz band but low relative permeability of about 10. The purpose of this study is to increase the permeability of such the composite magnetic core with low core loss, we investigated an effect of mixing Fe-AMO powder at different particle size distribution on the increase of packing density of Fe-AMO powder in the composite core. By using a hexagonal closely-packed (hcp) structure model, the appropriate different Fe-AMO particle diameter was estimated to obtain higher volume fraction of Fe-AMO powder for the fabrication of higher permeability composite core. When the spherical shape Fe-AMO particle with a single-size particle is assumed to be located according to the hcp structure in the composite core, there are two kinds of gaps (octahedral and tetrahedral gap) in the hcp structure. When the appropriate single-size Fe-AMO particles with smaller size are located at both octahedral and tetrahedral gap of the hcp structure, a theoretical volume fraction of the Fe-AMO powder in the composite core is estimated to be 76 %. We used a 2.56 μm median-diameter Fe-AMO powder (2.56 μm Fe-AMO) as the particles located at both octahedral and tetrahedral gap of the hcp structure because it was finest atomized-powder avaliable, where the particle size of Fe-AMO powder for making the hcp structure was calculated to be 11.39 μm from the hcp structure model. We used 10.94 μm median-diameter Fe-AMO powder (10.94 μm Fe-AMO) for making the hcp structure, which was closest to the calculated one. Fig. 1 shows the volume fraction and the permeability of a composite magnetic core with alternating mixing rate of 2.56 μm Fe-AMO and 10.94 μm Fe-AMO. The maximum volume fraction of Fe-AMO powder in a composite magnetic core was 71 vol.% when the Fe-AMO powder weight ratio of 25 wt.% of 2.56 μm median size and 75 wt.% of 10.94 μm median-size, which was 5 % lower than the theoretical volume fraction of 76 % because of the particle size distribution of Fe-AMO powder not having single-size particle. The relative permeability of the composite core with the maximum volume fraction of Fe-AMO powder was 21, which was 2.1 times higher than that of compsite core using 2.56 μm Fe-AMO only. The core losses were also evaluated using a BH analyzer (IWATSU, SY-8218). Since the dynamic losses, namely the eddy current loss in the composite magnetic core and residual loss in the Ni-Zn ferrite core, were dominant at around MHz band or above, where the dynamic loss was defined as W_{c0}-W_{h0}, W_{c0}; core loss per cycle and W_{h0}; hysteresis loss per cycle. In this study, the dynamic losses were evaluated for three kinds of the composite magnetic core with the maximum volume fraction 71 % of Fe-AMO powder, with 2.56 μm Fe-AMO only and with 10.94 μm Fe-AMO only. For comparison, the residual loss of the Ni-Zn ferrite core made by Fair-Lite was also evaluated. Fig. 2 shows frequency versus the dynamic losses per cycle of four kinds of the magnetic core under the constant maximum flux density B_m of 20 mT. From Fig. 2, at around 1MHz the composite magnetic core with the maximum volume fraction of Fe-AMO powder or with 2.56 μm Fe-AMO only exhibited the smallest dynamic loss than those of others. At 3 MHz frequency, the composite magnetic core with 2.56 μm Fe-AMO only exhibited the smallest dynamic loss. On the other hand, it was found that the dynamic loss of the composite magnetic core with the maximum volume fraction of Fe-AMO powder was closed to that of the composite core with 10.94 μm Fe-AMO only at 3 MHz. Such a dynamic loss measured at 3 MHz in the composite magnetic core with the maximum volume fraction of Fe-AMO powder was considered to be dominated by 10.94 μm Fe-AMO with larger eddy current inside. At around 1 MHz or below, the composite magnetic core, with the Fe-AMO powder maximum volume fraction and consisting of 2.56 μm and 10.94 μm Fe-AMO powder, had both 2.1 times higher permeability and the dynamic loss was similar to the conventional 2.56 μm Fe-AMO composite magnetic core [3].

[1] H. Wang, A. M. H. Kwan, Q. Jiang, and K. J. Chen, "A GaN pulse width modulation integrated circuit for GaN power converters," IEEE Trans. Electron Devices, vol. 62, no. 4, pp. 1143–1149, Apr. 2015. [2] A. León-Masich, H. Valderrama-Blavi, J. M. Bosque-Moncusí, and L. Martínez-Salamero, "Efficiency comparison between Si and SiC based implementations in a high gain DC-DC boost converter," IET Power Electron., vol. 8, no. 6, pp. 869–878, Jun. 2015 [3] K. Sugimura, D. Shibamoto, N. Yabu, T. Yamamoto, M. Sonehara, T. Sato, T. Mizuno, and H. Mizusaki, "Surface-Oxidized Amorphous Alloy Powder/Epoxy-Resin Composite Bulk Magnetic Core and Its Application to Megahertz Switching LLC Resonant Converter", IEEE Trans. Magn, Vol.53, no.11, #2801406, Nov.2017.

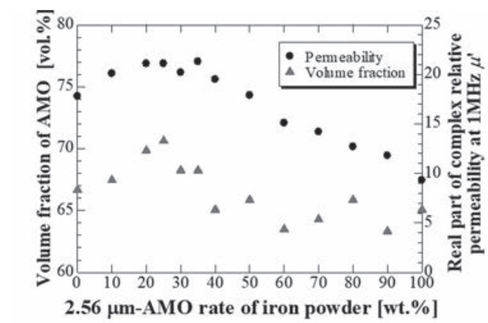

Fig. 1. Volume fraction of Fe-AMO powder and real part of complex relative permeability of a composite magnetic core with alternating mixing rate of 2.56 μm Fe-AMO and 10.94 μm Fe-AMO.

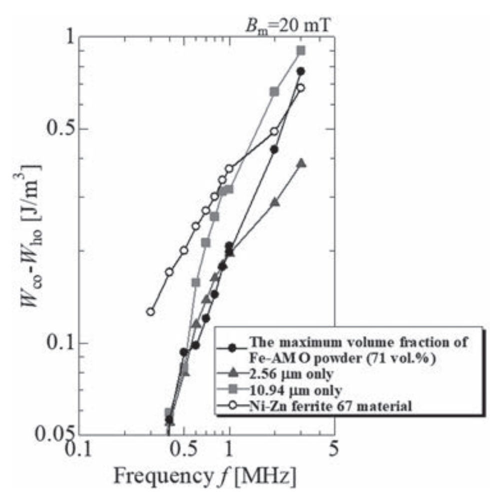

Fig. 2. Frequency versus the dynamic losses per cycle of a composite magnetic core with the maximum volume fraction of Fe-AMO powder, with 2.56 μm Fe-AMO only, and with 10.94 μm Fe-AMO only and Ni-Zn ferrite (67 material) measued under constant maximum flux density of 20 mT.

AV-05. Analysis of cutting technology influence on the magnetic anisotropy in grain-oriented steel based on the orientation distribution functions.

G. Paltanea[1], V. Manescu (Paltanea)[1], L. Dumitru[1] and H. Gavrila[1]
1. Electrical Engineering Department, University Politehnica of Bucharest, Bucharest, Romania

Grain-oriented electrical steel alloys have superior magnetic properties in the rolling direction (RD), due to its metallurgically induced Goss texture. The increased number of grains that have their easy magnetization axis of [001], oriented parallel to the RD, determines high values of the magnetic permeability and low energy losses. Anisotropy of their magnetic properties is intensively exploited nowadays, in order to manufacture electrical devices with high-energy efficiency [1, 2]. The magnetic cores of these electrical devices have parts with different orientations with respect to the RD, so the electrical engineers require knowing the path, where the magnetic reluctivity has a minimum value. A drawback of this approach is that the anisotropy of the grain-oriented silicon iron alloys is usually neglected and the catalogs provide only measured data for the RD and for the direction perpendicular to the rolling direction (TD) [111], in a good accordance with the international standards (EN 10107, JIS C 2553 and ASTM A876) [3]. The grain-oriented electrical steel sheets are generally cut through mechanical punching technology, which leads to induced mechanical stresses near the cut edge that influences the crystallographic texture and the magnetic properties of the device cores. The laser technology determines a burr free cut edge, which does not present mechanical deformations, while the magnetostrictive effect is absent in this area. The main disadvantage of the laser cutting is the induced thermal effect in the cutting zone that could have a negative influence on the grain orientations and, an unwanted oxidation could appear at the cut edge [4]. In the paper there were analyzed MOH commercially grain oriented samples with a thickness of 0.27 mm. Strips of 300 mm × 30 mm were cut through mechanical punching and laser at different angles ϕ with respect to the rolling direction, from 0° to 90° with a step of 15°. The samples were characterized with a unidirectional Single Strip Tester at a measuring frequency of 50 Hz. Pole figures and orientation distribution functions (ODFs) are considered today important in the polycrystalline material texture theory. It becomes almost a rule the fact that the magnetic properties of the crystalline materials are directly linked to their crystal structure and the crystal orientation is very important. The grain-oriented silicon iron strips are characterized by orthorhombic symmetry of body centered cubic crystals and the Goss texture (110)[001] samples could be analyzed with the ODFs theory. In [5, 6] it is put in evidence that all magnetic properties A could be described with three ODF parameters as $A = A_0 + A_1\cos(2\phi) + A_2\cos(4\phi)$, because they are usually a 4th order properties [5, 6, 7]. In [5, 7] is proposed a method to determine these three ODF coefficient, by considering the experimental data for the strips cut at 0°, 45° and 90° in the following assumption: $A_0 = 0.25[A(0°) + A(90°) + 2A(45°)]$, $A_1 = 0.5[A(0°) - A(90°)]$, $A_2 = 0.25[A(0°) + A(90°) - 2A(45°)]$. In the paper were determined the normal magnetization curves at a frequency of 50 Hz and at imposed values of the magnetic field strengths H ranging from 50 A/m to 10000 A/m, in the case of each angle ϕ and both cutting technologies. The model input data were experimental values of the magnetic polarization J at fixed H in the case of ϕ equal to 0°, 45° and 90°. In Fig. 1 are presented the polar diagrams $J(\phi)$ at 200 A/m and 2500 A/m; the last value is very important, because the magnetic polarization J_{25}, measured for H = 2500 A/m, is a direct function of the crystallographic texture, and the grains are monodomenial [7]. It can be noticed that the magnetic polarization distribution versus the cut angle has a 2nd fold variation, in the case of low magnetic field and a 4th fold distribution for high field strengths, fact that make very suitable the equation presented in [5, 6, 7]. The worst magnetic properties are observed at ϕ = 60°, which is in a good accordance with the theory that indicates an angle of 54.7° [8]. For both cutting technologies, the best magnetic properties are observed in the case of samples cut parallel to the rolling direction. It is obvious that the magnetization process is influenced by the cutting technology: the laser cut samples magnetize harder than the punched ones. In Fig. 2 there is presented the reconstructed normal magnetization curves, for punched strips, in the case of ϕ = 30°, 60° and 75° for both cutting technologies. The three computed ODF parameters lead to a good approximation of the experimental data and the cutting process affects in a substantial amount in low magnetic field region. The power losses evaluation is also performed based on the same algorithm. Finally, a prediction of the power losses for different angles at an imposed applied magnetic field strength is presented in the paper. Acknowledgment The work of Gheorghe PALTANEA has been funded by University Politehnica of Bucharest, through “Excellence Research Grants” Program, UPB-GEX 2017. Identifier: UPB-GEX2017, Ctr. No. 02/25.09.2017 (ANIZ-GO). The work of Veronica MANESCU (PALTANEA) has been funded by University Politehnica of Bucharest, through “Excellence Research Grants” Program, UPB-GEX 2017. Identifier: UPB-GEX2017, Ctr. No. 04/25.09.2017 (OPTIM-IE4).

[1] C. Demian, B. Cassoret, J.F. Brudny, T. Belgrand, AC magnetic circuits using nonsegmented shifted grain oriented electrical steel sheets: Impact on induction machine magnetic noise, IEEE Trans. Magn., vol. 48, no. 4, pp. 1409–1412, Apr. 2012. [2] H. Pfützner, E. Mulasalihovic, H. Yamaguchi, D. Sabic, G. Shilyashki, F. Hofbauer, Rotational magnetization in transformer cores—A review, IEEE Trans. Magn., vol. 47, no. 11, pp. 4523–4533, Nov. 2011. [3] S. V. Kulkarni and S. A. Khaparde, Transformer Engineering: Design and Practice. New York, NY, USA: Marcel Dekker, 2004. [4] L. Lanotte, C. Luponio, I. De Iorio, V. Tagliaferri, G. Tammaro, Effect of laser cutting on magnetic properties of grain-oriented Fe-Si ribbons, J. Sci. Technol., 8, pp. 252-256, 1992. [5] H.-J. Bunge, Texture analysis in materials science – mathematical methods. London, Butterworths, 1982. [6] H.-J. Bunge In: Advances and applications of quantitative texture analysis, H. J. Bunge, C. Esling, editors.. Clausthal, FRG, 1989. Oberursel, FRG, DGM Informationsgesellschaft – Verlag, 1991. p. 3-18. [7] M. F. de Campos, Anisotropy of steel sheets and consequence for Epstein test: I theory, in Proc. 28th IMEKO World Congr., Rio de Janeiro, Brazil, 2006, pp. 1–6. [8] M. Soinski, The anisotropy of coercive force in cold-rolled Goss texture electrical sheets, IEEE Trans. Magn., 23, 6, 1987.

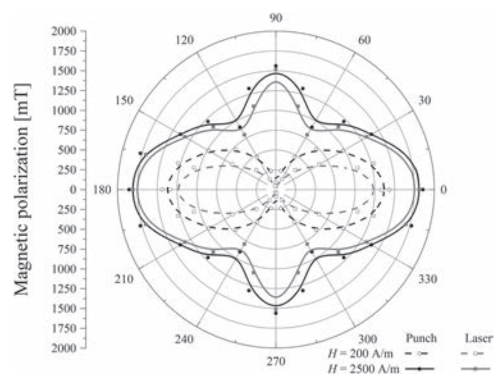

Fig. 1. Polar diagrams $J(\phi)$ at two values of the magnetic field strength, in the case of both cutting technologies.

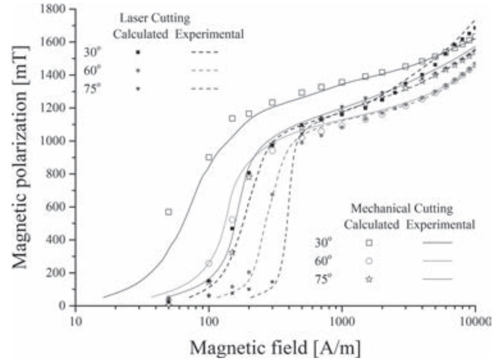

Fig. 2. Computed and experimental magnetization curves for the mechanically and laser cut samples.

AV-06. Effects of Annealing in Magnetic Field or under Tensile Stress on the Magnetic Properties of Fe-based Amorphous Magnetic Material.

T. Todaka[1], I. Uesugi[1] and T. Sato[1]
1. Division of Electrical and Electronic Engineering, Faculty of Science and Technology, Dept. of Innovative Engineering, Oita University, OIta, Japan

I. Introduction: Amorphous magnetic materials have been widely used as a core material of power transformers to reduce iron loss due to their excellent soft magnetic properties [1]. Also, from recent requirements of low loss and high speed electrical motors, considerable attention has been given to the amorphous magnetic materials that the iron loss is about 1/10 of one of the electrical steel sheets. However they have issues that the building factor (B.F.) and the magnetostriction are very large in comparison with those of the grain-oriented electrical steel sheets. As a solution of these issues, it is known that magnetic annealing after the magnetic-core processing is effective for reduction of B.F. of amorphous magnetic materials. However, reports on the magnetic annealing conditions of amorphous magnetic materials are very few and in the present circumstances they have been decided with intuition or experience of engineers. In order to effectively utilize the amorphous magnetic materials, we have tried to make clear a suitable magnetic annealing condition in a magnetic field, such as the temperature and the retention time. Furthermore, effects of a tensile stress adding during the heat treatment on the magnetic properties of the amorphous magnetic materials are examined. In this paper, knowledges about the annealing retention time to reduce the B.F. and the effects of annealing under tensile stress are reported. II. Measurements: Fig. 1 shows a schematic view of a special apparatus, which can apply a magnetic field and a tensile stress to a piece of 60 mm x 305 mm amorphous sheet, during annealing. The apparatus was put into an electric furnace as it is and heat treatment was performed. The amplitude of the exciting magnetic field strength in DC was controlled to be 800 A/m, the temperature was 320 degree-C. The retention time was changed from 0 min to 150 min with 30 minute step. The tensile stress depending on the attached weights was also changed from 9.8 MPa to 49.0 Mpa with 9.8 MPa step. The measurements of magnetic properties of the amorphous sheet (2605HB1M, Fe-Si-B) were conducted with a shingle sheet tester (H-coil method). Sinusoidal magnetic flux density conditions from 0.1 T to 1.55 T per 0.05 T at 50 Hz were kept during the measurements. III. Results and discussions: Fig. 2 shows an example of the iron loss reduction after magnetic annealing (320 degree-C, 150 min, 800 A/m) comparing with as cast one. As shown in this figure, the iron loss could significantly reduce after the magnetic annealing. Amorphous state after the magnetic annealing was also conformed from the XRD pattern. Fig. 3 (a) shows the iron loss as a fiction of the alternating magnetic flux density of 50 Hz and the annealing time (retention time) and Fig. 3 (b) shows the iron loss as a fiction of the alternating magnetic flux density of 50 Hz and the tensile stress. As shown in Fig. 3 (a), the iron loss became smaller with the retention time. As for the hysteresis loops, it was observed that the coercive force became smaller after the magnetic annealing. The reason can be considered as position stabilization of magnetic domain walls during the magnetic annealing [1,2]. Similar tendency should be observed for the annealing under tensile stress without magnetic field. As shown in Fig. 3 (b), the iron loss became smaller by adding only tensile stress. In this case, an optimal stress condition was observed at 32.9 MPa. The tensile stress was also effective to stabilize domain walls; however too much stress became a cause to increase pinning sites. The detailed results for the conditions mentioned above will be shown at the presentation and in the full version of paper.

[1] J. Marcin, M. Capik, et al., Tuning of Magnetic Properties and Domain Structure in FeCo- and FeSi- Soft Magnetic Alloys by Thermal Processing under Magnetic Field, Acta Electorotechnica et Informatica, Vol. 13, No. 1, DOI: 10.2478/aeei-2013-0020, 2013. [2] Y.S. Yang, Z.H. Li, Effect of Composite Magnetic Annealing in Amorphous Alloys, IEEE Trans. on Magn., Vol. 18, N0. 6, pp. 1397-1399, 1982.

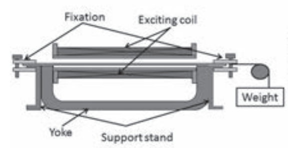

Fig. 1 Schematic view of the apparatus, which can apply a magnetic field and a tensile stress to amorphous sheets, during annealing.

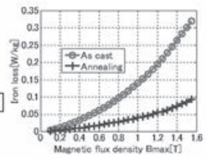

Fig. 2 An example of the iron loss reduction after magnetic annealing (320 degree-C, 150 min, 800 A/m) comparing with as cast one.

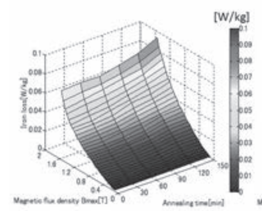

Fig. 3 (a) Iron loss as a fiction of the alternating magnetic flux density of 50 Hz and the annealing time (retention time).

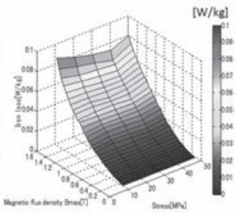

Fig. 3 (b) Iron loss as a fiction of the alternating magnetic flux density of 50 Hz and the tensile stress.

AV-07. Analysis of dynamic permeability and energy loss of ring-shaped Fe-Ga alloy.

L. Weng[1], W. Li[1], X. Cao[1], S. Liang[1] and B. Wang[1]
1. The State Key Laboratory of Reliability and Intelligence of Electrical Equipment, Hebei University of Technology, Tianjin, China

0. Introduction The dynamic permeability and loss of Fe-Ga alloy is an important index to determine the performance of Fe-Ga alloy. Permeability represents the ability of Fe-Ga alloy to conduct magnetic flux, and loss is the key factor affecting the operation performance of Fe-Ga alloy devices[1-2]. The high frequency-dependence characterization of ring-shaped Fe-Ga alloy including coercivity, loss and residual induction response to applied AC magnetic field is studied by Weng Ling[3]. The eddy current model to analyze the coercivity of ring-shaped Fe-Ga alloy at different heating temperatures is established by Grossinger R [4]. While they didn't analyze dynamic permeability which is important to design the Fe-Ga alloy transducers. In this paper, the dynamic permeability and loss model of ring-shaped Fe-Ga alloy based on the principle of electromagnetic is established. The results provide guidance for the design of high frequency Fe-Ga alloy transducers. 1. Dynamic Permeability and Loss Model of Ring-shaped Fe-Ga Alloy By the alternating magnetic field in the excitation coil induced electromotive force and Ohm's law can be obtained: $e=\mu_0N^2A\mu_m(\sin\delta+j\cos\delta)\omega I/l=(R+j\omega L)I$(1) From formula (1) can be obtained: $\mu'=\mu_m\cos\delta=Ll/\mu_0N^2A$(2) $\mu''=\mu_m\sin\delta=Rl/\mu_0N^2A\omega$(3) Where: *A* is the cross-sectional area of the ring-shaped sample,μ'is the real part of the complex permeability, it also known as elastic permeability. μ''is the imaginary part of the complex permeability, it also known as viscous permeability. As the phase difference between the voltage and current caused by the loss of magnetic core is δ, the loss factor, $\tan\delta=\mu''/\mu'=R/\omega L$(4) Through the above deduction, if the equivalent inductance and resistance of the ring-shaped Fe-Ga alloy are known, the variation of dynamic permeability and loss factor with frequency can be calculated by formula (2), (3) and (4). 2. Results and Analysis Using the equivalent inductance obtained experimentally, the elastic permeability of the ring-shaped Fe-Ga can be calculated from formula (2). The comparison between the model calculated value and the experimental measurement value is shown in Fig.1(a). When the magnetic field frequency is 1~12 kHz, the elastic permeability decreases greatly. When the magnetic field frequency is 12~28 kHz, the elastic permeability increases. Elastic permeability reflects the storage capacity of magnetic medium for magnetic energy. The calculated results of the model are basically consistent with the measured results, which verify the correctness of the model. Using the equivalent resistance obtained experimentally, the permeability of the ring-shaped Fe-Ga can be calculated from formula (3). The comparison between the model calculated value and the experimental measured value is shown in Fig.1 (b). As the frequency of the magnetic field increasing, the viscous permeability increases continuously. Viscous permeability characterizes the magnitude of the magnetic energy loss of the magnetic medium. The calculated results of the model are basically consistent with the measured results, which verify the correctness of the model. The loss factor that can be calculated from the formula (4). The change of the loss factor and relative loss with the frequency of the magnetic field is shown in Fig.2.As can be seen from Fig2, with the increase of the magnetic field frequency, the loss factor increases firstly and then decreases, finally it tends to be stable. While the relative loss shows a decreasing trend. The loss factor represents the size of the magnetic energy loss. The greater the loss factor, the greater the loss of magnetic energy in the magnetic medium. The intersection point of the relative loss and the loss factor curve represents the best working point of the Fe-Ga alloy device. It can be seen in Fig.2 that Fe-Ga alloy devices are at the best working efficiency when the magnetic field frequency is 3~4 kHz. Working in this frequency range, the ring-shaped Fe-Ga alloy device can minimize the loss of magnetic energy, Fe-Ga alloy medium magnetic energy storage capacity will not be too much. While the loss factor and relative loss are also in a balanced state, so Fe-Ga alloy devices maximizing the conversion of magnetic energy to other forms of energy can improve Fe-Ga alloy devices working efficiency. 3. Conclusions The elastic permeability, viscous permeability and loss factor of ring-shaped Fe-Ga alloy are calculated by the model. The correctness of the permeability model of ring-shaped Fe-Ga alloy is also verified by experiments. Finally, the optimum working magnetic field frequency of the ring-shaped Fe-Ga alloy device is about 3~4 kHz by analyzing the change of the loss factor and relative loss with the frequency of the magnetic field. The above theoretical analysis and experimental research provide a basis for the design of ring-shaped Fe-Ga alloy devices.

[1] Ktena A, Manasis C, Hristoforou E. On the Measurement of Permeability and Magnetostriction in Ribbons and Wires[J]. IEEE Transactions on Magnetics, 2014, 50(50):1-4. [2] Scheidler J J, Asnani V M, Dapino M J. Frequency-dependent, dynamic sensing properties of polycrystalline Galfenol (Fe81.6Ga18.4)[J]. Journal of Applied Physics, 2016, 119(24):043001-220. [3] Weng L, Li W, Sun Y, et al. High frequency characterization of Galfenol minor flux density loops[J]. Aip Advances, 2017, 7(5):056023. [4] Grossinger R, Mehboob N, Suess D, et al. An Eddy-Current Model Describing the Frequency Dependence of the Coercivity of Polycrystalline Galfenol[J]. IEEE Transactions on Magnetics, 2012, 48(11):3076-3079.

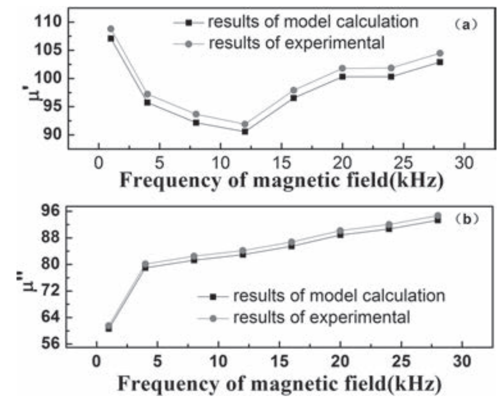

Fig. 1. Curves of permeability at different frequencies

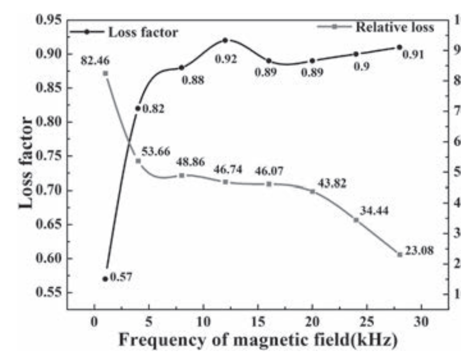

Fig. 2. Curves of loss factor and relative loss at different frequencies

AV-08. Magnetization reversal of helical Co and CoFe nanosprings.

D. Nam[1], A. Samardak[2], Y. Jeon[1], S. Kim[1], A. Davydenko[2], A. Ognev[2], L. Chebotkevich[2], A.S. Samardak[2,3] and *Y.K. Kim*[1]
1. Materials Science and Engineering, Korea University, Seoul, The Republic of Korea; 2. School of Natural Sciences, Far Eastern Federal University, Vladivostok, Russian Federation; 3. Center for Spin-Orbitronic Materials, Korea University, Seoul, The Republic of Korea

Introduction Helical nanostructures such as nanosprings (NSs) attract enormous attention owing to wide applications. In particular, magnetic helical nanosprings are promising among different systems, because of their additional advantage their motion can be controlled by magnetic field. As an example of application, under an external field, the helical NSs can be used as sensors, rotors and actuators [1]. We have presented the brief synthesis method for helical nanostructures and the difference of magnetic hysteresis behaviors [2]. In this study, we report magnetization reversal processes and magnetostatic interactions characterized of Co and CoFe NSs by first order reversal curves (FORCs) and micromagnetic simulations. Co and CoFe nanowires (NWs) were also fabricated and analyzed for comparison purposes. Experimental The NSs and NWs are fabricated by electrodeposition method utilizing anodized aluminum oxide nanotemplates which have nominal pore size of approximately 200 nm. Ag of 300 nm was deposited as a working electrode. The precursor solution is composed of cobalt sulfate heptahydrate, iron sulfate heptahydrate, vanadyl sulfate hydrate, L-ascorbic acid and a small amount of nitric acid to adjust acidity. However, Fe precursor was excluded for Co NSs and NWs. The NSs and NWs were synthesized under a constant current density. Magnetic properties were measured by vibrating sample magnetometry (VSM). Especially FORC analyses were employed to understand further magnetization reversal processes. Results and discussion A collection of electron microscopy images in Fig. 1 shows that NWs and NSs were uniformly synthesized into the nanotemplates [2]. To understand the interactions between neighboring NWs or NSs, the FORC method was used to observe the coercivity (H_c) and interaction field (H_i) distribution patterns. Magnetic fields in the parallel and perpendicular directions were applied. Compared to the NW array, the NS array shows unique distribution. The FORC diagram of parallel field to CoFe NS array has no distribution in H_i direction since there are a few interactions between neighboring NSs. In addition, defects, different length, and different H_c values of each NSs are responsible for long tail along the H_c direction. However, there is a large distribution in H_i direction due to interactions between the layers of the NSs themselves. The gaps between layers has more influence on magnetization reversal when perpendicular direction fields were applied to NSs.

[1] L. Liu *et al.,* Nanoscale 6, 9355 (2014). [2] D. Y. Nam *et al.,* IEEE Trans. Magn. 53, 2004104 (2016).

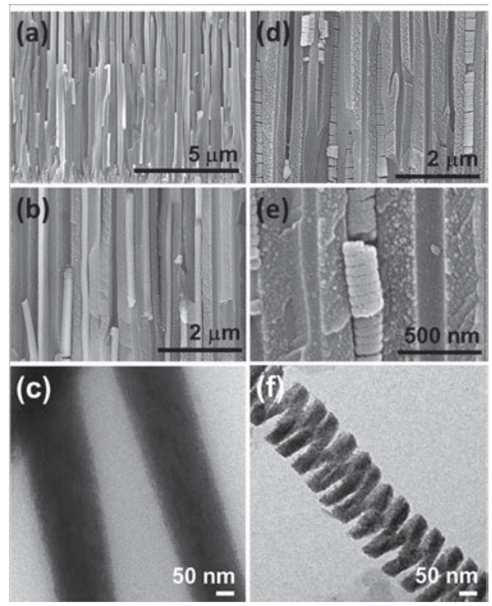

Fig. 1. Morphological shapes of CoFe NW arrays, (a)-(b), and NS arrays, (d)-(e), observed by SEM. (a) Low- and (b) high magnification images of CoFe nanowires embedded in the template. TEM images of free standing CoFe NW (c) and NS (f) specimens.

AV-09. Degradation of static and dynamic magnetic properties of non-oriented steel sheets by cutting.

V. Manescu (Paltanea)[1], G. Paltanea[1], E. Ferrara[2], F. Fiorillo[2] and I. Nemoianu[1]

1. Electrical Engineering Department, University Politehnica of Bucharest, Bucharest, Romania; 2. Nanoscience and Materials Division, Istituto Nazionale di Ricerca Metrologica, Torino, Italy

Shaping of laminated magnetic cores always implies cutting of the sheets and ensuing degradation, via localized plastic deformation, of their soft magnetic properties. The performances of fully processed non-oriented (NO) Fe-Si laminations can, in particular, be seriously impaired by the cutting operations required to form the slotted stator core of rotating machines. Because of its applicative impact, this problem has been amply treated in the literature, with focus on the specific magnetic properties of the mechanically damaged band at the cut edge [1] and on the phenomenological retrieval of the overall loss behavior, either by numerical methods [2] or analytical formulations [3], employing a suitable high number of parameters, to be found by experiments. These reveal somewhat awkward procedures, often limited to the assessment of the degradation of the quasi-static magnetic behavior of the material. In this work, which provides an extensive set of experimental results on different types of non-oriented Fe-Si sheets, we aim at a simple phenomenological assessment of the degradation of magnetization curve and magnetic losses enforced by cutting. This is based on the idea that, although the induction in a cut strip sample is not uniform, we can nevertheless invoke an equivalent uniform induction for the dynamic magnetic behavior, while providing simple relationships for the evolution of magnetization curve and losses with strip width. Four types of commercial non-oriented Fe-Si sheets, of thickness 0.192 mm $\le d \le$ 0.638 mm were cut as strips of different widths (5 mm $\le w \le$ 60 mm), using both guillotine punching and water-jet method. The measurements were performed under controlled sinusoidal flux by means of a calibrated single-strip tester, from DC to the maximum frequency f_{max} = 2 kHz, at the peak polarization values J_p = 0.5 T, 1.0 T, and 1.5 T. The normal magnetization curve (J_p, H_p) exhibited, in all materials, the expected rightward shift in the *J-H* plane upon decreasing strip width, with coercivity and hysteresis loop area correspondingly increased. By using a simple scheme, where the work-hardened region of the strip is identified with two defined bands of width L_c running along the cutting line at the edges, we can express the dependence of the magnetization J_p on the strip width w under an applied field H_p as $J_p(w) = J_{p0} - (J_{p0} - J_{pc})\times 2L_c/w$, $(w \ge 2L_c)$, where J_{p0} and J_{pc} are the magnetization values associated with the undamaged and damaged bands, respectively. It turns out that, by measuring the complete normal magnetization curves at two different w values, we can estimate the width of the damaged bands L_c and, for any H_p value, the associated magnetizations J_{p0} and J_{pc}. The full evolution of the curves with w is then obtained and found to agree with the experimental curves, in spite of the somewhat crude scheme involved. This is equally true for the hysteresis loss W_{hyst}, the area of the quasi-static loop, now evolving with w as $W_{hyst}(J_p, w) = W_{hyst}(J_{p0}) + (W_{hyst}(J_{pc}) - W_{hyst}(J_{p0}))\times 2L_c/w$, $(w \ge 2L_c)$. We show in Fig. 1 an example of energy loss versus frequency $W(J_p, f)$ behavior measured up to f = 400 Hz for J_p = 1.0 T on a 0.470 mm thick Fe-(2.6%)Si sheet and a 0.192 mm thick Fe-(3.5%)Si sheet. It is apparent that both the quasi-static (W_{hyst}) and the dynamic losses, the sum of the classical W_{cl} and the excess W_{exc} loss components, are affected by the cutting-induced strain hardening. Having estimated the quantity $2L_c$ through the previous analysis of the normal magnetization curves, we can immediately predict by the previous equation and knowledge of a couple of values of $W_{hyst}(J_p, w)$ at two strip widths, the whole $W_{hyst}(J_p, w)$ behavior versus w. This is observed in Fig. 2 to closely fit the experimental data, concerning the example shown in Fig. 1. It is also shown in Fig. 2 that a same inverse dependence on w as for $W_{hyst}(J_p, w)$ applies to the excess loss $W_{exc}(J_p, w)$. In deriving this quantity from the experimental $W(J_p, f)$ curve, we calculate the classical loss $W_{cl}(J_p, f)$ using the standard formula for uniform induction J_p. In fact, W_{cl} is chiefly associated with the macroscopic eddy current patterns circulating close and at the sheet surface, related to the time derivative of the flux averaged over the sample cross-section. W_{exc} has instead a local character, over distances basically connected with the grain size. It quite naturally follows a same dependence on w as $W_{hyst}(J_p, w)$, as illustrated in Fig. 2. It is understood, however, that the averaged sinusoidal $J(t)$ results from the composition of non-sinusoidal contributions from the damaged and undamaged regions. Actually, this appears to have a minor impact on the overall behavior of $W_{exc}(J_p, w)$, which is shown to be well described, up to the frequency limit imposed by skin effect, by the standard formulation provided by the statistical theory of losses [4], the effect of local distortion being in any case accounted for by the statistical parameter V_0. Acknowledgment The work of V. MANESCU (PALTANEA) and G. PALTANEA has been funded by U.P.B., through "Excellence Research Grants" Program, UPB-GEX 2017. Identifier: UPB-GEX2017, Ctr. No. 04/25.09.2017 (OPTIM-IE4) and Ctr. No. 02/25.09.2017 (ANIZ-GO).

[1] G. Crevecoeur, L. Dupré, L. Vandenbossche, and R. Van de Walle, "Local identification of magnetic hysteresis properties near cutting edges of electrical steel sheets," *IEEE Trans. Magn.*, vol. 44, no. 6, pp. 1010–1013, 2008. [2] M. Hofmann, H. Naumoski, U. Herr, and H. Herzog, "Magnetic properties of electrical steel sheets in respect of cutting: micromagnetic analysis and macromagnetic modeling," *IEEE Trans. Magn.*, vol. 52, no. 2, paper n° 2000114, 2016. [3] S. Steentjes. G. von Pfingsten, and K. Hameyer, "An application-oriented approach for consideration of materials degradation effects due to cutting on iron loss and magnetizability," *IEEE Trans. Magn.*, vol. 50, no. 11, paper n° 7027804, 2014. [4] E. Barbisio, F. Fiorillo, and C. Ragusa, "Predicting loss in magnetic steels under arbitrary induction waveform and with minor hysteresis loops," *IEEE Trans. Magn.*, vol. 40, no. 4, pp. 1810-1819, July 2004.

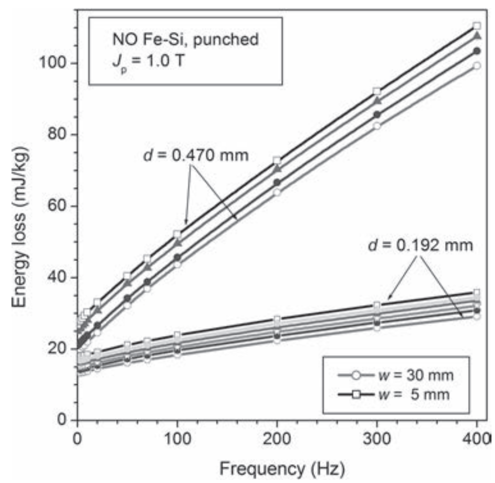

Fig. 1. Energy loss $W(f)$ measured at J_p = 1.0 T up to f = 400 Hz on guillotine punched strips of non-oriented Fe-Si sheets of different thickness d.

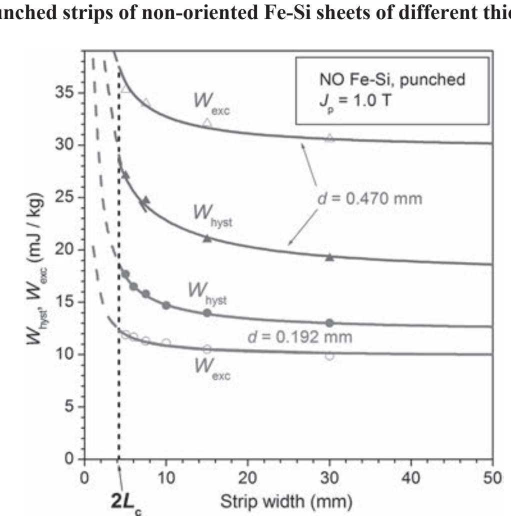

Fig. 2. Hysteresis loss W_{hyst} (full symbols) and excess loss W_{exc} (open symbols) at 400 Hz versus strip width w, as obtained by the experiments shown in Fig. 1.

AV-10. Magnetic properties of exchange coupled Fe-Ni/$Fe_{22}Ni_{78}$ double-layered films.

J. Kaji[1], H. Aramaki[1], K. Koda[1], K. Takashima[1], T. Yanai[1], M. Nakano[1] and H. Fukunaga[1]
1. Nagasaki University, Nagasaki, Japan

I. INTRODUCTION Soft magnetic materials are widely used in magnetic devices such as transformers, reactors and sensors. For application of the soft magnetic films to magnetic sensors, we have investigated Fe-Ni films prepared by an electroplating method and confirmed their good magnetic properties [1-3]. In general, the materials with high saturation magnetization are effective to reduce size of the devices. For Fe-Ni-system films, the increase in the Fe content of the films or substitution of Co for Ni is typically applied to increase the saturation magnetization. In the present study, we focused on magnetic exchange coupling as another method to increase the saturation magnetization, and considered that the total Fe contents in the films can be increased without abrupt increase in coercivity by preparing exchange coupled Fe-Ni/$Fe_{22}Ni_{78}$ multilayered films. This contribution reports the soft magnetic properties of double-layered Fe-Ni/$Fe_{22}Ni_{78}$ films prepared by an electroplating method. II. EXPERIMENTAL PROCEDDURES We carried out the electroplating to obtain the Fe-Ni double-layered films using two plating baths with different Fe ion concentration. The electrolyte of the plating bath contained the following: 20~117 g/L of $FeSO_4{\cdot}6H_2O$, 275 g/L of $NiSO_4{\cdot}7H_2O$, 10 g/L of $C_7H_4NNaO_3{\cdot}2H_2O$ (Saccharin), 15 g/L of NH_4Cl, 0.5 g/L of $C_6H_8O_6$ (Ascorbic acid), 3 g/L of $C_{12}H_{25}OSO_3Na$ (Sodium lauryl sulfate). $Fe_{22}Ni_{78}$ films were electroplated on the Cu plate from a plating bath with 53 g/L of $FeSO_4{\cdot}6H_2O$, and then Fe_xNi_{100-x} films were electroplated on the $Fe_{22}Ni_{78}$ ones using another plating bath. Bath temperature was set at 50°C during the plating, and current density was kept at 200 mA/cm^2 by using a computer-aided dc current source (Matsusada P4K-80). The dc-hysteresis loops of the Fe-Ni films were measured with a B-H tracer (Riken Denshi BHS-40), and the coercivity was determined from the loop. III. RESULTS AND DISSCUSSION Figure 1 shows the coercivity of the double-layered Fe-Ni/$Fe_{22}Ni_{78}$ films a function of total Fe content in the films. In this experiment, we controlled the thicknesses of each layer at 12 μm (total thickness: 24 μm) by the change in the plating time. As the Fe content in the Fe-Ni layer varied from 0 at. % to 68 at.% by the change in the $FeSO_4$ concentration, the total Fe content in the multilayered film consequently varied from 11 at.% to 40 at.%. For a comparison, the result for single-layered films (thickness: 24 μm) are also shown in Fig.1. As shown in Fig.1, all the double-layered films showed lower coercivity compared with the single-layered films. This result implies that the exchange coupling effectively works to reduce the coercivity. To confirm the effect of the exchange coupling on the coercivity, we changed layer thickness for the $Fe_{22}Ni_{78}$ magnetic phase from 1 to 18 μm. Figure 2 shows coercivity of the double-layered $Fe_{10}Ni_{90}$/$Fe_{22}Ni_{78}$ films as a function of thickness of the $Fe_{22}Ni_{78}$ layer. Since large variation of coercivity enables us to easily confirm the effect of the exchange coupling when the exchange coupling becomes weak, we determined the Fe content of the Fe-Ni layer at 10 at.% in this experiment. Total thickness of the double-layered $Fe_{10}Ni_{90}$/$Fe_{22}Ni_{78}$ film was kept at 24 μm. As shown in Fig.2, the coercivity dramatically decreased with increasing the thickness of $Fe_{22}Ni_{78}$ layer from 1 to 6 μm. This result implies that and $Fe_{10}Ni_{90}$ phase is effectively exchange coupled with $Fe_{22}Ni_{78}$ one to improve magnetic properties when the thickness of the $Fe_{22}Ni_{78}$ layer is more than 6 μm. From these results, we conclude that exchange coupled Fe-Ni/$Fe_{22}Ni_{78}$ multilayered films are one of attractive soft magnetic materials due to their improved magnetic properties.

[1]. T. Shimokawa, T. Yanai, K. Takahashi, M. Nakano, K. Suzuki, and H. Fukunaga, IEEE Transaction on Magnetics, Vol. 48 (2012) 2907. [2]. Y. Watanabe, M. Otsubo, A. Takahashi, T. Yanai, M. Nakano, H. Fukunaga, IEEE Transactions on Magnetics, Vol. 51, (2015) #4004104. [3]. T. Yanai, K. Kouda, K. Eguchi, T. Morimura, K. Takashima, M. Nakano, H. Fukunaga, "Electroplated Fe-Co-Ni films prepared in ammonium-chloride-based plating baths", AIP Advances, Vol. 8, (2018), to be published.

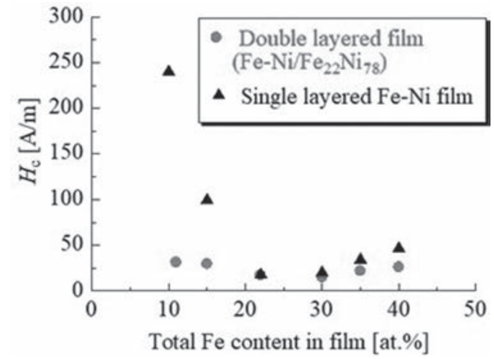

Fig. 1. Coercivity of double-layered Fe-Ni/$Fe_{22}Ni_{78}$ films as a function of total Fe content in the film. The result for single-layered Fe-Ni films is also shown in the figure.

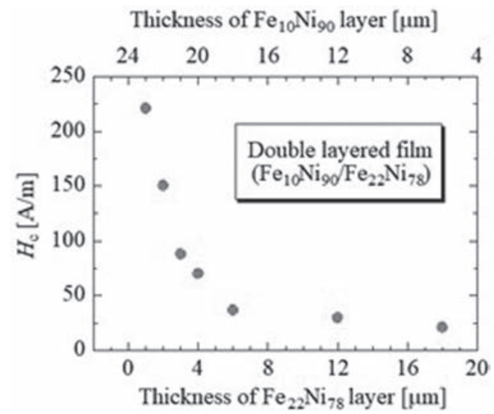

Fig. 2. Coercivity of double-layered $Fe_{10}Ni_{90}$/$Fe_{22}Ni_{78}$ films as a function of thickness of $Fe_{22}Ni_{78}$ layer.

AV-11. Investigation of dynamic and continuous heat treatment on the magnetic losses of non-oriented electrical steels.

J. Fuzer[1], P. Kollar[1], S. Martinkova[1], F. Kovac[2] and I. Petryshynets[2]
1. Institute of Physics, P.J. Safarik University, Kosice, Slovakia; 2. Division of Metals Systems, Institute of Materials Research, Kosice, Slovakia

Non-oriented steel (NO) sheets are materials with great engineering significance used in AC applications where the direction of magnetic flux is circular, such as electric motors and generators [1]. As an aspect of the worldwide trend towards energy consumption decrease and preservation of the environment, the reduction of electricity consumption has become an extremely crucial matter in recent years. The understanding of the dependence of power losses in electrical steels on frequency is of great importance [2]. Core losses are structure sensitive and depend on several metallurgical factors; such as chemical content, grain size, crystallographic texture, cleanliness and stress states in NO electrical steels. [3]. The aim of this work was to investigate the influence of dynamic and continuous heat treatment on the soft magnetic properties of NO electrical steels. The used experimental material was a NO electrical steel grade M530 – 50A after primary recrystallization. Experimental samples were temper rolled under laboratory conditions. The value of reduction was less than 8 %. After this the samples were subjected to dynamic or continuous annealing according to the patent SK 288322 [4] and European Norm EN 10126, respectively. The samples with primary recrystallized microstructure (R1) were characterized by average grain size about 20μm. The annealed samples at dynamic (R5 dyn) and continuous conditions (R6 cont) were characterized by coarse grained microstructure with average grain size 120μm and 100 μm, respectively. The strips of the NO electrical steels were used for the measuring of the specific electrical resistivity by the direct method and for the measurement of the coercivity by the Foerster Koerzimat HCJ 1.097. The ring samples were used for magnetic measurements. The AC/DC hysteresis loops were measured by the Permeameter AMH-1K-S at the frequency range from DC to 400 Hz at maximum induction of 1.0 T and 1.5 T, respectively. Fig.1 shows the differences between *B(H)* loops for 3 different samples for 1.0 T magnetic induction amplitude. These curves were obtained at 50 Hz. There is, clearly, enlargement of the locus area for sample R6 cont, which is related to the increase on the coercivity. The R1 sample requires higher field strengths to achieve the induction of 1.0 T in comparison to other samples, for 1.5 T sample R6 cont requires the highest field strength of the three samples. These steels are compared to find out the effect of thermal treatment on magnetic losses. Fig. 2 plots magnetic losses vs. frequency measured at 1.0 T inductions. It is evident from the Fig. 2 that sample R5 dyn has lowest core loss at all frequencies. The core losses dependences show the different ranking of the studied samples for 1.0 T and 1.5 T. The results show that the varied thermo-mechanical treatment affects the magnetic losses in NO electrical steel laminations and the comparison of the magnetic properties depends on the value of magnetic induction.

[1] Y. Oda, M. Kohno, A. Honda, *J. Magn. Magn. Mater.* 320, 2430, 2008. [2] S.E. Zirka, Y.I. Moroz, P. Marketos, A.J. Moses, *IEE Trans.on Magn.,* 46, 286, 2010. [3] A.J. Moses, *IEEE Proc*. 137 (Pt. A, No. 5) (1990) 233.. [4] F. Kováč, I. Petryshynets, V. Stoyka, T. Kvačkaj, I. Škorvánek, *Patent n.: 288322.* Banská Bystrica : ÚPV SR, 2015.

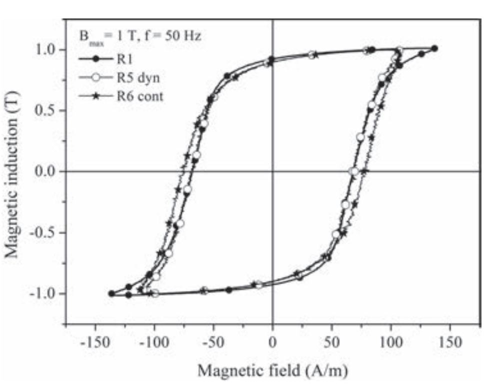

Fig. 1. Hysteresis loops of studied NO electrical steels measured at B_{max} =1.0 T, f = 50 Hz.

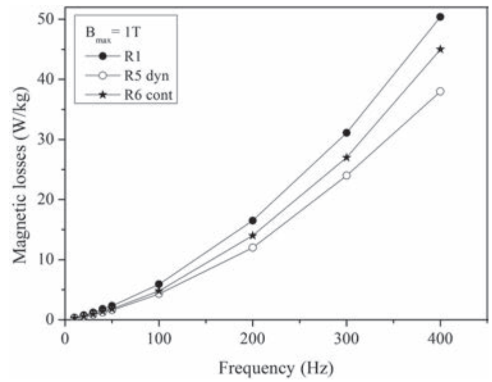

Fig. 2. Magnetic losses as a function of frequency of studied NO electrical steels measured at B_{max} =1.0 T.

AV-12. $NiFe_2O_4$ Nano-Hollow Spheres with Improved Magnetic and Dielectric Properties.

D. Mandal[1] and K. Mandal[1]
1. Condensed Matter Physics and Material Sciences, S.N.Bose National Centre for Basic Sciences, Kolkata, India

$NiFe_2O_4$ (NFO) is one of the most significant spinel ferrites due to its specific qualities such as low coercivity (H_C), high saturation magnetization (M_S) and Curie temperature (T_C), high electrical resistivity, low eddy current loss, and remarkable thermal and chemical stability [1]. Among the various morphologies of magnetic nanomaterials, nano-hollow spheres (NHS) are found to be very promising [2] because of their high M_S, large surface area and pore volume, low density, and ability to withstand volume changes due to temperature and pressure, which enable them to be used in wide varieties of applications in the fields of biomedical research, energy storage, high frequency magnetic devices and chemical sensors. The cavity inside and large surface enhances their capability of capturing and delivering drugs and also repeated internal reflections increase their applicability as microwave absorbers. Herein, the excellent properties of $NiFe_2O_4$ nano-hollow spheres (NFO NHS) synthesized in solvothermal method are reported. Figure 1(a) shows the X-Ray Diffraction plot of NFO NHS comparing with NFO Bulk indexing the crystal planes present and also confirming the single phase inverse spinel face centered cubic structure. Average crystallite size (= 23.5nm) and lattice constant (= 8.35Å) are calculated from Debye-Scherer formula and Bragg's law respectively from XRD spectra. The morphological analysis evidences the sample to be NHS with an average size of 200 nm, shown in SEM (Fig. 1(b)) and TEM (Fig. 1(c)) micrographs. EDX spectra (Fig. 1(d)) prove the constituents (Ni, Fe and O) present in the sample. M-H hysteresis loops of NFO NHS with maximum applied field up to 2kOe at temperatures 100K, 200K, 300K, 400K are described (Fig. 1(e)). At room temperature (300K), H_C and remnant magnetization (M_R) of NHS are 122Oe and 10.5emu/g respectively, displays the soft ferrimagnetic nature of NFO. The increase in H_C and magnetization on lowering temperatures are related to a growth of magnetic anisotropy preventing the alignment of the moment spins in an applied field [3]. A comparison between magnetic properties of NFO NHS, NFO nano particles (NPs) and Bulk NFO has been depicted in Fig. 1(f). It is found that T_C, H_C, and M_S values are increasing from bulk (H_C=78Oe, M_S=48.5emu/g) to NPs (H_C=93Oe, M_S=58.3emu/g) to NHS (H_C=122Oe, M_S=63.5emu/g). Both the increase in anisotropy and cationic movements are responsible for the higher H_C and M_S values of NPs than bulk NFO [3-4]. High temperature needed in solvothermal method to synthesize NHS and large surface to volume ratio of NHS are responsible for higher H_C and M_S values than NPs. The study of the dielectric properties (calculated from impedance (Z) – phase (θ) data [4]) gives information about the polarization behavior, conduction mechanisms and dielectric relaxation. Their variation with frequency (f) and temperature influences their applications for microwave devices e.g. in isolators, circulators etc [5]. Figure 2(a) shows the variation real (ε') and imaginary (ε'') values of dielectric constant with frequency (log(ω), ω=2πf) from 40 Hz-110 MHz at different temperatures from 30°C to 300°C. As the frequency increases ε' sharply falls and approaches to almost frequency independent nature due to inability of electric dipoles to comply with variation (i.e. frequency) of applied ac electric field, and increase in temperature facilitates more and more dipoles to be oriented along the field. The variation of ε' as well as ac conductivity ($\sigma_{ac}= \omega\varepsilon_0\varepsilon''$) (Fig. 2(b)) with frequency can be explained on the basis of Maxwell-Wagner two layers model for space charge, where ferrimagnetic materials are assumed to have larger grains and smaller grain boundaries as conducting and insulating layers, respectively. Dielectric loss ($\tan\delta = \varepsilon''/ \varepsilon'$) (absorption of energy) decreases with the increasing frequency of the applied electric field as after a certain frequency σ_{ac} increases and relaxation time constant also shrinks. Impedance spectra (Fig. 2(c), (d)) follows the above results and dielectric relaxation peak (80 kHz for 100°C) observed for each temperature shows its non-Debye type nature [4]. These improved properties [1, 3-5] make them suitable for uses in high-frequency devices as well as in bio-medical applications.

[1] K.M. Batoo, J. Phy. Chem. Solids 72 (2011) 1400–1407 [2] M. M. Goswami, Sci. Rep. 6, 35721. [3] G. Nabiyouni et al., CHIN. PHYS. LETT. 27, 12 (2010) 126401 [4] J. H. Joshi et al., Materials Research Bulletin 93 (2017) 63–73 [5] K. C. B. Naidu, W Madhuri, Bull. Mater. Sci., 40, 2 (2017) 417–425

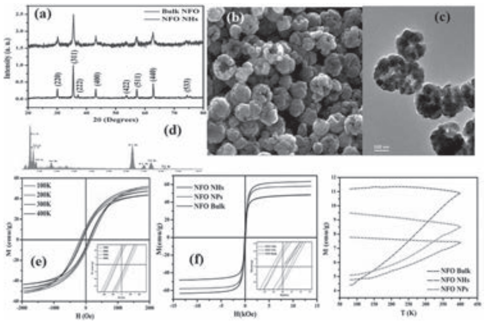

Fig. 1. (a) XRD of bulk NFO and NFO NHS (b) FESEM and (c) TEM micrographs of NFO NHS (d) EDX spectra (e) M-H curves of NFO NHS up to 2kOe at 100K, 200K, 300K, 400K (f) M-H curves at 300K and ZFC, FC magnetization vs. temperature curves at 100Oe within 80K to 400K of NFO bulk, NFO NPs, NFO NHS

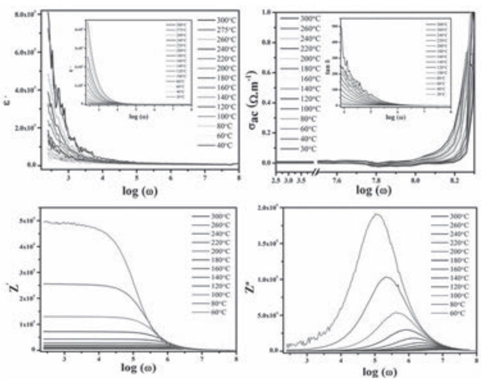

Fig. 2. (a) Variation of dielectric constant (ε') with log(ω) at different temperatures, Inset: ε'' vs. log(ω) (b) σ_{ac} vs. frequency at different temperatures, Inset: dielectric loss (tan δ) vs. log(ω) (c) Dependence of Real part of impedance (Z') and (d) Imaginary part of impedance (Z'') on frequency at different temperatures

AV-13. Magnetic material deterioration of non-oriented electrical steels as a result of plastic deformation considering residual stress distribution.

N. Leuning[1], S. Steentjes[1], H. Weiss[2], W. Volk[2] and K. Hameyer[1]
1. Institute of Electrical Machines (IEM), RWTH Aachen University, Aachen, Germany; 2. Institute of Metal Forming and Casting (utg), Technische Universität München, Munich, Germany

It is well known that magnetic properties of electrical steel are highly sensitive to mechanical stress [1-4]. Processing and manufacturing of magnetic cores lead to complex stress and strain distributions within the material. The stress covers different scales, i.e., residual stress within and between grains, local stress variations over several grains and global residual stress. The residual stress interacts with elastic stress due to magnetic and external forces during the operation, i.e., centrifugal forces. To account for the alteration of magnetization and loss due to mechanical stress in actual electrical machines, the basic relations have to be understood. A comprehensive description, respectively characterization of the magneto-elastic-plastic coupling is still missing in scientific literature. With a profound knowledge of the interrelations, improved material modeling and therefore the simulation of electromagnetic energy converters, such as electric motors or generators can be enabled. This study is aimed at the identification of the effect of plastic deformation and concurrent impact of residual elastic stress in this context. Previous research indicated that the magnetic deterioration through plastic deformation is caused mainly by elastic stress and not by the mechanism of dislocation formation [1,2]. Therefore, this study contributes to the general magneto-elastic as well as the magneto-elastic-plastic coupling. In contrast to complex processing impacts, for example cut edge effects, this study is performed on rectangular samples with a defined uniaxial tensile mechanical loading. The magnitude of the loading causes a homogenous stress state that is above the elastic limit and thus, leads to plastic deformation. The results of the experiments by reloading the material samples allow one to consider the different contributions of dislocations and internal stress. Further, mechanical finite-element (FE) simulations are conducted to evaluate the residual stress distribution in detail and link as well as quantify the magnetic deterioration with the integral components of the residual stress. Experimental The study is performed on samples of a conventional 0.35-mm, 2.4 wt.% FeSi, in rolling (RD) and transverse direction (TD). Three samples in each direction are stressed beyond the elastic limit with different maximum stress values. Next, the external force is removed and finally, the deformed samples are stressed again in the same direction as the initial deformation. The magnetic properties are characterized during the initial deformation process, and then again at reloading. With this approach, the effect of plastic deformation on the resulting magnetic property changes can be considered. In this consideration the different contributions of dislocations as the underlying mechanism of deformation and residual stress distribution as a direct consequence of plastic deformation, can be incorporated. Mechanical FE-simulations are used to correlate the global stress distribution with the elastic residual stress in the deformed samples. Results The presented work is based on the observation that the magnetic properties of uniaxially tensile-stressed samples above yield strength, deteriorate strongly when the external loading is removed [2, 4]. In [1] this effect is linked to long-range internal stress. In Fig.1 results are displayed for 1.0 T at 100 Hz. The experimental succession is represented by the path from 1→2→3. Here, two samples were tested with different peak stress σ_{max}. For the required magnetization H_{max} a linear increase with applied tensile stress at initial deformation is observed. The exceeding of the elastic limit is not perceived in the magnetization. When the external loading is removed a strong rise of H_{max} occurs. For the magnetic loss the behavior is similar, however the exceeding of the elastic limit can be observed in form of a steeper slope of the curve. A gradual reloading, path 3→4 shows an approximation of the reloading curve to the initial curve which results in the same behavior at peak stress. This indicates that the magnetic deterioration, e.g., of the magnetization ΔH_{max} between the initially deformed loaded and unloaded state due to the distribution of residual tensile and compressive stress as a consequence of plastic deformation is explainable as an equivalent tensile stress of σ_{max}. A comprehensive observation of the polarization dependence as well as a coupling to the residual stress distribution obtained from mechanical FE-simulations (comp. Fig. 2) is presented in the full paper. Conclusions The presented work highlights the necessity to improve the basic understanding of the magneto-elastic-plastic-coupling. This allows to incorporate the actual material behavior in material modeling, especially for models predicting the mechanical processing of NO electrical steel sheets. Even though the experimental study was performed on plastically deformed samples, vital information of elastic residual stress can be deduced. It was shown that the integral mechanical stress from mechanical simulations correlate with the magnetic deterioration and that a coupling of mechanical and magnetic simulations could be a promising approach to estimate magnetic deterioration. This work serves as a contribution towards the understanding of material deterioration on a physical level and for the development of quantification methods.

[1] V. E. Iordache, E. Hug, and N. Buiron, "Magnetic behaviour versus tensile deformation mechanisms in a non-oriented Fe-(3 wt.%)Si steel," Materials Science and Engineering: A, vol. 359, no. 1–2, pp. 62–74, 2003. [2] N. Leuning, S. Steentjes, and K. Hameyer, "Effect of magnetic anisotropy on Villari Effect in non-oriented FeSi electrical steel," International Journal of Applied Electromagnetics and Mechanics, vol. 55, no. S1, pp. 23–31, 2017. [3] Jan Karthaus, Simon Steentjes, Nora Leuning and Kay Hameyer, "Effect of mechanical stress on different iron loss components up to high frequencies and magnetic flux densities", COMPEL - The international journal for computation and mathematics in electrical and electronic engineering, vol. 36, no 3, pp. 580-592, 2017. [4] V. E. Iordache, F. Ossart, and E. Hug, "Magnetic characterisation of elastically and plastically tensile strained non-oriented Fe–3.2%Si steel," Journal of Magnetism and Magnetic Materials, vol. 254–255, pp. 57–59, 2003.

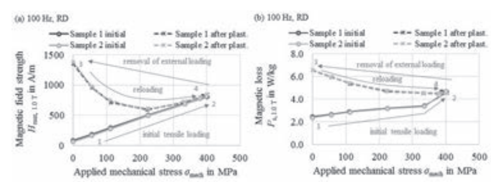

Fig. 1. H_{max} and P_s at 1.0 T for two samples at initial and reloading

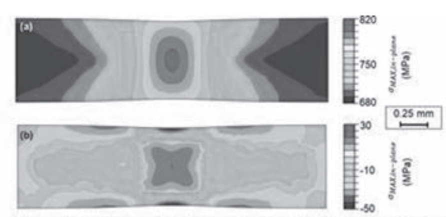

Fig. 2. Exemplary FE-simulation of a tensile test geometry, a) stressed, b) unstressed

AV-14. Magnetic properties and crystal structure of high-purity Fe-(6, 6.5, 7) mass%Si alloys.

K. Matsuyama[1], I. Sasaki[1], S. Nakagawa[1], H. Era[1], M. Takezawa[1], Y. Horibe[1], S. Hata[2], C. Kaidou[3], T. Ogawa[4] and S. Kubo[5]
1. Kyushu Institute of Technology, Kitakyushu, Japan; 2. Kyushu University, Fukuoka, Japan; 3. National Institute of Technology, Kitakyusyu College, Kitakyusyu, Japan; 4. Fukuoka Industrial Technology Center, Kitakyusyu, Japan; 5. Kagoshima University, Kagoshima, Japan

Introduction Electromagnetic steel sheets are used for iron core materials of various electric devices, and their performance improvement leads to high energy efficiency. Typically, electromagnetic steel sheets are based on Fe-Si alloys, and it is reported that purification of Fe-Si alloys is effective for improving their properties. Kaido et al. proposed the effectiveness of purification by high-purity Fe-3.1 mass%Si alloy by making a prototype motor and studying it.[1] Based on this research, Lei et al. fabricated high-purity Fe-(5, 6) mass%Si alloys with high concentration. Additionally, Lei et al. reported that the hysteresis loss of Fe-6 mass%Si is lower than Fe-5 mass%Si at low magnetic field, and increases more quickly at a high magnetic field.[2] From these results, it can be seen that as the amount of Si increases, the soft magnetic characteristics become better, but interest is given to what kind of magnetic behavior the high-purity Fe-Si alloy shows in the 6.5 mass%Si, which shows the best magnetic characteristics with Fe-Si alloy. The purpose of this study is to investigate the magnetic properties around the 6.5 mass%Si on the high-purity Fe-Si alloy and the crystal structure change by further increasing the amount of Si. Experiment and Calculation High-purity Fe-(6.5, 7) mass%Si ingots were made of 99.99 mass% electrolytic iron and 99.999 mass% silicon in a CCLM (Cold Crucible Levitation Melting) furnace in a high vacuum atmosphere. Samples with Si content of 6 mass% were those of a previous study. Ring samples were cut out from the manufactured ingots, and measurement was performed with a maximum applied magnetic field of 5000 A/m by using an Automatic DC Magnetization Analyzer. Magnetic domain behavior was observed with a Kerr effect microscope using a part of the ring sample used for magnetic property measurement. The crystal grains observed with the Kerr effect microscope have identified the crystal orientation by EBSD (Electron Back Diffraction Patterns). A sample for TEM (Transmission Electron Microscope) observation using samples with a diameter of 3 mm was prepared by ion milling. Magnetic domain behavior was observed with a Lorentz electron microscope using a sample for TEM. Additionally, an electron diffraction pattern was observed using TEM. Results Fig. 1 shows half hysteresis loops of high-purity Fe-(6, 6.5, 7) mass%Si alloys at a magnetic flux density of 1.5T. Coercivities of high-purity Fe-(6, 6.5, 7) mass%Si alloys are Hc=9.31 A/m, Hc=7.64 A/m, and Hc=7.92 A/m, respectively. Permeabilities of high-purity Fe-(6, 6.5, 7) mass%Si alloys are μ=12.3, μ=36.5, and μ=3.9, respectively. Hysteresis losses of high-purity Fe-(6, 6.5, 7) mass%Si alloys are Wh=0.27 W/kg, Wh=0.39 W/kg, and Wh=0.48 W/kg, respectively. The permeability and coercivity show the best values for high-purity Fe-6.5 mass%Si alloy shown in Fig. 1. Conversely, for hysteresis loss, high-purity Fe-6 mass%Si alloy shows the best value. Remarkably, there are large differences in the magnetic hysteresis loops behavior between the high-purity Fe-6.5 mass%Si alloy and the high-purity Fe-7 mass%Si alloy, but the hysteresis loss of the high-purity Fe-7 mass%Si alloy indicated good value. Compared with high-purity Fe-6.5 mass%Si alloy with the best soft magnetic properties and with commercially available Fe-6.5 mass%Si alloy, the high-purity Fe-6.5 mass%Si alloy we made had lower coercivity and lower hysteresis loss. From this result, it can be seen that soft magnetic characteristics are improved by purification. In the observation with the Kerr microscope, the high-purity Fe-(6, 7) mass%Si alloys have a single magnetic domain with the applied magnetic field of 120 kA/m (1.5 kOe). Additionally, the high-purity Fe-6.5 mass%Si alloy has a single magnetic domain with the applied magnetic field of 88 kA/m (1.1 kOe). In the observation with the Lorentz electronic microscope, movement of the domain walls is observed at the applied magnetic field of 24 kA/m for the high-purity Fe-7 mass%Si alloy. Furthermore, migration of the domain walls are confirmed at the applied magnetic field of 17 kA/m for the high-purity Fe-6.5 mass%Si alloy. Moreover, migration of the domain walls is confirmed at the applied magnetic field of 16 kA/m for the high-purity Fe-6 mass%Si alloy. Because the magnetic permeability is higher, the domain wall is more likely to move, so it can be said that the result is almost in agreement with the result of the magnetic characteristics from the results of the Kerr effect microscope image and the Lorentz electron microscope image. Fig. 2 shows the electron diffraction pattern of the high-purity Fe-7 mass%Si alloy. Fig. 2 also shows that the B2 and D03 structures appear. As a result of comparing the three compositions, it can be seen that the high-purity Fe-7 mass%Si alloy has the largest amount of B2 and D03 structures because the spots of B2 and D03 were diffracted more strongly as the Si amount was increased. It is argued that these structures may affect the large difference in magnetic properties of high-purity Fe-6.5 mass%Si alloy and high-purity Fe-7 mass%Si alloy.

[1]C.Kaido, T.Ogawa, Y.Arita, J.Yamasaki and Y.Shishido. Optimum Iron Loss of No-oriented Steel Sheets. J.Magn. Soc. Jpn. Vol. 31, No. 4, pp316-321, 2007 [2]Z.Lei, T.Horiuchi, Y.Mimura, I.Sasaki, C.Kido, M.Takezawa, S.Kubo, T.Ogawa, H.Era, Study on magnetic properties and domain structures of Fe-(5, 6) wt%Si alloys prepared with high purity metallurgy, 2015 IEEE International Magnetic Conference (INTERMAG) CD-09

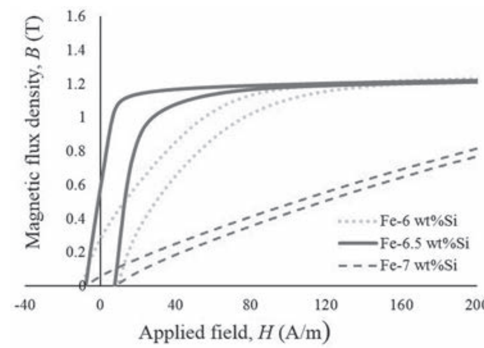

Fig. 1. Half hysteresis loops of high-purity Fe-(6, 6.5, 7) mass%Si alloys measured at maximum applied magnetic field of 5000 A/m

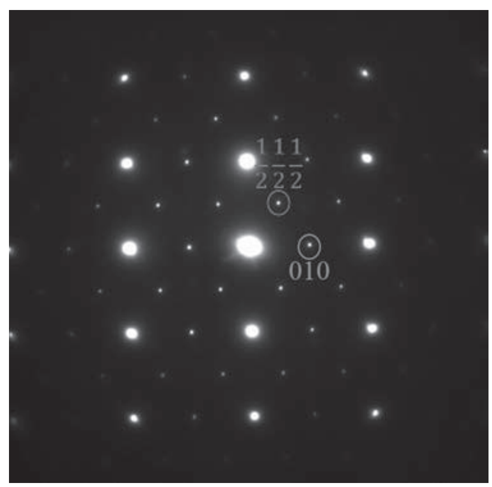

Fig. 2. The electron diffraction pattern of high-purity Fe-7 mass%Si alloy.

AV-15. Soft Magnetic Thin Films Laminations on Various Silicon Wafer Trench Geometries.

D.J. Cronin[1,2], P. McCloskey[1], A. Masood[1] and C. O'Mathuna[1]
1. Integrated Magnetics, Tyndall National Institute, Cork, Ireland; 2. University College Cork, Cork, Ireland

The recent surge in demand for miniaturisation of power transformers and inductors requires magnetic core materials with low energy loss, high saturation flux density, medium to high permeability, low coercivity and high operating frequency. With increasing switching frequencies for power supplies, the size and storage requirements for passive components is significantly lower. This is where the opportunity lies in using soft ferromagnetic thin films. Recent developments in magnetic materials such as CoZrO granular films, thin films and CoNiFe alloys have been evaluated by research groups such as George Loizos et al [1] for the next generation of integrated magnetic devices for high frequency applications. This work will focus on the development of thin film magnetic laminations for integrated magnetic trenches for applications to inductors on silicon. Lamination structures of CZTB magnetic material and an AlN insulator onto various microscale deep trenches were deposited onto silicon wafers by several fabrications processes and their properties analysed. These new trench shapes with an efficient magnetic material are expected to reduce eddy current and hysteresis losses compared to traditional cross-sectional shapes. Different trench designs were characterised for both magnetic and physical performance. The physical characterisation would include SEM and FIB imaging for layer uniformity of the magnetic material. Magnetic characterisation includes using a BH loop tracer to produce hysteresis loops in both easy and hard axes of the trenches to determine magnetic properties such as Coercivity (H_c) and anisotropy energy (H_k), the field required to fully magnetise the material in its hard axis. A permeameter was used to obtain its relative permeability vs frequency, μ_r vs f. Intrinsic properties of the material such saturation flux density and resistivity will not change with shape, whereas properties such as permeability or coercivity can be influenced by shape, surface structure and roughness etc. The shape designs fabricated were semi-circular, rectangular and quadrilateral. The fabrication processes used to etch the trenches were KOH bath, DRIE dry etching RF plasma and a dry vapour XeF_2 etch. A 'sandwich' of 10 layers of CZTB 200nm thick, each separated by a layer of 10nm was deposited into each trench. This lamination arrangement reduces eddy current losses. A profilometer was used to scan each trench to ensure the projected depth of 100 µm was observed. This work was done to see how coating trenches before copper deposition would influence their magnetic characteristics and efficiency when applied in integrated devices. Although defects and non-uniformity was seen in the SEM and FIB images, very promising results were obtained in particular for the rectangular shaped trench with H_c as low as 0.5 Oersteds. However after improving the fabrication process and eliminating defects and non-uniformity, H_c is expected to be even lower. Combined with a high B_{sat} of 1.3 T, this trench design is a favourable starting point for applications on a larger more complex scale. The full results show that the lamination coating could also be extended further to the surface of silicon wafers in inductor designs where flux lines are boosted through the components where inductance, L and permeability are increased. As cross-sectional area has a major role in increasing the inductance of a component, where is the magnetic path length, the shape of these trenches can play a major part in increasing its magnetic performance without changing its magnetic path length. Upon finding an ideal shape such as a rectangular trench, CZTB laminations can be applied to these magnetic components to improve their performance compared to their conventional cross-sectional geometry.

Gorge Loizos et al, 'Soft magnetic multi-layered thin films for HF applications' Science Direct, Volume 75, 2015, pg. 1096-1103. K. Mandl et al, 'The stress induced anisotropy in amorphous magnetic thin films' INTERMAG conference 2000 IEEE International. P. M. C. Ó. M. 2. a. S. K. Ansar Masood*1, "Tailoring the ultra-soft magnetic properties of sputtered FineMET thin films for high-frequency power applications," *8th Joint European Magnetic Symposia (JEMS2016).*

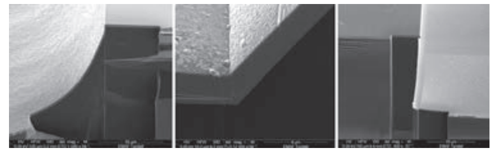

Fig. 1. (a) semi-circular trench. (b) A vertex of the quadrilateral trench. (c) The rectangular shaped trench. Roughness and defects can be eliminated in a further fabrication process. Images taken at a 54° angle to respective trench. CZTB present on the surfaces of each etched trench as seen in (b).

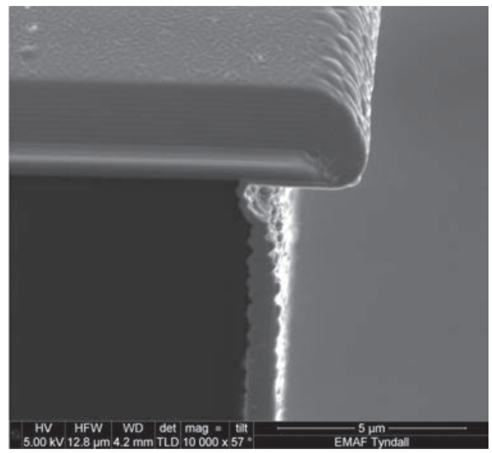

Fig. 2. SEM image at the corner of the rectangular trench shows the laminations between the CZTB and AlN, dark grey and light grey respectively.

AV-16. Effect of growth conditions on the Soft Magnetostrictive properties of thin Fe-Co-Cr films.

S. Baco[1], Q.A. Abbas[1], Z. Leong[1], T. Hayward[1], N. Morley[1] and T. Thomson[2]
1. Material Science and Engineering, The University of Sheffield, Sheffield, United Kingdom; 2. School of Computer Science, University of Manchester, Manchester, United Kingdom

Soft magnetic materials with low anisotropy and coercive fields, large magnetostriction constant and saturation magnetisation are required for microelectromechanical systems (MEMS) such as sensors and actuators [1]. One promising material for MEMS devices is FeCo, as not only is it cost effective compared to the rare earth element alloys but also has a high saturation magnetisation and magnetostriction constant [2]. Although FeCo has a high saturation magnetisation and magnetostriction constant, it can also have large coercive and anisotropy fields for as deposited films [3], which affect the performance of MEMS devices. One solution to produce soft magnetic FeCo films with small coercive and anisotropy fields is to alloy with other elements, such as B [4], Ni and Al [5]. The magnetostrictive properties of Fe-Co-Cr thin films in particular have not yet been reported, therefore the aim of this study was to investigate the magnetostrictive properties and microstructure of FeCoCr films. Since growth conditions strongly affect the microstructure, hence the magnetic properties, FeCoCr films were fabricated as a function of thickness and sputtering power by the RF Sputtering technique. The first film set varied the film thickness from 56nm to 165 nm, at constant power (75W) and pressure (4.8 mTorr). The second film set varied the sputtering power between 75 W and 150 W, with film thickness ~100nm and pressure (4.8 mTorr). The microstructure and magnetic properties were investigated by Atomic Force Microscopy (AFM), X-Ray Diffraction (XRD), and High-Field MOKE magnetometer respectively, while the Villari technique was used for the magnetostriction measurement. AFM analysis revealed that 56nm film had a rougher surface compared to the thicker films. For the first film set (different film thickness), all the films exhibited a wide XRD peak at 2θ ~44^0 associated with FeCoCr bcc (110). The same broad peak at 2θ ~44^0 was observe for the films grown at the lower powers (75W and 100W), while for the films grown at higher sputtering power (125W and 150 W), two sharp peaks were observed corresponding to FeCoCr bcc (110) at 2θ ~44^0 and bcc (211) at 2θ~82$^{0.}$ This indicates that crystallinity improved as the sputtering power increased. From the magnetisation hysteresis loops measured on the MOKE magnetometer, the soft magnetic properties of FeCoCr as function of thickness were observed, with the coercive fields reduced to H_c = 1.5 kAm^{-1} at 100nm and anisotropy H_k = 12 kAm^{-1} at 120 nm (Fig.1a). While the anisotropy and coercive fields were H_k <20 kAm^{-1} and H_c < 2 kAm^{-1} for the films grown at sputtering power between 75 W to 125 W, but rapidly increased for the films grown with 150W (Fig. 1b). This is likely to be due to the change in microstructure of the films at the highest sputter power. The magnetostriction constant of FeCoCr films was found to be the highest at 100 nm (λ = 28ppm) however it was significantly independent on film thicknesses (for all thicknesses λ was between 22 and 28 ppm). This means that the interfacial magnetostriction constant does not strongly influence the effective magnetostriction constant of these films. The magnetostriction constant decreased from 28ppm to 5 ppm, as the sputtering power increased for the 100nm films, which can be related to the changes in the microstructure of the films, as observed in XRD. For comparison, a 100nm FeCo film was grown at the same sputtering power (75W) and pressure (4.8 mTorr). The FeCo film had isotropic behaviour, with a considerably larger coercive field (H_c= 9.2 kA/m) (Figure 2) and slightly smaller magnetostriction (λ=25ppm) than the 100nm FeCoCr film. In summary, FeCoCr films have been successfully fabricated with remarkable good soft magnetostrictive properties. By adding Cr, the coercive fields reduced by factor of 6 compared to FeCo. The suitable sputtering parameter to produce the soft magnetic properties with low coercive and anisotropy fields, while maintaining high magnetostriction constant were grown at thicknesses between 100 and 125nm at a power of 75 W. Growing films at higher sputtering powers (150 W) resulted in better crystallinity, but with large coercive fields and low magnetostriction constant, due to their strong dependence on the microstructure.

[1] E. Quandt, "Giant magnetostrictive thin film materials and applications," *J. Alloys Compd.*, 258, 1–2, 126–132, (1997) [2] Bozorth RM, *Ferromagnetism*, IEEE, (NY): (1991). [3] M. D. Cooke, M. R. J. Gibbs, and R. F. Pettifer, "Sputter deposition of compositional gradient magnetostrictive FeCo based thin films," *J. Magn. Magn. Mater*., 237, 2, 175–180, (2001) [4] C.Das, S. Mohapatra, G.A. Vitthal, P. Alagarsamy "Magnetic properties of single-layer and multilayer structured $Co_{40}Fe_{40}B_{20}$ thin film," *Thin Solid Films* 616, 126-133, (2016) [5] F. Zheng, F. Luo, Y. Lou, Y. Wang, J. Bai, D. Wei, X. Liu, and F. Wei, "Magnetic properties and high-frequency characteristics of FeCoAlO gradient composition thin films," *J. Appl. Phys.*, 111, 7, 109–112, (2012).

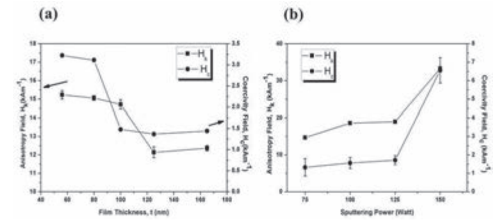

Fig. 1. Coercive and anisotropy fields as a function of (a) film thickness and (b) sputtering power.

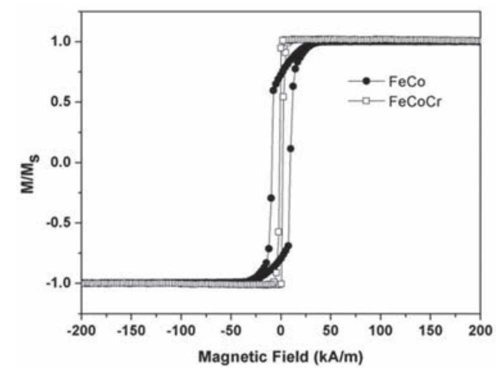

Fig. 2. Normalised Magnetisation of FeCo and FeCoCr films deposited with the same growth condition (thickness = 100nm ; power = 75 W and pressure = 4.8 mTorr)

Session AW
TRANSFORMERS AND INDUCTORS: MODELLING I
(Poster Session)

Cheng-Tsung Liu, Chair
National Sun Yat-Sen University, Kaohsiung, Taiwan

AW-01. Effect of Magnetic Annealing on Magnetic Characteristic of Amorphous Wound Core.

T. Sato[1] and T. Todaka[1]
1. Oita University, Oita, Japan

In this paper, an effect of a magnetic annealing on magnetic characteristics of an amorphous wound core is shown. Amorphous magnetic materials have been widely used as a core material of power transformers to reduce iron loss due to their excellent soft magnetic properties [1]. The amorphous core for transformer is wound core formed by stacking a plurality of amorphous sheet materials. Because a bending stress is generated at each of the corners of the wound core, the magnetic characteristic is deteriorated at the corners as shown in Fig.1 (a). As the result, the iron loss of the wound core becomes larger due to the effect of the bending stress. In order to remove the residual stress that is generated in the wound core including the bending stress, the wound core must be annealed in magnetic field by an electric furnace [2]. However, it hasn't become clear the effect of the magnetic annealing to the amorphous wound core in detail. Thus, we studied about the effect of the magnetic annealing to the bending stress. To express the bending stress at the corner of the wound core, 4 kinds of model wound cores formed by stacking the amorphous sheet were made. The model cores were formed by folding a cylindrical form, and the bending stress of model cores were adapted by changing the radius of the cylindrical cores. The values of radius of the model wound cores are 25mm, 35mm, 50mm, and 100mm. The bending stress was calculated by equations of shearing stress as shown in Fig.1 (b). When the bending stress is calculated by these equations, the value of the bending stress of the short radius model core becomes larger. The model wound cores were annealed by using the electric furnace as shown in Fig.2 (a). The holding time of the annealing conditions were adapted among 30 minutes to 480 minutes under annealing temperature 320 degree and the magnetic field 640 A/m. The magnetic characteristics of the model wound cores were measured by the system as shown in Fig.2 (b). The magnetic characteristics were measured before the magnetic annealing and after. Fig.2 (c) shows the iron loss curves of the model wound cores before the magnetic annealing. The iron loss increased in the bending stress applied state and the model core of higher bending stress became lager. It made clear that the iron loss of the wound core at the corner of inside in the non-magnetic annealing condition becomes lager than the outside due to the bending stress. Fig.2 (d) shows the relationship of iron loss between before and after the magnetic annealing. The iron loss after the magnetic annealing is smaller than before, the values of iron loss in the different bending stress conditions reduced to about same value 0.8 W/kg. These results show the effect of the magnetic annealing to the bending stress.

[1] J. Marcin, M. Capik, et al., Tuning of Magnetic Properties and Domain Structure in FeCo- and FeSi- Soft Magnetic Alloys by Thermal Processing under Magnetic Field, Acta Electorotechnica et Informatica, Vol. 13, No. 1, DOI: 10.2478/aeei-2013-0020, 2013. [2] Y.S. Yang, Z.H. Li, Effect of Composite Magnetic Annealing in Amorphous Alloys, IEEE Trans. on Magn., Vol. 18, N0. 6, pp. 1397-1399, 1982.

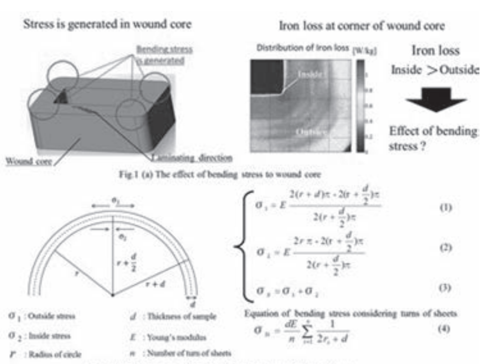

Fig.1 (a) The effect of bending stress to wound core
Fig.1 (b) Method of calculating bending stress to model wound core

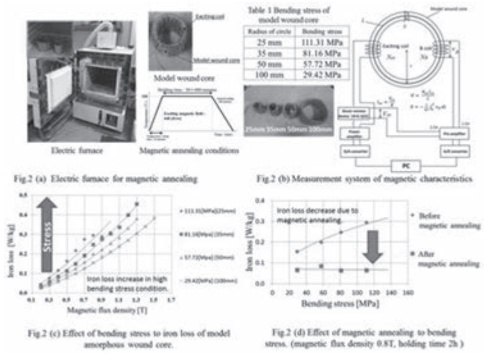

Fig.2 (a) Electric furnace for magnetic annealing
Fig.2 (b) Measurement system of magnetic characteristics
Fig.2 (c) Effect of bending stress to iron loss of model amorphous wound core.
Fig.2 (d) Effect of magnetic annealing to bending stress. (magnetic flux density 0.8T, holding time 2h)

AW-02. Numerical Simulation of Particle Motion Inside Nano-Modified Transformer by Multi-Scale LBM-FDM Method.

L. Xuan[1], F. Zeng[1], X. Guan[1] and H. Peng[1]
1. School of Electrical Engineering, Wuhan University, Wuhan, China

1. Introduction Applications of nanofluid has become more and more widespread. Then there's an idea of adding nanoparticles into transformer oil to form a stable suspension colloid. The method can improve heat transfer characteristics and insulating properties of transformer oil [1]. But it is inevitable that nanoparticles and inherent metallic particles inside transformer move continuously and have different electric charges in electric field, reducing insulation performance of transformer oil, even causing breakdowns [2]. Therefore, particle motion and distribution problems have received more and more concerns. Fu et al. presented a theoretical model for analyzing the movement of the conducting particles inside transformer oil [3]. Kumar et al. carried out simulation on particle movement with balanced and unbalanced voltages in a three phase common enclosure gas insulated busduct [4]. They proposed that a moving conducting particle in an external electric field will be subjected to a collective influence of several forces including electrostatic force, electrostatic force and drag force. Cui et al. proposed a novel particle tracing method to estimate the moisture in transformers [5]. Ma et al. simulated the distribution state of metal particles in the oil tract of traction transformer with the method of computational fluid dynamics [6]. However, the traditional calculation methods previous researches used have evident deficiencies, such as low calculation accuracy and enormous calculation quantity. After years of development, the lattice Boltzmann method (LBM) has become a promising method for fluid flows and heat transfer simulation [7]. The method is based on mesoscopic scale and has advantage of simplicity and high computational efficiency, which makes it popular and has been applied to many simulations of two-phase fluid flows. But owing to limit of its present application range, the algorithm has trouble solving macro problems such as analysis of electric field. In this study, a multi-scale LBM-FDM calculation model has been built. Motion characteristics of nanoparticles and metallic particles in a nano-modified transformer have been calculated. First, distributions of temperature rise and fluid flow inside transformer were calculated by mesoscopic LBM method. Secondly electrical field inside transformer was calculated by macro FDM method. Lastly movements of nanoparticles and metallic particles were simulated using results from previous analysis. 2. Numerical calculation method 2.1 Force analysis To figure out how a particle moves, force of a particle should be analyzed. In this study, it was enough for us to just consider gravity, viscous resistance and electric force, because magnitude of other forces was far smaller than those three forces. The motion equation is given by $ma+F_e+F_g+F_v=0$ where m is the mass of a particle, a is the acceleration, F_e is the electric force, F_g is the gravity, F_v is the viscous resistance. 2.2 Calculation process The numerical calculation process is shown in Fig. 1. As is shown, we firstly build a 2-D axisymmetric thermal-fluid and flow particle tracking multi-scale model. To get viscous resistance, velocity and temperature field is analyzed by LBM in mesoscopic dimension. To get electric force, electric field is analyzed by FDM in macroscale dimension. Then we should also consider gravity of a particle. Combining all three forces, movement tracks of a particle is finally obtained. 3. Results and discussion In the multi-scale calculation model, the iron core, primary windings and secondary windings were taken account for heat source, with transformer oil filled as medium. Distributions of temperature and velocity fields by LB analysis are shown in Fig. 2(a) and Fig. 2(b). At the time the voltage of primary winding access the peak, the distribution of electric field computed by FDM is shown in Fig. 2(c). Two nanoparticles of different positions were set as the research objects. Movement tracks of the nanoparticles under forces at 1500s are shown in Fig. 2(d). Blue lines represent the movement tracks and red circles represent the initial positions of one particle. As is shown, no matter where the starting position is, the nanoparticles will follow the flow of transformer oil, moving clockwise and cycle. In essence, it is found that the magnitude of viscous resistance is much larger than electric field force, thus the nanoparticle is mainly affected by the force of viscous resistance. Likewise, two metallic particles at different positions were set as research objects, and movement tracks of them at 3000s are shown in Fig. 2(e). As the figure shows, the movement tracks of the metallic particles differ from those of nanoparticles. Similar to the nanoparticles, the particles follow the flow of transformer oil at the place where the flow velocity of the oil is high. But at the place where the flow velocity of the oil is low, the particles are mainly affected by the gravity and may sink down. This is because the mass of a metallic particle is much larger than that of a nanoparticle. In addition, when a particle is near the windings, the effect of electric field force is obvious, and the alternating sinusoidal electric field under the power frequency causes a serious cyclic swing presents in the movement track of the particles (dense tracks in the figure).

[1] Liao, Rui Jin, et al. "Insulating properties of insulation paper modified by nano-Al_2O_3 for power transformer." Journal of Electric Power Science & Technology 1(2014):3-7. [2] Li, Junhao, et al. "Partial-Discharge Characteristics of Free Spherical Conducting Particles Under AC Condition in Transformer Oils." IEEE Transactions on Power Delivery 26.2(2011):538-546. [3] Fu, Shouhai, et al. "Calculation of Particles Moving Traces in Transformer Oil." Modern Electric Power (1999). [4] Kumar, G. V. Nagesh, et al. "Influence of unbalanced voltages on the movement of metallic particle in a three phase common enclosure gas insulated busduct." Sadhana 35.4(2010):393-406. [5] Cui, Yi, et al. "Particle tracing modelling on moisture dynamics of oil-impregnated transformer." Iet Science Measurement & Technology 10.4(2016):335-343. [6] Ma, S., Tang, J., et al. "Simulation study on distribution and influence factors of metal particles in traction transformer." High Voltage Engineering 41.11(2015):3628-3634. [7] Aidun, Cyrus K., and J. R. Clausen. "Lattice-Boltzmann Method for Complex Flows." Annual Review of Fluid Mechanics 42.1(2009):439-472.

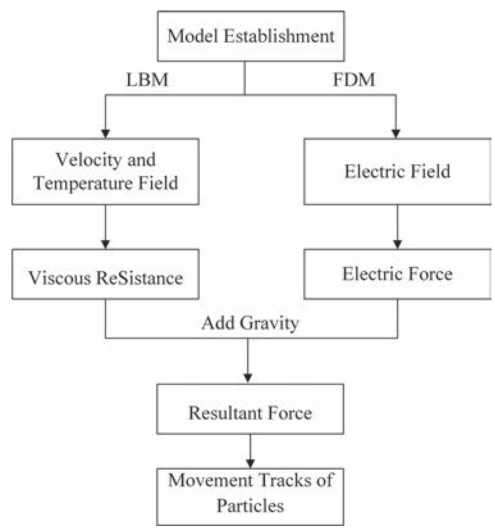

Fig. 1. Calculation procedures

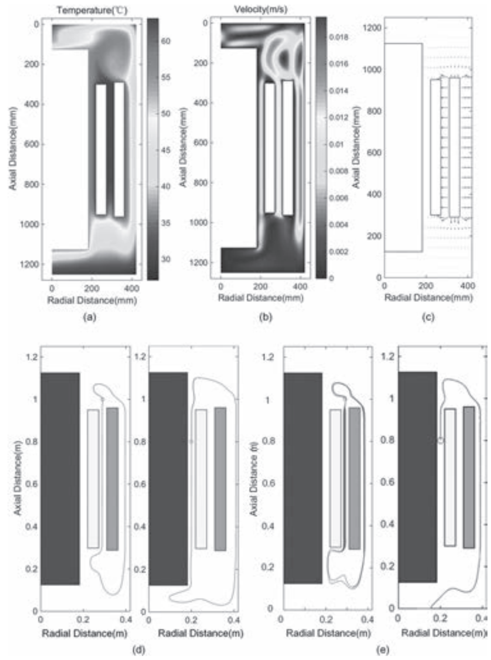

Fig. 2. Calculation results

AW-03. An Efficient Finite Element Modeling for Stray Loss Calculation in Power Transformer Tank Using Impedance Boundary Condition.

K. Park[1], S. Hahn[1] and H. Ahn[2]
1. Electrical Engineering, Dong-A University, BUSAN, The Republic of Korea; 2. R&D Center, Power & Industrial Systems Performance Group, Hyosung Corporation, Changwon, The Republic of Korea

1. Introduction A power transformer is one of the important power apparatuses for electric power transmission. Over the world, high efficient and low loss power transformer is widely studied. In a transformer, the electric power loss generated in the transformer is classified into copper loss, core loss, stray loss, and etc. The stray loss account for about 20% of the total loss in a power transformer. Especially, in case of a power transformer with large % impedance, the ratio of stray loss may be about 30~50% of the copper loss. The stray loss due to the eddy current induced by the leakage flux is occurred in the tank, steel structure, and localized part of whole winding. Previous work concerning the stray loss calculation of steel structure in a power transformer has been published by many researchers. Although many researchers produced some interesting results, they spent a lot of computing time in order to compute the stray loss of steel structure in a power transformer. To calculate the eddy currents, the skin effect must be considered. The transformer tank has a size of several meters, but the thickness of the tank is about ten millimetres and the skin depth of the tank is several millimetres. Therefore, a large number of meshes and a lot of calculation time are required to calculate the eddy current using FEM. Therefore, it needs to study the method to shorten computing time while maintaining the accuracy of analysis. In this paper, we propose the application of impedance boundary conditions to solve this problem. 2. Stray Loss Analysis 2.1 Stray Loss The transformer tank loss generated by the leakage flux from the windings are called stray loss. The losses on the transformer tank surface are as follows [1]. Loss = $\sqrt{(\omega\mu/8\sigma)}\int_s H_t H_t^* ds$ Where ω is the angular frequency, σ is the conductivity, μ is permeability, H_t is the tangential component of the magnetic field vector at the surface, *denotes complex conjugate. 2.2 Inpedance Boundary Condition If the skin depth is much thinner than the thickness of the conductor, the boundary condition for rough calculation without considering the effect inside the conductor is called the impedance boundary condition. At the surface of good conductors the tangential component of the electric field (E) is approximately proportional to the tangential component of magnetic field (H). This boundary condition can be written as the following equation [2]. $n \times E = Z_s n \times (n \times H)$ Where Z_s is the complex surface impedance. 3. Results and Discussion In our study, we proposed an efficient numerical method using the impedance boundary condition to reduce the computing time for the stray loss. The proposed method applies the impedance boundary condition to the tank wall that the leakage flux is penetrated into its surface. With this analysis method, we could calculate stray loss generating on 3-D transformer tank. The computation time of 3-D model depends on the number of mesh that one of several reasons. Therefore, in order to shorten the computation time, the number of mesh should be reduced. This result was compared with the number of shooters and the analysis time in case of applying the impedance boundary condition and considering the skin effect. Table 1 compares the total number of meshes and the computation time. In order to verify validity of proposed impedance boundary condition, compared with the computation value of stray loss for skin effect. Figure 1 shows the loss distribution of the two cases in the transformer tank. The proposed method is expected to be useful to reduce the computing time and to give the accurate results.

[1] Robert M. Del Vecchio, 'Transformer Design Principles: With Application to Core-Form Power Transformers", CRC Press, 2010. [2] S. A. Holland, G. P. O'Connell, and L. Haydock, "Calculating stray losses in power transformers using surface impedance with finite elements," IEEE Trans. Magn., vol. 28, no. 2, pp. 1355–1358, Mar. 1992.

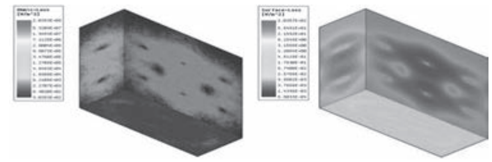

Fig. 1. (a) With Skin Effect (b) With Impedance Boundary Condition Fig 1. Stray Loss in Tank

Classification	Number of mesh	Computing time
3-D F.E.A.	2,500,622	2-hour 25 min 20 sec
Proposed method	539,833	24 min

Table 1. Comparison between 3-D F.E.A and Proposed method

AW-04. Relationship Between Drive Frequency and Load Characteristics in Bidirectional Contactless Power Transfer for Electric Vehicles.

T. Takura[1] and H. Matsuki[2]
1. Tohoku Institute of Technology, Sendai, Japan; 2. Tohoku University, Sendai, Japan

1. Introduction Recently, with the advent of vehicle-to-home (V2H), storage batteries of electric vehicles (EVs) have some roles of shifting the peak of electric power, making effective use of renewable energy, supplying the power in a disaster, and so on. In V2H, it is necessary to realize bidirectional power transfer between EVs and homes. Already, bidirectional power transfer can be realized by the plug-in method. The next generation V2H requires integration with bidirectional contactless power transfer (BCPT) technique in order to improve durability and convenience. BCPT needs to maintain the transmission performance even if the relationship between the power supply and the load is switched. By connecting the capacitor on the primary side and the secondary side symmetrically, the difference in performance depending on the direction can be reduced. In this study, SS method[1] is adopted as a symmetrical resonance circuit. However, SS method under the constant input voltage has a problem that, at light load, the current on the primary side increases to increase the voltage on the secondary side. Therefore, when the load fluctuates depending on the state of charge of the storage battery or the state of power usage at home, the strength of electromagnetic field leaking from the primary coil and the output voltage rise. In this study, we demonstrate suppressing the coil current and stabilizing the output voltage at the time of load fluctuation by changing the drive frequency that can be easily controlled from either the vehicle side or the home side. 2. Theory and experimental method The cause of the above problem in SS method is related to the reduction in the input impedance of the circuit. When driven at the resonance frequency, the input impedance approaches the winding resistance of the primary coil at light load. And, the current on the primary side becomes excessive. In order to solve this problem, changing the drive frequency is one of the effective ways. So, we confirmed the load characteristics to clear the effects of the drive frequency on the coil current and the output voltage. The specifications of the coils show Table I. The input voltage was constantly adjusted to 1 V (root mean square value), the resonance frequency was set at 86.6 kHz, and the secondary coil was located 100 mm vertically from the primary coil. 3. Results and conclusion The results of the load characteristics of the coil current and the output voltage when the drive frequency is changed to 86.6, 91.6, and 96.6 kHz are shown in Fig.1. At the resonance frequency, both the coil current on the primary side and secondary output voltage increased at light load. These results suggest the increase of leakage electromagnetic field and the risk of overvoltage at high power. On the other hand, by increasing the drive frequency, we succeeded in suppressing the coil current on the primary side and the output voltage. In particular, when transmitting at 96.6 kHz, the input voltage and the output voltage at light load are nearly equal, and the output voltage was stabilized. Therefore, the method of changing the driving frequency is extremely effective in suppressing leakage electromagnetic field and stabilizing the output voltage at the time of load fluctuation.

[1] N. Inagaki, "Theory of Image Impedance Matching for Inductively Coupled Power Transfer Systems," *IEEE Trans. Microw. Theory Tech.*, vol.62, no.4, pp.901-908, 2014

	Primary coil (air core)	Secondary coil (air core)
Outer diameter (mm)	285	290
Inner diameter (mm)	125	135
Number of windings	16	16
Frequency (kHz)	86.6	
Coupling coefficient	0.186 (air gap of 100 mm)	
Inductance (μH)	60.9	64.5
Resistance (mΩ)	50.9	55.8

TABLE I Coil specifications

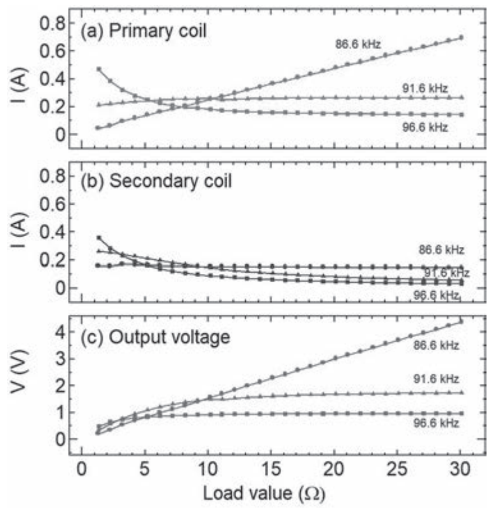

Fig. 1. Load characteristics ((a)coil current on the primary side, (b)coil current on the secondary side, and (c)output voltage)

AW-05. Insulation Materials Test and Electric Field Analysis for 330 kV IOCT used in Traction Network.

B. Bai[1], Q. Wang[1], D. Chen[1], X. He[1], T. Fu[2] and Q. Ma[2]
1. Shenyang University of Technology, Shenyang, China; 2. TBEA Shenyang Transformer Group Co. Ltd, Shenyang, China

Abstract. The insulation system of one 330kV Inverted-type Oil-immersed Current Transformer (IOCT) has broken down recently. In order to find the cause of the accident, the dielectric parameters of the IOCT insulation materials with different moisture content were tested at different temperature. Then, the electric field distribution of the IOCT insulation system was calculated using the data measured. The strongest electric field strength of main insulation was analyzed, and the extreme operating environment of IOCT was obtained. Keywords: IOCT, dielectric parameters test, moisture content, temperature, electric field strength 1. Introduction The IOCT working in the outdoor is a series device used in transmission network for measurement and protection purposes. The insulation system of one 330kV IOCT has broken down recently. This broken-down IOCT operates in high-speed rail traction network system in high latitudes, where the diurnal temperature variation is large and the air is humid. The polarization loss generated during IOCT operation will increase the temperature of the insulation system. As presented in previous research, with increase in temperature, greater dispersion of dielectric parameters of oil-paper were noticed [1,2]. With the increase of temperature, the average kinetic engergy of the conductive particles in the oil-paper samples increases, resulting in a larger dielectric loss factor [3], and the rising temperature will aggravate insulation aging [4,5]. During the IOCT operation, the moisture content of the insulation system will increase due to the insulation aging degradation and humid air invasion, and the insulation performance of oil-paper will deteriorate with the increase of moisture content [6]. The significance of water content is paramount: a humidity of 4% can shorten a transformer's operational lifetime by a factor of 40 (i.e., by 97.5%) [7]. The condition of oil-paper insulation is one of the basis factors determining the condition and life expectancy of many professional power appliances, including IOCT [8]. Therefore the temperature and moisture content dependence of the insulation materials should be taken into account in the calculation of the IOCT electric field distribution. In this paper, the relative permittivity of the IOCT insulation system with different moisture content was measured at different temperature, firstly. Then the IOCT FEM models were established according to the broken-down 330 kV IOCT. Finally, the data measured were taken into the material parameters of the models, and the electric field distribution of the IOCT was obtained at different temperature and moisture content. The strongest electric field strength of IOCT main insulation was analyzed, and the extreme operating environment of IOCT was obtained. 2. Measurement of the Dielectric Parameters The dielectric parameters (relative permittivity) of Minsk oil-immersed paper, and German semi-conductive paper with different moisture content were measured at different temperature, at 50Hz, using the Alpha-A broadband dielectric spectrometer. The results are shown in Fig. 1. More results will be shown in the full paper. 3. Calculation and Analysis The main insulation system of IOCT is consisted of Minsk oil-immersed insulation paper, German semi-conductive paper, and mineral oil. The outermost layer is oil storage tank. The innermost layer is shielding case, which is connected with ground, it is low potential. The conductive rod is connected in series in the traction system bus. Between the oil storage tank and the insulation system is the equalizing cage, which plays a role in balancing the voltage. The oil storage tank and equalizing cage are connected to the conductive rod, and they are high potential. The mineral oil filled in the gap in the oil storage tank, play insulation and heat dissipation. According to the structure of IOCT, the electric field distribution was obtained. The main results are shown in Fig. 2. Since the condition of the oil-immersed insulation paper determines the service life of the IOCT, the maximum electric field strength of each insulation layer is analyzed. More results will be shown in the full paper. 4. Conclusion The dielectric parameters of oil-immersed paper, and semi-conductive paper with different moisture content were measured at different temperature. Then, the IOCT model was established considering the temperature and moisture content dependence of the insulation materials. The influence of temperature on the electric field distribution of IOCT is more significant than that of moisture content. Although the temperature and moisture content rising is beneficial to equidistribution of the IOCT electric field, the too high temperature and moisture content will reduce the service life of insulation materials. The oil-paper damage of IOCT insulation system is generally not caused by electric breakdown but heat aging in high temperature. Therefore, the IOCT recommended operating temperature should not be higher than 383 K, and the moisture content should not be higher than 0.7%.

5. References [1] Poovamma P K, Sudhindra A, Mallikarjunappa K, et al. Evaluation of transformer insulation by frequency domain technique[C]. Solid Dielectrics, 2007. ICSD'07. IEEE International Conference on. IEEE, 2007: 681-684. [2] Ekanayake C, Gubanski S M, Graczkowski A, et al. Frequency response of oil impregnated pressboard and paper samples for estimating moisture in transformer insulation[J]. IEEE Transactions on Power Delivery, 2006, 21(3): 1309-1317. [3] Kozlovskis A, Rozenkrons J. Temperature dependence of return voltage characteristics[J]. IEEE transactions on power delivery, 1999, 14(3): 705-708. [4] Paraskevas C D, Vassiliou P, Dervos C T. Temperature dependent dielectric spectroscopy in frequency domain of high-voltage transformer oils compared to physicochemical results[J]. IEEE Transactions on Dielectrics and Electrical Insulation, 2006, 13(3): 539-546. [5] Lundgaard L E, Hansen W, Linhjell D, et al. Aging of oil-impregnated paper in power transformers[J]. IEEE Transactions on power delivery, 2004, 19(1): 230-239. [6] Ekanayake C, Gubanski S M, Mularachchi K D, et al. Diagnostic of power transformers in Sri Lanka application of dielectric spectroscopy in frequency domain[C]// Electrical Insulation Conference and Electrical Manufacturing & Coil Winding Conference, 2001. Proceedings. IEEE, 2001: 593-596. [7] Wolny S, Zdanowski M. Analysis of recovery voltage parameters of paper-oil insulation obtained from simulation investigations using the Cole-Cole model[J]. IEEE Transactions on Dielectrics and Electrical Insulation, 2009, 16(6):1676-1680. [8] Zaengl W S. Dielectric spectroscopy in time and frequency domain for HV power equipment. I. Theoretical considerations[J]. IEEE Electrical Insulation Magazine, 2003, 19(5): 5-19.

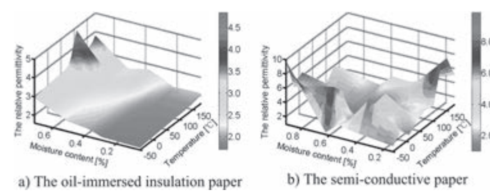

Fig. 1. The relative permittivity of insulation materials with different moisture content at different temperature

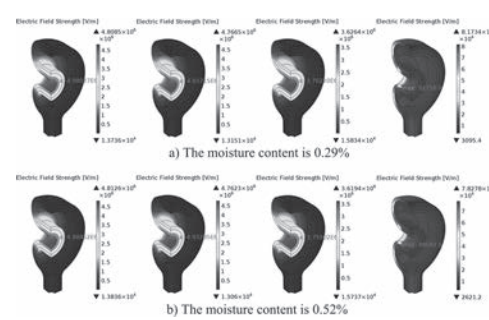

Fig. 2. The electric field distribution of insulation system with different moisture content at different temperature

AW-06. A Study on Increase of Core Loss Ratio and Inductance According to Construction of Induction Heater for Electric Vehicle.

J. Kang[1], Z. Wang[1] and K. Kim[1]
1. Dept. of Electrical Engineering, Hanbat National University, Daejeon, The Republic of Korea

In the automotive industry, PTC devices is used as a heat source for air conditioning systems. However, PTC devices have a disadvantage of high cost and heavy weight. On the other hand, Induction heater are characterized by faster heating rates and lower cost than conventional PTC devices [1]. However, in the automotive industry, research on induction heaters has not yet been conducted. At sub-zero temperatures, EV batteries have a feature of drastically decreasing capacity. The EV starts to operate without a separate preheating time at the start [2]. Therefore, the heating time is one of the most important factors for maintaining the battery temperature in winter. Therefore, induction heaters are more suitable than PTC devices as components for maintaining battery temperature in electric vehicles [3]. Important design parameters of the induction heater are the inductance and the loss. Increasing the inductance is an element to reduce the capacitance of the capacitor connected to the circuit. The price and size of the capacitor are proportional to the capacity. Therefore, reducing the capacitance is important to reduce fabrication cost and weight. The loss is largely divided into core loss from the work piece and copper loss form the coil. The ratio of core loss to total loss is very important. If the copp er loss is large, the coil generates a lot of heat, which is not good in durability and heat transfer. Therefore, it can be seen that high loss in the work piece is the most important factor for the efficiency of the induction heater. In this paper, we studied the improvement of the proportion of the core loss in the total loss and the inductance according to the structure of induction heater by using FEM. Analysis models are divided into three models in the paper. For comparison, the analysis models used the same turns of coil, wire diameter and used the Litz wire to reduce the skin effect and proximity effect of the coil at high frequency. Fig. 1 shows three proposed models. As shown in the figure, SUS430f is used as the material of the work piece. To reduce the skin effect and proximity effect of the coil, Litz wire(0.1 mm X 80reels) is used. The number of turns is 65 turns. Fig. 1-(a) shows a case where only one inner work piece and only an external coil are used. Fig.1-(b) shows a structure in which a work piece is formed inner and outer, and a coil is located therebetween. Fig. 1-(c) shows that the structure of the work piece is the same as Fig.1-(b), but the coil consists of the inner and outer parts. The three models are chosen to have the same number of turns and the size of inner work piece. To reduce the capacitance of the capacitors connected to the circuit, designing the induction heater to have large inductance is more advantageous for the manufacturing cost and weight. The capacitance for LC resonance can be estimated in advance by accurate inductance derivation. Therefore, it is one of the most important factors in design to accurately derive the value of inductance by simulation, magnetic equivalent circuit calculation, and actual measurement data. Fig. 2 shows the magnetic equivalent circuits of proposed models. As shown in the figure, the inductance value calculated by using the the magnetic equivalent circuit. Fig. 3 shows the magnetic flux distribution in the FEM simulation. As shown in Fig.3-(a), the magnetic flux leaks into the air. Thus, it can be seen that the inductance decreases due to leakage flux. On the other hand, Fig.3-(b) shows that the outer work piece blocks magnetic flux leaking into the air. Therefore, it can be seen that inductance is higher than model 1. Fig.3-(c) shows the magnetic flux leaking from outer to the air. Based on the above results, inductance analysis for three proposed models is conducted. As a result, we intend to derive a structure favorable to inductance among the three model structures. Fig. 4 shows the magnetic flux density distribution. As shown in the figure, model 2 has a small amount of magnetic flux leaking into the air and most of the flux flows through the work piece. Therefore, core loss is higher than model 1. Thus, when the number of turns and diameters of the coils are the same and the input power is the same, the copper loss of both models is the same, but the core loss ratio changes. As mentioned above, the output of the induction heater is divided into core loss and copper loss. Therefore the ratio of these losses is important to the design. If the copper loss ratio is high, the coil generates a lot of heat. However, coils are coated for insulation purposes. Therefore, when a large amount of heat is generated in the coil, the efficiency is low due to the durability of the coil and the low heat transfer rate. Therefore, FEM simulation has been carried to increase the ratio of core loss to tatal loss.

[1] Boadi, A, Tsuchida, Y, Todaka, T, and Enokizono, M, "Designing of suitable construction of high-frequency induction heating coil by using finite-element method," IEEE Trans. Magn., vol. 41, pp.4048-4050, Oct. 2005. [2] Acero, J, Carretero, C, Alonso, R and Burdio, J.M, "Quantitative Evaluation of Induction Efficiency in Domestic Induction Heating Applications", IEEE Transactions on Magnetics, vol. 45, pp.1382-1389, Apr. 2013. [3] M. Messadi, L. Hadjout, Y. Ouazir, H. Bensaidane, T. Lubin, S. Mezani, A. Rezzoug, N. Takorabet, "Eddy Current Computation in Translational Motion Conductive Plate of an Induction Heatre With Consideration of Finite Length Extremity Effects", IEEE Transac-tions on Magnetics, vol. 52, no. 3, pp. article 6300304, Mar. 2016.

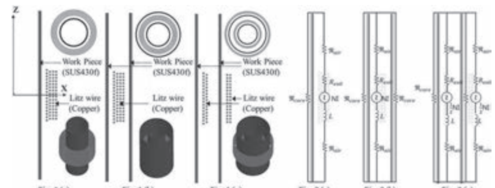

Fig. 1 (a) Fig. 1 (b) Fig. 1 (c) Fig. 2 (a) Fig. 2 (b) Fig. 2 (c)

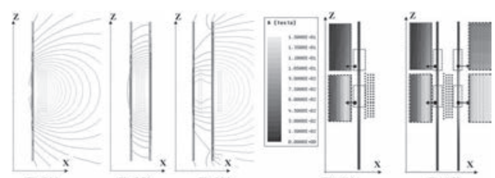

Fig. 3 (a) Fig. 3 (b) Fig. 3 (c) Fig. 4 (a) Fig. 4 (b)

AW-07. A Novel Magnetic Valve Structure for Magnetically Controlled Reactor.

M. Liu[1,2], S. Wang[2], Y. Li[1] and J. Li[2]
1. State Key Laboratory of Reliability and Intelligence of Electrical Equipment, Hebei University of Technology, Tianjin, China; 2. State Key Laboratory of Control and Simulation of Power System and Generation Equipments, Tsinghua University, Beijing, China

Abstract— Magnetically controlled reactor (MCR) is one type of saturable reactors (SR) that is based on the working principle of a magnetic magnifier, which is widely used in ultrahigh-voltage (UHV) power systems. The reactance of an MCR is changed by controlling the DC current through the control winding, to saturate the iron core by changing the thyristor conduction angle. In the traditional design, the valve structure has two different sections in MCR's magnetic valve, which leads to the increasing of the current harmonics. In the whole range of capacity adjustment (from the minimum to the rated capacity), only a small area of the reactor core is saturated, and the rest is working in an unsaturated state. The capacity of the reactor can be changed by changing the saturation degree of the magnetic path in the small section segment. Therefore, structure design of the magnetic valve is the key role for the MCR, which affects the adjustment performance directly. In this paper, a buffered structure and a mathematical model of the slope-stage saturable MCR (SSMCR) are proposed. This novel magnetic valve structure is shown in Fig. 1. There is a ramp in the middle of the valve core, which can compensate current harmonic generated by the main iron core when it is beginning to saturate. As a result, the total harmonics of the output current is reduced. The mathematical model that reveals the equivalent *B-H* characteristics of magnetic valve for the SSMCR is also presented. The deduction of the mathematical model indicates that there are two key factors affecting the total output current harmonics of the SSMCR. One is the parameter θ, which represents the slope of the ramp. The other one is the parameter *k*, which represents the ratio between the minimum length l_1 and the total length (l_1+l_2) of the magnetic valve. Meanwhile, the equivalent *B-H* curve is related to the two parameters, as shown in Fig. 2. Comparing the traditional magnetic valve structure, nearly 50% current harmonics amplitude is reduced during reactance adjustment according to the simulation. To calculate the equivalent *B-H* curve easier, the slope part of magnetic valve is divided into many stairs, as Fig.3a shown. The calculation is based on the two assumptions: (1) The magnetic flux density is uniform along the section of core. (2) Fringing and magnetic flux leakage is negligibly small. So the expression of equivalent *B-H* characteristics for the novel magnetic valves, as a function of *B*, can be written. The core is discretized into k elements (normally m=8 elements will suffice). The equivalent *B-H* characteristics is presented in Fig.2b. The simulation of SSMCR is presented that the 3rd current harmonic is maximum when t=0.1. Compared to the traditional MCR, the maximun current harmonic of SSMCR is 4.82% better than traditional MCR.

[1]. T. Wass, S. Hornfeldt and S. Valdemarsson, "Magnetic circuit for a controllable reactor," *IEEE Transactions on Magnetics*, vol. 42, no. 9, pp. 2196-2200, Sept. 2006. [2]. Baichao Chen and J. M. Kokernak, "Thyristor controlled two-stage magnetic-valve reactor for dynamic VAr-compensation in electric railway power supply systems," *APEC 2000. Fifteenth Annual IEEE Applied Power Electronics Conference and Exposition (Cat. No.00CH37058)*, New Orleans, LA, 2000, pp. 1066-1072 vol.2. [3].X. Chen, B. Chen, C. Tian, J. Yuan and Y. Liu, "Modeling and Harmonic Optimization of a Two-Stage Saturable Magnetically Controlled Reactor for an Arc Suppression Coil," *IEEE Transactions on Industrial Electronics*, vol. 59, no. 7, pp. 2824-2831, July 2012. [4].M. Nakano, K. Ishiyama and K. L. Arai, "Production of ultra thin grain oriented silicon steel sheets," *IEEE Transactions on Magnetics*, vol. 31, no. 6, pp. 3886-3888, Nov 1995. [5]. Y. Kawase *et al*., "Iron loss analysis in wound core of reactor with gap considering skin effect," *2016 19th International Conference on Electrical Machines and Systems (ICEMS)*, Chiba, 2016, pp. 1-4. [6]. C. Zhang, Y. Li, J. Li, Q. Yang and J. Zhu, "Measurement of Three-Dimensional Magnetic Properties With Feedback Control and Harmonic Compensation," *IEEE Transactions on Industrial Electronics*, vol. 64, no. 3, pp. 2476-2485, March 2017.

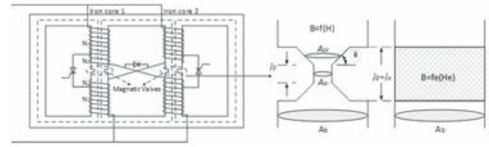

Fig. 1.

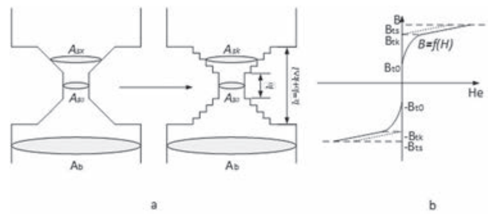

Fig. 2.

AW-08. Characteristic Analysis of a 100kW class High Frequency Transformer Using a Magnetic Equivalent Circuit Method.

H. Lee[2,1], S. Oh[2], J. Cho[2], S. Kim[2], J. So[1,3], Y. Park[1,3] and D. Kim[1,3]

1. Electrical Control Engineering, Sunchon National University, Suncheon, The Republic of Korea; 2. Korea Electronics Technology Institute, Gwanju, The Republic of Korea; 3. Greenenergy Laboratory, sunchon national university, Suncheon, The Republic of Korea

1. INTRODUCTION Considerable efforts have been made to improve the performance of power systems. In particular, the emphasis is on the power density, efficiency, and reduced passive elements in the inverter. A common method to reduce the size of passive elements is to increase the switching frequency of the inverter.[1] With the development of digital home appliances and renewable energy sources, interest in DC-based transmission and distribution has increased. Commonly used systems are based on alternating current. Therefore, the DC power generated from the renewable energy source is converted into the AC power and converted to another DC power for use in the digital device. The use of DC distribution reduces the unnecessary power conversion steps and improves the efficiency of power distribution. On the other hand, in the case of direct current distribution, the conversion from DC to a set DC voltage level is required. To achieve high efficiency in this process, the role of the DC / DC converter for distribution is important. The design of a high-frequency transformer, which is the main component of a DC / DC converter, is very important.[2] The transformer used in the current system, however, uses a high power and low frequency. In the case of a DC transmission system, such as HVDC, the transformer should use high power and high frequency, but there have been few studies in this area. Therefore, this study examined the design of the high frequency transformer. When a high frequency is used in a transformer, the magnetic flux is small. hence, the magnetic flux density, which is the magnetic flux passing through the same unit area, becomes small, which means that the size of the passive element can be reduced. When designing the transformer covered in this paper, it is necessary to consider the frequency components differently from a general transformer design. As a design method, the magnetic equivalent circuit method was used to simplify the design, and finite element method (FEM) analysis and comparative analysis were conducted for validation. The FEM analysis tool in MAXWELL was used. 2. MAIN SUBJECT 2.1 Structure and specification of transformer Fig. 1 (a), (b) presents the shape, specification and magnetic flux density of the 100kVA high frequency transformer model discussed in this paper. The shape of the transformer is a core type transformer: Across is the width of the core; Height is the height of the core; Lamination is the lamination thickness; Path is leg of the transformer; and is the amination length times the path is the cross-sectional area. 2.2 Magnetic equivalent circuit of the transformer The proposed method magnetic equivalent circuit provides the convenience of an analysis of the transformer. Fig. 2 (c), (d) presents the magnetic equivalent circuit. The reluctance, R_m, is caused by the resistance component in the relative magnetic field lines in the magnetic circuit, and corresponds to the electrical resistance in the electrical circuit. $R_m = F/\Phi = MPL/\mu_r\mu_0 A_c$ [A/Wb] (1) where F is the magnetomotive force; Φ is the magnetic flux; A_c is the effective cross section; μ_r is the relative permeability; μ_0 is the vacuum permeability; and MPL is the magnetic field pass length. The magnetic flux is bundle of magnetic lines, corresponding to the current in an electric circuit. $\Phi_m = V_1/4.44fN_1 = F/R_m$ [Wb] (2) f is the frequency; N_1 is the number of turns in primary; and V_1 is the input voltage. The magnetomotive force is a force for generating a magnetic field, and corresponds to the electromotive force in an electric circuit. $F = NI = \Phi_m R_m$ [AT] (3) The excitation current, I_0, at no-load of the transformer can be calculated by considering Φ_m in terms of the frequency in eq. 3. The magnetic flux density, B_m, will determine the design of the transformer material information in a magnetic flux passing through per unit area to be designed so that the core is not saturated. $B_m = \Phi_m/A_c$ [$T, Wb/m^2$] (4) The Composite magnetic reluctance, R_{mt}, $R_{mt} = 2*(R_{m1}+R_{m2})$ (5) 2.3 Analysis Results B_m and μ_r are determined by the core material properties; Φ_m is calculated using eq. 2; and R_m is calculated using eq. 1. Considering the frequency, I_0 can be derived from eq. 3. Φ_m and B_m can be calculated considering the frequency. Table 1 shows the comparison results of FEM and magnetic equivalent circuit. The exciting current and the error rate calculated by the magnetic equivalent circuit method in (c) was 3.5%. Fig. 1 (b) confirms that local saturation occurred only at the inner corner, which is the shortest path through which the flux of the transformer could flow, and the rest of the iron core was operated with a flux density < 0.4 [T]. This confirmed that it had been designed properly. 3. CONCLUSION In this study, a magnetic circuit equivalent method was applied to calculate the transformer characteristics more accurately considering the frequency. The validity of the proposed magnetic equivalent circuit method was confirmed by the FEM and comparative analysis. The proposed magnetic circuit equivalent method is a useful method for interpreting the fundamental characteristics of high-frequency transformers more efficiently. Acknowledgements This work was supported by NRF-2017R1A2B1009684

[1] COLONEL WM T. MCLYMAN, "TRANSFORMER AND INDUCTOR DESIGN HANDBOOK", CRC PRESS, 2011 [2] Su-Young Kim, Yoon-Seung Han, Ju-Hee Cho "Design and Experiment of 100kVA class High Frequency Transformer For DC/DC Converter", The Korean Institute of Electrical Engineers Vol.2015, No. 10, 2015

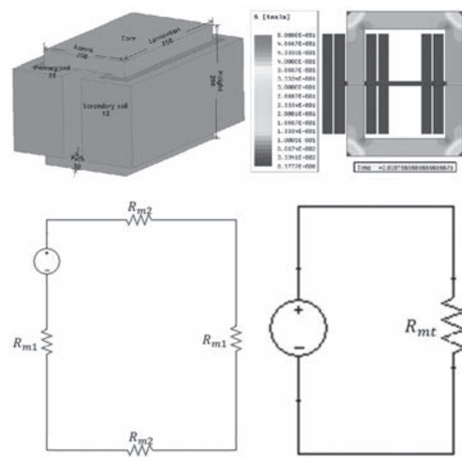

Fig. 1. Design model : (a) Shape, specifications, (b) Magnetic flux density Synthesis of the magnetic reluctance equivalent circuit : (c) First equivalent circuit, (d) Simplified equivalent circuit end

	units	Magnetic equivalent circuit	FEM
V_m	[V]	1500	1500
f	[Hz]	3000	3000
Φ_m	[Wb]	0.003128128	-
B_m	[$T, Wb/m^2$]	0.325	0.417
μ_r		3771.982	-
MPL	[m]	0.78	-
R_m	[AT/Wb]	15680	-
I_0	[A]	1.4346	1.3854
F	[AT]	51.6456	-
Φ_m	[Wb]	0.003293724	-
B_m	[$T, Wb/m^2$]	0.31368	-

Table 1: Magnetic equivalent circuit method and FEM analysis results

AW-09. Simulation and Impact Analysis of Remanent Flux on Power Transformer Inrush Current.

W. Ge[1] and Y. Wang[2]
1. School of Control and Mechanical Engineering, Tianjin Chengjian University, Tianjin, China; 2. State Key Lab of Reliability and Intelligence of Electrical Equipment, Hebei University of Technology, Tianjin, China

The electromagnetic characteristic of power transformers is a dynamic phenomenon. It is characterized by changes in current and magnetic flux state over time. Mathematically, the dynamic process of power transformers can be described by nonlinear differential equations. Analysis of electromagnetic equipment performance and accurate calculation of the magnetic field must consider the core nonlinear magnetic properties. By adding Jiles-Atherton (JA) model as shown in Fig. 1, the characteristics of transformer surge, including magnetic nonlinearity under transient conditions are simulated. In the final stage, the magnetizing inrush current is identified by the various characteristics of the fundamental wave amplitude, and the corresponding fundamental wave amplitude curves under different remanent fluxes are analyzed. To determine the effect of remanent flux on the inrush current, the single-phase and three-phase transformer no-load closing transient process is simulated. This paper has practical significance to provide an adequate theoretical basis for the identification and suppression of the inrush current. By reducing the remanent flux, the performance of the transformer, and furthermore the quality of the power system can be improved.

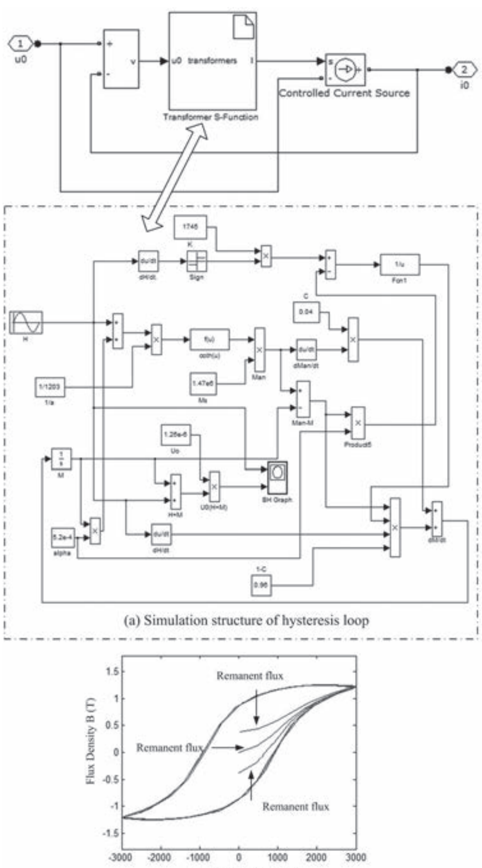

(a) Simulation structure of hysteresis loop

(b) Hysteresis loops under different initial remanent fluxes

AW-10. A Study on the Loss Analysis according to the Switching State of Single-Phase 3kW Transformerless Solar Inverter.

P. Je-Seok[1,2], P. Young-Un[1,2] and D. Kim[1,2]
1. Electrical Control Engineering, Sunchon National University, Suncheon, The Republic of Korea; 2. Sunchon National University, Greenenergy Laboratory, Sunchon, The Republic of Korea

Abstract - In this paper, we analyze the loss of a device depending on the switching state of a 3kW solar inverter circuit. IGBT and diode conduction losses and switching losses use PSIM's thermal module function and inductor loss analysis uses PSIM's MagCoupler function for more accurate analysis. 1. Introduction Power semiconductor losses take a lot of time to calculate using formulas. To solve these problems, various simulation tools such as PSIM, Jmag, and MATLAB have been developed and can easily and quickly analyze the loss using these simulation tools [1]. In this paper, a method for analyzing losses of power semiconductor devices and losses of diodes and inductors according to switching state of 3kW solar inverter circuit was studied. Power semiconductors and diodes are modeled by PSIM's Device Database Editor function using the information provided in the data sheet of the actual device to analyze the loss due to the switching state of the inverter using the thermal module function of the PSIM. The inductor is modeled as Jmag and combined with Psim to analyze losses[2][3]. 2. Analysis of solar inverter loss 2.1 inverter circuit Table 1 shows the specifications of the transformer type 3kW solar inverter circuit. Figure 1 shows the circuit constructed by PSIM according to this specification. It consists of Boost converter part and radio bridge type inverter part. The Boost converter part boosts the voltage input to the inverter and adjusts it to the inverter operating voltage range. The output voltage is always greater than the input voltage and when the switch is on, the diodes are reversed and disconnected from the output stage. The input supplies energy through the inductor, and when the switch is off, the output is supplied with energy through the inductor. The output filter capacitors are also very large to maintain a constant output voltage. The bridge type inverter consists of four IGBTs and controls the switch by PWM method [1]. 2.2 Inverter Loss Formula Inverter losses occur primarily in power semiconductor devices. The loss of the power semiconductor device IGBT is dispersed by conduction loss and switching loss. When the semiconductor switch element is OFF, current does not flow through the switch in the blocking area, so there is no loss of the element. When the switch is turned on, current flows through the switching element, and a voltage is applied to both ends of the element to cause a loss. The loss of the power semiconductor switching device is the sum of the conduction loss and the switching loss as shown in Eq. (1) [2] [3]. $P_{IGBT(loss)}=P_{c(IGBT)}+P_{sw(IGBT)}=P_{c(IGBT)}+P_{sw-on(IGBT)}+P_{sw-off(IGBT)}$ (1) $P_{c(IGBT)}$: Conduction Loss of IGBT $P_{sw(IGBT)}$: Switching Loss of IGBT The conduction loss of the IGBT is a loss occurring in the saturation region when the IGBT is ON, and is the value obtained by multiplying the current flowing through the switching element by the voltage across the device. $P_{c(IGBT)}=V_{ce(sat)}\times I_c$ (2) $V_{ce(sat)}$: Collector-Emitter Saturation Voltage I_c : Collector Current The switching loss of the IGBT is the loss caused by passing through the active region when the IGBT is turned on or off. It is the product of the current flowing through the switching element and the voltage across the IGBT. $P_{sw(IGBT)}=(E_{on}+E_{off})\times f_{sw}\times V_{cc}/V_{cc-datasheet}=1/T\int^{tr}V_{ce}(t)\times I_c(t)dt+1/T\int^{tf}V_{ce}(t)\times I_c(t)dt$ (3) E_{on} : Turn-on Energy Loss E_{off} : Turn-off Energy Loss f_{sw} : Switching Frequency V_{cc} : DC Input Voltage $V_{cc-datasheet}$: DC Input Voltage on Datasheet The loss of the diode is the sum of the conduction loss and the switching loss, and most of the switching loss is the turn-off loss. $P_{Diode}=P_{c(Diode)}+P_{sw(Diode)}+P_{c(Diode)}+P_{sw-off(Diode)}$ (4) $P_{c(Diode)}$: Conduction Loss of Diode $P_{sw(Diode)}$: Switching Loss of Diode The conduction loss of a diode is given by equation (5) as the product of the forward voltage drop of the diode and the current. $P_{c(Diode)}=V_F\times I_F$ (5) V_F : Foward Voltage Drop of Diode I_F : Foward Current of Diode The turn-off switching loss of the diode is determined by the reverse recovery current and the reverse recovery time of the diode and is given by Equation (6). $P_{rr(Diode)}=E_{rr}\times f_{sw}\times V_r/V_{r(datasheet)}=(1/4)\times Q_{rr}\times V_{rr}\times f_{sw}=(1/8)\times t_{rr}\times I_{rr}\times V_r\times f_{sw}$ (6) E_{rr} : Reverse Recovery Energy Loss V_r : Reverse Blocking Voltage $V_{r(datasheet)}$: Reverse Blocking Voltage on Datasheet Q_{rr} : Reverse Recovery Charge t_{rr} : Reverse Recovery Time I_{rr} : Reverse Recovery Current The loss of the Inductor is the sum of the iron loss and the copper loss, as shown in Equation (7). $Pt=P_c\times P_{cu}$ (7) P_c : Iron Loss P^{cu} : Copper Loss 2.3 IGBT and diode loss analysis The Thermal Module is a function that can simulate the loss of each device by inputting the value informed from data sheet of Diode, IGBT, MOSFET, Inductor etc through PSIM's Device Database Editor [5]. Figure 1 shows the circuit diagram of PSIM's thermal module to simulate the loss of the solar inverter. Figure 1 (d) is a thermal equivalent circuit with added thermal resistance to estimate the IGBT loss. 2.4 Modeling and Co-Analysis of Inductor Table 2 shows the simulation specifications. Figure 4 shows the inverter co-analysis results. 3. conclusion Through the PSIM and JMAG, the inductor design and the loss analysis for the solar inverter were obtained. Based on the results of this analysis, it is expected that it will be very helpful to design the inductor that can predict the loss and reduce the loss. Acknowledgements This work was supported by KEPCO Research Institute grant funded by Korea Electric Power Corporation(R16DA11).

[1] Yam P.Siwakoti, Frede Blaabjerg, Common-Ground-Type Transformerless Inverters for Single-Phase Solar Photovoltaic Systems, IEEE TRANSACTIONS INDUSTRIAL ELECTRONICS, VOL. 65, NO.3, MARCH 2018 [2] Marcelo C. Cavalcanti, A Feasible Loss Model for IGBT in Soft-Switching Inverters, Power Electronics Specialist Conference, 2003. PESC '03. 2003 IEEE 34th Annual Volume 4, 15-19 June 2003 Page(s):1845 - 1850 vol.4 [3] Powersim Instrument, PSIM User's Guide, 2017

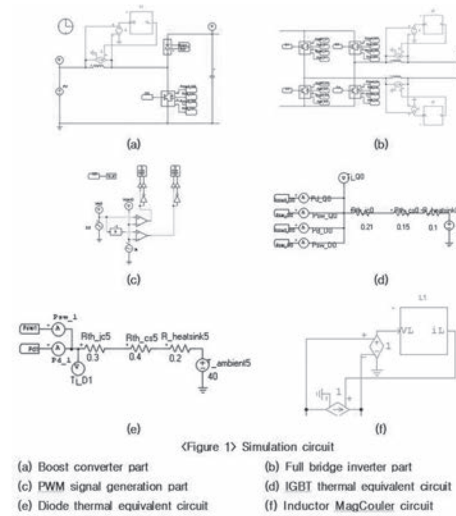

Fig. 1. Simulation circuit

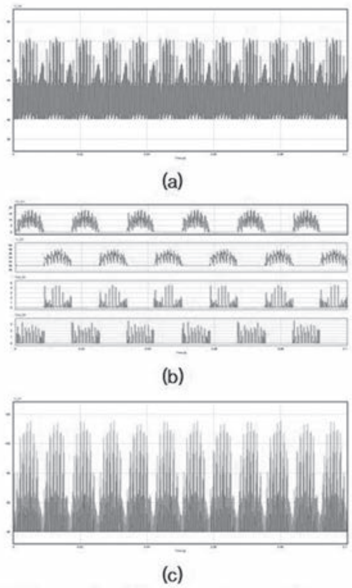

〈Figure 2〉 Loss Simulation Results of IGBT and Diode
(a) IGBT of Boost converter
(b) IGBT of Full bridge inverter
(c) Diode of Boost converter

Fig. 2. Loss Simulation Results of IGBT and Diode

AW-11. Design and Fabrication of Rotary Magnetostrictvie Energy Harvester for Knee-joint wearable applications.

B. Yan[1], J. Hong[1] and C. Zhang[2]
1. Guangdong University of Technology, Guangzhou, China; 2. Harbin Institute of Technology, Harbin, China

Energy generator used to harvesting the rotation of human knee-joint has got more attention, which has good application in self-powered design of wearable electronic devices. Consider the characteristics of human knee joint rotation, its rotation always appear as low frequency (1-2Hz), small angle deflection (0-90°) and huge drive torque (>50Nm) [1-2]. Traditional hybrid structure of electric machine and gearbox are always accompanied by high power density, but the size and mass are larger for its wearable. Harvesters based on piezoelectric ceramics exist smaller size and mass, but with lower output electricity. Magnetostrictive materials, such as TbDyFe alloy, shows relatively high power density and efficiency, also can be used to design of magnetostrictive/electromagnetic hybrid structure, which can help to improve the power density and output electricity. This paper presented an interest rotary magnetostrictive energy harvester, which is introduced in Fig.1. The harvester has two parts: stator and rotor. Six flat Terfenol-D rods surround by the picked up coils respective, are set in the stator uniformly. Rotary permanent magnet array are fixed in the rotor. The harvester rotates like as a stepper motor, which has rotary electromagnetic power generating effect and impacted magnetostrictive power generating effect in its rotation. Magnetic field and electromagnetic force in presented harvester are analyzed, rotary permanent magnet array and principal design parameters of harvester are optimally optimized. Then, the respectively harvesting effect of Terfenol-D rod induced by single ΔH and $\Delta\sigma$ are calculated, and its predicted hybrid harvesting effect is concluded. Lastly, a prototype of harvester is fabricated and tested. The size of proposed structure is control as 77cm^3, and its mass is about 0.21kg. The rotational harvester exists larger power density at 1-2Hz low frequency situation, can be generated up to 7.6V peak value voltage. Also more interest results will be introduced in our recently papers.

[1] A. Cervera, Z. Rubinshtein, M. Gad, R. Riemer, M. M. Peretz. Biomechanical Energy Harvesting System With Optimal Cost-of-Harvesting Tracking Algorithm. *Journal of Emerging and Selected Topics in Power Electronics*, 2016, 4(1): 293-302. [2] D. Wang, K. Lee, J. Ji. A Passive Gait-Based Weight-Support Lower Extremity Exoskeleton With Compliant Joints. *IEEE Transactions on Robotics*, 2016, 32(4): 933-942.

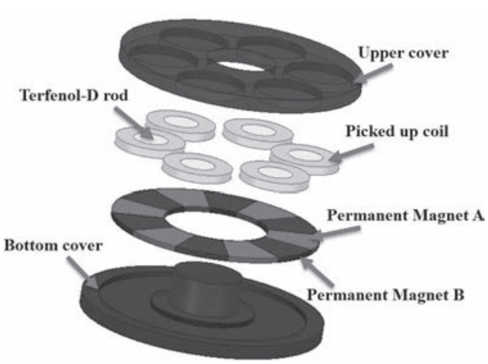

Fig. 1. Mainly structure of rotary magnetostrictive energy harvester

TUESDAY AFTERNOON, 24 APRIL 2018 ORCHID I, 2:00 TO 5:00

Session BA

SYMPOSIUM ON SYNCHROTRON X-RAY AND NEUTRON SCIENCES FOR MAGNETISM

Chengjun Sun, Chair
Argonne National Laboratory, Argonne, IL, United States

INVITED PAPERS

2:00

BA-01. New opportunities for characterizing magnetic systems using next-generation synchrotron radiation sources.

J. Lang[1]
1. X-Ray Science Division, Argonne National Laboratory, Argonne, IL, United States

The world-wide proliferation of synchrotron x-ray radiation light sources over the past 30 years has led to their routine application in investigations of the magnetic behavior of a wide-range of technologically relevant devices. The intense highly collimated x-ray beams with tunable polarization properties that these sources provide have enabled the development of various x-ray spectroscopic and scattering techniques, such as X-ray Magnetic Circular/Linear Dichroism (XMCD/XMLD) and X-ray Resonant Magnetic Scattering (XRMS), which have been applied to obtain key structural, electronic, and magnetic information from a variety of systems. Near core-shell resonances, such x-ray measurements probe particular electronic orbitals within individual atomic species, thereby offering unique insights into the multiple interactions present in multi-constituent materials. The current so-called "third-generation" synchrotron sources, such as the Advanced Photon Source in Chicago, USA, provide highly stable x-ray beams that can be focused to probe magnetic structures from a few hundred nanometers to microns. The evolution of modern technology, however, has led towards more complex hierarchical magnetic systems at much smaller length scales. Further, many correlated electron systems possess magnetic textures that order on the nanometer length scales. Over the next decade, many of the world's synchrotron sources will undergo significant upgrades and entirely new sources will be built as "fourth-generation" light sources in order to address these challenges. These machines will leverage new accelerator technologies to dramatically decrease the size of the electron bunches that produce the x-rays, which in turn will greatly increase the brightness of the available x-ray beams by factors of 50 or more. This will enable focusing of the full x-ray intensity to nanometer dimensions, and also greatly enhance the degree coherence of the x-ray beam. These vast improvements in photon beam properties, combined with rapid, ongoing advances in x-ray optics, insertion devices, and detectors, will provide transformative capabilities for utilizing x-rays to understand magnetic systems at unprecedented spatiotemporal time and length scales. Furthermore, it will enable studies of magnetism in the most extreme conditions such as high pressure, temperature, and applied fields. This talk will present examples of how synchrotron radiation light sources are currently applied understand magnetic systems, and the transformative capabilities that will be enabled by the new light sources on the horizon.

2:30

BA-02. Ultrafast and Very Small: Discover Nanoscale Magnetism With Picosecond Time Resolution Using X-Rays.

H. Ohldag[1]
1. Stanford Synchrotron Radiation Lightsource, SLAC National Accelerator Laboratory, Menlo Park, CA, United States

Today's magnetic device technology is based on complex magnetic alloys or multilayers that are patterned at the nanoscale and operate at gigahertz frequencies. To better understand the behavior of such devices one needs an experimental approach that is capable of detecting magnetization with nanometer and picosecond sensitivity. In addition, since devices contain different magnetic elements, a technique is needed that provides element-specific information about not only ferromagnetic but antiferromagnetic materials as well. Synchrotron based X-ray microscopy provides exactly these capabilities because a synchrotron produces tunable and fully polarized X-rays with energies between several tens of electron volts up to tens of kiloelectron volts. The interaction of tunable X-rays with matter is element-specific, allowing us to separately address different elements in a device. The polarization dependence or dichroism of the X-ray interaction provides a path to measure a ferromagnetic moment and its orientation or determine the orientation of the spin axis in an antiferromagnet. The wavelength of X-rays is on the order of nanometers, which enables microscopy with nanometer spatial resolution. And finally, a synchrotron is a pulsed X-ray source, with a pulse length of tens of picoseconds, which enables us to study magnetization dynamics with a time resolution given by the X-ray pulse length in a pump-probe fashion. For this purpose we designed and employed a dedicated scanning x-ray microscope at SSRL [3]. Over the past few years this microscope has been used to address spin transport across FM/NM interfaces [1], spin current induced dynamics [2,5] as well as controlling magnetic order in complex oxides with electric voltages [4]. In this presentation several examples will be given of how synchrotron based x-ray spectroscopy and microscopy can be used to directly address issues in magnetism research on fundamental length scales that are otherwise only accessible via indirect measurements. One important area for example is the field of interface magnetism. Complex magnetic multilayers have become more and more important over the past decade and are now an integral part of essentially every magnetic device. Often, we use structural characterization tools like high energy x-ray diffraction or transmission electron microscopy to quantify the quality of such interfaces. However, these methods only tell half of the story in the case of magnetic interfaces, since structural and magnetic interfaces can have a significantly different profile. To illustrate this issue figure 1 is shows magnetic domain images obtained using a Photoemission Electron Microscope at the Co and Cu L-resonance in a Cu(1nm)/Co(3nm) bilayer grown on a NiO(100) single crystal. The image of the left side shows rather large black and white areas representing magnetic domains in the Co layer. Corresponding Co soft x-ray absorption and circular dichroism spectra obtained from a single domains are shown in the lower half of the figure. These spectra can be used e.g. to quantitatively determine the number of holes in the 3d band as well as the spin and orbital momentum of Co in this sample. In this case, however, we would like to focus on the element specificity and the sensitivity to small magnetic moments of this technique. The panel on the right side shows an XMCD image acquired at the Cu absorption resonance at the same location. Surprisingly the Cu layer exhibits a net magnetization leading to an XMCD effect and the magnetization mimics the domain structure of the Co layer underneath. In this case the magnetization originates from Cu sites at the interface to the Co layer, that exhibit a small proximity moment of the order of 0.01 Bohr Magneton aligned with the Co layer. This means that the spontaneous magnetization does not abruptly end when moving across the interface from a ferromagnet into a non-magnet, but that the transition is rather gradual and may depend on the actual hybridization between ferromagnet and non-magnet at the interface. In any case the structural and magnetic profile of such an interface is different, which has implications for a wide area of effects, e.g. spin transport across interfaces [1]. Another area in which x-ray microscopy has made a significant impact is the field of magnetization dynamics, e.g. spin transfer torque oscillators. Figure 2 shows an image of a localized spin wave – or spin wave bullet – observed in a Co/Ni multilayer with perpendicular magnetic anisotropy. A spin polarized current is injected into the Co/Ni multilayer from an underlying FeNi film, which leads to localized precession of the magnetization in the Co/Ni layer that is restricted to the area of the current injection, roughly 150 nm in diameter. The magnetization precession leads happens on a cone-like orbit, which causes the projection of the magnetization along the surface normal to be reduced. This reduction of the projection can be detected in an x-ray microscope and leads to the contrast shown in the figure. The size of the contrast suggests that the opening angle of the precession cone is of the order of 30 degree. Here the fact that x-rays are able to penetrate different materials and one can chose to address the dynamic behavior of a particular layer via element sensitivity, allows us to study the dynamics of buried layer in a "real" multilayer structure. While transport measurements on these samples suggested the existence of a spin wave bullet, only the microscopic observation can conclusively confirm this behavior.

[1] R. Kukreja et al. Physical Review Letters 115 (9), 096601 (2015) [2] D. Backes et al. Physical Review Letters 115 (12), 127205 (2015) [3] S. Bonetti et al. Review of Scientific Instruments 86 (9), 093703 (2015) [4] B. K. Jang et al. Nature Physics 13 (2), 189-196 (2015) [5] S. Bonetti et al. Nature Communications 6 (2015)

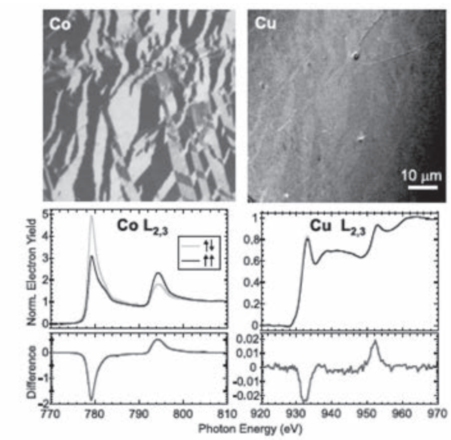

Fig. 1.

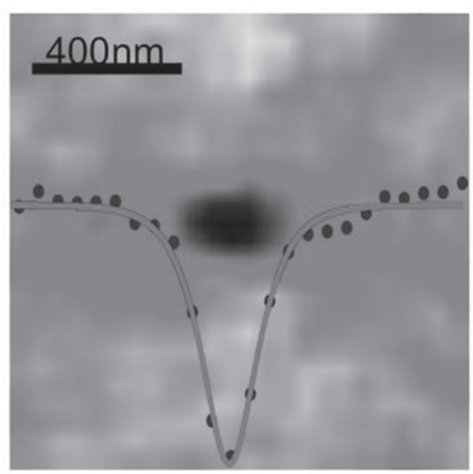

Fig. 2.

3:00

BA-03. Neutron Scattering on Magnetic Thin Films.

Y. Liu[1]
1. Neutron Sciences Directorate, Oak Ridge National Laboratory, Oak Ridge, TN, United States

Neutron scattering has played decisive roles in elucidating magnetic structures of crystalline materials in the last several decades, thanks to the relatively weak nature of the neutron scattering from materials and well-understood neutron-material interactions [1]. Historically, neutron scattering has dealt mostly with bulk magnetic materials, and magnetic thin films pose challenges because of their inherently small scattering volumes. With the advance in neutron sources and instrumentations, neutron scattering is more and more employed on magnetic thin film researches. Particularly, thanks to the increased flux and the reduced background, the critical mass of films has been pushed down to be less than 0.05 mg to use neutron diffraction to investigate atomic scale spin orders of functional antiferromagnetic oxide films. At the same time, polarized neutron reflectometry (PNR) has been widely used to determine the depth profile of the vector magnetization structure in magnetic heterostructures, especially at interfaces between dissimilar materials [2]. Interfaces can play a critical role in determining the properties of magnetic heterostructures, e.g. compositionally intermixed interfaces can enhance the energy product of ultra-strong exchange-spring permanent magnets, which consist of a high-magnetization soft phase and a high-anisotropy hard phase. Nanoscale variation of the micromagnetic properties at the interface is believed to be the underlying mechanism, but direct probing in a quantitative manner remains a challenge. We have determined spatially resolved profiles of micromagnetic properties via complementary studies of polarized neutron reflectometry and micromagnetic simulations [2], which we have coined the name "micromagnetic reflectometry" (Fig. 1). In comparison to the profiles estimated from the mixture model, the exchange stiffness is higher but the magnetic anisotropy is lower at the interface. Overall, the interfacial intermixing gives rise to new phases that efficiently couple the soft and hard layers but at the cost of the total magnetization. This result could not have been predicted from the nominal compositions. There are some important technical details in the data analysis. Particularly, significant spin-flip scattering was observed in large magnetic fields in the PNR experiments. The large applied magnetic field lifts the degeneracy of the vacuum energy states for spin-up and spin-down neutrons, i.e., the so-called Zeeman effect, which needs to be taken into account for PNR data analysis [3, 4]. Work at ORNL's Spallation Neutron Source was supported by the Scientific User Facilities Division, Office of Basic Energy Sciences, U.S. Department of Energy (DOE).

[1] Carpenter, John M., and C-K. Loong. *Elements of slow-neutron scattering*. Cambridge University Press, 2015. [2] Liu, Yaohua, and Xianglin Ke. "Interfacial magnetism in complex oxide heterostructures probed by neutrons and x-rays." *Journal of Physics: Condensed Matter* 27, 373003 (2015). [3] Liu, Yaohua, S. G. E. Te Velthuis, J. S. Jiang, Y. Choi, S. D. Bader, A. A. Parizzi, H. Ambaye, and V. Lauter. "Magnetic structure in Fe/Sm-Co exchange spring bilayers with intermixed interfaces." *Physical Review B* 83, 174418 (2011). [4] Maranville, Brian B., Brian J. Kirby, Alexander J. Grutter, Paul A. Kienzle, Charles F. Majkrzak, Yaohua Liu, and Cindi L. Dennis. "Measurement and modeling of polarized specular neutron reflectivity in large magnetic fields." *Journal of applied crystallography* 49, no. 4 (2016): 1121-1129.

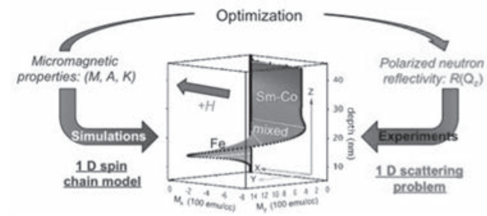

Fig. 1. Micromagnetic reflectometry determines the depth profiles of intrinsic magnetic properties of compositionally graded magnetic heterostructures via complementary studies of polarized neutron reflectometry and micromagnetic simulations.

3:30

BA-04. Polarized Neutron Reflectometry of Epitaxial Fe[0.25 + x] Pt[0.75 – x] Layers.

G.J. Mankey[1], G.L. Causer[2,3], D.L. Cortie[2,3], X. Wang[2], H. Zhu[3], M. Ionescu[3] and F. Klose[4]
1. Physics and Astronomy, University of Alabama, Tuscaloosa, AL, United States; 2. Institute for Superconducting and Electronic Materials, University of Wollongong, Lucas Heights, NSW, Australia; 3. Australian Nuclear Science and Technology Organisation, Lucas Heights, NSW, Australia; 4. Guangdong Technion-Israel Institute of Technology, Shantou, China

Abstract: Epitaxial Fe[0.25 + x]Pt[0.75 – x] layers can be either antiferromagnetic (AF) or ferromagnetic (FM) depending on the degree of chemical ordering controlled by the deposition temperature. Our neutron diffraction studies were the first to study AF phase transitions in these thin films [1] and we have also shown using PNR that a mixed AF-FM film is exchange biased with itself [2]. In AF-FM exchange-biased superlattices with a modulated chemical order parameter, PNR shows the magnetization can be modulated through the film thickness with no composition modulations [3]. Our recent results reveal that He+ ion bombardment and annealing can be applied toward controlling magnetic phases in epitaxial Fe[0.25]Pt[0.75] layers [4]. Introduction: The magnetic ordering of Fe[0.25 + x]Pt[0.75 – x] is a sensitive function of composition, crystal structure, and temperature. Chemically disordered epitaxial films with $-0.05 < x < 0.05$ are ferromagnetic with Curie temperatures of approximately 380 K. Epitaxial films in this range of composition prepared in the L12 crystal structure can exhibit two types of antiferromagnetism with ordering vectors along the (110) or (100) directions and Néel temperatures of approximately 160 K and 100 K, respectively. Nanostructured composite epitaxial films of ordered and disordered Fe[0.25 + x]Pt[0.75 – x] can be field-cooled through the Néel temperature resulting in chemically homogeneous material that exhibits a unidirectional anisotropy or exchange bias. In this talk, fabricating composite films by ion bombardment as well as characterizing their nanoscale magnetic structures will be discussed. Experimental: Epitaxial layers of chemically ordered single-crystalline material were deposited onto (001)-oriented MgO substrates by magnetron sputtering from a Fe[0.25]Pt[0.75] target. The film thickness was estimated from the sputtering rate and surface epitaxy was monitored by in-situ RHEED measurements. To determine the order parameter of the material, the intensity ratio between fundamental and superstructure x-ray diffraction peaks was measured. Magnetisation vs. field behaviours were measured using a Quantum Design PPMS vibrating sample magnetometer. Low temperature hysteresis curves were acquired after 10 kOe field-cooling from room temperature to establish a preferential exchange bias direction. Results and Discussion: Polarized neutron reflectometry (PNR) is used to aid in depth-profiling the magnetic modulation present in chemically continuous Fe[0.25]Pt[0.75] layers. By conducting a reflectivity measurement using two antiparallel neutron polarization states and taking the difference, the magnetization profile as a function of depth is determined. PNR data collection was performed on the PLATYPUS time-of-flight neutron reflectometer at ANSTO. All PNR measurements were performed in 10 kOe after field-cooling from 300 K in a 10 kOe external magnetic field. He+ ion irradiation was used to modify the chemical ordering in the film, and thus change the magnetic depth profile. Sample irradiation was performed on the SIRIUS tandem accelerator at ANSTO using 15 keV He+ ions, resulting in a FM (near-surface irradiated) / AFM (non-irradiated) FePt3 bilayer structure depicted in FIG. 1. Hysteresis loops of as grown and films irradiated with 15 keV He+ ions reveal changes in the magnetic properties of Fe[0.25]Pt[0.75] layers. The ion bombardment caused chemical disorder between Fe and Pt atoms and a subsequent increase in the 10 K magnetization is observed. Polarized neutron reflectivity was applied to probe the depth dependent magnetization and the data was analyzed to determine structures of films subjected to different ion bombardment and annealing conditions. PNR determines the depth of the disordered region of the irradiated films. These results were applied to further optimize the ion irradiation and annealing to produce tailored structures. A comprehensive model describing how the magnetic behavior is changed by varying degrees of local chemical disorder will be discussed. Acknowledgement: G.J. Mankey acknowledges funding from Bell South and shared equipment at the Center for Materials for Information Technology. Research was supported by the Australian Nuclear Science and Technology Organisation (ANSTO), the Australian Institute of Nuclear Science and Engineering (AINSE) Post-graduate Research Award (PGRA) and the Australian Government Research Training Program (AGRTP).

1. S. Maat, O. Hellwig, G. Zeltzer, E. E. Fullerton, G. J. Mankey, M. L. Crow and J. L. Robertson, Antiferromagnetic structure of FePt3 films studied by neutron scattering, Phys. Rev. B 63, 134426 (2001). 2. Z. Lu, M. J. Walock, P. R. LeClair, G. J. Mankey, P. Mani, D. Lott, F. Klose, H. Ambaye, V. Lauter, M. Wolff, A. Schreyer, M. Christen and B. C. Sales, Structural and magnetic properties of epitaxial Fe25Pt75. J. Vac. Sci. Technol. A 27, 770 (2009). 3. T. Saerbeck, H. Zhu, D. Lott, H. Lee, P. R. LeClair, G. J. Mankey, A. P. J. Stampfl and F. Klose, Tailoring exchange bias through chemical order in epitaxial FePt3 films, J. Appl. Phys. 114, 013901 (2013). 4. Grace L. Causer, David L. Cortie, Hanliang Zhu, Mihail Ionescu, Gary J. Mankey, Xiaolin Wang, Frank Klose, Towards 3D-Machined Ferromagnetic Nano-Elements: Direct Measurement of the Intrinsic Sharpness of Magnetic Interfaces Formed by Ion Beams, submitted (2018).

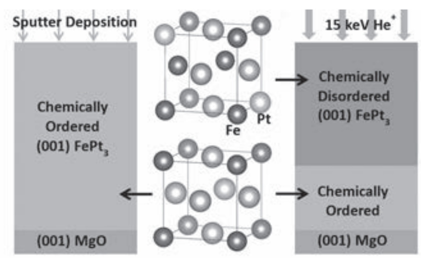

Fig. 1. Structures of as-deposited and ion irradiated films extracted from PNR measurements.

4:00

BA-05. Characterization of Magnetic Nanostructures with Polarized Neutron and Resonant X-ray scattering.

S. Sinha[1]
1. Physics, University of California San Diego, La Jolla, CA, United States

The basic physics of many magnetic nanostructures used for applications in magnetic information storage, read heads, etc. relates to the behavior of the spins at the interfaces. Measurement of the spatial distribution of magnetization at buried interfaces is often conveniently carried out via techniques such as polarized neutron reflectivity or resonant x-ray magnetic reflectivity and off-specular scattering. One example of a system where interface spins play a key role is an exchange-biased bilayer film, where the hysteresis loop of a ferromagnetic film in juxtaposition to an antiferromagnet is shifted, and this was assumed to be due to "frozen spins" in the antiferromagnet at the interface [1]. Neutron and X-Ray reflectivity have enabled the identification of these frozen spins and of the role they play in exchange bias. Examples will be given of two such systems, namely a Co film deposited on a film of antiferromagnetic FeF2 grown epitaxially on a MgF2 substrate [2]; and a permalloy film grown on a CoO substrate, where the interface interactions and thus the mechanism for exchange bias, are somewhat different [3]. Another example of magnetic nanostructures studied in thin films which have been studied with resonant magnetic X-ray scattering at synchrotrons are the topological entities known as skyrmions. While neutron scattering has played a major role in the discovery of skyrmions and of skyrmion lattices in a variety of materials, some unusual aspects of skyrmions have been discovered using synchrotron radiation. This includes the discovery of bound pairs of opposite helicity skyrmions in Fe-Gd thin films or "skyrmion molecules" [4]. Normally skyrmions are believed to arise as a result of the Dzyaloshinskii-Moriya interaction (DMI) in non-centrosymmetric magnetic materials competing with the regular exchange interaction, although topologically similar spin structures can be stabilized by the competition of long-range dipolar energy in a thin film geometry and domain wall energy [4]. We have shown how in Fe-Gd films, under the right conditions of magnetic field and temperature, one can trace the development of various phases, namely : a stripe domain phase; stripe-to-skyrmion transitions, a skyrmion lattice phase and a uniform magnetization phase. Diffuse magnetic neutron or X-ray scattering from interfaces can play an important role in determining the magnetic domain structure at interfaces and its correlation with interface roughness. We will illustrate this with an example of diffuse magnetic scattering from a Ni film on a V2O3 substrate, which has been shown [5] to yield a large enhancement in the magnetic coercivity at the temperature of the metal-insulator transition (MIT) of the V2O3. An explanation of this effect postulates the creation of a nano-domain structure in the Ni film patterned by the domain structure on the surface of the V2O3 that results from the crystallographic transition accompanying the MIT. Diffuse magnetic scattering utilizing polarized neutrons has enabled the determination of the sizes of these domains. Similarly diffuse magnetic resonant scattering from the interfaces of the Co/FeF2 exchange bias system has shown how the interface domain structure determines the exchange bias as a function of applied magnetic field and temperature. Finally, we shall show how resonant magnetic X-ray scattering using *coherent* X-rays have been used to study the dynamics of some of the spin systems discussed above. This is done using the technique of X-ray Photon Correlation Spectroscopy (XPCS) where the intensity pattern due to magnetic speckle on a two-dimensional detector is autocorrelated with the same pattern at a certain time delay later, yielding the so-called normalized intermediate scattering function f(q,t), which is related to the Fourier transform of the magnetic scattering function from the spins, namely S_{mag}(q, w). This provides an alternative to inelastic neutron scattering (INS) which is useful for looking at longer time-scales than those probed by INS, which are typically a fraction of a nanosecond or less. Thus, one may look at time scales from milliseconds to thousands of seconds using conventional synchrotron sources (used for studying slow fluctuations of magnetic domain walls or frustrated spin systems such as spin glasses), or use the novel double-pulse method with fixed, tunable delays developed at X-ray sources such as the Linear Coherent Light Source (LCLS) at the Stanford Linear Accelerator Center. Acknowledgement: This work was supported by U.S. Dept. of Energy, Office of Basic Energy Sciences (BES), under Award no. DE-SC0003678

[1] J. Nogués, I.K. Schuller, J. Magn. Magn. Mater. 192, 203 (1999). [2] S. Roy et al., Phys. Rev. Lett. 95, 047201 (2005) [3] A.E. Berkowitz et al., J. Appl. Phys. 117, 172607 (2015) [4] S.A. Montoya et al., Phys. Rev. B 95, 024415 (2017) [5] J. de la Venta et al., Appl. Phys. Lett. 102, 122404 (2013)

4:30

BA-06. Imaging the statics and dynamics of sub-10nm skyrmions using x-ray holography and scanning transmission x-ray microscopy.

F. Buettner[1]
1. Materials Science and Engineering, Massachusetts Institute of Technology, Cambridge, MA, United States

Skyrmions are topologically non-trivial spin textures with enormous potential for applications in computing and data storage technologies. Most of the present interest in these special types of magnetic domains derives from the possibly extraordinary small size of these features. For instance, at cryogenic temperatures, skyrmions down to 1 nm in size were observed already a few years ago [1]. More recently, room temperature skyrmions were observed in ferromagnetic multilayers [2–5]. The fact that all of these room-temperature skyrmions were observed by x-ray imaging illustrates how powerful and significant x-ray probes are for the skyrmion community. X-ray magnetic imaging is based on resonant photon aborption (x-ray magnetic circular dichroism), which provides element-specific magnetic contrast. The most established x-ray imaging techniques are Scanning Transmission X-ray Microscopy (STXM), TXM, and Photo-Emission Electron Microscopy (PEEM). All of these techniques were used to image skyrmions in the range of several tens of nanometers [3–5]. Key advantages of these established techniques are ease of use and rapid image acquisition. For instance, STXM has an unbeaten efficiency of time-resolved imaging. Full time-resolved videos can be acquired in less than 30 min. STXM is therefore a perfect tool for high throughput time-resolved magnetic imaging. The problem of STXM, TXM, and PEEM is that the resolution is limited to 15 nm and that this limit is not likely to be improved dramatically in the near future. In addition, all of these real space imaging techniques suffer from sample drift, which adds to the uncertainty. Therefore, real space imaging is most suitable to study skyrmions of several tens of nanometers in diameter. By contrast, most applications require skyrmions to be sub-10 nm in diameter at room temperature. We have recently derived by analytical modeling that sub-10 nm skyrmions can indeed be stabilized at room temperature [6]. The theory predicts that these sub-10 nm skyrmions exist in materials with close to zero stray field interactions, such as ferrimagnets and synthetic antiferromagnets. The unique capability of element-selective magnetic imaging offered by x-rays is crucial for imaging such antiferromagnetically ordered spin states. It is hence critical to advance x-ray imaging to detect the statics and dynamics of sub-10 nm skyrmions. The most promising route to achieve a breakthrough in high resolution x-ray imaging is to eliminate all lenses and optical elements. Instead, the diffraction pattern of the specimen is directly recorded on a CCD camera, see Fig. 1. The real space image is then reconstructed numerically. Fourier-Transform x-ray Holography (FTH) [7], coherent diffractive imaging (CDI) [8], and ptychography [9] are different strategies of performing this numerical task. The resolution of Fourier space imaging is fundamentally limited only by the wavelength of the incident light and the maximum recorded numerical aperture. An additional advantage of eliminating all lenses is that Fourier space imaging can be performed at next generation x-ray light sources with (sub)-femtosecond temporal resolution, such as free electron lasers [10] and high harmonic generation sources [11]. Furthermore, we have not observed any carbon deposition even after many days of imaging the same sample, which is most helpful when performing systematic studies on a particularly interesting sample. Finally, Fourier space imaging is intrinsically immune to sample drift, which we have recently exploited to track skyrmions with a precision of better than 3 nm in full time-resolved imaging [2]. Here, I will focus on the key advantages of STXM and FTH in the context of imaging small skyrmions. I will show how we applied STXM to measure the skyrmion Hall angle [12] and to systematically study the phase diagram of skyrmions and stripe domains in multilayers as a function of temperature, magnetic field, and applied current [13]. Using FTH, we have tracked the gyrotopic trajectory of a skyrmion with sub-3 nm precision and used this information to determine the skyrmion topology and its quasi-particle equation of motion [2]. Furthermore, we have found a deterministic and ultrafast way of creating skyrmions with spin-orbit torque current pulses [14]. Most recently, we have studied ferrimagnets in which we have observed skyrmions with ultrasmall diameters. Using a combination of apparent size and contrast of the observed features, we can conclude that they are indeed 10 nm in size. Finally, I will discuss strategies to advance Fourier space x-ray imaging to fully resolve sub-10 nm magnetic features in a reliable, robust, and fast way.

[1] Heinze, S. et al. Nature Physics 7, 713–718 (2011). [2] Büttner, F. et al. Nature Physics 11, 225–228 (2015). [3] Woo, S. et al. Nature Materials 15, 501–506 (2016). [4] Moreau-Luchaire, C. et al. Nature Nanotechnology 11, 444–448 (2016). [5] Boulle, O. et al. Nature Nanotechnology 11, 449–454 (2016). [6] Büttner, F., Lemesh, I. & Beach, G. S. D. arXiv:1704.08489 (2017). [7] Eisebitt, S. et al. Nature 432, 885–888 (2004). [8] Miao, J. et al. Nature 400, 342–344 (1999). [9] Thibault, P. & Menzel, A. Nature 494, 68–71 (2013). [10] Günther, C. M. et al. Nature Photonics 5, 99–102 (2011). [11] Kfir, O. et al. arXiv:1706.07695 (2017). [12] Litzius, K. et al. Nature Physics 13, 170–175 (2017). [13] Lemesh, I. et al. submitted (2017). [14] Büttner, F. et al. Nature Nanotechnology 12, 1040–1044 (2017).

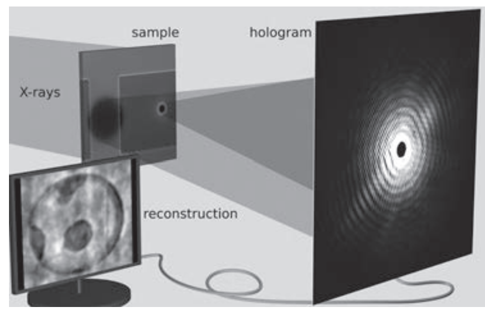

Fig. 1. Lensless Fourier space imaging of skyrmions via x-ray holography.

TUESDAY AFTERNOON, 24 APRIL 2018 ORCHID III, 2:00 TO 5:00

Session BB
SOFT MAGNETIC MATERIALS II: AMORPHOUS AND NANOCRYSTALLINE MATERIALS

Peter Kollar, Chair
P. J. Safarik University, Faculty of Science, Institute of Physics, Kosice, Slovakia

CONTRIBUTED PAPERS

2:00

BB-01. Influence of annealing time on structural and magnetic properties in Fe-Co-Si-B-P-Cu.

M. Kuhnt[1], M. Amalraj[2], K. Pradeep[2], M. Marsilius[3], T. Strache[3], C. Polak[3] and G. Herzer[3]
1. Department of Materials Science, Technische Unviersität Darmstadt, Darmstadt, Germany; 2. Materials Chemistry, RWTH Aachen University, Aachen, Germany; 3. Vacuumschmelze GmbH & Co.KG, Hanau, Germany

Nanocrystalline Fe-Co-Si-B-P-Cu alloys exhibit high saturation polarization J_s above 1.8 T combined with good soft magnetic properties and good glass forming ability [1,2]. In this work we investigated the influence of the annealing time on the structural and magnetic properties in Fe-Co-Si-B-P-Cu alloys. Amorphous ribbons of $Fe_{85.2-x}Co_xSi_{0.5}B_{9.5}P_4Cu_{0.8}$ (x=0, 4, 10, 15, 20, 25, 35, 40 and 57) have been produced by rapid solidification in 25 mm width and 22 μm thickness. The material was annealed at 470°C at various annealing times in the range from 10 s to 60 s [3]. As a result we obtained a nanocrystalline structure of bcc FeCo grains embedded in an amorphous matrix. The crystalline volume fraction (about 50% for all Co-contents), the saturation polarization and the saturation magnetostriction proved to be largely insensitive to the precise annealing time. However, the grain size D and, hence, the coercivity H_c increase significantly with increasing annealing times t_a. Figure 1 shows characteristic examples for the grain size dependence on annealing time, while Figure 2 depicts the corresponding grain size dependence of coercivity. For low Co contents H_c follows a D^6 law while a D^3 dependence is observed for intermediate Co concentrations. For the highest Co contents we observe a transition from a D^3 law for small, to a D^6 dependence for large grain sizes, respectively. These results can be understood from the corresponding contributions of magneto-elastic and magneto-crystalline anisotropy, respectively, which are both changing as a function of the Co-content [4, 5, 6].

[1] Zhang, Y. et al.: *IEEE Trans. Magn.* 50 (2014) 1-4 [2] Takenaka, K. et al.: *Mat. Trans.* 56 (2015) 372-376 [3] Herzer, G. et al.: *Phys. Stat. Sol. B* 248 (2011) 2382-2388 [4] Herzer, G.: *IEEE Trans. Magn.* 26 (1990), 1397-1402 [5] Suzuki, K. et al.: *J. Magn. Magn. Mater* 177-181 (1998) 949-950 [6] Herzer, G., *Acta Materialia* 61 (2013), 718-734

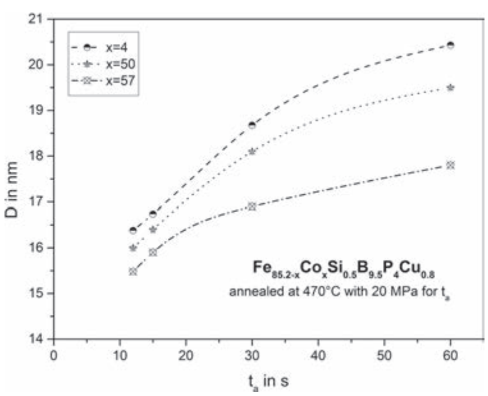

Fig. 1. Grain size in dependence of annealing time for (Fe,Co)-Si-B-P-Cu alloys.

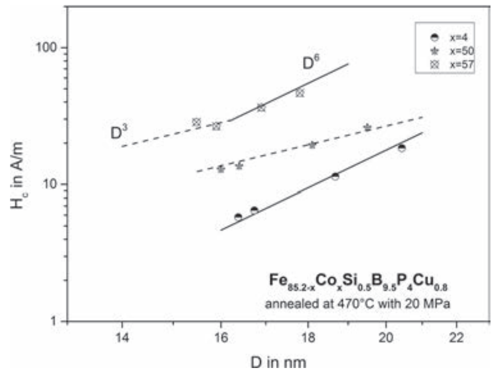

Fig. 2. Grain size dependence of coercivity for (Fe,Co)-Si-B-P-Cu alloys.

2:15

BB-02. Fabrication and properties of under 10 μm sized amorphous powders of high B_s soft magnetic alloy for high frequency applications.

T. Suzuki[1,2], P. Sharma[1], L. Jiang[1], Y. Zhang[3] and A. Makino[1]
1. Tohoku University, New Industry Creation Hatchery Center (NICHe), Sendai, Japan; 2. Sendai R&D Center, Sendai, Japan; 3. Tohoku University, Institute for Materials Research, Sendai, Japan

Small sized, light weight and high efficiency electrical devices are very important for green and low carbon society. The only way to reduce the size and weight of electrical devices is to operate them at higher frequencies (f) and high power levels. Unfortunately, the operating frequency range of present high magnetic flux density (B) core materials is below few kHz. This is due to various factors related to fabrication as well as fundamental magnetic properties. For example, at high frequencies, energy loss due to hysteresis ($W_h \propto f$) and eddy current ($W_e \propto f^2$) become too large. Generally the material which can be operated at several hundreds of kHz to MHz exhibit low saturation magnetic flux density (B_s). At present magnetic materials used for core applications in high frequency range (10 kHz to MHz) are ferrites. Ferrite has low conductivity, so their eddy current loss is low. That's why ferrite is suitable for high frequency applications. Recent developments in semiconducting components allow circuits to operate at higher frequencies and higher power levels, which force soft magnetic cores to be heavier and larger in size. This is due to low $B_s \leqq 0.5$T of ferrite. Therefore, to miniaturize electrical components and improve their performance at higher frequencies, materials with high B_s and low core loss (W) must be developed. Metallic alloys, such as amorphous and nanocrystalline have excellent soft magnetic properties ie. high B_s and low coercivity (H_c). Best high B_s (~1.85 T) and low core loss material with the ability to mass-produce is based on FeSiBPCu alloy (trade name NANOMET®) [1, 2]. There are some issues for applying this alloy to high frequency applications. For example, eddy current loss is high due to its high electrical conductivity. Developing the alloy in powder form can help in reducing the eddy current loss. Alloy with lower content of Fe (~76 at.%) can be produced in amorphous powder form by gas atomization process. However, it is difficult to produce amorphous powders with higher contents of Fe (>79 at.%) in the alloy, and it is due to low amorphous forming ability. A special technique like spinning water atomization process (SWAP) which has high cooling rate is required. The SAWP can produce amorphous powders of FeSiBPCu alloy with Fe content up to ~83.3 at.%. The average powder particle size produced with gas atomization and SWAP is ≥ 30 μm [3]. Size of the powder particles is very important for suppressing the eddy current loss at high frequencies. Therefore it is necessary to produce small size powder particles of FeSiBPCu alloy. Based on skin depth, the average powder particle size should be below 10 microns for the core operating at frequencies up to few tens of MHz. There is hardly any report on fabrication and magnetic properties of such small sized soft magnetic powders. We have attempted to produce the soft magnetic powder particles of size below 10 μm by gas atomization. Here, we report on the fabrication and magnetic properties. Two alloys were selected for the fabrication of powders; one (FeSiBP) with lower content of Fe (~76 at.%), and the other FeSiBPCCu with higher contents (~81.5 at.%) of Fe. This selection was made after analyzing the properties of these alloys in ribbon form. The cooling rate in gas atomization process is influenced by the type of the gas and its pressure, therefore we used Ar, N_2, and He gases with pressure up to 9 MPa. Size distribution of powder particles was measured by laser based particle size analyzer. Powders were classified in to different size ranges for example under 10 μm, under 20 μm, between 20-38 μm etc. Powders were analyzed in terms of their shape, structure, thermal and magnetic properties. Toroidal cores were made by mixing with a polymer resin. Atomization with He and N_2 gas is effective for increasing the cooling rate, when compared with Ar gas. The $Fe_{76}Si_9B_{10}P_5$ alloy powders made with different gases were amorphous, and it is due to high amorphous forming ability of this alloy. However, the results were quite different for high Fe content $Fe_{81.5}Si_{0.5}B_{4.5}P_{11.0}Cu_{0.5}C_{2.0}$ alloy. Processing with Ar gas only produces amorphous powders with size below 10 μm. The He and N_2 gasses showed significant improvement in cooling rate, and we could obtain amorphous powders with size below 20 μm. Intestinally the yield of powder particles with size below 10 μm was highest for He gas. The classified powders were mixed with polymer resin and molded under a pressure of 1500 MPa to make toroidal shaped cores (inner diameters: 13 mm, outer diameters: 8 mm). Pressed cores were annealed to optimize the magnetic properties by releasing the process related stress. Magnetic permeability was measured using impedance analyzer. Total core loss, which is the sum of hysteresis loss and eddy current loss was measured by ac B-H analyzer. Figure 1 shows the core loss at different frequencies (up to 1 MHz) under the magnetic induction B_m of 50 mT for $Fe_{76}Si_9B_{10}P_5$ alloy powder cores made under similar conditions. A significant decrease in coreloss at higher frequencies is noticeable. The core loss at 1 MHz is almost more than 4 times lower for a core with smaller particle size (under 10 μm) when compared with a core made from large sized particles (20 - 38 μm). The obtained results are important for the development of future high frequency and high power electronics. The details of the results and their analysis will be presented during the conference.

A. Makino, *IEEE Trans. Magn.*48, 1331 (2012). P. Sharma, X. Zhang, Y. Zhang and A. Makino, *Scripta Mater.* 95, 3 (2015). Y. Zhang, P. Sharma and A. Makino, *IEEE Trans. Magn.* 50, 2006804 (2014).

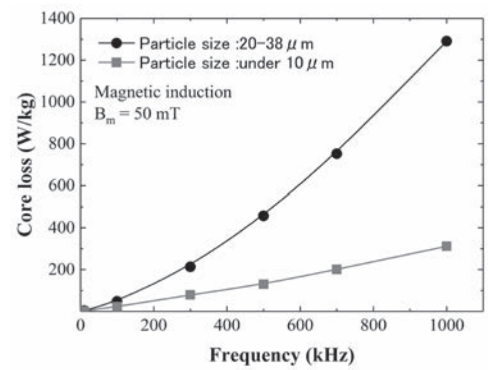

2:30

BB-03. Nanostructured Soft Magnetic Multilayers with Tunable Properties for On-Chip Micro-Magnetic Devices.

C. Falub[1], R. Hida[2], M. Meduna[3,4], M. Bless[1], J. Richter[1], H. Rohrmann[1], T. Nadig[1] and M. Padrun[1]
1. Evatec AG, Trübbach, Switzerland; 2. CEA-LETI/Minatec, Grenoble, France; 3. Department of Condensed Matter Physics, Masaryk University, Brno, Czechia; 4. CEITEC, Masaryk University, Brno, Czechia

Miniaturization of the RF passive devices and DC-DC converters is key to achieving lighter, faster and more efficient mobile devices, and high-conversion ratio DC micro-grids, as the 5th generation (5G) wireless network and Internet of Things (IoT) paradigms emerge. In order to realize this objective, however, the biggest challenge remains shrinking the size of the chip-integrated magnetic components (e.g. micro-inductors, micro-transformers). Due to their flux amplification properties and high operating frequencies, integrated thin film magnetic cores with high permeability based on amorphous and polycrystalline magnetic alloys promise further device miniaturization, lower energy loss and thus lower power operation [1,2]. Yet, integrating these magnetic films on the silicon complementary metal oxide semiconductors (Si-CMOS) platform is technologically very challenging, since for a significant inductance enhancement, several-micrometer-thick films with ultra-low losses need to be deposited. Moreover, leveraging this gain requires complex tailoring of the device architecture and magnetic thin film properties, since maximizing simultaneously the inductance, frequency bandwidth and peak quality factor is very difficult [3]. In this work, we present an economical method of manufacturing magnetic thin films, which allows combining soft magnetic materials with complementary properties, e.g. high saturation magnetization, low coercivity, high specific resistivity and low magnetostriction. Soft magnetic multilayered thin films based on the $Ni_{78.5}Fe_{21.5}$, $Co_{91.5}Ta_{4.5}Zr_4$, $Fe_{52}Co_{28}B_{20}$, $Fe_{65}Co_{35}$ alloy materials were deposited on 8" bare Si and Si/200nm-thermal-SiO_2 wafers in an industrial, high-throughput Evatec LLS EVO II magnetron sputtering system [4]. The sputtered multilayers consisted of stacks of alternating 80nm-thick ferromagnetic layers and 4nm-thick Al_2O_3 dielectric interlayers. Since the substrate cage rotates continuously, such that the substrates face different targets (e.g. NiFe, FeCoB, CoTaZr) alternatively (Fig. 1a), each ferromagnetic sublayer in the multilayer stack can exhibit a nano-layered structure with very sharp interfaces as revealed by X-ray reflectometry (XRR) and transmission electron microscopy (TEM) (Fig. 1b,c). We adjusted the thickness of these individual nanolayers by changing the cage rotation speed and the power of each cathode, which is an excellent mode to engineer new, composite ferromagnetic materials with tunable properties. The ferromagnetic layers were deposited by DC sputtering at a pressure of 1.7×10^{-3} mbar using Ni-21.5%Fe, Fe-28%Co-20%B (at.%) and Co-4.5%Ta-4%Zr long life (~250 kWh) targets, whereas the dielectric Al_2O_3 interlayers were deposited by RF sputtering from monoblock Al_2O_3 targets at a pressure of 5×10^{-3} mbar. We introduced the in-plane magnetic anisotropy in these multilayered thin films during sputtering by a linear magnetic field parallel to the wafer plane, which is designed such that the magnetic field of the magnetron located behind the opposite target is not perturbed. In-plane hysteresis loops (along the EA and HA directions) measured by means of magneto-opto Kerr effect (MOKE) and B-H looper revealed that the coercivity (H_c), anisotropy field (H_k) and magnetostriction of these thin films can be tuned with the thickness of the individual magnetic nanolayers (Fig. 2). The behavior of the coercive field for these nanolaminated films was explained by the random-anisotropy model based on grain size considerations (Fig. 2a). The nanolaminated structure exhibited a uniform magnetization throughout its structure with good microwave properties, as revealed by broadband (100 MHz - 10 GHz) RF spectra. The classical Landau-Lifschitz-Gilbert (LLG) model could describe well the experimental behavior of the magnetization dynamics of the multilayered structure (Fig. 2c,d). Since the nanolaminated multilayered structures exhibited no degradation upon post-annealing up to a temperature of 300°C, these materials are very promising for on-chip micro-magnetic devices.

[1] C.V. Falub, H. Rohrmann, M. Bless, M. Meduna, M. Marioni, D. Schneider, J.H. Richter, M. Padrun, *AIP Advances* 7, 056414 (2017). [2] C.V. Falub, R. Hida, M. Meduna, J. Zweck, J.-P. Michel, H. Sibuet, D. Schneider, M. Bless, J.H. Richter, H. Rohrmann, *IEEE Trans. Magn.* 53, 11, 2002906 (2017). [3] D. S. Gardner, G. Schrom, F. Paillet, B. Jamieson, T. Karnik, S. Borkar, *IEEE Trans. Magn.* 45, 10, 4760 (2009). [4] https://www.evatecnet.com/products/lls-evo-ii [5] C.V. Falub, M. Bless, R. Hida, M. Meduna, A. Ammann, *AIP Advances* 8, 048002 (2018).

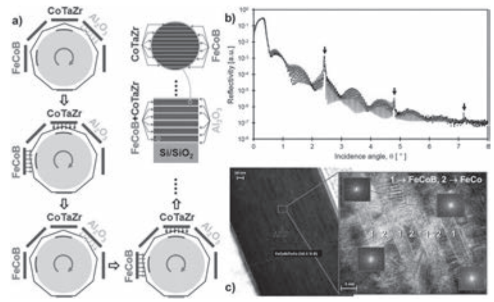

Fig. 1. (a) Schematic diagram showing the procedure for depositing nano-structured (FeCoB+CoTaZr)/Al_2O_3 soft magnetic multilayers at the LLS EVO II sputter tool; (b) Specular XRR scan for a (FeCoB+CoTaZr)/Al_2O_3 soft magnetic multilayer with ferromagnetic sublayers having a 2 nm bilayer period (25.8% Fe). Black solid symbols correspond to the experimental measurements, whereas the red, continuous line represents the fit within the kinematical scattering formalism. Nano-layering induces further intensity oscillations (indicated by black arrows). (c) TEM cross-section micrographs of the FeCoB/FeCo nano-structured multilayer with a 9.2 nm bilayer period (10.1 % B).

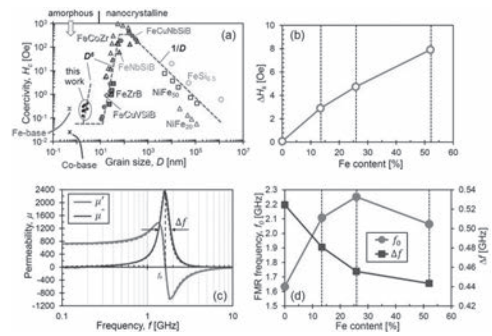

Fig. 2. (a) The increase of coercivity of (FeCoB+CoTaZr)/Al_2O_3 multilayers with grain size can be explained in the random anisotropy model for nanocrystalline ferromagnets. (b) Change of the anisotropy field (ΔH_k), which is a measure of magnetostriction, versus the Fe content in (FeCoB+CoTaZr)/Al_2O_3 multilayers. (c) Typical broadband RF spectra of real (μ') and imaginary (μ'') components of magnetic permeability of (FeCoB+CoTaZr)/Al_2O_3 multilayers. Dashed curves are the corresponding calculated permeability spectra in the LLG formalism. (d) Ferromagnetic resonance frequency (FMR) (f_0) and linewidth (Δf) versus the Fe content for (FeCoB+CoTaZr)/Al_2O_3 multilayers.

2:45

BB-04. Magnetic Properties of Annealed Amorphous Alloys (Fe-rich) Obtained by Gas Atomization Technique.

K.L. Alvarez[2,3], *J.M. Martín*[1,2], M. Ipatov[4], L. Dominguez[5] and J. Gonzalez[6]
1. Materials and Manufacturing, CEIT-IK4, San Sebastián, Spain; 2. Tecnun (University of Navarra), San Sebastián, Spain; 3. Escuela de Ingeniería Mecánica, Pontificia Universidad Católica de Valparaíso, Valparaíso, Chile; 4. SGIker (Magnetic Measurements), University of the Basque Country, San Sebastián, Spain; 5. Escuela de Ingeniería de Gipuzkoa, University of the Basque Country, San Sebastián, Spain; 6. Department Materials Physics, Faculty of Chemistry, University of the Basque Country, San Sebastián, Spain

Soft magnetic Fe-based Fe-Si-B amorphous alloys have been widely used as magnetic components in high frequency transformers, inductors, and sensors due to their magnetic behavior [1], [2]. These materials are typically produced by the "melt-spinning" technique, involving the rapid solidification process. It is important to remark that the amorphous ribbons obtained by the melt-spinning technique were widely introduced as soft magnetic materials in the 70s. One of the ways to advance in the research field of magnetic materials involves the exploration of new routes to fabricate them. Thus, a novel technique of rapid solidification that we have successfully used to produce soft magnetic amorphous alloys is gas atomization [3], which produces the material in powder form. In this technology, it is possible to reach average cooling rates of up to 10^6 K/s, depending on processing conditions and the atomizing gas. The soft magnetic character of gas atomized powders with composition $Fe_{70}Si_{18}B_{12}$ was reported by the authors in [3]. It was showed that particles <10 μm were amorphous and exhibited a low coercive field of around 7 Oe. Recently, the authors have produced a gas atomized powder of composition $Fe_{72.5}Si_{12.5}B_{15}$ that is fully amorphous for the whole particle size distribution, whose 90th percentile is 48.7 μm. Particles with a diameter <20 μm exhibit a coercivity of 3.26 Oe. It is well known that a thermal treatment below the crystallization temperature leads to structural relaxation with a significant improvement of the soft magnetic character [4]. In this work, we report the effect of the thermal treatment (at 250, 350, and 450 °C for 0 and 1 h) on the magnetic behavior of amorphous powder $Fe_{72.5}Si_{12.5}B_{15}$ with a particle size <20 μm. The annealing time of 0 h means that the sample was heated up to the annealing temperature and immediately cooled down without any holding. After such thermal treatments, the amorphous character of the annealed alloys was checked by X-ray diffraction technique. Fig. 1 shows the hysteresis loops of the annealed samples measured at room temperature, denoting the soft magnetic character associated with a very low value of coercive field. In fact, coercive field significantly decreases (see Fig. 2) from 3.26 Oe (as-atomized) to 0.44 Oe (annealed at 450 °C). There is an influence of the annealing time in this drop, with lower values of coercivity in the samples treated for 1 hour, except for the samples treated at 450 °C, whose coercivity is practically the same. The above mentioned behavior of the coercivity should be ascribed to the structural relaxation associated with thermal annealing without crystallization, decreasing the internal stresses and leading to a significant reduction of the magnetoelastic anisotropy.

[1] F. E. Luborsky, *Amorphous Metallic Alloys*. Butterworths, 1983. [2] A. Zhukov and J. Gonzalez, "Amorphous and nanocrystalline soft magnetic materials: Tailoring of magnetic properties, magnetoelastic and transport properties," in *Handbook of Advanced Magnetic Materials*, 2006, pp. 1091–1157. [3] K. L. Alvarez, J. M. Martín, M. Ipatov, and J. Gonzalez, "Soft magnetic amorphous alloys (Fe-rich) obtained by gas atomisation technique," *J. Alloys Compd.*, vol. 735, pp. 2646–2652, Feb. 2018. [4] F. Luborsky, J. Becker, and R. McCary, "Magnetic annealing of amorphous alloys," *IEEE Trans. Magn.*, vol. 11, no. 6, pp. 1644–1649, Nov. 1975.

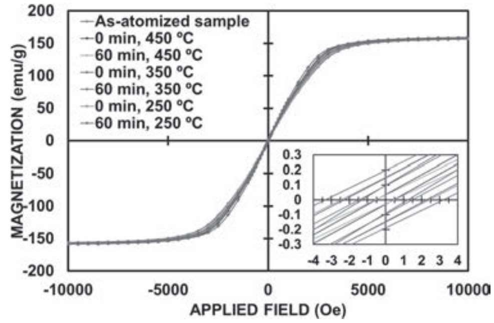

Fig. 1. Hysteresis loops of annealed amorphous samples at room temperature.

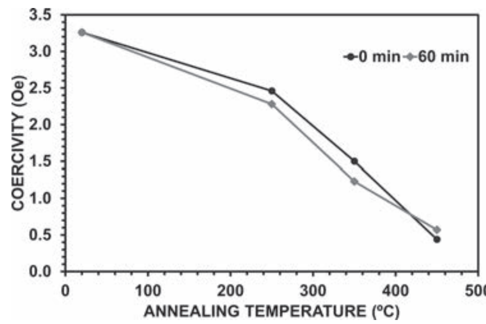

Fig. 2. Coercive field as a function of annealing temperature.

3:00

BB-05. Novel making method of high resistive surface layer of Fe-based amorphous alloy powder by surface-modification using two-step acid solution process.

K. Sugimura[1], N. Yabu[1], M. Sonehara[1] and T. Sato[1]
1. Faculty of Engineering, Shinshu University, Nagano, Japan

Silicon carbide (SiC) and gallium nitride (GaN) based power devices are well known for the application for high frequency switching converters, and their low on-resistance property is beneficial for the replacement of silicon (Si) based power devices [1], [2]. Application of these power devices to MHz switching DC-DC converters is expected to realize a compact and light-weight converter with a high conversion efficiency. Although the magnetic core for inductors and transformers must have low core-loss at MHz band to be applied to SiC/GaN based MHz switching converter, currently there are only Ni-Zn ferrite core available[3]. The authors reported an iron(Fe)-based metal composite magnetic core with 2.6 μm-diameter amorphous alloy powder (AMO-powder)/epoxy-resin and its application to MHz switching LLC resonant converter[4]. In order to reduce the core-loss at MHz band or above, the AMO-powder (Fe-Si-B-Cr-C) should have high electrical resistivity surface layer to suppress the over-lapped eddy current between the adjacent AMO-powders within the composite core. Silica (SiO_2) coating and surface oxidization are effective to make a high-resistive thin layer on the surface of such the metal powder[4], [5]. In this study, the authors have proposed a novel making method of the high-resistive thin layer on the water-atomized AMO-powder (Fe-Si-B-Cr-C) using the acid solution treatment. The novel method was based on the two-step acid solution treatment, the first-step phosphoric acid (H_3PO_4) treatment and the second-step hydrochloric acid (HCl) treatment. FIG. 1 shows the cross-sectional SEM image of a typical example of the surface-modified AMO-powder through the first-step treatment using 5 %-H_3PO_4 for 6 hours and the second-step treatment using 5 %-HCl for 4 hours. As shown in FIG. 1, two layers on the surface of the AMO-powder were observed. The inner layer was formed through the first-step phosphoric acid treatment and the outer layer was formed through the second-step hydrochloric acid treatment. The surface-modified layer thickness could be changed by the process conditions such as concentration of the acid solution and treatment time. The surface-modified two layers of the AMO-powder were analyzed by using X-ray photoelectron spectroscopy (XPS), where the XPS analysis targeted Fe-2p and Si-2p spectrum, the main reason for selection of Fe-2p and Si-2p spectrum was based on an idea that Fe and Si element in the AMO-powder were considered to contribute in the formation of a high-resistive surface layer composed of the iron-oxide and silicon oxide. FIG. 2 shows the XPS spectrum of Fe-2p and Si-2p evaluated for as-atomized AMO-powder and the two-step surface-modified AMO-powder. In the as-atomized powder, the peaks of metal-iron Fe(0), iron-oxide and oxygen deficient silicon-oxide near Si_2O_3 were observed. After the first-step phosphoric acid treatment, the peak of the metal-iron Fe(0) disappeared and the silicon-oxide changed to stoichiometric silicon-dioxide SiO_2. After the second-step hydrochloric acid treatment, the spectrum derived from the iron-oxide disappeared, and the SiO_2 peak became sharp with increasing the treatment time. From the above-mentioned results, the most outer surface layer of the two-step processed AMO-powder was considered to be high-resistive stoichiometric silicon-dioxide SiO_2. It was also thought that we could make a single-phase SiO_2 thin layer on the AMO-powder by an appropriate condition of the two-step acid solution treatment. The novel method for making the single-phase SiO_2 thin layer on the AMO-powder will be effective to suppress the eddy current over-lapped between adjacent powders within the composite magnetic core. The more detailed results will be presented at the conference.

[1] H. Wang, A. M. H. Kwan, Q. Jiang, and K. J. Chen, "A GaN pulse width modulation integrated circuit for GaN power converters," *IEEE Trans. Electron Devices*, vol. 62, no. 4, pp. 1143–1149, Apr. 2015. [2] A. León-Masich, H. Valderrama-Blavi, J. M. Bosque-Moncusí, and L. Martínez-Salamero, "Efficiency comparison between Si and SiC based implementations in a high gain DC-DC boost converter," *IET Power Electron.*, vol. 8, no. 6, pp. 869–878, Jun. 2015 [3] M. Harrison, "The future of power electronic design", in *Proc. IEEE Appl. Power Electron. Conf. Expo. (APEC) Plenary Sessions*, Long Beach, CA USA, 2016, accessed on Jan. 4, 2018. [4] K. Sugimura, D. Shibamoto, N. Yabu, T. Yamamoto, M. Sonehara, T. Sato, T. Mizuno, and H. Mizusaki, "Surface-Oxidized Amorphous Alloy Powder/Epoxy-Resin Composite Bulk Magnetic Core and Its Application to Megahertz Switching LLC Resonant Converter," *IEEE Trans. Magn*, Vol.53, no.11, #2801406, Nov. 2017. [5] K. Sugimura, Y. Miyajima, M. Sonehara, T. Sato, *et al*., "Formation of high electrical-resistivity thin surface layer on carbonyl-iron powder (CIP) and thermal stability of nanocrystalline structure and vortex magnetic structure of CIP," *AIP Adv*., vol. 6, no. 5, pp. 055932-1–055932-8, 2016.

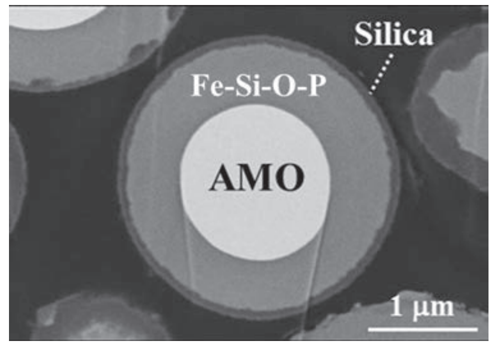

Fig. 1. Cross-sectional SEM image of surface-modified AMO-powder by two-step acid solution process.

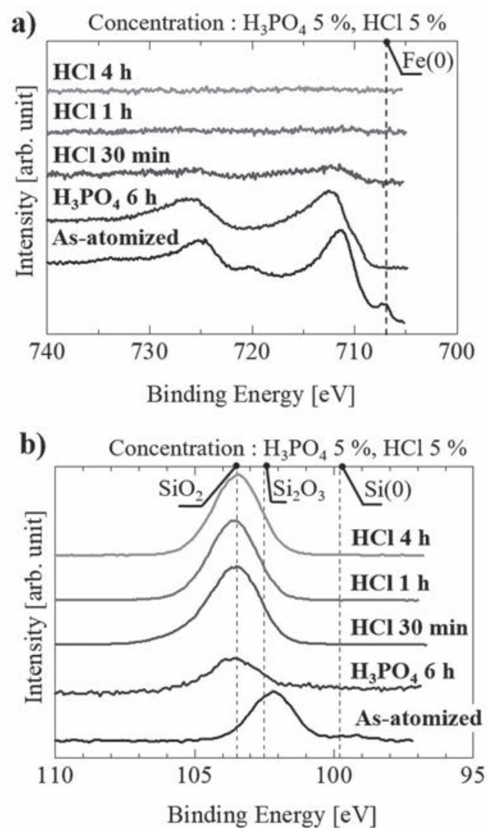

Fig. 2. XPS analysis results of surface-modified AMO-powder by two-step acid solution process. (a) Fe-2p spectrum, (b) Si-2p spectrum.

3:15

BB-06. Comparison of magnetostatic and magnetoimpedance properties for amorphous ribbons, wires and glass-coated microwires.

N.S. Perov[1,2], Y.A. Alekhina[1], L.A. Makarova[1], M.F. Khajrullin[1], I.A. Baraban[2] and V.V. Rodionova[2,3]
1. Faculty of Physics, magnetism department, Lomonosov MSU, Moscow, Russian Federation; 2. Institute of Physics & Technology and STP "Fabrika", Immanuel Kant Baltic Federal University, Kaliningrad, Russian Federation; 3. National University of Science and Technology «MISIS», Moscow, Russian Federation

The physical properties of the amorphous metallic alloys are useful for different practical applications. For example, corrosion resistance of amorphous Fe-based alloys with reduced Cr content is higher than corrosion resistance of the crystalline stainless steel. An electric resistivity of amorphous phase is 2-4 times higher than of crystalline one usually, as a result, the lower eddy current losses can be detected. Ferromagnetic amorphous metallic alloys are extremely soft. More other, amorphous alloys have good mechanical properties and they can be manufactured in different forms: ribbons, wires, powder, microwires etc. As a result of these properties combination, ferromagnetic amorphous metallic alloys are widely used as high-frequency cores of transformers, high performed sensors etc. [1-3] There is the stress distribution through the characteristic size (diameter or thickness) because of rapid cooling manufacturing processes, whose influence on magnetic properties has drastic role. Depending on fabrication technique, the value of stresses and the distribution are various even for the same composition of the alloy. In our research we compared properties of amorphous ribbons (up to 2 cm width and 29 micron thickness), rapid quenching method – microwires (up to 180 micron in diameter), Ulitovski-Taylor technique – glass-coated microwires (up to 23 micron of metallic diameter and 29 micron of total diameter) with similar composition. Amorphous structure and chemical composition were examined by XRD and EDX analysis, correspondingly. Magnetostatic properties were studied by Vibrating Sample Magnetometer (VSM), high frequency magnetic properties – by spectrum analyser. For hysteresis loops measurements by VSM the 15 mm length of the samples and magnetic field amplitude up to 2kOe were used. For magnetoimpedace measurements the following characteristics were used: I_{AC} till 20 mA, f_{AC} = 0.5-20 MHz, H_{ext} = 0-40 Oe. The comparison was made after length normalization. Depending on the stress distribution through the characteristic size of sample, its magnetic properties are quite different, shape of the hysteresis loops are drastic changed (see Fig. 1). Magnetoimpedance measurements allowed us, solving the inverse problem, to find the field dependences of the magnetic permeability of microwires with different diameters (see Fig. 2). Based the comparison we estimated the distribution of the permeability in the samples. Acknowledgement. The work was supported by the Russian Foundation for Basic research (grant No 18-02-00137)

[1] M. Hayashi, L.Thomas, R.Moriya, C.Rettner, S.S.P.Parkin, Science 320 (2008) 209–211. [2] M. Vazquez, Handbook of Magnetism and Advanced Magnetic Materials 4: Novel Materials, John Wiley&Sons, Ltd. 2007, pp.2192–2226. [3] A.Zhukov, J.Magn.Magn.Mater. 242–245 (PartI) (2002) 216–223.

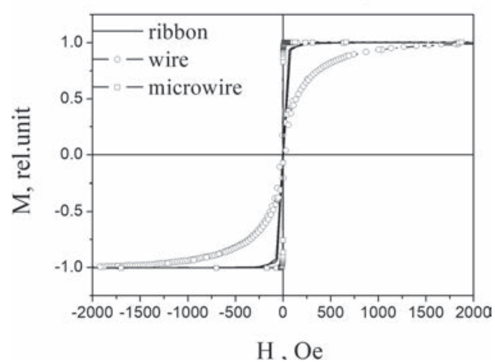

Fig. 1. Hysteresis loops of ferromagnetic amorphous Fe-Co-Si-B alloy in the form of ribbon, wire and glass-coated microwire.

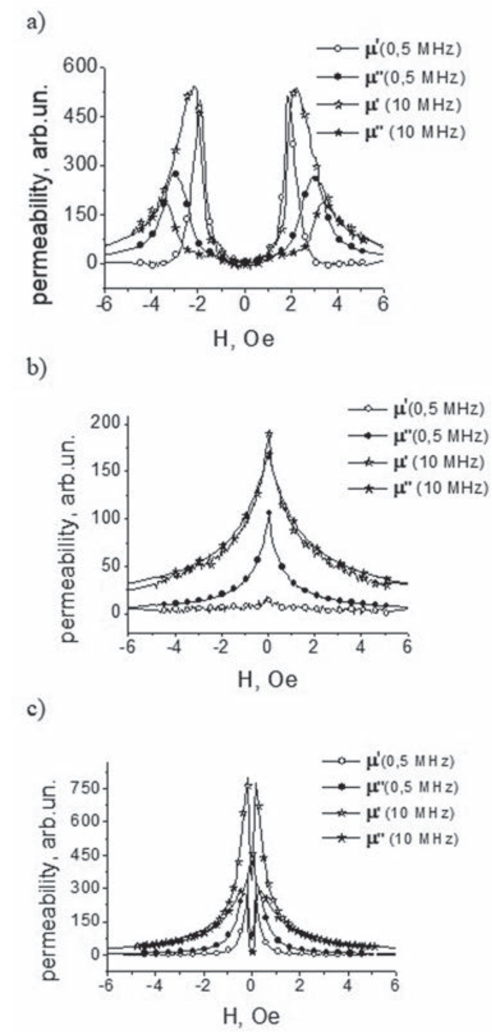

Fig. 2. Field dependences of the magnetic permeability of microwires with diameters 8.3(a), 12.4(b) and 36(c) micron measured at frequencies of 0.5 and 10 MHz

3:30

BB-07. Tunable structural and magnetic properties of single- and multiphase glass-coated microwires.

V. Rodionova[1,2], I.A. Baraban[1] and N.S. Perov[1,3]
1. STP "Fabrika", Immanuel Kant Baltic Federal University, Kaliningrad, Russian Federation; 2. National University of Science and Technology «MISIS», Moscow, Russian Federation; 3. Lomonosov Moscow State University, Moscow, Russian Federation

Cylindrical ferromagnetic glass-coated microwires are among the most studying types of the numerous family of wires consisted of objects with different dimensions and shapes [1-3]. A peculiar crystal state, and magnetic properties as a consequence, of the microwires are extremely sensitive to initial manufacturing conditions, which makes them convenient to tune required properties. The sensitivity of engineered magnetic properties to further external conditions makes microwires useful for a lot of practical applications. For instance, ferromagnetic glass-coated microwires show a number of outstanding effects depending on composition (Fe-, Co-, CoFe-based alloys, Heusler alloys etc.) and crystal state (amorphous, nanocrystalline or crystalline) of the ferromagnetic core [4, 5]. These effects include magnetic bistability [6] used in coding, logic, and memory systems (for example, [7, 8]), magnetoimpedance effect [9, 10] used in high-performance sensors [11, 12], shape memory and magnetocaloric effects [13, 14] for magneto-mechanical actuators [15]. The ability to produce partially crystalline microwires was demonstrated several years ago (for example, [3, 16, 17]) and is actively studied now (for example, [18, 19]). For obtaining nanocrystals in amorphous matrix different methods were used, for example, adding new components to initial alloy [16], or changing the manufacturing conditions [17, 19]. The possibility to switch magnetisation of different phases by varying magnetic field strength leads to a step-wise hysteresis loops. Magnetic properties of microwires which can be controlled and tuned in this way, are used for sensing and logical devices [20–22]. The purpose of this work is twofold: (i) to explore the effect of partial crystallisation in the metallic core on the magnetic properties of microwires and (ii) to find the manufacturing conditions for formation of single and multiphase metallic core of glass-coated microwires. We investigated glass-coated $Fe_{77.5}Si_{7.5}B_{15}$, $Fe_{45}Co_{30}Si_{10}B_{15}$ and $Co_{69}Fe_4Cr_4Si_{12}B_{11}$ microwires with metallic core diameter, d, from 8 mkm to 24 mkm, and total microwires diameter, D, from 12 mkm to 29 mkm. All samples were manufactured by quenching and drawing method. Changing technological parameters, such as a drawing velocity (1.3-9.1 m/sec) and cooling conditions (air and water cooling), leads to the variation of microwires diameters (both d and D) and enables production of microwires with tunable crystal structure of the magnetic metallic core: amorphous, nanostructured, the nanocrystals (can be with different crystal cells) inside the amorphous matrix [19]. The crystalline structure of the microwires was investigated by X-ray diffraction analysis and transmission electron microscopy. The Lake Shore vibrating sample magnetometer was used for evaluating magnetostatic properties. The length of the samples was 15 mm to exclude the influence of demagnetization factor. The rectangular hysteresis loops and amorphous structure – magnetic bistability – were found to be for all microwires prepared at high rate of cooling (water) independent of velocity of extraction and for $Fe_{77.5}Si_{7.5}B_{15}$ and $Co_{69}Fe_4Cr_4Si_{12}B_{11}$ microwires at low rate of cooling (air) and high velocity of extraction. The step-wise hysteresis loop in Figure ($Fe_{45}Co_{30}Si_{10}B_{15}$ microwire, air cooling) is typical for biphase microwires. The wide parts of the loop correspond to the crystal phase magnetisation reversal. By analyzing the step-wise hysteresis loop, we have estimated an amorphous phase volume (M_1/M_S) as well as coercive forces for each phase (Hc is estimated at half-height) depending on diameter of metallic core (see Figure). Our assumptions, based on the results of magnetic measurements, coincide with XRD and TEM analysis of the microwires. The same evaluation of properties can be trace for $Fe_{77.5}Si_{7.5}B_{15}$ wires. The magnetic response of different phases (amorphous, FCC and HCP Co modifications) of metallic core of $Co_{69}Fe_4Cr_4Si_{12}B_{11}$ wire is expressed as a change of the loop slope. The following tendency was found: if the volume of crystalline phase in the amorphous matrix is small (less than 20%) bistability is not suppressed: magnetisation reversal occurs mainly through the large Barkhausen jump, and a second phase arises, leading to a change in hysteresis loop shape to a step-wise one; formation of a larger volume of crystalline phase (more than 70%) in metallic core of microwire leads to a substantial change of magnetisation behavior: the multiphase behavior is expressed in the change of the hysteresis loop slope. In summary, we have found conditions to prepare single, bi- or multiphase glass-coated microwires (see table) and analyzed the role of structural properties on magnetic characteristics of glass-coated microwires [19]. Acknowledgments: This work was supported by the Russian Science Foundation (17-12-01569), the Ministry of Education and Science of the Russian Federation in the framework of government assignments 3.9002.2017/6.7 and 3.4168.2017/4.6.

[1] Manuel Vázquez, G. A. Basheed, Germán Infante, and Rafael P. Del Real, Phys. Rev. Lett. 108 (2012) 037201. [2] Mihail Ipatov, Valentina Zhukova, Arkady Zhukov, and Julian Gonzalez, Sci Rep. (2016) 6: 36180, doi: 10.1038/srep36180. [3] IG Serrano, A Hernando, P Marín, Journal of Applied Physics 115 (3) (2014) 033903. [4] M. Vazquez (Ed.), Magnetic Nano- and Microwires, Woodhead Publishing, Elsevier Ltd., Oxford, 2015. [5] M. Vazquez, H. Chiriac, A. Zhukov, L. Panina, T. Uchiyama, Phys. Status Solidi A 207 (2010) 1 [6] A. Zhukov, Domain wall propagation in a Fe-rich glass-coated amorphous microwire, Appl. Phys. Lett. 78 (2001) 3106–3108. [7] M. Hayashi, L. Thomas, R. Moriya, C. Rettner, S.S.P. Parkin, Science 320 (2008) 209–211. [8] M. Vazquez, Handbook of Magnetism and Advanced Magnetic Materials 4: Novel Materials, John Wiley & Sons Ltd, 2007, pp. 2192–2226. [9] V. Zhukova, M. Ipatov, A. Zhukov, Sensors 9 (2009) 9216–9240, https://doi.org/10.3390/s91109216. [10] L.V. Panina, Phys. Status Solidi A 206 (2009) 656. [11] F. Qin, H.-X. Hua-Xin, Prog. Mater. Sci. 58 (2013) 183. [12] Manh-Huong Phan, Hua-Xin Peng, Michael R. Wisnom, Yu. Seong-Cho, J. Appl. Phys. 98 (2005) 014316. [13] M. Ilyn, V. Zhukova, J.D. Santos, A. Zhukov, Phys. Status Solidi A 205 (2008) 1378. [14] V. Vega, L. Gonzsalez, J. Garcia, W.O. Rosa, D. Serantes, V.M. Prida, G. Badini, R. Varga, J.J. Sunol, B. Hernando, J. Appl. Phys. 112 (2012) 033905. [15] P. Mellner, V.A. Chernenko, G. Kostorz, Mater. Sci. Eng., A 387–389 (2004) 965–968. [16] A. Zhukov, C. Garcia, V. Zhukova, V. Larin, J. Gonzalez, J.J. Del Val, M. Knobel, J. M. Blanco, Solids 353 (2007) 922–924. [17] V. Rodionova, K. Chichay, V. Zhukova, N. Perov, M. Ipatov, P. Umnov, V. Molokanov, A. Zhukov, J Supercond Nov Magn, doi:10.1007/s10948-014-2777-8. [18] A.T. Morchenko, L.V. Panina, V.S. Larin, M.N. Churyukanova, M.M. Salem, H. Hashim, A.V. Trukhanov, V.V. Korovushkin, V.G. Kostishyn, Journal of Alloys and Compounds 698 (2017) 685-691; [19] I. Baraban, M. Gorshenkov, N. Andreev, K. Chichay, V. Rodionova. Journal of Magnetism and Magnetic Materials (2017) https://doi.org/10.1016/j.jmmm.2017.12.048. [20] A. Zhukov, Adv. Funct. Mater. 16 (5) (2006) 675–680. [21] J. Torrejon, G. Badini, K. Pirota, M. Vazquez, Acta Mater. 55 (13) (2007) 4271–4276. [22] A. Zhukov, V. Zhukova, Magnetic sensors and applications basedon thin magnetically soft wires with tunable magnetic proper-ties, Int. Freq. Sensor Assoc. Publishing 154 (2014).

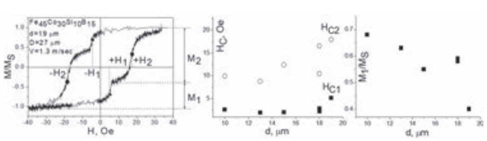

Fig. 1. Hysteresis loop of $Fe_{45}Co_{30}Si_{10}B_{15}$ microwire prepared at extraction rate of 1.3 m/sec under air cooling; an amorphous phase volume and coercivities of phases depending on microwire diameter.

Composition	Water cooling	Air cooling
$Fe_{77.5}Si_{7.5}B_{15}$	Singlephase (amorphous, bistable)	singlephase $V > 2.6$ m/sec biphase $V \leq 2.6$ m/sec
$Fe_{45}Co_{30}Si_{10}B_{15}$		biphase 1.3 m/sec $\leq V \leq$ 9.1 m/sec
$Co_{69}Fe_4Cr_4Si_{12}B_{11}$		singlephase $V \geq 6.5$ m/sec multiphase 2.6 m/sec $\leq V <$ 6.5 m/sec

Table. Manufacturing conditions to produce microwires in single or multiphase state.

3:45

BB-08. Magneto-optical observations of amorphous glass-coated microwires: role of topography.

K. Richter[2], A. Thiaville[1] and R. Varga[2]
1. Université Paris-Sud, Orsay, France; 2. University of Pavol Jozef Safarik, Kosice, Slovakia

Thin cylindrical wires attract considerable attention due to the interesting features of domain wall motion like absence of the Walker breakdown that makes possible to reach very high domain wall velocities [1]. While several experimental techniques allow for well controllable deposition of magnetic structures with complex geometries [2], a reliable determination of the surface magnetization usually meets several obstacles in case of samples with curved surface. Here, we provide a full analytical calculation of the Magneto-Optical Kerr Effect (MOKE) contrast for cylinders with reduced diameter. Understanding the underlying mechanisms allows devising a new approach for interpretation magneto-optical observations of amorphous glass-coated microwires. It is shown that the cylindrical shape of sample surface gives rise to a spatial distribution of the planes of incidence that are all tilted each to other [3]. Such mutual orientation of incident rays in combination with circumferential dependence of a local angle of incidence gives rise to apparent magneto-optical contrasts [3,4] that cannot be interpreted well without considering the curved surface of a cylinder. The magneto-optical contrast of magnetic cylinder is calculated for various angles of incidence, directions of surface magnetizations, directions of linear polarizations and as a function of an angle between polarizer and analyzer. Theoretical calculations [3] are tested experimentally on amorphous glass-coated microwires with well-defined cylindrical shape. Finally, our framework is used to study the shape of domain wall in FeSiB microwire characterized by very fast domain wall propagation that can reach up to several km/s. Our results show that a domain wall has tilted structure in these wires, which partially explains such high velocities.

[1] M. Yan, et al., *Phys. Rev. Lett.* 104 (2010), 057201. [2] A. Fernández-Pacheco, et al., *Sci. Rep.* 3 (2013), 1492. [3] K. Richter, et al., *Phys. Rev. B* 96 (2017), 064421. [4] K. Richter, et al., IEEE *Trans. Magn.* 50 (2014), 2501404. [5] K. Richter, et al., *Appl. Phys. Lett*. 96 (2010), 182507.

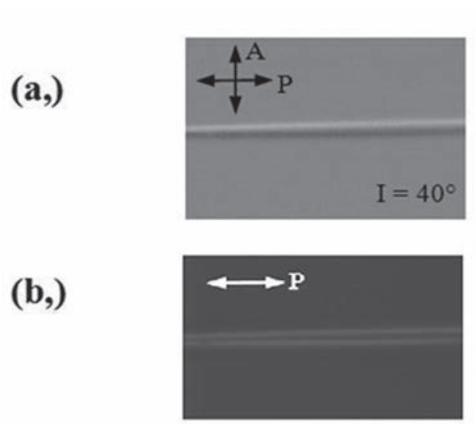

Fig. 1. (a,) Axial change of the surface magnetization generates black-and white magneto-optical contrast in MOKE microscopy. (b,) Optical image of corresponding place shows two intensity maxima.

4:00

BB-09. Comparison between two methods to measuring the magnetic fulx density in soft magnetic materials at high frequencies.

Y. Wang[1], X. Zhang[1], L. Chen[1], C. Liu[1] and Z. Wang[1]
1. Hebei University of Technology, Tianjin, China

I. INTRODUCTION In recent years, the application of nanocrystalline alloys in the field of electrical engineering is becoming more and more common. Nanocrystalline alloy materials have become one of the most important magnetic materials [1]. The nanocrystalline alloy has excellent electrical and magnetic properties and has been well developed in power, communications, medical, defense and civil products. At high frequencies, compared with the silicon steel sheet material for electrical workers, the nanocrystalline alloy not only has high permeability and low eddy current loss. The study of the magnetic properties of the nanocrystalline alloy, especially its properties in high-frequency rotating magnetic field, is of great significance for the use of this material. First of all, two-dimensional high-frequency rotating magnetic properties testing system is built. Secondly, two methods for measuring the magnetic flux density are compared, which are the probe method [2] and the capacitance method [3] Then, the magnetic properties of nanocrystalline alloys at high frequency were measured and compared respectively by the two methods of measuring the flux density. Finally, the advantages and disadvantages of the two methods were analyzed by the experimental results. II. TWO-DIMENSIONAL MAGNETIC PROPERTIES DETECTION SYSTEM The principle of the excitation is to pass the current signals 180 ° out of phase with each other in the orthogonal winding so as to generate a two-dimensional alternating magnetic field. Two-channel excitation signals are generated by LabVIEW programming software. As the excitation signal is weak enough to magnetize the excitation winding, the signal is amplified by two high-performance linear power amplifiers to drive the two axial excitation coils on the measurement device, For the excitation device to provide excitation current to ensure that the AMDA sample to be fully magnetized at a given frequency. The sample of the microcrystalline alloy is installed inside the BH composite sensor integrated module. After the sample is magnetized, the two sets of probes on the B sensor can measure two voltage signals corresponding to Bx and By, and the H coil can measure Hx and Hy corresponding to the two sets of voltage signal. Then, the collected four sets of voltage signals are amplified by a voltage preamplifier. Finally, through the four virtual input channels of the data acquisition card, the amplified voltage signal is collected and sent to the computer connected with it, and the data is processed and analyzed by LabVIEW software on the PC side. III. MAGNETIC FLUX DENSITY SENSOR AND H COIL During the experiment, the voltage signals corresponding to Bx and By, and Hx and Hy corresponding to Hx and Hy are measured by the sensor after the magnetization. Then, the signal is amplified by an amplifier. Finally, the voltage signal is collected by a data acquisition card and transmitted to Computer analysis and processing. A. probe method of measuring flux density NPT in the measurement process, the flux changes make the sample section eddy current, the sample has conductivity At the resistor), this creates a potential difference across the surface of the sample and the magnetic flux density B can be calculated from the induced voltage drop. The measurement principle shows that the method is suitable for monolithic measurement of magnetic materials. B. Capacitance flux density sensor In order to ensure good electrical contact, some force must be applied to the probe surface to the sample. The force is usually provided by a spring-connected probe that is pressed against the sample by a spring probe to maintain a constant force. The combination of force with the very sharp tip of the probe can lead to micro-damage on the surface of the material. The capacitance method is the probe for the conductive patch attached to the surface of the sample to be measured, the same use of eddy current pressure drop to derive the magnetic flux density. Its advantages are twofold: first, there is no need to insulate some samples; second, it does not introduce any micro-damage on the sample surface. C. H coil The principle of measuring the size of the magnetic field is the law of electromagnetic induction. There are two H coils for measuring the magnetic field strength, namely the Hx coil for measuring the magnetic field in the x direction. The structure of two H coils is exactly the same, the winding directions of the coils are perpendicular to each other, and used to measure the magnetic field strength in both directions of x and y. The coil is composed of a skeleton and enamelled fine copper wire. The skeleton is an insulating material and has a thickness of 0.5mm. The winding part is a square with a side length of 14mm. The diameter of the thin copper wire is 0.03mm, which is uniform and close Winding into a single layer, a total of winding 310 turns. In order to eliminate interline interference, H coil lead-out part also uses the form of twisted pair. IV. CONCLUTION It can be seen from the measurement results that the experimental data of the flux density measured by the capacitance method are very close to the data measured by the probe method. However, the capacitance method can obtain a sinusoidal waveform with better magnetic flux density, which is easy to control and reduces The complexity of the control method is a good way to obtain the nanocrystalline magnetic properties at higher magnetic flux densities.

1.International Electrotechnical Commission. IEC[S], 60404-6-2003, Methods of measurement of the magnetic properties of magnetically soft metallic and powder materials at frequencies in the range 20 Hz to 200 kHz by the use of ring specimens. Switzerland: 2007 2.Yamaguchi T, Senda K, Ishida M, et al. Theoretical analysis of localized magnetic flux measurement by needle probe[J]. Le Journal de Physique IV, 1998, 8(PR2): Pr2-717-Pr2-720 3.Zurek S, Meydan T. A novel capacitive flux density sensor[J]. Sensors and Actuators A: Physical,2006, 129(1–2): 121-125 4.Goričan V, Hamler A, Jesenik M, et al. Unreliable determination of vector B in 2-D SST[J]. Journal of Magnetism and Magnetic Materials, 2003, 254–255(0): 130-132

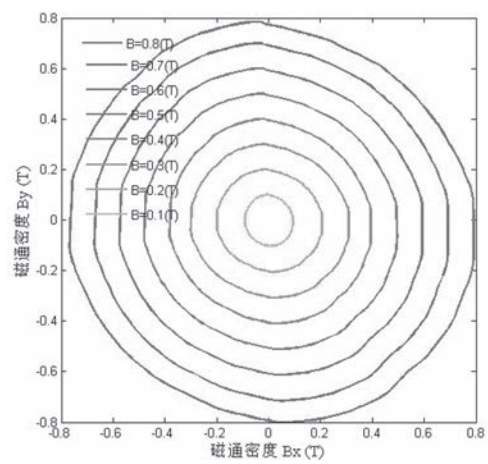

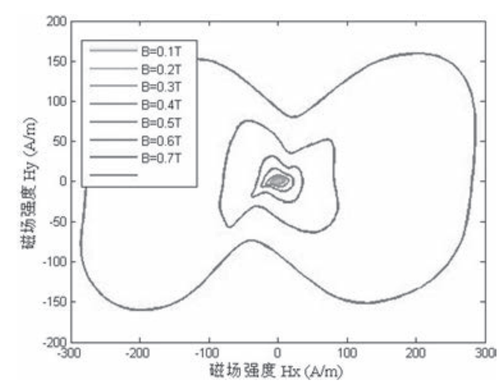

4:15

BB-10. Thickness dependent high frequency properties of multistripe patterned FeCoBSi magnetic films.

L. Zhang[1], Y. Liu[1], H. Zheng[1], W. Zhu[1], M. Zhang[1], P. Zhou[1], H. Chen[1], X. Wang[1], H. Lu[1], J. Xie[1] and L. Deng[1]
1. School of Microelectronics and Solid-State Electronics, University of Electronic Science and Technology of China, Chengdu, China

With the rapid development of telecommunication technology, the problems of electromagnetic inference (EMI), which deteriorate the performance of such systems in high frequency, attract public attentions significantly. EMI suppression materials, especially for magnetic shielding materials with noise suppression at high frequencies, pave the way for material scientists and RF engineers to protect susceptible devices. In order to satisfy requirements of EMI shielding materials, broadband and controllable resonances of magnetic films are desired. Meanwhile, a high damping factor at designed frequency would make contribution to realize promising EMI devices. Due to in-plane uniaxial anisotropy of a film could lead to well soft magnetic properties at Gigahertz frequency, hence better absorption properties, several methods including induced magnetic field, induced stress during deposition, multi-layer design, post annealing under external magnetic field were investigated. Besides, patterned magnetic films with induced shape anisotropy designed by artificial structure, draw great public attention due to its controllable and robust properties. Therefore, in this paper, in order to expand the resonance band furthermore, we introduced a unique multi-striped patterned FeCoBSi thin films and analyzed the novel broadened band phenomenon due to multiple resonance peaks with the Landau-Lifshitz-Gilbert (LLG) processional motion formulism. A series of $Fe_{66}Co_{17}B_{16}Si_1$ thin films were deposited on silicon (111) substrates by DC magnetron sputtering at room temperature. An external magnetic field of 500 Oe was applied along the short axis of the substrate to induce in-plane uniaxial anisotropy. Traditional ultraviolet (UV) lithography technology and lift off method were used to fabricate the multistriped patterns. A combined stripe patterned FeCoBSi films containing various stripes with different width were processed depending on thickness. The stripes were arranged successively with width sequence as 5um, 10um, 15um, 20um and 25um respectively. A separation gap of distinctive stripes was fixed at 5μm. The thickness of the patterned films varied from 45 nm to 135 nm. VSM measurement was operated at room temperature in order to characterize the static properties of magnetic films. The films with different thickness all possess a significant in-plane uniaxial anisotropy as figure 1 showed. Such uniaxial anisotropy was contributed by induced magnetic field as well as the stripe shape induced anisotropy. Furthermore, the hysteresis loops in figure 1 revealed well soft magnetic properties with coercivity as low as 13 Oe. With increase of film thickness, coercivity would decrease from 32 Oe at 45nm to 13 Oe at 135 nm, which was in accordance with random anisotropy model proposed by Herzer[1]. When the films were composed of amorphous or granular structure, if the grain size exceeded the exchange length (for FeCo-based alloys, the exchange length is approximately 46 nm[2]), the coercivity was inversely proportional to the former factor, hence decreased with increase of film thickness[3]. The broad resonance band phenomenon was enhanced with full width half maximum (FWHM) of 3.85 GHz at thin thickness, i.e. 45 nm for our experiments as showed in figure 2. The broaden band phenomenon was due to the different shape anisotropic field induced by different width stripe as our assumption. Consider the fixed width of the gap as 5um, which is large enough to magnetically separate the two consecutive stripes without coupling effect. Thus, each stripe was actually independent to each other leading to separate magnetic response under microwave excitation. The total response to the high frequency electromagnetic field should be a mathematical addition of every stripe[4]. Meanwhile, the alteration of resonance frequency could be predicted by the mathematic formula related to demagnetization factors. The results could be further illustrated by the shape induced effective anisotropy filed due to distinguished stripe width, which made it possible to control by the traditional lithography process in the actual application. In conclusion, multistripe patterned FeCoBSi thin films with different thickness were fabricated by DC sputtering and UV lithography technology. Band broadened phenomenon and multiple resonance peaks were observed in the experiment. Compared to the former double-striped patterned films, multistriped pattern could extend the resonance band (FWHM) furthermore to 3.85 GHz. By calculating the theoretical resonance frequency of different stripe, one can conclude that the band broadened phenomenon is contributed to supposition effect of various resonance peaks. The broaden band phenomenon could be controlled by tuning width of different stripe as well as thickness of magnetic films in order to meet the requirement in the actual application, which may be useful in the future EMI devices.

[1] G. Herzer, "Soft magnetic nanocrystalline materials, Scr. Metall. Mater". 33(1995) 1741. [2] M. A. Willard, D. E. Laughlin, and M. E. McHenry, "Recent advances in the development of (Fe,Co)88M7B4Cu1 magnets", J. Appl. Phys., vol. 87, no. 9, May 2000, Art. ID 7091. [3] S. Zhang, F. Xu, X. Ma, et al., "Thickness dependence of high-frequency magnetic properties in the oriented hcp-CoIr soft magnetic films with negative magnetocrystalline anisotropy", J. magnetism magnetic Mater. 299 (2014), 81-85. [4] Li Zhang, Hanyu Zheng, Wenbi Zhu, et al. "High frequency magnetic properties of multistriped patterned FeCoBSi thin films", Journal of Alloys and Compounds, vol.706, pp. 318-321, 2017.

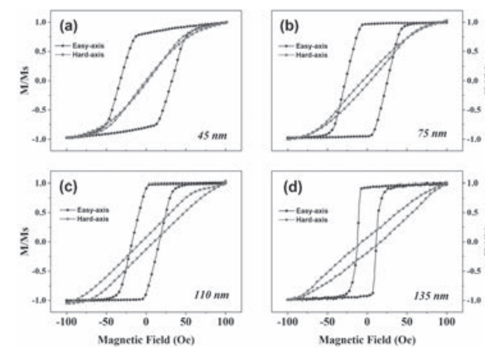

Fig. 1. The hysteresis loops of multistriped magnetic films with different thickness. The results are exhibited from easy-hard axis defined by induced magnetic field direction in each picture. From figure (a) to (d), the thickness of films varied from 45nm to 135nm.

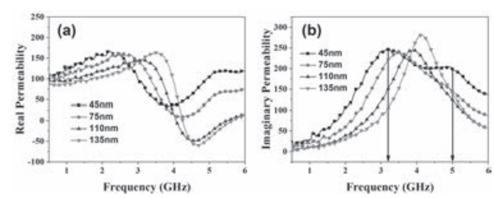

Fig. 2. The permeability spectrum of multistripe patterned FeCoBSi thin films. Figure (a) reveals the real permeability of films from thickness at 45nm to 135nm while figure (b) exhibits the imaginary permeability at each correspondent thickness, respectively.

4:30

BB-11. Microwave behaviour of metacomposites containing CNTs-coated ferromagnetic microwires.

Y. Luo[1], S. Wei[1], D. Estevez[1], F. Qin[1] and H. Peng[1]
1. Material Science and Engineering, Zhejiang University, Hangzhou, China

Metamaterials are featured with peculiar left-handed electromagnetic (EM) characteristics in favour of a wide range of interesting applications such as invisibility cloak, zero-loss imaging, perfect absorbers, etc.1,2 Nevertheless, conventional metamaterials are restricted to designs of periodical structures without considering the intrinsic materials' properties of building blocks. Fabrication technologies allow realising metamaterial properties from microwave to optical frequencies yet they are not cost-effective for mass production. We have proposed the term of 'metacomposites' to remedy these issues: (i)Metacomposites are 'true' piece of material possessing single/double negative left-handed features rather than a structure. (II) The eventual left-handed EM properties are manipulated by both dielectric/magnetic properties and geometrical arrangement of building blocks. (III) Metacomposites can be manufactured by an engineering technique. Microwires with ferromagnetic elements have been proved as desirable metamaterial building blocks due to their excellent soft magnetic properties and limited scattering effects to incident waves.3 It has been demonstrated that glass fibres reinforced composites containing ferromagnetic microwires display a double negative (DNG) feature evidenced by their transmission behaviour.4 However, such a metacomposite has rather limited response to external stimuli,5 e.g., magnetic fields, current, etc., which is crucial for practical applications. In the work, as a continuous effort, we design and manufacture rubber-based composites embedded with multiwall carbon nanotubes (MWCNTs) coated microwires. The magnetic properties of microwires can be optimised by a proper annealing dc current of 25 mA indicated by their giant magnetoimpedance (GMI) signature. The microwave properties of their composites show a remarkable on/off modes of left-handed behaviours tuned by external current bias. Experimentally, melt extracted amorphous $Co_{68.15}Fe_{4.35}Si_{12.25}B_{15.25}$ microwires with diameter of 70μm were used in the present work. MWCNTs (Cheaptube, purity 95%) were coated on the wires by electrophoretic deposition (EPD) technique in the following process.6 CNTs were chemically oxidised in a mixed solution of H_2SO_4, $KMNO_4$, $NaNO_3$, and H_2O_2 to generate carboxyl acid groups on the CNT surface in order to create negative surface charges. The deposition process was carried out at 10V bias for 120 seconds to ensure a homogeneous layer of CNTs on wire surface. Post current annealing was conducted by clamping microwires on a dc power supply with electrical current of 5mA, 10mA, 15mA, 20mA, 25mA, 30mA, respectively for 10 min. The impedance spectra Z(f, H) of microwires were extracted using a ZNB 20 vector network analyzer (VNA) (Rohde & Schwarz) with the probe current frequency within the range 1MHz $\leq$ f $\leq$ 200MHz.7 Testing frequencies are assigned as 1MHz, 10MHz, 100MHz and 200MHz, respectively with external fields swept in -40 $\leq$ H $\leq$ +40Oe. For the manufacture of composites, CNT-coated microwires were arranged into rubber matrix in a parallel manner with identical spacing of 2 mm, followed by an oven curing process at 125 oC for 30 min. Microwave measurement was conducted in WR-90 waveguide in the range of 8.2-12.4GHz. The complex permittivity was computed using the Reflection/Transmission Epsilon Fast Model.8 The low-frequency MI profiles (1 MHz) of CNT-coated wires (inset of Fig. 1) showcase a typical single peak feature, indicating that domain wall displacement dominates the magnetization process in the wires. Also, such mechanism is insensitive to CNTs-coating and annealing currents. Further, a double-peak transition appears (Fig. 1) as the measuring frequencies increases due to the stronger spin rotating therein. It is found that applying a dc bias up to 25 mA is beneficial in enhancing the GMI ratios arising from the increased volume of circular anisotropy of the used Co-based wires due to the relaxed surface stresses between CNT/wire interfaces. However, further increasing current to 30 mA is detrimental to GMI properties due to the possible crystallization on the wire surface that is unfavourable of magnetization rotation. Remarkably, the real part of permittivity of wire-composites shows a non-plasmonic signature as the annealing current is below 25 mA, suggesting a non-metamaterial medium. This is attributed to the discontinuous CNT islands that prevent the wires being as perfect electric conductor, which is a prerequisite for using Pendry's model.9 Further increasing annealing current to 30 mA induces dipole-dipole polarisation among CNTs and enhances the conductivity of CNT-coated wires and excited dielectric responses from the surface impedance (Fig. 1). Subsequently, plasmonic behaviour appears as evidenced in Fig. 2. The key features in the present study provides insights to design and fabricate tunable left-handed composites that are of potential engineering interest for cloaking and sensing applications.

1 D. R. Smith, J. B. Pendry, and M. K. Wiltshire, Science. 305, 788 (2004). 2 V.M. Shalaev, Optical negative-index metamaterials, Nat. Photon. 1, 41 (2007). 3 H. García-Miquel, J. Carbonell, J. Sánchez-Dehesa. Appl. Phys. Lett. 97, 094102 (2010). 4 Y. Luo, H. X. Peng, F. X. Qin, M. Ipatov, V. Zhukova, A. Zhukov, and J. Gonzalez, J. Appl. Phys.115, 173909 (2014). 5 Y. Luo, H. X. Peng, F. X. Qin, M. Ipatov, V. Zhukova, A. Zhukov, and J. Gonzalez, Appl. Phys. Lett.103, 251902 (2013). 6 A. R Boccaccini, J. Cho, JA Roether, B.J. C Thomas, EJ Minay and M.S.P Shaffer, Carbon. 44, 3149 (2006). 7 M. H. Phan, H.X. Peng. Prog. Mater. Sci. 53,323(2008). 8 F. X. Qin, Y. Quéré, C. Brosseau, H. Wang, J. S. Liu, J. F. Sun, and H. X. Peng, Appl. Phys. Lett.102, 122903 (2013) 9 J. Pendry, A. Holden, W. Stewart, I. Youngs. Phys. Rev. Lett. 76, 4773 (1996).

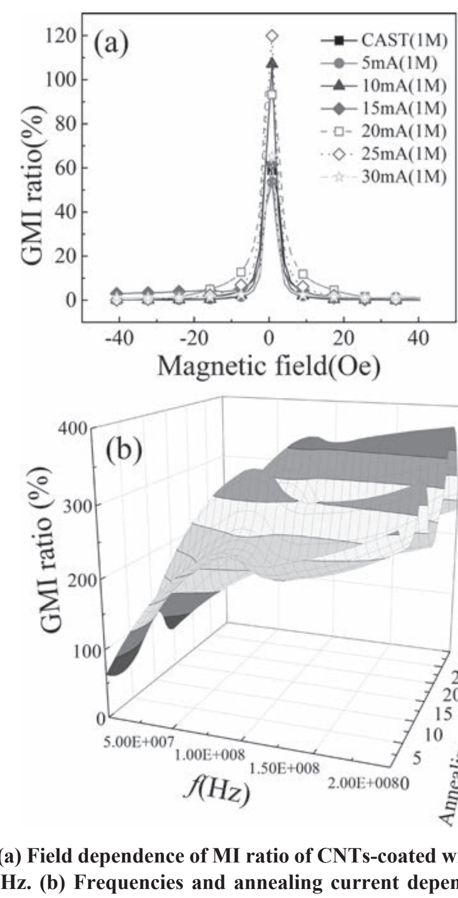

Fig. 1. (a) Field dependence of MI ratio of CNTs-coated wires measured at 1 MHz. (b) Frequencies and annealing current dependences of MI ratios of CNT-coated microwires.

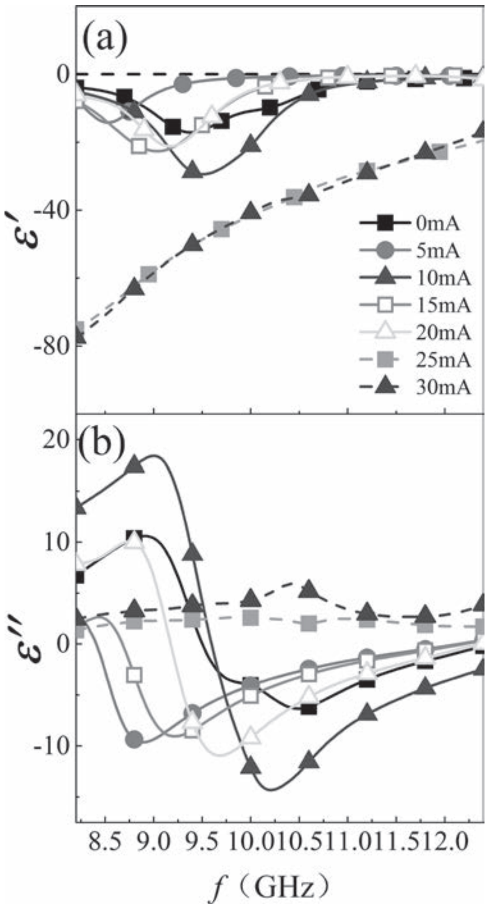

Fig. 2. Frequency dependence of (a) real part and (b) imaginary part of effective permittivity of rubber-based composites containing CNT-coated microwires annealing at different dc bias.

4:45

BB-12. Collective behavior of nanograins in Co-substituted Fe-based nanocrystalline alloys.

G. Manginas[1], G. Ababei[1], A. Damian[1], G. Stoian[1], M. Grigoras[1], M. Tibu[1], H. Chiriac[1], T.A. Ovari[1] and *N. Lupu*[1]
1. National Institute of Research and Development for Technical Physics, Iasi, Romania

The need for more efficient energy conversion and/or distribution systems is a challenging and strong demand nowadays. Among other materials, amorphous and/or nanocrystalline soft magnetic alloys are a viable alternative for both storage and transportation of the energy. In the recent years, they turned out to become competitive with silicon electrical steels and various ferrites for niche applications, mainly the ones involving working at high frequencies and temperatures [1]. The literature reports many attempts to improve the soft magnetic properties of Fe-based amorphous and/or nanocrystalline rapidly solidified materials, by modifying either the composition or annealing conditions. For example, it was shown that by replacing 22 at.% of Fe with Co, the Co-substituted FINEMET alloy can be used at 500^{0}C, the relatively low coercivity being preserved even at such high temperatures [2]. In order to study further these correlations and to understand why an amorphous and/or nanocrystalline material with nearly-zero magnetostriction has a large output response when subjected to a mechanical stress or vibration, in this work we will present comparatively our latest results on the collective behavior of nanograins in Co-substituted FINEMET and VITROPERM 800 rapidly quenched alloys, having nominal compositions $(Fe_{1-x}Co_x)_{73.5}Cu_1Nb_3Si_{13.5}B_9$ and $(Fe_{1-x}Co_x)_{73.5}Cu_1Nb_3Si_{15.5}B_7$, respectively (x = 0, 0.25, 0.5, 0.75 and 1), in the as-quenched state and after annealing at temperatures between 500 and 600°C. Our study mainly focusses on how Co influences the precipitation and anisotropies of the nanograins, as well as the temperature variation of magnetic and magnetoelastic properties of the 2 systems. In addition, we were interested to understand why the small compositional variations of Si and B in FINEMET and VITROPERM 800 alloys are inducing a strongly different magnetoelastic behavior in the as-quenched amorphous samples, with small positive magnetostriction values for FINEMET samples and zero magnetostriction for VITROPERM 800 ones. The as-quenched samples are fully amorphous as one can see from the TEM images shown in Fig. 1, while the ones subjected to annealing are nanocrystalline, with grains of 15-30 nm, randomly dispersed within the amorphous matrix, depending on the annealing temperature and Co content. The optimum magnetic properties are obtained at different annealing temperatures (between 510 and 550^{0}C), depending on Co content, as shown in Fig. 1; the larger the Co content, the lower is the optimum annealing temperature. The total substitution of Fe with Co is strongly influencing the microstructure and is hardening the material (Fig. 2). The substitution of Fe with Co followed by optimum annealing reduces drastically the saturation magnetostriction due to the more random distribution of internal micro-stresses in Co-substituted samples compared with the ones containing Fe only, but also due to the different orientation of the anisotropies of Fe(Co) grains relative to the matrix. The optimum magnetic properties are obtained for samples with Co contents ranging from 25 to 50 at.%, annealed at temperatures in the range of 530-540^{0}C, when the nanograins reach their optimum sizes (between 15 and 25 nm) and the percolation limit increases to 60-70%. In this case the collective behavior of the nanograins reaches the maximum strength, this being also influenced by the presence of Co in the DO_3 nanograins, which slightly shifts the nanograins structure from bcc towards fcc or even hcp. Such a specific behavior is also strongly dependent on the Si to B contents, a larger content of Si in VITROPERM 800 playing a more significant role in the exchange interactions between the grains through the amorphous residual matrix. *Financial support from the ITN-FP7 Marie Sklodowska-Curie program "VitriMetTech" N. 607080 and 3MAP NUCLEU Program (2018) is thankfully acknowledged.*

[1] G. Herzer, Acta Mater. 61 (2013) 718-734. [2] F. Mazaleyrat, Zs. Gercsi, J. Ferenc, T. Kulik, L.K. Varga, Mater. Sci. Eng. A 375–377 (2004) 1110–1115.

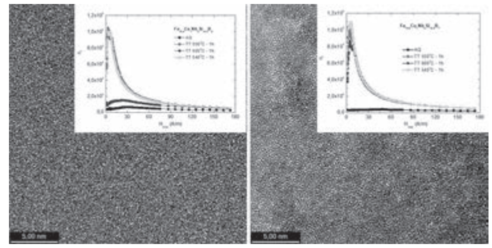

Fig. 1. HRTEM images of as-quenched FINEMET (left) and VITROPERM 800 (right) melt-spun ribbons and the variation of the relative magnetic permeability with applied magnetic field and annealing temperature for the same samples.

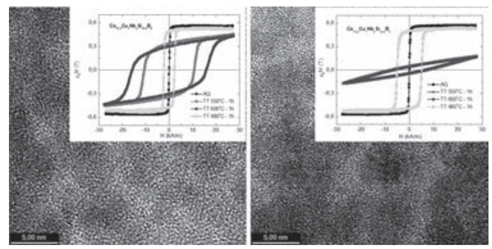

Fig. 2. HRTEM images of fully Co-substituted FINEMET (left) and VITROPERM 800 (right) melt-spun ribbons and the evolution of the magnetic hysteresis curves with annealing temperature for the same samples.

TUESDAY AFTERNOON, 24 APRIL 2018 ORCHID IV, 2:00 TO 5:00

Session BC
BIO-IMAGING AND BIO-DETECTION I

Daniel Ortega Ponce, Chair
IMDEA Nanociencia, Madrid, Spain

CONTRIBUTED PAPERS

2:00

BC-01. Magneto-paper composites for low-cost two-way valves and other active µPads.

M. Fratzl[1,3*], B. Chang[2], S. Oyola-Reynoso[2], G. Blaire[3], S. Delshadi[3,4], O. Cugat[3], M. Thuo[2], J. Bloch[5] and N. Dempsey[1]
1. Univ. Grenoble Alpes, CNRS, Grenoble INP, Institut Néel, Grenoble, France; 2. Department of Materials Science and Engineering, Iowa State University, Ames, IA, United States; 3. Univ. Grenoble Alpes, CNRS, Grenoble, France; 4. Univ. Grenoble Alpes, CNRS, Inserm, Grenoble, France; 5. Univ. Grenoble Alpes, CNRS, Grenoble INP, 3SR, Grenoble, France*

We present a magnetically actuated paper based microfluidic two-way valve that includes a neutral position — the first of its kind. The presented valves are highly robust, customizable, contact-free and fabricated using facile and cost effective methods suitable for microfluidic paper analytical devices (µPad) applications. The advent of a neutral position and ability to precisely control switching frequencies unlocks a new platform for highly controlled fluid flow in paper based microfluidic test assays. We demonstrate the feasibility of the two-way valves performing a fully automatized colorimetric assay on a Magnetic µPad (M-µPad). Portable and disposable diagnostic devices for Point-of-Care usage should be robust, lightweight, inexpensive, and easy to use. Microfluidic paper analytical devices (µPads) have emerged as an alternative to expensive glass or polymer based chips [1]. µPads offers numerous advantages compared to classical microfluidic approaches. Indeed, their capillary action eliminates the need for external pumps. Furthermore, µPads are bio-compatible for various applications including clinical diagnosis, food quality control, and environmental monitoring [2]. However, a downside to this promising technology is that many active elements used in microfluidic applications assuring robust fluid control such as valves and switches are hardly reproducible in disposable paper-based devices. Magnetism is widely used in microfluidics as it provides contactless and long-range forces that can be either repulsive or attractive. Li et al. reported on the fabrication of a paper-based magnetic valve by attaching an iron loaded PDMS film on one side of a paper cantilever [3]. By applying an external magnetic field, the cantilever deforms and closes a gap with an underlying paper, allowing fluid to flow downstream. However, this method presents numerous limitations. The preparation and deposition of the magnetic PDMS film adds a complexity to the µPad fabrication. The use of soft magnetic nanoparticles as magnetic structure implies that only attractive magnetic forces can be used to close the valve. While these two limitations could be solved by replacing the loaded PDMS with industrially produced permanent magnetic adhesive tape, the third is more problematic: as the magnetic film covers one side of the paper cantilever, fluid flow can only be assured through the opposite paper side. Recently, we have developed techniques to micro-pattern high-performance hard-magnet / polymer composites based on magnetic powders [4] or pillars [5], producing field gradient values as high as 10^6 T/m. We further managed to embed conducting polymer within paper thus making an active paper/polymer composite [6]. We are now integrating hard magnetic powders such as NdFeB and SmFeN directly into paper [Figure 1 a/b], so that both paper surfaces remain available for capillary fluid transport. To obtain a functional paper magnetic valve, both surfaces of the paper must remain accessible for capillary fluid transport. We present two different techniques to achieve paper magnetic valves: in the Deposit, Composite and Magnetize (DCM) technique, the magneto-active regions were directly integrated during the paper fabrication process. After fabricating a sheet of paper through an ISO 5269/1 TAPPI process, the outline of the valve was traced using a pen on the still-wet sheet. Hard-magnetic powders were deposited to form the magneto-active zone. A second sheet of paper with identical properties was fabricated and placed on the first one. The composite structure was subsequently dried in a sheet dryer at 60 °C, resulting in a stable valve without additional chemical binding substances (Figure 1 a). The second approach, the Emboss, Impregnate and Magnetize (EIM) technique consists of coating parts of one valve surface with hard magnetic powders without blocking capillary fluid transport through this surface. After cutting the valve out of the sheet we embossed the magneto-active region using a 3D printed mask prior to powder deposition. Hard magnetic powders dispersed in PDMS are spread on the embossed paper and due to the porosity of the paper, the PDMS eventually penetrated the embossed areas. After curing the PDMS at 80°C for 30 min, the magnetic powders were permanently fixed to the paper surface (Figure 1 b). We built an ELISA-compatible colorimetric assay M-µPad demonstrator compatible with both magnetic valve techniques. In our prototype, 2 reagent pads (red/blue fluids) were used, which are connected to a microfluidic syringe pumping fluid at a constant flow. In Figure 1 d, the valve was first opened towards reagent 1, filling up the strip zone with blue dye. After 120 s, the valve was switched towards reagent 2, which allows red dye to enter the test strip. Finally, the valve was closed towards position 0, stopping the fluid flow. Note that a microchip controlled the magnetic fields that were operating the entire sequence. We demonstrate the fabrication of a programmable 2-way paper based microfluidic valve - a missing element in the microfluidic circle. The highly customizable system remains robust, low cost and operates without external contact. We also demonstrated its applicability in an ELISA-compatible colorimetric assay.

[1] "Three-dimensional microfluidic devices fabricated in layered paper and tape," A.W. Martinez, S. T. Phillips, and G. M. Whitesides, PNAS 105, 19606–19611 (2008). [2] "Progress in the development and integration of fluid flow control tools in paper microfluidics," E. Fu and C. Downs, Lab on a Chip 17, 614-628 (2017). [3] "Magnetic timing valves for fluid control in paper-based microfluidics," X. Li, P. Zwanenburg, X. Liu, Lab on a Chip 13, 2609-2614 (2013). [4] "Micro-magnetic imprinting of high field gradient magnetic flux sources, " N. M. Dempsey, D. Le Roy, H. Marelli-Mathevon, G. Shaw, A. Dias, et al., Applied Physics Letters, 104, 262401 (2014). [2] [5] "Fabrication and characterization of polymer membranes with integrated arrays of high performance micro-magnets" M. M. Hamedi et al, Materials Today Communications, 6, 50-55 (2016). [6] "Electrically Activated Paper Actuators" M. M. Hamedi et al, Advanced Funct. Materials, 26, 2446 (2016).

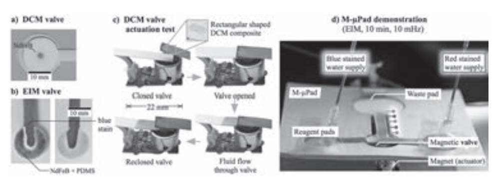

Fig. 1. a/b) DCM/EIM valves. c) Actuation of an EIM valve with an Arduino™ controlled electromagnet. d) ELISA-compatible colorimetric assay M-µPad demonstrator.

2:15

BC-02. Vertical hydrodynamic focusing for cell counting with a magnetoresistive cytometer.

A. Chicharo[4,1], L. Barnsley[2,3], M. Martins[4], A. Taouallah1[4], B. Silva[4], S. Cardoso de Freitas[5], L. Dieguez[4], B. Espiña[4] and P. Freitas[4,5]
1. Instituto Superior Técnico, Universidade de Lisboa, Lisbon, Portugal; 2. Jülich Centre for Neutron Science at Heinz Maier-Leibnitz Zentrum, Forschungszentrum Jülich GmbH, Garching, Germany; 3. Institute of Biomedical Engineering, University of Oxford, Oxford, United Kingdom; 4. INL - International Iberian Nanotechnology Laboratory, Braga, Portugal; 5. INESC-MN, Lisbon, Portugal

Cell counting has shown great impact across several areas of biological sciences: from clinical applications to environmental monitoring[1]. These devices are continuously being miniaturized[1,2], i.e. microcytometers, for automated cell couting[2,3]. Aligned with this goal, we present a magnetoresistive cytometer[4,5] that integrates spin-valves sensors(SVs), a new permanent magnet(PM) design for magnetization of magnetic beads(MBs), and, a new microfluidic feature to increase the system sensitivity. Magnetic sensing microcytometers, using SVs[4,5,6,7] or μHall sensors[8], present several advantages when compared to optical systems[8] or electrical impedance techniques[9]. Firstly that these devices rely on a more stable labelling by using magnetic beads (MBs), instead of fluorophores, to label the cells and secondly that specificity is attributed through magnetic labeling. The magnetic field of MBs in flow is quantified by the sensor, providing local signal detection from the MBs on the surface of the cells, even in the presence of other cells[10]. The sensors used are solid-state technology and are easily integrated with microfluidic channels to present the cells one-by-one in close proximity to the sensors. The magnetic detection is performed directly through a digital-to-analog electronic acquisition board without the need of integrating complex components such as microlenses in optical microcytometers[3]. Here we show an optimization for magnetic cytometers by developing an adaptable 3D flow focusing method into microfluidic channels that present the cells closer to the SVs. We demonstrate the two and three-dimensional confining capabilities of the fluid by hydrodynamic focusing on a microfluidic channel with 300μm in width and height of 50μm. This was achieved by observing the performance of a fluorescent focused sheath under a fluorescent and confocal microscopy and compared to simulation model(Fig.1(a)). The SVs, with 200μm in length, are located on the bottom of the microchannel. First, lateral focusing was set, using a combination of flow rates for the sample (Q_S) and lateral sheath (Q_L), to have a width of 100um (Q_L=2Q_S). The vertical flow rate (Q_V) can be adjusted accordingly to the cells size to be detected, from submicron up to 50μm diameter cells. The cells employed here have an average diameter of 20μm, thus a combination of vertical sheath flow Q_V=3Q_S=1.5Q_L was chosen to limit the sample height to 25um above the sensor. The microchip presented here(Fig.1(b)) incorporates 12 SVs located on a 2x6.5mm^2 area and are distributed in 6 microfluidic channels, with 2 sensors each. Typically, commercial permanent magnets(PM) are used for the magnetization of the superparamagnetic MBs. They are difficult to align and may reduce the SVs sensitivity due to the in-plane component of the magnetic field which drastically varies over the length-scale of the PM. We show the design of an innovative PM that presents a homogeneous, high out-of-plane magnetic field over the SVs (>1000 Oe out-of-plane and in-plane below 10 Oe). The SVs without a PM present average MR values of 8.07%±0.11 and sensitivity of 1.38±0.04 Ω/Oe. Using a commercial PM(N42 grade disc of 3cm and 3mm thick) below the chip, MR and sensitivity lowered significantly over all SVs to 6.45%±1.24 and 0.32±0.24 Ω/Oe and when subjected to the new custom-made magnet, MR ratios and sensitivity was increased, 7.55%±0.29 and 0.58±0.09Ω/Oe. The new magnet confers a high magnetization and can be used without careful alignment to ensure optimal operation on all SVs for the 6 microchannels. Afterwards, the effect of the 3D focusing in the detection biochip was verified with 1μm MBs flowing over the SVs. Signal bipolar peaks[4,5] were recorded and can be decomposed by two recognizable characteristics values: the amplitude of the peak(PA) and time-of-flight(TOF). Then, two SVs spaced by 300μm were used to measure the time between the signal peaks, on separate signal acquired channels, to obtain the linear velocity of the MBs. The system can be operated at high-speed flow conditions, reaching up to 7cm/s, and velocities with increasing vertical flow rates agrees with numerical microfluidic simulations. Finally, we demonstrated the system capability to increase a three-fold sensitivity of the device when cancer cells labelled with MBs are injected with vertical focusing over the sensors. The labelling of cancer cells were performed with 0.5um diameter MBs. Previous work with smaller cell sizes of myeloid leukemia cell line (5μm in diameter) [4] and *streptococcus agalactiae* cells (1μm in diameter) [5] using 50nm MBs for their detection. However, as cancer cells present higher sizes (around 20μm), larger MBs were required for the signal detection. Biotinylated anti-EpCAM antibodies against specific membrane receptors for the target cells were immobilized on the surface of the streptavidin -MBs and incubated with cells. The samples were analyzed in the same microchannel with and without vertical focusing and same output flow rate. Figure 2(a) and (b) shows the PA and TOF values for each detected signal with and without vertical focusing and compared to a sample composed only of MBs.

[1] Green and S. Wachsmann-Hogiu, *Development, History, and Future of Automated Cell Counters*, 2015. [2] P. K. Chattopadhyay and M. Roederer, "*Cytometry: Today's technology and tomorrow's horizons*," Methods, 2012. [3] D. A. Ateya, J. S. Erickson, P. B. Howell, L. R. Hilliard, J. P. Golden and F. S. Ligler, *The good, the bad, and the tiny: A review of microflow cytometry*, 2008. [4] J. Loureiro, P. Z. Andrade, S. Cardoso, C. L. Da Silva, J. M. Cabral and P. P. Freitas, "*Magnetoresistive chip cytometer*". [5] A. C. Fernandes, C. M. Duarte, F. A. Cardoso, R. Bexiga, S. Cardoso and P. P. Freitas, "*Lab-on-chip cytometry based on magnetoresistive sensors for bacteria detection in milk*," Sensors (Switzerland), 2014. [6] M. Reisbeck, M. J. Helou, L. Richter, B. Kappes, O. Friedrich and O. Hayden, "*Magnetic fingerprints of rolling cells for quantitative flow cytometry in whole blood*," *Scientific Reports,* 2016. [7] D. Issadore, J. Chung, H. Shao, M. Liong, A. A. Ghazani, C. M. Castro, R. Weissleder and H. Lee, "*Ultrasensitive clinical enumeration of rare cells ex vivo using a micro-hall detector*," *Science Translational Medicine,* 2012. [8] S. Etcheverry, A. Faridi, H. Ramachandraiah, T. Kumar, W. Margulis, F. Laurell and A. Russom, "*High performance micro-flow cytometer based on optical fibres*," Scientific Reports, 2017. [9]C. Petchakup, H. Li and H. W. Hou, *Advances in single cell impedance cytometry for biomedical applications*, 2017. [10] L. Mohammed, H. G. Gomaa, D. Ragab and J. Zhu, *Magnetic nanoparticles for environmental and biomedical applications: A review*, 2017.

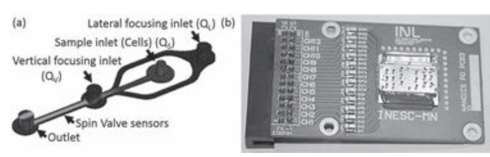

Fig. 1. (a) Schematic of the microfluidic channel with simulation of vertical focusing effect. (b) Microchip composed of SVs microchip with bonded polymer microfluidic channel module on top.

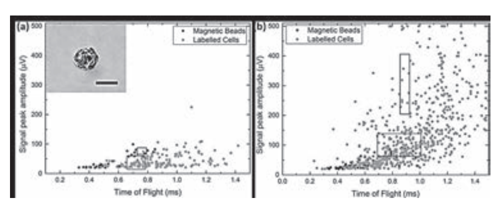

Fig. 2. PA vs TOF of detected events without (a) and with (b) vertical focusing. Inset of (a) presents an SW480 cancer cell labelled with 0.5μm magnetic beads. Scale corresponds to 20μm.

INVITED PAPER

2:30

BC-03. Magnetic Micro/Nano Structures for Biological Detection and Manipulations. ***(Invited)***

C. Li[1], B. Chen[1], Y. He[1], C. Hou[1], H. Huang[1] and *Z. Wei*[1]
1. National Tsing Hua University, Hsinchu, Taiwan

Magnetic micro-/nano-structures were designed and fabricated for bio-detection and bio-manipulation. First, some three dimensional micro-/nano-structures were proposed as biosensors. These three dimensional magnetic sensors can actively attract the magnetically labeled cells to the sensor position and fix the cells to be detected, which is advantageous over traditional two dimensional thin film biosensors.[1] Besides, by the integration of the spintronics and microfluidics, a Wheatstone bridge giant magnetoresistance (GMR) biosensor was also demonstrated for the detection and counting of magnetic cells.[2] Second, manipulating cells in specific positions is a very important issue for cell scaffold applications. In our study, by controlling magnetic domain walls in patterned magnetic thin films or by controlling the aligned direction of electrospun PVA-gelatin nano-fibers [3] with magnetic nanoparticles, the patterning of magnetic cells can be achieved. We also demonstrated that self-assembling of magnetic fluid or microdroplets can be used to form periodic lattice structures which can be employed for cell culture scaffolds. These research results can be applied to tissue engineering. Finally, the microstructured cone arrays made from ferrofluid molding technique as shown in Figure 1 were employed to systematically understand how the inclination of the trichome structures on leaf surface influences the wettability of leaves. By this engineering approach, it can also reveal how the inclination angle is optimized through natural selection. [4]

[1] H. T. Huang, T. R. Ger, Y. H. Lin, and Z. H. Wei*, "Single cell detection using magnetic zigzag nanowire biosensor," Lab on a Chip, 13, 3098-3104, 2013. [2] C. P. Lee, M. F. Lai, H. T. Huang, C. W. Lin, and Z. H. Wei*, "Wheatstone bridge giant-magnetoresistance based cell counter," Biosensors and Bioelectronics, 57, 48-53, 2014. [3] C. Y. Huang K. S. Hu, and Z. H. Wei*, "Comparison of cell behavior on pva/pva-gelatin electrospun nanofibers with random and aligned configuration," Scientific Reports, 6, 37960, 2016. [4] C. Y. Huang, M. F. Lai, W. L. Liu, and Z. H. Wei*, "Anisotropic wettability of biomimetic micro-/nanometer dual scale inclined cones fabricated by ferrofluid-molding method," Advanced Functional Materials, 25, 2670–2676, 2015.

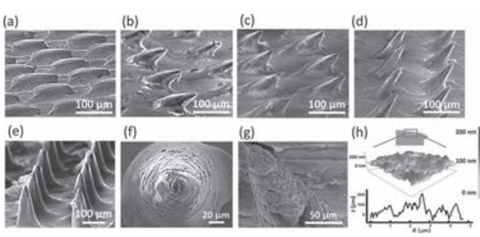

Fig. 1. (a)–(e) SEM images of the cone-shaped PDMS that deposited with nickel at different tilt angles (0°, 25°, 50°, 70°, and 90°). (f) Top-view and (g) the side view of high magnification SEM. (h) 3D surface AFM image of a cone (tilt angle = 0°) that deposited with nickel. The scanning area is 5 µm × 5 µm. Height profile taken from cross-section is also shown.

CONTRIBUTED PAPERS

3:00

BC-04. Magnetic sensing of Antimony bioactivity through Antimony bearing Ferrihydrite bioreduction.

A. Zegeye[1], C. Chang[2], m. Abdelmoula[3] and *T. Hauet*[2]
1. LIEC, Université de Lorraine, Nancy, France; 2. Institut Jean Lamour, Université de Lorraine, Nancy, France; 3. LCPME, Université de Lorraine, Nancy, France

Industrialization and related anthropogenic activities in the twentieth century have contributed to an unprecedented concentration of large quantities of heavy metals in the natural environment. Anthropogenic metal pollution poses significant risks to humans and ecosystems, in the form of contaminated soil and ground water, as well as reduction in food quality and land arability. The need to protect and restore ecosystems contaminated by anthropogenic metal pollution is at the forefront of environmental and public health advocates and policymakers. However, the current assessment methods are complex and hard to implement and fall short in fulfilling their intended purpose. As other groups [1,2], we are working on magnetic characterization methods to sense the metal mobility and the bioavailability, beyond the basic characterization of soil metallic pollution [3,4]. Indeed Fe(III) oxide such as ferrihydrite are ubiquitous in sediments and soils and due to their large surface area and reactive surface properties, they can be important sorbents of metal and metalloid such as antimony (Sb) [5]. Sorption and co-precipitation are considered to be the predominant processes by which most of the metals are scavenged by iron oxides, although co-precipitation appears to be more efficient for the removal of metals from solution. However, co-precipitated metals can be released to the surrounding environment as a direct or indirect consequence of dissimilatory iron reduction (DIR), which is a microbial reduction process of geochemical importance in natural systems. The aim of the present study was to investigate Sb behavior during DIR. Sb-bearing ferrihydrites, with variable Sb/(Fe+Sb) molar ratios, were synthezised by coprecipitation and incubated with an iron reducing bacteria, *Shewanella oneidensis* MR1 [4]. First, chemical and Transmission electron microscope analysis were undertaken to monitor the rate and the extent of the bioreduction and the mobilisation of Sb. Then Mössbauer and SQUID analysis were carried out to characterize the magnetite nanoparticles produced during the bioreduction. On the one hand, Mossbauer spectra at different temperature were fitted to obtain the isomer shift, quadrupole splitting and magnetic hyperfine field. On the other hand, field cooling (FC) and zero field cooling (ZFC) measurements, as well as hysteresis loop measurements were performed. The results revealed that the presence of Sb impacted the extent of reduction but no significant difference was measured in the rate of Fe(III) reduction. Sb is incorporated in the structure of the biogenic magnetite. The magnetite crystal structure is not modified but we were not able to distinguish if Sb cation occupies mainly octahedral or tetrahedral sites. The size of the biogenic magnetite decreases from 10 to 15nm with absence of Sb down to 2nm as the initial Sb concencentration in the ferrihydrite increases. As a consequence of both Sb incorporation and nanoparticle size decrease, magnetic features drastically changed at room and low temperature from ferromagnetic arrangement for zero Sb to superparamagnetic in the case of an initial concentration of few percent of Sb (see Fig. 1). Therefore, when a pollution in Sb is expected, macroscopic magnetometry measurements should be able to reveal the bioactivity of Sb in natural environment where bacteries can activate the bioreduction of ferrihydrite.

[1] D. Liu, *et al*., Catena 139, 53 (2016) [2] K. Porsch, *et al*., Env. Sci Technol 44, 3846 (2010) [3] A. Zegeye, M. Abdelmoula, M. Usman, K. Hanna, C. Ruby, Am. Mineral, 96, 1410 (2011) [4] A. Zegeye, C.S. Chang, M. Abdelmoula and T. Hauet, submitted (2018) [5] D. Maxbauer, *et al*., Earth Sci. Rev. 155, 28 (2016)

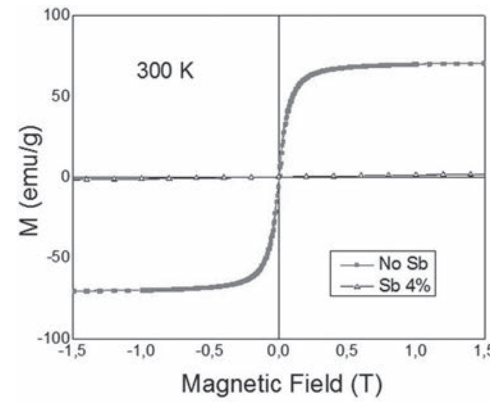

Fig. 1. Magnetization versus magnetic field measured at 300K for the product of bioreduction with zero Sb (red squares) and 4% of molar ratio Sb/(Fe + Sb) (blue triangles).

3:15

BC-05. Novel Electromagnet for MRI Applications.

J. Alonso-Valdesueiro[1], B. Sisniega[1] and J. Collantes[1]
1. Electricity and Electronics, University of the Basque Country (UPV/EHU), Leioa, Spain

Introduction: Magnetic Resonance Imaging is one of the most useful tools for medical diagnosis around the world. It is applied in diagnosis and treatment of many types of cancer, soft tissue injuries, *in-vivo* brain experiments and studies with drugs. Despite its development since the 70s [1], MRI still has to deal with problems that affect directly the sensitivity of the signal and the spatial resolution of the image. Some of these problems are related to the Nuclear Magnetic Resonance phenomenon in solid-state samples [2], and others come from the MRI technique itself [3]. Our work is focused on the development of a novel design of MRI magnet able to mitigate the spatial resolution problems in MRI experiments. RF-MAFS: Resolution problems in MRI are related to different inter and intramolecular phenomena [4] and experimental imperfections. In NMR, they are usually mitigated by applying the Magic Angle Spinning technique where the sample is tilted with respect to the main static magnetic field and spun around its principal axis, averaging to zero the effect of nuclear interactions on the NMR spectrum [5]. In MRI, the spatial resolution is also affected by changes in magnetic susceptibility along the sample, movements of the patient during the experiment and magnetic field inhomogeneities [3]. Applying MAS techniques in MRI experiments is not straightforward. Although some experiments have been performed on rats spun at very low spinning rate [6], the mechanical spinning of a human patient during MRI experiments looks extremely risky. A solution was proposed early in the 60s [7], thought for low-field NMR applications [8], [9] and implemented with permanent magnets for MRI purposes [10], where the main magnetic field is tilted with respect to the main axis of the sample and spun around it at very low spinning rates. The resultant field rotates around the sample at an angle of 54.74^{o} with respect to the sample main axis. Our approach follows the work developed in [9], where RF signals will produce a rotating magnetic field in the transverse plane with respect to the main axis of the sample and an optimized solenoid will produce a static field aligned with that axis. This is what we call RF-MAFS and it is able to achieve, in theory, ultra-high field spinning rates. To do so, we propose a magnet consisting of two Double-Helix Dipole coils [11] and an optimized solenoid [12] (see Fig. 1). RF-MAFS Magnet Development: Fig. 1 plots the concept for the RF-MAFS magnet. The magnet includes two Double-Helix Dipole coils of 81 turns, 10^{o} tilting angle and 1.5 mm effective conductor diameter with radii as specified. Theoretically (Biot-Savart integration) they produce two linearly polarized magnetic density fluxes of 2.4 mT/A 1.7 mT/A respectively. If the coils are placed in spatial "quadrature", the RF signals feeding the coils are compensated in amplitude and they are also phase shifted 90^{o} with respect to each other, the total magnetic flux density corresponds to a rotating magnetic field of B_{rot} = 1.7 mT/A over a large volume inside the coils. In practice, we have built two DHD coils with 5 mm spaced grooves (2x2 mm section) where we have placed 1.2 mm diameter copper wire. The grooves are carved on 4 G10 material tubes 3 mm thick resulting in two ~900 mm assemblies. Their impedances have been measured with a VNA in the 1 kHz-1.5 MHz band (see Fig. 1) for better tune and match. The optimized solenoid will be placed concentric to this assembly producing the static field component, B_z, needed to obtain the RF-MAFS field. Fig. 2 shows the measurement system developed to obtain the magnetic flux density generated by the DHD coils assemblies along their axis. The system consists of two pick-up coils of 5x5 mm section oriented in spatial "quadrature". The voltage induced by the time-varying magnetic flux is amplified by two instrumentation amplifiers working up to 15 kHz with G_v = 500 and filtered by a low-pass filter before going to an AGILENT-Infiniium oscilloscope. Fig. 2 also shows the normalized magnetic flux density, B_{rot}, produced by the two DHD coils when a 2 V_{pp} signal is amplified by an AR3501AH amplifier delivering ~1 A_{rms} (~10 W) when its gain is set to 50%. The measurement was taken every 2 mm along the *z*-axis with an almost constant SNR of 25 dB. The frequencies were kept in a range where the value of $|Z_L|$ reach a minimum keeping a considerable Signal to Noise Ratio ($|Z_L|_{int}$ @9 kHz = 6.72 Ωand $|Z_L|_{ext}$ @4 kHz = 10.35 Ω). B_{rot} was normalized to the value at the geometric center of the coil (*z* = 0 in Fig. 2). Fig. 2 demonstrates that the assembly produces a flat region of ~40 mm along the axis. In order to better evaluate the volume of homogeneity, a measurement system with 5 pairs of 2x2 mm pick-up coils placed on the surface of a 15 mm radius cylinder is being implemented at the moment. The coils will be moved 20 mm around the geometrical center of the assembly and a Cylindrical Harmonics Decomposition will be performed. The system will also include a hall detector per pair of coils in order to analyze in the same way the longitudinal magnetic field generated by the optimized solenoid, B_z. At the end, we will be able to deploy the RF-MAFS magnet optimized to provide a magnetic flux density ~2 mT/A with enough homogeneity to perform MRI experiments inside a cylindrical volume of 2.9x10^{-5} m^3.

[1] R. Damadian, «Tumor Detection by Nuclear Magnetic Resonance,» *Science,* vol. 171, nº 1, pp. 1151-1153, 1971. [2] M. J. Duer, Introduction to Solid-State NMR Spectroscopy, Oxford, UK: Blackwell Publishing Ltd, 2004. [3] E. M. Haacke ***et al.***, Magnetic Resonance Imaging: Physical Principles and Sequence Design, Hoboken, USA: John Wiley & Sons, Inc., 2014. [4] M. H. Levitt, Spin Dynamics: Basics of Nuclear Magnetic Resonance, Chichester, UK: John Wiley & Sons, Ltd., 2001. [5] E. Andrew, A. Bradbury and R. Eades, «Nuclear Magnetic Resonance Spectra from a Crystal rotated at High Speed,» *Nature,* vol. 182, p. 1659, 1959. [6] J. Z. Hu, D. N. Rommereim and R. A. Wind, «High-resolution 1H NMR Spectroscopy in Rat Liver using Magic Angle turning at 1 Hz Spinning Rate,» *Magn. Reson. in Med.,* vol. 47, p. 829, 2002. [7] E. R. Eades and R. G. Andrew, «Possibilities for high-resolution nuclear,» *Disc. Farad. Soc.,* vol. 34, p. 38, 1962. [8] C. Lee, D. Suter and A. Pines, «Theory of multiple-pulse NMR at low and zero field,,» *J. Magn. Reson.,* vol. 75, p. 110, 1987. [9] C. A. Meriles, D. Sakellariou, A. Moul, M. Goldman, T. F. Buding and A. Pines, «High-resolution NMR of static samples by rotation of the magnetic field,» *J. Magn. Reson.,* vol. 169, p. 13, 2004. [10] J. V. M. McGinley, M. Ristic and I. R. Young, «A permanent MRI magnet for magic angle imaging having its field parallel to the poles,» *J. Magn. Reson.,* vol. 271, p. 60, 2016. [11] C. Goodzeit, M. Ball and R. Meinke, «The double-helix dipole - a novel approach to accelerator magnet design,,» *IEEE Trans. on Appl. Supercond.,* vol. 13, nº 2, p. 1365, 2003. [12] H. Saint-Jaimes, J. Taquin and Y. Barhjoux, «Optimization of homogeneous electromagnetic coil systems: Application to whole-body NMR imaging magnets,» *Rev. Sci. Instrum.,* vol. 52, nº 10, p. 1501, 1981.

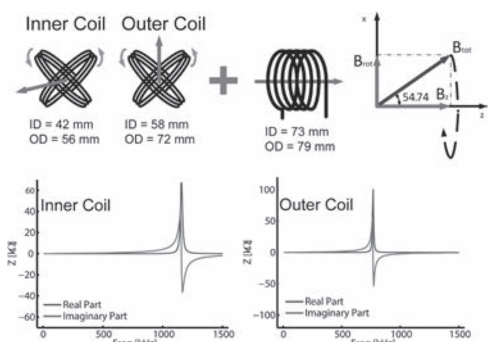

Fig. 1. RF-MAFS concept. The Inner coil shows a self resonance placed at ~1.2 MHz and the Outer coil at ~750 kHz.

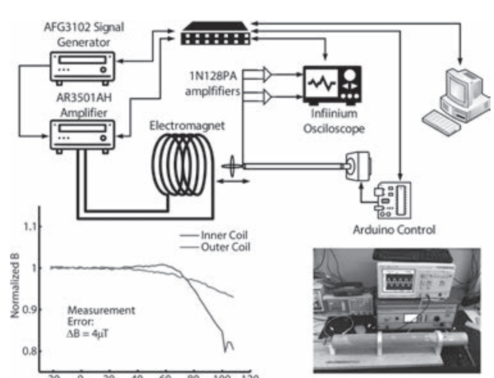

Fig. 2. Description of the Measurement System and the normalized B_{rot} produced by the DHDs built.

INVITED PAPER

3:30

BC-06. Marrying Nanomagnetics with RNA Sequencing of Single Cancer Cells.

S.X. Wang[1,2] and C. Ooi[3,4]

*1. Materials Science and Engineering, Stanford University, Stanford, CA, United States; 2. Electrical Engineering, Stanford University, Stanford, CA, United States; 3. A*STAR, Singapore, Singapore; 4. Chemical Engineering, Stanford University, Stanford, CA, United States*

Single-cell characterization techniques, such as mRNA-seq, have been applied to a diverse range of applications in cancer biology, yielding great insight into mechanisms leading to therapy resistance and tumor clonality. While single-cell techniques can yield a wealth of information, a common bottleneck is the lack of throughput, with many current processing methods being limited to the analysis of small volumes of single cell suspensions with cell densities on the order of 10^7 per mL. In this work [1], we present a high-throughput full-length mRNA-seq protocol incorporating a magnetic sifter and magnetic nanoparticle (MNP)-antibody conjugates for rare cell enrichment, and Smart-seq2 chemistry for sequencing. We evaluate the efficiency and quality of this protocol with a simulated circulating tumor cell system, whereby non-small-cell lung cancer (NSCLC) cell lines (NCI-H1650 and NCI-H1975) are spiked into whole blood, before being enriched for single-cell mRNA-seq by EpCAM-functionalized magnetic nanoparticles and the magnetic sifter. We obtain high efficiency (> 90%) capture and release of these simulated rare cells via the magnetic sifter, with reproducible transcriptome data, enabling highly predictive cancer diagnostics and treatment. We demonstrate the first integration of a high-throughput immunomagnetic cell separation platform (magnetic sifter), with a 96-well microplate-based single-cell full-length mRNA-seq technique (Smart-seq2 [2]), enabling rapid enrichment and sequencing of rare cells. This speed allows Smart-seq2 sequencing of a rare subset of cells ($\approx 10^2$) from a background of $\approx 10^9$ cells to start in under 4 hours. In contrast, recent notable papers reporting single-cell sequencing of circulating tumor cells (a notable rare cell of biological and clinical interest) have required longer overall processing times, separately due to incubation times [3], slower volumetric processing [4], or manual cell picking [5]. Our validation studies also demonstrate that our mRNA-seq data is of comparable quality to previous single-cell studies [6]. Additionally, we describe variant analysis on mRNA-seq data, capitalizing on the full-length reads from Smart-seq2, and illustrate how a combination of expression and variant analysis on single cells can help differentiate heterogeneous cells, in contrast to the current paradigm of thinking solely in terms of either variant (DNA-based) or expression (RNA-based) analysis. This is of interest to the single-cell sequencing community as it illustrates the strength of full-length mRNA-seq methods relative to 3'-biased methods, and might be a key consideration for future single-cell mRNA-seq studies. In summary, we present a unique MNP-based method of broad interest to the multidisciplinary research communities of cell separation and single-cell sequencing. We demonstrate a cell separation platform (magnetic sifter) that enables rapid single-cell sequencing of rare cells in complex biological systems, and envision this method would facilitate time-sensitive studies in areas such as immune or cancer biology, and liquid biopsies in diagnostics and immuno-therapy. This work was supported by US NIH through the Center for Cancer Nanotechnology Excellence (U54CA151459) and the Innovative Molecular Analysis Technologies (R33CA138330). CCO was supported by an A*STAR fellowship (Singapore).

[1] C. Ooi, G. L. Mantalas, S. R. Quake, and S. X. Wang, et al., High-throughput full-length single-cell mRNA-seq of rare cells, PLoS One, 12(11): e0188510 (2017) [2] Picelli, S. et al. Nat. Protocols 9(1), 171-81 (2014) [3] Ramsköld, D. et al. Nat. Biotech. 30(8):777-82 (2012) [4] Yu, M. et al. Nature. 487(7408):510-3 (2012) [5] Lohr, J.G. et al. Nat. Biotech. 32(5):479 (2014) [6] Wu, A.R. et al. Nat. Methods 11(1): 41-6 (2014)

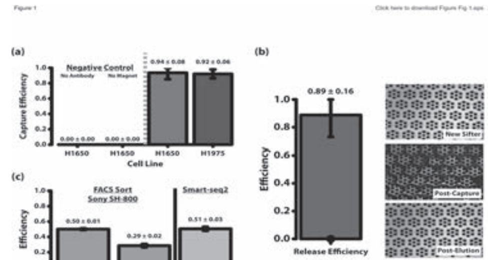

Fig. 1. Efficiencies of different steps in this method. (a) The sifter shows high capture efficiencies (> 90%) for 2 NSCLC cell lines tested (H1650 and H1975). (b) The sifter also exhibits good release properties of captured cells and magnetic nanoparticles (89%). Optical images illustrate the effectiveness of elution from the magnetic sifter. The sifter surface post-elution appears as pristine as the surface of a brand new sifter. (c) FACS sort efficiencies vary with sort purity settings. 2 sort settings on the Sony SH-800 cell sorter are tested. Efficiencies of 50% and 29% are observed for the semi-purity and ultra-purity modes respectively. A reduced purity setting is required for higher yields. By following the Smart-seq2 protocol exactly, we observed successful cDNA synthesis in 51% of the wells.

CONTRIBUTED PAPERS

4:00

BC-07. Development of Peak to Peak Voltage Detector Type MI Gradiometer for Magnetocardiography.

J. Ma[1] and T. Uchiyama[1]
1. Graduate School of Engineering, Nagoya University, Nagoya, Japan

1. Introduction Since the magnetic field generated by the human heart was detected for the first time, the magnetocardiography (MCG) has attracted considerable attentions in research and medical diagnostics. The ionic currents not only create the electric potential differences measured as the electrocardiogram (ECG), but generate a magnetic field (MCG signal) as well. According to the previous studies and clinical data, MCG has some advantages over ECG for the diagnosis of right atrial hypertrophy and right ventricular hypertrophy. It suffers from less limitations than ECG, because magnetic sensors can detect the signals directly related to undistorted cardiac electric current. The MCG has been gradually developed into a non-invasive technology for heart health screening [1], [2]. Up to now, the magnetometers based on SQUID are the main choices for detecting extremely week bio-magnetic signals. It has been developed as a medical instrument for diagnosing the ischemic cardiac disease and arrhythmias. Meanwhile, the SQUIDs are still limited by the need of cryogenic cooling liquids and a shielding room. Therefore, there are some miniature, low-cost, and highly sensitive magnetic sensor systems have been developed. As reported recently, a laser-pumped magnetometer and a pico-tesla resolution flux gate sensor are studied for MCG measurement. [3] In this study, we have proposed a peak to peak voltage detector type MI gradiometer (shortened: Pk-pk VD-type MI gradiometer), which is aimed to measure an extremely weak magnetic field. Meanwhile, we have demonstrated Pk-pk VD-type MI gradiometer for detecting magnetic cardiogram signals, with simultaneous measurement of cardiac electric activity. 2. Pk-pk VD-type MI gradiometer In the previous study, we had reported a high-performance MI magnetometer [5]. However, for detecting extremely weak magnetic field such as a bio-magnetic field, we have to cancel the background uniform noises such as geomagnetic field. For further improvement, in this study, we have developed the Pk-pk VD-type MI gradiometer for detecting the bio-magnetic signals in unshielded environment, based on the pk-pk VD-type MI magnetometer reported recently. The new MI gradiometer is composed of a pair of MI elements: a sensing element and a reference element. The pick-up coils are equipped in combination with the 30 um diameter CoFeSiB amorphous wire to realize a highly linear magnetic sensor by off-diagonal MI effect [6]. The distance between the coils is set to be 3cm. The figure 1 illustrates the block diagram of new MI gradiometer. The pulse generator produces a rectangular voltage wave to differential circuit. Then, the rectangular waves are transferred into three different positive pulses. As illustrated in Figure 1, we detect both the positive peak and negative peak of induced waves in each pick-up coil excited by rising edge and drop edge of the excitation pulse, by using the staggered pulses and analog switches. Finally, the Pk-pk VD-type MI gradiometer outputs the difference between the sensing element and reference element for canceling out uniform magnetic field noise. Therefore, we can achieve a highly sensitive, low noise level, and stable MI sensor system for bio-magnetic field measurement in unshielded environment, at room temperature. The field detection characteristics of two MI element are shown in Fig 1(b). Both of sensing and reference MI elements illustrate good linearity. The difference in the sensitivity of sensing and reference elements is within 1%. As illustrated in Fig 2(a), we investigate the magnetic noise spectral density of Pk-pk VD-type MI gradiometer, comparing with the environment magnetic noise spectral density measured by a commercial flux gate sensor, in an unshielded environment. The noise floor of the Pk-pk VD-type MI gradiometer is lower than 2 $pT/Hz^{1/2}$ in the frequency range from 1 Hz to 100 Hz. It is 1/5 of noise level of previous MI gradiometer in a 1-100 Hz frequency range [7]. Meanwhile, the Pk-pk VD-type MI gradiometer can cancel the environment magnetic noise by 34 dB. 3. MCG measurement MCG measurement by using the Pk-pk VD-type MI gradiometer is carried out on a male subject (aged 26) in siting position, without any magnetic shielding equipment. We set up the MI gradiometer on a wooden table, and the sensor head is perpendicularly placed to the chest surface, with a distance of 10 mm between the chest surface and sensor head. The measurement point is set at the chest surface, 25 mm to the left of the pit of stomach. The output superposing noise of new MI gradiometer is lower than previous MI gradiometer. Meanwhile, we have successfully measured the MCG signals in averaging over only 6 cycles. Comparing with the previous MCG measurements [8], we have markedly reduced the cycles for arithmetic average processing. The Fig.2(b) illustrates the simultaneously measured ECG and MCG signals in averaging over only 6 cycles. As illustrated in Fig.2(b), we can obviously identify a sharp magnetic peak, corresponding to the QRS complex of ECG. The amplitude of this magnetic peak related to the R peak is approximately 100 pT, which coincides well with the reported MCG value [3].

[1] Fiona E. Smith, Philip Langley, Peter van Leeuwen, Birgit Hailer, Lutz Trahms, Uwe Steinhoff, John P. Bourke, and Alan Murray, "Comparison of magnetocardiography and electrocardiography: a study of automatic measurement of dispersion of ventricular repolarization", EP Europace, Volume 8, Issue 10, 1 October 2006, Pages 887–893. [2] Yu.V. Maslennikov*, M.A. Primin, V.Yu. Slobodchikov, V.V. Khanin, I.V. Nedayvoda, V.A. Krymov, A.V. Okunev, E.A. Moiseenko, A.V. Beljaev, V.S. Rybkin, A.V. Tolcheev, A.V. Gapelyuk, "The DC-SQUID-based magnetocardiographic systems for clinical use", Phys. Procedia. 36, 88 (2012). [3] D. Robbes, "Highly sensitive magnetometers—A review," Sens. Actuators A, Phys., vol. 129, nos. 1–2, pp. 86–93, May 2006. [4] K. Mohri, T. Uchiyama, L. V. Panina, M. Yamamoto, and K. Bushida, "Recent Advances of Amorphous Wire CMOS IC Magneto-Impedance Sensors: Innovative High-Performance Micromagnetic Sensor Chip", Journal of Sensors Volume 2015, Article ID 718069, 8 pages. [5] J. Ma, and T. Uchiyama, "High Performance Single Element MI Magnetometer with Peak to Peak Voltage Detector by Synchronized Switching", IEEE TRANSACTIONS ON MAGNETICS, VOL. 53, NO. 11, NOVEMBER 2017. [6] S. Gudoshnikov, N. Usov, A. Nozdrin, M. Ipatov, A. Zhukov and V. Zhukova, "Highly sensitive magnetometer based on the off-diagonal GMI effect in Co-rich glass-coated microwire", Phys. Status Solidi A 211, No. 5, pp. 980–985 / DOI 10.1002/pssa.201300717, 2014. [7] T. Uchiyama, K. Mohri, Y. Honkura, and L. V. Panina, "Recent advances of pico-Tesla resolution magneto-impedance sensor based on amorphous wire CMOS IC MI sensor", IEEE Transactions on Magnetics, vol. 48, no. 11, pp. 3833–3839, 2012. [8] T. Uchiyama and T. Takiya, "Development of precise off-diagonal magnetoimpedance gradiometer for magnetocardiography," AIP Adv., vol. 7, no. 5, p. 056644, 2017.

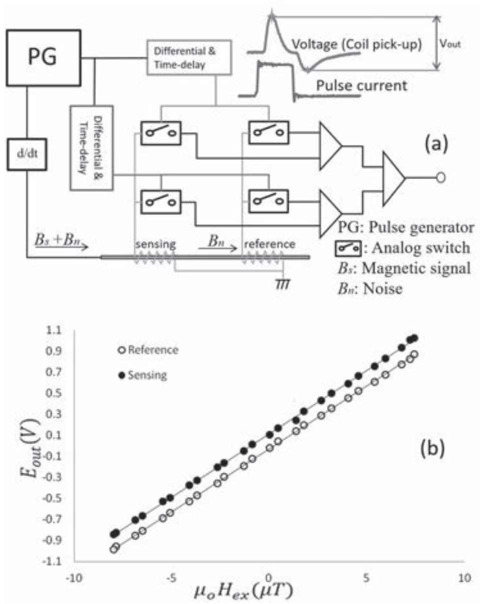

Fig. 1. (a) Block diagram of Pk-pk VD-type MI gradiometer. Fig. 1 (b) Field detection characteristics of two MI element in Pk-pk VD-type MI gradiometer.

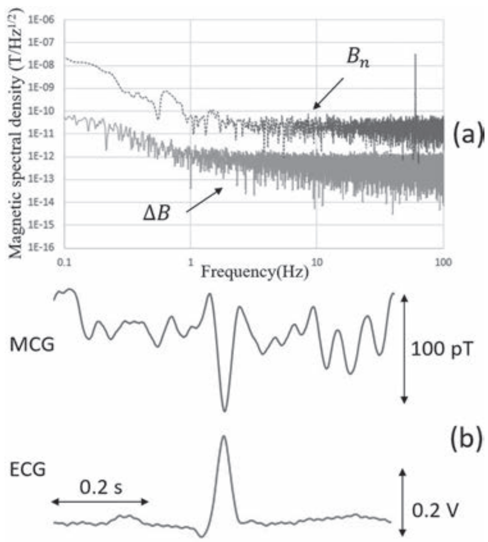

Fig. 2. (a) Comparison of the magnetic noise spectral density between Pk-pk VD-type MI gradiometer (ΔB) and environment magnetic noise (B_n). Fig. 2 (b) Simultaneously measured ECG and MCG signals in averaging over 6 cycles.

4:15

BC-08. Eddy Current-TMR Sensor for micro-motion detection of orthopaedic implants.

R.P. Khokle[1], S. Cardoso de Freitas[2], K. Esselle[1], M. Heimlich[1], F. Franco[2] and D. Bokor[3]
1. Engineering, Macquarie University, Sydney, NSW, Australia; 2. INESC-MN - Microsistemas e Nanotecnologias, Lisbon, Portugal; 3. Faculty of Medicine, Macquarie University, Sydney, NSW, Australia

Introduction Every year millions of people around the world undergo orthopaedic surgeries with partial or complete joint replacements. However, according to the various arthroplasty registers around the world, about 10 % of the implants require re-surgery at some point in their lifetime [1]. About 80-90% of implant failures occur due to mechanical reasons [1-2]. It is proposed in [2], that micromotion of the orthopaedic implants during the limb movement can provide insights on the possible implant failure in the future. For this purpose, it is necessary to monitor the motion of metallic orthopaedic implants with the resolution of the order of tens of microns when the person moves a limb. In this paper, it is proposed to use a small sensor embedded inside the bone at a distance from the orthopaedic implant. The space available for such a sensor is limited to the cylindrical hole of dimensions 3 mm x 10 mm. *Sensor Design and Experiment* A two-turn rectangular eddy current (EC) loop with trace width 0.2 mm is designed on Rogers RT Duroid 6010 substrate (e_r=10.2, tand = 0.0023) having dimensions 2.5 mm x 10 mm x 0.254 mm. For simulations, human male body model from Ansys HFSS is used. The electromagnetic tissue properties are used from IT'IS database [3]. A tibial metallic implant is assigned the properties of titanium which is one of the widely used materials for orthopaedic implants. The EC loop has a self-resonant frequency at 925 MHz. This high SRF ensures a stable performance of the sensor at low frequency. The simulation inside the human body showed that with increasing frequency the power absorption by the human tissue increases. Around 500 MHz, the power lost in tissue becomes equal to that dissipated in the current loop [2]. The operating frequency also depends upon the skin depth of the titanium implant which depends upon frequency. It is advantageous to keep the eddy currents on the surface of the implant which requires the frequency of operation to be high. A similar setup was also simulated without human body structure. It is observed that at 10 MHz, the difference of sensitivity between both the scenarios is negligible. Considering all these factors, therefore, operating frequency is decided to be kept in the range of 1 MHz – 10 MHz. The magnetic tunnel junction resistor offers very high sensitivity and low SNR. The MTJ stack is fabricated and characterised at INESC-MN by optical lithography and ion beam milling. The optimized stack is TJ937-940 – Si / 1000 SiO2/ 5 Ta / 15 Ru / 5 Ta / 15 Ru / 5 Ta / 5 Ru / 20 IrMn / 2 CoFe30 / 0.85 Ru / 2.6 CoFe40B20 / 1 MgO / 2 CoFe40B20 / 0.21 Ta / 4 NiFe / 0.20 Ru / 6 IrMn / 2 Ru /5 Ta/ 10 Ru/ 15 TiWN2 (Thickness in mm). The material resistance area product was set at RxA = 40kΩm^2. The linearity of the sensor is achieved by proper annealing steps that set the pinned layer perpendicular to the free layer. An array of 4x8 sensors per chip is fabricated. The chips were diced and wire bonded to a polyimide flexible PCB. Then the sensor is characterized to measure the TMR by using the same methods as in [4]. The TMR sensor IC is wire-bonded to the signal pads printed on a polyimide flexible substrate. Wire bonding is protected by a silicone-based glob top encapsulant. Since out of plane field detection is needed, the TMR sensor is mounted vertically on the horizontal EC loop by using a superglue. In the proposed range of frequency operation, the inductive coupling of EC-MR sensor assembly could produce higher voltage than the MR sensor response. Hence, to decouple this with the TMR response, heterodyne detection of the signal is proposed. The EC sensor is fed with a signal and TMR sensor is fed with a signal at using Agilent 33210 waveform generator. The TMR sensor response can, therefore, be obtained at 10 KHz difference signal using DSP 7265 signal recovery Lock-in amplifier. To ensure the synchronization of signals the internal clock reference was share between signal generators and a lock-in amplifier. Three signal generators and lock-in amplifier are controlled using LabView. The micromotion stage from Newport Corp. is actuated by using Conex CC controller. It is programmed for motion in 10 mm range using a MATLAB program. The entire measurement assembly is shown in figure 1. Figure 2a shows the shows the output response of the TMR sensor as measured by lock-in amplifier for the target moved from 1.65mm to 3.5mm. The output of the sensor is normalized and expressed at percent change with respect to the output at 1.65 mm standoff distance. Due to the chip size and vertical mount, it is not possible to have standoff distance shorter than 1.65 mm. As the stand-off increases, the change in output decreases. The output signal changes by 1.65% for 3 mm of total displacement. Figure 2b shows the MR percent change as the function of the applied field when the sensor is biased by 100 mA current. It shows 168.4 % TMR sensitivity. The resistance varies from 3.69KΩ to 9.9KΩ. These measurements verify the idea that TMR sensors in conjunction with eddy current loops can sense motion with high resolution at large standoff distances.

[1] Australian Orthopaedic Association National Joint Replacement Register, Annual Report 2016. [2] Rajas Khokle, Karu Esselle, Michael Heimlich, Desmond Bokor, "Orthopaedic Implant Micromotion Sensing Using An Eddy Current Sensor,"IEEE Life science conference, Sydney, Dec. 2017. [3] Hasgall P.A. et al., "IT'IS Database for thermal and electromagnetic parameters of biological tissues," Version 2.6, January 13th, 2015. www.itis.ethz.ch/database. [4] J. M. Almeida and P. P. Freitas, "Field detection in MgO magnetic tunnel junctions with superparamagnetic free layer and magnetic flux concentrators," Journal of Applied Physics 105, 07E722, 2009.

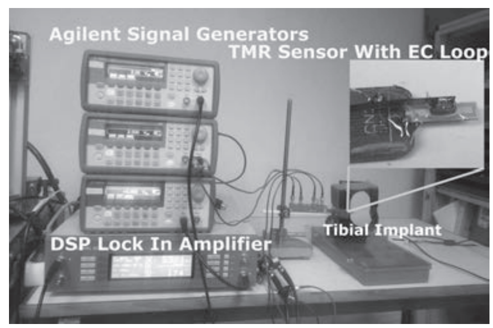

Fig. 1. Experimental setup of the EC-TMR sensor for heterodyne detection of micromotion of an implant.

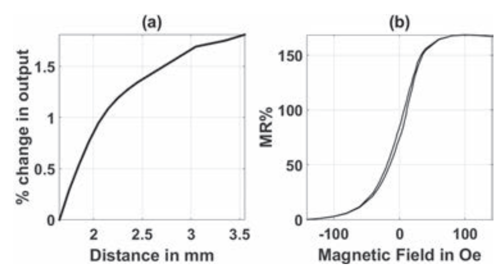

Fig. 2. (a) Output of EC TMR sensor for implant micromotion. (b) Characterization of MR % of fabricated TMR sensor.

4:30

BC-09. On-chip magnetophoretic concentration of Malaria-infected red blood cells and hemozoin nanocrystals.

M. Giacometti[2], L.B. Callegari[1], A. Collovini[2], M. Monticelli[1], C. Rinaldi[1], D. Petti[1], G. Ferrari[2], M. Sampietro[2], A. Dimasi[2], M. Piola[2], G.B. Fiore[2] and *R. Bertacco*[1]
1. Department of Physics, Politecnico di Milano, Milano, Italy; 2. DEIB, Politecnico di Milano, Milano, Italy

According to World Health Organization(WHO), 3.2 billion people are at risk for malaria. In 2015, 212 million new cases and 429000 deaths were estimated [1,2]. Despite treatment in the early stage of the disease is usually very effective, conventional diagnostic tests via optical microscopy examination of thick and thin blood smears are unsuitable for an effective screening of the population. On the other hand, the over-treatment of the disease due to the large percentage of false positives in currently available rapid diagnostic tests (RDTs) may increase the risk of drug resistance. In this scenario, there is a strong need of novel RTDs with (i) the same sensitivity of the gold standard (optical microscopy examination) and (ii) a reduced number of false positives. To fulfill the last requirement, a real improvement would be to move from the detection of antigens or antibodies, which can be hardly washed out in a patient living in an endemic zone even after many weeks from the last malaria episode, to the quantification of infected red blood cells in a blood smear (i-RBC). This essentially means to go back to the concept of gold standard tests, with the additional requirement of integrating i-RBC counting in lab-on-chip platforms suitable for low-cost, rapid and on-site wide screening of the population in endemic zones. It is well known that i-RBCs display a paramagnetic behavior with respect to blood plasma, so that they can be separated from healthy ones and other corpuscles in a high magnetic field gradient. [3] This is due to the fact that, during the intra-erythrocytic development, the parasite degrades hemoglobin into free heme. This molecule, highly toxic to the parasite, is converted in an insoluble form, known as hemozoin or malaria pigment, which crystallizes into paramagnetic nanocrystals found both within the i-RBCs and free in the blood, after RBCs lysis. Of course, both the concentration of free hemozoin crystals and i-RBCs can be used for the determination of the parasitemia. In this paper we present an on-chip magnetophoretic platform for the separation and concentration of i-RBC and hemozoin nanocrystals on pre-defined areas of a chip. This is a pre-requisite for the quantification of the relative percentage of i-RBC with respect to healthy ones (parasitemia) with high sensitivity. The blood drop is placed on a glass substrate, which is then put in close contact to the surface of a chip with Nickel micropillars, at a distance defined by an outer ring which defines also the volume of the cell where magnetophoretic separation takes place. The chip is placed face-down, so that magnetic attraction towards the nickel pillars, in the macroscopic field gradient produced by an external system of permanent magnets, opposes the gravity. In this configuration, i-RBCs and hemozoin crystals are attracted upwards, towards the micropillars, while non-infected erythrocytes and the other blood cells (i.e. white blood cells and platelets) sediment towards the glass substrate. Our design allows to obtain a macroscopic field gradient as high as 1×10^{15} A^2/m^3 up to a distance of 500 micron from the chip surface, strong enough to overcome gravity and attract i-RBCs and hemozoin crystals towards the chip surface. The chip consists of an array of Ni pillars, with 20-30 micron diameter and 20 micron height, fabricated by electroplating and arranged on a hexagonal closed packed lattice. In close proximity to the chip surface, Ni pillars produce a much stronger field gradient, up to 3×10^{16} A^2/m^3 at a few microns from their surface, which concentrate the i-RBCs and hemozoin crystals. We have tested this system using RBCs from bovine blood, treated with $NaNO_2$ in order to induce the transformation of hemoglobin into paramagnetic meta-hemoglobin.[4] In this way, we obtained suspensions in PBS of RBCs mimicking i-RBCs, suitable for experiments of capture. In figure 1 we report optical images from experiments performed in a direct configuration, where gravity and magnetic forces act in the same direction. Untreated RBCs (ut-RBCs) and treated ones with NaNO2 (t-RBCs) were stained with a red fluorophore to improve the quality of optical images. As evident from Figure 1, in case of t-RBCs we observed a capture efficiency of 100% by magnetic pillars in a lattice with center to center spacing of 80 microns. For hemozoin crystals the capture is even easier, because of their much larger volume susceptibility, 3.4×10^{-4} to be compared with 3.9×10^{-6} in case of i-RBCs. These results pave the way to the use of our magnetic chips as active slides for the magnetophoretic separation and concentration of malaria markers, both i-RBCs and hemozoin crystals, in well-defined areas of the chips where quantification can be performed with high sensitivity.

[1] World Health Organization, “Malaria Fact Sheet.” http://www.who.int/mediacentre/factsheets/fs094/en/. [2] World Health Organization, “Malaria Rapid Diagnostic Test Performance,” 2017. [3] C. C. Kim, E. B. Wilson, and J. L. De Risi, “Improved methods for magnetic purification of malaria parasites and haemozoin.,” Malar. J., vol. 17, no. 9, 2010. [4] J. Nam, H. Huang, H. Lim, C.-S. Lim, and S. Shin, “Magnetic separation of malaria-infected red blood cells in various developmental stages,” Anal. Chem., vol. 15, no. 85, pp. 7316–7323, 2013.

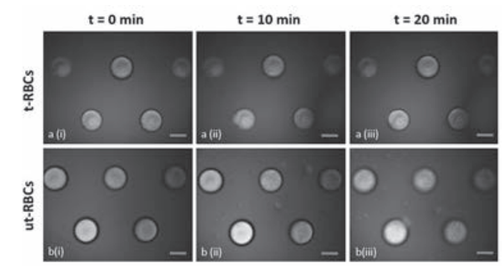

Fig. 1. Fluorescence images from magnetophoretic capture experiments of RBCs treated with NaNO2 (t-RBCs) and untreated ones (ut-RBCs) carried out using and hexagonal close packed array of Ni pillars with diameter d =30 m and spacing s =80 m. Each column represents a different time, 0 -10 - 20 minutes from the beginning of the observation. Scale bars are 20 microns.

4:45

BC-10. Effect of anti-LGR5 MicroBeads on CoFeB/Ta/CoFeB spin valve switching.

O. Koplak[1], A.A. Aristov[2], R. Morgunov[2,3] and S. Mangin[4]
1. Laboratory of Nanomaterials Spectroscopy, Institute of Problems of Chemical Physics, Chernogolovka, Russian Federation; 2. Tambov State Technical University, 392000, Tambov, Russia, Tambov, Russian Federation; 3. Institute of Problems of Chemical Physics, 142432, Chernogolovka, Moscow, Russia, Chernogolovka, Russian Federation; 4. Institut Jean Lamour, UMR 7198 CNRS, University de Lorraine, France, Nancy, France

The most researches are devoted to integrated response of GMR sensor to the significant amount of particles contributing to the detected magnetic field. Single magnetic nanoparticles and their ensembles cause locally inhomogeneous magnetization of the ferromagnetic CoFeB layer. This circumstance changes the magnetization dynamics of the films and domain walls propagation as well as integrated output of GMR sensor. Local impact of the nanoparticles ensemble can oversaturated microsized area of the FeCoB films resulting in nonlinear output of the scheme, not proportional to the particles amount. In this paper, we would like to propose monitoring of the GMR sensor surface during different stages of accumulation of protein–magnetic tag complexes binding to the antigen Anti-LGR5 fixed on the sensor surface. The LGR5 complex plays role of R-spondin receptor providing the modulation of Wnt/β-catenin signaling in normal and neoplastic stem cells. The LGR5-positive cells contribute to the nucleation and spreading of cancer in stomach, kidney, small intestine, colon, hair follicle being highly specific marker of stem cells. Scanning of the sensor surface by magnetic force microscope will allow us to distinguish the role of nucleation events, statistical distribution of the particles and effects on integrated GMR output. This work is aimed to analysis of magnetic response of CoFeB/Ta/CoFeB trilayer GMR platform to deposition of ferromagnetically labeled LGR5 cells on its surface. Two types of GMR platforms possessing perpendicular anisotropy were used in our experiments: MgO(2.5nm)/CoFeB(1.1nm)/Ta(0.75nm)/CoFeB(0.8nm)/MgO(2.5nm) bilayer and MgO(2.5nm) Ta(t)/CoFeB(0.8nm)/MgO(2.5nm) sinle layer (Figure 1). These systems were grown on a GaAs substrate by magnetron sputtering. The MFM method provides recording of the surface profile in the first scanning pass, while distribution of the second derivative of the normal component of magnetic field was mapped during second backward pass. Obtained images correspond to phase shift of cantilever vibrations caused by magnetic interaction of cantilever with the sample surface. Since CoFeB films possess comparatively low coercivity (~ 100 Oe), low magnetized high resolution CoCr magnetic tips, two times thinner compare to standard MFM tips were used. Low moment of the cantilever tip with reduced magnetic stray fields prevents magnetization of the surface by cantilever. Same surface of the sensor platform was measured three times: initial ultrasound cleaned surface, surface with deposited nanoparticles (with no biology cells), surface with cells labeled by the same nanoparticles. Surface with nanoparticles allowed one to distinguish separated a-Fe_2O_3 nanoparticles in AFM as well as in MFM mode (Figure 2). AFM profile of single nanoparticles was approximated by method proposed in. Frequency shift of the MFM canilever, *Df*, is known to be proportional to the magnetic moment of the individual nanoparticle *m* placed on nonmagnetic surface. Magnetic hysteresis loops of the reference trilayer and monolayer system at T = 300 K is presented on the Figure 1, 2. Four states M_1, M_2, M_3, M_4 sketched in the inserts corresponding to different combinations of layers magnetizations. The M_1 and M_4 states correspond to parallel orientation of top and bottom layers magnetizations M_U and M_D along and against positive direction of the field H, respectively; the M_2 and M_3 states correspond to antiparallel mutual orientations of M_U and M_D. Magnetic hysteresis loops of the trilayer and monolayer system with RA MicroBeads have been changed (Figure 2). Hysteresis appeared in contrast with absence of the hysteresis in the Si sample covered by same a-Fe_2O_3 nanoparticles. Following conclusions were proposed: Effects of cell microbead's labelled with commercial a-Fe_2O_3 nanoparticles on magnetic properties of MgO/CoFeB/Ta/CoFeB/MgO/GaAs spin valves and monolayer system MgO/CoFeB/MgO/GaAs wereobserved. Magnetic scattering fields of the ferromagnetic nanoparticles captured in cells shift critical switching magnetic controlled by competition magnetic anisotropy, interlayer exchange coupling and Zeeman energy in the synthetic ferrimagnet with strong perpendicular anisotropy. Local magnetic field of the nanoparticle and its effect on ferromagnetic film included in the spin valve were estimated accordingly with results of magnetic force microscopy. Scattering magnetic fields of NP's increases switching magnetic field of GMR sensor up to 240 Oe due to increase of free layer magnetization. Sensitivity of the switching field to the NP's is ~ 5 10^4 labeled cells per 1 Oe is well enough for reliable measurements of cells concentration. The work was supported by Ministry of Education and Science of the Russian Federation (grant 3.1992.2017/PCh)

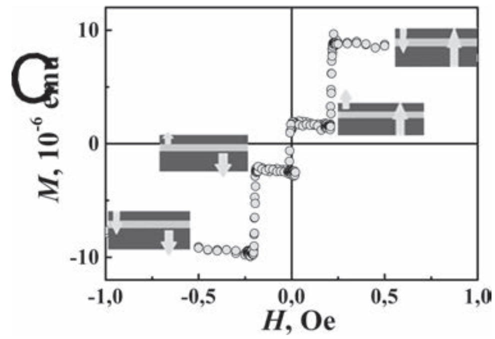

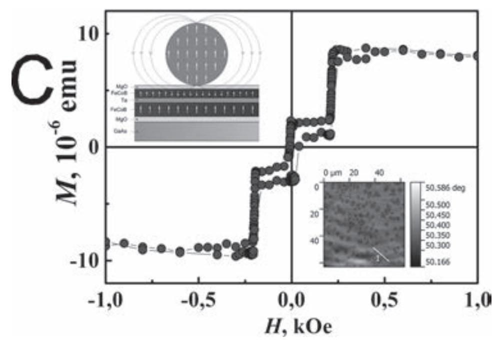

TUESDAY AFTERNOON, 24 APRIL 2018 PEONY IV, 2:00 TO 5:00

Session BD

MAGNETIC TUNNEL JUNCTION AND SPIN ORBIT TORQUE

Yihong Wu, Chair
National University of Singapore, Singapore

CONTRIBUTED PAPERS

2:00

BD-01. Voltage controlled magnetic tunnel junction based 3D-crosspoint memory with step shaped pulse for reliable write operation.

K. Ikegami[1], S. Fujita[1], T. Nozaki[3], T. Yamamoto[3], S. Yuasa[3] and Y. Suzuki[3,2]
1. Toshiba Corporation, Kawasaki, Japan; 2. Graduate School of Engineering Science, Osaka University, Osaka, Japan; 3. Spintronics Research Center, National Institute of Advanced Industrial Science and Technology (AIST), Tsukuba, Japan

Recently, STT-MRAM has been commercialized. MRAM with voltage controlled magnetic tunnel junction (VC-MTJ) has been expected as a post-STT-MRAM memory with faster speed and lower power [1-5]. Since read operation for VC-MTJ uses TMR as other MRAMs, conventional read can be used. On the other hand, VC-MTJ has specific write feature where write error rate (WER) is oscillatory dependent on pulse width. Hence, WER reduction for VC-MTJ is crucial. Previous studies have shown VC-MTJ applications for cache and main memory [6, 7]. Recently, storage class memory (SCM) has been introduced to mitigate memory gap between storage and main memory [8]. SCM is also a candidate for VC-MTJ utilization, since VC-MTJ has unipolar write suitable for 3D-crosspoint (3DX) configuration. This is the first paper to describe feasibility of VC-MTJ for SCM applications from the viewpoint of designs for memory cells and circuits. Typical SCM is characterized by 3DX structure with two-terminal selector device(SD) (Fig. 1(a)). SD has longer switching time than VC-MTJ[9-11]. Here, switching time variations of SD changes write pulse width of VC-MTJ that causes WER degradation. This is a major issue. To solve this, we propose a novel two-step pulse write method as described later. We evaluate WER improvement with this method by advanced circuit simulation. We further analyze WER reduction by interconnect and write driver. Major requirement for SD in 3DX memory is high on-off ratio to suppress sneak leakage current. Various SD have been intensively developed [9]. Among them, threshold type selector is considered to be promising due to large on-off ratio [10, 11] and several ten ns switching time. Figure 1(b) schematically shows conventional write pulse voltage (V_W), voltage across SD (V_{SEL}) and voltage across MTJ (V_{MTJ}). Initially, write voltage is applied to only SD, since off-state SD has much higher resistance than MTJ. After SD switches into on-state, write voltage is applied to only MTJ, since on-state SD has much lower resistance than MTJ. As SD has switching time variation, pulse width of V_{MTJ} (T_{MTJ}) varies and WER degrades severely. To suppress WER degradation, we propose two-step write pulse method (Fig. 1(c)), where write pulse has two voltage steps. First voltage is only for switching of SD and smaller than switch voltage of MTJ. Second voltage is for switching of MTJ. In this method, switch time variation of SD affects only the first voltage time, and not affects the second voltage time, T_{MTJ}. To evaluate WER with a proposed method, we firstly obtained V_{MTJ} shape in 3DX arrays by circuit simulation based on 2X nm 3DX memory[8]. WER was then calculated using the V_{MTJ} shape by Monte-Carlo simulation [3]. Figure 2 (a) shows WER of VC-MTJ in 3DX when 1024 bit cells are connected to a word line (WL). We calculated WER for various WL interconnect thickness, assuming interconnect material is tungsten[8]. The interconnect thickness was selected between 40 nm and 80 nm, since that of 3DX memory products is about 40 nm to 65 nm[8]. We also assumed damping constant, a = 0.025 and, diameter, f = 20 nm for MTJ, and external magnetic field to in-plane direction, H_{ext}= 152.6 Oe, so that switching time is about 1ns. Fig. 2(a) also shows WER when an idealistic trapezoidal pulse having no interconnect delay is directly applied to VC-MTJ for reference. These results indicate that as interconnect becomes thicker, WER of VC-MTJ is improved, and it becomes closer to a target WER for SCM (~1x10^{-4}). This reason is that the decrease in pulse rise and fall time by resistance reduction of interconnects. However, increasing interconnect thickness might make etching process difficult and obstacles further memory cell scaling. In case that interconnect thickness cannot be increased, we propose dual wordline (WL) driver circuit (DWD) shown in Fig. 2(b). When conventional single driver circuit is used for each WL, pulse distortion is largest at the other end. By driving WL from both ends using DWD, pulse rise and fall time become smaller than conventional ones. In this case, difference in activation time (t_{delay}) between the two WL drivers degrades WER (Fig. 2(c)), as shown in Fig. 2 (d). When t_{delay} is larger than 200 ps, WER becomes larger than single driver case. Therefore, we have to design interconnects and drivers so as t_{delay} to be ~0s. WER is, then, almost the same as that of direct pulse application, as shown in Fig. 2(d). As a result, DWD circuit can reduce WER considerably close to a target WER for SCM(~1x10^{-4}). These results thus indicate that WER of VC-MTJ for 3DX memory can be improved by proposed circuit designs. Figure 2 (e) compares write performance of various nonvolatile memories, which indicates VC-MTJ is superior to others, since it has higher-speed and lower-power write with higher-endurance compared with others. This work was partly supported by the ImPACT Program of the Council for Science, Technology and Innovation (Cabinet Office, Government of Japan). The authors would like to thank Yoichi Shiota for his contributions to VC-MTJ.

[1] J. Choe et al., in Proceedings of Flash Memory Summit. [2] T. Nozaki et al., Applied Physics Letters, vol. 96, no. 2, 022506, 2010. [3] Y. Shiota et al., Nature Materials, vol. 11, no. 1, pp. 39-43, 2011. [4] Y. Shiota et al., Applied Physics Express, vol. 9, no. 1, 013001, 2015. [5] P. Khalili Amiri et al., IEEE Trans. Magn. vol. 51, no. 11, 3401507 (2015). [6] C. Grezes et al., IEEE Magn. Lett. vol. 8, 3102705 (2017) [7] H. Noguchi et al., IEDM Tech. Dig., pp.675-678, 2016 [8] K. Ikegami et al., Intermag Conference, CF-11, Dublin, Ireland, 2016 [9] R. Aluguri et al., IEEE Journal of the Electron Devices Society vol. 4, issue 5, pp. 294-306 (2016) [10] S. H. Jo et al., IEEE Trans. Electron.Devices., vol. 62, no. 11, p. 3477 (2016) [11] H. Yang et al., IEDM Tech. Dig., pp. 836-839, 2017 [12] S. W. Fong et al., IEEE Trans. Electron Devices., vol. 64, no. 11, p. 4374 (2017)

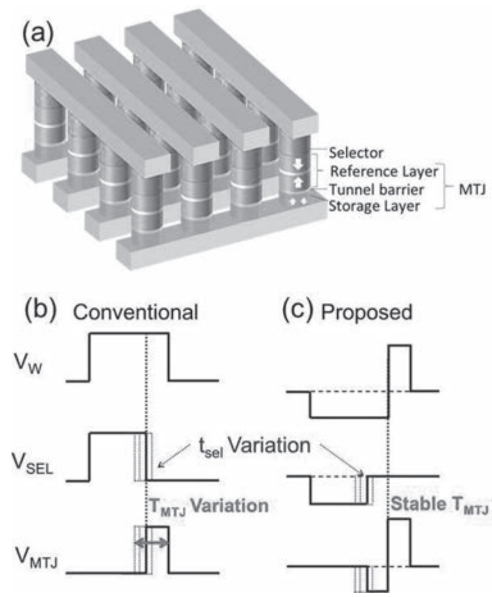

Fig. 1. (a) Schematics of VC-MTJ based crosspoint memory. (b) Conventional write pulse. (c) Proposed write pulse. T_{MTJ} of proposed write pulse does not affected by switch time variation of selector device.

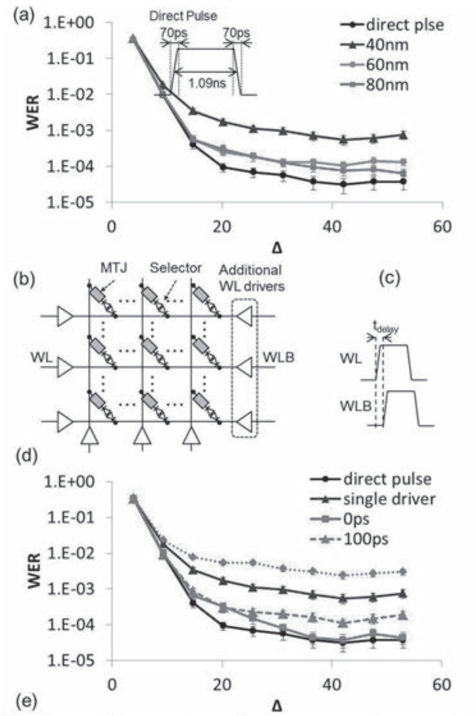

(e)

	VC-MRAM	STT-MRAM	PCM
Write Speed	<10ns (Selector Limited)	<10ns (Selector Limited)	~1us (reset)
Write Eenrgy	~1fJ	~10fJ	~100fJ [12]
Endurance	Practically unlimited	Practically unlimited	10^7 – 10^{11}[12]

Fig. 2. (a) WER of VC-MTJ of various interconnect thickness when α = 0.025, Φ = 20 nm and Hext = 152.6 Oe. For reference, WER of direct pulse application is shown. (b) DWD circuit. (c) Activation time difference (t_{delay}) (d) WER vs. t_{delay}. (e) Write performance for various crosspoint memories.

2:15

BD-02. Nanoscale spin-orbit torque devices with Co/Pt multilayers for wide-temperature range applications.

B. Jinnai[1], S. Fukami[1], H. Sato[1] and H. Ohno[1]
1. Tohoku University, Sendai, Japan

Spintronics memory devices utilizing spin-orbit torques (SOTs) to manipulate a magnetization direction as write operation [1-3] are promising for ultralow-power and high-performance integrated circuits owing to their non-volatility, fast operation capabilities, and design flexibility. Being integrated in leading-edge integrated circuits, SOT devices are required to have high thermal stability to secure enough data retention and large SOT efficiency generated by unit current to achieve low switching current in nanoscale dimensions. Especially considering those applications used in harsh conditions, such as automobile and aerospace, those requirements need to be met over a wide range of operation temperature, for example, –40 to 125°C according to one of automobile industry standards, i.e. AEC-Q100 Grade 1. To explore a material system meeting these requirements, we have been investigating Co/Pt multilayers for SOT devices [4], as they possess high magnetic anisotropy [5] and generate SOT despite of their symmetric structure [6]. The Co/Pt multilayers have high damping constant a [7,8], which is detrimental to device performances when they are used in a free layer of widely-studied spin-transfer torque (STT) switching devices. On the other hand, theoretical work predicts that a has little impact on threshold switching current of SOT devices with a perpendicular easy axis due to a different symmetry of the torques from that of STTs [9]. This allows to take advantage of Co/Pt multilayers in SOT devices. We have previously shown SOT-induced magnetization switching in micrometer-scale Hall-bar devices with Co/Pt multilayers and enhancements of switching efficiency and effective fields with increasing the number of Co/Pt stacking [4]. In this work, we study the SOT-induced magnetization switching in nanoscale SOT devices with Co/Pt multilayers down to 20 nm together with evaluation of their thermal stability over a wide range of operation temperature. Magnetization switching by current is observed in all the studied range of the width. A thermal stability factor Δ ($\equiv E/k_BT$, where E is an energy barrier against thermal fluctuation, k_B the Boltzmann constant, and T an absolute temperature) of more than 200 is obtained at 125°C in the device with 30-nm width. The feasibility of SOT devices with Co/Pt multilayers for those applications used in harsh conditions is discussed. The stacks of Ta(3)/Pt(3)/[Co(0.4)/Pt(0.4)]$_4$/Co(0.4)/Ta(0.2)/$(Co_{25}Fe_{75})_{75}B_{25}$(1)/MgO(1.2)/capping layers are prepared on Si substrates by dc/rf magnetron sputtering. The numbers in parentheses are nominal thicknesses in nanometer. The films are processed into nanowire devices with pairs of Ta/Pt channels and probes using EB-/photo-lithography, reactive ion etching, and Ar ion milling. Figures 1(a) and 1(b) show the schematic and top-down SEM image of a nanowire device. Nanowire widths are ranging from 20 to 400 nm with nanowire length of 300 nm. After the process, the device is annealed at 300°C under an application of perpendicular magnetic field of 0.4 T for an hour. To evaluate SOT-induced magnetization switching, dc current is applied to the channels under an in-plane field application in the collinear direction to the current while monitoring a Hall resistance R_{Hall}. Δ is determined by switching probability when repeating a sweep of perpendicular magnetic field. During the electrical measurements, stage temperature is controlled in order to examine the temperature dependence of the device properties. Width dependences of switching current I_{sw} and switching current density J_{sw} under an external in-plane field $|\mu_0H_{ext,in}|$ of 200 mT and Δ at room temperature are plotted in Figs. 1(c) and 1(d), respectively. While I_{sw} is scaled with the width, J_{sw} starts to increase below the width of 200 nm. The behavior is also observed in the previous report [10] and suggests that a magnetization reversal mode changes at the width of around 200 nm; as the width increases, a magnetization reversal mode involves incoherent magnetization dynamics, which may decrease J_{sw}. Δ exceeds 200 in the range of the width from 20 to 400 nm and has no clear trend with the width. Figures 2(a) and 2(b) show temperature dependences of I_{sw} under $|\mu_0H_{ext,in}|$ of 200 mT and Δ, respectively, in devices with the width of 30 nm. I_{sw} slightly decreases with increasing temperature due to thermal fluctuation. Δ also decreases with increasing temperature but Δ of more than 200 is obtained at 125°C. This means that the use of Co/Pt multilayers in nanoscale SOT devices can provide long enough data retention time at high temperature. Therefore, Co/Pt multilayers are promising to achieve reliable operations of nanoscale SOT devices over a wide range of temperature and consequently suitable for those applications that require high reliability even in harsh conditions. This work was partially supported by R&D Project for ICT Key Technology of MEXT, ImPACT Program of CSTI, and JST-OPERA.

[1] I. M. Miron *et al.*, Nature 476, 189 (2011). [2] L. Liu *et al.*, Science 336, 555 (2012). [3] S. Fukami *et al.*, Nature Nanotechnology 11, 621 (2016). [4] B. Jinnai *et al.*, Applied Physics Letters 111, 102402 (2017). [5] S. Ishikawa *et al.*, Journal of Applied Physics 115, 17C719 (2014). [6] K.-F. Huang *et al.*, Applied Physics Letters 107, 232407 (2015). [7] A. Barman *et al.*, Journal of Applied Physics 101, 09D102 (2007). [8] S. Mizukami *et al.*, Applied Physics Letters 96, 152502 (2010). [9] K.-S. Lee *et al.*, Applied Physics Letters 102, 112410 (2013). [10] C. Zhang *et al.*, Applied Physics Letters 107, 0121401 (2015).

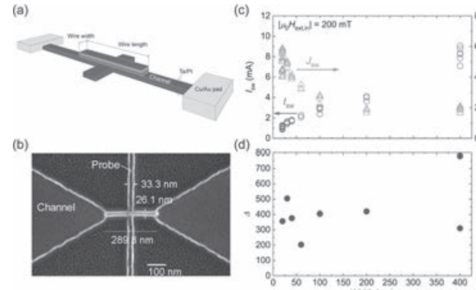

Fig. 1. (a) Schematic of a nanowire device and (b) top-down SEM image of the nanowire device with width of 30 nm and length of 300 nm. Width dependences of (c) I_{sw} and J_{sw} under $|\mu_0H_{ext,in}|$ = 200 mT and (d) Δ at room temperature.

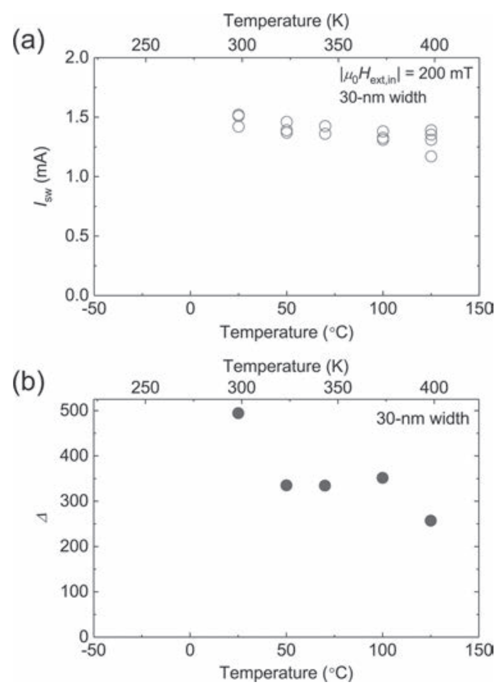

Fig. 2. Temperature dependences of (a) I_{sw} under $|\mu_0H_{ext,in}|$ = 200 mT and (b) Δ in the device with nanowire width of 30 nm.

INVITED PAPER

2:30

BD-03. Novel approach for nano-patterning magnetic tunnel junctions stacks: A route towards high density STT-RAM application.

I.L. Prejbeanu[1,2], V. Nguyen[1,2], P. Sabon[1,3], J. Chatterjee[1,2], N. Perrissin[1,2], S. Lequeux[1,2], L. Tillie[1,4], S. Auffret[1,2], R.C. Sousa[1,2], E. Gautier[1,3], L. Vila[1,2] and B. Dieny[1,2]
1. Université Grenoble Alpes, Grenoble, France; 2. INAC-SPINTEC, CEA, Grenoble, France; 3. SPINTEC, CNRS, Grenoble, France; 4. CEA-LETI, Grenoble, France

Spin-Transfer-Torque Magnetic Random Access Memories (STT-RAM) based on out-of-plane magnetized MTJ (pMTJ) are one of the most promising emerging non-volatile memory technologies as they combine a unique set of assets: quasi-infinite write endurance, high speed, low power consumption and scalability. Embedded STT-MRAM are about to enter in volume production for e-FLASH replacement. For this type of applications not requiring very high memory density, the preferred etching technique is still Ion Beam etching (IBE) [1]. However this technique is not appropriate for high density memory as it requires to etch the MTJ stack at specific angles to minimize the re-deposition on the sidewalls of the tunnel junctions. Etching at some angle leads to shadowing effects which give to the pillars a conical shape. This effect worsens as the memory pitch shrinks below typically 5F resulting in a poor control of the critical dimension at very dense pitch. Besides it is difficult to implement on large wafer with good uniformity [2]. Reactive ion etching (RIE) was also tried for MTJs with various gas but was found to be very complex due to the heterogeneous nature of the MTJ stacks and to cause corrosion of the magnetic materials [3]. Therefore, to be able to use STT-RAM as a dense working memory requires a new method for nanopatterning MTJ elements at small feature size (<20nm) and high pitch (~2F). In the approach we propose, the MTJ material is directly deposited on pre-patterned pillars (e.g Ta pillars prepared by RIE or Cu or W vias prepared by damascene process). The MTJ stack is then naturally patterned while being deposited thus not requiring any post-deposition etching. For the pre-patterned non-magnetic posts, we chose Ta as post-material since its reactive ion etching is very well controlled. In order to avoid the risk of electrical shorts between pillars due to the material deposited in the trenches between posts, the latter are given an undercut shape. Thanks to this shape, during the MTJ deposition, no metal gets deposited on the pillar sidewalls nor at the foot of the metallic posts. The process for fabricating the conducting non-magnetic Ta posts with undercut is depicted in Fig. 1. Ta is coated by Pt to form the top part of the post and protect the top Ta surface from oxidation. Then, following the formation of cylindrical Ta/Pt posts by an anisotropic RIE process, an isotropic RIE process is subsequently used in order to laterally trim the Ta part of the posts. Perpendicular MTJ stacks with MgO barrier were then deposited on these pre-patterned substrates. By depositing the MgO tunnel barrier at oblique incidence while rotating the substrate, it is possible to completely coat the MTJ bottom electrode with MgO and even to get thicker MgO deposit on the sidewall of the bottom electrode than on the horizontal part of the MTJ. This can help to concentrate the current away from the edge of the nano-patterned MTJ thus reducing the influence of possible edge defects. Similarly, lateral gradient of chemical composition can be induced in the storage or reference layers. Such gradient can be used to induce different properties at the edges and center of each dot in order for instance to reduce demagnetizing or nucleation effects at edges and improve STT switching efficiency. The magnetic properties of pMTJ stacks deposited on the pre-patterned substrate were evaluated by focused Kerr microscopy. Half-MTJ stacks were first deposited with bottom and top electrodes only to characterize the interfacial perpendicular anisotropy of the deposits on top of the posts CoFeB/MgO. The contribution of individual pillars and of the continuous deposit in the trenches could be distinguished. After optimizing the structural and magnetic properties, electrically characterization of these patterned MTJs were performed in terms of TMR and STT switching characteristics. The field-voltage switching phase diagram at room temperature was measured and is shown in Fig.2. At a constant applied field and even at zero field, the junctions can be switched from AP to P and from P to AP by STT. A switching voltage of 0.34 V for 100ns pulse was measured which is quite comparable or even slightly lower than similar MTJs patterned by IBE [4]. These electrical results demonstrate that functional patterned perpendicular MTJs can be obtained by this novel patterning process consisting in depositing the MTJ material on pre-patterned conducting posts. In conclusion, we have demonstrated a novel approach for nanopatterning MTJ down to sub-30nm dimensions at very narrow pitch by depositing the MTJ material on pre-patterned metallic posts. Remarkably, our approach allows to fabricate extremely dense arrays of very small size MTJs which is still impossible to achieve by IBE. This opens a possible route toward high density STT-MRAM application.

[1] M.Gajek et al, Appl.Phys.Lett.100, 132408 (2012) [2] http://www.memorystrategies.com/report/emerging/mram.htm [3] https://www.oxford-instruments.com/news/2016/february/new-etching-process-for-magnetic-ram [4] A. A. Timopheev et al., Phys. Rev. B 92, 104430 (2015)

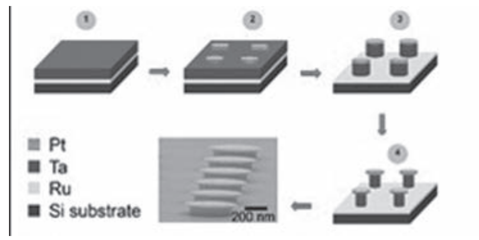

Fig. 1. Fabrication process of undercut Ta pillar using RIE. Typical SEM image of the undercut Ta pillars on Si wafer after RIE etching process.

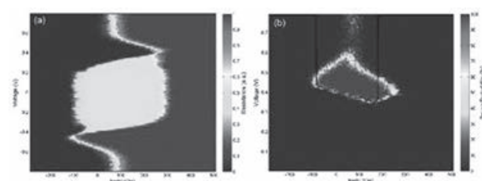

Fig. 2. (a) The field-voltage phase diagram of the junction measured at room temperature. At each field point, a 100-ns writing pulse with fixed amplitude is applied to the junction while measuring the resistance of the junction. In order to reduce the effect of stochasticity, the switching field values are averaged from 12 magnetoresistance loops. The same procedure is repeated for each pulse amplitude and the final phase diagram is constructed from these averaged magnetoresistance loops. (b) Probability of field-voltage switching window.

CONTRIBUTED PAPERS

3:00

BD-04. Voltage-control spintronics memory (VoCSM) with potential cell-size of 4F^2 using in-plane magnetic tunnel junction.

S. Shirotori[1], H. Yoda[1], Y. Ohsawa[1], M. Shimizu[1], A. Buyandalai[1], K. Koi[1], T. Inokuchi[1], N. Shimomura[1], H. Sugiyama[1], Y. Kato[1], S. Oikawa[1], M. Ishikawa[1], A. Tiwari[1] and A. Kurobe[1]
1. Toshiba corporation, Kawasaki, Japan

Magnetic random access memory (MRAM) is a candidate for memory applications because it offers advantages such as high density in the Gbit class and low energy consumption. Recently, voltage-control spintronics memory (VoCSM), which uses the voltage-control magnetic anisotropy (VCMA) effect as a selection method and the spin Hall effect (SHE) as a write method, has emerged as a promising candidate for high-speed and high-density applications, offering advantages such as ultra-low energy consumption, high-speed writing, read-disturb robustness, and unlimited endurance over conventional STT-MRAM [1]-[5]. VoCSM consists of a three-terminal configuration with a string-cell structure as shown in Fig. 1 (a), such that the ideal cell size is 4F^2 in the case of magnetic tunnel junction (MTJ) cells with perpendicular magnetic anisotropy (P-MTJ) as shown in Fig. 1 (b). The write mode is deterministic without application of magnetic field for precessional switching as shown in Fig. 1 (c). MTJ cells with in-plane anisotropy (I-MTJ) are normally used because the easy axis is perpendicular to the write-current direction [6], [7]. However, the conventional I-MTJ has the disadvantage of larger MTJ size than that of P-MTJ because of the shape anisotropy. In this study, MTJs with strain-induced in-plane magnetic anisotropy (SI-MTJ) were examined for use in memory cells. Figure 1 (d) shows a schematic diagram of our concept of the strain-induced VoCSM structure. An SI-MTJ can be produced by using an anisotropy control (AC) layer under the SHE electrode. We developed an AC layer that has the function of expanding the lattice of the storage layer using an SHE electrode. That is, the magnetic anisotropy of the storage layer is controllable by the strain and patterning of the AC layer and SHE electrode. Figure 2 (a) shows the measured resistance versus magnetic field (RH) hysteresis loops of MTJ in the VoCSM where the MTJ configuration consist of Ta (5.0 nm)/CoFeB (1.25 nm)/MgO (1.6 nm)/CoFeB (1.2 nm)/Co (0.6 nm)/Ru (0.84 nm)/CoFe (1.8 nm)/IrMn (8.0 nm) grown on a thermal oxide Si substrate with and without an AC layer, and patterned by using a two-step self-alignment (TSSA) process to form the 80 × 80 nm MTJ nanopillars on a 80-nm-wide Ta SHE electrode [4]. Even though the aspect ratio (AR) = 1, a clear switching behavior is observed. Moreover, a change in the coercive force (H_C) of over 300 Oe was observed due to the strain induced in the MTJ by using an AC layer. The stress (σ) along the magnetic easy-axis direction in the free layer in the MTJ was estimated to be 630 MPa by using the magnetostriction constant (λ) of the free layer of 17 ppm. This can also be controlled from 630 to 450 MPa, which is 0.2% to 0.3% of lattice expansion, by changing the configuration of the AC layer. The thermal stability factor has been measured to become around 2 times larger by controlling σ as shown in Fig. 2 (b). In summary, we successfully demonstrated that MTJs with strain-induced in-plane magnetic anisotropy had large unidirectional anisotropy even with an in-plane aspect ratio of 1. This work was partly supported by the ImPACT Program of the Council for Science, Technology and Innovation (Cabinet Office, Government of Japan).

[1] H. Yoda *et al.*, "Voltage-control spintronics memory (VoCSM) having potentials of ultra-low energy-consumption and high-density," in *Digests of 62nd IEDM*, session 27.6, San Francisco, CA, 3–7, December, 2016 [2] H. Yoda *et al.*, "High-speed voltage-control spintronics memory (high-speed VoCSM)," in *Proceedings of IMW 2017*, p. 165, Monterey, CA, 14 – 17 May, 2017 [3] T. Inokuchi *et al.*, "Improved read disturb and write error rates in voltage-control spintronics memory (VoCSM) by controlling energy barrier height," *Applied Physics Letters*, vol. 110, p. 252404, 2017 [4] S. Shirotori *et al.*, "Voltage-control spintronics memory with a self-aligned heavy-metal electrode," *IEEE Transactions on Magnetics*, vol. 53, p. 3401104, 2017 [5] H. Sugiyama *et al.*, "High-speed voltage-control spintronics memory focused on reduction in write current," *IEEE Xplorer 2017 17th Non-Volatile Memory Technology Symposium (NVMTS)* [6] S. Fukami *et al.*, "A spin-orbit torque switching scheme with collinear magnetic easy axis and current configuration," *Nature Nanotechnology*, vol. 11, pp. 621-625, 2016 [7] K. Koi *et al.*, "Switching mechanism design for high-speed voltage-control spintronics memory (VoCSM) considering the operation window," in *Digests of SSDM 2017*, session A-5-02, Sendai, Japan, 19–22 September, 2017

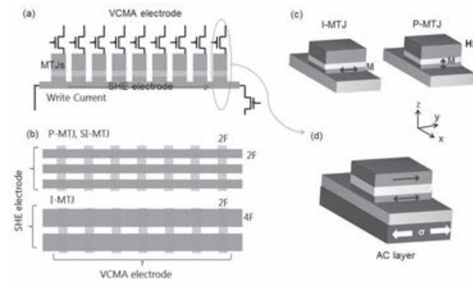

Fig. 1. (a) Schematic diagram of the VoCSM. (b) In plane image of the unit call. (c) Geometry of write modes. (d) Schematic diagram of our concept of strain-induced VoCSM.

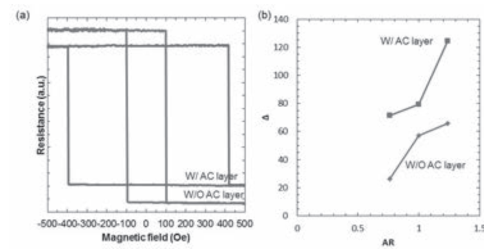

Fig. 2. (a) Hysteresis loop of an MTJ (80 × 80 nm size) with VoCSM structure as a function of magnetic field. The red line indicates VoCSM with an AC layer, and blue line indicates VoCSM without an AC layer. (b) Aspect ratio dependency of thermal stability factor Δ (MTJ width is 100 nm at AR =1).

3:15

BD-05. Ultra Low Power Composite Free Layer Spin-Orbit Torque MRAM.

W. Hsu[1], R. Bell[1] and R.H. Victora[1]
1. Electrical and Computer Engineering, University of Minnesota, Minneapolis, MN, United States

I. INTRODUCTION AND METHODS Spin-transfer torque MRAM (STT-MRAM) serves as a promising candidate for next generation memory. However, STT-MRAM suffers from tunnel barrier degradation under rapid operations and a poor spin polarization. In contrast, spin-orbit torque MRAM (SOT-MRAM) utilizes spin-orbit interaction at the interface of heavy metal (HM) and ferromagnetic (FM) layers via mechanisms such as the Rashba effect and spin Hall effect (SHE)[1,2]. Since current only flows through the heavy metal in SOT-MRAM, device performance is no longer limited by insulator breakdown. Because no charge current through the FM layer is needed in SOT devices, the other unrecognized benefit of SOT is its compatibility with low-damping magnetic insulators (MI). SOT experiments with YIG/Pt, YIG/Ta, and YIG/W have demonstrated the potential for ultra-low damped switching of YIG in SOT systems[3,4]. SOT switching has also been demonstrated in TmIG based system[5]. Here, we propose a composite free layer SOT-MRAM (Fig. 1a). The MTJ is a cylinder structure with a diameter D. The free layer consists of an easily switched YIG layer and a thermally stable high anisotropy (K_u~10^7 ergs/cc) $L1_0$-FePt or $L1_0$-FePd layer. These two layers are ferromagnetically coupled through the RKKY exchange provided by the Pd layer. It has been shown that exchange coupling between magnetic soft and hard layers can reduce the critical current[6]. Current CoFeB based devices necessitate larger diameters due to the low anisotropy. By adopting FePt or FePd, we can reduce the device area, which is favorable for high density applications. We optimized our device by running micromagnetic simulations in the macrospin approximation. A device of small diameter (D < 30nm) with low write energy (E_w < 1 fJ) can be achieved for 1 ns switching while maintaining thermal stability $\Delta = 60k_BT$ at room temperature. II. RESULTS When the charge current passes through the HM layer, a spin current transverses the HM/YIG interface due to spin-orbit interaction via the SHE. This spin current generates a torque to reverse the magnetization of the easily-switched YIG and eventually switches the hard layer (HL) through exchange coupling (Fig. 1b). An optimal design can be found under a fixed volume ($V=60k_BT/K_u$) and a fixed thickness of hard layer (t_{HL}) by varying the exchange coupling strength (J_{ex}) and the thickness of YIG layer (t_{YIG}). We found that the optimal $(t_{YIG}M_{s,YIG})/(t_{HL}M_{s,HL})$ and $J_{ex}/(2t_{HL}K_{u,HL})$ are fixed, where M_s is the saturation magnetization. For different hard layer thickness, we also found that the optimal write energy is proportional to the thickness of hard layer, i.e., inversely proportional to the device area at fixed hard layer volume. A write energy of ~17 aJ is achieved for 1 ns writing for a FePd/YIG composite free layer with diameter of 26.5 nm (t_{FePd} = 0.25 nm). The write energy as a function of the device size is shown in Fig. 2. The write energy of 17 aJ is within a factor 80 of the theoretical limit of $60k_BT$. When thermal fluctuations are included in the simulations, the write energy is only four times larger than the write energy obtained without thermal fluctuations even at a required bit error rate of 10^{-9}. Zhao et al.[7] found CoFeB based STT-MRAM to have E_w about 0.5 pJ with Δ = $50k_BT$. A CoFeB based SOT-MRAM proposed by Manipatruni et al.[8] has E_w about 100 aJ with $\Delta = 40k_BT$. These points are also plotted in Fig. 2 and suggest advantages for our proposed structure. In addition, the write energy of 17 aJ in our proposed structure represents 500× improvement relative to state-of-the-art DDR4 DRAM cells and 5×10^4× improvement when DRAM refresh energies are included.

[1] L. Liu, C.-F. Pai, Y. Li, H.W. Tseng, D.C. Ralph, and R.A. Buhrman, Science (80-.). 336, 555 (2012). [2] I.M. Miron, K. Garello, G. Gaudin, P.-J. Zermatten, M. V. Costache, S. Auffret, S. Bandiera, B. Rodmacq, A. Schuhl, and P. Gambardella, Nature 476, 189 (2011). [3] C. Hahn, G. de Loubens, O. Klein, M. Viret, V. V. Naletov, and J. Ben Youssef, Phys. Rev. B 87, (2013). [4] H.L. Wang, C.H. Du, Y. Pu, R. Adur, P.C. Hammel, and F.Y. Yang, Phys. Rev. B 88, (2013). [5] C.O. Avci, A. Quindeau, C.-F. Pai, M. Mann, L. Caretta, A.S. Tang, M.C. Onbasli, C.A. Ross, and G.S.D. Beach, Nat. Mater. 16, 309 (2016). [6] R. Bell, J. Hu, and R.H. Victora, IEEE Electron Device Lett. 37, 1108 (2016). [7] H. Zhao, A. Lyle, Y. Zhang, P.K. Amiri, G. Rowlands, Z. Zeng, J. Katine, H. Jiang, K. Galatsis, K.L. Wang, I.N. Krivorotov, and J.-P. Wang, J. Appl. Phys. 109, 07C720 (2011). [8] S. Manipatruni, D.E. Nikonov, and I.A. Young, Appl. Phys. Express 7, 103001 (2014).

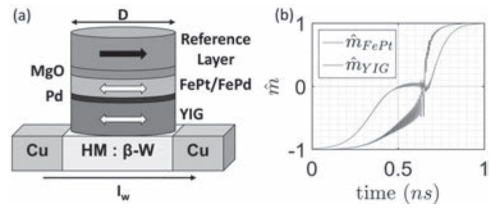

Fig. 1. (a) Schematic diagram of the proposed SOT-MRAM. (b) Magnetization reversal of proposed coupled composite structure.

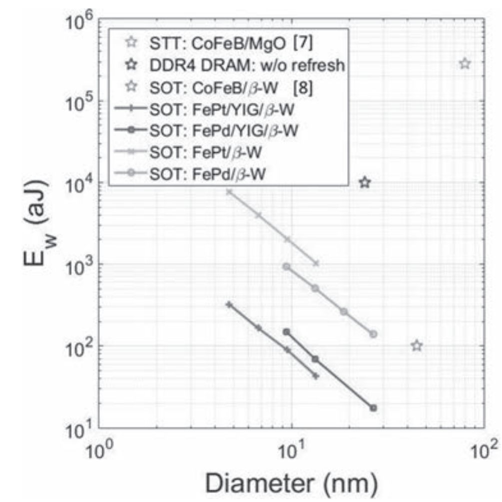

Fig. 2. Write energy (E_w) of the proposed SOT cell as a function of device diameter (with notable works included).

3:30

BD-06. Low frequency noise in vortex spin torque nano-oscillators.

S. Wittrock[1], S. Tsunegi[2], K. Yakushiji[2], A. Fukushima[2], H. Kubota[2], P. Bortolotti[1], U. Ebels[3], S. Yuasa[2], G. Cibiel[4], E. Rubiola[5] and V. Cros[1]
1. Unité Mixte de Physique CNRS/Thales, Palaiseau, France; 2. Spintronics Research Center, National Institute of Advanced Industrial Science and Technology (AIST), Ibaraki 305-8568, Japan; 3. Univ. Grenoble Alpes, CEA, CNRS, Grenoble INP, INAC, SPINTEC, 38000 Grenoble, France; 4. Centre National d'Études Spatiales (CNES), 31401 Toulouse, France; 5. Time-Frequency department, CNRS FEMTO-ST, Université de Franche Comté, 25030 Besançon, France

With their very rich static and dynamical properties, magnetic vortex dynamics excited by a spin polarized current represent not only a model system to study the physical mechanisms of spin transfer phenomena but could also give birth to a new generation of multi-functional micro-wave spintronic devices [1]. The key property of spin-torque nano-oscillators (STNOs) is their high nonlinearity [2] which gives rise to manifold phenomena such as injection locking to an external rf signal [3-4] or synchronization of multiple STNOs [5-7]. On the other hand, their large nonlinearity causes the oscillator's very poor spectral coherence and leads to a coupling between amplitude and phase noise [8]. While the noise distribution for offset frequencies far from the carrier frequency is reasonably well understood [8] and described by the general nonlinear autooscillator theory [2], low frequency noise remains under investigation as it limits the frequency stability of the oscillator. Extensively studied in GMR and TMR sensors [9-12], this work addresses the low frequency noise of a TMR-based spin-torque vortex oscillator in the regime of large amplitude steady oscillations. In detail, we present a precise experimental study of the TMR-based spin-torque vortex oscillator's low frequency noise, which remains poorly investigated for STNOs in the regime of large amplitude steady oscillations, as we propose here. The measured STNO's magnetic tunnel junction layer stack of PtMn/CoFe/Ru/ CoFeB/CoFe/MgO/FeB/MgO/Ta/Ru was realized by sputter deposition and nanopillar devices of 100-600nm were nanofabricated. The devices have a free running frequency from 100 MHz to 1 GHz depending on the diameter and the applied field value, with an integrated power of up to a few μW and a linewidth of typically ~100 kHz. In complement to the experimental measurements, we have also developed a phenomenological theory aiming to investigate the low frequency flicker noise in these vortex-STNOs. Starting from the corresponding nonlinear Langevin equations and a colored noise distribution, we find additional noise contributions to the white noise power spectral densities. This also gives an additional coupling term between amplitude and phase noise. Noteworthy, we find that this prediction agrees well to our experimental results of the gyrotropic mode's low frequency noise (fig. (a)). Furthermore, we analyze the noise dependence on the control parameter (the operating dc current) and the oscillator's active magnetic volume, reflected by the Hooge-formula for TMR sensors [12] and the oscillator's nonlinearity itself (fig. (b)). S.W. acknowledges financial support from Labex FIRST-TF. EU FP7 grant (MOSAIC No. ICT-FP7-8.317950) is also acknowledged for support.

[1] N. Locatelli, V. Cros, and J. Grollier, Nat Mater 13, 11 (2014). [2] A. Slavin and V. Tiberkevich, IEEE Transactions on Magnetics 45, 1875 (2009). [3] R. Lebrun et al, Phys. Rev. Lett 115, 017201 (2015) [4] A. Hamadeh et al., Appl. Phys. Lett. 104, 022408 (2014). [5] S. Kaka et al., Nature 437, 389 (2005) [6] N. Locatelli et al., Scientific Reports 5, 17039 (2015) [7] R. Lebrun et al, Nat. Comm. 8, 15825 (2017) [8] E. Grimaldi et al., Phys. Rev. B 89, 104404 (2014) [9] E.R. Nowak, M.B. Weissman, S.S.P. Parkin, APL 74, 600 (1999) [10] J.F. Feng, J.Y. Chen, H. Kurt, J.M.D. Coey, JAP 112, 123907 (2012) [11] D. Herranz et al., Appl. Phys. Lett. 99, 062511 (2011) [12] C. Fermon, M. Pannetier-Lecoeur, In: GMR-sensors, Vol. 6, edts: Reig et al., Springer, 2013 [13] L. Bianchini, et al., Appl. Phys. Lett. 97, 032502 (2010)

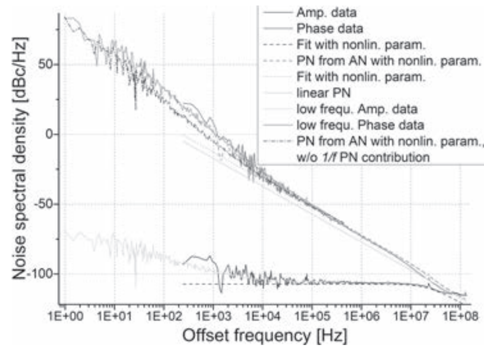

Fig. 1. Noise power spectral density of a spin torque vortex oscillator. The experimental data are shown together with the theoretical curves governed by the preliminarily determined nonlinear parameters [13] as well as the noise curve for a linear oscillator. Theoretical and experimental curves exhibit a good agreement. Here, the theoretical low frequency phase noise curve underestimates the experimental data because the low frequency pure phase noise contribution was neglected due to an experimentally hardly determinable parameter (the corresponding Hooge-factor). AN: Amplitude Noise, PN: Phase Noise.

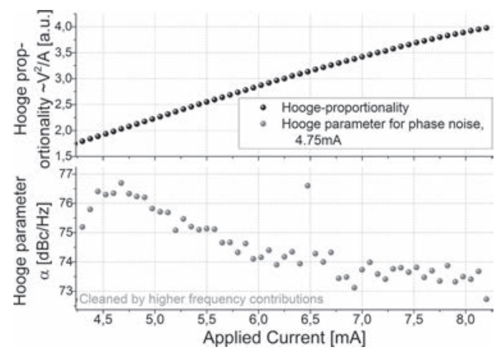

Fig. 2. Although the Hooge-proportionality, which mainly determines the 1/f noise in magnetic sensors, increases, the experimental Hooge-parameter decreases with higher applied current due to the dominant nonlinear effects. V: Voltage, A: Active magnetic surface.

3:45

BD-07. Non-local damping and perpendicular magnetic anisotropy in Hf/CoFeB/MgO.

J. Lourembam[1], A. Ghosh[1], M. Zeng[1], S. Wong[2], Q. Yap[1] and S. Lim[1]
1. Non volatile memory, Data Storage Institute, Singapore, Singapore;
2. Material Science Lab, Data Storage Institute, Singapore, Singapore

Perpendicular magnetic tunnel junctions (*p*-MTJs), based on CoFeB-MgO systems, are widely accepted as the key component for realizing high-density magnetoresistance random access memories (MRAMs).[1] Several experimental and theoretical research have been focused towards investigation of suitable "boron-sink" materials as a CoFeB underlayer to achieve high thermal stability, and low critical current in *p*-MTJs. [2–4] While Ta is the archetypal "boron-sink" underlayer for CoFeB-MgO systems, Hf has emerged as an alternative to Ta with the recent demonstration of 35% increase in interfacial perpendicular magnetic anisotropy (PMA) on replacing Ta.[2] However, important questions with regards to its spin properties such as interfacial magnetoelastic effects, role of orbitals in enhancing PMA, gilbert damping, spin-pumping, etc. remain which need to be addressed. Particularly, in the context of MRAM development, it is essential to investigate these properties in the ultra-thin limit of ferromagnetic thickness, t_F <1.3 nm. In this work, we report a comprehensive study on Hf/$Co_{20}Fe_{60}B_{20}$/MgO for t_F <1.3 nm, by investigating the crystallinity, PMA, and gilbert damping parameter supported by first principles calculations. First, high-resolution transmission electron microscopy (HRTEM), of the stack deposited by sputtering, reveals the crystallinity of the Hf underlayer as well as the MgO layer [Fig. 1 (a)]. Next, we observe a strong non-linear dependence of effective magnetic anisotropy on CoFeB thickness, which can be modelled by incorporating the contribution from magnetoelastic coupling in the standard Néel model [Fig. 1(b)].[5] The magnetic anisotropy energy reaches value as high as ~0.07 erg/cm^2, and PMA is observed for t_F <1.24 nm, significantly wider thickness range compared to Ta underlayer. First principles density-functional calculations (DFT) support the enhancement of PMA in Hf underlayer. Also, to understand the magnetization dynamics as a function of t_F, we use broadband ferromagnetic resonance spectroscopy. Within the PMA range of t_F, the damping is as low as ~0.012 [Fig. 2(a)]. By systematically comparing with MgO/CoFeB/MgO system, we account for non-local effects which contributes to enhancement of effective damping, and also follows a reciprocal relationship with t_F [Fig. 2(b)]. We model this enhanced non-local effect as originating from large spin-mixing conductance. Finally, with the help of DFT, and looking at the density of states, we discuss the true intrinsic damping in this system [Fig. 2(c)]. Our study opens up opportunities for niche applications in MRAM, where broad t_F range for PMA, and tunability in damping are desired.

[1] Z.H.U. Jian-Gang, Proc. IEEE 96, 1786 (2008). [2] T. Liu, J.W. Cai, and L. Sun, AIP Adv. 2, 32151 (2012). [3] T. Liu, Y. Zhang, J.W. Cai, and H.Y. Pan, 20, 1 (2014). [4] Y. Oh, K. Lee, J. Jeong, and B. Park, 724, 2012 (2014). [5] P.G. Gowtham, G.M. Stiehl, D.C. Ralph, and R.A. Buhrman, Phys. Rev. B 93, 24404 (2016).

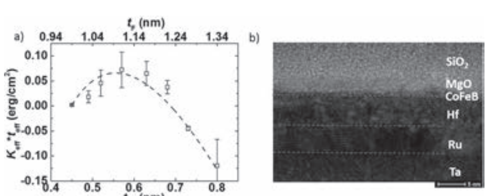

Fig. 1. a) Plot of effective anisotropy per unit area, $K_{eff} \times t_{eff}$ vs. effective thickness t_{eff} and true ferromagnetic thickness, t_F along with fitting model incorporating contributions from magnetoelastic coupling. Effective thickness is calculated by subtracting the dead layer thickness. b) Cross-section HRTEM image of the Hf/CoFeB/MgO film. The red dotted lines indicate guide to the eye for layer demarcation.

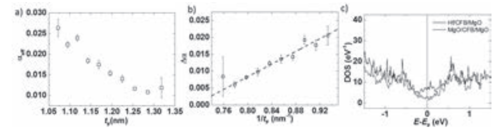

Fig. 2. a) The measured damping, α_{eff} as a function of t_F for Hf/CoFeB(t_F)/MgO films. b) Quantitative dependence of non-local contribution of damping, $\Delta\alpha$ on reciprocal of ferromagnetic layer thickness along with the linear fit. c) Calculated density of states for Hf/CoFeB/MgO and MgO/CoFeB/MgO.

4:00

BD-08. A thermally robust perpendicular magnetic tunnel junction with the FeTa decoupling layer.

J. Yu[1], X. Wang[1] and H. Fukuzawa[1]
*1. Emerging Memories, Institute of Microelectronics, A*STAR, Singapore, Singapore*

Spin-Transfer-Torque Magnetoresistive Random Access Memory (STT-MRAM) has attracted great attentions as an emerging non-volatile memory. For embedded application, its memory cell i.e. perpendicular magnetic tunnel junction (p-MTJ) needs to withstand the 400 °C thermal process which is involved in the semiconductor back-end-of-line (BEOL) process. Although several groups have reported 400 °C thermal robustness [1, 2], the key required atomic-level structure for p-MTJs has not yet been clarified. In this work, we have achieved 400 °C p-MTJ thermal robustness with an untrathin FeTa decoupling layer in the pinned layer, and analysed the atomic-level structure of the film. By comparing the crystal structures of thermally robust and thermally degraded p-MTJs, we have identified that decoupling the body-centered cubic (bcc) CoFeB reference layer and the face-centered cubic (fcc) Co/Pt superlattices is essential in achieving good thermal stability. Firstly, we have confirmed the thermal robustness of a thick p-MTJ against 400 °C as reported in Ref. [3]. The p-MTJ structure is Sub/Ta (1.2)/Pt (2.0)/[Co (0.3)/Pt (0.5)]$_6$/Co (0.5)/ Ru (0.85)/Co (0.5)/Pt (0.5)/[Co (0.3)/Pt (0.5)]$_4$/Ta (0.3)/$Co_{20}Fe_{60}B_{20}$ (1.2)/MgO(1.0)/$Co_{20}Fe_{60}B_{20}$ (1.2)/Mo(2.0)/Cap [thickness in nm]. However, for a thinner pinned layer p-MTJ by reducing the Co/Pt repetitions from 4 to 2 labelled as the conventional p-MTJ in Fig. 1(a), thermal stability degradation was observed from the major *M-H* loops [Fig. 1(b)]. Since the free layer exhibited sufficient thermal stability as shown in the inset of the figure, we speculated that thermal degradation could be initiated from the crystal interference in a thin region of Ta insertion layer where the bcc and fcc crystals meet each other. In order to solve this issue, we proposed a FeTa insertion layer to replace the Ta layer. The improved p-MTJ structure is shown in Fig. 1(a). FeTa was selected due to its amorphous structure as deposited. Under 400°C thermal annealing, it could nucleate and grow in an epitaxial manner along both bcc and fcc crystal boundaries of the neighbouring layers. This unique crystallization behaviour enables FeTa to act as a buffer to effectively decouple the bcc and fcc crystal structures. Regarding the magnetic function, the required ferromagnetic exchange coupling between the CoFeB reference layer and the Co/Pt superlattices was obtained thanks to the intrinsic magnetic property of FeTa alloy. As a result, the thermal robustness against 400 °C has been successfully achieved for the improved p-MTJ. Fig. 1(c) shows the decent major and minor *M-H* loops with little thermal degradation for the improved p-MTJ. To clarify the mechanism for achieving thermal robustness of the improved p-MTJ, we adopted the spherical aberration corrected Scanning Transmission Electron Microscope (Cs-corrected STEM) to visualize the atomic-scale structural difference at the Ta and FeTa interfaces (Fig. 2). Images show that a flat interface is present with the improved FeTa sample, and its CoFeB reference layer is more crystalline structured. In contrast, the conventional Ta sample shows a rougher crystal interface and the CoFeB reference layer tends to be amorphous. The structural difference suggests that the FeTa layer is more effective in decoupling the bcc and fcc crystal structures. This result could also account for the observation by another group that a thicker CoFeB reference layer resulted in thermal stability degradation [2]. Theoretically, a thicker film layer leads to a better thermal tolerance owing to its more robust crystal structure. However, when comes to a complex p-MTJ system consisting of both bcc and fcc lattices in an ultrathin region, a thicker CoFeB layer enhances the structural integrity of bcc lattice against the fcc Co/Pt superlattices. This subtle thickness change may break the thermodynamic equilibrium status between these two lattices during 400 °C thermal process, thus causing the degradation of perpendicular magnetic anisotropy originated from the Co/Pt superlattices. This also explained the slightly thermal degradation of the improved p-MTJ when thickening the CoFeB reference layer from 0.8 nm to 1.2 nm even though the FeTa insertion layer can realize more effective crystal decoupling between the bcc CoFeB and fcc Co/Pt superlattices. In summary, maintaining the crystal integrity of both the CoFeB bcc and Co/Pt fcc crystal structures and well control of their interface are essential in achieving good p-MTJ thermal tolerance for embedded STT-MRAM application.

[1] M. Gottwald et al., Appl. Phys. Lett. 106, 032413 (2015). [2] Y. Tomczak et al., Appl. Phys. Lett. 108, 042402 (2016). [3] J. Yu et al., Appl. Phys. Express 11, 013006 (2018).

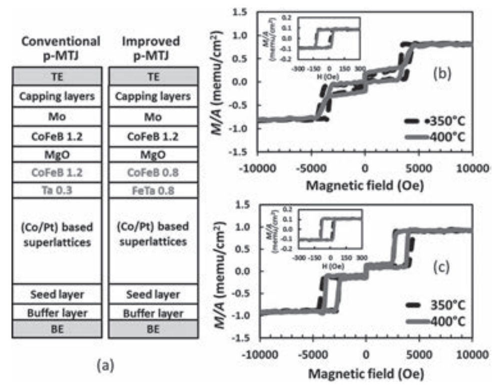

Fig. 1. (a) Schematic of the conventional and improved p-MTJs; and *M-H* loops for the (b) conventional p-MTJ, and (c) improved p-MTJ. The dashed black and solid blue lines represent the data for 350 °C and 400 °C samples respectively. The insets of the figures show their corresponding minor *M-H* loops.

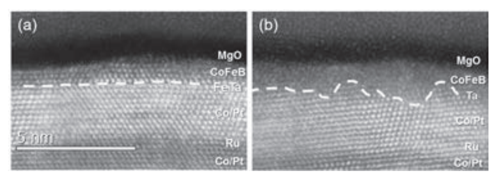

Fig. 2. Atomic-level dark field STEM images of p-MTJs focusing at the CoFeB and Co/Pt interfaces for (a) FeTa sample and (b) Ta sample.

4:15

BD-09. Effect of MgO interface in double barrier CoFeB MTJ structures.

S. Srivastava[1], A.P. Chen[1], T. Dutta[1], R. Ramaswamy[1], M. Saifullah[2], K. Yamane[3], J. Son[1,3], K. Lee[3], P. Yang[1] and H. Yang[1]
1. National University of Singapore, Singapore; 2. Agency for Science, Technology, and Research, Institute of Materials Research and Engineering, Singapore, Singapore; 3. GLOBALFOUNDARIES Singapore Pte. Ltd., Singapore, Singapore

The double barrier perpendicular MTJ system with CoFeB as the magnetic free layer and MgO as the barrier is the most preferred structure, due to its high thermal stability, for MRAM applications. In order to improve the MTJ free layer performance, it is essential to optimize magnetic properties of CoFeB. In literature, few works have studied the CoFeB composition dependence of the magnetic properties, however these studies are limited to either the bulk systems or a very few compositions. On the other hand, state of the art MTJs use ultrathin magnetic layers with the MgO interface, which show very different properties compared to the bulk systems. Thus, it is necessary to develop a comprehensive understanding of the effect of CoFeB composition with the MgO interface to identify the factors influencing the magnetic anisotropy and damping of the free layer, which are crucial factors for MRAM development. In this work, we have carried out a comprehensive study of various magnetic properties for different CoFeB compositions. We find that the saturation magnetization shows an anomalous trend with respect to CoFeB composition in contrast to conventional Slater-Pauling curve. Further, we also find a minimum in composition dependence of the damping parameter, which could not be explained using the theories and concepts established in previous studies. To explain these new observations, we theoretically calculated the density of states (DOS) and magnetic moments for different compositions. Figure 1 shows the composition transition of the nature of anisotropy from uniaxial to cubic anisotropy. Using this anisotropy information and the theoretical magnetic moments, we propose that this change in anisotropy is the predominant underlying mechanism for the observed anomalous magnetization behaviors. Furthermore, the theoretical calculations of DOS are also used to explain the minimum in the Gilbert damping parameter, which is shown in figure 2. Our results suggest that it is necessary to consider the structure of CoFeB ultra-thin films with MgO interface to understand the underlying physics of the magnetic properties in CoFeB/MgO based MTJs, which is important for scientific development. Our study also identifies the best CoFeB composition for the lowest spin transfer torque switching current, highest thermal stability and other characteristics which are important for applications.

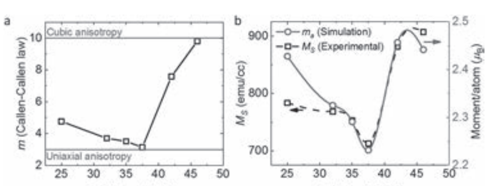

Fig. 1. (a) Composition dependence of degree of anisotropy. (b) Comparison of magnetization from experiments and average magnetic moment per atom calculated.

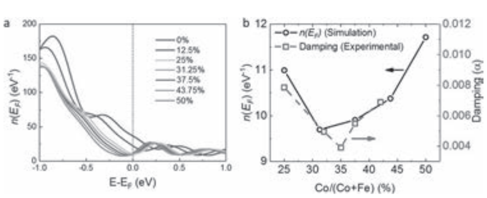

Fig. 2. (a) DOS calculation results for different Co compositions. (b) DOS at Fermi level ($n(E_F)$) and damping *a* obtained from experiments as a function of compositions.

4:30

BD-10. Withdrawn

4:45

BD-11. Effect of stray field from adjacent bits of high-density STT-MRAM on switching current.

S. Itai[1], T. Kai[1], M. Nakayama[1], T. Daibou[1] and J. Ito[1]
1. Institute of Memory Technology Research & Development, Toshiba Memory Corporation, Kawaksaki, Japan

Magnetoresistive random access memory (MRAM) has the potential to become the ultimate random access memory due to its non-volatility, high-speed operation, and unlimited read/write endurance. The experimental observation of spin-transfer torque (STT) switching [1-2] has stimulated considerable interest in high-density MRAM due to its simple cell structure. Last year, Toshiba and SKhynix reported [3] for the first time the realization of 4 Gbit high-density MRAM by employing perpendicular magnetic tunnel junctions (MTJs) with a 90 nm pitch between bits. However, enhancement of stray field between adjacent MTJ bits is expected to become a serious problem as the distance between MTJ bits decreases at higher densities. This effect causes degradation of various MTJ properties including thermal stability and the STT switching current. In this study, we investigate the effect of MTJ properties on the stray field from adjacent MTJ bits by using micro-magnetic calculations based on the Landau–Lifshitz–Gilbert equation [4]. We also investigate the dependence of STT switching current on the distance between bits. The micro-magnetic simulation that we used examines 9 to 25 bits that are modeled. Electric current is applied to only the center MTJ bit, which allows us to calculate the STT switching behavior for various configurations of the magnetization direction of the storage layer. We assume that the magnetization direction of the reference layer is fixed in the upward direction. The parallel configuration (P) has the magnetization direction of the storage layer pointing upward, and the anti-parallel configuration (AP) has the magnetization direction of the storage layer pointing downward. The storage layer parameters that we used are *Ms* (saturation magnetization) = 1400 emu/cc or 1700 emu/cc, *Ku* (magnetic anisotropy) = 17 Merg/cc or 14 Merg/cc, *D* (MTJ diameter) =14 nm or 20 nm, and *L* (distances between bits) = 2D nm or 3D nm. In general, the thermal stability factor, ΔE, is dependent on the external field and is given by $\Delta E_{eff} = \Delta E_{int} (1-H_{ext}/H_k)^2$ (1), where H_{ext} is the external field and H_k is the anisotropy field of the storage layer. Here, H_{ext} means the stray field from adjacent bits, the magnitude of which depends on the magnetization pattern of the adjacent storage layer. The switching current, *Ic*, of an MTJ with perpendicular magnetization is proportional to ΔE. Therefore, the value of *Ic* in the presence of stray field from adjacent MTJ bits is given by $Ic/Ic_{\_iso} = (1-H_{ext}/H_k)^2$ (2), where $Ic_{\_iso}$ is the calculated *Ic* of an isolated pattern without the adjacent MTJ bits. Figure 1 and 2 show $Ic/Ic_{\_iso}$ as a function of H_{ext}/H_k for various bit patterns. In this case, *Ic* is the P-AP switching current of the center bit, and H_{ext} is the average field over the z-direction estimated from a simple analytic model. In this report, we present calculations for two patterns. In one pattern, all the bits are in the AP configuration except the center bit as shown in Fig. 1, and the center bit is in the P configuration, which means that the storage layer magnetization direction of only the center bit shows a different direction. In this case, the direction of the stray field from the adjacent bits points upward, therefore the switching current *Ic* from P to AP increases for the disturbance of the STT switching with its stray field as compared to the switching current of the isolated pattern, *Ic_iso*. However, the quantitative dependence is different from Eq. (2), which may be due to the complex spatial distribution of the stray field from the adjacent bits. In another pattern, all the bits are in the P configuration as shown in Fig. 2, which means that all the bits show the same upward direction in the storage layer. In this case, the switching current exhibits very little change depending on the external field. We conclude that the effect of stray field from adjacent bits on the switching current is much larger than expected from a simple theoretical model. Importantly, these results suggest that it is necessary to carefully investigate the influence of adjacent bits when designing high-density MRAM devices.

[1] J. Katine *et al.*, Phys. Rev. Lett. 84, 3149 (2000). [2] M. Nakayama, *et al.*, J. Appl. Phys. 103, 07A710 (2008). [3] S.-W. Chung, *et al.*, IEDM 2016 Technical Digest, 27.1 (2016). [4] T. Kai, *et al.*, 53rd MMM conference, DC-07 (2008).

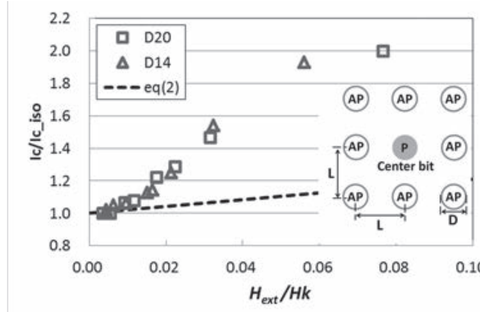

Fig. 1. ***Ic/Ic***$_{\_iso}$ **versus** ***H***$_{ext}$***/Hk*** **obtained in the case which all the bits are in the AP configuration except the center bit. D20 means that the MTJ diameter is 20 nm. D14 means that the MTJ diameter is 14 nm. The inserted figure is schematic diagram of the simulation structure in this case.**

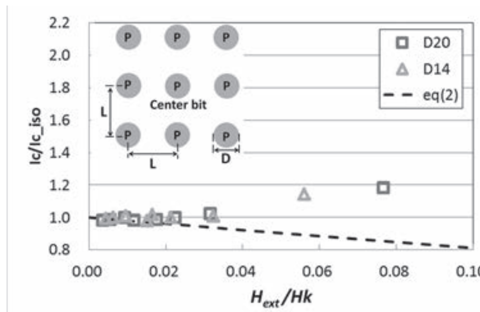

Fig. 2. ***Ic/Ic***$_{\_iso}$ **versus** ***H***$_{ext}$***/Hk*** **obtained in the case which all bits are in the P configuration. D20 means that the MTJ diameter is 20 nm and D14 means that the MTJ diameter is 14 nm. The inserted figure is schematic diagram of the simulation structure in this case.**

TUESDAY AFTERNOON, 24 APRIL 2018 ROSELLE II, 2:00 TO 5:00

Session BE
SPIN INJECTION AND SPIN TORQUE OSCILLATORS

Ciarán Fowley, Chair
Helmholtz-Zentrum Dresden-Rossendorf, Dresden, Germany

INVITED PAPER

2:00

BE-01. Effects of spin-orbit torque on the magnon gas.

V.E. Demidov[1], S. Urazhdin[2], B. Divinskiy[1] and S.O. Demokritov[1]
1. Institute for Applied Physics, University of Muenster, Muenster, Germany; 2. Emory University, Atlanta, GA, United States

Spin orbit torque (SOT) provides the possibility to control the magnetization state of conducting and insulating magnetic materials. Recently, it was shown that the influence of SOT on the spin system of ferromagnets results in either enhancement or suppression of magnetic fluctuations, depending on the polarization, which can be equivalently described as generation or annihilation of incoherent magnons. This mechanism is not specific to certain magnon states, and is expected to change magnon populations throughout the entire spectrum, thus avoiding the non-thermalized transient states inherent to other mechanisms used to drive magnon gases, such as the parametric pumping. Recent theoretical studies suggest that SOT can drive the magnon gas into a quasi-equilibrium state described by the Bose-Einstein statistics with non-zero chemical potential, suggesting the possibility of electrically-driven Bose-Einstein condensation (BEC) of magnons. These theories have been supported by the successful application of the developed theoretical framework to incoherent magnon transport. Variations of the chemical potential of the magnon gas were recently detected in measurements of spin relaxation rates of a nitrogen-vacancy center in diamond coupled to spin waves in a magnetic insulator. However, there was no direct experimental evidence that the magnon gas driven by SOT forms a quasi-equilibrium distribution, and the dependence of the effective thermodynamic characteristics has not been established. We studied the effects of SOT on the magnon distribution over a broad spectral range, by utilizing the micro-focus Brillouin light scattering (BLS) spectroscopy. The studied system comprises a 2 micrometers wide and 5 nm thick Pt strip overlaid by a 1 micrometer wide and 10 nm thick ferromagnetic Permalloy (Py) strip (Fig. 1a). The system is magnetized by the static magnetic field applied along the Py strip. The electric current I flowing in Pt is converted by the spin-Hall effect (SHE) into a spin current injected into Py through the Py/Pt interface. The magnetic moment carried by the spin current is either parallel or antiparallel to the Py magnetization M, depending on the direction of current, resulting in a decrease or an increase of the magnon population, respectively. The BLS spectra reflecting the current-dependent spectral density of magnons (Fig. 1b) allowed us to analyze the spectral magnon population function and determine the thermodynamic characteristics of the magnon gas. Our analysis clearly indicated that the magnon distribution can be described by the Bose-Einstein statistics expected for the quasi-equilibrium state. We determined the current-dependent chemical potential and effective temperature of the magnon gas (Fig. 2), and showed that, for one polarization of the spin current, the effective temperature of the magnon gas becomes significantly reduced, while the chemical potential stays almost constant (Fig. 2a). In contrast, for the opposite polarization, the effective temperature remains nearly unaffected, while the chemical potential linearly increases with current, until it closely approaches the lowest-energy magnon state (Fig. 2b), indicating the possibility of spin current-driven Bose-Einstein condensation. Our experimental results provide direct spectroscopic evidence that the magnon gas is driven by the SOT into a quasi-equilibrium state, which can be described by the Bose-Einstein distribution with current-dependent values of chemical potential and effective temperature. These findings support the theoretically proposed mechanism for the formation of current-induced magnetization auto-oscillations via the Bose-Einstein condensation of magnons. Our results should stimulate further experimental and theoretical exploration of the relationship between the thermodynamics of magnon gases driven by spin currents, and coherent magnetization dynamics.

S. O. Demokritov, et al., Nature 443, 430 (2006). V. E. Demidov, et al. Phys. Rev. Lett. 107, 107204 (2011). S. A. Bender, et al., Phys. Rev. Lett. 108, 246601 (2012). V. E. Demidov et al., Nature Mater. 11, 1028 (2012). L. J. Cornelissen, et al., Phys. Rev. B 94, 014412 (2016). C. Du, et al., Science 357, 195 (2016). V. E. Demidov et al., Phys. Rep. 673, 1 (2017). V. E. Demidov et al., Nat. Commun. 8, 1579 (2017).

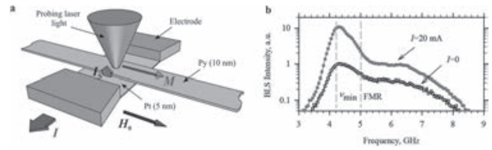

Fig. 1. (a) Schematic of the experiment. (b) BLS spectrum recorded at I=20 mA (solid symbols), together with the reference spectrum obtained at I=0 (open symbols).

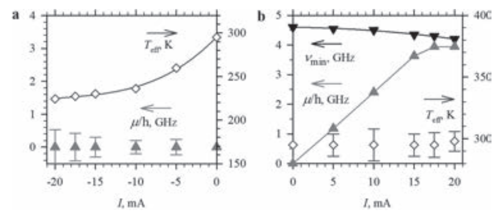

Fig. 2. (b) Current dependences of the chemical potential in the frequency units (point-up triangles) and of the effective temperature (diamonds) of the magnon gas for I<0 (a) and I>0 (b). Point-down triangles in (b) show the frequency of the lowest-energy magnon state.

CONTRIBUTED PAPERS

2:30

BE-02. Current-Induced Superparamagnetism in CoFeB Nanodots.

A.M. Abdelgawad[1], B. Parks[2] and *S. Majetich*[2]
1. Materials Science and Engineering, Carnegie Mellon University, Pittsburgh, PA, United States; 2. Physics, Carnegie Mellon University, Pittsburgh, PA, United States

Superparamagnetic tunnel junctions with perpendicular anisotropy have a fluctuation frequency that can be controlled by a voltage through voltage controlled magnetic anisotropy [1], but statistical mechanics limits the range of the time-averaged magnetoresistance. Here we describe how a much larger range can be achieved using nanostructures with in-plane magnetization. Such devices could be important for low power logic gates and probabilistic computing. [2,3]. The sample stack consists of an in-plane magnetic tunnel junction (MTJ) with a pinned synthetic antiferromagnet fixed layer: Pt(5)/Ta(10)/CoFeB(2.5) /MgO(1.0)/ CoFe(3)/Ru(0.8)CoFe(2)/PtMn(20)/Ta(50)/Si, where the numbers are in nanometers. In-plane hysteresis loops measured by alternating gradient magnetometry showed a 4 kOe switching field for the fixed layer. Out-of-plane loops indicated a free layer anisotropy field of ~ 600 Oe. The stack was patterned by electron beam lithography and etched down to the MgO tunnel barrier via ion milling, leaving arrays of circular 20 – 80 nm diameter CoFeB dots. After patterning the CoFeB layer, the sample was initialized with a permanent magnet along the pinning axis to orient the fixed layer. Conductive atomic force microscopy (CAFM) was then used to measure the magnetoresistance R as a function of in-plane magnetic field H, bias voltage V, and time t. Here positive bias corresponds to electrons flowing from tip to sample. At low voltage bias (50 mV) with no external magnetic field, the CoFeB dots were magnetically stable, for all sizes. Resistance as a function of magnetic field indicated coercivities on the order of 7 Oe, independent of size. In addition, there were small loop shifts due to orange peel coupling associated with interface roughness that varied with location and favored the parallel (P) state. Figure 1a shows resistance as a function of voltage bias measurements for a 40 nm tunnel junction, with H applied = 0. Figure 1b shows the result after an external field was used to cancel the local orange peel. There a high negative bias the device is stable in the P state, and at high positive bias it is stable in the antiparallel (AP) state. Between –50 mV and +250 mV the fluctuations indicate current-induced superparamagnetim of the 40 nm CoFeB dot. The threshold for fluctuating behavior is higher to stabilize the AP state than the P state. Similar asymmetric thresholds are also seen with stable MTJs and giant magnetoresistance spin valves. This, together with the current densities (here 3.4×10^6 A/cm^2 at –50 mV) suggest that spin transfer torque is the dominant cause of the superparamagnetic fluctuations. Interpretation of the superparamagnetism is complicated by the time-varying voltage bias (1.5 V/s) in Figure 1, and so the resistance as a function of time was measured at a series of fixed bias voltages within the fluctuating region (Figure 2). The data are consistent with those of Figure 1, but provide additional details. The change in *R(t)* as function of the applied bias reflects a gradual change in the direction of the normalized time-averaged magnetization of the free layer over the full range from 1 to -1, corresponding to P and AP states, respectively. Unlike with perpendicular MTJs, which have random telegraph noise between two levels [1], these in-plane MTJs have variable resistance between the P and AP limits, indicating incomplete reversal. For analysis of superparamagnetism in terms of a Neel-Brown model, the nanomagnet must spends most of its time in one of the ground states, and this is not necessarily true here. As an alternative approach, the fast Fourier transform (FFT) of the time trace was fit to a Lorentzian function to determine the average fluctuation time (t = 20 ms for the 40 nm device at +50 mV). This method avoids artifacts associated with thresholding that could obscure the underlying physics of current-driven superparamagnetism. The amplitude and frequency of these fluctuations are characterized as a function of the bias voltage and current density, for the different CoFeB dot diameters. The 20 nm diameter dots show more significant thermal effects, as expected. The statistical randomness of the signal and its use in probabilistic computing are discussed.

[1] B. Parks, M. Bapna, J. Igbokwe, H. Almasi, W. Wang, and S.A. Majetich, AIP Adv. 8, 55903 (2018). [2] M. Bapna and S.A. Majetich, Appl. Phys. Lett. 111, 243107 (2017). [3] K. Y. Camsari, R. Faria, B. M. Sutton, and S. Datta, Phys. Rev. X 7, 31014 (2017).

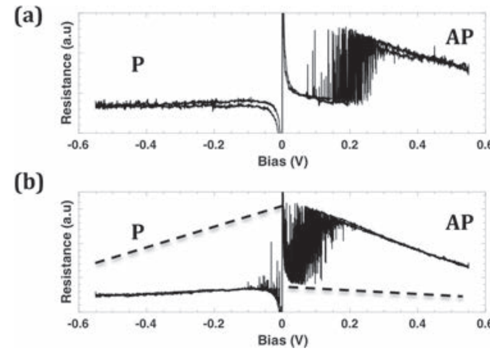

Fig. 1. R(V) curve for a 40 nm MTJ device at H_{net} =0. The large spike rear zero is an artifact due to the small current tunneling at low bias, and does not indicate switching. The critical switching bias from P to AP state is at ~ -50 mV. The dashed lines mark references for P state at positive bias and AP state at negative bias.

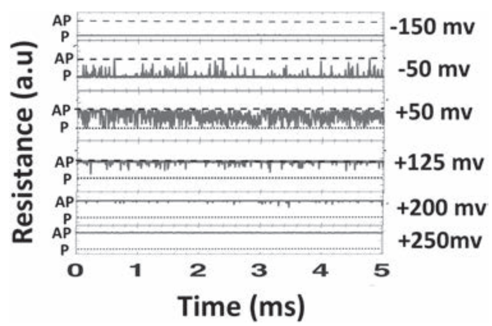

Fig. 2. Time traces of resistance at different bias voltages, for the 40 nm device of Fig. 1. with H_{net} = 0. All time traces are recorded for 150 ms at a 100 MHz acquisition rate, but here only 5 ms sections are shown. Dashed lines mark AP states while dotted lines mark P states.

2:45

BE-03. Out-of-plane auto-oscillation in spin Hall oscillator with additional polarizer.

T. Taniguchi[1]
1. Spintronics Research Center, National Institute of Advanced Industrial Science and Technology, Tsukuba, Japan

This theoretical work proposes an experimental scheme to excite an auto-oscillation in a perpendicular ferromagnet by the spin Hall effect. The spin-Hall effect [1] in nonmagnetic heavy metals has attracted much attention from the prospective of both fundamental physics and practical applications. The spin Hall effect in a nonmagnetic/ferromagnetic bilayer injects spin current from the nonmagnet to the ferromagnet, and excites spin torque acting on the magnetization. The spin torque induces magnetization dynamics such as switching and oscillation [2], which are applicable to practical applications such as magnetic memory, high sensitivity sensor, and brain-inspired computing [3]. A critical problem for further development of spintronics devices based on the spin Hall effect is the geometrical restriction on the direction of the spin torque. Let us assume that electric currents flow in the nonmagnet along the *x* direction, while the ferromagnet is set in the *z* direction. The spin polarization in spin current by the spin Hall effect is then fixed to the *y* direction. The designs and performances of the devices are subject to limitation due to this restriction of spin polarization. For example, the magnetization switching of a perpendicular ferromagnet solely by the spin Hall effect is impossible because the spin torque does not break the planar symmetry with respect to the film plane. Using external magnetic field, tilted anisotropy, or exchange bias has been proposed to overcome this issue [4]. It was also shown that an auto-oscillation in a perpendicular ferromagnet solely by the spin Hall effect is impossible due to the symmetry of the spin torque [5]. However, the auto-oscillation in a perpendicular ferromagnet is attractive because the large amplitude oscillation leads to a large emission power. In this work, we investigate the possibility to excite the auto-oscillation in a perpendicular ferromagnet by the spin Hall effect [6]. We focus on recent theoretical works on the spin Hall effect in the presence of an additional ferromagnet to the free layer [7]. It is predicted that the additional ferromagnet provides an additional spin torque excited in the free layer. In this study, we consider adding another ferromagnet, referred to as the pinned layer, on the top of the free layer, as shown in Fig. 1(a). The spin Hall effect in the bottom nonmagnet injects spin current into the free layer, and excites the conventional spin torque as a result of the absorption of the transverse spin current. On the other hand, the spin current survived during the transport from the bottom nonmagnet to the free layer moves to the pinned layer. Reflecting the spin current at the interface and inside the bulk, the pinned layer injects the reflected spin current into the free layer, and provides an additional spin torque. We evaluate the additional spin torque from the diffusive spin transport theory. The magnitude, direction, and angular dependence of the additional spin torque are found to depend on the magnetization direction in the pinned layer. By choosing an appropriate direction of the magnetization in the pinned layer, an auto-oscillation in the perpendicularly magnetized free layer can be excited. Figure 1(b) shows an example of the auto-oscillation obtained from the numerical simulation of the Landau-Lifshitz-Gilbert equation, where the magnetization in the free layer oscillates around the perpendicular axis within a frequency on the order of gigahertz. We notice that the direction of the magnetization in the pinned layer is an important parameter to stabilize the auto-oscillation. Figure 2 shows the dependences of the oscillation frequency of the magnetization in the free layer on the current in the bottom nonmagnet. Several values of the tilted angle of the magnetization in the pinned layer from the perpendicular axis are presented. In the low current region, the oscillation of the magnetization at the ferromagnetic resonance (FMR) frequency is excited by random torque originated from thermal fluctuation. The FMR frequency depends on the direction of the magnetization in the pinned layer through the stray field from the pinned layer. Above critical values of the current, two kinds of magnetization dynamics are excited in the free layer. When the tilted angle of the magnetization in the pinned layer is relatively large, the magnetization switching to an in-plane direction is achieved. In this case, the oscillation frequency discontinuously drops from the FMR frequency to a certain constant value. On the other hand, when the tilted angle of the magnetization in the pinned layer is relatively small, a stable auto-oscillation is excited, where the oscillation frequency changes continuously. The results provide a guideline to design an auto-oscillator based on the spin Hall effect.

[1] M. I. Dyakonov and V. I. Perel, Phys. Lett. A 35, 459 (1971). J. E. Hirsch, Phys. Rev. Lett. 83, 1834 (1999). [2] I. M. Miron *et al*., Nature 476, 189 (2011). L. Liu *et al*., Science 336, 555 (2012). V. E. Demidov *et al*., Nat. Commun. 5, 3179 (2014). [3] W. A. Borders *et al*., Appl. Phys. Express 10, 013007 (2017). K. Kudo and T. Morie, Appl. Phys. Express 10, 043001 (2017). [4] L. Liu *et al*., Phys. Rev. Lett. 109, 186602 (2012). L. Liu *et al*., Proc. Natl. Acad. Sci. U.S.A. 112, 10310 (2015). J. Torrejon *et al*., Phys. Rev. B 91, 214434 (2015). S. Fukami *et al*., Nat. Mater. 15, 535 (2016). [5] T. Taniguchi, Phys. Rev. B 91, 104406 (2015). [6] T. Taniguchi, Appl. Phys. Lett. 111, 022401 (2017). [7] W. T. Chen *et al*., Phys. Rev. B 87, 144411 (2013). T. Taniguchi *et al*., IEEE Trans. Magn. 52, 1400204 (2016). G. Go *et al*., Sci. Rep. 7, 45669 (2017).

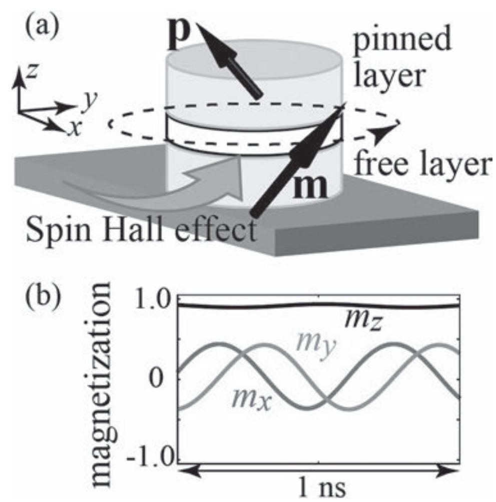

Fig. 1. (a) Schematic view of the system in this study. The spin Hall effect in the bottom nonmagnet injects spin current into the free layer, and excites spin torque on the magnetization. The pinned layer reflects the spin current, and excites an additional spin torque to the free layer. The magnetization directions of the free and pinned layers are denoted as m and p, respectively. (b) An example of the time evolution of the magnetization in the free layer in an auto-oscillation state.

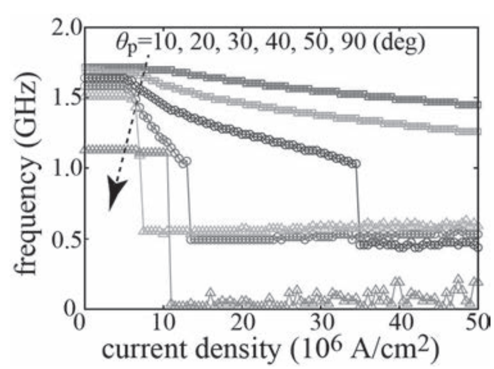

Fig. 2. Dependences of the oscillation frequency of the magnetization on the current in the bottom nonmagnet for several values of the angle θ_p. Here, θ_p is the tilted angle of the magnetization p in the pinned layer from the perpendicular (*z*) axis.

INVITED PAPER

3:00

BE-04. Engineering lateral nanostructures for the study of spin accumulation phenomena, giant magnetoresistance, spin Hall effect, and sensors.

J. Attané[1], L. Vila[1], A. Marty[1], G. Zahnd[1], T. Van Pham[1], P. Noel[1] and W. Savero-Torres[1]
1. Univ. Grenoble Alpes, CEA, CNRS, Grenoble INP, INAC, SPINTEC, Grenoble, France*

Spintronics is mainly based on the phenomenon of spin accumulation, which is inherent to the circulation of an electric current at the interfaces between ferromagnetic and non-magnetic materials. These accumulations are conventionally obtained in multilayers for which the thicknesses of the layers are smaller than the characteristic lengths of the spin-dependent transport. It is thus possible to generate in these multilayers magnetoresistances or spin transfer effects. The development of nanofabrication processes makes it nowadays possible to create nanodevices whose lateral dimensions are less than the characteristic lengths of the spin-dependent transport, and thus to bring into play similar phenomena. In this contribution, we show results obtained in different ferromagnetic/non-ferromagnetic lateral nanostructures, demonstrating that it is possible to take advantage of the three-dimensional geometry of the structures, and of the different possible orientations of the injected spins. In particular, transport studies have been carried out in collinear and non-collinear regimes, in order to study the consequences of the non-collinearity on the spin accumulations and magnetoresistances. The effect of non-collinearity is examined using spin absorption measurements and Hanle measurements. We also show that the flexibility offered by the lateral geometry allows designing the ferromagnetic and non-magnetic materials, to tailor the spin accumulation and magnetoresistance signals as well as the magnetic states[1]. After presenting some of our recent spin to charge inter-conversion experiments by spin Hall effects[2], Rashba interfaces[3] and topological surface states[4], we then show that lateral spin valves offer various experiments for accessing the spin polarization and spin diffusion length of ferromagnetic materials, the properties of interfaces or of spin conductors. Thus, lateral nanodevices are very interesting tools for studying materials, interfaces and surface states, and for harnessing the spin orbit coupling[5]. Finally, we show that by combining lateral and vertical geometries, it is possible to evidence a magnetoresistance due to the spin accumulation. This new magnetoresistance is based on the modulation of the additionnal spin resistance generated by the presence of a spin accumulation at the vicinity of an interface.

[1] G Zahnd *et al*., Scientific Reports 7, 9553 (2017) & Nanotechnology 27 (3), 035201 (2015) [2] P. Laczkowski *et al.*, Phys. Rev. B 96, 140405 (2017) [3] E. Lesne *et al.*, Nat. Mat. 15, 1261 (2016) [4] P. Noël *et al.*, arXiv preprint arXiv:1708.05470 (2017) [5] V.T. Pham *et al.*, Nano Lett. 16, 6755 (2016)

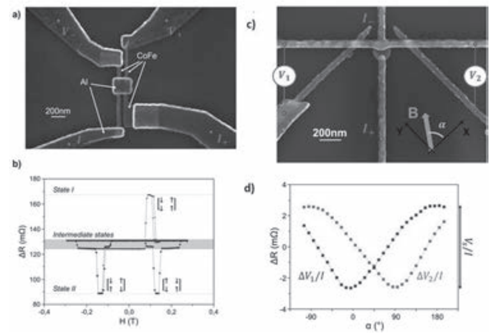

Fig. 1. (a,b) Multi-input/output nanodevices allowing large and multi-level GMR spin signals. (c,d) Ferromagnetic nanodisk with two non collinear spin injector/detector allowing an electrical control of the spin polarization axis.

CONTRIBUTED PAPERS

3:30

BE-05. Robust electrical mutual synchronization of spin torque oscillators.

S. Tsunegi[1], T. Taniguchi[1], R. Lebrun[2], K. Yakushiji[1], A. Fukushima[1], J. Grollier[2], V. Cros[2], S. Yuasa[1] and H. Kubota[1]
1. Spintronics Research Center, National Institute of Advanced Industrial Science and Technology (AIST), Palaiseau, France; 2. Unité Mixte de Physique CNRS, Thales, Univ. Paris Sud, Université Paris-Saclay, Palaiseau, France

Synchronization of spin torque oscillators (STOs) attracts much attention from fundamental and applied physics because it has a possibility to be used in practical devices such as the neuromorphic computing [1,2] and the phased array wave generator [3]. Recent studies have clarified that there are three key quantities determining the applicability of the synchronized STOs to the practical devices. First, it is necessary to synchronize a large number of STOs as the number of synchronized STOs determines the number of associative patterns in the associative memory [4]. Second, a fast transition from a given synchronous state to another is required because the transient time determines the operation speed of the devices. The third one is the robustness of the synchronization against the thermal fluctuations because the stability of the synchronization determines the output power. Very recently, we have successfully addressed these issues. First, we succeed to increase the number of the synchronized STOs up to eight [5]. This result guarantees the scalability of STOs. Moreover, we observe a fast transition time of STOs on the order of nanoseconds from asynchronous to synchronous states [6]. As for the robustness of the synchronization between STOs, a first approach has been to study the phase locking regime using a STO being synchronized to an external rf signal. The stability of the phase difference between the STO and the external signal is found to be of the order of milliseconds together with a phase noise level as low as -90 dBc/Hz at 1 MHz offset [7]. However, the stability of mutually synchronized STOs is expected to be relatively weaker as the phase noise of each STOs that are mutually synchronized shall affect the other ones. In fact, the robustness of the mutual synchronization has not been investigated yet and this is one of the main objectives of this study. Here, we aim at investigating the stability of the phase between the mutually synchronized STOs experimentally. To this purpose, we have measured the phase-slip time, during which the phase difference between the STOs is kept constant against the phase slip due to the thermal fluctuation. The circuit is composed of two vortex based STOs, each of them having a large emission power over 1 mW and a narrow linewidth being less than 300 kHz at the free running frequency around 330 MHz [8]. The STOs are electrically connected through directional couplers and attenuators. The coupling mechanism leading to the mutual synchronization originates from the emitted rf current from each STO which allows the efficient interaction between them [9] The directional couplers are used to characterize the individual signal of each STOs. The measured voltage signal is converted into the phase signal by the Hilbert transform. The attenuators are introduced to tune the coupling strength resulting in the synchronization force. Note that the individual magnets for each STO has been used in order to control separately the frequency of each STOs and make that the free running frequencies of the STOs are the same. In Figure 1(a), we show the time evolution of the phase difference Ψ between the synchronized STOs for several values of the attenuation A. The phase-slip time is determined by the shift of the phase difference with the factor of 2 π [9]. We confirm that the phase-slip time increases when the attenuation A is increased. In case of a strong coupling (A = 0 dB), it results in an extremely long stability of the phase difference. The stability is kept over one millisecond, corresponding to 10^5 oscillation periods. Unfortunately, we could not evaluate the phase-slip time for A = 0 dB because it is kept longer than the limit of the measurable time in our system. Therefore, we estimated the time between phase slips theoretically. The phase slip can be regarded as an escape of a Brownian particle from one stable state to the others in a periodic potential with the period of 2 π. We thus calculate the escape time as the phase-slip time by using the mean first passage time [10]. For a large coupling limit, the phase-slip time is given by $T_{slip}=\pi/\sqrt{AF_0}*\exp(\sqrt{AF_0}/D)$. Here, F_0 and D are related to the locking range at A=0 dB and the diffusion constant corresponding to the strength of the thermal noise. In Figure 1(b), we show the comparison of the phase-slip time evaluated from the experiments with the formula, where (F_0, D) =(3.73×10^7, 2.4×10^6) rad/s were determined by the fitting. These values correspond to a locking range of 6 MHz and a spectral linewidth of 630 kHz, which are consistent with our experimental results. According to the qualitative agreement between the experiments and theory, we predict that the phase slip time for A = 0 dB is 0.48 second corresponding to 10^8 oscillation periods. These results describe the first report highlighting a considerable long-time stability of the phase difference between the mutually synchronized STOs. We believe that it represents a crucial advances toward the development of the practical devices based on the STO arrays. Acknowledgments : the MIC/SCOPE # 162103105

[1] J. Torrejon *et al*., Nature 547, 428 (2017) [2] J. J. Hopfield, Proceedings of the National Academy of Sciences 79, 2554 (1982). [3] J. Sun *et. al*., Nature 493, 195 (2013) [4] T. Aonishi *et. al*, Phys. Rev. Lett. 82, 2800 (1999) [5] S. Tsunegi *et. al*., 61st Annual conference on MMM, HC-06 (2016) [6] S. Tsunegi *et. al*., 62nd Annual conference on MMM, CC-01 (2017) [7] R. Lebrun *et. al*., Phys. Rev. Lett. 115, 017201 (2015) [8] S. Tsunegi *et. al*., Appl. Phys. Express 7, 063009 (2014) [9] R. Lebrun *et. al*., Nat. Commun. 8, 15825 (2017) [10] H. Risken *The Fokker-Planck Equation*, 2nd edition. Springer, 1989.

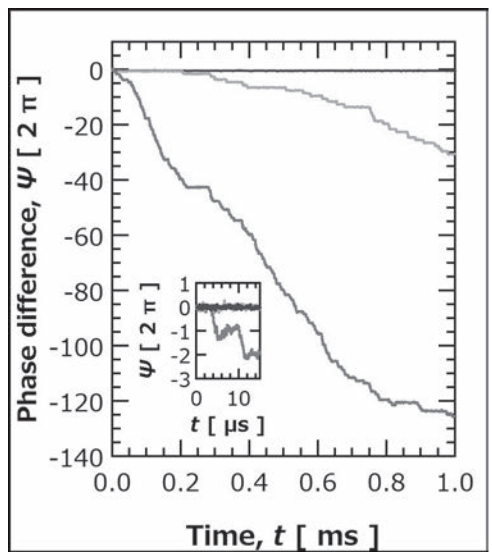

Fig. 1. (a) The evolution of the phase difference with the attenuations of 0 dB (blue),-10 dB (green), and -16 dB (red). The number of the phase slip increases with the increase of the attenuation.

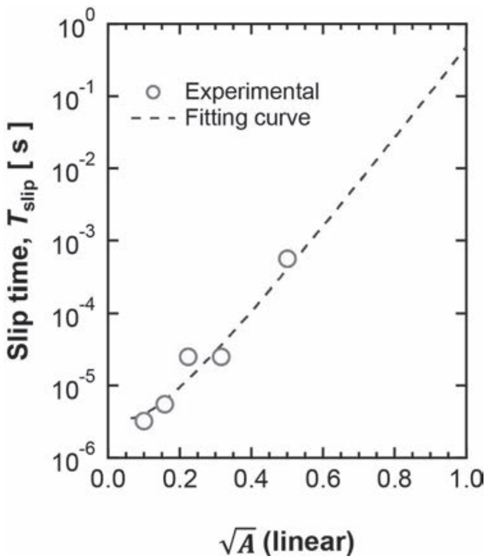

Fig. 1. (b) (b) Dependence of the phase slip time on the attenuation. The red circles are experimentally evaluated values, whereas the dashed blue line is the fitting by a theoretical equation.

3:45

BE-06. Micromagnetic Analysis of Emission Power in Spin Torque Oscillator: Influence of Diameter and Interlayer Exchange Coupling.

T. Tanaka[1], A. Furuya[1], Y. Uehara[1], K. Shimizu[1], J. Fujisaki[1], T. Ataka[1], C. Yoshida[1], H. Oshima[2], H. Kubota[3] and H. Imamura[3]

1. Fujitsu Limited, Kawasaki, Japan; 2. Fujitsu Laboratories Limited, Atsugi, Japan; 3. National Institute of Advanced Industrial Science and Technology (AIST), Tsukuba, Japan

INTRODUCTION The spin torque oscillators (STOs) are considered as the important devices, because the STOs are expected to be applied in many fields, such as a microwave generator or a magnetic field sensor. Therefore, the development of the STOs with the high emission power and the high Q-factor is in high demand. Considering a situation where a current density is constant, we can assume that a simple way to increase the emission power is to enlarge the STO device. Wang *et al.* have, however, reported that the emission power of a nano-pillar STO reaches to maximum around 300nm in the diameter [1]. They have speculated that the frequency of each magnetization oscillation of the free layer is same but the phase of that is different above 300nm in the diameter, which decreases the emission power of the STOs. To elucidate this phenomenon by simulations, it is essential to consider the size effect of the STOs. The micromagnetic simulation is key-tool because it can treat the geometry of the STOs and spatial magnetization dynamics. In this study, we simulate the STOs by using the micromagnetic simulations, analyze the emission power in various diameters and address a factor which enhances the emission power. METHOD The schematic picture of the model of the STO is shown in Fig. 1A. We prepared the STO models, the diameters of which are 200nm (D200), 250nm (D250), 300nm (D300), 350nm (D350) and 400nm (D400), respectively. The models are divided into unstructured hexagonal meshes, the size of which is about 3nm. The STO consists of five layers: FeB, MgO, FeCoB, Ru and FeCo. Hereafter, for simplicity, we call FeB, FeCoB and FeCo layers for the free layer (FL), reference layer (RL) and pinned layer (PL), respectively. To consider the current induced spin transfer torque effect, the magnetization dynamics of each layer is described by the Landau-Lifshitz-Gilbert equation including a spin transfer torque term[2].We consider that the spin transfer torque only acts between the FL and the RL through the MgO layer via a tunnel effect. In the FL, we use following physical properties: the saturation magnetization M_s is 1.82 T, the anisotropic constant K_U is 1.20 MJ/m^3, the exchange constant A_{ex} is 12.5 pJ/m, the damping constant α is 0.005 and the polarization p_0 is 0.54. As for the RL, M_s = 1.25 T, K_U = 0 MJ/m^3, A_{ex} = 10.0 pJ/m, α = 0.01 and p_0 = 0.54. As for the PL, M_s = 2.1 T, K_U = 0 MJ/m^3, A_{ex} = 10.0 pJ/m and α = 0.01. The external field, 300 mT, is applied onto the out-of-plane direction. The interlayer coupling constant, -0.1 mJ/m^2, is set between the RL and the PL. The exchange bias field, 100 mT, is applied to the PL. The current density is 200 GA/m^2 and flows through the STO from the PL to the FL. RESULTS Figure 1B shows the relation between the diameter of the STOs and the emission power obtained by the simulations. This result indicates that the peak of the emission power exists around D300. This is consistent with the reported experimental results [1]. Figure 1C shows the snapshot of magnetization states in D200 and D400, respectively. In the case of D200, although magnetization state is different between the center region and the edge region, the magnetization dynamics is relatively coherent. In contrast, the snapshot of D400 shows that the magnetization state is inhomogeneous. This indicates that oscillation phases at each area are non-uniform. Since the spatial phase difference reduces amplitudes of STO's oscillation, the emission power decreases at D400 and D350 (Fig.1 B). Figure 1D shows the time trajectories of the variance of an in-plane component of the FL's magnetization. This also indicates that the FL's magnetization of D400 is less coherent than of D200. Hence our simulations suggest that the degradation of the emission power is caused by the incoherent rotation of FL's magnetization. Figure 2 shows the emission powers of D200, D300 and D400 at various interlayer exchange coupling constants. In every diameter, the emission power is related to the strength of the interlayer coupling constant. We speculate that strengthening the interlayer coupling induces the coherent rotation of magnetization. This result suggests that increasing the interlayer exchange coupling by adjusting the Ru layer thickness can enhance the emission power of STOs.

[1]B. Wang, *et al.*, Applied Physics Letters 108, 253502 (2016) [2] T. Taniguchi, *et al.,* Applied Physics Express 6.12 (2013)

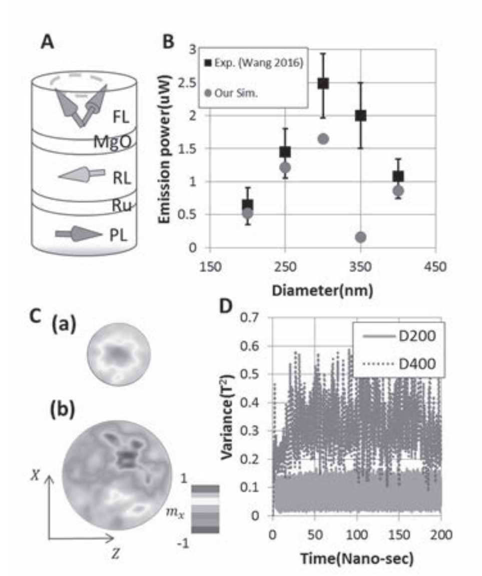

Fig. 1A. The schematic model of the STO used in this study.

Fig. 1B. Relation between the diameter and the emission power. The red circles and black squares show our simulation results and experimental results obtained by [1], respectively.

Fig. 1C. Magnetization states of the free layers of D200(a) and D400(b), respectively.

Fig. 1D. Time trajectories of the variances of the in plane magnetization of the FL. The cyan solid line and red dashed line represent the trajectories of D200 and D400, respectively.

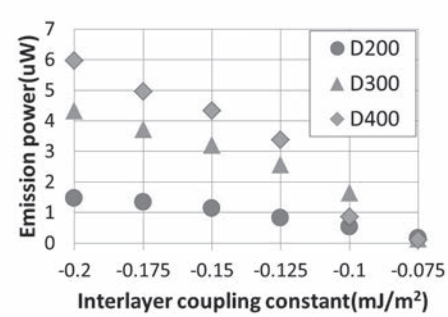

Fig. 2. The dependence of emission powers on various interlayer coupling constants. The red circle, green triangle and cyan diamond represent the emission powers of D200, D300 and D400.

4:00

BE-07. Influence of MgO Tunnel Barrier thickness in 3-terminal Spin Hall Nano-Oscillators.

M. Tarequzzaman[1,2], T. Boehnert[1], A. Jenkins[1], J. Borme[1], E. Paz[1], R. Ferreira[1] and P. Freitas[1,2]
1. Nanoelectronics (Spintronics), International Iberian Nanotechnology Laboratory (INL), Braga, Portugal; 2. Physics Department, Instituto Superior Tecnico (IST) – Universidade de Lisboa, Lisbon, Portugal

The Spin Hall Effect (SHE) can be used to generate pure spin currents, capable of exerting a spin transfer torque (STT) that induces oscillations in a ferromagnetic layer[1–3]. Until now, reported publications concern the STT effect induced from a spin Hall current on a fixed MgO barrier[1,4]. However, the influence of R×A on a performance of spin Hall current induced STT oscillations not been studied yet. To this end, we study the effect of spin Hall current induced STT on variable (wedge) MgO thickness. In this work, a 3-terminal MTJ stack incorporating MgO-wedge was deposited on a 200 mm, Si/100 nm Al_2O_3 wafer in a Timaris Singulus PVD deposition system, leading to a variable $R{\times}A$ over the wafer from 1 Ωμm^2 up to 70 Ωμm^2. The deposited stack was consisted of the following materials: 15 Ta/1.4 $Co_{0.4}Fe_{0.4}B_{0.2}$/[Wedged] MgO /2.2 $Co_{0.4}Fe_{0.4}B_{0.2}$/0.85 Ru/2.0 $Co_{0.7}Fe_{0.3}$/20 $Ir_{0.2}Mn_{0.8}$/5 Ru (thickness in nanometer). The stack was subsequently patterned into 30 different circular and ellipse-shaped nanopillars. The nanopillars patterning were done using electron beam lithography followed by etching in ion beam milling. The Hall bar (Ta layer (24 μm long and 1 μm wide)) geometry was engineered targeting a small DC current through the Ta line (I_{Ta}) should stimulate a magnetization dynamic effects caused by the SHE. Subsequent of nanofabrication, the nanopillars were measured in an automated 4-point geometry for statistical measurement. The devices were then measured in high-frequency setup (3-terminal device geometry) for pure spin Hall nano-oscillator measurement. Fig. 1(a) shows the measured TMR (%) distribution as a function of $R{\times}A$ in the final devices. The $R{\times}A$ ranging from 20 Ωμm^2 to 100 Ωμm^2, the change of TMR (%) is relatively small (160 % to 200 %) and exponentially decreases as the $R{\times}A$ decreases below 20 Ωμm^2. The exponential decrease in TMR (%) in low $R{\times}A$ region can be explained by the barrier imperfection (pin holes) due to thin MgO barrier. The 10% devices TMR (%) found to be below 40%, this is due to the incomplete planarization process of the sample. However, the TMR ratio of 90% devices was TMR (%) of above 80% clearly indicates that the nanofabrication process was successful. The Fig. 1(b) represents four TC for $R{\times}A$ values of 55, 11, 5 and 1.8 Ωμm^2 of nanopillar size: 200 nm. The plotted curves clearly show that for a high R×A value (55 μm^2) the characteristic carve (TC) is in the centre with high TMR ratio of 195% while decreasing the R×A values causes a certain decrease in TMR (%) and there are significantly shifted towards negative field values, which indicates ferromagnetic coupling (H_F) between the free and reference layer of the multilayer stack[5]. This shift in H_F in low $R{\times}A$ can be a result from either lateral magnetic flux arising from the synthetic antiferromagnet (SAF) that leads to stray fields and couple with the free layer or Néel coupling induced by the roughness of the MgO/CoFeB interface. In contrast, The H_F decreases with higher $R{\times}A$ as the thickness of the barrier increases and is due to reduced Néel coupling in the thicker barriers. To get the deeper insight role of the H_F dependence as a function of $R{\times}A$ values, for two nanopillar diameter 100 nm and 200 nm are plotted as shown in Fig. 1(c). Where 200 nm diameter nanopillars show the transition from positive to negative H_F as the $R{\times}A$ decreases. While for the 100 nm nanopillars, H_F dependence is not quite visible except the low $R{\times}A$ region. The reason behind this behavior is not completely understood. Although the possible explanation would be that the roughness on the nanopillars edges contributed to having multi-domain behavior which leads to this behavior. After the statistical and magnetic analysis of the devices, a set of 100 nm nanopillar diameter with different $R{\times}A$ was measured in a high-frequency measurement setup. The magnetic field H_{app} = -150 Oe is applied to set the MTJ nanopillar in the anti-parallel state while keeping the tunneling current ($I^{tunneling}$) at a low fixed bias of -50 μA during the measurement to transduce the magnetic oscillations. The power spectral density (PSD) measurements were done as a function of the spin Hall current ($I^{spin\ Hall}$) with an alternative sign of ± 5 mA in the step of 0.5 mA. The fact that only one polarity $I^{spin\ Hall}$ of was shown oscillations excludes the possibility of having thermal STT on the device. Fig. 2 (a) shows the $P_{matched}$ and TMR (%) distribution as a function of $R{\times}A$ (each dots and square represents a single device). All the $P_{matched}$ values were acquired from the highest (negative) values of $I^{spin\ Hall}$. From the acquired results, it can be confirmed that the increasing the thickness of the MgO barrier (increasing $R{\times}A$) leads to increases the TMR (%) and in turn increases the $P_{matched}$ of the device. To quantify the obtained results, $P_{matched}$ and f were extracted and plotted as a function of spin Hall current density ($J^{spin\ Hall}$) as shown in Fig. 2(b-c) for a particular device. The total $P_{matched}$ of 12 nW is obtained. The observed f indicates Red-shift behavior as increases which is a signature sign of steady state oscillations.

1. Liu, L., Pai, C. F., Ralph, D. C. & Buhrman, R. a. Magnetic oscillations driven by the spin hall effect in 3-terminal magnetic tunnel junction devices. *Phys. Rev. Lett.* 109, 1–5 (2012). 2. Demidov, V. E., Urazhdin, S., Zholud, A., Sadovnikov, A. V. & Demokritov, S. O. Nanoconstriction-based spin-Hall nano-oscillator. *Appl. Phys. Lett.* 105, 172410 (2014). 3. Demidov, V. E. *et al.* Spin-current nano-oscillator based on nonlocal spin injection. *Sci. Rep.* 5, 8578 (2015). 4. Ranjbar, M. *et al.* CoFeB-based spin Hall nano-oscillators. *IEEE Magn. Lett.* 5, 1–4 (2014). 5. Costa, J. D. *et al.* High power and low critical current density spin transfer torque nano-oscillators using MgO barriers with intermediate thickness. *Sci. Rep.* 7, 7237 (2017).

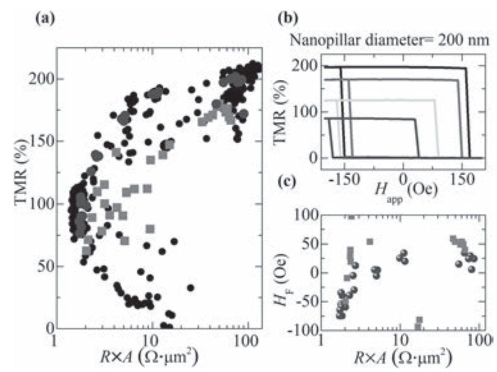

Fig. 1. (a) TMR (%) as a function of the resistance-area ($R{\times}A$) product. (b) TMR curves for different values of $R{\times}A$ (54, 11, 5, and 1.8) Ωμm^2 for nanopillar diameter of 200 nm. (c) Variation of H_F for two nanopillar diameter of 100 nm and 200 nm.

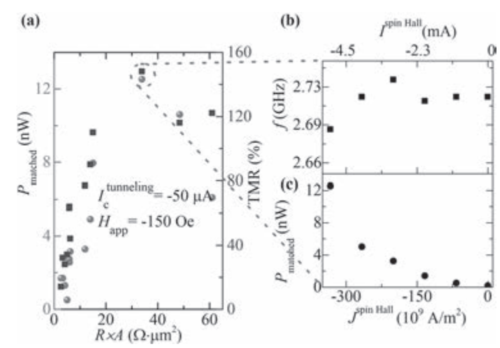

Fig. 2. (a) The $P_{matached}$ measured for $I^{spin\ Hall}$ ranging from +5 mA to -5 mA at a constant $I^{tunneling}$ of -50 μA and H_{app} = -150 Oe. (b-c) Frequency (f) and $P_{matached}$ as a function of $J^{spin\ Hall}$.

4:15

BE-08. Spin torque diode with perpendicular anisotropy used for passive demodulation of FM digital signals.

S. Louis[2], V.S. Tiberkevich[1], J. Li[2], O. Prokopenko[3] and A.N. Slavin[1]
1. Physics, Oakland University, Rochester, MI, United States; 2. Electrical and Computer Engineering, Oakland University, Rochester, MI, United States; 3. Faculty of Radio Physics, Electronics and Computer Systems, Taras Shevchenko National University of Kyiv, Kyiv, Ukraine

Recent advances in the spintronic design and fabrication techniques have led to the development of spin torque diodes having a *perpendicular magnetic anisotropy* (STD-PMA) in their free layer. Such STD-PMAs can act as energy harvesters of ambient microwave radiation [1], and when driven with a dc bias current, can operate as microwave generators [2]. The analytical formalism [3] has shown that STD-PMAs have a number of interesting properties. In particular: (i) in the presence of an external microwave current they can produce a rectified dc voltage that is linearly proportional to the external microwave frequency, and independent of the input power; (ii) the STD-PMA can perform a signal rectification without an independent power supply, drawing power entirely from the input signal; (iii) in contrast with the traditional spin torque diodes, the STD-PMA do not require an external bias magnetic field, and therefore can be easily integrated with CMOS and other microelectronic systems; (iv) the power threshold of operation of STD-PMA is rather low (several nanowatts), and thus, they can be used in applications where non-spintronic (e.g. Schottky-diode-based) devices fail; (v) above a particular threshold frequency, the STD-PMA does not produce a dc voltage, thus acting as a natural lowpass filter. Here, we propose a novel application for an STD-PMA: this device can perform *passive demodulation* for low-power frequency-modulated (FM) signals. To demonstrate this effect we performed a numerical simulation for an STD-PMA under the action of an external FM signal. The magnetization dynamics of the STD-PMA free layer, which performs the signal demodulation, was modeled using the Landau-Lifshift-Gilbert-Slonczewski equation in a macrospin approximation. We chose the following typical parameters of the system. We used a 1.65 nm-thick circular free layer having a radius of 50 nm, and made of $Co_{20}Fe_{60}B_{20}$. With this configuration, the effective field of the 1st order PMA was 1162 mT, and the field of the 2nd order PMA was 63 mT. The Gilbert damping parameter was 0.02, the spin-polarization efficiency was chosen to be 0.6, and the pinned layer of the STD-PMA was assumed to have the in-plane magnetization. With these parameters, the static magnetization of the free layer had an equilibrium out-of-plane angle of 45 degrees, a resistance of ≈ 800 Ω, and a tunneling magneto-resistance (TMR) of 112.5%. The two figures below demonstrate the numerically modeled STD-PMA performing both digital and analog FM demodulation. Fig. 1 shows the passive demodulation of a signal encoded with frequency shift keying (FSK). A short digital data sequence with a data rate of 2.5 MB is shown in Fig. 1(a), with voltages varying between a high and low state, and Fig. 1(b) shows this data encoded in the frequency of a signal, where f_{in} = 40 MHz is representing the "low" state and f_{in} = 60 MHz is representing the "high" state. The FSK signal has two powers, starting initially at 14 nW (-48dBm), increasing to 25 nW (-45 dBm), then again decreasing to 14 nW. When the FSK signal is incident on the simulated STD-PMA, it produces a dc voltage as shown in Fig 1(c). For the "low" state, the STD-PMA produces V_{out} = 400 μV, and in the "high" state the STD-PMA produces V_{out} = 600 μV. Note, that the voltage V_{out} is only dependent on the input frequency, and is independent of the input power. It is also important to emphasize, that despite the low power levels of this signal, the STD-PMA is powered entirely by the external signal, and that the magnetic anisotropy allows its operation in the absence of a bias magnetic field. The FM demodulation of an analog signal using an STD-PMA is demonstrated in Fig. 2. An analog signal with frequencies scanning a 5 MHz bandwidth (Fig. 2(a)) is FM modulated by a 50 MHz carrier signal. The power spectral density (PSD) of the signal after a single-sideband FM modulation is shown in Fig. 2(b), with a bandwidth in the 50-60 MHz frequency range. The curve presented in Fig. 2(c) shows that the STD-PMA output dc voltage faithfully reproduces the shape of the input analog signal. In summary, a spin torque diode with perpendicular magnetic anisotropy can act as a reliable FM demodulator that does not require any power and/or any bias magnetic field. The basis of its operation is the linear relationship between the input frequency and the STD dc voltage output. Our numerical simulation has shown that an STD-PMA can demodulate both a digital signal encoded by FSK, and an analog signal with a single-sideband FM modulation. We believe, that STD-PMAs will be useful in power-critical applications, which has growing relevance for autonomous devices and internet of things (IOT) applications.

[1] B Fang, M Carpentieri, S Louis, V Tiberkevich, A Slavin, I Krivorotov, R Tomasello, A Giordano, H Jiang, J Cai1, Y Fan, Z Zhang, B Zhang, J Katine, K Wang, P Amiri, G Finocchio, Z Zeng. Spintronic nano-scale harvester of broadband microwave energy. *arXiv preprint arXiv*: *1801.00445* (2018). [2] Z Zeng, G Finocchio, B Zhang, PK Amiri, JA Katine, IN Krivorotov, Y Huai, J Langer, B Azzerboni, KL Wang, et al. Ultralow-current-density and bias-field-free spin-transfer nano-oscillator. *Scientific Reports*, 3, 2013. [3] O Prokopenko, V Tyberkevych, A Slavin. "Microwave energy harvester based on a spin-torque diode with perpendicular magnetic anisotropy of the free layer," in *Magnetism and Magnetic Materials*, no. CC-02, Pittsburgh, PA, November 2017.

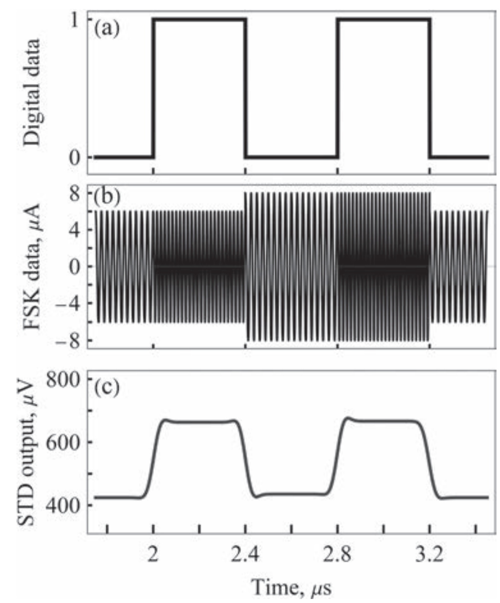

Fig. 1. Demodulation of an FSK (digital) FM signal: (a) Input digital logic signal, where the "high" state indicates "1", and the "low" state indicates "0"; (b) The input logic signal encoded with FSK, where 60 MHz is "1", and 40 MHz is "0". Note, that the signal amplitude increases from 6 to 8 μA, a power change from 14 nW to 25 nW. (c) STD-PMA response to the FSK input, where 600 μV is "1" and 400 μV is "0". The signal is dependent only on the signal frequency and is independent of the signal amplitude.

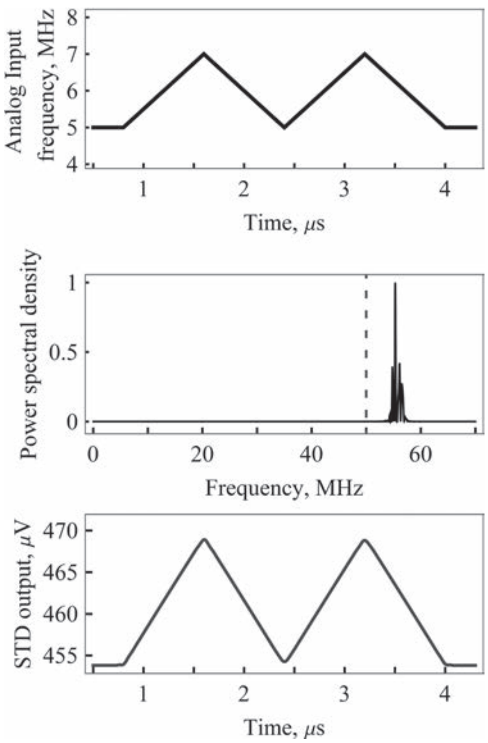

Fig. 2. Demodulation of an analog FM signal: (a) Frequency of the analog signal. Signal has a bandwidth of 2 MHz; (b) Black line shows the power spectral density (PSD) of the analog signal after it was single-side-band FM modulated by a 50 MHz carrier frequency, shown by a dashed purple line; (c) Demodulated dc voltage output of the STD-PMA.

4:30

BE-09. The reversible spin texture of ferroelectric GeTe for a tunable source of spin currents.

C. Rinaldi[1,2], S. Varotto[1], M. Asa[1], J. Slawinska[3], J. Fujii[4], G. Vinai[4], S. Cecchi[5], D. Di Sante[6], R. Calarco[5], I. Vobornik[4], G. Panaccione[4], S. Picozzi[3] and R. Bertacco[1]
1. Physics, Politecnico di Milano, Milano, Italy; 2. IFN-CNR, Milan, Italy; 3. CNR-SPIN, Chieti, Italy; 4. CNR-IOM, Trieste, Italy; 5. Paul-Drude-Institut für Festkörperelektronik, Berlin, Germany; 6. Institut für Theoretische Physik und Astrophysik, Universität Würzburg, Würzburg, Germany

Spin-orbit coupling effects in materials with broken inversion symmetry are responsible for peculiar spin textures. Moreover, ferroelectrics could enable the non-volatile control of the spin degree of freedom through the electrical switching of the spin texture, achievable by acting on the spontaneous polarization [1]. Such functionality holds potential for technological applications exploiting spin effects controlled by voltage pulses. Within this framework, Germanium Telluride may represent a ground-breaking multifunctional material belonging to FErroelectric Rashba SemiConductors [1]. Its *ferroelectricity* provides the non-volatile state variable able to generate and drive a giant *bulk Rashba-type spin-splitting* of the electronic bands, while its *semiconductivity* and CMOS-compatibility allow for the realization of spin-based transistors. In this paper we present the idea of using GeTe has a switchable and tunable source of pure spin currents. Indeed, in a Rashba system, a charge current can generate a perpendicular pure spin current by intrinsic spin Hall effect (SHE) [2]. The ferroelectric control of the Rashba effect would then allow to tune the generation of the spin currents by intrinsic SHE. The ferroelectric control of the spin texture in GeTe has been experimentally proved by combined use of Piezoresponse Force Microscopy and Spin and Angular Resolved Photoemission Spectroscopy [3, 4]. Separately, spin-to-charge conversion was previously investigated by spin-pumping experiments on GeTe/Fe bilayers, providing the first evidence of sizable interconversion from spin to charge currents [5]. Here we investigate the efficiency of the *charge-to-spin interconversion process* due to spin Hall effect. To this aim, we used the concept of unidirectional spin Hall magnetoresistance (USMR), introduced by Gambardella *et al.* [6] and sketched in Figure 1a for Fe/GeTe heterostructures. A charge current flowing in the plane of a non-magnetic (NM) thin film generates a spin current perpendicular to the film itself. A ferromagnetic layer (FM) grown on top serves as spin "detector". Spin accumulation and spin scattering at the NM/FM interface will depend on the relative orientation between magnetization and spins direction, resulting in a variation of the conductivity upon magnetization reversal. As shown in Ref. [6], the second harmonic resistance ($R_{2\omega}$) accounts for current-induced resistive terms, including both SHE and "spurious" thermoelectric effects [7]. Preliminary experiments on Fe/GeTe bilayers reveal the presence of sizable spin Hall effect in GeTe. We detected a non-negligible variation of the longitudinal resistance upon inversion of the in-plane iron magnetization at relatively low temperatures (120 K). The relative variation of the longitudinal resistance increases linearly with the current density J (Figure 1b), as expected for spin Hall effect in GeTe and ruling out the role of "spurious" thermal effects [7]. Moreover, the slope of the effect versus J is reduced when the GeTe layer thickness increases from 5 to 15 nm, pointing out the interfacial origin of the resistance variation. A detailed investigation of USMR in GeTe versus temperature and ferroelectric polarization is ongoing to eventually demonstrate the ferroelectric control of spin transport with the non-volatile inversion of spin Hall effect in ferroelectric Rashba semiconductors. The research looks towards the realization of non-volatile, electrically-controlled sources of pure spin currents. This element would open unprecedented perspectives for spintronic applications, such as the electric control of magnetization in nanostructures, the realization of spin-based neuromorphic devices and reconfigurable logic elements, as well as the excitation of spin waves in magnonic devices.

[1] D. Di Sante, *et al.*, Electric Control of the Giant Rashba Effect in Bulk GeTe, Adv. Mater. 25, 509-513 (2013). [2] J. Sinova *et al.*, Spin Hall effects, Reviews of Modern Physics 87, 1213 (2015). [3] M. Liebmann, C. Rinaldi *et al.*, Giant Rashba-Type Spin Splitting in Ferroelectric GeTe(111), Adv. Mater. 28, 560-565 (2016). [4] C. Rinaldi, *et al.*, Ferroelectric control of the spin texture in germanium telluride, Arxiv pre-print (arXiv:1707.0704). [5] C. Rinaldi, *et al.*, Evidence for spin to charge conversion in GeTe(111), APL Mater. 4, 032501 (2016). [6] C. O. Avci, P. Gambardella *et al.*, Unidirectional spin Hall magnetoresistance in ferromagnet/normal metal bilayers, Nature Phys. 11, 570 (2015). [7] J. E. Parrot, The Theory of the Nernst Effect in Semiconductors, Proc. Phys. Soc. 71(1), 82 (1958).

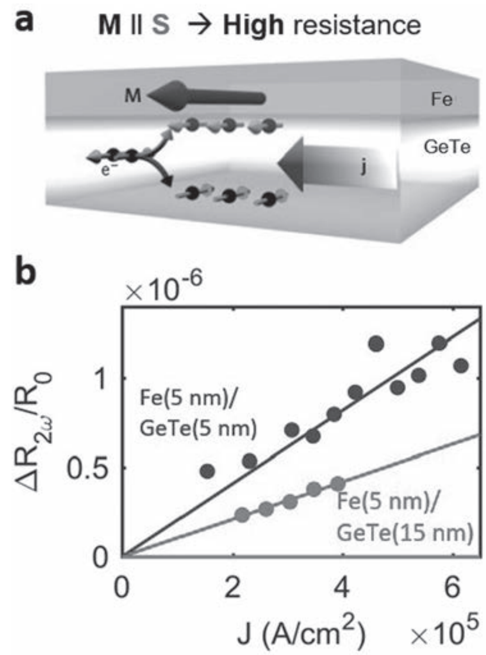

Fig. 1. (a) Sketch of the unidirectional Spin Hall Magnetoresistance concept (adapted from [6]). The longitudinal resistance in Fe/GeTe bilayers depends on the relative orientation of Fe magnetization and spins generated by Spin Hall Effect in GeTe. (b) Relative change of the longitudinal resistance (second harmonic signal) versus current density. The magnitude and the linear behavior confirm the presence of sizable charge-to-spin interconversion in GeTe.

4:45

BE-10. Withdrawn

Session BF

NANOWIRES, NANOPARTICLES AND CLUSTERS

Paola Tiberto, Chair
Istituto Nazionale di Ricerca Metrologica (INRIM), Torino, Italy

CONTRIBUTED PAPERS

2:00

BF-01. Anisotropy and coercivity analysis in tetragonal (Cu,Co)Fe_2O_4 particles.

H. Latiff[1,2], T. Devillers[1], H. Yanagihara[2], N. Dempsey[1] and D. Givord[1]
1. Université Grenoble Alpes, CNRS, Grenoble INP, Institut Néel, 38000 Grenoble, France; 2. Institute of Applied Physics, University of Tsukuba, 305-8573 Tsukuba, Japan

$CoFe_2O_4$ exhibits large magnetoelastic effects and a large magnetic anisotropy (MA) can be induced in the presence of strain, as demonstrated in epitaxially strained thin films [1-2]. The existence of MA in nanoparticle materials is desirable for many applications. The introduction of lattice distortion in nanomaterials was demonstrated by exploiting the Jahn-Teller (JT) effect of Cu^{2+} ions in (Cu,Co)Fe_2O_4 [3]. The considered samples are made of micron-sized particles, but the quadratic deformation due to the local strain occurs at the nanoscale. From the electronic configuration viewpoint, the high magnetic anisotropy is triggered by the activation of the spin-orbit interaction of the Co^{2+} ions on the B-site, in the presence of the Cu^{2+} with JT distortion. For the quantitative analysis of magnetic anisotropy in assemblies of (Cu,Co)Fe_2O_4 nanograins having various Co content, we have developed a software to model the applied field B_{app} dependence of the magnetization M. Coherent rotation of M is assumed in the model, and the two main physical parameters used to fit experimental data are the spontaneous magnetization M_s and the 2nd order anisotropy constant, K. By measuring $M(B_{app})$ for different applied field orientations, it was found that the grain orientation is fully isotropic. Under such circumstances, one expects that the ratio of the remanent magnetization M_r to M_s is equal to 0.5. In contrast, M_r/M_s>0.5 was systematically found and this suggests that some positive exchange interactions exist between individual nanograins. Adding a phenomenological exchange field between nanograins permitted excellent description of the experimental data (see Fig. 1). At 10 K, an anisotropy field $H_A \approx$ 2.8 MA/m is derived from M_s= 0.145×10^6 A/m and K= 0.25×10^6 J/m^3. While M_s is almost temperature independent, K shows a tendency to decrease with increasing temperature. This agrees with expected behavior. At 300K, $H_A \approx$ 1.9 MA/m, in fair agreement with the value estimated from rotational hysteresis measurements, where $H_A \approx$ 1.6 MA/m. From 10K to 300K, the exchange field decreases from 1.2 MA/m to 1.1 MA/m. Assuming that the exchange coupling is restricted to the first atomic layer of each nanograin, at low T, the exchange field value is renormalized to 40 MA/m, this is still 1-2 orders of magnitude less than the exchange field in the bulk of the grains, which is of the order of 10^3 MA/m. One of the main physical properties which is expected to be associated with magnetocrystalline anisotropy is coercivity, H_c. Tetragonally distorted $Cu_{1-x}Co_xFe_2O_4$ particles with x=0.1 showed an enhanced H_c value of up to 220 mT compared to non-distorted particles with x=0.2, for which H_c= 90 mT. It is well known that magnetic coercivity is not directly related to magnetic anisotropy but depends also in some poorly known manner on the sample's nanostructure. Under such circumstances, it is usual to relate the coercive field to the anisotropy field and demagnetizing field, assumed proportional to the spontaneous magnetization, $H_c = \alpha H_A - N_{eff} M_s$, within the so-called micromagnetic model [4], or to the domain wall energy, g, activation volume, v_a, and demagnetizing field (as above), $H_c = \alpha\ \gamma/(\mu_0 v_a^{1/3} M_s) - N_{eff} M_s$, within the so-called global model [5] (more rigorously, is replaced by, the coercive field in the absence of thermal activation effects, see below). In these expressions, α and N_{eff} are essentially phenomenological parameters. For the analysis, H_A was taken from the $M(B_{app})$ analysis described above. The domain wall energy may be expressed as $\gamma = 4\sqrt{AK}$, where A is the exchange constant related to the Curie temperature, taken as 6.57×10^{-12} J/m at low temperature and proportional to M_s^2. The activation volume, v_a, is related to the experimental viscosity coefficient S_v through $v_a = \mu_0 k_B T / S_v M_s$, where $S_v = S/\chi_{tot} - \chi_{rev}$, S being the logarithm dependence of the magnetization, χ_{tot} the total susceptibility and χ_{rev}, the reversible susceptibility [5]. The temperature dependence of the activation volume $v_a(T)$ derived from the magnetic viscosity measurements is shown in Fig. 2 (a) for two representative samples having the lowest (x=0.2) and highest (x=0.1) coercive field values considered in the present study; v_a increases from a value of around 2000 nm^3 at 10K for the two samples, up to around 175000 nm^3 for the low coercivity (almost cubic) sample and 5400 nm^3 for the strained tetragonal sample, at 300K. H_c was corrected for thermal activation to get $H_0 = H_c + 25S_v$ and H_0/M_s was plotted versus $\gamma/v_a^{1/3}\mu_0 M_s^2$ to extract α and N (Fig. 2 (b)). The dashed lines represent the linear fits for T=100–300K, giving the values for N and α: (α= 0.39; N= -0.24) for the tetragonal high H_c sample and (α= 0.29; N= -0.01) for the cubic low H_c sample. The parameter α has similar values in both samples, and the differences in finite temperature coercive field values between both samples is essentially due to the difference in the size of the activation volume. A simple physical argument explains this behavior. The activation volume is related to the cube of the domain wall thickness and it is obviously larger in the low anisotropy unstrained sample than in the tetragonally distorted one.

[1] A. Lisfi *et al*., *Phys. Rev. B,* 76 (2007) 054405. [2] T. Niizeki *et al*., *Appl. Phys. Lett.,* 103 (2013) 162407. [3] H. Latiff *et al.*, *IEEE Trans. Magn.,* 53 (2017) 9402304-1. [4] H. Kronmuller et al., J. Magn. Magn. Mater., 74 (1988) 291. [5] D. Givord et al., *IEEE Trans. Magn.,* 24 (1988) 1921.

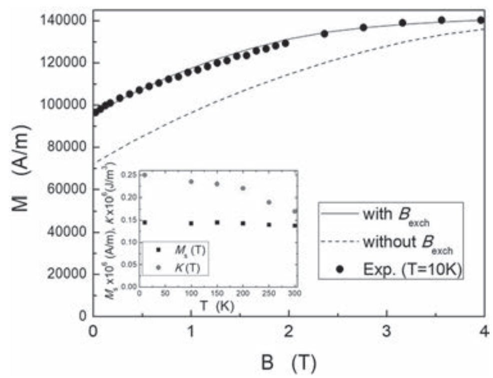

Fig. 1. Experimental dependence of the magnetization $M(B_{app})$ in x=0.1 sample (T=10K) and calculated curves (see text). Inset: M_s(T) and K(T) evaluated from the M(B_{app}) analysis.

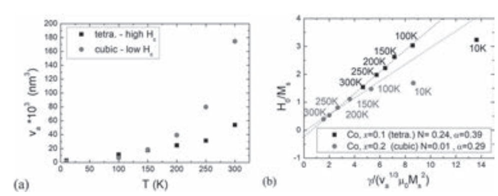

Fig. 2. (a) Activation volume as a function of temperature and (b) (H_c/M_s) vs ($\gamma/v_a^{1/3}\mu_0 M_s^2$), according to the global model analysis [5], for $Cu_{0.9}Co_{0.1}Fe_2O_4$ (high H_c) and $Cu_{0.8}Co_{0.2}Fe_2O_4$ (low H_c).

2:15

BF-02. The effect of surface spin disorder on magnetic properties of Fe/Fe_xO_y core-shell nanoparticles.

M. Lostun[1], D. Herea[1], M. Grigoras[1], G. Ababei[1], I. Ghemes[1] and *N. Lupu*[1]
1. National Institute of Research and Development for Technical Physics, Iasi, Romania

Fe-oxide nanoparticles are of considerable interest nowadays because of their unique characteristics, such as superparamagnetism, high saturation fields, and extra anisotropy contributions, which arise from the effects of finite size and large surface area. Usually they are obtained by chemical methods, but more recently some groups reported on their successful preparation by wet high-energy ball-milling. It is also well known that as the size of the nanoparticles decreases, surface effects would become more significant due to the increasing surface relative to their volume. We report here our recent results on the effect of ligands on the induced surface anisotropies and magnetic properties of Fe/Fe_2O_3 and Fe/Fe_3O_4 core-shell nanoparticles functionalized with 3-aminopropyltriethoxysilane (APTS) for biomedical applications (image contrast agents in magnetic resonance imaging (MRI) and magnetic carriers for drug delivery). Core-shell nanoparticles have been prepared by high-energy ball milling. In the presence of air or Ar, the Fe core was progressively covered with a Fe_2O_3 shell, and the obtained Fe/Fe_2O_3 nanoparticles have diameters of 200-300 nm after 68 h of milling. Fe/Fe_3O_4 nanoparticles of 20-60 nm were obtained by wet milling of Fe microparticles for 42 h. For milling times larger than 42 h the whole amount of Fe is transformed into Fe_3O_4, and the resulting magnetite nanoparticles have diameters ranging from 15 to 50 nm (Fig. 1). The magnetic properties of Fe/Fe_xO_y core-shell nanoparticles can be tailored from ferromagnetic Fe/Fe_2O_3 to weak ferromagnetic Fe/Fe_3O_4 and superparamagnetic Fe_3O_4 (Fig. 2). By choosing the appropriate milling conditions and starting materials is possible to tune the magnetic properties and make the Fe/FeO_x core-shell NPs suitable for different biomedical applications. The main advantage of such core-shell nanoparticles in biomedical applications, compared with simple Fe-oxides nanoparticles, resides in their easier use and manipulation for specific applications. To understand the surface spin disorder and its influence on the magnetic properties of Fe/Fe-oxide core-shell nanoparticles, their surface was systematically modified with APTS, by increasing progressively the concentration of the ligand. APTS was chosen as ligand because the bonding with the magnetic NPs is made through Si-O, NH_2 remaining free for bonding with different types of biomolecules. Low temperature magnetization measurements and ZFC/FC curves indicate a strong influence of the ligand on the magnetic properties. The change of the magnetic properties of nanoparticles also correlates with the specific coordinating functional group bound on the nanoparticles surface. The correlation suggests the decrease in spin-orbital coupling and surface anisotropy of magnetic nanoparticles due to the surface coordination. Because of the high saturation magnetization, these Fe/FeO_x core-shell NPs have a higher Specific Absorption Rate (SAR), making them suitable for hyperthermia applications. They can be also visualized by Magnetic Resonance Imaging because of the Fe-oxides shell. *This work was financially suported by the 3MAP NUCLEU Programme (2018).*

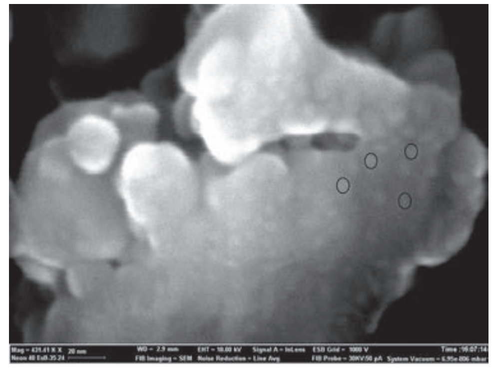

Fig. 1. HR-SEM image of the cross-section of Fe/Fe_3O_4 core-shell NPs. The bright spots represent the remaining Fe core (6-7 nm in diameter) and the dark matrix is the Fe_3O_4 shell.

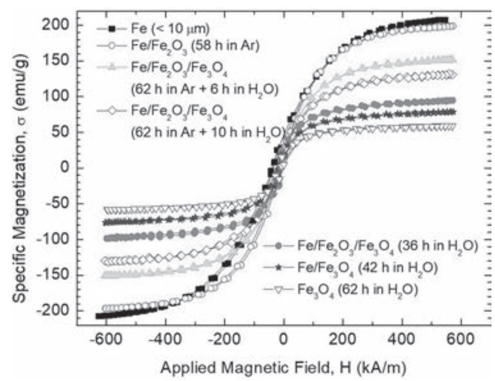

Fig. 2. The magnetic behavior of the core-shell nanoparticles depends strongly on the milling conditions.

2:30

BF-03. Magnetic Properties NFO-BTO and NFO-BSTO Nanocomposites.

T. Parida[1], M. B S[2] and *G. Markandeyulu*[1]
1. Physics, Indian Istitute of Technology Madras, Chennai, India;
2. Metallurgical and Materials Engineering, Indian Institute of Technology Madras, Chennai, India

I. INTRODUCTION Ever increasing technological necessities have enthused researchers to discover potential compounds (bulk/nano forms). Towards this, multiferroic materials have attracted various applications in the interdisciplinary fields of biomedical engineering and electronics [1-2]. These are useful in a wide range of applications starting with thin film devices such as magnetoelectric (ME) actuators, sensors, *etc.*, to the memory devices as well as carrier materials for drug delivery. Nanoparticles with core-shell structure have been reported to enhance the magnetoelectric properties depending on their size and nature of compounds chosen for core and shell. $NiFe_2O_4$ (NFO) core @ $BaTiO_3$ (BTO) shell structure is reported to have oxygen vacancies in BTO which enhance the magnetic permeability of the composites, one of the essential requirements for large magnetoelectric (ME) coupling [2]. The ME effect is a product property and it is mainly a strain mediated mechanism. When an electric field is applied, the piezoelectric phase changes its volume according to the piezoelectric coefficient, which exerts a force against the ferromagnetic counterpart. The latter being magnetostrictive, magnetization develops as a result of the mechanical strain. A similar effect is anticipated in case of NFO@BTO nanocomposite system with a better ME effect due to high surface to volume ratio. This system is then compared with NFO@$Ba_{0.66}Sr_{0.33}TiO_3$ (BSTO) system, with a view to exploring the possibility of a higher ME effect. The studies on BSTO materials have shown high permittivity, low dielectric loss, and high tunability coefficient [3]. Other than these, the foremost advantage is the fact that the BSTO family is lead-free and hence, compliance with the present requirements for environmentally benign materials can be met. The magnetic properties of the NFO@BTO nanocomposite system have been studied and the effect of Sr^{2+} doping on the magnetic properties is presented in this paper. II. EXPERIMENTAL DETAILS Synthesis of NFO@BTO core-shell structure was carried out using a two-step process. In the first step, NFO was prepared through the sol-gel process in which, $Ni(NO_3)_2.4H_2O$ and $Fe(NO_3)_3.9H_2O$ precursors were used as the starting materials in the ratio of 1:2. A 0.05M solution was prepared using ethanol as solvent. Subsequently, in the second step, the NFO particles were coated with the BTO shell. In order to prepare the BTO shell, 5 millimoles of $BaCO_3$ solution were mixed with 5 millimoles of Titanium isopropoxide. 7 millimoles of NFO solution were then mixed with the above BTO solution and the mixture was sonicated for 2 h and then was kept at 60°C in a magnetic stirrer for 12 h followed by a heat treatment at 750°C for 5 h. The composite system of NFO@BTO was confirmed by powder X-ray diffraction (XRD) studies. The core-shell structure was confirmed by Transmission electron microscopy (TEM). A similar procedure was carried out for the synthesis of NFO@BSTO nanocomposite system. The structure and morphology of the NFO@BSTO nanocomposites were investigated by XRD, TEM and magnetization measurements employing a vibrating sample magnetometer (VSM). III. RESULTS AND DISCUSSIONS From the powder XRD patterns, BTO phase was found to have formed in perovskite structure with the space group P4mm. The (001), (011), (111), (002), (012), (112), (022), (003) and (013) peaks were observed. The formation of NFO phase in spinel structure with Fd-3m is confirmed with (022), (311), (400) and (440) peaks. The crystallite size of NFO@BTO and NFO@BSTO nanocomposite is around 13-14 nm. There is clear peak shift of 0.3°-1.6° to higher angle on doping Sr^{2+} in A-site of ABO_3 phase indicating the reduction in lattice parameter. TEM studies revealed the core-shell structure with an average particle size of about 15 nm. The magnetization of as prepared NFO nanoparticles is found not to saturate and is 37 emu/g at 40 kOe. The existence of magnetic dead layer at the surface can cause a reduction in magnetization compared to crystalline particles. On addition of a non–magnetic shell of $BaTiO_3$, the magnetization has decreased further to 14.8 emu/g; can be attributed to the isolated $NiFe_2O_4$ particles with shell coated around them. Further, upon substitution of one-third of Ba^{2+} by Sr^{2+}, it is observed that the magnetization has increased to 18 emu/g. Substitution of Sr^{2+} doping leads to the development of coarser grains, as confirmed from the sharper XRD peaks. This leads to a reduction of the surface to volume ratio, taking the particle towards crystallinity that can cause the magnetization to increase. IV. CONCLUSION The XRD and TEM studies confirmed the formation of NFO@BTO core-shell nanoparticles. The magnetization of core-shell nanoparticles with Sr^{2+} substituted partially for Ba^{2+} increased.

[1] S. Betal, B. Shrestha, M. Dutta, L.F. Cotica, E. Khachatryan, K. Nash, L. Tang, A.S. Bhalla and R. Guo, *Sci. Rep.*, 6, 32019-32032, 2016. [2] A. Nagesetti, A. Rodzinski, E. Stimphil, T. Stewart, C. Khanall, P. Wang, R. Guduru, P. Liang, I. Agoulnik, J. Horstmyer and S. Khizroev, *Sci. Rep.*, 7, 1610-1619, 2017. [3] J. Zhou, L. Ly, Q. Liu, Y.X. Zhang and P. Liu, *Sci. Technol. Adv. Mater.*, 13, 045001-045013, 2012. [4] P.Z. Ge, X.G. Tang, Q.X. Liu, Y.P. Jiang, W.H. Li and B. Li, *J. Alloys Compd.*, 731, 70-77, 2018.

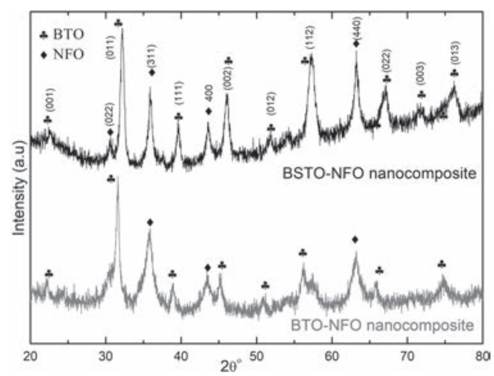

Fig. 1. XRD patterns confirm the formation of composite BTO-NFO and BSTO–NFO

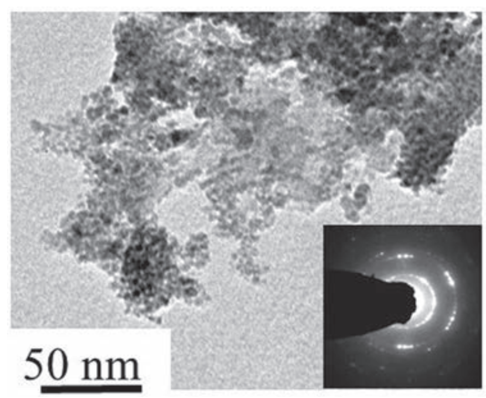

Fig. 2. TEM micrographs of BTO-NFO nanocomposite indicating nanocrystalline nature

2:45

BF-04. Topological control of the magnetic and magneto-transport properties of 3D interconnected nanofiber networks.

T. da Câmara Santa Clara Gomes[1], J. De La Torre Medina[2], Y. Velázquez-Galván[1], J. Martínez-Huerta[3], A. Encinas[1] and L. Piraux[1]
1. Institute of Condensed Matter and Nanosciences, Université catholique de Louvain, Louvain-La-Neuve, Belgium; 2. Instituto de Investigaciones en Materiales - Unidad Morelia, Universidad Nacional Autonoma de Mexico, Morelia, Mexico; 3. Division de Materiales Avanzados, Instituto Potosino de Investigacion Cientca y Tecnologica, San Luis Potosi, Mexico

Track-etched polymer membranes with crossed nanochannels have been revealed suitable as template for the synthesis of 3D interconnected magnetic nanofiber networks that present interesting magnetic and magneto-transport properties [1-4]. Successive track-etch process allows the control of the template geometry, including the angles between the nanochannels and the template normal, the volumetric porosity and the mean diameter that can be tuned between few tens of nm to few hundreds of nm. The host porous template is later filled from a previously sputtered metallic cathode by an electrodeposition process allowing the control of the material composition and nano-structuration. 3D networks of interconnected nanowires (Fig. 1a.), core-shell nanocables, nanotubes (Fig. 1b.) and multilayered nanowires have been successfully fabricated. As shown in the inset of Fig. 1a., the interconnected structure provides a reasonable mechanical stability to the 3D nano-architectures that are self-supported after dissolution of the porous template. In addition, the local removing of the cathode gives rise to a two-probe design suitable for electric measurements, as shown in Fig. 1c. Indeed, magneto-transport measurements can be easily performed on such interconnected nanofiber network films, with the current flow restricted along the nanofiber segments. The magnetic and magneto-transport properties of crossed homogeneous nanowire (CNW), crossed nanotube (CNT), and crossed multilayered nanowire networks have been investigated. A close relation between the CNWs magnetic properties and their topological and structural properties have been demonstrated in Co CNW networks, where the tuning of the crystalline structure using the electrolyte pH allows an accurate control of the magnetic anisotropy [2,5]. Similarly, it has been found that the magnetic anisotropy of NiCo CNW networks depends on the alloying composition, in agreement with previous results obtained on bulk materials and films [3,4,6,7]. An analytical model inherent to the topology of 3D nanowire networks has been validated, allowing to extract the AMR ratio from the measured magnetoresistance curves along the in-plane (IP) and out-of- plane (OOP) directions of the CNW network film [2-4]. The AMR ratio variation with respect to the Ni content for the NiCo CNWs has been found to be coherent with previous results obtained on bulk materials and films, exhibiting large ratio for about 75% atomic of Ni [3,8]. Ni CNT have been obtained using the electrochemical dealloying method and the modification of the magnetic and magneto-transport properties due to the inner hollow cores of the NTs have been investigated. By variating the reduction potential in the range of -0.8V to -1.1V, different NT wall thicknesses have been achieved, in good agreement with previous works [9-11]. The magnetic properties of the CNT network, such as the effective anisotropy field, the remanence and the coercive field, have been found to be dependent on the NT wall thickness, as depicted in Fig. 2a. Magneto-transport measurements revealed a modification of the magnetization reversal mechanisms for the CNT networks, contrasting with the CNW networks, as depicted in Fig. 2b. For the CNT network, a large decrease of the resistance is observed at the coercive field. It can be attributed to a magnetization reversal dominated by the curling (vortex) reversal mode, where magnetic moments rotate progressively via propagation of a large number of vortex domain walls. Conversely, the magneto-transport curve of the CNW network displays a decrease of the resistance that doesn’t correspond to the resistance at coercivity. Instead, it appears for positive field values, starting from the saturated positive state, contrasting with previous work on arrays of parallel NWs [12]. This effect can be ascribed to the interconnected NW architecture and the presence of domain walls that are formed at the magnetic junctions once the external field is reduced. Finally, 3D interconnected NiCo/Cu multilayered NWs network films have been successfully fabricated, displaying large GMR responses (up to 85.8% at 10K) measured with the current flowing perpendicularly to the plane of the layers in the nanowire segments. 3D nanofiber network architectures offer a wide range of controllable parameters that can be used to tune the magnetic and magneto-transport properties of mechanically stable 3D interconnected nanofiber networks that have potential applications in various fields.

[1] E. Araujo, A. Encinas, Y. Velázquez-Galván, J. M. Martínez-Huerta, G. Hamoir, E. Ferain, and L. Piraux, Nanoscale 7, 1485 (2015). [2] T. da Câmara Santa Clara Gomes, J. De La Torre Medina, Y. G. Velázquez-Galván, J. M. Martínez-Huerta, A. Encinas, and L. Piraux, Journal of Applied Physics, 120(4), 043904 (2016). [3] T. da Câmara Santa Clara Gomes, J. De La Torre Medina, M. Lemaitre and L. Piraux, Nanoscale Research Letters, 11(1), 466 (2016). [4] T. da Câmara Santa Clara Gomes, J. De La Torre Medina, Y. G. Velázquez-Galván, J. M. Martínez-Huerta, A. Encinas, and L. Piraux, IEEE Transactions on Magnetics, 53(11), 1-6 (2017). [5] M. Darques, A. Encinas, L. Vila and L. Piraux, Journal of Physics D: Applied Physics, 37(10), 1411 (2004). [6] N. Myung, and K. Nobe, Journal of the Electrochemical Society, 148(3), C136-C144 (2001). [7] B. G. Tóth, L. Péter, Á. Révész, J. Pádár and I. Bakonyi, The European Physical Journal B, 75(2), 167-177 (2010). [8] T. McGuire and R. L. Potter, IEEE Transactions on Magnetics, 11(4), 1018-1038 (1975). [9] Velazquez-Galvan Y, Martinez-Huerta J M, de la Torre Medina J, Danlée Y, Piraux L and Encinas A Journal of Physics: Condensed Matter, 26(2), 026001 (2014) [10] Wang Q, Wang G, Han X, Wang X and Hou J G, The Journal of Physical Chemistry B, 109(49), 23326-23329 (2005). [11] Antohe V A, Nysten E, Martinez-Huerta J M, Pereira de Sa P M and Piraux L, RSC Advances, 7(30), 18609-18616 (RSC Advances, 7(30), 18609-18616 (2017). [12] Pignard S, Goglio G, Radulescu A, Piraux L, Dubois S, Declémy A and Duvail J L 2000 Journal of Applied Physics 87(2) 824–829 (2000).

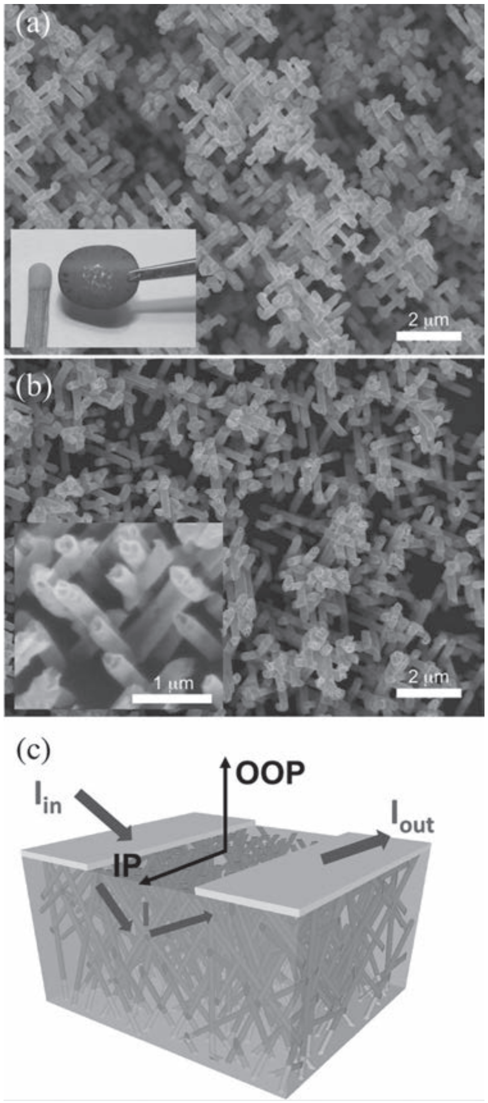

Fig. 1. SEM images of (a) a Ni CNW network and (b) a Ni CNT network obtained after the complete dissolution of the PC nanoporous host template. The inset displays in (a) shows its size and mechanical robustness. The inset in (b) displays a closer view of the tubular structure and crossing zones of the CNT network. (c) Schematic representation of the system after the local removing of the cathode used for electrodeposition leading to a suitable design for two-probe electrical measurement for magneto-measurement.

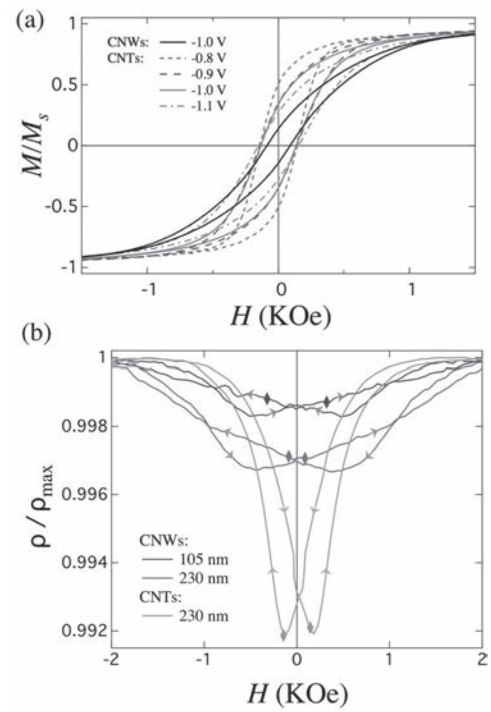

Fig. 2. (a) Hysteresis loops measured with the magnetic field applied along the out-of-plane (OOP) direction of the PC template and for CNT networks for different reduction potentials and for a CNW network (diameters = 230 nm). (b) Comparison of AMR curves recorded in the OOP direction for Ni CNW networks with NW diameters of 105 nm and 230 nm and for a CNT network with outer diameter of 230 nm. The lozenges in indicate the resistance state at the corresponding coercive field for each network.

INVITED PAPER

3:00

BF-05. Information Transfer and Trapping in a 3D Nano-printed Domain-wall Conduit. ***(Invited)***

D. Sanz-Hernández[1*], R.F. Hamans[2], J. Liao[1], A. Welbourne[1], R. Lavrijsen[2] and A. Fernández-Pacheco[1]
1. Cavendish Laboratory, University of Cambridge, Cambridge, United Kingdom; 2. Department of Applied Physics, Eindhoven University of Technology, Eindhoven, Netherlands

3D magnetic nanowire devices acting as domain wall conduits have long attracted attention. Devices in which domain walls move along a conduit have shown great potential for computing, biological and sensing applications, one example being the racetrack memory,[3] which could have a revolutionary impact in future computing devices. Until now, however, moving from 2D into 3D geometries has not been possible due to the limitations of traditional lithography and characterization techniques. In order to create and measure 3D nanowire devices, a leap in fabrication and characterization tools is required.[1] Two major experimental breakthroughs in nanofabrication and sensing of magnetic nanostructures are presented in this work: A first demonstration of a fabrication platform which can create functional high-quality 3D magnetic devices, and the development of a magneto-optical characterization method to probe individual 3D structures independently from the surrounding substrate.[2] These two breakthroughs will be presented by demonstrating how they can be used to produce and probe a functional 3D domain wall conduit. This device can extract magnetic domain walls from a 2D substrate and transport them vertically. In addition, we will provide a quantitative characterization of domain wall trapping mechanisms in such a 3D system, as well as showing how information flow can be controlled using 3D magnetic field sequences. Fabrication consists in a combination of state of the art non-magnetic 3D nanoprinting and traditional thermal evaporation of a thin film of magnetic material.[2] 3D nanoprinting is performed using Focused Electron Beam Induced Deposition, a technique in which the highly focused electron beam of a Scanning Electron Microscope is used to decompose a gas precursor in a very local and controlled way. By precise tuning of growth conditions, a high-quality interconnect region between the 2D substrate and the 3D interconnect can be achieved, critical for successful domain wall exchange between both. Precise control over conduit inclination over several micrometres with 300nm conduit widths is also demonstrated. Upon thermal evaporation of magnetic material (NiFe, 50nm) the nanoprinted 3D shape is fully transferred from the 3D scaffold onto the thin film. See Figure 1. Detection of individual 3D conduits is performed using a tailored dark-field magneto optical Kerr effect (MOKE) magnetometer.[2] In this instrument a linearly polarized laser is incident onto the conduit and surrounding 2D film. Due to the different inclination of the two systems, two separate reflections of the laser are obtained, a bright reflection corresponding to the large 2D film and a second 'dark-field' reflection corresponding to the 300nm wide conduit. The setup is tailored to detect both reflections, allowing to probe the magnetic state of the 2D film and the 3D conduit in parallel and without any cross-talk. By integrating the dark-field MOKE setup with a set of coils designed to apply magnetic fields in 3D we have been able to induce and detect the injection of domain walls from the 2D film into the 3D conduit. The low coercivity (0.2mT) 2D film is used as a source of domain walls and a systematic study of the fields necessary to inject the domain wall into the conduit has allowed us to identify the main domain wall pinning mechanisms in the system: pinning at the interconnection between the 2D film and the conduit, and pinning along the conduit.[2] In this talk we will describe how quantitative measurements of the pinning fields from 2D magnetic switching maps can be used to selectively trap domain walls either at the interconnect region or inside the 3D conduit. Finally, we will demonstrate how 3D field sequences may be used to further control information transfer in the system. As shown in Figure 2, a rotating field in the plane formed by the conduit and its supporting legs (x-z plane) may be used to periodically inject domain walls into the conduit, whereas a field along the plane of the film but perpendicular to the conduit (H_y) can be used to inhibit the creation an injection of domain walls, acting as a gate to information transfer. The methods presented in this work provide a new and powerful platform for the study of 3D magnetic nanostructures, naturally extensible to advanced materials and geometries. This presentation will therefore be of great interest to researchers and members of industry working in computing and sensing applications.

[1] Fernández-Pacheco et al, *Nat. Comm.,* 8, 15756 (2017) [2] Sanz-Hernández et al, ACS Nano, 11 (11), 11066 (2017) [3] Parkin and Yang, *Nat. Nano.*, 10 (3), 195-198 (2015)

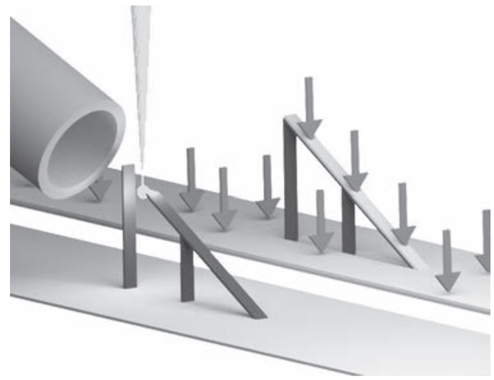

Fig. 1. Two step lithography combining 3D nanoprinting using a focused beam of electrons (left) and physical vapor deposition (right). The nanoprinted non-magnetic scaffold (black) transfers its 3D shape onto the magnetic thin film (lime) when the film is deposited. Conduit width 300nm.

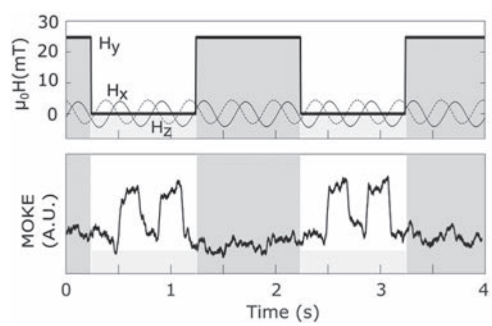

Fig. 2. Control of information injection into the 3D conduit. A rotating x-z field is applied to periodically inject domain walls into the 3D conduit, which are detected as a change in MOKE signal. A field perpendicular to the plane of rotation (H_y) is used to control the injection of walls into the conduit.

CONTRIBUTED PAPERS

3:30

BF-06. From vanishing interaction to superferromagnetic dimerization: Experimental determination of interaction lengths for embedded Co clusters.

F. Tournus[1], A. Hillion[1], A. Tamion[1], C. Albin[1] and V. Dupuis[1]
1. Institut Lumière Matière, Université Lyon 1 & CNRS, Villeurbanne, France

Magnetic nanoparticles are of great interest in a wide range of disciplines, including magnetic fluids, catalysis, biotechnology/biomedicine, magnetic resonance imaging, data storage, and environmental remediation. Successful applications of such magnetic nanoparticles in the areas listed above are highly dependent on the stability of the particles under a range of different conditions. In particular, these nanomagnets might be used as magnetic media in future high-density magnetic storage devices with ultimate recording bits (i.e. single nanoparticles). Reading and writing of such a system requires to know perfectly its magnetic properties in particular its anisotropy constant. It is then crucial to be able to characterize the magnetic properties of nanoparticles, and to be able to separate the intrinsic behavior from other effects coming from interparticle interactions in an assembly. In this study [6], we present magnetic measurements of Co clusters (around 2.5 nm diameter) embedded in different matrices: carbon and two metallic matrices (Au and Cu). We will first show that by using highly diluted samples prepared by low energy cluster deposition, we can reach a situation where no interactions are detected. The intrinsic magnetic properties of the particles can then be accurately determined thanks to a "global" fitting procedure (see figure 1) relying on the theoretical description of various magnetometry measurements [1-5]: low-temperature(hysteresis) and high-temperature (superparamagnetic) m(H) loops, zero- field cooled (ZFC)/field cooled (FC) susceptibility curves, and isothermal remanent magnetization (IRM) curves. We show how both the magnetic size and magnetic anisotropy energy (MAE) can be impacted by the nature of the matrix. Then, by considering nanoparticle assemblies of increasing concentrations (still remaining in a diluted range, lower than 10% in volume), we discuss the different effects of interactions between particles on the magnetic measurements (see figure 2). The evolution of Δm curves (deduced from remanence curves) is found to be very different from that of susceptibility curves. In order to account for the observed evolution of the measurements, we propose a simple model where magnetic dimers are formed for distances lower than a given interaction length [6]. This super-ferromagnetic correlation, which can be consistently inferred for each matrix, thus modifies the magnetic size distribution which has a drastic effect (in particular on ZFC/FC curves) as soon as particles are close enough from each other. The deduced interaction length (of the order of one nanometer) is found to be larger for metallic matrices and could be ascribed to RKKY interactions between neighboring magnetic nanoparticles.

[1] A.Tamion, M. Hillenkamp, F. Tournus, E. Bonet, and V.Dupuis, Appl. Phys. Lett. 95, 062503 (2009). [2] A. Tamion, E. Bonet, F. Tournus, C. Raufast, A. Hillion, O. Gaier, and V. Dupuis, Phys. Rev. B 85, 134430 (2012). [3] A. Hillion, A. Tamion, F. Tournus, O. Gaier, E. Bonet, C. Albin, and V. Dupuis, Phys. Rev. B 88, 094419 (2013). [4] F. Tournus, J. Magn. Magn. Mater. 375, 194 (2015). [5] F. Tournus, A. Tamion, A. Hillion, and V. Dupuis, J. Magn. Magn. Mater. 419, 1 (2016). [6] A. Hillion, A. Tamion, F. Tournus, C. Albin, and V. Dupuis, Phys. Rev. B 95, 134446 (2017).

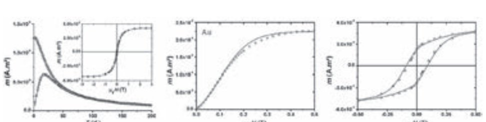

Fig. 1. From left to right, experimental and simulated ZFC/FC susceptibility curves, superparamagnetic magnetization loop (at 300 K), IRM curve and hysteresis loop at 2 K, for Co clusters embedded in Au (0.5% vol.).

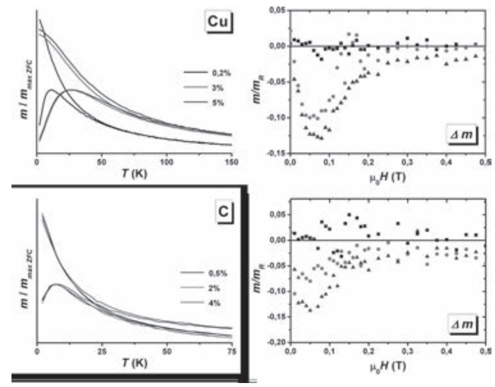

Fig. 2. ZFC/FC and Δm curves from samples of Co nanoparticles embedded in Cu and C at different concentrations. While the Δm evolution is qualitatively the same in both matrices, it is not the case of ZFC/FC curves. This can be interpreted in terms of a different "interaction length" in both matrices.

3:45

BF-07. The role of topologically non-trivial structures in magnetization processes of diameter modulated nanowires.

J. Fernandez-Roldan[1], C. Bran[1], R. Perez del Real[1], M. Vázquez[1] and *O. Chubykalo-Fesenko*[1]
1. Instituto de Ciencia de Materiales de Madrid, CSIC, Madrid, Spain

The future of domain-wall logic devices, registers or race-track-memories requires precise control of domain walls dynamics. The domain wall pinning can be achieved by artificial defects such as notches or by modulations in nanowire diameter. Cylindrical nanowires can be grown by electrodeposition inside the nanopores of anodic alumina templates and specifically designed for periodic diameter modulations [1,2] by a precise control of deposition parameters. Here, we consider the domain wall pinning in two-segment FeCo periodically diameter-modulated nanowire with large saturation magnetisation. The straight nanowires of this composition typically demagnetize through vortex domain wall propagation [3]. In addition, previous electron holography imaging at remanence has shown the presence of the vortex states at the ends of the large segments [4]. The measurements by Kerr-magnetometry on individual nanowires [1], when focusing on different spots along the wires, showed different local squared-shape hysteresis cycles with either a single or several jumps. With the aim to understand and to control the demagnetization processes and the pinning nature, we model the magnetization response under parallel applied field in FeCo periodically modulated polycrystalline nanowires varying the minor diameter. Our modelling indicates a complex behavior with a strong dependence on the polycrystalline disorder distribution and an important role of topologically non-trivial magnetization structures. The role of different non-trivial magnetization structures in hysteresis processes such as swirls, hedgehogs, helices have been discussed in the past. The helical magnetization domain wall, for example, has been introduced as possible magnetic configuration in iron whiskers [5]. In straight cylindrical nanowires topological defects in form of vortices nucleate at the nanowire ends due to curling magnetization instabilities [6]. Here we show that in modulated nanowires these structures nucleate at each segment end and as a consequence the whole magnetization process (and the pinning) is characterized by the existence of topologically non-trivial 3D magnetization configurations and their evolution and the applied field. In our model we consider magnetic nanowires modulated periodically in diameter with 5 segments. The largest segments have diameter D= 130 nm and length one micron (typical for the experimental situation), and the narrow segments have a variable diameter 40 nm < d <100 nm and length 300nm. The constriction between the two diameters is 50 nm long where the diameter is linearly varied from the smallest to the largest value. Nanowires are considered to have a granular bcc structure with random distributions. The latter is responsible for different nucleation-propagation sequences in each case due to the random vortex chirality patterns created at the end of each large segment for each particular distribution and different pinning sites. We demonstrate that modulated nanowires with a small diameter difference are characterized by an almost rectangular hysteresis loop but with an increased coercive field in comparison to the straight ones. The magnetization process is characterized by a formation of topologically protected walls formed initially by vortices with opposite chiralities at the end of each large segment. These structures propagate inside the whole nanowire in one field step and have the topology of 3D skyrmions (tubes). When two of these tubes with the opposite chiralities meet, the resulting structure is strongly topologically protected and the coercive field is increased. However, the most interesting case is when the diameter difference in modulations is large. The hysteresis cycle is characterized by an additional magnetization jump, a step corresponding to the depinning field. Here we report the occurrence of a novel pinning type called "corkscrew". As the field increases in the opposite direction, the initial vortices formed at the end of each modulation expand and form skyrmion tubes (with the magnetization core pointing against the field). Unlike the case above where the whole process is dynamical, in this case the tubes form a stable helicoidal structure along the large diameter segments only (see the Figure). The spiral amplitude and the oscilation frequency increases with the increase of the diameter difference and the tube core diameter size decreases. These structures are pinned at the constriction and the tube core size shrinks in order to penetrate into the narrow segments. In conclusion, the presence of topologically non-trivial configurations is inherent for the magnetization reversal processes in magnetic nanowires and defines the pinning nature in nanowires of modulated diameter. The magnetisation processes are characterized by the formation of skyrmion tubes. Unlike typical skyrmions stabilized by the Dzyaloshinkii-Moriya interaction, these "skyrmions" are of Bloch nature, i.e. have a pure dipolar origin and are stabilized by the finite-size effect in nano-objects. The new corkscrew pinning mechanism offers novel perspectives for nanowires engineering for multiple applications.

[1] E.M. Palmero, et al Nanotechnology 2015 26, 461001 [2] Y.P. Ivanov et al ASC Nano 2016 10, 5326 [3] C. Bran, et al *J. Appl. Phys*. 2013, 114, 043908. [4] L.A. Rodríguez, et al ASC Nano 2016, 10, 9669 [5] A.J. Hubert, J. Phys. Colloq. 1988, 49C8 [6] Y.P.Ivanov et al. J. Phys. D: Appl. Phys. 2013 46, 485001

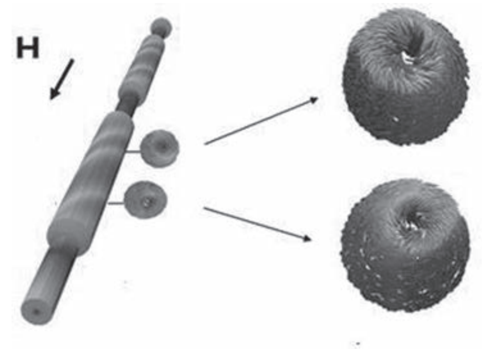

Fig. 1. Simulated magnetization distribution in two-segment nanowires with a particular disorder and small difference between diameters just before the switching field just before the switching showing the magnetization spiral and the skyrmion magnetization structure. The red color indicates magnetization opposite to the field direction while the blue one –parallel to the field.

INVITED PAPER

4:00

BF-08. Multisegmented cylindrical nanowires: from designed domain configuration to controlled stepped domain wall propagation.

C. Bran[1], E. Berganza[1], J. Fernandez-Roldan[1], M. Jaafar[1], R. Perez del Real[1], A. Asenjo[1], O. Chubykalo-Fesenko[1] and *M. Vázquez*[1]
1. Institute of Materials Science of Madrid, CSIC, Madrid, Spain

Magnetic cylindrical nanowires, NW, with constant diameter and multisegmented architecture are currently proposed in diverse nanotechnology applications as magnetoresistive reading heads, barcode units for security systems, specific tactile sensors, magnetoplasmonics, MRI markers or biochemical functionalization of different segments [1]. Interactions between adjacent segments have been recently proposed for engineering transport of information in logic devices and as 3D nanooscillators [2]. Such applications rely on a deep understanding and control on the magnetic response of individual NWs, particularly on the specific domain structure and remagnetization process in each magnetic segment. The magnetization reversal in uniform cylindrical NWs has been modeled to proceed by the nucleation of vortex-like structures at the ends of NWs followed by the propagation of a domain wall, DW, along the whole NW at given switching field [3]. In NWs with longitudinal uniaxial anisotropy (mostly shape anisotropy) the reversal requires the propagation of a Bloch-point like DW as a consequence of the singularity of the NW axis. For NWs with transverse anisotropy (overcoming crystalline anisotropy) the reversal also implies rotational processes. The reversal modes are also influenced by the NW diameter. The multisegmentation finally aims at the engineered periodical modulation of the magnetic anisotropy or the magnetic character of segments in order to control the magnetization reversal process. Cylindrical NWs were electrochemically grown under carefully controlled parameters inside self-assembled nanopores of anodic alumina membranes prepared by hard anodization. Afterwards, they were chemically released from the templates in order to investigate the magnetism of isolated nanowires. Magnetic characterization, at remanence and under longitudinal applied magnetic field, of those individual NWs was performed by magnetic force microscopy imaging, MFM, by magnetooptic Kerr effect, MOKE, and by photoemission electron microscopy, PEEM, combined with X-ray magnetic circular dichroism, XMCD. All these techniques supply magnetic information of the surface, while the latter one, XMCD-PEEM, provides in addition images that allow for the interpretation of the internal configuration of magnetic moments. The imaging of the magnetic domain configuration has been achieved at remanence and followed under constant applied field of variable amplitude [4]. Micromagnetic simulations were also carried out in order to further interpret and model the mainly vortex-promoted remagnetization process. Most recent results obtained in our laboratories will be overviewed for two families of multisegmented NWs: I) ferromagnetic/ferromagnetic, FM/FM (i.e., CoNi/Ni), and II) ferromagnetic/non-magnetic, FM/NM (i.e., CoFe/Cu). Importantly, the magnetic behavior finally depends on the crystalline nature of FM segments. Multisegmented individual cylindrical NWs with constant diameter (in the range of 100 to 150 nm) and total length up to 20 μm have been considered. The length of magnetic segments was up to 2 μm and that of non-magnetic segments was fixed to 20 nm. The analysis is focused on CoFe and CoNi FM segments exhibiting *bcc* or *fcc* cubic symmetry or *hcp* hexagonal structure depending on the relative Co content with significant magnetocrystalline anisotropy. That crystalline anisotropy can eventually enhance or balance the longitudinal shape anisotropy to result in segments from axial to transverse magnetization easy axis. After appropriate engineering of NWs (i.e., selection of segments composition and length), the following conclusions are outlined: Tipe I FM/FM NWs: a) The periodical modulation in magnetic anisotropy is observed (as an example, see the Figure), and b) Transverse or Axial domains are experimentally imaged together with Vortex domains (XMCD-PEEM), or Axial domains with Multivortex configurations (MFM) in CoNi/Ni NWs, as also confirmed by micromagnetic simulations. Tipe II FM/NM NWs: a) Vortex structures, with the same or opposite chirality, form at the ends of magnetic segments to determine the magnetic configuration and the magnetic switching of local segments which propagates under intersegments magnetostatic interactions, and b) Stepped and unidirectional propagation of the reversal process in CoFe/Cu NWs is confirmed (XMCD-PEEM, MFM, MOKE) by suitable geometric tailoring of magnetic segments. Micromagnetic modeling indicated that remagnetization takes place by complex vortex processes. Finally, the design and synthesis of nanowires with engineered multisegments represents a significant step forward towards advanced near-unidimensional magnetic nanostructures. They are intended for the controlled propagation of the magnetization reversal along the nanowires, which together with the role played by intersegments magnetostatic interactions, is expected to be of significant relevance in advanced media for transport of information.

[1] A. Mourachkine et al., Nano. Lett., 8, 3683 (2011); J.J. Park et al., IEEE Sensors Journal 17, 2015 (2017); B. Ozkale et al. ACS Appl. Mater. Interfaces 7, 7389 (2015); M. Bañobre et. al., J. Mater. Chemistry B, 5, 3338 (2017) [2] N. Locatelli et al., Sci. Rep. 5, 17039 (2015); C. Bran et. al., Nanotechnology 28, 095709 (2017) [3] S. Da Col et al., Phys. Rev. B 89, 180405 (2014); Y.P. Ivanov et al., J. Phys. D: Appl. Phys. 46, 485001 (2013) [4] C. Bran et al., Phys. Rev. B.96 (2017) 125415; E. Berganza et al., Sc. Rep. 7 (2017) 11576

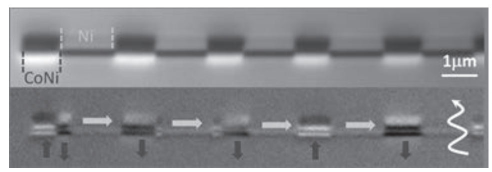

Fig. 1. Compositional XAS (upper panel) and magnetic XMCD-PEEM (bottom panel) images of CoNi/Ni NWs with modulations in anisotropy. Vortex (CoNi) and axial (Ni) domains are observed. The arrows point out the direction of magnetization in each segment.

CONTRIBUTED PAPERS

4:30

BF-09. Magnetic-field-induced domain wall propagation in modulated-diameter cylindrical nanowires.

J. Fernandez-Roldan[2], A. De Riz[1], B. Trapp[3], C. Thirion[3], J. Toussaint[3], *O. Fruchart*[1] and D. Gusakova[1]
1. SPINTEC, Univ. Grenoble Alpes, CNRS, CEA, Grenoble, France;
2. Institute of Materials Science of Madrid (ICMM-CSIC), Madrid, Spain;
3. Institut NEEL, Univ Grenoble Alpes, CNRS, Grenoble, France

Memory and logic concepts have been proposed, based on domain wall (DW) motion along one-dimensional conduits. In many designs it is important to be able to locate DWs at a specific location. In this context, the interaction of domain walls with protrusions and notches in nanostrips has been studied rather extensively(see eg [1,2]). Although the general trend is an increase of the pinning strength with the magnitude of the modulation, the physics sensitively depends on the nature of the wall: vortex or transverse, also with the circulation degree of freedom for the latter. Cylindrical nanowires is an alternative to flat strips. First, they provide a different physics due to the high magnetostatic energy and the occurence of novel walls such as the Bloch-point wall[3,4]. Also, due to the high magnetostatic energy it is expected that the type of DW matters less, and more general results may be derived. Second, from the synthesis point of view they would be the natural geometry for implementing conduits in 3D, such as for the original race-track proposal. On the side of theory there exists a handful of reports(see eg [5] as a pioneering work), however these concern specific geometries and do not provide a quantitative global picture. Experimental results are even more scarce, and again do not provide a quantitative picture[6]. We first report a theoretical study of DWs under the influence of a magnetic field within a cylindrical nanowire with diameter modulations. More specifically, we focus on a simple situation to highlight the physics at play: two long straight segments with different diameters, smoothly connected together in a fashion mimicking experimental cases (FIG1). This should provide a solid ground to understand more complex geometries. For both sakes of exchange and dipolar energy, it is expected that the DW tends to remain in the section with lower diameter, giving rise to a propagation field with finite value. We combine an analytical model and micromagnetic simulations performed in a finite-element scheme to smoothly describe curved geometries. The former is based on approximations to derive simple scaling laws, providing a global picture of the trends in terms of geometry and material parameter. Both exchange and magnetostatic energy are considered. We derive the very simple conclusion, that the DW depinning field is close to twice the magnetization value multiplied by the modulation slope (radius versus position)*. The latter is used to demonstrate the robustness of the scaling law, its range of application, and provide accurate figures. The two approaches agree particularly well in the case of gently sloping modulations (see eg FIG.2). These results validate the analytical scaling law, which may be useful to guide nanowire design and when analyzing experiments. Our approach is quite general and is being extended further to study the effect of other driving forces such as a spin-polarized current. * The exact scaling law reads: $H_c=[(9/20) * M_s(R_2-R_1)/\delta] * [1+(10/27)*(\Delta_d)^2\pi^2 /(R_1+R_2)^2]$. M_s is the material magnetization, Δ_d is the dipolar exchange length, and δ is one fourth of the modulation full width. This law is illustrated on FIG1.

[1] R. D. McMichael, J. Eicke, M. J. Donahue, D. G. Porter, J. Appl. Phys. 87, 7058 (2000) [2] L. K. Bogart, D. Atkinson, K. O'Shea, D. McGrouther, S. McVitie, Phys. Rev. B 79, 054414 (2009) [3] H. Forster, T. Schrefl, D. Suess, W. Scholz, V. Tsiantos, R. Dittrich, J. Fidler, J. Appl. Phys. 91, 6914 (2002) [4] A. Thiaville, Y. Nakatani, Domain-wall dynamics in nanowires and nanostrips, in Spin dynamics in confined magnetic structures III, B. Hillebrands & A. Thiaville*(Eds.)*, vol.101, *Springer* (2006) [5] S. Allende, D. Altbir, K. Nielsch, Phys. Rev. B 80, 174402 (2009) [6] O. Iglesias-Freire, C. Bran, E. Berganza, I. Mínguez-Bacho, C. Magén, M. Vázquez, A. Asenjo, Nanotech 26, 395702 (2015)

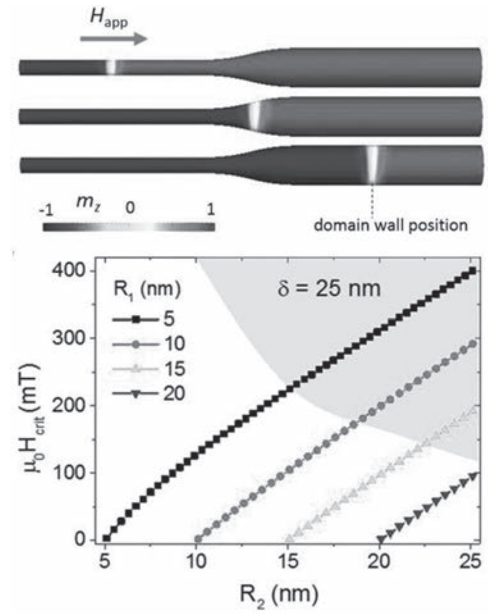

Fig. 1. Illustration for the type of modulation considered, and DW propagation. The graph shows the variation of the propagation field, versus the larger radius R_2, following the equation provided in the text.

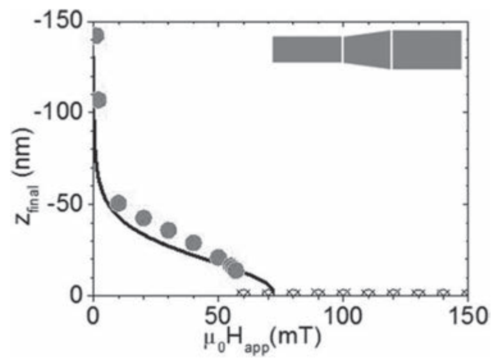

Fig. 2. Wall position versus applied field from the model (line) and simulations (dots). *z*=0 stands for the center of the modulation. Parameters are R_1=5nm, R_2=7.5nm, modulation full length 100nm, and Permalloy parameters (no adjustable parameter)

4:45

BF-10. Dominance of shape anisotropy among magnetostatic interaction and Magnetocrystalline anisotropy in electrodeposited $(FeCo)_{1-x}Cu_x$(X=0.1-0.5) Ternary Alloy Nanowires.

N. Ahmad[1,2], M. Zahid Shafiq[1], S. Khan[3], R. Sharif[4], A. Safeer[3], A. Majid[5], S.A. Shah[6] and K. Javed[6]
1. Physics, International Islamic University, Islamabad, Pakistan;
2. University of Chinese Academy of Sciences, Beijing, China;
3. Spintronics Laboratory,Department of Physics, International Islamic University, Islamabad, Pakistan; 4. Physics, University of Engineering and Technology, Lahore, Pakistan; 5. Physics, University of Gujrat, Gujrat, Pakistan; 6. Physics, FC College University, Lahore, Pakistan

The nanostructures based on templates fabrication have fascinated and provided facilities to researcher who work in material science to fabricate nanostructures such as nanotubes, nanoparticles and nanowires show optical, electrical and magnetic properties different from their bulk counterpart. Applications of ferromagnetic nanowires are in optical medium, electronic equipment and dense magnetic memories, [1,2]. Ferromagnetic nanowires arrays have applications in nanosensors [3], magnetic nanodevices [4] recording media[5]and micro circulator of magnetic nanowires is attracting a lot of attention[6]. In this method, magnetic nanowire arrays are produced by template-assisted electrodeposition into self-assembled anodic alumina pores, in which geometrical parameters as pore diameters, length, and center to center spacing between the pores can be easily controlled by varying the anodic electrochemical parameters. Highly arranged nanoporous alumina templates with pore diameters reaching from about 15 to 200nm and lengths from 100nm up to 50μm can thus be attained. Over the years, ferromagnetic non-magnetic multilayer nanowire arrays and CoAg, FeAg, CoCu, CoPd, CoPt binary systems, have been recorded in the literature [7] due to their motivating magneto transport and magnetic properties. From the vast variety of magnetic systems, FeCo nanowires show the necessary capability to be employed in generation of permanent magnets. FeCo magnetic alloy nanowires can be tuned by changing the alloy composition by adding further elements [8-10] or suitable thermal treatment [11]. In particular, high values of remanence and coercivity will be expected when the magnetic feild is applied parallel to the nanowires and will be assigned mainly to the magnetic shape anisotropy [12,13].Fabrication of FeCoCu nanowires into AAO templates by AC electrodeposition is very difficult due to mismatch of reduction potential and difference of ionic radii. It is the need of the hour to tune magnetic properties of FeCo alloy nanowires to discuss magnetization reversal process to abe employed in high density recording media and magnetic race track memory. Here in this work we have synthesized the $(FeCo)_{1-x}Cu_x$ (X=0.1-0.5) nanowire arrays by AC electrodeposition in anodic aluminum oxide templates (AAO). We also studied the effect of Cu substitution on structural, dielectric and magnetic properties of the nanowires. Surface properties, and particle size distribution was obtained by using a scanning electron microscope. The length and diameter of prepared nanowires is 18μm and 58nm respectively and the composition of Cu increased from 52 to 82 percentage as compared to Fe and Co atoms, was confirmed by energy dispersive X-ray spectroscopy (EDS). The crystallites size shows overall increasing trend from 44-54nm confirmed by XRD calculated using Scherer formula. The AAO seems to be amorphous while the metal nanowires are BCC and also observed FCC aluminum of substrate. The magnetic analysis was performed using a vibrating sample magnetometer, reveals that by increasing the Cu composition saturation magnetization and coercivity Hc of the nanowires decreased. Magnetic measurements exhibit strong magnetic anisotropy with magnetization easy axis parallel to the nanowires in as-prepared samples. The shape anisotropy remains dominant by overcoming on magnetostatic interactions and Magnetocrystalline anisotropy. The angle dependent coercivity and squareness decreases with the increase of angle and shows the maximum value at 0^0 and minimum. It is observed that magnetization reversal mechanism occurs by nucleation mode with the motion of domain walls. In order to use such nanowires in supercapacitor applications, the frequency dependent dielectric analysis of FeCoCu nanowire have been investigated thoroughly using an impedance analyzer in a wide range frequency. The behavior of dielectric parameters has been investigated using Maxwell-Wagner's model and Koop's theory.

[1]Al-Mawlawi, D., C. Z. Liu, and Martin Moskovits. "Nanowires formed in anodic oxide nanotemplates." Journal of materials research 04, 1014-1018.(1994) [2] Wäckelgård, Ewa. "A study of the optical properties of nickel-pigmented anodic alumina in the infrared region." *Journal of Physics: Condensed Matter* 8,5125 (1996): [3] Fodor, P. S., G. M. Tsoi, and L. E. Wenger. "Fabrication and characterization of Co 1− x Fe x alloy nanowires." Journal of Applied Physics10, 8186-8188.(2002) [4] Avella, Maurizio, Mariacristina Cocca, Maria Emanuela Errico, and Gennaro Gentile. "Nanotechnologies and Nanosensors: Future Applications for the Conservation of Cultural Heritage." In Nanotechnological Basis for Advanced Sensors 3,511-517. (2011) [5] Ramazani, A., M. Almasi-Kashi, E. Golafshan, and M. Arefpour. "Magnetic behavior of as-deposited and annealed CoFe and CoFeCu nanowire arrays by ac-pulse electrodeposition." *Journal of Crystal Growth* 402, 42-47(2014) [6] Darques, Michaël, J. De la Torre Medina, L. Piraux, Laurent Cagnon, and Isabelle Huynen. "Microwave circulator based on ferromagnetic nanowires in an alumina template." *Nanotechnology* 14,145208.(2010) [6] Dahmane, Y., L. Cagnon, Jean Voiron, S. Pairis, M. Bacia, L. Ortega, N. Benbrahim, and A. Kadri. "Magnetic and structural properties of electrodeposited CoPt and FePt nanowires in nanoporous alumina templates." *Journal of Physics D: Applied Physics* 21, 4523.(2006) [7] Bran, C., Yu P. Ivanov, J. García, R. P. Del Real, V. M. Prida, Oksana Chubykalo-Fesenko, and Manuel Vázquez. "Tuning the magnetization reversal process of FeCoCu nanowire arrays by thermal annealing." *Journal of Applied Physics* 4,043908.(2013) [8] Fodor, P. S., G. M. Tsoi, and L. E. Wenger. "Fabrication and characterization of $Co_{1-x}Fe_x$ alloy nanowires." *Journal of Applied Physics* 10, 8186-8188. (2002) [9] Wang, R. L., S. L. Tang, Y. G. Shi, X. L. Fei, B. Nie, and Y. W. Du. "Effects of annealing on the structure and magnetic properties of Fe 27 Co 23 Pb 50 nanowire arrays." *Journal of Applied Physics* 103, 07D507. (2008) [10] Shukla, Gaurav. "Magnetic and optical properties of epitaxial n-type Cu-doped ZnO thin films deposited on sapphire substrates." *Applied Physics A: Materials Science & Processing*1, 115-118.(2009)

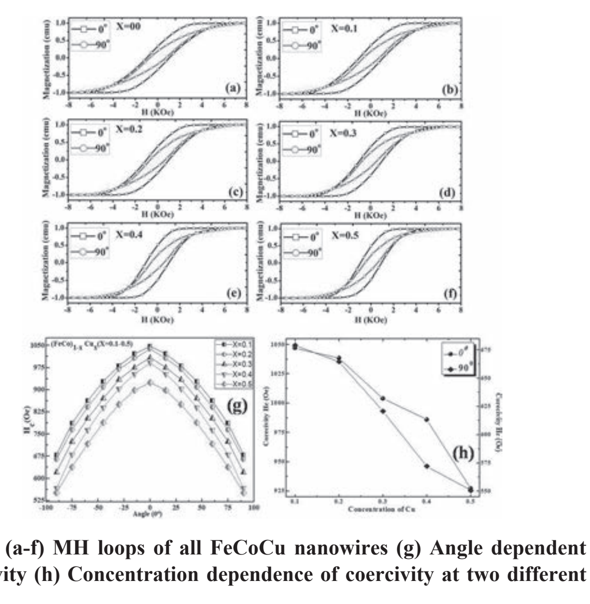

Fig. 1. (a-f) MH loops of all FeCoCu nanowires (g) Angle dependent coercivity (h) Concentration dependence of coercivity at two different angles

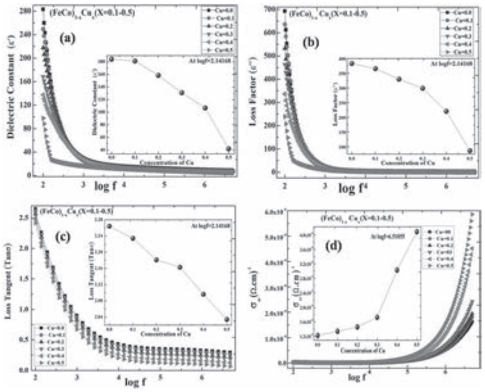

Fig. 2. Dielectric properties of FeCoCu nanowires (a) Dielectric constant (b) Loss Factor (c) Loss Tangent (d) AC Conductivity

TUESDAY AFTERNOON, 24 APRIL 2018 PEONY III, 2:00 TO 5:00

Session BG
LINEAR MOTORS I

Yacine Amara, Chair
Universite de Le Havre, Le Havre, France

INVITED PAPER

2:00

BG-01. Design Optimization and Performance Comparison of Two Linear Motor Topologies with PM-less Tracks. ***(Invited)***

S. Aleksandrov[1], T. Overboom[1] and E. Lomonova[1]
1. Electrical Engineering, Eindhoven Univercity of Technology, Eindhoven, Netherlands

I. Introduction Linear Permanent Magnet Synchronous Motor (LPMSM) topology is the preferable choice for a linear motor in terms of high force density and good overall performance. However, its main drawback is the relatively high price caused by the extensive usage of rare-earth materials in the track. This factor is critically important, especially when this type of motor has to be used in a long-stroke application, such as storage or airport transportation lines where the main prerequisite is a low-cost, passive and robust track. Therefore, Linear Induction Motor (LIM) and Linear Flux-Switching Permanent Magnet Motor (LFSPMM) are two possible alternatives suitable for long-stroke applications. Considering only the price of the track, LIM topology, with its flat aluminum secondary is most attractive. Nevertheless, the absence of rare-earth materials limits the propulsion force generated by the LIM. Another attractive alternative is the LFSPMM topology, which also has a passive secondary, but it incorporates a limited amount of rare-earth materials in its mover, improving its force generation capabilities. As a relatively new topology, the research on LFSPMM is still limited [1-2]. The existing design solutions for LIM having relatively small volume, have lower force density [3], compared to the designs having much larger overall dimensions [4]. Therefore, a direct comparison between LIM and LFSPMM is very difficult. Based on the volume of a benchmark LPMSM topology, in this paper, a comparison between LIM and LFSPMM is performed. To obtain optimal designs within this volume, a fast converging, semi-analytical methods are used for modelling both topologies and the results are used to compare LIM and LFSPMM topologies. II. Modelling Fig. 1a shows one periodical section of the investigated LIM topology, which contains a three-phase coil unit with distributed winding and an infinitely long flat aluminum secondary. The chosen semi-analytical modelling technique is Complex Harmonic Method (CHM) [5], where the magnetic field distribution is obtained while accounting for the eddy current effect in the conductive secondary. The primary core is considered infinitely permeable and the coils are modelled as current sheets on the top boundary of the airgap. The effective airgap length is adjusted using Carter's coefficient to account for the primary slotting. In Fig. 1b, the analyzed LFSPMM topology is shown. It represents one periodical section of the motor, where the primary incorporates two three-phase coil groups with concentrated windings and six tangentially magnetized permanent magnets. The secondary is considered as an infinitely long teeth structure made from laminated silicon steel. A Hybrid Analytical Method (HAM), which combines CHM with Magnetic Equivalent Circuit (MEC) [6], is chosen for modelling. The magnetic field distribution in the airgap is obtained by the CHM, while the mover and the track are modelled using MEC. In addition, to increase the accuracy and to allow coupling between the regions, the MEC-region is discretized. III. Design Optimization and Performance Comparison Both topologies are designed for the same volume as the LPMSM. The overall length, height and depth of the mover are kept the same. A fixed value of the input current density is used. The forces acting on the track, the secondary losses and also the primary copper losses are used for comparison between the performance of LIM and LFSPMM. As the speed of these linear motors is in the range of 10 m/s, which is relatively low compared to their rotary counterparts, the iron losses in the primary are neglected for the purpose of this comparison. Both topologies are optimized for maximum propulsion force. LIM is modelled and optimized, considering the optimal slip frequency for each variation of the pole pitch. Optimization parameters are the mechanical clearance, the thickness of the conductive secondary, the coil-to-tooth width ratio in the primary and the height of the mover. In Fig. 2a, the generated propulsion force for different pole pitches is shown, while in Fig. 2b the ratio between the force and the power losses is depicted. As the comparison between different topology variations is performed for a fixed length of the mover, the results for smaller pole pitches are multiplied with the number of periodic sections, which could fit in it. The results of the parameter sweep for the LFSPMM and the comparison with the results from the LIM topology will be presented in the full paper. IV. Conclusion The conducted research shows the comparison of LIM and LFSPMM topologies, optimized for maximum propulsion force while considering their losses. Both topologies are modelled using fast converging, semi-analytical modelling techniques. Finally, the results are compared to a benchmark LPMSM in terms of force density and power losses as low-cost alternatives for long-stroke applications.

[1] J. Cai, Q. Lu, X. Huang, Y. Ye, and Y. Fang, "Performance investigation of a novel multi-tooth switched-flux linear motor," in 2015 Tenth International Conference on Ecological Vehicles and Renewable Energies (EVER), pp. 1–7, March 2015. [2] R. Cao and W. Huang, "A double fed three-phase flux-switching linear motor with complementary magnet circuit for urban rail transit," in 2014 IEEE Conference and Expo Transportation Electrification Asia-Pacific (ITEC Asia-Pacific), pp. 1–5, Aug 2014. [3] A. Shiri and A. Shoulaie, "Design optimization and analysis of singlesided linear induction motor, considering all phenomena," IEEE Transactions on Energy Conversion, vol. 27, pp. 516–525, June 2012. [4] S. Nonaka and T. Higuchi, "Design of single-sided linear induction motors for urban transit," IEEE Transactions on Vehicular Technology, vol. 37, pp. 167–173, Aug 1988. [5] C. H. H. M. Custers, T. T. Overboom, J. W. Jansen, and E. A. Lomonova, "2-d semianalytical modeling of eddy currents in segmented structures," IEEE Transactions on Magnetics, vol. 51, pp. 1–4, Nov 2015. [6] E. P. Furlani, Permanent magnet and electromechanical devices: materials, analysis and applications. Academic Press, London, 2001.

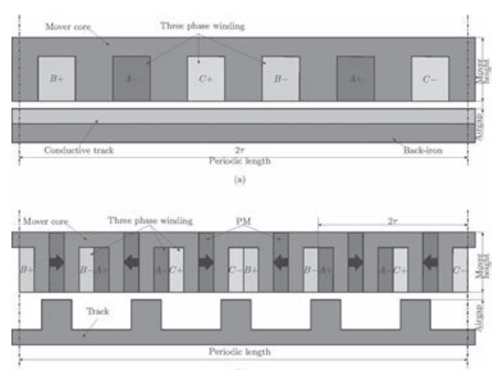

Fig. 1. Investigated topologies:
(a) LIM: a 3-phase motor with flat secondary,
(b) LFSPMM: a 3-phase, 6/5 pole motor.

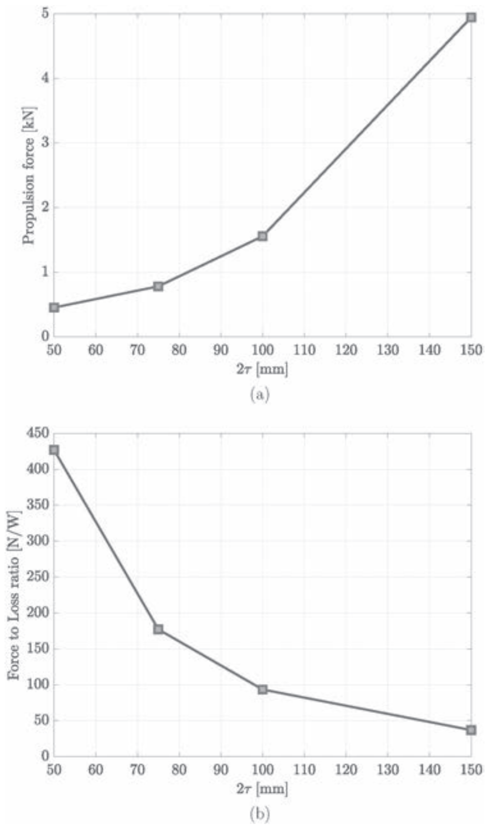

Fig. 2. Results for LIM topology:
(a) Maximum propulsion force for different pole pitches,
(b) Maximum force to loss ratio for different pole pitches.

CONTRIBUTED PAPERS

2:30

BG-02. A Three-Phase Tubular Permanent-Magnet Linear Machine with Hybrid Halbach/Axially-Magnetized Permanent Magnets.
Y. Sui[1,2], P. Zheng[1], Z. Yin[1] and J. Zhao[2]
1. School of Electrical Engineering and Automation, Harbin Institute of Technology, Harbin, China; 2. School of Mechatronics Engineering, Harbin Institute of Technology, Harbin, China

I. INTRODUCTION Free-piston energy converter, which integrates free-piston engine with a tubular permanent-magnet linear machine (PMLM), can generate electric power for applications like electric vehicles (EVs) [1]. As the key component of FPEC, the performance of the integrated PMLM has critical impact on the performance of FPEC. To improve the power density of the integrated tubular PMLM, the Halbach array which is composed by radially- and axially- magnetized PM rings is generally adopted. Since the radial magnetization of the homopolar PM ring is difficult, generally the homopolar PM ring is assembled by several cambered PM segments that are magnetized in radial direction, and these segments are banded by fabric bandages to improve the mechanical strength of the PM mover. But this manufacturing method will increase the air-gap length and compromise the performance of PMLM [1, 2]. To overcome the above disadvantages, we propose a kind of three-phase tubular PMLM which features hybrid Halbach/axially-magnetized permanent magnets (PMs), as shown in Fig. 1. II. MACHINE TOPOLOGIES AND OPERATING PRINCIPLE For the proposed machine, its mover structure can be regarded as a superposition of the conventional Halbach PM mover and the axially-magnetized PM mover, i.e., the proposed mover structure can be obtained by ringing the Halbach PM mover with an axially-magnetized PM mover. In comparison with the conventional Halbach array, the mover of the proposed machine has additional ferromagnetic poles which are sandwiched between the axially magnetized PMs. These additional ferromagnetic poles serve as magnetic path of the axially-magnetized PMs, and they also can confine the radial movement of the cambered radially-magnetized PM segments. Therefore, no extra fabric bandages are needed for the mover of the proposed machine, so the efficient air gap length can be smaller when it is compared with the conventional Halbach PMLM, i.e., higher power density can be obtained for the proposed machine. The stator of the proposed machine is similar to that of the conventional tubular PMLM, and annular windings are placed in the slotted stator. III. DESIGN AND OPTIMIZATION With the sinusoidal speed characteristic of the free-piston engine considered, the proposed machine is investigated under sinusoidal speed condition, and it is different from the design of the conventional PMLM which works under a constant speed. The back electro motive force (EMF), detent force, force, efficiency and power density, etc., are calculated by finite-element analysis (FEA). The main structural parameters, which include the outer radius of the mover, radial length of both the axially-magnetized PMs and the ferromagnetic poles, the axial length ratio of the radially-magnetized PMs to the pole pitch, etc., are optimized to improve the power density. To reduce the detent force which affects the dynamics of the mover, additional ferromagnetic teeth are attached on the stator core, and their dimensions are also optimized. IV. PERFORMANCE COMPARISON AND EXPERIMENTS Finally, the proposed machine is compared with two previously developed prototypes which are with the conventional Halbach mover and the axially-magnetized PM mover, respectively, as shown in Fig. 2. The tests of the conventional PMLMs have been done, and the mover of the proposed machine is still under construction, and the test results will be presented in the full paper. V. CONCLUSION A three-phase tubular PMLM with hybrid Halbach/axially-magnetized PMs is proposed and studied for FPEC. The machine topologies and operating principle are elaborately described. The influence of some main structural parameters on both the force capability and power density are investigated, and the detent force is reduced by attaching additional ferromagnetic teeth on the stator core. In comparison with the conventional Halbach and axially-magnetized PMLMs, the proposed machine features higher mass and volume power density. This machine topology is applicable to tubular PMLMs with any phases. This work was supported in part by National Natural Science Foundation of China (51607046, 51325701, 51377033, 51777013), in part by China Postdoctoral Science Foundation (2017M610204).

1. J. Wang, M. West, D. Howe, H. Zelaya-De La Parra, and W. M. Arshad. Design and experimental verification of a linear permanent magnet generator for a free-piston energy converter, IEEE Transactions on Energy Conversion, 2007, 22(2): 299-306. 2. Ping Zheng, Chengde Tong, Jing Zhao, Bin Yu, Lin Li, Jingang Bai, and Lu Zhang. Investigation of a 7-pole/6-slot Halbach-magnetized permanent-magnet linear alternator used for free-piston stirling engines. Journal of Applied Physics, 2012, 111: 07E711.

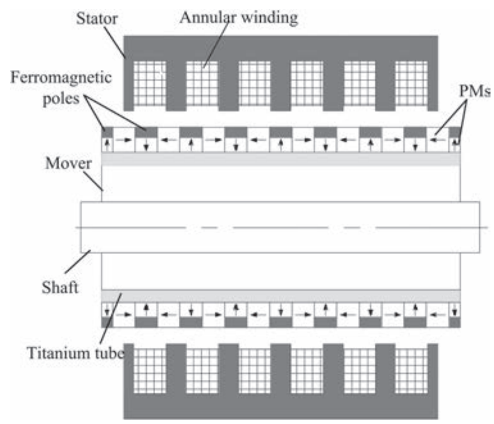

Fig. 1. Topology of the proposed tubular PMLM

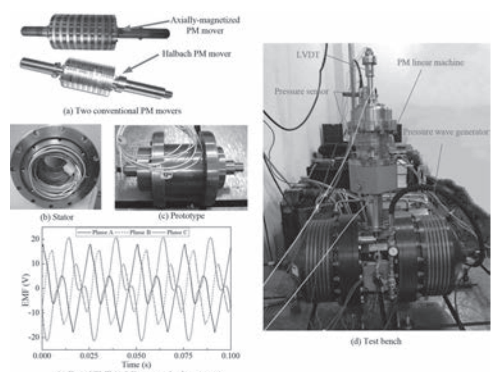

Fig. 2. Developed prototypes, test bench and tested results

2:45

BG-03. Design A Linear Flux-Switching Permanent Magnets Machine for Wave Energy Harvesting.

Y. Zou[1]
1. Electrical Engineering, The Hong Kong Polytechnic University, Hong Kong, China

I.INTRODUCTION Wave energy converters (WECs) that are considered to possess commercial values are the Pelamis from Ocean Power Delivery [1], the wave dragon from Wave Dragon APS [2], and the Archimedes Wave Swing from BV-AWS [3]. More and more researchers focus on oscillation wave energy harvesting by using linear machines such as linear synchronous permanent magnet generator (LSPMG) [4]. As a large number of permanent magnets (PM) are employed by the generator, the cost of the machines will be relatively high, compared with other PM-free machines. However, LSPMGs are hard to widely developed for large power volume application due to the limitation of the size of the PMs used for the machines. A linear flux-switching PM machine is designed in this study to create a cost-effective oscillation wave power generation. The machines, as a direct-drive generator, employs a few PMs so that the cost of the machine would be reduced dramatically. These PMs are embedded into the mover of the machine and it can generate electricity without excitation because of the utilization of the PMs. Without current excitation, the excitation current loss for the generator will be eradicated. The efficiency of the power generation system would be improved. Meanwhile, since the excitation current of the generator is zero and the excitation current loss can be ignored, this machine is suitable for low-speed operation. For wave power generation, the prominent feature is that the movement of the wave is rather low, around 1 m/s. Therefore, the designed machine is a promising candidate for wave energy harvesting. First, the structure of the machine is introduced and some basic principles for the machine are also given in this paper. Second, the structure of the power generation system based on the machine is introduced and the design procedure of the machine is elaborated. Also, the magnetic features of the machine are calculated by using finite element method (FEM). Last but not least, basic experiments for the machine is carried out, validated the effectiveness and feasibility of the designed machine for wave power generation. II.PROTOTYPE OF THE MACHINE The section view of the magnetic path of the machine and its prototype are shown in Fig.1(a) and (b). There are two phases of the machine, namely, phase A and phase B. The mover and the stator consist of a series of teeth. For the mover, PMs are sandwiched by two mover plates which are made of steel sheets. The mover is fixed by a solid aluminum. And this aluminum possesses eight wheels to guide the mover and guarantee the length of the air gap between the mover and the stator. The main specifications of the machine are listed in Table 1. The overall power generation system mainly consists of three parts: vertical flux-switching machine, energy converter, and storage part and a control part, as shown in Fig.1(d). A buoy can push the mover of the machine as the mechanical input. The stator is fixed on a spring installed at the end of the stator to avoid the colliding condition of the mover. The machine can absorb the wave energy via the buoy. The mover, pushed by the buoy, oscillates to against the magnetic force of the machine, generating electricity. A rectifier is used to regulate the generated electricity from alternative currents to direct currents and the electricity is stored by a capacitor. The operation principle of the machine is given in Fig.1 (e)~(f). When the mover moves, phase A and phase B will be induced terminal voltages and the voltages are alternative as the embedded PMs in the mover. III.BASIC THEORY According to Farad's law, the back EMF of each phase can be expressed as $d\Phi/dt=-N*v*d\Phi/dt$ (1) where λ is flux linkage of a phase and Φ is the flux of the phase. N represents the turns of the windings and x is the movement displace of the mover. v is the speed of the mover. It can be seen that the back EMF are proportion to N and v if the change rate of the flux keeps constant. If there is no local saturation for this machine, the flux of each phase without loading can be formulated as [5] $\Phi a=\Phi m*cos(2\pi x)$ (2) $\Phi b=\Phi m*cos(2\pi x+\pi/2)$ (3) where Φm and τ are the amplitude of flux of each phase with respect to the displacement and the length of the pitch. The flux distribution of the machine is given in Fig.2 (a). The density of the flux along the teeth aligned with the stator is bigger than that of the teeth unaligned. IV.EXPERIMENTAL VERIFICATION The experimental setup consists of the proposed machine, the energy storage system, the dSPACE DS1104 card based controller and loads, as shown in Fig.2(b). By using software package MATLAB/Simulink interfaced with DS1104, an emulated hardware controller for the power generation can be built quickly. The mover of the generator is driven by a linear machine via a metal rod. The generated electricity is stored in a capacitor. The open circuit voltage output and flux linkage of the machine are simulated as shown in Fig.2 (c), (d). The amplitude of the speed is 1 m/s. Under this speed, we can see that the maximum voltage is up to 12 V and the peak of the flux linkage is around 0.004 Wb. The linear machine is capable of producing electricity at such a low speed within 1 m/s. After rectifying, a controller is used to control the voltage by closed voltage control of the generator. The reference voltage is 6 V. the voltage response reaches the reference value and some fluctuations exist at the beginning. The mechanical force input for the machine is given in Fig.2 (f).

[1] R. Henderson, "Design, simulation, and testing of a novel hydraulic power take-off system for the Pelamis wave energy converter," Renew. Energy, vol. 31, pp. 271–283, 2006. [2] www.wavedragon.net, "Wave dragon official web site. [3] H. Polinder, M. E. C. Damen, and F. Gardner, "Linear PM generator system for wave energy conversion in the AWS," IEEE Trans. Energy Conversion, vol.19, no.3, 583-589, 2004. [4] J. Prudell, M. Stoddard, E. Amon, T. K. A. Brekken, and A. Jouanne, "A permanent-magnet tubular linear generator for ocean wave energy conversion," IEEE Trans. Industrial Applications, vol. 46, no. 6, 2392-2400, 2010. [5] Yue Hong; Mikael Eriksson; Valeria Castellucci; Cecilia Boström; Rafael Waters, "Linear generator-based wave energy converter model with experimental verification and three loading strategies," IET Renewable Power Generation, Vol. 10, Issue 3 Pages: 349 - 359, 2016.

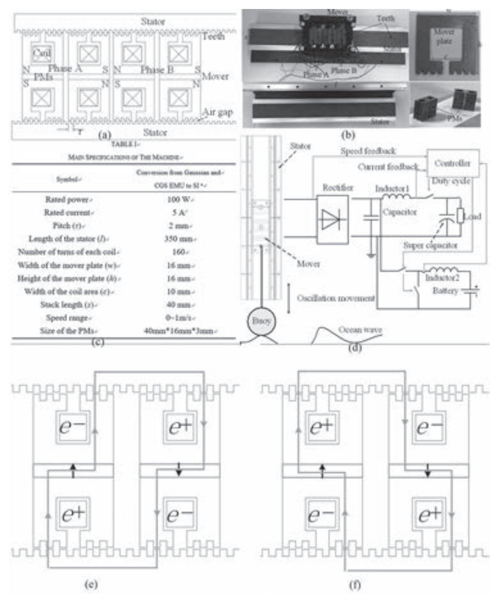

Fig. 1. Structure of the system

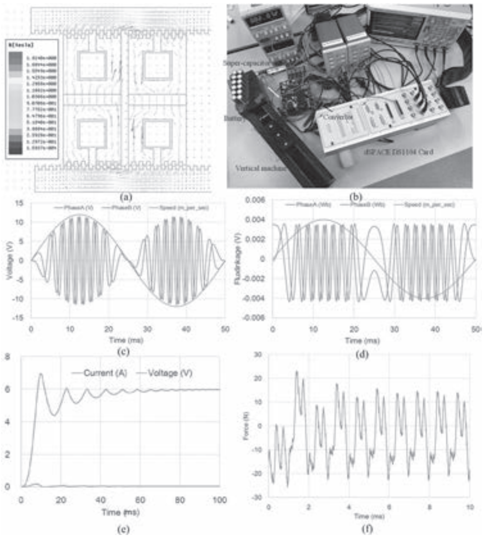

Fig. 2. Experimental results

3:00

BG-04. Torque Characteristics of Interior Permanent Magnet Spherical Actuators.

K. Takahara[1], K. Hirata[1] and N. Niguchi[1]
1. Osaka University, Suita, Japan

I. Introduction Actuating systems with multi degrees of freedom (multi-DOF) are composed of several single-DOF motors, which results in large, heavy and complicated structures. Therefore, multi-DOF actuators are expected to become a key technology to solve these problems, and various spherical actuators have been proposed [1]-[7]. We have proposed a surface permanent magnet (SPM) type outer rotor spherical actuator as shown in Fig. 1(a) [7]. In order to avoid the increase of the size, as shown in Fig. 1(b), the mover is supported using pillars with a spherical ball at their tip. Due to this support device, the inner surface of the mover must be covered with a resin part, and this increases the air gap length. In order to solve the problem, an interior permanent magnet (IPM) type is employed. By embedding the permanent magnets inside of the mover, the resin part is removed and the air gap length is decreased. Due to this structure, a high torque can be realized. In this paper, the torque constant characteristics of the IPM type spherical actuator is investigated and compared with those of SPM type spherical actuator. II. Proposed IPM Structure and Modeling Method of Torque Constant The proposed IPM type rotor is shown in Fig. 1(c). In the IPM model, cuboid-shaped permanent magnets are embedded into the mover, and form V-shape arrangements. Their poles change by every 22.5 degrees in the latitudinal direction, and every 30 degrees in the longitudinal direction. 32 coils are arranged in the stator, and 16-phase currents are applied to rotate the mover. A torque equation is defined as (1), where T is a torque vector, K_m is a magnet torque constant matrix, K_r is a reluctance torque constant matrix, T_{cog} is a cogging torque vector, and i is a current vector. Each torque constant can be calculated from (2), where T(0A) is the cogging torque, and T(1A), and T(-1A) are torques when 1-A, and −1-A currents are applied. The magnetic torque is proportional to the current. However, the reluctance torque is proportional to the square of the currents. III. Comparison of Torque Constant Characteristics The torque constants of SPM and IPM models are compared. The torque constant is evaluated by rotating a simple magnetic pole model shown in Fig. 1(d) around the X axis (latitudinal direction) along the arrangement of the permanent magnets. The pole of the permanent magnets changes every 22.5 degrees, and the simple magnetic pole model is rotated every 2.25 degrees around the X-axis. Considering the symmetry of the structure, the mover is rotated by 90 degrees around the X axis. The computed magnet, cogging, and reluctance torque constants are shown in Fig 2(a). From Fig. 2(a), the effective value of the magnet torque constant is decreased by approximately 7% although the total volume of the permanent magnets is reduced by approximately 35% in compared with the SPM model. This is because the permeance of the magnetic path is increased by using the IPM model, and the working point of the permanent magnets is increased. Next, the effective value of the cogging torque constant of the IPM type is about 72% less than that of the SPM type. This is because the path of magnetic flux has changed. The reluctance torque is not created in the SPM model, and it is created only in the IPM model. Therefore, if the reluctance torque can be effectively utilized, the torque can be increased. However, the ratio of the reluctance torque constant is only about 5% of the magnet torque, and the increase of the reluctance torque is required by changing the structure. Finally, the torque constants are compared. In this paper, they are evaluated by an evaluation function shown in (3), where F is an evaluation value and *rms* indicates an effective value. This evaluation value is higher as the current torque is larger and the cogging torque is smaller. The evaluation results of the SPM and IPM models are shown in Fig. 2(b). As shown in Fig. 2(b), the IPM model has an evaluation value 3 times or more higher than that of the SPM model. V. Conclusion In this paper, an IPM spherical actuator was proposed. Due to the comparison between the SPM and IPM models, it was found that the IPM model has better torque characteristics than the SPM model. In the final paper, the torque characteristics in other positions and the cause of the difference of the torque characteristics will be discussed.

[1] C. Xia, H. Li and T. Shi : "3-D Magnetic Field and Torque Analysis of a Novel Halbach Array Permanent-Magnet Spherical Motor", IEEE Transactions on Magnetics, Vol. 44, No. 8, pp. 2016-2020, 2008 [2] J. Wang, G. W. Jewell and D. Howe : ''A Novel Spherical Actuator: Design and Control'', IEEE Transactions on Magnetics, Vol. 33, No. 5, pp. 4209-4211, 1997 [3] K. Kahlen, I. Voss, C. Priebe and R. W. De Doncker : "Torque Control of a Spherical Machine With Variable Pole Pitch", IEEE Transactions on Power Electronics, Vol. 19, No. 6, pp. 1628-1634, 2004 [4] H. Son and Kok-Meng Lee : "Open-Loop Controller Design and Dynamic Characteristics of a Spherical Wheel Motor", IEEE Transactions on Industrial Electronics, Vol. 57, No. 10, pp. 3475-3482, 2010 [5] B. van Ninhuijs, J. W. Jansen, B. L. J. Gysen, and E. A. Lomonova : "Topology Comparison of Slotless Permanent Magnet Semispherical Actuators", IEEE Transactions on Magnetics, Vol. 50, No. 11, 2014 [6] Y. Sakaidani, K. Hirata, N. Niguchi and S. Maeda : "Experimental verification of feedback control of a 2-DOF spherical actuator", IEEE Transactions on Magnetics, Vol. 50, No. 11, 2014 [7] Y. Nishiura, K. Oya, K. Hirata : "3-DOF Outer Rotor Electromagnetic Spherical Actuator", Proceedings of the 2015 IEEE International Magnetics Conference (Intermag), 15303875, 2015

$$T = K_m i + K_r i^2 + T_{cog} \qquad \cdots (1)$$

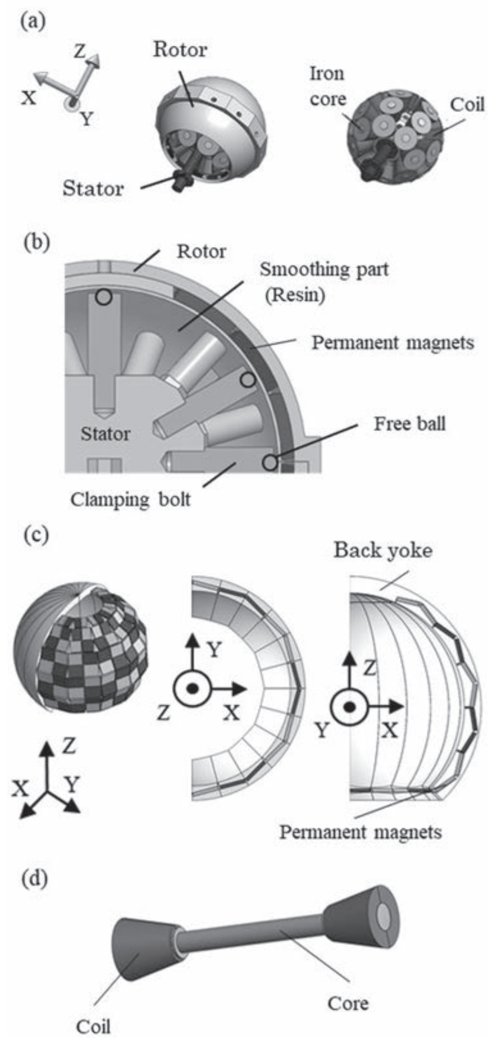

Fig. 1. Structure of (a)outer rotor spherical actuator, (b)support structure, (c)IPM model rotor and (d)simple magnetic pole model.

$$\begin{cases} \boldsymbol{K}_m = \dfrac{\boldsymbol{T}(1\mathrm{A}) - \boldsymbol{T}(-1\mathrm{A})}{2} \\ \boldsymbol{K}_r = \dfrac{\boldsymbol{T}(1\mathrm{A}) + \boldsymbol{T}(-1\mathrm{A}) - 2\boldsymbol{T}(0\mathrm{A})}{2} \\ \boldsymbol{T}_{cog} = \boldsymbol{T}(0\mathrm{A}) \end{cases} \quad \cdots(2)$$

$$F = \frac{\left[\boldsymbol{K}_m + \boldsymbol{K}_r\right]_{rms}}{\left[\boldsymbol{T}_{cog}\right]_{rms}} \quad \cdots(3)$$

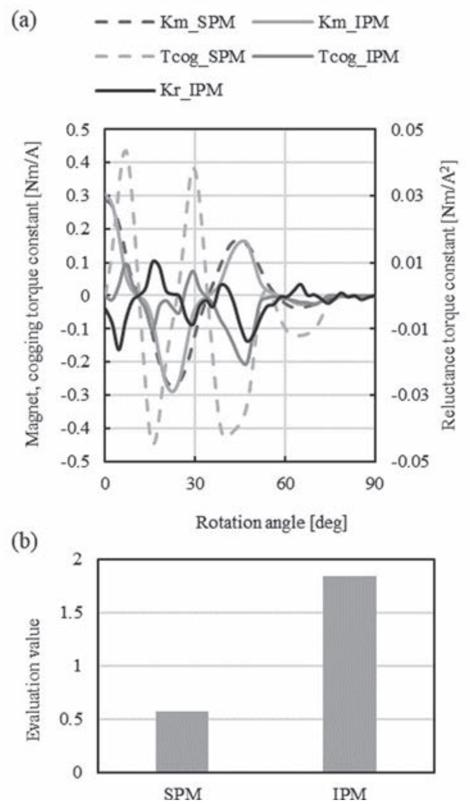

Fig. 2. Result of (a)torque constants and (b)evaluation value.

3:15

BG-05. Force Estimation Method for a Magnetic Lead-Screw-Driven Linear Actuator.

A. Heya[1], Y. Nakata[2], M. Sakai[1], H. Ishiguro[2] and K. Hirata[1]
1. Department of Adaptive Machine Systems, Osaka University, Suita, Japan; 2. Department of Systems Inovation, Osaka University, Toyonaka, Japan

I. Introduction A feed screw (e.g., slide-screw and ball-screw) is a transfer mechanism converting a rotation into a translation or vice versa, and is widely used in industrial fields. Some researchers developed muscle-like compliant actuators with a feed screw for robots [1][2]. The back-drivability of the feed screw is small because of the friction between the screw and the nut. Thus, the flexibility of the actuators is obtained by combining a mechanical spring. The actuators is expected to service robots and power-assist robots to increase the collision safety for human. However, a slide-screw and ball-screw have some problems such as a vibration, noise, and friction. In contrast, a magnetic lead screw (MLS) that can achieve a non-contact power transmission was developed [3][4]. Because of the power transition without contact, the MLS can be driven with a high efficiency, can achieve a maintenance-free operation, and has a force limiter function when overloaded. In addition, the MLS has a flexibility against external forces because it has the elastic characteristics due to a magnetic spring. Therefore, the MLS can be used as a flexible element of the actuator without using mechanical springs. Since conventional MLSs are composed of a spiral shape permanent magnet magnetized in the radius direction, they have problems of downsizing and low productivity. In order to solve these problems, we proposed a novel MLS that is composed of several pieces of arc-shaped permanent magnets and a linear actuator with the MLS. For realizing force control using the linear actuator, the force sensor is necessary. However, the size and weight of the actuator are increased by implementing the sensor system. In order to solve this problem, torque sensor-less control methods for electric motor have been proposed [5][6]. We have been studying about a force sensor-less control for the MLS driven linear actuator (MLSDLA). The force of the MLS is calculated by the magnetic phase difference between the nut part and screw part. Therefore, the output force of the MLSDLA is estimated by the phase difference of rotation and translation. In this paper, we propose a force estimation method using a magnetic phase difference for a force sensor-less control of the MLSDLA. The estimated force and measured force are compared, and the effectiveness of the proposed method is verified. II. Magnetic lead-screw-driven linear actuator (MLSDLA) The prototype of the MLSDLA is shown in Fig. 1 (a). The operating principle of the actuator is shown in Fig. 2 (b). The MLS consists a nut part and screw part. The permanent magnets are arranged only in the nut part. The actuator is driven by the translation of a screw thread caused by the rotation of the screw part using a rotary motor. A restoring force due to a magnetic attraction force is generated when a relative displacement between the nut and screw parts is created due to an external force. The nut part returns to an equilibrium position due to the restoring force. This restoring force works as an output force of the actuator. Since the MLS is composed of arc-shape permanent magnets, the MLS has the advantages of improving a productivity and is expected to be smaller than conventional MLSs. III. Force estimation method for MLSDLA In this section, a force estimation method using a magnetic phase difference is described. The magnetic phase difference is given as follows: $\phi = \theta-(2\pi/L)p$ where θ is the rotation angle of the screw part, p is the displacement of the nut part, and L is the lead of the screw. The estimated force expressed by a polynomial approximation using the least square method is given as follows: $F = 0.380\phi^5 + 0.172\phi^4 - 8.96\phi^3 - 2.55\phi^2 + 52.3\phi + 6.48$ IV. Comparison of the experimental and estimated results The comparison of the estimated and measured force by a force sensor is shown in Fig. 2. From these results, it is found that both show a good agreement with each other. The absolute average error of the estimated and measured force is 3.8 N. V. Conclusion In this paper, a force estimation method for the MLSDLA was proposed without a force sensor. The structure and operating principle of the MLSDLA were described. A force estimation method using a magnetic phase difference was described. In addition, the estimated and measured forces were compared, and it was found that both show a good agreement with each other. Our future goal is to develop a method for improving the estimation accuracy.

[1] J. E. Pratt and B. T. Krupp, “Design of a bipedal walking robot,” *Proceedings of SPIE*, vol. 6962, 2008. [2] C. Knabe, B. Lee, and D. Hong, “An inverted straight line mechanism for augmenting joint range of motion in a humanoid robot,” in *ASME International Design Engineering Technical Conferences*, 2014. [3] J. Wang, K. Atallah, and W. Wang, “Analysis of a Magnetic Screw for High Force Density Linear Electromagnetic Actuators”, IEEE Transactions on Magnetics, vol. 47, no. 10, pp. 4477-4480, Oct. 2011. [4] C. Knabe, B. Lee, and D. Hong, “An inverted straight line mechanism for augmenting joint range of motion in a humanoid robot,” in *ASME International Design Engineering Technical Conferences*, 2014. [5] A. Kato and K. Ohnishi, “Robust force sensorless control in motion control system”, *IEEE International Workshop on Advanced Motion Control*, pp. 165-170, 2006. [6] Y. Ohba, S. Katsuya, K. Ohishi, “Sensor-less force control for machine tool using reaction torque observer”, *Proceeding of the IEEE International Conference on Industrial Technology*, pp. 860-865, 2006.

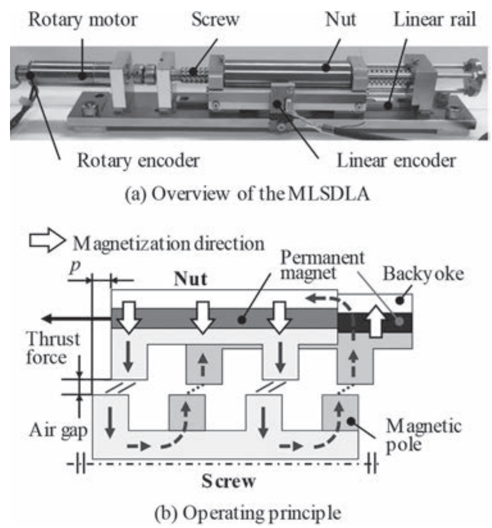

Fig. 1. Magnetic lead-screw-driven linear actuator.

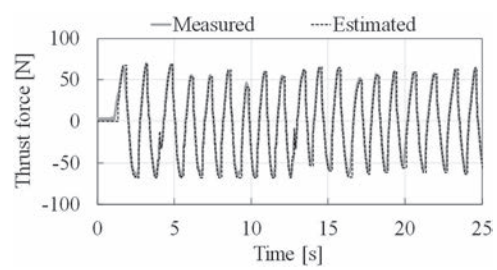

Fig. 2. Comparison of the experimental and estimated results.

3:30

BG-06. Performance Investigation of a five-phase Multi-segment primary PMLSM for Ropeless Elevator.

Q. Jiang[1] and Q. Lu[1]
1. Zhejiang University, Hangzhou, China

I. INTRODUCTION With the increasing advance of construction engineering, there are higher and higher buildings across the city at present, so the high performance elevator becomes very important. Normally they are mostly driven by a rotate motor with cable. However, if the buildings exceeding to 300m, the cable consumes a lot of power and causes some fluctuations in the process of moving. In order to overcome this problem, the elevator driven by multi-segment primary permanent magnet linear synchronous motor (MP-PMLSM) is adopted, which also has many other many obvious advantages, such as high efficiency, simple structure, save space occupancy, etc. Its key technologies are high thrust density PMLSMs and control system. Several PMLSMs have been proposed [1], [2], [3], mostly focusing on the motor structure and the switching control of primary section. The segment winding power feeding method is studied [4], [5]. which adopting sectional winding permanent magnet linear synchronous motor. The primary is divided into sections, but the iron corn is continuous, so they are not segment primary PMLSM in some ways. This paper proposed a 2t vertical hoist system driven by novel five-phase PMLSM with segment winding power supply. Compared to three-phase PMLSM, the five-phase PMLSM can reduce the thrust force ripple and noise during operation. Moreover, it has higher fault tolerance and thrust force when supplied with same voltage or current resource. Therefore, the five-phase PMLSM is the better candidate. In order to facilitate the installation, the primary and iron core are divided into sections. II. MODEL Fig.1 (a) shows the segment-primary ropeless elevator, comprised of several five-phase PMLSMs. The length of primary section should equal to the even multiple of pole pitch, the length of secondary should be the integral multiple of the length between adjacent primary sections. It is important to setting these parameters a proper value, then the initial phase angle of excitation source not need to be changed, which is convenient for control strategy to obtain steady thrust force. Fig.1 (b) shows the simplify structure of PMLSM, which is a 60-slots/12-poles five-phase structure and adopts surface-mounted PMs and full-pitch armature windings. It should be noted that full-pitch winding can achieve much high power density. Fig.1 (c) exhibits the winding power feeding method, which simplifies each primary as twelve sets five-phase windings. To ordinary method shown in Fig.1 (a), when the secondary entering into primary II, both primary I and II are energized at same time, and the primary I is kept energized untill secondary leaving primary I. Apparently, the uncoupled energized armature windings waste a lot of power. Adopting proposed winding power feeding method can overcome this shortcoming, which feeds the coupled windings and powered off the passing windings by switch according to the secondary position signal. III. ANALYSIS Fig.2 (a), (b) exhibit the magnetic flux distribution of the two power feeding methods, respectively. As known, the thrust force mainly produces by the coupled magnetic field, so the effective winding is only under the secondary. That is to say, many uncoupled windings are useless. However, the segment winding power feeding method gets higher efficiency due to lower the number of uncoupled winding. Based on power feeding supply, the thrust force and currents have been calculated by FEM under five phase sinusoidal voltage source. Fig.2 (c) shows the instantaneous thrust force for the vertical hoist by two methods. It can be seen that the average thrust forces are 22.96kN, 22.56kN and thrust ripples are 22.07%, 19.39% respectively. These two methods almost have same average thrust force, but the proposed method has lower thrust ripple. Since the input voltage values are 100V, 10V respectively, the proposed method can reduce the bus voltage to achieve higher thrust force. Fig.2 (d) shows the FFT analysis of thrust force within a polar intervals. Obviously, the amplitude of proposed method is slightly larger than that of ordinary one, and higher harmonic in two methods both have produced less thrust fluctuation. Fig.2 (e) show the equivalent q-axis current. Apparently, the instantaneous current produced by ordinary method is 1.5 time that of proposed method, which may damage the performance of inverter. However, the proposed method not have big instantaneous current.

IV. CONCLUSION This paper proposes a ropeless elevator driven by a novel five-phase PMLSM. To this vertical hoist system, a novel segment winding power feeding method is proposed. With this method, although the cost is a little expensive, the length of energized windings is effectively shorten, which not only can save approximately half of power consumption and lower bus voltage, but also improves the system efficiency.

[1] Qinfen Lu, Yihua Yao, Yunyue Ye, "Research on Ropeless Elevator driven by PMLSM," in 2016 Eleventh International Conference on Ecological Vehicles and Renewable Energies (EVER) [2] Shangguan X uan feng1, Li Qingfu1, Yuan Shiying2, Jiao Liucheng, "Analysis on Running Process of Permanent Linear Synchronous Motors with Discontinuous Stators," in JOURNAL OF XI′AN JIAOTONG UNIVERSIT Y, Vol.38,No.12,Dec.2004 [3] Shangguan X uan feng1, Li Qingfu1, Y uan Shiying, "The Vertical Hoist System Driven by PMLSM With Muliti-segment Primary,"in Proceedings of the CSEE,Vol.27,No.18,June.2007 [4] Hongwei Zhang, Xinhuan Wang, Fashan Yu and Qian Liu, "Characteristics of Segment Winding Permanent Magnet Linear Synchronous Motor Switching Failure," in Proceedings of 2014 IEEE International Conference on Mechatronics and Automation August 3 - 6, Tianjin, China [5] Junjie Hong, Liyi Li, *Member*, *IEEE*, Donghua Pan2 and Zijian Zong, "Comparison of two current predictive control methods for a segment winding permanent magnet linear synchronous motor,"

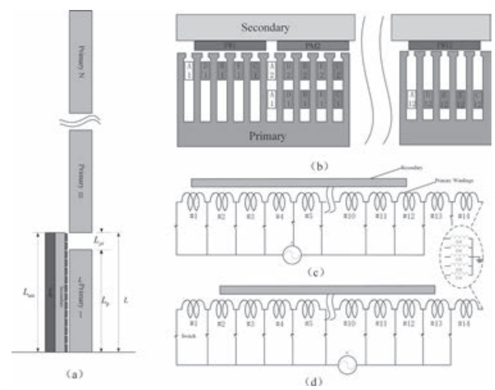

Fig. 1. (a) Vertical hoist system. (b) Simplified structure of five-phase PMLSM. (c) Starting position. (d) Entering into next winding

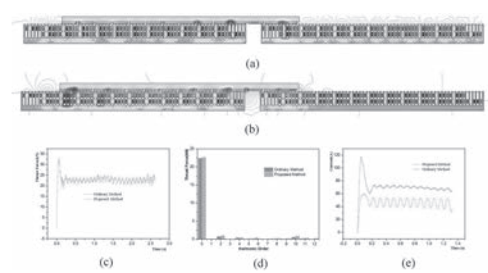

Fig. 2. (a) Flux distribution of ordinary method. (b) Flux distribution of proposed method. (c) Thrust force. (d) Thrust force spectra. (e) Equivalent *q*-axis current of inverter

3:45

BG-07. A Novel Linear Stator PM Vernier Machine with Spoke-Type Magnets.

A. Nematsaberi[1] and J. Faiz[1]
1. Electrical and Computer Engineering, University of Tehran, Tehran, The Islamic Republic of Iran

Introduction: The linear magnetic geared vernier machines offer high efficiency and good performance for low-speed applications such as direct-drive wave energy conversion due to the capability of low-speed high-force operation [1]. Linear permanent magnet (PM) vernier machines can be designed in both forms of translator PM and stator PM. In the second form, both the armature winding and PMs are located in the stator and the translator is only made of iron. Hence, the problems of mechanical integrity and thermal instability of the PMs have been surmounted in linear stator PM vernier (LSPMV) machines. It must be noted that all LSPMV machines which have been presented so far in the literature employ conventional surface-mounted PMs with radial or quasi-halbach magnetization and none of them have utilized spoke-type PMs [2]–[4]. Nevertheless, the spoke-type PMs have been recently proposed for the dual stator translator PM vernier (DSTPMV) machines [5], [6]. The reason is the flux-focusing effect of the spoke-type magnets leading to improved air-gap flux density and therefore higher thrust force. In this paper, a novel linear vernier machine is presented in which spoke-type PMs and armature winding are located in a single stator and only one air-gap exists in its topology. In addition, in order to reduce the leakage flux and increase the flux linkage of the armature windings, a non-magnetic space between pole shoes and PMs is introduced in the topology of the proposed machine. Machine configuration: Fig. 1a. illustrates the topology of the proposed machine. It can be observed that the conventional radial surface-mounted magnets are replaced by spoke-type magnets. Unlike the DSTPMV machines presented in [5], [6] in which the PMs are located in translator, the translator of the proposed machine contains only solid iron which offers a simpler and more robust structure. Also, it can be seen from Fig. 1a that there is a space between the stator pole shoe and the magnets specified by green color. Since this space is located between two stationary parts, there is no need to use bearings, and it can be filled with non-magnetic materials. In order to clarify the reason for the presence of this non-magnetic space in the proposed machine, using finite element analysis (FEA), the magnetic field distribution caused by PMs in no-load condition, when the thickness of non-magnetic space is 0 mm and 1 mm, are shown in Figs. 1b and 1c, respectively. In the absence of the non-magnetic space illustrated in Fig. 1b, the flux produced by the PMs, Φ_{PM1} is twice as high as the case illustrated in Fig. 1c, Φ_{PM2}, ($\Phi_{PM1}=2\Phi_{PM2}$). However, only 16.22% of Φ_{PM1} crosses the armature winding while for Φ_{PM2}, this value is equal to 63%. The reason for this phenomenon is a significant reduction in the leakage flux caused by embedding the non-magnetic space. Hence, it can be concluded that in Fig. 1b, the amount of $0.1622\Phi_{PM1}$ reaches the armature winding and stator yoke, whereas in Fig. 1c, this value is equal to $0.63\Phi_{PM1}0.5=0.315\ \Phi_{PM1}$. Machine performance and comparison: Fig. 1d depicts the variations of no-load back-EMF of the proposed machine with the PM volume. It is clear that as the PM volume increases, the back-EMF increases correspondingly. Considering a compromise between back-EMF and cost, the PM volume is determined to be 150cm^3. The proposed machine and the existing LSPMV machine [2] are designed and quantitatively compared in terms of their electromagnetic performance. Table I lists the fixed and designed parameters of both machines. Fig. 1e depicts the waveforms of the three-phase no-load flux linkages for both machines. The amplitudes of flux linkage of phase A for the existing and proposed machines are 0.2 T and 0.283 T, respectively. Thus, by using spoke-type PMs and the non-magnetic space the flux linkage is increased by 41.5%. Fig. 1f illustrates the thrust force waveforms of both machines. The average thrust force in the proposed and existing machines are 2.2 kN and 1.73 kN, respectively. Hence, as listed in Table I, although the number of armature winding turns per phase is higher in the existing machine, the proposed machine offers 27.16% higher thrust force which is due to the more utilization of the PMs in the proposed topology. Moreover, the thrust force ripples for existing and proposed machines are 4.06% and 4.33%, respectively, which are very acceptable. The effect of increasing the total PM volume on the average thrust force for both machines is investigated in Fig. 1g. It can be seen that unlike the proposed machine in which the average thrust force is directly proportional to the PM volume, the thrust force of the existing machine decreases as the PM volume increases. The optimal value of PM volume for the existing machine is 90 cm^3. However, it must be noted that at this point, the iron core of the existing machine is highly saturated. Furthermore, by decreasing the PM volume, the PM blocks will be subject to irreversible demagnetization. Therefore, the proposed machine exhibit a more promising electromagnetic performance than the existing one over different values of PM volume.

[1] J. Faiz and A. Nematsaberi, "Linear electrical generator topologies for direct-drive marine wave energy conversion- an overview," *IET Renew. Power Gener.*, vol. 11, no. 9, pp. 1163–1176, Jul. 2017. [2] Y. Du, K. T. Chau, M. Cheng, Y. Fan, Y. Wang, W. Hua, and Z. Wang, "Design and Analysis of Linear Stator Permanent Magnet Vernier Machines," *IEEE Trans. Magn.*, vol. 47, no. 10, pp. 4219–4222, Oct. 2011. [3] Y. Du, M. Cheng, K. T. Chau, X. Liu, F. Xiao, W. Zhao, K. Shi, and L. Mo, "Comparison of Linear Primary Permanent Magnet Vernier Machine and Linear Vernier Hybrid Machine," *IEEE Trans. Magn.*, vol. 50, no. 11, pp. 1–4, Nov. 2014. [4] Jinghua Ji, Wenxiang Zhao, Zhuoya Fang, Jianxing Zhao, and Jihong Zhu, "A Novel Linear Permanent-Magnet Vernier Machine With Improved Force Performance," *IEEE Trans. Magn.*, vol. 51, no. 8, pp. 1–10, Aug. 2015. [5] S. Khaliq, F. Zhao, and B. Kwon, "Design and analysis of a dual stator spoke type linear vernier machine for wave energy extraction," in *2015 IEEE Magnetics Conference (INTERMAG)*, 2015, vol. 11, pp. 1–1. [6] N. Baloch, S. Khaliq, and B.-I. Kwon, "A High Force Density HTS Tubular Vernier Machine," *IEEE Trans. Magn.*, vol. 53, no. 11, pp. 1–5, Nov. 2017.

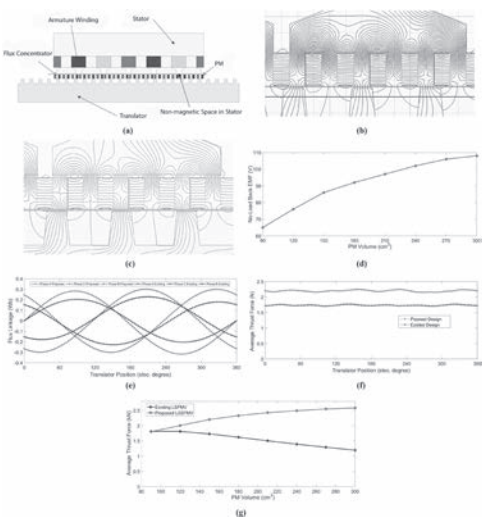

Fig. 1. (a) Machine configuration (b) Magnetic field distribution without non-magnetic space (c) Magnetic field distribution with 1mm non-magnetic space (d) Variation of back-EMF with PM volume (e) Flux linkages (f) Thrust Force (g) Variation of thrust force with PM volume

Fixed Parameters	Unit	Proposed	Existing
Stator armature teeth number		6	6
Translator tooth number		17	17
Flux modulation teeth number		18	18
Stack length	mm	100	100
Machine active width	mm	360	360
Air-gap length	mm	1	1
Slot current density	A/mm^2	4.3	4.3
Slot height	mm	27	27
PM volume	cm^3	150	150
Flux concentrator's width	mm	5	-
Translator tooth pitch	mm	21.17	21.17
Translator tooth height	mm	11	11
Design Parameters	**Unit**	**Proposed**	**Existing**
Armature winding slot width	mm	25	20
Thickness of non-magnetic space	mm	1.55	-
Number of winding turns per phase	mm	140	160
Stator yoke thickness	mm	64	58
Translator yoke thickness	mm	57	50
Performance Comparison	**Unit**	**Proposed**	**Existing**
Average thrust force	kN	2.2	1.73
Thrust force ripple	%	4.33	4.06
Back-EMF amplitude	V	86	61
Peak to peak value of cogging force	N	35.1	34
Iron loss	W	60	45.36
Copper loss	W	235.2	268
Shear stress	kN/mm^2	61.11	48.05
Force density	kN/mm^3	330.33	289.491
Output power	kW	2.2	1.73
Efficiency	%	86.58	81.88

Table I
Design parameters and Comparison of proposed and existing machines

4:00

BG-08. Development of a new rotary flux switching transverse flux machine with the ability of linear motion.

C. Liu[1,3], Y. Wang[1], J. Zhu[2], Y. Guo[2], G. Lei[2] and S. Wang[1]
1. Hebei University of Technology, Tianjin, China; 2. University of Technology Sydney, Sydney, NSW, Australia; 3. PMG Fussen GmbH, Fussen, Germany

I Introduction Soft magnetic composite (SMC) material is a new soft magnetic material, it is produced by using the powder metallurgy technology, and it has the advantages of the low eddy current loss and magnetic isotropy characteristic. With the SMC materials, various kinds of the electrical machines with 3D magnetic flux can be designed and prototyped [1-3]. Moreover, compared with the traditional electrical machines, the newly developed electrical machines with SMC cores can have higher efficiency and power density. Among them, the claw pole machine is a typical example, as the global winding and the 3D magnetic flux path are adopted. Nowadays, some special application are emerging, e.g. the robot arms with the capture ability, for this kind of application, the utilization of the rotary electrical machines with the ability of linear motion can save the required numbers of the electrical machines and reduce the complexity of the overall system, moreover the dynamic response characteristic can be improved. Thus, in this paper, a new rotary flux switching transverse flux machine (FSTFM) with the ability of linear motion is proposed. By using the finite element method, the basic electromagnetic properties of the proposed FSTFM are obtained; it can be found that the this machine can own the merits of the higher power density, low cost and good mechanical robust ability. II Topology and electromagnetic performance analysis The main topology of the proposed FSTFM is shown in Fig. 1(a) and Fig. 1(b), it can be found the complete machine includes the three single phase stator modules, and a long rotor module, each stator module shifts with the 120 degree electrically with the adjacent stator module. As shown in Fig. 1(b), the stator core is completed as the permanent magnets installed between the stator cores, and the adjacent PMs are magnetized along the opposite direction, and the winding of this machine is the global cylinder winding. By designed in this way, this machine can operate with the ability of not only the rotation motion but also the linear motion. Due to the very high flux concentration ability of the designed machine, the ferrite magnets are utilized to produce the PM flux, and the maximum flux density on the rotor teeth tips can reach to 2.0 T, as shown in Fig. 1(c) and Fig. 1(d). Fig. 2 shows the PM flux per turn of the designed FSTFM, it can be seen that the PM flux linkage of the FSTFM is in three phase distribution and each phase has the 120 degree in electrical with each other if the machine operated in the rotation way, however, if the machine operated in the linear motion way, the PM flux linkage of this machine is not distributed in the symmetrical three phase way. Moreover, accompanied with the linear motion, the PM flux magnitude of machine will be changed, and accompanied with the rotation motion; the PM flux magnitude of the machine will be changed as well, it is because of the FSTFM has the very strong magnetic coupled characteristic. III Conclusion With the designed structures of the FSTFM, this machine can have the ability in both rotation motion and the linear motion; it can be used in the special applications where both the rotary motion and linear motion are required. The designed structures of the FSTFM can be prototyped quite easy with the adoption of the SMC materials. However, the designed FSTFM has the strong magnetic coupled characteristic, and the electromagnetic force ripple of this machine in the linear motion is quite high, thus the rotor module of this machine is required to be optimized to make the machine have a overall good performance.

[1] C.C. Liu, J.G. Zhu, Y.H. Wang and et al. "Comparative Study of Small Electrical Machines With Soft Magnetic Composite Cores", IEEE transactions on industrial electronics, Volume: 64, Issue: 2, Feb. 2017 [2] Alan G. Jack, Barrie C. Mecrow, Phillip G. Dickinson, Dawn Stephenson, James S. Burdess, Neville Fawcett, and J. T. Evans, "Permanent-Magnet Machines with Powdered Iron Cores and Prepressed Windings", IEEE transactions on INDUSTRY APPLICATIONS, Volume: 36, no: 4, pp. 1077–1084,July. 2000 [3] Y. G. Guo, J. G. Zhu, and D. Dorrell, "Design and analysis of a claw pole PM motor with molded SMC core," IEEE Trans. Magn., vol. 45, no. 10, pp. 582–4585, Oct. 2009.

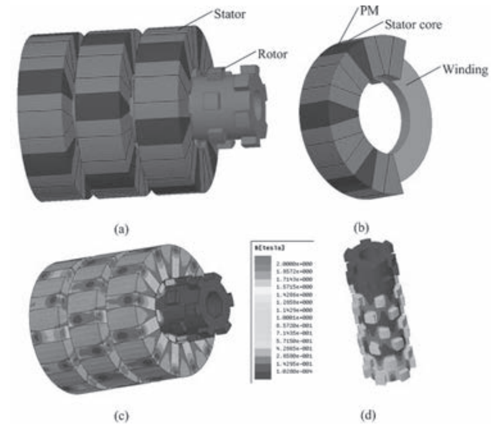

Fig. 1. Topology and no load magnetic flux density distribution of the machine, (a) complete three phase structure, (b) single phase structure, (c) and (d) no load magnetic flux density distribution

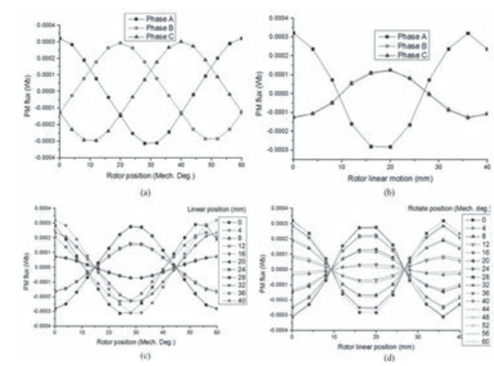

Fig. 2. PM flux per turn of the machine (a) three phase with the variation of the rotation motion, (b) three phase with the linear motion, (c) PM flux rotation motion with the variation of the different linear position, and (d) PM flux linear motion with the variation of the different rotation position

4:15

BG-09. Quantitative Comparison of Novel Dual-PM Linear Motors for Ropeless Elevator System.

H. Fan[1], *K. Chau*[1], C. Liu[2] and T. Ching[3]
1. Electrical and Electronic engineering, The University of Hong Kong, Hong Kong Island, Hong Kong; 2. School of Energy and Environment, City University of Hong Kong, Hong Kong, Hong Kong; 3. Faculty of Science and Technology, University of Macau, Macao, Macao

I. INTRODUCTION Due to high land prices in the metropolitans, such as Hong Kong, Tokyo and New York, high-rise buildings are mushrooming one after another. The conventional vertical elevators in multi-level or low-rise building, which usually adopt rotational electric motors plus hoist cables with counterweights, are no longer applicable. The cable for hoisting elevators have the strength and stability problems as it gets longer and longer [1, 2]. For solving these problems, a ropeless elevator system with self-propelled cars is proposed and testified. This system adopts the linear motor to drive the elevator car and omits the counterweight and cable [3, 4]. Thus, the efficiency and operation performances are dramatically improved. Moreover, areas of the elevator hoistway can be reduced [5]. According to the requirements, linear motors for ropeless elevators need to satisfy the following features: high power density, high force density, high reliability, high ratio of payload to self-weight and low force ripple. To achieve the above features, dual permanent magnet (PM) linear motors with fault-tolerant teeth (FTT) are good candidates. When the elevator car size is fixed, one way to further increase the force density with the same current density is to adopt the dual-PM structure [6]. Thus, in this paper, four dual-PM linear motors are proposed and compared for the application of ropeless elevator system. II. MACHINE TOPOLOGIES AND ANALYSIS The proposed linear machines have PMs on both the mover and stator, which can be termed as dual-PM structure. In this way, the internal space of the machine is fully utilized, leading to much higher force density and efficiency compared with the mover-PM or stator-PM motors. For ropeless elevator system, the proposed dual-PM linear motors are very suitable, owing to the high ratio of PM volume to the machine dimensions. In order to compare the machine performances, all four machine dimensions are designed to be the same, except for the installation position of mover PMs, as shown in Fig. 1. In general, the proposed dual-PM linear motors are designed with 24 slots and 22 poles. The double-stator or double-mover structure is adopted to reduce detent force, resulting in the reduction of propulsion force pulsation. Specifically, the double-stator slot-PM (DSSPM) linear machine is shown in Fig. 1(a), the double-mover slot-PM (DMSPM) linear machine is shown in Fig. 1(b), the double-stator tooth-PM (DSTPM) linear machine is shown in Fig. 1(c), and the double-mover tooth-PM (DMTPM) linear machine is shown in Fig. 1(d). In the stator, the iron cores are fixed to the hoist way, and the PMs are employed in the stator slot with upward magnetization direction. For the mover side, the fault-tolerant tooth (FTT) structure is used to improve the machine reliability. As can be seen, in the DSSPM and DMSPM linear machine, the PMs are placed on the mover slot openings with only the downward magnetization direction. For the DSTPM and DMTPM linear machine, the PMs are mounted on the mover teeth surface alternately, with only the downward magnetization direction. In order to apply the proposed machines for ropeless elevator system, there are practical space constraints. Thus, the mover length is chosen as 300 mm, the airgap is set as 1.5 mm and the mover velocity is 1 m/s. At first, the machine parameters are designed, such as the pole pitch, tooth length and semi-open slot size. Then four machines are optimized to achieve the best force performances. Furthermore, the mutual inductance characteristics are obtained to verify the fault-tolerant capability of the proposed machines. At last, the proposed four linear machines are compared. Fig. 2(a) shows the no-load EMF waveform of the proposed four dual-PM linear machines. The generated voltages of the DSSPM, DMSPM, DSTPM and DMTPM linear machines are 91.4 V, 92.7 V, 97.3 V and 97.8 V, respectively. As can be seen, the generated EMF of the tooth-PM machines are more symmetrical and sinusoidal than the slot-PM machines. Fig. 2(b) shows the thrust force waveform of the above four machine configurations. The generated average thrust forces of the DSSPM, DMSPM, DSTPM and DMTPM linear machines are 868.4 N, 1045.7 N, 1055.0 N and 1061.8 N, respectively. Since the PM volume in each machine configuration is the same, the average thrust force of the DSSPM machine is much lower than other three machines. In addition to the thrust force and force density, the force ripple is another important factor for the performance of the elevators. Furthermore, the force ripples of the above machines are 28.6%, 20.5%, 10.1% and 8.8 %, respectively. It shows that the force ripples of the tooth-PM machines are smaller than those of the slot-PM machines. More results such as force density and efficiency as well as experimental verification will be given in full paper. III. CONCLUSION A new class of linear machines, namely the dual-PM machine, has been proposed and analyzed, which is particularly designed for ropeless elevator system. By comparing four machine configurations, the double-mover tooth-PM (DSTPM) linear machine not only fully retains the advantages, but also achieves much higher force density, efficiency and lower force ripple. This work was supported by a grant (Project No. 17204317) from the Hong Kong Research Grants Council, HKSAR, China.

[1] T. Ishii, "Elevators for skyscrapers," *IEEE Spectrum,* vol. 31, pp. 42-46, Sep. 1994. [2] K.T. Chau, *Electric Vehicle Machines and Drives – Design, Analysis and Application*. Wiley-IEEE Press, 2015. [3] H. Lim and R. Krishnan, "Ropeless elevator with linear switched reluctance motor drive actuation systems", *IEEE Trans. Ind. Electron.*, *vol*. 54, no. 4, pp. 2209-2218, Aug. 2007. [4] S. G. Lee, S. A. Kim, S. Saha, Y. W. Zhu and Y. H. Cho, "Optimal Structure Design for Minimizing Detent Force of PMLSM for a Ropeless Elevator," *IEEE Transactions on Magnetics*, vol. 50, no. 1, pp. 1-4, Jan. 2014. [5] A. Onat, E. Kazan, N. Takahashi, D. Miyagi, Y. Komatsu and S. Markon, "Design and implementation of a linear motor for multicar elevators," *IEEE-ASME Transactions on Mechatronics,* vol. 15, pp. 685-693, Oct. 2010. [6] H. Fan, K. T. Chau, C. Liu and W. Li, "Doubly Salient Dual-PM Linear Machines for Regenerative Shock Absorbers," *IEEE Transactions on Magnetics*, vol. 53, no. 11, pp. 1-5, Nov. 2017.

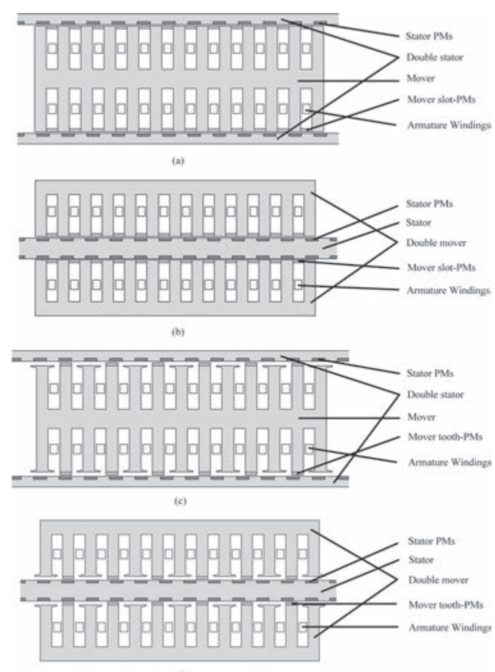

Fig. 1. Proposed dual-PM linear machines. (a) DSSPM machine. (b) DMSPM machine. (c) DSTPM machine. (d) DMTPM machine.

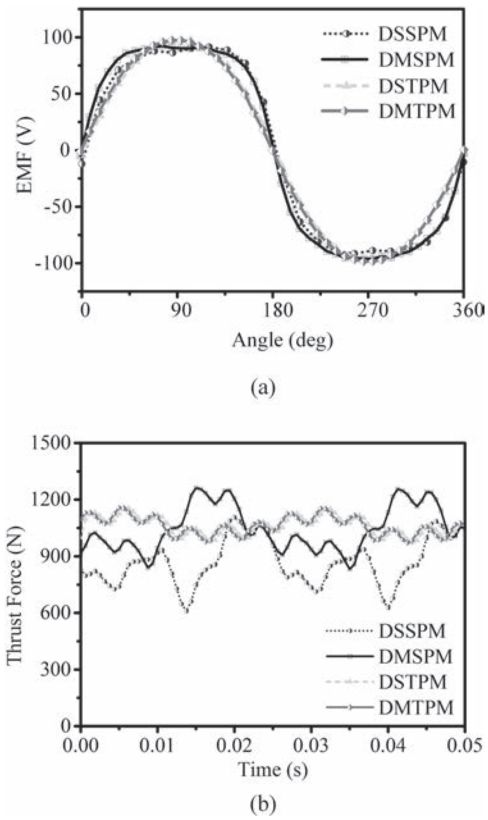

Fig. 2. Machine performance comparison. (a) EMF waveforms. (b) Thrust force waveforms.

4:30

BG-10. Design, control, and comparison of low-energy solenoid valve actuators.

J. van Dam[1], B. Gysen[1], M. Dhaens[2] and E. Lomonova[1]
1. Electrical Engineering, Eindhoven University of Technology, Eindhoven, Netherlands; 2. Advanced Chassis Research, Tenneco Automotive bvba, Sint-Truiden, Belgium

Introduction An automotive, fluid-control solenoid valve is composed of an electromagnetic reluctance actuator and a near-constant-force spring. Reluctance actuators are applied as electromagnetic brakes in aerospace applications [1], as valves that perform fast sorting tasks by means of short air-pulses in the manufacturing industry [2], as accurate fluid-control valves in petrochemical processes [3], and in the automotive industry to achieve variable valve timing in camless engines [4]. Common desires are a fast switching and low noise upon impact. Preferably, these objectives are met with minimized energy consumption, especially during constant position operation. In addition, minimizing the impact velocity improves valve lifetime and reduces the audible noise, vibration, and harshness (NVH). This paper considers cylindrical reluctance actuators due to their low cost. However, this complicates the use of laminations to minimize eddy current effects in a cost-effective manner. Proper analysis, design, and optimization of the reluctance actuator can, therefore, only be performed if these dynamic effects in the actuator are accounted for. This paper will focus on incorporating the eddy current effect in the models and their effect on performance, as well as control methods to improve the performance and minimize energy consumption. The performance of a classical reluctance actuator (Fig. 1a) is compared to a PM-biased topology (Fig. 1b) which reduces the energy consumption. Modeling is performed using transient, axisymmetric, nonlinear finite element (FE) simulations, coupled to Matlab-Simulink. Actuator topology and constraints Two single-coil reluctance actuators are shown in Fig. 1. One is a classical reluctance actuator with a stationary coil and a moving plunger (CLA). A second actuator includes a permanent magnet atop the core (PMB) to allow zero-power latching by means of a passive attraction force [1],[3],[5]. In addition, the actuator height and diameter are 16 and 13 mm, with a stroke of 0.25 mm. Moreover, the plunger of mass 1.2 g experiences an opposing force of 4 to 12N. Finally, the closed-to-open transition can last maximally 4 ms, with a typical valve-open time of several seconds. Open-loop simulation results In an open-loop co-simulation between Simulink and FE software, predefined voltage profiles are applied to the actuators, while the current is limited. In Fig. 2a, the electromagnetic force develops 0.075 ms slower in cases with eddy currents, and the final position is reached 0.115 ms later. This indicates the inherent eddy current damping in the device, slowing down the plunger. In addition, once the movement commences and the airgap closes, the developed electromagnetic force increases rapidly while the opposing force decreases, resulting in a quickly moving plunger. As a result of applying the voltage profiles in Fig. 2b, the corresponding coil currents develop. Note that equal voltages are applied to CLA and PMB until 1.15 ms, after which CLA requires a small hold voltage (1V) to hold the valve open (latch), whereas PMB achieves this passively. Therefore, the hold power can be reduced to zero using PMB. Fig. 2c shows the (in)ability of the actuators to passively latch the valve. The plunger in CLA retracts quickly after (<0.2ms) the supply voltage is removed, as the developed electromagnetic force drops below the opposing force. On the other hand, PMB latches indefinitely, under equal operating conditions, because of the passive attraction force provided by the PM. In general, the predefined voltage profiles produce unnecessarily high forces, indicating that additional control can greatly improve the energy efficiency. Moreover, a significant energy consumption reduction can be achieved by latching passively, and, therefore, reducing to zero the coil current and the hold power using PMB. In addition, plunger closed-to-open movement takes under 0.3ms without achieving a soft landing, while 4ms is allowed. Together, these considerations require to investigate closed-loop feedback control. Conclusions and future work Analyses on two reluctance actuators have shown that open-loop control using predefined voltage profiles results in high energy consumption and no soft-landing. Furthermore, the eddy current effects further deteriorate the timing performance and increase the losses. To achieve soft-landing and further minimization of energy consumption during movement and holding, the final paper will consider cascaded closed-loop control. Inner and outer feedback loops are considered to control the current and position, respectively. Simulations are performed using a closed-loop co-simulation using Simulink and transient FE software incorporating eddy current effects. These simulations will be performed on both actuator types and analysis will target possible reduction of energy consumption and the ability to achieve soft-landing. Acknowledgments The 3Ccar project has received funding from ECSEL JU under grant agreement No. 662192.

[1] B. V. Ravi Kumar, K. Sivakumar, Y. Srinivas Rao, and S. Karunanidhi (2017), "Design of a new electromagnetic brake for actuator locking mechanism in aerospace vehicle," in *IEEE Transactions on Magnetics*, vol. 53, no. 11, pp. 1–6. [2] T. Glück, W. Kemmetmüller, and A. Kugi (2011), "Trajectory optimization for soft landing of fast-switching electromagnetic valves," in *Proceedings of the 18th IFAC World Congress*, vol. 18, pp. 11532–11537. [3] F. Mach and T. Kaminský (2016), "Novel monostable fail-safe electromagnetic actuator for straight valve in high-speed operation," in *2016 ELEKTRO*, Strbske Pleso, pp. 186–191. [4] W. Hoffmann, K. Peterson, and A. G. Stefanopoulou (2003), "Iterative learning control for soft landing of electromechanical valve actuator in camless engines," in *IEEE Transactions on Control Systems Technology*, vol. 11, no. 2, pp. 174–184. [5] B. Gysen, S. Gibson, R. Clark, and G. Jewell (2008), "High temperature permanent magnet actuator for fail-safe applications," in *IEEJ Transactions on Industry Applications*, vol. 128, pp. 1198–1202.

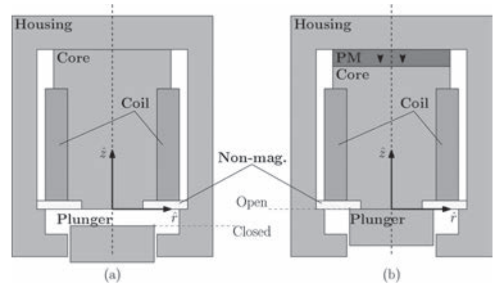

Fig. 1. (a) Classical reluctance actuator (CLA), and (b) permanent magnet-biased reluctance actuator (PMB).

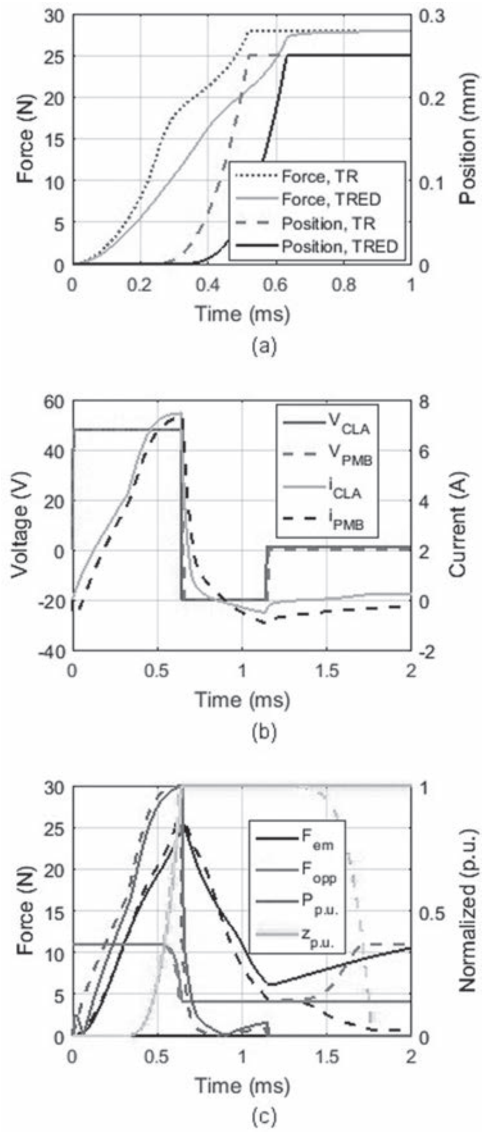

Fig. 2. Open-loop transient simulation results for predefined voltage profiles and equal maximal current to achieve closed-to-open plunger movement, with (a) force levels and plunger positions without (TR) and with (TRED) eddy currents for CLA, (b) predefined voltages and resulting current levels in TRED, and (c) electromagnetic and opposing force (left axis), input power and plunger position (right axis) in TRED, for CLA (- -) and PMB (---).

4:45

BG-11. Design and Analysis of a Planar Flux-Switching Permanent Magnet Motor.

H. Hu[1], G. Cao[1], S. Huang[1], C. Wu[1], J. Guo[1], D. Liang[2] and R. Mai[3]
1. Shenzhen Key Laboratory of Electromagnetic Control, Shenzhen University, Shenzhen, China; 2. School of Electrical Engineering, State Key Laboratory of Electrical Insulation and Power Equipment, Xi'an Jiaotong University, Xi'an, China; 3. School of Electrical Engineering, Southwest Jiaotong University, Chengdu, China

I. Introduction For precision positioning applications such as semiconductor lithography and microscale manufacturing, planar motor is an attractive positioning device, because of its advantages of simple structure, high precision, low friction, and low cost [1], [2]. Planar permanent magnet synchronous motor (PPMSM), which is one kind of planar motor, shows the obvious advantages of high efficiency and high thrust force density [3]. However, the cost is increased and the reliability is reduced inevitably for the PMSPM, because a vast majority of the material is permanent magnet (PM) for PPMSM [4]. As another kind of planar motor, planar switched reluctance motor (PSRM) possesses the merits of low cost and high reliability; however, the PSRM has the drawbacks of low efficiency and low thrust force density [5], [6]. Combining both superiorities of PSPMMs and PSRMs to develop a kind of planar motor showing high efficiency, high thrust force density, high reliability, and low cost is significant in precision positioning applications. At present, a new kind of stator PM brushless motor, namely the flux-switching permanent magnet motor (FPMM), has received more and more attention. For the FPMM and the permanent magnet synchronous motors, they feature high efficiency and high torque density [7]. Simple structure, low cost, and high reliability are shows for the FPMM and the switched reluctance motors [8], [9]. The FPMM have been applied to develop linear motors for precision positioning applications [10]. There are two main structures of the linear FPMMs. One is mover/stator pole pitch ratio approximately equal to one, the other is equal to three [11]. For the two structures, the linear FPMM with mover/stator pole pitch ratio of three would perform lower thrust force ripple [11], which is significant for precision positioning applications. Therefore, the linear FPMM with mover/stator pole pitch ratio of three could be suitable for developing a kind of planar motor with superiorities of high efficiency, high thrust force density, high reliability, and low cost. In this paper, a planar flux-switching permanent magnet (PFPMM) with mover/stator pole pitch ratio of three is proposed. II. Motor Design *A. Modeling* The magnetic field of the PFPMMs consists of two components: magnetic energy generated by permanent magnet W_p; magnetic energy generated by energized silicon iron W_e, which is given as $W_m=W_e+W_p$ (1) In terms of virtual work method, the one-axis electromagnetic thrust force under linear magnetic field can be deduced as $f(t)=dW_e/dx(t)+dW_P/dx(t)=\partial\int_0^i(\psi(t)di)+dW_P/dx(t)=0.5dL(x(t))/dx(t)i^2(t)+dW_P/dx(t)$ (2) where x, i, ψ, and L are the position, current, flux linkage, and inductance in one axis. *B. Design Consideration* For the PFPMM, the relation of the mover teeth pitch τ_u, the stator pole pitch τ_s, and the mover pole pitch τ_m is given as $\tau_u = 1.5\tau_s = 0.5\tau_m$ (3) The relation of the mover width w_m and the stator pole pitch τ_s is expressed as $w_m = k\tau_s$ (4) where k is the positive integer. The relation of the distance between the adjacent mover λ and the stator pole pitch τ_s is expressed as $\lambda=l\tau_s\pm\tau_s/3$ (5) where $\lambda>0$ and l is the nonnegative integer. The geometric dimension of PM is determined by using the finite element analysis. The material of PM is NdFeB30, and the remanence of PM is 1.1 T. The main geometric dimension of the PFPMM is then determined according to (3), (4), (5), and finite element analysis, which is listed in Table 1. The overall structure of the designed PFPMM is depicted in Fig. 1(c) and (d). For the designed PFPMM motor, the moving platform consists of six movers. Three movers are responsible for one-axis motion. The stator sets are a network structure constructed from stator blocks combination, which is shown in Fig. 1(a). Each stator block constituted by the laminated silicon steels. The mover is shown in Fig. 1(b). The iron core of mover is constituted by the laminated silicon steels. III. Results and Analysis The proposed PFPMM is analyzed based on three-dimensional finite element model (FEM) via ANSYS Maxwell software. The magnetic induction intensity distribution is shown Fig. 2 (a). The flux linkage of PM is shown in Fig. 2(b). A sinusoidal flux linkage of PM is illustrated, which is desired for the PFPMM. Fig. 2(c) depicts the Fourier analysis of the flux linkage. The amplitude of the fundamental frequency of the flux linkage is 92 % of that the total amplitude. The cogging force is shown in Fig. 2(d), which indicates that the maximum cogging force is 1.2 N. The thrust force and normal force of one mover versus current versus position is shown in Fig. 2(e) and Fig. 3(f), respectively. The change of the thrust force and normal force is small because of the magnetic saturation under the current larger than 7 A. The maximum thrust force of one mover is 20 N. The PFPMM generally operates with the sinusoidal current. The thrust force density versus current of the PFPMM and the PSRM presented in [5], [6] is shown in Fig. 3(g). Compared to the PSRM, the proposed PFPMM shows higher thrust force density. The effectiveness of the proposed PFPMM is verified.

[1] J. W. Jansen, J. P. C. Smeets, T. T. Overboom, J. M. M. Rovers, and E. A. Lomonova, "Overview of analytical models for the design of linear and planar motors," *IEEE Trans. Magn.*, vol. 50, no. 11, pp.1 –7, Nov. 2014. [2] T. Huang, K. Yang, C. Hu, Y. Zhu, and M. Li, "Integrated robust tracking controller design for a developed precision planar motor with equivalent disturbances," *IET Control Theory Appl.*, vol. 10, no. 9, pp. 1009–1017, May 2016. [3] L. Guo, H. Zhang, M. Galea, J. Li, and C. Gerada, "Multiobjective optimization of a magnetically levitated planar motor with multilayer windings," *IEEE Trans. Ind. Electron.*, vol. 63, no. 6, pp. 3522–3532, Jun. 2016 [4] J. M. M. Rovers, J. W. Jansen, and E. A. Lomonova, "Multiphysical analysis of moving-magnet planar motor topologies," *IEEE Trans. Magn.*, vol. 49, no. 12, pp. 5730–5741, Dec. 2013. [5] S. D. Huang, G. Z. Cao, Z. Y. H, C. Wu, J. A. Duan, N. C. Cheung, Q. Q. Qian "Maximum-force-per -ampere strategy of current distribution for efficiency improvement in planar switched reluctance motors," *IEEE Trans. Ind. Electron.*, vol. 63, no. 3, pp. 1665–1675, Mar. 2016. [6] G. Z. Cao, J. L. Fang, S. D. Huang, J. A. Duan, and J. F. Pan, "Optimization design of the planar switched reluctance motor on electromagnetic force ripple minimization," *IEEE Trans. Magn.*, vol.50, no.11, pp. 1–4, Nov. 2014. [7] M. Cheng, W. Hua, J. Zhang, and W. Zhao, "Overview of stator permanent magnet brushless machines," *IEEE Trans. Ind. Electron.*, vol. 58, no. 11, pp. 5087–5101, Nov. 2011. [8] Z. Xiang, L. Quan, X. Zhu, J. Huang and D. Fan, "Investigation of Optimal Split Ratio in Brushless Dual-Rotor Flux-Switching Permanent Magnet Machine Considering Power Allocation," *IEEE Trans. Magn.*, doi: 10.1109/TMAG.2017. 2769451, 2017. [9] Z. Xiang, L. Quan, X. Zhu, J. Huang and D. Fan, "Investigation of Optimal Split Ratio in Brushless Dual-Rotor Flux-Switching Permanent Magnet Machine Considering Power Allocation," *IEEE Trans. Magn.*, doi: 10.1109/TMAG.2017. 2769451, 2017. [10] H. Lin and J. A. Heilig, "Linear Hybrid Brushless Servo Motor," U.S. Patent 7 230 355, Jun. 12, 2007. [11] R. Cao, M. Cheng and W. Hua, "Investigation and General Design Principle of a New Series of Complementary and Modular Linear FSPM Motors," *IEEE Trans. Ind. Electron.*, vol. 60, no. 12, pp. 5436–5446, Dec. 2013.

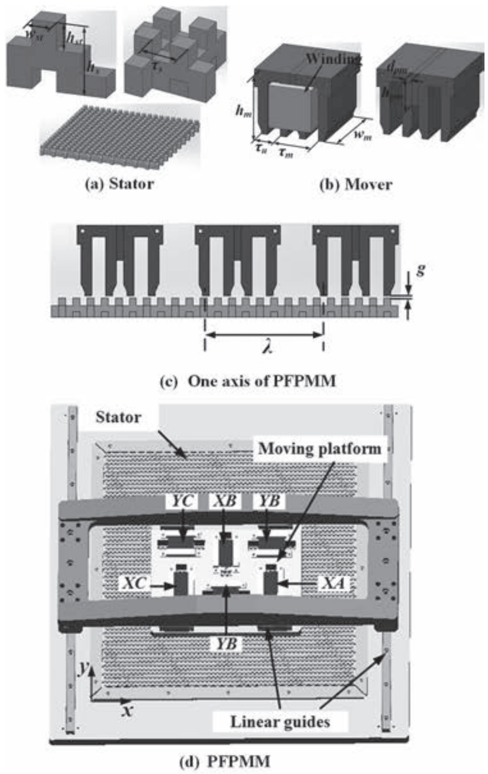

Fig .1 Structure of the PFPMM

Table 1 Parameters of the proposed PFPMM

Parameters	Value
τ_s (stator pole pitch)	7.2mm
w_{st} (width of stator teeth)	3.6 mm
h_s (high of the stator)	10 mm
h_{st} (high of the stator teeth)	4 mm
w_m (width of the mover)	43.2 mm
τ_m (mover pole pitch)	21.6 mm
h_m (high of the mover)	36 mm
l_{pm} (length of the PM)	18 mm
w_{pm} (width of the PM)	43.2 mm
d_{pm} (thickness of the PM)	3.6 mm
Number of turns	150
g (air gap of the PFPMM)	0.3 mm

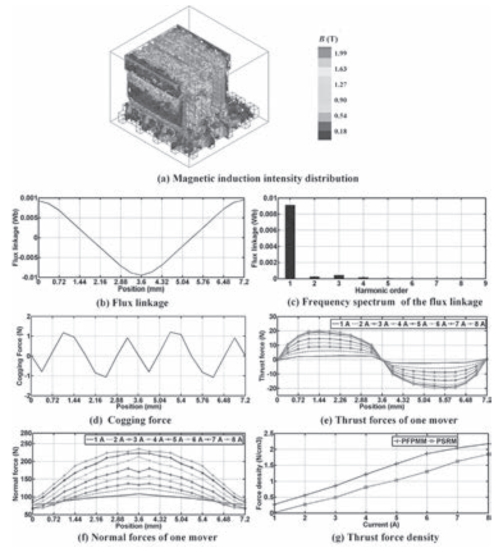

Fig.2 Simulation Results

TUESDAY AFTERNOON, 24 APRIL 2018 PEONY II, 2:00 TO 5:00

Session BH
SENSORS: FRONTIER APPLICATIONS I

Antonio Ruotolo, Chair
City University of Hong Kong, Kowloon, Hong Kong

CONTRIBUTED PAPERS

2:00

BH-01. The Ultimate Compact Packaging Technology based on Magnetoresistive devices for a minimum source-sensor distance.

F. Franco[1,2], R. Dias[3], J. Gaspar[3], T. Materne[4], T. Becker[4], S. Cardoso de Freitas[1,2] and P. Freitas[1,3]
1. INESC-MN, Lisbon, Portugal; 2. Instituto Superior Técnico, Lisbon, Portugal; 3. INL, Braga, Portugal; 4. BOGEN Electronic, Berlin, Germany

The magnetic field is a commonly used physical quantity to develop sensors for a broad range of industrial applications such as positioning systems based on magnetic encoders. Its dependence on the source-sensor distance imposes strong requirements in the sensor technology and packaging. Magnetoresistive (MR) sensors standout as a magnetic sensor technology that surpass other magnetic field detection techniques like inductive and hall effect sensors due to an enhanced spatial resolution and high sensitivity, achieving detection levels around the pT range at low frequency[1]. However, the packaging solution influences the optimum sensor performance level. The sensor packaging is mainly implemented to protect the device from mechanical damage, the intellectual property and establish electrical connection with outer electronics. The combination of silicon based sensor technologies with Complementary Metal Oxide Semiconductor (CMOS) technologies is a reduced footprint method to integrate a full electronic system[2], but the non-fabricated CMOS area for the sensor integration increases the production cost. Wirebonding technology is a reliable method used to connected independent components and it doesn't compromise the production cost[3]. However, a high density of contacts and the interconnections overlapment demand a larger chip area. Furthermore, the vertical volume occupied by the wirebonding loop increases the sensor-source distance. An alternative for connection on the back side of the substrate is the through-silicon-via(TSV) technology. Although its implementation is extremely affected by the via height-to-width ratio, state-of-the-art TSV technology can achieve a high density level of vias with 20μm diameter, upon reducing the wafer thickness to 200μm[4]. An alternative to bringing the sensor contacts towards the back side of the substrate while maintaining the wafer thickness at optimum levels for handling robustness is proposed in this work. A new approach was developed for planar sensor architectures, aiming to fulfill the demand for high accuracy technologies for positioning systems and motion control applications. The implementation of this sensor technology can push the magnetic encoders towards a competitive solution for applications with high constraints (reading distance, angular dependence and harsh environment). The prototype is based on a hybrid technology with a rigid Si chip combined with a flexible polyimide (PI) connector. The MR sensors are composed of a magnetic tunnel junction stack based on a MgO barrier deposited by magnetron sputtering in a N2000 tool [5] with the following structure: Ta 5/[Ru 18/Ta 3]x3/PtMn 20/CoFe 2.2/Ru 0.7/CoFeB 3/MgO 1.6/CoFeB 1.55/Ru 5/Ta 10 (nm). Consequently, they are defined in a standard top-down microfabrication process[6]. A 600nm AlSiCu/30nm TiW(N) thick metal layer is deposited between a double coated 10μm thick PI layer. The electrical contact between the two elements is established by opening vias along the 1st PI layer, while the 2nd PI layer is used as a protective layer and to define the pad layout for electrical contact with the external electronics through a ffc/fpc connector. Finally, the PI layers are patterned according to the flexible connector shape, being the Si substrate removed by opening tranches around the sensing chip using an DRIE technique combined with HF vapor that selectively removes the underlying SiO_2 sacrificial layer and detach the device from the wafer. Figure 1(a) display a schematic of the device cross section while Figure 1(b) shows the device top view after the microfabrication process. The prototype was implemented as a linear analog sin/cos encoder using a 80μm pole pitch incremental scale with an out-of-plane magnetization manufactured at BOGEN. The magnetic scales are commercial 1mm thick and 10mm wide elastomer filled with ferrite coated on top of a stainless steel carrier tape[7]. The sin/cos analog output is obtained through a double Wheatstone bridge in a full bridge configuration, which reduces the background noise, offset voltage and is translated into a higher signal to noise ratio. Furthermore, to minimize the impact of inhomogeneous interferences along the scale, each magnetic sensor is composed of several sensing elements distributed across different poles to obtain an average signal and a higher accuracy. The sensor exhibits a tunneling magnetoresistance of 123%, an intrinsic R-A product of 1.1MΩ.μm^2 and a minimum resistance of 1109±31kΩ. Despite a coercive field of 0.62±0.02mT, the sensor displays a sensitivity at zero field of 453±19 kΩ/mT in the most sensitive branch. Figure 2(a) shows the magnetotransport curve for a magnetic sensor of the Wheatstone bridge while Figure 2(b) displays the sin/cos output measured by the prototype along the magnetic scale at a reading distance around 80μm. Within a high yield microfabrication process, the sensors maintained all magnetic and electrical properties and were successfully implemented as a magnetic encoder. Furthermore, an outstanding configuration allows a 20μm sensor-source distance since the PI flexible connector establish electrical contact away from the Si chip since it can be bent towards a lower level or the opposite side.

[1] P. P. Freitas, R. Ferreira, S. Cardoso, and F. Cardoso, "Magnetoresistive sensors," *J. PhysicsCondensed Matter*, vol. 19, no. 16, p. 165221, 2007. [2] L. Zhang, X. He, Y. Wang, and Z. Yu, "A Fully Integrated CMOS Nanoscale Biosensor Microarray," *Cust. Integr. Circuits Conf. (CICC), 2011 IEEE*, 2011. [3] M. Antelius, A. C. Fischer, and F. Niklaus, "Unconventional applications of wire bonding create opportunities for microsystem integration," *J. Micromechanics Microengineering*, vol. 23, no. 8, 2013. [4] J. P. Gambino, S. A. Adderly, and J. U. Knickerbocker, "An overview of through-silicon-via technology and manufacturing," *Microelectron. Eng.*, vol. 135, pp. 73–106, 2015. [5] P.Wisniowski, S.Cardoso, N.Barradas and P.P.Freitas, "Effect of free layer thickness and shape anisotropy on the transfer curves of MgO magnetic tunnel junctions", J.Appl.Phys. 103, 07A910 (2008) [6] F. Franco *et al.*, "Advanced NDT Inspection Tools for Titanium Surfaces Based on High-Performance Magnetoresistive Sensors," *IEEE Trans. Magn.*, vol. 53, no. 4, p. 6200805, 2017. [7] www.bogen-electronic.com

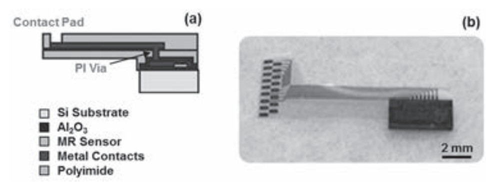

Fig. 1. a)Schematic of the device cross section.b) Device top-view after the microfabrication, showing the Si substrate with the sensors connected with the flexible PI cable.

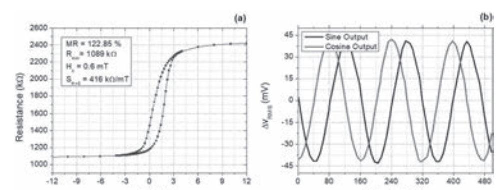

Fig. 2. a)Magnetotransport curve for a magnetic sensor of the Wheatstone bridge.b)Sin/Cos Output measured along the magnetic scale at a reading distance of 80μm.

2:15

BH-02. Busbar current transducer with suppression of external fields and gradients.

P. Ripka[1], A. Chirtsov[1] and J. Vyhnanek[1]
1. Czech Technical University, Prague, Czechia

Yokeless busbar current sensors are cheap and compact, but they are sensitive to external magnetic fields and field gradients [1,2]. We have described current transducer based on a couple of microfluxgate sensors [3] inside the cylindrical hole in the busbar [4,5]. The advantage of this transducer is high range and small size compared to similar transducer based on circular sensor array around the conductor [6]. Compared to Hall current sensors [7,8], fluxgate current sensor has 10-times better stability. Solution based on AMR has 10-times lower range due to the small saturation field of AMR sensors [9]. We have suggested that a partial suppression of the magnetic fields generated by external currents can be achieved by using four microfluxgate sensors: two of them are active and they measure y-component of the field at points A and C (B_{Ay} and B_{Cy}) the other two measure both field components at point B (B_{Bx} and B_{By}) [10]. This approach can be effective for the case of known geometry of the external currents or when the external currents are also measured. However, in general case the position and size of the external current is not always known and the interference field can be generated by several currents simultaneously. Significant magnetic fields can also by generated by coils and by magnetic materials (both hard and soft in external field) in the vicinity of the transducer. In this paper we therefore suggest current sensor which is immune to external homogeneous fields and first order field gradients. This means that our new solution does not perfectly compensate the field from external conductors, but effectively suppresses their influence, as higher order gradients from distant currents are small. Fig. 1 shows the current busbar with fluxgate sensor array inserted into the hole and field distribution shown on a busbar cross section. The size of the copper busbar is 6 x 1 cm and the hole diameter is 19 mm. The DC current value for this simulation was 1000 A. The sensor array shown on the photograph consists of six sensors - three of them are visible as a row with 6 mm pitch, which measures By in positions A,B and C. The other 3 sensors are on the opposite side of the PCB and they measure Bx at the same points. By moving the sensor array in y direction we can scan the field values at other positions above the central plane and verify the simulations. In general the fit between our measurements and FEM simulations is within 5%. After performing the simulation and measurement exercise we fixed the sensor optimum position for the final transducer design. All previously published current transducers of this type such as [3] and [7] used sensors in the central line (positions A and C) measuring By. The fact that B_{Ay} and B_{Cy} have opposite sign was used to suppress homogeneous external field B_0. However, field distribution of By along the A-C line is linear (Fig. 2 left) and this means that external dBy/dx field gradient cannot be suppressed. Possible solution of this problem would be to change the busbar geometry in order to achieve significantly non-linear field profile and evaluate second-order gradient from the measured current. We have made extensive simulations with various geometries but we never achieved significant non-linearity. Instead of that we decided to find alternative sensor positions. The novelty of our approach is that we use Bx instead of By. Bx response to the measured current does not change sign when mirroring around the y axis. At H and I points the sensitivity is the same, 5mT/1000 A. Due to the 2 mT maximum range of the DRV425 sensor the actual current range will be 400 A. Summing $B_{Hx} + B_{Ix}$ therefore does not suppress homogeneous external field B_{0x}, but instead of that it suppresses dBx/dx field gradient. This type of gradient is not typical for long conductors, but for dipolar sources such as coils and permanent magnets. This setup is also completely insensitive to external currents in x direction. The dependence on B_{0x} can be suppressed by using the third x-sensor at the central point A. Remaining is the dependence on dBx/dy field gradient. Here we face the similar problem as before, because Bx response to the measured current change sign when mirroring around the x axis. Fortunately, field distribution along the DE line is strongly non-linear and thus the external dBx/dy field gradient can be suppressed. This is documented by the Bx profile along the DE line (Fig. 2 right). We achieve the required compensation by using additional sensor located at J and eventually also K point. While $B_{Jy} - B_{hy}$ is insensitive to the measured current, this value depends only on dBy/dx field gradient. The resulting formula for the measured field B_m is $B_m = B_H + B_I - (B_J + B_K)/2 - B_B$ and in our example the lateral (x-direction) current is suppressed completely, while the superior (y direction) current in the vicinity of 20 cm is suppressed by the factor of 167. In conclusion, by using novel geometry of the fluxgate current transducer we achieve compensation of external fields and first order field gradients.

[1] P. Ripka, Electric current sensors: a review, Meas. Science and Technology 21 (2010) Iss. 11, pp.1-23. [2] P. Ripka; A.Chirtsov: Influence of External Current on Yokeless Electric Current Transducers, IEEE Transactions on Magnetics, 2017, Volume: 53, Issue: 11, paper # 4003904, pp. 1-4, [3] M. F. Snoeij, V. Schaffer, S. Udayashankar, Mikhail V. Ivanov: An Integrated Fluxgate Magnetometer for use in Closed-Loop/Open-Loop Isolated Current Sensing, IEEE J. Solid-state circuits 51 (2016), 1684-1694. [4] D. Lee, M. Eissa, A. Gabrys et al., "Fabrication and Performance of Integrated Fluxgate for Current Sensing Applications," IEEE Transactions on Magnetics, no. 99, 2017 [5] Pavel Ripka; Vaclav Grim; Vojtech Petrucha: A busbar current sensor with frequency compensation: IEEE Trans. Magn. Vol. 53 (2017), Issue 4, paper # 4000505 [6] R. Weiss, R. Makuch, A. Itzke, and R. Weigel, "Crosstalk in circular arrays of magnetic sensors for current measurement," IEEE Transactions on Industrial Electronics, vol. 64, no. 6, pp. 4903–4909, 2017. [7] K.-L. Chen and N. Chen, "A new method for power current measurement using a coreless Hall effect current transformer," IEEE Transactions on Instrumentation and Measurement, vol. 60, no. 1, pp. 158–169, 2011. [8] M. Blagojevic, U. Jovanovic, I. Jovanovic, D. Mancic, and R. S. Popovic, "Realization and optimization of bus bar current transducers based on Hall effect sensors," Measurement Science and Technology, vol. 27, no. 6, Article ID 065102, 2016. [9] P. Mlejnek, P. Ripka: Off-center error correction of AMR yokeless current transducer, Journal of Sensors, Volume 2017 (2017), Article ID 6057634 [10] P. Ripka, "4-sensor yokeless electric current transducer," 2017 IEEE International Magnetics Conference (INTERMAG), Dublin, 2017, pp. 1-1. doi: 10.1109/INTMAG.2017.8007975

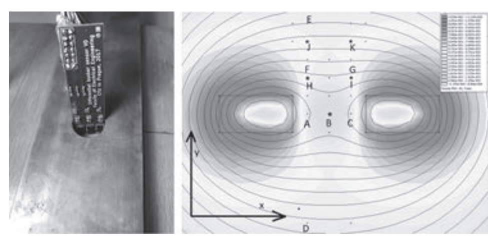

Fig. 1. Current busbar with fluxgate sensor array inserted into the hole (left). Field distribution shown on a cross section. The DC current value for this simulation was 1000 A (right). Final position of the sensors is marged by stars.

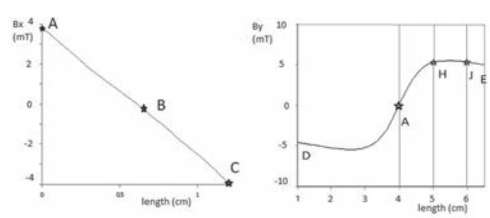

Fig. 2. Field profiles from the measured 1 000 A current: By along the A-C line (left) and Bx along the D-E line (right).

2:30

BH-03. Small Eddy Current Testing Sensor Probe using Tunneling Magnetoresistance Sensors for Detection of Cracks in Steel Structures.

K. Tsukada[1], M. Hayashi[1], Y. Nakamura[1], K. Sakai[1] and T. Kiwa[1]
1. Okayama University, Okayama, Japan

Eddy current testing (ECT) is a nondestructive testing (NDT) method, and is widely used to detect flaws in metal structures. ECT involves the use of a pair of detection and induction coils. The detection coil is used to measure the secondary magnetic field generated by the eddy current in the metal due to the applied AC magnetic field of the induction coil. In the case of a nonmagnetic material, since the magnetic field detected by the detection coil is generated only by the eddy current, ECT using a detection coil is suitable for detecting any abnormality in the eddy current distribution caused by a flaw. However, in the case of ferromagnetic materials, the magnetic field detected by the detection coil arises not only from the eddy current but also from the magnetization of the material itself, thereby making it difficult to apply ECT in such cases. The magnetization of the material can lead to detection errors in ECT; this is referred to as magnetic noise. Thus, a measuring technique that can minimize the signal arising from the magnetization of the material compared to that arising from the eddy current is required. Recently, instead of detection coils, magnetic sensors are being increasingly used for NDT. We also reported NDT using magnetoresistance sensors, such as extremely low-frequency ECT for evaluation of corrosion via thickness detection, and unsaturated AC magnetic flux leakage testing for detection of inner cracks. In this work, we have developed an ECT method using a small magnetic sensor probe with tunneling magnetoresistance (TMR) sensors to address the problem of magnetic noise in ferromagnetic materials. The signal arising from the magnetization of the material can be minimized with respect to the signal arising from the eddy current by minimizing the detection area and thereby, increasing the ratio of the area with a crack to the area without a crack. In our method, we reduce the detection area by using a micromagnetic sensor instead of a detection coil with a larger area. Thus, we developed a small single-channel magnetic sensor probe using TMR (Fig. 1(a)), and evaluated its performance by detecting cracks of different depths. The single-channel sensor probe consists of a TMR sensor mounted on a 2 mm wide amplifier circuit board and an induction coil. A nanogranular in-gap magnetic sensor, which is a type of TMR sensor with an even response function, was used. To obtain linear magnetic response, a magnetic bias was applied using a magnet, and a sensitivity of 0.3 V/mT was obtained in the sensor probe output. The induction coil was square-shaped with a cross-sectional area of 2.3×2.3 mm^2 and 32 turns. The applied magnetic field was maintained at a frequency of 1 kHz using a function generator. A 7 mm thick SS400 steel plate with 20 mm long and 1 mm wide cracks of different depths ranging from 0.5-7 mm was used as the test sample. To evaluate the performance of our detection system, the sensor probe was used to scan lines over the positions of the cracks. The output signal was detected using a lock-in amplifier, and analyzed using magnetic vectors with real and imaginary components. When the magnetic sensor is attached to the induction coil, the applied magnetic field is directly coupled to the former. Therefore, the applied magnetic vector signal in the absence of a sample was subtracted from the detected magnetic vector signal of the sample. Our analysis revealed an apparent signal change at the crack position in all the signals obtained after line scanning over the crack regions. However, a base line drift was observed in scanning experiments performed over a large distance. Such a drift can be attributed to an in-plane permeability fluctuation of the steel plate and the consequent magnetic noise. To address the problem of base line drift, a dual TMR sensor probe was developed (Fig. 1(b)). Two TMR sensors were attached to one long side of a rectangular induction coil with a cross-sectional area of 2.5×6.0 mm^2 and 60 turns. In Fig. 2, we show the magnetic vector intensity change observed in scanning experiments over a crack with a depth of 5 mm. Each signal change exhibited a waveform similar to that observed in case of a single-channel sensor probe. We also observed a drift, i.e., the base line showed different values at the start and end points (Fig. 2(a)). To determine whether the signal change arises due to the crack, knowledge of the absolute value of the signal at the crack position without any offset and base line drift is necessary. For this purpose, a differential magnetic vector (Fig. 2(b)) was calculated to obtain the true signal arising from the crack by subtracting one detected signal from the other. The line-scanned differential magnetic vector intensity exhibited a simple peak at the crack position without any base line drift. In conclusion, a reliable signal change due to a crack was obtained in ECT of a ferromagnetic material using a dual TMR sensor instead of a detection coil. The developed TMR sensor is small and can be easily incorporated inside the induction coil. Thus, ECT probes using multiple TMR sensors with only one induction coil can be easily realized.

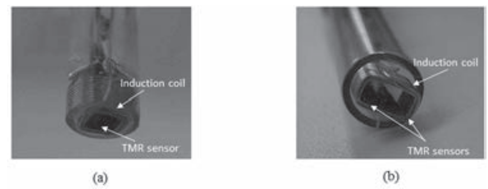

Fig. 1. Photographs of the sensor probe using a (a) single TMR, and (b) dual TMR sensor.

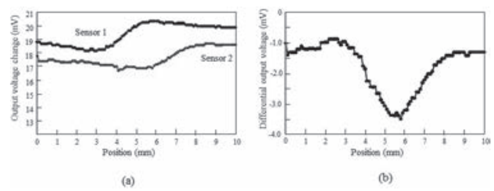

Fig. 2. Line-scanned magnetic field intensity of a steel plate with a surface crack (depth of 5 mm) using a dual TMR sensor probe: (a) individual sensor output, and (b) differential magnetic field intensity.

2:45

BH-04. Nondestructive testing of wire rope based on shoving magnetic field structure.

X. Yan[1] and D. Zhang[1]
1. Electrical Engineering and Electronics, Harbin Institute of Technology Shenzhen Graduate School, Shenzhen, China

I. INTRODUCTION The methods for wire rope or pipe nondestructive testing commonly include: eddy current testing, radiographic testing, optical testing, acoustic testing, electromagnetic testing, and so on. The structure of electromagnetic testing device is simple, and various types of magneto sensors can be used. In addition, the wire rope belongs to ferromagnetic components, with the application of electromagnetic excitation, the electromagnetic characteristics of the defects are different from the intact wire rope, where magnetic sensors can be used for data acquisition for defect detection. The electromagnetic testing is not affected by the oil or mud stains on the wire rope surface, so the internal and external defects can be detected. The electromagnetic testing of wire rope is common and cost effective for many wire rope operators, and it has been developed and recognized as the most reliable and effective wire rope NDT method [1,2]. At present, for wire rope or pipe nondestructive testing, usually uses the structure of magnets and a magnetic yoke as an excitation to excite the tested component to saturation state. A magnetic sensor [3] or magnetic sensor arrays [4] are used to pick up the defect electromagnetic signal, realizing the wire rope or pipe non-destructive testing. The participation of the yoke increases the weight of the detection probe and also increases the probe volume. In addition, the wire rope or the pipe is a rod-shaped structure, in order to achieve a better excitation effect, the arc-shaped magnet which is radical magnetizing needs to be designed for magnetization. This is increases the complexity of the magnetization. In this paper, a new excitation method based on shoving structure is proposed to simplify the magnetizing structure, and eliminate the use of magnetic yoke. The whole nondestructive testing probe is more compact and lightweight, at the same time can achieve a good detection effect. II. TOPOLOGY AND SIMULATION The nondestructive testing of ferromagnetic components based on shoving magnetic field structure is shown in Fig. 1. The two magnets is magnetized the tested component along its length. That is, the direction of the magnetic pole is along its thickness. In the field application, the structure of magnets can be two halves, and it is very easy for its magnetization. The two magnets should be as closer as better, in the premise that the magnetic sensors can be installed between them. The internal side polarity of the magnet should be same, are both N or both S. The simulation result is shown in Fig. 2. Conclusions obtained from it: in the squeeze structure, the magnetic sensor placed in the center of the two magnets can detect flaw magnetic flux leakage signal, which is used for defect inversion analysis. In the following simulation work, we will extract the magnetic flux leakage signal in the middle of the two magnets, and analyze the influence of sensor arrangement position on the test result to determine the optimal placement position of the sensor. III. EXPERIMENTAL RESULTS The prototype of the nondestructive testing probe based on shoving magnetic field is shown in Fig.3 (a). A steel iron rod whose diameter is 10mm is tested, there are 7 defects on it. 10 hall sensors is arranged around the pipe in the middle of the magnets. One of the hall test result is shown in Fig.3 (b). From the Fig3 (b), the defect signal has high signal-to-noise ratio, the defect size and the signal peak value has a proportion relationship. That means, the nondestructive testing of wire rope based on shoving magnetic field structure has remarkable detection effect.

[1]H.R. Weischedel and R.P. Ramsey, “Electromagnetic testing, a reliable method for the inspection of wire ropes in service”, NDT&E Int., vol. 3, no. 22, pp. 155-161, 1989. [2]X. L. Yan, D. L. Zhang, and S. M. Pan, “Online nondestructive testing for fine steel wire rope in electromagnetic interference environment”, NDT E Int., no. 92, pp. 75–81, 2017. [3]X. L. Yan, D. L. Zhang, and F. Zhao, “Improve the signal to noise ratio and installation convenience of the inductive coil for wire rope nondestructive testing”, NDT E Int., no. 92, pp. 221–227, 2017. [4]M. Le, J. Lee, and J. Jun, “Hall sensor array based validation of estimation of crack size in metals using magnetic dipole models”, NDT E Int., no. 52, pp. 18–25, 2013. [5]Y. L. Ma, R. Y. He, and J. Z. Chen, “A method for improving SNR of drill pipe leakage flux testing signals by means of magnetic concentrating effect”, IEEE Trans. Magn., vol. 51, no. 9, pp. 6201607, 2015.

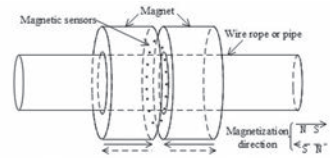

Fig.1 The diagram of the nondestructive testing of ferromagnetic components based on shoving magnetic field structure

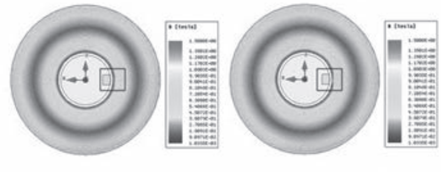

(a)When the defect is not under the sensor (b) When the defect is under the sensor
Fig.2 Simulation result

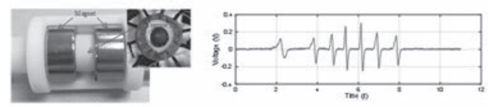

(a)The nondestructive testing probe based on shoving magnetic field (b)The hall sensors test result
Fig.3 Test result

3:00

BH-05. Magnetic detection of steel corrosion at a buried position near the ground level using a magnetic resistance sensor.

K. Tsukada[1], T. Tomioka[1], S. Wakabayashi[1], K. Sakai[1] and T. Kiwa[1]
1. Okayama University, Okayama, Japan

Accurate and easy inspection methods are in high demand to ensure the safety of social and industrial infrastructure. Corrosion and cracks are often detected in steel infrastructure, and they can be inspected using ultrasonic or magnetic testing. However, surface treatment, such as paint or rust stripping, is necessary to perform ultrasonic testing in order to maintain good acoustic matching contact. Therefore, it is difficult to apply ultrasonic testing to deteriorating and corroding steel structures, which are in serious requirement of corrosion detection. On the other hand, pulsed eddy current (PEC) testing methods and our recently reported extremely low frequency eddy current (ELECT) can be applied to perform thickness detection of thick steel plates without conducting surface treatment. Recently, the corrosion of steel structures, such as the illumination and road marker poles that are located in close proximity to the ground level, have become a social problem because serious traffic accidents may occur due to the collapse of poles that may be caused due to corrosion. Corrosion is observed to easily occur near the ground level. It is very difficult to detect corrosion because corrosion may be hidden by the soil, concrete, or tiles in many situations. Conventional inspection methods, such as digging to detect buried objects, requires a plenty of time along with a sufficient number of workers. Therefore, a method to detect such corrosion at hidden positions under the ground level is required. In this study, we develop a magnetic method that can be applicable to corrosion detection at the hidden positions under the ground. To achieve this objective, we use the noncontact characteristics of our developed ELECT method. For the purpose of detection, apart from the magnetic sensor probe, the probe was tilted in order to point it in a direction that is not perpendicular to the steel surface, but rather to the underground part (Fig. 1). This configuration produces an extensive exposure to the magnetic field. Subsequently, the eddy current occurs in the underground part. In many cases, it is located within 5 mm below the ground level. However, the location of corrosion is not always located just within the aforementioned region below the ground level. Therefore, we have developed two methods to detect the changes in location and thickness. The first method is the measurement of the changing distance from the ground level (Fig. 1(a)), while the second method performs the corresponding measurement with a different tilt angle (Fig. 1(b)). The developed measurement device consists mainly of a sensor probe, sensor circuits, current source for an induction coil, and personal computer for data acquisition and signal analysis. The sensor probe consists of an anisotropic magnetic resistance (AMR) sensor, induction coil, and a small cancellation coil, which was used to minimize the applied magnetic field at a particular position of the sensor to obtain a higher signal-to-noise ratio. Further, the applied magnetic field was operated using an AC current of 0.15 A, from 1 to 100 Hz. To analyze the thickness of the steel plate, we used our developed spectroscopic analysis of magnetic field (SAM). The test samples of the SS iron plate having a length of 350 mm, width of 200 mm, and thickness of 4 mm were used. Further, the test samples had a partially thinning zone from 0.5 to 3.0 mm, with a different length from 20 to 80 mm. The sensor probe was titled to the surface of the test sample by 30°, and the distance dependence of the magnetic spectrum was measured (Fig. 2). Each magnetic spectrum was adjusted to the zero point at a frequency of 1 Hz to reduce the magnetization signal of the ferromagnetic material. Fig. 2(a) depicts the distance dependence of the magnetic spectrum, when the test sample having a thinning depth of 3 mm and width of 60 mm were used to perform the measurement. The distance dependence was observed to be apparent and the magnetic strength gradually decreased, while the spectrum was shifted clockwise in order to be closer to the thinning part. Further, the magnetic spectrum was varied using the thinning depth. To evaluate the quantitative change of the magnetic spectrum, the differential magnetic vector was obtained by subtraction of a magnetic vector of 1Hz from the magnetic vector of 20 Hz. These dependencies of the thinning depth and distance on the differential magnetic vector's magnetic signal intensity are depicted in Fig. 2(b). Through the diagram that is depicted in Fig. 2(b), the corrosion depth and distance from the ground level were estimated using a pair of magnetic sensors that were separated by a constant distance. As an alternative method, corrosion detection was evaluated using a magnetic sensor with different tilt angles of 30° and 45° (Fig. 1(b)) by varying the tilt angle and eddy current distribution region. Further, similar results were obtained by performing the distance dependence test using a pair of separated magnetic sensors. To summarize, the change in thickness that was caused by corrosion was successfully detected using magnetic sensors with a different position or tilt angle.

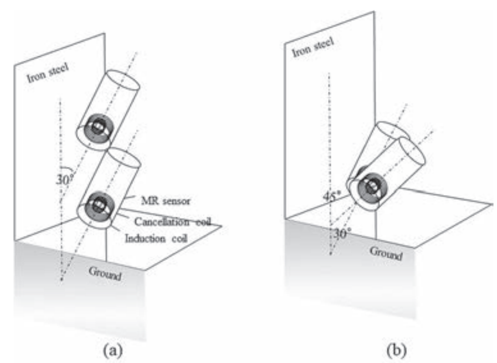

Fig. 1. Schematic of the sensor probe with changing (a) position and (b) tilt angle.

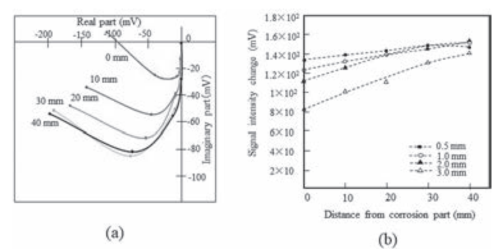

Fig. 2. Distance dependence of a (a) magnetic spectrum of the steel plate having a 3 mm thinning depth part, and (b) differential vector intensity of steel plate having a different thinning depth.

3:15

BH-06. Remote Underwater Animal Monitoring Magnetic Sensor System.

A. Kaidarova[2], S. Amara[2], M. Karimi[2], A. Shamim[2], N. Geraldi[1], C. Duarte[1] and J. Kosel[2]
1. Red Sea Research Center (RSRC), King Abdullah University of Science and Technology (KAUST), Thuwal;, Saudi Arabia; 2. Computer, Electrical and Mathematical Sciences & Engineering (CEMSE), King Abdullah University of Science and Technology (KAUST), Thuwal;, Saudi Arabia

Understanding the behavior of free-living marine species is essential for conservation efforts and predicting how environmental changes may influence marine ecosystems [1]. Despite the recent advances in autonomous recording tags, which are usually attached to free-living animals, acquiring quantitative datasets of their behavior is still technically challenging [2-4]. Magnetic sensing systems are recently becoming popular for underwater animal monitoring [5]. The main advantages of the magnetic approach are a high tolerance of fish to magnetic fields [6] and the measurable magnetic properties exhibited by magnets in water [7]. Such magnetic measuring systems typically consist of small neodymium magnets coupled with a magnetic field sensor to examine the feeding behavior [7], limb movements [8], respiration [9], defecation and heart rates of a number of underwater vertebrates [10]. We have optimized this system by introducing flexible, lightweight and less intrusive NdFeB-PDMS composite magnets, which conform to the body curvature of any marine animals and easily follow their body movement [11]. The corrosion-free composite magnets function effectively for monitoring the belly size of model fish in aquarium (Fig 1a) and study the behavior of the ecologically important giant clam (*Tridacna maxima*) (Fig 1b) in a wired configurational setup [11]. In order to provide a more versatile solution that can be applied to free ranging underwater animals, we have developed a wireless data acquisition system for the magnetic sensing system. To this end, a three-axial magnetometer (MAG3110, Sensors Freescale Semiconductor, Inc.) has been utilized to measure the magnetic stray field of flexible NdFeB-PDMS composite magnets. The magnetometer has been interfaced with a Bluetooth chip (nRF52832, Nordic Semiconductor) through a I^2C communication interface on a miniaturized PCB that was coated with 10 um biocompatible and waterproof Parylene C. The Bluetooth chip is utilized to wirelessly transmit the sensor's reading to any Bluetooth enabled smart device, such as smart phones or tablets. Three axes (x,y,z) of the vector magnetic field are sent over Bluetooth protocol at a refresh rate of 10 Hz (Fig 2a). An Android-based smart phone application was also developed to visualize the vector magnetic field in the form of its 3 (x,y,z) coordinates. The smart phone application scans for those Bluetooth devices, whose service UUID (Universal Unique Identifier) matches with the one assigned to our custom designed magnetometer service. The mobile application (acting as master) then connects to the Bluetooth device (acting as slave) and retrieves the data obtained by the magnetometer, once the notification is received from the devices. The data can be transferred to up to 100-150 meters, which is sufficient to realize real-time indoor monitoring applications. The developed system enables investigating the behavior of different marine species for which the traditional blogging devices, which use heavy, bulky and mechanically inflexible systems and satellite-linked dive recorders are not applicable. The system provides simple and cheap means for animal studies in aquariums. Due to the miniaturized PCB and lightweight, flexible composite magnets the opportunities have also greatly expanded to include tagging of smaller marine animals.

[1] Cooke, Steven J., et al. "Biotelemetry: a mechanistic approach to ecology." *Trends in Ecology & Evolution* 19.6 (2004): 334-343. [2] Block, Barbara A., et al. "Revealing pelagic habitat use: the tagging of Pacific pelagics program." *Oceanologica Acta* 25.5 (2002): 255-266. [3] Lander, Michelle E., et al. "Development and field testing a satellite-linked fluorometer for marine vertebrates." *Animal Biotelemetry* 3.1 (2015): 40.5): 112. [4] Franklin, Paul, and C. I. N. D. Y. Baker. "Fish passage research in the Southern Hemisphere: Challenges, lessons and the need for novel solutions." *International Symposium on Ecohydraulics, Melbourne, Australia*. 2016. [5] Raby, G. D., et al. "Evaluation of a simple technique for recovering fish from capture stress: integrating physiology, biotelemetry, and social science to solve a conservation problem." *Canadian Journal of Fisheries and Aquatic Sciences* 70.1 (2013): 90-100. [6] Rigg, Damian P., et al. "Do elasmobranch reactions to magnetic fields in water show promise for bycatch mitigation?." *Marine and Freshwater Research* 60.9 (2009): 942-948. [7] Wilson, R., et al. "Lip-reading in remote subjects: an attempt to quantify and separate ingestion, breathing and vocalisation in free-living animals using penguins as a model." *Marine Biology* 140.1 (2002): 17-27. [8] Wilson, R., and Nikolai Liebsch. "Up-beat motion in swinging limbs: new insights into assessing movement in free-living aquatic vertebrates." *Marine Biology* 142.3 (2003): 537-547. [9] Wilson, R. P., Simeone, A., Luna-Jorquera, G., Steinfurth, A., Jackson, S., & Fahlman, A. (2003). Patterns of respiration in diving penguins: is the last gasp an inspired tactic?. *Journal of Experimental Biology*, *206*(10), 1751-1763. [10] Wilson, R. P., Scolaro, A., Quintana, F., Siebert, U., thor Straten, M., Mills, K. & Müller, G. (2004). To the bottom of the heart: cloacal movement as an index of cardiac frequency, respiration and digestive evacuation in penguins. *Marine Biology*, *144*(4), 813-827 [11] Kaidarova, A. et al. "Tunable, flexible composite magnets for marine environment applications". *IEEE Journal of Oceanic Engineering, 2017.Under Review.*

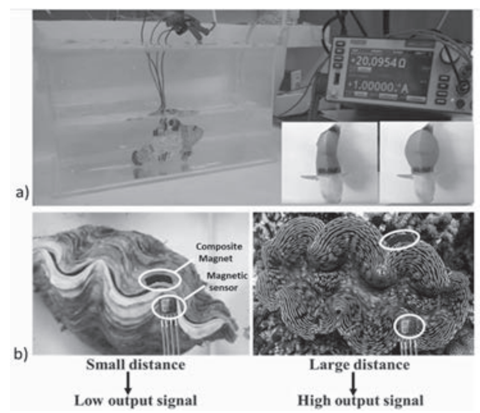

Fig. 1. a) Four-wire underwater monitoring setup with model fish. Inset shows a model fish without and with a gas filled cavity. b) Attachment of the magnetic sensor and composite magnet to a giant clam using biocompatible EpoPutty adhesive.

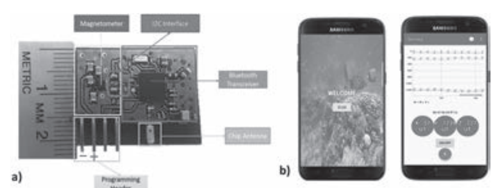

Fig. 2. a) Miniaturized PCB to sense magnetic field and transmitting data wirelessly using Bluetooth low energy (BLE) communication standard; b) Scanning screen which scans the magnetometer based Bluetooth devices and a screen displaying the 3-axes magnetometer data graphically as well as digitally in the units of Micro Tesla (μT).

INVITED PAPER

3:30

BH-07. High-performance micro magnetic sensors installed in wearable electronic compasses and I-o-T magnetic sensors promoting new information society - Amorphous Wire CMOS IC Magneto-Impedance Sensors -.

K. Mohri[1,2]

1. Graduate School of Engineering, Nagoya University, Nagoya, Japan;
2. Division of Research, Nagoya Industrial Science Research Institute, Nagoya, Japan

INTRODUCTION The Magnetics research, technology, and industry has been rapidly shifted in these years to the field of micro magnetic sensors due to the world-wide competing production of micro geo-magnetic sensors installed in the electronic compasses for Smart phones and mobile phones with the production number of more than 1 billion per year since 2014. OHSHIMA/ HARADA'S LEADING PRINCIPLE FOR CREATION OF MICRO GEO-MAGNETIC SENSORS A conception of "Electronic Compass" installed in mobile phones was proposed by Dr. S. Ohshima, late president of KDDI Corp., Japan on around 1985, the telecommunication liberalization year, after that Prof. K. Harada, Kyushu Univ. proposed a necessity of the creation of "magnetically sensitive and electrically high-impedance magnetic elements" for constitution of sensitive micro magnetic sensors. TEN REQUISITE CONDITIONS FOR MICRO MAGNETIC SENSORS INSTALLED IN WEARABLE ELECTRONIC COMPASSES We summarize the ten requisite conditions for micro geo-magnetic sensors installed in Smart phones and wrist watches : (1) micro sizing of the magnetic head less than 1 mm, (2) small power consumption less than 1 mW including the signal processing calculation power consumption in CPU, (3) high sensitivity with the resolution better than 0.1 mG, (4) high linearity (high directivity) with wide dynamic range more than ± 4 G, (5) anti magnetic shock of more than 40 G, (6) quick response, (7) high temperature stability, (8) high maximum operating temperature more than 80 deg.C, (9) mass productivity using Integrated Circuit processing, (10) reasonable cost. Only the high-performance micro magnetic sensors satisfying these ten conditions simultaneously can be adopted to the wearable micro magnetic sensors, that matches to human daily self-willed behavior. MAGNETO-IMPEDANCE EFFECT IN AMORPHOUS WIRE One of the most successful examples to create the high-performance micro magnetic sensors is the Amorphous Wire CMOS IC Magneto-Impedance Sensor based on the Magneto-Impedance effect in amorphous wires. The Magneto-Impedance effect in zero-magnetostrictive amorphous wires is a basic principle to create the magnetically sensitive and high-impedance element suitable for the high-performance micro magnetic sensors as expressed in the wire impedance Z_w : $Z_w = R_{dc}\, kr\, J_0(kr) / 2\, J_1(kr) \fallingdotseq (\rho\, L^2\, \omega\, \mu / 8\, \pi^2\, r^2)^{1/2}$ for δ sufficiently smaller than r (strong skin effect) (1), where J_0 and J_1 : 0^{th} and 1^{th} Bessel' s functions, respectively, R_{dc} : wire DC resistance, ρ : wire resistivity (130 μΩ–cm), L : wire length, ω : angular frequency of the wire current, μ : wire maximum differential permeability along the circumferential direction in the surface layer, r : wire radius, and δ $(= (2\rho/\omega\mu)^{1/2})$: skin depth. The wire impedance proportional to $(\mu(H_{ex}))^{1/2}$ sensitively changes with the external magnetic field H_{ex} at only the strong skin effect case (δ sufficiently smaller than r), in which the wire permeability μ sensitively and quickly changes with the magnetization rotation at the wire surface layer without any crystalline anisotropy, and simultaneously the wire impedance is very high. Thus the Magneto-Impedance effect in zero-magnetostrictive amorphous wire is suitable to constitute the sensitive and quick response micro magnetic sensors. Moreover, the zero-magnetostrictive amorphous wire is the highly robust material. AMORPHOUS WIRE AND CMOS IC MAGNETO-IMPEDANCE MICRO MAGNETIC SENSOR However, the Magneto-Impedance effect in amorphous wires using high-frequency wire current is so-called "Analog stage discovery" (science stage finding), which must be developed to so-called "Digital stage technology" (engineering stage) in order to use the Integrated Circuit processing technology for the mass productivity. We adopted the wire pulse current instead of the wire AC current having equivalent effect on the skin effect (Pulse current Magneto-Impedance effect). The unidirectional pulse train wire current forms the single domain structure for the magnetization rotation suppressing the Barkhausen magnetic noises, that results the high signal to noise ratio (S/N) magnetic sensors having a wide dynamic range. Furthermore, we adopted a pick-up coil set around the amorphous wire for constitution of a highly linear micro magnetic sensor suppressing the ringing electrical noises using an analog switch as a synchronous rectifying element. The digital type Magneto-Impedance micro magnetic sensor, named *MI sensor*, has been in mass production by Aichi Steel Corp, since 2002 as electronic compass chips for mobile phones, Smart phones, and wrist watches satisfying all the 10 requisite conditions expressed above. MULTI-DIFFERENTIAL OPERATION MI SENSOR ARRAY MODULE IN MAGNETIC GUIDANCE SYSTEM FOR CAR SELF DRIVING A robust magnetic guidance system for the car (bus) self driving has been developed by Aichi Steel Corp. and provided to the verification tests at Shiga pref. Hokkaido, and Okinawa pref. managed by Japanese Government on 2017. In the magnetic guidance, multi differential operation MI sensor array set to car underbody detects the weak magnetic field generated from a small ferrite magnet marker set on the road surface with 2 m interval cancelling road environmental various magnetic noises. Application of the MI sensors to the bio magnetic sensing using a pico-Tesla resolution and a high speed gyro sensing such as a Professional Baseball Pitching Ball Spin Analyzer with 50 rps detection (I-o-T sensing) have been also developed.

K. Mohri, T. Uchiyama, L..V. Panina, M. Yamamoto, and K. Bushida, "Review Article ; Recent Advances of Amorphous Wire CMOS IC Magneto-Impedance Sensors : Innovative High-Performance Micro Magnetic Sensor Chip," Journal of Sensors, Vol..2015, pp.1-8, 2015.

CONTRIBUTED PAPERS

4:00

BH-08. A localization method of submarines by using an airborne three-axis magnetometer carried on cruising aircraft.

Y. Shangguan[1], J. Yuan[1] and J. Zou[1]
1. Dept. of Electrical Engineering, Tsinghua University, Beijing, China

Abstract: A localization method for submarines is proposed in this paper, which can detect and locate submarines in a large area of sea rapidly by using an airborne three-axis magnetometer carried on cruising aircraft. The method is divided into three phases. First, a detection method based on the orthonormal basis function decomposition algorithm is applied in aircraft cruise to detect if submarines exist around. Second, a navigation method is to direct the aircraft flying toward the submarine to reduce the distance rapidly between the aircraft and the submarine. Third, a linear algorithm is to calculate the positon parameters of the submarine precisely. The theoretical analysis and numerical simulation examples are employed to verify the effectiveness of the method. 1. Introduction The submarine built of ferromagnetic materials will be magnetized by the geomagnetic field, resulting in an additional induction magnetic field, which can be detected and located by magnetic measurement. However, the geomagnetic field will seriously interfere with both the detection and the localization of submarines because it is much greater than the submarine induction field and will change slowly with the solar activity. Besides, the submarine induction magnetic field decays sharply with the distance, which results difficulties with accurate measurement in remote sensing. This paper presents a localization method for submarines, which takes advantage of the fast mobility of the airborne detection to achieve a wide range of detection and precise localization of submarines during aircraft cruise. 2. Localization method during aircraft cruise The method is divided into three phases: detection, navigation and localization. The first phase is based on the orthonormal basis function (OBF) decomposition method to determine whether submarines exist in the target area during aircraft cruise. After determining the existence of the submarine, a navigation method is proposed to direct the aircraft flying toward the submarine. When the aircraft is close to the submarine, the position parameters of the submarine are calculated with a linear algorithm. By alternate use of the navigation and the localization method in cruise, the direction of the aircraft cruise can be modified to be more accurate, which helps to achieve a result of localization with higher precision. The general flow-chart of the method is shown in Figure 1. 2.1 First phase : detection The first phase is based on the OBFs method to detect submarines in the target area during aircraft cruise. A detection point far from the target area is chose as the reference point and the geomagnetic field can be canceled by differential operation. The total field of the submarine induction magnetic field is decomposed into a set of orthonormal basis functions, out of which the dominant basis function is chosen as the detector. The detection occurs when the decision index value exceeds a predetermined threshold. In addition to determining whether the submarine exists, the minimum distance from the submarine to the cruise track, named the closest proximity approach (CPA), is estimated with a multi-channel manner. 2.2 Second phase : navigation When the detection occurs, a navigation method is proposed to guide the aircraft to approach the submarine to sense the submarine induction magnetic field at a close distance, as depicted in Fig. 2. First, the positon of the submarine is approximately estimated based on the CPA distance and parameters of the cruise. And then, a new cruise track is formed, where the CPA distance is remarkably reduced. At last, the aircraft is flying toward the submarine along the new track. 2.3 Third phase : localization When the aircraft is close to the submarine, the submarine induction field is relative stronger, and the accuracy of the measurement is high enough for localization calculation. In this paper, a linear localization formula is deduced based on the simplified mathematical model of the submarine in magnetic localization. A system of linear equations can be formed with the magnetic measurements of the three-axis magnetometer at four points on the cruise track. The position parameters of the submarine can be calculated by the solutions of the equations and the gradients of the magnetic field at a special point on the cruise track, where the horizontal components of the position parameter meet the direct proportion relationship. The simulation examples show that through this algorithm and a three-axis magnetometer with a sensitivity of 10pT, the relative error is less than 5.62% for localization when the CPA distance is 500m. The detailed results will be shown in the full text. 3. Conclusion (1)The orthonormal basis function decomposition method is suitable for detecting whether submarines exist by the measurement results of three-axis magnetometer, which can remarkably expand the effective detection range. (2)With the navigation method, the aircraft can be guided to approach the submarine, so that the localization of submarine with high accuracy can be achieved. (3)The linear localization algorithm presented in this paper has the advantages of low complexity, good real-time performance and easily implemented, which is suitable for locating submarines by cruising aircraft. (4)By the joint use of the three phases of the method in the aircraft cruise presented in this paper, submarines in a large area of sea can be detected and located rapidly.

[1] J. E. Mc Fee and Y. Das: Locating and identifying compact ferrous objects, IEEE Transactions On Geoscience and Remote Sensing, 28 (2) (1990), 182–193. [2] J. A. Baldoni and B. B. Yellen: Magnetic tracking system: Monitoring heart valve prostheses, *IEEE Transactions On Magnetics*, 43 (2007), 2430–2432. [3] Kazimierz Jakubiuk and Pawel Zimny, et al: Multi-dipoles model of ship's magnetic field, *International Journal of Applied Electromagnetics and Mechanics*, 39 (2012), 183–188. [4] E. Paperno, I. Sasada, and E. Leonovich: A new method for magnetic positioning and orientation tracking, *IEEE Transactions On Magnetics*, 37 (2001), 1938–1940. [5] M. Hirota, T. Furuse, K. Ebana, et al: Magnetic Detection of a Surface Ship by an Airborne LTS SUQID MAD, *IEEE Transactions On Applied Superconductivity*, 11 (2001), 884–887. [6] B. Ginzburg, L. Frumkis, and B. Z. Kaplan: Processing of magnetic scalar gradiometer signals using orthonormal functions, *Sens. Actuators A, Phys.*, 102 (2002), 67–75. [7] Arie Sheinker, Lev Frumkis, Boris Ginzburg, "Magnetic Anomaly Detection Using a Three-Axis Magnetometer," IEEE *Transactions on Magnetics*, vol. 45, pp. 160-167, No. 1, Jan. 2009. [8] Arie Sheinker, Boris Ginzburg, et al.: Magnetic Anomaly Detection Using High-Order Crossing Method, *IEEE Transactions Geoscience and Remote Sensing*, 50 (4) (2012), 1095–1103. [9] Chao Hu, Max Q.-H. Meng, and Mrinal Mandal, "A Linear Algorithm for Tracing Magnet Position and Orientation by Using Three-Axis Magnetic Sensors," IEEE *Transactions on Magnetics*, vol. 43, pp. 4096-4101, No. 12, Dec. 2007. [10] Yangyi Sui, Pan Kang, Defu Cheng, and Jun Lin, "Analysis and Simulation of Flight Effects on anAirborne Magnetic Gradient Tensor Measurement System," IEEE *Transactions on Instrumentation and measurement*, vol. 64, pp. 2657-2665, No.10, Oct. 2015.

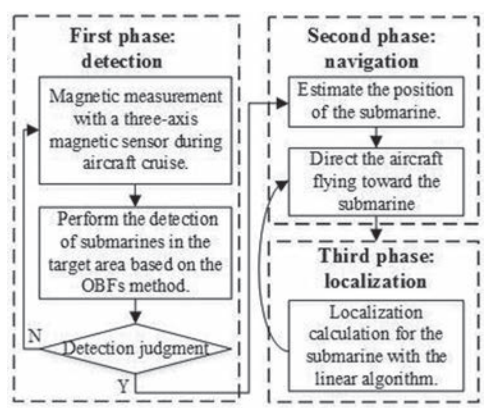

Fig. 1. General flow-chart of the localization method of submarines during aircraft cruise.

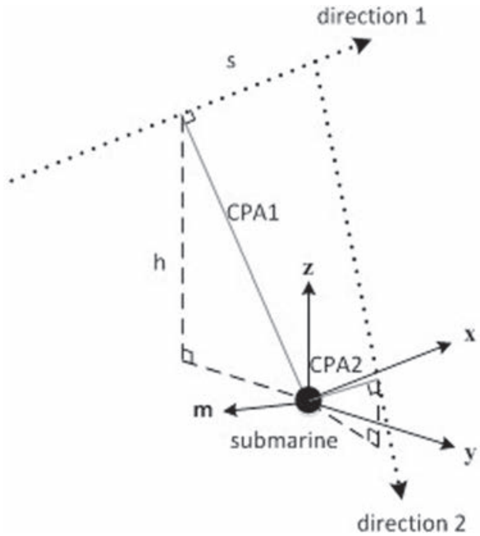

Fig. 2. The navigation process.

4:15

BH-09. Efficient wireless power transmission to medical implant using Wiegand sensor.

K. Takahashi[1], T. Yamada[1] and *Y. Takemura*[1]
1. Yokohama National University, Yokohama, Japan

1. Introduction We present a power receiving module of 21 mW using a magnetic wire as the core material in the detection coil. This power is equivalent to the power consumption of implantable medical devices, *e.g.*, capsule endoscopy. It is a novel concept and yields higher transmission efficiency than a conventional ferrite-core coil. Wireless power transmission to a medical implant deeply located in the human body is significant for developing therapeutic and diagnosis technology. It is normally difficult to design an excitation coil equal to the size of a human body for feeding sufficient power owing to the relatively high intensity and frequency requirements of the applied alternating magnetic field. The magnetic field required for achieving the power transmission of 21 mW was 4.8 kA/m at 10 kHz, which can be realized by a body-sized excitation coil [1]. The power receiving module developed in this study is also applicable to a battery-less sensor [2] and relating modules, which are the key devices designed for the Internet of Things. 2. Wiegand effect for power generation A magnetization reversal in magnetic wires with bistable magnetization states induces pulse voltage in a pick-up coil. The amplitude of the voltage is independent of the applied field down to zero frequency. This fast magnetization reversal is accompanied by a large Barkhausen jump, which is known as the Wiegand effect [3]. Currently, integrated circuits (ICs) powered by energy harvesting from Wiegand wires are commercially available for multiturn counters/encoders [4]. A twisted FeCoV wire, an optimum material yielding this effect, was used in this study. We achieved a battery-less Hall sensor operated by energy harvesting from a single Wiegand pulse [2]. As the pulse voltage induced in the pick-up coil is independent of the applied field frequency, a constant output voltage is generated even through a single event pertaining to the extremely slow movement of an excitation magnet, or through the application of an alternating magnetic field at low frequency. 3. Power receiving module using Wiegand effect An 11–mm-long $Fe_{0.4}Co_{0.5}V_{0.1}$ wire, supplied from Nikkoshi Co., Ltd., Japan, is used as the core material in the pick-up coil [5]. Its diameter is typically 0.25 mm. A pick-up coil with 400 turns is wound around the wire. When an alternating magnetic field is applied to the wire, a pulse voltage is induced in the pick-up coil. The peak voltage is approximately 1 mV per turn of the pick-up coil. The details related to the magnetic structure of the soft and hard layers in the wire and output voltage characteristics have been reported in Ref. 2. In this study, the positive and negative pulse voltages corresponding to the magnetization reversal of the wire under the applied alternating magnetic field were rectified and regulated to DC voltage as illustrated in Fig. 1. The configuration of the pick-up coil with a wire-core, excitation coil, rectifying circuit, and load resistor is also shown in the figure. Figure 2 shows the generated electric power, which was measured as power consumed at the load register of 2 kΩ. The applied alternating magnetic field was 4.8 kA/m in the frequency range of 0.01–50 kHz. The power was normalized by the area of the core. The power generation using a MnZn ferrite core with an effective permeability of approximately 50 was also evaluated. The frequency dependence of the result using the ferrite-core coil complies with the conventional theory of electromagnetic induction. As for the Wiegand wire core, the pulse voltage is independent of the applied field frequency, which results in efficient power generation at low excitation frequencies. The maximum power of 21 mW was achieved with using a 3000–turn pickup-coil. The wireless power transmission of 21 mW to a medically implantable device with a diameter on the order of 1 mm by an externally applied field of 4.8 kA/m at 10 kHz is a significant achievement because these field conditions are accomplished by a body-sized excitation coil with practical power supply. The experimental results of field intensity dependence, load resistance dependence, excitation by body-sized coil, and other possible applications including battery-less modules are also demonstrated in the presentation.

1) T. Aoto, K. Takahashi, H. Hoshiyama, Y. Yoshioka, T. Yamada, S. Ota, Y. Ikehata, S. Yamada, Y. Takemura, IEEJ, A137, 476, 2017. DOI: 10.1541/ieejfms.137.476 2) Y. Takemura, N. Fujinaga, A. Takebuchi, T. Yamada, IEEE Trans. Magn., 53, 4002706, 2017. DOI: 10.1109/TMAG.2017.2713837 3) J. R. Wiegand and M. Velinsky, U.S. Patent #3,820,090, 1974. 4) https://www.ichaus.de/product/iC-PM 5) A. Takebuchi, T. Yamada, Y. Takemura, J. Mag. Soc. Jpn., 41, 34, 2017. DOI: 10.3379/msjmag.1701R004

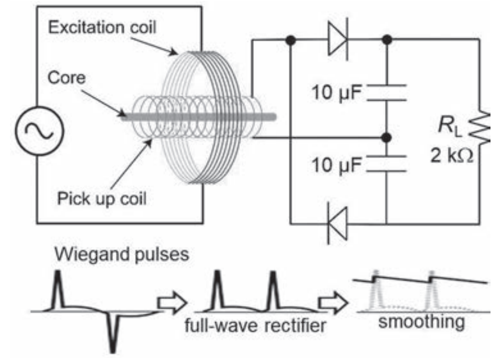

Fig. 1. Conversion of Wiegand pulse into DC voltage: Configuration of wire-core coil, excitation coil, full-wave voltage-doubling rectifier, and load resistor. Signal processing of Wiegand pulses to regulated DC voltage.

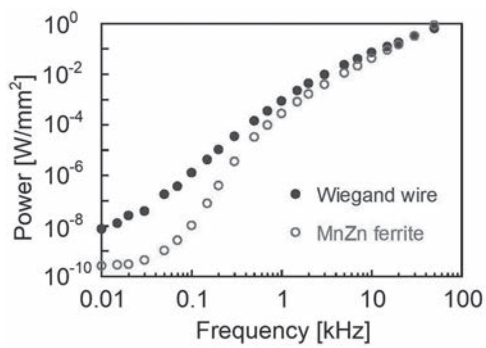

Fig. 2. Dependence of applied field frequency on electric power generated from wire-core and ferrite-core coils. The intensity of the applied magnetic field was 4.8 kA/m.

4:30

BH-10. Accurate Position Detection in Wireless Power Transfer Using Magnetoresistive Sensors for Implant Applications.

W. Han[1], K. Chau[1], C. Jiang[1] and W. Liu[1]
1. Electrical and Electronic Engineering, The University of Hong Kong, Hong Kong, Hong Kong

I. INTRODUCTION Recently, the utilization of magnetic resonant coupling (MRC) mechanism for wireless power transfer (WPT) has been actively investigated. Among numerous applications of WPT technology, the energization of implanted biomedical devices wirelessly and uninterruptedly from external supply is important because it can eliminate possible device replacement due to battery depletion. Given the implanted receiver is invisible from the external transmitter, the coil misalignment occurs easily which results in low transfer efficiency and high magnetic field leakage, and consequently endangers the human health [1]. Thus, the development of accurate position detection of the implanted receiver from the external transmitter is highly desirable. Presently, most studies of the position detection in WPT are focused on the application of electric vehicles. Although the corresponding technologies such as coil sets [2] or auxiliary multi-coils [3] have achieved fruitful outcome, they are too bulky and complicated to be used in implant applications. Due to the advantages of high stability, small size, low power consumption and high precision, the magnetoresistive (MR) sensor has been widely used in many industrial applications [4]. Generally, they are arranged in an array style to measure the magnetic field vector [5] or a moving magnetic object [6]. To the best of authors' knowledge, the application of MR sensors in WPT is absent in literature. In this paper, a new position detection approach in WPT is proposed and implemented, which is particularly suitable for implant applications. The key is to use a MR sensor array to directly measure the variation of magnetic field so as to precisely detect the relative position of the implanted receiver from the external transmitter. Therefore, the advantages of efficient and compact WPT for implant applications can be achieved. II. METHODOLOGY Fig. 1 shows the structure and equivalent circuit of the proposed WPT system using a MR sensor array. The transmitter and receiver are connected to their compensation capacitors in series, and operate at the same resonant frequency to achieve the desired MRC. And 12 single-axis MR sensors are distributed evenly along a circular array in the inner part of the transmitter. The MR sensor array is arranged along the vertical sensing direction and is energized by a low DC voltage. For simplicity, the coil misalignment is assumed to be along the horizontal direction only. Hence, the position detection can be considered as the detection of the misaligned orientation and departed displacement. The MR sensor output is amplified by the operational amplifier (OP) and then collected by the data acquisition (DAQ) card. Consequently, based on the proposed MR sensor array detection system, the external transmitter can be adjusted to achieve accurate alignment with the implanted receiver so that the transfer efficiency can be improved while the magnetic field leakage can be suppressed. Firstly, theoretical equations of the proposed system are deduced to assess the relationship between the distribution of magnetic field and the relative position of the implanted receiver. Secondly, the magnetic field distributions under different misalignments are analyzed by using finite element method based software JMAG. As shown in Fig. 2 (a), two typical cases of misalignment are analyzed: Case 1 is 30 mm misalignment along the 225^0 direction; Case 2 is 20 mm misalignment along the 90^0 direction. The corresponding magnetic field distributions are shown in Fig. 2 (b) and (c), respectively. Meanwhile, the magnetic flux densities at 12 points that can be captured by the MR sensor array are shown in Fig. 2 (d). It can be observed that the misaligned orientation is in coincidence with the location of the maximum sensor output and the departed displacement is in inverse proportion with the sensor output. Therefore, both the misaligned orientation and departed displacement can be detected by measuring the magnetic field distributions to accurately locate the position of the implanted receiver. III. CONCLUSION In this paper, an accurate position detection in WPT using MR sensors has been proposed and implemented for implant applications. The crucial point is to employ a MR sensor array to detect the variation of magnetic field so that the implanted receiver position can be accurately located. Theoretical analysis, numerical simulation and experimental results are given to validate the proposed system. This work was supported by a grant (Project No. SFBR 201511159096) from the University of Hong Kong, Hong Kong.

[1] K. Fotopoulou and B. W. Flynn, "Wireless power transfer in loosely coupled links: Coil misalignment model," *IEEE Trans. Magn*., vol. 47, no. 2, pp. 416–430, Feb. 2011. [2] Y. Gao, C. Duan, A. A. Oliveira, A. Ginart, K. B. Farley and Z. T. H. Tse, "3-D coil positioning based on magnetic sensing for wireless EV charging, " *IEEE Trans. Transport. Electrific.,* vol. 3, no. 3, pp. 578-588, Sept. 2017. [3] S. Y. Jeong, H. G. Kwak, G. C. Jang, S. Y. Choi and C. T. Rim, "Dual-purpose non-overlapping coil sets as metal object and vehicle position detections for wireless stationary EV chargers, " *IEEE Trans. Power Electron.*, vol. pp, no. 99, DOI: 10.1109/TPEL.2017.2765521, Oct. 2017. [4] K. Zhu, W. Han, W. K. Lee, P. W. T. Pong, "On-site non-invasive current monitoring of multi-core underground power cables with a magnetic-field sensing platform at a substation," *IEEE Sensors J*., vol. 17, no. 6, pp. 1837–1848, Mar. 2017. [5] G. Zhao, J. Hu, Y. Ouyang, W. Chang, Z. Wang, S. Wang, J. He and J. Bi, "Novel method for magnetic field vector measurement based on dual-axial tunneling magnetoresistive sensors, " *IEEE Trans. Magn*., vol. 53, no. 8, DOI: 10.1109/TMAG.2017.2655007, Aug. 2017. [6] C. Hu, M. Li, S. Song, W. Yang, R. Zhang, and M. Q.-H. Meng, "A cubic 3-axis magnetic sensor array for wirelessly tracking magnet position and orientation," *IEEE Sensors J*., vol. 10, no. 5, pp. 903–913, May 2010.

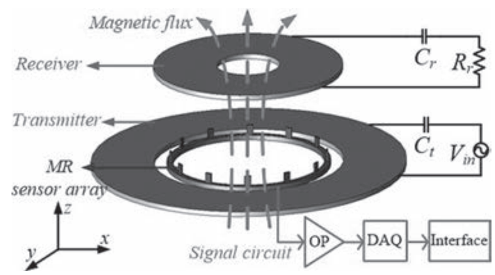

Fig. 1. Equivalent circuit of the proposed system.

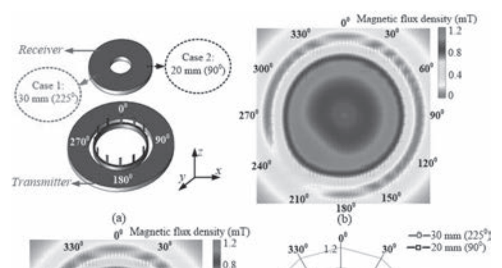

Fig. 2. Analysis of two misalignment cases. (a) Arrangement. (b) Magnetic field distribution of Case 1. (c) Magnetic field distribution of Case 2. (d) Measured magnetic flux densities using MR sensor array.

4:45

BH-11. Traffic Flow and Vehicle Speed Measurements using Magnetoresistive Sensors.

B. Santoso[1], Y. Bo[2], O. Chun Lian[1] and Y. Zhimin[1]
1. Non-volatile Memory, Data Storage Institute, Singapore, Singapore;
2. Institute of High Performance Computing, Singapore, Singapore

I.Introduction The magneto-resistive (MR) sensor is a good candidate for vehicle detection sensor which is low cost, scalable in deployment and reliable. Most vehicles have ferrous materials which distort the uniform earth magnetic field. A low field MR sensor can be used to detect this distorted field whenever vehicles are present [1]. In addition, when the MR sensors are deployed in an array, more information about the traffic flow can be obtained. This information is critical for the traffic light regulation used in traffic flow control. II.Experiment Setup A.Sensor Selection Magnetic sensor detects magnetic field and quantifies its magnitude by producing changes in electrical output. The state of art magnetic sensing element is made of layers of thin film material. The available magnetic sensors include Hall sensor, anisotropic magneto-resistive (AMR) sensor, giant magneto-resistive (GMR) sensor, and tunneling magneto-resistive (TMR) sensor [2]. The ambient earth magnetic field is uniform with a strength typically in the range of 0.5-0.6 Gauss. The AMR sensor fits the range with a good sensitivity. The 3-axis AMR sensor is preferred to map out magnetic field changes along *x, y and z* directions. Honeywell magnetometer HMC5883L is selected in this work. The sensor has a selectable operating range of minimum setting at +/-0.83G with 2mG typical root-mean-square (RMS) noise. B.Setup for Roadside Vehicle Detection Due to the spacing loss, the intensity of magnetic field is sensitive to the spacing between surface magnetic charges on vehicle body and the sensor [3]. In this work, we deploy the sensor nodes at the road side on curbs to demonstrate the feasibility of using magnetic sensors for the traffic flow and density measurements. A typical road lane in Singapore is about 3-4 m wide with a kerb height of 20 cm. The 3-axis sensor is installed in the directions of x axis cross the road, y axis down the road, and z axis out of ground. III.Results and Discussion When the vehicle passes by the sensor, all three channels of 3-axis AMR sensor measuring the change of magnetic field in *x,y,z* directions register as an event. To extract the precise vehicle information, the timestamp of detected vehicle signal must be as accurate as possible. Using the collected timestamp, the traffic flow or the number of vehicles passing through the road section per unit time can be calculated. The accuracy of timestamp is critical for the calculation of precise velocity of each passing vehicle. A.Signal Processing The signals of low cost sensors need to be processed to improve the signal-to-noise ratio and extract the velocity signal of the vehicle. A moving average window is used to remove the random and periodic noises. The processed signals are clean enough to identify the specific timestamp of the vehicles based on the signal profile, such as peaks or the steepest ascent/descent, etc. Both the sampling frequency and the signal amplitude resolution are critical to determine the accuracy of vehicle velocity. B.Velocity Accuracy Validation with High FPS Videos In the velocity measurement, two identical AMR sensor nodes are allocated at 1m spacing along the road. Concurrently, a video of the vehicle movement on the road is taken using a high resolution, high framerate video camera operating at 250 fps (frames per second) as shown in Fig. 2. There are 2 white markers placed on the road corresponding to the position of AMR sensors, which are also 1 meter apart. The white marker is used as the reference position to calculate the velocity from video images of the vehicle. The margin of timing error from the video is on the order of 4 ms, which has a speed accuracy of 0.04 m/s at 10 m/s velocity or of 0.12 m/s at 30 m/s velocity. It is accurate enough to validate the velocity accuracy measured by AMR sensors. C.Power Line Interference The AMR sensor is sensitive to the magnetic field being produced by various sources. In some cities, the electricity cables are buried right under the road. The powerline creates magnetic field alternating at 50/60 Hz. This interference field becomes a source of noise that manifests in the raw data of the sensor. The sensitive signals for vehicle detection lie in the *x-y* plane. First, cancellation of signals from both x-axis and z-axis is applied.The median filter is used to remove the spikes noise to get the final clean signal. The signals of y-axis and x-axis are used to calculate the vehicle velocity. D.Real Time Detection of Traffic Flow and Density For practical application, a software has been developed for the real-time processing and analysis of the traffic flow based on the raw data obtained from the AMR sensor nodes. The traffic flow is measured with one set of AMR sensor nodes at the side of a road for an hour. To understand real traffic behaviour, one can calculate the flow from the velocity of the detected vehicle as shown in Figure 2. The traffic flow time series indicates the number of vehicles passing through the road section per unit time and it is useful to deduce the traffic density on a particular road junction. IV.Conclusion Two of AMR sensor nodes separated at 1m spacing is able to measure the velocity of vehicles with good accuracy. The setup is of low cost and low power and is easily deployable in a large scale for traffic flow measurement. Due to the sampling frequency limit of on-the-shelf digital AMR sensor, the setup can only measure the vehicle speed below 100 Km/h.

[1] C.H Smith, M.J Caruso, R.W Schneider, T. Bratland, "A New Perspective on Magnetic Field Sensing", Sensors 5-12, pp 34-46, 1998 [2] Honeywell International Inc, "Vehicle Detection using AMR Sensors", Application Note AN218, August 2005 [3] Stanley V. Marshall, "Vehicle Detection Using a Magnetic Field Sensor", IEEE Trans. On Vehicular Technology, vol VT-27, no 2, pp65-68, 1978 [4] Rajko Horvat, Goran Kos and Marko Sevrovic, "Traffic Flow Modelling on the Road Network in the Cities", Tech Gazette 22, vol 2, pp475-486, 2016.

Fig. 1. Frame by frame images of the moving vehicle extracted with 250fps camera

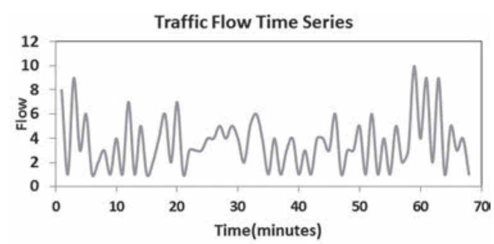

Fig. 2. Traffic flow time series

TUESDAY AFTERNOON, 24 APRIL 2018 ORCHID II, 2:00 TO 5:00

Session BI

COMPUTATIONAL MAGNETICS: MICROMAGNETICS AND AB-INITIO CALCULATIONS

Andrivo Rusdyi, Chair
National University of Singapore, Singapore

CONTRIBUTED PAPERS

2:00

BI-01. GPU-Accelerated Atomistic Energy-Barrier Calculations for Skyrmion Annihilation.

P.T. Heistracher[1], C. Abert[1], F. Bruckner[1], C. Vogler[1] and D. Suess[1]
1. Physics of Functional Materials, University of Vienna, Vienna, Austria

Isolated magnetic skyrmions have recently attracted a lot of attention in the scientific community as a potential candidate for storage and for logic devices. It has been demonstrated that an isolated skyrmion can be a stable configuration in a nanostructure, that it can be locally nucleated by injection of a spin-polarized current and that it can be displaced by current-induced spin torques, even in the presence of large defects [1]. According experiments demonstrate the applicability of topological charge as a carrier of information by showing the feasibility to write and erase such spin textures in a controlled fashion using local spin-polarized currents from a scanning tunnel microscope [2]. Single skyrmions or chains of skyrmions can be nucleated as a metastable state in thin films and the controlled creation and annihilation of these isolated skyrmions is opening a path to new concepts of spintronic devices. In these applications, the temporal stability of the encoded information is an important measure for their feasibility. The energy required to create or annihilate skyrmions is directly related to their stability and therefore is of high interest. Due to their topological protection, skyrmionic spin configurations cannot be continuously deformed to other magnetic configurations such as spin spirals or ferromagnetic states. This property gives rise to their comparably high annihilation energy and thus stability. Even though micromagnetic simulations are capable of describing skyrmion configurations, they cannot account for skyrmion creation or annihilation processes as they are mediated by a change of topological charge via Bloch points. This is in contradiction with the main assumption of micromagnetics, which states that the magnetic field can be approximated as a continuous field. Therefore, we consider an atomistic spin model to account for such skyrmion creation and annihilation processes. The atomistic model implies a considerably higher computational effort due to the increased number of elements in order to account for the high spacial resolution required by the atomic lattice. For this reason we develop a GPU-accelerated finite-difference code which solves the Landau–Lifshitz–Gilbert equation for an atomistic spin model considering dipole-dipole, exchange, uniaxial-anisotropy and Dzyaloshinskii-Moriya (DM) interactions. We further apply the improved string method [3] in order to calculate the creation and annihilation energy of magnetic skyrmions. The string method yields the most-probable transition path between two chosen magnetic configurations. This path corresponds to the minimum energy path in configuration space and therefore allows for the calculation of the energy barrier between those two configurations. For the calculation of skyrmion creation and annihilation energies a meta-stable skyrmionic magnetic configuration represents the first configuration and a homogeneous field configuration the latter configuration. Figure 1 depicts such an energy path for each iterative step performed in the string method. After several hundred iterations the string method converges and yields the energy-barrier. The performance gain obtained by the usage of a GPU-accelerator allows for an extensive parameter study. Figure 2 shows a phase diagram of the calculated annihilation energy for various values of the DM interaction energy d and the uniaxial-anisotropy energy k. High values of d favor the formation of domain walls whereas high values of k suppress domain walls. In the region with low values of d and high values of k, the creation of skyrmions is suppressed and no energy barrier occurs. In the region with high values of d and low values of k surrounded by a dashed polygon, the initial homogeneous configuration used in the string method is no longer a local energetic minimum and evolves to a skyrmionic configuration itself, thus yielding higher order transitions. Skyrmion annihilation processes mediated by a Bloch point are observed in the intermediate region and feature straight lines of equal energies in the phase diagram indicating a linear relation between the two trends.

[1] Sampaio, J., et al. "Nucleation, stability and current-induced motion of isolated magnetic skyrmions in nanostructures." *Nature nanotechnology* 8.11 (2013): 839-844. [2] Romming, Niklas, et al. "Writing and deleting single magnetic skyrmions." *Science* 341.6146 (2013): 636-639. [3] Weinan, E., Weiqing Ren, and Eric Vanden-Eijnden. "Simplified and improved string method for computing the minimum energy paths in barrier-crossing events." *The Journal of chemical physics* (2007).

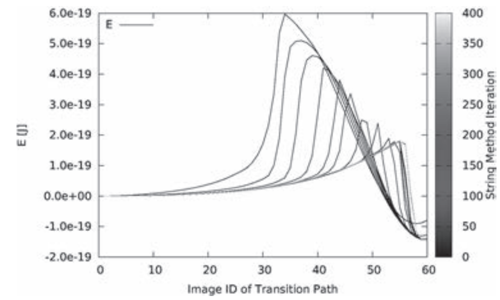

Fig. 1. Energies of transition paths for skyrmion annihilation as obtained by the string method. Image ID 1 represents a skyrmionic field configuration, Image 60 a homogeneous field configuration. Fast string convergence is observed and after several hundred iterations the termination criterion is met.

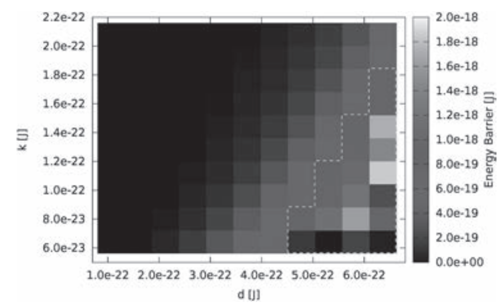

Fig. 2. Magnitude of the skyrmion annihilation energy as as function of the DM interaction energy d and uniaxial-anisotropy energy k. Values within the dashed polygon represent higher order transitions.

2:15

BI-02. Effect of dipolar interactions on magnetization reversal process using ultra-large-scale micromagnetics simulation.

H. Tsukahara[1], K. Iwano[1], C. Mitsumata[2], T. Ishikawa[1] and K. Ono[1]
1. High Energy Accelertaor Research Organization, Tsukuba, Japan;
2. National Institute for Materials Science (NIMS), Tsukuba, Japan

Importance of high-performance permanent magnets with high coercivity and remanence, which is indispensable for electric motors, increases due to shifting toward electric vehicles. Magnetization dynamics within the permanent magnet has been investigated over the years. However, there is a discrepancy between coercivities of theoretical calculations and experiments. When applied magnetic field exceeds the coercive field, magnetic nucleation cores are formed in some grains of the permanent magnet, and magnetization reversal regions expand into the magnet. Thus, it is important to reveal a mechanism of the formation of the nucleation cores. In this study, we performed ultra-large-scale micromagnetics simulations based on Landau-Lifshitz-Gilbert equation to clarify the mechanism of formation of the nucleation cores inside the hot-deformed permanent magnet. Figure 1(a) shows a simulation model for the hot-deformed permanent magnet with the size of 2048 × 2048 nm × 512 nm which consists of 3,391 tabular grains whose thickness is 32 nm and averaged diameter is 160 nm. We assumed magnetic materials of the grain is $Nd_2Fe_{14}B$ [1]. For inter-grain exchange interaction, the strength of exchange interaction was set as 1% of the intra-grain exchange interaction. The easy axis of each grain is tilted by 11.6 degrees on average from the c-axis. We simulated magnetization dynamics using our simulation code under periodic boundary condition to calculate magnetization inside the hot-deformed permanent magnet [2]. Figure 1(b) shows the simulated demagnetized curve. The hysteresis curve has a high square ratio, and coercivity of this simulation model is 28.0 kOe. When the external field reaches the coercive field, the nucleation cores are formed in some grains as shown in the inset of Fig1(b), and magnetization reversal regions expand across the grain boundaries. Finally, interaction domain structure appears inside the hot-deformed permanent model as shown Fig. 1(c) [3]. As can be seen from the inset of Fig. 1(b), the nucleation cores occur in grains with special characteristics. We plot the magnetization and the effective field under zero external field. Figures 2(a)-(d) show the magnetization and exchange, anisotropy and dipolar fields under zero external field. The magnetization of the grains in which the nucleation core are formed largely tilts from the z-axis. The tilt angle of magnetization does not affect the exchange and anisotropy fields in this simulation system. In contrast, the dipolar field is influenced by the tilt angle of the magnetization from adjacent grains in the z-direction that indicate white dotted lines. In this place, strong negative dipolar fields from the adjacent grains in contact at the top are applied onto edges of the grain where the nucleation core will be formed. The tilt angle of easy axis and the dipolar field at the edges on the top and bottom sides of the grains should be a good descriptor for the grains in which formation the nucleation cores are formed. Figures 2(e)-(g) are scatter plots as a function of the tilt angle of easy axis and minimum dipolar field at the edge of the grains during magnetization reversal process at 0.12 ns, 0.28 ns, and the interaction domain structure, respectively. Color indicates the magnetic domain configuration of the grains. The grains with multi-domain structure (blue circles) appear in large tilt angle and strong negative dipolar field region (a region surrounded by a dotted line) because the nucleation cores are formed in the grains. The number of the grain in this area is around 20. Thus, we can distinguish the grains that have a possibility of the formation of the nucleation core from other around 3000 grains using this scatter map. As time elapses, the grain having multi-domain structure appears in the high dipolar field region. Finally, the grains having the single-domain structure with positive or negative magnetization along the z-direction have almost same distribution.

[1] M. Sagawa, S. Fujimura, H. Yamamoto, Y. Matsuura, and S. Hirosawa, J. Appl. Phys. 57, 4094 (1985) [2] H. Tsukahara, K. Iwano, C. Mitsumata, T. Ishikawa, K. Ono, Comput. Phys. Commun, 207, 217 (2016). [3] H. Tsukahara, K. Iwano, C. Mitsumata, T. Ishikawa, K. Ono, 217 (2016). AIP Advance 7, 056224 (2017).

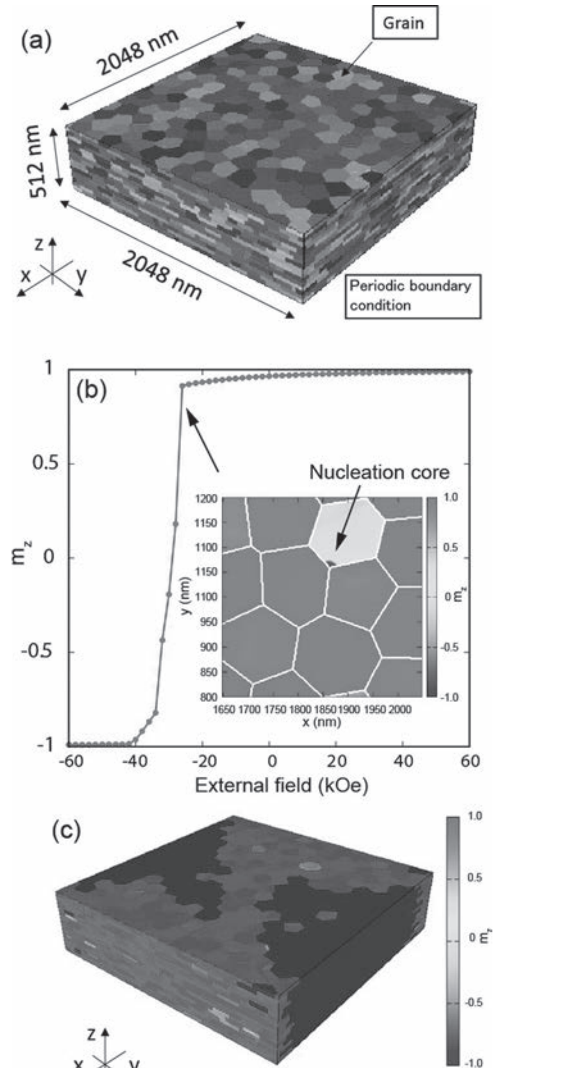

Fig. 1. (a) Simulation model for the hot-deformed permanent magnet. (b) Hysteresis curve and cross section of magnetization when nucleation cores are formed. White solid lines represent grain boundary. (c) Interaction domain structure at coercivity.

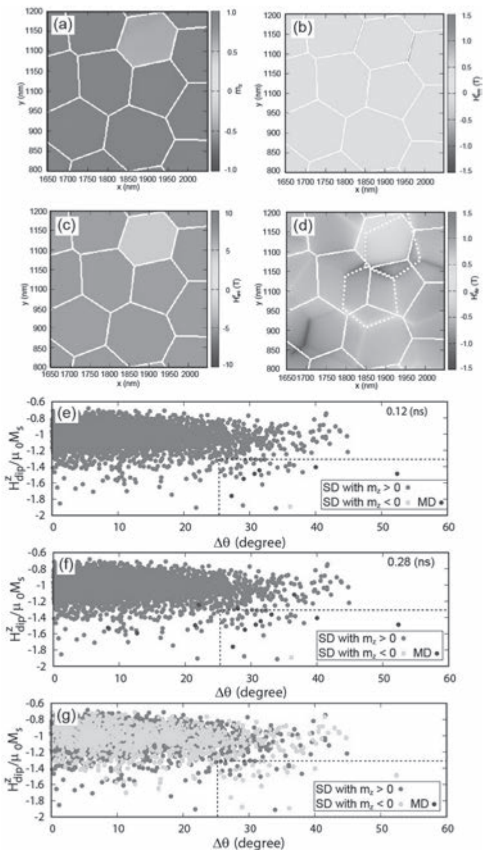

Fig. 2. Cross sections of (a) magnetization, and (b) exchange, (c) anisotropy and (d) dipolar fields under zero external field. White solid and dotted lines represent grain boundary within same and upper layers, respectively. Scatter maps as a function of the tilt angle of easy axis and minimum dipolar field during magnetization reversal progresses at (e) 0.12 ns, (f) 0.28 ns, and (g) interaction domain structure. Blue, red, and green circles represent the grains having multi- and single-domain structure with positive and negative orientation of magnetization along z-direction.

2:30

BI-03. Withdrawn

2:45

BI-04. Novel micromagnetic approach for self-consistent modeling of magnetization and temperature dynamics.

O. Chubykalo-Fesenko[1], D. Serantes[2], P. Nieves[3], C. Muñoz-Mendez[2] and R.W. Chantrell[4]
1. Instituto de Ciencia de Materiales de Madrid, CSIC, Madrid, Spain; 2. Universidad de Santiago de Compostela, Santiago de Compostela, Spain; 3. Universidad de Burgos, Burgos, Spain; 4. University of York, York, United Kingdom

The temperature plays an essential role in many novel and exciting phenomena such as domain wall motion under thermal gradients, temperature-assisted magnetization switching, ultra-fast magnetization dynamics, etc. In standard micromagnetics temperature is included as the white noise represented by random fields, however, this approach is valid for temperatures far from the Curie temperature only. At high temperatures the micromagnetics based on the Landau-Lifshitz-Bloch (LLB) equation which includes longitudinal magnetization dynamics has been developed in recent years [1,2]. Typically the influence of temperature on the magnetization dynamics is studied. However, there is an inverse effect when the magnetization dynamics produces temperature change, for example in the magnetocaloric effect or during the heating under an ac applied field. A promising application in this respect is the magnetic hyperthermia treatment for cancer. In the modeling of the temperature rise during the ac-field application, the released heat is usually evaluated in the global sense from the hysteresis cycle area, which corresponds to the whole thermodynamic ensemble. However this does not allow to describe, for example, the timescale of the temperature rise or the local individual heating around one nanoparticle, aspects that may play a key role in the development of accurate and safe biomedical protocols. As a different example, in the domain wall dynamics one can expect large local magnetization changes (especially if the domain wall has high velocity as is the case of antiferromagnets). These can lead to a local dynamical temperature rise. Recently, the self-consistent micromagnetic dynamical approach for both magnetization and temperature has been developed [3]. The approach consists in the simultaneous solution of the (quantum) LLB micromagnetic equation coupled to the equation for the temperature dynamics. The latter equation is derived from the self-consistent quantum mechanical treatment of the spin-phonon Hamiltonian and the density matrix approach. A more simple derivation considers simple thermodynamical reciprocity relations. In this talk we will discuss the main features of the novel micromagnetic approach. Not too close to the Curie temperature and in the absence of precessional effects, the global temperature rise coincides with that of the quasi-static hysteresis area evaluation. The temperature rise exists only for non-reversible processes, i.e. when the local magnetization torque is zero, consequently the magnetisation precession always produces some temperature change. Another source of the temperature change is the presence of the longitudinal relaxation term, active either in short timescale or close to the Curie temperature. Finally, any moving magnetic object (such as a domain wall) also produces some heat release. Furthermore, we will discuss some examples of recent modeling using this approach. Fig.1 presents modeling of dynamical temperature release during the ac-field treatment of an individual magnetite nanoparticle for several values of the energy relaxation times into the environment. The magnetization switches precessionally and during this time the temperature increase takes place. Importantly, the new approach allows to distinguish the individual heating of each interacting nanoparticle, for example, we study how the switching of one nanoparticle produces the temperature change on its neighbor. Particularly, we will present an example of coupled temperature/magnetization dynamics of two dipolar coupled nanoparticles. Here the magnetization switching of one nanoparticle produces a small irreversible change in magnetization of its neighbor during which the heat is also released. We believe that the model presented in this work constitutes a step forward towards more realistic modeling of many interesting phenomena where the magnetic and temperature dynamics are relevant, like heat-assisted magnetic recording, ultrafast magnetism, magnetic refrigeration, magnetic hyperthermia or spincaloritronics.

[1] N. Kazantseva, et al Phys. Rev. B 77, 184428 (2008). [2] J.Mendil et al, Sci. Rep. 4, 3980 (2014). [3] P. Nieves, D. Serantes, O. Chubykalo-Fesenko, Phys. Rev. B 94 (2016) 014409

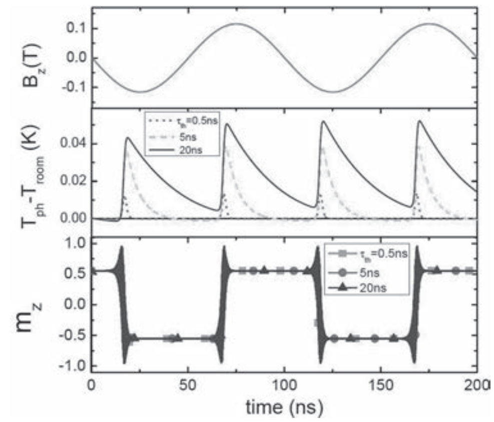

Fig. 1. The time evolution of the external applied magnetic field (upper panel), temperature (middle panel) and the magnetization component parallel to the field (lower panel) in a 20 nm magnetite nanoparticle for three different values of the characteristic energy relaxation time to the environment.

3:00

BI-05. Simulation of the Novel Magnetic Response of the Perpendicular Synthetic Ferrimagnet Ni_3Pt/Ir/Co using VAMPIRE.

J.N. Scott[1], W.R. Hendren[1], R. Bowman[1], R.W. Chantrell[2] and R.F. Evans[2]
1. Queen's University Belfast, Belfast, United Kingdom; 2. University of York, York, United Kingdom

Beyond the current envisaged roadmap for magnetic recording involving heat assisted magnetic recording (HAMR) and then potentially allied to bit patterned media (BPM) is the possibility of all optical magnetic switching (AOMS) as either a future or alternative, ultrafast, high density data storage mechanism. To date most studies in AOMS rely on rare earth alloys [1] or, more recently, complicated synthetic structures [2]. To design and create synthetic ferrimagnet systems requires knowledge and control of the interaction of several fundamental magnetic parameters such as M_S(T), H_c(T) and exchange J. Simulation of an idealised exchange-coupled Fe/FePt synthetic ferrimagnet demonstrated a short heat-pulse was sufficient to induce ultrafast heat-induced switching [3] but the simulation relied on inferred materials parameters such as weighted average to deduce the exchange J, between the two ferromagnetic layers. Therefore, there has been limited exploration and validation of atomistic models using data arising from realistic ferromagnet/metal/ferromagnet synthetic ferrimagnet structures. In this paper we have successfully corroborated, in simulation and experiment, unexpectedly novel, magnetic response of a simple perpendicular synthetic ferrimagnet Ni_3Pt/Ir/Co. The ferromagnetic layers being exchanged coupled via a metallic non-magnetic spacer layer through the Ruderman-Kittel-Kasuya-Yosida (RKKY) interaction and fabricated via UHV sputtering using the atomistic simulation package, VAMPIRE [4]. To do this we first describe the parametrisation of VAMPIRE from experimental data. It is necessary to obtained simulations of the constituent magnetic layers (Ni_3Pt & Co); this requires determination of the dimensions and simulation size that is appropriate for the individual layers but also representative of the synthetic structure to be designed. In Figure 1 we show both experimental and the simulated hysteresis loops for Ni_3Pt and Co layers. That along with M_S(T) experimental data, allows the identification of combinations of Ni_3Pt and Co that would lead to above room temperature magnetic compensation. Figure 2 shows the VAMPIRE simulation of a Ni_3Pt (100Å)/Ir (5Å)/Co (10Å) perpendicular ferrimagnet. The setup for the VAMPIRE simulation comprised 100Å x 100Å x 110Å cell, comprising ~106,000 spins, parameterised from experimental data and with the exchange parameter J, derived from a hysteresis loop taken at 10K for the Ni_3Pt (100Å)/Ir (5Å)/Co (10Å) multilayer. A suitable roughness at the interface of the magnetic layers is also included. In executing the simulation, the multilayer is perpendicularly statured, at each temperature point, and then allowed to relax to a remanence magnetisation determined at 2ns. The experimental SQUID derived M_R(T) data on Figure 2 agree very well with the simulation. Further, by adjusting the thickness of the Ir coupling layer the system was seen to remain ferromagnetically coupled across the temperature range. This gives us further confidence that both parametrisation and simulation are accurate. Unexpectedly, we observe that the overall simulated M_R(T) does not show a single 'compensation' point, but rather a magnetic reversal region between two temperatures where there is a magnetic compensation. This is confirmed by the SQUID data that shows negative remanence between these temperatures. In, addition, the SQUID data shows clear negative reversal switching [5] in that region as illustrated in the inset of Figure 2 and this will be discussed further. In summary, we demonstrate the integration of atomistic based modelling using VAMPIRE and experimental synthetic ferromagnetic structures to directly influence and direct the synthesis of novel magnetic materials.

[1] C. D. Stanciu et al, Phys. Rev. Letts. 99, 047601 (2007) [2] S. Mangin et al, Nature Materials 13, 286 (2014) [3] R. F. L. Evans et al, Appl. Phys. Lett. 104, 082410 (2014) [4] R. F. L. Evans et al, J. Phys.: Condens. Matter 26, 103202 (2014) [5] K. Takanashi et al, Appl. Phys. Lett. 63, 1585 (1993)

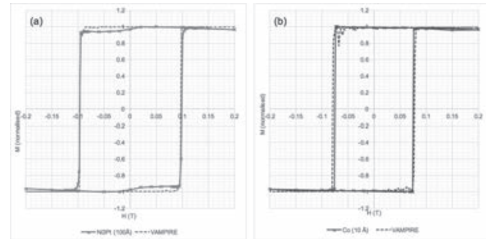

Fig. 1. Simulated and experimental hysteresis loops for the individual Ni_3Pt (a) and Co (b) films. The Ni_3Pt simulation was performed using ~96000 spins within a 100Å x 100Å x 100Å volume and the Co simulation with ~10000 spins and dimensions of 100Å x 100Å x 10Å.

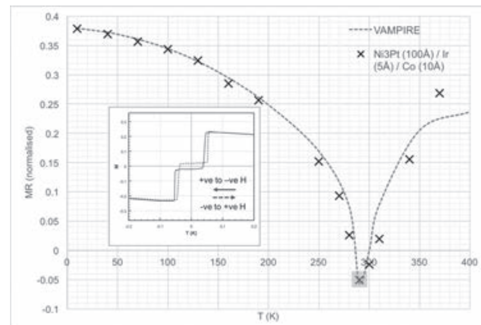

Fig. 2. M_R(T) VAMPIRE simulation compared to experimental SQUID measurements of Ni3Pt (100Å) / Ir (5Å) / Co (10Å) mulitlayer. Hysteresis loop recorded at 290K showing negative reversal is shown inset.

3:15

BI-06. Evaluation of Thermal Stability of Spin-Transfer Torque based Magnoresistive Random-Access Memory for Cache Applications in Advanced Technology Nodes.

H. Dixit[1], S. Agarwal[1], D. Datta[1], A. Jacob[2], D. Shum[3] and F. Benistant[3]
1. Globalfoundries Engineering Pvt. Ltd., Bangalore, India;
2. Globalfoundries, Malta, NY, United States; 3. Globalfoundries Singapore Pte. Ltd., Singapore, Singapore

Modern computing systems require enhanced performance; however, the conventional memories such as Static Random Access Memory (SRAM) are inadequate to support this demand. This is mainly due to the fact that SRAM density cannot be increased commensurately with Complementary Metal–Oxide–Semiconductor (CMOS) transistor scaling. For example, typically the six-transistor (6T) SRAM, which has long been the workhorse of high-performance caches, requires a cell size of 120-200F^2, where F is the feature size [1]. On the other hand, Spin-Transfer Torque based Magnetoresistive Random-Access Memory (STT-MRAM) have emerged as universal memory technology due to its non-volatility, endurance, low operating voltages and ultrafast switching [2]. Further, they occupy much less area with 1T design comparable to DRAM with cell size of 6-10 F^2 [1]. Thus, STT-MRAM is most suited for on-chip cache applications with highest possible density. One of the most important factors that determines the data retention time of STT-MRAM towards cache applications is the thermal stability of magnetization. It is known that with shrinking Magnetic Tunnel Junction (MTJ) dimensions, commensurate with CMOS scaling, the thermal stability of magnetization also decreases. This results in reduced retention times and increased bit error rates, posing significant challenges towards its application as cache memory. Hence, it is important to evaluate the thermal stability of magnetization as a function of decreasing MTJ diameter, to address their scalability and performance in advanced cache technology. In this article, we focus on perpendicular-MTJ and perform Micromagnetic simulations to evaluate the thermal stability factor at reduced MTJ diameter. Currently, the 22 nm nodes uses MTJ with 55-75 nm diameters [3]. First, we discuss the thermal energy barrier (E_b) necessary for 7/21 days of data retention for L3-cache applications at different failure in time (FIT) rates. The requirement for the thermal energy barrier is given by: E_b=-*ln*[-(t_0/t_p)**ln*(1-FIT/N_b)], where, FIT is failure in time, N_b are no. of bits, t_0 is the attempt frequency (assumed to be 1ns) and t_p is desired data retention time span (7/21 days). Figure 1 shows the calculated thermal energy barrier at different FIT's and data retention spans for various sizes of cache memories ranging between 1MB to 1GB. From this Figure, it is evident that the minimum thermal energy barrier should be greater than 20 KT for 1000 FIT's and 27 KT for 0.1 FIT's. Next, we calculate the thermal energy barrier of p-MTJ device to assess whether these demands can be satisfied with shrinking MTJ diameters. For this purpose, we use standard MTJ stack consisting of CoFeB as free layer with 0.85 nm thickness and its diameter varying between 5 - 60 nm to understand the scalability aspect. We perform E_b calculations using a monodomain and domain wall assisted switching mechanism as mentioned in Ref. [2]. The thermal energy barriers are evaluated at three different values of temperature namely, 25°C (room temperature), 100°C (operational temperature) and 260°C (solder reflow temperature). The required values, saturation magnetization (Ms), uniaxial anisotropy (Ks) and exchange constant (Aex) are used as measured in the GLOBALFOUNDRIES hardware [4]. Further, their temperature dependence is computed using Kinetic Monte Carlo simulations. The calculated thermal energy barriers, with varying MTJ diameters, are plotted in Figure 2 a). The MTJ diameters are varied between 5 - 60 nm which essentially encompasses 7, 10, 14 and 22nm CMOS technology nodes. The blue, red and green curves represent the data obtained at temperatures of 25, 100 and 260°C, respectively. We observe that the lowest thermal barrier of approximately 30 KT can be achieved at 15 nm diameter for the highest solder reflow temperature. This implies that the MTJ diameter can be scaled down to 15 nm without compromising the thermal stability as required by 0.1 FIT's for 21 days. However, the energy barriers are drastically reduced below 15 nm diameter. Figure 2b) shows the switching efficiency figure of merit for p-MTJs, which is defined as the ratio of the energy barrier and switching current. Here, the critical switching current is calculated using the macrospin model described in Ref. [5]. From this plot it can be observed that the switching efficiency of MTJ saturates at smaller diameters. These diameter values, at which the switching efficiency saturates, reduces with increasing temperatures. In summary, we presented a comprehensive benchmarking of STT-MRAM for cache applications. The data shows that STT-MRAM is indeed scalable and can be integrated with advanced CMOS nodes. Our results clearly show that the thermal stability requirements for L3-cache can be met at even smaller MTJ diameters. Finally, the critical diameter at which the switching efficiency saturates is also dependent on temperature.

[1] Mittal, S., & Vetter, J. S. "A survey of techniques for architecting DRAM caches", IEEE Transactions on Parallel and Distributed Systems, 27(6), pp. 1852-1863 (2016).. [2] D. Apalkov, B. Dieny, and J. M. Slaughter, "Magnetoresistive Random Access Memory," Proceedings of the IEEE, 104 (10) pp. 1796–1830, (2016). [3] Shum, D., et. al. "CMOS-embedded STT-MRAM arrays in 2x nm nodes for GP-MCU applications", 2017 Symposium on VLSI Technology, pp. T208-T209. IEEE (2017). [4] Naik, V. B., Meng, H., & Sbiaa, R. Thick CoFeB with perpendicular magnetic anisotropy in CoFeB-MgO based magnetic tunnel junction. AIP Advances, 2(4), pp. 042182 (2012). [5] Sato, H., et al. "Properties of magnetic tunnel junctions with a MgO/CoFeB/Ta/CoFeB/MgO recording structure down to junction diameter of 11 nm." Applied Physics Letters 105 (6), pp. 062403 (2014).

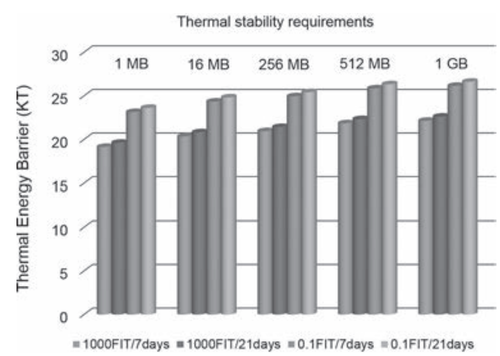

Fig. 1. Thermal energy barrier requirements for various sizes of cache memories.

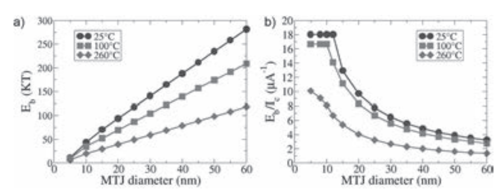

Fig. 2. a) Dependence of the thermal energy barrier on MTJ diameters and b) the switching efficiency figure of merit for advanced technology nodes.

3:30

BI-07. Stable Bloch point in helimagnetic nanostructures containing boundary between grains with different chirality.

M. Beg[1,2], D.I. Cortés-Ortuño[2], R.A. Pepper[2], M. Bisotti[2], G. Downing[2], B. Atie[2], O. Hovorka[2] and H. Fangohr[1,2]

1. European XFEL GmbH, Schenefeld, Germany; 2. Faculty of Engineering and the Environment, University of Southampton, Southampton, United Kingdom

Dzyaloshinskii-Moriya interaction (DMI) in helimagnetic materials can give rise to a large number of different non-trivial magnetisation configurations. One of them is the magnetic skyrmion. Recent research showed that confined helimagnetic nanostructures can host ground state skyrmionic states at zero external magnetic field and in the absence of magnetocrystalline anisotropy [1, 2]. However, the epitaxial growth of thin films from which the skyrmion hosting nanostructures should be etched, are usually granular. More precisely, they contain grains with different chirality and consequently different sign of the DMI constant. One of the questions is what magnetisation configurations can emerge in confined geometries containing such boundaries (interfaces). In order to address this, we perform finite element micromagnetic simulations on a 150 nm diameter FeGe disk containing grains with different chirality. The disk consists of two layers with different chirality and consequently different sign of DMI energy constant D. We fix the thickness of the bottom layer with D<0 to be 20 nm and vary the thickness of the top layer with D>0 between 2 nm and 18 nm. For every thickness of the top layer, we relax the system starting from the uniform magnetisation configuration. We use a full three-dimensional model, do not assume any translational invariance of magnetisation, and perform full demagnetisation field computation. We show the skyrmion number S values for individual layers in Fig. 1 (a). We notice that there is a sharp decrease in the S value for both layers at approximately 8.5 nm thickness of the top layer and in Fig. 1 (b), we investigate what is the difference between these two different magnetisation configurations. For thicknesses of the top layer below 8.5 nm, the energy contribution of the top layer in the total energy of the system is too small, and because layers with different sign of D are coupled by ferromagnetic exchange interaction, the top layer follows the magnetisation of the bottom layer. More precisely, both layers have the same chirality and the same orientation of the vortex state formed in them. However, above 8.5 nm, the energy contribution of the magnetisation state in the top layer becomes significant, and the system now relaxes to the state where both layers still have the same chirality, but now different orientation. The chirality-orientation states are now in accordance with the rules for different values of D in different layers. We find that between two layers (at the interface) a stable Bloch point (BP) [3, 4] is formed at zero external magnetic field and we show its detailed structure in Fig. 1 (c). Because micromagnetic models assume constant magnetisation magnitude, the precise magnetisation configuration at the BP cannot be obtained using micromagnetic simulations [5]. However, it is known how to identify the signature of the BP in such situations: the magnetisation direction covers any sufficiently small closed surface surrounding the BP exactly once [6, 7] and we illustrate that property in Fig 1 (c). After we explored the stability of a Bloch point at the interface between two grains with different chirality, we study the hysteretic behaviour of the system. We fix the thickness of the bottom layer to be 20 nm and set the thickness of the top layer to be 10 nm. The diameter of the disk is 150 nm. We vary the external magnetic field between −1 T and 1 T in steps of 100 mT. In Fig. 2 (a), we show the average out-of-plane magnetisation component as a function of external magnetic field and the hysteretic behaviour is evident. In Fig. 2 (b) we show the states at B=0 between which we can switch using an external magnetic field. We identify two different types of Bloch points. The first one is composed of two vortices with orientations pointing to each other which results in a head-to-head BP. However, in the other state vortices point away from each other and we name this state as a tail-to-tail BP. We conclude that the confined helimagnetic nanostructure containing the boundary between grains with different chiralities undergoes hysteretic behaviour when an external magnetic field is applied. Moreover, we can switch between two different zero-field stable BP (head-to-head and tail-to-tail) using an external magnetic field. Our demonstration of the stability and hysteretic behaviour of Bloch points, apart from being of fundamental physical interest, suggests a possible use in future spintronics, data storage and processing devices. We acknowledge the financial support from the Horizon 2020 European Research Infrastructures project (676541). The work is also supported by the EPSRC CDT in Next Generation Computational Modelling EP/L015382/1, and the EPSRC grant EP/N032128/1.

[1] Beg et al. Scientific Reports 5, 17137 (2015). [2] Zheng et al. Physical Review Letters 119, 197205 (2017). [3] E. Feldtkeller, Z. Angew. Phys. 19, 530 (1965). [4] W. Döring, Journal of Applied Physics 39, 1006 (1968). [5] C. Andreas et al. Physical Review B 89, 134403 (2014). [6] J. C. Slonczewski, In AIP Conf. Proc., vol. 24, 613–614 (1975). [7] A. Thiaville et al. Phys. Rev. B 67, 094410 (2003).

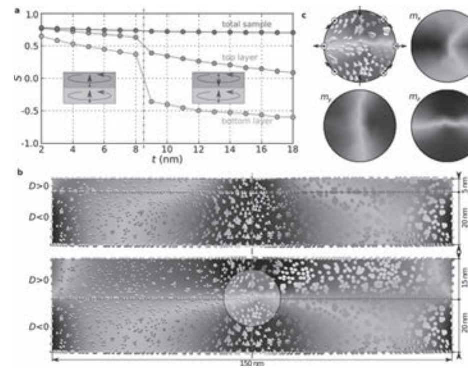

Fig. 1. (a) The skyrmion number S values for all individual layers in the studied structure. We notice that there is a sharp decrease in the S value for both layers at approximately 8.5 nm thickness of the top layer. (b) Different magnetisation configurations of both layers. For thicknesses below 8.5 nm the magnetisation in the top layer follows the magnetisation of the bottom layer. For larger thicknesses the orientation of the top layer reverses and a zero field stable Bloch point is formed. (c) Schematic representation of the Bloch point configuration.

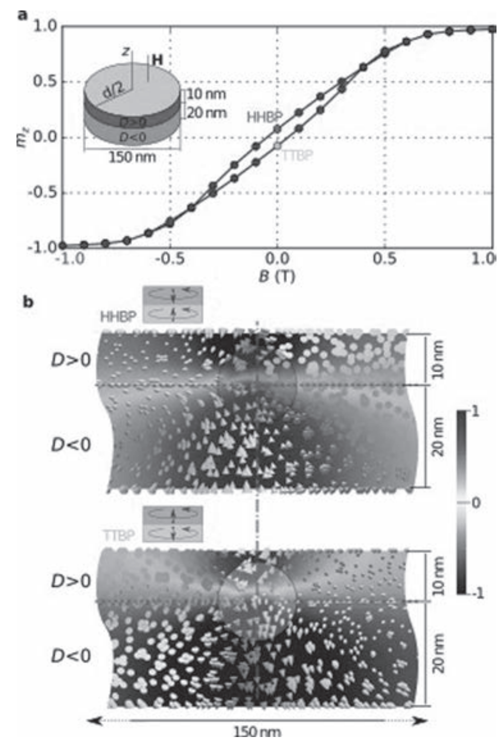

Fig. 2. (a) Average out-of-plane magnetisation as a function of external magnetic field. (b) The magnetisation configurations of two stable head-to-head and tail-to-tail Bloch points at zero external magnetic field.

3:45

BI-08. The effect of antisite disorder on magnetic and magnetocaloric properties of Ni-Co-Mn-In alloys: ab initio and Monte Carlo studies.

V. Sokolovskiy[1], V. Buchelnikov[1] and P. Entel[2]

1. Condensed matter, Chelyabinsk State University, Chelyabinsk, Russian Federation; 2. Duisburg-Essen University, Duisburg, Germany

Nowadays, the Ni-Co-Mn-In Heusler alloys have drawn a much attention due to a series of functional properties such as the shape memory effect, giant magnetoresistance and magnetocaloric effects etc., which are promising for future technologies [1-3]. Usually, the most of unique properties are associated with the martensitic transformation between the martensite with complex magnetic order and the austenite with ferromagnetic order. Moreover, there are strong competing magnetic interactions in the vicinity of magnetostructural phase transition, which are responsible for the change in magnetization. Evidently, the manipulation of magnetic interactions in both martensite and austenite leads to change the magnitude of the magnetization drop and to achieve the better magnetocaloric properties across the martensitic transformation. The present theoretical study is addressed the question of effect of competing magnetic interactions on magnetic and magnetocaloric properties of Ni-Co-Mn-In alloys through the addition of structural defects. Evidently, samples prepared experimentally without an additional annealing can contain many impurities and defects. Opposite, the influence of additional annealing can result to a highly ordered structure with minimum defect concentration. In this connection for compositions without additional annealing, we focused attention on the formation of structural (antisite) disorder between In and Mn atoms on the corresponding In and Mn sublattices with concentration *y* (which can be described by $Ni_2Mn_{1+x}In_{1-x}$ = $Ni_2Mn_{1-y}Sn_yMn_{x+y}In_{1-x-y}$, where *x* is the Mn excess concentration and *y* is the degree of antisite disorder) [4]. While for the samples upon additional annealing, the ordered structure (without defects, $y = 0$) is proposed. Our methodology consists of ab initio calculations and Monte Carlo (MC) simulations based on the Potts-Blume-Emery-Griffiths model allowing to simulate austenite-martensite transformation as well as magnetic and magnetocaloric properties [5-7]. Two subsequent steps were used in our calculations. Firstly, we calculated the exchange coupling constants (J_{ij}) using the SPR-KKR package [8] within the general gradient approximation in the form of Perdew-Burke-Ernzerhof. The chemical and structural disorders were simulated in the coherent potential approximation. The *Jij* calculations were done for cubic austenite (c/a = 1) and tetragonal martensite (c/a = 1.21) of $Ni_{43}Co_7Mn_{37+y}In_{13-y}$. Here, *y* takes values as follows: 1.5, 3.25, and 6.5. We note that the equilibrium lattice parameters for austenite and martensite were taken from our previous calculations (See Ref. [7]), and we supposed that lattice parameters change no with increasing degree of anisate disorder (*y*). Secondly, using the calculated exchange constants as a function of distance between interacting atoms, the MC simulations were performed. The model lattice that contains a real unit cell of Heusler alloy includes 3925 atoms with periodic boundary conditions. The configurations of excess Mn atoms (x + y) at the In sublattice and In atoms (y) at the Mn sublattice are chosen randomly and the total number of Mn and In atoms are fixed by a nominal composition $Ni_{43}Co_7Mn_{37+y}In_{13-y}$ (y = 1.5, 3.25, and 6.5). The MC simulations were performed using the Metropolis algorithm and 500 000 MC steps. Note that all model parameters expect the magnetic moments and J_{ij} constants were fixed and taken from [7]. Let us discuss the effect of additional annealing in the framework of theoretical approach assuming the presence of antisite disorder between In and Mn sublattice in $Ni_{43}Co_7Mn_{37}In_{13}$ alloy. In Fig. 1a we present calculated nearest exchange coupling constants for austenite of $Ni_{43}Co_7Mn_{37+y}In_{13-y}$ as a function of antisite defect concentration. As can be seen that all interactions with Mn_1 (Mn_2) atoms decrease (increase) with increasing *y*, respectively. Here $Mn_{1(2)}$ atoms denote Mn atoms located at Mn (In) sublattice, respectively. This observation is associated with the fact that the number of Mn_1 atoms becomes smaller with an increase of antisite disorder. MC simulations of thermomagnetization curves for $Ni_{43}Co_7Mn_{37+y}In_{13-y}$. (y = 0 and 1.5) in magnetic field of 2 T under the heating and cooling protocols are shown in Fig. 1b. The inset contains the M(T) curves for $Ni_{43}Co_7Mn_{37+y}In_{13-y}$ under heating. Thermal hysteresis between M(T) curves around the magnetostructural phase transition for the heating and cooling processes is clearly seen. Moreover, both the magnetization and Curie temperature of austenite are found to decrease compared to the ordered case (y = 0) with increasing degree of structural disorder. Generally, theoretical magnetization trend as a function of antisite disorder is provided by the recent experiments for both ordered and disordered $Ni_{50}Mn_{34.5}In_{15.5}$ alloys [9, 10]. In the framework of theoretical approach involving first-principles and Monte Carlo methods, a set of magnetization curves for the studied system are calculated. It is shown that the account of structural disorder (anti-site defects) results to decrease the magnetization and magnetocaloric properties around the magnetostructural transformation. This work is supported by RSF No. 17-72-20022.

[1] A. Planes, Ll. Manosa and M. Acet, J. Phys.: Condens. Matter 21 (2009) 233201. [2] V.D. Buchelnikov, V.V. Sokolovskiy, Phys. Met. Metallogr. 112 (2011) 633. [3] V.V. Sokolovskiy, M.A. Zagrebin, V.D. Buchelnikov, Materials Science Foundations 81 (2015) 38. [4] V. V. Sokolovskiy, V. D. Buchelnikov, M. A. Zagrebin et al. Phys. Rev. B 86 (2012) 134418. [5] V. Sokolovskiy, A. Grunebohm, V. Buchelnikov, et al., Entropy 16 (2014) 4992. [6] D. Comtesse, M. E. Gruner, M. Ogura, et al., Phys. Rev. B 89 (2014) 184403. [7] V.D. Buchelnikov, V.V. Sokolovskiy, M.A. Zagrebin et al. J. Phys. D: Appl. Phys. 48 (2015) 164005 [8] H. Ebert, SPR-KKR package Version 6.3 at http://ebert.cup.uni-muenchen.de. [9] J.M. Barandiaran, V.A. Chernenko, E. Cesari et al., Appl. Phys. Lett. 102 (2013) 071904. [10] J.M. Barandiaran, V.A. Chernenko, E. Cesari et al., J. Phys.: Condens. Matter 25 (2013) 484005.

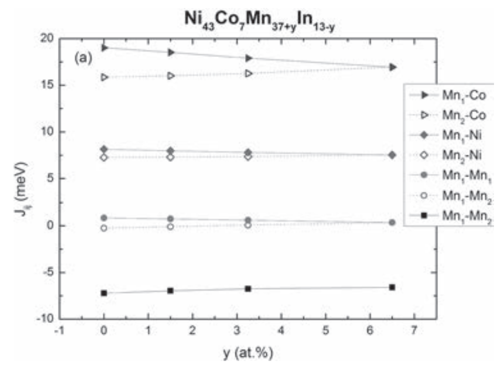

Fig. 1. Nearest exchange integrals for austenite of $Ni_{43}Co_7Mn_{37+y}In_{13-y}$ as a function of antisite defect concentration (y).

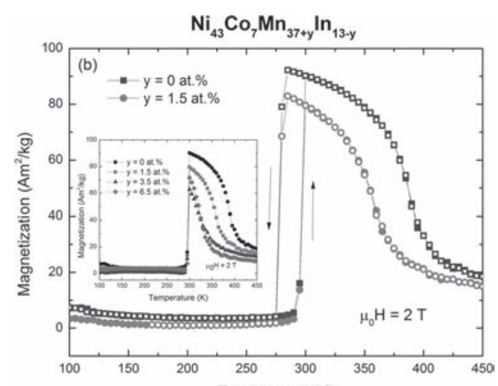

Fig. 2. Theoretical set of M(T) curves for $Ni_{43}Co_7Mn_{37+y}In_{13-y}$ alloy in magnetic field of 2 T. The inset presents M(T) curves for a series compositions under heating .

4:00

BI-09. Analysis of switching times distributions for uniaxial magnetic particles.

M. d'Aquino[1], C. Serpico[2] and V. Scalera[2]
1. Dipartimento di Ingegneria, Università degli Studi di Napoli "Parthenope", Napoli, Italy; 2. DIETI, University of Naples Federico II, Naples, Italy

Magnetization switching in nanoparticles and thin-films is the fundamental issue to deal with in order to obtain high speed and energy-efficient recording devices[1]. The optimization of switching mechanisms is constrained in the framework of the so-called magnetic recording trilemma. On one hand, one would like to have the magnetized bit occupying a smaller area on the recording medium and, at the same time, magnetization remaining stable over long enough time for reliable data retention. These two constraints are competing since thermal stability decreases with decreasing active volume of the magnetic bit. On the other hand, circumventing this issue would require higher coercivity of the magnetic material and, consequently, larger current feeding the write head. However, the maximum current amplitude is constrained by technological limits in the realizations of the pole tips and, thus, one cannot meet the aforementioned requirements. For these reasons, several strategies have been investigated in the last decades to realize fast magnetization switching with greater efficiency, such as microwave-assisted switching[2] and precessional switching[3]. In particular, the latter occurs through the application of a field transverse to the initial magnetization and yields much smaller switching times than conventional switching[4], [5]. However, to achieve successful switching, an extremely precise design of the field pulse is needed to switch off the field at the right moment [6]. Then, the equilibrium magnetization is reached after a relaxation from a high-to low-energy state[7]. This mechanism is probabilistic even when thermal fluctuations are neglected, due to multistability and small dissipation in magnetization dynamics[8]. When also thermal fluctuations are considered, the stochasticity of the switching process is even more pronounced[3]. On the other hand, magnetic recording devices must undergo strict reliability requirements in terms of extremely low write-error rates, which can be realized at expense of the speed of the write process. In this paper, we theoretically analyze the magnetization switching for a single magnetic grain of the recording medium subject to the write head field pulses and room temperature thermal fluctuations, as it is the case of perpendicular magnetic recording. This situation, in the absence of thermal fluctuations and for special symmetry of the magnetic particle, has been studied in a pioneering paper[9] and is referred to as damping switching. In this paper, by using analytical techniques, we derive expressions for the switching times distribution functions in terms of material, geometrical and external field properties. These analytical results provide a tool to quantify the write-error rates as function of design parameters, which may help the optimization of switching processes. To this end, we consider the Landau-Lifshitz-Gilbert (LLG) equation augmented with a thermal field of stochastic nature[10], whose intensity is given by the fluctuation-dissipation theorem. We assume that the magnetization is spatially-uniform during the dynamics, so that the magnetic particle can be described within a macrospin approximation. In the absence of excitation, the energy barrier separating the equilibria is much higher than the thermal energy. This hypothesis is suitable when the uniaxial anisotropy is large enough as it is the case for magnetic recording grains. The external field pulse amplitude is assumed to be above the critical switching field of the device. In this situation, the switching time can be evaluated considering the deterministic magnetization motion acting on a random initial magnetization distribution due to thermal fluctuations. In the absence of external field, the magnetization is distributed according to the stationary solution of the Fokker-Planck equation, which can be simply expressed in terms of the small tilting angle θ ($\sin\theta \approx \theta$) with respect to the particle's easy axis. Then, considering a rotationally-symmetric particle (z is the symmetry axis) and neglecting the thermal fluctuations during magnetization evolution, the LLG equation can be integrated by separation of variables[9] in order to determine the switching time t_s defined as the time interval between the application of the field pulse (the initial z-component of the magnetization is m_{z0}) and the time instant where the z-component of the magnetization is equal to a given value m_{zf}. By using appropriate derivation (details will be given in the full paper), it can be shown that the relationship $t_s(m_{z0},m_{zf})$ allows one to derive the probability and cumulative distribution functions for magnetization switching times as function of geometrical, material and excitation parameters. Such functions can be used to compute the write error-rate of the switching process for given switching duration t_s. The analytical predictions are compared with macrospin and micromagnetic simulations of magnetization switching (an example computation for a circular nanodot with 30nm diameter, 1nm thickness and perpendicular anisotropy is reported in fig. 1) in order to show the effectiveness of the approach.

[1] J.-P. Wang, "Magnetic data storage: Tilting for the top," Nature Mater., vol. 4, no. 3, pp. 191–192, 2005. [2] C. Thirion, W. Wernsdorfer, and D. Mailly, "Switching of magnetization by nonlinear resonance studied in single nanoparticles," Nature Mater., vol. 2, no. 8, pp. 524–527, 2003. [3] S. Kaka and S. E. Russek, "Precessional switching of submicrometer spin valves," Appl. Phys. Lett., vol. 80, no. 16, pp. 2958–2960, 2002. [4] G. Bertotti, I. D. Mayergoyz, C. Serpico, and M. d'Aquino, "Geometrical analysis of precessional switching and relaxation in uniformly magnetized bodies," IEEE Trans. Magn., vol. 39, no. 5, pp. 2501–2503, Sep. 2003. [5] M. Bauer, J. Fassbender, B. Hillebrands, and R. L. Stamps, "Switching behavior of a Stoner particle beyond the relaxation time limit," Phys. Rev. B, Condens. Matter, vol. 61, no. 5, p. 3410, 2000. [6] M. d'Aquino, W. Scholz, T. Schrefl, C. Serpico, and J. Fidler, "Numerical and analytical study of fast precessional switching," J. Appl. Phys., vol. 95, no. 11, pp. 7055–7057, Jun. 2004. [7] C. Serpico, M. d'Aquino, G. Bertotti, and I. D. Mayergoyz, "Analytical description of quasi-random magnetization relaxation to equilibrium," IEEE Trans. Magn., vol. 45, no. 11, pp. 5224–5227, Nov. 2009. [8] G. Bertotti, C. Serpico, and I. D. Mayergoyz, "Probabilistic aspects of magnetization relaxation in single-domain nanomagnets," Phys. Rev. Lett., vol. 110, p. 147205, Apr. 2013. [9] J. C. Mallinson, "Damped gyromagnetic switching", IEEE Trans. Magn. 36, 1976 (2000). [10] W.F. Brown, "Thermal Fluctuations of a Single-Domain Particle", Phys. Rev. 130, 1677 (1963).

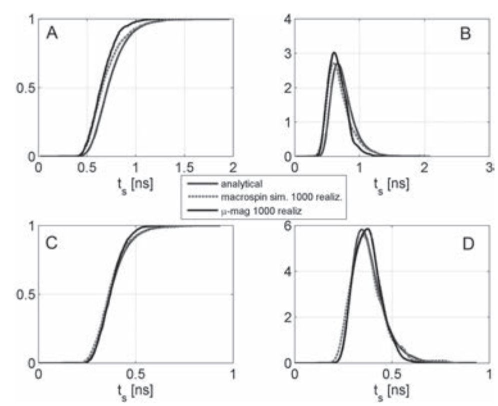

Fig. 1. Switching times probability and cumulative distributions as function of applied field pulse amplitude. Panels A, B refer to cdf and pdf computed for field amplitude equal to twice the critical field, whereas panels C,D refer to pulse amplitude equal to four times the critical field. Solid blue, dashed red, solid black lines refer to analytical theory, macrospin and micromagnetic simulations, respectively.

4:15

BI-10. *Ab initio* prediction of giant perpendicular magnetic anisotropy at Fe/$CuIn_{1-x}Ga_xSe_2$ interface.

K. Masuda[1], S. Kasai[1], Y. Miura[1,2] and K. Hono[1]
1. National Institute for Materials Science (NIMS), Tsukuba, Japan;
2. Electrical Engineering and Electronics, Kyoto Institute of Technology, Kyoto, Japan

Perpendicular magnetic anisotropy (PMA) at the interface between ferromagnetic and barrier layers is an essential property in magnetic tunnel junctions (MTJs) to realize sufficient thermal stability and low critical current in non-volatile spin transfer torque magnetic random access memories (STT-MRAMs) [1]. The PMA is also advantageous for reducing write error rates in voltage-controlled MRAMs [2].Therefore, it is of importance to find heterostructures which give rise to stronger interfacial PMA. Up to now, strong interfacial PMA has been observed in heterostructures consisting of ferromagnets (FMs) and insulator MgO. Ikeda *et al*. obtained a large interfacial anisotropy constant K_i of ~ 1.3 mJ/m^2 at the interface of CoFeB/MgO [3]. In a subsequent work, Koo *et al*. observed higher interfacial PMA with K_i ~ 2.0 mJ/m^2 in Fe/MgO [4]. However, no previous studies have reported such strong interfacial PMA on heterostructures with non-MgO barrier layers. Recently, Kasai *et al*. succeeded in fabricating novel MTJs where semiconductor $CuIn_{0.8}Ga_{0.2}Se_2$ (CIGS) is sandwiched between ferromagnetic Heusler alloys [5]. They observed both high magnetoresistance (MR) ratios and low resistance-area products (*RA*), which are also required for MRAM and hard disk drive (HDD) applications. In particular, when we consider the application of this MTJ to STT-MRAM cells, the possibility of obtaining high interfacial PMA should be investigated; however, no theoretical and experimental studies have focused on this issue. In this work, we theoretically studied interfacial magnetocrystalline anisotropies in various Fe/semiconductor(001) heterostructures including Fe/$CuIn_{1-x}Ga_xSe_2$(001). As semiconductor barriers, 14 types of semiconductors were considered in the present study (see Fig. 1 for details). We calculated values of K_i in these heterostructures by means of first-principles calculations based on density-functional theory, which is implemented in the Vienna *ab initio* simulation program (VASP). We first prepared supercells composed of 7 layers of Fe and 17 layers of the semiconductor barrier. Since quite thin Fe electrodes are used in experiments on PMA, we fixed the in-plane lattice constant of each supercell to the experimental lattice constant of the barrier. In all the supercells, we confirmed that Se, S, or As layer is energetically favored as the termination layer of the semiconductor barrier. In addition, all the atomic positions and the distance between ferromagnetic and barrier layers were optimized so that the total energy of the supercell is minimized. The values of K_i were calculated using the force theorem as $K_i = (E_{[100]}-E_{[001]})/2S$, where $E_{[100]}$ ($E_{[001]}$) is the sum of the eigenenergies of the supercell for the magnetization along the [100] ([001]) direction, S is the cross-sectional area of the supercell, and the factor 2 reflects the fact that two interfaces are included in the supercell. From this definition, a positive (negative) K_i shows the tendency toward perpendicular (in-plane) magnetic anisotropy. We used 10×10×1 k points to calculate total energies of the heterostructures with chalcopyrite semiconductors. We used more k points for other heterostructures owing to their smaller supercell sizes. Figure 1 shows the values of K_i obtained for various Fe/semiconductor systems. For comparison, we also show K_i for Fe/MgO(001) with a similar barrier thickness. It is found that most of the Fe/semiconductor systems investigated in this study have positive K_i. Particularly, Fe/$CuInSe_2$ has the largest K_i of 2.305 mJ/m^2, which is about 1.6 times as large as that of Fe/MgO (1.396 mJ/m^2). In Fig. 1, we also show the values of anisotropy of orbital magnetic moment $\Delta M_{orb,i}$ at interfacial Fe atoms. By comparing K_i and $\Delta M_{orb,i}$, we see that Bruno's relation ($K_i \alpha \Delta M_{orb,i}$) holds for almost all the systems considered in this study. This implies that the interfacial PMA in the present systems comes from the structure of the minority-spin local density of states (LDOS) of interfacial Fe atoms [6]. Figure 2 shows the projected *d*-orbital LDOSs of interfacial Fe atoms in Fe/$CuInSe_2$. We find some sharp peaks in the minority-spin LDOSs both just above and just below E_F, which enable excitations with quite small energies. In addition, these peaks have favorable *d*-orbital components for yielding large PMA [6]. These features are consistent with the largest K_i in Fe/$CuInSe_2$. Furthermore, we revealed that the positions of Se atoms at the interface is the key for such favorable *d*-orbital components in the LDOSs [6]. In summary, using *ab initio* calculations, we predict the largest K_i of 2.305 mJ/m^2 for Fe/$CuInSe_2$, which is about 1.6 times as large as that of Fe/MgO (1.396 mJ/m^2). Thus, Fe/$CuInSe_2$/Fe MTJ may be suitable for application as perpendicular MTJ for high capacity MRAM application with a small cell size. This work was partly supported by Grant-in-Aids for Scientific Research (S) (Grant No. 16H06332) and (B) (Grant No. 16H03852) from the Ministry of Education, Culture, Sports, Science and Technology, Japan, by NIMS MI2I, and also by the ImPACT Program of Council for Science, Technology and Innovation, Japan.

[1] B. Dieny, R.B. Goldfarb, and K. J. Lee, Introduction to Magnetic Random-access Memory (Wiley, Hoboken, NJ, 2016). [2] Y. Shiota *et al*., Appl. Phys. Express 9, 013001 (2016). [3] S. Ikeda *et al*., Nat. Mater. 9, 721 (2010). [4] J. W. Koo *et al*., Appl. Phys. Lett. 103, 192401 (2013). [5] S. Kasai *et al*., Appl. Phys. Lett. 109, 032409 (2016). [6] K. Masuda *et al*., Phys. Rev. B 96, 174401 (2017).

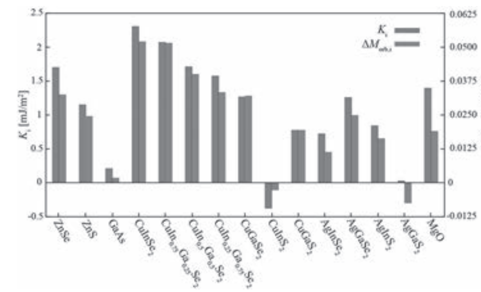

Fig. 1. Calculated values of anisotropy constant K_i and anisotropy of the orbital magnetic moment $\Delta M_{orb,i}$ at interfacial Fe atoms. The horizontal axis shows the materials *X* of the heterostructures Fe/*X*(001).

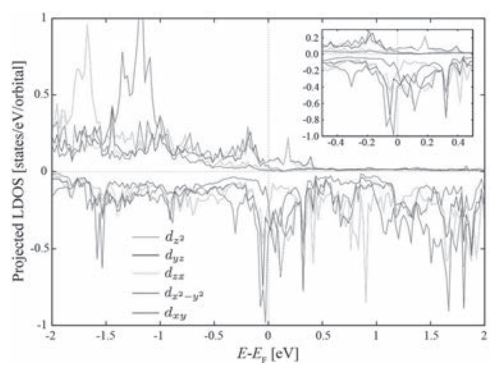

Fig. 2. Projected *d*-orbital LDOSs of interfacial Fe atoms in Fe/$CuInSe_2$(001). Positive and negative values indicate the majority- and minority-spin LDOSs, respectively. The inset shows a magnified view near the Fermi level.

TUESDAY AFTERNOON, 24 APRIL 2018 SIMPOR/ROSELLE BALLROOM, 1:30 TO 4:30

Session BP
TMR, VCMA AND MULTIFERROIC MATERIALS I
(Poster Session)

Xiufeng Han, Chair
Institute of Physics, Chinese Academy of Sciences, Beijing, China

BP-01. Coexistence of Large Voltage Controlled Magnetic Anisotropy, Large Surface Anisotropy, and Large TMR by a new MTJ structure having MgO/CoFeB/Ir/CoFeB.

S. Oikawa[1], Y. Saito[1], H. Yoda[1], Y. Kato[1], A. Tiwari[1], M. Ishikawa[1], N. Shimomura[1], K. Koi[1], T. Inokuchi[1], H. Sugiyama[1], M. Shimizu[1], S. Shirotori[1], A. Buyandalai[1], Y. Ohsawa[1] and A. Kurobe[1]
1. Corporate R&D Center, Toshiba Corporation, Kawasaki, Japan

In recent years, writing data in magnetic random access memory (MRAM) utilizing voltage controlled magnetic anisotropy (VCMA) has attracted much attention for its potential low power consumption [1]. We proposed voltage-control spintronics memory (VoCSM) which had high-efficient and deterministic writing properties [2]. In order to realize those memories, three features of a large VCMA, a large surface anisotropy Ks, and a large tunneling magnetoresistance (TMR) should coexist. In addition, a large spin-Hall angle is a must for VoCSM. Many challenges based on MgO tunneling barrier/ferromagnetic layer (FL) such as CoFeB thin films combined with various materials as an insertion layer at the MgO/FL interface or as an underlayer of FL showed improved VCMA but were concerned to fail in the coexistence of the feature because of very thin storage-layer or degraded lattice growth between MgO and CoFeB [3], [4], [5]. As a result, none of them have had a practical meaning as a memory cell so far. In this study, the experiments were conducted in which the insertion position of Ir was changed in MgO/CoFeB/Ta thin films. Each of the interface layer, the interlayer and the underlayer of Ir showed an increase in VCMA, and the largest VCMA was obtained in the case of inserting the Ir interlayer into the CoFeB layer. In addition, both the resistance-area product (RA) and TMR ratio decreased greatly when using the Ir interface layer, but clearly improved by employing the Ir interlayer. The base multilayer structure for VCMA measurement was Ta (5 nm)/MgO (~3 nm)/CoFeB (1–2 nm)/Ta (5–8 nm), which was deposited on a thermally oxidized Si substrate. The CoFeB layer was set to in-plane magnetization, and the base stack of IrMn/CoFe/Ru/CoFeB /MgO/CoFeB/Ta with a reference layer was prepared for RA and TMR measurement by using current in-plane tunneling (CIPT). The multilayers for VCMA were patterned and etched into the device size with one side of 3 to 50 μm and their hysteresis curves were measured using the magneto-optical polar Kerr effect. The effective perpendicular magnetic anisotropy field Hk_{eff} of the CoFeB layer was measured while bias voltage was applied to the device, and the variation of Ks depending on the electric field E was evaluated as the VCMA coefficient. Figure 1 shows the VCMA coefficients (–dKs/dE) of the MgO/CoFeB/Ta thin films as the “Base” sample, “Interface” sample in which Ir (0.2 or 0.3 nm) is layered at the MgO/CoFeB interface, “Interlayer” sample in which Ir (0.3 nm) is inserted in the middle of the CoFeB layer, and “Underlayer” sample in which Ir (0.5 nm) is formed between the CoFeB and the Ta layer. All coefficients of the “Interface”, “Interlayer”, and “Underlayer” samples increased more than that of the “Base” sample in terms of each average value, although each coefficient had a certain degree of dispersion. The Ks in the “Interface” sample also increased more than in the “Base” sample at each average value, however, the largest Ks (maximum of 2.2 erg/cm^2) and VCMA (maximum of 190 fJ/Vm) were obtained in the “Interlayer” sample. The relationship between RA and TMR ratio in the MTJ samples similar to Fig. 1 with the reference layer is plotted in Fig. 2. Both RA and the TMR ratio in the “Underlayer” sample were almost the same as those in the “Base” sample, but both decreased in the “Interface” sample and further decreased by increasing the Ir layer thickness from 0.2 to 0.3 nm. In the “Interlayer” sample, the deterioration of RA was not observed, and although the TMR ratio decreased, it still showed a high value of more than 120%. By comparison at the Ir thickness of 0.3 nm, it can be seen that both RA and TMR are clearly improved by changing from the Ir interface layer to the Ir interlayer. In summary, we successfully found the practical MTJ structure as a memory cell which realized coexistence of a large VCMA, a large Ks, and a large TMR for the first time. The structure is expected to have a large spin-Hall effect as well. This work was partly supported by the ImPACT Program of the Council for Science, Technology and Innovation (Cabinet Office, Government of Japan).

[1] W.-G. Wang et al., Nat. Mater. 11, 64 (2012). [2] H. Yoda et al., Digests of 62th IEDM, 27.6 (2016). [3] T. Nozaki et al., Phys. Rev. Appl. 5, 044006 (2016). [4] K. Nakamura et al., J. Magn. Magn. Mater. 429, 214 (2017). [5] W. Skowronski et al., Appl. Phys. Express 8, 053003 (2015).

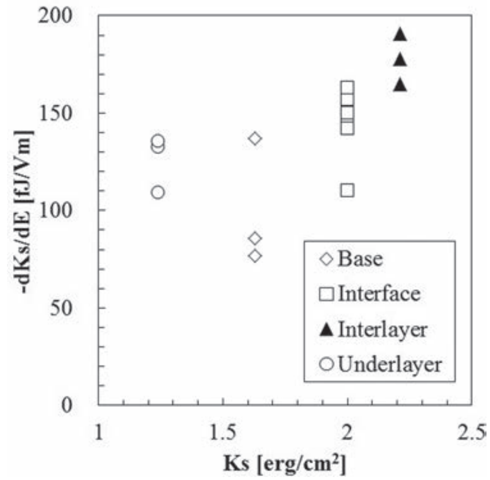

Fig. 1. Surface magnetic anisotropy Ks and VCMA coefficients (–dKs/dE) of MgO/CoFeB/Ta thin films with Ir layer insertion.

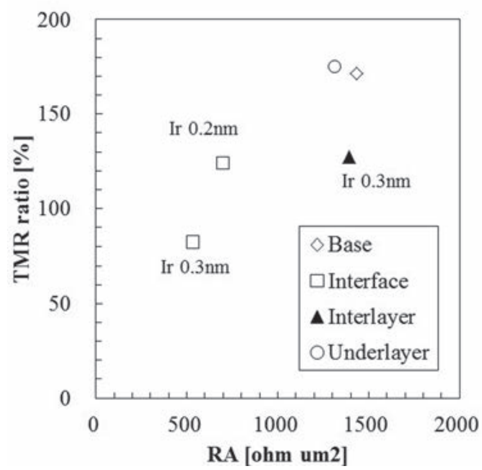

Fig. 2. Relationship between resistance-area product RA and TMR ratio in MTJ samples with Ir layer insertion.

BP-02. Ionic Liquid Gating Modulation of Diluted Magnetic Semiconductor (Zn, Mn)O Thin Films.

H. Wong[1], S. Ng[1], Y. Liu[1], K. Lam[1], K. Chan[1], W. Cheng[1], D. von Nordheim[2], C. Mak[1], B. Ploss[2] and *C. Leung*[1]

1. Department of Applied Physics, The Hong Kong Polytechnic University, Hong Kong, Hong Kong; 2. Department of SciTec, University of Applied Sciences Jena, Jena, Germany

Ionic liquid (IL) gating on functional oxide has drawn significant attention, since it can provide reversible changes in carrier concentration (~10^{14} cm^{-3}) at the interface, permitting the manipulation of electrical and magnetic properties via a low voltage [1-3]. In this work, we demonstrate the electric-field manipulation of transport properties in the dilute magnetic oxide (DMS) of $Zn_{0.98}Mn_{0.02}O$ (MZO) using an electric-double-layer transistor (EDLT) geometry through IL of N,N-diethy1-N-(2-methoxyethy1)-N-methylammonium (DEME+) and bis(trifluoromethylsulfony1)-imide (TFSI-). By the application of different gate voltages (V_g) through the top electrolyte, the accumulated and depleted charge carrier in the MZO channel lead to a reversible control in the transport phenomena at the interface. 10 nm-thick MZO thin films were deposited on (0001) Al_2O_3 single crystal substrates by pulsed laser deposition. The growth of MZO films was conducted at 300^{o}C with an oxygen pressure of 5 x10^{-4} Pa. To study electrical-field manipulation of MZO devices, the films were patterned into Hall bar patterns (channel width: 50 μm, channel length: 110 μm) by photolithography and wet etching using dilute HCl as etchants. Au (50 nm)/Ti (5 nm) coplanar electrodes for IL and contact electrodes for MZO were prepared by electron beam evaporation. Prior to the gating experiment, IL was baked at 80 ^{o}C in a high vacuum chamber to get rid of water contamination. A drop of IL was placed on the top of the as-grown film, serving as the top gate electrode. The devices were immediately cooled down to 230 K for the gating process. By applying different V_g (-2, 0 and 2 V), the charge carriers were accumulated and depleted in the channel surface. Then the devices were immediately cooled down to 180 K (below the freezing point of IL at 230 K) before V_g was removed. After the transport measurements, the devices were heated up to 230 K before changing the V_g for another measurement. Fig. 1 illustrates the profile of the longitudinal resistance (R_{xx}) of MZO EDLTs with alternating V_g between -2 and 2 V at 230 K. R_{xx} increases (decreases) sharply upon the application of V_g = -2 V (2 V), which is consistent with the scenario of accumulated (depleted) electron charge carrier at the MZO interfaces [4]. Such modulations of R_{xx} are due to electron charge movement in MZO rather than the contribution of gate current: the drain-source current is higher than the gate-source current by at least two orders of magnitude. Magnetotransport behavior of MZO at 10 K after the application of different V_g (-2, 0 and 2 V) are shown in Fig. 2, which shows the magnetoresistance (MR) with out-of-plane applied field for MZO EDLT. Here MR is defined as MR=(R_{xx}(H)-R_{xx}(0))/R_{xx}(0), where $R_{xx}(H)$ and R_{xx}(0) are the R_{xx} values with external magnetic fields of *H* and zero, respectively. The peak positive MR increases from 0 to 1.8% and the negative-MR (measured at 9 T) decreases from –4.5% to -0.6% when V_g increases from -2 to 2 V. Enhancement in positive MR in the low field regime (<1 T) implies that the ferromagnetic state of MZO is enhanced, as the electron carrier concentration in MZO increases upon switching the V_g from -2 to 2 V [5]. The present results, therefore, demonstrate controllable movement of anions and cations in IL by electric-field effect plays an important role in the manipulation of magnetism in the MZO. Financial support by RGC, HKSAR (PolyU 153015/14P) and PolyU (1-ZE25) are acknowledged.

[1] C. Ge, K.J. Jin, L. Gu, L.C. Peng and Y.S. Hu *et al.*, Adv. Mater. Interfaces, 2, 1500407 (2015). [2] B. Cui, C. Song, G. Wang, Y. Yan and J. Peng *et al.*, Adv. Funct. Mater., 24, 7233 (2014). [3] A. Verma, K. Nomoto, W.S. Hwang, S. Raghavan and S. Stemmer *et al.*, Appl. Phys. Lett., 108 183509 (2016). [4] H. Yuan, H. Shimotani, A. Tsukazaki, A. Ohtomo and M. Kawasaki *et al.*, Adv. Funct. Mater., 19, 1046 (2009). [5] L.T. Chang, C.Y. Wang, J. Tang, T. Nie and W. Jiang *et al.*, Nano Lett., 14 1823 (2014).

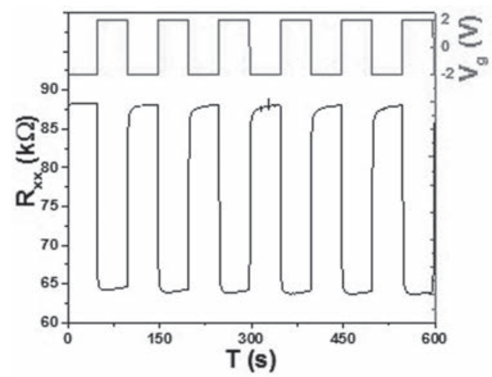

Fig. 1. Time profile of longitudinal resistance (R_{xx}) of MZO EDLTs, during the application of different V_g (profile at top).

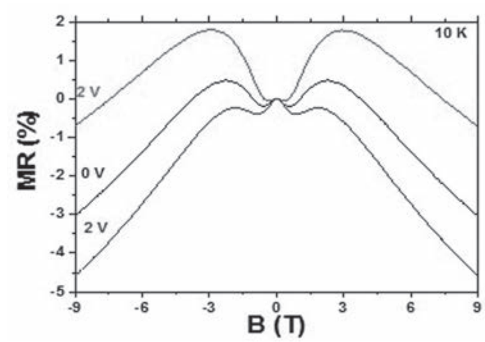

Fig. 2. Magnetoresistance of MZO EDLTs for V_g = -2, 0 and 2 V measured at 10 K.

BP-03. Development of all spinel magnetic tunnel junctions: epitaxial $Fe_3O_4/MgAl_2O_4/Fe_3O_4(001)$ structure.

T. Tainosho[1], H. Yanagihara[1] and H. Sukegawa[2]

1. Applied physics, University of Tsukuba, Tsukuba, Japan; 2. Research Center for Magnetic and Spintronic Materials, National Institute for Materials Science (NIMS), Tsukuba, Japan

Introduction Utilizing highly spin-polarized materials is a key to enlarge tunnel magnetoresistance (TMR) ratio of a magnetic tunnel junction (MTJ) and therefore, half metallic materials have been eagerly studied for decades. Among the various candidate substances of half metals, magnetite (Fe_3O_4) is attractive because of its high Curie temperature of ~850 K. Although much efforts had been paid for fabricating MTJs with Fe_3O_4 electrodes, the reported TMR ratios were not as high as ones expected for its half metallicity[1]. The origin of the significantly lower TMR of the MTJs with Fe_3O_4 electrodes is still controversial, but the characteristic film growth of $Fe_3O_4(001)$, particularly generation of high-density anti-phase boundaries (APBs) in $Fe_3O_4(001)$, could significantly reduce the local spin polarization at the interface. In order to solve the issue, building an all-spinel-type epitaxial MTJ by introducing a magnesium-aluminate $MgAl_2O_4$ tunnel barrier would be effective. Since ultra-thin $Fe_3O_4(001)$ films on $MgAl_2O_4(001)$ show the fewer anti-phase boundaries[2], we can simply expect to improve the microstructure at $Fe_3O_4(001)$ and $MgAl_2O_4(001)$ interfaces. In this study, we developed the growth technique of a fully epitaxial $Fe_3O_4/MgAl_2O_4/Fe_3O_4(001)$ structure by optimizing reactive sputtering method. Experiment We deposited $Ru(10)/Co(14.4)/Fe_3O_4(21.2)/MgAl_2O_4(3)/Al(0.3)/Fe_3O_4(127.2)$/substrate (thickness in nm) films on MgO(001) substrates. All the oxide layers were deposited by a reactive RF magnetron sputtering technique and the metal layers were deposited by a DC sputtering technique. The $MgAl_2O_4$ barrier with a nominal thickness of 3 nm was deposited at room temperature (RT). Both the top- and bottom-Fe_3O_4 electrodes were deposited at 573 K. The thin Co layer was deposited on the top Fe_3O_4 electrode to obtain different coercivities between the top and bottom electrodes. During the deposition, the surface structures were monitored by reflection high energy electron diffraction (RHEED). Magnetization(M)-magnetic field(H) curves of the MTJ stacks as well as a single Fe_3O_4 layer on an MgO(001) substrate were measured at RT. The magnetic field was applied along in-plane easy axis of [110] of Fe_3O_4. The film was patterned into ellipsoidal pillars (size: 20x10 mm^2) by photolithography and Ar ion milling. Magnetotransport properties were characterized by a DC four-probe method at RT. Results and discussion Figure 1(a) shows the RHEED pattern of the MgO(001) substrate. The spacing between the streaks indicated by the arrows corresponds to the lattice spacing of MgO (a~0.4 nm). Figures 1 (b), (c), and (d) show the patterns of bottom Fe_3O_4, $MgAl_2O_4$ barrier, and top Fe_3O_4, respectively. They indicate that the epitaxial growth of the electrodes and the barrier; therefore, an all-spinel structured MTJ was achieved. From the MH-curve of the single Fe_3O_4 on MgO(001), the saturation magnetization M_s of Fe_3O_4 was estimated to be 463 kA/m, comparable to the bulk value (480 kA/m) within an experimental error. Figure 2 shows the MH-curve of the MTJ stack. Both top and bottom electrodes showed sharp and independent magnetization reversal, and thus magnetically parallel/antiparallel configurations were realized. This behavior is in contrast to the results in most of previous reports, where an incomplete magnetic separation in MTJs was observed. Therefore, the achievement of the all-spinel MTJ using an $MgAl_2O_4$ barrier may promote the formation of high crystallinity and small interfacial flatness of an MTJ. However, the $MgAl_2O_4$ barrier of this MTJ stack is too thick to evaluate its TMR ratio due to its very large resistance-area-product (RA) > 20 GΩ●μm^2. The inset of Fig. 2 shows a typical current-voltage (IV)-curve of the MTJ. The nonlinear IV curve indicates the tunneling behavior of the $MgAl_2O_4$ between the Fe_3O_4 electrodes. Using the Simmons model[3], the effective barrier height and the effective thickness were estimated to be 1.1 eV and 2.4 nm, respectively. The barrier height is smaller than the reported values of $MgAl_2O_4$ (2-3 eV)[4], indicating that further improvement in the $MgAl_2O_4$ crystallinity may be needed for good spin-dependent transport properties. Summary In this study, we developed an all-spinel-type MTJ structure with $MgAl_2O_4$ and Fe_3O_4. The RHEED patterns indicated that both the $MgAl_2O_4$ and Fe_3O_4 were epitaxially grown with a spinel structure. In addition, the good magnetization process between top- and bottom-$Fe_3O_4(001)$ layers was demonstrated. Since a TMR ratio could not be evaluate due to the significantly large RA, further optimization of each film thickness and growth condition is necessary. This study suggests that the use of an all-spinel structure will be promising for improving microstructures of Fe_3O_4-based MTJs toward better TMR performance.

[1] M. Opel, S. Geprags, E.P. MenzelA, N. Nielsen, D. Reisinger, K.-W. Nielsen, A. Brandlmaier, F.D. Czeschka, M. Althammer, M. Weiler, S.T.B. Goennenwein, J. Simon, M. Svete, W. Yu, S.-M. Huhne, W. Made, and R. Gross, Phys. Status Solidi A 208, 232 (2011). [2] M. Luysberg, R.G.S. Sofin, S.K. Arora, and I. V. Shvets, Phys. Rev. B 80, 024111 (2009). [3] J.G. Simmons, J. Appl. Phys. 34, 1793 (1963). [4] H. Sukegawa, Y. Kato, M. Belmoubarik, P.-H. Cheng, T. Daibou, N. Shimomura, Y. Kamiguchi, J. Ito, H. Yoda, T. Ohkubo, S. Mitani, and K. Hono, Appl. Phys. Lett. 110, 122404 (2017).

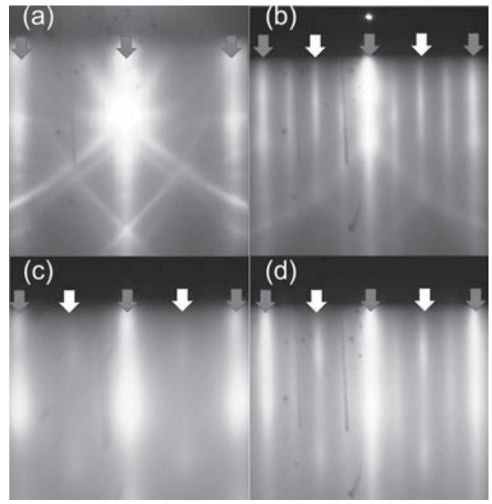

Fig. 1. RHEED patterns into [100] azimuth at each surface. (a) MgO substrate (b) bottom Fe_3O_4 electrode (c) $MgAl_2O_4$ barrier and (d) top Fe_3O_4 electrode. Spinel structure are confirmed in both the barrier and the electrodes.

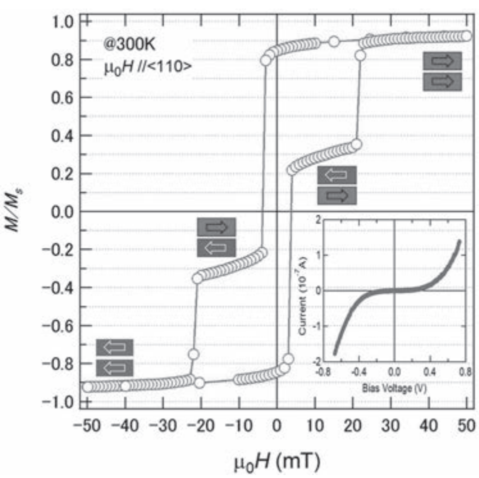

Fig. 2. An MH-curve of the $Fe_3O_4/MgAl_2O_4/Fe_3O_4(001)$ MTJ stack. A typical IV-curve of MTJ is shown in the inset

BP-04. Large enhancement of magneto-dielectric effect in Co–MgF_2 nano–composites by small addition of Si.

Y. Cao[1], N. Kobayashi[2], S. Ohnuma[1,2] and H. Masumoto[1]
1. Frontier Research Institute for Interdisciplinary Science, Tohoku University, Sendai, Japan; 2. Research Institute for Electromagnetic Materials, DENJIKEN, Sendai, Japan

I. Introduction The scarcity of room-temperature multiferroics has led researchers to develop two-phase magnetoelectric (ME) composites combining the ferroelectric and ferromagnetic phases via strain engineering [1, 2]. However, the process is involved in high temperature sintering and may create defects and diffusion, which will hamper their practical use. Recently, a new tunnel-type magneto-dielectric (TMD) effect was discovered by our group at room temperature [3]; this provides new dawn for ME effect, which is caused by the oscillation of the charge carriers between super-paramagnetic granules in films. Nevertheless, the reported TMD ratio ($\Delta\varepsilon'/\varepsilon'_0$), to date, attained 3% under magnetic field $H = 10$ kOe [3]. Even though we have realized the low-field enhancement of TMD effect in a two-dimensional Co/AlF granular nanostructures [4], the TMD response is still far from satisfactory and their further enhancements remain an open question. Here, we have, for the first time, realized large enhanced TMD response (3.7% at $f =$ 15 kHz) in Co–MgF_2 granular nano-composites by means of nonmagnetic Si dopant. This work may be of importance in high-performance ME device applications. II. Experimental The Co–MgF_2 films with different concentration of Si (x) were deposited on Si(100) and Pt/Ti/SiO_2/Si substrates by a triple-source magnetron sputtering method in a sputtering Ar gas pressure of 0.5 Pa, wherein the Co target, MgF_2 target and Si target were used. Film thickness was regulated at ca. 350 nm and Si concentration (x) was regulated in the range of 0–3.7 at. %. HAADF–STEM was used for structural characterization. Chemical compositions and state of all samples were analyzed by XRF and XPS, which revealed a stoichiometric MgF_2 matrix and Co granule contents of *ca.* 16 at. %. Magnetic, dielectric and magneto-dielectric properties were measured by VSM and LCR meters. III. Results and discussion The Co–MgF_2 film shows a nano-granular structure, wherein the bright areas correspond to Co granules because of its high Z number, and the areas with the dark contrast is probably related to Mg–fluorides (MgF_2) (Fig. 1a). To verify this suggestion and analyze the dispersion of Si, EDX mapping and spectra for several granules are shown in Figs. 1(b–e), indicating that there is an ubiquitous match between Co and Mg, and the Si is distributed uniformly. XPS spectra has confirmed the pure Si instead of Si-oxides in as-deposited samples. Frequency dependence on the real part of dielectric constant (ε'_0) show that there is no obvious change in ε'_0 as increasing the Si content. With the application of magnetic field $H = 10$ kOe, there is a slight increase in ε'_0, denoted as positive TMD ratio $\Delta\varepsilon'/\varepsilon'_0$. $\Delta\varepsilon'/\varepsilon'_0$ of the Co–MgF_2 films retains at 0.7%, and it increases to a maximum value of 3.7% with small Si addition of 0.7 at.% (Fig. 2a). Further increasing the Si content led to a decrease in $\Delta\varepsilon'/\varepsilon'_0$, concluding that there exists an optimum Si dopant content for a given Co content. By fixing the frequency of ac field to 15 kHz, magnetic field dependence of $\Delta\varepsilon'/\varepsilon'_0$ is shown in Fig. 2b. A gradual increase in $\Delta\varepsilon'/\varepsilon'_0$ with the application of magnetic field is observed. It is noted that samples with $x = 0.7$ has largest magnetization values ($M_s = 1.4$ kG). We may infer that the enhanced $\Delta\varepsilon'/\varepsilon'_0$ by means of Si dopant is related to the increase in magnetization values, which is probably caused by the change in the size and atomic ordering of magnetic granules. This study offers a new route for high room temperature magneto-dielectric response in nano-composites and may have potential application in spintronic devices.

[1] J. Wang, et al, *Science* 299, 1719 (2003). [2] N. Ikeda, et al, *Nature* 436, 1136 (2005). [3] N. Kobayashi, et al. *Nat. Commun.* 5, 4417 (2014). [4] Y. Cao, et al. *Appl. Phys. Lett.* 110, 072902 (2017).

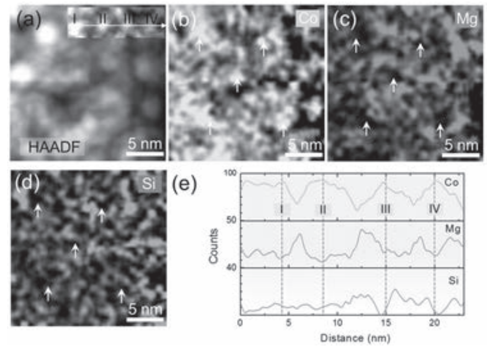

Fig. 1. (a) Cross sectional HAADF–STEM image of the Co–MgF_2 films with Si content of 1.3% and the elemental maps of (b) Co, (c) Mg, and (d) Si; arrows indicated the bright areas in (b) for clarification. (e) Associated energy-dispersive X-ray spectra for several granules as marked in the upper inset of (a).

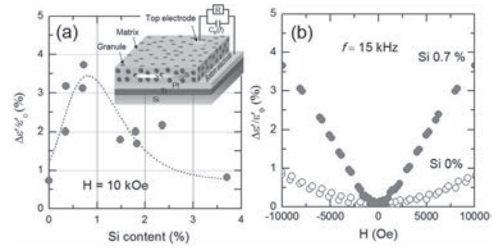

Fig. 2. (a) TMD ratio $\Delta\varepsilon'/\varepsilon'_0$ under H = 10 kOe as function of Si atomic percent; the dashed curve show the fitting results guided to the eyes. Inset presents the schematic overview for TMD measurement. (b) Magnetic field dependence of $\Delta\varepsilon'/\varepsilon'_0$ for Co–MgF_2 films with and without Si dopant at frequency of 15 kHz.

BP-05. Giant zero-biased magnetoelectric coupling characteristics in flexible Metglas/poly(vinylidene fluoride) heterostructures.

Y. Long[1], *J. Qiu*[1], X. He[1], Q. Chang[1], Z. Hu[1] and H. Liu[1]
1. College of Optoelectronic Engineering, Chongqing University, Chongqing, China

Magnetoelectric (ME) effect have intrigued dramatic research interests in the past decades, owing to its potential applications in a large number of new multifunctional devices, including magnetic storage, energy harvesters, magnetic field sensors, transformers, and microwave devices, among other. [1,2] It exists in materials by different principles: through the elastic coupling between magnetostrictive and piezoelectric phases (in ME composites) or through the coupling of electric dipole and magnetic moment (in single-phase ME material). In general, ME single-phase materials are not suitable to be utilized in technological application, owing to their low ME response which typically occurs at low temperatures. Compared with single-phase ME materials, ME composites have exhibited commendable ME coupling characteristic at room temperature. Furthermore, among ME composites, laminates show the largest ME response, thus being the most suitable structure for industrial applications. However, in spite of laminated ME composites have shown high ME conversion coefficient and strong ME responses, the external dc bias magnetic field (H_{dc}) is indispensable due to the saturation magnetostrictive coefficient of magnetostrictive material can be obtain only under a high H_{dc}, which will improve production costs and increase technical difficulty in industrial production. To overcome these shortcomings, some researchers have focused on zero-biased ME composites. In particular, Mandal *et al*. have reported zero-bias ME coupling for samples of PZT and magnetization-graded ferromagnetic layers, the grading in the magnetization is achieved with the use of Ni and Metglas. [3] Chen *et al*. demonstrated that a multiferroic heterostructure consisting of piezoelectric ceramic PZT, giant magnetostrictive material Terfenol-D, and different thickness soft magnetic alloy FeCuNbSiB shows an enhancement in the ME coefficient at zero bias. [4] Although those works have investigated zero-biased ME response of the laminates, they require complicated synthesis process. Moreover, conventional ceramic based laminated ME composites consisting of piezoelectric ceramics (e.g., PZT and (PMN-PT)) are usually fragility, non-bendable, fatigue, and expensive, which do not meet the increasing industry demands in terms of flexibility, complicated shape, and cost, hindering them from being used in rapidly growing technological areas such as wearable devices. Bearing these in mind, in this paper, the flexible zero-biased laminated ME composites consisting of FeSiB (Metglas)/poly(vinylidene fluoride) (PVDF) is presented, whose zero-biased ME coupling characteristics and ME sensing performance have been investigated. The optimum size of composites have determined by optimizing the resonance magnetoelectric voltage coefficient, αME,r, values. It is found that an appropriate size of composites is propitious to the zero-biased ME coupling characteristics due to the demagnetization effect. In addition, to evaluate the ability of composites to be used in bend status, the relationship between the resonant MEVC with H_{dc} under different bend conditions have also been investigated, for which have never been or just partially discussed. As shown in Fig. 1, the zero-biased resonant MEVC showed an attenuation of approximately 76%, with increasing θ up to 50°. Although the zero-biased resonant MEVC shows substantial decline under bend status, it still has very large value. Meanwhile, the proposed composites also have a commendable ac magnetic field (H_{ac}) sensing performance. The induced zero-biased ME voltage have an excellent linear relationship to ac magnetic field both at the low frequency (1kHz) and the resonant frequency (57.3kHz) as shown in Fig. 2. Obviously, it clearly indicated that the proposed zero-biased FeSiB/PVDF composite have great potential of being applied to wearable devices.

[1] S. Reis, M. P. Silva, N. Castro, V. Correia, P. Martins, A. Lasheras, J. Gutierrez, J. M. Barandiarán, J. G. Rocha, and S. Lanceros-Mendez, "Characterization of Metglas/poly(vinylidene fluoride)/Metglas magnetoelectric laminates for AC/DC magnetic sensor applications", Mater. Design. 92, 906 (2016). [2] P. Martins and S. Lanceros-Méndez, "Polymer-based magnetoelectric materials", Adv. Funct. Mater. 23, 3371 (2013). [3] S. K. Mandal, G. Sreenivasulu, V. M. Petrov, and G. Srinivasan, "Magnetization-graded multiferroic composite and magnetoelectric effects at zero bias", Phys. Rev. B. 84, 014432 (2011). [4] L. Chen, Y. Wang, F. J. Qin, and D. Y. Li, "Enhanced sensitivity with five-phase heterostructure magnetoelectric sensor at low magnetic bias field", IEEE Trans. Magn. 52, 2501304 (2016).

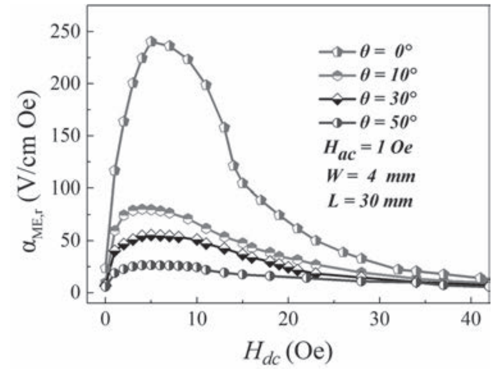

Fig. 1. The resonant MEVC of transducers as a function of H_{dc} under different bend status.

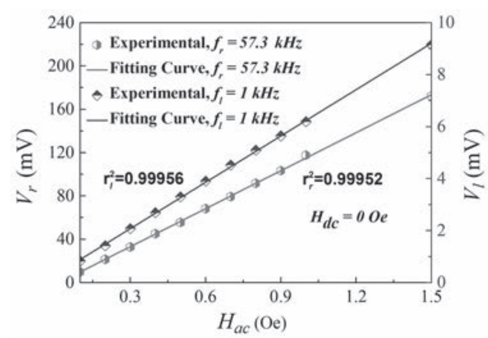

Fig. 2. The zero-biased ME voltage as a function of ac magnetic field H_{ac} at low frequency and resonant frequency.

BP-06. Study of magnetic and electrical properties of $Zn_{0.9}Mn_{0.1}Fe_2O_4$-$BaTiO_3$ multiferroic composites.

A. Farheen[1] and R. Singh[1]
1. School of Physics, University of Hyderabad, Hyderabad, India

Generally, magnetic and electric dipoles are mutually exclusive in crystalline materials. But the composite multiferroics offers a way to attain magnetic and ferroelectric ordering simultaneously. Also, the composites are important for the advancement of magneto-electronic devices, magnetoelectric sensors, random access memory, etc. [1]. In the present work, the room temperature multiferroic property was verified through magnetic hysteresis (M(H)) and ferroelectric hysteresis (P(E)) loop measurements. The composites (1-x) BaTiO3+(x) Zn0.9Mn0.1Fe2O4 (x = 0, 0.10, 0.20 and 1) were synthesized by using the nanoparticles of Zn0.9Mn0.1Fe2O4 (ZMF) and BaTiO3 (BTO) by sintering at 1200°C for 6 hours. The nanoparticles of BTO and ZMF were synthesized by hydrothermal method and by co-precipitation method respectively as described in our earlier works [2,3]. The crystal structure of the nanoparticles of ZMF and BTO are cubic spinel and tetragonal phase respectively as confirmed by X-ray diffraction (XRD) analysis (Fig.1a). The XRD of the composite (x = 0, 0.10, 0.20 and 1) samples confirm the co-existence of BTO and ZMF phases. It is observed from the field emission scanning electron microscope (FESEM) micrographs (fig.1a inset) that the composite system consists of two kinds of regions: one corresponds to ferromagnetic (FM) phase and the other one to ferroelectric (FE) phase. Fig. 2(a) shows the magnetization vs. magnetic field (M(H)) plots for the FM-FE composites at 300K with x = 0.10, 0.20 and 1 respectively. An increase in magnetization is observed with the inclusion of ZMF. The samples exhibit magnetic hysteresis behaviour with very low coercivity values indicating their soft ferromagnetic nature with much lower magnetization value than pure ZMF (inset of Fig. 2(a)). This indicates the existence of non-magnetic FE phase along with FM phase. The ferroelectric particles surrounding the magnetic particles influence the magnetic coupling among the magnetic particles. The presence of M(H) hysteresis loop confirms the magnetic ordering in the FM-FE composites. Fig. 2(b) shows the change of saturation magnetization (Ms) and coercivity (Hc) as a function of ZMF percentage (x %) for all the FM-FE composites. The gradual increase in Ms-values with the increase in ZMF content indicates that the Ms-values for the composites follow the mixture rule. Therefore, the magnetic response of composites depends on ZMF percentage [3]. Also, the increase in coercivity observed with decreasing ferrite percentage may be due to the diamagnetic nature of BTO. The observed multiple resonance in the ferromagnetic resonance (FMR) spectra (Fig.2(c)) of the composites is attributed to the coexisting magnetic states of the cations and cation distribution between A and B sublattices of spinel ferrites. It can also be attributed to the presence of heterogeneities in the composites. The decrease in resonance field (Hr-value) is related to the increase in internal magnetic field which indicates the increase in magnetic response with increasing ZMF percentage. Fig. 1(b) shows the ferroelectric hysteresis (P(E) loop) at room temperature for FM-FE composites (x=0.10 and 0.20). The shape of P(E) loop confirms the ferroelectric ordering of the composites at room temperature. The positive curvature of the P(E) loop shows that the leakage current contribution is minimal. The remnant polarization and coercive field increases with increase in ZMF percentage. Since in the FM-FE composites, the ferroelectric grains are surrounded by the ferrite grains or vice versa. Therefore, the heterogeneous microstructure may be a possible reason for alteration in the interaction among the internal poles of the FM-FE composite. The FM-FE composites show a decrease in dielectric constant (ε) value (solid lines in fig.1c) with an increase in dielectric loss (tan δ) (symbol lines in fig.1c) with an increase in ZMF-content. It is observed that the dielectric constant and loss values decrease with increasing frequency approaching to a lower saturation value at high frequencies. The variation of ε-value with frequency is attributed to the fact that the electric dipoles are unable to follow the fast alternate electric field oscillations under high frequencies. At lower frequencies, the FM-FE composites have higher ε and loss values. The FE-FM distribution makes two types of inter grain connectivity impling two types of ionic relaxations in the low frequency region confirming the results from FESEM micrographs. It is clear from the results that magnetic, electric and dielectric properties of composites strongly depend on the microstructure of the sample. And the multiferroic properties of ferromagnetic-ferroelectric composites are due to the induced electric polarization in the magnetic order or vice versa.

1. C. W. Nan, M. I. Bichurin, S. Dong, D. Viehland and G. Srinivasan, Multiferroic magnetoelectric composites: Historical perspective, status, and future directions, J. Applied. Physics 103, 031101 (2008). 2.G. Thirupathi and R. Singh, Crystal Structure and Magnetic Properties of Mn-Doped Zn-Ferrite Nanoparticles, IEEE transactions on magnetics, vol. 50, no. 11 (2014). 3.A. Farheen, T. Gadipelly and R. Singh, Multiferroic properties of ferromagnetic and ferroelectric coupled Mn-Zn Ferrite and BaTiO3 composites, Ferroelectrics 516, 82-89 (2017).

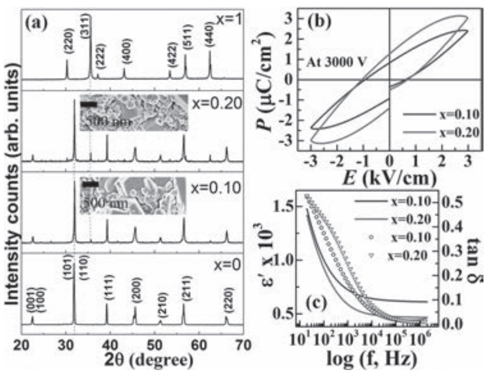

Fig. 1. The XRD and FESEM micrographs of FM-FE composites

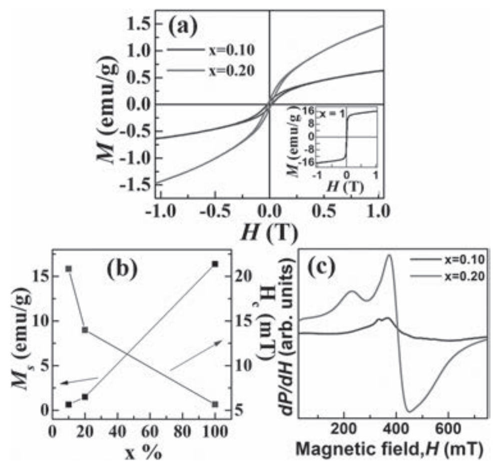

Fig. 2. The M(H) loop, FMR spectra, P(E) loop and dielectric plots of FM-FE composites.

BP-07. Theory of electrically tunable thin-film electromagnetic crystals based on a coplanar waveguide.

A.A. Nikitin[1,2], A. Nikitin[1,2], A.B. Ustinov[1], E. Lähderanta[2] and B.A. Kalinikos[1]

1. Physical Electronics and Technology, St. Petersburg Electrotechnical University, St. Petersburg, Russian Federation; 2. Laboratory of Physics, Lappeenranta University of Technology, Lappeenranta, Finland

Artificial magnetic materials with a spatial periodic modulation of their physical properties or geometry, known as magnonic crystals, are promising for new microwave devices such as phase shifters [1, 2], various spin-wave logic elements [3, 4], high-sensitivity magnetic sensors [5, 6], and others [7, 8]. Recent advances related to the thin-film technology have resulted in fabrication of the multilayered *multiferroic structures* that combine advantages of the ferrites and ferroelectrics. Owning to the dual tunability of wave spectra by both electric and magnetic fields, such structures were widely used in microwave devices [9]. Different kinds of ferrite-ferroelectric all-thin-film structures were suggested based on coplanar or slot transmission lines [10-12]. In these structures, spin-electromagnetic waves (SEW) are originated from the electrodynamic coupling of the electromagnetic wave propagating in the transmission line with the spin waves (SW) propagating in the ferrite film. However, up to now the periodic multiferroic structures based on coplanar waveguides (CPW) were investigated only experimentally [10]. The purpose of this work is to develop a theory of hybridized spin-electromagnetic waves in the thin-film regular and periodic multiferroic waveguiding structures based on CPW. In order to distinguish the *periodical* multiferroic waveguides from known ferrite magnonic crystals, as well as from photonic crystals, below we name them as *electromagnetic crystals* (EMC). A studied EMC structure is shown in Fig. 1. It is composed of several layers enumerated with index j, namely, a sapphire substrate ($j = 1$), a barium strontium titanate (BST) ferroelectric film ($j = 2$), an epitaxial yttrium iron garnet (YIG) film ($j = 3$), and a gadolinium gallium garnet substrate ($j = 4$). The periodic segments of the CPW form the thin-film EMC. Here the central metal strip of width h and two conducting ground planes are positioned in the plane z between *ferroelectric* and *ferrite* layers. The segments of narrow w_1 and wide w_2 slots has the period Λ. Application of control voltage U to the periodic CPW electrodes provides a reduction of the ferroelectric film permittivity ε_2 and so maintains an electric tunability. The hybridized waves are considered to propagate along x-axis, i.e. along CPW, which is magnetized to saturation by a uniform magnetic field H along z-axis. Due to the symmetry of the fundamental CPW mode its dispersion relation can be found through analytical solution of the full set of Maxwell's equations utilizing the method of approximate boundary conditions described in details in Ref. [12]. The obtained dispersion relation for a *regular* CPW was used for a numerical calculation of the transmission characteristics of the EMC using the transfer-matrix method [13]. Note that this method takes into account the insertion losses and is suitable for the finite-length periodic structures. Following the outlined theory, Fig. 2(a) illustrates the effect of hybridization of two principal electromagnetic modes for the *regular* CPW and *regular* slot-line structure. One can clearly see that the area of the maximum hybridization of SEWs in the CPW shifts to the higher wavenumbers in comparison to the slot-line structure. This behavior is determined by a sufficient reduction of the phase velocity of the microwave electromagnetic waves due to additional "magnetic wall" boundary condition applied at the central metal strip. Note that the calculations were carried out for the typical parameters of YIG and BST films commonly used in microwave devices (see, e.g., Ref. [9]). A reduction of the CPW slot width w shifts the SEW dispersion characteristic to the higher wave numbers. Consequently, the SEW formed in the EMC accumulate the different phase shifts in different segments of the periodic structure at a fixed frequency (see Fig. 1). The band-gaps appear at the frequencies where this phase shift is a multiple of π. As a result, a major part of the spin-electromagnetic wave power will be reflected from the electrodes of EMC at the frequencies that satisfy to the Bragg condition. This effect is visible on the transmission characteristic shown in Fig. 2(b). The characteristic was calculated for the EMC with number of periods $N = 10$ and $\Lambda = 1$ mm with the use of the transfer matrix method. In this case, the width of the first band gap (denoted by I in Fig. 2(b)) is 24.6 MHz at a level of 3 dB from the maximum loss at 33 dB. In addition, this figure illustrates electric tuning of the EMC band gap positions for a reduction of the ferroelectric film permittivity ε_3 from 1500 to 750. In summary, a novel EMC based on CPW were studied. In particular, it was found that a high microwave signal rejection of more than 30 dB appears for the periodic structures. Furthermore, the electric tuning for the first band-gap reaches values of 10.45 MHz by the dielectric permittivity reducing of the ferroelectric film by half. All these advantages make this kind of EMC perspective for development of new microwave devices. The work in SPbETU was supported in part by the Russian Science Foundation, Grant 14-12-01296P. The work in LUT was supported by the Academy of Finland.

1. Y. Zhu, K. H. Chi, and C. S. Tsai, "Magnonic crystals-based tunable microwave phase shifters," Appl. Phys. Lett., 2014, Vol. 105, Iss. 2, p. 022411. 2. S. Louis, I. Lisenkov, S. Nikitov, V. Tyberkevych, and A. Slavin, "Bias-free spin-wave phase shifter for magnonic logic," AIP Advances, 2016, Vol. 6, Iss. 6, p. 065103. 3. A. A. Nikitin, A. B. Ustinov, A. A. Semenov, A. V. Chumak, A. A. Serga, V. I. Vasyuchka, E. Lähderanta, B. A. Kalinikos, and B. Hillebrands, "A spin-wave logic gate based on a width-modulated dynamic magnonic crystal." Appl. Phys. Lett., 2015, Vol. 106, Iss. 10, p. 102405. 4. T. Fischer, M. Kewenig, D. A. Bozhko, A. A. Serga, I. I. Syvorotka, F. Ciubotaru, C. Adelmann, B. Hillebrands, and A. V. Chumak, "Experimental prototype of a spin-wave majority gate," Appl. Phys. Lett., 2017, Vol. 110, Iss. 15, p. 152401. 5. M. Inoue, A. Baryshev, H. Takagi, P. B. Lim, K. Hatafuku, J. Noda, and K. Togo, "Investigating the use of magnonic crystals as extremely sensitive magnetic field sensors at room temperature," Appl. Phys. Lett., 2011, Vol. 98, Iss. 13, p. 132511. 6. H. Takagi, J. Noda, T. Ueno, N. Kanazawa, Y. Nakamura, and M. Inoue, "Monolithic Structure and Multiaxis Magnetic Sensing with Magnonic Crystals," Electron. Commun. Jpn., 2014, Vol. 97, Iss. 10, p. 11-16. 7. M. Krawczyk and D. Grundler, "Review and prospects of magnonic crystals and devices with reprogrammable band structure." J. Phys.: Condens. Matter., 2014, Vol. 26, Iss. 12, p. 123202. 8. A.V. Sadovnikov, S.A. Odintsov, E.N. Beginin, S.E. Sheshukova, Yu. P. Sharaevskii, S.A. Nikitov, "Toward nonlinear magnonics: Intensity-dependent spin-wave switching in insulating side-coupled magnetic stripes" Phys. Rev. B 96, 144428 (2017). 9. M. M. Vopson, "Fundamentals of multiferroic materials and their possible applications," Crit. Rev. Solid State Mater. Sci., 2015, Vol. 40, Iss. 4, p. 223-250. 10. J. H. Leach, H. Liu, V. Avrutin, E. Rowe, Ü. Özgür, H. Morkoç, Y.-Y. Song, M. Wu, "Electrically and magnetically tunable phase shifters based on a barium strontium titanate-yttrium iron garnet layered structure," J. Appl. Phys., 2010, Vol. 108, Iss. 6, p. 064106. 11. A. A. Nikitin, A. B. Ustinov, A. A. Semenov, B. A. Kalinikos, and E. Lähderanta, "All-thin-film multilayered multiferroic structures with a slot-line for spin-electromagnetic wave devices," Appl. Phys. Lett., 2014, Vol. 104, Iss. 9, p. 093513. 12. A. A. Nikitin, A. B. Ustinov, V. V. Vitko, A. A. Semenov, P. Yu. Belyavskiy, I. G. Mironenko, A. A. Stashkevich, B. A. Kalinikos, and E. Lähderanta, "Dispersion characteristics of spin-electromagnetic waves in planar multiferroic structures", J. Appl. Phys., 2015, Vol. 118, Iss. 18, p. 183901. 13. Li Zhi-Yuan, Lin Lan-Lan, "Photonic band structures solved by a plane-wave- based transfer-matrix method," Phys. Rev. E, 2003, Vol. 67, Iss. 4, p. 046607.

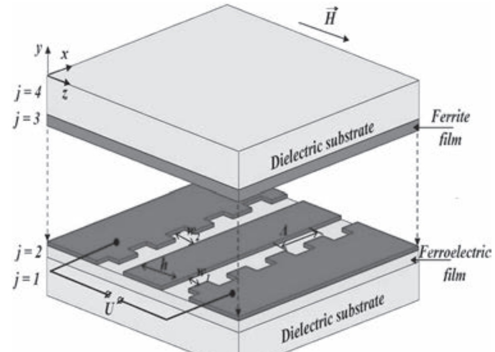

Fig. 1. The thin-film electromagnetic crystal based on CPW

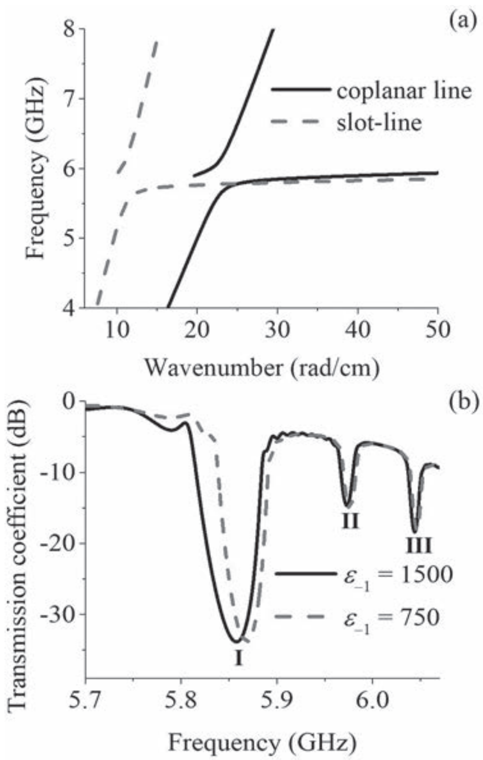

Fig. 2. (a) The spectra of the hybrid SEW in the all-thin-film multiferroic structure with a slot-line (dashed curve) and coplanar line (solid curve). (b) Electric tuning of the transmission characteristic for the EWC

BP-08. Dielectric relaxation and conduction mechanism of magneto-electric hexaferrite $BaFe_{10.2}Sc_{1.8}O_{19}$.

R. Tang[1], Q. Zhu[1] and X. Su[1]
1. College of Physics, Optoelectronics and Energy, Soochow University, Suzhou, China

The dielectric relaxation process, conduction mechanism and the micro-structure-electrical property relationship in the multiferroic M-type hexaferrites have not been well understood until now[1-2]. In this work, the dielectric relaxation and conduction properties of polycrystalline hexaferrite BaFe10.2Sc1.8O19 (BFSO) have been investigated as a function of temperature from 253 to 473 K with impedance spectroscopy. The frequency dependent impedance and modulus spectra show that the dielectric responses of BFSO are thermally activated. In addition, there is a distribution of relaxation times in the sample. The scaling behaviors of Z^" and M^" spectra further suggest that the distribution of relaxation times is temperature independent. The frequency dependent conductivity spectra follow the universal power law at high temperatures but deviate slightly at low temperatures. The large increase of activation energy above 413 K indicates that at high temperatures, relaxation/conduction processes may be contributed mainly by the diffusive oxygen vacancies, while at low temperatures electron hopping dominates. The fitting results of σ' spectra further suggest that electron/oxygen vacancy-related small polaron hopping is the most probable conduction mechanism for BFSO.

[1] R.J.Tang ; C.Jiang; J.Jian; X.Zhang; H.Y.Wang; H. Yang, Appl. Phys. Lett. 106, 022902 (2015). [2] R.J.Tang; H.Zhou; W. L.You; H.Yang; Appl. Phys. Lett. 109, 082903 (2016).

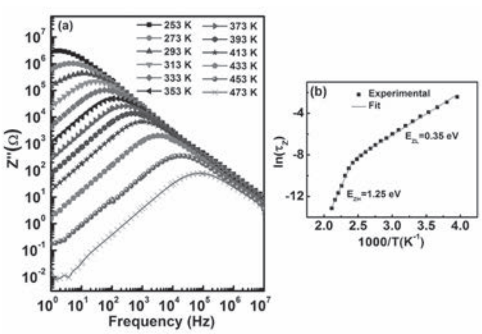

Fig. 1. (a) Frequency dependence of Z^'' at different temperatures, (b) the temperature dependence of the relaxation times obtained from the peak frequencies of Z^''.

BP-09. Magnetodielectric effects in multiferroic M-type hexaferrite thin films.

R. Tang[1], Q. Zhu[1], X. Su[1] and H. Yang[2]
1. College of Physics, Optoelectronics and Energy, Soochow University, Suzhou, China; 2. School of Science, Nanjing University of Aeronautics and Astronautics, Nanjing, China

Materials exhibiting large magnetodielectric (MD) couplings could be potentially used in many devices, such as tunable filters and magnetic sensors. Hexaferrites has been discovered as a class of multiferroic materials [1]. The MD properties of the bulk Z-type and M-type hexaferrites have been studied [2-3]. It has been shown that the physical properties of the oxide thin films, especially epitaxial thin films, could be drastically different from those of the polycrystalline bulk materials due to the differences in size and microstructures. However, the MD properties of multiferroic hexaferrite thin films have not been well understood, especially at room temperature. In this work, the MD effects of epitaxial hexaferrite $BaFe_{10.2}Sc_{1.8}O_{19}$ (BFSO) thin film have been investigated around the room temperature. The frequency dependent dielectric constant and MD analysis at room temperature show that in the low frequency regime (f <100 Hz), the MD effect exists but it is very small. When the frequency is higher than 1 kHz, two strong MD peaks exist which should be contributed by the magnetic field dependent sample/electrode interface polarizations (1 kHz < f <100 kHz) and electric dipole rotations in the film (f >100 kHz), respectively. Further temperature dependent MD analysis at 1 MHz shows that the magnetic-field-induced electric dipoles dominate the MD effect below the conical magnetic transition temperature (T_{cone} = 306 K), while the lattice-type dipoles dominate the MD effect above T_{cone}. The above findings further the potential applications of multiferroic hexaferrite thin films in the magnetoelectric devices.

[1] T. Kimura, Annu. Rev. Condens. Matter. Phys. 3, 93 (2012). [2] X. Zhang, Y. G. Zhao, Y. F. Cui, L. D. Ye, J. W. Wang, S. Zhang, H. Y. Zhang, and M. H. Zhu, Appl. Phys. Lett. 100, 032901 (2012). [3] R.J. Tang, H. Zhou, W. L. You, and H. Yang, Appl. Phys. Lett. 109, 082903 (2016).

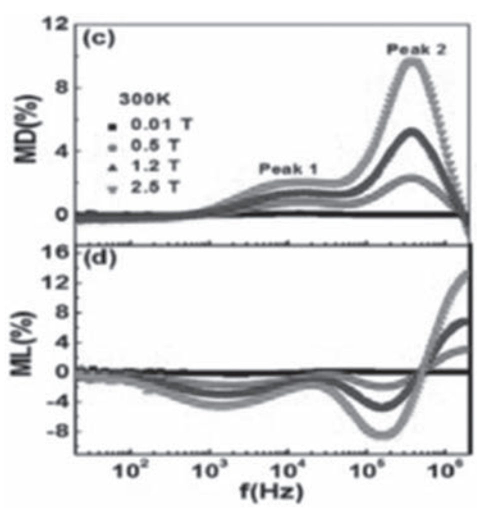

Fig. 1. Frequency dependences of MD and ML effects of $BaFe_{10.2}Sc_{1.8}O_{19}$ epitaxial thin film at 300 K. The magnetic field is 0.01 T, 0.5 T, 1.2 T and 2.5 T respectively.

BP-10. Room-temperature multiferroic properties of $0.5LaFe_{0.5}Co_{0.5}O_3$-$Bi_4Ti_3O_{12}$ thin films.

J. Su[1,2]
1. Qingdao University, Qingdao, China; 2. Nanjing Unversity, Nanjing, China

Multiferroic materials, which exhibit rich and fascinating physics such as the combination of ferroelectric and ferromagnetic characteristics, have gripped considerable attention due to their unusual physical properties in new device application [1]. $0.5LaFe_{0.5}Co_{0.5}O_3$-$Bi_4Ti_3O_{12}$ (0.5LFC-BTO) multiferroic thin films were prepared via a sol-gel method on (111)Pt/Ti/SiO_2/Si(100) substrates. Bismuth nitrate [$Bi(NO_3)_3.5H_2O$], lanthanum oxide (La_2O_3), iron acetylacetonate ($C_{15}H_{21}FeO_6$), Cobalt acetylacetonate ($C_{15}H_{21}CoO_6$), and Tetrabutyl orthotitanate [$Ti(OC_4H_9)_4$] were used as the precursors materials for Bi, La, Fe, Co, and Ti, respectively. The La_2O_3 was dissolved in nitric acid (HNO_3) by constant stirring. Both $C_{15}H_{21}FeO_6$ and $Bi(NO_3)_3.5H_2O$ were dissolved in a compound solution of n-propanol ($CH_3CH_2CH_2OH$) and glacial acetic acid (CH_3COOH) was used to regulate the stability of solution as a stable agent. About a 4% excess of bismuth nitrate was added to compensate because of the volatilization of Bi during annealing process in high temperature. Precursor solution was spin-coated on substrates at 3500 rpm for 30 s. After that, the wet films were pulpless at 200 °C for 240 s and pyrolyzed at 320 °C for 360 s. Then the deposited films were followed by the rapid thermal annealing process at 780 °C for 480 s in oxygen atmosphere. The above steps were repeated six times to obtain the ultimate thickness of ~ 400 nm. To measure the electric properties, Au dots were sputtered on the film surface as top electrodes through the shadow masks. The hysteresis loops reach saturation gradually with the amplitude of applied electric field E being increased (Fig. 1(a)). The remanent polarization $2P_r$ and the coercive field $2E_c$ are 48 μC/cm² and 196 kV/cm under E of 360 kV/cm. The spontaneous polarization vector P_s is ~ 50 μC/cm², as much as 2.5 times over that of $Bi_5FeTi_3O_{15}$ thin films (~ 20μC/cm²) [2], larger than that of $0.5LaFeO_3$-$Bi_4Ti_3O_{12}$thin films (~ 37μC/cm²) nearly by 35% [3]. The better ferroelectric property of $0.5LaFe_{0.5}Co_{0.5}O_3$-$Bi_4Ti_3O_{12}$ thin films may owe to the reduction of chemical defects such as oxygen and bismuth vacancies, which is caused by the substitution of La^{3+} for Bi^{3+}. The $2P_r$ has a very slight trend with increasing f which indicates that the ferroelectric domain in 0.5LFC-BTO thin film has good frequency stability (Fig. 1(b)). In addition, the 0.5LFC-BTO thin films show weak ferromagnetism with the saturation magnetization M_s ~ 2.0 emu/cm³ (Fig. 2(a)), which is larger than that the $0.5LaFeO_3$-$Bi_4Ti_3O_{12}$ thin films (M_s ~ 0.90 emu/cm³) and BFTO films (M_s ~ 1.7 emu/cm³) [3,4]. The 0.5LFC-BTO thin films with layered perovskite structure is similar to that of $Bi_6Fe_{2-x}Co_xTi_3O_{18}$ [5], the concentration ratio of Fe/Co is also 1: 1, therefore, we speculate that the magnetic enhancement of 0.5LFC-BTO thin films is mainly related to the ferromagnetic interaction between the adjacent Fe-O and Co-O octahedrons. It is evident that the dielectric constant of 0.5LFC-BTO thin films change after H is applied at room temperature, indicating a magnetic dielectric coupling effect (MDC). The MDC can be defined as MDC = %, where $e_r(H)$ and $e_r(0)$ are the dielectric constants at magnetic field and zero field, respectively. The MDC coefficient is about 0.75% under H = 0.5 T (Fig. 2(b)). The MDC may stem from the spin reorientation under the magnetic field by affecting the interaction between the local dipoles of Fe^{2+} and Fe^{3+}. The MDC weakens with increasing frequency. It is because that the response of local dipoles of Fe^{2+} and Fe^{3+} to applied electric field needs longer time [6]. The coexistence of Fe^{2+} and Fe^{3+} was further confirmed by X-ray photoelectron spectroscopy (not shown here). Lorentzian-Gaussian curve fitting was used to evaluate the Fe^{2+}: Fe^{3+} ratio, which is ~80: 20 as estimated from the integrated intensities. In conclusion, 0.5LFC-BTO thin films were prepared via a sol-gel method. The films have a single-phase Aurivillius perovskite structure with space group *Fmm2*. As expected, the room-temperature multiferroic properties with $2P_r$ of ~48 μC/cm² and M_s of ~ 2.0 emu/cm³ were detected. Furthermore, a MDC effect with MDC ~ 0.75% was observed under a low magnetic field of 0.5 T at room temperature, resulting from the charge ordering of Fe^{2+} and Fe^{3+}.

References [1] R. Ramesh, N.A. Spaldin, Multiferroics: progress and prospects in thin films, Nat. Mater. 6 (2007) 21-29. [2] H.Y. Zhao, H. Kimura, Z.X. Cheng, M. Osada, J.L. Wang, X.L. Wang, S.X. Dou, Y. Liu, J.D. Yu, T. Matsumoto, T. Tohei, N. Shibata, Y. Ikuhara, Large magnetoelectric coupling in magnetically short-range ordered $Bi_5Ti_3FeO_{15}$ film, Sci. Rep. 4 (2014) 5255. [3] D.J. Zhang, J. Su, C.J. Lu, Y.C. Zhang, C. Zhang, Y. Li, L.Y. Feng, Room-temperature multiferroic properties of sol-gel derived $0.5LaFeO_3$-$Bi_4Ti_3O_{12}$ thin films with layered perovskite, J. Alloys Compd. 709 (2017) 729-734. [4] F.X. Wu, Z. Chen, Y.B. Chen, S.T. Zhang, J. Zhou, Y.Y. Zhu, Y.F. Chen, Significant ferrimagnetism observed in Aurivillius $Bi_4Ti_3O_{12}$ doped by antiferromagnetic $LaFeO_3$, Appl. Phys. Lett. 98 (2011) 212501. [5] Z. Liu, J. Yang, X.W. Tang, L.H. Yin, X.B. Zhu, J.M. Dai, Y.P. Sun, Multiferroic properties of Aurivillius phase $Bi_6Fe_{2-x}Co_xTi_3O_{18}$ thin films prepared by a chemical solution deposition route, Appl. Phy. Lett. 101 (2012) 122402. [6] H. Sun, B.W. Zou, X.R. Ni, X.Y. Mao, X.B. Chen, J.S. Zhu, Ferroelectric properties and the origin of the magnetism in the $Bi_6Fe_2Ti_3O_{18}$ thin films, J. Mater. Sci. 50 (2015) 5475-5481.

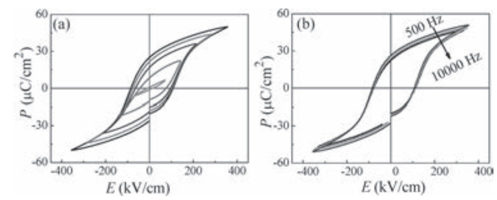

Fig. 1. *P-E* hysteresis loops at room temperature of the $0.5LaFe_{0.5}Co_{0.5}O_3$-$Bi_4Ti_3O_{12}$ films (a) under various applied electric fields *E* with fixed frequency *f*. (b) under different *f* with fixed *E*.

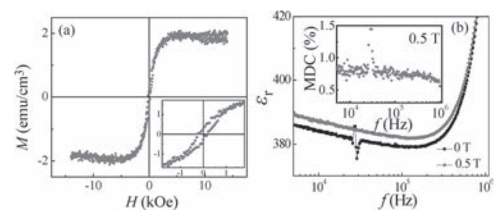

Fig. 2. (a) The *M-H* curve of the $0.5LaFe_{0.5}Co_{0.5}O_3$-$Bi_4Ti_3O_{12}$ thin films measured at room temperature. (b) The frequency dependence of the dielectric constant under 0 T and 0.5 T in the $0.5LaFe_{0.5}Co_{0.5}O_3$-$Bi_4Ti_3O_{12}$ films at room temperature. The inset is the MDC value with a different frequency.

TUESDAY AFTERNOON, 24 APRIL 2018 SIMPOR/ROSELLE BALLROOM, 1:30 TO 4:30

Session BQ
ENERGY ASSISTED RECORDING AND RECORDING MEDIA
(Poster Session)

Stephanie Hernandez, Chair
Seagate Technology, Shakopee, MN, United States

BQ-01. Micromagnetic model analysis of spin-torque oscillator (STO) integrated into recording write head for microwave-assisted magnetic recording–Oscillation of STO vs. rise time of in-gap field–.

Y. Kanai[1], R. Itagaki[1], S. Greaves[2] and H. Muraoka[2]

1. Information and Electronics Engineering Department, Niigata Institute of Technology, Kashiwazaki, Japan; 2. RIEC, Tohoku University, Sendai, Japan

Introduction Microwave-assisted magnetic recording (MAMR) [1] is one candidate for next-generation perpendicular magnetic recording [2]. Stable oscillation is one of the most important factors for spin-torque oscillators (STOs) used in a MAMR system. We performed micromagnetic simulations and found that stable STO oscillations were hard to obtain when the STO was inserted into the main pole – trailing shield (MP–TS) gap, primarily due to the strong magnetostatic interactions between the STO and write head [3]. We also showed that the rise time of the field applied to an isolated STO greatly affected the STO oscillation [4], i.e. a shorter rise time gave better, more consistent STO oscillation. In this paper, we show that the rise time of the in-gap field acting on the STO is critical to stable STO oscillation. We also show that the combination of a tilted STO and a tilted main pole – trailing shield gap results in stable STO oscillation due to weaker magnetostatic interactions between the STO and write head. Calculation Model A micromagnetic model analysis was carried out considering a double-layered STO utilizing transmission spin torque. We used commercial micromagnetic software (Fujitsu, EXAMAG v.2.1) [5]. The thickness of the field generation layer (FGL) was 10 nm, whilst the spin injection layer (SIL) was 2 nm thick. A 2 nm thick, non-magnetic inter layer was located between the FGL and SIL. The saturation magnetization ($4\pi M_s$) was 20 kG for the FGL and 6 kG for the SIL. The anisotropy fields (H_k) of both the FGL and SIL were 31.4 Oe. The exchange constants, A, were 2.5×10^{-6} erg/cm^3 for the FGL and 0.75×10^{-6} erg/cm^3 for the SIL. The Gilbert damping factor, α, was 0.02 for both the FGL and SIL. The write head model had overall dimensions close to those of commercial write heads (3.25 μm × 2.55 μm × 4.5 μm). Results and Discussion When the Gilbert damping factor, α, of the write head was increased from 0.02 to 0.2 the rise time of the MP–TS in-gap field (0 – 90 %) was shortened from 0.23 ns to 0.15 ns, and the stability of the FGL rotation improved, as shown in Fig. 1. The obtained FGL rotation frequencies were 23 GHz for α = 0.02 and 34 GHz for α = 0.2. The primary reason for the improved rotation came from the applied field reaching equilibrium with the spin-torque field in a shorter time. The second model we considered was a write head with a 20 nm MP–TS gap and a small STO (20 nm wide × 20 nm high). It is necessary to generate a high head field gradient to obtain high linear recording densities. In that regard, the MP–TS gap should be as small as 10 nm [6], while maintaining space to accommodate the STO. It is often believed that a large STO is needed to generate a large high-frequency FGL field. However, using an isolated STO model we found that the FGL field did not decay in proportion to the area of the STO facing the medium and it was easier to obtain coherent, stable oscillation in smaller STOs. In the head model with a 20 nm MP-TS gap, changing α did not affect the rise time (0.15 ns for α = 0.02 and 0.14 ns for α = 0.2) and the FGL rotation was unstable. The reason for this was that reducing the MP–TS gap made the magnetic circuit of the write head more efficient and there was no further room to reduce the rise time by changing α. In addition, the magnetostatic interactions between the STO and write head were larger compared with the 30 nm gap model, making the STO oscillation unstable. To decrease the magnetostatic interactions, we used a third write head model whose MP–TS gap was tilted with respect to the medium surface [7]. The STO was also tilted at the same angle. In the model, the trailing edge of the main pole was perpendicular to the medium surface, while the edge of the trailing shield was tilted. We varied the angle of tilt from 0° to 50° and found that 40° was the best with respect to obtaining stable FGL oscillation. Note that the applied field perpendicular to the FGL became weaker, but more uniform, as the angle of tilt increased. In Fig. 2, the FGL oscillations are shown for (a) a perpendicular STO and (b) a STO tilted by 40° with respect to the medium surface. It was found that the FGL magnetization rotated stably in the tilted STO model. The obtained FGL rotation frequencies were 24 GHz for the perpendicular STO and 30 GHz for the tilted STO. This shows that tilting the STO was quite effective to realize stable STO oscillation. It was also noted that a smaller head coil current and a smaller injected current density, J, to the STO were sufficient. Acknowledgment Financial support from JSPS Kaken-hi (16K06321) and Advanced Storage Research Consortium. Software support from JSOL, Japan.

[1] J.-G. Zhu, X. Zhu, and Y. Tang, "Microwave assisted magnetic recording," *IEEE Trans. Magn.*, vol. 44, no. 1, pp.125-131, Jan. 2008. [2] Energy-assisted Recording Technology, https:// play.vidyard.com/ JZLozr2ujb2jR964BaFNPW. [3] Y. Kanai, R. Itagaki, S. J. Greaves, and H. Muraoka, "Micromagnetic model analysis of various spin torque oscillators with write head for microwave-assisted magnetic recording," *IEEE Trans. Magn.*, vol. 53, 2017, Art ID 3001105. [4] Y. Kanai, R. Itagaki, S. Greaves, and H. Muraoka, "Micromagnetic model analysis of spin torque oscillators integrated into write head gap vs. head field response," *MMM Conf.*, BQ-08, Pittsburgh, PA, U.S.A., Nov. 2017, unpublished. [5] http://www. fujitsu.com/global/about/resources/news/press-releases/2015 /0324-01.html [6] Y. Kanai, Y. Jinbo, T. Tsukamoto, S. J. Greaves, K. Yoshida, and H. Muraoka, "Finite-element and micromagnetic modeling of write heads for shingled recording," *IEEE Trans. Magn.*, vol. 46, no. 3, pp. 715 - 721, Mar. 2010. [7] T. Katayama, Y. Kanai, K. Yoshida, S. Greaves, and H. Muraoka, "Micromagnetic model analysis of integrated single-pole-type head with tilted spin-torque oscillator for high-frequency microwave-assisted magnetic recording," *J. Appl. Phys.*, vol. 117, pp. 17C503-1 - 17C503-4, May 2015.

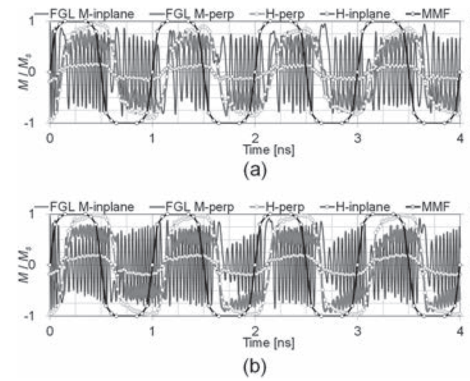

Fig. 1. FGL rotations vs. time for write head α = 0.02 (a) and 0.2 (b). MP-TS gap = 30 nm, MP width = 30 nm. $J = 6.0\times10^8$ A/cm^2. FGL: 30 nm × 30 nm. Black line (MMF) shows head coil current of 0.4 AT$_{pp}$; green (H-perp): perpendicular component of MP-TS in-gap field to FGL; purple (H-inplane): in-plane component of MP-TS in-gap field to FGL; blue (FGL M-inplane): in-plane component of FGL magnetization; red (FGL M-perp): perpendicular component of FGL magnetization. The obtained FGL rotation frequencies were (a) 23 GHz and (b) 34 GHz.

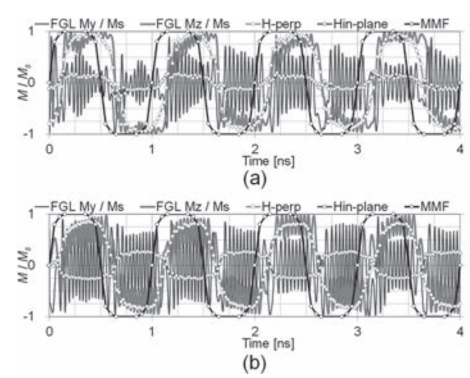

Fig. 2. FGL rotations vs. time for (a) perpendicular STO with perpendicular gap and (b) tilted STO. Write head α = 0.02. MP-TS gap = 20 nm, MP width = 40 nm. Head coil current (MMF) was 0.12 AT$_{pp}$, $J = 3.0\times10^8$ A/cm^2. FGL: 20 nm × 20 nm. The obtained FGL rotation frequencies were (a) 24 GHz and (b) 30 GHz.

BQ-02. ***Effect of SIL magnetic design on STO optimization in MAMR.***

I. Tagawa[1]
1. Electrical and Electronics, Tohoku Institute of Technology, Sendai, Japan

Uniform and stable oscillation of magnetization is one of the most important factors for the spin-torque oscillator (STO) in microwave assisted magnetic recording (MAMR) [1][2]. Impact of magneto-static interaction between STO and recording head have been discussed often [3][4], but the interaction including spin torque effect is not understood well even just between the field generation layer (FGL) and the spin injection layer (SIL) in STO. In this paper, we focused upon an effect of SIL magnetic design, i.e. the saturation magnetization and layer thickness, on STO optimization for uniform and stable oscillation and tried to understand the magnetic interaction with spin torque. A commercial micromagnetics software (Fujitsu Examag v2.1.1) was used, in which the effective field due to spin transfer torque is considered by the equation shown in Fig.1. In this analysis, a uniform alternative field was applied to STO and magneto-static interaction between STO and head was neglected as shown in Fig.1. The dimensions and magnetic properties are as the followings; FGL&SIL width and height= 30x30 nm, FGL thickness= 6 nm, FGL Bs= 2 or 1 T, FGL&SIL Hk= 1 Oe, Polarization= 0.5, Exchange= 1.0E-6 erg/cm, Damping= 0.02, SIL thickness and SIL Bs are variables. An alternative rectangular field with 1 GHz frequency and 14 kOe magnitude was applied and the injection current density was set at 4.0E+8 A/cm^2 with a direction to SIL from FGL. Results are shown in Fig.2 for (a) FGL Bs= 2 T and (b) FGL Bs= 1 T, respectively. Here, since the reduced cross-track component (My/Ms) of averaged FGL magnetization alternates at a microwave frequency, the root mean square (rms) value was calculated and multiplied by √2 to get 1 at the perfect sine-wave oscillation. In Fig.2(a) for the FGL Bs= 2 T, we can see that the optimum Bs of SIL is around at 1.5, 0.8, 0.6 and 0.4 T for the SIL thickness of 6, 3, 2 and 1, respectively. It's very interesting that the optimum Bs of SIL decreases simply according as SIL thickness increases, and these SIL design impacts significantly to FGL oscillation. In the case for FGL Bs= 1 T, as shown in Fig.2(b), all optimum points have moved to larger Bs positions compared to Fig.2(a). Mechanism for these characteristics is not fully understood yet, but it should relate to both the magneto-static effect and the spin transfer effect, which interact each other. From these figures, once FGL Bs is given, the optimum Bs and the thickness for SIL can be designed. We also confirmed that these optimum positions for the SIL doesn't change even if FGL thickness was changed, and it depends only upon the FGL Bs.

[1] J. -G. Zhu, X. Zhu, Y. Tang, "Microwave assisted magnetic recording", IEEE Trans. Magn., vol.44, no.1 (2008) [2] *A. Takeo, K. Koi, G. Koizumi, et. al., "MAMR - R/W performance improvement by mag-flip STO assist" Intermag 2014 Dresden, AD-02* [3] *Y. Kanai, K. Yoshida, S. Greaves, H. Muraoka, "Micromagnetic model analysis of spin-transfer torque oscillator and write heads for microwave-assisted magnetic recording" IEEE Trans. Magn., vol. 53, no.2 (2017)* [4] Y. Kanai, R. Itagaki, S. Greaves, H. Muraoka, "Micromagnetic model analysis of various spin torque oscillators with write head for microwave-assisted magnetic recording" IEEE Trans. Magn., Intermag 2017, AQ-03, to be published

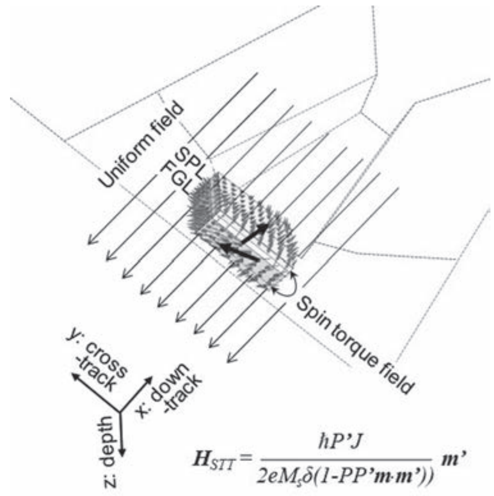

Fig. 1. (a) the coordinate system and allocation of FGL and SIL, and (b) assumption for the simulation, where, H_{STT}, P, P', h, J, e, Ms, δ, m, m', are the spin torque field vector, self-cell polarization, adjacent-cell polarization, Dirac constant, current density, electron charge, saturation magnetization, self-cell thickness, unit magnetization vector at adjacent-cell, respectively.

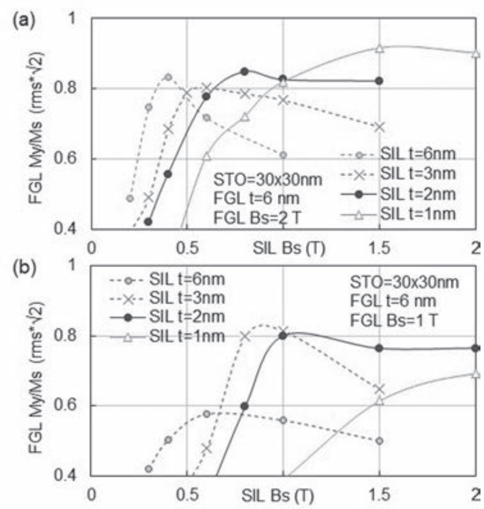

Fig. 2. the cross-track component RMS value of averaged magnetization of FGL as a function of SIL Bs with a parameter of SIL thickness in the case (a) for FGL Bs= 2T and (b) for FGL Bs= 1 T.

BQ-03. Magnetic recording using a spin torque oscillator.

S. Greaves[1]
1. Tohoku University, Sendai, Japan

Introduction Microwave-assisted magnetic recording (MAMR) is a promising technology that may be introduced into recording systems in the future. In a MAMR system a spin torque oscillator (STO) generates a high frequency (HF) field that assists the head field during recording. However, it is also possible to reverse the magnetisation of a grain using only the HF field [1], [2]. This work investigates how the probability of magnetisation reversal can be maximised using only the field from a STO, i.e. when no head field or other external magnetic fields are present. The Model In most of this work the STO was assumed to consist of only a uniformly-magnetised field generating layer (FGL) in which the magnetisation rotated at a constant frequency. The FGL was 30 nm wide, 30 nm high and 10 nm thick with M_s of 1591 emu/cm^3. Subsequently, a full micromagnetic model of the STO and grain was used to confirm the results. In the full model a 5 nm thick spin injection layer (SIL) with M_s of 637 emu/cm^3 and K_u of 8×10^6 erg/cm^3 with an easy axis along the *y* (down-track) direction was used in addition to the FGL. A single magnetic grain, 8 nm across and with M_s of 750 emu/cm^3, was placed at various positions underneath the STO, with a 4.5 nm vertical spacing between the two. The grain had an exchange coupled composite (ECC) structure with magnetically hard and magnetically soft layers exchange coupled together. A 4 ns field pulse from the STO was applied to the grain and the switching probability was calculated as a function of STO position, HF field frequency, soft layer thickness (d_{soft}) and soft layer K_u (K_u soft). The temperature was 300 K in all simulations. Results First, the switching probability of the hard layer by itself was calculated as a function of thickness and K_u. It was possible to achieve switching probabilities close to 1, but only when the hard layer K_u was sufficiently small and under such conditions the thermal stability would be inadequate for long-term data storage. Next, the hard layer thickness was fixed at 4 nm with K_u of 7.7×10^6 erg/cm^3. The optimum STO frequency was sought for various soft layer thicknesses and soft layer K_u. Fig. 1 shows the switching probability as a function of STO position, where the position $\Delta y = 0$ nm indicates the centre of the STO was directly over the centre of the grain. Due to the chirality of the HF field acting on the grain, switching of the magnetisation (from "up" to "down") was only observed when the STO was to the left of the grain ($\Delta y \leq 0$). Similarly, switching from "down" to "up" was only possible when the STO was to the right of the grain. In a recording system it is the sharpness of the left edges of the curves in fig. 1 that will determine the minimum transition width. For a grain with K_u soft of 1×10^6 erg/cm^3 the transition from $P = 1$ to $P = 0$ took place over a width of 7 nm. Fig. 1 shows that switching probabilities of 1 (after 100 trials) were possible for a wide range of STO positions when K_u soft was between 0.5×10^6 erg/cm^3 and 1×10^6 erg/cm^3. When K_u soft was too large the switching probability began to decrease and when K_u soft was zero the areas where the switching probability was 1 became non-contiguous. Also, the optimum soft layer thickness increased as K_u soft decreased, suggesting that the magnetisation reversal process was linked to the width of the domain wall in the soft layer. Meanwhile, the optimum HF field frequency was found to increase with K_u soft. A more detailed switching probability plot for a grain with K_u soft = 0.5×10^6 erg/cm^3 is shown in fig. 2. In addition to the large region of high switching probability centred around HF field frequencies of ≈11 GHz, several other regions of high switching probability were also observed, e.g. for HF field frequencies of ≈6 GHz. The inset to fig. 2 shows the in-plane magnetisation dynamics of the soft layer when the STO frequency was 6.2 GHz, a frequency which fell within the second-largest region of high switching probability in fig. 2. To examine the state of the grain magnetisation just prior to switching the FGL M_s was reduced to 1100 emu/cm^3 and the temperature was reduced to 4.2 K. The plot in fig. 2 shows the soft layer magnetisation over a period from 50 ns to 60 ns after the application of the STO field. It was clear that although the STO oscillation frequency was 6.2 GHz the soft layer magnetisation completed two revolutions for every one rotation of the STO, doubling the soft layer oscillation frequency to 12.4 GHz. The origin of the frequency doubling was exchange coupling with the hard layer and also the strength of the field from the STO. Finally, the simulations were repeated with a full STO model and magnetostatic interactions between the grain and the STO. A current density of 1×10^{18} esu/cm^{2}s caused the FGL magnetisation to oscillate at about 12 GHz, which was sufficient to switch the magnetisation of a grain with K_u soft of 1×10^6 erg/cm^3. One issue identified from these simulations was the amount of time required for the STO oscillation to stabilise at the required frequency.

[1] T. Taniguchi, Appl. Phys. Expr. 8, 083004, (2015). [2] H. Suto, T. Kanao, T. Nagasawa, K. Mizushima and R. Sato, Sci. Rep. 7, 13804, (2017).

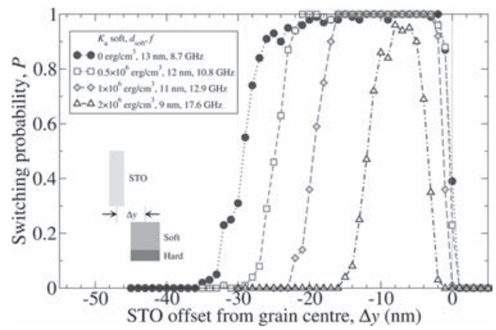

Fig. 1. Switching probability vs. STO position relative to the grain for grains with various K_u soft. Optimum d_{soft} and HF field frequency shown on graph.

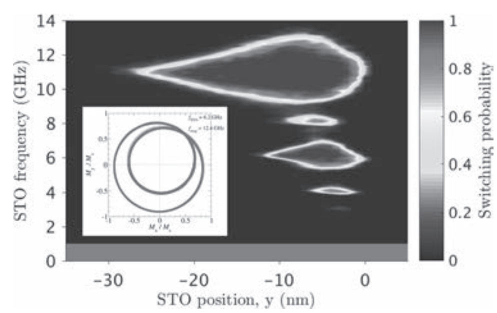

Fig. 2. Switching probability map for a grain with K_u soft = 0.5×10^6 erg/cm^3 and d_{soft} = 12 nm as a function of STO position and HF field frequency. Inset: in-plane magnetisation dynamics of soft layer for a STO frequency of 6.2 GHz and Δy = -6 nm.

BQ-04. Columnar Structural FePt films with Good Perpendicular Anisotropy Grown on TiNZrO Intermediate Layer.

K. Dong[1], F. Jin[1], W. Mo[1] and J. Song[1]
1. School of Automation, China University of Geosciences, Wuhan, China

FePt based heat assisted magnetic recording (HAMR) medium has drawn a lot of attention because of its ability to extend the areal density to 5 Tb/in^2 in theory due to the high magnetocrystalline anisotropy of FePt. For the practical application of FePt thin film in future heat assisted magnetic recording, the FePt films should exhibit good (001) texture, large magnetocrystalline anisotropy, and small grain size with a narrow size distribution and well isolated columnar structure. In order to achieve this aim, great progresses have been made in the fabrication of columnar FePt thin films by selecting various materials to introduce into the FePt films to isolate and reduce the grain size. However, the results reported showed that the columnar structural FePt films exhibited poor perpendicular anisotropy. The objective of this work is introduced a new TiNZrO intermediate layer to improve the perpendicular anisotropy of columnar FePt-ZrO_2 films. FePt (8 nm)-ZrO_2 30 vol.% films were fabricated on TiON, TiN-ZrO_2 and TiNZrO intermediate layers by a magnetron sputtering system with a base pressure better than 2×10^{-8} Torr, respectively, and the films structure are shown in Fig.1(c). The TiNZrO intermediate layer was formed by cosputtering TiN and ZrO_2 at substrate temperature of 500°C, and the analysis of the Zr 3d spectra of the TiNZrO intermediate layer are shown in Fig.1(b). It can be seen that the FePt grains of FePt-ZrO_2 thin films grown on these three intermediate layers exhibited columnar structure (Fig.1g, h and i), and very good epitaxial growth had been observed between FePt and TiNZrO. However, with using TiON and nanogranular TiN-ZrO_2 intermediate layer, very clear FePt (200) peaks were appeared (Fig.1a) and large opening-up of in-plane M-H loops (Fig.1d and e) were obtained, suggesting the perpendicular anisotropy was poor. By introducing the TiNZrO intermediate layer, the FePt (200) peak was disappeared and the FePt film exhibited obvious perpendicular anisotropy (Fig.1f). The $H_c\perp/H_c\|$ratio of 3.27 was larger than that with using TiON (around 1.84), TiN-ZrO_2 (around 1.76). All these indicate the perpendicular anisotropy and the (001) orientations were both improved a lot with using TiNZrO intermediate layer, as compared to the common used TiON and TiN-ZrO_2 intermediate layer.

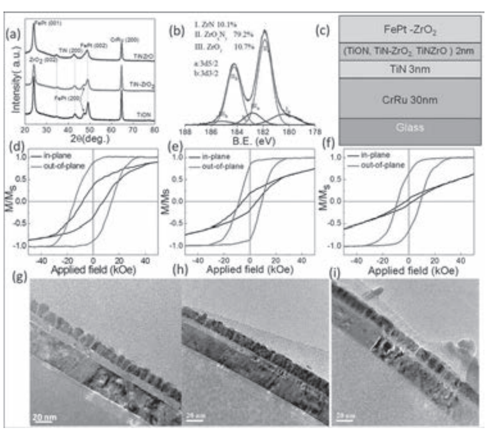

Fig. 1. XRD spectra (a), M-H loops (d, e, f) and Low magnification cross-sectional TEM images (g, h, i) of FePt (8 nm)-ZrO_2 30 vol.%/ (TiON, TiN-ZrO_2, TiNZrO)/TiN/CrRu/glass films, as well as (b) XPS analysis of the Zr 3d spectra of the TiNZrO intermediate layer and (c) films structure. (d) and (g) for TiON, (e) and (h) for TiN-ZrO_2, (f) and (i) for TiNZrO.

BQ-05. Study of Erase Band and Write Performance in Shingled Magnetic Recording with Exchanged Coupled Composite Media.

J. Chen[1,4], *G. Xie*[1,2], K. Luo[1], W. Cheng[1], P. Lu[1,4] and Y. Wang[3]
1. Wuhan National Laboratory for Optoelectronics, Huazhong University of Science and Technology, Wuhan, China; 2. Key Lab of Jiangxi Province for Numerical Simulation and Emulation Technology, Gannan Normal University, Ganzhou, China; 3. Electrical and Computer Engineering Department, Carnegie Mellon University, Pittsburgh, PA, United States; 4. Key Laboratory of Information Storage System (School of Computer Science and Technology, Huazhong University of Science and Technology), Ministry of Education of China, Wuhan, China

I. Introduction The shingled magnetic recording (SMR) with $L1_0$-FePt based exchange coupled composite (ECC) media is a promising way to achieve ultra-high recording density [1] [2]. With the increasing track density, shingled writing inevitably causes the adjacent tracks erasure (ATE) and corresponding erase band noise (EBN), which deteriorates the write performance and introduces more write errors. During the shingled write process, our study indicates the skew and corner angles of wide main pole affect the EBN, moreover the insensitive angular dependence of switching field of ECC media is found to play an important role in mitigating transition noise and ATE [2]. Compared to our previous digest presented in Intermag2015 [3], this paper improves the calculation method of erase band width (EBW) by considering the overwriting side in SMR, more importantly the impact of ECC media on mitigating ATE is explored with EBW and bit error rate. Furthermore, the shingled write heads with different corner angle (*CA*), tip tapered angle (*TA*) and skew angle (*SA*) are studied to reach a tradeoff between adequate write field and moderate EBW. The investigation indicated that the combination of relatively smaller *CA*, larger *TA* and smaller *SA* was beneficial for reducing the EBN, while it weakened the write field. Hence we suggested that an optimized writer design (*CA*=78°, *TA*=50°, -10°<*SA*<10° in our simulation) with ECC media $L1_0$-FePt(6nm)/$[Co/Ni]_5$(4nm) could provide adequate write field and minimize the EBN simultaneously. II. Models and Methodology A) The ECC media is modeled by Voronoi grains and each single grain consists of two-layer composite structure, shown in FIG.1(a). The thermal stability factor $\Delta E/k_BT$ is set as 60 to ensure the thermal stability for more than 10 years. The energy barrier of grain (ΔE) is given as below according to [4] $\Delta E=(K_u^h+K_u^s)(1-H/H_{sw})^\gamma$ where V is the volume of layer, H is the write field, H_{sw} is the switching field, and γ=1.5, the hard layer (index h) of $L1_0$-FePt and soft layer (index s) of $[Co/Ni]_5$ are investigated for ECC media. The magnetic parameters are given as follows according to [5]: the saturation magnetizations (M_s) are set as $M_{[Co/Ni]5}$=750emu/cc and M_{FePt}=500emu/cc. The exchange coupling constants are set as $A_{FePt}=1.2\times10^{-6}$erg/cm and $A_{[Co/Ni]5}=1.0\times10^{-6}$erg/cm. The anisotropy constant (Ku) are set as $K_{[Co/Ni]5}=2.5\times10^6$erg/cc and $K_{FePt}=1.61\times10^7$erg/cc, while the thickness of FePt and $[Co/Ni]_5$ are set as 6nm and 4nm in order to keep $\Delta E=60k_BT$. Hence, the H_{sw} of ECC media is calculated as 16.44kOe according to our simulation. B) The shingled write head is designed to provide both sufficient write field and high field gradient, as shown in FIG.1(b). The writer comprises of a single main pole, return yoke and shield. The *SA* is the angle between recording track and normal direction of trailing side; the *CA* is the angle between trailing side and flaring side from the air bearing surface view (ABS); the *TA* is the angle between the ABS and side of pole tip. The geometric and magnetic parameters of writer are similar to our previous works [3] [6]. III. Results and Discussions The shingled write head is implemented to micromagnetically write grains on ECC media to evaluate EBW and writing performance using the finite element method. The field distribution is evaluated in the center plane of recording layer (10nm below the ABS). For a write head with *CA*=80°, *TA*=40° and *SA*=0°, the effective write field (H_{eff}) and H_{sw} variations are shown in FIG.2(a). The results reveal that $P_{erasure}$ is less than 5×10^{-4} when the EBW equals to 14nm, here $P_{erasure}$ is defined as the probability that adjacent track bit is erased when writing the target bit. It is worth noting that EBW can be reduced in two ways according to FIG.2(a): 1) For the writer part, the H_{eff} decreases away from the writer corner, hence it is possible to generate the H_{eff} with an optimum magnitude (slightly larger than H_{sw}), considering excessively large H_{eff} tends to increase the fringing field and erase adjacent track more severely; 2) For the media part, the angle between the write field and easy axis of ECC media varies away from writer corner and the corresponding H_{sw} varies with the cross-track distance. Hence it is also possible to utilize the ECC media's insensitive angular dependence to reduce ATE. For a write head with *CA*=78°, *TA*=50°, the H_{eff} and EBW versus different *SA* are shown in FIG.2(b). As illustrated, the H_{eff} and EBW increase with the increase of *SA* because the skew effect stretches the field contour, hence the side-erasure field increases and the adjacent track's bits suffer more fringing field. The writer cannot provide adequate H_{eff} to reverse recording bit when *SA* is smaller than lower bound. While when the *SA* is larger than upper bound, the slope of EBW curve will increase sharply, result in a remarkable increase in the EBW and deteriorate the write performance severely. Hence the tolerable range of *SA* (-10° to 10° marked with dash line) is found by taking the tradeoff between adequate H_{eff} and small EBW. ACKNOWLEDGMENT This work was supported by the National Natural Science Foundation of China under the Grant No.61672246, No.61432007, No.51001051.

[1] Y. Kanai, Y. Jinbo, T. Tsukamoto, and S. J. Greaves, "Finite-element and micromagnetic modeling of write heads for shingled recording," *IEEE Trans. Magn.,* vol. 46, no. 3, pp. 715-721, Mar. 2010. [2] R. H. Victora and X. Shen, "Exchange coupled composite media," *Proc. IEEE,* vol. 96, no. 11, pp. 1799-1809, Nov. 2008. [3] G. Xie, J. Chen, G. Yu, and W. Cheng, "Skew and corner angle induced erase band noise for shingled magnetic recording," in *Proc. Digests Intermag. Conf.,* pp. FQ-02, May. 2015. [4] D. Goll, S. Macke, and H. N. Bertram, "Thermal reversal of exchange spring composite media in magnetic fields," *Appl. Phys. Lett.,* vol. 90, no. 17, pp. 172506-1-172506-3, Apr. 2007. [5] J. Wang, H. Sepehri-Amin, Y. K. Takahashi, S. Okamoto, S. Kasai, and J. Y. Kim, *et al.* "Magnetization reversal of FePt based exchange coupled composite media," *Acta Mater.,* vol. 111, pp. 47-55, Mar. 2016. [6] G. Yu and J. Chen, "Skew Effect-Induced Track Erasure of Shingled Magnetic Recording System," *IEEE Trans. Magn.,* vol. 50, no. 11, pp.1-4, Nov. 2014.

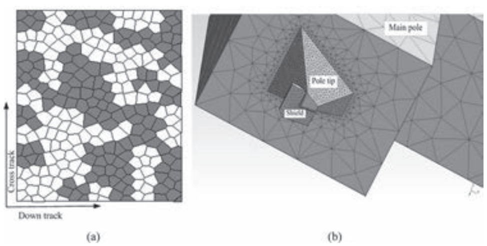

Fig. 1. (a) The ECC media modeled by Voronoi grains of 5nm average diameter, targeting an areal density of 20Tgrains per square inch. (b) The schematic structure of shingled write head.

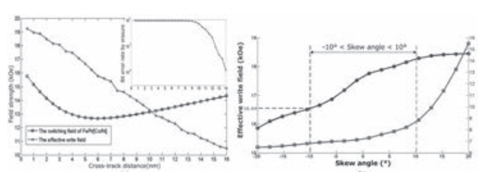

Fig. 2. (a) The H_{sw} and H_{eff} vs. distance away from writer corner along cross-track direction. Inset: BER by erasure vs. offset distance across the track. (b) H_{eff} and EBW as function of skew angle.

BQ-06. Lattice Mismatch Induced Oscillatory Feature Size and its Impact on the Physical Limitation of Grain Size.

J. Deng[1], H. Li[1], K. Dong[5], R. Li[2], Y. Peng[3], G. Ju[3], J. Hu[4], G. Chow[1] and J. Chen[1]
1. Materials Science and Engineering, National University of Singapore, Singapore; 2. Key Laboratory of Magnetic Materials and Devices & Zhejiang Province Key Laboratory of Magnetic Materials and Application Technology, Ningbo, China; 3. Seagate Technology, Fremont, CA, United States; 4. Singapore Institute of Manufacturing Technology, Singapore, Singapore; 5. School of Automation, China University of Geoscience, Wuhan, China

Since the early 1990's, with the arrival of the Information era, the digital data is being created exponantially every year. The need to accomodate the rapidly increasing data urges the advancement of the data storage technology by increasing the storage capacity. It hence requests for the reduction in the grain size and size distribution of heteroepitaxial recording medium. As the grain size is scaled down, the decisive factors for size limitation in a heteroepitaxial nanostructure are the strain energy brought by the lattice mismatch and the significant surface energy contribution due to high surface-to-volume ratio [1]. The misfit strain plays a particularly important role in the microstructure evolution of large lattice-mismatched systems. However, the strain effect on the size evolution of the epilayer in a heteroepitaxial system and the corresponding mechanism are still elusive. In this study, we demonstrate that the misfit strain can lead to the oscillation of size distributions in heteroepitaxial nanostructures, revealing the power of the strain in controlling the shape of the heteroepitaxial nanostructures. The samples were prepared by magnetron sputtering (AJA Orion 8) with a base pressure lower than 2×10^{8} Torr. The FePt layer with thickness of 4 nm, 6 nm, 8 nm, 10 nm was deposited on single crystal MgO (100) substrate at 400°C and at Ar working presure of 10 mTorr. The deposition rate of FePt film was fixed at 18 Å/min. 10 nm FePt thin film deposited on MgO has a maze-like pattern with <110> oriented grain boundaries as observed in the scanning electron microscopy (SEM) images as shown in Fig. 1. A statistics analysis on the feature size of the rectangular grains were carried out. The feature sizes distribution exhibits a periodical multi-peak behavior. As shown by the peak distances labelled between two neighboring peaks, the period is about 3.3 ± 0.5 nm. From the cross-sectional TEM images shown in Fig. 2, the trapezoidal shape of FePt islands indicates that the equilibrium crystal shape formed on MgO is a square truncated pyramid with top (001) and lateral (111) facets. A 12/11 domain matching epitaxy (DME) of FePt/MgO system could be observed in the inverse fast fourier transform images. With the formation of dislocations, the strain energy can be completely released in a DME system. The period of the misfit dislocations coincides well with the oscillation period of the size distributions of FePt islands, suggesting that is related to the oscillatory nature of the misfit strain energy. Based on the experimental findings, a simple model was established to investigate the correlations between the misfit strain energy and the size oscillation. The results tell us that when the FePt island size is an integer times of the misfit dislocation period, the misfit strain can be nearly cancelled by the misfit dislocations. Therefore, these discrete sizes are preferred in heteroepitaxial FePt nanostructures.

[1] L. B. Freund and S. Suresh, *Thin Film Materials: Stress, Defect Formation and Surface Evolution* (Cambridge University Press, New York, 2004).

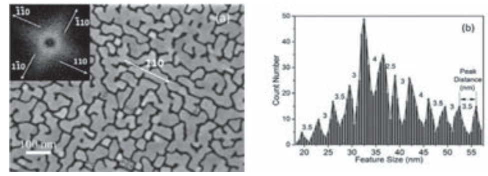

Fig. 1. (a) SEM image of the FePt 10 nm thin film grown on MgO single crystal substrate. Inset is the corresponding fast Fourier transform (FFT) image. The red arrows explain how to measure the feature sizes of rectangular FePt islands. (b) The statistical feature size distributions for FePt maze-like patterns. The peak distances are labelled by the number between each pair of peaks.

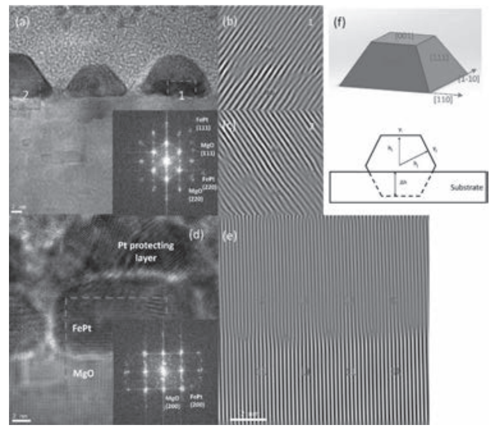

Fig. 2. (a) High resolution cross-sectional TEM image of 4 nm FePt thin film taken along [-110] zone axis. Inset is the corresponding fast Fourier transform (FFT) image. (b) & (c) Inverse Fourier-filtered images taken from location 1 and 2 in (a). (d) High resolution cross-sectional TEM image taken along [010] zone axis. Insert is the corresponding fast Fourier transform (FFT) image. (e) Inverse Fourier-filtered images taken from the red box in (d). (f) Schematic drawing of a truncated square pyramidal island with edges and facets labelled, and the equilibrium shape of a supported crystal. The Wulff shape of the free crystal is truncated at the interface by Δh, which is proportional to E_{adh}.

BQ-07. Magnetic properties and microstructure of [FePt-Mg(Ti, Ta, Zr, Nb, B)O] granular films.

J. Tsai[1], Y. Chen[1], C. Pi[1], Y. Wu[1], C. Chang[1] and G. Varvaro[2]
1. Department of Materials Science and Egineering, National Chung Hsing University, Taichung, Taiwan; 2. nM2-Lab, Istituto di Struttura della Materia, CNR, Monterotondo Scalo (Roma), 00015, Roma, Italy

I. INTRODUCTION $L1_0$ FePt-based thin films with a (001) crystallographic texture have been largely investigated over the last two decades as potential materials for next generation ultra-high density magnetic recording media (>1Tbit/in2), due to the high magneto-crystalline anisotropy (5-10 MJ/m^3), which ensures room temperature thermal stability of grains with in-plane size down to 3 nm. Moreover, due to the moderate Curie temperature (650-750K) of the FePt-based alloys, such a material is currently the best candidate for Heat Assisted Magnetic Recording (HAMR), an emergent technology close to the commercialization, which is expected to increase the areal density in hard disk drives beyond 2 Tbit/in^2. To achieve thermally stable recording media for HAMR with an area density as large as 2 Tbit/in^2, FePt granular films consisting of columnar and well separated grains with a high microstructural uniformity and small in-plane size are required. For this purpose, single and multiple segregants such as carbon, transition metal-oxide and carbide have been extensively discussed but further work is still necessary to achieve the required morpho-structural and magnetic properties for recording densities up to 2 Tbit/in^2 and beyond. In this work a novel Mg(Ti, Ta, Zr, Nb, B)O segregant without carbon is proposed as a potential material for next generation FePt-based high density recording media. II. EXPERIMANTAL [FePt-Mg(Ti, Ta, Zr, Nb, B)O]/MgTiON/CrRu films were deposited by magnetron sputtering on glass substrates. The background pressure of sputtering system was below $5x10^{-7}$ Torr and the working pressure was set to 10^{-3} Torr. The CrRu seed layer with a (002) texture was first grown on the glass substrate to induce the formation of a (002) textured MgTiON intermediate-layer. To investigate the effect of the Mg(Ti, Ta, Zr, Nb, B)O segregant material, two different series of samples were prepared. In series (I), a Mg(Ti, Ta, Zr, Nb, B)O interlayer with a thickness *t*=0, 2, 4, 6, 13 nm was deposited under a 10 nm thick FePt layer (i.e. FePt(10nm)/Mg(Ti, Ta, Zr, Nb, B)O(*t*)/MgTiON/CrRu) in series (II), a FePt(2nm)/$[Mg(Ti, Ta, Zr, Nb, B)(t)/FePt(4nm)]_2$ (t=0, 0.5, 1, 1.5 nm) multilayer stack was deposited on top of the MgTiON intermediate-layer. In both the cases the deposition was carried out by using a $(MgO)_{70}(Ti_6Ta_6Zr_6Nb_6B_6)$ target and at a deposition temperature of 470^{o}C to favor the formation of the $L1_0$-FePt phase and the diffusion of the segregant material in the FePt layer. The crystal structure of the samples was identified using a standard X-ray diffraction (XRD) technique (BRUKER, D8 Discover). In-plane and out-of-plane field-dependent magnetization loops were measured at room temperature by using superconducting quantum interference device (SQUID) magnetometer. The film microstructure was studied by using transmission electron microscopy (TEM, JEOL JEM-2010). III. RESULTS AND DISCUSSIONS XRD spectra of series (I) are reported in Figure 1(a). Besides the (002) reflection peaks of the CrRu seed layer and the MgTiON intermediate layer, the (001) superlattice diffraction peak and the (002) fundamental reflection of the $L1_0$ FePt are present suggesting that the $L1_0$ FePt film has a (001) preferred orientation. However, the disordered FePt (200) peak is also present thus indicating that the Mg(Ti, Ta, Zr, Nb, B) interlayer has deteriorated the epitaxial growth of the FePt film. In series (II), only the (001) and (002) FePt peaks are present in the XRD spectra (Fig 1b), thus suggesting that such a deposition process does not affect the epitaxial growth of the FePt film. The out-of-plane and in-plane field dependent magnetization loops of representative samples of series I(a) and II(b) measured at room temperature are reported. In both the series, the FePt films present a preferential perpendicular anisotropy, samples from series (I) showing a larger in-plane loops area, which origins from the contribution of disordered FePt regions as evidenced by XRD results. Overall, samples of series (I) present a larger out-of-plane coercivity (H_c, up to 14.4 kOe for t= 2 nm) with respect to samples of series (II) (H_c= 10.7kOe for t=1 nm) as a consequence of a different microstructure as discussed below. Figure 2 shows the cross-sectional TEM images of FePt(2nm)/[Mg(Ti, Ta, Zr, Nb, B)O(*t*)/FePt $(4nm)]_2$ (t= 0.5, 1, 1.5 nm) multilayers (series II). The FePt film was more continuous with Mg(Ti, Ta, Zr, Nb, B)O(*t*=0, 0.5nm) interlayer for two pairs shown in Fig. 2(a-b) and the FePt grains with dark contrast were appeared in the large island and the coercivity is 8.6kOe. In Fig. 2(c-d), the FePt grains were more separated when the thickness of Mg(Ti, Ta, Zr, Nb, B)O interlayer increased to 1 nm and 1.5 nm for two pairs and the FePt films show higher coercivity(10.7kOe). The FePt grains morphology were in the dorm shape with almost perpendicular grains contact. In sample series I, the separation of FePt grains were much better than series II and illustrated much higher coercivity(14.4kOe). In summary, when a Mg(Ti, Ta, Zr, Nb, B)O interlayer is deposited under FePt layer, the FePt (001) orientation is deteriorated but the grains separation is enhanced and the films show higher coercivity but also a larger in-plane magnetization. In sample series (II), where the Mg(Ti, Ta, Zr, Nb, B)O is inserted between FePt layers, the [001] orientation was improved but the FePt grains separation is weaker, thus leading to a lower coercivity.

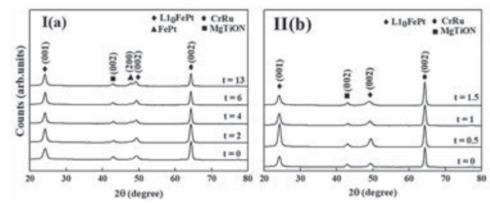

Fig. 1. XRD patterns of (a) series I,(b) series II

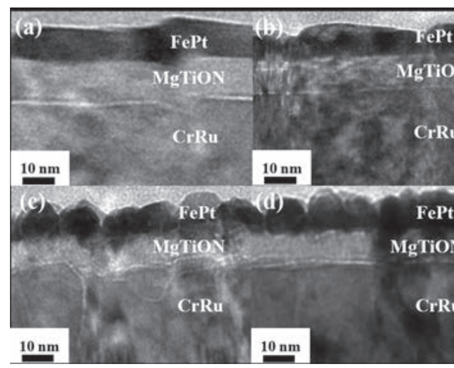

Fig. 2. TEM images of series (II), t= (a)0,(b)0.5,(c)1,(d)1.5 nm

BQ-08. First order reversal curves and intrinsic parameter determination for magnetic materials: limitations of hysteron-based approaches in correlated systems.

S. Ruta[1], O. Hovorka[2], K. Wang[3], P. Huang[3], G. Ju[3] and R.W. Chantrell[1]
1. Physics, University of York, York, United Kingdom; 2. Faculty of Engineering and the Environment, University of Southampton, Southampton, United Kingdom; 3. Seagate Technology, Fremont, CA, United States

I) Introduction The intrinsic switching field distribution (SFD) is a fundamental characteristic of granular magnetic materials and it determines the quality of recording media used in hard disk drives. Being able to evaluate the thermal SFD of a system of coupled grains dominated by thermally activated hysteresis behaviour remains a challenge and is an essential practical step for developing and optimising the present-day and future magnetic recording technology. SFD is defined as a distribution of irreversible switching events of magnetic grains in the absence of inter-granular interactions. If there are no reversible components of magnetization the SFD corresponds directly to the differentiated hysteresis loop. If thermal relaxation is absent, then the SFD provides direct information about the distributions of intrinsic material properties of grains, such as anisotropy and volume. This relatively simple physical picture becomes complicated 1) by the presence of thermal relaxation, when the SFD also includes a component from thermal activation and becomes non-linearly dependent on the sweep rate of external field applied during the hysteresis loop measurement, and 2) by inter-particle interactions leading to correlated switching of magnetic grains, when the intrinsic switching thresholds of individual grains can no longer be resolved. In this work we have investigated the range of validity of first order reversal curves (FORC) technique, as is widely used for the applications mentioned above. II) Methods and Results First Order Reversal curve (FORC) method is extensively applied as a tool to qualitatively capture the general aspects of a magnetic system: mixed magnetic phases, cluster/long-range ferromagnetic state, magnetic characterization of geological mixtures minerals and different magnetization reversal mechanisms[1]. The method is also used as a quantitative approach for determination of thermal intrinsic switching field distributions (SFD), and interaction field distribution (IFD) in magnetic systems with hysteresis, such as in recording media. The attractiveness of the FORC method is in its simplicity and its straightforward applications to a wide range of systems displaying hysteresis. The correct SFD identification of the FORC based techniques originate in the work of Mayergoyz [2]. He mathematically proved that for any hysteresis system (magnetic or non-magnetic) that satisfies the Preisach model condition, the input SFD (or the equivalent quantity for non-magnetic system) can be accurately re-obtained using the FORC method. As a benchmark for validating the methods we consider a kinetic Monte-Carlo (kMC) model of exchange and magnetostatic interacting Stoner-Wohlfarth grains, including self-consistently the volume and anisotropy distributions, and thermal activation. Using kinetic Monte-Carlo framework we developed a model of increasing layers of complexity to describe realistic devices, from non-interacting system, to mean-field approximation and to grain-grain interaction, where intercalation are calculated taking into account the grain geometry (shape, size, position). Our results show that the reliability of the FORC technique is critically affected by the presence of interaction (magnetostatic and exchange), when there is correlated behaviour of magnetic entities. The nature of correlations are irrelevant, as we show with a 'toy model' in which the correlations are artificially induced. This toy model, gives the possibility to explore the effects of correlation in a general system, as the interaction strength is always the same and just the degree of correlation is systematically varied [3]. This is a fundamental limitation of the FORC method, independent of the benchmark model. We quantify the limiting model parameter range (in terms of magnetostatic and exchange interaction) of the FORC methods for a perpendicular magnetic recording system (Fig. 1). Figure (1a) shows the dependence of the maximum value of the correlation function in absolute value as function of the exchange and magnetostatic field magnitudes. The results show that the parameter space having the best determination of the SFD from the Preisach-based FORC analysis corresponds to that having weak spatial correlation of the magnetization structure. In these work we demonstrate that FORC methods can be applied only when interaction induced correlations are negligible (Fig. 1).

[1] A. Stancu, C. Pike, L. Stoleriu, P. Postolache, and D. Cimpoesu, "Micromagnetic and Preisachanalysis of the First Order Reversal Curves (FORC) diagram," Journal of Applied Physics, vol. 93, no. 10, p. 6620, 2003. [2] I. D. Mayergoyz. Mathematical Models of Hysteresis. Springer New York, New York,NY, 1991. [3] Ruta, S. *et al*. *Sci. Rep.* 7, 45218; doi: 10.1038/srep45218 (2017).

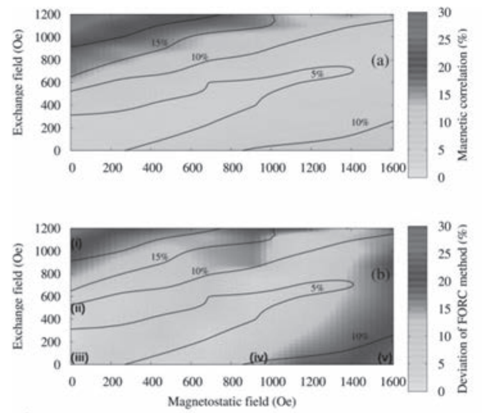

Fig. 1. Diagram showing the deviation of σ_{SFD} from the FORC method in comparison with the expected value (b). The contour line indicate the correlations for the same interactions (a).

BQ-09. Magnetization Reversal of antiferromagnetically coupled (Co/ Ni) and (Co/ Pt) Multilayers.

A.Y. AlSubhi[1]
1. Physics, Sultan Qaboos University, Muscat, Oman

The antiferromagnetic coupling (AF) between two ferromagnetic layers separated by nonmagnetic spacer has been investigated due to its importance in magnetic recording and spintronic devices. For instance, in magnetic tunnel junction with perpendicular anisotropy, the stray field from reference layer could reach large values which could affect the stability of the free layer. The AF structure is a good way to minimize the magnetostatic field. In this study, the AF coupling between a soft $(Co_{0.3}/ Ni_{0.6})_{xN}$ multilayers and a hard $(Co_{0.3}/ Pt_{0.8})_{12}$ multilayer is investigated. The number of repeats of the soft multilayer is varied from 4 to 8 while it is fixed to 12 for the hard one. The AF coupling is induced by a thin Ru of 0.8 nm between the two multilayers. Fig 1 shows the major and minor loops of the coupled structure for N = 4 at room temperature. In this case a clear two steps switching is observed. The coercivity of the $(Co/Ni)_4$ soft layer H_{C1} and $(Co/Pt)_{12}$ hard layer H_{C2} were measured for both single and exchange coupled cases. The antiferromagnetic exchange coupling H_{ex} measured from the shift of the minor hysteresis loops. In the inset of Fig 1 $J_{ex} = H_{ex} M_{S\times}t_f$ is plotted as a function of temperature where M_S and t_f are the saturation magnetization and thickness of the soft layer respectively. This behavior is different from the case of two AF coupled (Co/ Pd) multilayers [1]. The maximum exchange coupling is observed at around 150 K. For low temperature, a gradual increase of J_{ex} following an Arrhenius law was revealed. The non-monotonous dependence of J_{ex} with temperature is unusual in such films. Recently Xiao et al reported a similar behavior in antiferromagnetically coupled $[Pt/CoFeB]_{N1}/Ru/[CoFeB/Pt]_{N2}$. Where N_1 and N_2 are the number of repetetions [2] For large (Co/Ni) with 8 bilayers, the two steps magnetization reversal disappears and a rotation of the magnetization of the soft layer from out-of plane to in-plane is observed as can be seen in Fig 2. This hysteresis loop is characterized by cooperative reversal of all the layers instead of layer-by-layer switching. This type of the hysteresis is seen for different temperatures ranging from 4 K to 300 K. For an understanding of the magnetization reversal of AF structure, magnetic force microscopy and micromagnetic simulation will be presented.

1-R. Sbiaa et al Journal of Applied Physics 118, 063902 (2015) 2- Yili Xiao et al, Journal of Applied Physics 113, 17A325 (2013)

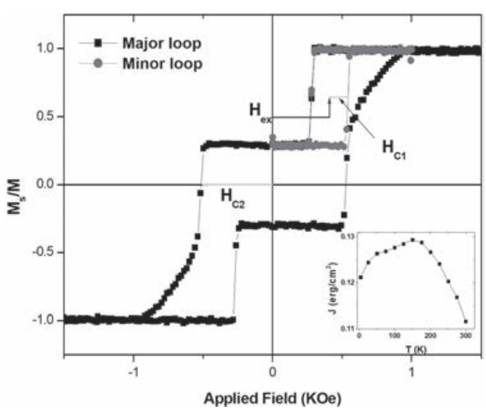

Fig. 1. Major and minor loops of $[(Co_{0.3}/ Ni_{0.6})_4/ Ru_{0.8}/ ((Co_{0.3}/ Pt_{0.8})_{12}]$ at room temperature. The inset is the temperature dependence of interlayer exchange coupling.

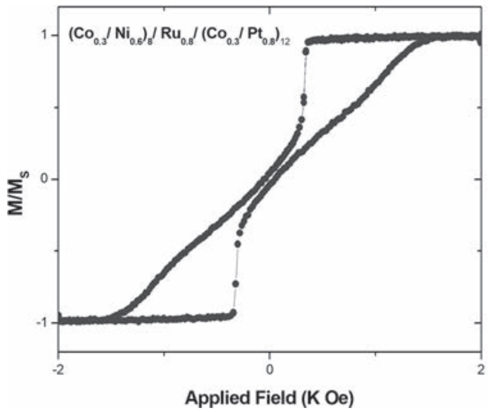

Fig. 2. Out of plane magnetic hysteresis loop of $[(Co_{0.3}/ Ni_{0.6})_8/ Ru_{0.8}/ ((Co_{0.3}/ Pt_{0.8})_{12}]$ at room temperature.

BQ-10. Withdrawn

BQ-11. Reduction of intergranular exchange coupling for CoPt-B_2O_3 granular media by employing a RuCoCr-oxide buffer layer with oxide of various melting points.

K. Tham[1], R. Kushibiki[1], T. Kamada[1], S. Hinata[2] and S. Saito[2]
1. Tanaka Kikinzoku Kogyo, Sendai, Japan; 2. Tohoku University, Sendai, Japan

INTRODUCTION CoPt-oxide granular films have been widely used for perpendicular magnetic recording media. To further increase recording density of the media, enhancement of magnetocrystalline anisotropy (K_u) to overcome the thermal stability issue and reduction of media noise to increase signal-to-noise-ratio are essential. The requirements can be realized through the promotion of columnar growth of magnetic grains which are phase separated with oxide boundary material and intergranular exchange decoupling[1)], respectively. Generally, for the grain boundary materials of the granular media, oxides with amorphous phase which do not dissolve into CoPt metal have been utilized. The oxide is expected to segregate into the trench of Ru underlayer so that CoPt grains can grow heteroepitaxially on the bump of Ru underlayer. Many authors have proposed various kinds of oxide materials to be segregated into the grain boundaries, like SiO_2[2)], TiO_2[3)], Ta_2O_5[3)], Nb_2O_5[4)], WO_3[4)], MgO[5)], Cr_2O_3[5)], and Y_2O_3[5)]. Previously, we had found that a granular medium with high magnetocrystalline anisotropy (K_u) was successfully realized when B_2O_3 was applied for the grain boundary material[6)]. However, the separation between magnetic grains at the initial growth region in the Ru trench by low melting point oxide such as B_2O_3 is not sufficient[7)]. Therefore, we have carried out an investigation on the deposition of a buffer layer (BL) with non-ferromagnetic metal and oxides of various melting points (T_m) on the Ru underlayer to grow the non-ferromagnetic metal and oxide on the Ru bump and trench, respectively, aiming to intergranular exchange decouple the magnetic grains. In this paper, we will discuss about the effect of utilizing BL with oxide of various T_m on the intergranular exchange decoupling of CoPt-B_2O_3 granular media in relation with magnetic properties. RESULT AND DISCUSSION Samples structure used in this study: Sub./ Ta (5 nm)/ $Ni_{90}W_{10}$ (6 nm)/ Ru (0.6 Pa, 10 nm)/ Ru (8.0 Pa, 10 nm)/ BL/ $Co_{80}Pt_{20}$-30vol%B_2O_3 (16 nm)/ C (7 nm). $Ru_{50}Co_{25}Cr_{25}$-30vol%TiO_2 (0-4 nm) was used for the BL. Here for the BL, a non-ferromagnetic Ru alloy which consists of the metal element of underlayer (Ru) and granular media (Co) was adopted for the metal material to maintain hetero-epitaxial growth of CoPt alloy on Ru. While TiO_2 was chosen as a typical material used for the grain boundaries in the granular media. Fig. 1 shows dependence of H_c on the BL thickness (d_{BL}). When d_{BL} is increased from 0 to 1.5 nm, a large increase of H_c around 20%, from 7.5 to 9.0 kOe can be observed. Further increase of d_{BL} to 4.0 nm will decrease H_c from 9.0 to 8.7 kOe. This indicates that the employment of the BL is quite effective to increase H_c of the medium. To find out the origin of H_c variation according to various BL thickness, anisotropy field (H_k), thermal stability and degree of intergranular exchange coupling were investigated. Here, thermal stability and degree of intergranular exchange coupling are determined from $v_{act}K_u^{grain}/kT$ and a, where v_{act} is the activation volume measured from time dependence of remanence coercivity[8)] and K_u^{grain} is evaluated from K_u of the granular media when 30vol% B_2O_3 is excluded. Fig. 2 shows dependence of (a) H_k and K_u, (b) $v_{act}K_u^{grain}/kT$ and (c) a on d_{BL}. When d_{BL} is varied from 0 to 4.0 nm, H_k and K_u remain constant at around 18.5 kOe and 8.0×10^6 erg/cm^3, respectively. On the other hand, $v_{act}K_u^{grain}/kT$ and a decrease from 160 to 140 and from 1.7 to 1.2, respectively, when d_{BL} is increased from 0 to 1.5 nm. This reveals that the granular medium is thermally stable and the intergranular exchange decoupling is promoted. This result suggests that the decrease of degree of intergranular exchange coupling when d_{BL} is increased from 0 to 1.5 nm induces larger H_c. From these results, the introduction of RuCoCr-TiO_2 BL underneath the high K_u CoPt-B_2O_3 granular media is quite effective to increase H_c through reduction of intergranular exchange coupling. In the conference, the effect of melting point of the oxide for RuCoCr-oxide BL on magnetic properties and microstructure of CoPt-B_2O_3 granular media will be reported.

[1] G. Choe, M. Zheng, E.N. Abarra, B.G. Demczyk, J.N. Zhou, B.R. Acharya, and K.E. Johnson, *J. Magn. Magn. Mater.*, 287, 159 (2005). [2] T. Oikawa, M. Nakamura, H. Uwazumi, *T.* Shimatsu, H. Muraoka, and Y. Nakamura*, IEEE Trans. Magn.,* 38, 1976 (2002). [3] J. Ariake, T. Chiba, and N. Honda, *IEEE Trans. Magn.*, 41, 3142 (2005). [4] T. P. Nolan, J. D. Risner, S. D. Harkness IV, E. Girt, S. Z. Wu, G. Ju, and R. Sinclair, *IEEE Trans. Magn.*, 43, 639 (2007). [5] V. M. Sokalski, J. G. Zhu, and D. E. Laughlin, *IEEE Trans. Magn.*, 46, 2260 (2010). [6] K. K. Tham, R. Kushibiki, S. Hinata, and S. Saito, *Jpn. J. Appl. Phys*., 55, 07MC06 (2016). [7] R. Kushibiki, K. K. Tham, S. Hinata, and S. Saito, *AIP Advances*, 7, 056512 (2017) [8] K. Yamanaka, T. Takayama, Y. Ogawa, A. Yano, and T. Okuwaki, *J. Magn. Magn. Mater.*, 145, 255 (1995).

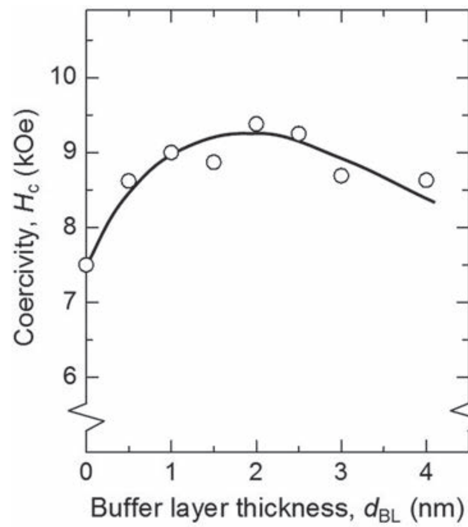

Fig. 1. Dependence of coercivity (H_c) on the buffer layer thickness (d_{BL})

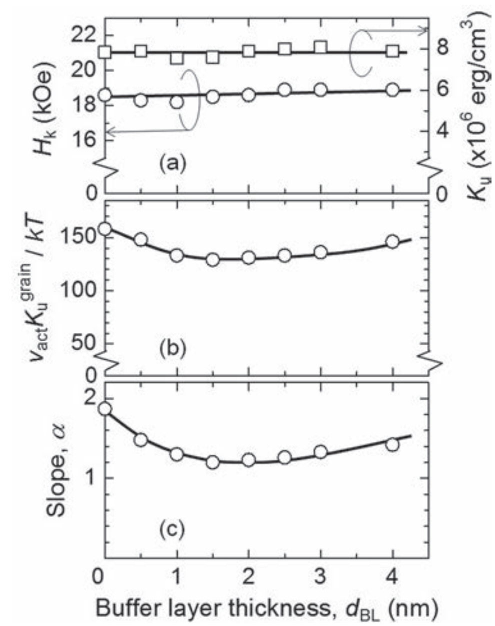

Fig. 2. Dependence of (a) H_k and K_u, (b) $v_{act}K_u^{grain}/kT$ and (c) Slope (a) on buffer layer thickness (d_{BL}).

BQ-12. Ion beam patterning of ultrathin $L1_0$-MnGa (001) film grown on CoGa buffer layer.

Y. Horie[1], D. Oshima[1], T. Kato[1] and S. Iwata[1]
1. Nagoya University, Nagoya-shi, Japan

Bit patterned media (BPM) are considered to extend the areal density of magnetic recording to more than 5 Tbit/in^2 by combining it with heat or microwave assisted magnetic recording. One of the major issues for the practical use of BPM is the development of a low-cost and high-yield fabrication process. We reported that magnetism of MnGa was altered from ferromagnetic to paramagnetic associated with the phase change from $L1_0$ ordered to A1 disordered phase by 30 keV Kr^+ ion irradiation and that bit patterned media with a pitch size down to 80 nm were realized by the ion beam patterning [1]. For further high-density patterning, thinner resist masks and incident ions with lower kinetic energy should be used. In order to pattern using low energy Kr^+ ions, e.g., < 10 keV, the growth of ultrathin $L1_0$-MnGa layer is necessary. Recently, an ultra-thin MnGa film was reported to be grown successfully on a nonmagnetic CoGa buffer layer [2]. In this report, we also used the CoGa buffer layer to grow the ultrathin MnGa layer and fabricated bit patterned MnGa with a pitch size less than 80 nm by using 10 keV Kr^+ ion irradiation. The MnGa film with a stack of Cr (2) / MnGa (5) / CoGa (30) / Cr (20) / MgO(001) (thickness in nm) was prepared by rf magnetron sputtering. The Cr buffer layer was deposited at a temperature at 400 °C, and post-annealed at 600 °C for 60 min. After cooling down to 400 °C, the CoGa layer was deposited and post-annealed at 600 °C for 30 min. The MnGa layer was deposited by co-sputtering of $Mn_{40}Ga_{60}$ and $Mn_{60}Ga_{40}$ targets at 300 °C, and post-annealed at 400 °C for 60 min. The composition of the MnGa was tuned to $Mn_{50}Ga_{50}$ by controlling the sputtering power of the two targets. Ion-beam bit-patterned film was fabricated by e-beam lithography and an ion implantation system. Anisole-diluted ZEP520A resist with a thickness of 40 nm was used as a mask for patterning. The energy of the Kr^+ ion irradiation was set to be 10 keV. Figure 1 (a) shows the *M-H* out of plane loop of the CoGa-buffered MnGa film. *M* represents the magnetization per unit volume of the MnGa layer. It is expected that there are two components in the *M-H* loop; one is square hysteresis with H_c = 2 kOe and another is superparamagnetic hysteresis with zero coercivity and remanence. From the surface-sensitive Kerr loop measurements, 5-nm thick MnGa was confirmed to have square hysteresis, indicating a large perpendicular anisotropy and smooth wall propagation in spite of the ultrathin thickness of the MnGa. The superparamagnetic component is considered to come from the CoGa buffer layer. The saturation magnetization of the ultrathin MnGa film can be estimated to be 320 emu/cc by excluding the contribution of CoGa in the *M-H* loop. Figure 1 (b) shows the dependence of the saturation magnetization M_s on the dose of 10 keV Kr^+ ion irradiation. The M_s gradually decreased with the dose and became a constant at the dose of 1×10^{14} ions/cm^2 or more. The residual magnetization is considered to come from the contribution of the CoGa buffer layer as discussed in Fig. 1 (a), and the ferromagnetism of the MnGa layer disappeared by the 10 keV Kr^+ ion dose of 1×10^{14} ions/cm^2 just as our previous report [1]. Figure 2 shows the MFM images of the bit patterned MnGa film with pitch sizes of (a) 100 nm and (b) 60 nm. As shown in Fig. 2 (a) and (b), bright and dark signals were observed in non-irradiated regions indicating the existence of the perpendicularly magnetized $L1_0$-MnGa. On the other hand, no magnetic signal was seen in the irradiated regions. Thus, magnetically patterning with a pitch size of 60 nm was successfully realized by using ultrathin MnGa, and 10 keV Kr^+ ion irradiation.

[1] D. Oshima et al, IEEE Trans. Magn., 49, 3610 (2013). [2] K. Z. Suzuki et al, J. Appl. Phys., 55, 010305 (2016).

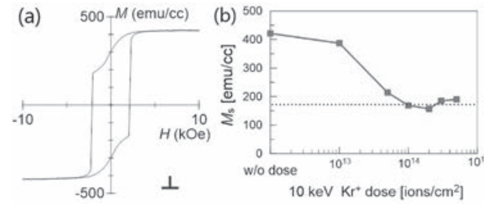

Fig. 1. (a) out of plane *M-H* loop of the 5 nm-thick MnGa film grown on CoGa buffer layer. (b) dependence of the saturation magnetization M_s of the 5 nm-thick MnGa on the dose of 10 keV Kr^+ ion irradiation

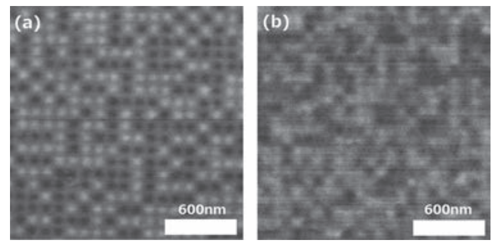

Fig. 2. MFM images of the bit patterned MnGa (5 nm) film with pitch sizes of (a) 100 nm and (b) 60 nm

BQ-13. Exchange coupling through a Pt spacer to enable ultrafast memory devices.

C.A. Lambert[2,1], J. Gorchon[1], Y. Yang[1], A. Pattabi[1], R. Wilson[1], J. Bokor[1] and S. Salahuddin[1]
1. EECS, UC Berkeley, Berkeley, CA, United States; 2. Materials Science, ETH Zürich, Zürich, Switzerland

A single femto-second optical pulse can fully reverse the magnetization of a film within picoseconds [1]. Such fast operation hugely increases the range of application of magnetic devices. However, so far, this type of ultrafast switching has been restricted to ferri-magnetic GdFeCo films and, in contrast, ferro-magnetic films require multiple pulses [2], thereby being slower and less energy efficient. Here, we demonstrate magnetization switching induced by a single laser pulse in various ferromagnetic Co/Pt multilayers grown on GdFeCo, by exploiting the exchange coupling between the two magnetic films. We have shown that, despite using thick (up to 5 nm) metallic Pt spacers to separate a Co/Pt multilayer from a GdFeCo layer, we can still achieve single-shot AOS of the ferromagnetic layer by exploiting the exchange interaction [3]. Moreover, we demonstrated a 7 ps switching time on a sample with a 1.5 nm Pt spacer. This rather general method can be extended to other ferromagnets, ferrimagnets and even antiferromagnets. We believe that this approach will greatly expand the range of materials and applications for ultrafast magnetic switching.

[1] Stanciu, C. D. *et al.* All-optical magnetic recording with circularly polarized light. *Phys. Rev. Lett.* 99, 47601 (2007). [2] Lambert, C.-H. *et al.* All-optical control of ferromagnetic thin films and nanostructures. *Science* 345, 1337–1340 (2014). [3] Gorchon, J., Lambert, C.H., Yang, et al., Single shot ultrafast all optical magnetization switching of ferromagnetic Co/Pt multilayers. Appl. Phys. Lett. 111, 042401 (2017).

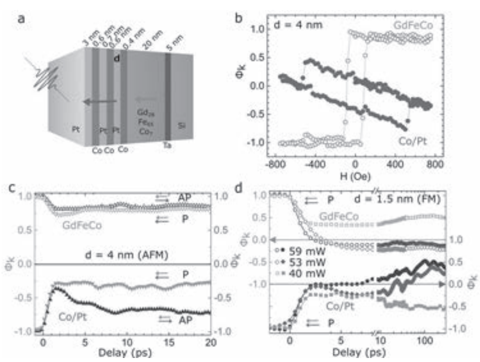

Fig. 1. Time-resolved depth-sensitive magneto-optical measurements of laser induced dynamics. a, GdFeCo/Co/Pt(d nm)/[Co/Pt]$_2$ stack series with Pt spacer of thickness d. b, Depth-sensitive MOKE magnetic hysteresis loops on sample d=4 nm. c, Depth-sensitive time-resolved demagnetization curves for antiparallel (AP) or parallel (P) initial states of the stack d=4 nm. Green and blue arrows represent GdFeCo and Co/Pt magnetizations, respectively. d, Depth-sensitive demagnetization and AOS experiments at various fluences on sample d=1.5 nm.

BQ-14. Thermodiffusion and the replenishment phenomena of PFPEs for the application of heat-assisted magnetic recording.

P. Chung[1]
1. Energy Engineering, Inje University, Gimhae-si, The Republic of Korea

New design and component materials of head-disk interface are required to satisfy stringent operating conditions including heating and cooling cycles that occur within the order of nanosecond to achieve the necessary data rates and to generate a large thermal gradient for sharp bit edge for heat assisted magnetic recording (HAMR). During the HAMR operation, the locally heated lubricant experiences evaporation as well as thermal flow-out. The stumbling block in HAMR technology is to fully understand the system behavior under large thermal gradient in addition to elevated temperature. We introduce the Soret effect for the first time in HAMR research to rigorously analyze diffusional flux in continuum level. The temperature gradient can cause mass flux via process known as thermodiffusion or Soret effect. At the same time the concentration gradient can also contribute heat transfer via Dufour effect and these effects modifies temperature and concentration profile (Fig 1a). We examine these two effects using molecular dynamics (MD) by hybridizing aforementioned continuum model using PFPE replenishment phenomena as benchmark example. Marchon and Saito examined local thermal diffusion phenomena of nonfunctional PFPE lubricant by studying the lubricant removal at the center and the formation of a rim at the edge of hot spot using MD as well as computational fluid dynamics [1]. Dahl and Bogy investigated the recovery of the depleted lubricants for functional PFPEs have been investigated as functions of temperature and the hot spot size using continuum based Reynold's equation [2]. Although there exists previous attempt, the thermodiffusion mechanism at the rim, where the drastic temperature gradient exists, and this phenomena has not been fully understood. We examine replenishment phenomena for various PFPEs controlled by the temperature gradient at the rim (Fig.1b). Specifically, chemical functionalities covering linear functional PFPEs (*e.g.*, Zdol and Ztetraol) as well as other chemically complex PFPEs (*e.g.*, ZTMD, TA30, and QA40) will be examined using coarse-grained MD. The local heating and cooling in molecular scale were simulated by propagating the kinetic energy of PFPE molecules adjacent to the heat source. We also investigated the reflow process of the lubricant film by analyzing time-dependent evolution of the thin lubricant film profile and correlated to the thermodiffusion coefficient via hybridizing continuum model including Soret coefficientMolecular weight dependence is also examined in addition to the functionality effect to demonstrate the significance of the thermodiffusion contribution. In-depth analysis on the lubricant behavior with heating and cooling cycle with large temperature gradient will provide better molecular design criteria of HAMR lubricants.

1. B. Marchon and Y. Saito, *IEEE Trans. Magn.*, 48, 4471 (2012). 2. J.B. Dahl and D.B. Bogy, *Tribol. Lett.*, 52, 163 (2013).

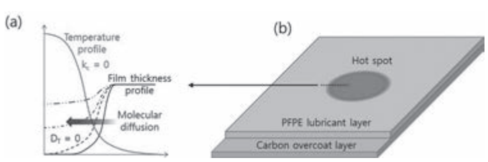

Fig. 1. (a) The relative importance of Soret & Dufour terms in heat & mass fluxes. (b) Isometric view of the confined PFPE lubricant lm on the carbon surface with hot spot (red).

BQ-15. Investigation Nonlinear GPR Target for BCJR Algorithm on Perpendicular HAMR Channel with Volterra Model.

W. Wongtrairat[1], T. Sopon[1], S. Wongsuthavas[2], S. Sophan[1] and *P. Supnithi*[3]
1. Faculty of Engineering and Architecture, Rajamangala University of Technology Isan (RMUTI), Nakhonratchasima, Thailand; 2. Faculty of Science and Liberal Arts, Rajamangala University of Technology Isan (RMUTI), Nakhonratchasima, Thailand; 3. Faculty of Engineering, King Mongkut's Institute of Technology Ladkrabang (KMITL), Bangkok, Thailand

Abstract: In this work, we propose the nonlinear generalized partial response (GPR) targets for the perpendicular heat-assisted magnetic recording (HAMR) channels with Volterra model (VM). We consider the trellis of nonlinear values for BCJR based detector, which is used to estimate the probability of the data bits. The bit error rate (BER) simulation is based on various parameters of the perpendicular HAMR system in linear and nonlinear channels at the areal density of 5 Tb/inch^2. The simulation results show the BER performance of the BCJR based detector with nonlinear GPR target better than the nonlinear PR1 target. Heat-assisted magnetic recording (HAMR) system requirements achieve high areal densities about to 1 Tb/inch^2. The medium of HAMR system is temporarily heated during the recording process [1]. However, as grain sizes are reduced, thermal fluctuations can reverse spontaneously the grain magnetization direction. As an alternative to the Bahl-Cocke-Jelinek-Raviv (BCJR) algorithm [2] method, a trellis based detector is proposed for the HAMR channels. In this research, we apply the nonlinear generalized partial response (GPR) targets for the state trellis diagram of BCJR based detector [3] on perpendicular HAMR system with Volterra model (VM) [4] for the readback signal, as shown in Figure 1. We modify the PR1 target to nonlinear PR1 target for the 1st VM kernel. After that, the nonlinear GPR target of channel has been adjusted by the designed 2nd VM, in which the readback signal is the VM actual waveform signal. We improve the branch values of trellis from linear GPR target to nonlinear GPR targets. The received signal y_i and the readback signal r_i with AWGN signal n_i can be expressed as $r_i = y_i + n_i = a_i * h_i + n_i$ The received signal y_i is updated by paper [4], which is modify the linear target to nonlinear target for the trellis diagram, as shown in Figure 2. We can define the equations of a state branch in the trellis for BCJR detection as $g_i(a,q) = 1/\mathrm{sqrt}(2\pi\sigma^2)\times\exp(-(r_i - y_i\ (a,q))^2/2\sigma^2)$ $g_i(b,q) = 1/\mathrm{sqrt}(2\pi\sigma^2)\times\exp(-(r_i - y_i\ (b,q))^2/2\sigma^2)$ Forward in trellis, calculate each branch values in equation $a_q = a_{a-1}(Q) \times g_i(a,q) + a_{b-1}(Q) \times g_i(b,q)$ $a_Q = a_q/\mathrm{SUM}(a_q)$ In addition, calculate each branch values in backward of trellis are as follows: $b_q = b_a \times g_{i-1}(q,a) + b_b \times g_{i-1}(q,b)$ $b_Q = b_Q/\mathrm{SUM}(b_q)$ After that, we calculate the sum of the probability values between forward and backword to update the soft information as $\Pr[u_i=1|r_i] = a_Q \times g_i(a,q) \times b_Q + a_Q \times g_i(b,q) \times b_Q$ In the simulation, we consider the HAMR system at the areal density of 5 Tb/inch^2, which the parameters are described previously by P. Tueku, et al, [5]. The parameters of VM kernel determine the constant coefficients $K_1 = 1$ and $K_2 = 0.3$. The jitter noise is 20 percents. The additive white Gaussian noise (AWGN) has zero mean and variance $\sigma^2 = 0.5\times10^{-(SNR/10)}$. We define the range of signal-to-noise ratio (SNR) is 15 to 25 dB. In Figure 3, we compare the improved BCJR based detection with nonlinear GPR target and PR1 target. The BCJR based detection with nonlinear GPR target achieves the gain of 0.1 dB over the BCJR based detection with nonlinear PR1 target based detector at the BER of 10^{-5}. Conclusions We propose the method to improve the branch values of trellis by using linear GPR target to nonlinear GPR target for BCJR detector on HAMR system with VM kernel. In the simulation results, we found the BER performance of the BCJR detector with nonlinear GPR target is better than the BCJR detector with nonlinear PR1 target.

[1] A. Q. Wu, et al., "HAMR Areal Density Demonstration of TBPSI on Spinstand," *IEEE Trans. on Magn.*, vol.49, pp.779-782, 2013 [2] L. Bahl, et al., "Optimal Decoding of Linear Codes for Minimizing Symbol Error Rate," *IEEE Trans. on Infor. Theory*, vol. IT-20(2), pp.284-287, March 1974 [3] M. P. C. Fossorier, et al., "Simplified Trellis Diagram for a Simple Partial Erasure Model," *IEEE Trans. Magn.*, vol.34, no.1, pp. 320-322, 1998. [4] I. Ozgunes, et al., "Modeling of the Nonlinear Perpendicular Recording Readback Signal," *Journal of Magnetism and Magn. Mate.*, vol.287, pp.442-448, 2005. [5] P. Tueku, et al., "Target and Equalizer Design for Perpendicular Heat-Assisted Magnetic Recording," *Int. Journal of Electrical, Computer, Energetic, Electronic and Communication Engineering*, vol.8, no.3, pp.534-540, 2014

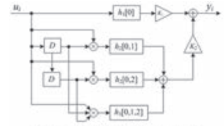

Fig.1. Block diagram of Volterra model

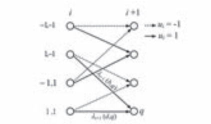

Fig.2. Trellis of nonlinear GPR target with designed 2nd of VM kernel

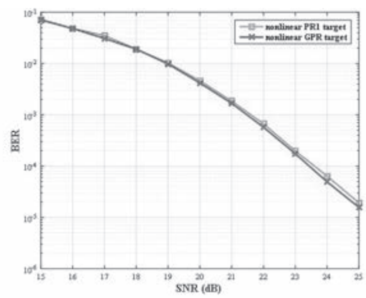

Fig.3. BER performance comparison between BCJR detector with nonlinear PR1 and GPR targets

TUESDAY AFTERNOON, 24 APRIL 2018 SIMPOR/ROSELLE BALLROOM, 1:30 TO 4:30

Session BW
TMR, VCMA AND MULTIFERROIC MATERIALS II
(Poster Session)

Shiheng Liang, Chair

Institute of physics, Chinese Academy of Sciences, Beijing, China

BW-01. Voltage control of perpendicular exchange bias in Pt/IrMn/Co/$(Co/Pt)_2$/Ta/PMN-PT(011) multiferroic heterostructures.

Q. Yang[1], *Z. Hu*[1], Z. Zhou[1], S. Zhao[1] and M. Liu[1]
1. Xi'an Jiaotong University, Xi'an, China

Exchange bias (EB), as an internal magnetic bias induced by a ferromagnetic-antiferromagnetic exchange coupling, is extremely important in many magnetic applications such as memories, sensors and other devices. [1, 2] Voltage control of exchange bias in multiferroics provides an energy-efficient way to achieve a rapidly 180° deterministic switching of magnetization, which has been considered as a key challenge in realizing next generation of fast, compact and ultra-low power magnetoelectric memories and sensors. [3] Although there are some researches related to the voltage controlled EB, [4-6] few of them focus on the regulation of perpendicular EB which is of great technological relevance for high-density spintronics. In this study, we demonstrated E-field control of perpendicular EB based on Pt 4nm/IrMn 4nm/Co 0.7 nm/(Co 0.7nm/Pt 0.95 nm)$_2$/Ta 3nm/PMN-PT (011) multiferroic heterostructure at room temperature. Angular dependences of EB with different applied voltage were studied through vibrating sample measurements (VSM) and ferromagnetic resonance (FMR) measurements respectively. For each method, maximal E-field induced exchange field change of ΔH_{eb} = 47 Oe and 95 Oe were obtained at θ=0° and 10° while under the compressive stress. Since VSM and FMR have different measurement principle, the difference of ΔH_{eb} is predictable.[7] We related this phenomenon to the strain induced lattice distortion, which can influence the Co 3d - Pt 5d interfacial hybridization [8, 9] and then the change of interlayer exchange bias. This voltage manipulation of perpendicular EB should offer new possibilities towards novel magnetic devices and memories with great energy-efficiency and ultra-high densities.

[1] E. Lage, C. Kirchhof, V. Hrkac, L. Kienle, R. Jahns, R. Knöchel*, et al.*, "Exchange biasing of magnetoelectric composites," *Nature materials,* vol. 11, pp. 523-529, 2012. [2] C. A. F. Vaz, J. Hoffman, C. H. Ahn, and R. Ramesh, "Magnetoelectric Coupling Effects in Multiferroic Complex Oxide Composite Structures," *Advanced Materials,* vol. 22, pp. 2900-2918, Jul 20 2010. [3] M. Liu, J. Lou, S. Li, and N. X. Sun, "E-Field Control of Exchange Bias and Deterministic Magnetization Switching in AFM/FM/FE Multiferroic Heterostructures," *Advanced Functional Materials,* vol. 21, pp. 2593-2598, 2011. [4] R. Ramesh and N. A. Spaldin, "Multiferroics: progress and prospects in thin films," *Nat Mater,* vol. 6, pp. 21-29, 01// print 2007. [5] Y. Yang, Y. Gong, S. Ma, C. Shen, D. Wang, Q. Cao*, et al.*, "Electric-field control of exchange bias field in a Mn 50.1 Ni 39.3 Sn 10.6/piezoelectric laminate," *Journal of Alloys and Compounds,* vol. 619, pp. 1-4, 2015. [6] S. Wu, S. A. Cybart, P. Yu, M. Rossell, J. Zhang, R. Ramesh*, et al.*, "Reversible electric control of exchange bias in a multiferroic field-effect device," *Nature materials,* vol. 9, pp. 756-761, 2010. [7] J. Geshev, L. G. Pereira, and J. E. Schmidt, "Angular dependence of the exchange bias obtained from magnetization and ferromagnetic resonance measurements in exchange-coupled bilayers," *Physical Review B,* vol. 64, p. 184411, 10/17/2001. [8] B. Peng, Z. Zhou, T. Nan, G. Dong, M. Feng, Q. Yang*, et al.*, "Deterministic Switching of Perpendicular Magnetic Anisotropy by Voltage Control of Spin Reorientation Transition in (Co/Pt)3/Pb(Mg1/3Nb2/3)O3–PbTiO3 Multiferroic Heterostructures," *ACS Nano,* vol. 11, pp. 4337-4345, 2017/04/25 2017. [9] Q. Yang, T. Nan, Y. Zhang, Z. Zhou, B. Peng, W. Ren*, et al.*, "Voltage Control of Perpendicular Magnetic Anisotropy in Multiferroic (Co/Pt)3/Pb(Mg1/3Nb2/3)O3–PbTiO3 Heterostructures," *Physical Review Applied,* vol. 8, p. 044006, 10/16/ 2017.

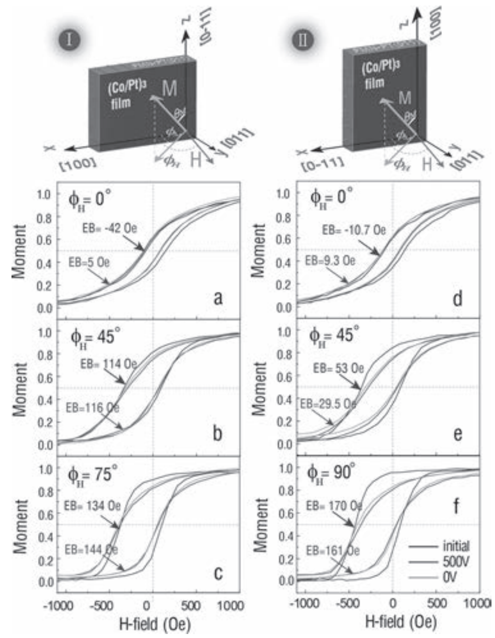

Fig. 1. (a–c) Magnetic hysteresis loops in the configuration I (θ=0° is the [100] direction) with and without external voltage for θ=0°, 45°, 75°. (d–f) Magnetic hysteresis loops in configuration II (θ=0° is the [011] direction) with and without external voltage for θ=0°, 45°, 90°.

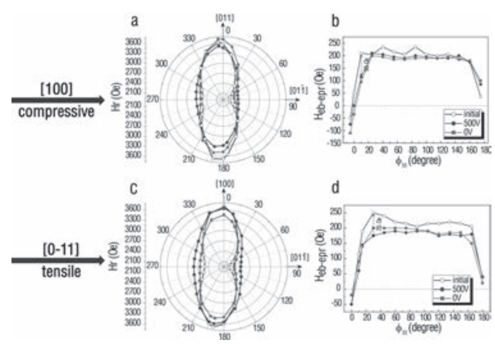

Fig. 2. Angular dependence of FMR (a,c) and exchange bias (c,d) for PMN-PT(011) /Ta 3nm/(Pt 9.5A/Co 7A)$_2$/Co7A/IrMn 4nm/Pt 4nm multiferroics heterostructure based on configuration I (a,b) and configuration II (c,b) respectively.

BW-02. Voltage switching of perpendicular magnetic anisotropy in $(Co/Pt)_3$/PZN-PT heterostructures at room temperature.

B. Peng[1], M. Feng[1], Q. Yang[1], Y. Zhang[1] and M. Liu[1]
1. Xi'an Jiaotong University, Xi'an, China

One of the central challenges in realizing multiferroics based magnetoelectric memories is the ability to non-volatilely switch magnetization between the in-plane and out-of-plane directions with a control voltage.[1] This switching often requires overcoming a large demagnetization field, which is hardly achieved by a relatively small voltage-induced magnetic anisotropy in conventional multiferroic laminates.[2,3] However, in ultra-thin ferromagnetic/ferroelectric heterostructures, given the effect of spin reorientation transition, voltage induced-lattice strain can tip the balance between the surface anisotropy and demagnetization field, leading to a deterministic switching of magnetization between the in-plane and out-of-plane directions.[4] In this work, we demonstrate a voltage switching of perpendicular magnetic anisotropy in $(Co/Pt)_3$/(011) PZN-PT multiferroic heterostructures at room temperature. Electric field control of magnetic anisotropy was quantitatively studied by ferromagnetic resonance (FIG. 1a) Taking the advantage of large electric field induced strain during phase change in PZN-PT piezoelectric single crystalline substrates, a large electric field-induced effective magnetic field up to 670 Oe was observed(FIG. 1b), leading to a switching of magnetization easy axis rotation from out-of-plane to in-plane that demonstrated by angular dependence of ferromagnetic resonance fields (FIG. 1c and 1d). In addition, it was also confirmed by the magnetic hysteresis loops(FIG. 1e and 1f). The strong magnetoelectric coupling in $(Co/Pt)_3$/PZN-PT at room temperature provides a new platform for realization of voltage control of perpendicular magnetic anisotropy that will enable power efficient multiferroic memories.

[1] N. A. Spaldin, S. W. Cheong, and R. Ramesh, "Multiferroics: Past, present, and future", Phys. Today 63 (10), 38 (2010). [2] M. Liu, J. Lou, S. D. Li, and N. X. Sun, "E-Field Control of Exchange Bias and Deterministic Magnetization Switching in AFM/FM/FE Multiferroic Heterostructures", Adv. Funct. Mater. 21 (13), 2593 (2011). [3] M. Liu, B. M. Howe, L. Grazulis, K. Mahalingam, T. Nan, N. X. Sun, and G. J. Brown, "Voltage-Impulse-Induced Non-Volatile Ferroelastic Switching of Ferromagnetic Resonance for Reconfigurable Magnetoelectric Microwave Devices", Adv. Mater. 25 (35), 4886 (2013). [4] B. Peng, Z. Zhou, T. Nan, G. Dong, M. Feng, Q. Yang, X. Wang, S. Zhao, D. Xian, Z. D. Jiang, W. Ren, Z. G. Ye, N. X. Sun, and M. Liu. "Deterministic Switching of Perpendicular Magnetic Anisotropy by Voltage Control of Spin Reorientation Transition in $(Co/Pt)_3$/$Pb(Mg_{1/3}Nb_{2/3})O_3$-$PbTiO_3$ Multiferroic Heterostructures." ACS Nano 11(4), 4337 (2017)

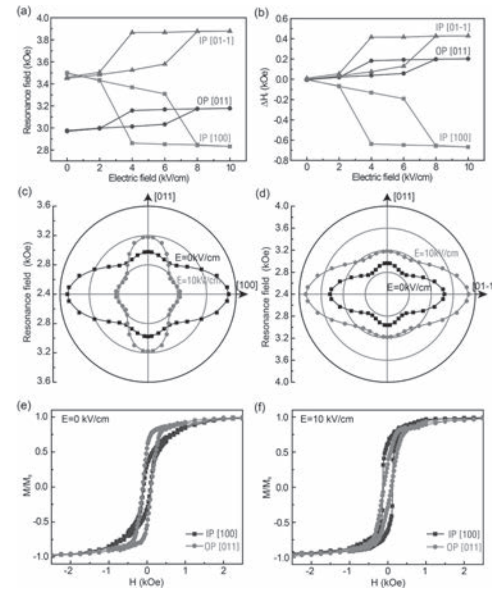

Fig. 1. Voltage switching of perpendicular magnetic anisotropy in $(Co/Pt)_3$/(011) PZN-PT multiferroic heterostructures: (a) Electric field dependent ferromagnetic resonance field and (b) electric field induced effective magnetic field along in-plane (IP) [100] and [01-1] directions as well as out-of-plane (OP) [011] direction, (c) angular dependent ferromagnetic resonance fields in the [100]-[011] plane, (d) angular dependent ferromagnetic resonance fields in the [01-1]-[011] plane, magnetic hysteresis loop measured along in-plane [100] and out-of-plane [011] directions at (e) E=0 kV/cm and (f) E=10 kV/cm.

BW-03. High isotropic Terfenol-D/PZT magnetoelectric sensor based on ring nested structure.

X. Wu[1], J. Ouyang[1], W. Wang[1], Y. Ren[1], S. Chen[1] and X. Yang[1]
1. School of Optical and Electronic Information,Huazhong University of Science and Technology, WuHan, China

Magnetoelectric sensors with high sensitivity and the easy preparation of structure, etc, have broad application prospects in the weak magnetic signal detection and other fields. In recent years, scholars [1-4] studied the dependence of the magnetoelectric effect on the magnetic field direction. The results show that the output of the magnetoelectric composites change with the angle of the magnetic field, and the ratio of the maximum value to the minimum value of the output signal is recorded as K. When K is very large, the magnetoelectric composites have high anisotropy, which means they are very sensitive to magnetic field in a particular direction and are therefore suitable for vector magnetic field measurements; in contrast, when K is very small, the magnetoelectric composites are highly isotropic, which means their outputs are less affected by the direction of magnetic field and thus are suitable for the scalar field measurement. Dong et al [1] and our team [2] made highly anisotropic magnetoelectric sensors (K values between 100 and 1000), and it was found that K values were related to the shape anisotropy of piezoelectric materials and magnetostrictive materials. But so far, high isotropic magnetoelectric sensors have not been reported yet. In this respect, Terfenol-D/PZT magnetoelectric sensor based on ring nested structure is studied in this paper, both of which have shape isotropy, as shown in Fig 1(a). We tested the relationship between the voltage (V) output of the structure and the DC bias magnetic field (Fig 1(b)). The structure was placed in the horizontal AC magnetic field generated by the coil, and the electromagnet provided a DC bias magnetic field in the horizontal direction. When the AC magnetic field (H_{AC}) is 1Oe at 10kHz, and DC bias magnetic (H_{DC}) field increases from 280Oe to 10920Oe, the output curve of the structure (Fig 1(c)) shows that the rapid increase before 2520Oe of H_{DC}, and then decreased slowly. The voltage reaches a maximum of 364.055mV when H_{DC} is 2520Oe. In order to miniaturize the sensor probe, we changed the electromagnet to a small cylindrical magnet with a diameter of 10 mm and a height of 10 mm, making it a sensor as shown in Fig 2(a). It consists of Terfenol-D/PZT structure, two magnets with the same polar direction and a frame. In order to study the output linearity of the sensor, we use the instruments shown in Fig 2(b) to test the relationship between V and H_{AC}, by adjusting the distance between magnets and material, the probe response reaches its maximum. At this time, the output voltage of the sensor, which in the magnetic shield barrel, increases linearly with the increasing AC magnetic field at 10kHz, which generated by the coil, as shown in Fig 2(c). In order to study the magnetoelectronic isotropy of the sensor, keeping the H_{AC}=1Oe at 10kHz, each time the sensor is rotated by 30°, the relationship between V and the rotation angle shown in Fig 2(d) is obtained and fitted by our proposed finite element model, and it can be calculated that K equals 1.99. According to the results of finite element method, we found the test values were in agreement with the theoretical values, which proved experimentally and simulatively the ring nested structure sensor was highly isotropy. And it was also found that magnetoelectronic isotropy could be affected by the shape isotropy of the piezoelectric and magnetostrictive materials, as well as the direction of the bias magnetic field by the finite element method.

[1] Dong, S., Zhai, J., Li, J., & Viehland, D. (2006). Near-ideal magnetoelectricity in high-permeability magnetostrictive/piezofiber laminates with a (2-1) connectivity. Applied Physics Letters, 89(25), 252904. [2] Chen, S., Yang, X., Ouyang, J., Lin, G., Jin, F., & Tong, B. (2014). Fabrication and characterization of shape anisotropy AlN/FeCoSiB magnetoelectric composite films. Ceramics International, 40(2), 3419-3423. [3] Palneedi, H., Annapureddy, V., Lee, H. Y., Choi, J. J., Choi, S. Y., Chung, S. Y., & Ryu, J. (2017). Strong and anisotropic magnetoelectricity in composites of magnetostrictive Ni and solid-state grown lead-free piezoelectric BZT–BCT single crystals. Journal of Asian Ceramic Societies, 5(1), 36-41. [4] Chu, Z., Shi, H., Shi, W., Liu, G., Wu, J., Yang, J., & Dong, S. (2017). Enhanced Resonance Magnetoelectric Coupling in (1-1) Connectivity Composites. Advanced Materials, 29(19).

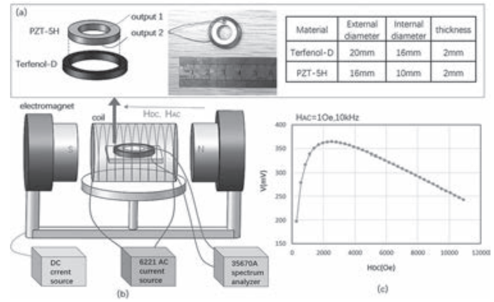

Fig. 1. (a) Material structure and dimensions; (b) Schematic diagram of the magnetoelectric composites experimental instruments; (c) Test curve of the relationship between composite voltage output and the DC bias magnetic field.

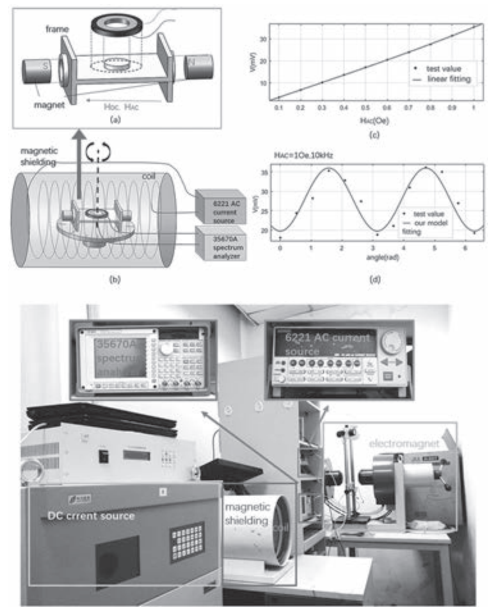

Fig. 2. (a) Sensor structure; (b) Schematic diagram of the sensor experimental instruments; (c) Test and fitting curve of the relationship between sensor output and AC magnetic field; (d) Test and fitting curve of the relationship between sensor output voltage and AC magnetic field direction.

BW-04. Preparation and Characterization of Permalloy and Cobalt Doped $BiFeO_3$ Hybrid Core-shell nanostructures.

K. Javed[1,2], N. Ahmad[3], M. Shahzad[1] and S. Shah[1]
1. Physics, Forman Christian College, Lahore, Pakistan; 2. Institute of Physics, Chinese Academy of Sciences, Beijing, China; 3. Department of Physics, FBAS, International Islamic University, Islamabad, Pakistan

Nanowires and Nanotubes have got considerable attention because of their novel potential applications in ultrahigh magnetic recording media, ultrasmall magnetic sensors, drug delivery etc.[1] The properties of nanostructures are highly dependent on their size, which makes them very attractive for industrial applications[2] Hybrid coreshell nanostructures have attracted ever-increasing interest due to its potential for applications as multifunctional devices[3-4]. Hybrid interfaces comprising ferromagnetic metals and ferroelectric/multiferroic oxides are of particular interest for the next generation magnetoelectric memories, in which magnetism can be tuned electrically via strain-/spin-mediated couplings across the interfaces[5]. Hybrid one-dimensional core-shell nanowires and coreshell nanotubes consisting of Permalloy core and Cobalt doped $BiFeO_3$ multiferroic shell were synthesized using a two-step method (Sol-gel and DC electrodeposition). Doping effect has been studied by structural and magnetic characterization. The results have shown a significant exchange bias and coercivity, particularly for hybrid coreshell nanotubes. This may be attributed to effective reduction of domain size between coreshell adjacent layers. SEM and TEM showed excellent surface morphology for both coreshell nanowires and coreshell nanotubes, with shell thickness ~20nm. At low temperature, super-paramagnetic contribution plays an important role to control magnetic behavior. Easy magnetization axis aligned parallel to axis of coreshell nanowires due to dominant shape anisotropy. The results have shown that by site engineering method the properties of multiferroic composition can be improved. This multipurpose method can be used to blend several hybrid one dimensional core-shell nanowires as well as for coreshell nanotubes.

[1] K. Javed, W. J. Li, S. S. Ali, D. W. Shi, U. Khan, S. Riaz, and X. F. Han, Scientific Reports, 5, 18203 (2015). [2] U. Khan, W. J. Li, N. Adeela, M. Irfan, K. Javed, C. H. Wan, S. Riaz and X. F. Han, Nanoscale, 8, 6064 (2016). [3] S. S. Ali, W. J. Li, K. Javed, D. W. Shi, S. Riaz, G. J. Zhai, and X. F. Han, Nanotechnology, 27, 045708 (2016). [4] S. S. Ali, W. J. Li, K. Javed, D. W. Shi, S. Riaz, Y. Liu, Y. G. Zhao, G. J. Zhai, and X. F. Han, Nanoscale, 7, 13398 (2015). [5] Qintong Zhang, and Xiufeng Han et. al. Adv. Mater., 27, 6934 (2015).

BW-05. Large Magnetoelectric coupling in a Y-type hexaferrite.

Y. Yang[1,2], K. Jiang[1], J. Li[1], C. Duan[2], X. Wang[1] and H. Ge[1]
1. College of Materials Science and Engineering, Zhejiang Province Key Laboratory of Magnetism, China Jiliang University, Hangzhou, Hangzhou, China; 2. Key Laboratory of Polar Materials and Devices, Ministry of Education, East China Normal University, Shanghai, Shanghai, China

We report the multiferroicity and large magnetoelectric coupling in a Y-type hexaferrite, $Ba_{0.5}Sr_{1.5}Zn_2(In_{0.08}Fe_{0.92})_{12}O_{22}$.By applying an electric field, the magnetization, planar helix transition temperature, coercivity and magnetization reversal of $Ba_{0.5}Sr_{1.5}Zn_2(In_{0.08}Fe_{0.92})_{12}O_{22}$ are effectively modified. As shown in Figure.1, two peaks are observed at 315 and 337 K, corresponding to T_S and T_N, respectively. The inset shows the temperature dependence of magnetization (M-T) for In-BSZFO measured at 50 Oe. The sample undergoes an AFM phase transition at T_N = 337 K followed by a PH transition around T_S = 315 K, agreeing well with the DSC results. Remarkable electrical controlling of magnetism is observed at 315 K. According to the M-T curves for In-BSZFO at 2 kOe with or without DC electric field (E_{dc}) shown in Figure. 2(a), it is clear that M is almost unchanged below 280 K, but decreases distinctly with E_{dc} in the vicinity of T_S, suggesting that E_{dc} can affect M more easily around the PH to AFM phase transition region. As a result, T_S shifts toward the lower temperature about 7 K, which can be seen from the inset of Fig. 2(a). Interestingly, cross-control of magnetism and ferroelectricity is simultaneously realized in this magnetoelectric hexaferrite[Fig.2(b)]. Large direct and converse magnetoelectric effects in In-BSZFO give a valuable contribution to the study of magnetoelectric effect, which is of great importance in promising its practical applications in the future.

[1] S. W. Cheong, M. Mostovoy, Nat. Mater. 6(2007)13–20. [2] D. Khomskii, Physics 2 (2009)20. [3] Y. Tokura, S. Seki, Adv. Mater. 22 (2010) 1554–1565. [4] T. Arima, J. Phys. Soc. Jpn. 80(2011)052001. [5] Y. Kitagawa, Y. Hiraoka, T. Honda, et.al, Nat. Mater. 9(2010)797–802. [6] Y. Tokunaga, Y. Kaneko, D. Okuyama, et.al, Phys.Rev.Lett.105(2010)257201. [7] S. H. Chun, Y. S. Chai, B. G. Jeon, et.al, Phys.Rev.Lett.108(2012)177201. [8] T. Kimura, Annu. Rev. Condens. Matter Phys. 3(2012)93–110.

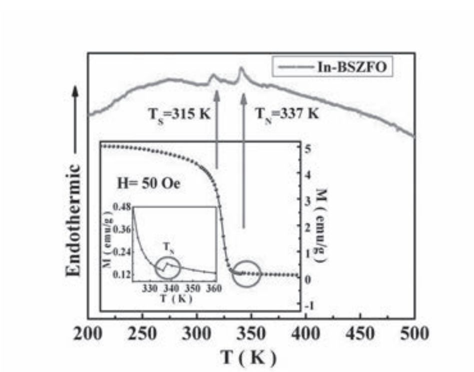

Fig. 1. The DSC curve of In-BSZFO in the temperature range of 200-500 K. The inset shows the M-T curves measured at 50 Oe.

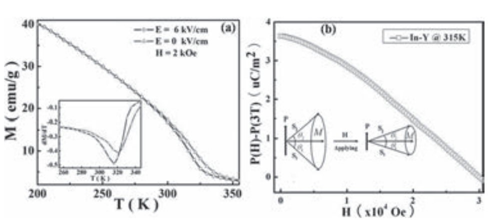

Fig. 2. M-T curves measured at 2 kOe with E_{dc} = 0 and 6 kV/cm, respectively. Inset: dM/ dT–T curves near the transition temperature; (b)The H dependence of P at 315 K. Inset: the dependence of the spin cone angle on H.

BW-06. Resistive switching in Pt/$BiFeO_3$/$SrRuO_3$/$SrTiO_3$ heterostructures.

T. Wang[1], *W. Cheng*[1,2], C. Wang[1], H. Wang[2], Y. Hao[1] and X. Miao[1,2]
1. School of Optical and Electronic Information, Huazhong University of Science and Technology, Wuhan, China; 2. Wuhan National Research Center for Optoelectronics, Huazhong University of Science and Technology, Wuhan, China

1. Introduction The demand for high speed, high storage density, and low power consumption nonvolatile memory technology has stimulated extensive research into new functional materials. Resistive switching has been reported in multiferroic bismuth ferrite (BFO), in which the resistance can be switched between a high resistance state (HRS) and a low resistance state (LRS) [1-2]. These two resistance states can stand for binary 0 and 1 in resistive-switch memory. In general, the metal/BFO/metal cell shows bipolar resistive switching that the set to a LRS occurs at one voltage polarity and the reset to the HRS appears at reversal voltage polarity. It has been widely recognized that this so-called bipolar resistive switching is usually connected with a voltage-driven oxygen vacancy movement.However, BFO films exhibit p-type conduction as a result of Bi loss[3], and a Schottky junction or a p-n junction may be formed at the metal/BFO interface and can be modulated by the ferroelectric polarization, which induces blocking or non-blocking interfaces for the transport of carriers and consequent the resistive switching behavior [4-5]. Here, we prepared Pt/BFO/$SrRuO_3$/$SrTiO_3$ resistive device units and observed a repeatable and switchable resistive effect of BFO films with a tunable HRS/LRS ratios and a low resistance switching voltage of ±1.5 V, apart from the high forming voltage. 2. Experiments The BFO films of 25 nm were deposited on $SrTiO_3$ (001) substrates with 40 nm $SrRuO_3$ buffered layer via RF magnetron sputtering. The substrate heating temperature and the working pressure of oxygen gas were maintained at degree centigrade and 1 Pa, respectively. To fabricate a metal/insulator/metal cell, top electrodes of Pt (100 nm) with diameters of 100μm, 200μm and 300μm were sputtered onto the as-deposited BFO films through a shadow mask shown as Fig1. The I–V curves of the devices were measured by an Agilent B1500 source meter and the maximum current is limited by a compliance current to avoid permanent hard breakdown while unipolar HRS switches to LRS. 3. Results and Discussion Fig 1 shows the I–V measurements by sweeping the bias voltage from 0 to -2V, back to +2 V and returning to 0, repeatedly. The large hysteresis in I–V curves is clearly observed and the Pt/BFO/SRO cell changes from low conducting state (OFF) to high conducting state (ON) at about -1.5 V. Moreover, when sweeping bias voltage transforms from negative value to positive value, we find that the Pt/BFO/SRO cell changes from ON to OFF at about ±1.5 V. Furthermore, I-V curves exhibit good repeatability within nine testing cycles and the resistance switching does not need the forming process, which indicates that resistive switching does not origin from a voltage-driven oxygen vacancy movement, but is possibly correlated with the change of the potential barrier height in the interface between BFO and SRO [3]. Fig 2 presents the OFF/ON resistance ratio at different testing cycles and stimulated voltage range. It is easily seen that the ON resistance almost keeps the same value, but the OFF/ON resistance ratio significantly depends on the maximum value of negative voltage. The OFF/ON resistance ratios reach about 100, 30 and 10, when the negative voltages are -2V, -1.8V and -1.6V, respectively, probably due to the different degree of ferroelectric polarization in the BFO films[4]. More research details for the ferroelectric polarization induced resistive switching will be bring out in the conference. 4. Conclusion We demonstrated a significant resistive switching at a low operating voltage of ±1.5V with ON/OFF ratios as high as 100 in Pt/BFO/SRO/STO (001) heterostructures, and can successfully tune ON/OFF ratios from 10 to 100 by applying different negative voltages. By further optimizing its cell structure, BFO film based device may become a promising candidate for non-volatile memories due to the advantages of low power consumption, multi-value storage and high stability. ACKNOWLEDGMENTS This work was supported by the National Natural Science Foundation of China (Grant Nos. 61432007 and 61474050) and the Fundamental Research Funds for the Central Universities, HUST (Grant No.2016YXMS204).

[1] Yao S, Zhou S, Bürger D, et al. Nonvolatile bipolar resistive switching in Au/$BiFeO_3$/Pt. Journal of Applied Physics, 2011, 109(12):95. [2] Li M, Zhuge F, Zhu X, et al. Nonvolatile resistive switching in metal/La-doped $BiFeO_3$/Pt sandwiches. Nanotechnology, 2010, 21(42):425202. [3] Hu Z, Li Q, Li M, et al. Ferroelectric memristor based on Pt/$BiFeO_3$/Nb-doped $SrTiO_3$ heterostructure[J]. Applied Physics Letters, 2013, 102(10):076502. [4] Bruno F Y, Boyn S, Fusil S, et al. Millionfold Resistance Change in Ferroelectric Tunnel Junctions Based on Nickelate Electrodes. Advanced Electronic Materials, 2016, 2(3): 1500245. [5] Boyn S, Douglas A M, Blouzon C, et al. Tunnel electroresistance in $BiFeO_3$ junctions: size does matter. Applied Physics Letters, 2016, 109(23):232902.

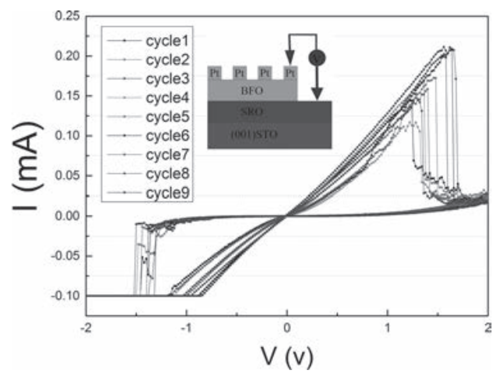

Fig. 1. I-V curves for Pt/BFO/SRO/STO at the voltage range of ±2V

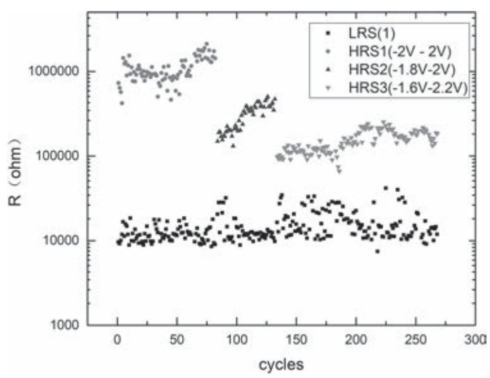

Fig. 2. the high and low resistance stability at different stimulated negative voltages

BW-07. Integrated Thin-Film Magnetoelectric Waveguide with Tunable Resonance Frequency.

A. El-Ghazaly[2], J. Evans[3], N. Sato[1], N. Montross[3], R.M. White[4] and S.X. Wang[1,4]
1. Electrical Engineering, Stanford University, Stanford, CA, United States; 2. Electrical Engineering and Computer Science, University of California Berkeley, Berkeley, CA, United States; 3. Radiant Technologies, Inc., Albuquerque, NM, United States; 4. Materials Science and Engineering, Stanford University, Stanford, CA, United States

Magnetoelectrics offer the ability to electrically control magnetic material and device properties. This feature has the potential to provide numerous benefits to electronic systems and motivate the integration of magnetic devices into mainstream electronics [1-3]. Most work on magnetoelectrics thus far, however, has involved either specialized crystalline multiferroic materials [1,4-6] or bulk piezoelectric/magnetic composite layers [7-13]. Here, we attempt to bridge the gap between magnetoelectricity and silicon-integrated electronics by producing the first fully-integrated thin-film magnetoelectric resonant waveguides for tunable radio frequency (RF) systems [14]. Tunability of these devices is achieved through electric field control of magnetic permeability in order to change the phase velocity and resonance frequency of coplanar waveguides. The devices were fabricated on a conventional silicon substrate and incorporate thin-film magnetoelectric composites, made up of both magnetic and piezoelectric material layers for strain-control of magnetic anisotropy. The fabricated devices achieved reversible tunability of the resonance frequency with a large converse magnetoelectric coupling coefficient of up to 24 mG-cm/V using just thin films. The tunable waveguide device, shown in Fig. 1, was designed as an RF quarter-wavelength resonator, whose resonance is based on the total effective permeability and permittivity of the material stack. To provide the capability of tuning the resonance frequency, a thin-film magnetoelectric composite was created using a magnetostrictive ferromagnetic layer on top of a piezoelectric/electrodes combined layer, with the silicon substrate on the bottom. A coplanar waveguide on the surface of the structure carries the wave such that its propagation is influenced by the properties of the underlying magnetoelectric stack. Electric field control of piezoelectric strain couples to the magnetic layer for strain control of magnetization and permeability, therefore influencing the propagating phase velocity and resonance frequency of the waveguide. Fig. 1a illustrates the simplified integrated structure as well as the electric field lines from the interdigitated electrodes controlling the piezoelectric. Fig. 1b shows scanning electron microscope images of the cross-section of the fabricated devices, produced by focused-ion beam. Platinum interdigitated electrodes (IDE) [11] apply an approximately in-plane electric field, as shown in Fig. 1a, to the piezoelectric PNZT and take advantage of the d_{33} strains, which are typically larger than d_{31} strains. The ferromagnetic material, $Co_{43}Fe_{43}B_{14}$ (At%) [12] was selected for its high magnetostriction value of $\lambda s \sim 55 \times 10^{-6}$ and high ferromagnetic resonance frequency (~ 2 GHz for a square film). These two properties allow for a large degree of electrical control (via strain) of magnetization and a material resonance frequency well separated from that of the device resonance. In addition, the magnetic film was laminated and patterned into a narrow bar parallel to the wave propagation direction, such that the shape anisotropy contributed to aligning the magnetization uniformly along the length direction, with permeability measured along the orthogonal (width) direction. Fig. 2 presents measurement results from the magnetoelectric resonator device. The polarization measurements around the remanence point, indicate that the polarization (and related strain) is fairly linear and reversible, despite some hysteresis. The corresponding RF resonance shifts for the magnetoelectric waveguide follow a similar trend but with opposite polarity. This is due to the fact that the strain causes a rotation of the magnetization and an increase in the permeability with electric field; permeability is inversely related to the phase velocity and resonance frequency, therefore leading to a decrease in the resonance frequency with applied electric field. Neglecting contributions due to stray fields or temperature effects, we extract an effective magnetoelectric coefficient for the composite device equal to approximately 24 mG-cm/V, which is comparable with many other multiferroic and magnetoelectric composites. Acknowledgement Research for this project was conducted with government support under FA9550-11-C-0028 and awarded by the Department of Defense, Air Force Office of Scientific Research, National Defense Science and Engineering Graduate (NDSEG) Fellowship, 32 CFR 168a. Part of this work was performed using the Stanford Nanofabrication Facility (SNF) and the Stanford Nano Shared Facilities (SNSF) at Stanford University.

[1] C. Israel, N. D. Mathur, and J. F. Scott, "A one-cent room-temperature magnetoelectric sensor," *Nat. Mater.*, vol. 7, no. February, pp. 93–94, 2008. [2] M. Bibes and A. Barthélémy, "Multiferroics: towards a magnetoelectric memory," *Nat. Mater.*, vol. 7, no. June, pp. 425–426, 2008. [3] J. F. Scott, "Multiferroic memories," *Nat. Mater.*, vol. 6, no. April, pp. 256–257, 2007. [4] W. Eerenstein, N. D. Mathur, and J. F. Scott, "Multiferroic and magnetoelectric materials.," *Nature*, vol. 442, no. 7104, pp. 759–65, 2006. [5] R. Ramesh and N. A. Spaldin, "Multiferroics: progress and prospects in thin films," *Nat. Mater.*, vol. 6, no. 1, pp. 21–29, 2007. [6] J. Wang, J. B. Neaton, H. Zheng, V. Nagarajan, S. B. Ogale, B. Liu, D. Viehland, V. Vaithyanathan, D. G. Schlom, U. V Waghmare, N. a Spaldin, K. M. Rabe, M. Wuttig, and R. Ramesh, "Epitaxial BiFeO3 multiferroic thin film heterostructures.," *Science (80-.).*, vol. 299, no. 5613, pp. 1719–1722, 2003. [7] G. Yu, Z. Wang, M. Abolfath-Beygi, C. He, X. Li, K. L. Wong, P. Nordeen, H. Wu, G. P. Carman, X. Han, I. A. Alhomoudi, P. K. Amiri, and K. L. Wang, "Strain-induced modulation of perpendicular magnetic anisotropy in Ta/CoFeB/MgO structures investigated by ferromagnetic resonance," *Appl. Phys. Lett.*, vol. 106, no. 7, p. 72402, 2015. [8] J. Lou, D. Reed, M. Liu, and N. X. Sun, "Electrostatically tunable magnetoelectric inductors with large inductance tunability," *Appl. Phys. Lett.*, vol. 94, no. 11, p. 112508, 2009. [9] S. Dong, J. Zhai, S. Priya, J.-F. Li, and D. Viehland, "Tunable features of magnetoelectric transformers," *IEEE Trans. Ultrason. Ferroelectr. Freq. Control*, vol. 56, no. 6, pp. 1124–7, Jul. 2009. [10] K. I. Arai, C. S. Muranaka, and M. Yamaguchi, "A new hybrid device using magnetostrictive amorphous films and piezoelectric substrates," *IEEE Trans. Magn.*, vol. 30, no. 2, pp. 916–918, Mar. 1994. [11] G. A. Lebedev, B. Viala, J. Delamare, and O. Cugat, "Voltage-Controlled Uniaxial Magnetic Anisotropy in Soft Magnetostrictive Ferromagnetic Thin Films," *IEEE Trans. Magn.*, vol. 47, no. 10, pp. 4037–4040, Oct. 2011. [12] G. A. Lebedev, B. Viala, T. Lafont, D. I. Zakharov, O. Cugat, and J. Delamare, "Converse magnetoelectric effect dependence with CoFeB composition in ferromagnetic/piezoelectric composites," *J. Appl. Phys.*, vol. 111, no. 7, p. 07C725, 2012. [13] J. L. Hockel, T. Wu, and G. P. Carman, "Voltage bias influence on the converse magne- toelectric effect of PZT/terfenol-D/PZT laminates," Journal of Applied Physics, vol. 109, no. 6, p. 064106, 2011. [14] A. El-Ghazaly, J. T. Evans, N. Sato, N. Montross, H. Ohldag, R. M. White, and S. X. Wang, "Electrically- Tunable Integrated Thin-Film Magnetoelectric Resonators," Advanced Materials Technologies, vol. 2, no. 8, p. 1700062, 2017.

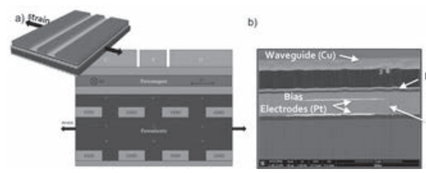

Fig. 1. Diagrams of the magnetoelectric composite waveguide, including a) 3D model and cross-sectional electric field diagram of the coplanar waveguide structure on top of the magnetoelectric composite; b) cross-sectional SEM image of the material layers.

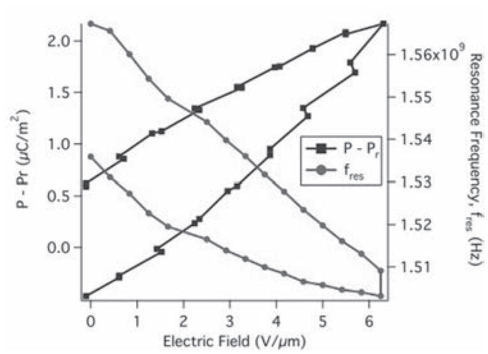

Fig. 2. Measurements of the magnetoelectric waveguide results, showing a) polarization change and b) tunable resonance frequency as a function of electric field.

BW-08. Study of magneto-dielectric behaviour in Haldane spin chain Ho_2BaNiO_5.

S.K. Upadhyay[1] and E.V. Sampathkumaran[1]
1. Department of Condensed Matter Physics and Material Science, Tata Institute of Fundamental Research, Mumbai, MUMBAI, India

In search of new multiferroic materials, researchers have discovered various rare earth based multiferroic materials $RMnO_3$, $R_2Mn_2O_5$ (where, R= rare earth) in the past decade, due to its interesting physics as well as promising application in the field of memory devices[1]. During last few years, our group has explored multiferroicity in Haldane spin chain based system R_2BaNiO_5 (R=Gd, Dy, Tb, Er, Sm etc.) [2, 3]. This family of insulating oxides, crystallizing in *Immm*-type orthorhombic structure, occupy a special place in the area of magnetism. In this family, Ni^{2+} ions (spin = 1) form linear chains which are well separated by R ions. For R= Y, there is no magnetic ordering from Ni sublattice, but for magnetic rare-earth members, ordered magnetic moments appear simultaneously for R and Ni ions with a complex antiferromagnetic structure [4]. We noted that, for R= Gd, Dy and Er, onset of short-range or long-range magnetic order triggers ferroelectricity due to the distortion of Ni-O bond distances, whereas, for the Tb member, multiferroicity appears well below its Néel temperature (T_N) associated with different magnetic structure. Focussing on the Ho member, it was reported in the literature [5] that there are two meta-magnetic transitions in this compound. We have studied its magnetic, dielectric and magneto-dielectric behavior in detail, the results of which are reported here. The polycrystalline sample of Ho_2BaNiO_5 was prepared by a standard solid-state reaction route as reported in ref.[5]. The x-ray powder diffraction pattern (Cu-K_α radiation) at room temperature confirmed the single phase formation of the sample. The observed diffraction pattern was analyzed by Rietveld fitting by using Fullproof program. The lattice parameters obtained by the best fitting (a= 3.760(1) Å, b= 5.758 (4) Å and c= 11.329 (3) Å) match well with the literature [5]. Ac magnetic susceptibility (χ) and isothermal M measurements were carried out by a commercial superconducting quantum interface device (SQUID, Quantum design, USA). Agilent E4980A LCR meter with a home-made sample holder integrated with the PPMS (Quantum Design, USA) was used for the complex dielectric permittivity measurements. Isothermal dielectric constant (ε¢) as a function of magnetic field (H) was measured at some selected temperatures. Figure 1 reveals the one to one correspondences between the dielectric constant (electrical susceptibility) and magnetic susceptibility of the studied sample. A careful analysis of dielectric data as a function of temperature showed that around 12 K, there is an anomaly in dielectric data for the frequency of 100 kHz as shown in the left frame of figure 1. The first derivative of the ac-susceptibility data shows peak close to 12 K (right frame of figure.1), suggesting a new magnetic transition following anti-ferromagnetic transition around 52 K (please see the inset of figure1). In order to support the existence of a magnetic transition around 12 K, we measured isothermal magnetization at various temperatures (not all temperature shown here). We observe a distinct upturn in $M(H)$ near (H_{cr1} =) 29 kOe and (H_{cr2}=55 kOe) for T= 10 K, attributable to the existence of a field induced transition as shown in the left frame of the figure2. Further support for magnetodielectric coupling is obtained from isothermal magnetodielectric data, shown in the right frame of Fig. 2. For 10 K, ε [defined as = {ε (H) – ε (0)}/ε (0)] undergoes a sharp increase with H and achieve a maximum near H_{cr1}; there is another upturn at H_{cr2}, supporting the existence of two (broad) meta-electric transition. The field at which this upturn happens decreases with increasing temperature. No such meta-electric like feature is observed for the curves well above 12 K. Magnetic, dielectric and magneto-dielectric behaviour have been studied for the Haldane chain based system Ho_2BaNiO_5. The strange behaviour of dielectric in the presence of magnetic field is manifested by the possible field induced change in magnetic structure and due to the existence of magneto-dielectric coupling. Neutron measurements are underway for understanding the magnetic structure to relate to magneto-dielectric coupling differences above and below 12 K.

1) T. Kimura, T. Goto, H. Shintani, K. Ishiazaka, T. Arima, and Y. Tokura, Nature (London) 426, 55 (2003). 2) K. Singh, Tathamay Basu, S. Chowki, N. Mohapatra, Kartik K Iyer, P.L. Paulose, and E.V. Sampathkumaran, Phys Rev. B 88, 094438 (2013). 3) Sanjay Kumar Upadhyay, P.L. Paulose, and E.V. Sampathkumaran, Phys. Rev. B 96, 014418 (2017). 4) E. Garcia-Matres, J. L. Martinez and J. Rodriguez-Carvajal, Eur. Phys. J. B. 24, 59-70 (2001). 5) G. Nenert and T.T.M. Palstra, Phys. Rev. B 76, 024415 (2007).

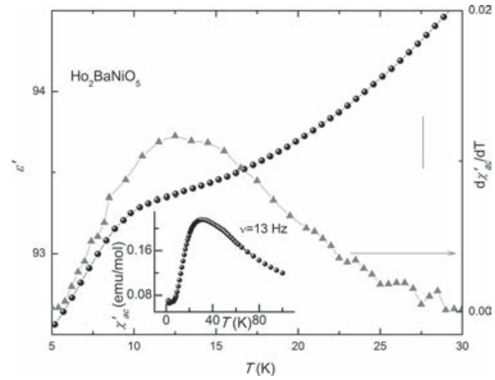

Fig. 1. Left frame presents the dielectric data in zero magnetic field with frequency of 100 kHz. Right frame shows first derivative of ac-χ data in zero field with frequency of 13 Hz. Inset shows the ac-χ data to highlight the antiferromagnetic transition around 52 K.

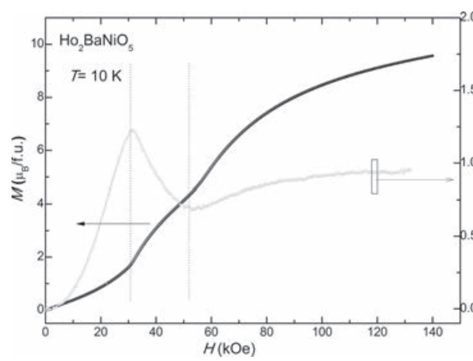

Fig. 2. Left frame presents the *M-H* data while right frame presents the magneto-dielectric data depicting the one to one correspondence.

BW-09. Prediction of Room Temperature Oxygen Vacancy-mediated Multiferroicity in a Cobalt-substituted Perovskite.

M.C. Onbasli[1]
1. Dept. of Electrical and Electronics Engineering, Koc University, Istanbul, Turkey

Multiferroic materials are a source of novel physics as well as enablers of memory and logic devices that are unattainable using conventional semiconductors. Most of the known single-phase multiferroic materials, however, are only multiferroic at low temperatures, are antiferromagnetic instead of ferro- or ferrimagnetic, or present either sinusoidal (with negligible magnetization) or screw-type magnetism with low Curie temperature. Here, we predict through density functional theory calculations that both magnetism and electric polarization can originate from the interactions between oxygen vacancies and the B-site cations in cobalt-substituted $SrTiO_3$, and we show experimentally that oxygen-deficient polycrystalline and single crystal thin films of $SrTi_{0.70}Co_{0.30}O_{3-\delta}$ can exhibit mixed Co valence states giving rise to room temperature ferromagnetism. The experimental and modeling results suggest a class of multiferroic materials with properties controlled by their oxygen stoichiometry. There has been intense interest in voltage-controlled magnetism and other magnetoelectric phenomena that can occur in multiferroic oxide thin films [1–4]. For integrated memory and logic applications, materials with significant room temperature (RT) polarization and magnetization, as well as coupling between the magnetic and ferroelectric order parameters, are desirable. Out of the wide range of multiferroic materials studied, many of them are multiferroic only at cryogenic temperatures [5–9], are antiferromagnetic at RT [10–12], or exhibit high magnetic field or voltage bias points [13]. $Bi_{0.75}Sr_{0.25}FeO_3$ [10] and $BiFeO_3$ and its derivatives [11,12] are both antiferromagnetic and strongly ferroelectric. Significant RT multiferroicity and low-field magnetoelectric coupling has been observed in $Sr_4Co_2Fe_{36}O_{60}$ [14], $Sr_3Co_2Fe_{24}O_{41}$ [15] and Y-type $BaSrCo_{2-x}Zn_xFe_{11}AlO_{22}$ ceramics [16], and RT electric control of magnetism has been achieved in $SrCo_2Ti_2Fe_8O_{19}$ [17]. $Sr_3Co_2Fe_{24}O_{41}$, a ferroelectric hexaferrite, has a spiral spin structure and is magnetoelectric at moderate fields [15]. Magnetoelectric coupling has been observed in oxygen-deficient ferroelectric domain walls in $PbTiO_3$ [18] and in PZTFT ($(PbZr_{0.53}Ti_{0.47}O_3)_{0.6}$-$(PbFe_{0.5}Ta_{0.5}O_3)_{0.4}$) [19], and Co-doped TiO_2 exhibited ferromagnetism [20] and magnetoelectric coupling [21] at RT. Despite these advances, obtaining a material which is both magnetic and ferroelectric at room temperature remains an important challenge. A path towards RT magnetoelectrics may exist by control of both magnetic substitution and defect engineering in perovskites. Substitutional doping of magnetic cations into the B sites of perovskite films has been shown to induce intrinsic RT magnetism without metallic precipitates, as in the case of $Sr(Ti,Co)O_{3-\delta}$ [22–24], (La or Ba,Sr)$(Ti,Co)O_{3-\delta}$ [25,26], and $Sr(Ti,Fe)O_{3-\delta}$ [23,27]. Perovskites can support large oxygen deficiency [28] and it is known that oxygen vacancies and other defects promoted by vacancies affect the electronic properties by introducing lattice distortion, lowering symmetry, and stabilizing mixtures of cation valence states. For example, ferroelectricity in $SrTiO_3$ (STO) is promoted by strain [29,30] and Sr-vacancy defects [31–33]; magnetism is promoted by oxygen vacancies [34–38]; and oxygen vacancies were also found to strongly affect mobility and resistivities in $SrTiO_3$. $SrMnO_3$ films exhibit strain-induced coupling of electrical polarization and defects [39]. Oxygen vacancies were found to interact with ferroelectric domain walls to cause magnetism in $PbTiO_3$ thin films [18]. Resistive switching dynamics and polarization in $BaTiO_3$ were controlled by varying oxygen vacancy concentrations [40], and polarization gradients were created across multiferroic $SrMnO_3$ films by introducing oxygen vacancy gradients [41]. The combined effects of strain and oxygen vacancies on resistivity and magnetism were also shown for $SrCoO_x$ thin films [42]. Changing oxygen partial pressure (vacancy concentrations) alter the strain by lowering the symmetry and alter the multiferroic coupling coefficient in $(BaTiO_3)_{1-x}(BiFeO_3)_x$ films [43]. Oxygen vacancies affected both ferroelectricity[44] and magnetism [45] in $YMnO_3$. One may therefore intuit that the simultaneous substitution of magnetic B-site ions, introduction of oxygen off-stoichiometry and strain in a perovskite could trigger both ferroelectricity and magnetism, and presumably coupling between them. Here, we predict through density functional theory (DFT) calculations that both magnetism and ferroelectricity can coexist in oxygen-deficient $SrTi_{1-x}Co_xO_{3-\delta}$ (STCo) with $x = 0.25$ arising from the interplay between oxygen vacancies, B-site ions and structural distortions of the material, suggesting a route to multiferroicity in a class of oxides. We experimentally support several key ideas of this prediction with measurements on $SrTi_{0.70}Co_{0.30}O_{3-\delta}$ (STCo30) deposited as single crystal films on STO or as polycrystalline films on Si and SiO_2, which demonstrate the presence of mixed-valence Co and RT magnetism, though ferroelectricity was not observed above 77 K. The DFT modeling predicts magnetic and polarization order parameters in oxygen-deficient STCo, and identifies the complex V_O interactions that lead to magnetism and polarized charge in this material. We find that both magnetism and ferroelectricity are intrinsically derived from the same structural and electronic features, i.e., the non-centrosymmetrically-distributed spin and charges around the ions. This observation presents a general feature that may be used to identify and manipulate other multiferroic systems.

1. Scott, J. F. Room-temperature multiferroic magnetoelectrics. *NPG Asia Mater.* 5, e72 (2013). 2. Martin, L. W., Chu, Y.-H. & Ramesh, R. Advances in the growth and characterization of magnetic, ferroelectric, and multiferroic oxide thin films. *Mater. Sci. Eng. R Reports* 68, 89–133 (2010). 3. Ramesh, R. & Spaldin, N. a. Multiferroics: progress and prospects in thin films. *Nat. Mater.* 6, 21–9 (2007). 4. Eerenstein, W., Mathur, N. D. & Scott, J. F. Multiferroic and magnetoelectric materials. *Nature* 442, 759–765 (2006). 5. Matsubara, M. *et al.* Magnetoelectric domain control in multiferroic $TbMnO_3$. *Science* 348, 1112–1115 (2015). 6. Kimura, T. *et al.* Magnetic control of ferroelectric polarization. *Nature* 426, 55–58 (2003). 7. Lee, J. H. *et al.* Epitaxial stabilization of a new multiferroic hexagonal phase of $TbMnO_3$ thin films. *Adv. Mater.* 18, 3125–3129 (2006). 8. Lee, S. *et al.* Direct observation of a coupling between spin, lattice and electric dipole moment in multiferroic $YMnO_3$. *Phys. Rev. B - Condens. Matter Mater. Phys.* 71, 1–4 (2005). 9. Lee, J. H. *et al.* A strong ferroelectric ferromagnet created by means of spin-lattice coupling. *Nature* 466, 954–8 (2010). 10. Kundys, B., Maignan, A., Martin, C., Nguyen, N. & Simon, C. Magnetic field induced ferroelectric loop in $Bi_{0.75}Sr_{0.25}FeO_3$. *Appl Phys Lett* 92, 112905 (2008). 11. Wang, J. *et al.* Epitaxial $BiFeO_3$ Multiferroic Thin Film Heterostructures. *Science.* 299, 1719– 1722 (2003). 12. Lee, D., Kim, M. G., Ryu, S., Jang, H. M. & Lee, S. G. Epitaxially grown La-modified BiFeO3 magnetoferroelectric thin films. *Appl. Phys. Lett.* 86, 1–3 (2005). 13. Hamasaki, Y. *et al.* Epitaxial growth of metastable multiferroic $AlFeO_3$ film on $SrTiO_3$ (111) substrate. *Appl. Phys. Lett.* 104, 0–5 (2014). 14. Okumura, K. *et al.* Magnetism and magnetoelectricity of a U-type hexaferrite $Sr_4Co_2Fe_{36}O_{60}$. *Appl. Phys. Lett.* 98, 1–4 (2011). 15. Kitagawa, Y. *et al.* Low-field magnetoelectric effect at room temperature. *Nat. Mater.* 9, 797–802 (2010). 16. Hirose, S., Haruki, K., Ando, A. & Kimura, T. Mutual control of magnetization and electrical polarization by electric and magnetic fields at room temperature in Y-type $BaSrCo_{2-x}Zn_xFe_{11}AlO_{22}$ ceramics. *Appl. Phys. Lett.* 104, (2014). 17. Wang, L. *et al.* Electric control of magnetism at room temperature. *Sci. Rep.* 2, 1–5 (2012). 18. Xu, T., Shimada, T., Araki, Y., Wang, J. & Kitamura, T. Multiferroic Domain Walls in Ferroelectric $PbTiO_3$ with Oxygen Deficiency. *Nano Lett.* 16, 454–458 (2015). 19. Evans, D. M. *et al.* Magnetic switching of ferroelectric domains at room temperature in multiferroic PZTFT. *Nat. Commun.* 4, 1534 (2013). 20. Matsumoto, Y. *et al.* Room-Temperature Ferromagnetism in Transparent Transition Metal – Doped Titanium Dioxide. *Science.* 291, 854–857 (2001). 21. Yamada, Y. *et al.* Electrically Induced Ferromagnetism at Room Temperature in Cobalt-Doped Titanium Dioxide. *Science* 332, 1065 (2011). 22. Florez, J. M. *et al.* First-principles insights on the magnetism of cubic $SrTi_{1-x}Co_xO_{3-\delta}$. *Appl. Phys. Lett.* 100, (2012). 23. Kim, D. H., Bi, L., Jiang, P., Dionne, G. F. & Ross, C. A. Magnetoelastic effects in $SrTi_{1-x}M_xO_3$ (M = Fe, Co, or Cr) epitaxial thin films. *Phys. Rev. B* 84, 1–9 (2011). 24. Bi, L., Kim, H. S., Dionne, G. F. & Ross, C. A. Structure, magnetic properties and magnetoelastic anisotropy in epitaxial $Sr(Ti_{1-x}Co_x)O_3$ films. *New J. Phys.* 12, (2010). 25. Fix, T. *et al.* Ferromagnetism in Co-doped $(La,Sr)TiO_3$. *New J. Phys.* 11, 073042 (2009). 26. Luo, L. B. *et al.* Room-temperature ferromagnetism in the Co-doped $Ba_{0.5}Sr_{0.5}TiO_3$ thin films. *Appl. Phys. Lett.* 92, 232507 (2008). 27. Da Silva, L. F. *et al.* Insight into the effects of fe addition on the local structure and electronic properties of $SrTiO_3$. *J. Phys. Chem. C* 118, 4930–4940 (2014). 28. Jeen, H. *et al.* Reversible redox reactions in an epitaxially stabilized $SrCoO_x$ oxygen sponge. *Nat. Mater.* 12, 1057–63 (2013). 29. Haeni, J. H.

et al. Room-temperature ferroelectricity in strained $SrTiO_3$. *Nature* 430, 758–761 (2004). 30. Warusawithana, M. P. *et al.* A Ferroelectric Oxide Made Directly on Silicon. *Science.* 324, 367–370 (2009). 31. Lee, D. *et al.* Emergence of room-temperature ferroelectricity at reduced dimensions. *Science.* 349, 1314–1317 (2015). 32. Kim, Y. S. *et al.* Observation of room-temperature ferroelectricity in tetragonal strontium titanate thin films on $SrTiO_3$ (001) substrates. *Appl. Phys. Lett.* 91, 2005–2008 (2007). 33. Yang, F. *et al.* Room-temperature ferroelectricity of $SrTiO_3$ films modulated by cation concentration. *Appl. Phys. Lett.* 107, 0–4 (2015). 34. Rice, W. D. *et al.* Persistent optically induced magnetism in oxygen-deficient strontium titanate. *Nat. Mater.* 13, 481–7 (2014). 35. Zhang, Y., Wang, J., Sahoo, M., Shimada, T. & Kitamura, T. Mechanical control of magnetism in oxygen deficient perovskite $SrTiO_3$. *Phys. Chem. Chem. Phys.* 17, 27136–27144 (2015). 36. Lopez-Bezanilla, A., Ganesh, P. & Littlewood, P. B. Magnetism and metal-insulator transition in oxygen-deficient $SrTiO_3$. *Phys. Rev. B* 92, 115112 (2015). 37. Lee, H. N., Seo, S. S. A., Choi, W. S. & Rouleau, C. M. Growth control of oxygen stoichiometry in homoepitaxial $SrTiO_3$ films by pulsed laser epitaxy in high vacuum. *Sci. Rep.* 1–7 (2016). doi:10.1038/srep19941 38. Huang, W., Nechache, R., Li, S., Chaker, M. & Rosei, F. Electrical and Optical Properties of Transparent Conducting p -Type $SrTiO_3$ Thin Films. *J. Am. Ceram. Soc.* 99, 226–233 (2016). 39. Becher, C. *et al.* Strain-induced coupling of electrical polarization and structural defects in $SrMnO_3$ films. *Nat. Nanotechnol.* 10, 661–665 (2015). 40. Li, M. *et al.* Controlling Resistance Switching Polarities of Epitaxial $BaTiO_3$ Films by Mediation of Ferroelectricity and Oxygen Vacancies. *Adv. Electron. Mater.* 1: 1500069 (2015). doi:10.1002/aelm.201500069 41. Guzmán, R. *et al.* Polar-Graded Multiferroic $SrMnO_3$ Thin Films. *Nano Lett.* 16, 2221–2227 (2016). doi:10.1021/acs.nanolett.5b04455 42. Petrie, J. R. *et al.* Strain Control of Oxygen Vacancies in Epitaxial Strontium Cobaltite Films. *Adv. Funct. Mater.* 26, 1563–1563 (2016). doi:10.1002/adfm.201504868 43. Lorenz, M. *et al.* Correlation of high magnetoelectric coupling with oxygen vacancy superstructure in epitaxial multiferroic $BaTiO_3$-$BiFeO_3$ composite thin films. *Materials (Basel).* 9, 44 (2016). 44 Shaobo Cheng, Menglei Li, Qingping Meng, Wenhui Duan, Y. G. Zhao, X. F. Sun, Yimei Zhu, and Jing Zhu, Electronic and crystal structure changes induced by in-plane oxygen vacancies in multiferroic $YMnO_3$, *Phys. Rev. B* 93, 054409 (2016) 45 Shaobo Cheng, Menglei Li, Shiqing Deng, Shanyong Bao, Peizhe Tang, Wenhui Duan, Jing Ma, Cewen Nan, and Jing Zhu, Manipulation of Magnetic Properties by Oxygen Vacancies in Multiferroic $YMnO_3$, *Adv. Funct. Mater.* 26, 3589–3598 (2016)

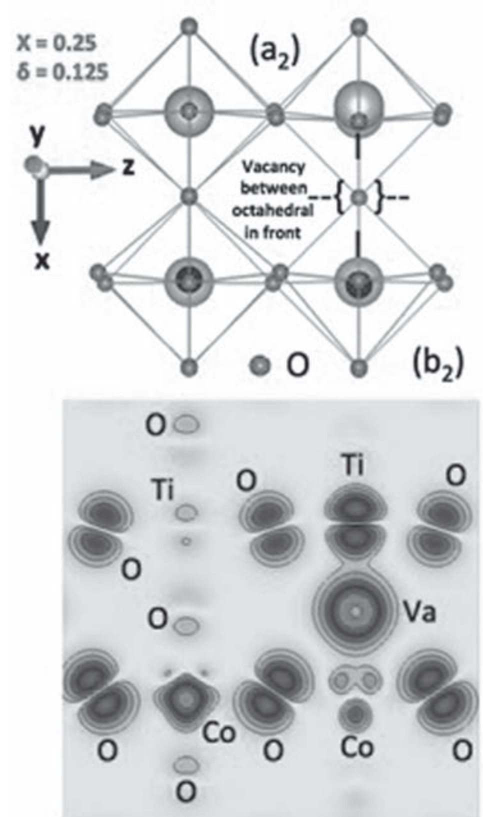

BW-10. Magnetoelectric characteristics in three–phase magnetostrictive/piezoelectric composites with different high permeability materials.

L. Chen[1] and Y. Wang[2]
1. Key Lab of Computer Vision and IntelligentInformation System, Chongqing University of arts and sciences, ChongQing, China; 2. School of Electronic Information and Electric Engineering, Shanghai Jiao Tong University, Shanghai, China

The magnetostrictive/piezoelectric laminate composites consisting of Ni, Permendur, Metglas or Terfenol-D as magnetostrictive phase and PVDF, PZT or PMN-PT as piezoelectric phase demonstrate strong magnetoelectric effect due to the product property, which provide effective conversion between electric field energy and magnetic field energy. The superior performances make them potential applications in novel multifunctional devices, such as multiple-state storages, energy harvesting transducers, tunable microwave devices, magnetic field sensors, and transformers. Recently, it has been found that the magnetic permeability for magnetostrictive material directly affects its effective piezomagnetic coefficient and corresponding magnetoelectric effect. Combining traditional magnetostrictive/piezoelectric laminate composites and high permeability materials can significantly enhance the effective permeability, which produce the self-biased ME effect. However, in previous reports, most researchers have focused on the preparation method and testing composite structure consisting of specific high permeability materials, which is lack of comparisons and analysis for composites with different high permeability material. Actually for the practical applications of magnetoelectric composites, it is both physically interesting and technologically important to systematically investigate the ME composites with different high permeability materials. Hence in this study, by bonding three different high permeability materials FeCuNbSiB, FeSiB and CoNiFeSiB into Terfenol-D/PZT laminate, the FeCuNbSiB/Terfenol-D/PZT, FeSiB/Terfenol-D/PZT, and CoNiFeSiB/Terfenol-D/PZT laminate composites are prepared. The influences of the different high permeability materials on the ME characteristics of the composites have been investigated, as shown in Fig.1. On one hand, the experimental results demonstrate that the maximum zero-bias ME voltage coefficient for FeCuNbSiB/Terfenol-D/PZT achieves 1.105V/Oe due to the larger magnetic permeability of FeCuNbSiB, which is ~2 times higher than that of CoNiFeSiB/Terfenol-D/PZT and ~ 3 times higher than that of Terfenol-D/PZT. On the other hand, the maximum ME voltage coefficient for FeSiB/Terfenol-D/PZT achieves 2.108V/Oe at low bias field H_{dc}=175Oe due to the higher saturation magnetostriction of FeSiB, while the maximum ME voltage coefficients for Terfenol-D/PZT, CoNiFeSiB/Terfenol-D/PZT, FeCuNbSiB/Terfenol-D/PZT achieve 1.893V/Oe at H_{dc}=510Oe, 1.742V/Oe at H_{dc}=439Oe, 2.065V/Oe at H_{dc}=598Oe, respectively. Correspondingly, the study indicates both the saturation magnetostriction and magnetic permeability of high permeability materials have noticeable influences on the ME characteristics of the laminate composites, which should be taken into consideration when selecting the suitable material.

[1] D. T. H. Giang, P. A. Duc, N. T. Ngo, N. T. Hien, and N. H. Duc, "Spatial angular positioning device with three-dimensional magnetoelectric sensors," Rev. Sci. Instrum., vol. 83, no. 9, p. 095006, 2012. [2] D. T. H. Giang, P. A. Duc, N. T. Ngoc, and N. H. Duc,"Geomagnetic sensors based on metglas/PZT laminates," Sens.Actuators A. Phys., vol. 179, pp. 78–82, Jun. 2012.

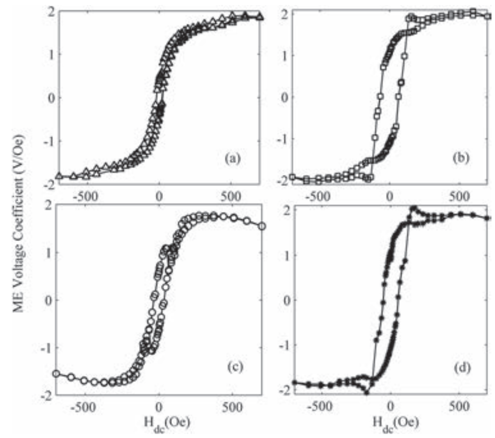

Fig. 1. ME voltage coefficients as a function of H_{dc} for (a)Terfenol-D/PZT,(b)FeCuNbSiB/Terfenol-D/PZT,(c)CoNiFeSiB/Terfenol-D/PZT,(d) FeSiB/Terfenol-D/PZT.

BW-11. High-Performance Photovoltalic Readable Ferroelectric Non-volatile Memory Based on La Doped $BiFeO_3$ Films.

D. Li[1], D. Zheng[1], C. Jin[1] and H. Bai[1]
1. Tianjin University, Tianjin, China

Abstract: To seek the approach for nonvolatile storage, the ferroelectric dependent transport properties and ferroelectric switchable photovoltaic effects have been widely studied in recent years [1-3]. However, the solutions for realizing high performance electrical writing and optical reading are still limited. As one of the most potential lead-free ferroelectric materials and the unique singular room-temperature multiferroic material, $BiFeO_3$ (BFO) has a very large remnant ferroelectric polarization [4]. Moreover, BFO is particular for its relatively narrow band gap of about 2.7 eV, which supports the photovoltaic effect in the visible range [5]. To optimize the polarization related device performance, it is essential to reach the balance between ferroelectricity and conductivity. It has been demonstrated that the 10% doping of La at the Bi site can effectively avoid the formation of Bi vacancy and improve the crystallization and stabilize the crystal structure [6]. Therefore, $La_{0.1}Bi_{0.9}FeO_3$ (LBFO) was chosen as the ferroelectric layer for its smaller leakage current and lower coercivity compared with BFO. Epitaxial LBFO films with $SrRuO_3$ bottom electrodes were fabricated on $SrTiO_3$ (001) substrates by magnetron sputtering. The LBFO thin films exhibit strong ferroelectric properties (Figure 1a). Electric field controlled nonvolatile reversible resistance switchings (Figures 1b and 1c) and switchable photovoltaic effects (Figure 2a) have been observed in Pt/LBFO/SRO heterostructures, which have been proved to be modulated by the ferroelectric reversal. With 88-nm-thick LBFO layer, the observed room temperature pulsed-read resistance switching ratio can reach 10^5 % magnitude by applying ±2.7 V pulse voltages (Figure 1d). Besides, Figure 2b shows the ferroelectric switchable photovoltaic effect in the visible wavelength range, which exhibits a large tunable open-circuit photovoltage (V_{OC}) from –75 to –330 mV. The switching mechanisms in resistance and photovoltaic effects can be attributed to the polarization reversal modulated interfacial barriers and deep trap states. Our result has demonstrated a high-performance photovoltalic readable ferroelectric nonvolatile memory, which should be helpful in designing novel multifunctional memory devices with high manipulating speed, high density and lower power assumption. Acknowledgements: Financial support from the National Natural Science Foundation of China (11434006, 51772207, 51272174).

[1] A. Tsurumaki, et al. Adv. Funct. Mater. 2012, 22, 1040-1047. [2] I. Pintilie, et al. ACS Appl. Mater. Interfaces 2014, 6, 2929-2939. [3] T. Choi, et al. Science 2009, 324, 63. [4] J. Wang, et al. Science 2003, 299, 1719–1722. [5] M. Yang, et al. Appl. Phys. Lett. 2017, 110, 183902. [6] Y. Chu, et al. Nano Lett. 2009, 9, 1726–1730.

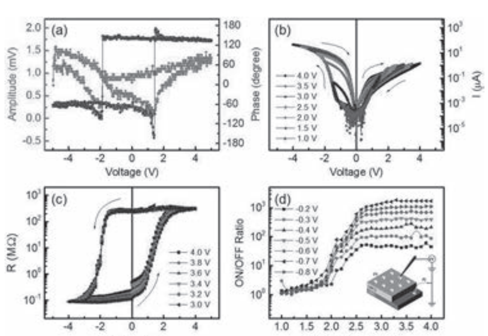

Fig. 1. (a) PFM ramp curves (phase and amplitude) for the LBFO (88 nm)/SRO heterostructure. (b) and (c) Room temperature *J-V* curves and pulsed-read *R-V* loops of the corresponding heterostructure with the scanning directions illustrated by arrows. (d) Pulse voltage amplitude related ON/OFF ratios measured by increasing the read voltages. Inset of (d) shows the device architecture of the Pt/LBFO/SRO heterostructures.

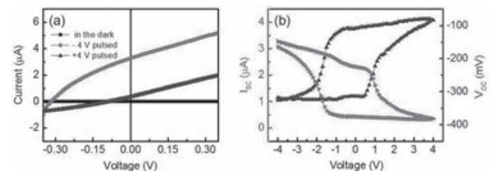

Fig. 2. (a) *I-V* curves of the Pt/LBFO/SRO/STO heterostructures in the dark and after –4 V and +4 V pulses poling under the illumination of 200 mW/cm². (b) Pulsed-read I_{SC} (blue) and V_{OC} (red) loops under the illumination.

Session BR
MAGNETIC OXIDE AND ALLOY FILMS
(Poster Session)

Jiafeng Feng, Chair
Institute of Physics, Chinese Academy of Sciences, Beijing, China

BR-01. Enhancement of magnetoresistance by cobalt substitution in double exchange ferromagnets: $Pr_{0.6}Sr_{0.4}Mn_{1-x}Co_xO_3$ (x = 0, 0.05 and 0.1).

A. Chanda[1] and R. Mahendiran[1]
1. Department of Physics, National University of Singapore, Singapore

The perovskite manganites having the general formula $R_{1-x}A_xMnO_3$ [R = La^{3+}, Pr^{3+}, etc., and, A = Sr^{2+}, Ba^{2+}, etc.] have enticed considerable attention during the last three decades because of colossal negative magnetoresistance and mutiferroicity.[1,2] The parent compound $RMnO_3$ containing Mn^{3+}:$t_{2g}^3 e_g^1$ ion is an antiferromagnetic insulator but the introduction of charge carrier (e_g hole in Mn^{4+}:t_{2g}^3) by Sr^{2+} substitution for R (= La^{3+}, Pr^{3+}, Nd^{3+}) induces ferromagnetism and also metallic like resistivity for x = 0.2- 0.5.[3] The simultaneous occurrence of ferromagnetism and metallic resistivity is understood in terms of Zener's double exchange interaction [4]. On the other hand, cobaltites of the formula $RCoO_3$ are nonmagnetic insulator at low temperatures but they also show ferromagnetism and metallic resistivity when holes (Co^{4+}) are introduced by partial substitution of Sr^{2+} for R^{3+} ion for x = 0.2-0.5 [5]. The occurrence of ferromagnetism in hole-doped cobaltites is can be understood without recourse to the Zener's double exchange interaction but by Stoner's type - band ferromagnetism [6]. Hole-doped cobaltites show much smaller magnetoresistance (5-7% for H = 7 T) at the ferromagnetic transition temperature (T_C) compared to colossal magnetoresistance (= 50-100 %) for the same field at T_C [7]. Hence, it will be interesting to investigate the effect of Co substitution for Mn on magnetism, electrical resistivity and magnetoresistance. Zero-field cooled and field-cooled magnetization and *ac* susceptibility measurements in $La_{0.7}Sr_{0.3}Mn_{1-x}Co_xO_3$ were interpreted in terms spin glass (SG) or cluster glass (CG) state that evolves with Co substitution for the doping range x =0.3-0.9.[8]. Magnetic and magnetoresistance in rare earth cobaltites other than R = La are still scarce. Tryonchuck *et al*.,[9] investigated $Pr_{0.5}Sr_{0.5}Mn_{1-x}Co_xO_3$ by neutron diffraction and revealed that the magnetic ground for the compounds with composition range 0.1 £ x £ 0.25 is SG or CG state, whereas, a new inhomogeneous FM state appears for higher Co doped compounds. While $Pr_{0.5}Sr_{0.5}MnO_3$ shows paramagnetic to ferromagnetic transition (T_C = 250 K) followed by antiferromagnetic transition. On the other hand, $Pr_{0.6}Sr_{0.4}MnO_3$ undergoes only a temperature driven PM to FM transition near room temperature (T_C = 305 K), however, a first order magneto-structural transition occurs at a still lower temperature (T_{MST} = 86 K) which causes a step-like decrease in the temperature dependence of magnetization[10]. Here, we investigate the effect of Co substitution on magnetism, electrical resistivity and magnetoresistance in $Pr_{0.6}Sr_{0.4}Mn_{1-x}Co_xO_3$ (x = 0 to 0.1). We observed that the long range FM order persists for low doping (x = 0.05) with a radical downshift in T_C (260 K). Surprisingly, the magnetostructural transition of the parent compound shifts down to low temperature with 5% Co doping, but disappears for 10% doping. A decrease in magnetization as well as increase in electrical resistivity (r) [from ~0.055 W-cm for x = 0.0 to ~ 0.15 W-cm for x = 0.1 at room temperature] with Co doping have been observed, which clearly indicates destabilization of ferromagnetic DE interaction. For both the compounds x = 0.0 and 0.05, r shows a clear peak at their respective T_C, whereas, such feature is absent in x = 0.1 (Fig. 1. (a)-(c)). The temperature dependent magnetoresistance (MR), defined as MR = [r (7T) - r (0T)]/r (0T) x 100 %, also shows a peak at T_C for both the compounds x = 0.0 and 0.05. However, the MR for x = 0.1 does not show a peak at T_C but a huge enhancement in MR at low temperatures occurs with increasing Co doping [from 45 % for x = 0.0 to 65 % for x = 0.1 at 10 K under 7 T magnetic field] (Fig. 1. (d) and (e)). The origin of large MR at low temperatures for Co doped compounds will be explained in the framework of spin dependent transport between neighbouring FM grains (tunneling magnetoresistance). Acknowledgement: R. M. thanks the Ministry of Education, Singapore for supporting this work (R144-000-373-112).

[1] Y. Tokura, Reports on Progress in Physics 69, 797 (2006). [2] N. A. Spaldin, S.-W. Cheong, and R. Ramesh, Phys. Today 63, 38 (2010). [3] E. Wollan and W. Koehler, Physical Review 100, 545 (1955). [4] C. Zener, Physical Review 82, 403 (1951). [5] G. Jonker and J. Van Santen, Physica 19, 120 (1953). [6] J. B. Goodenough, Journal of Physics and Chemistry of Solids 6, 287 (1958). [7] R. Mahendiran and A. Raychaudhuri, Physical Review B 54, 16044 (1996). [8] X. G. Chen *et al.*, Journal of Applied Physics 116, 103907 (2014). [9] I. Troyanchuk, A. Chobot, N. Tereshko, O. Mantytskaya, and E. Efimova, Physics of the Solid State 53, 1340 (2011). [10] D. Maheswar Repaka, T. Tripathi, M. Aparnadevi, and R. Mahendiran, Journal of Applied Physics 112, 123915 (2012).

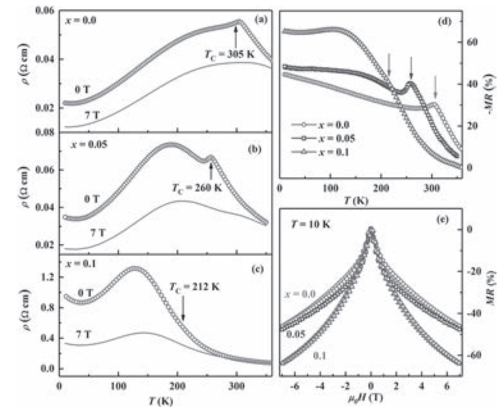

Fig. 1. (a), (b) and (c): Temperature dependent resistivity of the compounds x = 0.0, 0.05 and 0.1, respectively, under both 0 and 7 T magnetic fields, (d) and (e) temperature and magnetic field dependence of magnetoresistance, respectively of those compounds.

BR-02. Increased Curie temperature induced by orbital ordering in $La_{0.67}Sr_{0.33}MnO_3/BaTiO_3$ superlattices.

Z. Quan[1], F. Zhang[1], B. Wu[1], G. Zhou[1] and X. Xu[1]
1. Shanxi Normal University, Linfen, China

A common observation in perovskite manganite films is that the Curie temperature (T_C) decreases with the reduction of film thickness, which limits their potential for spintronic devices, such as field-effect transistors, magnetic tunnel junctions, and nonvolatile magnetic memory [1,2]. This is the so-called "dead layer" effect. Recently, many efforts have been made to increase the T_C of ultrathin perovskite manganite films by superlattice interface control and precise strain tuning [3]. $La_{0.67}Sr_{0.33}MnO_3$ (LSMO) films have drawn increasing interest due to their colossal magnetoresistance effect, high T_C, and half metallicity [4,5]. First principle calculations indicate that the T_C of LSMO films can be increased by more than an order of magnitude by controlling orbital ordering in LSMO/$BaTiO_3$(BTO) superlattices [6]. Here, we synthesized (001) oriented $[LSMO(3u.c.)/BTO(3u.c.)]_n$ superlattices (denoted as SL-n, where n = 3, 4, 10 is the number of cycles and u.c. is the shortening of unit cells) using pulsed laser deposition (PLD) and reveal the relationship between the origin of high T_C and manganese e_g orbital occupancy through the use of x-ray linear dichroism (XLD) measurements. It is found that the regular intercalation of BTO layers between LSMO layers can effectively enhance ferromagnetic order and increases the T_C of ultrathin LSMO films due to the orbital occupation of $e_g(x^2–y^2)$ in Mn^{3+} ions. Figure 1(a) shows the cross-sectional high-resolution transmission electron microscopy (HRTEM) of the SL-3 sample on a (001) oriented $SrTiO_3$ substrate, endorsing high quality epitaxial growth of LSMO/BTO superlattice. The image shows atomically sharp interfaces between the LSMO and BTO layers highlighted by red arrows. There is no obvious interdiffusion at the interfaces, and the LSMO and BTO layers are fully strained to the $SrTiO_3$ substrates. The temperature-dependent magnetization for SL-n films with n = 3, 4, 10, as well as a LSMO(3) sample with the thickness of 3 u.c., are shown in Fig. 1(b). The T_C of the superlattices is significantly improved compared to the LSMO(3) film, of which T_C is around 45 K (see the inset). For the SL-10 sample, the T_C reaches a maximum value of $T_C \sim 310$ K. For (001) oriented LSMO films, supposing that $e_g(x^2–y^2)$ is occupied in Mn^{3+} ions, the intralayer double exchange between Mn^{3+} and Mn^{4+} will become very strong and the interlayer double exchange will decline in strength. This can result in a high T_C of thin film samples. In our LSMO/BTO films, the lattice parameter of the BTO (a = 0.397–0.403 nm from a tetragonal to rhombohedral phase) is larger than that of LSMO (a = 0.387 nm), resulting in a ~ 4% lattice mismatch. The LSMO layers are in a high tensile strain state ($c < a$), causing occupancy in the $e_g(x^2–y^2)$ orbital. We have confirmed the manganese e_g orbital occupancy in relation to XLD measurements, which is an extremely sensitive probe for the electronic structure and the d orbital (e_g) electron occupancy. Fig. 1(c-d) show the XLD spectra of Mn, as well as the in-plane and out-of-plane x-ray absorption spectroscopy (XAS) spectra, of SL-3 and SL-10 samples. The area under the XLD curve at the L_2-edge peak (DXLD) representing the difference between the relative occupancies of the $e_g(x^2–y^2/3z^2–r^2)$ orbitals, is negative, implying a preferential occupancy of the $e_g(x^2–y^2)$ orbital. Thus, the interfacial tensile strain induces in-plane orbital ordering of the $e_g(x^2–y^2)$ orbital occupancy in the LSMO layers, achieving in-plane double exchange ferromagnetic coupling between Mn^{3+} and Mn^{4+} ions with high T_C. Our findings create new opportunities for the design and control of magnetism in artificial structures and offer considerable potential for applications in novel magnetoelectronic applications, including nonvolatile magnetic memory working far above room temperature.

1. S. Thiel, G. Hammerl, A. Schmehl, C. W. Schneider, and J. Mannhart, *Science* 2006, 313:1942. 2. L. E. Hueso, J. M. Pruneda, V. Ferrari, G. Burnell, and J. P. Valdes-Herrera *et al.*, *Nature* 2007, 445:410. 3. J. X. Ma, X. F. Liu, T. Lin, G. Y. Gao, J. P. Zhang, W. B. Wu, X. G. Li, and J. Shi, *Phys Rev B* 2009, 79:174424. 4. M. Bowen, M. Bibes, A. Barthelemy, J. P. Contour, A. Anane, Y. Lemaitre, and A. Fert, *Appl Phys Lett* 2003, 82:233. 5. Z. Quan, B. Wu, F. Zhang, G. Zhou, J. Zang, and X. Xu, *Appl Phys Lett* 2017, 110:072405. 6. A. Sadoc, B. Mercey, C. Simon, D. Grebille, W. Prellier, M. B. Lepetit, *Phys Rev Lett* 2010, 104:046804.

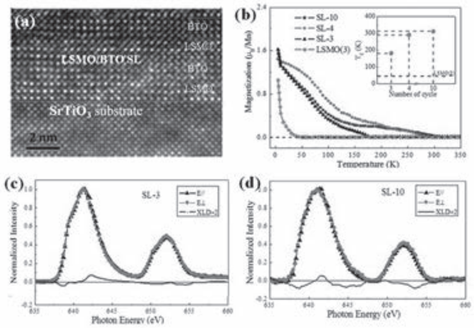

Fig. 1. (a) A cross-section HRTEM image of the SL-3 sample with the interfaces between the LSMO and BTO layers indicated by red arrows. (b) Temperature-dependent magnetization of the SL-n samples (n = 3, 4, 10) and an ultrathin LSMO film with a 3 u.c. thickness. The inset shows cycle number dependence on the T_C. (c and d) Normalized XAS and XLD curves for samples SL-3 and SL-10 measured at room temperature.

BR-03. Electrical Conduction Mechanism for Investigation of Charge Ordering in $Nd_{0.5}Ca_{0.5}MnO_3$.

A. Swain[1] and V. Gorige[1]
1. School of Physics, University of Hyderabad, Hyderabad, India

Colossal magnetoresistance in manganites has been extensively investigated for the last two decades. However, the phenomenon of charge ordering (CO) and its consequent effects do not seem to have been fully explored [1]. The parent manganite, $LnMnO_3$ (Ln = rare earth cation) is an antiferromagnetic-insulator (AFMI) due to superexchange interaction with nearest neighbor Mn^{3+} ions. The partial substitution of divalent cation at Ln site results in two valence state of Mn (i.e. Mn^{3+} and Mn^{4+}) and the physical properties are controlled by Mn^{3+}/Mn^{4+} ratio. Particularly, the equal concentration of Mn^{3+} and Mn^{4+} in manganites leads to localization of conduction electron by resulting in AFMI behavior, called charge ordering (CO) [2]. The destabilization of CO by some means may lead to a ferromagnetic-metal (FMM) behavior with huge magnetoresistance (MR) and mostly this can be achieved by applied magnetic field, which is power consuming process [3]. There is a quest for alternative approaches to suppress the CO other than the magnetic field for low power consumption. In view of this, an attempt was made to demonstrate the suppression of CO by reducing particle size in $Nd_{0.5}Ca_{0.5}MnO_3$ (NCMO) manganite system. Even though the magnetic and electrical properties are strongly correlated in these manganites, unfortunately, there is no comprehensive study on CO suppression by analyzing electrical transport mechanism. In this work, we are presenting a detailed investigation of the effect of particle size as well as the applied magnetic field on CO behavior in NCMO manganite system by studying electrical transport properties. The samples with different particle sizes (20-400 nm) were synthesized by using a citrate-based sol-gel method by sintering at different temperatures (700-1350 °C). The samples were characterized by physicochemical characterization techniques. The electrical transport measurements were carried out by using PPMS (Quantum Design) in an applied magnetic field ranging from 0-12 T. The electrical resistivity data were analyzed by considering appropriate theoretical models in different temperature regimes. The phase purity of all the samples was confirmed by x-ray diffraction (XRD) and the Rietveld refinement of the data reveals that all the samples crystallize in orthorhombic structure with '*Pnma*' space group. The crystallite size of the samples was estimated from full-width at half-maxima of the XRD peaks by adopting Williamson Hall method. In addition, the grain and particle sizes were obtained by scanning and transmission electron microscopy techniques, respectively. The crystallite, grain, and particle sizes were found to increase with increasing sintering temperature. Since the samples crystallized in orthorhombic structure, it was expected that the variation in particle size might cause changes in orthorhombic strain (OS), which may result in considerable changes in physical properties [1]. The estimated OS (*ac*-plane and along *b*-axis) of the unit cell versus particle size plot shows a significant change around 50 nm, which can be attributed to the CO crossover in these samples. In fact, the CO crossover is in agreement with data obtained from temperature dependent magnetization, which appears as a broad hump (T_{CO}) ~ 240 K [4]. As the charge and spin degrees of freedom of electrons are strongly coupled in these systems, the temperature dependent electrical resistivity (ρ-T) is expected to show CO signatures around T_{CO}. Unfortunately, the ρ-T data is not showing any anomaly around T_{CO}. It is known that the activation energy of charge carriers is more sensitive as compared to resistivity. However, surprisingly, when the temperature-dependent activation energy curves were plotted, a hump around 240 K was noticed signifying CO behavior. Interestingly, it is getting suppressed for the samples with a particle size below 50 nm and with the applied magnetic fields above 4 T. To understand more clearly CO crossover as a function of particle size as well as applied fields, the ρ-T curves were obtained in presence of magnetic fields. The FMM behavior along with metal-insulator transition (T_P) started appearing in the applied field ≥ 4 T, which signifies the CO melting. The ρ-T data around T_{CO} was fitted with Small Polaron Hopping (SPH) and Variable Range Hopping (VRH) models in different temperature regimes. Well above the T_P, the data were fitted with SPH model and the polaron activation energy was calculated. Further, just above T_P the ρ-T data was fitted with VRH model and charge carrier density values were estimated. The variation of the obtained parameters with particle size and applied magnetic fields were showing significant change around 50 nm as well as the applied fields ~ 4 T. Further, field-induced FMM behavior in these samples was analyzed in terms of grain/domain boundary, electron-electron, and electron-magnon interactions. The effect of the relative contributions of these terms on CO melting is discussed in the full paper. Finally, the MR% was calculated around T_{CO} and it was found that the value of MR% is double for CO samples (particle size > 50 nm) when compared to CO suppressed samples (particle size < 50 nm). In conclusion, the observed CO crossover in NCMO around 50 nm particle sizes can be attributed to the prominent surface spin disorder, planar discommensurations and induced lattice strain effects arising due to large surface to volume ratio of the nanoparticles.

[1] T. Zhang, X. P. Wang, Q. F. Fang, and X. G. Li, "Magnetic and charge ordering in nanosized manganites," *Appl. Phys. Rev.*, vol. 1, no. 3, p. 31302, 2014. [2] Z. Jirak, E. Hadova, O. Kaman, K. Knizek, M. Marysko, and E. Pollert, "Ferromagnetism versus charge ordering in the $Pr_{0.5}Ca_{0.5}MnO_3$ and $La_{0.5}Ca_{0.5}MnO_3$ nanocrystals," *Phys. Rev. B*, vol. 81, no. 2, p. 24403, 2010. [3] M. Tokunaga, N. Miura, Y. Tomioka, and Y. Tokura, "High-magnetic-field study of the phase transitions of $R_{1-x}Ca_xMnO_3$," *Phys. Rev. B*, vol. 57, no. 9, p. 5259, 1998. [4] B. Sudakshina, K. D. Chandrasekhar, H. D. Yang, and M. Vasundhara, "Observation of complex magnetic behaviour in calcium doped neodymium manganites," *J. Phys. D. Appl. Phys.*, vol. 50, no. 6, p. 65004, 2017.

BR-04. Withdrawn

BR-05. Large Magnetoresistance in Diode Assisted ZnCoO Device.

K. Zhang[1,2], Y. Zhang[1,2], Z. Zhang[1,2], Z. Zheng[1,2], *J. Nan*[1,2], G. Wang[1,2], Y. Wang[1,2], W. Yun[1,2] and W. Zhao[1,2]

1. Fert Beijing Institute, Beihang University, Beijing, China; 2. School of Electronics and Information Engineering, Beihang University, Beijing, China

Magnetoresistance (MR) effect is at the heart of modern information storage, which represents the electrical resistance change ratio of materials or devices under the application of external magnetic field. In order to realize large MR value, lots of promising materials and structures were proposed. Extraordinary MR (EMR) [1, 2] in some non-magnetic semiconductors has gained much attention owing to the large MR magnitude and linear magnetic field dependence, which can be ascribed to inhomogeneity of carrier density or mobility. Recently, large MR value was realized by exquisitely coupling the magnetic response of materials and the nonlinear transport effect of diode [3, 4]. However, these devices could not satisfy the requirement of high sensitivity at low magnetic field and small work current simultaneously. Here, we utilized the negative MR and large resistivity of ZnCoO magnetic semiconductor films to realize high magnetic-field sensitivity with small work current at room temperature. In our experiments, ZnCoO magnetic semiconductor films of 60 nm were cut into a stripe with 7 mm in length and 2 mm in width. As shown in Fig. 1(a), linear voltage-current (V-I) curves and about -13% MR values were observed. Here, MR is always defined as $MR=(V_H-V_0)/V_H$, where V_H and V_0 are the voltage detected with and without applied magnetic field respectively. Then a Zener diode was connected between electrode 1 and 4 to fabricate a diode assisted ZnCoO device (DAZD). Fig. 1(b) shows the V-I curves and MR value of the DAZD with 9.1V Zener diode under different magnetic fields. A sharp increase in voltage by several orders was observed at critical transition current I_C=0.375 mA under 0T, which is directly related with the Zener Diode. When the applied current is smaller than 0.375 mA, the voltage dropped on the diode is smaller than the critical voltage (U_C) of Zener diode and the diode could be considered as open circuit, which results in a small measured voltage because of the voltage attenuation with the increase of distance. When the voltage dropped on the diode is larger than U_C, the diode can be considered as short circuit and electrode 4 and 1 turn into short-connected, which results in a sudden increase in the detected voltage. As shown in Fig. 1(b), the MR value of the DAZD is high up to -1539% at 0.1T, -3958% at 0.4T, -5359% at 1T and -6850% MR at 6T with small work current, which is a higher sensitivity in low magnetic field compared with the Si, Ge, GaAs nonmagnetic semiconductor. As shown in Fig. 1(c), the MR value and the shape of MR curve could be tuned by the applied current. For I = 0.380 mA and I = 0.428 mA, the MR value is almost the same (~ -850%), but the former one is much higher than the later one in magnetic field sensitivity and the shape of the MR curves changes from sharp to obtuse. Generally, the MR value of DAZDs was closely related to the transport property of Zener diode and ZnCoO films. Here, we measured the MR value of DAZDs connected by Zener diodes with different threshold voltage. With the increase of Zener diodes' threshold voltage, the MR_{max} value increases at first, then remains nearly unchanged as shown in Fig. 2(a). This is because that the Zener diodes' sharpness of resistance transition increases with the increase of U_C and keeps the same when U_C larger than 6.8V as shown in Fig. 2(b). This work may have potential application in the area of magnetic sensor industry with the advantage of low power consumption.

[1] R. Xu, A. Husmann, T. F. Rosenbaum, M.-L. Saboungi, J. E. Enderby, and P. B. Littlewood, Large magnetoreisitance in non-magnetic silver chalcogenides, *Nature*, vol. 390, pp. 57-60 (1997). [2] M. P. Delmo, S. Yamamoto, S. Kasai, T. Ono, and K. Kobayashi, Large positive magnetoresistive effect in silicon induced by the space-charge effect, *Nature*, vol. 457, pp. 1112-1115 (2009). [3] Z. C. Luo, C. Y. Xiong, X. Zhang, Z. G. Guo, J. W. Cai, and X. Z. Zhang, Extremely Large Magnetoresistance at Low Magnetic Field by Coupling the Nonlinear Transport Effect and the Anomalous Hall Effect, *Adv. Mater.*, vol. 28, pp. 2760-2764 (2016). [4] J. J. Chen, X. Z. Zhang, H. G. Piao, J. M. Wang, and Z. C. Luo, Enhanced low field magnetoresistance in germanium and silicon-diode combined device at room temperature, *Appl. Phys. Lett.*, vol. 105, pp. 193508 (2014).

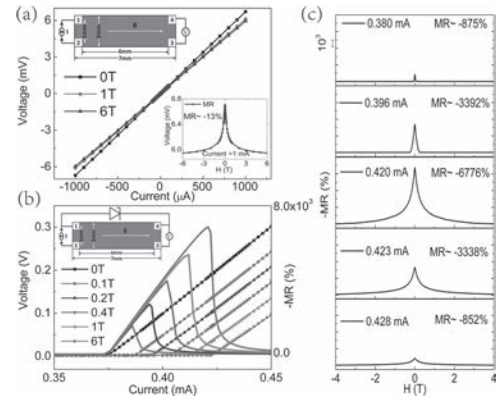

Fig. 1. (a) The V-I curves of ZnCoO film under magnetic field 0T, 1T, 6T. The inset in bottom right corner shows the voltage dependence on magnetic field with current I = 1 mA. The inset in top left corner shows the schematic graph of ZnCoO film. (b) The V-I curves and corresponding MR value of our DAZD measured under different magnetic field. Inset in (b) shows the schematic graph of our DAZD. (c) MR performance under different applied currents.

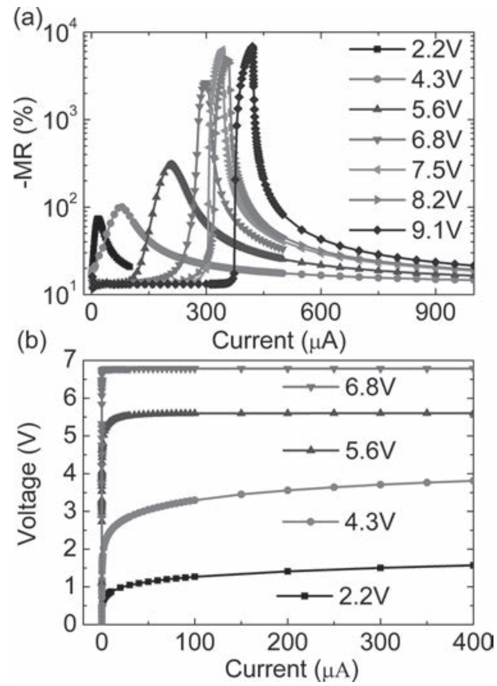

Fig. 2. (a) The MR performance of DAZD connected with different Zener diodes. (b) The V-I curves of Zener diodes with different threshold voltage.

BR-06. Negative spin Hall magnetoresistance in antiferromagnetic Cr_2O_3/Ta bilayer at the low temperature region.

Y. Ji[1], J. Miao[1], K. Meng[1], J. Chen[1], X. Xu[1], Y. Wu[1] and Y. Jiang[1]
1. School of Materials Science and Engineering, University of Science and Technology Beijing, Beijing, China

Spin Hall magnetoresistance (SMR) is a MR effect that there is no charge current in the ferromagnetic (FM) layer, which depends on the relative orientation between the magnetic moments of FM layer and the spin direction injected from normal metal (NM), therefore ferromagnetic insulators (FMIs) are widely applied in SMR.[1] Recently, A. Manchon investigated the physical origin of SMR in antiferromanets and predicted that should be observable with other antiferromagnetic insulators such as NiO, CoO, Cr_2O_3 etc. [2] Unsurprising, we observed a nearly 0.1% SMR ratio in Cr_2O_3/W with 9 T.[3] Soon after that, a negative SMR has been observed in both NiO bulk crystal and films.[4-6] 50 nm Cr_2O_3 film was grown on Al_2O_3 (0001) substrate by pulse laser deposition and a 5 nm thickness of Ta layer was in-situ grown on the surface of Cr_2O_3 film by magnetron sputtering. Then, we manufactured 400 μm×40 μm hall bar for electrical measurements by electron beam lithography and Ar ion etching. A 400 μm×40 μm hall bar for electric measunremts was patterned on the surface of sample. Fig. 1(a) show the angle-dependent magnetoresistance measurements on Cr_2O_3/Ta bilayer with a constant field 3 T. Fig. 1(b) shows the angle dependence of SMR for Cr_2O_3/Ta bilayer with 3 T at various temperature, where the corresponding temperature dependence of SMR is described in Fig. 1(c). Interestingly, as the temperature decreases, SMR changed from positive to negative monotonically. In order to explain above observations, the magnetization structure of Cr_2O_3 need to be taken into account. As known, a surface magnetization exists at the (0001) surface of the magnetoelectric antiferromagnet Cr_2O_3.[7] Therefore, Cr_2O_3 can be divided into two parts: surface ferromagnetism and bulk antiferromagnetism, both will contribute to SMR. The surface ferromagnetism leads to the positive SMR, while the negative SMR origins from the bulk antiferromagnetism. To confirm this conclusion, the Hall resistance measurements were carried out in Cr_2O_3/Ta bilayer at different temperature, shown in Fig. 2(a) and Fig. 2(b). When the temperature is higher than 250 K, the slopes of hall curves are all positive and abnormal Hall effect (AHE) can be observed. In addition, AHE signals get stronger with the increasing temperature, which origins from surface ferromagnetism of Cr_2O_3. On the other hand, as the temperature is lower than the transition temperature, the slopes of hall curves are all negative and no AHE signals can be found. In other words, surface ferromagnetism may vanish, or bulk antiferromagnetism may cover the surface ferromagnetism up.[7] In conclusion, we observed a negative SMR ratio in Cr_2O_3/Ta bilayer below 250 K, which is attributed to magnetization of Cr_2O_3The observations of negative SMR in antiferromagnet, like NiO, Cr_2O_3, pave the way for applications in antiferromagnetic spintronic devices.

1) H. Nakayama, M. Althammer, Y.-T. Chen, K. Uchida, Y. Kajiwara, D. Kikuchi, T. Ohtani, S. Geprägs, M. Opel, S. Takahashi, R. Gross, G. E. W. Bauer, S. T. B. Goennenwein, and E. Saitoh, *Phys. Rev. Lett.* 110 (20), 206601 (2013). 2) A. Manchon, *Phys. Status Solidi RRL* 11, 1600409 (2017). 3) Y. Ji, J. Miao, K. K. Meng, Z. Y. Ren, B. W. Dong, X. G. Xu, Y. Wu, and Y. Jiang, *Appl. Phys. Lett.* 110, 262401 (2017). 4) G. R. Hoogeboom, A. Aqeel, T. Kuschel, T. T. M. Palstra, and B. J. van Wees, *Appl. Phys. Lett.* 111, 52409 (2017). 5) J. Fischer, O. Gomonay, R. Schlitz, K. Ganzhorn, N. Vlietstra, M. Althammer, H. Huebl, M. Opel, R. Gross, S. T. B. Goennenwein, and S. Geprägs, *preprint arXiv:* 1709.04158 (2017). 6) L. Baldrati, A. Ross1, T. Niizeki, C. Schneider, R. Ramos, J. Cramer1, O. Gomonay, M. Filianina, T. Savchenko, D. Heinze, A. Kleibert, E. Saitoh, J. Sinova, and M. Kläui, *preprint arXiv:* 1709.00910 (2017). 7) X. He, Y. Wang, N. Wu, A. N. Caruso, E. Vescovo, K. D. Belashchenko, P. A. Dowben, and Ch. Binek, *Nat. Mater.* 9, 579 (2010).

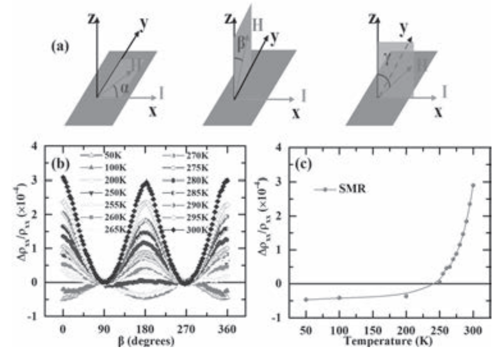

Fig. 1. (a) Notations of rotations of the angular α, β, and γ. (b) β dependence of the resistance in Cr_2O_3 (25)/Ta (5) with 3 T magnetic field at different temperature. (c) Temperature dependence of SMR signals in Cr_2O_3 (25)/Ta (5) under 3 T.

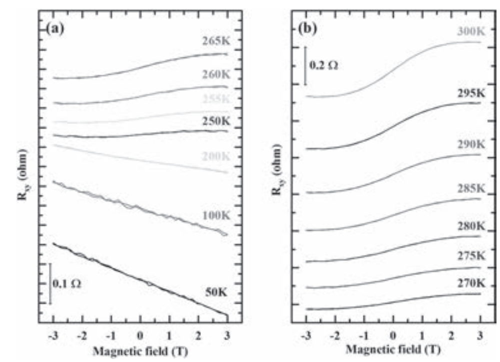

Fig. 2. (a) and (b) AHE measurements of Cr_2O_3 (25)/Ta (5) at 50 K-265 K (a) and at 270 K-300 K (b).

BR-07. Effect of sputtering conditions on the in plane and out of plane magnetic properties of tetragonal Mn_2VGa Heusler alloy films.

P. Midhunlal[1], A. Chelvane[2], A. Talapatra[3], J. Mohanty[3], J. Joseph[4], A. Rajani Kanth[4] and N. Harish Kumar[1]

1. Department of Physics, IIT Madras, Chennai, India; 2. Defense Metallurgical Research Laboratory, Hyderabad, India; 3. Department of Physics, IIT Hyderabad, Hyderabad, India; 4. School of Physics, Univesity of Hyderabad, Hyderabad, India

Abstract: A systematic investigation on the effect of sputtering power, substrate temperature and film thickness on the structural and magnetic properties of DC magnetron sputtered Mn_2VGa Heusler alloy films have been carried out by using x-ray diffraction, SQUID magnetometry and magnetic force microscopy (MFM). In plane (IP) and out of plane (OOP) magnetization measurements carried out on tetragonal Mn_2VGa thin films shows strong OOP magnetization (which is absent in the reported cubic Mn_2VGa films) which is close to the IP magnetization value. The observed IP and OOP magnetic moment at 5 T is 1.62 μ_B and 1.26 μ_B respectively and the IP and OOP coercivity is 2 KOe and 2.2 KOe for 100 nm thick film deposited at 75 W power and 450˚C substrate temperature. The crystallinity and magnetization (both IP and OOP) was found to decrease as the substrate temperature and film thickness was reduced due to the off stoichiometric film growth. MFM images shows patch like domain pattern with decreasing magnetic phase contrast with decrease in substrate temperatures and thickness. A disorder dependent scattering below 67 K and a minimum around 25 K is observed in resistivity measurement for the film deposited at 400 ˚C substrate temperature. Introduction Half-metallic ferromagnetic Heusler alloy films are being used as spin injection electrodes in spintronic devices such as magnetic random access memory (MRAM) and read head of hard disc drives due to their peculiar electronic band structure where majority (minority) carriers exhibit conductive nature and minority (majority) carriers exhibit semi conductive or insulative nature [1]. This gives 100% spin polarization at the Fermi level for these alloys (half-metallicity). Ramesh Kumar *et al*. have shown the ferrimagnetic nature and half-metallicity in Mn_2VGa alloy through neutron diffraction, magnetic, transport and magneto-transport studies [2,3]. The reported Curie temperature for Mn_2VGa is 783 K which is well above the room temperature and the magnetic moment is 1.88 μ_B which is suitable for spintronic applications. For device applications, it is essential to fabricate thin films of this material with desirable physical properties. In this paper, first time we report the existence of OOP magnetization along with the IP magnetization in tetragonal Mn_2VGa Heusler alloy films .A systematic investigation on the effect of thickness and substrate temperature on the IP and OOP magnetization has been carried out. Results and discussion XRD measurements showed tetragonal crystal structure for the films irrespective of the sputtering parameters. Better crystallinity was observed for films deposited at elevated power (75 W) and substrate temperature. Figure 1a shows the XRD patterns of 100 nm thick films deposited at 75 W power and different substrate temperatures. The interesting observation from the magnetization measurement is the presence of strong OOP magnetization along with the in plane component in the films as shown in figure 1b which was absent in the cubic Mn_2VGa films [4]. The magnetization value at 5 T (M_{5T}) for the film deposited at 500 ˚C substrate temperature is 255.2 emu/cc (1.62 μ_B/f.u) for the IP and 198.9 emu/cc (1.26 μ_B/f.u) for the OOP configuration. Even though the IP magnetic moment value of 1.62 μ_B/f.u is different from the expected integer value of 2 μ_B/f.u (as per Slater-Pauling rule) for the cubic Mn_2VGa, it is better than the earlier reported value of 1.56 μ_B/f.u for the cubic Mn_2VGa film [4]. The coercivity value at 5 K for the IP and OOP configurations are 2 KOe and 2.24 KOe respectively for the film deposited at 500 ˚C substrate temperature which differ significantly from the reported soft magnetic behavior of bulk sample. Magnetic moment (IP&OOP) was found to decrease with the decreases in substrate temperatures as shown in figure 1b. This could be due to the poor crystallinity of the films at lower substrate temperatures. The M-H curve for the room temperature deposited film shows a diamagnetic behavior (possibly dominated by the Si substrate) both in IP and OOP measurements. It was observed that the IP and OOP magnetization has gradually decreased as the substrate temperature and thickness was lowered. Temperature variation of resistivity shows a metallic behavior with a dominant disorder dependent scattering for T < 67 K and electron–phonon scattering in the high temperature regime (T > 67 K). A minimum was observed around 25 K, possibly due to the disorder enhanced coherent scattering of conduction electrons.

1. I Galanakis, Ph Mavropoulos and P H Dederichs, J. Phys. D: Appl. Phys. 39,765 (2006). 2. K Ramesh Kumar, N Harish Kumar, P D Babu, S Venkatesh and SRamakrishnan, J. Phys.: Condens. Matter 24, 336007 (2012). 3. K. Ramesh Kumar, N. Harish Kumar, G. Markandeyulu, J. AroutChelvane, V. Neu, P.D.Babu, J. Magn. Magn. Mater. 320, 2737 (2008). 4. Christoph Klewe, Markus Meinert, Jan Schmalhorst and Günter Reiss, J. Phys.: Condens. Matter 25, 076001(2013).

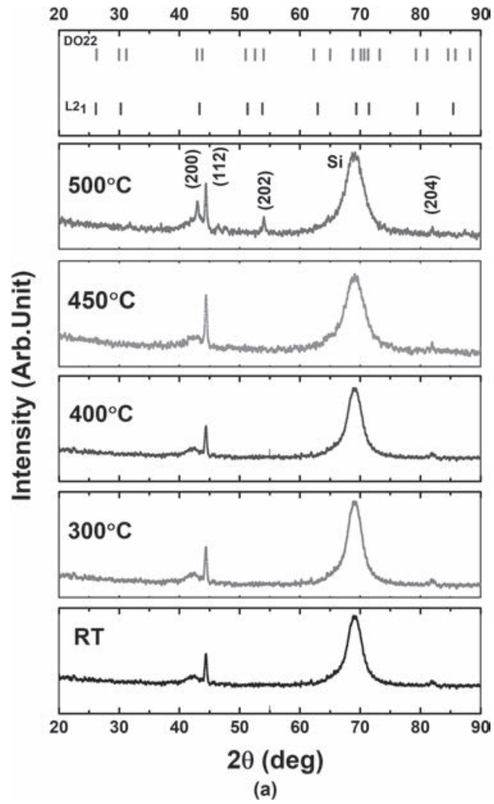

Fig. 1. (a) XRD patterns of films deposited at different substrate temperatures. Simulated XRD spectrums for cubic and tetragonal structure also has shown on the top of figure 1a.

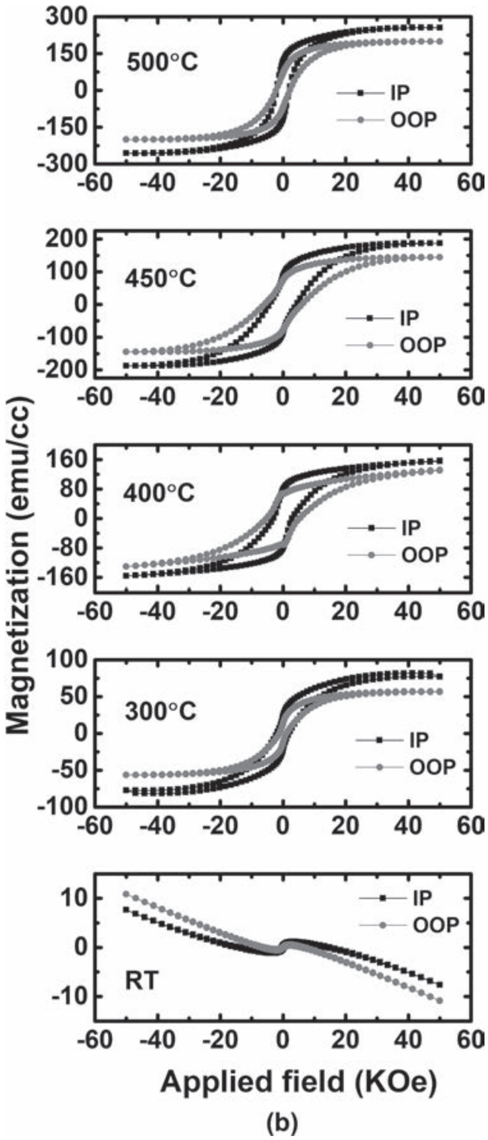

Fig. 1b. Corresponding in plane and out of plane M-H curves for films deposited at different substrate temperatures.

BR-08. Structural, magnetic and transport properties of half-metallic quaternary Heusler alloy CoRuMnSi: Theory and Experiment.

V. Yenugonda[1], D. Rani[1], S. Samatham[1], A. Alam[1] and K. Suresh[1]
1. Departmnet of Physics, Indian Institute of Technology Bombay, Mumbai, India

Introduction: Spintronics is the spin based technology which utilizes the electronic spin degree of freedom in addition to its charge [1,2]. For realization of spintronic devices, special materials are required; i.e., their electrical conduction should be by only one type of spin carriers. Realization of spin-polarized transport occurs in materials classified as half-metals, spin gap-less semiconductors and magnetic semiconductors. These materials can be either ferro-, ferri- or fully compensated ferrimagnets. The necessary condition in all these materials is that they show integer magnetic moment. In order to retain spin polarization at room temperature, these materials should also possess high magnetic ordering temperature. From the last decade, quaternary Heusler alloys (QHAs) gained importance in the search for spintronics materials [3]. Kundu *et. al.* studied certain Co-based QHAs such as CoRuMnSi [4]. We probe this alloy using a joint experimental and theoretical study. Experimental techniques: Polycrystalline CoRuMnSi alloy was prepared by arc-melting followed by annealing for 7 days at 800 °C. Room temperature powder X-ray diffraction (XRD) pattern was analyzed usign Fullprof suite. There are three nondegenerate crystal arrangements in the Y-type structure [5]. By keeping Si at 4a site in F-43mspace group, the configurations are I) Mn at 4b, Co at 4c and Ru at 4d sites, II) Mn at 4c, Co at 4b and Ru at 4d sites, and III) Mn at 4d, Co at 4c and Ru at 4b sites respectively. Reitveld refinement was carried out for all the configurations including disorder. Magnetization measurements were carried out using Physical property measurement system. Electrical resistivity (ρ) measurements were done using four probe contact method by applying 5 mA current. Theoretical details: Spin resolved band structure calculations were carried out with the help of Quantum ESPRESSO [6]. Exchange correlations were taken in GGA approximation. Four atomic face centred cubic primitive cell was used. All the three configurations were fully relaxed with different initial magnetic states. The parameters such as energy cutoff, charge density cutoff, kpoints sampling in Brillowin zone etc. used in simulations are same as mentioned elsewhere [7]. Results and Discussion: (i) Crystal structure: XRD pattern of CoRuMnSi can be indexed in LiMgPdSn type structure with lattice parameter of 5.78 Å. However, due to 50% anti-site disorder between tetrahedral site atoms (as revealed from refinement), the crystal symmetry reduces to $L2_1$. Refinement considering 50% anti-site disorder of tetrahedral atoms gives the best fit [Fig. 1 (a) and (b)]. In configuration I, Co and Ru occupy tetrahedral sites while in configuration II, it is between Mn and Ru. XRD refinement is unable to distinguish between these two configurations. However on the basis of electronegativities, one can conclude that Mn occupies octahedral site and hence configuration I with 50% antisite disorder (between Ru and Co) is the actual structure [1,5]. Theoretical simulations also confirm the configuration I as the ground state. (ii) Magnetization and electrical transport: For QHAs composed of at least two elements having more than half-filled d electrons, the saturation moment obeys the following Slater Pauling rule [2,5] M_s=N-24, where N is the total number of valence electrons. The alloy has a moment of nearly 4 μ_B at 3 K (see Fig.2(a)), which is consistent with the SP rule as it contains 28 valence electrons. It is found to be ferromagnetic with T_C > 400 K(see Fig.2(b)). In Fig. 2c, ρ-T data is shown, which indicates metallic nature above 50 K. Theoretical results: Configuration I with ferromagnetic state is found to be the ground state among the three configurations. It has spin moments of 0.99 μ_B, 0.16 μ_B and 2.85 μ_B on Co, Ru and Mn respectively. Its spin resolved DOS and band structure are shown at the bottom panel of the Fig. 2. Minority spin band has a gap of 0.58 eV and the Fermi level lies nearly 23 meV above the top of the valence band. Minority spin band has metallic bands crossing the Fermi level. The energy differences among the three configurations is quite large (> 16 mRy/atom) and hence no disorder is expected to occur in atomic sites other than on the tetrahedral ones. Conclusion: CoRuMnSi crystallizes in $L2_1$ structure as revealed by XRD pattern. Magnetization measurements reveal that it is ferromagnetic with a moment ~ 4 μ_B/f.u. and T_C of more than 400 K. Absence of T^2 contribution to ρ(T) indirectly suggests the half-metallic nature. Theoretical simulations predicts that the material is a half-metallic ferromagnet in the ground state configuration with a moment that is consistent with the experimental value. Energy differences among the three configurations is quite large and hence disorder in the atomic positions is not possible. In view of these, this alloy appears to be a promising candidate for spintronics applications.

[1] C. Felser, G. H. Fecher, and B. Balke, Angew. Chem., Int. Ed. 46, 668(2007). [2] Half-Metallic Alloys, edited by I. Galanakis and P. H. Dederichs (Springer, Berlin, 2005). [3] L. Bainsla and K. G. Suresh, Applied Physics Reviews 3, 031101 (2016). [4] A. Kundu, S. Ghosh, R. Banerjee, S. Ghosh, and B. Sanyal, Scientific Reports 7, 1803 (2017). [5] Enamullah, Y. Venkateswara, Sachin Gupta, Manoj Raama Varma, Prashant Singh, K. G. Suresh, and Aftab Alam, Phy. Rev. B. 92, 224413 (2015). [6] P. Giannozzi et al., Journal of Physics: Condensed Matter 21, 395502 (2009). [7] Y. Venkateswara, Sachin Gupta, S. Shanmukharao Samatham, Manoj Raama Varma, Enamullah Khan, K. G. Suresh, adn Aftab Alam, arXiv:1707.04854.

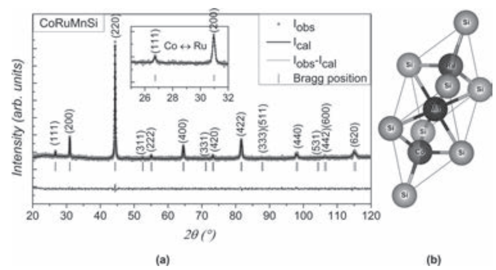

Fig. 1. (a) Reitveld refined room temperature powder XRD pattern of CoRuMnSi along with the best fit obtained for the configuration I with 50% anti-site disorder between Co and Ru. The inset shows the fit near (111) and (200) peaks. (b) Crystal structure.

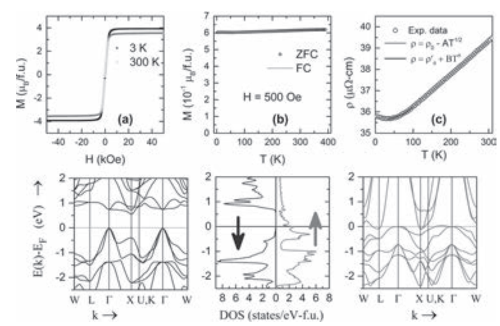

Fig. 2. (a) Isothermal M-H data at 3 K and 300 K for CoRuMnSi alloy. (b) M-T data in 500 Oe for CoRuMnSi in ZFC and FC modes. (c) ρ-T data in zero field. Results of spin resolved band structure simulations for configuration I are shown in the bottom panel: band structure for spin down band (left side) and spin up band (right side) along with their DOS (middle).

BR-09. Possible spin gapless semiconductor type behaviour in CoFeMnSi epitaxial thin films.

V.K. Kushwaha[1], J. Rani[1], A. Tulapurkar[2] and C. Tomy[1]
1. Physics Department, Indian Institute of Technology Bombay, Powai, India; 2. Department of Electrical Engineering, Indian Institute of Technology Bombay, Mumbai, India

Spintronics is the emerging field of electronics, utilizing not only the charge of electrons but also their spins, which offers many advantages (such as non-volatility, high speed, low power consumption, etc.) over conventional electronics. For driving the spintronics devices, fully polarized spin current is essential, which can be generated using the special type of magnetic materials such as half-metallic ferromagnets (HMF), spin-gapless semiconductors (SGS), etc. However, SGS materials, because of their unique band structure, have gained a lot of interest for potential spintronics applications due to their exceptional magnetic and transport properties over HMF. SGS materials exhibit a band gap in one spin channel and a zero band gap in the other spin channel at the Fermi level (E_F), which leads to 100% spin-polarization at the Fermi level. SGS properties have been observed in Heusler alloys (e.g., CoFeMnSi, Mn_2CoAl, CoFeCrAl, Ti_2MnAl, etc.), oxides (Co-doped $PbPdO_2$), zigzag silicene nanoribbons, and strained Ti_2C monolayer. Among the known SGS candidates, Heusler alloys have attracted much attention due to their very high Curie temperature (T_C). CoFeMnSi is an equiatomic quaternary Heusler alloy (EQHA), which crystallize in the Y-type structure, and is experimentally confirmed as a SGS material in bulk form. However, for spintronics applications, the unique properties of SGS have to be realized in thin films. Here, we report the structural, magnetic and transport properties of CoFeMnSi (CFMS) epitaxial thin film grown on single crystal MgO (001) substrate using pulsed laser deposition (PLD) system. The temperature dependence magnetization (M-T) indicates that the Curie temperature (T_C) of the film is well above 400 K. The magnetic field (H) dependence magnetization (M-H) measurements gives the saturation magnetization (M_s) value of 3.28 μ_B/f.u. at 300 K. The electrical resistivity of the film is indicating a semiconducting behaviour with TCR value of -7×10^{-10} Ω.m/K which is comparable with the TCR values reported for SGS Heusler alloys and is much less than the TCR values of classical semiconductors. Nearly temperature independent and low electrical conductivity of the order of 2.86×10^3 S/cm indicates a possible SGS behaviour and in agreement with experimentally reported SGS behaviour. One of the main impacts of the SGS materials is that they can be used as the SGS/semiconductor heterostructures to enhance the spin injection efficiency due to smaller conductivity mismatch as compared to the HMF/semiconductor heterostructures. Therefore, SGS behaviour with high Curie temperature (T_C) makes CFMS thin films as a potential candidate for fabricating the practical spintronics devices. (e.g., spin vale, magnetic tunnel junctions etc.).

Varun K. Kushwaha, Jyoti Rani, Ashwin Tulapurkar, and C. V. Tomy, Appl. Phys. Lett. 111, 152407 (2017)

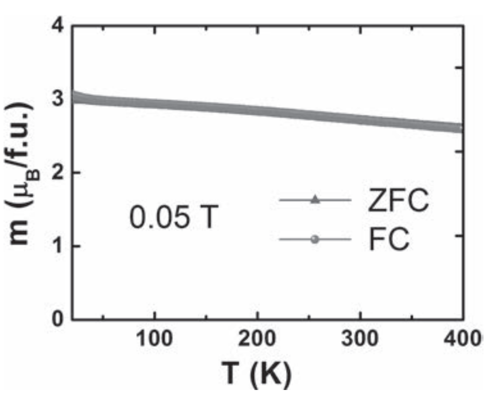

Fig. 1. Temperature dependence magnetization (M-T) in the temperature range of 5-400K, indicating Curie temperature (T_C) of the film well above 400 K.

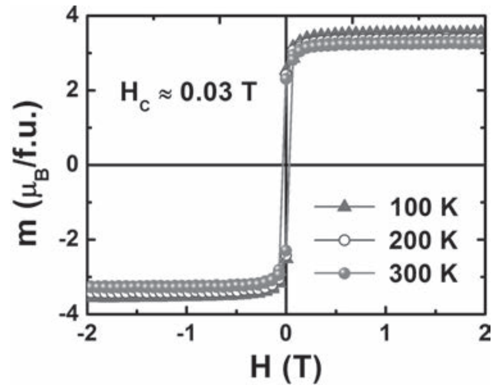

Fig. 2. Magnetic field dependence magnetization (M-H) fo the film at 100 K, 200 K, and 300 K.

BR-10. Interplay between structure and anisotropic magnetoresistance in Ta/NiFe/Ta thin films.

H.W. Chang[1], M. Chan[2], D. Wei[2], C. Wang[3] and C. Ouyang[4]
1. Department of Physics, National Chung Cheng University, Taichung, Taiwan; 2. National Taipei University of Technology, Taipei, Taiwan; 3. Department of Applied Physics, Tunghai University, Taichung, Taiwan; 4. Department of Materials Science and Engineering, National Tsing Hua University, Hsinchu, Taiwan

Anisotropic magnetoresistance (AMR) effect, resulted from the anisotropic scattering of conduction electrons due to the spin-orbit interaction, has been extensively investigated due to wide applications in advanced spintronic devices, magnetoresistance heads, and magnetic field sensor [1-3]. Because of its relatively large AMR ratio and excellent soft magnetic properties, permalloy (NiFe) is the most adopted material for AMR devices. Ta was reported being able to improve microstructure and AMR ratio of NiFe films [3], and the sensing component typically contains a Ta/NiFe/Ta multilayer for desired microstructure and performance. In this study, in order to further understand relationship between the AMR rato and the microstructure, Ta/NiFe/Ta trilayer films are prepared on SiO_2/Si(100) substrates at room temperature (RT) by sputtering at the external magnetic field of 1 kG induced NdFeB sintered magnets. Structure, surface morphology, magnetic properties, and AMR of Ta/NiFe/Ta films with various working pressure and thickness of Ta underlayer and post-annealing temperature are reported, and the relationship between the AMR ratio and the microstructure is also discussed. X-Ray diffraction analysis show that the crystallinity of the NiFe(111) texture strongly depends on the working pressure (P_{Ta}) in the range of 2-8 mtorr, thickness (t_{Ta}) in the range of 0-5 nm of Ta underlayer and post-annealing temperature (T) of 150-400 ^{o}C at magnetic field of 1500 Oe. The studied films at P_{Ta} of 2-5 mtorr and t_{Ta} of 0-5 nm through proper post annealing (T = 150-300 ^{o}C) exhibit smooth interface and flat surface with low root-mean-square roughness. The in-plane magnetic anisotropy, induced by the applied magnetic field during deposition, with good soft magnetic property is obtained, and it is improved through post-annealing at appropriate T = 150-300 ^{o}C. Figure 1 (a) shows MR ratio versus magnetic field curves of Ta/NiFe/Ta films post annealed at various temperatures (T), and MR ratio of the films with various T, t_{Ta}, and P_{Ta} are summarized in Fig. 1(b)-(d), respectively. All studied Ta/NiFe/Ta films exhibit a typical MR ratio and good MR properties. As shown in Fig.1 (b), with increasing T, MR ratio is improved from 1.5 % at T = RT to 2.5% at T = 300 ^{o}C resulted from enhanced NiFe(111) texture at first, and then reduced to 1.3 % and 0.9% at T = 350 ^{o}C and 400 ^{o}C, respectively, because of interdiffusion between NiFe and Ta layers. The above result indicates the optimal annealing temperature here is 300 ^{o}C. As shown in Fig. 1(c) and (d), for as-deposited films, the change of MR ratio with either t_{Ta} or P_{Ta} is similar to that of peak intensity and d_{csd} of NiFe(111) texture, and the MR ratio is significantly enhanced through post annealed at T = 300 ^{o}C due to improved NiFe(111) texture. Finally, the relationship between the structure and MR property is also revealed, except for the samples with rougher surface. MR ratio is found to increase with increasing d_{csd} as shown in Fig. 2. MR ratio increases from 1.3% to 2.5 % as d_{csd} grows from 11.1 nm to 15.6-16.0 nm. The results indicate that the structural defects especially planar defects suppress the MR ratio of the studied Ta/NiFe/Ta films. This study suggests that proper Ta underlayer and post-annealing are crucial in the MR properties for Ta/NiFe/Ta system.

[1] T. R. McGuire and R. I. Potter, IEEE Trans. Magn. 11, 1018 (1975). [2] Y. F. Liu, J. W. Cai and L. Sun, Appl. Phys. Lett. 96, 092509 (2010). [3] G. Choe and M. Steinback, J. Appl. Phys. 85, 5777 (1999).

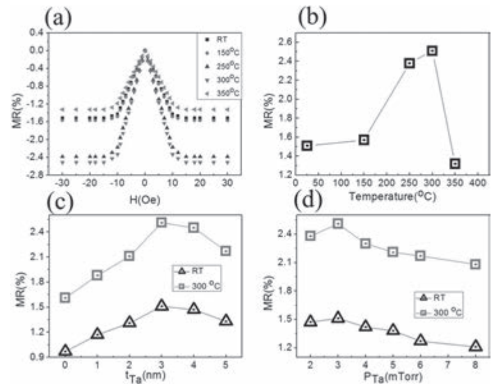

Fig. 1. MR-H curves and MR ratio of Ta/NiFe/Ta films with various conditions.

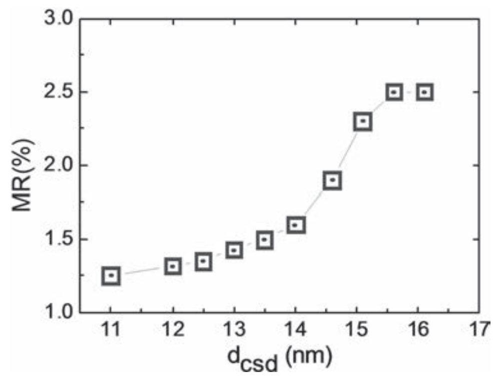

Fig. 2. MR ratio versus d_{csd} plot for Ta/NiFe/Ta films in this present study.

BR-11. Different Phase Mn_2Ga films introduced by varying the Cr buffer thickness.

Y. Zheng[1], Y. Liu[1], L. Ren[1] and K. Teo[1]
1. Electrical and Computer Department, National University of Singapore, Singapore

I. INTRODUCTION Tetragonal Mn_xGa alloys in $L1_0$ or $D0_{22}$ phase have small α, high P and high PMA, tunable M_s which perfectly meet the requirement for STT-MRAM.[1-4] Cubic Mn_xGa alloys are not energetically favored and observed in the bulk, but can be deposited in thin films on certain substrate or buffer layer.[5] Usually, the cubic Mn_xGa can form half-Heusler or Heusler structure, in which a 100% spin polarization is predicated. Especially cubic Mn_3Ga is considered as a potential "half-metallic antiferromagnet" with zero spin magnetization moment from the modified Slater-Pauling rule m = Nv–24, where Nv is the number of valence electrons per formula. The "half-metallic antiferromagnet" could be useful because the material would be fully spin polarized, yet would be free from shape anisotropy and create no stray field. Kurt has realized the "half-metallic antiferromagnet" by doping Ru or Pt in the cubic Mn_2Ga materals.[5, 6] *II. EXPERIMENTS AND RESULT* Mn_2Ga films were deposited on MgO (100) substrate with a Cr buffer layer in an ultrahigh vacuum MBE chamber. Before depositing Mn_2Ga film, MgO substrate was annealed at 600 °C. Different thickness of Cr buffer layer was deposited at ambient temperature and subsequently *in-situ* annealed at 600 °C. The 7 nm Mn_2Ga film was then deposited at ambient temperature and subsequently *in-situ* annealed at temperature T_a = 400 °C. The film stack was finally capped with MgO layer of 4 nm at room temperature to prevent oxidation. The composition of the films was controlled by the Mn and Ga fluxes. The structural analysis was performed by x-ray diffractometer (XRD). Magnetization measurements were carried out using a vibrating sample magnetometer (VSM). Figure 1 shows XRD patterns for 7 nm thick Mn_2Ga films with different thickness of Cr buffer layer. For the films with Cr thickness larger than 5 nm, both Cr (002) and tetragonal Mn_2Ga (002) peaks can be clearly observed, indicating the films are tetragonal structure. For the films with ultrathin Cr thickness (1 nm and below), two $C1_b$-Mn_2Ga (001) and $C1_b$-Mn_2Ga (002) are observed. For the Mn_2Ga film with 3 nm Cr buffer layer, no Cr or any other Mn_2Ga peaks are observed, which means both Mn_2Ga phases are not overwhelmed. For the cubic phase of Mn_2Ga, lattice constant of 6.00 Å is found for the films with 1 nm Cr buffer layer or without buffer layer. The epitaxial relationship should be MgO(001)[100]//Mn_2Ga(001)[110]. For tetragonal phase of Mn_2Ga, the lattice constant decrease with the increase of the thickness of the Cr buffer layer for the tensile stress change. Usually the lattice constant varies much with the thickness of the Cr buffer layer or tetragonal MnGa since large lattice mismatch between Cr and MnGa (nearly 4%). However, it keeps nearly constant for cubic Mn_2Ga condition (5.99 Å is found for 30 nm Mn_2Ga on MgO substrate) since there is only about a 1% lattice mismatch between Cr and cubic Mn_2Ga. Hysteresis loops measured at 300 K for Mn_2Ga film with different Cr buffer layer thickness are shown in figure 2. The Hysteresis loops for the films with Cr buffer layer below 1 nm present the superparamagnetic state, which may be come from the small size ferromagnetic manganese compound clusters. All the Mn_2Ga films with Cr thickness larger than 1 nm show the PMA and the saturated magnetization value increase with the Cr thickness. This reflect the more and more tetragonal Mn_2Ga phase exist in the films. The square perpendicular hysteresis loop in figure. 2 (e) means rather pure tetragonal phase Mn_2Ga film when it is deposited on the 13 nm Cr buffer layer. The hysteresis loop shape change for the film with 40 nm Cr buffer layer may come from the strain relax. In summary, thin Mn_2Ga films were grown on MgO substrate with varying thickness of Cr buffer layer using molecular beam epitaxy. Cubic Mn_2Ga films with the half-Heusler $C1_b$ structure obtained when the thickness of Cr buffer layer is below 3 nm. Tetrogonal Mn_2Ga phase with high perpendicular magnetic anisotropy are obtained when the thickness of Cr buffer layer is above 3 nm.

1. S. Mizukami, F. Wu, A. Sakuma, J. Walowski, D. Watanabe, T. Kubota, X. Zhang, H. Naganuma, M. Oogane, Y. Ando, and T. Miyazaki, Phys. Rev. Lett., 106, 117201 (2011). 2. H. Kurt, K. Rode, M. Venkatesan, P. Stamenov, and J. M. D. Coey, Phys. Status Solidi B 248, 2338 (2011); Phys. Rev. B 83, 020405(R) (2011). 3. L. J. Zhu, S. H. Nie, K. K. Meng, D. Pan, J. H. Zhao, and H. Z. Zheng, Adv. Mater., 24, 4547 (2012). 4. Y. H. Zheng, G. C. Han, H. Lu, and K. L. Teo, J. Appl. Phys., 115, 043902 (2014) 5. H. Kurt, K. Rode, P. Stamenov, M. Venkatesan, Y.-C. Lau, E. Fonda, and J. M. D. Coey, Phys. Rev. Lett., 112, 027201 (2014). 6. S. Singh1, S.W. D. Souza1, J. Nayak1, E. Suard2, L. Chapon2, A. Senyshyn3, V. Petricek4, Y. Skourski5, M. Nicklas1, C. Felser1 & S. Chadov1, Nat. Commun. 7, 12671(2016).

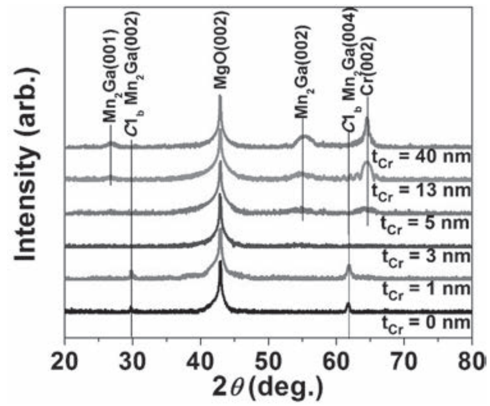

Fig. 1. XRD 2θ patterns for Mn_2Ga films.

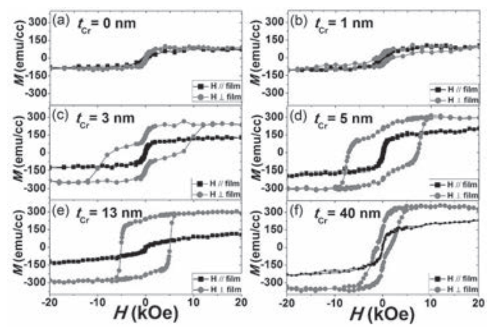

Fig. 2. Perpendicular hysteresis loops measured at 300 K for Mn_2Ga film with different thickness of Cr buffer layer (t_{Cr}): (a) 0 nm; (b) 1 nm; (c) 3 nm; (d) 5 nm; (e) 13 nm; (f) 40 nm.

BR-12. Generation of Néel field in anti-ferromagnetic nanowire by a sloped electric field.

K. Kubota[1], K. Yamada[2] and Y. Nakatani[1]
1. Graduate school of Informatics and Engineering, University of Electro-Communications, Chofu, Japan; 2. Faculty of Engineering, Gifu University, Gifu, Japan

Since a proposal of a racetrack memory, a magnetic domain wall motion in a magnetic nanowire has attracted attention as a novel technique for memory development [1]. Recently, it has reported that the domain wall motion velocity in Anti-ferromagnets (AFM) is much faster than that in ferromagnets [2-6] and, the DW motion in AFM has been gathering attentions. The DW in AFM with Dzyaloshinskii-Moriya interaction (DMI) can be moved by an external magnetic field and a spin-orbit spin transfer torque[4-5]. Whereas the DW in AFM without DMI can be moved by Néel field generated by Néel Spin Orbit Torque (NSOT) [7,8]. In this study, we propose a method to generate Néel field by using a sloped electric field (SEF) and demonstrate the DW motion in AFM by micromagnetic simulations. We used one dimensional nanowire with 360 nm of length and 1.0 nm of thickness. The nanowire is divided by rectangular prisms with dimension of 2.0×1.0 nm^2. The material parameters used in the simulations are as follows: the saturation magnetization M_s = 10000/4π emu/cm^3, the perpendicular magnetic anisotropy K_u = 2.0 Merg/cm^3, the homogeneous exchange stiffness constant A = 1.6 μerg/cm, the inhomogeneous exchange stiffness constant A_0 = 1.0/π Gerg/cm^3, and the Gilbert damping constant a = 0.01. In the simulation, we assumed that K_u is decreased by the electric field, therefore K_u is decreased linearly from left edge to the right edge in the wire by SEF (Fig. 1) [9]. The reduction rate of K_u is defined asΔKu (erg/cm^4) [9]. Because K_u changes by SEF, the DW energy ($\sigma = 4\sqrt{(AK_u)}$) [10] changes with the position in the nanowire. The DW moves in the direction of decreasing DW energy (K_u) even in AFM wire. An effective magnetic field should be applied to the moving DW. The directions of the effective field to M_1 and M_2 sublattices in moving DW in AFM should be opposite (Néel field) (see Fig.1). In this way, the Néel field is generated by SEF. To confirm the generation of the Néel field by SEF, we simulated the DW motion in AFM by SFE. Figure 2 shows the effect of the ΔK_u on the DW motion velocity (v). The Néel field (H_k) generated by the SEF can be obtained in the same method as [9]; $H^{\mathrm{eff}}_k = (\partial\sigma/\partial x)/2M_s$ (1). Figure 2 also shows the effective Néel field (H^{eff}_k) generated by the SEF and the DW motion velocity obtained by (where g and D are the gyromagnetic ratio and DW width, respectively). The simulation results agree very well with the DW velocity of $v_{\mathrm{Anlay.}}$ obtained by Eq. (1). It shows that Néel Field can be generated in AFM by SEF.

[1] Stuart S. P. Parkin, *et al.*, Science 320, 190 (2008). [2] T. Jungwirth, *et al.*, Nat. Nanotechnol. 11, 231 (2016). [3] A. F. Andreev and V. I. Marchenko, Phys. Usp. 23, 21 (1980). [4] V. G. Bar'yakhtar, B. A. Ivanov, and M. V. Chetkin, Sov. Phys. Usp. 28, 563 (1985). [5] T. Shiino, *et al.*, Phys, Rev, Lett. 117, 087203 (2016). [6] Louis Néel, Nobel Lecture (1970). [7] J. Zelezný, *et.al.*, Phys. Rev. Lett. 113, 157201 (2014). [8] O. Gomonay, *et al.*, Phys. Rev. Lett. 117, 017202 (2016). [9] K. Yamada, *et al.*, Appl. Phys. Lett. 108, 202405 (2016). [10] A. P. Malozemoff, Phys. Rev. B 35, 3679 (1987).

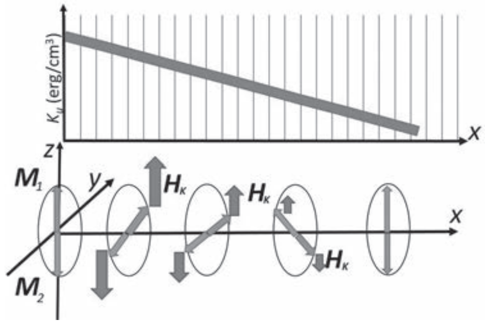

Fig. 1. Generation of Néel field in AFM by SEF.

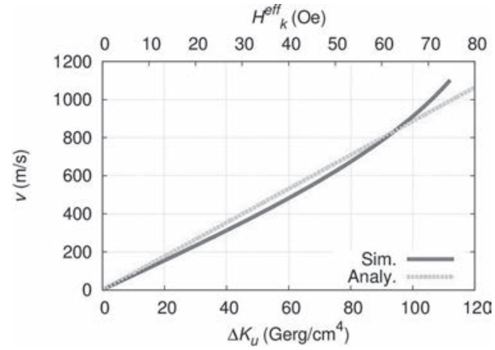

Fig. 2. Domain-wall motion velocity by SEF (Simulations and Analysis).

BR-13. XMCD study of ultra-thin Co_2FeAl film.

X. Zhang[1], W. Liu[2], L. He[1] and Y. Xu[1,2]
1. Nanjing Unversity, Nanjing, China; 2. University of York, York, United Kingdom

Spintronic devices rely on thin layers of magnetic materials, for they are designed to control both the charge current and the spin current of the electrons. Half-metallic ferromagnets (HMFs) have only one spin channel for conduction at the Fermi level, thus in principle this kind of material has 100% spin polarization for transport properties. Combined with the unique elemental selectivity of x-ray magnetic circular dichroism (XMCD), we can determine the local symmetries, the electronic configuration and the values of orbital and spin moments of specific element. X-ray absorption spectroscopy (XAS) measurements at the Co and Fe $L_{2,3}$ absorption edges were performed on beamline I06 at Diamond Light Source, U.K. Oppositely circular polarized X-rays with 100% degree of polarization were used to successively resolve XMCD signals from the respective elements. The light-helicity was switched in a saturating magnetic field of 1 T, which was applied at 60 degrees with respect to the film plane and in parallel with the incident beam. The XMCD was obtained by taking the difference of the XAS spectra, that is, $\sigma^- - \sigma^+$ by flipping the X-ray helicity.[1] Typical XAS and XMCD spectra of the 2.5-uc-thick Co_2FeAl film using total electron yield detection (TEY) are presented in Fig. 1. Both Co and Fe show a white line at each spin-orbit split core level without prominent splitting for both left- and right-circularly polarized X-rays, shown in Fig. 1a & 1d, indicating that the samples have been well protected from oxidation. The XMCD signals of Co (Fig. 1c) and Fe (Fig. 1f) point to the same direction, which indicates a ferromagnetic coupling between the two elements. The shoulder structures appear in the higher photon energy region of Co L_3 peaks, which is corresponding to the B2 structures due to the Co-Co bonding states. One of the most powerful aspects of the XMCD technique is that the average magnetic moment of each element can be calculated by applying the sum rules using the integrated intensity of the XAS and XMCD spectra. The orbital moment (m_l) of Co atom (0.17 μ_B/atom) and Fe atom (0.14 μ_B/atom) is a little bit large, compared with a previous study.[2] We believe the enhancement of orbital magnetic moment, implying the possibility of enhanced spin-orbit coupling (SOC), is derived from the interfacial contribution of Co_2FeAl/GaAs. The presence of Al decreases the localized magnetic moment on both Co and Fe sites, which is due to the empty majority bands. Therefore, the magnetic moment of Al is negative and is about -0.10 μ_B/f.u. In our 2.5-uc-thick sample, considering the calculated value of the moment at Al site, the total magnetic moment of the Co_2FeAl thin film has been evaluated as 3.41 μ_B/f.u. The theoretically predicated magnetic moment for Co_2FeAl thin films is very different, such as 3.8 μ_B/f.u., 4.89 μ_B/f.u.,[3] and 5.0 μ_B/f.u[4]. Compared with the data reported by S. Soni *et al*.,[5] an obvious reduction of Fe spin magnetic moments was observed. This loss could be attributed to either the site disorder in the bulk of the film, or the existence of a non-ferromagnetic interlayer close to the Al_2O_3 capping layer. The unique elemental selectivity of the XMCD technique has enabled direct observation of the relative magnetization of the Co and Fe, which indicates a ferromagnetic coupling of Co and Fe atoms.

1. Liu, W.; He, L.; Xu, Y.; Murata, K.; Onbasli, M. C.; Lang, M.; Maltby, N. J.; Li, S.; Wang, X.; Ross, C. A.; Bencok, P.; van der Laan, G.; Zhang, R.; Wang, K. L. *Nano letters* 2015, 15, (1), 764-9. 2. Elmers, H. J.; Wurmehl, S.; Fecher, G. H.; Jakob, G.; Felser, C.; Schönhense, G. *Applied Physics A* 2004, 79, (3), 557-563. 3. Galanakis, I.; Dederichs, P. H.; Papanikolaou, N. *Physical Review B* 2002, 66, (17). 4. Nie, S.; Chin, Y.; Liu, W.; Tung, J.; Lu, J.; Lin, H.; Guo, G.; Meng, K.; Chen, L.; Zhu, L. *Physical review letters* 2013, 111, (2), 027203. 5. Soni, S.; Dalela, S.; Sharma, S. S.; Liu, E. K.; Wang, W. H.; Wu, G. H.; Kumar, M.; Garg, K. B. *Journal of Alloys and Compounds* 2016, 674, 295-299.

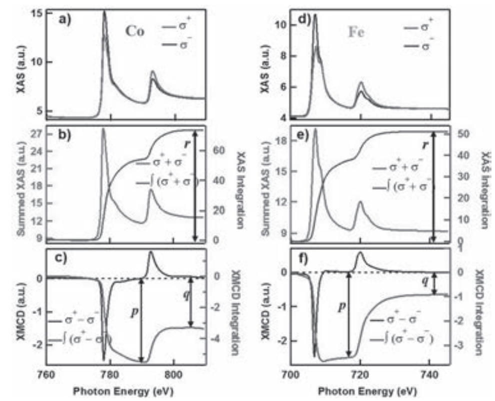

Fig. 1. XAS and XMCD measurements. X-ray absorption spectra of Co_2FeAl films at the (a) Co $L_{2,3}$ edge & (d) Fe $L_{2,3}$ edge averaged from TEY intensities measured at 300 K. σ+ and σ- stand for the XAS probed by left and right X-ray helicities, respectively. (b, e) Summed XAS spectra and its integration. (c, f) Corresponding XMCD spectra and its integration.

Session BS

PERMANENT MAGNET AND RELUCTANCE MACHINES III
(Poster Session)

Xiao Liu, Co-Chair
Hunan University, Changsha, China
Xiaofeng Ding, Co-Chair
Beihang University, Beijing, China

BS-01. Reliability Comparison of Stator-Permanent Magnet Machine and Rotor Permanent Magnet Machine.

W. Li[1] and M. Cheng[1]
1. School of Electrical Engineering, Southeast University, Nanjing, China

I. INTRODUCTION Recently, flux-switching permanent magnet (FSPM) machines have attracted wide interests due to the merits of high power density and high efficiency, etc.[1]-[4]. The reliability of FSPM machine is qualitatively analyzed by changing the phase number of the motor, thermal calculation and fault tolerance control in some literature. However, the reliability quantitative analysis of FSPM machines has never been reported although it is an important issue for electrical machines. Hence, in this paper, a reliability assessment model of FSPM machine is established based on Markov method. Then, a reliability comparison between FSPM machine and Prius machine is conducted. The relationship between the reliability and the position of the PM is determined. Finally, the comparison results are essentially useful to guide the selection of application field for the stator-PM machine. II. THE RELIABILITY MODEL AND ANALYSIS OF MACHINE Reliability analysis, not only need to consider the health state and failure state of components and subsystems, but also need to consider their main faults on the system work. The reliability state of machine system are determined by comparing reliability criteria with the effects of every faults. Markov process is a non-aftereffect stochastic process and based on the change of system state. The next state is only associated with the present state and regardless of all previous states. The Chapman-Kolmogorov equations is the most commonly used method for calculating the Markov method[5] (1) where, the superscript T, and represents the transpose of the matrix, derivatives of state probability matrix and state transition matrix, respectively. $P(t)$ can be represented by a row vector. The elements in the state transition matrix represent the probability of state transition. The sign indicates the state transition direction, "-" means transfer out and "+" means transfer in. The sum of each reliable working state is equal to the system reliability: (2) The biggest characteristics of stator-PM machine is that PMs are located on stator. It is necessary to discuss the influence of the PM position on the reliability. The heat dissipation of the PMs are relatively easy due to the PMs are located on stator. Compared with the PM failure rate of three-phase FSPM machine, the PM failure rate of Prius machine is relatively big. Therefore, the PM failure rate multiplied by a coefficient w to represent the impact of heat dissipation on the failure rate. (3) where, λ_{PMPD} represent permanent magnet performance degradation. Using the Markov method, the reliability equation of FSPM machine system and Prius machine system are calculated. Comparing the reliability of these two machine systems, the curves and the difference between them are illustrated in Fig.1. There is almost no difference in their reliability. The reliability varied with *w* are illustrated in Fig. 2. With the increase of *w*, the rate of decline of surface increases. The reliability of three-phase FSPM machine system (w=1) is bigger than that of Prius machine system (w>1). Therefore, the PM on the stator is helpful to improve the reliability of the PM-machine. III. CONCLUSION The Markov method are used to evaluate the reliability of FSPM machine system and Prius machine system. The effect of every component fault on the reliability assessment is considered. The biggest difference between their structure is the PM position, which indicates that the PM position can influence the reliability. The effect of temperature on the failure rate of PM is considered in the process of reliability evaluation. By comparing their reliability, the application field of FSPM machine system is wide. The detailed process of reliability assessment and analysis will be elaborated in the full-paper.

1)M. Cheng, L. Sun, G. Buja, L. Song, "Advanced electrical machines and machine-based systems for electric and hybrid vehicles," *Energies.* vol. 8, no. 9, pp. 9541-9564, Sept. 2015. 2)M. Villani, M Tursini, G. Fabri, L. Castellini, "High Reliability Permanent Magnet Brushless Motor Drive for Aircraft Application," *IEEE Trans. Ind. Electron.*, vol. 59, no. 5, pp. 2073–2081, Jun. 2012. 3)M. Cheng, Y. Zhu, "The state of the art of wind energy conversion systems and technologies: A review," *Energy Convers. Manage.*, vol. 88, pp. 332–347, Dec. 2014. 4)Fahad S. Al Badawi; Mohammad AlMuhaini; Reliability modelling and assessment of electric motor driven systems in hydrocarbon industries[J]. IET Electric Power Applications. 2015, 9(9): 605-611. 5)Ali M. Bazzi, Alejandro Dominguez-Garcia and Philip T. Krein, Markov Reliability Modeling for Induction Motor Drives Under Field-Oriented Control[J]. IEEE Trans. on Ind. Electron. 2012, 27(2):534-546.

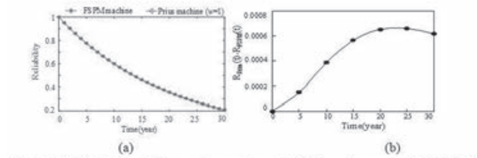

Fig.1. Reliability between Prius machine system and FSPM machine system. (a) Reliability curves. (b) Reliability gap between Prius machine system and FSPM machine system

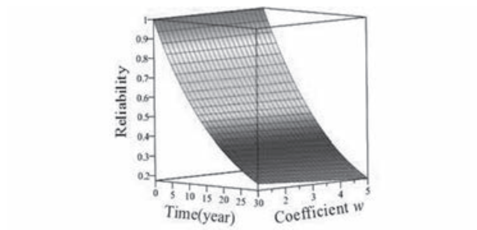

Fig. 2. Reliability of machine system varies with coefficient *w*

BS-02. Torque Analysis and Improvement of Single-Phase Asymmetric-Stator-Pole Doubly Salient Permanent Magnet Machine.

M. He[1], W. Xu[1] and C. Ye[1]

1. School of Electrical and Electronic Engineering, Huazhong University of Science and Technology, Wuhan, China

Abstract—Doubly salient permanent magnet machine (DSPMM) has received extensive attentions recently due to its simple structure, high reliability, high torque density, *etc.* An improved 4/4 stator/rotor single-phase asymmetric-stator-pole doubly salient permanent magnet machine (SP-ASPDSPMM) is proposed in this paper. Firstly, it investigates the topologies and operation principle based on graphical description and torque expression. Then, the effect of main structure parameters on the torque is studied based on two-dimensional finite element algorithm (2-D FEA). And then, comprehensive comparison on main electromagnetic performances for the two machines is made. Finally, one prototype for the improved structure is made and tested. It indicates that lower cogging torque, lower torque ripple and stronger starting performance can be obtained by the improved structure. The theoretical results are well validated by the experiments. I. Introduction Doubly salient permanent magnet machine (DSPMM) has been studied extensively in recent years due to its high torque density, high efficiency, high reliability, *etc.* [1]. However, the torque density of traditional DSPMM with concentrated windings is limited by its unipolar flux linkage. To obtain bipolar flux linkage and improve the electromagnetic performances, one 4/6 stator/rotor single-phase DSPMM with full-pitch winding configuration is developed in [2, 3]. They could offer higher efficiency and lower copper cost with the same output power. But they suffer from low material utilization ratio and poor starting performance. To solve the problems mentioned above, one 4/4 stator/rotor single-phase asymmetric-stator-pole doubly salient permanent magnet machine (SP-ASPDSPMM) is proposed in [4]. Based on the analysis results of [4], the torque density can be further improved by the SP-ASPDSPMM. But the torque ripple of it is relatively high and may deteriorate its operation performance. Therefore, one improved SP-ASPDSPMM is proposed in this paper to further improve its electromagnetic torque performance and other electromagnetic performances. This paper is organized as follows. In Section II, the topologies and operation principle for the SP-ASPDSPMMs are investigated. After that, the effect of main structure parameters on torque is performed based on two-dimensional finite element algorithm (2-D FEA) in Section III. In Section IV, comprehensive comparison of the original and improved structures on main electromagnetic performance indexes is made. Then, one prototype for the improved machine is made and tested in Section V. In Section VI, some conclusions are drawn. II. Topologies and Operation Principle Topologies for the original and improved 4/4 stator/rotor SP-ASPDSPMM are shown in Fig.1. It is known that the pole shoe, step air gap and auxiliary teeth are introduced in the improved structure. For limited space, more details will be given in the full paper. III. Effect of Main Structure Parameters on Electromagnetic Torque In this section, some design specifications are given and the effect of designed structure parameters on electromagnetic torque is studied based on 2-D FEA. More details will be given in the full text. IV. Performance Comparison In this section, the no-load air-gap flux density, output torque, torque ripple, starting torque, losses and other performances of the two machines are compared comprehensively. Fig. 1 shows the components of torque of both machines. The average torque for the original and improved structure is 0.72 and 0.59 Nm, respectively. However, the peak-to-peak value of torques for both machines are 2.67 and 1.29 Nm, respectively. Thus, the average torque for the improved structure is 18% lower than that of original one and the torque ripple for the former is 52% lower than that of the latter. Compared with the original machine, the value of reluctance torque for the improved model is higher around the θ=0°&45°rotor position and it reaches the minimum at θ=22.5°&67.5°rotor position, where the reactive torque reaches its maximum. Besides, the peak-to-peak value of cogging torque for the improved structure, 0.39 Nm, is 65% lower than that of the original one, 1.11Nm. Thus, the torque ripple could be much reduced. More results will be given in the following full paper due to the limited space. V. Experiment To verify the feasibility of proposed machine, a prototype with 750W and 25,000 rev/min is manufactured. The static torque, starting torque with different currents and other performances are tested and the measured results will be given in the full manuscript in details. VI. Conclusion An improved 4/4 stator/rotor SP-ASPDSPMM is proposed in this paper. The special topology and operation principle are investigated. The effect of designed structure parameters on the electromagnetic torque is analyzed based on 2-D FEA. The performance comparison of main electromagnetic performance indexes between the original and improved structure is made. It indicates that the average torque, cogging torque and torque ripple are 18%, 65% and 52% lower than those of original one, respectively. One prototype for the improved structure is made and the measured results are in good agreement with the theoretical analysis results based on 2D FEA with considerably small errors.

[1] M. Cheng, W. Hua, J. Zhang, and W. Zhao, "Overview of stator permanent magnet brushless machines," *IEEE Trans. Ind. Electron.,* vol. 58, no. 11, pp. 5087-5101, Nov. 2011. [2] D. Bian, Q. Zhan, "A novel single phase doubly salient permanent magnet motor," *Proc. Int. Conf. on Power Electronics and Drive Systems (PEDS),* 1999, pp. 725-729. [3] J. Z. Zhang, M. Cheng, and Y. Zhang, "Single phase doubly salient permanent magnet generator with full-pitched winding," *Proc. Int. Conf. on Electrical Machines and Systems (ICEMS)*, 2009, pp. 311 - 316. [4] M. He, W. Xu, and C. Ye, "Novel 4/4 stator/rotor single-phase asymmetric-stator-pole doubly salient permanent magnet machine," *Proc. Int. Conf. on Energy Conversion Congress and Exposition (ECCE)*, 2017, pp. 5049 - 5056.

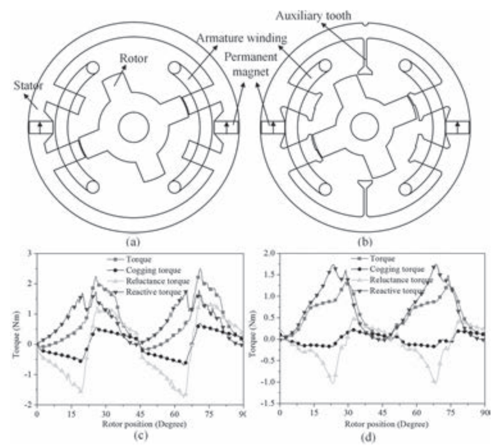

Fig. 1. Topologies and torque for both machines. (a). Original structure. (b). Improved structure. (c). Torque for original structure. (d). Torque for improved structure.

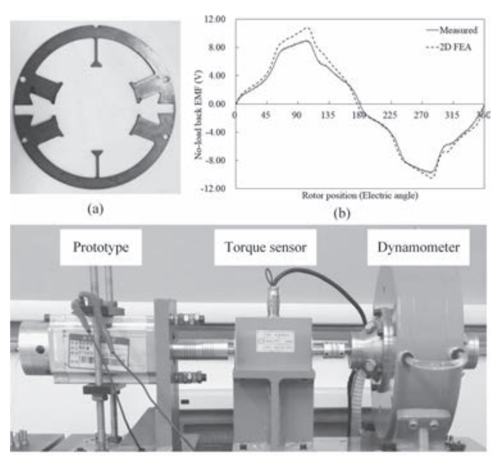

Fig. 2. Prototype and test bed. (a). Stator lamination. (b). No-load back-EMF@1736 rev/min. (c). Test bed.

BS-03. Suppression of Irreversible Demagnetization under Motor Operation by Preliminarily Demagnetizing of Neodymium Bonded Magnet in In-Wheel Axial-Gap Motor.

S. Nagano[1], M. Takemoto[1], S. Ogasawara[1], K. Orikawa[1], W. Hino[2] and K. Takezaki[2]
1. Graduate School of Information Science and Technology, Hokkaido University, Sapporo, Japan; 2. Dynax Corporation, Chitose, Japan

I. INTRODUCTION Small electric vehicles called city commuters travelling short distances have attracted much attention because of its small battery and low price. However, as the small city commuters have limited space inside the car, it is important to develop an in-wheel motor that incorporates a traction motor inside the wheel in order to utilize effectively space inside the car [1-2]. As one of the in-wheel motor, an in-wheel axial-gap motor, which is flat shape and can insert a reduction gearbox into the center of the stator core, has been proposed [3-5]. Cost reduction is required for traction motors in addition to the high performance such as small size, high output, high efficiency, and wide operation range of constant output. A neodymium sintered magnet has been used in conventional traction motors to satisfy the above strict required performance. The neodymium sintered magnet has high residual magnetic flux density and high coercive force, and a good squareness of B-H curve. However, it has a disadvantage of high price. Inexpensive electric city commuters are required to further reduce the motor cost. Therefore, in this study, the neodymium bonded magnet is adopted for a proposed in-wheel motor. Although characteristics of the neodymium bonded magnet is lower than that of the neodymium sintered magnet, the neodymium bonded magnet is inexpensive and have relatively high residual magnet flux density. One of the advantages of neodymium bonded magnet is that eddy current loss does not occur. Therefore, it is possible to suppress the heat generation of the magnet and rotor which is difficult to cool. However, neodymium bonded magnets have disadvantages of poor squareness, and irreversible demagnetization occurs even under normal operation. For this reason, the performance of the motor varies depending on different irreversible magnetization due to the different operating condition. This paper discusses that irreversible demagnetization in motor operation of the neodymium bonded magnet used in the in-wheel axial-gap motor is suppressed by improving the apparent squareness of B-H curve by applying reverse magnetic field at manufacturing the magnet. II. STRUCTURE OF PROPOSED MOTOR Fig.1 (a) shows an overall view of the proposed motor. The rotor is structured by inserting neodymium bonded magnets into a spoke shape rotor support using non-magnetic stainless steel to maximize the magnetic torque. This coreless rotor structure can suppress iron loss because of decreasing the magnetic flux density in the stator core. III. RESULTS OF ANALYSIS Fig. 1 (b) shows the B-H characteristics of the neodymium bonded magnet. FE analysis is carried out with two magnets: an ordinary neodymium bonded magnet and an irreversibly demagnetized neodymium bonded magnet previously subjected to reverse magnetic field after magnetization. The B-H characteristic of the magnet with preliminarily demagnetizing was created assuming that a reverse magnetic field of -222000 A/m is applied at manufacturing the magnet. The strength of this reverse magnetic field was determined from the magnetic field strength at the center of the magnet in the demagnetization analysis with the current density of 11.0 A/mm^2 and current phase angle β = 90 deg in order to withstand irreversible demagnetization under motor operation which is a maximum current density of 8.4 A/mm^2. Fig. 2 (a) shows the analysis results of torque characteristics using ordinary magnet without preliminarily demagnetizing when the magnet thickness is changed to 10, 15, 20 mm under maximum current density of 8.4 A/mm^2. The torque decreases due to demagnetization during the rotation angles from 0 deg to approximately 10 deg, and the torque decreases greatly as the magnet thickness is thinner. In case of the magnet thickness of 20 mm which becomes the smallest torque reduction, the average torque of the steady state between rotation angles from 30 deg to 45 deg was 113.2 Nm. Fig. 2 (b) shows reduction rates of U-phase magnetic flux linkage both models with and without preliminarily demagnetizing under the demagnetization analysis. The magnet thickness of both models is constant at 20 mm. The condition of demagnetization analysis was: the rotor does not rotate, current phase angle is β = 90 deg. The reduction rates of U-phase magnetic flux linkage at the maximum current density of 8.4 A/mm^2 was 3.2% in the model without preliminarily demagnetizing, while 0.3% in the model with preliminarily demagnetizing. It is evident that the demagnetization resistance is improved by preliminarily demagnetizing. Fig. 2 (c) shows the analysis result of torque characteristic using the model with preliminarily demagnetizing. The average torque between rotation angles from 30 deg to 45 deg was 111.1 Nm, and slightly 1.9% lower than the average torque of 113.2 Nm of the model without preliminarily demagnetizing. In contrast to the decrease in the residual magnetic flux density of 6.9% by preliminary demagnetization, the decrease in torque can be suppressed, and the occurrence of irreversible demagnetization under motor operation can be suppressed. IV. SUMMRY In this paper, irreversible demagnetization in motor operation of the neodymium bonded magnet used in the in-wheel axial-gap motor was suppressed by improving the apparent squareness by applying reverse magnetic field at manufacturing the magnet.

[1] K. Roumani, and B. Schmuelling, "Topology selection for low voltage PMSM for in-wheel direct-drive application," in *Proc. 2017 19th International Conference on Electric Drives and Power Electronics (EDPE)*, Oct. 2017. [2] S. Chung, S. Moon, D. Kim, and J. Kim, "Development of a 20-Pole–24-Slot SPMSM With Consequent Pole Rotor for In-Wheel Direct Drive," *IEEE Transaction on Industry Applications*, vol. 63, Issue 1, pp. 302-309, Jan. 2016. [3] K. Sone, M. Takemoto, S. Ogasawara, K. Takezaki, and H. Akiyama, "A Ferrite PM In-Wheel Motor Without Rare Earth Materials for Electric City Commuters," *IEEE Transactions on Magnetics*, vol. 48, No. 11, pp. 2961-2964, Nov. 2012. [4] T. Takahashi, M. Takemoto, S. Ogasawara, W. Hino, and K. Takezaki, "Size and Weight Reduction of an In-Wheel Axial-Gap Motor Using Ferrite Permanent Magnets for Electric Commuter Cars," *IEEE Transaction on Industry Applications*, vol. 53, No. 4, pp. 3927-3935, Jul./Aug. 2017. [5] R. Tsunata, M. Takemoto, S. Ogasawara, A. Watanabe, T. Ueno, and K. Yamada, "Development and Evaluation of an Axial Gap Motor using Neodymium Bonded Magnet,", *IEEE Transaction Industry Applications*, Issue 99, 2017.

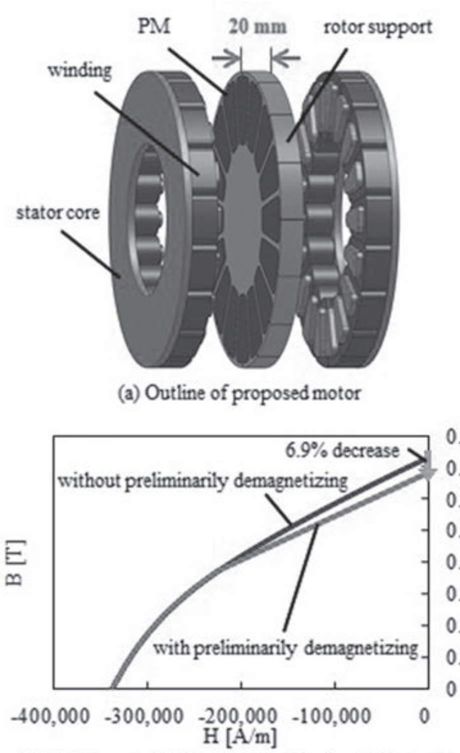

(b) B-H characteristics of neodymium bonded magnets

Fig. 1. Structure and magnet chracteristics

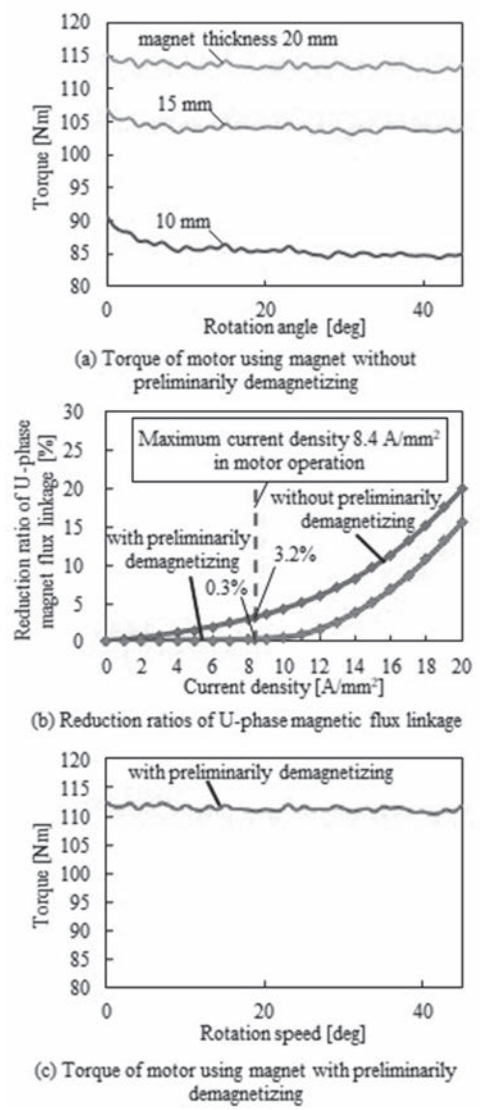

Fig. 2. Analysis results

BS-04. Study of Dual Airgap Stator and Rotor Permanent Magnet Machines with Halbach Array Configurations Using Phase-group Concentrated-coil Windings.

D. Chen[1], L. Fang[1], Z. Feng[1] and B. Bai[1]
1. School of Electrical Engineering, Shenyang University of Technology, Shenyang, China

Abstract— This paper presents a new structure of dual airgap stator and rotor permanent magnet machines to improve the electromagnetic performance and reduce torque ripple by incorporating the halbach array magnet configurations, phase-group concentrated-coil windings, and an unaligned arrangement of two stators. Firstly, the electromagnetic and mechanical structure of the dual airgap stator and rotor permanent magnet machines with halbach array (DASHAPMM) is designed, and the stator structure, rotor structure and winding distribution are given. Secondly, a quantitative comparison is performed between the proposed DASHAPMM and DASSTPMM (dual airgap stator and rotor permanent magnet machines with spoke-type configurations using phase-group concentrated-coil windings). The machine performance including back electromotive force, cogging torque, and electromagnetic torque are first analyzed by a finite element method under the same operating conditions. Finally, a prototype of the DASHAPMM and DASSTPMM is manufactured, and some key simulation results are verified by experimental tests. *Index Terms*— Dual airgap stator, machine, halbach array, spoke-type, phase-group concentrated-coil windings, comparison. I Introduction In recent year, to achieve wide speed range and high torque density in a constrained space of direct-drive applications, permanent magnet synchronous machines (PMSMs) are commonly applied comprising all power ranges due to their significant advantages such as high torque, power density and high efficiency[1]-[2]. Many novel topologies of PMSMs with high torque density have been proposed. However, a common challenge for both types of PMSMs exists from the viewpoint of production cost since the raw materials of rare earth PMs have the problem of high price and limited supply. In addition, another challenge in terms of pulsating torques, including cogging torque and torque ripple, is an important issue in PMSMs, especially in those PMSMs with dual airgap structures or spoke-type configurations featuring flux focusing effects [3]. However, although various traditional approaches, such as skewing, as well as tooth or magnet shaping, have been demonstrated to effectively reduce cogging torque and torque ripple, these approaches inevitably introduce performance degradation and manufacturing difficulties. Furthermore, these approaches are commonly considered independently after fulfillment of the requirements for torque/power densities. In this paper, an advanced design procedure for PMSMs, including both stator-PM and rotor-PM machines, is proposed to comprehensively improve machine performance including torque/power density, efficiency, cogging torque, and torque ripple. The DASHAPMM interior PM machine termed the rotor-PM machine configuration, are investigated for the direct-drive applications, in which the phase-group concentrated-coil windings and an unaligned arrangement of the two rotors/stators are utilized. Adoption of phase-group concentrated-coil windings is implemented to obtain a unity displacement winding factor, and enhance the flux focusing effects together with the use of halbach array PM configurations. The unaligned arrangement of two rotors/stators will help to not only achieve further flux magnification by alternating the PM flux from one air gap to the other while keeping the flux relatively constant in the magnet, but also suppress the cogging torque and torque ripple. A quantitative comparison is performed between the proposed DASHAPMM and DASSTPMM. The machine performance including back electromotive force, cogging torque, and electromagnetic torque are first analyzed by a finite element method under the same operating conditions. Finally, a prototype of the DASHAPMM and DASSTPMM is manufactured, and some key simulation results are verified by experimental tests. II. Study of simulation and experiment and discussion of result The structure of DASHAPMM and DASSTPMM as in Fig. 1 and Fig. 2. The magnet width, rotor and stator teeth width as well as the stator slot width within one group phase are designed to be the same as θ equaling $\pi/2$(elec.) for obtaining the unity displacement winding factor, while the stator slot width between the two different phases will be $5\theta/3$ equaling $5\pi/6$ (elec.) for producing a balanced three-phase back EMF. Thus, a specific combination of stator slots and rotor/magnet poles depending on the stator winding construction can be deduced. The structure of rotor for DASHAPMM is halbach array, and the structure of rotor for DASSTPMM is spoke-type. Fig. 3 shows a comparison of the magnetic flux density distribution. Fig. 4 shows a comparison of the back EMF. Fig.5 shows the manufactured motor and experimental system for DASSTPMM and DASHAPMM.The rotor of DASHAPMM is in the process of being manufactured. III. Conclusion This paper has proposed a design technique for DASHAPMM, incorporating the advantages of the halbach array magnets, phase-group concentrated-coil windings, and an unaligned arrangement of two rotors/stators. A quantitative comparison has been carried out among the investigated machines with the aid of 2-D FEM. The prototype of the proposed DASHAPMM has been manufactured based on the specifications of a standard washer motor, and some key simulation results are validated by experimental tests.

[1] Wenliang Zhao, Dezhi Chen, Thomas A. Lipo, Byung-il Kwon. “Dual airgap stator- and rotor- permanent magnet machines with spoke-type configurations using phase-group concentrated-coil windings,” *IEEE Trans. Ind. Appl*., Vol.53, no.4, pp.3327-3335, July./Aug. 2017. [2] D. G. Dorrell, M.-F. Hsieh, and A. M. Knight, “Alternative rotor designsfor high performance brushless permanent magnet machines for hybridelectric vehicles,”*IEEE Trans. Magn*., vol. 48, no. 2, pp. 835-838, Feb.2012. [3] S. Ooi, S. Morimoto, M. Sanada, and Y. Inoue, “Performance evaluationof a high power density PMA SynRM with ferrite magnets,”*IEEE Trans.Ind. Appl*., vol. 49, no. 3, pp. 1308-1315, May/Jun. 2013.

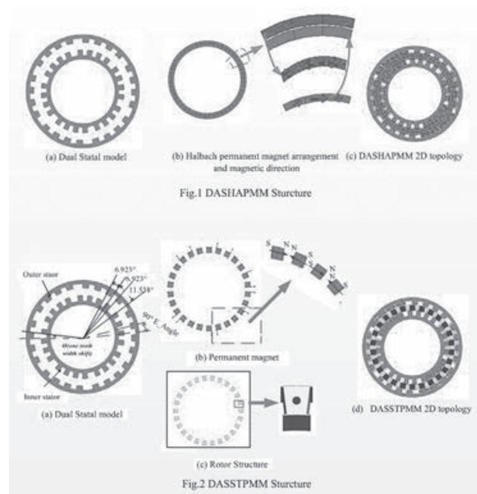

Fig. 1. a Structure of DASHAPMM and DASSTPMM

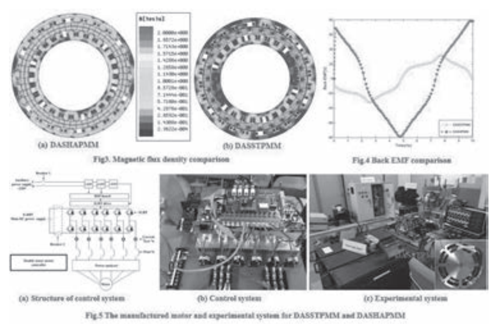

Fig. 2. b Simulation result and experimental system

BS-05. Unexpected Parasitic Torque Ripple Component Analysis in PMSM according to Parallel Winding Pattern Considering Eccentricity.

D. Lee[2], C. Jeong[2], S. Lee[2] and J. Hur[2]
2. Electrical Engineering Incheon National University, Incheon, China

Permanent magnet synchronous motor (PMSM) is widely used because of its high efficiency and high torque density [1], [2]. However, PMSM has a critical issue about torque ripple. The cause of the torque ripple of the permanent magnet motor is mainly divided into two types: one is structural reason and the other is harmonic component of the input power source (such as inverter output) [3]. In motor design perspective, the structural reason of torque ripple is the only factor that can be handled. The most popular phenomenon of torque ripple component caused by the structural reason of motor is cogging torque and thus, many researchers studied reduction methods of cogging torque [4]–[8]. As a result of these studies, many mitigation techniques of cogging torque were addressed. Since those techniques solve the cogging torque issue to some extent, this paper does not cover about the cogging torque. Instead, we investigated on torque component that had not drawn much attention and underestimated so far. It is the torque generated by circulating current in the parallel branch. This torque component is defined as 'unexpected parasitic torque' in this paper. In ideal condition, it is impossible to have circulating current in parallel winding. In reality, on the other hand, it is not possible to manufacture the motor in ideal condition. Therefore, the motors which have parallel branch can possibly produce unexpected parasitic torque component. To understand the phenomenon of parasitic torque generation, it is necessary to pay attention to the circulating current of the parallel windings. As mentioned above, the circulating current occurs by imperfect condition of motor; such as asymmetric magnetic strength of each pole, machining error of rotor and stator, unbalanced winding of each slot, rotor eccentricity and so on. Among these many imperfect conditions, in this paper, the eccentricity is considered which happens often in manufacturing process. In this analysis, the motor with 8pole and 12slot is used which is one of the most typical combinations of pole-slot number. The 8pole/12slot motor can have four possible cases of winding connection with double layer winding. Those cases are demonstrated in Fig. 1 with conceptual diagram of eccentric motor. As it is shown in Fig. 1 (a), the airgap lengths from each stator tooth (l_{g_U1}, l_{g_U2}, l_{g_U3}, l_{g_U4}) are different to each other when there is eccentricity. Thus, induced voltages by flux of permanent magnet at each slot winding will be clearly different. And then, since these slot windings are connected in series and parallel, those voltages of each winding will be superpositioned. Here, we can find the source of circulating current. When there is voltage difference between parallel windings, electrical potential occurs between those windings and this gives generation of the circulating current. Of course, the circulating current can be different according to the pattern of winding connection. Fig. 2 (a)–(d) shows the variation of circulating current under various eccentric conditions according to each winding connection cases and Fig. 2 (e)–(h) shows the parasitic torque component as a resultant of those circulating current. Here, winding connection case1 is omitted because it does not have parallel branch. The most noticeable point in Fig. 2 is that it is possible to have nearly zeroed circulating current and parasitic torque even though it has parallel circuit and eccentric rotor by looking at case 3. Other parallel connections, except the case3, show parasitic torque components that cannot be ignored. Since the parasitic torque increases in proportion to the rotation speed of the motor, it can be a fatal defect, particularly when high-speed operation is required. Thus in the case of high speed motor, the winding connection pattern of case3 is recommended. In the future, more detailed explanation about the correlation between parallel windings and eccentricity will be addressed. In such a process, it will be revealed that why there is minimum parasitic torque in the case3.

[1] S. T. Lee, and J. Hur, "Detection technique for stator inter-turn faults in BLDC motors based on third harmonic components of line currents," IEEE Transactions on Industry Applications, vol. 53, no. 1, pp.143-150, Jan/Feb. 2017. [2] J. K. Park, C. L. Jeong, S. T. Lee, and J. Hur, "Early detection technique for stator winding inter-turn fault in BLDC motor using input impedance," IEEE Transaction on Industry Applications, vol. 51, no. 1, pp. 7655-7665, Jan/Feb. 2015. [5] J. F. Gieras, "Analytical approach to cogging torque calculation of PM brushless motors," IEEE Transaction on Industry Applications, vol. 40, no. 5, pp. 1310-1316, Sep. 2004. [4] I. Petrov, P. Ponomarev, Y. Alexandrova, and J. Pyrhonen, "Unequal teeth widths for torque ripple reduction in permanent magnet synchronous machines with fractional-slot non-overlapping windings," IEEE Transaction on Magnetics, vol. 51, no. 2, Feb. 2015. [5] G. J. Li, B. Ren, Z. Q. Zhu, Y. X. Li, and J. Ma, "Cogging torque mitigation of modular permanent magnet machines" IEEE Transaction on Magnetics, vol. 52, no. 1, Jan. 2016. [6] Y. U. Park, J. H. Cho, and D. K. Kim, "Cogging torque reduction of single-phase brushless DC motor with a tapered air-gap using optimizing notch size and position," IEEE Transaction on Industry Applications, vol. 51, no. 6, pp. 4455-4463, Nov. 2015. [7] W. Ren, Q. Xu, Q. Li, and L. Zhou, "Reduction of cogging torque and torque ripple in interior PM Machines with asymmetrical V-type rotor design," IEEE Transaction on Magnetics, vol. 52, no. 7, Jul. 2016. [8] Y. D. Yao, D. R. Huang, J. C. Wang, S. H. Liou, S. J. Wang, T. F. Ying, and D. Y. Chiang, "Simulation study of the reduction of cogging torque in PM motors," IEEE Transaction on Magnetics, vol. 33, no. 5, pp. 4095-4097, Sep. 1997.

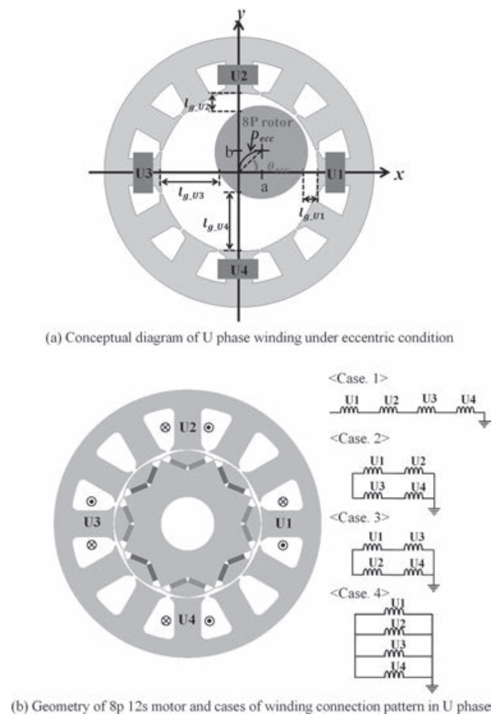

Fig. 1. Conceptual diagram of U phase winding under eccentric condition and cases of winding connection pattern in 8p 12s motor

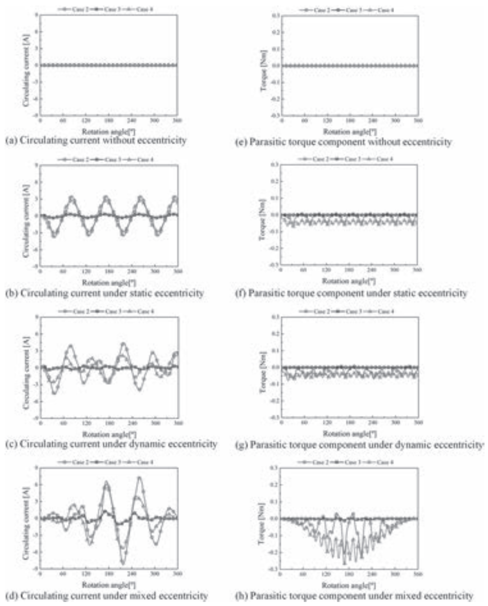

Fig. 2. Circulating current and parasitic torque component of each case under various eccentricity condition

BS-06. A Study of New Design Process of Spoke Type Permanent Magnet Synchronous Motor Considering Post Assembly Magnetization Performance.

S. Lee[1], H. Kong[2] and W. Kim[3]

1. Intelligent Information Technology Fusion, Busan University of Foreign Studies, Busan, The Republic of Korea; 2. Gachon University, Seongnam, The Republic of Korea; 3. Gachon University, Seongnam, The Republic of Korea

Permanent magnet synchronous motors (PMSM) have been used for various applications due to its high efficiency and power density [1-2]. The advantage of PMSM is based on the fact that permanent magnet (PM) can be used to generate field flux without external current. As a result, the ability to generate the magnetic flux of the PM is a direct indicator of the performance characteristics of the PMSM. The Demagnetization, which means a decrease in magnetic flux generated in PMs, is one of the important considerations in the design of PMSM. Several studies have discussed the design of PMSM that take into account the demagnetization of PMs [3-5]. However, the studies of the design of PMSM that take into account the magnetization performance was relatively insufficient. This is because both the surface permanent magnet synchronous motor (SPMSM) and the interior permanent magnet synchronous motor (IPMSM), which are mainly used in industry, do not have any difficulty in post assembly magnetization. The post assembly magnetization is a method in which a rotor is assembled with PMs without magnetization and then magnetized using a magnetizing yoke. This magnetization method is used as a standard in mass production motors because of its high mass productivity and the ability to completely magnetize PMs. As a result, in the conventional SPMSM and IPMSM, there was no problem in the magnetization of the PMs, so it was not necessary to consider the magnetization performance in the design process. However, the spoke type PMSM which has been largely investigated in recent years, because it has high power density and low cost by using a concentrated flux structure [6-7], is difficult to be magnetized by post assembly magnetization unlike the conventional motors [8]. This is because the rotor structure for the magnetic flux concentration of the spoke type PMSM acts as a cause of deterioration of the magnetization performance in the post assembly magnetization. As a result, the performance such as power density and efficiency is inversely related to the magnetization performance related to mass production. In order to design the spoke type PMSM with high mass productivity and high performance, it is necessary to consider the magnetizing performance in the design process. In this paper, we propose a new design process of spoke type PMSM considering not only the demagnetization of PMs but also magnetism performance. Using the proposed design process, we designed a spoke type PMSM that provides equal mass production and high performance compared to existing motors. The designed spoke type PMSM improved the output density by about 20% and the price was about 25% lower than the SPMSM of the same specification.

[1] J. Du, X. Wang, and H. Lv, "Optimization of magnet shape based on efficiency map of IPMSM for EVs," IEEE Trans. Appl. Supercond., vol. 26, no. 7, Oct. 2016, Art. no. 0609807. [2] Hui Li and H. Zhu, "Design of bearingless flux-switching permanentmagnet motor," IEEE Trans. Appl. Supercond., vol. 26, no. 4, Jun. 2016, Art. no. 5202005. [3] B. M. Ebrahimi and J. Faiz, "Demagnetization fault diagnosis in surface mounted permanent magnet synchronous motors," IEEE Trans. Magn., vol. 49, no. 3, pp. 1185–1192, Mar. 2013 [4] K. C. Kim, S. B. Lee, D. H. Kim, and J. Lee, "The shape design of permanent magnet for permanent magnet synchronous motor considering partial demagnetization," IEEE Trans. Magn., vol. 42, no. 10, pp. 3485–3487, Oct. 2006 [5] J. D. McFarland and T. M. Jahns, "Investigation of the rotor demagnetization characteristics of interior PM synchronous machines during fault conditions," IEEE Trans. Ind. Appl., vol. 50, no. 4, pp. 2768–2775, Jul./Aug. 2012 [6] P. Zhang, G. Y. Sizov, D. M. Ionel, and N. A. O. Demerdash, "Establishing the relative merits of interior and spoketype permanentmagnet machines with ferrite or NdFeB through systematic design optimization," IEEE Trans. Ind. Appl., vol. 51, no. 4, pp. 2940–2948, Jul./Aug. 2015. [7] S. J. Galioto, P. B. Reddy, A. M. EL-Refaie, and J. P. Alexander, "Effect of magnet types on performance of high-speed spoke interior-permanentmagnet machines designed for traction applications," IEEE Trans. Ind. Appl., vol. 51, no. 3, pp. 2148–2160, May/Jun. 2015. [8] H. S. Seol, T. C. Jeong, H. W. Jun, Ju Lee, and D. W. Kang, "Design of 3-Times Magnetizer and rotor of Spoke-Type PMSM Conidering Post-Assembly Magnetization," IEEE Trans. Magnetics, vol. 53, no. 11, Article Sequence No. 8208005, Nov. 2017.

BS-07. Development of IE4 Class Line-Start Permanent Magnet Motor from a Small Three Phase Induction Motor.

S. Rhyu[1], S. Khaliq[1], K. Lee[1] and R. Kim[1]
1. Intelligent Mechatronics Research Center, Korea Electronics Technology Institute, Bucheon, The Republic of Korea

Small three phase Induction Motors (IMs) are widely used in many industrial applications, such as blower and compressors, due to its lower cost, robustness and line start capability. However, IMs suffer from overall lower efficiency due to excitation penalty and higher rotor losses. On the other hand, PM synchronous motor can achieve higher power factor and efficiency; it lacks the line starting ability like IM. Line Start Permanent Magnet (LSPM) motor is developed to combine the advantages of direct line start ability and higher efficiency. LSPM motors can start directly from the grid due to the electromagnetic induction in the rotor cage bars, which produces cage torque during the asynchronous starting operation. Once the motor achieves rated speed, cage torque vanishes, and it behaves like permanent magnet synchronous motor (PMSM). Most of the LSPM motors developed in literature are 4-pole [1]. The manufacturing of a 4-pole LSPM motor is easier compared to 2-pole since it is not required to surround the shaft with PM and flux barriers to achieving higher performance, as it is essential in the latter. Furthermore, small-size IM (< 7.5 kW) have a significant potential for efficiency improvement due to a higher rotor loss component, however, at the same time, have limited space for PM insertion and flux barriers due to the presence of rotor cage [2]. However, 2-pole motors are considered suitable for the high-speed applications. In this paper, an LSPM motor is developed by modification to the small scale IM rotor with the aim to achieve almost unity power factor and operational efficiency to an IE4 or higher class motor. The 2-pole LSPM model is developed by inserting PMs in an off the shelf IM, HHT-05, considering minimum manufacturing cost. Stator outer dimension and slot design are kept same as in the basic IM model. Fig. 1 (a) shows the rotor assembly of the LSPM model. Only rectangular shaped PMs are utilized to mitigate the manufacturing cost associated with the unconventional PM shapes. PM thickness was kept 3 mm to withstand the stator magnetomotive force (MMF) during asynchronous starting which can cause irreversible demagnetization. Rotor cage bars were skewed by one slot pitch for a smooth back EMF and torque ripple reduction. Initially, the LSPM model was analyzed with Steady state Finite Element Analysis (FEA) to assess the no-load output back EMF. Then, dynamic starting performance and synchronizing ability was examined by directly applying line voltage to the stator in FEA simulation. Firstly, no load back EMF of the LSPM is analyzed by rotating the rotor at the rated speed. Back EMF, induced by PMs in steady state, is a crucial parameter to improve the performance of LSPM, i.e., high efficiency and unity power factor. Therefore, one winding turn/slot is increased in the LSPM compared to the basic IM to improve the back EMF while keeping a reasonable slot fill factor for feasible manufacturing. Fig. 1 (b) shows the back EMF of the unskewed and skewed rotor bars by one slot pitch. It shows that due to the slotting structure of stator and the presence of rotor cage produces higher order harmonics in the back EMF, which are smoothed out through skewing of the rotor bars. Furthermore, it is essential to analyze the dynamic starting performance of LSPM to verify the starting ability. Therefore, a dynamic simulation was performed with the FEA. The stator was supplied with the line voltage and frequency, i.e., 220 V and 60 Hz. Fig. 1 (c) exhibits the output load torque. The negative peaks in the torque output are due to the braking effect produced by the PMs during starting and affect the synchronization of LSPM with the stator MMF. However, the developed model achieves the rated torque after almost 0.3 S of starting. Fig. 1 (d) shows the load current waveform, which was also obtained through dynamic simulation. When LSPM is connected to the grid, it draws large unbalanced currents at the start. As the rotor starts rotating, it induces the voltage in the stator winding, and the stator currents become balanced finally at the rated speed as shown in fig. 1 (d). Table I (Fig. 2) summarizes the design specifications of basic IM and LSPM models and compares the output performance. Stator outer diameter and slot design are kept same in both models. Furthermore, the stack length was reduced by 15 mm in the LSPM model, which was enough to achieve the required efficiency and almost unity power factor. Additionally, smaller stack length also reduced the material cost in LSPM. Rated speed in both models is also different as IM rotor runs at a slip while LSPM rotor rotates in synchronism with the stator field during steady state. Therefore, a small increase in output power of LSPM is expected, as shown in table I. Rated current in the LSPM is found to be 19 % lower than the basic IM model, which in turn decreased the copper losses and also caused the improvement in power factor. Table I shows that IM exhibits 57 % higher copper losses compared to LSPM model. Also, the power factor in LSPM is 0.985 which is almost unity and 0.18 higher than IM. Furthermore, the efficiency of the LSPM at the rated condition in 94.7 %, which is 7.2 % higher than the basic IM model. Therefore, it is evident that the performance improvement in LSPM is remarkable with only small modifications. The detailed design of the developed model along with the experimental analysis will be presented in the full manuscript.

[1] R. T. Ugale and B. N. Chaudhari, "Rotor Configurations for Improved Starting and Synchronous Performance of Line Start Permanent-Magnet Synchronous Motor," in IEEE Transactions on Industrial Electronics, vol. 64, no. 1, pp. 138-148, Jan. 2017.doi: 10.1109/TIE.2016.2606587 [2] D. Mingardi and N. Bianchi, "Line-Start PM-Assisted Synchronous Motor Design, Optimization, and Tests," in IEEE Transactions on Industrial Electronics, vol. 64, no. 12, pp. 9739-9747, Dec. 2017.doi: 10.1109/TIE.2017.2711557

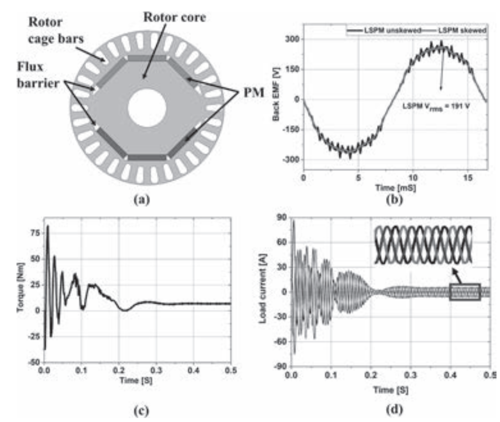

Fig. 1. (a) LSPM rotor (b) Steady-state back EMF (c) Output torque (d) Load current

Table. I Design Specifications and FEA performance

ITEM	IM	LSPM Model
Outer diameter (mm)	148	
Stack length (mm)	100	85
Supply voltage (V)	220/380	
No. of poles	2	
No. of rotor bars	30	
Rotor bar material	Aluminum	
Magnet volume (mm^3)	-	30,600
PM material	-	NdFeB
FEA PERFORMANCE COMPARISON		
Rated speed (rpm)	3530	3600
Output Power (kW)	2.55	2.6
Rated current (A_{rms})	5.32	4.30
Copper losses (W)	170	108
Power factor	0.81	0.985
Efficiency (%)	87.5	94.7

Fig. 2.

BS-08. Design and Analysis of a Two-phase BLDC Motor with Hybrid Permanent Magnet Material for Only-pull Drive Technique.

T. Yazdan[1] and B. Kwon[1]
1. Electronic Systems Engineering, Hanyang University, Ansan-si, The Republic of Korea

I. INTRODUCTION Permanent magnets with high energy density are widely used for high performance permanent magnet (PM) machines. However, the cost increase of rare-earth magnets demand the effective utilization or the use of relatively thin magnets in PM machines. To reduce the consumption of rare-earth magnets, hybrid permanent magnets arrangements (combined with ferrite) have been used in various PM motors, and the demagnetization endurance has been investigated [1]-[2]. The surface type and the spoke type magnets forming the parallel and serial magnetic circuits have been employed for the purpose of torque improvement. However, spoke type magnets and the thin surface magnets suffer the greater risk of irreversible demagnetization. Traditionally, the thick magnets are utilized to ensure the healthy operation of PM machines without irreversible demagnetization [3]. Recently, an only-pull drive technique have been developed in [4] to protect the thin magnets from irreversible demagnetization and discussed a surface mounted PM (SPM) motor to validate the effectiveness. This paper proposed a two-phase radial flux brushless DC (BLDC) motor comprising of hybrid permanent magnet material on the rotor; NdFeB in SPM type and ferrite in spoke type configuration. The purpose of this hybrid topology is to improve the output torque and to save both types of magnets from irreversible demagnetization at a time. The electromagnetic performance of the proposed motor has been compared with that of a basic two-phase SPM type motor driven by the only-pull drive technique. Further, the operating point of the both magnet types has been analyzed to confirm the safe operation of the proposed motor without irreversible demagnetization. The merits and demerits of the proposed operation are also discussed. II. THE PROPOSED MOTOR TOPOLOGY AND PRINCIPLE OF OPERATION The topology of the basic and the proposed two-phase BLDC motors driven by the only-pull drive technique is shown in Fig. 1(a) and Fig. 1(b) respectively. The proposed motor contains a stator equipped with group concentrated winding [5] with an additional slot width between the phase groups to produce balanced back-EMF and a rotor decorated with thin surface type (NdFeB) and spoke type (ferrite) magnets. The flux flows from spoke magnets to the iron-poles, and passes from the surface magnets towards stator core, and returns back through the other surface magnet forming a serial magnetic circuit. All the conventional PM machines operate under both the magnetizing process (pull process) and demagnetizing process (push process) of the flux linkage at the risk of irreversible demagnetization of the magnets, which may result in the failure of machine operation. In the operation principle of the proposed motor, current is injected only for the increasing flux linkage that is only-pull process and will not go under decreasing flux linkage (push-process) which is caused by repulsion of alike poles from stator and rotor. The basic concept of pull process and push process is shown in Fig.1 (c). Each phase conducts for the span of 90 electrical degrees only in the region of pull process of flux linkage. Thus, one phase produces the torque alternately at any time. Regardless of applying the only-pull drive technique, the trailing edges of the standalone spoke type magnets are vulnerable to the external opposite fields that causes the partial demagnetization. Whereas, in the proposed motor, the surface magnets provide a shield to the trailing edges of the spoke type magnets and protects from intensive reverse fields during the operation. III. RESULTS AND DISCUSSION Using the only-pull drive technique for the proposed motor, the demagnetization profile and the electromagnetic performance are primarily investigated. To investigate the demagnetization profile, the motors are subjected to the overload current of 4.5A that is multiple of rated current of 1.5A and back-EMF is analyzed after the occurrence of overload current. However, the proposed motor having a hybrid permanent magnet material and driven with only-pull technique, executes safe operation without risk of irreversible demagnetization. The comparison is summarized in Fig. 2. As a result, the proposed motor topology can be a better solution for only-pull drive technique where spoke type magnets are involved. Further, the improved torque in the proposed motor has been observed. The detailed analysis and comparison results based on magnetic operating point will be presented in the full paper.

[1] Q. Chen, G. Liu, W. Zhao, M. Shao and Z. Liu, “Design and Analysis of the New High-Reliability Motors With Hybrid Permanent Magnet Material,” *IEEE Trans on Magnetics*, vol. 50, no. 12, pp. 1-10, Dec. 2014. [2] Gaohong Xu, Guohai Liu, Xinxin Du, and Fangfang Bian “A novel PM motor with hybrid PM excitation and asymmetric rotor structure for high torque performance”, *American Institute of Physics advances,* Mar 2017. [3] S. Zhang et al., “Permanent magnet technology for electric motors in automotive applications,” 2012 *2nd International Electric Drives Production Conference (EDPC)*, *Nuremberg*, 2012, pp. 1-11. [4] T. Yazdan, W. Zhao, T. A. Lipo and B. I. Kwon, “A Novel Technique for Two-Phase BLDC Motor to Avoid Demagnetization,” *IEEE Trans on Magnetics*, vol. 52, no. 7, pp. 1-4, July 2016. [5] W. Zhao, T. A. Lipo and B. I. Kwon, “Comparative Study on Novel Dual Stator Radial Flux and Axial Flux Permanent Magnet Motors With Ferrite Magnets for Traction Application,” *IEEE Trans on Magnetics*, vol. 50, no. 11, pp. 1-4, Nov. 2014.

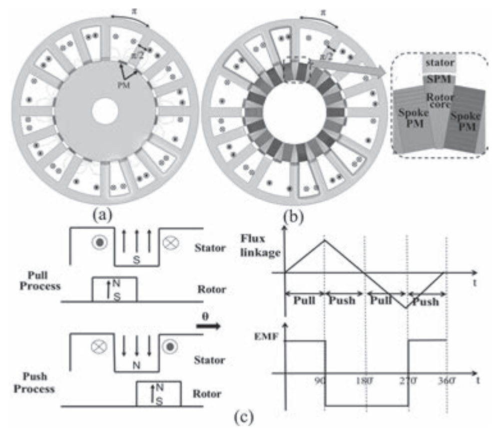

Fig. 1. Topology of 16slots/18poles two-phase PM motor (a) SPM type with NdFeB magnets (b) hybrid type with NdFeB (SPM) and ferrite type (spoke) (c) basic pull and push process of PM machine

Table. 1 Design data and FEA results for two-phase BLDC motor

Items	Basic model	Proposed model
Slots/Poles	16/18	
Drive type	Only-pull	Only-pull
Rated speed, rpm	1580	
Back-EMF E_{rms}, V	440	552
Rated current I_{rms}, A	1.5	
Output Torque, Nm	4.89	5.74
Demagnetization protection on overload current	Yes	Yes

Fig. 2.

BS-09. Comparative Studies of Modular PMSMs with Symmetrical or Asymmetrical Six-Phase Windings.

L. Cheng[1], Y. Sui[1], *P. Zheng*[1], Z. Yin[1] and R. Ma[1]
1. Harbin Institute of Technology, Harbin, China

Nowadays, multiphase permanent-magnet synchronous machines (PMSMs) equipped with fractional-slot concentrated windings (FSCWs) are increasingly attractive for the industrial applications due to their high torque density, high efficiency and high fault-tolerant capacity [1, 2]. Meanwhile, owing to their characteristics of easy manufacturing, convenient transportation and high fault-tolerant capacity, the modular permanent magnet synchronous machines (PMSMs) are also favored by various industrial applications, such as electric vehicle and wind turbine applications [3]. Fortunately, the FSCWs, especially the single-layer FSCWs, are inherently easy to modular manufacture. However, due to the manufacturing tolerance, the additional mechanical gaps between the modules are inevitable which will affect the magnetic field distribution and hence the electromagnetic performances. The influences of the additional mechanical gaps on electromagnetic performances of three-phase modular PMSM have been investigated [4]. Nevertheless, the influences of the additional gaps between the modules in a six-phase modular machine have not been covered. Moreover, the influences of the mechanical gaps on the performances under post-fault operating conditions in a six-phase PMSM have not been investigated in current literature. Therefore, in this paper, the influences of the additional mechanical gaps on the performance under healthy, faulty and post-fault operating conditions of modular PMSM with symmetrical or asymmetrical six-phase windings are investigated. In this paper, firstly, by analyzing the slot star diagram of a conventional 12-slot/14(10)-pole three-phase PMSM with double-layer FSCW, three different six-phase winding layouts can be obtained by dividing the conventional 12-slot/14(10)-pole three-phase winding into two sets of independent three-phase windings as shown in Fig. 1. It can be found that the winding of scheme I is asymmetrical six-phase winding with an electrical angle of 30° between the two sets of three-phase windings and the other two schemes are symmetrical six-phase winding with an electrical angle of 60° between the two sets of three-phase windings. Scheme III will be abandoned because the electromagnetic performances of scheme III are all the same with II while its magnetic isolation capacity is much lower than scheme II. To enhance their magnetic isolation capacity further, the 12 double-layer slots are divided into 24 single-layer slots so that three 24-slot/14(10)-pole six-phase PMSM with unequal teeth can be obtained. And, the modular stators are used to enhance their practicability and fault-tolerant capacity, as shown in Fig. 2. It can be seen that for scheme I, there is only one modular method—one module with one coil. On the other hand, there can be two different modular methods—one modular with one coil and one modular with one-phase (one phase possesses two adjacent coils). The different modular methods will introduce different additional mechanical gaps which cannot be avoided resulting from the manufacture limitations and tolerances, as shown in Fig. 2. The influences of these mechanical gaps on the electromagnetic performances, such as the winding factor, average torque, torque ripple and stator magnetomotive distribution, are fully investigated. Moreover, the influences of these gaps under faulty operating conditions, such as one-phase open-circuit, two-phase open-circuit and one-phase short-circuit failure, and under post-fault operating conditions are also investigated.

[1] V.I. Patel, J. Wang, and D.T. Nugraha et al, “Enhanced availability of drivetrain through novel multiphase permanent-magnet machine drive,” *IEEE Trans. on Ind. Electron.*, vol. 63, no. 1, pp. 469-480, 2016. [2] A.M. EL-Refai, J.P. Alexander, and S. Galioto et al, “Advanced high-power-density interior permanent magnet motor for traction applications,” *IEEE Trans. on Ind. Appl.*, vol. 50, no. 5, pp. 3235–3248, 2014. [3] B. Bickel, J. Franke, and T. Albrecht, “Manufacturing cell for winding and assembling a segmented stator of PM-synchronous machines for hybrid vehicles,” *in Proc. 2nd Int. EDPC*, Oct. 2012, pp. 1–5. [4] G. J. Li, Z. Q. Zhu, W. Q. Chu, M. P. Foster, and D. A. Stone, “Influence of flux gaps on electromagnetic performance of novel modular PM machines,” *IEEE Trans. Energy Convers.*, vol. 29, no. 3, pp. 716–726, Sep. 2014.

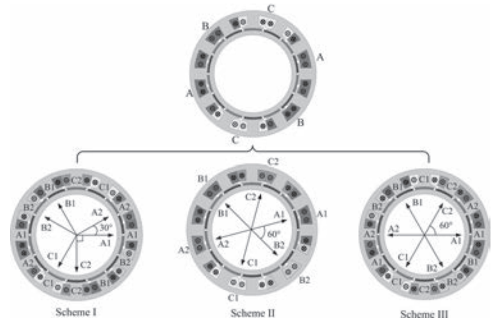

Fig. 1. Three 12-slot/14-pole six-phase winding layouts derived from the conventional three-phase winding

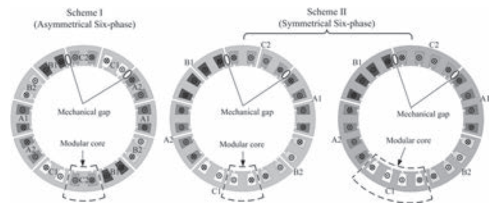

Fig. 2. Modular stators for different six-phase FSCW configurations

BS-10. Reaserch on Flux Density Fluctuation for Brushless Double Rotor Flux-Switching Permanent Magnet Motor Considering Low Magnetic Coupling.

Z. Xiang[1]
1. School of electrical and information engineering, Jiangsu University, Zhen Jiang, China

I. INTRODUCTION. A type of machines family with feature of double rotors, in recent years, has attracted increasing attention due to its advantages of high power density, high efficiency, and high PM utilization [1]. And when the double rotors concept was put forward, various motor topologies have been proposed for obtaining the improved torque capability. Among the existing double rotors motors, a type of double-output double rotor permanent magnet (DO-DRPM) motors are particularly favored by the researchers, which because they can be connected with engine to achieve a highly-integrated hybrid powertrain and realize the function of power split and combination. Since the DO-DRPM motor generally has two independent rotors, the multi-operational modes can be performed in one motor frame, such as the four-quadrant energy transducer (4QT) [2]. It is noted that the 4QT usually needs brushes and slip rings to feed current, which causes the frequent maintenance and friction loss. Recently, an alternative brushless scheme is developed purposely for the DO-DRPM motor [3]. The new resulting motor can not only manage the power split and combination, but also avoid the brush and slip ring. However, regardless of the 4QT or the brushless DO-DRPM motor, their flux lines distribution between the inner and outer airgaps exhibits a certain extent of magnetic coupling. It will result in an irregular variation of the magnetic field, which brings difficulties to the independent control of the inner and outer motors, especially when they are designed with different pole pairs. Therefore, the analysis and evaluation of magnetic coupling is crucial and necessary for the type of the DO-DRPM motors. The purpose of this paper is to investigate the magnetic coupling for a brushless double rotor flux-switching permanent magnet (BDR-FSPM) motor. And by introducing the concept of flux density fluctuation, the magnetic coupling degree between the inner and outer motor can be evaluated accurately and conveniently, which lays a foundation for the high reliability operation and flexible controllability of the BDR-FSPM motor. II. MOTOR TOPOLOGIES AND MAGNETIC FIELD DISTRIBUTION In this paper, four topologies are presented and investigated for low magnetic coupling, as shown in Fig. 1. From Fig. 1 (a) to (d), among the four motor topologies, the common grounds are the same pole-slot combinations of 22-pole /12-slot /10-pole and the same locations of armature winding and PMs. Meanwhile, the differences of them are the various designs of the PM topology, flux barrier, magnetic bridge, and relative position between the inner and outer stators. Then the magnetic field distributions of the four motor topologies are depicted in Fig. 2. It can be seen from Fig. 2 (a) to (d) that the motors of type I, type II and type III present obvious serial magnetic path between the two air-gaps, while the majority of magnetic flux lines in Type IV motors is closed in the middle stator, enjoying a desired parallel magnetic path and indicating a lower magnetic coupling to some extent. Additionally, to quantitatively evaluate the flux density fluctuation caused by magnetic coupling, four referenced points are selected for calculating the flux density fluctuation, respectively setting in the outer rotor, outer stator, inner rotor, and inner stator, as illustrated in Fig. 2. III. SIMULATION AND EXPERIMENT Fig. 3 shows the no-load flux densities of the four points for the four motor topologies. When the inner motor works alone, the flux densities variations of point 1 in outer rotor and point 2 in outer stator are respectively depicted in Fig. 3 (a) and (b). Similarly, at the condition of outer motor working alone, Fig. 3 (c) and (d) respectively show the flux densities variations of point 3 in inner stator and point 4 in inner rotor. Obviously, under the four points, the type IV motor has the lowest flux density variation. For better presentation, Fig. 3 (e) illustrates the peak to peak (P-P) values of the flux densities in all points. And to present a fair comparison, the total flux density fluctuations of the four motors are further calculated, and it is defined as the average value of the flux density P-P values of the four points, as shown in Fig. 3 (f). As expected, among the four topologies, the type IV motor has the smallest flux density fluctuations, indicating that it possesses the lowest magnetic coupling degree between the inner and outer motors. Moreover, the partial performances of the type IV motor are given in Fig. 4. From Fig. 4 (a) and (b), the inner coupling-EMF accounts for 2.5% value of the outer back-EMF, while the percentage of the outer coupling-EMF on the inner back-EMF is also low, only accounting for 1.8%, manifesting a low magnetic coupling. Meanwhile, the steady torque of outer and inner motors is presented in Fig. 4 (c) and (d). Then a prototype motor with the type IV topologies is manufactured, as shown in Fig. 5(a). And Fig. 5 (b) depicted the measured back-EMF of outer motor and its coupling-EMF, which is agreed with the results in Fig. 4 (a). In conclusion, the simulation and experiment results shows that the BDR-FSPM motor with the topologies IV offers low magnetic coupling, providing the guarantee for the flexible controllability of the motor. More detailed performances analysis and experimental results will be presented in the full paper to verify the validity.

[1] L. Sun, M. Cheng, H. Wen, and L. Song, "Motion control and performance evaluation of a magnetic-geared dual-rotor motor in hybrid powertrain," *IEEE Trans. Ind. Electron.* vol. 64, no. 3, pp. 1863-1872, Mar. 2017. [2] P. Zheng, R. Liu, P. Thelin, E. Nordlund, and C. Sadarangani, "Research on the cooling system of a 4QT prototype machine used for HEV," *IEEE Trans. Eenrgy Convers.*, vol. 23, no. 1, pp. 61-67, Mar. 2008. [3] Y. Yeh, M. Hsieh, D. G. Dorrell, "Different Arrangements for Dual-Rotor Dual-Output Radial-Flux Motors," *IEEE Trans. Ind. Appl.*, vol. 48, no. 2, pp. 612-622, Mar./Apr. 2012.

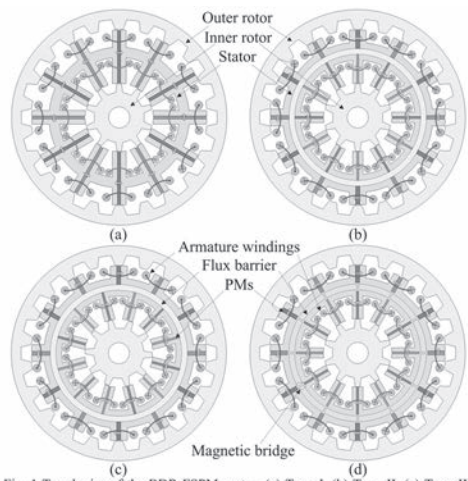

Fig. 1 Topologies of the BDR-FSPM motor. (a) Type I. (b) Type II. (c) Type III. (d) Type IV.

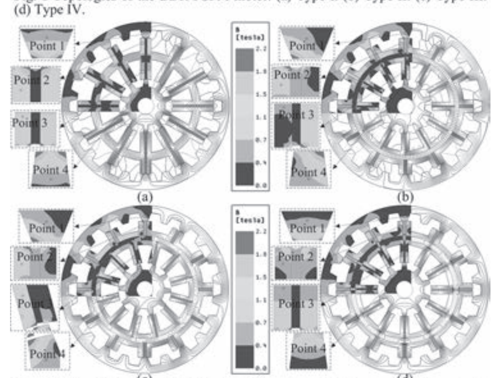

Fig. 2 No-load Magnetic distributions of the BDR-FSPM motor. (a) Type I. (b) Type II. (c) Type III. (d) Type IV.

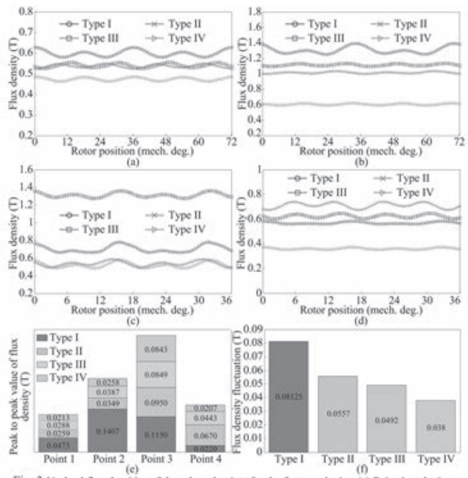

Fig. 3 No-load flux densities of the selected points for the four topologies. (a) Point 1 at the inner motor working alone. (b) Point 2 at the inner motor working alone. (c) Point 3 at the outer motor working alone. (d) Point 4 at the outer motor working alone. (e) Peak to peak value of flux densities. (f) Flux density fluctuation.

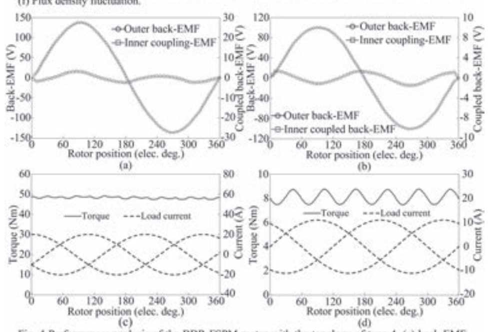

Fig. 4 Performances analysis of the BDR-FSPM motor with the topology of type 4. (a) back-EMF of outer motor and its coupling-EMF. (b) back-EMF of inner motor and its coupling-EMF. (c) Steady torque of outer motor. (d) Steady torque of inner motor.

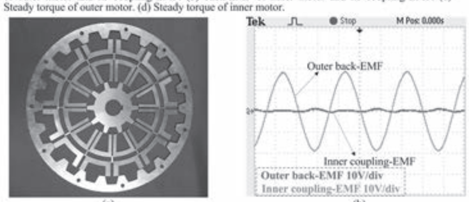

Fig. 5 Experimental validation of the BDR-FSPM motor with the topology of type 4. (a) Silicon steel sheet. (b) Measured back-EMF of outer motor and its coupling-EMF.

BS-11. Development of Differing Extent Mesh Adaptive Direct Search applied for Optimal Design of Spoke-Type PMSM.

D. Lee[2] and S. Jung[1]
1. Sungkyunkwan University, Suwon, The Republic of Korea; 2. Department electrical and computer engineering, University of Illinois at Urbana-Champaign, Champaign, IL, United States

Introduction The spoke type permanent magnet synchronous machines (PMSM) have a buried PMs on both sides of poles in rotor, which has characteristics of high torque density and high power density by concentrated magnetic flux [1,2]. However, torque ripple and cogging torque is generated higher than other type motors. Hence, spoke type PMSM is required for reduction design of torque ripple and cogging torque [3]. This paper presents newly differing extent mesh adaptive direct search (MADS) to minimize torque ripple and cogging torque for spoke type PMSM. MADS is a mesh-based approach for heuristic search methods and generates random trial points to search the best local minima [4]. Multistart strategy can be adopted in MADS to search the global optimum, which enables an algorithm to select the global optimum among several solution candidates. In conventional multistart scheme, each solution starts to search for a local optimum after a convergence of the previous one. This consumes excessive function calls at local regions that are irrelevant to the global optimum. This study aims to solve these problem by introducing Differing Extent MADS, which it is an intelligent method that conducts parallel multistart methods and shares information between each solution in the same search step. It can distinguish whether the points are close to the global optimum and stops the search if not, to reduce the computation time. Furthermore, each solution is classified as three group (p1~3), which have distinct characteristics as: p1 has large searching flame and mesh size, which can strengthen the searching performance for a global optimum. p3 has small of that, which can convergence fast to local optimum than others. p2 have intermediate feature between these, which can complement both global optimum and speed. Also, three group search to share an information each other for effective searching. Fig.1 show the concept of proposed algorithms. In full paper, the performance of proposed algorithm would be verified by benchmark function and electric machine in terms of global searching and a computation time, which it compared with other algorithms. For rotating machine with high speed, PMs get centrifugal force and it causes serious damage to the rotor core. Also, changed slot sharp and current density by optimal design causes temperature rising. In accordance, it is recommended to include mechanical stress according to modified designs. In this paper, the proposed optimization algorithms have been applied for optimal design of spoke type PMSM for multi-objective with reducing the torque ripple and cogging torque considering mechanical stress. The performance is analyzed for reliable accuracy based on nonlinear FEA as shown Fig. 2. In the process for optimal design, rotor dimension is designed for mechanical stress from optimization algorithms and it is evaluated for safety factor according to maximum rotor speed. Electromagnetic analysis starts until satisfying a safety factor iteration on. Second, average torque is calculated by electromagnetic field. If it is not satisfied, input current is increased one until average torque is satisfied. 'The results will be presented at full paper.

D. Y. Kim, J. K. Nam, and G. H. Jang," Reduction of Magnetically Induced Vibration of a Spoke-Type IPM Motor Using Magnetomechanical Coupled Analysis and Optimization," *IEEE Trans. Magn.,* vol. 49, no. 9, pp. 5097-5105, 2013. Y. Demir, O. Ocak, M. Aydin, "Included in Your Digital Subscription Design, optimization and manufacturing of a spoke type interior permanent magnet synchronous motor for low voltage-high current servo applications," IEEE International, IEMDC, pp. 9-14, 2013. K. Y. Hwang, J. H. Jo, and B. I. Kwon, "A Study on Optimal Pole Design of Spoke-Type IPMSM With Concentrated Winding for Reducing the Torque Ripple by Experiment Design Method," *IEEE Trans. Magn.,* vol. 45, no. 10, pp. 4712-4715, 2009. D. Lee, S. Lee, J.-W. Kim, C.-G. Lee, and S.-Y. Jung, "Intelligent memetic algorithm using GA and guided MADS for the optimal design of interior PM synchronous machine," IEEE Trans. Magn., vol. 47, no. 5, pp. 1230–1233, May 2011

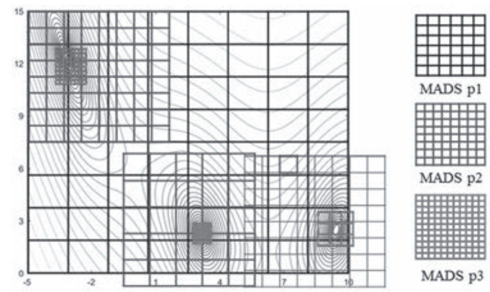

Fig. 1. Concept of Differing Extent Mesh Adaptive Direct Search

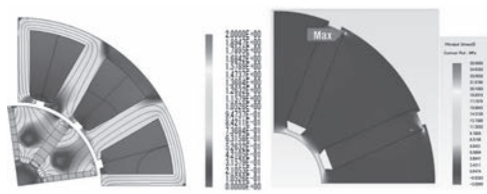

Fig. 2. Flux density and mechanical stress of spoke-Type PMSM

BS-12. Comparative Study of Serial and Parallel PM Axial Field Flux-switching Memory Machines.

N. Li[1,2], *M. Lin*[1], J. Zhu[2], G. Yang[1] and Y. Kong[1]
1. School of Electrical Engineering, Southeast University, Nanjing, China; 2. School of Electrical and Data Engineering, University of Technology Sydney, Sydney, NSW, Australia

Abstract This paper mainly investigates two axial field flux-switching memory (AFFSM) machines with serial and parallel permanent magnets (PMs) configurations. Hysteresis model is adopted to present the flux regulation principle in both configurations. Finite element method is used analyze influence of design parameters on the working of hybrid PM.The flux regulation characteristics are obtained and compared. Results show that both configurations can obtain a good flux regualtion capacity by coordinating two PMs. Introduction Memory machines using low coercive force (LCF) nonlinear permanent magnets (PMs) for flux regulation are attracting great research interests [1-6].The LCF PMs in memory machines can be demagnetized and re-magnetized by short pulse current with negligible energy dissipation. As a result, it shows benefit in improving the efficiency and extending the speed range of PM machines when magnetization levels of LCF PMs are controlled at the optimal levels [1], [2]. However, some advantages of PM machines such as high torque density may disappear due to the lower energy product of LCF PMs. Another drawback is that LCF PMs can get easily demagnetized by armature field even under normal load [3]. To take the advantages of the flux controllability of LCF PMs and overcome the disadvantages, additional high coercive force (HCF) PM is introduced into memory machine to assist the LCF PM. By incorporating two types of PM in parallel or serial to provide hybrid excitation, the PM memory machines can not only provide magnetic flux controllability but also maintain the high torque/force density [4-6]. However, interactions between two types of PMs in two PM configurations exist and are different. LCF PM can be either magnetized or demagnetized by HCF PM even without magnetization control current [4], [6]. Thus, working of both PMs must be coordinated and carefully evaluated. The purpose of this paper is to develop the hybrid PM memory machines based on axial field flux-switching (AFFS) machines. Two axial field flux-switching memory (AFFSM) machines with different hybrid PM configurations, i.e. series PM (SPM) and parallel PM (PPM) types are proposed and compared. Hysteresis model coupling magnetic circuit is proposed to present the flux regulation principle of the SPM and PPM. For simplicity, the main specifications of two investigated memory machines such as the inner diameter, outer diameter and axial length are the same. The total usage of hybrid PM and the ratio between HCF PM and LCF PM are adjusted in order to achieve the same torque when LCF PMs are at fully magnetization state. The impacts of different PM dimensions on the magnetization requirement are also investigated. In particular, flux regulation characteristics and maximum flux regulation capacities of two memory machines are analyzed and compared. Machine Configuration and Operating Principle of Hybrid PM Fig. 1 a) and c) shows the 3-D views of the proposed double stator single rotor SPM- and PPM-AFFSM machines. Two stators are symmetric along the axis and have a 12/10 pole combination. Two PMs are arranged adjacent to each other and are tangential magnetized. Each stator adopts the same armature winding arrangement. To change the magnetization state of LCF PM, an additional DC excitation winding is introduced into the stator. By imposing pulse current with different amplitudes in the DC excitation winding, the LCF PMs can be magnetized and demagnetized. The working processes of LCF PM in two configurations during magnetizing and demagnetizing process are shown in Fig. 1 b) and d) respectively. As can be seen, the load line of LCF PM in SPM configuration moves towards the first quadrant, which means LCF PM can be magnetized by adjacent HCF PM. In contrast, LCF PM will be demagnetized by adjacent HCF PM, moving its load line towards the second quadrant. Comparison of Flux regulation characteristics Fig. 2 shows the minor loops of LCF PM in SPM and PPM configurations from different initial magnetization states. As shown in Fig.2 a) and b), magnetic flux of LCF PM in SPM configuration can be decreased up to 40% of its fully magnetized value. As two types of PMs are connected in series, variation range of total magnetic flux will be directly determined by the change of magnetic flux in LCF PM. One thing should be notice is that maximum demagnetizing current is almost identical with fully magnetizing current due to the magnetizing of HCF PM. By contrast, LCF PM can be total demagnetized from the completely magnetization in PPM configuration. However, total flux regulation capacity will be smaller as HCF provides part of fixed magnetic flux. Since LCF PM produces magnetic field opposing that of LCF PM, demagnetizing of LCF PM will be easier compared with SPM configuration. However, fully magnetizing LCF PM in PPM configuration will be more difficult. Conclusion In this paper, two AFFSM machines with SPM and PPM configurations are proposed and investigated. Flux regulation characteristics are presented. Results show that by adjusting the usage of PMs both configurations can obtain good flux regulation capacity. Working of LCF PM in SPM configuration is more stable. However, larger demagnetizing current is required. By contrast, fully demagnetizing current is much smaller in PPM configuration.

[1] N. Limsuwan, T. Kato, K. Akatsu, and R. D. Lorenz, "Design and Evaluation of a Variable-Flux Flux-Intensifying Interior Permanent-Magnet Machine," *IEEE Transactions on Industry Applications*, vol. 50, no. 2, pp. 1015–1024, Mar. 2014. [2] X. Zhu, Z. Xiang, L. Quan, W. Wu, and Y. Du, "Multi-Mode Optimization Design Methodology for a Flux-Controllable Stator Permanent Magnet Memory Motor Considering Driving Cycles," *IEEE Transactions on Industrial Electronics*, vol. PP, no. 99, pp. 1–1, 2017. [3] M. Ibrahim and P. Pillay, "Design of high torque density variable flux permanent magnet machine using Alnico magnets," presented at the 2014 IEEE Energy Conversion Congress and Exposition (ECCE), 2014, pp. 3535–3540. [4] K. Sakai, K. Yuki, Y. Hashiba, N. Takahashi, and K. Yasui, "Principle of the variable-magnetic-force memory motor," in *International Conference on Electrical Machines and Systems, 2009. ICEMS 2009*, 2009, pp. 1–6. [5] D. Wu, Z. Q. Zhu, X. Liu, A. Pride, R. Deodhar, and T. Sasaki, "Cross coupling effect in hybrid magnet memory motor," presented at the 7th IET International Conference on Power Electronics, Machines and Drives (PEMD 2014), 2014, pp. 1–6. [6] H. Hua, Z. Q. Zhu, A. Pride, R. Deodhar, and T. Sasaki, "A Novel Variable Flux Memory Machine with Series Hybrid Magnets," *IEEE Transactions on Industry Applications*, vol. PP, no. 99, pp. 1–1, 2017.

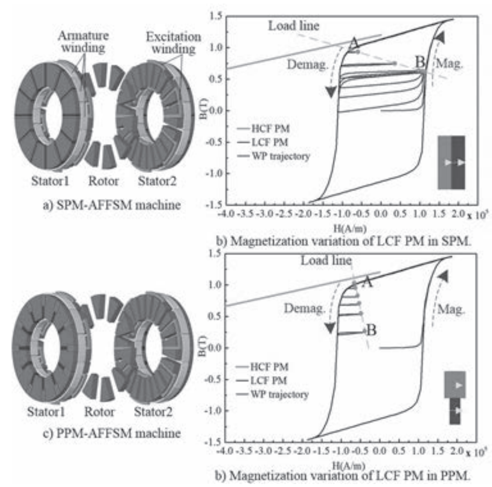

Fig. 1. 3-D views of proposed memory machines and working point trajectory of LCF PMs during magnetizing and demagnetizing in different PM configurations.

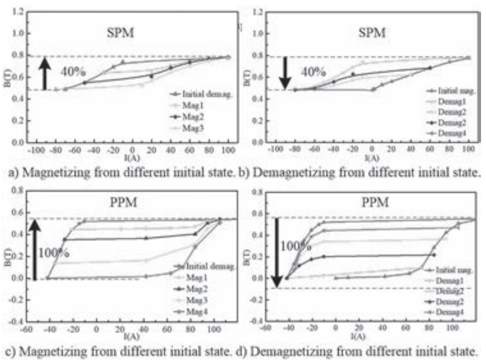

Fig. 2. Minor loops after magnetizing and demagnetizing from different initial magnetization states.

BS-13. Magnetic and Mechanical Characteristics of Electric Motor according to the Weld-laminated Core and the Bond-laminated Core.

D. Kim[1], M. Park[1], M. Yoon[1], J. Sim[1] and J. Hong[1]
1. Automotive engineering, Hanyang University, Seoul, The Republic of Korea

Today, electric motors are used in a variety of fields such as automotive, consumer electronics, and industrial applications. The demand for these motors is also increasing [1]. Especially, we have come closer to everyday life, such as automotive (e.g., traction, EPS, and ISG), household appliances (e.g., refrigerators, washing machines and elevator motors). Because the vibration and noise caused by the motor cause anxiety and discomfort to people, studies are being actively carried out to clarify and reduce the cause of motor vibration and noise. The factors that affect the vibration and noise can be largely divided into magnetic, electronic, aerodynamic, and mechanical sources [2]. First, the magnetic source generates excitation force through the magnetic field that passes through the airgap to create deformation in a stator, and if the frequency of this force matches the natural frequency, resonance occurs, and the sound vibrations are amplified. The studies on the vibration and noise created by the magnetic source are as follows. In [3-5], the vibration and noise were analyzed in accordance with the stator shape, pole angle, skew, overhang, and barrier of the rotor. In [6-10], the vibration orders by pole and slot combination were compared, optimization for vibration and noise reduction was performed, and the unbalanced magnetic forces were analyzed according to the winding method used to compare and analyze the vibration and noise. As a result, these studies helped reduce the vibration and noise by controlling the spatial harmonics of the airgap magnetic flux density in the motor design. Second, the vibration and noise caused by electronic sources occur as the input (including the harmonics) rather than the sinusoidal input is applied during the motor control. Especially, when the force generated by the harmonic input is generated near the natural frequency, the vibration and noise are further increased. In related studies [11], the vibration and noise were reduced through a method of avoiding the natural frequency of the stator by adjusting the magnitude and frequency of the PWM voltage. In [12, 13], harmonics were injected into the current to generate additional forces of the same magnitude and frequency as those that cause the vibration and noise in the opposite phase, thereby offsetting the two forces and reducing the vibration and noise. Most of these studies analyzed the vibration and noise for their design and control, but as mentioned earlier, the mechanical property of the stator is one of the main factors affecting the vibration and noise. Also, the stacking of the stator affects its mechanical characteristics [14-15]. The effects of lamination have been studied steadily. A study on the change of magnetic properties when welding lamination was performed [16-17], and a study on the change of magnetic properties due to mechanical stress applied during lamination was also studied [18]. However, further studies on the change of mechanical properties by lamination are needed In this regard, this paper presents the differences in the magnetic and mechanical characteristics depending on the stator lamination method used during the manufacturing process of the motor, and we propose a lamination method to improve the vibration of an electric motor based on the analysis of magnetic and mechanical characteristics of weld-laminated core and bond-laminated core. In Section II, the B-H curve and iron loss of an electric steel sheet according to two lamination methods are measured and the output characteristics of the induction motor are compared using finite element analysis (FEA). In Section III, modal tests of weld-laminated core and bond-laminated core are performed to compare the mode shape, stiffness and damping ratio, and the influence of this on the vibration of the motor is verified through FEA. Fig. 1 is a comparison of the frequency response function (FRF) of a weld-laminated core and a bond-laminated core through a modal test. The difference in the natural frequency of the two models is approximately the same at 0.51% based on circumferential mode shape 2. However, the attenuating band at the FRF peak is wider, ie, gradually attenuated, in the bond-laminated core. This means that the damping ratio is larger than the weld-laminated core. In section IV, the vibration reduction effect mentioned above is verified experimentally at a load of 4Nm, the rated output of the target motor, and a rotational speed of 3500rpm. As can be seen in Figure 2, the overall vibration of the bond-laminated motor at the same load was reduced by 2.5 dB. Finally, Section V concludes this paper.

[1] M. R. Park, H. J. Kim, Y. Y. Choi, J. P. Hong and J. J. Lee, “Characteristics of IPMSM According to Rotor Design Considering Nonlinearity of Permanent Magnet,” *IEEE Trans. Magn.*, vol. 52, no. 3, pp. 1-4, March 2016. [2] P. Vijayraghavan and R. Krishnan, “Noise in electric machines: a review,” *IEEE Trans. Ind. Appl.*, vol. 35, no. 5, pp. 1007-1013, Sep.-Oct. 1999. [3] J. W. Jung, S. H. Lee, G. H. Lee, J. P. Hong, D. H. Lee and K. N. Kim, “Reduction Design of Vibration and Noise in IPMSM Type Integrated Starter and Generator for HEV,” *IEEE Trans. Magn.*, vol. 46, no. 6, pp. 2454-2457, June 2010. [4] J. W. Jung, D. J. Kim, J. P. Hong, G. H. Lee and S. M. Jeon, “Experimental Verification and Effects of Step Skewed Rotor Type IPMSM on Vibration and Noise,” *IEEE Trans. Magn.*, vol. 47, no. 10, pp. 3661-3664, Oct. 2011. [5] A. Cassat *et al*., “A Practical Solution to Mitigate Vibrations in Industrial PM Motors Having Concentric Windings,”, “ *IEEE Trans. Ind. Appl.*, vol. 48, no. 5, pp. 1526-1538, Sept.-Oct. 2012. [6] Z. Q. Zhu, Z. P. Xia, L. J. Wu and G. W. Jewell, “Analytical Modeling and Finite-Element Computation of Radial Vibration Force in Fractional-Slot Permanent-Magnet Brushless Machines,”, “ *IEEE Trans. Ind. Appl.*, vol. 46, no. 5, pp. 1908-1918, Sept.-Oct. 2010. [7] G. Verez, G. Barakat, Y. Amara and G. Hoblos, “Impact of Pole and Slot Combination on Vibrations and Noise of Electromagnetic Origins in Permanent Magnet Synchronous Motors,” *IEEE Trans. Magn.*, vol. 51, no. 3, pp. 1-4, March 2015. [8] Z. Q. Zhu, Z. P. Xia, L. J. Wu and G. W. Jewell, “Influence of slot and pole number combination on radial force and vibration modes in fractional slot PM brushless machines having single- and double-layer windings,” in *Proc. Energy Convers. Congr. Expo. (ECCE)*, 2009, pp. 3443-3450. [9] S. Zuo, F. Lin and X. Wu, “Noise Analysis, Calculation, and Reduction of External Rotor Permanent-Magnet Synchronous Motor,” in *IEEE Trans. Ind. Electron.,* vol. 62, no. 10, pp. 6204-6212, Oct. 2015. [10] D. Y. Kim, M. R. Park, J. H. Sim, J. P. Hong, “Advanced method of selecting number of poles and slots for low-frequency vibration reduction of traction motor for elevator,”, “ *IEEE/ASME Trans. Mechatronics.*, vol. 22, no. 4, pp. 1554-1562, August. 2017. [11] H. Stemmler and T. Eilinger, “Spectral analysis of the sinusoidal PWM with variable switching frequency for noise reduction in inverter-fed induction motors,” in *Proc. IEEE PESC’94*, Taipei, Taiwan, 1994, pp. 269-277 vol.1. [12] D. Torregrossa, D. Paire, F. Peyraut, B. Fahimi and A. Miraoui, “Active Mitigation of Electromagnetic Vibration Radiated by PMSM in Fractional-Horsepower Drives by Optimal Choice of the Carrier Frequency,” *IEEE Trans. Ind. Electron.,* vol. 59, no. 3, pp. 1346-1354, March 2012. [13] D. Belkhayat, D. Roger and J. F. Brudny, “Active reduction of magnetic noise in asynchronous machine controlled by stator current harmonics,” in *Proc. 8th Int. Conf. Electrical Machines and Drives*, 1997, pp. 400-405. [14] Z. Tang, P. Pillay, A. M. Omekanda, C. Li and C. Cetinkaya, “Young’s modulus for laminated machine structures with particular reference to switched reluctance motor vibrations,” *IEEE Trans. Ind. Appl.*, vol. 40, no. 3, pp. 748-754, May-June 2004. [15] Y. Gao, K. Muramatsu, M. J. Hatim and M. Nagata, “The Effect of Laminated Structure on Coupled Magnetic Field and Mechanical Analyses of Iron Core and Its Homogenization Technique,” *IEEE Trans. Magn.*, vol. 47, no. 5, pp. 1358-1361, May 2011. [16] K. Bourchas, A. Stening, J. Soulard, A. Broddefalk, M. Lindenmo, M. Dahlen, and F. Gyllensten, “Quantifying effects of cutting and welding on magnetic properties of electrical steels,” *IEEE Trans. Ind. Appl.*, vol. 53, no. 5, pp. 4269-4278, Sept.-Oct. 2017. [17] A. Krings, S. Nategh, O. Wallmark, and J. Soulard, “Influence of the welding process on the performance of slotless PM motors with SiFe and NiFe stator laminations,” *IEEE Trans. Ind. Appl.*, vol. 50, no. 1, pp. 296-306, Jan.-Feb. 2014. [18] X. Ding, S. Ren, Y. Xiong, F. Chen, and J. Xu, “2-D magnetic properties measurement system for electrical steel sheets considering laminated direction mechanical stress,” *IEEE Trans. Magn.*, vol. 53, no. 10, Oct. 2017.

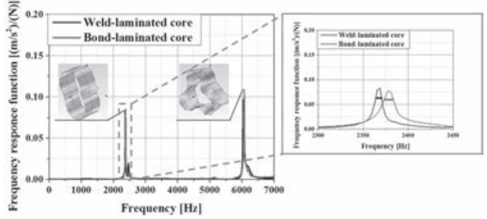

Fig. 1. Modal test result (FRF)

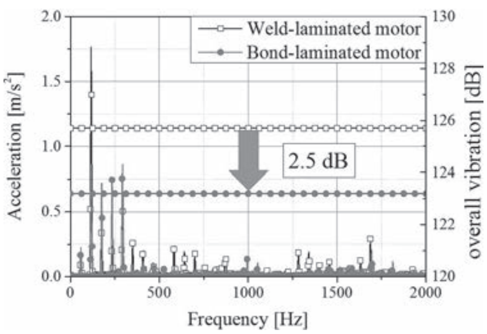

Fig. 2. Vibration test result

BS-14. A Novel Demagnetization Fault Detection Technique for IPMSM using Voltage angle.

Z. Ullah[1] and J. Hur[1]
1. Department of electrical engineering, Incheon National University, Incheon, The Republic of Korea

Owing to its high efficiency and torque density interior permanent magnet synchronous motor (IPMSM) is widely used [1]. However, IPMSM has a critical issue of irreversible demagnetization fault (IDF). It is among the most frequently occurred fault in PM motors. IDF means that the strengths of PM in IPMSM decrease, and it generates a low output torque. Various reason can cause IDF, such as high temperature, uneven magnetization, aging, and the reverse magnetic field [2].It has a very intensive effect on the operation of the motor. It severely decreases the back electromotive force of the PMSM.Furthermore, it causes variations in the air gap flux density, stator voltages, currents, and the output torque. Consequently, the vibrations and the acoustic noise in the motor also increase. A higher input current for the constant torque and speed, rise in winding temperature, and drop in magnetic flux are results of this fault [3].Several strategies are proposed for the diagnosis of IDF. Stator current Frequency-based [4], Frequency-time distribution based [5], [6], coil sensing based [7], and electromagnetic analysis based [8], techniques are proposed. However, these methods lack accuracy and are too complex. Furthermore, the frequencies used in mentioned techniques can also be caused by other faults such as eccentricity [9].In addition, in the nonstationary condition, the frequency domain analysis is extremely difficult to extract. This paper proposed a new method, which is very simple and relatively faster way for the detection of IDF.The reduction in magnetic flux due to weaken-magnet change the dq-axis voltages and hence the angle (δ) of the voltage vector also change. We exploit this property of δ for the detection of IDF. The proposed method is verified by conducting simulation and experiments on a 400-watt IPMSM (rated parameter: 10.32A, 1.1Nm, 3500rpm). To maintain the accuracy and avoid false alarm the data obtained at several operating conditions is processed using linear discriminant analysis (LDA) and quadratic discriminant analysis (QDA) method. The IPMSM model in the d-q frame is given by the following equation: $V_d=R_ai_d+d\lambda_d/dt-\lambda_q\omega_e$ (1) $V_q=R_ai_q+d\lambda_q/dt+\lambda_d\omega_e$ (2) $\lambda_d=\lambda_{PM}+L_di_d$ (3) $\lambda_q=L_qi_q$ (4) In steady state, the derivative terms are zero. Hence we can write the eq. (1) and (2) as follow: $V_d=R_ai_d-\lambda_q\omega_e$ (5) $V_q=R_ai_q+\lambda_d\omega_e$ (6) Here V_{dq}, i_{dq}, L_{dq}, and λ_{dq} represent the dq-axis voltages, currents, inductances, and flux. λ_{PM}, R_a, and ω_e are PM flux, stator resistance, and angular speed. When the IDF occurs the IPMSM draw more current for the same load at constant speed. Furthermore, L_d and L_q get bigger with the severity of IDF because the reluctance of the IPMSM become smaller. The decrease in λ_{PM} cause reduction in total λ_d.The effect of demagnetized region is similar as an air gap, forcing the magnetic flux towards q-axis and this phenomenon causes an increase in λ_q and hence the V_d in (5) increase on negative side while V_q in (6) decrease. The variation of flux and voltage vectors under healthy and IDF for an IPMSM is shown in Fig. 1(a). It is shown that as a result of IDF the δ_h (healthy) increase to δ_f (IDF). Thus, this increase in δ can be utilized as a signature of IDF. If the condition $\delta>\delta+\Delta\delta$ is true, so we can conclude that IDF has occurred. Where $\Delta\delta$ is a threshold value decided by the variation of δ in the healthy condition by noise factor. During analysis of δ, the change in magnitude and angle (β) of the stator current is kept under consideration. Because δ is proportional to β. A practical problem of the detection of reversible demagnetization exists. However, this fact is already verified that the IDF does not arise under steady state [10], [11]. To verify this idea simulation and experiments are performed. The magnetic flux density of single pole demagnetized model in Finite element method (FEM) is shown in Fig. 1(b). A 6 poles / 9 slots IPMSM for the experiment can be seen in Fig. 1 (c). To realize the different severities of IDF different size of magnets are used in each pole of the rotor, Fig. 1(d). Each pole has 14mm width. Therefore, 14mm (0% IDF), 11mm (21% IDF), 8mm (42% IDF), 5mm (64% IDF), and 2mm (86% IDF) wide magnets are used in each pole to realize the fault. FEM simulation is conducted on different operating points to get the values of the dq-axis inductances. It is impossible to obtain and process the data on all operating points. Therefore, the operating points exist within our calculated one are obtained using interpolation. The simulation and experiment are carried out for the constant load and speed (1.1 Nm, 3500 rpm) and observed the effect of DF on dq-axis current, flux and voltages. Fig. 2(a) shows the λ_{dq} on full load and 50% load with different severities of DF.The V_{dq} for the healthy and faulty motor can be seen in Fig. 2(b) with rated load and two different speeds. The corresponding change in δ is shown in Fig. 2(c). It is clear that as the DF increases the value of δ also increase. Fig. 2(d) shows the result of LDA and QDA based analysis. A generalized expression for the δ valid for every motor model, variation stator resistance, uniform magnetization and more detail of operating conditions will be added in full paper.

[1] T. M. Jahns et al. "Interior permanent magnet synchronous motors for adjustable-speed drives," IEEE Trans. Ind. Appl., vol. IA-22, no. 4, pp. 738–747, Jul. 1986. [2] J. Faiz, and H. Nedjadi-Koti, "Demagnetization fault indexs in permanent magnet synchronous motors-An overview," *IEEE Trans. Mag.*, vol. 52, no. 4, pp. 8201511-8201511, April 2016. [3] M. Zhu *et al.*, "Torque-ripple-based interior permanent-magnet synchronous machine rotor demagnetization fault detection and current regulation," *IEEE Trans. Ind. App.*, vol. 53, no. 3, pp. 2795-2804, May 2017. [4] Reemon Z. Haddad et al., "On the accuracy of fault detection and separation in permanent magnet synchronous machine using MCSA/MVSA and LDA," IEEE Trans. Energy Conversion, vol. 31, no. 3, pp.924-934, April 2016. [5] A. G. Espinosa et al., "Fault detection by means of Hilbert-Huang transform of the stator current in a PMSM with demagnetization," IEEE Trans. Energy Conversion, vol. 25, no. 2, pp.312-318, June 2010. [6] J. Riba Ruiz *et al.*, "Detection of demagnetization faults in permanent-magnet synchronous motors under nonstationary conditions," *IEEE Trans. Mag.*, vol. 45, no. 7, pp. 2961-2969, July 2009. [7] J. Bisschop et al., "Demagnetization fault detection in axial flux PM machine by using sensing coils and an analytical model," IEEE Trans. Mag., vol. 53, no. 6, pp. 8203404-8203404, June 2017. [8] Yao Da, et al, "A new approach to fault diagnostics for permanent magnet synchronous machines using electromagnetic signature analysis," IEEE Trans. Power Electronics, vol. 28, no. 8, pp. 4104-4112, Nov. 2012. [9] S. moon *et al.*, "Demnetization fault diagnosis of a PMSM based on structure analysis of motor inductance," *IEEE Trans. Ind. Elec.*, vol. 63, no. 6, pp. 3795-3803, June 2016. [10]T. Hosoi, H. Watanabe, K. Shima, T. Fukami, R. Hanaoka, and S. Takata, "Demagnetization analysis of additional permanent magnets in salientpole synchronous machines with damper bars under sudden short circuits," IEEE Trans. Ind. Electron., vol. 59, no. 6, pp. 2448–2456, Jun. 2012. [11]S. S. Moosavi, A. Djerdir, Y. Ait. Amirat, and D. A. Khaburi, "Demagnetization fault diagnosis in permanent magnet synchronous motors: A review of the state-of-the-art, " Elsevier J. Magn. Magn. Mater., vol. 391, pp. 203–212, Oct. 2015.

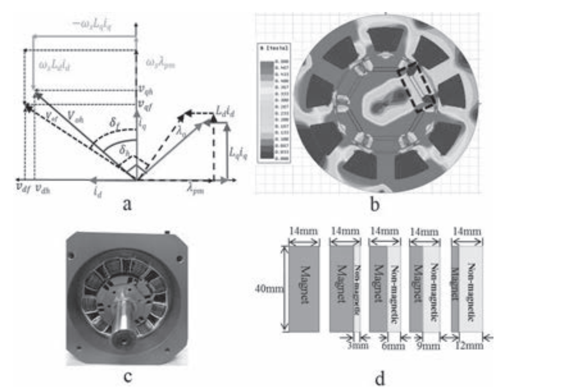

Fig. 1. (a) Phasor diagram of healthy and faulty IPMSM, (b) FEM model of one pole demagnetized motor, (c) 400-watt case study IPMSM (d) Combination of magnets to realize different severities of DF

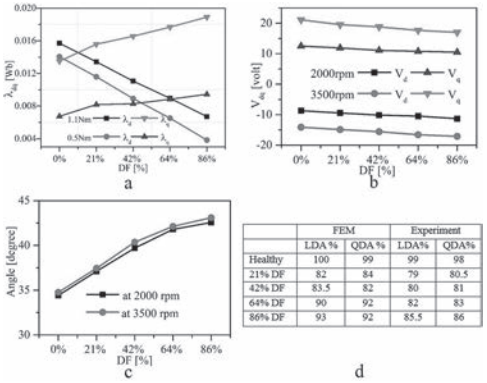

	FEM		Experiment	
	LDA %	QDA %	LDA%	QDA%
Healthy	100	99	99	98
21% DF	82	84	79	80.5
42% DF	83.5	82	80	81
64% DF	90	92	82	83
86% DF	93	92	85.5	86

d

Fig. 2. Experimental results. (a) λ_{dq} under full and half load with DF, (b) Variation of V_{dq} with DF (c) Variation of δ with DF (d) FDA and QDA results for FEM and experimental data.

BS-15. Design of IPMSM for Minimization of Electromagnetic Vibration.

I. Jang[1]
1. Hyundai Mobis, Yongin-si, The Republic of Korea

1. Introduction The vibration occurring in an electric motor can be largely divided into mechanical vibration due to nonaligned bearings and shafts, and electromagnetic vibration by the electromagnetic force. For existing industrial electric motors, the mechanical vibration associated with the life of the motor was the most important concern. However, in recent years, electric motors—such as the ones used for electric cars and hybrid cars—have high-torque density by using the rare-earth permanent magnet. Thus, the relative importance of electromagnetic noise and vibration is increasing. Electromagnetic vibration and noise affect people emotionally, so it has become very important to reduce vibration when designing a motor. The electromagnetic vibration can be predicted by analyzing radial force as a vibration source when designing the electromagnetic field of an electric motor. Thus, analyzing the spatial and time harmonics of the radial force enables us to find the harmonic that most influences the vibration. In this study, the optimum design of a 10-pole, 12-slot IPMSM for vibration reduction was performed. The optimum design was created by analyzing the radial force and finding the design variables that affect vibration. Additionally, to verify the validity of the design results, the results were compared using an electromagnetic-vibro coupled analysis. 2. Review of Electric Motor Design Parameters (Variable Selection Process) In an electric motor, torque is affected by the fundamental frequency components of the airgap flux density. Electromagnetic vibration is affected by the fundamental frequency component of the air gap flux density, as well as by time harmonics and spatial harmonics of the same density. The velocity of the vibrations generated in a motor is a function of the magnitude of the vibration source and mechanical geometry of the motor. The vibration caused by the electromagnetic force has the radial force density as a vibration source, and is calculated by squaring the airgap flux density, as shown in equation (1). The airgap flux density can be expressed as a function of the magnetomotive force generated in the stator and rotor, and the slot relative permeance is given as shown in Equation (2). Fig. 1(a) shows the airgap flux density of the 10-pole, 12-slot motor and 10-pole, slotless motor. The results of the FFT analysis are shown in Fig. 1(b). The absence of the stator slot demonstrates that only the 5th, 15th, and 25th harmonics exist, which are the multiple orders of the pole pair number. But the presence of the stator slot shows that the harmonics of other orders also exist. If the variable geometries of the rotor and the stator change, the magnitude of harmonic components of the flux density also changes. Therefore, to achieve the optimum design while considering vibration, the shape parameters should be selected. This affects the harmonic factors of the air gap magnetic flux density. 3. Optimum Design (Design Elements, Objective Function) In this chapter, the optimum design was found by selecting the design variables that minimize the vibration velocity for the initial design model. Table I shows the specification of the 10-pole, 12-slot IPMSM used for the optimum design. Fig. 2 shows the 10-pole, 12-slot IPMSM and design variables. For the design variables, the barrier angle $\theta_{barrier}$ that affects the harmonic waveforms of the magnetic flux density due to a permanent magnet was selected, along with the slot opening width W_{so} that affects the harmonics of the stator slot relative permeance. The objective function was designed to minimize vibration. The optimum design was created by maintaining the torque T and, at the same time, minimizing its vibration velocity V_m in the initial model. In this paper, vibration velocities were calculated by extracting the radial force densities for individual time steps from the results of an electromagnetic finite element analysis, and dividing those densities into a time harmonic and a spatial harmonic [1]. Table II shows the results on the torque and vibration velocity, and presents initial values and optimum values. For the 10-pole, 12-slot model, the 2nd spatial harmonics of the radial force density in the 2nd vibration frequency have the greatest impact on vibration velocity. As shown in Fig. 3, the 2nd spatial harmonics of the radial force density in the 2nd time harmonics of vibration velocity decreased 4.52%, and thus the overall vibration velocity decreased as well. 4. Verification Through Coupled Analysis During actual measurement of vibration velocity, it is also possible to identify a cause of electromagnetic force and to observe that mechanical vibration actually occurs. Thus, it is difficult to distinguish the mechanical vibration from the electromagnetic vibration by using tests. Therefore, in this study, the validity of the results was verified using an electromagnetic-vibro coupled analysis on the 10-pole, 12-slot model. Fig. 4 shows a comparison of vibration velocities by time harmonics in the initial model and the optimum model. 5. Conclusion In this study, an analysis was made to identify the shape parameters that affect the magnetic flux density of rotor and slot relative permeance in a permanent magnet motor. Using these parameters, optimal design was performed to minimize the vibration velocity in a 10-pole, 12-slot IPMSM initial model. As a result, vibration velocity was reduced by 5.5%. In addition, electromagnetic field-vibration interaction analysis was performed, and thus the results of the optimum design were verified.

I.-S. Jang, S.-H. Ham, W.-H. Kim, C.-S. Jin, S.-Y. Cho, K.-D. Lee, J.-J. Lee, D. Kang, and J. Lee, "Method for Analyzing Vibrations Due to Electromagnetic Force in Electric Motors," *Magn. IEEE Trans.*, vol. 50, no. 2, pp. 297–300, 2014.

Table I
Specification of 10-poles-12slots IPMSM

Description	Symbol	Value	Unit
Number of poles and slots	Np/Ns	10p 12s	-
Peak value of the phase current	Imax	550	Apeak
Rotation speed	-	2,843	rpm
Stator outer diameter	Dso	0.26	m
Stator inner diameter	Dsi	0.164	m
Rotor outer diameter	Dro	0.162	m
Stacking length	Lstk	0.16	m

Table II

Design variable Objective function	Initial Values	Optimum Values	Unit
Slot open width	12	10	mm
Barrier Angle	100	98	deg
Torque	412.5	412.5	Nm
Vibration Velocity	0.256	0.242	mm/s

Equation 1 : $p(\theta_m,t)=\frac{1}{\mu_0}B^2(\theta_m,t)$ $[N/m^2]$

Equation 2 : $B(\theta_m,t)=F(\theta_m,t)G(\theta_m)$ $[T]$

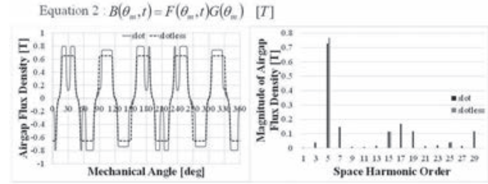

(a) FEM results (b) Magnitude of space harmonics
Fig. 1. Airgap flux density of 10-poles-12-slots and 10-poles-slotless

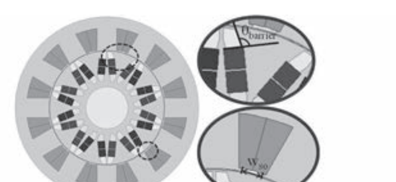

Fig. 2. Model shape of 10-poles-12slots IPMSM

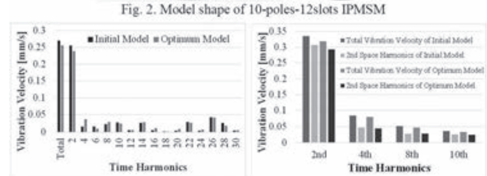

Fig. 3. Analysis of vibration by harmonics.

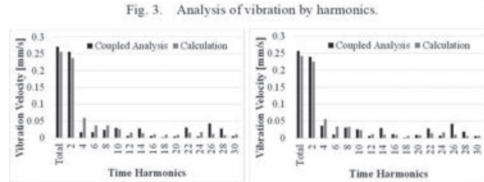

(a) Initial model (b) Optimum model
Fig. 4. comparison of vibration velocities by time harmonics.

BS-16. Optimal Design of a Switched Reluctance Motor with Magnetically Disconnected Rotor Modules Using a Design of Experiments - Differential Evolution (DOE-DE) Finite Element Analysis (FEA) based Method.

V. Rallabandi[1], J. Wu[1], *D.G. Dorrell*[2], P. Zhou[3] and D. Ionel[1]
1. Electrical and Computer Engineering, University of Kentucky, Lexington, KY, United States; 2. Discipline of Electrical, Electronics and Computer Engineering, University of KwaZulu-Natal, Durban, South Africa; 3. ANSYS Inc., Pittsburgh, PA, United States

Introduction Switched reluctance (SR) machines are attractive because they present relatively high efficiencies and torque densities but have no permanent magnets. Their limitations include high torque ripple, mitigated in large inertia applications such as electric vehicles. This digest focuses on the multi-objective optimization of an external rotor switched reluctance motor. The stator has concentrated coils and the rotor is configured with magnetically isolated modules. The experimental methodology tries to identify the variables affecting the objectives of loss and active mass. After this, differential evolution is used for optimization. The digest illustrates the optimal design process associated with the development of a prototype machine and its systematic comparison with a conventional SR motor design. Improvements with respect to the chosen objectives over a reference machine are quantified through finite element analysis. Further, a method for comparing the different designs on the Pareto front and identify the best compromise designs is proposed. *Background* Switched reluctance motors employing rotors with magnetically disconnected modules are shown to have higher specific torque and efficiency. This is primarily because of the shorter flux paths, which lead to a larger difference of aligned and unaligned position inductances for the same dimensions [1-2]. In such machines, the stator has wide main and narrower auxiliary stator teeth (Fig. 1 (a)). Only the main teeth are wound with concentrated coils, and the auxiliary teeth serve as return paths for the flux. The specific torque and efficiency increase with rotor module number in this type of machine. The machine considered in this study has 12 stator teeth and 26 rotor poles. A prototype demonstrator of this type was presented in [2] and is illustrated in Fig. 1(b). The increase in performance when a higher number of rotor modules is used is because of the reduction in the required volume of magnetic core material, which provides more room for the coils. This allows an increase in the ampere-turns for the same dimensions or the use of a larger split ratio, both of which contribute to a higher torque output. *Problem Formulation and Solution* A two-objective function unconstrained optimization is used in this study. The loss, including copper and core loss and active mass are considered as objectives to be minimized. The average torque output of the machine depends on geometrical parameters, and in this context, nine dimensionless independent variables are identified. The outer diameter is kept constant for all designs. For the better performing designs, the machine axial length is modified to ensure that all the studied candidates provide the same torque. A variation of ±20% from the dimensions of a reference design is considered for this study. The number of candidate designs that need to be studied to find an optimum solution if all nine design variables are considered would be very large, and therefore, the experimental methodology identifies which of the input variables have a significant impact on the objectives [3]. The variables that do not have a statistically significant effect on the outputs are fixed at their reference values and not considered in the optimization study. Multi-objective differential evolution (DE) is used in this study. *Systematic Method for Best Compromise Design Selection* Following an optimization study using DE, a method for systematically comparing the designs is proposed. The results of an example DE based study are shown in Fig. 2(a). The method allocates scores and ranks designs based on a directed graph, developed by representing each design with co-ordinates corresponding to the values of its objective functions; this is shown in Fig. 2(b). Arrows on the directed graph point towards designs with smaller co-ordinates. The score of each candidate design is evaluated by taking normalized weighted sums of the scores of other designs. The weight is calculated using the difference between the co-ordinates. If the difference is found to be against the direction of the arrows then the corresponding weights are set to zero. The scores are evaluated by the solution of an equation of the type Ax=x. To illustrate the capability of the algorithm, eleven designs marked in Fig. 2(a) are selected and compared. The proposed directed graph based technique eliminates the designs labeled x_6, x_7, x_8, x_9 and x_{11}, and retains the remaining six. The remaining designs are found to be on the Pareto front, which validates its successful operation. This method can be used to compare different designs on the Pareto front. Weighing factors can be included depending on which objective is more important, and this can be used to study different scenarios which aids the selection process.

[1] B. C. Mecrow, E. A. El-Kharashi, J. W. Finch and A. G. Jack, "Segmental rotor switched reluctance motors with single-tooth windings," in IEE Proceedings - Electric Power Applications, vol. 150, no. 5, pp. 591-599, 9 Sept. 2003. [2] S. P. Nikam, V. Rallabandi and B. G. Fernandes, "A High-Torque-Density Permanent-Magnet Free Motor for in-Wheel Electric Vehicle Application," in IEEE Transactions on Industry Applications, vol. 48, no. 6, pp. 2287-2295, Nov.-Dec. 2012 [3] P. Zhang, G. Y. Sizov, D. M. Ionel and N. A. O. Demerdash, "Establishing the Relative Merits of Interior and Spoke-Type Permanent-Magnet Machines With Ferrite or NdFeB Through Systematic Design Optimization," in IEEE Transactions on Industry Applications, vol. 51, no. 4, pp. 2940-2948, July-Aug. 2015.

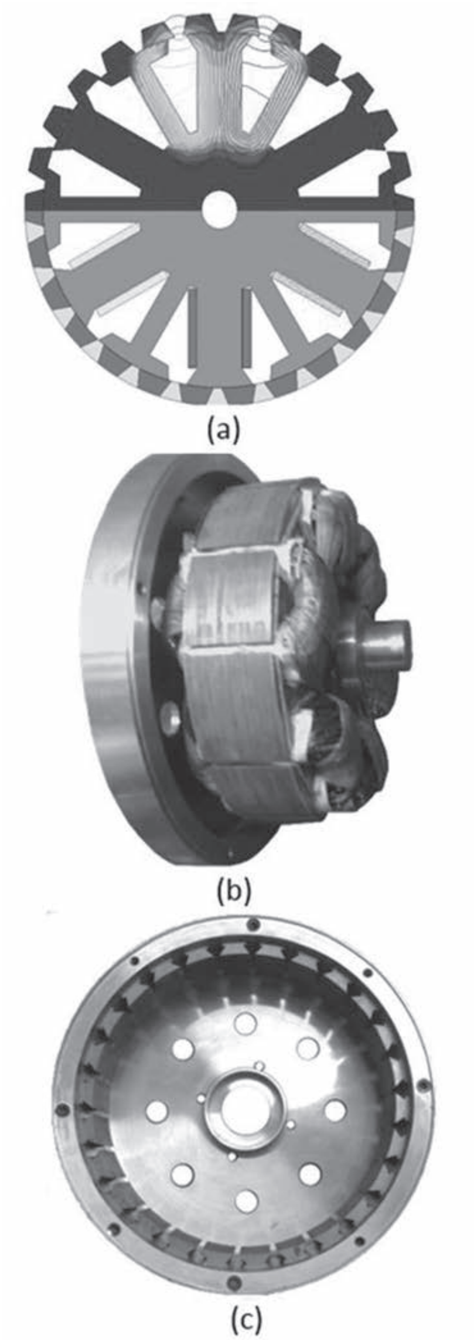

Fig. 1: (a) Geometry, flux paths of the SR motor with disconnected rotor modules. The coils are purposely represented disproportionately thin in order to illustrate that only alternate stator teeth are wound. (b) Stator and (c) rotor, of a prototype 1.5 kW motor. The rotor modules are placed in a non-magnetic stainless steel frame.

Fig. 1.

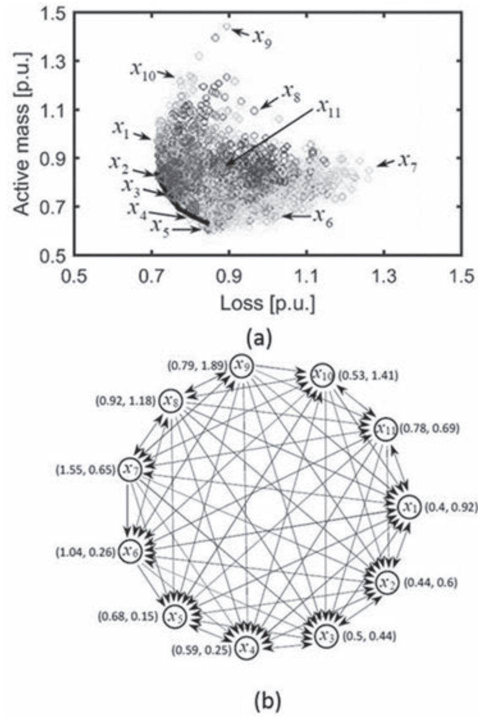

Fig. 2: (a) Example two-objective differential evolution optimization results with 1 p.u. corresponding to a conventional machine. The Pareto front is identified on the black curve and includes designs for which improvement in a given objective can be achieved though the deterioration of the second one (b) Schematic illustration of the proposed method for systematically selecting best compromise designs from the Pareto front.

Fig. 2.

Session BT
PERMANENT MAGNET AND RELUCTANCE MACHINES IV
(Poster Session)

Zhejie Liu, Chair
ARTC, Singapore, Singapore

BT-01. A novel variable flux permanent magnet synchronous machine with quasi-series magnet configuration and passive flux barrier.

S. Zhang[1], *P. Zheng*[1], Y. Liu[1], M. Wang[1], G. Qiao[1] and F. Liu[1]
1. School of Electrical Engineering and Automation, Harbin Institute of Technology, Harbin, China

I. Introduction Variable flux permanent magnet synchronous machine (VF-PMSMs) has drawn considerable attention due to the capability of operating in a wide speed range with overall high efficiency. The conceptual machine firstly proposed employs AlNiCo magnets characterized by low H_c and $(BH)_{max}$ as sole magnetomotive force (MMF) source [1]. Various topologies have been further developed to enhance the torque density by employing both low coercive-force PMs (AlNiCo) and high coercive-force PMs (NdFeB) [2,3]. The magnet configuration could be classified to parallel configuration and series configuration, as shown in Fig. 1(a) and (b). In parallel configuration, part of MMF generated by NdFeB magnets exerts on AlNiCo magnets, which leads to low working point and even unintentional demagnetization of AlNiCo magnets under on-load operation. Preceding defects could be avoided in series configuration due to the support of NdFeB magnets to AlNiCo magnets, but several times of demagnetizing current are required to fulfill the demagnetization process and the magnetization state variation range is usually limited. In this paper, a topology of VF-PMSM with quasi-series magnet configuration and passive flux barrier is proposed, which exhibits both advantages of high torque density of series configuration and easily achievable demagnetizing current of parallel configuration. II. Machine topology and operating principle A 48-slot/8-pole proof-of-concept machine is illustrated in Fig. 1 (c). AlNiCo magnets and NdFeB magnets are arranged in V type and spoke type, respectively. A flux barrier playing a crucial role of passively regulating magnetic flux during the demagnetization process is arranged between the NdFeB magnets and the shaft. The flux distribution under no-load operation, demagnetization regulation and after regulation are shown in Fig. 2 (a) to (c). In the case of no-load operation, most magnetic flux of NdFeB magnets flows through AlNiCo magnets to the airgap, while little magnetic flux of NdFeB magnets are short circuited through the passive flux barrier. The support of NdFeB magnets as existing in series configuration enables AlNiCo magnets to keep a high working point to enhance the torque density of the proposed machine. During the demagnetization process, 1 p.u. d-axis current pulse (J=5.24 A/mm^2) is applied to demagnetize AlNiCo magnets. In contrast to no-load operation, most magnetic flux of NdFeB magnets yields to flow through the passive flux barrier due to the applied opposite MMF. The flux barrier acts as a passive closed path of NdFeB magnets' flux during the demagnetization process. There is no need for the demagnetizing MMF to overcome the magnetizing MMF generated by NdFeB magnets and hence AlNiCo magnets are more easily demagnetized than the traditional series configuration. After the demagnetizing pulse is removed, most magnetic flux of NdFeB magnets flows through AlNiCo magnets again. However, the proportion of this part magnetic flux decreases when compared with that before demagnetization. This results from the decrease of working point as well as magnetic flux of AlNiCo magnets, and thus the magnetic flux of NdFeB magnets in series with AlNiCo magnets decreases. Such effect benefits extending the magnetization state variation range. III. Comparative study between different magnet configurations To further demonstrate the merit of the proposed machine, a quantitative study between three configurations is carried out. As shown in Fig. 1, same volumes of both AlNiCo magnets and NdFeB magnets are consumed in three configurations. Working point variations of AlNiCo magnets during demagnetization process are shown in Fig 2(d) to (f). A moderate demagnetization from 0.89 T to 0.52 T is obtained in the proposed topology by employing 1 p.u. demagnetizing pulse. In the parallel configuration, AlNiCo magnets are demagnetized reversely at -0.24 T by the same amplitude of demagnetizing pulse. What's more, the working point of parallel configuration with 1 p.u. load current locates at -0.06 T demonstrating the unintentional demagnetization at load operation. In the series configuration, it can be seen that the working point of AlNiCo magnets is demagnetized from 1 T to 0.96 T in a fairly tight range. IV. Influences of passive flux barrier on demagnetization and torque capability Demagnetization ratio and torque capability with different thicknesses of passive flux barrier ranging from 0 mm to 3 mm are summarized in Fig. 2(g). Demagnetization ratio used to evaluate the magnetization state variation range is defined as $k=|B_r-B_{ave}|/B_r\times100\%$, where B_r is the remanence of AlNiCo magnet, B_{ave} is the average flux density of AlNiCo magnet after being demagnetized. When 1 p.u. demagnetizing pulse is employed, demagnetization ratio increases with the thickness of flux barrier decreases. However, the torque with small thickness of flux barrier decreases due to the leakage flux, and particularly the torque with 2 p.u. load current is very limited in this situation. The thickness of passive flux barrier ranging from 1.5 mm to 2 mm is preferred, which could obtain about fifty percent demagnetization ratio at 1 p.u. demagnetizing pulse and exhibit overload capability. V. Conclusion The proposed topology of VF-PMSM could accomplish the demagnetization manipulation with an achievable level of demagnetizing pulse. Meanwhile, the quasi-series magnet configuration enables the proposed machine to offer a high torque density and overload operating capability.

[1] V. Ostovic, "Memory motors—A new class of controllable flux PM machines for a true wide speed operation," in Proc. 36th IAS Annu. Meeting Ind. Appl. Conf., 2001, vol. 4, pp. 2577–2584. [2] A. Athavale, K. Sasaki, B. S. Gagas, T. Kato, and R. D. Lorenz, "Variable Flux Permanent Magnet Synchronous Machine (VF-PMSM) Design Methodologies to Meet Electric Vehicle Traction Requirements with Reduced Losses," IEEE Trans. Ind. Appl., vol. 53, no. 5, pp. 4318-4326, Sept.-Oct. 2017. [3] B.S. Gagas, K. Sasaki, A. Athavale, T. Kato, R.D. Lorenz, "Magnet Temperature Effects on the Useful Properties of Variable Flux PM Synchronous Machines and a Mitigating Method for Magnetization Changes," IEEE Trans. Ind. Appl., vol. 53, no. 3, pp. 2189-2199, May-June 2017.

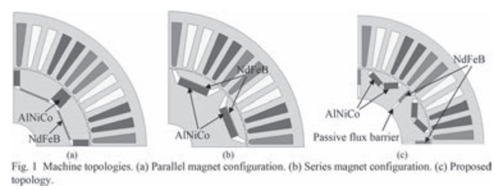

Fig. 1. Machine topologies.

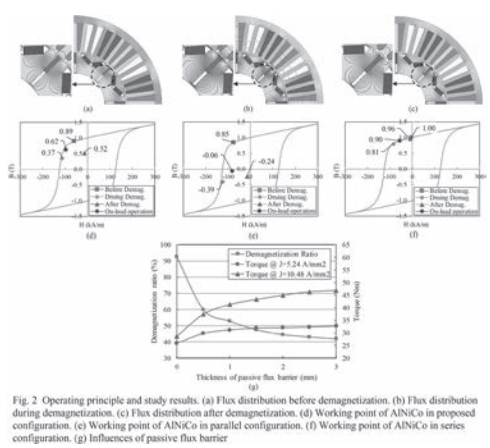

Fig. 2. Operating principle and study results.

BT-02. Torque Improvement of External-Rotor Permanent Magnet Machine Using Flux Concentrated Rotor.

Q. Li[1] and T. Fan[1]
1. Institute of Electrical Engineering, Chinese Academy of Sciences, Bei-Jing, China

I.Introduction In recent decades, due to high specific torque, external rotor permanent magnet synchronous machines (ER-PMSM) have been widely applied for in-wheel direct-driving electric vehicle (EV) [1]. The torque enhancement of the external rotor SPM becomes research hotspot and has been discussed intensively [2]-[3]. Ref. [2] investigated the effect of the stator tooth width, magnet depth and Halbach array to the external rotor motor, through analyzing the torque and the efficiency characteristic. In [3], the influence of the motor design parameters on the characteristics of the external rotor PMSM was researched. The relationships of pole number and teeth height ratio on the torque, losses and winding temperature rise are derived from analytical calculation method. In this paper, an external rotor PMSM using flux concentrated rotor is proposed to enhance the output torque. The output toque characteristic of the proposed motor is compared with the conventional motor, calculated by the finite element analysis (FEA). To evaluate the peak torque capacity, the instantaneous temperature contour of the proposed motor under the peak torque condition is also compared with the conventional external rotor motor. II.Introduction Topology of ER-PMSM with Flux Concentrated Rotor Fig.1(a) illustrates a conventional ER-PMSM, which is optimized for peak torque 240Nm by the method proposed in [3], under the effective weight limitation for 6 kg and the space constraints. The outer diameter of the rotor core is limited to 220mm, and inner diameter of the stator core is constrained to 150 mm, while the length of the core is fixed to 45mm. In order to enhancing the specific torque, the flux concentrated rotor is used by spoke magnet, and this proposed motor is shown as Fig.1(b). Both of these two motors have 48 slots, and almost the same stator diameters and winding, except the slot opening. It means these two motor have the same phase resistance and same copper losses with the same current excitation. The conventional motor has 40 poles with surface mounted permanent magnet, while the proposed motor has 56 poles with spoke permanent magnet utilizing flux concentrated character. III. Electromagnetic and Thermal Analysis The electromagnetic characteristics of the two motor are calculated by the finite element analysis (FEA). For the proposed motor, the fundamental component of the no-load induced voltage increases 32% than that of the conventional motor, because of the flux concentrated rotor. Therefore under the same current excitation, the output torque of the proposed motor is obviously bigger than the conventional motor. Considering the temperature constraint of the peak torque, which is should operating 30 second, the peak current is limited to 105 Arms. The peak torque of the conventional motor is 240.1 Nm, while using flux concentrated rotor, the peak torque of the proposed motor is enhanced to 309 Nm, increase nearly 29%, shown as Fig2. (a). To evaluate the peak torque capacity, the temperature contour of the two motor under peak torque condition with operating 30s are predicted by the FEA. As a water jacket with a coolant temperature of 40 °C is assumed to be mounted in the candidate machines and the winding insulation is C-class (220°C), so the maximum winding temperature under peak torque condition should be under 190°C. As the two motor have same phase resistance, so the copper losses are the same and the winding hottest points of the two motor under peak torque condition are almost equal to 188°C, shown as Fig.2(b) and (c). IV. Conclusion In this paper, an ER-PMSM with flux concentrated rotor is proposed to improve the output torque. A conventional ER-PMSM is optimized as baseline motor under 6 kg effective weight limitation. By utilizing flux concentrated rotor, the no-load air-gap flux density can be obviously increased, compared with that of the conventional ER-PMSM. Therefore, the peak torque the proposed motor increases about 29% than the prototype motor, and the temperature contour of the two motor under peak torque condition are also evaluated by FEA. The specific torque of the proposed motor under effective weight is up to 50 Nm/kg under effective weight, It can be found that using flux concentrated rotor can obviously enhance the torque capacity.

[1]J. Wang, K. Atallah, Z. Q. Zhu, and D. Howe, "Modular Three-Phase Permanent-Magnet Brushless Machines for In-Wheel Applications," *IEEE Transactions on Vehicular Technology,* vol. 57, no. 5, pp. 2714-2720, 2008. [2]L. Li, J. Zhang, C. Zhang, and J. Yu, "Research on Electromagnetic and Thermal Issue of High-Efficiency and High-Power-Density Outer-Rotor Motor," *IEEE Transactions on Applied Superconductivity,* vol. 26, no. 4, pp. 1-5, 2016. [3]Q. Li, T. Fan, X. Wen, and P. Ning, "A rotor design method of external rotor surface permanent magnet machine for in-wheel application," in *Electrical Machines and Systems (ICEMS), 2015 18th International Conference on*, 2015, pp. 1498-1501.

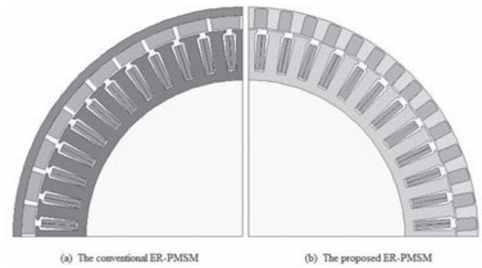

Fig. 1. The two motor cross sections

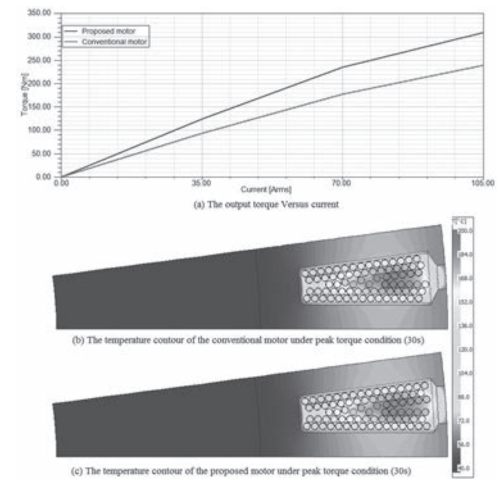

Fig. 2. The comparison of the torque and temparature characteristics for the two motors

BT-03. Robust hybrid type permanent magnet traction motor against irreversible demagnetization at high temperature.

C. Jeong[1] and J. Hur[1]
1. Incheon National University, Incheon, The Republic of Korea

Permanent magnet (PM) motors have been applied for a traction motor, because they have great efficiency, high power density, and wide power-speed range. Despite of these advantages, in case of all motors using PM, there is a common concern, which is irreversible demagnetization generated by current armature reaction. This is because the demagnetization has directly a bad effect on performance, reliability, and safety. Although many studies have already analyzed the demagnetization phenomenon [1]-[3], the risk of irreversible demagnetization in the traction motor is still remained, since the traction motor should endure at high temperature over 180°C, which can lead to irreversible demagnetization. Therefore, it is necessary to develop a robust PM motor to withstand at high temperature. For developing the PM traction motor, neodymium PM has been generally applied, because of its advantages such as high flux density per PM volume, durability, and downsizing. Nevertheless, various researches are currently studying the ways to decrease the dependence on neodymium PM in order to reduce the cost of electrical and hybrid vehicles and ensure reliability of material supply. As a result, the motors with less- or non-rare earth material are suggested in [4]-[6]. Especially, a hybrid type PM motor is recently considered to substitute for neodymium PM motor [7], [8]. Here, the hybrid type PM denotes that both of neodymium and ferrite PMs are simultaneously used in a rotor. This is because, comparing the output characteristics per identical rotor volume at same operation condition, the hybrid type PM motor is better than ferrite PM motor. In this paper, it is proposed that the hybrid type PM motor employed in a traction motor is robust against the irreversible demagnetization at high temperature, compared with neodymium PM motor. First, a novel motor using hybrid type PM is demonstrated and suggested to be an alternative motor, as the output characteristics between neodymium PM and hybrid type PM motors are compared by using results through finite element analysis (FEA). Furthermore, the irreversible demagnetization of each motor at high temperature is analyzed for verifying reliability of proposed motor. Fig. 1 shows the performance comparison of neodymium PM and proposed hybrid type PM motors. In case of the hybrid type PM, all length of stator, rotor, and stack is maintained, compared with that of neodymium PM motor, as shown in Figs. 1(a) and (b); whereas, the volume of neodymium PM in motor using hybrid type PM is only used about 60% of neodymium PM motor. Comparing Fig. 1(c) with Fig. 1(d), even though the amount of neodymium PM is decreased, the back electro motive force (BEMF) of motor using hybrid type PM is higher than that of motor using neodymium PM, because of assisted ferrite PMs. As a result, when input current of both neodymium and hybrid type PM motors is identical, the average torque of hybrid type PM motor is higher than that of neodymium PM motor. Consequently, it is evaluated for hybrid type PM motor to be appropriate for replacing the neodymium PM motor as a traction motor. In case of traction motor, it is essential to analyze irreversible demagnetization, since the traction motor have to be able to withstand high temperature in accordance with operating environment. The demagnetization aspects according to magnet type embedded in PM motor are changed in spite of same input current and temperature, because neodymium and ferrite PMs have different characteristic of BH curve about temperature. Therefore, for comparing the demagnetization aspects at each motor, the irreversible demagnetization of two motors is analyzed, as shown in Fig. 2. When beta angle, temperature, and input current are 90°, 140°C, and 240A_{rms}, the severity of irreversible demagnetization is demonstrated through demagnetization ratio in PM, as shown in Figs. 2(a) and (b). In case of neodymium PM motor, the average demagnetization ratio at overall magnets is enhanced about 15%; on the other hand, in case of hybrid type PM motor, the demagnetization ratio at PM corner is partially increased about 35%. At that time, comparing the change of BEMF value between two motors, the BEMF of neodymium PM motor is decreased about 7.6%, but that of hybrid type PM motor is almost constant, as shown in Figs. 2(c) and (d). Moreover, Fig. 2(e) shows that the reduction rate of BEMF value by increasing temperature is indicated. As a result of this analysis, it is verified that the hybrid type PM motor can endure at higher temperature than neodymium PM motor. In future work, detail information of each motor and the fluctuation of radial flux density by armature reaction leading to irreversible demagnetization will be described. Furthermore, the analysis of irreversible demagnetization according to various beta angles will be discussed.

[1] H. Kim and J. Hur, "Dynamic characteristic analysis of irreversible demagnetization in SPM- and IPM-type BLDC motors," IEEE Transactions on Industry Applications, vol. 53, no. 2, March/April 2017. [2] D. Kang, "Analysis of vibration and performance considering demagnetization phenomenon of the interior permanent magnet motor," IEEE Transactions on Magnetics, vol. 53, no. 11, November 2017. [3] J. Faiz and E. Mazaheri-Tehrani, "Demagnetization modeling and fault diagnosing techniques in permanent magnet machines under stationary and nonstationary conditions: an overview," IEEE Transactions on Industry Applications, vol. 53, no. 3, May/June 2017. [4] A. Fasolo, L. Alberti, and N. Bianchi, "Performance comparison between switching-flux and IPM machines with rare-earth and ferrite PMs," IEEE Transactions on Industry Applications, vol. 50, no. 2, March/April 2014. [5] T. Masuko, S. Miyamoto, and I. Miki, "Development of a novel rotor structure for reducing rare earth use in permanent magnet synchronous motor," International Symposium on Power Electronics, Electrical Drives, Automation and Motion, 22-24 June 2016. [6] S. S. R. Bonthu, AKM Arafat, and S. Choi, "Comparisons of rare-earth and rare-earth-free external rotor permanent magnet assisted synchronous reluctance motors," IEEE Transactions on Industrial Electronics, vol. 64, no. 12, December 2017. [7] C. Jeong and J. Hur, "Optimization design of PMSM with hybrid-type permanent magnet considering irreversible demagnetization," IEEE Transactions on Magnetics, vol. 53, no. 11, November 2017. [8] X. Zhu, X. Wang, C. Zhang, L. Wang, and W. Wu, "Design and analysis of a spoke-type hybrid permanent magnet motor for electric vehicles," IEEE Transactions on Magnetics, vol. 53, issue 11, December 2017.

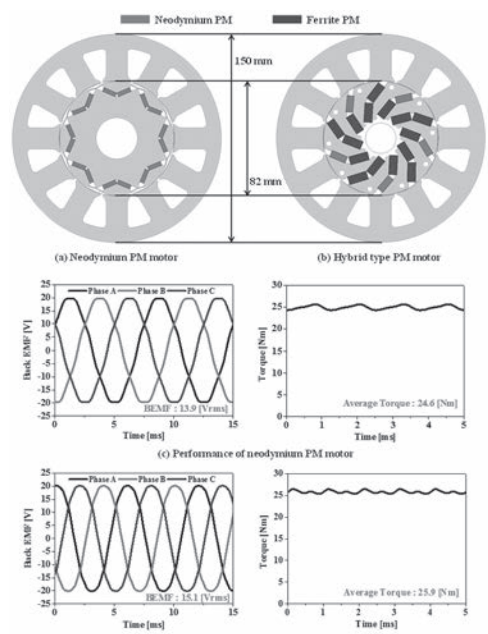

Fig. 1. Comparison of performance between neodymium PM motor and hybrid type PM motor

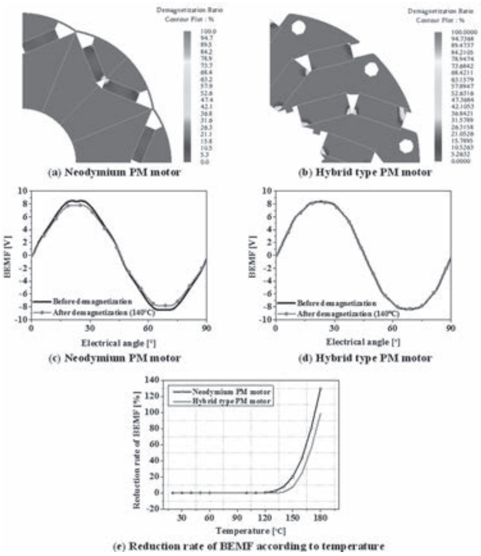

Fig. 2. Analysis of irreversible demagnetization of neodymium PM motor and hybrid type PM motor.

BT-04. Elimination of Sub-harmonic in Stator MMF of 18-slot/10-pole PM Machines by Employing Unequal Slot and Uneven Turns per Coil.

H. Sun[1] and X. Chen[1]

1. Electrical Engineering, Nanjing University of Areonautics and Astronautics, NanJing, China

I.Introduction Surface-mounted permanent magnet (SPM) machines with fractional-slot non-overlapping windings offer several key features, such as high torque density, high efficiency, and low cogging torque, and have been widely used in these high performance applications [1]. However, the associated parasitic effects, i.e., significant rotor loss (rotor core loss and PM loss), high localized stator saturation and large noise and vibration, have always been obstacles, which are mainly due to the non-sinusoidal stator magnetomotive force (MMF), especially the sub-harmonic and super-harmonic [2]. Recently, SPM machines with fractional-slot overlapping windings (FSOW), for example, 18-slot/10-pole machines, have been paid lots of attention since they prove to be competitive in reducing rotor eddy current loss resulting from the harmonic in MMF [3]-[4]. For 12-slot/10-pole machine, the winding factors of 1st (sub-harmonic), 5th (working harmonic), and 7th (super-harmonic) are 0.067, 0.933, and 0.933, respectively, whilst for 18-slot/10-pole machines, they are 0.061, 0.945, and 0.139, respectively. It is clear to see that by employing the 18-slot/10-pole FSOW machine, the 7th harmonic can be suppressed significantly, whilst the 1st harmonic can still be large whose rotating speed is high, which will induce large rotor loss especially at high speed. The purpose of this paper is to reduce the sub-harmonic in stator MMF of 18-slot/10-pole FSOW machine by employing novel stator with unequal slot and uneven coil turns while the torque density is not effected. The comparison of electromagnetic performance including the back-EMF waveforms, cogging torque, average torque, torque ripple, rotor eddy current loss between the conventional and novel 18-slot/10-pole FSOW machines are carried out, which will be shown in full paper. II.Structures and Features of Conventional and Novel 18-Slot/10-Pole SPM Machines Fig. 1 (a) shows the conventional 18-slot stator with coil pitch equal to 2. Each slot shares the same areas and the coil turn number N is identical. The mechanical angle between adjacent teeth is 20 degree. Fig. 1 (b) depicts the structure of novel 18-slot stator. Tooth 1, 4, 7, 10, 13, 16 are shifted by 1 degree clockwise whilst Tooth 3, 6, 9, 12, 15, 18 by 1 degree anti-clockwise. During the shifting, the slot opening width keep unchanged, being 2mm. The slot area of novel stator slot is no longer the same, which is beneficial for designing coils belonging to one phase with different turns for reduction of stator MMF space harmonic. Take one of the coil groups of phase A for example, which consists of coil A_1, coil A_2, and coil A_3. The number of turns of coil A_1, A_2, and A_3 is N for conventional stator, whilst for the novel stator, turns of coil A_1 and A_3 is N_2 and turns of coil A_2 is N_1, whose values are set for reduction of the sub-harmonic in stator MMF. Fig. 1 (c) shows a part of the novel 18-slot stator with only the coils of phase-A drawn. Tooth 1 and tooth 4 are shifted by b to the right side, whilst tooth 3 and tooth 6 are shifted by β to the left side. Fig. 2 shows the stator MMF and torque comparison between 18-slot/10-pole machines with conventional and novel stator. It can be seen that compared with the conventional stator, the novel stator can reduce the 1st harmonic of stator MMF to zero with the 7th harmonic increasing about 40%. The average torque of the two is about the same. III.Conclusion This paper proposes a method for elimination of the sub-harmonic in 18-slot/10-pole FSOW SPM machine. The subharmonic in stator MMF can be total eliminated by employing the novel stator with unequal slot and uneven coil turns. Rotor eddy current loss can be reduced and the torque density of the novel machine can maintain to be the same as that of the conventional one.

[1] A. M. EL-Refaie, "Fractional-slot concentrated-windings synchronous permanent magnet machines: Opportunities and challenges," *IEEE Trans. Ind. Electron.*, vol. 57, no. 1, pp. 107–121, Jan. 2010. [2] M. Freddy and L. Heinz, "Parasitic effects in PM machines with concentrated windings," *IEEE Trans. Ind. Appl.*, vol. 43, no. 5, pp. 1223–1232, Sep./Oct. 2007. [3] K. Wang, Z. Q. Zhu, and G. Ombach, "Synthesis of high performance fractional-slot permanent-magnet machines with coil-pitch of two slot-pitches," *IEEE Trans. Energy Convers.*, vol. 29, no. 3, pp. 758–770, May 2014. [4] J. Wang, V. I. Patel and W. Wang, "Fractional-Slot Permanent Magnet Brushless Machines with Low Space Harmonic Contents," *IEEE Trans. Magn.*, vol. 50, pp. 1-9, 2014.

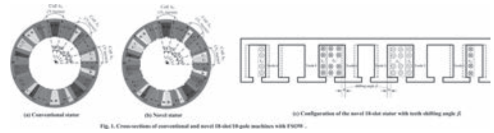

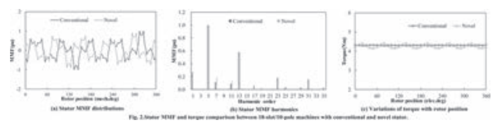

BT-05. A high continuous torque density external rotor surface permanent magnet machine for in-wheel application.

Y. Li[1], T. Fan[1], Q. Li[1], X. Wen[1] and X. Zhuang[2]
1. Institute of Electrical Engineering,Chinese Academy of Sciences, Beijing, China; 2. Beijing First-rate New Energyedrive Technology, Beijing, China

I.Introduction Since the growing shortage of energy and environmental problems, electric vehicle (EV) is getting increasing attention of researchers. In China, the number of EV has double during the past six years from 2010 to 2015 [1]. In particular, [2], [3] and [4] researched and developed the in-wheel motor technology for electric vehicles. However, the motor requirements of the in-wheel driving EV are not only high peak torque and small size, but also high continuous torque density, which is limited by the winding temperature. In this paper, a new cooling method is proposed for the external rotor SPM to improve the continuous torque capability, by enhancing heat dissipation at the end-winding. The finite element analysis (FEA) is used to evaluate the effect of the proposed cooling method. Two motors are manufactured, one is used the proposed cooling method, another motor is conventional motor. The experiment results of the two motors show that the continuous torque increased by 28.5% after using the proposed cooling method, under the same winding temperature constraint, and basically consistent with the simulation results. II.The proposed cooling construction For the conventional external rotor SPM, the winding is cooling by the water jacket, and the water jacket is fixed to the stator inner diameter. Therefore the hottest point is in the end-winding. So to improve the continuous torque, decrease the end-winding temperature is an attractive approach. In this paper, new cooling method is proposed for the external rotor SPM to improve the continuous torque capability. Fig.1(a) illustrates the proposed cooling construction. For the motor with the proposed cooling construction, the path of the heat transfer at the end winding is changed from the "the end winding – the winding – the stator – the water jacket" to "the end winding – the water jacket", which reduces the heat transfer resistance. III.electromagnetic and thermal characteristics To evaluate the proposed cooling method, a conventional external rotor SPM is optimized for a micro-EV, which continue torque is 70 Nm and Dimension is constrained. The outer diameter of the rotor core is limited to 220mm, and the inner diameter of the stator core is limited to 150mm, while the length of the core is limited to 45mm. the optimization method proposed in [5] is carried out, and the maximum winding temperature under continuous torque condition should be under 140°C, while the water jacket with a coolant temperature of 20 °C. Two motor models are built, one is the conventional motor, and another is the proposed motor using the new cooling construction. The design parameters of the two motor are the same, which cooling constructions are different. The Computational fluid dynamics (CFD) was used to evaluate the thermal characteristics of the two motors, under the same temperature limitation on continuous torque condition. The simulation results show that the continuous current of the proposed motor increase 30% compared with the conventional motor, as well as continuous torque. IV.Experiment and validation Two prototype motors are manufactured, the proposed motor is shown as Fig.1(b). As the experimental results in Fig.2 shows, the final winding temperature of the conventional motor is 134.2 °C with continuous torque 70 Nm during 600 rpm, while the final winding temperature of the proposed motor is 136 °C with continuous torque 91 Nm during 600 rpm. The winding temperature of the proposed motor calculated by CFD is quiet agree with the experimental results, shown as Fig.2. V.Conclusion This paper proposed a new cooling method, by enhancing heat dissipation at the end-winding. Utilizing the new cooling construction, the continuous torque increased by 30%. Both numerical simulation and experiment results validate the proposed cooling method.

[1] Fei Lei, Bin Du, Xin Liu, Xiaoping Xie, Tian Chai, "Optimization of an implicit constrained multi-physics system for motor wheels of electric vehicle," Energy, 2016, pp980-990 [2] Kazim Cakir and A. Sabanovic, In-wheel Motor Design for Electric Vehicles, AMC'06-Istanbul, Turkey, 2006, pp. 613-618 [3] Manu Jain, and Sheldon S. Williamson, Suitability Analysis of In-Wheel Motor Direct Drives for Electric and Hybrid Electric Vehicles, IEEE Electrical Power & Energy Conference, 2009 [4] Shinichiro Sakai, Hideo Sado, and Yoichi Hori, 1999, Motion Control in an Electric Vehicle with Four Independently Driven In-Wheel Motors, IEEE/ASME Transactions on Mechatronics, March 1999, Vol. 4, No. 1 [5] T. Fan, Q. Li, Y. Li, X. Wen, and X. Zhuang, "Influence of design parameters on characteristics of external-rotor permanent magnet synchronous machine," in *International Conference on Electrical Machines and Systems*, 2017, pp. 1-6.

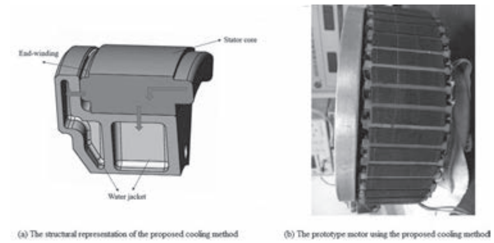

Fig. 1. The proposed cooling construction

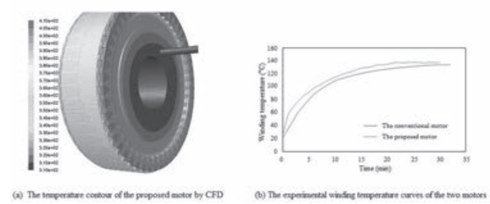

Fig. 2. The thermal characteristics during the continuous torque conditon

BT-06. Design and Analysis a New Wide Speed Range Permanent Magnet Motor Capable of High Efficiency Over Wide Speed Ranges.

X. Zhu[1] and L. Ge[1]

1. School of Electrical and Information Engineering, Jiangsu University, Zhenjiang, China

I. Introduction. Permanent magnet (PM) motors have attracted considerable attention for their advantages of high torque density and high efficiency [1]. However, it is difficult to regulate the air-gap field, thus the narrow speed range of the PM motor limits their application especially in electric vehicles, where wide speed range is often needed [2]. Currently, several methods have been proposed to achieve the capability of flux adjustment, including applying a negative *d*-axis current or introducing extra DC field windings to PM motor [3], and yet additional losses may lead to degraded efficiency especially under the deep flux-weakening region. In this paper, a new wide speed range permanent magnet motor with special flux barriers design in rotor core is proposed, where a new design concept of variable main flux and leakage flux are both obtained at different load conditions successfully. The key novelty lies in that the saturation level of the leakage flux path can be controlled by applying different level of *q*-axis load current and thus the *d*-axis magnetic field can be controlled without any additional *d*-axis current and copper losses. So the proposed motor can achieve a high efficiency over wide speed and torque ranges. II. Topologies and Principles. Fig. 1 shows the proposed motor with leakage flux controllable characteristics. For comparison, the similar characteristics of a conventional PM motor are also proposed in Fig. 1. As seen from the figure, the leakage flux branch in the proposed motor is skillfully designed to be two arc-shaped bridges. Generally, to make full use of main magnet flux and to obtain high torque, the leakage flux is expected as small as possible. However, in this proposed motor, a leakage flux branch between two adjacent magnets is designed for a wider speed operation range. In high speed region, magnet flux has a trend of flowing through the leakage flux branch rather than into the air-gap, naturally forming a flux-weakening effect without additional *d*-axis current, thus the motor can realize magnetic field self-controlling under various conditions. Due to the decreasing of magnet flux, efficiency in high speed region can be advanced along with the reduction of iron losses. Moreover, the extra arc-shaped flux barriers can not only guarantee the output capability of the motor, but also make saliency ratio large, resulting in decreasing back electromotive force (EMF) at high speed operation. On the other hand, in low speed region, the leakage flux in the rotor core can be passively reduced by the *q*-axis current effect and more flux gets into the stator for high torque capability. III. Performance analysis. To confirm the unique characteristic, the relationship between *q*-axis current and *d*-axis flux is evaluated in Fig. 2 (a). Compared with the conventional PM motor, the *d*-axis flux variation of the proposed motor is fairly large, which is about 20%. From Fig. 2 (b), it can be obtained that the conventional motor has large saliency ratio, however, the proposed motor has relatively small saliency ratio due to the large *q*-axis reluctance by the extra arc-shaped flux barriers design. The corresponding motor torque distribution with motor speed is described in Fig. 3 according to a driving cycle. It can be seen that the motor works mainly at low torque operation and high-speed region. Hence efficiency characteristics of both the proposed motor and the conventional motor are investigated. In Fig. 4, the 95% efficiency contour line of both two motors is illustrated to protrude the high efficiency area. The high efficiency area of the conventional motor is mainly concentrated in the low-medium speed and large torque area, whereas the proposed new motor is mainly concentrated in the middle-high speed and low torque area. In order to verify the wider high efficiency region performance, iron loss and copper loss properties of both two motors are evaluated. Fig. 5 shows the iron loss difference map. It can be seen that the proposed motor achieves smaller iron loss property all over the operation ranges. This feature can be explained by the smaller magnet flux linkage under flux-weakening control due to the leakage flux property. Fig. 6 shows the copper loss of the proposed motor in high speed region is relatively reduced compared to the conventional motor when the speed is over 2500rpm. Under high speed operation with flux-weakening control, the magnetic flux can be passively decreased by up to 20% caused by leakage flux property, resulting in achieving small amount of flux-weakening current i_d. From these results, the proposed motor is suitable for high speed application in terms of improving average efficiency. More detailed analysis will be presented in the full paper.

[1] X. Zhu, Z. Xiang, C. Zhang, L. Quan, Y. Du, and W. Gu, "Co-reduction of torque ripple for outer rotor flux-switching PM motor using systematic multi-level design and control schemes," *IEEE Trans. Ind. Electron*., vol. 64, no. 2, pp. 1102-1112, Feb. 2017. [2] N. Limsuwan, T. Kato, K. Akatsu, and R. D. Lorenz, "Design and evaluation of a variable-flux flux-intensifying interior permanent-magnet machine," *IEEE Trans. Ind. Appl.*, Vol. 50, No. 2, pp. 1015-1024, Mar./Apr. 2014. [3] W. Hua, X. M. Yin, G. Zhang, and M. Cheng, "Analysis of two novel five-phase hybrid-excitation flux-switching machines for electric vehicles," *IEEE Trans. Magn.*, vol. 50, no. 11, Nov. 2014, Art. ID. 8700305.

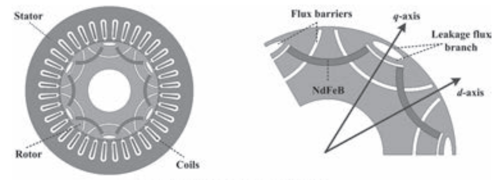

(a) Topology of the new proposed motor

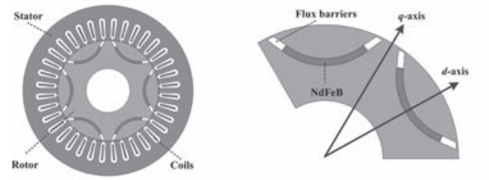

(b) Topology of the conventional motor

Fig. 1 Topologies of the new proposed motor and the conventional motor.

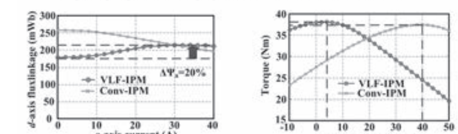

(a) Relationship between i_q and *d*-axis fluxlinkage (b) Torque versus current angle

Fig. 2 Theoretical analysis for the proposed motor.

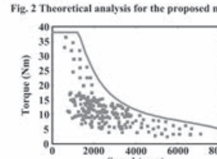

Fig. 3 EVs driving cycle torque distribution versus speed.

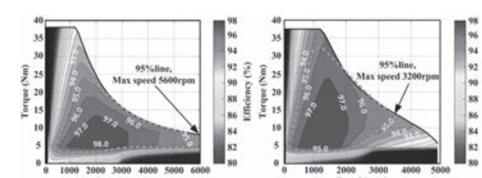

(a) Efficiency map of the proposed motor (b) Efficiency map of the conventional motor

Fig. 4 Comparison of efficiency map.

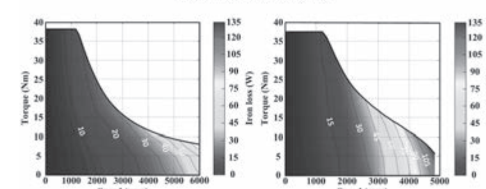

(a) Iron loss of the proposed motor (b) Iron loss of the conventional motor

Fig. 5 Comparison of iron loss map.

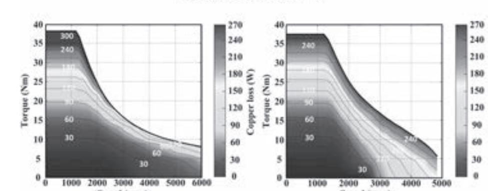

(a) Copper loss of the proposed motor (b) Copper loss of the conventional motor

Fig. 6 Comparison of copper loss map.

BT-07. Design method of permanent magnetic loop return magnetic system and application in vehicle relay.

H. Liang[1], *H. Yu*[1], X. Ye[1] and G. Zhai[1]
1. Harbin Institute of Technology, Harbin, China

1 Preface Lots of vehicle relay is used to realize the function of signal transmission and logic control in high speed rail and urban rail transit. A certain type of traditional clapper type relay started running on the locomotive for a few months, the contact point is closed, however, the test results showed that the contact was broken, which greatly affected the normal operation of the locomotive. The SEM test results show that the contact is in the disconnected state, the moving contact surface is worn and polluted, C and O contents are lot. Therefore, the main failure mode failure mechanism leads to high contact surface film growth caused by contact resistance. Reducing the contact resistance is an effective way to solve this problem. Approaches to reduce the contact resistance divide in two, one is the seal of the relay contact surface in order to inhibit the growth of surface film, but it is not good for heat dissipation, high temperature will affect the service life of electronic components nearby; the other one is to increase the contact pressure, to decreases the contact resistance. The sealed coil has large power consumption and high temperature rise, which will reduce the service life of the surrounding electronic components. Therefore, the only solution of the problem is to increase the contact pressure. 2 Solution based on permanent magnet return circuit The static characteristics of fault traditional patted relay are shown in Figure1(a), when the contact pressure increases, the counter force increases (in Fig. 1(b) in force increases from the black line to the red dotted line), in order to ensure the regular operating (actuation: attractive force greater than the counter force; release: counter force greater than attractive force), needs the increasing of the electromagnetic attractive force (attractive force characteristic in Figure 1 increased from the solid black curve to red dotted curves), it is necessary to improve the current in the coil in order to obtain large attractive force, which will cause the rise of coil power consumption. In order to keep the power consumption of the coil constant and increase the contact pressure DFj at the same time, as shown in Figure 1(b), the counter force characteristics can be moved downward (black dotted broken line in Figure 1(b)) and then increased contact pressure, however, the holding force DFb of the relay at the release position (DFb is the difference between the counter force and the electromagnetic force at 0V, and the electromagnetic force at 0V is zero for the conventional clapper magnetic system) will decrease at this time, so that the relay vibration index is affected. If the electromagnetic force at 0V is a negative value besides zero. DFb can keep the original value unchanged, so that the contact pressure is increased and the coil power consumption and anti-vibration index is unchanged. If the reaction force characteristics continue to move down to obtain the expected absorption characteristics shown in Figure 3, the relay power consumption won't rise, while the contact pressure increases, DFb remains unchanged, and it can still meet the requirements of vibration resistance. Figure 1(c) shows the static characteristics is the typical suction characteristic curve shape of the permanent magnetic loop return magnetic system. In the existing relay products, the Balance Force relay magnetic system from Leach is the typical representative of this magnetic system. The characteristics of the permanent magnet loop return magnetic system are: (1) three working air gaps; (2) a permanent magnetic flux gap smaller closure path at the release location; (3) a permanent magnetic flux gap bigger closure path at the suction location. According to the characteristics of permanent-magnet-loop-return magnetic-system, combined with the structure of traditional clapper type magnetic system, a new type of magnetic system with permanent magnetic loop return magnetic circuit structure is showed. Carry out the static characteristic simulation of the new permanent magnetic loop return clapper magnetic system, and compared with the traditional type, see table 1. As can be seen from it, the contact pressure is increased, the rated power consumption of the new magnetic system is unchanged, the power consumption of the absorbing part is reduced, and the retaining force of the releasing side remains constant, which achieves the goal of improvement. Contact pressure(N) Retention(N) Act consumption(10-3J) Power rating(W) Fault relay 0.3 7.4 8.69 1.78 Improved relay0.4 7.44.12 1.77 3 conclusion (1) Three characteristics of the permanent magnet loop return magnetic system are presented: three working air gaps, a permanent magnetic flux gap closed path at the release location, and a permanent magnetic flux gap closure path at the suction location. (2) Based on the characteristics of the permanent magnet loop return magnetic system, a method of constructing a new permanent magnet loop return magnetic system is presented. This method can also be used in other permanent magnet magnetic systems. (3) Proposed a new type of permanent magnet loop back clapping magnetic system, the simulation results show that this kind of magnetic system of relay with high contact pressure, low power consumption, pull off the electrical characteristics of permanent magnet coil on loop back, solves the traditional capping relay fault due to high contact resistance failure problems.

[1] Mathematical model to simulate an arc erosion of electrical contact in switchgear device. Kale A,Ranade M,Singh A. Electrical Con-tacts (Holm),2015 IEEE 61st Holm Conference on. 2015 [2] A virtual factory based approach to on-line simulation and scheduling for an FMS and a case study[J]. Ming-Hung Lin,Li-Chen Fu. Journal of Intelligent Manufacturing. 2001 (3)

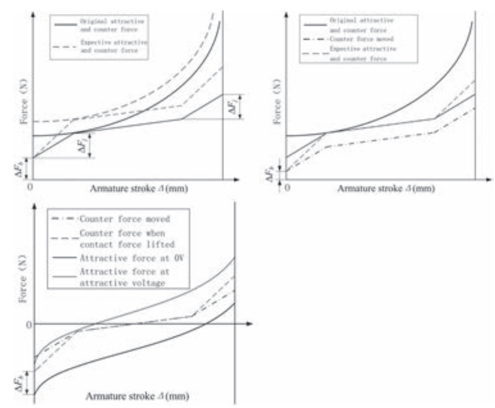

Fig. 1. Static characteristics

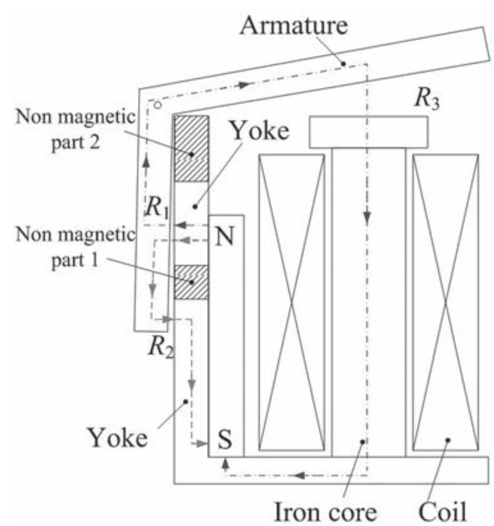

Fig. 2. New type of clapping magnetic system

BT-08. Analysis on the starting and Synchronization Capabilities for a Novel 6/8 Pole Changing Line-Start Permanent Magnet Synchronous Motor.

M. Tian[1], X. Wang[1], W. Zhao[1] and C. Li[1]
1. School of Electrical Engineering, Shandong University, Ji'nan, China

I. Introduction Line-start permanent magnet synchronous motor (LSPMSM) has been widely used in applications such as pumps, fans and compressors for its high torque and power density, efficiency and power factor [1]-[2]. However, it suffers from the poor starting and synchronization capabilities, and always a compromise between the starting and synchronization capabilities is adopted because of the conflict with each other [3]-[4]. So far, several different rotor configurations, such as squirrel-cage rotor, solid rotor, slotted solid rotor, two-part rotor geometry and so on [5]-[7], and different magnet, cage bars shapes [8]-[9], were presented and discussed to improve the starting and synchronization capabilities. But the starting capability cannot get fundamentally improved for the existence of the braking and pulsating torques. In [10]-[12], the pole changing method was presented, and the drawbacks of PMSM got overcame. However, more switches were used, and the reliability was reduced for the proposed 2/4 pole changing winding. In addition, the turn numbers cannot be adjusted to balance the starting and running performance. In this paper, a 6/8 pole changing LSPMSM is designed based on the novel 6/8 pole changing stator winding. As the different pole numbers between stator winding and rotor PMs during 6-pole starting process, the inherent braking torque and pulsating torque for conventional LSPMSM can get effectively eliminated, and the starting capability can be fundamentally improved. Furthermore, as the effective improvement of the starting capability, the rotor resistance can be optimized to be smaller to improve the synchronization capability simultaneously. II. The Structures of the Motor and 6/8 Pole Changing Winding Fig.1(a) and (b) show the structures of a 380V, 30kW, 8-pole LSPMSM and the proposed 6/8 pole changing winding respectively. At the beginning of the starting, 1U, 1V, 1W are connected with the applied source, and the winding is 6-pole. When the motor reaches a certain speed, 1U, 1V, 1W are disconnected and 2U, 2V, 2W are switched on, the winding is switched to 8-pole. Keep the 8-pole state until the motor runs stably. The structure of the proposed winding is more simple and easier to control because of the less use of switches, the reliability is also get higher and service life is longer. Meanwhile, the performance of the starting and steady running can also get balanced by adjusting the winding turns of the two pole states. III. The Analysis of the Starting Process Firstly, the no-load back electromagnetic force (EMF) of the proposed 6-pole and 8-pole winding are calculated respectively. The results show that the value of the 6-pole winding is nearly zero, which can fundamentally explain the reason for the elimination of the braking torque. Then the comparison of the locked-rotor torque with two winding shows that the values are 900 Nm and 909 Nm respectively, but the torque fluctuation rate is reduced by 40.4% for the 6-pole winding. Finally, the speed, current and electromagnetic torque during the entire starting process between the proposed pole changing and conventional LSPMSM are compared. The results show that the starting time is shorter, speed and torque fluctuation is smaller, and even the time to pull into synchronization is also shorter for the proposed one. IV. The Improvement of the Synchronization Capability Under the premise that the starting capability has been effectively improved, the rotor resistance R can be appropriately reduced to improve the synchronization capability simultaneously. Fig.2(a) shows the torque-speed (T-s) curve with two different rotor resistance R_1 and R_2, and R_1>R_2. As the starting torque T_{st} is proportional to R, so T_{st1}>T_{st2}. The maximum torque T_{max} and the corresponding critical slip s_m are, $T_{max}\approx m_1U_1^2/(2\Omega_s(X_{1\sigma}+X'_{2\sigma}))$, $s_m\approx R/(X_{1\sigma}+X'_{2\sigma})$, where m_1, U_1, Ω_s, $X_{1\sigma}$, $X'_{2\sigma}$ are phase numbers, input voltage, angular velocity of rotation, stator leakage reactance and rotor leakage reactance, respectively. So T_{max1}=T_{max2}, s_{m1}>s_{m2}. And during the synchronization process, for an arbitrary slip s_0, the smaller rotor resistance corresponds to the larger torque, T_1<T_2, which is more advantageous for pull-into synchronization. To reduce the rotor resistance, the cross-sectional area of the cage bar is designed larger. And then the comparison of the synchronization capability between the original and the new proposed 6/8 pole changing LSPMSM is analyzed by comparing the maximum inertia of moment J_{max} (the rated inertia of moment is J_r) that motor can pull into synchronization. The speeds of two motors with different J is shown in Fig.2(b), and the results show that J_{max} is 15J_r for original 6/8 motor while for the proposed new designed 6/8 pole motor, J_{max} is 19J_r. The synchronization capability gets well improved. V. Conclusion This paper has proposed a novel 6/8 pole changing LSPMSM. Based on the pole changing starting method, the starting capability gets fundamentally improved. Furthermore, under the premise of guaranteeing the starting capability, the synchronization capability is considered by reducing the rotor resistance. Through processing, both the starting and synchronization capabilities have been improved.

[1] S. Shamlou, M. Mirsalim, "Design, optimization, analysis and experimentally verification of a new line-start permanent magnet synchronous shaded-pole motor," *IET Elect. Power Appl.*, vol.7, no. 1, pp.16-26. 2012. [2] R. T. Ugale, B. N. Chaudhari. "Rotor Configurations for Improved Starting and Synchronous Performance of Line Start Permanent-Magnet Synchronous Motor," *IEEE Trans. Ind. Electron*., vol. 64, no. 1, pp. 138-148, 2017. [3] A. H. Isfahani and S. -Z. Vaez, "Line start permanent magnet synchronous motors: Challenges and opportunities," *Elsevier J. Energy*, vol. 34, no. 11, pp. 1755–1763, Nov. 2009. [4] T. T. Ding, N. Takorabet, F. M. Sargos, X. H. Wang, "Design and analysis of different line-start PM synchronous motors for oil-pump applications," *IEEE Trans. Magn*., vol. 45, no. 3, pp. 1816-1819, 2009. [5] M. N. Azari and M. Mirsalim, "Line start permanent magnet motor synchronization capability improvement using slotted solid rotor," *IET Elect. Power Appl*. vol. 7, no. 6, pp. 462–469, 2013. [6] E. P. Sanchez, A.C. Smith. "Steady-State Analysis of a Canned Line-Start PM Motor. *IEEE Trans. Magn*., vol. 47, no. 10, pp. 4080-4083. 2011. [7] R. T. Ugale, A. Bhanuji, and B. N. Chaudhari. "A novel line start permanent magnet synchronous motor using two-part rotor". *TENC. IEEE Reg. 10 Conf.,* pp. 1–5. 2009. [8] M. Niazazari, M. Mirsalim, S. Mohamadi. "Effect of rotor slots parameters on synchronization capability of slotted solid rotor line start permanent magnet motor". *IEEE Power. Elect. Drive Syst. Tech. Conf.*, Tehran, pp. 60-65. Feb. 2013. [9] E. G. Shehata. "Design tradeoffs between starting and steady state performances of line-started interior permanent magnet synchronous motor". *IET Int. Conf. Power Elect. Mach. Drives*. Manchester, UK, pp. 1-6. Apr. 2014. [10] C. M. Stephens, G. B. Kliman, J. Boyd. "A line-start permanent magnet motor with gentle starting behavior". *IEEE Trans. Ind. Appl*., vol. 1, pp. 371-379. 1998. [11] N. F. Ershad, M. Mirsalim, A. D. Aliabad. "Line-start permanent magnet motors: proper design for pole-changing starting method". *IET Elect. Power Appl.*, vol.7, no. 6, pp.470-476. 2013. [12] A. D. Aliabad, M. Mirsalim, N.F. Ershad. "Line-Start Permanent-Magnet Motors: Significant Improvements in Starting Torque, Synchronization, and Steady-State Performance". *IEEE Trans. Magn*., vol. 46, no. 12, pp. 4066-4072. 2010.

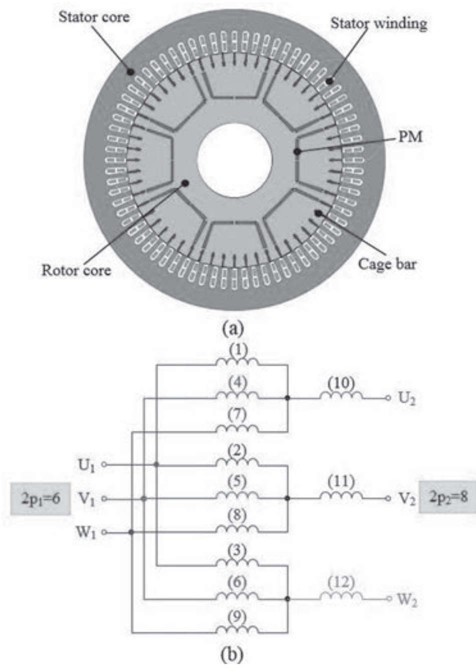

Fig. 1. The structures of (a) the proposed motor, and (b) the novel 6/8 pole changing stator winding.

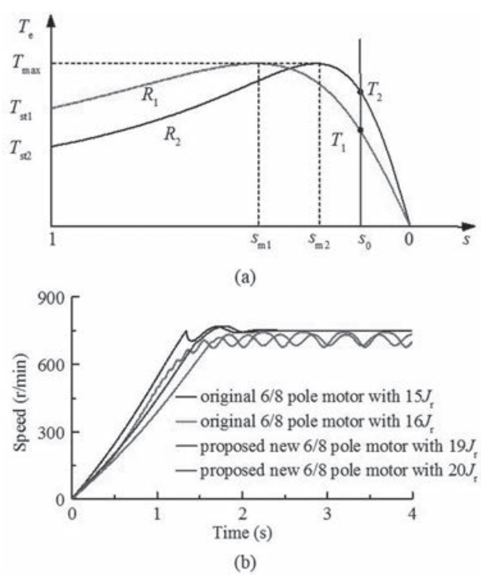

Fig. 2. (a) The *T-s* curve with different rotor resistance and $R_1 > R_2$, (b) the comparison of the synchronization process with different inertia *J* between the original and proposed new 6/8 pole changing LSPMSM.

BT-09. Investigation of a Transverse-flux Flux-reversal Motor with Consequent-pole Configuration.

B. Kou[1], *X. Yang*[1], Y. Zhou[1], J. Luo[1] and H. Zhang[1]
1. Harbin Institute of Technology, Harbin, China

I. INTRODUCTION With the advantages of high torque/power density and high feasibility for multi-pole/multi-phase design, the transverse flux motor has been widely investigated for low-speed large-torque direct-drive applications [1][2]. Nevertheless, the previous transverse flux motors always face the problem of high manufacturing cost that is caused by using of a large amount of expensive rare-earth permanent magnet and complex motor core structure. For avoiding those shortcomings, a transverse-flux flux-reversal motor (TF-FRM) is proposed in [3]. Both stator and rotor of the TF-FRM can be fabricated by silicon steel sheet that simplifies the manufacturing of core, meanwhile, the total volume of PMs used in TF-FRM is fewer and the provided torque density is considerable. In this paper, a transverse-flux flux-reversal motor with consequent-pole configuration (TF-CFRM) is proposed based on the forgoing TF-FRM, which can further reduce the volume of PMs and provide high torque density. Firstly, the basic structure and working principle are introduced. Secondly, the analytical expression of the electromagnetic torque is derived by a 3-D equivalent magnetic circuit model. Then the influences of structural dimensions on torque density is analyzed by finite element method. At last, the torque performance of the proposed TF-CFRM is compared with TF-FRM and flux reversal motor [4]. *II. BASIC STRUCTURE AND WORKING PRINCIPLE* The fundamental structures of traditional flux reversal motor, forgoing TF-FRM and proposed TF-CFRM are shown in Fig.1. The proposed TF-CFRM is a three-phase machine which is combined by three single-phase units along axial direction. The stator radial-flux cores have tooth-slot configuration in the inner surface, the center line of 'tooth' in one core is aligned to the center line of 'slot' in another core in one single-phase unit. The PMs are fixed in the 'slot' area of stator radial-flux cores, all PMs of the same polarity and they are magnetized along radial direction. Like the traditional flux reversal PM motor, the proposed motor works on the principle of variable flux linkage, inducing a back electromotive force that interacts with an alternating armature current in torque generation. *III.PRELIMINARY ANALYSIS BY 3-D EQUIVALENT MAGNETIC CIRCUIT MODEL* A 3-D equivalent magnetic circuit model is built for preliminary analysis of TF-CFRM. Since the magnetic field of different phases of TF-CFRM are decoupled, and the model has a periodicity along rotational direction, the magnetic circuit model under two pole-pitch is built for simplify the calculation. Then the analytical expressions of flux linkage in coil, no-load back electromotive force and electromagnetic torque are divided. *IV. INFLUENCE OF KEY DIMENSIONS AND TORQUE PERFORMANCE COMPARISON* Since the length of PM in the rotational direction, the thickness of PM in the magnetized direction and the rotor core length in rotational direction (l_{pm}, h_{pm} and l_{rt} respectively) have significant effects on the magnetic reluctance of TF-CFRM, then resulting in the influences on the torque performances. The ratio of PM rotational length on pole-pitch k_{pm} (l_{pm}/τ_{pm}), the radio of rotor core rotational length on pole-pitch k_{rt} (l_{rt}/τ_{pm}) and the PM thickness h_{pm} are listed as three key dimensions. The analysis of key dimensions are done by finite element method, and the results are shown in Fig.2a and 2b. From the results, the optimal value range of the three dimensions are selected as 1.1~1.2, 0.6~0.7 and 3~4mm. The torque performance such as cogging torque, electromagnetic torque and torque ripple of the proposed TF-CFRM is compared with TF-FRM and flux reversal motor which have same dimensions, the results are shown in Fig.2c. *V. CONCLUSION* A transverse-flux flux-reversal motor with consequent-pole configuration is introduced in this paper. The expressions of electromagnetic torque is derived by equivalent magnetic circuit model. The influences of three key dimensions on torque performance are investigated by finite element method, the optimal value ranges of key dimensions are presented which provides useful information for future design process. And the torque performance of proposed motor is compared with TF-FRM and FRM by FEM. The torque density per volume of TF-CFRM is 8.07kN.m/m^3 when the RMS current density is 4.3A/mm^2, which is similar to the ones of TF-FRM and FRM. Meanwhile, the total volume of PMs used in TF-CFRM is 77% of TF-FRM and 57% of FRM. That means TF-CFRM is a considerable solution of direct-drive motor which can reduce the manufacturing cost and provide acceptable large torque density.

[1] Ueda Y, Takahashi H, Akiba T, et al. Fundamental Design of a Consequent-Pole Transverse-Flux Motor for Direct-Drive Systems[J]. *IEEE Trans. Magn.*, 2013, vol. 49, no. 7, pp. 4096-4099. [2] Zou J, Zhao M, Wang Q, et al. Development and Analysis of Tubular Transverse Flux Machine With Permanent-Magnet Excitation[J]. *IEEE Trans. Ind. Electron.*, 2012, vol. 59, no. 5, pp. 2198–2207. [3] Kou B, Yang X, Luo J, et al. Modeling and Analysis of a Transverse-flux Flux Reversal Motor[J]. *IEEE Trans. Energy Convers*, 2016, vol. 31, no. 3, pp. 1121–1131. [4] Gao Y, Qu R, Li D, et al. Design of Three-Phase Flux-Reversal Machines With Fractional-Slot Windings[J]. *IEEE Trans. Ind. Appl.*, 2016, vol. 52, no. 4, pp. 2856-2864

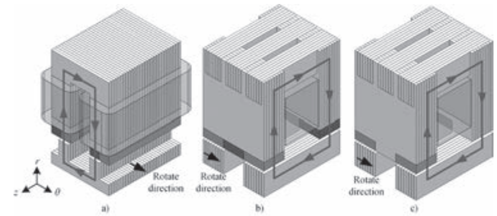

Fig.1. Fundamental motor structure. a) Flux reversal motor; b) TF-FRM; c) TF-CFRM.

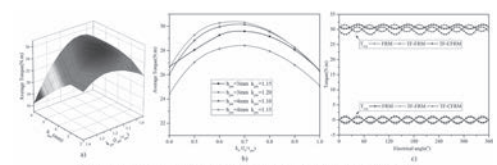

Fig.2. Results of finite element analysis. a) Influence of k_{pm} and h_{pm} on average torque; b) Influence of k_{rt} on average torque; c) Torque performance comparison between FRM, TF-FRM and TF-CFRM.

BT-10. Torque Improvement of Five-Phase Halbach Permanent Magnet Machines Considering Third-Harmonic Flux Density.

L. Zhang[1] and L. Liu[1]
1. Nanjing University of Aeronautics and Astronautics, Nanjing, China

I. INTRODUCTION Multi-phase machines have obtained wide applications in aerospace, rail transient, electric vehicle, etc. due to the advantages of high torque density, high efficiency, and high reliability [1]-[2]. The five-phase permanent magnet (PM) machines, as one of such machines, can improve the torque density by injecting third-harmonic current into the fundamental one. This is mainly due to the additional output torque can be contributed by the interaction of third-harmonic back-EMF and injected third-harmonic current [3]. Therefore, the third-harmonic component in phase back-EMF is the basic conditions of torque density improvement by third-harmonic current injection. The Halbach PM array technique, which can provide approximate sine air-gap flux density to suppress the torque ripple, has been widely applied to obtain excellent static and dynamic performance in the PM machines [4]-[5]. However, due to the lack of third-harmonic component in phase back-EMF for this structure,it is no of effect to improve the torque density by injecting third-harmonic current in the five-phase PM machines. Therefore, this paper proposes a third-harmonic Halbach PM array structure based on the conventional Halbach PM array, in which the more third-harmonic contents in phase back-EMF can be provided. The torque characteristics of the five-phase PM machines with the proposed structure and the conventional structure are compared by finite element method, when the sine with third-harmonic (SIN+3rd) current is supplied under the current constraints of the same amplitude (AMP) and the same root-mean-square (RMS), respectively. II. MACHINE STRUCTURES AND FINITE ELEMENT ANALYSIS The proposed third-harmonic Halbach PM array structure consists of two sets of conventional discrete Halbach PM array for one pole, and the evolution schematic of the proposed structure is shown in Fig.1 (a). The analogous saddle shaped air-gap flux density can be produced in the proposed structure, and the corresponding back-EMF is induced, which can improve the contents of third-harmonic component in the phase back-EMF. Therefore, the output torque can be improved by the additional torque contributed by the third-harmonic components. In order to verify the torque improvement of the proposed structure compared to the conventional structure, the 10-slot/8-pole five-phase PM machines with unequal teeth and single-layer non-overlapping winding are employed. The two five-phase PM machines structures are shown in Fig.1 (b) and (c). The output torque waveforms of the two five-phase PM machines are given in Fig. 2 (a) and (b). It can be observed that the average torque of the five-phase PM machines with proposed third-harmonic Halbach PM array can be improved by 6.57% compared to that of the conventional Halbach PM array five-phase PM machines, when the SIN+3rd current is supplied under the same AMP constraint. For the same RMS constraint, the average torque can be improved by 5.99% of the conventional Halbach PM array five-phase PM machines. Meanwhile, it should be noted that the corresponding torque ripple is hardly deteriorated.

[1] E. Levi, R. Bojoi, F. Profumo, H. A. Toliyat, and S. Williamson, “Multiphase induction motor drives - A technology status review,” IET Elect. Power Appl., vol. 1, no. 4, pp. 489-516, Jul. 2007. [2] G. K. Singh “Multi-phase induction machine drive research-a survey,” Elect Pow Sys Res., vol. 61, no. 2, pp. 139-147, Mar. 2007. [3] K. Wang, Z. Q. Zhu and G. Ombach, “Torque improvement of five-phase surface-mounted permanent magnet machine using third-order harmonic,” IEEE Trans. Energy Convers., vol. 29, no. 3, pp. 735-747, Sep. 2014. [4] M. Markovic, and Y. Perriard, “Optimization design of a segmented Halbach permanent-magnet motor using an analytical moel,” IEEE Trans. Magn., vol. 45, no.7, pp. 2955-2960, Jul. 2009. [5] K. J. Meessen, B. J. Gysen, J. H. Paulides, and E. A. Lomonova, “Halbach permanent magnet shape selection for slotless tubular actuators,” IEEE Trans. Magn., vol. 44, no.11, pp. 4305-4308, Nov. 2008.

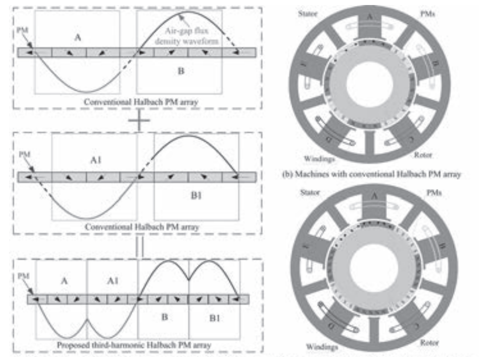

(a) Evolution schematic of proposed third-harmonic Halbach PM array (c) Machines with proposed third-harmonic Halbach PM array

Fig.1 Evolution schematic of proposed structure and five-phase PM machines structures

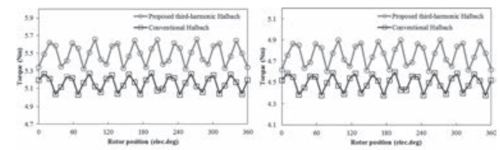

(a)Same AMP constraint (b) Same RMS constraint

Fig.2 Comparison of output torque under different current supply

BT-11. A High Power Factor Vernier Machine with Coil-Pitch of Two Slot Pitches.

Y. Liu[1], H. Li[1] and Z. Zhu[1]
1. The University of Sheffield, Sheffield, United Kingdom

Abstract--In this paper, an 18-slot/26-pole Vernier permanent magnet synchronous machine (VPMSM) with coil-pitch of two slot pitches is proposed based on a 9-slot/18-flux-modulation-pole/26-pole VPMSM with concentrated tooth-coil windings. Compared with the original VPMSM, the number of slots is doubled and the phase winding connection is adjusted to reduce the space harmonic content, the phase inductance and hence, improve the power factor. The study shows that the proposed VPMSM has a higher power factor of 93% with a torque improvement. Moreover, a series of VPMSMs with high power factor is proposed from the same design principle. 1. Introduction Vernier permanent magnet synchronous machine (VPMSM) has become a promising candidate in direct drive application because of its high torque density [1] and low torque ripple [2]. However, different from traditional PMSMs, Vernier machines suffer from low power factor which increases the cost of power converters [3] and hinder their application. Compared with the traditional PMSM with higher power factors, the low power factor of VPMSM is caused by the increased number of rotor PM poles and the relatively large phase inductance. There are some papers trying to improve the power factor of VPMSMs by using Halbach PM rotor [3] or dual-rotor structure [4]. However, special techniques or complicated structures are needed, hindering their application to common VPMSM designs. In this paper, an 18-slot/26-pole VPMSM with coil-pitch of two slot pitches is evolved and proposed based on a 9-slot/18-flux-modulation-pole (FMP)/26-pole VPMSM with concentrated tooth-coil windings. Compared with the original machine, the slot number is doubled and the phase winding connection is adjusted in the proposed one to reduce the space harmonic content, and hence, decrease the phase inductance. The study shows that such design can effectively decrease the phase inductance and improve the power factor from 73% to 93% with a torque improvement. Moreover, a series of VPMSMs with high power factor will be proposed from the same design principle. 2. Machine structure and performance comparison A 9-slot/26-pole VPMSM with 18 FMPs and concentrated windings is shown in Fig. 1 (c). This is a typical VPMSM with concentrated tooth-coil windings [5] since it satisfies p_r=N_f-p_s, where p_r is the number of PM pole-pairs in the rotor, N_f is the number of FMPs in the stator and p_s is number of the armature winding pole pairs in the stator. This machine suffers from low power factor as a result of high PM pole number and relatively large phase inductance. In this paper, an 18-slot/26-pole VPMSM with coil-pitch of two slot pitches is proposed based on the 9-slot/26-pole VPMSM. The proposed machine is evolved from the original machine via the following steps: (1) Double the number of slots so that in the proposed machine the number of stator slots N_s equals to N_f in the original machine, as shown in Figs. 1 (a) and (b). (2) Divide the windings of phase (A, B, C) in Fig 1 (c) into two groups denoted as (A1, B1, C1) and (A2, B2, C2) in Fig. 1 (d). (3) In the proposed machine, configure (A1, B1, C1) in the same way with (A, B, C), with the coil spanning two slot pitches. (4) In the proposed machine, configure (A2, B2, C2) 180 mechanical degree away from (A1, B1, C1), with opposite polarity. By doing this, the armature reaction space harmonics of even orders can be effectively eliminated without affecting the fundamental harmonic [6], as shown in Fig. 1 (e). The reduction of armature reaction space harmonic content can directly reduce the phase inductance per turn, and hence, improve the power factor. Both the 9-slot and the 18-slot/26-pole VPMSMs are globally optimised under the same overall size, same copper loss considering the end windings and PM volume. The performance of the optimised machines are shown in Table 1. It shows that the proposed machine increases the power factor from 73% to 93%, with a torque improvement. 3. Design principle and guidelines It is proved that for the VPMSM with concentrated windings, as long as it satisfies $1/2N_f = N_s = 2(N_f - p_r) \pm 1$, it can be evolved into a VPMSM with $N_s = (4p_r \pm 2)/3$ and coil-pitch of two slot pitches. In this way, the space harmonic content as well as the inductance will be reduced, and hence, the power factor will increase. Detailed design principle and guidelines will be presented in the full paper. 4. Experiment validation The prototype of the 18-slot/26-pole machine with coil-pitch of two slot pitches will be manufactured and tested. 5. Conclusion In this paper, an 18-slot/26-pole VPMSM with coil-pitch of two slot pitches is proposed from a 9-slot/18-FMP/26-pole VPMSM with concentrated windings. Compared with the original VPMSM, the proposed design reduces the armature reaction space harmonic content and phase inductance without affecting the fundamental harmonic, and hence increases the power factor with a torque improvement. The study also shows that a series of VPMSMs with coil-pitch of two slot pitches can achieve high power factor based on the same design principle.

[1] A. Toba and T. a Lipo, "Generic torque-maximizing design methodology of surface permanent-magnet Vernier machine," *IEEE Trans. Ind. Appl.*, vol. 36, no. 6, pp. 1539–1546, Nov./Dec. 2000. [2] D. Li, R. Qu, and J. Li, "Analysis of torque capability and quality in Vernier permanent-magnet machines," *IEEE Trans. Ind. Appl.*, vol. 52, no. 1, pp. 125–135, Jan./Feb. 2016. [3] D. Li, R. Qu, and T. A. Lipo, "High-power-factor vernier permanent-magnet machines," *IEEE Trans. Ind. Appl.*, vol. 50, no. 6, pp. 3664–3674, 2014. [4] Y. Kataoka, M. Takayama, Y. Matsushima, and Y. Anazawa, "Comparison of three magnet array-type rotors in surface permanent magnet-type vernier motor," in Proc. Int. Conf. Elect. Mach. Syst., pp. 1–6, Oct. 2012, [5] K. Okada, N. Niguchi, and K. Hirata, "Analysis of a vernier motor with concentrated windings," *IEEE Trans. Magn.*, vol. 49, no. 5, pp. 2241–2244, 2013. [6] J. Wang, V. I. Patel, and W. Wang, "Fractional-slot permanent magnet brushless machines with low space harmonic contents," *IEEE Trans. Magn.*, vol. 50, no. 1, pp. 1–9, 2014.

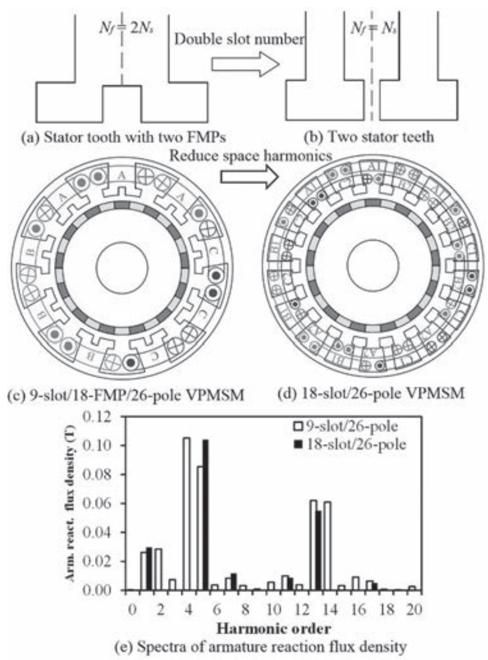

Fig. 1. Machine topology and evolution.

	9-slot/26-pole	18-slot/26-pole
Inductance per turn (mH)	0.019	0.010
Torque (Nm)	5.9	6.0
Power factor	0.73	0.93

Table 1. Performance comparison.

BT-12. A study on hall sensor fault signal compensation algorithm to prevent irreversible demagnetization by hall sensor faults.

D. Lee[1], B. Kim[1], S. Lee[1], J. Lee[1] and D. Kang[1]
1. Convergence System Engineering, keimyung university, Daegu, The Republic of Korea

BLDC motors are similar to DC motors, but they use semiconductor switches to implement commutator and brush functions. Therefore, it is the motor that solves the disadvantages of the mechanical structure of DC motor. BLDC motors have a simple structure and high torque and high speed operation.[1][2] In order to realize this function, it is essential to know the position of the permanent magnet. Normally, a permanent magnet motor uses a Hall sensor. The three Hall sensors are arranged at intervals of 120 ° of the machine angle to detect the position of the rotor.[3][4] From the detected signal, the position of the rotor can be divided into six sections. In the six sections, two phases should be selected to excite current. So that the rotor continually rotates in one direction. However, this hall sensor has frequent faults according to the usage environment and has a disadvantage that an error signal can be generated due to the influence of an external magnetic field. The magnetic field sensing capability may be degraded in a high temperature environment. In addition, an error signal may be generated by the leakage magnetic flux generated by the magnetic saturation of the iron core.[5] Fault of a position sensor such as a Hall sensor in a permanent magnet synchronous motor drive system rotating at high speed is an important factor that lowers the reliability of the control system.[6] In addition, the fault of the hall sensor may generate an overcurrent in each. The overcurrent increases in proportion to the speed of the motor. The overcurrent generated in each phase is one of the fatal factors that can cause Irreversible demagnetization in the permanent magnet synchronous motor. Failure analysis studies are under way to solve these problems. Sensorless control switching studies in the event of faults are also underway. A sensorless position estimator is usually used to compensate for the failure signal of the position sensor. The sensor output value is compared with the output value from the sensorless controller. If the error is over a certain range, the sensor is judged to be faulty and switched to sensorless control. If the error range for judging the failure of the sensor is small, an error is determined to be a failure even in a normal state. On the contrary, if the error range for judging the failure of the sensor is too large, a large current ripple occurs when switching to the sensorless control. In this paper, we use the method of comparing and analyzing the interval data from the first triggered point in real time. Therefore, the failure of the hall sensor can be detected immediately, and the hall sensor in which the failure has occurred can also be grasped. In this paper, the signal of the failed Hall sensor is compensated by using two Hall sensors operating normally. Therefore, it has higher reliability than sensorless control by using a normal sensor. The circuit that compensates the signal uses a logic circuit and a phase shift circuit. Two normally operating Hall sensors are input to the logic gate circuit to generate an inverted waveform of one hall sensor. The phase shift circuit is constructed using resistors, capacitors, and op amps. The inverted waveform from the logic gate circuit is input to the phase shift circuit to generate two waveforms delayed by a specified angle. The delayed two waveforms are used to generate the faulty hall sensor waveform through the op amp. The simplorer circuit consists of a motor, a controller, and an inverter. And the Hall sensor was forced to generate a fault at 200[ms]. We have detected the fault by constructing the algorithm as described above. Identify the failed hall sensor and enter the remaining normal operating Hall sensor into the phase shifting circuit. The signal generated through the phase shift circuit compensates the signal of the failed Hall sensor. As a result, we confirmed that the motor operates normally through the compensated Hall sensor and two normally operating Hall sensors. Irreversible demagnetization of the permanent magnet is also reduced when the Hall sensor fails.

[1]Jianhui Hu, Jibin Zou, Fei Xu, Yong Li, and Yanchao Fu, "An Improved PMSM Rotor Position Sensor Based on Linear Hall Sensors" IEEE TRANSACTIONS ON MAGNETICS, VOL. 48, NO. 11, NOVEMBER 2012 [2]Sam-Young Kim, Chinchul Choi, Kyeongjin Lee, and Wootaik Lee, "An Improved Rotor Position Estimation With Vector-Tracking Observer in PMSM Drives With Low-Resolution Hall-Effect Sensors" IEEE TRANSACTIONS ON INDUSTRIAL ELECTRONICS, VOL. 58, NO. 9, SEPTEMBER 2011 [3]Nikolay Samoylenko, Qiang Han and Juri Jatskevich, "Dynamic Performance of Brushless DC Motors With Unbalanced Hall Sensors" IEEE TRANSACTIONS ON ENERGY CONVERSION, VOL. 23, NO. 3, SEPTEMBER 2008 [4]Giacomo Scelba, Giulio De Donato, Mario Pulvirenti, Fabio Giulii Capponi, and Giuseppe Scarcella, "Hall-Effect Sensor Fault Detection, Identification, and Compensation in Brushless DC Drives" IEEE TRANSACTIONS ON INDUSTRY APPLICATIONS, VOL. 52, NO. 2, MARCH/APRIL 2016 [5]Myung-Hyuk Jang, Kwang-Woon Lee," Hall Sensor Fault Detection and Fault-Tolerant Control of High-Speed PMSM Drive System" THE TRANSACTIONS OF KOREAN INSTITUTE OF POWER ELECTRONICS 18(3), 2013.6, 205-210 (6 pages) [6]Yao Da, Xiaodong Shi, Mahesh Krishnamurthy,"A Novel Universal Sensor Concept for Survivable PMSM Drives" IEEE Transactions on Power Electronics VOL. 28, NO. 12, Dec. 2013

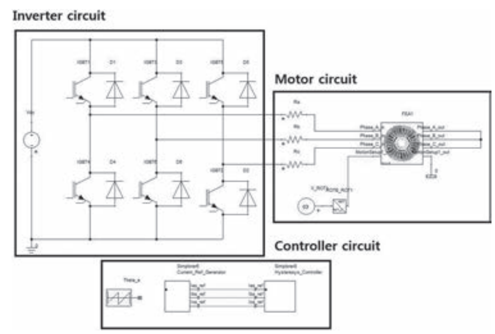

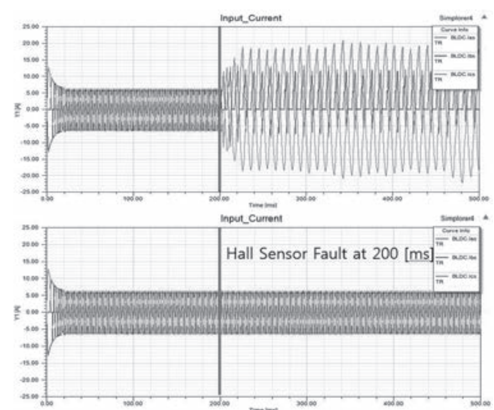

BT-13. Efficiency Optimization for IPMSM Considering Hysteresis Loss.

T. Ishikawa[1]
1. Electronics and Informatics, Gunma University, Kiryu, Japan

1. Introduction It is very important to maximize the efficiency of electric motors, because electric motors consume more than 50 % of total energy produced in the world. One way to achieve this goal is to apply control techniques to reduce the motor losses. Interior permanent magnet motors (IPMSMs) exhibit better efficiency than induction motors. Therefore, this paper treats IPMSMs. IPMSMs have two types of loss such as copper loss due to the winding resistance and iron loss due to eddy current and hysteresis losses in the core and permanent magnet materials. However, the references which treated loss minimization of IPMSMs take into account a constant core-loss resistance only [1] [2]. This paper proposes d- and q-axis equivalent circuits which take into account eddy-current-loss resistance and hysteresis-loss resistance. The characteristics of an IPMSM are clarified when the loss minimization algorithm is used. 2. Loss minimization algorithm In order to use a vector control strategy, three-phase stationary frame is transformed to a two-phase synchronously rotating d-q frame. Figure 1 shows the d-q axis equivalent circuits of IPMSMs including copper, eddy-current and hysteresis losses. In this figure, R_a: stator resistance, R_e: eddy-current-loss resistance, R_h: hysteresis-loss resistance, ω: electrical rotor speed, ϕ_f: magnetic flux linkage, L_d, L_q: d-q axis self-inductances, R_{h0}: R_h when $\omega=\omega_0$, v_d, v_q: d-q axis stator voltages, i_d, i_q: d-q axis stator currents, i_{od}, i_{oq}: d-q axis magnetizing currents, i_{ed}, i_{eq}: d-q axis eddy-current-loss currents, i_{hd}, i_{hq}: d-q axis hysteresis-loss currents in the synchronous rotating frame. In the equivalent circuit shown in references [1] and [2], hysteresis-loss resistance R_h is omitted. The terminal voltage ignoring stator resistance is expressed as at a steady state, V_o=sqrt($v_{od}^2+v_{oq}^2$)=ω*sqrt(($L_d*i_{od}+\phi_f)^2+(L_q*i_{oq})^2$)=ω*ϕ. Therefore, copper loss is given by $P_c = R_a*(i_d^2+i_q^2)$. Eddy current loss is given by $P_e = V_o^2/R_e = \omega^2*\phi_f^2/R_e \propto f^2*B^2$. Hysteresis loss is also given by $P_h = V_o^2/R_h = \omega^2*\phi_f^2/(R_{h0}*\omega/\omega_0) \propto f*B^2$. It is noted that if hysteresis-loss resistance $R_h = R_{h0}*\omega/\omega_0$, hysteresis loss is proportional to frequency f times the square of flux density B. The d-axis magnetizing current iod for minimizing loss is given by $d(P_c+P_e+P_h)/d(i_{od}) = 0$. As a result, iod is represented as a function of ω and torque T_e, and then ioq, id, iq, and the efficiency can be represented as a function of ω and torque T_e. 3. Characteristics at loss minimization situation As derived in the previous section, i_d, i_q, and efficiency become a function of only iod when load torque and speed are considered to be constant. The stator current id and iq of a IPMSM producing minimum loss are plotted in Figure 2 for three different speeds and four different torque, in which ω0 is set to 1000 min^{-1}. The stator current id and iq without considering the hysteresis-loss resistance are also plotted to clarify the effect of hysteresis loss resistance, in which R_h is set to be infinite and Re is set to be half. It is found from figure 2(a) that id becomes large when speed is high and becomes a little bit small when speed is low by considering the hysteresis-loss resistance. Figure 2(b) shows that motor efficiency becomes low when speed is high and becomes low when speed is high by considering the hysteresis-loss resistance. Therefore, the hysteresis-loss resistance should be taken into account when the loss minimization algorithm is used. 4. Conclusions This paper has proposed d- and q-axis equivalent circuits which take into account eddy-current-loss resistance and hysteresis-loss resistance, which is proportional to the speed. It has been clarified that the hysteresis-loss resistance should be taken into account when the loss minimization algorithm is used.

[1] M. N. Uddin and R. S. Rebeiro, "Online Efficiency Optimization of a Fuzzy-Logic-Controller-Based IPMSM Drive", EEE Trans. on Industry Applications, Vol. 47, No. 2, pp. 1043-1050, 2011 [2] F. C. F. Azevedo and M. N. Uddin, "Recent Advances in Loss Minimization Algorithms for IPMSM Drives", 2014 IEEE Industry Application Society Annual Meeting, pp1-9, 2014

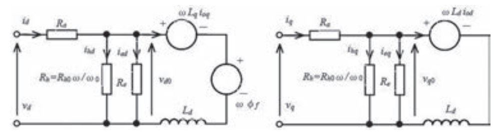

Fig. 1. d-q axis equivalent circuits for IPMSMs including eddy current loss and hysteresis loss. (a) d-axis, (b) q-axis

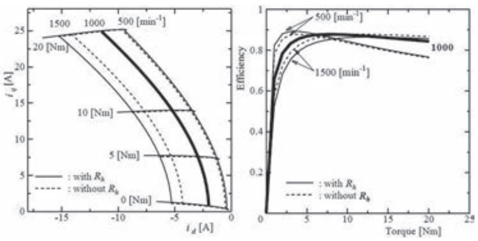

Fig. 2. (a) Current vector loci for maximum efficiency, (b) Efficiency characteristics

BT-14. Comparison of the Power Factor of SMPM and SM Vernier Outer Runner Machines for Traction Applications.

D. Thyroff[1], C. Hittinger[1] and I. Hahn[1]
1. Institute of Electrical Machines and Drives, University of Erlangen-Nuremberg, Erlangen, Germany

1. Introduction In traction applications high torques at low speeds and in standstill are required. Therefore, often a high speed machine is combined with a gear to adapt torque and speed of the machine [1, 2]. However, gears need maintenance and lubrication, while creating noise and increasing the inertia of the machine. Using direct drives instead of high speed drives allows removing the gear. Yet, the used direct drives need a very high standstill torque and a high torque density [1, 2]. Besides the PM machine, the Vernier machines, a group of the flux modulation machines, offer machine topologies with higher torque densities [4]. In comparison to the PM machine, a very low power factor of the Vernier machine is reported [5 - 7]. The power factor of both machine types is mostly compared in the corner speed point. But in traction applications it is not sufficient to focus on a single point and on a single objective, as the drive is dynamically driven over the whole torque and speed range. Therefore, this paper investigates on a performance comparison of both machines designed as outer runner machines with surface mounted magnets [3], while applying the same objectives and requirements. The calculation method bases on FEM and includes the evaluation of iron losses by the IGSE model [8]. The final paper will include pictures and data of the machines geometry *2. Control strategies and machine design objectives* The control of an electrical machine splits into the base speed region and into the field weakening area. In the base speed region the machine is driven following the MTPA (= maximum torque per ampere) control strategy, while the MTPA is found by following the trajectory of maximum torque per current amplitude through the Id- and Iq-map [9, 10]. Figure 1 shows the Id- and Iq-map for the investigated Vernier machine. The MTPA connects the zero point and the current limit circle in the Id- and Iq-map, as shown in figure 1. In the field weakening area the machine is operated following the MTPV (=maximum torque per voltage) control strategy, while the MTPV is found by following the maximum torque per voltage amplitude trajectory through the Id- and Iq-map [9, 10]. The MTPV connects the current limit circle and the ideal short circuit point (= SCP) by a nearly vertical trajectory, as shown in figure 1. Only if the machine is operated following the MTPV a constant power output in the field weakening area is possible. Therefore, it is necessary that the ideal SCP lies inside the current limit circle of the machine. Otherwise the output power of the machine will decrease in the field weakening area [9, 10]. However, offering constant power at higher speeds is a significant objective in traction applications, therefore it is an important design objective to locate the ideal SCP inside the current limit circle. Doing so also allows a safe runout with tolerable currents in case of an inverter failure. Both trajectories are connected by traveling on the current limit circle, resulting in the Id and Iq limit curve. The resulting speeds and torques along the limit curve are shown in figure 2. The final paper will also include the MTPA and MTPV Id- and Iq-map plots for the PM machine. *3. Power factor comparison of the PM and Vernier Machine* As it is mandatory for traction applications to locate the ideal SCP point inside the current limit circle, the design of both machines needs to fulfil this requirement. It is fulfilled, if the winding is able to fully compensate the magnet flux linkage. Due to the theory of flux modulation the amplitude of the flux linkage in the Vernier machine is smaller than in the PM machine, since not the whole flux is linked. However, due to the speed difference between stator and rotor the back-EMF and the torque are higher, which is the known as the magnetic gearing effect. In summary, the Vernier machine achieves a higher torque and a higher back-EMF compared to the PM machine, while developing a smaller flux linkage [7]. During the design of both machines it is noticeable that the magnet volume in the PM machine needs to be decreased to locate the ideal SCP point inside the current limit circle. Due to the necessary reduction of magnet volume in the PM machine it is obvious that the power factor is strongly reduced. However, to achieve acceptable power factors with the Vernier machine the machine current needs to be reduced. Nevertheless, the Vernier machine accomplishes nearly twice the torque of the PM machine with only 60% of the current, while both machines locate the ideal SCP point inside the current limit circle. The power factor of the Vernier machine at the corner point is 0.65, see figure 2, and the power factor of the PM machine at the corner point is 0.7. Finally, the power factor of the Vernier machine is in a similar range when it comes to traction applications, while the Vernier machine shows significant improvements in torque. The power factor plot for the PM machine will be included in the final paper. Furthermore equations supporting the named arguments will be included in the final paper. *4. Conclusion* The general claim, that Vernier machines exhibit poor power factors is not true if it comes to traction applications and the objective is to locate the ideal SCP point inside the current limit circle. As in this case, the power factor of the PM machine is in a very similar range as the one of the Vernier machine. It even is shown that Vernier machines are advantageous as the flux linkage is smaller, wherefore it is easier to fulfill the design objective.

[1] O. S. Chirilă, D. Stoia, M. Cernat and K. Hamayer, “High-performance magnetic gears topologies,” *Optimization of Electrical and Electronic Equipment (OPTIM), 2010 12th International Conference on*, Basov, 2010, pp. 1091-1096. [2] K. Atallah, J. Rens, S. Mezani and D. Howe, “A Novel “Pseudo” Direct-Drive Brushless Permanent Magnet Machine,” in *IEEE Transactions on Magnetics*, vol. 44, no. 11, pp. 4349-4352, Nov. 2008. [3] D. Thyroff and I. Hahn, “Investigation on different pole configurations of an outer rotor integrated magnetic gear,” *IECON 2017 - 43rd Annual Conference of the IEEE Industrial Electronics Society,* Beijing, China, 2017, pp. 2040-2045. [4] D. Li, R. Qu and J. Li, “Topologies and analysis of flux-modulation machines,” *2015 IEEE Energy Conversion Congress and Exposition (ECCE)*, Montreal, QC, 2015, pp. 2153-2160. [5] B. Kim and T. A. Lipo, “Operation and Design Principles of a PM Vernier Motor,” in *IEEE Transactions on Industry Applications*, vol. 50, no. 6, pp. 3656-3663, Nov.-Dec. 2014. [6] B. Kim and T. A. Lipo, “Analysis of a PM Vernier Motor With Spoke Structure,” in *IEEE Transactions on Industry Applications*, vol. 52, no. 1, pp. 217-225, Jan.-Feb. 2016. [7] D. Thyroff, C. Hittinger and I. Hahn, “Analytic power factor calculation for vernier machines with concentrated windings,” *2017 IEEE International Electric Machines and Drives Conference (IEMDC)*, Miami, FL, 2017, pp. 1-6. [8] Jieli Li, T. Abdallah and C. R. Sullivan, “Improved calculation of core loss with nonsinusoidal waveforms,” *Conference Record of the 2001 IEEE Industry Applications Conference. 36th IAS Annual Meeting (Cat. No.01CH37248)*, Chicago, IL, USA, 2001, pp. 2203-2210 vol.4 [9] P. Y. Lin, W. T. Lee, S. W. Chen, J. C. Hwang and Y. S. Lai, “Infinite speed drives control with MTPA and MTPV for interior permanent magnet synchronous motor,” *IECON 2014 - 40th Annual Conference of the IEEE Industrial Electronics Society*, Dallas, TX, 2014, pp. 668-674. [10] C. M. Hackl, J. Kullick, H. Eldeeb and L. Horlbeck, “Analytical computation of the optimal reference currents for MTPC/MTPA, MTPV and MTPF operation of anisotropic synchronous machines considering stator resistance and mutual inductance,” *2017 19th European Conference on Power Electronics and Applications (EPE'17 ECCE Europe)*, Warsaw, 2017, pp. P.1-P.10.

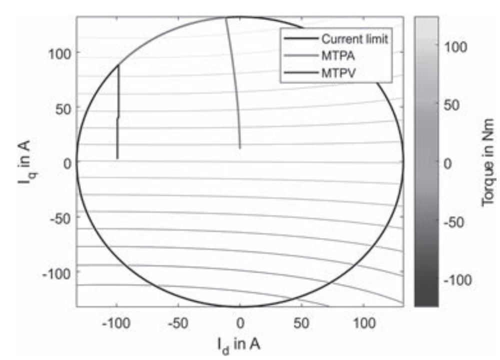

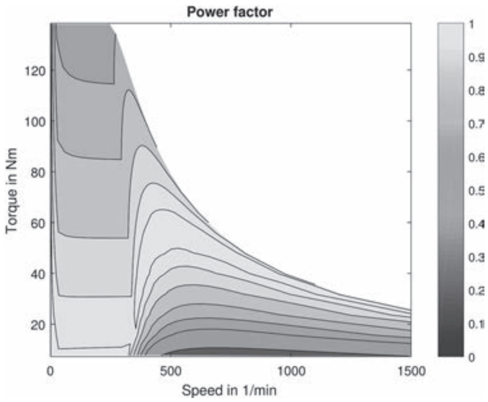
Power factor
Torque in Nm
Speed in 1/min
0
500
1000
1500
20
40
60
80
100
120
1
0.9
0.8
0.7
0.6
0.5
0.4
0.3
0.2
0.1
0

BT-15. Comparative Parameters Investigation of Composite Solid Rotor Applied to Line-Start Permanent-Magnet Synchronous Motors.

B. Yan[1], Y. Yang[1] and X. Wang[1]
1. School of Electrical Engineering, Shandong University, Ji'nan, China

I. INTRODUCTION Besides the desirable properties of high power factor and high power density, the line-start permanent-magnet synchronous motor (LSPMSM) features another capability of self-starting due to the cage embedded in the rotor. However, the starting behavior of such motors remains sensitive to heavy loads, and the braking torque caused by the permanent-magnets (PMs) constitutes the main reason for the load sensitivity [1]. Decreasing the PMs content will surely restrain the braking torque, whereas the motor steady-state performances, such as the working efficiency and synchronous torque, will be worsened by the PMs decrement. To solve this conflict, a composite solid rotor (CSR) applicable for the LSPMSM is designed in [2] by the authors. As shown in Fig. 1(a), the solid steel rather than laminated one is used in the designed rotor for its inherently high starting torque [3]. Meanwhile, a squirrel cage and some narrow slots are attached on the rotor surface, by which the rotor energy conversion is strengthened [2] and the motor starting capability is hence improved. II. PARAMETERS DETERMINATION BASED ON EEC Aimed at a further research on the cage and slots covered in the CSR, a parameters comparison between the CSR and three other rotors (named as I-III) is performed in this paper. Fig. 1(b) gives the cross-sectional views of rotor I-III. In contrast to the CSR, rotor I and II are not equipped with the slots and cage, respectively. Rotor III embraces neither cage nor slots on its surface. Parameters determination of the CSR and rotor I-III relies on an electric equivalent circuit (EEC) established for the motors. Configuration and parameters definition of the EEC are depicted by Fig. 1(c). It should be noted that all of the compared rotors exhibit heavy structural unbalance due to the solid steels split by PMs. Consequently, the rotor parameters of the EEC are divided into the *q*- and *d*-axis components, and the rotor unbalance is reflected in detail by the parameters division. A two-dimensional (2-D) finite element method (FEM) is utilized to calculate the circuit elements covering the rotor parameters. During the calculation, the PMs are treated as air blocks since the rotor parameters are merely dependent on the conductive rotor segments. However, the effects of the PMs on the reluctivity distribution are kept unchanged by the frozen-permeability method [4], [5]. III. PARAMETERS COMPARISON AND ANALYSIS The rotor parameters derived from the EEC are compared in Fig. 2(a). Based on the comparison, two remarkable value relations can be concluded as: (1) the *q*-/ *d*-axis resistances and leakage reactance of the CSR and rotor I are smaller than those of rotor II and III, (2) the *q*-axis resistance of the CSR is smaller than that of rotor I, and the *q*-axis resistance of rotor II is smaller than that of rotor III. The upper half of Fig. 2(b) gives reasons for relation (1). Compared to rotor II and III, both of the CSR and rotor I additionally contain a cage on the surface. The added cage carrying eddy currents makes up a branch in parallel with the solid steel, and the resistance and leakage reactance of the whole rotor is decreased due to the parallel connection. The lower half of Fig. 2 (b) provides explanations for relation (II). Compared to rotor I and III, both of the CSR and rotor II furtherly include the slots on their surface. The added slots located on the *d*-axis central lines enlarge the eddy-current area of the *q*-axis rotor region and hence reduce the *q*-axis rotor resistance. By using the parameters given in Fig. 2(a), the induction torques of the LSPMSPMs with the four compared rotors are calculated and then displayed in Fig. 2(c). It can be found that the highest torque value is involved by the motor with the CSR, which is generated by its smaller rotor parameters than those of motors with rotor I-III. A further comparison among the motors with the CSR and rotor I-III is carried out through the FEM calculations of start-ups under heavy load conditions. As shown in Fig. 2(d), only the motor with the CSR reaches synchronization under 1.2 times of normal load torque and 6.5 times of rotor inertia. The above comparisons of rotor parameters (Fig. 2(a)), induction torques (Fig. 2(c)) and start-ups (Fig. 2(d)) validate the rotor parameters decrement and the resultant torque enhancement by attaching the cage and slots on the CSR, and thus the starting performance improvement by applying the CSR in the LSPMSM.

[1] A. H. Isfahani and S. Vaez-Zadeh, "Line start permanent magnet synchronous motors: challenges and opportunities," Elsevier J. Energy, vol. 34, no. 11, pp. 1755-1763, Nov. 2009. [2] B. Yan, X. H. Wang and Y. B. Yang, "Starting performance improvement of line-start permanent-magnet synchronous motor using composite solid rotor," will to be published in IEEE Trans. Magn., vol. 54, no. 3, pp. 1-4, 2017. [3] M. N. Azari and M. Mirsalim, "Line-start permanent-magnet motor synchronisation capability improvement using slotted solid rotor," IET Electr. Power Appl., vol. 7, no. 6, pp. 462-469, Jul. 2013. [4] W. Q. Chu and Z. Q. Zhu, "Average torque separation in permanent magnet synchronous machines using frozen permeability," IEEE Trans. Magn., vol. 49, no. 3, pp. 1202-1210, Mar. 2013. [5] W. Q. Chu and Z. Q. Zhu, "On-load cogging torque calculation in permanent magnet machines," IEEE Trans. Magn., vol. 49, no. 6, pp. 2982-2989, Jun. 2013.

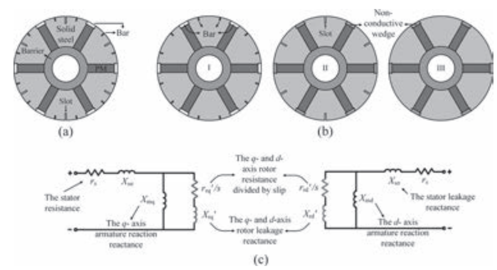

Fig. 1. (a) Structure of the CSR, (b) cross-sectional views of rotor I-III, and (c) configuration and parameters definition of the EEC.

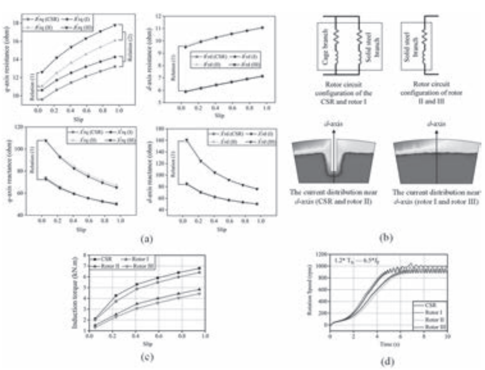

Fig. 2. (a) The rotor parameters comparison, (b) reason illustrations of relation (1) and (2), (c) the induction torques comparison, and (d) the start-ups comparison.

BT-16. Multi-sensor Fusion Based Permanet Magnet Demagnetization Detection in Permanet Magnet Synchrounous Machines.

M. Zhu[1], W. Hu[1], *S. Mukundan*[1] and N. C. Kar[1]
1. Electrical and Computer Engineering, University of Windsor, Windsor, ON, Canada

I.Introduction Most of the demagnetization detection techniques are based on single sensor diagnosis such as analysis of stator current [1], acoustic noise [2], or torque [3]. However, single sensor demagnetization detection has inherent uncertainties due to fault models and motor operating environments. Hence, multi-sensor information fusion is an effective way to solve such uncertainties and improve demagnetization detection accuracy and improve motor control stability. This paper explores the use of acoustic noise and torque ripple for on-line PM demagnetization detection by using the multi-sensor information fusion method. Both noise and torque signals are first analyzed and processed by wavelet transforms for de-noising and feature value extraction. Moreover, multi-sensor information fusion is applied to estimate the demagnetization ratio based on the support vector machine (SVM) training set. The proposed demagnetization detection approach is experimentally verified on a laboratory PMSM and compared with single-sensor detection method. II.Multi-Sensors Information Fusion Multi-sensors information fusion technology is based on the idea that sensors with different information have complementary characteristics and results in more accurate estimation than a single source. The multi-sensors fusion method can effectively improve the robustness of diagnostic decision-making. The information can be fused at different levels such as signal-level, feature-level and decision-level. For a medium-sized permanent magnet synchronous machine (PMSM) in electric vehicle (EV), there is not much choice in terms of sensor accuracy or feature extraction. So, in this paper, decision-level fusion is more suitable and efficient and hence a human artificial network based fusion method is implemented. III.Multi-Sensors Information Fusion Based Demagnetization Detection During motor operation, the rotor magnet demagnetization distorts the magnetic flux distribution resulting in noise, vibrations and torque ripple in the machine. In order to use those multi-source information as the demagnetization indexes, a demagnetization detection model is proposed and shown in Fig. 1(a). The detailed procedure is explained as follows. A. Signal Pre-process The measured noise and torque from individual sensors are non-stationary and are generally disturbed by the noises from inverter and flux linkage harmonics. To eliminate or reduce those electromagnetic noises and interferences, the initial signals should be filtered first. The example of torque measurement processing is shown inFig.1 (b). B. Feature Extraction Power spectral density (PSD) is chosen as the characteristic which shows the strength of the variations as a function of frequency and calculated according to (1), where $R_X(\tau)$ is the auto-correlation function. The example of torque PSD is shown in Fig. 2(a). C. Initial Demagnetization Diagnosis via Individual Sensor The process of individual sensor classification can be implemented by support vector machine based on LIBSVM algorithm. In order to analyze the ability of classification association, the training sample set for the rotor demagnetization is divided into three types: health, demagnetization 1 (17% magnets loss) and demagnetization 2 (33% magnets loss). The data samples are first transformed to [-1,1] through scaling transformation, and then optimal penalty factor C and parameter γ of the kernel function is optimized by performing grid search. The posterior probability of each classifier can be determined according to (2), where $p_i(x)$ is the normalized posterior probability of x to the i^{th} class. D. Fusion analysis After the posterior probability of each classifier is combined to construct the decision profile for decision-level fusion, a BP NN is applied for decision-level making based on the decision profile. Then the demagnetization detection results are diag nosed consistently with the corresponding decision rules. IV.Demagnetization Detection Model Validation A laboratory 12.5 kW PMSM shown in Fig. 2(b), with rated torque of 50 Nm and rated speed of 3,000 rpm, is employed for validating the performance of the proposed method. The test motor was demagnetized by increasing the motor internal temperature through long period of operation. After a series of testing, a look-up table has been established, based on which the PM demagnetization ratios can be referred to the relevant motor internal temperature. By applying the proposed method, the SVM result is shown in Fig. 2(c), and the demagnetization result can be estimated from decision-level fusion. Fig. 2(d) shows the BPNN training performance. More results will be shown in the full paper. V.Conclusion This paper presents a non-invasive approach to detect the PM demagnetization based on multi-sensor fusion. Two sensors information are measured to evaluate the rotor flux linkage individually at first. Then fusion method is employed to detect the PM demagnetization at the decision-level. The experimental results have demonstrated that the detection accuracy is significantly improved by fusing the individual detection on decision-level compared with single sensor methods. If there is a priori knowledge of demagnetization, detection can be achieved without the need for data fusion. However, due to the complexity of the motor, many environmental conditions affect the certainty of the diagnosis. Therefore, under constant load condition, the diagnostic accuracy can be achieved up to 100%, while under variable load conditions, the diagnostic accuracy drops to 90.24%.

[1] S. Ruoho, J. Kolehmainen, and A. Arkkio, "Interdependence of Demagnetization, Loading, and Temperature Rise in a Permanent Magnet Synchronous Motor," *IEEE Trans. Magn*., vol. 46, pp. 949 -953, 2009. [2] M. Zhu, W. Hu, and N. C. Kar, "Acoustic Noise Based Uniform Permanent Magnet Demagnetization Detection in Surface Mounted PMSM for High-Performance PMSM Drive," *IEEE Trans. on Transportation Electrification*, vol. PP, no. 99, pp., 2017. [3] M. Zhu, W. Hu, and N. C. Kar, "Torque Ripple Based Interior Permanent Magnet Synchronous Machine Rotor Demagnetization Fault Detection and Current Regulation," *IEEE Trans. on Indus. App.*, vol. 53, no. 3, pp.2795-2804, 2017.

$$S_x(f)=\int_{-\infty}^{+\infty} R_X(\tau)e^{-2j\pi\tau}d\tau \quad (1)$$

$$p_i(x)=\frac{P_i(x)}{\sum_{i=1}^{k} P_i(x)} \quad (2)$$

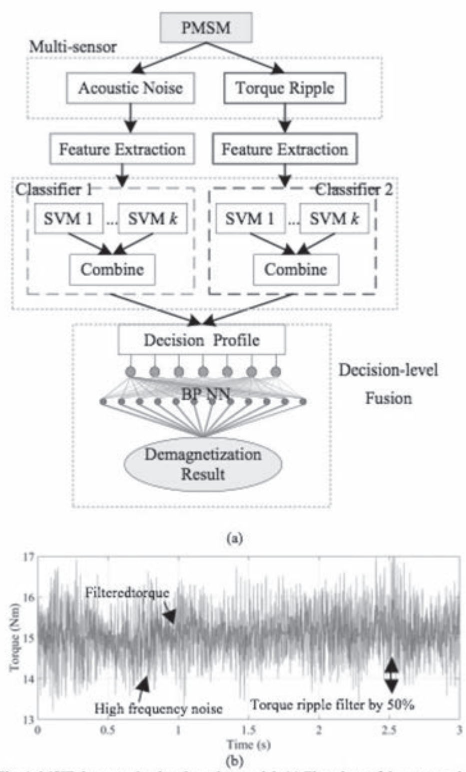

Fig. 1. MSIF demagnetization detection model. (a) Flowchart of the proposed MSIF demagnetization detection. (b) Torque signal filtering from a healthy motor at 1,500 rpm.

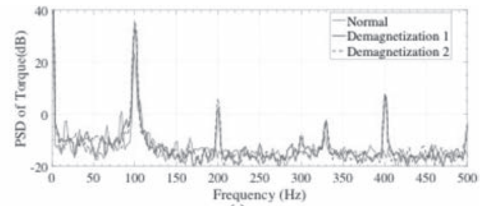

(a)

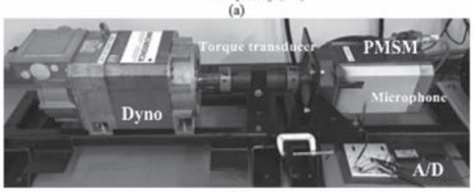

(b)

TABLE I.SVM CLASSIFIER PARAMETERS

Classifier	SVM number	b	C	γ
Healthy	26	4.60927	22.6	0.03521
Demag 1	30	7.75903		
Demag2	16	6.97892		

(c)

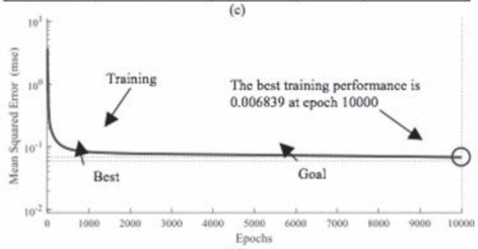

(d)

Fig. 2. Demagnetization detection of a PMSM. (a) PSD spectrum of PMSM torque with demagnetization faults. (b) Experimental setup. (c) SVM classifier results under variable motor operation. (d) BP NN training performance.

TUESDAY AFTERNOON, 24 APRIL 2018 SIMPOR/ROSELLE BALLROOM, 1:30 TO 4:30

Session BU
RARE EARTH TRANSITION METAL BORIDES II
(Poster Session)

Satoshi Hirosawa, Co-Chair
National Institute for Materials Science (NIMS), Tsukuba, Japan
Minggang Zhu, Co-Chair
Central Iron & Steel Res., Beijing, China
Zhongmin Chen, Co-Chair
Neo Performance Materials (S) Pte Ltd, Singapore, Singapore

BU-01. PLD-fabricated Nd-Fe-B film magnets on Si substrates with Si oxide layer.

Y. Yamaguchi[1], D. Shimizu[1], A. Yamashita[1], T. Yanai[1], M. Nakano[1] and H. Fukunaga[1]
1. Nagasaki University, Nagasaki, Japan

Although a sputtering method is one of promising methods to obtain an anisotropic Nd-Fe-B film magnet on a Si substrate with a Ta buffer layer [1][2], the maximum thickness of the films is mainly 20 microns because peeling phenomenon occurred during a deposition or an annealing process, and an increase in thickness is required in order to apply them to various miniaturized devices. On the other hand, we reported an isotropic Nd-Fe-B film magnet deposited on a Si substrate with a 500 nm-thick thermal oxide layer using PLD (Pulsed Laser Deposition) method and succeeded in enhancing the thickness up to approximately160 microns [3]. In our previous experiment, the exfoliation of a Nd-Fe-B film couldn't be confirmed and mechanical destruction occurred from the inside of a Si substrate. In this report, we investigated the adhesion between a PLD-fabricated Nd-Fe-B film and a Si substrate with a Si oxide layer such as a natural and a thermal oxide one. It was clarified that the sufficient thickness of the oxide layer is indispensable to avoid the peeling phenomenon. We also paid attention that a glass has an intermediate thermal expansion coefficient (10.0×10^{-6} K^{-1}) between a Si substrate (2.6×10^{-6} K^{-1}) and a $Nd_2Fe_{14}B$ phase (14.7×10^{-6} K^{-1}), and therefore the fabrication of a thick glass film instead of the use of a Si oxide layer was carried out. Resultantly, we could improve the magnetic properties of a Nd-Fe-B film deposited on a Si substrate. A rotated target was ablated using a Nd-YAG pulse laser (wave length=355 nm, frequency : 30 Hz) in the vacuum atmosphere of approximately 10^{-5} Pa. The deposition of a Nd-Fe-B film magnet on a Si substrate was carried out using a $Nd_XFe_{14}B$ (X=2.0~3.5) target. Four Si substrates with a 1 nm-thick natural oxide layer together with three thermal oxide layers with the thickness 20, 100 and 500 nm, respectively, were used. Moreover, in order to prepare a glass film on a Si substrate using a Nd-YAG pulse laser in the vacuum atmosphere, a glass plate on a bulk metal was used as a target. The glass film was deposited followed by a Nd-Fe-B film on a Si substrate. A flash annealing (PA) method followed the deposition to crystallize an as-deposited Nd-Fe-B film with amorphous structure. The magnetic properties of the samples were measured with a vibrating sample magnetometer (VSM) under the maximum applied magnetic field of 2.5 T after magnetizing each sample with a pulsed magnetic field of 7 T. All the films had isotropic magnetic properties, therefore in-plane ones were only shown in the paper. The thickness of each film was measured with a micrometer or estimated by measuring each weight. The compositions of glass films together with Pr-Fe-B films was analyzed with an X-ray photoelectron spectroscopy (XPS) and an energy dispersive X-ray spectrometry (EDX), respectively. Figure 1 shows the obtained maximum thickness of PLD-fabricated Nd-Fe-B film magnets without mechanical destruction deposited on Si substrates with various thicknesses of Si oxide layers. Here, Nd content (Nd / (Nd + Fe)) in each Nd-Fe-B film was fixed at approximately 20 at. %. As the thickness of the oxide layer increased, the thickness of the film magnets could be enhanced after an annealing process. In addition, the peeling of a Nd-Fe-B film occurred in the case of each Si substrate with a natural oxide together with a 20 or 100 nm-thick thermal oxide klayer. On the other hand, mechanical destruction from the inside of a Si substrate was always observed as the thickness of a Si oxide layer became 500 nm. It is considered that the dependence of the thickness of an oxide layer on the adhesion is attributed to the existence of a Fe-Si-O compound. We have already reported that an increase in Nd contents of a Nd-Fe-B film compared with a stoichiometric composition enabled us to enhance the thickness of the film deposited on a Si substrate without a mechanical destruction [3]. The phenomenon is considered to be attributed that Nd element precipitated around a Nd_2Fe_4B grain boundary has an intermediate linear expansion coefficient between a Si and a $Nd_2Fe_{14}B$ phase. On the other hand, the reduction in Nd contents of a Nd-Fe-B film is required because a large amount of Nd degraded the values of residual magnetization and $(BH)_{max}$. Here, we focused on the linear expansion coefficient of glass and prepared a glass film with the thickness range from 20 to 130 microns, which is thicker than that of the previously mentioned thermal Si oxide layers. Figure 2 shows the M-H loops of two Nd-Fe-B films deposited on each Si substrate with a 500 nm thick thermal oxide layer and a 64 µm-thick glass film, respectively. The thicknesses of the both Nd-Fe-B films were almost 60 µm. It was clarified that the use of a thick glass film is effective to decrease the Nd amount and $(BH)_{max}$ value of a Nd-Fe-B film deposited on a Si substrate could be improved by approximately 20 kJ/m^3.

[1] R. Fujiwara, T. Shinshi, and E. Kazawa, Sens. Actuators A Phys., Vol. 220, 298-304 (2014) [2] Y. Zhang, D. Givord, and N. M. Dempsey, Acta Mater., Vol. 60, 3783-3788 (2012). [3] M. Nakano Y. Chikuba, M. Oryoshi, A. Yamashita, T. Yanai, R. Fujiwara, T. Shinshi, and H. Fukunaga, IEEE Trans. Magn., Vol. 51, 2102604 (2015).

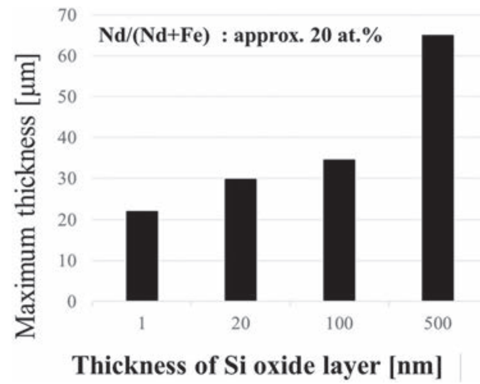

Fig. 1. Relationship between thicknesses of Si oxide layer and obtained maximum thickness of Nd-Fe-B film magnets with the Nd content of about 20 at. % without mechanical destruction.

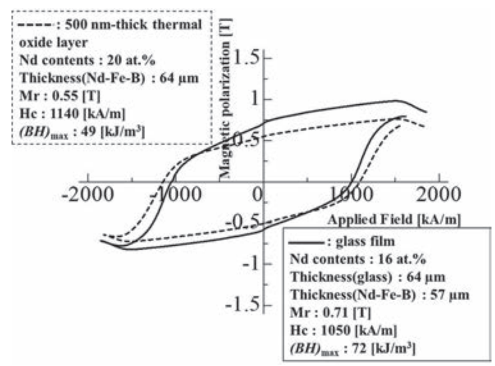

Fig. 2. Two M-H loops of Nd-Fe-B films deposited on each Si substrate with a 500 nm thick thermal oxide layer and a 64 µm-thick glass film, respectively. The use of a glass film enabled us to enhance the values of residual magnetization and $(BH)_{max}$.

BU-02. Increase in nucleation field of nanocrystalline Nd-Fe-B magnets due to strengthening of exchange interaction - computer simulation –.

T. Harada[1], T. Yanai[1], M. Nakano[1] and H. Fukunaga[1]
1. Nagasaki University, Nagasaki, Japan

An improvement in coercivity H_c is strongly needed for N-Fe-B magnets, because their H_c values deteriorate remarkably at high temperatures and this deterioration raises difficulty in their applications at high temperatures. As H_c is affected by a microstructure of a magnet, effects of microstructures on H_c have been reported. Previously, we carried out micromagnetic simulation of demagnetization process for nanocrystalline Nd-Fe-B magnets with non-magnetic inclusions with varying the size of the inclusions and reported that the nucleation field H_N is affected by not only the strength of local demagnetizing field but also the spatial size of the region where the local demagnetizing field exists [1]. It was also clarified that the nucleation of the reversal domain occurs when the above size exceeds a critical value depending on the exchange length, L_{ex} (= $\sqrt{(A/K_u)}$), where A and K_u are the exchange stiffness coefficient and the anisotropy constant, respectively. The above results strongly suggest that A as well as K_u affect H_N. In this contribution, the effect of A on H_N was investigated with varying temperature for nanocrystalline Nd-(Fe,Co)-B magnets by computer simulation, and it was found that strengthening of A effectively increases H_N of nanocrystalline Nd-Fe-B magnets. The simulation model was shown in the inset of Fig.1. We assumed a model magnet composed of $Nd_2Fe_{14}B$ grains (48 or 96 nm in size), a tetrahedral non-magnetic multi-junction phase, and non-magnetic grain boundary phase covering the $Nd_2Fe_{14}B$ grain. The periodic condition was adopted for three directions, and resultantly a tetrahedral non-magnetic multi-junction phase contacts with neighboring four $Nd_2Fe_{14}B$ grains. The grain was divided into 64×64×64 cubic elements, and micromagnetic simulation of demagnetization process was carried out with varying A, the size of the tetrahedral non-magnetic multi-junction phase, T, and temperature. Details of the calculation method were described elsewhere [1]. The non-magnetic multi-junction generated a local demagnetizing field and H_N decreased with increasing T. The calculated decrease in H_N corresponds to the increase in the effective demagnetizing factor N_{eff}, because H_N is described as $H_N = aH_A - N_{eff} J_s / \mu_0$ [2], where a, H_A, J_s, and m_0 were the microstructure factor, the anisotropy field, the saturation polarization, and the permeability of vacuum, respectively. Therefore, we calculated N_{eff} with varying T, L and temperature, and the results are shown in Fig.1 as a function of T/L_{ex}. As seen in the figure, N_{eff} was plotted on one curve independently of L and temperature, and increased with the increase in T/L_{ex}. The increase in N_{eff} corresponds to the decrease in H_N. This result clearly suggests that the effect of demagnetizing field is determined by the ratio of T and L_{ex}, and that the effect of demagnetizing field can be suppressed by decreasing T/L_{ex}. Therefore, for fixed T and K_u values, an increase in A is expected to decrease N_{eff} and resultantly to increase H_N. To confirm the above idea, H_N was calculated for the model Nd-Fe-B magnet with L = 96 nm, T = 60 nm and K_u = 4.5 MJ/m^3 with varying A. Consequently, it was confirmed that the increase in A from 8.7 to 17.4 pJ/m results in the increase in H_N from 4.46 to 4.82 MA/m. The above results strongly suggest that the enhancement in the exchange interaction is one of effective methods for improving H_N of Nd-Fe-B magnets composed of fine grains. The replacement of Fe with Co is effective in increasing A and it has been reported the replacement up to 10 at. % does not decrease K_u remarkably [3]. Therefore, we simulated H_N for the magnet composed of $Nd_2(Fe_{0.9}Co_{0.1})_{14}B$. Figure 2 shows H_N and N_{eff} for L = 96 nm and T = 60 nm as a function of temperature. H_N is reduced by the anisotropy field H_A. It is clearly seen that the replacement decreases N_{eff} and increases H_N/H_A. In conclusion, strengthening of the exchange interaction is effective in increasing H_N and resultantly improving H_c.

[1] H. Fukunaga, R. Hori, M. Nakano, T. Yanai, R. Kato and Y. Nakazaki, *J. Appl. Phys*. 117, 17A729 (2015). [2] H. Kronmüller, K.-D. Durst, S. Hock and G. Martine, *J. Phys. Colloq*. 49, C8-623 (1988). [3] M. Sagawa, S. Hirosawa, H. Yamamoto, S. Fujimura and Y. Matsuura, *Jpn. J. Appl. Phys.* 26, 785 (1987).

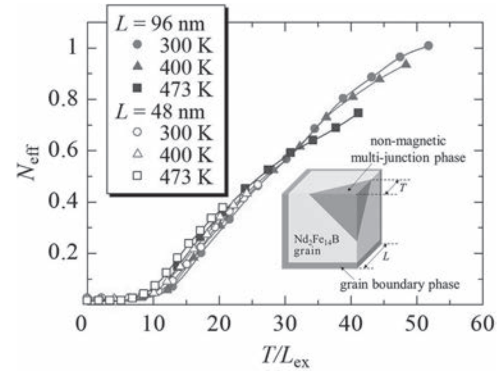

Fig. 1. Effective demagnetizing factor N_{eff} as a function of T/L_{ex}, where T and L_{ex} are the multi-junction size and the exchange length, respectively. The inset shows the simulation model.

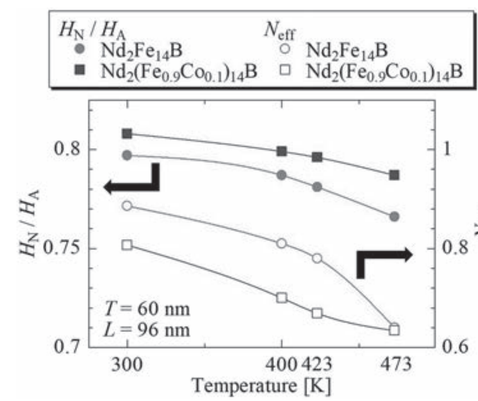

Fig. 2. Effect of Co substitution on H_N/H_A and effective demagnetizing factor N_{eff}, where H_N and H_A are the nucleation field and the anisotropy field, respectively.

BU-03. Investigation on texture, magnetic properties and inhomogeneities of hot deformed Nd–Fe–B magnet.

H. Li[1], Q. Wu[1], M. Yue[1], X. Xu[1], J. Liang[1] and J. Zhang[1]
1. College of Materials Science and Engineering, Beijing University of Technology, Beijing, China

I. INTRODUCTION The hot deformed Nd–Fe–B permanent magnets have drawn widely attention due to their high magnetic performance[1]. It is important to understand the relevance between the local magnetic properties and the local orientation texture features in hot deformed Nd–Fe–B magnets. Detailed investigation have revealed that its magnetic performance was inhomogeneous along axial directions which are parallel with the press directions[2]. However, the systematic investigations on the inhomogeneities of the magnetic performance in hot deformed Nd–Fe–B bulk permanent magnet along the radial directions are insufficient. In this paper, hot deformed Nd–Fe–B bulk magnets have been prepared by spark plasma sintering (SPS) method. The relationship between magnetic properties and inhomogeneities of orientation texture in the different locations along radial directions in hot deformed Nd–Fe–B magnet has been investigated. II. EXPERIMENTS Commercial Nd–Fe–B magnetic powders (MQP-F) were used as initial materials. The magnetic powders were poured into a tungsten carbide (WC) mold and fast consolidated into columnar samples by using the spark plasma sintering (SPS) method. The temperature and pressure of sintering were 650°C and 500 MPa, respectively. The size of compaction isotropic magnet is 7.5 mm in radius and 15 mm in height. After compaction, the columnar samples were hot-deformed into disc-shaped samples with a height reduction of 60% via SPS in 750°C. The size of final anisotropic bulk magnet is 12 mm in radius and 6 mm in height. From the hot-deformed magnet, three samples were selected by their distances to the center in radial directions, named "center region", "subcenter region", and "edge region". The crystal structure and microstructure were characterized by X-ray diffractometry (XRD, Bruker D8 ADVANCE) and scanning electron microscopy (SEM, FEI NANO200), respectively. The magnetic properties at room temperature were measured by vibrating sample magnetometry (VSM, Lakeshore 7410) with a magnetic field up to 30 kOe. The electron back-scattered diffraction (EBSD) measurements were performed using a high-speed detector (EDAX Hikari camera) incorporated in the scanning electron microscope. III. RUSULTS AND DISSUSION XRD patterns of the three samples are shown in Fig. 1(a). The magnets were examined with the surface perpendicular to the radial direction of the disc. All diffraction peaks could be indexed to the standard patterns of $Nd_2Fe_{14}B$. The intensity ratios of (0 0 6) and (1 0 5) peaks which indicate the degree of texture of c-axis crystallographic alignment are 3.13, 1.90 and 0.66 for "center region", "subcenter region" and "edge region" magnet, respectively. The XRD patterns of the "edge region" are similar to that of the isotropic magnets. However, the intensity ratio is obviously increased in the "center region". The changes of intensity ratios reveal that the degree of crystal alignment along the easy c-axis is different in the various locations of radial directions. The magnetic hysteresis loops of the three samples are shown in Fig. 1(b). For all samples, the high remanence ratio indicates that c-axis texture forms throughout the whole sample via hot deformation, leading to strong magnetic anisotropy in the entire magnet. However, the maximum energy product sharply increases to 43.72 MGOe, while coercivity slightly decreases to 12.06 kOe from the edge to the center along the radial direction, which illustrates that the magnetic performances are heterogeneous at different locations in the bulk magnet. The quantitative texture analysis is carried out based on the calculation of pole figure (PF) and inverse pole figure (IPF) of the normal direction (ND). Fig. 2 shows the {001} PFs and the IPFs obtained from the EBSD data of the three samples. The maximum intensities of the "center region" sample is the highest which is approximately 48.0 MRD (Multiple of a Random Distribution) in PF and 47.7 MRD in IPF, while those of the "edge region" sample are the lowest. The low MRD values suggest a weak texture in the sample. IV. CONCLUSION In summary, anisotropic Nd–Fe–B magnets were prepared by hot deformation methods. The hot deformed permanent magnets exhibit inhomogeous magnetic performance in radial directions along which the maximum energy product increases obviously from the "edge" to the "center", while coercivity decreases slightly. The XRD and EBSD characterizations suggest that the enhanced c-axis texture in "center region" results in the stronger magnetic anisotropy and increased maximum energy product.

[1] T. Wang, M. Yue, Y. Q. Li, M. Tokita, Q. Wu, D. T. Zhang, et al., "Tuning of Microstructure and Magnetic Properties of Nanocrystalline Nd-Fe-B Permanent Magnets Prepared by Spark Plasma Sintering," Ieee Magnetics Letters, vol. 6, 2015. [2] A. H. Li, W. Li, B. Lai, H. J. Wang, M. G. Zhu, and W. Pan, "Investigation on microstructure, texture, and magnetic properties of hot deformed Nd-Fe-B ring magnets," Journal of Applied Physics, vol. 107, 2010.

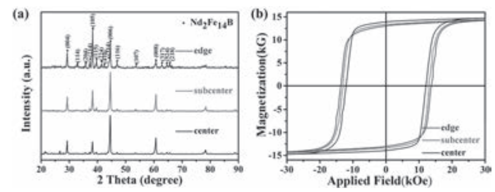

Fig. 1. XRD patterns (a) and magnetic hysteresis loops (b) of the three samples.

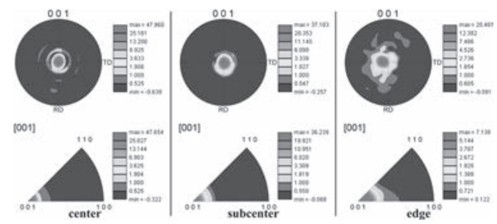

Fig. 2. The {001} pole figure (PF) and the inverse pole figure (IPF) of normal direction (ND) in the three samples.

BU-04. The effect of ambient pressure of annealing process on magnetic properties and surface microstructure of sintered Nd-Fe-B magnet.

X. Yang[1,2], S. Guo[1], J. Zeng[1,2], Q. Zhang[1,2], G. Ding[1], J. Di[1,2] and A. Yan[1]
1. Ningbo Institute of Industry Technology, CAS, Ningbo, China; 2. University of Chinese Academy of Sciences, Beijing, China

It is well known that the magnetic properties of Nd-Fe-B sintered magnets are microstructural sensitive. Post-sintered annealing is an important process to improve magnetic properties, and appropriate post-sintered annealing can effectively enhance coercivity without HRE elements introduction[1-4]. So, many researches have been carried out to explain the change in coercivity during the post-sintered annealing in order to further improve coercivity, including the evolution of rare earth oxides [1, 2]and Cu-rich phase[3, 4]. Ambient pressure has huge influence on the microstructure, but the relationship of ambient pressure between microstructure and magnetic properties has never been revealed. Therefore, it is meaningful to investigate the effect of ambient pressure on microstructure and magnetic properties. The original magnets with the nominal composition of $Nd_{31.5}Fe_{bal}B_{0.91}Cu_{0.2}$ (wt. %) was prepared by traditional metallurgy route. As shown in Fig. 1(a), the as-sintered magnets were divided into two groups, one group was annealed at 900 °C for 2 h in 0.2 MPa Ar atmosphere, marked as Sample A, while another group treated in vacuum, marked as Sample B, then two groups both annealed at 500 °C for 2 h. Fig. 1(b) shows the demagnetization curves of Sample A & B. It can be clearly seen that the coercivity of the Sample A, 10.79 kOe, is 0.51 kOe higher than that of Sample B, 10.28 kOe, without any difference of remanence. Fig. 2 expresses the secondary electron (SE) SEM images of the magnets surface. From the Fig. 2(a), we can find that the $Nd_2Fe_{14}B$ grains are still obviously visible and a small amount of granular material appears on the grains. Moreover, we can distinguish that the granular material is agglutinated with another phase. On the contrary, in Fig. 2(b), the whole magnet surface of Sample B is wrapped by a newly formed phase and no distinct $Nd_2Fe_{14}B$ grains can be found. According to the EDS analysis (not show here), the chemical composition of the granular matter and surrounding gelatinosa matter is closed to NdO and $Nd_6Fe_{13}Cu$. These two phases are common part of the grain boundary phase, so we can conclude that the grain boundary phase volatilize during 1st post-sintered annealing and the higher ambient pressure is beneficial to suppress the volatilization. Furthermore, the relationship between the quantity of volatilization, microstructure and magnetic properties is comprehensively investigated.

[1] D.W. Park, T.-H. Kim, S.-R. Lee, D.H. Kim, T.S. Jang, Effect of annealing on microstructural changes of Nd-rich phases and magnetic properties of Nd–Fe–B sintered magnet, J. Appl. Phys. 107(9) (2010) 09A737. [2] T.-H. Kim, S.-R. Lee, S. Namkumg, T.-S. Jang, A study on the Nd-rich phase evolution in the Nd–Fe–B sintered magnet and its mechanism during post-sintering annealing, J. Alloys Compd. 537 (2012) 261-268. [3] W.F. Li, T. Ohkubo, K. Hono, Effect of post-sinter annealing on the coercivity and microstructure of Nd–Fe–B permanent magnets, Acta Mater. 57(5) (2009) 1337-1346. [4] H. Sepehri-Amin, T. Ohkubo, T. Shima, K. Hono, Grain boundary and interface chemistry of an Nd–Fe–B-based sintered magnet, Acta Mater. 60(3) (2012) 819-830.

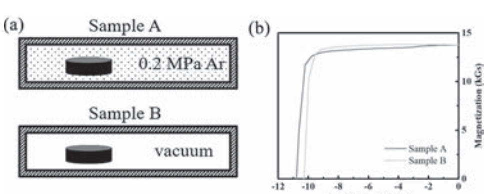

Fig. 1. (a) Schematic diagram and (b) demagnetization curves of Sample A and B.

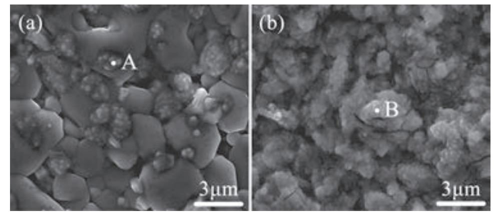

Fig. 2. Magnets surface SE SEM images of (a) Sample A and (b) Sample B.

BU-05. Improved coercivity enhancement of sintered Nd-Fe-B magnets by TbH_2 grain boundary diffusion with Al aiding.

J. Di[1,2], S. Guo[1], G. Ding[1], L. Cai[3], X. Yang[1,2], K. Chen[1,2], R. Chen[1] and A. Yan[1]

1. Ningbo Institute of Material Technology and Engineering, Chinese Academy of Sciences, Ningbo, China; 2. University of Chinese Academy of Sciences, Beijing, China; 3. Ningbo Jinji Magnetic Material Co., Ltd, Ningbo, China

High thermal stability and enhanced coercivity (H_{ci}) of sintered Nd-Fe-B permanent magnets have attracted a lot of research interest driven by the demand for motor applications in hybrid electric vehicles (HEV) and generators such as wind turbines. The heavy rare earth (HRE) Tb and Dy substitution for Nd has been developed as a common method for the H_{ci} enhancement, but it leads to the decrease in magnetization saturation and their criticality impedes the application in the long term. To solve the problem, grain boundary diffusion process (GBDP) has been developed as a more efficient method. By GBDP, the grains were magnetically hardened by the $(Nd,HRE)_2Fe_{14}B$ shell with higher anisotropy field and the surface region was magnetically hardened by such grains. However, the high amount of Tb in the outermost surface grains lead to the substantially reduced remanence compared to the initial state prior to GBDP and thus has to be removed. To improve HRE efficiency, a method to reduce the Tb enrichment in the near surface region without detrimental effect on H_{ci} is desired. In this study, the influence of TbH_2 powder GBDP with Al powder aiding (TbH_2-Al) through dip-coating 30 at.%TbH_2 and 70 at.% Al in alcohol on the magnetic properties and the microstructure of sintered Nd-Fe-B magnets were investigated. The H_{ci} was enhanced from 13.70kOe to 22.26 kOe and 23.29 kOe for the magnets GBDP by TbH_2 and TbH_2-Al, respectively, as shown in Fig. 1(a). The increase in H_{ci} enhancement with Al aiding was 1.03 kOe though the TbH_2 amount in the source was reduced. The distribution of Tb concentrations of the GBDP magnets versus depth are shown in Fig. 1 (b). For both the TbH_2 and TbH_2-Al GBDP magnets, Tb concentrations in the near surface area were higher than that in the inner area. The accumulation of Tb in the near-surface region was substantially reduced with Al aiding. The improved H_{ci} enhancement and the reduced accumulation in the near surface region indicate highly effective GBDP by TbH_2 with Al aiding. Compared to the microstructure of a typical sintered Nd-Fe-B magnets GBDP by TbH_2 as shown in Fig.2(a) which consist of $(Nd,Tb)_2Fe_{14}B$ shell and the less visible grain boundary phases (GBs), the TbH_2-Al GBDP magnets exhibit distinct differences. First, the grains are surrounded by the uniform Nd-rich phase along the GB. Secondly, the thickness of the shell structure was reduced. Analysis of the domain pattern by Kerr microscopy combined with the uniform Nd-rich phase along the GB and the core-shell structure is of importance for the understanding of the mechanism for H_{ci} enhancement. The Al and Tb distribution in the grains and the GBs is helpful for understanding the phase evolution during GBDP by SEM with EDS and TEM.

[1] K. Loewe, C. Brombacher, M. Katter, O. Gutfleisch, Temperature-dependent Dy diffusion processes in Nd-Fe-B permanent magnets, Acta Materialia, 83 (2015) 248-255. [2] X.J. Cao, L. Chen, S. Guo, R.J. Chen, G.L. Yan, A. Yan, Impact of TbF3 diffusion on coercivity and microstructure in sintered Nd-Fe-B magnets by electrophoretic deposition, Scripta Materialia, 116 (2016) 40-43.

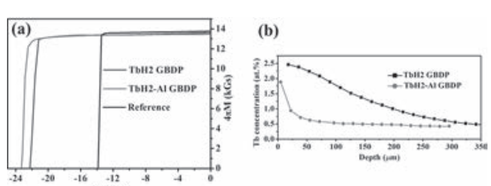

Fig. 1. (a) Demagnetization curves of the magnets GBDP by TbH_2 and TbH_2-Al and the reference magnet and (b) Tb concentration depth profile of the magnets GBDP by TbH_2 and TbH_2-Al by GDA

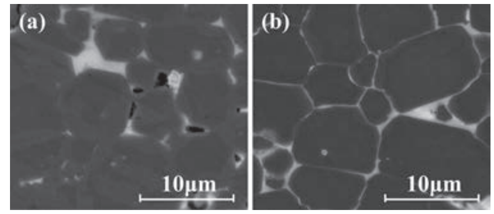

Fig. 2. SEM images of the magnets GBDP by TbH_2 (a) and TbH_2-Al (b) in the near surface region

BU-06. Thermal resistance of hot-deformed Nd-Fe-B magnets doped with Pr-Cu powders.

X. Tang[1], C. Jin[1], W. Yin[1], R. Chen[1] and M. Li[1]
1. Ningbo Institute of Industrial Technology, Chinese Academy of Science, Ningbo, China

Due to the excellent magnetic properties of Nd-Fe-B magnets, the usage of the magnets has been spread in various applications, such as sensors, motors and generators. However, because of the poor thermal stability of $Nd_2Fe_{14}B$ magnets, the expansion of application field is largely limited. The most effective ways to solve this problem are considered to be the additions of Co or heavy rare earth (HRE) elements of Dy or Tb to increase the Curie temperature or coercivity of magnets, respectively. However, the cost of the magnets would be increased because of the scarcity and shortage crisis of Co and RE elements. Besides, the excessive addition of Co elements will deteriorate the magnetic properties. So at present days, the enhancement of coercivity is considered to be the most popular methods to optimize the thermal stability. For now, the optimization of grain boundary is the most economically feasible method, such as grain boundary diffusion process, to obtain high coercivity magnets without abundant usage of HRe. In hot-deformed Nd-Fe-B magnets, the coercivity of magnets could be largely enhanced by covering low eutectic RE-rich alloys and then annealing. However, in this way, the remanence and maximum energy product are decreased simultaneously. In this paper, the melt spun powders mixed with $Pr_{70}Cu_{30}$ powders are hot pressed to obtain fully density precursor. And then the hot-deformed magnet is obtained by die-upset process with a height reduction of 70%. The coercivity of the magnets with 1 wt.% and 2 wt.% $Pr_{70}Cu_{30}$ addition is 20.3 and 22.7 kOe while the remanence is 13.45 and 13.32 kGs, respectively. The coercivity and remanence coefficients of temperature of the specimen with 2 wt.% $Pr_{70}Cu_{30}$ addition are β=-0.537%/^{o}C and α=-0.108 %/^{o}C slightly better than that of sintered HRe-free magnets which are β=-0.617%/^{o}C and α=-0.12 %/^{o}C. The irreversible flux losses of the hot-deformed magnets and sintered magnets with and without HRe are also obtained as shown in Fig.1. It can be seen that the irreversible flux loss of the hot-deformed magnets with Pr-Cu addition is comparable to that of sintered-HRe magnets while is much better than that of sintere-HRe free magnets. In order to analysis the thermal stability of the hot-deformed magnets with Pr-Cu addition, the temperature dependence of magnetic domain structure is also carried out using the Magneto-optic Kerr microscope.

1. H. Sepehri-Amin, T. Ohkubo, S. Nagashima, M. Yano, T. Shoji, A. Kato, T. Schrefl, K. Hono, Acta Mater. 61 (2013) 6622–6634. 2. X. Tang, R.J. Chen, W.Z. Yin, C.X. Jin, D. Lee, A. Yan, Appl. Phys. Lett. 107 (2015) 202403.

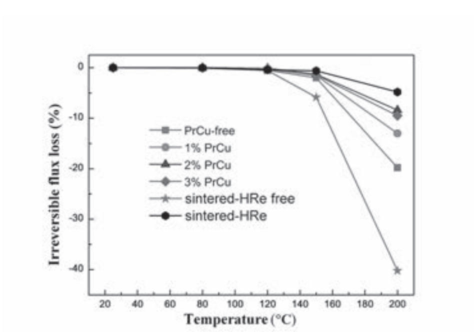

BU-07. Enhanced coercivity of Nd-Ce-Y-Fe-B sintered magnets by adding (Pr, Nd)-H powders.

B. Peng[1], Y. Liu[1], J. Jin[1] and M. Yan[1]
1. Department of Materials Science and Engineering, Zhejiang Unviersity, Hangzhou, China

Incorporating cheaper and more abundant rare earth (RE) elements Ce, La or Y into the Nd-Fe-B based magnets has stimulated considerable research efforts [1-2]. Among them, one promising candidate is the Y/Ce co-substituted Nd-Ce-Y-Fe-B sintered magnet, for which the Y-rich 2:14:1 phase with positive temperature coefficient of magnetocrystalline anisotropy can improve the thermal stability of magnetic properties. However, the inferior anisotropic field (H_A) of $Ce_2Fe_{14}B$ and $Y_2Fe_{14}B$ to $Nd_2Fe_{14}B$ leads to low coercivity of the Nd-Ce-Y-Fe-B magnets when Y/Ce substitution for Pr/Nd exceeds 25 wt%. To further enhance the coercivity, in this work, $(Pr_{20}Nd_{80})$-H_x powders were introduced into the $(Nd,Pr)_{22.8}(Y,Ce)_{7.7}Fe_{bal}B_1$ sintered magnets. Fig. 1 shows the room temperature coercivity H_{cj} and remanence B_r for the starting Y/Ce co-substituted magnet and the magnets added with 1, 2 and 3 wt% (Pr, Nd)-H powders, respectively. The coercivity can be effectively enhanced with the increase of (Pr, Nd)-H powders amount, for example, H_{cj} is 10.3 kOe when added with 3 wt% (Pr, Nd)-H, which is 10.8% higher than that for the starting magnet. The coercivity increment is accompanied with very slight reduction in B_r and $(BH)_{max}$. After (Pr, Nd)-H powders is added, the intergranular RE-rich phase becomes clearer and more continuous when compared to the starting magnet, isolating well the adjacent grains. As shown in Fig.2, the grain boundary layer is ~10 nm, which may play an important role to decouple the adjacent 2:14:1 phase grains during magnetization reversal. Meanwhile, the dehydrogenation of (Pr, Nd)-H during sintering promotes the diffusion of Nd and Pr towards the 2:14:1 phase grains. The formation of (Nd, Pr)-rich shell with locally enhanced magnetocrystalline anisotropy also contributes to the coercivity enhancement.

[1] A.K. Pathak, M. Khan, K.A. Gschneidner Jr., R.W. McCallum, L. Zhou, K. Sun, M.J. Kramer and V.K. Pecharsky, Acta Mater. 103 (2016) 211-216. [2] Y.J. Zhang, T.Y. Ma, J.Y. Jin, J.T. Li, C. Wu, B.G. Shen, M. Yan, Acta Mater. 128 (2017) 22-30. [3] B.X. Peng, T.Y. Ma, Y.J. Zhang, J.Y. Jin, M. Yan, Scr. Mater. 131 (2017) 11-14.

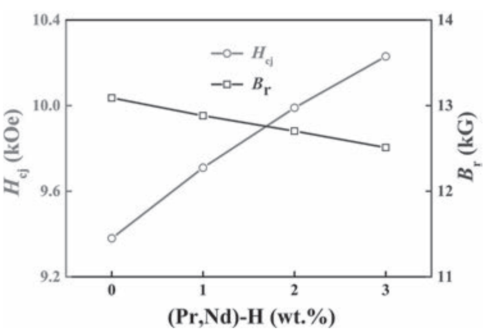

Fig. 1. Room temperature coercivity H_{cj} and remanence B_r for the starting Y/Ce co-substituted magnet and the magnets added with 1, 2 and 3 wt% (Pr, Nd)-H powders, respectively.

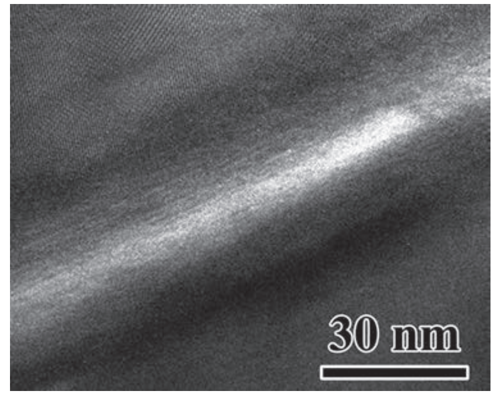

Fig. 2. High resolution transmission electron microscopy characterization of typical grain boundary for the magnet added with (Pr, Nd)-H powders.

BU-08. Spin reorientation, magnetic viscosity and exchange coupling effects of the Nd-Ce-Fe-B sintered magnets prepared by single-main-phase and dual-main-phase alloy methods.

Z. Jiang[1], *Y. Fang*[1], R. Han[1], T. Liu[1], M. Zhu[1] and W. Li[1]
1. Functional Materials Research Institute, Central Iron and Steel Research Institute, Beijing, China

Introduction Achievement of high performance Nd-Fe-B magnets is highly dependent on Nd and Pr elements, which are only occupied small quantity in the natural rare earth resources. From commercial and resource utilization consideration, low cost compounds with tolerable less or same magnetic properties are generally welcomed. Ce element, which is abundant in rare earth ore, is considered as a potential substitute [1-3]. In 1991, D. Li *et al.*[2] reported magnetic properties of $(Ce_{1-x}Nd_x)_{13.5}(Fe,Co,Si,)_{80}B_{6.5}$ sintered magnets. Zhou *et al.* [3] have investigated the influence of Si, Co and didymium oxide on the magnetic properties of 40%Ce-50%Nd-10%Pr magnets. These previous magnets were prepared by a single-main-phase alloy method. Recently, Zhu *et al.*[4] have reported $(Nd_{0.7}Ce_{0.3})(Fe,TM)_{bal}B$ sintered magnets with the maximum energy product of over 43 MGOe by a dual-main-phase alloy method. More recently, Susner *et al.*[5] have discussed Ce-substituted $Nd_2Fe_{14}B$ single crystals, showing only small decrease with increasing Ce content in intrinsic magnetic properties. To further reveal the influence of Ce on the magnetic properties of Nd-Ce-Fe-B sintered magnets, the temperature dependence of magnetic properties were investigated systematically, especial for a wide temperature range from 50K to 360K. The effect of heat-treatment conditions on the magnetic properties (spin reorientation, magnetic viscosity, exchange coupling) were discussed for the magnets prepared by single-main-phase alloy method and dual-main-phase alloy method as well. Experimental Magnets with nominal composition of $(Nd_{0.8}Ce_{0.2})_{30}(Fe,TM)_{69}B_1$ were prepared by single-main-phase (SMP) alloy method and dual-main-phase (DMP) alloy method [4], respectively. In order to reveal the effect of annealing process on the magnetic properties of the magnets, two kinds of specimens were fabricated. One was as-sintered magnet only sintered at 1323K for 2h, the other was tempering magnet, which was obtained for the as-sintered magnet tempered at 773K for 2-5h. Magnetic measurements were performed using Physical Property Measurement System with the maximum field of 9T. Results and Discussion The temperature dependence of magnetic properties of the SMP and DMP specimens were measured in the range of 60K to 360K for the as-sintered and tempering states (Fig.1). The saturation magnetization M_s and remanent magnetization M_r of all the specimens decreases gradually with increasing temperature. Moreover, the M_s and M_r of the as-sintered specimens are more than that of tempering one whatever it is SMP or DMP method. As shown in Fig.1(b), It is found that the curves take on peak around 100K, indicating an abnormal temperature coefficient of M_r, which is related to be the spin orientation discussed bellow. For intrinsic coercivity H_{cj}, it show different story. As for SMP specimen, the as-sintered one shows higher H_{cj} than that of the tempering one. However, for DMP specimen the as-sintered state has lower H_{cj} comparing to tempering state. Taking the room temperature H_{cj} as example, from as-sintered to tempering state, H_{cj} decreases from 7.51 to 3.90kOe for SMP specimens, and increases from 4.96 to 7.34kOe for DMP specimens. The enhanced coercivity for the DMP tempering state specimen maybe due to the smooth transition between grains to intergranular phase reduced the exchange coupling interaction between the matrix grains with different magnetocrystalline anisotropic field. The temperature dependence of ac susceptibility χ_{ac} of the specimens with perpendicular c-axis direction was shown in Fig. 2. The χ_{ac} peak represents minimum magnetocrystalline anisotropy. It is the temperature of easy-magnetization direction turning point, or spin reorientation temperature (T_{sr})[7]. The anomalies in the χ_{ac} curves reflect T_{sr}. Compared the specimens prepared in different methods, the T_{sr} of SMP specimens is about 80K, while the T_{sr} of DMP specimens is relatively higher, about 90K, indicating that the anisotropy field of the specimens has changed, and their grains real composition should be different. The SMP specimens should make a cerium substitution of Nd in the Nd-Fe-B main phase. Time dependence of the magnetization was furthor investigated. The specimens are kept in an magnetic field H_0 equal to H_{cj} for 2400 seconds. Time dependent of magnetization follows the expression $M(t)=M_0-S\,ln(t+t_0)$, where S is the magnetic viscosity parameter, M_0 a constant and t_0 a fitting parameter to establish a reference time. From 0 to 120 seconds, the M/M_0 curves show a non-linear change, indicating that the M rapidly decreases at the initial stage of time and then reaches a steady state. The magnetic viscosity parameter of DMP as-sintered specimens is the highest among the specimens, which is 4.23emu/(g.s); while DMP tempering specimen is only 2.07 emu/(g.s), indicating that tempering reduces magnetic viscosity, which is related to exchange coupling interaction between grains. Conclusions Magnetic measurements indicate that the M_s and M_r represent different temperature dependence comparing to intrinsic coercivity H_{cj} for SMP and DMP specimens. The ac susceptibility χ_{ac} investigation shows that the spin reorientation changes from 80K in SMP specimens to 90K in DMP specimens, which is lower than Nd-Fe-B sintered magnets. Moreover, the magnetic viscosity characterization indicates that tempering could reduce exchange coupling interaction between grains.

[1] A. K. Pathak, M. Khan, K. A. Gschneidner, Jr., R. W. McCallum, L. Zhou, K. Sun, et al., *Adv. Mater.*, vol. 27, pp 2663, 2015. [2] D. Li and Y. Bogatin, *J. Appl. Phys.*, vol. 69, pp5515, 1991 [3] S. X. Zhou and Y. G. Wang, *J. Appl. Phys.*, vol. 75, pp. 6268, 1994. [4] M. Zhu, W. Li, J. Wang, L. Zheng, Y. Li, K. Zhang, H. Feng, T. Liu, *IEEE Trans. Magn.*, vol.50, pp.1, 2014. [5] M. A. Susner, B. S. Conner, B. I. Saparov, M. A. McGuire, E. J. Crumlin, G. M. Veith, H. Cao, K. V. Shanavas, D. S. Parker, B. C. Chakoumakos, and B. C. Sales, *J. Magn. Magn. Mater.*, vol.434, pp.1, 2017. [6] M. Zhu, R. Han, W. Li, S. Huang, D. Zheng, L. Song and X. Shi, *IEEE Trans. Magn.*, vol.51, pp.1,2015. [7] W. L. Zuo, S. L. Zuo, R. Li, T. Y. Zhao, F. X. Hu, J. R. Sun, X. F. Zhang, J. P. Liu, B. G. Shen, *J. Alloy. Compd.,* vol.695, pp.1786,2017.

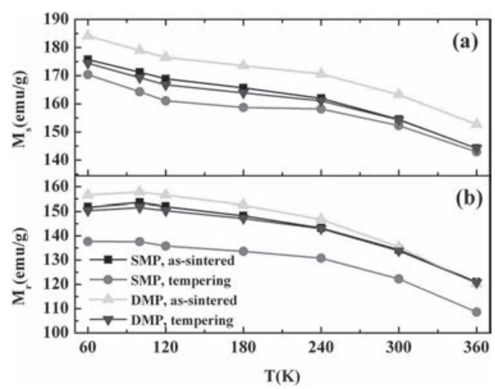

Fig. 1. Temperature dependence of M_s (a) and M_r (b) of the specimens.

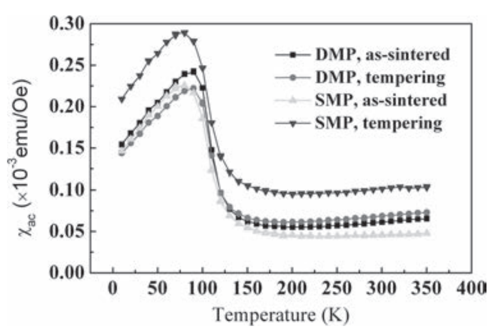

Fig. 2. Temperature dependence of ac susceptibility χ_{ac} of the specimens.

BU-09. Effects of Ta doping and Ce reduction on the magnetic properties and thermal stability of Ce-Fe-B alloys.

J. Zhang[1], L. Zhao[1], X. Liao[1], H. Zeng[1] and *Z. Liu*[1]
1. South China University of Technology, Guangzhou, China

Recently, the abundant and inexpensive RE elements like La and Ce have been employed for developing high performance/price permanent magnets. Ce is the only RE element which not only has trivalent (3^+) $4f^1$ and tetravalent (4^+) $4f^0$ electronic states but also exhibits phases with enormous (15-17%) volume differences[1, 2]. Although the intrinsic magnetic properties of $Ce_2Fe_{14}B$ are inferior to those of $Nd_2Fe_{14}B$, they are sufficient for producing the magnets with hard magnetic properties higher than ferrites. Herbst[3] et al. obtained the appropriate magnetic properties in melt spun $Ce_{17}Fe_{78}B_6$ alloy with intrinsic coercivity ${}_iH_c$=429.9 kA/m, remanence J_r=0.49 T, and energy product $(BH)_{max}$=33 kJ/m^3. To further improve their performance, it is essential to modify the composition, control the phase constitution, and refine the microstructure. Our previous work suggested that in ternary Ce-Fe-B alloy, $Ce_2Fe_{14}B$ phase precipitates first during rapid quenching, while α-Fe phase precipitates first from the amorphous matrix during annealing[4]. The $CeFe_2$ phase behaves as a soft magnetic phase below 230(±2) K[5] and its presence is thought to be harmful to the hard magnetic properties but beneficial to the wettability of 2:14:1 phase when the magnets are sintered [6]. For composition modification, Co substitution for Fe was used to increase the curie temperature T_c of $Ce_2Fe_{14}B$ phase[7]. Zr, Hf doping could refine grain size and optimize the microstructure. Jiang et al. [8] reported that Ga doping could also improve the magnetic properties and curie temperature (T_c) attributed to the increase of Ce^{3+} ratio. On the other hand, another transition metal Ta has been frequently employed in soft magnetic materials for improving thermal stability and glass formability. However, the effects of Ta doping on the structure and magnetic properties of RE-Fe-B alloys received little attention. Liu et al.[9] showed that Ta plays an important role in producing an appropriate combination of magnetic properties in $Nd_9Fe_{86-x}Ta_xB_5$ alloys. In this work, the effects of Ta element doping and Ce reduction on the phase constitution, microstructure and magnetic properties of melt spun $Ce_{17}Fe_{78}B_6$ alloy were systematically investigated. The XRD refinement results for the optimized $Ce_{17-y}Fe_{78-x+y}Ta_xB_6$ alloys indicate that the alloys composed of $Ce_2Fe_{14}B$ phase and $CeFe_2$ phase. With the Ta substitution for Fe, the lattice constants *a* and *c* of 2:14:1 phase keep constant, but a decreasing trend is observed for grain size of 2:14:1. The volume fraction of $CeFe_2$ phase decreases by reducing Ce content in $Ce_{17-y}Fe_{77.25+y}Ta_{0.75}B_6$ alloys and only 2:14:1 phase can be detected in y=5 alloy. The *x* dependent magnetic properties are shown in Fig. 1. The highest H_c of 553 kA/m obtained in $Ce_{17}Fe_{77.25}Ta_{0.75}B_6$ alloy is attributed to the increase of RE/Fe ratio and the grain refinement. Further substitution of Fe by Ta deteriorates the magnetic properties perhaps due to the formation of an unknown phase. The deterioration of thermal stability (temperature coefficient of coercivity β and temperature coefficient of coercivity α) is observed in the Ta substituted alloys in the temperature range between 300 K and 400 K, which is inconsistent with the effects shown in Ta substituted (Nd,Dy)-(Fe,Co)-B alloys reported by Chin et al.[10].The reason could be attributed to the decreasing Curie temperature T_c from 424 K for x=0 alloy to 416 K for x=0.75 alloy. As Ta element does not enter 2:14:1 phase, the decrease of T_c might because of the increase of vacancies in the Fe sublattices for higher Ce content and low Fe content reported by Li et al.[11]. By reducing the Ce content in the $Ce_{17-y}Fe_{77.25+y}Ta_{0.75}B_6$ alloys, H_c value decreased monotonously, but the remanence (J_r) was significantly enhanced by increasing Fe content, as shown in Fig. 2. The H_c value of y=5 alloy is quite low since the decoupling effect between $Ce_2Fe_{14}B$ grains was weakened due to its low amount of intergranular phase. As a result, good magnetic properties i.e. H_c=514 kA/m, J_r=0.49 T, $(BH)_{max}$=36 kJ/m^3 and 448 kA/m, 0.54 T, 41 kJ/m^3 were obtained in the $Ce_{15}Fe_{79.25}Ta_{0.75}B_6$ and $Ce_{14}Fe_{80.25}Ta_{0.75}B_6$ alloys, respectively, which are superior to those of recently reported $Ce_{17}Fe_{78-x}M_xB_6$ (Zr, Ga and Hf) alloys. The present work shows that a minor substitution of Ta could further improve the magnetic properties of Ce-Fe-B alloys, which is beneficial for composition design.

[1] ALAM A, KHAN M, MCCALLUM R W, et al. Site-preference and valency for rare-earth sites in (R-Ce)$_2$Fe$_{14}$B magnets [J]. Applied Physics Letters, 2013, 102(4): 042402. [2] ALAM A, JOHNSON D D. Mixed valency and site-preference chemistry for cerium and its compounds: A predictive density-functional theory study [J]. Physical Review B, 2014, 89(23): 235126. [3] HERBST J, MEYER M, PINKERTON F. Magnetic hardening of $Ce_2Fe_{14}B$ [J]. Journal of Applied Physics, 2012, 111(7): 07A718. [4] ZHANG Z, ZHAO L, ZHONG X, et al. Phase precipitation behavior of melt-spun ternary $Ce_2Fe_{14}B$ alloy during rapid quenching and heat treatment [J]. Journal of Magnetism and Magnetic Materials, 2017. [5] PAOLASINI L, DERVENAGAS P, VULLIET P, et al. Magnetic response function of the itinerant ferromagnet $CeFe_2$ [J]. Physical Review B, 1998, 58(18): 12117. [6] ZHANG Y, MA T, JIN J, et al. Effects of $REFe_2$ on microstructure and magnetic properties of Nd-Ce-Fe-B sintered magnets [J]. Acta Materialia, 2017, 128(22-30). [7] SKOUG E J, MEYER M, PINKERTON F, et al. Crystal structure and magnetic properties of $Ce_2Fe_{14-x}Co_xB$ alloys [J]. Journal of Alloys and Compounds, 2013, 574(552-5). [8] JIANG Q, ZHONG M, LEI W, et al. Effect of Ga addition on the valence state of Ce and magnetic properties of melt-spun $Ce_{17}Fe_{78-x}B_6Ga_x$ (x= 0-1.0) ribbons [J]. AIP Advances, 2017, 7(8): 085013. [9] LIU Z, LIU Y, DEHERI P, et al. Improving permanent magnetic properties of rapidly solidified nanophase RE–TM–B alloys by compositional modification [J]. Journal of Magnetism and Magnetic Materials, 2009, 321(15): 2290-5. [10] CHIN T, LIN C, HUANG Y, et al. Enhanced thermal stability of sintered (Nd, Dy) (Fe, Co) B magnets by the addition of Ta or Ti [J]. IEEE transactions on magnetics, 1993, 29(6): 2788-90. [11] LI Z-B, ZHANG M, SHEN B-G, et al. Variations of phase constitution and magnetic properties with Ce content in Ce-Fe-B permanent magnets [J]. Materials Letters, 2016, 172(102-4).

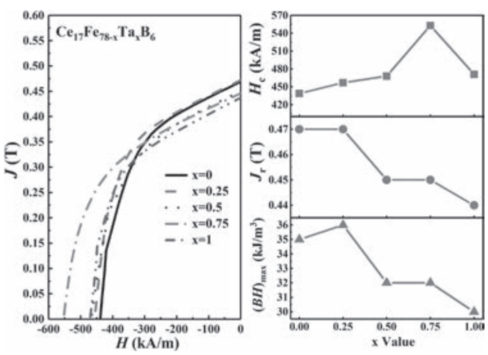

Fig. 1. Magnetic properties as a function of Ta content for as-spun $Ce_{17}Fe_{78-x}Ta_xB_6$ (x=0, 0.25, 0.5, 0.75, 1.00) alloys

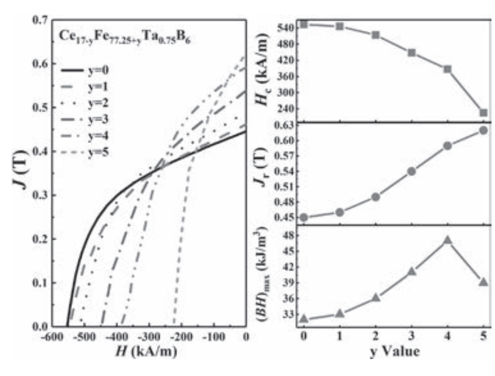

Fig. 2. Magnetic properties as a function of Ce content for as-spun $Ce_{17-y}Fe_{77.25+y}Ta_{0.75}B_6$ (y=0, 1, 2, 3, 4, 5) alloys

BU-10. Coercivity enhancement of hot-deformed NdFeB magnets by doping $R_{80}Ga_{20}$ (R= Pr, Dy, Tb) alloys.

Y. Lee[1], Y. Wong[1], H.W. Chang[1] and W.C. Chang[1]
1. Department of physics, National Chung Cheng University, Chiayi, Taiwan

$Nd_2Fe_{14}B$-type magnets have attracted considerable attention and widely used in many fields due to the highest magnetic energy product ($(BH)_{max}$) among all the developed permanent magnetic materials. The hot deformation method is a potential and simple method to obtain anisotropic Nd-Fe-B magnets with high $(BH)_{max}$ [1]. However, the intrinsic coercivity ($_iH_c$) of hot-doformed Dy-free Nd-Fe-B magnets is normally smaller than 15 kOe, $_iH_c$ enhancement is crucial and necessary for the applications at high temperature. In order to enhance the coercivity, a noticeable amount of heavy rare earth (HRE) element, such as Dy or Tb, is added to obtain $(Nd, HRE)_2Fe_{14}B$ phase with a higher magnetocrystalline anisotropy field (H_a) [2]. In addition, Ga addition into the hot deformed magnets is also effective in coercivity enhancement [3]. In this work, $R_{80}Ga_{20}$ (R=Pr, Dy and Tb) alloy powders were adopted to be mixed with the commercial NdFeB MQU-F powders as the raw material to make hot deformed NdFeB magnets for the purpose of improving the coercivity especially. $R_{80}Ga_{20}$ (R = Pr, Dy, and Tb) alloys powders were prepared by arc-melting and subsequently melt spun at wheel speed of 30 m/s. Two weight % of the crushed $R_{80}Ga_{20}$ powders with size of about 200 μm were mixed with the commercial NdFeB MQU-F powders. The as-mixed powders were pressed at 650 °C under 250 MPa in vacuum to form a dense disk, and then deformed at 810 °C under 100 MPa with 70% reduction in thickness. Furthermore, the hot deformed magnets were post-annealed at various temperatures for 2 hours to optimize the microstructure and magnetic properties. The magnetic properties were measured by a B-H loop tracer. To understand phase distribution and microstructure, X-ray diffraction (XRD), scanning electron microscopy (SEM), and transmission electron microscopy (TEM) were employed, respectively. Magnetic properties of the hot deformed NdFeB magnets by doping $R_{80}Ga_{20}$ (R=Pr, Dy and Tb) powders are studied. As shown in Fig. 1(a), the magnet made from pure MQU-F powder exhibits good magnetic properties of remanence (B_r) = 13.0 kG, $_iH_c$ = 15.0 kOe, and $(BH)_{max}$ = 41.5 MGOe. Coercivity are enhanced by doping $R_{80}Ga_{20}$ (R=Pr, Dy and Tb) powders. Coercivity enhancement (Δ_iH_c) of the magnets doped with $R_{80}Ga_{20}$ (R=Pr, Dy and Tb) powders is highly related to H_a of $R_2Fe_{14}B$ phase. For hot deformed $Pr_{80}Ga_{20}$ and $Dy_{80}Ga_{20}$-doped magnet followed by 600 °C annealing, Δ_iH_c are 2.2 kOe and 2.7 kOe, respectively, but B_r and $(BH)_{max}$ are decreased to 12.0 kG and 34.1-35.5 MGOe. Especially, $Tb_{80}Ga_{20}$-doped magnet exhibits larger Δ_iH_c of 3.7 kOe with higher $_iH_c$ = 18.7 kOe and slightly decreased B_r (= 12.5 kG) and $(BH)_{max}$ (= 39.4 MGOe). Quite importantly, increasing annealing temperature to 700 °C could remarkably enhance the coercivity to 24 kOe (Δ_iH_c =9 kOe) and slightly reduce $(BH)_{max}$ to 37.5 MGOe. As shown in Fig.1 (b) and (c), the platelet-shape grains observed in studied samples contribute to high B_r and $(BH)_{max}$. The size of magnetic grains approached to single-domain size results in coercivity enhancement and the improvement of the squareness of demagnetization curves shown in Fig. 1(a). Figure 2 shows XRD patterns of the studied NdFeB magnets. All diffraction peaks of the studied samples belong to 2:14:1 phase, and no other phase is detected. In addition, all studied magnets show a good (00L) texture. High I(006)/I(105) of 1.7 for the hot deformed magnet made from pure MQU-F powders results in higher B_r and thus $(BH)_{max}$. The reduced I(006)/I(105) value to 1.2 for the samples with R = Pr and Dy, and 1.5 for the magnet with R= Tb leads to the decrease of B_r to 12.0 kG and 12.5 kG, respectively. TEM and EDX analysis show that Tb and Ga prefer to appear at grain boundary for the $Tb_{80}Ga_{20}$-doped magnets post annealed at 600 °C, while Tb diffuses into grain interior and Ga also prefer to stay at grain boundary with increasing annealing temperature to 700 °C. The appearance of Ga decreases Fe content at the grain boundary phase, and therefore reduces number of nucleation sites and also increases pinning strength of the domain wall movement. H_a of 2:14:1 phase is improved by Tb diffusion into 2:14:1 grains. Both above effects lead to remarkable coercivity enhancement. This study provided economic way for mass production a thicker MQ 3 magnets which are suitable for the application at high temperature.

[1] R. W. Lee et al., Appl. Phys. Lett. 46, 790 (1985).. [2] M. Sagawa et al., J. Appl. Phys. 61, 3559 (1987). [3] M. Endoh et al., IEEE Transactions on Magnetics. 25(5), 4114 (1989).

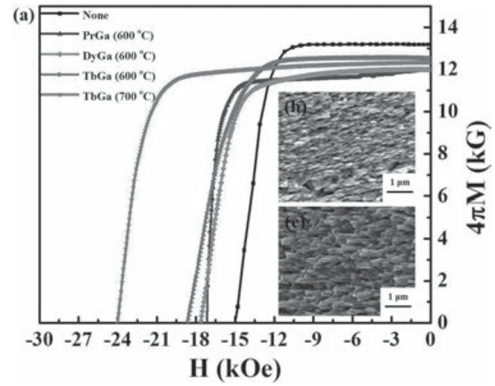

Fig. 1. (a) Magnetic properties of the hot deformed NdFeB magnets made from commercial MQU-F powders doped with $R_{80}Ga_{20}$ (R=Pr, Dy and Tb) and post-annealed at 600 °C or 700 °C for 2 hours. SEM images of hot deformed magnets (b) made from pure MQU-F powders, (c) $Tb_{80}Ga_{20}$-doped magnets annealed at 700 °C for 2 hours.

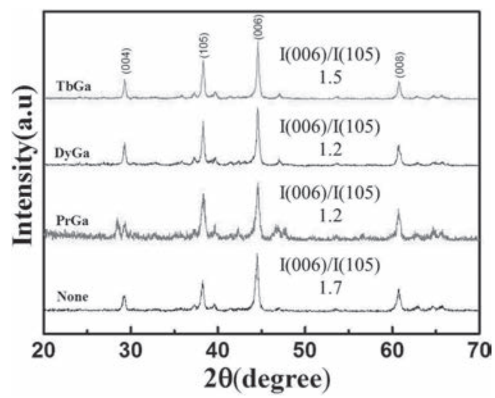

Fig. 2. XRD patterns of hot deformed NdFeB magnets without and with $R_{80}Ga_{20}$ alloy powders (R=Pr, Dy and Tb) doping.

BU-11. Distinctive diffusion behaviors observed in Dy-Fe-Ga intergranular added sintered Nd-Fe-B.

J. Zeng[1,2], S. Guo[1], X. Yang[1,2], G. Ding[1] and A. Yan[1]
1. Ningbo Institute of Industrial Technology, CAS, Ningbo, China; 2. University of Chinese Academy of Science, Beijing, China

Doping HRE-rich powders has been proved to be an effective way to improve coercivity in sintered bulk Nd-Fe-B magnet. Dy-Fe-Ga powders with a fine grain size were prepared though hydrogenation–disproportionation–desorption–recombination and a further jet-milling. The powders were added in conventional Dy-free powders and a high increase rate of coercivity for adding Dy-rich additives is achieved by 3.59 kOe/wt. % Dy. During sintering, redistribution of liquid phase leads to distinctive Dy diffusion behaviors. A model is proposed to explain the process. In order to acquire fine grain size, HDDR is introduced in processing Dy-Fe-Ga powder. The initial alloy with a composition of $Dy_1(Fe_{0.8}Ga_{0.2})_2$ was prepared through high-frequency induction melting. The alloy was directly processed in hydrogen furnace and the disproportionation condition is set as 800°C in 2 hours. After HDDR, the powder was further refined through jet milling. By blending the refined Dy-Fe-Ga power in conventional Dy-free powder, the coercivity of the sintered magnet increased 7.17kOe, which equals 3.59kOe increase for 1% Dy adding. The demagnetization curves are shown in Fig. 1. The detailed microstructure changes during sintering was investigated via observation in samples quenched at 800°C, 1000°C and 1030°C which corresponds to different sintering stages till achieving final sintering temperature. SEM images of samples processed at 800°C and 1000°C both show a relatively denser area containing less holes and more Nd-rich phase. SEM areal composition analysis shows the dense areas in the sample of 800°C contains more than 36 wt.% Nd, and the area outside contains much less Nd of 28 wt.% which is closed to the stoichiometric Nd content of 26.68 wt.% in $Nd_2Fe_{14}B_1$, however, the Dy and Ga content shows opposite distribution tendency as follows: in the dense area, less than 2.5 wt.% of Dy is recorded compared with more than 3.5 wt.% outside, more than 1.3 wt.% of Ga is recorded compared with less than 0.7 wt.% outside. The sample processed at 1000°C shows a much more homogenized elemental distribution but with the same tendency of the sample processed at 800°C. The sample processed at 1000°C showed a more obvious core-shell structure outside the dense area, detailed compositional analysis of points also reveals this. Through investigating the sample without adding Dy-Fe-Ga powder, no agglomerated liquid phase was detected though the whole sintering process. Based on this, The liquid phase which contains less than 5 wt.% Dy and more than 50 wt.% Nd forms as the diffusion of Dy into the 2:14:1 phase. Excessive Nd-rich phase liquidifies and agglomerates, which prompt the diffusion of Dy deep into the 2:14:1 phase. To be noticed that Dy content outside the dense area is much higher than that in the dense area, the uneven mixing of powder, which might be conceivable, do not directly leads to the agglomerated liquid phase. The whole diffusion process is schematically shown in Fig 2. It is interesting though, comparing with the grains in the porous area, dense area features a much lower Dy concentration difference between the inner and outer parts of the grains than the dense area. The excessive liquid phase should be the cause of that considering the liquid sintering process accompanied in 1000 °C. Study reveals that dissolution and re-precipitation of $Nd_2Fe_{14}B$ reaction with the RE-rich liquid phase features the liquid sintering process [1]. The ternary eutectic reaction, $L \leftrightarrow Nd + Nd_2Fe_{14}B + Nd_{1+\varepsilon}Fe_4B_4$, reacts at 655 °C, which is much lower than 1000 °C, so the dissolution and re-precipitation process should be violent in the dense area. The reaction causes not only reshape of grains but also exchanges of large amount of atoms, [2] as for the main phase grain, prompting Dy atoms diffusing deep into the center part of grain. Besides the solid-liquid reaction, diffusion follows the Fick's second law, but the diffusion constant without liquid phase at 1000 °C should be relatively low, so for the porous area, a much more obvious core-shell structure is observed.

[1] L. Xianglian and Z. Shouzeng, Journal of Rare Earths 25 (3), 329-335 (2007). [2] W. D. Kingery, J Appl Phys 30 (3), 301-306 (1959).

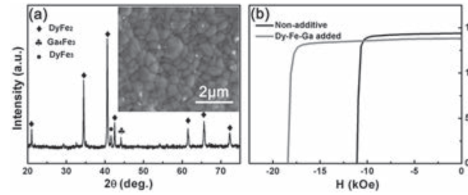

Fig. 1. (a) XRD patern of HDDR Dy-Fe-Ga alloy, insect figure is Secondary electron (SE) image of HDDR Dy-Fe-Ga alloy, (b) Demagnetization cureves of the sample with/without HDDR Dy-Fe-Ga powders addition.

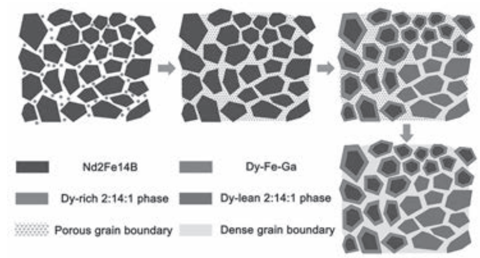

Fig. 2. Schematic depiction of the liquid-redistribution and diffusion process.

BU-12. Effects of La substitution on the crystal structure and intrinsic magnetic properties of MM-Fe-B alloy (MM = La, Ce, Pr, Nd).

W. Liu[1], *Z. Zhang*[1], Z. Li[1], D. Zhang[1], H. Zhang[1], M. Yue[1], Q. Lu[1], Q. Wu[1] and Y. Li[1]
1. Beijing University of Technology, Beijing, China

I. INTRODUCTION Since the discovery of NdFeB in 1983 by Sagawa [1], permanent-magnet materials develop rapidly and become the heart of modern technology, such as wind power generators and electric cars. Misch metal (MM) is mined as raw ore with a composition of $La_{25}Ce_{55}Pr_5Nd_{15}$, but Pr and Nd are overused which causes idle of La and Ce. It must also be mentioned that sintered magnets made using of MM can greatly reduce costs. Yu et al. reported the $MM_{33}Fe_{66}B$ alloys yield M_s of 11.3 kG, H_A of 48.4 kOe, and T_c of 502.9 K[2]. The intrinsic magnetic properties of MM-Fe-B are not very low, but it has a lower price. In some researches [3-4], $CeFe_2$ phase exists in the magnet as harmful phases and decreases the magnetic properties. In our study, alloy ingot with nominal composition of $(La_xMM_{1-x})_{33}Fe_{66}B$ were prepared, the effects of La substitution on the crystal structure and intrinsic magnetic properties of MM-Fe-B alloy were investigated. It is found that the addition of La could suppress the $CeFe_2$ phase. II. EXPERIMENTS Alloy ingot with nominal composition of $(La_xMM_{1-x})_{33}Fe_{66}B$ (x=0, 0.025, 0.05, 0.075, 0.1, 0.15) was prepared by induction melting, and the ingots were then homogenized by annealing at 1273 K under Ar for 24 h. Misch-metal containing about 23.8 wt.% La and 55.2 wt.% Ce and 4.1 wt.% Pr and 16.6 wt.% Nd with a purity of about 99.7 wt.% was used in this experiment. The crystal structure and phase relations of the $(La_{1-x}MM_x)_{33}Fe_{66}B$ system were investigated by X-ray powder diffraction (XRD), scanning electron microscopy (SEM) equipped with energy dispersive X-ray spectroscopy (EDS). Measurements of magnetization-field curves (M-H) along both magnetically easy and hard direction of the alloy and magnetization-temperature curves (M-T) were carried out in a vibrating sample magnetometer (VSM) (Quantum Design) with a maximum magnetic field of 3 T. III. RESULTS AND DISCUSSIONS Fig. 1 shows the XRD diagram of the $(La_xMM_{1-x})_{33}Fe_{66}B$ ingots. It can be found that there are the peaks of $CeFe_2$ phase at 21 degrees, 34.6 degrees and 40.8 degrees when the substituted amount of La is 0-7.5 wt.%. With the increase of La to 10 wt.% in $(La_xMM_{1-x})_{33}Fe_{66}B$, the peaks of $CeFe_2$ phase disappear. Therefore, it is concluded that the addition of La can inhibit formation of $CeFe_2$ phase. The addition of La will consume some Ce to preferentially form La-Ce solid solution, and then it would suppress the formation of 1:2 phases. As a result, the massive $CeFe_2$ phase disappears when La replaces 10 wt.% MM. This is consistent with the observation from SEM–EDS. There is no denying that $(La_xMM_{1-x})_{33}Fe_{66}B$ alloy have four main phases including $Nd_2Fe_{14}B$, $Pr_2Fe_{14}B$, $La_2Fe_{14}B$ and $Ce_2Fe_{14}B$. Another interesting finding is that La substitution would cause the change of Nd, Pr, La and Ce content in main phase, which means the four main phases ratio changes with the La substitution. The Pr+Nd/La+Ce ratio as function of La substitution is shown in Fig.2(a). With increase of La content, the Pr+Nd/La+Ce ratio decreases first, peaks at 7.5 wt.% La substitution, and then increases. At 295 K, the M_s of $Nd_2Fe_{14}B$, $Pr_2Fe_{14}B$, $La_2Fe_{14}B$ and $Ce_2Fe_{14}B$ alloy is 16, 15.6, 13.8 and 11.7 kG. Therefore, the M_s of $(La_xMM_{1-x})_{33}Fe_{66}B$ alloy would be determined by the different main phase ratio. As a result, it exhibits the same tendency to Pr+Nd/La+Ce ratio as shown in fig. 2(b). It should be pointed out that the Pr+Nd/La+Ce ratio in the alloy with 15 wt.% La is less than that of the alloy without La substitution. However, M_s of $(La_{0.15}MM_{0.85})_{33}Fe_{66}B$ alloy is bigger than that of $MM_{33}Fe_{66}B$ alloy. Given that $CeFe_2$ phase disappears in the $(La_xMM_{1-x})_{33}Fe_{66}B$ alloy with La substitution more than 7.5 wt.%, and the $CeFe_2$ phase has low M_s, $(La_{0.15}MM_{0.85})_{33}Fe_{66}B$ alloy with higher M_s is reasonable. To further explore this concept, the M_s of $(La_xMM_{1-x})_{33}Fe_{66}B$ alloy was calculated according the M_s of four main phases and $CeFe_2$ phase, the Pr+Nd/La+Ce ratio and the $CeFe_2$ content. As shown in fig.2(c), the calculation data is in accord with experimental results. IV. CONCLUSIONS The alloy with nominal composition of $(La_xMM_{1-x})_{33}Fe_{66}B$ were prepared, and the rule of La substitution on the crystal structure and intrinsic magnetic properties of MM-Fe-B alloy were obtained. It is found that La substitution could suppress the $CeFe_2$ phase and cause the change of Pr+Nd/La+Ce ratio in main phase of $(La_xMM_{1-x})_{33}Fe_{66}B$ alloy, therefore, reflect in the M_s of $(La_xMM_{1-x})_{33}Fe_{66}B$ alloy. With increase of La content, the M_s decreases first, peaks at 7.5 wt.% La substitution, and then increases. The M_s of $(La_{0.15}MM_{0.85})_{33}Fe_{66}B$ alloy is bigger than that of $MM_{33}Fe_{66}B$ alloy due to restrain of the $CeFe_2$ phase. ACKNOWLEDGEMENT This work was supported by the National Key Research and Development Program of China (2016YFB0700902).

[1] M. Sagawa, S. Fujimura, N. Togawa, H. Yamamoto, & Y. Matsuura, (1984). New material for permanent magnets on a base of Nd and Fe (invited). Journal of Applied Physics, 55(6), 2083-2087. [2] X. Q. Yu, M. Yue, W. Q. Liu, Z. Li, M. G. Zhu, and S. Z. Dong. (2016). Structure and intrinsic magnetic properties of $MM_2Fe_{14}B$ (MM=La, Ce, Pr, Nd) alloys. Journal of Rare Earths, 34(6), 614-617.. [3] Y. Z. Jin, T. Ma, and M. Yan. (2016). Mechanical properties of La–Ce-substituted Nd–Fe–B magnets. IEEE Transactions on Magnetics, 52(7), 1-4. [4] W. L. Zuo, S. L. Zuo, R. Li, T. Y. Zhao, F. X. Hu, J. R. Sun, et al. (2017). High performance misch-metal (MM)-Fe-B magnets prepared by melt spinning. Journal of Alloys & Compounds, 695, 1786-1792.

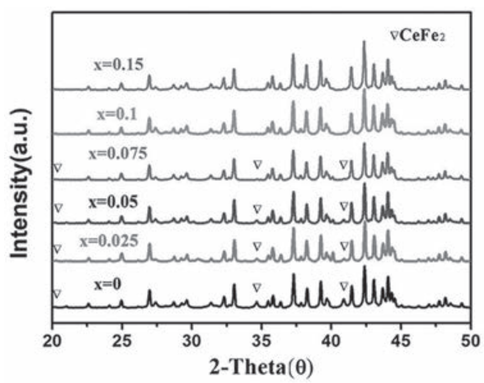

Fig. 1. XRD diagram of (LaxMM1-x)33Fe66B ingot (x=0-0.15)

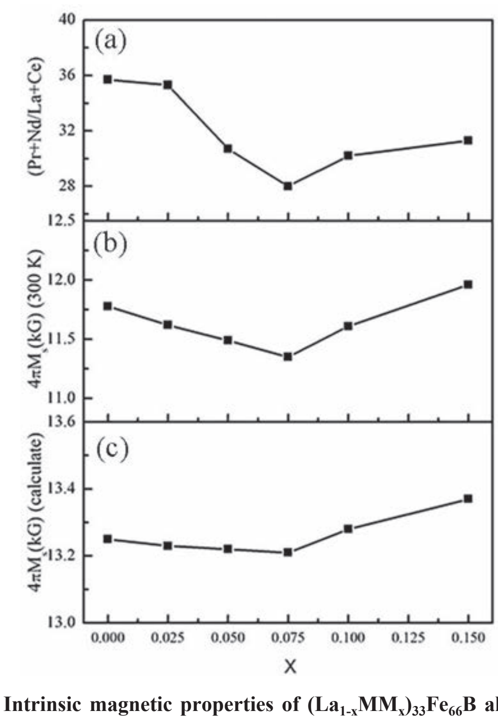

Fig. 2. Intrinsic magnetic properties of $(La_{1-x}MM_x)_{33}Fe_{66}B$ alloy (x=0-0.15), (a) the ratio of Pr+Nd/La+Ce, (b) the experiment value of M_s, (c) the calculated values of M_s.

BU-13. Effects of (Nd,Pr)H_x intergranular addition on the mechanical properties of Nd-Pr-Ce-Fe-B sintered magnets.

J. Jin[1], Z. Qian[1], G. Bai[1], B. Peng[1], Y. Liu[1] and M. Yan[1]
1. material science and engineering, Zhejiang University, Hangzhou, China

Incorporating Ce into the $Nd_2Fe_{14}B$-type sintered magnet has attracted growing attention due to its high crustal abundance and low material cost [1-3]. The inferior intrinsic magnetic properties of $Ce_2Fe_{14}B$ to $Nd_2Fe_{14}B$ compound, however, pose a big challenge for the Nd-Ce-Fe-B permanent magnets to exhibit equivalent magnetic properties. Fortunately, the multi main phase (MMP) magnet, by mixing the Ce-free and Ce-rich 2:14:1-type components has been demonstrated to possess preferable magnetic performance recently [4-6]. For instance, maximum energy product $(BH)_{max}$ of 36.7 MGOe has been obtained upon a high level of Ce substitution for Nd (45 wt. %) [6]. Considering that the gap in the coercivity between Nd-Fe-B commercial magnets and Nd-Ce-Fe-B MMP ones still exist, Nd hydrides have been introduced as intergranular additives into the Nd-Ce-Fe-B sintered magnets. Results revealed that the coercivity can be significantly enhanced from 8.3 to 12.2 kOe upon 3 wt.% (Nd,Pr)H_x additives. Besides the magnetic performance, other properties including the mechanical performance of 2:14:1-type permanent magnets also determine the end-product application in various areas, such as high-speed motors. As the introduction of (Nd,Pr)H_x into Nd-Pr-Ce-Fe-B magnets may exert complex influences on the traditional intergranular fracture behavior, whether the mechanical properties suffer severe deterioration or not is still left unknown. Understanding the relationship between (Nd,Pr)H_x content, microstructure and mechanical properties changes is of great significance in mass production of Nd-Pr-Ce-Fe-B sintered magnets and hence requires detailed investigations. In the present work, 20 wt.% $(Nd,Pr)_{30.8}Fe_{bal}M_{1.39}B$ and 80 wt. % $[(Nd,Pr)_{0.5}Ce_{0.5}]_{30.8}Fe_{bal}M_{1.39}B$ magnetic powders have been mixed to prepare the MMP magnet with 40 wt. % Ce substitution. Here 0~3 wt.% (Nd,Pr)H_x has been added before compressing, sintering and annealing. Dependences of fracture toughness K_{IC} and bending strength σ_{bb} on the (Nd,Pr)H_x addition are shown in Fig. 1. Clearly, the increasing (Nd,Pr)H_x content from 0 to 3 wt.% can gradually enhance both the fracture toughness and the bending strength. At 3 wt.% (Nd,Pr)H_x incorporation, high value of 2.0 $MPa \cdot m^{1/2}$ and 229 MPa can be obtained for the 40 wt. % Ce-containing MMP magnets. It suggests that the Nd-Pr-Ce-Fe-B MMP magnets with (Nd,Pr)H_x intergranular addition are promising to be new substitutes for low-to-medium Nd-Fe-B commercial magnets. The enhanced mechanical properties can be attributed to the increased volume fraction of the intergranular regions upon (Nd,Pr)H_x addition and the modified distribution of RE-rich intergranular phases, as shown in Fig. 2a and b. Additionally, thick grain boundary layers can also be found in the fractograph of Nd-Pr-Ce-Fe-B MMP magnets after (Nd,Pr)H_x addition (Fig. 2d). It is in good agreement with the aforementioned results that (Nd,Pr)H_x intergranular additives can enhance both the fracture toughness and the bending strength simultaneously.

[1] S. Massari, and M. Ruberti, Resour. Pol. 38, 36 (2013). [2] Z.B. Li, B.G. Shen, M. Zhang, F.X. Hu, and J.R. Sun, J. Alloys Compd. 628, 325 (2015). [3] A.K. Pathak, M. Khan, K.A. Gschneidner Jr., R.W. McCallum, L. Zhou, K. Sun, K.W. Dennis, C. Zhou, F.E. Pinkerton, M.J. Kramer, and V.K. Pecharsky, Adv. Mater. 27, 2663 (2015). [4] E. Niu, Z. A. Chen, G. A. Chen, Y. G. Zhao, J. Zhang, X. L. Rao, B. P. Hu and Z. X. Wang, J. Appl. Phys. 115, 113912 (2014). [5] J.Y. Jin, T.Y. Ma, Y.J. Zhang, G.H. Bai, M. Yan, Sci. Rep. 6, 32200 (2016). [6] Y.J. Zhang, T.Y. Ma, J.Y. Jin, J.T. Li, C. Wu, B.G. Shen, and M. Yan, Acta Mater. 128, 22 (2017).

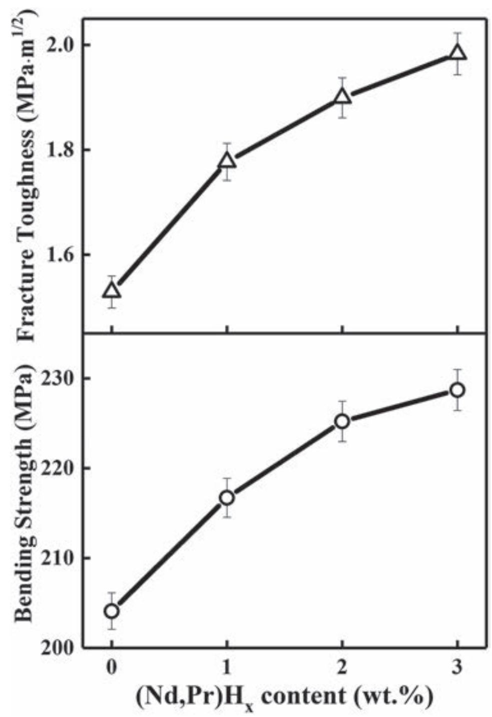

Fig. 1. Dependences of fracture toughness and bending strength on the (Nd,Pr)H_x contents for the 40 wt.% Ce-containing MMP magnets.

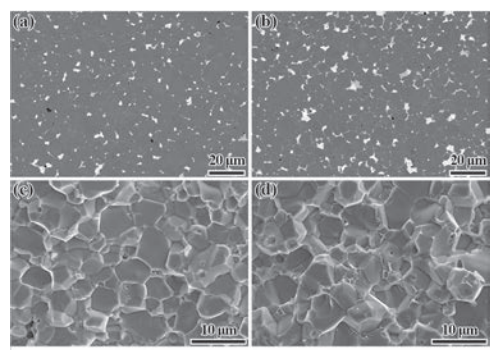

Fig. 2. Back-scattered SEM images for the 40 wt. % Ce-containing Nd-Pr-Ce-Fe-B MMP magnet (a) without (Nd,Pr)H_x addition and (b) with 3 wt.% (Nd,Pr)H_x addition. The corresponding fractographs are shown in (c) and (d), respectively.

BU-14. Study on recycling technology for waste MQ bonded Nd-Fe-B magnets.

M. Liu[1], Y. Zhang[1], W. Liu[1], D. Zhang[1] and M. Yue[1]
1. Beijing University of Technology, Beijing, China

I. INTRODUCTION Nowadays, the Nd-Fe-B bonded magnets are playing a crucial role in many aspects, such as hard disk drive magnet (HDD), optical disk drive magnet (ODD) [1]. So more and more waste Nd-Fe-B bonded magnets are produced and filled into land due to their short lifetime and difficult recovery techniques. Recent increasing prices of rare-earth elements and concerns over the security of supply are making it highly attractive to recycle these magnets. However, those available techniques for recovering sintered magnets cannot be applied to bonded magnets due to different contaminants in two kinds of waste magnets [2]. Therefore, a novel recovering technique is adopted to remove the epoxy resin in waste bonded Nd-Fe-B magnets in this paper. II. METHOD Firstly, the waste magnet bulks were demagnetized in the vacuum environment. Then, the demagnetized magnet bulks were swelled in the mixed solvent of acetone, N-butyl alcohol, Dimethyl Formamide in the ratio of 1.43:1:1.47 to obtain MQ magnetic powders. Acetate acetone and mixed solutions of acetone, N-butyl alcohol, Dimethyl Formamide were used to remove oxides impurities and the epoxy resin by water bath heating and stiring, respectively. Finally, recycled magnetic powders were obtained by vacuum drying at 40°C after being washed in acetone. The microstructure and phase of the samples were examined by scanning electron microscopy (SEM) and X-ray diffraction (XRD), respectively. Magnetic properties at room temperature were measured using a physical property measurement system (PPMS) with a magnetic field up to 3T. III. RUSULTS AND DISSUSION After waste bonded magnets are treated by above process, the main phase is still $Nd_2Fe_{14}B$ with no being destroyed. However the content of carbon and oxygen are reduced to 54%,25.7%, respectively, because the large amount of epoxy resin are removed. It can be seen from Fig.1.(a) that a large amount of epoxy resin (white part) are agglomerated on the surface of the waste magnetic powders. Contrarily, the surface of the recovered powders is clear and smooth due to epoxy resin particles disappearing. The magnetic hysteresis loops of three magnetic powders are shown in Fig.2. The recycled magnetic powders possess the best magnetic properties with M_r of 98 emu/g, M_s of 151.5 emu/g, H_{cj} of 7.139 kOe, and $(BH)_{max}$ of 13.741 MGOe, which were greatly improved compared to those of the waste magnetic powders. When compared with the commercial magnetic powder, the M_r, M_s, H_{cj} and $(BH)_{max}$ of recycled magnetic powder reached 102%, 107%, 102%, 105% of commercially powder, respectively, which are satisfied to the standard of commercial application. IV. CONCLUSION A method for recycling the magnetic powder from the waste MQ bonded Nd-Fe-B magnets has been proposed, which does not destroy the magnetic particles itself. The obtained recycled magnet powders have attained the demand of commercial application and can be applied to the preparation of bonded magnets, such as hard disk drive magnet, automotive motor and magnetic sensor products.

[1] E. Anagnostopoulou, B. Grindi, L. M. Lacroix, F. Ott, I. Panagiotopoulos, and G. Viau, "Dense arrMehmet Ali Recainal, Chenna Rao Borra, Hydrometallurgical recycling of NdFeB magnets: Complete leaching, iron removal and electrolysis, 2017, 12(5):574-583. [2] Vemic M, Bordas F, Comte S, Guibaud G, Lens P N L, van Hullebusch E D. Recovery of molybdenum, nickel and cobalt by precipitation from the acidic leachate of a mineral sludge. Environ. Technol., 2016, 37(17): 2231.

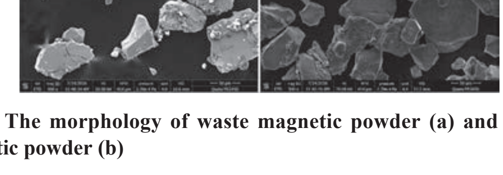

Fig. 1. The morphology of waste magnetic powder (a) and recycled magnetic powder (b)

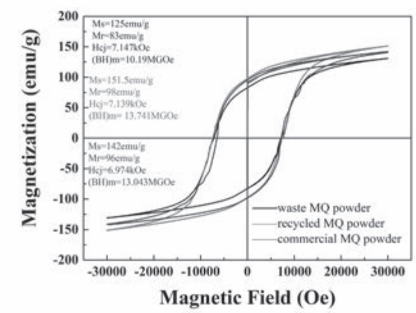

Fig. 2. Comparison of magnetic properties between waste magnetic powder, recycled magnetic powder and commercial powder

Session BV
SPIN-ORBITRONICS II
(Poster Session)

Pan He, Chair
National University of Singapore, Singapore

BV-01. Negative spin Hall magnetoresistance effect in Pt/GdIG.

H. Zhao[1] and D. Wu[1]
1. Physics, Nanjing Unversity, Nanjing, China

We fabricate high-quality ferrimagnetic thin film Gd3Fe5O12 (GdIG) via pulsed laser deposition and study the spin Hall magnetoresistance effect (SMR) in Pt/GdIG. GdIG has a minimal magnetization below Curie temperature, called magnetic compensation temperature (T_{comp}). We study the magnetoresistance of Pt around and far away from T_{comp} of GdIG thin film. In comparison to the positive SMR, a negative SMR is observed around T_{comp}. In this unique temperature range, magnetic moment of Gd approaches to net magnetic moment of two different Fe which are tetrahedrally and octahedrally coordinated with oxygen atom. The antiferromagnetic exchange coupling no longer dominates, leading to canted phase between Gd moments and Fe moments. Therefore, the negative SMR is explained by the changes of magnetic moment obliquity in size around T_{comp} on account of weak antiferromagnetic exchange coupling.

Bernasconi, J. and D. Kuse (1971). “Canted Spin Phase in Gadolinium Iron Garnet.” Physical Review B 3(3): 811-815. Ganzhorn, K., et al. (2016). “Spin Hall magnetoresistance in a canted ferrimagnet.” Physical Review B 94(9): 094401. Geprägs, S., et al. (2016). “Origin of the spin Seebeck effect in compensated ferrimagnets.” Nature Communications 7. Marmion, S. R., et al. (2014). “Temperature dependence of spin Hall magnetoresistance in thin YIG/Pt films.” Physical Review B 89(22): 220404. Meyer, S., et al. (2014). “Temperature dependent spin transport properties of platinum inferred from spin Hall magnetoresistance measurements.” Applied Physics Letters 104(24): 242411. Miao, B. F., et al. (2014). “Physical Origins of the New Magnetoresistance in Pt/YIG.” Physical Review Letters 112(23): 236601.

BV-02. Injection locking of constriction-based spin Hall nano-oscillators.

T. Hache[1,2], T. Weinhold[1,3], S. Arekapudi[2], O. Hellwig[1,2], J. Fassbender[1,3] and H. Schultheiss[1,3]
1. Institute of Ion Beam Physics and Materials Research, Helmholtz-Zentrum Dresden - Rossendorf, Dresden, Germany; 2. Institute of Physics, TU Chemnitz, Chemnitz, Germany; 3. TU Dresden, Dresden, Germany

Spin Hall nano-oscillators show great promise for future communication technologies. Recently, the experimental and theoretical fundamental research yielded different geometries and ways to synchronize them mutually or to an external stimulus for increasing coherency and output power [1,2,3,4]. Here, we report on the injection locking in constriction based spin Hall nano-oscillators measured by μBLS. Auto-oscillations of the magnetization are excited within a 150 nm wide constriction of a 1 micron wide wire consisting of a double layer of Pt(7)/Co40Fe40B20(5). Due to the constriction, the generated pure spin current via the spin Hall effect in the Pt reaches its highest value within a laterally confined area. This pure spin current is injected in the CoFeB layer where the magnetization is aligned under an angle of 170° with respect to the spin current polarization by an external magnetic field of 50 mT. There, the spin current density exceeds the critical value and creates a torque on the magnetization which compensates the intrinsic Gilbert damping stabilizing a certain precession trajectory of the magnetization. As a consequence, for a fixed direct current a certain auto-oscillation amplitude and frequency is achieved. With the injection locking experiment we were able to influence the frequency, line width and amplitude of the auto-oscillations for fixed values of the direct current. We added an alternating current (12 dBm) to the direct charge current leading to a spin current modulation and effective field modulation due to the generated alternating Oersted field. The alternating current was swept from a frequency below the auto-oscillation frequency to a frequency above the autooscillation frequency (Fig 1). Coming closer to the auto-oscillation, a significant frequency pulling of the auto-oscillations towards the external stimulus was observed indicating the interaction. Within the locking range the frequency of the auto-oscillation was synchronized with the external stimulus and the amplitude was strongly amplified. The line width of the auto-oscillations was decreased significantly below the value of the free running state indicating an increase of coherency of the oscillating magnetization volume. The authors acknowledge financial support from the Deutsche Forschungsgemeinschaft within programme SCHU 2922/1-1. K.S.

[1]: V. E. Demidov, S. Urazhdin, A. Zholud, A. V. Sadovnikov, and S. O. Demokritov, Applied Physics Letters 105, 172410 (2014) [2]: V.E. Demidov, H. Ulrichs, S.V. Gurevich, S.O. Demokritov, V.S. Tiberkevich, A.N. Slavin, A. Zholud and S. Urazhdin, Nat. Commun. 5:3179 (2014) [3]: A. A. Awad, P. Dürrenfeld, A. Houshang, M. Dvornik, E. Iacocca, R. K. Dumas and J. Åkerman, Nature Physics 13, 292–299 (2017) [4]: Andrei Slavin and Vasil Tiberkevich, IEEE TRANSACTIONS ON MAGNETICS, VOL. 45, NO. 4, APRIL 2009

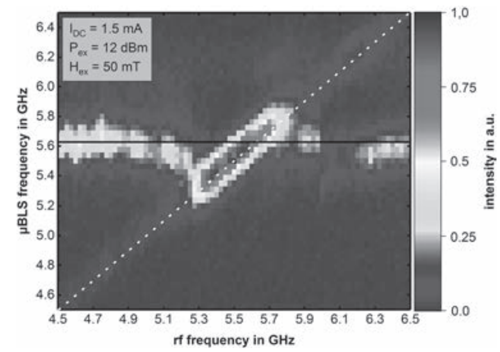

Fig. 1. Plot of the auto-oscillation frequency measured by μBLS. Outside the locking range the auto oscillations have a frequency of about 5.63 GHz (black line). The frequency of the alternating current is swept from 4.5 GHz to 6.5 GHz indicated by the dotted white line and a weak increase of the spin wave intensity. Within the locking range the auto-oscillation intensity is increased strongly and controlled by the external stimulus indicated by a shift of the auto-oscillation frequency (5.25 GHz to 5.75 GHz).

BV-03. Vectorial Observation of the Spin Seebeck Effect in $NiFe_2O_4$ Thin Films.

Z. Li[1,4], A.V. Singh[1], J. Krieft[2], A. Rastogi[3], T. Mewes[1,4], T. Kuschel[2] and A. Gupta[1]

1. MINT Center, The University of Alabama, Tuscaloosa, AL, United States; 2. Department of Physics, Bielefeld University, Center for Spinelectronic Materials and Devices, Bielefeld, Germany; 3. Materials Science and Technology Division, Oak Ridge National Laboratory, Oak Ridge, TN, United States; 4. Department of Physics & Astronomy, The University of Alabama, Tuscaloosa, AL, United States

I. Introduction The spin Seebeck effect (SSE) can generate spin current by a temperature gradient and first observed by K. Uchida et al. in 2008. The longitudinal spin Seebeck effect (LSSE) refers to the generation of spin current from an out-of-plane temperature gradient. The generated spin voltage can be detected in two perpendicular in-plane film dimensions, which depends on the orientation of spin polarization vector, magnetic anisotropy and magnetic domain state. We show how magnetization reversal process can be understood by analyzing the voltages from LSSE in two perpendicular in-plane directions. This method may present an alternative to vectorial magnetometry using the magneto-optic Kerr effect. II. Experimental Nickel ferrite ($NiFe_2O_4$, NFO) films were prepared on (110) or (100) oriented MGO and CGO substrates ($5 \times 5 \times 0.5$ mm^3) by PLD technique in an oxygen environment with a background pressure of 10 mTorr. The temperature of the substrates was kept constant at 700 °C during the film growth. For LSSE measurements, a 5 nm thick Pt film was deposited *in-situ* on top of the PLD grown NFO films by DC sputtering at 20 W power and 5 mTorr Ar pressure. All films were structurally characterized using a Philips X′Pert diffractometer with a Cu-Kα source and their thicknesses were determined from X-ray reflectivity (XRR) measurements. Magnetization hysteresis loops of the samples were also measured by VSM in a PPMS® DynaCool™ system (Quantum Design). For four-point vectorial LSSE measurements, it is shown in Fig. 1. III. Results & Discussion Magnetization measurements were performed on 450 nm thick NFO film grown on (110)-oriented MGO and CGO substrates to examine the magnetic in-plane anisotropy. As shown in Fig. 2(a), we observe a sharp switching of the magnetization when the external magnetic field is applied along the magnetic easy axis [1 -1 0] direction with a squareness of approximately one. With the external magnetic field applied along the hard axis [0 0 1] direction, we obtain a switching behavior with magnetic hard axis and an anisotropy field of about 2000 Oe, with squareness far lower than one. Similar with magnetization measurements, we measured the V_{LSSE} signal in two perpendicular configurations. In the first configuration (in Fig. 2(b)), we measure the voltage signal along the magnetic hard axis ([0 0 1]). When the magnetic field is applied along the magnetic easy axis ([1 -1 0]), the magnetization of the NFO film also aligns along in the same direction. When the magnetic field direction changes polarity, the magnetization of the film also switches into the same direction. This results in a sharp switching in the V_{LSSE} signal (90° in Fig. 2(b)) and it is comparable to the corresponding magnetization measurement when the magnetic field in the [1 -1 0] direction (Fig. 2(a)). In saturation, the magnetization of the NFO film is aligned along the direction of external magnetic field for all θ angles. The direction of the voltage measurement is sensitive to detect the spin current that is spin polarized along the x-direction. The voltage generation due to the ISHE is caused by the projection of magnetization in the x-direction. Upon lowering the angle between the external magnetic field and the x-direction, the saturation voltage decreases in correspondence with cross product in the ISHE equation. In the second configuration (in Fig. 2(c)), we changed the position of voltage contacts to the magnetic easy axis direction and then measured the V_{LSSE} signal. When the external magnetic field is applied along the magnetic hard axis of NFO thin film, we observe a LSSE voltage curve similar to the magnetization curve along the magnetic hard axis direction ([0 0 1] direction in Fig. 2(a)). The voltage signal saturates at the highest applied external magnetic field. When the external magnetic field is reduced, the voltage signal does not show a sharp switching, but favors the curved shape of the magnetization measurement in the [0 0 1] direction with low remanence, which is very different from that from the first configuration (in Fig. 2(b)). The similar magnetization and LSSE measurements were done in NFO/CGO (110) film. From Fig. 2(d), we can see the magnetizations on two perpendicular directions are almost the same, since less lattice mismatch between the film and the substrate leads to weak magnetic anisotropy according to our analysis of samples' lattice structure data. Moreover, the voltage signals from LSSE measurement are shown in Fig. 2(e) & 2(f), and we can see the similar results from both directions if ignoring some misalignment during measurement. IV. Conclusions Two perpendicular LSSE measurements were carried out simultaneously for the first time. The lattice mismatch between the film and the substrate leads to strain anisotropy in the NFO thin film, which is higher for MGO substrate compared with CGO substrate. Moreover, the voltages obtained from two perpendicular LSSE measurements reveal the complete reversal process of magnetization, which shows potential application for a new alternative vectorial magnetometry for magnetization reversal.

[1] K. Uchida *et al.*, J. Phys.: Condens. Matter. 26, 389601 (2014). [2] T. Kuschel *et al*., J. Phys. D: Appl. Phys. 44, 265003 (2011). [3] K. Uchida *et al*., Appl. Phys. Lett. 97, 172505 (2010).

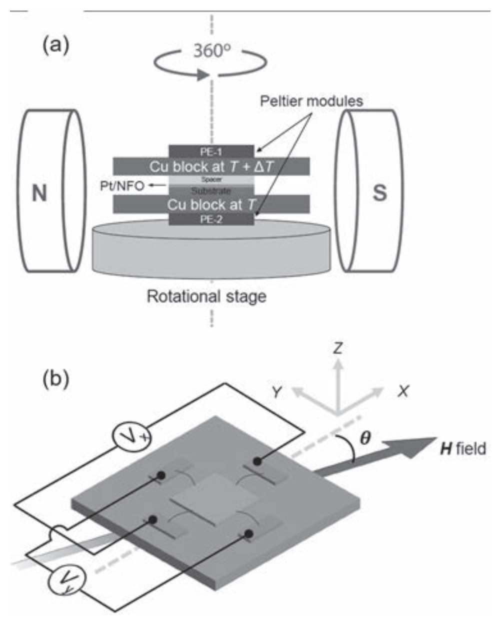

Fig. 1. (Color online) (a) LSSE setup. (b) The geometry for for-point vectorial LSSE measurements.

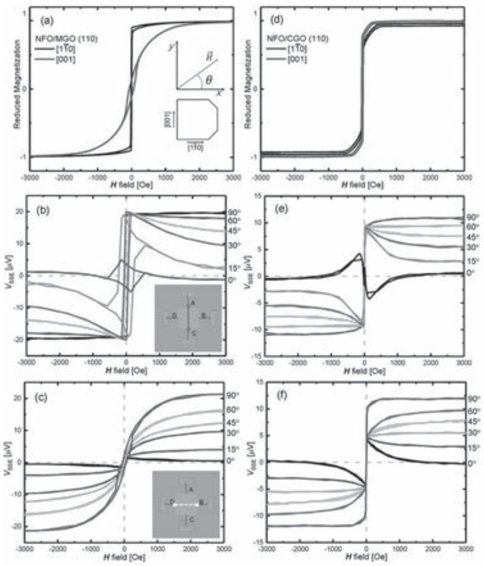

Fig. 2. (Color online) (a) & (d) Normalized in-plane (IP) magnetization versus magnetic field for Pt/NFO/MGO (110) and Pt/NFO/CGO (110), respectively. LSSE measurements at various angles for Pt/NFO/MGO and Pt/NFO/CGO with voltage measured (b) & (e) along the [0 0 1] direction and (c) & (f) along the [1 -1 0] direction, respectively.

BV-04. Amplification of spin waves in ultra-thin Yttrium Iron Garnet microwaveguides by the spin-orbit torque.

M. Evelt[1], V.E. Demidov[1], V. Bessonov[2], S.O. Demokritov[1], J.L. Prieto[3], M. Muñoz[4], J.B. Youssef[9], V. Naletov[5], G. de Loubens[6], O. Klein[7], M. Collet[8], K. Garcia-Hernandez[8], P. Bortolotti[8], V. Cros[8] and A. Anane[8]
1. Institut für Angewandte Physik, Westfälische Wilhelms-Universität Münster, Münster, Germany; 2. M.N. Miheev Institute of Metal Physics of Ural Branch of Russian Academy of Sciences, Yekaterinburg, Russian Federation; 3. Instituto de Sistemas Optoelectronicos y Microtecnologa (UPM), Ciudad Universitaria, Madrid, Spain; 4. IMM-Instituto de Microelectrónica de Madrid (CNM-CSIC), Madrid, Spain; 5. Institute of Physics, Kazan Federal University, Kazan, Russian Federation; 6. Service de Physique de l'État Condensé, Université Paris-Saclay, Gif-sur-Yvette, France; 7. INAC-SPINTEC, CEA/CNRS and Univ. Grenoble Alpes, Grenoble, France; 8. Unité Mixte de Physique CNRS, Univ. Paris-Sud, Université Paris-Saclay, Palaiseau, France; 9. Laboratoire de Magnétisme de Bretagne CNRS, Université de Bretagne Occidentale, Brest, France

Spin-orbit torque (SOT) produced by the Spin Hall effect (SHE) is currently considered as a promising mechanism for the excitation and control of the magnetization dynamics in magnetic nano-systems. The significant advantage of SOT for the emerging field of magnonics utilizing spin waves as a signal carrier in nano-circuits, is the possibility to exert spin-transfer torque over extended areas. In contrast to the spin transfer torque produced by spin-polarized electric currents, the SOT provides an opportunity not only to excite local magnetization oscillations, but also to control the propagation length of spin waves. Another important advantage of SOT is the possibility to implement spin-torque devices based on insulating magnetic materials, such as Yttrium Iron Garnet (YIG). In the past years, the applicability of this material was limited by the large micrometer-range thickness of high-quality YIG films. Only very recently, with the developments in preparation of high-quality nanometer-thick YIG films, the implementation of insulator-based spin-torque devices became practically feasible. We studied the effects of SOT on the propagation of spin waves in 1 micrometer wide waveguides prepared from a 20 nm thick YIG film grown by the pulsed laser deposition. The film was covered by an 8 nm thick layer of Pt deposited using dc magnetron sputtering and the YIG/Pt bylayer was patterned by e-beam lithography. Spin waves in the waveguide were excited by a broadband 3 micrometer wide microwave antenna made of 250 nm thick Au. A dc electrical current I flowing in the plane of the Pt film was converted by the SHE into the transverse spin accumulation. The associated pure spin current was injected into the YIG film resulting in a spin-transfer torque on its magnetization. Depending on the relative orientation of the current and the static magnetic field, the SOT either compensated or enhanced the effective magnetic damping in the YIG film. Propagating spin waves were detected with the submicrometer spatial resolution by using micro-focus Brillouin light scattering (BLS) spectroscopy, which allows the direct characterization of the spatial decay of propagating spin waves. The results of the measurements clearly demonstrated that, in the studied system, the propagation length of spin waves can be efficiently controlled by SOT. In particular, we observed an increase of the propagation length by nearly a factor of 10, when the electric current was applied. This variation corresponds to the SOT-induced increase of the spin-wave intensity at the output of a 10 micrometer long transmission line by three orders of magnitude. Additionally, the high efficiency of our system allowed us to study the regime, where the damping is overcompensated by SOT and the true amplification of spin waves is expected. We show that, in this regime, the spin system of the YIG film is strongly overdriven, which results in the suppression of the spin-wave amplification. Our observations should stimulate both the development of advanced magnonic devices and theoretical work to deepen the understanding of the interaction of spin currents with spin waves.

V. E. Demidov, et al., Appl. Phys. Lett. 104, 152402 (2014). A. Hamadeh, et al., Phys. Rev. Lett. 113, 197203 (2014). M. Collet, et al., Nat. Commun. 7, 10377 (2016). M. Evelt, et al., Appl. Phys. Lett. 108, 172406 (2016). V. E. Demidov et al., Phys. Rep. 673, 1 (2017). M. Collet et al., Appl. Phys. Lett. 110, 092408 (2017).

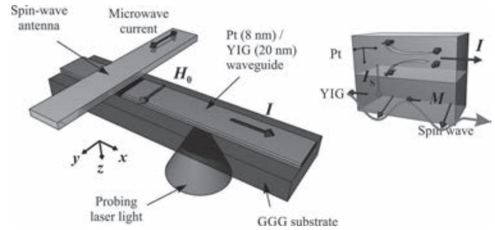

Fig. 1. Schematic of the experiment

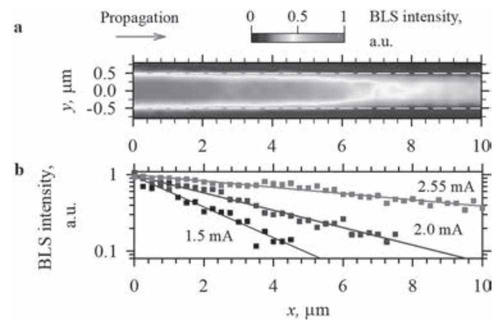

Fig. 2. (a) Measured spatial map of the spin-wave intensity. (b) Decay characteristics of spin waves measured for different currents in the Pt layer.

BV-05. A precise analytical method of harmonic Hall voltage measurement for spin-orbit torque.

S. Yun[1], E. Park[2], K. Lee[1,2] and S. Lim[1]
1. Materials Science and Engineering, Korea University, Seoul, The Republic of Korea; 2. KU-KIST Graduate School of Converging Science and Technology, Korea University, Seoul, The Republic of Korea

In-plane currents in a nonmagnetic/ferromagnetic bilayer nanostructure can generate a torque due to the spin-orbit coupling, known as the spin-orbit torque, which is sufficient enough to reverse the magnetization in the ferromagnetic layer [1]. Numerous studies have been conducted to identify the principal origin of the spin-orbit coupling as being either the spin Hall effect in the nonmagnetic layer [2] or the interfacial spin-orbit coupling—frequently referred to as the Rashba effect—at the nonmagnetic/ferromagnetic interface [3]. The precise analysis of the spin-orbit torque as a function of the magnetization angle can provide important information about the physical origin. Theoretically, the spin-orbit torque induced by the spin Hall effect is known to be independent of the magnetization angle of the ferromagnetic layer, whereas that induced by the interfacial spin-orbit coupling is dependent on the magnetization angle [4, 5]. In this study, an accurate method is developed to extract the spin-orbit effective fields, over a wide range of the polar magnetization angle, through an analysis of the results of harmonic Hall voltage measurements by deriving detailed analytical equations, in which both the *z*-component of the applied magnetic field and the second-order perpendicular magnetic anisotropy are taken into account [6]. The method is tested by analyzing the results of a macrospin simulation. The spin-orbit effective fields extracted from the proposed analytical method are found to be in excellent agreement with the input spin-orbit effective fields used for the macrospin simulation over the entire range of the polar magnetization angle and a wide range (0–2) of the ratio of the planar to the anomalous Hall voltage considered in this study. The accuracy of the proposed method is demonstrated more clearly via a systematic study involving a comparison of its results with those of the conventional analytical method (refer to Fig. 1) [6]. A further test of the proposed method, made by analyzing the experimental results for a stack with Si substrate (wet-oxidized)/Ta (5 nm)/Pt (5 nm)/Co (0.6 nm)/MgO (2 nm)/Ta (2 nm), also demonstrates the accuracy of the new analytical method (refer to Fig. 2) [6]. This research was supported by the Creative Materials Discovery Program through the National Research Foundation of Korea (No. 2015M3D1A1070465). Presenting author: Seok Jin Yun, e-mail: yunsj111@korea.ac.kr

[1] M. Miron, K. Garello, G. Gaudin, P.-J. Zermatten, M. V. Costache, S. Auffret, S. Bandiera, B. Rodmacq, A. Schuhl, and P. Gambadella, *Nature* 476, 189–193 (2011). [2] M. I. Dyakonov and V. I. Perel, *Phys. Lett. A* 35, 459–460 (1971). [3] Y. A. Bychkov and E. I. Rashba, *J. Phys. C* 17, 6039–6045 (1984). [4] K. Garello, I. M. Miron, C. O. Avci, F. Freimuth, Y. Mokrousov, S. Blugel, S. Auffret, O. Boulle, G. Gaudin, and P. Gambardella, *Nat. Nanotechnol.* 8, 587–593 (2013). [5] K.-S. Lee, D. Go, A. Manchon, P. M. Haney, M. D. Stiles, H.-W. Lee, and K.-J. Lee, *Phys. Rev. B* 91, 144401 (2015). [6] S. J. Yun, E.-S. Park, K.-J. Lee, and S. H. Lim, *NPG Asia Mater.* 9, e449 (2017).

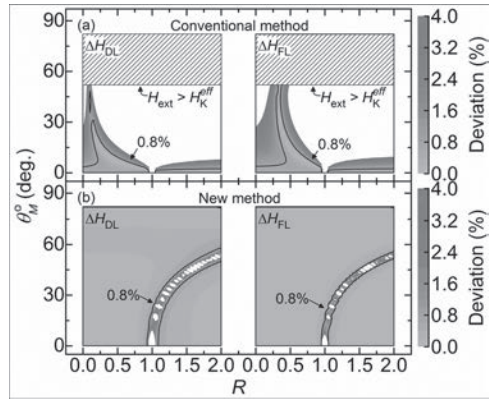

Fig. 1. Contour plots showing deviation (in %) from input values of the damping-like and field-like spin-orbit effective fields [ΔH_{DL} (left panel) and ΔH_{FL} (right panel)] as a function of the polar magnetization angle (θ_M°) and the ratio of the planar to the anomalous Hall voltage (*R*). The results obtained from the conventional analytical method are shown in (a), and those obtained from the new analytical method are shown in (b).

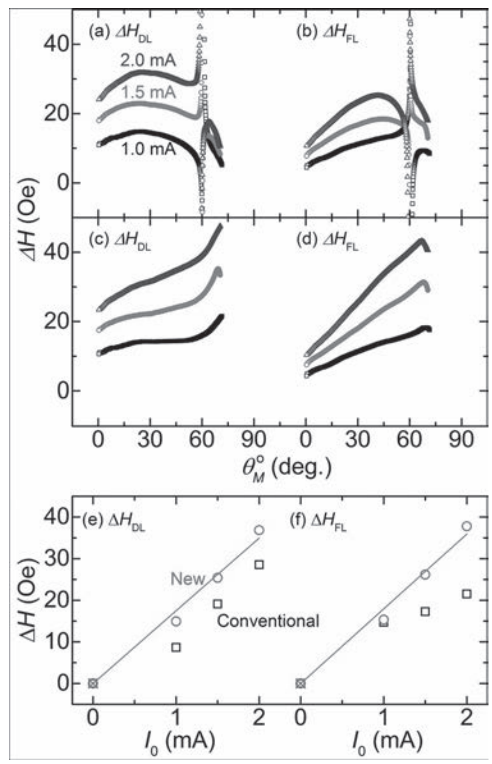

Fig. 2. Results for ΔH_{DL} [(a) and (c)] and ΔH_{FL} [(b) and (d)] as functions of θ_M° at three different in-plane charge current (I_0) of 1.0 mA (black squares), 1.5 mA (red circles), and 2.0 mA (blue triangles), which are calculated using the conventional [(a) and (b)] and new [(c) and (d)] analytical methods. Results for ΔH_{DL} [(e)] and ΔH_{FL} [(f)] obtained at a θ_M° value of 55° as functions of I_0 calculated using the conventional (black squares) and new (red circles) analytical methods. Lines in (e) and (f) are the least squares fit to the new results.

BV-06. Magnon dragged Magnetoresistance and Spin Seebeck Effect in YIG/IRMN bilayer.

Y. Cai[1], W. Li[1], *Y. Wu*[1], K. Meng[1], J. Miao[1], X. Xu[1] and Y. Jiang[1]
1. University of Science and Technology Beijing, Beijing, China

I. INTRODUCTION Much effort has been dedicated to investigate the magnon transport in insulating magnetic films (such as yttrium iron garnet Y3Fe5O12 (YIG)) due to its long diffusion length and decay time. By means of the spin Hall effect (SHE) and the inverse SHE (ISHE) of heavy metal materials(such as platinum (Pt)), the magnon can be generated and detected in insulating magnetic layer/heavy metal layer hybrids. Recently, a magnon dragged magnetoresistance (R_{drag}) are discovered in the nonlocal YIG/Pt layers [1]. Most of the experimental studies of R_{drag} focus on a planar nonlocal YIG/Pt bilayer system with Pt as the injector and detector due to its strong SOC. It has been demonstrated that metallic antiferromagnets (such as IrMn) also exhibit spin Hall properties similar to that of Pt[2]. Thus, metallic antiferromagnets would be good candidates for investigation of magnon transport in insulating magnetic films. Here, we report a systematical study of R_{drag} and spin Seebeck effect (R_{SSE}) induced by DC current in nonlocal YIG/IrMn heterostructures. II. EXPERIMENT YIG (50 nm)/IrMn (5 nm) was grown by pulsed laser deposition and magnetron sputtering. After electron beam lithography and Argon ion etching, different gapped devices with the same injector (w_i = 600 nm, L_i = 150 μm) and detector (w_d = 600 nm, L_d = 120 μm) were prepared. DC current (I) was sent though the injector using a Keithley 6221 sourcemeter and the non-local voltage (V_{ISHE}) was recorded simultaneously by Keithley 2182A nanovoltmeters. By reversing the current, we can obtain $R_{drag} = [V_{ISHE}(+I)- V_{ISHE}(-I)] /2I$ and $R_{SSE} = [V_{ISHE}(+I) + V_{ISHE}(-I)] /2I$. The magnetic field is applied inplane with an angle θ to the current. III. RESULT AND DISCUSSION As shown in Fig. 1(a) and (b), the angular dependence of R_{drag} and R_{SSE} on the magnetic field exhibits $\cos^2\theta$ and $\cos\theta$ relationship since the former includes SHE and ISHE while the latter only involves ISHE in the detector. A clear linear R_{SSE} on current is observed which demonstrates the origin of SSE is the Joule heating effect. R_{drag} is almost the same with the current increasing for the drag effect is caused by spin accumulation at the interface. All the results confirm that IrMn could act as an ideal spin injector and detector. Fig. 2 (a) and (b) present the magnetic field dependence of V_{drag} and V_{SSE} in different gapped devices. All of them shown similar suppression by field. δV_{drag} = V(H=10 kOe)-V(H=0.1 kOe)/ V(H=0.1 kOe) increases from 40% to 70% with the injector-detector separation distance increasing, which is consistent with the diffusion model because the field will decrease the diffusion length of magnons [3]. The diffusion length can be obtained by fitting the signal with $V=V_0\exp(-d/\lambda_m)$ and we extracted λ_m = 1.2 μm at H = 0.1kOe which is within the values reported in YIG/Pt layers. The result is reasonable for our nano-thick YIG because the magnons scattering to the surface maybe enhanced due to the ultra-thin film. The same behavior of V_{SSE} is observed when the field increases from 1 kOe to 10 kOe. While a slight increase of V_{SSE} can be figured out when the magnetic field increases from 0.1 kOe to 1 kOe except for d = 1500 nm. The Joule heating in nonlocal structure is radical and maybe a local temperature appeared in the detector, therefore the thermally excited magnons are more complex than simple diffusive model which need to be explored in the future. Fig. 2 (c) shows the temperature dependences of R_{drag} and R_{SSE}. R_{drag} grows rapidly in nearly a $T^{2.3}$ trend with the temperature increasing from 125 K to 400 K while R_{SSE} saturated from 300 K to 400 K. Though electrically and thermally excited magnons both transport in the YIG channel, their distinct dependences on temperature indicate the spin accumulation for R_{drag} and R_{SSE} is very different. IV. SUMMARY We observed the magnon dragged magnetoresistance and spin Seebeck effect in YIG/IrMn nonlocal structures. According to their different dependences on applied current, R_{drag} and R_{SSE} can be separated as the antisymmetric and symmetric part of nonlocal inverse spin Hall voltages. The magnetic field and temperature dependences of magnon transport are systematically studied and the different temperature dependences demonstrate their distinct origin of spin Hall effect and spin Seebeck effect.

1) L. J. Cornelissen, J. Liu, R. A. Duine, J. Ben Youssef and B. J. van Wees, "Long-distance transport of magnon spin information in a magnetic insulator at room temperature", *Nature Phys.*, vol. 11, no. 12, pp. 1022–1026, (2015). 2) J. B. S. Mendes, R. O. Cunha, O. A. Santos, P. R. T. Ribeiro, F. L. A. Machado, R. L. Rodríguez-Suárez, A. Azevedo, S. M. Rezende, "Large inverse spin Hall effect in the antiferromagnetic metal $Ir_{20}Mn_{80}$", *Phys. Rev. B,* vol. 89, no. 14, pp. 140406(R)/1–140406(R)/5, (2014). 3) L. J. Cornelissen and B. J. van Wees, "Magnetic field dependence of the magnon spin diffusion length in the magnetic insulator yttrium iron garnet", *Phys. Rev. B*, vol. 93, no. 2, pp. 020403(R)/1–020403(R)/5, (2016). 4) L. J. Cornelissen, J. Shan, and B. J. van Wees, "Temperature dependence of the magnon spin diffusion length and magnon spin conductivity in the magnetic insulator yttrium iron garnet", *Phys. Rev. B,* vol. 94, no.18, 180402(R)/1-180402(R)/6, (2016)

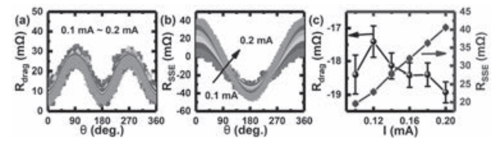

Fig. 1. Angular dependence of (a) R_{drag} (b) R_{SSE} on magnetic field at different current. (c) Current dependence of R_{drag} and R_{SSE}. All data are obtained in the device with d = 600 nm at room temperature.

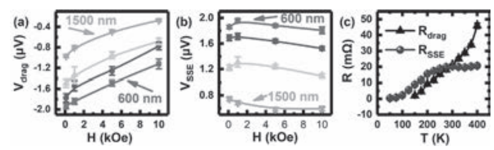

Fig. 2. Magnetic field dependence of (a) V_{drag} (b) V_{SSE} at I = 0.1 mA. (c) Temperature dependence of R_{drag} and R_{SSE} at I = 0.1 mA.

BV-07. Theory of capping layer effect on spin-orbit torque in multilayers.

C. Sun[1], Z. Siu[1], S. Tan[2], H. Yang[1] and M.B. Jalil[1]
1. Department of Electrical and Computer Engineering, National University of Singapore, Singapore; 2. Department of Physics, National Taiwan University, Taipei, Taiwan

Spin-orbit torque (SOT) is conventionally realized by applying an in-plane current passes through the heavy metal (HM)/ ferromagnet (FM) multilayers. In order to enhance the magnitude of SOT, considerable experimental works have been devoted to studying HM material properties and thickness variation of HM and FM layer [1-4]. Recently, it was shown experimentally that the capping layer can strongly influence the SOT [1]. Hence, the objective of our study is to develop a model based on spin-drift-diffusion (SDD) theory to analyze the effect of capping layer on SOT in perpendicularly magnetized HM/FM/Cap systems (Fig. 1) and other experimentally observed trends. Our model shows close correspondence to experimentally observed trends. Here we considered two cases: i) capping layer only acts as a protective layer, e.g. normal metal (NM) with zero spin Hall angle (θ_{Cap}=0); ii) capping layer behaves as another HM or spin polarized current source, i.e., θ_{Cap}<0 (we have assumed HM possesses positive spin Hall angle, i.e., θ_{HM}>0). Firstly, we studied capping layer thickness dependence. For case i) θ_{Cap}=0, we get that SOT decreases with increasing capping layer thickness (t_{Cap}) in Fig. 2(a), which corresponds to the experimental results from [1] in which they use Cu as capping layer. In the same figure, we also plot the case with θ_{Cap}>0 (yellow dotted line) for comparison, the capping layer thickness dependence shows a similar trend to the case when θ_{Cap}=0 (the blue solid line), but with reduced magnitude. However, as can be seen from Fig. 2(b), in the case of ii) capping layer made of W which acts as another HM with opposite spin Hall angle (i.e., θ_{Cap}<0), SOT achieves a maximum value at t_{Cap}~2 nm, at which the general decreasing trend starts to overcome the second spin Hall source from the capping layer. This behavior corresponds closely to that observed from another experimental work [3], in which a torque maxima occurs at t_{Cap}~2 nm, as shown in the inset of Fig. 2(b). Comparing cases i) and ii), besides the presence of a torque maxima, it can also be seen that the magnitude of SOT has been generally enhanced by the presence of spin Hall effect in the capping layer. We also investigated FM layer thickness dependence for the above two cases in Fig. 2(c) and (d), both of them give similar trends: the spin torque decreases with increasing FM layer thickness (t_{FM}) after achieving a peak at t_{FM} that is comparable to transverse spin diffusion length of FM (l_{sf}^T). This trend corresponds to the experimental data [1] as shown in the inset, where MgO or Ru were used as capping layer. Note that the experimental measurements were done for thickness of t_{FM}=0.9 nm or thicker, because a FM layer is needed to realize magnetization switching. As a result, the decreasing trend seen experimentally to some extent corresponds to our simulation results for t_{FM} larger than 1 nm. In addition, by comparing the two curves in Fig. 2(d), it can be seen that a shorter l_{sf}^T (stronger spin relaxation in FM) results in increased magnitude of SOT. In addition to the thickness dependence, we also assessed how other physical properties of capping layer (i.e., spin diffusion length and resistivity) affect SOT, which may lead to further enhancement of SOT.

[1] X. Qiu, W. Legrand, P. He, Y. Wu, J. Yu, R. Ramaswamy, A. Manchon, and H. Yang, Physical review letters 117, 217206 (2016). [2] R. Ramaswamy, X. Qiu, T. Dutta, S. D. Pollard, and H. Yang, Applied Physics Letters 108, 202406 (2016). [3] J. Yu, X. Qiu, W. Legrand, and H. Yang, Applied Physics Letters 109, 042403 (2016). [4] J. Kim, J. Sinha, M. Hayashi, M. Yamanouchi, S. Fukami, T. Suzuki, S. Mitani, and H. Ohno, arXiv preprint arXiv:1207.2521 (2012).

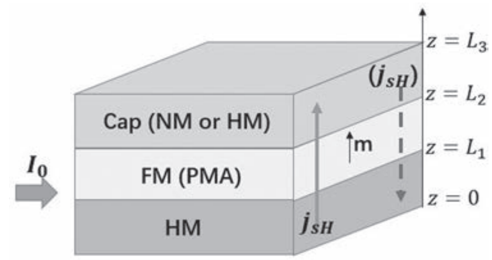

Fig. 1. Schematic diagram of the HM/FM/Cap multilayers discussed in this work. Here FM possesses perpendicular magnetic anisotropy (PMA), thus we assume the local magnetization direction is perpendicular to plane (i.e. along z direction) in FM. The charge current I_0 flows in-plane and introduces spin polarized current due to spin Hall effect (SHE) in HM. Here we will focus on transport perpendicular to plane or along z axis.

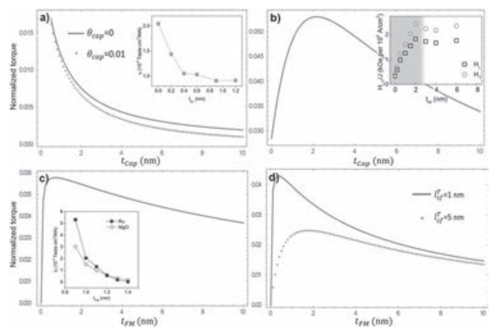

Fig. 2. Layer thickness dependence of SOT. The normalized torque as a function of capping layer thickness t_{Cap} from 0 nm to 10 nm with a) Cu as capping layer (i.e., θ_{Cap}=0), in which we also plot the case for θ_{Cap}>0 for comparison as the yellow dotted line shows; b) W as capping layer (i.e., θ_{Cap}<0). c) and d) plot of normalized torque as a function of FM layer thickness t_{FM} from 0 nm to 10 nm with Cu as capping layer (i.e., θ_{Cap}=0) and W as capping layer (i.e., θ_{Cap}<0), respectively. In (d), we also plot the case for longer l_{sf}^T (i.e., l_{sf}^T=5 nm) for comparison as shown by the yellow dotted line. The insets are experimental results with corresponding capping materials adapted from experimental works [1] and [3], which indicate close correspondence between our simulation results and experiments.

BV-08. Spin accumulation in asymmetric topological insulator thin films in out-of-plane magnetic fields.

Z. Siu[1], D. Chowdhury[2], B. Basu[3] and M.B. Jalil[1]
1. National University of Singapore, Singapore; 2. Ben-Gurion University, Beer Sheva, Israel; 3. Indian Statistical Institute, Kolkata, India

Topological insulator (TI) thin films[1] differ from bulk TI in that the former possess both top and bottom surfaces where the states localized at different surfaces can couple to each other due to the finite thickness. In this work, we calculate the spin accumulation resulting from an in-plane electric field in the *y* direction to a TI thin film system with an adjoining ferromagnetic (FM) layer magnetized in the *x* direction on top, and a magnetic field in the *z* direction (Fig 1). The spin accumulation exerts a torque on the magnetization which may be utilized for magnetization switching. The inter-surface coupling and out-of-plane magnetic fields each has distinct effects on the physics of the system. The inter-surface coupling opens up a band gap in the dispersion relation. The gap size is reduced by the magnetization coupling. The out-of-plane magnetic field, on the other hand, collapses the continuum spectrum of stattes into discrete Landau levels. The asymmetry between the top and bottom surfaces of the TI due to the presence of the FM layer at only the top surface results in two possible effects - (i) the top surface experiences a contact potential with the FM layer absent in the lower surface, and (ii) the top surface is more strongly coupled to the FM magnetization. We model the system and these effects via the Hamiltonian $H = v(\pi_y\sigma_x-\pi_y\sigma_x)\tau_z + \lambda\tau_x + \Delta_z\sigma_z + (M_x + \delta M_x\tau_z)\sigma_x + E_z\tau_z$. Here the τs indicate whether the states are localized nearer the top or bottom surface ($<\tau_z>=\pm1$), the $\lambda\tau_x$ term represents the inter-surface coupling, $\Delta_z\sigma_z$ the combined effects of the Zeeman splitting and out-of-plane magnetization, $\delta M_x\tau_z\sigma_x$ the difference in magnetization between the upper and lower surface, and $E_z\tau_z$ the potential energy difference between the two surfaces. In the absence of asymmetry ($E_z=\delta M_x=0$), the spin y accumulation due to the electric field is equal and opposite between the top and bottom surfaces so the net non-equilibrium spin accumulation summing over both surfaces, $<\delta\sigma_y>$ vanishes. Introducing either a finite value of either E_z or δM_x breaks this antisymmetry and leads to a finite spin y accumulation (Fig 2). The features appearing in the variation of the spin accumulation with energy can be related to the features in the dispersion relation. We argue that this spin accumulation may be explained by Berry curvature effects[2] as illustrated in Fig. 2. The Landau levels in the presence of the field may be thought of as resulting from the collapse of the continuum of states in the absence of the field into discrete levels, so that the spin accumulation of each Landau level is the sum of the contributions of its constituent continuum states. For each of these continuum states, applying an electric field causes a momentum shift, and the spins of the states rotate along with the changing momentum-dependent spin-orbit interaction field. The rotation of the spins can be thought of as being due to an effective magnetic field (inset of panel b) that both provides the torque to rotate the spins as well as confers an out-of-plane spin accumulation. Our results suggest that the amount of spin torque hence exerted can thus be controlled by modulating both or either of the scalar potential difference or magnetization magnitude difference between the top and bottom surfaces of the film. This offers an additional avenue to control the spin torque exerted on the FM magnetization independent of the in-plane current.

1. J. Linder, T. Yokoyama and A. Sudbö, Phys. Rev. B 80, 205401 (2009); C.-X. Liu et al, Phys. Rev. B 81, 041307 (2010); H.-Z. Lu et al, Phys. Rev. B 81, 115407 (2010). 2. H. Kurebayashi et al, Nature Nanotechnology 9, 211 (2014); S.G. Tan et al, Sci. Reps. 5, 18409 (2015).

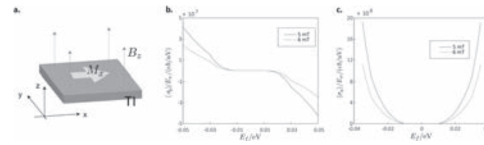

Fig. 1. a. A schematic representation of the TI thin film system with an out-of-plane magnetic field and an adjoining ferromagnetic layer magnetized in an in-plane direction.
The other two panels show the in-plane spin accumulation for the two values of applied magnetic field indicated in the caption as a function of the Fermi energy when b. only the magnetization coupling is asymmetrical without a potential energy difference between the two surfaces and c. only a potential energy difference between the two surfaces is present without the magnetization asymmetry.

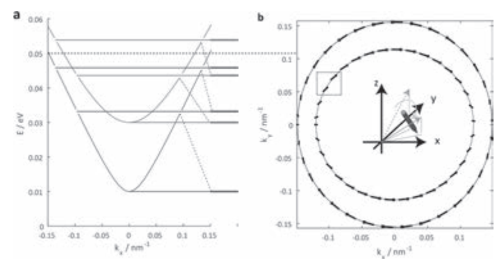

Fig. 2. a. The collapse of the continuum of states in the absence of the magnetic field into discrete Landau levels, and b. the spin polarizations of the states at 0.05 eV without the magnetic field. The inset shows the electric-field induced effective magnetic field which causes the rotation of the spins and confers an out-of-plane spin accumulation.

BV-09. Tuning the spin orbit torque efficiency and Dzyaloshinskii-Moriya interaction by inserting a Pt spacer in Ta/CoFeB/MgO structures.

Y. Chen[1], J. Jia[1], Y. Zheng[1], Y. Wang[1] and *J. Cao*[1]
1. Lanzhou Univercity, Lanzhou, China

In Recent years, the magnetization switching induced by spin-orbit torques (SOT) in ferromagnetic (FM)/Heavy metal (HM) structure has drawn much attention for their potential application in magnetic memory and logic devices. In general, when a current passes through the FM/HM structure, both a damping-like (DL) and a field-like torque can be present. However, theoretical and experimental work have verified that the DL torque, arising from the spin-Hall effect (SHE), is most relevant to magnetization switching. The transformation efficiency from charge current to spin current is normally expressed by the spin Hall angleθ_{SH}=j_s/j_e. Different values of θ_{SH} were reported for various HM films β-Ta (0.12), Pt (0.07), and β-W(0.4). However, in recent works, people found that the FM/HM interface also plays an important role to determine the spin torque efficiency.[1] The interlayers between the HM and FM layers can significantly alter the spin transmission and thereby lead to a change in the observed θ_{SH}. Therefore, from application viewpoint, it is more meaningful to express the transformation efficiency by "SOT efficiency", instead of an intrinsic "spin Hall angle". In addition, Dzyaloshinskii-Moriya Interaction (DMI) at the FM/HM interface is another important factor for SOT-induced switching. DMI is capable of stabilizing Neel-type domain walls, and thereby alter the required in-plane field for a deterministic switching. So a further investigation and control of interfacial DMI still requires for much work. Recently, Pai et al[2] developed an indirect way to estimate SOT efficiency and DMI simultaneously. In this work, we measured the DL torque efficiency and DMI with respect to the thickness of Pt (t_{Pt}) in Ta/Pt/CoFeB/MgO structures by this method. We find that both the DL torque and DMI decreases with t_{Pt} in the range between 0-1nm. It is supposed that opposite sign of spin Hall angle and DMI in Ta and Pt could lead to this behavior. Laterly, SOT-induced switching under different in-plane bias fields were studied. We find that small SOT efficiency and DMI may result in larger switching current and small required in-plane field for a deterministic switching. The experiments were carried out in Ta(5)/Pt(t_{Pt})/CoFeB(1)/MgO(1)/Ta(1) structures(thickness in nanometer), where t_{Pt} various from 0 to 4 nm. All the stacks were deposited at room temperature on thermally oxidized Si substrates by using a magnetron sputtering system. These film stacks were subsequently patterned into Hall bar devices. M-H hysteresis loops of stacks were obtained by VSM and it is found that when t_{Pt} is less than 1.0nm, all the stacks exhibit significant PMA. As schematically shown in Fig. 1(a), we measured the R_H *vs* H_z loops in the Hall-bar devices as a function of applied dc current density (J_{dc}) and in-plane bias field (H_x). Representative R_H vs H_z loops with H_x =600 Oe and J_{dc} = ±5.6MA/cm^2 are shown in Fig. 1(b) for Ta(5)/CoFeB(1)/MgO(1)/Ta(1). Current-induced effective field H_z^{eff}, the outcome of DL torque, push the AHE curve to deviate from the original symmetric form and shift it to the left or right according the polarity of J_{dc} and H_x. Since SOT is proportional to the current, larger current indicates more obvious AHE-curve shift, as shown in Fig.1(c). By reversing the polarity of H_x, the slope of H_z^{eff} /J_{dc} is also reversed and H_z^{eff}/J_{dc} is almost zero at H_x=0. This is consistent with the prediction from the SHE +DMI scenario [3]. In Fig. 2(d), we summarized the measured effective field per current density (χ= H_z^{eff}/J_{dc}) as a function of H_x. We find that χ increases quasi-linearly with H_x and saturates at H_x≈±500 Oe, at which the DW moment in the Néel-type walls realign parallel to H_x, and therefore the $|H_z^{eff}|$ attains a maximum. This facilitate us to estimate the intensity of DMI by D = $m_0 H_{DMI} M_S \Delta$, where D is the DW width obtained from Δ=$(A/K_{eff})^{1/2}$. The χ-H_x curves were measured for all the samples with t_{Pt}=0, 0.3, 0.7, 1nm, as shown in Fig.2(a). The maximum spin torque efficiency (χ_m) and H_{DMI} can be subtracted from the saturation value and saturation field in χ-H_x curves, which are plotted in Fig.2(b). We find that both the DL torque and DMI decreases with t_{Pt} in the range between 0-1nm. Becasue Ta and Pt have opposite spin Hall angle, the Pt layer partially cancelled out the spin current produced in the Ta layers and results in a small χ_m. We expect that the DMI should change sign when a thin Pt layer was inserted because DMI is an interface effect. However, this did not happen until t_{Pt}=1nm. Recently, S. Tacchi et al[4] has proved that several monolayers heavy metals near the interface of HM/FM play paramount role in DMI. As we know, Pt with fcc structure is of lattice parameter a=0.39nm; thus, if Pt is thinner than 1nm which is approximately equal to 3 monolayers, the bottom Ta layer will remarkably affect the interfacial DMI and its contribution will weaken with increasing t_{Pt}. In the other hand, while Pt is thicker than 1nm, Pt insertion layer will shield the influence of Ta, dominates the interfacial DMI and enhances D.

[1] S. G. Je, D. H. Kim, S. C. Yoo, B. C. Min, K. J. Lee, & S. B. Choe, Phys. Rev. B *88*(21), 214401. (2013). [2] C.-F. Pai, M. Mann, A. J. Tan, and G. S. D. Beach, Phys.Rev. B 93, 144409 (2016). [3] O. J. Lee, L. Q. Liu, C. F. Pai, Y. Li, H. W. Tseng, P. G. Gowtham, J. P. Park, D. C. Ralph and R. A. Buhrman, Phys.Rev. B 89, 024418 (2014). [4] S.Tacchi, et al. *Phys. Rev. Lett.*118, 147201 (2017).

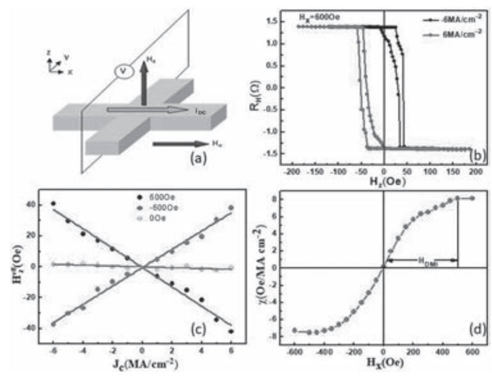

Fig. 1. (a) Schematic of AHE measurements. (b) AHE loops with dc currents density J_{dc}=±6MA/cm^2 and H_x=600 Oe applied. (c) H_z^{eff} as a function of J_{dc} under different H_x. (d) Measured effective χ as a function of H_x.

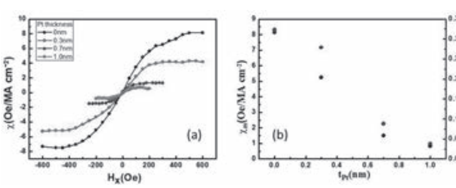

Fig. 2. (a) Comparison of χ as the function of H_x for t_{Pt}=0, 0.3,0.7 and 1.0nm. (b) χ_m and D as a function of t_{Pt}.

BV-10. Spin-Orbit Torque Induced Magnetization Switching In Co/Pt Multilayer-based Synthetic Antiferromagnets.

L. Zhu[1], X. Xu[1], K. Meng[1], Y. Wu[1], J. Miao[1] and Y. Jiang[1]
1. School of Materials Science and Engineering, University of Science and Technology Beijing, Beijing, China

Spin-orbit torques (SOTs) switching have been observed in Co/Pt multilayers with strong perpendicular magnetic anisotropy (PMA).[1] In bilayers system made of heavy-nonmagnetic metals (HMs) and ferromagnets (FMs), SOTs are derived from spin Hall effect (SHE) and interfacial Rashba spin-orbit coupling. However, in multilayers, SOTs arise from the global imbalance of the spin currents from the top and bottom interfaces for each Co layer.[1] Moreover, synthetic antiferromagnets (SyAFs) can be switched by SOTs, and the switching mechanism does not obey the usual SOTs switching rule[2] of the macrospin model[3]. Therefore, it is important to clarify the mechanism of SyAFs based SOTs switching. In this work, we report SOTs switching in Co/Pt multilayer-based SAFs with the stacking structure of Si/SiO_2/Ta (2)/Pt (5)/[Pt (1)/Co (0.4)]$_3$/Ru (0.8)/[Co (0.4)/Pt (1)]$_5$ (thickness in nanometer). The film was deposited by magnetron sputtering and patterned into a Hall bar using electron beam lithography (EBL) and an Ar ion milling technique. Figures 1(a) and (b) present the normalized magnetization curve (M/Ms) and the Hall resistance curve (R_{AHE}) as a function of the out-of-plane magnetic field with a DC current of 1 mA, respectively. It is obvious that both of the M-H and R-H loops indicate an antiferromagnetic (AFM) interlayer coupling as well as a strong PMA in the multilayer structure. The current-induced magnetization switching is presented in Fig. 2. As shown in Fig. 2(a), the saturated R_H increases with increasing the applied maximum channel current under an external field of +300 Oe, which indicates that more domains can be reversed under a large current. Fig 2.(b) presents that the magnetization can be switched and the orientation depends on the direction of the external field. The anomalous switching behavior is also shown in Fig 2.(b). The switching orientation changes with a larger in-plane external field, indicating the anomalous switching mechanism in SyAFs. According to our study, the total thickness of magnetic layer Co is up to 3.2 nm, which is much thicker than previous reports, which is meaningful for real application in spintronics devices.

[1] Huang, K. F., Wang, D. S., Lin, H. H., & Lai, C. H. (2015). Engineering spin-orbit torque in Co/Pt multilayers with perpendicular magnetic anisotropy. Applied Physics Letters, 107(23), 232407. [2] Bi, C., Almasi, H., Price, K., Newhouse-Illige, T., Xu, M., Allen, S. R., ... & Wang, W. (2017). Anomalous spin-orbit torque switching in synthetic antiferromagnets. Physical Review B, 95(10), 104434. [3] Liu, L., Lee, O. J., Gudmundsen, T. J., Ralph, D. C., & Buhrman, R. A. (2012). Current-induced switching of perpendicularly magnetized magnetic layers using spin torque from the spin Hall effect. Physical review letters, 109(9), 096602.

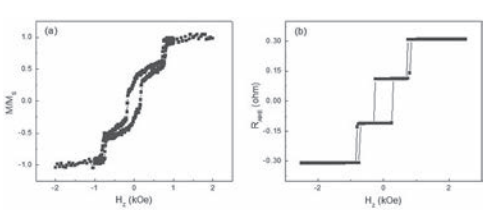

Fig. 1. Magnetization curve (a) and the Hall resistance curve (b) as a function of the out-of-plane magnetic field.

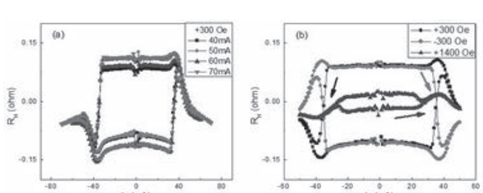

Fig. 2. The current-induced magnetization switching (a) with various maximum channel current and (b) under different in-plane external field.

BV-11. Impact of Hydrogen Gas on the Inverse Spin Hall Effect in Palladium-Cobalt Bi-Layer Films.

S.I. Watt[1], R. Cong[1,2], M. Sushruth[1], C. Lueng[1], P. Metaxas[1] and *M. Kostylev*[1]
1. University of Western Australia, Crawley, WA, Australia; 2. University of Science and Technology of China, Hefei, China

Palladium/cobalt bi-layer films demonstrate a host of important magnetic and spintronic effects, namely strong perpendicular magnetic anisotropy (PMA) induced at the interface [1] and a strong Spin Hall Effect. It has been shown that a strong spin-pumping effect across the interface [2] during driven ferromagnetic resonance (FMR) in the Co layer leads to a strong inverse Spin Hall Effect (iSHE) in the Pd layer [3]. In these conditions, iSHE is seen as a sharp peak in the dependence of a *dc* voltage across the Pd layer on the static magnetic field applied to the sample. Unique for Pd is its strong affinity to hydrogen gas making it useful for gas sensing applications. In particular, sensors exploiting FMR-based probing of the interfacial PMA in Pd/Co bi-layer films have an important advantage: demonstrated capability of hydrogen gas concentration measurements in a very wide concentration range, including near 100% [4]. It has been demonstrated that absorption of hydrogen gas affects the effective field of interface PMA [5, 6, 7], resulting in a downward shift (in field) of the in-plane FMR peak for the Co layer [8]. In the present work we explore the effect of hydrogen gas on the iSHE response of Co/Pd films when their Co layers are driven to FMR. We demonstrate that the iSHE voltage across the Pd layer is altered in the presence of the gas [9]. This demonstrates the potential for FMR-based hydrogen gas sensing using a device-generated *dc* output, as opposed to the microwave voltage generated from the FMR measurements as in previous studies [10], simplifying the design of the magnetic gas sensor. Palladium/Cobalt bilayer films were deposited onto Silicon substrates using DC magnetron sputtering. Each sample consists of a 10 nm Co layer with a capping Pd layer of varying thickness. Leads were attached to opposite edges of each sample using a conductive epoxy. Similar to [3], the samples were mounted in the center of a microwave cavity and subject to an in-plane external magnetic field. The microwave power source was tuned to the cavity resonance and the external field swept to induce FMR in the Co layer. The iSHE-induced voltage across the sample length perpendicular to the in-plane field was measured using a nanovoltmeter. We also measure conventional field-resolved FMR spectra. Each Pd/Co sample is measured first in N_2 gas atmosphere and then exposed to a 3% concentration Hydrogen gas atmosphere (“3% H_2” from here). Upon exposure of the sample to 3% H_2, a distinct shift to lower fields of both iSHE and FMR peaks is evident. The minimum resonance field corresponds to a sample with a 7.5 nm thick Pd cap (Fig. 1(a)). The smallest FMR field corresponds to the largest effective PMA. Interestingly, this sample shows the smallest FMR and iSHE peak shift in the presence of Hydrogen gas (Fig. 1(b)). This may be related to a change in the crystal structure of the Pd layer as a function of thickness, similar to that previously observed for other heavy metals [10]. We find a consistent decrease in the resonance field upon hydrogenation (Fig. 1(b)). The peak shift to lower fields is related to a decrease in the effective field of the interface PMA. The hydrogen gas induced shift of the iSHE peak is the main finding of this work. The fits demonstrate a very good agreement between the FMR and iSHE peak positions for all the samples, consistent with spin pumping effect by the precessing magnetization in the Co layer underlying the iSHE response [3, 12, 13]. We also find that absorption of H_2 induces a decrease in the linewidth (Fig. 2(b)) of both FMR and iSHE peaks. This observation is consistent with our previous studies in which we also saw a decrease in the linewidth of the FMR peak [8, 14]. However we observe a difference in the linewidths measured through the iSHE and FMR channels (Fig. 2(a)). Also, from comparison of Fig. 2(b) and 1(b) one sees that the decrease in the linewidth correlates with the change in the peak position. In our previous work, we consistently observed an increase in the height of the FMR peak upon H_2 gas absorption [4, 8, 14, 15]. The same occurs here however the change in the height of the iSHE peaks is smaller. Fig. 2(c) shows the ratio of resonance peak heights for the FMR and ISHE traces in 3% H_2 and N_2 atmospheres. To understand the difference between the changes to the heights of the iSHE and FMR peaks we attempt to quantify the changes to the iSHE response using a method similar to that employed in [3], where the same cavity FMR approach was used to measure the iSHE response of Pd/Co films. Our analysis suggests that one possible reason for the decrease in the iSHE peak amplitude is a decrease in the Spin Hall Angle in the presence of H_2. However, the absolute value of the decrease in the angle could not be extracted, because the registered change in the iSHE amplitude due to absorption of H_2 is comparable with a numerical error which accumulates during the multi-step calculation of the Spin Hall Angle based on the raw FMR and iSHE data. The finding of this experiment opens up a pathway to design a magnetic-film based hydrogen gas sensor whose output signal will be a *dc* voltage.

[1] H J G Draaisma, W J M de Jonge, F J A den Broeder, “Magnetic interface anisotropy in Pd/Co and Pd/Fe multilayers”, *J. Magn. Magn. Mater.*, vol. 66, pp. 351-355, 1987. [2] J M Shaw, H T Nembach, T J Silva, “ Determination of spin pumping as a source of linewidth in sputtered Co 90 Fe 10 /Pd multilayers by use of broadband ferromagnetic resonance spectroscopy “, *Phys. Rev. B*, vol. 85, 2012. [3] K Ando, E Saitoh, “Inverse spin-Hall effect in palladium at room temperature”, *J. Appl. Phys.*, vol. 108, 2010. [4] C Lueng, P J Metaxas, M Sushruth, M Kostylev, “Adjustable sensitivity for hydrogen gas sensing using perpendicular-to-plane ferromagnetic resonance in Pd/Co bi-layer film”, *Int. J. Hydrogen Energy*, vol. 42, pp. 3407-3414, 2017. [5] D Lederman, Y Wang, E H Morales, R J Matelon, G B Cabrera, U G Volkmann, A L Cabrera, “Magnetooptic properties of Fe/PdFe/Pd and Co/PdCo/Pd bilayers under hydrogen absorption”, *Appl. Phys. Lett.*, vol. 85, pp. 615-617, 2004. [6] K Munbodh, F A Perez, D Lederman, “Changes in magnetic properties of Co/Pd multilayers induced by hydrogen absorption”, *J. Appl. Phys.*, vol. 111, 2012. [7] W.-C Lin, C J Tsai, B-Y Wang, C-H Kao, W-F Pong, “Hydrogenation induced reversible modulation of perpendicular magnetic coercivity in Pd/Co/Pd films”, *Appl. Phys. Lett.*, vol. 102, 2013. [8] C S Chang, M Kostylev, E Ivanov, “Metallic spintronic thin film as a hydrogen sensor”, *Appl. Phys. Lett.*, vol. 102, 2013. [9] S. Watt, R. Cong, C. Lueng, M. Sushruth, P. J. Metaxas and M. Kostylev, “Impact of Hydrogen Gas on the Inverse Spin Hall Effect in Palladium/Cobalt Bilayer Films,” in *IEEE Magnetics Letters*, vol. 9, pp. 1-4, 2018. [10] C Lueng, P J Metaxas, M Kostylev, “Sensitivity enhancement of a Pd/Co bilayer film for hydrogen gas sensing using a perpendicular-to-plane ferromagnetic resonance configuration”, *IEEE Trans. Magn.*, vol. 52, 2016b. [11] J Liu, T Ohkubo, S Mitani, K Hono, M Hayashi, “Correlation between the spin Hall angle and the structural phases of early 5d transition metals”, *Appl. Phys. Lett.*, vol. 107, 2015. [12] W T Soh, B Peng, C K Ong, “An angular analysis to separate spin pumping-induced inverse spin Hall effect from spin rectification in a Py/Pt bilayer”, *J. Phys. D: Appl. Phys.*, vol. 47, 2014. [13] O Mosendz, J E Pearson, F Y Fradin, G E W Bauer, S D Bader, A Hoffmann, “Quantifying spin Hall angles from spin pumping: Experiments and theory”, *Phys. Rev. Lett.*, vol. 104, 2010. [14] C Lueng, P J Metaxas, M Kostylev, “Pd/Co bi-layer films for microwave-frequency hydrogen gas sensing applications”, *Proc. 2014 Conf. Optoelectron. Microelectron. Mater. Devices*, pp. 27-29, 2015. [15] C Lueng, P Lupo, P J Metaxas, M Kostylev, A O Adeyeye, “Nanopatterning-enhanced sensitivity and response time of dynamic palladium/cobalt/palladium hydrogen gas sensors”, *Adv. Mater. Techn.*, vol. 1, 2016a.

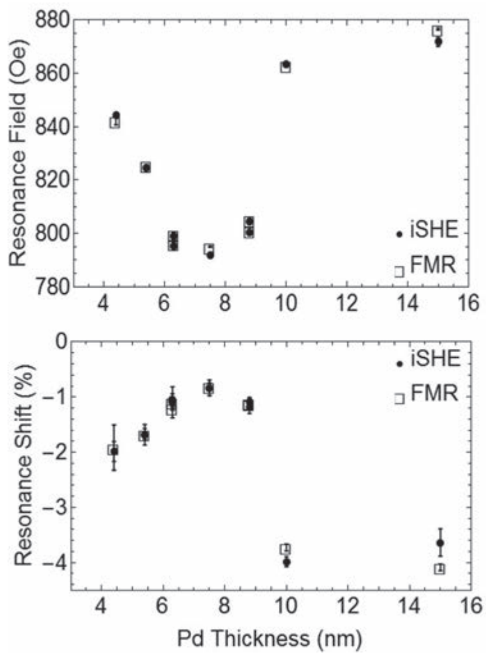

Fig. 1. (a) FMR peak positions for the samples in their virgin state (N_2 atmosphere). (b) Percentage shift in resonance position upon hydrogenation.

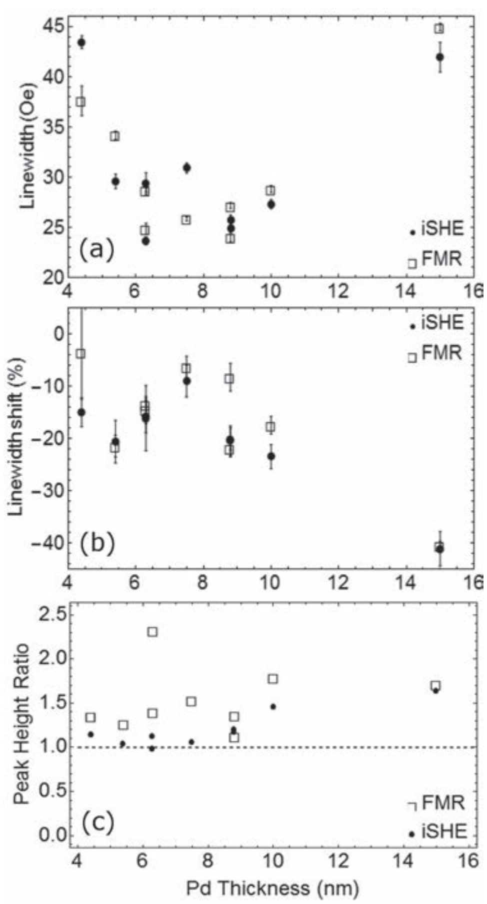

Fig. 2. (a) Resonance linewidth for the samples in their virgin state (N_2 atmosphere). (b) Change in FMR and iSHE linewidths upon hydrogenation. (c) Ratio of peak heights between N_2 and 3% H_2.

BV-12. The effect of inserting a Pt layer in Pt/Co/Ta structure on spin orbit torque.

S. Li[1], G.J. Lim[1] and W. Lew[1]
1. School of Physics and Physical Science, Nanyang Technological University, Singapore, Singapore

Spin-orbit torque (SOT) arising from ferromagnetic heterostructures consisting of an ultra-thin ferromagnet (FM) sandwiched between a heavy metal (HM) and an oxide layer has attracted extensive attention for low power spintronics devices applications.[1-3] The charge current flowing through the HM can influence the magnetization of the adjacent FM layer via the SOT effect that collectively contributed by the effects of spin Hall[4] and Rashba[5]. To quantify the magnitude of the SOT, two effective fields, a damping-like term alone the current direction, and a field-like term transverse to the current direction, are introduced. The Pt/Co/Ta structure has an enhancced SOT generating from both Pt and Ta layers as they have opposite spin Hall angles.[6] In this work, a Pt layer with different thicknesses was inserted between the Co/Pt and its effect on the SOT effective fields was investigated. Our measurements show that the field-like term is negligibly small after inserting the Pt layer because the Rashba effect at the Pt/Co interface counteracts the effect at the Co/Pt interface. However, the damping-like term can be continuously tuned by inserting the Pt layer, including both the sign and magnitude of the SOT effective fields. When the Pt thickness is small, the damping-like term are contributed by both the Pt and Ta layers, however, when the Pt thickness increases, the contribution from the bottom and top Pt layers became significant. The deposited stacks are Pt (3 nm)/Co (0.9 nm) /Pt (t)/Ta (3 nm), where t = 0.9, 2, 2.5, 3, 3.5 and 4 nm. Harmonic Hall voltage measurement technique was used to characterize the SOT effective fields. Figure 1 shows the first and second harmonic Hall voltage signals for t = 0.9 nm sample under longitudinal and transverse magnetic fields, for both up and down magnetized states. The slope of the second harmonic Hall voltage under the transverse magnetic fields is zero, indicating that the field-like SOT is negligibly small, which applied to all measured samples. The damping-like effective fields were plotted as a function of the Pt thickness for up and down magnetized states, as shown in Fig. 2. The result show that the damping-like term can be tuned continuously by the inserted Pt layer. The sign of the damping-like fields is inversed when t < ~2.1 nm and t > ~2.1 nm. The magnitude of the damping-like fields is firstly decreased with the increse of t under 2.1 nm, and becomes greater when the Pt thickness is larger than 2.1nm. The change of the damping-like fields is small at Pt thickness greater than 3 nm.

1. Katine, J. A., Albert, F. J., Buhrman, R. A., Myers, E. B. & Ralph, D. C. Current-driven magnetization reversal and spin-wave excitations in Co /Cu /Co pillars. *Phys. Rev. Lett.* 84, 3149 (2000). 2. Parkin, S. S. P., Hayashi, M. & Thomas, L. Magnetic domain-wall racetrack memory. *Science* 320, 190-194 (2008). 3. Goolaup, S., Ramu, M., Murapaka, C. & Lew, W. S. Transverse domain wall profile for logic applications. *Sci. Rep.* 5, 9603 (2015). 4. Liu, L. Q., Lee, O. J., Gudmundsen, T. J., Ralph, D. C. & Buhrman, R. A. Current-Induced Switching of Perpendicularly Magnetized Magnetic Layers Using Spin Torque from the Spin Hall Effect. *Phys. Rev. Lett.* 109, 096602 (2012). 5. Miron, I. M. *et al.* Perpendicular switching of a single ferromagnetic layer induced by in-plane current injection. *Nature* 476, 189 (2011). 6. Woo, S., Mann, M., Tan, A. J., Caretta, L., Beach & G. S. D. Enhanced spin-orbit torques in Pt/Co/Ta heterostructures. Appl. Phys. Lett. 105, 212404 (2014).

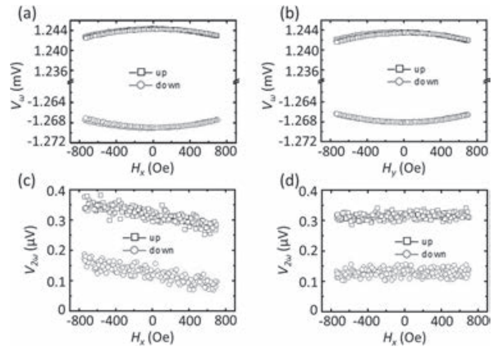

Fig. 1. The first (a) and second (c) harmonic Hall voltage signals under longitudinal magnetic fields for both up and down magnetized states. The first (b) and second (d) harmonic Hall voltage signals under transverse magnetic fields for both up and down magnetized states.

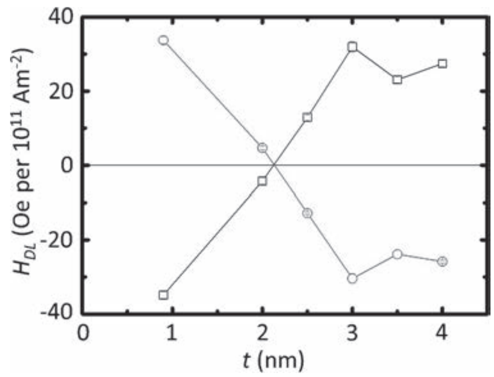

Fig. 2. The damping-like fields as a function of Pt thickness for up and down magnetized states.

BV-13. Spin current pump-probe effect in Yttrium iron garnet plate with different thickness.

Y. Chen[1], J.G. Lin[1] and S. Huang[2]
1. Center for Condensed Matter Sciences, National Taiwan University, Taipei, Taiwan; 2. Department of Physics, National Taiwan University, Taipei, Taiwan

The spin pumping phenomenon attracts intensive interest for the applications of pure spin current devices with high energy-efficiency. With the excitation of ferromagnetic resonance (FMR) in a bi-layer system, spin torque is transferred from a ferromagnetic (FM) layer to a non-magnetic metal (NM) layer, activating the spin current in NM. Spin current reveals itself as an inverse spin Hall Effect (ISHE) induced DC voltage along the transversal direction of magnetic polarization. It has been demonstrated that beside the coherent excitation, individual spin-wave resonance (SWR) mode can also induce a spin pumping effect. [1] Previous studies mostly focused on the semi-2D excitations of SWR, such as in the magnetic insulator $Y_3Fe_5O_{12}$ (YIG) films on $Gd_3Ga_5O_{12}$ substrate. In this work, we report SWR induced spin pumping effect in YIG single crystal plates for the first time. 10 nm of Pt film is deposited on 1.5 x 1.5mm YIG plates with thickness (t) of 80, 220, 270 and 320 μm. 9.8 GHz of microwave is applied with a cavity of TE_{102} mode. Fig. 1(a) shows the microwave absorption intensity vs. in-plane DC field (H) for YIG plate with t = 320 μm. Both backward-volume magnetostatic modes (bulk mode) and Damon–Eshbach modes (surface mode) are observed at H higher and lower than resonance field of uniform mode, respectively. However, the bulk modes have an unusually low intensity at the second peak compared with the first (B1) and third (B2) peak. It is called V1 and doesn't belong to the series of bulk SWR mode along the H direction. Both surface and bulk modes generate the correspondent inverse spin Hall voltage as displayed in Fig. 1 (b). The Power-dependent voltage for each SWR mode is plotted in Fig. 2. The surface mode, S1, shows a linear behavior with power. On the other hand, in bulk mode region, B1 and B2 intend to saturate at high power. The V1 mode induced voltage is linear with power, which may exceed the B1-induced one at the power higher than 15mW. The solid curves in Fig. 2 are the theoretical fits using spin-backflow model. The sample displays a systematic change in the resonance-field/linewidth of both bulk and surface modes with decreasing the thickness, which will be discussed further in the text.

1 Y. Kajiwara et. al, Nature 464, 11, 262 (2010)

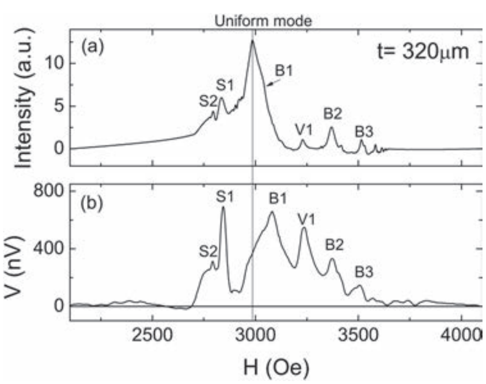

Fig. 1. H-dependent FMR spectrum (a) and inverse spin Hall Voltage (b) for t = 320 μm.

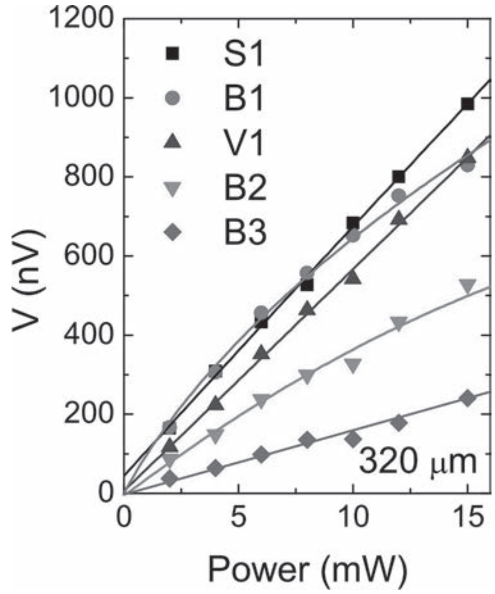

Fig. 2. Power dependent Inverse spin Hall Voltage for each spin-wave mode for t = 320 μm.

BV-14. Anomalous Nernst effect in $Ir_{22}Mn_{78}/Co_{20}Fe_{60}B_{20}$/MgO layers with perpendicular magnetic anisotropy.

S. Tu[1], J. Hu[1], G. Yu[2], H. Yu[1], C. Liu[1], F. Heimbach[1], X. Wang[3], J. Zhang[1], Y. Zhang[1], A. Hamzic[4], K. Wang[2], W. Zhao[1] and J. Ansermet[5]
1. Beihang University, Beijing, China; 2. University of California, Los Angeles, CA, United States; 3. Hong Kong University Science & Technology, Kowloon, Hong Kong; 4. University of Zagreb, Zagreb, Croatia; 5. Ecole Polytechnique Federale de Lausanne, Lausanne, Switzerland

The anomalous Nernst effect in perpendicularly magnetized $Ir_{22}Mn_{78}/Co_{20}Fe_{60}B_{20}$/MgO thin film is measured using well-defined in-plane temperature gradients. The geometry with out-of-plane magnetic field and in plane temperature gradient is the natural configuration to avoid longitudinal spin Seebeck effect and allow a precise determination of the temperature gradient. The anomalous Nernst coefficient reaches 1.8 μV/K at room temperature, which is almost 50 times larger than that of $Ta/Co_{20}Fe_{60}B_{20}$/MgO thin film with perpendicular magnetic anisotropy. The anomalous Nernst and anomalous Hall results in different sample structures reveal that the large Nernst coefficient of $Ir_{22}Mn_{78}/Co_{20}Fe_{60}B_{20}$/MgO thin film is related to the interface between CoFeB and IrMn. Finally, we point out a possible application of ANE that takes advantage of the perpendicular magnetization to obtain large Nernst voltage, owing to the in-plane geometry of the device.

1, G. E. W. Bauer, E. Saitoh, and B. J. van Wees, Nat. Mater. 11, 391–399 (2012). 3, A. von Bieren, F. Brandl, D. Grundler, and J.-P. Ansermet, Appl. Phys. Lett. 102, 052408 (2013). 2, D. Wu, G. Yu, C.-T. Chen, S. A. Razavi, Q. Shao, X. Li, B. Zhao, K. L. Wong, C. He, Z. Zhang, P. K. Amiri, and K. L. Wang, Appl. Phys. Lett. 109, 222401 (2016).

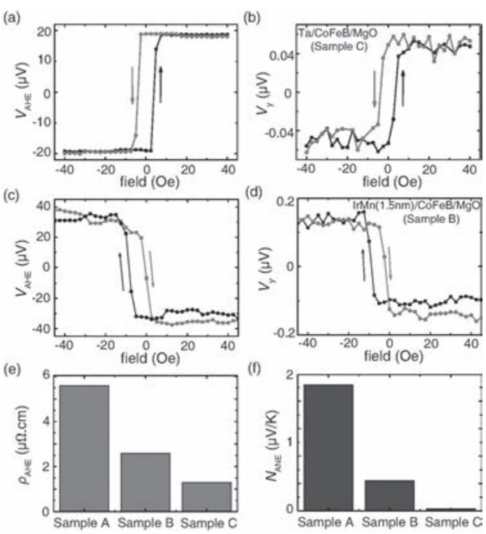

Fig. 1. Magnetic field H_x dependence of the AHE voltage V_{AHE} with -50μA DC in (a) and the Nernst voltage V_y under an applied temperature gradient ∇T_x of -4.7K/cm in (b) for the perpendicularly magnetized Ta/CoFeB/MgO layers. (c) and (d) The AHE voltage V_{AHE} with -50μA DC and the Nernst voltage V_y under an applied temperature gradient ∇T_x of -1K/cm in perpendicularly magnetized Ta/IrMn(1.5nm)/CoFeB/MgO layers, respectively. (e) AHE resistivity and (f) Anomalous Nernst coefficients in different samples. Here, sample A, sample B, and sample C represent $Ta/Ir_{22}Mn_{78}(2.5nm)/Co_{20}Fe_{60}B_{20}$/MgO, $Ta/Ir_{22}Mn_{78}(1.5nm)/Co_{20}Fe_{60}B_{20}$/MgO, and $Ta/Co_{20}Fe_{60}B_{20}$/MgO thin films with all being Ta capped.

BV-15. Spin pumping effect via an evanescent state in ferromagnetic insulator.

K. Hoshi[1] and J. Ohe[1]
1. Physics, Toho University, Narashino-shi, Japan

To generate and control the spin current such as the conduction electrons spin current and the spin- wave spin current is the key task of the spintronics field. Spin pumping effect in the normal metal/ferromagnetic metal junction system is typical mechanism for generating the conduction electrons spin current. The spin pumping effect in variety junction systems such as the antiferromagnetic insulators/normal metal and ferromagnets/topological insulators/ferromagets have been also experimentally reported. The spin pumping current in the normal metal is induced by the precession of the magnetization. The spin pumping current in normal metal is converted into the charge voltage via the inverse spin Hall effect due to spin-orbit interaction. The spin pumping effect was theoretically researched by Mizukami et al. by using the spin diffusion equation. On the other hand, Tserkovnyak et al. has applied the scattering theory including the spin mixing conductance to the spin pumping effect. These theories predicted the spin current polarized in the direction of the spin precession axis and are difficult to investigate the microscopic origin of the spin pumping effect. Recent analytical work has clarified that the mechanism of spin pumping effect is different between the ferromagnetic metal case and the ferromagnetic insulator case. For the ferromagnetic metal case, spin pumping effect was presented by using a quantum mechanical picture and field theoretical derivation. On the other hand, for the insulating case, the proximity effect causing the additional spin accumulation in the normal metal is required to generate the spin current. The conventional approach of the scattering matrix theory also show the absence of the spin pumping effect when the electron state does not exist in the magnetic region such as ferromagnetic insulators. When the electron energy is close to the potential energy of the insulator, however, the electron wave function can penetrate into the region of ferromagnetic metal and feels the s-d coupling via the evanescent mode of the electron conductions. In this report, we investigate numerically the spin pumping effect by using the normal metal/ferromagnetic insulator (NM/FI) junction system with the additional gate voltage. In order to calculate the spin current from the FI with the precessional magnetization to the NM, We employ the quantum pumping current formula based on scattering matrix approach. We calculate the scattering matrix by using the Green's function technique by which the evanescent mode of the electron in the FI is treated precisely. The ferromagnetic system under the static potential due to gate voltage can represents both the metallic system and the insulating system by comparing the Fermi energy of the injected conduction electrons in NM. Numerical results show that the pumping spin current is generated even in the insulating regime. By increasing the static potential, the spin pumping current diminishes as a results of the conventional scattering theory. In order to clarify the mechanism of the spin pumping effect, we develop the numerical technique that can solve both the Landau-Lifshitz- Gilbert equation and the Schrödinger equation simultaneously. We calculate the dynamics of the conduction electrons wave packet that is injected to the ferromagnetic insulator. Although the static magnetization does not induce the spin current, we obtained the pumped spin current when the magnetization processes due to the applied magnetic field. The wave packet dynamics reveals that the spin-dependent scattering via the evanescent mode of the electrons in the ferromagnetic insulator plays an important role for generating the spin current. We also investigate the modulation of the Gilbert damping in the FI due to the spin pumping effect. Proposed effect gives us the possibility of new type of the spintronics devices that can control of the spin current by the additional gate voltage.

S. Mizukami, Y. Ando, and T. Miyazaki, Phys. Rev. B 66, 104413 (2002). Y. Tserkovnyak, A. Brataas, and G. E. Bauer, Phys. Rev. B 66, 224403 (2002). G. Tatara and S. Mizukami, Phys. Rev. B 96, 064423 (2017). Y. Kang et al., Chin. Phys. B 26, 047272 (2017). T. Inoue, G. E. Bauer, and K. Nomura, Phys. Rev. B 94, 205428 (2016). P. W. Brouwer, Phys. Rev. B 58, R10135 (1998).

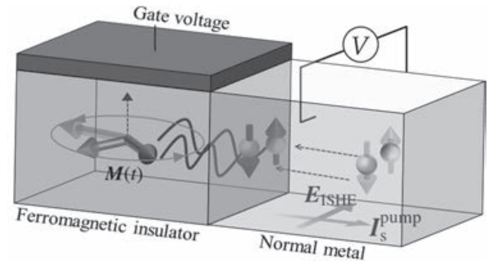

Fig. 1. Schematic view of the spin pumping effect in the NM/FI junction system with additional gate voltage.

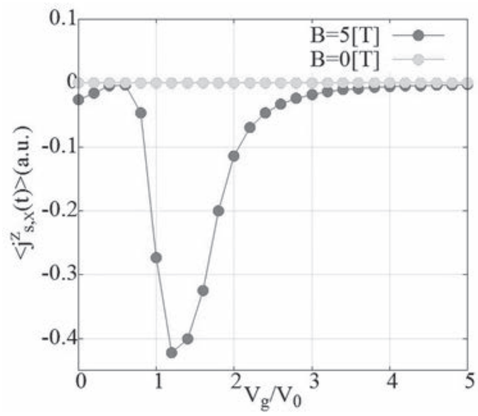

Fig. 2. The expected value of the pumped spin current density in the NM as a function of the static potential due to gate voltage. Red points denotes the case of the precessional magnetization. Green points denotes the case of the static magnetization.

TUESDAY EVENING, 24 APRIL 2018 ORCHID I, 5:30 TO 7:00

Session XA

HOW TO GET A JOB IN INDUSTRY, ACADEMIA OR GOVERNMENT LAB

Albrecht Jander, Co-Chair
Oregon State University, Corvallis, OR, United States
Usha Varshney, Co-Chair
National Science Foundation, Arlington, VA, United States

WEDNESDAY MORNING, 25 APRIL 2018 ORCHID I-II, 9:00 TO 12:00

Session CA
SYMPOSIUM ON SKYRMIONS FOR THE FUTURE

Wei Han, Chair
Peking University, Beijing, China

INVITED PAPERS

9:00

CA-01. Skyrmions in magnetic multilayers at room temperature: electrical creation, detection and manipulation, 3D shaping.

A. Fert[1,2], W. Legrand[1,2], D. Maccariello[1,2], J. Chauleau[3,4], N. Reyren[1,2], S. Collin[1,2], K. Bouzehouane[1,2], K. Garcia[1,2], N. Jaouen[3] and V. Cros[1,2]
1. UMP CNRS-Thales, CNRS, Palaiseau, France; 2. UMP CNRS-Thales, Université Paris-Saclay, Orsay, France; 3. Synchrotron SOLEIL, Gif-sur-Yvette, France; 4. SPEC, CEA, Gif-sur-Yvette, France

Up to the last years, skyrmions were observed only at low temperature but an important effort of research has been recently devoted in several groups to stabilize small (< 100 nm) skyrmions above room temperature (RT) in magnetic multilayers having additive interfacial DMI [1]. The talk will present experimental results at RT on small skyrmions (30-80 nm) in several types of multilayers associating magnetic layers of Co and nonmagnetic layers of heavy metals (Pt, Ir, W, Ta, Ru). First, the talk will be devoted to the electrical creation, detection and manipulation of skyrmions in narrow tracks. We will describe and discuss: i) the creation of skyrmions by current pulses and its mechanism (spin transfer torque vs thermal effects) [2], ii) the detection of skyrmions (one by one) by Anomalous Hall Effect measurements [3], iii) the current-induced motion of skyrmions, the influence of defects on velocity and Skyrmion Hall Angle [2]. Then, we will present results [4] on skyrmions shaped in 3D by a control of the relative values of DMI and dipole interactions for a given number of layers (3D structure experimentally determined by x-ray magnetic scattering, XRMS). We will discuss the impact of a 3D structure on spin torque induced dynamics. A list of pending problems will conclude the talk. Acknowl: EU grant MAGicSky No. FET-Open-665095, SoGraph (ANR-15-GRFL-0005) and ANR grant TOPSky (ANR-17-CE24-0025-01) for financial support.

[1] Review article: A. Fert, N, Reyren and V. Cros, Nature Review Materials 2, 17031 (2017). [2] W. Legrand *et al.*, Nano Letters 17, 2703 (2017) [3] D. Maccariello *et al.*, arXiv:1706.05809 ; accepted for publ. in Nat. Nanotechnol (2018) [4] W. Legrand *et al.*, arXiv: 1712.05978

9:30

CA-02. Atomic-Scale Observation and Manipulation of Individual Nanoscale Skyrmions by Local Spin Currents and Electric Fields.

R. Wiesendanger[1]
1. Dept. of Physics, University of Hamburg, Hamburg, Germany

Nanoscale skyrmions in metallic ultrathin films and multilayers [1,2], stabilized by interfacial Dzyaloshinskii-Moriya (DM) interactions [3], have recently become of significant interest due to their great potential for future magnetic memory and logic devices [4]. Based on the first observation and manipulation of individual skyrmions in Pd-Fe bilayers epitaxially grown on Ir substrates [5-7] by spin-polarized scanning tunneling microscopy (SP-STM) techniques [8], a large number of skyrmion-based device concepts have been proposed which profit from the small size, enhanced stability and easy movement of skyrmions in nanostructured magnetic films and multilayer structures. Atomic-resolution three-dimensional spin maps of nanoscale skyrmion lattices [9-11] as well as individual skyrmions [5-7] by SP-STM were found to be in excellent agreement with early pioneering theoretical predictions of chiral magnetic skyrmions [12,13]. Magnetic-field dependent SP-STM studies of individual magnetic skyrmions allowed for a determination of material-specific parameters such as the exchange stiffness, the magnetic anisotropy, and the DM constant [6]. The properties of magnetic skyrmions can widely be tuned, e.g. by multiple interface engineering, leading to skyrmionic states in metallic multilayer systems being stable up to room temperature [14-16] and in zero magnetic field. In this case, however, magnetic dipolar interactions play an additional important role for the stabilization of magnetic skyrmions. Alternatively, chemical treatments, e.g. by oxidation or hydrogenation of ultrathin magnetic thin films can serve as a simple route towards tailored skyrmionic states. Recent investigations by our group show that hydrogenation can induce skyrmionic phases in ultrathin magnetic films which do not exhibit such phases in the pristine state [17]. Any kind of storage and logic applications of magnetic skyrmions requires the ability to write, manipulate, and to delete individual skyrmions. This can be achieved by various experimental approaches: By locally injecting spin-polarized electrons from an atomically sharp SP-STM tip, writing and deleting of individual skyrmions has been demonstrated, making use of spin-transfer torque exerted by the injected high-energy spin-polarized electrons [5]. Alternatively, individual skyrmions can be created and deleted by local electric fields [18], which can be of great advantage in view of energy-efficient skyrmionic device concepts. The subsequent detection of the written skyrmions can also be achieved by electrical means rather than by using a magnetic sensing element [19,20]. Recently, it has been demonstrated that it is also possible to drive trains of individual room-temperature skyrmions along magnetic nanowire tracks at speeds exceeding 100 m/s using short current pulses [16]. These results highlight the potential of current-driven skyrmions for future racetrack-type memory applications [21]. However, detailed investigations of the role of pinning [22] and edge effects [23] are required in order to achieve a reliable operation of skyrmion-based racetrack memories. An interesting challenge for the future is the observation and manipulation of interface-stabilized nanoscale magnetic skyrmions in oxide-based thin films and heterostructures. In this case, SP-STM cannot be applied to reveal the atomic-scale spin texture of such magnetic skyrmions due to the electrically insulating nature of the materials. However, our group recently demonstrated the successful application of Magnetic Exchange Force Microscopy (MExFM) [24,25] to non-collinear spin textures such as skyrmion lattices [26]. Since this particular atomic-resolution imaging technique is not limited to electrically conducting materials, it can be very useful for the discovery of yet unknown skyrmionic states in novel classes of insulating material systems including multiferroics.

[1] R. Wiesendanger, Nature Reviews Materials 1, 16044 (2016). [2] Focus Issue on Magnetic Skyrmions, eds. A. Fert, N. Nagaosa, M. Thorwart, and R. Wiesendanger, New J. Phys. (2016). [3] A. A. Khajetoorians et al., Nature Commun. 7, 10620 (2016) and refs. therein. [4] A. Fert et al., Nature Nanotechnology 8, 152 (2013). [5] N. Romming et al., Science 341, 6146 (2013). [6] N. Romming et al., Phys. Rev. Lett. 114, 177203 (2015). [7] A. O. Leonov et al., New J. Phys. 18, 065003 (2016). [8] R. Wiesendanger, Rev. Mod. Phys. 81, 1495 (2009). [9] S. Heinze et al., Nature Physics 7, 713 (2011). [10] A. Sonntag et al., Phys. Rev. Lett. 113, 077202 (2014). [11] J. Brede et al., Nature Nanotechnology 9, 1018 (2014). [12] A. N. Bogdanov, M. V. Kudinov, and D. A. Yablonskii, Sov. Phys. Solid State 31, 1707 (1989). [13] A. Bogdanov and A. Hubert, Phys. Stat. Sol. B 186, 527 (1994). [14] G. Chen et al., Appl. Phys. Lett. 106, 242404 (2015). [15] C. Moreau-Luchaire et al., Nature Nanotechnology 11, 444 (2016). [16] S. Woo et al., Nature Materials 15, 501 (2016). [17] P.-J. Hsu et al., (submitted). [18] P.-J. Hsu et al., Nature Nanotechnology 12, 123 (2017). [19] C. Hanneken et al., Nature Nanotechnology 10, 1039 (2015). [20] A. Kubetzka et al., Phys. Rev. B 95, 104433 (2017). [21] S. Krause and R. Wiesendanger, Nature Materials 15, 493 (2016). [22] Ch. Hanneken et al., New J. Phys. 18, 055009 (2016). [23] J. Hagemeister et al., Phys. Rev. Lett. 117, 207202 (2016). [24] U. Kaiser, A. Schwarz, and R. Wiesendanger, Nature 446, 522 (2007). [25] R. Schmidt et al., Nano Lett. 9, 200 (2009). [26] J. Grenz et al., Phys. Rev. Lett. 119, 047205 (2017).

10:00

CA-03. Skyrmion Dynamics – from thermal diffusion to ultra-fast motion.

M. Kläui[1,2]
1. Universität Mainz, Mainz, Germany; 2. Materials Science in Mainz, Johannes Gutenberg University, Mainz, Germany

Spintronics promises to be a paradigm shift from using the charge degree of freedom to using the spin degree of freedom. To this end three key requirements are: (i) stable spin structures for long term data retention; (ii) efficient spin manipulation for low power devices and (iii) ideally no susceptibility to stray fields as realized for antiferromagnets. We explore different materials classes to tackle these challenges and explore the science necessary for a disruptive new technology. To obtain ultimate stability, topological spin structures that emerge due to the Dzyaloshinskii-Moriya interaction (DMI), such as chiral domain walls and skyrmions are used. These possess a high stability and are of key importance for magnetic memories and logic devices [1,2]. We have investigated in detail the dynamics of topological spin structures, such as chiral domain walls that we can move synchronously with field pulses [3]. We determine in tailored multilayers the DMI [4], which leads to perfectly chiral spin structures. For ultimately efficient spin manipulation, spin transfer torques are maximized by using highly spin-polarized ferromagnetic materials that we develop and we characterize the spin transport using THz spectroscopy [2]. Furthermore, we use spin-orbit torques, that can transfer 10x more angular momentum than conventional spin transfer torques [4-6]. We then combine materials with strong spin-orbit torques and strong DMI where novel topologically stabilized skyrmion spin structure emerge [5]. Using spin-orbit torques we demonstrate in optimized low pinning materials for the first time that we can move a train of skyrmions in a "racetrack"-type device [1] reliably [5,6]. We find that skyrmions exhibit a skyrmion Hall effect leading to a component of the displacement perpendicular to the current flow [6]. We study the field - induced dynamics of skyrmions [7] and find that the trajectory of the skyrmion's position is accurately described by our quasi particle equation of motion. From a fit we are able to deduce the inertial mass of the skyrmion and find it to be much larger than inertia found in any other magnetic system, which can be attributed to the non-trivial topology [7]. While thus highly reproducible driven skyrmion motion is possible, we have recently developed new ultra-low pinning multilayer stacks, which exhibit thermally activated dynamics of skyrmions. Here the energy landscape is sufficiently flat so that we observe pure diffusive motion of skyrmion quasiparticles. In contrast to predictions where diffusion was expected to be largely suppressed [8], we find that skyrmions exhibit diffusion at a range of temperatures. Furthermore, in contrast to the analytical calculations, we find a strong temperature and size dependence of the diffusion and we can explain these observations based on thermally activated excitations of the skyrmions. By varying the temperature and drive, we finally probe the transition from thermally activated diffusion to the viscous flow regime for the first time and quantify the skyrmion Hall angle across the full dynamics range.

References: [1] S. S. P. Parkin et al., Science 320, 190 (2008); O. Boulle et al., Mater. Sci. Eng. R 72, 159 (2011). [2] M. Jourdan et al, Nat. Comm. 5, 3974 (2014); Z. Jin et al, Nat. Phys. 11, 761 (2015). [3] J.-S. Kim et al., Nat. Comm. 5, 3429 (2014). [4] R. Lo Conte et al.; Phys. Rev B 91, 014433 (2015); D. Han et al., Nano Lett. 16, 4438 (2016). [5] S. Woo et al., Nat. Mat. 15, 501 (2016); S. Jaiswal et al., Appl. Phys. Lett. 111, 022409 (2017). [6] K. Litzius et al., Nat. Phys. 13, 170 (2017) [7] F. Büttner et al., Nat. Phys. 11, 225 (2015) [8] C. Schütte et al., Phys. Rev. B 90, 174434 (2014); J. Zazvorka, M. Kläui et al., (under review)

10:30

CA-04. Skyrmions in magnetic multilayers.

W. Jiang[1], X. Zhang[2], P. P. Upadhyaya[3], X. Wang[4,5], S. Zhang[4], C. Phatak[4], G. Yu[3], Q. Wang[4], Z. Wei[4], M. Jungfleisch[4], J. Pearson[4], A. Petford-Long[4], X. Cheng[5], O. Heinonen[4], Y. Tserkovnyak[6], K. Wang[3], Y. Zhou[2], S. te Velthuis[4] and A. Hoffmann[4]
1. Department of Physics, Tsinghua University, Beijing, China; 2. School of Science and Engineering, The Chinese University of Hong Kong at Shenzhen, Shenzhen, China; 3. Department of Electrical Engineering, University of California, Los Angeles, CA, United States; 4. Materials Sciences Division, Argonne National Laboratory, Lemont, IL, United States; 5. Department of Physics, Bryn Mawr College, Bryn Mawr, PA, United States; 6. Department of Physics, University of California, Los Angeles, CA, United States

Symmetry breaking together with a strong spin-orbit interaction give rise to many exciting opportunities for the condensed matter physics community. Topologically protected magnetic skyrmions are one of the examples [1-3]. In this talk, I will first present our experimental results in the electric creation and manipulation of magnetic skyrmions at room temperature in a common material system - heterostructures with an interfacial inversion symmetry breaking. This is enabled by the inhomogeneous current induced spin-orbit torques in a Ta/CoFeB/TaO_x trilayer [4-6]. Secondly, I will demonstrate experimentally a real space spin-topology driven dynamics of magnetic skyrmion – the skyrmion Hall effect [7-8]. Namely, an accumulation of skyrmions at the transverse side of the device is experimentally achieved. Thirdly, investigation of sub-50 nanometer skyrmions in a Pt/Co/Ir multilayer [9] in the absence of magnetic field was conducted, through which we further demonstrated a robust skyrmion phase existing for temperature up to 245 °C. Finally, some open questions and future focus points will be addressed.

[1] A. Fert, et al., *Nature Nanotechnology*, 8, 152 (2013). [2] N. Nagaosa, et al., *Nature Nanotechnology* 8, 899-911 (2013). [3] W. Jiang, *et al.*, *Physics Reports*, 704, 1-49 (2017). [4] W. Jiang, *et al.*, *Science* 349, 283 (2015). [5] W. Jiang, *et al.*, *AIP Advances* 6, 055602 (2016). [6] O. Heinonen, *et al.*, *Physical Review B* 93, 094407 (2016). [7] W. Jiang, *et al.*, *Nature Physics*,13, 162 (2017). [8] K. Litzius, *et al.*, *Nature Physics*,13, 170 (2017). [9] C. Moreau-Luchaire, et al., *Nature Nanotechnology* 11, 444-448 (2016).

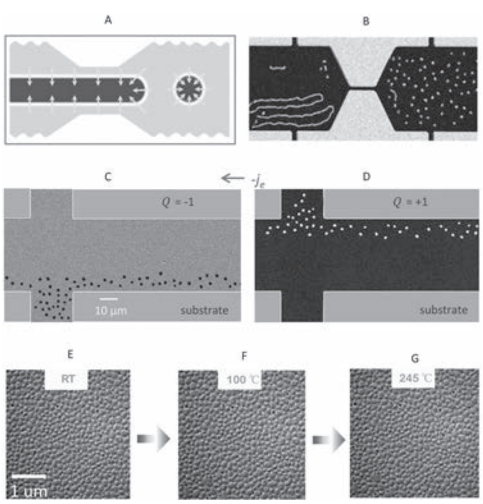

Fig. 1. Figures A-B are the corresponding illustration of generation of skyrmions by inhomogeneous spin-orbit torques. Figures C-D are the experimental demonstration of skyrmion Hall effect. Figures E-G are the Lorentz transmission electron microscope images acquired at different temperatures.

11:00

CA-05. Chiral Bobbers and Skyrmions in Epitaxial B20 Thin Films and Superlattices.

R. Kawakami[1], A.S. Ahmed[1], J. Rowland[1], B.D. Esser[2,4], S.R. Dunsiger[3,5], D.W. McComb[2,4] and M. Randeria[1]
1. Physics, Ohio State University, Columbus, OH, United States;
2. CEMAS, Ohio State University, Columbus, OH, United States;
3. Physics, Simon Fraser University, Burnaby, BC, Canada; 4. Materials Science and Engineering, Ohio State University, Columbus, OH, United States; 5. Center for Emergent Materials, Ohio State University, Columbus, OH, United States

Skyrmions are localized spin textures that exist in magnetic materials where spatial inversion symmetry is broken. In such systems, the Dzyaloshinskii-Moriya interaction (DMI) favoring perpendicular alignment of neighboring spins competes with the ferromagnetic exchange interaction and magnetic anisotropy to form a variety of non-collinear spin textures including skyrmion, helical, and conical phases, whose stability depends on the external magnetic field (H) and temperature (T). The most well-studied materials are the non-centrosymmetric B20 crystals such as MnSi [1,2] and FeGe [3], where the broken bulk inversion symmetry generates a bulk Dresselhaus DMI. While most of the initial work on B20 materials has focused on bulk crystals, the advent of B20 thin films via sputter deposition and molecular beam epitaxy (MBE) has opened up the possibility for new interface-stabilized spin textures due to the presence of interface Rashba DMI and interface magnetic anisotropies. One of the fascinating predictions for thin films of non-centrosymmetric materials is the presence of new spin textures forming at the surfaces and interfaces including the "chiral bobber" [4] and "stacked spiral" [5] phases. In Fig. 1, we illustrate the interfacial chiral bobber crystal (Fig. 1a) and compare with the well-known bulk skyrmion crystal (Fig. 1b). The skyrmion phase consists of a hexagonal array of skyrmion tubes that extend throughout the crystal and are aligned with the external magnetic field. Like skyrmions, chiral bobbers (Fig. 1a) have moments that wind around a centerline. However, unlike skyrmions, chiral bobbers are localized to the surface of a film in a region with thickness $\sim L_D/2$, where L_D is the helical pitch length (~70 nm for FeGe). Here, we report experimental and theoretical evidence for a stable chiral bobber region through magnetization measurements on a series of epitaxial FeGe thin films grown by MBE [6]. We first establish the presence of skyrmions in our FeGe/Si(111) samples with thickness below $L_D/2$ through Lorentz transmission electron microscopy, and also demonstrate similar topological Hall characteristics as in previous studies on sputter deposited FeGe films. The experimental evidence for chiral bobbers comes through magnetization measurement on FeGe films as a function of film thickness. Specifically, we investigate the magnetic phase diagram through magnetization measurements (M vs. H) and analysis of the susceptibility curves (c vs. H) for different temperatures and film thicknesses (L). Fig. 2a-2c show representative susceptibility curves at 10 K for FeGe thickness of 35 nm, 80 nm and 500 nm. Notably, the susceptibility exhibits a negative slope in the field range between 2.5 kOe and 5.0 kOe (blue shaded regions), and Fig. 2d summarizes the susceptibility curves in this range for FeGe thicknesses from 14 nm to 1000 nm. As shown in Fig. 2e, we find that the experimentally measured susceptibility has a slope ($d\chi/dH$) that is constant for $L < L_D/2$, and scales as $1/L$ for $L > L_D/2$. This implies an interfacial spin texture which penetrates a distance $L_D/2$ into the sample. We then use micromagnetic calculations to identify this spin texture as a skyrmion lattice in the very thin films and a chiral bobber lattice on the surface of a bulk cone phase in the thicker samples. We need to include two new ingredients – interface DMI and magnetic anisotropy – in the simulations to understand the experimental observations. It is known that the bulk Dresselhaus DMI of B20 materials leads only to metastable [4] chiral bobbers in the thin film geometry. We show that interface Rashba DMI, arising from broken surface inversion symmetry in a thin film, together with the bulk DMI leads to stable interfacial chiral bobbers. Further, an analysis of our experimental saturation fields indicates an effective easy-plane magnetic anisotropy in our films. We show that this too is an important input parameter in the simulations that give us insight into the evolution from skyrmions to chiral bobbers with increasing film thickness. The combination of experimental susceptibility data and micromagnetic simulations provide strong evidence for chiral bobbers at the interfaces of FeGe thin films. Beyond individual FeGe layers, new possibilities are enabled by the synthesis of a new class of artificial skyrmion materials, namely B20 superlattices. We report the successful growth of B20 superlattices comprised of single crystal thin films of FeGe, MnGe, and CrGe on Si(111) substrates [7]. Thin films and superlattices are grown by MBE and are characterized through a combination of reflection high energy electron diffraction, X-ray diffraction, and cross-sectional scanning transmission electron microscopy. X-ray energy dispersive spectroscopy distinguishes layers by elemental mapping and indicates good interface quality with relatively low levels of intermixing in the [CrGe/MnGe/FeGe] superlattice. This demonstration of epitaxial, single-crystalline B20 superlattices is a significant advance toward tunable skyrmion systems.

[1] A. Neubauer, *et al.*, Phys. Rev. Lett. 102, 186602 (2009). [2] M. Janoschek, *et al.*, J. Phys. Conf. Ser. 200, 032026 (2010). [3] X. Z. Yu, *et al.*, Nat. Mater. 10, 106 (2011). [4] F. N. Rybakov, *et al.*, Phys. Rev. Lett. 115, 117201 (2015). [5] F. N. Rybakov, *et al.*, New J. Phys. 18, 45002 (2016). [6] A. S. Ahmed, *et al.,* arXiv:1706.08248 (2017). [7] A. S. Ahmed, *et al.,* J. Cryst. Growth 467, 38 (2017).

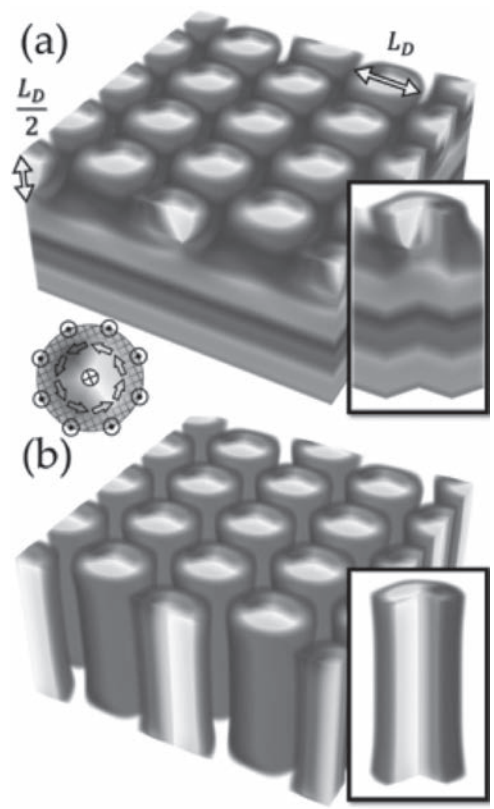

Fig. 1. (a) Chiral bobber crystal confined to the surface where the bulk is the conical phase. (b) Skyrmion crystal consisting of tubes aligned along the external magnetic field.

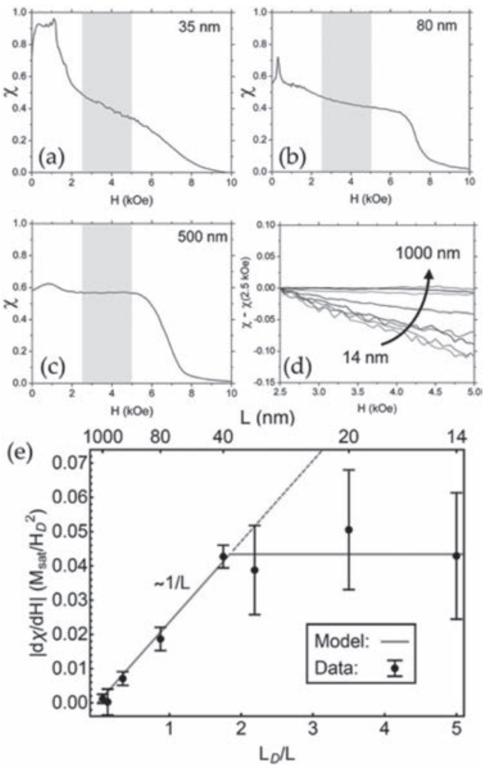

Fig. 2. (a-c) Susceptibility curves at 10 K for 35 nm, 80 nm, and 500 nm thickness of FeGe, respectively. (d) Susceptibility curves plotted between [2.5 and 5 kOe] for film thickness from 14 nm to 1000 nm. (e) Magnitude of *dχ/dH* plotted versus inverse thickness L_D/L.

11:30

CA-06. Magnetic antiskyrmions above room temperature in tetragonal Heusler materials.

S. Parkin[1]
1. NISE, Max Planck Institute for Microstructure Physics, Halle (Saale), Germany

Over the past few years there have been remarkable discoveries in spin-based phenomena that rely on *spin-orbit coupling* that could spur the development of advanced magnetic memory devices [1-3]. These include the formation of *chiral* spin textures in the form of Néel domain walls and topological spin textures, and skyrmions, that are stabilized by a Dzyaloshinskii-Moriya exchange interaction. The Dzyaloshinskii-Moriya exchange interaction is derived from broken symmetries and spin-orbit interactions at interfaces or within the bulk of materials. Recently we have discovered magnetic *antiskyrmions* in a tetragonal Heusler compound, $Mn_{1.4}Pt_{0.9}Pd_{0.1}Sn$ using Lorentz transmission electron microscopy [4]. Direct imaging by Lorentz transmission electron microscopy shows field- stabilized antiskyrmion lattices and isolated antiskyrmions from 100 K to well beyond room temperature, and zero-field metastable antiskyrmions at low temperatures. We show that the anti-skyrmions become more stable as the thickness of the slab in which the antiskyrmions are imaged is increased, in contrast to previous work on the thickness dependence of skyrmions. We discuss the origin of this important difference. Finally, we discuss the observation of antiskyrmions in thin films of Mn_2RhSn, another inverse tetragonal Heusler which has D_{2d} symmetry, using variable temperature magnetic force microscopy.

1 Parkin, S. S. P. & Yang, S.-H. Memory on the Racetrack. *Nat. Nano.* 10, 195-198, (2015). 2 Ryu, K.-S., Thomas, L., Yang, S.-H. & Parkin, S. S. P. Chiral spin torque at magnetic domain walls. *Nat. Nano.* 8, 527–533, (2013). 3 Yang, S.-H., Ryu, K.-S. & Parkin, S. S. P. Domain-wall velocities of up to 750 ms-1 driven by exchange-coupling torque in synthetic antiferromagnets. *Nat. Nano.* 10, 221-226, (2015). 4 Nayak, A. K. *et al.* Magnetic antiskyrmions above room temperature in tetragonal Heusler materials. *Nature* 548, 561-566, (2017).

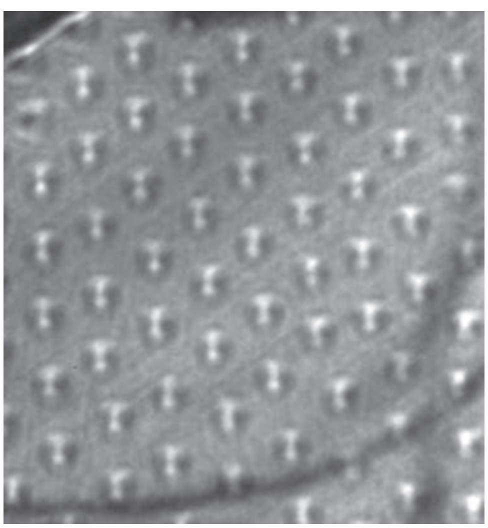

WEDNESDAY MORNING, 25 APRIL 2018 ORCHID III, 9:00 TO 12:00

Session CB
SOFT MAGNETIC MATERIALS III: CRYSTALLINE MATERIALS

Nicoleta Lupu, Chair
National Institute of Research and Development for Technical Physics, Iasi, Romania

INVITED PAPER

9:00

CB-01. Magnetic properties and microstructure of newly developed iron-based soft magnetic powders. ***(Invited)***

N. Imaoka[1], S. Yamamoto[1] and K. Ozaki[1]
1. Magnetic Powder Metallurgy Research Center, National Institute of Advanced Industrial Science and Technology (AIST), Nagoya, Japan

The world market for electric vehicles is expected to reach 15 million by 2020. With the expansion of this market, the sales of soft magnetic materials for drive motor applications will increase to several hundred million dollars [1]. Currently, soft magnetic stators for electric motors in automotive applications are typically assembled by stacking several hundred rolled electrical steel sheets with surface insulating layers (each about 300-μm-thick). The high cost of drive motors arises from the complex process of assembling the stators, and the resolution of this problem is one of the several challenges that need to be addressed for the wide usage of electric vehicles. We have attempted to develop novel high-performance soft magnetic powders using a simple and low-cost fabrication process for solidification of powders without rolling and stacking. In this paper, we report high-magnetization Fe-Mn powders, which can be easily solidified by conventional powder metallurgy processes [1–3]. The Fe-Mn powders doped with 0.1 and 33 atomic-percent manganese (hereafter denoted as Mn0.1 and Mn33, respectively) were fabricated by the reduction of manganese-doped ferrite $(Fe,Mn)_3O_4$ nano-powders with a hydrogen gas at 900–1100 °C. The sample powders were ground using an agate mortar and pestle to an average particle size of about ten to several tens of microns. The starting manganese-doped ferrite nano-powders with a particle size of 5–50 nm were prepared by our aqueous process [2–5]. The magnetization curves of these samples were measured using a vibrating sample magnetometer (VSM) at 300 K, and the magnetic field was applied up to 9 T. The value of saturation magnetization was determined by the law of approach to saturation using the magnetization curve in fields between 2 and 9 T. The saturation magnetization of the Mn0.1 sample was about 2.2 × 100 emu/g, which is comparable to those of pure iron powders. Mn0.1 and Mn33 powders exhibited a coercivity of 0.1–1 Oe, as measured by VSM. These values are much lower than those of iron powders of the same size. Fig. 1 shows the characteristic X-ray map of manganese for about 100-nm-thick cross-section of Mn33 coagulation powders by transmission electron microscopy (TEM) combined with energy-dispersive X-ray spectroscopy (EDS). The Mn33 specimens for TEM were milled using a focused ion beam (FIB) system. The content fluctuation of manganese was observed in the plane of the specimen surface, and the size of the content fluctuation was 20–100 nm. A similar content fluctuation was observed in the Mn0.1 specimen, and the size of the content fluctuation was close to that of the Mn33 sample. Furthermore, the crystallite sizes of these powders were estimated between 30 and 100 nm by X-ray diffraction (XRD), which is consistent with the TEM-EDS results. Fig. 2 shows the relationship between the contents of iron or oxygen and manganese in the pixel regions (20 × 20 nm) of the same Mn33 specimen as Fig. 1, which were measured on a pixel-by-pixel basis by EDS. The results from the EDS measurement of 65,536 pixels revealed that Mn33 powders were a composite of Fe-Mn metal phases and MnO phases in areas of about 20 × 20 nm and thickness of about 100 nm. The coexistence of the MnO oxide phase in the Fe-Mn metal phase of the Mn33 sample was confirmed by XRD. However, the size of the Fe-Mn metal phase is rather large, if the coercivity is assumed to be controlled by the random anisotropy model [6]. The Fe-Mn metal phase in our powders includes only a small amount of manganese [1, 2]; therefore, the magnetic crystalline anisotropy energy of the metal phase is almost the same as that of iron, and much higher than that of the Fe-Si phase reported in Ref. 6. Consequently, the ideal crystal size of the Fe-Mn metal phase should be much smaller than that of the Fe-Si phase (about 10 nm) under the control of a magnetic reversal via the random anisotropy model. We predict a novel mechanism of magnetic reversal functions in our Fe-Mn powders.

[1] N. Imaoka and S. Yamamoto et al., Abstract 120th Annual meeting of Japan Society of Powder and Powder Metallurgy, Kyoto, Japan, 2017, pp. 62–63. [2] N. Imaoka et al., PCT/JP2017/12035. [3] S. Yamamoto et al., JPA2017-222157. [4] N. Imaoka et al., J. Appl. Phys., 103 (7), 07E129 (2008). [5] N. Imaoka et al., AIP Advances, 6, 056022 (2016). [6] G. Herzer, IEEE Trans. Magn., 26(5), 1397 (1990).

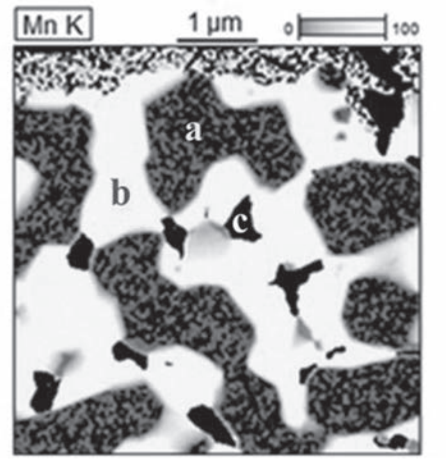

Fig. 1. Characteristic X-ray map of manganese for about 100-nm-thick cross-section of Mn33 coagulation powders using TEM-EDS. a) Fe-Mn metal main phase, b) MnO main phase, c) void.

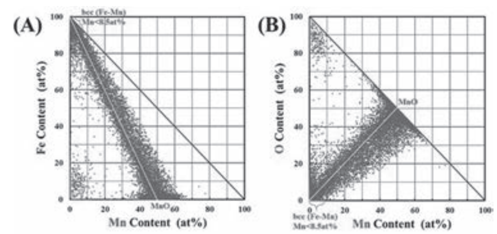

Fig. 2. Relationship between contents of (A) iron and (B) oxygen and manganese content in the pixel regions (20 × 20 nm area; 100-nm thick; 65,536 data points) of the same Mn33 specimen as Fig. 1, which were measured on a pixel-by-pixel basis by EDS.

CONTRIBUTED PAPERS

9:30

CB-02. XAFS studies of the newly developed iron-based soft magnetic powders.

S. Yamamoto[1], N. Imaoka[1] and K. Ozaki[1]
1. National Institute of Advanced Industrial Science and Technology (AIST), Nagoya, Japan

As environment-friendly modes of transportation, vehicles which consume less or no fossil fuels such as electric and hybrid vehicles have been gaining much attention. The global market for such environment-friendly vehicles is expected to reach 15,000,000 by 2020, which is almost ten times as large as that in 2015 [1]. The global market for high performance soft magnetic materials necessary for high efficiency motors is expected to grow up to US $ 6.6 billion by 2020 [1]. Such global trends accelarate development of new soft magnetic materials which realize further higher efficiencies as well as lower cost of production. Currently, relatively large soft magnetic components of car motors such as a stator are fabricated by stacking hundreds of insulation coating-fitted thin magnetic steel sheets. Their typical thicknesses are around a few hundred micrometers and thus complicated and costly processes are necessary for fabrication. Further larger saturation magnetic flux density (B_s) and lower iron losses have been strongly demanded to improve efficiency. In order to fulfil these requirements, we have tried to develop new powdery soft magnetic materials featuring high B_s, low iron losses and easiness to be compacted/sintered by conventional powder metallurgy processes [2-5]. Our newly developed iron-based powders, especially those doped with tiny amount of manganese (*ca.* 0.1 atomic%), are found to have excellent soft magnetic properties, *e.g.*, B_ss of more than 2.1 T and coercivities of less than 10 A/m. Possible origins of such good soft magnetic properties are believed to the fine microstructures induced by the doped manganese, although detailed mechanisms are not clear at present. As part of our efforts to clarify the mechanisms underlying such good soft magnetic properties, we carried out X-ray absorption fine structure (XAFS) measurements on our manganese-doped iron powders. In this presentation, we will show the results from the XAFS measurements with particular emphasis on chemical states of the doped manganese. The manganese-doped iron powders were prepared by reduction of manganese-doped ferrite nanoparticles with H_2 gas at 900-1100 ^{o}C. The starting manganese-doped ferrite nanoparticles were prepared by the coprecipitation method under basic conditions. Details of the preparation methods were reported elsewhere [2]. XAFS measurements at the Fe-K and Mn-K edges were carried out at BL14B2 of SPring-8. Fig.1 shows the X-ray absorption near edge structure (XANES) spectrum of the sample doped with 0.1 atomic% manganese (hereafter denoted as Mn0.1) measured at the Mn K-edge. The XANES spectra of the MnO and α-Mn standards measured at the Mn-K edge are also shown for comparison. The spectrum from the Mn0.1 sample is clearly different from that of the MnO standard, but is similar to that of the α-Mn standard, interestingly. These data strongly indicate that a considerable fraction of the doped manganese in the Mn0.1 sample is in metallic state. It is quite surprising if we remember the preparation method, *i.e.*, reduction of the manganese doped ferrite nanoparticles with H_2 gas. Results from structural analyses using the extended X-ray absorption near edge structure (EXAFS) spectra will also be shown in the presentation.

[1] S. Yamamoto et al., 120th Annual meeting of Japan Society of Powder and Powder Metallurgy (3-17A). [2] N. Imaoka et al., PCT/JP2017/12035. [3] N. Imaoka et al., PCT/JP2017/12032. [4] S. Yamamoto et al., JPA2017-222157. [5] S. Yamamoto et al., JPA2017-222145.

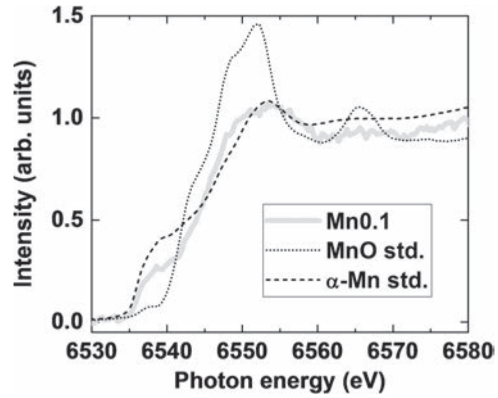

Fig. 1. XANES spectra of Mn0.1, and MnO and α-Mn standards.

9:45

CB-03. Irreversible permeability of Fe and Ni based soft magnetic powder compacts.

P. Kollar[1], Z. Bircakova[1], J. Fuzer[1], D. Oleksakova[2], R. Bures[3] and M. Faberova[3]
1. Department of Condensed Matter Physics, Institute of Physics, Faculty of Science, P. J. Safarik University, Kosice, Slovakia; 2. Department of Sciences and Humanities, Institute of Manufacturing Management, Faculty of Manufacturing Technologies, Technical University of Košice, Presov, Slovakia; 3. Institute of Material Research, Slovak Academy of Science, Kosice, Slovakia

Soft magnetic materials exhibit typical properties as low coercivity, high permeability or low energy losses and comprise various kinds of materials (e.g. electrical steels, soft ferrites, various alloys or powder compacted and composite materials), being used in a wide range of applications. At present the powder compacted materials are still more attracting the research interest and are progressively replacing e.g. electrical steels in many applications [1]. The magnetization reversal is characteristic for each ferromagnetic material. The goal of this work was to propose and verify the relations for irreversible relative permeability at initial magnetization curve for selected soft magnetic powder compacts – the compacted and sintered NiFe powder and the non-sintered warm compacted Fe powder. The relations were derived based on the well-known Steinmetz law [2] for DC energy losses: $W_{DC} = K_{DC} B^x$, where K_{DC} and x are the Steinmetz coefficients and [H, B] denote the magnetic field and induction of the maximum point of minor DC hysteresis loop. The DC losses W_{DC} depend on the amount of structural imperfections in material, surface roughness and stress regions – the possible pinning centres for moving domain walls [1,3,4]. W_{DC} characterize the amount of irreversible magnetization processes within the magnetizing cycle of minor DC hysteresis loop, as they are accompanied by energy dissipation. The quantity irreversible relative permeability μ_{irr} is the difference between the differential one μ_{diff} and the reversible one μ_{rev} [3,4]. Irreversible relative permeability at initial curve μ_{irr}^{IN} reflects the proportion of irreversible processes at particular point of the initial curve. The relations for μ_{irr}^{IN} were expressed on the basis of Steinmetz law. Two types of soft magnetic powder compacted materials have been investigated, prepared in the form of a ring of outer diameter ~ 24 mm, inner diameter ~ 18 mm and height ~ 2.5 mm. The first one was the polycrystalline NiFe (50 wt.% Ni and 50 wt.% Fe) powder obtained by high-energy ball milling of the ribbon (for 6 h, ball to powder ratio 9:1, RPM 200) and annealed at 800°C in air atmosphere for 1 h in order to relieve the stresses induced during milling process. The powder was compacted at uniaxial pressure 800 MPa, followed by a sintering at 400°C for 30 min and at 1180°C for 1 h in electric furnace in air atmosphere. The second sample was the pure polycrystalline Fe ASC 100.29 powder (from producer Höganäs AB Sweden [5]), which was compacted at a temperature 290 °C for 5 min (the compaction pressure was 700 MPa) without follow-up sintering. The samples represent different kinds of powder compacts – differing in the composition, the porosity content (~ 20 % and ~ 10 %, respectively) and the preparation conditions resulting in the qualitatively different contacts between ferromagnetic particles. W_{DC}, μ_{tot} and μ_{diff} values were obtained from the measurements of initial magnetization curves and DC hysteresis loops, by the fluxmeter-based hysteresisgraph, the magnetic induction was measured referred to the ferromagnetic material in sample. μ_{rev} was measured at each point of the initial curve by the developed setup based on the lock-in amplifier, described in [6], according to general definition of μ_{rev} [3,4]. The proposed relations were verified by the comparison of the calculated dependences of μ_{irr}^{IN} vs. H with the experimental ones, where the function F_{Stein} was found for each sample, within the range of validity of Steinmetz law of given material. The form of F_{Stein} revealed its significant dependence on the magnetic interaction between ferromagnetic particles, which is given by the inner demagnetizing fields and characterized by μ_{tot} of material. For the non-sintered warm compacted Fe powder this interaction was slightly worsen compared to the sintered NiFe sample (with μ_{tot} approximately 10-times higher), due to the worse contacted particles. The derived relations enabled to calculate μ_{irr}^{IN} as a function of H or B, fitting the experimental data in the range of validity of Steinmetz law with a good accuracy (relative standard deviation ~ 5 %). In Fig. 1 the comparison of calculated dependence μ_{irr}^{IN} vs. H with the measured one is shown for the non-sintered iron powder. We assume the relations may be helpful to find the irreversible permeability values and the proportions of irreversible magnetization processes within the whole magnetization process in selected powder compacts. Acknowledgement This work was realized within the frame of the project "The progressive technology for the preparation of microcomposite materials for electrotechnics" ITMS 26220220105, supported by Operational Program "Research and Development" financed through European Regional Development Fund; further by Slovak Research and Development Agency under the contract APVV-15-0115 and by Scientific Grant Agency of Ministry of Education of Slovak Republic and Slovak Academy of Science – projects VEGA 1/0330/15 and VEGA 1/0377/16.

[1] K.H.J. Buschow, *Concise encyclopedia of magnetic and superconducting materials*, Elsevier, Oxford, UK, 2005 [2] C.P. Steinmetz: originally published in 1892, *Proc. IEEE* 72, 2, 1984 [3] J.M.D. Coey, *Magnetism and magnetic materials*, Cambridge University Press, 2009 [4] R.M. Bozorth, *Ferromagnetism*, third edition, IEEE Press, Piscataway, New Jersey, 1993 [5] www.hoganas.com [6] Z. Birčáková, P. Kollár, B. Weidenfeller, J. Füzer, M. Fáberová, R. Bureš, *J. Alloys. Comp*. 645, 283-289, 2015

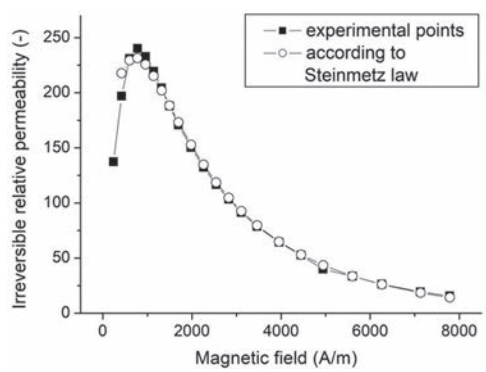

Fig. 1. The dependence μ_{irr}^{IN} vs. H for warm compacted Fe powder – experimental data compared with the calculated ones according to Steinmetz law

10:00

CB-04. Effect of ordering on the antiferromagnetic properties of near-equimolar FeCr-based magnetic alloys.

Z. Leong[1], S. Baco[1] and N. Morley[1]
1. University of Sheffield, Sheffield, United Kingdom

The magnetic properties of multi-components alloys (>4 components, near equimolar) have received modest attention; the strain fields in these alloys may play a role in the partial ordering of these alloys. In the equimolar FeCoCrNi system, the Cr site occupancy is observed to be dependent on the fabrication process [1,2]. Similarly Wei *et al.* reported the cooling-rate dependency of the coercive field of a $Fe_{26.7}Co_{28.5}Ni_{28.5S}Si_{4.6}B_{8.7}P_3$ multi-component alloy [3]. The reported results suggest that Cr additions to an alloy system may be tuned by control of both the amount of addition, and the fabrication method. Magnetostrictive FeCo thin films are used for a variety of applications, such as in artificial multiferroic structures, sensors and actuators. However, one disadvantage is their large coercive field (>10kA/m), which means that 100% switching is not achievable. The effect of Cr addition to FeCo has not been fully explored, and previous results in the literature investigate only small amounts of Cr addition to equiatomic FeCo [4–6]. In this work, we investigate the phase structure and magnetic properties of equimolar $Fe_{0.25}Co_{0.25}Cr_{0.25}Ni_{0.25}$ and near-equimolar $Fe_{0.4}Co_{0.4}Cr_{0.2}$ samples (henceforth designated as FeCoCrNi and $FeCoCr_{0.5}$) synthesised as both bulk and thin film samples, to try and understand the co-dependency of alloying and processing on structure and the coercivity field. Both bulk alloy compositions (equimolar FeCoCrNi and $FeCoCr_{0.5}$) were synthesised into 2.5g ingots *via* arc-melting in a copper hearth, while the thin films were evaporated from the synthesised ingots onto a cleaned Si substrate at a deposition rate of 0.07Å/s. All four samples were characterised using x-ray diffraction (XRD) and magneto-optic Kerr effect (MOKE) magnetometer (*cf.* Figure 1). The FeCoCrNi and $FeCoCr_{0.5}$ compositions possess a rule-of-mixtures Mulliken electronegativity of 4.06 and 4.11 respectively; following previous work, this suggests that their as-cast structures will possess the FCC structure, or a mixed FCC+BCC structure [7]. These predictions deviate from the indexing of the XRD patterns of the bulk specimens (3.56A FCC and 2.53A/4.08A HCP for FeCrCrNi and $FeCoCr_{0.5}$ respectively); the HCP and FCC phases are very close to one another as both are close-packed structures, which may explain the inaccuracies in the prediction [8]. A diffused halo/peak was observed for the $FeCoCr_{0.5}$ thin-film composition, suggesting a disordered structure, while peak broadening was similarly observed for the FeCrCrNi thin film composition, suggesting a semi-ordered structure. The breakdown in structure is expected to reduce spin-orbit coupling effects. Accordingly, a decrease in coercivity is observed for the thin films, as compared to the bulk samples (a decrease from 200 to 37 A/m and 150 to 35 A/m for the $FeCoCr_{0.5}$ and FeCoCrNi compositions, respectively). The structural dependency and stability of HCP and FCC Co is reported be dependent on its magnetic state (whether ferromagnetic, paramagnetic, and non-magnetic) [9], which may be correlated to the observations here, highlighting the possible complexity of structural relationship with processing methods [1]. Further understanding of this relationship will lead to and allow the design of stoichiometric compositions with specific magnetic properties.

[1] C. Niu, A.J. Zaddach, A.A. Oni, X. Sang, J.W. Hurt, J.M. LeBeau, C.C. Koch, D.L. Irving, Spin-driven ordering of Cr in the equiatomic high entropy alloy NiFeCrCo, Appl. Phys. Lett. 106 (2015) 161906. doi:10.1063/1.4918996. [2] B. Niu, F. Zhang, H. Ping, N. Li, J. Zhou, L. Lei, J. Xie, J. Zhang, W. Wang, Z. Fu, Sol-gel Autocombustion Synthesis of Nanocrystalline High-entropy Alloys, Sci. Rep. 7 (2017). doi:10.1038/s41598-017-03644-6. [3] R. Wei, H. Sun, C. Chen, Z. Han, F. Li, Effect of cooling rate on the phase structure and magnetic properties of Fe 26.7 Co 28.5 Ni 28.5 Si 4.6 B 8.7 P 3 high entropy alloy, J. Magn. Magn. Mater. 435 (2017) 184–186. doi:10.1016/j.jmmm.2017.04.017. [4] R.A. Buckley, Microstructure and Kinetics of the Ordering Transformation in Iron–Cobalt Alloys, FeCo, FeCo–0.4%Cr, FeCo–2.5%V, Met. Sci. 9 (1975) 243–247. doi:10.1179/030634575790445080. [5] R.A. Buckley, Ordering and recrystallization in Fe-50Co-0.4%Cr, Met. Sci. 13 (1979) 67–72. doi:10.1179/msc.1979.13.2.67. [6] T. Sourmail, Near equiatomic FeCo alloys: Constitution, mechanical and magnetic properties, Prog. Mater. Sci. 50 (2005) 816–880. doi:10.1016/j.pmatsci.2005.04.001. [7] Z. Leong, Y. Huang, R. Goodall, I. Todd, Electronegativity and enthalpy of mixing biplots for High Entropy Alloy solid solution prediction, Mater. Chem. Phys. (2017). doi:10.1016/j.matchemphys.2017.09.001. [8] A new semi-empirical method based on a distorted tetragonal scheme for the structure prediction and alloy design of multiple-component alloys, University of Sheffield, 2017. http://etheses.whiterose.ac.uk/id/eprint/17022 (accessed February 1, 2018). [9] R. Lizárraga, F. Pan, L. Bergqvist, E. Holmström, Z. Gercsi, L. Vitos, First Principles Theory of the hcp-fcc Phase Transition in Cobalt, Sci. Rep. 7 (2017). doi:10.1038/s41598-017-03877-5.

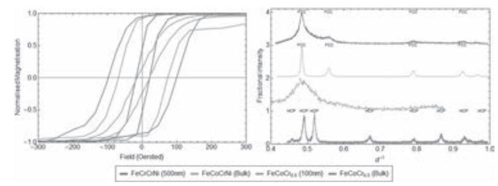

Fig. 1. (Left) MOKE hysteresis loops of the FeCoCrNi and $FeCoCr_{0.5}$ compositions (Right) XRD patterns of the FeCoCrNi and $FeCoCr_{0.5}$ compositions, with identified phases shown.

10:15

CB-05. Anisotropy and demagnetizing effects on the magnetic behavior of polycrystalline gadolinium across the spin-reorientation revealed by a magneto-thermal protocol.

V. Provenzano[2], R. Witte[4], H. ElBidweihy[1], A. Arrott[3], C. Radu[5] and H. Hahn[4]
1. Department of Electrical and Computer Engineering, United States Naval Academy, Annapolis, MD, United States; 2. National Institute of Standards and Technology (NIST), Gaithersburg, MD, United States; 3. Simon Fraser University, Burnaby, BC, Canada; 4. Institute of Nanotechnology, Eggenstein-Leopoldshafen, Germany; 5. Lake Shore Cryotronics Inc., Westerville, OH, United States

Polycrystalline samples of high purity gadolinium (Gd) exhibit memory of fields applied during cooling to low temperatures starting from above the Curie temperature (T_C). Such cooling effects were first seen by Miekeljohn and Bean for cobalt with a surface coating of cobalt oxide and explained by exchange anisotropy arising from the coupling of the ferromagnetic cobalt to the anti-ferromagnetic cobalt oxide [1]. In an ideally soft magnetic material, as there is no anisotropy, the magnetic charge density is all on the surface, from which it creates a shape-dependent demagnetizing field equal and opposite to the applied field. A magnetically soft polycrystalline material with a small anisotropy, like gadolinium, approximates the ideally soft magnetic material when the magnetic charge density near the grain boundaries creates magnetic fields perpendicular to the magnetization equal and opposite to the anisotropy fields perpendicular to the magnetization in each grain [2]. If the magnetization in two adjacent grains do not have the same component perpendicular to the grain boundary, local energy densities of magnetic charge near the grain boundary increase as the square of the difference in the components perpendicular to the interface. The anisotropy energy in each grain is decreased linearly with decrease in angle between the magnetization direction and the preferred anisotropy axis. This rotation is small. Anisotropy-dependent buildup of charges gives rise to magnetic hysteresis, both at constant field with varying temperature and at constant temperature with varying field. Memory effects can be erased at low temperature by application of a field in the opposite direction that is sufficiently larger in magnitude than the cooling field. Like many uniaxial magnetic materials, the first order anisotropy constant K_1 of Gd changes sign at what is known as the spin reorientation temperature, T_{SR}. This temperature dependence of the uniaxial anisotropy, particularly the change in sign in a narrow temperature range, allows insight into the role of anisotropy in polycrystalline materials [3]. The essence of the magneto-thermal protocol adopted here is shown in Figure 1 for an irregularly-shaped sample (roughly a thin rectangular platelet) in the as-received condition from Alfa Aesar (99.9% purity). The measurements are shown for the sample oriented either with its long axis or with its intermediate axis along the field direction. Figure 1(a) curve C1 shows the magnetization (multiplied by -0.1 for graphic comparison) in a negative applied field $\mu_0 H_{FC}$=-50 mT as the sample is cooled from 300 K to 5 K. When the susceptibility is large, the magnetization is given by M = <mv>/V + χ_D H_A, where <mv> is the averaged moment of the trapped magnetization from field cooling, v/V is the volume fraction of trapped magnetization, and $1/\chi_D$, the magnetic stiffness, is the demagnetizing factor. This is the case below 210 K where the first uniaxial anisotropy constant is negative and the magnetization rotates in the easy plane perpendicular to the anisotropy axis. The lower internal susceptibility χ_i between 250 K and 290 K is more easily seen for the field along the Long Axis where χ_D is larger, as $1/\chi = 1/\chi_i + 1/\chi_D$. The trapped magnetization is less for the Intermediate Axis as the internal field is less because of the greater demagnetizing field. The choice of -50 mT for field cooling was based on the smaller demagnetizing factor, for which higher applied fields produces less trapped magnetization, a measure of which is the difference in each of the C1 curves between 210 K and 5 K. The curves W1 are for warming from 5 K to 380 K in a positive applied field of $\mu_0 H_A$=5 mT. This field is small enough not to erase the trapped moment at low temperatures, yet provides the comparison shown in Figure 1(b) in the second cooling C2 and second warming W2 in the same field from 380 K to 5 K and back to 380 K. The measure of the trapped magnetization on warming is the difference between W1 and W2 for the same orientations. This sequence is our standard protocol for revealing the role of grain boundary trapped magnetization. Measuring in the same field as the cooling field is not informative when the demagnetizing factors are large. Yet one can still discern the effect of field cooling for the data along the Long Axis. Note that the magnetization at 210 K is almost fully determined by the demagnetizing field even though there still is trapped moment at that temperature. To isolate the effects of the several temperature regions of different anisotropy, the cooling field $\mu_0 H_{FC}$=-50 mT was applied at a series of lower starting temperatures (270 K, 255 K, 235 K, and 150 K) and the W1, C2, and W2 sequences were measured (Figure 2). It is clear from analyzing this data, that the blocking temperature is close to 270 K. The details of freezing the magnetization at the grain boundaries changes with the temperature range. When in the temperature regions of an easy plane of magnetization, it is more likely the magnetization is frozen in directions other than that of the applied field. If polycrystalline Gd is to be employed in operations below 270 K, it will be important to understand these effects.

[1] W. H. Meiklejohn, C. P. Bean, Phys. Rev. 105, 904 (1957). [2] V. Provenzano, et al., IEEE Trans. Magn. 53, 1000905 (2017). [3] A. S. Arrott, T. L. Templeton, AIP Advances 8, 047301 (2018).

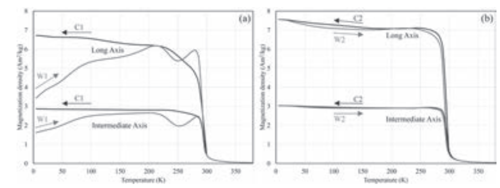

Fig. 1. The temperature dependence of the magnetization density for a polycrystalline gadolinium sample subjected to the magneto-thermal protocol explained in the text.

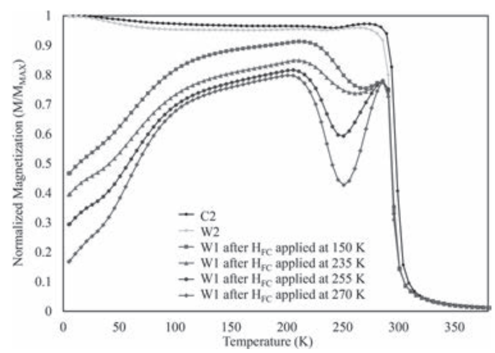

Fig. 2. Normalized magnetization versus temperature showing the effect of applying $\mu_0 H_{FC}$=-50 mT during C1 at series of lower starting temperatures (270 K, 255 K, 235 K, and 150 K).

10:30

CB-06. Design, Fabrication and Performance Evaluation of Magneto-Dielectric Based Electromagnetic Wave Absorbers Optimized Using Biologically Inspired Optimization Strategies.

R. Panwar[1] and D. Singh[2]
1. Electronics & Communication Engineering, IIIT, Jabalpur, India; 2. IIT, Roorkee, India

A lot of efforts have been devoted in the past few decades to realize electromagnetic (EM) wave absorbers for commercial and military applications [1]-[8]. Certain practical applications require a broadband absorber with the constraint of lower coating thickness. But it is a very challenging task to design a lightweight and wideband absorber using the material alone due to certain physical limitations. However, the multilayering based EM technique can be utilized to overcome the limitations of single layer materials [3]-[5]. Therefore, in this work, magneto-dielectric materials based dual and triple layer structures with wide bandwidth and a lower coating thickness have been designed, fabricated and measured for their EM wave absorbing performance. A thickness restriction ($t \leq 2.0$ mm) and wide bandwidth of reflection loss (*RL*)$\leq$ -10 dB are the main design constraints for this study. The optimization of multilayered structures is a very complex problem, due to the involvement of several design parameters, i.e., selection of suitable materials, layer preferences, and their thicknesses etc. However, a good prediction of their effective dielectric and magnetic properties can simplify the task. It is well known that the design of an absorbing material depends upon the selection and proper arrangement of dielectric and magnetic components, which can provide a proper impedance matching. The dielectric and magnetic properties of a material depends on its composition, particle shape & size, etc. [6], [8]. The material selection is a very important aspect in the development of multilayered structures. The materials utilized for this study are ferrite-graphene and Fe_3O_4-Ti based heterogeneous composites developed using bottom up and top-down nanaofabrication approaches. The frequency dependent complex permittivity and permeability values of materials have been measured using a vector network analyzer, N5247A PNA series network analyzer, 10 MHz - 67 GHz. Genetic Algorithm (GA) has been employed for the optimization of dual & triple layer structures. Further, results obtained from GA are validated with the help of Particle Swarm Optimization (PSO) and HFSS based EM simulator. Figure 1 (a) and (b) depicts the frequency dependent reflection loss (RL) characteristics of dual and triple layer EM wave absorbing structures. One can notice a quite good agreement between GA, PSO and HFSS data in terms of peak RL values, -10 dB absorption bandwidth and coating thickness. The dips in RL-frequency spectra's indicates the occurrence of absorption or minimum reflection of the EM wave for the particular thickness and frequency. The occurrence of the dips has been found to be due to a successive odd number multiple of the quarter wavelength thickness of the absorber, which is known as matching thickness and it can be expressed as: $t_m=n\lambda_g/4$ (n = 1,3,5….), where n = 1 corresponds to the first dip at low frequency [7]. In general, matching thickness t_m corresponds to the minimum RL value. The coating thickness greatly affects the EM wave absorption characteristics. Here, the matching thickness for dual and triple layer absorbers has been obtained using GA and PSO. The optimal thickness values for dual and triple layer absorbing structures are 1.4 mm and 1.6 mm, respectively. The next step was the fabrication and performance evaluation of optimum structures with corresponding matching thickness only. A flat rectangular aluminum alloy plate with dimensions of 94.5 mm (length) × 74.2 mm (width) × 2.0 mm (thickness) has been used for the coating purpose. The Al alloy substrate was properly polished with belt followed by different grades of emery papers and cleaned with the help of distilled water and acetone. Subsequently, optimum material (70 wt%) has been uniformly mixed into the epoxy resin (30 wt%) in order to form an EM wave absorbing paint. The prepared paint was coated on a conducting Al alloy sheet to study its absorption property. An indigenously developed single port waveguide measurement setup has been employed for the performance evaluation of fabricated absorbing coatings. Figure 2 (a) and (b) shows an image of measurement setup and corresponding fabricated sample. A triple layer absorber is found to possess a measured RL of -36.61 dB at 11.0 GHz with an effective absorption bandwidth of 3.0 GHz (9.0-12.0 GHz) for 1.6 mm absorber layer coating thickness as shown in Figure 2 (c). There is a slight deviation in RL curve, that may have arose due to fabrication errors. The concept of multi-layering benefits from the change of effective impedance with the distance into the composite, so that the reflections can be minimized. Multilayered structures have varying properties, such that their surface impedance is as close as possible to the incident wave impedance, which results in a change in their intrinsic impedance inside by gradually increasing their conductivity to provide minimum reflections at the boundary of each layer. The EM wave can go deeper into the multilayered structures as compared to single layer absorber and may result in more scattering within the absorber. This phenomenon prolongs the propagation path of EM wave in the structures and more absorption of the wave takes place.

[1] S. Piersanti, F.D. Paulis, A. Orlandi, S. Connor, Q. Liu, B. Archambeault, P. Dixon, M. Khorrami, J. L. Drewniak, Near field shielding performances of EMI noise suppression absorbers, IEEE Transactions on Electromagnetic Compatibility, vol. 59, pp. 654-661, 2017. [2] R. U. Nair, R.M. Jha, Electromagnetic design and performance analysis of airborne radomes: Trends and perspectives, IEEE Antennas & Propagation Mazagine, vol. 56, pp. 276-298, 2014. [3] M. Najim, S. Puthucheri, V. Agarwala, and D. Singh, ANN based two layer absorber design using Fe-Al hybrid nanocomposites for broad bandwidth microwave absorption, IEEE Transactions on Magnetics, vol. 52, pp. 4003208, 2016. [4] R. Panwar, S. Puthucheri, D. Singh, V. Agarwala, Design of a ferrite-graphene based thin broadband radar wave absorber for stealth application, IEEE Transactions on Magnetics, vol. 51, pp. 1-4, 2015. [5] D. Micheli, C. Apollo, R. Pastore, D. Barbera, R.B. Morles, M. Marchetti, G. Gradoni, V.M. Primiani and F. Moglie, Optimization of multilayer shields made of composite nanostructured materials, IEEE Transactions on Electromagnetic Compatibility, vol. 54, pp. 60-69, (2012). [6] F. Qin and C. Brosseau, A review and analysis of microwave absorption in polymers composites filled with carbonaceous particles, Journal of Applied Physics, vol. 111, pp. 061301, (2012). [7] R. Panwar, S. Puthucheri, V. Agarwala, D. Singh, Fractal frequency selective surface embedded thin broadband microwave absorber coatings using heterogeneous composites, IEEE Transactions on Microwave Theory & Techniques, vol. 63, pp. 2438 -2448, 2015. [8] V. Mishra, S. Puthucheri, and D. Singh, Development of analytical approach to fabricate composites for microwave absorption, IEEE Transactions on Magnetics, vol. 53, pp. 2800710, 2017.

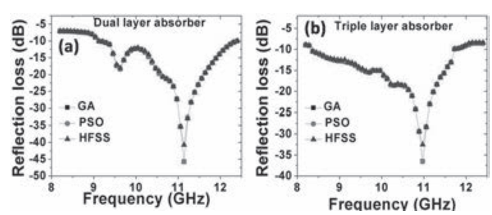

Fig. 1. Frequency dependent RL spectra's of(a) Dual and (b) triple layer absorbers optimized using GA and validated through PSO and HFSS.

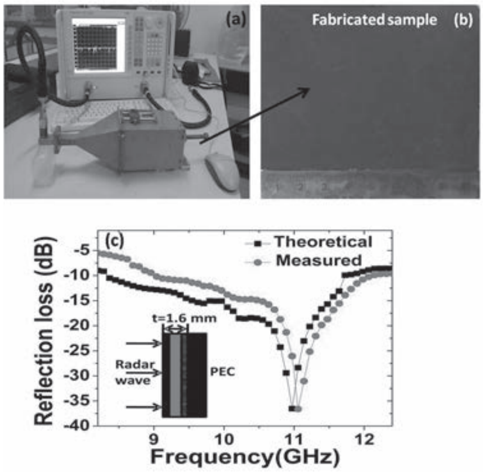

Fig. 2. Measured EM wave absorption characteristics (a) single port microwave measurement setup, (b) fabricated sample and (c) RL-frequency spectra's for 1.6 mm thick multilayered structure.

10:45

CB-07. The influence of cobalt content on structure and magnetic properties of Fe-Si soft magnetic composites.

C. Zhou[1], C. Wu[1] and M. Yan[1]
1. Zhejiang University, Hangzhou, China

Fe-Co-Si soft magnetic composites (SMCs) containing Fe-Co-Si powers were firstly prepared by ball milling, phosphorus acid passivation and compaction. Phase composition with the Co content varied from 0 to 20 at% has been investigated and A2 + $D0_3$ phases have been obtained for the Fe-Co-Si alloy. The influence of Co content on saturation magnetization (M_s) of Fe-Co-Si powers have been investigated and the highest M_s was 175.9 emu/g obtained at 4 at% Co content. The effect of Co content on permeability and core loss of Fe-Co-Si SMCs have also been revealed. The optimal performances with the highest permeability of 110 and lowest core loss of 280.7 mW/cm^3 (50 mT, 100 KHz) were obtained at 12 at% cobalt content. Core loss was separated into eddy current loss (P_e) and hysteresis loss (P_h), indicated that the variation of core loss was determined by P_h. The mechanism of the variation of permeability and P_h was investigated through magnetocrystalline anisotropy constant (K_1) and saturation magnetostriction constant (λ_s). The λ_s.was proved to be the decisive role and it determined the variation of permeability and P_h, which was influenced by the couple effect between A2 and $D0_3$ phase.

11:00

CB-08. The effect of mechanical stress on the static hysteresis loop shape in NO electrical steel.

B. Schauerte[1], S. Steentjes[1], N. Leuning[1] and K. Hameyer[1]
1. Institute of electrical machines (IEM), RWTH Aachen University, Aachen, Germany

Magnetic properties of soft magnetic steel sheets alter significantly mainly due to mechanical stress [1]. This mechanical stress originates either from the different manufacturing processes [2-4] or the operation of electrical machines, e.g., centrifugal force or magnetic forces. Static hysteresis models that are used in the design process to represent the constitutive relation between the magnetic flux density and magnetic field are usually parametrized by means of standardized magnetic measurements on a single-sheet tester or Epstein frame according to the *IEC 60404-2* and *IEC 60404-3* standards. During these measurements either stress-relief annealed samples or samples that are made by a gentle method of cutting, e.g., wire or water jet cutting, are used. Commonly, the samples are not subjected to any external mechanical stress or specific residual stress during the measurements. However, when measuring the hysteresis loops of samples that are processed by a specific non-gentle method of cutting, such as blanking or laser cutting, samples of different width or assembled magnetic components, various hysteresis loop shapes can be obtained. These can deviate significantly from the hysteresis loop shapes of unprocessed (or gently-processed) soft magnetic material. The neglection of stress effects leads to a strong simplification that is often inadequate when considering the influence of the varying magnetic properties on the hysteresis loop shape and its dynamic behavior [5]. The underlying magneto-mechanical coupling is the result of intricate mechanisms at different spatial scales and is typically modelled by using micromagnetic or multiscale approaches. However, these are not suitable for an implementation in numerical tools such as Finite Element simulation packages due to their prohibitive huge computational effort. Simplified thermodynamic approaches were developed which are based on a phenomenological definition of a free energy density [6]. However, these approaches require a huge amount of measured data to represent the magneto-mechanical free energy density. This paper presents a thorough analysis of the effect of internal mechanical stress state on the static hysteresis loop and an efficient approach to include the magneto-elastic coupling in an energy-based hysteresis model, which allows one to replicate the material behavior based on a reduced amount of measured data. This energy-based hysteresis model is based on the decomposition of total field strength into reversible and irreversible components. The values of the model parameters are determined by using experimental data obtained at a uniaxial single-sheet tester which is equipped with a tensile and compression hydraulic loading unit. This enablesthe application of uniaxial mechanical stress collinear to the magnetic flux up to a maximum force of 5 kN. For the model parameter identification, two different schemes are developed: (i) a semi-physical scheme that uses the anhysteretic curve to identify the reversible field component and coercivity to identify the irreversible components and (ii) a mathematical scheme based on the least-square error minimization by means of a Levenberg-Marquardt and a differential evolution algorithm. The model's accuracy and predictive capability is analyzed in terms of energy loss and hysteresis loop shape prediction. The hysteresis model uses the magnetic flux density B as the independent field variable. The magnetic field H is separated into an anhysteretic component H_{An}, and a hysteretic component H_H, that considers the energy loss linked to the jerky domain-wall motion. In contrast to [7], this paper utilizes a set of two Langevin functions [8] to represent the anhysteretic field H_{An}: $H_{An} = B/\mu_0 - M_S\,[w\,(\coth(\lambda_a) - 1/\lambda_a) + (1 - w)\,(\coth(\lambda_b) - 1/\lambda_b)]$ with $\lambda_{a,b} = [H_{An}\,(1 - \alpha_{a,b}) + B\,(\alpha_{a,b} / \mu_0)] / a_{a,b}$ The hysteretic component H_H can be derived by the solution of the implicit function [7]: .$I_D Y_H\,(H_H - H_{H,0}) = (B_H - B_0)(H_{HS}£(\lambda_H) - H_H)$. I_D denotes the sign of the magnetic-flux-density change from the value at the previous step B_0 to the current step B. Y_H is a model parameter. $H_{H,0}$ denotes the previous value of H_H. The sought-after H_H has to be determined by iterative algorithms, such as Newton's method. £ is short for the Langevin function. The input variable for the Langevin function λ_H can be calculated by means of H_{HS} and model parameter a_H. $\lambda_H = [H_H - I_D H_{HS}] / a_H$ H_{HS} and a_H are model parameter. The proposed hysteresis model requires a set of eight parameter. Fig. 1 depicts a comparison of model prediction and measured data at three different stress levels. The full paper will show the model parameters with respect to the different mechanical stress levels and a parameter sensitivity analysis in which the parameters will be set in relation to characteristic values and the shapes of the modeled hysteresis curves. The energy-based hysteresis model allows one to gather an improved understanding of the magneto-mechanical modeling and to efficiently replicate the hysteresis loops for mechanical stress values between the examined operation points. This will be discussed in detail in the full paper.

[1] C. S. Schneider; "Effect of stress on the shape of ferromagnetic hysteresis loops," *Journal of Applied Physics*, vol. 97, 10E503, 2005. [2] N. Leuning, S. Steentjes, K. Hameyer, M. Schulte, and W. Bleck, 'Effect of Material Processing and Imposed Mechanical Stress on the Magnetic, Mechanical, and Microstructural Properties of High-Silicon Electrical Steel', steel research int., vol. 87, no. 12, pp. 1638-1647, 2016. [3] H. A. Weiss, N. Leuning, S. Steentjes, K. Hameyer, T. Andorfer, S. Jenner, W. Volk, 'Influence of shear cutting parameters on the electromagnetic properties of non-oriented electrical steel sheets', Journal of Magnetism and Magnetic Materials, vol. 421, no. Supplement C, pp. 250–259, Jan. 2017. [4] V. Maurel, F. Ossart, R. Billardon, "Residual stresses in punched laminations: Phenomenological analysis and influence on the magnetic behavior of electrical steels," *Journal of Applied Physics*, vol. 93, iss. 10, pp. 7106 - 7108, 2003. [5] M. Petrun; S. Steentjes; K. Hameyer, D. Dolinar; "Modeling the influence of varying magnetic properties in soft magnetic materials on the hysteresis shape using the flux tube approach, " *Journal of Applied Physics*, vol. 117, 17A708, 2015. [6] P. Rasilo et al., "Modeling of hysteresis losses in ferromagnetic laminations under mechanical stress," *IEEE Trans. Magn.*, vol. 52, no. 3, Mar. 2016, Art. no. 7300204. [7] P.I. Koltermann, L.A. Righi, J.P.A. Bastos, R. Carlson, N. Sadowski, N.J. Batistela, "A modified Jiles method for hysteresis computation including minor loops," *Physica B: Condensed Matter*, vol. 275, no. 1–3, pp. 233-237, 2000. [8] S. Steentjes, M. Petrun, G. Glehn, D. Dolinar, and K. Hameyer, "Suitability of the double Langevin function for description of anhysteretic magnetization curves in NO and GO electrical steel grades," *AIP Advances* vol. 7, no. 5, Art. no. 056013, 2017. [9] N. Sadowski, N. J. Batistela, J. P. A. Bastos and M. Lajoie-Mazenc, "An inverse Jiles-Atherton model to take into account hysteresis in time-stepping finite-element calculations," *IEEE Transactions on Magnetics*, vol. 38, no. 2, pp. 797-800, 2002.

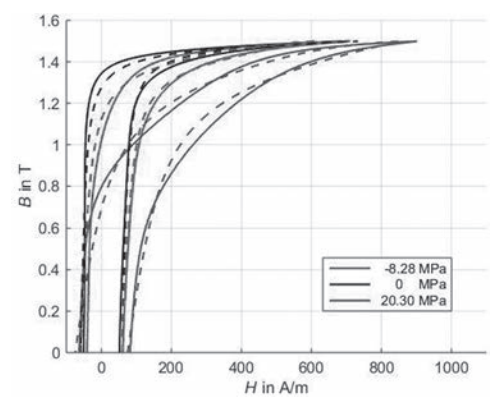

Fig. 1. Comparison of measured data (continuous lines) and simulation data (dashed lines) for three different stress levels: reference state (0 MPa), tensile (20.30 MPa) and max. compressive stress (-8.28 MPa).

11:15

CB-09. Improvement of Grain-Oriented Electrical Steel Sheet by Hyperfine Processing Magnetic Domain Structure on Vector Magnetic Characteristics.

M. Enokizono[1], D. Wakabayashi[3], T. Sato[2] and Y. Mamiduka[1]
1. Vector Magnetic Characteristic Technical Laboratory, Usa-city, Japan;
2. Faculty of Science and Technology, Oita University, Oita, Japan;
3. Mechanical and Electrical Engineering, Nippon Bunri University, Oita, Japan

Grain oriented electrical steel sheet has strong uniaxial anisotropy by grain orientation. The strong magnetic anisotropy using the tension effect of the coat has been manifested. The scratch sheet treated by the laser stress was developed so that this loss may decrease. However it increases the rotational loss in T-joint corner parts of three-phase transformer core. Furthermore the anomalous eddy current loss is large due to the effect of large grain and large magnetic domain size. We developed the new grain-oriented electrical steel sheet with low rotational power loss by hyperfine processing magnetic domain. According to this minute effect, faces store core loss were made to decrease to over 40%. According to this hyperfine processing effect of magnetic domain, it was possible the rotational power losses were made to decrease to over 40%. And the core loss of arbitrary direction decrease, also. The size of magnetic domain by hyperfine processing is within 0.25mm × 0.25mm. This hyperfine magnetic domain facilitates magnetization rotation. In this paper, we provide the vector magnetic characteristics of this steel sheet. HYPERFINE PROCESSING MAGNETIC DOMAIN STRUCTURE Figure 1 shows the sheet specimen which is high grade grain-oriented electrical steel for vector magnetic measurement. The specimen size is 80mm x 80mm rectangular sheet, 0.27mm thickness. The center area 40mm x 30mm is treated by hyperfine processing magnetic domain. The pitch width of this treatment by the fiber laser is defined PL in this paper. The pitch width was treated from 2mm to 0.125mm, as sown in Fig. 1. We could not improve over 0.25mm. Then best treated steel sheet was named the vector magnetic controlled steel sheet by hyperfine processing magnetic domain structure. Furthermore, Figure.1.shows the effect of pitch width (PL) on magnetic domain structure. The size of magnetic domain structure has been segmented small with decreasing pitch width size (PL). The magnetic domain structure was observed by magnetic viewer. This structure size by treatment of PL=0.25mm x 0.25mm has been segmented small, as the observation is more difficult. This hyperfine processing was carried by fiber laser system and suppresses the effect of the thermal stress for steel plate. This processing treatment is different from conventional scratch processing [1] [2]. Figure.2. shows the effect of pitch width (PL) on rotational magnetic power loss. The loss decreases with decreasing PL, the optimum effect in PL=0.25mm x 0.25mm are obtained and 26.7% loss reduction was obtained for the before treatment. In order to understand the parameter depend on magnetic power loss can be expressed. $W\theta_{BH}$ due to θ_H decrease but W_H due to |H| increases. That the difference in $W\theta_{BH}$ and W_H will be shown as follow $W_P = - \Delta W\theta_{BH} + \Delta W_H$, $\Delta W\theta_{BH} \rangle \Delta W_H$ Figur.3. shows the relation among B, H and θ_{BH} by hyperfine processing magnetic domain structure. θ_{BH} has been reduced, though H is increased by this effect as shown in this figure. It is indicated that this facilitates the rotation of the magnetization. CONCLUSION The hyperfine processing treatment of magnetic domain facilitates the magnetization rotation. This new improvement steel sheet can be easily design without considering the effect of anisotropic phenomena and high orientation. The advantage of this steel sheet is summarized in the following. (1)Anisotropic property by high grain orientation is eased by the hyperfine treatment of magnetic domain. (2)Rotational magnetic power loss decrease by the hyperfine magnetic domain. (3)The effect of transverse direction with hard magnetizing is large and effective. (4)The main factor of magnetic power loss(iron loss, core loss) reduction I the specific difference angle θ_{BH} between vector B and vector H. (5)By localized treatment near T-joint area of three-phase transformer core, total loss will decrease and upgrade efficiency. The conventional one-dimensional scalar magnetic characteristic measurement is insufficient for the materials development. Vector magnetic characteristic measurement is very important about research and development for reduction of loss and upgrading efficiency of electric power machines.

[1] M. Nakamura, K. Hirose, T. Iuchi, S. Yamaguchi, and Y. Ohya, Characteristics of laser irradiated grain oriented silicon steel, *IEEE Trans. Magn*., vol. 18, pp. 1508-1510, Nov 1982. [2] M. Nakamura, K. Hirose, T. Nozawa, and M. Matsuo, Domain refinement of grain oriented silicon steel by laser irradiation, *IEEE Trans. Magn*., vol. 23, pp. 3074-3076, Sep 1987.

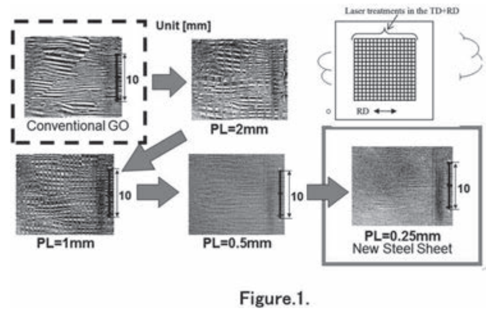

Fig. 1. Treatment specimens

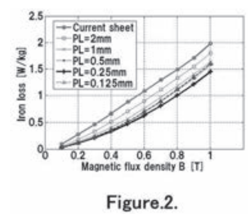

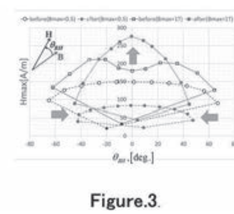

Fig. 2. Effect of hyperfine processing and Fig.3. Relation of B - H - θ_{BH}

11:30

CB-10. Improvement of Grain-oriented Electrical Steel Sheet by Hyperfine Technique on Two-dimensional Magnetostriction.

D. Wakabayashi[1] and M. Enokizono[1]
1. Nippon Bunri University, Oita, Japan

It is known that high iron loss and large magnetostriction occur due to rotating magnetic flux at T-joint part of transformer core. Grain-oriented electrical steel sheet usually is used as the transformer core. In order to decrease the iron loss and the magnetostriction under rotating magnetic flux condition, we developed a newly vector magnetic characteristic control electrical steel sheet[1]. It was developed by laser processing to an existing steel sheet. In this paper, the measurement results of the new steel sheet are reported. Fig.1 (a) shows the laser processing equipment and the vector magnetic characteristic control electrical steel sheet. Three-axial stain gauge was passed on the steel sheet to measure two-dimensional magnetostriction. It is processed on the back of the steel sheet. The laser traces are 0.25 mm wide square. Fig.1 (b) shows magnetic domain images before and after laser treatment. The magnetic domain is oriented in rolling direction before the treatment. On the other hand, the magnetic domain is hyperfine after treatment. We call the hyperfine technique, vector magnetic characteristic control technique. Fig. 2 shows the measurement results before (conventional grain-oriented electrical steel sheet) and after (vector magnetic characteristic control electrical steel sheet) laser treatment. Fig. 2 (a) shows vector magnetic characteristic and two-dimensional magnetostriction. The direction of 0 deg.-180deg. is the rolling direction. The red arrow, blue arrow, pink line and black line in the patterns show the magnetic flux density vector, the magnetic field strength vector, expansion and contraction of two-dimensional magnetostriction respectively. These figures show relationship between direction of B-vector, H-vector and maximum magnetostriction[2-4]. Fig. 2 (b) shows iron loss and magnetostriction dependence on maximum magnetic flux density. Both the iron loss and magnetostriction are decreasing due to laser treatment. These results show the laser treatment is effective to lower the iron loss and magnetostriction of the transformer core. The full paper presents the detailed measurement results of two-dimensional mgnetostriction under vector magnetic characteristics on the new control steel sheet.

[1] T. Kajiwara, K. Ooka, M. Enokizono. “A new electrical steel sheet developed by vector magnetic characteristic control”, IEEE Trans. Magn., Vol. 50, No. 11, 2014. [2] M. Enokizono, T. Todaka and S. Kanao, “Two-dimensional magnetic properties of silicon steel sheet subjected to a rotating field”, IEEE Trans. Magn., Vol. 29, No. 6, Nov, pp.3550-3552, 1993. [3] M. Enokizono, S. Kanao and G. Shirakawa, “Measurement of arbitrary dynamic magnetostriction under alternating and rotating field”, IEEE Trans. Magn., Vol. 31, No. 6, Nov, pp.3409-3411, 1995. [4] D. Wakabayashi, M. Enokizono. “Two-dimensional magnetostriction under vector magnetic characteristic”, Journal of Applied physics, 117, 17A926, 2015.

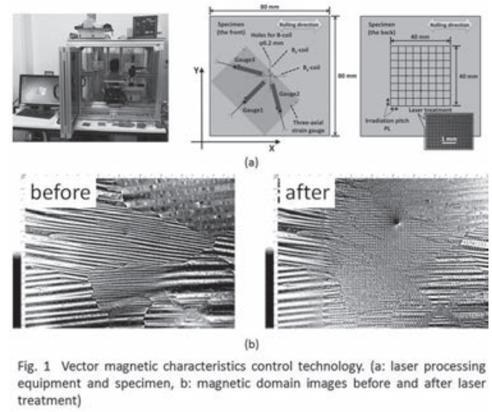

Fig. 1. Vector magnetic characteristics control technology. (a: laser processing equipment and specimen, b: magnetic domain images before and after laser treatment)

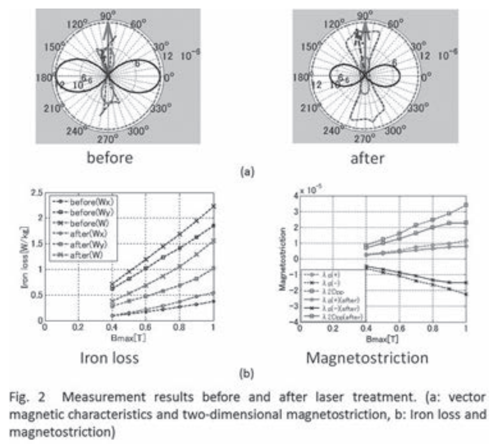

Fig. 2. Measurement results before and after laser treatment. (a: vector magnetic characteristics and two-dimensional magnetostriction, b: Iron loss and magnetostriction)

11:45

CB-11. Evolution of Residual Magnetic Field of U75V Steel Induced by Uniaxial Tensile Load with Increasing Amplitudes.

M. Fu[1], S. Bao[1] and Z. Zhao[1]
1. College of Civil Engineering and Architecture, Zhejiang University, Hangzhou, China

With a strong demand for methods to evaluate safety of engineering structures, there has been an increased interest in the investigation of the residual magnetic field (RMF) of ferromagnetic materials induced by external loads. Nevertheless previous work were mainly focused on the investigation of the unidimensional RMF variations of demagnetized materials, experimental research on the multidimensional RMF distribution characteristics induced by external loads in undemagnetized materials is scarce. To this end, in this research, the evolution of the RMF signals of initially undemagnetized U75V steel specimen under tensile load with increasing amplitudes was investigated. It was found that the fluctuation of the unidimensional RMF reduces with increase in load in the elastic stage, and remains relatively stable during the plastic stage. An effective way for characterizing deformation stages of the undemagnetized specimen was proposed. The two-dimensional vector distribution of the RMF indicates that the specimen tends to be magnetized as a rectangular magnet with an N pole and S pole at two ends with the increase of load. The possible reasons underlying the experimental results were discussed as well.

J. W. Wilson, G. Y. Tian, and S. Barrans, Sensors & Actuators A Physical. 135, 381 (2007). Z. D. Wang, Y. Gu, and Y. S. Wang, Journal of Magnetism & Magnetic Materials. 324, 382 (2012). L. M. Li, S. L. Huang, X. F. Wang, K. R. Shi, and S. Wu, Journal of Magnetism & Magnetic Materials. 261, 385 (2003). M. Roskosz, and P. Gawrilenko, NDT & E International. 41, 570 (2008). L. H. Dong, B. S. Xu, S. Y. Dong, L. Song, Q. Z. Chen, and D. Wang, NDT & E International. 42, 323 (2009). C. L. Shi, S. Y. Dong, B. S. Xu, and P. He, Journal of Magnetism & Magnetic Materials. 322, 413 (2010). J. C. Leng, M. Q. Xu, M. X. Xu, and J. Z. Zhang, NDT & E International. 42, 410 (2009). K. Yao, B. Deng, and Z. D. Wang, NDT & E International. 47, 7 (2012). L. H. Dong, B. S. Xu, S. Y. Dong, Q. Z. Chen, and D. Wang, NDT & E International. 41, 184 (2008). M. Roskosz, and M. Bieniek, NDT & E International. 54, 63 (2013). L. H. Dong, B.S. Xu, S. Y. Dong, Q. Z. Chen, and D. Wang, International Journal of Fatigue. 30, 1599 (2008). K. Yao, B. Deng, and Z. D. Wang, NDT & E International. 47, 7 (2012). S. Bao, W.L. Jin, and M. F. Huang, Journal of Zhejiang University-Science A. 11, 580 (2010). S. Bao, and D. Zhang, Insight-Non-Destructive Testing and Condition Monitoring. 57, 401 (2015). S. Bao, S. N. Hu, L. Lin, Y. B. Gu, and M. L. Fu, Insight-Non-Destructive Testing and Condition Monitoring. 57, 683 (2015). L. H. Dong, B. S. Xu, S. Y. Dong, and Q. Z. Chen, Nondestructive Testing and Evaluation. 25, 145 (2010).

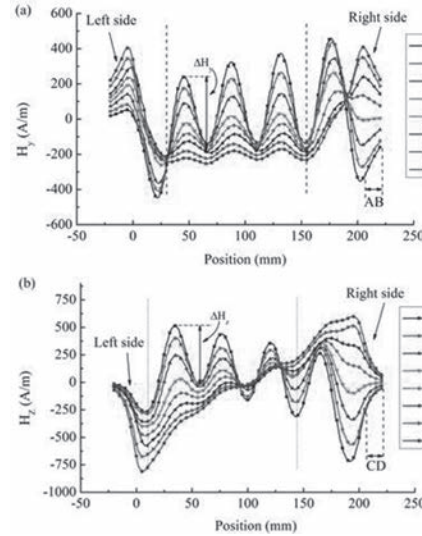

Fig. 1. Variation of the RMF components along the scanning line with the increase of load in the elastic stage: (a) tangential component H_y; (b) normal component H_z

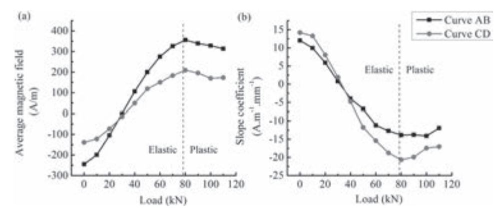

Fig. 2. Variations of the average magnetic field and the slope coefficient of curves AB and CD at various applied loads in different deformation stages: (a) average magnetic field; (b) slope coefficient

WEDNESDAY MORNING, 25 APRIL 2018 ORCHID IV, 9:00 TO 12:00

Session CC
MICROSCOPY, IMAGING AND CHARACTERIZATION II

Yaohua Liu, Chair
Oak Ridge National Laboratory, Oak Ridge, TN, United States

INVITED PAPERS

9:00

CC-01. Nanoscale Magnetic Imaging using Circularly Polarized High-Harmonic Radiation.

O. Kfir[1,2], S. Zayko[1], C. Nolte[3], M. Sivis[1], M. Möller[1], B. Hebler[4], S. Arekapudi[4], D. Steil[3], S. Schäfer[1], M. Albrecht[4], O. Cohen[2], S. Mathias[3,5] and C. Ropers[1,5]
1. IV. Physical Institute, University of Göttingen, Göttingen, Germany; 2. Department of Physics and Solid State Institute, Technion - Israel Institute of Technology, Haifa, Germany; 3. I. Physical Institute, University of Göttingen, Göttingen, Germany; 4. Institute of Physics, University of Augsburg, Augsburg, Germany; 5. International Center for Advanced Studies of Energy Conversion (ICASEC), University of Göttingen, Göttingen, Germany

Magnetic structures exhibit a rich variety of nanometric scale patterns, textures and topological states, governed by various spin-coupling and spin-orbit-coupling mechanisms [1,2]. Mapping magnetization features in space and their dynamics is essential to understand magnetic behavior at the smallest scale. To date, imaging of the spin-state with high spatial and ultrafast temporal resolution is exclusively accessible in synchrotrons and free-electron lasers (FELs), providing for extreme-UV and soft-X-ray beams with circular polarization [3-5]. These large scale facilities enable magneto-optical microscopy since their high flux compensates for the small probability of the magneto-optical scattering. Sources of nanometric-wavelength radiation based on high-order harmonic generation (HHG) from visible and infra-red lasers are very appealing for dynamical imaging applications since they provide for exquisite spatial coherence [6], few-femtosecond pulse duration, controllable polarization [7-9], with a footprint of a standard optical table. In the last decade, the imaging capabilities of HHG were repeatedly demonstrated [6,11,12] for high-contrast micro-machined samples, however, imaging of material systems capable of pico- and femtosecond dynamics remained elusive. This work demonstrates the first magnetic imaging with high-harmonic radiation [10]. The XMCD (X-ray magnetic circular dichroism) phase and amplitude contrast of cobalt are independently mapped for a Co/Pd multilayer structure, revealing a worm-like ordering of the magnetic domains. The magnetic spatial features are retrieved from the diffraction pattern of a circularly-polarized high-harmonic beam passing through the magnetic multilayer and a partly transmissive mask, using coherent diffractive imaging (CDI) methods [12]. The ratio between the complex exit-waves recorded with left- and right-handed circular polarizations provided for a quantitative mapping of the magnetization components parallel (or anti-parallel) to the beam, with a resolution below 50 nm. To enhance the weak magneto-optical scattering signal, we use heterodyning with a strong auxiliary field, thereby overcoming the weak scattering probability. The experimental system is illustrated in Fig. 1a. Amplified pulses from a Ti:Sapphire laser system (repetition rate, 1 kHz; central wavelength, 800 nm; pulse energy, 2 mJ; pulse duration, 45 fs) are converted to a bi-circular field (circularly polarized field propagating with a counter-rotating second harmonic) by a MAZEL-TOV apparatus [9] for the generation of circularly polarized high harmonics [7,8] in a He-filled gas cell. The harmonics are focused and spatially dispersed by a toroidal grating, where the 38th order (21 nm, 59 eV) illuminates the sample. The sample (see Fig. 1b) is a free-standing 200-nm-thick Si membrane coated with a Co/Pd multilayer on the front and an opaque gold layer on the back-side. Using ion-beam milling, the gold is removed from the central aperture (4 um diameter) and 4 auxiliary holes are drilled through. The high quality diffraction and the resulting flat contrast reconstruction (see Fig. 2) allows to quantitatively evaluate the magneto-optical refraction for the cobalt in our multilayer, $\Delta\delta_{Co}$=0.022±0.002. To conclude, this approach will facilitate quantitative, spatially-resolved studies of ultrafast magnetization dynamics, that offer new opportunities in nanoscale magnetism. We believe that the increasing interest in ferrimagnets materials and structures for data-related applications may benefit a great deal from such a compact magneto-optical microscope, accessing the nanoscale, element-specific magnetization, even in the absence of a stray magnetic field.

[1] Mühlbauer, S., et al., Science 323, 915–919 (2009). [2] Soumyanarayanan, A., et al., Nature 539, 509–517 (2016). [3] Eisebitt, S., et al., Nature 432, 885–888 (2004). [4] Van Waeyenberge, B. et al., Nature 444, 461–464 (2006). [5] Büttner, F. et al., Nat. Phys. 11, 225–228 (2015). [6] Zayko, S. et al., Opt. Exp. 23, 19911 (2015) [7] Fleischer, A., Kfir, O., et al., Nat. Phot. 8, 543–549 (2014). [8] Kfir, O., et al., Nat Photon 9, 99–105 (2015). [9] Kfir, O., Appl. Phys. Lett. 108, 211106 (2016). [10] Kfir, O., Zayko, S., et al., Science Adv. 3, eaao4641 (2017). [11] Sandberg, R. L., et al., Phys. Rev. Lett. 99, 098103 (2007). [12] Miao, J., et al., Science 348, 530–535 (2015).

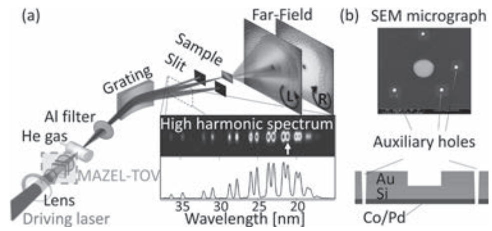

Fig. 1. Experimental system for magnetic imaging with circularly polarized HHG (see full details in [10]). (a) The driving laser is manipulated by a "MAZEL-TOV" apparatus [9] for the generation of circularly polarized high harmonics in a He-filled gas cell. The harmonics (inset, top: beam shape, bottom: vertically integrated lineout) are focused onto the sample by a toroidal grating, and a slit selects the 38th harmonic order (white arrow). The far-field diffraction pattern is recorded with left-hand and with right-hand circularly polarized illumination to isolate the magnetic features from the non-magnetic background. (b) Top: a SEM micrograph shows the central aperture, and the four surrounding auxiliary holes. Bottom: the illustration of the sample's cross section shows the Si-membrane and the Co/Pd multilayer deposited on the front side, as well as drilled-through auxiliary holes, allowing for the transmission of an intense auxiliary field for heterodyning.

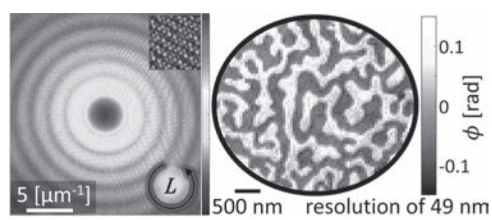

Fig. 2. Experimental data and retrieved domain structure. (left) Log-scale of the far-field diffraction pattern for left-handed circularly polarized illumination (L), demonstrating a high speckle visibility across the detector (see zoomed top corner). A similar diffraction pattern is recorded for right-handed (R) polarization. The strong auxiliary field (note the concentric rings) enhances the weak magneto-optical signal through their interference over the entire detector. (right) Quantitative XMCD phase contrast image of worm-like magnetic domains, with resolution of a single pixel (49 nm). The flat contrast within the domains and the sharp domain edges allows to retrieve the magneto-optical refraction in the cobalt, $\Delta\delta_{Co}$=0.022±0.002.

9:30

CC-02. Exploring magnetism at the nanoscale with a single spin microscope.

V. Jacques[1]
1. Laboratoire Charles Coulomb, UMR5221, CNRS and Université de Montpellier, Montpellier, France

In the past years, it was realized that the experimental methods allowing for the detection of single spins in the solid-state, which were initially developed for quantum information science, open new avenues for high sensitivity magnetometry at the nanoscale. In that spirit, it was proposed to use the electronic spin of a single nitrogen-vacancy (NV) defect in diamond as an atomic-sized magnetic field sensor [1,2]. This approach promises significant advances in magnetic imaging since it provides non-invasive, quantitative and vectorial magnetic field measurements, with an unprecedented combination of spatial resolution and magnetic sensitivity under ambient conditions. In this talk, I will show how scanning-NV magnetometry can be used as a powerful tool for exploring exotic spin textures in thin magnetic materials focusing on (i) domain walls and magnetic skyrmions in ultrathin ferromagnets [3,4] and (ii) cycloidal antiferromagnetic order in multiferroic materials [5].

[1] G. Balasubramanian *et al.,* Nature 455, 648 (2008) ; J. Maze *et al.,* Nature 455, 644 (2008). [2] L. Rondin *et al.,* Rep. Prog. Phys. 77, 056503 (2014). [3] Tetienne *et al.,* Nat. Commun. 6, 6733 (2015) [4] Gross *et al.*, arXiv:1709.06027 (2017) [5] Gross *et al.,* Nature 549, 252 (2017)

CONTRIBUTED PAPERS

10:00

CC-03. Atomic scale magnetic and structural imaging by achromatic electron microscopy.

X. Zhong[1], Z. Wang[1], L. Jin[2], J. Rusz[3], H. Jiang[1], Y. Moritomo[4], J. Mayer[2,5], R. Dunin-Borkowski[5], R. Yu[1] and J. Zhu[1]
1. National Center for Electron Microscopy in Beijing, School of Materials Science and Engineering, Tsinghua University, Beijing, China; 2. Ernst Ruska-Centre for Microscopy and Spectroscopy with Electrons and Peter Grünberg Institute, Forschungszentrum Jülich GmbH, Jülich, Germany; 3. Department of Physics and Astronomy, Uppsala University, Uppsala, Sweden; 4. Graduate School of Pure & Applied Science and Faculty of Pure & Applied Science, University of Tsukuba, Ibaraki, Japan; 5. Central Facility for Electron Microscopy, RWTH Aachen University, Aachen, Germany

The atomic-level knowledge of local spin configuration of the magnetic materials is of great importance to predict and control their physical properties, in order to meet the challenges of ever-increasing demands on performance of functional materials. However, it is highly challenging to experimentally characterize magnetic properties of such materials with atomic scale spatial resolution. The leading techniques in spatially resolved magnetic imaging are magnetic exchange force microscopy and spin polarized scanning tunneling microscopy. However, as they are surface sensitive, very little information can be obtained regarding bulk or buried materials. The X-ray magnetic circular dichroism (XMCD) combined with photoelectron emission microscopy (PEEM) technique is a very attractive alternative because it has the spatial resolution as high as the polarized x-ray beam size besides element specific feature, as it is less surface sensitive and can be used to look at the interior of the thin films. However, the length scale of magnetic contrast using highly brilliant left and right circularly polarized X-ray beams is around 15nm [1]. The best option to push the spatial resolution of the spectromicroscopies lies in the electron beam equivalent technique electron energy-loss magnetic chiral dichroism (EMCD) [2], which is also called electron magnetic circular dichroism. Physically, XMCD and EMCD shares the same underlying physics in which the angular momentum transferred during X-ray absorption or inelastic electron scattering can selectively excite magnetic sublevels in atoms. The structured electron beams generated through interference of suitably phased plane waves can produce beams with orbital angular momentum. Electron beams can be easily focused compared with X-rays, allowing for atomic scale magnetism to be probed. Previously, we have found a strong EMCD signal in transition metal oxides allowing them to use standing wave methods to identify the different spin states of Fe atoms with site specificity [3]. In principle EMCD can offer higher spatial resolution and greater depth sensitivity due to the short de Broglie wavelength and penetration of high-energy electrons compared to XMCD. Recently by using EMCD and achromatic electron microscopy, we are able to access the magnetic circurlar dichroism with unit-cell resolution and even with atomic resolution [4,5]. Combining with advanced capobility of structural and chemical imaging by using aberration-corrected transmission electron microscopy, all the information including magnetic polarization, atomic configurations, chemical states can be simultaneously accessed from the very same sample region. In the examples of complex oxides including Sr_2FeMoO_6, $NiFe_2O_4$ and $La_{0.7}Sr_{0.3}MnO_3$[3-6], we would like to show how to achieve local atomic-scale magnetic, chemical and structural information and understand the structure-property relationship of these magnetic materials at the atomic level.

1. W. L. Chao, B. D. Harteneck, J. A. Liddle, E. H. Anderson, and D. T. Attwood, Soft X-ray microscopy at a spatial resolution better than 15nm, *Nature* 435 (2005), 1210-1213. 2. Schattschneider, P. *et al.* Detection of magnetic circular dichroism using a transmission electron microscope. *Nature* 441, 486–488 (2006). 3. Z. Q. Wang, X. Y. Zhong*, R. Yu, Z. Y. Cheng, J. Zhu*, Quantitative experimental determination of site-specific magnetic structures by transmitted electrons. *Nature Communications,* 4 (2013), 1395,. 4. Z. C. Wang, A. H. Tavabi, L. Jin, J. Rusz, D. Tyutyunnikov, H. B. Jiang, Y. Moritomo, J. Mayer, R. E. Dunin-Borkowski, R. Yu, J. Zhu and X. Y. Zhong*, Atomic scale imaging of magnetic circular dichroism by achromatic electron microscopy, Nature Materials, https://doi.org/10.1038/s41563-017-0010-4, 2018. 5. L. Jin, C. L. Jia, I. Lindfors-Vrejoiu, X. Y. Zhong, H. C. Du, R. E. Dunin-Borkowski, Direct Demonstration of a Magnetic Dead Layer Resulting from A-Site Cation Inhomogeneity in a (La,Sr)MnO3 Epitaxial Film System, *Advanced Materials Interfaces*, 3 (2016), 1600414. 6. Z. C. Wang, X. Y. Zhong*, L. Jin, X. F. Chen, Y. Moritomo, and J. Mayer. Effects of dynamic diffraction conditions on magnetic parameter determination in a double perovskite Sr_2FeMoO_6 using electron energy-loss magnetic chiral dichroism. *Ultramicroscopy* 176, (2017) 212.

10:15

CC-04. Smart Magnetic Probes with Controllable States for Quantitative MFM.

O. Kazakova[1], V. Panchal[1], H. Corte-León[1], R. Puttock[1], L. Rodríguez[2] and V. Neu[3]
1. National Physical Laboratory, Teddington, United Kingdom;
2. Universidad del Valle, Cali, Colombia; 3. IFW Dresden, Dresden, Germany

A novel method for quantitative magnetic force microscopy (MFM) using smart functional magnetic probes with controllable states is presented [1-3]. A comprehensive method for visualisation and quantification of the magnetic stray field is applied to the particular cases of smart custom-made multi-layered (ML) and domain wall (DW) based probes with high/low magnetic moment states. ML probes were fabricated by deposition of Co/Si/Co layers on one side of a commercial Si probe (Fig. 1 a-b). V-shaped DW-probes were modified out of commercial magnetic probes using focused ion beam lithography (Fig. 1d). Both types of probes can controllably produce 4 stable magnetic states as confirmed by *in situ* MFM studies and e-holography visualisation of the probe states (Fig. 1 d left). *In situ* MFM studies of reference samples are used to define the probe switching fields and magnetization spatial resolution [1]. Quantitative values of the probe magnetic moments are obtained by determining their real space tip transfer function (Fig. 1c). The outcomes of the methods are introduced as inputs into a numerical model. The modelling results fully match the experimental measurements, outlining an all-inclusive method for the calibration of complex magnetic probes with a controllable low/high magnetic moment [1, 3]. Furthermore, a smart probe in the low moment state provide complementary information about the in-plane component of the sample's magnetization, which is not achievable by standard methods, thus allowing for 3D reconstruction of the sample's magnetisation. Through additional development of multivariate statistical methods this approach also provides a route to secure, traceable and authenticated digital solutions.

1. V. Panchal, et al., 'Calibration of multilayered magnetic force microscopy probes' Sci Reports 7, 7224 (2017) 2. T. Wren, et al., 'Switchable bi-stable multilayer magnetic probes for imaging of soft magnetic structures' Ultramicroscopy, 179, 41 (2017) 3. R. Puttock, et al., 'V-shaped domain wall probes for calibrated magnetic force microscopy' IEEE Trans Magn. 53, 6500805 (2017)

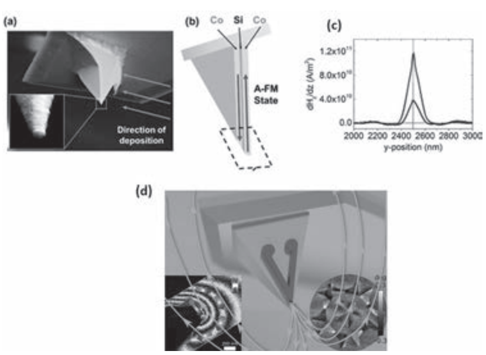

Fig. 1. a) SEM image of a ML probe (yellow colour represents Co layers); b) schematics of the ML probe in the A-FM state; c) real space tip transfer function of the 4 superimposed magnetisation states of the ML probe, i.e. large magnitude for FM and low magnitude for A-FM states; d) schematics of the DW probe with magnetic flux image of the probe in the 'curl' state obtained by e-holography (left) and an MFM image of the penrose pattern obtained by the DW probe in the head-to-head state.

INVITED PAPER

10:30

CC-05. Single Atom Magnets at Surfaces – State-of-the-art and Future Perspectives.

H. Brune[1]
1. Phyics, Swiss Federal Institute of Technology Lausanne (EPFL), Lausanne, Switzerland

Single ion magnets, or more generally single molecular magnets (SMMs), where the magnetic unit comprises more then one atom, are reality since many years. They are discussed as candidates for magnetic information storage, molecular spintronics, and quantum bits [1, 2]. Surface Science has opened up an alternative approach to this field which are single atoms adsorbed onto surfaces and investigated under ultra-high vacuum conditions. Ho atoms on two monolayer thick MgO(100) films grown on Ag(100) where found to exhibit magnetic remanence up to 30 K and relaxation times of at least one hour at 2 K [3]. This result was obtained from ensemble measurements using X-ray magnetic circular dichroism (XMCD). Spin-polarized scanning tunnelling microscopy (STM) measurements demonstrated reading and writing of individual Ho atoms and confirmed their long magnetic lifetimes [4]. Very recent STM experiments show stable magnetization over two hours in external fields of 8 T that are applied opposite to the magnetization of the atoms and at temperatures of 8 K [5]. We have identified two more systems that exhibit permanent magnetism in single adatoms, namely a superlattice of Dy atoms on the moiré pattern formed by graphene on Ir(111) [6] and for Tb/MgO/Ag(100) [7]. Recently, electron paramagnetic resonance (ESR) has been realized on individual Fe atoms with the STM [8]. We elaborate on the Physics giving rise to extremely stable magnetic quantum states of single adatoms and discuss the perspectives opened up by the combination of long magnetic relaxation times in single adatoms with the availability of ESR-STM measurements of magnetic coherence times.

[1] S. Thiele, F. Balestro, R. Ballou, S. Klyatskaya, M. Ruben, and W. Wernsdorfer, Science 344, 1135 (2014). [2] R. J. Blagg *et al*., Nat. Chem. 5, 673 (2013). [3] F. Donati *et al.*, Science 352, 318 (2016). [4] F. D. Natterer *et al.* Nature 543, 226 (2017). [5] F. D. Natterer, F. Donati, F. Patthey and H. Brune, arXiv:1712.07871 (2018). [6] R. Baltic *et al.* Nanolett. 16, 7610 (2016). [7] L. Persichetti *et al.*, to be published. [8] S. Baumann, W. Paul, T. Choi, C. P. Lutz, A. Ardavan, and A. J. Heinrich, Science 350, 417 (2015).

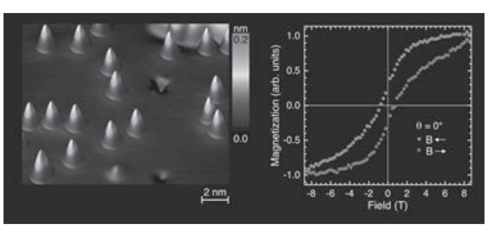

Fig. 1. Left: STM image of individual Ho atoms on two monolayers (ML) MgO(100) grown on Ag(100) (4.7 K, Ho coverage 0.005 ML). Right: Magnetization curve recorded with XMCD for ensemble of individual Ho atoms on 7 ML MgO on Ag(100) (6.5 K, 8 mT/s, Ho coverage 0.01 ML). Taken from [3].

CONTRIBUTED PAPERS

11:00

CC-06. Investigation of anisotropic quadratic magneto-optic Kerr ellipticity of Fe(100) grown on Ir(100).

A.V. Pradeep[1,2], K.G. Ajesh[1], S. Ghosh[1,3] and P. Kumar[1]
1. Department of Physics, Indian Institute of Science, Bangalore, India; 2. Dept. of Collegiate Education Kerala, RWPC, Kannur, India; 3. Department of Physics, Cornell University, Ithaca, NY, United States

Magneto-optic Kerr effect (MOKE) is widely used as a tool to investigate anisotropic constants, coercivity, exchange bias field, domain structure and magnetization reversal of magnetic thin films and single crystals. In most of its application, the magneto-optic coupling (M-O) is assumed to be linearly dependent on magnetization. But, this assumption is not always valid. Recently, it is found that the dependence of M-O coupling is not only linear but also quadratic on magnetization. The second order dependence of M-O coupling on magnetization was observed recently from ferromagnetic metals[1], [2], Heusler alloys[3], [4] and half-metallic ferrimagnets[5]. Therefore, the analysis of MOKE measurements based on the assumption that magneto-optic coupling is linear on magnetization, are being modified up to quadratic terms. In addition quadratic magneto-optic Kerr effect (QMOKE) is useful in the investigation of higher order spin-orbit interaction and for measuring spin-orbit induced torque in ferromagnetic/heavy-metal interface[6]. Heavy-metal/ferromagnetic multilayer are the promising candidates in spintronics due to their higher efficiency in manipulating magnetism via electrical means[7]. The knowledge of QMOKE from such systems will be useful in designing spintronics devise. We have investigated the QMOKE signal from Fe(100) grown on Ir(100). We have already reported the real part of the quadratic Kerr angle (Quadratic Kerr rotation) from Fe(100)/Ir(100) system[8]. Here we discuss the imaginary part of quadratic Kerr angle (Quadratic Kerr ellipticity) and its anisotropy with sample rotation. Iron film of thickness 13 nm is grown on a clean (100) surface of a single crystal Iridium, using an e-beam evaporator inside a UHV chamber. The growth condition and deposition system were discussed elsewhere[9]. The substrate and film qualities are monitored using Auger electron spectroscopy (AES). The crystal structure is analyzed using LEED and XRD. Film growth is monitored using medium energy electron diffraction (MEED) and is found to be layer by layer up to 20 monolayer. Fe grows pseudomorphically on Ir(100) with Fe(100) plane parallel to Ir(100) surface and the in-plane [100] direction of Fe(100) parallel to the in-plane [110] direction of Ir(100). QMOKE signal are extracted using a full rotating field method at saturation. For this, we have used a simple QMOKE measurement system discussed elsewhere[5]. In order to extract the imaginary part of the complex Kerr angle, which is the Kerr ellipticity, a quarter wave-plate is installed between the sample and the analyzer of the QMOKE measurement system. Then, at a particular angle of sample rotation (r=90°), the Kerr ellipticity (e) is measured as the function of angle of magnetic field. This is shown in Fig.1(a). The linear Kerr ellipticity (e^L) and quadratic Kerr ellipticity (e^Q) are obtained by symmetrizing and anti-symmetrizing the measured Kerr ellipticity respectively. The linear Kerr ellipticity is shown in Fig.1(b) and quadratic Kerr ellipticity is shown in Fig.1(c). Since the measurements are done at saturation, the magnetization vector follows the magnetic field. Fig.1(d) shows the angle of magnetization (x_M) vs. angle of magnetic field (x_H). This curve is obtained using the relation $e^L(x_H)=L^*\cos(x_M)$ where L^* is the maximum value of linear Kerr ellipticity. Fitting the quadratic Kerr ellipticity with $e^Q=Q^*_1\mathrm{Cos}(x_H)\mathrm{Sin}(x_H)+Q^*_2\mathrm{Cos}(2x_H)$, the Q_1^* and Q_2^* are obtained. Then we systematically rotated the sample and above procedure is repeated to quantitatively measure the imaginary part of linear (L^*) and quadratic (Q_1^* and Q_2^*) components of MOKE for every angle of sample rotation. We followed the sign convention of ref [1]. Kerr ellipticity is measured using both s and p-polarized light. Kerr ellipticity averaged between the s and p-polarized light is plotted against the angle of sample rotation, which is shown as open symbols in Fig.2. Here open black squares represent the imaginary part of linear component of MOKE, which is isotropic with sample rotation and the black solid line represents the linear fit. Red open circles and the blue open triangles represent the imaginary part of quadratic component of MOKE Q_1^* and Q_2^* respectively. The quadratic component of MOKE are anisotropic with respect to the sample rotation. The red and blue solid lines represent the fit to the data using equations $Q_1^*=b^*+c^*\cos(4r)$ and $Q_2^*=(-c/2)\sin(4r)$ respectively. From the fit, the parameter L^*, b^* and c^* which relate the linear (K) and quadratic (G and ΔG) magneto-optic coupling coefficients are obtained. The value of L^*, b^* and c^* are +6.37±0.04 mdeg, −5.95±0.09 mdeg and −4.2±0.2 mdeg respectively.

[1] M. Buchmeier, R. Schreiber, D. E. Bürgler, and C. M. Schneider, "Thickness dependence of linear and quadratic magneto-optical Kerr effects in ultrathin Fe(001) films," *Phys. Rev. B*, vol. 79, no. 6, p. 064402, Feb. 2009. [2] J. H. Liang, Y. L. Chen, L. Sun, C. Zhou, Y. Yang, and Y. Z. Wu, "The anisotropic linear and quadratic magneto-optical Kerr effects in epitaxial Fe/GaAs(110) film," *Appl. Phys. Lett.*, vol. 108, no. 8, p. 082404, Feb. 2016. [3] G. Wolf, J. Hamrle, S. Trudel, T. Kubota, Y. Ando, and B. Hillebrands, "Quadratic magneto-optical Kerr effect in Co2MnSi," *J. Appl. Phys.*, vol. 110, no. 4, p. 043904, Aug. 2011. [4] J. Hamrle, S. Blomeier, O. Gaier, B. Hillebrands, H. Schneider, G. Jakob, K. Postava, and C. Felser, "Huge quadratic magneto-optical Kerr effect and magnetization reversal in the Co 2 FeSi Heusler compound," *J. Phys. D. Appl. Phys.*, vol. 40, no. 6, pp. 1563–1569, Mar. 2007. [5] A. V. Pradeep, S. Ghosh, and P. S. Anil Kumar, "Simple quadratic magneto-optic Kerr effect measurement system using permanent magnets," *Rev. Sci. Instrum.*, vol. 88, no. 1, p. 013901, Jan. 2017. [6] X. Fan, A. R. Mellnik, W. Wang, N. Reynolds, T. Wang, H. Celik, V. O. Lorenz, D. C. Ralph, and J. Q. Xiao, "All-Optical Vector Measurement of Spin-Orbit-Induced Torques Using Both Polar and Quadratic Magneto-Optic Kerr Effects," p. 17, Sep. 2015. [7] G. Yu, P. Upadhyaya, Y. Fan, J. G. Alzate, W. Jiang, K. L. Wong, S. Takei, S. A. Bender, L.-T. Chang, Y. Jiang, M. Lang, J. Tang, Y. Wang, Y. Tserkovnyak, P. K. Amiri, and K. L. Wang, "Switching of perpendicular magnetization by spin–orbit torques in the absence of external magnetic fields," *Nat. Nanotechnol.*, vol. 9, no. 7, pp. 548–554, May 2014. [8] A. V. Pradeep, S. Ghosh, K. G. Ajesh, and P. S. A. Kumar, "Quadratic Magneto-Optic Kerr Effect Investigations of Fe(100) Grown on Ir(100)," *IEEE Trans. Magn.*, vol. 53, no. 11, pp. 1–5, Nov. 2017. [9] A. V. Pradeep, A. Roy, P. S. A. Kumar, and J. Kirschner, "Development of a spin polarized low energy electron diffraction system," *Rev. Sci. Instrum.*, vol. 87, no. 2, p. 023906, Feb. 2016.

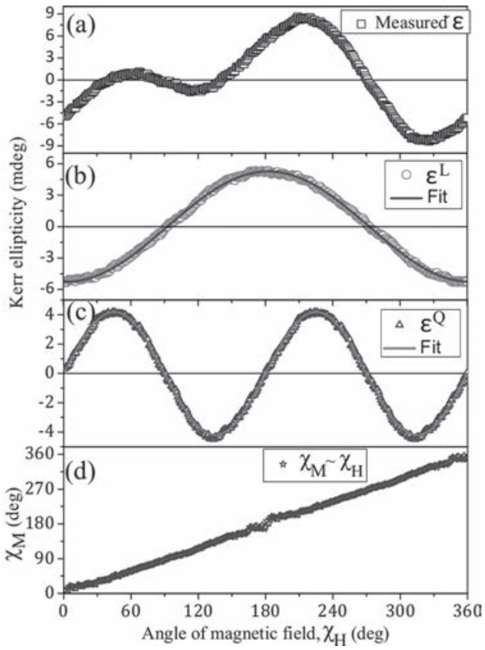

Fig. 1. (a) Magneto-optic Kerr effect measured as the function of the angle of in-plane magnetic field at a fixed angle of sample rotation of 90°. (b) The open circle represents the extracted linear part of Kerr ellipticity and solid line represents the theoretical fit. (c) The open triangle represents the quadratic part of the Kerr ellipticity and solid line represents the theoretical fit. (d) Open symbol show the angle of magnetization vs. angle of magnetic field. All angles are measured with respect to the light scattering plane. The angle of incidence is ~5°.

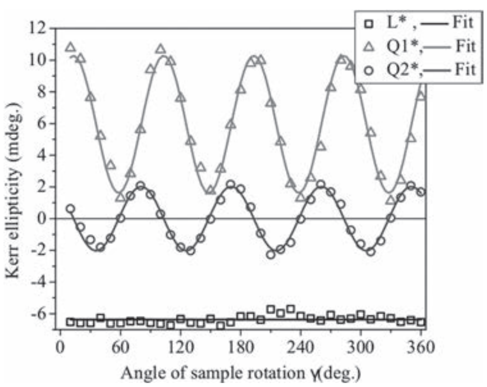

Fig. 2. Open square represents the linear part of Kerr ellipticity, open triangle and open circle represents the quadratic component of MOKE Q_1^* and Q_2^* as the function of the angle of sample rotation with respect to the light scattering plane.

11:15

CC-07. Spatially-resolved electric-field manipulation of magnetism in multiferroic heterostructures.

Y. Ba[1], *Y. Zhao*[1], Y. Liu[1], P. Li[1], L. Wu[2], J. Unguris[3], D. Pierce[3], D. Yang[4], C. Feng[1], Y. Zhang[1], H. Wu[5], D. Li[5], Y. Chang[5], J. Zhang[4], X. Han[5], J. Cai[5] and C. Nan[2]
1. Department of Physics and State Key Laboratory of Low-Dimensional Quantum Physics, Tsinghua University, Beijing, China; 2. School of Materials Science and Engineering, Tsinghua University, Beijing, China; 3. National Institute of Standards and Technology, Gaithersburg, MD, United States; 4. Beijing Normal University, Beijing, China; 5. Beijing National Laboratory for Condensed Matter Physics, Chinese Academy of Sciences, Beijing, China

With the fast development of information storage, exploiting new concepts for dense, fast, and non-volatile random access memory with low energy consumption is a significant and challenging task. To realize this goal, electric-field control of magnetism is crucial. In this regard, multiferroic materials are important and have attracted much attention due to their interesting new physics and potentials for exploring novel multifunctional devices [1,2]. In the multiferroic materials, electric polarization can be tuned by applying an external magnetic field or vice versa. This magnetoelectric (ME) effect originates from the coupling of the magnetic and ferroelectric orders. However, single-phase multiferroic materials are rare and the multiferroic heterostructures, composed of ferromagnetic (FM) and ferroelectric (FE) materials, provide an alternative way for exploring the ME coupling effect. One of the key issues in the study of the FM/FE heterostructures is the control of magnetism via electric fields, which is essential for the new generation information storage technology. We have carried out electric-field control of magnetism in different FM/FE heterostructures in our previous work [3,4]. Although a lot of work have been carried out on electric-field control of magnetism in multiferroic heterostructures via interfacial strain coupling, most of the previous reports on electric-field control of magnetism in FM/PMN-PT through strain-mediated interaction are volatile with a *butterfly-like* behavior. Recently, for the first time, we reported a large and nonvolatile *loop-like* bipolar-electric-field-controlled magnetization at room temperature in $Co_{40}Fe_{40}B_{20}$(/$Pb(Mg_{1/3}Nb_{2/3})_{0.7}Ti_{0.3}O_3$(001) (CoFeB/PMN-PT(001)) and it was proposed that the unusual nonvolatile behavior is related to the 109° FE domain switching in PMN-PT[3]. So far, CoFeB/PMN-PT(001) has been one of the widely studied multiferroic heterostructures. However, one important issue remains to be solved — the magnetic responses of CoFeB corresponding to the different FE domain switching of PMN-PT(001), namely 109°, 71° and 180° domain switching, under bipolar electric fields along the [001] direction. The reason is that in the previous reports, macroscopic magnetic measurements on CoFeB films got the total magnetization from the magnetic responses of CoFeB corresponding to the different FE domain switching of PMN-PT(001). Even using techniques with spatial resolution, it could not get the distinct magnetic behavior of CoFeB related to the different FE domain switching of PMN-PT(001) as shown in our previous work [5] because the intralayer magnetic interactions hinder the complete response of magnetic domain to the strain induced by FE domain switching. This issue is very important for understanding the mechanism of electric-field control of magnetism in FM-FE multiferroic heterostructures and it's also very important for applications in terms of domain engineering for designing devices based on distinct magnetic response of CoFeB related to different FE domain switching. We solve this problem by patterning the CoFeB film of CoFeB/PMN-PT(001) into separated and small non-interacting discs whose size is comparable to the FE domains [6]. Such mesoscopic structures are essential for observing the distinct behaviors of electric-field control of magnetism corresponding to the different types of FE domain switching because the behavior of electric-field control of magnetism for these discs depends on the type of FE domain switching underneath them. By using spatially-resolved techniques including magneto-optic Kerr effect (MOKE) and scanning electron microscopy with polarization analysis (SEMPA) with in situ electric fields, we uncover the distinct behaviors of electric-field control of magnetism corresponding to the different types of FE domain switching in CoFeB mesoscopic discs on PMN-PT(001). For the first time, the 90° rotation of the magnetic easy axis induced by 109° FE domain switching was observed. Both MOKE and SEMPA demonstrate three types of magnetic responses to electric fields, with type I and type II attributed to 109°, 71°/180° FE domain switching, respectively, and type III attributed to a combined behavior of multi-FE-domain switching. In addition, for the first time, we systematically studied the variations of effective magnetic anisotropy field with electric field and correlated them with the proposed different FE domain switching paths. This work is significant for understanding the distinct magnetic responses to different FE domain switching, and shedding light on the path of FE domain switching. The spatially-resolved study of electric-field control of magnetism on the mesoscale paves the way for further nanoscale research, which is important for the realization of low-power consumption and high-speed MRAM utilizing these materials.

1. W. Eerenstein, N. D. Mathur, and J. F. Scott, Nature 442,759 (2006). 2. R. Ramesh and N. A. Spaldin, Nature Mater. 6, 21 (2007). 3. S. Zhang et al., Phys. Rev. Lett. 108, 137203 (2012). 4. S. Zhang et al., Scientific Reports 4, 3727 (2014); L. F. Yang et al., Scientific Reports 4, 4591 (2014); P. S. Li et al., Adv. Mater. 26, 4320 (2014); A. T. Chen et al., Adv. Mater.28, 363 (2016) 5. P. S. Li et al., ACS Appl. Mater. Interfaces 9, 2642 (2017). 6. Y. Ba et al., to be published.

11:30

CC-08. An Aparatus and Method for Full-Vector Inductive Mapping of Radio Frequency Magnetic Field Distributions in the Vicinity of RFID Tags.

P.S. Stamenov[1], K. Ackland[1], M. Lotya[2] and D.J. Finn[2,1]
1. School of Physics and CRANN, Trinity College, Dublin, Ireland;
2. Amatech Group Limited, Galway, Ireland

RFID has become very widespread in both everyday life and specific scientific applications for the exchange data or the identification and/or tracking of transponders (tags). The performance of a short-range (0 - 1 m) RFID system generally depends on both the properties of the tag(s), and the qualities of the reader antenna and host electronics. The most prolific passive tag-based system, uses tags with no internal power source, which use the EM field emitted by the reader to power their internal circuits [1]. Here we describe and demonstrate the capabilities of an inductive magnetic field mapping platform designed to aid the characterisation and optimisation of passive near-field RFID tags for financial payment and national identity smartcards (ID-1), operating at 13.56 MHz (HF) as defined by the ISO/IEC 14443 standard [2]. Smaller modules are currently being integrated in smaller devices, such as wrist-bands, watches and items of jewlery. Limited flux-integration areas of the antena lead to smaller coupled power and a shorter communication range. One possible counter-measure is the use of flux-concentrating magnetic material. In the HF region, there are two main competing soft magnetic families - low-permeability insulating ferrites and high-permeability metallic micro patricle systems such as sendust. Sendust is a magnetically soft ($H_c \sim 5$ A m^{-1}) iron-rich alloy of Fe, Al and Si of general composition 6-11 wt. % Si, 4-8 wt% Al, discovered by researchers in Sendai, Japan, in 1936 [3] as a higher permeability (max. ~ 1.4 10^5) cheaper alternative to permalloy in inductor and magnetic flux concentrator applications. Other essential properties of sendust are its high resistivity (~ 10^2 μΩ cm) and low loss within the low RF ranges, 0.1-1000 kHz. Unsurprisingly, as the frequency of operation increases, the real part of the magnetic permeability decreases and the losses (hysteretic, eddy current and anomalous) increase. The integration of sendust components in RFID tags is therefore subject to a number of constraints and poses a non-trivial multiple-parameter optimisation problem, which requires the detailed and quantitative understanding of the near field RF distributions created. The quantitative RF field imaging system, presented on fig. 1a is comprized of two main sub-systems: a stepper motor-driven 4-axial table, which holds the measured RFID tag-assembly, and a source coil (2 turns of 0.5 mm diameter wire, with an overal diamater of 21 cm), powered by an RF broadband amplifier (constant 40 dB gain, 50 Ω coupled). The second main sub-system is comprized by a 4-micro-coil assembly, allowing for the measurement of H_x, H_y, H_z and dH_z/dz and a 4-channel Vector Network Analyser (VNA), which produces the excitation waveforms and acquires the in- and out-of-phase signals. The individually insulated sensing coils on their poly-carbonate carriers are glued together in one monoblock assembly (see fig. 1b), which is in turn mounted on a transparent poly-carbonate carrier, allowing for easy optical alignment to the Device Under Test (DUT). The VNA used is of the R&S ZVB series with a front-end band-width of 20 GHz and allows for the rapid and simultaneous acquisition of 4 complex transmission spectra (S41 to S44). The measurment consist of acquiring 4 complex transmission spectra (of at least 101 frequency points each) for each spatial point of a rectangular (x, y) grid - i.e. a constant z-cut. The postprocessing of the data involves corrections for direct inductive pick-up between the source coil and the sense coils, corrections for non-orthogonality of the vector components and calibration of the source and measured field magnitudes. An example of a vector field map of the HF magnetic field is shown on fig. 1c. The region of the copper RFID module coils is clearly seen around the perimeter, as are the CMOS chip (at the bottom of the visible field) and the 200 μm thick, sendust film of lateral dimenions (3 x 40 mm). The vector reconstruction corresponds to the peak-resonance frequency region of 13.6-13.7 MHz. As expected, the imaginery components, at resonance, are small and only contain useful information about a small region of space between the sendust strip and the CMOS chip. As frequency spectra are obtained at every spatial point of the scanned field, these can be processed and fitted to simple analytical models or compared to finite element calculations as required. Fig. 2 represents thesimultaneous fitting of the real and imaginery parts of the frequency spectra, for a point just above the copper coils of the tag, half-way up the length of the coil, to a model comprised of two damped harmonic oscillators. The type of complete spatial, full-vector, complex magnetic susceptibility imaging presented here should open pathways to the integration of magnetic materials in near-field short-range communication sysytems, including, but not limited to RFID.

[1] V. Chawla and D. S. Ha, *An overview of passive RFID*, IEEE Commun. Mag., vol. 45, no. 9, pp. 11–17, Sep. 2007. [2] Identification cards - Contactless integrated circuit(s) cards - Proximity cards - Part 1: Physical characteristics, ISO/IEC 14443-1, 2000. [3] H. Masumoto and T. Yamamoto, *"On a New Alloy "Sendust" and its Magnetic and Electric Properties,"* Journal of the Japan Institute of Metals, vol. 1, pp. 127-135, 1937.

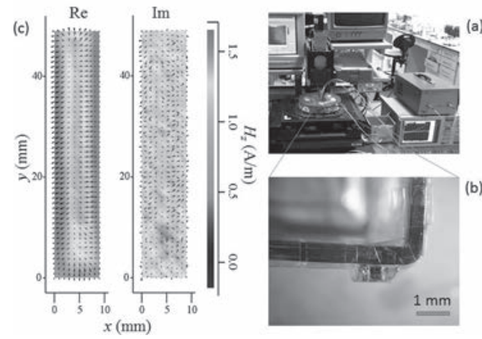

Fig. 1. An overview of the RF field mapper (a), together with a detailed view of the assembly of the measurement micro-coils. b) Vector profiles of the real and imaginery components of the RF field in a plane 0.5 mm above the RFID tag, at resonance. The colorscale corresponds to the H_z component of the field.

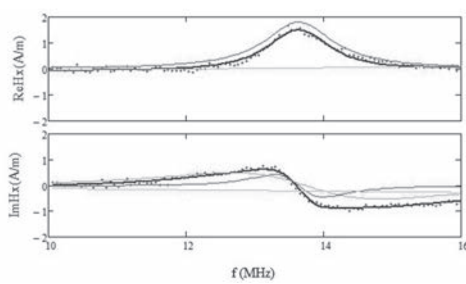

Fig. 2. Single spatial point, frequency spectra of the real and imaginery components of the H_x field component (obtained in 0.2 s). The fits have been executed simultaneously for the real and imaginery components. Fitting curve is in bold-line, the Lorentzian and Lorentzian derivative resonance components and the linear inductive background are also shown for clarity.

11:45

CC-09. A Sensitive AC Magnetometer using A Resonant Excitation Coil for Characterization of Magnetic Fluid in Nonlinear Magnetization Region.

M. Saari[1], N. Suhaimi[1], N. Che Lah[2], K. Sakai[3], T. Kiwa[3] and K. Tsukada[3]
1. Faculty of Electrical & Electronic Engineering, Universiti Malaysia Pahang, Pekan, Malaysia; 2. Faculty of Manufacturing Engineering, Universiti Malaysia Pahang, Pekan, Malaysia; 3. Graduate School of Natural Science and Technology, Okayama University, Okayama, Japan

Characterization of magnetic nanoparticles (MNPs) is important for their standardization and optimization for specific applications[1]–[3]. One of the characterization methods is AC susceptibility measurement where this method can provide fast information of MNPs on dynamic magnetization, size distribution and magnetic anisotropy[1], [2], [4], [5]. In this study, we report a development of a sensitive AC magnetometer using induction coils for characterization of MNPs in nonlinear magnetization region. The developed AC magnetometer system consists of two main parts: magnetic field excitation unit and magnetic response detection unit. Using a cylindrical surface current model [6], the excitation coil of the magnetic field excitation unit was designed to produce a high homogeneity and strong excitation magnetic field for a 1-ml cylindrical sample. The excitation coil was wound to be 300 turns with an inner diameter of 30 mm using a Litz wire. To prevent voltage breakdown and sparks, and mitigate the temperature rise of the excitation coil during excitation of high magnitude and frequency of current, a specific fabrication design was adopted. To generate high excitation magnetic field at high frequency, a resonant technique was applied where multiple values of polypropylene film capacitors were connected in series to the excitation coil. The resonant frequency was determined from the selected value of capacitance. For the magnetic response detection unit, an induction detection coil was fabricated using a 0.25-mm Cu wire. The detection coil was configured to be a first-order axial differential coil, whose inner diameter was 15 mm and one coil had 1000 turns. The detection coil was placed into the excitation coil and the cancellation rate of the excitation magnetic field was improved by manually tuning the position of the detection coil at the axis of the excitation coil. The detection coil was connected to a lock-in amplifier (LI5640, NF Corporation) for a phase-sensitive detection. We first measured the complex impedance of the excitation coil. The resistance of the excitation coil showed a constant value of 1.3 Ω until 1 kHz and increased in a higher frequency region. The measured reactance of the excitation coil increased linearly with respect to frequency and the inductance was measured to be 1.52 mH. The increase of impedance at high frequency was found to be due to the inductance of the excitation coil where the increase of the impedance can be compensated using a LCR resonant circuit. To evaluate the effectiveness of the resonant technique, the current magnitude of the excitation coil connected with a current supply and resonant capacitors was measured when the current supply was operated in a constant voltage mode at different resonant frequencies. Compared to the case when the resonant technique was not applied, the current magnitude was maintained to a constant value up to 18 kHz. The homogeneity of the excitation field for a region of 15 mm × 10 mm was measured to be 95%, which was in good agreement with the simulation result. The excitation coil showed a high efficiency of 5.2 mT/ampere at the high homogeneity region, enabling characterization of MNPs in the non-linear magnetization region.[7] The DC resistance and inductance of the detection coil were measured to be 41.46 Ω and 16.76 mH. The complex impedance of the detection coil increased when the frequency was greater than 1 kHz and a self-resonant characteristic was observed at 70 kHz. Using a small 30-turn coil, the gradient characteristic and the sensitivity of the detection coil were measured, where detection sensitivity of a sample can be improved when the sample is placed at an optimized position relative to the detection coil. The developed system showed a sensitivity of 5×10^{-10} $Am^2/\sqrt{Hz}$ at 100 Hz. The feasibility of the developed system was demonstrated by measuring the dynamic magnetization of a commercial multi-core iron oxide nanoparticles, namely nanomag-D-spio D100 (Micromod Partikeltechnologie GmbH, Rostock-Warnemuende, Germany), having a mean hydrodynamic size of 100 nm. Different solutions of iron concentration were prepared from 0.24 mg/ml to 300 ng/ml by diluting the stock solution with purified water. The developed system successfully measured the harmonics response of the iron oxide nanoparticles at different iron concentrations where a linear relation of third, fifth and seventh harmonics were observed with respect to iron concentration. The non-linear magnetization characteristic of the iron oxide nanoparticles was observed when the amplitude of the excitation field was greater than 3 mT. We also demonstrated the ability of the developed to measure the complex susceptibility of the iron oxide nanoparticle solutions. The real component of magnetization m' showed a constant response until 18 kHz while the imaginary component of magnetization m'' slightly increased with increasing frequency, inferring that the Neel relaxation was dominant in the iron oxide nanoparticles. Therefore, a sensitive characterization of magnetic fluid can be expected by using the developed system. This work was supported by Ministry of Higher Education of Malaysia under grant number of RDU 160115 and Research Management Center of Universiti Malaysia Pahang under grant number of RDU 170377.

[1] J. Wells *et al.*, "Standardisation of magnetic nanoparticles in liquid suspension," *J. Phys. D. Appl. Phys.*, vol. 50, no. 38, p. 383003, Sep. 2017. [2] K. Enpuku, T. Sasayama, and T. Yoshida, "Estimation of magnetic moment and anisotropy energy of magnetic markers for biosensing application," *J. Appl. Phys.*, vol. 119, no. 18, 2016. [3] M. M. Saari, K. Sakai, T. Kiwa, T. Sasayama, T. Yoshida, and K. Tsukada, "Characterization of the magnetic moment distribution in low-concentration solutions of iron oxide nanoparticles by a high- T <inf>c</inf> superconducting quantum interference device magnetometer," *J. Appl. Phys.*, vol. 117, no. 17, 2015. [4] F. Ahrentorp *et al.*, "Sensitive high frequency AC susceptometry in magnetic nanoparticle applications," *AIP Conf. Proc.*, vol. 1311, no. 2010, pp. 213–223, 2010. [5] V. Connord, B. Mehdaoui, R. P. Tan, J. Carrey, and M. Respaud, "An air-cooled Litz wire coil for measuring the high frequency hysteresis loops of magnetic samples - A useful setup for magnetic hyperthermia applications," *Rev. Sci. Instrum.*, vol. 85, no. 9, 2014. [6] N. S. Suhaimi, M. M. Saari, A. I. Mohamed, N. A. C. Lah, and M. Samykano, "Development of a compact and sensitive AC magnetometer for evaluation of magnetic nanoparticles solution," in *2017 IEEE 8th Control and System Graduate Research Colloquium (ICSGRC)*, 2017, no. August, pp. 221–224. [7] Z. W. Tay, P. W. Goodwill, D. W. Hensley, L. A. Taylor, B. Zheng, and S. M. Conolly, "A High-Throughput, Arbitrary-Waveform, MPI Spectrometer and Relaxometer for Comprehensive Magnetic Particle Optimization and Characterization," *Sci. Rep.*, vol. 6, no. March, p. 34180, 2016.

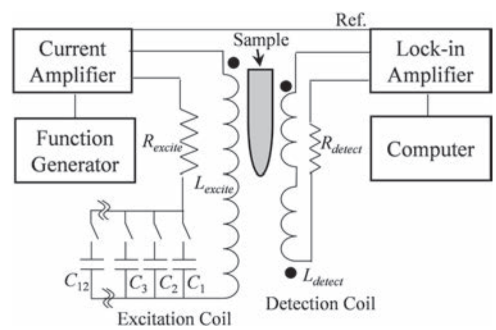

Fig. 1. Schematic diagram of the developed AC magnetometer system with a resonant excitation coil.

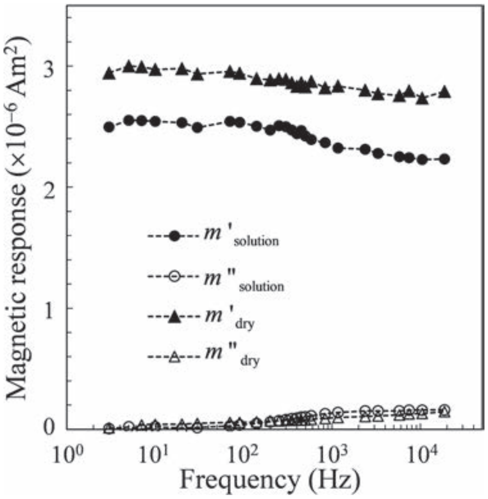

Fig. 2. Real (*m*') and imaginary (*m*") magnetic response versus excitation frequency of the multi-core iron oxide nanoparticles in dry and solution states.

Session CD
DOMAIN WALL DYNAMICS

Tiejun Zhou, Co-Chair
Hangzhou Dianzi University, Hangzhou, China
Dunhui Wang, Co-Chair
Nanjing University, Nanjing, China

CONTRIBUTED PAPERS

9:00

CD-01. Domain wall properties and spin transfer torque in perpendicularly magnetized Mn_4N ferrimagnet thin films.

T. Gushi[1], L. Vila[2], J. Attané[2], O. Fruchart[2], A. Marty[2], S. Pizzini[3], J. Vogel[3], F. Takata[1], A. Anzai[1] and T. Suemasu[1]
1. Institute of Applied Physics, University of Tsukuba, Tsukuba, Japan; 2. INAC/SPINTEC, CEA, Grenoble, France; 3. Institut Néel, CNRS, Grenoble, France

Current induced domain wall motion (CIDWM) is attractive for several applications arising from spintronics. Since its discovery, the spin-transfer torque (STT) allows one to envision several memory candidates, or magnetic based computation technologies, combining, for example, tunability, high density, rapid operation, altogether with inherent magnetic non-volatility and energy efficient read/write/store operations. CIDWM can be achieved through the spin-transfer torque (STT) given by spin polarized carriers to the local magnetic states [1,2]. Lower threshold current density j_{th} for CIDWM and higher domain wall (DW) velocity v_{DW} are expected if spontaneous magnetization M_S gets smaller as the amount of torque for magnetization reversal should scale with M_S. In addition, j_{th} is expected to be smaller in perpendicularly magnetized layers than in-plane magnetized layers [3,4]. Therefore, magnetic materials possessing perpendicular magnetic anisotropy (PMA) and small M_S are very interesting candidates for spintronic devices based on CIDWM. We are interested in ferrimagnetic Mn_4N thin films. First, Mn_4N has a large perpendicular magnetic anisotropy (μ_0H_K about 3 T) and a small μ_0M_S (0.14 T) [5,6]. So Mn_4N is in principle a promising candidate for CIDWM in materials with strong PMA and small M_S. Second, it is a ferrimagnetic material composed of only abundant, light and cheap elements. In this paper, we characterize and compare domain wall (DW) properties of Mn_4N thin films grown on MgO or $SrTiO_3$ (STO) substrates. Single crystalline Mn_4N films have been deposited at 450 °C using molecular beam epitaxy [6], with a 3-nm-thick SiO_2 cap. The magnetic properties have been evaluated by Magneto-transport, and the magnetic configuration has been observed by magnetic force microscopy (MFM) or Kerr microscopy. We observe large Extra-Ordinary Hall effect (~2%) despite Mn_4N is being made of only light elements. Moreover we show that we can achieve magnetization reversal with millimeter sized magnetic domains in Mn_4N thin layers. Finally, we report very efficient CIDWM properties in Mn_4N nanostrips. Figure 1 presents the hysteresis loops (minor for B) measured by Extra-Ordinary Hall resistivity ρ_{EHE} for the fabricated Mn_4N films. Focusing on the two films grown on MgO, the 30 nm one (A) has better magnetic properties than the 10 nm one (B), with a lower coercive field and a higher remanence. The sample (C), grown on STO, possess a full remanence (M_r/M_S=1.0), a quite sharp magnetization switching and even a smaller coercive field, compared to (A). The higher quality of the films deposited on STO can be seen when imaging its magnetic domains. Figures 2 show domain structures of Mn_4N films captured by MFM or Kerr microscopy after partial magnetization reversal process from the saturated state. The sample deposited on MgO shows small magnetic domains, despite the small M_S and large K_u of Mn_4N which should lead to large equilibrium domain size. We attribute this to the presence of a large distribution of pinning defects, also responsible for the higher coercivity of thinner sample (B). The sample grown on STO has far larger magnetic domains, propagating with incredibly big domain sizes (larger than 1 mm). In addition, the smoothness of the DWs in this layer indicates that there are few intrinsic DW pinning sites, which agrees with the sharp magnetization switching in the hysteresis loop. We attribute the differences observed between the Mn_4N/MgO and Mn_4N/STO systems to the large misfit between Mn_4N and MgO (-7.6%) compared with STO (-0.4%), which leads to defects that can trap DWs. As the relaxation of the strain occurs at the vicinity of the interface, the importance of these defects is clearer in the thinnest film deposited on MgO. We successfully observed the effect of STT on the coercive field and will report very efficient CIDWM in Mn_4N wire. Though the detail will be presented at the conference, STT efficiency ε, calculated by the equivalency between the magnetic field and the electrical current density for magnetization reversal is found to be around 7×10^{-12} Tm^2/A. The threshold current density for CIDWM is observed at 2×10^{11} A/m^2, and the DW velocity v_{DW} reaches over 200 m/s in first attempts, without any assistance of external field or spin-orbit torque from the cap layer. In summary, this paper reports the first investigation of CIDWM in Mn_4N. DW properties in Mn_4N film were drastically improved by changing substrate from MgO to STO. We report magnetization reversal with extremely large domain size, due to few domain nucleation centers and smooth DW propagation. In addition, the Mn_4N/STO system shows great potential for application to CIDWM devices with low threshold current and ultrahigh DW speed. This work was financially supported in part by JSPS (No. 26249037) and JSPS Fellows (No. 16J02879).

[1] L. Berger, J. Appl. Phys. 55, 1954 (1984). [2] J. C. Slonczewski, J. Magn. Magn. Mater. 159, L1 (1996). [3] S. Fukami, T. Suzuki, N. Ohshima, K. Nagahara, and N. Ishiwata, J. Appl. Phys. 103, 07E718 (2008). [4] S.-W. Jung, W. Kim, T.-D. Lee, K.-J. Lee, and H.-W. Lee, Appl. Phys. Lett. 92, 202508 (2008). [5] K. Kabara, and M. Tsunoda, J. Appl. Phys. 117, 17B512 (2015). [6] Y. Yasutomi, K. Ito, T. Sanai, K. Toko, and T. Suemasu, J. Appl. Phys. 115, 17A935 (2014).

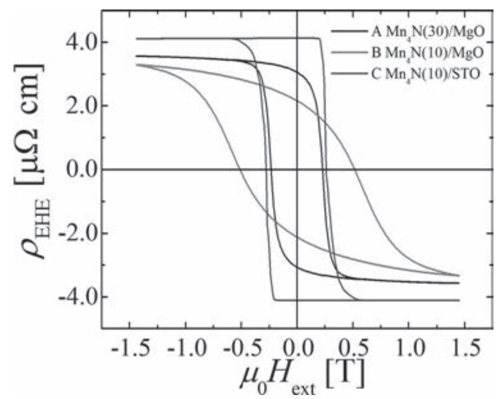

Fig. 1. Hysteresis loops of the samples A-C obtained by Extra-Ordinary Hall effect. The samples on MgO have smooth curves, and thinner sample B cannot be saturated by only 1.5 T. In contrast, sample C on STO has well squared loop with full remanence. The sharp switching around 0.2 T indicates that DW motion in sample C is easier than in the one deposited on MgO.

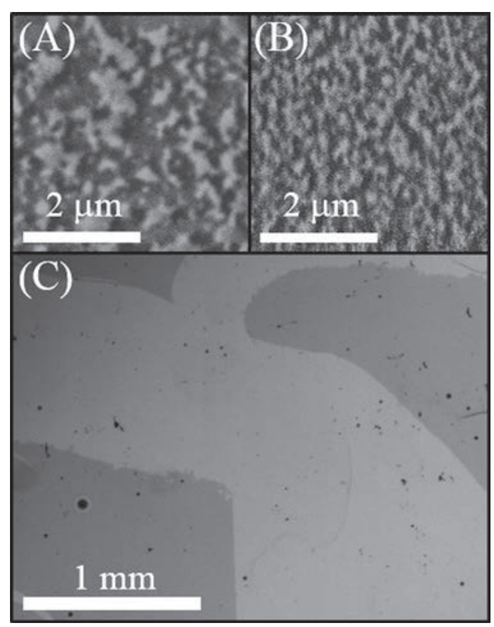

Fig. 2. RMFM (A, B) and Kerr microscopy images (C) of the domain structure after demagnetization. The films on MgO have small and not continuous domains, while that on STO has extremely large domains wider than 1 mm, which indicates few nucleation centers and DW pinning sites.

9:15

CD-02. Anomalous Nernst effect related to magnetic domains in a microfabricated thermoelectric element made of noncollinear antiferromagnet Mn_3Sn.

H. Narita[1], M. Ikhlas[1], M. Kimata[2], A.A. Nugroho[3], S. Nakatsuji[1,4] and Y. Otani[1,4]
1. Institute for Solid State Physics, The University of Tokyo, Kashiwa, Japan; 2. Tohoku University, Sendai, Japan; 3. Faculty of Mathematics and Natural Sciences, Institut Teknologi Bandung, Bandung, Indonesia; 4. JST CREST, Tokyo, Japan

Recently, antiferromagnetic materials have attracted increasing attention because of their large magnetotransport and thermomagnetic effects, in which the electronic band structure associated with the noncollinear spin configuration is responsible for generating Berry curvature through spin-orbit coupling[1-3]. The anomalous Nernst effect (ANE) is a thermoelectric phenomenon typically observed in ferromagnets under the application of a temperature gradient, in which a transverse voltage is induced perpendicular to both the temperature gradients and the magnetization. Recent experimental studies have shown large ANE in a noncollinear antiferromagnetic metal Mn_3Sn with a vanishingly small magnetization of 0.002 μ_B per Mn atom[4,5], whose band structure has the Weyl points near [6,7]. In previous studies, the fabrication of thermoelectric devices with the enhanced Seebeck effect has proven to be complicated, owing to the requirement for alternately aligned p- and n-type semiconductor pillars[8]. On the other hand, the ANE allows the design of much simpler thermopiles composed of laterally series-connected wires. Toward realizing a thermopile made of the chiral anti-ferromagnet Mn_3Sn, focused ion beam (FIB) lithography was employed to microfabricate a thermoelectric element consisting of a $Ta/Al_2O_3/Mn_3Sn$ layered structure[9]. Figures 1(a) and (b) show a schematic illustration of the microfabricated Mn_3Sn device structure for measuring ANE and the magnetic structure of the Mn_3Sn when the magnetic field is applied along the [01-10] axis, where the thermal gradient is applied along the [0001] axis. In this device, the Ta layer acts as a heater producing Joule heat diffusing across the Al_2O_3 insulating layer into the thin Mn_3Sn layer. All measurements were performed at room temperature in vacuum. Figure 2 shows the ANE results for the configuration shown in Fig. 1(a) obtained for a dc current of ±1.5 mA applied to the Ta heater. The measured AN signal exhibits a clear hysteresis in an applied temperature gradient and magnetic field. The V_{ANE} is indeed independent of the direction of the applied electrical current in the Ta heater. This indicates that the hysteresis loop in Fig. 2(a) is arising from the ANE in Mn_3Sn. The observation of the spontaneous, zero field value is essential for construction of the thermopile element. Figure 2(b) shows the electrical current dependence of V_{ANE}. The voltage increases with the electrical current in the Ta heater. The sign and magnitude do not depend on the direction of the electrical current. The magnitude is also proportional to the square of the electrical current applied to the Ta heater. In addition, the angular dependence of ANE in the configuration shown in Figure 1(a) shows a small anomaly around 60° when the magnetic field is rotated from the [2-1-10] axis (0°) to the [01-10] axis (90°). On the other hand, in another ANE-measurement device of Mn_3Sn, the shape of the hysteresis of ANE has a step structure depending on the electrical current in the Ta heater just beside the microfabricated Mn_3Sn. According to the theoretical study, six magnetic domains that are different at each 60° are proposed in Mn_3Sn[10]. However, an additional study is required to clarify the origin of this structure. In summary, we evaluated the ANE in a microfabricated device comprised of the chiral antiferromagnet Mn_3Sn as a first step to realize a thermopile device. The spontaneous, zero field voltage signal in the device is of the order of a few μV, which is almost the same order of magnitude as observed in the bulk single-crystal Mn_3Sn under a temperature gradient. The anomalous Nernst coefficient S_{ANE} of the microfabricated element was determined using a temperature gradient simulated by finite-element modeling. The experiment and simulation revealed that the ANE coefficient is 0.27 μV/K which is in good agreement with the bulk value. This result indicates that the FIB microfabrication does not significantly alter the thermoelectric properties of bulk Mn_3Sn. As the chiral antiferromagnet produces almost no stray field, our study opens the avenue for the fabrication of an efficient thermopile by densely packing the microfabricated antiferromagnetic elements. In this work, the Mn_3Sn microdevice was fabricated from a bulk crystal, rather than through the deposition of thin films. This approach enables us to investigate thermoelectric phenomena on the nanoscale in wider range of materials than conventional materials used in thin film based devices.

[1]S. Nakatsuji, N. Kiyohara and T. Higo, Nature 527, 212–215 (2015). [2]N. Kiyohara, T. Tomita, and S. Nakatsuji, Phys. Rev. Applied, 5, 064009 (2016). [3]A. K. Nayak, J. E. Fischer, Y. Sun, B. Yan, J. Karel, A. C. Komarek, C. Shekhar, N. Kumar, W. Schnelle, J. Kübler, C. Felser, S. S. P. Parkin, Sci. Adv. 2, 1501870 (2016). [4]M. Ikhlas, T. Tomita, T. Koretsune, M. Suzuki, D. Nishio-Hamane, R. Arita, Y. Otani, S. Nakatsuji, doi:10.1038/nphys4181 (2017). [5]X. Li, L. Xu, L. Ding, J. Wang, M. Shen, X. Lu, Z. Zhu and K. Behnia, Phys. Rev. Lett. 119, 056601 (2017). [6]G. Sharma, P. Goswami, and S. Tewari, Phys. Rev. B 93, 035116 (2016). [7]K. Kuroda, T. Tomita, M.-T. Suzuki, C. Bareille, A. A. Nugroho, P. Goswami, M. Ochi, M. Ikhlas, M. Nakayama, S. Akebi, R. Noguchi, R. Ishii, N. Inami, K. Ono, H. Kumigashira, A. Varykhalov, T. Muro, T. Koretsune, R. Arita, S. Shin, Takeshi Kondo, S. Nakatsuji, Nat. Mater. 16, 1090–1095 (2017). [8]LeBlanc, S. Thermoelectric generators: Linking material properties and systems engineering for waste heat recovery applications. Sustain. Mater. Technol 1-2, 26–35 (2014). [9]H. Narita, M. Ikhlas, M. Kimata, A. A. Nugroho, S. Nakatsuji, YoshiChika Otani, Appl. Phys. Lett. 111, 202404-1-5 (2017). [10]J. Liu and L. Balents, PRL 119, 087202 (2017).

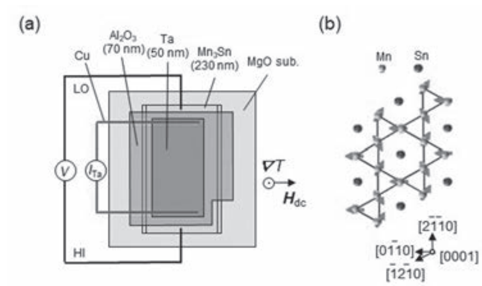

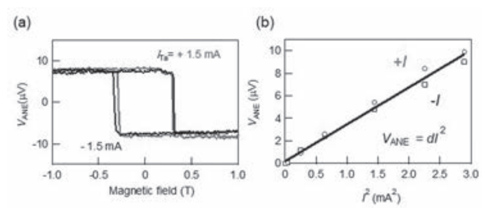

9:30

CD-03. Direct observation of domain wall surface tension by deflating or inflating a magnetic bubble.

X. Zhang[1,2*], N. Vernier[2], W. Zhao[1], L. Vila[3] and D. Ravelosona[2]
1. Fert Beijing Institute, School of Electronic and Information Engineering, Beihang University, Beijing, China; 2. Center for Nanoscience and Nanotechnology, Université Paris-Sud, Orsay, France; 3. Université Grenoble Alpes, Grenoble, France

The behavior of a magnetic domain wall (DW) is similar to that of many other types of interfaces in physics, such as vortices in superconductors, soap films or surfaces of liquids. The main parameter required to explain the observed behavior is the surface energy γ. This energy plays a very important role in the dynamics and statics of the DW, such as the topological transition of magnetic textures from domain stripes to skyrmionic bubbles[1]. Moreover, the stabilization and the size of these skyrmionic bubbles is directly determined by the competition between the DW surface tension and the dipolar interaction[2]. Another example, in the artificial pinning of DWs at constrictions, the depinning process is directly related to the increase of the surface energy γ due to the modification of the DW length to move out of the constriction. However, it is difficult to directly observe the effect of the DW surface energy and determine its value. In this presentation, we report the direct observation and measurement of magnetic DW surface tension in CoFeB thin films with perpendicular anisotropy. In small magnetic squares, we observed that semicircular domain bubbles could spontaneously collapse in zero magnetic fields, as shown in Fig. 1(a). This can be explained by the Laplace-Young pressure on the DW induced by its curvature and the associated surface energy, read $P=\gamma/R$, where R is the radius of curvature. Then, an external magnetic field was applied to stabilize these semi-circular domain bubbles. We found that when the external field is larger than a critical value, the bubble expands; when the external is smaller than this value, the bubble collapses. A clear boundary (representing the stabilizing field) between the expanding field and contracting field was found. The stabilizing fields change linearly with the inverse of the radius of bubbles, as shown in Fig. 1(b). This relationship enables us to determine the surface energy of the DW quantitatively. Our experiments further showed that the surface energy could lead to a geometrically induced pinning when the DW propagates in a Hall cross or from a narrow wire into a nucleation pad, as shown in Fig. 2(a). We further demonstrate that the measurement of the depinning field as a function of the wire width, as shown in Fig. 2(b), is another way to estimate the surface energy of the DW. In addition, some other interesting phenomena, such as the interplay of two adjacent bubbles under the competition between the dipole interaction and the unbalanced Laplace pressure were observed. The dynamic process will be presented. Moreover, a new type of magnetic sensors, which can detect the magnetic field based on the surface tension (or elasticity) of the DW is proposed based on the above experiments. In summary, our experiments reveal that the surface tension can be an important fundamental parameter dominating the behavior of DWs, and thus be directly observable. Two new methods to directly measure the surface energy of the DW are proposed and verified. This accurate measurement of the DW surface energy is very helpful to estimate intrinsic parameters such as Dzyaloshinskii-Moriya Interactions (DMI) or exchange stiffness in magnetic materials and to better understand the role played by the different energy terms involved in the physics of DWs. Note that the DMI results in an additional term in the expression of the surface energy γ that is proportional to the DMI coefficient[3]. Moreover, understanding of the dynamic behavior of DWs governed by its surface tension is important to develop novel devices such as racetrack memory and the DW based magnetic sensors[4,5].

[1] W. Jiang *et al.*, "Blowing magnetic skyrmion bubbles," *Science*, vol. 349, no. 6245, pp. 283–286, 2015. [2] A. Fert, N. Reyren, and V. Cros, "Magnetic skyrmions: advances in physics and potential applications," *Nat. Rev. Mater.*, vol. 2, p. 17031, 2017. [3] S. Rohart and A. Thiaville, "Skyrmion confinement in ultrathin film nanostructures in the presence of Dzyaloshinskii-Moriya interaction," *Phys. Rev. B*, vol. 88, no. 18, p. 184422, 2013. [4] X. Zhang et al "Direct observation of domain wall surface tension by deflating or inflating a magnetic bubble"ArXiv:1708.06719 (2018) [5] X. Zhang et la. "Magnetoresistive sensors based on the elasticity of domain walls" ArXiv (2018)

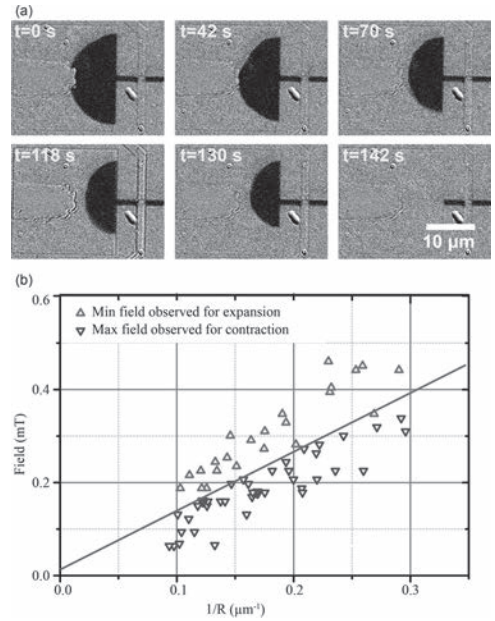

Fig. 1. (a) Kerr images showing the spontaneous contraction of the semicircular domain bubble in a zero external field. (b) Critical fields for expansion and contraction as a function of the inverse of the radius of the semicircular domain bubble. The green line is plotted along the boundary between the expansion field and contraction field, indicating the critical field required to stabilize the semicircular bubble.

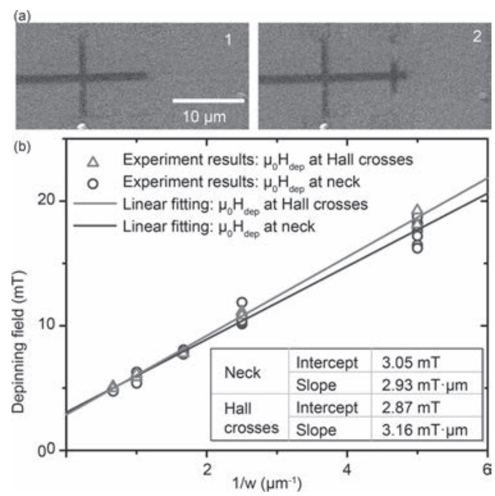

Fig. 2. (a) DW depinning at the neck (Hall cross): Image n°1 shows the pinned DW after a field pulse of 5.9mT and 5 μs; image n°2 shows the profile of the DW depinned after the magnitude of the field pulse increased to 6.0 mT; (b) DW depinning field as a function of the inverse of the wire width.

9:45

CD-04. Tailoring the Current Driven Domain Wall Motion by Engineering Two Heavy Metal Underlayers.

Y. Liu[1,3], X. Liu[2,3] and J. Zhu[2,3]

1. Materials Science and Engineering, Carnegie Mellon University, Pittsburgh, PA, United States; 2. Electrical and Computer Engineering, Carnegie Mellon University, Pittsburgh, PA, United States; 3. Data Storage Systems Center, Carnegie Mellon University, Pittsburgh, PA, United States

The ability to move magnetic domain walls by electrical current enlightens novel ways for developing non-volatile memory and logic devices [1], [2]. The realization of current driven domain wall motion (DWM) in heavy metal (HM)/ ferromagnet (FM)/ oxide heterogeneous structures can be attributed to the combined effect of spin Hall effect from HM and Dzyaloshinskii-Moriya interaction (DMI) at HM/FM interface [3], [4]. Different combinations of spin Hall angle (positive or negative) and effective DMI field (left or right) determine the direction of DWM with respect to the current direction [5]–[7]. Alternating the direction of DWM often requires the selection of different HM or FM materials. Here, we show that it's able to control the direction as well as velocity of the current induced DWM by varying the relative thicknesses of two heavy metal underlayers. In our experiments, all films were deposited by magneton sputtering (DC for metals, RF for oxide) with base pressure ≤ 2×10^{-8} Torr. The film stacks were substrate/ Ta(0.5)/ Pt(3)/ W(0.6, 0.8, 1, 1.5)/ FeCoB (1.2)/ MgO(2)/Ta(1) with units in nanometers. Note that the bottom and top thin Ta layers are for film adhesion and capping purposes, and the effect of spin Hall torques from these layers on the FeCoB layer are negligible. The films were then annealed at 305 ^{0}C under 0.4 T magnetic field perpendicular to the film surface. Magnetization curves were measured by Alternating Gradient Field Magnetometer and all films exhibited perpendicular magnetic anisotropy. Magnetic bubble domain testing [8] was conducted to measure the domain wall chirality at the W/ FeCoB interface. Figure 1 shows the velocity of down-up and up-down domain walls as a function of in-plane magnetic field under $\mu_0H_z = 0.5$ mT. The results show that the domain wall has right-handed chirality at the W/ FeCoB interface, which agrees with previous observations by other group [5]. The minima in Figure 1 indicate the effective DMI field is around 43 mT. Next, films were lithographically patterned into 4 μm-wide 26 μm-long wires with bowtie-like contact pads on each side. The domain wall motion under nanosecond current pulses was tracked by Kerr microscope, where the velocity of domain wall motion was determined with the sequences of Kerr images. The velocity of current driven domain wall is plotted in Figure 2 as a function of W layer thickness, where positive velocity indicates domain wall motion along the current direction. We observe that the domain wall moves in the same direction as the current when W layer thickness is above 0.8 nm. Meanwhile, the domain wall velocity is linearly dependent on W layer thickness. Once the thickness is reduced below 0.8 nm, however, the motion direction switch to that against the current direction. Such phenomenon arises from the injection of two spin currents into the FeCoB layer with opposite signs of spin polarization (Figure 2 inserted), which further causes the competition of two opposite spin orbit torques. The two spin currents are generated by the spin Hall effect of the two heavy metal underlayers, where they reach balance at 0.8 nm thick W layer, as indicated by the zero domain wall velocity. In summary, we have demonstrated that by changing the relative thicknesses of two heavy metal underlayers we are able to control the direction and velocity of current driven domain wall motion. It results from the competition of two pure spin currents with opposite signs of spin polarization generated by the spin Hall effect of the heavy metal underlayers. Such way of manipulating current driven DWM would spark novel designs in spintronic devices and applications.

[1] D. M. Bromberg, M. T. Moneck, V. M. Sokalski, J. Zhu, L. Pileggi, and J.-G. Zhu, "Experimental demonstration of four-terminal magnetic logic device with separate read- and write-paths," *Electron device Meet.*, no. October 2015, pp. 792–795, 2014. [2] S. Parkin and S.-H. Yang, "Memory on the racetrack," *Nat. Nanotechnol.*, vol. 10, no. 3, pp. 195–198, 2015. [3] O. J. Lee, L. Q. Liu, C. F. Pai, Y. Li, H. W. Tseng, P. G. Gowtham, J. P. Park, D. C. Ralph, and R. A. Buhrman, "Central role of domain wall depinning for perpendicular magnetization switching driven by spin torque from the spin Hall effect," *Phys. Rev. B - Condens. Matter Mater. Phys.*, vol. 89, no. 2, pp. 1–8, 2014. [4] K.-S. Ryu, S.-H. Yang, L. Thomas, and S. S. P. Parkin, "Chiral spin torque arising from proximity-induced magnetization.," *Nat. Commun.*, vol. 5, no. May, p. 3910, 2014. [5] J. Torrejon, J. Kim, J. Sinha, S. Mitani, M. Hayashi, M. Yamanouchi, and H. Ohno, "Interface control of the magnetic chirality in CoFeB/MgO heterostructures with heavy-metal underlayers," *Nat. Commun.*, vol. 5, p. 4655, 2014. [6] L. Liu, "Spin-torque switching with the giant spin Hall effect of tantalum," *Science (80-.).*, vol. 336, pp. 555–558, 2012. [7] C. F. Pai, L. Liu, Y. Li, H. W. Tseng, D. C. Ralph, and R. A. Buhrman, "Spin transfer torque devices utilizing the giant spin Hall effect of tungsten," *Appl. Phys. Lett.*, vol. 101, no. 12, pp. 1–5, 2012. [8] D. Lau, V. Sundar, J. G. Zhu, and V. Sokalski, "Energetic molding of chiral magnetic bubbles," *Phys. Rev. B*, vol. 94, no. 6, pp. 1–5, 2016.

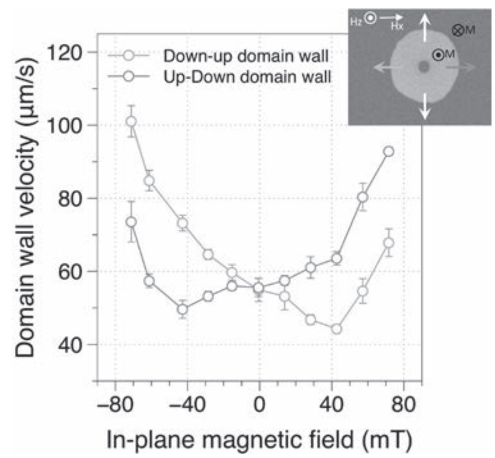

Fig. 1. Velocity of down-up and up-down domain walls as a function of in-plane magnetic field for the film with 1 nm W layer. Inserted: Kerr image showing an initialized magnetic bubble domain. Arrows at the domain walls illustrate right-handed chirality.

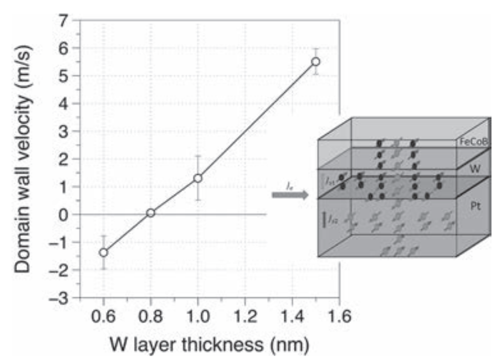

Fig. 2. Domain wall velocity vs. W layer thickness, under applied voltage of 0.75 V/μm. Positive velocity indicates domain walls move along the current direction. Inserted: illustration of injection of the spin currents with opposite signs of spin polarization (J_{s1} and J_{s2}) generated by the two heavy metal layers. Grey dots: electron flow in the Pt layer. Black dots: electron flow in the W layer. Red and green arrows: spin polarization directions.

INVITED PAPER

10:00

CD-05. Magnetic domain wall dynamics and its application.

T. Ono[2,1]
1. CSRN, Osaka University, Toyonaka, Japan; 2. ICR, Kyoto University, Uji, Japan

Current-induced magentic domain wall motion in ferromagnetic materials has been attracted much attention both from scientific and technological points of view [1,2]. When a magnetic DW is driven by electric current via adiabatic spin torque, the theory predicts a finite threshold current even for a perfect wire without any extrinsic pinning [3]. We have shown that this intrinsic pinning determines the threshold current, and thus that the adiabatic spin torque dominates the DW motion resulting in DW motion along electron flow direction, in a perpendicularly magnetized Co/Ni system sandwiched by a symmetric capping and seed layers [4-10]. On the other hand, current-induced DW motion against electron flow direction has been observed in ultrathin magnetic films in which the structural inversion symmetry (SIA) was broken [11, 12].This DW motion against electron flow direction has been explained by the combination of a chiral DW and spin Hall torque [13, 14]. Antiferromagnets are expected to show much faster spin dynamics than ferromagnets because they have higher resonance frequencies than ferromagnets. However, experimental investigations of antiferromagnetic spin dynamics have remained unexplored mainly because of the immunity of antiferromagnets to magnetic fields. Furthermore, this immunity makes field-driven antiferromagnetic DW motion impossible despite rich physics of field-driven DW dynamics as proven in ferromagnetic DW studies. We show that fast field-driven antiferromagnetic spin dynamics is realized in ferrimagnets at the angular momentum compensation point T_A [15]. Using rare-earth–3d-transition metal ferrimagnetic compounds where net angular moment is nonzero at T_A, the field-driven DW mobility remarkably enhances up to 20 km/sT. This remarkable enhancement is a consequence of antiferromagnetic spin dynamics at T_A. Such a high DW velocity leads to coherent terahertz spin-wave emission [16]. Our finding allows us to investigate the physics of antiferromagnetic spin dynamics and highlights the possibility of ferrimagnets for DW devices. Acknowledgment This work was partly supported by JSPS KAKENHI Grant Numbers 15H05702, 26870300, 26870304, 26103002, 25220604, 2604316, Collaborative Research Program of the Institute for Chemical Research, Kyoto University, Cooperative Research Project Program of the Research Institute of Electrical Communication, Tohoku University, and R & D project for ICT Key Technology of MEXT from the Japan Society for the Promotion of Science (JSPS).

[1] A. Yamaguchi et al., Phys. Rev. Lett. 92 (2004) 077205. [2] S. S. P. Parkin, M. Hayashi, and L. Thomas, Science 320 (2008) 190. [3] G. Tatara & H. Kohno, Phys. Rev. Lett. 92 (2004)086601. [4] T. Koyama et al., Nature Materials 10 (2011) 194. [5] T. Koyama et al., Appl. Phys. Lett. 98 (2011) 192509. [6] D. Chiba et al., Appl. Phys. Express 3 (2010) 073004. [7] T. Koyama et al., Appl. Phys. Express 1 (2008) 101303. [8] T. Koyama et al., Nature Nanotechnology 7 (2012) 635. [9] Y. Yoshimura et al., Appl. Phys. Express 5 (2012) 063001. [10] K-J. Kim et al., Nature Communications 4, (2013) 2011: doi:10.1038/ncomms3011. [11] I. M. Miron et al., Nature Materials. 10, (2011) 419. [12] T. Koyama et al., Appl. Phys. Express 6 (2013) 033001. [13] S. Emori, et al., Nat. Mater. 12, (2013) 611. [14] K. S. Ryu, et al., Nat. Nanotech. 8, (2013) 527. [15] K.-J. Kim et al., Nature Materials 16 (2017) 1187. [16] Se-Hyeok Oh et al.,Phys. Rev. B 96, 100407(R) (2017)

CONTRIBUTED PAPERS

10:30

CD-06. Field- and current-driven motion of domain walls in cylindrical nanowires.

A. Wartelle[2], B. Trapp[2], S. Bochmann[3], C. Thirion[2], S. Martin[1,2], M. Stano[2], M. Schöbitz[1,2], M. Foerster[4], L. Aballe[4], T.O. Mentes[5], A. Locatelli[5], A. Sala[5], L. Cagnon[2], J. Toussaint[2], J. Bachmann[3] and *O. Fruchart*[1]
1. SPINTEC, Univ. Grenoble Alpes, CNRS, CEA, Grenoble, France; 2. Institut Néel, Univ. Grenoble Alpes, CNRS, Grenoble, France; 3. Friedrich-Alexander Universität Erlangen-Nürnberg, Erlangen, Germany; 4. Alba Synchrotron Light Facility, Barcelona, Spain; 5. Elettra-Sincrotrone Trieste, S.C.p.A., Trieste, Italy

The motion of domain walls(DWs) in one-dimensional conduits is expected to sensitively depend on the geometry of the cross-section of the conduit. In flat strips, DWs may be of either transverse or vortex type. These DWs share the same topology, which permits the easy transformation of one into another during motion. This is the Walker breakdown, which results in strongly reduced wall velocities above a few mT[1], and also limits the velocity under current. In cylindrical nanowires, transverse-vortex walls also exist (TVW), however a wall with a different topology has been predicted: the Bloch point domain wall (BPW): a quasi-orthoradial curling of magnetization around the core of the DW, where magnetization vanishes for symmetry reasons. The BPW is named after this micromagnetic singularity[2]. Above a threshold diameter of about 7*Δ_d (where Δ_d is the dipolar exchange length), the BPW should be of lowest energy. When motioned under magnetic field, related to their special topology BPWs are expected [3] to remain locked and reach a steady-state motion with a high mobility (proportional to $1/\alpha$, α being the damping parameter). Besides, the chirality of the BPW, i.e. the sense of its orthoradial curling, should be right with the direction of motion [3]. We report results on wires made of soft magnetic alloys (Ni, Fe_xNi_{1-x} and Co_xNi_{1-x}) electroplated in insulating templates with cylindrical holes. The latter are dissolved so that individual wires can be collected and inspected at a wafer surface. We were first to provide the experimental evidence for BPWs[4], using shadow XMCD-PEEM. Here we report several key advancements of the topic. First, we improved the material quality, exploring composition and annealing conditions. This allowed to decrease extrinsic pinning to propagation fields around 10mT or below. Second, we performed experiments of DW motion under magnetic field, from quasistatic to down to nanosecond pulses. Imaging the DW before and after the pulse allows us to track changes in its configuration with shadow XMCD-PEEM, accessing the type, and chirality in case of BPW. We confirm the tendency for the selection of the chirality depending on the direction of motion. Also, beyond a threshold in the range 10-20mT, we evidenced transformation of DW topology, from TVW to BPW and vice-versa. While the transformation from TVW to BPW could be reproduced with micromagnetic simulations and seems intrinsic, the reverse transformation from BPW to TVW may also be related to material defects. This possibility of change of topology had never been reported nor predicted before. It has importance consequences as the mobility of the two topologies of walls is expected to differ by α^2. Third, we developed a nanofabrication process to contact electrically individual wires in a two- or four-probes geometry. The process was optimized to minimize the contact resistance, so that current pulses of magnitude $2.5x10^{12}$ A/m^2 can be sent with up to 100ns duration. Uniformly-magnetized wires display an anisotropic magnetoresistance of several percent, similar to bulk values. DWs could be moved with a threshold current around $1.0x10^{12}$ A/m^2. The lower estimate for the DW speed is 350m/s, which suggests a high mobility of BPWs also under spin-polarized current

[1] Geoffrey S. D. Beach, et al., Nat. Mater. 4, 741 (2005) [2] S. Jamet, et al., chapter in “Magnetic Nano- and Microwires: Design, synthesis, properties and applications”, Woodhead (2015) [3] A. Thiaville, Y. Nakatani, chapter in “Spin Dynamics in Confined Magnetic Structures III”, SpringerVerlag Berlin Heidelberg, 2006 [4] S. Da Col, et al., Phys. Rev. B 89, 180405 (2014)

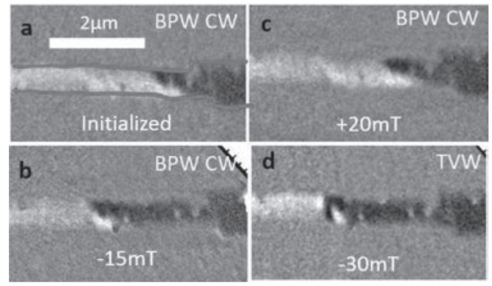

Fig. 1. Shadow XMCD-PEEM magnetic microscopy, revealing the type of wall (TVW or BPW), and the circulation (CW or CCW) for the latter. a-d is a sequence of images performed at rest, separated by application of quasistatic pulses of magnetic field.

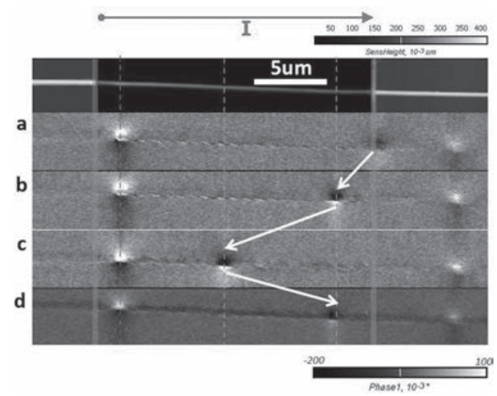

Fig. 2. Atomic (top) and Magnetic Force Microscopy (sequence a-d) images of a Ni wire with diameter 180nm: initial state (a) and after: full-width 30ns current pulse ($9.4x10^{11}$ A/m^2) (b) and a second similar one (c); quasistatic field pulse with strength -15mT.

10:45

CD-07. Inertial and Supermagnonic Dynamics of Domain Walls driven by Spin-Orbit Fields in an Antiferromagnet.

R. Otxoa[1,2], P. Roy[1] and *J. Wunderlich*[1,3]
1. Hitachi, Ltd., Cambridge, United Kingdom; 2. Donostia International Physics Center, Donostia, Spain; 3. Institute of Physics ASCR, Prague, Czechia

Magnetic domain wall dynamics in the layered antiferromagnet such as Mn_2Au and CuMnAs, driven by staggered field-like current-induced spin-orbit torques [1], is investigated by analytical theory and atomistic spin dynamics simulations. Our findings unveil the inertial character of the moving domain wall when the driving mechanism is of field-like torque type. For experimentally feasible excitation strengths, once the excitation is off, we observe inertial domain wall displacements that can be greater than 100 nm. Additionally, spin waves emission only occur under rapid acceleration/deceleration. Once the domain wall reach state motion even though travelling at speeds of 98% of the maximum magnon group velocity no signature of spin-waves emission is observed [2]. This means that the main reason for a given maximum steady-state velocity at a given excitation amplitude is here not due to dissipation via spin-waves [3]. Instead, at these high speeds, the natural response of the system to release the exchange energy stored within the contracted domain wall is to nucleate a domain wall pair with trivial winding number preserving the overall topological charge. The impact of the new domain wall pair is of great consequence onto the initially moving domain wall. We observe that, the system is able to sustain a moving domain wall at speeds higher than the maximum magnon group velocity revealing a super-magnonic regime of motion. These new observed features challenge the applicability of relativistic principle in such a system at very strong excitation. Additionally, we provide a plausible scenario extending the current theory based on dispersive media to explain this regime of motion based on the repulsive ferromagnetic exchange interaction among the neighbouring domain walls.

[1] J. Zelezny, H. Gao, K. Vyborny, J. Zemen, J. Masek, A.Manchon, J. Wunderlich, J. Sinova, and T. Jungwirth, Phys. Rev. Lett. 113, 157201 (2014). [2] O. Gomonay, T. Jungwirth, and J. Sinova, Phys. Rev. Lett. 117, 017202 (2016). [3] T. Shiino, S.-H. Oh, P. M. Haney, S.-W. Lee, G. Go, B.-G. Park, and K.-J. Lee, Physical review letters 117, 087203 (2016).

11:00

CD-08. Current-induced domain-wall motion in pinned magnetic wires.

M. Samiepour[1], J. Kim[1], I. Polenciuc[1], T. Hayward[2], D. Allwood[2], G. Vallejo-Fernandez[1], K. O'Grady[1] and A. Hirohata[1]
1. University of York, York, United Kingdom; 2. University of Sheffield, Sheffield, United Kingdom

In racetrack memory [1] digital data is stored in a series of magnetic domain walls (DWs) in ferromagnetic nanowires. The racetrack memory operates on the base that the DWs can be moved along the nanowires by passing a current through the wire. When a current is applied to a ferromagnetic nanowire, it becomes spin-polarised. The interaction between angular momentum of spin-polarised electrons and the DW, induces a torque on the magnetic moments in the DW and move the DW. Therefore, the racetrack memory is a solid state device without moving parts and can operate faster than hard disk drives (HDDs). In our previous work, we have fabricated a simple pinning scheme for the DWs in straight wires using exchange bias. We have patterned IrMn antiferromagnetic (AF) wires with different widths perpendicularly above and below the CoFe ferromagnetic (F) wires. The AF wires induce exchange bias at AF/F crossing points which act as pinning sites. In the racetrack memory having uniform domain wall pin is essential to control the motion of DWs along the nanowires [3]. Prior to the fabrication of our devices, a vibrating sample magnetometer (VSM, ADE, Model10) was used to characterise an unpatterned continuous film to estimate the pinning strength. The magnetisation curves for the unpatterned films exhibits a loop shift of Hex=46 Oe which is induced by the exchange bias at the CoFe (10nm) / IrMn (5nm) interface [2]. Focused Magneto-Optical Kerr Effect (MOKE) was used to measure local magnetic properties of the FM wires in different devices with four AF wire widths of 1, 1.5, 2, 2.5 µm. The unset racetrack devices show a very small degree of pinning as expected. For the bottom-biased devices, pinning fields increase only slightly with increasing AF wire width. For the top-biased devices, the pinning is larger than that for the bottom-biased structure. These previous results prove that such a structure is ideal for producing DW pins with controlled strength. Following this study we designed a L-shaped magnetic wire with a round corner with a diameter of 650µm, in which one end of the wire is connected to a diamond shaped pad (1.5 µm square) to inject DW and the other end is a sharp arrow to prevent the nucleation of DW. The SEM image of device is shown in Figure 1. We observed that exchange bias gives rise to the domain wall pin therefore we used IrMn bars to pin the DW in our new devices. In this study we fabricated a variety of devices with different AF widths between 100 nm and 500 nm deposited on the 500 nm width F layer. We will report details of current-induced domain wall displacement measured in these devices.

[1] S. S. P. Parkin, M. Hayashi, and L. Thomas, *Science* 320 (2008) 190. [2] M. Hayashi, L. Thomas, R. Moriya, C. Rettner, and S. S. P. Parkin, *Science* 320 (2008) 209. [3] I. Polenciuc, A. J. Vick, D. A. Allowood, T. J. Hayward, G. Vallejo-Fernandez, K. O'Grady, and A. Hirohata, *Applied Physics Letters* 105 (2014) 162406.

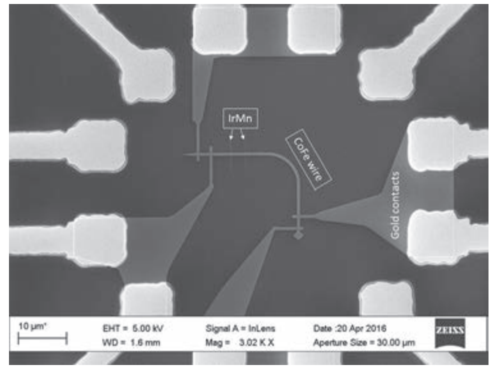

Fig. 1. SEM image of actual device. The L-shaped CoFe wire contains the injector diamond shaped pad and the sharp arrow at the end. The two IrMn bars are 100 nm and 200 nm wide. The electrical current are applied to the wire by the gold contacts.

11:15

CD-09. Action of current on ferrimagnetic domain wall: 2 propagation regimes in creep and influence of domain wall structure.

E. Haltz[1], J. Sampaio[1], R. Weil[1], Y. Dumont[2] and *A. Mougin*[1]
1. CNRS, Univ. Paris-Sud, Université Paris-Saclay, Laboratoire de Physique des Solides, Orsay, France; 2. Université de Versailles St-Quentin-en-Yvelines, Versailles, France

The possibility of manipulating magnetic domain walls (DWs) using electrical current is very attractive for magnetic devices that store and process non-volatile information [1]. To estimate the efficiency of current acting on a magnetic texture (by Spin Transfer Torque for instance), the relevant quantity is a drift speed $u=(g\mu_B P)/(2eMs)$ J where J is the current density, P its spin polarisation in the magnetic media, Ms the net magnetisation, g the Landé factor, μ_B the Bohr magneton, e the electron charge [2]. The analytical q-ϕ model of DW motion along 1D wire shows that DW motion induced just by field or just by STT exhibits 2 different DW propagation regimes [3]. For low field or low current (low u), the DW moves steadily with just a tilt of its central magnetisation. This regime is called translational regime. For stronger field or current (strong u), the DW moves with a continuous precession of its central magnetisation. This regime is called precessional regime. In both regimes, speeds are proportional to H or u. The 2 regimes are separated by a critical field (or critical current) called Walker field (or current). Since the velocity is linear with H or u, it is possible to convert a current density acting on the DW into an equivalent field Heq defined as the field necessary to induce the same macroscopic velocity as the current density. In this equivalent field approach, Heq is proportional to u, with a proportionality constant for each regime. In classical ferromagnetic materials that have been mostly studied, P and Ms have the same physical origin and thermal dependence. Therefore, for those materials, the ratio P/Ms entering u which governs efficiency of STT is fixed. To play with P/Ms, we focused on more exotic materials namely Rare Earth/ Transition Metal (RETM) ferrimagnetics alloys [4] in which it is possible to tune independently Ms or P by composition or temperature. Indeed, in RETM, two populations of magnetic moments are antiferromagnetically coupled: 3d TM moments are antiparallel to 5d and localised 4f RE moments. The alloys net magnetisation is the difference of moments of the 2 populations whereas spin polarisation P arises only from that of RE and TM conduction electrons. We measured amorphous ferrimagnetic TbFe alloys thin films grown by coevaporation. They exhibit perpendicular magnetic anisotropy and P and Ms have clearly different thermal dependence (Fig 1a). The propagation of DWs in TbFe microtracks was analysed using Kerr microscopy. In a first step, we measured the velocity under continuous field (without current pulses) at different temperatures. We observed a nonlinear behaviour of velocity versus field and a strong dependence with temperature (Fig 1b). This type of DW dynamic is called creep regime. In this regime, the DWM is characterised by discrete hopping of the DW between weak pinning centres acting collectively and the DW velocity is described by an Arrhenius law. The energy barrier to overcome by thermal activation depends on the applied field H weighted by a universal exponent (μ=-1/4) that describes the motion of 1D elastic system in 2D random disorder media [5]. Fig 2a illustrates our original results demonstrating Current Induced DW Motion in TbFe wires under combined field and current and Fig 1c shows DW velocities for a few current densities. Two main observations can be done. The STT-like action pushes DWs along the electrons flow and can add or substract to the field action: a signature of STT is the increase of the split between fast (up-triangle) and slow (down-triangle) DWs. Joule heating modifies the creep dynamic and makes DWMs easier in both directions: the mean speed increases. A very careful analysis of the creep velocity was performed taking into account field, current and temperature versus time. We could evaluate Joule heating and the current contribution in terms of equivalent field Heq. In Fig 2b, Heq is reported versus current density (J) and clearly presents 2 regimes. Heq is not proportional to J P/Ms over the entire range (dashed line - material parameters from Fig 1a), as expected in conventional STT [3]. Based on an extended q-ϕ 1D model, we describe two regimes separated by a Walker-like threshold above which the CIDWM is more efficient, maybe thanks to changes of DW structure such as the creation of Néel lines [6]. This allows a determination of both the adiabatic STT parameter and of the damping constant. Investigations of the shape of the DW at sub-micron scale level are under progress. This could further elucidate the mechanisms responsible for motion and depinning under current and validate our theory thermally activated DW depinning after current pulses with the evidence of Bloch/Néel lines.

[1] I. Miron et al., *Nat Mat* 9, 230 (2010); [2] A. Thiaville et al., *EPL* 100, 57002 (2012) [3] A. Thiaville et al., *EPL* 69 (2005) ; A Mougin et al., EPL 78 (2007) [4] P. Hansen et al., *J Appl Phys* 66, 756 (1989) [5]: V. Jeudy et al., *PRL* 117, 057201 (2016) [6] J. Slonczewski, *J Appl Phys* 45, 2705 (1974)

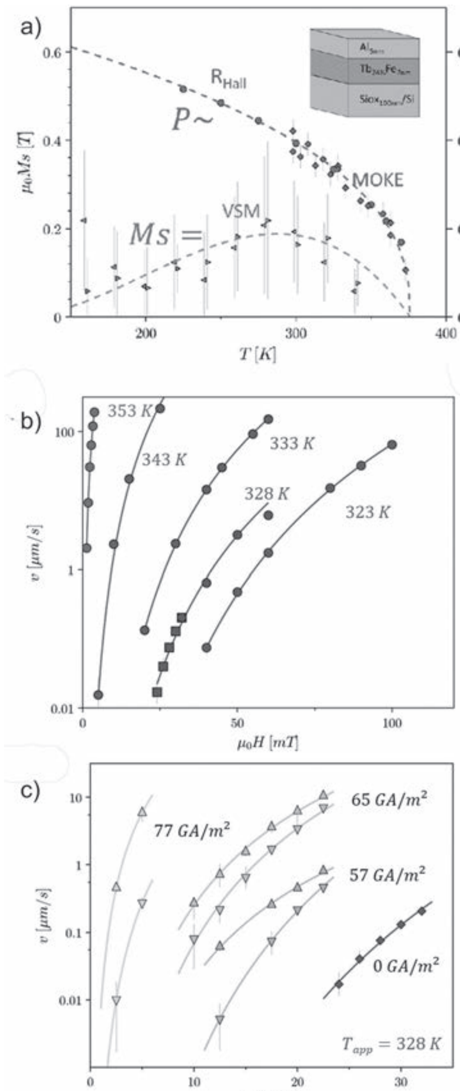

Fig. 1. a) Magnetic properties of TbFe thin films vs temperature. Reds circles and diamonds: Hall resistivity and MOKE hysteresis loops amplitude mainly proportional to polarisation P. Green triangles: VSM hysteresis loops amplitude proportional to magnetisation Ms.
b) DW velocities induced by field at different T in logarithm scale.
c) DW velocity versus field at different current densities and at T=328K. Up-triangles: fast DWs. Down-triangles: slow DWs.
Continuous lines correspond to fits using the creep law.

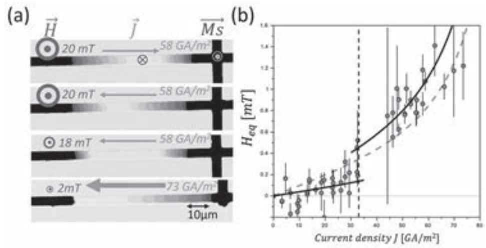

Fig. 2. a) Superimposed Kerr images showing the propagation of two DWs in a TbFe wire under current and magnetic field; b) Heq vs current density. The vertical threshold is the Walker-like limit estimated from material parameters using the 1D model. Dashed line corresponds to the single-regime STT and the continuous lines to the 2 regimes model.

11:30

CD-10. Asymmetric domain wall motion in Pt/Co/Pt induced by electric current.

M. Nsibi[1], J. Nath[1], I. Joumard[1], S. Auffret[1], I. Miron[1] and G. Gaudin[1]
1. SPINTEC, CEA-INAC/CNRS/Université Grenoble Alpes, Grenoble, France

Novel device concepts, for data storage [1] and logic operations, based on current driven magnetic domain wall (DW) propagation have regained attention after evidencing spin-orbit torques (SOT) in ferromagnetic thin layers. The significant contributions of SOT to magnetization switching [2, 3] and to DW dynamics [4] have been demonstrated in [Heavy Metal (HM)/ Ferromagnetic (FM)/ Oxide] stacks. These stacks exhibit a Structural Inversion Asymmetry (SIA). Owing to the combination of spin-orbit coupling and exchange interactions, an electric current flowing in the plane of these stacks gives rise to torques acting on the magnetization of the FM layer. In addition, Dzyaloshinskii-Moriya Interaction (DMI) is present in SIA stacks, and plays a role in forming a Néel-type DW in the FM [5]. In stacks with large SIA, the combined action of SOT and DMI was proposed to account for the fast and efficient propagation of DWs [6, 7], making these stacks promising for spintronic applications. In the present work, we study a $Pt_{3\ nm}/Co_{0.6\ nm}/Pt_{1.5\ nm}$ stack with the magnetic anisotropy perpendicular to the plane. Because a layer of Pt is at both sides of the Co layer, this stack is expected to have a low SIA. Unlike large SIA stacks where DMI and SOT are considered the dominant mechanisms of current-driven DW dynamics, Pt/Co/Pt is a good candidate to investigate DMI and SOT contributions to DW dynamics with other possible relevant mechanisms. Furthermore, such stacks have been demonstrated to exhibit the chiral damping mechanism [8]. SOT act on the magnetization of the DW core [5-7]. We intend to study this by following a non-collinear DW propagation. A non-collinear DW propagation occurs when the direction of the current and the direction of the DW propagation are not parallel. Using wide-field Kerr microscopy, we follow the motion of DWs by applying current pulses to an-initially prepared magnetic circular domain. A circular domain allows us to probe the motion of DWs at all angles simultaneously. The displacements are found to be asymmetric with respect to the collinear configuration where the direction of the current and the direction of the DW propagation are parallel (see figure.1). At a certain angle, the DW is at its largest displacement. Whereas, it is shorter at its corresponding conjugate angle. This asymmetry is qualitatively equivalent to the one reported in Pt/Co/AlOx structure [9]. Now we consider the case where the current is applied in the presence of an external in-plane magnetic field. The magnetic in-plane field acts on the internal configuration of a DW and at a sufficient strength saturates the DW core magnetization along the direction of the field. This alters the action of SOT on the magnetization. We aim then to follow the DW motion asymmetry as we vary the strength and the direction of the applied magnetic field. The obtained results from this study are only partially accounted for by the combined action of DMI and SOT. Hence, the purely model based on DMI and SOT is found to be insufficient to explain all our observations in Pt/Co/Pt. Our findings uncover new aspects of the dynamics of DWs in 2D in SIA stacks. There is a need for an extended model including more and new mechanisms besides DMI and SOT to understand the magnetization interactions. The asymmetry of DW dynamics presented here offer also new ways to manipulate ferromagnetic pillars useful for spintronic devices.

[1] S.S.P. Parkin et al. Science 320, 190 (2008) [2] I.M. Miron et al. Nature Materials 9, 230-234 (2010) [3] I.M. Miron et al. Nature 476, 189-193 (2011) [4] I.M. Miron et al. Nature Materials 10, 419-423 (2011) [5] A. Thiaville et al. EPL, 100 (2012) 57002 [6] K-S. Ryu et al. Nature Nanotechnology 8, 527-533 (2013) [7] S. Emori et al. Nature Materials 12, 611-616 (2013) [8] E. Jué et al. Nature Materials 15, 272-277 (2016) [9] C.K. Safeer et al. Nature Nanotechnology 11, 143-146 (2016)

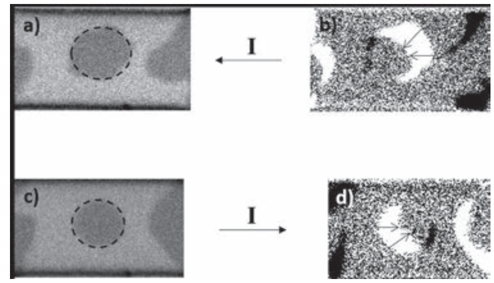

Fig. 1. Kerr microscopy images of DW displacements induced by current I. a and c are images of the initial states before injecting the current I. In a and c, dark regions (resp. bright) correspond to magnetic domains where the magnetization is pointing up (resp. down) with respect to the plane of the image. The initial up magnetic circular domains are emphasized by dots in a and c. b (resp. d) is the differential image obtained by subtracting a (resp. c) from the final Kerr microscopy image after the injection of the current I. In b and d, dark contrast (resp. bright) correspond to the growth of up (resp. down) domains. Both semicircular DWs in b and d moved asymmetrically along the direction of current I. The final domains did not then conserve their initial circular shapes. DWs did not propagate equivalently due to magneto-static interactions resulting in smaller domains.

11:45

CD-11. Influence of the Tb layer on current driven domain wall motion in Pt / Co / Tb magnetic wire.

H. Awano[1], W.C. Ying[1], R. Yoshimura[1], S. Sumi[1] and P.V. Thach[1]
1. Graduate School, Toyota Technological Institute, Nagoya, Japan

We have reported that the critical current density can be reduced in current driven domain wall motion of magnetic wire composed of (rare earth-transition metal alloy or multilayer/Pt) hetero structure[1, 2]. This may be due to the small magnetization and the high efficiency of the spin orbit torque effect[3,4]. On the other hand, the rare earth metals are heavy metals and cause large spin orbital interaction, so we need to investigate this effect as well. Therefore, Pt / Co / Tb three-layered magnetic were is prepared and the influence of the Tb in current driven domain wall motion was investigated. The specimen wires were establish by conventional fabrication process with different Tb layer thinness (t nm) from 0 to 5 nm. Layers of Ta(3 nm)/Pt(3 nm)/Co (0.9)/Tb (t nm)/Ta(3 nm)/Pt(1.5 nm) were deposited on the thermally oxidized silicon substrates, Pt layer and Ta layer were deposited by DC magnetron sputtering and Co layer and Tb layer were deposited by RF magnetron sputtering. Fig.1 shows Tb layer thickness dependence of satulate magnetization (Ms) per Co in Pt/Co/Tb magnetic wire. In general. when the Tb layer and the Co layer are in contact with each other, a TbCo alloy is formed at the interface and a ferrimagnetic material. That is, since the magnetic moments of Tb and Co sub-networks are opposite to each other, the net magnetic moment shows a small value. When the Tb layer thickness is 0 nm, Ms shows that of Co alone, but as the Tb layer thickness becomes 1 nm, Ms decreases slightly because the TbCo alloy can be formed at the interface. However, when the Tb layer thickness is 2 nm or more, Ms shows a constant value, so it can be considered that the alloy layer thickness at the interface is 2 nm or less. In order to investigate current-induced DW motion by applying voltage pulses of 100-ns duration between two electrodes. The results are shown in Fig.2 for a wire width of 3μm. The slope of domain wall velocity (V) versus current density (J) curves increases when Tb thickness increases. The highest slope was obtained for Tb 5 nm thickness specimen wire. In addition, the critical current density (J_C) *decrease when the Tb thickness increasing. I observed the increasing Tb layer thickness will enhance the spin-orbit torque.*

[1] D. Ngo *et.al*., Appl. Phys. Express, 4 093002 (2011) [2] H. Awano, J. Magn. Mat., Mater, 383 50 (2015) [3] D. Bang *et.al*., Phys. Rev. B, 93 174424 (2016) [4] R. Mishra, *et.al*., Phys. Rev. Lett., 118 167201 (2017)

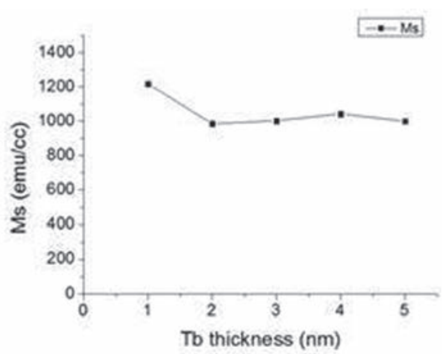

Fig.1 Tb layer thickness dependence of Ms in the Pt/Co/Tb magnetic wire

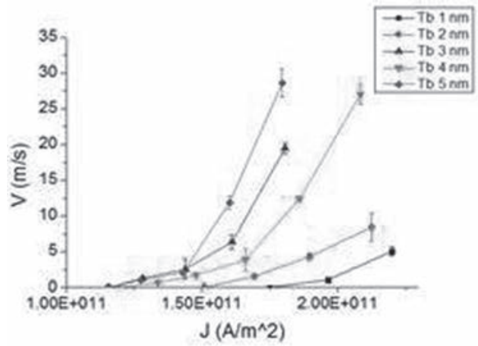

Fig.2 Current density dependence of domain wall velocity in the Pt/Co/Tb magnetic wire

WEDNESDAY MORNING, 25 APRIL 2018 ROSELLE II, 9:00 TO 12:00

Session CE

HIGH FREQUENCY MAGNETIC MATERIALS AND DEVICES II

Jianbo Wang, Co-Chair
Lanzhou University, Lanzhou, China
Masahiro Yamaguchi, Co-Chair
Tohoku Unviersity, Sendai, Japan

INVITED PAPER

9:00

CE-01. Dispersion Engineering of Nonreciprocal Composite Right/Left Handed Metamaterials Using Ferrite Materials in Microwave Region.
T. Ueda[1] and T. Itoh[2]
1. Electrical Engineering and Electronics, Kyoto Institute of Technology, Kyoto, Japan; 2. Electrical Engineering Department, University of California, Los Angeles, CA, United States

Metamaterials are artificial electromagnetic structures which are composed of smaller elements compared to the wavelength, referred to as unit cell, where macroscopic constitutive relation such as effective permittivity and permeability have been designed and controlled in order to manipulate electromagnetic wave propagation for various applications. Specifically, nonreciprocal metamaterials have been investigated to discover new electromagnetic phenomena and to invent state-of-the-art functional circuits and antennas. Nonreciprocity manifests itself as a result of a combination of two factors; the one is broken time reversal symmetry and another is broken space inversion symmetry. The former factor is realized by using gyrotropic materials such as ferrite in microwave region or magneto-optic media in optical region. For example, a microstrip line constructed on a normally magnetized ferrite substrate supports an edge guided mode [1] showing the field displacement effect in which the fields are asymmetrically concentrated at one of strip edges. The field concentration side can be switched by changing the directions of wave propagation or the externally applied dc magnetic field. In such cases, when stubs are asymmetrically inserted at the strip edges to provide geometrical asymmetry to the wave-guiding structure for broken space inverse symmetry, the propagating wave regards the line as different structures for two anti-parallel propagation directions, which results in nonreciprocal transmission. In the earlier work on nonreciprocal metamaterials, nonreciprocity appearing in the magnitude of transmission coefficients was studied for applications to isolators and circulators [2]. More recently, nonreciprocity appearing in the phase of transmission coefficients was focused on, from the metamaterial point of view [3],[4]. By using the phase-shifting nonreciprocal metamaterials, we can have fascinating situations where forward wave mode is dominant with positive refractive index in one propagation direction and backward wave mode is dominant with negative refractive index in the opposite direction at the same frequency. In the special cases, we can have field profiles with unidirectional wavenumber vectors along the wave-guiding structures regardless of the transmitted power directions. Such nonreciprocal metamaterials were implemented to transmission-line resonators providing unique characteristics in that the resonance frequency is independent of the resonators' size and that the field profiles have uniform magnitude and linearly-varying phase distribution, referred to as pseudo-traveling wave resonators [5]. The phase gradient of the fields along the resonators can be arbitrarily varied by changing the nonreciprocity of the lines under the resonant condition. This tunable phase gradient along the resonant structures was implemented to highly-efficient beam scanning leaky wave antennas [6], and to polarization switchable circularly polarized antennas [7],[8]. Nonreciprocal metamaterials can provide potential solutions to improvement of performance in microwave circuits and antennas. For beam steering antennas based on nonreciprocal metamaterials, the beam angle is determined by magnitude of the nonreciprocity in the metamaterial lines. For circularly polarized antennas based on the nonreciprocal metamaterial rings, the phase shift for one circulation corresponds to 360 degrees. Therefore, the enhancement of nonreciprocal phase gradient along the metamaterial line leads to wider beam swing in the leaky wave antennas and miniaturization of the circularly polarized antennas. Recently, it was demonstrated that an appropriate combination of curvatures of lines and asymmetric insertion of stubs enhances the geometrical asymmetry of the line, resulting in the enhancement of the nonreciprocity [9]. Not only magnitude but also dispersion of phase-shifting nonreciprocity in metamaterials have been designed and controlled for improvement of microwave circuits and antennas. For example, beam scanning leaky wave antennas generally suffer from beam squint problem where the beam direction varies with the operational frequency. For the nonreciprocal metamaterial based beam scanning antennas, the beam squint originates from the frequency dependence of phase-shifting nonreciprocity. To eliminate the beam squint, metamaterials with dispersion-less nonreciprocity was proposed and demonstrated to show the phase-shifting nonreciprocity proportional to the operational frequency [10].

[1] M. E. Hines, "Reciprocal and nonreciprocal modes of propagation in ferrite strip line and microstrip devices," IEEE Trans. Microw. Theory Tech., vol. 19, no. 5, pp. 442–451, May 1971. [2] T. Ueda and M. Tsutsumi, "Nonreciprocal left-handed transmission characteristics of microstrip lines on the ferrite Substrate," IET Proc. Microwaves, Antennas & Propag., vol. 1, no. 2, pp. 349-354, April 2007. [3] T. Ueda, K. Horikawa, M. Akiyama, and M. Tsutsumi, "Nonreciprocal phase-shift composite right/left handed transmission lines and their application to leaky wave antennas," IEEE Trans. Antennas Propag., vol. 57, no. 7, pp. 1995-2005, July 2009. [4] T. Ueda and M. Akiyama, "Nonreciprocal phase-shift composite right/left handed transmission lines using ferrite-rod-embedded substrate." IEEE Trans. on Magnetics, vol. 45, no. 10, pp. 4203-4206, Oct. 2009 [5] T. Ueda and H. Kishimoto, "Pseudo-traveling wave resonator based on nonreciprocal phase-shift composite right/left handed transmission lines," in 2010 IEEE MTT-S Int. Microw. Sym. Dig., pp. 41-44, May 23-28, 2010 [6] T. Ueda, S. Yamamoto, Y. Kado, T. Itoh, "Pseudo-traveling wave resonator with magnetically tunable phase gradient of fields and its applications to beam steering antennas," IEEE Trans. Microw. Theory Tech., vol. 60, no. 10, pp. 3043-3054, Oct. 2012. [7] A. Porokhnyku, T. Ueda, Y. Kado, and T. Itoh, "Beam antenna with circular polarization rotation switching based on passive components," Proc. 44th Eur. Microw. Conf., pp. 327-330, Oct. 2014. [8] K. Ninomiya, T, Ueda, A. Porokhnyuk, T. Itoh, "Demonstration of circularly-polarized leaky-wave antenna based on pseudo-traveling wave resonance", Proc. 45th Eur. Microw. Conf., pp. 450-453, 2015. [9] J. Yamamuchi, T. Ueda, Y. Kubo, T. Itoh, "Enhancement of phase-shifting nonreciprocity in microstrip-line-based metamaterials by using a combination of their curvatures and asymmetrical insertion of stubs," IEEE Trans. on Microw. Theory Tech., vol. 65, no. 12, pp. 5123-5132, Dec. 2017. [10] T. Ueda, K. Ninomiya, K. Yoshida, T. Itoh, "Design of dispersion-free phase-shifting nonreciprocity in composite right/left handed metamaterials," in 2016 IEEE MTT-S Inter. Microw. Sym. Dig., pp. 1-4, May 2016.

CONTRIBUTED PAPERS

9:30

CE-02. AlN Interlayers Allow Robust Hexagonal Barium Ferrite Heteroepitaxy on 6H-SiC.

A.S. Sokolov[1], C. Yu[1], E. Beam[2], X. Gu[2], Y. Obi[3] and V. Harris[1]
1. ECE, Northeastern University, Burlington, MA, United States; 2. Qorvo, Richardson, TX, United States; 3. Metamagnetics, Inc., Westborough, MA, United States

Virtually all electronic and microwave components have been constantly shrinking, including the ones used in Transmit/Receive Modules. The microwave circulator is an essential part of every T/R module and has largely remained unchanged since the inception. The concept of T/R module crystalized in the 1970s and became practical in the 1980s with the emergence of GaAs monolithic integrated circuits. Circulators are not solid state components and have ferrites at their cores. The first attempts to integrate the ferrites and semiconductor platforms have been made in the 1990s, but mostly failed - GaAs substrates could not withstand high temperatures required for spinel ferrite processing. Further work focused on wide band gap semiconductors that offered better temperature stability, such as SiC or GaN. These semiconductors were used as substrates to grow crystallographycally textured hexagonal barium ferrite films (BaM) by means of pulsed laser deposition due to their lattice parameters. Several buffer layers have been explored, including MgO and Pt. A number of promising results on SiC substrates have been published in the 2000s [1-2]. Eventually, it turned out that even SiC coated with magnesium oxide (MgO) is not stable under barium hexaferrite films at elevated temperatures [3]. Z. Chen et al. concluded that this phenomenon is due to the chemical affinity of Si and Fe. In fact, the eutectic transition in the Fe–Si phase diagram occurs at about 875^{o}C, and barium hexaferrite films are usually grown at temperatures exceeding 900^{O}C. To address this problem, we investigated the behavior of buffer layers commonly used between SiC and BaM at elevated temperatures, and also explored novel options. The primary function of a nucleation layer is to improve the crystalline quality of the overlying hexaferrite. This is achieved by providing a surface that improves the wetting and adhesion of the PLD seed layers, adjusting the lattice constant to a closer match to the hexaferrite, mitigating interfacial strain and controlling interfacial chemical reactions between the hexaferrite seed layers and SiC. In addition to providing a seed for hexaferrite deposition, nucleation layers are needed to protect the SiC substrate during the high temperature and potentially corrosive hexaferrite growth process. As such the nucleation/protection layers must be chemically stable and robust. To this end, traditional magnesium oxide and platinum, as well as the novel (with respect to BaM) aluminum nitride interlayers were studied. Our approach to achieving the nucleation and growth of protective MgO or Pt thin films is based on Atomic Layer Deposition (ALD). The advantages of this process include the ability to conformally coat structured substrates free from pinholes and other surface defects. Novel AlN layers were deposited by means of Metal-Organic Chemical Vapor Deposition (MOCVD). To study temperature stability of these nucleation layers, coated 6H-SiC wafers were annealed at temperatures between 600 and 900^{O}C, in air, oxygen, and nitrogen atmospheres. Further analysis included scanning electron microscopy (SEM), atomic force microscopy (AFM), X-Ray diffractometry (XRD), and surface resistivity measurements. As deposited nucleation layers had the thickness of about 30nm, surface roughness Ra of about 0.4nm, and high degrees of crystalline orientation. Pt nucleation layers mostly preserved their properties after annealing at 600^{o}C, but experienced boil off at temperatures approaching 900^{o}C. Although MgO interlayers on SiC substrates demonstrated much better thermal stability, BaM films grown on MgO faced a number of problems, including low density, delamination, and cracking. AlN interlayers are widely used in semiconductor manufacturing to reduce the tensile stress and cracks, but have never been used as nucleation layers for magnetic films. Our annealing study demonstrated that AlN on SiC retains its properties after annealing at elevated temperatures even in oxygen atmosphere. However, we were not able to grow high quality hexaferrite films directly on AlN due to poor epitaxy, poor adhesion, and cracking. Therefore, an additional layer of MgO has been introduced on top of AlN by means of ALD. Such heterostructures (MgO/AlN/SiC) exhibited excellent temperature stability, the surface roughness remained unchanged after the annealing at 900^{o}C and equaled 2.4nm (Figure 1). We were able to reliably produce high quality, perpendicularly textured BaM films on these structures under varying pulsed laser deposition conditions. Optimal PLD parameters can be found elsewhere [1-3]. As deposited 1.5um thick BaM films on MgO/AlN/SiC heterostructures have been rigorously tested and demonstrated excellent functional properties. Vibrating sample magnetometery (VSM), XRD, and pole figures confirmed a high degree of crystalline orientation ((00n) texture). The surface of these films, as well as ion milled holes, were analyzed by SEM and AFM, and appeared to have a near theoretical density. This conclusion was supported by the VSM analysis that revealed a near theoretical saturation magnetization and a low magnetic coercively of about 200 Oe. The FMR linewidths were measured by a coplanar waveguide connected to a Vector Network Analyzer (VNA) and equaled 500 to 600 Oe [4-5]. As demonstrated in prior art, microwave magnetic properties of as-deposited BaM films can be further improved by subsequent annealing in oxygen atmosphere.

[1] Oliver, S.A., Yoon, S.D., Kozulin, I., Chen, M.L. and Vittoria, C., 2000. Growth and characterization of thick oriented barium hexaferrite films on MgO (111) substrates. *Applied Physics Letters*, *76*(24), pp.3612-3614. [2] Chen, Z., Yang, A., Yoon, S.D., Ziemer, K., Vittoria, C. and Harris, V.G., 2006. Growth of Ba-hexaferrite films on single crystal 6-H SiC. Journal of magnetism and magnetic materials, 301(1), pp.166-170. [3] Chen, Z., Yang, A., Mahalingam, K., Averett, K.L., Gao, J., Brown, G.J., Vittoria, C. and Harris, V.G., 2010. Structure, magnetic, and microwave properties of thick Ba-hexaferrite films epitaxially grown on GaN/Al 2 O 3 substrates. Applied Physics Letters, 96(24), p.242502. [4] Sokolov, A.S., Geiler, M. and Harris, V.G., 2016. Broadband ferromagnetic resonance linewidth measurement by a microstripline transmission resonator. Applied Physics Letters, 108(17), p.172408. [5] Sokolov, A.S., Andalib, P., Chen, Y. and Harris, V.G., 2016. Single-Point FMR Linewidth Measurement by TE 10 Rectangular Transmission Cavity Perturbation. IEEE Transactions on Microwave Theory and Techniques, 64(11), pp.3772-3780.

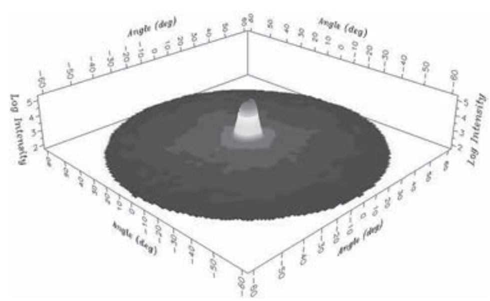

Fig. 1. BaM on MgO/AlN/SiC. (008) Peak. Pole Figure.

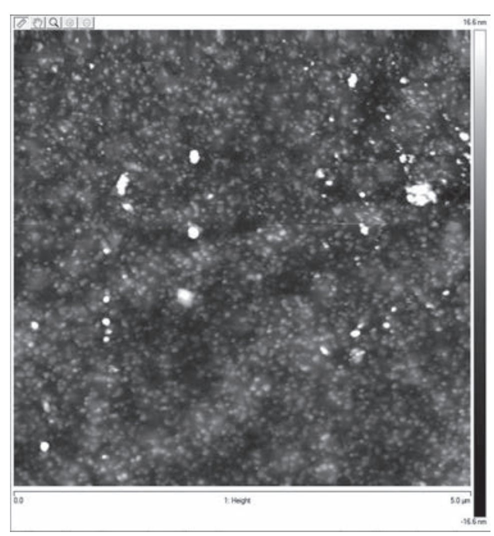

Fig. 2. MgO/AlN/GaN annealed at 900^{O}C for 60min. AFM analysis. Ra=2.43nm.

9:45

CE-03. Thin-Film Magnetic Inductors for Gigahertz Integrated Applications.

A. El-Ghazaly[2], R.M. White[3] and S.X. Wang[1,3]
1. Electrical Engineering, Stanford University, Stanford, CA, United States; 2. Electrical Engineering and Computer Science, University of California, Berkeley, CA, United States; 3. Materials Science and Engineering, Stanford University, Stanford, CA, United States

While thin-film magnetic cores provide significant enhancement to integrated passive circuit elements, including inductors and transformers [1-10], often their operating frequency limits their applications to mainly power management [1-6]. The growing field of mobile electronics, however, demands higher inductances than achievable by air-core inductors [11], [12] and higher operating frequencies than previously achievable by magnetic materials. This work aims to meet the needs of radio frequency mobile applications, by providing high frequency inductors with large inductance enhancement due to a magnetic core, all in a small form factor. As illustrated by pervious works [7-10], the trade-off between inductance enhancement and high operating frequency is challenging to overcome. Although magnetic cores contribute high permeability for inductors, at the intrinsic ferromagnetic resonance (FMR) frequency of magnetic materials (typically between 1 and 2 GHz for large blanket films), the relative permeability drops to unity, thereby making the inductance enhancement due to the material negligible. Extending the operating frequency, however, by means of patterning the magnetic core and increasing the FMR frequency through shape anisotropy has the consequence of also decreasing the permeability. In this work, we analyze the most crucial considerations regarding material selection and the fabrication process as well as magnetic-core and device design in order to produce and inductor offering a magnetic enhancement over air core extending beyond 6 GHz, a low frequency inductance of 1 nH, and a peak quality factor of four at approximately 3 GHz [13]. Both air-core and magnetic-core solenoid inductors of the same topology, shown in Fig. 1, were fabricated and measured. First, a 40 μm thick polymer insulating layer (SU-8 2015) was formed on the silicon substrate to provide isolation of the inductor from the parasitic substrate. 3 μm thick bottom inductor windings were electroplated starting from a thin Ti/Cu seed layer. Planarization and insulation was completed using two layers of the SU-8 2002 polymer to first fill the gaps between windings for planarization and then provide an additional 1.5 μm insulation layer between the windings and the magnetic layer. The magnetic material $Co_{43}Fe_{43}B_{14}$, selected its excellent high frequency properties [14], [15], was sputter deposited with laminations such that 63 nm CoFeB layers were alternated with 6 nm SiO_2 insulating layers to form a total of 1 μm thick magnetic core. The core was then patterned into a narrow shape for high shape anisotropy and high FMR frequency, where laminations further improved broadband performance by reducing high frequency losses due to eddy currents. Finally, the vias and top inductor windings were again formed by an electroplating process. The comparison of measured inductance from the air-core and magnetic-core inductors of the same design provided a direct evaluation of the performance enhancement of the inductor due to the magnetic material. Fig. 2 shows the measured permeability of the blanket film as well as the calculated permeability of the patterned magnetic core used in the inductor. The shape anisotropy is seen to increase the bandwidth of the inductor by approximately 1 GHz. The inductance of the fabricated inductors, shown on the same graph, was approximately 1 nH for the magnetic-core inductor and 0.5 nH for the air-core version. Thus, incorporation of the magnetic core is seen to experimentally double the inductance of the air-core inductor well into the high frequency mobile electronics range. The decreasing inductance at higher frequencies and suppression of the ferromagnetic resonance peak is likely due to a combination of misalignment of the applied magnetic field during deposition of the cores [15], parasitic capacitances, and eddy currents along the length of the core. Nevertheless, these results show that, with continued optimizations, magnetic materials may indeed satisfy the needs of mobile electronics applications. Acknowledgement Research for this project was conducted with government support under FA9550-11-C-0028 and awarded by the Department of Defense, Air Force Office of Scientific Research, National Defense Science and Engineering Graduate (NDSEG) Fellowship, 32 CFR 168a. Part of this work was performed using the Stanford Nanofabrication Facility (SNF) and the Stanford Nano Shared Facilities (SNSF) at Stanford University.

[1] G. J. Mehas, K. D. Coonley, and C. R. Sullivan, "Design of microfabricated inductors for microprocessor power delivery," in *IEEE Applied Power Electronics Conference*, 1999, pp. 1181–1187. [2] N. Wang, T. O'Donnell, S. Roy, P. McCloskey, O', and C. Mathuna, "Micro-inductors integrated on silicon for power supply on chip," *J. Magn. Magn. Mater.*, vol. 316, 2007. [3] S. Prabhakaran, C. R. Sullivan, T. O'Donnell, M. Brunet, and S. Roy, "Microfabricated coupled inductors for DC-DC converters for microprocessor power delivery," *PESC Rec. - IEEE Annu. Power Electron. Spec. Conf.*, vol. 6, pp. 4467–4472, 2004. [4] N. Sturcken, E. J. O. Sullivan, N. Wang, P. Herget, B. C. Webb, L. T. Romankiw, M. Petracca, R. Davies, R. E. Fontana, G. M. Decad, I. Johnkymissis, A. V Peterchev, L. P. Carloni, W. J. Gallagher, and K. L. Shepard, "A 2.5D Integrated Voltage Regulator Using Coupled-Magnetic-Core Inductors on Silicon Interposer," *IEEE J. Solid-State Circuits*, vol. 48, no. 1, pp. 244–254, 2013. [5] D. W. Lee, K. Hwang, and S. X. Wang, "Fabrication and Analysis of High-Performance Integrated Solenoid Inductor With Magnetic Core," *IEEE Trans. Magn.*, vol. 44, no. 11, pp. 4089–4095, 2008. [6] J. Mullenix, A. El-Ghazaly, and S. X. Wang, "Integrated Transformers With Sputtered Laminated Magnetic Core," *IEEE Trans. Magn.*, vol. 49, no. 7, pp. 4021–4027, 2013. [7] K. Ikeda, K. Kobayashi, K. Ohta, R. Kondo, T. Suzuki, and M. Fujimoto, "Thin-film inductor for gigahertz band with CoFeSiO-SiO/sub 2/2 multilayer granular films and its application for power amplifier module," *IEEE Trans. Magn.*, vol. 39, no. 5, pp. 3057–3061, Sep. 2003. [8] D. S. Gardner, G. Schrom, P. Hazucha, F. Paillet, T. Karnik, and S. Borkar, "Integrated on-chip inductors with magnetic films," *IEEE Trans. Magn.*, vol. 43, no. 6, pp. 2615–2617, 2007. [9] J. Salvia, J. A. Bain, and C. P. Yue, "Tunable on-chip inductors up to 5 GHz using patterned permalloy laminations," *IEEE Int. Electron Devices Meet. 2005*, vol. 0, no. 1, pp. 963–966, 2005. [10] Y. Gao, S. Z. Zardareh, X. Yang, T. X. Nan, Z. Y. Zhou, M. Onabajo, M. Liu, A. Aronow, K. Mahalingam, B. M. Howe, G. J. Brown, and N. X. Sun, "Significantly enhanced inductance and quality factor of GHz integrated magnetic solenoid inductors with FeGaB/Al2O3 Multilayer Films," *IEEE Trans. Electron Devices*, vol. 61, no. 5, pp. 1470–1476, 2014. [11] R. Meere, N. Wang, T. O'Donnell, S. Kulkarni, S. Roy, and S. C. O'Mathuna, "Magnetic-core and air-core inductors on silicon: A performance comparison up to 100 MHz," *IEEE Trans. Magn.*, vol. 47, no. 10, pp. 4429–4432, 2011. [12] "International Technology Roadmap for Semiconductors," Tech. Rep., 2011. [13] A. El-Ghazaly, R. M. White, and S. X. Wang, "Gigahertz-Band Integrated Magnetic Inductors," *IEEE Transactions on Microwave Theory and Techniques*, vol. 65, no. 12, pp. 4893–4900, 2017. [14] L. H. Chen, T. J. Klemmer, K. A. Ellis, R. B. van Dover, and S. Jin, "Soft-magnetic properties of Fe – Co – B thin films for ultra-high-frequency applications," *J. Appl. Phys.*, vol. 87, no. 9, pp. 1–4, 2000. [15] G. A. Lebedev, B. Viala, T. Lafont, D. I. Zakharov, O. Cugat, and J. Delamare, "Converse magnetoelectric effect dependence with CoFeB composition in ferromagnetic/piezoelectric composites," *J. Appl. Phys.*, vol. 111, no. 7, p. 07C725, 2012. [16] A. El-Ghazaly, J. M. Mullenix, R. M. White, and S. X. Wang, "Kerr-Imaged Edge-Curling Wall Effects of Narrow Magnetic Cores," *IEEE Trans. Magn.*, vol. 49, no. 7, pp. 4017–4020, Jul. 2013.

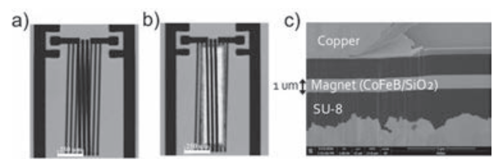

Fig. 1. Inductor images, showing a) air-core topology, b) magnetic-core topology, and c) cross-sectional SEM of the layers in the magnetic-core inductor.

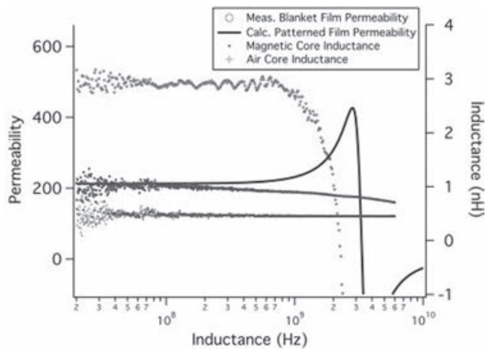

Fig. 2. Frequency-domain results, combining the permeability spectra measured for the blanket film of CoFeB and calculated for the patterned CoFeB magnetic core. On the same graph are the measured inductance results for the magnetic-core and air-core inductors.

10:00

CE-04. Ultra-wide Band (10 MHz- 26 GHz) Permeability Measurements of Magnetic Films.

Y. Chen[1], X. Wang[2], H. Chen[2], Y. Gao[1] and *N. Sun*[2]
1. Winchester Technologies, Burlington, MA, United States;
2. Northeastern University, Boston, MA, United States

I. Introduction Magnetic materials are the necessary components of the modern rf components. The demand for higher communication speed such as the upcoming 5G network requires higher operation frequency of rf components. For example, the future spectrum band of mobile network will be extended above 24 GHz [1]. Permeability measurements provide a basis for the design and characterization of magnetic materials and the development of RF devices. However, permeability measurement results and commercially available permeameters have been limited to 9GHz or below [2-7]. Conventional broadband permeameters use a vector network analyzer (VNA), and a pick-up coil or an electric short [2,3], or a broadband transmission line [4,6] for magnetically exciting the materials under test. Inductance changes are measured at zero magnetic field and at saturation magnetic field through a vector network analyzer for extracting the permeability spectrum. The bandwidth of Pick-up coil is limited to several hundred MHz. Transmission-lines [4-6] are widely used for broadband permeameters. However, the transmission-line type permeameters are noisy in the frequency range below 100MHz due to the low inductance. In addition, all these broadband permeameters based on vector network analyzers are expensive, and not reliable in measuring thin films or materials with low permeability because of the low signal to noise ratio (SNR). In this article, we demonstrate a new type of permemeter for ultra-wide band permeability measurements with significantly enhanced signal to noise ratio (SNR), and demonstrate the measurements on a 50nm FeGaB film up to 22GHz and an ultra-thin 2nm NiFe film. This permeameter enables the characterization of the complex permeability between 10MHz-26GHz, as well as many other typical magnetic parameters including linewidth, saturation magnetization, effective anisotropy field, Gilbert damping, and inhomogeneous linewidth broadening. In addition, the new permeability measurement system shows 40 ~ 50dB higher SNR over the conventional permeameters. II. Measurement and Results The proposed permeability measurement system is established from the broadband ferromagnetic resonance (FMR) spectrometer [8], which uses a microwave source without a VNA. Before measuring the permeability of magnetic films, the in-plane magnetic anisotropy field H_k and saturation magnetization $4\pi M_s$ of a 50nm FeGaB film are evaluated from FMR as 11.6Oe and 13934Gs, which are comparable to the reported results of FeGaB [10] measured by VSM. The complex permeability is defined as $\mu = \mu' + j\times\mu''$, where are μ' and μ'' the real and imaginary part of permeability respectively. The low-frequency permeability equals to the theoretical initial permeability as $\mu_{lowf}'=1+4\pi M_s/(H_k+H)$ when H is applied along the magnetic in-plane easy axis. One can calculate the low-frequency permeability from the saturation magnetization and anisotropy field that are determined from FMR characterization initially. The complex permeability as a function of frequency at fixed bias field is determined by the frequency-swept measurement, as detailed in Ref [8]. Fig.1 shows the measured spectrum of complex permeability of a 50nm FeGaB sample at zero bias field and 2000Oe bias field. The resonance shifts from 2GHz to 20GHz with the increase of bias field. The profile of the complex permeability agrees well with the theoretical permeability calculated from Landau–Lifshitz–Gilbert (LLG) equation, which validates the results. To further investigate the detection limit of the system, we measured the permeability on a 2nm ultrathin NiFe sample. NiFe is a commonly used ferromagnetic material with weaker magnetization than FeGaB. The saturation magnetization and anisotropy field are extracted to be 7735G and 7.5Oe following the same analyzing procedure for FeGaB sample. The resonance peak is near 700MHz that is lower than the resonance frequency of FeGaB because of the smaller saturation magnetization of NiFe. Again, there is a good agreement in profile and amplitude between the measured permeability spectrum and theoretical permeability from LLG equation. III. Performance Comparison A comparison between the reported permeability measurements on magnetic films is summarized in Table I. The new method presented in this study can measure samples through a much wider frequency bandwidth than any other permeability measurements using microwave transmission line or cavity with vector network analyzer. Moreover, our permeameter has shown much higher SNR, particularly in the low-frequency region (~100MHz). We analyzed the SNR of the real part of permeability for all the studies listed in Table I. The measurements on 50nm FeGAB film lead to S/N ratio of 72dB, indicating the highest sensitivity among all the permeability measurement techniques that we know. In addition, our system is able to detect a 2nm ultra-thin NiFe film with a SNR of 28dB, which is beyond the capability of other methods. IV. Conclusion A new permeability measurement system has been demonstrated with ultra-wide frequency band from 10MHz up to 26GHz. The measurements on 50nm FeGaB and 2nm NiFe thin films have shown excellent SNR, which is 40~50dB higher than conventional permeameters, and the measured permeability spectrum matches well with the theoretical permeability simulated by LLG equation.

[1] GSMA, “5G Spectrum,” 2016. [2] P. A. Calcagno and D. A. Thompson, “Semiautomatic permeance tester for thick magnetic films,” *Review of Scientific Instruments,* vol. 46, pp. 904-908, 1975. [3] M. Yamaguchi, T. Kawazu, and K. I. Arai, “Resonance analysis of figure-8 coil type permeance meters,” *IEEE Transactions on Magnetics,* vol. 29, pp. 2986-2988, 1993. [4] E. Salahun, P. Queffelec, M. L. Floc’h, and P. Gelin, “A broadband permeameter for “in situ” measurements of rectangular samples,” *IEEE Transactions on Magnetics,* vol. 37, pp. 2743-2745, 2001. [5] D. Pain, M. Ledieu, O. Acher, A. L. Adenot, and F. Duverger, “An improved permeameter for thin film measurements up to 6 GHz,” *Journal of Applied Physics,* vol. 85, pp. 5151-5153, 1999. [6] Y. Ding, T. J. Klemmer, and T. M. Crawford, “A coplanar waveguide permeameter for studying high-frequency properties of soft magnetic materials,” *Journal of Applied Physics,* vol. 96, pp. 2969-2972, 2004. [7] M. Yamaguchi, Y. Miyazawa, K. Kaminishi, and K.-I. Arai, “A New 1 MHz-9 GHz Thin-Film Permeameter Using a Side-Open TEM Cell and a Planar Shielded-Loop Coil,” *Transactions of the Magnetics Society of Japan,* vol. 3, pp. 137-140, 2003. [8] S. Beguhn, Z. Zhou, S. Rand, X. Yang, J. Lou, and N. X. Sun, “A new highly sensitive broadband ferromagnetic resonance measurement system with lock-in detection,” *Journal of Applied Physics,* vol. 111, p. 07A503, 2012. [9] C. Kittel, “On the Theory of Ferromagnetic Resonance Absorption,” *Physical Review,* vol. 73, pp. 155-161, 01/15/ 1948. [10] J. Lou, R. E. Insignares, Z. Cai, K. S. Ziemer, M. Liu, and N. X. Sun, “Soft magnetism, magnetostriction, and microwave properties of FeGaB thin films,” *Applied Physics Letters,* vol. 91, p. 182504, 2007. [11] J. M. Beaujour, D. Ravelosona, I. Tudosa, E. E. Fullerton, and A. D. Kent, “Ferromagnetic resonance linewidth in ultrathin films with perpendicular magnetic anisotropy,” *Physical Review B,* vol. 80, p. 180415, 11/17/ 2009. [12] O. Obi, M. Liu, J. Lou, S. Stoute, X. Xing, N. X. Sun, et al., “Spin-spray deposited NiZn-Ferrite films exhibiting ‘>?50 at GHz range,” Journal of Applied Physics, vol. 109, p. 07E527, 2011/04/01 2011. [13] J. Lou, D. Reed, C. Pettiford, M. Liu, P. Han, S. Dong, et al., “Giant microwave tunability in FeGaB/lead magnesium niobate-lead titanate multiferroic composites,” Applied Physics Letters, vol. 92, p. 262502, 2008/06/30 2008. [14] S. X. Wang, N. X. Sun, M. Yamaguchi, and S. Yabukami, “Properties of a new soft magnetic material,” Nature, vol. 407, p. 150, 09/14/online 2000. [15] D. I. Mircea and T. W. Clinton, “Near-field microwave probe for local ferromagnetic resonance characterization,” Applied Physics Letters, vol. 90, p. 142504, 2007/04/02 2007

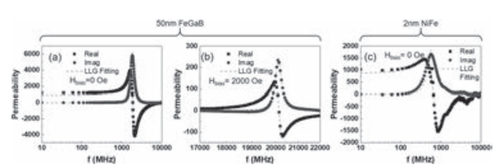

Fig. 1. The complex permeability spectrum of (a) 50nm FeGaB at zero bias field, (b) 50nm FeGaB at 2000Oe bias field and (c) 2nm NiFe at zero bias field. The dashed lines are the theoretical permeability from LLG equation.

TABLE I

S/N ratio and bandwidth of different permeability measurement methods on various magnetic films

Sample under Test	Bandwidth	Estimated SNR	
700nm NiZn Ferrite	45MHz-10GHz	13dB @ 300 MHz	Ref [12]
100nm FeGaB	500MHz-3GHz	27db @ 500 MHz	Ref [13]
100nm FeCoN	1MHz-1.2GHz	30dB @ 10MHz	Ref [14]
100nm NiFe	100MHz-6GHz	14dB @ 100MHz	Ref [6]
100nm NiFe	500MHz-6GHz	16dB @ 500MHz	Ref [15]
200nm CoNbZr	1MHz-9GHz	27dB @ 10MHz	Ref [7]
50nm FeGaB	10MHz-26GHz	72dB @ 10MHz	This study
2nm NiFe	10MHz-26GHz	28dB @ 10MHz	This study

10:15

CE-05. In-site measurement of permeability and magnetostrtriction constant of magnetic films deposited on Si wafers.

O. Mori[1], Y. Endo[2,3], Y. Shimada[1], S. Yabukami[4] and R. Utsumi[1]
1. Toei Scientific Industrial Co., LTD, Natori, Japan; 2. Graduate School of Engineering, Tohoku University, Sendai, Japan; 3. Center for Spintronics Research Networks, Tohoku University, Sendai, Japan; 4. Tohoku Gakuin University, Tagajo, Japan

1. Introduction This paper proposes a new technique to measure simultaneously and non-distractively both permeability and saturation magnetostriction constant of magnetic thin films deposited on Si wafers. Generally in order to evaluate permeability and magnetostriction of magnetic thin films, samples with adequate size and shape have to be prepared separately for each measurement. This new measurement technique allows for in-site measurement of these material properties for a magnetic thin film on a large-sized Si wafer substrate. 2. Experimental procedures In addition to permeability measurement using the microstrip line probe that was already reported[1)] this technique measures ferromagnetic resonance (FMR) of the same sample. In the FMR measurement, a Si wafer is bent with well controlled curvature radius giving uniaxial tensile stress to the magnetic film on the Si wafer. The FMR frequency ($f_{r\sigma}$) shifts due to the uniaxial anisotropy caused by magneto-elastic effect and the shift reflects the strength of magnetostriction of films. From dependence of fr_{σ} on an external magnetic field (H_{ex}) the saturation magnetostriction constant λ_s is available by graphical fitting and calculation. The following is an example of the measurement. The film to be measured is Co-Zr-Nb amorphous with thickness of 500 nm deposited on a 4 inch diameter Si wafer by RF sputtering. As shown in Fig. 1, the sample was set on a substrate holder with a curvature radius of 300 mm with the film surface upside. The film in this state is under a uniaxial tensile stress that induces uniaxial anisotropy through magnetostrictive effect. The resonance frequency shift is plotted as a function of H_{ex}. The relation between the resonance frequency and H_{ex} is $(f_{r\sigma}^2 - f_{r0}^2) / f_{r0}^2 = (3\lambda_s h_s E_f / 2rM_s) / (H_{kf} + H_{ex})$ (1) where $f_{r\sigma}$ and f_{r0} are resonance frequencies under tensile stress and in stress free state, respectively. r is curvature radius determined by position censor (278mm for the present sample), M_s is saturation magnetization, H_{kf} is other kind of uniaxial anisotropy field such as induced anisotropy, h_s is a substrate thickness, and E_f is Young's modulus. 3. Results and discussion The resonance frequency was defined as the peak frequency of resonance power loss profile, which was determined from s_{21} measured with a network analyzer. Fig. 2 shows $(1-s_{21})/ s_{21}$ which means an effective resistive component of resonance. The solid and broken lines are profiles under tensile stress and in stress free state, respectively. Under the stress, $f_{r\sigma}$ shifts to lower values and difference ($f_{r\sigma}– f_{r0}$) tends to decrease from 30 MHz to 4 MHz with increase of H_{ex}. Fig.3 shows plotting of $(f_{r\sigma}^2–f_{r0}^2)/fr_0^2$ as a function of $1/(H_{kf}+H_{ex})$. The value of λs was determined by fitting the plot with a linear line with proportionality $(3\lambda_s h_s E_f/2rM_s)$, that is, $-7.2x10^{-7}$. A film sample deposited on a thin glass rectangular substrate simultaneously with that of the Si substrate was measured with the optical cantilever technique and λs was found to be $-13x10^{-7}$. Table 1 summarizes the results of two methods of λs measurement for Co- Zr-Nb films with different compositions. They are in good agreement confirming that the technique proposed here is reliable for film characterization on Si wafers. Conclusion The experiments described here give good evidence that the technique proposed here has a high potential as a measurement method of in-site characterization of magnetic thin films on large size Si wafers. Compared to the conventional optical cantilever method, this proposed technique has the following advantages. 1. Permeability and saturation magnetostriction properties can be evaluated simultaneously and non-distractively. When the probe size is reduced in future, information on local distribution of these properties on Si wafers becomes available. 2. In the conventional optical cantilever method rotatable or bi-directional H_{ex} is needed. This limits the external field strength, while H_{ex} of the proposed method is unidirectional without limitation to the strength, making application to magnetically hard samples possible.

Reference 1) S. Yabukami, K. Kusunoki, H. Uetake, H. Yamada, T. Ozawa, R. Utsumi, T. Mori izumi, Y. Shimada, "Permeability Measurements of Thin Film Using a Flexible Microstrip Line-Type Probe Up To 40 GHz", *Journal of the Magnetics Society of Japan*, Vol. 41, No. 2, pp. 25-28 (2017).

Table 1 Results for different film thicknesses.

samples	film thickness [nm]	λs (this measurement)	λs (cantilever method)
Co-Zr-Nb	500	-7.19×10^{-7}	-1.36×10^{-6}
Co-Zr-Nb	250	-2.31×10^{-6}	-3.07×10^{-6}
Co-Zr-Nb	50	-4.29×10^{-6}	-6.44×10^{-6}

Fig. 1 Schematic of the measurement system.

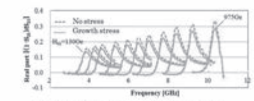

Fig. 2 FMR of CoZrNb film (on 4inch Wafer, 500nm thick).

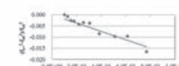

Fig. 3 Magnetic field dependence of resonance frequency.

10:30

CE-06. Skin Effect Suppressed NiFe/Cu Electroplated Multilayer Wiring for High Data-Rate and Low Delay-Time I/O Interface Board.

M. Yamaguchi[1,4], T. Yanai[2], H. Nakayama[3], R. Sai[4], H. Fujiwara[5], Y. Kitai[5], M. Sato[5] and U. Sangawa[5]
1. Department of Electrical Engineering, Tohoku Unviersity, Sendai, Japan; 2. Division of Electrical Engineering and Computer Science, Graduate school of Engineering, Nagasaki University, Nagasaki, Japan; 3. Department of Electronics and Control Engineering, National Institute of Technology, Nagano College, Nagano, Japan; 4. New Industry Creation Hachery Center, Tohoku University, Sendai, Japan; 5. Electronic Materials Business Division, Automotive & Industrial Systems Company, Panasonic Corporation, Kadoma, Japan

INTRODUCTION - This paper proposes a new application of skin effect suppression technology [1]-[4] for long wiring on high-speed & low-delay I/O board (typical wiring length; 200 to 1000 mm). This proposal will overcome the difficulty to further reduce the transmission losses on the I/O board with >50 Gbps data rate, which is currently performed by lowering dielectric substrate losses and surface smoothing of Cu conductor. A major challenge in this paper is to demonstrate the skin effect suppression by electroplated magnetic/conductor multilayer, instead of sputter-deposited thin film in literature [2]-[4], in order to meet coming cost-effective, thick (>5 μm), large area, and high throughput mass productivity requirements. High frequency (>10 GHz) estimation of complex permeability and measurements of low resistance devices are also investigated. *EXPERIMENTAL PROCEDURE* - Cu was selected as metal conductor material, and NiFe the magnetic material. The target frequency to demonstrate skin effect suppression is selected as 15 GHz. The Cu and Ni80Fe20 films are alternately electroplated to form the NiFe/Cu multilayer, as Shown in Fig. 1. The top and bottom surface layers of the multilayer are Cu layers. The skin effect can be suppressed in the multilayer provided that the real part of the relative permeability of NiFe, μ_r' is negative and the volume average of the relative permeability, μ_{rav}, becomes zero(refer equation (1) as inset in Fig. 1). The μ_{rav} can be zero when the ratio r of the Cu thickness t_N to the NiFe thickness t_F, equals $r = t_N/t_F = -\mu_r'$ ($\mu_r<0$). The imaginary part of the relative permeability μ_r'' must be small enough. Thicknes of each of Cu and NiFe layer is so designed not to exceed skin depth δ of the material (refer equation (2) as inset in Fig. 1). In order to design the film thickness ratio, r, complex permeability of NiFe film with thin Cu back layer was measured by a shielded-loop type thin film permeameter up to 9 GHz[5]. Static hysteresis loop was also measuerd. Then parametes necessary to estimate higher frequency comprex permeabililty by the known Landau-Lifshitz-Gilbert equation [6] were extracted as 4πMs=8000 G, Hc = 0.5 Oe, FMR frequency = 0.9 GHz, and damping parameter α=0.1. This calculation lead μ_r'= -2 at 15 GHz. Accordingly, Cu thickness t_N = 0.51 μm and NiFe thickness t_F=0.25 μm are targetted. Total number of layers is 21 and total thickness is 7.85 μm. Maximum size of electroplating area was 75 x 75 mm^2. Film-substrate bending was reduced by electric deposition parameters [7] and additives to solution. *RESULTS AND DISCUSSION* - Fig. 2(a) shows simulated cross-sectional current distribution at 15 GHz by a full wave FEM simulator (Ansis Co, HFSS) [8]. Within the multilayer, current density is high in Cu and low in NiFe because of the electric conductivity difference. Compared with Cu conductor, it is seen that the top and bottom surface curernt densities become low, and depth-center current density becomes slightly high for the multilayer, showing the skin effect is suppressed. The suppression is not perfectly because of large damping (α=0.1) and noticeable contribution from imaginary part of the relative permeability μ_r''. Accordingly it was estimated that the degree of transmission loss decrease at 15 GHz would be 5 %. In Fig. 2(b), this is clearly demonstrated in experiments. Provided a lower damping material with low imaginary part permeability, the degree of skin effecrt suppresion would be more significant.

[1]B. Rejaei and M. Vroubel, “Suppression of skin effect in metal/ferromagnet superlattice conductors,” J. Appl. Phys. 96, 6863 (2004). [2] Y. Zhuang, B. Rejaei, H. Schellevis, M. Vroubel, J. N. Burghart, “Magnetic-Multilayered Interconnects Featuring Skin Effect Suppression,” IEEE Electron Device Letters, 29, (4), pp. 319-321 (2008). [3]M. Yamaguchi, N. Sato, and Y. Endo, Proceedings of EuMC 2010, Poster 10-1, Paris, France (2010). [4]N. Sato, Y. Endo, M. Yamaguchi, “Skin effect suppression for Cu/CoZrNb multilayered inductor,” J. Appl. Phys.,111(7), 07A501-07A501-3 (2012). [5]M. Yamaguchi, Y. Miyazawa, K. Kaminishi, and K. I. Arai, “A New 1 MHz-9GHz Thin-FilmPerm eameter Using a Side-Open TEM Cell and a Planar Shielded-Loop Coil,” Trans. Magn. Soc. Jpn. 3, 137 (2003). [6] Y. Shimada, K. Yamada, S. Hatta, and H. Fukunaga, Jisei Zairyou(Magnetic Materials)[in Japanese], Koudansha Scientific, Tokyo (1999). [7] T. Yanai K. Azuma, K. Eguchi, Y. Watanabe, T. Ohgai, M. Nakano, H. Fukunaga, “Effects of annealing and pulse plating on soft magnetic properties of electroplated Fe-Ni films”, AIP Advances, 6 (5), #055923 (2016). [8] T. Hiraguri, H. Nakayama et al, “Design of Multiband Planar Antenna for Wireless LAN with Finite Element Method,” Proc. 2016 IEEE 5th Global Conf. on Consumer Electronics (GCCE), pp. 19 - 22 (2016).

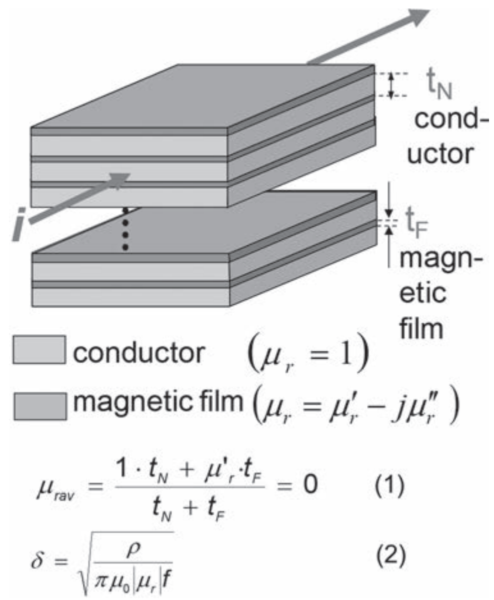

Fig. 1. Structure of counductor/magnetic film multilayer.

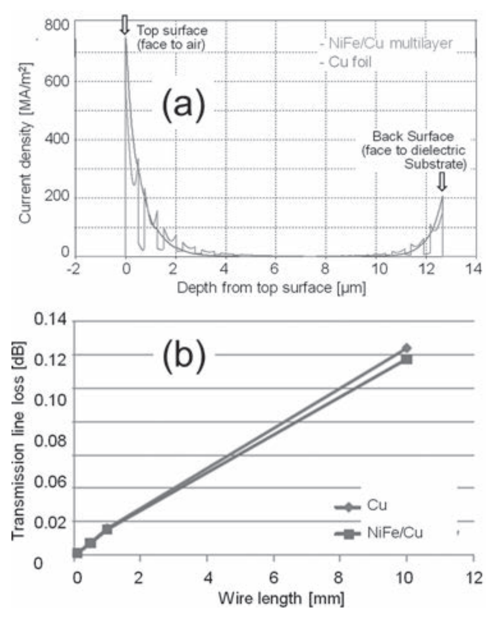

Fig. 2. Simulated and Measured Results; (a)Simulated cross-sectional conduction current distribution. Multilater is located at 0 - 12.4 μm. (b) Measured transmission line losses at 15 GHz.

10:45

CE-07. Angular dependence of single sideband generation in spin torque nano-oscillators.

R. Sharma[1], N. Sisodia[1] and P.K. Muduli[1]
1. Physics, Indian Institute of Technology Delhi, Delhi, India

Spin torque nano-oscillators (STNOs) [1-3] are useful to generate high frequency GHz range carrier signal for transmitting the low-frequency information signal through analog frequency modulation. [4-7] Recently a single sideband (SSB) generation [7], which uses transmitter power and bandwidth more efficiently, has been demonstrated in magnetic tunnel junction (MTJ) based STNOs using nonlinear dependence of STNO frequency and amplitude on the bias current (I_{dc}). The SSB generation is well described by nonlinear frequency and amplitude modulation (NFAM) theory. [5,8] This study shows a strong dependence of onset modulation frequency (f_{onset}) required for seeing the SSB on the STNO frequency (f_0) tunability with bias current at a fixed in-plane angle (ϕ = angle between fixed and free layer). Furthermore, macrospin simulation showed that field like torque, which is a device property, can manipulate the frequency tunability and thus the f_{onset}. In this work, we present macrospin simulations to show a strong dependence of SSB generation and f_{onset} on varying in-plane field angle, which is easy to control in the experiments. We show that ϕ strongly alters the red-shift of STNO frequency with the bias current, which changes the onset frequency for SSB generation. We performed the macrospin simulation for the same CoFeB/MgO/CoFeB based device used in Ref [7]. All the simulation parameters are same as in Ref [7]. Electrons are assumed to flow from fixed layer to free layer. Field angle is measured with respect to fixed layer which is pinned in x direction (ϕ=0°). Magnetization is initially aligned along the direction of externally applied field (H_{app}) and later relaxes in the direction of effective field (H_{eff}) according to the LLG equation. Here, the effective field (H_{eff}) contains contributions from external field, demagnetizing field and thermal field. The Slonczewski term is then added to the system to account for the torque generated due to spin polarized current. Figures 1(a-c) show the modulation spectra at H_{app} = 400 Oe and I_{dc} = 7 mA three in-plane field angles of 190°, 195° and 200°. The Fig.1 (a-c) shows that the onset frequency required to see the SSB generation (shown by white line) strongly depend on the angle between free and fixed layer even in a narrow range of 10°. In order to understand this behavior, free running STNO frequency is plotted in Fig. 2(a). It can be clearly observed that change in ϕ changes the STNO frequency red shift at higher dc bias current. The maximum frequency of operation of the STNO, f_{max} is shown by black dotted lines in Fig 2(a). Whenever upper sideband frequency [f_0 + modulation frequency (f_m)] lies above f_{max} only lower sideband is generated. Since red shift of STNO frequency with I_{dc} strongly depends on the ϕ angle [Fig 2(a)], SSB onset frequency (f_{onset}) also varies as a function of ϕ, which is shown in fig 2(b). In particular, frequency tunability is negligible at high in-plane field angle, which are not suitable for SSB generation. The value of f_{onset} is approximately equal to f_{max}-f_0. Another important factor for SSB transmission is the power generated by the STNO which is shown as a function of ϕ, in Fig 2 (c) at I_{dc} = 7 mA. At higher angles, power of the STNO becomes relatively low and STNO frequency reaches the f_{max} region (shown by red dotted lines). So, an optimum value of ϕ=210° is suitable for the SSB application. We will discuss these simulation results by the NFAM theory, which includes the nonlinear variation in STNO frequency and amplitude as a function of modulation current around the bias dc current at different values of ϕ. In conclusion, we present an angular dependence of SSB generation in MTJ-STNOs, which gives a liberty to the experimentalist to tune the SSB generation by an external parameter i.e. the in-plane field angle.

1. S. I. Kiselev et al.,"Microwave oscillations of a nanomagnet driven by a spin-polarized current", Nat. 425, 380–383 (2003). 2. A. M. Deac et al.,"Bias-driven high-power microwave emission from MgO-based tunnel magnetoresistance devices", Nat. Phys. 4, 803–809 (2008). 3. P. Villard et al.," A GHz Spintronic-Based RF Oscillator", IEEE J. Solid-State Circuits 45, 214–223 (2010). 4. M. R. Pufall et al."Frequency modulation of spin-transfer oscillators", Appl. Phys. Lett. 86, 082506 (2005). 5. P. K. Muduli et al.,"Nonlinear frequency and amplitude modulation of a nanocontact-based spin-torque oscillator", Phys. Rev. B 81, 140408 (2010). 6. Pogoryelov, Y. et al.," Frequency modulation of spin torque oscillator pairs", Appl. Phys. Lett. 98, 192501 (2011). 7. Raghav Sharma et al.," A high-speed single sideband generator using a magnetic tunnel junction spin torque nano-oscillator", Nature Scientific Reports 7, 13422 (2017). 8. G. Consolo et al.,"A Generalized Model of Nonlinear Dynamics in Combined Frequency-Amplitude Modulators", IEEE Trans. Magn. 46, 3629–3634 (2010).

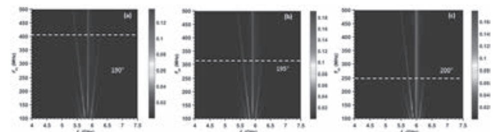

Fig. 1. Map of power vs. modulation frequency (f_m) and frequency (f_0) for I_m = 1 mA at ϕ = (a) 190°, (b) 195°, and (c) 200°. The white dashed lines separate the NFAM and SSB regions.

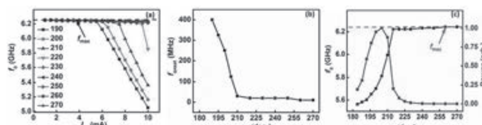

Fig. 2. (a) STNO frequency vs. bias current for various values of the ϕ. (b) onset modulation frequency, f_{onset} for observing lower single side band (LSSB) at H_{app} = 400 Oe and I_{dc} = 7 mA with varying ϕ. (c) STNO frequency vs. bias current H_{app} = 400 Oe and I_{dc} = 7 mA with varying ϕ.

INVITED PAPER

11:00

CE-08. Broadband antenna using strain-mediated spin Hall nano-oscillator. *(Invited)*

Q. Wang[1], J. Domann[2], J. Hu[1] and G.P. Carman[1]
1. Department of Mechanical and Aerospace Engineering, University of California, Los Angeles, Los Angeles, CA, United States; 2. Department of Biomedical Engineering and Mechanics, Virginia Tech, Blacksburg, VA, United States

The magnetic nano-oscillator is a promising candidate for microwave generator due to its high tunability and wide range of working temperature. Usually the steady precession in the nano-oscillator is achieved by applying spin-transfer torque (STT) to cancel the intrinsic Gilbert damping of the magnetic oscillator. As an energy-efficient alternative to STT, the spin-orbit torque (SOT) can also be used to compensate the intrinsic magnetic damping and induce steady magnetic oscillation in the spin-Hall nano-oscillator (SHNO). However, there are few studies on tuning frequencies in SHNO without using external bias field, which is crucial for practical on-chip application. Here, we present a new control method of SHTO by using voltage-induced strain in a multiferroic system (i.e., coupled piezoelectric and magnetoelastic effects). A macrospin model is developed to simulate the piezoelectric/heavy metal/magnetoelastic structure. Applying voltage to the piezoelectric layer induces strain, which in turn generates an effective magnetoelastic field inside the magnetoelastic element (e.g., CoFeB). It is shown that both the frequency and amplitude of the oscillation can be tuned within wide ranges by tuning strain and the SOT current applied to the heavy metal layer. The strain-mediated SHNO provides a platform of a potential antenna system with wide-range frequency and amplitude modulation. Fig. 1a illustrates an array of strain-mediated STNO for antenna transmitter application. The magnetic nano-oscillators (shown in blue) are attached to a heavy metal thin film (e.g., Ta), which is then attached to a piezoelectric substrate such as PMN-PT or PZT ($Pb_y[Zr_xTi_{1-x}]O_3$). The SOT current is applied to the heavy metal to compensate the Gilbert damping, and the voltage is applied to the bottom of the piezoelectric layer to generate strain. The voltage-induced strain is estimated using a finite element model and input into the macrospin model to calculate the magnetic dynamics of a single magnetic oscillator. Each nano-oscillator is a CoFeB element with 50nm diameter and 1.5nm thickness. For specific ranges of strain/current combinations (as shown Fig. 1b and 1c), the SOT completely compensates the CoFeB's Gilbert damping and leads to steady out-of-plane magnetic oscillation. The upper left plot in Fig. 1a shows the temporal change of the perpendicular magnetization in a representative steady oscillation. It is shown that the amplitude of the perpendicular magnetization is invariant with time. Fig. 1b shows the oscillation frequency diagram with different voltage induced strains and current density values. For the strain and current range studied, the frequency can be tuned from 500MHz ~ 5GHz, which is within the microwave range. The minimum strain to initiate continuous oscillations is ~1000, while the minimum current density is ~1×10^6 A/cm^2. For the oscillating cases with fixed current, the applied strain has negligible influence on oscillation frequency. However, with fixed applied strain, tuning the current density causes large changes in oscillation frequency. More specifically, higher current density leads to higher oscillating frequency. When the current exceeds 3×10^7 A/cm^2, further increasing the current will increase the threshold strain, causing the oscillation more and more difficult to initiate. Fig. 1c shows the oscillation amplitude diagram with varying strain and current densities. The oscillation region is the same as in Fig. 1b. The color bar represents the amplitude of the perpendicular magnetization under a steady out-of-plane oscillation as shown in Fig. 1a. It is shown that both current density and strain have strong impact on the oscillation amplitude. For a given strain level, increasing the current will decrease the oscillation amplitude. In contrast, for a given current density, increasing the strain will increase the oscillation amplitude. Combining the frequency and amplitude diagrams in Fig. 1b and 1c, one can design the system to have a wide range of frequency and amplitude outputs by choosing a specific strain/current combination. In conclusion, the strain-mediated SOT control has a potential application of broadband antenna with large frequency-modulation (FM) and amplitude-modulation (AM) abilities.

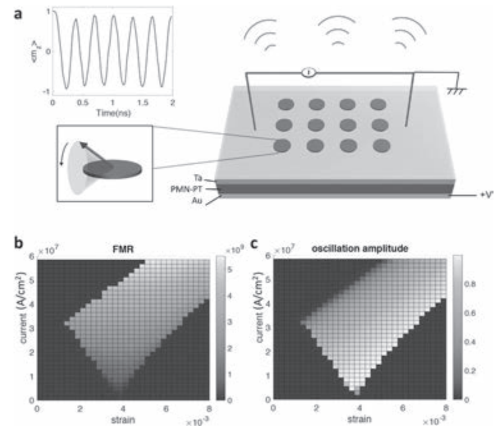

Fig. 1. (a) Illustration of the antenna design based on the strain-mediated spin Hall nano-oscillator. (b) Oscillation diagram of frequencies for different applied strain and current. (c) Oscillation diagram of perpendicular magnetization amplitudes for different applied strain and current.

CONTRIBUTED PAPERS

11:30

CE-09. Experimental demonstration of broadband spintronic diodes for harvesting of sub-μWatt microwave energy.

B. Fang[1], M. Carpentieri[2], A.N. Slavin[5], P. Khalili Amiri[3], G. Finocchio[4] and *Z. Zeng*[1]

1. Key Laboratory of Nanodevices and Applications, Suzhou Institute of Nano-tech and Nano-bionics,CAS, Suzhou, China; 2. Department of Electrical and Information Engineering, Politecnico di Bari, Bari, Italy; 3. Northwestern University, Evanston, IL, United States; 4. University of Messina, Messina, Italy; 5. Oakland University, Rochester, MI, United States

Energy harvesting technologies offer a promising approach to capture energy from ambient sources, such as vibration, heat, and electromagnetic waves. Among them, the ambient radio-frequency (RF) electromagnetic signals provide an attractive energy source for applications in self-powered portable electronics in the "internet of things" era [1, 2]. However, currently available microwave detectors based on semiconductors do not meet the practical requirements for energy harvesting applications. The key challenges that need to be addressed are: (i) Miniaturization: Electromagnetic devices currently used for microwave energy harvesting could be efficient but are difficult to miniaturize, and (ii) Low input-power operation: Here we show the development of a *bias-field-free* nanoscale spintronic diode (NSD) based on a magnetic tunnel junction (MTJ) having a *canted magnetization* in the free layer, and demonstrate that this NSD could be an efficient harvester of broadband ambient RF radiation, capable to efficiently harvest microwave powers of microWatt and below. The stack composition of the MTJs is PtMn (15) /$Co_{70}Fe_{30}$ (2.3)/Ru (0.85)/$Co_{40}Fe_{40}B_{20}$ (2.4)/MgO (0.8)/$Co_{20}Fe_{60}B_{20}$ (1.65) (thickness in nm) patterned into ellipse-shaped pillars using electron-beam lithography and ion milling techniques. The free layer is composed of $Co_{20}Fe_{60}B_{20}$ capped by Ta and exhibits interfacial perpendicular anisotropy [3]. It is designed in order to have a tilted out-of-plane easy axis, due to the competition of shape anisotropy with the first and second-order magnetic anisotropies of the free layer. The perpendicular magnetic anisotropy (PMA) in the MgO/$Co_{20}Fe_{60}B_{20}$/Ta free layer is caused by an interfacial effect that arises from the hybridization between the O (of the MgO) and Fe (of the CoFeB) orbitals, and can be controlled by the CoFeB composition, the capping material, and the thickness of the free layer. We have measured the rectified voltage with an RF current in the absence of an applied magnetic field by applying an RF current to the device through a bias tee using a signal generator, while the rectification voltage V_{DC} across the MTJ is recorded with a nanovoltmeter. The frequency response of the NSD shows that a novel type of frequency behaviour, i.e. broadband response, is achieved. Figure 1 displays an example with a RF input power of P_{RF} = 10 μW, showing that the NSD rectifies a nearly constant voltage across a 100 to 550 MHz range. To evaluate the performance for energy harvesting applications, the rectified DC voltages obtained at a frequency of 500 MHz for several Schottky diodes and two spintronic diodes were compared. Figure 2 summarizes the calculated efficiency for a constant frequency of 500 MHz. The efficiency in the high-barrier Schottky diodes is extremely low (< 10^{-8}%), as expected [4]. The spintronic diode exhibits better efficiency than the low-barrier Schottky diodes at low input power (< 5 μW). For example, at an RF input power of 3.2 μW, the spintronic diode has a conversion efficiency of 0.005%, compared to less than 0.001% for low-barrier Schottky diodes. Therefore, our results suggest that the spintronic diode offers a prospective approach for energy harvesting applications.

[1] Priya, S. & Inman, D. J. Energy harvesting technologies (Springer, 2009). [2] Hemour, S. & Wu, K. Radio-frequency rectifier for electromagnetic energy harvesting: development path and future outlook. *Proc. IEEE* 102, 1667-1691(2014). [3] Ikeda, S. *et al*. A perpendicular-anisotropy CoFeB-MgO magnetic tunnel junction. *Nat. Mater*. 9, 721-724 (2010). [4] Hagerty, J. A., Helmbrecht, F. B., McCalpin, W. H., Zane, R. & Popovic, Z. B. Recycling ambient microwave energy with broad-band rectenna arrays. *IEEE Trans. Microwave Theor. Tech*. 52, 1014-1024 (2004).

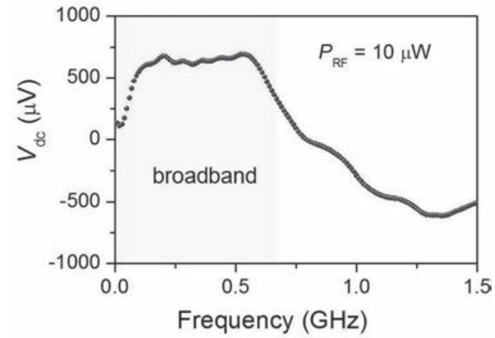

Fig. 1. Generated voltage (V_{DC}) as a function of RF frequency for RF powers of 10 μW

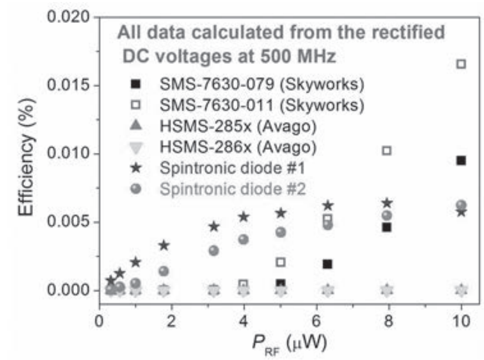

Fig. 2. Efficiencies for Schottky diodes and spintronic diode at a frequency of 500 MHz

11:45

CE-10. Intrinsic permeability of composites filled with nickel powders.

S.N. Starostenko[1], K.N. Rozanov[1] and A.O. Shiryaev[1]
1. Theoretical, Institute for Theoretical and Applied Electromagnetics, Moscow, Russian Federation

The microwave permeability of nickel (Ni) is reconstructed from constitutive parameter measurements of paraffin–binded composites filled with flakes or spheres of carbonyl nickel. The metal permeability is assumed to be equal to the intrinsic permeability of inclusions. The mean diameter of spheres is about 12μm, the mean diameter of flakes obtained from spheres by ball milling is about 50μm, the thickness is about 2μm. The shape and size are determined by microscopy and by laser particle sizer Analysette 22. The measurements of composite permittivity ε_{mix} and permeability μ_{mix} are performed with MS2028 VNA applying the reflection-transmission coaxial-line technique within 0.05-20GHz frequency band. The calculations are performed for isotropic mixtures filled with spheres and for plane-isotropic mixtures filled with flakes. The assumption of plane isotropy for flake-filled samples is reasonable as for the pressed washer sample the thickness (~0.8mm) is much smaller than the diameter (7mm). The effects of filling factor, particle shape and size on permittivity and permeability are analyzed. The reconstruction of inclusion permeability μ_{incl} is based on treatment of the measured dependence of ε_{mix} and μ_{mix} on frequency *f* and volume fraction of inclusions *p*.The procedure is based on generalized Sihvola mixing model [1] simplified for a plane-isotropic composite. The model is valid for wide range of susceptibility contrast and accounts for inclusion shape and geometric spectral linewidth [2] described by parameter *a* in equation (Eq.1). The dependence of composite susceptibility χ_{32} on frequency is defined by the corresponding dependence of inclusion susceptibility χ_{12}. The susceptibilities χ_{12} and χ_{32} are normalized by the corresponding constitutive parameter of a binder: permittivity ε_2 or permeability μ_2 of polymer. Equation (Eq.1) relates susceptibility of a composite χ_{32} to the filling factor *p*, inclusion susceptibility χ_{12}, inclusion depolarization factor *N* and mixture structure characterized by parameter *a*. $\chi_{m32}/\chi_{m12}=p(1+a\chi_{m32})/[1+ a\chi_{m32}+ N\chi_{m12}(1-p)]$ (1) Indexes 1, 2 and 3 relate to inclusion, binder and mixture. The inclusions are assumed to be identical spheres or identical oblate ellipsoids of rotation; their shape defines the depolarization factor *N* [3]. The similar equation (Eq.2) describes composite electric susceptibility χ_{e32}. As metal conductivity is about 10^8Ohm×m,thus $\chi_{e12} >>\chi_{e32}$ at practicable fillings, and Eq.1 may be simplified as shown below. $\chi_{e32} = p\chi_{e12}\ (1+a\chi_{e32})/[1+ a\chi_{e32} + N\chi_{e12}\ (1-p)] \approx p/[N\ (1-p)-ap]$ (2) The difference in electric and magnetic susceptibility of metals $\chi_{e12} /\chi_{m12} >>1$ makes it possible to estimate intrinsic permeability of metals at microwaves, where the measurements with bulk metals are impossible because of skinning. Moreover the mixing model (Eq.1) makes it possible to estimate from the measured data the spectral linewidth *a* as well. It is easy to show that for metal inclusions ($\chi_{\varepsilon12}\rightarrow\alpha\infty$) the inclusion depolarization factor *N* and percolation threshold p_c are related to linewidth parameter *a* as Eq.3 $a=N(1-p_c)/p_c$ (3) The parameters *N* and p_c are readily determined experimentally and are used in the generalized Maxell Garnett (Odelevskiy) equation to relate a composite susceptibility to that one of inclusion [4]. The measured at 50MHz quasistatic permittivity and permeability $\varepsilon_{mix}(p)$ and $\mu_{mix}(p)$ data are shown in Fig.1 by circles and squares correspondingly. As the imaginary permeability μ''_{mix} at 50MHz is comparable to real part μ'_{mix}, the value $\mu_{mix}(p)$ is presented by the absolute value of μ_{mix}. In the vicinity of percolation threshold p_c the samples become electrically conductive and the measured permittivity has poor reprodusability and jumps from high positive to negative values. The effect of negative permittivity is known [5] but we relate it to inductive resistance of long clusters similar to that of wire sections [6]. The dashed lines in Fig.1 present the permittivity curves calculated from Eq.2 with *N* and p_c as fitted parameters. The fitted values of depolarization factor N_{sph}=0.149 and N_{flk}=0.04 agree with microscopic measurements. The percolation threshold values are correspondingly $p_{c\text{-}sphere}$=0.56, and $p_{c\text{-}flake}$=0.19; thus Eq.3 gives a_{sphere}=0.111 and a_{flake}=0.167. The measured frequency dependence of microwave permeability for composites filled with flakes and spheres (the data in Fig.2 are selected for composites with approximately the same ε_{mix}-values) shows that the absorption peak shape and frequency strongly depend on inclusion shape and on thickness because of skinning. The absorption frequency is much lower than that of composites with carbonyl iron [1] and the permeability values measured at 50MHz are far from static ones. The reconstructed inclusion permeability at this frequency is also far from the static one as the loss tangent for spheres and flakes is close to unity, while the permeability real value is about 5 for both inclusion types; the value is about 2 times lower than the reported data [7]; the difference may be attributed to skinning and structural defects introduced in flakes while ball milling. The measured microwave constitutive parameters of composites show that Ni flakes and spheres both are promising fillers for interference suppressors and UHF-band absorbers similar to sendust powders [4].

1) A.H. Sihvola, J.A. Kong, IEEE Trans. on Geoscience and Remote Sensing, vol. 26, no. 4, 420, 1988 2) D.J. Bergman, Phys. Rev. B, vol. 19, no. 4, p.2359, 1979 3) S.F. Lomayeva, A.V. Syugaev, A.N. Maratkanova, A.A. Shakov, K.N. Rozanov, D.A. Petrov, C.A. Stergiou, J. Alloys Compounds, 721, p.18, 2017 4) S.N. Starostenko, K.N. Rozanov, A. O. Shiryaev, A.N. Shalygin, A. N. Lagarkov, J. Appl. Phys. 121, p.245107, 2017 5) Z. Zhang, K.S. Yao, L.Z. Kuang, S. Sun, X. Ji, Ceramics International, vol.42, p.19063, 2016 6) S. N. Starostenko, K. N. Rozanov, PIER, 99, p.405, 2009 7) S. Lucyszyn, Microwave Characterization of Nickel, PIERS on line, vol.4, p.686, 2008

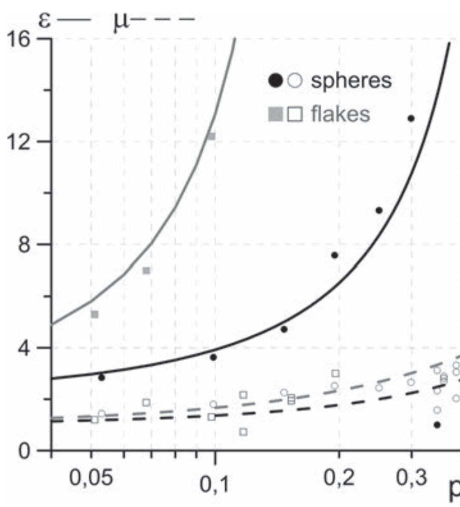

Fig. 1. Measured and calculated quasistatic permittivity and permeability of composites filled with Ni spheres and flakes.

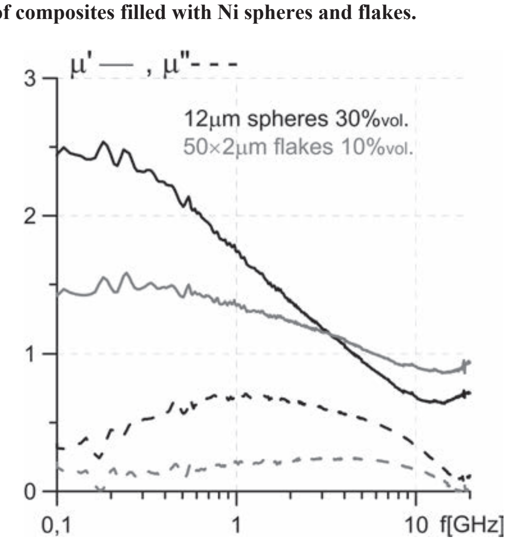

Fig. 2. Measured dependence of complex permeability on frequency for composites filled with 30% vol. of Ni spheres and 10%vol. of flakes.

WEDNESDAY MORNING, 25 APRIL 2018 PEONY I, 9:00 TO 12:00

Session CF

MAGNETISATION DYNAMICS I

Zongzhi Zhang, Chair

Fudan University, Shanghai, China

CONTRIBUTED PAPERS

9:00

CF-01. Magnetic damping in metallic and half-metallic Co_2MnGe thin films.

J.M. Shaw[1], E.K. Delczeg-Czirjak[2], E.R. Edwards[1], Y. Kvashnin[2], D. Thonig[2], M. Schoen[1], M. Pufall[1], M. Schneider[1], T. Silva[1], O. Karis[2], K. Rice[3], O. Eriksson[2] and H. Nembach[1]
1. Quantum Electromagnetics Division, NIST, Boulder, CO, United States; 2. Department of Physics, Uppsala University, Uppsala, Sweden; 3. CAMECA Instruments, Madison, WI, United States

One class of material that currently shows promise for spintronic and magnonic applications is Heusler compounds. Of importance is the fact that many of these compounds are half-metallic, meaning that one of the spin bands has a bandgap at the Fermi energy (i.e., insulating) while the other spin band is metallic in nature (i.e., conducting). This property leads to highly efficient generation of spin currents and large values of giant magnetoresistance, even at room temperature. [1,2] In addition, many half-metallic Heusler compounds are expected to have exceptionally low values of the damping parameter. We show that low values of the magnetic damping parameter can be achieved in sputter deposited poly-crystalline films of Co_2MnGe annealed at relatively low temperatures up to 400 °C. Such a low processing temperature for sputter deposited films is advantageous for many applications in spintronics that have limited thermal budgets. Measured damping values as low as 0.0014 are achieved with an intrinsic value of 0.0010 after spin-pumping contributions are taken into account. Of importance to applications is the low value of inhomogeneous linewidth that yields measured linewidths of 1.8 mT and 5.1 mT at 10 GHz and 40 GHz, respectively. The damping parameter is found to monotonically decrease as the annealing temperature increases, as shown in Figure 1. X-ray diffraction reveals that the increase in annealing temperature results in an increase in the B2 order of the films, suggesting that the damping parameter depends on the crystalline order of the CMG. This hypothesis was investigated via calculations of the damping parameter from density functional theory as implemented in the SPR-KKR code [3,4] combined with linear response theory. [5] Here, the damping parameter is calculated as the structure evolves from A2 to B2 to $L2_1$ orders as shown in Figure 2. The largest decrease in the damping parameter occurs during the A2 to B2 transition as the half-metallic phase becomes established. Finally, it is important to point out that our results show excellent *quantitative* agreement between the calculated and experimentally determined values of the damping parameter as the crystalline order is varied. Having the ability to quantitatively predict damping in materials can lead to the discovery of new materials with ultra-low values of the damping parameter.

[1] M. Zhu, B. D. Soe, R. D. McMichael, M. J. Carey, S. Maat, and J. R. Childress, Appl. Phys. Lett. 98, 072510 (2011). [2] T. Kubota, Y. Ina, Z. Wen, H. Narisawa, and K. Takanashi, Phys. Rev. Mater. 1, 044402 (2017). [3] http://ebert.cup.uni-muenchen.de/sprkkr, (2017). [4] H. Ebert, D. Ködderitzsch, and J. Minár, Rep. Prog. Phys. 74, 096501 (2011). [5] H. Ebert, S. Mankovsky, D. Ködderitzsch, and P. J. Kelly, Phys. Rev. Lett. 107, 066603 (2011).

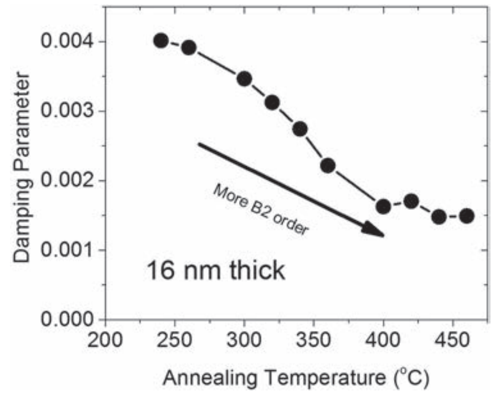

Fig. 1. The magnetic damping parameter as a function of annealing temperature. As the temperature is increased, the B2 order also increases.

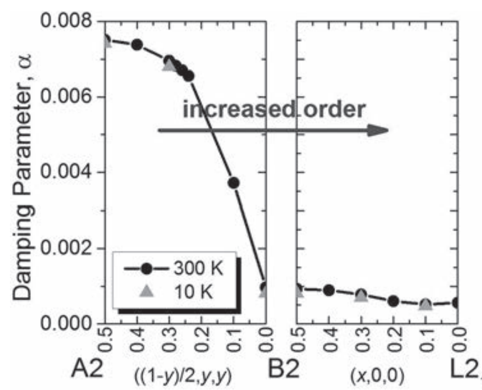

Fig. 2. DFT calculations of the magnetic damping as the crystalline structure evolves from A2 (left) to B2 (center) to $L2_1$ (right)

9:15

CF-02. Enhanced magnetostatic and dynamic properties in Fe/Co substituted Ni-Mn-In alloy films.

R. Modak[1] and *A. Srinivasan*[1]
1. Department of Physics, Indian Institute of Technology, Guwahati, India

Multifunctional properties [1-3] and half metallic character [4] of Ni-Mn-In alloys have projected them as promising candidates for fabricating magnetoelectronic devices (MED) [5,6]. Since MEDs operating at microwave frequencies consume very little energy and are capable of achieving higher speeds, the search is on for new prospective materials for such applications. Understanding the magnetodynamic properties of thin films of these prospective alloys is very important for these applications. Substitution of magnetic elements in Ni-Mn-In is expected to enhance its magnetic properties. Here, Ni-Mn-X-In (X = Fe, Co) alloy films of thickness 500±5 nm were deposited on Si (100) substrate by dc magnetron sputtering from a $Ni_{48}Mn_{39}In_{13}$ alloy target. The fourth element (X) was introduced in the films by symmetrically placed 2 × 2 mm^2 X chips on the Ni-Mn-In target. As-deposited films were annealed *ex situ* at 550 °C under residual Ar gas pressure of 10^{-3} Pa for 1 h. Composition of the three annealed films were found to be $Ni_{49.2}Mn_{39.6}In_{11.1}$ (F1), $Ni_{49.1}Mn_{36.9}Fe_{2.9}In_{11.1}$ (F2) and $Ni_{49.0}Mn_{36.8}Co_{3.0}In_{11.2}$ (F3). The corresponding valence electron to atom (*e*/*a*) ratio of F1, F2 and F3 are 8.02, 8.09 and 8.08, respectively. Grazing incidence X-ray diffraction patterns of the films confirmed single phase austenite structure with $L2_1$ ordering (space group Fm-3m). Room temperature isothermal magnetization (*M-H*) curves recorded as a function of applied field showed paramagnetic behavior in all as-deposited films due to their amorphous structure. However upon annealing, ferromagnetic order was induced in the films with the formation of a polycrystalline structure (*c.f.* Fig.1(a)). It can be noticed from the figure that substitution of Fe or Co for Mn increases the magnetization upto ~120 emu/cc. It is evident from the typical *M-H* loops depicted as inset in Fig. 1(a) that the easy axis of magnetization is along the plane of the films. Room temperature ferromagnetic resonance (FMR) spectra recorded using an electron spin resonance spectrometer for different polar angles (θ_H) with applied magnetic field oriented along the film plane are shown in Fig. 1(b). The FMR spectra were analyzed using the well-known theoretical model discussed in Refs [7-9]. Effective magnetization ($4\pi M_{eff}$) and perpendicular effective anisotropy (K_1) have been extracted from the numerical fitting to resonance field (H_r) recorded from in plane orientation (90°) to out of plane (0°) of the film with respect to the applied magnetic field, using the above model. The analysis shows that H_r varies from a low to a higher value when the applied field is rotated in steps from in-plane to out-of-plane orientation. The saturation magnetization (M_s) of the films estimated from the H_r versus θ_H plots shown as inset in Fig. 1(c), are in good agreement with the dc magnetometry measurements. Fig. 1(c) represents the numerically fitted FMR linewidth (ΔH) data as a function of θ_H. It can be seen that the numerically modeled curves yield a good fit to experimental data with three crucial factors contributing to the observed linewidth. These are the (1) Gilbert damping term (ΔH_α) which is an internal property of the material, (2) 2-magnon scattering term ($\Delta H_{2\text{-}Mag}$), and (3) ΔH_0 term which depends on various extrinsic parameters related to the material nature. A careful look in Fig. 1(c) would reveal that with Fe (or Co) substitution, ΔH increased (or decreased) as compared to the ternary alloy film even though the Gilbert damping constant (α) remained almost invariant for both elemental substitutions. Through these studies, we show for the first time Co substituted Ni-Mn-In films with low Gilbert damping constant, higher saturation magnetization, high perpendicular anisotropy and easy axis along film plane which are very promising attributes for application in MED.

1. S. Fähler, U. K. Rößler, O. Kastner, J. Eckert, G. Eggeler, H. Emmerich, P. Entel, S. Müller, E. Quandt, and K. Albe, Adv. Eng. Mater. 14, 10 (2012). doi:10.1002/adem.201100178. 2. S. Y. Yu, Z. H. Liu, G. D. Liu, J. L. Chen, Z. X. Cao, G. H. Wu, B. Zhang, and X. X. Zhang, Appl. Phys. Lett. 89, 162503 (2006). doi:10.1063/1.2362581. 3. T. Sakon, S. Yamazaki, Y. Kodama, M. Motokawa, T. Kanomata, K. Oikawa, R. Kainuma, and K. Ishida, Jpn. J. Appl. Phys. 46, 995 (2007). doi:10.1143/JJAP.46.995. 4. M. T. Johnson, P. J. H. Bloemen, F. J. A. den Broeder, and J. J. De Vries, Reports Prog. Phys. 59, 1409 (1996). doi:10.1088/0034-4885/59/11/002. 5. L.B.-P. and R.S. Bernard Dieny, Cristian Papusoi, Ursula Ebels, Dimitri Houssameddine, Spin polarised magnetic device, 2012. U. S. Patent 8279666 B2 (2 October 2012). 6. R. Sato, Magneto resistive effect element with a magnetic film generating spin fluctuation of conduction electrons, U. S. Patent 8411394 B2 (2 April 2013). 7. S. Mizukami, Y. Ando, and T. Miyazaki, Phys. Rev. B 66, 104413 (2002). doi:10.1103/PhysRevB.66.104413. 8. R. Yilgin, M. Oogane, Y. Ando, and T. Miyazaki, J. Magn. Magn. Mater. 310, 2322 (2007). doi:10.1016/j.jmmm.2006.11.032. 9. R. Modak, B. Samantaray, P. Mandal, and A. Srinivasan, J. Alloys Compd. 692, 529 (2017). doi:10.1016/j.jallcom.2016.09.036.

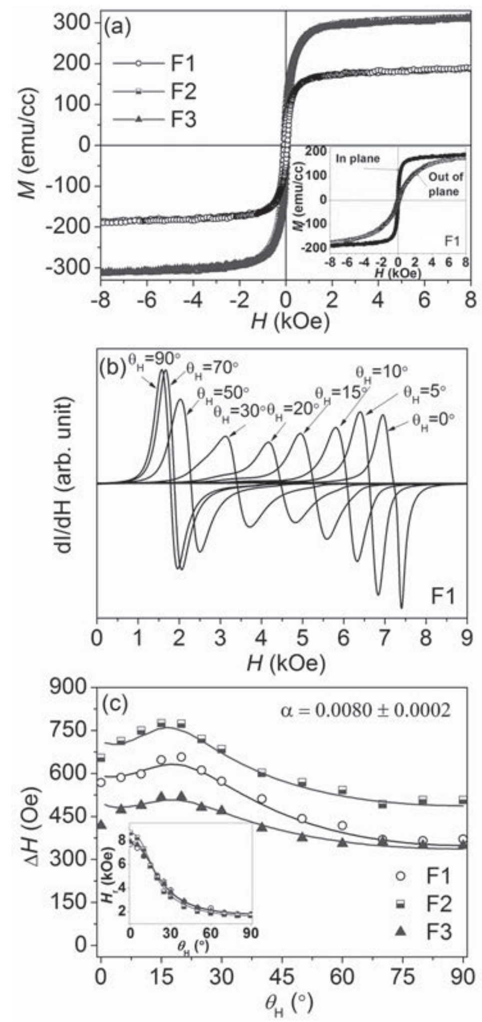

Fig. 1. (a) Room temperature in-plane *M-H* loops of 550 °C annealed F1, F2 and F3 films. Inset shows in-plane and out-of-plane *M-H* loops of F1. (b) Room temperature FMR spectra for F1 film recorded at 9.44 GHz. (c) θ_H dependence of ΔH for all the films. Solid lines represent fits to the experimental data. Inset shows variation of H_r with θ_H for all films.

9:30

CF-03. Manipulation of Gilbert Damping Parameter by Annealing Sputtered Deposited Co/Pt Bilayer Thin Films.

A. Kumar[1], N. Pandey[2], D.K. Gupta[2], M. Gupta[2], S. Chaudhary[1] and P.K. Muduli[1]

1. Department of Physics, IIT Delhi, New Delhi, India; 2. UGC-DAE Consortium for Scientific Research, Indore, India

Ferromagnet/ heavy metal (FM/HM) systems have attracted considerable attention due to the presence of current-induced spin-orbit torques (SOT) at their interface. The SOT allows the manipulation of magnetization of the ferromagnet when sufficient high current density is used [1,2]. An important parameter for potential applications of these heterostructures is the Gilbert damping constant of the FM, which can be affected by the details of the interface. Here we study the damping constant of Co thin films in Co/Pt multilayers as a function of post-growth annealing. Such post-growth treatment is expected to affect the SOT and hence knowledge of the damping constant as a function of annealing temperature (T_A) is useful for applications. Co (10 nm)/Pt (5 nm) bilayer structure was prepared using DC magnetron sputtering on a Si (100) n-type substrate at 3 mTorr working pressure with base pressure of $<1\times10^{-7}$ mbar. The Si substrates were cleaned using RF cleaning with RF bias of 50 W for 15 min. We used 3-inch sputter targets with 99.99% purity for better uniformity over a large area of the substrate. We also performed pre-sputtering for 2 minutes before every deposition. Co and Pt thin films were sputtered at a very low growth rate of 5 Å/min and 25 Å/min, respectively. Structural characterization of as-deposited Co/Pt bilayers was performed using X-ray Diffraction (XRD) and X-ray reflectivity (XRR) measurements (Fig. 1). XRD spectra show the polycrystalline growth of Co/Pt bilayer thin film. XRR measurements show the high-quality growth of thin film with roughness <1 nm, this is further confirmed by atomic force microscopy (AFM). After growth, samples were annealed at zero field in a high vacuum chamber for 300, 400 and 500 °C with vacuum $<5\times10^{-6}$ Torr for 1hour. Figure 1 (c)-(e) shows AFM images for as-deposited and post-annealed samples. The AFM measurements show an increase of grain size with increase in annealing temperature, T_A, which predict high inter-diffusion of Pt and Co thin films with increase in T_A [3,4] Figure 2 (a) shows ferromagnetic resonance (FMR) spectra of as-grown Co/Pt bilayer thin films for 9 GHz RF frequency, the red line is fitted with derivative of the Lorentzian equation, fitting provides the value of linewidth and resonance field for a particular fixed frequency. Similar measurements are repeated for a frequency range of 6-12 GHz. The FMR linewidth vs. frequency was fitted to determine the Gilbert damping constant (α_{eff}). Frequency vs. resonance field was fitted with Kittle's formula to determine effective saturation magnetization (M_{eff}) [5]. Gilbert damping parameter is found to increases with increase in T_A while the effective saturation magnetization shows opposite behavior [Fig. 2(b)]. No FMR signal was observed for the sample annealed at T_A= 500 °C. These results can be understood by possible intermixing of Pt and Co at the interface. This study predicts that Gilbert damping constant of Co/Pt bilayer thin films can be manipulated by annealing the heterostructures at high temperature. We will show a detailed study of interface and inverse spin Hall effect measurements for understanding the possible effect on SOT due to annealing.

1. Luqiao Liu *et al.*, "Spin-Torque Switching with the Giant Spin Hall Effect of Tantalum", Science, 336, 555, (2012). 2. Luqiao Liu *et al.*, "Spin-Torque Ferromagnetic Resonance Induced by the Spin Hall Effect", Phys. Rev. Lett. 106, 036601, (2017). 3. Masahiro Kitada, "Annealing behavior and magnetic properties of Co/Pt and Fe/Pt bilayer thin films", Thin Solid Films, 146, 21-26, (1987). 4. Chin-Chung Yu *et al.*, Annealing Effect on the Structure and Magnetism of Co/Pt Single- and Bi-Crystal Multilayers, IEEE Transactions on Magnetics, 41, 2, (2005). 5. Nilamani Behera *et al.*, Effect of Ru thickness on spin pumping in Ru/Py bilayer, Journal of Applied Physics 117, 17A714 (2015).

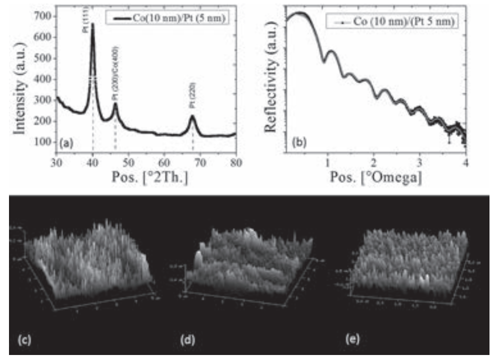

Fig. 1. (a) XRD spectra and (b) XRR spectra of as-deposited Co (10 nm)/ Pt (5 nm) thin film. (c), (d) and (e) AFM images of the Co/ Pt surfaces for as-deposited, 300 °C-annealed and 400 °C-annealed, respectively.

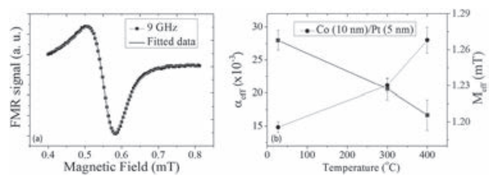

Fig. 2. (a) FMR spectra for Co/Pt as-deposited bilayer thin film for 9 GHz RF frequency. (b) Variation of Gilbert damping parameter and effective saturation magnetization with annealing temperature (T_A).

9:45

CF-04. Spin-orbit-torque and magnetic damping in ferromagnetic bilayers.

D. Lee[1], J. Kim[1], K. Lee[1], B. Ju[1], H. Koo[1], B. Min[1] and *O. Lee*[1]
1. Korea Institute of Science and Technology, Seoul, The Republic of Korea

Electrical manipulation of magnetization has been of great importance because of its scientific interest and potential application for low-power and high-speed spintronic devices. More recently, a number of works have demonstrated that in-plane charge currents generate spin-orbit torques (SOTs) that can directly switch the magnetization in hetero-structures with a strong spin-orbit coupling (SOC). For the practical use of SOT-MRAMs, it is required to reduce the write current density (J_c) significantly for minimization of Joule heat effect, low power consumption and CMOS compatibility. It is, hence, important to employ a multilayer system exhibiting a low resistivity, a large conversion efficiency from charge currents to spin currents (i.e. spin-Hall angle, θ_{SH}), a small magnetic damping (α) and a low demagnetization field (or effective out-of-plane magnetization) as much as possible to minimize J_c. Especially the achievement of a larger θ_{SH} and a lower α at the same time is of importance to implement successful SOT-devices. However, the recent spin-transparency model [1,2] suggests that the simultaneous achievement of a large θ_{SH} and a low α might be improbable. In the model, the interface transparency of the spin current between a heavy metal and a ferromagnetic layer plays an important role in determining both the effective magnitude of the spin-Hall angle and the increased amount of a magnetic damping due to the spin-pumping effect; e.g. θ_{SH}(Pt|Co)~0.11 vs θ_{SH}(Pt|Py)~0.05 but $\Delta\alpha_{sp}$(Pt|Co)~2 $\Delta\alpha_{sp}$(Pt|Py) from the Ref. [1,2]. This model indicates that the increase in θ_{SH} with a higher spin transparency will be counteracted by an increase in α so that the variation of the transparency would not be helpful for lowering J_c. Here we present one strategy to relieve this issue by utilizing ferromagnetic bilayers, consisting of Co and Py, instead of a single ferromagnetic layer, sandwiched between MgO and Pt layers [3]. We used DC/RF magnetron sputtering to deposit two series of multilayer films having different stack orders, Pt|Co|Py|MgO or Pt|Py|Co|MgO, on a thermally oxidized Si substrate at room temperature. The multilayers consist of, from the bottom to the top, Ta(1)/Pt(5)/Co(*t*)/Py(5-t)/MgO(2)/Ta(2) and Ta(1)/Pt(5)/Py(5-*t*)/Co(t)/MgO(2)/Ta(2) (thickness in nm) where the thickness of cobalt (t_{Co}) layer was varied from 0 to 5 nm. We considered Co|Py or Py|Co magnetic layers as a single ferromagnetic layer in our analysis because the total thickness of the bi-layers (5 nm) is comparable or less than the exchange length of each Co or Py. We, first of all, characterized the multilayer films by using our vibrating sample magnetometer (VSM). The saturated magnetization (M_s) monotonously increases with the t_{Co} as expected while the stack order (Pt|Co|Py|MgO or Pt|Py|Co|MgO) has little effect on the M_s. However the perpendicular magnetization anisotropy (PMA) is strongly dependent on the stacking order: Pt|Co|Py series have much stronger PMA than Pt|Py|Co|MgO series, resulting in the effective out-of-plane demagnetization field ($4\pi M_{eff}$) of Pt|Co|Py|MgO lower than $4\pi M_{eff}$ of Pt|Py|Co|MgO. We note that the magnitude of $4\pi M_{eff}$ is also one of the key material parameters in determining the switching current density for the anti-damping SOT induced magnetization switching. Next we utilized spin-torque ferromagnetic resonance (ST-FMR) method to investigate their spin-Hall angle's (θ_{SH}), magnetic damping's (α), inhomogeneous linewidth broadening's (ΔH0), and effective out-of-plane demagnetization field's ($4\pi M_{eff}$) as functions of their stacking order and relative thicknesses. Figure. 1 summarizes the measured $4\pi M_{eff}$, α, ΔH0 and θ_{SH} from the ST-FMR. The $4\pi M_{eff}$'s are in good agreement with the ones from the *M-H* hysteresis; the $4\pi M_{eff}$'s for Pt|Co(t)|Py(5-t)|MgO is lower than the ones for the Pt|Py(5-t)|Co(t)|MgO. Our results show that the value of θ_{SH} was determined by the type of interface mostly in contact to the Pt layer (Pt|FM), i.e. θ_{SH}(Pt|Co) > θ_{SH}(Pt|Py), which is consistent with the spin-transparency model. However we found that the FM|MgO interface also plays a substantial role in determining the dynamical dissipation parameters, along with the spin-pumping effect through the Pt|FM interface. The Co|MgO interface significantly increases both α and ΔH0 probably due to more developed two-magnon scattering process while the Py|MgO interface has a negligible effect on their enhancements. Figure 2 summarizes the determined α *vs* ΔH0 from all our ST-FMR devices having ferromagnetic bi- or tri-layers. Interestingly α increases with increasing ΔH0 quasi-linearly for samples with a Co|MgO interface, whereas for those with a Py|MgO interface, α remains nearly constant with increasing ΔH0, which is mostly distributed at low values. The measured data definitely indicates that a new magnetic relaxation channel is developed at the Co|MgO interface. We, based on the measured parameters, estimate the current density as functions of the stack order and the t_{Co} for the SOT induced in-plane magnetization switching. Overall for a low J_{c0} the multilayer configuration of Pt|Co|Py|MgO has more preferable material parameters than the stack of Pt|Py|Co|MgO. Our approach suggests one promising method to optimize θ_{SH}, α, ΔH0, and $4\pi M_{eff}$ by engineering both interfaces contacting to the Pt and the MgO layers. In this talk, we shall present the detailed our results for the various stacking order and thickness ranges. And we will discuss about possible mechanism to the magnetic damping from the interface with MgO layer.

[1] W. Zhang et al., Nature Physics, 11, 496 (2015). [2] C. F. Pai et al, Physical Review B 92, 064426 (2015) [3] DongJoon Lee et al. under review (2017)

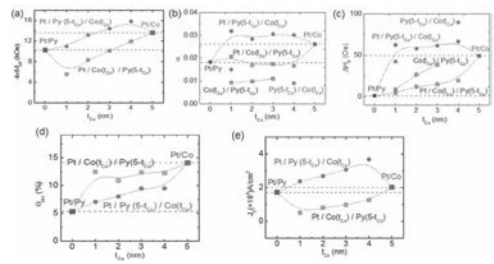

Fig. 1.

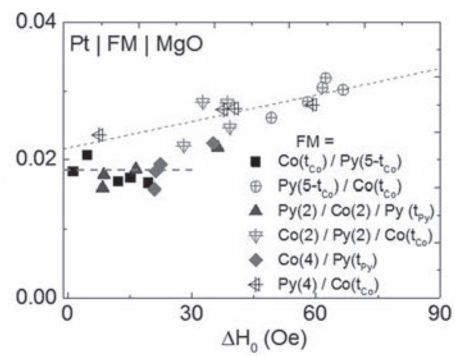

Fig. 2.

10:00

CF-05. Tetragonally Distorted Ultrathin $Fe_{50}Co_{50}$ Epitaxial Film with High Magnetic Anisotropy and Gilbert Damping.

R. Mandal[1], J. Jung[1], Y. Takahashi[1], Y. Sakuraba[1], S. Kasai[1], T. Ohkubo[1] and K. Hono[1]
1. Research Center for Magnetic and Spintronic Materials, National Institute for Materials Science (NIMS), Tsukuba, Japan

Perpendicular magnetic anisotropy (PMA) thin films have attracted considerable interest due to their potential application in the field of spintronics such as spin transfer torque magnetic random access memory (STT-MRAM) [1]. To increase the capacity of STT-MRAM, high PMA material is required for both of the reference and free layers in order to overcome the thermal agitation problem. One of promising PMA materials is the tetragonally distorted FeCo alloy. Large PMA of 0.2 MJ/m^3 was reported for tetragonally distorted FeCo grown on Rh [2, 3]. To further investigate the potential of this material for the ferromagnetic layer in STT-MRAM, the estimation of Gilbert damping (α) is necessary. Here we report unusually high α of 0.04 in 1.0-nm-thick FeCo film grown on a Rh underlayer. Based on the microstructure observation, we conclude that large value of α is due to the Rh diffusion as well as the large lattice distortion. The $Fe_{50}Co_{50}$ films were deposited by ultra-high vacuum magnetron sputtering system at a base pressure of 2×10^{-7} pa. The stacking structure of the film is MgO/Rh (50)/$Fe_{50}Co_{50}$ (t)/Rh (3), where the numbers in the parentheses indicate the thickness in nm. The thickness (t) of $Fe_{50}Co_{50}$ was varied from 1.0-nm to 10.0-nm. The Rh buffer layer was deposited at room temperature followed by post annealing at 573 K. $Fe_{50}Co_{50}$ (t) layer and the capping Rh (3) layer were also deposited at room temperature (RT). The magnetization curves were measured using a vibrating sample magnetometer whereas the crystalline structure and microstructure were verified by using X-ray diffraction (XRD) and transmission electron microscopy (TEM) with energy dispersive spectroscopic (EDS) analysis. α was estimated by time-resolved magneto optical Kerr effect (TRMOKE) method based on an all-optical two-color pump-probe setup [5]. Here the pump pulse used as an excitation pulse to excite the magnetization whereas the probe beam used to measure the change of magnetization *w.r.t.* the time in phase sensitive manner. Fig. 1 (a) shows a cross-sectional STEM-HAADF image of 1.0-nm-thick FeCo sample. The zone axis is Rh [110] and FeCo [100]. From the lattice spacing in this image, c/a is determined to be 1.3, in agreement with that estimated by XRD data. No misfit dislocations are observed in this area of view, indicating that there is a large strain in the FeCo layer. Fig. 1 (b) and (d) shows an elemental mapping and the composition profile. Although the deposition of FeCo was carried out at RT, the serious interdiffusion of Rh is observed because of the good solubility in the Fe-Rh system. Fig. 1 (c) shows the magnetization curve of the perpendicular and in-plane directions of the 1.0-nm-thick sample. The film shows strong PMA and K_u is about 0.6 MJ/m^3 which is the highest value ever reported for FeCo [4]. With the increase of the film thickness of FeCo, the c/a, K_u and Rh interdiffusion decreases (data is not shown here). Thicker than 2.0-nm, the film shows in-plane magnetic anisotropy. The inset of Fig. 2 shows the typical TRMOKE signals for 1.0-nm-thick sample at various strength of external bias magnetic fields ($\mu_0 H$). Using the linearized LLG equation [6] α was estimated as a function of the inverse film thickness 1/t. We found that the value of α for t = 1.0-nm is 0.04, unusually high value for FeCo, and later α decreases to 0.01 at t = 10.0-nm-thick film. The value of α shows a linear trend as shown by the blue dotted line in Fig. 2 from in-plane to PMA samples. From the microstructure observation, we can conclude that the large α in 1.0-nm-thick FeCo PMA sample is due to the Rh diffusion as well as the large lattice distortion. Judging from the large PMA and α, 1.0-nm-thick FeCo film is suitable for the reference layer in STT-MRAM, because it has high PMA and α in the very thin region. However, it is not suitable for a free layer as its damping and magnetization are too large for low current STT switching.

[1] S. Mangin et al. *Nat. Mater.* 5, 210 (2006). [2] T. Burkert et al. *Phys. Rev. Lett.* 93, 027203 (2004). [3] H. Oomiya et al. *J. Phys. D:Appl. Phys.* 48, 475003 (2015). [4] B. Lao et al., *IEEE Trans. Magn.* 50, 2008704 (2014). [5] Y. K. Takahashi et al. *Appl. Phys. Lett.* 110, 252409 (2017). [6] S. Iihama et al. *Phys. Rev. B* 89, 174416 (2014).

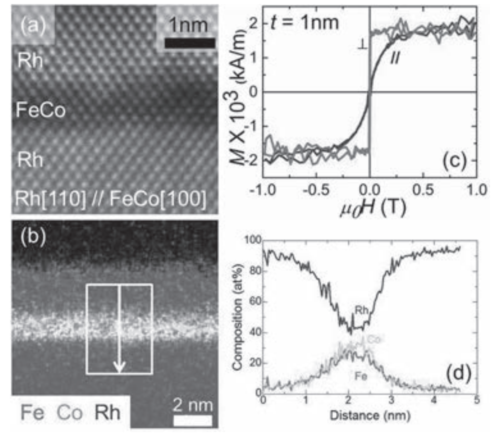

Fig. 1. (a) Cross-sectional STEM-HADDF image, (b) Elemental mapping and (d) the depth profile of the atomic species for t = 1.0-nm $Fe_{50}Co_{50}$ thin film. (c) The magnetization curve of t = 1.0-nm $Fe_{50}Co_{50}$ sample where the red and blue curve correspond to the out-of-plane and in-plane directions.

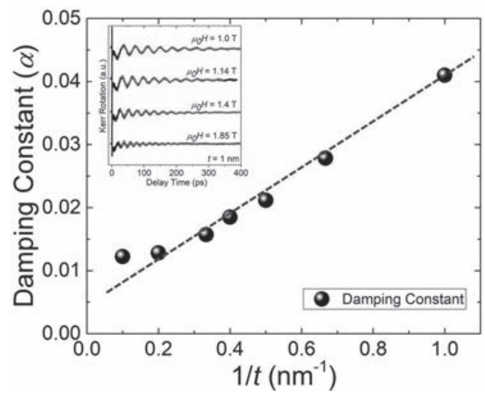

Fig. 2. The damping constant α as a function of inverse film thickness 1/t. Black dot corresponds to the damping value. The TR-MOKE signals from 1.0-nm-thick $Fe_{50}Co_{50}$ film under an external magnetic field ($\mu_0 H$) with different strength is shown at inset.

10:15

CF-06. Magnetic field dependence of ferromagnetic resonance of Ni wires fabricated on ferroelectric $LiNbO_3$ substrate for studying magnetic anisotropy induced by the heterojunction.

A. Yamaguchi[1], A. Nakao[2], Y. Utsumi[1], T. Saiki[3], Y. Takizawa[3] and K. Yamada[4]
1. Laboratry of Advanced Science and Technology for Industry, University of Hyogo, Ako-gun, Japan; 2. RIKEN, Wako, Japan; 3. Hyogo Prefectural Institute of Technology, Kobe, Japan; 4. Gifu University, Gifu, Japan

Understanding and controlling magnetism in laterally confined micro/nano-structures has been attracted much attention because of both the fundamental magnetism and engineering applications such as magnetoresistive sensors and microwave oscillators. [1] One of the interesting magnetic domain structure is vortex core, being the most obvious example. [2] To understand and control the magnetism, the magnetization dynamics in the artificially confined magnets have been investigated using various techniques including time-resolve Kerr microscopy [3], Brillouin light scattering [4, 5] and electrical detection techniques. [6 – 10] Recently, control of the magnetization structure or dynamics using electric fields, spin currents or strain that is electrically induced via piezoelectric effect has been focused to achieve the electric control of magnetic characteristics in the spintronics devices. [11] One simple idea is creation of an artificial multiferroic materials induced by the heterojunction between ferromagnetic and ferroelectric materials. [12, 13] This idea has been tried by a number of researchers, and a considerable advance in knowledge and technique has been obtained. The study on magnetization dynamics in artificial nano/micro-magnets with the heterojunction is a significant important subject for many applications of magnetic materials, examples of which include nonvolatile magnetic random access memory, microwave-detector and oscillator. The electrical techniques allow the indirect detection of the resistance oscillation as a function of the input microwave signal. The homodyne detection using rectifying effect can provide an excellent probe for the intrinsic magnetization dynamics influenced by the additional contributions derived from the heterojunction in the nano.micro-magnets. In this investigation, we demonstrated ferromagnetic resonance of a Ni wire with magnetic anisotropy induced by the magnetoelastic effect derived from the heterojunction between the Ni layer and ferroelectric single crystalline $LiNbO_3$ substrate. We fabricated the 30-nm-thick Ni wire onto the $LiNbO_3$ substrate by means of electron-beam lithography and lift-off methods using a magnetron sputtering. [12, 13] The Ni wire is placed in the aperture between the conductive strip lines of the coplanar waveguide (CPW) comprising of a Cr (5 nm)/Au (80 nm). The wire prepared between the CPW strip lines is 5 μm in width and 100 μm in length as show in the inset of Fig. 1(a). In this study, the Ni wire is oriented perpendicular to the orientation flat (OF) direction of the substrate. The alignment allows the formation of zebra-stripe domain structure near the absence of external magnetic field. The rectifying spectra are dependent on the magnetic field strength, angle, and internal domain structure. In this study, we focused on the magnetic response for the microwave current excitation in the Ni wire with zebra-stripe domain structure under the external magnetic field. First, we measured the magnetoresistances (MRs) of the Ni wire in the application of magnetic field at θ = 0° (magnetic field // Ni wire) and 90° (magnetic field Ni wire) as shown in Fig. 1(b). In this study, we defined MR ratio as MR ratio = $[R(H)\text{-}R(H_{sat})]/R(H_{sat})\times 100$ %, where H_{sat} denotes the saturation magnetic field at which the MR was saturated. As shown in Fig. 1(b), focusing the MR behaviors of the cases : θ = 0 and 90°, we found the hysteresis and possibility of domain structure formation near the absence of magnetic field in both cases. Next, the field angle dependence of rectifying spectra are measured. The magnetic field was applied at angle *q* relative to the longitudinal axis of Ni wire. Figures 2(a) and 2(b) show the typical rectifying spectra in Ni wire oriented perpendicular to the OF direction in the application of magnetic fields at the angles θ = 0 and 90°, respectively. The clear rectifying signals are observed as shown in Fig. 2(a), while almost signals are independent of the magnetic fields in Fig. 2(b). Based on the analytical calculations of the rectifying spectra, we could estimate the uniaxial magnetic anisotropy derived from the heterojunction. Our results manifest that the electrical detection techniques of MR and rectifying effect are very useful for understanding and evaluating the magnetic properties induced by the heterojunction between ferromagnetic and ferroelectric materials. This study will open a door to develop the novel artificial multiferroic materials [14] and devices using the heterojunction.

[1] B. Hillebrands and K. E. Ounadjela edit., *Spin Dynamics in Confined Magnetic Structures*, Springer, Berlin, Heidelberg, 2002, Vol. I - III. [2] T. Shinjo, T. Okuno, R. Hassdorf, K. Shigeto, and T. Ono, Science 289, 930 (2000). [3] M. Belov, Z. Liu, R. D. Sydora, and M. R. Freeman, Phys. Rev. B 69, 094414 (2004). [4] C. Bayer, S. O. Demokritov, B. Hillebrands, and A. N. Slavin, Appl. Phys. Lett. 82, 607 (2003). [5] S. O. Demokritov, B. Hillebrands, and A. N. Slavin, Phys. Rep. 348, 41 (2001). [6] A. A. Tulapurkar, Y. Suzuki, A. Fukushima, H. Kubota, H. Maehara, K. Tsunekawa, D. D. Djayaprawira, N. Watanabe, and S. Yuasa, Nature 438, 339 (2005). [7] J. C. Sankey, P. M. Braganca, A. G. F. Garcia, I. N. Krivorotov, R. A. Buhrman, and D. C. Ralph, Phys. Rev. Lett. 96, 227601 (2006). [8] A. Yamaguchi, H. Miyajima, T. Ono, Y. Suzuki, and S. Yuasa, Appl. Phys. Lett. 90, 182507 (2007). [9] A. Yamaguchi, K. Motoi, A. Hirohata, H. Miyajima, Y. Miyashita, and Y. Sanada, Phys. Rev. B 78, 104401 (2008). [10] N. Mecking, Y. S. Gui, and C.-M. Hu, Phys. Rev. B 76, 224430 (2007). [11] J. Dean, M. T. Bryan, J. D. Cooper, A. Virbule, J. E. Cunningham, and T. J. Hayward, Appl. Phys. Lett. 107, 142405 (2015). [12] A. Yamaguchi, T. Ohkochi, A. Yasui, T. Kinoshita, K. Yamada, IEEE Trans. Magn. 53, 8108504 (2017). [13] A. Yamaguchi, A. Nakao, T. Ohkochi, A. Yasui, T. Kinoshita, Y. Utsumi, T. Saiki, and K. Yamada, AIP Advances 8, 056411 (2018). [14] M. Fiebig, Th. Lottermoser, D. Meier, M. Trassin, Nature Review Materials 1, 16046 (2016).

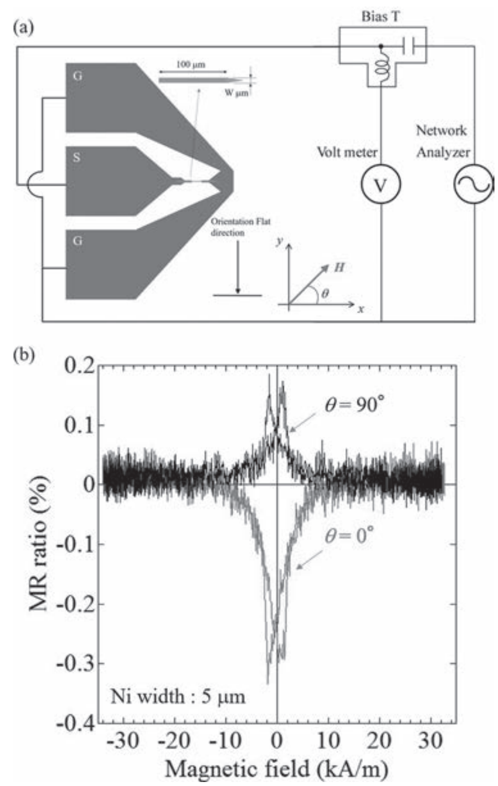

Fig. 1. (a) The rf electric circuit and the schematic of measurement system. The 30-nm-thick Ni wire with length of 100 μm and width of 5 μm is fabricated onto a single crystal lithium niobate substrate. (b) The magnetoresistances of the Ni wire in the cases that the magnetic fields are applied parallel (θ = 0°) and perpendicular (θ = 90°) to the longitudinal axis of the Ni wire.

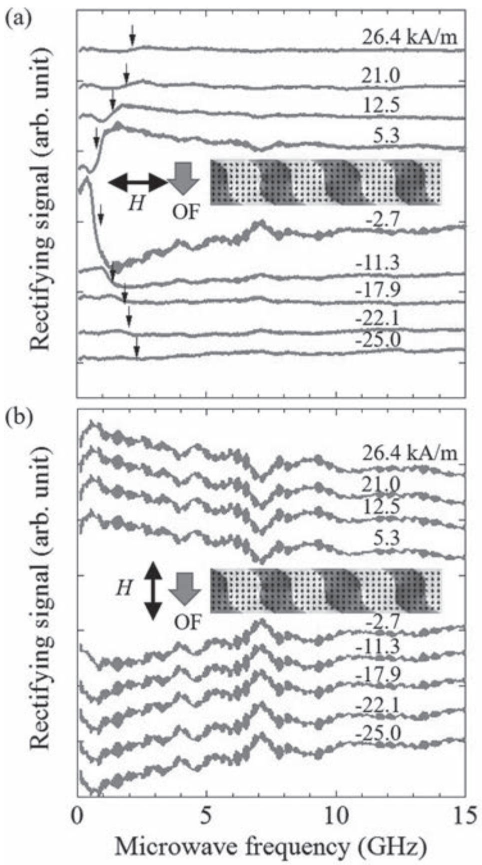

Fig. 2. Rectifying signals as a function of an external magnetic field in plane at angles (a) θ = 0° and (b) θ = 90° with respect to the longitudinal axis of the Ni wire, respectively. Each signal is vertically shifted for clarity.

10:30

CF-07. Spin orbit torque switching process with nonuniform micromagnetic states in three terminal devices.

J. Zhang[1,2], C. Garg[2,3], T. Phung[2], C. Rettner[2], B. Hughes[2], S. Yang[2], Y. Jiang[1] and S. Parkin[2,3]
1. University of Science and Technology Beijing, Beijing, China; 2. IBM Almaden Research Center, San Jose, CA, United States; 3. Max Planck Institute for Microstructure Physics, Halle, Germany

Spin orbit torques have attracted interest for use in manipulation of magnetization of magnetic memory devices[1]. Tungsten-oxide (W(O)) is a new material to generate spin orbit torque which has highest spin hall angle up to -0.5[2] to date for conventional metal materials. Whilst much work has focused on improving the spin hall angle of new materials, there is much less work investigating the application of this W(O) material as the highly efficient spin orbit torque generator for memory devices. Here, we explore switching dynamics of the magnetic tunnel junction in use of spin obit torque in three terminal magnetic devices which use W(O) as the spin hall layer. We investigate the role of non-uniform micromagnetic states in achieving deterministic switching in a novel scheme where the magnetization of the magnetic element and spin polarization are non-collinear without external field. We also confirm the -50% spin hall angle of W(O) as the spin orbit torque generator in three terminal devices. Lastly, we show the potential of using this novel spin orbit torque scheme in non-volatile magnetic logic application

1. Aradhya, S. V., Rowlands, G. E., Oh, J., Ralph, D. C. & Buhrman, R. A. Nanosecond-Timescale Low Energy Switching of In-Plane Magnetic Tunnel Junctions through Dynamic Oersted-Field-Assisted Spin Hall Effect. Nano Lett. 16, 5987–5992 (2016). 2. Demasius, K.-U. *et al.* Enhanced spin–orbit torques by oxygen incorporation in tungsten films. Nat. Commun. 7, 10644 (2016).

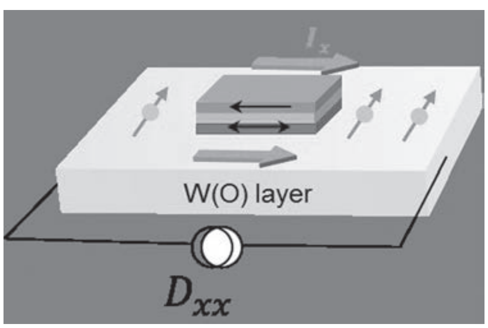

Fig. 1. Schematic diagram of the three-terminal SOT device studied in the D_{xx} configuration where the easy axis of the magnetic nano-element is along the x direction, and the current I_x is collinear to the easy axis direction.

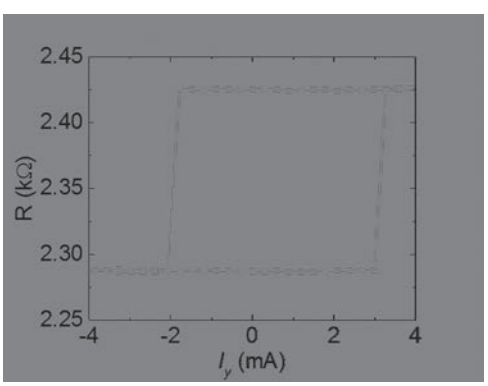

Fig. 2. RI loop measured with current applied along y axis, and magnetic field applied along x to symmetrize the switching currents.

10:45

CF-08. Tuning interfacial Dzyaloshinskii-Moriya interaction and Gilbert damping parameter with Py/$Cu_{1-x}Pt_x$ layers.

H. Bouloussa[1], R. Ramaswamy[2], Y. Roussigné[1], M. Belmeguenai[1], A. Stashkevich[1], H. Yang[2] and S. Chérif[1]
1. LSPM (CNRS-UPR 3407), Université Paris 13, Sorbonne Paris Cité, Villetaneuse, France; 2. Department of Electrical and Computer Engineering, National University of Singapore, Singapore

Spin Hall effect (SHE) is known to be a good way to generate spin currents taking advantage of spin-orbit (SO) interaction in non-magnetic (NM) materials [1]. Since the origin of SHE is based on SO coupling and SO coupling is expected to be larger for heavier elements, several studies on SHE have been conducted with heavy metals such as Pt [2]. Recent studies have also been carried out by adding NM impurities with strong SO coupling in light metals to enhance and tune the spin Hall angle θ_{SH}, a parameter allowing the quantization of the spin current generation efficiency of a material by SHE [3]. Besides, in direct contact with a ferromagnetic layer, the interfacial Dzyaloshinskii-Moriya interaction (DMI), introduced by broken inversion symmetry and strong SO coupling, can be arised. This phenomenon, which plays an important role in the creation of skyrmions [4], combined to the SHE should be understood for applications, particularly the behaviour of magnetic parameters with SO coupling variation in such systems. In this work, we study the effects on the DMI constant D_s and the Gilbert damping parameter α of the addition of Pt into a light metal Cu mostly used in spintronic devices nowadays. The structure of the studied films is Si substrate/ Py (5 nm)/$Cu_{1-x}Pt_x$ (6 nm)/MgO (1 nm)/SiO_2 (3 nm). We first studied the DMI using Brillouin light scattering (BLS) technique. The BLS data were analysed for ultrathin films leading to a Stokes (F_S) and anti-Stokes (F_{AS}) frequency difference: $\Delta F = F_S - F_{AS} = (2\gamma D_s k_{sw})/(\pi M_s t_{FM})$, with the saturation magnetization M_s deduced from VSM measurements, the ferromagnetic layer thickness t_{FM} and the gyromagnetic ratio γ ($\gamma/2\pi$ = 29.5 GHz/T for Py [5]). The slope d(DF)/dk_{sw} is given by $(2\gamma Ds)/(\pi M_s t_{FM})$ .The analysis of the BLS results leads to an increasing of the D_s values with the Pt concentration (figure 1a) due to the appearance of more strong SO coupling sites. We obtained an expected D_s value for the Py/Pt structure [5]. The full width at half maximum of the Stokes and anti-Stokes peaks was also measured (figure 1b) providing direct information of the α by their proportionality [6]. Ferromagnetic resonance (FMR) measurement were performed in order to extract α (figure 1c) and effective magnetization $4\pi M_{eff}$ (figure 1d) depending on Pt concentration. The addition of Pt into Cu induces a large increase of α until saturating at ~ 75% of Pt as also observed by BLS. This increase can be explained by the spin pumping contribution brought by the Pt. The Pt also induces a dead layer deduced from the M_s for different Py thicknesses. The reduction of Py thickness leads to a higher anisotropy H_a in line with the decrease of the $4\pi M_{eff}$ (= $4\pi M_s - H_a$) with Pt concentration. In our CuPt system, the DMI and the Gilbert damping parameter could be engineered depending on Pt concentration for different applications.

[1] J. E. Hirsch, Phys. Rev. Lett. 83, 1834, (1999) [2] E. Saitoh, M. Ueda, H. Miyajima, G. Tatara, Appl. Phys. Lett. 88, 182509 (2006) [3] L. Q. Liu, T. Moriyama, D. C. Ralph, and R. A. Buhrman, Phys. Rev. Lett. 106, 036601 (2011) [4] A. Thiaville, S. Rohart, E. Jùe, V. Cros, and A. Fert, Europhy. Lett.100, 57002 (2012). [5] A. Stashkevich, M. Belmeguenai, Y. Roussigné, S. M. Chérif, M. Kostylev, M. Gabor, D. Lacour, C.Tiusan, M. Hehn, Physical Review B 91 (21), 214409 (2015) [6] N.-H. Kim, J. Jung, J. Cho, D.-S. Han, Y. Yin, J.-S. Kim, H. J. M. Swagten, C.-Y. You, Appl. Phys. Lett. 108, 142406 (2016)

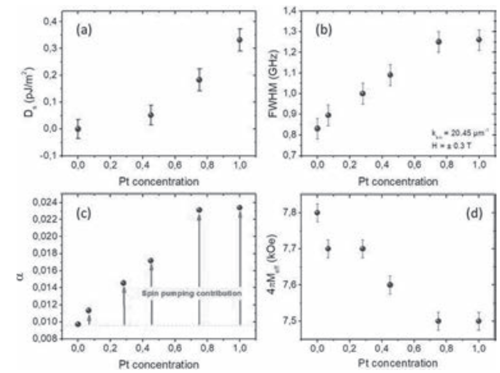

Fig. 1. (a) DMI constant D_s dependence on Pt concentration. (b) Full width at half maximum (FWHM) of BLS peaks dependence on Pt concentration. (c) Gilbert damping parameter α dependence on Pt concentration, extracted from FMR measurements. The red arrows represent the spin pumping contribution induced by Pt. (d) Effective magnetization $4\pi M_{eff}$ dependence on Pt concentration, extracted from FMR measurements.

11:00

CF-09. Microresonator-ferromagnetic resonance investigation of thermal spin-transfer torque in Co_2FeAl/MgO/CoFeB magnetic tunnel junctions.

H. Cansever[1,2], R. Narkowicz[1], K. Lenz[1], C. Fowley[1], L. Ramasubramanian[1], O. Yildirim[1,4], A. Niesen[3], T. Huebner[3], J. Lindner[1], J. Fassbender[1,2] and A. Deac[1]
1. Institute of Ion Beam Physics and Materials Research, Helmholtz-Zentrum Dresden Rossendorf, Dresden, Germany; 2. Institute of Solid State Physics, Technical University of Dresden, Dresden, Germany; 3. Center for Spinelectronic Materials and Devices, Bielefeld University, Bielefeld, Germany; 4. EMPA-Swiss Federal Laboratories for Materials Science and Technology, Dübendorf, Switzerland

Similar to electrical currents flowing through magnetic multilayers [1,2], thermal gradients applied across the barrier of a magnetic tunnel junction may induce pure spin currents and generate 'thermal' spin-transfer torques large enough to induce magnetization dynamics on the free layer [3, 4]. The relation of spin current, charge current and heat current was theoretically described by Bauer et al. using Onsager's reciprocity rule [5]. According to Onsager's law, spin currents can be produced by bias voltages or thermal gradients and investigated in terms of spin-Seebeck effect in magnetic multilayers. First, Hatami et al. theoretically studied the spin-Seebeck effect in spin-valves and introduced the concept of thermal spin-transfer torques. They predicted that the thermally induced spin current creates an imbalance on the interface between non-magnetic and ferromagnetic layers due to collisions (electron-electron and electron-phonon interactions) [3]. Thermal spin-transfer torques were studied experimentally within asymmetric Co/Cu/Co nanowire spin-valves which exhibit switching field changes under varying a.c. currents causing Joule heating [6]. In magnetic tunnel junctions, it was theoretically predicted that temperature differences of around 10 K over an ultrathin barrier (1 nm) can create magnetization dynamics in Fe/MgO/Fe magnetic tunnel junctions [4]. The spin-Seebeck effect has been studied on CoFeB/MgO/CoFeB magnetic tunnel junctions using different heating methods such as Joule heating, heating with Peltier elements, as well as laser heating [8-14]. Recently, it was shown that using Co_2FeAl as a reference layer improves tunneling magneto-Seebeck ratio (TMS) in the magnetic tunnel junctions [7]. Here, we describe a novel experimental approach and setup to observe effects of thermal gradients within magnetic tunnel junctions with Heusler compounds by using the microresonator ferromagnetic resonance (μR-FMR) method under laser heating. Initially, microresonators (shown in figure 1) were introduced by Narkowicz et al. for electron paramagnetic resonance (EPR) experiments to achieve optimal sensitivity for small objects [8]. Detecting the FMR signal of nano- to micron-sized samples in conventional cavities (cm^3) is not possible, due to the too small ferromagnetic volume, and therefore low filling factor. A planar microresonator, by definition, is a two-dimensional structure, its diameter can be tailored to match the order of the sample's size (shown as a black ellipse in the microresonator loop in figure 1). Two stubs are attached to the inductive loop. The capacitive radial stub in first approximation may be viewed as an element to tune the loop to the operation frequency, while the rectangular stub matches the structure to the 50 Ω impedance of the microstrip feedline. We investigated magnetic tunnel junctions (MTJs) fabricated out of Co_2FeAl/MgO/CoFeB stacks. The sample and microresonator fabrication consist of multiple steps of lithography, ion etching, and lift-off processes. The sample is finally patterned into a 6x9 μm^2 elliptical shape using electron beam lithography (EBL) and ion beam etching is used to etch down the sample to the substrate. Microresonators are then fabricated around the sample using UV lithography. For laser heating, a continuous-wave (CW) laser at 532 nm wavelength and with tunable power up to 33 mW is focused on the sample. "Hot-FMR" measurements were performed on unpatterned multilayers between 300 K and 450 K (figure 2) to understand the effect of global heating. It is clearly seen that the FMR signal of Co_2FeAl exhibits a shift with increasing temperature. As seen in the inset graph, it is difficult to quantify the changes for the CoFeB signal, due to its small intensity. Subsequent, measurements in the presence of a thermal gradient were performed on 6x9 μm^2 MTJs, integrated into microresonator loops with an inner diameter of 20 μm. The MTJs were submitted to laser irradiation, up to a maximum power of 33 mW. Unlike the Hot-FMR measurements, the resonance field and linewidth did not show clear changes with increasing laser power. The results suggest that the laser power is neither sufficient to induce magnetization dynamics via thermal gradients across the barrier nor lead to significant changes of the magnetic parameters due to global heating of the sample. As a conclusion, the effect of a global temperature change on the resonance frequency and linewidth of Co_2FeAl was analyzed. With regards to the μR-FMR results, the higher laser power is needed to induce magnetization dynamics. Moreover, the lateral heat transport might reduce the vertical thermal gradients, thus similar measurements on smaller structures are required. This study was funded by the German Research Foundation (DFG) via priority program SpinCaT (SPP 1538). We thank H. Schultheiss for helping with the optical part of the experimental setup and S. Zhou for giving the access to the VSM setup.

[1] J.C. Slonczewski, J. Magn. Magn. Mater. 159, L1, (1996) [2] L. Berger, Phys. Rev. B 54, 9353, (1996) [3] M. Hatami, G.E.W. Bauer, Q. Zhang and P.J. Kelly, Phys. Rev. Lett. 99, 066603 (2007). [4] X. Jia, K. Xia and G.E.W. Bauer, Phys. Rev. Lett. 107, 176603 (2011). [5] G.E.W. Bauer, E. Saitoh, B.J. van Wees, Nature Mater. 11, 391, (2012). [6] H. Yu, S. Granville, D.P. Yu and J.-Ph. Ansermet, Phys. Rev. Lett. 104, 146601 (2010). [7] A. Boehnke, U. Martens, C. Sterwerf, A. Niesen, T. Huebner, M. von der Ehe, M. Meinert, T. Kuschel, A. Thomas, C. Heiliger, M. Münzenberg M, *Nature Communications* 8,(1),1626, (2017). [8] R. Narkowicz, D. Suter and R. Stonies, J. Magn. Reson.175, 275 (2005)

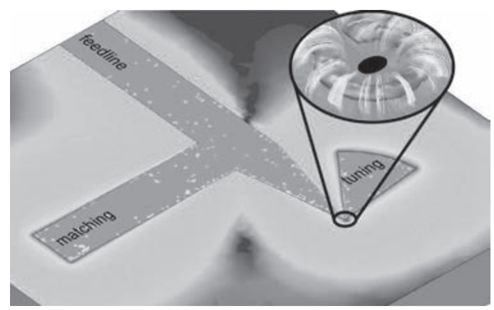

Fig. 1. The layout of a planar microresonator with simulated electric field distribution at the resonance frequency. The inset shows the current and magnetic field distribution (out-of-plane direction) in the loop containing a sample (black ellipse).

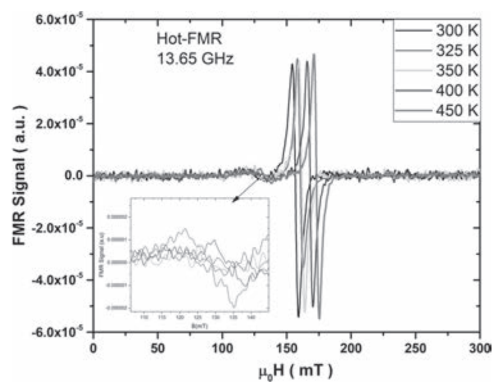

Fig. 2. FMR spectra of the extended film measured in the in-plane direction at different temperatures.

11:15

CF-10. Gilbert Damping Enhancement in Ion-Beam Sputtered Co_2FeAl/Mo Bilayer thin films.

S. Husain[1], A. Kumar[2], V. Barwal[1], N. Behera[2], S. Akansel[2], P. Svedlindh[2] and S. Chaudhary[1]
1. Physics, Indian Institute of Technology, New Delhi, India; 2. Material Science and Engineering, Uppsala University, Uppsala, Sweden

Full Heusler alloys such as Co_2FeAl (CFA) are promising candidate for lowest damping among the Heusler compounds and the manipulation of the damping constant is the key requirement for the study of spin transfer torque [1-3]. In this work, the spin dynamics properties of CFA/Mo bilayer thin films grown on Si(100) substrate by the ion-beam sputtering system are analysed in detail. Ferromagnetic resonance (FMR) has been used to investigate the Mo(0-10nm) layer thickness dependence gilbert damping parameter enhancement (spin pumping) in CFA(8)/Mo(t_{Mo}) bilayer system. The spin pumping then confirmed by inserting various Cu layer thickness (For brevity Cu(1nm) is shown in Fig.1(d)) at CFA(8nm)/Mo(5nm) interface which terminates the spin pumping into the Mo layer. The gilbert damping is found to increase up to 0.0084±0.0003 which is ~68% enhancement of original Gilbert damping (0.0050±0.0002) of CFA(8nm)/Al(Al(4nm)) [Fig.1(c)]. This enhancememt of Gilbert damping is comparable to the Pt nonmagnetic metal. The experimental data have been analyzed using a model for spin pumping that includes the effective spin mixing conductance and the spin-diffusion length. The spin mixing conductance and spin-diffusion length were calculated and found to be 1.19×10^{19} m^{-2} and 3.5±0.35nm, respectively. PPMS VSM was used to measure the saturation magnetization. The thickness, interface width and the surface roughnesses were evaluated by the XRR and AFM respectively. From these These results are indispensable for Mo as spin pumping material in spin dynamic devices.

[1] D.C. Ralph and M.D. Stiles, J. Magn. Magn. Mater. 320, 1190 (2008). [2] S. Husain, S. Akansel, A. Kumar, P. Svedlindh, and S. Chaudhary, Sci. Rep. 6, 28692 (2016). [3] A. Kumar, F. Pan, S. Husain, S. Akansel, Rimantas Brucas, Lars Bergqvist, S. Chaudhary, and P. Svedlindh, Phys. Rev. B 96, 224425 (2017).

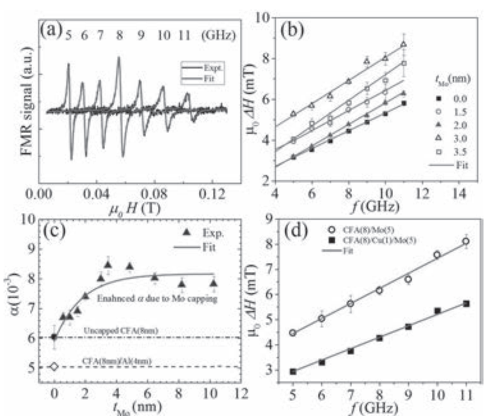

Fig. 1. (a) FMR spectra recorded at various frequencies for the sample Si/SiO_2/CFA(8nm)/ Mo(5nm) bilayer system. (b) Linewidth vs. Frequency plots for the various samples Si/SiO2/CFA/Mo(*t*) (*t*=thickness of Mo mentioned in the figure legend). (c) Extracted damping constant vs. thickness of Mo and damping constant for CFA(8nm)/Al(4nm) shown by dashed line for comaprision of enhancement of Gilbert damping by spin pumping. (d) The ΔH Vs *f* for CFA(8nm)/Mo(5nm) and CFA(8nm)/Cu(1nm)/Mo(5nm) systems.

11:30

CF-11. Study of Static and Dynamic Properties of Dumbbell Shaped Structures.

P.N. Sherpa[1], S. Khanal[1] and L. Spinu[1]
1. Physics/ Advanced Materials Science Institute, University of New Orleans, New Orleans, LA, United States

Metamaterials such as magnonic crystals (MC) have been of great interest in the past years as its easily tunable magnetic properties provide new possibilities for exciting technologies. Information transformation, signal processing, spintronic devices, high-density data storage and sensors [1-4] are a few examples where MC show the promising application. MCs are also a perfect candidate for on-chip data communication, phase shifters, splitters, and non-linear networks as well as magnonic logic devices [5-9]. The unique non-reciprocal properties of spin waves have possible application in microwave devices such as isolators, circulators and microwave filters [10, 11]. The beauty of MC is that the static and dynamic properties can be easily tuned by simply the changing the shape, size, spacing, and symmetry of the structure. Saturation magnetization, anisotropy constant, exchange stiffness, and damping constant is no longer only intrinsic properties of the magnetic structure because of different boundary condition for different structures. Controlling these parameters in a systematic manner to achieve distinctive properties is highly important from a technological perspective. For this, extensive studies on structures such as nanowires, dots, rings, grooves, antidots, modulated wires, etc. have been performed. Periodic modulations on one or both sides of nanowires to study the effect on static and dynamic properties is shown in detail in reference [12, 15]. In this study, we combined two different structures, wires and dots in a dumbbell configuration, to study the static and dynamic properties collectively. Joining the planer symmetric structured dot to the non-planer symmetric wire should be interesting to study how static and dynamic properties would change from individual to a combined form of varying structures. Magnetic nanowires where magnetization reversal (MR) generally takes place by nucleation and propagation of domain walls are different from the dot structure where MR takes place depending on the aspect ratio as well as size [13]. Understanding MR on these combined structures and effect on both static and dynamic properties is main drive of this study. Magneto-Optic Kerr Effect (MOKE) and vector network analyzer- ferromagnetic resonance (VNA-FMR) were used to study the static and dynamic properties respectively. Ground-signal-ground (G-S-G) type coplanar waveguides (CPW) were prepared by the combined method of photolithography, DC sputtering and liftoff process. Titanium (Ti), copper (Cu) and gold (Au) having thickness 5 nm, 150 nm, and 10 nm, respectively, were deposited on silicon substrate. The dimensions and shape of CPW were designed by the CST MICROWAVE STUDIO to achieve the nominal characteristic impedance of 50 Ohm. Then periodic Ni80Fe20 (Permalloy - Py) arrays of dumbbell were fabricated on the top of the signal line of CPW with the help of electron beam lithography, sputtering and liftoff process. Six sets of samples are prepared on top of a CPW, three parallel and three perpendicular to the signal line (since the dot is symmetric, parallel and perpendicular refer to the orientation of the wire axis with respect to the signal line). The samples parallel to the signal line are named D-1-PA, D-2-PA, D-4-PA, which means the diameter of the dots are 1, 2, and 4 micrometers, respectively. D-1-PE, D-2-PE, D-4-PE refers to samples with dot diameter 1, 2 and 4 micrometers, oriented perpendicular to the signal line. In all samples, the wire has a length of 4 micrometers and a width of 1 micrometer. The thickness of all samples was 50 nm and the gap between individual dumbbell was kept more than 1 micrometer to ensure the structures did not interact with each other. MOKE was used to study static properties, such as collective magnetization reversal, sweeping the external magnetic field in different directions, for example. VNA-FMR was used to study the dynamic properties at room temperature. The ac magnetic field and dc applied field were always kept perpendicular to each other to satisfy the condition of FMR. The microwave frequency was swept from 1 to 15 GHz while keeping the dc magnetic field constant. The dc field was swept from 1500 to -1500 Oe with a step of 10 Oe. The scattering parameter transmission coefficient (S21) was collected as a function of frequency. The 3-dimensional contour plot of frequency, dc field, and S21, where the highest absorption of microwave field is shown in black, is presented in the figure. To better understand the experimental results, micromagnetic simulations were performed with graphics processing unit (GPU) accelerated micromagnetic simulation software Mumax [14] on LONI Queen Bee supercomputer, from LONI (Louisiana Optical Network Initiative - http://www.loni.org/), with a 1.5 Petaflop peak performance cluster containing 504 compute nodes with 960 NVIDIA Tesla K20x GPU's and over 10,000 Intel Xeon processing cores.

[1] A. Haldar, A.O. Adeyeye, Deterministic Control of Magnetization Dynamics in Reconfigurable Nanomagnetic Networks for Logic Applications, Acs Nano, 10 (2016) 1690-1698. [2] <Spinwave logic circuits UCLA.pdf>. [3] K. Vogt, F.Y. Fradin, J.E. Pearson, T. Sebastian, S.D. Bader, B. Hillebrands, A. Hoffmann, H. Schultheiss, Realization of a spin-wave multiplexer, Nat Commun, 5 (2014) 3727. [4] L.E. Hueso, J.M. Pruneda, V. Ferrari, G. Burnell, J.P. Valdes-Herrera, B.D. Simons, P.B. Littlewood, E. Artacho, A. Fert, N.D. Mathur, Transformation of spin information into large electrical signals using carbon nanotubes, Nature, 445 (2007) 410-413. [5] V.V. Kruglyak, A. Barman, R.J. Hicken, J.R. Childress, J.A. Katine, Picosecond magnetization dynamics in nanomagnets: Crossover to nonuniform precession, Physical Review B, 71 (2005). [6] Y. Au, M. Dvornik, O. Dmytriiev, V.V. Kruglyak, Nanoscale spin wave valve and phase shifter, Applied Physics Letters, 100 (2012) 172408. [7] S.-K. Kim, K.-S. Lee, D.-S. Han, A gigahertz-range spin-wave filter composed of width-modulated nanostrip magnonic-crystal waveguides, Applied Physics Letters, 95 (2009) 082507. [8] S. Kaka, M.R. Pufall, W.H. Rippard, T.J. Silva, S.E. Russek, J.A. Katine, Mutual phase-locking of microwave spin torque nano-oscillators, Nature, 437 (2005) 389-392. [9] J. Ding, M. Kostylev, A.O. Adeyeye, Realization of a mesoscopic reprogrammable magnetic logic based on a nanoscale reconfigurable magnonic crystal, Applied Physics Letters, 100 (2012). [10] F. Garcia-Sanchez, P. Borys, A. Vansteenkiste, J.-V. Kim, R.L. Stamps, Nonreciprocal spin-wave channeling along textures driven by the Dzyaloshinskii-Moriya interaction, Physical Review B, 89 (2014). [11] K. Di, S.X. Feng, S.N. Piramanayagam, V.L. Zhang, H.S. Lim, S.C. Ng, M.H. Kuok, Enhancement of spin-wave nonreciprocity in magnonic crystals via synthetic antiferromagnetic coupling, Sci Rep-Uk, 5 (2015) 6. [12] L.L. Xiong, A.O. Adeyeye, Dynamic behavior of Ni80Fe20 nanowires with controlled periodic width modulation, Applied Physics Letters, 108 (2016) 262401. [13] C.A. Ross, M. Hwang, M. Shima, J.Y. Cheng, M. Farhoud, T.A. Savas, H.I. Smith, W. Schwarzacher, F.M. Ross, M. Redjdal, F.B. Humphrey, Micromagnetic behavior of electrodeposited cylinder arrays, Physical Review B, 65 (2002). [14] A. Vansteenkiste, J. Leliaert, M. Dvornik, M. Helsen, F. Garcia-Sanchez, B. Van Waeyenberge, The design and verification of MuMax3, Aip Adv, 4 (2014) 107133. [15] S. Khanal, P. Sherpa and L. Spinu, "Splitting of Ferromagnetic Resonance Spectra in Periodically Modulated 1-D Magnonic Crystal," in *IEEE Transactions on Magnetics*, vol. 53, no. 11, pp. 1-4, Nov.2017.doi: 10.1109/TMAG.2017.2707281

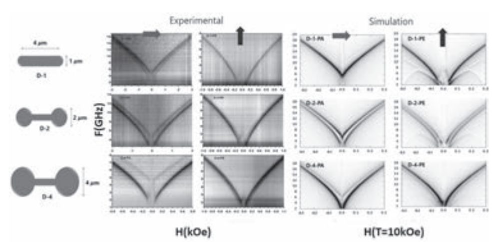

Fig.1: (Left Side) Contour plots of experimental broadband FMR spectra for samples D1, D2 and D3 at 0 and 90 deg. (Right Side) Contour plots of micromagnetic simulation FMR spectra for samples D1,D2 and D3 at 0 and 90 deg.

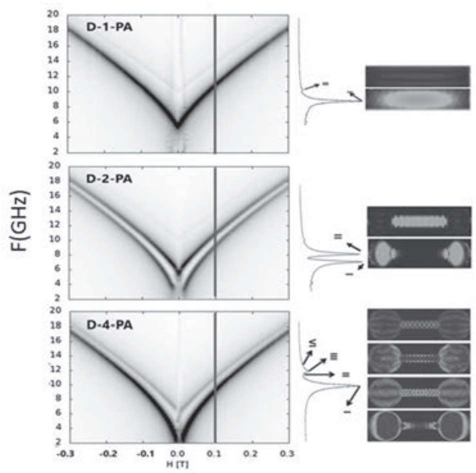

Fig. 2: Micromagnetic simulation results for geometries similar to D-1, D-2 and D-3. The spectra at external field 1kOe are shown in the middle column with the corresponding spectra in the right column.

11:45

CF-12. Magnetization and FMR studies of Si/Ni multilayers with varying Ni layer thickness.

D. Singh[1], R. Roy[1] and M. Senthil Kumar[1]
1. Department of Physics, Indian Institute of Technology Bombay, Mumbai, India

Magnetic properties of ferromagnetic multilayers are influenced by their structure and composition. In ferromagnetic materials, the spontaneous magnetization is well explained by Bloch's law occurs from the spin wave theory for bulk ferromagnets[1]. In many cases the Bloch's law is also verified for ultrathin two dimensional ferromagnetic films with $T^{3/2}$ dependency[2]. The magnetic field dependent MH-loops and ferromagnetic resonance (FMR) spectra technique are extensively used as useful tools to determine effective spontaneous magnetization, Lande's factor, magnetic anisotropy effect ($2K/M_s$) and interlayer exchange coupling between ferro-magnetic layers separated by non-magnetic spacer layer[3] The Si/Ni multi-layers were prepared using a DC magnetron sputtering system at 300K. After achieving a base pressure of $2x10^{-6}$ mbar, the deposition was taken place on to the both glass and Si (111) wafer at $4x10^{-3}$ mbar of Ar pressure. The nominal thickness of the Si layer was fixed at 10Å and that of the Ni layer varied from 10 Å to 100Å. We have investigated the influence of the Ni layer thickness on the structural and magnetic field dependent magnetization, spin wave excitations and ferromagnetic resonance properties of the Si/Ni multilayers (ML). The GIXRD pattern obtained within the annular region 10° to 90° at 300K shows a strong texture along Ni (111) plane. There are no peaks originating from Si layer explaining that Si layer is amorphous whereas Ni layer is nanocrystalline. The field dependent in plane magnetization measurements were carried out at 300K, 200K, 100K, 77K, 10K and 4.2K with magnetic field up to 20 kOe. The variation in M_S with temperature T of the ML is shown in the Fig. 1 (a). To study the spin wave excitation, we have fitted the M_S versus T data using Bloch's equation i.e. $M(T) = M(0)(1-BT^{3/2})$. The spin wave constant (B) and stiffness coefficient (D) are related by the equation $B = 0.0587(g\mu_B/M(0))(k_B/D)^{3/2}$ [4]. Where g and μ_B are the spectroscopic splitting factor and Bohr magnetron respectively. It can be clearly seen in Fig. 1 (a) that M_S versus T data is well fitted using Bloch's equation. The deduced B parameter's values are much higher than that of bulk Ni ($7.5x10^{-6}K^{-3/2}$). The B values are found to increase from $18.4x10^{-6}K^{-3/2}$ to $132.4x10^{-6}K^{-3/2}$ by decreasing t_{Ni} from 100Å to 10Å, respectively. Furthermore, the B parameter is dependent with t_{Ni} through the equation $B(t_{Ni}) = B_{Bulk} - (B_{Surface}/t_{Ni})$ where B_{Bulk} and $B_{Surface}$ are the bulk and surface spin wave parameters [5]. It is evident in Fig. 1 (c) that the B parameters fit reasonably well to a straight line with respect to the t_{Ni}. The extrapolation to $1/t_{Ni} = 0$ is in good agreement to that of bulk for Ni which is equal to $5.8x10^{-6}K^{-3/2}\pm 0.6x10^{-6}K^{-3/2}$. From the slope of the linear fit of B versus $1/t_{Ni}$, is deduced to be $1.3x10^{-3}ÅK^{-3/2}$. The FMR study is carried out at 9.443 GHz. The FMR spectra of the Si/Ni ML were recorded at 300K in both parallel and perpendicular direction. The effective spontaneous magnetization (M_{eff}) is calculated using Kttlel's equations[6]. The variation in M_S and M_{eff} at 300K obtained from S-VSM and FMR spectra respectively is shown in Fig. 2 (a). The difference between the M_S and $M_{eff,}$ in Fig. 2 (a), could be due to the demagnetization field and interface magneto crystalline anisotropy. If the interface anisotropy is contributing towards the first order anisotropy energy K_1, then the perpendicular anisotropy (including demagnetization term) can be estimated according to the equation $K_{eff} = K_V + (2K_S/t_{Ni})$ Where K_S, $K_V = K_U-2\pi(M_S)^2$ and $K_{eff} = K_1-2\pi(M_S)^2$ are the surface anisotropy, volume anisotropy and effective anisotropy energies, respectively. We have report the t_{Ni} dependency of K_{eff} in Fig. 2 (b). The data fitted between $K_{eff}*t_{Ni}$ and t_{Ni} follow a well approximated linear line. The deduced K_V and K_S from the straight line fit of Fig. 2 (b) at 300 K are $-1.09x10^6$ erg/cm^2 and 0.12 erg/cm^2, respectively. The positive vale of K_S indicates that the surface anisotropy energy try to confine magnetization perpendicular to the film surface [1][7]. The negative value of K_V ascribes that the volume anisotropy energy tends to confine magnetization in the plane of the film. From Fig. 2 (b) the intersection on the x-axis is deduced to be 23 Å indicating that the major contribution to the anisotropy comes from the interfaces of the multilayer. Therefore in the low thickness regime (t_{Ni} < 23Å) the interface anisotropy dominating and favoring confinement of magnetization to the out of the film surface whereas with that of higher thickness (t_{Ni} > 23Å) volume anisotropy dominates indicating easy axis of magnetization along the film surface.

[1] M. Lassri, H. Salhi, R. Moubah, and H. Lassri, *Bull. Mater.* 39, 1085–1089, 2016. [2] H. Hamouda, M. Lassri, M. Abid, H. Lassri, D. Saifaoui, and R. Krishnan, *J. Mater. Sci. Mater. Electron.*, 15, 395–398, 2004. [3] M. Erkovan *et al.*, *J. Appl. Phys.*, 110, 023908, 2011. [4] F. Keffer, Handbuch der Physik, vol. 18, Springer-Verlag, Berlin, p. 130, 1966. [5] H. Salhi, K. Chafai, K. Benkirane, H. Lassri, M. Abid, and E. K. Hlil, *Phys. B Condens. Matter*, 405, 1312–1315, 2010. [6] C. Kittel, *Introduction to solid state physics*, 8th ed., vol. 3. John Wiley & Sons, Inc., 2005. [7] M. Lassri, M. Omri, H. Ouahmane, M. Abid, M. Ayadi, and R. Krishnan, *Phys. B Condens. Matter*, 344, 319–324, 2004.

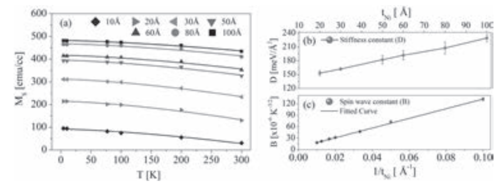

Fig. 1. (a) The variation in M_S with temperature. The solid symbols are experimental data points whereas solid lines are the fitted cures using Bloch's equation. (b) and (c) are the t_{Ni} dependent variations in spin wave constant and stiffness constant.

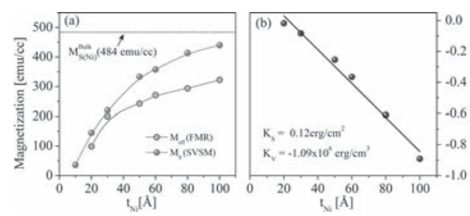

Fig. 2. (a) Variation of saturation magnetization with t_{Ni} obtained from S-VSM and FMR data at 300K, (b) t_{Ni} dependency of K_{eff} multiplied by Ni layer thickness at 300K.

WEDNESDAY MORNING, 25 APRIL 2018 PEONY III, 9:00 TO 12:00

Session CG
MODELLING OF MACHINES I

Ping Zheng, Chair
Harbin Institute of Technology, Harbin, China

CONTRIBUTED PAPERS

9:00

CG-01. An Improved Core-Loss Calculation Method with Variable Coefficients Based on Equivalent Frequency.

W. Jia[1] and X. Lan[1]
1. Nanjing University of Aeronautics and Astronautics, Nanjing, China

Abstract: A concept of equivalent frequency is proposed for arbitrary waveforms. A determination method of core-loss coefficients based on the equivalent frequency is established, together with an improved core-loss calculation method for electric machines. Finally, a doubly salient motor is used as a prototype to verify the improved core-loss calculation method. I. Introduction Due to the uneven distribution and local super-saturation of flux density, together with the high frequency of fundamental and harmonic components, the core loss of non-sinusoidal electric machines is prominent and difficult to predict. The core-loss prediction of non-sinusoidal electric machines is an important and challenging subject. Many calculation models has been proposed and improved in many researches [1-6].The most widely used one is the dynamic model proposed by D. Lin in [6], which has been used in ANASYS Maxwell. However, the core-loss coefficients varies with frequency and flux density, the calculation results with constant core-loss coefficients can only valid in a certain operating condition. Some core-loss calculation methods with variable coefficients have been studied in some researches [7-8]. However, most of them only consider the influence of frequency or flux density. Besides, if the time-domain dynamic model is used, only the fundamental frequency of a periodic waveform is considered. So, the core loss of electric machines cannot be calculated precisely, especially for aperiodic waveforms. II. The Equivalent Frequency of Arbitrary Flux Density In order to predict the core loss of arbitrary flux density precisely, the concepts of equivalent frequency and period are proposed, which are defined according to the equivalent values of average flux-density change rate. An arbitrary flux density can be deemed as a sinusoidal waveform with the amplitude equaling to half of the peak-to-peak value of the arbitrary flux density, and the equivalent sinusoidal waveform has the same average value of absolute flux-density change rate with the arbitrary flux density waveform. Fig. 1 shows an arbitrary flux density waveforms and the associated equivalent sinusoidal waveforms. For a sinusoidal flux density waveform expressed as $B=B_m\sin\omega t$ *T*he average value of the flux-density change rate for the sinusoidal waveform equals to $4B_mf$. For an arbitrary flux density waveform, the average value of the flux-density change rate can be expressed as $\sum(|\Delta B/\Delta t|)/(N\Delta t)$. Let the average change rate of arbitrary flux density equal that of the sinusoidal flux density, the equivalent frequency can be deduced as $f_{eq}=\sum(|\Delta B|)/(4B_{m.eq}N\Delta t)$, where $B_{m.eq}$ equals half of the peak-to-peak value of the arbitrary flux density. III. Improved Core Loss Model with Equivalent frequency Based Variable Coefficients According to the two-term model, the coefficients satisfy the expression below: $P_{fe}/(fB_m^2)=k_h+k_cf$ So, the coefficient k_h is the vertical intercept of the curves, which can be calculated by ignoring the nonlinearity of the curves during the low frequency. The coefficient k_c can be calculated according to the expression below: $k_c=P_{fe}/(f^2B_m^2)-k_hf$. By analyzing the changing pattern of k_c, it can be obtained that k_c changes with the frequency more obviously than with the flux density. Besides, k_c decreases with the frequency monotonously, which can be explained by the skin effect. By fitting the data of k_c, a mathematic model expressing the variations of k_c versus frequency can be shown below: $k_c=k_{c0}f^a\ln(f)+k_{c1}f^b$ where k_{c0}, k_{c1}, a, and b are flux density–dependent variables, which can be obtained by fitting the data of k_c with different frequency at every flux density point. The waveform of flux density can be deemed as a combination of many hysteresis loops, and each hysteresis loop contributes to the hysteresis loss independently. Therefore, the hysteresis loss of a electric machine can be expressed as $P_h=\sum[(m_i/T)\sum(k_hB_{m\_r.j}^2+k_hB_{m\_t.j}^2)]$ where m_i is the mass of the element i;$B_{m\_r.j}$ and $B_{m\_t.j}$ are the amplitudes of the radial and tangential flux density components of the jth hysteresis loop, respectively. The improved eddy loss of an electric machine with the time-stepping FEA method can be expressed as $P_c=\sum\{(m_if/(2\pi\Delta t))[(k_c(f_{eq},B_{eq})\sum(B_{k+1\_r.i}-B_{k+1\_r.i})^2+k_c(f_{eq},B_{eq})\sum(B_{k+1\_t.i}-B_{k+1\_t.i})^2\}$ IV. Experimental Verification In order to verify the improved core-loss calculation method, a DSEM is used as a prototype for core-loss calculation. Rotor-lock experiments are carried out and used for comparing with the calculated results. Fig.2 presents the core-loss comparison obtained from two different methods, i.e. the ANSYS results and the improved time-stepping FEA method proposed above. Obviously, the improved time-stepping FEA method can estimate core loss more accurately. V. Conclusions An improved core loss calculation method is proposed and verified. The conclusions can be obtained: 1)The proposed concept of equivalent frequency can be used to calculate coefficients in time-domain models so as to improve the accuracy of the core loss prediction. 2)A determination method of core-loss coefficients is established. By adopting the function-fitting method together with the looking-up table method, the influences of frequency and amplitude of flux density on core-loss coefficients are both considered. Besides, due to the effects of skin effects, the eddy-loss coefficient reduces significantly with the frequency. 3)The core loss with improved calculation method can predict core loss with high accuracy.

[1] I. Villar, U. Viscarret, I. Etxeberria-Otadui and A. Rufer, "Global Loss Evaluation Methods for Nonsinusoidally Fed Medium-Frequency Power Transformers," in IEEE Transactions on Industrial Electronics, vol. 56, no. 10, pp. 4132-4140, Oct. 2009. [2] J. Muhlethaler, J. Biela, J. W. Kolar and A. Ecklebe, "Improved Core-Loss Calculation for Magnetic Components Employed in Power Electronic Systems," in IEEE Transactions on Power Electronics, vol. 27, no. 2, pp. 964-973, Feb. 2012. [3] J. Reinert, A. Brockmeyer and R. W. A. A. De Doncker, "Calculation of losses in ferro- and ferrimagnetic materials based on the modified Steinmetz equation," in IEEE Transactions on Industry Applications, vol. 37, no. 4, pp. 1055-1061, Jul/Aug 2001. [4] J. V. Leite, M. V. Ferreira da Luz, N. Sadowski and P. A. da Silva, "Modelling Dynamic Losses Under Rotational Magnetic Flux," in IEEE Transactions on Magnetics, vol. 48, no. 2, pp. 895-898, Feb. 2012. [5] A. Brockmeyer and L. Schulting, "Modelling of dynamic losses in magnetic material," 1993 Fifth European Conference on Power Electronics and Applications, Brighton, UK, 1993, pp. 112-117 vol.3. [6] D. Lin, P. Zhou, W. N. Fu, Z. Badics and Z. J. Cendes, "A dynamic core loss model for soft ferromagnetic and power ferrite materials in transient finite element analysis," in IEEE Transactions on Magnetics, vol. 40, no. 2, pp. 1318-1321, March 2004. [7] Q. Yu, B. Bilgin and A. Emadi, "Loss and Efficiency Analysis of Switched Reluctance Machines Using a New Calculation Method," in IEEE Transactions on Industrial Electronics, vol. 62, no. 5, pp. 3072-3080, May 2015. [8] S. Zhu, M. Cheng, J. Dong and J. Du, "Core Loss Analysis and Calculation of Stator Permanent-Magnet Machine Considering DC-Biased Magnetic Induction," in IEEE Transactions on Industrial Electronics, vol. 61, no. 10, pp. 5203-5212, Oct. 2014.

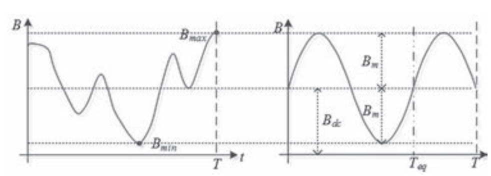

Fig. 1. equivalent frequency of arbitrary flux density

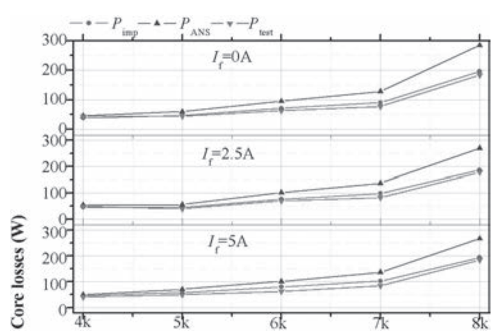

Fig. 2. Core-loss comparison results

9:15

CG-02. Design of a High Power density Halbach BLDC Motor for Electric Vehicle Propulsion.

V.R. Bommadevara[1]
1. Electrical Engineering, IIT, Hyderabad, India

Abstract: Electric vehicles (EV) are the need of the day for future transportation. The electric drives used for vehicle propulsion need to be highly efficient and high power dense to improve the performance of EVs and make them competent in transportation applications. In the similar lines this paper proposes a Radial Flux BLDC motor with surface magnet rotor with a halbach array. The complete design of motor is carried out, nonlinear magnetic analysis carried out and arrived at performance characteristics. The proposed topology is compared with conventional BLDC motor and found an increment of 20% in torque density. The hardware is realized and tested for its performance I. Introduction: Improved power density topologies for electric drives are need of the day which will lead to energy efficient drives for critical applications. BLDC motors are commonly used as drive in EV propulsion applications due to their high power density and efficiency [1]. In BLDC family, axial flux BLDC with dual stator and dual rotor structure is capable of producing high torque densities [2]-[5]. In radial flux BLDC family dual rotor permanent magnet brushless DC motor (DR-BLDC) is proposed which is capable of producing high torque density [6]-[7].This paper proposes a high power density BLDC motor with radial flux configuration and rotor employing surface mount magnets forming a Halbach array. II. Proposed Topology: Fig.1 shows the complete construction and specifications of Halbach BLDC (HB-BLDC) motor. The motor is configured as radial Flux BLDC motor; rotor is employed with surface mount magnets forming a Halbach array. A. Magnetic design: The magnetic equivalent circuit of the motor is derived and solved for parameters like air gap flux density, flux density in stator core and flux density in stator teeth. The main magnet and auxiliary magnet is modeled as a current source and the circuit is solved. The equivalent circuit is given in Fig.2 along with equations and solved parameters. B. No-Load Magnetic analysis: The magnetic material characteristics are non-linear in nature and have to be taken care in arriving at magnetic parameters of the motor. Finite element(FE)analysis is carried out on the motor by taking the nonlinear B-H characteristics of the material into account. The magnetic parameters of the machine are derived at no load using the magnetic analysis and shown in table-I of fig.3.The flux density profile in the complete motor, rotor and stator is shown in fig.3. C. Load analysis: Once the no load magnetic design is completed to arrive at overall dimensions of the machine, the electrical design is carried out to arrive at important parameters of winding, current density, stator resistance and inductance. FE analysis is carried out to analyze the effect of armature reaction during peak load of the motor. The average flux density distribution in stator, rotor core is shown in fig.4 along with air gap flux density curve. The max. Flux density in stator core is 2.2T and rotor core is 1.95T. D. Current-torque characteristics: The machine is loaded with peak current density corresponding to 16A i.e. 50A/mm^2 and FE analysis is carried out to arrive at current-torque characteristics of the motor and is shown in fig.5.The characteristics of the both proposed and conventional configurations are compared and found that there is an increment of 24% in power density with the proposed halbach BLDC motor. D. Development of prototype and test results: The prototype is realized and complete developed stator and rotor are shown in fig.6. The hardware is tested for its performance and the results are in line with designed values. III. Conclusion: A halbach BLDC motor is proposed for high power densiyty application of EV propulsion. Complete design of motor carried along with non linear electro-magnetic analysis on no-load and load conditions. The Current-Torque characteristics of the proposed motor is compared with conventional motor and found an increment of 24% in the power density with same volume and weight. The hardware is realised as per the design and tested for its perfrroamnce. The proposed motor will be right choice for high power density applications like elecctric vehicles.

[1] Z.Q.Zhu, David Howe, "Electric machines and drives for electric, hybrid and fuel cell vehicles", Proceedings of IEEE, vol.95,issue.4,pp.746-765,Apr 2007. [2]R.Qu, M.Aydin, and T.A.Lipo, "Performance comparison of dual-rotor radial-flux and axial-flux permanent-magnet BLDC machines," *in proc. IEEE Int. Elect. Mach. Drives Conf.*, M Adison, WI, pp.1948-1954, 2003. [3] K.Sitapati and R.Krishnan, "Performance comparisons of radial and axial field permanent magnet brushless machines," *IEEE Trans. Ind. Appl.*, Vol. 37, No. 5, pp.1219-1226, 2001. [4] N.B.Simisie and H.B.Ertan, "A comparison of torque capabilities of axial flux and radial flux type of brushless dc (BLDC) drives for wide speed range applications," *in proc. IEEE PEDS, Honk Kong*, pp.719-724, 1999. [5]A.Cavangninto, M.Lazzari, F.Profumo and A.Tenconi, "A comparison between the axial Flux and Radial flux structures for PM synchronous motors," *IEEE IAS Annual Meeting*, Chicago, IL, Vol.3, pp.1611-1618, 2001. [6] Qu R and Lipo T A, "Dual-rotor, radial-flux, torodially wound, permanent-magnet machines" *IEEE Trans. Industry Applications*, vol. 39, no. 6, pp. 1665-1673, 2003. [7] R.Qu and T.A.Lipo, "Design and parameter effect analysis of dual-rotor radial flux, toroidally wound, permanent magnet machines," *IEEE Trans. Industry Applications*, vol. 40, no. 3, pp.771-779, 2004.

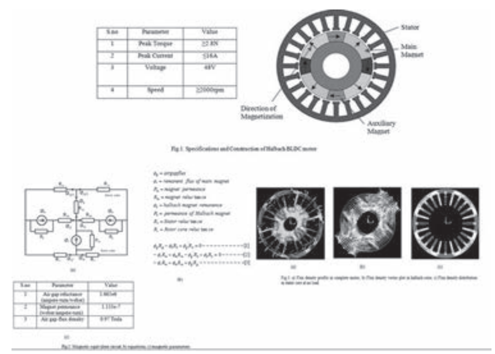

Fig. 1. Specifcations and construction,2.magnetic circuit,equations,3. FE plots

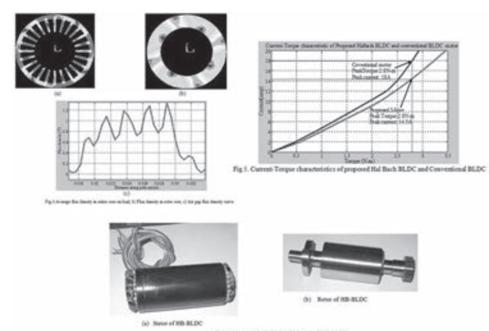

Fig. 2. Flux density profile on load,5.Current-Torque charateristics,6. Realized hardware

9:30

CG-03. High Frequency Characterization of Magnetic Rod Cores with Anisotropic Power Loss.

B.A. Reese[1] and C.R. Sullivan[1]
1. Dartmouth College, Lebanon, NH, United States

New low-loss magnetic flake composite materials are emerging which are well suited for high frequency (> 1 MHz) power electronic converters [1-4]. Much like laminated magnetic materials, magnetic flake composites have low eddy current loss only if flux travels through the long dimensions of the flakes (as opposed to through the thickness). Thus, in order to properly optimize the fabrication processes, a method of accurately measuring the power loss in each direction of flux travel is essential. Core loss is typically measured on a closed magnetic circuit, which is an ideal arrangement if the material can be easily formed into a closed shape (e.g., toroidal) and has low power loss in the two directions of flux travel. However, these conditions are not always met and a rod or bar core sample must be used. Forcing the magnetic field within a sample into only one direction can be accomplished with a high permeability return path as long as the power loss of the return path is significantly lower than the material under test. If the return path loss is on the same order as the test sample loss, then separating the two loss mechanisms becomes very difficult due to the nonlinear nature of the core losses. Since the goal of this work is to produce materials that will have power loss lower that typical high permeability materials, the magnetic return path is not a viable option. In this work we consider an open magnetic circuit characterization method so that the parasitic loss mechanisms can be more easily removed from the measurement. The key challenge for open circuit measurements is the flux fringing effect at the ends of the sample, which cause flux to travel in directions other than the intended measurement direction. This effect can be minimized by making the sample long compared to its diameter. However, a sufficiently large aspect ratio may also be difficult to achieve in a given process. Here we describe a core test fixture which properly aligns the field within a low aspect ratio rod core sample without introducing nonlinear power loss mechanisms. The magnetization at the center of a long solenoid inductor is $(\mu_r\text{-}1)NI/L$, where μ_r is the relative permeability of the core, N is the number of turns, I is the coil current, and L is the length of the coil. The end portions of the magnetic core can be emulated with additional solenoid windings, as shown in Fig. 1. In order to maintain constant flux through the core test sample, the emulation coils must generate a field equal to the magnetization of the core: $(\mu_r\text{-}1)N_x I_x/L_x = N_e I_e/L_e$ (1) Where the x subscript indicates parameters for the outer excitation coil and the e subscript indicates parameters for the core emulation coils on each side of the test sample. This arrangement is beneficial because the portions of the core which experience flux perpendicular to the intended measurement direction are now replaced with windings which have isotropic, linear, and predictable power loss. The excitation and core emulation coils should be connected in series to ensure the coil currents have the same phase. Since $I_x = I_e$, the currents drop out of (1). We then define an optimal turns ratio, a_{opt}, between the core emulation and excitation coils as $a_{opt} = N_e/N_x = (\mu_r\text{-}1)(L_e/L_x)$ (2) Fig. 2 shows finite element simulation results for different values of the turns ratio a, where the vertical axis is the amount of flux that is perpendicular to the intended measurement direction divided by the total amount of flux. The $a = a_{opt}$ line assumes that the fixture's turns ratio is changed for each permeability, according to (2). The perpendicular flux ratio reaches up to 0.5% because a nonzero gap between the core and emulation coils was assumed for the simulation. Since continually adjusting the turns ratio is impractical, we also consider using discrete values of a over restricted ranges. The $a = 0$ line, where only the excitation coil is connected, approaches 0% flux ratio at $\mu_r = 1$ and 15% at $\mu_r = 100$. When only the emulation coils are connected ($a = \infty$) the flux ratios become 21% at $\mu_r = 1$ and 1% at $\mu_r = 100$. A combination of the two configurations, where $a = 0$ is used for $\mu_r < 4.5$ and $a = \infty$ is used for $\mu_r > 4.5$ reduces the maximum flux ratio to 9.5%. Note that the best performing magnetic materials for high frequency (> 1 MHz) power electronics applications have permeabilities in the 15-40 range [5]. Thus, the core fixture must address the high flux ratio in this middle range. One way this could be achieved is to add a third configuration at the crossover point of $\mu_r = 4.5$ with $a_{opt} = 1.5$. This keeps the flux ratio to within 5%. Fourth and fifth configurations can also be added at the new crossover points of $\mu_r = 2.1$ and $\mu_r = 12.3$ (with a_{opt} of 0.5 and 5, respectively) to keep the flux ratio to within 2.5%.

[1] Endo et al., "Study on the Electric Performances of Planar Inductor with Fe-system Magnetic Flake Composite Integrated for SiP DC-to-DC Converter Applications," IEEE Transactions on Magnetics, vol. 51, no. 11, Nov. 2015. [2] Zhou et al., "Loss characterization of Mo-doped FeNi flake for DC-to-DC converter and MHz frequency applications," Journal of Applied Physics 111, 2012. [3] T. Suetsuna, S. Suenaga, and K. Harada, "Bulk nanogranular composite of magnetic metal and insulating oxide matrix," Scripta Materialia 113 (2016) 89–92. [4] Y. Shirakata, N. Hidaka, M. Ishitsuka, A. Teramoto, and T. Ohmi, "High Permeability and Low Loss Ni–Fe Composite Material for High-Frequency Applications," IEEE Transactions on Magnetics, vol. 44, no. 9, Sept. 2008. [5] A. J. Hanson, J. Belk, S. Lim, C. R. Sullivan, and D. J. Perreault, "Measurements and performance factor comparisons of magnetic materials at high frequency," IEEE Transactions on Power Electronics, 2016.

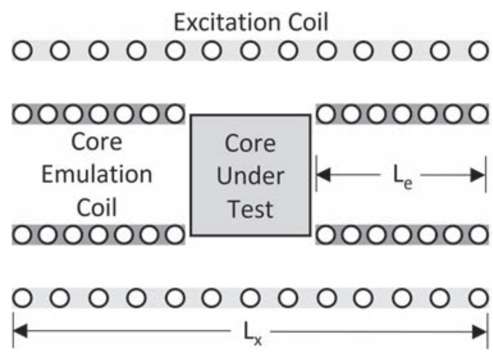

Fig. 1. Diagram of the proposed core test fixture.

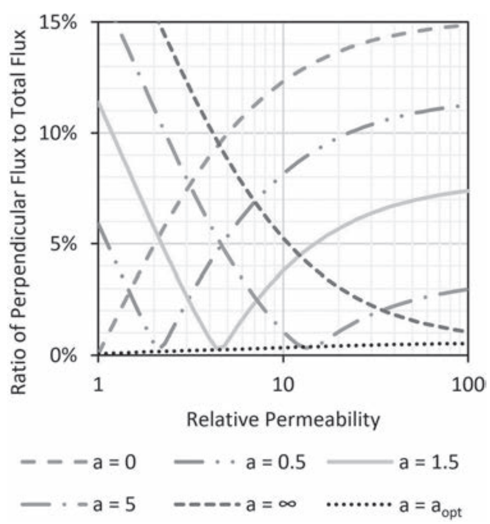

Fig. 2. Finite element simulation results of the core test fixture for different values of the turns ratio *a*.

9:45

CG-04. Freeze-Cast Magnetic Composites for High Frequency Power Conversion.

B.A. Reese[1], C.R. Sullivan[1] and U.G. Wegst[1]
1. Dartmouth College, Lebanon, NH, United States

While emerging thin-film magnetic materials [1] offer significantly lower power losses than ferrites in the 1-100 MHz range, they are very expensive to manufacture and difficult to scale up to higher power levels. Composite materials composed of magnetic flakes embedded in an insulating binder have the potential to achieve low power loss at high frequency [2-5], while maintaining lower cost and better scalability than thin-films. The flakes can have low eddy current loss due to their small cross sectional area; however, precise alignment of the flakes is required to minimize the loss. A common theme for reducing power loss in magnetic core materials is to interleave thin layers of magnetic material with thin layers of an electrical insulator. When a time varying magnetic flux passes through a conductor (including many magnetic materials), it generates eddy currents which lead to power loss. Thin laminations of magnetic material decrease the amount of flux passing through a conductive region, thus reducing the magnitude of induced eddy currents. Instead of continuous laminations, some cores are composed of small magnetic particles in an insulating binder. Commercially available powder cores are composed of individually insulated magnetic particles that are approximately 100 μm in size and offer lower loss than laminated tape wound cores but higher loss than ferrites. Several groups have made composite cores with magnetic flakes that have thicknesses in the 0.1-0.5 μm range. Since the cross-sectional area of these flakes is so small, they can potentially allow significant reduction of eddy current loss. However, the flakes must be precisely aligned with the magnetic field to have any benefit. Misalignment not only increases power loss, but could result in localized heating and thermal stress on the component. [2] formed the magnetic flake composite around a winding. The authors attempted to align the flakes with (a) a magnetic field generated from the winding and (b) applying pressure to the assembly. Pressure alignment achieved better alignment of the flakes than magnetic field alignment; however, there were still large regions which were not aligned correctly and the performance peaked at 4 MHz. [3] hot pressed bare cores (i.e., without an embedded winding) and achieved better alignment of the flakes. The permeability of this material started to roll of at approximately 10 MHz. [4] and [5] achieved very good, yet still imperfect alignment with hot pressing which led to permeability rolloff at 100 MHz and 1 GHz, respectively. These results show that the performance of flake composites is highly dependent on flake alignment and there is still some room for improvement. Thus, processes that can better control flake alignment could greatly extend the capability of magnetic components. A promising approach to achieve improved particle alignment is the use of the freeze-casting process for the manufacture of the magnetic composite materials. The process has been shown to produce highly aligned "brick-and-mortar" structures with alumina platelets in a polymer binder [6]. Figure 1 shows a schematic representation of the freeze-casting of the magnetic composite, where a water-based slurry (a) with magnetic flakes and an insulting binder (not shown) is directionally solidified. As the ice crystals grow, the flakes align along the freezing direction due to a shear flow between the dendritic ice crystals (b). The ice is then removed by sublimation (lyophilized) and a porous scaffold of the flakes and binder remains (c). Finally, the sample is compressed to collapse the pores (d). The binder provides isolation between the flakes to prevent eddy current conduction paths. A freeze-cast magnetic composite was fabricated with a slurry of nanocellulose from the University of Maine and 0.6 μm thick permalloy flakes from Novamet. The slurry was mixed in a shear mixer, directionally solidified, and then lyophilized. Scanning electron microscopy revealed that the majority of the magnetic flakes within the sample's pore walls were indeed aligned with each other, as shown in Fig. 2. Hysteresis curves were measured with a vibrating sample magnetometer, resulting in permeability of 11.0 and saturation flux density of 180 mT, both of which are comparable to commercially available high frequency (>1 MHz) magnetic materials.

[1] C. R. Sullivan, D. V. Harburg, J. Qiu, C. G. Levey, and D. Yao, "Integrating magnetics for on-chip power: A perspective," IEEE Transactions on Power Electronics, vol. 28, no. 9, pp. 4342–4353, 2013. [2] Endo et al., "Study on the Electric Performances of Planar Inductor with Fe-system Magnetic Flake Composite Integrated for SiP DC-to-DC Converter Applications," IEEE Transactions on Magnetics, vol. 51, no. 11, Nov. 2015. [3] Zhou et al., "Loss characterization of Mo-doped FeNi flake for DC-to-DC converter and MHz frequency applications," Journal of Applied Physics 111, 2012. [4] T. Suetsuna, S. Suenaga, and K. Harada, "Bulk nanogranular composite of magnetic metal and insulating oxide matrix," Scripta Materialia 113 (2016) 89–92. [5] Y. Shirakata, N. Hidaka, M. Ishitsuka, A. Teramoto, and T. Ohmi, "High Permeability and Low Loss Ni–Fe Composite Material for High-Frequency Applications," IEEE Transactions on Magnetics, vol. 44, no. 9, Sept. 2008. [6] Philipp M. Hunger, Amalie E. Donius, Ulrike G. K. Wegst, "Platelets self-assemble into porous nacre during freezecasting," Journal of the Mechanical Behavior of Biomedical Materials 19, pp. 87-93, 2013.

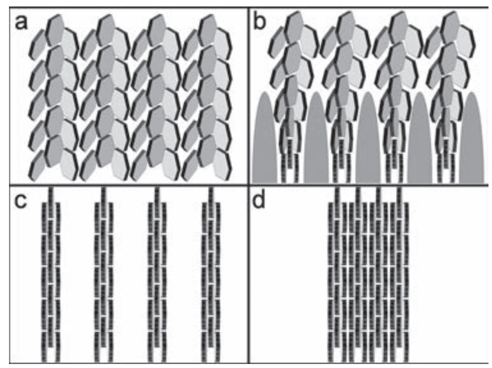

Fig. 1. Schematic of magnetic flake self-assembly during freeze-casting.

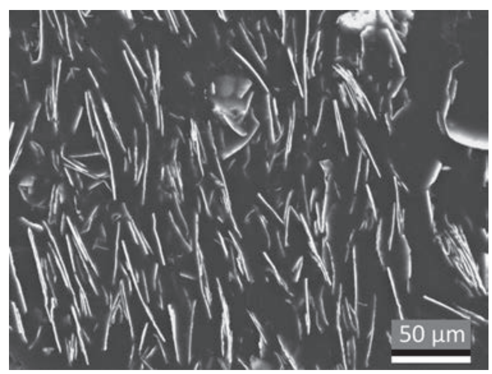

Fig. 2. Cross section of freeze-cast magnetic flakes in a nanocellulose binder.

10:00

CG-05. Electromagnetic Torque Analysis for All-Harmonic-Torque Permanent Magnet Synchronous Motor.

J.W. Zhang[1]
1. Changsha University, Changsha, China

I. Introduction With the advanced industrial development, such as robots and aerospace, the requirements for permanent magnet synchronous motors (PMSM) applied in these fields are increasing, especially the high torque density. There also have been a lot of research activities in developing new techniques for improving the torque performance of the PMSM, and the use of magneto motive force (MMF) harmonic components is approved effectively [1-5]. The torque is improved by >6% with the optimal third-harmonic-shaped rotor of interior PMSM [2]. The authors in [3] proposed to inject third harmonic into both the PM shape and current waveform of the five-phased PMSM is proposed, and consequently the torque could be improved significantly. This paper presents a novel all-harmonic-torque PMSM (AHT-PMSM) including special winding and commutation model. For this PMSM, the stator MMF (F_s) possesses the same harmonic components as the rotor MMF (F_r), and all the MMF harmonic components could be used to generate the effective electromagnetic torque. In theory, the electromagnetic torque of AHT-PMSM can be improved by 23% compared with that generated only by fundamental MMFs. The results of FE simulation and experiment show that compared to that of the normal sinusoidal PMSM, the torque of the AHT-PMSM is significantly improved by > 20% with the same size. II. Topology and Principle The rotor structure of AHT-PMSM is the same as the conventional PMSM, but the configuration of stator winding is quite different. The number of phases is decided by $Q/2p$, where Q is the number of slots and p is the number of pole pairs, and each slot under a pole is classified as different phase. Each phase winding is equipped with a hall sensor to detect the flux field position. Fig. 1(b) shows the phase winding distribution of a 24-slot/4pole AHT-PMSM. The configuration of the power supply for the 24-slot/4-pole AHT-PMSM is shown in Fig. 1 (a). Each stator phase winding is supplied by a half-bridge DC/DC converter which can supply positive or negative current. For AHT-PMSM, the conductors under the same pole are fed the currents with the same direction. In order to maintain the orthogonality between the F_s and F_r, when the rotor rotates from one slot to the next slot, a phase winding current would be commuted due to the hall signal of this phase. Fig. 1(b) shows the polarity of armature currents versus the position of PMs. The effective electromagnetic torque of PMSM is generated only by the interaction between the F_s and F_r harmonic components with the same order, and when the angles between them are $\pi/2$, the electromagnetic torque is maximum. For the conventional concept of the sinusoidal PMSM, the electromagnetic torque is produced only by fundamental MMFs, and the maximum electromagnetic torque could be calculated as $T_{esin}=K_{str}pF_{r1}F_{s1}$ where K_{str} is the structure constant, and F_{r1} and F_{s1} are the amplitude of fundamental components of F_r and F_s. The F_r of surface-mounted PMSM is a square wave, which includes all the odd order harmonics. For ATH-PMSM, F_s is approximated as triangular wave according to the Ampere's law, which also includes all the odd order harmonics. The waveforms also with fundamental and 3rd harmonics of F_r and F_s are shown in Fig. 1 (c). The angles between all the same order harmonics between F_s and F_r are the constant of $\pi/2$. So all the harmonic components of MMF can generate the maximum effective electromagnetic torque, which could be calculated as $T_{eAHT}=\pi^2/8{*}K_{str}pF_{r1}F_{s1}\approx 1.23T_{esin}$ It is obvious that the electromagnetic torque of AHT-PMSM is improved by 23% compared with that of normal sinusoidal PMSM theoretically. III. FE Analysis and Experiment A 2-D FEM model of a 24-slot/4-pole AHT-PMSM is used to verity the previous analysis. Fig. 2 (a) shows the flux density waveforms produced by PMs and stator currents separately, which agrees well with the theoretical analysis. Fig. 2 (b) shows the torque waveforms of the AHT-PMSM and normal PMSM versus the armature currents amplitude of 10A, 20A and 30A. The average torque values of the two PMSMs are 3.62Nm and 3.01Nm with 30A, 2.42Nm and 2.0Nm with 20A, 1.23Nm and 1.04Nm with 10A. It is obvious that the average torque values of AHT-PMSM are improve by > 20% compared with those of conventional PMSM. A prototype of AHT-PMSM according to the FEM models is manufactured, and the stator core with the stator windings is shown in Fig. 2 (c). The torque values with the armature currents of 10A, 15A, 20A, 25A and 30A of the AHT-PMSM and a normal PMSM with same size are measured. The test results are shown in Fig. 2 (d), which shows that the torque of AHT-PMSM is improved by at least 20% compared with that of the normal PMSM due to each stator current value.

[1] Jonathan Michael Crider,Scott D.Sudhoff, "A inner rotor flux-modulated permanent magnet synchronus machine for low-speed high-torque applications," *IEEE Trans.Energy Conversion*, vol.30, no.3, pp.1247-1254, Sep.2015 [2] K.Wang, Z.Q.Zhu,Grzegorz Ombach, "Average torque improvement of interior permanent-magnet machine using third harmonic in rotor shape," *IEEE Trans.Industrial Electronics*, vol.61, no.9, pp.5047-5057, Sep.2014 [3] Mario J.Duran,Francisco Salas,Manuel R.Arahal, "Bifurcation analysis of five-phase induction motor drives with third harmonic injection," *IEEE Trans.Industrial Electronics*, vol.55, no.5, pp.2006-2014, May.2008 [4] K.Wang, Z.Q.Zhu, G.Ombach, "Torque enhancement of surface-mounted permanent magnet machine using third-order harmonic," *IEEE Trans.Magn*., vol.50, no.3, Mar.2014 [5] Wenliang Zhao, Fei Zhao, Thomas A.lipo, "Optimal design of a novel V-type interior permanent magnet motor with assisted barriers for the improvement of torque characteristics," *IEEE Trans.Magn*., vol.50, no.11, Nov.2014

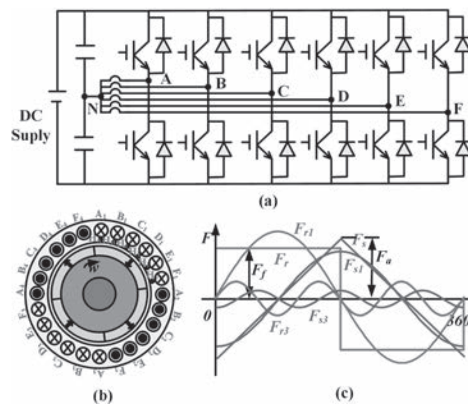

Fig. 1. Principle of AHT-PMSM
(a) Configuration of the power supply for AHT-PMSM
(b) Distribution of armature currents versus the rotor position
(c) Waveforms of F_r and F_s with a pair pole pitch

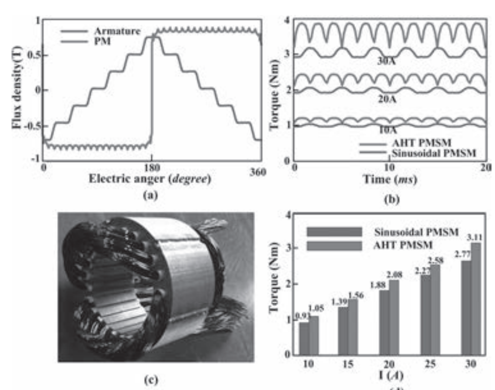

Fig. 2. Results of simulation and experiment
(a) Simulation waveforms of PM and armature flux density
(b) Simulation waveforms of torque versus different armature currents
(c) Stator core with winding of AHT-PMSM prototype
(d) Experimental torque values with different armature currents

10:15

CG-06. Performance Optimization of a Novel DC Fault Current Limiter Combining Different Magnetic Materials and Topologies.

H. Zhou[1], J. Yuan[1], L. Wei[1,2], P. Gan[1], F. Chen[1], Y. Zhong[1], C. Tian[1], B. Chen[1], Y. Gao[3] and K. Muramatsu[3]
1. School of Electrical and Engineering, Wuhan University, Wuhan, China; 2. Department of Electrical Engineering, Graduate School of Engineering, Kyoto University, Kyoto, Japan; 3. Department of Electrical and Electronic Engineering, Saga University, Saga, Japan

I. Introduction For future high voltage direct current (HVDC) grids, the dc protection system is often considered as one of the main challenges due to the difficulty in interrupting a large dc current and the stringent time constraint imposed by the fast rising fault current[1]. Therefore, a novel DC system fault current limiter based on saturable core reactor theory (DCSFCL) was proposed previously. In order to obtain better performance of DCSFCL that is unable to be accomplished by single magnetic material, mixed magnetic materials were applied to take advantages of different magnetic materials. Furthermore, magnetic valves were also added to original DCSFCL topology, which is a good way to optimize clipping performance and reduce the usage of both magnetic materials and permanent magnets (PM). ANSYS models were built and finite element analysis were carried out to verify the feasibility of these deductions. II. Configuration and Principle Study From previous studies, permalloy and nanocrystalline alloy are chosen to combine their fine magnetic characteristics and improve the performance. Fig.1 shows basic configuration and working principle of proposed mix material model with magnetic valve structure. According to Faraday's law of electromagnetic induction and the constitutive relationship between voltage and inductance, inductance of DC coils L_{fcl} can be calculated as: $L_{\mathrm{fcl}}=(4N_{\mathrm{dc}}^2)/(2R_{\mathrm{e11}}+2R_{\mathrm{e12}}+R_{\mathrm{e21}}+R_{\mathrm{e22}}+2R_{\mathrm{m}}+4R_{\mathrm{u}})$, where N_{dc} is turn number of DC coil, while R_{e11}, R_{e12}, R_{e21}, R_{e22}, R_{m} and R_{u} are magnetic resistance of both limbs, PM and iron yokes. Since magnetic valve are often used to generate iron-core reactor[2], fast responding material, i.e., nanocrystalline alloy, is added into original limbs and magnetic valve structure is applied to enhance the performance of DCSFCL. Given that two materials have different working points (1.51T for permalloy and 1.1T for nanocrystalline alloy), the limb structure needed to be properly designed based on the flux continuity theorem($B_{\mathrm{I}}S_{\mathrm{A}}=B_{\mathrm{II}}S_{\mathrm{B}}+f_{l\mathrm{II}}$, $B_{\mathrm{II}}S_{\mathrm{B}}=B_{\mathrm{III}}S_{\mathrm{C}}+f_{l\mathrm{III}}$), where $f_{l\mathrm{II}}$ and $f_{l\mathrm{III}}$ are leakage flux of iron core II and III, while B_{I}, B_{II} and B_{III} are flux density inside the core. In that case, two materials can desaturate simultaneously and therefore, clipping performance can be improved. On the other hand, magnetic valve means smaller cross-sectional area, which leads to larger flux density inside the valve. In that case, less PM and magnetic material will be needed to get the limb into critical saturation state. Therefore, this valve structure can also reduce the usage of both PM and permalloy, which is cost efficient. III. Simulation Results Fig.2 shows the electromagnetic models built in ANSYS and simulation results. Considering that valve structure is applied, it can be seen from Fig.2(a) and (b) that flux density distribution of the limb is not continuous along the limb and those two materials work at their own critical saturation point. The sunken part, shown in Fig.2(a), demonstrates the separate critical saturation state of different materials, which is a solid prove for effectiveness of magnetic valve structure. Hence, the inductance value of the coils, shown in Fig.2(c), is 31.9% larger than single permalloy model due to the fast desaturate speed of inserted nanocrystalline alloy. Clipping performance is shown in Fig.2(d). It can be found that the new valve model has 55.1% and 4.9% drop in fault current compared with fixed smoothing reactor and single permalloy model, respectively. Besides, usage of permalloy and PM decrease by 22.9% and 50.9% compared with single permalloy model. Therefore, proposed mixed valve model is both better in performance and economy. IV. Conclusion In this digest, a novel structure and material modified HVDC transmission system saturable core fault current limiter is proposed. The combination of different magnetic materials makes use of fine characteristics of those materials and applied magnetic valve structure further enhance the clipping performance. Detailed information and investigation will be shown in the full paper.

[1] M. Wang, W. Leterme, J. Beerten and D. V. Hertem, "Robustness evaluation of fast breaker failure backup protection in bipolar HVDC grids," in *13th IET International Conference on AC and DC Power Transmission (ACDC 2017), 2017 IET*, Manchester UK, 14 February-16 February 2017, pp. 1-7. [2] X. Chen, B. Chen, C. Tian, J. Yuan, and Y. Liu, "Modeling and Harmonic Optimization of a Two-Stage Saturable Magnetically Controlled Reactor for an Arc Suppression Coil," *IEEE Transactions on Industrial Electronics*, vol. 59, no. 7, pp. 2824-2831, July 2012.

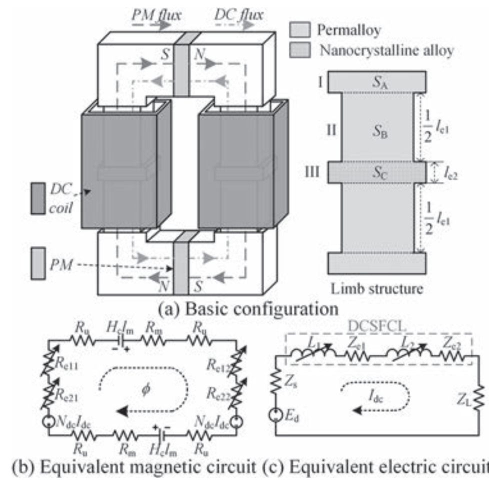

Fig. 1. Configuration and equivalent circuits

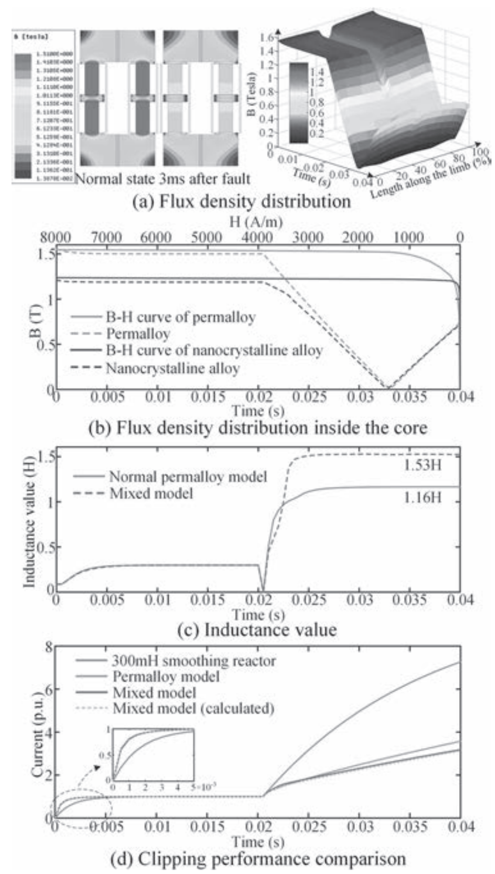

Fig. 2. Simulation and comparison

10:30

CG-07. Dynamic Modeling and Control of Three-Degree-of-Freedom Electromagnetic Actuator for Image Stabilization.

A. Heya[1], K. Hirata[1] and N. Niguchi[1]
1. Department of Adaptive Machine Systems, Osaka University, Suita, Japan

I. Introduction Recently, the demand of an environment recognition using cameras mounted on autonomous mobile systems such as an unmanned aerial vehicle and walking robot has been rapidly increasing. However, the decrease of the recognition accuracy attributed an image quality deterioration due to vibrations has become a problem [1-3]. In order to solve this problem, a lens-unit-swing system which consists of a lens and imaging device has been developed. This system can suppress camera shakes over wide rotation ranges around three axes. Nevertheless, the increase of the size and weight has become a problem because several motors and links are required. Three-degree-of-freedom (3-DOF) actuators are expected to become a solution for these problems. However, conventional 3-DOF actuators are large in size, and need a complicated control system [4-6]. We proposed a novel 3-DOF electromagnetic actuator for an image stabilization, and an electromagnetic field analysis using 3-D FEM was conducted to verify the dynamic characteristics [7]. However, the calculation time of a high-speed motion increases because the time step of the analysis is small. In addition, the image stabilization system requires a high robustness for disturbances, and a robust control system is required. In this paper, we propose a dynamic modeling method of the actuator for reducing the calculation time, and a robust control system using its dynamic model is created. The basic structure and operating principle of the actuator are described. The decrease of the calculation time is achieved using state equations. In addition, an attitude stabilization system is created using a sliding mode control. Finally, the impulse disturbance response of the actuator is calculated, and the effectiveness of the control system is verified. II. 3-DOF actuator for image stabilization The basic structure of the proposed actuator is shown in Fig. 1 (a) [7]. This actuator is mainly composed of an inner mover and an outer stator. The mover consists of six permanent magnets and an inner yoke. The stator consists of outer yokes and coils. The rotation angle around the x-axis and y-axis is ±25 deg., and that around z-axis is ±5 deg. The basic operating principle of the actuator is shown in Fig. 1 (b). A tilting torque is due to Lorentz force. The coils carrying currents generate tangential direction forces that cause the tilting torque, and the mover makes a tilting motion. Similarly, the panning and rolling torques are generated and the mover makes panning and rolling motions. This actuator can be controlled by only 3 sets of the coils. Therefore, 3-DOF motions can be achieved by a simple control system. III. Dynamic modeling In this research, the rotor attitude is expressed by XYZ Euler angles. The equations used for the derivation of the state equation is show in Fig. (a). The motion equation with a generalized coordinate q is given by (1), where τ is the output torque, c and s represent a cosine and sine, respectively, and the relationship of $I_1=I_{xx}=I_{yy}$, $I_3=I_{zz}$ is satisfied. The torque generation equation is given by (2), where K_T, K_D and D are the torque constant, detent constant and viscosity friction coefficient, respectively, τ_f is the friction torque, and I_a is the current. The circuit equation is given by (3), where R_c, L and K_B are the coil resistance, inductance and back-electromotive force constant, respectively. The state equation can be derived to couple (1), (2), and (3) with each other. The state equation is given by (4).The comparison of the dynamic characteristics calculated by the state equation and the dynamic analysis of an electromagnetic field analysis using 3-D FEM is conducted to verify the validity of the state equation. An AC voltage of an amplitude of 5 V and frequency of 100 Hz is applied. The analysis results are shown in Fig. 2 (b). From these results, it is found that both shows a good agreement with each other. In the steady response, the maximum amplitude error of the panning and tilting motions are 24%, and that of the rolling motion is 21%. These errors are caused by the linearization of the torque characteristics in the torque generation equation. In this analysis, the calculation time of the dynamic analysis using the state equation is 1.53 s, and that of the dynamic analysis using 3D-FEM is 66.7 h. From these results, the state equation could shorten the calculation time by 1/157000. IV. Comparison of control systems An attitude stabilization system using a PID control, optimal regulator and sliding mode control is compared in terms of the control performance for a disturbance. The impulse disturbance response of each control system are shown in Fig. (c). From these results, it is found that the attitude can be stabilized, and the sliding mode control has the highest convergence. V. Conclusion In this paper, a dynamic modeling method was proposed for reducing the calculation time, and a robust control system using a dynamic model was created. The state equation of the actuator was derived, and the decrease of the calculation time was achieved. In addition, an attitude stabilization system using a PID control, optimal regulator and sliding mode control was compared. It was found that the control system using the sliding mode control has the highest robustness. In the final paper, the detail of the state equation, the controller design method and the verified results for comparing a control performance will be shown.

[1] W. G Aguilar, and C. Angulo, “Real-time video stabilization without phantom movements for micro aerial vehicles,” *EURASIP J. on Image and Video Processing*, vol. 46, Dec. 2014. [2] R. Kurazume, and S. Hirose, “Development of image stabilization for remote operation of walking robots,” *Proc. of the 2000 IEEE Inter. Conf. on Robotics and Automat.*, pp. 1856-1861, San Francisco, CA, Apr. 2000. [3] S.-C. Hsu, S.-F. Liang, K.-W. Fan, and C.-T. Lin, “A Robust In-Car Digital Image Stabilization Technique,” *IEEE Trans. on Systems*, *Man*, *and Cybernetics*, Part C: Applications and Reviews, vol. 37, no. 2, pp. 234-247, Mar. 2007. [4] W. Wang, J. Wang, G. W. Jewel and D. Howe, “Design and Control of a Novel Spherical Permanent Magnet Actuator With Three Degrees of Freedom,”*IEEE/ASME Trans. on Mechatron.,* vol. 8, no. 4, pp. 457-468, Dec. 2003. [5] K. Kahlen, I. Voss, C. Priebe and R. De Doncker, “Torque Control of a Spherical Machine With Variable Pole Pitch,” *IEEE Trans. on Power Electron.,*vol. 19, no. 6, pp. 1628-1634, Nov. 2004. [6] L. Yan, I-M. Chen, C. K. Lim, G. Yang, W. Lin and K.-M. Lee, “Design and Analysis of a Permanent Magnet Spherical Actuator,” *IEEE/ASME Trans. Mechatron.,*vol. 13, no. 2, pp. 239-248, Apr. 2008. [7] A. Heya, K. Hirata, N. Niguchi, T. Yoshimoto and T. Ota, “Dynamic Analysis of High-Speed Three-Degree-of-Freedom Electromagnetic Actuator for Image Stabilization”, *IEEE Trans. on Magn.*, vol. 53, no. 11, 2706942, Nov. 2017.

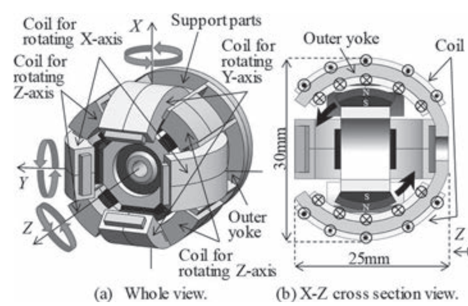

Fig. 1. Basic structure of the actuator.

$$H\ddot{q} + C\dot{q} = \tau \qquad (1)$$

$$\tau = K_T I_a - K_D q - D\dot{q} - \tau_f \qquad (2)$$

$$V = R_c I_a + L\frac{dI_a}{dt} + K_B \dot{q} \qquad (3)$$

$$H = \begin{bmatrix} I_1 c^2\beta + I_3 s^2\beta & 0 & I_3 s\beta \\ 0 & I_1 & 0 \\ I_3 s\beta & 0 & I_3 \end{bmatrix}, C = \begin{bmatrix} 2\dot{\beta}(I_3 - I_1)s\beta c\beta & \dot{\gamma} I_3 c\beta & 0 \\ \dot{\alpha}(I_1 - I_3)s\beta c\beta & 0 & -\dot{\alpha} I_3 c\beta \\ \dot{\beta} I_3 c\beta & 0 & 0 \end{bmatrix}$$

$$\dot{q} = \begin{bmatrix} \dot{q}_1 \\ \dot{q}_2 \\ \dot{q}_3 \end{bmatrix} = \begin{bmatrix} \mathbf{0} & \mathbf{1} & \mathbf{0} \\ -H^{-1}K_D & -H^{-1}C & H^{-1}K_T \\ \mathbf{0} & -L^{-1}K_B & -L^{-1}R_c \end{bmatrix} \begin{bmatrix} q_1 \\ q_2 \\ q_3 \end{bmatrix} + \begin{bmatrix} \mathbf{0} \\ \mathbf{0} \\ L^{-1} \end{bmatrix} V \qquad (4)$$

$$q_1 = [\alpha\ \beta\ \gamma]^T,\ q_2 = [\dot{\alpha}\ \dot{\beta}\ \dot{\gamma}]^T,\ q_3 = [I_{ax}\ I_{ay}\ I_{az}]^T$$

(a) State equation of the actuator.

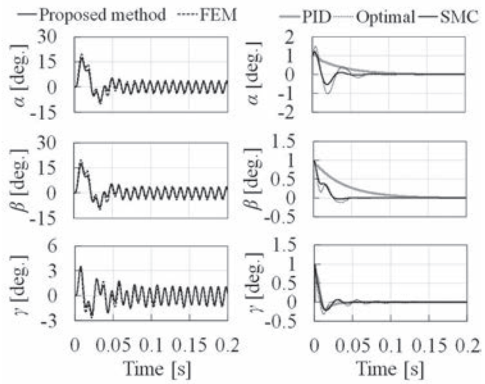

(b) Comparison of the proposed method and 3-D FEM.

(c) Comparison of the PID control, optimal regulator, sliding mode control (SMC).

Fig. 2. State equation and calculation results.

10:45

CG-08. Investigation of a High Corner-Power Modular Fault-Tolerant Permanent-Magnet In-Wheel Motor.

Y. Tang[1], F. Chai[1], Z. Song[1] and P. Liang[1]
1. Department of Electrical Engineering, Harbin Institute of Technology, Harbin, China

I. INTRODUCTION To acquire high reliability and corner-power of electric vehicles, modular fault-tolerant permanent-magnet synchronous motors (PMSMs) are becoming promising candidates[1,2], especially for the vehicles adopting in wheel PMSM schemes[3]. In this paper, a novel three-phase modular fault-tolerant modular in-wheel is proposed and investigated. The motor consist of some sub-motors, and each sub-motor is controlled by an independent drive. The applicable slot/pole combinations and module number are recommended for the motor, and the 24-slot/16-pole and 4-modules scheme is selected for the wheel driver application in this paper. The electromagnetic structure was designed, and the fault-tolerant slot was optimized to obtain reasonable fault-tolerant performance and torque curve. The fault-tolerant ability was analyzed under some conditions, including one phase open-circuit of a sub-motor, one sub-motor open, one single phase short-circuited. The result indicates that the drive system can survive these fault conditions through proper current control strategies. The proposed scheme is proved to have satisfying electromagnetic and fault-tolerant performances. II. THE CHOICE OF ELECTROMAGNETIC SCHEMES The corner-power is proportional to the product of maximum speed and maximum torque, the proper maximum speed and maximum torque can get a high corner-power. Design for fault-tolerant motor to achieve electric isolation, effective magnetic isolation, effective thermal isolation and physical isolation, the ability to reduce the bad influence of fault sub-motor on the other normal sub-motors[4]. 1) The Choice of Winding Form The promising winding forms for fault-tolerant motor are double layer fractional slot concentrated winding and single layer integer slot distributed winding. The former has a shorter end winding and a higher winding factor than these of the latter, however, the latter have a better performance on electric-magnetic-thermal isolation. 2) The Choice of Slot/Pole Combination and Module Number: Each sub-motor should be an independent module, the slot and pole are integer multiples of module number. The pole should not be too much because of the high maximum speed. The slot number is determined by pole number and winding form. III. DESIGN OF MODULAR FAULT-TOLERANT MOTOR A. Model Design of the Motor In this section, 24-slot/16-pole double layer fractional slot concentrated winding is investigated. The motor model is shown as Fig.1. The maximum speed is 4100 rpm and the maximum torque is 1500 Nm. B. Shape of the Fault-Tolerant Slot The deep slot has large inductance but bad high speed performance. The stator slot obtains large leakage inductance adopting small slot opening and big tooth tip depth, the ability to limit short-circuit current, however the torque decreases. Design for slot has overall consideration about electromagnetic performance and fault-tolerant ability of the motor. C. Electromagnetic Performance of the Motor FEM is used to calculate the main working point, including rated operation, maximum speed operation and overload operation. The motor get the technical indicators and has a high corner. IV. FAULT-TOLERANT ABILITY 1) Open Circuit of One Phase in a Sub-Motor: Fig. 2 shows the average torque is 466 Nm and the torque pulsation get 12% under open-circuit of one phase in a sub-motor; the through the compensation measure, the average torque value is 507 Nm, with 4.8% pulsation. The average torque is a slightly decreased, but the torque pulsation is reduced dramatically, which demonstrates that the motor can work well under condition of one phase open circuit. 2) Open Circuit of three Phases in a Sub-Motor Under the condition, the average torque drops to 381 Nm, but the torque pulsation is a slightly decreased, which demonstrates that the motor can work well even though lack of a sub-motor. 3) Inter-Turn Short Circuit One Phase in a Sub-Motor: The amplitude of short circuit current is 163 A which is slightly bigger than the rated current. When the number of short-turn is one, the average torque value is 505 Nm, with pulsation 4.5%. V. CONCLUSIONS 1) The 24-slot/16-pole combination is selected for the wheel driven application in this paper, and the electromagnetic design shows that it can meets the requirements in EV application. 2)The fault-tolerant slot was optimized with FEM, and better torque curve and ability of suppression short-circuit current are achieved. 3)The fault-tolerant ability was analyzed under three fault conditions; research results indicate that the drive system can survive these fault conditions. 4)Through proper current control strategies, different fault-tolerant performances can be obtained.

[1]Ping Zheng, Yi Sui, Jing Zhao,"Investigation of a Novel Five-Phase Modular Permanent-Magnet In-Wheel Motor".IEEE Trans. Magn., 47(10) 4042-4087, (2011). [2]G. J. Li, B. Ren, Z. Q. Zhu, "Cogging Torque Mitigation of Modular Permanent Magnet Machines". IEEE Trans. Magn., 52(1) 1-10, (2016). [3]Chukwuma J. Ifedi, Barrie C. Mecrow, Simon T. M. Brockway, "Fault-Tolerant In-Wheel Motor Topologies for High-Performance Electric Vehicles". IEEE Trans. Ind. Appl., 49(3) 1249-1257, (2013). [4]H. Zhang, O. Wallmark, M. Leksell, "An iterative FEA-based approach for the design of fault-tolerant IPM-FSCW machines"., 17th European Conference on Power Electronics and Applications (EPE'15 ECCE-Europe), 1-7(2015)

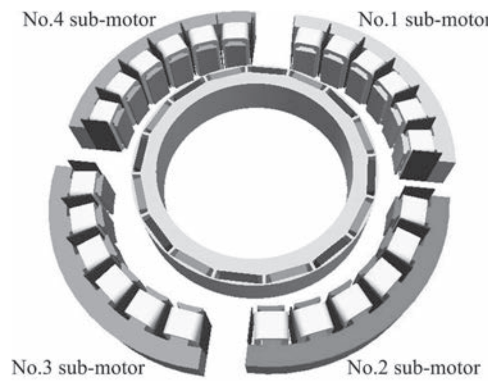

Fig. 1. Modular fault-tolerant motor model.

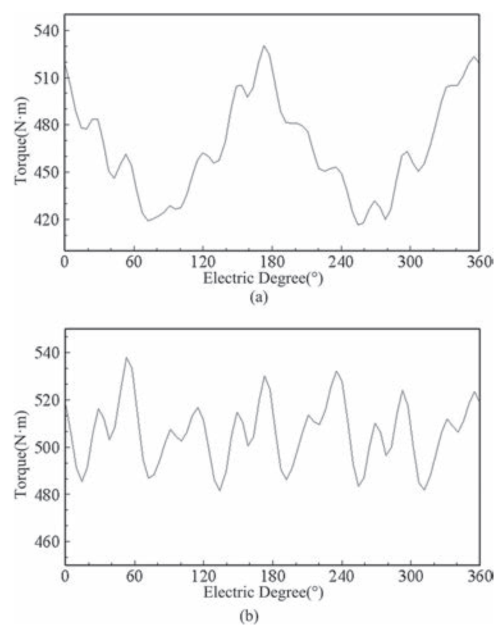

Fig. 2. Open Circuit of One Phase in a Sub-Motor: (a) Torque performance without compensation measure, (b) Torque performance with compensation measure.

11:00

CG-09. An Effective Method with Copper Ring for Vibration Reduction in Permanent Magnet Brush DC Motors.

J. Hong[1], S. Wang[1], Y. Sun[1] and J. Li[1]
1. Tsinghua University, Beijing, China

Abstract:This paper presents a new method by sticking the copper ring on the permanent magnet brush DC motor (PMDC) to reduce the electromagnetic noise. Firstly, the air gap flux density distribution and radial force density distribution are derived in detail and the principle of such electromagnetic noise reduction technique is presented. Then, finite element method (FEM) and experimental results are given to validate the proposed technique, by testing the vibration spectrum of the two prototype PMBDC. It is shown that the acceleration in modified motor has about one-third of that in the origin motor. 1 introduction Vibration and noise become important specifications for many applications, and research on vibration and noise keeps hot for long time. The electromagnetic vibration of motors is mainly caused by the electromagnetic exciting force [1-2]. Electromagnetic exciting force wave on the stator changes with time and space, causes deformation of mechanical structure, and excites the motor to vibrate [3-8]. Existing research mainly focused on PM motors, switched reluctance motors, and induction motors. Many literatures [9-12] studied the accurate predictions of the vibration and noise behaviors by modeling precisely the magnetic forces and the mechanical structures for PM motors. But few papers show the vibration reduction method of PMBDC. This paper proposed a novel method by sticking the copper ring to reduce the vibration and noise on the PMBDC motor whose cross section is shown in Fig.1(a). 2 analysis of magnetic field 2.1 magnetic field generated by permanent magnet When ignoring magnetic saturation, the flux density distribution in the air gap under no load can be expressed as $b(\theta,t)=\pm(B_\delta\Lambda_0+\sum B_\delta\Lambda_k\cos kZ(\theta-\omega_r t))$ $\theta\epsilon[-\alpha\pi/(2p)+j2\pi/(2p),\alpha\pi/(2p)+j2\pi/(2p)]$ Where Z is the number of rotor slots,Λ_0 andΛ_k are the amplitude of average and k-th harmonic magnetic permeability.α is the pole arc coefficient. When j=2m,m=0,1,2,.., the sign in the equation takes a positive value; When j=2m+1, the sign is negative. The term$B_\delta\Lambda_0$ represents the main pole magnetic field excited by the permanent magnets, which does not change with time, and the second term represents the additional magnetic field caused by periodically changing of the permeance due to slotted rotor. 2.2magnetic field inducted by eddy current in copper ring Fig. 1(b) shows the solving region, which is half length of the motor. The direction y is the circumferential direction, and the direction z is the axial direction of the motor. Region 1 is the copper ring portion covered by the stator, and Region 2 is the end of the copper ring. In order to simplify the analysis, let $k=\pi/\tau$ The high frequency magnetic field can be written as: $Hs=H_m\exp(j(wt-ky))$ Where w is the rotation frequency. The magnetic field induced by the eddy current in the coppering is: $H_r=H_p\exp(j(wt-ky))$ So, the magnetic field in the air-gap is the interaction between the two magnetic fields. $H_x=H_p\exp(j(wt-ky))+H_m\exp(j(wt-ky))$ The Maxwell's equation can be written as: $\partial E_z/\partial y-\partial Ey/\partial z=-\partial B_x/\partial t$, $J_y=\partial Hr/\partial z$, $J_z=\partial Hr/\partial y$ The magnetic field can be deduced: $\partial^2 Hp/\partial z^2-(k^2+j\omega\sigma_e\mu_0)H_p-j\omega\sigma_e\mu_0 H_{m=0}$ The general solution of the equation is $Hp=C_1\exp(\lambda z)+C_2\exp(-\lambda z)+CH_m$ Where, C,C_1,C_2 and λ are undetermined coefficients, which can be solved by the boundary conditions. 2.3 The eddy current in copper ring Some works have been done about the simulation of flux density in the air-gap in the different copper ring thickness. The results show that the copper ring is thicker, the stronger ability to weaken the high frequency magnetic field in the motor. The eddy current and the copper loss are also analyzed in detail. 2.4 analysis of radial force density The radial force density distribution under one pole shoe calculated by Maxwell stress tensor method is $p_n=b^2(\theta,t)/(2\mu_0)$ For different copper ring thickness, the radial force is carefully analyzed and compared. 3 Modal and vibration analysis It is important to complete the modal analysis or modal test of the structure of the motor. This will decide whether the resonance occurs on the motor. In the modal testing, the test DC motor is suspended by the elastic rope to simulate the free support-condition. The natural frequencies corresponding to the circumferential modes 1 to 5 are identified to be 474Hz, 1496Hz, 2498Hz, 4185Hz, and 5241Hz, respectively. In the 3D structural finite-element analysis, the harmonic responses are calculated by using the mode-superposition method, and Five different thickness of copper ring are simulated and analyzed. 4 Experimental results In order to validate this proposed method, experimental verification of two sample motors has been performed by measuring the acceleration. The motor is hanged on the bracket by elastic rope. Seven accelerometer sensors are evenly attached on the stator in the circumferential direction, and the average of the acceleration is adopted.Fig.2 shows the vibration result of the simulated and measured when the motor run at 1500 rpm. It can be seen that the measured acceleration of 36^{th} harmonic component of prototype is 1.81m/s^2, which is approximately 3-times greater than the modified motor, 0. 56m/s^2. 5 conclusions This paper presents a new method by sticking the copper ring on the permanent magnet brush DC motor (PMBDC) permanent magnet to reduce the electromagnetic noise. The aim of the proposed strategy is to decrease the vibration and acoustic caused by the rotor slot harmonics. The FEM and experimental results show that the vibration in the modified motor is only one-third of that in the origin one.

[1] J. P. Hong, K. H. Ha, and L. Ju, "Stator pole and yoke design for vibration reduction of switched reluctance motor," *IEEE Trans. Magn.*, vol. 38, DOI 10.1109/20.996239, no. 2, pp. 929-932, Mar. 2002 [2] T. Sun, J. M. Kim, G. H. Lee, J. P. Hong, and M. R. Choi, "Effect of Pole and Slot Combination on Noise and Vibration in Permanent Magnet Synchronous Motor," *IEEE Trans. Magn.*, vol. 47, DOI 10.1109/TMAG.2010.2093872, no. 5, pp. 1038-1041, May. 2011 [3] T. Ishikawa, M. Yamada, and N. Kurita, "Design of Magnet Arrangement in Interior Permanent Magnet Synchronous Motor by Response Surface Methodology in Consideration of Torque and Vibration," *IEEE Trans. Magn.*, vol. 47, DOI 10.1109/TMAG.2010.2091399, no. 5. pp. 1290-1293, May. 2011. [4] D. Torregrossa, A. Khoobroo, and B. Fahimi, "Prediction of Acoustic Noise and Torque Pulsation in PM Synchronous Machines with Static Eccentricity and Partial Demagnetization Using Field Reconstruction Method," *IEEE Trans. Ind. Electron.,* vol. 59, DOI 10.1109/TIE.2011.2151810, no. 2, pp. 934-944. Feb. 2012 [5] S. Yu, and R. Tang, "Electromagnetic and mechanical characterizations of noise and vibration in permanent magnet synchronous machines," *IEEE Trans. Magn.,* vol. 42, DOI 10.1109/TMAG.2006.871637, no. 4, pp. 1335-1338, Apr. 2006 [6] D. Torregrossa, F. Peyraut, B. Fahimi, J. M. Boua, and A. Miraoui, "Multiphysics Finite-Element Modeling for Vibration and Acoustic Analysis of Permanent Magnet Synchronous Machine," *IEEE Trans. Energy Convers.,* vol. 26, DOI 10.1109/TMAG.2006.871637, no. 2, pp. 490-500. Jun. 2011 [7] S. K. Lee, G. H. Kang, and H. Jin, "Finite Element Computation of Magnetic Vibration Sources in 100 kW Two Fractional-Slot Interior Permanent Magnet Machines for Ship," *IEEE Trans. Magn.,* vol. 48, DOI 10.1109/TMAG.2011.2176323, no. 2, pp. 867-870, Feb. 2012. [8] Z. Q. Zhu and J. H. Leong, "Analysis and mitigation of torsional vibration of PM brushless DC drives with direct torque controller," in *Proc. Energy Convers. Congr. Expo.,* DOI 10.1109/ECCE.2011.6063959, pp. 1502-1509, Sept. 2011. [9] J. Krotsch, and B. Piepenbreier. "Radial Forces in External Rotor Permanent Magnet Synchronous Motors With Non-Overlapping Windings," *IEEE Trans. Ind. Electron.,* vol. 59, DOI 10.1109/TIE.2011.2151827, no. 5, pp. 2267-2276, May. 2012. [10] J. W. Jung *et al*. "Reduction Design of Vibration and Noise in IPMSM Type Integrated Starter and Generator for HEV," *IEEE Trans. Magn.,* vol. 46, DOI 10.1109/TMAG.2010.2041434, no. 6, pp. 2454-2457, June. 2010. [11] M. Furlan, A. Cerigoj, and M. Boltezar, "A coupled electromagnetic-mechanical-acoustic model of a DC electric motor," *COMPEL*. Vol. 22, DOI 10.1108/03321640310483075, no. 4, pp. 1155 – 1165, 2003. [12] G. He, Z. Huang, R. Qin and D. Chen, "Numerical Prediction of Electromagnetic Vibration and Noise of Permanent-Magnet Direct Current Commutator Motors With Rotor Eccentricities and Glue Effects," *IEEE Trans. Magn*, vol. 48, DOI 10.1109/TMAG.2011.2178100, no. 5, pp. 1924-1931, May. 2012.

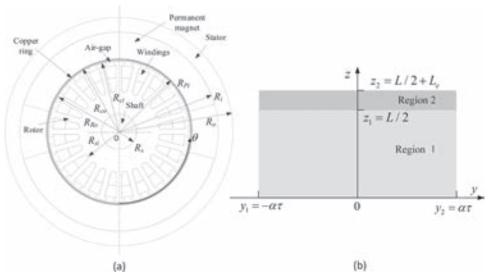

Fig. 1. cross section of the motor

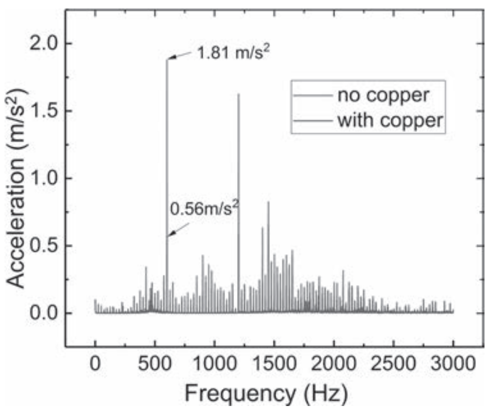

Fig. 2. experiment results

11:15

CG-10. High Transmission Capacity P.U.A. Wireless Power Transfer for AUV Using an Optimized Magnetic Coupler.

C. Cai[1], Z. Yang[1], M. Qin[1] and s. Wu[1]
1. School of Information and Electrical Engeering, Harbin Institute of Technology at Weihai, Weihai, China

The Autonomous Underwater Vehicle (AUV) is an important maritime equipment widely used. Its endurance is limited by space as well as battery technology, which leads to poor flexibility and concealment. Wireless power transfer(WPT) is a proper approach to solve this problem effectively. Nowadays, there are some problems AUV wireless power transmission facing as low coupling capacity, undesirable AUV shape change and insufficient energy density[1-2]. To solve these problems, inductively coupled power transfer technology(ICPT) is applied to propose an ε-type core with strong coupling capacity, large energy density and none changing shape needs,which can improve transmission capacity per-unit-area(p.u.a.). The power formula[3] and efficiency formula based on the mutual inductance model are given respectively: $P_{out}=V_{in}\,I_1k^2Q$(1) $\eta=R_r/(R_1+R_r)=R_{ac}/(L_sR_1/k^2L_p+R_{ac})$(2) where $V_{in}I_1$ is the input power, k is the coupling coefficient, Q is the quality factor, R_1 and R_r are the primary coil resistance and the secondary reaction resistance, L_p and L_s are the primary and secondary coil self-inductance, and R_{ac} is the AC equivalent impedance. Based on formula (1) and (2), the power and efficiency will be enhanced with the coupling coefficient k increased and other parameters fixed. In the magnetic circuit model, the coupling coefficient k is expressed as[4]: $k=0.25R_{E2}/(R_{E1}+0.25R_{E2})=0.25R_{E2}/(l/\mu_0S+0.25R_{E2})$(3) where R_{E1}, R_{E2} are the main magnetic resistance and leakage magnetic circuit reluctance, l is the gap length, μ_0 is the absolute permeability and S is the equivalent cross-sectional area. R_{E2} can be regarded as a fixed value, so the coupling coefficient k is affected by l and S. When the cross-sectional area S is fixed, reducing air gap l can increase the coupling coefficient k. Therefore, the coupling coefficient of coupling device needs to be increased as much as possible. The addition of magnetic core can significantly enhance the coupling capability[1]. In this paper, a new type of coupling device is proposed pointing at the shape characteristics of a cylindrical AUV. It consists of coils and an ε-type core that is closely fitted to the AUV arc surface, as shown in Fig. 1 (a). Moreover, the ε-type core significantly reduces the air gap and makes it uniform therefore its coupling coefficient k is higher than other cores'. When AUV thickness together with air gap is approximately 8mm, the ε-type core coupling coefficient k can be 0.55. By contrast, the E-type and U-type cores in similar situations are less possible to reduce due to arc shape obstruction. The tapered core in [2] has a very high coupling coefficient with a small air gap. However, a partial modification of the AUV is required and the coupling device needs to be precisely aligned during charging. Compared with the toroidal core, moreover, less ferrite is used in the ε-type core. Therefore, the ε-type core is superior to the current coupling device. Practical application should consider its dimension fitting specific application objects. The coupler design in [3] also involves the iteration approach. The specific design process is as followings. Firstly, core shape as well as the compensation circuit are selected. The maximum length and height of the core could be decided according to the AUV diameter. Secondly, the minimum dimension is calculated with the area product method (AP method). In this interval, the coupling coefficient is taken as the goal based on the main variables including the core length, window width and column height. Maxwell 3D simulation software is used to perform the finite element analysis(FEA). Besides, a core with a smaller Aw/Ae ratio is preferred. The edge flux is small, which will contribute to a high efficiency. After figuring out the dimension, the inductance of the winding is calculated in conjunction with the relevant formula. The re-iterate designed is required if the winding cross-sectional area exceeds the window area, or power and efficiency requirements fail. The final optimal solution could be chosen from the calculation. This paper is applied to AUV with a diameter of 300mm. According to the requirement that transmission power is 600W and efficiency ratio should be higher than 0.8, the minimum length is 65mm. In this interval, the core length, window width and column height are taken as variables, and parametric analysis is carried out in the simulation. The ε-type 200mm is selected to meet the requirements. To reduce the volume quality, the final length is set to 100mm by reducing its size gradually. Meanwhile the corresponding inner and outer curvature radius are 154mm and 200mm. The secondary side is symmetrical with the primary, and the optimal dimensions are shown in Fig. 1 (b). With this design, the 17 turns with an inductance of 107μH are selected. Following the 136nF capacitance is calculated when resonant frequency is 50kHz. The results of ε-type core hardware experimental verification are shown in Fig. 2. As the input voltage gradually increases, the output power reaches 600W, and the efficiency is stable at 0.86. More importantly, the ε-type core has strong coupling ability, small volume and light mass. Meanwhile the transmission capacity p.u.a. is approximate 0.2W/mm^2, which is greatly improved in comparison to 0.083W/mm^2 for the EV. The improvement of transmission capacity p.u.a. will facilitate the AUV with an intense surface area for WPT. At the same time, the ε-type core is valuable in other WPT system where there is curvature.

[1] J. Manikandan, A. Vishwanath, V. K. Agrawal, and Manu Korulla, "Indigenous design and development of underwater wireless power transfer system," Twenty Second National Conference on Communication. 2016:1-6. [2] T.Kojiya, F. Sato, H. Matsuki and T. Sato, "Automatic power supply system to underwater vehicles utilizing non-contacting technology," IEEE Mtts/ieee Techno-Ocean '04., 2004:2341-2345 Vol.4. [3] M.Budhia, J. T. Boys, G. Covic, and Chang-Yu Huang, "Development of a Single-Sided Flux Magnetic Coupler for Electric Vehicle IPT Charging Systems," IEEE Trans. Ind. Electron., 2013, 60(1):318-328. [4] C. G. Kim, D. H. Seo, J. S. You, J. H. Park and B. H. Cho, "Design of a contactless battery charger for cellular phone," IEEE Trans. Ind. Electron., 2001, 48(6):1238-1247.

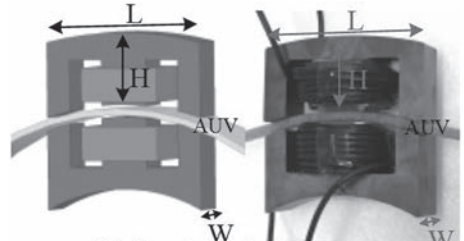

(a) Structure of ε-type core

Size	
Length×Width×Height	100×29×48 mm
The radius of curvature of the outside of the primary side	200mm
The radius of curvature of the inside of the primary side	154mm
The radius of curvature of the outside of the secondary side	146mm
The radius of curvature of the inside of the secondary side	100mm
Coil parameters	
Primary, secondary inductance	107μH
Mutual inductance	55μH
Capacitance parameters	
Primary, secondary capacitance	136nF

(b) Parameters of ε-type core

Fig.1 Structure and parameters of ε-type core

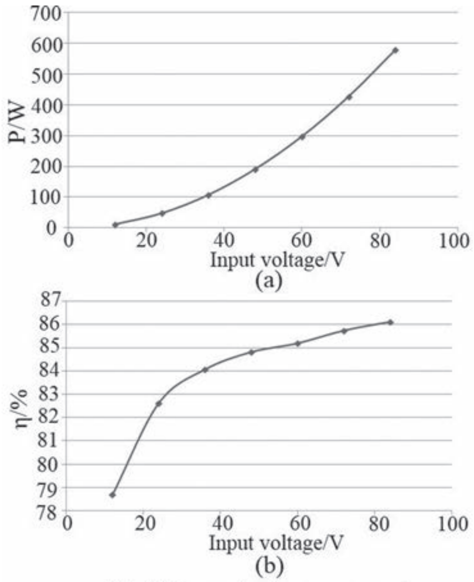

Fig.2 Transmission power and efficiency diagram for ε-type core

11:30

CG-11. An Economical Three-Phase Fault Current Limiter Considering Different Types of Fault.

J. Yuan[1], *P. Gan*[1], L. Wei[1,2], H. Zhou[1], Y. Zhong[1], Z. Zhang[1], C. Tian[1], Y. Gao[3], K. Muramatsu[3] and B. Chen[1]
1. Electrical and Engineering, Wuhan University, Wuhan, China;
2. Department of Electrical Engineering, Graduate School of Engineering, Kyoto University, Kyoto, Japan; 3. Department of Electrical and Electronic Engineering, Saga University, Saga, Japan

I.Introduction With the rapid development of the power system, the fault current becomes a big problem. The current limiting measures become more and more important. The saturated-core fault current limiter(SFCL) is one of the promising methods[1]. The most serious fault in electric power system is three-phase short-circuit fault, and the fault current is more likely to exceed the circuit breaker's capacity. The use of three single-phase current limiters at the same time will need a lot of ferromagnetic material and space. A compact three-phase SFCL was proposed in [2], but it cannot limit three-phase fault current[2]. So we propose a novel structure of Economical Three-phase Saturated-core Fault Current limiter(ETSFCL). The novel structure has good clipping performance at three-phase fault conditions. Compared to three single-phase SFCLs proposed in [3], it saves a lot of ferromagnetic material and reduces the AC flux through the permanent magnet. The stability of the permanent magnet is greatly improved and the risk of demagnetization is reduced. In this paper, the operating principle of the proposed structure is explained by analyzing its equivalent magnetic circuit and electrical circuit. FEA models were established in ANSOFT to verify the its effectiveness. II.Configuration and Working Principle The novel concept of ETSFCL studied in this digest is shown in Fig.1(a). It consists of an iron core, three-phase limbs, two permanent magnets (PM) and DC/AC coils. Six AC coils are in series with power system and conduct the current of it. They are wounded on the six outer limbs equally. And six DC coils are also wounded on the outer limbs for biasing the iron core into saturation. An inductance is connected in the DC circuit. The inner limbs with air-gap are used to provide paths for AC flux. Equivalent electric circuit of economical SFCL is shown in Fig.1(b). USi (i=A, B, C) are the three-phase voltage sources of the simple three-phase system. ZSi and ZLi are the system impedances and load impedances of three phases. Lf is the fault-limiting reactor. Ed is the DC voltage source. Nac, Ndc are the number of turns of the AC and DC coils. Idc is the current of DC coils. IA_ac, IB_ac and IC_ac are the currents of three-phase AC coils, respectively. I is the amplitude of load current of each phase. Equivalent magnetic circuit of ETSFCL is shown in Fig.1(c). Re1_i (i=A, B, C), Re2_i (i=A, B, C), Rm, and Rg refer to the reluctances of the left outer limbs, the right outer limbs, the PM and the air-gap branch, respectively. The reluctance of the unsaturated yoke (Ru) is small and can be ignored. Hc, mm, lm are the coercive force, permeability, and the length of PM respectively. Under normal conditions, six outer limbs are deeply saturated. Based on Faraday's law of electromagnetic induction and the constitutive relationship between voltage and inductance (U=Ndf/dt=Ldi/dt), inductance of the ETSFCL (Lfcl) can be derived: Lfcl=NI(1/3bc+2abRm+1/2ac)/[Res(1/3bc+2abRm+1/2ac)+1/6c2+acRm], where a=1/3Res+Rg, b=1/2Res+Rg, c=Res×Rg. Res, Rg and Rm is very large, so the impedance is very small under normal conditions, having little effect on power system. When the fault occurs, the two outer limbs of the fault phase(s) will turn out of saturation alternatively. The impedance of ETSFCL can be adjusted by changing the values of Lf. The increased impedance of the ESFCL can limit the fault current. ESFCL can normally work on any short-circuit fault conditions because of its Six discrete limbs. III.Comparative Study and Simulations To validate the effectiveness of CSFCL, a 220 V model was designed and established in ANSOFT based on the structure proposed above. The flux density distribution is shown in Fig.2(a). The comparison of change of magnetic flux in the permanent magnet is shown in Fig. 2(b). As is shown in Fig. 2(a), at normal conditions, the limbs are all in deep saturation, and at fault conditions the limbs can independently turn out of saturation, which means it can work at any fault condition. And when fault occurs, the AC flux through the PM is 0.01T, much less than 0.06T in the single-phase SFCL in [3]. Therefore, the loss and the risk of demagnetization can be further reduced, the stability of the permanent magnet is improved. Compared to the 120A in system without FCL, the fault current is limited to less than 70A at single-phase fault and two-phase fault condition with ETSFCL. When three-phase fault occurs, the current is less than 80 A. In this study, we compare parameters of the ETSFCL with three single-phase FCLs[3] when they have the similar clipping performance. The economical use a common yoke, and its compact structure reduces the length of the equivalent air gap, improving the utilization ratio of permanent magnet. So the ETSFCL saves about 39% silicon steel and 40% permanent magnet. IV.Conclusion This digest briefly introduces a novel economical three-phase fault current limiter and explained the basic operating principle. The proposed ETSFCL has a good performance in limiting three-phase fault current. Compared to three single phase SFCLs, ETSFCL saves about 40% ferromagnetic material The AC flux in PM is reduced to 1/6, which means the loss and the risk of demagnetization can be further reduced, the stability of the permanent magnet is improved. Detailed comparisons and experimental results will be shown in the full paper

[1]J. C. Knott and J. W. Moscrop, "Increasing Energy Efficiency of Saturated-Core Fault Current Limiters with Permanent Magnets," *IEEE Trans. Magn.*, vol. 49, no. 7, July 2013, pp: 4132-4136. [2]J. Yuan, Y. Zhong, S. Liao, L. Wei, Y. Gao, K. Muramatsu, J. Jia, B. Chen, and L. Bai. "A Novel Three-Phase Compact Saturated-Core Fault Current Limiter," *IEEE Trans. Magn.*, vol. 53, no. 11, Nov. 2017, Art. no. 8401104. [3]J. Yuan, Y. Zhong, Y. Lei, C. Tian, W. Guan, Y. Gao, K. Muramatsu and B. Chen, "A novel hybrid saturated core fault current limiter topology considering permanent magnet stability and performance," *IEEE Trans. Magn.*, vol. 53, no. 6, Jun. 2017, Art. no. 8400304.

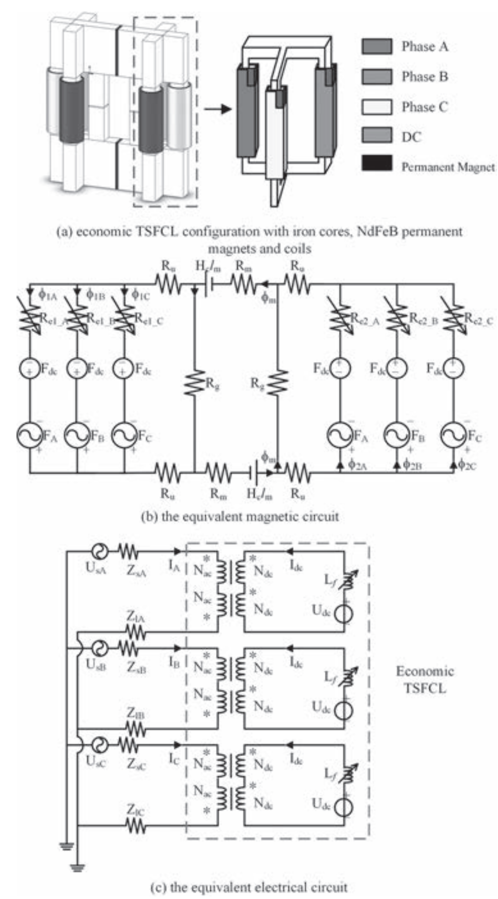

Fig. 1. the configuration and equivalent circuit

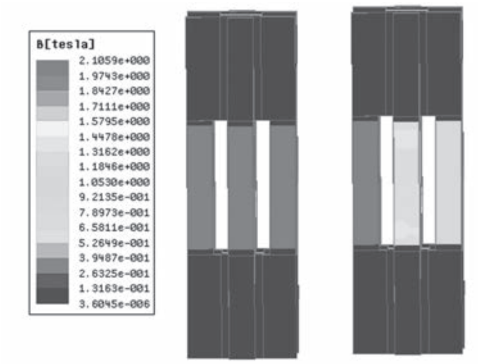

(a) flux density distribution in normal and fault conditions

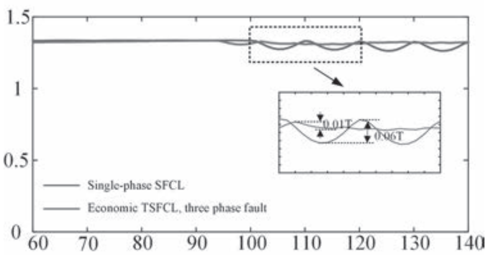

(b) the comparison of the magnetic flux in PMs

Fig. 2. the flux density distribution and the comparison of magnetic flux in PMs

11:45

CG-12. Electromagnetic Vibration Analysis of Surface-Mounted Permanent Magnet Synchronous Machine.

Z. Xing[1], X. Wang[1] and W. Zhao[1]
1. School of Electrical Engineering, Shandong University, Ji'nan, China

1.Introduction Because of its simple structure, high power density and high efficiency, the applications of permanent magnet synchronous machine (PMSM) gain continual expansion, and the low-noise and high-performance PMSM has also become one of the hot research spots. In [1]-[4], the analytical calculation of the air-gap magnetic field of PMSM is studied in detail, and the transient magnetic field distribution of the surface permanent magnet brushless DC machine is obtained. Accordingly, an analytical model of analyzing the radial electromagnetic force wave in fractional-slot PMSM is established, and the influence of stator slotting, etc. on electromagnetic force waves are calculated in [5]. In [6], the vibration characteristics of four different types of interior PMSMs are analyzed by the finite element method (FEM), and the influence of winding configurations on the vibration characteristics is obtained, however, it is difficult to distinguish the source of exciting wave. In this paper, a method of calculating radial electromagnetic force combining analytical method and FEM is proposed. With this method, the influence of slot size is considered, meanwhile, the integral expression of radial electromagnetic force wave is calculated accurately and conveniently. Further, the influences of slot opening width, skewed slot rate, pole arc coefficient, eccentricity on the electromagnetic force wave are analyzed, which lay the theoretical foundation for the weakening of electromagnetic vibration. 2.Electromagnetic force wave calculation principle Electromagnetic vibration is excited by the exciting force wave, the key to calculate the exciting force wave is calculate the air gap flux density accurately. The magnetic potential drop on the stator core could be ignored with the assumption that the permeability of the iron core is infinite. Thus, the air gap magnetic flux density along the circumference could be described as $B_{ag}(\theta,\alpha)=\mu_0 F(\theta)/\delta(\theta,\alpha)$, where μ_0 represents the vacuum permeability, $F(\theta)$ is the air gap magnetomotive force, $\delta(\theta,\alpha)$ is the effective air gap length. The air gap magnetomotive force is divided into two parts, one is the magnetomotive force generated by the PM, and the other is the magnetomotive force generated by the winding. Fig.1(a) shows the machine structure without slots. With this structure, the magnetomotive force generated by the PM can be calculated as $F(\theta)=B_0(\theta)\times\delta/\mu_0$, where the $B_0(\theta)$ is the magnetic flux density of the air gap when the stator slots are neglected. The magnetomotive force generated by the winding can be obtained directly by analytical calculation. As shown in the Fig.1(b), the length of the air gap corresponding to the tooth is uniform and the magnetic flux density is basically the same. Thus, in range of the entire tooth pitch, the magnetic potential drop on the air gap is basically unchanged, and it can be calculated as $F\approx F_{\delta t}=B_{\delta t}\times\delta/\mu_0$, where $B_{\delta t}$ is the magnetic flux density corresponding to the stator tooth, so the effective air gap length can be calculated as $\delta(\theta,\alpha)=\mu_0\times F/B_{\delta t}(\theta,\alpha)$, where the $B_{dt}(\theta,a)$ is the distribution of the magnetic flux density of air gap along the circumference in range of a tooth pitch. 3.Electromagnetic force wave analysis According to Maxwell's tensor method, the radial force density acting on the inner surface of the stator is $f_r=(B_r^2-B_t^2)/(2\mu_0)\approx B_r^2/(2\mu_0)$. the expression of radial electromagnetic force wave can be calculated accurately. For the 24-pole/72-slot machine studied in this paper, the minimum order of the wave force is 24. 4.Influences of machine structure parameters on electromagnetic vibration Based on the above analysis, this paper proposes to reduce the lower-order electromagnetic force waves through the reasonable choice of machine structure parameters. Changing the slot opening width can affect the alternating component of the air gap permeance, as shown in the Fig.2(a), the amplitude of the exciting force wave will increase with the increase of slot opening width. Adopting skewed slot structure will cause phase differences between the radial forces at different axial positions, so the average radial force acting on a line will decrease. As shown in the Fig.2(b), the amplitude of the exciting force wave will decrease when the stator adopts skewed slot structure. As shown in the Fig.2(c) and (d), when the skewed slot rate is constant, the amplitude of the 24-order exciting force wave decreases with the increase of the pole arc coefficient, but the amplitude of the 48-order exciting force wave increases firstly and then decreases with the increase of the pole arc coefficient. As shown in the Fig.2(e) and (f), When the polar arc coefficients are different, the law of change of low-order force waves with eccentricity is also different. So only in a specific pole arc coefficient can we change the eccentricity to weaken the electromagnetic vibration. 5.Conclusion In this paper, the radial electromagnetic force has been calculated accurately by combining the analytical method and FEM. The influences of machine structure parameters on the electromagnetic force wave are analyzed. The study found that the lower-order electromagnetic force wave can be decreased by decreasing slot opening width, increasing the pole arc coefficient and adopting skewed slot. Adopting eccentric magnet pole can only weaken the electromagnetic force wave with a specific arc coefficient.

[1]Z. Q. Zhu, D. Howe, E. Bolte, B. Ackermann, Instantaneous magnetic field distribution in brushless permanent magnet DC motors, Part I: open-circuit field, IEEE Trans. Mag., Vol. 29, No. 1, pp. 124-135, 1993. [2]Z. Q. Zhu, D. Howe, Instantaneous magnetic field distribution in brushless permanent magnet DC motors, Part II: armature-reaction field, IEEE Trans. Mag., Vol. 29, No. 1, pp. 136-142, 1993. [3]Z. Q. Zhu, D. Howe, Instantaneous magnetic field distribution in brushless permanent magnet DC motors, Part III: effect of stator slotting, IEEE Trans. Mag., Vol. 29, No. 1, pp. 143-151, 1993. [4]Z. Q. Zhu, D. Howe, Instantaneous magnetic field distribution in brushless permanent magnet DC motors, Part IV: magnetic field on load, IEEE Trans. Mag., Vol. 29, No. 1, pp. 152-158, 1993. [5]Z. Q. Zhu, Z. P. Xia, L. J. Wu, Geraint W. Jewell, Analytical modeling and finite element computation of radial vibration force in fractional-slot permanent magnet brushless machines, IEEE Trans. Industry Applications, Vol. 46, No. 5, pp. 1908-1918, 2010. [6]Takeo Ishikawa, Hironobu Inaba, Michio Matsunamiet, Comparison of vibration characteristics of several interior permanent magnet synchronous motors, Proceedings of the International Conference on Electrical Machines and Systems, pp. 314-319, 2008.

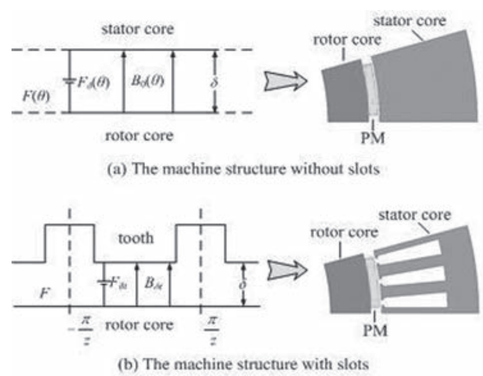

Fig. 1. Schematic diagram of machine structure

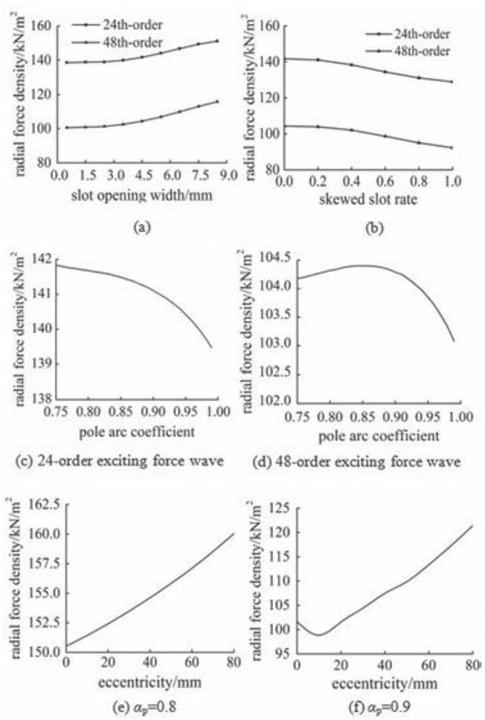

Fig. 2. Influence of machine structure parameters on the radial force density

WEDNESDAY MORNING, 25 APRIL 2018 PEONY II, 9:00 TO 12:00

Session CH
TRANSFORMERS AND INDUCTORS

Yasushi Endo, Chair
Tohoku University, Sendai, Japan

CONTRIBUTED PAPERS

9:00

CH-01. Reduced EMI Noise with the Consideration of Magnetic Material Design in the Grid-Connected Inverter for More Electric Aircraft.

Y. Liu[1], Y. Liu[2], H. Wang[1], G. Wang[1] and J. Peng[1]
1. Shenzhen University, Shenzhen, China; 2. Nanyang Technological University, Singapore, Singapore

1.Introduction The concept of more electric aircraft (MEA) is based on the increasing use of electric power to replace the non-electric subsystems in the traditional aircraft. It provides significant improvements in reliability, maintenance cost, fuel consumption and overall weight for the aircraft [1]. The LCL filter is widely used in the grid-connected inverter due to its harmonic attenuation performance and system stability [2, 3]. Compact and efficient magnetic components design in the power inverter results in its total size and weight minimization. Winding technology [4, 5], switching frequency [6] and core selection [7] are three important issues in the size reduction of magnetic components in the LCL filter. Furthermore, besides power quality of the power grid, another important issue is the conducted EMI which is mainly generated due to the high frequency transistor switching and parasitic components in the noise conduction path [8, 9]. The differential mode (DM) EMI is dominant compared with the common mode (CM) EMI in the inverter side, thus the LCL filter can be treated as an EMI filter [10] if the self-resonant frequency in the filtering inductor is high enough. Thus, if THD and EMI can be reduced at the same time with one filter, the power density would be increased pronouncedly. 2. LCL filter design The output LCL filter is a necessary part as shown in Fig. 1 (a) for the harmonic limit requirement [11, 12]. The LCL filter is expected to attenuate the grid side current complied with the IEEE 519-std as shown in [13]. To increase the power density, the silicon carbide (SiC) power module is employed in the grid-connected inverter so that switching frequency can be pushed to 60 kHz or higher [14]. The Low core loss, high saturation flux density, wider operation frequency and high operation temperature Amorphous core take advanced power conditioning applications with high power. 3D printing technology is adopted for the bobbin fabrication with the purpose of compactness. 4. Inductor winding design The Amorphous core with low loss and high saturation flux density is chosen for the filtering inductors design. The impedance of the two types of inductors with different winding technology that is measured by Hewlett Packard 4194A Impedance analyzer. In order to reduce the parasitic components at higher frequency range, the conventional copper wire for inductor winding is replaced by copper foil with an EE Amorphous core. The copper foil inductor has larger resonant frequency than copper wire inductor. Larger resonant frequency means that it has better noise attenuation for the conducted EMI noise in the range of 150 kHz to 30 MHz. Fig. 1 (b) and (c) show the commond mode (CM) and differential model (DM) EMI noise model with the LCL filter consideration. It can be found that larger impedance of L_i denotes the smaller noise voltage and the EMI filter requirement can be reduced. Thus, the weight of the copper foil inductor is smaller than the copper wire inductor in the system requirement for the inverter. Copper foil inductor has more efficient high frequency noise attenuation ability and save more space for the EMI filter design. According to above analysis, the copper foil inductor will be designed and applied in the experiment to verify its THD and EMI noise attenuation effect. 5. Experiment results The LCL filter design is verified in a 30 kW, 750 V (DC) and 230 V/400 Hz two-level three-phase grid-connected inverter based on the early works [15]. The SiC power module is employed to achieve a high switching frequency with the commercial product CAS100H12AM1 (1.2 kV, 100 A) from Wolfspeed. It achieves 97.9% energy conversion efficiency at 30 kW input power and 60 kHz switching frequency. Fig. 2 (a) shows the simulated flux distribution at full load by FEA software, in which the maximum flux in the core is 4/5 of the saturation flux 1.56T. Fig. 2 (b) shows the temperature distribution in the filtering inductor after one hour full load running, the maximum temperature is 155^{o}C which is lower than the its Curie Temperature. Fig. 2 (d) shows the experimental current in the inverter with foil-wound inductor. The LCL filter can not only reduce the THD but also reduce the DM EMI noise at higher frequency range. Smaller resonant frequency can lead to larger noise attenuation performance. Fig. 2 (c) compares the grid side current spectrum in the two kinds of LCL filter with copper wire and copper foil inductor. It can be found that the high frequency current spectrum in the LCL filter with copper foil wound is smaller than copper wire wound. Thus, the foil wound inductor is used in the high power density inverter that would result in a smaller EMI filter requirement. 6. Conclusion This paper proposes the LCL filter design in a grid-connected system using foil-wound, 3D printing and SiC-based power converter. The experimental inverter and grid side currents' spectrums are used to evaluate the noise attenuation comparison of the copper foil-wound and traditional copper wire-wound inductors in the LCL filter. Due to the higher resonant frequency, smaller EMI noise and less space requirement in the foil-wound inductor, it is highly recommended for the high power density inverter design.

[1] J. Rosero, J. Ortega, E. Aldabas, and L. Romeral, "Moving towards a more electric aircraft," *IEEE Aerospace and Electronic Systems Magazine,* vol. 22, pp. 3-9, 2007. [2] Z. Xin, X. Wang, P. C. Loh, and F. Blaabjerg, "Grid-Current-Feedback Control for LCL-Filtered Grid Converters With Enhanced Stability," IEEE Transactions on Power Electronics, vol. 32, pp. 3216-3228, 2017. [3] X. Fu and S. Li, "Control of Single-Phase Grid-Connected Converters With LCL Filters Using Recurrent Neural Network and Conventional Control Methods," Power Electronics, IEEE Transactions on, vol. 31, pp. 5354-5364, 2016. [4] K. Nakamura, Y. Yamada, R. Nono, T. Ohinata, K. Arimatsu, and O. Ichinokura, "A Novel 3-D Concentric-Winding-Type Three-Phase Variable Inductor for Reactive Power Compensation in Electric Power Systems," IEEE Transactions on Magnetics, vol. 53, pp. 1-4, 2017. [5] A. Stadler, R. Huber, T. Stolzke, and C. Gulden, "Analytical calculation of copper losses in litz-wire windings of gapped inductors," IEEE Transactions on Magnetics, vol. 50, pp. 81-84, 2014. [6] R. M. Burkart, H. Uemura, and J. W. Kolar, "Optimal inductor design for 3-phase voltage-source PWM converters considering different magnetic materials and a wide switching frequency range," in *2014 International Power Electronics Conference (IPEC-Hiroshima 2014-ECCE ASIA)*, 2014, pp. 891-898. [7] F. Zheng, Y. Pei, Y. Liu, L. Wang, X. Yang, and Z. Wang, "Design coupled inductors for interleaved converters using a three-leg core," IEEE Transactions on Magnetics, vol. 44, pp. 4697-4705, 2008. [8] W. Cheng, X. He, S. Xu, and W. Sun, "Analysis of common-mode electromagnetic interference noise in a flyback converter using a self-supply power control integrated circuit," *IET Power Electronics,* vol. 8, pp. 1749-1757, 2015. [9] A. Frikha, M. Bensetti, H. Boulzazen, and F. Duval, "Influence of PCB and Connections on the Electromagnetic Conducted Emissions for Electric or Hybrid Vehicle Application," IEEE Transactions on Magnetics, vol. 49, pp. 1841-1844, 2013. [10] M. Liserre, F. Blaabjerg, and S. Hansen, "Design and control of an LCL-filter-based three-phase active rectifier," *IEEE Trans. Ind. Appl.,* vol. 41, pp. 1281-1291, 2005. [11] M. Sanatkar-Chayjani and M. Monfared, "Design of LCL and LLCL filters for single-phase grid connected converters," *IET Power Electronics,* vol. 9, pp. 1971-1978, 2016. [12] X. Zheng, L. Xiao, Y. Lei, and Z. Wang, "Optimisation of LCL filter based on closed-loop total harmonic distortion calculation model of the grid-connected inverter," *IET Power Electronics,* vol. 8, pp. 860-868, 2015. [13] "IEEE Recommended Practice and Requirements for Harmonic Control in Electric Power Systems," *IEEE Std 519-2014 (Revision of IEEE Std 519-1992),* pp. 1-29, 2014. [14] S. Yin, K. J. Tseng, R. Simanjorang, Y. Liu, and J. Pou, "A 50-kW High-Frequency and High-Efficiency SiC Voltage Source Inverter for More Electric Aircraft," *IEEE Trans. Ind. Electron.,* 2017. [15] S. Yin, K. Tseng, C. Tong, R. Simanjorang, Y. Liu, A. Nawawi*, et al.*, "Evaluation of power loss and efficiency for 50 kW SiC high power density converter," in *Energy, Power and Transportation Electrification (ACEPT), Asian Conference on*, 2016, pp. 1-6.

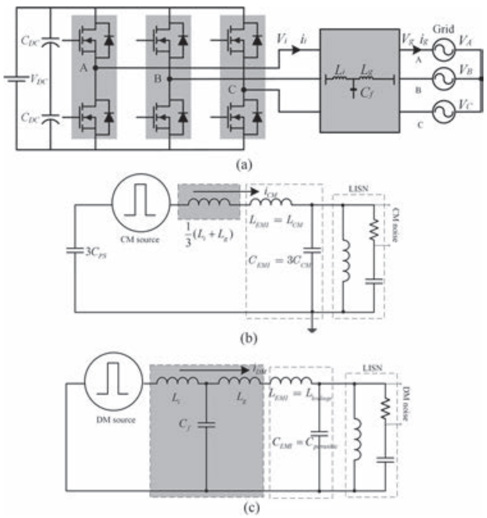

Fig. 1. (a) Grid-connected system, (b) equivalent CM noise model, (c) equivalent DM noise model

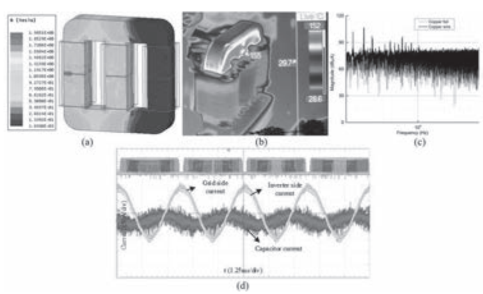

Fig. 2. Experiment results, (a) FEA analysis for flux distribution, (b) Inductor temperature distribution, (c) Comparison of high frequency current spectrum in the grid side, (d) Inverter and grid sides current

9:15

CH-02. All-Metal Domestic Induction Heating Using Single-Frequency Double-Layer Coils.

W. Han[1], K. Chau[1], C. Jiang[1] and W. Liu[1]
1. Electrical and Electronic Engineering, The University of Hong Kong, Hong Kong, Hong Kong

I. INTRODUCTION In the past few decades, induction heating based on near-field magnetic coupling has been actively developed, aiming to improve the efficiency, controllability and safety. For traditional induction heating, the heating coil is energized by an AC power source to generate an alternating magnetic field, which in turn induces the eddy current in the workpiece to produce the heating effect [1]. Nevertheless, the workpiece made of non-ferromagnetic materials like stainless steel, aluminum and copper cannot be properly heated, which dramatically limits its application as compared with traditional open-fire heating. There was an attempt to heat the non-ferromagnetic workpiece using a strong magnetic field provided by superconducting windings [2], but it was not practical for domestic induction heating. By using low-frequency AC (around 20 kHz) to heat the ferromagnetic pan and high-frequency AC (over 70 kHz) to heat the non-ferromagnetic pan, the selective operating frequency technique was developed for all-metal domestic induction heating [3]. However, the corresponding switching and winding losses significantly increased, which inevitably resulted in low heating efficiency. In addition, the frequency selection caused serious electromagnetic interference and increased complexity and cost. Recently, the homogeneity and flexibility of induction heating has been improved by adopting the magnetic resonant coupling (MRC) mechanism [4]-[5]. In this paper, a new all-metal domestic heating system is proposed and implemented. The key is to employ double-layer coils and utilizes the MRC mechanism to induce a high current in the resonant coil when heating the non-ferromagnetic pans, thus successfully heating both the ferromagnetic and non-ferromagnetic pans at 30 kHz resonant frequency. Consequently, the advantages of simplicity, high heating efficiency and single operating frequency can be attained for all-metal induction heating. II. METHODOLOGY The proposed approach employs double-layer coils and utilizes the MRC mechanism in a new way. Fig. 1 shows the structure and equivalent circuit of the proposed induction heating in which two coils are laid on lower and upper sides of the ceramic glass plate concentrically, thus dubbed as lower and upper coils and the pan is regarded as the load coil. Unlike normal MRC for wireless power transfer, the resonant coil (the upper coil) not only serves to boost the power transfer from the transmitter to the receiver but also provides high current to strengthen the magnetic coupling and hence the dissipated power in the non-ferromagnetic pan. Since the equivalent impedances of the upper and lower coils are affected by the material of the pan, two sets of switched capacitors are introduced so that the coil inductances can be properly compensated when loaded with the ferromagnetic and non-ferromagnetic pans at the same operating frequency. Additionally, some ferrite slabs are placed beneath the lower coil to enhance the heating performance. Hence, the lower coil is directly excited by a low-frequency AC source which in turn excites the upper coil indirectly via the MRC mechanism. Given that the inductances of the coils are fully compensated by the capacitors, both high power factor in the lower coil and high resonant current in the upper coil are achieved simultaneously. Meanwhile, since the resistances of the coils which are made of Litz-wire are quite small, high power transfer efficiency can be achieved. Both the lower and upper coils transmit power to the pan and the upper coil plays a major role because of much higher current and stronger magnetic coupling. Firstly, theoretical equations based on the equivalent circuit are deduced to assess the currents flowing in two coils loaded with the ferromagnetic and non-ferromagnetic pans. Hence, the corresponding dissipated power and power transfer efficiency can be calculated. Secondly, the magnetic field and thermal field analyses of the proposed heating system when using the iron, stainless steel, aluminum and copper pans are carried out using finite element method based software JMAG. Finally, an experimental prototype has been constructed and tested to verify the feasibility and efficiency of the proposed all-metal domestic induction heating. As shown in Fig. 2, the thermal images of various metallic pans are captured by a thermal scanner (FLUKE TiS 40) after heating for 120 s in the proposed heating system. It illustrates that the average temperatures along the pan diameter of the iron, stainless steel, aluminum and copper pans are 105.1^{o}C, 102.5^{o}C, 108.5^{o}C and 104.1^{o}C, respectively, at the same operating frequency of 30 kHz. It confirms that all metallic pans can be heated successfully in the proposed induction heating system. More simulation and experimental results will be given in the full paper. III. CONCLUSION In this paper, an all-metal domestic induction heating system has been proposed and implemented. The key is to newly employ double-layer coils and utilizes the MRC mechanism so that both the ferromagnetic and non-ferromagnetic pans can be effectively heated. Theoretical analysis, numerical simulation and experimentation are given to validate the proposed system. This work was supported by a grant (Project No. SPF 201409176054) from the University of Hong Kong, Hong Kong.

[1] O. Lucía, P. Maussion, E. J. Dede, and J. M. Burdio, "Induction heating technology and its applications: past developments, current technology, and future challenges," *IEEE Trans. Ind. Electron*., vol. 61, no. 5, pp. 2509–2520, May 2014. [2] T. Lubin, D. Netter, J. Leveque, and A. Rezzoug, "Induction heating of aluminum billets subjected to a strong rotating magnetic field produced by superconducting windings," *IEEE Trans. Magn*., vol. 45, no. 5, pp. 2118–2127, May 2009. [3] I. Millán, J. M. Burdío, J. Acero, O. Lucía, and S. Llorente, "Series resonant inverter with selective harmonic operation applied to all-metal domestic induction heating," *IET Power Electr.*, vol. 4, no. 5, pp.587-592, May 2011. [4] W. Han, K.T. Chau, and Z. Zhang, "Flexible induction heating using magnetic resonant coupling," *IEEE Trans. Ind. Electron.*, vol. 64, no. 3, pp. 1982-1992, Mar. 2017. [5] W. Han, K. T. Chau, Z. Zhang, and C. Jiang, "Single-source multiple-coil homogeneous induction heating," *IEEE Trans. Magn.*, vol. 53, no. 11, pp. 7207706:1-6, Nov. 2017.

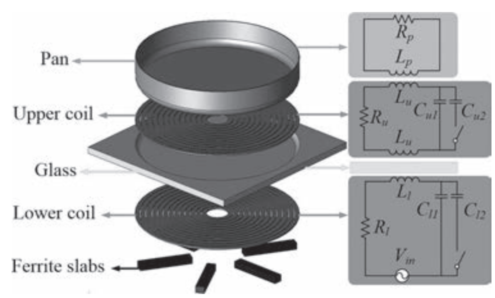

Fig. 1. Structure and equivalent circuit of the proposed induction heating.

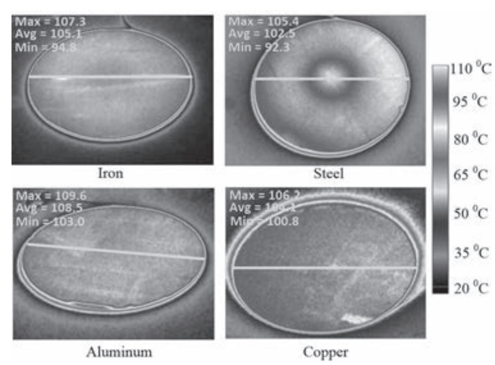

Fig. 2. Temperature distributions in various metallic pans.

9:30

CH-03. Analytic Computation of Power-Line Voltage Drop Produced by Magnetic Energy Harvesting Device.

K. Kim[1], B. Park[1], J. Kim[1], J. Koo[2] and S. Ahn[1]
1. Korea Advanced Institute of Science and Technology (KAIST), Deajeon, The Republic of Korea; 2. Ferrarispower, Seongnam, The Republic of Korea

1. INTRODUCTION For power-line monitoring, autonomous wireless power-line sensors are hung from overhead power-lines and transmit the data collected from measurement systems using internet-of-things technology. Since these sensors require a continuous power supply, some have proposed using self-powered monitoring devices to harvest magnetic energy using a current transformer (CT) with a toroidal core structure, as shown in Fig. 1a [1], [2]. However, those studies only focused on the power transfer efficiency of the CT without considering the effect of eddy-current loss in the CT and impedance matching for maximum power transfer to the load. Even though this device produces voltage drop and impedance changes in the power-line, no analysis of the CT impact on the power quality of the power-line has been done. The power quality is very important issue that power supplier cannot ignore. Impedance changes by CT in power-lines can induce power factor distortions in the electric power system. This paper presents analytical methods for calculating voltage drop and impedance changes in power-lines. Voltage drop and impedance change were found to increase as load impedance decreased under the impedance matching condition. 2. ELECTRICAL MODEL OF POWER-LINE AND ENERGY HARVESTING DEVICE A. COMPUTATION OF CURRENT DENSITY AND VECTOR POTENTIAL Unlike previous works which calculated the magnetic field distribution in the CT [3], [4], current density and vector potential are useful for calculating the impedances of the power-line and CT. In conductors, the current density J_z can be expressed as Fig. 2a from Maxwell's equation and Ohm's law. Assuming that the field emission in the air region is the transverse electromagnetic, the vector potential A_z can be expressed as Fig. 2b. The general solutions of these Helmholtz equations in cylindrical coordinates can be obtained as Fig. 2c. The current densities inside the power-line and CT can be expressed as Bessel functions and the vector potential of air regions is simplified by the logarithm function, where I_s denotes the current in the power-line, the current I_p in the CT and the coil turns N_p. The constants c_0, c_1, c_2 and c_3 can be determined by Ampere's law, while c_4 is not needed since it will be eliminated in computational procedure for the impedances. B. EQUIVALENT CIRCUIT MODEL Fig. 1b shows the equivalent circuit model. In a quasi-magnetostatic field [5], the scalar potential per unit length can be expressed as Fig. 2d. This is valid because the structure parameters in CT are much less than 1/4 wavelength (5×10^6m at 60Hz). The power-line impedances Z_{s_in}, $j\omega L_{s\_ext}$ and Z_{sc} can be obtained by applying the integral form of Faraday's law in Fig. 2d. The CT impedance Z_p consists of Z_{pc} due to the self-induced voltage in the coil and the wire wound resistance R_p, while Z_{pc} can be calculated by Faraday's law in the differential form and R_p is obtained from the resistance model of round wire [6]. The magnetic coupling between power-line and CT can be represented by M_{sp} in Fig. 2h, which not only makes the induced voltage for magnetic energy harvesting, but also causes the voltage drop in the power-line. M_{sp} can be obtained in a similar way to Z_{pc}. Z_{sc}, M_{sp} and Z_{pc} includes the losses due to the eddy-current inside the CT. 3. VOLTAGE DROP IN POWER-LINE As shown in Fig. 1c, the total impedance Z_{s_tot} viewed from the power-line referred to the primary side must include the effective impedance Z_{s_eff} due to magnetic coupling. Using I_s/I_p=j$\omega M_{sp}/(Z_{pc}+R_p+Z_L)$ [7], Z_{s_eff} is expressed as Fig. 2g. The inductance of the power-line without CT for magnetic energy harvesting is $\mu_0 h/8\pi$. Compared to the power-line with CT, the variation in impedance ΔZ can be expressed as Fig. 2i. To maximize power transfer by minimizing losses due to signal reflection from the load, the impedance matching circuit has the absolute difference between Z_L and Z_p, as shown in Fig. 2j. Under the condition of impedance matching, the denominator in Fig. 2i is doubled of Z_L. If there is no load connected to the magnetic energy harvesting device (open circuit or Z_L=inf), the voltage drop across the power-line is minimized since Z_{s_eff} is zero. Although there is no power dissipated at the load, a voltage drop still occurs on the power-line due to the eddy-current loss of CT ($Z_{sc}\neq0$). On the other hand, when Z_L is connected to the magnetic energy harvesting device ($Z_L\neq$inf), the voltage drop in the power-line increases as Z_L decreases. In order words, the power consumption of the load increases since Z_L decreases at P=$V^2/4Z_L$. When the structure parameters of CT are inner radius ρ_1=17.1mm, outer radius ρ_2=37.9mm, height h=45mm, coil turns N_p=90, permeability in the CT μ_c=50000 and conductivity in the CT $\sigma_c=2.2\times10^5$S/m, the voltage drop $\Delta V=\Delta Z\times I_s$ of the power-line is as follows. - I_s=60A, no load (Z_L=inf), ΔV = 0.54V - I_s=60A, Z_L=5Ω (impedance matching), ΔV = 5.12V - I_s=60A, Z_L=2Ω (impedance matching), ΔV = 13.33V

[1] W. Wang, X. Huang, L. Tan, J. Guo, H. Liu, "Optimization Design of an Magnetic Energy Harvesting Device for Wireless Power Supply System Overhead High-Voltage Power Lines", *Energies*, vol. 9, no. 4, April 2016. [2] Z. Wu, Y. Wen, P. Li, "A power supply of self-powered online monitoring systems for power cords", *IEEE Trans. Energy Convers.*, vol. 28, no. 4, pp. 921-928, Dec. 2013. [3] C. Jaschke, P. Schegner, "Analytic computation of the magnetizing inductance of current instrument transformers under consideration of eddy currents", *IEEE Trans. Magn.*, vol. 51, no. 11, Nov. 2015. [4] K. V. Namjoshi, J. D. Lavers, P. P. Biringer, "Eddy current power loss in toroidal cores with rectangular cross section", *IEEE Trans. Magn.*, vol. 34, no. 3, pp. 636-641, May 1998. [5] J. D. Jackson, *Classical Electrodynamics*, 3rd ed. New York: Wiley, 1998, pp. 218-223. [6] M. M. Al-Asadi, A. P. Duffy, A. J. Willis, K. Hodge, and T. M. Benson, "A simple formula for calculating the frequency- dependent resistance of a round wire," *Microw. Optical Technol. Lett.*, vol. 19, no. 2, pp. 84–87, 1998. [7] J. Shin, S. Shin, Y. Kim, S. Ahn, S. Lee, G. Jung, S.-J. Jeon, D.-H. Cho, "Design and implementation of shaped magnetic-resonance-based wireless power transfer system for roadway-powered moving electric vehicles", *IEEE Trans. Ind. Electron.*, vol. 61, no. 3, pp. 1179-1192, Mar. 2014.

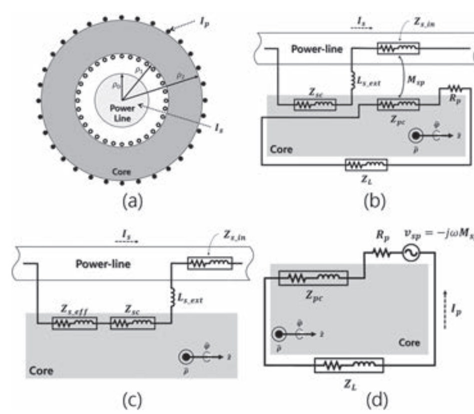

Fig. 1. Current transformer (a) with a rectangular cross section. The equivalent circuit model (a) can be divided into an equivalent circuit (b) of the power-line referred to the primary side and an equivalent circuit (c) of CT referred to the secondary side.

$$\nabla^2 J_z + k^2 J_z = 0 \quad \text{(a)} \qquad \nabla_t^2 A_z = 0 \quad \text{(b)}$$

$$J_z(\rho) = \begin{cases} c_0 \mathrm{J}_0(k_s\rho) = \frac{k_s I_s}{2\pi\rho_0}\cdot\frac{\mathrm{J}_0(k_s\rho)}{\mathrm{J}_1(k_s\rho_0)} \\ c_1\mathrm{H}_0^{(1)}(k_c\rho) + c_2\mathrm{H}_0^{(2)}(k_c\rho) = (I_s - N_p I_p)\cdot\gamma(\rho) \end{cases} \quad \text{(c)}$$

$$A_z(\rho) = c_3\ln\rho + c_4 = -\frac{\mu I_s}{2\pi}\ln\rho + c_4$$

$$-\frac{d\phi}{dz} = E_z + j\omega A_z = \frac{J_z}{\sigma_c} + j\omega A_z \quad \text{(d)}$$

$$Z_{s\_tot} = Z_{s\_in} + j\omega L_{s\_ext} + Z_{sc} + Z_{s\_eff} \quad \text{(e)} \quad Z_p = Z_{pc} + R_p \quad \text{(f)}$$

$$Z_{s\_eff} = \frac{\omega^2 {M_{sp}}^2}{Z_{pc}+R_p+Z_L} = \frac{\omega^2 {M_{sp}}^2}{2Z_L} \quad \text{(g)} \quad M_{sp} = \frac{jN_p h}{\omega\sigma_c}\{\gamma(\rho_1) - \gamma(\rho_2)\} \quad \text{(h)}$$

$$\Delta Z = \left| j\omega\left(L_{s\_ext} - \frac{\mu_0 h}{8\pi}\right) + Z_{sc} + Z_{s\_eff} \right| \quad \text{(i)} \quad |Z_m| = |Z_L - Z_p| \quad \text{(j)}$$

Fig. 2. Calculation results (c) for Helmholtz equation (a) and (b). Impedance variation (i) in the power-line and impedance matching (j) for the magnetic energy harvesting device, calculated by (d)-(h).

9:45

CH-04. Matrix formulation of Cauer Ladder Network Method for Efficient Eddy-Current Analysis.

T. Matsuo[1], A. Kameari[2], K. Sugahara[3] and Y. Shindo[4]
1. Kyoto University, Kyoto, Japan; 2. Science Solutions International Laboratory, Inc., Tokyo, Japan; 3. Kindai University, Higashiosaka, Japan; 4. Kawasaki Heavy Industries, Ltd., Akashi, Japan

1. Introduction Advanced power control often requires detailed eddy-current analyses of electric machines handling thin skin depth due to high frequency switching. The Cauer circuit [1][2] is a very efficient and exact representation of the eddy-current field in magnetic sheets and cylinders for wide frequency range, where magnetic and electric fields are optimally expanded by orthogonal polynomials. Recently, the Cauer circuit representation is extended to describe general eddy-current fields powered by the finite element method (FEM). This method is called Cauer ladder network (CLN) method [3][4] and still retains clear physical meaning based on the orthogonal function expansion. The generality of CLN method has a similarity to model order reduction (MOR) methods [5][6]. The relation between the CLN method and other MOR methods has not been clear yet because of the physics-based derivation of CLN method. This article derives a matrix formulation of CLN method for clear understanding of mathematical aspects of the CLN method. **2. Matrix based formulation of CLN method** In the matrix form based on the FEM, the governing equation of eddy-current field is given as $\boldsymbol{Ka} = \sigma\boldsymbol{e}$, $\boldsymbol{Ce} = -\,\mathrm{j}\omega\boldsymbol{Ca}$, $\boldsymbol{K} = \boldsymbol{C}^{\mathrm{T}}\boldsymbol{vC}$ (1) where $\boldsymbol{a}$ and $\boldsymbol{e}$ are the variable vectors representing vector potential and electric field, $\boldsymbol{C}$ is the edge-face incidence matrix [7], $\boldsymbol{v}$ is the reluctivity matrix, and σ is the conductivity matrix. The CLN method is described by the recurrence formulae below to generate orthogonal basis vectors as $\boldsymbol{K}(\boldsymbol{a}_{2n+1}-\boldsymbol{a}_{2n-1}) = \sigma\boldsymbol{e}_{2n}/\lambda_{2n}$ (2) $\boldsymbol{e}_{2n+2} - \boldsymbol{e}_{2n} = -\,\boldsymbol{a}_{2n+1}/\lambda_{2n+1}$ (3) where $\boldsymbol{a}_{2n-1}$ and $\boldsymbol{e}_{2n}$ are orthogonal basis vectors for vector potential and electric field and $\lambda_{2n} = \boldsymbol{e}_{2n}{}^{\mathrm{T}}\sigma\boldsymbol{e}_{2n}$, $\lambda_{2n+1} = \boldsymbol{a}_{2n+1}{}^{\mathrm{T}}\boldsymbol{Ka}_{2n+1}$. (4) The initial conditions for the recurrence formulae are given by $\boldsymbol{a}_{-1} = 0$, $\boldsymbol{Ke}_0 = 0$ (5) where it is assumed that a unit voltage is given as the boundary condition. As derived later, the eddy-current field is equivalently represented by the Cauer circuit shown in Fig. 1(a), where $R_{2n} = 1/\lambda_{2n}$, $L_{2n+1} = \lambda_{2n+1}$. (6) **3. Derivation of orthogonality** The orthogonality of basis vectors is derived by induction as follows. The multiplication of (2) and (3) gives $-(1/\lambda_{2k-1})\boldsymbol{a}_{2k-1}{}^{\mathrm{T}}\boldsymbol{K}(\boldsymbol{a}_{2n+1}-\boldsymbol{a}_{2n-1}) = (1/\lambda_{2n})(\boldsymbol{e}_{2k}-\boldsymbol{e}_{2k-2})^{\mathrm{T}}\sigma\boldsymbol{e}_{2n}$. (7) From (4), (5) and (7) with $n = 0$, $k = 1$, it holds that $\boldsymbol{a}_{-1}{}^{\mathrm{T}}\boldsymbol{Ka}_1 = 0$, $\boldsymbol{e}_2{}^{\mathrm{T}}\sigma\boldsymbol{e}_0 = 0$. (8) It is supposed that $\boldsymbol{a}_{2i-1}{}^{\mathrm{T}}\boldsymbol{Ka}_{2j-1} = 0$, $\boldsymbol{e}_{2i}{}^{\mathrm{T}}\sigma\boldsymbol{e}_{2j} = 0$ ($i < j \le n$). (9) From (4) (9) and (7), $\boldsymbol{a}_{2k-1}{}^{\mathrm{T}}\boldsymbol{Ka}_{2n+1} = 0$ ($k \le n$) (10) is obtained. By replacing (k, n) in (7) by (n+1, k), it holds that $-(1/\lambda_{2n+1})\boldsymbol{a}_{2n+1}{}^{\mathrm{T}}\boldsymbol{K}(\boldsymbol{a}_{2k+1}-\boldsymbol{a}_{2k-1}) = (1/\lambda_{2k})(\boldsymbol{e}_{2n+2}-\boldsymbol{e}_{2n})^{\mathrm{T}}\sigma\boldsymbol{e}_{2k}$. (11) From (4), (9) and (11), $\boldsymbol{e}_{2k}{}^{\mathrm{T}}\sigma\boldsymbol{e}_{2n+2} = 0$ ($k \le n$) (12) is obtained. Thus, the orthogonality below is proven by induction: $\boldsymbol{a}_{2i-1}{}^{\mathrm{T}}\boldsymbol{Ka}_{2j-1} = \boldsymbol{h}_{2i-1}{}^{\mathrm{T}}\boldsymbol{v}^{-1}\boldsymbol{h}_{2j-1} = \delta_{ij}\lambda_{2i+1}$, $\boldsymbol{e}_{2k}{}^{\mathrm{T}}\sigma\boldsymbol{e}_{2j} = \delta_{ij}\lambda_{2i}$ (13) where δ_{ij} is Kronecker's delta and $\boldsymbol{h}_{2i+1} = \boldsymbol{vCa}_{2i+1}$. The full paper will reveal the similarity to other MOR methods and will discuss the benefit of the CLN method based on comparison with the Lanczos algorithm. **4. Derivation of circuit equations** Electromagnetic fields are expanded as $\nu Ca = \boldsymbol{h} = \Sigma_n H_{2n+1}\boldsymbol{h}_{2n+1} = \Sigma_n H_{2n+1}\boldsymbol{\nu Ca}_{2n+1}$, $\boldsymbol{e} = \Sigma_n E_{2n}\boldsymbol{e}_{2n}$. (14) The substitution of (14) into (1) gives $\boldsymbol{K}\Sigma_n H_{2n+1}\boldsymbol{a}_{2n+1} = \sigma\Sigma_n E_{2n}\boldsymbol{e}_{2n}$. (15) $\boldsymbol{C}\,\Sigma_n E_{2n}\boldsymbol{e}_{2n} = -\,\mathrm{j}\omega\,\Sigma_n H_{2n+1}\boldsymbol{Ca}_{2n+1}$. (16) From (16), the electric field is given as $\Sigma_n E_{2n}\boldsymbol{e}_{2n} = -\,\mathrm{j}\omega\,\Sigma_n H_{2n+1}\boldsymbol{a}_{2n+1} - V_{\mathrm{S}}\boldsymbol{G}\phi$ (17) where V_{S} is the source voltage, $\boldsymbol{G}$ is the node-edge incidence matrix corresponding to the grad-operator, and ϕ is the variable vector representing scaler potential satisfying $\boldsymbol{e}_0 = -\,\boldsymbol{G}\phi$. (18) Multiplying (17) by $(1/\lambda_{2k})\boldsymbol{e}_{2k}$ gives $(1/\lambda_{2k})\boldsymbol{e}_{2k}{}^{\mathrm{T}}\sigma\,(\Sigma_n E_{2n}\boldsymbol{e}_{2n} - V_{\mathrm{S}}\boldsymbol{e}_0) = -\,\mathrm{j}\omega(\boldsymbol{a}_{2k+1}-\boldsymbol{a}_{2k-1})^{\mathrm{T}}\boldsymbol{K}\,\Sigma_n H_{2n+1}\boldsymbol{a}_{2n+1}$. (19) From (13) and (19), it holds that $E_0 = V_{\mathrm{S}} - \mathrm{j}\omega\lambda_1 H_1$, $E_{2k} = -\,\mathrm{j}\omega(\lambda_{2k+1}H_{2k+1} - \lambda_{2k-1}H_{2k-1})$ (k = 1, 2, …). (20) Multiplying (15) by $-(1/\lambda_{2k+1})\boldsymbol{a}_{2k+1}$ gives $-\,(1/\lambda_{2k+1})\boldsymbol{a}_{2k+1}{}^{\mathrm{T}}\boldsymbol{K}\,\Sigma_n H_{2n+1}\boldsymbol{a}_{2n+1} = (\boldsymbol{e}_{2k+2}-\boldsymbol{e}_{2k})^{\mathrm{T}}\sigma\Sigma_n E_{2n}\boldsymbol{e}_{2n}$. (21) From (13) and (21), it holds that $-\,H_{2k+1} = \lambda_{2k+2}E_{2k+2} - \lambda_{2k}E_{2k}$ (k = 0, 1, …). (22) Eqs. (20) and (22) represent the Cauer circuit in Fig. 1(a). Inversely, the substitution of (20) and (22) into (15) and (17) results in (2) and (3), which confirms the equivalence of the CLN and the eddy-current field. **5. Computation example** To demonstrate the efficiency and accuracy of the CLN method, a sample eddy-current problem is solved. A square iron bar [Fig. 2(a)] has the conductivity and permeability of $2*10^6$ S/m and 0.01 H/m. The unit electric filed is imposed at the surface of iron bar. The analytical solution is given by the Fourier expansion, which is represented by the Foster circuit shown in Fig. 1(b) where (m, n)-th R-L pair corresponds to the ($2m-1$, $2n-1$)-th sinusoidal basis function. Fig. 2(b) compares the frequency dependence of admittance per unit length. The Cauer circuit with only 3 or 6 R-L pairs accurately reconstructs the wide range of frequency dependence whereas the Foster circuit requires a large number of R-L pairs. The magnetic flux distributions due to $\boldsymbol{a}_1$, $\boldsymbol{a}_3$ and $\boldsymbol{a}_5$ are shown in Fig. 1(a). Using expansions (14) with these distributions, the CLN method can reconstruct the magnetic and electric fields. In the full paper more practical application will be presented.

[1] Y. Shindo, T. Miyazaki, T. Matsuo, "Cauer circuit representation of the homogenized eddy-current field based on the Legendre expansion for a magnetic sheet," IEEE Trans. Magn., vol. 52, no. 3, 6300504, Mar. 2016. [2] Y. Shindo, A. Kameari, T. Matsuo, "Efficient circuit representation of eddy-current fields," COMPEL, vol. 36, Iss: 5, pp. 1457-1473, 2017. [3] A. Kameari, H. Ebrahimi, K. Sugahara, Y. Shindo, and T. Matsuo, "Cauer ladder network representation of eddy-current fields for model order reduction using finite element method," IEEE Trans. Magn. (accepted for publication). [4] K. Sugahara, A. Kameari, H. Ebrahimi, Y. Shindo and T. Matsuo, "Finite element analysis of unbounded eddy-current problem with Cauer ladder network method," IEEE Trans. Magn. (accepted for publication). [5] P. Feldmann and R. W. Freund, "Efficient linear circuit analysis by Padé approximation via the Lanczos process," IEEE Trans. Comput.-Aided Design Integr. Circuits Syst., vol. 14, no. 5, pp. 639–649, May 1995. [6] Y. Sato, and H. Igarashi, "Generation of equivalent circuit from finite-element model using model order reduction," IEEE Trans. Magn., vol. 52, no. 3, 1100304, Mar. 2016. [7] A. Bossavit, Computational Electromagnetism, Academic Press, 1998.

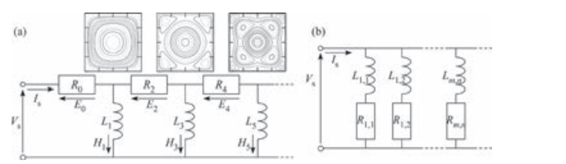

Fig. 1. Circuit representation: (a) Cauer circuit, (b) Foster circuit

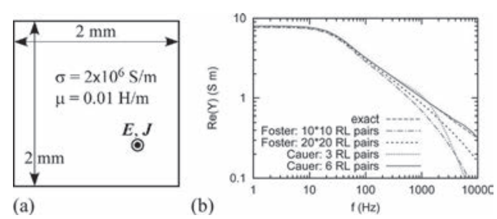

Fig. 2. Eddy-current analysis (a) square bar, (b) frequency dependence of admittance $Y = I_{\mathrm{S}}/V_{\mathrm{S}}$ per unit length

10:00

CH-05. Design of Rotary Transformer Based on Transient Field-Circuit Coupled Model.

H. Zhong[1], Y. Wang[1], B. Peng[1] and Y. Yang[1]
1. Electrical Engineering School, Shandong University, Jinan, China

I. Introduction It is necessary to transmit electrical power from a stationary source to a rotating load or circuit in many industrial applications such as wound-rotor synchronous[1], doubly fed induction generator[2]-[4], radar power supplies[5] and so on. Although using of the brushed equipments is a simple, compact and low-cost solution, the presence of brushes and slip rings increases the maintenance costs and limits the machine only to non-explosive environments due to the mechanical wearing. To make a contactless maintenance-free solution, different brushless structures are proposed. This paper presents a novel rotary transformer for power supplying rotatable parts of electrical applications as a robust alternative to sliding contacts. The stator winding of the electrical machine is directly connected to the power grid while the stator(primary) winding of the rotary transformer is connected to power grid through power electronics converters and integrated control unit. This configuration can realize the indirect control of the torque, speed, power factor and current of induction by controlling the amplitude, frequency and phase of the rotary transformer primary winding voltage. The rotor winding of the electrical machine is electrically connected to the secondary winding of the transformer; consequently their currents have the same electric frequency. II. Structure Design of Rotary Transformer The structure of the rotary transformer in the plane is shown in Fig.1. One design challenge of the rotary transformer is the air gap of radial freedom to allow a small axial movement without affecting the electrical characteristics too much. The possible designs are limited by the constructive constraints such as the axial length l_{ax}, the outer diameter d_{out}, the desired air gap length c or the rotational speed n. A 3kVA rotary transformer parameters are designed using the core geometry Kg approach. Structural parameters and efficiency are two of the most important design specifications of the rotary transformer. Following with the traditional transformer design procedure and taking into account the characteristics of the rotary transformer, a transient calculation method coupling field-circuit mehtod is used in the design flow. The dimension calculation is performed by accurately analyzation the size and distribution of the magnetic field in the transformer core silicon steel laminations. The effect of the air gap is considered in the design to ensure that sufficient core area provided to prevent the core from saturation. III. Transient Nonlinear and Anisotropic Field-circuit Coupled Method A transient calculation method coupling field-circuit is presented considering nonlinear anisotropic magnetic properties of ferromagnetic materials in the transformer core silicon steel laminations. Transient calculation method coupling field-circuit has been improved compare with the traditional calculation method. The expressions of FE discretization are deduced in 3D transient eddy current field coupling field-circuit considering the electromagnetic characteristics of different materials such as anisotropy and isotropy and nonlinearity respectively. Nonlinear algebraic equations are solved by Newton-Raphson method which is common method to solve these equations, calculation accuracy of magnetic field of the rotary transformers can be improved greatly using this method. The field control equation is described as equation (1), where W_t is the turns of the transformer windings, S_t is the cross-sectional area of windings, A is the vector magnetomotive force. The discrete matrix is obtained by the Galerkin finite element method as equation (2), where j is the scalar magnetomotive force, N_j is the basis interpolated function, J_s is the source current density. The derivation of the nonlinear isotropic coefficient matrix by complex coefficient Newton - Raphson method was presented in [5]. Followed the similar derivation, the nonlinear anisotropic coefficient matrix of the field coupled equations is derived as equation (3), where c_e is determined by lamination coefficient c, shown in equation (4). Defined f_j as equation (5), the element of unit Jacobian matrix [J] is shown in equation (6). IV. Analysis and Verification The rotational speed of the rotary transformer is set to be 1200r/min in the calculation. The transient magnetic field of transformer core, distribution of loss density of no-load and the difference and size of exciting current change with time are analyzed. Magnetic flux density and no-load loss of the transformer model is calculated and analyzed. The validity and the correctness of the field-circuit coupled method is verified compared with the experimental results.

[1] Patin, N., Monmasson, E., Louis, J.P.: Modeling and control of a cascaded doubly fed induction generator dedicated to isolated grid, IEEE Trans. Ind. Electron., 2009, 56, (10). pp. 4207–4219 [2] H. Zhong, L. Zhao, and X. Li, Design and analysis of a three-phase rotary transformer for doubly fed induction generators, IEEE Trans. Ind. Appl., vol. 51, no. 4, pp. 2791–2796, Jul./Aug. 2015 [3] M. Ruviaro and F. Rüncos, "Analysis and test results of a brushless doubly fed induction machine with rotary transformer," IEEE Trans. Ind. Electron., vol. 59, no. 6, pp. 2670–2677, Jun. 2012. [4] M. Ruviaro, F. Runcos, and N. Sadowski, Wound Rotor Doubly Fed Induction Machine with Radial Rotary Transformer, Journal of Microwaves, Optoelectronics and Electromagnetics Applications, vol. 12, no. 2, pp. 1–16, 2013. [5]Zhu X Y, Cheng M, Zhao W X. A transient cosimulation approach to performance analysis of hybrid excited doubly salient machine considering indirect field-circuit coupling[J]. IEEE Transactions on Magnetics, 2007, 43(6):2558-2560

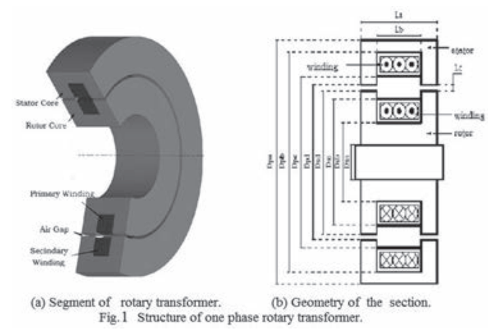

Fig. 1. Structure of one phase rotary transformer.

$$\frac{W_t}{S_t}\frac{\partial}{\partial t}\int_{\Omega} A h \mathrm{d}\Omega + RI + L\frac{dI}{dt} = u \qquad (1)$$

$$\begin{bmatrix} \int_V [\frac{1}{\mu}\nabla\times N_j\cdot\nabla\times() + \frac{1}{\mu}\nabla\cdot N_j\nabla\cdot() + \frac{1}{\mu}\frac{\partial N_j}{\partial t}\cdot()]\mathrm{d}V & \int_V \frac{1}{\mu}\frac{\partial N_j}{\partial t}\cdot\nabla()\mathrm{d}V \\ \int_{V_1}\frac{1}{\mu}\frac{\partial N_j}{\partial t}\cdot()\mathrm{d}V & \int_{V_1}\frac{1}{\mu}\frac{\partial N_j}{\partial t}\cdot\nabla()\mathrm{d}V \end{bmatrix}\begin{bmatrix} A \\ \varphi \end{bmatrix} = \begin{bmatrix} \int_V N_j\cdot J_s \mathrm{d}V \\ 0 \end{bmatrix} \qquad (2)$$

$$\sum_{e=1}^{NE}\int_{\Delta_e} c_e\left(\frac{\partial N_j^e}{\partial x}\frac{\partial A_z}{\partial x} + \frac{\partial N_j^e}{\partial y}\frac{\partial A_z}{\partial y}\right)\mathrm{d}x\mathrm{d}y + \sum_{e=1}^{NE}\int_{\Delta_e}\frac{\partial}{\partial t}\frac{1}{\mu_e}N_j^e A_z \mathrm{d}x\mathrm{d}y = \sum_{e=1}^{NE}\int_{\Delta_e} N_j^e J_{sz}\mathrm{d}x\mathrm{d}y \qquad (3)$$
$$(j = 1,2,3,\cdots,n)$$

$$c_e = \frac{3}{\frac{\mu_0}{1\ \ c} + c\mu_x + c\mu_y} \qquad (4)$$

$$f_j = \sum_{e=1}^{NE}\int_{\Delta_e} c_e\left(\frac{\partial N_j^e}{\partial x}\frac{\partial A_z}{\partial x} + \frac{\partial N_j^e}{\partial y}\frac{\partial A_z}{\partial y}\right)\mathrm{d}x\mathrm{d}y + \sum_{e=1}^{NE}\int_{\Delta_e}\frac{\partial}{\partial t}\frac{1}{\mu_e}N_j^e A_z \mathrm{d}x\mathrm{d}y \qquad (5)$$
$$(j = 1,2,3,\cdots,n)$$

$$\begin{aligned} J_{gh}^e\frac{\partial f_k^e}{\partial A_{zh}} &= \int_{\Delta_e} c_e \frac{\partial}{\partial A_{zh}}\left(\frac{\partial N_k^e}{\partial x}\frac{\partial A_z}{\partial x} + \frac{\partial N_k^e}{\partial y}\frac{\partial A_z}{\partial y}\right)\mathrm{d}x\mathrm{d}y \\ &+ \int_{\Delta_e}\left(\frac{\partial c_{ey}}{\partial A_{zh}}\frac{\partial N_k^e}{\partial x}\frac{\partial A_z}{\partial x} + \frac{\partial c_{ex}}{\partial A_{zh}}\frac{\partial N_k^e}{\partial y}\frac{\partial A_z}{\partial y}\right)\mathrm{d}x\mathrm{d}y \\ &+ \frac{\partial}{\partial t}\frac{1}{\mu_e}\int_{\Delta_e}\frac{\partial}{\partial A_{zh}}(N_k^e A_z)\mathrm{d}x\mathrm{d}y \end{aligned} \qquad (6)$$
$$(k = 1,2,3,\cdots,n) \qquad (g,h = i,j,m)$$

Fig. 2. Equations1-6

10:15

CH-06. Benefits of Synthetic Polymer Bonded Soft Magnetic Composites for Inductive Wireless Power Transfer Receivers in Electric Vehicles.

D. Barth[1], B. Klaus[1] and T. Leibfried[1]
1. Institute of Electric Energy Systems and High-Voltage Technology (IEH), Karlsruhe Institute of Technology (KIT), Karlsruhe, Germany

Abstract This paper displays the application of synthetic polymer bonded soft magnetic composites (SMC) as an alternative to ferrite backplates in inductive wireless power transfer (WPT) receivers. We analyze the influence of different shapes and the materials relative permeability on the coupling factor. Proximity effect loss and material processing are taken into account. Introduction Wireless charging is a crucial technology to increase the consumer acceptance of electric vehicles. Several publications present the investigation of WPT systems with a nominal power of several kilowatts, e.g. [1][2]. To increase coupling, the coils do usually have a high-permeable ferrite backplate or ferrite bars [3]. Soft magnetic ferrites are brittle, thus they are difficult to shape. Embedding the coil windings and the ferrite in a plastic housing keeps them in place. A soft magnetic polymer combines the magnetic benefits of ferrites and the structure and fabrication of synthetics. For this purpose, high-permeable ferrite is powdered and added to the polymer. The material must be compound to reach the desired permeability. It also has to be injection-moldable to receive the advantage of unlimited shaping. [4]. An existing application of such material is the flux guide in electrical machines [5]. For WPT systems, a similar approach to combine ferrite and concrete is presented in [6]. Analysis We use the magnetic resistance to describe the requirements of a good shape for the SMC. Assuming a current linkage Θ is given, the magnetic flux in a magnetic circuit is $\Phi=\Theta/R_m$, where R_m is the magnetic resistance. We can rewrite the magnetic coupling factor of two coils: $k = \mathrm{sqrt}(\Phi_{12}\ \Phi_{21}/\Phi_{11}\Phi_{22}) = \mathrm{sqrt}(R_{m,11}R_{m,22}/R_{m,21}R_{m,12})$ Because of symmetry, the magnetic circuits through both coils are identical, so we get $R_{m,21}=R_{m,12}=R_{m,h}$. The equation shows that increasing the coupling factor means decreasing the magnetic resistance of the main flux $R_{m,h}$ without decreasing the magnetic resistances of the stray flux. Figure 1 presents the proposed shape of the receiver unit ferrite. The figure is rotationally symmetric to the z-axis and shows two identical receiver coils with ten turns. While the coil on the top has a pure ferrite backplate, the second one contains SMC. Covering the windings with SMC from all sides would decrease the coupling factor, for it offers a path of low magnetic resistance for the stray flux. If the downside is left open, the SMC operates as a shielding in all directions besides towards the transmitter unit. Thereby it increases the coupling factor. Simulation The SMC is modeled as a distributed air-gap with an equable relative permeability [7]. To compare its shape to a ferrite backplate with varying permeability, we place the two receiver coils in figure 1 above the same transmitter coil. The coupling factor is calculated depending on the relative permeability of the receiver ferrite. Figure 2 shows that in this setup, the SMC with μ_r=30 achieves a better coupling factor than any possible backplate made of pure ferrite. Additionally, the coupling factor in this setup is already 94% of the maximum value that can be reached with μ_r>10000. Synthetic Polymer Bonded Soft Magnetic Composites, which allow complex shaping, do not have to be high-permeable as pure ferrites. The coupling factor increases only slightly if the permeability exceeds 100. The complex shaping of ferrite material has another advantage in high-power WPT systems. The SMC separates the windings. A layer of a material with μ_r>1 between the windings causes the magnetic flux not to be conducted in the windings and reduces the proximity effect loss. The external proximity effect loss that describes eddy current loss in a winding, caused by an external magnetic field, can be calculated using [8]: $P_{p,ext}=2*G*H_{rms}^2*l$ where G is the specific proximity effect factor depending on the conductor design and the frequency, H_{rms} is the average magnetic field strength (rms) in the winding and l is the length of the winding. To compare the setups in figure 1 regarding the average magnetic field strength in the conductors, the receiver designs must achieve the same coupling factor to have equal conditions. We choose μ_r=30 for the SMC and μ_r=3000 for the ferrite backplate. The average magnetic field strength in the conductor is about 30% less if we use the SMC. The equation above indicates that the external proximity effect loss reduces by more than 50%. Conclusion and details to come Synthetic polymer bonded soft magnetic composites can improve the performance and reduce proximity effect loss in inductive WPT systems although the relative permeability is low compared to pure ferrite. It is lightweight and its shaping is inexpensive using die casting. In high-performance applications, it can be combined with a ferrite backplate to maximize coupling. The full paper will contain a further analysis of the ferrite shape and how to optimize it, based on FEA-simulation. The saturation flux density and the coupling factor in case of coil misalignment will be included. Experimental validation of the simulation results is to come. The manufacturing of coils, embedded in ferrite composite, is in process. Due to the lack of SMC material that is purchasable, we will test only one product with μ_r=8.

[1] T. Shijo, K. Ogawa, M. Suzuki, Y. Kanekiyo, M. Ishida and S. Obayashi, "EMI reduction technology in 85 kHz band 44 kW wireless power transfer system for rapid contactless charging of electric bus," *2016 IEEE Energy Conversion Congress and Exposition (ECCE)*, Milwaukee, WI, 2016, pp. 1-6. [2] T. D. Nguyen, S. Li, W. Li and C. C. Mi, "Feasibility study on bipolar pads for efficient wireless power chargers," *2014 IEEE Applied Power Electronics Conference and Exposition - APEC 2014*, Fort Worth, TX, 2014, pp. 1676-1682. [3] M. Budhia, G. A. Covic and J. T. Boys, "Design and Optimization of Circular Magnetic Structures for Lumped Inductive Power Transfer Systems," in *IEEE Transactions on Power Electronics*, vol. 26, no. 11, pp. 3096-3108, Nov. 2011. [4] M. Anhalt and B. Weidenfeller, "Magnetic properties of polymer bonded soft magnetic particles for various filler fractions," *Journal of Applied Physics*, 101(2):023907, 2007. [5] M. Sarasa, "Einsatz neuer weichmagnetischer Werkstoffe bei elektrischen Maschinen im Kraftfahrzeug," *Dissertation*, Fakultät für Elektrotechnik und Informationstechnik, Universität der Bundeswehr München, Munich, 2005. [6] M. Esguerra and R. Lucke, "Anordnung magnetisierbarer Strukturen zur Maximierung der kontaktlos übertragbaren Leistung," *Patent*, Apr. 13, 2017, dE Patent App. DE201,510,012,950. [7] L. Michalowsky, "Weichmagnetische Ferrite: zum Aufbau von Präzisions-Hochfrequenzbauelementen für Kommunikationstechnik, Automobilindustrie und Industrieautomatisierung," expert-Verlag, 2006. [8] C. R. Sullivan and L. W. Losses, "Analytical model for effects of twisting on litz-wire losses," 2014 IEEE 15th Workshop on Control and Modeling for Power Electronics (COMPEL), Santander, 2014, pp. 1-10.

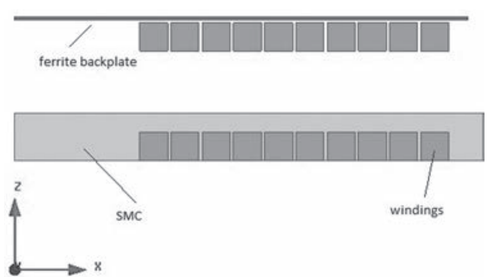

Fig. 1. Inductive WPT receivers with 10 windings and a ferrite backplate (top) or a SMC bonding (bottom).

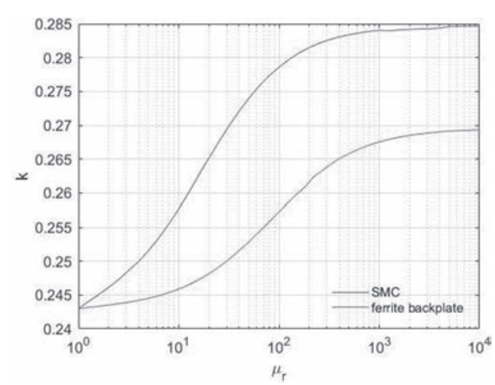

Fig. 2. The coupling factor depending on the relative permeability and different ferrite shapes in the receiver unit.

10:30

CH-07. Winding Losses Analysis of a 4 KVA High Frequency Coaxial Transformer Used in the Bi-Directional DC-DC Converter.

W. Water[1] and J. Lu[1]
1. Griffith University, South Brisbane, QLD, Australia

ABSTRACT This paper examines the winding losses characteristic of a 4 kVA high frequency coaxial transformer used in the bi-directional DC-DC converters. With consideration of nonlinear behavior of the magnetic material, the winding losses of the transformer can now be estimated more accurately. Three-dimensional (3-D) simulation techniques, in conjunction with the Finite Element Method (FEM) technique, were deployed. These techniques significantly improve the calculation accuracy of the winding resistance under any specific condition. Prototypes were built to validate the effectiveness of the simulation and computation results. The simulation result and the measurement result are consistent with less than 10% error. I INTRODUCTION The most common type of high frequency coaxial transformer (HFCT) only has a two cylinder copper winding within a stacked core tube, which is composed of numbers of ring cores [1]. A similar design was introduced by replacing the inner copper tubes with Litz wires as shown in [2]. This makes it suitable for MHz range and high power applications, but there are not too many advantages when implemented in lower power and middle frequency range applications. The improved structure HFCT with symmetrical multi-turns winding deployment was introduced in [3]. This enables the HFCT to operate at a lower frequency range of 100 to 300 kHz while having a scalability with a power range from hundreds of watts to dozens of kilowatts. Much research has been undertaken to study the HFCT, such as structural optimizations, magnetic and electric field simulations, and the analysis of the Faraday shield [4], [5]. However, a comprehensive winding loss analysis of the HFCT has not yet been conducted. This is mainly due to the complex geometrical structure of the HFCT and the nonlinearity characteristics of the magnetic materials. The analysis and simulation of the HFCT performance requires more comprehensive modelling and computation and it is now presented in this paper. II APPLICATION AND PROTOTYPES A.Application The introduced HFCT can be used in many applications that operate at high frequencies and high power conditions while requiring the galvanic isolation for safety purposes. An example of this is the ongoing project involving the high power density on-board Electric Vehicle (EV) charger. This bi-directional four-quadrant DC/AC converter has many functions, such as battery charging and discharging, power factor correction, active and reactive power compensation and uninterrupted power supply [6]. B.Final Transformer Prototype Two prototypes have been built to validate the design's effectiveness. To reduce the common-mode noise propagating to the secondary side, one prototype was built with the Faraday shield. The final prototype (right) weighs about 820 grams with a volume of 84.5 mm x 52 mm x 99.5 mm. In comparison, the HFCT without the Faraday shield is 10 mm lower in height and 30 grams lighter. III WINDING LOSS ANALYSIS A.Eddy Current Simulation Result It can also be justified from the result shown in Fig. 3 that the winding structure of the HFCT is optimal because of the evenly distributed current. Hot spots are observed on the turning corner of the windings, where the end region and coaxial section windings are connected. However, the variation of peak current density is relatively small at about 26.2% to 37.8% when compared with the average value. B.Winding Losses Breakdown With the assistance of the 3-D FEM technique, the HFCT winding losses breakdown can be obtained (results will be showed in full paper). Under the condition of 400 V and 10 A, the eddy current losses of different regions of the HFCT can be analyzed across a broad operating frequency range. The thickness of the Faraday shield is 0.1 mm, which is equivalent to 0.485 skin depth at 100 kHz. However, it still contributes approximately 21.6% loss to the overall loss under full load conditions. The eddy current loss of the Faraday shield is largely due to the coaxial. The AC/DC resistance ratio at 100 kHz is 3.9 for the round conductor implemented according to *Dowell's* equations [7]. However, the resistance AC/DC ratio of the secondary and the primary winding are 5.65 and 5.91 respectively in the simulation result. It can be justified that the proximity effect and eddy current effect are contributing an additional 44.8% to 51.54% in losses. C.Winding Resistance Measurement The impedance measurements were conducted with the use of a high frequency Microtest Transformer Analyzer. The ambient temperature is stable at roughly 20 to 25°C, and both the open circuit and short circuit calibrations were conducted prior to testing. As expected, the winding resistance increases with the increased operating frequency. Results of the winding resistance comparison are shown in Fig. 2. The winding resistance does not increase dramatically until the operating frequency is above 200 kHz. Grounding or ungrounding of the Faraday shield had little effect on winding resistance. A comparison of the winding resistance measurement result with the simulation result indicates that they are consistent whereas the variation in difference is only 3.5% to 7.2% for the non-shielded case and 0.3%~2.3% for the shielded case. V ACKNOWLEDGMENT The work was supported by the *Advance Queensland Research Fellowship Program* from the Queensland Government, Elevare Energy and Griffith University.

[1] D. M. Divan, "Design considerations for high power high frequency transformers," *21st Annual IEEE Conference on Power Electronics Specialists*, San Antonio, TX, USA, 1990, pp. 734-742 [2] M. S. Rauls, D. W. Novotny and D. M. Divan, "Design considerations for high-frequency coaxial winding power transformers," in *IEEE Transactions on Industry Applications*, vol. 29, no. 2, pp. 375-381, Mar/Apr 1993. [3] Junwei Lu and Fu Wong, "High frequency coaxial transformer with faraday shield," *INTERMAG 2000 Digest of Technical Papers. 2000 IEEE International Magnetics Conference*, Toronto, ON, Canada, 2000, pp. 442-442. [4] W. Water and J. Lu, "Shielding Analysis of High-Frequency Coaxial Transformers Used for Electric Vehicle On-Board Charging Systems," in *IEEE Transactions on Magnetics*, vol. 49, no. 7, pp. 4005-4008, July 2013. [5] J. Li, W. Water, B. Zhu and J. Lu, "Integrated High-Frequency Coaxial Transformer Design Platform Using Artificial Neural Network Optimization and FEM Simulation," in *IEEE Transactions on Magnetics*, vol. 51, no. 3, pp. 1-4, March 2015. [6] E. Sortomme and M. A. El-Sharkawi, "Optimal Charging Strategies for Unidirectional Vehicle-to-Grid," in *IEEE Transactions on Smart Grid*, vol. 2, no. 1, pp. 131-138, March 2011. [7] P. L. Dowell, "Effects of eddy currents in transformer windings", *Proceedings of the Institution of Electrical Engineers*, vol. 113, no. 8, pp. 1387-1394, Aug. 1966.

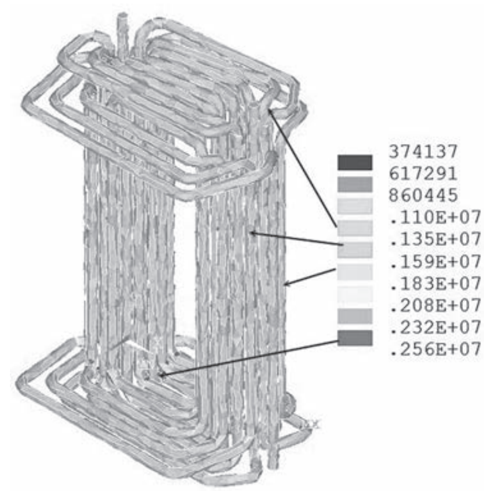

Fig. 1. Current distribution of windings under full load conditions (A/m²)

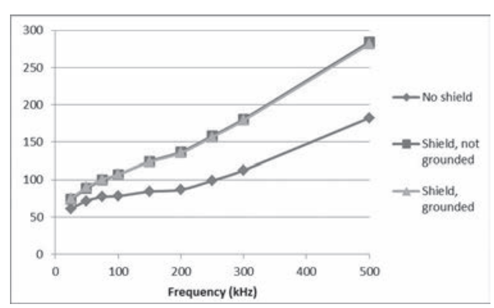

Fig. 2. Comparison of HFCT winding resistance (mΩ)

10:45

CH-08. Leakage Flux based turn-to-turn Fault Detection for Shunt Inductor.

B. Chen[1], *J. Dong*[1], C. Tian[1] and Q. Chen[1]
1. Wuhan University, Wuhan, China

I INTRODUCTION Dry-type iron-core inductors in urban high-voltage substation reactive power local balance and reasonable control of voltage fluctuations plays an important role [1]. As its number of applications and uptime increase, the amount of failure must also increase. The most common events of dry-coil devices are interturn faults, which can damage the insulation of the coil and even burn the device when a large current generated in the short-circuit loop. Right now, the low-voltage dry-type iron-core inductors lack a special inter-turn fault detection method and generally use overcurrent protection and temperature detection protection. The zero-sequence and negative-sequence power direction protection are mostly used for ultrahigh-voltage inductors protection[2-3]. Therefore, this paper proposes to use the difference of the distribution characteristics of space magnetic field in normal operation and inter-turn fault as the criterion of on-line detection algorithm for turn-to-turn fault [4-5]. In this paper, a field-circuit coupled finite element model of a three-phase iron-core inductor is established. The distribution characteristics of the spatial magnetic field under normal operating conditions and different inter-turn fault conditions are simulated and analyzed. This result provides a theoretical basis for the inductor on-line detection algorithm of non-contact turn-to-turn fault. II SIMULATION RESULTS UNDER NORMAL CONDITIONS In this paper, field-coupled finite element model of BKSC-5000/10 parallel core inductor is simulated. Fig.1 (a) shows a half-length longitudinal cross-sectional view of a dry core inductor and its simplified simulation. Fig.1(b) shows the amplitude of magnetic flux density, the radial component BX and the axial component BY curve in the axial path from the outermost layer of inductor A phase winding 10mm. The calculated path is the same height as the windings in Fig.1 (a), with coordinates of 0-1550 mm from bottom to top. The axial component of magnetic flux density on this path is symmetrical about the horizontal axis L1, and its value is approximately the same in the middle section of the winding but varies greatly at the end. The radial component BX of the magnetic flux density is odd-symmetrical about the horizontal axis L1. The component direction of the field at the symmetry point of the horizontal axis L1 is opposite and the value of the end position is larger. The amplitude curve of the magnetic flux density is symmetrical about the central axis L1, and the strength of the leakage magnetic field at the end of the winding is significantly greater than that of the mid-section. III INTERTURN FAULT SIMULATION RESULTS Fig.2 (a) shows the core inductor windings occur in different turns of the inter-turn short when the reference path of the magnetic flux density curve. As the number of shorted turns increases, the magnetic flux leakage flux of the path increases as a whole. Meanwhile, the degree of asymmetry of the path along the horizontal axis L1 gradually increases, and the field asymmetry Diff1<Diff6 <Diff10 <Diff13. Fault detection algorithm can be based on changes in the degree of asymmetry of the magnetic field to determine the occurrence and severity of inter-turn short circuit. Fig.2 (b) shows the induced voltage curves of two symmetrical induction coils on the measurement path outside the winding when turn-to-turn fault occurs in the iron-core inductor windings. From Fig.2 (b), under normal operating conditions (0-20ms), the induced voltage of the coil is approximately zero. After the inter-turn fault occurs in the winding (20-100ms), the induced voltage Vfault of the coil at the fault position and the symmetrical position coil Induced voltage Vsys phase opposite and greater amplitude, Vout coil output voltage in series, much larger than the measured values under normal conditions. IV CONCLUSION In this paper, based on the field-coupled finite element simulation model, the distribution of magnetic field in the iron-core inductor under normal operating conditions and inter-turn fault conditions is analyzed. The following conclusions are drawn: under normal operating conditions, the leakage flux density of core reactors is small, and their spatial magnetic fields are longitudinally symmetrical. Under asymmetrical turn-to-turn conditions, the asymmetry of the magnetic field increases with the increase of short turns. The asymmetry of the space magnetic field under the inter-turn fault can be used as the criterion of the interturn fault detection algorithm.

[1] Haghjoo F, Mostafaei M. Flux-based method to diagnose and identify the location of turn-to-turn faults in transformers[J]. IET Generation Transmission & Distribution, 2016, 10(4):1083-1091. [2] Haghjoo F, Mostafaei M, Mohammadi H. A New Leakage Flux Based Technique for Turn to Turn Fault Protection and Faulty Region Identification in Transformers[J]. IEEE Transactions on Power Delivery, 2017, PP(99):1-1. [3] Haghjoo F, Mohammadi H. Planar Sensors for Online Detection and Region Identification of Turn-to-Turn Faults in Transformers[J]. IEEE Sensors Journal, 2017, PP(99):1-1. [4] Cabanas M F, González F P, Melero M G, et al. Insulation Fault Diagnosis in High Voltage Power Transformers by Means of Leakage Flux Analysis[J]. 114,(2011), 2011, 114(8):211-234. [5] GE Shaojie, DONG Wanguang. Burnout Fault Analysis of 10 kV Dry-type Reactor[J]. Power Capacitor and Reactive Power Compensation, 2015, 36(2):89-92.

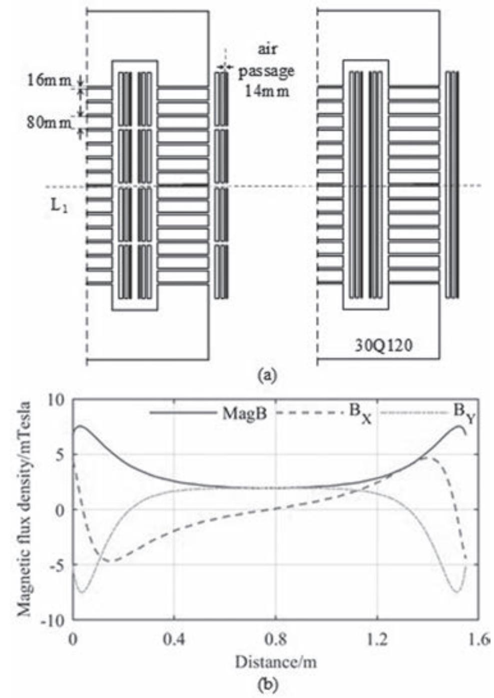

Fig. 1. (a) Longitudinal section diagram of an iron-core reactor (b) The amplitude of magnetic induction intensity and B_X and B_Y components on the axial path

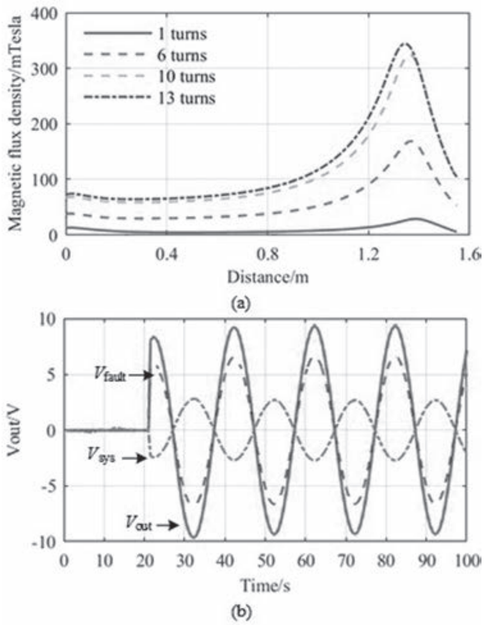

Fig. 2. (a) Magnetic induction intensity of different number of short turns (b) Turn-to-turn short circuit to measure the coil induced voltage

11:00

CH-09. Auto-transformer and Magnetic Control Soft Start Method of Super Large Capacity and High Voltage Motor Considering the Cost and Performance Optimization.

J. Yuan[1], *C. Wang*[1], Y. Zhu[1], H. Zhou[1], L. Wei[1,2], C. Tian[1], Y. Gao[3], K. Muramatsu[3] and B. Chen[1]
1. Electrical and Engineering, Wuhan University, Wuhan, China;
2. Department of Electrical Engineering, Graduate School of Engineering, Kyoto University, Kyoto, Japan; 3. Department of Electrical and Electronic Engineering, Saga University, Saga, Japan

I. Introduction The start current can reach up to as high as 4-7 times of the motor's rated current when high voltage motors start directly. For super large capacity motors (voltage above 6 kV, power above 10000 kW), the direct start current could reach 5000 Ampere or more[1]. Such large start current will not only have a huge impact on the motor itself but also cause a sudden decline of the grid voltage[2]-[3]. The main way is the step-down start method such as auto-transformer soft start and magnetic control soft start. However, the secondary impact exists during auto-transformer soft starting and the cost of magnetic control starter is too high[4]. This paper proposed a novel auto-transformer and magnetic control (ATMC) soft start method of super large capacity and high voltage induction motor. Firstly, the basic working principle of the proposed method is analyzed. In addition, the calculation formulas of cost for magnetic control soft starter and ATMC soft starter are deduced, and specific examples are analyzed and compared. Finally, simulation results verify the effectiveness of the proposed soft start method. II. Basic Principle Fig.1 (a) shows the topological diagram of auto-transformer and magnetic control soft starter. The starting procedure can be divided into the following three parts. At first, thyristor T of the magnetic control reactor (MCR) is turned off, the winding N_1 of MCR and the additional winding N_2 constitute an auto-transformer to reduce motor terminal voltage. After it, motor terminal voltage is gradually increasing, disconnect from the winding N_2 and the motor is connected in series with MCR. By controlling the turn-on angle of the thyristor T, the DC control current is generated, so that the core of the reactor is magnetically saturated, and the equivalent reactance value is reduced to achieve constant current start. When the motor is approaching the rated speed, disconnect the soft starter. III. Cost Comparison Here are the calculation formulas of C_1(cost for magnetic control soft starter) and C_2(cost for auto-transformer and magnetic control soft starter): $C_1=xk_{set}^2I_n^2(((U_1/(k_{set}I_n))^2\text{-}R_k^2)^{0.5}\text{-}X_k\text{-}X_s)$ (1) $C_2=(xk_{set}^2I_n^2(R_k^2+(X_k+X_s)^2)^{0.5})/k+(xk_a^2U_1^2X_{L2})/(R_{ck}^2+(X_{ck}+X_s)^2)$ (2). Take 12500kW/10kV motor for example, we get the comparison diagram for C_1, C_2 and C_1-C_2 versus start current multiple k_{set} when the tap ratio of auto-transformer k_a is equal to 0.8 shown in Fig.1 (b). When k_{set}=1.25, C_1 minus C_2 reaches the maximum which is 0.91×106x, C_1 is 32% higher than C_2. Therefore, we can get the conclusion: the choice of auto-transformer with appropriate tap ratio can greatly reduce the cost of ATMC soft starter compared with the cost of magnetic control soft starter under the same starting requirement. IV. Simulation Results and Conclusion According to the conclusion of the cost calculation, the total cost of the auto-transformer and magnetic control soft starter is reduced as much as possible by selecting the appropriate tap ratio of the auto-transformer. Motor parameter setting is given as follows: rated power is 18MW, rated voltage is 10kV, rated current is 1.039kA, rated speed is 1500r/min. The simulation results for three start methods, namely direct start, auto-transformer soft start and auto-transformer and magnetic control soft start, are shown in Fig.2. Fig.2 (a) shows that when the motor starts directly, the stator current reaches as high as more than 5000 A. It is about 5 times of the rated current. Such large start current will be harmful to the grid and the motor. The starting current can be reduced to about 2.5 times of the rated current when using ATMC soft start method. Fig.2 (a) and (b) show that there is obvious secondary current and torque impact during auto-transformer soft starting. Fig.2 (c) shows that start time of ATMC soft starter is about 15s which is 5s less than auto-transformer soft starter. Therefore, the auto-transformer and magnetic control soft start method can effectively reduce the starting current, eliminate the secondary impact, have fast response speed and starting performance is smooth and stable. In addition, more detailed analysis and experimental studies will be analyzed in the full paper.

[1] W. Huang, Y. Yuan, Y. Chang, "A Novel Soft Start Method Based on Autotransformer and Magnetic Control," *International Conference on Industrial Technology*, pp. 2108-2113, March 2016.[2] S.-K. Kim and T.-K. Kim, "A Novel Hybrid Sequential Start Control System for Large Inductive Loads," *Jouranl of Electeical Engineering & Technology*, vol. 10, no. 1, pp. 388-394, January 2015.[3] M. Falahi, K. Butler-Purry, and M. Ehsani, "Induction Motor Starting in Islanded Microgrids," *IEEE Transactions on Smart Grid*, vol. 4, no.3, pp. 1323-1331, September 2013.[4] X. Chen, B. Chen, C. Tian, J. Yuan, and Y. Liu, "Modeling and harmonic optimization of a two-stage saturable magnetically controlled reactor for an arc suppression coil,". *IEEE Transactions on Industrial Electronics*, vol. 59, no. 7, pp. 2824–2831, July 2012.

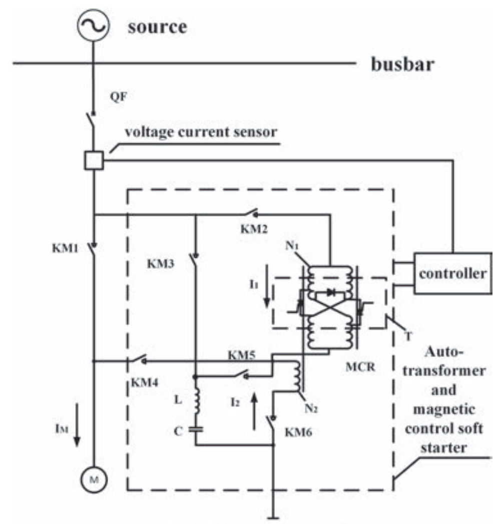

(a) Topological diagram of ATMC soft starter

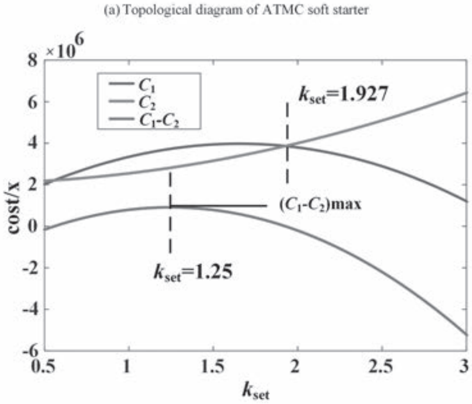

(b) Comparison diagram for C_1, C_2 and C_1-C_2 versus k_{set} when k_a=0.8

Fig. 1. Theoretical analysis of ATMC soft starter and cost comparison

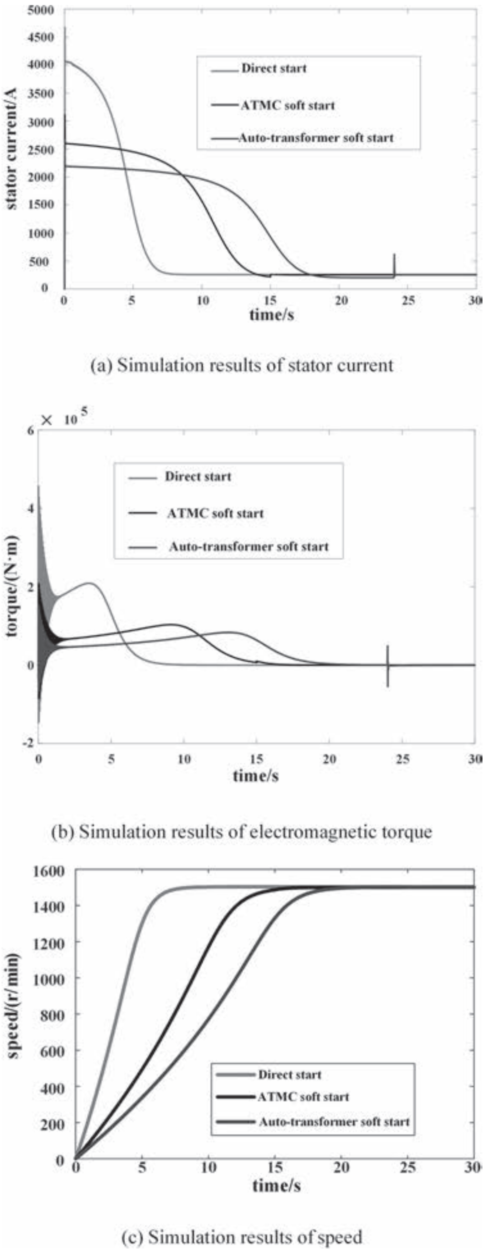

(a) Simulation results of stator current

(b) Simulation results of electromagnetic torque

(c) Simulation results of speed

Fig. 2. Simulation results for three start methods

11:15

CH-10. Fast Three-dimensional Optimization of Magnetic Cores for Loss and Volume Reduction.

S. Shimokawa[1], H. Oshima[1], K. Shimizu[2], Y. Uehara[2], J. Fujisaki[2], A. Furuya[2] and H. Igarashi[3]
1. Fujitsu Laboratories Ltd., Atsugi, Japan; 2. Fujitsu Limited, Kawasaki, Japan; 3. Hokkaido University, Sapporo, Japan

I. INTRODUCTION Power electronic devices have been widely applied such as in consumer devices and electrical vehicles, and improvement of their efficiency is strongly required. One of the main factors of energy loss in the devices is the magnetic core loss in inductors and transformers. Therefore, simulation technology that realizes accurate energy loss estimation based on magnetic characteristics of the materials has been highly demanded. For this reason, we have been developing large-scale magnetic field simulation technology by combining micromagnetic models and the finite element method (FEM) [1]. One the other hand, structural design optimization for devices with complicated shapes requires huge man-hours, and it is difficult to judge whether the designed shape is sufficiently optimized. Genetic algorithm (GA) is widely used in various optimal design problems for its excellent global search capabilities. However, GA generally requires large numbers of simulations, and it takes a long time to search the optimal solution. To solve this problem, neural networks (NN) are applied as surrogate models instead of physics models to reduce computing time in some previous work [2]. In this work, we perform shape parameter optimization of an EI-shaped inductor using GA and NN surrogate models designed from magnetic simulation results. Magnetic loss and volume of the cores are chosen to be objective functions. Few previous works have been reported on optimization studies with magnetic core loss as an objective function [3]. Here we solve multi-objective optimization problems, and Pareto optimal fronts for various inductance values are obtained. We also show that experiment that employs one of the optimal design parameters presents good agreement within 10% with the simulation results. II. METHOD Fig. 1 shows a structure of the EI-shaped ferrite core. In general, larger inductance value can be realized by expanding the cross-sectional area of a magnetic flux flow under the condition of fixed external dimensions. However, it also causes increase in magnetic loss and volume (mass) of the core. Therefore, in this work, magnetic loss and volume are set as objective functions under constraints of various inductance values (lower limit) as well as external dimensions and minimum coil winding space. In magnetic simulation, we employed the FEM that includes the dielectric effect at grain boundaries in ferrite material to take account of the size effect at high frequency [4]. For magnetic hysteresis modeling, we adopted the play model [5] and fitted parameters of the model by using experimental results of B-H curves of a Mn-Zn ferrite toroidal core measured at a low frequency (10 kHz). The average magnetic flux density in the center pole of the E-shaped core was set to be 200 mT at the driving frequency of 100 kHz. For multi-objective optimization search, we employed SPEA2 (Strength Pareto Evolutionary Algorithm-II) combining with NN surrogate models designed using magnetic simulation results. To design the surrogate models of inductance and magnetic loss, one thousand magnetic simulation data with randomly generated six shape parameters were used. The number of the intermediate layer and its size was set to 1 and 10, respectively. As a result of the NN design for both inductance and magnetic loss, we obtained the coefficient of determinations R^2 of more than 0.999 between magnetic simulation results and NN outputs. Volume of the core is calculated from shaped parameters. III. RESULTS Fig.2 shows the results of multi-objective optimization for minimum magnetic loss and volume of the core. For optimization settings, number of population and generations are both set to 50, while crossover rate and mutation rate are set to 0.7 and 0.3. In addition, lower limit of inductance value L_{LC} is set to 41, 43, 45, 47 and 49 μH. The black plots and the red plots show Pareto optimal fronts obtained by the NN surrogate models and the magnetic simulation, respectively. One optimal search takes about 0.1 hours by the NN surrogate models, while it needs 83 hours by the magnetic simulation. As can be seen from the figure, the Pareto optimal fronts are obtained for each L_{LC} by the NN surrogate models. When L_{LC} becomes smaller, the Pareto optimal fronts become wider and the degrees of freedom in the design for minimizing both magnetic loss and volume become larger. It is also confirmed that the Pareto optimal fronts obtained from the NN surrogate models and the magnetic simulation at L_{LC} = 49 μH are reasonably similar. We conducted experiment in one condition of the Pareto optimal fronts at L_{LC} = 49 μH to verify the simulation results. As a result, the inductances evaluated from the experiment and the simulation are 48.6 μH and 48.8 μH (+0.4%), respectively, and the losses evaluated from the experiment and the simulation are 3.68 W and 3.34 W (-9.2%), respectively. These results show good agreement, and we also found that the error in the loss is reduced by using finer mesh in the FEM model of core. In further simulation studies with more shape parameters, we found that the reduction of the volume while keeping the loss can be achieved by cutting off the four external corners, where magnetic flux density significantly decreases compared to the main magnetic flux paths.

[1] H. Oshima, Y. Uehara, K. Shimizu, K. Inagaki, A. Furuya, J. Fujisaki, M. Suzuki, K. Kawano, T. Mifune, T. Matsuo, K. Watanabe and H. Igarashi, "Experimental and Simulation Modeling Studies of Magnetic Properties of Ni-Zn Ferrite Cores", Abstract of ICF11, (2013). [2] H. Sasaki and H. Igarashi, "Topology optimization of rotating machines using deep learning: a fundamental study", The Papers of Joint Technical Meeting on "Static Apparatus" and "Rotating Machinery", IEE Japan, SA-17-081, RM-17-112, (2017). [3] T. Sato, S. Aya, H. Igarashi, M. Suzuki, Y. Iwasaki and K. Kawano, "Loss Computation of Soft Magnetic Composite Inductors Based on Interpolated Scalar Magnetic Property", IEEE Trans. Magn., vol. 51, 3, (2015). [4] K. Shimizu, A. Furuya, Y. Uehara, J. Fujisaki, T. Ataka, T. Tanaka, and H. Oshima, "Method of Finite Element Analysis Considering Dimensional Resonance under High Frequency Excitation", The Annual Meeting Record, IEE Japan, (2017). [5] T. Matsuo and M. Shimasaki, "Two Types of Isotropic Vector Play Models and Their Rotational Hysteresis Losses", IEEE Trans. Magn. vol. 44, 6 (2008).

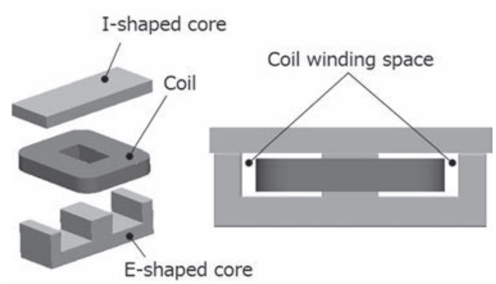

Fig. 1. Structure of the EI-shaped ferrite core.

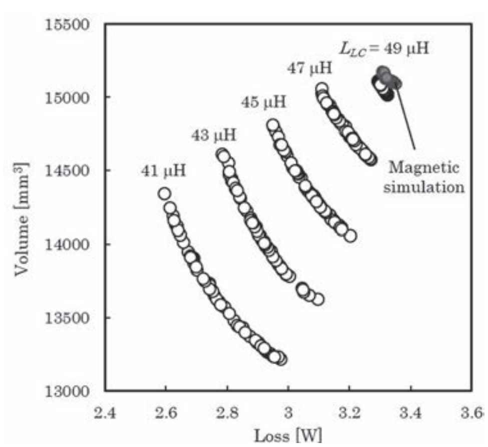

Fig. 2. Results of multi-objective optimization for minimum magnetic loss and volume of the core.

WEDNESDAY MORNING, 25 APRIL 2018 SIMPOR/ROSELLE BALLROOM, 8:30 TO 11:30

Session CP
MAGNETIC THERAPIES AND NANOMEDICINE I
(Poster Session)

Yuko Ichiyanagi, Chair
Yokohama National University, Yokohama, Japan

CP-01. Alteration in motor cortical excitability induced by peripheral stimulation with magnetic stimulation.

A. Sato[1], T. Torii[1], M. Iwahashi[1] and K. Iramina[2]
1. Medical Care and Welfare Engineering, Tokai University, Kumamoto, Japan; 2. Graduate School of Systems Life Sciences, Kyushu University, Fukuoka, Japan

1. Introduction In recent years, the conditioning of cortical excitability has attracted attention as a valuable function to the recovery of motor function after stroke. Motor cortical excitability can be altered by transcranial magnetic stimulation (TMS), and by peripheral stimulation [1-3]. This study focused attention on the effects of peripheral stimulation on cortical excitability because TMS is not provided for all patients. Many studies of peripheral stimulation have not focused on the inhibition of cortical excitability. This study investigated the possibility that peripheral stimulation has an adjustment effect of motor cortical excitability, by examining the inhibition of cortical excitability induced by peripheral stimulation. This study used magnetic stimulation as peripheral stimulation, because the eddy currents induced by magnetic stimulation stimulate deeper tissue regions. 2. Methods A total of 26 healthy participants (right-handedness) were enrolled. The experimental paradigm was divided into three phases. In the first phase, TMS (0.1 Hz, 105% of each participant's resting motor threshold) was delivered to the left or right primary motor cortex to evoke motor evoked potential (MEP) from the contralateral first dorsal interosseous muscle. The measured MEPs in this phase were used to evaluate the effect of the peripheral stimulation as a baseline. In the second phase, peripheral stimulation (1 Hz magnetic stimulation, 100 pulses) was applied over the contralateral or ipsilateral forearm for the target motor cortex, immediately after the first phase. Finally, in the third phase, TMS was performed according to the same set up as in the first phase, and MEPs induced by TMS were also recorded. The effects of peripheral stimulation on motor cortical excitability were evaluated by comparing the mean MEP amplitudes recorded in the first phase and third phase. 3. Results Fig. 1 shows the normalized average MEP amplitude. Because there were individual differences in the MEP amplitudes induced by TMS, we performed normalization using each control condition (before peripheral stimulation). For the contralateral forearm for the left motor cortex, the average MEP amplitude after peripheral stimulation was significantly decreased compared with the average MEP amplitude before peripheral stimulation ($n=13$, $p<0001$). In contrast, no significant difference was observed in the contralateral forearm for the right motor cortex ($n=12$, $p=0.3$). The mean decrease in average MEP amplitude was approximately 65 %. For the ipsilateral forearm for left and right motor cortex, the average MEP amplitude after peripheral stimulation was significantly increased compared with the average MEP amplitude before peripheral stimulation (for the left motor cortex: $n=15$, $p<0.01$, for the right motor cortex: $n=11$, $p<0.05$). The mean increases in average MEP amplitude were approximately 142 % (left motor cortex) and 154 % (right motor cortex). 4. Discussion Previous TMS studies have reported that the inhibition of motor cortical excitability elicited by suprathreshold repetitive TMS may be based on afferent feedback activation related to peripheral muscle twitch induced by TMS [4,5]. This study provided magnetic stimulation of the forearm to induce the inhibition of motor cortical excitability. This study found an alteration in MEP amplitude following peripheral stimulation. Because MEP amplitude is used to evaluate the excitability of the corticospinal tract [6], changes of the MEP amplitude observed in this study may have an influence on motor cortical excitability. In the contralateral forearm for the left motor cortex, a decrease in MEP amplitude was observed after peripheral stimulation. This result suggests that the inhibition of cortical excitability of the left motor cortex was induced via peripheral stimulation over the contralateral forearm. A previous rTMS study incorporating functional magnetic resonance imaging (fMRI) suggested that the afferent feedback from muscle movements induced by supra-threshold rTMS may represent the dominant input to the motor system via the primary motor cortex [7]. Thus, we expected that the afferent feedback due to muscle twitch such as suprathreshold rTMS caused inhibition of cortex excitability due to the peripheral stimulation. In contrast, in the contralateral forearm for the right motor cortex, no significant changes in mean MEP amplitude were observed after peripheral stimulation. In this result, it should be noted that all participants in the current experiment were right-handedness. Right-handed has been associated with distinct anatomical asymmetry of the left hemisphere [8]. Thus, this study speculates that handedness-related cerebral asymmetry may be associated with the differences in cortical excitability observed in this study. Next, in the ipsilateral forearm for each motor cortex, increases in MEP amplitude were observed after peripheral stimulation. This increased MEP amplitude suggests that peripheral stimulation may have affected the facilitation of motor cortical excitability. The stimulation due to peripheral stimulation for the ipsilateral forearm may be caused by excitatory information to the cerebral cortex of the dominant side, and then transmitted to the cerebral cortex of the non-dominant side through the corpus callosum. The results of this study suggested that peripheral stimulation may have an adjustment effect on motor cortical excitability by the change of the stimulation site.

[1] F. Maeda, J. P. Keenan et al.: Modulation of corticospinal excitability by repetitive transcranial magnetic stimulation. Clin Neurophysiol 111, pp. 800-805 (2000) [2] Pascual-Leone A, Valls-Solé et al.: Responses to rapid-rate transcranial magnetic stimulation of the human motor cortex. Brain 1117 (Pt 4), pp, 847-858 (1994) [3] Struppler A, Binkofski et al.: A fronto-parietal network is mediating improvement of motor function related to repetitive peripheral magnetic stimulation: A PET-H2O15 study. NeuroImage 36, pp. T174-T186 (2007) [4] Chen R, Classen J et al.: Depression of motor cortex excitability by low-frequency transcranial magnetic stimulation. Neurology, 48(5), pp. 1398-1403 (1997) [5] Lang N, Harms J et al.: Stimulus intensity and coil characteristics influence the efficacy of rTMS to suppress cortical excitability. Clin Neurophysiol, 117(10), pp. 2292-2301 (2006) [6] Petersen NT, Pyndt HS, Nielsen JB: Investigating human motor control by transcranial magnetic stimulation. Exp Brain Res., 152(1), pp. 1-16 (2003) [7] Bestmann S, Baudewig J et al.: Functional MRI of the immediate impact of transcranial magnetic stimulation on cortical and subcortical motor circuits. Eur J Neurosci, 19(7), pp. 1950-1962 (2004) [8] Corballis MC,: Cerebral asymmetry: motoring on.", Trends Cogn Sci., 2(4), pp. 152-157 (1998)

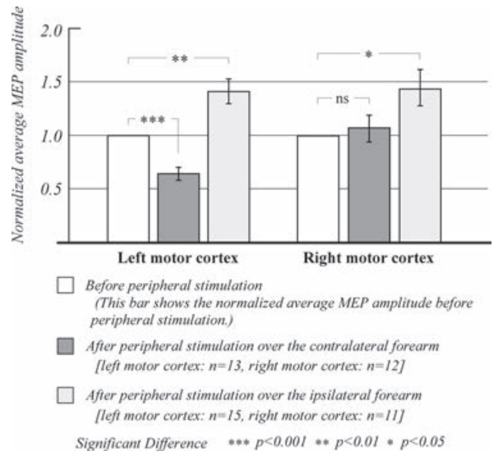

Fig. 1. Comparison of MEP amplitude evoked by peripheral stimulation

CP-02. Transcranial magnetic stimulation: design of a high current magnetic pulse generator with custom coil for the application on small animals.

J. Selvaraj[1], P. Rastogi[1], N. Prabhu Gaunkar[1], *R.L. Hadimani*[2,1] and M. Mina[1,3]

1. Department of Electrical and Computer Engineering, Iowa State University, Ames, IA, United States; 2. Dept. of Mechanical and Nuclear Engineering, Virginia Commonwealth University, Richmond, VA, United States; 3. Department of Industrial Design, Iowa State University, Ames, IA, United States

Transcranial Magnetic Stimulation (TMS) is a non-invasive and outpatient treatment for Major Depressive Disorder (MDD)[1]. It has also proven to produce beneficial effects for other neurological and psychiatric disorders including: Parkinson's Disease (PD), Obsessive Compulsive Disorder (OCD), Anxiety, Post-Traumatic Stress Disorder (PTSD) and Schizophrenia [2]–[6]. Recently, researchers have shown interest in investigating the effect of TMS in neurological disorders which have not been explored by utilizing animal studies [7]. Animal studies are required to test the efficacy and safety of the treatments before using the new treatment in human subjects. Furthermore, animal studies can reduce research cost and speed up the development of new TMS treatment procedures. That is why it is important to have flexible and tunable hardware/coil solutions that allow tenability of power, current, and the shape of the signals needed for experimentation. TMS is based on the principal of Faraday's law of induction, in which time-varying magnetic fields are used to induce an electric field in the brain. Substantial research has been published related to the improvement of coil designs, using head models and clinical studies. However, few publications are available on TMS stimulators and even less on TMS stimulators for use on small animals such as rodents and mice. Current commercial TMS stimulators are very expensive and they have limited usage due to the coil's unique geometry and size. Perhaps an important contrasting is that commercial coils are large enough to stimulate the entire body of the small animal, so studies needed to focally stimulate part of the brain are impossible. Hence, in this article a novel design for a small size TMS stimulator has been proposed. TMS stimulator has been designed for the stimulation of small animals, namely mice and other rodents. This new design was created to focally stimulate parts of rodent brain instead of stimulating their whole body when a commercial coil is used. This will provide researchers an opportunity to choose small TMS coils since commercial TMS stimulators do not support small inductive loads [8]. Mice brains are very small in size when compared with human brains that consist of approximately 2 cm^2 surface area, whereas human brains have about 100 times more surface area [9]. This small area allows the distance between the coil and the surface of the brain to be small hence the field needed to stimulate the brain to initiate action potential is about 0.1Tesla [7]. This means the circuit designed has to be capable of handling current more than 300 A. In addition, the proposed design provides additional flexibility, so that the coil can be changed to match the required specification of other coil designs for different locations of stimulation. Figure 1 shows the TMS stimulator and a coil positioned on a mice model.

[1] R. R. Ji, T. E. Schlaepfer, C. D. Aizenman, C. M. Epstein, D. Qiu, J. C. Huang, and F. Rupp, "Repetitive transcranial magnetic stimulation activates specific regions in rat brain.," Proc. Natl. Acad. Sci. U. S. A., vol. 95, no. 26, pp. 15635–15640, 1998. [2] M. E. Keck, I. Sillaber, K. Ebner, T. Welt, N. Toschi, S. T. Kaehler, N. Singewald, A. Philippu, G. K. Elbel, C. T. Wotjak, F. Holsboer, R. Landgraf, and M. Engelmann, "Acute transcranial magnetic stimulation of frontal brain regions selectively modulates the release of vasopressin, biogenic amines and amino acids in the rat brain," Eur. J. Neurosci., vol. 12, no. 10, pp. 3713–3720, 2000. [3] F. Paes, T. Baczynski, F. Novaes, T. Marinho, O. Arias-Carrión, H. Budde, A. T. Sack, J. P. Huston, L. F. Almada, M. Carta, A. C. Silva, A. E. Nardi, and S. Machado, "Repetitive Transcranial Magnetic Stimulation (rTMS) to Treat Social Anxiety Disorder: Case Reports and a Review of the Literature.," Clin. Pract. Epidemiol. Ment. Health, vol. 9, pp. 180–8, 2013. [4] M. S. George, S. H. Lisanby, D. Avery, W. M. McDonald, V. Durkalski, M. Pavlicova, B. Anderson, Z. Nahas, P. Bulow, P. Zarkowski, P. E. Holtzheimer, T. Schwartz, H. A. Sackeim, R. AJ, S. AF, F. E, S. N, T. T, G. H, Z. A, S. M, and S.-L. C, "Daily Left Prefrontal Transcranial Magnetic Stimulation Therapy for Major Depressive Disorder," Arch. Gen. Psychiatry, vol. 67, no. 5, p. 507, May 2010. [5] M. Isserles, A. Y. Shalev, Y. Roth, T. Peri, I. Kutz, E. Zlotnick, and A. Zangen, "Effectiveness of deep transcranial magnetic stimulation combined with a brief exposure procedure in post-traumatic stress disorder--a pilot study.," Brain Stimul., vol. 6, no. 3, pp. 377–83, May 2013. [6] M. Kobayashi and A. Pascual-Leone, "Transcranial magnetic stimulation in neurology," Lancet Neurol., vol. 2, no. 3, pp. 145–156, 2003. [7] P. Rastogi, R. L. Hadimani, and D. C. Jiles, "Investigation of Coil Designs for Transcranial Magnetic Stimulation on Mice," IEEE Trans. Magn., vol. 52, no. 7, pp. 1–4, Jul. 2016. [8] C. Hovey, C. Hovey, R. Jalinous, and R. Jalinous, "The guide to magnetic stimulation," Polym. Contents, vol. 20, no. 4, pp. 284–287, 2006. [9] R. Ward and R. L. Collins, "Brain Size and Shape in Strongly and Weakly Lateralized Mice," Brain Res., vol. 328, pp. 243–249, 1985.

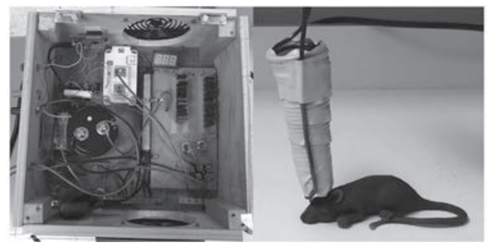

Fig. 1. Illustrate a TMS stimulator and a focused coil positioned on a mice model.

CP-03. Effects of Pulsed Magnetic Field on the Flowing Red Blood Cells using Microvascular Model.

Y. Jo[1], H. Ahn[1], K. Shin[1] and *H. Lee*[1]
1. Sangji University, Wonju, The Republic of Korea

Introduction:It is known that red blood cells (RBCs) aggregation would significantly impede the blood flow and increase the vascular flow resistance contributing to peripheral vascular diseases. For many years, the use of pulsed magnetic field (PMF) was proposed as an alternative non-invasive medical treatment for influencing human physiology, via inducing electric current in deep tissue with the rapidly changing field of the magnetic impulses. Since various cardiovascular diseases such as hypertension, diabetes and thrombosis are also highly correlated to RBC aggregation, many researches concerning the effects of magnetic field on biological systems, especially, on the blood circulation were done. [1] However, the exact physiological role of disaggregation and mobility of RBCs in the blood microcirculatory network has not been clearly elucidated yet. The aim of the present study was to investigate the effects of PMF on the changes of blood flow in the microvascular model, simulated the human capillary. Since the capillaries represent the major site of oxygen delivery from RBCs to tissues, it is very important to know the velocity of blood flow of RBCs, blood viscosity, and shear rate in microvascular model for the microcirculation system. In addition, it is necessary to explore how the magnetic field affects hemorheology of RBCs. Experimental Method: PDMS(DC-184A/B,Dow Corning) was used for microvascular device model because of its blood compatibility, its transparency, and ease of use. The devices are fabricated with nano wire and mounted on a glass slide by 2 days dried at 25^{o}C. The channel diameter is 10~15 μm. All blood samples were collected by venipuncture in New Zealand white female rabbits, weighing 1.5–1.8 kg and 10 weeks of age, and anticoagulated using EDTA. Our PMF stimulator system consisted of single layered coil of 10 turns with an elliptical shape of 12.0 x 4.5 cm. The maximum intensity is 0.27 T at a transition time of 0.102 ms, with pulse intervals of 1 Hz. Images of blood flow are obtained with video camera attached to the microscope. In order to see the improvement of rouleaux formation of RBCs before and after PMF, erythrocyte sedimentation rate (ESR) was measured. To see how the magnetic field affects the oxygen transport capacity of RBCs, using free radicals, tBHP, oxidative stress was induced in the erythrocyte membrane to observe changes in blood flow. Results and Discussion: Fig.1 shows ESR with time before and after PMF. Preliminary study in our group has showed that PMF improved the rouleaux formation of RBCs with comparison of aggregation morphologies before and after stimulus. [2] The larger the value of ESR, the faster the erythrocyte sedimentation starts and sedimentation speeds up. The value of ESR is small after PMF stimulus, which proved the rouleaux formation of RBCs were improved. Fig.2 shows microscopic observation of flowing RBCs using microvascular model (a) before and (b) after PMF. The velocities of blood cell in microvascular model are 15.5 μm/s and 19.2 μm/s, before and after PMF stimulus, respectively. According to Einstein's theory, large rouleaux formation of RBCs is main factor affecting the viscosity of blood. And the blood viscosity along the flow direction is significantly reduced by the use of high magnetic field of 1 T [3]. Our results have demonstrated that PMF might reduce blood viscosity, and blood flow faster. It was also observed that the blood velocity of erythrocytes exposed to oxidative stress increased from 8.3 μm/s to 12.2 μm/s after PMF. In this study, PMF stimulus is proposed to achieve improvement of RBCs aggregation, increase of blood velocity, and reducing blood viscosity. Since non-Newtonian character of blood play a role in the microcirculation, for expanding our results, we need more experiments in diverse microvascular model in the size of 5 to 100 μm and inlet pressure and injection rate of blood.

[1] Y.J. Kim, J. S. Yoo, D.G. Hwang, and H. S. Lee, J. of Magn. 19(1), 32(2014). [2] D.G. Hwang, H.J. Park, W. Kim, J, Lee and H. S. Lee, J of Applied Phys. 117, 17D156(2015). [3] R.Tao, and K. Huang, Phys. Rev. E 84, 011905(2011).

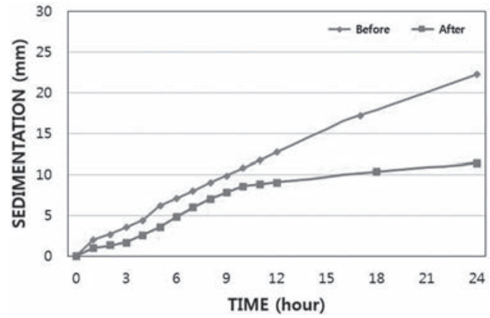

Fig. 1. Showing the sedimentation of RBC with time before and after PMF.

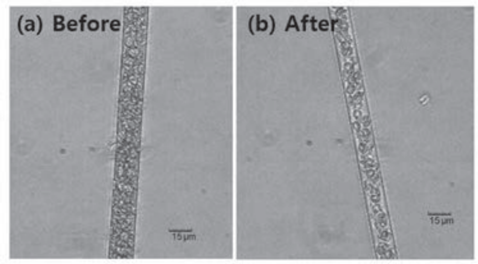

Fig. 2. Microscopic observation of flowing RBCs using microvascular model (a) before and (b) after PMF

CP-04. Transcranial magnetic stimulation: comparison of 15 coils with 50 MRI derived head models.

P. Rastogi[1], Y. Tang[1], B. Zhang[1], E.G. Lee[2], R.L. Hadimani[3,1] and D.C. Jiles[1]

1. Department of Electrical and Computer Engineering, Iowa State University, Ames, IA, United States; 2. Department of Psychiatry, Massachusetts General Hospital, Harvard Medical School, Charleston, MA, United States; 3. Department of Mechanical and Nuclear engineering, Virginia Commonwealth University, Richmond, VA, United States

Transcranial Magnetic Stimulation (TMS) has been gaining popularity for the treatment of Major Depressive Disorder (MDD) due to its non-invasive, painless and out-patient nature[1]. It also under investigation as a therapeutic tool for treating other psychiatric and neurological disorders such migraines, Schizophrenia, Parkinson's disease, and Post Traumatic Stress Disorder (PTSD). TMS is based on the principal of Faraday's law in which a large amount of current is passed through coils to generate time varying magnetic fields, thus inducing electric fields in the brain. There are several coils commercially available for both clinical and research studies which provide stimulation profiles that are characteristically unique in both stimulation intensity and focality. Understanding how stimulation characteristics differ between coils is important for researchers and clinicians as they attempt to choose a coil whose stimulation profile is best for a specific use case. Differences in coils have been characterized in detail in both spherical models, and in a single heterogeneous head model, but never with a population-based modeling approach [2][3]. It is well known within the TMS community that anatomical variability, including brain-scalp distance, cerebrospinal fluid, and gyral anatomy, exists between individuals and thus contributes to varying stimulation profiles[4–6]. Population-based modeling approaches that utilize many head models, can illustrate the effects of this anatomical variability in order to see group average stimulation characteristics. Here, we use population-based modeling with 50 unique, heterogeneous head models to calculate the induced electric field in TMS from 15 coil designs. The models used in this study were taken from the Population Head Model repository [5], and contain anatomical components for skin, skull, cerebrospinal fluid, grey matter, white matter, cerebellum, and ventricles. Simulations utilizing low-frequency magneto-quasi-static solvers were used in SEMCAD X to calculate the induced electric field from various coil designs. Parameters were calculated in post-processing describing stimulation intensity (both in brain and scalp), spread (both surface and volumetric), and "hot spot" location are used to illustrate similarities and differences between these coils. Figure 1 illustrates four coils positioned on the vertex of a MRI derived head model. In this study, simulations were ranboth over the vertex and dorsolateral prefrontal cortex for all subjects and all coil designs to give perspective from two different locations of stimulation. The results described in this study will serve as a guide for both researchers and clinicians wanting to understand the differences between coils stimulation profiles.

1 Pascual-Leone A, Rubio B, Pallardó F, Catalá MD. Rapid-rate transcranial magnetic stimulation of left dorsolateral prefrontal cortex in drug-resistant depression. Lancet 1996;348:233–7. doi:10.1016/S0140-6736(96)01219-6. 2 Deng Z De, Lisanby SH, Peterchev A V. Electric field depth-focality tradeoff in transcranial magnetic stimulation: Simulation comparison of 50 coil designs. Brain Stimul 2013;6:1–13. doi:10.1016/j.brs.2012.02.005. 3 Lu M, Ueno S. Comparison of the induced fields using different coil configurations during deep transcranial magnetic stimulation. PLoS One 2017:1–12. 4 Thielscher A, Opitz A, Windhoff M. Impact of the gyral geometry on the electric field induced by transcranial magnetic stimulation. Neuroimage 2011;54:234–43. doi:10.1016/j.neuroimage.2010.07.061. 5 Lee EG, Duffy W, Hadimani RL, Waris M, Siddiqui W, Islam F, et al. Investigational Effect of Brain-Scalp Distance on the Efficacy of Transcranial Magnetic Stimulation Treatment in Depression. IEEE Trans Magn 2016;52:52–5. doi:10.1109/TMAG.2015.2514158. 6 Miranda PC, Hallett M, Basser PJ. The electric field induced in the brain by magnetic stimulation: A 3-D finite-element analysis of the effect of tissue heterogeneity and anisotropy. IEEE Trans Biomed Eng 2003;50:1074–85. doi:10.1109/TBME.2003.816079.

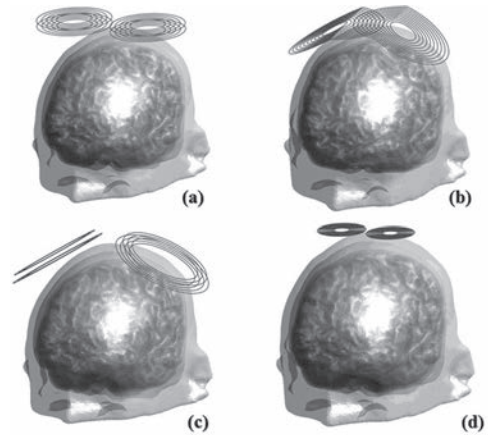

Fig. 1. Illustrate four coil positioned on a MRI derived head model (a) MagVenture B65 coil (b) MagVenture B70 coil (c) MagVenture D-380 coil (d) Magstim 25 mm double coil.

CP-05. Magnetohydrodynamic Approach to Effective Blood-Flow Control Utilizing ELF fields.

H. Nakagawa[1] and M. Ohuchi[1]
1. Department of Electrical and Electronic Engineering, Tokyo Denki University, Adachi-ku, Japan

Abstract To describe the broad potential opportunities in magnetohydrodynamic (MHD) studies for magnetic therapies, we examined the MHD effects of extremely low frequency (ELF) magnetic fields produced by a prototype diverted from an existing alternating magnetic therapy apparatus (AMTA), employing functional near-infrared spectroscopic (fNIRS) analyses. Experimental Five healthy male subjects ranging in age from 33 to 68 (two subjects each in their 30 s and 40 s, and one subject in his 60 s) took part in this experiment. For ELF stimulations to the subjects, we used a prototype equipped with two additional coils for twisting the ELF field of a commercial AMTA (NIKKEN, Biobeam 21). The flux-density (B_{eff}) distribution from the AMTA is shown in Fig. 1. The maximum density was revealed as 60 mT at each center of the internal iron core. We were able to obtain the B_{eff} of 60 mT on the coil surface, under a constant current of 0.34 A. Then the field frequencies of all the coils were fixed at 50 Hz, and the sinusoidal waveform signals from the additional coils were synchronized in phase in accordance with the axis of a part of the human body. All measurements on fNIRS (Hitach HOT121B) were carried out while the subjects were sitting on a chair in a quiet room at a temperature of 23°C and humidity of 50%. Discussion Our experimental results showed the fact that the proper twisted ELF fields induced from the prototyped machine were able to control the autonomic nervous system, depending on the field strength. We therefore estimated that the mechanism of blood-flow accelerations induced by ELF stimulations is due to a little temperature increase generated by an induced eddy current, and the following joule-heat gradient of the current. Consequently, the blood flow is probably accelerated in the process of human bioactivity via the autonomic nervous system [1–4], in order to reduce the induced fever and/or the heat gradient. On the other hand, there were no significant differences across the two mounting positions (Fig. 2A and 2B) in the behaviors of arterial/venous blood flows. It is quite probable that the arterial blood flows (Fig. 2A) could not generate an eddy current necessary for activations of the autonomic nervous system, although the flows grasping as a pulsating flow might induce an electromagnetic induction phenomenon in a fluid. We firmly believe that MHD effects for a virtual magnetic therapy are induced by moderately swept turbulence in the blood.

[1] M. D. Spranger, A. C. Krishnan, P D. Levy, D. S. O'Leary, and S. A. Smith, "Blood flow restriction training and the exercise pressor reflex: a call for concern," *Am. J. Physiol. Heart Circ. Physiol.*, vol. 309, no. 9, pp. H1440-1452, 2015. [2] I. Gibbins, "Functional organization of autonomic neural pathways," *Organogenesis*, vol. 9, no. 3, pp. 169-175, 2013. [3] J. F. Thayer, F. Ahs, M. Fredrikson, J. J. Sollers 3rd, and T. D. Wager, "A meta-analysis of heart rate variability and neuroimaging studies: implications for heart rate variability as a marker of stress and health," *Neurosci. Biobehav. Rev*. vol. 36, no. 2, pp. 747-756, 2012. [4] C. Cheyuo, A. Jacob, R. Wu, M. Zhou, G. F. Coppa, and P. Wang, "The parasympathetic nervous system in the quest for stroke therapeutics," *J. Cereb. Blood Flow Metab.*, vol. 31, no. 5, pp. 1187-1195, 2011.

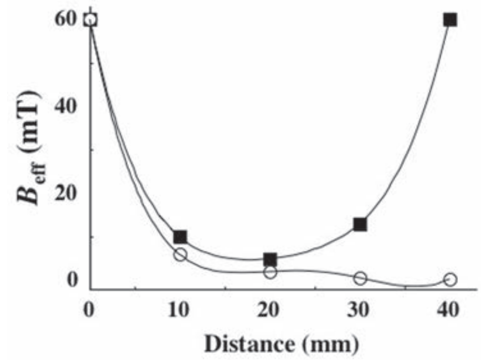

Fig. 1. Magnetic flux distributions from internal coil cores in Biobeam 21. The flux density (B_{eff}) was measured every 10 mm vertically (○) and horizontally (■) from the center of the coil surface. The maximum density was revealed to be 60 mT at each center of the iron cores. The densities at the horizontal points were measured within the space between the two internal cores (40 mm).

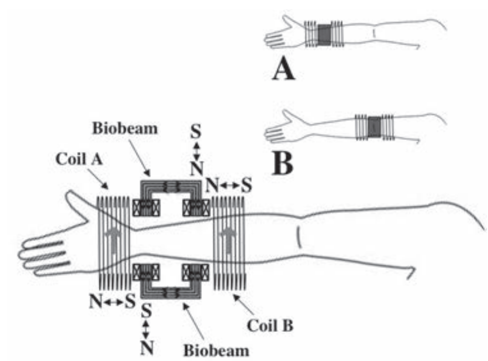

Fig. 2. Arrangements of additional coils and AMTA. Two additional coils were equipped at both ends of the Biobeam. The field frequencies of both the coils were fixed at 50 Hz out of phase along the axis of each subject's forearm.

CP-06. High Focality Stimulation on Primary Auditory Cortex.

J.R. Germick[1], Y. Alkheder[2], P. Rastogi[1], A. Pandurangi[3], D.C. Jiles[1] and R.L. Hadimani[2]

1. Dept. of Electrical and Nuclear Engineering, Iowa State University, Ames, IA, United States; 2. Dept. of Mechanical and Nuclear Engineering, Virginia Commonwealth University, Richmond, VA, United States; 3. Dept. of Psychiatry, School of Medicine, Virginia Commonwealth University, Richmond, VA, United States

Transcranial magnetic stimulation (TMS) is a non-invasive neuromodulation method that can be used to depolarize cortical neurons. TMS is used as a therapy for many neurological disorders, in fact TMS treatment has already been FDA approved to treat major depressive disorder. This is achieved by applying high current pulses through TMS coils to produce sufficiently high electric fields across the neuronal membrane. Even though the manifestation of auditory hallucinations are complex, there is evidence that the Primary Auditory Cortex plays a role as studies by Shi et. al.1 As the Primary Auditory Cortex is relatively small, the need for a coil that can stimulate small regions of the brain without stimulating neighboring regions is an apparent need for many researchers. The induced electric field depends on the coil geometry, which can be modified to suit specific applications. For example, two coils with very different geometry, the Figure-of-Eight (FOE) and the H-coil, while both FDA approved do not provide focused stimulation however, there is another coil design that claims to provide higher focused stimulation than the FOE. The Quadruple Butterfly coil (QBC) introduced by Rastogi et al. showed that there was improvement in focality over the dorsolateral prefrontal cortex in 50 head models.2 In the current work the authors have compared the volume stimulated (defined as the total volume of grey and white matter with at least half the maximum electric field calculated in the brain) by both the FOE and the QBC in 15 healthy head models and 15 Schizophrenic head models. The healthy models were created from MRI scans of healthy patients, while the Schizophrenic models were fabricated from the scans of Schizophrenic patients obtained from the SchizConnect database. Each model consists of 7 distinct anatomic structures: the skin, skull, Cerebrospinal fluid, grey matter, white matter, cerebellum, and ventricles. Simulations were performed using Sim4Life, a finite element tool used for the calculation of induced electric fields on GM.3 Electrical conductivities for each anatomical layer of the models were assigned based on Lee et al.4 In the computer modeling, the coils were placed 5mm from the scalp as shown in Fig 1, this displacement accounts for the insulation thickness around the coils. Additionally, the current in the QBC was scaled down relative to the FOE so that the maximum induced electric field on the cortex of each model were nearly identical. The results have shown that the QBC coil has 35 percent less stimulation volume than the FOE coil on average for the same induced electric field on the surface of the cortex. On each model the QBC proved to have lower volume of stimulation than the FOE. These results can be seen in Fig 2 for 15 models. Even with the reduced stimulation volume the QBC maintains the same depth of penetration as the FOE coil.

[1] Shi Wei Xing. The Auditory Cortex in Schizophrenia. Biological psychiatry. 2007;61(7):829-830. doi:10.1016/j.biopsych.2007.02.007. [2] Rastogi, E.G. Lee, R.L. Hadimani and D. C. Jiles, "Transcranial Magnetic Stimulation-coil design with improved focality", A.I.P Advances, Volume 7, Issue 5, December 2016. [3] Schmid & Partner Engineering AG, "Sim4life." [4] E. G. Lee et al., "Investigational Effect of Brain-Scalp Distance on the Efficacy of Transcranial Magnetic Stimulation Treatment in Depression"; in IEEE Transactions on Magnetics, vol. 52, no. 7, pp. 1-4, July 2016.

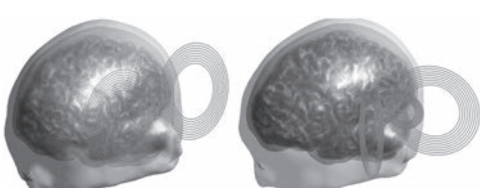

Fig. 1. Shows the position of the FOE, left, and QBC, right, over the left Primary Auditory Cortex.

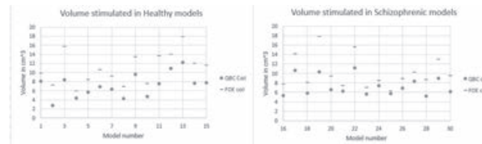

Fig. 2. The volume of stimulation of the QBC and the FOE in the Healthy model set.

CP-07. Efficacy of Investigating Mirror Neuron Activity in Schizophrenics Using Transcranial Magnetic Stimulation.

J.R. Germick[1], E. Cheng[2], P. Rastogi[1], R.L. Hadimani[3,1], U. Mehta[4], A. Pandurangi[5] and D.C. Jiles[1]
1. Dept. of Electrical and Nuclear Engineering, Iowa State University, Ames, IA, United States; 2. Dept. of Biomedical Engineering, Virginia Commonwealth University, Richmond, VA, United States; 3. Dept. of Mechanical and Nuclear Engineering, Virginia Commonwealth University, Richmond, VA, United States; 4. Department of Psychiatry, National Institute of Mental Health and Neurosciences, Bangalore, India; 5. Dept. of Psychiatry, School of Medicine, Virginia Commonwealth University, Richmond, VA, United States

Transcranial Magnetic Stimulation, TMS, has been gaining considerable traction as a viable therapy for many neurological disorders. TMS utilizes a large capacitance that is charged to a high voltage to be discharged into a coil that is held on the scalp. The resulting magnetic field induces electrical current in the brain greater in magnitude to the currents produced chemically. In practice the level of voltage applied to the coils is derived on a per-patient basis using Resting Motor Potential, RMT. The RMT is defined as the minimum dose required to evoke at least 50 microvolt MEP's, motor evoked potentials by stimulation over the motor cortex. This is measured using electromyography on the muscle group stimulated. Once the RMT is established this voltage level is used in all areas of the brain under the assumption that the excitability of neurons elsewhere in the brain is similar to that of the motor cortex. For example, in Mehta et al.1 RMT was established as described above to investigate Mirror neuron activity of Schizophrenic patients in the inferior frontal gyrus, IFG, and related areas. In this study the authors have received T1 weighted MRI scans from over 50 schizophrenic patients who have received TMS stimulation over their IFG as well as the RMT's used during stimulation. Using the MRI scans, head models were created of the patients consisting of 7 distinct anatomical structures. These include: the skin, skull, Cerebrospinal fluid, grey matter, white matter, cerebellum, and ventricles. Simulations were performed using Sim4Life, a finite element tool used for the calculation of induced electric fields in the brain.2 Electrical conductivities for each anatomical layer of the models were assigned based on Lee et al.3 In the computer modeling, the coils were placed 5mm from the scalp as shown in Fig 1, this displacement accounts for the insulation thickness around the coils. To measure the excitability of cortical neurons the authors have used Sim4Life to calculate the maximum induced electric field in the brain, and the volume of stimulation on the IFG. Where the volume of stimulation is defined as the volume of the brain with induced electric field above half the maximum induced electric field in the brain as seen in Fig 2. If RMT is indeed proportional to the excitability of neurons in all areas of the brain, the value of the maximum induced electric field should be proportional to the RMT. The authors have found that a higher maximum electric field was calculated in models with correspondingly low RMT's. This is as expected due to the fact that a lower RMT is directly related to higher excitability of cortical neurons. The authors plan to further solidify this conclusion by running simulations on a total of 50 anatomically accurate MRI derived heterogeneous head models.

[1]Mehta, U M, et al. "Reduced Mirror Neuron Activity in Schizophrenia and Its Association with Theory of Mind Deficits: Evidence from a Transcranial Magnetic Stimulation Study."Schizophrenia Bulletin, Volume 40, issue 5, November 2013 [2] Schmid & Partner Engineering AG, "Sim4life." [3] E. G. Lee et al., Investigational Effect of Brain-Scalp Distance on the Efficacy of Transcranial Magnetic Stimulation Treatment in Depression, IEEE Transactions on Magnetics, vol. 52, no. 7, pp. 1-4, July 2016.

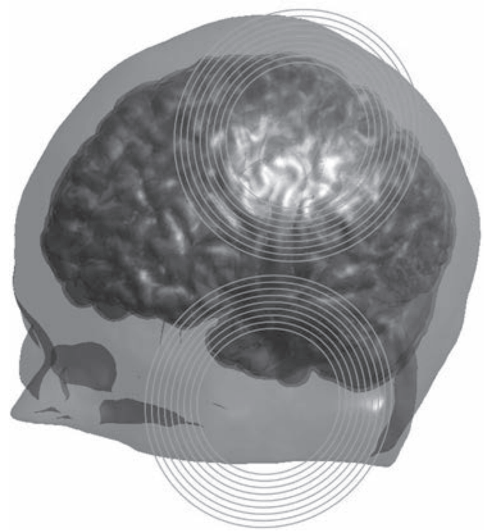

Fig. 1. Shows the position of the Figure-of-Eight coil above the IFG

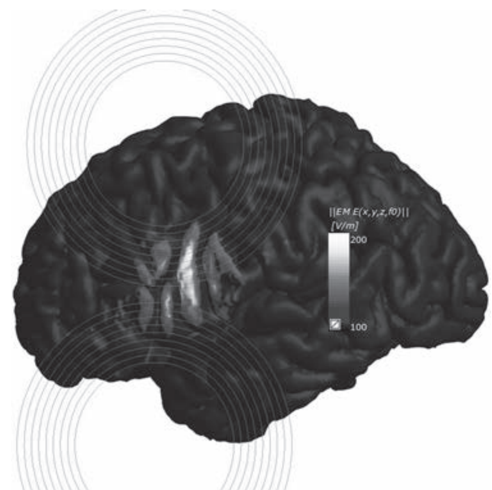

Fig. 2. The highlighted area is the volume stimulated above one half the maximum induced electric field.

CP-08. Simulation study of Magnetic Response of Magnetic Nanoparticles for different temperature under different selection gradient field.

J. Zhu[1], X. Lu[1], S. Wei[1], Z. Wang[1] and W. Yang[1]
1. School Electronic, Electrical and Communication Engineering, University of Chinese Academy of Sciences, Beijing, China

INTRODUCTION In the past ten years, magnetic particles (MNP) have been developed into functional materials of therapeutic platform for integrated diagnosis of disease diagnosis, targeted drug delivery and magnetic thermal therapy [1, 2]. The thermal effect of MNP under alternating electromagnetic field can be widely used in targeted magnetic thermal therapy [3, 4]. Quantitatively obtain of the distribution of the magnetic nanoparticales temperature is one of the current challenges of magnetic nanoparticles based cancer hyperthermia. Besides, the current commonly used invasive methods, such as infrared optical fiber temperature measurement, not only cause damage to the tissue, but also difficult to obtain the temperature distribution of the lesions. In 2009, John B.Weaver and his partners offered a direct method for temperature measurement based on MNP [5].They found that the magnetic response of MNP has monotonic linear relationship with temperature and therefore it can detect the temperature of MNP itself. However, this method has limitations in obtaining the temperature distribution. In 2016, Christian Stehning and his partners presented a simultaneous imaging and temperature mapping method using a 'multi-color' reconstruction approach by applying a field free point (FFP) selection [6]. However, it is still unclear how the implied gradient field for FFP will impacts the temperature detection. In this study, we proposed to simulate the MNP magnetic response of the 3rd and 5th order harmonics under different temperatures in the presence of an applied gradient field. METHOD In this study, according to the Langevin function, the non-linear response of one dimensional MNP solution was simulated according to Equ (1). $M(t)=\int\Phi(x)*(\pi/6)*M_s*D^3*L(\pi/(6kT)*Ms*D^3*H(x,t))\,dx$ (1) Where $\Phi(x)$ is the distribution of the MNP concentration distribution and D is the diameter of the MNP.Ms is the saturation magnetization of the magnetic nanoparticles. H(x,t) is the applied selection and drive field.k is the Boltzmann constant and T is the temperature(K). L is the the Langevin function. The radius of magnetic nanoparticle is 20nm. The selection field is an infinite one-dimensional gradient magnetic field, and the field-free point (FFP) is the center point of the solution. The gradient of selection field is taken at 0T/m, 1T/m, 2T/m and 3T/ m. The drive field amplitude is 20 mT and the frequency is 25 khz. To show the relationship of the gradient and the harmonics, the Fourier transform was implied to obtain the first 10 harmonics. To study the relationship between the the gradient and temperature, the peak of each harmonic was detected by finding local max of the data and then the peak of the 3rd and 5th harmonic was subdivided to obtain a ratio for temperature detection. RESULTS AND DISCUSS As shown in Fig 1, we found that even order response exists when adding background selection gradient field, and the harmonics are lower than those with no gradient field. Considering the 3rd and 5th order harmonics, they all decreased when gradient increased. Furthermore, we studied the ratio of 3rd and 5th order harmonics with different temperatures by adding gradient field. It is shown in Fig 2 that this ratio has linear relationship when the gradient of selection field is 2T/ m. This linear relationship offer the basis for the feasibility of temperature distribution detection. The basic theory of magnetic particles imaging mention that by adding gradient field the magnetization response produced by magnetic nanoparticles under the alternating current electromagnetic field only reflects the information of magnetic nanoparticles in unsaturated space. It implies gradient field helps to spatial localization, which offers the possibilty of detection for temperature distribution. Meanwhile the slope of the line is deeper when adding 2T/m gradient field compared with that with no gradient field. So we can deduce that an additional selection field can further increase the sensitivity of temperature measurement. In the future studies, more detailed theoretical studies will be implied for better understanding the mechanism and the detecting system will be setup and experiments will be carried out for the validation of the simulation results. CONCLUSION In this study, aimed for a better understanding for the temperature distribution detection of the magnetic particles for hyperthermia, based on the Langevin function, a simulation study for the relationship of temperature and implied gradient field for field selection was studied. The results show that increased selection gradient strength will improve the detection sensitivity of the temperature detection of the MNPs. ACKNOWLEDGMENT This work was supported by the NSFC 51607169.

[1] Laurent S, Forge D, Port M, Roch A, Robic C, Vander Elst L, Muller RN: Magnetic iron oxide nanoparticles: synthesis, stabilization vectorization, physicochemical characterization and biological applications. Chem Rev [J] 2008, 108:2084-2110. [2] Xie J, Liu G, Eden HS, Ai H, Chen X: Surface-engineered magnetic nanoparticles platforms for cancer imaging and therapy. Acc Chem Res. [J] 2011, 44:883-892. [3] Xie J, Jon S. Magnetic nanoparticles-based theranostics. Theranostics. [J] 2012, 2:3-121. [4] Challa S.S.R. Kumar, Faruq Mohammad. Magnetic nanomaterials for hyperthermia-based therapy and controlled drug delivery. Advanced Drug Delivery Reviews. [J] 2011, 63, 9, 14: 789–808 [5]John B.Weaver, Adam M. Rauwerdink, Eric W.Hansen. Magnetic nanoparticle temperature estimation. Med. Phys. [J] 2009, 36: 1822 [6]Stehning C, Gleich B, Rahmer J. Simultaneous magnetic particle imaging (MPI) and temperature mapping using multi- color MPI [J]. International Journal on Magnetic Particle Imaging, 2016:2(2)

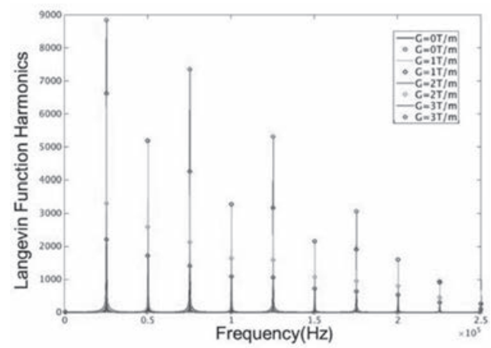

Fig. 1. magnetic nanoparticles magnetization response spectrum with different gradients

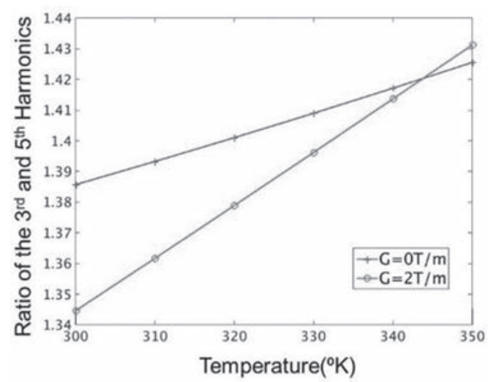

Fig. 2. the ratio of 3rd and 5th has linear relationship when the gradient of selection field is 2T/m

CP-09. Gradient/ELF magnetic Field Affects Metamorphic Behaviors in T_4-Administrated Axolotls: Regulation of Amphibian Metamorphosis Depending on Field Strength and Exposure Timing.

H. Nakagawa[1] and M. Ohuchi[1]
1. Department of Electrical and Electronic Engineering, Tokyo Denki University, Adachi-ku, Japan

Introduction Juvenile axolotls (*Ambystoma mexicanum*) can be readily metamorphosed to mature salamanders by a function of thyroxine (T_4) [1]–[5]; therefore, the experimental applications utilizing axolotls must be favorable for a direct examination with respect to aquatic-terrestrial transformations. But, there are almost no previous studies of the observations of axolotl metamorphosis under exposure to magnetic fields. The purpose of this study is to investigate the influences of a gradient or an extremely low frequency (ELF) magnetic field on the T_4-inducing forced metamorphosis of axolotls. Materials and Methods Thirty-six axolotls (about 120 mm) were bred under the same condition as group feeding. Before performing this experiment, all the axolotls were individually kept in 0.85-L square boxes containing dechlorinated water (0.7 L) without aeration under an illumination of 250 $mEm^{-2}s^{-1}$ on a 12 : 12 h L : D photocycle. The water temperature was also strictly controlled at 24°C, employing an original water-renewing system equipped with siphonage (siphon effect) and temperature controls (Fig. 2). After the adaptation of the axolotls to our experimental environment at least a week, they were kept in 0.32–0.80 mM T_4 and were exposed to a gradient magnetic field of 250 mT or an ELF magnetic field of 5.0 mT at 10 Hz. The gradient/ELF exposure was continued up to the morphological completions of all the T_4-administrated axolotls. The axolotls had become accustomed to being given food rotating of a solid / a tubifex worm. The morphological changes of the axolotls influenced by the presence of the T_4 were monitored every day, and the changes were evaluated minutely based on the reported method [1]. Discussion To begin with, we will discuss the influences of an ELF field of 5.0 mT at 10 Hz on axolotl metamorphosis, from the viewpoints of a metamorphic rapidity and a morphological change. The earliest completion of axolotl metamorphosis in a control experiment was observed at Day 13, and the remaining axolotls completed their metamorphoses by Day 17. However, none of the metamorphoses were completed by Day 14 under exposure to the ELF field. Moreover, there were morphological delays of up to 26% compared with a control. Concerning the timeframe of the morphological changes in the axolotls under our experimental conditions, we detected no particular change in connection with the ELF field. On the other hand, we found that the initiation timings of gradient-field exposure did affect the survival rates of the salamanded axolotls. Our data greatly support the idea that gradient/ELF exposures might modify axolotl metamorphosis minutely, depending on the exposure timing, the field strength, and the frequency, and so on.

[1] R. B. Page, J. R. Monaghan, J. A. Walker, and S. R. Voss, “A model of transcriptional and morphological changes during thyroid hormone-induced metamorphosis of the axolotl,” *Gen. Comp. Endocrinol*., vol. 162, no. 2, pp. 219-232, 2009. [2] P. Huggins, C. K. Johnson, A. Schoergendorfer, S. Putta, A. C. Bathke, A. J. Stromberg, and S. R. Voss, “Identification of differentially expressed thyroid hormone responsive genes from the brain of the Mexican Axolotl (*Ambystoma mexicanum*),” *Comp. Biochem. Physiol. C Toxicol. Pharmacol.*, vol. 155, no. 1, pp. 128-135, 2012. [3] H. L. Thurston, S. Prayaga, A. Thomas, V. Guharoy, S. Dube, B. J. Poiesz, D. K. Dube, “Expression of Nkx2.5 in wild type, cardiac mutant, and thyroxine-induced metamorphosed hearts of the Mexican axolotl,” *Cardiovasc. Toxicol.*, vol. 9, no. 1, pp. 13-20, 2009. [4] R. B. Page, S. R. Voss, A. K. Samuels, J. J. Smith, S. Putta, and C. K. Beachy, “Effect of thyroid hormone concentration on the transcriptional response underlying induced metamorphosis in the Mexican axolotl (*Ambystoma*),” *BMC Genomics*, vol. 11, no. 9, p. 78, 2008. [5] D. D. Brown, “The role of thyroid hormone in zebrafish and axolotl development,” *Proc. Natl. Acad. Sci. USA*, vol. 94, no. 24, pp. 13011-13016, 1997.

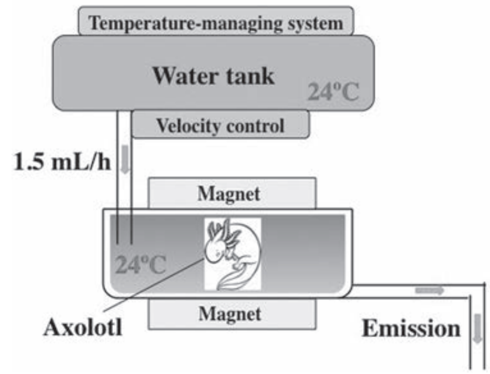

Fig. 1. Water-renewing system equipped with temperature controls.

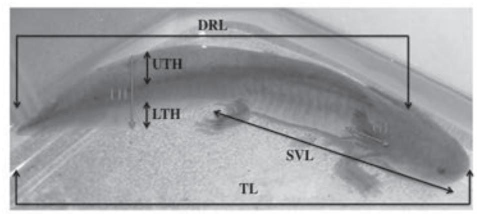

Fig. 2. Seven morphometric traits monitored during axolotl metamorphosis. TL, total length; DRL, dorsal ridge length; TH, tail height; UTH, upper tailfin height; LTH, lower tailfin height; SVL, snout-vent-length; GL, gill length.

CP-10. Reaserch on Influence of the Electric Vehicle on Body During the Wireless Charging Process.

S. Jiang[1]
1. Tianjin Polytechnic University, Tianjin, China

I. INTRODUCTION In recent years, the development of electric vehicles (EV) is becoming more and more rapid, but the current charging method of plug-in has the disadvantages of time consuming, unsafe, the interface that is not unified and so on. Therefore, a new energy supply mode-wireless power charging is proposed[1.2]. The advantages of wireless charging are high space utilization, high security, more convenient, stronger user experience compared to the plug-in charging. As the research hotspot of the new charging mode of EV, wireless charging has attracted more and more attention and research at home and abroad. For the development of EV charging, the effect of charging on life safety is the most important factor. The safety influence to the carrying life is also more important, but it is still in its infancy in our current research. Hunter H.Wu et al[3] designed a 5kW inductive wireless charging device for EV. The experiment was used to measure the magnetic induction intensity of 4 different positions at the man of 1.5 meters high. The result accorded with the ICNIRP electromagnetic safety standard. Omer C et al[4] measure the magnetic induction of the floor, seat, and head occipital positions when the transmitted and received coils are position offset. The measurement results conform to ICNIRP. The research of this topic not only provides a theoretical foundation for the safety analysis of the EV's wireless charging life, but also conducive to the future application development and promotion. In this study, the actual EV model, the adult model and the coils model are built. Under the condition of transmission frequency and output power of 85kHz and 15.2kW respectively, the magnetic induction intensity and electric field intensity of the human body in different positions are obtained. An experimental prototype of EV wireless charging and a measurement method for electromagnetic exposure on EV are set up to confirm the reliability of the simulation results. Finally the electromagnetic safety evaluation of EV charging system is carried out from the perspective of molecular biology. II. SIMULATION ANALYSIS The structure of the EV wireless charging system is to install the transmitter on the ground or underground, and the receiver is installed on the chassis of the car. When the EV needs charging, the transmitter and the receiver need to put the correct position. The electrical energy through the primary coil (TX) is transmitted to the secondary coil(RX), which realizes non-contact power transmission. At present, resonant coupling mode is applied in the EV charging. so the system can work normally when TX and RX are in a certain degree of dislocation, which improves the flexibility of the power supply. In order to reduce the leakage inductance, the volt ampere capacity of the system, and improve the system performance, Series- Series compensation is generally applied to the structure. The model of wireless charging system of EV is built by using finite element simulation software. The charging frequency, output power and distance between TX and RX are 85kHz,15.2kW,20cm respectively. The magnetic induction intensity and electric field intensity distribution sectional graph of the coils can be obtained. According to the same method, the contour that meets the international electromagnetic safety limit can be obtained by making sections in the two diagonal space of the charging device, as shown in Fig.1. The magnetic induction intensity of the green line represents the safety value of 27μT. Outside green area, space magnetic induction is less than 27μT, according to ICNIRP electromagnetic safety limit. The value of magnetic induction intensity and the electric field intensity are calculated and analyzed on the different positions at the top of the charging device center. The results show the magnetic induction intensity in some regions is not satisfied with the safety limit, and electric field intensity in all regions is satisfied, as shown in Fig.2. III. EXPERIMENT AND DISCUSSION A prototype of the EV wireless charging device is built, including power supply, transmitter, receiver, rectifier receiver and load. A three-dimensional electromagnetic radiation analyzer is used to measure the setting points. The measured values of the experiment are in close agreement with the simulated values. The experiment results verify the correctness of the simulation. A total of 12 healthy mice divided into the control group and the experimental group are selected in the experiment. The control group is placed in a thermostat at 37 degrees without magnetic field radiation. The experimental group is placed in the location below the long edge of the wireless charging device. It is exposed to electromagnetic radiation for 30 days, and 2 hours every day. Other experimental conditions remain unchanged. Results the changes of blood routine and blood biochemical indexes of mice are observed. The statistical analysis software of SPSS is used to make a significant analysis of the above data. The experimental results show the $P>0.05$ of each index. There is no significant difference in biochemical index between the control group and the experimental group in the wireless charging space. According to the analysis of the experimental data, it can be considered that the electromagnetic field of the EV in this paper is not harmful to the body.

[1] Zhang X., Yuan Z., Yang Q., et al, Coil Design and Efficiency Analysis for Dynamic Wireless Charging System for Electric Vehicles[J]. IEEE Transactions on Magnetics,2016, 52(7): 1-4. [2] Xian Zhang, Hang Su, Pengcheng Zhang, et al, Modeling and Validation for Electromagnetic–Mechanical Synchronous Resonance via Wireless Power Transmission[J]. IEEE Transactions on Magnetics,2015, 51(3): 1-4. [3] H. Wu H., Gilchrist A., D. Sealy K., et al, A High Efficiency 5 kW Inductive Charger for EVs Using Dual Side Control[J]. IEEE Transactions on Industrial Informatics,2012, 8(3): 585-595. [4] C. Onar O., M. Miller J., L. Campbell S., et al. A novel wireless power transfer for in-motion EV/PHEV charging[C]. 2013 Twenty-Eighth Annual IEEE Applied Power Electronics Conference and Exposition (APEC), 2013: 3073-3080.

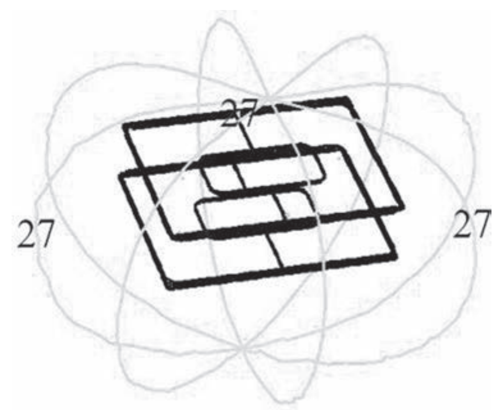

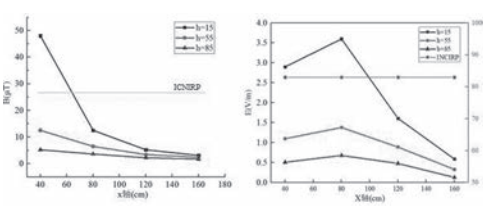

CP-11. Biogenic micro-mirrors of aquatic species display enhanced light reflection upon exposure to a magnetic field.

H. Kashiwagi[1], H. Asada[2] and M. Iwasaka[3]
1. Graduate School of AdSM, Hiroshima University, Higashihiroshima, Japan; 2. Graduate School of Science and Technology for Innovation, Yamaguchi University, Ube, Japan; 3. RNBS, Hiroshima University, Higashihiroshima, Japan

Elaborate materials and systems found in living organisms provide a basis for generating biomimetic technologies in newly developing industries. Among these, micro crystals discovered in body surfaces and eyes of various aquatic organisms have been found to possess unprecedented optical functions [1]-[3] with potential application in biocompatible micro electro-mechanical systems (MEMS) and biomedical diagnosis and treatment. We previously investigated the remarkable camouflaging ability of the marine copepod *Sapphirina*, whose body produces various colors enabling it to vanish into the background. This brilliant coloring appears to be controlled by the structural arrangement of regular hexagonal guanine crystals and cytoplasm alternately situated beneath the dorsal cuticle [4]-[8]. We also investigated the iridescent eyes of the scallop, which are situated on the mantle tissue. We surmised that a multilayer guanine crystal structure in these eyes plays an important role in gathering and amplifying external light [9]-[11]. Guanine crystals are a type of biogenic photonic crystal with very high refractive index (n = 1.83) [12], [13]. Although the crystals themselves are colorless, they emanate iridescent colors whose value is determined mainly by the quantity of light transmitted, reflected and/or optically disrupted, factors which can be attributed to the thickness of the crystal, or, in the case of *Sapphirina*, the cytoplasm [8]. Therefore *Sapphirina* and the scallop may serve as reasonable models for further investigating biological optical coloring and light gathering properties. Extending our investigations to include the behavior of guanine crystals derived from various other marine animals, we found that fish-derived guanine crystals (dozens of micrometers in size) suspended in water have a highly-functional magnetic response, aligning themselves along the direction of the magnetic field [14]-[19]. By further examining the relationship between different crystalline structure arrangements and optical coloring, we hope to clarify the mechanism of brilliant colorization in animal camouflage utilizing natural light. In the present study we investigated the optical and magnetic properties of guanine crystals obtained from *Sapphirina* and the scallop. Guanine crystal suspensions enclosed within a cuvette were fixed between two opposing electromagnets and illuminated by halogen light. Guanine crystal behavior, with and without application of the magnetic field, was observed from directly above with a real-time, charge-coupled device (CCD) microscope and high-resolution spectrophotometer. Electron microscopy showed the distinctive honeycomb-like guanine crystals from *Sapphirina* to be overlapped or scattered. Scallop suspensions, on the other hand, were found to contain a majority of micron/submicron angular and spherical shaped crystal granules. Reflection intensity of both types of guanine crystals increased when exposed to a 0.5T magnetic field, and remained so throughout exposure. When the magnetic field was turned off again, reflection intensity returned to its original state. These changes were seen to occur instantaneously. Although in a previous study we mentioned that no such responses were observed with guanine crystals from *Sapphirina* [20], in the present study we increased the guanine crystal concentration of *Sapphirina* and enclosed suspensions in a thicker vessel. Although the shape of the crystals from these two species were different, magnetic response and light reflection switching properties were the same, and corresponded to those previously observed with the larger fish-derived guanine crystals. *Sapphirina* crystals in particular displayed a sort of flickering structural color. This was most noticeable when ultrasonic cleaning was performed before centrifugation. But cleaning also tended to reduce the intensity of structural color and the amount of reflected light. Time-series spectroscopic analysis quantitatively confirmed the CCD microscope results. This paper also describes the diamagnetic rotational energy of guanine crystals under magnetic exposure. In conclusion, guanine micro crystals were seen to enhance light reflection upon exposure to a magnetic field, a response that was not dependent on size or shape. Biogenic microcrystals seem to be new candidate optical materials, and should lead to new insights into various optical MEMS and biomedical applications, such as a convectional tracer for micro fluidic circuits, a highly sensitive optical biosensor for bacterial detection combining a light-gathering element, as well as stem cell manipulations for traumatic bone regeneration utilizing the diamagnetic rotational properties of guanine crystals. This work was supported by JST-CREST "Advanced core technology for creation and practical utilization of innovative properties and functions based upon optics and photonics (Grant number: JPMJCR16N1)."

[1] Shulei Zhao, Parrish Clawson Brady, Meng Gao, Robert Ian Etheredge, George W. Kattawar, Molly E. Cummings, J R Soc Interface. 12, 20141390 (2015). [2] T. M. Jordan, J. C. Partridge & N. W. Roberts, Nature Photonics 6, 759 (2012). [3] Parrish C. Brady, Alexander A. Gilerson, George W. Kattawar, James M. Sullivan, Michael S. Twardowski, Heidi M. Dierssen, Meng Gao, Kort Travis, Robert Ian Etheredge, Alberto Tonizzo, Amir Ibrahim, Carlos Carrizo, Yalong Gu, Brandon J. Russell, Kathryn Mislinski, Shulei Zhao, Molly E. Cummings, Science 350, 965 (2015). [4] Chae J, Nishida S, Marine Biology 119, 205 (1994). [5] Chae J, Nishida S, Journal of the Marine Biological Association of the UK 79, 437 (1999). [6] Jinho Chae, Kumiko Kita-Tsukamoto, Shuhei Nishida and Kouichi Ohwada, Journal of Crustacean Biology 16, 20 (1996). [7] Jinho Chae, Shuhei Nishida, Journal of the Marine Biological Association of the United Kingdom 84, 727 (2004). [8] Gur D, Leshem B, Pierantoni M, Farstey V, Oron D, Weiner S, Addadi L, J. Am. Chem. Soc. 137, 8408 (2015). [9] V. C. Barber, Eileen M. Evans, M. F. Land, Z Zellforsch Mikrosk Anat 76(3), 25-312 (1967). [10] M. F. Land, Journal of Experimental Biology 45, 433-447 (1966). [11] Dvir Gur, Benjamin A. Palmer, Steve Weiner, Lia Addadi, Advanced Functional Materials 27, 1603514 (2017). [12] Avital Levy-Lior, Boaz Pokroy, Berta Levavi-Sivan, Leslie Leiserowitz, Steve Weiner and Lia Addadi, Cryst. Growth Des. 8, 507 (2008). [13] Jérémie Teyssier, Suzanne V. Saenko, Dirk van der Marel & Michel C. Milinkovitch, Nature Communications 6, 6368 (2015). [14] Masakazu Iwasaka, Yuito Miyashita, Yuri Mizukawa, Kentaro Suzuki, Taro Toyota and Tadashi Sugawara, Applied Physics Express 6, 037002 (2013). [15] M. Iwasaka, J. Appl. Phys. 107, 09B314 (2010). [16] Y. Mizukawa, M. Iwasaka, IEEE Transactions on Magnetics 49, 3480 (2013). [17] M. Iwasaka, Y. Mizukawa, Langmuir 29, 4328 (2013). [18] Masakazu Iwasaka, Yuri Mizukawa, and Nicholas W. Roberts, Langmuir 32, 180 (2016). [19] H. Kashiwagi, A. Kashiwagi, and M. Iwasaka, AIP Advances 7, 056426 (2017). [20] H. Kashiwagi, Y. Mizukawa, M. Iwasaka and S. Ohtsuka, AIP Advances 7, 056731 (2017).

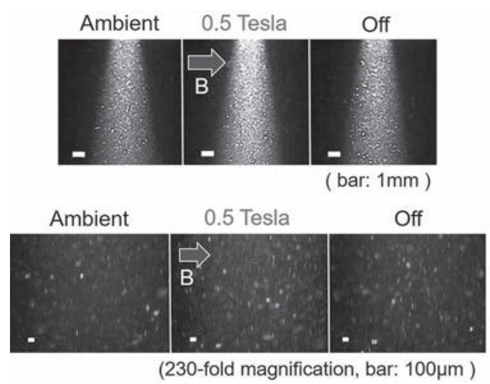

Fig. 1. Behavior of guanine crystals (CCD microscope)

CP-12. Numerical investigation of biconical transcranial magnetic stimulation coil.

Y. Wu[1] and *Z. Liu*[1]
1. School of Materials Science and Engineering, South China University of Technology, Guangzhou, China

Transcranial magnetic stimulation, also known as TMS, is rapidly developed as a no-invasive, non-painful and safe tool for studying the physiology of human brain and brain therapy [1,2]. TMS is based on the principle of electro-magnetic induction of an electric field in the brain, which is of sufficient magnitude and density to depolarize neurons. Depending on the parameters of stimulation, TMS pulses can decrease or increase the cortical excitability even beyond the duration of the train of stimulation, and this produces behavioral consequences and prospect therapeutic potential [2-4]. Since electric field induced is an important parameter in stimulation process, this work investigates the 3-dimensional electric field distribution in human brain using the finite element method. Fig 1 shows the cross section of two-layer human head model and the investigated biconical TMS coils. The human head is modeled with harnpan and tissue fluid, and TMS coils consisted of two separated cones. The model is located in a solution region, in which the solution is generated and the mesh is refined, with proper boundary condition applied to determine the unique solution of the electromagnetic field. The magnitude of the induced electric field in the head is used for evaluating the stimulation effect. By investigating the influences of the distance between two cones, included angle, current frequency and the location of the coils, the optimized TMS coil sep-up for deep stimulation and good stimulation accuracy has been obtained. Fig 1. TMS model of biconical coil model Simulation result shows that high current frequency is beneficial for effectively deep stimulation, with 0.2V/m as threshold for effective electric field. Since the distribution of electric field is determined by the projection of TMS coil on the human head, decreasing the distance between two cones of biconical TMS coil can increase the magnitude of electric field along the symmetric axis, which is directing to the human head. The higher electric field means that the deeper tissue in the human head can be stimulated, as shown in Fig 2 a). Electric field in tissue fluid is decaying in an exponential form, which leads to a slightly improved stimulation depth by decreasing the distance between two cones. On the other hand, the decreasing the distance can also stimulate the human brain with a shaper peak of the magnitude of electric field, as shown in Fig 2 b) shows, which gives a better stimulation accuracy. The included angle between two cones has also been investigated, and the smaller angle generally leads to the larger electric field induced along the symmetric axis directing to the human head. In addition, to get good stimulation, TMS coil should be as close to the head as possible in the desired stimulation region. Fig 2. Influences of distance between coils on the magnitude of electric field on the distribution of the magnitude of electric field along symmetric axis directing to human head (a) and distribution of the magnitude of electric field in tissue fluid parallel to the connection of the center of the two cones (b).

[1] Hallett M. Transcranial magnetic stimulation[J]. Nature, 2000, 406(6792):147-150. [2] Rossi S, Hallett M, Rossini P M, et al. Safety, ethical considerations, and application guidelines for the use of transcranial magnetic stimulation in clinical practice and research. Clinical neurophysiology, 2009, 120(12): 2008-2039. [3] O'Reardon J P, Solvason H B, Janicak P G, et al. Efficacy and safety of transcranial magnetic stimulation in the acute treatment of major depression: a multisite randomized controlled trial. Biological Psychiatry, 2010, 67(2):15-7. [4] Nicolo P, Ptak R, Guggisberg A G. Variability of behavioural responses to transcranial magnetic stimulation: Origins and predictors. Neuropsychologia, 2015, 74:137.

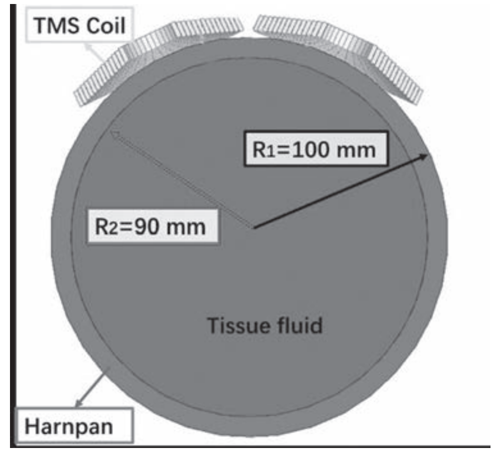

Fig. 1. TMS model of biconical coil model

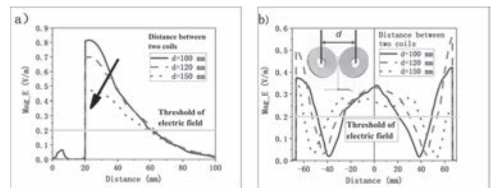

Fig. 2. Influences of distance between coils on the magnitude of electric field on the distribution of the magnitude of electric field along symmetric axis directing to human head (a) and distribution of the magnitude of electric field in tissue fluid parallel to the connection of the center of the two cones (b).

CP-13. Effects of Magnetic Stimulation on Insomnia Based on Brain Functional Networks.

H. Yu[1], W. Zheng[1], W. Xia[1], W. Ding[2], G. Xu[1] and L. Guo[1]
1. Hebei University of Technology, Tianjin, China, Tianjin, China; 2. Tianjin Beichen District Chinese Medicine Hospital, Tianjin, China

Abstract: Sleep disorders, particularly insomnia, affect a great percentage of the population. Electroacupuncture (EA) and transcutaneous electric stimulation (TES) have been introduced into clinical practice to treat insomnia. Magnetic stimulation has more advantages than electric stimulation. In this paper, magnetic stimulation was used to stimulate acupuncture points (acupoints), 32-channel electroencephalography (EEG) signals were recorded before and after stimulation. Brain functional networks were constructed based on EEG data to determine whether magnetic stimulation at acupoints could treat insomnia or not. The results suggested that magnetic stimulation at acupoints might be an effective treatment for insomnia. Keywords: magnetic stimulation, brain network, acupuncture point, insomnia I.Introduction Magnetic stimulation has the advantage of being less painful and uncomfortable than electric stimulation, and it is possible to convey impulses toward the deep tissues without attenuation of the stimulus intensity [1]. And now, transcranical magnetic stimulation (TMS) offers promising non-invasive, surgery-free medical treatment of neurological ailments [2]. Peripheral magnetic stimulation has been gradually developed [3]. II.Materials And Methods Eighteen right-handed (9 insomnia, 9 healthy) subjects were chosen, with consent obtained before the study. Magnetic stimulation was used to stimulate PC6 (Neiguan), HT7 (Shenmen) and SP6(Sanyinjiao) acupoints, respectively. Frequency of stimulation was 1Hz. Intensity of stimulation was 80% of the maximal (2.2 T). Each insomnia subject was stimulated 6 minutes each time for 3 days. 32-channel EEG signals were recorded before and after magnetic stimulation. Brain functional networks at different stages were constructed and analyzed to explore the effects of magnetic stimulation at acupoints. III.Results Compared to healthy subjects, insomnia subjects' brain functional connections between frontal and other lobes decreased, and the efficiency of brain information transmission were reduced. For insomnia subjects, after magnetic stimulation at acupoints, the connections and the information transmission efficiency of corresponding brain regions were improved, as shown in Fig.1 and Fig. 2. IV.Discussion For insomnia subjects, after magnetic stimulation at acupoints, the correlation between different cerebral cortex regions was strengthened in contrast with that of before stimulation. The results indicated that after magnetic stimulation at acupoints, the synchronization of each relevant cortex functional regions was increased. Temporal synchronization of cerebral electrical activity plays an important role in brain function [4]. It suggested that magnetic stimulation at acupoints might be an effective treatment for insomnia. Acknowledgment This work was supported by the Natural Science Foundation of China under Grant No.31400844.

M. Sekino, S. Ueno. "Comparison of current distributions in electroconvulsive therapy and transcranial magnetic stimulation," *J Appl Phys*, vol. 91, pp. 8730-8732, 2002. D. M. Stephen, J. S. Spencer, L. H. Ravi, et al. "Thermal and Mechanical Analysis of Novel Transcranial Magnetic Stimulation Coil for Mice," *IEEE Trans. Magnetics*, vol. 50, 5100805, 2014. B. Luber, S. H. Lisanby. "Enhancement of human cognitive performance using transcranial magnetic stimulation (TMS)," *NeuroImage*, vol. 85, pp. 961-970, 2014. S. T. Marzieh, J. Mahdi, G. K. Maria. "synchronizability of EEG-Based Functional Networks in Early Alzheimer's Disease," *IEEE Trans. Neural Systems and Rehabilitation Engineering*, vol. 20, pp. 636-641, 2012.

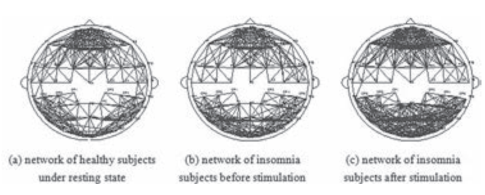

Fig. 1. brain functional networks under different states.

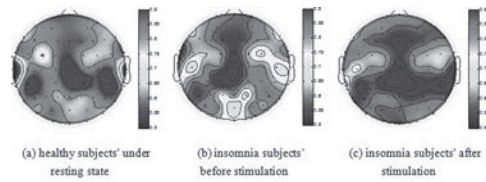

Fig. 2. information transmission efficiency of brain functional networks under different states.

CP-14. Effects of Magnetic Stimulation on the Proliferation of Dopaminergic Neuronal Cells Grown in Extracellular Matrix.

X. Zhong[1], J.C. Boldrey[1], I.C. Schneider[2], L. Que[1] and D.C. Jiles[1]
1. Electrical and Computer Engineering, Iowa State University, Ames, IA, United States; 2. Chemical and Biological Engineering, Iowa State University, Ames, IA, United States

Transcranial Magnetic Stimulation (TMS) is a neuromodulation technique which is capable of non-invasively activating the neurons in the brain. TMS has been an approved method of treatment for major depressive disorders by the US Food and Drug Administration (FDA) since 2008. The major principle in TMS is electromagnetic induction. The time-varying magnetic field generated by the TMS stimulator induces an electric field in conductive brain tissues which activates neurons by depolarization. However, limited studies have reported the effects of the magnetic fields used in TMS on individual neurons and in cell cultures, especially on neuronal cells grown in a three-dimensional extracellular matrix (3D ECM). The main function of a 3D ECM is to provide the biochemical and structural support to the surrounding cells that is found in vivo. The protein collagen is the major component of the ECM that plays an important role in giving cells strength and structural integrity. Hyaluronon is a polysaccharide found in the ECM of all vertebrates. It is known to provide support and protection to the cells within the ECM. Poly-D-Lysine (PDL) is a positively charged amino acid polymer used to help cells bind to substrates such as glass and plastic. Based on these theories, we investigated the effects of magnetic fields generated by a monophasic TMS stimulator using a 90 mm circular coil on the N27 rat dopaminergic neuronal cell line grown on two-dimensional (2D) and in three-dimensional (3D) ECMs. In our experiments, collagen-coated functionalized glass cover slips and PDL coated cover slips were used as 2D ECM for cell growth. Images of both, stimulated group and non-stimulated group, were captured at five time points from the stimulation time (0 hour) to 72 hours. Cells were counted, averaged and plotted. The results of our experiments showed that the magnetic stimulation decreased the growth rate of the N27 cells in comparison to the non-stimulated control group. However, it was observed that the collagen coating helped the cells to be more resistant to this negative effect caused by magnetic stimulation. We concluded that the magnetic stimulation used in our study decreased the proliferation of N27 dopaminergic neuronal cells and that collagen plays a role in protecting the cells from adverse effects of strong magnetic fields. Experiments currently underway are studying the effects that magnetic fields have on N27 cells within 3D ECM of collagen and 3D ECM of collagen/hyaluronon.

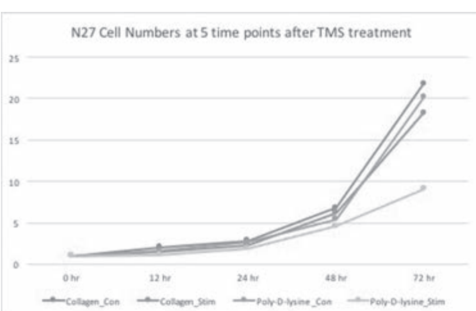

Fig. 1. N27 cell numbers at 5 time points after stimulation in each treatment and control group

CP-15. Computational Safety Study of Combination Treatment: Deep Brain Stimulation and Transcranial Magnetic Stimulation.

F. Syeda[1], C.H. Serrate[1], H. Magsood[1], K. Holloway[2,3] and R.L. Hadimani[1]
1. Mechanical and Nuclear Engineering, Virginia Commonwealth University, Glen Allen, VA, United States; 2. McGuire Research Institute, Hunter Holmes McGuire Veterans Affairs Medical Center, Richmond, VA, United States; 3. Department of Neurosurgery, Virginia Commonwealth University Health System, Richmond, VA, United States

Patients of Parkinson's Disease (PD) suffer from debilitating symptoms and complications, including bradykinesia, resting tremor, shuffling gait, and rigidity as well as non-motor symptoms including speech and swallowing difficulties. [1] [2] [3] PD patients often receive deep brain stimulation (DBS) surgery, in which one or two electrical leads are inserted into the subthalamic nucleus (STN) or globus pallidus internus (GPi), and current is continuously delivered to these nuclei from a battery pack inserted into a chest pocket.[4] [5] [6] DBS has been shown to effectively eliminate motor symptoms in patients of both PD as well as Essential Tremor. [4] [5] [7] However, one of the more crippling symptoms of PD that is not treated by DBS is hypophonic speech and swallowing difficulty (dysphagia). The mouth motor area of the primary motor cortex is thought to play a role in the pathophysiology of these symptoms and manipulation of this cortex through repetitive Transcranial Magnetic Stimulation (rTMS) has been proposed as a treatment option. [2] [8] [9] [10] [11] [12] rTMS is a non-invasive neuromodulation therapy which utilizes time-varying magnetic fields to induce electric fields in the patient's brain, thus stimulating neurons in the targeted region. [13] [14] [15] However, the potential for electromagnetic interference from the magnetic fields of rTMS with the conductive leads of DBS has prevented serious consideration of the combination therapy. Primarily, there is concern regarding eddy currents, which are induced on conductive surfaces caused by time-varying magnetic fields. It is hypothesized that B-fields from rTMS may induce such currents on the surface of any conductive part of the lead, and this current would travel along the lead down to the contacts, in turn stimulating the deep brain nuclei which the contacts target. We posit that this issue has yet to be studied with proper models and parameters. The objective of this study is to calculate induced current and temperature increase from TMS in DBS leads that have been implanted in the patient's brain. We have developed a novel, highly complex DBS lead in SolidWorks, using parameters from commercially available Medtronic lead 3387. It is composed of the insulating sleeve, four independent wires with wire insulation, and 4 contacts at the lead tip. Additionally, we use newly-developed head models created using MRI images of real patients, downloaded from the online database ADNI PPMI. These models include separate geometries for grey matter, white matter, cerebrospinal fluid, skin, skull, and cerebellum.[16] We perform simulations using the Finite Element Analysis software known as Sim4Life, which has been developed by Zurich Medtech for the purposes of simulating the effects of EM fields on biological tissue. Using simulation results, we calculate voltage values in the DBS lead, as can be seen in Figure 1. Note that in all cases the induced voltage values are on the order of mV, three orders of magnitude below the typical voltage values of DBS stimulation (about 1 V). For this reason, it is clear that our simulations show that for a DBS lead positioned medially in the patient's head, TMS in the mouth area of the primary motor cortex is safe and will not induce a voltage comparable to DBS stimulation. Additionally, thermal simulations were performed for t = > 30 min, with TMS being in the "on" state from t = 20 min to t = 50 min. The initial time of 20 minutes was given for the simulation to bring all tissue to their respective initial conditions, which place various parts of the brain between 37 and 37.3° C. TMS was then switched on, and left on for 30 minutes, until t = 50 min. Cooldown was then observed. The results show that although there is slight increase in temperature in the tissue close to TMS coils (T_{max} = 37.45° C)as well as the DBS lead (T_{max} = 37.3° C), maximum temperature does not exceed 37.45° C in any part of the brain, which is a negligible increase in temperature. Temperature variation over time on the gray matter surface can be seen in Figure 2. Therefore, our simulations suggest that TMS in the presence of DBS leads is safe, both in terms of electromagnetic interference as well as temperature increase. However, experimental verification is required to be certain that TMS/DBS combination therapy will not cause any harm to the patient in a real-world scenario.

[1] J. Jankovic, "Parkinson's disease: clinical features and diagnosis.," *Journal of neurology, neurosurgery, and psychiatry*, vol. 79, no. 4, pp. 68– 76, 2008. [2] L. Hartelius and P. Svensson, "Speech and swallowing symptoms associated with Parkinson's disease and multiple sclerosis: A survey," *olia Phoniatrica et Logopaedica*, vol. 46, no. 1, pp. 9– 17, 1994. [3] K. R. Chaudhuri, D. G. Healy, and A. H. Schapira, "Non-motor symptoms of Parkinson's disease: diagnosis and management," *The ancet Neurology*, vol. 5, no. 3, pp. 235–245, 2006. [4] R. J. Coffey, "Deep brain stimulation devices: A brief technical history and review," 2009. [5] J. S. Perlmutter and J. W. Mink, "DEEP BRAIN STIMULATION," *Annual Review of Neuroscience*, vol. 29, no. 1, pp. 229–257, 2006. [6] A. M. Lozano and N. Lipsman, "Probing and Regulating Dysfunctional Circuits Using Deep Brain Stimulation," vol. 77, no. 3, pp. 406–424, 2013. [7] W. C. Koller, K. E. Lyons, S. B. Wilkinson, a. I. Troster, and R. Pahwa, "Long-term safety and efficacy of unilateral deep brain stimulation of the thalamus in essential tremor.," *Movement disorders : official journal of the Movement Disorder Society*, vol. 16, no. 3, pp. 464–468, 2001. [8] M. Kobayashi and A. Pascual-Leone, "Transcranial magnetic stimulation in neurology," *The Lancet Neurology*, vol. 2, no. 3, pp. 145–156, 2003. [9] A. Pascual-Leone, J. Valls-Sole, E. M. Wassermann, and M. Hallett, "Responses to rapid-rate transcranial magnetic stimulation of the human motor cortex.," *Brain : a journal of neurology*, vol. 117 Pt 4, pp. 847–58, 1994. [10] A. Pascual-Leone, D. Nguyet, L. G. Cohen, J. P. Brasil-Neto, A. Cammarota, and M. Hallett, "Modulation of muscle responses evoked by transcranial magnetic stimulation during the acquisition of new fine motor skills.," *Journal of neurophysiology*, vol. 74, no. 3, pp. 1037–45, 1995. [11] S. C. Blank, S. K. Scott, K. Murphy, E. Warburton, and R. J. Wise, "Speech production: Wernicke, Broca and beyond," *Brain*, vol. 125, no. 8, pp. 1829–1838, 2002. [12] P. T. Fox, a. Huang, L. M. Parsons, J. H. Xiong, F. Zamarippa, L. Rainey, and J. L. Lancaster, "Location-probability profiles for the mouth region of human primary motor-sensory cortex: model and validation.," *NeuroImage*, vol. 13, pp. 196–209, 2001. [13] M. S. George, S. H. Lisanby, and H. A. Sackeim, "Transcranial magnetic stimulation: Applications in neuropsychiatry.," *Archives of General Psychiatry*, vol. 56, no. 4, pp. 300–311, 1999. [14] M. S. George, Z. Nahas, M. Molloy, A. M. Speer, N. C. Oliver, X. B. Li, G. W. Arana, S. C. Risch, and J. C. Ballenger, "A controlled trial of daily left prefrontal cortex TMS for treating depression," *Biological Psychiatry*, vol. 48, no. 10, pp. 962–970, 2000. [15] M. Hallett, "Transcranial magnetic stimulation and the human brain.," *Nature*, vol. 406, pp. 147–150, 2000. [16] F. Syeda, H. Magsood, E. G. Lee, A. A. ElGendy, D. C. Jiles, and R. L. Hadimani, "Effect of anatomical variability in brain on transcranial magnetic stimulation treatment," *AIP Advances*, vol. 7, p. 056711, may 2017.

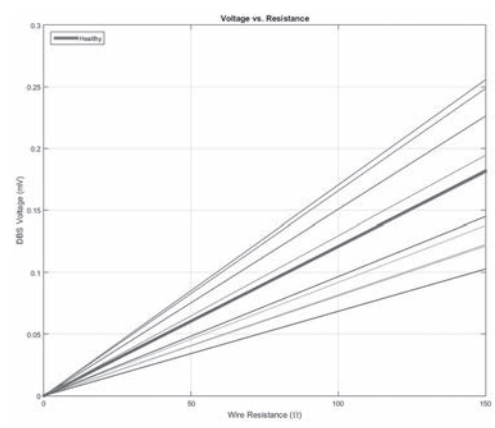

Fig. 1. Voltage induced in lead wire for 11 models across a range of resistance values. Note the scale of induced voltage is in mV.

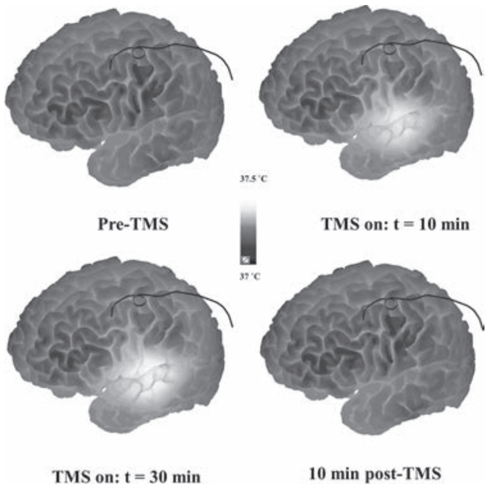

Fig. 2. Temperature variation on gray matter surface when TMS is turned on for 30 min.

CP-16. Study on the Effects of Magnetic Stimulation on K-Ras-Driven Lung Cancer in Mice.

N. Zhang[1,2], S. Ning[3], *S. Wang*[1], C. Zhang[2], S. Wang[1] and P. Hao[1]
1. State Key Laboratory of Electrical Insulation and Power Equipment, Faculty of Electrical Engineering, Xi'an Jiaotong University, Xi'an, China; 2. Department of Oncology, Johns Hopkins University School of Medicine, Baltimore, MD, United States; 3. College of Electrical and Information Engineering, Shaanxi University of Science and Technology, Xi'an, China

I. INTRODUCTION Mutations in the K-Ras gene are more common in primary lung adenocarcinoma than others. The effects of chemotherapy and radiation therapy to K-Ras mutation lung cancer are not ideal. Decades of research have proved that there are significant differences in electrical characteristics between cancer cells and normal cells. According to this phenomenon, the positive effect of electromagnetic stimulation on cancer treatment is receiving increasing attention [1]. The electric field could change the direction of dipoles within the target cells and lead to tumor cell apoptosis [2]. Clinical trials lead to Food and Drug Administration approval for the Tumor treating field treatment of recurrent glioblastoma. However, the electric field could not penetrate into biological tissues very deeply due to the various of impedance. Because of the disadvantages of the electric field, the biological effect of magnetic field stimulation is receiving increasing attention. For a similar relative permeability, the magnetic field can easily reach the position deep inside the tissue, avoiding the problems that were caused by an electric field. Previous studies have shown that the extremely low-frequency magnetic field significantly inhibited cell growth and induced apoptosis of prostate cancer cells in vitro [3]. Based on the A549 lung tumor cell experiment that was carried out in our preceding study, the initial frequency for tumor suppression was also studied [4]. Although the principle has not been fully discovered, magnetic field stimulation suggests a new way of tumor inhibition. In this research, a variable magnetic field stimulation system and a pair of stimulation coil were designed to find the inhibition effect of magnetic field stimulation on K-Ras-driven lung cancer in mice. The magnetic field distribution was calculated by the finite element method. The biological experiments were carried out to verify the inhibition of cell growth. The western blotting result showed that the magnetic stimulation inhibited the K-Ras-driven lung cancer cells noninvasively. II. SIMULATIONS AND MAGNETIC STIMULATION SYSTEM During the experiments, as shown in Fig. 1(a), stimulation coils were set on both sides of the holder. Mice holder can provide a dark environment at the end of the other side; the mouse keeps calm and peace during the magnetic stimulation. Based on the sensitive frequency and the intensity of the A549 cell line, the stimulation coil is designed by FEM calculation. The stimulation coil can be regarded as many single-turn coils of different radius. The magnetic flux density generated by the single-turn coil current can be determined by Biot-Savart's law. In the animal experiment, the RMS voltage of the stimulation coil is 30V. According to the previous study on the magnetic flux density calculation, the maximum magnetic flux density at the position of the lung in mice is 2.2 mT by programming. The visual simulations were carried out in Fig.1 (b). As shown in Fig. 1(a) and (c), the system consisted of a signal generator and a pair of stimulation coils. The signal generator was composed of a microchip, a keyboard, and an H-type circuit. The frequency of the magnetic stimulation could be changed easily by changing the value of the timer on the microchip. The stimulus intensity could also be adjusted by regulating the voltage of the H-type circuit. III. EXPERIMENTS AND RESULTS Experiments: All the tumors in mice were activated by using adenovirus-based delivery of Cre recombinase into lung epithelial cells. After four weeks, mice with tumors were ready for magnetic stimulation. The selected 20 mice were divided into the stimulation group and control group. Stimulation group is given 2 hours' magnetic field stimulation every day and none of the control group. Results: Nuclear factor erythroid-2 related factor-2 (Nrf2) is a redox-sensitive transcription factor that confers cytoprotection against oxidative stress and apoptosis in normal cells [5]. After two weeks, the dimension of tumor in stimulation group is 13.7% lower than that of the control group. As shown in Fig. 2, the Nrf2 gene was suppressed in lung tumor cells, and measured by western blotting. Therefore, the growth of K-Ras-driven lung cancer has been slowed down. IV. CONCLUSION In this paper, a magnetic stimulation system with stimulation coil for K-Ras-driven lung cancer in mice was proposed. The principle of magnetic stimulation on cancer cells is analyzed. The parameters of stimulation coils were calculated and optimized for animal experiments. The magnetic flux density at lung of mice was simulated by numerical calculation and the finite elements method. The biological experiments were conducted by two week's stimulation. The animal experiment results showed that the expression of Nrf2 had been suppressed. This approach could also suggest another way to treat cancer noninvasively.

[1] Swanson, Kenneth D., Edwin Lok, and Eric T. Wong. "An overview of alternating electric fields therapy (NovoTTF therapy) for the treatment of malignant glioma," *Current neurology and neuroscience reports*, Vol. 16, no. 1, pp. 8, 2016. [2] Kirson, Eilon D., et al. "Alternating electric fields arrest cell proliferation in animal tumor models and human brain tumors," *Proceedings of the National Academy of Sciences*, Vol. 104, no. 24, pp. 10152-10157, 2007. [3] Koh, Eui Kwan, et al. "A 60-Hz sinusoidal magnetic field induces apoptosis of prostate cancer cells through reactive oxygen species," *International journal of radiation biology*, Vol. 84, no. 11, pp. 945-955, 2008. [4]Zhang, Naming, et al. "Theoretical Analysis and Design of a Variable Frequency Magnetic Field Stimulation System for Tumor Suppression," *IEEE Transactions on Applied Superconductivity*, Vol. 26, no. 7, pp. 1-4, 2016. [5] Singh, Anju, et al. "RNAi-mediated silencing of nuclear factor erythroid-2–related factor 2 gene expression in non–small cell lung cancer inhibits tumor growth and increases efficacy of chemotherapy," *Cancer research*, Vol. 68, no. 19, pp. 7975-7984, 2008.

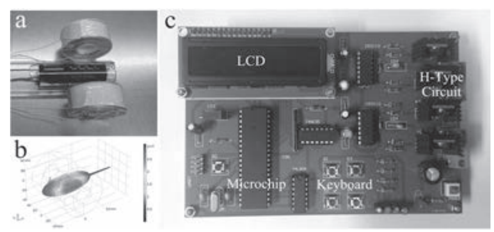

Fig. 1. (a)The mice holder with Stimulation coils. (b) Visual simulations of magnetic flux density. (c)Prototype of magnetic field generator for vivo experiment.

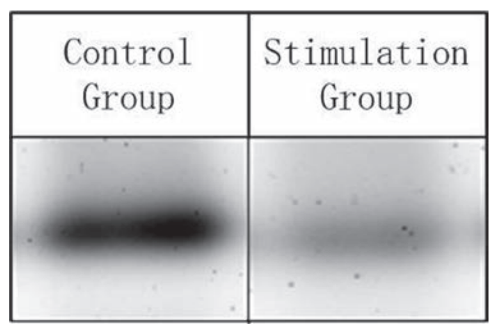

Fig. 2. Nrf2 Gene expression (by Western Blot)

WEDNESDAY MORNING, 25 APRIL 2018 SIMPOR/ROSELLE BALLROOM, 8:30 TO 11:30

Session CQ
DOMAIN WALLS AND SKYRMIONS
(Poster Session)

Yan Zhou, Chair
The Chinese University of Hong Kong, Shatin, Hong Kong

CQ-01. Measurement of tilted magnetic anisotropy of quasi-perpendicularly magnetized Ta/Pt/CoFeB/Pt multilayers.

S. Guddeti[1] and P. Kumar[1]
1. Department of Physics, Indian Institute of Science, Bangalore, India

In the field of ultra thin film magnetism, the study of domain wall dynamics in perpendicularly magnetized systems has garnered significant attention. These offer improved functionalities like lower energy consumption for data storage technologies than current TMR based MRAM and possible three dimensional storage [1]. In such systems where the magnetization reversal is mediated by the Spin Hall effect, the chirality of the domain wall becomes critical [2,3,4]. However, due to the stochastic nature of nucleation, domain wall of either chirality is equally likely. An external biasing magnetic field is required to deterministic generation of domain wall of particular chirality leading to deterministic reversal. Recent studies on quasi-perpendicularly magnetized Pt/Co/Pt trilayers with tilted anisotropy have shown it is possible for deterministic reversal thereby eliminating the need for a biasing field [5]. In the present paper, we have studied tilted magnetic anisotropy in quasi perpendicularly magnetized Ta/Pt/CoFeB/Pt system using vibrating sample magnetometry (VSM). We also performed Magneto-Optic Kerr Effect (MOKE) microscopy to study the effect of the tilt in the anisotropy on the domain wall motion mediated reversal. Ta/Pt/CoFeB/Pt is well known perpendicularly magnetized system [6]. A tilt in the anisotropy can be obtained with a thickness gradient in CoFeB layer. We have grown quasi-perpendicularly magnetized Ta/Pt/CoFeB/Pt multilayer films on SiO_2 substrate using oblique-angle sputter deposition technique. We perform detailed investigations on two sets of multilayer thin films of Ta(3 nm)Pt(3 nm)CoFeB(x nm)Pt(1 nm) corresponding to with and without thickness gradient in CoFeB layer. In order to have uniform thickness of the layers, the substrate is rotated in-situ using stepper motor. Polar-MOKE measurements indicate perpendiculary magnetized films for x varying from 0.6 nm to 1.5 nm. There is no ferromagnetic hysteresis at room temperature for films below thickness 0.6 nm of CoFeB layer. Above 1.5 nm thickness of CoFeB layer, films show in-plane anisotropy. High field in-plane and low field out-of-plane M-H measurements are performed to calculate the anisotropy constant 8.93 x 10^5 J/m^3 for Ta(3 nm)Pt(3 nm)CoFeB(0.7 nm)Pt(1 nm) thin film. For the set of samples with thickness gradient in CoFeB layer, we calculate the tilt in anisotropy in quasi-perpendicularly magnetized films using Kerr microscopy by applying an additional biasing in-plane field H_x. Component of H_x along the tilted anisotropy axis acts as a bias field, $H_{tilt} = H_x \sin(\theta)$, where θ is the tilt angle. H_{tilt} contributes to shift in the hysteresis loop observed in Kerr microscopy. The shift in hysteresis loop is shown in Fig 1. The effect of tilt is captured by the slope of shift(H_{tilt}) vs in plane field (H_x) as shown in Figure 1. The effect of the tilt can be maximised by rotating the sample in-plane such that the in-plane component of the tilt axis lies along the direction of in-plane field. Figure 2 gives the variation of slope with azimuthal orientation for Ta(3 nm)Pt(3 nm)CoFeB(0.6 nm)Pt(1 nm) sample, from which the tilt is estimated to be 0.7°. To capture the effect of tilt on domain wall motion, Ta(3 nm)Pt(3 nm)CoFeB(0.6 nm)Pt(1 nm) thin film is patterned into a wire of width 10 um with an extended pad for domain wall nucleation as shown in Figure 2. The devices are patterned using optical lithography and ion beam etching. After patterning the switching fields are increased due to possible degradation of sample during etching. Preliminary current induced reversal measurements using a pulsed current density of 5.9 x 10^{11} A/m^2 of 100 μs pulse width indicate partial switching of the wire as shown in Figure 2. Due to the limitation of applying out-of-plane fields not higher than 150 Oe in the in-house instrumentation, the device is partially reversed. In conclusion, we report estimation of tilt in anisotropy of quasi-perpendicularly magnetized Ta(3 nm)Pt(3 nm)CoFeB(x nm)Pt(1 nm) thin films and preliminary measurements of current induced domain wall dynamics.

1.Parkin *et. al.* "Magnetic domain wall racetrack memory" *Science* 320,5873,190-194 (2008) *2.Haazen et. al.* "Domain wall depinning governed by the spin Hall effect" *Nature Materials* 12, 299–303 (2013) 3.Emori *et. al.* "Current-driven dynamics of chiral ferromagnetic domain walls" *Nature Materials* 12, 611–616 (2013) 4.Torrejon *et. al.* "Interface control of the magnetic chirality in CoFeB/MgO heterostructures with heavy-metal underlayers" *Nature Communications* 5, Article number: 4655 (2014) 5. Vineeth *et. al.* "Spin Hall effect mediated current-induced deterministic switching in all-metallic perpendicularly magnetized Pt/Co/Pt trilayers" *Physical Review B* 96, 104412 (2017) 6.Kai *et. al.* "Asymmetric spin-wave dispersion due to Dzyaloshinskii-Moriya interaction in an ultrathin Pt/CoFeB film" *Applied Physics Letters* 106, 052403 (2015)

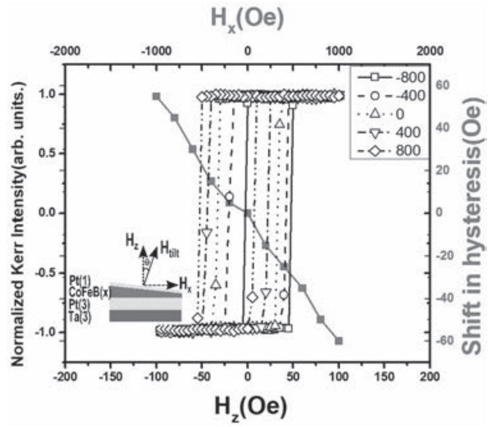

Fig. 1. Out-of-plane hysteresis loop in black are measured under a fixed biasing in-plane field shows shift of the loop as the biasing field varies from 800 to -800 Oe in Ta(3 nm)Pt(3 nm)CoFeB(0.6 nm)Pt(1 nm) thin film. This shift(top axis) with respect to the in-plane field H_x(right axis) is plotted in red.

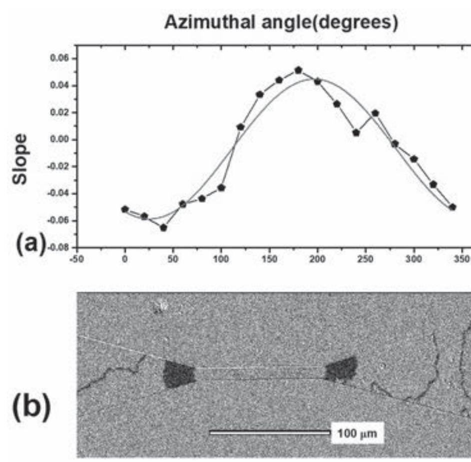

Fig. 2. (Top) The slope of the shift vs in-plane field is plotted with respect to rotation of the sample. The data is fit to $H_z \cos(\theta) + H_x \sin(\theta) \cos(\Phi) = H_c$ where θ is the tilt as shown in Figure 1,Φ is the azimulthal angle and H_c is the switching field. This gives tilt of 0.7°. (Bottom) Kerr micrograph of wire of width 10 μm with an extended pad of Ta(3)Pt(3)CoFeB(0.6)Pt(1). On passing 100 μs of 5.9 x 10^{11} A/m^2 current, there is a partial reversal of domains.

CQ-02. Pinning sites with tilted magnetization for domain wall motion control in racetrack memory.

T. Jin[1], F. Tan[1], C.C. Ang[1], W. Gan[1], J. Cao[2], W. Lew[1] and S. Piramanayagam[1]
1. Nanyang University, Division of Physics and Applied Physics, School of Physical and Mathematical Sciences, Singapore, Singapore; 2. Lanzhou University, Lanzhou, China

Domain wall based devices such as racetrack memory have been proposed as promising candidates for high capacity, non-volatile information storage [1,2]. In these devices, multiple domain walls can be propagated through nanowires at speeds of many hundreds m/s using spin transfer torque, thus allowing data to be written, read and processed. One of the main challenges towards the commercial realization for domain wall memory is the stochasticity of domain wall motion. In thin film systems, where domain wall motion is the dominant reversal mechanism, the magnetization reversal does not happen in a controlled fashion but instead forms zig-zag domains extending over several micrometers in length to form. Such stochastic behavior limits the maximum data density. To overcome this issue, researchers have used lithographically fabricated notches to act as domain wall pinning centers [3]. The other method to form pinning centers is based on exchange bias [4]. In our previous study, we proposed the use of non-magnetic metal diffusion or ions implanted locally to control and pin domains in nanowires [5]. In this report, we demonstrate the formation of pinning centers by using exchange interaction between films with perpendicular magnetic anisotropy and in-plane magnetization to create locally tilted magnetization. The perpendicular magnetic anisotropy (PMA) material Ta (1)/ Pt (5)/[Co (0.3)/ Ni (0.4)]$_3$ (all thickness values are in nm) multilayers were deposited on Si (SiO_2) substrate and the in-plane magnetic (IMA) anisotropy material $Co_{10}Ni_{90}$ (2.5 nm) alloy was grown on top of the PMA layer. The thickness of a Pt spacer layer between the PMA layer and IMA layer was varied to tune the angle of magnetization. Figure 1 (a) shows film stack studied in this report. The hysteresis loops of films with various Pt spacer layer thickness in the in-plane direction and out-of-plane direction are shown in (b) and (c) respectively. At Pt layer thickness below 2 nm, the switching behavior of the PMA and IMA layer suggests the presence of exchange interaction between the layers. While a thicker Pt layer of 5 nm causes the switching behavior to be independent of each other and thus increasing the coercivity [6]. Mumax3 simulation was performed to study the domain wall pinning effect and depinning current with various tilt angles. Figure 2 (a) shows the domain wall propagation without pinning. Figure 2 (b) shows domain wall propagation with a pinning center, where the magnetization is tilted at 5 degrees from the perpendicular axis. The result shows that the domain wall is pinned at the edge of the pinning center. Our results further indicate that the magnetization tilt angle can be increased to decrease the barrier energy, which reduces the depinning current as demonstrated in figure 2 (c).

[1] S. Parkin, *et al.* Magnetically engineered spintronic sensors and memory. *Proceedings of the IEEE* 91 5, 661-680, (2003). [2] R. Sbiaa, & S. N. Piramanayagam, Multi-level domain wall memory in constricted magnetic nanowires. *Applied Physics a-Materials Science & Processing* 114 4, 1347-1351, (2014). [3] D. Atkinson, D. S. Eastwood, and L. K. Bogart, Controlling domain wall pinning in planar nanowires by selecting domain wall type and its application in a memory concept, *Appl. Phys. Lett.* 92, 022510 (2008). [4] I. Polenciuc, A. J. Vick, D. A. Allwood, T. J. Hayward, G. Vallejo-Fernandez, K. O'Grady, and A. Hirohata, Domain wall pinning for racetrack memory using exchange bias. *Appl. Phys. Lett.* 105, 162406 (2014). [5] T. L. Jin, M. Ranjbar, *et al.* Tuning magnetic properties for domain wall pinning via localized metal diffusion, *Sci. Rep.* 7, 16208 (2017). [6] K. K. M. Pandey, J. S. Chen, *et al.* Interlayer coupling and switching field of exchange coupled media, J. Appl. Phys. 105, 07B733 (2009).

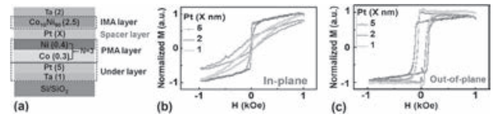

Fig. 1. (a) Schematic diagram of film stack. (b) The hysteresis loops with various Pt spacer layer thickness in the in-plane direction and (c) out-of-plane direction.

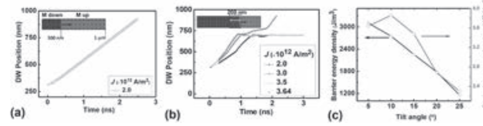

Fig. 2. (a) Domain wall propagation without pinning and (b) domain wall propagation with pinning center forming by tilting magnetization (M) of 5 degrees. (c) Change in barrier energy density and depinning current density with various tilt angles.

CQ-03. Role of Effective Anisotropy in Temperature Gradient-induced Skyrmion Motion.

X. Wang[1], W. Gan[2], T. Jin[2] and W. Lew[2]
1. School of Science, Lanzhou University of Technology, Lanzhou, China; 2. School of Physical and Mathematical Sciences, Nanyang Technological University, Singapore, Singapore

Skyrmions are promising candidates for information storage applications due to its small size and high thermal stability. While current-induced skyrmion motion has been the focus of many scientific efforts,[1] we show that skyrmion motion induced by thermal gradient is also significant. Several works have already shown that the skyrmion moves towards the hotter region and its speed is proportional to the temperature gradient. However, most existing theories cannot explain the phenomena completely,[2] such as the strong dependence of velocity on skyrmion size. In this work, we propose an intuitive yet comprehensive explanation: the thermal gradient creates a gradient in effective perpendicular magnetic anisotropy, leading to an inhomogeneous energy landscape that creates a driving force. Fig. 1(a) shows that the effective anisotropy field (H_K) and saturation magnetization (M_s) of skyrmion system decrease with the increase of temperature. As effective perpendicular magnetic anisotropy $K_{u,eff}=\mu_0 M_s H_K$, the increase of temperature causes the decrease anisotropy. The energy attributed to the K_u is given by: [3] $E_{Ku}=-K_u(m\bullet z)^2\pi R_{sk}^2 d$ (1) where d is the thickness of skyrmion system, R_{sk} is the radius of skyrmion. These indicate that the increase of temperature leads to the decrease of energy in skyrmion system, which means the total energy of a skyrmion is lower at high temperatures and the skyrmion will drift towards a region of higher temperature to minimize energy. Considering the inhomogeneous energy landscape caused by temperature gradient as a force acting on skyrmion, larger temperature gradient leads to higher average speed of skyrmion motion, which can be verified by Fig.1 (b). Estimating the anisotropy gradient caused by temperature gradient, we demonstrate the anisotropy gradient-induced skyrmion motion, which shows the same trend with temperature gradient-induced, as shown in Fig.1 (b). Furthermore, it was observed that the speed of the skyrmion increases slightly with its size. This phenomenon cannot be explained by the magnon current model developed by previous studies.[2] As we discussed above, positive temperature gradient leads to the decrease of magnetic anisotropy, the domain wall width is expected to increase, leading to a bigger skyrmion during the motion. To verify the effect of skyrmion size, in-plane and out-of-plane magnetic fields were applied. As shown in Fig. 2(a), the size of skyrmion change as a function of the external magnetic field applied in the direction of magnetic moment in the skyrmion center (z-axis), and there is no obvious impact of in-plane field on skyrmion size. The skyrmion velocity indeed changes proportionally to the skyrmion radius, shown in Fig. 2(b). This is consistent with our model, in which a larger skyrmion experiences larger inhomogeneous energy, leading to the increase in skyrmion velocity. In conclusion, we have developed a robust model describing the skyrmion motion in a temperature gradient. Such an understanding is critical for the design of skyrmion devices where pulsed currents are expected to generate temperature gradients.

[1] THIAVILLE A, NAKATANI Y, MILTAT J, et al. Micromagnetic understanding of current-driven domain wall motion in patterned nanowires [J]. EPL (Europhysics Letters), 2005, 69(6): 990. [2] KONG L, ZANG J. Dynamics of an insulating Skyrmion under a temperature gradient [J]. Physical review letters, 2013, 111(6): 067203. [3] BOULLE O, VOGEL J, YANG H, et al. Room-temperature chiral magnetic skyrmions in ultrathin magnetic nanostructures [J]. Nature nanotechnology, 2016, 11(5): 449-54.

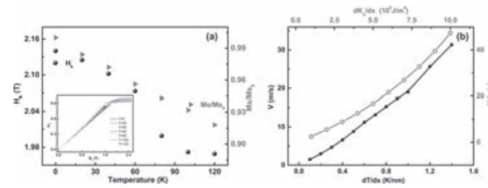

Fig. 1. (a) H_K, M_s decrease with the increase of temperature, indicating that the decrease of $K_{u,eff}$. Inset shows the hysteresis loops with different temperature. (b) Average velocity of skyrmion motion as a function of temperature gradient/ magnetic anisotropy gradient, showing the dependence of skyrmion motion.

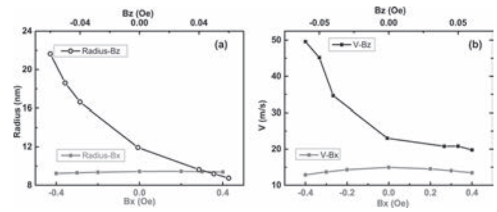

Fig. 2. (a) The change of skyrmion radius with respect to B_x/B_z. (b) The in-plane field (B_x) and out-of-plane field (B_z) as a function of velocity under $dK_u/dx=8\times10^{11}J/m^4$. indicating that the velocity of skyrmion motion corresponds to its size, which is determined by the effective anisotropy energy.

CQ-04. Multilevel Storage Based on Magnetic Skyrmion.

S. Luo[1] and L. You[1]
1. School of Optical and Electronic Information, Huazhong University of Science & Technology, Wuhan, China

Magnetic tunnel junction (MTJ) is the storage element of spin-transfer torque magnetic random access memory (STT-MRAM), consisting of two ferromagnetic (FM) layers separated by a tunneling layer. Generally, with the magnetization direction of two FM layers parallel or antiparallel, the MTJ exhibits two resistances R_p or R_{ap} due to the tunneling magnetoresistance (TMR) effect. The improvement on the TMR as well as the distinction between R_p and R_{ap} offers the possibility to divide the resistance of MTJ into multiple levels, so as to explore multilevel storage technology that is an efficient method to enhance the integration density of STT-MRAM [1,2]. Furthermore, magnetic skyrmion is also considered as the storage unit in new magnetic memory devices, which is an essentially topological spin texture with whirling configuration generated at the FM/heavy metal (HM) bilayer with Dzyaloshinskii–Moriya interaction (DMI) effect. From a practical application point of view, building MTJ stacks to locally address skyrmions is of great promise for future skyrmion based devices [3]. In this work, initialization-free multilevel storage can be implemented based on MTJ structure with an extended free layer (Fig. 1a), and is demonstrated by micromagnetic simulation. We find four resistance states of such a MTJ structure that are distinguished by changing the magnetization configurations with the coexistence of magnetic switching and skyrmion creation/annihilation by applying a current via spin-transfer torque (STT) effect. Comparing with conventional MTJ, the generation of skyrmion in free layer gives rise to another two resistance states except for R_p and R_{ap}, thanks to the non-linear configuration of skyrmion and this topological-phase-like transition. As expected, there exist four states in studied MTJ structures (Fig. 1b-e), according to the magnetization of two FM layers, namely, parallel (P), antiparallel (AP), quasi-parallel (Quasi-P) and quasi-antiparallel (Quasi-AP) states, the latter two denoted as the core of skyrmion is either in parallel or antiparallel with the fixed layer. We calculate the relative resistance R/R_p of the four states dependence on the ratio between the lateral diameter of MTJ stack (d_{MTJ}) and the diameter of skyrmion (d_{sk}). The results indicate that it is optimal to set $d_{MTJ}/d_{sk} \sim 1.2$, where the difference between any two resistance states is larger than 0.2 R_p to distinguish the four states as much as possible. The initialization-free operation of four states are obtained. P can be realized by a negative current with density of J_1 and duration of Δt_1 (Fig. 2a) while AP realized by a positive current of the same density and duration (Fig. 2b). Quasi-AP and Quasi-P can be realized by creating a skyrmion based on P and AP, respectively, with another current pulse of J_2 and Δt_2 (Figs. 2c-d). We find that the required current densities J_1 and J_2, of the order of $\sim 10^8$-10^9 A/cm^2 (Fig. 2e), are relatively large, mainly because of the mismatch between the fixed layer and free layer in dimension and the topological energy barrier for skyrmion creation. The delays Δt_1 and Δt_2, of the order of $\sim 10^1$-10^2 ps (Fig. 2f), are rather small, which is favorable for high-speed spintronics. The results presented in this work provide a completely new strategy for multilevel storage based on magnetic skyrmion that could not only lead to multi-functional applications but also provide novel insight into topological magnetism.

[1] X. Lou, et al., Appl. Phys. Lett. 93, 242502 (2008) [2] Y. Kim, et al., IEEE Trans. Electron. Dev. 62, 561 (2015) [3] W. Jiang, et al., Phys. Rep. 704, 1 (2017)

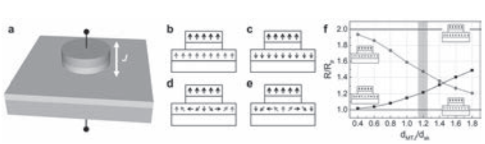

Fig. 1. (a) Structure of a MTJ stack with an extended free layer contacted with a heavy metal layer. (b-e) Four states of the studied MTJ, namely, (b) parallel (P), (c) antiparallel (AP), (d) quasi-antiparallel (Quasi-AP), and (e) quasi-parallel (Quasi-P). (f) Relative resistance R/R_p dependence on the ratio between the lateral diameter of MTJ stack (d_{MTJ}) and the diameter of skyrmion (d_{sk}).

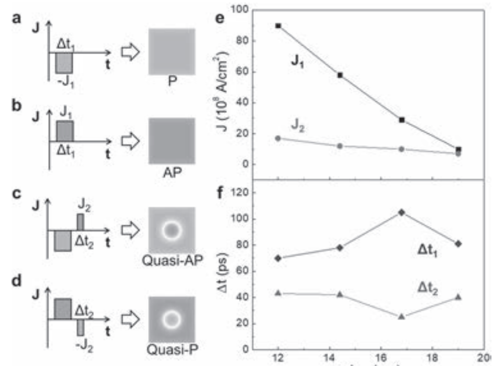

Fig. 2. Operations for (a) P, (b) AP, (c) Quasi-AP, and (d) Quasi-P states. (e) Required current density (J) and (f) duration (Δt) as functions of d_{MTJ}/d_{sk}.

CQ-05. Spin-hall effect-driven motion of chiral skyrmions in an anisotropy gradient.

R. Tomasello[1], S. Komineas[2], G. Siracusano[3], M. Carpentieri[4] and G. Finocchio[5]
1. Department of Engineering, University of Perugia, Terni, Italy;
2. Department of Mathematics and Applied Mathematics, University of Crete, Heraklion, Greece; 3. Department of Electric, Electronic and Computer Engineering, University of Catania, Catania, Italy; 4. Department of Electrical and Information Engineering, Politecnico di Bari, Bari, Italy;
5. Department of Mathematical and Computer Sciences, Physical Sciences and Earth Sciences, University of Messina, Messina, Italy

Magnetic skyrmions are localized non-uniform configurations of the magnetization with a unique fundamental feature to be topologically protected, i.e. they are characterized by an integer winding number Q[1]. According to the type of Dzyaloshinskii-Moriya interaction (DMI) and the material properties, different skyrmion patterns can be stabilized, such as Bloch and Néel[1] as well as antiskyrmions[2]. In this work, we will focus on Néel skyrmions, which are the most promising for applications. In fact, on the technological side, the possibility to electrically manipulate skyrmions[3–6] by means of spin-polarized currents, opens the way for many promising applications as information carriers in low-power microelectronic technologies[4,7]. To this aim, the analysis of the current-driven skyrmion motion becomes crucial. In particular, this motion is characterized by an in-plane angle with respect to the direction of the applied current, i.e. the skyrmion Hall angle. In an ideal system, micromagnetic simulations and the theoretical approach based on Thiele's equation[5,8] predict a constant skyrmion Hall angle independent of the value of the applied current. On the contrary, recent experimental observations[6] have shown that the presence of a perpendicular anisotropy linear gradient can strongly affect the spin-Hall effect (SHE)-driven skyrmion motion, and hence the skyrmion Hall angle, which cannot be predicted theoretically by the current form of Thiele's equation[5,8]. Here, we have combined micromagnetic simulations with an analytical model based on Thiele's formalism to investigate, from a fundamental point of view, the SHE-driven skyrmion motion in presence of a new force arising from a perpendicular anisotropy linear gradient. We have observed two key dynamics: (*i*) the presence of only the gradient leads the skyrmion to mainly move in the direction perpendicular to the gradient itself; (*ii*) the simultaneous action of gradient and SHE yields a skyrmion expansion while it moves, consequently leading to an accelerated motion. We consider a ferromagnet in a square geometry with side lengths L_x=L_y=400 nm and a thickness t_{FM}=1 nm (Fig. 1). This is coupled to a heavy metal layer (Pt) in order to achieve a sufficiently large interfacial DMI. Statics and dynamics of the magnetization are modeled by the Landau-Lifshitz equation where we add a Gilbert damping term and a Slonczewski term that models the spin-torque effect deriving from the SHE. We consider a current j_{HM} flowing along the *x*-axis and a spin polarization in the *y*-axis. We study the dynamical behavior of the skyrmion where a constant anisotropy gradient exists along the-direction (Fig. 1). Hence, the anisotropy coefficient K can be written as K=K_u+Gy, where K_u is the perpendicular anisotorpy constant at the center of the sample. In order to study this dynamical behavior, we assume a rigid skyrmion configuration that travels with a constant velocity v=(v_x,v_y). We also apply an out-of-plane field H_{ext}=50 mT. Figs. 2(a) and (b) show the effect of only the perpendicular anisotropy linear gradient G on the skyrmion motion. Both velocity components increase with the gradient. However, the skyrmion is characterized by a larger positive v_x and a very small negative v_y. The latter is due to a torque linked to the damping term. Heuristically, the skyrmion motion induced by the anisotropy gradient can be understood as follows. The presence of the anisotropy gradient gives rise to two different values of the effective field for the upper and lower in-plane magnetization of the skyrmion domain wall, where the magnetization is mainly oriented along the *y*-direction, thus generating two different conservative torques acting on the skyrmion (see inset in Fig. 2(a)). These torques do not balance each other leading to a resulting torque along the *x*-direction which induces the skyrmion motion. The larger is the skyrmion and/or the larger is the gradient, the faster is the motion. Moreover, the key result concerns the effect of the *y*-component of the velocity. The presence of the negative v_y leads the skyrmion to move towards a region with lower K_u, thus inducing its expansion[7,9]. For what explained above, a larger skyrmion undergoes a larger gradient, and hence, the torque from the gradient increases while the skyrmion moves along the negative *y*-direction. This induces an accelerated motion of the skyrmion. In order to describe correctly such a motion within the analytical framework, the Thiele's equation has to take into account a variable skyrmion diameter. This key analytical advance becomes more important when the skyrmion motion is driven by the SHE in presence of G, due to a larger expansion of the skyrmion. Figs. 2(c) and (d) show the velocity components as a function of the local K_u value linked to the linear gradient, for j_{HM}=10 MA/cm^2 and G=0.5 TJ/m^4. Analytics and micromagnetics agree well in predicting an increase of the velocity with the decrease of the K_u, and, therefore, in describining the accelarated motion of the skyrmion.

[1] G. Finocchio, F. Büttner, R. Tomasello, M. Carpentieri, and M. Kläui, J. Phys. D. Appl. Phys. 49, 423001 (2016). [2] A.K. Nayak, V. Kumar, T. Ma, P. Werner, E. Pippel, R. Sahoo, F. Damay, U.K. Rößler, C. Felser, and S.S.P. Parkin, Nature 548, 561 (2017). [3] J. Iwasaki, M. Mochizuki, and N. Nagaosa, Nat. Nanotechnol. 8, 742 (2013). [4] J. Sampaio, V. Cros, S. Rohart, A. Thiaville, and A. Fert, Nat. Nanotechnol. 8, 839 (2013). [5] R. Tomasello, E. Martinez, R. Zivieri, L. Torres, M. Carpentieri, and G. Finocchio, Sci. Rep. 4, 6784 (2014). [6] G. Yu, P. Upadhyaya, Q. Shao, H. Wu, G. Yin, X. Li, C. He, W. Jiang, X. Han, P.K. Amiri, and K.L. Wang, Nano Lett. 17, 261 (2017). [7] G. Finocchio, M. Ricci, R. Tomasello, A. Giordano, M. Lanuzza, V. Puliafito, P. Burrascano, B. Azzerboni, and M. Carpentieri, Appl. Phys. Lett. 107, 262401 (2015). [8] A.A. Thiele, Phys. Rev. Lett. 30, 230 (1973). [9] J. Ding, X. Yang, and T. Zhu, J. Phys. D. Appl. Phys. 48, 115004 (2015).

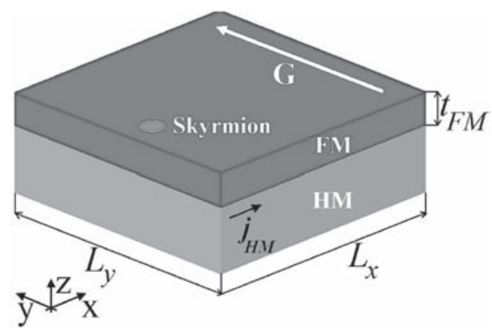

Fig. 1. a schematic representation of the ferromagnet/heavy metal bilayer under investigation, where the current j_{HM} and the gradient G are also indicated.

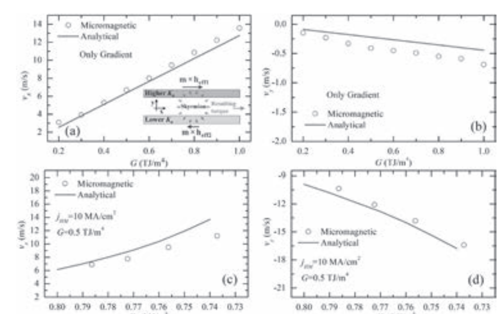

Fig. 2. skyrmion velocity components (v_x and v_y, respectively) as a function of (a) and (b) G with no current applied, (c) and (d) the perpendicular anisotropy constant along the gradient (G=0.5 TJ/m^4) for j_{HM}=10 MA/cm^2. Inset in (a): schematic representation of the skyrmion circular domain wall in presence of the anisotropy gradient. The two different conservative torques are indicated.

CQ-06. Spectroscopic Evaluation of Non-Adiabatic Spin Transfer Torque Using Coupled Oscillation of Magnetic Vortices.

T. Horaguchi[1], T. Tanazawa[1] and Y. Nozaki[1,2]
1. Department of Physics, Keio University, Yokohama, Japan; 2. Center for Spintronics Research Network, Keio University, Yokohama, Japan

We demonstrated a reliable evaluation of a non-adiabatic spin-transfer torque coefficient β by an electrical detection of coupled oscillation of magnetic vortices in NiFe gourd-shaped thin film. The value of β was evaluated to be which was 9.3 times larger than the Gilbert damping constant α. It is noted that our method is not affected by a spin polarization of driving current and can exclude the contribution of magnetic torque owing to the magnetic field produced by the current. Spin polarized current in a ferromagnetic metal can transfer a spin angular momentum to the local magnetization via s-d exchange interaction. The consequent torque on magnetization is called as spin-transfer torque (STT). It has been suggested that there are two processes in the transfer mechanism; i.e. adiabatic and non-adiabatic processes. Non-adiabatic contribution which is generally scaled by β is important to understand the STT related phenomena. For example, it determines a velocity of domain wall [1] and an amplification ratio of spin waves [2]. The non-adiabatic STT is considered to depend on both the value of α and a spatial gradient of magnetization [3]. However, the previously reported values of β are widely scattered because it is difficult to exclude the magnetic torque owing to the magnetic field produced by the current. Thus, we need more reliable method to measure β precisely. In this study, the value of β is evaluated by analyzing spectra of translational mode in coupled magnetic vortices which is causes by not only spin transfer torque but also the Oersted field torque. In the coupled oscillation of vortices, the eigenfrequencies of translational modes owing to STT and Oersted field torque are totally different. In general, a coupled oscillation has two classes of oscillation, i.e. a center-of-mass and relative motions. Moreover, when a magnetic vortex is confined in an ellipsoidal disk of ferromagnet, a restoring force acting on the vortex core depends on the oscillation direction. As a consequence, there are four resonant modes with different eigen frequencies in the coupled oscillation. Hata et al. analytically calculated that not only the relative orientation of core magnetization (p_1=p_2 or -p_2) but also the applied directions of electrical current (u_x or u_y) and Oersted field (h_x or h_y) determined which mode was excited in the coupled magnetic vortices [4]. The spectrum of coupled oscillation is, therefore, suitable to evaluate a non-adiabatic STT coefficient β which is generally difficult to be distinguished from the Oersted field contribution. Figure 1 shows our experimental setup where a self-homodyne technique is used to measure a spectrum of coupled oscillation of magnetic vortices in a NiFe gourd-shaped thin film. The self-homodyne measurement of the STT-induced translational mode in a magnetic vortex is a powerful tool to evaluate the value of β. The rectified voltage V_{det} is in proportion to the complex amplitude of coupled oscillation via anisotropic magnetoresistance (AMR) effect. An alternating current produced by a radio-frequency signal synthesizer was applied to the NiFe gourd-shaped thin film. A direct current (dc) rectified voltage between electrodes was measured via dc port of bias-tee while the external alternating current was applied to the longitudinal direction of the gourd-shaped thin film. At that time, the Oersted field according to the Ampere's law was simultaneously generated. Figure 2 shows a rectified voltage as a function of frequency of alternating current applied to the gourd-shaped thin film. As indicated by arrows in Fig. 2(a) and 2(b), we observed two different spectra consisting of 1 and 2 resonant peaks which are associated with the translational modes for p_1=p_2 and p_1=-p_2, respectively. From the analytical calculation, we found that the rectified voltage spectra consist of the sum of Lorentzian and anti-Lorentzian (dispersion) functions, $A_L f_L(f)$ and $A_{AL} f_{AL}(f)$, and the value of β can be evaluated from the relative amplitude of A_L/A_{AL}. The evaluated value of β is 0.14±0.02 (9.3α) which is comparable to the previous β evaluated from a direct tracing of single vortex core motions. The ratio between β and α is also consistent with the previous study [5]. The similarity in β suggests that the spatial gradient of core magnetization is significant to determine the magnitude of β.

[1] M. Hayashi et al., Phys. Rev. Lett. 96, 197207 (2006). [2] S. M. Seo et.al, Phys. Rev. Lett. 102, 147202(2009). [3] G. Tatara et.al., Phys. Rev. B 78, 064429 (2008). [4] H.Hata et.al., Phys. Rev. B 90, 104418 (2014). [5] S. D. Pollard et.al., Nat.Commun. 3, 1028 (2012).

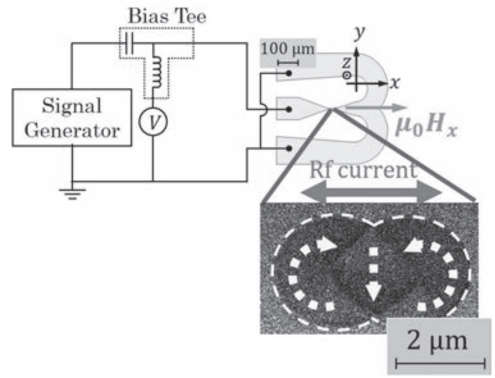

Fig. 1. Schematic measurement setup. Sample consisted of 50-nm-thick NiFe gourd-shaped thin film electrically connected to 100-nm-thick Au electrodes. The inset is the magnetic force micrograph at remanent state. White dotted line and yellow arrows are guide to identify NiFe disk and the magnetization direction, respectively.

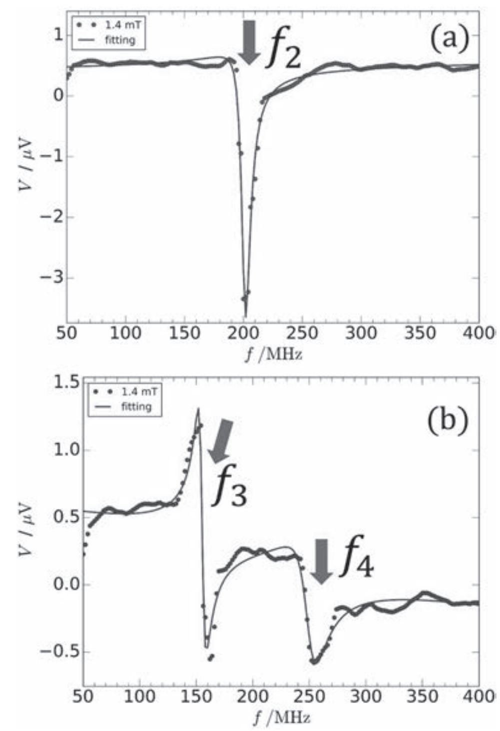

Fig. 2. Spectra of rectified voltage measured for coupled oscillation of vortices with relative orientations of core magnetization (a)p_1=p_2 and (b)p_1=-p_2 .

CQ-07. Over 100,000-times variation of domain-wall speed with respect to ferromagnetic layer thickness.

D. Kim[1], M. Park[1], Y. Park[1,2], J. Yu[1], J. Kim[1], D. Kim[1,3], B. Min[2] and S. Choe[1]
1. Physics, Seoul National University, Seoul, The Republic of Korea; 2. Korea Institute of Science and Technology, Seoul, The Republic of Korea; 3. Kyoto University, Kyoto, Japan

Magnetic domain-wall (DW) motion has been attracted a great attention due to its promising application toward the next-generation magnetic memory/logic devices [1,2]. For a better performance of these DW-based devices, achievement of fast DW speed is of necessity. For this purpose, various studies have been conducted using various materials and structure engineering [3-5]. Here, we report the ferromagnetic-layer-thickness dependence of the DW speed in ultra-thin non-magnet/ferromagnet/non-magnet multilayer films. For this study, 5.0-nm Ta/2.5-nm Pt/-nm Co/1.5-nm TiO_2/2.0-nm Pt films were fabricated on a Si/100-nm SiO_2 substrate using dc and ac magnetron sputtering, where the Co layer thickness t_{Co} varied from 0.65 to 1.00 nm with a 0.05-nm increment. The TiO_2 layer was formed by Ti-layer deposition, followed by oxidation under 3.3-Torr O_2 pressure for 1 h. All films exhibited strong perpendicular magnetic anisotropy and clear DW motion under the application of a magnetic field. The DW speed v_{DW} was then measured by use of magneto-optical Kerr effect microscope equipped with an electromagnet. Figure 1 shows the creep-scaling plots of v_{DW} as a function of $H^{-1/4}$ for films with different t_{Co}'s, as denoted in the plot. All curves showed typical creep-scaling behavior with linear dependence in the present scaled axes. The plot also shows the existence of an overall tendency between t_{Co} and v_{DW}; thinner t_{Co} exhibits faster v_{DW}. It is worthwhile to note that v_{DW} varies even more than 10^5 times depending on v_{DW}, as indicated by the vertical arrow. To investigate the origin of this significant variation of the DW speed with respect to t_{Co}, variation of creep scaling constant α with respect to t_{Co} was investigated, which was determined by the slope of creep curves (Figure 1). Interestingly, as shown by Figure 2, α exhibited clear linear dependence on t_{Co}. This linear dependence was then finally demonstrated by the creep theory, which will be discussed in the presentation. We expect that our present observation may provide a guide for an optimal design rule of the ferromagnetic layer thickness for better performance of DW-based spintronics devices.

[1] S. S. P. Parkin, M. Hayashi, and L. Thomas, Science 320, 190 (2008). [2] R. Lavrijsen, J.-H. Lee, A. Fernández-Pacheco, D. C. M. CC. Petit, R. Mansell, and R. P. Cowburn, Nature 493, 647 (2013). [3] P. J. Metaxas, J. P. Jamet, A. Mougin, M. Cormier, J. Ferré, V. Baltz, B. Rodmacq, B. Dieny, and R. L. Stamps, Phys. Rev. Lett. 99, 217208 (2007). [4] I. M. Miron, T. Moore, H. Szambolics, L. D. Buda-Prejbeanu, S. Auffret, B. Rodmacq, S. Pizzini, J. Vogel, M. Bonfim, A. Schuhl, and G. Gaudin, Nature Mater. 10, 419 (2011). [5] S.-H. Yang, K.-S. Ryu, and S. Parkin, Nature Nanotech. 10, 211-226 (2015).

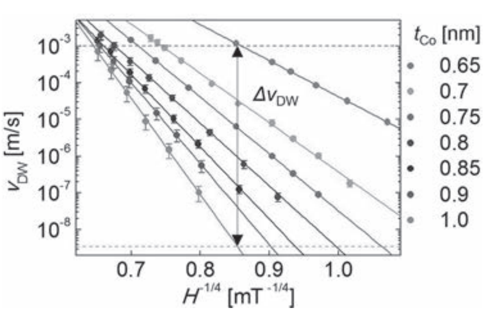

Fig. 1. Plot of v_{DW} with respect to $H^{-1/4}$. The solid lines indicate the best fitting with the creep-scaling law. The vertical black arrow indicates the DW speed deviation between t_{Co}=0.65 nm and 1.00 nm.

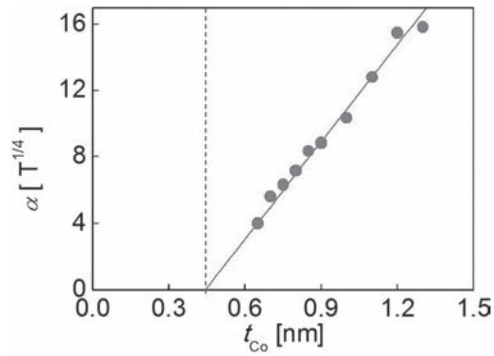

Fig. 2. Plot of α with respect to t_{Co}. The solid line shows the best linear fitting and the vertical dashed line indicates the intercept to the abscissa.

CQ-08. Coherent terahertz spin-wave emission associated with ferrimagnetic domain wall dynamics.

S. Oh[1], S. Kim[2], D. Lee[3], G. Go[3], K. Kim[4,5], T. Ono[5], Y. Tserkovnyak[2] and K. Lee[1,3]

1. Department of Nano-Semiconductor and Engineering, Korea University, Seoul, The Republic of Korea; 2. Department of Physics and Astronomy, University of California, Los Angeles, CA, United States; 3. Department of Materials Science and Engineering, Korea University, Seoul, The Republic of Korea; 4. Department of Physics, Korea Advanced Institute of Science and Technology (KAIST), Daejeon, The Republic of Korea; 5. Institute for Chemical Research, Kyoto University, Kyoto, Japan

In modern communications, information is carried by electromagnetic waves whose frequency is limited to ≈0.1 terahertz (THz), the frequency of oscillating circuits based on high-speed transistors [1]. On the other hand, semiconductor lasers generate coherent light with a frequency >30 THz [2]. The terahertz gap refers to the fact that no relevant technology exists in the frequency range between these two limits (0.1–30 THz). Therefore, it is of critical importance to find relevant physical phenomena that fill in the terahertz gap. In this respect, antiferromagnets whose resonance frequencies are in the THz range [3,4] are of interest [5,6]. It has been reported that coherent THz magnons or spin waves are generated in antiferromagnets, driven by a laser [7,8] or an electrical current [9,10]. However, THz spin-wave excitations by a dc magnetic field are in principle not possible for antiferromagnets as their magnetic moments are compensated on an atomic scale. In this presentation, we theoretically show that the generation of coherent THz spin waves can be achieved by field-driven domain wall (DW) motion in ferrimagnet/heavy metal bilayers in which the interfacial Dzyaloshinskii-Moriya interaction (DMI) is present. The DMI is shown to facilitate THz spin-wave emission in a wide range of the net angular momentum by increasing the Walker breakdown field. Moreover, we show that spin-orbit torque combined with the DMI also drives fast ferrimagnetic domain wall motion by emitting terahertz spin waves. Figure 1 shows domain wall velocity V_{DW} with external field H_z. The numerically obtained values (symbols) of V_{DW} are in good agreement with theoretical solutions (solid lines) except for the case of angular momentum compensation temperature T_A. Because net angular momentum is vanished at T_A, Walker breakdown does not occur resulting in linear increase in V_{DW} with H_z. In the high H_z regime at T_A, however, nonlinearity of V_{DW} appears, and it is analogous with relativistic kinematics. The maximum spin wave group velocity $v_{g,max}$ (dashed line) acts as the speed of light and the domain wall width shrinks as V_{DW} approaches $v_{g,max}$ via Lorentz contraction. Moreover, domain wall emits terahertz range spin wave to dissipate the raised domain wall energy. Red line in Fig. 1 represents the 'relativistically' modified solution. For the cases showing nonlinearity at T_A, we observe spin-wave emission from the DW (Fig. 2). We confirm that the emitted spin-wave frequency is in the THz range. To elaborate the nonlinearity and associated THz spin-wave emission, we derive the spin-wave dispersion for ferrimagnets on top of a uniform ground state as $\omega_{\pm}=\{\pm\delta_s+[\delta_s^2+4\rho(Ak^2+K-h)]^{1/2}\}/2\rho$, where the upper (lower) sign corresponds to the right-handed (left-handed) circular mode. δ_s is the net angular momentum, ρ parametrizes the inertia of the dynamics, A is the exchange energy constant, k is the wave vector, K is the easy-axis anisotropy energy constant, and h represents the Zeeman energy. We note that the DMI does not contribute to spin-wave dispersion as it is effective only for the y component of magnetization, which is negligible for perpendicularly magnetized ferrimagnets. From the dispersion, we obtain the maximum spin-wave group velocity $v_{g,max}=A/ds$, where d is the lattice constant, $s=(s_1+s_2)/2$, and s_i is the spin density for each site i. In conclusion, we have shown field-driven THz spin-wave emission for ferrimagnetic DWs, which is not possible for ferromagnetic or antiferromagnetic DWs. Our finding suggests that ferrimagnetic DWs are potentially useful for high-speed and high-frequency spintronics devices.

[1] C. Sirtori, Nature (London) 417, 132 (2002). [2] M. Beck, D. Hofstetter, T. Aellen, J. Faist, U. Oesterle, M. Ilegems, E. Gini, and H. Melchior, Science 295, 301 (2002). [3] T. Nagamiya, Prog. Theor. Phys. 6, 342 (1951). [4] F. Keffer and C. Kittel, Phys. Rev. 85, 329 (1952). [5] T. Jungwirth, X. Marti, P. Wadley, and J. Wunderlich, Nat. Nanotechnol. 11, 231 (2016). [6] V. Baltz, A. Manchon, M. Tsoi, T. Moriyama, T. Ono, and Y. Tserkovnyak, arXiv:1606.04284. [7] T. Satoh, S.-J. Cho, R. Iida, T. Shimura, K. Kuroda, H. Ueda, Y. Ueda, B. A. Ivanov, F. Nori, and M. Fiebig, Phys. Rev. Lett. 105, 077402 (2010). [8] T. Kampfrath, A. Sell, G. Klatt, A. Pashkin, S. Mährlein, T. Dekorsy, M. Wolf, M. Fiebig, A. Leitenstorfer, and R. Huber, Nat. Photonics 5, 31 (2011). [9] R. Cheng, D. Xiao, and A. Brataas, Phys. Rev. Lett. 116, 207603 (2016). [10] T. Shiino, S.-H. Oh, P. M. Haney, S.-W. Lee, G. Go, B.-G. Park, and K.-J. Lee, Phys. Rev. Lett. 117, 087203 (2016).

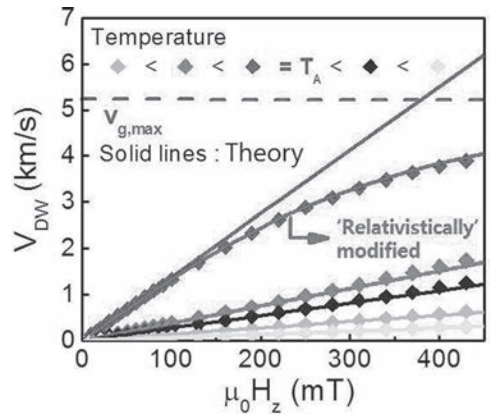

Fig. 1. Domain wall velocities as a function of external field in the vicinity of T_A. Symbols indicate numerical results, and solid lines indicate theoretical solutions.

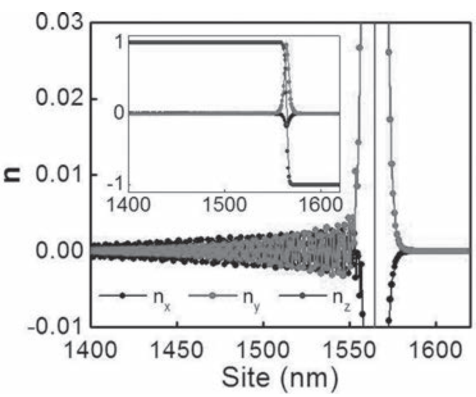

Fig. 2. Configuration of domain wall and spin waves for the staggered vector n. The inset shows the overall shape of the domain wall.

CQ-09. Domain wall configurations in amorphous ferromagnetic nanowires with cylindrical symmetry.

C. Rotarescu[1], H. Chiriac[1], N. Lupu[1] and *T.A. Ovari*[1]
1. National Institute of Research and Development for Technical Physics, Iasi, Romania

Long amorphous glass-coated magnetic nanowires with metallic nucleus diameters down to 90 nm have been recently prepared by an enhanced glass-coated melt spinning method [1]. These nanowires with cylindrical symmetry are composite materials, obtained in a single-step fabrication process, in which a ferromagnetic material (the actual nanowire) is embedded in a glass coating. Their main characteristic is a magnetically bistable behavior, i.e. a single step reversal of the axial magnetization when the applied field reaches a threshold value called switching field, and which appears irrespective of the sign and magnitude of the alloy's magnetostriction constant, λ, i.e. in both nearly zero magnetostrictive samples, e.g., $(Co_{0.94}Fe_{0.06})_{72.5}Si_{12.5}B_{15}$ with $\lambda \approx -1 \times 10^{-7}$, considered as $\lambda \approx 0$, and highly magnetostrictive ones, e.g., $Fe_{77.5}Si_{7.5}B_{15}$ with $\lambda = +25 \times 10^{-6}$, considered as $\lambda >> 0$. Here we report on the magnetization process and domain wall configurations in such bistable amorphous nanowires with cylindrical symmetry by taking into account the nonlinear distribution of their intrinsic magnetoelastic anisotropy, K_{me}. We investigated the axial magnetization process through a novel, finite element-based micromagnetic model, in order to describe the magnetization process and associated hysteresis loops in such rapidly solidified ultrathin samples. In this study, we have employed the parallel computing implementation of the MAGPAR finite element micromagnetics package [2]. Figure 1 shows the calculated loops in case of a zero-magnetostrictive sample ($\lambda \approx 0 \Rightarrow K_{me} \approx 0$), as well as for a highly magnetostrictive one ($\lambda >> 0 \Rightarrow K_{me} \neq 0$) in two cases: (i) for a standard anisotropy distribution given by $K_{me}(r) = K_{max} \times \cos[\pi(r/R)]$, in which K_{max} is the maximum anisotropy, r the radial coordinate and R the nanowire radius, and (ii) for a radially shifted anisotropy distribution, $K_{me}(r) = K_{max} \times \cos\{\pi[(r-r_0)/R]\}$, respectively. The radial shift $r_0 = 0.3R$ was included in order to get the shape of the distribution as close as possible to the one expected to emerge from the distribution of internal stresses found in this type of nanowires [3]. These results have been compared to experimentally measured inductive hysteresis loops, showing that the radially shifted anisotropy distribution offers a far more precise description of the magnetic behavior than the standard anisotropy distribution. The proposed model allows one to visualize the configurations of the magnetic moments, which are difficult to see experimentally. Figure 2 shows the distributions of magnetic moments at remanence for the case $K_{me} \approx 0$. One observes that the magnetization at the nanowire end displays an open vortex-like structure. Such a structure minimizes the magnetostatic energy at the nanowire ends and decreases the shape anisotropy. If the external field is increased or further rotated, these structures suffer depinning from the end of the nanowire and subsequently propagate as vortex domain walls. These vortex walls appear spontaneously at room temperature due to demagnetization. Their actual propagation at magnetization switching allows one to consider these ultrathin cylindrical amorphous nanowires as potential nanoconduits for the displacement of domain walls with vortex configurations. This is a key result, given the large domain wall propagation velocities that have been experimentally found in this novel type of nanowires, i.e. well over 1200 m/s [4]. Therefore, it is expected to have a significant impact on the applications of these cylindrical ferromagnetic nanowires, opening up extremely promising opportunities for their use in magnetic logic applications. Acknowledgements - Work supported by the Romanian Executive Agency for Higher Education, Research, Development and Innovation Funding (UEFISCCDI) under project PN-III-P4-ID-PCE-2016-0358 – Contract no. 149/2017.

[1] Chiriac, H. *et al.* Rapidly solidified amorphous nanowires. *J. Appl. Phys.* 109, 063902 (2011). [2] Scholz, W. *et al.* Scalable parallel micromagnetic solvers for magnetic nanostructures. *Comp. Mat. Sci.* 28, 366-383 (2003). [3] Óvári, T.-A., Lupu, N., Corodeanu, S. & Chiriac, H. Magnetostatic and magnetoelastic interactions in glass-coated magnetostrictive nanowires. *IEEE Trans. Magn.* 50, 2006904 (2014). [4] Corodeanu, S., Chiriac, H. & Óvári, T.-A. Accurate measurement of domain wall velocity in amorphous microwires, submicron wires, and nanowires. *Rev. Sci. Instrum.* 82, 094701 (2011).

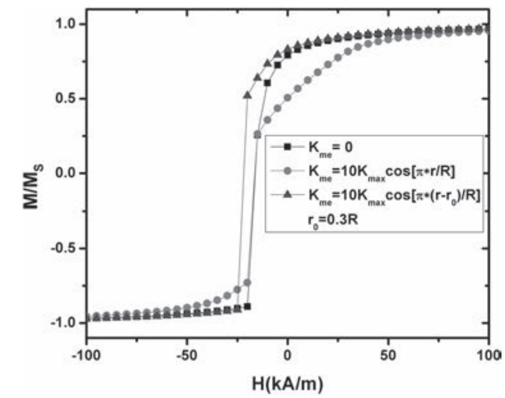

Fig. 1. Calculated hysteresis loops for various magnetoelastic anisotropy distributions: (i) nearly zero magnetostrictive sample; (ii) standard distribution; and (iii) radially shifted distribution.

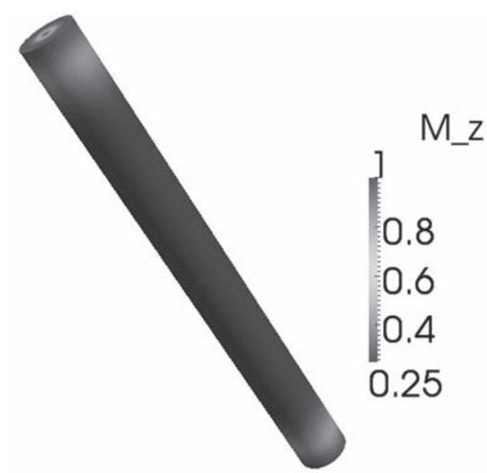

Fig. 2. Configuration of the magnetic moments at remanence for a nanowire with $K_{me} \approx 0$.

CQ-10. Thermally assisted domain wall motion in the presence of spin torque.

J. Chureemart[2] and P. Chureemart[1]
1. Physics department, Mahasarakham University, Kantarawichai, Thailand; 2. Physics department, Mahasarakham University, Kantarawichai, Thailand

Utilizing a spin-polarized current to manipulate the magnetization has become the subject of intensive study leading to the development of novel spintronic devices [1–3]. The future domain wall (DW) based spintronic devices rely on the ability to accurately manipulate the position of domain wall which can be controlled by injecting the spin current. In addition, there is a new possibility to represent the data bits by DWs themselves [4]. Therefore, it is necessary for device design to understand underlying interplay between the spin-polarized current and the local magnetization giving rise to the spin-transfer torque (STT) acting on DW. In often-used micromagnetic model, spin torques are generally represented by the coefficients μ and β describing the adiabatic and non-adiabatic torques [5-6]. The adiabatic and non-adiabatic torques are empirical constants which are assumed to be spatial independent and their magnitudes are still a matter of discussion. Recently, these spin torque coefficients can be calculated directly from the spin accumulation [7–8] and the results demonstrated that μ and β are nonuniform throughout the structure due to the fact that they strongly depend on the gradient of magnetisation. Although there are several studies of spin transfer torque but the effect of thermal fluctuation on magnetisation dynamic has not been comprehensively investigated. In previous studies [5-6], the effect of thermal fluctuation is represented by the random fluctuating field taken into account the micromagnetic model. It can be used to represent the thermal fluctuation but the magnitudes of spin torque coefficients are still assumed which may lead to the missing some of relevant physics. In this work, the spin accumulation is suggested to describe the effect of spin transfer torque directly as well as the atomistic model will be used to investigate the magnetisation dynamic which is able to deal with the interface properties instead of using the standard micromagnetic model. We will also investigate the effect of spin transfer torque and thermal fluctuation on DW motion by using atomistic modeling coupled with the spin accumulation model. To investigate the thermally domain wall motion driven by injecting spin current, the generalized spin accumulation model coupled with atomistic model is employed. The magnetization dynamic can be considered by performing the atomistic model via the Landau-Lifshitz-Gilbert (LLG) equation using a transfer matrix approach proposed by P.Chureemart *et.al.* [9] and thermal field is introduced into the LLG equation as the additional field. The bilayer structure with a pinned layer providing a spin-polarized current and a free layer are created with dimensions of 60 nmx 30nm x 1.5nm in order to calculate the spin accumulation and spin torque the system is discretized into macrocells at 1.15 nm x1.15 nmx1.15 nm in size. We first investigate the effect of uniaxial anisotropy on domain wall motion by introducing the current density of 5×10^{11} A/m^2 for athermal case. The anisotropy constant is varied from 6 K_U to 80 K_U where K_U is the uniaxial anisotropy constant based on cobalt, $K_U = 4.644 \times 10^{-24}$ J/atom. As shown in Fig. 1(a), it is found that DW can move easily for higher anisotropy as expected. Next observation is to study the effect of current density, the system with high anisotropy constant of 40K_U is chosen. Increasing current density tends to shift DW easily due to high spin polarized current as demonstrated in Fig. 1(b). In addition, we also observe that the equilibrium time becomes shorter for the case of high current density. Finally, we now consider the effect of thermal fluctuations taken into account the atomistic model on DW translation. The temperature dependence of DW displacement and initial DW velocity of the system with current density of $j_e = 10^{12}$ A/m^2 are investigated as shown in figure 2 (a) and (b) respectively. It interestingly shows that the thermal fluctuation can assist DW motion. The initial DW velocity increases with increasing temperature. At 300K, the DW velocity is up to 900 m/s which is consistent with previous experimental studies. The atomistic model coupled with spin accumulation model is proposed to be a new route to use for DW-based devices design.

[1] S. S. P. Parkin, M. Hayashi, and L. Thomas, Science 320, 190, (2008). [2] R. P. Cowburn, Nat Mater 6, 255, (2007). [3] B. Beyersdorff et al., Phys. Rev. B 86, 184427, (2012). [4] K. A. Omari and T. J. Hayward, Phys. Rev. Applied 2, 044001 (2014). [5] J. Shen, M. Shi, T. Tanaka, and K. Matsuyama, Journal of Applied Physics 117, (2015). [6] R. Sbiaa, Applied Physics Letters 105, 2014 (2014). [7] D. Claudio-Gonzalez, A. Thiaville, and J. Miltat, Phys. Rev. Lett. 108, 227208, (2012). [8] P. Chureemart, I. D'Amico, and R. W. Chantrell, Journal of Physics: Condensed Matter 27, 146004, (2015). [9] P. Chureemart, R.F.L. Evans, I.D'Amico, and R.W. Chantrell, Phys. Rev. B, 92, 054434 (2015)

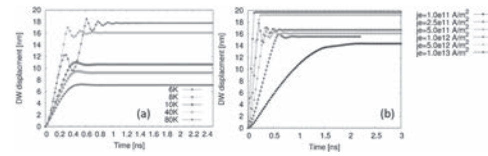

Fig. 1. The time-dependent variation of the DW displacement in terms of (a) K_U and (b) j_e.

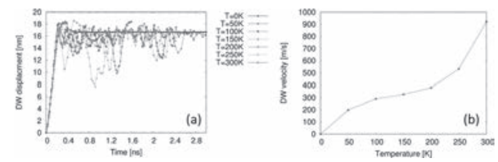

Fig. 2. (a) The time-dependent variation of the DW displacement with different temperature (b) the temperature dependence of DW velocity at 1 ns.

CQ-11. Magnetic skyrmion motion in the presence of defect.

I. Hong[1] and K. Lee[1,2]
1. KU-KIST graduate school of converging science and technology, Korea University, Seoul, The Republic of Korea; 2. Department of materials science and engineering, Korea University, Seoul, The Republic of Korea

In the magnetic system, defect can be occurred by impurity or faulty at the process. Study of defect carried out in various ways with magnetic texture, such as domain walls, vortices, and magnetic skyrmions[1]. Among these texture, skyrmion has emerged as a major interest for the reason of topological protection and high speed with low current. In the thin films, magnetic skyrmion stuructures are stabilized by the competition of magnetic energy terms like exchange interaction, Dzyaloshinskii-Moriya interaction(DMI), anisotropy. In the last work, we studied about domain wall motion at the step of DMI[2], which induced a different energy landscape for a domain wall. In the same way, one can expect that the step of DMI or anisotropy change the energy landscape of magnetic skyrmions. We performed the two dimensional micromagnetics simulation with the following parameters: exchange stiffness constant $A=1.3\times10^{-6}$ erg/cm, uniaxial anisotropy constant with z easy axis $K=7\times10^{6}$ erg/cm^3, DMI constant $D=2.5$ erg/cm^2. Skyrmion can be moved by the spin-transfer-torque(STT), which induced by the spin-polarized current. STT is described by the two torques; adiabatic term, $(j\ \nabla)m$, and non-adiabatic term, $\beta m\times(j\ \nabla)m$. First, we studied about point defect of DMI constant and anisotropy. We find that, in both cases, skyrmions scattered with defects and moved to y direction while scattering with defects (see Figure. 1). Both –y and +y direction motion appear while skyrmion pass through the defects. On the other hand, in the plannar defect, large y motion can be arise, but back motion has not generated. We find that the defect causes a skyrmion motion transverse to the external driving force. The transverse for a point defect is consistent with the previously reported skyrmion Hall effect[1]. On the other hand, the transverse motion for a planar defect is found to have a much larger deflection of magnetic skyrmion in addition to the skyrmion Hall effect.

[1] C. Reichhardt and C. J. O. Reichhardt, New J. Phys. 18, 095005 (2016)
[2] I.-S. Hong, S.-W. Lee, and K.-J. Lee, Curr. Appl. Phys. 17, 1576-1581 (2017)

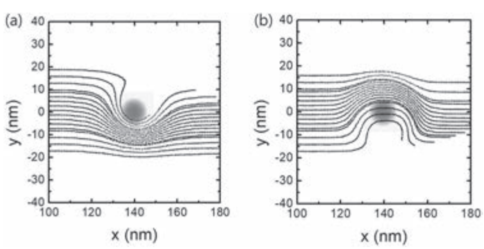

Fig. 1. Black dots shows trajectory of skyrmion which has different initial position of y axis. Red circle indicate point defect of (a)DMI and (b)anisotropy.

CQ-12. Mechanism of skyrmionium nucleation by local spin-orbit torque.

A. Kolesnikov[1], M. Stebliy[1], A. Ognev[1], A.S. Samardak[1] and L. Chebotkevich[1]
1. School of Natural Science, Far Eastern Federal University, Vladivostok, Russian Federation

Magnetic skyrmionium [1,2] is novel topological protected state without skyrmion Hall effect (SkHE) [3] in ferromagnets. This state represents a skyrmion surrounded by circular domain wall with opposite topological charge (Q), this structure is elastically coupled due to magnetostatic repulsion. Since the direction of deviation from longitudinal motion due to SkHE depends on a sign of Q. Therefore the topological inhibition of Magnus effect is observed in this composite structure. Skyrmionium moves directly along the nanotrack under the action small current density [4]. These advantage make skyrmionuim useful for application in racetrack memory. Firstly, we need to control the processes of nucleation and annihilation of skyrmoinium, for its application in real racetrack memory devices. In previous works the spin-transfer torque effect was used for this goal [4]. Spin current polarized along z was locally injected perpendicularly to disk plane. However, the experimental implementation of this method is rather problematic, because of the complexity of creating a nanocontact of an annular shape. We propose a novel method of skyrmionium nucleation using the spin-orbit torque (SOT) effect [5,6]. For nucleation of the domain with required shape, for example annular, we offer locally change the magnitude of SOT effect. It can be realized in system ferromagnetic/heavy metal (FM/HM) by addition of HM with opposite Spin hall angle on the second interface (HM_1/FM/HM_2) [7]. Based on the system Pt/Co/Ta investigated in the article [7] we studied trilayer structure with consist of continuous films Pt/Co and nanostructured capping layer Ta (Fig. 1a). Capping layer has nanoring shape with diameter 100 nm and width 25 nm. This nanostructured layer allows enhance local spin current density which will be injected perpendicularly Co film. Taking in account geometry, conductive parameters and local Spin Hall effect engineering the spin current density distribution map was calculated (Fig. 1b). Simulation of the process of the skyrmionium nucleation was carried out for a nanotrack with a size of 1000×400×0.6 nm^3 and the magnetic parameters were chosen according to data in article [7]. Initially ferromagnetic film was saturated along z. Then external magnetic field B_x=0.6 T and 20 ps impulse spin current with distribution accordingly Fig. 1b were applied. Under the action of current and magnetic field the m_z component of the magnetization decreases (Fig 1c), which corresponds to the incline of the magnetization under the influence of a plane magnetic field and the nucleation and growth of a domain under the SOT effect. Since the distribution of the spin current is non-uniform, the density is higher in the region under the nanoring, the nucleated domain also has an annular shape (Fig. 1d). Drag force acting from spin current on domain wall shifts the domain. Therefore the external action is removed (j_s=0 A/m^2 and B_x=0 T) to prevent further growth and displacement of the domain. The self-organization of the magnetization configuration occurs after disabling the external influence. In thin FM layers with high perpendicular magnetic anisotropy (PMA) and positive Dzyaloshinskii-Moriya interaction (DMI), Neel's domain walls with left-handed chirality are stabilized [8]. The stabilized skyrmionium had an asymmetric shape and a large size for these magnetic parameters (Fig. 1d). Therefore, the transition to the equilibrium state takes some time, with a decreasing the size of the skyrmionium, the value of m_z in the considered region increases (Fig. 1c). The complete process of nucleation and stabilization of the skyrmionium for these magnetic parameters is 700 ps. Also we studied static and dynamic properties of skyrmionium in comparison with free skyrmion. The stability regions and the dependences of radii for skyrmion and skyrmiounium on magnetic parameters are presented on Fig. 2a,b. Under the action of perpendicular spin current j_s polarized along y simple skyrmion moves with non-zero velocities V_x and V_y (Fig. 2c). In the case of skyrmion full compensation of Magnus force leads to rectilinear motion along the nanotrack. We found that skyrmionium has higher dissipation efficiency, in comparison with free skyrmion, consequently greater drag force acts on skyrmionium and it moves faster. Support by RFBR (grants 17-52-50060, 15-02-05302, 17-52-45135, 18-02-00205), the state task (3.5178.2017) and the Grant program of the Russian President (MK-2643.2017.2, MK-5021.2018.2) are acknowledged.

[1] S. Komineas and N. Papanicolaou, Skyrmion dynamics in chiral ferromagnets, *Phys. Rev. B* 92, 064412 (2015). [2] S. Komineas and N. Papanicolaou, Skyrmion dynamics in chiral ferromagnets under spin-transfer torque, *Phys. Rev. B* 92, 174405 (2015). [3] J. Iwasaki, M. Mochizuki, N. Nagaosa, Universal current-velocity relation of skyrmion motion in chiral magnets, *Nature Communications* 4, 1463 (2013). [4] X. Zhang, J. Xia, Y. Zhou, et al. Control and manipulation of a magnetic skyrmionium in nanostructures, *Phys. Rev. B* 94, 094420 (2016). [5] I.M. Miron, et al. Perpendicular switching of a single ferromagnetic layer induced by in-plane current injection, *Nature* 476, 189–193 (2011). [6] M. Cubukcu, et al. Spin-orbit torque magnetization switching of a three-terminal perpendicular magnetic tunnel junction, *Appl. Phys. Lett.* 104, 042406 (2014). [7] S. Woo, M. Mann, et al. Enhanced spin-orbit torques in Pt/Co/Ta heterostructures, Phys. Rev. Lett. 105, 212404 (2014). [8] M. Heide, G. Bihlmayer, S. Blügel Dzyaloshinskii-Moriya interaction accounting for the orientation of magnetic domain in ultrathin films: Fe/W(110), *Phys. Rev. B* 78, 140403(R) (2008).

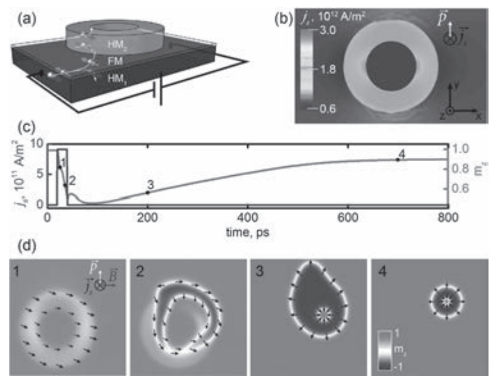

Fig. 1. (a) Scheme of Spin Hall effect in trilayer structure HM_1/FM/HM_2. (b) The distribution of the spin current density (j_s) injected into the ferromagnetic layer. (c) The time dependence of the spin current density passing through the ferromagnetic layer, the corresponding changes of the perpendicular component of magnetization m_z. (d) Visualization of the process skyrmionium nucleation in the ferromagnetic layer for the chosen instants of time (1-4).

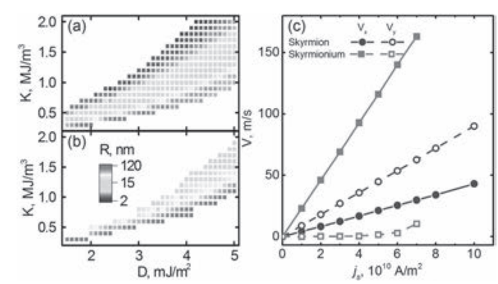

Fig. 2. Diagrams of radii for (a) skyrmion and (b) skyrmionium in coordinates of DMI and PMA. (c) Plot of the dependencies V_x and V_y components of the velocity on the current density for the skyrmion and skyrmionium.

CQ-13. Controllable transport of a skyrmion in a ferromagnetic narrow channel with voltage-controlled magnetic anisotropy.

J. Wang[1], J. Xia[2], X. Zhang[2], G. Zhao[3], J. Wu[4], Y. Xu[2], L. Ye[5], Z. Zou[6] and Y. Zhou[1]

1. Department of Electronic Engineering, University of York, York, United Kingdom; 2. School of Science and Engineering, The Chinese University of Hong Kong, Shenzhen, Shenzhen, China; 3. College of Physics and Electronic Engineering, Sichuan Normal University, Chengdu, China; 4. Department of Physics, University of York, York, United Kingdom; 5. College of Communication Engineering, Chongqing University, Chongqing, China; 6. Department of Physics, Nanjing University, Nanjing, China

Magnetic skyrmions are nanoscale particle-like topological configurations, which have been found in certain magnetic bulks, films and nanowire. The skyrmion is stabilized by delicate competitions among the ferromagnetic exchange coupling, perpendicular magnetic anisotropy (PMA) and Dzyaloshinskii-Moriya interaction (DMI) in magnetic systems.[1-2] In this work, we report the dynamics of a skyrmion in a narrow ferromagnetic nanotrack channel with voltage-controlled perpendicular magnetic anisotropy(VCMA), which can be used to build the skyrmion diode and ratchet memory and avoid from the skymion hall effect.[3] The pinning and depinning of the magnetic skyrmion in the nanotrack through the VCMA gate are investigated. This work will be useful for the design and development of the skyrmion transport channel, which is a building block for any future skyrmion-based information devices. The simulation model is an ultrathin ferromagnetic nanotrack, 1000 nm * 80 nm * 0.4 nm, as shown in Fig. 1a.[4] The model is discretized into tetragonal volume elements with the size of 2 nm * 2 nm * 0.4 nm. The micromagnetic simulations are performed with the Object Oriented MicroMagnetic Framework (OOMMF). The dynamic of magnetization is described by Landau-Lifshitz-Gilbert LLG (LLG) equation. The parameters for the micromagnetic simulation the saturation magnetization M_S = 580 kA/m, the damping coefficient α = 0.3, the DMI constant D = 3 mJ/m^2, and the exchange constant A = 15 pJ/m. For the simulation of the motion of skyrmion, two types of VCMA profile are considered, period wedge-shape and sinusoidal functions, as shown in Figs. 1c and d respectively. The function for the period wedge-shape profile is given as: Ku(x) = $K_{u0} + K_{uv} - K_{u0wx}$ (1) Ku(x) = $K_{u0} + K_{uv} - K_{u0}2(1 + \sin(2\pi x = w - \phi))$ (2) where w is the period length w, ϕ is the phase, and x is the longitudinal coordinate. The period wedge-shape is given in the Eq. 1 and the sinusoidal function is given in the Eq. 2. The linear anisotropy profile and the sinusoidal function profile are given in the Figs. 1b and c. The motion of the magnetic skyrmion in the nanotrack with VCMA driven by the current pulse also be simulated. The initial position the skyrmion is x = 86 nm which is the middle of a voltage gate. Fig. 2 shows the motion of the skyrmion in the nanotrack with a periodical wedge-shaped profile with Kuv = 0.750 MJ/m^3 with the period length w = 50 nm. The current density of the pulse is 20MA = cm^2. The pulse is applied at t = 0.5 ns. For one period of the current pulse, te is the time interval applying the current and tr is the relax time without applying current. tr = 5 ns in the simulations. When te = 1 ns, the skyrmion cannot pass the voltage gate and moves in a circle trajectory as shown in Figs. 3a and b. For te = 2 ns, the trajectory of the skyrmion is shown in Fig. 2c. The time-dependence of the position in the x direction and the current density are shown in Fig. 2d. At t = 14.5 ns, the skyrmion is located at x = 187 nm. After applying the pulse, x = 241 nm at t = 16.5 ns. Then the applied current is off. The skyrmion further relax to x = 236 nm before the next pulse. The displacement of skyrmion is 50 nm after a pulse is applied. For te = 3 ns, Figs. 2e and f, one current pulse results in a displacement of 100 nm. In this work, the skyrmion motion in a ferromagnetic nanotrack with single or multiple VCMA gates is studied. This work shows the trajectory and location of the skyrmion can be controlled by periodically located VCMA gates as well as the driving current pulse. The unidirectional motion of the skyrmion realized by the VCMA effect can be used to build the skyrmion-based one-way information channel and the skyrmion diode. Our results are useful for the design and development of the skyrmion-based spintronic devices.

[1] S. Mühlbauer, B. Binz, F. Jonietz, C. Pfleiderer, A. Rosch, A. Neubauer, R. Georgii, and P. Böni, Science 323, 5916 (2009). [2] C. Pfleiderer, T. Adams, A. Bauer, W. Biberacher, B. Binz, F. Birkelbach, P. Böni, C. Franz, R. Georgii, M. Janoschek, F. Jonietz, T. Keller, R. Ritz, S. Mühlbauer, W. Münzer, A. Neubauer, B. Pedersen, and A. Rosch, J. Phys: Condens. Matter 22,16 (2010). [3] W. Kang, Y. Huang, C. Zheng, W. Lv, N. Lei, Y. Zhang, X. Zhang, Y. Zhou, W. Zhao, Sci. Rep. 6, 23164 (2016) [4] M. J. Donahue and D. G. Porter, OOMMF User Guide, Version 1.0, Interagency Report NIST IR 6376, Gaithersburg, MD (1999).

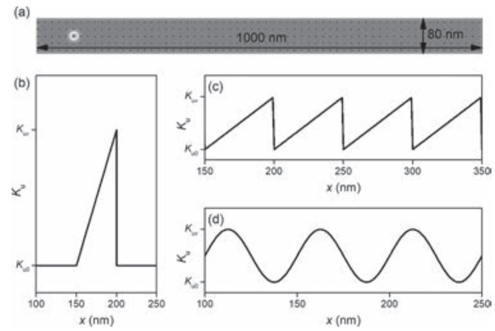

Fig. 1. (a) A Schematic of the magnetic nanotrack where a magnetic skyrmion is initially placed. The out-of-plane magnetization component is represented by the red (-z)-white (0)- blue (+z) color scale. (b) A linear anisotropy profile. (c) A periodical repetition of a linear anisotropy profile with a period w. (b) Sinusoidal function of x with a period w.

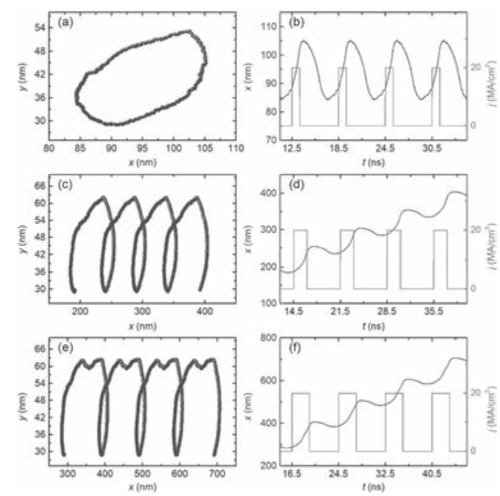

Fig. 2. The skyrmion motion driven by the current pulse in the nanotrack with the wedge shaped Ku with Kuv = 0.75 MJ/m^3. The left panel shows the trajectories of the skyrmion. The right panel shows the x position of the skyrmion and the current density as functions of time t. For one period of the current pulse, te is the pulse time and tr is the relax time without applying current. tr = 5 ns in the simulations. (a), (b) te = 1 ns. (c), (d) te = 2 ns. (c), (d) te = 3 ns.

CQ-14. Current-induced skyrmion dynamics in a frustrated magnetic film.

X. Zhang[1,2], J. Xia[1], Y. Zhou[1], X. Liu[2], H. Zhang[3] and M. Ezawa[4]
1. School of Science and Engineering, The Chinese University of Hong Kong, Shenzhen, Shenzhen, China; 2. Department of Electrical and Computer Engineering, Shinshu University, Nagano, Japan; 3. College of Optoelectronic Engineering, Shenzhen University, Shenzhen, China; 4. Department of Applied Physics, The University of Tokyo, Tokyo, Japan

The magnetic skyrmion is an exotic and versatile topological object in condensed matter physics, which promises novel applications in electronic and spintronic devices [1-2]. Recently, a rich phase diagram of an anisotropic frustrated magnet and properties of frustrated skyrmions with arbitrary vorticity and helicity were investigated [3]. Other remarkable physical properties of skyrmions in the frustrated magnetic system have also been studied theoretically [4-6]. Here, we explore the skyrmion dynamics in a frustrated magnet based on the J_1-J_2-J_3 classical Heisenberg model explicitly by including the dipole-dipole interaction [7]. The skyrmion energy acquires a helicity dependence due to the dipole-dipole interaction, resulting in the current-induced translational motion with a fixed helicity. The lowest-energy states are the degenerate Bloch-type states, which can be used for building the binary memory. By increasing the driving current, the helicity locking-unlocking transition occurs, where the translational motion changes to the rotational motion. Furthermore, we demonstrate that two skyrmions can spontaneously form a bound state. The separation of the bound state forced by a driving current is also studied. In addition, we show the annihilation of a pair of skyrmion and antiskyrmion. Our results reveal the distinctive frustrated skyrmions may enable new applications.

[1] Jiang, W. et al. Skyrmions in magnetic multilayers. Phys. Rep. 704, 1–49 (2017). [2] Kang, W., Huang, Y., Zhang, X., Zhou, Y. & Zhao, W. Skyrmion-electronics: an overview and outlook. Proc. IEEE 104, 2040–2061 (2016). [3] Leonov, A. O. & Mostovoy, M. Multiply periodic states and isolated skyrmions in an anisotropic frustrated magnet. Nat. Commun. 6, 8275 (2015). [4] Leonov, A. O. & Mostovoy, M. Edge states and skyrmion dynamics in nanostripes of frustrated magnets. Nat. Commun. 8, 14394 (2017). [5] Lin, S.-Z. & Hayami, S. Ginzburg-Landau theory for skyrmions in inversionsymmetric magnets with competing interactions. Phys. Rev. B 93, 064430 (2016). [6] Batista, C. D., Lin, S.-Z., Hayami, S. & Kamiya, Y. Frustration and chiral orderings in correlated electron systems. Rep. Prog. Phys. 79, 84504 (2016). [7] Zhang, X., Xia, J., Zhou, Y., Liu, X., Zhang, H. & Ezawa, M. Skyrmion dynamics in a frustrated ferromagnetic film and current-induced helicity locking-unlocking transition. Nat. Commun. 8, 1717 (2017).

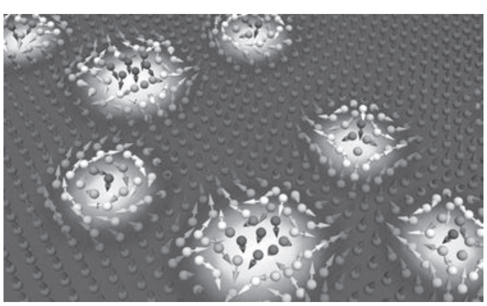

Fig. 1. Skyrmions and antiskyrmions with different topological charges in a frustrated magnetic thin film.

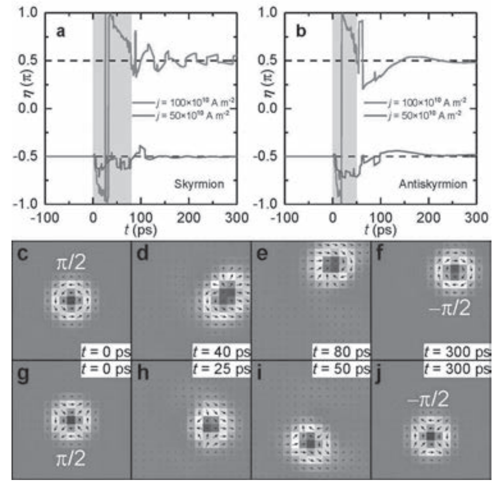

Fig. 2. Flip of the skyrmion (antiskyrmion) helicity induced by a current pulse. (a) Skyrmion helicity as a function of time. A skyrmion is at rest with the helicity being $\eta = -\pi/2$. The helicity is flipped by a strong 80-ps-long current pulse and becomes $\eta = \pi/2$. Such a flip does not occur by applying a small current pulse with the same duration. (b) A similar flip occurs also for an antiskyrmion. (c)-(f) Snapshots of the skyrmion during the helicity flip process. (g)-(j) Snapshots of the antiskyrmion during the helicity flip process.

CQ-15. Bidirectional propagation of tilting domain wall due to the interfacial Dzyaloshinskii-Moriya interaction in perpendicularly magnetized T-junction.

J. Kwon[1], H. Hwang[1], J. Hong[1] and C. You[1]
1. Department of Emerging Materials Science, Daegu Gyeongbuk Institute of Science and Technology, Daegu, The Republic of Korea

The use of field-driven magnetic domain wall (DW) in one-dimensional wire is one of the crucial development element for the spin-based logic or memristor devices.[1,2] The presence of interfacial Dzyaloshinskii-Moriya interaction (iDMI) in the inversion symmetry breaking structure induces an asymmetrical DW configuration with respect to the direction of in-plane field.[3,4] The dynamics of field-driven DW motion in perpendicular magnetic anisotropy (PMA) influenced by DW tilt due to iDMI effect, edge defects, and roughness in the T-shaped structure. The dependence of DW configuration and location in a T-shaped junction structure has been investigated with visualizing the DWs configuration and position by utilizing Kerr microscopy technique. Thin film stacks $Si/SiO_2/Ta/Pt/[Co/Pt]_{x4}$ with Ta capping were used for T-shape device fabrication. Images from Kerr microscopy reveal that the iDMI effective field contributes a right-hand tilt of the DW configuration along its propagation direction in Fig. 1(b)-1. Due to the influence of the iDMI and the edge defects in the input line, a DW enables to change its tilt angle responding to the initial types of DW (up-down or down-up DW) respect to its propagation direction. At the junction, due to the initial tilting orientation, the expansion of DW having a crescent profile extends towards B2 output such as elongated DW profile, as shown in Fig. 1(b)-2. A DW configuration in the two-dimensional T-shaped structure changes from right or left-hand tilting DW to dendritic-domain wall at the junction. Then, DW restores the tilting DW configuration due to the iDMI and propagates through branches, B1 and B2. The elongation direction of DW towards branches at the junction can play a significant role that one of DWs in the branches approaches first to the destination pad, as shown in Fig. 1(b)-6. Accordingly, the DMI constant has been estimated by measuring circular DW expansion on the film utilizing Kerr microscopy technique.[5] In addition to, micromagnetic simulation result provides a clue to understand for dynamics of the DW configuration in the structure.

[1] D. A. Allwood, G. Xiong, C. C. Faulkner, D. Atkinson, D. Petit, and R. P. Cowburn, Science 309 (5741), 1688 (2005). [2] S. Lequeux, J. Sampaio, V. Cros, K. Yakushiji, A. Fukushima, R. Matsumoto, H. Kubota, S. Yuasa, and J. Grollier, Sci. Rep. 6, 31510 (2016). [3] I. E. Dzyaloshinskii, Sov. Phys. JETP 5, 1259 (1957). [4] S.-G. Je, D.-H. Kim, S.-C. Yoo, B.-C. Min, K.-J. Lee, and S.-B. Choe, Phys. Rev. B 88 (21) (2013). [5] K.-S. Ryu, L. Thomas, S.-H. Yang, and S. S. Parkin, Appl. Phys. Express 5 (9), 093006 (2012).

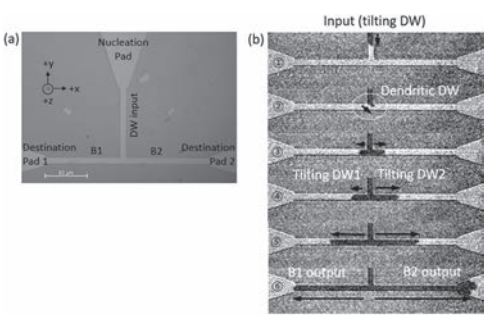

Fig. 1. (a) Microscopy image of a T-shaped device, which has a wire width, 5μm. (b) 1 - 6 Kerr microscopy images for DW dynamics in the structure as DW has a creep motion by field pulse. DW tilting angle has been oriented due to the propagation directions from an input wire to two outputs. Black arrows indicate the propagation direction of DW.

WEDNESDAY MORNING, 25 APRIL 2018 SIMPOR/ROSELLE BALLROOM, 8:30 TO 11:30

Session CR
FUNDAMENTAL PROPERTIES AND COOPERATIVE PHENOMENA I
(Poster Session)

Baomin Wang, Chair
Ningbo Institute of Materials Technology & Engineering, Ningbo, China

CR-01. Mechanism of spin re-orientation phase transition in $SmCrO_3$.

M. Tripathi[1], T. Chatterji[2], R.J. Choudhary[1], D.M. Phase[1] and H.E. Fischer[2]
1. Thin film magnetization, UGC DAE Consortium for Scientific research, Indore, India; 2. Institut Laue-Langevin, Grenoble, France

Understanding the mechanism of Spin reorientation phase transition (SRPT) plays an important role in designing of ultrafast switching equipment as well as in learning the fundamental aspects of complex magnetic exchange interactions [1,2]. The phenomenon of SRPT in $SmCrO_3$ has been considered as a process comprising continuous rotation of magnetic moments of chromium ions, the belief which is incompetent to explain the intrinsically associated thermal hysteresis and magnetic glassy state below SRPT [3-5]. The presence of highly neutron absorbing natural Sm atoms has prevented to record neutron diffraction patterns and consequently getting a microscopic insight of SRPT so far. In the present work, we have utilized high energy 'hot neutrons' with λ= 0.4997 Å, a value which is much higher than corresponding resonance energy width responsible for high absorption of neutrons, and succeeded to probe the evolution of microscopic spin configuration with temperature. Unambiguously three distinct phases were observed : Γ_4 or G_x A_y F_z configuration where uncompensated magnetic moments lie along c-cyrstallographic axis just below Neel temperature (T_N = 191 K); Γ_1 or A_x G_y C_z fully compensated spin structure below T< 10 K ; and non-equilibrium configuration with co-existing Γ_4 and Γ_1 phases in the vicinity of SRPT (10 K < T < 40 K). The transfer of magnetic scattering intensities associated with $(011)_m$ and $(101)_m$ Bragg's planes is observed in the vicinity of SRPT indicating the reorientation of magnetic moments from b-c to a-c crystallographic plane. In addition, the intensities related to $(010)_m$ and $(100)_m$ planes significantly increase below 40 K. The emergence of $(010)_m$ and $(100)_m$ planes correspond to the ordering of Sm moments [6,7]. In Γ_4(G_x, A_y, F_z) antiferromagnetic structure, the magnetic moments on neighboring atomic sites point exactly opposite to each other along x || a and y || b directions whereas, the z || c components are parallel, giving rise to weak ferromagnetism along c axis. Very small canting with respect to z || c axis results in a small (0.18-0.39 μ_B) uncompensated moment along -c axis. Γ_1 is a collinear antiferromagnetic structure not allowing any uncompensated moment. The temperarute driven magnetic phase diagram along with evolution of magnetic moments with temperature is constructed in Fig.1. The phase co-existence in the vicinity of SRPT reveals the discontinuous nature of transition and thus we divulge that $SmCrO_3$ possess a discontinuous first order SRPT and uncompensated antiferromagnetic ground state in contrast to the earlier predictions [3,4,8]. In addition, we qualitatively estimated the free energy in the vicinity of SRPT in the functional form of Sm^{3+}- Cr^{3+} antisymmetric-anisotropic exchange interactions and canting angles of moments, a value equivalent to the magneto-crystalline anisotropy, revealing the mechanism of SRPT is governed by completion between exchange interactions and anisotropy energy [8]. To summarize by the present studies, we determined the magnetic structure of $SmCrO_3$ for the first time, evidencing the uncompensated canted antiferromagnetic phase below Néel temperature, collinear antiferromagnetic ground state and the co-existence of both phases in the SRPT regime. Moreover, this is the first time in our knowledge to present the neutron diffraction of Sm- containing polycrystallites using high energy neutrons and we insist that this approach would be in general helpful for any Sm-containing insulating material where Sm moment is significantly high.

1. A. Kimel, B. Ivanov, R. Pisarev, P. Usachev, A. Kirilyuk and T. Rasing, Nature Phys. 5, 727 (2009). 2. A. Kirilyuk, A. V. Kimel and Theo Rasing, Rev. Mod. Phys. 82, 2731 (2010). 3. G. Gorodetsky, R. Hornreich, S. Shaft, B. Sharon, A. Shaulov, and B.Wanklyn, Phys. Rev. B 16, 515 (1977). 4. X. Qian, L. Chen, S. Cao, and J. Zhang, Solid State Commun.,195, 21 (2014). 5. M. Tripathi, R. Choudhary, and D. Phase, RSC Adv. 6, 90255 (2016). 6. P. Mandal, C. Serrao, E. Suard, V. Caignaert, B. Raveau, A. Sundaresan, and C. Rao, J. Sol. State Chem. 197, 408 (2013). 7. N. Shamir, H. Shaked, and S. Shtrikman, Phys. Rev. B, 24, 6642 (1981) 8. M. Tripathi, R. J. Choudhary, D. M. Phase, T. Chatterji, and H. E. Fischer, Phys. Rev. B 96, 174421 (2017).

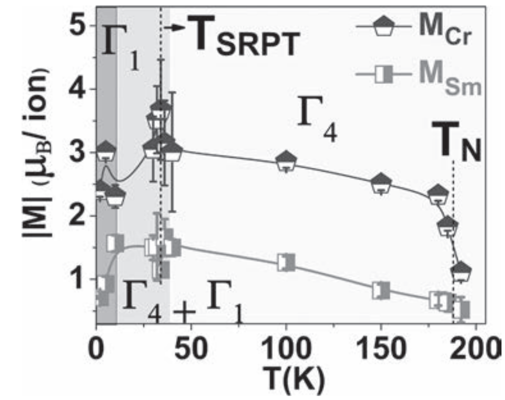

Fig. 1. Thermal evolution of magnetic moments of chromium and samarium ions and temperature driven magnetic phase diagram of $SmCrO_3$.

CR-02. Unusual Critical Behaviors in $La_{1.2}Sr_{1.8}Mn_2O_7$ Single Crystal.

D. Tran[1,2], X. Kieu[1], D. Pham[1], V. Tien[1], S. Yu[1], T. Phan[3], A. Telegin[4] and S. Naumov[4]

1. Chungbuk National University, Cheongju, The Republic of Korea;
2. Institute of Materials Science, Vietnam Academy of Science and Technology, Hanoi, Vietnam; 3. Hankuk University of Foreign Studies, Yongin, The Republic of Korea; 4. Institute of Metal Physics, RAS, Russian Federation

$Ln_{2-2x}A_{1+2x}Mn_2O_7$ (*Ln* and *A* are lanthanide and alkaline-earth metals, respectively) is a member of the Ruddlesden-Popper family ($Ln_{n+1}Mn_nO_{3n+1}$ with *n* is the dimension), which have attracted considerable interest due to their rich electrical-magnetic phase diagram. Previous reports have pointed that with $n = 1$, such as $La_{2-x}Sr_xMnO_4$, it has a layered perovskite structure and is a two-dimensional anti-ferromagnetic [1]. Meanwhile, with $n = 2$, it has a double-layered perovskite structure and is considered to be a two dimensional ferromagnetic (FM). Its structure is a stack of FM metal sheets composed of MnO_2 bilayers separated by a $(Ln,A)_2O_2$ rock-salt layer, thus forming a natural array of FM-insulator-FM junctions. Thus, the materials usually exhibit strongly anisotropic and complex physical properties [2, 3]. Though the anisotropy and the dimensionality of $Ln_{2-2x}A_{1+2x}Mn_2O_7$ are well known to play key roles in the magnetoresistance effect, but detailed analyses related to the ferromagnetic-paramagnetic (FM-PM) critical region have not yet been carried out. In this report, we present a detailed analysis on the critical behaviors in a single crystal of $La_{1.2}Sr_{1.8}Mn_2O_7$ via isothermal magnetization measured at different temperatures in the magnetic phase transition. Our results reveal that the material exhibits a single FM-PM phase transition corresponding to a second-order phase transition, takes place at $T_C = 85$ K. An analysis of the Landau-Lifshitz coefficients from the Arrott plots ($H/M = a(T) + b(T)M^2$) showed that $a(T)$ changed from the positive to the negative values at different temperatures in the field ranges of $H =$ 0-10 kOe, 10-30 kOe, and 30-50 kOe, indicating that the critical behavior could not be described with a single model under different applied fields. Using the Kouvel-Fisher and the critical isotherm analysis methods [4], we determined the values of the critical exponents for $La_{1.2}Sr_{1.8}Mn_2O_7$ around its FM-PM phase transition over different ranges of the magnetic field (Fig. 1). The critical exponent β value is found to be 0.51, 0.417, and 0.371 under field ranges of $H =$ 0-10, 10-30, and 30-50 kOe, respectively. Meanwhile, the value of the critical exponent γ is quite stable (γ = 0.973-1.074). It almost in-depends on the choice of field fitting range. This means that the critical exponent β depends strongly on the choice of the field's range, shifting from the value approaching that of the mean field model (β = 0.5) [5] to the value approaching that of the 3D-Heisenbeg model (β = 0.365) [5]. Additionally, with the obtained critical exponents, almost $M(H, T)$ data measured in the vicinity of T_C obeys the scaling equation $M(H, \varepsilon) = \varepsilon^\beta f_\pm(H/\varepsilon^{\beta+\gamma})$, where f_+ for $T > T_C$ and f_- for $T < T_C$ are regular analytic functions, and $\varepsilon = (T - T_C)/T_C$ is the reduced temperature [5]. Fig. 2 shows the $M/|\varepsilon|^\beta$ versus $H/|\varepsilon|^{\beta+\gamma}$ curves in a log-log scale for $La_{1.2}Sr_{1.8}Mn_2O_7$ single crystal. The natures of these phenomena are discussed thoroughly by means of the crystal structure and magnetic anisotropy of the material.

[1]. Y. Moritomo, Y. Tomioka, A. Asamitsu, Y. Tokura and Y. Matsui, Phys. Rev. B 51, 3297 (1995). [2]. K. Hirota, S. Ishihara, H. Fujioka, M. Kubota, H. Yoshizawa, Y. Moritomo, Y. Endoh and S. Maekawa, Phys. Rev. B 65, 064414 (2002). [3]. H. Asano, J. Hayakawa and M. Matsui, Phys. Rev. B 56, 5395 (1997). [4]. J. S. Kouvel and M. E. Fisher, Phys. Rev. 136, A1626 (1964). [5]. H. E. Stanley, *Introduction to Phase Transitions and Critical Phenomena* (Oxford University Press, London, 1971).

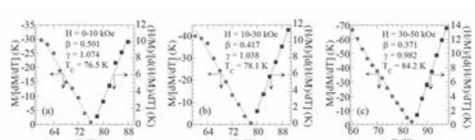

Fig. 1. Kouvel-Fisher plots of $M[dM/dT]^{-1}$ and $(H/M)[d(H/M)/dT]^{-1}$ versus *T* at different field ranges chosen for fitting: (a) *H* = 0-10 kOe, (b) *H* = 10-30 kOe, and (c) *H* = 30-50 kOe.

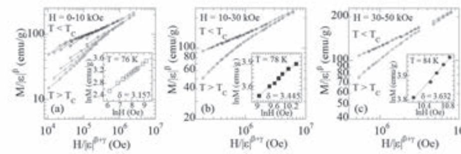

Fig. 2. $M/|\varepsilon|^\beta$ versus $H/|\varepsilon|^{\beta+\gamma}$ curves in a log-log scale obtained at different magnetic field range: (a) *H* = 0-10 kOe, (b) *H* = 10-30 kOe, and (c) *H* = 30-50 kOe. Insets show the ln*M* versus ln*H* curves at $T \approx T_C$.

CR-03. Critical behavior in $La_{0.75}Ca_{0.2}Ag_{0.05}MnO_3$ Exhibiting the Griffiths Phase.

D. Tran[1,2], D. Pham[1], X. Kieu[1] and S. Yu[1]
1. Chungbuk National University, Cheongju, The Republic of Korea;
2. Vietnam Academy of Science and Technology, Hanoi, Vietnam

Although $LaMnO_3$ is an insulating antiferromagnetic material, $La_{1-x}A_xMnO_3$ (A is an alkali earth and/or alkali element) exhibits some the electrical and the magnetic phase transitions, such as the ferromagnetic-paramagnetic (FM-PM) and the metal-insulating phase transitions, the magnetoresistance and the magnetocaloric effects [1, 2, 3]. However, detailed analyses related to the FM-PM critical region in a compound exhibiting the presence of the Griffiths phase have not yet been carried out. In this work, we have investigated the critical properties in the vicinity of the FM-PM phase transition in a polycrystalline sample of La0.75Ca0.2Ag0.05MnO3, which was prepared by a solid-state reaction method. The Rietveld refinement technique has been used to analyze the structure at room temperature, indicating all X-ray diffraction peaks belong to an orthorhombic structure (space group *Pnma*) with a = 4.486 Å, b = 7.767 Å, and c = 5.493 Å. Temperature dependence of the inverse of the susceptibility $\chi^{-1}(T)$ proves an existence of the Griffiths phase well above Curie temperature (Tc = 230 K) [4]. Detailed analyses of the isothermal magnetization $M(H, T)$ data reveal the sample exhibiting a second-order phase transition (SOPT), and its the temperature dependences of the saturation magnetization and the initial susceptibility obey the asymptotic relations. Using the Kouvel-Fisher and the critical isotherm analysis methods [5], the critical parameters (β, γ, δ, and Tc) for sample in two representative regions of low (below 15 kOe) and high (above 15 kOe) magnetic fields in the case of the no-subtracting and subtracting the demagnetization field (H_d) have been estimated. Experimental results suggest that the values of the critical exponents in the low magnetic field region are quite close to those expected for the 3D-Heisenberg model (β = 0.365 and γ = 1.336) [6]. Meanwhile, in the high magnetic field region, an unusual critical behavior has been observed, both β and γ values are found to be about 0.5. Using these critical exponent values, almost $M(H, T)$ data measured at different temperatures around FM-PM phase transition are collapsed onto two universal curves of $M/|\varepsilon|^{\beta}$ versus $H/|\varepsilon|^{(\beta+\gamma)}$ corresponding to the regular functions for $T > T_C$ and $T < T_C$, respectively. The natures of these phenomena are discussed thoroughly by means of a contribution of the Griffiths phase [4] and a coexistence of the short-range and the long-range magnetic interactions in material.

[1]. B.C. Hauback, H.Fjellvag, and N. Sakai, J. Solid State Chem. 124, 43 (1996). [2]. A.P. Ramirez, J. Phys., Condens. Matter 9, 8171 (1997). [3]. M.H. Phan and S.C. Yu, J. Magn. Magn. Mater. 308, 325 (2007). [4]. W.Jiang, X.Zhou, G.Williams, Y.Mukovskii, R.Privezentsev, Journal of Physics: Condensed Matter 21, 415603 (2009). [5]. J.S. Kouvel and M.E. Fisher, Phys. Rev. 136, A1626 (1964). [6]. H.E. Stanley, *Introduction to Phase Transitions and Critical Phenomena* (Oxford University Press, London, 1971).

CR-04. Observation of Griffiths like phase above room temperature in antiferromagnetic double perovskite Pr_2CoFeO_6.

A. Pal[1], V. Gangwar[1] and S. Chatterjee[1]
1. Physics, Indian Institute of Technology BHU, Varanasi, India

: Rare earth and transition metal oxides with rock-salt ordered doubleperovskite structure ($A_2B^{/}B^{//}O6$, A being rare earth and $B^{'}$& $B^{''}$ are transition metal ions) have been extensively studied for last few decades due to their technologically attractive and wide spectrum of physical properties. In these double perovskite systems B-site ordering and anti-site disorder play the crucial role in deciding its magnetic ground state. Depending on the magnetic interactions between B-site ions, double perovskite systems are reported to show ferromagnetism, exchange bias, spin-glass, magneto-resistance and magneto-capacitance etc. We report a spectrum of unusual magnetic properties including near room temperature antiferromagnetism (AFM) with existence of Griffiths like phase above neel temperature in double perovskite Pr2CoFeO6. In most of the previous studies in double perovskites, people have studied with $B^{/}$ and $B^{//}$ having oxidation states +2 and +4 respectively which give rise to ferromagnetic ordering following Goodenough-Kanamori (GK) rule[1]. In our sample, the nominal valency of both the B-site cations (Co and Fe) is +3 which is expected to produce antiferromagnetic ordering according to GK rule. In the temperature dependent magnetization study, we observed a AFM transition near room temperature at 270K, which is supported by observation of sharp and frequency independent peaks in ac susceptibility data, Fig-1. Inset of figure-1, showing isothermal magnetization as a function of magnetic field at temperatures 250K and 265K. The linear non-saturating behaviour of the magnetization curves clearly suggesting antiferromagnetic ordering. The dominant AFM behaviour is associated to the AFM exchange interactions occurring in Co^{3+}/Co^{3+}, Fe^{3+}/Fe^{3+} and Co^{3+}/Fe^{3+}. Most interestingly, a Griffiths like phase is observed above neel temperature (T_N 270K). Griffiths phase is usually observed in ferromagnetic systems but a paradigm shift occurred since few groups recently have reported existence of Griffiths phase in antiferromagnetic system [2]. In figure-2, a down turn behaviour is observed below a temperature T_G 370K in field dependent "temperature (T) variation of inverse susceptibility $1/\chi$" study,- which is the signature pattern of typical Griffiths phase. In typical Griffiths phase region, the temperature variation of inverse susceptibility follows a characteristic dependence given by χ^{-1} α $(T-T_N)^{1-\lambda}$, where T_N is ordering temperature and the range of λ lies between 0 to 1 in Griffiths phase regime[3]. Inset of figure 2, showing the fitted curve for applied magnetic field 250 Oe, the value obtained for λ is 0.9 which confirms the existence of Griffiths phase in PCFO.

1.J B Goodenough, Phys. Rev. 100 (1955) 564 2.Jitender Kumar, Soumendra Nath Panja,Shanu Dengre, and Sunil Nair, Phys. Rev B 95 (2017) 054401 3.Z. W. Ouyang et. al. Phys. Rev B 74, (2006) 094404

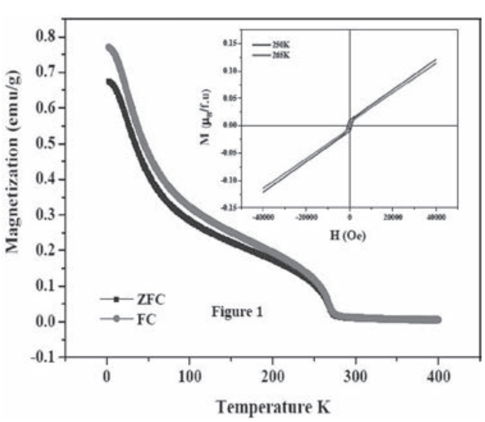

Fig. 1. Magnetization Vs temperature curves with ZFC and FC protocols at H=250 Oe. Inset: M-H curves at 250K and 265K.

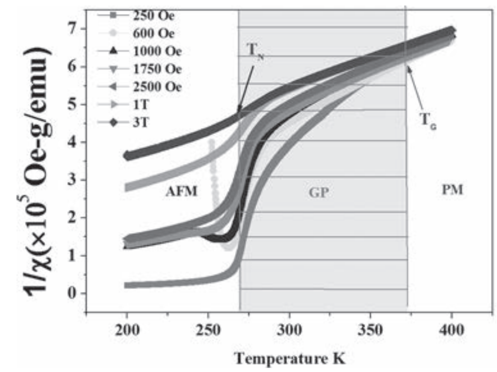

Fig. 2. Inverse susceptibility vs temperature curves at different fields. Inset: $\log_{10}\chi^{-1}$ Vs (T/T_N-1) plot at H=250 Oe.

CR-05. Low Temperature Magnetic Properties of Pyrochlore $Nd_2Ru_2O_7$.

D. Kumar[1], S.T. Ku[1], M.R. Lees[2], W.T. Lee[3], R.J. Aldus[3], A. Studer[3], I. Paolo[3], S. Asai[4], T. Masuda[4], S.W. Chen[5], J.M. Chen[5] and L.J. Chang[1,6]
1. Department of Physics, National Cheng Kung University, Tainan, Taiwan; 2. Department of Physics, University of Warwick, Coventry, United Kingdom; 3. Australian Nuclear Science and Technology Organization, Kirrawee, NSW, Australia; 4. Institute of Solid State Physics, The University of Tokyo, Chiba, Japan; 5. National Synchrotron Radiation Research Center, Hsinchu, Taiwan; 6. Advanced Science Research Center, Japan Atomic Energy Agency, Ibaraki, Japan

Frustrated pyrochlore compounds with general formula $A_2B_2O_7$ [1-5], where A is a trivalent rare-earth ion and B is a tetravalent transition-metal ion [1], with space group *Fd-3m*, is constituted by two individual interpenetrating A_2O' and B_2O_6 sublattices, composed by corner-sharing tetrahedra. Pyrochlore oxides have been extensively studied in the past few decades, and various novel magnetic behaviors have been discovered, including metal-insulator transition, spin glass [2], spin ice [3,4], and spin liquid [5]. These behaviors come from the geometrical frustration of pyrochlore lattice, which may lead to the macroscopic magnetic degenerate ground states rather than conventional long-range ordered ground states. We have performed x-ray diffraction, dc and ac magnetic susceptibilities, isothermal magnetization, heat capacity and neutron diffraction measurements of polycrystalline $Nd_2Ru_2O_7$ down to 0.4 K. Synchrotron x-ray studies confirm the phase purity and face-centered-cubic (space group *Fd-3m)* pyrochlore structure with lattice parameter, a = 10.3544 Å (5×10^{-4}). Three anomalies are observed in the dc magnetic susceptibility measurements at 146 K, 21 K and 1.8 K, which are due to the ordering of the Ru^{4+} moments into an antiferromagnetically coupled state, a weak canting of the ferromagnetic spins attributed to both Nd^{3+} and Ru^{4+} ions and a long-range-ordering of Nd^{3+} spins, respectively. A bifurcation of ZFC-FC susceptibility curves are observed at 146 K and 21 K, indicating spin canting which leads to weak ferromagnetism. We clarify the ambiguity regarding 21 K anomaly in $Nd_2Ru_2O_7$ reported in ref. [6,7] and we discussed 21 K anomaly on the pretext of spin canting. We fit $\chi(T)$ for T < 20 K with modified Curie-Weiss behavior $\chi(T) = \chi_0 + C/(T - \theta_{CW})$, where temperature independent term χ_0 represents Van Vleck contribution. The fit yields $\mu_{eff} = 2.37\ \mu_B$/Nd for Ising ground state of $Nd_2Ru_2O_7$ and $\theta_{CW} = +0.11(4)$ K. The positive value of θ_{CW} indicates weak ferromagnetic coupling among Nd spins. The isothermal magnetization data behavior at 2 K indicates significant single-ion anisotropy, expected for a local <111> Ising anisotropic system. The nearest neighbor dipole-dipole interactions D_{nn} is estimated to be ≈ 0.16 K. The nearest neighbor exchange interaction J_{nn} between the <111> Ising moments is estimated to be ≈ -0.77 K, from the dc susceptibility data. The value of J_{nn} indicates that antiferromagnetic exchange interactions dominate over dipolar interactions in $Nd_2Ru_2O_7$. A long-range ordering of Nd^{3+} spins is observed and confirmed at 1.8 K in all the measurements, indicating the ground state of the compound was not the glassy transition at ~ 21 K. Low temperature magnetic entropy is accumulated as *R*ln2 up to 5 K, suggesting Nd^{3+} doublet ground state. Lattice distortions are accompanied along with the transitions as revealed by the neutron and synchrotron x-ray diffraction measurements [8]. The magnetic moment of Nd^{3+} ion at 0.4 K is estimated as 1.54(2) μ_B and the magnetic structure is all-in all-out as determined by the powder neutron diffraction measurements. This is the first report on long range ordering of Nd^{3+} in $Nd_2Ru_2O_7$.

1. A. Harrison, J. Phys. Condens. Matter 16, S553 (2004). 2. J. E. Greedan, M. Sato, Xu Yan, and F. S. Razavi, Solid State Commun. 59, 895 (1986). 3. H. W. J. Blöte, R. F. Wielinga, and W. J. Huiskamp, Physica 43, 549 (1969). 4. M. J. Harris, S. T. Bramwell, D. F. McMorrow, T. Zeiske, and K. Godfrey, Phys. Rev. Lett. 79, 2554 (1997). 5. J. Gardner, B. Gaulin, S.-H. Lee, C. Broholm, N. Raju, and J. Greedan, Phys. Rev. Lett. 83, 211 (1999). 6. N. Taira, M. Wakeshima, and Y. Hinatsu, J. Solid State Chem. 152, 441 (2000). 7. M. W. Gaultois, P. T. Barton, C. S. Birkel, L. M. Misch, E. E. Rodriguez, G. D. Stucky, and R. Seshadri, J. Phys. Condens. Matter 25, 186004 (2013). 8. S.-W. Chen, S.-W. Fu, C.-W. Pao, J.-M. Lee, S.-A. Chen, S.-C. Haw, J.-F. Lee, C.-H. Liu, C.-K. Chang, Y.-C. Chuang, H.-S. Sheu, K.-T. Lu, S.-T. Ku, L.-J. Chang and J.-M. Chen, Phys. Chem. Chem. Phys. 17, 23667 (2015).

CR-06. Magnetic excitation, partial gap opening and chemical pressure effect in $CeNiGe_2$.

K. Singh[1] and *K. Mukherjee*[1]
1. School of Basic Sciences, Indian Institute of Technology, Mandi, India

The hybridization of 4*f*-electrons with conducting electrons results in fascinating ground state due to the competition between inter-site Ruderman-Kittel-Kasuya-Yosida (RKKY), and intra-site Kondo interaction in Ce-based intermetallics compound [1]. In such systems, parameters like magnetic field, external and/or chemical pressure is used to tune the ground state, leading to intriguing phases, such magnetic instability, non-Fermi liquid behavior, unconventional superconductivity, etc [2-3]. Literature report suggests that beyond the oxide family, it is relatively rare to observe the phenomenon of spin density wave (SDW) and itinerant antiferromagnetism [3, 4]. In some heavy fermionic system, the phenomenon of SDW is reported owing to the presence of a partially gapping of Fermi surface [5, 6]. The heavy fermion antiferromagnetic compound $CeNiGe_2$ is investigated by Jung et al., due to the intriguing physics exhibited by this compound [7]. Recent studies indicate that external pressure and high magnetic field are incapable to repress the long range ordering, resulting in the absence of Quantum critical point (QCP) and that the behavior of this compound is not in accordance to the Doniach model, which is widely used to classify heavy fermion compounds [8, 9]. Kim et al., reported that partial replacement of Ge in place Si leads to magnetic order being suppressed and some sign of Quantum critical point (QCP) is observed [10]. However to the best of our knowledge there are no literature reports about whether QCP or signature of non-fermi liquid behavior is observed due to Ce-site dilution by a nonmagnetic ion. Also, the low temperature ground state of $CeNiGe_2$ which has received considerable attention in the past decade remains undetermined. Here, we report the results of our investigation of magnetization, transport, thermodynamic and non-linear dc susceptibility measurements for the Y-substituted heavy fermion system $CeNiGe_2$. Y-substitution results in sequential suppression of magnetic ordering temperature below 1.8 K and also increases itinerancy among the spins. In $CeNiGe_2$ below ordering temperature, our results point towards the observation of SDW due to the presence of partial gap over a portion of the Fermi surface. Non linear dc susceptibility indicates the presence of multipolar magnetic order due to the coexistence of itinerant and localized moment in this compound. Our results indicate that the quadupolar orders leads to magnetic excitation, which is accountable for the development of the gap. This gap opening is suppressed and also is shifted down in temperature with the increase in Y-substitution. Signature of non Fermi liquid behavior or quantum critical point is absent even after 40% dilution of Ce-site, unlike to that, observed for Si substituted $CeNiGe_2$. Further, investigation of Gruneisen parameter gives an indication of fluctuations among spins which increases in itinerant state as observed for Y-0.4 compound.

[1] See, for example, N. Grewe and F. Steglich, in Handbook on the Physics and Chemistry of Rare Earths, edited by K. A. Gschneidner, Jr. and L. Eyring (Elsevier, Amsterdam, 1991), Vol. 14, p. 343 [2] H. v. Lohneysen, A. Rosch, M. Vojta, and P. Wolfle, *Rev. Mod. Phys.* 79, 1015 (2007) [3] G. Baym, and C. Pethick, Landau Fermi liquid theory (Wiley, New York, 1991) [4] A. Yeh, Y-Ah Soh, J. Brooke, G. Aeppli, T. F. Rosenbaum, and S. M. Hayden, *Nature London* 419, 459 (2002) [5] R. Movshovich, A. Lacerda, P. C. Canfield, J. D. Thompson, and Z. Fisk, *Phys. Rev. Lett.* 73, 492 (1994) [6] H-F. Li, C. Cao, A. Wildes, W. Schmidt, K. Schmalzl, B. Hou, L-P Regnault, C. Zhang, P. Meuffels, W. Loser, and G. Roth *Sci Rep.* 5, 7968 (2015) [7] M. H. Jung, N. Harrison, A. H. Lacerda, H. Nakotte, P. G. Pagliuso, J. L. Sarrao, and J. D. Thompson, *Phys. Rev. B* 66, 054420 (2002); V. K. Pecharsky and K. A. Gschneidner, Jr. *Phys. Rev. B* 43, 10906 (1991) [8] A. T. Holmes, T. Muramatsu, D. Kaczorowski, Z. Bukowski, T. Kagayama, and K. Shimizu, *Phys. Rev. B* 85, 033101 (2012) [9] Karan Singh and K. Mukherjee *Phys. Lett. A*, 381, 3236-3240 (2017) [10] D. Y. Kim, D. H. Ryu, J. B. Hong, J-G Park, Y. S. Kwon, M. A. Jung, M. H. Jung, N. Takeda, N. Takeda, M Ishikawa and S. Kimura, *J. Phys.: Condens. Matter* 16, 8323- 8334 (2004)

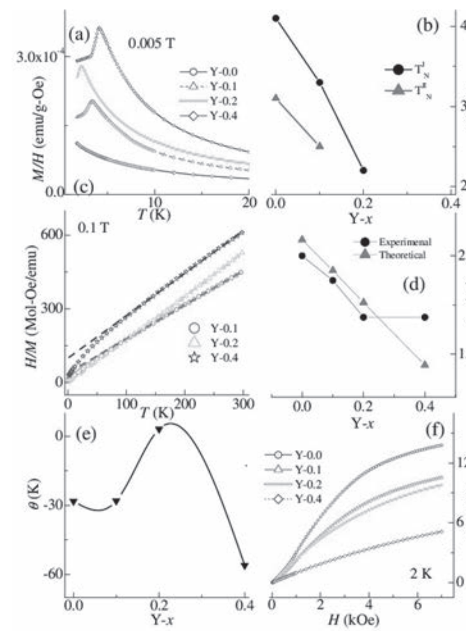

Fig. 1. (a) Temperature response of dc susceptibility (*M*/*H*) under zero field cooling condition at 0.005 T for all the compounds. (b) Variation of transition temperature with Y-concentration. (c) Temperature (*T*) response of inverse magnetic susceptibility (*H/M*) at 0.1 T. Straight lines through the curves shows the Curie Weiss law fitting. (d) and (e) Variation of effective moment (u_{eff}) and Curie Weiss temperature (θ (K)) with Y-concentration, respectively. (f) Isothermal magnetization versus magnetic field at temperature 2 K for all the compounds.

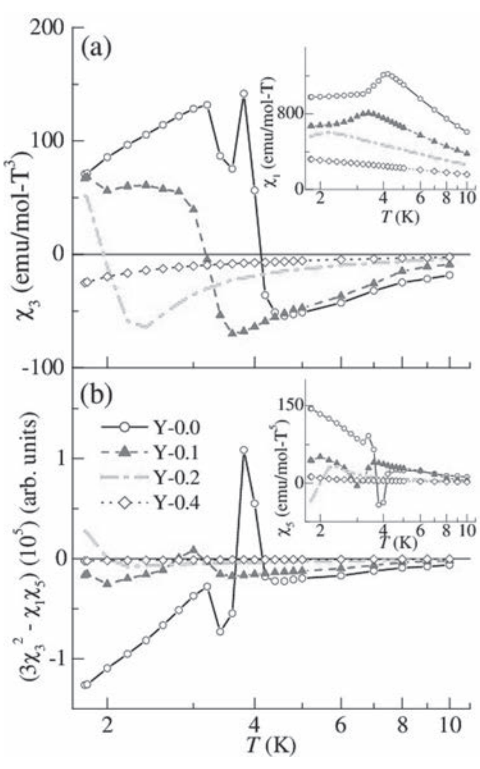

Fig. 2. (a) and its inset: Temperature response of third order susceptibility (χ_3) and first order susceptibility (χ_1) for the series of compounds $Ce_{1-x}Y_xNiGe_2$ (x = 0.0, 0.1, 0.2, and 0.4) respectively. (b) and its inset: Temperature response of the quantity ($3\chi^2_3 - \chi_5\chi_1$) and fifth order susceptibility (χ_5) for the same compounds respectively.

CR-07. Orthorhombic Ti_2O_3: A Polymorph-Dependent Narrow-Bandgap Ferromagnetic Oxide.

Y. Li[2,1], Y. Weng[3], X. Yin[4], X. Yu[4], S. Kumar[2], N. Wehbe[5], H. Wu[1], H. Alshareef[2], S.J. Pennycook[1], M.B. Breese[4], J. Chen[1], S. Dong[3] and T. Wu[2]
1. Material Science and Engineering, National University of Singapore, Singapore; 2. Material Science and Engineering, King Abdullah University of Science and Technology (KAUST), Jeddah, Saudi Arabia; 3. Department of Physics, Southeast University, Nanjing, China; 4. Singapore Synchrotron Light Source (SSLS), National University of Singapore, Singapore; 5. Imaging&Characterization Core Lab, King Abdullah University of Science and Technology (KAUST), Jeddah, Saudi Arabia

Magnetic semiconductors are highly sought in spintronics, which allow not only the control of charge carriers like in traditional electronics, but also the control of spin states. However, almost all known magnetic semiconductors are featured with bandgaps larger than 1 eV, which limits their applications in long-wavelength regimes. In this work, we report the discovery of orthorhombic-structured Ti_2O_3 (R-Ti_2O_3) films as a unique narrow-bandgap (~0.1 eV) ferromagnetic oxide semiconductor. In contrast, the well-known corundum-structured Ti_2O_3 (C-Ti_2O_3) polymorph has an antiferromagnetic ground state.[1] Our comprehensive study on epitaxial Ti_2O_3 thin films reveals strong correlations between structure, electrical, and magnetic properties. The new orthorhombic Ti_2O_3 polymorph was found to be n-type with very high electron concentration, while the bulk-type trigonal-structured Ti_2O_3 was p-type.[2] More interestingly, in contrast to the antiferromagnetic ground state of trigonal bulk Ti_2O_3, unexpected ferromagnetism with a transition temperature well above room temperature was observed in the orthorhombic Ti_2O_3, which was confirmed by X-ray magnetic circular dichroism (XMCD) measurements.[3] The room-temperature ferromagnetism observed in orthorhombic-structured Ti_2O_3 demonstrates a new route towards controlling magnetism in epitaxial oxide films through selective stabilization of polymorph phases. Both Ti_2O_3 polymorph thin films were deposited on Al_2O_3 (001) single crystal substrates at different temperatures using pulsed laser deposition, with a corundum Ti_2O_3 target. As shown in Fig. 1, two polymorphs of Ti_2O_3 epitaxial films were characterized by X-ray diffraction and Raman spectroscopy, with well-distinguished polymorph-dependent characteristics. Moreover, X-ray magnetic circular dichroism (XMCD) was performed to investigate the magnetism of both polymorphs. As shown in Fig. 2, a clear ferromagnetic behaviour was observed by Ti L-edge XMCD in R-Ti_2O_3, while C-Ti_2O_3 shows no XMCD signal. Using n_{3d}=1 for Ti^{3+} and taking into account the circular polarization, the value of total magnetic moment 0.16 μ_B/Ti was obtained for R-Ti_2O_3. Although both Ti_2O_3 polymorphs share the similar narrow bandgap of ~0.1 eV, their spin configurations are quite different. Since the ferromagnetic R-Ti_2O_3 polymorph has a bandgap as narrow as 0.1 eV, it might enable the exploration of interaction with polarized infrared light in new types of spintronic devices. Furthermore, the contrast of physical properties in these two polymorph phases of Ti_2O_3 demonstrates a new route to engineering charge and spin ground states in semiconductors, which may inspire the exploration of selective stabilization of polymorph phases in other materials relevant to electronic and spintronic applications.

[1] D. Adler. Antiferromagnetism in Ti_2O_3. *Phys. Rev. Lett.* 17, 139 (1966). [2] J. Yahia, H. P. R. Frederikse. Electrical Conduction in p-Type Titanium Sestluioxide. *Phys. Rev.* 123, 1257 (1961). [3] Y. Li, Y. Weng, X. Yin, X. Yu, S. R. S. Kumar, N. Wehbe, H. Wu, H. N. Alshareef, S. J. Pennycook, M. B. H. Breese, J. S. Chen, S. Dong, T. Wu, Orthorhombic Ti_2O_3: A Ploymorph-Dependent Narrow-Bandgap Ferromagnetic Oxide, *Adv. Funct. Mater.* 2018, 1705657.

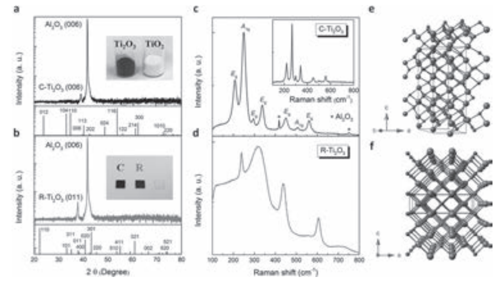

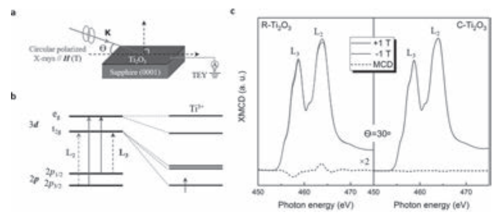

CR-08. Inverted magnetic hysteresis loop and strong magnetoelectric coupling in mixed ferrimagnetic-multiferroic phases of a double perovskite.

D. Oh[1], M. Kim[1], J. Moon[1], S. Oh[1], Y. Choi[1] and N. Lee[1]
1. Yonsei University, Seoul, The Republic of Korea

Exploring new magnetic materials is essential for finding advantageous functional properties such as magnetoresistance, magnetocaloric effect, spintronic functionality, and multiferroicity. Versatile classes of double perovskite compounds have been recently investigated because of intriguing physical properties arising from the proper combination of several magnetic ions. In this study, we examined magnetic and dielectric properties of single-crystalline double-perovskite Er_2CoMnO_6. In addition to the ferromagnetic order arising at T_C = 67 K from the dominant Co^{2+} and Mn^{4+} superexchange interactions, the long-range order of Er^{3+} moments below T_{Er} = 10 K activates the ferrimagnetic order, characterized by compensated magnetization at T_{Comp} = 3.15 K. The inverted magnetic hysteresis loop observed below T_{Comp} can be described by an extended Stoner–Wohlfarth model that is established from contrasting magnetic anisotropy and moments between Er^{3+} and ferromagnetic Co^{2+}/Mn^{4+} sublattices. From the measurement of dielectric properties, an additional small portion of the multiferroic phase, as found in Lu_2CoMnO_6, is identified at T_C. The coexisting ferrimagnetic and multiferroic phases appear to be strongly correlated in that metamagnetic and dielectric transitions occur simultaneously. Our results based on intricate magnetic correlations and phases in Er_2CoMnO_6 enrich fundamental and applied research on magnetic materials through the scope of distinct magnetic characteristics in double perovskites.

CR-09. Study of Spin Polarized Tunneling in Magnetoresistance and Low Temperature Anomaly in Nanoparticles of $La_{0.5}Ca_{0.5}MnO_3$.

A.K. Saw[1], G. Channagoudra[1], H. Fu[2], *R.L. Hadimani*[3] and V. Dayal[1]
1. Department of Physics, Maharaja Institute of Technology-Mysore, Mandya, India; 2. University of Electronic Science and Technology of China, Chengdu, China; 3. Department of Mechanical and Nuclear Engineering, Virginia Commonwealth University, Richmond, VA, United States

Perovskite oxides are typical correlated electron systems and important functional materials, owning fascinating physical properties and promising potential for applications [1–4]. Half doped manganites with generic formula $R_{0.5}A_{0.5}MnO_3$ (where R, trivalent rare earth and A, divalent alkaline earth element) are topic of significant interest in both theoretical and experimental frontiers. The ground state of half doped manganites show contrasting behavior where the charge ordering (CO), orbital ordering (OO) coupled with antiferromagnetic insulating (AFI) state favored by the localizing effects and ferromagnetic metallic (FMM) state driven by the delocalizing effects. The low-temperature electronic transport in some manganites presents a feature of weak insulating/semiconducting behavior and has been explained using different mechanisms [5-9]. Furthermore, physical properties are also modified to a considerable extent subject to the reduction of particle size. This occurs mainly due to the finite size effect, surface and interface effect in magnetic nanoparticles. In this digest, the low temperature resistivity and magnetoresistance (MR) in polycrystalline half doped $La_{0.5}Ca_{0.5}MnO_3$ of ~25.9 nm size nanoparticle synthesized using citrate route has been investigated in the absence and presence of the magnetic field (H = 0T, 4T and 8T). As shown in Fig 1 (a). X-ray diffraction data along with fitting using Rietveld Fullprof software [10] to the orthorhombic unit cell structure crystallizes in Pnma space group (No. 62).The lower value of χ^2 =1.48 indicated a good agreement between observed and calculated patterns. The average crystallite size calculated to be 25.9 nm using the Scherrer's formula [11] after correcting for instrumental contribution to line broadening. Fig. 1 (b) and (c) depicts images elucidating the surface morphology of the sample obtained using Scanning Electron Microscopy at 1μm and 3 μm respectively taken 15KeV. It can be seen that, the grains are in average spherical shaped nano size possessing fine and clear grain boundaries with a small neck between two adjacent grains. From the temperature dependence of resistivity plot shows metal–insulator (MI) transitions at temperature (T_{MI}) = 89 K at 0T as shown in Fig. 2. With the application of magnetic field, the decrease in resistivity and shifting of T_{MI} towards higher temperatures suggests consolidation of Double Exchange mechanism [12]. The significant decreases in resistivity with field over a wide temperature range, for example, from lowest temperature of measurement to ~250 K indicates that FM interaction starts dominating well above observed T_{MI}. This is further supported by isothermal MR measurement which shows PM like behaivour at 300 K and FM like below 200 K discussed later. Based on the phenomenon of phase coexistence in ferromagnetic metallic and paramagnetic insulating regions in the doped manganites, the temperature variation of the resistivity between 50 K and 300 K are in agreement with combined contributions of empirical [13,14] and Small Polaronic Conduction (SPC) model written as; $\rho_{whole}(T)=(\rho_0+\rho_1 T^2+\rho_2 T^{4.5}).f+(1-f).B.T.\exp(E_a/k_B T)$..... (1), where $f=\{[\exp(T-T^M_c/\text{delta})+1]^{-1}$ is the Boltzmann's distribution function of charge carriers in the metallic state. And the characteristic T_{MI} is denoted as T^M_c and delta as the effective transition width over the interval of T^M_c. At temperature below 40 K, a shallow minimum (T_{min}) appears in resistivity plot. The application of the magnetic field suppresses the effect and gradually decreases T_{min} with increasing magnetic field. However application of even 8T could not diminish the effect and is explained considering intergrain tunneling of the charge carriers between anti-ferromagnetically coupled grains. Inset of Fig. 2 shows the magnetic field (H) dependent magnetoresistance [MR % =ρ(H)-ρ(0)/ρ(0)×100] isotherms. At 5 K and H=0.5 T (<1T), the observed MR is ~ 30 %, which increases with the increasing H. At highest measured H= 8 T, the MR is ~ 65%, 60%, ~30% and ~10% at 5 K, 100 K, 250 K and 300 K respectively. MR plot also suggest PM like behavior (concave shape) at 300 K and FM like below 200 K (Convex shape). At 250 K MR behavior seems to be typical of PM near FM transition temperature as discussed earlier. The lower T_{MI} appears to be due to nanoparticle nature of the sample where surface could be insulating. The evidence of metallic seem in isothermal MR as at 8T field MR is about 30%, which is expected due to spin polarized tunneling between two FM grains. Similar such behavior was suggested by Rawat et al. [15] for $GdPd_2Si$ and Lee et. al.[16] for perovskite manganites. The disappearance of the MR at higher temperature regime in insulating state can be ascribed to the weakening of the DE mechanism because of the paramagnetic (PM) state. The present results are discussed and possible explanations are given based on the allied theory.

1. E. Dagotto, T. Hotta, and A. Moreo, Phys.Rep. 344(1), 1 (2001). 2. Y. Tokura, Rep. Prog. Phys. 69(3), 797 (2006). 3. C. Sen, G. Alvarez, and E. Dagotto, Phys.Rev. Lett. 98(12) 127202 (2007) 4. C. Sen, G. Alvarez, and E. Dagotto, Phys. Rev. Lett. 105(9) 097203 (2010). 5. Kondo J. Prog Theor Phys 32:37 (1964). 6. Ziese M. Phys Rev B;68:132411 (2003) 7. Kumar D, Sankar J, Narayan J, Singh RK, Majumdar AK. Phys Rev B 65 094407 (2000). 8. E. Rozenberg, M Auslender., I. Felner and G Gorodetsky., *J Appl. Phys*. 88 2578 (2000). 9. J.S. Helman, B. Abeles, Phys. Rev. Lett. 37 1429 (1976). 10. J. Rodriguez Carvajel, FULLPROF version 3.0 Laboratorie Leon Brillioun, CEACNRS,(1995) 11. Patterson, A L., Phys. Rev. vol. 56, pp. 978–982 (1939). 12. C. Zenner, Phys. Rev. 82 403 (1951). 13. M.Jaime, P.Lin, M.B. Salamon, P.D. han, Phys. Rev. B 58 (1998) R5901;A.S. Alexandrov, A.M. Bratkovsky, Phys. Rev. Lett. 82 141(1999). 14. G. Jeffrey Snyder, R. Hikes, S. DiCarolis, M.R. Beasley, T.H. Geballe, Phys. Rev. B 53 14434(1996) 15. R. Rawat and I. Das, J. Phys.: Condens. Matter 13 L57–L63 (2001) 16. S. Lee,H. Y. Hwang,Boris I. Shraiman,W. D. Ratcliff II and S-W. Cheong, Phys. Rev. Lett, 82, 22 (1999)

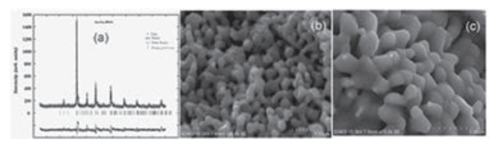

Fig. 1. (a) Rietveld fitted Xray diffraction pattern of $La_{0.5}Ca_{0.5}MnO_3$ at room temperature. (b) and (c) Scanning Electron micrograph at different Magnifications.

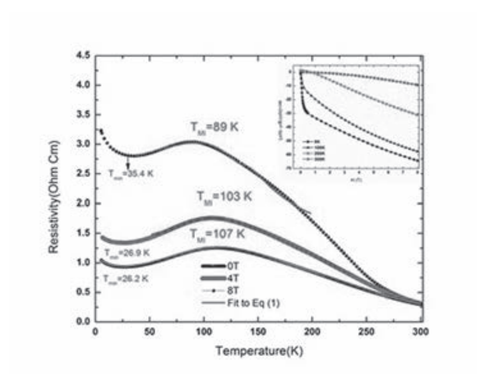

Fig. 2. Temperature dependence of resistivity at 0, 4 and 8 T fitted to equation (1). (Inset) Feld dependence MR isotherms.

CR-10. Non-collinear spin structure at ultrathin magnetic interfaces and its evolution by the oxygen adsorption.

T. Chuang[1], C. Huang[2], C. Lu[1] and D. Wei[1,2]
1. National Synchrotron Radiation Research Center, Hsinchu, Taiwan;
2. National Sun Yat-sen University, Program for Synchrotron Radiation and Neutron Beam Applications, Kaohsiung, Taiwan

The study of non-collinear spin structures has recently attracted much attention, since manipulating these magnetic textures offers a possibility to achieve fast ultrahigh-density data manipulation. The origin of the chirality is caused by the anti-symmetric exchange interaction, i.e. Dzyaloshinskii-Moriya interaction (DMI). Large DMI has been predicted and observed at interfaces between heavy metals and transition metal ferromagnets, resulting in asymmetric spin wave dispersion relation [1-2] and chiral spin structures, such as Skyrmions within external magnetic field at low temperature [3]. Recently, these chiral spin textures have been observed by X-ray magnetic circular dichroism (XMCD) based photoemission electron microscope (XPEEM) at room temperature without external field in the system of MgO covered Co/Pt [4], demonstrating the possibilities of investigating chiral spin structures by XPEEM. In the other hand, a real-space imaging of magnetic stripe domain structures in epitaxial Fe/Ni bilayers grown on Cu(001) [5] and Co/Ni multilayers grown on Pt(111) or Ir(111) [6] has suggested the existence of Néel-type chiral domain walls with a fixed chirality at room temperature by spin-polarized low energy electron microscopy (SPLEEM), which indicates that the underlying mechanism is the DMI [5]. Recently, it has been predicted that the DMI in the Fe/Ir system can be tuned and even controlled by the adsorption of electronegative ions, such as oxygen or nitrogen [7], due to the hybridization of transition metals and the ions, which alters the degree of electronic asymmetry at the interface. However, at this moment there is still no direct experimental proof. Here we report that by using XPEEM with XMCD contrast at BL05B2 end-station at Taiwan Light Source a Néel-type out-of-plane chiral magnetic domain wall structure was observed in epitaxial Fe/Ni/Cu(001) across stripe domains within the spin reorientation transition (SRT) (see Fig. 1 (a)). The information of a fixed right-handed chirality can be obtained from a high-resolution XPEEM image with a line-profile of the intensity of the XMCD contrast (Fig. 1 (b)), which is in line with the result of SPLEEM [5]. Furthermore, by taking the advantage of the synchrotron-based element-selective technique, it is found that the spin structure in Fe films is ferromagnetically coupled to the one in Ni films in this system. In addition, the evolution of the stripe domains by the oxygen adsorption is also presented and discussed (see Fig. 1 (c)-(e)). It is found that the domain periodicity becomes larger and averaged domain width is increased when the thickness of oxygen passivation is increased from 0 to 1 Langmuir. It is an evidence that the DMI-magnitude is decreased when the oxygen atoms are passivated on top of the Fe surface, which has been predicted by calculation [7]. Moreover, the X-ray absorption spectra (XAS) of oxygen *K*-edge and Fe *L*-edge indicate that the oxygen atoms are only passivated on the Fe surface without having Fe-O state. Realizing the control of the DMI in ultrathin metal films is of great importance in the surface/interface physics and it will pave the way towards the design of chiral magnetic properties through interface engineering.

[1] Kh. Zakeri, *et al.*, *Phys. Rev. Lett.* 104, 137203 (2010). [2] Kh. Zakeri, *et al.*, *Phys. Rev. Lett.* 108, 197205 (2012). [3] N. Romming, *et al.*, *Science* 314, 636 (2013). [4] O. Boulle, *et al.*, *Nat. Nanotech.* 11, 449 (2016). [5] G. Chen, *et al.*, *Phys. Rev. Lett.* 110, 177204 (2013). [6] G. Chen, et al., *Nat. Commun.* 4, 2671 (2013). [7] A. Belabbes, et al., Sci. Rep. 6, 24634 (2016).

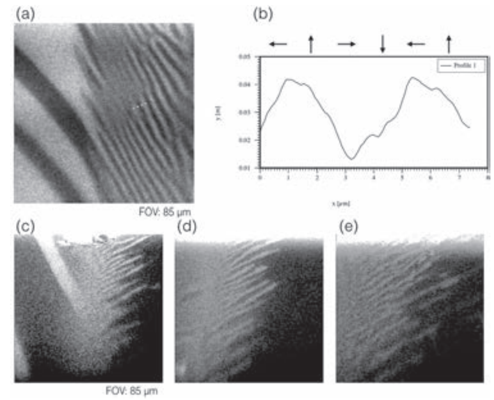

Fig. 1. | (a) XMCD-PEEM image of stripe domains in 2.3 ML Fe/2 ML Ni/Cu(001) and (b) the intensity line-profile of the yellow dashed line. (c)-(e) XMCD-PEEM images of stripe domains in 2.3 ML Fe/2 ML Ni/Cu(001) with 0, 0.5, and 1 Langmuir oxygen adsorption.

CR-11. Role of Fe-doped effect in two-dimensional MoS_2 magnetic semiconductor.

C. Kao[2], C. Yang[2], H. Kao[2], Y. Tung[2], T. Hsu[2], W. Wu[2] and K. Lin[1]
1. Chemical Engineering and Material Science, Yuan Ze University, Taoyuan City, Taiwan; 2. Physics, Chung Yuan Christian University, Taoyuan City, Taiwan

Two two-dimensional $Mo_{1-x}Fe_xS_2$ (x=0, 0.01) nanosheets were fabricated by the hydrothermal method. High-resolution TEM images show both samples were composited with amount 12 layers. As Figure 1(a) show the Raman peaks were broadening in the iron-doped sample. In the two-dimensional MoS_2, the 1 % Fe^{4+} doping means the irons were separated by eight Mo^{4+} alone *a* or *b* axis in the *a-b* plane. The larger Mo^{4+} ion (r_{ion} = 0.65 Å) were replaced by smaller Fe^{4+} (r_{ion}=0.585 Å), and caused the structural distortion. The imperfect periodicity will cause the soften of the phonon mode and make Raman peaks broadening. Ac conductivity experiments revealed both samples obeyed small polaron hopping model as Fig. 1(b). The activation energies of x=0 are 0.121(3) eV and 0.066(1) eV above and below 200 K. Similar two difference activation energies, 0.140(2) eV and 0.082(1) eV above and below 240 K are also found in x=0.01 sample. The effect of iron-doped may raise the activation energies of small polaron. Figure 2 (a) show the magnetic susceptibility of both samples. The diamagnetism is observed in pure MoS_2 between 20 K and 300 K.[1] In contrast, the x=0.01 sample exhibited paramagnetism from 5 K to 300 K. The χ^{-1}-T plot shows the magnetic correlation started at about 270 K. Figure 2 (b) displayed the magnetic hysteresis experiments. No hysteresis loops were found in both samples. For x=0.01 sample, this is an evidence that the doped iron are not aggregated and formed as a magnetic domain. Furthermore, the Brillouin function plus a linear term can be utilized to describe the collected curves of x=0 and 0.01 samples. Small positive and negative slopes of the linear term were found in x=0 and 0.01, respectively. These results revealed both samples contain two origins of magnetism. For x=0, the paramagnetic behavior is found at low field and low temperature. But the diamagnetism is observed at all temperature region. The temperature independent diamagnetic behavior is associated with Langevin diamagnetism. For x=0.01 sample, the Brillouin term is coming from the doped iron ions. The fitted $<m_z>$ of the x=0.01 sample is about 0.019 $m_B/f.\ u.$, which matched the value of 1 % Fe^{4+} (S=2) ion-doped.

[1] Shiming Yan, Wen Qiao, Xueming He, Xiaobing Guo, Li Xi, Wei Zhong, and Youwei Du, Appl Phys Lett. 106, 012408 (2015)

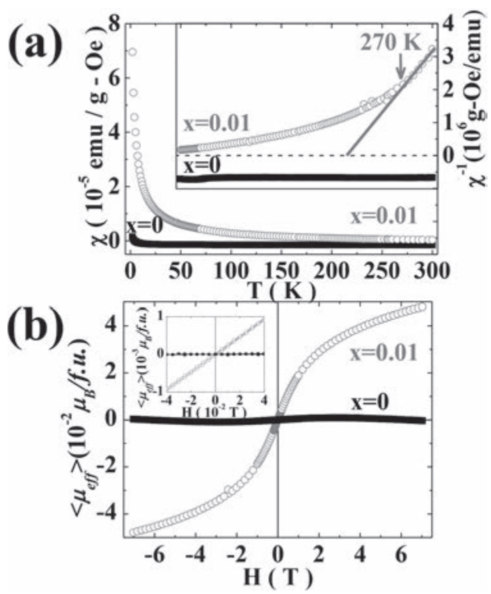

Fig. 1. (a) Raman spectra and (b) ac conductivity of $Mo_{1-x}Fe_xS_2$ (x=0 and 0.01). The inset of (b) show the ln-T^{-1} plot of both samples.

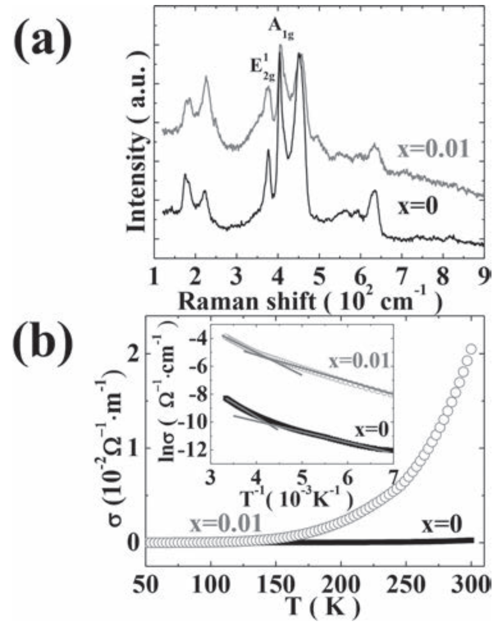

Fig. 2. Magnetic experiments of $Mo_{1-x}Fe_xS_2$ (x=0 and 0.01) of (a) ac susceptibility and χ^{-1}-T plot (as inset) and (b) hysteresis loop and low field region (as inset).

CR-12. Reversible 90-Degree Rotation of Fe Magnetic Moment Using Hydrogen.

W. Lin[1], C. Hsu[1], P. Chang[1], Y. Chen[1] and C. Liu[1]
1. Department of Physics, National Taiwan Normal University, Taipei, Taiwan

$[Pd/Fe]_2$ multilayers were deposited on a flat MgO(001) to study the effect of hydrogen on magnetic interlayer coupling. Complex magnetic hysteresis behavior, including single, double, and triple loops, were measured as a function of the azimuthal angle in a longitudinal and transverse direction. With a combination of a 2-fold magnetic anisotropy energy in the bottom-Fe and a 4-fold MAE in the top-Fe, the complex magnetic hysteresis behavior could be clearly explained. Two well-split hysteresis loops with almost zero Kerr remanence were measured by choosing a suitable Pd thickness and applying the magnetic field perpendicular to the easy axis of the bottom-Fe. The split double loops originated from the 90°-rotation of the top-Fe moment. On exposure to a hydrogen gas atmosphere, the separation of the two minor loops increased, indicating that Pd-hydride formation enhanced the ferromagnetic coupling between the two Fe layers. Based on these observations, we proposed that, by applying a suitable constant magnetic field, the top-Fe moment could undergo reversible 90°-rotation following hydrogen exposure. The results suggest that the Pd space layer used for mediating the magnetic interlayer coupling is sensitive to hydrogen, and therefore, the multilayer system can function as a giant magnetoresistance-type sensor suitable for hydrogen gas.

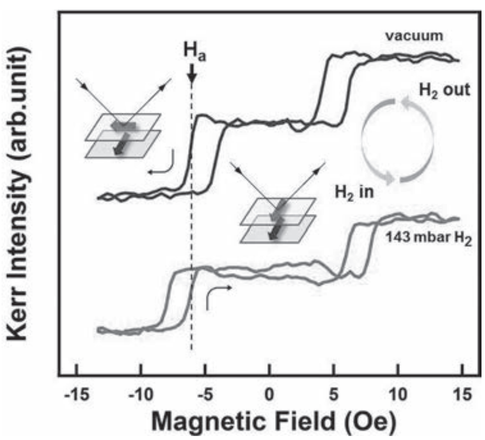

Fig. 1. Reversible 90° rotation of the magnetic moment in the top Fe layer through hydrogen charging. Following H_2 gas absorbtion or desorption, the magnetization minor hysteresis loop shifted toward a larger or smaller coercivity field. When a suitable constant field H_a (as indicated by the dashed line) was applied, the hydrogen charging or discharging reverses the top-Fe layer by 90°.

CR-13. The Role of Graphene Oxide Precursor on Magnetic and Microwave Properties of Nitrogen-doped Graphene.

L. Quan[1], *F. Qin*[1], H. Wang[1] and H. Peng[1]
1. Zhejiang University, Hangzhou, China

Two-dimensional nanomaterials, owing to their excellent physical, chemical and electronic properties, have been extensively explored[1]. Graphene, among others, has attracted tremendous attention since its discovery in 2004[2]. It has outstanding thermal conductivity, electrical conductivity, mechanical properties and high specific surface area with ultrathin thickness, all these properties make graphene a star material. However, pristine graphene is diamagnetic due to the lack of local magnetic moments, which limited its application in many spintronic and magnetic devices. According to the first principle calculations, different kinds of defects (etc. vacancies, adatoms, heteroatoms) can induce different magnetic moments[3]. Nitrogen falls into our best choice as the doping element, in that it is adjacent to carbon in the periodic table and hence has the similar atom size and valence, thus, the introduction of nitrogen will not cause excessive distortion to graphene lattice. Besides, the electronegativity divergence between C atom (2.55) and N atom (3.04) can breach the electroneutrality of graphene material and lead to the change of atomic charge distribution and spin density, which may serve as the resource of graphene magnetism[4]. In this work, a facile thermal annealing method was conducted for two types of GO (GO-1 stands for monolayer; GO-2 stands for multi-layer) to synthesize the nitrogen-doped graphene (NG), through the programmed temperature to achieve a control between doping and reduction process. Several factors that influence the doping and reduction degree have been investigated to reveal the dominant factor that affect the magnetic properties of NG. Table 1 showed that the lower doping is attained with higher reduction degree, which suggests that the doping process is closely related with the oxygen-containing groups in graphene sheets. It is also found that the precursor GO-1 with a slightly lower C/O ratio than GO-2 can be so much more reduced to the extent with C/O ratio obtained more than twice than that of GO-2. This is consistent with the AFM characterization (Fig.1(c,d)): GO-1-NG obtained has more layers than GO-2-NG, which is attributed to less oxygen-containing functional groups left likely leading to a restacking. Also, as indicated in the Raman spectra (Fig.1(a)), I_D/I_G of GO-1 is decreased after reduction, which is opposite to the case of GO-2. Such a striking contrast points to the fact that the graphitic sp^2 hybrid structure was better restored after the reduction and doping process for monolayer than multilayer. Since the doped N does not vary much for these two types of GO, it follows that the increasing number of GO layers has little influence on the doping degree but may suppress the reduction process. With respect to the magnetic properties (Fig.1(b)), both NG samples obtained affords improved magnetization at 2K than their precursor GO, respectively. But the M_s of GO-1-NG reaches 1.31 emu/g, which is far larger than that of GO-2-NG, which indicates that a well restored graphitic structure plays a determinant role here on magnetization of graphene.

1. J. Hong, C. Jin, J. Yuan and Z. Zhang, *Advanced materials*, 2017, 29. 2. K. S. Novoselov, A. K. Geim, S. V. Morozov, D. Jiang, Y. Zhang, S. V. Dubonos, I. V. Grigorieva and A. A. Firsov, *Science*, 2004, 306, 666-669. 3. C. Ma, X. Shao and D. Cao, *Journal of Materials Chemistry*, 2012, 22, 8911. 4. Z. Yang, Z. Yao, G. Li, G. Fang, H. Nie, Z. Liu, X. Zhou, X. a. Chen and S. Huang, *ACS Nano*, 2012, 6, 205-211. 5. Z.-H. Sheng, L. Shao, J.-J. Chen, W.-J. Bao, F.-B. Wang and X.-H. Xia, *ACS Nano*, 2011, 5, 4350-4358.

	C1s	O1s	N1s	C/O	N/C
GO-1	79.75	20.25		3.938	
GO-1-NG	91.29	2.33	6.38	39.18	6.98
GO-2	75.82	24.18		3.136	
GO-2-NG	88.07	4.54	7.39	19.40	8.39

Table 1 C1s, N1s, O1s content and C/O, N/C ratio of GO-1, GO-1-NG, GO-2, GO-2-NG.

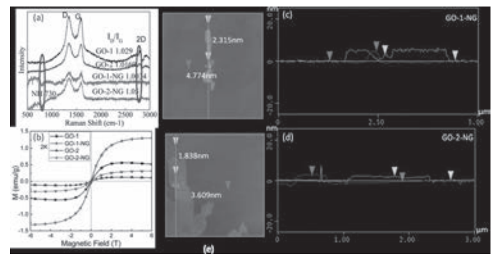

Fig. 1. (a) the Raman spectra; (b) M-H profiles; AFM images of (c) GO-1-NG and (d) GO-2-NG.

WEDNESDAY MORNING, 25 APRIL 2018 SIMPOR/ROSELLE BALLROOM, 8:30 TO 11:30

Session CS
HARD MAGNETS I
(Poster Session)

Aru Yan, Chair
Ningbo Institute of Materials Technology & Engineering, Ningbo, China

CS-01. Magnetic properties of Fe-Pt thick-film magnets electroplated on Cu substrates.

Y. Omagari[1], J. Honda[1], R. Hamamura[1], H. Yamada[2], N. Fujita[2], K. Takashima[1], T. Yanai[1], M. Nakano[1] and H. Fukunaga[1]
1. Nagasaki University, Nagasaki, Japan; 2. National Institute of Technology, Nara College, Nara, Japan

I. INTRODUCTION $L1_0$ ordered Fe-Pt films are attractive film-magnets for small-sized medical devices due to their high crystalline anisotropy and high biological safety, and some researchers have been reported the $L1_0$ ordered Fe-Pt thick films (> 1 μm) prepared by sputtering methods [1-2]. For applying the films to the devices, fabrication processes with high deposition rate are effective. Thus, we have employed an electroplating method using high current density (> 0.5 A/cm^2). Although we realized 23 μm-thick Fe-Pt films with high coercivity (approx. 700 kA/m) in the past study [3], partial peelings of the films from Ta substrates, which is attributed to many cracks on the film surface, prevented us from accurate evaluation of the magnetic polarization of the films. Recently, we employed Cu substrates instead of the Ta ones for the electroplating, and clarified that the Cu substrates are hopeful for the electroplated Fe-Pt thick films to reduce the cracks and the partial peelings [4]. In the present study, we electroplated Fe-Pt thick films (> 10 μm) on the Cu substrates and evaluated their magnetic properties. II. EXPERIMENTAL PROCEDDURES We carried out an electroplating to obtain Fe-Pt thick films by using a direct current. The electrolyte of the plating bath contained the following: 10 g/L of $Pt(NO_2)_2(NH_3)_2$, 5-10 g/L of $FeSO_4 \cdot 7H_2O$, 25 g/L of $H_6N_2O_3S$ or NH_4Cl, 30 g/L of $C_6H_8O_7$-H_2O (Citric acid). 5 mm-wide Pt mesh and 500 μm-thick Cu plate were used as the anode and the cathode, respectively. 75 mm^2 (5 mm × 15 mm) Fe-Pt films were electroplated on the Cu plate. The current density of 1 A/cm^2 and the plating time from 10 to 60 min were controlled by using a computer-aided dc current source. The bath temperature was kept at 70°C during the plating. To promote $L1_0$ ordering of the Fe-Pt crystalline phase, we annealed as-plated Fe-Pt films at 700°C for 30 min in a vacuum (< 10^{-2} Pa). The compositions of the as-plated Fe-Pt films and the hysteresis loops of the annealed ones were measured with a SEM-EDX system and a VSM, respectively. III. RESULTS AND DISSCUSSION Figure 1 shows thickness of the $Fe_{50}Pt_{50}$ films plated on the Cu substrates as a function of plating time. Typical hysteresis loop of an annealed thick films is also shown in Fig.1 as an inset. As shown in Fig.1, the thickness increases with increasing plating time, and the deposition rate, which is calculated by the slope of the linier fitting line, is 0.5 μm/min. Owing to high deposition rate, we could obtain 30 μm-thick Fe-Pt films in 60 min. This thickness is much higher than 1 μm of electroplated Fe-Pt films reported by S. Thongmee *et al.* [5] and 23 μm for our previous study [3]. Figure 2 shows coercivity and remanence of the annealed Fe-Pt films as a function of Fe content in the film. As shown in Fig.2, high coercivity values of approximately 1,000 kA/m were obtained at the Fe content of approximately 50 at.%. The coercivity values are much higher than 446 kA/m [1] and 580 kA/m [2] for thick Fe-Pt films prepared by sputtering methods, and are also much higher than 700 kA/m for our previous study, in which Ta substrates were employed [3]. From the result for the coercivity, we found that the Cu substrate is more effective to obtain Fe-Pt films with high coercivity. The remanence slightly increased with increasing the Fe content, and approximately 0.7 T was obtained when the coercivity is almost the same as those for the sputtered films [1-2] (approx. 500 kA/m). Although the remanence value is slightly smaller than 0.9 T [1] and 0.8 T [2], deposition rate of our process (0.5 μm/min) clearly higher than 0.08 μm/min [2]. Therefore, we concluded that the electroplating is one of attractive methods for high speed preparation of the Fe-Pt thick-film magnets with high coercivity.

[1] P.L. Wu, X.H. Li, W. Li H.Y. Sun, Y. Chen, X.Y. Zhang, "Magnetic properties of Fe-Pt thick-film magnets prepared by RF sputtering," *Mater. Lett.*, 62 (2008) 309. [2] H. Aoyama, Y. Honkura, "Magnetic properties of Fe–Pt sputtered thick film magnet," *J. Magn. Soc. Jpn.*, 20, (1996), pp.237-240. [3] T. Yanai, K. Furutani, T. Ohgai, M. Nakano, K. Suzuki, H. Fukunaga, "Fe-Pt thick-film magnets prepared by electroplating method," *J. Appl. Phys.*, 117, #17A744, (2015) [4] T. Yanai, J. Honda, R. Hamamura, Y. Omagari, H. Yamada, N. Fujita, K. Takashima, M. Nakano, H. Fukunaga, "Improvement in surface conditions of electroplated Fe-Pt thick-film magnets", *AIP Advances*, 8, (2018), to be published. [5] S. Thongmee, J. Ding, J. Y. Lin, D. J. Blackwood, J. B. Yi, J. H. Yin, "FePt films fabricated by electrodeposition," *J. Appl. Phys.*, 101, 09K519, (2007).

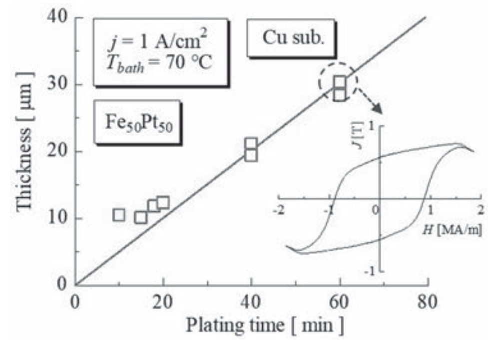

Fig. 1. Thickness of the as-plated $Fe_{50}Pt_{50}$ films as a function of plating time.

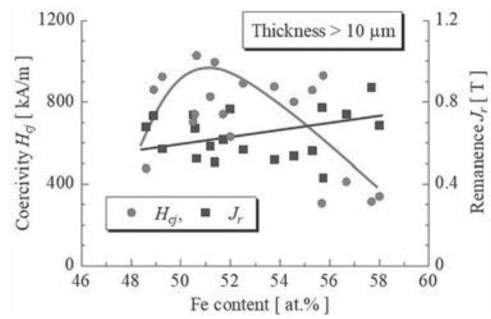

Fig. 2. Coercivity and remanence of the annealed Fe-Pt films as a function of Fe content in the film.

CS-02. Mossbauer studies and magnetic properties of Fe-doped MnAl(C) alloys.

V. Nguyen[1,2], F. Calvayrac[1] and N. Randrianantoandro[1]
1. Institut des Molécules et Matériaux du Mans – UMR CNRS n°6283, Le Mans Université, Le Mans, France; 2. Advanced Materials Science and Nanotechnology, University of Science and Technology of Hanoi, Vietnam Academy of Science and Technology, Hanoi, Vietnam

The manganese aluminum (MnAl) alloy, which was first reported by Kono [1] and Koch *et al.* [2], is one of the promising rare-earth-free magnets as having interesting intrinsic properties. The τ–phase is normally formed from the high-temperature ε-phase by cooling the ε-phase at an appropriate rate or annealing it at 400-600^{o}C [1, 3]. Through ε to τ transformation, stable phases like γ_2-Mn_5Al_8 and the β-Mn phase can appear (Fig.1). Doping of carbon has been proved to improve the stabilization of the ferromagnetic τ–phase MnAl ($L1_o$) [4-6]. Mossbauer spectrometry is based on the resonant effect of absorption and emission of gamma rays of nuclei of the same isotope in solid. It is a very sensitive technique, being capable of detecting changes in the order of 10^{-11} thanks to its extremely narrow line widths of gamma rays. In particular, Mossbauer spectrometry allows to probe microscopically at the atomic scale, and therefore it is very efficient for studying atomic environment in solid materials. Normally, three kinds of nuclear interactions are recorded by Mossbauer spectrometry: - Isomer shift (δ): It describes a positive or negative shift of the spectra depending on the increase or decrease of s-electron density at the nucleus of the absorber in comparison with the source. It is often used for examining oxidation state, valency states, electron shielding and the electron-drawing power of electronegative groups. - Quadrupole splitting (Q.S.): It is caused by the interaction between the nuclear quadrupole moment with the surrounding electric field gradient (EFG), causing the splitting of the nuclear energy level. Oxidation state, spin state, and site symmetry can be determined by measuring the Q.S. - Magnetic hyperfine field (B_{hf}): This interaction is based on the nuclear Zeeman effect that occurs when a magnetic field exists at the nucleus. This magnetic field may come from within the crystal by exchange interaction or by applying an external magnetic field. In the topic of the metastable MnAl(C) τ-phase, our aim is to probe the local behavior of Mn atoms when its environment is perturbed by the presence of atomic insertion (C atoms), change of temperature or application external magnetic field. In the absence of Mossbauer isotope for manganese, we substituted some Mn atoms in MnAl(C) alloys by ^{57}Fe atoms. Therefore, four nominal compositions with ^{57}Fe enrichment: ε-$Mn_{50.5}Fe_{0.5}Al_{47}C_2$, and its corresponding τ-$Mn_{50.5}Fe_{0.5}Al_{47}C_2$, γ_2-$Mn_{40}Fe_{0.5}Al_{59.5}$, and β-$Mn_{60}Fe_{0.5}Al_{39.5}$ were mechanically synthesized for Mossbauer studies. A non-iron $Mn_{50.7}Al_{47.3}C_2$ was also synthesized for magnetic properties comparison. Fig.2 shows the X-ray diffraction diagrams of the samples. As can be seen, high purities of all the phases were obtained under 10h of milling by tungsten carbide (WC) vials of a planetary ball mill (PULVERISETTE 7 premium line), the balls-to-powder weight ratio is 25:1, followed by an appropriate heat treatment. A trace of Al_2O_3 was found in ε and τ phases, and a small amount of $MnAlC_3$ was found in the β phase, which is due to a small carbon contamination from the WC vials during the milling process. Further results and discussion on the microstructure, Mossbauer spectra analysis, and magnetic properties will be presented at the conference.

[1] H. Kono, On the Ferromagnetic Phase in Manganese-Aluminum System, Journal of the Physical Society of Japan, 13 (1958) 1444-1451. [2] A. J. J. Koch, P. Hokkeling, M. G. v. d. Steeg, K.J.d. Vos, New Material for Permanent Magnets on a Base of Mn and Al, Journal of Applied Physics, 31 (1960) S75-S77. [3] W. Koester, Aufbau und magnetische Eigenshaften der Aluminium-Mangan-Legierungen mit mehr als 25 At.%Mn, Z.Metallk, 51 (1960) 271-280. [4] Z.W. Liu, C. Chen, Z.G. Zheng, B.H. Tan, R.V. Ramanujan, Phase transitions and hard magnetic properties for rapidly solidified MnAl alloys doped with C, B, and rare earth elements, Journal of Materials Science, 47 (2012) 2333-2338. [5] Q. Zeng, I. Baker, J.B. Cui, Z.C. Yan, Structural and magnetic properties of nanostructured Mn–Al–C magnetic materials, Journal of Magnetism and Magnetic Materials, 308 (2007) 214-226. [6] O. Obi, L. Burns, Y. Chen, T. Fitchorov, S. Kim, K. Hsu, D. Heiman, L.H. Lewis, V.G. Harris, Magnetic and structural properties of heat-treated high-moment mechanically alloyed MnAlC powders, Journal of Alloys and Compounds, 582 (2014) 598-602. [7] A. McAlister, J. Murray, The (Al– Mn) Aluminum-Manganese system, Journal of Phase Equilibria, 8 (1987) 438-447.

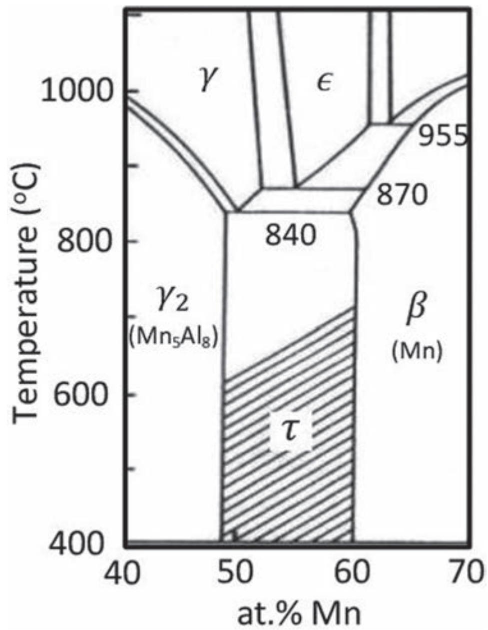

Fig. 1. Phase diagram of MnAl alloy [7].

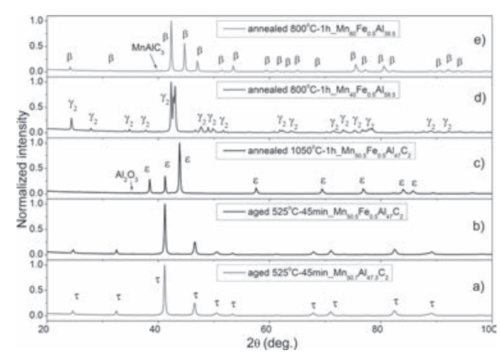

Fig. 2. XRD diffraction diagrams of a) τ-non-iron-$Mn_{50.7}Al_{47.3}C_2$, b) τ-$Mn_{50.5}Fe_{0.5}Al_{47}C_2$, c) ε-$Mn_{50.5}Fe_{0.5}Al_{47}C_2$, d) γ_2-$Mn_{40}Fe_{0.5}Al_{59.5}$, e) β-$Mn_{60}Fe_{0.5}Al_{39.5}$.

CS-03. Magnetic properties and morphologies of synthesized strontium ferrite powders by the molten salt method.

M. Kim[1], K. Lee[1], M. Choi[1] and J. Kim[1]
1. Materials Science and Chemical Engineering, Hanyang University, Ansan, The Republic of Korea

M-type ferrite magnets have been widely used in various applications in electronic devices such as motors, sensors, and etc., because of their relatively good magnetic characteristics and very low manufacturing cost. In addition, compared with $Nd_2Fe_{14}B_1$ magnets, the ferrite magnets possess excellent high temperature properties and corrosion resistance properties [1]. Thus, the ferrite magnets have been widely used under severe operating conditions, such as magnetic core powders for encoders in automobile motors. In recent, these encoders are strongly required to increase the angular resolution for more precise control. This indicates that these M-type ferrite powders should be homogeneously distributed in a composite matrix to reduce the positional errors. In addition, the composite magnet with ferrite powders is required to increase the remanence and coercivity. Therefore, it is critical to develop new M-type ferrite powders with homogeneous shape, dimensions and excellent magnetic properties. To synthesize ferrite powders, various methods, such as solid state reaction, sol-gel and molten salt method have been commonly used. Among them, the molten salt method is known to have an advantage of preventing the aggregation and controlling the shape and dimensions of powders. Thus, in this experiment, strontium hexa-ferrite powders were synthesized by the molten salt method and subsequent two step heat treatment. The morphological changes depending on processing conditions were analyzed using X-ray diffractometer and electron microscopes and then the relationship between their morphologies and magnetic properties measured by a vibrating sample magnetometer and a B-H analyzer were investigated. In this experiment, strontium ferrite powders were synthesized by a molten salt method for controlling the size and shape of synthesized powders. Before calcination, strontium carbonate ($SrCO_3$, 97.0%, DAEJUNG, Korea) with an average size of 1μm, α-hematite (Fe_2O_3, 99.9%, KOJUNDO, Japan) with an average size of 1μm and sodium chloride (NaCl, 99.0%, DUKSAN Pure Chemical, Korea) with the mole ratio of 1:5.7:x (x=0, 10, 20, 30, 40) were mixed by planetary centrifugal mixer at 1500 rpm for 60 min. These mixed raw materials were calcined using an alumina crucible in a box furnace under O_2 atmosphere. During calcination, the flow rate of O_2 gas was maintained at 3 L/min and the heating rate was controlled at 10°C/min. After the calcination process, these synthesized powders were furnace-cooled to the room temperature. In order to control the morphology of powders, the calcination process consisted of two successive annealing steps. At the first step, the first annealing was carried out over the melting temperature of NaCl for the dissolution. This dissolution process should enhance the dispersion of the Fe_2O_3 and the $SrCO_3$ powders to be dispersed in the liquid NaCl matrix, which induces the homogeneous nucleation and suppresses excessive growth of strontium ferrite powders. At the second step, the temperature increased to form the strontium hexa-ferrite phase at the elevated temperature. In this calcination process, it is expected to control the size and shape of strontium ferrite powders by changing the temperature and time. After the calcination process, these synthesized powders were washed 10 times with distilled water using a sonicator to remove the residual NaCl powders and then dried at 60°C for 24 hr. The microstructures of the strontium ferrite powders were analyzed by an X-ray diffractometer (XRD, Rigaku, D/MAX-2500) using CuKα radiation. The magnetization(M_S), remanence value(M_r) and coercivity(H_C) were measured by a vibrating sample magnetometer (VSM, LakeShore 7404) under 15 kOe. The morphology of the strontium ferrite powders was observed by a scanning electron microscope (SEM, Tescan MIRA3) Figure 1 shows the XRD patterns and VSM results of strontium ferrite powders synthesized with different NaCl ratios at the calcination condition of 850°C for 60 min and 1050°C 90 min. As shown in the figure, the peak positions of strontium ferrite powders were well matched with those of JCPDS card (#01-080-1197) although the small amount of residual Fe_2O_3 powders still existed. As shown in the attached table, the magnetic properties of these powders clearly demonstrate the formation of M-type hexa-ferrite. Despite the same annealing condition, the coercivity and remanence were increased with increasing the NaCl ratio. In order to investigate the changes in the magnetic properties of these two ferrite powders, the SEM morphologies were observed and shown in figure 2. As shown in the figure, the size of synthesized powders became smaller and the shape became more uniform as the NaCl ratio increased. In addition, the aspect ratio of hexagonal type powders is shown to be dependent on the NaCl ratio. Thus, it is expected that these ferrite powders with controlled shape and dimensions enhance the magnetic properties of the composite magnets used in magnetic encoders. A more detailed discussion on the effects of various heat treatment conditions on the morphology of ferrite powders will be presented.

[1] Kyumin Kim, Kwang-Won jeon, Ki Woong Moon, Min Kye Kang, Jongryoul Kim, IEEE Transactions on Magnetics, Vol. 52, NO. 7, 2101604, July, 2016

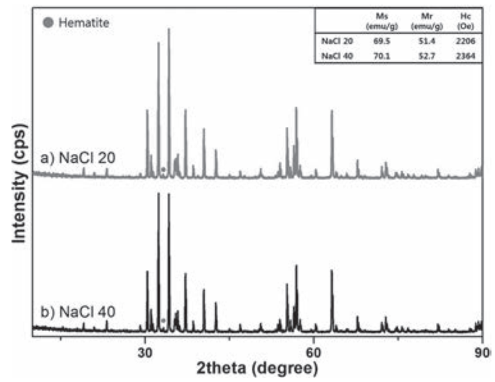

Fig. 1. X-ray diffraction analysis of synthesized strontium ferrites with different NaCl ratio by molten salt method at a) x=20 and b) x=40

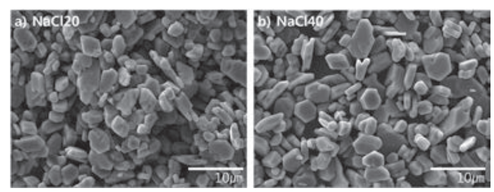

Fig. 2. SEM images of synthesized strontium ferrites with different NaCl ratio by molten salt method at a) x=20 and b) x=40

CS-04. Synthesis of high-purity spherical core-shell α"-$Fe_{16}N_2/SiO_2$ magnetic nanoparticles.

J. Li[1], L. Guo[1], X. Peng[1], Y. Yang[1], X. Wang[1] and H. Ge[1]
1. Department of Materials Science & Engineering, China Jiliang University, Hangzhou, China

Introduction Incorporating shells on magnetic nanoparticles (NPs) has received much interest because a shell offers protections of the active core component against oxidation, corrosion, magnetic lateral interaction among magnetic nanoparticles, and sintering phenomena.[1]Moreover, the core-shell structured NPs has potential applications in high density data storage, the biomedical field, catalysis, etc.[2-3] Recently, one of the attractive shell applications is for surface modification of α"-$Fe_{16}N_2$ NPs, in which they are used for creating a permanent magnetic material with a giant magnetic moment as an alternative to rare-earth-free magnetic material.[4] In this work, we report an effective and simple way for synthesizing well-dispersed spherical core-shell α"-$Fe_{16}N_2/SiO_2$ ferromagnetic NPs from core-shell Fe_3O_4/SiO_2 NPs. The influences of coating process on the formation of α"-$Fe_{16}N_2$ were studied, the magnetic properties of the synthesized α"-$Fe_{16}N_2/SiO_2$ NPs were also investigated. Experimental Core-shell α"-$Fe_{16}N_2/SiO_2$ NPs were synthesized by means of two-step process: (1) to prepare core-shell Fe_3O_4/SiO_2 NPs by Stöber method, (2) low temperature nitridation of α-Fe/SiO_2 obtained from the reduction of Fe_3O_4/SiO_2 NPs. In the first step, Fe_3O_4 NPs were dispersed in 50 ml of hydrochloric acid solution with a concentration of 0.1 mol/L, with ultrasonic stirring for 10 min at room temperature. After that, the above solution was washed with distilled water to remove the residual hydrochloric acid, which were then dissolved in the mixed solution that contains 80 ml ethanol and 20 ml distilled water. A certain amount of ammonia water and teraethoxysilane was successively added to the above mixture in drop and stirring for 6 h at certain temperature. Subsequently the mixture solution was washed several times with ethanol and distilled water successively to remove the suspended solids. Finally, the sample was dried in vacuum drying oven at 60 °C for 6 h. For the second step, the core-shell Fe_3O_4/SiO_2 NPs were reduced with hydrogen gas for 4 h at a temperature of 400 °C, after which the furnace was purged for 5min with argon gas. The temperature of the furnace was then reduced to 170 °C, after which a nitriding treatment was performed in a flow of ammonia gas. Results and Discussion The core-shell Fe_3O_4/SiO_2 samples were characterized via X-ray diffraction and infrared spectroscopic analysis, which demonstrated the Fe_3O_4 NPs were well coated with SiO_2. The XRD patterns of nitriding products obtained at 170 °C with various time are exhibited in figure 1. The proportion of α"-$Fe_{16}N_2$ gradually increases with increasing nitridation time, when the nitridation time was 12 h, high-purity α"-$Fe_{16}N_2$ /SiO_2 was obtained. However, with longer nitriding time, the proportion of α"-$Fe_{16}N_2$ decreases then. When the nitriding time is 12h, the saturation magnetization of α"-$Fe_{16}N_2/SiO_2$ is 138.2 emu/g. Fig. 2 shows the TEM images of the Fe_3O_4 and α"-$Fe_{16}N_2/SiO_2$ NPs respectively, a transparent layer of silica dioxide coated on the surface of α"-$Fe_{16}N_2$ can be clearly seen, indicating core-shell α"-$Fe_{16}N_2/SiO_2$ was successfully prepared.

[1] S. Peng, C. Wang, J. Xie and S. Sun, J. Am. Chem. Soc., 2006,128, 10676-10677. [2] Y. Sasaki, N. Usuki, K. Matsuo and M. Kishimoto, IEEE Trans. Magn., 2005, 41, 3241-3243. [3] T. Seto, K. Koga, F. Takano, H. Akinaga, T. Orii, M. Hirasawa and M. Murayama, J. Phys.: Conf. Ser., 2007, 59, 255. [4]T. Ogi, Q. Li, S. Horie, A. Tameka, T. Iwaki, K. Okuyama, High-purity core-shell α″-$Fe_{16}N_2/Al_2O_3$ nanoparticles synthesized from a-hematite for rare-earth-free magnet applications, Adv. Powder. Technol., 2016,27,2520-2525.

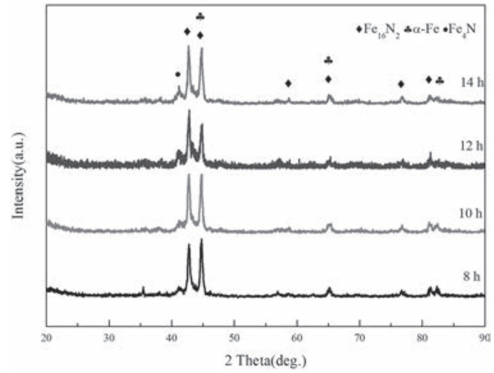

Fig. 1. XRD patterns of the nitrided products prepared under different nitridation time at 170 °C

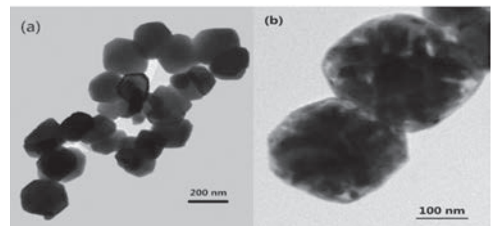

Fig. 2. TEM micrographs of the raw material (a)Fe_3O_4, and nitrided core-shell product (b) $Fe_{16}N_2/SiO_2$

CS-05. Coercivity and phase evolution in mechanically milled $(FeCo)_2B$-type hard magnetic alloy.

K. Kim[1], *H. Kwon*[1], M. Kang[3], C. Yang[3], J. Lee[2] and J. Yu[2]
1. Pukyong National University, Pusan, The Republic of Korea; 2. Korea Institute of Materials Science, Changwon, The Republic of Korea; 3. Sungkyunkwan University, Suwon, The Republic of Korea

INTRODUCTION Permanent magnet is an essential functional material in the area of energy saving and clean environment technology. Current extensive research activities on the permanent magnetic materials can be categorized into three domains : First and most of all, maximizing performance, in particular coercivity, of the current Nd-Fe-B-type magnet using less or no heavy rare-earth element (Dy, Tb). Secondly, searching for new rare-earth compound having high magnetocrystalline anisotropy (MCA) and saturation magnetization (Ms). Finally and equally important, finding new 3d transition metal compound alloy with high MCA and Ms. The latter one seemingly comes into spotlight in relation to next generation permanent magnetic material, and much attention has been paid to Fe-Co alloy having high Ms. First-principles calculations have predicted that tetragonal Fe-Co alloy could have high MCA, provided that high degree of order and large tetragonality are secured in the alloy, which are understood not to be as straightforward. In the meantime, it has long been known that $(FeCo)_2B$-type compound had uniaxial MCA with considerably high magnetocrystalline anisotropy energy (MAE). Recently, it was reported that the Re-substituted $(FeCo)_2B$-type compound had good hard magnetic properties such that it caught much attention as new permanent magnetic material being free of rare-earth metals [1]. In the present study, realization of coercivity in the Re-substituted $(FeCo)_2B$-type compound alloy prepared mainly by mechanical milling was investigated. Phase evolution in the $(FeCo)_2B$-type alloy by mechanical milling and annealing was also investigated. EXPERIMENTAL Re-substituted $(FeCo)_2B$-type alloy with composition of $(Fe_{0.675}Co_{0.3}Re_{0.025})_2B$ was melted in an arc-melting furnace and then the melt was suctioned onto a cold mold to prepare flake-form material by suction cast technique. Prepared flakes were mechanically milled and annealed in various conditions. Annealing of some milled alloy samples was performed in a thermomagnetic analyzer (TMA) to accomplish simultaneously annealing and phase analysis. On annealing in the TMA, sample was swiftly heated to the annealing temperature by pushing into hot zone in the oven, which was heated beforehand to the desired temperature, and held there for desired time. No sooner did the sample temperature arrive and stay at the desired temperature than cooling-down toward room temperature started by cutting off the power for heating oven. In the course of cooling the magnetization variation was monitored. Magnetic, microstructural characterization and phase analysis of the material were performed by using VSM, TMA, SEM, TEM, and XRD. RESULTS AND DISCUSSION The Re-substituted $(FeCo)_2B$-type alloy in suction-cast condition consisted of $(FeCo)_2B$-type and (FeCo) B-type phases. Phase constitution in the mechanically milled alloy varied according to the condition of mechanical milling and subsequent annealing. The material milled for short period (3 hrs) consisted of $(FeCo)_2B$-type, (FeCo)B-type, $(FeCo)_3B$-type, and amorphous phases. The (FeCo)B-type and $(FeCo)_3B$-type phases disappeared as milling time increased, and the material milled for longer than 12 hrs consisted of $(FeCo)_2B$-type and amorphous phases. Fig. 1 (a) and (b) show phase analysis results in the Re-substituted $(FeCo)_2B$-type alloy in as-milled (24 hrs) and annealed (890 °C, 15 min) conditions examined by means of XRD and TMA. In XRD patterns of the material in as-milled condition a broad hump appeared in the low angle range and peaks corresponding to the $(FeCo)_2B$-type phase were extensively broadened, indicating that the material consisted of very finely crystallized $(FeCo)_2B$-type phase and amorphous phase. This phase constitution in the material in as-milled condition was also evidenced by the phase analysis results by TMA. Magnetic transitions occurring at around 375 °C and above 600 °C were corresponding to the Curie temperature of the amorphous and $(FeCo)_2B$-type phases, respectively. The sufficiently milled material being consisted of $(FeCo)_2B$-type and amorphous phases could be converted into $(FeCo)_2B$-type single phase material by brief annealing at elevated temperature above 740 °C. As can be seen in Fig. 1(a) and (b), the as-milled material converted into $(FeCo)_2B$-type single phase by brief annealing at 890 °C for 15 min. This finding is interesting in that single phase $(FeCo)_2B$-type material can be obtained by rather easily by combination of suction casting and mechanical milling with respect to standard alloy preparation technique. The Fe_2B-type compound is known to form at high temperature over 1400 °C via peritectic reaction between solid and liquid phases in Fe-B alloy system, which is basically very sluggish metallurgical process. A prolonged annealing of the cast alloy at high temperature is, therefore, required as a matter of course to acquire single phase $(FeCo)_2B$-type alloy in standard alloy preparation route. The alloy in as-milled condition (24 hrs) exhibited low coercivity of 0.2 kOe, and the coercivity was increased up to around 1 kOe by brief annealing (890 °C, 15 min). In this article, phase evolution and coercivity development in the mechanically milled and subsequently annealed Re-substituted $(FeCo)_2B$-type alloy are to be discussed.

[1] A. Edstrom, M. Werwinski, D. Iusan, J. Rusz, O. Eriksson, K. P. Skokov, I. A. Radulov, S. Ener, M. D. Kuz'min, J. Hong, M. Fries, D. Yu. Karpenkov, O. Gutfleisch, P. Toson and J. Fidler "Magnetic properties of $(Fe_{1-x}Co_x)_2B$ alloys and the effect of doping by 5d elements," Phys. Rev., B 92, 174413, 2015.

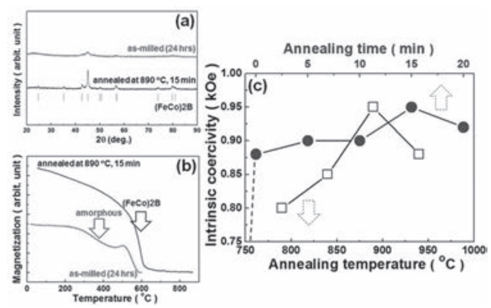

Fig. 1. (a) XRD patterns and (b) TMA tracings of the Re-substituted $(FeCo)_2B$-type alloy in as-milled and annealed condition. (c) Variations of coercivity of the mechanically-milled Re-substituted $(FeCo)_2B$-type alloy as a function of annealing temperature and time (at 890 °C).

CS-06. Hard magnetic property improvement of melt spun $PrCo_5$ ribbons by Fe and C doping.

H.W. Chang[1], H. Wang[1], Y. Lee[1], C. Shih[1], W.C. Chang[1], C. Shaw[2] and C. Yang[3]
1. Department of Physics, National Chung Cheng University, Chia-Yi, Taiwan; 2. Superrite Electronics Co. Ltd., Taipei, Taiwan; 3. Chung-Yuan Christian University, Chungli, Taiwan

Development of novel permanent magnetic materials is very important in modern technology due to ever-increasing demand for the wide applications in consumer electronics, hybrid electric vehicles, wind power generators, and robotics, etc. Rare earth (R) cobalt alloys, such as $SmCo_5$ and Sm_2Co_{17}, with excellent magnetically hard intrinsic properties have attracted much attention for decades. Unlike $SmCo_5$, the developed $PrCo_5$ alloys so far showed low coercivity due to relatively smaller magnetocrystalline anisotropy field, though $PrCo_5$ has the highest the saturation magnetization and therefore theoretical energy product among RCo_5 systems [1-2]. Limited report related to the magnetic and microstructural characterizations for $PrCo_5$ system in ribbon form is available till today. Proper Fe addition into YCo_5 system has been reported to effectively improve the magnetically hard intrinsic properties, especially the saturation magnetization, and appropriate C doping in various permanent magnetic alloys, i.e. $R_2Fe_{14}B$ and $SmCo_7$, is helpful in microstructure refinement and the improvement of magnetic properties [3-5]. It is of interest to find out whether these effects contribute to the improvement of the hard magnetic performance of $PrCo_5$ alloys or not. Accordingly, doping effects of Fe and C on the magnetic properties, crystal structure, and microstructure of $PrCo_5$ alloys are studied. The melt spinning process is adopted to prepare the $PrCo_{5-x-y}Fe_xC_y$ (x=0-0.3; y=0-0.4) ribbons at a wheel speed of 10-40 m/s. All samples were magnetized by a 50 kOe peak pulse field before magnetic measurement. No demagnetization field correction was made in this study. Curie temperature (T_C) of magnetic phase was determined by thermo-gravimetric analysis with an applied magnetic field at a heating rate of 20 ^oC/min. At first, effect of quenching rate on the magnetic properties and microstructure of $PrCo_5$ ribbons has been studied. At lower wheel speed of 10-20 m/s, the coexistence of 2:17 phase with magnetic hard 1:5 phase leads to low coercivity of below 0.5 kOe, while increasing wheel speed to 40 m/s improves the coercivity to 3.3 kOe due to the suppression of 2:17 phase. Most importantly, magnetic properties of melt spun $PrCo_5$ ribbons are significantly enhanced by doping Fe and C. Listed in Table 1, lower permanent magnetic properties of B_r = 6.4 kG, $_iH_c$ = 3.3 kOe, and $(BH)_{max}$ = 5.0 MGOe are obtained for binary $PrCo_5$ ribbon, and improved to B_r = 6.1-6.9 kG, $_iH_c$ = 7.3-13.5 kOe, $(BH)_{max}$ = 7.3-8.9 MGOe by doping C, yet slightly decreased to B_r = 5.1 kG, $_iH_c$ = 4.5 kOe, $(BH)_{max}$ = 4.2 MGOe by doping Fe, respectively. Most interestingly, the optimal magnetic properties of B_r = 5.8 kG, $_iH_c$ = 16.2 kOe, $(BH)_{max}$ = 8.0 MGOe are achieved for C and Fe co-doped $PrCo_{4.6}Fe_{0.3}C_{0.1}$ ribbons, where the coercivity is the highest value in $PrCo_5$ system ever reported. Shown in Fig.1, x-ray diffraction analysis indicates that all studied ribbons consist of hexagonal 1:5 phase and minor 2:17 phase. Fe or C-doping could suppress the 2:17 phase and stabilize 1:5 phase, and therefore enhance coercivity but decrease the remanence of $PrCo_5$ ribbons. The slightly changed lattice constants of the 1:5 phase by doping Fe or C, i.e. enlarged *a* and reduced *c*, reveals the entrance of Fe and C into the crystal structure of 1:5 phase. The *c/a* ratio of 1:5 phase are decreased from 0.825 to 0.800 by doping C, to 0.797 by doping Fe, and to 0.801 by co-doping Fe and C, respectively. The change in *c/a* ratio of 1:5 phase may improve magnetocrystalline anisotropy field to contribute the coercivity enhancement. Besides, the Rietveld refinement finds that about 3 volume percentage of nonmagnetic Pr_2C_3 phase appears for the ribbons co-doped with Fe and C. T_C of 1:5 phase is increased from 609 ^oC to 650 ^oC by doping C, to 646 ^oC by doping Fe, and to 673 ^oC by co-doping Fe and C, respectively. The different degree of the increment of T_C with Fe and C substitution is related to different strength of exchange interaction for neighboring magnetic atoms. Importantly, the increased T_C of 1:5 phase by co-doping Fe and C is beneficial in improving the thermal stability of the magnet. Transmission electron microscopy (TEM) images of $PrCo_{5-x-y}Fe_xC_y$ ribbons are shown in each inset of Fig.1. The large grain size of 100-120 nm is observed for $PrCo_5$ ribbon, and it is refined to 30-70 nm by doping Fe, to 10-30 nm by doping C, and to 5-20 nm by co-doping Fe and C, respectively. The microstructure refinement is helpful in improving $_iH_c$, the squareness of demagnetization curve, and therefore $(BH)_{max}$. Besides, some small precipitates found for the sample co-doped with Fe and C is Pr_2C_3, identified by energy dispersive x-ray spectroscopy, which well agrees with XRD analysis. The nonmagnetic Pr_2C_3 precipitates impede the magnetization reversal and thus enhance coercivity. Summarized with the above results, the increased volume fraction of 1:5 phase, the strengthened H_A, and the refined microstructure, the induction of nonmagnetic Pr_2C_3 precipitates by co-doping Fe and C make $PrCo_{4.6}Fe_{0.3}C_{0.1}$ ribbons exhibit high permanent magnetic performance of $_iH_c$ = 16.2 kOe and $(BH)_{max}$ = 8.0 MGOe. They are promising candidate materials for making bonded magnets.

[1] B. Yang et al., J. Phys. D: Appl. Phys. 41, 015003 (2008). [2] W.Q. Liu et al., J. Appl. Phys. 109, 07A731 (2011). [3] H.W. Chang et al., J. Appl. Phys. 101, 09K508 (2007). [4] C.H. Chiu et al., Scripta. Mater. 56, 429 (2007). [5] C. C. Hsieh et al., J. Appl. Phys. 107, 09A710 (2010)

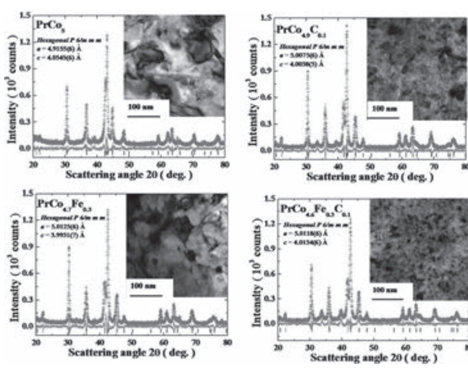

Fig. 1. XRD patterns and TEM images of melt spun $PrCo_{5-x-y}Fe_xC_y$ ribbons.

x	y	B_r (kG)	$_iH_c$ (kOe)	$(BH)_{max}$ (MGOe)	T_C (^oC)
0	0	6.4	3.3	5.0	609
0	0.1	6.2	13.5	8.9	650
0	0.2	6.1	8.8	7.3	-
0	0.3	6.5	7.8	7.4	-
0	0.4	6.9	7.3	8.0	-
0.3	0	5.1	4.5	4.2	646
0.3	0.1	5.8	16.2	8.0	673

Table 1 Magnetic properties of melt spun $PrCo_{5-x-y}Fe_xC_y$ ribbons.

CS-07. First-principles study of spin-wave dispersion in $Sm(FeCo)_{12}$.

T. Fukazawa[1,2], H. Akai[3,2], Y. Harashima[1,2] and T. Miyake[1,2]
1. National Institute of Advanced Industrial Science and Technology (AIST), Tsukuba, Japan; 2. ESICMM, National Institute for Materials Science (NIMS), Tsukuba, Japan; 3. ISSP, The University of Tokyo, Kashiwa, Japan

Introduction Behavior of magnetic properties at finite temperatures is important in applications of hard magnets, and *ab initio* modeling of spins for them has become one of the standard techniques for addressing it today. In construction of such a model, intersite magnetic interaction is evaluated based on first-principles calculation. The spin-wave dispersion derived from the interactions offers information of magnetic collective modes that are related to finite temperature properties in an intuitive way, and the dispersion can be compared directly to that obtained by experiments. Magnetic compounds with the $ThMn_{12}$ structure have regained attention since their potential as the main phase in a hard magnet was reevaluated by a first-principles study [1] and experimental works [2, 3] in these years. Hirayama et al. have recently synthesized $Sm(Fe_{1-x}Co_x)_{12}$ films for $x = 0$, 0.1, 0.2, and shown that $Sm(Fe_{0.8}Co_{0.2})_{12}$ has favorable magnetic properties, including the spontaneous magnetization of 1.78 T at room temperature [4]. We in this paper present spin-wave dispersion in $Sm(FeCo)_{12}$ calculated based on first-principles to address magnetic properties of the system at finite temperatures. Because there is no experiment clarifying its spin-wave dispersion to the best of our knowledge, we compare our values of the spin-wave stiffness with those obtained from the experiment by Hirayama et al. We also discuss anisotropy in the lowest branch around the Gamma point: spin-waves are more easily propagate along a*-axis than along c*-axis especially in $SmFe_{12}$. Methods We use the Korringa–Kohn–Rostoker Green function method for solving the Kohn-Sham equation of density functional theory. The exchange–correlation functional is approximated within the local density approximation. The f-orbitals at the Sm site are treated as a trivalent open core, and the self-interaction correction is applied to the orbitals. We assume the Fe and Co atoms randomly occupy the 8f, 8i and 8j site in the $ThMn_{12}$ structure and their site preference is disregarded. We treat the randomness with the virtual crystal approximation (VCA). The magnetic coupling is calculated by using Liechtenstein's formula [5]. For the calculation of spin-wave dispersion, we refer readers to Ref. 6. We use the experimental lattice constant *a* and *c* given in Ref. 4. For the lack of experimental data to fix the inner freedom of the coordinate, we use the calculated values of the inner parameters for $SmFe_{12}$ given in Ref. 7. Results and Discussion Figure 1 shows the spin-wave dispersion in $SmFe_{12}$ (purple) and $Sm(Fe_{0.8}Co_{0.2})_{12}$ (green). The green lines are aligned comparatively upward because the introduction of Co in $Sm(Fe_{0.8}Co_{0.2})_{12}$ enhances the magnetic exchange interaction and makes the excitation energy for the collective modes higher than in $SmFe_{12}$. The energy difference between $SmFe_{12}$ and $Sm(Fe_{0.8}Co_{0.2})_{12}$ at the Z point = (1 0 0) on the lowest branch is especially noteworthy. In $SmFe_{12}$, the curvatures around the Gamma point is larger along c*-axis than that along a*-axis (see also Fig. 2), and the smallness of the excitation energy of the Z mode is typical of this anisotropy (the shortest path of Γ–Z is along a*-axis, which is shown in Fig. 1). As for the $Sm(Fe_{0.8}Co_{0.2})_{12}$, the curvatures become more isotropic due to the enhancement of the exchange interaction. We also calculated the spin-wave stiffness from the dispersion. Figure 2 shows values of them calculated by $D = (D_a^2 D_c)^{1/3}$ where D_a and D_c is the curvature along the a*- and c*-axis, respectively, so that D gives the coefficient of $T^{2/3}$ in Bloch's law with the expression derived for the isotropic case. Those are in adequate agreement with the value obtained by Hirayama et al [4]. Conclusion We presented calculation of the spin-wave dispersion in $SmFe_{12}$ and $Sm(Fe_{0.8}Co_{0.2})_{12}$, and discussed how the introduction of Co enhances the exchange interaction. Our calculation predicted anisotropy in the curvatures of the lowest branch around the Gamma point in $SmFe_{12}$ and weakening of the anisotropy when Co is introduced into the system. We also calculated the spin-wave stiffness of the systems, which values are in adequate agreement with the experimental values by Hirayama et al [4].

[1] T. Miyake, K. Terakura, Y. Harashima, H. Kino, S. Ishibashi, J. Phys. Soc. Jpn. 83 (2014), 043702. [2] Y. Hirayama, Y.K. Takahashi, S. Hirosawa, K. Hono, Scr. Mater. 95 (2015) 70. [3] Y. Hirayama, T. Miyake, K. Hono, JOM 67 (2015) 1344. [4] Y. Hirayama, Y. K. Takahashi, S. Hirosawa, K. Hono, Scr. Mater. 138 (2017) 62. [5] A. I. Liechtenstein, M. I. Katsnelson, V. P. Antropov, V. A. Gubanov, J. Magn. Magn. Mater. 67 (1987) 65. [6] M. Pajda, J. Kudrnovsky, I. Turek, V. Drchal, P. Bruno, Phys. Rev. B 64 (1998) 174402. [7] T. Fukazawa, H. Akai, Y. Harashima, T. Miyake, arXiv:1711.05137 (submitted to J. Phys. Soc. Jpn).

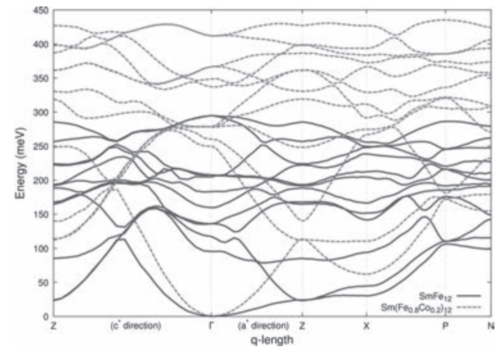

Fig. 1. The spin-wave dispersion in $SmFe_{12}$ (purple) and $Sm(Fe_{0.8}Co_{0.2})_{12}$ (green).

x	D ($D_{\mathrm{Exp.}}$)	D_a	D_c
0	118 (179)	91.6	194
0.1	252 (251)	220	332
0.2	324 (351)	290	407

Fig. 2. Calculated values of the spin-wave stiffness for $Sm(Fe_{1-x}Co_x)_{12}$ compared with the experimental values by Hirayama et al [4]. The curvatures around the Gamma point in the lowest branch and along the a*- and c*-axis are also shown as D_a and D_c. The stiffness values are in the unit of meVÅ².

CS-08. Site probability of substituted Titanium in 1:12 phase structures SmFe12, NdFe12, and SmCo12.

C. Skelland[1], G. Hrkac[1,6], T. Schrefl[3], T. Ostler[4], S. Westmoreland[5], R.W. Chantrell[5], R.F. Evans[5], M. Yano[2], T. Shoji[2], A. Kato[2] and A. Manabe[2]

1. University of Exeter, Exeter, United Kingdom; 2. Toyota Motor Corporation, Toyota City, Japan; 3. Danube University, Krems, Austria; 4. Sheffield Hallam University, Sheffield, United Kingdom; 5. University of York, York, United Kingdom; 6. TU Vienna, Vienna, Austria

1:12 phase structures are an alternative candidate to the current high temperature magnets $Nd_2Fe_{14}B$. Work by T. Mikyake et al.[1] showed that with minor Ti substitution and nitrogenation, $NdFe_{12}$ could be changed to $NdFe_{11}TiN$ which has comparable magnetic properties to $Nd_2Fe_{14}B$ at room temperature, but a higher curie temperature making it ideal for high temperature applications. To study the formation energy of 1:12 phase structures and how it changes with Titanium percentage, ab initio calculations on the lattice structure must be performed. In order to calculate the minimum energy from first principle one has to calculate first the site probability of the substituted Titanium in the 1:12 structure. We use molecular dynamics with potentials derived from first principle to calculate the site probability for Titanium using GULP[2]. Atom interaction was modelled using Morse potentials[3]. The Titanium substitution was permutated through all possible substitution positions and the lowest energy configuration was derived and from that the site probability calculated. The results of these simulations are shown in figure 1. Figure 1 shows the probability distribution of Ti as function of atom percentage and site preference. For $NdFe_{12-x}Ti_x$ and $SmFe_{12-x}Ti_x$, the preferred position of Titanium in all investigated 1:12 phase structures follows the same probability pattern, and fills in the different atomic positions by group. There are three groups associated with the 1:12 phase the 8i, 8j, and 8f groups. The groups contain atomic sites that are equally likely to be filled at any Titanium substitution when the precise path to that substitution is unknown, see figure 2. For $NdFe_{12-x}Ti_x$ and $Sm_{12-x}Ti_x$; there is no preference for any particular atom within the groups at any Titanium substitution as shown in figure 2 for the Sm based system. There it can be seen that the Ti atom has the same probability energy wise to populate any of the 8 possible 8i sites, lowest energy of -142.6eV, followed by the 8j site of -141.5 eV and the least probable one the 8f site with -140.6 eV. The statistical distribution of the Titanium substitutions by atomic site grouping is shown in figure 1 at various Titanium at. %. The graphs show how Titanium switches preference between atomic group sets as the Titanium percentage in the structure increases. An initial preference for the 8i atoms is followed by a switching preference between the 8j and 8i atomic groups every 2 atoms filled, until all 8i positions are filled. For $SmCo_{12-x}Ti_x$, the system follows a similar probability distribution to the RFe_{12} structures, but due to Cobalt's different electronic structure the cohesive energy difference of the $SmCo_{12}$ structure is greater than the Iron based one with one Titanium substitution. For $SmFe_{12}$ the cohesive energy changes from -157.4eV to -158.9eV, a gain of 1.5eV where for $SmCo_{12}$ the cohesive energy changes from -140.2eV to -142.6eV a gain of 2.4eV. This indicates, due to the larger gain in energy, that the Cobalt system is more stable than the Iron based one. In the future we will explore supercell structures and calculate the total formation energy according to the Born Haber cycle and add additional substitutes such as V, C, etc. to improve the phase stability and formation energy.

[1] T. Miyake et al., J. Phys. Soc. Jpn. 83, 043702 (2014) [2] J. D. Gale, J. Chem. Soc., Faraday Trans., 1997, 93, 629-637 [3] P. M. Morse, Phys. Rev. 34, 57, 1929

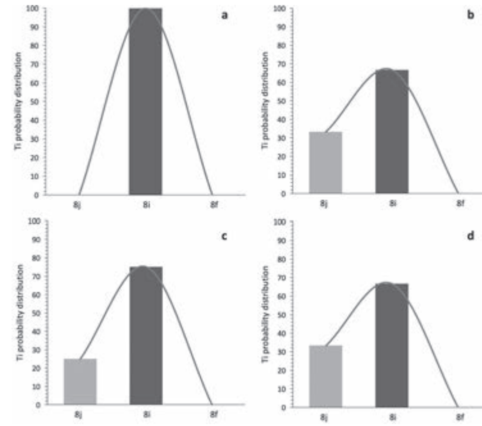

Fig. 1. (a) Statistical distribution of Titanium substitutions at 4 at. % Ti in Nd2Fe23Ti, Sm2Fe23Ti, and Sm2Co23Ti, (b) Statistical distribution at 25 at. % Ti in NdFe9Ti3, SmFe9Ti3, and SmCo9Ti3, (c) Statistical distribution at 33 at. % Ti in NdFe8Ti4, SmFe8Ti4, and SmCo8Ti4, (d) Statistical distribution at 50 at. % Ti in NdFe6Ti6, SmFe6Ti6, and SmCo6Ti6.

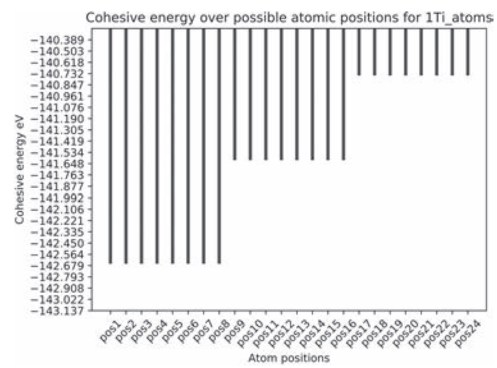

Fig. 2. Cohesive energy of the different atomic positions in SmCo12 with one Titanium substitution. The different energy levels correspond to different atomic site groups, positions 1 to 8 are part of the 8i group, positions 9 to 16 are part of the 8j group, and positions 17 to 24 are part of the 8f group.

CS-09. Magnetic properties of $(Sm,Zr)_5(Fe,Co)_{17-x}Ti_x$ melt-spun ribbons.

T. Saito[1], *T. Horita*[1] and D. Nishio-Hamane[2]
1. Chiba Institute of Technology, Chiba, Japan; 2. Institute for Solid State Physics, The University of Tokyo, Kashiwa, Japan

The Sm_5Fe_{17}-type phase is a new ferromagnetic intermetallic compounds in the binary Sm-Fe system [1-3]. The Sm_5Fe_{17}-type phase has been shown to be a metastable phase that can be prepared by the annealing of amorphous Sm-Fe melt-spun ribbon [4]. Although the Sm_5Fe_{17}-type phase exhibits high coercivity comparable to that of Nd-Fe-B magnets, the reported values of its remanence are relatively low. It is therefore essential to increase the remanence of the Sm_5Fe_{17}-type phase. Several efforts have been made to achieve this objective, but it has been reported that the large compositional modification of the Sm_5Fe_{17}-type phase resulted in its decomposition [5]. In the present study, melt-spun ribbons were prepared containing small amounts of cobalt and zirconium added to Sm_5Fe_{17}-type phase. Small amounts of titanium were also added to the $(Sm,Zr)_5(Fe,Co)_{17}$ phase to improve the magnetic properties. The structures and magnetic properties of these $(Sm,Zr)_5(Fe,Co)_{17-x}Ti_x$ melt-spun ribbons are discussed here. $(Sm_{0.8}Zr_{0.2})_5(Fe_{0.75}Co_{0.25})_{17-x}Ti_x$ (x = 0–2.0) ingots were prepared by induction melting under an argon atmosphere. The molten alloy ingots were then ejected through an orifice with argon onto a copper wheel rotating at a surface velocity of 40 ms^{-1}. The melt-spun ribbons thus obtained were annealed under an argon atmosphere at 773–1273 K for 1 h. The phases in the specimens were investigated by X-ray diffraction (XRD) using Cu Kα radiation. The microstructures of the specimens were examined using a transmission electron microscope (TEM) after ion-beam thinning. The magnetic properties of the specimens were measured at room temperature using a vibrating sample magnetometer (VSM) with a maximum applied field of 25 kOe. The crystalline phases of the $(Sm_{0.8}Zr_{0.2})_5(Fe_{0.75}Co_{0.25})_{17-x}Ti_x$ (x = 0–2.0) melt-spun ribbons were examined in the XRD study. The XRD pattern of the $(Sm_{0.8}Zr_{0.2})_5(Fe_{0.75}Co_{0.25})_{17}$ melt-spun ribbon showed only a fairly broad halo-like peak, which is a characteristic of an amorphous structure. However, the XRD patterns of the $(Sm_{0.8}Zr_{0.2})_5(Fe_{0.75}Co_{0.25})_{17-x}Ti_x$ (x = 0.5–2.0) melt-spun ribbons exhibited small crystalline peaks together with the broad halo-like peak. Thus, the $(Sm_{0.8}Zr_{0.2})_5(Fe_{0.75}Co_{0.25})_{17-x}Ti_x$ (x = 0–2.0) melt-spun ribbons consisted of the amorphous phase either alone or together with small amounts of the crystalline phase. The resultant $(Sm_{0.8}Zr_{0.2})_5(Fe_{0.75}Co_{0.25})_{17-x}Ti_x$ (x = 0–2.0) melt-spun ribbons showed low coercivity values regardless of the Ti content. Heat treatment of these specimens was carried out to increase the coercivity. Figure 1 shows the dependence of the coercivity of the $(Sm_{0.8}Zr_{0.2})_5(Fe_{0.75}Co_{0.25})_{17-x}Ti_x$ (x = 0–2.0) melt-spun ribbons on the annealing temperature. The specimens annealed at 873 K or lower showed a low coercivity value comparable to that of the as-quenched melt-spun ribbons, while the specimens annealed at 973 K and above exhibited high coercivity. The highest coercivity, H_c = 13.3 kOe, was obtained in the $(Sm_{0.8}Zr_{0.2})_5(Fe_{0.75}Co_{0.25})_{15.5}Ti_{1.5}$ specimen after annealing at 1073 K. In order to clarify the origin of the coercivity in the annealed $(Sm_{0.7}Zr_{0.3})_2(Fe_{0.7}Co_{0.3})_{17-x}Ti_x$ (x = 0–2.0) melt-spun ribbons, the structures were examined by XRD and thermomagnetic studies. Figure 2 shows the XRD patterns of the $(Sm_{0.8}Zr_{0.2})_5(Fe_{0.75}Co_{0.25})_{17-x}Ti_x$ (x = 0–2.0) melt-spun ribbons annealed at 1073 K. The $(Sm_{0.8}Zr_{0.2})_5(Fe_{0.75}Co_{0.25})_{17}$ melt-spun ribbon consisted of the Sm_5Fe_{17}-type phase. To our surprise, the specimens with added Ti did not consist of the Sm_5Fe_{17}-type phase but rather the $SmFe_3$-type phase. In other words, the achieved high coercivity in the annealed $(Sm_{0.8}Zr_{0.2})_5(Fe_{0.75}Co_{0.25})_{15.5}Ti_{1.5}$ melt-spun ribbon was not due to the Sm_5Fe_{17}-type phase but to the $SmFe_3$-type phase. This indicates that the addition of Ti to the $(Sm_{0.8}Zr_{0.2})_5(Fe_{0.75}Co_{0.25})_{17}$ melt-spun ribbon impeded the formation of the metastable Sm_5Fe_{17}-type phase and led to the formation of the stable $SmFe_3$-type phase. In conclusion, it was found that the addition of Ti to $(Sm_{0.8}Zr_{0.2})_5(Fe_{0.75}Co_{0.25})_{17}$ melt-spun ribbon changed the metastable Sm_5Fe_{17}-type phase into the stable $SmFe_3$-type phase. The resultant $(Sm_{0.8}Zr_{0.2})_5(Fe_{0.75}Co_{0.25})_{15.5}Ti_{1.5}$ melt-spun ribbon with the $SmFe_3$-type phase exhibited a high coercivity of 13.3 kOe. This work was supported by Grant-in Aid for Scientific Research (KAKENHI) No. 17K06776 from the Japan Society for the Promotion of Science (JSPS). The use of the facilities of the Materials Design and Characterization Laboratory at the Institute for Solid State Physics, The University of Tokyo, is gratefully acknowledged.

[1] F. J. Cadieu, H. Hegde, R. Rani, A. Navarathna, and K. Chen, Mater. Lett. 11, 284 (1991). [2] R. Rani, H. Hegde, A. Navarathna, K. Chen, and F. J. Cadieu, IEEE Trans. Magn. 28, 2835 (1992). [3] A. C. Neiva and F. P. Missell, Proceedings of the 8th International Symposium on Magnetic Anisotropy and Coercivity, edited by C.A.F. Manwaring, pp.315-324, (1994). [4] T. Saito, J. Alloys Compd., 440, 315 (2007). [5] T.Saito and D. N. Hamane, IEEE Trans. Magn., 49, 3345 (2013).

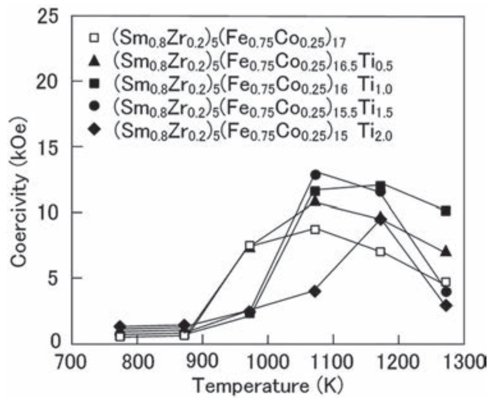

Fig. 1. Dependence of the coercivity of the $(Sm_{0.8}Zr_{0.2})_5(Fe_{0.75}Co_{0.25})_{17-x}Ti_x$ (x = 0–2.0) melt-spun ribbons on the annealing temperature.

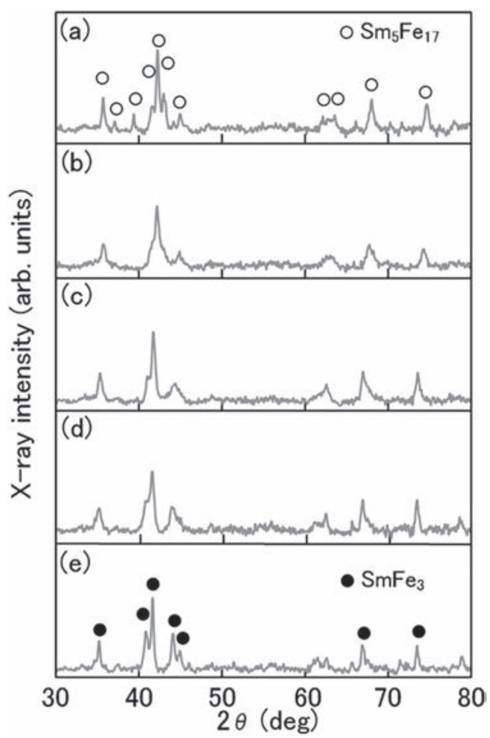

Fig. 2. XRD patterns of the $(Sm_{0.8}Zr_{0.2})_5(Fe_{0.75}Co_{0.25})_{17-x}Ti_x$ (x = 0–2.0) melt-spun ribbons annealed at 1073 K: (a) $(Sm_{0.8}Zr_{0.2})_5(Fe_{0.75}Co_{0.25})_{17}$, (b) $(Sm_{0.8}Zr_{0.2})_5(Fe_{0.75}Co_{0.25})_{16.5}Ti_{0.5}$, (c) $(Sm_{0.8}Zr_{0.2})_5(Fe_{0.75}Co_{0.25})_{16}Ti_{1.0}$, (d) $(Sm_{0.8}Zr_{0.2})_5(Fe_{0.75}Co_{0.25})_{15.5}Ti_{1.5}$, and (e) $(Sm_{0.8}Zr_{0.2})_5(Fe_{0.75}Co_{0.25})_{15}Ti_{2.0}$.

CS-10. Coercivity Mechanism of SrO●6Fe_2O_3 Ferrite Magnets.

Y. Matsuura[1]
1. Research Institute for Applied Sciences, Kyoto, Japan

1. Introduction In our previous work[(1), (2)] we found that the alignment dependence of the coercivity (ALDC) of ferrite magnets behaves similar to that of Nd-Fe-B sintered magnets. The coercivity of ferrite magnets decreases as the alignment (α) improves, where α is defined by Br/Js, and Br and Js are the residual and saturation magnetizations. α is also calculated using the alignment distribution function (ADF) ($P(\theta)$), which is obtained by electron back-scattered diffraction (EBSD). θ indicates the angle from the alignment direction. Further, $P(\theta)$ was found to be similar to the Gaussian distribution function (GDF) from EBSD. It was found that the calculated α agreed well with the experimental results.[(2)] From the ALDC in Nd-Fe-B sintered magnets, the coercivity decrease ratio (β) is defined by as follows, $\beta=((H_{cJ} - H_{cJisotropy}) / H_{cJisotropy})$ x 100. where H_{cJ} and $H_{cJisotropy}$ are the coercivities of the aligned and isotropic magnets, respectively. The value for β is also calculated using $P(\theta)$. The coercivity is determined by the magnetic field at zero magnetization. The value of H_{cJ} is determined by the magnetic field at J=0 in the calculation using $P(\theta)$. θ_1 is defined as the angle of the magnetization reversal area (AMRA). The calculated and measured results for β exhibit a large discrepancy, demonstrating the invalidity of the postulation that every grain independently reverses by the magnetic domain wall motion or the 1/cos θ law. Instead, it is suggested that the simultaneous reversal of a number of grains is induced by the magnetic domain wall jump. The measured θ_1, which is defined as the angle of the magnetization reverse area, is obtained using the measured β and, when compared with the calculated θ_1, the measured θ_1 is found to be larger than the calculated θ_1.[(3)] Further, the measured θ_1 is more similar to that of a lower-alignment magnet of calculation than the measured θ_1. Thus, in the magnetization reversal process, the coercivity of the aligned magnets behaves like that of low-aligned magnets: by the pinning and de-pinning of the magnetic domain walls. When a GDF with a standard deviation (σ) is used for calculation of the angular dependence of the coercivity (ANDC), where the GDF has same θ_1 value as that obtained by experiment, it was found that the experimental results of the ANDC are qualitatively explained. It is important to determine whether the ANDC of ferrite magnets can also be explained using same logic used for Nd-Fe-B sintered magnets. 2. Experiment Ferrite magnets with a composition of $Sr_{0.6}Fe_2O_3$ and α=0.5, 0.57, 0.87 and 093 were cut in 7×7×7 mm cubes for magnetic property measurements of the ALDC, and into $^{\Phi}4\times4$ mm cylinders to measure ANDC. The Br and Js values are measured by a permeameter with a 2 T maximum magnetic field. ANDC is measured by a vibrating sample magnetometer with a 1.7 T magnetic field. 3. Results and Discussion Figure 1 shows the calculated values of θ_1, and the θ_1 values of the $Sr_{0.6}Fe_2O_3$ magnets calculated using the measured β value. The calculated values for θ_1 imply that every grain independently follows the 1/cos θ law. However, the measured θ_1 values in the actual magnets are greater than the calculated ones, suggesting that a number of grains reverse simultaneously by pinning and de-pinning of the magnetic domain walls. It was found that $Sr_{0.6}Fe_2O_3$ with α=0.93 has a θ_1 of 41°, similar to the calculated results with the GDF of σ=70°. Using σ=70°, the ANDC is calculated and is then compared with the experiment. Figure 2 shows the calculated and experimental results. The ANDC of $Sr_{0.6}Fe_2O_3$ decreases with increasing magnetic field angle until 40°, after which the coercivity gradually increases until 70°. At a glance, this behavior of the ANDC seems like a coherent rotation of magnetization, but the calculation results using σ=70° and θ_1=41°, obtained from the ALDC, agrees well with the experiment until Φ=40°. These results reinforce our speculation that the coercivity of ferrite magnets is also determined by the pinning and de-pinning of magnetic domain walls.

(1) Y. Matsuura, R. Ishii and J. Hoshijima, J. Magn. Magn. Mater. Vol. 336, 88-92 (2013) (2) Y. Matsuura, N. Kitai, R. Ishii, M. Natsumeda and J. Hoshijima, J. Magn. Magn. Mater. Vol. 346, 113 (2013) (3) Y. Matsuura, IEEJ Technical Meeting, MAG-17-094, 43-46, 2017

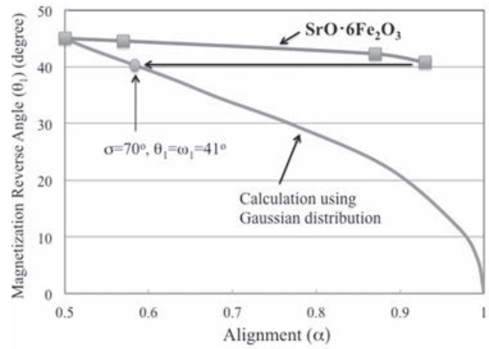

Fig. 1. Angle of magnetization reversal area of SrO·6Fe_2O_3 and the calculation results using a Gaussian distribution.

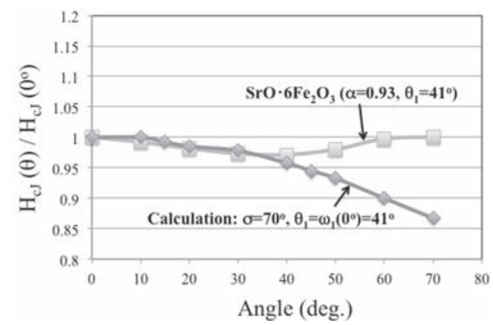

Fig. 2. Angular dependence of the coercivity of SrO·6Fe_2O_3 and the calculation results using a Gaussian distribution with s=70°.

CS-11. Electronic structure and magnetic property of $Ba_{1-x}Sr_{x}CoFe_{11}O_{19}$ hexaferrites.

N. Tran[1], D. Kim[1], H. Kim[1], S. Lee[1], T. Phan[1] and B. Lee[1]
1. Department of Physics and Oxide Research Center, Hankuk University of Foreign Studies, Yongsi-si, The Republic of Korea

Ferrite materials play an important role in promoting the development of modern electrical and electronic devices. In the oxide form, two ferrite systems are usually interested to be cubic spinel ferrites (*Me*Fe_2O_4, where *Me* is a divalent cation) and hexagonal ferrites (hexaferrites). Though the hexaferrites were discovered since 1950s, there has been an exponentially increasing interest until now [1]. Among the hexaferrites, M-type barium hexaferrite ($BaFe_{12}O_{19}$) has attracted a special interest because this material can be fabricated by simple techniques and has many intriguing properties. For example, with the large coercive force (H_c), high Curie temperature (T_C, above 700 K [2]), corrosion resistance, and high chemical stability, $BaFe_{12}O_{19}$ is usually used to fabricate permanent magnets. One has also found its promising applications in high-density recording media, microwave-related devices, and energy conversion and storage devices [1, 3]. Because the magnetic property of $BaFe_{12}O_{19}$ can easily tuned as expected upon changing fabrication conditions, crystal sizes, and dopants, its application range is remarkably widened. It has been found that the changes in fabrication conditions and dopants would create different intrinsic defects (such as crystal defects, impurities, and grain morphology), which influences the magnitude of H_c and the saturation magnetization (M_s). For the doping case, Ba and Fe in $BaFe_{12}O_{19}$ can be substituted with alkaline-earth (or rare-earth) and 3*d* transition metals, respectively [2-5]. To explain the magnetic property of these compounds, it is necessary to know the crystal and electronic structures. Such works are usually based on X-ray diffraction, X-ray photoelectron spectroscopy, and Mössbauer technique [2, 4]. To the best of our knowledge, there is no work on X-ray absorption spectroscopy (XAS) to find out the relation between the electronic structure and magnetic property of doped $BaFe_{12}O_{19}$. Taking into this problem, we have prepared $Ba_{1-x}Sr_{x}CoFe_{11}O_{19}$ samples. Their crystalline/electronic structures and magnetic property were then studied. $Ba_{1-x}Sr_{x}CoFe_{11}O_{19}$ (x = 0-1) nanoparticles (NPs) were prepared by co-precipitation method, using $Ba(NO_3)_2$, $Sr(NO_3)_2$, $Co(NO_3)_2.6H_2O$, and $Fe(NO_3)_3.9H_2O$ as precursors. These chemicals with stoichiometric ratios were dissolved in 100 mL DI water at 90 °C. After that, 50 mL NaOH solution (1 M) was added to the mixtures and continuously stirred for 2 h. The products after chemical reactions were filtered, washed by ethanol and DI water, and annealed at 900 °C for 3 h in air. Finally, the products were checked the grain morphology by a scanning electron microscope (SEM, JSM-5410LV). Their crystal and electronic structures were studied by an X-ray diffractometer (Rigaku, MiniFlex) and XAS (the 8C nano-XAFS beamline, Pohang Light Source). The magnetic property was studied by a vibrating sample magnetometer. All investigations were carried out at room temperature. Results revealed that fabricated $Ba_{1-x}Sr_{x}CoFe_{11}O_{19}$ NPs with average particle sizes of 100~300 nm crystallized in a hexagonal structure (P6$_3$/mmc space group). When Sr content (x) increases, the shape of crystals modifies very much while the unit-cell parameters decrease due to the replacement of Sr^{2+} (1.18 Å) for Ba^{2+} (1.35 Å). Detailed analyses for the Fe and Co *K*-edge XAS spectra prove oxidation numbers of Fe and Co to be 3+ and 2+, respectively, which are stable versus an x change in $Ba_{1-x}Sr_{x}CoFe_{11}O_{19}$, Fig. 1. Our study has also found a small change of the Fe-O bond length in between 1.89 and 1.91 Å. Though both the hexagonal and electronic structures are almost unchanged by Sr doping (excepting for the lattice parameters), our study on the magnetic property has indicated the x dependence of magnetic parameters, as seen in Fig. 2. While M_s decreases from 46.1 emu/g for x = 0 to 34.2 emu/g for x = 1, H_c tends to increase from 1630 Oe for x = 0 to ~2200 Oe for x = 0.5, but slightly decreases to 2040 Oe as x = 1. We think that such M_s changes are related to in the exchange interactions between Fe^{3+} and/or Co^{2+} ions located at the octahedral, tetrahedral, and bipyramid sites, which are sensitive to the changes related to local structures, such as Fe/Co-O bond lengths and Fe/Co-O-Fe/Co bond angles. Meanwhile, the H_c change is mainly due to different grain sizes, morphology, and shapes. Our work also reviews recent reports on M-hexaferrites, and discuss in detail their magnetic property, particularly $BaFe_{12}O_{19}$-related compounds.

[1] R. C. Pullar, *Prog. Mater. Sci.,* 57, 1191-1334 (2012). [2] S. Y. An *et al.*, *J. Magn. Magn. Mater.,* 242–245, 413–415 (2002). [3] C. X. Hu *et al.*, *RSC Adv.,* 5, 70749 (2015). [4] M. Cernea *et al.*, *J. Alloys Compd.,* 561, 121-128 (2013). [5] C. Singh *et al.*, *Mater. Lett.,* 63, 1921-1924 (2009).

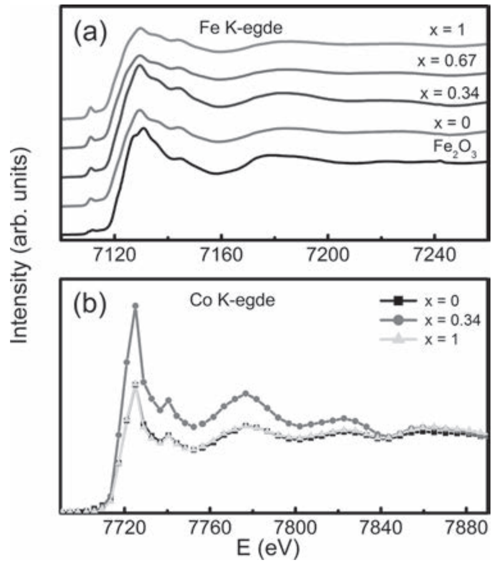

Fig. 1. XAS spectra of NPs recorded at (a) Fe and (b) Co *K*-edges.

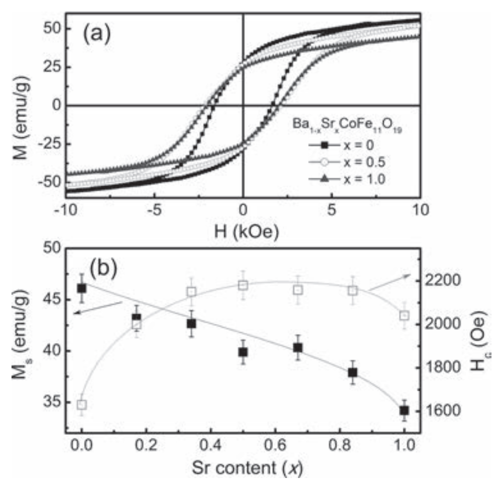

Fig. 2. (a) Typical *M-H* loops and (b) *x*-dependent M_s and H_c of NPs.

Session CT
LINEAR MOTORS II
(Poster Session)

Fei Zhao, Chair
Harbin Institute of Technology (Shenzhen), Shenzhen, China

CT-01. Characteristic Analysis and Design of a Novel Ironless Halbach-magnetized Permanent Magnet Linear Synchronous Motor.

L. Zhang[1] and B. Kou[1]
1. Department of Electrical Engineering, Harbin Institute of Technology, Harbin, China

Abstract —This paper proposes an ironless permanent magnet linear synchronous motor (ILPMLSM) with a novel Halbach array. The magnetic flux density distribution of the Halbach array is solved analytically by using the equivalent magnetization current method (EMCM). Expressions of the no-load back-EMF and the electromagnetic thrust are obtained. The design of the coils and permanent magnet are studied respectively, the effects of the parameters of the magnets on the electrical properties of the ILPMLSM are analysed. A prototype motor is manufactured, and some experiments were carried out with it. I. Introduction At the present time, there exist many various applications with linear motor in all parts of the industry. In some special applications, the low torque ripple and high precision position control are needed. In this case, the permanent magnet linear synchronous motor with moving ironless windings seems to be as suitable electrical machine. In this paper, an ironless permanent magnet linear synchronous motor (ILPMLSM) with a novel double side Halbach array is analysed, as shown in Fig. 1. Electromagnetic analysis and design method investigation of the ILPMLSM are the main contribution of this paper. II. Analytical Model of the ILPMLSM Based on the equivalent magnetization current method, the air-gap flux density distribution of the motor is obtained by calculating the vector sum of the field generated by all the magnets in the array. The y-component of air-gap flux density distribution can be obtained. Based on the Lorentz law, the thrust of the ironless permanent magnet linear synchronous motor can be derived. Assuming the ironless windings moving in the x-direction with a velocity v, the expression of the back-EMF of coils with *N* turns can be also derived. III. Design and Optimization of the ILPMLSM The main dimensions of the ILPMLSM are derived. The design of the coils and permanent magnet are studied respectively, the effects of the parameters of the magnets on the electrical properties of the ILPMLSM are analyzed. The fundamental component of the air-gap flux density affects directly the amplitude of the average thrust, and the magnetic flux density is mainly affected by the top width and the top height of the PMs, the bottom width and the bottom height of the PMs, and the air-gap length. The relationships between the fundamental air-gap flux density and the five dimension coefficients are investigated. IV. Prototype and Experiment Based on the previous analysis in this paper, a prototype of the ILPMLSM has been designed and manufactured, as shown in Fig.2. And some experiments are carried out with the prototype to verify the satisfactory design of the ILPMLSM. Fig. 2 shows the prototype and experimental results. V. Conclusion This paper investigates an ironless Halbach-magnetized permanent-magnet linear synchronous motor. The air-gap flux density distribution was obtained by using equivalent magnetization current methods and the analytical model of the ILPMLSM was established. Design method and optimization of the ILPMLSM were investigated. Based on the analysis, a prototype motor was designed, built and tested. Experimental data indicated satisfactory design.

[1] Z. Q. Zhu, and D. Howe, "Halbach permanent magnet machines and applications: A review," *IEEE Proc. Electr. Power Appl.*, vol. 148, no. 4, pp. 299-308, Jul. 2001. [2] Gan Zhou, Xueliang Huang, Hao Jiang, Li Tan, and Jianning Dong, "Analysis method to a Halbach PM ironless linear motor with trapezoid windings," IEEE Transactions on Magnetics, Vol. 47, No.10, pp. 4167-4170, Oct. 2011.

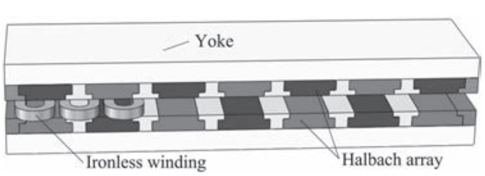

Fig. 1. Scehme of the ILPMLSM with a novel double side Halbach array.

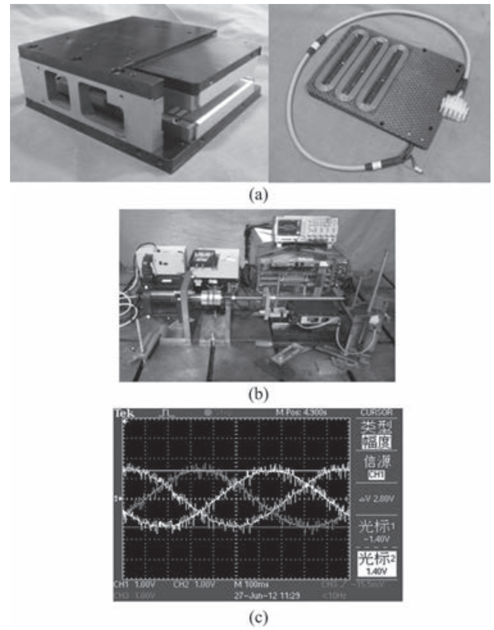

Fig. 2. The prototype and experimental result. (a) the protype test platform, (b) the no-load back-EMF waveform.

CT-02. Power Factor Improvement of Linear Permanent-Magnet Vernier Motor by Using Dual-Inverter.

D. Xu[1], *W. Zhao*[1] and P. Zhao[1]
1. School of Electrical and Information Engineering, Jiangsu University, Zhenjiang, China

INTRODUCTION Linear permanent-magnet vernier motor (LPMVM) has the merits of high efficiency, high force density and low cost, which is very suitable for long stroke applications [1]. However, it suffers from relatively lower power factor [2]. Recently, open-winding (OW) motor fed by dual-inverter with a floating capacitor was presented by opening the neutral point of three-phase stator windings and then connecting two inverters to two winding ends respectively [3]-[5]. The purpose of this paper is to improve the power factor of the LPMVM by using the dual inverter OW technique. METHOD Fig. 1 shows the block diagram of the proposed control method. The terminal voltage vector of the OW-LPMVM is decomposed into two orthogonal quantities to drive the dual-inverter. The active and reactive powers required by the motor are produced by main inverter (MI) powered the DC power and compensation inverter (CI) powered the floating capacitor respectively, so the power factor of the LPMVM system can be improved. In this work, an acquisition method of orthogonal voltage vectors is proposed based on instantaneous power theory, which can avoid the use of the trigonometric and inverse trigonometric functions. Consequently, the proposed method can be easily implemented without heavy computational load. RESULTS Laboratory prototype of an OW-LPMVM is shown in Fig. 2. Fig. 3 shows the experimental results of the electromagnetic force, the mover velocity, and the floating capacitor voltage of the OW-LPMVM dual-inverter drive system. It can be seen from Fig. 3(a) and Fig. 3 (b) that the LPMVM has a good performance when system enters a steady state with v_{ref} = 0.32 m/s and F_L = 100 N. It can be seen from Fig. 3(c) that the capacitor voltage can be controlled to dynamically keep as a constant value that is the same as the DC-link power voltage. Fig. 4 shows the experimental results of the low-pass filtered pole voltages of dual-inverter and armature current. It can be observed from Fig. 4 that pole voltage u_{a1} of the MI is in phase with armature current i_a while pole voltage u_{a2} of the CI approximately lag i_a by 90 degrees. Therefore, the proposed power factor improvement method exhibits a good effect in improving the equivalent power factor of the LPMVM. More details will be given in the full paper.

[1] W. Zhao, J. Zheng, J. Wang, G. Liu, J. Zhao, and Z. Fang, "Design and analysis of a linear permanent-magnet vernier machine with improved force density," *IEEE Trans. Ind. Electron*., vol. 63, no. 4, pp. 2072-2082, Apr. 2016. [2] S. Lee, S. Kim, S. Saha, Y. Zhu, and Y. Cho, "Optimal structure design for minimizing detent force of PMLSM for a ropeless elevator," *IEEE Trans. Magn.*, vol. 50, no. 1, Jan. 2014. [3] J. Ewanchuk, J. Salmon, and C. Chapelsky, "A method for supply voltage boosting in an open-ended induction machine using a dual inverter system with a floating capacitor bridge," *IEEE Trans. Power Electron.*, vol. 28, no. 3, pp. 1348–1357, Mar. 2013. [4] D. Pan, F. Liang, Y. Wang, and T. A. Lipo, "Extension of the operating region of an IPM motor utilizing series compensation," *IEEE Trans. Ind. Appl.*, vol. 50, no. 1, pp. 539–548, Jan./Feb. 2014. [5] Y. Lee and J. Ha, "Hybrid modulation of dual-inverter for open-end permanent magnet synchronous motor," *IEEE Trans. Power Electron.*, vol. 30, no. 6, pp. 3286–3299, Jun. 2015.

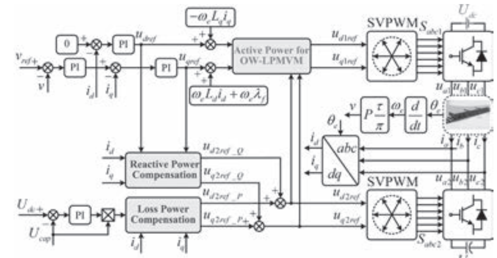

Fig. 1. Block diagram of the proposed control method.

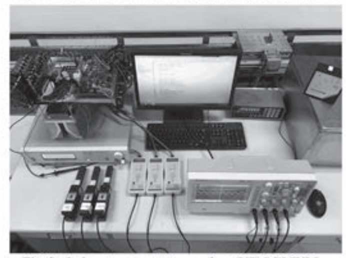
Fig. 2. Laboratory prototype of an OW-LPMVM.

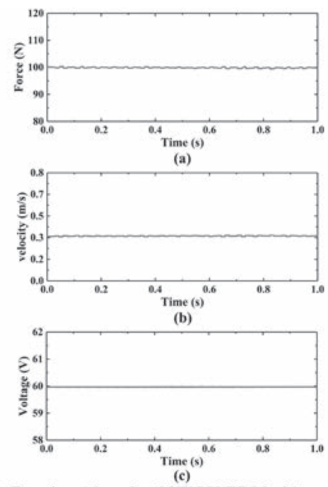

Fig. 3. Experimental results of OW-LPMVM dual-inverter system. (a) Electromagnetic force. (b) Mover velocity. (c) Capacitor voltage.

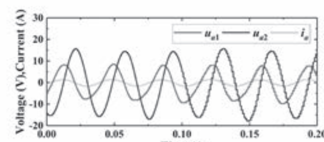

Fig. 4. Experimental results of voltages of dual-inverter and motor current.

CT-03. Detent Force Investigation in Long-stator PM Linear Machines with Non-ideal Mechanical Airgap Condition.

M. Ma[1]
1. School of Electrical Engineering and Automation, Hefei University of Technology, Hefei, China

I. Introduction The end effects of detent force is inherent characteristic of permanent magnet (PM) linear machines, and it is also the significant drawbacks for motion control and high-precision applications. Many foregoing efforts have been proposed to reduce detent force [1]. For the long-stator (Moving-magnet) linear machines, it is widely adopted modular segments, which is easy to assemble and maintain. But the assembled structure will causes non-ideal mechanical airgap condition inevitably, and it brings significant effects on detent force, which is comparatively less observed by researchers. Because of the uneven actual airgap situation, the calculation model and the suppression method of detent force should be discussed and determined. Hence, in this paper the non-ideal mechanical airgap condition in long-stator linear machines is generalized and simplified. And then, the detent force characteristics are studied based on the variable airgap analysis model. Finally the the measures to eliminate the detent force in the non-ideal mechanical airgap condition are analyzed. II. non-ideal mechanical airgap condition analysis The uneven mechanical airgap condition in long-stator linear machines is mainly caused by the deformation of the mover and the assembly errors shown in Fig.1 a). Generally the large normal force exits between PM mover and stator core, so the mover yoke will be deformed. In addition, the multi-segments stator appears in an assembled array, and the air gap length of boundary between two stator segments is hard to control. To sum up, the non-ideal air-gap condition appears. First, the actual air gap situation in long-stator prototype are tested, and the data is listed as shown in Fig. 1 b). The measured point 1 and point 7 are located ends of stator, while point 3 and point5 are located at the junction of segments. The other points are distributed in equally space. It is well known that accurate calculated results can be obtained by finite element method. However, the actual air gap situation for long-stator linear prototype is very complex for the whole stroke, modeling analysis will face the meshing problem of irregular air gap. Hence, based on the actual data the non-ideal mechanical air gap conditions are categorized into two types: linear deviation air gap situation and V shaped airgap situation. III. detent force calculation and suppression Based on the above categories, the detent force characteristics in different non-ideal mechanical air gap condition are analyzed by finite element method. In numerical model, a wedge-shaped air gap develops because of uneven air gap conditions. The wedge-shaped air gap needs to be divided into several combinations of entities, and corresponding mesh lengths are set for different entities different. The sub-regional triangulation technology are adopted to ensure the quality of narrow area of grid. The results show that: 1) the positive and negative amplitude of detent force waveforms are asymmetrical in linear deviation air gap situation. The deviation in one direction occurs, and the positive or negative deviation will produce corresponding changes. 2) The V shaped air gap includes two conditions: V mouth up and V mouth down. In V shape air gap it can be seen that the positive and negative amplitude of detent force are still asymmetrical, but they gradually tend toward uniformity in middle region. For the detent force in non-ideal airgap condition, the suppression method of skewing is effective, and the optimal skewing length are obtained. The experiment of detent force shown in Fig. 2 are carried out to verify the correctness of the analysis results. IV. Conclusion This paper presents detent force characteristics analyses for long-stator PM linear machines with non-ideal mechanical air gap situation. The non-ideal mechanical air gap condition is categorized depending on measured data of actual airgap length. And then corresponding calculated models with sub-regional triangulation technology are established. The skewing method is an efficient way for detent force suppression. The analysis results can provide references to operational analysis and assembly process for long-stator PM linear machines.

[1] Yu-wu Zhu, Yun-Hyun Cho. Thrust Ripples Suppression of Permanent Magnet Linear Synchronous Motor[J]. IEEE Trans. on Magnetics, 2007, 43(6):2537-2538.

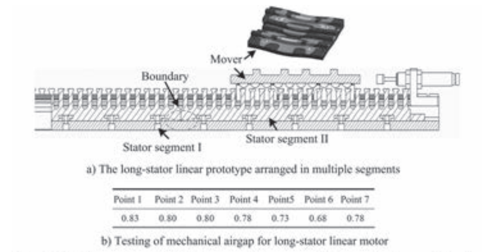

Fig. 1. The long-stator PM linear prototype and its actual air gap situation.

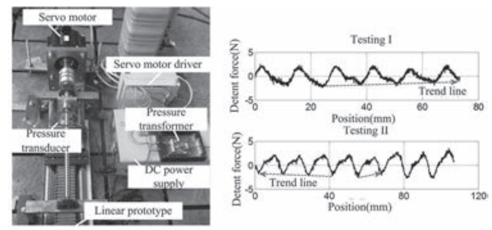

Fig. 2. The experimental results of detent force.

CT-04. Algorithm of Linear Induction Motor Control Considering End-effect of Magnetic Levitation Train Propulsion System.

H. Seo[2], J. Jeong[1], G. Choe[3] and J. Lim[4]

1. Dept. of Electrical Engineering, Chungnam National University, Daejeon, The Republic of Korea; 2. EV Team, R&D Center, VCTech, Gunpo, The Republic of Korea; 3. Dept. of Electrical Engineering, Konkuk University, Seoul, The Republic of Korea; 4. Dept. of Magnetic Levitation and Linear Drive, Korea Institute of Machinery & Materials, Daejeon, The Republic of Korea

This paper proposes a propulsion control algorithm considering End-effect of a linear induction motor (LIM) used in a magnetic levitation train. Indirect field oriented control (IFOC) technique is one of the popular control techniques widely applied to LIM drive control. The main idea of IFOC in a LIM is the decoupling of the flux and torque. Therefore, IFOC has a higher dynamic characteristic than the scalar control [1]. The LIM applied to the magnetic levitation trains should control the thrust force and also take into account the normal force for levitation stabilization. When the LIM is driven, normal force is inevitable. The normal force is a function of the speed, the slip frequency and the current of the train. In the rotary type induction motor, the normal force is canceled due to its symmetrical structure. Therefore, IM could operate in a low slip and high efficiency range. However, in the case of LIM, a high attraction force is generated in a low slip region, which cause the instability of the levitation system. Therefore, the propulsion control for magnetic levitation trains must operate in a higher slip region than the slip used in conventional IFOC. In this paper, the slip characteristics of the LIM are analyzed to improve the efficiency and safety of the magnetic levitation train by FEM analysis. A constant slip frequency propulsion control algorithm is proposed for operation in the analyzed slip region. The proposed algorithm can be controlled by separating magnetic flux and thrust from IFOC. The proposed algorithm is verified in 250 kW test bench. The results of FEM analysis according to speed and slip at constant voltage condition are shown on Fig. 1. The dotted lines of Indirect Field Oriented Control(IFOC) and Constant Slip Indirect Field Oriented Control(CSIFOC) are shown on the figure. The slip of the IFOC is low and that leads to operate near the maximum thrust and efficiency. However, the normal force of LIM is also increase, which could not be allowed in maglev application. On the other hand, when CSIFOC is performed considering normal force, the slip is higher than the conventional algorithm. Although the CSIFOC is not operated in maximum thrust slip, the normal force could be greatly reduced. Fig. 2 (a) shows the CSIFOC algorithm considering the end-effect of the linear induction motor. In general IFOC, the d-axis current reference is calculated through the magnetic flux reference value, and the q-axis is calculated based on thrust. However, the CSIFOC for the LIM generates the d-axis and q-axis current references along with the slip frequency and thrust. Fig. 2 (b) shows the waveform of the experimental results based on the general IFOC and the proposed algorithm. Both IFOC and CSIFOC were tested with the same rate pattern of the same load. It is confirmed that CSIVC has larger slip than conventional IFOC and low normal force in all regions. In this paper, a constant slip frequency IFOC algorithm is proposed considering the end effect of LIM used for magnetic levitation trains. The efficiency, thrust and normal force according to the speed and slip through the FEM analysis of the LIM were analyzed and the slip condition suitable for the magnetic levitation train is proposed. In addition, a current reference generation algorithm based on the thrust and slip is proposed in the IFOC considering the end effect to operate under the proposed slip condition. In the full paper, the detailed formulas of the proposed algorithm are developed and will be verified through simulation and experimental results.

[1] P. Hamedani and A. Shoulaie, “Indirect field oriented control of Linear Induction Motors considering the end effects supplied from a Cascaded H-Bridge inverter with multiband hystersis modulation,” in 4th Annual International Power Electronics, Drive Systems and Technologies Conference, 2013, pp. 13–19.

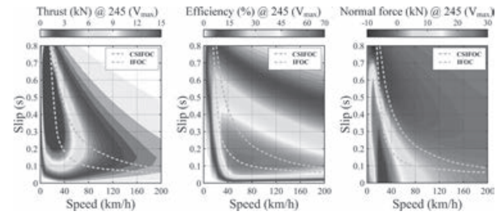

Fig. 1. Analysis results of magnetic characteristics considering speed and slip at maximum voltage condition

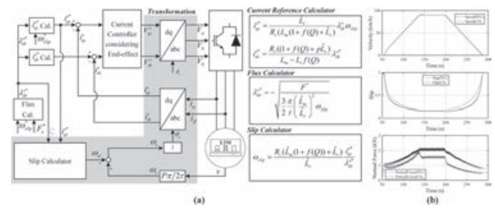

Fig. 2. (a) Constant sleep frequency propulsion control algorithm based on IFOC (b) Normal force comparison experiment results of IFOC and CSIFOC

CT-05. Experimental Verification of Characteristic Analysis and Performance Verification of Double-Sided Permanent Magnet Linear Synchronous Generator Designed with Three-Dimensional Effects for Ocean Wave Energy Converter.

S. Seo[1], G. Jang[1], M. Koo[1], K. Kim[2], K. Hong[2] and J. Choi[1]
1. Electrical Engineering, Chung-nam National University, Daejeon, The Republic of Korea; 2. Offshore Plant Research Division, Korea Research Institute of Ships & Ocean Engineering, DaeJeon, The Republic of Korea

In this study, a three-dimensional (3D) analysis method and a manufacturing model are used for generating performance analysis and experimental verification on a double-sided permanent magnet linear synchronous generator (PMLSG) with a slotless stator, as shown in Fig. 1(a) [1]. The PMLSG with a slotless stator has a moderately large magnetic air gap; thus, it should be analyzed considering the end effects, such as fringing and leakage flux. Due to these effects, the PMLSG requires a 3D analysis method and a variety of other approaches, including the numerical and analytical methods that have been used in previous studies, for electromagnetic field analysis [2-4]. The 3D finite element (FE) analysis is a highly reliable numerical method; however, the design parameters increase the analysis time, as shown in Fig. 1(b). Conversely, there are methods to reduce the analysis time along with increased reliability, such as the 3D analytical approach. For the 3D analytical approach, the PMLSG can be simplified and represented on an xy-plane and a yz-plane, as shown in Fig. 1(c). As the fringing and leakage flux emerge in the z direction, its end effects should be considered to improve the accuracy. Further, the flux density results of the open circuit and armature reaction fields are generated by permanent magnets (PMs) in a mover and by currents in stator windings. Articles designed in this manner have already been published in reference paper [1]. However, reference paper [1] addressed the results up to the counter-electromotive force at no load. Therefore, in this paper, we will cover the details of the process subsequent to those outlined in the reference paper [1]. For the PM linear generator to be applied to the ocean wave energy converter, highly efficient energy conversion is important; however, maximum power generation is more important considering the wave motion to change in real-time. Therefore, we propose the characteristic map of the generating performance, that is, the characteristic results of power, losses, efficiency, force, and power take-off (PTO) damping coefficient. The conditions for optimum performance and the range of maximum power generation can be obtained from these results. Further, when regular wave energy is generated, the heaving motion of the buoy is changed by the PTO damping coefficient from the PM linear generator, and the input velocity of the PM linear generator is affected by this phenomenon. Therefore, the condition selection for maximum power in regular wave energy is very important for the ocean wave energy converter. Therefore, this paper deals with the generating characteristics of the PM linear generator, with the heaving motion of the buoy coupled with the generator according to the ocean wave variation. Finally, we deal with the generating results of the PM linear generator for the ocean wave energy converter according to the irregular input wave. Fig. 2 shows the experimental results of two cases with the no-load and load tests (load resistance condition, 2 Ω). Here, the two cases represent the difference in the irregular velocity. The irregular velocity is simulated using irregular wave energy and heaving buoy motion equation. In the detailed manuscript, firstly, we will present a simple summary process of the 3D analysis method and various experimental results of the manufactured model; and all the analytical procedures are specially designed to contribute to related research and industrial applications. ACKNOWLEDGMENTS This work was supported by the Basic Research Laboratory (BRL) of the National Research Foundation (NRF-2017R1A4A1015744) funded by the Korean government.

References [1] *M. M. Koo, J. Y. Choi, H. J. Shin, J. M. K, "No-Load Analysis of PMLSM With Halbach Array and PM Overhang Based on Three-Dimensional Analytical Method," IEEE Trans. Appl. Superconductivity., vol. 26, no. 4, Jun. 2016.* [2] O. de la Barrière, S. Hlioui, H. B. Ahmed, M. Gabsi, and M. LoBue, "3-D formal resolution of Maxwell equations for the computation of the no-load flux in an axial flux permanent-magnet synchronous machine," IEEE Trans. Magn., vol. 48, no. 1,. Jan. 2012. [3] B. L. J. Gysen, K. J. Meessen, J. J. H. Paulides, and E. A. Lomonova, "3-D analytical and numerical modeling of tubular actuators with skewed permanent magnets," IEEE Trans. Magn., vol. 47, no. 9, Sep. 2011. [4] J. Azzouzi, G. Barakat and B. Dakyo, "Quasi-3-D Analytical Modeling of the Magnetic Field of an Axial Flux Permanent-Magnet Synchronous Machine," IEEE Trans. Magn., vol. 20, no. 4, pp. 746-752, Dec. 2005.

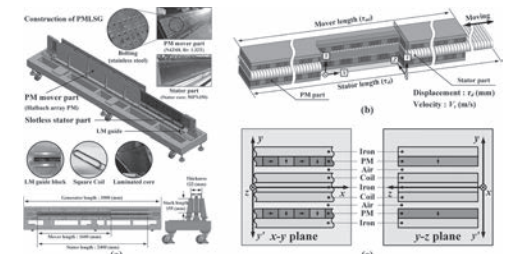

Fig. 1. Construction and analysis model of double-sided PMLSG: (a) Materials and the manufactured plan of the mover and stator parts, (b) 3D FE analysis model, and (c) simplified analytical model according to the analysis plane.

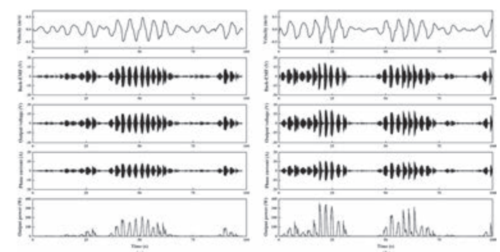

Fig. 2. Experimental results of the irregular wave condition under each case (load resistance condition, 2Ω). (a) Case 1, (b) Case 2.

CT-06. Novel Propulsion Control Algorithm considering Magnetic Field Analysis Results of Linear Induction Motor for High Performance Operating.

J. Jeong[1], H. Seo[2], J. Lim[3] and J. Choi[1]
1. Electrical Engineering, Chungnam National University, Daejeon, The Republic of Korea; 2. EV Team, R&D Center, VCTech, Gunpo, The Republic of Korea; 3. Magnetic Levitation and Linear Drive, Korea Institute of Machinery & Materials, Daejeon, The Republic of Korea

Single-sided linear induction motors (SLIMs) have merits such as high initial thrust, simple structure, flexible mechanism, absence of dust emission, and low noise [1]. Thus, SLIMs are broadly adopted as a traction component in many industrial applications, especially in magnetic levitation (maglev) transportation systems or urban train systems [2]. The 200km/h-class semi-high-speed maglev train currently being developed in Korea uses SLIMs to propel it. SLIMs are widely used for the propulsion of maglev trains, as they are lightweight and inexpensive to produce. However, their driving characteristics are inferior to those of linear synchronous motors (LSMs) because of their low power factor and the presence of slip. Therefore, to increase the operation efficiency of maglev trains using SLIMs, it is important to analyze the characteristics of speed and slip and identify the optimal operating points. This study analyzes the thrust, normal force, and efficiency characteristics of semi-high-speed maglev train LIMs in detail, using two-dimensional (2D) finite element method (FEM). The maximum thrust and efficiency range were determined using this analysis. An efficiency map was derived based on the operating conditions in the constant-thrust region. Furthermore, the thrust based on the constant power region was analyzed to demonstrate the overall operating capabilities of the LIM. The thrust, normal force, and efficiency were analyzed in detail according to the overall driving speed and slip condition, and it was presented as a contour map. Based on the characteristics map of LIM derived, we proposed a new thrust control algorithm by reflecting the optimum slip frequency in the control algorithm. Among the characteristics of the analyzed LIM, a new propulsion algorithm was proposed to minimize the energy consumption, and the feasibility was verified by simulation and experiment. Finally, the consumption energy of the new algorithm was calculated to confirm that the energy was reduced compared to the existing algorithm. A diagram of the semi-high-speed maglev train and the associated LIM is shown in Fig. 1 (a). Fig. 1 (b) is a plot of the thrust, normal force, and efficiency with respect to slip at the rated speed of 90 km/h. Fig. 1 (c) is an efficiency map created by FEM analysis of slip for various speeds. In this analysis, the variation of efficiency with respect to slip can be observed for speeds of up to the maximum speed of 200 km/h. The map shows very high efficiency values for slip values between 0.1 and 0.3, and the trend indicates that efficiency increases as speed increases at lower speeds. At the points where efficiency increases, the thrust and the normal force values can be referenced for high-efficiency operation of the maglev train. Fig. 2 (a) is a block diagram of the optimal slip indirect vector control (OSIVC) algorithm. The basic configuration is consistent with the constant slip frequency control, but the part of inputting the slip frequency command depending on the optimal slip modeling according to speed is different. Fig. 2 (b) compares the power consumption of thrust control algorithm. The highest power consumption is shown when using regular IVC. When SCFIVC and IVC are compared, the final amount of power can be reduced by 12%, and it was finally found that 2% is reduced more when using OSIVC. This energy difference is caused by the fact that it was operated with the best slip for the motor and driven with the highest slip frequency. The constant slip frequency control in the acceleration/deceleration regions yields maximum efficiency points different from the constant-speed region, so the energy consumption is greater than in the constant-speed region. These characteristics are valuable to semi-highspeed Maglev trains, as they experience a considerable amount of acceleration and deceleration during their operation. Fig. 2 (c) is a manufacturing model for performance evaluation, and we will present the results on a full paper.

[1] I. Boldea, "Linear Motion Electromagnetic Devices," New York, USA: Taylor & Francis, 2001. [2] H. W. Lee, C. B. Park, and S. Won, "A Study on transient analysis of linear induction motor with ununiform airgap for shallow-depth underground train," Trans. of KIEE., vol. 62, no. 5, pp. 723 729, 2013.

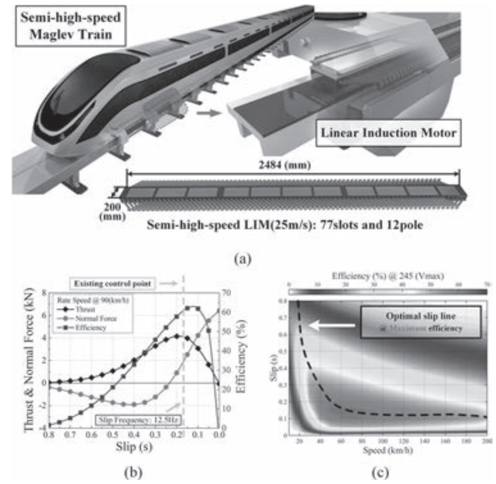

Fig. 1. (a) Schematic and manufactured model of LIM, (b) thrust, normal force, and efficiency as a function of slip, and (c) efficiency contour map considering speed and slip condition.

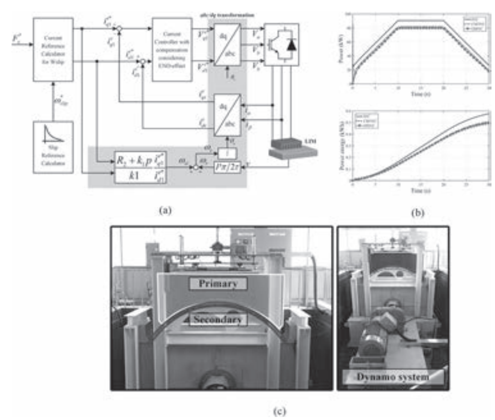

Fig. 2. (a) Block diagram for optimized slip indirect vector control, (b) comparison of power energy, and (c) manufactured dynamo system for LIM.

CT-07. Design and Reduction of Thrust Ripple in Transverse Flux Permanent Magnet Linear Machine.

M. Zhao[1,2], K. Liu[3], H. Yang[1], N. Feng[1], D. Hou[1], P. Zhang[1] and M. Xu[1]
1. Ludong University, Yantai, China; 2. Harbin Institute of Technology, Harbin, China; 3. Southeast University, Nanjing, China

This paper proposed a tubular transverse flux permanent magnet linear machine with the quasi-distributed stator segments, due to the problem of larger thrust force ripple in the machine, which has some merits higher force density and better controllable characteristic etc. Firstly, the structure and operating principle of tubular transverse flux permanent magnet linear machine was presented. Secondly, the influence of the quasi-distributed stator segments on the motor performance is analyzed in detail. Special attention is paid to the Back-EMF, cogging force and electromagnetic force etc. The paper investigates the influence of different arrangements in transverse flux permanent magnet linear machine, including theoretical analysis and numerical calculation. The results show that the thrust ripple can be decreased by the quasi-distributed stator segments in transverse flux permanent magnet linear machine. I.Introduction With the concept of shipboard electrical ejection system being put forward, the studies of high thrust permanent magnet linear motor are carried out by international scholars, which are focused on moving-magnetic type permanent magnet linear motor at present [1]. However, as a new type of high thrust density linear motor, the permanent magnet linear motor (PMLM) is still on the stage of exploring study [2-5]. The structure parameters of machine were optimized by 3-D magnetic grid method and response surface method, in order to improve the thrust density of the machine. A novel bidirectional cross-linking transverse flux tubular PMLM was investigated, which has solved the lower utilization rate of secondary permanent magnet in transverse flux PMLM. However, the motor has some disadvantages, such as complicated structure, higher requirements of processing technology and troublesome in winding placement. In a word, this type of motor has a good application prospect in the field of linear direct drive system. II.ICONSTRUCTION AND PRINCIPLE OF TUBULAR TRANSVERSE FLUX PERMANENT MAGNET LINEAR MACHINE The novel stator segment axial distribution arrangement transverse flux PMLM has been investigated in this paper. Fig. 1 shows the physical model of tubular transverse flux PMLM with four core segments on the stator and six pairs of poles on the mover. II.TRANSVERSE FLUX PERMANENT MAGNET LINEAR MACHINE WITH QUASI-DISTRIBUTED STATOR SEGMENTS In general, the stator core stacks of transverse flux linear machine are axially arranged in a distance of a double pole pitch. However, this paper proposed a novel stator stacks distribution, called as class distribution, as shown in Fig.2. One thing to note here is that the class distribution arrangement comes from traditional motor distributed winding while it is different from the definition of distributed winding at the same time. The theoretical derivation process will be presented with more detail in full paper. III.Conclusions A novel tubular transverse flux PMLM with the quasi-distributed stator segments is proposed in this paper. It investigates the influence of different distribution mode on the machine performance including back-EMF, cogging force and electromagnetic force. (1) The 5th and 7th harmonic of back-EMF can be eliminated when the distance of laminations group y1 are $9\tau/5$ and $27\tau/14$ respectively for the given pole pitch of τ and the stator segment number q of 4. Furthermore, it proves the validity of theoretical derivation by using numerical calculation. (2) The amplitude of cogging force is decreasing with the decrease of distances of stator laminations group by using numerical calculation of cogging force. (3) The amplitude of 6th ripple force can be obviously reduction when the distance of stator laminations group is $23\tau/12$ by using numerical calculation of electromagnetic force.

[1] Luo Honghao, Wu Jun, Chang Wensen. "Minimization of Cogging Force in Moving Magnet Type PMBLDCLM, "*Proceedings of the CSEE*, vol.27, no.6, pp.12-16, 2007. [2] Zou Ji-bin, Zhao Mei. "Development and Analysis of Tubular Transverse Flux Machine with Permanent Magnet Excitation," *IEEE Transactions on Industrial Electronics*, vol.59, no.5, pp. 2198-2207, 2012. [3] Do-Kwan Hong, Byung-Chul Woo, Dae-Hyun Koo, et al. "Optimum Design of Transverse Flux Linear Motor for Weight reduction and Improvement Thrust Force Using Response Surface Methodology," *IEEE Transactions on Magnetics*, vol.44, no.11, pp.4317-4320, 2008. [4] Li Peng. "Basic research on bidirectional cross linking transverse flux tubular linear permanent magnet synchronous motor," Harbin: Harbin institute of technology, 2011. [5] Kou Baoquan, Yang Guolong, Zhou Weizheng, Zhang He. "Bidirectional Crosslinking Transverse Flux Flat Type Permanent Magnet Linear Synchronous Motor," *Proceedings of the CSEE*, vol.32, no.33, pp.75-82, 2012.

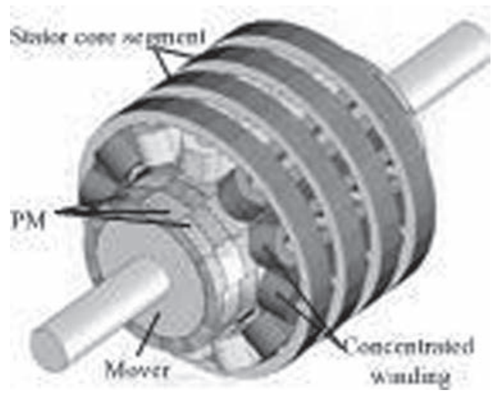

Fig. 1. Arrangement of winding and permanent magnets.

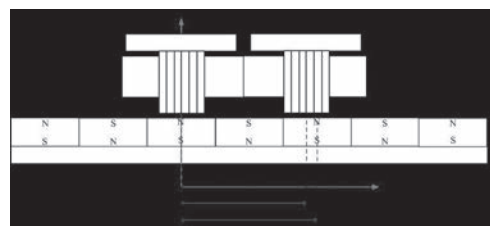

Fig. 2. The axial view of TFPMLM

CT-08. Design and Implementation of Amorphous Magnetic Material-Based Common Magnetic-Bus for the Replacement of Common DC-Bus.

M. Islam[1], K. Muttaqi[1], D. Sutanto[1] and J. Zhu[2]
1. Faculty of Engineering and Information Sciences, University of Wollongong, Wollongong, NSW, Australia; 2. Faculty of Engineering and Information Technologies, University of Technology, Sydney, NSW, Australia

In recent years, smart microgrid technologies are gaining considerable interest, where a common dc-bus is generally used to interconnect multiple power sources, e.g. solar photovoltaic (PV) modules [1]– [3]. In a dc-bus based solar microgrid system, multiple PV modules deliver power the dc-bus through maximum power point tracker (MPPT) and dc/dc converters. The MPPT ensures the operation of solar PV modules at maximum power point (MPP) but provides output voltage that is not constant. The dc/dc converter is used to control the output voltage at the dc-bus level. The operating point of all MPPTs may not be the same as the radiation or temperature levels on PV modules are not always the same. Therefore, the generation of common dc-link voltage from different PV modules limit the range of MPPT operation, i.e. some MPPT fails to extract the maximum power. In this paper, a high-frequency (about 10 kHz) common magnetic-bus as a replacement for common dc-bus has been proposed to overcome the restriction of MPPT and complication of the PV inverter operation. The design process of the high-frequency magnetic-link leads to multi-physics problems with some critical decision making tasks and thereby affects the power converter efficiency and cost. Optimal design of high-frequency magnetic-links with advanced soft magnetic materials having high saturation flux density and low specific core loss, is requested to improve the power conversion efficiency. For large capacity high-frequency transformers, it is desirable to have a high saturation flux density to avoid large volume and low core loss to achieve high efficiency. Because of these superior characteristics, e.g. the saturation flux density, specific core loss, cost, and availability of various size strips (wide) the Fe-based amorphous magnetic alloy 2605S3A has been used in high power applications [4]–[8]. Moreover, the price for iron-based Metglas magnetic material has decreased significantly in recent years. The high-frequency magnetic-links are usually excited with square wave voltage which significantly increases the core losses compared with that obtained under sinusoidal voltage excitation. The vendors, e.g. Metglas Metals, provide only the core loss data under sinusoidal voltage excitations. Using the given data (measured under sinusoidal voltage excitation), it is really difficult to obtain an optimal design of high-frequency magnetic-links [9]. In order to obtain an optimal design, the magnetic material 2605S3A is characterise under square-wave voltage excitation. In the ANSOFT Maxwell 3D environment, a magnetic core is modelled using the optimal parameters obtained from optimization and square-wave voltage high-frequency characteristics of amorphous alloy 2605S3A. The ANSOFT Maxwell 3D gives the electromagnetic field distributions for a specific model with given magnetic material, boundaries, and source conditions, applying Maxwell's equations over a finite region of space. To verify the feasibility of the proposed concept a high-frequency magnetic-bus is developed. Based on the optimization results, amorphous alloy 2605S3A sheet (2.5 cm wide and 20 μm thick) was collected from Metglas Metals Inc., USA. For the electrical insulation and mechanical bonding, the Metglas sheet was glued with Araldite 2011 on the surface of each layer. During the wrapping of Metglas stripes of 2605S3A, equal and opposite forces were applied to make a uniform distribution of Araldite. Fig. 1 shows a photograph of the magnetic-bus with inner and outer frames. After wrapping, the frames were removed before the Araldite dried up, e.g. within 2 hours. To minimize the proximity effect, Litz wires are used for windings with single layer placement. Fig. 2 shows a photograph of developed four windings high-frequency magnetic-bus. The high-frequency inverter generates square-wave voltage which is used to energize the primary coil of high-frequency magnetic-bus. The core losses of amorphous alloy 2605S3A in terms of flux density and frequency with square-wave voltage excitation were measured. All secondary windings show similar total loss characteristics. Such a similarity of characteristics is also necessary to ensure balance three dc-supplies for the modular multilevel inverter, which helps to eliminate the extra control circuit to mitigate the imbalancing problem. These design and implementation techniques would have great potential for the development of new medium or high-voltage inverters for solar PV systems and smart micro-grid applications, especially in replacing common dc-buses by magnetic-buses. The detail developmental process of high-frequency magnetic-bus using amorphous magnetic alloys will be explicitly described in full paper.

[1] Vithayasrichareon, P., MacGill, I. F., Valuing large-scale solar photovoltaics in future electricity generation portfolios and its implications for energy and climate policies, IET Renew. Power Gener., 2016, 10, (1), pp. 79–87 [2] Shahrbabak, Z. M., Tabesh, A., Yousefi, G. R., Economical design of utility-scale photovoltaic power plants with optimum availability, IEEE Trans. Ind. Electron., 2014, 61, (7), pp. 3399–3406 [3] Azmi, S. A., Adam, G. P., Ahmed, K. H., Finney, S. J., Williams, B. W., Grid interfacing of multimegawatt photovoltaic inverters, IEEE Trans. Power Electron., 2013, 28, (6), pp. 2770–2784 [4] Fan, T., Li, Q., Wen, X., Development of a high power density motor made of Amorphous alloy cores, IEEE Trans. Ind. Electron., 2014, 61, (9), pp. 4510–4518 [5] Zhang, Z., Sharma, P., Makino, A., Role of Si in high Bs and low core-loss Fe85.2B10-xP4Cu0.8Six nanocrystalline alloy, J. Appl. Phys., 2012, 112, (10), art. 103902 [6] Makino, A., Kubota, T., Yubuta, K., Inoue, A., Urata, A., Matsumoto, H., Yoshide, S., Low core losses and magnetic properties of Fe85-86Si1-2B8P4Cu1 nanocrystalline alloys with high B for power applications, J. Appl. Phys., 2011, 109, (7), art. 07A302 [7] Azuma, D., Hasegawa, R., Core loss in toroidal cores based on Fe-based amorphous Metglas 2605HB1 alloy, IEEE Trans. Magn., 2011, 47, (10), pp. 3460–3462 [8] Hsu, C. H., Lee, C. Y., Chang, Y. H., Lin, F. J., Fu, C. M., Lin, J. G., Effect of magnetostriction on the core loss, noise, and vibration of fluxgate sensor composed of amorphous materials, IEEE Trans. Magn., 2013, 49, (7), pp. 3862–3865 [9] Boglietti, A., Cavagnino, A., Lazzari, M., Pastorelli, M., Predicting iron losses in soft magnetic materials with arbitrary voltage supply: an engineering approach, IEEE Trans. Magn., 2003, 39, (2), pp. 981–989

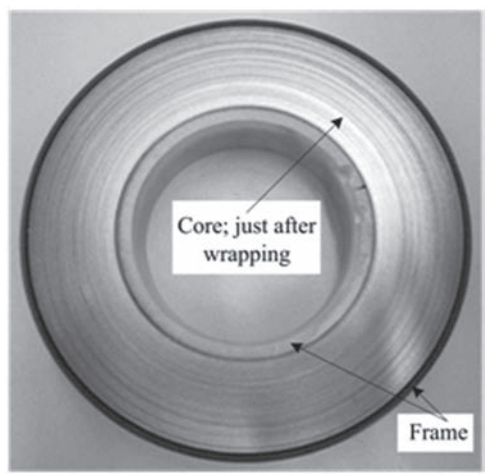

Fig. 1. A photograph of the magnetic-bus with inner and outer frames, maid by amorphous alloy 2605S3A sheet (2.5 cm wide and 20 μm thick) which was collected from Metglas Metals Inc., USA.

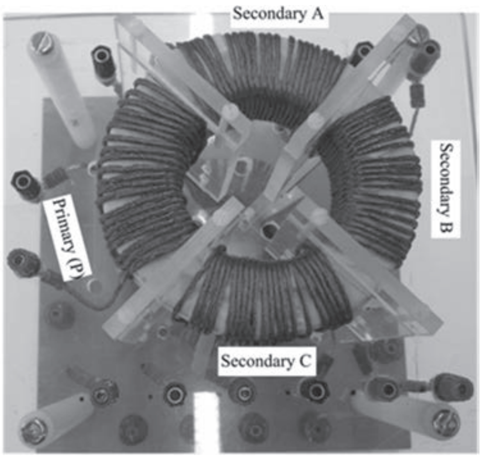

Fig. 2. A photograph of the developed four windings high-frequency magnetic-bus, core was maid by amorphous alloy 2605S3A sheet (2.5 cm wide and 20 μm thick) and Litz wires are used for windings with single layer placement.

CT-09. Research on Detent Force for Tubular Permanent Magnet Linear Motor with Skewed Core End.

G. Zhao[1], Y. Wang[1], B. Bai[1] and X. Gao[1]
1. Shenyang University of Technology, Shenyang, China

I. INTRODUCTION Detent force is a major concern in the linear motor, which is brought by the discontinuity of the core end. The detent force can reduce the positioning accuracy in servo system, so many people have done many work to weaken it [1][2]. The method for reducing the cogging force by auxiliary slots is mentioned in [3], in which the analytic relationship between the auxiliary slot number and the cogging force is derived and the selection of the auxiliary slot number is also discussed. The end effect detent force of permanent magnet linear motor (PMLM) is analyzed based on the lateral force method [4]. The analytical expressions describing the position and the width of auxiliary poles are derived. In this paper, a method of skewed primary core end for the tubular PMLM is proposed and the prototype is designed and manufactured. The analytical relation between the skewed primary core end length and the detent force is derived, from which the best skewed end length can be obtained. Subsequently, the detent force is analyzed by finite element method (FEM) and the detent force of the tubular PMLM with the skewed primary core end has been significantly reduced compared to the direct core end one. II. Analysis of tubular PMLM with skewed ends As shown in Fig.1, a common tubular PMLM that its primary core end (called motor 1 below) is direct is designed and the motor have 12 slots 11 poles. Several factors influencing the detent force such as the primary core length, pole arc coefficient and the tooth width have been optimized by FEM. But the peak detent force still exceeds 20N. The design and analysis details will be given in full paper. Based on the motor above, a tubular PMLM scheme with skewed primary core end (called motor 2 below) is proposed as shown in Fig.2. The two motors have the same secondary core in order to compare the influence of skewed core end. For the motor 2, phase difference will be generated between the skewed primary core end and the permanent magnet poles. So if the appropriate length of skewed primary core end is chosen, end force can be reduced significantly because of the phase difference. The analytical equation of the detent force can be deduced according to analyzing the model of motor 2, shown in equation (1), Where F_{slot}, F_{end} is the cogging force and the end force, respectively. d, δ, Φ_m, μ_0, τ is the length of skewed primary core end, the length of the air gap, the maximum magnetic flux, the vacuum permeability, the pole pitch, respectively. S is a half of a magnetic pole area; D is the shaft radius of tubular PMLM; C is an equivalent length that is equal to the product of slot number and slot pitch; α is the equivalent angle between tooth and the permanent magnet if the tubular TMLM is regarded as a rotational motor; Z is the slot number; p is pole pair. The derivation process will be given in full paper. From the equation, the detent force is composed of three parts, the third part is cogging force and it is a constant when the number of slots and poles are certain, but the first and second parts change as the d varies. When different d is chosen, the detent force is also different. When $d=\tau$, the detent force is the minimum. In order to verify the validity of the analytical equation, the 3D model of the tubular PMLM with the skewed primary core end is established in the finite element software Ansys Maxwell, as shown in Fig.3. Fig.4 shows the calculation results for the detent force of the tubular PMLM with different length of skewed primary core end. The peak detent force is extracted and shown in Fig.5. According to Fig.4 and Fig.5, both the fluctuation of detent force waveform and the peak detent force are minimum when the length of skewed core end is one pole pitch. Compared to the direct primary core end motor, the peak detent force of the skewed primary core end motor is reduced from 22.7N to 11.4N, which is reduced by about 50%, when the length of skewed primary core end is one pole pitch. According to Fig.5 the detent force variation versus d is not linear, so not each length of the skewed primary core end is effective to reduce the detent force. The two kinds of prototypes are manufactured for proving the validity, as is shown in Fig.6. The testing results accord with the analytical and calculation results. More testing detail will be given in full paper. III. CONCLUSIONS The method of reducing detent force of the tubular PMLM is proposed through skewing the primary core end. The analytical equation for the detent force of tubular PMLM with skewed primary core end is derived. The validity of the analytical method is verified by the finite element method and the prototype test. The detent force can be reduced effectively through skewing the primary core end, especially the peak detent force is minimum when the length of skewed primary core end is one pole pitch.

[1] Sung-Jin Kim, Eui-Jong Park, Sang-Yong Jung, and Yong-Jae Kim, “Optimal Design of Reformed Auxiliary Teeth for Reducing End Detent Force of Stationary Discontinuous Armature PMLSM”, IEEE Transactions on Applied Superconductivity, vol. 26, no. 4, Jun. 2016. [2] M. Wang, L. Li, D. Pan, “Detent Force Compensation for PMLSM Systems Based on Structural Design and Control Method Combination”, IEEE Transactions on Industrial Electronics, vol. 62, no. 11, pp. 6845-6854, Nov. 2015. [3] Huang K.F, LI H.S, Zhou Y., “Method research for reducing the cogging force by auxiliary slots”, Electric Machines and Control, vol. 18, no. 3, pp. 54-59, Mar. 2014. [4] Kou B.Q, Zhang H.G. “End Effect Detent Force Reduction for Permanent Magnet Linear Synchronous Motors with Auxiliary Poles One-Piece Structure”, Transactions of China electrotechnical society, vol. 30, No.6, pp. 106-113. Mar. 2015.

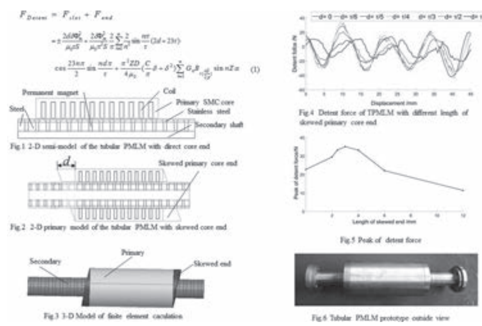

CT-10. Thermal Design of a Toroidally Wound Mover Linear Switched Reluctance Machine using 3D Equivalent Thermal Network.

D. Zhang[1], X. Du[1], D. Wang[1] and C. Peng[1]
1. Shandong University, Jinan, China

Abstract-- Thermal analysis is an important issue in machine design which allows to have a knowledge of the machine temperature rise. This paper presents the thermal modeling, analysis and experiments of a linear switched reluctance machine (LSRM) with toroidally wound mover and segmental structure. Firstly, a 3-D heat flow model with the homogenized region for the presented LSRM is established using the thermal equivalent circuit. Then the 3-D thermal model for the presented LSRM is build by FEA which can give the detailed temperature profile of the entire machine. At last, the actual experiment on a prototype is carried out, validating the accuracy and feasibility of the thermal equivalent model above. I.Introduction Linear Switched Reluctance Machine(LSRM) features a double salient structure as its rotary counterpart which has neither magnets nor copper in the secondary, thus resulting in a simple and robust structure, and ultimately exhibiting low cost and high reliability [1]-[2]. Thermal problem has a major impact on the operation performance of the motor because there is always a design objective which requires the windings to supply as much current as possible to achieve high thrust density [3]. So the temperature rise of the machine should be simultaneously observed in the operation as it cannot exceed the maximum value. The accurate method to predict the temperature rise is Finite Element Analysis (FEA) [4]-[5]. However, it is usually very time consuming and cannot give policy to quickly identify the sensitivity of the machine parameters to the temperature rise. This paper put forward the thermal analysis, modeling and experimental validation of a LSRM. A 3-D thermal resistance network model is established to analyze the thermal field. The numerical 3-D heat flow model are developed by FEA and the results are compared to that obtained of thermal resistance network model. Finally, the experiment on a prototype machine is given to validate the analysis and results above. II.Configuration of the LSRM and thermal network Linear switched reluctance machine(LSRM) adopts double salient pole structure, which has 3-phase windings with a 3-pole mover and 2-pole stator. This LSRM has an annular phase winding wound around the mover yoke. The stator consists of series of individual segments embedded in an aluminium base. A.Thermal resistance The thermal field refers to the thermal of all the points in a space at a time. That mains $T=f(x,y,z,t)$ (1) $Q=k_x(\partial T/\partial x)i+ k_y(\partial T/\partial y)j+ k_z(\partial T/\partial z)k$ (2) where T is thermal in K, k_x, k_y and k_z are thermal conductivities in W/m●K. Consider the one-dimensional situation, we assume that the heat can only come in or out in the x direction. The thermal of the cubic region on the plane at $x=0$ is T_{0x} and on the plane at $x=l_x$ is T_{lx}. The steady-state conditions with temperature variation in the x-coordinate is $d^2T(x)/dx^2=-p/k_x$ (3) $Q_x=k_xS_x/l_x\times(T_{lx}-T_{0x}+1/2\times p/k_x\times l_x^2)$ (4) where p is power dissipation density. S_x is the surface area in the x-direction. It is easy to define the thermal resistance of the region in the x-direction as $R_x=l_x/(2k_xS_x)$ (5) B.Thermal equivalent network Assuming that the heat flow is transmitted in all directions equally, the thermal network can form a three-dimensional model. The configuration of the equivalent thermal circuit is shown in Fig. 1. As the linear motor structure is symmetrical, no heat flow will cross the central plane of the motor by thermal symmetry. Due to the symmetry, only a quarter of the move part need to considered. Since the air gap is only 0.5mm, the influence of the stator and aluminum base on the heat dissipation must be considered. The entire areas are divided into 15 parts, where part 5, 7 are coil windings, part 1, 2, 3, 4, 6 and 8 are mover yoke, part 9, 10 are mover teeth, part 11, 12 are stator and part 13, 14 and 15 are aluminium segment, and the temperature of each part is T_1 to T_{15}. For the presented LSRM, the iron loss of silicon steel sheet can be ignored. The dominant heat source of the presented LSRM is generated by the windings, i.e. copper loss $P=I^2R$ (6) where I is rated phase current and R is the resistance of phase winding. III.FEA result and experiment verification To verify the thermal model presented above, the 3-D heat flow model of the LSRM is established by FEA. In the FEA thermal simulation, the ambient temperature is 25°C, and the heat convection factor is 10 W/m²●K. The thermal distribution of the LSRM is shown in Fig. 2. In the 3-D thermal model, the highest temperature is 125.1°C which appears in center of phase B winding(T_5). Mover tooth(T_{10}) and aluminium base(T_{13}) temperature are 108.3°C and 98°C. Which is consistent with the results of the thermal network. To further validate the results of the thermal analysis above, the practical thermal experiment of the prototype is done. The measured temperature of the winding(T_5) is close to that of FEA and thermal equivalent circuit, which is 114.7°C. IV.Conclusions This paper develops a 3-D thermal circuit model of a linear switched reluctance machine with segmental structure stator and toroidal winding. The thermal field and temperature rise of the specific component of the machine is obtained. Then the numerical FEA heat flow models of the machine are established, and the results are compared to that obtained of thermal resistance network model. Finally, the experiment on a prototype machine is done to validate the analysis and results above.

[1] Zou, Y., Cheng, K.W.E., Cheung, N.C., and Pan, J.: 'Deformation and Noise Mitigation for the Linear Switched Reluctance Motor With Skewed Teeth Structure', *IEEE Transactions on Magnetics*, vol. 50, no. 11, pp. 1-4, Nov, 2014. [2] H. K. Yeo, H. J. Park, J. M. Seo, S. Y. Jung, J. S. Ro and H. K. Jung, "Electromagnetic and Thermal Analysis of a Surface-Mounted Permanent-Magnet Motor with Overhang Structure,", *IEEE Transactions on Magnetics*, vol. 53, no. 6, pp. 1-4, June, 2017. [3] J. F. Pan, Y. Zou, G. Cao, N. C. Cheung and B. Zhang, "High-Precision Dual-Loop Position Control of an Asymmetric Bilateral Linear Hybrid Switched Reluctance Motor,", *IEEE Transactions on Magnetics*, vol. 51, no. 11, pp. 1-5, Nov. 2015. [4] G. Zhang, W. Hua, M. Cheng, B. Zhang and X. Guo, "Coupled Magnetic-Thermal Fields Analysis of Water Cooling Flux-Switching Permanent Magnet Motors by an Axially Segmented Model," *IEEE Transactions on Magnetics*, vol. 53, no. 6, pp. 1-4, June, 2017. [5] J. Dong *et al*., "Electromagnetic and Thermal Analysis of Open-Circuit Air Cooled High-Speed Permanent Magnet Machines With Gramme Ring Windings," *IEEE Transactions on Magnetics*, vol. 50, no. 11, pp. 1-4, Nov. 2014.

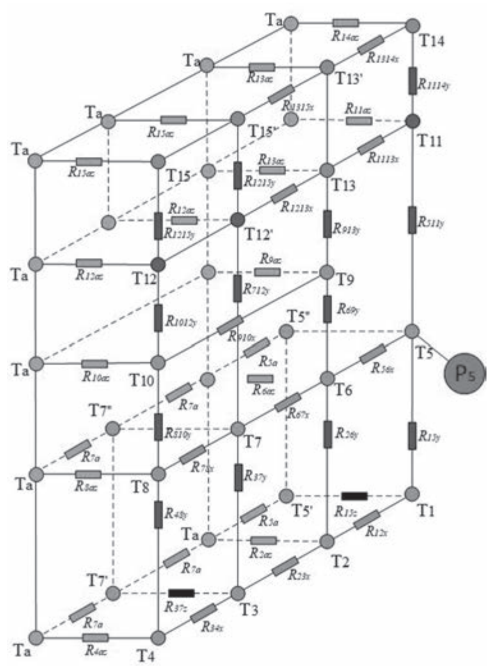

Fig. 1. 3-D thermal equivalent circuit of the presented LSRM

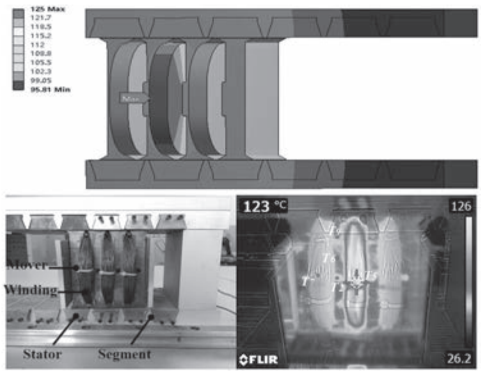

Fig. 2. FEA result and experiment verification

CT-11. A New Decoupled RotLin Motor with Fuzzy Sliding Mode Control.

Y. Zou[1] and E. Cheng[1]
1. Electrical Engineering, The Hong Kong Polytechnic University, Hong Kong, Hong Kong

I. INTRODUCTION Rotary-linear (RotLin) machines are usually employed in industrial devices such as boring machines, grinders and mechanical carving machines [1]. In the past, the primitive investigation on a brushless direct current (BLDC) rotary-linear motor presented the design approach and proposed the coupled output issue for this kind of motor [2]. Also, an inductive rotary-linear motor is studied in [3], elaborating the design procedure and analyzing the end effect of the motor. A voice coil motor combining a linear motor and a rotary motor is studied to improve the acceleration and precision of the movements [4]. A permanent magnet synchronized rotary-linear motor is also investigated, with a prototype shown in the literature [5]. However, the interaction between the linear part and the rotational part deteriorates the performance of these motors, including the accuracy of its position control. In this study, a decoupled RLSRM is designed and manufactured to improve the performance of the motor for practical applications. The motor possesses a decoupled magnetic structure in the linear part and the rotary part, avoided the mentioned coupling effect. It can realize the linear and the rotational movements simultaneously, with experimental results illustrated a spiral motion by using the motor. A sliding mode control (SMC) combined with a fuzzy logic controller (FLC) is designed for the motor against its nonlinear magnetic curves of soft materials. Experiments prove the effectiveness of the controller for the RLSRM considering the nonlinearity, outweighing the traditional proportional-integral-derivative (PID) control. II. STRUCTURE OF THE MOTOR This motor can be considered as a two-stator motor that merges a linear switched reluctance motor (LSRM) and a rotating switched reluctance motor (SRM). The outside stator is responsible for linear movements and the inner stator generates the torque of the mover, as shown in Fig 1.(a). The mover is a solid part stacked by steel sheets. By designing the structure, the size of the motor can be reduced. As the mover is very simple, its manufacturing and assembling will be easy. Consequently, the manufacturing cost of the motor can be also reduced. Meanwhile, short flux paths for the outside stator and the inner stator can avoid the coupling effect from the two stators. Some flux barriers are added for the mover. Therefore, the magnetic decoupling structure has been devised by the simple structure. The linear movements and the rotation can be controlled and realized simultaneously with no coupling effect. Figure 1(b) shows the structure of the mover. This mover has poles and slots deployed alternatively and their lengths are listed in Table I. The section view of the motor including the mover, the outside stator and the inner stator is shown in Fig.1 (c). The flux lines of the motor are plotted in Fig.1 (d). The flux lines pass closed along the stators and the mover with short magnetic circuit paths, which shows the magnetically decoupled structure of the motor. Main specifications are listed in Table I. III. CONTROL OF THE MOTOR The control block of the system is shown in Fig.2. For the linear motion, a proportional- derivative controller gets the control outputs from the FLC block, and outputs force commands for the force distibution funciton (FDF) of the motor. After the FDF converts the force to the reference current for a driver, the drive will supply the regulated power for the motor according to the reference current. Similarly, The SMC is designed for the rotating part. After obtaining the outputs from the FLC block, the SMC outputs torque references for the torque sharing function (TSF) that supplies references for the driver of the motor. The sliding surface of the SMC can be expressed by $s=de/dt+\lambda e,\ \lambda>0$. (1) e is the error of the input and the output and its changing rate is de. The phase plane is (e, de). The first-order equation to represent the sliding mode $(s,ds)=0$. We can obtain $e=-e\lambda$. The solution of this equation is $e(t)=e(t)*e$^-$\lambda(t)$. (2) According to Lyapunov's principle, the following equation needs to be guaranteed if the solution can reach the sliding surface. $s*ds<0,\ V=0.5*s^2(e,t),\ dV<0$. (3) And the control law of the controller can be obtained $u(t)=(\alpha|e|+\beta(de/dt))*sgn(S)$. (4) α and β are constants that can be adjusted by the FLC block. $sgn(S)$ is the signal function. IV. EXPERIMENTAL RESULTS The whole experimental set up consists of a computer, a dSPACE DS1104 card, a power supplier, a driver and the motor, as shown in Fig.3. The static torque and force outputs are measured and given in Fig.4. The control scheme, as well as the controllers, is built using the software package MATLAB/Simulink. After programming and debugging the control scheme into the dSPACE card, the card will output commands for drivers of the motor, getting the feedbacks of position and rotational angle from two encoders and constructing a closed loop control. The mover can move in linear and rotating directions simultaneously and it can realize a spiral movement. The experiments are carried out when the mover rotates at a constant speed of 500 rpm and the reference to the linear movement scope is 20 mm under 0.5 Hz. In Fig.5 (a), the linear movement response is plotted, and position error is given in Fig.5 (b). From Fig.5 (c), the error of the controlled speed is around 1 rpm.

[1]J. F. Pan, Yu Zou, and Norbert C. Cheung, "Performance Analysis and Decoupling Control of an Integrated Rotary–Linear Machine With Coupled Magnetic Paths", IEEE Transactions on Magnetics, Vol. 50, No. 2, Feb. 2014. [2]Lei Xu, Mingyao Lin, Xinghe Fu, Xiaoyong Zhu, Chao Zhang, and Wenye Wu, "Orthogonal Magnetic Field Analysis of a Double-Stator Linear-Rotary Permanent Magnet Motor With Orthogonally Arrayed Permanent Magnets ", IEEE Transactions on Magnetics, Vol. 53, No. 11, Nov. 2017. [3]Jikai Si, Haichao Feng, Liwang Ai, Yihua Hu, and Wenping Cao, "Design and Analysis of a 2-DOF Split-Stator Induction Motor ", IEEE Transactions on Energy Conversion, Vol. 30, No. 3, pp.1200-1208, Sep. 2015. [4]Zijiao Zhang, Haibo Zhou, and Ji-an Duan, "Design and Analysis of a High Acceleration Rotary-Linear Voice Coil Motor ", IEEE Transactions on Magnetics, Vol. 53, No. 7, Jul. 2017. [5]Lei Xu, Mingyao Lin, Xinghe Fu, and Nian Li, "Design and Analysis of a Double-Stator Linear–Rotary Permanent-Magnet Motor ", IEEE Transactions on Applied Superconductivity, Vol. 26, No. 4, Jun.2016.

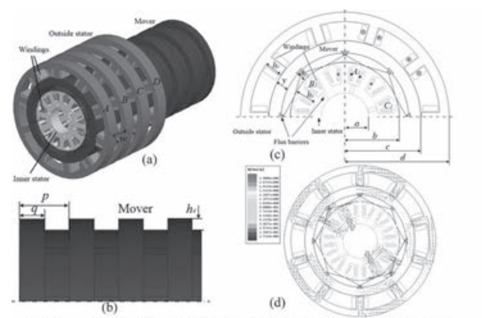

Fig.1 The structure of the proposed motor (a) and section views the mover (b) as well as the motor (c), and flux lines distribution of the motor (d).

TABLE I THE MAIN SPECIFICATIONS OF THE MOTOR

Symbol	Value (unit)	Symbol	Value (unit)
P	500 W	*h1*	19.2 mm
U	80 V	*h2*	9.5 mm
I	6 A	*h3*	22.4 mm
y	10 mm	*h4*	10 mm
a	25 mm	*g1*	0.8 mm
b	60 mm	*g2*	0.3 mm
c	80 mm	Length of outside stator	92 mm
d	110 mm	Length of inner stator	200 mm
p	46 mm	Length of the mover	400 mm
q	24 mm	Encoder accuracy	1μm

Fig. 1. The structure of the motor

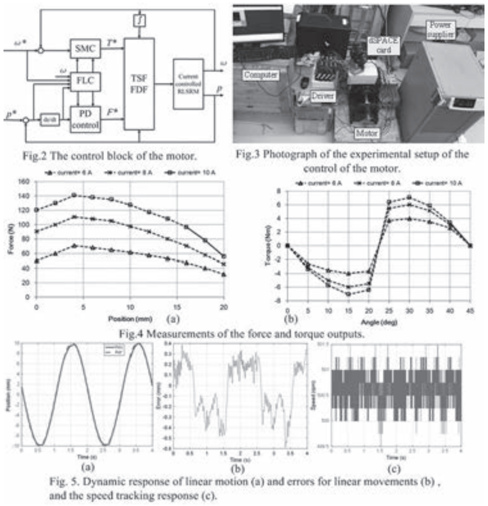

Fig. 2. Experiments of the motor

CT-12. Design of VCM actuator with optical zoom for smartphone cameras.

Y. Chang[1], C. Hu[1], C. Hsieh[1] and *C. Liu*[1]
1. National Chung Cheng University, Chiayi County, Taiwan

In recent years, compact and multifunction smartphones have changed the way people live and replaced many electronic products because of their powerful camera features. Smartphones are pretty convenient to be brought to everywhere and smartphones could capture and upload pictures to social networking sites at any time. In addition, the performances of smartphone cameras are as good as digital cameras. Therefore, smartphone cameras have almost replaced digital cameras nowadays. Comparing to the four major functions of the digital cameras: auto-focusing (AF), optical image stabilization (OIS), digital zoom and optical zoom, smartphone cameras has been equipped maturely in terms of AF, OIS, and digital zoom functions, but in the aspect of optical zoom, the optical zoom is restricted by the appearances and dimensions of smart phones. Therefore, the function of optical zooming is really rare in smartphone cameras so far. However, the evolution of cellphones grows intensely, so the manufactures need to provide a better optical performance and make a new gimmick to attract consumers. As a result, it could be predicted that the optical zoom function will be the next focus attention on smartphone cameras. Consequently, this paper proposes a novel smartphone camera with optical zoom. Zoom is a method to get a closer view of far-away objects without moving legs when people are taking a picture. Although the optical zoom has already widely used on digital cameras, most smartphones have only digital zoom because of size limit. The digital zoom is a simple image processing to enlarge the center image, and it causes image quality decreasing [1]. By contrast, the optical zoom enlarges the image through changing the distances of lenses without image quality decreasing [2]. For the purpose of AF, OIS, and optical zoom, many kinds of actuators have been developed for smartphone cameras in the literature. These devices include piezoelectric motors [3], stepping motors [4], ionic polymer metal composites, and voice coil motors (VCMs) [5.6], etc. Because VCMs have the advantage of high-performance dynamic characteristics, simple structure, and low cost, VCMs are the most common actuators in smartphone AF and OIS cameras. However, stepping motors could provide a longer stroke for zoom with small size, so only stepping motors are applied in commercial optical zoom smartphone cameras so far. In this paper, we propose a novel VCM actuator with optical zoom for smartphone cameras. The proposed VCM actuator has a long zoom stroke through specific optical structure layout. Moreover, it has a simpler structure when compared to stepping motor smartphone cameras. Figure 1(a) and 1(b) illustrate the 3D CAD model and laboratory-built prototype of the proposed VCM actuator, respectively. As shown, there are two lens groups, two prisms and two independent VCMs. The light goes through the first lens group, is reflected by these two prisms for changing direction, and then goes through the second lens group to image plane. When two individual currents are passed through to two independent VCMs, the optical zoom actuator could change the distances of these two lens groups to achieve optical zoom function. In addition, the proposed VCM actuator has shorter length and could generate uniform Lorentz force F_{VCM} with shorter magnets. The dynamic performance of the proposed VCM actuator is then verified experimentally using a laboratory-built prototype. Figure 2(a) presents the simulation and experimental results of F_{VCM} with the displacement under the same input current of 30 mA. As shown, the curve "simulation of real module" indicates that the simulation results are obtained using an actual prototype module in which its manufacturing and assembly tolerances are considered. It can be observed that simulation and experimental results are consistent form displacement -3 mm to 3 mm (stroke of 6 mm). Figure 2(b) illustrates the performance verification of the response time with the positive stroke. The dynamic performance of the proposed VCM actuator is is then verified experimentally using a laboratory-built prototype. As shown in Fig. 2(b), the experimental results have shown that the proposed VCM actuator has a good positioning accuracy of 0.01 mm and fast response time of 40 ms with the advantage of long-stroke and simpler structure.

1. R. Lukac, K. Martin, and K.N. Platanoitis,"Digital camera zooming based on unified CFA image processing steps," IEEE Trans. Consum. Electron. vol.50, no. 1, pp 15 – 24, 2004. 2. A. Miks and J. Novak, "Analysis of two-element zoom systems based on variable power lenses," Opt. Express, vol. 18, pp. 6797-6810, 2010. 3. H. P. Ko, H. Jeong, and B. Koc, "Piezoelectric actuator for mobile auto focus camera applications," J. Electroceram., vol. 23, pp. 530-535, 2009. 4. A. Milecki and J. Ortmann, "Electrohydraulic linear actuator with two stepping motors controlled by overshoot-free algorithm," Mech. Syst. Signal Proc., vol. 96, pp.45-47, 2017. 5. C. S. Liu, Y. H. Chang, and L. H. Fei,"Design of an open-loop controlled auto- focusing VCM actuator without spring plates," Int. J. Appl. Electromagn. Mech., vol. 51, no. 1, pp. 61-70, 2016. 6. C. L. Hsieh, Y. H. Chang, Y. T. Chen, and C. S. Liu," Design of VCM actuator with L-shape coil for smartphone cameras," Microsyst. Technol., .https://doi.org/10.1007/s00542-017-3454-1, 2017.

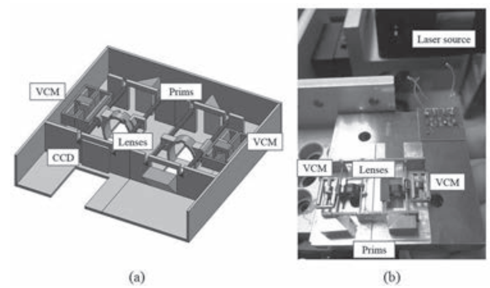

Fig. 1. (a) 3D CAD model and (b) laboratory-built prototype of proposed VCM actuator.

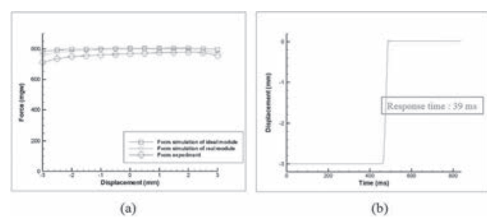

Fig. 2. (a) Comparison of simulation and experimental values of F_{VCM} with displacement; (b) experimental results for variation of response time with positive stroke.

CT-13. Design and Analysis of a Tubular Hybrid-Excited Flux-Modulated PM Motor with Improved Power Factor.

H. Zhou[1], J. Zhang[1], W. Tao[1] and G. Liu[1]
1. School of Electrical and Information Engineering, Jiangsu University, Zhenjiang, China

I. Introduction Tubular permanent magnet motors have been applied to many direct drive applications such as electromagnetic suspension due to their zero net radial force and volumetrically efficient [1]. Vernier permanent-magnet motors have attracted much more attention recently for their low speed and high thrust force features [2]. However, the power factor of vernier permanent-magnet motors is usually lower than that of conventional PM motors [3]. To solve the problem, a new tubular hybrid-excited flux-modulated PM motor with improved power factor is proposed in this paper. II. Proposed motor Fig. 1 shows the structure of the proposed motor. It consists of one stator and one mover. PM excitations are both employed on the stator and the mover. Halbach arrays are used in the stator to solve the problem of the flux leakage. A consequent pole is adopted in the mover, which can reduce the number of PMs required. The armature windings and DC field windings are housed in the stator slots and mover slots, respectively. The main air-gap fluxes are generated by the PMs. The air-gap magnetic field can be modulated by each stator split-poles and mover teeth. Therefore, the proposed motor can offer much higher force capability than the existing ones at low speed. The auxiliary DC field excitation is used to strengthen or weaken the air gap magnetic field, and then the power factor of the proposed motor is improved. Therefore, with incorporation the merits of the flux-modulated structure and the auxiliary DC field excitation, the performances of the proposed motor are flexible and controllable. III. Results The electromagnetic performances of the proposed motor are analyzed by using the finite-element method. Fig. 2 shows the no-load air-gap flux density under operating conditions of flux strengthening (I_{dc}=+5 A), no additional flux control (I_{dc}=0), and flux weakening (I_{dc}=-5 A), respectively. The magnetic field can be regulated from 1.02 T to 1.75 T. Fig. 3 shows the back-EMF waveforms under different states mentioned above. It can be seen that the back-EMF reaches 69 V at I_{dc}=+5 A, which increases by 21.1% compared without DC field excitation (only PM excitations). Fig. 4 shows the steady thrust force when the phase current is 5 A. It can be noted that the average thrust force increases from 701 N to 794 N while I_{dc} increases from 0 to 5 A. Moreover, the power factor increases by 29.5% from 0.454 to 0.588 in the same circumstances. Therefore, the proposed motor can achieve high thrust force and also improve power factor. More detailed content will be discussed in the full paper.

[1] J. Wang and D. Howe, "Design optimization of radially magnetized, iron-cored, tubular permanent magnet machines and drive systems," *IEEE Trans. Magn.*, vol. 40, no. 5, pp. 3262-3277, Sep. 2004. [2] W. Zhao, X. Sun, J. Ji, and G. Liu, "Design and analysis of new vernier permanent-magnet machine with improved torque capability," *IEEE Trans. Magn.*,vol. 26, no. 4, Jun. 2016, Art. ID 5201505. [3] T. W. Ching, K. T. Chau, and W, Li, "Power factor improvement of a linear vernier permanent-magnet machine using auxiliary dc field excitation," *IEEE Trans. Magn.*,vol. 52, no. 7, Jul. 2016, Art. ID 8204804.

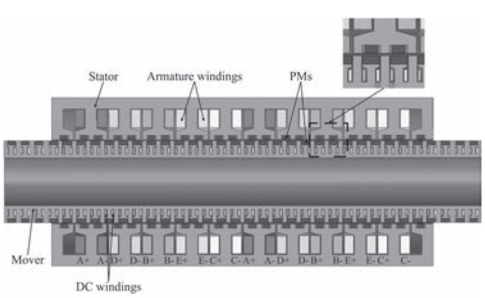

Fig. Proposed motor

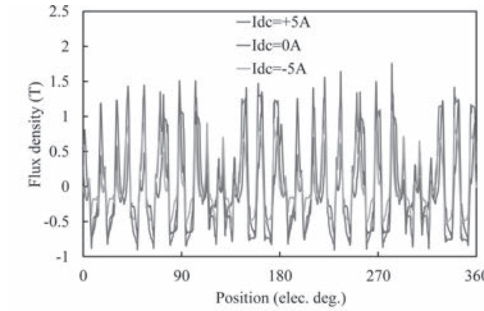

Fig. 2 Air-gap flux density.

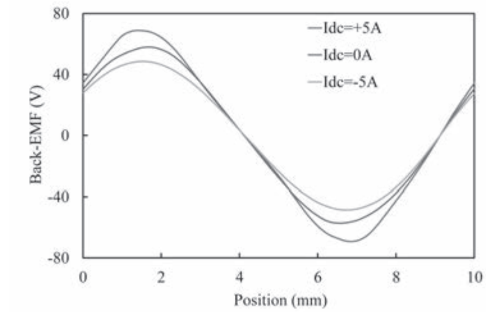

Fig. 3 Back-EMFs at mover speed of 1 m/s.

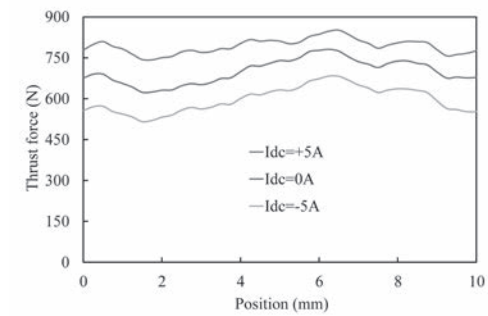

Fig. 4 Thrust force.

CT-14. Design a Spherical Motor and Its Drive.

Y. Zou[1] and N. Cheung[1]
1. Electrical Engineering, The Hong Kong Polytechnic University, Hong Kong, China

I. Introduction Compared with traditional machines that realize two-dimensional motion usually by using several motors and mechanical devices, two-degree of freedom motors performance outweigh these traditional ones in speed control or positioning tracking. For example, in the paper [1], linear-rotary motors have been investigated to realize linear and rotating motion. It is convenient for automatic machines such as curving machines, print circuit board machines and laser welding machines to get high position responses. Spherical motors are also investigated for two-degree of freedom movement [2,3]. Therefore, direct drive two degrees of freedom motors are helpful both in developing compact structure and outstanding performance in industrial applications. In this study, a direct drive two-freedom of degree spherical motor is proposed. This motor inherits the advantages of DC motors and variable reluctance motors. An elaborated design method for this motor is given and discussed and FEA is used to accurately calculate main parameters for the motor. II. Structure and principles of the motor This motor mainly consists of three parts as shown in Fig.1 (a). The first part is a silicon steel sheets stacked rotor fixed on a shaft supported by two bearings. The two bearings fixed on a crust embrace four moving units, constructing the mover as the second part. The third part is the stator comprised of two circles that sandwich the mover in the direction perpendicular to the shaft. The mover and the stator can be considered as a stepping motor. Interestingly, the mover and the stator can be also treated as an entire part which provides a constant magnetic field consisting two pairs of magnetic poles for the rotor. The rotor rotates along the direction shown in Fig.1(a). The rotor is operated as a DC motor. In the vertical direction, the mover can move along the stator possessing curved teeth, as shown in Fig.1(b). The mover and the stator are curbed and guided by two cone bearings. This motor combines a variable reluctance moving units to adjust the direction of the shaft and a DC motor based rotor rotating at a high speed along the shaft. The motor can be controlled in two modes that are variable reluctance mode and DC mode. Based on the principles, the stator, the movers and the rotor can be simplified as Fig.1 (c). For the variable reluctance mode, the flux lines are closed in a short path shown in phase B of Fig.1 (c). For DC mode, flux lines are shown in lower part of Fig.1 (c). The prototype of the motor is shown in Fig.1 (d). This prototype mainly consists of two stators, four movers and a rotor. The mutual influence between the coils from the mover and the rotor under the two modes can be analyzed by Fig.1 (e) and (f). The premise is that the air gaps in short flux path are identical and there is no saturation in the path. According to the simplified mode Fig.1 (e), it can be seen that source of the flux lines are identical and connected in parallel. Therefore, all flux lines will pass through the long magnetic paths. Assuming that the whole magnetic circuit has no saturation part, when the motor works in short flux path and simplified magnetic circuit is given in Fig.1 (f), the fluxes can be calculated as: $\Phi 1+\Phi 2+\Phi 3=0$,(1) $2Fm+\Phi 2*Rmg-\Phi 1*Rmg=0$,(2) $Fm+\Phi 3*Rrg-Fr-\Phi 1*Rmg=0$,(3) $Fr-\Phi 3*Rrg+Fm+\Phi 2*Rmg=0$.(4) Here, $\Phi 1$,$\Phi 2$ and $\Phi 3$ are flux linkages of the three paths. *Fm* is the magnetic potential force from coils of the stator. *Fr* is the magnetic potential force from the coil of the rotor. *Rmg* and Rrg are magnetic reluctances of the stator and the rotor, respectively. III. Drive topology The magnetic flux distribution of the motor is partly shown in Fig.2 (a). The two modes mentioned can be realized by a parallel-series topology. A simple topology of the electric driver, taking one mover (coil 1 and coil 2) as an example, can realize the connection by using the switch 3 shown in Fig.2 (b). A half bridge topology is mainly controlled by two switches (S1 and S2) that are usually high frequent MOSFETs and two diodes (D1 and D2). S1 and S2 are used to conduct the coils to the power supply of the motor and D1and D2 are freewheeling diodes when S1 and S2 turn off. As shown in Fig.2 (c), when S1 and S2 turn on, if S3 turns to the upper points, the two coils will be connected in series, and the current passing through the two coils will be in series. Flux lines will pass through the mover and the stator along the short path. If S3 turns to the low points, the two coils will be connected in parallel and the current will pass through the two coils parallelly. Flux lines will pass through the rotor, the mover and the stator along the long path as shown in Fig.2 (d). IV. Torque output The inductance profiles of the coils are shown in Fig.2 (e). And torque outputs with the variety of current excitation levels in coils on the movers and the rotor are given in Fig2 (f). Current1 and current2 are current values of the coils on the mover and the rotor, respectively. When the current1 is at 1000 ampere-turns, the torque output from the rotor will be on the rise with the increase of the current of the coils on the rotor. The torque outputs from the rotor with the excitations (current1=current2=1000ampere turns) are larger than the condition (current1=2000, current2 =500), which suggests that the current in the coils of the rotor makes more contributions to the rotating torque and this torque can exceed 6 Nm.

[1]J. F. Pan, Yu Zou and Norbert C. Cheung, "Performance analysis and decoupling control of an integrated rotary–linear machine with coupled magnetic paths", IEEE Transactions on Magnetics, Vol.50, no.2, 2014, pp.7018804. [2]Masahito Tsukano, Yo Sakaidani, Katsuhiro Hirata, Noboru Niguchi, Shuhei Maeda and Ariff Zaini, "Analysis of 2-degree of freedom outer rotor spherical actuator employing 3-D finite element method", IEEE Transactions on Magnetics, Vol.49, no.5, 2013, pp.2233-2236. [3] Shuhei Maeda, Katsuhiro Hirata and Noboru Niguchi, "Dynamic analysis of an independently controllable electromagnetic spherical actuator", IEEE Transactions on Magnetics, Vol.49. no.5, 2013, pp.2263-2266.

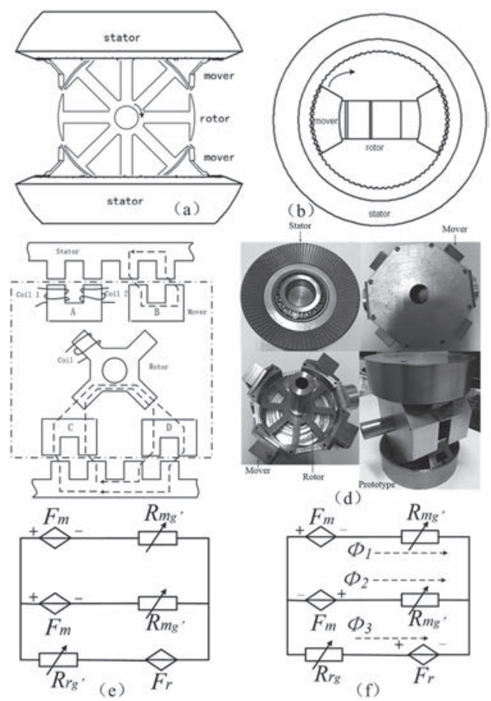

Fig. 1. Principles of the motor

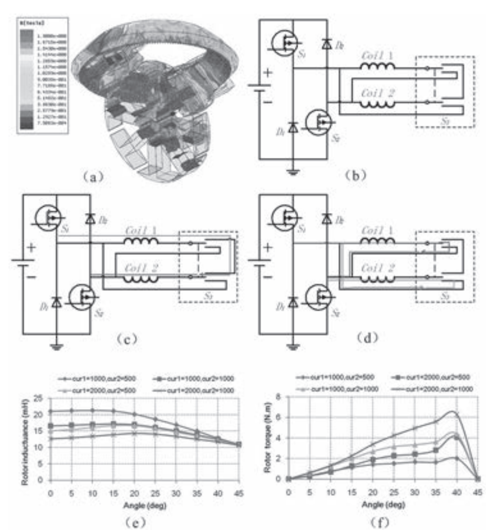

Fig. 2. Drive topology for the motor

CT-15. Proposal and Design of Primary-PM Transverse-Flux Linear Motor with Enhanced Secondary-PM Structure for High Power Density.

J. Luo[1], B. Kou[1], X. Yang[1], L. Zhang[1] and H. Zhang[1]
1. Electrical Engineering, Harbin Institute of Technology, Harbin, China

I. INTRODUCTION Linear motor has shown its essentiality in industrial applications such as semiconductor manufacturing, high-grade CNC machine tools, rail transportation systems. Nowadays, the urgent demands for high power density linear direct drive system has been proposed. The traditional linear motors are subjected to serious competition between electric loading and magnetic loading. Further improvement of its power density seems uneasy to realize. The transverse-flux motors (TFM) have the peculiarity of decouple of electromagnetic loadings[1]-[3]. The TFMs are considered to be potential candidate for high power density systems. However, there are several common drawbacks need to be addressed before its practical applications. Leakage flux has led to poor utilization of permanent magnets. Owing to the structure peculiarity, TFMs experience more disadvantages from leakage flux. It was reported that the leakage flux would produce negative force in the operating process, led to poor power factor[4]. Up to now, several approaches have been brought forward to inhibit the leakage flux. One possible way is to use high permeability material to enclose the leakage flux, preventing it from interlinking the armature[5]. Another way is to use magnet shield technology. The magnets are placed in the leakage flux path in a direction against the leakage flux[6]. But they all increase the complexity of the motors, making it hard to manufacture and increasing the prime cost. II. BASIC STRUCTURE AND OPERATING PRINCIPLE The proposed primary-PM transverse-flux linear motor is shown in Fig.1. The primary side is comprised of laminated primary core, armature windings intertwined on each primary tooth, and primary magnets. The primary teeth are notched along the direction of motion. There are two types of steel sheets used to construct the primary core as shown in the figure. The upper steel sheet has notched tooth on the second and fourth teeth while the lower steel sheet on the first and third teeth. The two kinds of steel sheets are laminated along the longitudinal direction by turns and retuse slots are formed on the primary teeth. The primary magnets are inserted into these slots with the same polarity. The secondary core is also composed of high permeability materials. And the secondary magnets are embedded into notched slots on the secondary core with the same direction of magnetization as the primary magnets. The long secondary side short primary structure is employed in this paper. Hence, the secondary side is the stator while the primary side is the mover. A minimum element model is employed to explain the operation mechanism as shown in Fig. 1. The flux paths are depicted in Fig. 2. The airgap region faced by the primary is divided into four subregions. Since all the magnets have the same magnetized direction, each magnet will complete its circuit loop by the subregion without magnets located. As the secondary magnet aligns different primary magnet, the magnetic flux will reverse its direction interlinking the coil. III. PARAMETER OPTIMIZATION AND PERFORMANCE EVALUATION In this part, the leading parameters will be analyzed by 3-D finite element method. Based on the optimized dimensions, the static and dynamic performance are investigated, including the magnetic field distribution, the back-EMF waveform, the armature reaction field distribution, thrust force and detent force. The thrust force density is addressed by comparing to the transverse-flux flux-reversal linear motor (TF-FRLM) in [7]. The results show that the proposed motor can achieve a 1.6-times force density than the TF-FRLM and also with lower detent force. IV. CONCLUSION Several conclusions will be drawn in this section. The full paper will be accomplished about 4-5 pages. A prototype motor is also under design at present. The merits of the proposed motor are list as fallows: 1)The leakage flux paths are suppressed from interlinking the armature coils, increasing the power density. 2)Both the primary and secondary cores can be made of steel sheets, which simplifies the manufacturing process and saves the prime cost. 3)The back EMF is highly sinusoidal waveform by star connection, and the proposed motor can be easily driven by conventional controllers. 4)Compared to the traditional linear motors, the proposed motor use fewer magnets to achieve the same power level.

[1]H. Weh and H. May, "Achievable force densities for permanent magnet excited machines in new configurations," *in Proc*. *Int*. *Conf*. *Electron*. Mach., Munchen, Germany, 1986, pp. 1107-1111. [2]Pan J F, Cheung N C, and Zou Y. "Design and analysis of a novel transverse-flux tubular linear machine with gear-shaped teeth structure," *IEEE Trans. Magn.*, 2012, 48(11): 3339-3343. [3]R. Watanabe, J. S. Shin, T. Koseki, et al. "Optimal design for high output power of transverse-flux-type cylindrical linear synchronous generator," *IEEE Trans. Magn.*, 2014, 50(11): 1-4. [4]Anglada J R, Sharkh S M, "An insight into torque production and power factor in transverse-flux machines," *IEEE Xxii Int. Conf. Electrical Machines*., 2016:1-1. [5] Wang Q, Xu Y, Hu J, et al, "Enhancement of a thrust force of a tubular electromagnetic launcher with transverse flux configuration by leakage flux suppression," *IEEE Trans. Plasma Sci.*, 2013, 41(5):1150-1155. [6] Qu S C, Li H B, Ma X G, "A design of transverse flux switched reluctance motors with permanent magnet shield," *IEEE Int. Conf. Electrical Machines and Systems*., 2008:3367-3369. [7]B. Kou, J. Luo, X. Yang and L. Zhang, "Modeling and analysis of a novel transverse-flux flux-reversal linear motor for long-stroke application," *IEEE Trans*. *Ind*. *Electron*. vol. 63, no. 10, pp. 6238-6248 2016.

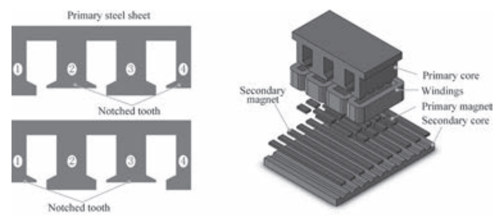

Basic structure of proposed motor

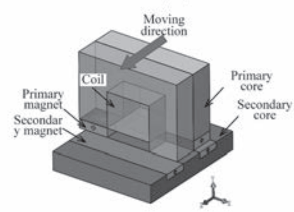

Minimum element model of proposed motor

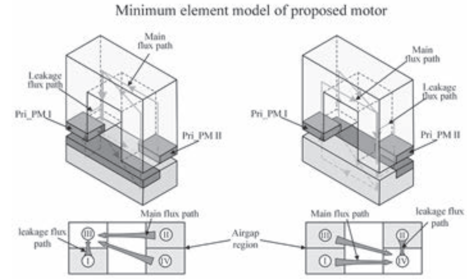

Operation principle of proposed motor

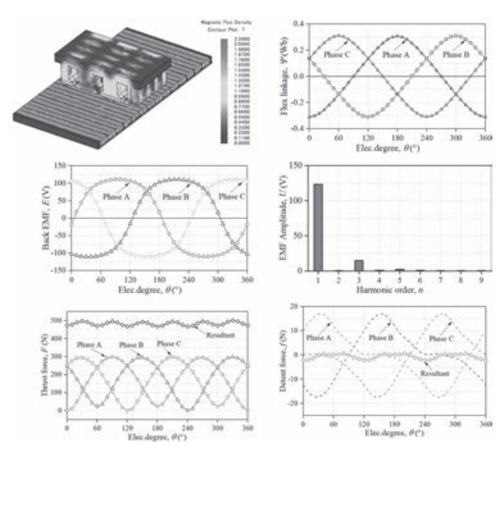

CT-16. Improvement of the self-propelled rotary actuator in consideration of shape and rolling direction of steel sheets.

N. Soda[1], T. Kawano[1] and M. Enokizono[2]
1. College of Engineering, Ibaraki University, Hitachi, Japan; 2. Vector Magnetic Characteristic Technical Laboratory, Usa, Japan

It is very important for prevention of accidents to detect cracks and defects inside of steam generator tubes in the industrial plants as typified by nuclear power plants. In order to detect the defects inside of tube with complicated structure, it is necessary to develop an electromagnetic actuator self-propelled inside of tube [1-5]. The easiest method of applying an exciting magnetic field to the electromagnetic actuator from the outside of tube is how to wind copper wire around tube and form a solenoid coil on the surface of tube. However, in this case, an exciting magnetic field is induced in parallel to the axis direction of tube by the coil. Therefore, as shown in Fig. 1(a), we had fabricated the self-propelled rotary actuator whose rotational axis is parallel to the exciting magnetic field [6-8]. In this actuator, the stator has pole pieces which are made of grain-oriented electrical steel sheet (35G155), and the rotor has permanent magnets (Ne-Fe-B) which are fixed on cylinder made from acrylic. Moreover, as a feature of this actuator, the shape of steel sheet of this stator was not a rectangle but a triangle, as shown in Fig. 1(a). It was thought that a triangle steel sheet generates larger starting torque than a rectangle steel sheet, because magnetic flux distribution at the base of triangle steel sheet under an exciting magnetic field is asymmetrical to the rotational direction of the rotor [7-8]. However, by setting the rolling direction of a grain-oriented electrical steel sheet in the different direction from the exciting magnetic field direction, magnetic flux distribution at the end of the steel sheet becomes asymmetric even if the shape of stator is a rectangle. Accordingly, we clarified that the starting torque of the actuator is improved by setting the rolling direction of rectangle steel sheet appropriately [9]. In this paper, we attempt to improve the starting torque of the actuator by setting the rolling direction of triangle steel sheet. In order to calculate the actuator in consideration of the rolling direction of the steel sheet, we carry out finite element analysis which introduced the complex E&S model [9]. Fig. 1(b) shows the analysis model of actuator's stator with triangle steel sheet and the definition of inclination angle ϕ of rolling direction in the steel sheet. Inclination angle ϕ = 90 deg. means the rolling direction of steel sheet is parallel to the direction of exciting magnetic field H_o. In addition, we analyze the rectangle steel sheet model shown with the dashed line in Fig. 1(b), for comparison. As a result of experiment, when the exciting magnetic field H_o is not applied, the permanent magnet is stationary at the right angle corner of the triangle steel sheet, and is stationary in the middle of the rectangle steel sheet [8]. The magnitude of starting torque of the actuator is dependent on the magnitude of x-component (i.e., the rotational direction of the rotor) of magnetic flux density within the stationary position when the exciting magnetic field H_o is applied. Therefore, we calculate the average of B_x (i.e., x-component of magnetic flux density) within the region of stationary position. The exciting magnetic field H_o is a sign waveform of the peak amplitude 500 Oe, and the frequency is 50 Hz. Fig. 2(a) shows the relationship between the average of B_x within the region of stationary position and the inclination angle ϕ of the rolling direction in the triangle and rectangle steel sheet. In every inclination angle ϕ, the average of B_x of the triangle steel sheet is large than that of the rectangular steel sheet. In both the triangle and the rectangle steel sheet, the average of B_x becomes the maximum when ϕ = 60 deg. At the inclination angle ϕ = 60 deg., the average of B_x of the triangle steel sheet is more than 1.5 times that of the rectangle steel sheet. Therefore, we consider the starting torque of the actuator which used the triangle steel sheet of ϕ = 60 deg. is about 1.5 times as large as that which used the rectangle steel sheet. Next, we evaluate the total iron loss of the steel sheet in actuator's stators. We can calculate directly the iron loss from results obtained by finite element analysis which introduced the complex E&S model. Fig. 2(b) shows the relationship between the total iron loss of the stator core and the inclination angle ϕ. The total iron loss in the rectangle steel sheet becomes large with decrease in the inclination angle ϕ, and takes the minimum value in ϕ = 90 deg. The total iron loss in the triangle steel sheet changes little in inclination angle ϕ from 60 deg. to 90 deg., it increases in inclination angle ϕ less than 60 deg. The difference in the total iron loss between the triangle and the rectangle steel sheet occurs because both shape and rolling direction of steel sheet affect iron loss distribution. As a result, in order to improve the starting torque of the actuator and decrease the total iron loss of that, we consider that the shape of steel sheet in the stator core is a triangle and the optimum inclination angle ϕ of the rolling direction of steel sheet from the rotational axis is 60 deg.

[1] T. Honda, N. Miyazaki, and J. Yamasaki, "Development of a Magnetic Linear Motor Based on a Friction Drive," *IEEE Trans. on Magnetics*, Vol. 35, No. 5, pp. 4004-4006, Sept. 1999. [2] Se-gon Roh and Hyouk Ryeol Choi, "Differential-Drive In-Pipe Robot for Moving Inside Urban Gas Pipelines," *IEEE Trans. on Robotics*, Vol. 21, No. 1, pp. 1-17, Feb. 2005. [3] Jungwan Park, Dongjun Hyun, Woong-Hee Cho, Tae-Hyun Kim, and Hyun-Seok Yang, "Normal-Force Control for an In-Pipe Robot According to the Inclination of Pipelines," *IEEE Trans. on Industrial Electronics*, Vol. 58, No. 12, pp. 5304-5310, Dec. 2011. [4] Jinwei Qiao, Jianzhong Shang, and Andrew Goldenberg, "Development of Inchworm In-Pipe Robot Based on Self-Locking Mechanism," *IEEE/ASME Trans. on Mechatronics*, Vol. 18, No. 2, pp. 799-806, April 2013. [5] Hiroyuki Yaguchi, "Magnetic Actuator Capable of Inspection in a Complex Pipe by Phase Control of Multiple Electromagnetic Vibration Components," *IEEE Trans. on Magnetics*, Vol. 51, No. 11, Nov. 2015, Art. ID 8205704. [6] M. Enokizono, T. Todaka, and K. Goto, "Fabrication of a Magnetic Drive Unit for that Moves in the Same Direction of the Exciting Magnetic Field," *IEEE Trans. on Magnetics*, Vol. 34, No. 4, pp. 2087-2089, July 1998. [7] M. Enokizono, T. Todaka, K. Goto, and Y. S. Chew, "Improvement of a Magnetic Rotary Element for Propulsion of a Self-Running Actuator," *IEEE Trans. on Magnetics*, Vol. 35, No. 5, pp. 4016-4018, Sept. 1999. [8] M. Enokizono, T. Todaka, and K. Goto, "Fabrication of A Rotary device for Self-Running Magnetic Actuator," *Trans. IEE Japan*, Vol. 120-E, No. 2, pp. 45-51, Feb. 2000. [9] N. Soda and M. Enokizono, "Magnetic Field Analysis of Self-Propelled Rotary Actuator's Stator in Considering of the Rolling Direction of the Steel Sheet," *IEEE Trans.* on *Magnetics*, Vol. 52, No. 3, Article #:7000404, March 2016.

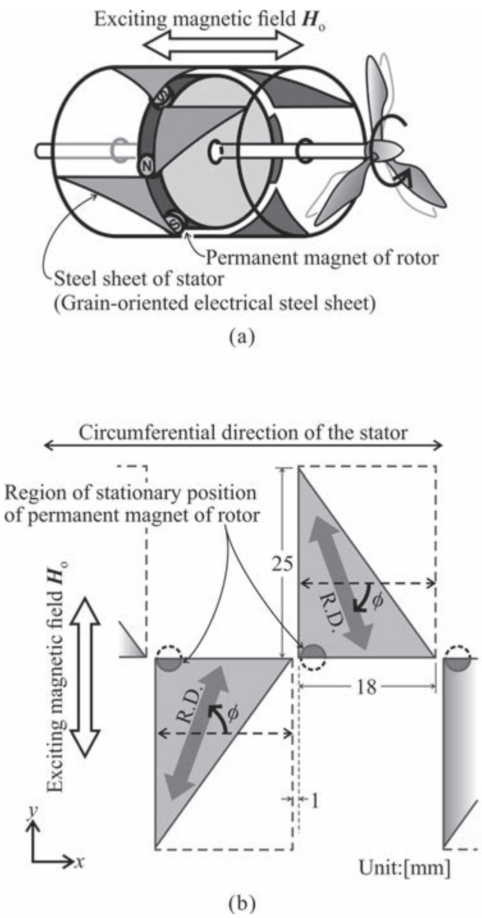

Fig. 1. (a)The model of self-propelled rotary actuator. (b)The analysis model and the definition of the inclination angle ϕ of rolling direction.

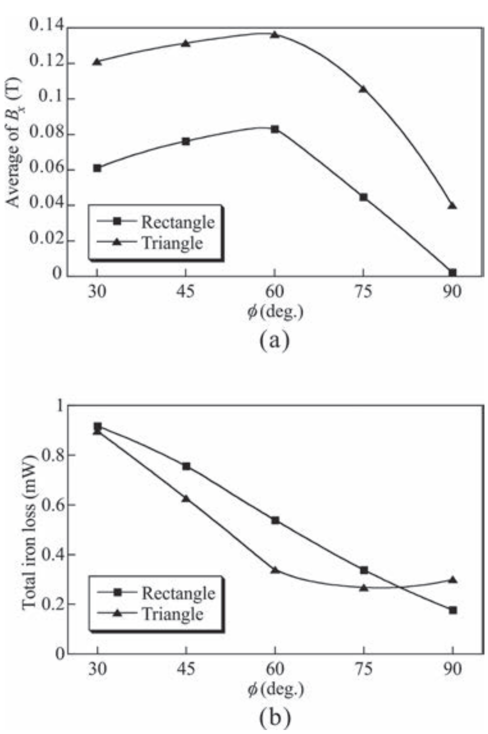

Fig. 2. (a)The relationship between the average of B_x within the region of stationary position and the inclination angle ϕ. (b)The relationship between the total iron loss of the stator core and the inclination angle ϕ.

WEDNESDAY MORNING, 25 APRIL 2018 SIMPOR/ROSELLE BALLROOM, 8:30 TO 11:30

Session CU
LINEAR MOTORS III
(Poster Session)

Wei Xu, Co-Chair
Huazhong University of Science and Technology, Wuhan, China
Feng Chai, Co-Chair
Harbin Institute of Technology, Harbin, China

CU-01. Design and Analysis of a Novel Modular Linear Double Stator Biased Flux Machine.

Y. Mao[1] and *S. Niu*[1]
1. Electrical Engineering, The Hong Kong Polytechnic University, Hong Kong, Hong Kong

I. Introduction Wave energy is a kind of renewable energy. It has advantages like other renewable energy such as clean, inexhaustible and widespread. In addition, it exhibits higher power density than other renewable resources [1]. Linear motors have good adaptability to wave motion, because they can produce a direct thrust force without the need of a gearbox that converts the oscillation into rotation which can reduce system cost and complexity [2]. The modular linear double stator biased flux (LDSBF) machine is a novel linear machine which exhibits high torque density in low speed applications. It is promising to generalize the use of LDSBF machine in wave power generation for it can effectively capture the low frequency and high force wave energy. To further improve the power density of linear PM machine, the modular linear double stator biased flux (LDSBF) machine is proposed in this paper. The double stator biased flux machine is researched and developed on the basis of conventional linear biased flux PM (LBFPM) machine [3]. In general, they are both stator PM machines that employ concentrated windings. The flux polarity in an independent coil is whether bipolar or unipolar. II. Configuration and Operating Principle of the Modular LDSBF Machine Fig. 1 shows the configuration of the proposed modular linear double stator biased flux machine. It mainly consists of an inner stator, an outer stator and a rotor sandwiched between the stators. The outer stator has salient structure and coils are wound on the teeth. PMs are set in the inner stator. This linear machine is constituted of several modular units. Each modular consists a π-shaped lamination core, a magnet and two sets of concentrated coil. Adjacent modular are separated by flux-barrier made of nonmagnetic material. The working principle of this machine is due to the flux bias effect. When the mover's position changed, the flux path in each slot also changed. These procedures will keep going and repeating. Motivation of the mover will lead to variation of direction and intensity of flux-linkage in the winding, thus inducing the back electromotive force. Theoretically, the mutual inductance between coils in the outer stator is zero. Since the mutual inductance is insignificant, the proposed linear machine can be regarded as set of several independent single phase machines. Each unit of single phase machine consists one PM piece and two stator teeth with coils wound on it. So it is reasonably to make modular design of the linear double stator bias flux machine. To build a modular LDSBF machine, flux barriers are introduced in the yoke. Modular design can further cut down flux leakage and improve efficiency in usage of magnets. In addition, manufacture cost can be reduced because each unit is easily assembled by a π-shaped lamination core, a magnet and two sets of concentrated coils. III. Slot/Rotor Combination Analysis The stator/ rotor pole combinations 24/20, 24/22, 24/26 and 24/28 are analyzed and compared by finite element method (FEM) in this study. To analyze electromagnetic performance open circuit flux of each coil is measured which is shown in Fig. 2. Partition the coils that have similar flux distribution into one group, it can be seen from Fig. 2 (a), (c), (d) that each group have 4 coils and the phase difference between each group is 120 degree. While in Fig. 2 (b), each group have 2 coils and the phase difference is 60 degree. The coil arrangement method should follow the principle of evenly maximizing the fluxes per phase winding. So for the former type, each group of coils belongs to different phase. And the group of coils that have opposite value (symmetrical parts along the y=0 in the figure) will be connected in reverse series. After arrange the coils according to this approach, waveform of the total flux linkage of three phase is shown in Fig.3 It can be seen from Fig. 3 that coil flux distribution of 24/22 is bipolar while it is unipolar for 24/20, 24/26 and 24/28 combinations. In addition, the three phase flux linkage of 24/22 combinations is more sinusoidal. The reason is mainly caused by the individual coil flux and the connection pattern. For the former type of linear machines, phase fluxes are unipolar with DC component, and all of the harmonics are kept. While in 24/22 combination, the DC component and the even older harmonics of fluxes are eliminated, so the phase flux waveform is more symmetrical. So the 24/22 combination is the best choice. The LDSBF machine is also optimized and compared with its counterpart LBFPM machine. The FEM result presented in Fig. 4 shows that LDSBF machine has better performance than LBFPM machine.

[1] M. Lejion. R. Waters. M. Rahm, O. Svennson, C. Bostrom. E. Stromstedt, J. Engstrom, S. Tyberg, A. Savin, H. Gravrakmo, H. Bernhoff, l. Sundberg, l. Isberg, O. Danielsson, M. Eriksson, E. Legerskog, B. Bolund, and K. Thorbun, "Catch the wave to electricity", IEEE Power Energy Magazine, vol. 7, no. 1, pp. 50-54, 2009. [2] Amal Souissi, Imen Abdennadher, Ahmed Masmoudi, "On the stator magnetic circuit design of tubular-linear PM synchronous machines: A comparison between three topologies", *Sustainable Mobility Applications, Renewables and Technology (SMART), 2015 International Conference on*, February 2016. [3] D. Wu, J. T. Shi, Z. Q. Zhu and X. Liu, "Electromagnetic performance of novel synchronous machines with permanent magnets in stator yoke,"*IEEE Trans. Magn.,* vol. 50, no. 9, September 2014.

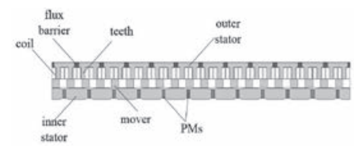

Fig. 1

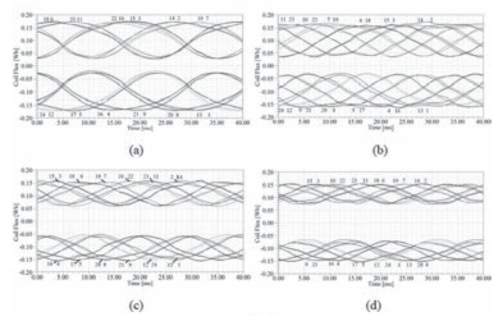

Fig. 2

Fig. 1. Configuration of proposed modular LDSBF machine

Fig. 2. Open circuit flux waveform of each coil for modular LDSBF machines with (a) 24/20 (b) 24/22 (c) 24/26 (d) 24/28 stator/slots combinations.

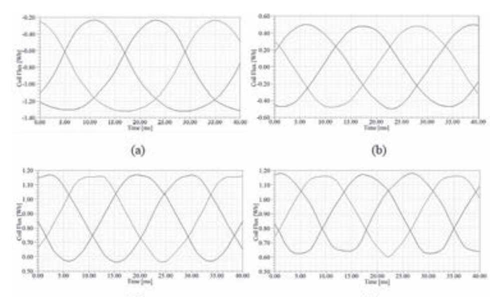

Fig. 3

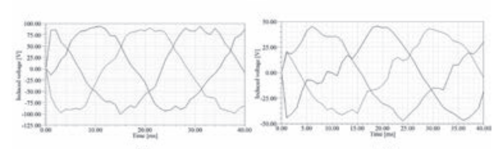

Fig. 4

Fig. 3. Three phase flux linkage waveform of modular LDSBF machines with (a) 24/20 (b) 24/22 (c) 24/26 (d) 24/28 stator/slots combinations.

Fig. 4. Induced voltage waveform of (a) modular LDSBF machine (b) LBFPM machine

CU-02. Experimental investigation of a new type of oscillation based linear capsule actuator.

L. Wu[1], K. Lu[1] and Y. Xia[1]
1. Department of Energy Technology, Aalborg University, Aalborg, Denmark

Abstract This paper studies new vibration-based linear actuation mechanism for potential active in-vivo capsule applications. The new actuator is very simple in structure, consisting of coil and magnets only. This simple structure contributes to the design of a sealed linear locomotion system, avoiding to damage the intestinal tissue caused by the paddle or leg sticking outside the capsule. In addition, the new capsule actuator utilizes pulsed force source to create controllable oscillation for realizing linear movement. The feasibility of the new actuator structure and driving confirmed experimentally in the laboratory on a prototype and analysis results by using 3D Finite Element Model are provided. 1. Introduction The current capsule endoscopy can only passively travel inside the GI tract, which is propelled by natural peristalsis to travel through the entire GI tract, and it cannot be controlled and stopped at a precise position for diagnosis due to the peristalsis frequency is not controllable. Therefore, a locomotion system needs to be added to improve the current capsule endoscopy, namely, an active capsule endoscopy. The actuator is the key component to achieve an active capsule endoscopy. The main disadvantage of the current capsule is its poor manipulation ability, which can be demonstrated by some peculiarities, such as the movement speed, position as well as orientation of the capsule are out of control. The present capsule, in the existing literature, can achieve an active movement inside the human body by means of a micro DC motor or shape memory alloy (SMA) wire. For example, in [1], SMA can realize inchworm-like actuation achieving forth and backwards movements. But it needs to consume high power in the range of 450-1700wM and increase consequently the temperature by 12°C in 3 minutes, which may damage the intestinal tissue. In [2], a micro-DC motor is employed to drive paddled/legged-type capsule; but this mechanism generates large velocity in a range of several times the desired velocity of 15 cm/min, which may not allow enough time for picturing folds inside the GI tract. The sharp paddles or legs of the paddled/legged-based capsule may also damage the body tissue. Compared with the conventional capsule actuators, the main advantage of a moving coil-magnetic type linear actuator is its simplicity in structure [3]. The other advantages are recognized to be consisting of relatively few components, quick response time, and a long lifetime [4]. Furthermore, this linear actuator can be design as a sealed locomotion system. Therefore, there will be no paddle or leg sticking outside the capsule that may damage the intestinal. 2. The Proposed New Structure The new actuator proposed in this paper consists of three PMs and one small solenoidal coil. Two of the PMs are attached to the two ends of the capsule while the third PM is attached to the small coil in the middle as shown in Fig. 1. When a pulsed current shown as e.g. in Fig. 2(b), is supplied to the small coil, it will produce an electromagnetic force between the small coil and the magnets. The small coil and PM3 will then move towards PM1 due to the attractive (/repelling) force between PM1 (/PM2) and the small coil. Upon suddenly stopping the current supplied to the small coil, the repelling (/attracting) force between PM1 (/PM2) and PM3 will then push the small coil and PM3 to its original position as indicated in Fig. 2(a). This will cause the entire capsule to move forward according to the Momentum Conservation Law. Repeating the pulsed current supply will force the actuator run into a stable vibration state. The vibration frequency and amplitude of this actuator is controllable by controlling the duty ratio and amplitude of the current supplied to the small coil. The linear vibration can be well used to generate controllable linear movement of the capsule, such phenomenon will be demonstrated further in this project. This new linear actuator has strong manipulation ability. It has also the potential to realize more therapeutic functions, such as biopsy tissues, unclogging lumen, coagulating, ablating, and apposing tissue. More details explaining this vibration based linear motion and 3D FEA results will be given in the final paper.

[1] L. Liu, S. Towfighian, A. Hila, "A review of locomotion systems for capsule endoscopy", IEEE Rev. Biomed. Eng. 8 (2015) 138–151. [2] M. Quirini and A. Menciassi, "Design and fabrication of a motor legged capsule for the active exploration of the gastrointestinal tract," IEEE/ASME Trans. Mechatron., vol. 13, no. 2, pp. 169–179, Apr. 2008. [3] R. Olaru, C. Astratini-Enache and C. Petrescu, Analysis and design of a moving-magnet type linear actuator with repulsive magnetic forces, International Journal of Applied Electromagnetics and Mechanics 38(2–3) (2012), 127–137. [4] Szczesny S, Jetzki S, Leonhardt S. Review of Current Actuator Suitability for Use in Medical Implants. Conf Proc IEEE Eng Med Biol Soc. 2006;1:5956–9.

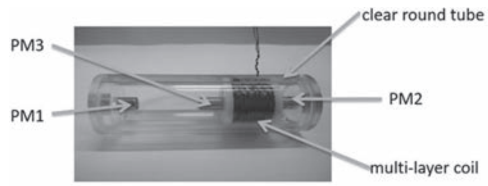

Fig. 1 Diagram of the capsule prototype

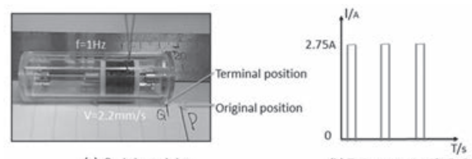

(a) Prototype status (b) T=1s, current ratio D=0.3

Fig. 2 The prototype moves periodicity when the multi-coil input pulse current

CU-03. Dry Run Test of the In-vessel CEDM.

J. Park[1], M. Baek[2], W. Lee[1], M. Lee[1], Y. Cho[1], H. Kim[1], C. Maeng[1] and C. Chung[1]
1. KEPCO E&C, Daejeon, The Republic of Korea; 2. Woojin Inc., Hwaseong, The Republic of Korea

1. Introduction The control element drive mechanism (CEDM) is an electromechanical device to control the reactivity of the nuclear reactor by withdrawing, inserting or holding the control rods. The conventional CEDMs have been installed outside the reactor vessel. However, there have been demands for locating the CEDM inside reactor vessels because it provides significant benefits in respect of safety of the nuclear reactor. Accordingly, an in-vessel CEDM has been developed to meet the harsh environmental condition inside nuclear reactor. The in-vessel CEDM is based on the conventional magnetic jack type external CEDM for commercial reactors in order to take advantage of the proven technologies as much as possible. However, the in-vessel CEDM is differentiated from the conventional CEDM as follows: 1) Mineral-insulated cable was adopted for windings as the enamel-coated wire of the conventional CEDM is not operable in such harsh environment. 2) The in-vessel CEDM has no pressure boundary as the whole assembly is submerged. 3) The latch assembly was designed to meet the driving pitch requirement of 10 mm, which is almost double precision comparing to the conventional CEDM. The fine motion pitch was achieved by changing the double steps per-pitch concept to single step per-pitch concept [1]. 4) Martensitic stainless steel is used for the coil housing to provide magnetic flux path in submerged condition. 5) Diameter of the CEDM assembly was reduced to assign one control rod assembly for each and every fuel assembly. 6) A high-temperature position indicator was designed to monitor the operation inside the reactor. This paper introduces a preliminary test to check the operability of the proposed in-vessel CEDM in dry condition. 2. Prototype Test A prototype of the in-vessel CEDM was manufactured, and it was then installed in a specially designed fixture for dry run test as shown in Figure 1. A prototype of the in-vessel position indicator was also manufactured and installed on the top of the prototype CEDM to monitor the operation. A dummy weight was attached at the bottom of the drive shaft to provide the lifting load of 100kgf. The prototype was run by a control system designed to provide sequential electrical power. The prototype in-vessel CEDM withdrew and inserted the dummy weight at the required speed. Successful operation was monitored by the current traces as shown in Figure 2 together with the position indicator. 3. Concluding Remarks A magnetic jack type in-vessel CEDM was developed for a small modular reactor. A prototype was manufactured to verify its feasibility. A dry run test was performed with the prototype. The prototype in-vessel CEDM was proved to be capable of withdrawing and inserting the required weight at the required speed. The prototype will be tested in high temperature, high pressure and submerged condition in the near future. ACKNOWLEDGMENT This work was supported by the Nuclear Power Core Technology Development Program of the Korea Institute of Energy Technology Evaluation and Planning (KETEP), granted financial resource from the Ministry of Trade, Industry & Energy, Republic of Korea. (No. 20131510101680).

[1] Magnetic Jack Type Control Element Drive Mechanism for Precision Position Control of the Control Element Assembly, by Park Jinseok, Jang Yongtae, Lee Myounggoo, Chang Sanggyoon, Lee Daehee, U.S Patent 9,711,245 B2, 2017.

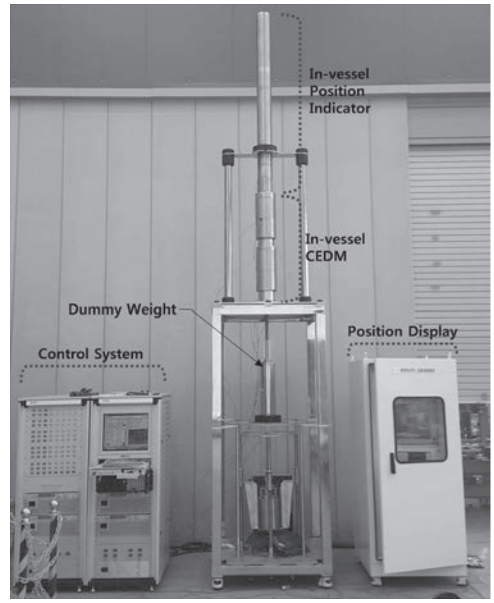

Fig. 1. Dry run test setup

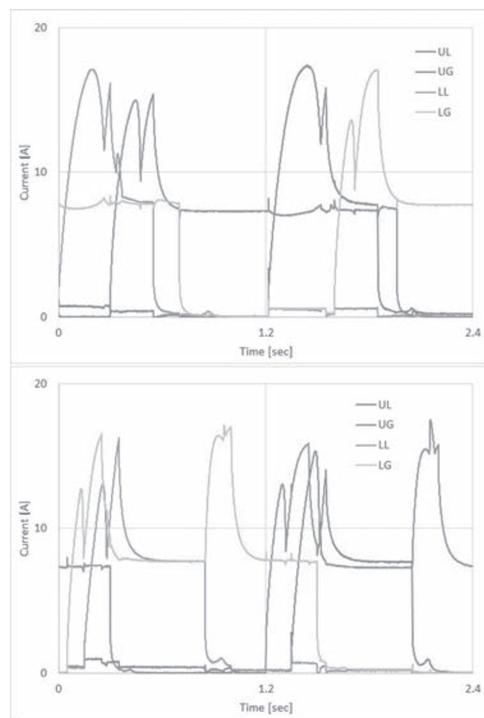

Fig. 2. Current traces (withdrawal: upper, insertion: lower)

CU-04. Design and Analysis of Linear Hybrid-Excited Slot Permanent Magnet Machines.

Y. Shen[1] and Q. Lu[1]
1. College of Electrical Engineering, Zhejiang University, Hangzhou, China

I. INTRODUCTION Linear switched reluctance machines (LSRMs) have been extensively researched and applied to long distance direct-drive applications due to their low cost and simple structures [1]-[3]. However, they still suffer from unavoidable high force ripple, acoustic noise and vibration due to the unipolar excitation, as well as relatively low force density [4]. In order to solve these problems, this paper proposes a novel linear hybrid-excited slot permanent magnet machine (LHESPMM). It is modified from a three-phase unipolar excited LSRM by adding non-overlapping DC field windings and PMs in the primary and exciting the armature windings with sinusoidal bipolar currents [5], [6]. Since the PMs are inserted in the primary slots and magnetized in parallel with the motion direction, the PM flux is only located in the primary at open circuit, which makes the cogging force negligible. It is also low PM consumption and especially beneficial to long stroke, and has good flux regulation capability and higher force density with a dual parallel excitation sources of DC current and PMs. Moreover, the excitation with sinusoidal bipolar currents makes it possible to operate in four quadrants and can be supplied with a bidirectional three-phase inverter rather than the asymmetric bridge converter. Therefore, the force ripple, vibration and acoustic noise can be reduced. II. OPTIMIZATION AND PERFORMANCE Fig. 1(a) shows the topology of the proposed 12-slots LHESPMM. Its primary accommodates PMs, DC field and armature windings, while the secondary is only made of slotted lamination. The DC field windings are identically wound on each primary tooth. Moreover, the PMs are magnetized in the opposite direction against the DC-excited flux and then inserted into the primary slots approaching the air gap. In addition, the armature windings are excited with sinusoidal bipolar currents. Fig. 1(b) shows the key geometric parameters of this machine. With the simplified models, the operating principle can be explained. At open circuit, as shown in Fig. 1(c), the PMs are short-circuited by adjacent primary teeth, so that there is very small sinusoidal bipolar variation of the flux-linkage in the coil, which changes 360 electrical degrees with a moving distance of pole pitch. If the PMs are removed and the tooth is excited by a DC coil, the flux links both the primary and secondary, as shown in Fig. 1(d). When both DC coil and PMs are present, as shown in Fig. 1(e), the fluxes from both the DC coil and PMs link both the primary and secondary because of the magnetic pull, which makes induced EMF in the armature windings. For slot/pole combinations, LHESPMM is similar to conventional PMLM, e.g., 12-slots/10-poles (12s/10p), 12s/11p, 12s/13p, 12s/14p, etc. Fig. 1(f) shows the fundamental coil back-EMF phasors of LHESPMM. It can be deduced that the coils for every phase consist of coil back-EMFs in phase or 180° phase shifted, which is indicated with the symbol “’”. The proposed 12s-10/11/13/14p LHESPMMs are globally optimized by 2D finite-element analysis (FEA), where genetic algorithm (GA) is used for maximum average force. The key geometric parameters, including split ratio, primary tooth width, PM height, back iron height, the width and height of secondary tooth, and the auxiliary tooth width have been optimized. When optimizing, the current density is fixed to 7.0 A/mm^2, the coil filling factor is fixed to 0.83, and the number of turns per DC coil is equal to that of armature coil. The other fixed parameters are as follows: slot pitch is 20mm, the machine height is 43.8mm, the active length is 50mm and the air gap length is 0.8mm. The average force and force ripple are shown in Fig. 2(a), where 12s/13p and 12s/14p exhibit higher average force than that of 12s/10p and 12s/11p. Moreover, the machine with odd number secondary poles, e.g., 12s/11p and 12s/13p, exhibit relatively lower force ripple. Therefore, 12s/13p is an optimal choice in order to obtain high force density and relatively low force ripple. The cogging force of the 12s/13p LHESPMM is negligible when DC current is small, as shown in Fig. 2(b). Fig. 2(c) and 2(d) show the phase flux-linkage and back-EMF with different DC currents. Apparently, the flux-linkage and back-EMF in three phases are bipolar and sinusoidal, which can reduce the force ripple. When DC current is 9A, the amplitudes of flux-linkage and back-EMF are smaller than those of 6A, due to the saturation of the primary. Fig. 2(e) shows the force-current characteristic of this machine. It can be deduced that a good flux regulation capability and higher force density can be achieved with DC field windings. Finally, a 12s/13p prototype machine is manufactured to validate the 2D FE predicted results, as shown in Fig. 2(f) and 2(g). III. CONCLUSION This paper proposes a novel 12s/13p LHESPMM. After global optimization with GA, the average force is improved to 88.7N and the force ripple is reduced to 3.2% with the rated phase and DC currents of 3A. This machine exhibits negligible cogging force, a good flux regulation capability and high force density. Finally, the results are validated by a prototype machine.

[1] Byeong-Seok Lee, Han-Kyung Bae, P. Vijayraghavan and R. Krishnan, “Design of a linear switched reluctance machine,” *IEEE Trans. Ind. Appl.*, vol. 36, no. 6, pp. 1571-1580, Nov./Dec. 2000. [2] N. S. Lobo, H. S. Lim and R. Krishnan, “Comparison of Linear Switched Reluctance Machines for Vertical Propulsion Application: Analysis, Design, and Experimental Correlation,” *IEEE Trans. on Ind. Appl.*, vol. 44, no. 4, pp. 1134-1142, Jul./Aug. 2008. [3] J. G. Amoros and P. Andrada, “Sensitivity Analysis of Geometrical Parameters on a Double-Sided Linear Switched Reluctance Motor,” *IEEE Trans. Ind. Electron.*, vol. 57, no. 1, pp. 311-319, Jan. 2010. [4] J. F. Pan, N. C. Cheung and Y. Zou, “An Improved Force Distribution Function for Linear Switched Reluctance Motor on Force Ripple Minimization With Nonlinear Inductance Modeling,” *IEEE Trans. on Magn.*, vol. 48, no. 11, pp. 3064-3067, Nov. 2012. [5] P. Andrada, B. Blanqué, E. Martínez, M. Torrent, J. García-Amorós and J. I. Perat, “New linear hybrid reluctance actuator,” *in Proc. ICEM*, Berlin, 2014, pp. 585-590. [6] Y. Shen, Q. Lu and X. Huang, “Analysis of a Novel Linear Doubly Salient Slot Permanent Magnet Motor,” *IEEE Trans. Magn.*, vol. 53, no. 11, pp. 1-4, Nov. 2017.

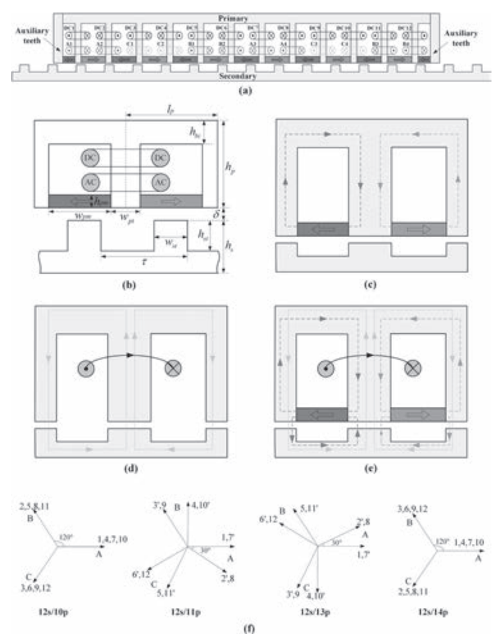

Fig. 1. The topology and slot/pole combinations of the 12-slots LHESPMMs. (a) Topology. (b) Parameters. (c), (d), (e) Operation principle. (f) Back-EMF phasors.

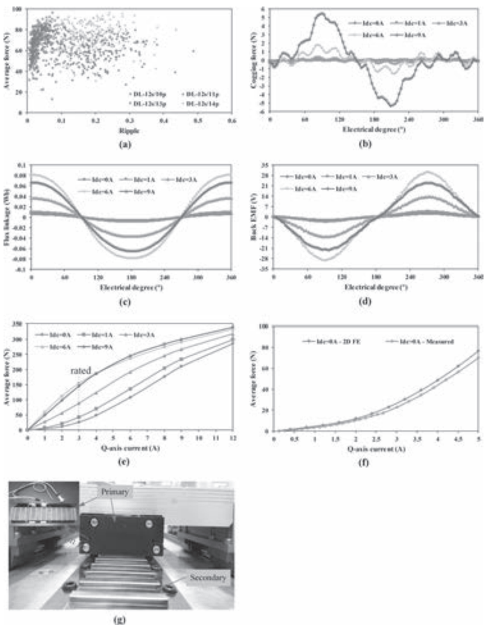

Fig. 2. The performance of the 12s/13p LHESPMM. (a) Global optimization. (b) Cogging force. (c) Flux-linkage. (d) Back-EMF. (e) Force-current characteristic. (f) Experimental validation. (g) Prototype Machine.

CU-05. Investigation of Novel Linear Multi-tooth Variable Flux Reluctance Machines.

Y. Shen[1] and Q. Lu[1]
1. College of Electrical Engineering, Zhejiang University, Hangzhou, China

I. INTRODUCTION Due to the high price of rare-earth permanent magnet (PM), non-PM linear switched reluctance machines (LSRMs) attract more and more attention and have been used in direct-drive applications with the merits of their low cost and robust structures [1], [2]. However, since the excitation is unipolar and non-sinusoidal, LSRMs still suffer from high force ripple and relatively low force density. In order to reduce the force ripple meanwhile enhancing the force density, novel linear variable flux reluctance machine (LVFRMs) are developed from LSRMs by splitting the windings into non-overlapping armature and DC field windings [3]. LVFRMs exhibits sinusoidal phase flux linkage and back-EMF, where higher force density and lower force ripple can be achieved compared to LSRMs [4], [5]. However, the force density of LVFRMs is still limited by high copper losses due to both the armature and field windings. Multi-tooth is one of the topology innovations to further improve the thrust force capability, which can also be introduced in LVFRMs [6]. This paper aims to propose a novel three phase multi-tooth LVFRM to further improve the force density. A fair comparison between multi-tooth and single-tooth LVFRMs is implemented under the same copper loss. Moreover, the electromagnetic performance of 4-tooth LVFRMs with different slot/pole combinations is compared. Finally, the merits and drawbacks of multi-tooth LVFRM are drawn. II. ANALYSIS AND COMPARISON Doubly salient structure is adopted in single-tooth LVFRM, where both DC field and armature windings are identically wound on each primary tooth while the secondary is slotted lamination [5]. When splitting each primary tooth into *n* small teeth, multi-tooth LVFRM can be obtained, as shown in Fig. 1(a). The choice of slot/pole combination in multi-tooth LVFRMs is also flexible, where odd number secondary poles also can be employed. Fig. 1(b) and 1(c) show the topologies and winding configurations of single-tooth 6-slots/7-poles (6s/7p) and 4-tooth 6s/25p LVFRMs, respectively. As it can be seen, with $Ns=nNp+1$, these two machines exhibit the same winding configuration. The coil connections of the armature winding are determined by fundamental coil back-EMF phasors, as shown in Fig. 1(d). It can be deduced that the coils for every phase consist of coil back-EMFs in phase or 180° phase shifted that indicated with the symbol "’". The outer geometric parameters of multi-tooth LVFRM are as follows: slot pitch is 20mm, the machine height is 43.8mm, the active length is 50mm and the air gap length is 0.8mm. Due to the constraints of the rated total copper loss and the slot area, the average force varies with the ratio of excitation and armature copper losses. When these two copper losses are equal, i.e., Pf=Pa, the average force will be maximum. In this paper, the total copper loss is fixed to 30W. Fig. 2(a) shows the variation of average force with the number of small teeth when slot/pole combination is determined by $Ns=nNp+1$. It can be seen that 4-tooth LVFRM exhibits the highest average force. Hence, 4-tooth LVFRM will be adopted to compare with single-tooth one. Fig. 2(b) shows the air-gap flux density of 6s/7p and 6s/25p LVFRMs at open circuit (Pf=15W). The flux modulation effect of each primary small teeth can be seen based on the peak number of flux density. Moreover, more sinusoidal back-EMF can be obtained in 6s/25p LVFRM, as shown in Fig. 2(c). Fig. 2(d) shows the cogging force of 6s/7p and 6s/25p LVFRMs. It can be seen that the cogging force will increase with the influence of end effect. Moreover, multi-tooth structure will aggravate the end-effect. At rated copper loss of 30W, the average force of 6s/25p LVFRM is 18.4N and 6s/7p is 14.2N, which increases nearly 30%. However, the force ripple in 4-tooth LVFRM also increases, as shown in Fig. 2(e). Fig. 2(f) shows the variation of average force with total copper loss (Pf=Pa). It can be seen that multi-tooth LVFRM saturates more quickly at high electric load. For 4-tooth LVFRM, the slot/pole combination can be 6s/22p, 6s/23p, 6s/25p and 6s/26p. Fig. 2(g) and 2(h) show the back-EMF at v=0.24m/s and average force at 30W, respectively. It can be deduced that odd number secondary poles exhibit more sinusoidal back-EMF and higher average force than even ones. Finally, a 3D model of 6s/25p LVFRM is built to validate the 2D predicted results and further analyze the end effect. III. CONCLUSION This paper makes a fair comparison between single- and multi-tooth LVFRMs. At rated copper loss, the average force of 6s/25p (4-tooth) LVFRM is 18.4N, which increases nearly 30% compared with single-tooth one. Moreover, odd number secondary poles also exhibit more sinusoidal back-EMF and higher average force in multi-tooth LVFRMs. In terms of thrust force performance, multi-tooth LVFRMs can be adopted at low electric load.

[1] Byeong-Seok Lee, Han-Kyung Bae, P. Vijayraghavan and R. Krishnan, "Design of a linear switched reluctance machine," *IEEE Trans. Ind. Appl.*, vol. 36, no. 6, pp. 1571-1580, Nov./Dec. 2000. [2] N. S. Lobo, H. S. Lim and R. Krishnan, "Comparison of Linear Switched Reluctance Machines for Vertical Propulsion Application: Analysis, Design, and Experimental Correlation," *IEEE Trans. on Ind. Appl.*, vol. 44, no. 4, pp. 1134-1142, Jul./Aug. 2008. [3] J. Ou, Y. Liu, M. Schiefer and M. Doppelbauer, "A Novel PM-Free High-Speed Linear Machine With Amorphous Primary Core," IEEE Trans. Magn., vol. 53, no. 11, pp. 1-8, Nov. 2017. [4] X. Liu and Z. Q. Zhu, "Comparative Study of Novel Variable Flux Reluctance Machines With Doubly Fed Doubly Salient Machines," *IEEE Trans. Magn.*, vol. 49, no. 7, pp. 3838-3841, Jul. 2013. [5] J. T. Shi, X. Liu, D. Wu and Z. Q. Zhu, "Influence of Stator and Rotor Pole Arcs on Electromagnetic Torque of Variable Flux Reluctance Machines," *IEEE Trans. Magn.*, vol. 50, no. 11, pp. 1-4, Nov. 2014. [6] Y. Shen, Q. Lu, H. Li, J. Cai, X. Huang and Y. Fang, "Analysis of a Novel Double-Sided Yokeless Multitooth Linear Switched-Flux PM Motor," *IEEE Trans. Ind. Electron.*, vol. 65, no. 2, pp. 1837-1845, Feb. 2018.

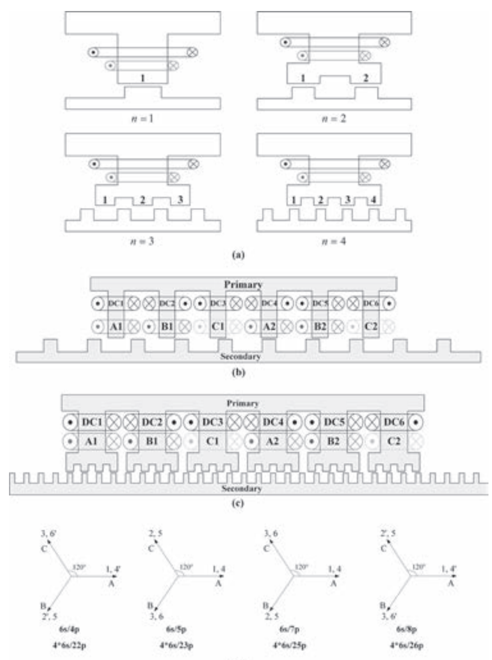

Fig. 1. The topology and coil back-EMF phasors of single- and multi-tooth LVFRMs. (a) Schematic of multi-tooth. (b) 6s/7p LVFRM. (c) 6s/25p LVFRM. (d) Coil back-EMF phasors.

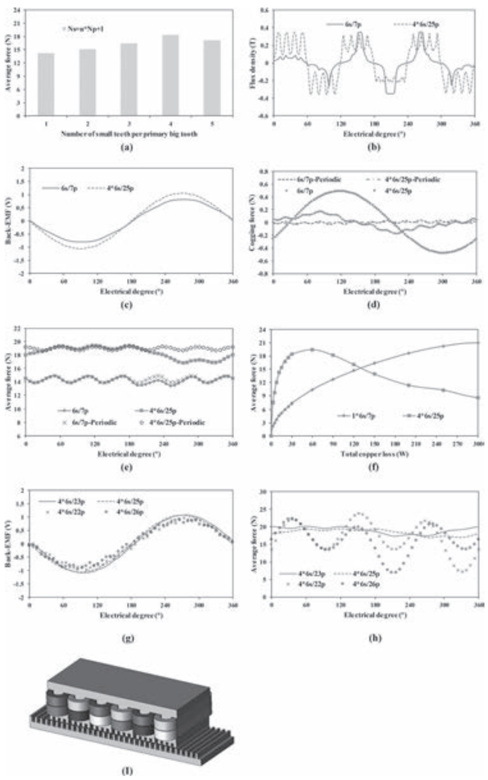

Fig. 2. The performance of the 6s/25p LVFRM. (a) Comparison with different small teeth. (b), (c), (d), (e) Air-gap flux density, back-EMF, cogging force and average force of 6s/7p and 6s/25p LVFRMs. (f) Force-total copper loss characteristic. (g), (h) Back-EMF and average force of 6s-22/23/25/26p LVFRMs. (I) 3D model.

CU-06. A Study of Non-symmetric Double-sided Linear Induction Motor for Hyperloop All-in-one system(Propulsion, Levitation, Guidance).

W. Ji[1], G. Jeong[2], H. Kim[2] and H. Lee[1]
1. Railway Vehicle System Engineering, Korea National University of Transportation, Incheon, The Republic of Korea; 2. Hanyang University, Seoul, The Republic of Korea

1. Introduction Currently demand on environment-friendly ultrahigh speed long distance transportation is increasing, so that Hyperloop is getting attention globally. Hyperloop is a new innovative transportation that a levitated subsonic speed train travels through vacuum cylindrical tube. Hyperloop needs functions of propulsion, levitation and guidance for its service and also many device is necessary for those functions. In high speed maglev train, generally, linear synchronous motor is applied for propulsion and permanent magnet is used for passive levitation, and Electromagnet or permanent magnet is used for guidance. In tube, constrained space, many device makes entire system complicated and size of vehicle, tube is increased. Therefore, costs of maintanace, manufacture, construction are increased and control of each devices is very difficult. This study proposes Non-symmetric Double-sided Linear Induction Motor (NSDLIM) as propulsion, levitation, guidance All-in-one system for Hyperloop. Requirements of NSDLIM was investigated considering special structure and operating environment and basic model was designed. Then force of propulsion, levitation, guide depending on are analyzed by using finite element method (FEM). By adjusting parameters such as materials, shape, slip frequency, validation and possibility of NSDLIM was examined. 2. NSDLIM for Hyperloop All-in-one System Every system of high speed maglev that has been studied and developed requires two or more devices for propulsion, levitation and guidance. MLX in Japan applys a linear synvhronous motor for propulsion, and uses 8-coil on both sides of the guideway and superconducting electromagnets on both sides of the vehicle for levitation and guidance. Trans Rapid in Germany is propelled by a linear synchronous motor and using attractive force by electromagnets and magnetic substances to levitate and guide. Conventional maglev train systems has many devices and large vehicle, guideway so it is hard to be applied to hyperloop As shown in Fig. 1, NSDLIM, the subject of this study, has a primary coil on both sides of the bottom of the tube and vertical secondary reaction plate attached to under the vehicle. NSDLIM is designed based on linear induction motor (LIM) and utilizes three charateristics of a linear induction motor. Thrust force by the propulsion principle of a conventional linear induction motor, levitation force by transverse end effect, guide force by normal force are generated in NSDLIM. Therefore, just one All-in-one system can conduct 3 functions so has advantages small sized vehicle and tube, low cost of maintanance and construction, simple control etc. 3. Design of NSDLIM Hyperloop has unusual structure and operating environment such as vacuum cylindrical tube guideway, so that requirements are different from conventional highspeed maglev train. As shown in Table. 2, very hign speed, acceleration and power are required and length is limited. Basic model of the NSDLIM was designed by using magnetic equivalent circuit and considering analyzing time, it is 1/2 sized. The primary material of the NSDLIM is 35SPN230 and pole pitch is 450mm by considering winding because of thick wire due to high current, winding method is double layer short pitch distributed winding by considering thrust and levitation force ripple. And seconday reaction plate material is aluminum and airgap is 20mm, thickness of plate is 30mm. 4. Analysis of NSDLIM NSDLIM was analyzed by using FEM. Because of its structural characteristics, thrust and guide force by 2D FEM, levitation force by 3D FEM are analyzed. By investigating effects of parameters on force of propulsion, levitation and guide, parameters such as conductivity of secondary plate, teeth width, slot width, airgap, direction of magnetic field, slip, input current, slot per phase per pole were adjusted to improve 3 forces. Fig. 2,3 shows thrust force – slip and levitation force – slip with vertical displacement and input current is 7kA and frequency is 386Hz. Displacement 0mm means that primary and secondary are center arranged. As the displacement increases, the thrust force deceases and levitation force increases. As shown, thrust force is high despite its required force is 27.5kN, but levitation force is low. Fig 3 shows thrust and levitation force of model of different slot per phase per pole. It is seen that thrust force decreases but levitation force increases. So by adjusting parameters NSDLIM model that meet forces requirements could be derived. 5. Conclusion This paper is study of non-symmetric double-sided linear induction motor for Hyperloop All-in-one system. There is 2 or more devices for propulsion, levitation and guidance in hyperloop system. Therefore, entire system is compligated and size of tube and vehicle increase so cost increases and control is difficult. To replace conventional system with NSDLIM, validation and possibility of NSDLIM was examined. Design, analyze, of NSDLIM was conducted and model that meets required thrust force was derived and by adjusting parameters force of propulsion, levitation and guide was improved. The possibility of NSDLIM was verified and through detail design and consider other parameters such as ladder type of secondary plate, NSDLIM could be realized as All-in-one system for Hyperloop.

[1] H.W. Lee, C.B Park, and B.S Lee, "Thrust performance improvement of a linear induction motor", JEET., vol.6, pp.81-85 (2011) [2] Boldea, S. A. Nasar, "Linear motion electromagnetic devices", Taylor & Francis, New York (2001) [3] S. Nonaka and S. T. Higuchi, "Elements of linear induction motor design for urban transit," IEEE Trans. Magn., vol.MAG-23, no. 5, pp.3002–3004, Sep. (1987)

Fig. 1. Concept of NSDLIM

Table. 1. Requirements of NSDLIM

Content	Specification	Unit
Weight	20	ton
Maximum speed	1000	km/h
Acceleration	4.9	m/s²
Required thrust force	110	kN
Power	30.6	MW
Number of NSDLIM	2	-
NSDLIM length	26	m

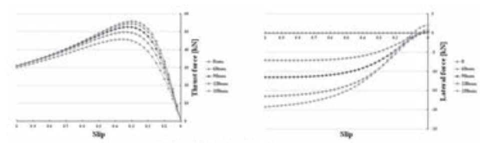

Fig. 2. Thrust and levitation force with displacement

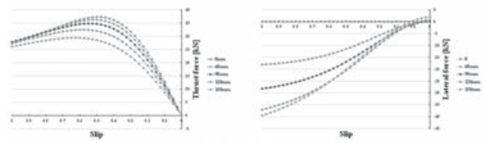

Fig. 3. Thrust and levitation force with displacement
(different slot per phase per pole)

CU-07. Design and analysis of a novel rotary-linear motor with voice coil structure.

F. Xing[1] and B. Kwon[1]
1. Hanyang University, Ansan, The Republic of Korea

I. INTRODUCTION With the greatly development of the industry, such as the field of integrated circuit and high-precision robot arm, they always require multidimensional complex movements and posture adjustments. Therefore, the multi-degree-of-freedom motion platform is among the most important research topics to advance precision machining. As one of them, the rotary-linear motors have the advantages of two degree-of-freedom motions and simple structures, which can facilitate high performance [1], [2]. However, the conventional rotary-linear motor has the disadvantages of low acceleration, big size, no-smooth force, slow actuation and so on. Therefore, a novel type of rotary linear motor overcoming these disadvantages with high controllability is an increasing necessity. In this paper, a rotary-linear motor combined the SPM motor and the voice coil motor [3] structure (RL-SVCM) is proposed here to achieve rotary and linear motion independently and fully decoupling control with smooth linear force. Furthermore, the voice coil structure of the mover allows the motor to provide a high acceleration and quick response. Especially, the novel unique structure in the linear motion part can make the linear force approaching constant value, which proves a big convenience for the control of the voice coil motor. This motor features a small size, which makes the motor especially suitable for PCB drilling, pick-and place systems, tooling machine, precision operated robot arm and so on. II. MODELING AND FEM ANALYSIS RESULTS Fig. 1 shows the novel structure of the RL-SVCM in 3D, which based on the double stators and one rotor (mover) structure, as well as the sectional views can be found in it. From Fig. 1, it can be found that the outside stator is prepared for the rotating working part of the RL-SVCM, which is a SPM motor with four pole pairs. The outside stator is designed with the concentrated winding in 12 slots, and two different colors of the magnets on the outside of the rotor/mover representing the different magnet direction work for the SPM motor rotating part. Also in Fig. 1 the inside stator is prepared for the linear working part of the RL-SVCM, which is a voice coil motor. The inside stator is designed with the voice coil and the magnet matching with the linear motion is with the single magnet direction shown in green color equipped in the inside of the rotor/mover. Surround the rotor/mover part, the outside is one straight air gap used for the rotating motion part, and the three segments air gap in the inside of the rotor/mover are working for the linear motion part. Meanwhile, the magnetic circuit of the rotary motion and linear motion are shown in the two sectional views of the Fig. 1. The FEM analysis results are shown in the Fig. 2. Fig. 2(a) shows the torque distribution under the max current point of the rotary motion, and Fig. 2(b) shows the linear mover force and force ripple under different currents. The table 1 shows the torque, torque ripple of the rotary motion; the forces, force ripples of the linear motion; and also the detail of the RL-SVCM. III. CONCLUSION This paper proposed a novel rotary-linear motor combined the SPM motor and the voice coil motor structure. The detail structure of the electrical motor is presented here. Also the FEM analysis results are shown in the paper. From the analysis result, the most important advantage of this paper is the smooth constant force in the linear motion and quick response, which is great convenient for the control of it. And also the high acceleration, small size are the advantage of the two degree-of-freedom motions rotary-linear motor. About the detail analysis of the motor will be shown in the full paper.

[1] Xu, Lei, Mingyao Lin, and Xinghe Fu. “End-effects analysis and experimental study of a double stator linear-rotary permanent magnet motor with long mover.” IET Electric Power Applications 11.9 (2017): 1601-1609. [2] Zhang, Zi-jiao, Hai-Bo Zhou, and Ji-an Duan. “Design and analysis of a high acceleration rotary-linear voice coil motor.” IEEE Transactions on Magnetics (2017). [3] R. T. Ratliff and P. R. Pagilla, “Design, modeling, and seek control of a voice-coil motor actuator with nonlinear magnetic bias,” IEEE Trans. Magn., vol. 41, no. 6, pp. 2180–2188, Jun. 2005.

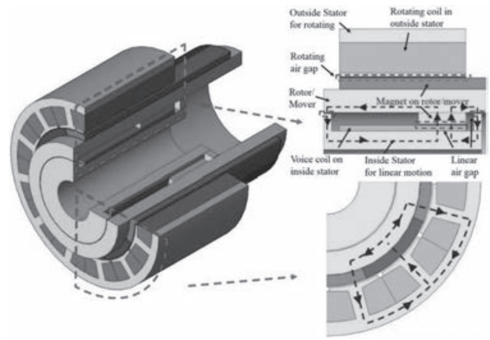

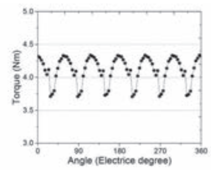

Fig. 2(a) Rotary torque under max point

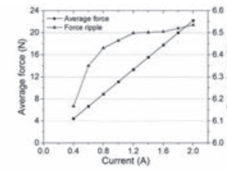

Fig. 2(b) Force and force ripple of linear motion

Table 1 Motor size and FEM analysis result

Item	Unit	Value
Stator slots/Magnet poles	V	12/8
Outside stator/ inside stator/ rotor(mover) axial length	mm	80/100/ 150
Rotor/mover outside air gap diameter	mm	90
Two rotor/mover inside air gap diameter	mm	60/50
Linear motion length	mm	50
Torque(average)	Nm	4.08
Torque ripple	%	15.3
Linear force under 1.6A	N	17.8
Linear force ripple under 1.6A	%	6.53

CU-08. Design and Experimental Analysis of a 3kW Single-Phase Linear Permanent Magnet Generator for Stirling Engines.

K. Lee[1,2], S. Lee[1], J. Park[1], J. Choi[2] and K. Sim[3]
1. Korea Institute of Industrial Technology, Gwangju, The Republic of Korea; 2. Electrical engineering, Chungnam National University, Daejeon, The Republic of Korea; 3. Seoul National University of Science and Technology, Seoul, The Republic of Korea

I. INTRODUCTION Recently, there has been an increasing demand for technological development in the field of renewable energy. This is because of the abnormal climate change on Earth due to greenhouse gas emissions caused by the continuous use of fossil fuels. Among these technologies, cogeneration systems using free-piston Stirling engines (FPSEs) are one of the most effective alternatives to cope with the climate change. The FPSEs can be used with various power sources such as gas, liquid, solid fuel, and thermal energy from both nuclear and solar energies. The FPSEs can also be used for recycling waste heat [1], [2]. The FPSEs consist of linear generators ; this structure has the advantage of less mechanical friction loss because there is no mechanism restricting the motion of the piston. Additionally, linear generators are better than rotating machines in terms of efficiency and maintenance because they have the advantage of generating a linear thrust in a short stroke range [3], [4]. In this study, the optimum design and load characteristics of a linear generator for an FPSE system were discussed. To design a suitable generator for an FPSE system, a single-phase linear permanent magnet generator (SPLPMG) was designed considering the operation speed and stroke characteristics of the engine. Further, no-load and load characteristics were analyzed by the finite element method (FEM) considering the manufacturing process and design parameters of the SPLPMG. In addition, to evaluate the performance of the linear generator, a test rig composed of a crankshaft, whose rotation was converted into a linear motion, was evaluated. The prototype SPLPMG was driven by a servo motor or a gasoline engine to evaluate the operation speed and load resistance characteristics. Finally, the optimum design and characteristics measurement results of the SPLPMG were compared. II. OPTIMAL DESIGN AND EXPERIMENTAL Fig. 1(a) shows the position of SPLPMG in the internal structure of an FPSE system. Fig. 1(b) shows the detailed shape of the SPLPMG. The generator has a stator composed of 12 pieces of iron core, and the inner core is made of radial lamination. It is a generator with an outer stator structure and has two airgaps. The mover in the generator converts the mechanical energy into electric energy by reciprocating the short stroke interval, ±20 mm. Since the stroke length of the generator was very short, it was designed as the SPLPMG rather than a three-phase generator. Moreover, considering the stacking factor due to both the stator manufacturing process and the radial stacking of the inner core, the no-load and load analysis of the SPLPMG was performed according to the frequency. The measurement system was constructed to verify the characteristics of the designed linear generator. Because the designed linear generator was reciprocating, it was more difficult to evaluate than the rotary generator. In this study, a test rig composed of a crankshaft that converts rotational motion into linear motion was fabricated, and the load of the linear generator was tested. To minimize the mechanical loss due to the reciprocating movement of the linear generator, the noncontact air bearing was used instead of the mechanical linear bearing while evaluating the performance of the linear generator. The load evaluation was carried out by serially connecting the resonant capacitor and the load resistor, in accordance with the resonant frequency of the SPLPMG. The linear generator evaluation system is shown in Fig. 2(a). As a result of the load evaluation, it was confirmed that the generator output is 3046 W when the generator operated at a frequency of 27 Hz, the resonant capacitor is 300 uF, and the load resistance is 10 Ω. Fig. 2(b) shows the FEM and measurement results according to the operating frequency and the load resistance of the linear generator. III. RESULTS In this study, the design, analysis, and evaluation methods of a 3 kW-class SPLPMG for an FPSE system were presented. To evaluate the no-load and load characteristics of the optimized generator, a characteristic evaluation system equipped with a motion conversion mechanism was installed, so that the ±20 mm stroke displacement could be linearly operated. As a result, it was confirmed that the generator output was 3046 W when the resonant capacitor was 300 uF, and the load resistance was 10 Ω at a generator driving frequency of 27 Hz. Further, considering the operating frequency deviation between them, the FEM and load test results were confirmed to be almost similar.

[1] Y. C. Hsieh, T. C. Hsu, and J. S. Chiou, “Integration of a free-piston Stirling engine and a moving grate incinerator,” *Renew. Energy*, vol. 33, no. 1, pp. 48–54, Jan. 2008. [2] Ping Zheng, Chengde Tong, Jingang Bai, Bin Yu, Yi Sui, and Wei Shi, “Electromagnetic Design and Control Strategy of an Axially Magnetized Permanent-Magnet Linear Alternator for Free-Piston Stirling Engines,” *IEEE Trans. Ind. Appl.,* vol. 48, no. 6, pp. 2230-2239, Nov/Dec. 2012. [3] Cristofaro Pompermaier, Kalluf Flavio Jorge Haddad, Alexandre Zambonetti, M. V. Ferreira da Luz and Ion Boldea, “Small Linear PM Oscillatory Motor: Magnetic Circuit Modeling Corrected by Axisymmetric 2-D FEM and Experimental Characterization,” *IEEE Trans. Ind. Electron*., vol. 59, no. 3, pp. 1389–1396, Mar. 2012. [4] Thu Thuy Dang, Marie Ruellan, Laurent Prevond, Hamid Ben Ahmed, and Bernard Multon, “Sizing Optimization of Tubular Linear Induction Generator and Its Possible Application in High Acceleration Free-Piston Stirling Microcogeneration,” *IEEE Trans. Ind. Appl.,* vol. 51, no. 5, pp. 3716-3733, Sep/Oct. 2015.

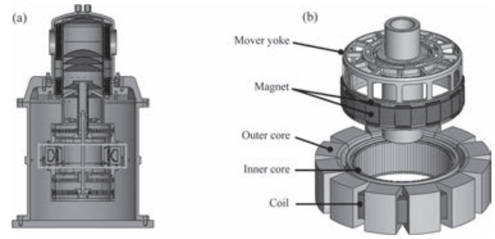

Fig. 1. (a) The position of SPLPMG in the FPSE. (b) SPLPMG.

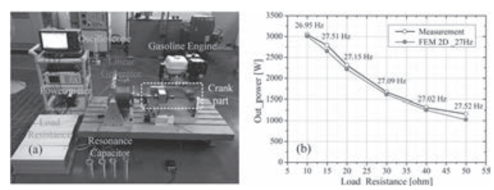

Fig. 2. (a) Linear generator evaluation system. (b) Comparison of the FEM and measurement results for SPLPMG.

CU-09. Cost and detent force reduction in a permanent magnet linear motor by using different PM materials.

X. Liu[1,2], D. Gerada[2,3], Z. Xu[2,3], C. Gerada[2,3] and *H. Yu*[1]
1. Department of Electrical Engineering, Southeast University, Nanjing, JiangSu, China; 2. Power Electronics, Machines and Control Group, The University of Nottingham, Nottingham, United Kingdom; 3. Department of Electrical and Electronic Engineering, University of Nottingham, Ningbo, China

Abstract : The bigger cogging force and higher cost are the two main problems for optimizing the design and application of the permanent magnet linear motor (PMLM). This paper proposes a new method of adopting two types of permanent magnet materials applied in a PMLM to decrease the cogging force and cost. Three PM material configurations are considered in this paper, namely (i)NdFeB only poles, (ii)alternate NdFeB and Ferrite poles, and (iii) NdFeB poles with Ferrite edges. Firstly, the PMLM using NdFeB only is designed, then through replacing the adjacent NdFeB pole with a Ferrite pole, or placing Ferrite at the edges of the NdFeB magnets the performances are investigated. It is found that the PMLM with two different permanent magnet materials can achieve a similar magnetic force as the NdFeB only design, and moreover the cogging force can be reduced to under 5% of the rated magnetic force. It is shown that a PMLM with sectional lower magnetic energy magnets can improve performance and lower the overall mass of the rare-earth elements (hence improving the cost). Keywords: PMLM, permanent magnet materials, ferrite, cost I Introduction Permanent magnet electric machines are widely used in industrial manufacture, railway transportation etc. due to the advantages of simple structure, reliable operation, high performance and small size. There are two main design challenges, being reducing the cogging force and lowering the cost cost. Many methods are proposed in [1], [2], [3], [4] to reduce the cogging force. The cost of the permanent magnet motors is still a sensitive issue and a barrier to mass proliferation is some markets, because of the heavy use of the rare earth permanent magnet materials, such as NdFeB, SmCo, etc. In 2017, motor's main manufacturing materials, such as copper, silicon steel and Rubidium metal are experiencing a price increase in different levels, most alarmingly the price of the rubidium which increased by up to 81%. In light of this it is necessary to research on the higher performance and smaller volume motors to decrease the use of Nd-Fe-B permanent magnetic materials, or find other materials to replace the higher cost permanent magnet (PM). In this paper, a method of using the low price permanent magnet materials of Ferrite to replace sections of the NdFeB is proposed. Although the coercivity force and magnetic energy is only 10% of the NdFeB, performance/cost benefits are found when they are used in combination. Starting with a designed PMLM with NdFeB PMs only, shown in Fig.1a, two methods are applied to reduce the cost of the PMLM. In the first method, the alternate poles (in this case being the South pole) are replaced by the Ferrite, with the width and height of these Ferrite PMs optimized to tailor the magnetic flux. Through the optimization, the aforesaid PMLM achieves the same average force as the NeFeB only design, and because of the replacement of the NdFeB, the whole cost of the PMLM will decrease considerably. In this staggered arrangement, shown in Fig.1 (c), the size of the adjacent Ferrite PMs are different, which affects the magnetic flux in the air gap - this principle is similar to change the magnet shape to optimize the cogging force of the PM motors[5]–[7]. Another method is replacing sectional edges of the NdFeB with Ferrite, as shown in Fig.1(b) and through changing the ratio of the Ferrite and NdFeB in one pole pitch, the cogging force is reduced, and the cost of the PMLM is also reduced. II Optimizing of the PMLM with NdFeB and Ferrite edges Two methods are adopted in this paper, as shown in Fig.1 (b) and Fig.1 (c). The optimization the configuration shown in Fig.1(b) will be described in this section. III Optimization results of the PMLM with alternate Ferrite pole The PMLM with the NdFeB only of Fig.1(a) is optimized, and the mean force is 345N, the cogging force being about 2.5%. With the same envelope of the original machine of Fig.1a, another PMLM with Ferrite only, and using alternate NdFeB and Ferrite magnets as shown in Fig1c are built, and the force is compared in Fig.2. Through the optimization the PMLM with NdFeB only and with the alternate Ferrite pole can have a same force level with the PMLM with NdFeB only, as shown in Fig.2, and the cogging force can also be reduced. IV Experiment A PMLM only with the NdFeB is manufactured, and the cogging force is measured, which can be used to verify the modelling for this newly proposed PMLM. V Conclusion In this paper, in order to reduce the manufactured cost and improve the force quality of the permanent magnet electric machines, a PMLM with two types of PM materials is proposed. Through the simulation, it is found that the force of this new PMLM with two magnet types is of the same level of the PMLM with NdFeB magnets only. This structure can reduce the use of the NdFeB, the cost of the PMLM unit, and reduce the force ripple. The final paper will describe and quantify these benefits further.

[1] Q. Wang and J. Wang, 'Assessment of cogging-force-reduction techniques applied to fractional-slot linear permanent magnet motors equipped with non-overlapping windings', *IET Electr. Power Appl.*, vol. 10, no. 8, pp. 697–705, 2016. [2] Z. Zhang, H. Zhou, J. Duan, and B. Kou, 'Design and Analysis of a New Ring Winding Structure for Permanent Magnet Linear Synchronous Motors', *IEEE Trans. Plasma Sci.*, vol. 44, no. 12, pp. 3311–3321, 2016. [3] C. Liu, H. Yu, M. Hu, Q. Liu, and S. Zhou, 'Detent Force Reduction in Permanent Magnet Tubular Linear Generator for Direct-Driver Wave Energy Conversion', *IEEE Trans. Magn.*, vol. 49, no. 5, pp. 1913–1916, 2013. [4] X. Huang, Q. Tan, Q. Wang, and J. Li, 'Optimization for the Pole Structure of Slot-Less Tubular Permanent Magnet Synchronous Linear Motor and Segmented Detent Force Compensation', *IEEE Trans. Appl. Supercond.*, vol. 26, no. 7, pp. 1–5, 2016. [5] S. Ruangsinchaiwanich, Z. Q. Zhu, and D. Howe, 'Influence of magnet shape on cogging torque and back-emf waveform in permanent magnet machines', in *2005 International Conference on Electrical Machines and Systems*, 2005, vol. 1, p. 284–289 Vol. 1. [6] K. Wang, Z. Q. Zhu, and G. Ombach, 'Torque improvement of five-phase surface-mounted permanent magnet machine using third-order harmonic', in *2016 IEEE Power and Energy Society General Meeting (PESGM)*, 2016, pp. 1–1. [7] H. Fang and D. Wang, 'A Novel Design Method of Permanent Magnet Synchronous Generator From Perspective of Permanent Magnet Material Saving', *IEEE Trans. Energy Convers.*, vol. 32, no. 1, pp. 48–54, Mar. 2017.

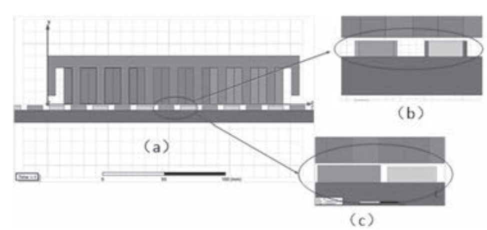

Fig. 1. PMLM with NdFeB and Ferrite

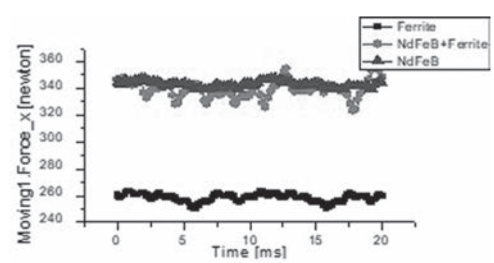

Fig. 2. Force comparison for the three types PMLMs

CU-10. Torque Analysis and Optimal Design of a Three-Degrees-of-Freedom Maglev Permanent Magnet Linear Motor.

F. Xing[1], B. Kou[1], T. Wang[1], C. Zhang[1] and Y. Zhou[1]
1. Harbin Institute of Technology, Harbin, China

I. INTRODUCTION The maglev permanent magnet linear motor has the advantages of no mechanical friction and high stiffness, and it is widely researched by many scholars for the great application in high speed, large acceleration and high precision linear positioning movement[1],[2], Compared with the linear motor supported by the air flotation system or mechanical structure, the maglev linear is more suitable for working in dust-free vacuum environment, which makes it a promising research field[3]. The maglev linear motor has three degrees of motion freedom, which are respectively realized by the horizontal thrust force in the *x*-aixs, the normal force in the *z*-aixs and the torque around the *y*-aixs. The horizontal thrust and normal force can be controlled by the conventional *dq* composition method, but both *q*-axis current and *d*-axis current will generate additional torque to rotate the motor mover. In the control process this additional torque can be seen as disturbance. One of the key issues to realize the optimal control of the maglev linear motor control system is to decrease or eliminate this additional torque. To achieve this, a new linear motor structure has been proposed in this paper. First, the analytical model of the maglev linear motor is constructed. The above additional torque can be analyzed, based on which the new-structure maglev linear motor is proposed. Finally, the optimal design for the proposed linear motor is done in this paper. II. MODELING AND TORQUE ANALYSIS First, the coordinate system of the maglev linear and the coordinate transformation system of position and vector are constructed. Second, the electromagnetic force and torque on three degrees of freedom have been numerically analyzed. Finally, the finite element method has been used to validate the analytical analysis. Fig.1 shows the structure of the maglev linear motor model. It consists of the stator, mover and the gap between them. τ is the pole pitch. The stator has ABC three-phase windings and non-conductive plate. The distance between the two winding centers is τ. The three-phase windings are arranged in the *x*-direction with the electrical degree gap of 240. The width of the windings is 4τ. Moreover, the mover consists of permanent magnet and conductive plate. III. DESIGN OF A NEW MAGLEV LINEAR MOTOR Based on the analysis of the additional torque in the above section, two motor units can be combined to cancel out the additional torque. To make sure that two additional torques are in the opposite direction and the horizontal and levitation forces for the two motor units are in the same direction, the phase angle difference between them should be $1/2\tau$. Fig. 2 shows the arrangement of the windings. Moreover, the size of the main and auxiliary permanent magnets of a Halbach permanent magnet array can influence the distribution of the magnetic flux density in the air gap, and therefore the structural optimization of the permanent magnets needs to be performed according to the required performance index. Furthermore, the thickness of the permanent magnets can also affect the motor force coefficient, which will be analyzed in the next section. IV. VALIDATION AND ANALYSIS Fig. 3 shows the electromagnetic force and torque of two motor units as a function of the *x* position. It can be seen that the horizontal force and levitation force of the two motor units always maintain a nearly constant output with the change of the position of the mover, while the torque changes with the change of the mover position. Fig.4a shows that the horizontal force and levitation force produced by the levitation linear motor are the sum of the respective horizontal force and the levitation force produced by the two units. From Fig.4b it can be seen that the additional torques acting on the centroid of the mover are in the opposite directions, and thus cancel each other out. From the simulation analysis it can be obtained in the magnetic levitation linear motor current can offset the additional torque ripple. V. CONCLUSIONS In this paper, a new-structure magnetic levitation linear motor is proposed to reduce the additional torque generated by coil. The new topology makes the additional torques generated by two different units cancel each other out. With this problem solved the commonly used *dq* decoupling strategy can be adopted realize the control of the proposed maglev linear motor. The finite element simulation shows that the new-structure magnetic levitation linear motor can effectively reduce the additional torque fluctuation.

[1] T. J. Teo, H. Zhu, and C. K. Pang," Modeling of a two degrees-of-freedom moving magnet linear motor for magnetically levitated positioners," *IEEE Trans. Magn*., vol.50, no 12, 8300512, Dec. 2014. [2] C. M. M. van Lierop, J. W. Jansen, A. A. H. Damen, E. A. Lomonova, P. P. J. van den Bosch, and A. J. A. Vandenput, "Model-based commutation of a long-stroke magnetically levitated linear actuator," *IEEE Trans. Ind. Appl*., vol.45,no 6, pp.1982–1990, Nov./Dec. 2009. [3] T.T. Overboom, J.P.C. Smeets, J.W. Jansen, and E. Lomonova, "Semianalytical calculation of the torque in a linear permanent- magnet motor with finite yoke length," *IEEE Trans. Magn*., vol.48, no 11, pp.3575–3578, Nov.2012.

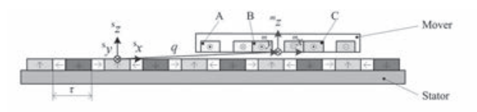

Fig.1 Coordinate definition of the maglev linear motor.

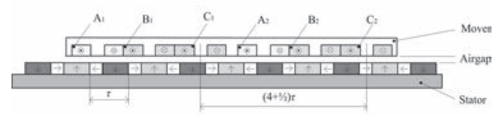

Fig.2 Proposed structure of the maglev linear motor.

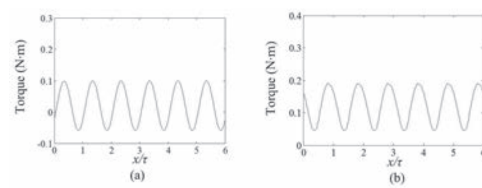

Fig.3 (a) Torque of the motor unit I , and (b) torque of the motor unit II.

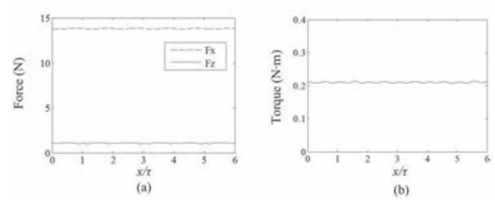

Fig.4 (a) Force of the motor, and (b) torque of the motor.

CU-11. A Robust Multimodal Optimization Strategy for a Tubular Voice Coil Motor Design in Linear Slit Stage.

J. Lim[1] and D. Lim[2]

1. Magnetic Levitation and Linear Drive, Korea Institute of Machinery & Materials (KIMM), Daejeon, The Republic of Korea; 2. Electrical Engineering, University of Ulsan, Ulsan, The Republic of Korea

Introduction This paper describes the design optimization of the voice coil motor(VCM) for linear slit stage. Linear slit stage is a device that serves the aperture of the laser equipment for removing defective pixels in the LED display panel. The VCM acts to open and close the aperture at high speed. The slit stage itself is driven by a gantry system to find the approximate location of the large display. After gantry system finds approximate position, the VCM corrects precise location to determine the position and size of laser beam. The gantry system of the operating equipment moves at high acceleration to shorten a tac time. Due to the lack of thrust to overcome the high acceleration of the gantry, the VCM often loses its exact position. In order to solve this problem, it is necessary to maximize the thrust of the VCM. The VCM should have a thrust that can overcome the acceleration of the gantry so that it can maintain precise position even when moving in a high speed. The problem of reducing the thrust losses at both ends of the stroke and reducing the settling time should also be considered, which are related with minimizing thrust ripple and minimizing mass respectively. Therefore, optimal design considering various objective functions such as thrust, thrust ripple, and mass is required. Main Body The 3D modeling of linear slit stage and optimization flow chart are shown on Fig. 1. The VCM's stator consists of a cylindrical magnet and a linear scale. A mover of the VCM is made up of moving coil and a linear encoder head. In order to reduce the tac time, a settling time minimization is required, which can be achieved by a large thrust, a small moving mass, and a low time constant of the moving coil. Since VCM has various design variables and objective functions, it is impossible to apply optimization to all variables of VCM. For this reason, we propose a robust multimodal optimization (RMO) strategy that can consider for various objective functions and a robust solution with minimal analysis. The objective function of the design is the force, force ripple, and mass that are most important in the design of the VCM, and the design variables are the dimensions of VCM components. In the first stage of the RMO strategy, the Taguchi method [1] is used to derive initial design and select sensitive design variables. The residual magnetic flux is selected as a noise factor because it is an uncontrollable factor that has a great influence on the distribution of performance and the objective function. Through the calculation of the synthetic SNR, a rough optimal design for seven design variables is derived, and two sensitive design variables are selected. In the second stage of the RMO strategy, kriging assisted multimodal optimization[2] is applied to search multiple optima of the two sensitive variables sorted by the initial stage. The initial surrogate model is constructed by applying the objective function values of the Latin Hyper Cube Sampling[3]. After searching the local peaks of the generated surrogate model, the object function values are calculated for the local peaks of the surrogate model. Then the surrogate model is updated with the calculated object function values. This process is repeated until the global peak value converges to within a certain criteria. In order to solve the problem of being trapped at the local peak, perform a blank fill algorithm[1] which can scatter the variables to unrevealed area. In the third stage optimization, the robustness of the solution is evaluated to analyze the noise factor. The final solution should have a high value of the objective function and a robust value for the change of the variable. In this digest, Robust algorithm is verified by test function. In order to determine the optimal solution, we introduce k which internally divides the maximum and minimum values for a certain peak range. The internal division value determines the weight value at maximum value and difference of maximum and minimum. The test function and the objective function are shown below. The results are shown in Fig. 2. The largest 6 peaks are described. $F(X,Y) = X^{0.25}*\sin(X^2)*Y^{0.25}*\sin(2*Y^2)$ opt = k * Max + (1-k) * MIN The first and third candidates show that the rank is changed according to the sensitivity domain of the peak. Peak value of candidate 1 is high, but candidate 3 can be better solution when sensitivity is considered. Therefore, candidate 3 can be an optimal solution to reduce variation in performance of equipment caused by uniformity and production tolerance of control gains of mass-produced VCMs. Conclusion In the design for the VCM applied to the linear slot stage, various design variables, objective functions, and design reliability should be considered simultaneously. In order to derive the robust optimal design result of the VCM, we propose a RMO strategy. Furthermore, we analyze the robustness of the proposed peak and present the criterion for selecting the optimal solution. The proposed optimal design strategy is very meaningful because it can not only consider various design variables and objective functions but also derive a robust solution with minimum analysis. In the final paper, we will present the details of the proposed design including the verification of manufactured product.

[1] Dong-Kuk Lim, Sang-Yong Jung, Kyung-Pyo Yi, and Hyun-Kyo Jung. A novel sequential-stage optimization strategy for an interior permanent magnet synchronous generator design. IEEE Transactions on Industrial Electronics, vol. 65, no. 2, pp. 1781-1790, Feb. 2018. [2] Bin Xia, Ziyan Ren, and Chang-Seop Koh. Utilizing kriging surrogate models for multi-objective robust optimization of electromagnetic devices. IEEE Transactions on Magnetics, vol. 50, no. 2, pp. 693-696, 2014. [3] Ronald L Iman. Latin hypercube sampling. John Wiley & Sons, Ltd, 2008.

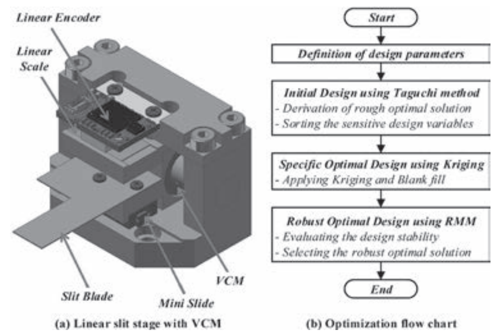

Fig. 1. Linear Slit Stage and flow chart of RMO strategy.

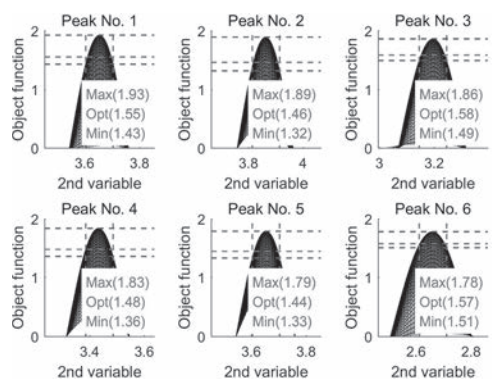

Fig. 2. Result of multimodal peak searching

CU-12. A Study on Performance Improvement of Spherical Multi-DOF Motor.

S. Cho[1], J. Lim[1], *K. Joo*[1], S. Oh[1], D. Kang[2] and j. Lee[1]
1. Electrical Engineering, Hanyang University, Seoul, The Republic of Korea; 2. Keimyung University, Daegu, The Republic of Korea

I. Introduction Development of humanoid is actively proceeding with increasing interest in robot development around the world. Eyeballs and joints of the humanoid are implemented with multi-degrees-of-freedom (DOF) systems using multiple actuators to achieve similar degrees of freedom to the human body.[1]-[2] However, these systems have the weak point of increasing size and weight. Therefore, in recent years, researches have been actively conducted on motors capable of multi-axis drive with one motor in order to replace several actuator systems. [3]-[5] This paper presents a spherical multi-DOF motor as the motor for application to the eyes of robots. It is possible to operate three axes with one motor. In addition, research was conducted to improve the output characteristics of the spherical multi-DOF motor and tilting stability analysis for stable tilting drive. II. Study on performance improvement of multi-DOF motor A. Basic model The structure of the spherical multi-DOF motor proposed in this paper is shown in Fig. 1. In order to reduce the eddy current loss, the inner rotor and the outer rotor are composed to move at the same time. The stator has coils for tilting driving and coils for rotational driving. Since the spherical multi-DOF motor is driven by three axes, the three-axis coordinate system is defined as shown in Fig. 2. B. Output characteristics according to change of the number of phases and pole arc angle In order to improve the output characteristics of the spherical multi-DOF motor, the characteristics of the output according to the change of the number of phases and pole arc angle under the same magneto-motive force condition were analyzed. The currents of the coils for tilting and rotating are applied as shown in equation (1). The analysis results of the output characteristics according to the change of the number of phases and pole arc angle are shown in Fig. 3. It can be seen that the three-phase system is superior in terms of average torque and torque ripple characteristics. C. Tilting stability according to change of the number of phases and pole arc angle Since the spherical multi-DOF motor is driven by three axes, it is essential to analyze the stability according to the command position. Fig. 4 and Fig. 5 show the stability characteristics of 3-phase and 4-phase motors when α and β are 0 ° at arbitrary positions. From these figures, it can be confirmed that a torque curve having a negative slope is formed and the generated torque is 0Nm at a point of α = 0 °. III. Conclusion This paper presents the spherical multi-DOF motor for three-DOF implementation. The analysis was performed according to the change of the number of phases and pole arc angle to improve the output characteristics. Through these process, it was confirmed that the three-phase system has better output characteristics than the other phase systems, and the output torque improved through detailed design of the pole arc angle. Further, stability analysis for three-axis drive was carried out, and it was confirmed that the proposed motor can drive three-axis drive. The full paper will provide additional analysis for improving output torque, and additional stability analysis based on the position of the coils and permanent magnets.

[1] Y. Sakaidani, K. Hirata, and N. Niguchi, "Characteristics Analysis of a 2-D Differentially Coupled Magnetic Actuator," IEEE Trans. Magn., vol. 52, no. 3, Art No. 8200904, Mar. 2016. [2] H. Kim and J. Song, "Multi-DOF counterbalance mechanism for a service robot arm," IEEE/ASME Trans. Mechatronics, vol. 19, no. 6, pp. 1756–1763, Dec. 2014. [3] H. J. Lee, H. J. Park, G. H. Ryu, S. Y. Oh, and J. Lee, "Performance improvement of operating three-degree-of-freedom spherical permanent-magnet motor," IEEE Trans. Magn., vol. 48, no. 11, pp. 4654–4657, Nov. 2012. [4] Y. Bai, Q. Wang, Y. Yu, and M. Yang, "Design methods of the spherical quadrupole magnets and sextupole magnets,"IEEE Trans.Magn., vol. 42, no. 4, pp. 1187–1190, Apr. 2006. [5] S. H. Won, "A Study on the Analysis and the Control Characteristics of a 3 D.O.F Spherical Motor for Robotic Joints," Ph.D. thesis, Electr. Dept., Hanyang Univ., Seoul, 2007.

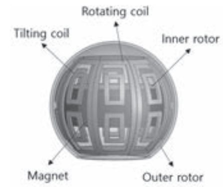

Fig. 1. Structure of double cavity multi-degree-of-freedom motor.

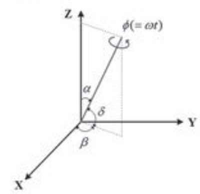

Fig. 2. 3-axis coordinate system.

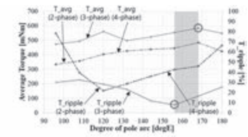

Fig. 3. Torque characteristics according to the change of the number of phases and pole arc angle.

$$\begin{cases} i_{pole(d'),n} = I_d I_p \cos\left(\frac{\pi}{4} - I_p \frac{\pi}{4}\frac{\alpha}{\theta_m}\cos\left(\beta - \frac{4\pi}{mP}(n-1)\right)\right) \\ i_{pole(a),n} = -i_{pole(d'),n} \end{cases}$$
$$\begin{cases} i_{rot,n} = I_m \cos\left(\frac{P}{2}(\omega t + \beta) - \frac{\pi}{2}\left(\sin\frac{(n-1)\pi}{2}\right)\right), m = 2 \\ i_{rot,n} = I_m \cos\left(\frac{P}{2}(\omega t + \beta) - \frac{2\pi}{m}(n-1)\right), m > 2 \end{cases} \quad (1)$$

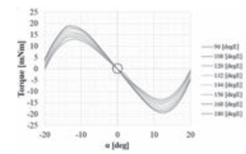

Fig. 4. Stability characteristics of three-phase multi-degree-of-freedom motor (α=0°, β=0°).

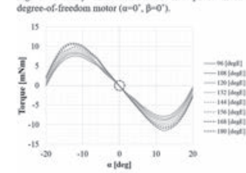

Fig. 5. Stability characteristics of four-phase multi-degree-of-freedom motor (α=0°, β=0°).

CU-13. A novel Switched Halbach Electro-magnetic linear actuating valve for Aerospace vehicle.

V.R. Bommadevara[1]
1. Electrical Engineering, IIT, Hyderabad, India

Abstract—A novel Switched Halbach electro-magnetic linear actuating valve is proposed to reduce the battery power consumption and improve the reliability of the total system.2-D Finite element analysis is carried out on the proposed topology and simulation results are promising which make this novel valve as an efficient solution in place of conventional solenoid valves. The hardware is realized and tested for its performance. I. Introduction:Reliability and energy efficiency are two major important areas in any aerospace vehicle. In satellite launch vehicles and guided missiles Reaction control system (RCS) is widely used in exo-atmospheric region for attitude control of the vehicle [1].Actuating valve is major element in the reaction control system which controls the oxidizer/fuel flow and hence the thrust in on/off control mode. Solenoid valves are used widely in RCS as control element. Continuous research in the area of solenoid valve to improve its response time, reliability and energy efficiency of total system is on and arrived at various configurations in terms of control and valve topologies [2]-[6]. In this paper a novel linear actuating valve based on switched Halbach topology is proposed which improves the energy efficiency and reliability of the total system. II. Proposed Topology: Fig.1 shows the complete model of Halbach magnetic valve (HB-valve). The stationary member of the valve is built with two co-axial permanent magnets magnetized along horizontal axis. Soft Magnetic material is embedded in between two magnets which is magnetized by a coil in the required direction along vertical axis. The moving member is plunger made of soft magnetic material. A. Principle of operation: The operation of this valve can be divided into three stages as shown in fig.1(c), (d) & (e). Stage-I: Coil is not powered on: In this stage the flux density in both top and bottom air gaps will be same as the flux from both the magnets distribute equally in both sections of plunger through air gaps. Equal and opposite forces F1 and F2 are exerted on the plunger in vertical direction (y-axis) and hence the plunger will be its Null position. Stage-II: Coil is excited with negative polarity: In this stage the flux density in top air gap is less than flux density in bottom air gap as the soft magnet is magnetized in -ve y-direction due to coil excitation. This makes both magnets and soft magnet as an Halbach array and the force F1 is less than force F2 and the net force tends to move the plunger up along vertical direction (+ve y-axis) and this is valve off position. And once the excitation is removed the Halbach is switched off and there is asymmetry in the top and bottom air gaps (bottom air gap is less than top). This makes F2 more than F1 and always there is force to move plunger up. The same function is done by a mechanical spring in conventional solenoid valve during off condition. Hence in HB-valve no spring is required. Stage-III: Coil is excited with positive polarity: In this stage the flux density in top air gap is more than flux density in bottom air gap as the soft magnet is magnetized in +ve y-direction due to coil excitation. The force F1 is more than force F2 and the net force tends to move the plunger down along vertical direction (-ve y-axis) and this is valve on position. And once the excitation is removed the Halbach is switched off and there is asymmetry in the top and bottom air gaps (top air gap is less than bottom). This makes F1 more than F2 and always there is force to move plunger down. This means there is no power required to hold the valve in on condition which improves the reliability and overall energy efficiency of the system. B. 2-D Finite element analysis (FE): Non linear magnetic analysis is carried on the HB-valve using FE (finite element) analysis to validate the design concept. The HB-valve is modeled as a 2-D axis-symmetric model along y-axis. The FE analysis results are shown in fig.2 for different stages of the valve operation. Electrical design is carried out to arrive at important parameters of winding i.e. Current density, resistance and inductance. The maximum current density of the coil required to switch the Halbach array direction is 80AT/mm^2. FE analysis on load is carried out to arrive forces exerted on plunger during transient and hold conditions of valve. III PRoTOTYPE HARDWARE: Proto hardware has been realized based on the design of HB-Valve. The hardware is shown in fig.3.The performance evaluation on hardware is carried out and test results are matching with design parameters. IV. Conclusion: Concept of a novel Switched Halbach electro-magnetic linear actuating valve (HB-valve) is proposed which can be used as an alternative to conventional solenoid valves for Reaction control system in aero-space vehicles. The design concept is validated using FE analysis and all stages of operation are analyzed by deriving the air gap flux densities and forces on the plunger. The main advantage in this valve is it eliminates use of mechanical spring and requires no power during hold condition of valve. The proto hardware is realized and tested for its performance which fairly matches with design.

[1]Warren J.Boord, John B.Hoffman. “Missile Defence Systems Engineering” CRC press@2015. [2] Xun Zhao; Liang Li; Jian Song; Chenfeng Li; Xiang Gao,” Linear Control of Switching Valve in Vehicle Hydraulic Control Unit Based on Sensorless Solenoid Position Estimation” IEEE Transactions on Industrial Electronics, vol. 63, issue 7, pp.4073-4085, 2016. [3] Chan-Se Jeong; Hak-Sun Kim; Soon-Yong Yang, “A study on the development of multi-stage solenoid valve”, ICCAS 2010, pages 1552-1555. [4] Wang Yupeng; Liu Xinghua; Chen Yuhang; Liu Fushui “The Optimal Drive Current of Solenoid Valve and Its Effect on Fuel Injection Characteristics,” 2010 International Conference on Electrical and Control Engineering, pp. 2383 – 2387, 2010. [5] Zeljko Situm; Tihomir Zilie; Mario Essert, “High speed solenoid valves in pneumatic servo applications”, 2007 Mediterranean Conference on Control & Automation, pp.1-6, 2007. [6] lll-Yeong Lee, “Switching Response Improvement of a High Speed On/Off Solenoid Valve by Using a 3 Power Source Type Valve Driving Circuit”, 2006 IEEE International Conference on Industrial Technology, pages: 1823-1828, 2006.

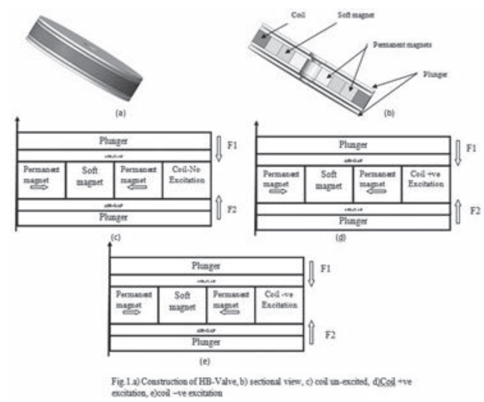

Fig. 1. a) construction of HB valve,b)sectional view,c)Coil un excited state,d)Coil +ve excited,e)coil -ve excited

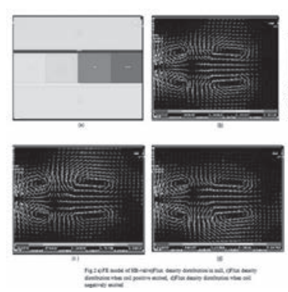

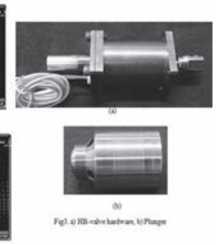

Fig. 2. FE model and flux density plots
Fig.3 Hardware of HB valve

CU-14. Electromagnetic optimization and minimization of detent force for linear permanent magnet vernier motor.

Y. Shao[1], *H. Zhang*[1] and B. Kou[1]
1. Harbin Institute of Technology, Harbin, China

I. Introduction Currently, linear motors have widely applications in direct drive system due to the advantages of transmission chains elimination. The detent force is an essential parameter for linear motors which is relative to the resultant thrust ripple. In this paper, a linear permanent magnet vernier motor(LPMVM) is analyzed which has high thrust density and low thrust ripple. Meanwhile, and the detent force is analyzed by Maxwell's tensor method. Finally, detent force and electromagnetic thrust are analyzed by a simplified three-phase model with a symmetry boundary in the 3-D finite element analysis (FEA) [1]-[3]. II. Basic Structure The basic structure of LPMVM is shown in Fig. 1. The proposed motor has double-sided structure which is comprised of one primary and two secondaries. The primary is comprised of one primary core and three-phase toroidal armature windings. The secondary is comprised of two iron yokes and permanent magnets (PMs), while the PMs are parallel magnetized and fixed on the surface of iron yoke, and the double-side structure adopts N-N relative arrangement form. The 6-slots/10-pole structure is used in this motor, which can generate 5th harmonic in air-gap magnetic field. III. Analysis and Optimization Detent force consists of cogging force and end force. Cogging force is generated by the interaction between primary tooth and secondary PMs. In this paper, through the shape optimization of the stator teeth and the permanent magnet to reduce the detent force. End effect is an important problem of linear motor electromagnetic properties. In this paper, the Maxwell tensor method is used for analyzing the end force. The relationship between the end force and the length of the primary core is obtained. For linear servo system, both thrust density and thrust ripple features should be taken into account. Among them, the influences of relative parameters on thrust and thrust ripple are shown in Figure 2. IV. Conclusion The proposed LPMVM has advantages of high thrust density and low thrust ripple. By comparison, the electromagnetic character is better than traditional linear permanent magnet synchronous motor. Moreover, the method of detent force analysis and optimization can be used to relative linear motor design.

[1] Zhao W, Zheng J, Wang J, et al. Design and Analysis of a Linear Permanent- Magnet Vernier Machine With Improved Force Density[J]. IEEE Transactions on Industrial Electronics, 2016, 63(4):2072-2082. [2] Zhang R, Li J, Hai R, et al. A novel triple-rotor axial-flux vernier permanent magnet machine[C]// IEEE International Conference on Applied Superconductivity and Electromagnetic Devices. IEEE, 2016:537-538. [3] Li D, Qu R. Sinusoidal back-EMF of vernier Permanent Magnet machines[C]// International Conference on Electrical Machines and Systems. IEEE, 2013:1-6.

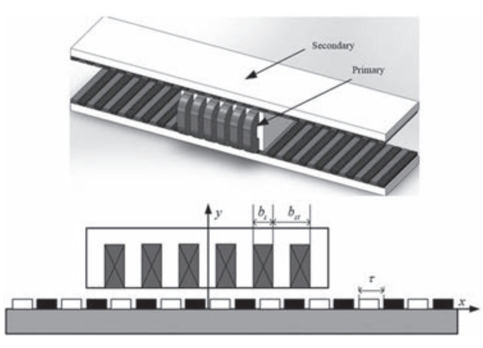

Fig. 1. Basic structure and parameters of LPMVM.

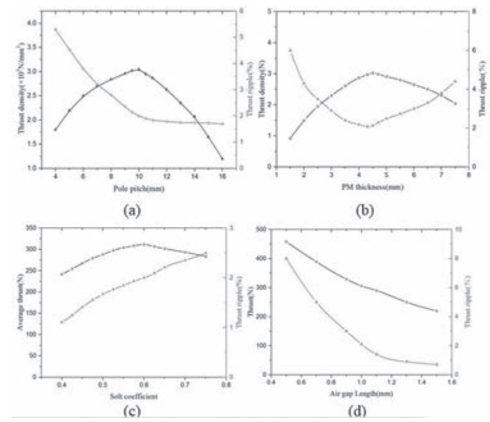

Fig. 2. Influence of relative parameter on thrust density and thrust ripple. (a) Pole pitch. (b) PM thickness. (c) Slot coefficient. (d) Air gap length

CU-15. Design Optimization of High Force Density Linear Switched Reluctance Motor with Segmental Stator for Long Distance Propulsion Applications.

H. Zheng[1], X. Du[1], D. Zhang[1], D. Wang[1], L. Wang[1] and X. Wang[1]
1. Shandong University, Tsinan, China

Abstract—Linear Switched Reluctance Motor with Segmental Stator (LSRMSS) has been studied and proved to provide higher efficiency and force density than conventional LSRM. Since LSRMSS features significant local saturation and fringing effects, the geometric dimensions of the machine can not be determined by analytical design method. This paper introduces an overall design optimization process of LSRMSS which aims to improve the payload ratio of the machine both considering the copper loss and force ripple ratio. The optimization algorithm is combined with FEA to determine the optimal region of the machine dimensions. The results show that the active payload ratio of the machine is significantly enhanced by the design optimization process as well as the commutation force and force ripple ratio. INTRODUCTION In recent years, there is a surge of interests for Linear Switched Reluctance Motor (LSRM) due to the features of the robust and simple structure, the capability of fault tolerance and working under hostile environment [1]. LSRMSS has been studied and proved to be an alternative to the linear driving system due to its high efficiency, high force density and low cost [2]. In addition, LSRMSS is more applicable to long distance translations due to its low manufacturing and maintenance cost [3]-[5]. This paper is focused on the optimization process of geometric parameters of the original LSRMSS mentioned. The main target is to make progress in some propulsion forces calculated by different methods. OPTIMIZATION PROCEDURE A. Establishment of Geometric Parameters The 3D view of the original LSRMSS model and the experimental machine is pictured in Fig. 1. This is a LSRMSS with 3 phases, 2 stator poles and 4 mover teeth, which stack length is 60 mm. Several parameters are proposed to determine the final geometric model of the LSRMSS. The parameters within the range have some constrains with each other to make the LSRMSS feasible. The authors have updated the Constraints during the process of optimization. B. Optimization of Single Objective On the basis of the original motor, the authors optimize the machine dimensions to enhance the 3 objectives which are mean thrust, commutation thrust and thrust density. Firstly, mean thrust is the average of one single-phase operating thrust in one period, and is, to a certain extent, one of a basic performance in LSRMSS. Secondly, commutation thrust is the thrust obtained by the motor by controlling the switch of the three-phase electrical circuit. Then, the thrust density is defined as the thrust per unit mass of the mover, and it is considered vitally when the LSRM is used in vertical conditions. Finally, the authors have also considered the copper loss, which is a crucial performance in the fields of energy saving. The data results have been combined with Design of Experiment (DOE) and Finite Element Analysis (FEA). RESULTS ANALYSIS The results of the 3 optimization objectives are displayed in Fig. 2. The contour graphs of every optimization objective are also showed as well as the scatter plot 2D graphs. It reflects the relation between the parameters in the optimization algorithm and the optimization objectives. Every proposed LSRMSS model has a superior performance in a certain objective above. The analysis of LSRMSS by FEM showed an obvious improvement. Mean thrust is increased by 20.6%, commutation thrust is increased by 16.6% and thrust density is increased by 37.4%. In addition, the optimal solution of the approximate function is verified by the magnetic circuit and finite element analysis, which further proves the rationality of the range of the parameters. CONCLUSION This paper presents design optimization of the LSRMSS by using the DOE and FEM. Three new geometric models are proposed, which have superiority over the original model in terms of mean thrust, commutation thrust and thrust density, validating the rationality of the design optimization.

[1] Wenlong Li; Chau, K.T.; Chunhua Liu; Chun Qiu, "Design and Analysis of a Flux-Controllable Linear Variable Reluctance Machine," IEEE Transactions on Applied Superconductivity, Vol. 24, No. 3, pp. 1-4. [2] Daohan Wang, Xingfei Du, Dengxu Zhang, Xiuhe Wang, "Design, Optimization and Prototyping of Segmental Type Linear Switched Reluctance Motor with a Toroidally Wound Mover for Vertical Propulsion Application," IEEE Transactions on Industrial Electronics, 2017, pp. 1865-1874. [3] H. S. Lim and R. Krishnan, "Ropeless Elevator with Linear Switched Reluctance Motor Drive Actuation Systems," IEEE Transactions on Industrial Electronics, 2007, pp.2209-2218. [4] EI Manâa Barhoumi, Mansour Hajji, Boujemâa,Ben Salah, "Influences analysis of geometrical parameters on propulsive force of LSRM", Systems, Signals & Devices (SSD), 2013 10th International Multi-Conference on, pp.1-6. [5]X. Xu, X. Wang, S. Yuan, and H. Feng, "Optimization of vertical linear synchronous motor for ropeless elevator with INGA method," ICECE, Wuhan, 2010, pp. 3965-3968.

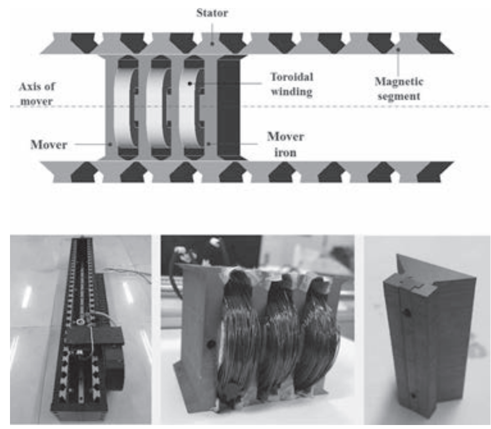

Fig. 1. The 3D view of the original LSRMSS model and the experimental machine

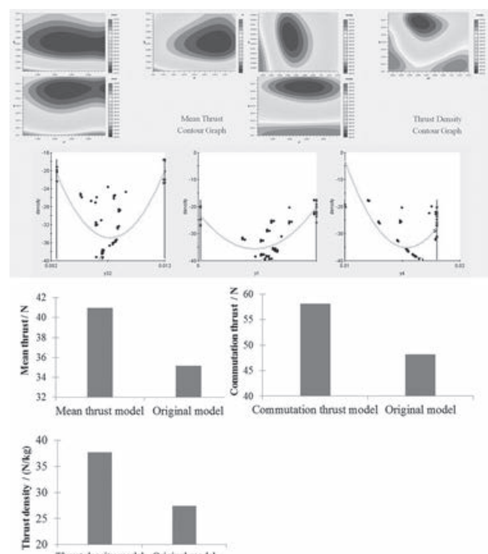

Fig. 2. The contour graph of optimization, the scatter plot 2D graph and the optimal results

CU-16. Design of 2-Phase Slotless Actuator with New Winding Structure for Position Control of Multi-DOF Motor.

H. Hong[1], *H. Kim*[1], S. Oh[1] and j. Lee[1]
1. Hanyang University, Seoul, The Republic of Korea

An electric motor, which is a typical energy conversion device that generates mechanical output by receiving electrical input, is now an indispensable device in our daily life and is being used in many fields. Applications range from highly efficient direct drive motors for industrial and consumer applications to traction motors for vehicle and train applications. In addition, multi-degree-of-freedom motors, which are emerging as the next generation of motor technology, are capable of driving three-dimensional motions of more than 2 degrees of freedom and are currently undergoing research in leading countries such as the US, Japan and Germany. The multi-degree-of-freedom electric motors have been studied focusing on spherical electric motors in which the driving axes rotating in three directions of yaw, pitch and roll are matched to one driving point. In recent years, multi-degree-of-freedom systems having three drive axes and three drive points have been actively applied to various industries. However, spherical electric motors have limitations in practical use due to their difficult fabrication and controllability, and the multi-degree-of-freedom system applied to industry has a complicated structure by combining a general single-axis drive motor and a drive shaft structure in degrees of freedom. In order to solve the problems of existing multi-degree-of-freedom systems, the proposed structure is the hybrid type discussed in this paper. This paper introduces the advantages and disadvantages of various types of position control actuators that can be applied to such a hybrid multi-degree of freedom system, and studies on the design of slotless actuators and tilting structure for more precise and improved position control performance. For this purpose, a 3phase actuator with a cogging torque applied to a conventional hybrid type multi-degree of freedom system is replaced with a 2phase slotless actuator which has no cogging torque and can be advantageous in terms of responsiveness. In the design, a new winding structure that can solve the difficult manufacturing and proprietary technical rights of the advanced companies, which was the problem of the existing slotless winding, was applied to the 2phase actuator. And the validity of this is verified by theory, interpretation and experiment. In addition, unlike the 1st generation hybrid type multi-degree-of-freedom system, which applied inner rotor actuator, the proposed 2nd generation system enables the improvement of the output density by improving the position drive range and joint structure by applying the outer rotor actuator. Finally, the validity of this paper is verified by performing no-load test for design verification of the designed 2phase slotless actuator, speed control for position characteristic verification, and position control test.

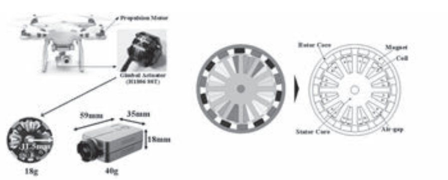
Fig 1. Commercial gimbals actuators selected as comparative group

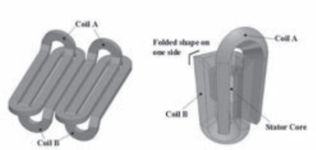

Fig 2. Proposed slotless winding structure of 2-phase drum winding type

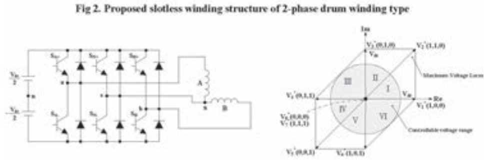
Fig 3. 3-leg inverter for 2-phase actuator drive & the output voltage vector according to the switching state


Fig 4. The final model of the 2-phase actuator

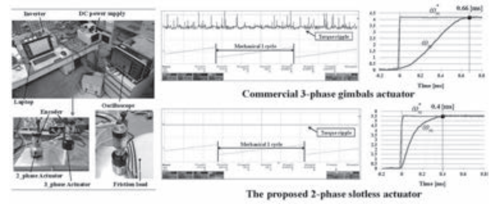

Fig 5. Load test set of tilting actuator

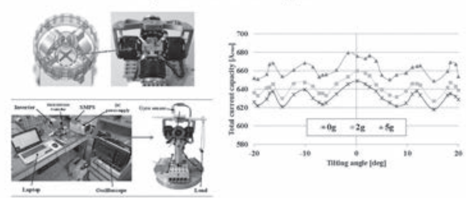
Fig 6. Relation between weight load and input current capacity by tilting angle

WEDNESDAY MORNING, 25 APRIL 2018 SIMPOR/ROSELLE BALLROOM, 8:30 TO 11:30

Session CV
SENSORS: FRONTIER APPLICATIONS II
(Poster Session)

Yuan-Chieh Tseng, Chair
National Chiao Tung Universoty, Hsin-chu, Taiwan

CV-01. Nondestructive Testing for Shallow Defect of Ferromagnetic Objects Based on Magnetic Probe Structure.

S. Pan[1], D. Zhang[1] and E. Zhang[1]
1. Power Electronic and Motion Control Research Center, Harbin Institute of Technology Shenzhen Graduate School, Shenzhen, China

I. INTRODUCTION The Electromagnetic inspection technique plays an important role in the nondestructive testing (NDT) for many decades. Today, this NDT area is rather wide and significant. The magnetic flux leakage (MFL) technology is one of the most widely used electromagnetic nondestructive testing (NDT) techniques. MFL tools use permanent magnets to magnetize the detected object near to saturation flux density [1], [2]. Generally, the magnetizer mechanism of MFL are bulky and heavy. Although the shape of the opening and the depth profile of an arbitrary three-dimensional (3-D) defect from MFL measurements can be estimated [3], the inversion method is complicated and susceptible by the magnetization factors. For different shapes and different sizes of detected object, the magnetizer mechanism of MFL should be designed individually, and this requires a lot of time and experimentation. In this paper, a simple and portable magnetic detection device is designed with permanent magnets, magnetic probe structure and the Hall sensors. Compared with the magnetizer mechanism of MFL, the magnetic detection device is very light, low cost and easy to design and manufacture. The magnetic detection device can make qualitative, and quantitative evaluation for shallow defect of ferromagnetic objects. II. DESIGN PRINCIPLES AND SIMULATION The designed magnetic detection device is made of permanent magnets, magnetic probe structure and the Hall sensors in Fig. 1a. The designed magnetic detection device is not to magnetize the detected object near to saturation flux density, instead use the permanent magnets to generate the magnetic field that perpendicular to the surface of the detected object. The magnetic probe structure is made of high permeability materials, is used to gather the magnetic field. Through the magnetic probe structure, the direction of magnetic field is better, and the magnetic field intensity is stronger than generated by permanent magnets. During the testing process, there is no defect on the detected object, and there is no change of the direction of magnetic field under the probe structure. If there is defect on the detected object and nearby the magnetic probe structure. Because the magnetic resistance of the defect is far greater than the magnetic resistance of the intact surface, the balance of the magnetic circuit of detection system is destroyed, it causes the direction of magnetic field under the probe structure be changed. The Hall sensors detect the changes of the magnetic field under the probe structure to qualitative and quantitative evaluation the shallow defect of ferromagnetic objects. In this paper, the above phenomenon is analyzed by FEM in Fig. 1b, and through the simulation analysis, we optimized the magnetic circuit to high sensitivity and precision of the detection system. III. EXPERIMENTAL RESULTS The magnetic detection device based on magnetic probe structure for the plate, wire-rope and pipe are designed (in Fig. 2a and 2b). Through simulations and experiments, we find the magnetic detection device can make qualitative and quantitative evaluation for shallow defect of ferromagnetic objects. The waveform of defect on the plate is shown in Fig. 2c, and the result of detection of wire-rope is shown Fig. 2d. For wire-rope detection, the weight of the detection device is one thirtieth of the weight of the magnetic leakage detector, and the qualitative detection rate of defect is the same as the magnetic leakage detection. At the same time, it has certain quantitative detection precision.

[1] Feng J, Lu S, Liu J, et al. A Sensor Liftoff Modification Method of Magnetic Flux Leakage Signal for Defect Profile Estimation[J]. IEEE Transactions on Magnetics, 2017. [2] Zhang D, Zhao M, Zhou Z, et al. Characterization of wire rope defects with gray level co-occurrence matrix of magnetic flux leakage images[J]. Journal of Nondestructive Evaluation, 2013, 32(1): 37-43. [3] Ravan M, Amineh R K, Koziel S, et al. Sizing of 3-D arbitrary defects using magnetic flux leakage measurements[J]. IEEE Transactions on magnetics, 2010, 46(4): 1024-1033.

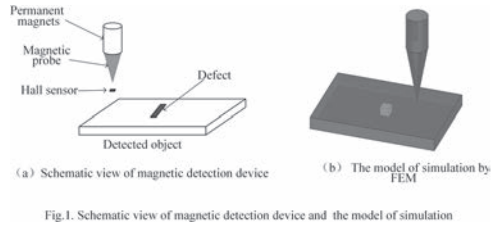

Fig. 1. Schematic view of magnetic detection device and the model of simulation.

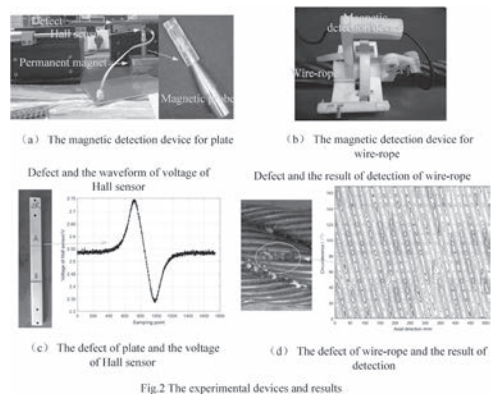

Fig. 2. The Experimental devices and results.

CV-02. DC-arcing detection by noise measurement with magnetic sensing by TMR sensors.

W. Miao[1], X. Liu[1], S.K. Lam[1] and P. Pong[1]
1. The University of Hong Kong, HK, Hong Kong

1. Introduction An arc fault establishes a current path in the air which may cause malfunction of DC system and even a fire hazard. Arc fault detection is essential to improving the reliability, efficiency and safety of the DC system. However, the randomness of DC arc faults makes it difficult to define their characteristics [1]. Various detection techniques have been widely researched. There are mainly three methodologies to detect DC arc faults: frequency-spectrum analysis, wavelet transformation and electromagnetic radiation. The wavelet transformation attains the arc information in a time-frequency domain for arc detection but the accuracy depends on the correct selection of the 'mother wavelet' [2]. The electromagnetic radiation of DC arc from 1 MHz to 100 MHz could be used for arc detection [3]. However, the appearance and amplitude of the arc signals are arbitrary leading to the difficulties in identifying DC arc. Although the frequency-spectrum analysis detecting arc through the signatures of the frequency domain is of higher accuracy and is widely adopted [4, 5], the aimed frequency range and the threshold of power spectra to differentiate between DC arc and normal operation are unspecific. Thus, reliable techniques to detect DC arc faults are still lacking. In this paper, a magnetic-sensing-based technique is proposed to detect DC arc. This work developed a promising DC-arcing detection technique based on the analysis of frequency domain features of the magnetic field measured by a magnetic sensor. This technique is cost-effective because it can be implemented with low-cost magnetoresistive sensors which are capable of measuring electric current [6], and it does not require expensive current transformers. In the presence of an arc fault, the frequency spectrum of the load current is composed of both pink and white noise [7]. The frequency spectra from 0 to 50 kHz can be numerically fitted by a superposition of pink and white noise characterized by the fitting parameters of slope (γ) and magnitude (*A*). These fitting parameters can then be used to distinguish the characteristics of arc. The effect of supply voltage on the frequency domain of the arc current was investigated. The effects of the load current and electrode diameter were also examined. The detection technique was tested under various load conditions to demonstrate that the detection technique could reliably discriminate the normal operation and arc fault. The measurement results obtained with tunnelling magnetoresistance (TMR) sensors were compared with that obtained with a current probe to verify the effectiveness of the proposed technique. 2. Experiments The experimental setup mainly consists of an arc generator, a 10-kW DC power supply, a TMR sensor (TMR2001), the current probe, and an oscilloscope as shown in Fig. 1 (a). The DC arc was induced between the two copper electrodes by operating the stepper motor to create a gap length of 0.3 mm. As shown in Fig. 1, from a period of 0.5 s of their time-domain current waveforms respectively (Fig. 1b), the frequency spectra (Fig. 1c) of normal operation current and sustained arcing current were extracted. The characteristics of arcing were investigated from 48 V to 300 V in step of 12 V. The experiments were carried out at a load current of 5 A with the 3-mm diameter of copper electrodes. The pink noise equation (1) was applied to fit the FFT spectra of the current in normal operation and sustained arcing. $S(f) = A/f^{\gamma} + c$ (1) where f is the frequency, A, γ and c are constants. 3. Results and Discussion The measurement results in Fig. 1 (b) suggest that the current in normal operation and sustained arcing can be measured by both the TMR sensor and the current probe. Although the arc current detected by TMR sensor is larger in oscillations, the magnitude and variations are consistent with the results from the current probe. Therefore, the FFT spectra of the current waveform measured from the TMR sensor and the current probe are similar as Fig. 1 (c) depicts. According to Fig. 1 (c), the presence of arc causes a significant increase of the power spectral density (PSD) from 0 to 1 kHz which can be attributed to the pink noise. This phenomenon is particularly pronounced for the arcing at a lower voltage (e.g. 48 V). As the voltage increases, the arc current becomes more similar in nature to the normal operation current. Thus, the strength of the pink noise of the arc current decreases with the voltage. This trend is shown by the results at 48 V, 108 V, 180 V and 300 V in Fig. 2 (a). The effect of voltage on arcing was investigated from 48 V to 300V as shown in Fig. 2 (b) and (c). The parameter differences between normal operation and arcing can be applied to determine arc. The parameter P derived from γ and A using equation (2) (Fig. 2 d) is capable of identifying arc from 48V to 300V as Fig. 2 (e) shows. 4. Conclusion The TMR sensor can effectively measure the frequency spectrum of the arc current by sensing the magnetic field emanated. Since the differences of the parameter P between normal operation and arcing are unambiguous, it is ideal for determination of the DC arc. In the full paper, the influences of load current and the electrode diameter on the proposed technique will be reported. The details of the experimental results on arc detection of DC system from 48 V to 300V with the current up to 30 A will be presented.

[1] X. Yao, L. Herrera, S. Ji, K. Zou, and J. Wang, "Characteristic study and time-domain discrete-wavelet-transform based hybrid detection of series DC arc faults," *IEEE Transactions on Power Electronics,* vol. 29, no. 6, pp. 3103-3115, 2014. [2] Z. Wang and R. S. Balog, "Arc fault and flash signal analysis in DC distribution systems using wavelet transformation," *IEEE Transactions on Smart Grid,* vol. 6, no. 4, pp. 1955-1963, 2015. [3] C. J. Kim, "Electromagnetic radiation behavior of low-voltage arcing fault," *IEEE transactions on power delivery,* vol. 24, no. 1, pp. 416-423, 2009. [4] T. Instruments, "AN-2154 RD-195 DC Arc Detection Evaluation Board," *Dallas: TI,* 2012. [5] S. McCalmonit, "Low cost arc fault detection and protection for PV systems," *Contract,* vol. 303, pp. 275-3000, 2013. [6] C. Reig, M.-D. Cubells-Beltrán, and D. Ramírez Muñoz, "Magnetic field sensors based on giant magnetoresistance (GMR) technology: Applications in electrical current sensing," *Sensors,* vol. 9, no. 10, pp. 7919-7942, 2009. [7] F. Schimpf and L. E. Norum, "Recognition of electric arcing in the DC-wiring of photovoltaic systems," in *Telecommunications Energy Conference, 2009. INTELEC 2009. 31st International*, 2009, pp. 1-6: IEEE.

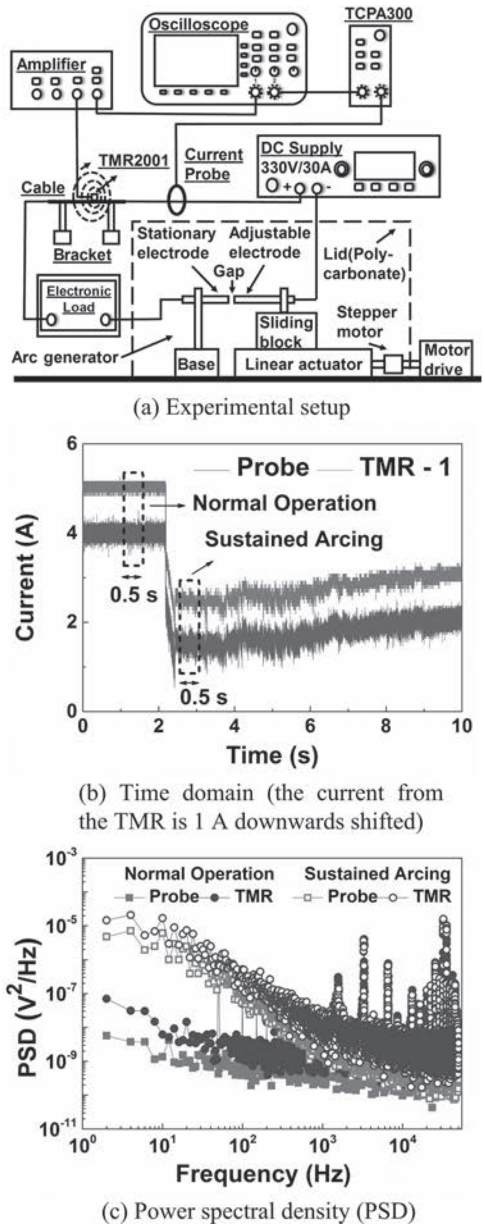

(a) Experimental setup

(b) Time domain (the current from the TMR is 1 A downwards shifted)

(c) Power spectral density (PSD)

Fig. 1. The current from the TMR2001 and current probe when supply with 48V and 5A

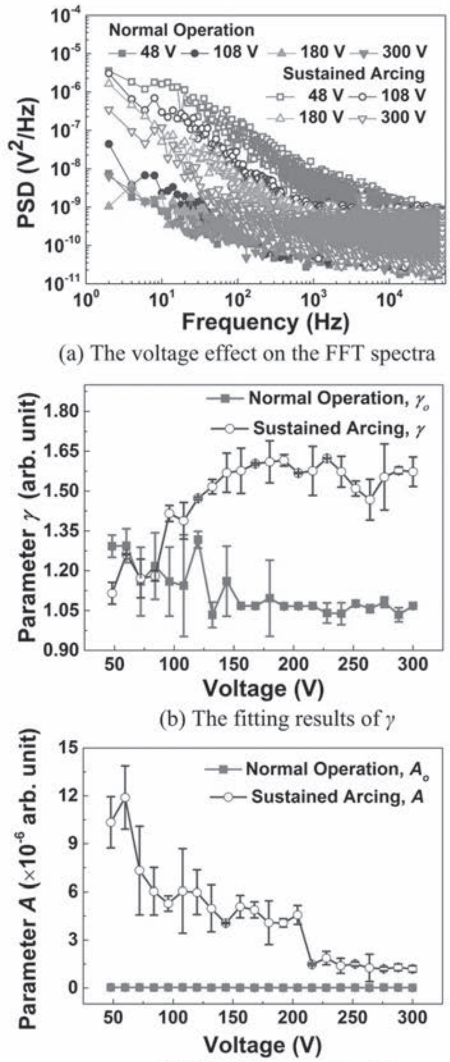

(a) The voltage effect on the FFT spectra

(b) The fitting results of γ

(c) The fitting results of A

$$P = (\gamma_s - 1.9\times10^{-6})\times 10 + A \qquad (2)$$

$$\gamma_s = \frac{\gamma}{k} \qquad k = \frac{\sum_{n=1}^{N} \frac{\gamma_n}{A_n}}{N}$$

where P is the derived parameter,
k is the mean value of γ divided by A.

(d) The equation to combine γ and A

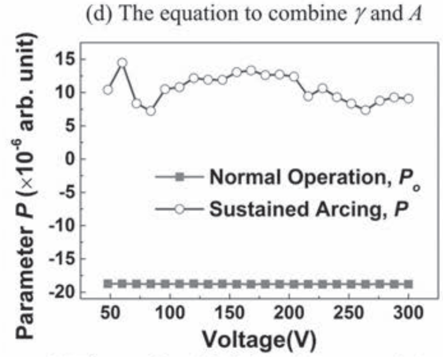

(e) The results of P derived from γ and A

Fig. 2. The frequency spectra and fitting results of normal operation and sustained arcing

CV-03. Structural Health Monitoring using magnetostrictive sensors.

Z. Leong[1], L. Chan[1], W. Holmes[1], J. Clarke[1], N. Walters[1], S. Hayes[1] and N. Morley[1]

1. Materials Science and Engineering, University of Sheffield, Sheffield, United Kingdom

Composites, although possessing good structural properties are subject to complicated modes of failure. These damages are often barely visible as they may be located between composite layers. Thus Structural Health Monitoring (SHM) of aircraft composite is required to determine when barely visible impact damage (BVID) occurs during flight, as if caught early before the damage becomes irreparable, it can be repaired *in-situ*, so saving money and time. BVID causes a strain within the composite, which can be measured, using surface mounted techniques such as fibre optics and piezoelectric sensors [1]. This project investigated an alternative technique using magnetostrictive ribbons in a sensor-actuator setup (henceforth referred to as sensors) to measure the BVID of carbon composites. Computer modelling and experimental research were used to determine the sensitivity and limitations of these magnetostrictive sensors. Composite samples were fabricated from a 2×2mm twill weave pre-impregnated carbon fibre epoxy system (VTC401®) from SHD Composites, with $Fe_{77.5}Si_{7.5}B_{15}$ (FeSiB) magnetostrictive ribbons mounted on both the surface and within the composite in different grid arrangements as sensing elements. Two methods were used to measure the strain response of the fabricated composite samples: through induction measurements, as well as a Hall-effect sensor. Tests were performed to determine if the magnetostrictive sensor could detect composite damage, strain in different conditions and composite delamination. The uniform strain sensitivity of the magnetostrictive sensor was tested using an inductance method utilising a 112 turn pick-up coil connected to an Atlas LCR45 analyser [2]. Passive induction measurements were used to determine how the magnetostrictive sensor responded to a uniform strain applied via bending jigs with different bend radii [3]. Further investigations into the magnetostrictive sensor strain response after mechanical vibrations and temperature cycling were also carried out. Local damage was achieved using impact testing and Figure 1 shows the change in response of the magnetostrictive ribbon before and after damage to the composite. It is observed that for while undamaged (solid shapes), the variation in the inductance is ±2 μH across the length of the composite. After damage, there is a change of 6 μH when the damage is between the ribbons and 14 μH when the damage is on the ribbon. Thus this shows that BVID can be detected using magnetostrictive ribbons. Another consideration is the amount of ribbon attached to the composite for detecting damage, thus an optimised grid design is necessary, which has a spacing that is small enough to detect damage, but not too small that large quantities of ribbon are required, which increase the composite mass. It was found from both modelling and experimental work (Type A in Fig. 1) that 20 mm spacing between the ribbons, provided the ideal weight trade-off for the required detection level. To determine whether the magnetostrictive sensors could detect delamination (which is a primary source of aerospace damage), a series of *in-situ* measurements using a Hall-effect sensor were carried out to measure the change in magnetisation of the magnetostrictive ribbons, during a stress-strain measurement of a composite sample (Fig. 2) obtained from three-point bending tests on an Instron machine. It is observed in the stress-strain curve that delamination occurs at a strain of 0.004, which corresponds to a change in the magnetisation gradient at ~140 secs. At 0.014 strain the composite breaks, and this is observed as a large positive jump in the magnetisation. This was repeated for a large number of samples, and it was determined that the magnetostrictive sensor can give a measurable change in magnetisation that corresponds to a delamination in the composite. Thus, the magnetostrictive ribbons are also able to detect delamination of composites, before failure. In conclusion, magnetostrictive ribbon sensors for structural health monitoring are a real alternative to existing methods. They are able to detect both barely visible damage and delamination within composites. Acknowledgements: Part of this research was funded under the Cleansky2 scheme, for the project SHERLOC JTI-CS-2009-01-GRA-01-005

[1] Backman, B F, 2005, *Composite structures, design, safety and innovation*, (Amsterdam: Elsevier) [2] Al-Taher A et al, *Journal of Physics: Conference Series*, 903, 012010, (2017) [3] Jones RM, 1998 *Mechanics of composite materials*, (Philadelphia, PA: Taylor & Francis)

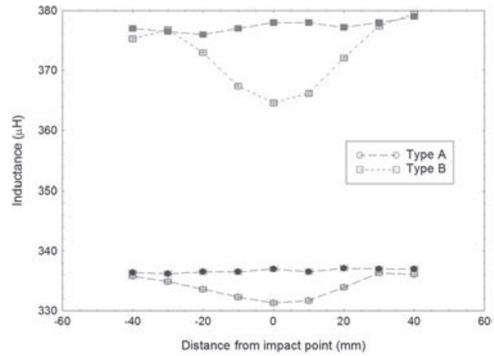

Fig. 1. BVID impact response profile for inductance against distance to impact point. FeSiB ribbons Type A (damage between ribbons) and B (damage on ribbon) configuration. Closed shapes are for no damage and open shapes are for damaged samples.

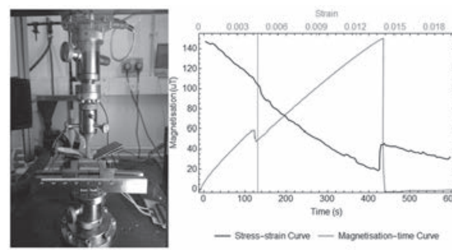

Fig. 2. a. 3-point bend set-up of a composite sample with delamination observed. 2b. Overplot of a stress vs strain curve of a 4-ply composite, with a magnetostrictive ribbon attached and Magnetisation vs time measured simultaneously with the stress-strain curve.

CV-04. Serial MTJ sensors for detection back-side defects by eddy current testing.

Z. Jin[1], M. Oogane[1], M.b. Mohd Noor Sam[1], K. Fujiwara[1] and Y. Ando[1]
1. Applied Physics, Tohoku University, Sendai, Japan

In recent years, magnetic tunnel junctions (MTJs) based on MgO barrier have been attracted attention due to their high tunnel magneto-resistance (TMR) effect. MTJ based sensors enable us to measure very small magnetic field because of their high sensitivity and can be used in various industry fields [1]. Nondestructive eddy current testing (ECT) have been investigated using MTJ sensors for detection of surface defects. However, it is necessary to develop sensors to detect defects not only on the surface but also in deep. A serial MTJ sensor can realize a high signal-to-noise ratio (SNR) during inspection of deep defects due to improvement of sensitivity by optimizing number of MTJs [2]. In order to obtain high SNR for detection of deep defects in ECT measurements, we fabricated serial MTJ sensors with various numbers of MTJ. Furthermore, we systematically investigated their sensor performance on ECT measurements. The film structure of MTJ devices was SiO_2-sub./Ta(5)/Ru(10)/Ta(5)/$Ni_{80}Fe_{20}$(70)/Ru (0.9)/$Co_{40}Fe_{40}B_{20}$(3)/MgO(2)/$Co_{40}Fe_{40}B_{20}$(3)/Ru(0.9)/$Co_{75}Fe_{25}$(5)/$Ir_{22}Mn_{78}$(10)/Ta(8) (in nm). The series of 4, 16, 28, 40, and 52 MTJs with 10×10 μm^2 top pinned layers and 15×60 μm^2 bottom free layers were fabricated with photolithography and ion milling processes. After fabrication, the fabricated MTJs were annealed twice in a vacuum chamber using different directions and temperatures for obtaining a linear *R-H* curve [3]. An automatic ECT system was composed of an excitation coil with a function generator and sensing probe with the prepared MTJ device. The back-side pits with various diameter (from 4 mm to 8 mm) and depth (2.5, 5.0 and 7.5 mm from the detection surface) in 10 mm-thick copper specimens were inspected by using fabricated MTJ sensors. Figure 1(a) shows the MTJs number (*N*) dependence of detectivity in serial MTJ sensors measured by uniform magnetic field using a Helmholtz coil. The result shows that detectivity of MTJ sensors improves with increasing number of MTJs, which indicates that the fabricated sensor with 52 serial MTJs can offer high SNR for the uniform magnetic field. As shown in Fig. 2(b), the defect signal is observed when using ECT probe with a serial MTJs sensor ($N = 28$). However, since the secondary magnetic field induced from eddy currents in specimens is not uniform, the SNR strongly depends on distance between MTJ sensors and specimens. As shown in Figure 2(a), when an excitation field with low frequency (100 Hz) was used to detect back-side pits with various depths, the signals were almost saturated at $N > 28$. Fig. 2(b) shows SNR for inspection of defects with various depths. The serial MTJ sensor with 28 serial MTJs exhibited the highest SNR for detection of back-side pits regardless of the depth. This study confirmed that the optimized MTJ sensor can be used to detect deep defects in conductive materials with a high SNR in ECT measurements.

[1] J. Lenz and A. S. Edelstein, IEEE Sens. J. 6, 631 (2006) [2] R. Guerrero, M. Pannetier-Lecoeur, C. Fermon, S. Cardoso, R. Ferreira, and P. P. Freitas, J. Appl. Phys. 105, 113922 (2009). [3] K. Fujiwara, M. Oogane, F. Kou, D. Watanabe, H. Naganuma, and Y. Ando, Jpn. J. Appl. Phys. 50, 013001 (2011).

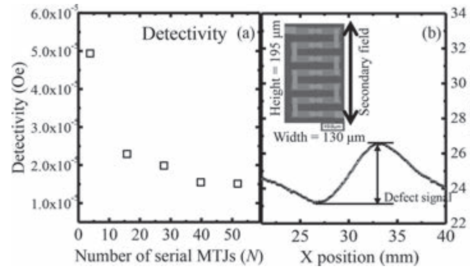

Fig. 1. Detectivity of different fabricated sensors and detection result. (a)Relationship of detectivity and serial MTJ number *N*. (b)Detection of back-side pit (5 mm deep and 6 mm diameter) using probe with 28 serial MTJs sensor at excitation field (100 Hz). The insets are microscopic image of 28 serial MTJs in 7 rows. Owing to small width (130 μm) of sensor, the "point-like" ECT measurement can be conducted, and the rows and height of sensor increased with increasing MTJ number *N* for different sensors.

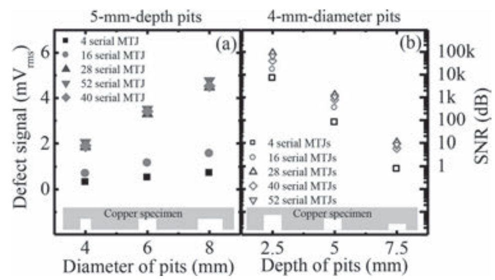

Fig. 2. The specimen that contains various back-side pits was inspected by using ECT probes with different sensors. (a)Output signal variation for back-side pits with various diameters but same wall thinning rate. (b)SNR for detection of back-side pits with various depths but same diameter. Here, the depth was defined as the distance from the bottom of pit to detection surface.

CV-05. Detection of Slit Defects on Backside of Steel Plate Using Low-Frequency Eddy-Current-Testing.

W. Yoshimura[1], R. Tanaka[1], *T. Sasayama*[1] and K. Enpuku[1]
1. Kyushu University, Fukuoka, Japan

INTRODUCTION Ferromagnetic materials such as steel have high magnetic permeability, and thus their skin depth is shallower than that of non-ferromagnetic materials. Therefore, inspection at low frequency is required to examine a thick steel plate using eddy current testing (ECT) [1], [2]. Previously, we have demonstrated, using an electromagnetic simulation in conjunction with the finite element method, that the slit defect in the backside of the steel plate can be detected when the excitation frequency is low enough [3]. In this study, we propose a system that detects slit defects in the backside of the steel plate using low-frequency-ECT (LF-ECT). *METHODS* Figure 1 shows the developed LF-ECT system. Two excitation coils were arranged on the upper side of the steel plate, and one detection coil was placed between these excitation coils to obtain the magnetic flux density B. The amplitude and frequency of the excitation were set to 2 A and 4 Hz, respectively. The output voltage of the detection coil was amplified with a low-noise preamplifier (SA-400F3, NF Co.) and then fed to a lock-in amplifier (LIA) (LI5640, NF Co.) to obtain the in-phase (real part of the magnetic flux density) and out-of-phase (imaginary part of the magnetic flux density) components. The excitation and detection coils were moved simultaneously by 5 mm using two-axis motorized stages (OSMS26-300(XY), Sigma-koki Co., Ltd.). We used an SM490A steel plate as a test specimen. The thickness of the steel plate was 10 mm. A crack of length 50 mm and width 10 mm was made on the back of the steel plate. The thickness of the crack, d, was 6 mm. In this study, we also established the more suitable current direction to detect the defects in these coils, as shown in Fig. 1. *RESULTS* Figure 2 shows the imaginary part of the magnetic flux density distribution Im[B] obtained by the detection coil. The distribution when the excitation current is in opposite direction in the two excitation coils is shown in Fig. 2(a), whereas the distribution when the excitation current is in the same direction in the two coils is shown in Fig. 2(b). In Fig. 2(a), the positive and negative values of Im[B] are observed in the vicinity of the edges of the defect. In contrast, only the positive value of Im[B] is observed at the defect in Fig. 2(b). These results suggest that the method to flow the excitation current in the same direction as shown in Fig. 1(b) is more suitable to detect the position of the defects. *ACKNOWLEDGMENTS* This work was supported in part by the Cross-Ministerial Strategic Innovation Promotion Program (SIP), Cabinet Office, Government of Japan.

[1] T. Sasayama, T. Ishida, M. Matsuo, and K. Enpuku, IEEE Trans. Appl. Supercond. 26, 9001305 (2016). [2] K. Tsukada, Y. Haga, K. Morita, N. Song, K. Sakai, T. Kiwa, and W. Cheng, IEEE Trans. Magn. 52, 6201504 (2016). [3] R. Tanaka, T. Sasayama, M. Matsuo, and Keiji Enpuku, Proc. Intermag, BN-05 (2017).

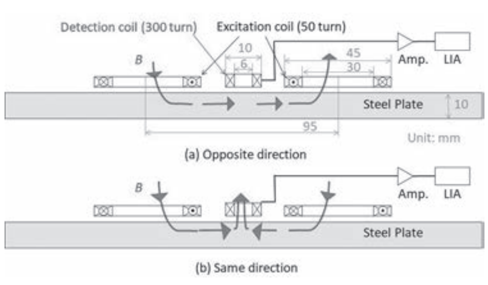

Fig. 1. Developed LF-ECT system when the excitation current in the two excitation coils is in the (a) opposite and (b) same direction.

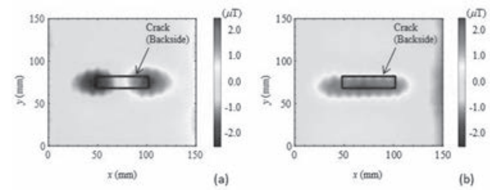

Fig. 2. Imaginary part of the magnetic flux density distribution when the excitation current in the coils is in the (a) opposite and (b) same direction.

CV-06. Detection and identification of object based on a magnetostrictive tactile sensing system.

B. Zhang[1], B. Wang[1], Y. Li[1], W. Huang[1] and L. Weng[1]
1. Hebei University of Technology, Tianjin, China

Tactile sensing is important for the exploration and manipulation of object, and a lot of research work has been done on the design and characteristic testing of the tactile sensor[1]. The research work mainly focuses on piezoresistive and piezoelectric tactile sensors[2-4], while theoretical and experimental studies are a little on piezomagnetic tactile sensors. In fact, the piezomagnetic tactile sensor has the advantages of high precision, simple signal processing circuit and less influence on temperature, compared with piezoresistive and piezoelectric sensors. The tactile information can be used to detect the hardness of objects, and then, to identify the degree of hardness. Here, a magnetostrictive tactile sensing system has been founded for acquiring tactile information corresponding to the pressure and stiffness. The magnetostrictive tactile sensing system can be used to test the grasp force of manipulator and detect the stiffness of object. The system consists of magnetic field regulating device, sensor, oscilloscope, manipulator, signal acquisition and control circuit. The core component is a tactile sensor based on the inverse magnetostrictive effect, and it is mainly composed of hard touch rod, Galfenol cantilever beam, permanent magnet and Hall element. The magnetic flux loop formed by permanent magnet and Galfenol cantilever beam. The sensor is mounted on a mechanical finger and move toward the sample object slowly. When the fingers touch the surface of the object, the mechanical fingers press a distance of 6mm. The mechanical finger torque controller provides a clamping force correlating to control value. We record the time series that the sensor provides during a full palpation procedure. Based on this dynamic information, different objects can be detected and identified. Fig.1 shows the relationship between the tactile sensor output voltage and time for four samples of different hardness, in the bias magnetic field of 2.56 kA/m. Four samples are sponge, foam 1, silica gel and foam 2 respectively. Simultaneously, the four samples are cubes with size of 3 centimeters. The steady-state output voltage of sponge, foam 1, silica gel and foam 2 is about 54 mV, 130 mV, 165 mV and 225 mV respectively. From Fig.1, the output voltage rising gradient and steady-state voltage of the sensor increase with the hardness of the samples, which is able to reflect the hardness degree of samples. A robotic gripper with sensor mounted on its finger performs a palpation procedure on a set of objects. By gripping an object, the robot explores the material properties, and acquires tactile information. Each object is grasped 30 times, and the corresponding sensor characteristic distributions of the four objects with different hardness are obtained as shown in Fig. 2. A number of training examples are stored for each object, and the objects are divided into four hardness grades of A, B, C and D. After the training samples are determined, a new observation is compared to the training data, and is assigned the label using the Extreme Learning Machine classifier algorithm. Because the shape of the observations are not the same, grasping process is slightly changed. After the object is detected to be contacted, it is further pressed into 6mm for hardness identification. An object is detected and identified, based on the Extreme Learning Machine classifier algorithm, the output voltage rising gradient and steady-state voltage. The complex matrixes at the best classification accuracy are plotted to show the recognition rate of each object. This kind of algorithm can be applied to real time operation, and the object can be recognized during the grasping process. It means that the system is able to identify object successfully.

[1]Drimus A, Kootstra G, Bilberg A, et al. "Design of a flexible tactile sensor for classification of rigid and deformable objects". Robotics & Autonomous Systems, 62(1) 3-15, (2014). [2]Kawamura T, Nejigane K, Tani K. "Force Response Characteristics for Fine Deformation of CMC Touch Sensor in a Hybrid Tactile Sensor System". Vojnosanitetski Pregled, 23(12) 817-822, (2017). [3]Kirthika S K, Ponraj G, Ren H. "Fabrication and Comparative Study on Sensing Characteristics of Soft Textile-Layered Tactile Sensors". IEEE Sensors Letters, 1(3) 1-4, (2017). [4] Wang Z, Jiang R, Li G, et al. "Flexible Dual-Mode Tactile Sensor Derived from Three-Dimensional Porous Carbon Architecture". Acs Applied Materials & Interfaces, 9(27) 22685-22693, (2017).

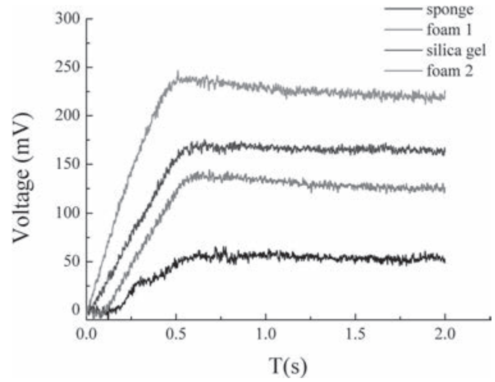

Fig. 1. Relationship between the tactile sensor output voltage and time for four samples of different hardness

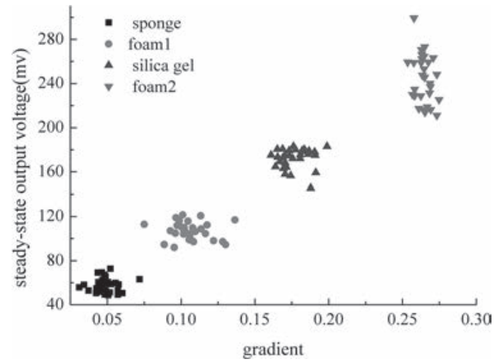

Fig. 2. Feature distribution of four samples

CV-07. Strategy for determining a magnet position in a 2D space using 1D sensors.

P.M. Ribeiro[1], M. Neto[1] and S. Cardoso de Freitas[1]
1. INESC - Microssistemas e Nanotecnologias and IN, Lisbon, Portugal

Various useful applications arise from detecting the position of a magnet (e.g. encoders) [1], or transduce this position into another interesting physical quantity (e.g. force) [2]. To determine these quantities, the magnetic field of the reference magnet is measured in all spatial directions, using one magnetic sensor to measure the magnetic field generated by the magnet on each of the spatial directions. However, the fabrication of monolithic 2D and 3D magnetic sensors pose some fabrication challenges [3], particularly, the inability to anneal these sensors and retain two or three dimensional sensitivity, limiting the fabricated sensors performance and behaviour uniformity over large area samples or wafers. In this work, we present a strategy to detect the position of a magnet within a plane through the magnetic field it generates in another parallel plane in space, detected using an array of strategically placed TMR (tunnelling magnetoresistive) sensors. This strategy consists in placing the magnet over the sensor, with its magnetic moment direction (Y direction) orthogonal to both the sensor plane normal vector (Z direction) and sensitive direction (X direction). When placed in this configuration, the magnetic field intensity in the sensor sensitive direction will be that of a quadrupole, within the sensor plane (Figure 1). The magnetic field data is then captured at four points in the sensitive plane and used as the input parameters of a magnetic field vs position fit, which can then be used to determine the position of the magnet that would generate the magnetic field measured at each of the four sensitive elements. To optimize the design of this setup, a simulation was performed using COMSOL Multiphysics, assuming the magnetic field was generated by a cylindrical NdFeB magnet with 1 mm in diameter and height and characterized by a remanence of 13.2 kG. From this analysis, we determined that the best configuration to take advantage of the whole sensitive range of the sensor without reaching saturation would be to place this magnet at a 3 mm distance from the sensitive plane, which in turn resulted in the maximums and minimums of the quadrupolar field to be located at 1.5 mm in the X coordinate and 1.5 mm in the Y coordinate from the centre of the magnet, with intensities of $\pm$ 15 Oe. By placing four sensitive elements approximately where the maximum and minimum magnetic fields generated by the quadrupolar field are, one can achieve the maximum variability of the signal and therefore, the maximum sensitivity. The TMR sensor stack (from bottom to top: Ta 50/[Ru 150/Ta $50]_{x3}$/NiFe 30/CoFe 30/Al_2O_3 14/CoFe 30/Ru 6/NiFe 30/MnIr 180/Ru 150/Ta 50, thicknesses in Å) was deposited at INESC-MN by ion beam [4] and patterned into 4 sensitive regions, at a distance of 1.5 mm from the centre of the die in both X and Y, with each sensitive region consisting of 49 magnetic tunnel junctions (with 20x2 μm^2 area) in series, yielding a sensitivity of 886 Ω/Oe. The magnetic field was generated by a cylindrical magnet with the aforementioned characteristics. This magnet was fixed 3 mm over the sensor, which was attached to a precision motorized stage that moved within an area of 2x2 mm^2 with a step resolution of 20 μm in both planar directions. 10000 experimental resistance/position points were acquired for each of the four TMR sensors, which were used to train various predictive algorithms, while an ensemble of 100 resistance/position points were measured independently from the training ensemble to test the data fits. The best performing algorithm consisted in using two bootstrapped-aggregated prediction trees [5], one for each output coordinate, yielding a root mean square (RMS) error of 96 μm between the real position of the magnet and the value predicted by this method (Figure 2). The use of artificial neural networks (ANN) [6] was also tested. The ANN architecture yielding the best fit was a feed-forward network comprised of a 4-neuron input layer (one for each sensor signal), a hidden layer of 20 neurons, and a 2-neuron output layer (for the X and Y positions of the sensor). The RMS error achieved by this method was of 191 μm between the real position of the magnet and the position predicted by this method. Despite the loss in precision, it is computationally less demanding to extracting predictions, and requires less memory (2.9 kB vs 10 MB required by the prediction tree), allowing the possibility of being implemented on embedded processors, and consequently, in miniaturized devices.

[1] A. J. Fleming, *Sensors and Actuators A: Physical, vol. 190, pp. 106-126, 2013* [2] T. Paulino *et al.*, *2017 IEEE International Conference on Robotics and Automation (ICRA), pp. 966-971, 2017* [3] Y. Lee *et al., Journal of Applied Physics, vol. 117, 17A320, 2015* [4] S. Knudde *et al.*, *Journal of Magnetism and Magnetic Materials*, vol. 412, pp. 181-184, 2017 [5] L. Breinman, *Machine Learning*, vol. 45, pp. 5-32, 2001 [6] H. Simon, *Neural Networks: A Comprehensive Foundation*, 2nd Ed., Prentice Hall, 1998

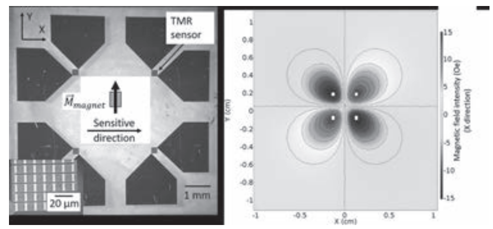

Fig. 1. Left: Fabricated sensor and device setup. The magnet is fixed 3 mm above the die, with its magnetization point in the direct normal to both the vector normal to the plane and the sensing direction of the MTJs (Inset: microphotograph of the TMR sensor array). Right: Simulation results using with the simulation parameters mentioned in the text. The white squares represent the points where the sensing elements were placed (corresponding to the maximum values of magnetic field).

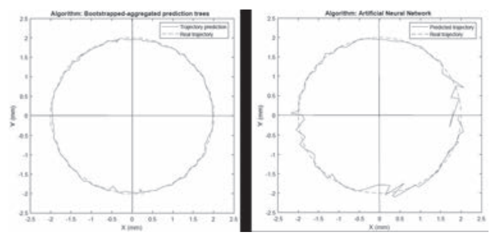

Fig. 2. Comparison between the real trajectory of the magnet over the sensor and the trajectory predicted by the algorithms, given the signal of the four sensors. Left: Real vs predicted trajectory by the bootstrapped-aggregated prediction tree fit. Right: Real vs predicted trajectory by the ANN fit.

CV-08. Analysis of a Defect Signal Deformations Induced by Eddy Current in RFECT System for Pipeline Inspection.

H. Kim[1], H. Yoo[2] and G. Park[3]
1. Electrical and Computer Engineering, Pusan National University, Busan, The Republic of Korea; 2. Korea Gas Corporation, Incheon, The Republic of Korea; 3. Electrical Engineering, Pusan National University, Busan, The Republic of Korea

1. Introduction The remote field eddy current testing (RFECT) system is generally used for inspection of ferromagnetic and conductive tubes such as pipelines. One main advantage of this technique is the high sensitivity to detect a defect on the external surface of pipe wall even if systems are located inside the pipelines [1]. This system consists of an exciting coil to generate the alternating magnetic field and receiving sensor coils for detecting defect signals. Both coils could be wound coaxially or vertically with respect to the tested pipe. Based on the RFEC phenomenon, there is remote field zone that the circumferential eddy currents induced by the source field are spread in the external surface of the pipe [2]-[3]. In general, this remote fields are located about two times of pipe diameters from the exciter coil [3]-[5]. Hence, the receiving coil should be placed in the remote field zone to detect the defect signal efficiently. In previous study, the unknown defect size is being mainly estimated by using phase angle difference between sensing signal and reference input signal because the amplitude of sensing signals is too small [6]-[7]. In such a small signals, eddy current signals imposing the size and shapes of defects are mixed with induced magnetic fields of defects, which causes the distortions of sensing signals. To increase the sizing accuracy of defects, it is important to measure the peak amplitude variation of defect signals at receiving coils exactly and analyze the distribution patterns of eddy currents in the pipeline. In this paper, the distribution of eddy currents on the pipe wall is computed by finite element method to predict the electromagnetic field signal deformations in the vicinity of the defect. And then, the effects of the induced magnetic field on defect signals in receiving coils are analyzed with respect to the different depth size of defects. The amplitude and the distribution pattern of defect signals are computed by 3D finite element method and the method to eliminate the signal distortions caused by induced magnetic fields are presented. Simulated results in this paper agreed well with measuring ones. 2. The Structure of RFECT System Fig. 1(a) shows the basic structure and diagram of RFECT system for inspecting 8 inches gas pipelines. An exciter coil is fed the AC voltage source with a low frequency to induce the alternating magnetic field on the pipe wall considering effects of wall thickness and eddy current distribution. Sensing coils are arranged along the full periphery in the interior of the pipe for detecting localized defects. Both coils are separated by a distance greater than twice the diameter of pipe. 3. Analysis of Defect Signal Deformations 3.1. Numerical analysis To predict electromagnetic field signal at the position of receiving coils efficiently, it is necessary to analyze the distribution of eddy current density on the pipe wall near the defect. The variation of eddy current distribution around the defect causes the magnetic field induced on the receiving coils to be distorted. As a result, both the amplitude and phase difference of the induced voltage on the receiving coils are affected by the reduction of pipe thickness. The distribution and magnitude of magnetic flux density for inspection system are computed by numerical analysis to derive defect signals. Assuming a quasi-stationary approach, the eddy current analysis is performed by 3-D finite element method. 3.2. Effects of induced magnetic field on the defect signal The background voltage signal in a receiver coil is defined as the offset of induced magnetic fields caused by eddy currents on the pipe wall with no defects. In general, both the amplitude and distribution of offset signal are changed with respect to the defect depth. Therefore, the defect signal is determined by combining the offset signal with the effects of induced magnetic field distortion in the vicinity of a defect. However, the pattern of defect signal distribution varies with the depth size. 4. Experimental Verification Fig. 1(b) show the experimental setup of RFECT system to verify the characteristics of defect signals. The RFECT system is pulled by the traction system from one side to the other side of the pipe specimen. Measured signals passing through the lock-in amplifier board from the receiving coil is converted as DC output voltage signals. Fig. 2 shows results that patterns of defect signals depend on defect depth. The defect signal includes the background offset with components of signal deformations. 5. Conclusion The advantage of RFECT is to detect the defect on the external surface of the pipe wall. It is used to be good method for inspecting gas pipelines. For the maintenance, it is essential to predict and analyze the amplitude variation of defect signals precisely because the amplitude of defect signals includes a lot of information to estimate the size of defects. This paper focused on the analysis of defect signal deformations induced by eddy current on the pipe around sensor coils with respect to the different depth size of defects. From the result of numerical simulation and experimental measurement, the defect signal was determined by the background offset with components of local field distortion. Eventually, it turned out that the pattern of defect signal distribution could be varied with defect depth.

[1] T. R. Schmidt, "Instrument Promises to Permit Measuring Wall Thickness of Pipelines in Place," Materials Protection, vol. 2, no. 1, pp. 8-12, January 1963. [2] T. R. Schmidt, "The Remote Field Eddy Current Inspection Technique," Materials Evaluation, vol. 42, pp. 225-300, February 1984. [3] S. P. Sullivan, A Description of the Remote Field Eddy Current Effect in Metallic Tubes, Ph.D. thesis, Queen's University, Canada, 1989. [4] T. R. Schmidt, D. L. Atherton, and S. P. Sullivan, "Use of One-Dimensional Skin-Effect Equations for Predicting Remote-Field Characteristics, Including Wall-Thickness versus Frequency Requirements," Materials Evaluation, vol. 47, no. 1, pp. 76-79, January 1989. [5] S. P. Sullivan, D. L. Atherton, and T. R. Schmidt, "Comparing a One-Dimensional Skin Effect Equation with Through Transmission Eddy Current Phenomena," British Journal of Non-Destructive Testing, vol. 32, no. 2, pp. 71-75, February 1990. [6] H. Ostermeyer, D. Stegemann, "New Aspects for Remote Field Eddy Current Probe Development," 7th ECNDT, vol. 4, no. 8, August 1999. [7] Albert Teitsma, Julie Maupin, "Reduced Mandated Inspection by Remote Field Eddy Current Inspection of Unpiggable Pipelines," Technical Final Report, pp. 12-15, October 2006.

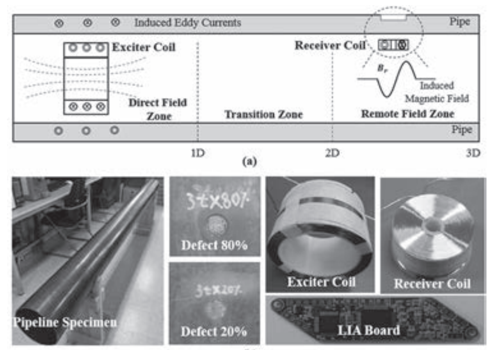

Fig. 1. The structure of RFECT System. (a) Schematic diagram. (b) Experimental setup.

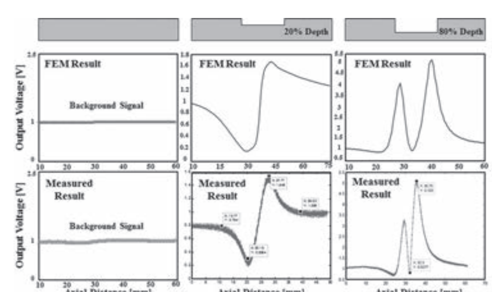

Fig. 2. Effects of the induced magnetic field on defect signals with respect to defect depth.

CV-09. Fault Line Identification of HVDC Transmission Line by Frequency Spectrum Correlation Based on Capacitive-Coupling and Magnetic-Field-Sensing.

K. Zhu[1], W. Lee[1] and P. Pong[1]
1. Electrical and Electronic Engineering, The University of Hong Kong, Hong Kong, Hong Kong

The proliferation of high-voltage direct current (HVDC) system is growing fast thanks to its distinct technical advantages such as long-distance bulk-power delivery at a lower cost, asynchronous interconnections, and reduced power loss [1]. The protection system of HVDC system must detect, identify and isolate the fault quickly to keep the system stable by isolating only the components that are under fault, whilst leaving the rest of the network in operation [2]. However, the criteria of under-voltage and voltage derivative protection systems may fail because there also arises a large voltage drop/variation on the healthy transmission line due to the electromagnetic coupling between HVDC transmission lines incurred by the sharp transient current from the faulty one [3, 4]. Thus the healthy line could be mistakenly identified and isolated, resulting in further disruption and delaying system restoring time. In order to distinguish the healthy HVDC transmission line from the faulted one, a fault line identification technique based on the frequency spectrum correlation is developed in this paper. Firstly, the equivalent circuit of a single-circuit HVDC system was established in Fig. 1(a) to analyze the electromagnetic coupling between HVDC transmission lines based on voltage and current of the positive (U_p, I_p) and negative (U_n, I_n) polarity, respectively (Fig. 1(a)). As such, the voltage of one transmission line can be correlated with the current of the other line as (taking the voltage of negative polarity as an example) [3] $U_{n\_m}(t_2) = U_n(t_2)-(I_n(t_2) \times R_n + L_n (dI_n/d_t) - M_{pn}(dI_p/d_t))$ (1) where R_n (L_n) is the line resistance (self-inductance), M_{pn} is their mutual inductance, dI_n/d_t (dI_p/d_t) is the current change rate within a time from t_1 to t_2. By taking the Fourier Transform of Eq. (1), the frequency spectrum of voltage (£($U_{n\_m}(t_2)$)) must exhibit a similar pattern with the one of the varied current (£(dI_p/d_t)) if this voltage variation is incurred by the current change. For example, the frequency spectrum of line current (I_p, I_n) and voltage at the measurement point (U_{p_m}, U_{p_n}) after a grounding short-circuit (lasting 0.03s) of the negative transmission line is analyzed in Fig. 1(b). Since the voltage variation of the positive pole is incurred by the current change of the negative pole, the frequency spectrum of the voltage for positive pole (U_{p_m}) exhibits a high similarity with the current of the negative (I_n) while the voltage of negative pole (U_{n_m}) with the current of positive pole (I_p) is not. Therefore, the similarity degree of frequency spectrum between voltage of a line and current of another can be used to identify reliably whether the voltage variation is incurred by electromagnetic coupling or fault, and thus avoiding false operation of protection system. In order to verify this technique, a single-circuit HVDC system was established in PSCAD/ EMTDC [5] as shown in Fig. 2(a). A grounding short-circuit fault was simulated with the system operating in the normal status under 2 kA rated current. The frequency spectrum correlation coefficient (C_1 describes the spectrum similarity between the voltage of positive polarity and current of the negative polarity, and C_2 vice versa) after the fault was calculated (Fig. 2 (b) and (c)). The result shows that the voltage of the positive polarity and the current of the negative polarity are highly correlated (C_1 remains large and C_2 drops sharply) after the fault happens at 1.00 s, indicating this voltage is induced by the current variation of negative polarity rather than by the short-circuit fault itself. As such, despite the fact that a large voltage variation on the positive polarity occurred by electromagnetic coupling, this healthy line would not be identified as the faulty line. By comparing the sampling window of 0.01, 0.005, 0.001s, it can be observed that the shorter time window for frequency spectrum analysis can provide a faster response time based on a higher spectrum resolution [6]. A capacitive-coupling and magnetic-field-sensing assisted platform composing of two paralleled induction bars, and an array of magnetic sensors at both ends was previously developed in [7, 8], and it is capable of measuring overhead line voltage and current. This platform was adopted to implement this identification technique, and the details of simulation results will be reported in the full paper. This identification technique can further enhance the reliability of HVDC system by avoiding the unnecessary outages due to accidental shut down of healthy lines, fostering the interconnection of load centers with the use of HVDC system for increased power transmission capacity.

[1] M. P. Bahrman and B. K. Johnson, “The ABCs of HVDC transmission technologies,” *IEEE Power Energy Mag.,* vol. 5, pp. 32-44, 2007. [2] P. M. Anderson, *Power Sys. Prot.*: Wiley, 1998. [3] H. Guo, Q. Wu, S. Li, Y. Lu, A. Zhang, and T. Li, “Study on the influence of electromagnetic coupling of UHVDC power transmission lines on the voltage derivative protection,” *Power Sys. Prot. Ctrl.,* vol. 43, pp. 1-6, 2015. [4] R. Benato and F. Dughiero, “Solution of coupled electromagnetic and thermal problems in gas-insulated transmission lines,” *IEEE Trans. Magn,* vol. 39, pp. 1741-1744, 2003. [5] P. Liu, R. Che, Y. Xu, and H. Zhang, “Detailed modeling and simulation of+ 500kV HVDC transmission system using PSCAD/EMTDC,” in *IEEE Conf. Pwr. Nrg. Engineering*, 2015. [6] R. N. Bracewell and R. N. Bracewell, *The Fourier transform and its applications,* vol. 31999: McGraw-Hill New York, 1986. [7] K. Zhu and P. W. T.Pong, “Non-Contact Electric-Coupling-Based and Magnetic-Field-Sensing-Assisted Sensing Technique for Monitoring Voltage of HVDC Transmission Lines,” presented at the *IEEE Sens. 2017*, Glasgow, Scotland, UK, 2017. [8] X. Sun, Q. Huang, Y. Hou, L. Jiang, and P. W. T. Pong, “Noncontact operation-state monitoring technology based on magnetic-field sensing for overhead high-voltage transmission lines,” *IEEE Trans. Power Del.,* vol. 28, pp. 2145-2153, 2013.

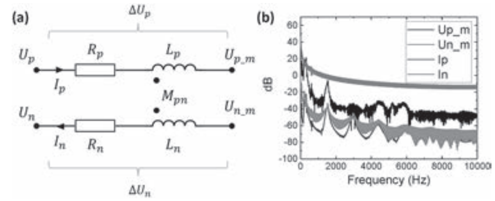

Fig. 1. Frequency spectrum analysis. (a) An equivalent circuit consisting of line resistor, inductor, and mutual inductor for HVDC transmission lines. (b) Frequency spectrum (time window = 0.005 s) for voltage (U_{p_m}, U_{p_n}) and current (I_p, I_n) of positive and negative polarity, respectively.

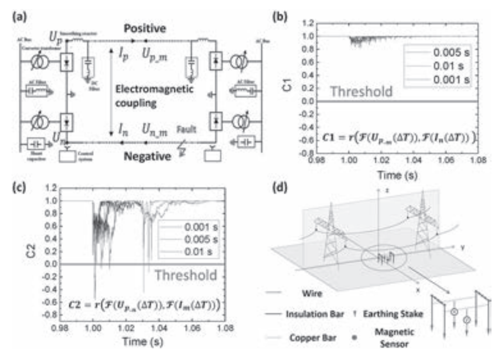

Fig. 2. Validation of the proposed identification technique by simulation. (a) a ±500 kV single-circuit HVDC system simulating a grounding short-circuit on the negative pole. (b) Frequency spectrum correlation between the positive polarity voltage and negative current (C_1). (c) Frequency spectrum correlation between the negative polarity voltage and positive current (C_2). (d) Capacitive-coupling and magnetic-field-sensing assisted platform consisting of induction bars and magnetic sensors.

CV-10. Searching an avalanche victim using a transmitter with a rotating magnetic dipole.

A. Chiba[1] and T. Nara[1]
1. The University of Tokyo, Tokyo, Japan

1. Introduction Avalanche beacons are transmitters and receivers of 457 kHz magnetic field which are widely used for rescue of avalanche victims. Conventionally, a dipolar magnetic field is created by using one of three, orthogonal coils in a victim's transmitter, and then a searcher measures its magnetic flux density by using all three coils of a receiver to find a victim. A problem, however, is that a searcher should make a detour along the magnetic line of force to reach the victim. In this paper, we propose to use all the three coils of a transmitter in order to navigate searchers linearly to a victim. Detecting the posture of a transmitter by using accelerometers, we create a magnetic dipole equivalently rotating in the xy-plane. Then, the searcher can determine the direction to linearly proceed toward the victim by quadrature detection of the x- and y-components of the magnetic flux density. Although the use of a rotating magnetic dipole was proposed by Paperno [1] for magnetic tracking, their method needs to know the phase of a signal input to the transmitter, which is not applicable to avalanche rescue. Our method can navigate the searcher irrespective of the phase of the transmitter's signal. 2. Method As shown in Fig.1, the xyz-axes are set along the receiver's orthogonal coils, where the xy-plane is a searching plane. The aim is to find a direction of a transmitter viewing from the receiver, ϕ. By putting three orthogonal accelerometers, a rotating matrix R from the xyz-frame to the transmitter's XYZ-frame can be obtained. Then, in order to create a magnetic dipole rotating in the xy-plane with frequency of $f = \omega/(2\pi)$, the current proportional to Ri is input to three orthogonal coils of the transmitter, where $i = \cos \Omega t * (\cos(\omega t + \theta_0), \sin(\omega t + \theta_0), 0)^T$ where $F = \Omega/(2\pi)$= 457 kHz and θ_0 is an initial phase. As shown in Fig.1, denote the envelopes of the x- and y-components of the magnetic flux density measured by a receiver by Bx and By, respectively. Let $I_k = \int B_k \cos \omega t\, dt$ and $Q_k = \int B_k \sin \omega t\, dt$ for $k = x$ and y. Then, we can show that $\tan 2\phi = \{(Q_x+I_y)(I_x+Q_y)+(I_x-Q_y)(I_y-Q_x)\}/\{-(Q_x+I_y)(I_y-Q_x)+(I_x-Q_y)(I_x+Q_y)\}$. Note that this equation holds irrespective of θ_0, showing that the direction of a line along which the searcher should proceed to reach the victim can be determined from the quadrature detection of the magnetic flux density without knowing the initial phase of the transmitter signal. Although ϕ itself is determined up to π, the direction to proceed can be decided by measuring $|B|$. The goal of search, that is, the place just above the victim, can be also judged by detecting the maximum of $|B|$. 3. Experimental results The orthogonal bar coils (BA-200) and variable capacitors (CBM-223) tuned with F = 457 kHz were used as a transmitter. Modulation frequency $f = \omega/(2\pi)$ was 5 Hz. The other, same-type coils were used as a receiver to measure the magnetic flux density. After obtaining its envelope by a quadrature detection with frequency F, the quadrature detection with frequency f was conducted to obtain I_k and Q_k, from which $\tan 2\phi$ was estimated. The transmitter was moved on circles of radius r = 300 mm centered at the receiver, where ϕ = 0, 45, 90, 135, and 180 degrees. Fig. 2 shows the angle errors between the estimated line and the line connecting the transmitter and receiver. The mean and maximum error was 10.7 degrees and 24.3 degrees, respectively, which shows the validity of our method. Experimental results for wider search range has been preliminarily conducted and will be shown in the paper.

[1] E. Paperno, I. Sasada and E. Leonovich, "A new method for magnetic position and orientation tracking," in IEEE Transactions on Magnetics, vol. 37, no. 4, pp. 1938-1940, Jul 2001.

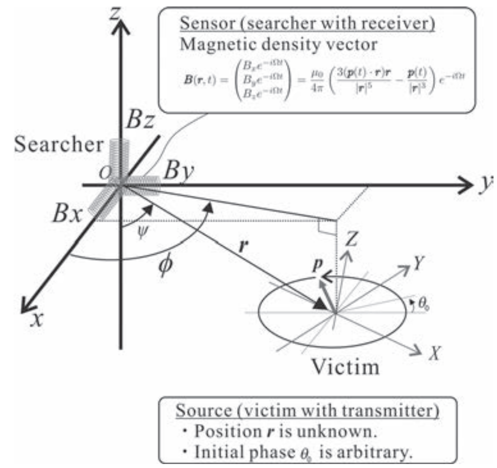

Fig. 1. Problem setting.

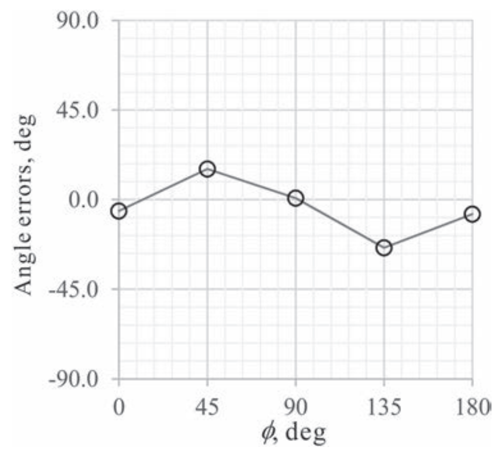

Fig. 2. Angle errors between the estimated line and the line connecting the transmitter and receiver.

CV-11. Determination Scheme for Accurate Defect Depth in Underground Pipeline Inspection by Using Magnetic Flux Leakage Sensors.

H. Kim[1], C. Heo[1], S. Cho[3] and G. Park[2]
1. Electrical and Computer Engineering, Pusan National University, Busan, The Republic of Korea; 2. Electrical Engineering, Pusan National University, Busan, The Republic of Korea; 3. Korea Gas Corporation, Incheon, The Republic of Korea

1. Introduction The magnetic flux leakage (MFL) type nondestructive testing (NDT) has been applied for inspection of defects in ferromagnetic materials such as underground gas pipelines [1]. In this system, the magnetic field is applied to magnetize a steel pipe so as to induce the magnetic leakage fields in the vicinity of defects on the pipeline. A strong magnetic field produced by the permanent magnet could saturates the pipeline so as to leak the magnetic field around the defect sufficiently. Hall sensors equipped along the pipeline measure the leakage fields, then the size of defects could be estimated by the measured signals [2]-[3]. Form the measured sensing signals, decomposing or estimating sizes and shapes of defects are necessary because sensing signals contain the size and shape information of defects [4]-[5]. For the maintenance of pipelines, the estimation of depth size is the most important procedure for the management of safety accident. However, the previous depth estimation contains high error rate inevitably because the depth signal implies the width and length error simultaneously [5]. In conventional method, the depth size of defect is depend on the variables for the axial length and circumferential width of defects, which makes it hard to estimate defect depth independently. So, the previous work for depth estimation showed some errors especially in the large size of depth [5]. This paper focused on the enhanced method for the depth sizing in various defects by using decoupling algorithm to improve the sizing accuracy of defect depth. The functional relationship between signal amplitude and shape factors of defects are derived by the polynomial surface fitting with respect to defect's length and width so as to decouple the errors. To derive a decomposing algorithm, magnetic leakage signals are computed by nonlinear 3-D FEM and measured by hall sensors from standard defects on the 16 inches diameter pipe specimen. Estimated results show good agreements with measured ones. 2. System Structure The structure of MFL system is shown in Fig. 1. It is designed for inspection of the small diameter gas pipeline. Because small pressure of a gas inside the small pipeline is not enough to push and run the NDT system, it is necessary to adopt snake type robot modules to drive the NDT system as shown in Fig. 1(a). NDT system has ten MFL modules inside the pipe. In Fig. 1(b) and Fig. 1(c), every module consists of Nd-Fe-B magnets with steel back-yoke for generating a magnetic field on the pipe. Hall sensors are arranged along the full periphery of each MFL module to detect axial component signal of magnetic leakage flux. 3. Estimation of Defect Depth 3.1. Numerical analysis of defect signal The distribution and magnitude of magnetic flux density for MFL system was computed by using 3D finite element analysis. From simulated results, it is possible to predict the distribution and magnitude variation of defect signal with respect to various shapes of defects by computing the leakage flux density at the sensor position. 3.2. Measurement of defect signal From both FE simulation and experimental measurement, the peak amplitude of defect signal is detected by a hall sensor passing through the center of defects. The signal amplitude of leakage fields is dependent on the shape of defects such as length, width and depth. Especially, the peak amplitude of leakage signal with respect to axial distance is closely dependent on the variation of defect depth. It has a quadratic functional relationship between depth size and peak amplitude of leakage signal when it comes to various shapes of defects. 3.3. New Algorithm for estimating the defect depth A new estimation algorithm to enhance the sizing accuracy of defect depth is presented in this paper. The key point is that if each peak value of maximum depth size could be determined from known data groups instead of obtaining each incorrect coefficient, estimated results could be more reliable. Proposed method is attributed from that the rate of amplitude variation with respect to depth size is almost same even if the shape of defects is different. It is easily verified by using normalization method to data groups about peak amplitude. 4. Experimental Verification Fig. 2 show the experimental results that estimated sizes of defect depth are compared to actual sizes of defect depth. Estimated results are presented by using both the previous and enhanced mechanism for depth estimation. The admitted error bound for defect depth is generally 20%. In Fig. 2(b), most estimated results are well fitted within bound to the actual size, whereas there are some errors in case of more than 50% depth of defects as shown in Fig. 2(a). 5. Conclusion In this paper, an enhanced estimation algorithm is presented for the sizing of defect depth which has coupled error mixing data in pipeline inspection. By using decoupling algorithm, the functional relationship between signal amplitude and shape factors of defects are derived by the polynomial surface fitting with respect to defect's length and width. Magnetic leakage signals computed by nonlinear 3-D FEM are correlated with enhanced algorithm. The experimental results showed that the estimated values from enhanced algorithm reduces error efficiently than conventional works.

[1] Z. Zhang, L. Udpa, S. S. Udpa, Y. Sun, J. Si, "An Equivalent Linear Model For Magnetostatic Non-destructive Evaluation," IEEE Trans. Magn, vol. 32, no. 3, May 1996. [2] H. Haines et. Al., "Advanced MFL Signal Analysis Aids Pipe Corrosion Detection," Pipeline & Gas Industry, pp. 49-63, Mar 1999. [3] G. S. Park, "Analysis of the velocity-induced eddy current in MFL type NDT," IEEE Trans. Magn, vol. 40, no. 2, pp. 663-666, March 2004. [4] R. C. Ireland and C. R. Torres, "Finite element modeling of a circumferential magnetizer," Sensors and Actuators, vol. 129, issue 1-2, May 2006. [5] Hui Min Kim, Gwan Soo Park, "A Study on the Estimation of the Shapes of Axially Oriented Cracks in CMFL type NDT System," IEEE Trans. Magn, vol. 50, no. 2, 7002504, February 2014.

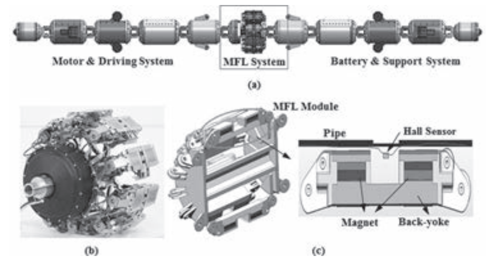

Fig. 1. The structure of MFL System. (a) In-pipe robot system. (b) Total veiw. (c) Side view.

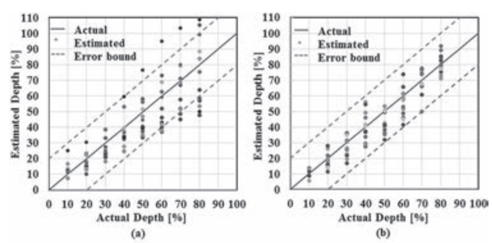

Fig. 2. Estimation results of defect depth. (a) Result from previous work. (b) Result from enhanced work.

CV-12. ***Detecting method of hardened depth in surface hardened steel by magnetic field on steel.***

Y. Gotoh[1], S. Onita[2], T. Horino[2] and Y. Misaka[2]
1. Innovative Engineering, Faculty of Science and Technology, Oita University, Oita, Japan; 2. Research and Development Center, Neturen Co., Ltd., Hiratsuka, Japan

Introduction The surface hardened steel is used in a large-sized ball bearing part or the gear part in a large-sized heavy industrial machine, etc. The inspection of the surface hardened depth is important in the intensity or the guarantee of quality of these parts. Especially, since the size of the hardened steel parts in a large-sized heavy industrial machine is large, the destructive inspection using the Vickers hardness tester, etc. is made difficult. Therefore, the non-destructive inspection method is needed for the evaluation of its hardened depth. The maximum permeability and the conductivity of the hardened domain are smaller than the non-hardening domain inside the steel [1]. Therefore, the electromagnetic non-destructive methods for detecting the surface hardened depth by the difference of flux density inside the surface hardened steel are proposed [2,3]. In this paper, the high sensitivity inspection method using the detecting of the magnetic field on the surface of the hardened steel is investigated. The detection sensitivity of this proposal technique is higher than the method [3] of detecting the flux density inside the hardened steel. The magnetic field is estimated by 3-D nonlinear finite element method (FEM) taking account of the electromagnetic characteristics of the layers with and without hardening. Moreover, the optimal design of the search coil in the proposal sensor for raising detection sensitivity is carried out using the evolution strategy method [4]. The usefulness of this proposal inspection method is shown also from comparison with an experimental verification. Inspection method and modeling of magnetic properties Fig.1 shows the 1/2 domain of the proposed the inspection model for detecting the surface hardened depth inside the hardened SCM440 steel plate. The proposal electromagnetic sensor is composed of a magnetic yoke of lamination of silicon steel plates with an alternating exciting coil, and a search coil for the detecting of the magnetic field on the surface of the hardened steel. As for a search coil in this sensor, the *x*-direction of the magnetic field (B_x) on the surface of the steel plate is detected. The width (*Sw*), length (*Sl*) and height (*Sh*) of the search coil are 9.4mm, 6mm and 1.2mm, respectively. The distance (lift-off : L_o) between the yoke of the sensor and the surface of the hardened steel is equal to 0.5mm. The exciting frequency and ampere-turns are 15Hz and 126AT, respectively. Fig.2 shows the initial magnetization curves of the layer with and without hardening inside the SCM440 steel. And, since the conductivities of the steel plate with and without hardening are 3.61×10^6 S/m and 3.98×10^6 S/m, the permeability and conductivity are decreased with the increase of the hardness. The flux density and eddy current density are analyzed by 3-D electromagnetic FEM taking account of the initial magnetic curves and conductivities of the layers with and without hardening inside the steel. Moreover, the initial magnetic curve and conductivity in the layer between the hardened layer and non-hardened layer in the steel are calculated by interpolation using the electromagnetic property of each layer. Inspection of surface hardened depth in steel plate Fig.3 shows the distribution of flux density inside surface hardened steel plate when the hardened depth is 0mm and 3mm, respectively. This figure denotes that since the permeability and conductivity in surface hardened domain is decreased the flux density in the surface domain in the steel plate is decreased when the hardened depth is increased. Fig.4 shows the effect of the surface hardened depth on the value of the change rate of B_x in the search coil. The figure denotes that B_x is increased when the hardened depth is increased. This is, because the B_x from the impression magnetic field is increased since the permeability and conductivity in surface domain of the steel plate is decreased when the hardened depth is increased. As for B_x in the search coil, the calculated result is in agreement with measurement. In this research, comparison of the detection sensitivity of the inspection method [3] by the detecting of the flux density (B_z) inside the magnetic yoke as shown in Fig.5, and this proposal method by the detecting of the magnetic field (B_x) on the steel is investigated. In this model of Fig.5, a magnetic closed loop is formed between the sensor and the steel, and the flux density in the steel is detected with a search coil of the yoke. Fig.6 shows the comparison result of absolute values of B_x and B_z for the detecting of the hardened depth of the surface hardened steel by experiment. This figure denotes that the detection sensitivity of the proposal method by $|B_x|$ is higher than the method by $|B_z|$. Optimal design of search coil The optimal dimension of a search coil for detecting the magnetic field B_x in the proposal sensor is determined using the evolution strategy [4]. Fig.7 shows the inspection result in the optimal search coil form determined by the evolution strategy. The width (*Sw*), length (*Sl*) and height (*Sh*) of the optimal search coil are 20.36mm, 6mm and 1.8mm, respectively. The inspection result by the initial search coil model as shown in Fig.1 is also shown in this figure. This figure denotes that the detection sensitivity of the optimal search coil is increased from the initial model. The optimal search coil is the form which detects more magnetic fields on the steel plate distributed between the magnetic poles of the magnetic yoke.

[1] J.Marcus, *Electromagnetic Nondestructive Evaluation (IX)*, 2005, pp.135-142, 2005. [2] Y.Kai, *Electromagnetic Nondestructive Evaluation (VIII)*, 2004, pp.153-158, 2004. [3] Y.Gotoh, N.Sasaguri, and N.Takahashi, *IEEE Transactions on Magnetics,* vol.46, no.8, pp.3137-3144, 2010. [4] T.K.Chung, S.K.Kim, S.Y.Hahn, *IEEE Transactions on Magnetics*, vol. 33, no.2, pp.1908-1911, 1997.

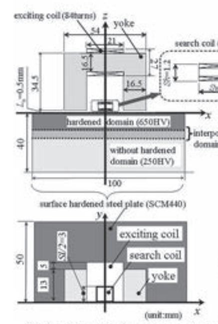

Fig.1. Inspection model of surface hardened steel plate (1/2domain, 15Hz, 126AT, SCM440 steel).

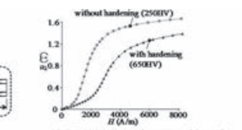

Fig.2. Initial magnetization curves of the steel with and without hardening (SCM440 steel).

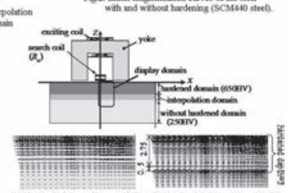

(a) the depth is 0mm(B_{max}=1.52T) (b) the depth is 3mm(B_{max}=1.24T)

Fig.3. Distribution of flux density inside the hardened steel plate (15Hz, 126AT).

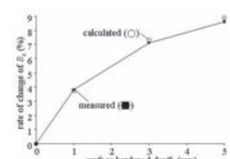

Fig.4. Effect of surface hardened depth on the value of the change rate of Bx in the search coil (15Hz, 126AT).

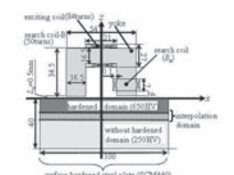

Fig.5. Inspection model using a search coil (Bz) with the yoke.

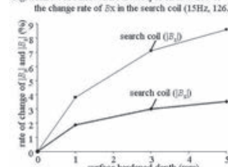

Fig.6. Comparison result of $|Bx|$ and $|Bz|$ for the detecting of the hardened depth (measured, 15Hz, 126AT).

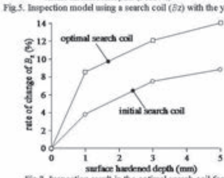

Fig.7. Inspection result in the optimal search coil form determined by the evolution strategy(calculated).

CV-13. Electromagnetic inspection for detecting defect of underground part in road sign pillar.

Y. Gotoh[1], *M. Tohara*[2] and R. Nakamura[3]

1. Innovative Engineering, Faculty of Science and Technology, Oita University, Oita, Japan; 2. Mechanical and Energy Systems Engineering, Oita University, Oita, Japan; 3. Division of Technical administration, Japan Non-Destructive Inspection Inc., Kurashiki, Japan

Introduction The steel pipe in a road sign pillar and an illumination pillar is built on the ground. Since the road sign pillar etc. was built and many years have passed, the underground part of its steel pipe may be corroded. In recent years, the accident from which the road sign pillar falls down is increased owing to the generating of the corrosion or the defect in the underground part of the steel pipe. Therefore, the inspection of the corrosion or the defect in the underground part of its steel pipe is demanded. However, since the position of its defect etc is underground part, it is necessary to dig up the ground for the inspection of its part. On the other hand, the non-destructive inspections by the ultrasonic wave method using the guided wave or the electromagnetic acoustic transducers (EMATs) are examined [1,2]. However, by these methods, since the detection signal is changed by the adhesion degree of the ground and the steel pipe, the quantitative evaluation of the defect is made difficult. In this paper, the non-destructive inspection method using the alternating magnetic field by low exciting frequency is proposed for the quantitative evaluation of the defect. Since the position of the defect in the steel pipe of a road sign pillar is in the underground part, it can't see the defect position from the ground. Therefore, in the actual inspection, it is necessary to detect both the distance (d_i) from a sensor to the defect position and the depth (d_e) of the defect. In this research, both the distance (d_i) from the proposal sensor to the defect and the depth (d_e) of the defect are presumed. The flux density and eddy current in the steel pipe is estimated by 3-D nonlinear finite element method (FEM). The usefulness of this proposal inspection method is shown also from comparison with an experimental verification. *Proposed electromagnetic sensor and detecting signal* Fig.1 shows the inspection model for evaluating both the distance (d_i) from a proposed electromagnetic sensor to the defect and depth (d_e) of the defect in the steel pipe (STK400). This inspection sensor is composed of two magnetic yokes of steel material (SS400) with an exciting coil, and a search coil. The search coil is arranged at the yoke of the side of the defect. The exciting frequency and ampere are 20Hz and 6A, respectively. The distance (lift-off : L_o) between the sensor and the steel pipe is equal to 0.1mm. Fig.2 shows distribution of flux density near the sensor when there is the steel pipe without defect. The flux density is analyzed by 3-D finite element method (FEM) of the step-by-step method taking account of B-H curves of the steel pipe and magnetic yoke. The figure denotes that the impressed magnetic field from two yokes is distributed to both of ±z-direction of the steel pipe. Fig.3 shows the effect of the defect depth (d_e) on the calculated output voltage in the search coil when the distance (d_i) from the sensor to a defect is changed. The figure denotes that since the ferromagnetic domain in the steel pipe is decreased when the defect depth (d_e) is increased, the flux density in the search coil is decreased. Moreover, when the distance (d_i) between a sensor and the defect is increased, the output voltage in the search coil with defect depth (d_e) is decreased. *Evaluating both the distance (d_i) from the sensor to the defect and depth (d_e) of the defect* In this research, the output voltage of the arbitrary two positions on the z-axis line in the steel pipe is measured at the intervals of 10mm by one sensor as shown in Fig.4. Then, both distance (d_i) and the depth (d_e) are presumed from these two measured output voltages and the calculated curves as shown in Fig. 3. Table I show the presumed results of both distance (d_i) and the depth (d_e) when the defect depth is 40% and 60%, respectively. This table denotes that the maximum error of the distance and depth are 3mm and 1.6%, respectively. Therefore, the usefulness of this proposed method using alternating magnetic field was shown in this table.

[1]J.L.Rose, *Journal of Pressure Vessel Technology*, vol.24, pp.273-282, 2002. [2]H.Nakamto, D.Nakamura, F.Kojima, K.Komatsu, and H.Tomita, *Proc. of the 18th International Symposium on Applied Electromagnetics and Mechanics* (ISEM), SP-284, 2017.

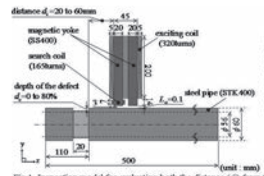

Fig.1. Inspection model for evaluating both the distance (di) from the sensor to the defect and depth (de) of the defect in a steel pipe (STK400).

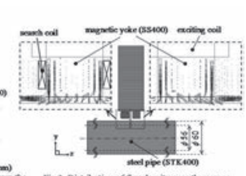

Fig.2. Distribution of flux density near the sensor when there is the steel pipe without defect.

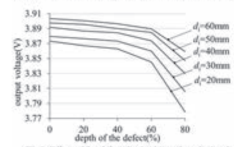

Fig.3. Effect of the defect depth (de) on the calculated output voltage in the search coil (20Hz, 6A).

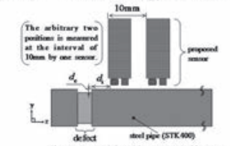

Fig.4. Measured the arbitrary two positions on the steel pipe z-axis at interval of 10mm.

Table I Presumed results of both distance (d_i) and the depth (d_e)

case	true value		estimated value		error	
	d_i(mm)	d_e(%)	d_i(mm)	d_e(%)	d_i(mm)	d_e(%)
1	45 & 55	40	45 & 55	39.2	0	0.8
2	27 & 37	60	30 & 40	61.6	3	1.6

CV-14. Investigation of Magnetic Tunnel Junction Sensor for Magnetic Flux Leakage Testing of Reinforced Concrete.

M.b. Mohd Noor Sam[1], Z. Jin[1], M. Oogane[1], K. Fujiwara[1] and Y. Ando[1]
1. Applied Physics, Tohoku University, Sendai, Japan

Magnetic flux leakage (MFL) testing a popular method for detection of defects such as the metal loss due to the corrosion in steel bars located in reinforced concrete. The magnetic flux leak cause by the defect is then measured by a magnetic sensor, which gives information to the user of the presence of the defect [1]. However, as the distance between the defect and magnetic sensor (lift-off) increases, the strength of the leaked magnetic flux drops significantly, making it difficult to detect. A candidate of highly sensitive magnetic sensor to detect defects at the condition of large lift-off is the magnetic tunnel junction (MTJ) sensor. In this research, the MFL testing was carried out by MTJ sensor with high sensitivity. The MTJ structure used in this research consists of a film structures of SiO_2sub./Ta(5)/$Ni_{80}Fe_{20}$(70)/Ru(0.85)/$Co_{40}Fe_{40}B_{20}$(3)/MgO(2)/$Co_{40}Fe_{40}B_{20}$(3)/Ru(0.8)/$Co_{75}Fe_{25}$ (5)/$Ir_{22}Mn_{78}$ (10)/Ta (8) (in nm) with a sensitivity of 87.8 mV/mT. Each MTJ was fabricated into the device with an area of 8080 μm^2 and 5550 MTJ devices (1110 in series and 5 in parallel) were integrated to obtain a high signal-to-noise (SNR) ratio [2]. The fabricated sensor was attached to an acrylic push car and the scan was done along the length of reinforced concrete specimen (length is 2.0 meter with the defect at the 1.0 meter mark). The output of the MTJ sensor was measured by conventional DC four-terminal method. Fig. 1 shows the change of the output voltage from the MTJ sensor measured at various lift-off values according the magnetic flux leaking from the specimen. As shown in Fig. 1, the defect's location can be identified as the change of the voltage from the MTJ sensor. Fig. 2 shows the SNR for measurements with and without a magnetic flux concentrator. Averaging of 50 times measurements was carried out to improve the SNR. The result indicates that the defects were detected by our MTJ sensor with a high SNR and installing a magnetic flux concentrator significantly improved the SNR until lift-off of 18 cm. We demonstrated the MFL testing with a high SNR using the MTJ sensor and the detection of defects under the condition with larger lift-off value can be realized by the improvement of sensitivity of the MTJ sensor. This work was partly supported by the Center of Innovative Integrated Electronic Systems (CIES) and the Center for Spintronics Research Network (CSRN).

[1] M. Hirose, T. Maeda, K. Matsuda, M. Yokota, A. Hattori and T. Miyagawa, Journal of Structural Engineering, 58A, p. 867-878 (2012) [2] K. Fujiwara, M. Oogane, F. Kou, D. Watanabe, H. Naganuma, and Y. Ando, Jpn. J. Appl. Phys. 50, 013001 (2011).

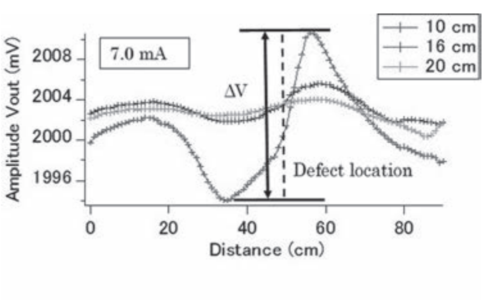

Fig. 1. The relationship between the lift-off value and the amplitude of signal output (mV). The defect location is defined as the halfway point between the highest peak and the lowest peak

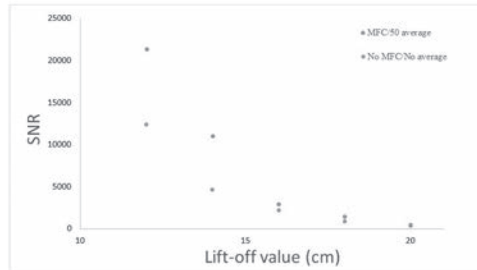

CV-15. A New Design of MFL Sensors for Self-Driving NDT Robot to Avoid Getting Stuck in Curved Underground Pipelines.

H. Kim[1], H. Yoo[2] and G. Park[3]
1. Electrical and Computer Engineering, Pusan National University, Busan, The Republic of Korea; 2. Korea Gas Corporation, Incheon, The Republic of Korea; 3. Electrical Engineering, Pusan National University, Busan, The Republic of Korea

1. Introduction Magnetic Flux Leakage (MFL) type Pipelines Inspection Gauge (PIG) is commonly used to detect defects on underground pipeline as one of nondestructive testing (NDT) instruments. In-line inspection of MFL PIG is commonly used to examine a large portion of the long distance transmission pipeline which transports natural gas from gathering points to local companies [1]-[3]. The operating pressure of this pipeline is over 20 atm and the diameter of pipe is more than 20 inches. So, MFL PIG which is called MFL sensor could be driven automatically by operating gas flow inside the pipe and it has been proved to be a reliable and effective ways for inspection of pipelines. Although it is effective for the inter-city scale large size pipelines, it is hard to be applicable for the curved pipelines with small size installed inside the city. That is because these pipelines have limited gas pressure and flow conditions, some obstacles such as bent region, welded joints, 90 degree miter. For these reasons, it is necessary to adopt self-driving robot system to drive MFL sensors as shown in Fig. 1. The basic principle of MFL method is that it generates a strong magnetic field on the pipe wall to be magnetically saturated. That's because the leakage field signal from defects on the pipe could be maximized [4]-[5]. The common structure consists of a fixed permanent magnet as the source of magneto-motive force and it cannot change the path of magnetic fields on the pipe. In the previous structure of MFL PIG, a strong magnetic attractive force is always generated between the pipe and MFL PIG [5]-[6]. Even though the previous MFL sensor is enough to pass in straight line, when this module passes through curved pipelines, the magnetic force between pipe and inspection module is increased sharply so that the PIG module could be stuck eventually. This paper proposed a new design structure of MFL PIG to decrease stuck forces on the pipe wall. All structural parameters for MFL sensors were designed to minimize the magnetic force and maximize the detection sensitivity of defect signals. The magnetic forces on the pipe was computed by numerical analysis to estimate necessary traction forces in self-driving robot. Also, the performance of proposed system was verified by experiments in the pipeline simulation facility. 2. Design and Structure The structure of MFL sensors with in-pipe robot system is shown in Fig. 1(a) and Fig. 1(c). The system is designed for inspection of 16 inches diameter pipelines and it consists of ten MFL modules, every module has Nd-Fe-B magnets with back yokes which are used to generate and transfer the magnetic field on the pipe. Also, every MFL Module has hall sensors to detect axial component of flux leakage signal. Fig. 1(d) shows the structure diagram of a conventional MFL module and that of a proposal module. The proposed system is designed to minimize the attachment force on the pipe and maximize the detection sensitivity of defect signals. In proposed system, each magnet has rotary magnets for the shunting mechanism so that it prevents the magnetic energy from being channeled into the pipe. 3. Numerical Analysis of MFL Sensors 3.1. Magnetization on the pipe The distribution and magnitude of magnetic flux density of MFL system are computed by using numerical analysis to derive the magnetic force acting on the pipe. The magnetic flux density on the pipe could be analyzed by using conventional 3D nonlinear finite element method. 3.2. Effects of magnetization on the defect signal From both FE simulation and experimental measurement, the peak amplitude of defect signal is detected by a hall sensor passing through the center of defects. The signal amplitude of leakage flux is dependent on the shape of defects such as length, width and depth. 3.3. Effects of magnetic force on the pipe To compute the magnetic force on the pipe in a given MFL module, the equation of magnetic energy stored in magnetic field space is used. There is an air gap between the pipe and MFL module, so the magnetic energy accumulated in an air gap is computed by the numerical results of magnetic flux. The magnetic force is proportional to the square of air gap flux density. 4. Experimental Verification When the MFL module passes through bent pipe or welded pipe joint, the distance of air gap between pipe and module is decreased. At that time, not only the air gap flux density is relatively increased but also the magnetic force is exponentially increased. So, the magnetic force has considerable influence on the traction force of driving robot. In Fig. 2, the proposed system generates sufficient magnetic fields to detect the defect signal even if it didn't saturate the steel pipe magnetically. 5. Conclusion In this paper, we introduced MFL sensors equipped with robotic platforms for inspection of low pressure gas pipelines. First of all, to verify the performance of MFL system, it is necessary to check the magnetization of the pipe wall. There are ten MFL modules in robotic platforms and each module consists of magnet bars. Each magnet bar generates sufficient magnetic fields to detect the defect signal even if it didn't saturate the steel pipe magnetically. Therefore, we propose the novel structure type of MFL module for reducing magnetic force on the pipe.

[1] P. A. Ivanov, Z. Zhang, C. H. Yeoh, L. Udpa, Y. Sun, S. S. Udpa, W. Lord, "Magnetic Flux Leakage Modeling for Mechanical Damage in Transmission Pipelines", IEEE Trans. Magnetics, vol. 34, no. 5, pp. 3020-3023, September 1998. [2] Y. K. Shin and W. Lord, "Numerical Modeling of Moving Probe Effects for Electromagnetic Nondestructive Evaluation", IEEE Trans. Magnetics, vol. 29, no. 2, pp. 1865-1868, March 1993. [3] S. Lukyanets, A. Snarskii, M. Shamonin and V. Bakaev, "Calculation of magnetic leakage field from a surface defect in a linear ferromagnetic material : an analytical approach", NDT & E International, vol. 36, issue 1, pp.51-55, Jan. 2003. [4] G. S. Park, "Analysis of the velocity-induced eddy current in MFL type NDT", IEEE Trans. Magnetics, vol. 40, no. 2, pp.663-666, March 2004. [5] P. Laursen, G. Vradis, and C. Swiech, "First Robotic Device To Inspect Unpiggable Gas Transmission Pipeline", Pipeline & Gas Journal, November 2009, vol. 236, No. 11. [6] Rejesh T. Keshwani, "Analysis of Magnetic Flux Leakage Signals of Instrumented Pipeline Inspection Gauge Using Finite Element Method", IETE Journal of Research, vol. 55, issue. 2, pp. 73-82, March 2009.

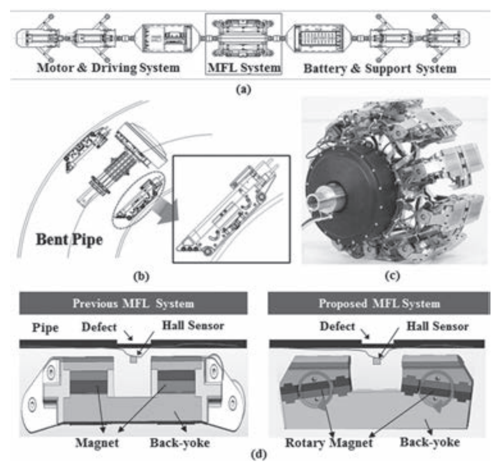

Fig. 1. MFL Sensors for inspection of small diameter pipelines. (a) MFL sensors integrated with in-pipe robot. (b) Bent pipe. (c) Total structure. (d) Proposed design.

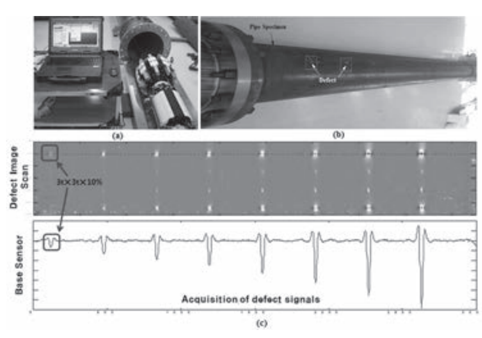

Fig. 2. Experimental setup and measurement. (a) MFL Instruments. (b) Pipe specimen. (c) Defect signals.

CV-16. A High-Field Tunneling Magnetoresistive Angle Sensor.

J. Deak[1] and I. Jin[2]
1. R&D, MultiDimension Technology Co., Ltd, Zhangjiagang, China;
2. Wafer Front End, MultiDimension Technology Co., Ltd, San Jose, CA, United States

Magnetoresistive sensors combined with permanent magnets are becoming increasingly popular for measuring mechanical displacement, velocity, rotation, etc. [1] In the case of magnetic angle sensors, a permanent magnet is attached to a rotating component, such as a shaft, and a magnetoresistive sensor detects the magnetic field change as the permanent magnet rotates with the shaft. [2] The measured magnetic field value is converted into a measure of shaft rotation angle. Because this is a non-contact measurement, it provides an inherently wear-free means of monitoring the rotation of a mechanical component. There are other advantages, for example, unlike optical sensors that require a powered optical source and transparent medium through which the measurement is made, magnetic sensors are low power and can tolerate dirt, dust, and other unavoidable contamination that may occur during its operational lifetime. Anisotropic magnetoresistance (AMR), giant magnetoresistance (GMR), and tunneling magnetoresistance (TMR) sensors are often used in angle sensor applications, but TMR is preferred due to its higher output and full 360 degree measurement capability. [3] Unfortunately, the accuracy and linearity of 360 degree GMR or TMR angle sensors are known to degrade as the applied field from the moving permanent magnet is increased. [4] Figure 1 illustrates the response of a TMR angle sensor as a function of the strength of a rotating magnetic field. It shows nearly ideal sinusoidal behavior at 50 Oe applied field, but the sensor output becomes a triangle wave with undesired harmonics when a field of 400 Oe is used. This is unfortunate, since the ability to tolerate larger magnetic field makes an angle sensor more immune to external field interference and to displacement between the permanent magnet and the sensor. It is thus desirable to find a means for increasing the operating field range. We will show the reason for the change to the triangular waveform, which degrades angle measurement accuracy, is a result of motion of the pinned layer magnetization in response to the rotating magnetic field. In order to overcome this effect, we modeled, designed, fabricated, and tested a novel 360-degree TMR angle sensor which includes a circular attenuator placed above each TMR element. The design concept is illustrated in the inset of Figure 2. These novel TMR angle sensors consist of a conventional stack comprising Seed/PtMn/CoFe/Ru/CoFe/CoFeB/MgO/CoFeB/NiFe/Cap, which is a bottom-pinned synthetic antiferromagnet pinned layer, MgO tunnel barrier, and simple bilayer free-layer structure. The attenuator is composed of plated permalloy, with thickness of about 5 microns. The attenuation was modeled using finite elements software. Figure 2 compares the angular error measured on an attenuated and a standard TMR angle sensor at various values of applied magnetic field ranging from 50 to 1500 Oe. The angle error is calculated by fitting a sinusoid to the voltage as a function of magnetic field angle curves. Note that the standard TMR angle sensor shows optimal performance over a range of about 25 to 100 Oe. The attenuated angle sensor uses an attenuator with an attenuation ratio of about 12x. As a result, the optimal field range is shifted from less than about 300 to about 800 Oe, but the error remains low, even from 100 to 1400 Oe. This experiment also shows the linearity of the angle sensor seems improved over the standard design. There are likely two main reasons for this. First, the pinning layer is well shielded, which reduces the motion of the pinned layer magnetization. Second, the attenuators may make the field at the location of the TMR elements more uniform. In summary, a 360-degree TMR angle sensor capable of operating with low error and high linearity in magnetic fields ranging from 100 Oe to over 1.4 kOe was designed, fabricated, and tested. The results agree well with modeling, and the resulting sensors are ideally suited for precise angle measurement in magnetically harsh environments.

[1] Herbert Schewe and Wolfgang Schelter, "Industrial Applications of Magnetoresistive Sensors," Sensors and Actuators A: Physical vol. 59, issue 1–3, pp. 165-167, April 1997. [2] Dexin Wang, Jay Brown, Tim Hazelton, and Jim Daughton, "Angle Sensor Using Spin Valve With SAF Structure," *IEEE Trans. Magn.*, vol. 41, no. 10, pp. 3700-3702, October 2005. [3] Manfred Ruehrig, Robert Seidel, Ludwig Baer, Michael Vieth, Guenter Rupp, Joachim Wecker, "Angular Sensor Using TMR Junctions with an AAF (Artificial Antiferromagnet) Reference Electrode and Improved Thermal Stability," *IEEE Trans. Magn.*, vol. 40, no. 1, January 2004. [4] Yosuke Komasaki, Hiraku Hirabayashi, and Shunji Saruki, "Rotating Field Sensor," US Patent US8736256 B2, May 2014.

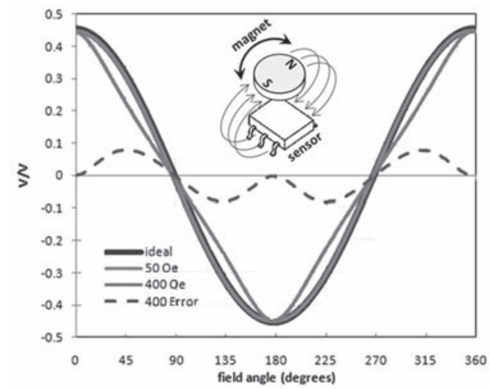

Fig. 1. A plot of the ideal sinusoidal response of a TMR angle sensor, compared with data measured using a 50 Oe rotatingn field and a 400 Oe rotating field. Note the 400 Oe response form the sensor appears as a triangle wave, rather than a sinusoid. The inset of the figure shows the geomery of a rotating permanent magnet with respect to the sensor.

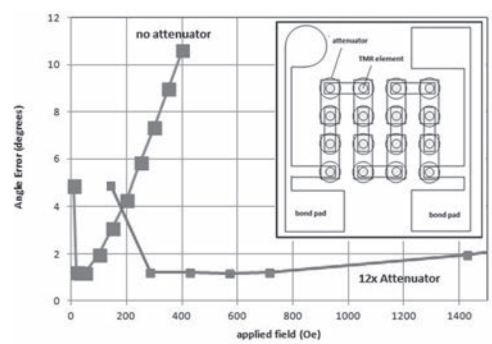

Fig. 2. The inset shows a schematic diagram of a singe magnetoresistor angle sensor die. The die consists of a string of circular TMR element interconnected in series as a two port network. A permalloy disk is placed over top of each TMR element in order to attenuate the external magnetic field. Four such single magnetoresistor dice may be arranced in a semiconductor package in order to implement a full bridge, or alternatively, a full bridge may be built onto a single chip. The blue curve shows angle measurement error as a function of applied field strength measured on an angle sensor with no attenuators. The red curve shows the result measured on an identical angle sensor die that includes attenuators over the TMR elements.

WEDNESDAY MORNING, 25 APRIL 2018 SIMPOR/ROSELLE BALLROOM, 8:30 TO 11:30

Session CW
SENSORS: FUNDAMENTAL DEVELOPMENTS AND MATERIALS II
(Poster Session)

Alexander Sergeevich Samardak, Chair
Far Eastern Federal University, Vladivostok, Russian Federation

CW-01. Frequency Characteristics of an Optical Current Sensor Based on Rare Earth Materials.

W. Sima[1], *Y. Wang*[1], M. Yang[1] and R. Zheng[1]
1. State Key Laboratory of Power Transmission Equipment & System Security and New Technology, Chongqing University, Chongqing, China

Traditional electromagnetic current transformers are widely used in power systems and have exposed insurmountable weaknesses: large volumetric and heavy weight, ferromagnetic resonance, magnetic saturation, high requirement for insulation, and harmonics. One of the most important problems is that the high-frequency current is hard to be accurately measured by the current transformers due to their poor frequency performance. Many optical current transducers (OCTs) have been proposed and designed to provide solutions to the problem. Now, most of the OCTs are mainly focused on improving the accuracy, practicality, and stability by using low reverse-magnetic materials. The frequency performances of these OCTs cover 0-20 kHz. However, some of the transient currents, such as the lightning current, in power systems contain frequency components as high as MHz. To further increase the high frequency performance of the OCTs to meet the requirement of practical utilization, there is still a room for the improvement of the OCTs. With the rapid development of materials science in recent years, the performance of paramagnetic magneto-optical materials which were neglected in the past has been greatly improved. Application of the rare-earth-doped magneto-optical glass material can improve the response sensitivity and high frequency performance of OCTs. In this paper, an OCT is designed by using rare-earth-doped magneto-optical glass materials. Then, theoretical and simulation analysis are conducted to evaluate the frequency characteristic of the OTCs. Finally, an optical experimental platform is established to verify the analysis above. The OCT is based on Faraday magneto-optical effect: when the linearly polarized light travels through a magneto-optical media along the direction of the magnetic field generated by the current, the polarization direction of the light will be rotated. The overall structure is a straight through path. A linear polarization is generated by a laser,and goes through the optical media. The optical detector converts the light intensity into a voltage to establish the relationship between light intensity and current. The angle between the two polarizers is analyzed theoretically based on Marius's law, the positive (negative) Verdet constant with the included angle equal to $3\pi/4(\pi/4)$ has the perfect amplitude response. The output and input waveforms are the same in a large frequency range and have no phase differences. Combined with the actual situation, the dynamic characteristics of the Faraday rotation angle is different from the static characteristics; the main reasons are the absorption of light and the magnetic loss of materials. The absorption of light by the material causes the outgoing linearly polarized light to become elliptically polarized light, and the magnetic loss will make an alternating magnetization relative to the alternating magnetic field strength have a phase lag. Both of them will change the Faraday rotation angle to a plural form: $\theta=\theta'+i\theta''$, leading to the unsatisfactory frequency characteristics. Therefore, the optical absorption and magnetic loss of the magneto-optical material should be considered for the design of the OCTs. Through the study of the frequency characteristic, the paramagnetic magneto-optic glass MR3-2 doped with rare earth Tb^{+3} ions has a light absorption coefficient which is less than 1% and negligible magnetic loss is applicated to the OCT, it also has high Verdet constant to increase the sensitivity further. Amplitude-frequency characteristics and phase-frequency characteristics of the OCT are evaluated by simulation, they are ideal. Then, an optical experiment platform is built up to test the frequency response. A signal generator and a power amplifier generate a 0-50kHz sinusoidal current with a magnitude of 1.7A. The current flowing through the solenoid (930 turns per meter in double layers) is used to generate a magnetic field, which is equivalent to the magnetic field that 2kA wire at its 10cm position. An oscilloscope is used to acquire the output voltage waveform from the photodetector. The experiments show that the OCT using new materials have a significant increase in sensitivity. The acquired waveforms remain the same amplitude without phase shift and show no distortion in the frequency range from 0 Hz to 50kHz. Therefore, the frequency response is considered to be ideal, which is consistent with the theoretical analysis and simulation results. In this paper, an OCT using rare earth paramagnetic glasses with excellent magneto-optical properties is designed to measure harmonics and transient currents. Experiments show that the OCT has ideal frequency characteristics within 50 kHz range, the maximum measurable amplitude can reach 2000A, it is suitable for measuring most of the currents in the field.

Stephan Mohr, Thomas Bosselman, "A high dynamic range magneto-optic current transformer with advanced signal processing," *IEEE Sensors Journal*, 2003, 3(6): 744-751.

CW-02. Current annealing of glass-coated amorphous wire for noise reduction of low-offset fundamental mode orthogonal fluxgate.

N. Murata[1,2] and R. Nomura[1]

1. Environmental Test Technology Unit, Japan Aerospace Exploration Agency (JAXA), Tsukuba, Japan; 2. Department of Space and Astronautical Science, The Graduate University for Advanced Studies, Sagamihara, Japan

Introduction Several kinds of compact magnetic sensors such as fundamental mode orthogonal fluxgate (FM-OFG) and GMI sensors utilize amorphous wires as magnetic cores [1]. There are mainly two types of amorphous wires: one created by so called in-water spinning method and the other created by Taylor–Ulitovsky method with glass coating over metallic core [2]. The former wire has been commonly used for FM-OFG sensors, and in some cases annealing is introduced to improve the performances of the sensors [3]. However, it is pointed out in [2] that those wires require very sensitive annealing process to obtain repeatable magnetic characteristics, and have disadvantages in cost and fabrication complexity compared to the glass-coated wires. In this research, 60-μm-diameter glass-coated Co-Fe-Si-B-Cr wire bent in hairpin shape was newly adopted to a 45mm-long FM-OFG sensor head. Current annealing [4] was then performed to the wire, and the noise and offset characteristics of the sensor were evaluated. Low-offset FM-OFG FM-OFG is known as the low-noise orthogonal fluxgate invented by Sasada [5] which operates with DC-biased sinuous excitation current, in other words, sinuous AC current (*Iac*) of small amplitude superposed on large DC current (*Idc*), directly passing through a magnetic wire core. However, uniaxial anisotropy in the wire affects the motion of magnetization and causes large offset. A technique called bias switching [6] periodically flips the polarity of DC bias and AC excitation current to obtain induced signals that become complementary to each other in which the offset components attributed to the anisotropy are modulated in the opposite polarity while the sensor sensitivity components are modulated in the same polarity. That way, averaging those two signals by a low-pass filter brings offset-free output. Application of the as-cast glass-coated wire The glass-coated amorphous wire in as-cast form was implemented to the sensor head and operated by FM-OFG circuit in feedback configuration with the following conditions: *Iac* (38 kHz) = 14 mArms, *Idc* = 22 mA, and the bias switching frequency = 2.4 kHz. The circuit was designed to have a cutoff frequency of 20 Hz. Then the sensor head was placed in a 4-layer magnetic shield and noise spectral density was measured. As a result, the measured noise at 1 Hz was 45.8 pT/Hz$^{1/2}$ (dashed line in Fig. 1). To investigate the source of the noise, the bias switching frequency was set to be as low as 0.1 Hz so that two complementary signals obtained under alternating excitation modes directly appear as an output, without being averaged by the low-pass filter. Since the sensor head is placed in the magnetic shield, the output corresponds to the intrinsic offset of the sensor. The result is shown in Fig. 2 (a). In a theory, a completely symmetrical waveform should be obtained under ideal behavior of the bias switching technique, but it can be observed that output levels asymmetrically vary in the order of several mV (which corresponds to several nT) every time the polarity of excitation current returns to the original state after inversion. Those random, asymmetrical variations of the output levels obviously could not be canceled by averaging, and thus lead to increase in the output noise. The variations imply that there is considerable non-repeatability in magnetization when the periodical inversions of excitation field occur, which should be attributed to the fluctuation of M-H curves observed in amorphous cores [7]. Current annealing of the glass-coated wire To improve the magnetic property of the glass-coated amorphous wire, current annealing was performed with very simple method. With the sensor head kept in the magnetic shied, its cable was connected to DC power supply to apply current of 100 mA to the wire core for 40 minutes. The resistance of the wire core was 64 Ω. Then the same experiment as above was carried out. The obtained result shown in Fig. 2 (b) presented more than 10-fold improvements in variations of output levels, showing symmetrical and uniform behavior against periodical inversions of the excitation field. This improvement implies that stress relaxation brought by current annealing changed the magnetic property of the wire to have better repeatability in its M-H curve. The absolute value of output levels, which corresponds to the intrinsic sensor offset, is also reduced, meaning that the anisotropy in the wire is induced strongly to the circumferential direction by the annealing current. The spectral noise density obtained using the current-annealed sensor head is shown in Fig. 1 with a solid line. The noise at 1 Hz was reduced to 11.7 pT/Hz$^{1/2}$ confirming the efficacy of the current annealing. Then current annealing was performed to several sensor heads under different current conditions. It was discovered that 200 mA current deteriorated the magnetic property of the wire, possibly due to partial crystallizations. As far as the current level is kept around 100 mA, noise characteristics of all the five tested sensors improved to similar level as the solid line in Fig. 1, meaning that the current annealing is also an effective way to obtain stable level of performances among sensor heads.

[1] A. Grosz *et al.*, Eds., *High Sensitivity Magnetometers*. Basel, Switzerland: Springer, 2017, pp. 63-126. [2] V. N. Murray, Ed., *Progress in Ferromagnetism Research*. Hauppauge, NY, USA: Nova Science Publishers, 2005, pp.255-292. [3] M. Butta *et al.*, “Method for offset suppression in orthogonal fluxgate with annealed wire core,” *Sensor Lett.*, vol. 12, no. 8, 2014. [4] V. A. Zhukova *et al.*, “Processing of magnetic properties of nearly-zero magnetostrictive glass coated microwires by current annealing,” *IEEE Trans. Magn.*, vol. 39, no. 6, 2003. [5] I. Sasada, “Orthogonal fluxgate mechanism operated with dc biased excitation,” *J. Appl. Phys.*, vol. 91, no. 10, 2002. [6] F. Koga *et al.*, “Low Offset Orthogonal Fluxgate Operating in Fundamental Mode,” *Journal of the Magnetics Society of Japan*, vol.27, no. 4, 2003. [7] T. Sonoda *et al.*, “Measurement of fluctuations of magnetized loop in amorphous cores,” *IEEE Trans. Magn.*, vol. 22, no. 5, 1986.

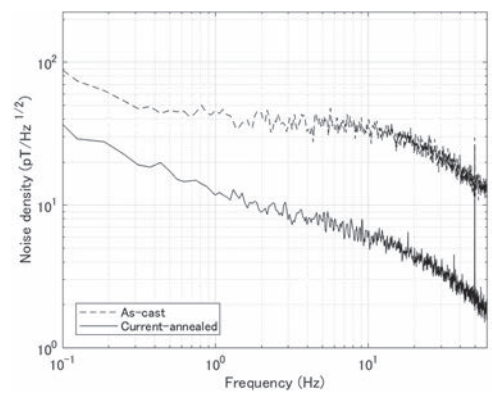

Fig. 1. Noise spectral density of FM-OFG obtained with the sensor head using the as-cast wire (dashed line) and the current-annealed wire (solid line).

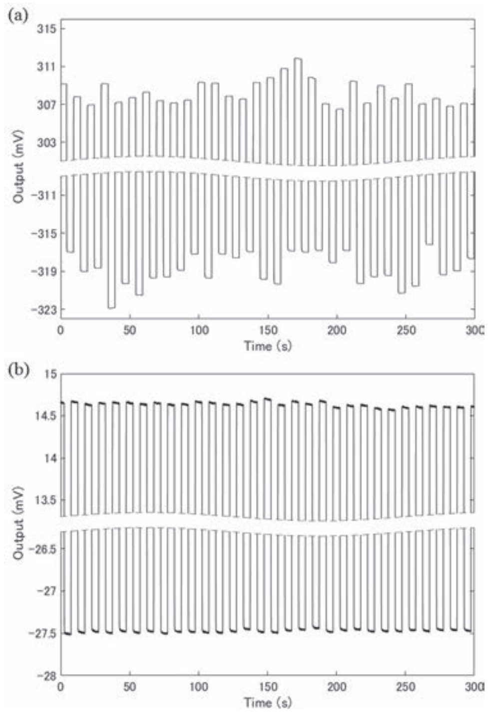

Fig. 2. Output of FM-OFG under 0.1 Hz bias switching with the sensor head using the as-cast wire (a) and the current-annealed wire (b). In both cases, sensor heads are placed in the magnetic shield.

CW-03. High frequency and sensitivity magnetic core with amorphous HB1-M operate at electromagnetic interface characteristic.

C. Hsu[1], C. Chang[3] and C. Tseng[2]

1. Department of Mechanical Engineering, Oriental Institute of Technology, New Taipei city, Taiwan; 2. Division of Physics, Institute of Nuclear Energy Research, Taoyuan, Taiwan; 3. Department of Information and Telecommunications Engineering, Ming Chuan University, Taoyuan, Taiwan

1. Abstract Body: This paper presents the EMI impact on the current transformer with amorphous HB1-M core, printed circuit board (PCB) power transformer and the filter of inductor for Internet of Things (IoTs) device. According to the antenna principle, the radiation emission power responses of PCB transformer and current transformer are estimated and found to be negligible due to the EMI experimental report. The current transformer with amorphous HB1-M core is annealed at 350 °C and soaks for 1.5 h. The simulation results of electromagnetic field is to display the power electronic circuit shield response, which also presented resistance EMI signal for power inductor in magnetic flux density and electric potential. According to the major radiated EMI source in the frequency range between of 50 MHz to 400 MHz is found to be the filter of the power circuit, where antenna emission energy transients occur, rather than the PCB transformer. Experimental results have confirmed that the application of PCB transformer in electronic circuit might not be have seriously EMI problem on the power electronic circuit. 2. Introduction There is the most of important application of Internet of Things (IoTs) in sensor device with high permeability magnetic core material providing a current in its secondary winding proportional to the alternating current flowing in its primary [1-2]. A common development way in metering and protective relaying for smart grid and power substations is useful where it facilitate the safe measurement of large currents, often in the presence of high voltages [3]. Also, some case in electronic circuit application and minor current signal detection is not only provided typically signal measurement but it can transmit stable signal by using communication system and also support as well analog-digital signal to behind receiver to user application [4,5]. It is well-known that basic principle of SMS is satisfied with several characteristics including fast switching of high current and voltage signals within power converter systems. Regarding to the electromagnetic interference (EMI) problems, it becomes more critical problem due to the compromise between efficiency and power density [6]. In aspect of electromagnetic response, the printed circuit board (PCB) with magnetic core device performed SPS induced a significant EMI source; it should face their intrinsic switching properties and the generated EMI noise levels. Moreover, electromagnetic compatibility (EMC) regulations need to satisfy as follow rules, for example, line-current harmonic standards and IEC 61000-3-2 [7]. 3. Simulation, Experimental and Discussion Results This study presents an amorphous alloy with HB1-M and SA1 material which is made by Hitachi Co., This product, the parameter of physics characteristic includes HB1-M and SA1 with thicknesses of 0.025μ-meter and widths of 20 mm. Besides, both magnetic cores annealed at 320°C (for HB1-M) and 350°C (for SA1), and soaked around 1.5 h are performed. For magnetism properties for different material in crystalline phase and microstructure, are measured by using X-ray diffraction (XRD) and a vibrating sample magnetometer (VSM) as shown in Figure 1 (a)-(b). Besides, energy dispersing spectroscopy (EDS) is used to detect material compositions, as shown in Fig. 1 (c). EMI noise sources within power-line or radiation emission of antenna equipment, operated at duty cycle characteristic of currents, is made. The critical PCB continuously turning loops (*di/dt*) and the pulsating voltages of the phase nodes (*dv/dt*) are defined. The common (CM) and differential (DM) noise sources and the corresponding noise propagation paths can be obtained. The inductor need to withstand the rated current without saturating while simultaneously providing the required CM/DM noise attenuation. The core of inductor is chosen from typical material. Also, the permeability curves $\mu r(f)$ is referred by datasheets or impedance measurements. EMI analysis is performed as follows: first, define EMI noise sources, including to identify fast rates of change of currents *di/dt* and voltages *dv/dt*. Next, it should be concerned noise propagation paths, i.e., CM/DM conduction paths. Before that step, it is most well-known that numerical techniques for power inductor and electronics component applications is simulated by finite element analysis (FEA), as shown in Figure 2(a)-(b). This paper presents the EMI impact on the current transformer with amorphous HB1-M core, a fully sensing magnetic core development in core structure and EMI testing results, as shown in Figure 2(c)-(d). According to the antenna principle, the radiation emission power responses of PCB transformer and current transformer are estimated and found to be negligible due to the experimental report of EMI. The major radiated EMI source in the frequency range between of 50 MHz to 400 MHz is found to be the filter of the power circuit, where antenna emission energy transients occur, rather than the PCB transformer. Experimental results have confirmed that the application of PCB transformer in electronic circuit might not be seriously EMI problem on the power electronic circuit.

[1] K. Yamaguchi, et. al., "Characteristics of a thin film microtransformer with circular spiral coils," *IEEE Trans. Magn.,* vol. 29, pp. 2232–2237, Sept. 1993. [2] C. O. Math, N. Wang, S. Kulkarni, and S. Roy, "Review of integrated magnetics for power supply on chip (PwrSoC)," *IEEE Trans. Power Electron*., vol. 27, no. 11, pp. 4799–4816, Nov. 2012. [3] M. Brunet, et. al., "Electrical performance of microtransformers for DC-DC converter applications," *IEEE Trans. Magn*., vol. 38, no. 5, pp. 3174–3176, Sep. 2002. [4] J. Lu., Jia, X. Wang, K. Padmanabhan, W. G. Hurley, and Z. J. Shen, "Modeling, design, and characterization of multiturn bondwire inductors with ferrite epoxy glob cores for power supply system-on-chip or systemin-package applications," *IEEE Trans. Power Electron*., vol. 25, no. 8, pp. 2010–2017, Aug. 2010. [5] H. Jia, J. Lu, X. Wang, K. Padmanabhan, and Z. J. Shen, "Integration of a monolithic buck converter power IC and bondwire inductors with ferrite epoxy glob cores," *IEEE Trans. Power Electron*., vol. 26, no. 6, pp. 1627–1630, Jun. 2011. [6] S.-Y.-R. Hui, et. al., "Coreless PCB-based transformers for power MOSFETS/IGBT gate drive circuits," *IEEE Trans. Power Electron*., vol. 14, no. 3, pp. 442–430, May 1999.

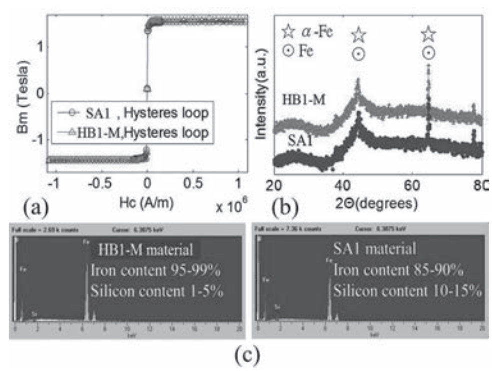

Fig. 1. The measured results of the magnetic properties for amorphous materials HB1-M and SA1: (a) VSM, (b) XRD and (c) EDS.

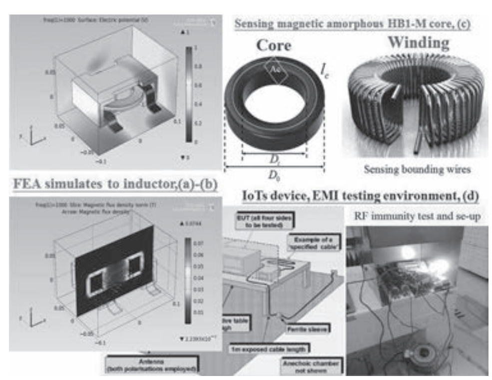

Fig. 2. Sensing magnetic core device with amorphous HB1-M material in IoTs application: (a) FEA in electrical potential, (b) FEA in magnetic flux distribution,(c) amorphous HB1-M design, (d) magnetic core perform EMI testing and environment.

CW-04. Noise suppression and sensitivity manipulation of magnetic tunnel junction sensors with soft magnetic $Co_{70.5}Fe_{4.5}Si_{15}B_{10}$ layer.

L. Huang[1], Z. Yuan[1], B. Tao[1], C. Wan[1], P. Guo[1], Q. Zhang[1], L. Yin[1], J. Feng[1], T. Nakano[2], H. Naganuma[2], H. Liu[1], Y. Yan[3] and *X. Han*[1]
1. State Key Lab of Magnetism, Institute of Physics, Beijing, China;
2. Tohoku University, Sendai, Japan; 3. Jilin University, Changchun, China

Magnetic tunnel junction (MTJ) sensors have exhibited a strong competitiveness in low-field sensing applications such as biomagnetic sensing and read head for hard disk drives due to their high sensitivity. As is known that ultimate field detection limits depend on both voltage noise character and sensitivity of MTJ sensors, which are thus crucial for ultra-low field (such as nT and pT) detection. Low frequency noise of MTJs is usually dominated by $1/f$ noise which is attributed to either charge traps within barrier or fluctuations of magnetization of free layer [1]. Random telegraph noise (RTN) is observed in the free layer with multi-domain state, resulting in Barkhausen noise in $R(H)$ loop [2]. In order to realize lower detection limit, the above two main kinds of noises should be suppressed as much as possible. Besides, soft magnetic materials with low anisotropy such as NiFe, CoFeSiB, NiFeCuMo have been developed to improve the field sensitivity. Especially, amorphous CoFeSiB alloy shows ultralow anisotropy field and high crystallization temperature (790K), making it a good candidate for sensing layer in MTJ sensors. In this work, the MTJ sensors with CoFeSiB and NiFe were fabricated and linear response to applied field was realized by using two-step annealing process and applying a bias field along easy axis of free layer. The bias field was used to stabilize single domain of free layer and eliminate Barkhausen noise in MTJ sensors. The samples with CoFeSiB electrode show much better thermal stability, higher sensitivity and better detectivity than that of NiFe electrode. A sensitivity of 3.9 %/Oe and detectivity of 4.5 nT/√Hz at 10Hz are achieved for samples with CoFeB/Ru/CoFeSiB free layer under bias field of 10 Oe [3]. Besides, the linear range can be widened as the bias field increases at the cost of sensitivity. This property might be useful for some special application, in which larger linear area is much more important than the sensitivity. With bias field along easy axis of free layer, the noise suppression and sensitivity manipulation are realized, which are beneficial for applications in industrial control, biomagnetic sensing, etc. The MTJ sensors with CoFeSiB amorphous soft magnetic layer can be an excellent candidate for sensors with high sensitivity in weak magnetic field detection applications.

[1] Z. H. Yuan, J. F. Feng, P. Guo, C. H. Wan, H. X. Wei, S. S. Ali, X. F. Han, T. Nakano, H. Naganuma, Y. Ando, *J. Magn. Magn. Mater.* 398, 215 (2016). [2] S. C. Das, *J. Appl. Phys.* 69, 5411 (1991). [3] L. Huang, Z. H. Yuan, B. S. Tao, C. H. Wan, P. Guo, Q. T. Zhang, L. Yin, J. F. Feng, T. Nakano, H. Naganuma, H. F. Liu, Y. Yan, X. F. Han, *J. Appl. Phys.* 122, 113903 (2017).

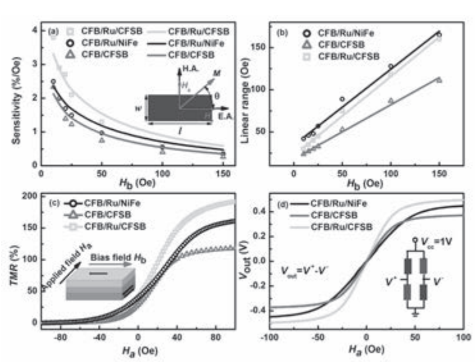

Fig. 1. (a) The measured (scatters) and calculated (solid line) sensitivity dependence on different bias fields. (b) The measured linear range dependence on bias field. The solid line is the linear fitting curve. (c) The *TMR* ratios versus applied field H_a with bias field H_b along easy axis of free layer. The bias field is 10 Oe for CFB/CFSB and CFB/Ru/CFSB samples and 15 Oe for CFB/Ru/NiFe samples. (d) The calculated output of Wheatstone bridge with 1 V bias voltage. The inset figure shows the Wheatstone bridge circuit.

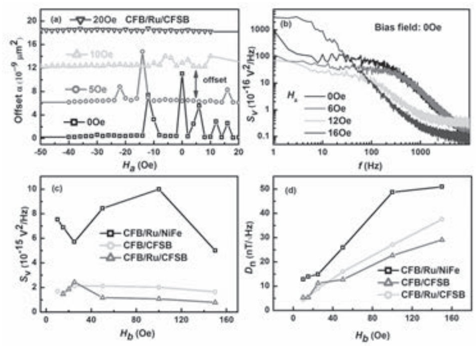

Fig. 2. (a) Hooge parameter of CFB/Ru/CFSB samples dependence on applied field with different bias field at 102 Hz. The curves are offset by 6×10^{-9} μm². (b) The noise power spectrum corresponding the measurement condition of peaks in (a). The voltage noise (c) and field detectivity (d) with different bias field at frequency of 10 Hz and bias current of 103 μA.

CW-05. Tuning antiparallel pinned spin valves with modified artificial antiferromagnetic layer for full-bridge magnetic sensors.

V. Luong[1], A. Nguyen[1] and H. Tran Thi[1]
1. International Training Institute for Materials Science, Hanoi University of Science and Technology, Ha Noi, Vietnam

A full-bridge magnetoresistive spin valve (SV) sensor scheme for applications of linear magnetic measurement is fabricated and analyzed with the sign of magnetoresistance (MR) can be tuned by the modified the artificial antiferromagnetic (AAF) layer. In the last two decades, SV sensors have shown their crucial roles in the life. The common applications of SV sensors are used in position, angle sensors [1, 2], electronic compasses, and contactless current sensors [3]. To build a sensor, especially for resistive sensors, a Wheatstone-bridge is always a good solution for its advantages of the lessening dc-offset, and temperature errors [4]. In the MR sensor fabrication, the bias direction is also the main factor that decides the sensor architectures. For instance, a half-bridge was realized by two active cells, whereas shielding the other two cells [5, 6] or killing their sense by the roughened surfaces [7]. However, the effective sensitivity and linearity of the sensor are reduced [8]. There are several methods to form a full-bridge that provides a maximum output of the sensor. For example, the current strap was directly fabricated on the surface of the device to induce the local bias magnetic field during the cool-field post-annealing process [9]. Using an appropriate location of MR cells within the gap of the flux guide, a full-bridge could be established [10]. An antiparallel alignment of the pinned direction of the two pairs of MR cells was carried out by a microscopic focused laser heating during cool-field treatment [11]. Another method is that the usage of two deposition processes for two pairs of MR cells in the opposite applied magnetic field [12]. In this work, we propose a method to tune the bias direction of two neighboring meanders in the full-bridge by varying the thickness of Ru in AAF layers of patterned SV cells with a single post-field annealing step. In order to implement the proposed design, the two deposition processes were carried out. First one, two normal magnetoresistance SV cells are the structure of (Si/SiO_2)/Ta(50Å)/NiFe(30Å)/Co(15Å)/Cu(24Å)/CoFe(25Å)/IrMn(100Å)/Ta(50Å), whereas, the other two cells are the inverse magnetoresistance with an AAF layer of structure of (Si/SiO_2)/Ta(50Å)/NiFe(30Å)/Co(15Å)/Cu(24Å)/[CoFe(15Å)/Ru(7Å)/CoFe(25Å)]/IrMn(100Å)/Ta(50Å). The normal MR and inverse MR curves of the different SV structures are shown in Fig. 1. The SV films were prepared by RF magnetron sputtering. The conventional lift-off method was used to pattern the MR cells. A tiny permanent magnet was used to adjust the sensor operating point. To estimate an appropriate MR ratio for an expectation sensitivity, the hyperbolic tangent model was introduced by author *et al.* [13], a required MR correspondences a sensitivity and a saturation field range was given by $MR = (2.(dV/V/dB).B_s)/(G_m-(dV/V/dB).B_s)$ (1) where MR is the magnetoresistance ratio, $dV/V/dB$ is the sensitivity of the bridge (V/V/Oe), B_s is the saturation field, and G_m is the flux amplification factor. Suppose, $G_m = 1$ (no gain flux density), and the B_s is about 50 Oe, in order to yield a sensitivity of 1 mV/V/Oe, the MR ratio should be at least 10.5 %. The SV cells were patterned to the dimensions of 200 μm × 2 μm. The resistance of individual SV cell is about 10 kΩ. The cut chip dimension is 2 mm × 1 mm was attached to a printed circuit (PCB) board using the aluminum wire bonding method. The voltage output of the bridge was amplified by a preamplifier using AD620 from Analog Device, Inc., and connected to a data acquisition device (MyDAQ). The data was recorded using a software coded in the LabVIEW. The performance of the SV full-bridge was verified by setting up the sensor in a sweeping magnetic field of ±150 Oe induced by a Helmholtz coil. The response curve of the full bridge to the external fields are shown in Fig. 2. The obtained sensitivity is 0.23 mV/V/Oe with B_s is about 100 Oe and a patterned MR ratio of 4.5% is in agreement with the hyperbolic tangent model in Eq. (1) [13]. Further experiments to increase the resistance of GMR elements using the advanced microfabrication methods are still ongoing. The sensitivity of the bridge can be further enhanced by the patterning SV cells in series [14] or the usage of a flux amplification (flux concentrators) [15].

[1] M. M. Miller, P. Lubitz, G. A. Prinz, J. J. Krebs, A. S. Edelstein, S. F. Cheng, and F. G. Parsons, "Development of a high precision absolute linear displacement sensor utilizing GMR spin-valves," *IEEE Transactions on Magnetics,* vol. 33, pp. 3388-3390, 1997. [2] H. A. M. v. d. Berg, G. Rupp, W. Clemens, G. Gieres, M. Vieth, J. Wecker, and S. Zoll, "Hard-soft GMR sensors with Co-Rh based artificial antiferromagnetic subsystem," *IEEE Transactions on Magnetics,* vol. 34, pp. 1336-1338, 1998. [3] M. Vieth, W. Clemens, H. van den Berg, G. Rupp, J. Wecker, and M. Kroeker, "Contactless current detection with GMR sensors based on an artificial antiferromagnet (AAF) subsystem," *Sensors and Actuators A: Physical,* vol. 81, pp. 44-48, 2000. [4] A. De Marcellis, G. Ferri, and P. Mantenuto, "Resistive Sensor Interfacing," in *Giant Magnetoresistance (GMR) Sensors: From Basis to State-of-the-Art Applications*, ed Berlin, Heidelberg: Springer Berlin Heidelberg, 2013, pp. 71-102. [5] J. M. Daughton and Y. J. Chen, "GMR materials for low field applications," *IEEE Transactions on Magnetics,* vol. 29, pp. 2705-2710, 1993. [6] Q. Zhenghong, W. Dexin, J. M. Daughton, M. Tondra, C. Nordman, and A. Popple, "Linear spin-valve bridge sensing devices," *IEEE Transactions on Magnetics,* vol. 40, pp. 2643-2645, 2004. [7] J. Daughton, J. Brown, E. Chen, R. Beech, A. Pohm, and W. Kude, "Magnetic field sensors using GMR multilayer," *IEEE Transactions on Magnetics,* vol. 30, pp. 4608-4610, 1994. [8] P. P. Freitas, J. L. Costa, N. Almeida, L. V. Melo, F. Silva, J. Bernardo, and C. Santos, "Giant magnetoresistive sensors for rotational speed control," *Journal of Applied Physics,* vol. 85, pp. 5459-5461, 1999. [9] J. K. Spong, Speriosu, R. E. Fontana, M. M. Dovek, and T. L. Hylton, "Giant magnetoresistive spin valve bridge sensor," *IEEE Transactions on Magnetics,* vol. 32, pp. 366-371, 1996. [10] J. Chen, M. C. Wurz, A. Belski, and L. Rissing, "Designs and Characterizations of Soft Magnetic Flux Guides in a 3-D Magnetic Field Sensor," *IEEE Transactions on Magnetics,* vol. 48, pp. 1481-1484, 2012. [11] O. Ueberschär, M. J. Almeida, P. Matthes, M. Müller, R. Ecke, R. Rückriem, J. Schuster, H. Exner, and S. E. Schulz, "Optimized Monolithic 2-D Spin-Valve Sensor for High-Sensitivity Compass Applications," *IEEE Transactions on Magnetics,* vol. 51, pp. 1-4, 2015. [12] K. M. H. Lenssen, D. J. Adelerhof, H. J. Gassen, A. E. T. Kuiper, G. H. J. Somers, and J. B. A. D. van Zon, "Robust giant magnetoresistance sensors," *Sensors and Actuators A: Physical,* vol. 85, pp. 1-8, 2000. [13] V. S. Luong, Y. H. Su, C. C. Lu, J. T. Jeng, J. H. Hsu, M. H. Liao, J. C. Wu, M. H. Lai, and C. R. Chang, "Planarization, Fabrication and Characterization of Three-dimensional Magnetic Field Sensors," *IEEE Transactions on Nanotechnology,* vol. PP, pp. 1-1, 2017. [14] M. Tondra, J. M. Daughton, D. Wang, R. S. Beech, A. Fink, and J. A. Taylor, "Picotesla field sensor design using spin-dependent tunneling devices," *Journal of Applied Physics,* vol. 83, pp. 6688-6690, 1998. [15] A. Guedes, J. M. Almeida, S. Cardoso, R. Ferreira, and P. P. Freitas, "Improving Magnetic Field Detection Limits of Spin Valve Sensors Using Magnetic Flux Guide Concentrators," *IEEE Transactions on Magnetics,* vol. 43, pp. 2376-2378, 2007.

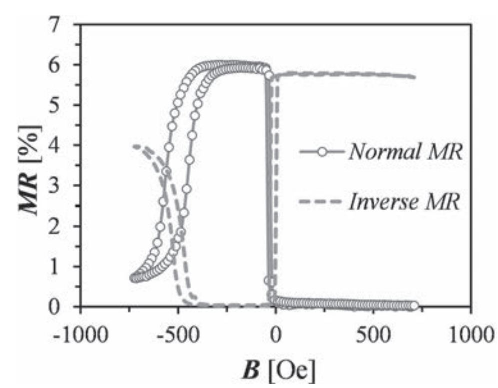

Fig. 1. *M-R* loops of the different SV structures with a normal MR and an inverse MR.

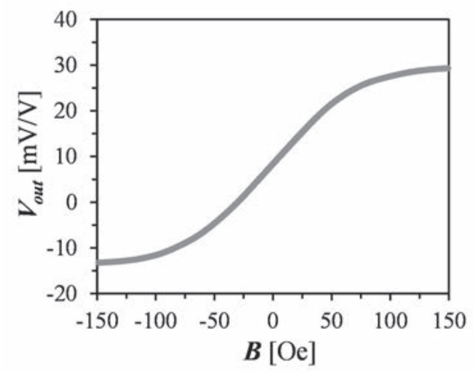

Fig. 2. The response of the proposed full-bridge output to the magnetic field.

CW-06. Hybrid planar hall effect and giant magnetoresistance sensors based on ferromagnetic/nonmagnetic/ferromagnetic multi-domain structures.

A. Elzwawy[1,2], A. Talantsev[1,3] and C. Kim[1]
1. Emerging materials science, Daegu Gyeongbuk Institute of Science & Technology (DGIST), Daegu, The Republic of Korea; 2. Ceramics Department, National Research Centre, Cairo, Egypt; 3. Institute of Problems of Chemical Physics, Moscow, Russian Federation

Magnetic sensors based on planar and out-of-plane magnetoresistance (MR) response to the applied magnetic field are the objects of interest in modern spintronics. The main advantage of MR sensors based on magnetic metal layers, in comparison with semiconductor Hall sensors is the independence of the carrier concentration on temperature. Magnetoresistance response of NiFe/M/NiFe (M = Au, Ta, Ag) sensors to DC magnetic field is studied for a wide range of angles α between magnetic field direction and sensing current direction. The anisotropic magnetoresistance (AMR) and giant magnetoresistance (GMR) contributions to magnetic field dependence of along with current V_{AMR} and perpendicular-to-current V_{PHE} (planar Hall) voltages are distinguished. The AMR contribution results in the steady changes of V_{AMR} and V_{PHE}, while GMR contribution may result in as steady, as well as jump wise response of V_{AMR} and V_{PHE}, dependently on the angle α. The correlation ratio r between magnetic fields of V_{AMR} and V_{PHE} jumps is found to be governed by the orientation of magnetic field in respect to the current direction. The V_{AMR} and V_{PHE} jumps become uncorrelated (r = 0) at α = 0° and 90°. The angular dependence of the correlation between V_{AMR} (H) and $V_{PHE}(H)$ jumps will be discussed in terms of bidirectional domain wall motion model. This work is supported by the grant of Ministry of Trade, Industry, and Energy (MOTIE, Korea, grant 10064089).

[1]. P. P. Freitas, F. A. Cardoso, V. C. Martins, et al., Lab on a Chip 12 546 (2012). [2]. P. P. Freitas, R. Ferreira, S. Cardoso, F. Cardoso, J. Phys.: Cond. Mat. 19 165221 (2007). [3]. S. Cardoso, D. C. Leitao, T. M. Dias, J. Valadeiro, M. D. Silva, A. Chicharo, V. Silverio, J. Gaspar, P. P. Freitas, J. Phys. D: Appl. Phys. 50 213001 (2017). [4]. F. W. Østerberg, G. Rizzi, A. D. Henriksen, M. F. Hansen. J. Appl. Phys. 115 184505 (2014). [5]. D. L. Graham, H. A. Ferreira, P. P. Freitas, Trends in Biotechnology 22 455 (2004).

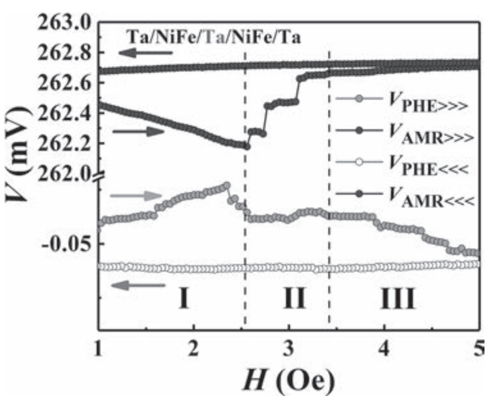

Fig. 1. Detailed V_{PHE} (H) and V_{AMR} (H) dependences at 0.1 Oe/s magnetic field ramping velocity for α = 0°. The vertical dashed lines show correspondence between $V_{PHE}(H)$ and $V_{AMR}(H)$ jumps. “>>>” and “<<<” symbols point magnetic field ramping direction.

CW-07. Anisotropy control of magnetostrictive film using thermal stress ant its application for sensor device.

S. Hashi[1], D. Sora[1], Y. Kubo[1], K. Arai[1] and K. Ishiyama[1]
1. Resarch Institute of Electrical Communication, Tohoku University, Sendai, Japan

We proposed an arbitrary control method of the anisotropy of magnetostrictive film employing a residual stress of lamination structure after annealing, which was considered mechanical properties such as coefficient of thermal expansion and Young's modulus of substrate, nonmagnetic layer and the magnetostrictive film. In addition, a high sensitive strain sensor using the anisotropy controlled FeSiB film by the method and inverse magnetostriction effect (Villari effect) was realized and demonstrated [1, 2]. This sensor can detects the strain by high frequency impedance change associated with high frequency permeability change of FeSiB. However, because dynamic range and working point of the sensor was in almost tensile strain region, the sensor was required a comparatively large bias stress to use as a vibration sensor. Therefore, we tried to arrange the dynamic range and working point of the sensor to suitable state for using vibration sensor by adjusting structure of the sensor element. The sensor element composed of 1 turn meander-patterned molybdenum (Mo) film as conductive layer and FeSiB magnetostrictive films that laminated a part of the meander. Both ends of the meander-pattern were used as electrodes to measure the high frequency impedance by using network analyzer. The element was fabricated on 150 μm-thick glass substrate by photolithography using lift-off process and RF sputtering. Then, it was annealed at 360 °C for 2 hours under a rotating magnetic field of 240 kA/m. Thickness of Mo layer and FeSiB layer were 1 μm. After annealing the element, the FeSiB films of the sensor element were subject to residual stress from Mo film and thin glass substrate, which induced a magnetic anisotropy to width direction (Fig. 1) of the rectangular shaped FeSiB film via magnetoelastic coupling. Fig. 2 shows the variation of high frequency impedance of the sensor element according to applied strain. The impedance change exhibited a peak value at around 100 ppm of applied strain and decreased steeply until at around 0 ppm. In addition, from the high frequency impedance change of the element under tensile strain the sensor exhibited a gauge factor of about 6,300 at a carrier frequency of 200MHz. Around 100 ppm reduction of working point of the strain sensor was realized. It is thought that the thermal stress to the FeSiB film was weakened by adjusting the ratio of layer thickness. At the conference, further quantitative discussion of properties of the sensor and evaluation results of vibration sensor will be presented.

[1] Y. Suwa, S. Agatsuma, S. Hashi, K. Ishiyama, IEEE Trans. Magn., 46, (2010) 666. [2] Y. Miwa, J. Shin, Y. Hayashi, S. Hashi, K. Ishiyama, IEEE Trans. Magn., 51, (2015) 2000604.

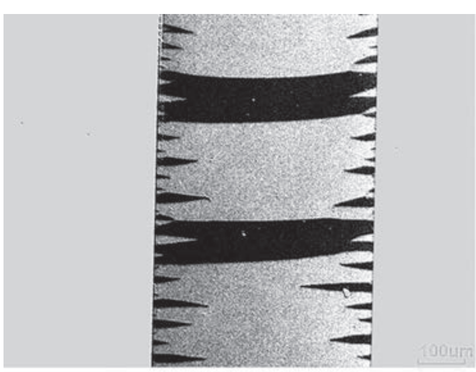

Fig. 1. Magnetic domain structure of FeSiB film after annealing.

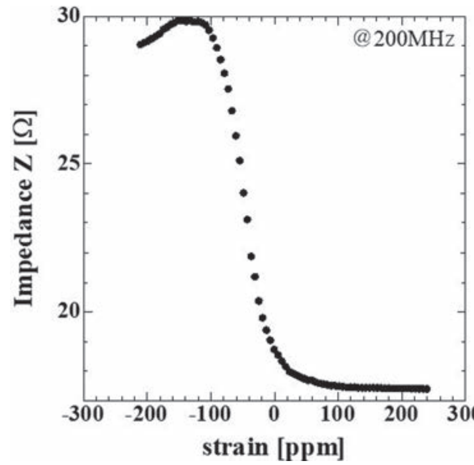

Fig. 2. High frequency impedance of the sensor according to applied strain.

CW-08. A Self-biased Anisotropic Magnetoresistive (AMR) Magnetic Field Sensor on Flexible Kapton.

C. Wang[1], W. Su[1], J. Pu[1], Z. Hu[1] and M. Liu[1]
1. Electronic Materials Research Laboratory, Key Laboratory of the Ministry of Education & International Center for Dielectric Research, Xi'an Jiaotong University, Xi'an, China

Magnetic sensors have attracted extensive attention due to their highly sensitive, e.g., navigation,[1] medical diagnosis (magnetoencephalography, magneto-cardiography, etc.), [2-4] and data storage.[5] Flexible substrates have received a great deal of attention due to their outstanding portability and wearability. A great fabrication of magnetic sensors on flexible substrates can make a big difference in our lives. AMR magnetic sensor has a simple structure and high sensitivity, when magnetization M and current density J are parallel ($R_{//}$), the resistance of Permalloy is at maximum and when magnetization M and current density J are perpendicular with each other ($R_{\perp}$),[6] the resistance is at minimum. In this work, we fabricated a self-biased anisotropic magnetoresistive (AMR) magnetic field sensor on flexible Kapton and it shows excellent stability and sensitivity even in the case of larger deformation. Here, we designed the Wheatstone bridge and barber pole structures, the current flow can be rotated by an angle of 45° or 135° with respect to the magnetic easy axis. We made AMR magnetic sensors on flexible Kapton by lift-off. First, the flexible substrates were cleaned by sequentially rinsing in acetone and ethanol. Then, we made a specific size of the pattern on the substrate by photolithography. Permalloy, Gold, Pt layers were sequentially deposited by sputtering method with base pressure $<10^{-7}$ torr. The magnetoresistance effect is characterized using typical four point probe resistivity measurement, as shown in Figure 1. Figure 1 shows that when there is an applied magnetic field, the resistance of the magnetoresistive sensor will change, the AMR ratio is probably 1.2%. Figure 2(a) shows that when the applied magnetic field is 114 Oe, the resistance of the magnetic field sensor varies with the angle of the magnetic field with a bending radius of 5 mm. Figure 2(b) shows that when the same magnet passes over the sensor at a same height, the resistance of the sensor have a different change with a different bending radius. In summary, we fabricated flexible AMR sensors on Kapton substrates. It shows excellent stability and sensitivity with a bending radius of 5 mm. With a great advantage of high sensitivity, excellent flexibility, and stability, the flexible AMR sensor provides a platform capable where wearable electrics for navigation, medical diagnosis and health monitoring can be realized.

[1] T. M. Liakopoulos, C. H. Ahn, Sens. Actuators A-Phys. 1999, 77, 66. [2] R. C. decharms, Nat. Rev. Neurosci. 2008, 9, 720. [3] D. H. Kim, N. S. Lu, R. Ghaffari, Y. S. Kim, S. P. Lee, L. Z. Xu, J. A. Wu, R. H. Kim, J. Z. Song, Z. J. Liu, J. Viventi, B. de Graff, B. Elolampi, M. Mansour, M. J. Slepian, S. Hwang, J. D. Moss, S. M. Won, Y. G. Huang, B. Litt, J. A. Rogers, Nat. Mater. 2011, 10, 316. [4] D. Karnaushenko, B. Ibarlucea, S. Lee, G. Lin, L. Baraban, S. Pregl, M. Melzer, D. Makarov, W. M. Weber, T. Mikolajick, O. G. Schmidt, G. Cuniberti, Adv. Healthcare Mater. 2015, 4, 1517. [5] J. Akerman, Science 2005, 308, 508. [6] C. Moron, C. Cabrera, A. Moron, A. Garcia, M. Gonzalez, Sensors 2015, 15, 28340.

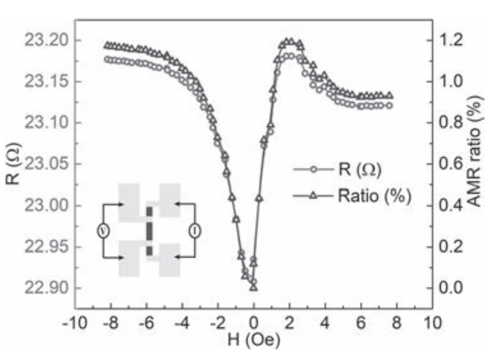

Fig. 1. Resistance of the magnetic sensor in different magnetic fields.

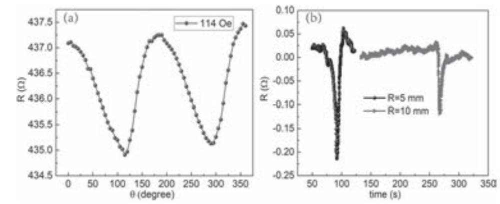

Fig. 2. (a) Resistance of the magnetic sensor varies with the angle; (b) Sensor response to an applied magnetic field.

CW-09. A flexible magnetoelectric transducer based on FeCuNbSiB/ poly (vinylidene fluoride) (PVDF) laminate composites for wearable magnetic sensors.

X. He[1], *J. Qiu*[1], Y. Long[1], Q. Chang[1], Z. Hu[1] and H. Liu[1]
1. College of Optoelectronic Engineering, Chongqing University, Chongqing, China

In recent years, flexible wearable equipment has attracted more and more attentions, and has made great development. Wearable electronics are expected to be one of the most active research areas in the next decades. There are more and more studies about flexible wearable sensors [1] and some of them have been used in life. However, there are few studies on flexible wearable magnetic sensors. Magnetic sensors [2] are useful and influential for human life, and kinds of sensors have been utilized in practice. To date, the new magnetic field detecting technologies with more excellent performance has been still the focused issues and trends. Magnetoelectric (ME) composite sensor was proposed as a candidate for the next-generation magnetic field sensors, due to its high sensitivity, compact size and room-temperature operation. Among the ME composites, laminate composites display the highest ME response, particularly those fabricated with magnetostrictive alloys and piezoceramic materials. However, piezoelectric ceramics have low electrical resistivity, high dielectric losses and are expensive, dense and brittle, which can lead to fatigue and failure, hindering their incorporation into technological applications. The piezoelectric polymer-based ME laminates [3] have several advantages over the ceramic based ones. They are easily fabricated by conventional low-temperature processing into a variety of forms, such as thin sheets or moulded shapes, and exhibit improved mechanical properties. The nanocrystalline FeCuNbSiB was elected as magnetostrictive material owing to its large piezomagnetic coefficient at low magnetic fields, high mechanical quality factor and large interface stress-strain coupling effect. For sensor applications, the optimization of the element responsible for the coupling between magnetostrictive and piezoelectric components plays a crucial role. However, coupling between the different phases is not the only parameter that requires optimization prior to their incorporation into technological applications: characteristics such as size, structure and relative geometry of the components may allow tailoring the applicability of ME composite materials. Furthermore, there is an increasing interest in fabricating smaller devices mainly in communication systems and wearable devices, which reduces the cost and improves the functionality [4]. For these reasons, it is essential to study the influence of the size on the ME coupling properties of the laminate composite. On the other hand, it is necessary to study its bending performance as the flexible ME transducer for better application for wearable magnetic sensors. In this paper, a series of flexible ME transducers based on nanocrystalline alloy (FeCuNbSiB)/poly (vinylidene fluoride) (PVDF) laminate composites for wearable magnetic sensors were fabricated. The effects of the composites size, geometry and structure on the ME coupling properties were investigated. Just as shown in Fig. 1, it is concluded that the ME voltage coefficient increases with decreasing transversal size aspect ratio (TAR) (from 3 to 1), reaching a maximum ME voltage coefficient of 203 V/cm Oe. The ME laminate composites with lowest longitudinal size aspect ratio (LAR) resulted in better ME voltage coefficient when compared with higher LAR. By investigating the ME coupling properties under different angles, it is also found that the optimal resonant ME voltage will decrease with the bending angle (θ) increases, getting the minimum of 11.56 V/cm Oe when θ=50°, which is shown in Fig. 2. The effects of thickness and fatigue properties for the ME coupling properties also were investigated. All these results provide an experimental basis for posterior research and practical application, which is very useful for science and advanced applications.

[1] E. Singh, M. Meyyappan, and H. S. Nalwa, "Flexible Graphene-Based Wearable Gas and Chemical Sensors," ACS Appl. Mater. Interfaces. Vol. 9, pp. 34544–34586 (2017). [2] S. Reis, M. P. Silva, N. Castro, V. Correia, P. Martins, A. Lasheras, J. Gutierrez, J. M. Barandiar_an, J. G. Rocha, and S. Lanceros-Mendez, "Characterization of Metglas/poly(vinylidene fluoride)/Metglas magnetoelectric laminates for AC/DC magnetic sensor applications," Mater. Des. Vol. 92, pp. 906-910 (2016). [3] A. Lasheras, J. Guti_errez, S. Reis, D. Sousa, M. Silva, P. Martins, S. Lanceros-Mendez, J. M. Barandiar_an, D. A. Shishkin, and A. P. Potapov, "Energy harvesting device based on a metallic glass/PVDF magnetoelectric laminated composite," Smart. Mater. Struct. Vol. 24, pp. 065024 (2015). [4] A. Lasheras, J. Gutierrez, and J. M. Barandiaran, "Quantification of size effects in the magnetoelectric response of metallic glass/PVDF laminates," Appl. Phys. Let., vol. 108, no.22, pp. 222903 (2016).

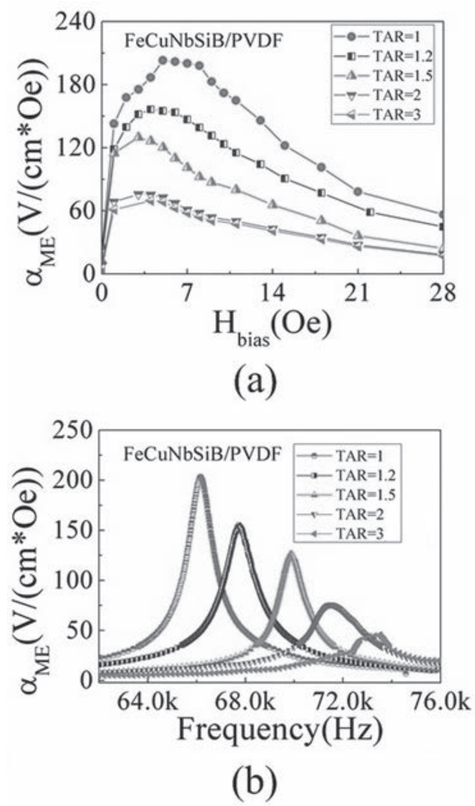

Fig. 1. (a)The resonant ME voltage coefficients as a function of dc bias magnetic field and (b)the ME voltage coefficients near resonance frequency at optimal bias magnetic field for the FeCuNbSiB/PVDF laminate composites with different transversal size aspect ratios (TARs) between PVDF and FeCuNbSiB layers.

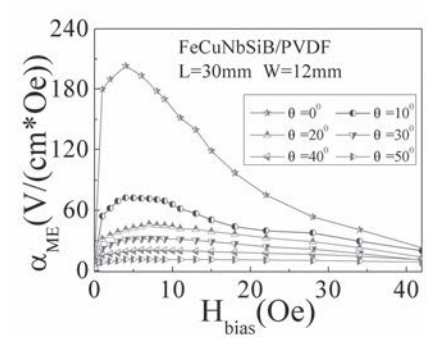

Fig. 2. The resonant ME voltage coefficients as a function of dc bias magnetic field for the ME transducer based on FeCuNbSiB/PVDF laminate composites with different bending angles (θ).

CW-10. Flat bandwidth expansion for spin-valve GMR magnetic field sensors.

Y. Chiang[1], X. Trinh[1] and *J. Jeng*[1]
1. Mechanical Engineering, National Kaohsiung University of Applied Sciences, Kaohsiung, Taiwan

The solid-state magnetic field sensors developed in recent years are transducers that convert magnetic fields under test into digital or analog voltage outputs. [1] The system consists of the front-end sensing element and the rear-end signal processing unit. The key performances of magnetic field sensor are demonstrated by its sensitivity, noise, linear range, and frequency bandwidth. The ultimate frequency response and noise behavior of the sensing system are determined by the driving method for the front-end sensing element. For quasi-static geomagnetic applications, flipping or modulation techniques is used to minimized the hysteresis for high accuracy measurement of DC field [2], but the available flat bandwidth is limited to less than one tenth of modulation frequency [3]. In contrast, a flat bandwidth over 30 kHz is observed for the DC-field-biased GMR sensor with a magnetic field feedback [4], which is ideal for high frequency applications, e.g. eddy-current sensing. However, the output under a DC-biased field is hysteretic and hence it is not suitable for DC measurement. For industry and high-end consumer applications, a magnetometer with a large bandwidth is necessary for mixed AC and DC measurement. A straight forward implementation of high bandwidth DC/AC magnetometer is to combine the DC sensor with and an AC induction coil [5]-[6]. However, the hybrid magnetometer of this kind has a feature size much larger than the solid-state sensor in it. In addition, the output levels for the two element sensors could be very different, inducing more complexity in signal processing. In this work, we explore the flat bandwidth expansion technique using two spin-valve GMR magnetic field sensors driven by different schemes, i.e. field modulation and DC-field-bias. Fig.1 shows the block diagram for the analog signal processing of the system. The low-frequency GMR sensor (LF sensor) is driven by AC magnetic modulation field to achieve high linearity and low hysteresis. A low-pass filter is used to extract the DC output induced by the nonlinear voltage-field relation of spin valve. In this way, the complexity of driving circuit with the inclusion of synchronous detection is avoided. The high-frequency GMR sensor (HF sensor) driven by a DC magnetic field bias has higher hysteresis in the low frequency range, but it exhibits high sensitivity and good linearity for high frequency field measurement. The LF sensor is suitable for detection of DC and low frequency magnetic field, while the HF sensor is capable of AC measurement at higher frequencies. The combined sensor output of the system has a wide bandwidth and is suitable for both DC and AC measurement. To combine the output of the two sensors, the output of HF sensor is high-pass (6 dB/oct) filtered at 100 Hz, and the output of LF sensor is low-pass (6 dB/oct) filtered at 100 Hz. The amplifier gains of the two outputs are fine tuned to achieve a uniform sensitivity, and the two outputs are combined with a summing amplifier. The observed outputs of LF and HF sensors as well as the combined signals are shown in Fig.2. It was found that the front-end sensitivities are 9.8 V/T for LF sensor and 251 V/T for HF sensor. The total sensitivity of the combined GMR sensing system is 2312 V/T with the total amplifier gains of 500 for the LF sensor and 20 for the HF sensor, supply voltage is 0.69 V for LF sensor and 2.61 V for HF sensor. The linearity error of the combined output signal is 2.2% within the ±4 μT range. The field noise spectral density is 65 nT/√Hz at 1 Hz. The output of summing amplifier is well consistent with theoretical values predicted by numeral calculations from the circuit model. The flat bandwidth of the combined output is expanded to the range from DC to above 10 kHz. The maximum deviation of normalized sensitivity is 1.7% at 100 Hz and the 3-dB flat bandwidth is 40 kHz. The phase lag of the combined output changes slowly to from 0° to -15° with an increasing frequency from 1 Hz to 1 kHz. The phase lag increases to -130° at 10 kHz and becomes random at frequencies above 100 kHz. Further improvement in the uniformity of frequency response is possible by optimizing the circuit parameters of low-pass and high-pass filters to fine tune their characteristic frequencies and gains. The observed frequency response of our system surpasses the existing GMR sensing systems reported by Tyler et al. [7], for which the 5% flat bandwidth is 530 Hz, and 10% flat bandwidth is 1.515 kHz. Our system exhibited a 5% flat bandwidth of 1.7 kHz and a 10% flat bandwidth of 8.3 kHz, while the response to quasi-static sweeping field at frequencies below 0.1 Hz shows negligible hysteresis. The broad bandwidth of our system makes it suitable for detecting the DC and AC magnetic fields in nondestructive evaluation [4]. It is also suitable for monitoring the environmental field in transient motion tracking with the software gyroscope [8] consisting of magnetic sensor and accelerometer. This work is supported by the Ministry of Science and Technology of Taiwan under Grant No. MOST MOST 105-2221-E-151-038.

[1] P Ripka, M Janosek, "Advances in Magnetic Field Sensors", Advanced Materials, IEEE Sensors Journal, 10(6), 1108-1116. [2] Van Su Luong, Anh Tuan Nguyen, Anh Tue Nguyen, "Exchange biased spin valve-based gating flux sensor" Measurement, Vol.115, pp.173-177 (2018). [3] Jen-Tzong Jeng, Ting-Yu Hsu, and Chih-Cheng Lu, "Odd-Harmonic Characteristics of the Field-Modulated GMR Magnetometer", IEEE Trans. Mag. 47, pp.3538-3541 (2011). [4] Jen-Tzong Jeng, Guan-Shiun Lee, Wen-Chu Liao, and Chia-Lun Shu, "Depth-resolved eddy-current detection with GMR magnetometer," Journal of Magnetism and Magnetic Materials, vol. 304, e470–e473 (2006). [5] P. Leroy, C. Coillot, V. Mosser, A. Roux, & G. Chanteur, "An AC/DC magnetometer for space missions: Improvement of a Hall sensor by the magnetic flux concentration of the magnetic core of a search coil", Sensors and Actuators A: Physical, 142(2), 503-510 (2008). [6] F. Han, S. Harada & I. Sasada, "Fluxgate and Search Coil Hybrid: A Low-Noise Wide-Band Magnetometer", IEEE Transactions on Magnetics, 48(11), 3700-3703 (2012). [7] Tyler J. Brauhn, Minhao Sheng, Bryan Allison Dow, Hiroyuki Nogawa, and Robert D. Lorenz, "Module-Integrated GMR-Based Current Sensing for Closed-Loop Control of a Motor Drive," IEEE Transactions on Industry Applications, Jan.-Feb. 2017, Vol.53(1), pp.222-231 [8] "Gyroscope apparatus", US patent, Publication No. 20170293368 A1, 2017.

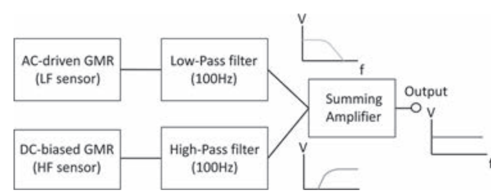

Fig. 1. Schematics of the signal processing unit

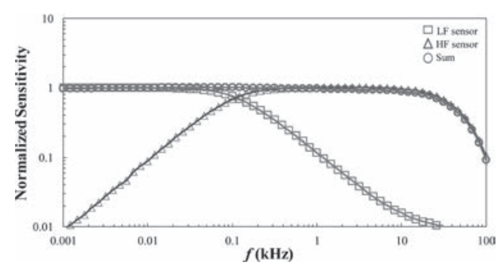

Fig. 2. Normalized sensitivity of LF sensor, HF sensor, and combined output of two sensors. Brown: LF sensor, Purple: HF sensor, Blue: Output of summing amplifier.

CW-11. High isotropic magnetic sensor based on ring Terfenol-D / PZT composites.

W. Wang[1], J. Ouyang[1], X. Wu[1], Y. Ren[1], J. Liang[1], S. Chen[1] and X. Yang[1]
1. School of Optical and Electronic Information, Huazhong University of Science and Technology, Wuhan, China

The magnetoelectric sensor has the characteristics of high sensitivity, wide response frequency range, low power consumption and easy preparation. It has broad application prospects in the detection of weak magnetic field such as geomagnetic field, biological magnetic field etc. In recent years, the related research[1-4] shows that the output of the magnetoelectric composites vary with the angle of the measured magnetic field, in which the ratio of the maximum value to the minimum value of the output signal is denoted as K. When K is large, the magnetoelectric composites have high anisotropy. For example, Dong et al. [1] and our group [2] prepared magnetoelectric sensors with high anisotropy (100 ≤ K ≤1000), and found that K values are related to the shape anisotropy of piezoelectric materials and magnetostrictive materials respectively. It means that the magnetoelectric sensor is very sensitive to the magnetic field in a specific direction and is suitable for vector magnetic field measurement. In contrast, when K is small, the magnetoelectric composites are highly isotropic, which means that their outputs are less affected by the direction of the magnetic field, and are suitable for scalar magnetic field measurements. However, highly isotropic magnetoelectric sensors were seldom reported. For this reason, this paper studies a Terfenol-D / PZT highly isotropic magnetoelectric sensor based on ring-shaped composite structure. As shown in Figure 1 (a), we first prepared magnetoelectric composites using Terfenol-D and PZT-5H, both of which were annular in shape. The resonant frequency of the material is shown in Figure 1 (b). The sensor was placed in a solenoid with AC current, held by a foam, and fixed on a platform. In the case of the electromagnet to provide DC bias magnetic field, the spectrum analyzer measured the output signal of the magnetoelectric sensor. The frequency of the AC signal was changed continuously to record the output of the magnetoelectric composites, and the resonance frequency of the composites can be analyzed through the curve to be about 32 kHz. Fig. 1 (c) shows the relationship between the output of composites and the DC bias magnetic field, when the frequency of AC resonant magnetic field is 32 kHz, as well as the DC bias magnetic field Hdc is from 200 to 3360Oe. The result shows that the composites output increased first, then kept stable after. Next step, we measured the linearity and isotropy of the sample in a shield tube. Figure 2 (a) introduces the testing instruments, and the micro-sensor device was placed in the magnetic shield tube. Fig. 2 (b) show the linearity of the sensor. When the DC bias magnetic field is is about 280Oe by bias magnet, the output of the magnetoelectric sensor at the AC frequency of 32 kHz has a linear relationship with the amplitude of the AC signal, as well as the sensitivity is 24 mV / Oe, indicating that it has a good linear relationship. Finally, we analyzed this model with finite method, the finite element results show that the magnetoelectric isotropy could be influenced mainly by the shape of the magnetostrictive and piezoelectric material, and the position of the bias magnetic field. Then we measured the isotropic characteristics of the ring-shaped sensor. The result is shown in Figure 2 (c). We placed the sensor device in the shield tube and rotated the sensor 360 ° in steps of 30 ° to measure the change of the output signal. The isotropy ratio of the magnetoelectric sensor (K) was fitted with finite method, and the result shows that the result approximately is 13: 1. As can be seen from the figure, the test values were in agreement with the theoretical values with finite method. This is because both the Terfenol-D and PZT-5H materials are isotropic in shape, which greatly increases the isotropic effect of the magnetoelectric sensor.

[1] Dong, S., Zhai, J., Li, J., & Viehland, D. (2006). Near-ideal magnetoelectricity in high-permeability magnetostrictive/piezofiber laminates with a (2-1) connectivity. Applied Physics Letters, 89(25), 252904. [2] Chen, S., Yang, X., Ouyang, J., Lin, G., Jin, F., & Tong, B. (2014). Fabrication and characterization of shape anisotropy AlN/FeCoSiB magnetoelectric composite films. Ceramics International, 40(2), 3419-3423. [3] Palneedi, H., Annapureddy, V., Lee, H. Y., Choi, J. J., Choi, S. Y., Chung, S. Y., & Ryu, J. (2017). Strong and anisotropic magnetoelectricity in composites of magnetostrictive Ni and solid-state grown lead-free piezoelectric BZT–BCT single crystals. Journal of Asian Ceramic Societies, 5(1), 36-41. [4] Chu, Z., Shi, H., Shi, W., Liu, G., Wu, J., Yang, J., & Dong, S. (2017). Enhanced Resonance Magnetoelectric Coupling in (1-1) Connectivity Composites. Advanced Materials, 29(19).

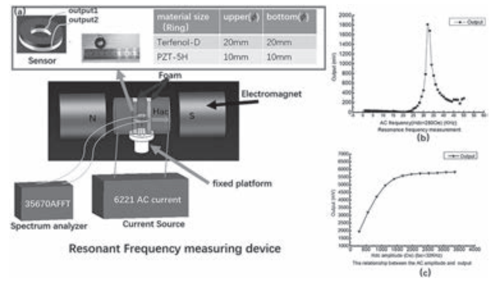

Fig. 1. The Resonant Frequency measuring instruments and the results. The relationship between Hdc amplitude and output.

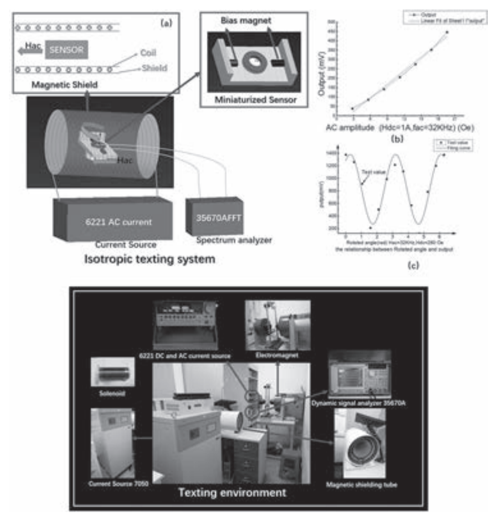

Fig. 2. The Linearity and Isotropy testing system of the sensor, and the testing results. The real testing system and instruments.

CW-12. Incident power dependence on magnetoimpedance element with domain wall resonance.

C. Sumida[1] and *H. Kikuchi*[1]
1. Iwate University, Morioka, Japan

I. INTRODUCTION Magnetoimpedance(MI) sensor utilizes permeability changes of the material through skin effect and ferromagnetic resonance when the sensor is applied to a magnetic field, and it has a higher sensitivity [1]. The sensors, which are composed of amorphous wires, are currently commercialized as compasses in mobile phones, and researches advance their sensitivity still continue for application of biomedical research [2] and nondestructive testing [3]. On the other hand, thin-film MI elements which has the compatibility with miniaturized integrated electronic devices such as driving and detecting circuits, contributes to the miniaturization of sensor device with higher spatial resolution. However, one problem of using thin-film elements is higher operating frequency. Typically, operating frequency is above 100 MHz to GHz range for elements with several μm thickness; this is unsuitable for general-purpose driving and detecting circuits, which normally operate below 20–30 MHz. During our investigations about thin-film MI elements, we found an interesting behavior that the frequency profile of impedance shows double peak depending on the applied bias field, that is, another peak appears at lower frequency region [4]. Then we analyzed this profile based on the domain wall equation and indicated the changes in impedance is attributed to the domain wall resonance (DWR) [5]. We also showed a potential of the phenomenon applied for developing a highly sensitive sensor operated at frequencies around the dozen megahertz region. In such cases, more detailed investigations about incident power is required because the behavior of impedance changes strongly depends on input high frequency power and this behavior is not still clear. Thus, in this study, we evaluated experimentally the impedance profile around frequency where the DWR occurs when the incident ac power modulated, and discussed about the sensitivity of impedance changes. II. EXPERIMENTAL PROCEDURE The thin-film element having 20-μm wide, 2-μm thick and 1-mm long was fabricated using an amorphous $Co_{85}Nb_{12}Zr_3$ film by photolithography and sputtering processes. The element was then annealed in vacuum by applying a field of 3 kOe at 400 °C and its easy axis is controlled parallel to the width direction. After field annealing, a Cu/Ti electrode with 2-μm thick, was fabricated. The impedance of fabricated element was measured by a network analyzer and a wafer probe. The incident ac power was changed from –20 to 5 dBm. During impedance measurements, a dc external magnetic field was applied to the element along the longitudinal direction by a Helmholtz coil. III. RESULTS AND DISCUSSION Fig. 1(a) shows an example of a frequency profile of impedance and inductance with/without DWR and it also includes the definition of parameters evaluated here; resonance frequency f_r, and changes in impedance peak ΔZ_p. When incident power is –10 dBm, the profile shows a peak for impedance and a rapid reduction of inductance due to DWR around 8.5 MHz, while the profile does not show DWR for –20 dBm (we applied magnetic field of 6.5 Oe to the element). Fig. 1 (b) shows the applied dc field dependence of f_r when the ac incident power altered. If the plotted data does not exist, which means we cannot observe DWR on the impedance profile. The values of f_r increase with increasing applied dc field and we confirmed ΔZ_p shows similar tendency to the changes in f_r. If the incident power is smaller, the field range where DWR occurs becomes smaller; e.g. the DWR appears from 7 to 8 Oe for –15 dBm while from 2 to 6 Oe for 5 dBm. On the other hand, the changing range of f_r and ΔZ_p has maximum point: in this case, f_r changes 55 MHz and ΔZ_p changes 14 Ω for –5 or –7 dBm. Then we investigated the impedance change against applied dc field and the sensitivity, defined as the maximum slope of the impedance profile, at a fixed frequency. Fig. 2 (a) shows the field dependence of impedance at 30 MHz when incident power changes. In the results of –20 dBm, we cannot observe DWR in this case, the impedance has a peak of 7.5 Ω at around 8.5 Oe. When incident power is –10 dBm, the peak value of impedance change becomes maximum (12 Ω at 8 Oe), then the peak intensity decreases with increasing incident power (See Fig. 2(b)). Also, the field intensity where the impedance has a peak shifts to lower field as the incident power increases (See Fig. 2(b)). When the incident power becomes –10 dBm, the sensitivity becomes maximum (38 Ω/Oe), which indicate DWR enhances the sensitivity of thin-film MI elements at the relatively lower frequency compared with the case without DWR (5.5 Ω/Oe for –20 dBm). IV. CONCLUSION The dependence of incident ac power on thin-film MI profile when the DWR occurs were investigated. If incident power is smaller, the profile did not show DWR, whereas larger incident power induces DWR, which brings abnormal impedance peak and rapid inductance reduction at relatively lower frequency region. Additionally, the DWR enhances the sensitivity of MI elements around the dozen megahertz region compared with the change without DWR.

[1] K. Mohri, K. Bushida, M. Noda, H. Yoshida, L. V. Panina, T. Uchiyama, "Magneto-Impedance Element", *IEEE Trans. Magn.*, Vol. 31, 2455–2460 (1995). [2] T. Wang, Z. Yang, C. Lei, J. Lei, Y. Zhou, "An integrated giant magnetoimpedance biosensor for detection of biomarker", *Biosens. Bioelectron.*, Vol. 58, 338–344 (2014). [3] W. Cheng, "Magnetic Flux Leakage Testing of Reverse SideWall-Thinning by Using Very Low Strength Magnetization", *J. Nondestruct. Eval.*, Vol. 35: 31 (2016). [4] H. Kikuchi, S. Kamata, C. Sumida, T. Nakai, S. Hashi, K. Ishiyama, "Enhancement of impedance change in low frequency on thin-film magnetoimpedance element", *J. Magn. Magn. Mater.,* Vol. 420, 269–274 (2016). [5] H. Kikuchi, C. Sumida, H. Uetake, S. Yabukami, S. Hashi, K. Ishiyama, "Analysis of thin-film magnetoimpedance behavior at low MHz region based on domain wall equation and bias susceptibility theory", *AIP Advances*, Vol. 7, 056617- 1–6 (2017).

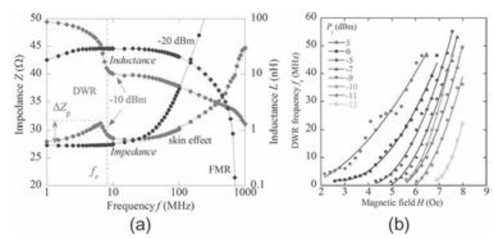

Fig. 1. (a) Example of frequency dependence with/without DWR and definition of parameters, DWR frequency f_r and peak in impedance change ΔZ_p. DWR occurs for –10 dBm while not for –20 dBm. (b) Relation between DWR frequency, f_r and applied dc field.

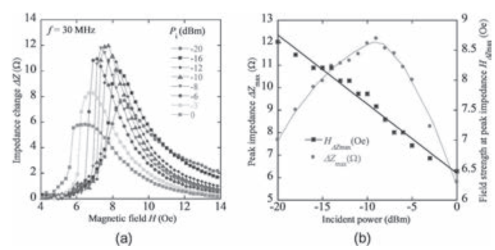

Fig. 2. (a) Applied field dependence of impedance at 30 MHz. (b) Incident power dependence of peak value of impedance and field intensity where impedance has maximum at 30 MHz.

CW-13. Influence of substrate material and geometry on giant magnetoimpedance of NiFe composite wires.

K. Roy[1] and *V. Srinivas*[1]

1. Department of Physics, Indian Institute of Technology Madras, Chennai, India

The giant magnetoimpedance (GMI) effect has been reported in soft magnetic materials at higher frequencies essentially due to the changes in skin effect as a consequence of applied external magnetic field [1]. The GMI element with zero-magnetostriction can be used to fabricate new sensitive, quick response and low power consumption micro-magnetic sensors [2]. Different geometries of GMI elements have been investigated to improve the sensitivity [3]. On the other hand, electroplated composite wires consisting of a highly conductive inner core and an outer soft magnetic shell have been predicted to exhibit GMI [1], which are suitable for the development of low magnetic field sensor. Further the soft magnetic properties which depend on microstructure of the film can be controlled by varying deposition parameters like additive(s) concentration in electrochemical bath. It was shown that deposition parameters have significant role in stabilizing the permalloy composition of NiFe thin films [4]. Main objective of the present investigation is two fold i.e, to study the MI response (i) of magnetic films deposited on different substrate material (Cu, Ag and Ni wires) (ii) when MI elements are connected in series and parallel geometry. The electrolytic compositions used are 0.36 M nickel sulphate, 0.05 M iron sulphate per litre and boric/citric acid concentration varied 10 to 60 g/lt. The NiFe films were deposited on ~100 mm diameter Cu (Cooper), Ni (Nickel) and Ag (Silver) wires and impedance was measured under dc magnetic field. The MI is defined as, $[Z(H_{ext})\text{-}Z(H_{max})]/Z(H_{max})$, where H_{ext} is the external magnetic field applied, H_{max} is the maximum applied magnetic field. Deposition was carried on all wires by optimizing the deposition parameters. The MI elements were deposited using identical deposition parameters and are connected in series and parallel geometry to study the cascading effect on MI. The composition and thickness of the films was determined by SEM. Subsequently MI as a function of applied field was measured at different frequencies and shown in Fig.1. Since the MI depends skin effect which in turn depends on the conductivity the MI characteristics are expected to be different. It is observed that the films deposited of Cu and Ag wires show a maximum MI of ~500% at field of 0 Oe (100 kHz) and 2.4 Oe (60 kHz) respectively. While a maximum MI of ~200% at field 2.4 Oe (200 k Hz) was observed for film deposited on Ni wire. Although Ni wire itself is a ferromagnetic sample the MI for Nickel is found to be negligibly small. From all the substrate variation studies, it is clear that the material of the substrate plays a major role not only on magnitude of MI but also frequency at which the maximum MI is observed. In the case of two wire series connection the maximum MI is 215%, while for four wire the maximum MI of 360% was observed at 4 Oe (500 kHz frequency). We have observed a significant change in magnitude of series combination. On the other hand in comparison to the single wire, the maximum MI frequency is shifted from 60 kHz to 500 kHz for both the double and four wire connections. Interestingly the H_k value is same for all the cases, which is expected since the films are deposited under identical conditions. These results suggest that the magnetic response is similar but the higher initial impedance could possibly be shifting the frequency at which the maximum MI is observed. This is important observation that emerges out of this study, which means a magnetic field sensor can be designed for suitable frequency range by choosing the series combination of MI elements. On the other hand two wire parallel combination the maximum MI is 300% at 4.8 Oe (90 k Hz) and for four wire the maximum MI of 120% observed at 2.4 Oe (200 k Hz). Here the MI value is decreased as the number of wires are increased. Also the maximum MI frequency is shifted from 60 kHz (single wire), 90 kHz(double wire) to 200 kHz(four wire). This is also a strong evidence of the fact that for high MI value the sample needs to have lower z, as well as highly soft magnetic in nature. These features can be understood on the basis of standard Maxwell equations and the Landau-Lifshitz-Gilbert equation [5]. A detailed experimental and numerical simulations will be presented in order to explain the observed changes MI with substrate material.

[1] M.L.A. Machado and S.M. Rezende, "A theoretical model for the giant magnetoimpedance in ribbons of amorphous soft ferromagnetic alloys", J. Appl. Phys. 79 (1996) 6558. [2]K. Mohri, T. Uchiyamaa, L.P. Shena, C.M. Caia, L.V. Panina, "Amorphous wire and CMOS IC-based sensitive micromagnetic sensors (MI sensor and SI sensor) for intelligent measurements and controls", J. Magn. Magn. Mater 249 (2002) 351. [3] T. Wang, C. Lei, Z. Yang, X. Sun, Y. Liu, and Y. Zhou, "Meander-shaped magnetoimpedance sensor for measuring inhomogeneous magnetic fringe fields of NiFe films" Appl. Phys. Let. 105 (2014)172404. [4] A. A. Chlenova, A. A. Moiseev, M. S. Derevyanko, A. V. Semirov, V. N. Lepalovsky and G.V. Kurlyandskaya, "Permalloy Based Thin Film Structures: Magnetic Properties and the Giant Magnetoimpedance Effect in the Temperature Range Important for Biomedical Applications" Sensors 17 (2017) doi:10.3390/s17081900 [5] S. K. Manna and V. Srinivas, "AC magnetic and magnetoimpedance properties of CoFe(NbMnNi)BSi amorphous ribbons" J. Magn.Magn. Mater. 449 (2018) 467–474

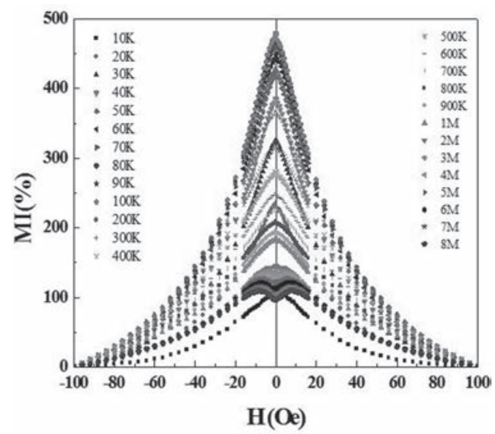

Fig. 1. (a) MI vs H plot of NiFe film on Cu wire at different frequencies.

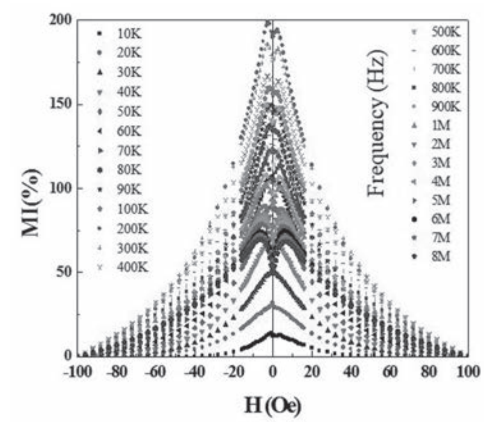

Fig. 2. (b) MI vs H plot for NiFe film on Ni wire at different frequencies.

CW-14. Fabrication of ferromagnetic Co-MgF$_2$ granular film with high transmittance and large Faraday-effect for optical magnetic field sensor.

M. Miyamoto[1,2], T. Kubo[2], Y. Fujishiro[1], K. Shiota[1], M. Sonehara[1] and T. Sato[1]
1. Shinshu University, Nagano, Japan; 2. Citizen Finedevice Co., Ltd., Kitasaku-gun, Japan

The Faraday-effect has been used for the measurement of magnetic field induced by electric current. Actually, an optical fiber sensor using the Faraday-effect has been developed as an alternative method of the current-transformer in the substation of the AC electric power system. However, in the optical fiber electric current sensor, it is difficult to minimize the sensor head because the optical fiber must be wound to a conductor wire. Recently, we proposed an optical magnetic field sensor with a small head [1] for the switching current measurement for the SiC/GaN power-devices, which consisted of a Faraday-element using a magnetic thin film. Such a magnetic thin film for the Faraday-element must have both higher transmittance for the light (transparency) and large Faraday-effect. Rare earth substituted yttrium iron garnet film (R:YIG) with high transmittance and large Faraday-effect has been widely studied, and a cerium substituted film (Ce:YIG) with high performance has recently been reported [2]. However, Ce:YIG film has a temperature-dependent magnetization owing to the low Curie temperature around or below 300 deg C. In this study, we focus on a granular film with ferromagnetic fine metal particles dispersed in an insulator matrix to obtain high transmittance and large Faraday-effect. Actually, N. Kobayashi *et al.* [3] reported a FeCo-AlF granular film with high transmittance. J. L. Dorman *et al.* [4] also reported a Fe-Al$_2$O$_3$ granular film with large Faraday rotation angle of 3000 to 4000 deg./cm at 1550 nm wavelength. In our study, to develop the Faraday-element for the optical magnetic field sensor, the granular film was fabricated by co-evaporation method using cobalt (Co) and magnesium fluoride (MgF$_2$). The evaporation rate ratio was kept to Co : MgF$_2$ = 1 : 2 (Co volume fraction of 0.33). The substrate- temperature during co-evaporation was R.T. to 450 deg C. The magnetic and magneto-optical properties of the film were characterized. The substrate-temperature dependences of the cobalt particle diameter and the extinction coefficient k in the Co-MgF$_2$ granular film deposited by co-evaporation are shown in Fig. 1. The Co particle diameter became large proportional to the substrate-temperature during the deposition. At low substrate-temperature during the deposition, average Co-granule diameter was about 3 nm and the granular film exhibited a superparamagnetism. On the other hand, not shown here in detail, at the substrate-temperature during the deposition of 350 deg C or above, the granular film exhibited a magnetization curve with a hysteresis as an evidence of the ferromagnetic behaviour. O. Kitakami *et al*. [5] reported a superparamagnetic critical diameter of hcp-Co, it was estimated to be about 7 nm, in our study, such the critical Co diameter was estimated to be about 4 nm. The cobalt particle size became large and the k of the film became low with increasing the substrate-temperature during the deposition. The minimum k of the film was 0.028 at the substrate-temperature of 450 deg C, which was much smaller than those of previous studies. Even in constant concentration of Co or MgF$_2$ in the film, the k changed by substrate-temperature during the deposition. We considered that the distance between the adjacent cobalt particles became wider when the cobalt particle became larger, and such a relationship between cobalt particle size and the distance between the adjacent particles was considered to be strongly related to the low k of the Co-MgF$_2$ granular film. Fig. 2 shows the magnetization curve of Co-MgF$_2$ granular film deposited at 350 deg C measured in the film plane and perpendicular to the film plane, and the Faraday-rotation angle versus applied magnetic field. From Fig. 2, the Co-MgF$_2$ granular film had the in-plane aligned magnetization, and the perpendicular magnetization process was considered to be due to the magnetization rotation by the perpendicular demagnetizing effect. Although not shown here, even at ambient temperature of 350 deg C, the decrease of saturation magnetization M_s of the Co-MgF$_2$ granular film deposited at 350 deg C was a little 10 %. Therefore, the Co-MgF$_2$ granular film was considered to have a Curie temperature much higher than 350 deg C. In Fig. 2, the Faraday-rotation loop was corresponding to the magnetization curve well. The Faraday-rotation angle was linearly proportional to the applied magnetic field within ±2 kOe. The upper limit of magnetic field 2 kOe of the linear relation was considered to be due to the perpendicular demagnetizing magnetic field H_d, where H_d was estimated to be about 4 kOe from the saturation magnetization M_s of 4 kG. Since the H_d was considered to be dependent only on the M_s with the curie temperature much higher than 350 deg C. Therefore, the Co-MgF$_2$ granular film will be useful for the Faraday-element of the optical magnetic field sensor used in high ambient temperature.

[1] T. Hanada *et al*.: *40th Annual Conf. on Magnetics in Japan*, 6pB-13 (2016). [2] Mehmet C. Onbasli *et al*.: *Nature*, Scientific Reports 6, Article number 23640 (2016). [3] N. Kobayashi *et al*.: *Nature*, Scientific Reports 6, Article number 34227 (2016). [4] J. L. Dorman *et al*.: *J. Appl. Phys.*, Vol.67, No.9, 1 May (1990). [5] O. Kitakami *et al*.: *Jpn. J. Appl. Phys.*, Vol.35, pp.1724-1728 (1996).

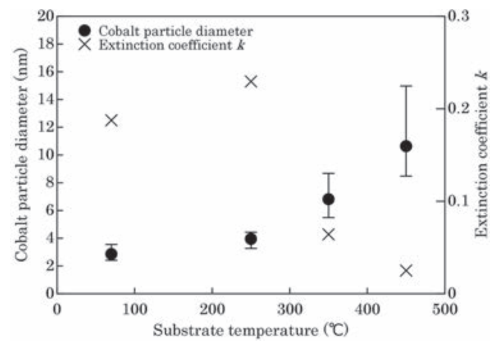

Fig. 1. Cobalt particle diameter and extinction coefficient *k* of Co-MgF$_2$ granular film deposited at different substrate- temperature.

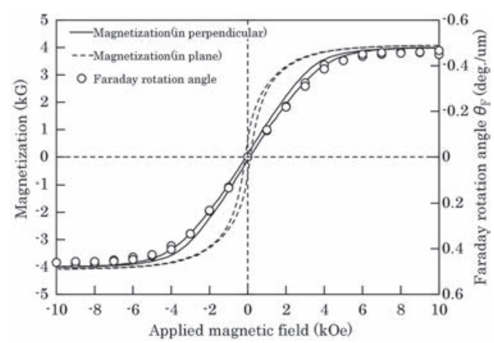

Fig. 2. Magnetization curves and Faraday-rotation loop of 350 deg C deposited Co-MgF$_2$ granular film. Faraday rotation angle was measured at 1550 nm wavelength.

CW-15. Effect of Annealing Temperature on GMI in NiFe Thin Films.

L. Zhu[1], F. Jin[1], K. Dong[1], W. Mo[1] and J. Song[1]
1. China University of Geosciences, Wuhan, China, Wuhan, China

Soft magnetic amorphous films have the giant magneto-impedance (GMI) effect, which is of great significance to realize miniaturized and integrated GMI micro-magnetic sensor [1]. So it is the hotspot to improve the GMI effect and sensitivity of amorphous soft magnetic films nowadays. In this work, we studied the effects of different annealing temperatures on soft magnetic properties and GMI effect of NiFe films. We used the magnetron sputtering to prepare NiFe single layer thin films with a thickness of 80nm which were deposited onto a glass substrate. Then the films were annealed at different certain temperatures. The annealing temperatures were 200°C, 500°C and 600°C respectively. The magnetization curves at 200°C, 500°C and 600°C and XRD 2θ spectra at 500°C of the NiFe single layer film were shown in figure 1 (a) and (b). The in-plane easy magnetization direction was not obvious when the annealing temperatures was 200°C, while the annealing temperature reached 500-600°C, there were good in-plane easy magnetization directions. Annealing can effectively eliminate the films' magnetic anisotropy and optimize the soft magnetic properties of the film [2]. On the outcome of the analysis, a sample with a sandwiched multilayer structure defined as Ta/$(NiFe/Ag)_5$/Ag/$(NiFe/Ag)_5$/Ta had been prepared by magnetron sputtering. It had a total thickness of 5nm/$(80nm/2nm)_5$/200nm/$(80nm/2nm)_5$/5nm and a dimension of 1mm×10mm. The MI effect was measured in a network analyzer using a microstrip test-fixture. Figure 2 (a) and (b) showed the structural diagram and the sample of the multilayered film respectively. At present, the GMI curve test at room temperature has been completed, and the GMI curve test under the annealing conditions will continue.

[1] García-Arribas A, Fernández E, Svalov A, et al. Thin-film magneto-impedance structures with very large sensitivity[J]. Journal of Magnetism & Magnetic Materials, 2016, 400:321-326. [2] Xiao S Q, Liu Y H, Yan S S, et al. Giant magnetoimpedance and domain structure in FeCuNbSiB films and sandwiched films[J]. Physical Review B, 2000, 61(8):5734-5739.

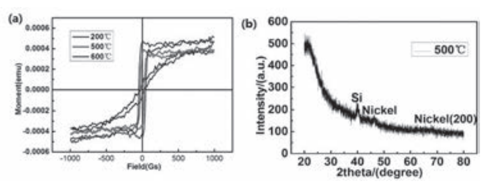

Fig. 1. (a) The magnetization curves at 200°C, 500°C and 600°C of the NiFe single layer film (b) XRD 2θ spectra at 500°C of the NiFe single layer film

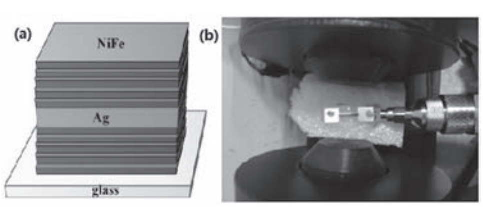

Fig. 2. (a) the structural diagram of the NiFe multilayered film (b) the sample of the NiFe multilayered film

CW-16. Effect of amorphous wire core diameter on the noise of an orthogonal fluxgate.

M. Butta[1], M. Janosek[1], B. Schutte[1], M. Vázquez[2], R. Perez del Real[2], E. Calle[2] and A. Jimenez[2]
1. Faculty of Electrical Engineering, Czech Technical University in Prague, Praha, Czechia; 2. Institute of Materials Science of Madrid (ICMM-CSIC), Madrid, Spain

Orthogonal fluxgates have been proved to provide low noise measurement of quasi-static magnetic field. Typically Co-based amorphous wires are used because they allow to reach noise as low as 2.5 pT/√Hz noise at 1 Hz for as-cast wires and 1 pT/√Hz noise for annealed wires [1]. So far, however, only one diameter has been used for such wires, namely 125 μm. This is due to the fact that commercially available magnetic wires manufactured by Unitika™ are available only in this diameter. In this paper we investigate the possibility to reduce the noise of an orthogonal fluxgate by increasing the diameter of the magnetic wires used as core of the sensor. We manufactured (Co0.94Fe0.06)72.5Si12.5B15 in-water solidified amorphous wires with diameter in a range from 80 μm to 220 μm by changing the diameter of the ejecting hole of the crucible where the alloy was melted [2]. For different holes diameter we adjusted the value of argon pressure inside the crucible and speed of the water wheel in order to obtain a continuos casting of the magnetic wire. We then analized the magnetic behaviour of the wire by measuring the hysteresis loop by means of VSM: the coercivity keeps between 80 A/m and 180 A/m for wires with diameter up to 190 μm, then it rises up to 4300 A/m for wires with diameter higher than 200 μm. This indicates that we can produce amorphous wires only with diameter up to 190 μm. For larger diameter the central part of the wire is nanocristalline. This is cause by limited cooling rate during casting (about 10^6 K/s) which does not allow to cool fast enough the inner portion of the wire making possible the development of crystals. The wires where then used as core for orthogonal fluxgate in fundamental mode [3]. The length of the wires was 8 cm, the pick-up coil was composed of 900 turns and it was 6 cm long (to avoid the effects of the terminations). The wire where excited by 50 mA dc current and 45 mA ac current. We characterized the noise for different values of excitation current frequency and we found out that is it slightly higher at resonance frequency, therefore for all wires we selected a frequency for excitation curret out of resonation. This lead us to different frequency for different wires, given that the resonance frequency depends on the wire's diameter. In order to obtain a fair comparison we selected a frequency (between 60 and 90 kHz) which returned the lowest achivable noise for every sensor. Fig. 1 shows the noise spectra of orthogonal fluxgates based on amorphous wires with 80 μm, 130 μm and 180 μm. As we can see the noise drops down from 12 pT/√Hz at 1 Hz to 2 pT/√Hz. Interestingly, this noise decrease is achieved despite the less favourable demagnetizing factor of the wires with high diameter (1.12×10^{-3} for 180 μm vs. 5×10^{-4} for 80 μm). Wires with larger diameter which contain a nanocrystalline core do not show any output signal, indicating they do not work as orthogonal fluxgate anymore. Therefore, we derive that the magnetic wires for orthogonal fluxgates have to be casted with the largest possible diameter, for this reduces the noise, despite less favourable demagnetizing factor; the upper limit of the maximum diameter the casting method allows to achieve fully amourphous wires.

[1] Butta, M. and Sasada, I., Method for offset suppression in orthogonal fluxgate with annealed wire core, Sensor Letters, 2014, Vol. 12, n. 8, pp. 1295-1298, doi 10.1166/sl.2014.3311 [2] Waseda Y., Ueno S., Hagiwara M. and Aust K, Formation and mechanical properties of Fe- and Co-based amorphous allow wires produced by in-rotating-water spinning method, Progress in Material Science Vol. 34, pp. 149-260, 1990 [3] Sasada I., Orthogonal fluxgate mechanism operated with DC biased excitation, Journal of Applied Physics 91(10):7789-7791

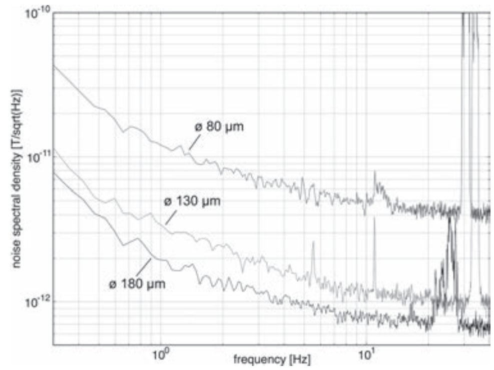

WEDNESDAY AFTERNOON, 25 APRIL 2018 ORCHID I-II, 2:00 TO 4:00

Session DA
SYMPOSIUM ON MAGNETISM IN BIOMEDICINE: WHERE NEXT?

Montserrat Rivas, Chair
Universidad de Oviedo, Gijón, Spain

INVITED PAPERS

2:00

DA-01. In-situ Studies of the Dynamical Magnetic Response of Iron Oxide Nanoparticles in Cellular Environments.

D. Cabrera[1,2], *N. Telling*[1], A. Coene[3], J. Leliaert[4], E. Artés-Ibáñez[2], L. Dupré[3] and F. Teran[2]
1. Institute for Science and Technology in Medicine, Keele University, Stoke-on-Trent, United Kingdom; 2. Campus Universitario de Cantoblanco, iMdea Nanociencia, Madrid, Spain; 3. Department of Electrical Energy, Metals, Mechanical Constructions and Systems, Ghent University, Zwijnaarde, Belgium; 4. Department of Solid State Sciences, Ghent University, Ghent, Belgium

Magnetic nanoparticles (MNPs) offer unique and important capabilities applicable to both fundamental research and technology based applications in biomedicine and the life sciences. In particular, their interaction with suitable static or alternating magnetic fields means that they can act as conduits for the remote application of mechanical forces to cells, as well as delivering local heating through the magnetic hyperthermia effect. In addition, their magnetic properties make it possible to not only track the particles *in vivo*, but also to probe their local environment using techniques such as magnetic particle imaging. However, in order to achieve their full potential, it is essential to understand how the cellular environment the magnetic nanoparticles occupy affects their behaviour and ultimately performance. MNPs exposed to alternating (AC) magnetic fields offer potential applications as hyperthermia mediators for cancer treatment [1,2], providing a complementary physical technique to therapies using pharmacological and immunological treatments. An important property of magnetic hyperthermia is that it produces a localised heating affect which can be used to induce apoptosis and necrosis of cancer cells. In fact, the ability to associate magnetic nanoparticles with individual cells, either by cellular uptake or by binding the nanoparticles to cell membranes, gives unrivalled potential for treating cancer on a cell by cell basis. An example of the uptake of iron oxide magnetic nanoparticles by breast cancer cells (MCF-7 cell line) is shown in the TEM image in Figure 1. Despite the exciting possibilities for cancer treatments offered by magnetic hyperthermia, there are still some significant challenges to overcome before this can become a viable therapy. Perhaps most significantly, recent experiments have shown a reduction in the MNP heating efficiency when the particles are located inside cells or tissues [3,4]. It has been suggested that the enhancement of nanoparticle aggregation and/or immobilization after interaction with cells could cause this effect, although a quantitative description is currently lacking. MNP aggregation can be caused following internalisation and subsequent sequestering of the MNPs into intracellular vesicles known as lysosomes [4,5], as can be clearly seen in Figure 1. In this talk I will describe the results of our recent experiments to use a combination of AC magnetic susceptibility [6,7] and AC magnetometry [8,9] to probe the in situ dynamic magnetic response of nanoparticles following their association with live cancer cells. Measurement of the AC hysteresis loop area provides a direct method for assessing the heating efficiency of the nanoparticles (known as the Specific Absorption Rate or SAR), without the heat dissipation complications associated with calorimetric methods [8]. Furthermore, the shape of the hysteresis loops provides crucial information on how the dynamic magnetic response of the nanoparticles is affected by their local biological environment. Complementary to this, AC susceptibility measurements probe the mobility and aggregation state of the particles, as well as their effective magnetic anisotropy. By combining these techniques, we were thus able to evaluate the behaviour of two different MNP core sizes following cell internalisation, and to compare this to experimental model systems where either the aggregation or the mobility of the particles was systematically varied. By fitting the AC susceptibility data with a computational model, we also obtained values for the effective magnetic anisotropy of the MNPs in their different environments. The SAR results shown in Figure 2, revealed that the heating efficiency was indeed reduced following cellular internalisation (by comparison with aqueous suspension), but that the effect was only significant for the larger (21 nm) particles. The origin of this reduction was found to be a corresponding decrease in the effective anisotropy of the particles, once they were associated with cells. Experiments on the model MNP systems revealed similar qualitative and quantitative trends to those seen in the cellular experiments, but caused predominately by increasing MNP aggregation rather than reducing nanoparticle mobility. The results discussed here are important for progress in magnetic hyperthermia research as they enhance our understanding of the dynamic magnetic response of MNPs in cells, which in turn defines their heating efficiency. The use of AC magnetic techniques to probe the MNP response in situ, also offers a method for assessing future MNP designs such that barriers to exploiting magnetic hyperthermia can ultimately be overcome.

1. Espinosa, A. *et al.* Duality of Iron Oxide Nanoparticles in Cancer Therapy: Amplification of Heating Efficiency by Magnetic Hyperthermia and Photothermal Bimodal Treatment. *ACS Nano* 10, 2436-2446, doi:10.1021/acsnano.5b07249 (2016). 2. Maier-Hauff, K. *et al.* Efficacy and safety of intratumoral thermotherapy using magnetic iron-oxide nanoparticles combined with external beam radiotherapy on patients with recurrent glioblastoma multiforme. *Journal of Neuro-Oncology* 103, 317-324, doi:10.1007/s11060-010-0389-0 (2011). 3. Arami, H. *et al.* Invivo multimodal magnetic particle imaging (MPI) with tailored magneto/optical contrast agents. *Biomaterials* 52, 251-261, doi:10.1016/j.biomaterials.2015.02.040 (2015). 4. Di Corato, R. *et al.* Magnetic hyperthermia efficiency in the cellular environment for different nanoparticle designs. *Biomaterials* 35, 6400-6411, doi:http://dx.doi.org/10.1016/j.biomaterials.2014.04.036 (2014). 5. Levy, M. *et al.* Nanomagnetism reveals the intracellular clustering of iron oxide nanoparticles in the organism. *Nanoscale* 3, 4402-4410, doi:10.1039/c1nr10778j (2011). 6. Soukup, D., Moise, S., Céspedes, E., Dobson, J. & Telling, N. D. In Situ Measurement of Magnetization Relaxation of Internalized Nanoparticles in Live Cells. *ACS Nano* 9, 231-240, doi:10.1021/nn503888j (2015). 7. Moise, S. *et al.* The cellular magnetic response and biocompatibility of biogenic zinc- and cobalt-doped magnetite nanoparticles. *Scientific Reports* 7, doi:10.1038/srep39922 (2017). 8. Ovejero, J. G. *et al.* Effects of inter- and intra-aggregate magnetic dipolar interactions on the magnetic heating efficiency of iron oxide nanoparticles. *Physical Chemistry Chemical Physics* 18, 10954-10963, doi:10.1039/c6cp00468g (2016). 9. Cabrera, D. *et al*, Unraveling viscosity effects on the hysteresis losses of magnetic nanocubes. *Nanoscale* 9, 5094-510 (2017).

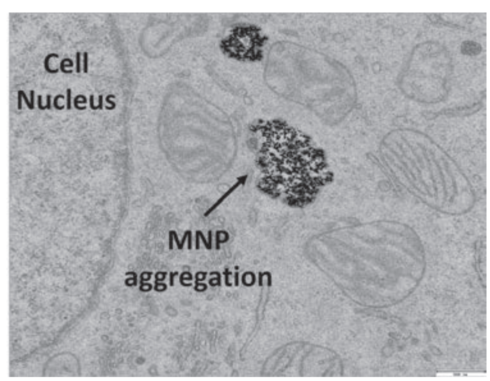

Fig. 1. TEM image showing MNP aggregation in intracellular lysosomes.

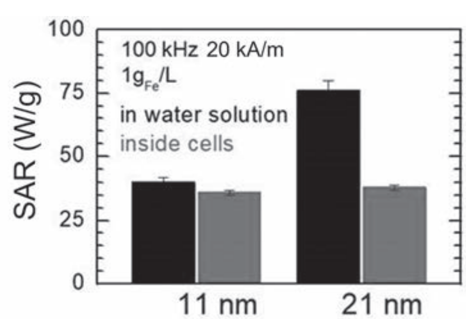

Fig. 2. Specific Absoption Rate (SAR) of iron oxide MNPs in water and in cells

2:30

DA-02. Design and Medical Applications of a Platform for Image-Guided Non-Invasive Brain Delivery of Magnetic Particles.

J. Benlloch[1] and *I. Weinberg*[1]
1. I3M, Valencia, Spain

The first successful clinical trial for shallow focussing of magnetic nanoparticles was performed in the mid 1990s to treat inoperable surface tumours [1]. Since then, much clinical progress has been achieved in the treatment of diseases with magnetic nanoparticles. In particular, a private company has obtained CE mark in 2014 for the therapy of some tumours, after treating 90 patients with brain tumors and about 80 patients with other tumors such as pancreatic, prostate or esophageal cancer [2]. The fluid containing magnetic particles is injected into a tumor and then it is heated through external application of alternating magnetic fields. Heating sensitizes tumor cells to radiotherapy and/or chemotherapy. However, injecting the fluid into a brain tumor, implies a considerable risk due to the potential functional damage in the brain areas traversed by the needle. Moreover, an optimally efficient hyperthermia or drug delivery system involves a perfect control on the particle delivery to achieve, for instance, an even distribution of the nanoparticles throughout the tumor. In order to reach that objective, a device that allows simultaneous visualization of the tumor and the magnetic nanoparticles is required. Therefore, a good question to ask is whether it is possible to deliver therapy to the right place through any biological tissue. In order to most efficiently deliver nanoparticles to specific foci in the brain and central nervous system, it would be helpful to have anatomic guidance at the time of administration and delivery. Magnetic particle imaging (MPI) does not allow simultaneous MRI guidance because the static field disrupts the ability to demagnetize the particles. We have built a low-profile electro-permanent MRI system [3] that can be quenched in milliseconds and then reconfigured to guide magnetic particles (Fig. 1). Particles can be designed and manufactured specifically to take advantage of the properties of this delivery system, for example with nano-engineered features that permit rotation of the particles during translation. A combination of custom magnetic pulses and particle shapes enables unprecedented capabilities: concentration and de-aggregation [4], rotation [5] and penetration through viscous materials [6]. This combined rotation and translation eliminates the corona formation that would otherwise hinder the motion of particles through biological tissues. We have shown (in rodents) that it is possible to administer the neuroparticles™ intra-nasally and then to guide them into and through the brain using magnetic gradients that can concentrate the particles (Fig. 2) [7]. Once in place, the particles can deliver drugs and nucleic acids as needed clinically. Using wearable electromagnets programmed securely in the field, it will be possible to stimulate the relevant brain foci mechanically to accomplish clinical missions (e.g. addiction therapy). Therefore, this platform is able to: Image with high spatial resolution [8] and in real time both the magnetic nanoparticles and the target in the human head. Move through tissue effectively. Traverse physiological barriers. Concentrate particles on target. Carry diverse payloads that are released in controlled fashion. Ablate target when needed. The platform could be used as a device to drive magnetic nanoparticles to a specific target and then perform a physical task, like treating refractory sinusitis or intracranial aneurisms. The platform could be also used as a drug delivery device through magnetic carriers. Potential indications of the use of the new Platform as a drug-device are the following: treat deep brain tumors, Parkinson disease, addiction therapy and severe depression treatment. The Platform might be used simply as diagnostic imaging device for head diseases.

[1] Lübbe AS, Bergemann C, Riess H, Reichardt P, Possinger K, Matthias M, Dörken B, Herrmann F, Gürtler R, Hohenberger P, Haas N, Soor R, Sander B, Lemke AJ, Ohlendorf D, Huhnt W, Huhn D. "Clinical experiences with magnetic drug-targeting: a phase-I study with 4'-epi-doxorubicin in 14 patients with advanced solid tumours". *Cancer Research* 56, 4694-4701, 1996. IF 9,0. [2] Etheridge ML et al. The Big Picture on Small Medicine: The State of Nanomedicine Products Approved for Use or in Clinical Trials. Nanomedicine 2013 9(1):1-14. [3] A. Nacev, R. Hilaman, S. Jafari, D. Patel, S. Chowdhury, L. Mair, P. Stepanov, and I. Weinberg, "Tunable Electropermanent System for Magnetic Resonance Imaging and Magnetic Particle Propulsion," in *Gordon Research Conference, In-vivo Magnetic Resonance Imaging*, 2016. [4] Dynamic Magnetic Inversion Circumvents a Century-Old Theorem and Concentrates Ferromagnetic Rods to Central Targets. A Nacev, et al. ACS NanoLetters 15(1):359-364 (2015). [5] Biofilm Ablation: Rotating Nanorods Remove Microbes from Surfaces, Enhancing Antimicrobial Efficacy. LO Mair, et al. Proceedings of the Scientific and Clinical Applications of Magnetic Carriers Meeting, June 2016, Vancouver, Canada. [6] Analysis of Driven Nanorod Transport Through a Biopolymer Matrix. LO Mair, IN Weinberg, R Superfine. Journal of Magnetism and Magnetic Materials 380:295-298 (2015) [7] A Nacev, P Stepanov, S Kupfer, L Mair, MG Urdaneta, M Shimoji, ST Fricke, B Shapiro, IN Weinberg. ACS NanoLetters 15(1):359-364 (2015). [8] A quiet, fast, high-resolution desktop MRI capable of imaging solid-bound water. A Nacev, E Anashkin, JP Rigla, JM Benlloch, MG Urdaneta, A Sarwar, PY Stepanov, IN Weinberg, and ST Fricke, ISMRM Proceedings (2014).

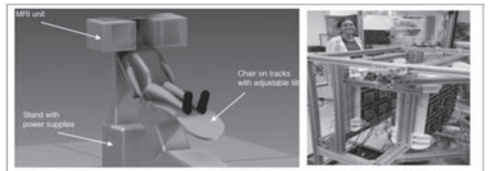

Fig.1. (Left) Conceptual Scheme of Combined Imaging/ Delivery Platform. (Right) Current Implementation of the Platform showing the Electro-Permanent Magnets.

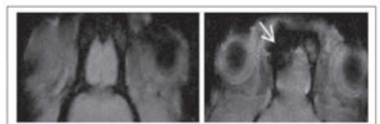

Fig.2 Magnetic delivery of particles into rat brain from intra-nasal administration.

3:00

DA-03. Magnetoelectric biomaterials for advanced tissue engineering applications.

S. Lanceros-Mendez[1], C. Ribeiro[2], S. Ribeiro[2], M. Fernandes[2], N. Castro[1] and V. Correia[2]
1. BCMaterials, Leioa, Spain; 2. Universidade do Minho, Braga, Portugal

Tissue engineering and regenerative medicine is a multidisciplinary research field that typically involves a biocompatible biomaterial, which can be combined with stem cells and different stimuli with the objective of repairing failing organs. In this context, it is increasingly recognized the need of active or smart scaffolds in order to properly regenerate specific tissues. Among the most relevant clues that active scaffolds can provide are electrical and electromechanical ones[1], as they are among the most relevant clues determining tissue functionality in tissues such as muscle and bone, among others. Thus, electroactive materials and, in particular, piezoelectric ones[1], demonstrate strong potential for novel tissue engineering strategies, in particular taking also into account the existence of these phenomena within some tissues, indicating their requirement also during tissue regeneration[1,2]. Piezoelectric materials can provide an electrical signal to the cells in response to a mechanical input[3], but also a mechanical excitation upon electrical input, being therefore suitable for both electrical and mechanical cell stimulation, being mechano-transduction other of the main clues determining cell differentiation and proliferation. In many situations the mechanical stimulation necessary for the electroactive response[2,3] cannot be provided by the human body and the electrical excitation of the piezoelectric material, necessary for the mechanical response, needs the use of wires and electrodes, which makes difficult the applicability of the materials. Those situations can be overcome by the use of magnetoelectric materials[4], that produce an electrical output upon magnetic stimulation and that can be also used to provide just mechanical stimulation in response to the magnetic field, due to the magnetostrictive effect. This talk will reports on magnetoelectric materials used for tissue engineering applications[4,5]. The most used materials and geometries[6] for tissue engineering strategies are reported together with the main achievements, challenges and future needs for research and actual therapies[4,5]. A compilation of the most relevant results and strategies will be provided as start point for novel research pathways in the most relevant and challenging open questions. Further, this novel approach has led to the need of novel bioreactor concepts to perform *in-vitro* studies in cell differentiation and proliferation. In this context, the main developed bioreactors will be also summarized as well as their adequacy to the developed magnetoelectric materials. It will be demonstrated that magnetoelectric cell stimulation is a novel, suitable and needed approach for tissue engineering allowing magnetic, mechanical and electrical stimuli. Acknowledgements The authors thank the Portuguese Fundação para a Ciência e Tecnologia (FCT) for financial support under Strategic Funding UID/FIS/04650/2013 and project PTDC/EEI-SII/5582/2014, including FEDER funds, UE. The authors also thank the FCT for financial support under grants SFRH/BPD/90870/2012 (CR), SFRH/BD/111478/2015 (SR), SFRH/BPD/121464/2016 (MMF) and SFRH/BPD/97739/2013 (VC). Financial support from the Spanish Ministry of Economy and Competitiveness (MINECO) through the project MAT2016-76039-C4-3-R (AEI/FEDER, UE) (including the FEDER financial support) and from the Basque Government Industry Department under the ELKARTEK Program is also acknowledged.

Ribeiro, C.; Sencadas, V.; Correia, D. M.; Lanceros-Méndez, S. "Piezoelectric polymers as biomaterials for tissue engineering applications". Colloids and Surfaces B: Biointerfaces 2015, 136, 46-55. Ribeiro, C.; Correia, D.M.;, Rodrigues, I.; Guardão, L.; Guimarães, S.; Soares, R.; Lanceros-Méndez, S.; In vivo demonstration of the suitability of piezoelectric stimuli for bone reparation; Materials Letters, 209; 118-121; 2017 Ribeiro, C.; Parssinen, J.; Sencadas, V.; Correia, V.; Miettinen, S.; Hytonen, V. P.; Lanceros-Mendez, S. "Dynamic piezoelectric stimulation enhances osteogenic differentiation of human adipose stem cells". J. Biomed. Mater. Res. Part A 2015, 103, 2172-2175. Lanceros-Méndez, S.; Martins, P. "Magnetoelectric Polymer-Based Composites: Fundamentals and Applications"; Wiley, 2017. Ribeiro, C.; Correia, V.; Martins, P.; Gama, F. M.; Lanceros-Mendez, S. "Proving the suitability of magnetoelectric stimuli for tissue engineering applications". Colloids and Surfaces B: Biointerfaces 2016, 140, 554 430-436. Correia, D. M.; Goncalves, R.; Ribeiro, C.; Sencadas, V.; Botelho, G.; Ribelles, J. L. G.; Lanceros-586 Mendez, S. "Electrosprayed poly(vinylidene fluoride) microparticles for tissue engineering applications". RSC 587 Advances 2014, 4, 33013-33021.

3:30

DA-04. *In Vivo* Magnetic Recording of Neuronal Activity.

M. Pannetier-Lecoeur[1], V. Trauchessec[1], T. Wunderle[2], L. Caruso[1], J. Trejo-Rosillo[1], C.M. Lewis[2], J. Valadeiro[3], J. Ni[2], P. Jendritza[2], C. Fermon[1], S. Cardoso de Freitas[3], P. Freitas[3] and P. Fries[2]
1. SPEC, CEA Saclay, Gif sur Yvette, France; 2. Ernst Strüngmann Institute (ESI) for Neuroscience in Cooperation with Max Planck Society, Frankfurt, Germany; 3. Instituto de Engenharia de Sistemas e Computadores – Microsistemas e Nanotecnologias, Lisbon, Portugal

Currents circulating in excitable cells like neurons or nerve fibers may be measured by the radiated magnetic field. At the organ level, these magnetic fields can be detected by non-invasive experiments using highly sensitive magnetometers such as SQUIDS [1], atomic magnetometers [2] or mixed sensors [3], the latter using spin electronics. This technique, called cammed Magneto-Encephalography, allows measuring neuronal activity at a millisecond resolution and for collective response of population of typically 10 000 neurons and more. To understand the genesis of the signals obtained in brain areas, it is relevant to investigate the fields generated at the level of one or few cells. This requires small and sensitive field sensors, operating at physiological temperatures, which has long been out of reach from existing technologies. Spin electronics allow now developing small size and very sensitive magnetometers, reaching the sub-nanotesla field range on micron-size sensors. These devices operate from low temperature to hundreds of °C, so they can be used at physiological temperature. Furthermore, spin electronics sensors, based on thin film technology, can be deposited on silicon or glass substrates which can be shaped in needle-type devices to allow penetration in tissues with reduced damages. We have designed and fabricated magnetic sensors called magnetrodes, as a magnetic equivalent of electrodes, to probe locally the information transmission of excitable cells. These probes contain one or several GMR elements in embodiment compatible with recordings in contact with tissues or within tissues. Two types of sensors have been evaluated on living tissues; planar probes to investigate the Action Potential propagation in *in vitro* preparation of muscle cells, which have demonstrated the first local biomagnetic recordings with GMR sensors [4], and sharp probes for *in vivo* recordings of cortical activity. Here we present the first *in vivo* experiments performed, which have paved a new way to a local description of electrical activity, without direct contact to the cell and which allow accessing not only the amplitude of the activity but also its direction of propagation, at any depth within the tissues. Magnetrodes have demonstrated their ability to detect neuronal signals such as Evoked Response Fields, which correspond to electrical Local Field Potentials in response to an external stimulus [5] as well as Action Potential, which are related to the activity of a single neuron.

[1] John Clarke and Alex I. Braginski. The SQUID Handbook: Vol. II *Applications of SQUIDs and SQUIDs Systems*. WILEY-VCH, 2006. [2] I. K. Kominis, T. W. Kornack, J. C. Allred, and M. V. Romalis. *A subfemtotesla multichannel atomic magnetometer*. Nature, 422 (6932):596–599, 04 2003. [3] M. Pannetier-Lecoeur, L. Parkkonen, N. Sergeeva-Chollet, H. Polovy, C. Fermon and C. Fowley (2011) *Magnetocardiography with sensors based on giant magnetoresistance*, Appl. Phys. Lett. 98 153705. [4] Barbieri, F. *et al.* Local recording of biological magnetic fields using Giant Magneto Resistance-based micro-probes. *Sci. Rep.* 6, 39330; doi: 10.1038/srep39330 (2016). [5] L. Caruso *et al.* Neuron, Volume 95, Issue 6, 1283 - 1291.e4 (2017).

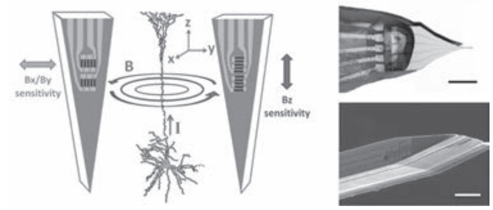

Fig. 1. Left: Schematic configuration of a sharp magnetrode for recordings within the tissue, indicating the sensitivity axis of the probes (straight arrows) and the field generated around the responding neuron. Top right: Optical picture of a sharp magnetrode, scalebar 5mm; Bottom right: SEM picture of a magnetrode containing two sensing elements for in vivo recordings. Scalebar 100µm.

WEDNESDAY AFTERNOON, 25 APRIL 2018 ORCHID III, 2:00 TO 4:00

Session DB
MAGNETIC FLUIDS AND ORGANIC MAGNETIC MATERIALS I

Guoqiang Yu, Chair
Institute of physics, Chinese Academy of Sciences, Beijing, China

CONTRIBUTED PAPERS

2:00

DB-01. Organic Ligand Induced Ferromagnetism in Ni doped ZnO films.

s. Nallusamy[1] and G. Nammalvar[1]
1. Physics, National Institute of Technology, Tiruchirappalli, India

Diluted Magnetic Semiconductors (DMS) are one of the most prominent classes of materials in spintronics with certain interesting properties such as magnetic, magneto-optical, magneto-electronic and semiconducting behavior for memory device applications. ZnO based DMS have been paid great attention owing to their plausible magnetic and optical properties. There are numerous reports available on the improved optical and magnetic properties of ZnO upon doping transition metal (TM) ions like Mn^{2+}, Co^{2+} and Cu^{2+} [1-3]. However, many of these reports lack the device fabrication process even though the magnetic properties of the ZnO material was found enhanced. One way to improve the ferromagnetic behavior of ZnO is to use dopants of appropriate magnetic nature such as Ni, Fe and further surface functionalization using organic ligands[4-6]. Here, we present Amine functionalized (3, 5, & 7 mol. %) Ni doped ZnO thin films grown by RF magnetron sputtering. The Ni doped ZnO targets of 3,5 & 7 mol.% were prepared by mixing appropriate amount of NiO powder with ZnO powder. These pellets were used for the thin film deposition on Si (100) substrate by RF Magnetron sputtering. Before deposition, 10^{-6}mbar vacuum was achieved from rotary and diffusion pumps. The RF power of 120 W & Ar and O_2 pressures, 0.015 mbar and 0.02 mbar, were maintained during the deposition process. The optimized substrate temperature, 450°C and sputtering time of 40 minutes w maintained during the depositions of all the thin films. The deposited film has been subsequently functionalized with Amine by the spin coating technique. Using micro pipette, Amine was spread over on the grown film. After an adsorption time of 60 seconds, the spin coater was ramped to 3000 rpm at 500 rpm intervals. The above process was repeated for 10 cycles to achieve a uniform coverage of organic molecules on the grown Ni doped ZnO films. After completion of the process, the films were annealed in air at 80 °C for 5 min. Fig.(1a) shows the schematic diagram of the entire process. The structural properties were analyzed by XRD (Rigaka Ultima III) using Cu-kα. The defect level and vacancies present in the Ni doped ZnO thin films were identified by Photoluminescence measurement (Perkin elmer Ls55). The presence of chemical bond and functionalization of Amine (N) molecule has been examined by X-ray photoelectron spectroscopy using Al K_{α} radiation. The surface morphology and elemental composition were investigated using the SEM attached with EDX. The magnetic properties of the films were analyzed by VSM at room temperature. The hexagonal wurtzite structure was confirmed by X-ray diffraction analysis. The grain size was found to decrease from 44.35 to 23.10 nm at various Ni doping concentration. The PL emission intensity at 2.8 eV reveals the presence of Oxygen vacancies in Ni^{2+} doped ZnO films which in turn originates the ferromagnetism. The green emission further blue shifted to 3 eV upon Amine capping. The magnetic saturation of 5 mol.% of Ni^{2+} doped ZnO films measured as 12.09 emu/cm^3 and 22.20 emu/cm^3 for Amine functionalized Ni doped ZnO thin films. This clearly shows the enhancement of ferromagnetism due to functionalization. The functionalization of Amine was confirmed the appearance of Zn-N bond observed in the XPS spectrum reveals the formation of surface layer between Zn and N atom. Fig(1b) shows the Magnetization (M) - Magnetic field (H) hysteresis loop of Amine functionalized and unfunctionalized (3,5 & 7 mol%) Ni doped ZnO thin film samples measured at room temperature. It was noticed that the saturation magnetization values are increases up to 5 mol% Ni doped ZnO films and then decreases. The higher stauration magnetisation might be due to the exchange interaction between oxygen vacancies and doped Ni ions in the Ni doped ZnO films. The decrease of Saturation Magnetization for 7 mol% is due to the compensation effect of oxygen vacancies combined with the increase of antiferromagnetic interaction between the Ni ions due to the shortening of distance between ionic distance in the lattice[7,8]. Upon Amine functionalisation on these Ni doped ZnO films shows enhanced ferromagnetism. In particular, Amine functionalized 5 mol% Ni doped ZnO films exhibit maximum enhanced Saturation Magnetization. The enhancement of ferromagnetism in amine functionalized Ni doped ZnO films is attributed to the lowering electronegativity value of N atoms than that of O atom. Also, there is an expansion of the Zn-O bond nearest to the N atom is due to the charge redistribution caused by the ligands. As the Zn atom transfers part of its charge to the N atom, the charge transfer to the neighboring atom decreases, thus weakening the Zn-O bond while simultaneously creating a hole in the O 2p orbital. The accompanying changes in the Zn-O bond, there is a hybridization between the Zn s orbitals with N p orbitals. The resulting unpaired P electrons in O, N sites lead to the enhance the magnetic moments and make the system more magnetic[9,10]. The enhanced ferromagnetism is well justified by the difference in XRD, PL, and XPS results of unfunctionalized and functionalized Ni doped ZnO films. The ligand induced magnetic materials are much useful in magnetic sensor and biomedicine applications.

1) Q.shao C.wang, J.A.Zapin, C.W.Leung, and Ruotolo (2015), " Ferromagnetism in Ti doped ZnO thin films", Journal of Applied Physics 117, 17B908(2015) doi:10.1063/1.4917514. 2) Dianwu Wu; Mei Yang, Zhongbing Huang, Guangfu Yin, Xiaoming Liao, Yunqing Kang; Xianfu Chen, Hui Wang, (2009), "preparation and properties of Ni doped ZnO rod arrays from aqueous solution", Journal of colloid and interface science 330(2009) 380-385 doi: 10.1016/j.jcis.2008.10.067. 3)Yalu Zuo, shihui ge, Zhongqiang chen, Li zhang, Xueyun Zhou, Shiming yan (2009), " Morphology, optical and magnetic properties of $Zn_{1-x}Ni_xO$ nanorods arrays fabricated by hydrothermal method", Journal of Alloys and compounds, 470(2009)47-50 doi: 10.1016/j.jallcom.2008.03.010. 4) Sivanantham Nallusamy, Gopalakrishnan Nammalvar (2017), "Fabrication of Thiol-Functionalized Ni-Doped ZnO Thin Films for Room-Temperature Ferromagnetism" IEEE MAGNETICS LETTERS, Volume 8 (2017) 2109304. 5) S.Yilmaz; E. McGlynn, E. Bacakz, J. Cullen, R.K. Chellappan (2012), "Structural, optical and magnetic properties of Ni doped ZnO micro rods grown by the spray pyrolysis method", Chemical physical letters 525-526(2012)72-76 doi: 10.1016/j.cplett.2012.01.003. 6) R.siddheswaran (2015) Siddheswaran, R., Netrvalová, M., Savková, J., Novák, P., Očenášek, J., Šutta, P., ... & Jayavel, R. (2015). Reactive magnetron sputtering of Ni doped ZnO thin film: Investigation of optical, structural, mechanical and magnetic properties. Journal of Alloys and Compounds, 636, 85-92 doi: 10.1016/j.jallcom.2015.02.142 7) Liu, X., Lin, F., Sun, L., Cheng, W., Ma, X., & Shi, W. (2006). Doping concentration dependence of room-temperature ferromagnetism for Ni-doped ZnO thin films prepared by pulsed-laser deposition. Applied Physics Letters, 88(6), 062508. Doi: 10.1063/1.2170420 8) Wakano, T., Fujimura, N., Morinaga, Y., Abe, N., Ashida, A., & Ito, T. (2001). Magnetic and magneto-transport properties of ZnO: Ni films. Physica E: Low-Dimensional Systems and Nanostructures, 10(1), 260-264. Doi: 10.1016/S1386-9477(01)00095-9 9) Wang, Q., Sun, Q., & Jena, P. (2008). Ligand induced ferromagnetism in ZnO nanostructures. The Journal of chemical physics, 129(16), 164714. Doi: 10.1063/1.3001925 10)Liu, E. Z., & Jiang, J. Z. (2009). Magnetism of O-terminated ZnO (0001) with adsorbates. The Journal of Physical Chemistry C, 113(36), 16116-16120.doi: 10.1021/jp9037304

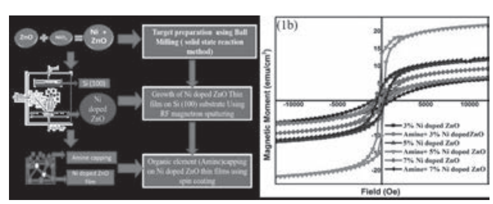

Fig. (1a). Schematic diagram of the experimental procedures
Fig. (1b). M-H loop for functionalized and unfunctionalized Ni doped ZnO film

DMS	Saturation magnetization value, M_s (emu/cm^3)		
	3%	5%	7%
Ni doped ZnO	6.70	12.09	9.69
Amine Functionalized Ni doped ZnO	7.09	22.20	12.59
Enhancement percentage	17%	83%	30%

Fig. 2. Saturation Magnetization values of unfunctionalised and functionalised Ni doped ZnO thin film

2:15

DB-02. Uniaxial 2D Superlattice of Fe_4 Molecular Magnets on Graphene.

M. Fonin[1], F. Paschke[1], L. Gragnaniello[1], P. Erler[1], H. Brune[2] and S. Rusponi[2]
1. University of Konstanz, Konstanz, Germany; 2. EPFL, Lausanne, Switzerland

We demonstrate that electrospray deposition enables the preparation of monolayers of intact Fe_4H single molecule magnets on graphene/Ir(111) [1]. Topographic information obtained by using scanning tunneling microscopy confirms the realization of high-quality 2D assembly on the graphene/Ir(111) substrate. From the magnetic field dependence of the x-ray magnetic circular dichroism signal, we infer that the magnetic easy axis of each Fe_4H molecule is oriented perpendicular to the sample surface with the value of the uniaxial anisotropy being unaffected upon the deposition on graphene. Furthermore, we observe inelastic features in scanning tunneling spectroscopy, due to spin-flip excitations from the magnetic ground state, giving access to the intramolecular exchange coupling J_1 on the single-molecule level, which is unprecedentedly close to the bulk value. Our findings suggest that Fe_4H molecules undergo only negligible interaction with the graphene/Ir(111) substrate, resulting in a two-dimensional array of molecular magnets that retain their bulk magnetic properties.

[1] L. Gragnaniello et al., Nano Lett. 17, 7177 (2017).

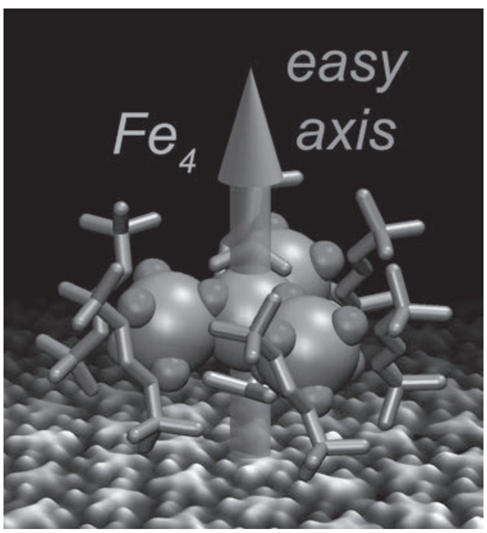

2:30

DB-03. Spin dependent charge trapping in a MnO_2/C_{60} heterojunction.

T. Moorsom[1], M. Rogers[1], G. Teobaldi[2], M. Valvidares[3], S. Lee[4], R. Stewart[4], T. Prokscha[5], H. Leutkens[5], P. Gargiani[3], D. Bromley[1], M. Ali[1], F. Al Ma'Mari[6], G. Burnell[1], B. Hickey[1] and O. Cespedes[1]
1. University of Leeds, Leeds, United Kingdom; 2. Stephenson Institute of Renewable Energy, University of Liverpool, Liverpool, United Kingdom; 3. ALBA Synchrotron, Barcelona, Spain; 4. University of St Andrews, St Andrews, United Kingdom; 5. Paul Scherrer Institut, Villigen, Switzerland; 6. Sultan Qaboos University, Muscat, Oman

Spin injection in molecule-metal heterojunctions is dominated by interfacial effects. [1] At the interface between semi-conducting molecular films and metal or semi-conducting substrates, hybrid states emerge which can then be occupied through charge transfer across an interfacial potential. Where the conduction bands of the substrate are spin split, such as in ferromagnetic or half-metallic metals, hybrid interface states can also be spin polarised leading to emergent magnetism in surface molecules. [2, 3, 4] Over the last decade, there has been a concerted effort to understand these interfacial effects and their potential impact on molecular spintronics. However, a persistent challenge in molecular spintronics is how to utilise these interfacial effects as a toolbox to develop multifunctional devices which can compete with conventional spintronics. [5] One method for controlling interfacial effects is to utilise the coupling of ionic and charge current in a manner similar to a memristor. When the electrode material in a molecular heterojunction is a metal oxide such as a manganate, it has been observed that the diffusion of oxygen ions into the molecular film has a profound effect on spin injection and transport characteristics. [6] By controlling the flow of oxygen ions between a molecular semi-conductor and a metal oxide electrode, it is possible to reliably switch interfacial effects on and off in a two terminal device. Here we present such a multifunctional device based on a MnO_2/C_{60}/ferromagnet heterojunction. The interfacial properties of this system are dominated by the exohedral bonding of oxygen to C_{60} which produces half-metallic surface states and a strongly rectifying contact barrier. During transport across this device, spin polarised charges become trapped in surface states due to the spin filtering action of this half-metallic interface causing charge and spin to accumulate in highly stable interfacial trap states. Where interfacial polarisation is stabilised by a magnetic electrode, spin polarised charge can be stored over timescales in excess of 30 minutes as measured by X-ray Magnetic Circular Dichroism (XMCD). The capacitance of these heterojunctions is also shown to follow the magnetisation of the ferromagnetic electrode, being maximised when the electrode is saturated and minimised when it is demagnetised. Because the half-metallic surface states are dependent on interfacial chemistry, diffusion of oxygen into the molecular film quenches these behaviours by screening the interfacial potential and switching the character of the C60 from n-type to p-type through the formation of a mid-gap acceptor band. Because C60 can repeatably absorb and desorb exohedral oxygen without destruction of the cage, the interfacial effects can be switched on and off through bias cycling. [7] This system also exhibits photovoltaic effects due to the p-n junction formed at the interface. The photovoltaic properties can also be controlled through bias cycling wherein the interfacial potential is quenched by the formation of the mid-gap acceptor band. It has not yet been established whether the spin-filtering interface means that the photovoltaic effect is dependent on the polarisation of incident light or the magnetisation of the ferromagnetic electrode though it is expected that there should also be a spin dependence in the open circuit voltage. The MnO_2/C_{60} system provides unprecendented multifunctionality which is applicable to molecular spintronics. In a single two terminal device, it is possible to realise spin dependent charge trapping and spin filtering, photovoltaic effects and a strongly rectifying barrier all of which can be reliably switched on and off through voltage cycling.

[1] - C Barraud et al, Nat. Phys. 6, 615-620, 2010. [2] - F Al Ma'Mari et al, Nature, 524, 69-73, 2015. [3] - T Moorsom et al, Phys. Rev. B. 90, 125311, 2014. [4] F Djeghloul et al, J. Phys. Chem. Lett. 7, 2310 – 2315, 2016. [5] M Cinchetti et al, Nat. Mat. 16, 507-515, 2017. [6] H Xie et al, Appl. Phys. Lett. 108, 011603, 2016. [7] T Arai et al. Solid State Comm. 84, 8, 1992.

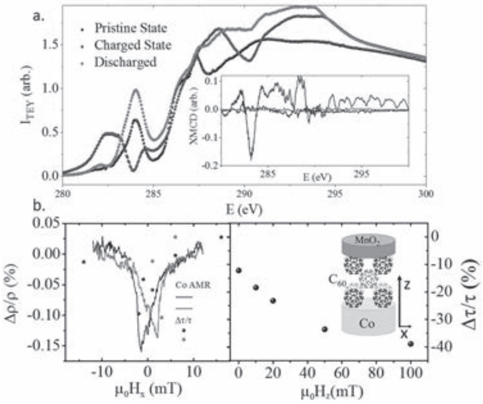

Fig. 1. a. XAS and XMCD measured in a heterojunction of $Co/C_{60}/MnO_2$. XAS is measured in TEY mode and primarily measures the upper three monolayers of the C_{60} film closest to the MnO_2. After applying a bias, the K-edge is significantly altered with the LUMO supressed and a peak emerging 1eV lower. This state is predicted by density functional theory and occurs due to the accumulation of interfacial charge. This state shows a spin polarisation observable in XMCD which is stable over timescales of 30 minutes. b. Measurements of the decay time constant for the open circuit voltage (VOC) after the interface is charged by a pulse of light from a XeHg lamp. The solid lines show AMR in the cobalt electrode and the points show the percent change in time constant. The decay of VOC is fastest around the coercivity. When a field is applied out of plane, larger out of plane field leads to faster decay.

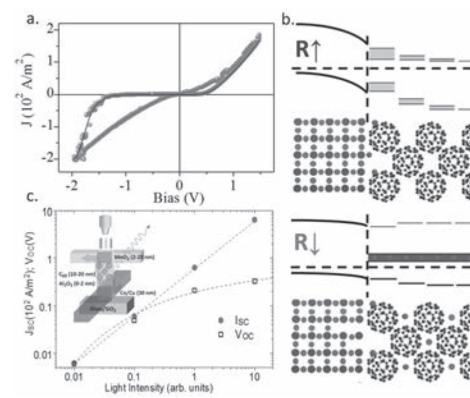

Fig. 2. a. IV characteristic of a $Co/C_{60}/MnO_2$ heterojunction. The MnO_2/C_{60} interface creates a strongly rectifying barrier making the IV asymmetric. At high negative bias (<-1.5 V) the junction breaks down as oxygen begins to diffuse into the molecular film forming a mid-gap acceptor band, b. The accetor band compensates donor transport, reducing mobility and increasing resistivity. However, because it also quenches the interfacial barrier it leads to an apparent drop in resistance and symmetric IV. Above the breakdown voltage, the resistivity of C60 oxide is higher than the as deposited film as expected. c. When in the asymmetric state, the interfacial potential leads makes the device a high ideality (>2) low efficiency (<0.1 %) photovoltaic.

2:45

DB-04. Carbon-coated nanoparticles of zinc-doped iron oxides for magnetic separation of organic pollutants: structure, magnetism and separation performance.

L. Kubickova[1,2], J. Koktan[1], T. Korinkova[1], M. Klementova[1], T. Kmjec[2], J. Kohout[2], P. Rezanka[3] and O. Kaman[1]

1. Department of Magnetics and Superconductors, Academy of Sciences of the Czech Republic, Prague, Czechia; 2. Department of Low-Temperature Physics, Charles University, Prague, Czechia; 3. Department of Analytical Chemistry, University of Chemistry and Technology, Prague, Czechia

Magnetic nanoparticles with high magnetization and high surface-to-volume ratio provide attractive platform for magnetic separation in wastewater treatment, analytical chemistry, catalysis, and sorting of cells in medical research. The separation of analytes from dilute samples poses a crucial step in chemical analysis of organic pollutants such as steroid compounds. Magnetic nanoparticles with suitable surface modifications offer an excellent sorbent for this purpose. Importantly, zinc-doped ferrimagnetic systems of magnetite/maghemite exhibit higher magnetization than their undoped counterparts, and they can be prepared by the thermal decomposition method as fine particles with almost bulk-like magnetic properties [1]. Moreover, such products can be easily transformed to carbon-coated nanoparticles, whose surface might be efficient for adsorption of organic compounds. Zinc-doped iron oxide nanoparticles were synthesized by thermal decomposition of zinc acetylacetonate and iron(III) acetylacetonate in octadecene [2], and the as-prepared particles were stabilized by addition of surfactants, namely oleic acid and oleylamine. The nanoparticles with surfactants were thermally treated at 500 °C under argon flow to achieve carbon-coated particles (ZF@C). In addition, the original particles were thoroughly purified, whereby magnetic cores (ZF) with only a residual organic component were obtained. The analysis of ZF and ZF@C samples by XRD revealed only a single phase of the spinel structure (*Fd*-3*m*). The Rietveld refinement evidenced that lattice parameter a and the mean size of crystallites d_{XRD} remained unchanged after the carbonization of surfactants since almost the same values of a = 8.4026(5) Å and 8.4039(5) Å and d_{XRD} = 22 nm and 21 nm were found for ZF and ZF@C, respectively. Further, XRF analysis of ZF cores was used to determine the Zn:Fe ratio. The actual oxygen stoichiometry was inferred from the Mössbauer spectra, and the composition of magnetic cores was refined to $(Fe^{3+}_{0.81}Zn^{2+}_{0.19})_T[Fe^{3+}_{1.19}Fe^{2+}_{0.63}Zn^{2+}_{0.18}]_O O_4$ for ZF and $(Fe^{3+}_{0.72}Zn^{2+}_{0.28})_T[Fe^{3+}_{1.40}Fe^{2+}_{0.45}Zn^{2+}_{0.09}Ø_{0.06}]_O O_4$ for ZF@C, where Ø denotes the vacancy. Interestingly, zinc ions migrated preferably to tetrahedral sites during the thermal treatment of particles. Finally, TGA measurements were performed in an inert atmosphere and in air on the particles stabilised by surfactants to simulate the process of carbonization, and the content of carbon in the ZF@C product was estimated to ≈5% wt. The TEM inspection of ZF showed predominantly spheroidal shape of particles and rather narrow size distribution with the mean size of 15 nm and s_d = 2 nm. Practically identical size of particles was found for the ZF@C sample, whose HRTEM analysis demonstrated high crystallinity of the cores, presence of a thin amorphous surface layer of carbon nature, and formation of particle clusters. Magnetic behaviour of the samples was probed by SQUID magnetometry; selected properties are demonstrated in Fig. 1. Hysteresis loops evidenced high magnetization for the ZF@C particles as well as for the comparative ZF sample (Fig. 1a). The loops show coercivity ≈0.25 kOe at 5 K and almost negligible coercivity at 300 K. The investigation of the blocking behaviour by the ZFC/FC susceptibility measurements revealed that the ZF@C sample was almost completely in the superparamagnetic state at 300 K (Fig. 1b). However, the carbonization shifts the ZFC/FC bifurcation to higher temperature, which hinders the onset of full superparamagnetic relaxation. This finding might be explained in relation to stronger dipolar interactions among magnetic cores in the ZF@C sample with only a thin carbon layer compared to the initial particles where a residual layer of bulky surfactants may persist. Finally, the performance of ZF@C nanoparticles in separation of organic pollutants was tested. First, methylene blue was selected as a model compound to determine the adsorption isotherm. Aqueous solutions of methylene blue of different concentrations were incubated with ZF@C particles (0.5 mg mL^{-1}), and the decrease of the dye concentration in the supernatant was analysed spectrophotometrically (see Fig. 2). The adsorption isotherm was fitted by the Langmuir model for a monomolecular layer of a sorbate on a homogeneous sorbent [3]. Second, the separation of ß-estradiol and the reusability of the sorbent were studied by repeated application of ZF@C particles (5 mg) into 1 L of the steroid solution (0.27 mg L^{-1}), followed by magnetic separation and spectrophotometric determination of ß-estradiol eluted from the sorbent (see inset of Fig. 2). High performance and reusability of the ZF@C nanoparticles suggest their prospective applications in separation of steroid and other organic pollutants.

1. Sun, S. H., Zeng, H., Robinson, D. B., Raoux, S., Rice, P. M., Wang, S. X., and Li, G. X., 2004. Monodisperse MFe2O4 (M = Fe, Co, Mn) nanoparticles. *Journal of the American Chemical Society*, 126(1): 273-279. 2. Kaman, O., Korinková, T., Jirak, Z., Marysko, M., and Veverka, M., 2015. The superspin glass transition in zinc ferrite nanoparticles. *Journal of Applied Physics*, 117: art. no. 17C706 (4 pp.). 3. Langmuir, I., 1916. The constitution and fundamental properties of solids and liquids. Part I. *Journal of the American Chemical Society*, 38 (11): 2221–2295

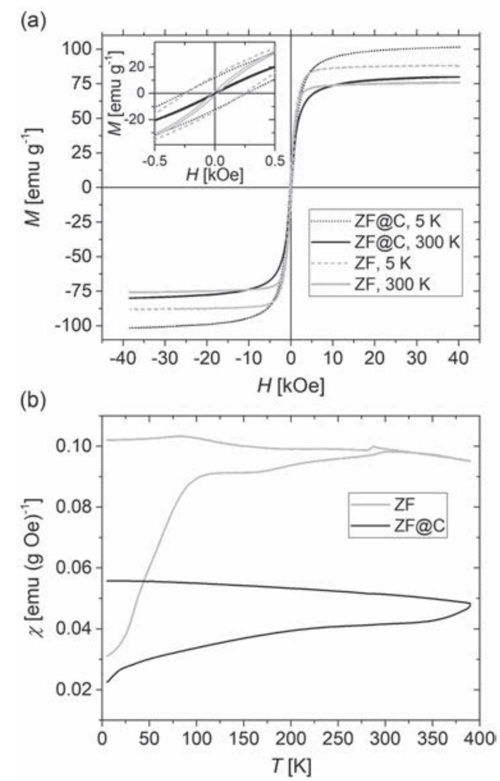

Fig. 1. Magnetic behaviour of carbon-coated particles (ZF@C) and original magnetic cores (ZF): (a) hysteresis loops at 5 K and 300 K, (b) ZFC-FC susceptibility studies at H = 20 Oe.

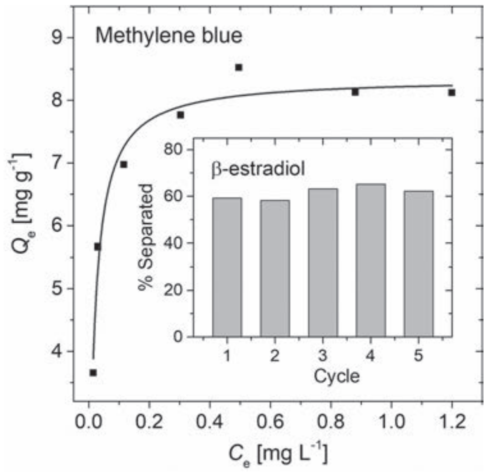

Fig. 2. **Separation of organic compounds by ZF@C particles: the adsorbed amount of methylene blue per gram of the sorbent Q_e as a function of the equilibrium concentration of the compound in solution C_e, the data are fitted by the Langmuir isotherm; the inset demonstrates the adsorption of ß-estradiol (percentage of the compound separated from solution) in repeated use of the sorbent in five cycles.**

3:00

DB-05. Singlet ground state in the spin-1/2 weakly coupled dimer compound $NH_4[(V_2O_3)_2(4,4'\text{-bpy})_2(H_2PO_4)(PO_4)_2].0.5H_2O$.

A. Unnikrishnan[1], V. Kumar[4], P. Anjana[2], A. Thirumurugan[2], J. Sichelschmidt[3], A. Mahajan[4] and R. Nath[1]
1. School of Physics, Indian Institute of Science Education and Research, Thiruvananthapuram, India; 2. School of Chemistry, Indian Institute of Science Education and Research, Thiruvananthapuram, India; 3. Max Planck Institute for Chemical Physics of Solids, Dresden, Germany; 4. Department of Physics, Indian Institute of Technology Bombay, Mumbai, India

We present the synthesis and a detailed investigation of structural and magnetic properties of polycrystalline $NH_4[(V_2O_3)_2(4,4'\text{-bpy})_2(H_2PO_4)(PO_4)_2]$. $0.5H_2O$ by means of x-ray diffraction, magnetic susceptibility, electron spin resonance, and ^{31}P nuclear magnetic resonance measurements. Temperature dependent magnetic susceptibility could be described well using a weakly coupled spin-1/2 dimer model with an excitation gap Δ/k_B = 26.1 K between the singlet ground state and triplet excited states and a weak inter-dimer exchange coupling J'/k_B = 4.6 K. A gapped chain model also described the data well with a gap of about 20 K. The ESR intensity as a function of temperature traces the bulk susceptibility nicely. The isotropic Lande g-factor is estimated to be about g = 1.97, at room temperature. We are able to resolve the ^{31}P NMR signal as coming from two inequivalent P-sites in the crystal structure. The hyperfine coupling constant between ^{31}P nucleus and V^{4+} spins is calculated to be $A_{hf}(1)$ = 2963 Oe/ μ_B and $A_{hf}(2)$ = 1466 Oe/μ_B for the P(1) and P(2) sites, respectively. Our NMR shift and spin-lattice relaxation rate for both the ^{31}P sites show an activated behaviour at low temperatures further confirming the singlet ground state. The estimated value of the spin gap from the NMR data measured in an applied field of H = 9.394 T is consistent with the gap obtained from the magnetic susceptibility analysis using the dimer model. Because of a relatively small spin gap, $NH_4[(V_2O_3)_2(4,4'\text{-bpy})_2(H_2PO_4)(PO_4)_2]$. $0.5H_2O$ is a promising compound for further experimental studies under high magnetic fields.

1. U. Arjun et al., Phys. Rev. B, 95, 174421 (2017) 2. L.-I. Hung et.al., Inorg. Chem., 41, 3929 (2002) 3. D. C. Johnston, Handbook of magnetic materials, Vol. 10 (1997) 4. Y. Singh and D. C. Johnston, Phys. Rev. B 76, 012407 5. S. Sachdev and K. Damle, Phys. Rev. Lett. 78, 943 (1997)

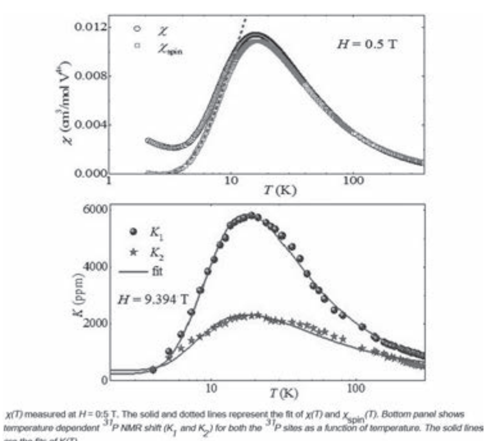

Fig. 1. χ(T) measured at H = 0.5 T. The solid and dotted lines represent the fit of χ(T) and χ_{spin}(T). Bottom panel shows temperature dependent ^{31}P NMR shift (K_1 and K_2) for both the ^{31}P sites as a function of temperature. The solid lines are the fits of K(T).

3:15

DB-06. Spinterface induced magnetic properties in Fe or Co thin films.

S. Mallik[1], S. Mattauch[2], M.K. Dalai[3], T. Brückel[2] and *S. Bedanta*[1]
1. Physics, National Institute of Science Education and Research (NISER), Bhubaneswar, India; 2. Jülich Centre for Neutron Science (JCNS), Munich, Germany; 3. CSIR–National Physical Laboratory, New Delhi, India

Study of spinterface between organic semiconductor (OSC) and ferromagnetic (FM) layers has drawn significant research interest in recent years because of their potential in spintronic applications [1,2]. Different aspects of organic spintronics such as magnetoresistance, induced interface moment etc. have been studied extensively in the last decade [2,3]. Among various available OSCs, Buckminsterfullerene (C_{60}) has drawn immense research interest in organic spintronics because it exhibits the following properties viz. low spin-orbit coupling, large spin diffusion length at room temperature, thermal and mechanical resilience, absence of hyperfine interaction etc.[4, 5]. An induced moment of 1.2 μ_B per cage of C_{60} and suppression of ferromagnetic moment of Co up to 21% have been observed for Co/C_{60} multilayers by X-ray magnetic circular dichroism (XMCD) and polarized neutron reflectivity (PNR) measurements [6]. Similarly, the hybrid interface between Fe and C_{60} leads to magnetic moments of the C_{60} to $\mu_S = -0.21$ and -0.27 μ_B per molecule where it was aligned antiparallel on Fe(001) substrate and Fe on W(001) substrate, respectively [7]. We have studied the magnetic interface in bilayers and trilayers of FM/C_{60} and FM/C_{60}/FM samples where FM is either Fe or Co. These samples are prepared on both MgO (001) and Si (100) substrates using DC magnetron sputtering and thermal evaporation for FM and C_{60}, respectively. The thicknesses of the FM and the C_{60} layers were varied between 5 nm to 15 nm and 15 nm to 40 nm, respectively. Investigation of structural interfaces has been performed by secondary ion mass spectroscopy (SIMS). Structural characterization by SIMS revealed a few angstrom of inter-diffusion between all the layers. PNR was performed on the samples at MARIA reflectometer in Heinz Maier-Leibnitz Zentrum, Germany. The PNR fits for MgO(001)/Fe(15 nm)/C_{60}(40 nm)/Au(6 nm) sample along the cubic hard axis ($\phi = 45°$) (Figure 1(a)) indicates spin-polarized charge transfer at the interface between Fe and C_{60} layer. It has been observed that ~ 1.9 nm of C_{60} layers exhibit a magnetic moment of 3 μ_B per cage [8] probably due to the sp hybridization between Fe and C_{60} molecules [6, 7]. The layer structure of the sample obtained from the PNR fit is shown in figure 1(b). However, in case of the PNR fits for the sample with similar structure but prepared on Si (100) substrate exhibits a decrease in induced magnetic moment of C_{60} cage by 34% due to the presence of strain in the Fe layer arising from the lattice mismatch between Si and Fe. The thickness of the magnetic C_{60} layer is also reduced in this sample. The induced magnetic moment in C_{60} gets increased for the samples having lower thicknesses of the Fe layers (5 nm and 10 nm). PNR fits for similar samples with Co as the FM layer also exhibits hybridized interface with a decrease in the Co magnetic moment near the interface. The hysteresis loops along with the domain images were measured for all the samples at room temperature by a magneto optic Kerr effect (MOKE) based microscope in longitudinal mode by varying the angle (ϕ) between the easy axis and the applied field direction at an interval of 10°. For the samples prepared on MgO substrates, we have observed a uniaxial anisotropy superimposed on the cubic anisotropy due to the oblique deposition geometry and the epitaxial growth of Fe on MgO (001) substrate, respectively [9]. However, due to the large lattice mismatch between Fe and Si (100), Fe grows in polycrystalline nature. Therefore, samples prepared on Si (100) substrate exhibit only uniaxial anisotropy due to the oblique deposition geometry. For the control sample prepared without C_{60} layer i.e. MgO(001)/Fe(15 nm)/Au(6 nm), the magnetization reversal occurs either via two 90° or 180° domain wall motions combined with partial rotation depending on ϕ [9]. However, for MgO(001)/Fe(15 nm)/C_{60}(40 nm)/Au(6 nm), a significant change in the magnetization reversal process as well as in the domain structures has been observed in comparison to the control sample due to the presence of C_{60} layer on top of the Fe layer. Similarly, a significant change in the domain size and structure have been observed between the samples prepared on Si (100) substrates. Understanding the spinterface induced magnetization reversal mechanism and domain structures will have a significant impact on the fundamental physics as well as various device engineering.

[1] S. Sanvito, Nat. Phys. 6, (2010) 562–564. [2] W. J. M. Naber *et al*., J. Phys. D: Appl. Phys. 40, (2007) R205. [3] T. Tran *et al*., ACS Appl. Mater. Interfaces 5, (2013) 837. [4] D. M. Gruen, Nucl. Instrum. Methods Phys. Res. 78, (1993) 118. [5] X. M. Zhang et al., Nat. Commun. 4, (2013) 1392. [6] T. Moorsom *et al.*, Phys. Rev. B 90, (2014) 125311. [7] T. Tran et al., ACS Appl. Mater. Interfaces 5, (2013) 837. [8] S. Mallik *et al*., AIP Advances, 4, (2014) 097118. [9] S. Mallik *et al*., Scientific Reports (Under review).

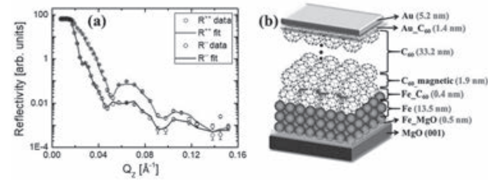

Fig. 1. (a) Polarized neutron reflectivity data and the fit for MgO(001)/Fe(15 nm)/C_{60}(40 nm)/Au(6 nm) sample measured at saturation. (b) The model layer structure of the sample obtained from the PNR fit shown in (a).

3:30

DB-07. Evaluation of Local Anisotropy of Magnetic Response from Non-oriented Electrical Steel by Magnetic Barkhausen Noise.

Y. He[2], M. Mehdi[1,2], E. J. Hilinski[3], A. Edrisy[1], *S. Mukundan*[4], A. Mollaeian[4] and N. C. Kar[4]
1. Mechanical, Automotive, and Materials Engineering, University of Windsor, Windsor, ON, Canada; 2. CanmetMATERIALS, Hamilton, ON, Canada; 3. Tempel Steel Co, Chicago, IL, United States; 4. Electrical and computer engineering, University of Windsor, Windsor, ON, Canada

Abstract Non-oriented electrical steels are indispensable materials for use in electric motors as magnetic cores. It is desired that the magnetic properties of the steel sheets be optimal and uniform in all the directions in the sheet plane. Thus, knowing the magnetic properties of the steel sheets in all the directions is crucial for the design of the electric motors. However, the magnetic properties of non-oriented electrical steels are usually measured by standard Epstein frame method, which normally only gives the overall magnetic properties in the rolling and transverse directions, and the magnetic properties in other directions are usually not known. In this research, magnetic Barkhausen noise (MBN) technique is utilized to characterize the local magnetic response of the processed non-oriented electrical steel. By rotating the MBN sensor to all the directions in the sheet plane, the local magnetic responses are obtained. The measured MBN is then directly compared to the crystallographic texture (texture factor) measured in the same direction. In this way, the local magnetic response of the steel sheet can be correlated to the crystallographic texture. It was found that magnetic Barkhausen noise technique was able to detect the difference in magnetic response induced by magnetocrystalline anisotropy if the effect of the residual stress can be eliminated. This would provide a potential technique for the characterization of magnetic properties of non-oriented electrical steel. *I. Introduction and Methodology* Non-oriented electrical steel sheets used in electric motors are usually produced from cast ingots through a series of thermomechanical processing steps such as hot rolling, cold rolling, and annealing. The thin steel sheets are then punched and stacked to form the magnetic core, which is subsequently wound with wires around the radial teeth. To maximize the magnetic flux density and reduce the core loss, it is desired that the easy axes (<100> for iron) be aligned to the magnetization directions (i.e. along all the teeth in the magnetic core) [1]. This requires that the magnetic properties in all the directions of the rolled sheet be optimal and uniform. However, during thermomechanical processing, anisotropy in magnetic properties is inevitably induced, while the magnetic properties of non-oriented electrical steels are usually measured in the rolling and transverse directions only [2]. For the better design of electric motors, the magnetic properties of the steel sheets in all the directions should be known. In this paper, a relatively new technique, i.e. magnetic Barkhausen noise analysis, is utilized to characterize the local magnetic response of electrical steel sheet in all the directions of the sheet plane. The measured magnetic Barkhausen noise is then correlated to the crystallographic texture, which is one of the factors that affect the anisotropy of the material. *II. Material and Experimental procedure* The material used in this study is a non-oriented electrical steel containing 0.9 wt% Si. The steel was cast, hot rolled, annealed and cold rolled to sheets of 0.5 mm in thickness [3]. The thin sheets were then annealed at different temperatures to produce microstructures with various fractions of recrystallization. The textures of the steel sheets were measured by electron backscatter diffraction and the texture factor at all the directions was calculated based on the orientation distribution functions. The magnetic Barkhausen noise was measured in various angles (0°-360°) to the rolling direction, and the root mean square values of the MBN are directly compared to the texture factor in the same directions. *III. Results and discussion* The angular magnetic Barkhausen noise shows apparent anisotropy in various angles from the rolling direction, indicating differences in the magnetic response of the material and in magnetic properties. For samples after complete recrystallization, the angular MBN results correspond well with the texture factors measured in the same directions, while for partially recrystallized samples, the correspondence between the MBN and the texture factor is disrupted because of the existence of residual stress in the microstructure. *IV. Conclusion* Using MBN, it is able to characterize the local anisotropy of magnetic response of non-oriented electrical steel. By directly comparing the angular MBN results to the measured texture, it is able to explain the correspondence between the MBN signal and the easy magnetization axes of the steel. This would provide a potential method for the characterization of directional magnetic properties for magnetic cores.

[1] L. Kestens, S. Jacobs, Texture Control During the Manufacturing of Nonoriented Electrical Steels, Texture, Stress, and Microstructure, (2008), Article ID: 173083: 1-9. [2] ASTM A343/A343M, Standard Test Method for Alternating-Current Magnetic Properties of Materials at Power Frequencies Using Wattmeter-Ammeter-Voltmeter Method and 25-cm Epstein Test Frame, ASTM International, West Conshohocken, PA (2014). [3] Y. He, E.J. Hilinski, Texture and magnetic properties of non-oriented electrical steels processed by an unconventional cold rolling scheme, J. Magn. Magn. Mater. 405 (2016) 337-352.

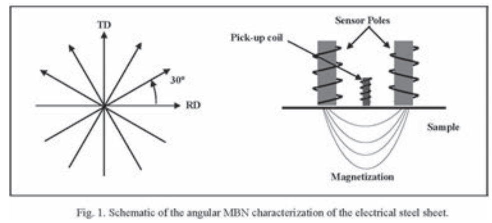

Fig. 1. Schematic of the angular MBN characterization of the electrical steel sheet.

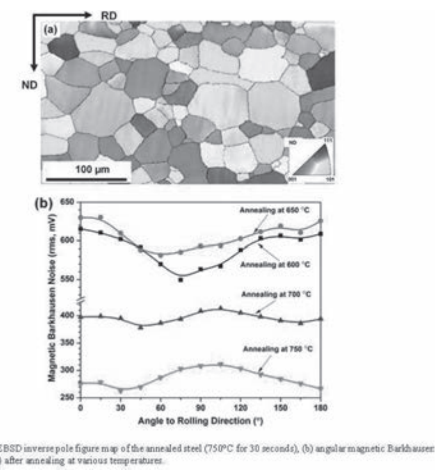

Fig. 2. (a) EBSD inverse pole figure map of the annealed steel (750°C for 30 seconds), (b) angular magnetic Barkhausen noise (rms) after annealing at various temperatures.

3:45

DB-08. 5% Superelasticity in Ferromagnetic FeNiCoAl Cold-Drawn Rapidly Quenched Microwires for Medical Applications.

F. Borza[1], V. Dobrea[1], L. Bujoreanu[2], M. Grigoras[1], G. Ababei[1] and N. Lupu[1]
1. National Institute of Research and Development for Technical Physics, Iasi, Romania; 2. Faculty of Materials Science and Engineering, "Gheorghe Asachi" Technical University of Iasi, Iasi, Romania

Superelasticity is the shape memory property that has been most explored for commercial use. Its application is guided by the ability of SMAs to sustain large elastic strains at certain temperatures during use. The storage of large amount of energy when stress is applied accompanied by constant unloading of this stress is the basis for applications employing this property [1]. Applications of superelastic alloys includes guide wires, catheters, and stents to be used, for instance, in minimally invasive surgery such as endovascular peripheral surgery or neurosurgery. There is a strong demand to improve the maneuverability, reliability, and safety of these devices as well as to improve advantages over the NiTi alloy system through increase in superelastic properties [2]. Thus, Fe-based shape memory alloys have been developed since they offer relatively cheap alloying constituents and ease of fabrication and facilities for conventional steel making can be employed. These novel, intelligent, high-performance shape memory materials are expected to possess multifunctionality, fast response, smaller size, and reliability for application as integrated multifunctional sensing-actuating systems. Recently a FeNiCoAlTaB SMAs, which exhibits remarkable tensile superelastic strains higher than 13% at room temperature in the polycrystalline state and strengths of >1GPa, was reported by Tanaka et. al. [3]. In the attempt to reduce the steps involved in the thermo-mechanical processing of this materials, a cost effective technique, rapid quenching from the melt, has been reported by our group for the fabrication of these magnetic superelastic materials as wire-shaped materials [4]. We have reported up to 2% superelasticity in wire-shaped $Fe_{40.95}Ni_{28}Co_{17}Al_{11.5}Ta_{2.5}B_{0.05}$ materials with the diameter of about 200 micrometers which have been subjected to successive cold-drawing down to 50 micrometers and and ageing by thermal annealing at 800°C for one hour. In this work we report 5% superelasticity in rapidly quenched $Fe_{43.5}Ni_{28}Co_{17}Al_{11.5}$ microwires cold drawn 50 μm in diameter and subsequently annealed at 800°C for one hour. $Fe_{43.5}Ni_{28}Co_{17}Al_{11.5}$ microwires with the diameter of about 200 micrometers have been prepared by in rotating water quenching technique and subsequently subjected to successive cold-drawing down to 50 micrometers (aprox. 93% reduction of diameter) followed by annealing at 800°C for one hour. Scanning electron microscopy (SEM, Transmission Electron Microscopy (TEM), thermomagnetic, and magnetic measurements have been performed to assess the structural and magnetic differences between the cold-drawn as-cast samples and samples annealed at 800°C for one hour. The magnetic measurements have been performed using the PPMS and VSM. The SEM investigations revealed an amorphous-like structure in the as-cast state for 200μm which transforms into a polycrystalline structure with some elongated grains after cold-drawing, the grains increasing in number and size (up to micrometers) after subsequent annealing at 800°C for 1h. Thermomagnetic curve of as-cast microwire, presented in Figure 1, measured at low fields of 20 Oe present a maximum at 325°C which is abruptly decreasing until 370°C (Curie temperature of austenite phase). Within this temperature range the martensitic transformation takes place and it is also accompanied by a relaxation of the stresses induced during cold drawing, fact which is accordance with the results of the measurements of resistivity vs. temperature. When cooling the curve does not follow the same path, showing irreversible transformation. An increase in magnetization can be observed. In the case of annealed microwires, a more definite curie temperature has been observed indicating that the stresses have been released through annealing and the martensitic transformation took place. Superelastic tensile stresses (Figure 2) of up 5 % have been achieved in the annealed FeNiCoAl cold-drawn microwires. Potential uses of superelastic alloys also include miniature stents, catheters or guide wires in minimally invasive medicine due to their small dimensions.
Acknowledgements: Financial support from Ministry of Research and Innovation, NUCLEU programme, 3MAP/2018 project is highly acknowledged.

[1] M.H. Wu, L.M. Schetky, Proceedings of the International Conference on Shape Memory and Superelastic Technologies, Pacific Grove, California, 2000, pp. 171–182. [2] K.K. Alaneme, E. Anita OkoteteEngineering Science and Technology, an International Journal 19 (2016) 1582–1592. [3] Y. Tanaka, Y. Himuro, R. Kainuma, Y. Sutou, T. Omori, K. Ishida, Science 327 (2010) 1488-1490. [4] F. Borza, N. Lupu, V. Dobrea, H. Chiriac, Journal of Applied Physics 117 (2015) pp. 17E512.

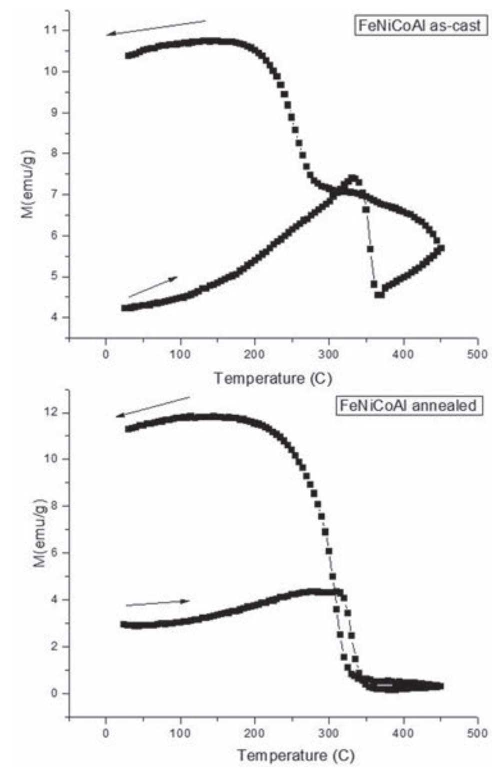

Fig. 1. Magnetization vs. temperature for FeNiCoAl as-cast and annealed microwires

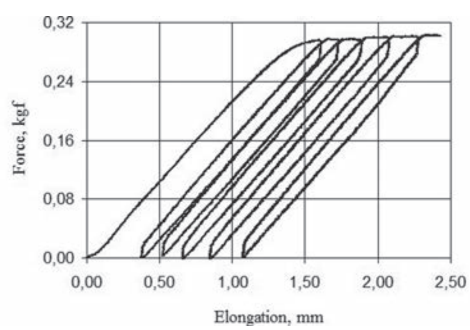

Fig. 2. Stess-strain curve of FeNiCoAl annealed microwire

Session DC

SPIN-TRANSPORT WITH TOPOLOGICAL MATERIALS

Kyung-Jin Lee, Chair

Korea University, Seoul, The Republic of Korea

CONTRIBUTED PAPERS

2:00

DC-01. Bilinear magnetoelectric resistance for spin texture detection in topological insulators.

P. He[1], S. Zhang[2,3], D. Zhu[1], Y. Liu[1], Y. Wang[1], G. Vignale[2] and H. Yang[1]
1. National University of Singapore, Singapore; 2. Department of Physics and Astronomy, University of Missouri, Columbia, MO, United States; 3. Materials Science Division, Argonne National Laboratory, Lemont, IL, United States

The discovery of three-dimensional (3D) topological insulators (TIs) has triggered research activities for the physical properties of this new state of matter[1], and exploring its applications to spintronics and optoelectronics[2]. The most remarkable property of TIs is their topologically protected surfaces states characterized by a tight correlation between spin orientation and momentum, known as spin-momentum locking. The resulting spin texture has been mapped by spin- and angle-resolved photoemission spectroscopy (SR-ARPES)[3]. When the topological surface states (TSS) are hexagonally deformed (Fig. 1a), the spin texture acquires a momentum-dependent out-of-plane component[4]. This hexagonally warped helical spin texture, depicted in Fig. 1b, has been observed in various TI materials by SR-ARPES[5]. In addition to the optical methods, electrical detection of the spin-polarized TSS has been achieved with the use of ferromagnetic contacts as spin detectors[6]. However, only the in-plane spin component could be detected by this method. In this work, we report the observation of a new magneto-resistance effect in a single layer of nonmagnetic 3D TI Bi_2Se_3, which scales linearly with the applied electric current and magnetic field: we thus name it "bilinear magneto-electric resistance" (BMER)[7]. In contrast with other magneto-resistance effects in TIs, the BMER effect originates from a nonlinear spin current J_s (E^2) induced by the variation of electron distribution at the second order in the applied electric field E, δf_2, which, contrary to the electron distribution at the first order in E (δf_1), has equal signs for surface states of opposite momenta and spins. The nonlinear spin current is partially converted to a nonlinear charge current by the external magnetic field, giving rise to the BMER effect. Making use of the BMER effect, we demonstrate that a mapping between momentum-dependent spin textures and the angular dependence of the BMER can be established (Fig. 2), which enables transport measurements of the 3D spin texture in the TSS with hexagonal warping.

[1] M. Z. Hasan and C. L. Kane, *Rev. Mod. Phys.* 82, 3045 (2010). [2] D. Pesin and A. H. MacDonald, *Nat. Mater.* 11, 409 (2012). [3] D. Hsieh *et al.*, *Nature* 460, 1101 (2009). [4] L. Fu, *Phys. Rev. Lett.* 103, 266801 (2009). [5] M. Nomura, S. Souma, A. Takayama, T. Sato, T. Takahashi, K. Eto, K. Segawa, and Y. Ando, *Phys. Rev. B* 89, 045134 (2014). [6] C. H. Li, O. M. J. van 't Erve, J. T. Robinson, Y. Liu, L. Li, and B. T. Jonker, *Nat. Nanotech.* 9, 218 (2014). [7] P. He, S. S.-L. Zhang, D. Zhu, Y. Liu, Y. Wang, J. Yu, G. Vignale, and H. Yang, arXiv:1706.09589v1 (2017).

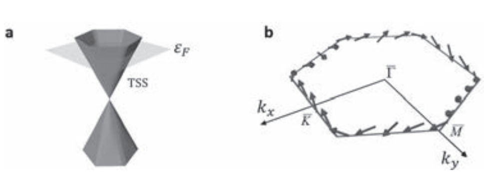

Fig. 1. (a) Hexagonally warped energy dispersion for the surface states with Fermi surface lying in the conduction band. (b) Hexagonally warped spin texture at the Fermi contour of the surface states.

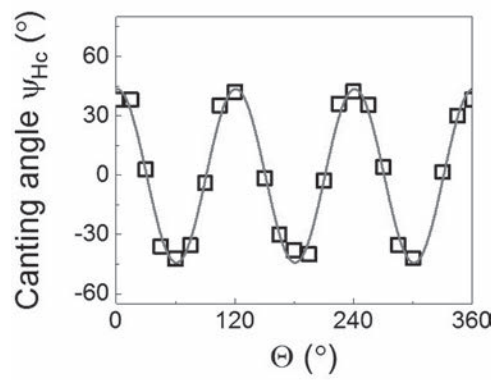

Fig. 2. Magnetic field canting angle as a function of the angle between the current direction and the line.

2:15

DC-02. Ultra-low-power spin-orbit-torque switching using the colossal spin Hall effect in BiSb topological insulator.

K.H. Nguyen[1], Y. Ueda[1] and N. Pham[1,2]
1. Electronic and Electrical Engineering, Tokyo Institute of Technology, Tokyo, Japan; 2. Center for Spintronics Research Network (CSRN), The University of Tokyo, Tokyo, Japan

Spin-orbit-torque (SOT) switching using the spin Hall effect (SHE) in heavy metals and topological insulators (TIs) has great potential for ultra-low power magnetoresistive random-access memory (MRAM). To be competitive with conventional spin-transfer-torque (STT) switching, a pure spin current source with large spin Hall angle ($\theta_{SH} > 1$) and high electrical conductivity ($\sigma > 10^5\ \Omega^{-1}m^{-1}$) is required. While heavy metals (such as Pt, Ta, and W) have high $\sigma > 10^5\ \Omega^{-1}m^{-1}$, their spin Hall effect is not strong enough ($\theta_{SH} \sim 0.08$-0.4) [1-4] for practical SOT-MRAM. In contrast, TI have been shown to have large $\theta_{SH} > 1$ at room temperature [5], but their $\sigma \sim 10^4\ \Omega^{-1}m^{-1}$ is low and thus not compatible to realistic SOT-MRAM. There is no spin Hall material so far that can satisfy both conditions simultaneously. Here, we demonstrate such a pure spin current source: BiSb narrow-gap topological thin films with $\sigma \sim 2.5\times10^5\ \Omega^{-1}m^{-1}$, $\theta_{SH} \sim 52$, and spin Hall conductivity $\sigma_{SH} \sim 1.3\times10^7\ (h/4\pi e)\ \Omega^{-1}m^{-1}$ at room temperature. We show that BiSb thin films can generate a colossal spin-orbit field of 2770 Oe/(MA/cm^2). In term of σ_{SH}, BiSb outperforms the nearest competitor (Pt) by a factor of 30, and other TIs by a factor of 100. Therefore, BiSb is the best candidate for the pure spin current source in ultra-low power SOT-MRAM [6]. To demonstrate SOT switching with ultra-low current density using the colossal spin Hall effect of BiSb, we prepare a 100 μm × 50 μm Hall bar of a $Bi_{0.9}Sb_{0.1}$ (5nm) / $Mn_{0.45}Ga_{0.55}$ (3nm) bi-layer. Figure 1(a) and 1(b) demonstrate the SOT switching of the MnGa layer when applying 100 ms pulse currents to the Hall bar and an in-plane H_{ext} = + 3.5 kOe and -3.5 kOe, respectively. We observed clear switching at an average critical current density of $J = 1.5\times10^6$ A/cm^2 ($J_{BiSb} = 1.1\times10^6$ A/cm^2). Here, the critical current density is defined at which the Hall resistance changes sign. Furthermore, the switching direction is reversed when the in-plane H_{ext} direction is reversed, consistent with the behavior of SOT switching. The observed critical current density is much smaller than those of Ta (5 nm) / MnGa (3 nm) ($J = 1.1\times10^8$ A/cm^2) [7], IrMn (4 nm) / MnGa (3 nm) ($J = 1.5\times10^8$ A/cm^2) [8], and Pt (2 nm) / MnGa (2.5 nm) ($J = 5.0\times10^7$ A/cm^2) [9]. Note that this low critical current density was observed even though the MnGa ferromagnet used in our bi-layer has higher perpendicular anisotropy energy $H_K^{eff} \approx 50$ kOe by one order of magnitude than those used in previous room-temperature SOT switching experiments in Bi_2Se_3 / CoTb [10] and Bi_xSe_{1-x} / CoFeB [11], double-checking the colossal spin Hall effect of BiSb. We estimate that the critical switching current for a BiSb-based SOT-MRAM with size of 37 nm and a 5 nm-thick BiSb layer as the spin current source was estimated only 2.2 μA, which is one order of magnitude smaller than that of STT-MRAM at the same size fabricated by the industries [12]. Therefore, the switching power can be reduced by at least one order of magnitude. Furthermore, since SOT-MRAM can be switched one order of magnitude faster than STT-MRAM, the switching energy can be reduced by at least two orders of magnitude. That means BiSb-based SOT-MRAM can be very competitive to even static random-access memory, and is the suitable ultra-low-power memory for internet-of-thing applications.

[1] L. Liu et al., Science 336, 555 (2012). [2] I. M. Miron et al., Nature 476, 189 (2011). [3] L. Liu et al., Phys. Rev. Lett. 109, 096602 (2012). [4] Q. Hao and G. Xiao, Phys. Rev. Appl. 3, 034009 (2015). [5] A. R. Mellnik et al, Nature 511, 449 (2015). [6] N. H. D. Khang, Y. Ueda and P. N. Hai, arXiv:1709.07684. [7] K. K. Meng et al., Sci. Rep. 6, 38375 (2016). [8] K. K. Meng et al., Phys. Rev. B 94, 214413 (2016). [9] R. Ranjbar et al., Jpn. J. Appl. Phys. 55, 120302 (2016). [10] J. Han et al, Phys. Rev. Lett. 119, 077702 (2017). [11] DC. Mahendra et al, preprint at arXiv:1703.03822. [12] L. Thomas, MSST 2017 Mass Storage Conference (2017).

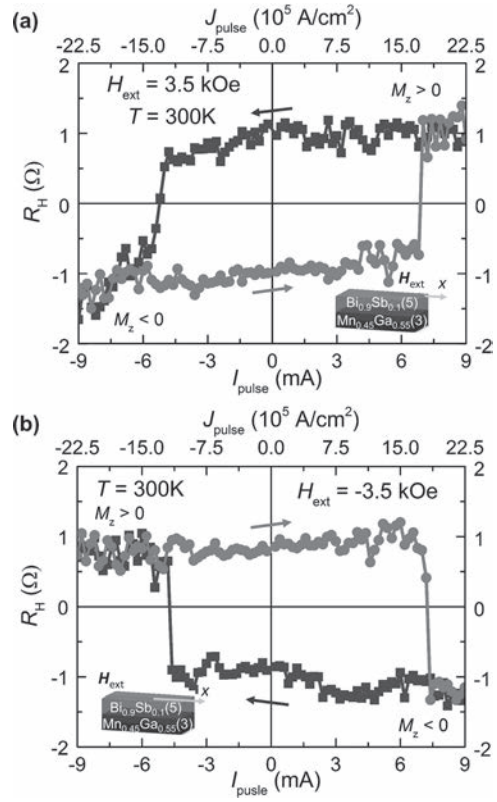

Fig. 1. Room-temperature current induced magnetization switching in a 100 μm×50 μm Hall bar of $Bi_{0.9}Sb_{0.1}$(5nm)/$Mn_{0.45}Ga_{0.55}$(3nm) bi-layer under 100 ms pulse current and an in-plane H_{ext} of +3.5 kOe (a) and -3.5 kOe (b).

2:30

DC-03. Role of surface states in the generation of the colossal spin Hall effect in BiSb topological insulator.

K. Yao[1], T. Shirokura[1] and N. Pham[1,2]
1. Electrical&Electronic Engineering course, Tokyo Institute of Technology, Tokyo, Japan; 2. Center for Spintronics Research Network, The University of Tokyo, Tokyo, Japan

Spin-transfer-torque (STT) magnetoresistive random access memory (MRAM) is a non-volatile memory technology that is gaining steam in various applications with no idling power consumption, un-limited endurance, and fast read/write time. However, STT-MRAM still has some fundamental problems, such as large writing current as well as considerable asymmetry between the read and write current. Recently, spin-orbit-torque (SOT) switching using the spin Hall effect (SHE) in heavy metals [1,2] and topological insulators (TIs) [3,4] has attracted much attention as an alternative writing method for MRAM. SOT-MRAM can overcome the problems of STT-MRAM thanks to separated writing and reading path. For practical SOT-MRAM, a spin current source with large spin Hall angle θ_{SH} (>1) and sufficiently large electrical conductivity σ ($>10^5\Omega^{-1}m^{-1}$) is required to achieve efficient spin current generation. Heavy metals, such as Pt, Ta, and W have large σ, but their reported values of θ_{SH} are smaller than 1. Recently, giant SHE with θ_{SH} larger than 1 has been observed in several TIs [5,6], which are exotic materials with insulating bulk states and spin-momentum locking surface states. Since TIs are essentially insulators, σ of many of TIs is limited to $10^4\Omega^{-1}m^{-1}$, almost one order of of magnitude smaller than that of ferromagnets used in MRAM. Recently, we have shown that BiSb can have both giant SHE and σ. BiSb is a TI with very small band gap [7][8], thus it has much larger σ (σ~$2.5\times10^5\Omega^{-1}m^{-1}$) than other TIs [9]. Furthermore, colossal SHE with θ_{SH} ~ 52 has been observed in MnGa/BiSb(012) bi-layer at room temperature, and ultra-low current magnetization switching of MnGa using SHE of BiSb(012) has been demonstrated [10]. In this work, to explore the role of the surface states as well as the surface orientation in the generation of SHE, we have systematically investigated the spin Hall angle of BiSb as a function of temperature. Figure 1(a) shows the conduction model of BiSb, where carriers are transported through two surface states with conductivity σ_S, spin Hall angle θ_S and total thickness t_S, and bulk states with conductivity σ_B, spin Hall angle θ_B and total thickness t. The ratio between the surface conductance and the total conductance $\Gamma = \sigma_S t_S / (\sigma_S t_S + \sigma_B t)$ can be deduced from the temperature dependence of the conductivity of a single BiSb layer [11]. From the temperature dependence of Γ and θ_{SH}, we can deduce the role of the surface states in the generation of θ_{SH}. We have prepared a 50 nm-thick $Bi_{0.6}Sb_{0.4}$(001) / 4.7 nm-thick MnAs bi-layer on GaAs(111)A substrates by molecular beam epitaxy method. The sample was patterned into a 50 μm width Hall bar structure by photolithography and Ar ion milling. To evaluate θ_{SH}, we used the in-plane magnetization rotation technique [12]. Figure 1(b) shows our measurement setup, with I the applied dc current along the x axis, σ the unit vector of the spin polarization direction of the injected spin current, H_{ext} the in-plane rotating magnetic field, H_T the transverse field-like effective magnetic field, H_{SO} the perpendicular damping-like effective magnetic field, m the magnetization of MnAs, θ the angle between I and H_{ext}, and ϕ the angle between I and m. In our case, $H_T << H_{ext}$, thus $\phi = \theta$ and H_{SO} is proportional to cosθ. By measuring the Hall resistance R_H as a function of θ under various current density and temperature, we can deduce H_{SO} and θ_{SH}. Figure 1(c) shows representative $R_H(\theta)$ curves measured at 8 K with an applied current of +5mA (left) and – 5 mA (right). Blue circles and red solid lines correspond to measured data and fitting curves, respectively. Clear difference between them can be seen, reflecting the effect of H_{SO}. Figure 2(a) shows the temperature dependence of θ_{SH} and Γ. We observe that θ_{SH} increases much faster than Γ. At room temperature, θ_{SH} is 3 but becomes as large as 166 at 8 K. In Figure 2(b), we plot the nominal sheet spin Hall angle of the whole layer $q_{SH} = \theta_{SH}/t$, and the sheet spin Hall angle of the surface states $q_S = \theta_S/t_S$ as functions of temperature. We observed almost similar trend of q_{SH} and q_S, indicating the dominance of the surface state spin Hall effect in the generation of θ_{SH} in BiSb. The maximum q_S of BiSb(001) is $3.3nm^{-1}$ at 8K, which is smaller than that (q_S = $5.2nm^{-1}$) of BiSb(012) at room temperature. This indicates that the surface orientation is critical for observation of colossal SHE at room temperature.

[1] L. Liu, T. Moriyama, D. C. Ralph, and R. A. Buhrman, Phys. Rev. Lett., 106 (2011) 036601. [2] L. Liu, C. F. Pai, Y. Li, H. W. Tseng, D. C. Ralph, and R. A. Buhrman, Science, 336 (2012) 555. [3] J. Han et al., Phys. Rev. Lett. 119 (2017) 077702. [4] DC. Mahendra et al., arXiv: 1703.03822v1. [5] Y. Fan et al., Nature Mater. 13 (2014) 699. [6] A. R. Mellnik, J. S. Lee, A. Richardella, J. L. Grab, P. J. Mintun, M. H. Fischer, A.Vaezi, A.Manchon, E. A.Kim, N. Samarth, and D. C. Ralph, Nature 551 (2014) 449. [7] D. Hsieh, D. Qian, L. Wray, Y. Xia, Y. S. Hor, R. J. Cava, and M. Z. Hasan, Nature 452 (2008) 970. [8] L. A. Wray et al., Nature Phys.7 (2011) 32. [9] Y. Ueda, N. H. D. Khang, K. Yao, and P. N. Hai, Appl. Phys. Lett. 110 (2017) 062401. [10] N. H. D. Khang, Y. Ueda, P.N. Hai, arXiv:1709.07684. [11] S. Xiao and X. Jin, Phys. Rev. Lett. 109 (2012)166805. [12] M. Kawaguchi, K. Shimamura, S. Fukami, F. Matsukura, H. Ohno, T. Moriyama, D. Chiba, and T. Ono, Appl. Phys. Express 6 (2013) 113002.

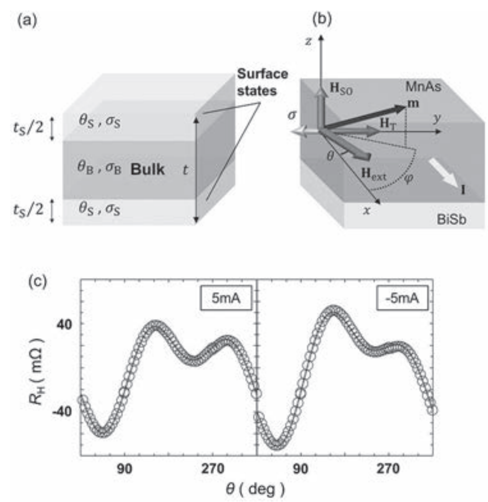

Fig. 1. (a) Conduction model of BiSb. (b) Schematic diagrams of the measurement setup. (c) Representative $R_H(\theta)$ curves measured at 8 K with an applied current of +5 mA (left) and – 5 mA (right). Blue circles and red solid lines correspond to measured data and fitting curves, respectively.

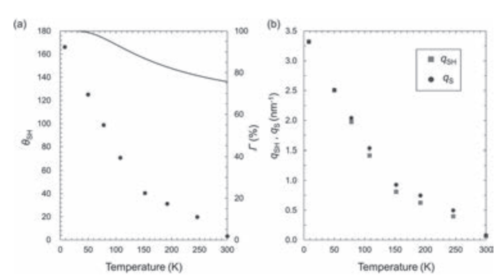

Fig. 2. (a) Spin Hall angle θ_{SH} of the whole layer and the ratio Γ between the surface conductance and the total conductance as functions of temperature. (b) Sheet spin Hall angle of the whole layer $q_{SH} = \theta_{SH} / t$ and the surface states $q_S = \theta_S / t_S$ as functions of temperature.

2:45

DC-04. High spin-orbit torque efficiency of *in-situ* fabricated Bi_2Se_3/Fe heterostructures.

D. Zhu[1], Y. Wang[1], S. Shi[1], K. Teo[1], Y. Wu[1] and H. Yang[1]
1. Department of Electrical and Computer Engineering, National University of Singapore, Singapore

Due to the spin-momentum-locked topological surface states (TSS), three dimensional topological insulators (3D-TI) have attracted much attention for realizing highly efficient charge-spin interconversion and current induced magnetization switching in the adjacent ferromagnet (FM) layer [1-6]. Especially, extensive efforts have been devoted to evaluate the spin-orbit torque (SOT) efficiency in TI/FM heterostructures by using different techniques such as spin torque ferromagnetic resonance (ST-FMR) [1-3], second harmonic magnetometry [4], and spin pumping [5]. However, a large variation of the SOT efficiency values has been reported, even in the same TI material Bi_2Se_3. The different quality of the interface between Bi_2Se_3 and FM layers might be one important reason for the reported discrepancy of SOT efficiency in the Bi_2Se_3 due to the *ex-situ* deposition of the FM layer on top of TI or the involvement of capping/decapping processes for the Se protection layer. In this study, we employ an *in-situ* film growth of Bi_2Se_3/Fe heterostructures in a MBE system. We investigate the SOT efficiency of the Bi_2Se_3/Fe heterostructures by the ST-FMR technique. From conventional analysis of the ST-FMR spectra [2, 3, 7], the effective SOT efficiency $\theta_{||}$ has been obtained at different temperatures, as shown in Fig. 1. The $\theta_{||}$ is ~0.7 at 300 K, and it increases remarkably with decreasing the temperature and reaches ~5.1 at 15 K. Moreover, an *interface* SOT efficiency $\lambda_{TSS}= J_S/J_{C\text{-}TSS}$ is evaluated to extract the TSS originated SOT efficiency, where J_S is the spin current density (A/cm^2) with in-plane spin polarization at the Bi_2Se_3/Fe interface, and $J_{C\text{-}TSS}$ (A/cm) is the surface charge current density flowing in the TSS. The λ_{TSS} is determined to be ~1.53 nm^{-1} at 20 K. Both the $\theta_{||}$ of ~5.1 and λ_{TSS} of ~1.53 nm^{-1} are significantly enhanced as compared with those obtained from traditional *ex-situ* film deposition methods in Bi_2Se_3/FM heterostructures by ST-FMR measurements. The higher SOT efficiency we have obtained is attributed to the high quality interface and thus the enhanced interface spin transparency due to the *in-situ* fabrication and the low kinetic energy of Fe flux in the sample deposition process. Our *in-situ* deposition can reduce the contamination, degradation, and interdiffusion of the interface between the Bi_2Se_3 and Fe. Our results reveal that the interface can play an important role in the SOTs in TI/FM structures, and the interface engineering may serve as an effective pathway for exploring highly efficient TI based spintronic devices.

[1] A. R. Mellnik *et al.*, Spin-transfer torque generated by a topological insulator. Nature 511, 449 (2014). [2] Y. Wang *et al.*, Room temperature magnetization switching in topological insulator-ferromagnet heterostructures by spin-orbit torques. Nat. Commun. 8, 1364 (2017). [3] Y. Wang *et al.*, Topological Surface States Originated Spin-Orbit Torques in Bi_2Se_3. Phys. Rev. Lett. 114, 257202 (2015). [4] Y. Fan *et al.*, Magnetization switching through giant spin-orbit torque in a magnetically doped topological insulator heterostructure. Nat. Mater. 13, 699 (2014) [5] Y. Shiomi *et al.*, Spin-Electricity Conversion Induced by Spin Injection into Topological Insulators. Phys. Rev. Lett. 113, 196601 (2014). [6] J. Han *et al.*, Room-Temperature Spin-Orbit Torque Switching Induced by a Topological Insulator. Phys. Rev. Lett. 119, 077702 (2017). [7] Y. Wang *et al.*, Determination of intrinsic spin Hall angle in Pt. Appl. Phys. Lett. 105, 152412 (2014).

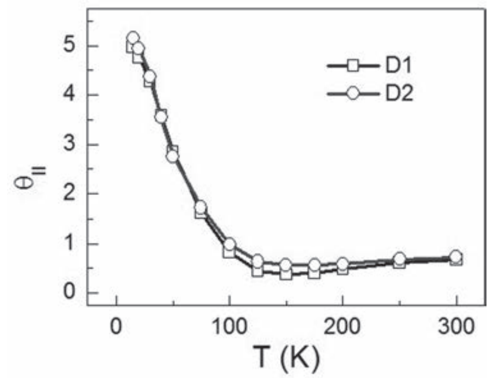

Fig. 1. Temperature dependent effective SOT efficiency $\theta_{||}$ of Bi_2Se_3 (10 QL)/Fe (16 nm) heterostructures. D1 and D2 represent two ST-FMR devices.

INVITED PAPERS

3:00

DC-05. Spin and charge conversion in topological surface states and oxide interface states.

W. Han[1]
1. International Center for Quantum Materials, Peking University, Beijing, China

Spin and charge conversion has attracted a lot of interest in the field of spintronics. Edelstein effect refers to spin current conversion from charge current flowing in inversion asymmetric two-dimensional electron gases (2DEGs) with large Rashba spin orbit coupling. In this talk, I will present the spin and charge conversion using the topological surface states and Rashba-split 2DEG. In the first one [1], I will describe our experimental results that demonstrate the spin injection and the inverse Edelstein effect in the spin-momentum locked surface states of a topological Kondo insulator, SmB_6 (Figure 1). I will also discuss the spin pumping efficiency between the topological surface states and a ferrimagnetic insulator due to interfacial s-d exchange interaction. In the second part of my talk, I will discuss the gate-tunable spin and charge conversion (Figure 2) at room temperature of the Rashba-split 2DEG between $SrTiO_3$ and $LaAlO_3$ via the inverse Edelstein effect [2]. These results are important for the generation and manipulation of the pure spin current for future spintronics applications.

[1] Q. Song, J. Mi, D. Zhao, T. Su, W. Yuan, W. Xing, Y. Chen, T. Wang, T. Wu, X. H. Chen, X. C. Xie, C. Zhang, J. Shi, and Wei Han, "*Spin Injection and Inverse Edelstein Effect in the Surface States of Topological Kondo Insulator SmB_6*", Nature Communications, 7:13485 (2016). [2] Q. Song, H. Zhang, T. Su, W. Yuan, Y. Chen, W. Xing, J. Shi, J. R. Sun, and Wei Han, "*Observation of Inverse Edelstein Effect in Rashba-Split 2DEG between SrTiO3 and LaAlO3 at Room Temperature*", Science Advances, 3, e1602312 (2017).

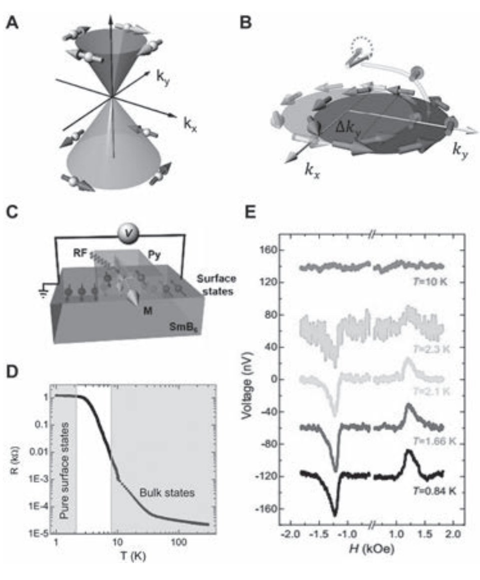

Fig. 1. Spin and charge conversion in the pure topological surface states of SmB6.

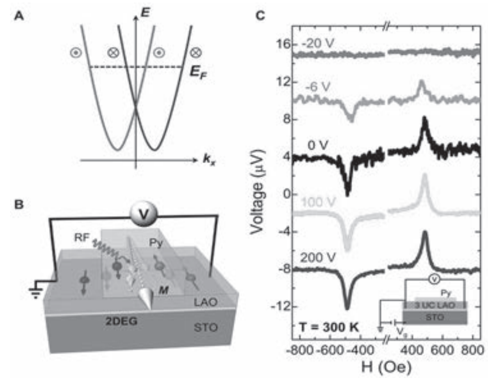

Fig. 2. Gate tunable spin and charge conversion for Rashba-split 2DEG at the oxide interface.

3:30

DC-06. Highly efficient spin-to-charge current conversion at room temperature in strained HgTe surface states. ***(Invited)***

P. Noel[1], C. Thomas[2,3], *L. Vila*[1], T. Meunier[3], P. Ballet[2] and J. Attané[1]
1. INAC, Spintec, Université Grenoble Alpes, Grenoble, France; 2. Leti/Dopt, CEA, Grenoble, France; 3. Institut Néel, C.N.R.S. and Université Grenoble Alpes, Grenoble, France

We report the observation of spin-to-charge current conversion in strained mercury telluride at room temperature, using spin pumping experiments. The conversion rates are found to be very high, with inverse Edelstein lengths up to 2.0 +/- 0.5 nm. The influence of the HgTe layer thickness on the conversion efficiency has been studied, as well as the role of a HgCdTe barrier inserted in-between the HgTe and NiFe layers. These measurements, associated to the temperature dependence of the resistivity, allow ascribing these high conversion rates to the spin momentum locking property of HgTe surface states [1], promising electronic states for spintronics. Spintronics devices need efficient ways to transform charge current into spin current or to make the opposite conversion to detect spin current. Classical spintronics generally uses magnetic materials and exchange interaction. Such manipulation can also be achieved by harnessing the Spin Orbit Coupling (SOC) in non-magnetic materials. For instance, the Spin Hall Effect permits to convert charge currents into spin currents in the bulk of heavy metals, such as Pt or Ta [2]. Yet a more efficient conversion can be obtained in two dimensional electron gas (2DEG) at surfaces and interfaces such as Rashba Interfaces [3] and newly discovered topological insulator materials. The main interest of topological insulators lies in their surface states, which possess a linear Dirac-like dispersion, and a spin momentum locking as seen on figure 1. A flow of electric current in the 2DEG would cause a perpendicular spin accumulation. This effect is known as the Edelstein Effect [4], while the reverse spin-to charge-conversion effect is known as the Inverse Edelstein Effect (IEE). Recent results suggest that surfaces of topological insulators as Bi_2Se_3 [5] or strained α-Sn [6] have a strong potential for spintronics, both for the generation or detection of spin currents through direct or inverse Edelstein effects. Among these newly discovered class of material strained HgTe is a promising one. Gap opening and Topological insulator properties can be induced in HgTe by applying a tensile strain that can be achieved by epitaxy of HgTe on a substrate with a larger lattice constant, such as CdTe [7]. Moreover large mobility and mean free path has been reported. The spin to charge current conversion was studied in strained HgTe thin films by ferromagnetic resonance spin pumping in cavity as described on figure 2. The spin to charge current conversion rate, the inverse Edelstein length [8], was measured to be up to 2 nm, one to two orders of magnitude larger than in Bi-based topological insulators [9]. Such high conversion rate can be related to the large value of the mobility [10] and mean free path of the surface states of strained HgTe and the lower bulk to surface conductivity ratio at room temperature compared to Bi_2Se_3. Moreover the non-conventional thickness dependence of the conversion rate allows ascribing this conversion to the topological surface states.

[1] P. Noel, C. Thomas, Y. Fu, L. Vila, B. Haas, P.H. Jouneau, S. Gambarelli, T. Meunier, P. Ballet, J.P. Attané, arXiv:1708.05470 [2] J. E. Hirsch, Physical Review Letters 83, 9 (1999) [3] C. R. Ast, J. Henk, A. Ernst, L. Moreschini, M. Falub, D. Pacilé, P. Bruno, K. Kern, and M. Grioni, Phys. Rev. Lett. 98, 186807 (2007) [4] V. M. Edelstein, Solid State Commun. 73, 233 (1990) [5] A. R. Mellnik, J. S. Lee, A. Richardella, J. L. Grab, P. J. Mintun, M. H. Fischer, A. Vaezi, A. Manchon, E.-A. Kim, N. Samarth and D. C. Ralph, Nature 511, 449–451 (2014) [6] J.-C. Rojas-Sanchez, S. Oyarzun, Y. Fu, A. Marty, C. Vergnaud, S. Gambarelli, L. Vila, M. Jamet, Y. Ohtsubo, A. Taleb-Ibrahimi, P. Le Fèvre, F. Bertran, N. Reyren, J.-M. George, and A. Fert, Phys. Rev. Lett. 116, 096602 (2016) [7] L. Fu and C. L. Kane, Phys. Rev. B 76, 045302 (2007) [8] J.-C. Rojas-Sanchez, L. Vila, G. Desfonds, S. Gambarelli, J. P. Attané, J. M. De Teresa, C. Magén, and A. Fert, Nat. Commun. 4, 2944 (2013) [9] H. Wang, J. Kally, J.S. Lee, T. Liu, H. Chang, D.R. Hickey, K.A. Mkhoyan, M. Wu, A. Richardella, and N. Samarth Phys. Rev. Lett. 117, 076601 (2016) [10] D.A. Kozlov, Z.D. Kvon, E.B. Olshanetsky, N.N. Mikhailov, S.A. Dvoretsky, and D. Weiss, Phys. Rev. Lett. 112, 196801 (2014)

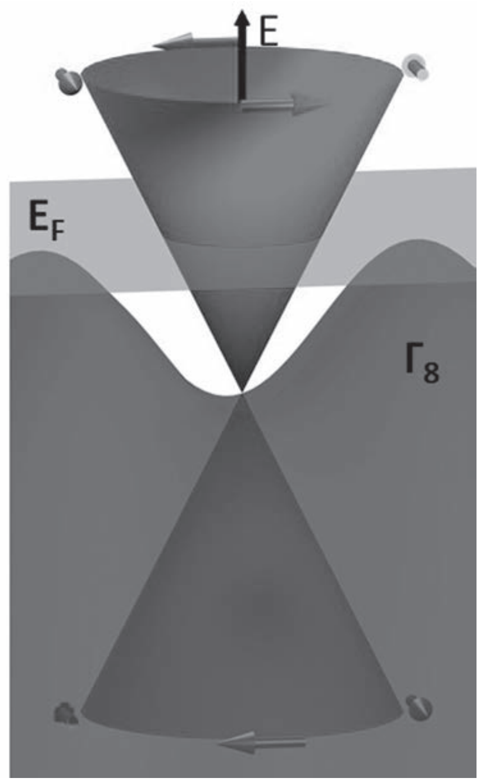

Fig. 1. Schematic representation of the band structure of strained HgTe, with the Dirac dispersion cone of the surface states, and the bulk Γ8 band. The arrows represent the helical spin configuration.

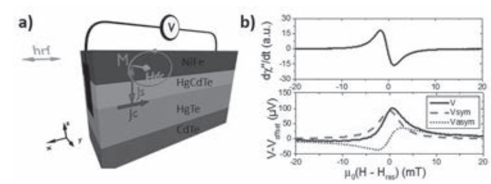

Fig. 2. a) Geometry of the spin pumping by ferromagnetic resonance (FMR) measurement setup and stack used for the measurement. b) FMR and DC voltage from spin pumping FMR measurement. The symmetric (dashed line) and antisymmetric (dotted line) contributions have been extracted from the measured signal (in blue). The symmetric contribution corresponds to the inverse Edelstein Effect contribution

WEDNESDAY AFTERNOON, 25 APRIL 2018 PEONY IV, 2:00 TO 4:00

Session DD
NEUROMORPHIC COMPUTING

Susana Cardoso de Freitas, Co-Chair
INESC-MN, Lisboa, Portugal
Myriam Pannetier-Lecoeur, Co-Chair
CEA Saclay, Gif sur Yvette, France

INVITED PAPER

2:00

DD-01. Neuromorphic computing with spintronic devices.

J. Grollier[1]
1. Unité Mixte CNRS/Thales, Palaiseau, France

Today, neural networks are everywhere: they are the virtual assistants in our smartphones, they are powering our search engines and they are the key to big data classification. They can even beat humans at image recognition or at strategy games such as Go. However neural networks are still running as software on our current computers, consuming tens of kilowatts and working rather slowly. In comparison, the brain from which they are inspired, operates with 20 W and can realize incredibly complex tasks in fractions of seconds. Building chips more closely inspired from the brain architecture is the path to cognitive computing at low energy cost. Applications of such chips span from embedded automatic pattern recognition for big data management, going through unmanned vehicle control to bio-medical prosthesis. The challenge of fabricating brain-inspired hardware relies in the ultra-high density networks that have to be built, out of complex processing units interlinked by tunable connections providing memory. Magnetic nanodevices can be a key technology in this context thanks to their ability to provide massive access to memory, their multiple and tunable functionalities, their non-linear dynamics and compatibility with CMOS [1]. In this talk I will give an overview of recent advances in the field of hardware brain-inspired computing. I will show how magnetic nanodevices can be used for brain-inspired computing, and discuss the working principle of neuromorphic models that can be implemented in Spintronics. Finally, I will show our first results of cognitive pattern recognition with magnetic oscillators [2,3].

[1] J. Grollier, D. Querlioz and M. D. Stiles, PIEEE 104, 2024 (2016) [2] J. Torrejon et al, Nature 547, 428-431 (2017) [3] M. Romera et al, ArXiv :1711.02704 (2017)

CONTRIBUTED PAPERS

2:30

DD-02. Low energy implementation of feedforward neural network with backpropagation algorithm using a spin orbit torque driven skyrmionic device.

U. Saxena[1], D. Kaushik[1], M. Bansal[1], H. Chandel[1], U. Sahu[1] and *D. Bhowmik*[1]

1. Electrical Engineering, Indian Institute of Technology Delhi, New Delhi, India

Non-volatility of spintronic devices opens up possibility of implementation of Artificial Neural Networks (ANN) in hardware and thereby take advantage of the parallel architecture of the system similar to human brain [1,2,3]. Spin orbit torque driven domain wall based devices that act as synapse have been shown to be much more energy efficient than CMOS devices that implement neural networks [2,4]. Here, we have considered the role of defects in ferromagnetic layer and thereby proposed a spin orbit torque driven skyrmionic device, which consumes even lower energy compared to domain wall based device for synaptic behavior. We perform micromagnetic simulations on mumax3 [5] to demonstrate motion of Neel skyrmion and transverse Neel domain wall in a ferromagnet layer of thickness 1 nm, driven by spin orbit torque from current flowing through layer of heavy metal (Pt, spin Hall angle = 0.07) underneath [6,8,9]. We observe (as shown in Fig. 1a) that in the presence of triangular notch defects of 6 nm depth and modified anisotropy 1.2 MJ/m^3 (the magnet has uniform perpendicular anisotropy of 0.8 MJ/m^3 elsewhere) on the two edges of the magnet at a separation of 60 nm each, domain wall is pinned up to a current density of 24 MA/cm^2 through the heavy metal. But a skyrmion is depinned by current density as low as 1 MA/cm^2 though its velocity at such small current density is also very small [6,7]. Based on this result, we propose a skyrmionic device as shown in Fig. 1b, which can act as a synapse. A Magnetic Tunnel Junction (MTJ) structure is present at the right end of the device. Based on magnitude and duration of current pulse through heavy metal layer (applied between terminal T3 and T1) certain number of skyrmions moves to the region of the ferromagnet below the MTJ. Hence Tunneling Magneto-Resistance of MTJ measured between terminal T2 and T1 is a function of the current between T3 and T1 and corresponds to the weight of the synapse, which can be controlled by the current and stored subsequently since skyrmions won't move once current pulse is removed just like domain walls (Fig. 1b). The resistance vs current behavior of the skyrmionic synapse (Fig. 1c), obtained through micromagnetic simulations, shows that in the presence of defects a very small range of current (3.5 μA to 6.5 μA) can modulate the resistance from its lowest to highest value, corresponding to weight of synapse varying from -1 to 1. On the other hand a much larger range of current (-300 μA to 380 μA) is needed to do the same for domain wall based synapse proposed in Ref. 4 if defects are present. Next we solve the standard digit recognition problem (Fig. 2b) by simulating a feedforward neural network with backpropagation algorithm [10] (Fig. 2a) using the domain wall device (Ref. 4) or skyrmion based device (Fig. 1b) as synapses. A three layer feedforward network is trained to identify digits 0-4 across 10 computer generated variations for each digit, that mimic variations due to different handwriting. 35,000 iterations are needed to train the network and total number of synapses is 425. Error generated at the output layer after every iteration needs to be used to change the weights of all the synapses for subsequent iteration through the back-propagation algorithm. This is implemented by passing currents proportional to the generated error through the heavy metal layer of the synaptic devices (between terminal T3 and T1) and move the domain wall/ skyrmion to change the resistance of the MTJ (between T2 and T1) and thus change the weight value of the synapse.The energy dissipation due to this current flow in the heavy metal layer is called the "write" energy consumption, which is the most dominant energy contribution in the system. Fig. 2c is our key result which compares the total "write" energy consumption to train the network with synaptic devices being of the following four types: i. domain wall without defect (write current pulse width: 1 ns) ii. Skyrmion without defect (write pulse width: 15 ns) iii. Domain wall with defect (write pulse width: 0.5 ns) iv. Skyrmion with defect (write pulse width: 550 ns). We see that in the absence of defect, domain wall synapses consume less energy than skyrmion based synapses because domain wall moves faster than skyrmion for a given current density (Fig. 1a). But in presence of defects, since domain wall is pinned till current density of ~24 MA/cm^2 while skyrmions do not get pinned at current density even much smaller than that, if we "write" the skyrmion synapses with current pulses of very long duration (≥ 500 ns) and very small magnitude (3-6 μA) the skyrmion synapse based network can be trained at 2 orders of magnitude lower energy consumption than domain wall synapse based network. Thus in this paper we propose and simulate a skyrmion based synaptic device and show it to be much more energy efficient than domain wall based device. It will be particularly suitable for solving problems where time is not a major constraint.

1. LeCun, Y. *et al.* Nature 521, 436-444 (2015). 2. Sengupta, A. *et al.* Applied Physics Reviews 4, 041105 (2017). 3. Grollier, J. *et al.* Proceedings of the IEEE 104 (10), 2024-2039 (2016). 4. Sengupta, A. *et al.* IEEE Transactions on Biomedical Circuits and Systems 10 (6) (2016). 5. Vansteenkiste, A. *et al.* AIP Advances 4, 107133 (2014). 6. Sampaio, J. *et al.* Nature Nanotech. 8, 839-844 (2013). 7. Dutta, S. *et al.* AIP Advances 5, 127206 (2015). 8. Emori, S. *et al.* Nature Mater. 12, 611-616 (2013). 9. Bhowmik, D. *et al.* Scientific Reports 5, 11823 (2015). 10. Haykin, S. Neural Networks, Pearson (1994).

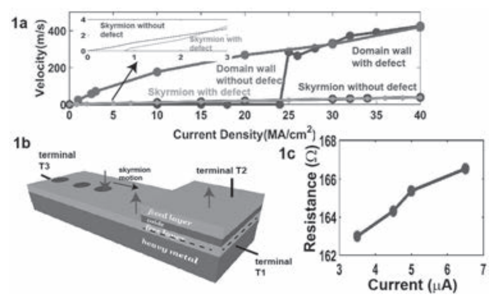

Fig. 1. a) Velocity of domain wall/ skyrmion vs current density obtained from micromagnetic simulations b) Proposed skyrmionic device that act as synapse c) Resistance between terminal T2 and T1 as function of current applied between T3 and T1, showing synaptic behavior

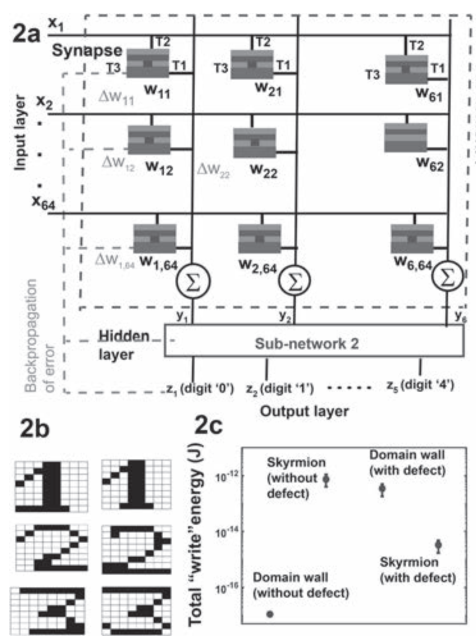

Fig. 2. a) Feedforward neural network using domain wall device or skyrmionic device b) Variations of different digits. The network is trained to identify the digits despite variations. c) Total "write" energy consumption to train the network for different domain wall and skyrmionic devices with or without defects

2:45

DD-03. Circuit-level Design and Evaluation of STT-MRAM based Binary Winner-Takes-All Network for Image Recognition.

C. Wang[1,2], *D. Zhang*[1,2], Y. Hou[1,2], L. Zeng[1,2], J. Klein[3] and W. Zhao[1,2]
1. Fert Beijing Institute, BDBC, Beihang University, Beijing, China; 2. School of Electrical and Information Engineering, Beihang University, Beijing, China; 3. Centre de Nanoscience et de Nanotechnologies (C2N-Orsay), University of Paris-Sud, Orsay, France

Recently it has been demonstrated that binary neural network (BNNs) can achieve satisfying accuracy on various databases with the significant reduction of computation and memory resources [1], which provides a promising way for on-chip implementation of deep neural networks (DNNs). To storage synaptic weights, the SRAM is traditionally utilized in the CMOS based ASIC designs for hardware acceleration implementation of DNNs. However, it has been proved to be extremely area- and power-inefficiency due to its large cell area (>200F^2) and volatility, respectively. To overcome these issues, the emerging non-volatile spin transfer torque magnetoresistive RAM (STT-MRAM) with small cell area (<10F^2) recently has been proposed to implement synaptic weights instead of SRAM [2]. Moreover, STT-MRAM has been demonstrated at Gb chip-level by industry [3]. In this paper, a single-layer binary perceptron (BP) is proposed for image recognition, which can be implemented via the pseudo-crossbar array of 1T-1MTJ (STT-MRAM cell) as shown in Fig. 1(a). With the learning rule in [1], such BP was trained in an off-line manner on a set of N=30 patterns, including three stylized letters ('z', 'v', 'n') as shown in Fig. 1(b) [4], which also was used for testing. To classify these three stylized letters, we design a winner-takes-all (WTA) circuit as shown in Fig. 1(c), which is used as the peripheral inference circuit of proposed BP. Based on a physics-based STT-MTJ compact model and a commercial CMOS 40 nm design kit, the functionality of the proposed BP and WTA circuit have been demonstrated as shown in Fig. 2(a). Additionally, we also investigate the impact of TMR and device variations on the recognition rate as shown in Fig. 2(b) and Fig. 2(c), respectively. In summary, a STT-MRAM based binary synaptic array with a WTA circuit has been proposed for image recognition, which provides a promising solution for hardware implementation of BNNs on-chip.

[1] M. Courbariaux, I. Hubara, D. Soudry, R. El-Yaniv, and Y. Ben-gio, "Binarized neural networks: Training deep neural networks with weights and activations constrained to+ 1 or-1," arXiv preprint arXiv:1602.02830, 2016. [2] D. Zhang, L. Zeng, K. Cao, M. Wang, S. Peng, Y. Zhang, Y. Zhang, J.-O. Klein, Y. Wang, and W. Zhao, "All spin artificial neural networks based on compound spintronic synapse and neuron," IEEE transactions on biomedical circuits and systems, vol. 10, no. 4, pp. 828–836, 2016. [3] S.-W. Chung, T. Kishi, J. Park, M. Yoshikawa, K. Park, T. Nagase, K. Sunouchi, H. Kanaya, G. Kim, K. Noma et al., "4gbit density stt-mram using perpendicular mtj realized with compact cell structure," in Electron Devices Meeting (IEDM), 2016 IEEE International. IEEE, 2016, pp. 27–1. [4] M. Prezioso, F. Merrikh-Bayat, B. Hoskins, G. Adam, K. K. Likharev, and D. B. Strukov, "Training and operation of an integrated neuromorphic network based on metal-oxide memristors," Nature, vol. 521, no. 7550, pp. 61–64, 2015.

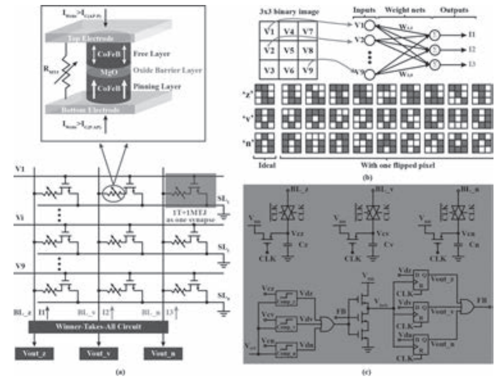

Fig. 1. (a) The diagram of the proposed single-layer binary perceptron based on the pseudo-crossbar array of 1T-1MTJ; (b) The image pattern set for both training and testing; (c) The schematic of proposed winner-takes-all circuit.

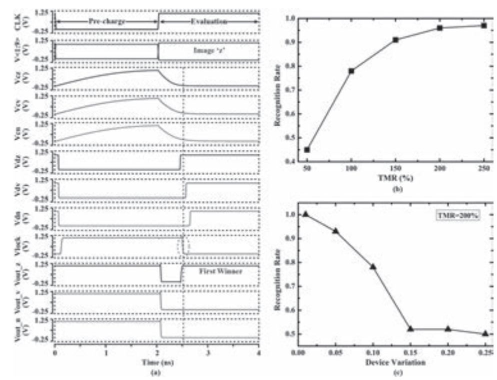

Fig. 2. (a) The voltage waveforms of the proposed single-layer binary perceptron and winner-takes-all circuit; The influence of the TMR (b) and device variations (c) on the recognition rate.

INVITED PAPER

3:00

DD-04. AFM-based artificial neurons for ultrafast neuromorphic computing.

O. Sulymenko[3], R. Khymyn[2], V.S. Tiberkevich[1], J. Åkerman[2] and *A.N. Slavin*[1]

1. Physics, Oakland University, Rochester Hills, MI, United States;

2. Physics, University of Gothenburg, Gothenburg, Sweden;

3. Radiophysics, Taras Shevchenko National University of Kyiv, Kyiv, Ukraine

Neuromorphic signal processing is one of the most promising post-von Neumann computational paradigms. Neuromorphic circuits mimic the brain functionality using artificial "neurons" and "synapses" and provide superior performance for cognitive tasks like, e.g., image or speech recognition. Currently, several commercial neuromorphic circuits built using conventional CMOS technology are available. However, the CMOS-based elements are better suited for digital logic operations than for analog nonlinear processing necessary for neuromorphic computing. Therefore, an intensive search for alternative neuromorphic elements is performed by many research groups worldwide. In particular, promising results demonstrating potential of spintronic spin-torque oscillators for neuromorphic computing have been recently reported [1]. In this work, we show that antiferromagnetic (AFM) spin Hall oscillators (SHO) [2, 3] can serve as ultrafast and energy efficient neuromorphic "neurons". The AFM neurons can operate at frequencies around 100 GHz, can be coupled in complex synchronized networks, can perform complex logical operations, and can have small power consumption about 1 μW per oscillator. The sketch of an AFM-based SHO is shown in Fig. 1(a). Similarly to ferromagnetic SHOs, the AFM oscillator is based on a bi-layer consisting of an active layer (AFM) and a heavy metal (e.g., Pt) layer which serves as a spin Hall polarizer. In the considered oscillator, the AFM material should have a bi-axial type of anisotropy (e.g., NiO) with the hard axis lying in the film plane [3]. In this geometry, the bias DC current creates a constant torque on the AFM sublattice magnetizations. When this spin-torque exceeds the restoring torque created by the in-plane AFM anisotropy (supercritical regime), the AFM magnetizations start to rotate with frequency proportional to the DC current [3]. The neuromorphic operation of the AFM SHO is achieved in the subcritical regime, when the DC bias current below the threshold current. Although the subcritical DC spin-torque is not sufficient to overcome the anisotropy energy barrier, it rotates the AFM magnetizations close to the direction of the maximum of the anisotropy energy (see Fig. 1(c)). In this state the AFM SHO is extremely sensitive to weak input signals, which can move the magnetizations over the energy barrier. Then, the AFM magnetizations will make one full rotation until they again stop near the energy maximum. During this rotation, the AFM generates an output spike due to the spin-pumping effect. It is important to note, that this AFM rotation is governed by the intrinsic ultra-fast AFM dynamics, and, therefore, the output spike is ultra-short (about 4 ps for NiO-based AFM oscillator), rather intense, and its characteristics are independent of the characteristics of the input signal. The output spike of the AFM SHO can be used to initiate other AFM-based neurons. Our simulations show, that the amplitude of the output spike and the coupling strength provided by a common Pt layer are sufficient to initiate a second AFM-based neuron, thus providing possibility for a multi-stage neuromorphic processing without any intermediate amplifiers. An example of such simulations is shown in Fig. 1(b), which shows the dynamics of 2 mutually coupled AFM SHOs. The first oscillator ("input", upper panel) was driven by an externally set sequence of pulses. The second oscillator ("output", lower panel) received input only from the 1st oscillator, and, in response, produced a completely synchronized sequence of spikes. By changing the amplitude of the DC bias current, it is possible to change the sensitivity of the AFM neuron, and to realize various logical gates (i.e., AND, OR, and MAJ) using just one AFM element. Inversion of the sign of the input signal (which can be done using the control "synapse" part of a neuromorphic circuit) further increases the set of possible operations performed by a single AFM neuron, and allows one to create rather sophisticated logical circuits with just a few elements. In particular, we demonstrate that a full adder can be realized with only 3 AFM oscillators. By employing two-way mutual coupling between the AFM oscillators, it is possible to go beyond standard logical functions, and create, for example, controllable memory loops. The simplest loop consists of 2 mutually coupled AFM neurons. When an input "write" signal is applied to the 1st neuron, it will initiate the 2nd one, which, in turn, will again initiate the 1st neuron, resulting in continuous generation of the spike sequence, which can be controllably terminated by external "erase" signal (see simulation results in Fig. 2). Finally, our estimations show that the minimal energy consumption of an AFM neuron, determined by the ohmic losses in the Pt layer, can be as low as 1 μW, and can be further reduced if more efficient spin Hall materials are used. Thus, the proposed AFM-based spin Hall oscillators look very promising candidates for the practical realization of ultra-fast and energy efficient artificial neurons in the future neuromorphic circuits.

[1] J. Torrejon *et al.*, Nature 547, 428 (2017). [2] R. Cheng, et al., Phys. Rev. Lett. 116, 207603 (2016). [3] R. Khymyn *et al.*, Sci. Rep. 7, 43705 (2017).

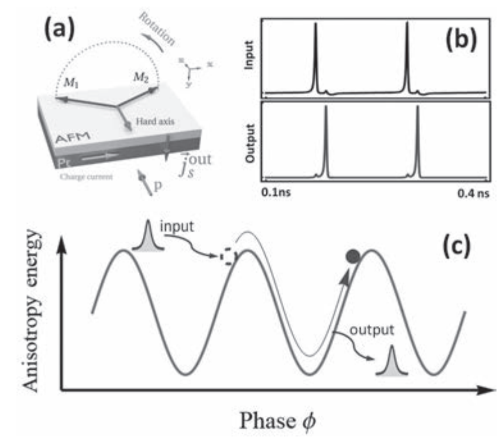

Fig. 1. (a) A sketch of AFM-based SHO. (b) Dynamics of two coupled AFM SHOs. The 1st SHO (upper panel) is driven by an external signal and serves as input for the 2nd SHO (lower panel), which produces synchronized spike sequence. (c) Illustration of operation principle of AFM-based neuron.

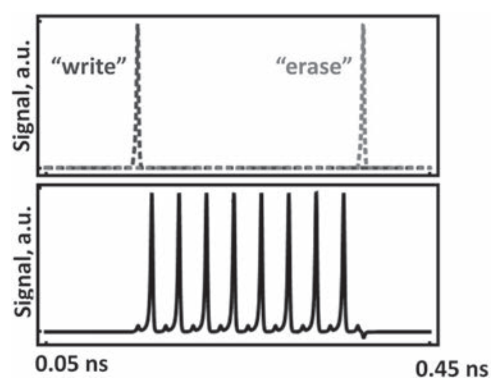

Fig. 2. Simulations of a memory loop consisting of 2 AFM neurons. Upper panel: external "write" and "erase" signals. Lower panel: spike sequence generated by one of the AFM neurons.

CONTRIBUTED PAPERS

3:30

DD-05. Domain wall based Mackey-Glass oscillator for neuromorphic applications.

J. Williame[1] and J. Kim[1]
1. Centre de Nanosciences et de Nanotechnologies, CNRS, Université Paris-Sud, Université Paris-Saclay, Orsay, France

Delayed feedback in dynamical systems, whereby the output signal of a system is sent back into its input with amplification and delay, can stabilize a system or, on the contrary, result in a variety of nonlinear behaviors [1]. One example of delayed feedback loop to stabilize a system are the phase lockings loops used to enhances the spectral properties of an oscillator [2]. You can also use time delayed feedback loops to control the chaos in some systems. On the other hand we can use such loops to increase the complexity and destabilize a system. As such one important consequence of delayed feedback is the possibility of inducing chaotic dynamics, even in low-dimensional systems. From a mathematical perspective, the delayed feedback expands the phase space of the dynamical system, which means that phenomena such as chaos can appear. We then can use chaos for various applications like chaos computing, chaos multiplexing for encryption, random number generation or neuromorphic applications like reservoir computing. In traditional reservoir computing we use a reservoir of many interconnected units called neurons to mimic the human brain and perform tasks like pattern recognition. The main problems to implement such reservoir is the large number of required neurons and connections. This is where the time delayed feedback loops come in. Indeed, it was demonstrated that we can use only one non-linear neuron with such loop to mimic an entire reservoir. A good canditate for such neuron is the Mackey-Glass oscillator [4], which is described by a first-order delay-differential equation and can exhibit a variety of different dynamical states, including limit-cycle and aperiodic states, and complex transients. Indeed, such a dynamical system has recently been implemented in an optoelectronic circuit to perform reservoir computing [3]. This optoelectronic circuit is very efficient and can perform spoken word recognition up to one million word per second but is not easy to implement in our everyday devices like smartphones and laptops. This is due to the intrinsically big optic part of this system which is very hard to scale down. Our approach to solve this problem is to use an already micro or nanoscale device as our non linear neuron. And because we know that a Mackey-Glass oscillator system can perform the pattern recognition we are looking for it makes sense to look for a device behaving like a Mackey-Glass. We then decided to use the oscillations of a pinned domain wall [5] as we believed it could exhibit a Mackey-Glass like behavior. In this work we simulated such domain wall with the opensource micromagnetic simulations software Mumax3 [6]. In the first part of our work we present the device we simulated and we demonstrate that its behavior is indeed very close to a Mackey-Glass oscillator. The system is a permalloy racetrack with an inverted notch on one side of the track in order to pin the domain wall. Thanks to the asymmetry the domain wall is strongly pinned to the notch side of the racetrack but can move relatively easily along the other side. We then have a diagonal wall anchored to the notch and with a slope changing with the injected current along the racetrack. In order to make the time delayed feedback loop we have to get an output. We assume the racetrack to be along the x axis and in the xy plane. The output we chose to use for the feedback is the average value of the magnetization along the y axis in the region just after the inverted notch, ie the area where our diagonal wall is, which is a value that could be measured experimentally with a proper device design. With the proper parameters for the racetrack dimensions and for the feedback loop we show that our device can have a transfer function very close to the one of a Mackey-Glass oscillator as shown in the first figure. In the second part of our work we explore the different dynamics our device can exhibit with a large array of feedback parameters. With the feedback we can modulate the amplitude of the wall oscillations or stop them. We can also induces near chaos oscillations which is interesting for pattern recognition since reservoir computing works better with neurons in a state at the edge of chaos. A example of this behavior is shown in the second figure. In this second part we will also see if our device is able to perform neuromorphic tasks like spoken digit recognition or chaotic number series prediction.

[1] G. Khalsa, M. D. Stiles, and J. Grollier, Applied Physics Letters 106,242402 (2015). [2] S. H. Strogatz, Nonlinear Dynamics and Chaos (Perseus Books, Reading, MA, 1994). [3] L. Appeltant, M. C. Soriano, G. Van der Sande, J. Danckaert, S. Massar, J. Dambre, B. Schrauwen, C. R. Mirasso, and I. Fischer, Nature Commu- nications 2, 468 (2011). [4] M. C. Mackey and L. Glass, Science 197, 287 (1977). [5] S. Weinberg, *The Quantum Theory of Fields*, Vol. 2. Chap 23, Cambridge University Press (1995). [6] A. Vansteenkiste, J. Leliart, M. Dvornik, M. Helsen, F. Garcia-Sanchez and B. V. Waeyenberge. AIP Advances 4, 107133 (2014).

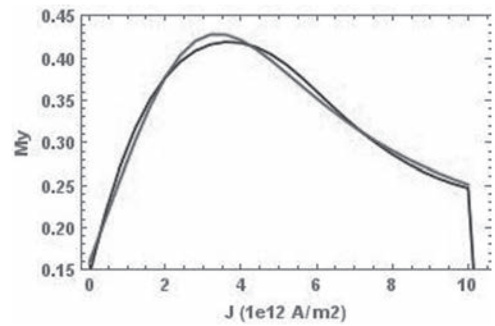

Fig. 1. Domain wall oscillator transfer function (Blue) and fitted Mackey Glass oscillator transfer function (Red).

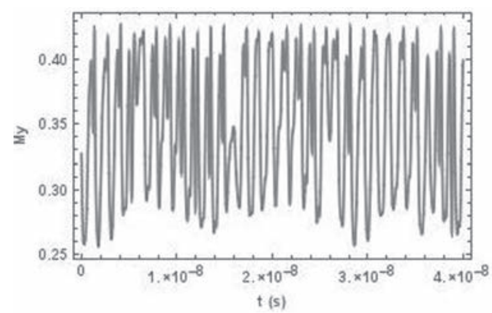

Fig. 2. Time trace of the domain wall oscillator with time delayed feedback in near-chaos regime.

3:45

DD-06. Neuromorphic computing using spin-transfer torque magnetic random access memory (STT-MRAM).

J. Moon[1] and K. Lee[1,2]
1. Department of Materials Science and Engineering, Korea University, Seoul, The Republic of Korea; 2. KU-KIST Graduate School of Converging Science and Technology, Korea University, Seoul, The Republic of Korea

The most notable difference between neuromorphic system and conventional information processing system is their use of memory structures. Von Neumann architecture (conventional information processing system) have one (or more) central processing unit (CPU) which is separated from the main memory. Therefore, bottleneck of von Neumann architecture is given by memory-related constraints such as latency and bandwidth. The brain-inspired computing offers an attractive solution for implementing an alternative non von Neumann computing because biological (or bio-inspired, neuromorphic) system has a colocalized memory and computation. The synapses of (artificial) neural network act as memory storage and nonlinear operator at the same time for parallel computation. Restricted Boltzmann machines (RBMs) is a generative stochastic energy-based model of artificial neural network [1]. It has been introduced as bi-directionally connected networks of stochastic processing units as shown in following figure. The RBM has only connections between the layer of hidden (or latent) and visible (or observable) variables but not between two variables of the same layer. Spin-transfer torque magnetic random access memory (STT-MRAM) is one of the most promising nonvolatile memories with low power consumption. The binary information (high resistance or low resistance) is recorded in the magnetic state of nanomagnets via spin current. Magnetization reversal (switching) of STT-MRAM is a probabilistic process due to thermal fluctuations and the switching probability of STT-MRAM can be changed by applying an electric field because energy barrier of STT-MRAM can be modulated using an electric field [2]. In this work, we numerically demonstrated RBM composed of STT-MRAMs. By virtue of stochastic binary states and non-linearity of STT-MRAM, it is possible to build RBM without additional random number generator which cannot be easily achieved. We believe that our work is helpful to develop artificial neural network using emerging technology and would open the way for unexplored applications of STT-MTJs in robust, low power, cognitive-type systems.

[1] G. E. Hinton *et al.*, Neural Computation 18(7), 1527 (2006). [2] F. Matsukura *et al.*, Nature nanotechnology 10, 209 (2015).

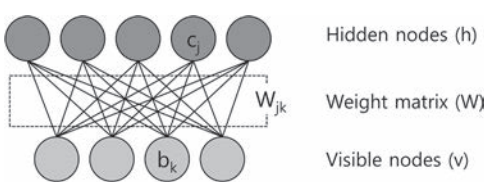

Fig. 1. The schematic structure of Restricted Boltzmann machines (RBMs) is shown. RBMs are composed of two layers which are commonly referred to as visible (or observable, yellow circle) layer and hidden (or latent, blue circle) layer. The black line indicates the weight matrix between connected nodes.

WEDNESDAY AFTERNOON, 25 APRIL 2018

ROSELLE II, 2:00 TO 4:00

Session DE
ANTIFERROMAGNETIC SPINTRONICS

Young Sun, Chair
Institute of Physics, Chinese Academy of Sciences, Beijing, China

CONTRIBUTED PAPERS

2:00

DE-01. Role of thermal activation in the electrical switching of antiferromagnetic Mn_2Au and CuMnAs.

T. Matalla-Wagner[1], D. Graulich[1], M. Rath[1] and *M. Meinert*[1]
1. Faculty of Physics, Bielefeld University, Bielefeld, Germany

Electrical manipulation of antiferromagnets with specific symmetries offers the prospect of creating novel, antiferromagnetic spintronic devices [1]. Such devices aim to make use of the insensitivity to external magnetic fields and the ultrafast dynamics at the picosecond timescale intrinsic to antiferromagnets. The possibility to electrically switch antiferromagnets was first predicted for Mn_2Au [2] and then experimentally observed in tetragonal CuMnAs [3]. We report on the electrical switching of magnetron-sputtered films of Mn_2Au and CuMnAs. The switching in Mn_2Au is observed in simple Hall-cross structures with a parallel pulsing scheme, see Fig. 1. An exponential dependenc of the switching amplitude on the current density is observed and a saturating behaviour with pulse widths approaching 1ms is seen. We analyze the switching with a macroscopic stochastic switching model and propose an analytical expression for the critical curent density required to switch the Néel vector in the presence of thermal activation. Furthermore, an expression for the switching amplitude is derived in the linear response regime. A kinetic Monte Carlo technique is applied to simulate the switching and quantitative agreement between experiments and model calculations is obtained, see Fig. 2. It is found that the switching is thermally assisted by the Joule heating of the current pulses, which facilitates the switching of Mn2Au. The model analysis shows that the electrically set magnetization state of Mn_2Au is long-term stable at room temperature ($\Delta = E_B / k_BT = 64$), paving the way for practical applications in memory devices [4]. We estimate the spin-orbit torque efficiency as 0.4 ... 1.05 mT / (10^{11} A/m^2), in reasonable agreement with the prediction by Zelezny et al. [2]. In the case of CuMnAs, we find a notable dependence of the switching amplitude per pulse on the temperature, with a pronounced peak around 260K. This is similar to usually observed distributions of the blocking temperature in exchange-coupled antiferromagnet / ferromagnet systems, which are related to the grain size distribution in the antiferromagnets [5]. The switching is observed even in films with rather poor crystalline quality and does not seem to rely on excellent crystal quality. Similar switching behaviour as compared to Mn_2Au is observed, however at much smaller current densities and in agreement with the previously reported switching in epitaxial CuMnAs [3].

[1] O. Gomonay et al., Phys. Status Solidi RRL RRL 11, 1700022 (2017) [2] J. Zelezny et al., Phys. Rev. Lett. 113, 157201 (2014) [3] P. Wadley et al., Science 351, 587–590 (2016) [4] M. Meinert et al., arXiv:1706.06983 [5] K. O'Grady et al., J. Magn. Magn. Mater. 322, 883 (2010)

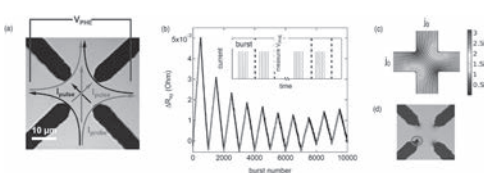

Fig. 1. (a), Optical micrograph of the Hall cross used for the switching experiment. Current pulses are injected as indicated by red and black curved arrows, resulting in an effective current flow in the center of the Hall cross as indicated by small straight arrows. The Néel vector is thus switched at ± 45° with respect to both the probe current and the voltage pickup lines, so that the planar Hall effect can be measured at maximum efficiency. (b), Demonstration of the Néel vector switching at $j_0 = 2 \times 10^{11}$ A/m^2 and $\Delta t = 200\mu s$. Each burst consists of 100 pulses, i.e. 1.92mC are transferred per burst. The inset represents the pulsing and measurement scheme (not to scale). (c), finite-element simulation of the current flow. (d), Optical micrograph of a Hall cross after heavy electrical stress.

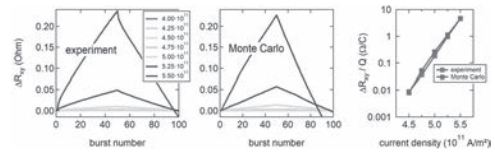

Fig. 2. (a), switching amplitude as a function of the current density j_0 (given as A/m^2). Experiment with $\Delta t = 1\mu s$ and 1mC per burst. (b), Monte Carlo simulations with grain diameter D = 15.0nm and K = 17.3μeV per cell. (c), extracted switching amplitudes per unit charge.

2:15

DE-02. Spin transport thru antiferromagnetic NiO in Bi_2Se_3/NiO/Py heterostructures.

Y. Wang[1], D. Zhu[1], J. Lee[1], Y. Yang[1], R. Ramaswamy[1], K. Teo[1], Y. Wu[1] and H. Yang[1]
1. Department of Electrical and Computer Engineering, National University of Singapore, Singapore

The spin current transport has been extensively studied in the conductive materials, in which spin current is carried by the itinerant electrons. It has been recently shown that spin current can pass through or even be amplified with a layer of the antiferromagnetic (AF) insulator NiO inserted between a ferromagnet (FM) and a heavy metal [1-5]. In this case, there is no itinerant electron in the NiO layer due to its insulating nature. It has been suggested that the spin current is conducted through NiO via the thermally excited AF magnons [2,4,6]. Thus it is of importance to experimentally prove the spin transmission thru the NiO layer. Furthermore, a highly efficient SOT driven magnetization switching at room temperature has been recently demonstrated in topological insulators (TIs)/FM bilayer [7,8], in which the switching efficiency is about two orders of magnitude larger than that in heavy metals. However, current shunting is an unavoidable issue in the TI/FM bilayer due to the higher resistance of TI than FM layer. To solve this issue, we propose to insert an AF insulator NiO between the TI and FM layers, by which we can confine the flow of charge current within only TI layer, and the spin currents generated in TI can still be transmitted through the NiO layer and reach the FM layer. In this study, we show that the spin current is carried thru a moderately thick NiO layer by using spin-torque ferromagnetic resonance (ST-FMR) measurements in the Bi_2Se_3 (8 nm)/NiO (t_{NiO} = 0–17.5 nm)/NiFe (6 nm) structures at room temperature as shown in Fig. 1(a). The SOT efficiency ($\theta_{\|}$) as a function of NiO thickness is plotted in Fig. 1(b). It is observed that $\theta_{\|}$ abrupt decreases from ~0.9 to ~0.18 with only a 2-nm NiO insertion layer. As t_{NiO} increases above 10 nm, an enhancement of SOT efficiency to ~0.5 ($t_{NiO} \geq 14$ nm) is observed. Our results reveals that the AF magnons may carry the spin currents in thicker NiO layers. In addition, we achieve the SOT-induced magnetization switching, imaged by a magneto-optic Kerr effect (MOKE) microscope, in the Bi_2Se_3/NiO/NiFe heterostructures with t_{NiO} up to 17.5 nm at room temperature by injecting a pulsed dc current. We find J_C in the thicker NiO region ($t_{NiO} \geq 12$ nm) is about 2 times larger than that in the region of $t_{NiO} \leq 2$ nm. Further, no full magnetization switching can be achieved as 2 nm < t_{NiO} < 12 nm. This is in line with the results in Fig. 1(b). Moreover, we find that the switching efficiency (η) for $t_{NiO} \geq 12$ nm is ~6 times higher than that for $t_{NiO} \leq 2$ nm. Here, η is defined as $M_s t\alpha(H_c + M_{eff}/2)/J_C$, where M_s, t, α, H_c and M_{eff} are the saturation magnetization, thickness, damping constant, coercivity field and effective magnetization of NiFe layer, respectively. We have successfully demonstrated SOT induced magnetization switching in Bi_2Se_3/NiO/NiFe by utlilizing the spin transport in an AF insulator, which might pave the way for high performance TI based magnetic devices.

[1] C. Hahn, G. De Loubens, V. V. Naletov, J. B. Youssef, O. Klein, and M. Viret, EPL (Europhysics Letters) 108, 57005 (2014). [2] H. Wang, C. Du, P. C. Hammel, and F. Yang, Phys. Rev. Lett. 113, 097202 (2014). [3] T. Moriyama, S. Takei, M. Nagata, Y. Yoshimura, N. Matsuzaki, T. Terashima, Y. Tserkovnyak, and T. Ono, Appl. Phys. Lett. 106, 162406 (2015). [4] W. Lin, K. Chen, S. Zhang, and C. Chien, Phys. Rev. Lett. 116, 186601 (2016). [5] D. Hou *et al.*, Phys. Rev. Lett. 118, 147202 (2017). [6] S. Rezende, R. Rodríguez-Suárez, and A. Azevedo, Phys. Rev. B 93, 054412 (2016). [7] J. Han, A. Richardella, S. A. Siddiqui, J. Finley, N. Samarth, and L. Liu, Phys. Rev. Lett. 119, 077702 (2017). [8] Y. Wang *et al.*, Nat. Commun. 8, 1364 (2017).

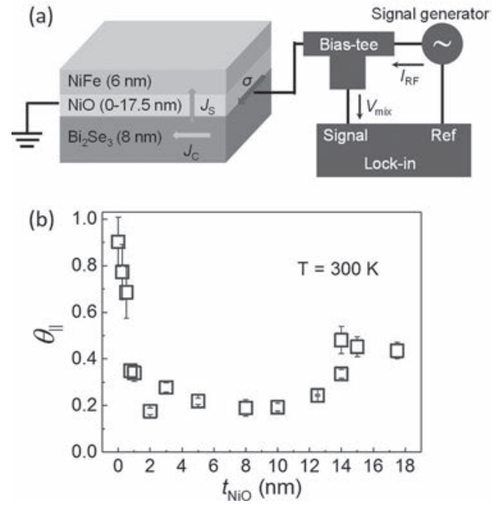

Fig. 1. (a) Schematic diagram of the ST-FMR measurement setup. J_C, J_S and σ represent charge current density in the Bi_2Se_3 layer, spin current density from Bi_2Se_3 to NiFe layer and the spin polarization at the topological surface states in the Bi_2Se_3 layer, respectively. (b) SOT efficiency as a function of NiO layer thickness measured by ST-FMR technique at room temperature.

2:30

DE-03. Giant Spin-Hall Angle in Epitaxial $L1_0$-IrMn.

J. Zhou[1], X. Wang[3], J. Yu[1], Q. Qin[1], L. Liu[1], S. Chen[1], J. Deng[1], H. Yoong[1], P. Yang[2], X. Han[3] and J. Chen[1]
1. Material Science & Engineering, National University of Singapore, Singapore; 2. Singapore Synchrotron Light Source, National University of Singapore, Singapore; 3. Institute of Physics and Beijing National Laboratory for Condensed Matter Physics, Chinese Academy of Sciences, Beijing, China

Metallic antiferromagnets are taking an increasingly critical role in research of spintronics due to their high conductivity, strong exchange bias and large spin-orbit torques (SOT). Zhang *et al* have shown that the spin Hall angle (SHA), which is believed to be positively related to SOT, of alloys of Mn is comparable to Pt [1]. Among other antiferromagnetic alloys, IrMn is an appealing medium to study SOT in metallic antiferromagnets because of its well-defined crystallographic phases and the correspondingly unique magnetic configurations. In 2016, Zhang *et al* demonstrated that the SHA of $L1_2$-$IrMn_3$ can be as large as 0.35 [2]. Moreover, IrMn could be a promising material for applications of spintronics. Tapping on the merits of exchange bias and SOT in IrMn, Oh *et al* observed field-free switching in a bilayer structure of IrMn/CoFeB, taking a big step towards low-energy spintronics [3]. Currently the mechanisms of SOT in IrMn are yet well understood. In addition, there exists a gap between empirically observed SOT and theoretical frameworks. Past reports were frequently based on polycrystalline IrMn thin films but the models relate to the long-range structural or magnetic orders of IrMn. Keep these in mind, this work will demonstrate that the SHA of epitaxially deposited $L1_0$-IrMn shows an unprecedented high value of 0.7, in sharp contrast to its polycrystalline counterpart. Thin film stacks of IrMn(25)/Permalloy(Py)(20)/SiO_2(2), from left to right, were deposited using DC magnetron sputtering. Numbers in the brackets indicate thickness in nanometers. The layer of IrMn was deposited at high temperature while Py and SiO_2 were deposited at room temperature. The films was subject to X-ray diffraction (XRD) measurement to characterize the crystallographic structure of IrMn. The thin film stack was then patterned to micro bars with a combination of photolithography and ion-beam etching. The patterned device was subject to spin-torque ferromagnetic resonance (STFMR) measurement: a microwave was applied along the long axis of the micro bar and an external magnetic field was swept parallel to the sample plane at 45 degrees with the microwave. Using methods presented in ref. [4], the measured rectifying voltage was fitted against external field to extract the SHA. Fig. 1 shows the two-theta scan of the epitaxially deposited $L1_0$-IrMn. The $L1_0$ phase was further verified using reciprocal lattice space mapping. Fig. 2 (a) shows the typical STFMR measurement results and the quality of fitting. The collected data points are well fitted with symmetric and anti-symmetric components clearly separated. Fig. 2 (b) shows the calculated SHA for $L1_0$-IrMn, which is approximately around 0.7 over the microwave frequency range of 8-12 GHz. The error bars reflect the spread of 5 devices on the same sample.

[1] Wei Zhang, Matthias B. Jungfleisch, Wanjun Jiang, John E. Pearson, and Axel Hoffmann, *Phys. Rev. Lett*, 113, 196602 (2014) [2] Weifeng Zhang, Wei Han, See-Hun Yang, Yan Sun, Yang Zhang, Binghai Yan, Stuart S. P. Parkin, *Sci. Adv*. 2, e1600759 (2016) [3] Young-Wan Oh, Seung-heon Chris Baek, Y.M. Kim, Hae Yeon Lee, Kyeong-Dong Lee, Chang-Geun Yang, Eun-Sang Park, Ki-Seung Lee, Kyoung-Whan Kim, Gyungchoon Go, Jong Ryul Jeong, Byoung-Chul Min, Hyun-Woo Lee, Kyung-Jin Lee, Byong-Guk Park, *Nat. Nanotechnol.* 11, 878–884 (2016) [4] L. Liu, T. Moriyama, D. C. Ralph, R. A. Buhrmanby, *Phys. Rev. Lett*. 106, 036601 (2011).

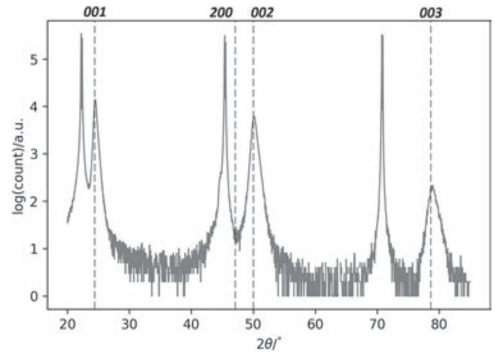

Fig. 1. Two-theta scan of $L1_0$-IrMn. Vertical lines show the reference bulk values.

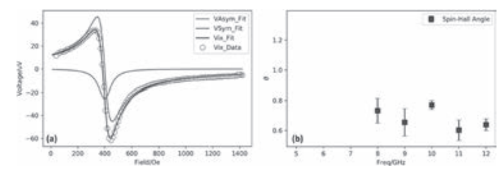

Fig. 2. STFMR results. (a) Typical fitting of STFMR measurement on $L1_0$-IrMn/Py at 9GHz and 18dBm input power. VAsym stands for anti-symmetric component; Vsym stands for the symmetric component; Vix stands for the overall mixed voltage. (b) Calculated spin Hall angle of $L1_0$-IrMn over different microwave frequency. The points and error bars are based on 5-device average.

2:45

DE-04. Spin-Hall and Anisotropic Magnetoresistance effects in Layered Structures with Ferrimagnetic Co-Gd alloys.

T. Seki[1], W. Zhou[1], T. Kubota[1] and K. Takanashi[1]
1. Tohoku University, Sendai, Japan

Introduction: Antiferromagnetic spintronics is an emerging research field and has attracted much attention because of the unique properties of antiferromagnets: zero net magnetization and small magnetic susceptibility that enable us to develop the ultrahigh density magnetic memory devices. Also antiferromagnets exhibit the high speed magnetization dynamics compared with those for ferromagnets used in the conventional spintronic devices. Recent studies demonstrated that the flow of spin angular momentum, *i.e.* spin current (J_s) was generated from the antiferromagnet and J_s also interacts with the magnetic moments of antiferromagnet [Ref. 1]. However, the detailed mechanism of the interaction between J_s and the antiferromagnetic structure has not fully been understood yet. We consider that the ferrimagnetic Co-Gd amorphous alloys, in which the Co and Gd moments (m^{Co} and m^{Gd}) are coupled antiferromagnetically, are a promising system for the systematic investigation of the interaction between J_s and the antiferromagnetic structure. Since the net magnetic moment of Co-Gd (m^{Co-Gd}) is given by $| m^{Co} - m^{Gd} |$, which of m^{Co} or m^{Gd} is dominant for m^{Co-Gd} strongly depends on the composition of Co-Gd. In addition, the compensated ferrimagnet is obtained at the Co-Gd composition showing $m^{Co} = m^{Gd}$. The ferrimagnetic structure at the compensation point is similar to an antiferromagnetic structure from the viewpoint of zero net magnetization. Recently, several studies reported the interaction between J_s and local spins of Co-Gd or Gd-Fe-Co near the compensation points [Ref. 2,3]. In this study, we investigated the composition dependence of spin-Hall magnetoresistance (SMR) for the in-plane magnetized $Co_{100-x}Gd_x$ amorphous alloys sandwiched by the Cr and Pt layers. In addition to the SMR, we also measured the composition dependence of anisotropic magnetoresistance (AMR) of the Cr / $Co_{100-x}Gd_x$ / Pt layers, and we found the different composition dependences of SMR and AMR. Experimental Results: Thin films were deposited on a thermally oxidized Si substrate using a magnetron sputtering system. First, a 4 nm-thick Cr buffer was deposited on the Si-O substrate. Then, Co and Gd were co-deposited to form $Co_{100-x}Gd_x$ layers with a thickness of 30 nm. Finally, a 4nm-thick Pt layer was deposited. All the layers were deposited at room temperature. By tuning the sputtering powers of Co and Gd targets, the Gd concentration was widely varied from $x = 0$ to $x = 45$. Except $x = 0$ corresponding to the pure Co, all the Co-Gd layers were amorphous alloys. The top Pt layer serves as not only the capping layer to prevent the Co-Gd from oxidation, but also the layer generating transverse J_s from the charge current (J_c) via the spin-Hall effect owing to its large spin-orbit coupling. Magnetic properties were measured using a superconducting quantum interference device magnetometer and a longitudinal magneto-optical Kerr effect (L-MOKE) equipment with a laser wavelength of 680 nm. The *M-H* curves showed the magnetization (M) was changed with x. As x was increased from 12 to 37, the local minimum of M appeared at $x = 25$. In contrast to the M - H curves, the L-MOKE loops showed the gradual decrease in the magnitude of Kerr rotation angle with x. A remarkable point observed in the L-MOKE loops was that the sign of Kerr rotation angle reversed at $x = 25$. In other words, the discontinuous change in the Kerr rotation angle versus x was observed at $x = 25$. These experimental facts indicate that the compensation point (composition) of the present Co-Gd exists around x = 25. The composition dependence of AMR showed the sign change from positive to negative as x was increased, and zero AMR was observed near the compensation composition. It is well known that the pure Co shows the positive AMR while the pure Gd showed the negative AMR. Our experimental result suggests that both *d*-electrons of Co and Gd contribute the magnitude of AMR. We consider that the AMR disappears when the positive AMR from Co and the negative AMR from Gd cancel each other. On the other hand, the non-zero SMR was obtained even when the AMR became almost zero. Our experimental results clearly indicate the different scattering mechanisms for AMR and SMR. In contrast to the AMR effect based on the *s-d* scattering in the bulk, SMR depends on other parameters such as spin mixing conductance at the interface that do not play an important role for the AMR effect. That is a possible reason for the different composition dependences between SMR and AMR. Consequently, our experimental results and findings using the ferrimagnetic Co-Gd alloys are useful and important to reveal the underlying physics of SMR and AMR.

[Ref. 1] T. Jungwirth, X. Marti, P. Wadley and J. Wunderlich, *Nature Nano*. 11, 231 (2016). [Ref. 2] T. Okuno, K.-J. Kim, T. Tono, S. Kim, T. Moriyama, H. Yoshikawa, A. Tsukamoto, and T. Ono, *Appl. Phys. Exp.* 9, 073001 (2016). [Ref. 3] R. Mishra, J. Yu, X. Qiu, M. Motapothula, T. Venkatesan, and H. Yang, *Phys. Rev. Lett.* 118, 167201 (2017).

3:00

DE-05. Spin-orbit torque in antiferromagnets.

C. Song[1], X. Zhou[1], X. Chen[1], P. Zhang[1], G. Shi[1] and F. Pan[1]
1. Department of Materials Science and Engineering, Tsinghua University, Beijing, China

Antiferromagnets with zero net magnetic moment, strong anti-interference and ultrafast switching speed have potential competitiveness in high-density information storage [1,2]. Electrical switching of antiferromagnets is at the heart of device application [3]. We will present our recent progress in the current-driven magnetization switching through spin-orbit torque (SOT) in three antiferromagnetic systems, including Mn_2Au, and [Co/Pd]/Ru/[Co/Pd] synthetic antiferromagnets (SAF). Body centered tetragonal antiferromagnet Mn_2Au with opposite spin sub-lattices is a unique metallic material for Néel-order spin-orbit torque (SOT) switching. The SOT switching in quasi-epitaxial (103), (101) and (204) Mn_2Au films prepared by a simple magnetron sputtering method will be discussed. We demonstrate current induced antiferromagnetic moment switching in all the prepared Mn_2Au films by a short current pulse at room temperature, whereas different orientated films exhibit distinguished switching characters. A direction-independent reversible switching is attained in Mn_2Au (103) films due to negligible magnetocrystalline anisotropy energy, while for Mn_2Au (101) and (204) films, the switching is invertible with the current applied along the in-plane easy axis and its vertical axis, but becomes attenuated seriously during initially switching circles when the current is applied along hard axis, because of the existence of magnetocrystalline anisotropy energy [4]. SAF were proposed to replace ferromagnets in magnetic memory devices to reduce the stray field, increase the storage density and improve the thermal stability. We will discuss the SOT in a perpendicularly magnetized Pt/[Co/Pd]/Ru/[Co/Pd] SAF structure, which exhibits completely compensated magnetization and a high exchange coupling field of 2200 Oe. The magnetizations of two Co/Pd layers can be switched by spin-orbit torque between two antiparallel states simultaneously. The magnetization switching can be read out due to much stronger spin-orbit coupling at bottom Pt/[Co/Pd] interface compared to its upper counterpart without Pt. Both experimental and theoretical analyses unravel that the torque efficiency of antiferromagnetic coupled stacks is significantly higher than the ferromagnetic counterpart, which conquers the exchange coupling field, leading to the critical switching current of SAF comparable to the ferromagnetic coupled one [5,6]. Besides the fundamental significance, the efficient switching of antiferromagnets by current would advance magnetic memory devices with high density, high speed and low power consumption.

[1] T. Jungwirth, X. Marti, P. Wadley, and J. Wunderlich, Nat. Nanotechnol, 11, 231 (2016). [2] X. Z. Chen, C. Song, et al., Nat. Commun. 8, 449 (2017). [3] P. Wadley, et al. Science 351, 587 (2016). [4] X. F. Zhou, C. Song, et al. submitted. [5]G. Y. Shi, C. Song, et al. Phys. Rev. B 95, 104435 (2017). [6] P. X. Zhang, C. Song et al. submitted.

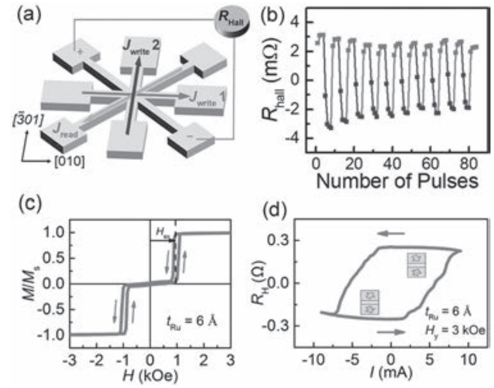

Fig. 1. (a) and (b) are the schematic of the switching measurement and current-driven SOT switching of Mn_2Au; (c) and (d) are normalized out-of-plane hysteresis loops and current-induced SOT switching of [Co/Pd]/Ru/[Co/Pd].

3:15

DE-06. Micromagnetic simulations of spin-Hall driven dynamics in an antiferromagnet.

V. Puliafito[1], M. Carpentieri[2], B. Azzerboni[1], V.S. Tiberkevich[3], A.N. Slavin[3] and G. Finocchio[4]
1. Department of Engineering, University of Messina, Messina, Italy; 2. Department of Electrical and Information Engineering, Politecnico di Bari, Bari, Italy; 3. Department of Physics, Oakland University, Rochester, MI, United States; 4. Department of Mathematical and Computer Science, Physical Sciences and Earth Sciences, University of Messina, Messina, Italy

In the last decades, the research in spintronics has mainly concentrated on ferromagnetic materials, which respond to the different kinds of spin-transfer torques with gigahertz-frequency dynamics [1-3]. A jump to higher-frequency devices, working in the range of terahertz, is promised by the use of antiferromagnets (AFM) [4-6]. AFM materials will, probably, be in the research spotlight in the near future. In order to study their behavior, however, a new theoretical approach is needed, which, for instance, has to account for the strong internal exchange field in AFMs, for the absence of macroscopic magnetization, and possibility to operate without an external bias field. When it comes to modeling, AFMs are generally studied by considering the magnetizations M_1 and M_2 of the two sublattices. Dynamics of M_1 and M_2 is ruled by two coupled Landau-Lifshitz-Gilbert equations [6]. In this work, we model micromagnetically an antiferromagnetic spin-Hall oscillator (ASHO). This device consists of an AFM layer coupled to a layer of a heavy metal, as sketched in Fig. 1, where a coordinate system *x-y-z* is also shown. The AFM layer is square-shaped, with dimensions 40x40 nm^2, whereas the dimension along *z*, namely its thickness *d*, varies from 1 to 5 nm. The heavy metal is designed with 4 terminals that can be used to apply a charge current, and/or to read the device resistance [7]. According to the well-known spin-Hall effect, when a current is applied (in our case in the plane *x-y*), it creates a spin polarization in the heavy metal. The consequent spin current, flowing along the *z* direction, creates a spin accumulation at the interface with the AFM, and, therefore, a torque on the AFM. The direction of the spin-Hall polarization p is perpendicular to the plane of the charge and spin currents, namely, if the charge current is applied along the axis *x* and the spin current is along the axis *z*, the spin polarization is along the axis *y* [2,7]. The spin-Hall-driven torque, therefore, acts on the magnetizations M_1 and M_2 of the two AFM sublattices in the same direction, thus allowing dynamics with a non-zero net magnetization. We investigate this dynamics, solving the equations of motion for the two sublattices by means of a custom-developed micromagnetic code. The following parameters are used in our simulations: saturation magnetization M_S=350x10^3 A/m, spin-Hall angle θ_{SH}=0.10. The exchange constant *A* is a variable parameter in our simulations, and assumes the values of 0.5, 1.0 and 1.5x10^{11} J/m. Similarly, the Gilbert damping constant α is set equal to 0.01, 0.05 and 0.1. The AFM is assumed to have the in-plane anisotropy along the *x* direction, the corresponding constant is K_u=10^5 J/m^3, and simulations start from the equilibrium AFM configuration of M_1 and M_2 along the easy axis, shown in Fig. 1. Last, but not least, the current is applied differently at the terminals, in order to modify the direction of the spin-Hall polarization with respect to the easy axis *x*. We consider three cases: (i) current at the terminals A-A' along *x* direction (p along *y*), (ii) current at the terminals B-B' along -*y* direction (p along *x* axis), and (iii) current at both A-A' and B-B' with equal intensity (p is directed 45° w.r.t. to x and y axes). By means of this configuration, it is, therefore, possible to manage the direction of the spin-Hall polarization with respect to the AFM easy axis, simply by tuning the two currents at the two couples of terminals. The above described systematic study has provided important data on the behavior of an AFM under the action of the spin-Hall effect. Dynamics of magnetization is excited above a certain threshold current. However, the same dynamics is turned off at the lower values of the driving current, highlighting a clear hysteretic behavior of the excitation. The values of the threshold currents and the width of the hysteresis region depend on different parameters. For instance, the threshold current increases with the increase of the AFM thickness, or the damping, or the exchange constant. When the polarization is moved from the axis *y* to the AFM easy axis, the threshold current slightly increases, and to get the excitation of dynamics we need to include a small thermal field. Above the threshold, the magnetizations of the two AFM sublattices show a precession around the spin-polarization direction, as shown in the inset of Fig. 2. The net magnetization is, mainly, given by the sum of the components of M_1 and M_2 along the spin polarization p, whereas the other two components give almost zero contribution when the sum of M_1 and M_2 is evaluated. The frequency of the net magnetization dynamics shows a blue-shift with the increase of the applied current (see the example in Fig. 2). The values of the generated frequency are from hundreds of GHz up to several THz, as expected. The hysteretic excitation, the blue-shift of the frequency, the order of threshold current, and of output frequencies confirm the predictions of the previous analytical studies [6], and confirm the validity of our numerical approach.

[1] W. H. Rippard, M. R. Pufall, and S. E. Russek, Phys. Rev. B 74, 224409, 2006. [2] L. Liu, T. Moriyama, D. C. Ralph, and R. A. Buhrman, Phys. Rev. Lett. 106, 036601, 2011. [3] Z. Zeng, G. Finocchio, and H. Juang, Nanoscale 5, 2219, 2013. [4] S. Baierl, et al., Phys. Rev. Lett. 117, 197201, 2016. [5] R. Cheng, D. Xiao, and A. Brataas, Phys. Rev. Lett. 116, 207603, 2016. [6] R. Khymin, et al., Sci. Rep. 7, 43705, 2017. [7] I. M. Miron, et al., Nature 476, 189, 2011.

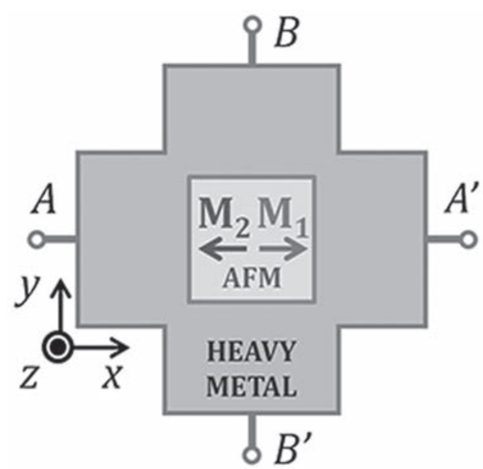

Fig. 1. Schematics of the simulated device: a 4-terminal bi-layered spin-Hall oscillator made of an antiferromagnet coupled to a heavy metal. Terminals A-A' and B-B' can be used for the application of a charge current, and for the measurement of the Hall resistance of the device.

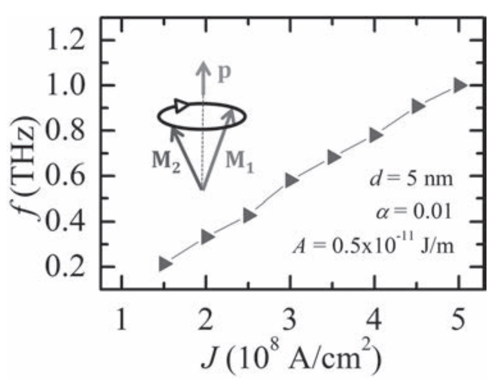

Fig. 2. Oscillation frequency of the AFM sublattices vs. current for a particular set of parameters. Inset: sketch of the precession of the two AFM sublattices around the direction of the spin-Hall polarization.

3:30

DE-07. Terahertz-frequency AC signal source based on antiferromagnetic tunnel junction.

O. Sulymenko[1], *O. Prokopenko*[1], A.N. Slavin[2] and V.S. Tiberkevich[2]
1. Faculty of Radio Physics, Electronics and Computer Systems, Taras Shevchenko National University of Kyiv, Kiev, Ukraine; 2. Department of Physics, Oakland University, Rochester, MI, United States

Spintronic nano-oscillators [1, 2] are now considered as promising nano-scale AC signal sources for the future energy-efficient electronics. However, nowadays such sources mainly utilize ferromagnetic materials (FM), and, therefore, their operation frequencies are limited to the interval of 1–50 GHz [1, 2], which is not sufficiently high for many practical applications. To substantially increase the frequency of the spintronic AC signal sources one could use antiferromagnets (AFMs), where characteristic operation frequencies, typically, lie in the terahertz range (0.1–10 THz) [3-5]. The theoretically proposed AFM-based nano-oscillators can operate in the absence of a bias dc magnetic field, and can be driven by a dc electric current [6-8]. However, the problem of a practical development of AFM-based AC signal generators, and, in particular, the problem of a power extraction from such AFM generators, has not been solved yet. In [7] an AFM-based spin Hall oscillator (SHO), where the power of the generated AC signal is extracted through the inverse spin-Hall effect (ISHE), has been proposed. The other power extraction mechanism, based on the reception of the magneto-dipolar radiation from a current-driven canted AFM attached to the high-Q resonator has been analyzed in [8]. Both these methods of the THz-frequency signal extraction have some disadvantages: for an SHO utilizing ISHE the AFM material must be bi-anisotopic with a weak perpendicular anisotropy [7], while in the case of a canted AFM embedded in a resonator, the device has a large size (~ 10 μm) defined by the wavelength of the generated signal [8]. In this paper we consider an alternative mechanism of the THz-frequency signal extraction from an AFM-based SHO, where the signal power is collected through the AC variation of the tunneling anisotropic magnetoresistance (TAMR) in an AFM tunnel junction (ATJ), the electrical switching of which has been experimentally observed in the recent works [9, 10]. We consider an AFM SHO based on an IrMn/Pt bilayer structure, where the driving dc current I_{drive} flowing in the Pt layer forces a flow of a spin current I_{SH} into the AFM layer. This spin current excites the rotation of magnetizations of the IrMn AFM sublattices through the spin-Hall effect (SHE) [5], which gives rise to the AC variations of the TAMR [10]. Thus the junction resistance changes in time as $R(t) = R_0 + \Delta R \sin(\omega t)$ (Fig. 1). At the same time, the simultaneously supplied bias dc current I_{dc}, traversing the junction cross-section, results in the generation of the AC voltage of the magnitude $U_{ac} = I_{dc}\Delta R$ across the whole structure. Thus, when such a dc biased ATJ is connected through a bias tee to a load, having the resistance of $R_L = 50\ \Omega$, the AC voltage generated in the ATJ excites an AC current in the load, allows one to extract an AC power P_L of the excited signal from the load. Our theoretical model of the proposed AC source based on an ATJ is very simple. We consider an ATJ as a circuit consisting of an AC voltage source (generating AC voltage of the magnitude U_{ac}) with the internal resistance R_0 shunted by a capacitor of the capacitance C. This equivalent circuit is connected through an ideal bias tee to a resistive load of the resistance R_L. Using Kirchhoff's laws, we found the following expressions for the powers: $P_{dc} = I_{dc}^2 R_0$ is the dc power injected in the ATJ, $P_L = (R_L U_{ac}^2)/[2(R_L + R_0)^2 + R_L^2\beta^2)]$ is the power emitted in the load, where $\beta = \omega R_0 C$. Then, the efficiency of the AC power extraction can be estimated as $\zeta = P_L/P_{dc}$. The frequency dependences of the P_L and ζ, calculated for a junction having experimental parameters (resistance-area product, tunnel magneto-resistance ratio, etc.) taken from [10], are shown in Fig. 2. They demonstrate that both these characteristics are decreasing with the increase of the generated frequency. The calculations also demonstrated, that the output power P_L, injected into the load in the frequency range 0.1 – 1 THz, is comparable to, or may even exceed, the power extracted via ISHE and magneto-dipole emission mechanism, while the efficiency of the power extraction mechanism via AC TAMR variations is about 1%, which may be sufficient for some practical applications. Also, it should be noted, that a substantial advantage of the proposed AFM-based AC signal source with signal extraction through TAMR lies in the simplicity and reliability of its experimental realization at micro- and nano-scale. In conclusion, we proposed a method of the AC signal extraction from an ATJ-based SHO based on TAMR, which can be easily experimentally realized at micro- and nano-scale, and can provide an output AC power of the order of $P_L \sim 10\ \mu W$ and an efficiency of about 1%.

[1] S.I. Kiselev et al., Nature 425, 380 (2003). [2] V.E. Demidov et al., Nat. Mater. 11, 1028 (2012). [3] H.V. Gomonay and V.M. Loktev, Phys. Rev. B 81, 144427 (2010). [4] E.V. Gomonay and V.M. Loktev, Low Temp. Phys. 40, 17 (2014). [5] J. Sinova et al., Rev. Mod. Phys. 87, 1213 (2015). [6] R. Cheng, D. Xiao, A. Brataas, Phys. Rev. Lett. 116, 207603 (2016). [7] R. Khymyn et al., Sci. Rep. 7, 43705 (2017). [8] O. Sulymenko et al., Phys. Rev. Applied 8, 064007 (2017). [9] P. Wadley et al., Science 351, 587 (2016). [10] B.G. Park et al., Nat. Mater. 10, 347 (2011).

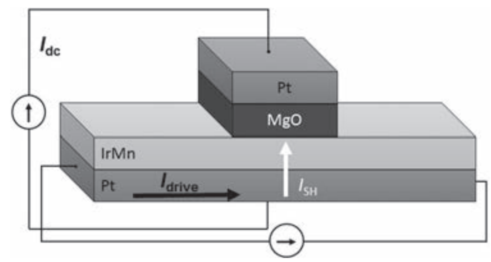

Fig. 1. AFM SHO structure with signal extraction using TAMR.

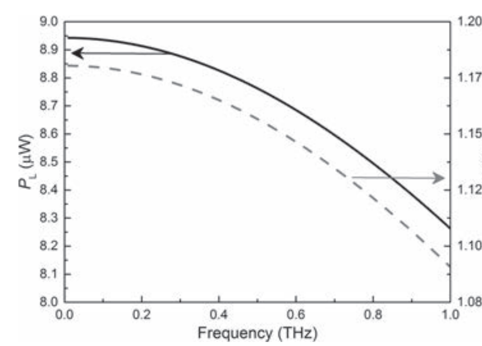

Fig. 2. Output power emitted in the load (solid curve) and power conversion efficiency (dashed curve) of the proposed THz-frequency AFM generator with TAMR as functions of the generated signal frequency.

3:45

DE-08. Injection-locking of a nonlinear sub-THz antiferromagnetic spin-Hall oscillator.

R. Khymyn[1], V.S. Tiberkevich[2], A.N. Slavin[2] and J. Åkerman[1,3]
1. Department of Physics, University of Gothenburg, Gothenburg, Sweden; 2. Department of Physics, Oakland University, Rochester, MI, United States; 3. Department of Applied Physics, KTH Royal Institute Technology, Stockholm, Sweden

We demonstrate theoretically that a spin-Hall oscillator (SHO) based on a thin layer of an antiferromagnetic (AFM) material can be effectively phase-locked to a driving ac electrical signal at both the fundamental frequency, and the frequencies of higher harmonics. The latter phenomenon is a direct consequence of the strongly nonlinear dynamics of the AFM SHO. The nano-oscillators based on the spin transfer torque (STNO) and spin-Hall (SHO) effects are of a considerable interest for modern spintronics as tunable generators of microwave signals. For practical applications, a critically important property is the ability of oscillators to synchronize to the external driving signal and with each other. The STNOs and SHOs have hitherto been based on ferromagnetic materials, and their generation and synchronization properties, are relatively well-known. Recently, however, it was proposed to use AFM materials as active layers of SHOs, because the strong internal exchange field in AFMs allows one to achieve generation frequencies belonging to the THz range [1-4]. In an AFM-based SHO, the spin current created by the spin-Hall effect (SHE) in adjacent current-driven heavy metal layer induces a torque on the Neel vector l of the AFM. If the spin polarization of the current p is *perpendicular* to the equilibrium orientation of the Neel vector l_0, the Neel vector starts to rotate in the plane perpendicular to p [1,3]. The extraction of the ac signal caused by this rotation using the inverse SHE (ISHE) is, however, nontrivial, because it requires that the rotation of the Neel vector is non-uniform in time. Several approaches were proposed to solve this problem [2-4], for instance, it was shown in Ref. [3], that the non-uniform rotation of the Neel vector could be achieved in AFM materials with bi-axial type of anisotropy (e.g., NiO). The generation of the ac signal starts when the spin transfer torque caused by the SHE overcomes the energy barrier caused by the anisotropy-induced potential. This competition determines the critical (threshold) value of the electric current density j_{th} in the adjacent layer of a heavy metal [3]. At low values of the supercriticality $\xi = j_{dc} - j_{th}$ the AFM dynamics is strongly *nonlinear*, which is reflected in the nonlinear dependence of the generation frequency $f(j_{dc})$ on the applied current j_{dc} (see dashed line on Fig. 1). This makes our AFM SHO a fundamentally nonlinear oscillator. The injection-locking of an AFM SHO to an external ac signal in the *linear* region of $f(j_{dc})$ dependence has been studied in Ref. [5] for the case when dc and ac spin currents acting on the AFM layer have orthogonal polarization. In the current work, we are focused on the *nonlinear* dynamics of the oscillator, and we are interested in the case when both dc and ac components of the spin current have the same polarization (i.e., when the ac component of the electrical current with the carrier frequency f_{ac} is directly mixed with the dc current, $j(t) = j_{dc} + j_{ac}\sin(2\pi f_{ac} t)$), which is much easier to realize experimentally. To investigate the synchronization properties of an AFM SHO we solve a set of two coupled Landau-Lifshitz equations for each magnetization sublattice of the AFM with the parameters typical for the nickel oxide. The generation frequency of an SHO driven by the ac with f_{ac}=0.3 THz as a function of j_{dc} is shown on Fig. 1 by a solid line. As one can see from the comparison with the free-running SHO (j_{ac}=0, dashed line in Fig. 1), this dependence exhibits a series of flat plateaus, which correspond to the injection-locking to the external signal. The plateaus are observable when the frequency of the free-running SHO is close to integer divisors of the frequency of the driving signal - f/f_{ac}=1,1/2,1/3... We also observe a narrow synchronization regions for other rational numbers, e.g. 2/3, 4/5. Therefore, the nonlinear AFM SHO can be effectively synchronized not only at the fundamental frequency, but also at the frequencies of higher harmonics. We investigated the maximum detuning frequency of the injection-locked SHO, i.e. the synchronization bandwidth, for the fundamental frequency, and for the second harmonic. The corresponding plots for f_{ac}=0.3 THz are shown in Fig. 2. Both synchronization bandwidths are approximately linear functions of the amplitude of the driving ac signal j_{ac}, and can reach values of several GHz for reasonable current amplitudes j_{ac}. Unexpectedly, it turned out, that the synchronization bandwith for the second harmonic is *higher* than for the fundamental frequency, which can be explained by a strongly nonlinear behavior of the AFM SHO in the region of small generation frequencies f. These results show, that an AFM SHOs operating in the nonlinear regime can be efficiently phase-locked to an external current, and can be used for the detection and frequency conversion of sub-THz external signals.

[1] H. V. Gomonay and V. M. Loktev, Phys. Rev. B 81, 144427 (2010). [2] R. Cheng, D. Xiao, and A. Brataas, Phys.Rev. Lett. 116, 207603 (2016). [3] R. Khymyn, I. Lisenkov, V. Tiberkevich, B. A. Ivanov, and A. Slavin, Sci. Rep. 7, 43705 (2017). [4] O. R. Sulymenko et al., Physical Review Applied 8, 064007 (2017). [5] O. Gomonay, T. Jungwirth and J. Sinova, https://arxiv.org/pdf/1712.02686.pdf (2017)

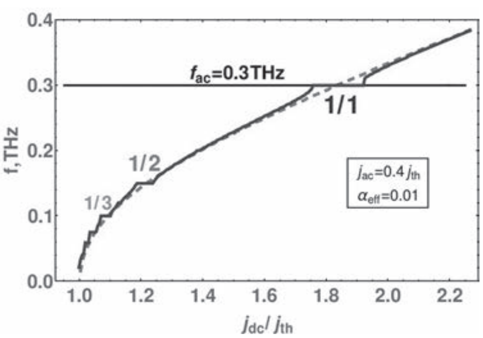

Fig. 1. The calculated generation frequency of an oscillator as a function of applied dc electrical current. The dashed line corresponds to the free running oscillator, while the solid one - to the oscillator with applied ac electric current. The frequency of the external current (f_{ac}=0.3 THz) is shown by the black horizontal line.

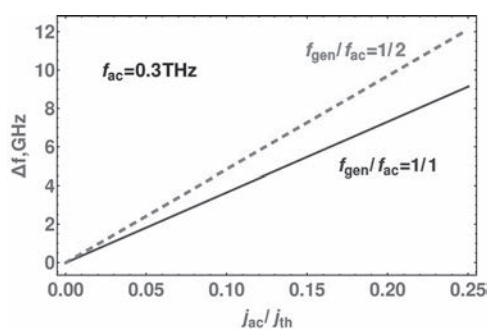

Fig. 2. The dependence of the synchronization bandwidth on the amplitude of the applied ac current. The blue solid line shows the case of phase-locking at the frequency of the external ac, while the red dashed one - at the half frequency of the driving signal.

WEDNESDAY AFTERNOON, 25 APRIL 2018 PEONY I, 2:00 TO 4:00

Session DF
HEAT ASSISTED RECORDING PHYSICS

Kaizhong Gao, Chair
Argonne National Laboratory, North Oaks, MN, United States

INVITED PAPERS

2:00

DF-01. Thermally induced magnetisation switching: basic physics and potential for a new storage technology.

R.F. Evans[1], T. Ostler[3], O. Chubykalo-Fesenko[2] and *R.W. Chantrell*[1]
1. Physics, The University of York, York, United Kingdom; 2. Institute of Materials Science of Madrid (ICMM-CSIC), Madrid, Spain; 3. Faculty of Arts, Computing, Engineering and Sciences, Sheffield Hallam University, Sheffield, United Kingdom

Ultrafast magnetisation processes are generally observed as a response of the magnetisation to a femtosecond laser pulse. This pump-probe technique uses a high power pump pulse to excite the system with a low power (probe) beam split off and used, after a time delay, to measure the magnetic state via MOKE. Since the pioneering demonstration of ultrafast demagnetization in Ni [1], the field has produced a series of remarkable discoveries, including that of magnetization reversal driven by circularly polarized light [2] giving rise to the intriguing concept of all-optical magnetic recording on the picosecond timescale. We have investigated the physics of this phenomenon using an atomistic model as described by Evans et.al. [3]. This approach models the dynamic response at the atomic scale using Langevin Dynamics, with the interatomic exchange based on the Heisenberg form. It was shown [4] that all-optical reversal was achieved due to the elevated temperatures achieved in the pulsed laser process, which accessed the so-called 'linear' reversal mechanism capable of switching on the sub-picosecond timescale. Linear reversal is a high-temperature phenomenon where reversal proceeds via magnetisation collapse to a highly non-uniform state and is not accessible to conventional micromagnetic models. Linear reversal is important in the ultrafast processes because it accesses the longitudinal relaxation time of a few hundred fs around 2 orders of magnitude faster than conventional precessional switching. We will firstly outline the physics of these processes, leading to the discovery of Thermally Induced Magnetisation Switching (TIMS) [5] in ferrimagnets, in which magnetization switching occurs in the absence of an externally applied field. This effect is shown to arise from the excitation of a 2-magnon bound state, which is responsible for the transfer of angular momentum between sublattices. This gives rise to a transient ferromagnetic-like state which drives magnetization reversal. The basic requirements for TIMS are antiferromagnetically coupled sublattices or layers, with differential relaxation times. Formation of the transient ferromagnetic-like state and the subsequent thermally induced switching can be interpreted as arising from a large effective field due to the strong inter-sublattice exchange. In terms of recording technology this field has considerable significance since it has been shown [6] that basic thermodynamic considerations lead to the requirement of fields larger than those accessible to conventional inductive switching in order to avoid errors due to thermally induced back switching. The implications of TIMS for future magnetic storage devices is considerable, in terms of the reduction in complexity of write transducers, increased data rate and power reduction. Until recently, such magnetisation switching could only be triggered by ultrafast laser pulses. Arguably, a recent paper [7] has brought the technology closer by demonstrating TIMS using ultrafast (non-polarised) current pulses, potentially accessible to CMOS technology. The results suggest that relatively slow current pulses are required, which will be discussed in terms of the atomistic model approach. We will finally consider potential recording densities and the materials required for their realisation.

[1] Beaurepaire et.al., *Phys. Rev. Lett.,* 76 (1996) 4250–4253. [2] C.D Stanicu et.al., *Phys. Rev. Lett.,* 99 (2007) 217204. [3] RFL Evans et al., J. Phys.: Condens. Matter, 26, 103202 (2014) [4] K Vahaplar et al Phys. Rev. Lett., 103, 117201 (2009)[5] T Ostler et.al, *Nat. Commun*., 3 (2012) 666 doi: 10.1038/ncomms1666. [6] RF Evans et. al., *Appl. Phys Lett*., 100 (2012) 102402. [7] Yang Yang et.al., https://arxiv.org/abs/1609.06392.

2:30

DF-02. Micromagnetics at Finite Temperature.

D. Wei[1]
1. School of Materials Science and Engineering, Tsinghua University, Beijing, China

Micromagnetics include two main parts: "magnetization curve theory" and "domain theory" [1]. In 1935, the Landau-Lifshitz equations were brought up to analyze the domain wall motion [2]. Since the early works by Brown Jr. in 1960s, micromagnetics had considerable progress in 1980s, including the utilization of the Landau-Lifshitz-Gilbert (LLG) equations to calculate the thin film's magnetization curve [3], and the establishment of the Finite-Difference-Method Fast-Fourier-Transform (FDM-FFT) micromagnetics to highly speed up the computation of the most time consuming magnetostatic interactions among total number N micromagnetic cells [4]. Recent developments of computational magnetism require the ability to calculate the magnetics at finite temperature [5], to calculate domains at large scales, i.e. three-dimensional micromagnetics at finite temperature are the target for the development of computational magnetics. In 2016, the author and collaborators developed a new micromagnetic method based on the Hybrid Monte Carlo (HMC) algorithm, which can calculate M-H loops and domains at finite temperature below Curie point [6], after two years' testing in explaining experiments, and in the characteristics of computational costs, it is found that the simulations using the HMC micromagnetics method can explain M-H loops and domains from 0K to the Curie temperature, even with superparamagnetic properties calculated. It costs roughly $O(N)$ computational time with a faster convergence time than the conventional Landau-Lifshitz equations. The Hybrid Monte Carlo method is a numerical simulation method used extensively in lattice field theory community which is capable of generating a Boltzmann-like distribution of the form $e^{-S[\Phi]}$, where Φ denotes the collection of all degrees of freedom of the system and $S[\Phi]$ is known as the Euclidean action (energy) of the system. The way to perform this simulation is to mimic what Nature does for the molecules in the air. For our purpose, the field variables Φ are just all magnetization vectors $\{M_i\}$ for various micromagnetic cells and the action $S[\Phi]$ is replaced by $F[\{M_i\}]$--the Landau magnetic free energy divided by k_BT. In the micromagnetic simulation, the ferromagnetic material is discretized into a regular mesh, similar as the FDM-FFT method. The Hamiltonian for the HMC algorithm is given by Eq. (2) in Ref. [6], where V_c is the volume of a micromagnetic cell, M_i is the magnetization vector in the ith cell and Π_i is the corresponding conjugate momentum, two of which forming a conjugate pair similar to that of coordinate and momentum in mechanics. The equation of motion for the system is Hamilton equations Eq. (3) in Ref. [6] for the magnetization vector M_i and the corresponding conjugate momentum Π_i. The whole simulation time is divided into trajectories. In each trajectory, this set of Hamilton equations will be utilized to generate the configurations of $\{M_i\}$ versus Monte Carlo time τ according to Eq. (2); at the end of the trajectory, a Monte-Carlo judgment is performed (if the total energy is lower than that at the beginning of the trajectory, the new configuration is accepted, if the total energy is higher than that at the beginning of the trajectory, the new configuration is accepted with a probability $e^{-\Delta E/kT}$), finally at a certain temperature T the equilibrated distribution $e^{-F[\{Mi\}]/kT}$ can be achieved. The expression for the effective field H^i_{eff}, as we will see below, is quite similar to the effective field in traditional micromagnetic models using LL equations, except for terms related to the newly added constraint potential to confine the magnitude of M_i near a sphere $|M_i|$=Ms(T). The magnetic free energy is Eq. (4)-(9) in Ref. [6], where the anisotropy energy and the constraint potential form a double-well potential that usually appears in the Landau's second-order phase transition theory, with $\{M_i\}$ as the order parameter. For a $(40nm)^3$ magnetic cube with 8*8*8 micromagnetic cells, the simulation result is unchanged at a chosen K for λ=bK in the shaded area, as seen in Fig.1. HMC micromagnetic method can also be utilized to study non-equilibrium problems such as time-dependent coercivity. If we compare the simulated $M_i(t)$ versus the Sharrock's law, we can determine that a trajectory ($\tau=10^{-3}$) in the HMC algorithm roughly equals to t=1 ns in the real time scale [7]. We cooperate with NIMS Japan [8] to study the M-H loops of FePt-C media at different temperature. It is found that the power η for $K(T)/K(0)=[Ms(T)/Ms(0)]^{\eta}$ has correlation to the alloys, in FePt-C media η is around 2.5, the calculated magnetization loops at temperatures 300K, 400K, 500K, 600K agree well with the experimental results; at 700K, no experimental M-H loops are measured because the magnetic signal is so weak comparing with the noise, but using HMC micromagnetics, the superparamagnetic properties can be simulated. This confirms the validity of the HMC micromagnetic method in the polycrystalline thin film.

[1] Brown Jr. W. F., "Micromagnetics". Wiley, New York, London (1963). [2] Landau L. and Lifshitz E, "On the theory of the dispersion of magnetic permeability in ferromagnetic bodies", Phys. Zeitsch. Der Sow., 8, 153 (1935), reprinted in English by Ukr. J. Phys. 53, 14 (2008). [3] Victora, R. H. "Micromagnetic predictions for magnetization reversal in CoNi films", J. Appl. Phys. 62, 4220-4225, 1987. [4] Bertram, H. N., Zhu, J. G. "Micromagnetic studies of thin metallic films", J. Appl. Phys. 63, 3248-3253, 1988. [5] N. Kazantseva, D. Hinzke, U. Nowak, R. W. Chantrell, U. Atxitia, and O. Chubykalo-Fesenko, Phys. Rev. B 77, 184428 (2008). [6] Wei D, Song Junjie, Liu C. Micromagnetics at Finite Temperature. IEEE Transactions on Magnetics, 52(11): 1-8, (2016). [7] Jingyue Miao, Dan Wei, and Chuan Liu, "Micromagnetic studies of Time-Dependent Coercivity", IEEE Transactions on Magnetics, VOL.53, NO.11, 8204404, (2017). [8] Song Junjie, J. Wang, Dan Wei, Y. K. Takahashi, and K. Hono, "Micromagnetic studies at finite temperature on FePt-C granular films",IEEE Transactions on Magnetics, VOL.53, NO.11, 7100504, (2017).

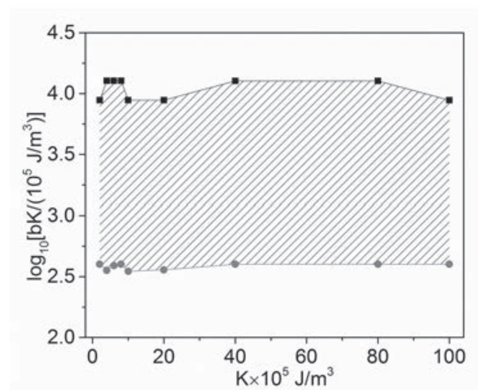

Fig. 1. In a (40nm)^3 cube with 8*8*8 cells, at a chosen *K*, the simulated magnetic properties will not change for bK in the shaded area.

3:00

DF-03. Impact of intergrain spin transfer torques due to huge thermal gradients on the performance of heat assisted magnetic recording.

B. Dieny[1], M. Chshiev[1], B. Charles[1], N. Strelkov[1,2], A. Truong[1], O. Fruchart[1], A. Hallal[1], J. Wang[3], Y. Takahashi[3], T. Mizuno[4] and K. Hono[3]
1. SPINTEC, Grenoble Alpes Univ/CEA/CNRS, Grenoble, France; 2. Physics Department, Lomonosov Moscow State University, Moscow, Russian Federation; 3. National Institute for Materials Science, Tsukuba, Japan; 4. Headway Technologies, Milpitas, CA, United States

Heat assisted magnetic recording (HAMR) is a new technology which uses temporary near field laser heating of the media during write to increase hard disk drive storage density. By using plasmonic antenna embedded in the write head, an extremely high thermal gradient is created in the recording media (up to 10K/nm). State of the art HAMR media consists of grains of $L1_0$-FePt exhibiting high perpendicular anisotropy separated by 1 to 2 nm thick carbon segregant. Next to the plasmonic antenna, the difference of temperature between two nanosized FePt grains in the media can reach 80K across the 2 nm thick grain boundary. This represents a gigantic local thermal gradient of 40K/nm across a carbon tunnel barrier. In the field of spincaloritronics, much weaker thermal gradient of ~1K/nm was shown to cause a thermal spin-transfer torque capable of inducing magnetization switching in a magnetic tunnel junction. Considering on one hand that two neighboring grains separated by an insulating grain boundary in a HAMR medium can be viewed as a magnetic tunnel junction and on the other hand that the thermal gradients in HAMR are one to two orders of magnitude larger than those used in conventional spincaloritronics, one may expect a strong impact from these thermal spin-transfer torques on magnetization switching dynamics in HAMR recording. This issue has been overlooked in the previous investigations on the development of HAMR technology. This study combines theory, experiments aiming at determining the polarization of tunneling electrons across the media grain boundaries and micromagnetic simulations of recording process taking into account these thermal gradients. It is shown that the thermal in-plane torque can have a detrimental impact on the recording performances by favoring antiparallel magnetic alignment between neighboring grains during the media cooling. Implications on media design are discussed in order to overcome the influence of these thermal torques. Suggestions of spincaloritronics experiments taking advantage of these huge thermal gradients produced by plasmonic antenna will also be given.

B.Dieny, M.Chshiev, B.Charles, N.Strelkov, A.Truong, O.Fruchart, A.Hallal, J.Wang, Y.K.Takahashi, T.Mizuno, K.Hono, arXiv:1712.03302

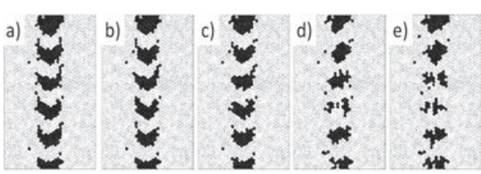

Fig. 1. Simulated images (300nm x 440nm) of tracks of alternating 0 and 1 bits assuming various amplitudes of the thermal spin transfer torques (TST) ranging from 0 to100% of the calculated torques expected for FePtC media. a) No TST; b) 25% TST c) $T_{//}$ = 50% calculated TST ; d) 75% TST ; e) 100% TST

CONTRIBUTED PAPERS

3:30

DF-04. Effect of Recording Conditions on the Downtrack Thermal Gradient in Heat Assisted Magnetic Recording.

S. Hernandez[1], Z. Liu[1], S.D. Granz[1], P. Huang[2], I. Gilbert[1], D. Mader[1], M. Blaber[3], C.J. Rea[3], G. Ju[2], T. Rausch[1] and E. Gage[1]
1. Seagate Research Group, Seagate Technology, Shakopee, MN, United States; 2. Recording Media Operations, Seagate Technology, Fremont, CA, United States; 3. Recording Head Operations, Seagate Technology, Bloomington, MN, United States

Written-in transition jitter is the dominant source of media noise in Heat Assisted Magnetic Recording (HAMR) systems. The down-track thermal gradient observed in the media is believed to be one of the key contributors to transition quality. In general, this gradient is defined as the change in temperature in the downtrack direction in the vicinity of the write position. This write position, and consequently the thermal gradient, is determined by media properties such as anisotropy field and Curie temperature, as well as the magnitude of the applied magnetic field from the head. The thermal gradient also depends on the near field transducer (NFT): its geometry, its material properties, and its interaction with the media and heat sink. Recently, a reliable estimation of the down-track thermal gradient has been obtained via the laser current modulation [1],[2],[3] method. In this method, the laser current is modulated during the recording of a single tone pattern. By changing the laser power, the size of the thermal spot changes thereby changing the location of the transition. This minor shift in position is related to the change of temperature near the transition, namely the thermal gradient. By measuring the shift in transition position and knowing the amplitude of the laser power modulation, the thermal gradient can be calculated. This study elucidates the effect of recording conditions, such as relative head to media velocity, on this measurement by comparing single tone patterns captured from a drive and a spin-stand to micromagnetically modeled patterns. Dynamic recording system models have had much success in predicting phenomena observed at spin-stand and drive [4] via common performance metrics such as transition and remanence SNR. However, this is the first effort to use a laser current modulation method in a micromagnetic model in order to directly compare to thermal gradient measured experimentally. Figure 1 compares measured and modeled downtrack thermal gradient as a function of relative head to media velocity under different laser power and writer current conditions. At spin-stand, the thermal gradient is characterized using the side band ratio (SBR) method described in reference [1]. A single tone pattern is recorded with laser power modulation. This modulation produces a phase modulation of the signal, resulting in sidebands in the signal frequency spectrum. The transition displacement, and by association the thermal gradient, can be calculated from the amplitude of these sidebands. Measurements are captured at zero skew, a radius of 23 mm and an active clearance of 1 nm. Simulated data is obtained using a micromagnetic model that employs the renormalized Landau Liftshitz Gilbert equation [5] to represent high temperature magnetization dynamics. The media and magnetic writer/NFT configurations used are consistent with the designs used in the experiment. The peak spot temperature in the model is chosen such that the track widths obtained are similar to those measured. In the model, like in the measurement, a single tone pattern is recorded with modulated peak laser temperature. The change in phase of the signal due to this modulation is extracted using a Hilbert transform. The shift in the transition is calculated from phase jump at the location of the laser temperature step .This shift was then used to calculate the thermal gradient. In the data set shown in figure 1(a), the laser power is kept constant at each head velocity and writer current condition. This means that the track width, and therefore the signal, will change with changing velocity. As the velocity increases there is less time for grains to switch, meaning that writing occurs at a higher temperature than when the velocity is low. The thermal gradient decreases near the peak temperature of the hot spot, accounting for the decrease observed in both the spin-stand and the model. Figure 1(b) shows measurement and modeling results where the track width is kept constant at each head velocity and writer current condition by varying the laser power. As velocity increases, the maximum thermal spot temperature must be increased to compensate for the decreased time grains experience the effect of the heat spot. Since the write temperature increases with velocity to maintain the track width, and the maximum thermal spot temperature increases at each velocity condition, the effective thermal gradient at the write point tends to remain constant. The spin-stand data also shows increasing thermal gradient with increasing write current. This is a reasonable observation, given that increasing the write current produces an increasing applied magnetic field, as long as the write pole is far away from saturation. This in turn results in a lower write temperature and a higher thermal gradient, since the gradient is higher further away from the peak temperature. Given that the model accurately describes the effects of recording conditions such as laser power, writer fields and head to media velocities on thermal gradient, the effect of skew and thermal spot properties can be explored in depth.

[1] Saunders et. Al, “Thermal Gradient Measurments and Analysis”, IEEE Trans Mag. 2017 [2]J. Hohlfeld, X. Zheng, and M. Benakli, “Measuring temperature and field profiles in heat assisted magnetic recording,” J. Appl. Phys., vol. 118, no. 6, p. 064501, 2015. [3] H. J. Richter et al., “Direct measurement of the thermal gradient in heat assisted magnetic recording,” IEEE Trans. Magn., vol. 49, no. 10, pp. 5378–5381, Oct. 2013 [4] Hernandez et. Al, “Using Ensemble Waveform Analysis to Compare Heat Assisted Magnetic Recording Characteristics of Modeled and Measured Signals”, IEEE Trans Mag. 2017 [5] R.H. Victora, P. Huang, “Simulation of Heat Assisted Magnetic Recording Using Renormalized Media Cells”, IEEE Trans Magn. 49, 751-757 (2013)

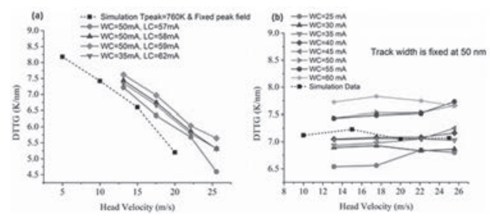

Fig. 1. Downtrack thermal gradient as a function of relative head to media velocity for (a) constant laser power at each head velocity (varying track width) and (b) constant track width at each head velocity (varying laser power). The solid lines show spin-stand data at different writer current (WC) and laser current (LC) conditions, while the dashed lines show data obtained through micromagnetic simulation.

3:45

DF-05. Understanding of Different Noises in HAMR.

Y. Jiao[1] and R.H. Victora[1]
1. Electrical and Computer Engineering, University of Minnesota, Minneapolis, MN, United States

I. INTRODUCTION AND METHODS As Perpendicular Magnetic Recording (PMR) technology reaches its areal density limit, the commercial introduction of Heat-Assisted Magnetic Recording (HAMR) [1], considered to be the most promising candidate to push areal density forward to 4 Tb/in^2, becomes more imminent. However, as the areal density increases, concerns about noise become more important. In Seagate's recent presentation [2], remanence noise appears to be a very important factor for HAMR's jitter, unlike the case of PMR. In this work, we try to understand the different contributions to noise in HAMR, especially the remanence noise and transition noise. Then we discuss how they will affect the performance of HAMR. II. NOISE DEFINATION AND CALCULATION Separation of the different types of noise from the playback signal can be a difficult and arbitrary task. When bit length is large and uniform (tone), a simple division based on distance to the transition can suffice. Seagate has introduced a technique [3] that splits the noise into transition and remanence components for a more realistic bit length and pseudo-random bit sequence. It is based on the general understanding that transition noise always exists around the transition region, while remanence noise exists all over the media and should be independent of the patterns recorded on the media. However, when bit length is small, it is a challenge to apply this method because it is difficult to unambiguously define a transition region so as to get an appropriate window function. Instead, we propose principle components analysis (PCA) [4], which is a statistical method based on signal variances, with these two assumptions: 1. δSignal > δNoise_rem > δNoise_trans. δSignal means the standard deviation of original signals without any noise; δNoise_rem means the standard deviation of remanence noise and δNoise_trans means standard deviation of transition noise. It is obvious that signals have the largest fluctuations, so the first components in the new coordinate system should describe signals, and then comes the remanence noise, and finally transition noise. This is because the standard deviation of transition noise is non-zero only near the transition region. 2. All three parts in the playback signals should comply with linear superposition, which means that they can be added directly together. Here, we show simulated [5] data for eight repetitions of the recorded signal on different media samples for a minimum bit length of 25.5 nm with 20-m/s head-moving velocity and 5.5-nm grain pitch. We use Singular Value Decomposition (SVD) to determine eight principal components of the playback signals. The sorted eigenvalues are shown in Figure 1. It is found that the first eigenvalue is much larger than the other seven after doing PCA, which means the signals have the largest variance in playback signals. Then we choose the first R principal components (columns) of the left singular matrix to reconstruct signals. Figure 2 shows the reproduced signals after we did PCA with different values of R. In Figure 2(a), we show only signal components with little noise when R = 1. When R = 4 (Figure 2(b)), we can see larger fluctuations among the reproduced signals, especially in the vicinity of peaks and valleys. These fluctuations are considered to be remanence noise. When R = 8 (Figure 2(c)), all eight components were counted to reproduce playback signals and these signals are exactly the same as our original playback signals.

[1] Kryder M H, et al. Proceedings of the IEEE, 2008, 96(11): 1810-1835. [2] Hohlfeld J, Benakli M et al. TMRC 2017, D1. [3] Hernández S, Lu P L, Granz S, et al. IEEE Transactions on Magnetics, 2017, 53(2): 1-6. [4] Wall M E, Rechtsteiner A, Rocha L M. Springer US, 2003: 91-109. [5] Victora R H, Huang, P W. IEEE Transactions on Magnetics, 2013, 49(2), 751-757.

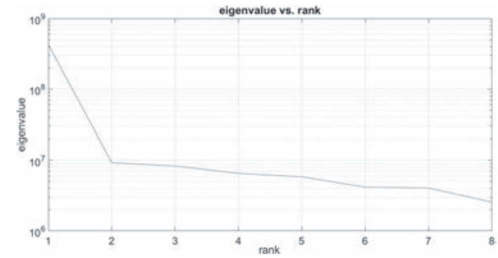

Fig. 1. Sorted eigenvalues from the largest to the smallest

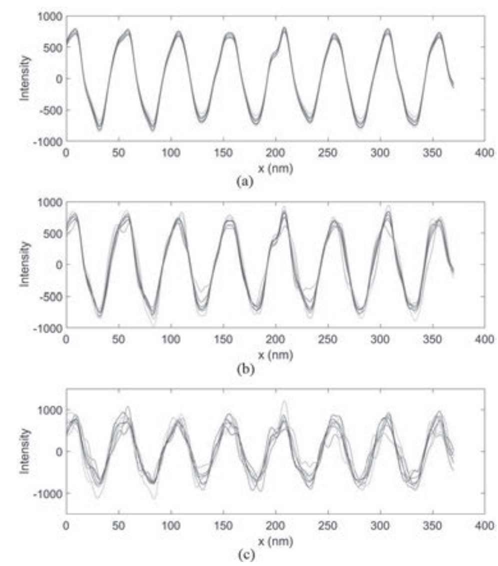

Fig. 2. Reconstructed playback signals by using the first R principle components in the left singular matrix. (a) R = 1; (b) R = 4; (c) R = 8

WEDNESDAY AFTERNOON, 25 APRIL 2018 PEONY III, 2:00 TO 4:00

Session DG
ENERGY HARVESTERS AND GENERATORS I

Christopher H. T. Lee, Chair
Massachusetts Institute of Technology, Cambridge, MA, United States

CONTRIBUTED PAPERS

2:00

DG-01. Design and analysis of an integrated electromagnetic energy harvester from water flow.

T. Wang[1], Y. Zhang[1] and S. Zhu[1]
1. Zhejiang University, Zhoushan, China

1. Introduction Energy harvesting is an attractive technique for a wide variety of wireless network sensors and nodes, which have strong demand for being battery free. Hydrokinetic energy is a remarkable energy source which comes in two forms, vertical in waves and horizontal in currents and tides. This work focuses on harvesting the kinetic energy from water flow with relatively low velocity in oceans or rivers for remote sensors and robots. A direct idea is the miniaturization of conventional blade water turbine and electrical generator. However, this energy harvester usually has large volume because the independent turbine and generator are required to be coupled coaxially or by using gearbox. Moreover, the relatively high viscous drag on the blades at low Reynolds numbers may deteriorate the generation performance. In this work, an electromagnetic energy harvester is designed and analyzed by using Tesla disk turbines which have the advantages of easy manufacture, low noise, and no blades. In addition, axial-flux permanent magnet generation technique is applied to make the machine compact. 2. Schematic Figure 1 presents the schematic diagrams of the cylindrical electromagnetic energy harvester on radial and axial cross sections respectively. The turbine rotor mainly consists of a series of disks installed with uniform gaps on a shaft which is supported by a pair of bearings. Permanent magnets with alternative axial magnetization direction are mounted on the end surfaces of the turbine rotor, and coils are fixed in the end caps correspondingly. The permanent magnets and the coils form a miniature axial-flux permanent magnet generator. A ring cover with symmetrical grooves is fixed on the outer of the energy harvester so as to convert water flow with random direction to the direction almost tangential to the disks. The physical process of flow energy harvesting is illustrated as follows. When the electromagnetic energy harvester is located in regions with horizontal water flow, an amount of water will flow into the gaps between disks through the grooves of the ring cover. Then viscous drag force will be generated to drive the turbine rotor as well as the attached permanent magnets to rotate according to Newton viscous law, which results in periodic variation of the flux through the coils. Based on electromagnetic induction theory, electromotive forces will be induced in the coils and current will be generated when the coils are connected with electrical loads. 3. Analytical model In the ironless axial-flux permanent magnet generator, the magnetic field is mainly produced by a series of cubical permanent magnets distributed axial symmetrically. Therefore, the flux density in three-dimensional coordinate can be derived as a function of position based on Coulombian model and rotation transformation. Then the flux through a coil turn can be calculated by integrating the flux density over the corresponding area, and the total flux through the coil can be obtained as a sum of the flux through every turn at the specific location. According to the law of electromagnetic induction, the induced electromotive force can be derived by calculating the derivative of the coil flux with respect to time. Assuming a resistive load is connected, the output voltage and power can also be expressed. 4. Prototype and test A prototype is fabricated by using plastic material and 3D printing technique with precision of 0.1 mm. It has diameter of 6.5 cm, height of 4.6 cm, and approximate weight of 140 g. In the turbine rotor, there are 8 disks with diameter of 5.2 cm and thickness of 0.15 cm, and the adjacent disks are separated by sleeves with thickness of 0.15 cm. The number of rectangular NdFeB permanent magnets on each end surface is 12 and the dimension is 1.0 cm × 0.5 cm × 0.3 cm. The coils are wound by using copper wires with diameter of 0.1 mm, and the turn number per coil is about 200. There are total 8 grooves set in the ring cover. An experimental setup is developed to test the prototype and verify the analytical model. No-load experiments show that the prototype can operate at flow velocity down to 0.61 m/s and induce peak-to-peak electromotive force of 2.64~11.92 V at flow velocity of 0.61~1.87 m/s. Figure 2 presents the comparison between the measured waveform and the analytical waveform of the induced electromotive force at the rotating speed of about 500 rpm. It can be observed that the two waveforms are in good accordance. Loaded experiments show that the output electrical power is 23.1 mW at flow velocity of 1.87 m/s when the load resistance is approximately equal to the coil resistance. 5. Conclusion In conclusion, an integrated electromagnetic energy harvester is designed and analyzed for remote sensors and robots in oceans or rivers. The compact structure is beneficial to integrate with remote wireless electronic devices such as autonomous oceanographic sampling networks. Experimental results validate the effectiveness of the analytical model and the harvesting capability of the energy harvester for water flow with relatively low velocity.

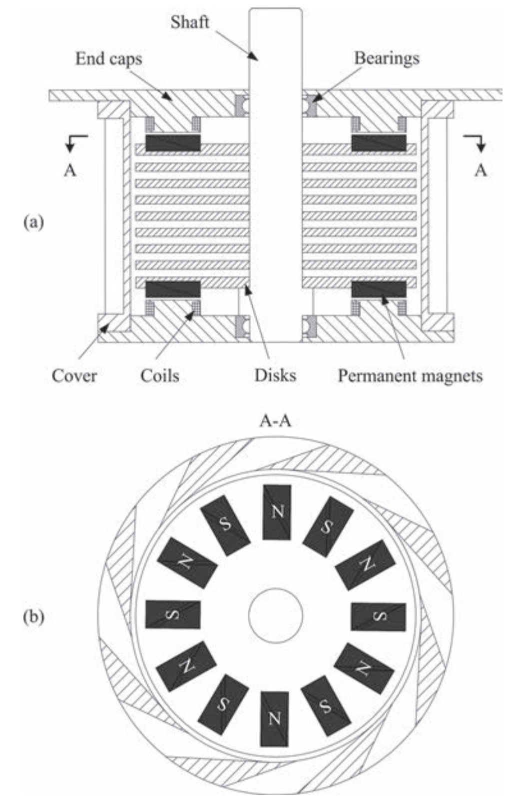

Fig. 1. Schematic diagrams of electromagnetic energy harvester on radial and axial cross sections

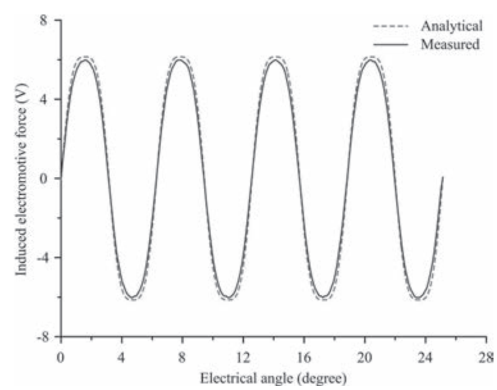

Fig. 2. Measured and analytical waveforms of induced electromotive force at rotating speed of 500 rpm

2:15

DG-02. Investigation of a Novel Dual-PM Partitioned-primary Hybrid-excited Flux-switching Linear Machine.

Z. Zeng[1] and *Q. Lu*[1]
1. College of Electrical Engineering, Zhejiang University, Hangzhou, China

Introduction: Hybrid-excited flux-switching linear machine (HEFSLM) has become a research hotspot due to the merits of high thrust force density, wide operation area, robust secondary, etc. Recently, several topologies have been proposed [1], [2], but all these structures accommodate excitation winding, armature winding and PMs on the primary, which makes the primary crowded. Consequently, both flux-adjusting ratio and thrust force density may be confined. In order to solve the aforementioned contradiction, this paper proposes a novel dual-PM partitioned-primary HEFSLM (PP-HEFSLM) featuring dual-PM and dual-primary structure, thus excitation windings and armature windings are separately amounted in corresponding slot areas [3-5]. Since these two kind slots are increased simultaneously, both thrust force performance and speed-adjusting area can be improved effectively. Topology and Optimization: Fig. 1(a) shows the topology of conventional 6-slot/11-pole (6s/11p) E-core HEFSLM. Fig. 1(b) shows the topology of the proposed 6s/7p dual-PM PP-HEFSLM. Apparently, the former HEFSLM makes the excitation windings, armature windings and PMs located in the single-primary, thus the areas of excitation slots and armature slots are limited. However, to latter HEFSLM, the primary is partitioned into two separated parts with excitation slots aligned to PM I. PM I is sandwiched between two U-shaped steel lamination, while PM II is inset in the excitation teeth. The magnetization direction of PM I and PM II are parallel and perpendicular to moving direction respectively. Moreover, to make armature flux-linkage caused by PM I and PM II have same polarity, the magnetization direction of two adjacent PM II and their middle PM I should be clockwise or anti-clockwise. The operation principle of the proposed HEFSLM is similar to the E-core HEFSLM, that is to say, based on flux-switching mechanism. Along with a secondary-pitch movement, the armature coil flux changes an electrical circle, so brushless AC operation is suitable for the proposed machine. Its feasible slot/pole combinations can be 6s/4p, 6s/5p, 6s/7p and 6s/8p, among which 6s/5p and 6s/7p structures exhibit larger winding coefficient. To E-core counterpart, the corresponding values are 6s/11p and 6s/13p. Therefore, these two HEFSLMs with their own two suitable slot/pole combinations are globally optimized for maximal average thrust force based on genetic algorithm under fixed armature copper loss 30 W, maximal excitation current density 15 A/mm^2, and identical volume for an unbiased comparison. It is found that 6s/7p and 6s/11p are the optimal slot/pole combinations for PP-HEFSLM and E-core HEFSLM, respectively. Comparative Investigation: For the globally optimized 6s/7p PP-HEFSLM and 6s/11p E-core HEFSLM, the electromagnetic performances are comparatively investigated. The PP-HEFSLM exhibits 13.27% larger fundamental back-EMF amplitude and smaller harmonics as shown in Fig. 1(c), and *d*-axis flux-linkage of PP-HEFSLM can be adjusted from 75.38% to 116.66%, while it is only 91.64% to 112.35% for E-core one as shown in Fig.1(d). Apparently, PP-HEFSLM greatly improves both back-EMF waveform and flux-adjusting capability. The thrust force performances and loss curves are shown in Fig.2 (a)-(d). As it can be seen, the PP-HEFSLM exhibits relatively big average thrust force especially at heavy load, while E-core one seems to be more easily saturated. At zero *d*-axis current control method, it also exhibits bigger average thrust force and maximal average thrust force, which indicates its reluctance force can be negligible. In addition, due to double-sided PM structure, its normal force is very low compared with that of E-core structure, which greatly simplifies installment and simultaneously avoids uneven airgap caused by big normal force. Along with the increasing of velocity, the losses of both structures drastically increase due to the increased electrical frequency, but this phenomenon is more evident for E-core structure and the loss is also larger at same velocity because of larger secondary pole number. Conclusion: This paper proposes a novel dual-PM PP-HEFSLM. Its optimal slot/pole combination is investigated, and then the electromagnetic performances are calculated. By comparing with corresponding optimal E-core structure, the results show the proposed machine exhibits better thrust force performance, wider flux-adjusting range, greatly reduced normal force and smaller loss. Detailed descriptions will be given in the full paper.

[1] R. Cao, M. Cheng, C. Mi, W. Hua and W. Zhao, “A hybrid excitation flux-switching permanent magnet linear motor for urban rail transit,” *2011 IEEE Vehicle Power and Propulsion Conference*, Chicago, IL, 2011, pp. 1-5. [2] C. C. Hwang, P. L. Li and C. T. Liu, “Design and Analysis of a Novel Hybrid Excited Linear Flux Switching Permanent Magnet Motor,” in IEEE Transactions on Magnetics, vol. 48, no. 11, pp. 2969-2972, Nov. 2012. [3] Z. Q. Zhu, A. L. Shuraiji and Q. F. Lu, “Comparative Study of Novel Tubular Partitioned Stator Permanent Magnet Machines,” in IEEE Transactions on Magnetics, vol. 52, no. 1, pp. 1-7, Jan. 2016. [4] A. L. Shuraiji, Z. Q. Zhu and Q. F. Lu, “A Novel Partitioned Stator Flux Reversal Permanent Magnet Linear Machine,” in IEEE Transactions on Magnetics, vol. 52, no. 1, pp. 1-6, Jan. 2016. [5] H. Hua, Z. Q. Zhu and H. Zhan, “Novel Consequent-Pole Hybrid Excited Machine With Separated Excitation Stator,” in IEEE Transactions on Industrial Electronics, vol. 63, no. 8, pp. 4718-4728, Aug. 2016.

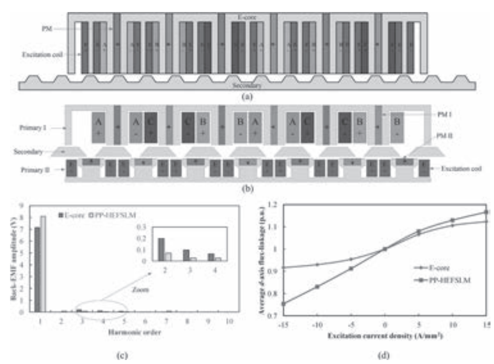

Fig. 1. (a) Topology of E-core structure. (b) Topology of proposed dual-PM PP-HEFSLM. (c) Phase back-EMF spectra under rated velocity and zero excitation current. (d) Flux-adjusting range.

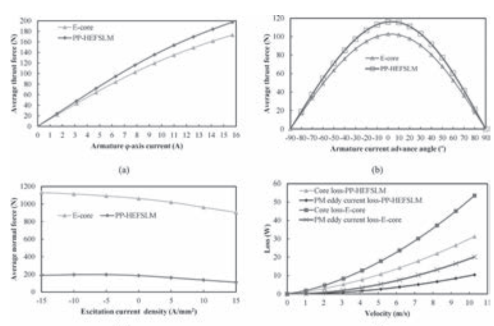

Fig. 2. (a) Average thrust force - *q*-axis current characteristic under zero excitation current. (b) Average thrust force - current advance angle characteristic under rated armature current and zero excitation current. (c) Open-circuit normal force. (d) Losses.

2:30

DG-03. A novel two-degree-of-freedom electromagnetic vibration energy harvester: design, modeling and experiments.

Z. Wang[1], S. Wu[1], T. Yao[2], D. Lv[1] and H. Zhang[1]
1. State Key Laboratory of Reliability and Intelligence of Electrical Equipment, Hebei University of Technology, Tianjin Municipality, China; 2. School of Mechanical Engineering, Hebei University of Technology, Tianjin Municipality, China

1. Introduction With the rapid development of Internet of Things(IoT) technology, a large number of microprocessors, sensors and other small power electronic devices are widely used, inexhaustible vibration energy often exist in the working environment of these electronic devices. If the vibration energy is collected, the power supply problem of these electronic devices can be solved. Green vibration energy harvesting technology can not only greatly reduce the battery consumption, but also help to extend the working time of electronic devices. This technology has received much attention over the past few years. The traditional single-degree-of-freedom vibration energy harvester has low electromechanical conversion efficiency which hinders the engineering application of this technology. A novel vibration energy harvester that has linear motion part and rotary motion part is proposed to improve the electromechanical conversion efficiency. The harvester can be modelled as a two-degree-of-freedom (TDOF) mechanical system containing linear springs and rigid pendulum. The system response can be calculated based on the derived model for a given excitation. The maximum electromechanical conversion can be obtained by parametric resonance analysis. The output electromotive force (EMF) can be calculated by Faraday Law, and the magnetic field is solved by Finite Element Method and the TDOF model. A prototype is fabricated accordingly, and is tested on the vehicle running on the urban road. 2. Mathematical analysis The proposed vibration energy harvester is shown in Figure 1. The device mainly consists of a shell, two springs, two wheels, a pendulum and coils. The wheels move left and right under the vibration excitation applied on the shell, and then the mover swings accordingly. The flux of the coils varies with the relative motion between the coils and the permanent magnets inside the mover. The EMF can be generated in the coils. And part of the vibration energy can be conversed into electrical energy by supplying power to load. The Lagrange theorem is applied to analyze the proposed model with given displacement excitation. If the mass of pendulum is omitted, the system kinetic energy can be expressed by the mass of all parts and the length of the pendulum. Potential energy depends on the stiffness of the spring and the location of the mover. Further more, the system TDOF motion differential equation is deduced. 3. Simulation and Test The vibration energy harvester, contain 4 cylindrical permanent magnets and 8 coils with 300 turns each, are simulated in the follow. In general, our test results show that the vibration frequency focus on about 20Hz on the condition of the vehicle is running on the urban road. Therefore, $X(t)=10\sin(40\pi t)$ mm is set as the vibration excitation. The wheels' displacement x (Figure.2(a)) and the swing angle of pendulum θ (Figure.2(b)) can be calculated. Figure.2(a) shows the maximum x is about 35mm, which is nearly 3.5 times greater than that of the X. That means the proposed harvester can amplify the vibration. Figure.2(b) shows the maximum θ is up to 60 degrees. The output EMF (Figure.2(c)) can be calculated on the basis of θ and magnetic field distribution which analyzed by finite element method. As shown in Figure.2(c), the peak-to-peak value and the effective value of the output EMF are 13.02V and 3.59V, respectively. The average output power is 344.65mW under impedance matching conditions. The prototype is designed and fabricated on the basis of simulation analysis. The coils are made of copper enameled wire coil. And permanent magnets are NdFeB with grade N35. The prototype is tested in the vehicle running on the urban road. This work was supported in part by the National Natural Science Foundation of China under Grant No. 51107030 and 51775166, in part by the Hebei Province Foundation for Recruiting Returned Scholars under Grant No. CL201708

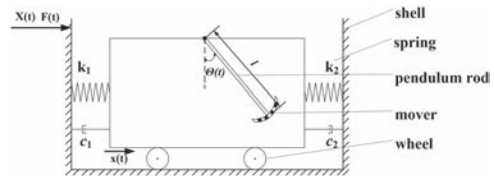

Fig. 1. The structure of vibration energy harvester

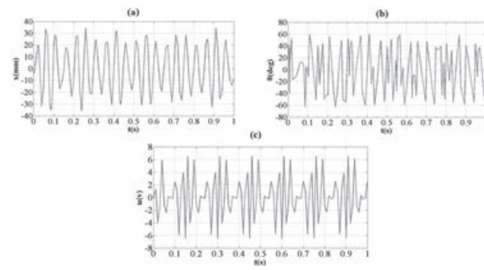

Fig. 2. (a)The wheels' displacement *x* under sinusoidal excitation 2(b) The swing angle θ of pendulum under sinusoidal excitation 2(c)The output EMF under sinusoidal excitation

2:45

DG-04. A planar translational permanent magnet generator for an inertial wave energy converter.

M. Trapanese[1]
1. DEIM, Palermo University, Palermo, Italy

Amongst renewable energy sources, sea wave energy is definitely the less developed. Wave energy converter technology is still at an immature stage. This is probably caused by two reasons: i) the strong technical novelties that are required to extract the energy that is contained in a highly and stochastically variable motion; ii) the difficulty to find a suitable electrical system able to convert the energy contained in the motion of the sea into electrical energy. Several approaches to harvest sea wave energy have been proposed; almost all of them introduce a mechanical conversion device between the waves and the electromagnetic generator. This stage converts the mechanical energy contained in the motion modes of the converter placed on the waves (heave, sway, surge, yaw, pitch and roll) into a more usable mechanical energy; it may be a hydraulic coupling device or a mechanical gear and, in any case, introduces additional losses, weakness in the reliability of the system and additional maintenance requirements. In order to solve these issues a generator directly coupled to the sea waves entirely contained in a vessel has been proposed. These systems are known as Inertial Wave Energy Converter and up to know they have been designed to exploit only one motion mode of the wave converter. The most proposed solutions are linear generators for heave motion in point absorber technology and rotating generator coupled to a fly wheel for rolling motion mode. This paper presents a permanent magnet planar translational generator able to exploit more motion modes of the mechanical converter coupled to the waves. Linear electrical generator has been recently studied for the exploitation of sea wave energy [1-2] but, to our best knowledge, no planar translational generator has been proposed. In this paper in order to maximize the energy extraction all the motion modes of the waves have been considered and included in the mathematical model of the system. The principle of operation of the generator can be summarized as follows: the moving part (translator) of the generator is driven from the sea waves and induces and emf on the winding mounted on the armature. The movement of the translator is two dimensional and therefore all the movement modes of the wave, but heave motion, can be exploited. The mathematical model includes the dynamic equations of the moving part of the generator and the electric equations of the windings. The coupling parameters (inductances, fluxes etc.) have been determined by a FEM analysis (which includes a careful analysis of the boundary conditions, because of the fact that the machine is working in a conductive medium). The design has been optimized by including in the mathematical model used for the optimization the following aspects: 1. the dynamic and stochastic features of the waves; 2. a dynamic model of the mechanical system; 3. a parametric circuit model of the magnetic circuit as well as of the electric windings; 4. A circuit model of the power electronics converter used to connect the generator to the utility. The main innovation of the optimisation approach proposed is that the speed of the machine is neither supposed known nor supposed fixed, but the stochastic features of the imposed movement are the factors that mostly influence the optimisation process. The optimization has been performed by finding the maximum of an objective function that has been built on the basis of the mathematical model developed. The variables of the function were related to the magnetic circuit of the converter, the parameters to the stochastic features of the waves as well as to the characteristics of the hydraulic system and of the power electronics converter. The results show several maxima that indicate several possible alternative designs. In order to verify the results, a reconfigurable machine has been built and tested in laboratory. The tests have verified the value of the emf, of the magnetic induction as well as of the power production in several configuration of the machine. In a scaled down version of the machine, it has been possible to generate almost 10 watt and to reach an output voltage of 25 V peak to peak. These values were in agreement with the design values within an error of 15%.

[1] Leijon, M.; Bernhoff, H.; Agren, O.; Isberg, J.; Sundberg, J.; Berg, M.; Karlsson, K.E.; Wolfbrandt, A. “Multiphysics simulation of wave energy to electric energy conversion by permanent magnet linear generator”, IEEE Transactions on energy conversion vol. 20, N.1, pp. 219- 224, 2005. [2] Polinder H., Gardner F. and Vrisema V., “Linear PM generator for wave energy conversion in the AWS”, in Proc. ICEM 2000, Espoo, Finland, 2000.

3:00

DG-05. Ultra small and thin energy-harvesting device based on electromagnetic induction.

K. Morii[1] and S. Koganezawa[2]
1. Kansai University Graduate School, Suita-shi, Japan; 2. Kansai University, Suita-shi, Japan

1. Introduction Energy harvesting devices (EHDs), which generate a small amount of electric power from energy sources in the environment, are expected to be power sources for Internet-of-Things (IoT) devices or wearable electronic devices to realize a high-grade sensor-network society. Many EHDs suitable for various applications have been reported so far and are being developed. In this study, we propose a novel EHD with an extremely small and thin structure. A potential application of the proposed EHD is its installation in the soles of shoes to generate electric power by the repeated loading and unloading of weight during walking to drive health-monitoring sensors. Such an application requires the EHD to be small and lightweight. We applied electromagnetic induction to the proposed EHD, although electromagnetic-induction based devices are generally considered difficult to be miniaturized. To our knowledge, the smallest electromagnetic EHD for application to shoes has a volume of 8.8 cm^3 and thickness of 16 mm [1]; these dimensions are too large to allow embedding in a shoe sole. However, electromagnetic induction generates much lower voltage than power generators based on piezoelectric transducers and electrostatic induction, which are often used for small structures. Therefore, an electromagnetic generator can easily be used with an integrated circuit and electronic components, which are small but need to take into account electro-static discharge susceptibility. Based on this idea, we have developed a small electromagnetic generator with sufficient power generation capacity. 2. Design We set the target EHD design to a 4-cm^2 footprint and 7.5-mm thickness; these dimensions render the device extremely small and thin compared to those in previous studies [1]–[3]. Because recent low-power wireless sensors can be driven with 100-μW power, we set the target power generation amount to >100 μW. The prototype of the designed EHD is shown in Figure 1. Figure 2 illustrates the design with some parts transparentized for a better understanding of the structure. The device consists of a base, covers, eight coils with iron cores, four springs, moving parts, and yokes. The moving part receives the input force in the z direction, and two neodymium magnets and yokes are fixed to the moving parts. Note that the maximum energy product of each magnet is approximately 320 kJ/m^3, and its dimensions are 7 mm × 1 mm × 1.3 mm. The moving part is supported by four springs, whose total spring constant is 6864 N/m. Each coil is wound around a 1-mm-diameter iron core, and the number of turns of each coil is 206. Eight coils are connected in series, thus the impedance of the EHD is 16 Ω at 500 Hz. The footprint of the EHD is 20 mm × 20 mm. The height to the top of the cover is 5 mm, and that of the moving part is 7.5 mm. There is a 2.5-mm difference in height between the cover and moving part, and this difference determines the range of movement of the magnets. The volume of the device is 2.4 cm^3. Figure 2 (b) depicts a cross-section of the EHD, which facilitates an understanding of the power generation mechanism. When a force in the z direction is applied to the upper surface of the moving part, the moving part is pushed down toward the base. The magnets mounted on the moving part pass over the iron cores of the coils with a small gap of approximately 0.1 mm. Consequently, the magnetic flux density going through the iron cores varies corresponding to the distance between the magnet and cores (i.e., the permeance of the magnetic circuit). Once the force is released, the moving part returns to its initial position by the restoring force of the springs supporting the moving part. The magnets pass over the iron cores again. Thus, when the force is exerted or released, electric power is generated. To obtain a large power generation, the variation of magnetic flux density due to the reciprocating motion should be as large as possible. Because the minimum air gap between the magnet and the yoke is very narrow (approximately 0.1 mm), the maximum magnetic flux density achieved is 1.0 T. In contrast, when the moving part is at either the top or bottom position, the magnets are the farthest from the iron cores, and the magnetic flux density is only 0.27 T. Therefore, the variation of the magnetic flux density during a stroke of the moving part is 0.73 T. Such a large variation is an advantageous feature of the proposed structure and the source of the large power generation. 3. Experimental result We measured the power generation amount by applying an impact force to the moving parts. An external resistor of 16 Ω was connected in series with the coils of the EHD. Then, an impact force was applied to the top of the moving part, and the voltage generated between both ends of the external resister was measured. The power generation amount was defined as the energy consumption in the external resistor. The impact acceleration was measured using a small acceleration sensor. When a half-sine impact pulse with a maximum force and duration of 161 N and 2 ms, respectively, was applied, the generated voltage was 2.1 V, and the power generation amount was calculated as 119 μJ (49.6 μJ/cm3). Assuming that such input repeats at 1 Hz during walking, the power generation performance is 119 μW. Therefore, the performance of proposed EHD exceeded the target power generation amount required to drive a low-power wireless sensor.

[1] Elvio Bonisoli, Maurizio Repetto, Nicolò Manca, Alessandro Gasparini “Electromechanical and Electronic Integrated Harvester for Shoes Application” JOURNAL OF LATEX CLASS FILES, vol. 14, no. 8, August 2015 [2] K Ylli, D Hoffmann, A Willmann, P Becker, B Folkmer and Y Manoli “Energy harvesting from human motion: exploiting swing and shock excitations” Smart Materials and Structures, vol. 24, no. 2, January 2015 [3] D Carroll, M Duffy “Modelling, design, and testing of an electromagnetic power generator optimized for integration into shoes” Proceedings of the Institution of Mechanical Engineers, Part I: Journal of Systems and Control Engineering. 226 (2) 256–270, September 2011

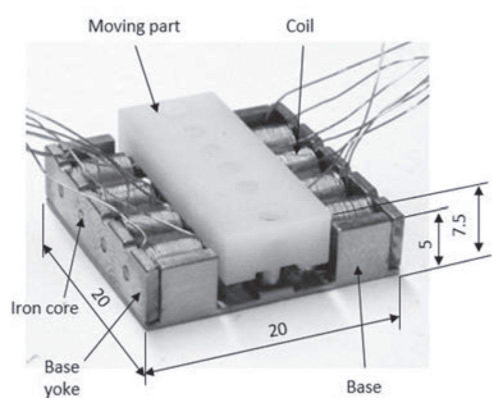

Fig. 1. The prototype of the designed EHD

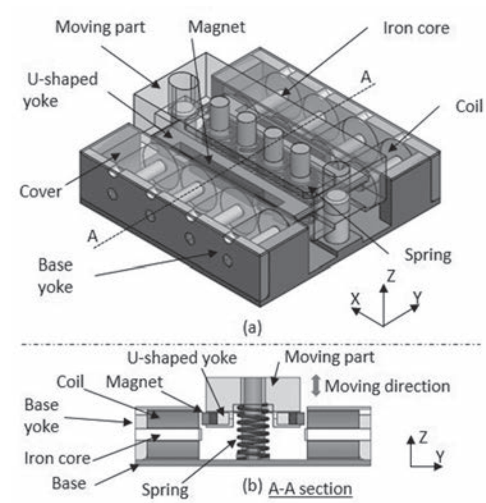

Fig. 2. (a) Illustration of the EHD (b) A cross-section of the EHD

3:15

DG-06. Performance Analysis of a Novel Fall-Back Transverse-Flux Permanent-Magnet Generator with Outer Rotor Design Suitable for Direct-Coupling Wind Turbine.

M.A. Patel[1] and S.C. Vora[1]
1. Department of Electrical Engineering, Institute of Technology, Nirma University, Ahmedabad, India

A fall-back transverse-flux permanent magnet generator (FB-TFPMG) with inner rotor design preferred for wind power applications, employs half the number of PMs (as against conventional TFPMG), elliptical shaped stator core and toroidal shaped coil. In this manuscript, a novel concept of FB-TFPMG with outer rotor design, suitable for direct coupling to wind turbine, is explored with a possibility to improve the power to volume ratio in comparison with the inner rotor FB-TFPMG. In the proposed configuration, the blades of the wind turbine are directly fastened to the drum to perceive the direct coupling between the wind turbine and the outer rotor FB-TFPM generator. This leads to immediate benefit of lower weight and better cooling. The dynamic performance of a novel concept of the proposed topology is analysed using 3-D finite element tool and the results are compared with the inner rotor FB-TFPMG. With expeditious penetration of wind power generator technologies and remarkable wind power generation capacity installed worldwide, numerous concepts of wind generator have been proposed and assembled. In [1]-[2], possible future wind generation systems and topologies are reviewed. A conventional transverse-flux permanent-magnet generator (TFPMG) with U-shaped stator core [3]-[4] is chosen as the best generator among all direct-drive PM generators because of its higher power density and simple coil design. The main drawbacks of conventional TFPMG has a complex design, an uneven magnetic flux distribution and high flux leakage due to multi-dimensional magnetic flux pattern. An iron bridge is employed between adjacent stator cores, as a solution to prevent the excessive leakage flux [5]-[6]. An improvement to the concept of conventional transverse-flux permanent-magnet generator, with a fall-back rotor is presented in [7]. A fall-back transverse-flux permanent-magnet generator (FB-TFPMG) with *inner* rotor design reduces the number of PMs to half, possess elliptical shaped stator cores and toroidal shaped coil in comparison to conventional TFPMG. Fall-back path of the rotor offers several advantages, importantly it avoids the losses in inactive magnets and the reduction in overall cost of the generator. Various outer rotor configurations of permanent magnet generators are deliberated in the literature i.e. radial flux, axial flux, transverse flux design, claw pole type and superconducting generators [8]-[10]. Transverse flux PM generator with outer rotor designs are compared in [11]-[12]. In this paper, a novel concept of FB-TFPMG is extended with outer rotor design, suitable for direct-coupling of wind turbine. This design is explored with a possibility to improve the performance and power to volume ratio in comparison with the inner rotor FB-TFPMG. The detailed cut section of the one phase of a novel FB-TFPM generator with outer rotor design is depicted in Fig. 1. The FB-TFPMG is basically a multi-phase configuration with circumferential toroidal shaped coil per phase in the stator. It possesses half of the total magnets with outer rotor for benefits of the availability of the space in it and possibility to modify the PM rotor pole position for better performance. It comprises of inner stator core assembly, which is mounted on the fixed shaft. Soft magnetic composite material is used for stator structure with even number of U-shaped magnetic circuits (cores) placed circumferentially inside a rotor core assembly. Rotor possesses number of magnetic pole pairs (NdFeB) exactly equal to the number of stator cores. The rotor back is made of mild steel. PM fluxes of all N-poles add up in the stator core in one direction and as the rotor travels one PM pole angle, all fall-back part (S-poles) add up their fluxes in the stator core in the reverse direction. As the rotor travels, the magnets and fall-back part of the rotor change their polarities and hence alternating emf is induced in the toroidal shaped coil. PM flux paths are bi-directional in the stator and three-dimensional in the rotor. The results of a novel outer rotor FB-TFPMG are focused on the most important parameters such as electromagnetic field analysis and induced emf under no-load condition and on-load condition. The induced emf plots under no-load and on-load condition are shown in Fig. 2 and are in good agreement with the inner rotor FB-TFPMG. Outer rotor design with 10.27% reduction in volume gives the equivalent output power as compared with the inner rotor design.

[1] Yicheng Chen, P. Pillay and A. Khan, "PM wind generator topologies," in *IEEE Trans. on Industry Applications*, vol. 41, no. 6, pp. 1619-1626, Dec. 2005. [2] Li, H. and Chen, Z., "Overview of different wind generator systems and their comparisons," in IET Renewable Power Generation, vol.2, no.2, pp.123-138, Jun. 2008. [3] A. Lange, "Transverse flux machine," U.S. Patent 5 773 910, Jun. 30, 1998. [4] Jacek F. Gieras, "Transverse Flux Machine," U. S. Patent 7,830,057 B2, Nov. 09, 2010. [5] Dobzhanskyi, O., Mendrela, E.E.; and Trzynadlowski, A.M., "Analysis of Leakage Flux Losses in the Transverse Flux Permanent Magnet Generator," in IEEE Green Technologies Conference (IEEE Green), vol., no., pp.1-6, 14-15 Apr. 2011. [6] O. Dobzhanskyi, R. Gouws and E. Amiri, "On the Role of Magnetic Shunts for Increasing Performance of Transverse Flux Machines," in IEEE Transactions on Magnetics, vol. 53, no. 2, pp. 1-8, Feb. 2017. [7] M. A. Patel and S. C. Vora, "Analysis of a Fall-Back Transverse-Flux Permanent-Magnet Generator," in *IEEE Transactions on Magnetics*, vol. 53, no. 11, pp. 1-5, Nov. 2017. [8] B. Anvari, Y. Li and H. A. Toliyat, "Comparison of outer rotor permanent magnet and magnet-less generators for direct-drive wind turbine applications," *2015 IEEE International Electric Machines & Drives Conference (IEMDC)*, Coeur d'Alene, ID, 2015, pp. 181-186. [9] X. M. Li, Z. X. Yang and D. L. Song, "A novel outer rotor axial primary magnetic circuit permanent magnet generator," *2015 International Conference on Advanced Mechatronic Systems (ICAMechS)*, Beijing, 2015, pp. 20-23. [10] H. Bai, F. Zhang, H. P. Gruenberger and E. Nolle, "Study on Novel Claw Pole Automobile Generator with Outer PM Rotor," *2007 2nd IEEE Conference on Industrial Electronics and Applications*, Harbin, 2007, pp. 632-635. [11] O. Dobzhanskyi, R. Gouws and E. Amiri, "Comparison analysis of PM transverse flux outer rotor machines with and without magnetic shunts," *2016 IEEE Energy Conversion Congress and Exposition (ECCE)*, Milwaukee, WI, 2016, pp. 1-8. [12] O. Dobzhanskyi, R. Gouws and E. Amiri, "Analysis of PM Transverse-Flux Outer Rotor Machines With Different Configuration," in *IEEE Transactions on Industry Applications*, vol. 53, no. 5, pp. 4260-4268, Sept.-Oct. 2017.

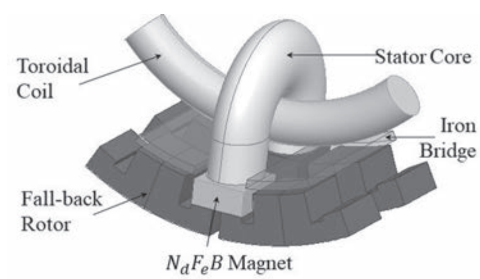

Fig. 1. Cut section of one of the phases of outer rotor fall-back transverse flux permanent magnet generator.

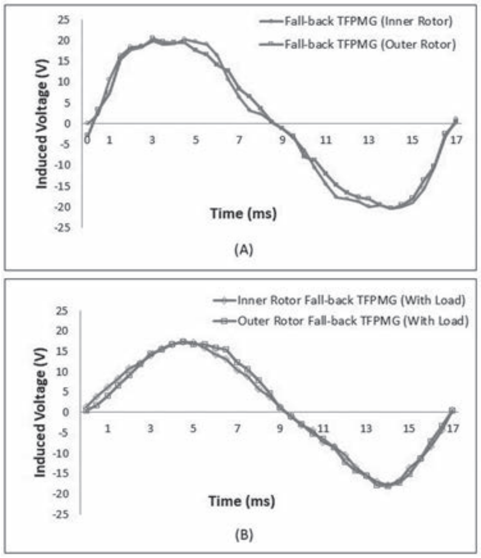

Fig. 2. Induced emfs plots under (a) no-load and (b) on-load condition of outer rotor and inner rotor fall-back transverse flux permanent magnet generator (FB-TFPMG).

3:30

DG-07. Magnetic field modelling of an Ironless Wind Power Microgenerator.

V. Verdum[1], R.P. Homrich[1], A.F. Flores Filho[1], M.A. Silveira[2] and *D.G. Dorrell*[3]

1. Engenharia Elétrica, Universidade Federal do Rio Grande do Sul, Porto Alegre, Brazil; 2. Engenharia Elétrica, Universidade Luterana do Brasil, Canoas, Brazil; 3. University of KwaZulu-Natal, Durban, South Africa

I. INTRODUCTION Microgeneration wind turbines often have starting problems due to cogging torque. Since small turbines for urban use are often located near or on top of buildings, they are subjected to a lower level the wind speed and to a more turbulent wind. The wind turbine presented in this digest is rated at only 1 kW; to increase the wind speed through the turbine, a diffuser is proposed. This can increase the speed in about 30% and improve the power coefficient C_w by about 70 %. The rotor is integrated into the turbine by fixing the turbine blade tips to an outer rotor ring which avoids shading by a centre rotor hub [1]. This ensures that the turbine reaches rated speed in less time and with greater regularity, i.e. it improves the starting. The turbine micro generator has an induced volts-per-phase of 94 V at 450 rpm. It is formed from a rotor with 100 surface mounted magnetic poles with no back iron, and an ironless three-phase stator. The inner diameter of the rotor is 1500 mm and determined by the length of the blades. The outer diameter of the rotor is 1546 mm. Each magnetic pole measures 30×40×5 mm (w× l × h). The outer diameter of the micro generator is 1554 mm. The pole pitch is very small due to the pole pair number and the diameters of the rotor. Therefore, the permanent magnets poles do not need to be arc shaped and rectangular shapes can be employed. Fig. 1 presents a view of the wind turbine with the electrical generator, the blades, and the diffuser. II. ANALYSIS OF THE MICROGENERATOR In the machine design process, experimental data can help determine the magnitude of the magnetic induction produced by the NdFeB permanent magnets [2]. To perform the design of the machine and understand the distribution of the internal magnetic flux, it is proposed an analytical model based on the magnetic scalar potential applied to a coreless configuration. In the analytical model, the magnetic field equations allow one to preview the behaviour of the magnetic flux density in terms of its distribution (Fig. 2). Values for the induced voltage across the windings can also be obtained. The formulation of the magnetic scalar potential assumes that all regions are free from current. The analytical model employs rectangular coordinates because the pole pitch arc is very short compared to the large diameter of the machine. Hence, the machine is considered linear. The magnetic circuit of the machine is divided in boundaries, each one with appropriate conditions for the field. These boundaries define the permanent magnets, the inner air volume where the blades are located, and the outer air volume where the armature windings are placed. In the air-gaps, the Laplacian of the magnetic scalar potential is null (Laplace's equation) [3]. The permanent magnet may be characterized by a fixed magnetization, so that the respective Poisson's equation equals the divergence of the magnetization vector. By means of the magnetic potential equation of each region, and by the imposed magnetic field boundary conditions, it is possible to obtain the equations for the magnetic flux density vectors in all regions. The magnetic flux-per-pole when the micro generator is running is obtained by integration of the normal component of the magnetic flux density vector over a pole pitch. The induced voltage-per-phase in the windings is computed using the normal component of the magnetic flux density vector. Fig. 2 presents a graph of the induced voltage-per-phase as a function of the wind turbine speed. The analytical model results are compared to numerical analysis calculations for validation and good correlation is found. The non-sinusoidal wave in Fig. 2 is the first step to study the magnitude of the voltage under load. In this project, the AWG 12 wire employed offers a very low resistance calculated in 0.48Ω per phase. With a line current density of 2.29 kA/m and a current density of $1.08\text{x}10^6 \text{A/m}^2$ in the armature conductors, the magnetic field produced in the winding is too weak to distort or reduce the permanent magnets field. The inductance in the absence of ferromagnetic material and proportional to a seven-turn coil is also low and computed to be 100 μH. It results in a very good regulation for the machine with losses of 20 W at rated power output. III Conclusions This digest outlines a method for predicting the magnetic field produced by a permanent-magnet coreless machine. Compared to machines with a substantial back iron, the proposed machine has lower magnetic induction in the windings and no cogging torque. Using magnetic scalar potential, it is possible to determine the magnitude of the magnetic field as a function of the tangential distance along the pole pitch and the coil span. It allows an approach in terms of rectangular coordinates. The analytical method provides means to optimize the machine without complex and time consuming numerical methods, which can speed up the design process and allow automated design. The induced voltage calculation achieves good agreement with numerical analysis in a 2D arrangement with a mean percentage error of 2.73 %, as seen with the aid of Fig. 2. Likewise, the armature reactance has good agreement, and that will also be presented in more details by the full paper. This work, therefore, makes a good contribution to the rapid and automated design of these small turbines.

[1] V. Verdum, R. P. Homrich, A. F. Flores Filho and D. G. Dorrell, "Ironless Machine Design for Wind-Based Microgeneration," in IEEE Transactions on Magnetics, vol. 53, no. 11, pp. 1-4, Nov. 2017. doi: 10.1109/TMAG.2017.2699621 [2] I. Stamenkovic, N. Milivojevic, N. Schofield, M. Krishnamurthy and A. Emadi, "Design, Analysis, and Optimization of Ironless Stator Permanent Magnet Machines," in IEEE Transactions on Power Electronics, vol. 28, no. 5, pp. 2527-2538, May 2013. doi: 10.1109/TPEL.2012.2216901 [3]K. J. Binns, P. J. Lawrenson, and C. W. Trowbridge. The Analytical and Numerical Solution of Electric and Magnetic Fields. West Sussex, U.K.: Wiley, 1992.

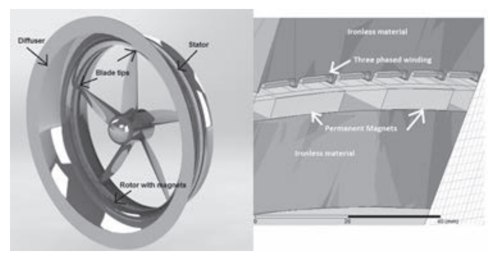

Fig. 1. Shrouded wind turbine with generator fixed on the blades tip and two poles detail

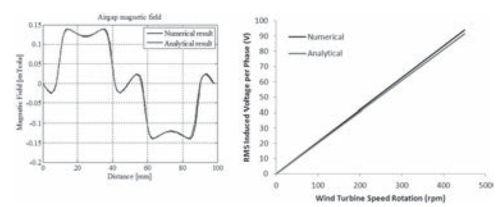

Fig. 2. Magnetic field in the winding and induced voltage-per-phase (RMS) as a function of the turbine speed

3:45

DG-08. Multiple-Objective-Based Optimal Energy Distribution for Wireless Power Transfer.

Z. Zhang[1], H. Pang[1], R. Tong[1], W. Ai[1], *S. Chang*[1] and J. Wang[1]
1. School of Electrical and Information Engineering, Tianjin University, Tianjin, China

I. Introduction Along with the increasing popularity of smart home, multi-coupling wireless power transfer (WPT) technique has shown significant potentials for portable electric-driven appliances. Accordingly, there existing growing diversity of charging requirements from various household appliances like mobile phones, iPad or laptop, for examples quick charging, the State of Charge (SoC), etc., therefore, the multi-coupling WPT system needs to deal with various charging requests simultaneously. Besides, the security of the wirelessly transmitted energy attracts attentions from researchers as well, especially for multiple WPT receivers coupling with the identical transmitting coil. Previously proposed energy encryption scheme utilized the characteristic of frequency sensitivity to encrypt the transmission channel [1]. Consequently, the key point of delivering the maximum power is to ensure the impedance matching, especially adjusting the resonant capacitor of primary unit while the frequency is regulated randomly. As aforementioned, this paper proposes an optimal-distribution and maximum-power based system which can distribute the limited transmitted power to different receivers simultaneously based on the proposed multi-coupling energy distribution scheme utilizing a novel control algorithm, meanwhile the proposed system is able to compensate the change of capacitance voltage due to the change of resonant frequency on account of various standard of charging equipment. More importantly, the proposed compensation which can extend the range of resonant frequency significantly only need one capacitor with a brand new current injection topology named capacitance buffer rather than the traditional capacitor array, so the system can continuously adjust the impedance to the resonate state to maintain the maximum output power. II. Proposed Optimal Energy Distribution Fig. 1 depicts the prototype of proposed optimal energy distribution based WPT system. Fig.2 shows four different working conditions regarding to this system. Fig. 2 (a) represents the average energy distribution where the RMS voltage of load 1 and load 2 are 1.89V and 1.93V, respectively, it means the energy is divided into two equivalent part. Fig. 2 (b) stands for the situation that load 1 is at the high priority through the proposed energy distribution algorithm so it need to be charged quickly, meanwhile load 2 is at the bottom of the charging list which is likely to receive the less quotient energy since the majority of transmitted energy is received by load 1, where the RMS voltage of load 1 and load 2 are 2.67V and 0.141V, respectively. Both these two situations are operating at the resonant state thus the inductance voltage and the capacitance voltage equal the same, which is 78.3V and 79.2V in Fig. 2 (a) with 117.6V and 118.9V in Fig. 2 (b). Fig. 2 (c) and Fig. 2 (d) both operate at the average energy distribution mechanism. Fig. 2 (c) shows the operating frequency is adjusted to the random frequency of 22kHz, however, the compensation capacitor is still 81.22nF which is the value of resonant state at 20kHz. In such a case, the inductance voltage and the capacitance voltage are 50.0V and 36.1V, respectively. So the difference between inductance voltage and capacitance voltage equals 14V which means the primary circuit works at the non-resonant state due to the frequency deviation and the excitation current will decrease dramatically as well. Besides, the RMS voltage of load 1 and load 2 are 0.779V and 0.766V, respectively, which drop to an extremely low level compared to the situation in Fig. 2 (a). Fig.2 (d) shows the same situation in Fig. 2 (c) but with the capacitance buffer utilizing the current injection topology where the RMS voltage of load 1 and load 2 are 1.67V and 1.62V, respectively, it means the transmitted power reverts to the resonant level in Fig.2 (a) and the inductance voltage and the capacitance voltage are 71.9V and 72.4V, respectively. It illustrates the ideal functionality of the proposed capacitance buffer to fine tune the compensation impedance so as to maintain the maximum power. III. Conclusion This paper has proposed an optimal-distribution and maximum-power based WPT system. It means that the wirelessly-transmitted energy could be distributed more effective and more intelligent, which is almost unexplored in other WPT researches. The proposed energy distribution algorithm provides an effective charging strategy for multi-coupling WPT systems, meanwhile the capacitance buffer with the current injection topology promotes the load voltage for about 214.4% at the frequency of 22kHz by means of tune the capacitance compensation. In addition, the measured results are in good agreements with the theoretical designs and simulated results, which verify the feasibility and correctness of the proposed approach in this paper, thus effectively enhancing the performance of multi-coupling WPT systems. Besides, the detailed parameters, distribution algorithm, current injection topology, simulated results, and experimental waveforms will be presented in the full manuscript.

[1] Z. Zhang, K. T. Chau, C. Qiu, and C. Liu, "Energy encryption for wireless power transfer," *IEEE Trans. Power Electron.*, vol. 30, no. 9, pp. 5237-5246, Oct, 2015.

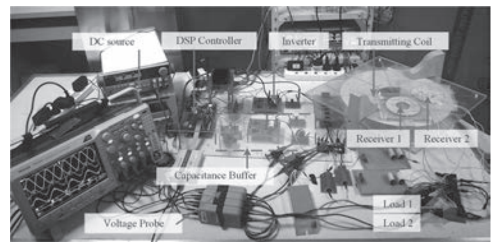

Fig. 1. Experimental prototype.

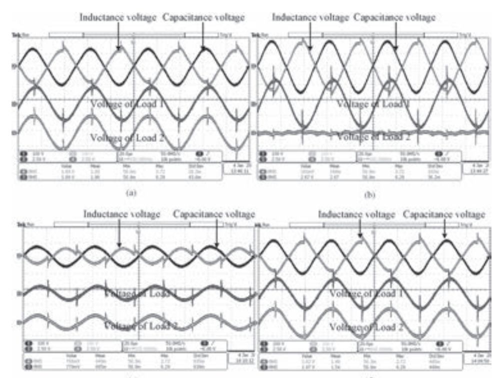

Fig. 2. Measured steady-state waveforms with Ch1: primary capacitor voltage (100V/div), Ch2: primary inductor voltage (100V/div), Ch3: voltage of load 1 (2.5V/div), and Ch4: voltage of load 2 (2.5V/div), (20µs/div): (a) f = 20kHz with average energy distribution (b) f = 20kHz with energy priority distribution (c) f = 22kHz without current injection topology (d) f = 22kHz with current injection topology.

WEDNESDAY AFTERNOON, 25 APRIL 2018

PEONY II, 2:00 TO 4:00

Session DH
PERMANENT MAGNET AND RELUCTANCE MACHINES V

E.A. Lomonova, Chair
Technische Universiteit Eindhoven, Eindhoven, Netherlands

CONTRIBUTED PAPERS

2:00

DH-01. Design and Analysis for Torque Ripple Reduction in Synchronous Reluctance Machine.

D. Yan[1], C. Xia[1,2], L. Guo[1], H. Wang[2] and *T. Shi*[1]
1. School of Electrical and Information Engineering, Tianjin University, Tianjin, China; 2. Tianjin Engineering Center of Electric Machine System Design and Control, Tianjin, China

I. Introduction The rotor of transversally laminated synchronous reluctance motor is constructed with multi-flux barriers by stamping the laminated steel sheets and the machine is short for TLR-SynRM. It has obvious advantages of smooth rotor surface, and the lower copper loss, et al. [1]. Nevertheless, TLR-SynRM has the drawback of high torque ripple, and one of the main reasons is the non-sinusoidal distribution of the air-gap flux density caused by the spatial harmonics of stator magnetic potential and flux-barrier rotor configuration. In [2], it has been carried out the genetic algorithm (GA) optimizations to improve the angles of the flux-barrier ends to reduce the torque ripple. In this paper, it proposes the step-shaped gradient flux barriers in TLR-SynRM for torque ripple reduction .A method is presented to compute the reluctances of each layer of flux barriers through conformal mapping method. Based on this calculation, it is shown how the air-gap flux density distribution of TLR-SynRM can be analytically computed through magnetic equivalent circuit (MEC) method. Combining with the two methods, the flux-barrier parameters for torque ripple reduction can be improved and the final improved flux-barrier parameters are obtained. II. The Rotor Configuration of the Step-shaped Gradient Flux Barriers In Fig.1(a), each layer of the gradient flux barriers is divided by region Q_1,Q_2,Q_3. Where $w_{ins}(z)$ is the width of the z_{th} layer of flux barrier in region Q_3; $w_{iron}(z)$ is the width of the z_{th} layer of silicon steel sheets between the z_{th} layer of flux barrier and the$(z+1)_{th}$ layer of flux barrier, z=1,2,…,n_w-1, where x_{0z} is the z_{th} layer salient flux-barrier width; n_w is the total layers of flux barriers. This rotor configuration has two remarkable features. First, its flux barriers are step-shaped and the parameter X=[x_{01}, x_{02}, …, x_{0nw}] that makes the each layer of the gradient flux barriers change in steps has a great influence on the air-gap flux density distribution, where x_{0k} is the k_{th} layer salient flux-barrier width, k=1,2,3…,n_w. The units of the parameter X is millimeter. Second, the widths of multi-flux barriers in the middle regions are changing in a gradient fashion. III. Computed the Reluctance using Conformal Mapping The conventional method may be hardly extended to the proposed non-uniform width of the step-shaped gradient flux barriers in this paper. A method is presented to compute the reluctance through conformal mapping [3].In Fig.1(b), the k_{th} layer salient flux-barrier width x_{0k} in complex plane w is mapped into the k_{th} layer salient flux-barrier width x_k in complex plane z_1. It needs to fix Neumann and Dirichlet boundary conditions to calculate the reluctances in rectangular region Q_1, Q_2, Q_3, and the field solution inside rectangle region is given by a uniform flux density of constant magnitude B_x. IV. MEC Model The step-shaped gradient flux-barrier MEC model is established in Fig.1(c). Within each air-gap region, a MMF source F_{ij}(with i and j equal to 1,2,3 or 4) and the flux Φ_{ij} passing through an air-gap reluctance R_{gij}. The whole air-gap of TLR-SynRM is subdivided into various regions, marked as 11,12,13,14,21,31,41,22 and delimited by the end points of flux barriers. According to the last section and the formulation for the reluctance, it can be concluded that the values of R_{b11} and R_{b21} are hardly changed with x_1 and x_2 respectively, and the values of R_{b31} and R_{b41} decrease to zero along with x_3 and x_4 growing. V. The Air-Gap Flux Density Distribution and FEM Assessment Combining with the configuration characteristic of rotor, the stator inner surface is further subdivided into nine different regions, marked as S_ϕ (ϕ=1, 2…, 9), as shown the gray and white regions in Fig.1 (a). According to the last section, it can be obtained multi-group parameters X, therefore the multi-group distributions of $B_g(\theta)$ are obtained from the MEC model in Fig.1(c). It can summarize the rules as follows. First, it can be concluded that the distributions of $B_g(\theta)$ from region S_1 to region S_4 do not change with x_3 and x_4. Second, it can be concluded that the distributions of $B_g(\theta)$ from region S_5 to region S_9 are monotonically increasing along with x_3 and x_4 growing and the results are in accordance with the linear variation of the reluctances R_{b31} and R_{b41} along with x_3 and x_4 growing. In this paper, the value of the parameter X is [1.230, 1.257, 4.223, 1.493] for guaranteeing the sinusoidal distribution and continuity of $B_g(\theta)$. The air-gap flux density computed by the analytical method and FEM are shown in Fig.1 (d). A comparative observation between Fig.2 (a) and Fig.2 (b) shows that the fundamental amplitude of $B_g(\theta)$ with the step-shaped gradient flux barriers in TLR-SynRM is increased by 5.1% than the conventional rotor flux barriers in TLR-SynRM. The torque ripple is 3.76%, whereas it is decreased by 15.74% when compared with the conventional rotor flux barriers in TLR-SynRM. VI. Conclusion It can be concluded that the torque ripple of TLR-SynRM with the step-shaped gradient flux barriers can be reduced effectively and it can make the torque waveform smoother.

[1] Marco F, Nicola B, Alberto D, Emanuele F, "Design of synchronous reluctance motor for hybrid electric vehicle," *IEEE Trans. Ind. Appl.*, vol.51, no.4, pp.3030-3040, Jul./Aug.2015. [2] Christopher M.Spargo, Barrie C. Mecrow, James D.Widmer, "A seminumerical finite-element postprocessing torque ripple analysis technique for synchronous electric machines utilizing the air-gap Maxwell stress tensor," *IEEE Trans. Magn.*, vol.50,no.5,pp.237-242, May.2014. [3] Alberto Tessarolo, "Modeling and analysis of synchronous reluctance machines with circular flux barriers through conformal mapping," *IEEE Trans. Magn.*, vol.45, no.4, pp.1-11, Apr.2015.

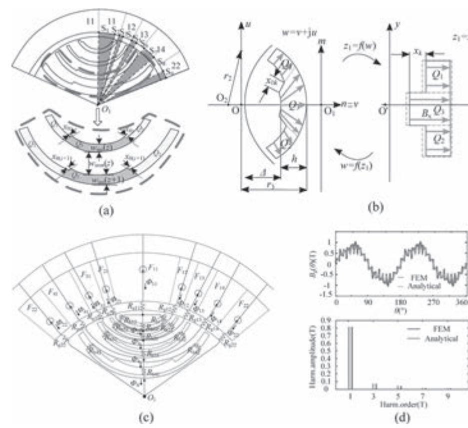

Fig. 1. Design produces of the step-shaped gradient flux-barrier in TLR-SynRM (a) The step-shaped gradient flux barriers (b) Transformation by conformal mapping method (c) Magnetic equivalent circuit (d) The distribution of $B_g(\theta)$ computed by the analytical method and FEM

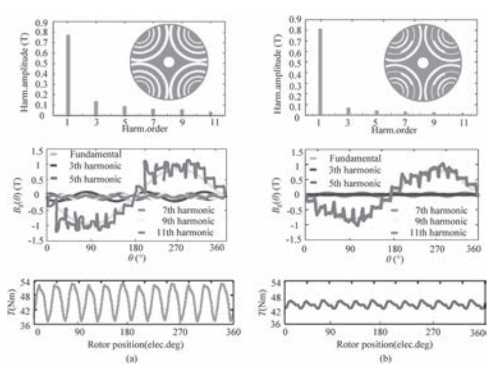

Fig. 2. The waveforms of the air-gap flux density, harmonic content and torque (a) The conventional flux barriers with equal width (b) The step-shaped gradient flux barriers

2:15

DH-02. Printed Circuit Axial-Flux Permanent Magnet Machines: A Comparative Analysis of Their PCB Topologies and Performance Characteristics.

S. Paul[2,1], M. Farshadnia[1], A. Pouramin[1], J. Fletcher[1] and J. Chang[2]
1. Electrical Engineering and Telecommunications, University of New South Wales, Kensington, NSW, Australia; 2. Electrical Engineering, Dong-A University, Busan, The Republic of Korea

Abstract — The aim of this paper is to provide a detailed comparison of three stator topologies for wave-type printed circuit board (PCB) winding axial flux permanent magnet machines (AFPMSMs). This comparison is performed based on the generated back electromotive force (EMF), winding inductances, and torque production capabilities of these machines. Three topologies are investigated, overlapping radial wave, non-overlapping radial wave, and overlapping parallel wave PCB windings. 3D finite element analysis (FEA) is used for these investigations. *Introduction:* Recently the axial flux permanent magnet synchronous machines (AFPMSMs) have gained wide attention because of their planer geometries, high number of pole pairs, short end windings, and high torque density which facilitates their use in applications such as hybrid and electric vehicles, aerospace actuation, and micromachines [1-2]. The existing literatures mostly focus on the design and comparison of conventional AFMSMs. However, not many documented works are found on AFPMSMs with printed circuit board (PCB) windings. PCB winding AFPMSMs are attractive for various applications that require thinner designs. The cornerstone and main challenge in design of such machines is their PCB windings which ultimately influences the electromotive force (EMF) and electromagnetic torque of the motor. Various layouts such as spiral or rhomboidal [3-5] PCB windings are mentioned in the literature. However, these topologies suffer from having a shorter active conductor length, increased joule losses, and inefficient use of the PCB surface that is facing the magnetic field. An alternative topology can be the use of wave-type PCB windings which sufficiently use the PCB surface, while keeping the joule losses to a minimum. Thus, there is a need to have a detailed survey of wave-type PCB winding topologies for PCB AFPMSMs which would be helpful while considering innovative designs of these machines. Therefore, this paper proposes a comparative study on novel wave-type PCB winding topologies for AFPMSMs in terms of their back-EMF, inductances, and torque production capabilities. *Stator Topologies for PCB Axial-Flux PMSMs:* A double-sided 10 pole AFPMSM as shown in Fig. 1(a) is used in this study. Three two-layer three-phase PCB stator topologies are chosen for the comparison, namely: 1) overlapping radial wave winding; 2) non-overlapping radial wave winding; and 3) overlapping parallel wave winding, as shown in Fig. 1(b) to (d), respectively. In Fig. 1(b) to (d), only one side of the two-layer PCB windings are presented for better visualization; the track widths of the windings are also exaggerated for clear illustration. In all the PCB topologies, the track width is equal to 7 mil (0.178 mm) with a minimum track clearance of 6 mil (0.152 mm). Track thickness is equal to 2 oz/ft^2 (equivalent to 0.07 mm thickness). The PCBs are designed to have the maximum number of turns per phase for the given track width and clearance. Other design parameters of the machines are shown in Table I. *Evaluation of back-EMF, Electromagnetic Torque, and Inductances:* Performance characteristics of different PCB winding topologies of Fig. 1 are obtained using 3D FEA at the synchronous speed of 600rpm. The generated three-phase back-EMFs by these topologies are shown in Fig. 2(a)-(c). A comparison between the harmonic content of the generated voltages is shown in Fig. 2(d). It is observed that the non-overlapping radial wave winding generates the highest fundamental voltage harmonic; however, it contains high third harmonic content, hence the back-EMF is trapezoidal. The overlapping radial wave winding on the other hand has a lower fundamental value and third harmonic. The overlapping parallel wave PCB winding generates the lowest fundamental voltage and is the least efficient topology among the three topologies of Fig. 1. PCB AFPMSMs are air-cored motors, thus the electromagnetic torque originates only from the alignment torque which is directly proportional to the fundamental component of the back-EMF. Therefore, for a given current, among the three compared PCB winding topologies, the non-overlapping winding produces the highest electromagnetic torque. The lowest electromagnetic torque belongs to the parallel wave PCB winding which has the lowest fundamental back-EMF harmonic. The inductances for air-cored AFPMSMs are generally small, in μH since the cumulative effective airgap is high and the number of turns is limited. Among the studied PCB AFPMSMs, the non-overlapping radial wave PCB topology has the highest self-inductance and lowest mutual inductance since the adjacent windings do not overlap. The overlapping radial wave and the parallel wave windings have higher mutual inductances due to the adjacent winding tracks overlapping. However, self-inductances for these two PCB winding topologies are in the same range. *Conclusion*: A comparative study on the performance characteristics of different PCB winding topologies for PCB AFPMSMs was presented in this research. The analysis considered three PCB winding topologies and compared them in terms of their back-EMF, electromagnetic torque, and inductances. Among the three studied topologies, the non-overlapping radial wave winding has the highest fundamental back-EMF harmonic and electromagnetic torque. On the other hand, the overlapping parallel wave winding had the worst performance in terms of torque production capability. Full evaluation of the studied winding topologies will be added in the extended manuscript.

[1] A. Pop, M. M. Radulescu, H. Balan, M. Chirca, and V. Zaharia, “Electromagnetic design and finite-element analysis of an axial-flux permanent magnet machine,” in *Proc. Int. Conf. Appl. Theoretical Elect.*, pp. 1–4, Oct. 2014. [2] J. Wu, “Design of a miniature axial flux flywheel motor with PCB winding for nanosatellites,” *in Proc. Int. Conf. Optoelectron. Microelectron*., pp. 544–548, Aug. 2012. [3] Y. C. Chuo, C. C Wang, C. S. Liu, H. C. Yu, Y. H. Chang and J. B. Horng, “Development of a Miniature Axial-Field Spindle Motor,” *IEEE Trans. on Magn*., Vol. 41, No. 2, 2005. [4] G. H. Jung and J. H Chang, “Development of an Axial Gap Spindle Motor for Computer Hard Disk Drives using PCB Winding and Dual Air Gaps,” *IEEE Trans. on Magn*., Vol. 38, No. 5, pp. 3297-3299, 2002. [5] M. C. Tsai and L. Y. Hsu, “Design of a Miniature Axial Flux Spindle Motor with Rhomboidal PCB winding,” *IEEE Trans. on Magn*., Vol. 42, No. 10, pp. 3488-3490, 2006.

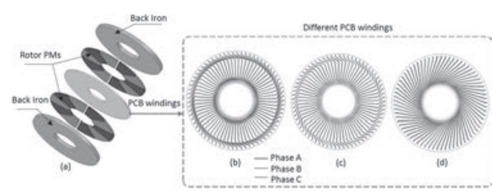

Fig. 1. (a) A double side 10 pole PCB AFPMSM with the different stator winding topologies (b) Overlapping radial wave winding (c) Nonoverlapping radial wave winding (d) Overlapping parallel wave winding.

Table I
Design Specification for The Studied PCB Winding AFPMSM

Parameter	Value	Unit
Stator outer diameter	100	mm
Stator inner diameter	40	mm
PM thickness	3.0	mm
PCB thickness	1.6	mm
Airgap length	0.85	mm
Number of poles	10	--

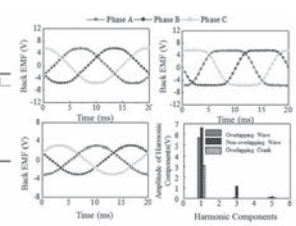

Fig. 2 Back EMF plot for (a) Overlapping radial wave, (b) Non-overlapping radial wave, (c) Parallel wave PCB windings and (d) the harmonic analysis.

2:30

DH-03. Electromagnetic Performance Analysis of a New Hybrid Excitation Synchronous Machine for Electric Vehicle Applications.

Y. Liu[1], Z. Zhang[1], C. Wang[1] and W. Geng[1]
1. Nanjing University of Aeronautics and Astronautics, Nanjing, China

I. INTRODUCTION Permanent magnet synchronous machines (PMSMs) have been attracting wide attentions and extensively applied in many fields due to their high torque density, high power density and high efficiency. However, the traditional PMSMs with constant air-gap flux hardly achieve perfect performances in an EV drive system which simultaneously requires both high output torque density and wide flux weakening range. Hybrid excitation synchronous machines (HESMs) are recently proposed as the potential candidates for EV drive systems, for the air-gap flux can be regulated by field current efficiently. The PM excitation is beneficial to improve torque density, and the field excitation brings good flux regulation capability, which is crucial for the wide flux weakening range in EV drive systems [1]. This paper studies the electromagnetic performance of a new HESM topology and the applicability of the HESM to a drive system for EV applications. A 100kW prototype HESM has been designed and developed for experimental verification. The contribution of this paper is to propose a promising solution where an HESM replaces a PMSM as a drive system in EV applications. II. OPERATION PRINCIPLE AND MACHINE SPECIFICATION Fig.1 shows the configuration of the new HESM with dual-end built-in field windings. The machine assembly axial length is not increased due to the built-in field windings. Compared to the HESM with extended magnetic bridge to embed field windings depicted in Fig. 2(a), the torque density and flux regulation capability of the new HESM are both improved with the optimized excitation structure. The operation principle of the HESMs depicted in Fig. 2(a) and (b) in a simplified form is illustrated in Fig. 3. Table I presents the design requirements of a drive motor for EV applications. Table II provides the main parameters of the designed HESM with dual-end built-in field windings. III. ELECTROMAGNETIC PERFORMANCE ANALYSIS In order to verify the applicability of the new HESM to a drive system for EV applications, the electromagnetic performance analysis mainly focuses on the torque characteristics and flux regulation capability. Fig. 4 shows the cogging torque waveforms with different field current. As shown in Fig. 5, the cogging torque magnitude increases with field current. Fig. 6 shows the torque-current characteristics with i_d=0 control strategy under different modes. As shown in Fig. 7, the rated output torque can be achieved by different combinations of armature current and field current. The output torque ripple can be optimized by the coordinated operation between field current and armature current. Fig. 8 shows the no-load flux regulation capability with field current. As shown in Fig. 9, the flux regulation capability of the new HESM can improved by the coordinated operation between field current and *d*-axis current. IV. EXPERIMENTAL VERIFICATION A 100kW prototype HESM with dual-end built-in field windings has been designed and developed for experimental verification. The prototype HESM and experimental setup are shown in Fig.10. Fig. 11 shows the back-EMF waveforms, no-load flux regulation capability and output torque capability. It can be seen that the simulated results agree well with the measured results. V. CONCLUSION In this paper, the electromagnetic performance of a new HESM with dual-end built-in field windings is investigated to verify the applicability of the HESM to a drive system for EV applications. A 100kW prototype HESM with dual-end built-in field windings has been designed and developed based on the requirements of a drive motor for EV applications, which simultaneously requires both high output torque density and wide flux weakening range.

Y. Liu, Z. Zhang and X. Zhang, "Design and Optimization of Hybrid Excitation Synchronous Machines With Magnetic Shunting Rotor for Electric Vehicle Traction Applications," in *IEEE Transactions on Industry Applications*, vol. 53, no. 6, pp. 5252-5261, Nov.-Dec. 2017.

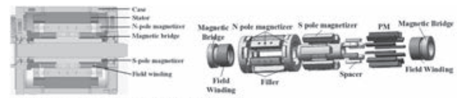

Fig. 1 Configuration of the HESM with dual-end built-in field windings.

Fig. 2 PM flux paths in the HESMs with magnetic shunting rotor. (a) HESM with extended magnetic bridge. (b) HESM with dual-end built-in field windings.

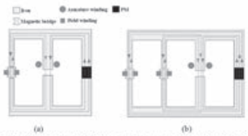

Fig. 3 Simplified operation principles of the HESMs. (a) HESM with extended magnetic bridge. (b) HESM with dual-end built-in field windings.

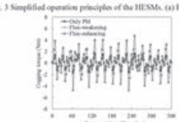

Fig. 4 Cogging torque waveforms with different field currents.

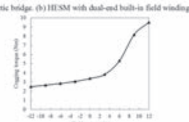

Fig. 5 Cogging torque against field currents.

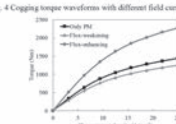

Fig. 6. Output torque against current density characteristics.

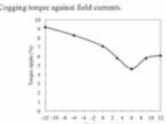

Fig. 7. Torque ripple against field current with the rated output torque.

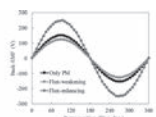

Fig. 8. No-load flux regulation capability.

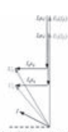

Fig. 9. Torque ripple against field current with the rated output torque.

Fig. 10. 100kW prototype HESM. (a) S poles rotor core. (b) Rotor. (c) Assembly.

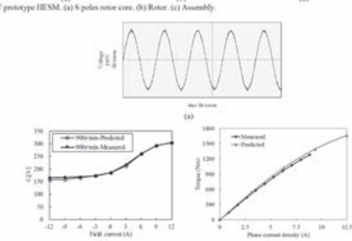

Fig. 11. Torque ripple against field current with the rated output torque. (a) No-load back-EMF waveforms. (b) No-load flux regulation capability (c) Output torque capability under flux-enhancing mode.

TABLE I
DESIGN REQUIREMENTS OF A DRIVE MOTOR

Parameter	Value
Phase number, *m*	3
Rated torque (Nm)	960
Max torque (Nm)	2400
Rated output power (kW)	100
Maximum output power (kW)	200
Rated speed (r/min)	1000
Maximum speed (r/min)	2800

TABLE II
PARAMETERS OF HESMS WITH DUAL-END BUILT-IN FIELD WINDINGS

Parameter	Value
Out diameter of the stator (mm)	400
Inner diameter of the stator (mm)	290
Length of stator core (mm)	240
Length of rotor core (mm)	360
Motor axial length (mm)	400
Main air-gap length (mm)	2
Magnet dimensions (thickness, width, length) (mm)	(14,40,240)
Rated current density (A/mm^2)	6.6
Max current density (A/mm^2)	20

2:45

DH-04. A New Variable Step Skew Approach for Minimizing Torque Pulsations in Permanent Magnet Synchronous Motors.

O. Ocak[1,2] and M. Aydin[2]
1. R&D, Akim Metal A.S., Kocaeli, Turkey; 2. Department of Mechatronics Engineering, Kocaeli University, Kocaeli, Turkey

I. INTRODUCTION There are several methods in order to reduce the torque pulsations for synchronous permanent magnet (PM) motors in literature [1]. These methods include design modifications both at rotor and stator sides such as using different slot/pole combinations, skewing rotor or stator, magnet grouping and adding auxiliary slots. One of the most common methods used in practice is step skew rotor. In general, adding one slot pitch step skew with several equal rotor segments increase torque quality and also decrease both cogging and ripple torque components for integer slot PM motors [2-7]. However, the skew angle and the step skew length could be optimized to get better torque quality. In this study, a new step skew technique is proposed with different segment lengths and skew angles between the segment pieces. Optimization comprising both parameters are carried out and the results compared with traditional step skew approach. 2D FEA results are obtained for conventional step skew rotor for a reference motor. Rotor optimization with varying rotor segment lengths and skew angles are attained and the optimized results are compared with the reference PM motor. II. MODELING OF PROPOSED STEP SKEW ROTOR AND ROTOR OPTIMIZATION In this study, a previously designed integer slot, 7.5kW, 4.000rpm surface mounted PM synchronous motor is used as a reference motor. 2D FEA model and mesh structure is shown in Fig 1. Both no-load and on-load FEA are performed and cogging torque, back EMF and torque output are obtained as shown in Fig 2. As observed from the analyses, the peak-to-peak cogging torque is 2.63Nm, peak back EMF voltage is 121.95V with a TDH of 8.24% and torque output is 18.75Nm with 16.2% ripple. Conventional step skew approach is applied to the reference motor. Several step skew up to 5 segments are investigated with FEA and the results are provided in Fig 3. By using 4 step skew rotor, %0.75 cogging torque, 115.85V line back EMF voltage with 0.8% THD and 3.7% torque ripple are obtained. An optimization code is developed in order to find the optimum step skew angle and the segment of the rotor segments. The flow chart is shown in Fig 4. With the developed optimization approach, the length of the rotor segments and the skew angles are varied to find the optimum torque pulsating components. 2D and 3D CAD models for standard step skew and the proposed step skew approaches are shown in Fig 5. Taking results from 2D FEA, necessary scaling and phase shifting are applied according to magnet lengths and skewing angles and results are summed to obtain the results of the proposed approaches. Rotor optimization to get minimum cogging for different segment numbers are summarized in Fig 7. As seen from the figure, optimum result for minimum cogging torque is close to the results with standard 3 step skew structure with 0.27Nm. Same analysis is repeated for torque output as seen in Fig 8 and it is found that 4 segmented rotor structure provide 17.7Nm average torque output with 1.74% torque ripple. The analyses show that manufacturing a prototype with 4 rotor segments and optimum skew angles and segment lengths provides minimum torque ripple. 3D FEA analyses are also performed for the optimized rotor. 3D FEA results and comparison with 2D FEA are also shown in Fig 9. It is seen that results are in good agreement. III. PROTOTYPE MANUFACTURING AND EXPERIMENTAL RESULTS Prototype manufacturing for the reference PM motor and the proposed PM motor are completed. Motor housing parts and sample laminations are illustrated in Fig 10. Experimental results and comparison between the test data and FEA simulations will be provided in the paper. IV. CONCLUSION In this study, a new step skew approach for surface PM motors is proposed for the first time in literature. The proposed step skew approach relies on varying both the length of the step skew and the angle between the rotor segments. It is shown that it is possible to optimize both parameters and obtain less torque pulsations as opposed to the conventional step skew. Prototypes are built for both the reference and the proposed motors. Detailed test results and the comparison with FEA will be provided in the final version of the paper.

1) T.M. Jahns and W. L: Soong, "Pulsating Torque Minimization Techniques for Permanent Magnet AC Motor Drives-A review," *IEEE Trans. Ind. Appl*., vol. 43, no. 2, pp. 321-330, Apr. 1996. 2) N. Bianchi and S. Bolognani, "Design Techniques for Reducing the Cogging Torque in Surface-Mounted PM Motors," *IEEE Trans. Ind. Appl*., vol. 38, no. 5, pp. 1259-1265, Sep./Oct. 2002. 3) X. Ge, Z. Q. Zhu, G. Kemp, D. Moule and C. Williams, "Optimal step-Skew Methods for Cogging Torque Reduction Accounting for Three-Dimensional Effect of Interior Permanent Magnet Machines," *IEEE Trans. On Energy Conversion*, vol. 32, no. 1, pp. 222-232, Mar. 2017. 4) W. Q. Chu and Z. Q. Zhu, "Investigation of Torque Ripples in Permanent Magnet Synchronous Machines with Skewing," *IEEE Trans. On Magnetics*, vol. 49, no.3, Mar. 2013. 5) W. Q. Chu and Z. Q. Zhu, "Reduction of On-Load Torque Ripples in Permanent Magnet Synchronous Machines by Improved Skewing," *IEEE Trans. On Magnetics*, vol. 49, no.7, pp. 3822-3825, Jul. 2013. 6) T. Li and G. Slemon, "Reduction of Cogging Torque in Permanent Magnet Motors," *IEEE Trans. On Magnetics*, vol. 24, no.6, pp. 2901-2903, Jul. 2013. 7) L. Dosiek and P. Pillay, "Cogging Torque Reduction in Permanent Magnet Machines," *IEEE Trans. Ind. Appl*., vol. 43, no. 6, pp. 1565-1571, Now.-Dec., 2007.

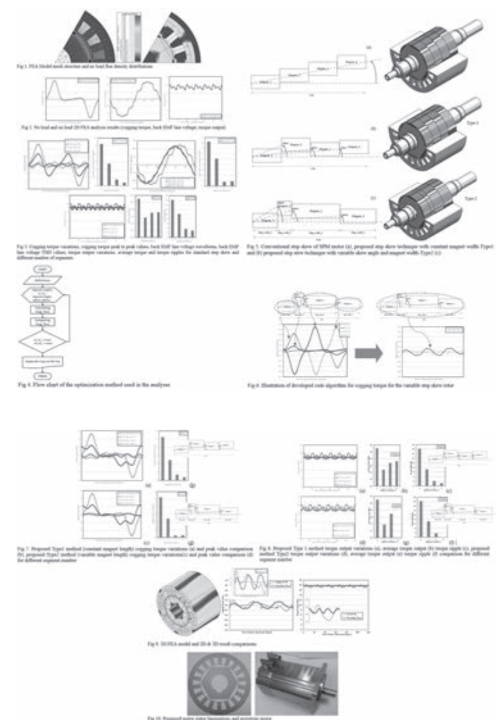

3:00

DH-05. Suppression of Even-Order Harmonics and Torque Ripple in Outer Rotor Consequent-Pole PM Machine with Multilayer Windings.

F. Li[1] and H. Zhang[1]
1. Institute of automation, Nanjing University of Aeronautics and Astronautics, Nan Jing, China

I. Introduction Due to the excellent performance of permanent magnet (PM) machine with high power density, small volume and high efficiency, they are widely used in the aerospace field, high performance servo field, distributed power generation and flywheel energy storage [1-2]. But the use of rare earth materials especially the high energy product PM, such as NdFeB, is expensive. To reduce the cost, the research on the less-PM machines has drawn much attention over the last few years. The consequent pole rotor was proposed for low speed direct drive [3-5], where its electromagnetic performance was analyzed. However, for some specific slot and pole combinations of CP PM machines, the even harmonics exist in the phase back-EMFs can't be counteract and this will increase the torque ripple. In order to suppress its even harmonics, the multilayer windings are employed. The purpose of this paper is to suppress even-order harmonics in Back-EMFs and torque ripple in out rotor CP PM machine by multilayer winding and the principle is verified by FEA and experiment results. Compared with the traditional 27-slot/30-pole 2 layer PMSM, the average torque of 27-slot/30-pole 4 layer PMSM with CP rotor can maintain 98.47% by saving 28.2% amount of PM. Furthermore, the efficiency of the 27-slot/30-pole 4 layer CP SPM machines is almost the same as the traditional 27-slot/30-pole 2 layer SPM machine when operate at rated speed. However, the torque ripple of the 2 layer CP SPM machines is highest of the analyzed machines. The prototype of traditional 27-slot/30-pole with 2 layer winding and CP rotor with 4 layer winding are fabricated to verify the FEA results. II. MACHINE TOPOLOGIES, FEA RESULT AND EXPERIMENTAL VALIDATION The traditional 27-slot/30-pole 2 layer PMSMs with traditional and CP rotor and 27-slot/30-pole 4 layer PMSMs with CP rotor are employed to analyze the electromagnetic characteristics of the machines. Figs. 1 (a), (b), (c) shows the rotor, the stator together with the winding connections employed for the three machines respectively. The star of slot of the unit machine for the 27-slot/30-pole 4 layer SPM machine is given in Fig. 1 (d). The Back-EMFs phasors A+, A- and A++, A-- belongs to phase-A defined as the first and second set winding of the machine, respectively. Figs. 2 (a), (b) show the Back-EMFs waveform and harmonics contents of 27-slot/30-pole CP SPM machine, it can be seen the resultant Back-EMF of the first and second set windings suppressed the even harmonics contents effectively in the 27-slot/30-pole CP SPM machine with 4 layer winding. The electromagnetic torque varies with rotor position for the three machines are given in Fig. 2 (c). As can be seen average torque of the 27-slot/30-pole 4 layer CP SPM machine can maintain 98.47% by saving 28.2% amount of PM compared with the traditional SPM machine, while the torque ripple is 5% lower than the 27-slot/30-pole 2 layer CP SPM machine and 0.98% higher than the 27-slot/30-pole 2 layer SPM machine. The prototype of 27-slot/30-pole 2 layer SPM machine is shown in Fig. 2 (d). The prototype of 27-slot/30-pole 4 layer SPM machine with CP rotor is in manufacture and will be shown together with the experimental results in the full paper.

III. REFERENCES [1] A. M. EL-Refaie, "Fractional-slot concentrated-windings synchronous permanent magnet machines: Opportunities and challenges," IEEE Trans. Ind. Electron., vol. 57, no. 1, pp. 107–121, Jan. 2010. [2] J. Wang, K. Atallah, Z. Q. Zhu, and D. Howe, "Modular three-phase permanent-magnet brushless machines for in-wheel applications," IEEE Trans. Veh. Technol., vol. 57, no. 5, pp. 2714–2720, Sep. 2008. [3] S. U. Chung et al., "Fractional slot concentrated winding permanent magnet synchronous machine with consequent pole rotor for low speed direct drive," IEEE Trans. Magn., vol. 48, no. 11, pp. 2965–2968, Nov. 2012. [4] S. U. Chung, J. W. Kim, Y. D. Chun, B. C. Woo, and D. K. Hong, "Fractional slot concentrated winding PMSM with consequent pole rotor for a low-speed direct drive: Reduction of rare earth permanent magnet," IEEE Trans. Energy Convers., vol. 30, no. 1, pp. 103–109, Mar. 2015. [5] S. U. Chung, S. Moon, D. Kim, and J. Kim, "Development of a 20-Pole– 24-slot SPMSM with consequent pole rotor for in-wheel direct drive," IEEE Trans. Ind. Electron., vol. 63, no. 1, pp. 302–309, Jan. 2016.

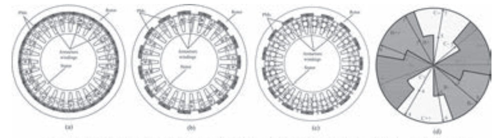

Fig. 1 Diagram and star of slot of the analyzed machines. (a) 27/30-2 layer SPM machine. (b) 27/30-2 layer CP SPM machine. (c) 27/30-4 layer CP SPM machine. (d) Star of slot of 9/10 4 layer unit machine.

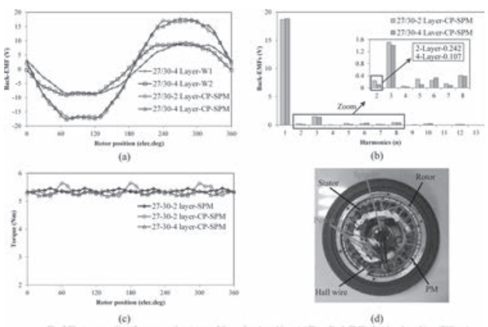

Fig. 2 Electromagnetic performance and prototype of the analyzed machines. (a) Phase Back-EMF of analyzed machines (300rpm). (b) Harmonics of Back-EMFs. (c) Variation of torque with rotor position (BLAC). (d) 27/30 2 layer traditional SPM machine.

3:15

DH-06. A Unified Design Approach of a Direct Drive External-Rotor Switched Reluctance Motor (Ex-R SRM) and its Implementation for a Low-Speed Domestic Appliance with R-dump Converter.

R. Azhagar[1] and A. Kavitha[1]
1. Electrical and Electronics Engineering, College of Engineering, Anna University, Chennai, India

ABSTRACT This paper demonstrates a unified design approach of an 8/6 External-Rotor Switched Reluctance Motor developed for a 150 RPM domestic application as direct drive. Here, the initial sizing of dimensions is determined by the analytical design calculation. The feasibility of the analytical design has been verified through Finite Element Analysis (FEA) under static and dynamic conditions. Further, a detailed fractional factorial design study has been conducted using Design of Experiments (DOE) to identify the critical design parameters which are sensitive to peak and average torque. This data from DOE is analysed through regression technique and fit a transfer function. This transfer function is helpful in finding the optimum design without spending much time in finite element analysis. Finally, the design is further optimized for conduction angles with R-dump converter to reduce the torque ripple. As a consequence, an optimum on/off angle has arrived which gives high average torque compared to the initial design. A prototype has been developed for the domestic appliance and tested with the actual load. INTRODUCTION The external rotor configuration of the motor provides many advantages over internal rotor such as it provides higher air gap radius, higher torque to ampere ratio hence increased efficiency. Additionally, it is well suited for high torque density applications and allows direct integration with the load like a fan, in wheel direct drives, hybrid electric vehicles, and wind turbines. In these applications, the mechanical construction is not a difficult one [1]. So, here, the application requires high torque at low speed where this motor can be directly coupled to the load. Also, the external motor with 6/8 pole switched reluctance motor has been developed and tested for a fan application at a minimum speed of 200 RPM [2]. In this digest, a unified design approach of an 8/6 Ex-R Switched Reluctance Motor and its implementation to use it as a direct drive for a low speed of 150 RPM in a domestic appliance has been proposed in detail. DESIRED DOMESTIC APPLIANCE REQUIREMENTS AND CONSTRAINTS To design an Ex-R SRM, the specification of the motor has to be defined first from application requirements. The domestic application considered for the study is a wet grinder. The grinders have a drum with stones which is driven by the conventional induction motor. The belt or gear mechanism is used for speed reduction [4]. Basically, wet grinder uses stone for grinding and the drive runs at low speed. The low-speed grinding is advantageous over high-speed grinding appliances (mixers or blenders) since it does not generate much heat which is very important for better food quality [5]. The motor design has to meet both electrical requirements and mechanical constraints of the application. Since the motor is going to be used as direct drive it should fit within the periphery of drum[5]. The drum diameter is 250 mm. Also, the height of the motor should be as low as possible to have a better mechanical stability. So, its axial length is restricted to 40 mm. The proposed direct drive Ex-R SRM based wet grinder is shown Figure 9. The rated torque required for the application is 12 Nm at the low speed of 150 RPM with the peak torque of 14 Nm. The peak current of the motor should not exceed 10 A. UNIFIED DESIGN APPROACH INITIAL DESIGN OF Ex-R SRM The initial dimensions of the 4-phase, 8/6 Ex-R SRM is calculated from the analytical design equation modified from Inner rotor configuration[6]. VERIFICATION WITH FINITE ELEMENT ANALYSIS (FEA) The SR motor model shown in Fig.1 with initial and final design dimensions are modeled and analyzed using a 2-Dimensional (2D) FEA under static and transient conditions. The static torque, inductance profile and flux linkages for various currents with respect to rotor position are predicted through static simulation by exciting the phase coil with the current value of up to 10 Amps. In order to study the effect of on/off conduction angles on torque ripple are simulated during transient conditions by energizing semiconductor switches in R- dump converter circuit model at speed of 150 RPM. SENSITIVITY ANALYSIS USING DESIGN OF EXPERIMENTS (DOE) It has been identified from the initial study that there are 6 parameters which directly affect both peak and average torque of motor output. A.Fractional factorial design As the FE analysis is a time-consuming one, in order to save the simulation time, the full factorial has been converted into fractional factorial with 32 runs and the average and torque results are tabulated. B.ANOVA Analysis The simulation results of fractional factorial are further analyzed using ANOVA method and main and interaction effects are predicted. The main effects plot (Fig.4) show that the 3 factors which significantly affect the torque such as Outer diameter, stack length and no of turns. From the regression fit, optimum dimensions are finalised based on the high average and peak torque. EXPERIMENTAL VERIFICATION Finally, a prototype of the domestic appliance has been developed and tested with the actual load conditions. CONCLUSION In this digest, an 8/6 External-Rotor Switched Reluctance Motor for a low-speed has been designed and developed. This motor used as direct in the actual domestic application and tested with the actual load.

[1] M. D. Hennen, and R. W. De Doncker, “Comparison of Outer- and Inner-Rotor Switched Reluctance Machines,” in 7th International Conference on Power Electronics and Drive Systems, PEDS, 2007,pp.702-706. [2] Chen, Hao, and Jason J. Gu, “Switched reluctance motor drive with external rotor for fan an air conditioner,” IEEE/ASME Transactions on Mechatronics, vol. 18, no. 5, pp.1448 - 1458, July. 2013. [3] Jianing Lin, Nigel Schofield, and Ali Emadi, “External-Rotor 6–10 Switched Reluctance Motor for an Electric Bicycle”, IEEE Transactions on Transportation Electrification, Vol. 1, No. 4, December 2015. [4] Masazumi Suzuki, “Direct Drive Technology and its impact on Generator business”, Power Transmission Engineering, www.powertransmission.com, December 2009. [5] L.Initha, J.Jegan, R.Kumar, “Analysis and Improvement of Quality in Wet Grinder Manufacturing Industry Through Customer Complaint Investigation”, International Journal of Innovative Research in Science, Engineering, and Technology, Vol. 4, Issue 1, January 2015. [6] R. Krishnan, Switched Reluctance Motor Drives: Modeling, Simulation, Analysis, Design, and Application. Boca Raton, FL, USA: CRC Press, 2001.

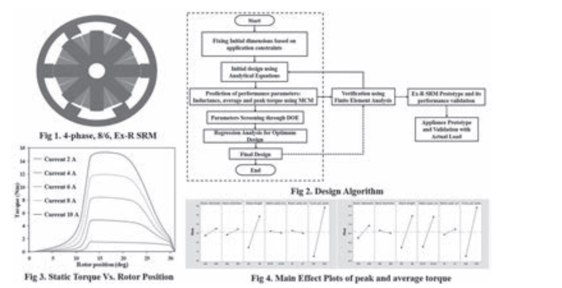

Fig. 1. 4-phase, 8/6, Ex-R SRM
Fig. 2. Design Algorithm
Fig. 3. Static Torque Vs. Rotor Position
Fig. 4. Main Effect Plots

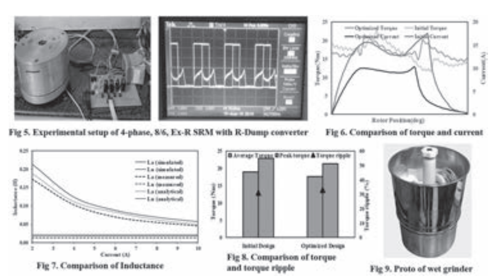

Fig. 5. Experimental setup
Fig. 6, 7 & 8. Comparison plot of Inductance, torque, and torque ripple
Fig. 9. Proto of wet grinder

3:30

DH-07. Characteristic Analysis of Turn-to-turn Short Circuit Current Mitigation Method for Concentrated Winding Permanent Magnet Machines.

Y. Jiang[1], Z. Zhang[1], W. Jiang[1], J. Huang[1] and Y. Xu[1]
1. Nanjing University of Aeronuatics and Asrtonautics, Nanjing, China

I. INTRODUCTION Fractional slot concentrated winding (FSCW) permanent magnet synchronous machines (PMSMs) with high power density, fault tolerance and wide constant-power speed range are gaining increasing attention in the aircraft starter generator (SG) system. However, the short circuit (SC) fault, especially the turn-to-turn SC fault, is the obstruct crux in aviation applications. The high reluctance permanent magnet machine (HRPMM) can inherently limit the SC current with high self-inductance and low mutual inductance. Combining with the current injection mitigation method, it can limit turn-to-turn SC current to a permissible level [1] [2]. But higher reluctance always leads to lower power density. So far there has been no numerous criteria on trading off between the two characteristics. In this paper, analytical model based on flux distribution [3] is established to estimate the SC current. The requirement for HRPMMs to survive the turn-to-turn SC fault is deducted. The derived expression is aimed to provide guidelines for designing HRPMMs. The theoretical analysis is verified by finite element analysis (FEA) and experiments on a 24-slot, 16-pole PMSM. The paper provides guidelines for designing high-performance HRPMM for aviation power system. II. ANALYSIS OF THE SC CURRENT FOR PMSMS For PMSMs with series windings, it is assumed that the full-stage turn-to-turn SC fault occurs in winding a_1, as shown in Fig.1-2. The SC current I_s is shown in equation (1), where E_2 is back electromotive force (BEMF), I_a, I_b and I_c are phase currents, M_{hs} is mutual inductance between the healthy and faulty turns, L_s is faulty turns self-inductance, r_s is faulty turns resistor, M_{sb} and M_{sc} are mutual inductances between B, C phases and the faulty turns. The magnitude of no load SC current is shown as equation (2). For FSCW-PMSMs, the phase mutual inductance can be ignored. The typical current mitigation method is injecting flux-weakening current (i_d) to reduce flux linkage of the faulty turns, as shown in in equation (3). Analytical model is established according to the flux distribution as shown in Fig.3. Equation (4) is used to compute L_s and M_{hs}. Where, x is the ratio of healthy turns and faulty turns number in one slot. γ is coupling factor of different windings in a phase, as illustrated in Fig.3 and equation (5). The factor represents the influence of stator and rotor core reluctance on the inductance. L_{sm} and L_{sl} are winding self-inductance and leakage inductance, as derived by equation (6). Where L_m and L_l are phase self-inductance and leakage inductance, n is number of the windings in a phase. By replacing (4) into (3), the SC current can be expressed as equation (7). An ideal post-fault condition for the HRPMM is that the SC current and i_d share the same magnitude I_1. Under this condition, the no-load SC current can be expressed as equation (8). In the SG system with high speed, the resistance of armature winding can be neglected. Furthermore, the winding leakage inductance is far more less than self-inductance, leading to equation (9). To ensure long-term operation after the SC fault, I_1 should be no more than the rated current. Since the single-turn SC fault is the most critical condition, it can be inferred that HRPMM should satisfy equation (10) to guarantee survival of turn-to-turn SC fault. For PMSMs with parallel winding connection in Fig.4, the SC fault lowers the impedance in the faulty winding, affecting the current distribution. Thus, the designing equation is shown as equation (11). III. FINITE ELEMENT ANALYSIS AND EXPERIMENT VERIFICATION FEA and experiments are carried out on a 24-slot, 16-pole series-connected FSCW-PMSM as shown in Fig.5 and Tab.I. For the coils' safety, two-turn SC fault is conducted under no-load condition at 600rpm. The control structure is shown in Fig.6. Once the fault is detected, i_d would be injected to reduce the BEMF in the shorted turns, thus diminishing the SC current. The PMSM prototype and experiment platform are shown in Fig.7. Two turns of the same slot are brought out and shortened externally to emulate turn-to-turn SC current. The contact resistor is 29mΩ. Varied i_d is injected to observe the respond of SC current. Equation (3) is used to calculate the SC current. Figure 8 and 9 illustrate the analytical, simulation and experiment results. The results are in accordance with each other. When i_d varies from 0A to -150A, the SC current can be reduced from 130.5A to 83.1A. The FEA results and the experiment results are slightly higher than the analytical results because of the neglected core saturation in analytical model. The experiment results are slightly lower than the FEA results because the heat produced during the rotation magnifies the resistance of the copper conductors, reducing the SC current. From the results, it can also be seen that I_1 is about 80A. The value agrees with the equation (12). The FEA and experiment results verify the conclusion in part II. IV. CONCLUSION In this paper, analytical models of the SC current of the FSCW-PMSMs with series and parallel winding connections are established. Analytical expression is derived for designing HRPMM which could ensure long-term operation under turn-to-turn SC fault. FEA and experiments on a 24-slot, 16-pole PMSM are conducted to verify the deduction. The paper provides guidelines to trade off between the high power density and high reliability when designing HRPMM for the safety critical application. It widens the application foreground of PMSM for the aviation power system.

[1]A. El-Refaie, M. Shah, and K.-K. Huh, "High-power-density fault-tolerant PM generator for safety-critical applications," *IEEE Trans. Ind. Appl.*, vol. 50, nol. 3, pp. 1717-1728, 2014. [2]Z. Zhang, J. Huang, Y. Jiang, W. Geng, Y. Xu, "Overview and analysis of PM starter/generator for aircraft electrical power systems," *CES TEMS*, vol. 1, no. 2, pp. 117-131, 2017. [3] B.-G. Gu, J.-H. Choi, and I.-S. Jung, "Development and analysis of interturn short fault model of PMSMs with series and parallel winding connections," *IEEE Trans Power Electron.*, vol. 29, no. 4, pp. 2016-2026, 2014.

$$\dot{I}_s = -\frac{\dot{E}_2}{r_s + jwL_s} - \frac{jwM_{hs}}{r_s + jwL_s}\dot{I}_a - \frac{jwM_{sb}}{r_s + jwL_s}\dot{I}_b \frac{jwM_{sc}}{r_s + jwL_s}\dot{I}_c \tag{1}$$

$$\left|\dot{I}_{s0}\right| = \frac{\left|\dot{E}_2\right|}{\sqrt[2]{r_s^2 + (jwL_s)^2}} \tag{2}$$

$$\left|\dot{I}_s\right| = \left|\dot{I}_{s0}\right| - \frac{wM_{hs}}{\sqrt[2]{r_s^2 + (wL_s)^2}}\left|\dot{I}_a\right| \tag{3}$$

$$\begin{gathered} L_s = (1-x)^2 * (L_{sm} + L_{sl}) \\ M_{sh} = x(1-x)(L_{sm} + L_{sl}) + \gamma(1-x)L_{sm} \end{gathered} \tag{4}$$

$$\gamma = \gamma_{12} + \gamma_{13} + \ldots + \gamma_{1n} \tag{5}$$

$$\begin{gathered} L_{sm} = \frac{L_m}{n(1-\gamma)} \\ L_{sl} = L_l / n \end{gathered} \tag{6}$$

$$\left|\dot{I}_s\right| = \left|\dot{I}_{s0}\right| - \frac{w(x(1-x)L_{sm} + x(1-x)L_{sl})}{\sqrt[2]{r_s^2 + (jwx(1-x)(L_{sm} + L_{sl}))^2}}\left|\dot{I}_a\right| \tag{7}$$

$$\left|\dot{I}_{s0}\right| = \left[1 + \frac{w(x(1-x)L_{sm} + x(1-x)L_{sl})}{\sqrt[2]{r_s^2 + (jwx(1-x)(L_{sm} + L_{sl}))^2}}\right]\left|\dot{I}_1\right| \tag{8}$$

$$I_{s0} = \frac{1}{1-x}(1+\gamma)I_1 \tag{9}$$

$$I_{s0} \le N_{slot}(1+\gamma)I_{rated} \tag{10}$$

$$I_{s0} \le N_{slot}(1+\gamma)\frac{I_{rated}}{1+x^2} \tag{11}$$

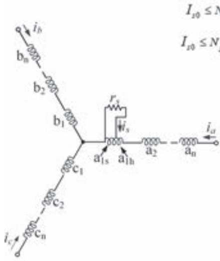

Fig.1. Illustration of series connected winding with turn-to-turn fault.

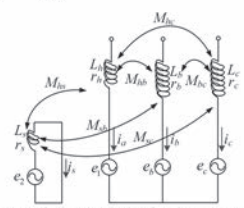

Fig.2. Equivalent circuit of series connected winding with full-stage turn-to-turn SC fault.

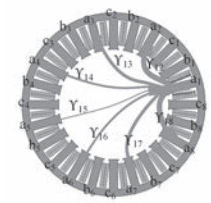

Fig.3. Magnetic flux flow generated by a_1 to the other windings of phase A.

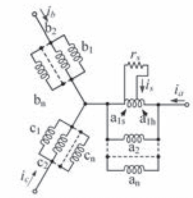

Fig.4. Illustration of parallel connected winding with turn-to-turn SC fault.

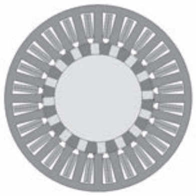

Fig.5. Cross section view of 24-slot, 16-pole PMSG.

Tab.1. Specifications of the PMSG

Slots/Poles	24/16
Rated voltage/V	540
Rated power/kW	50
Rated speed/rpm	2800
Turns per slot	16
Phase self-inductance/mH	1.8
Phase mutual inductance/uH	184

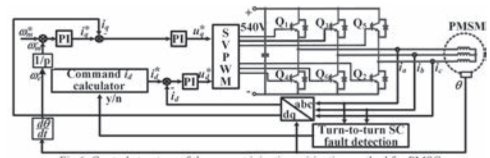

Fig.6. Control structure of the current injection mitigation method for PMSG in the motoring mode.

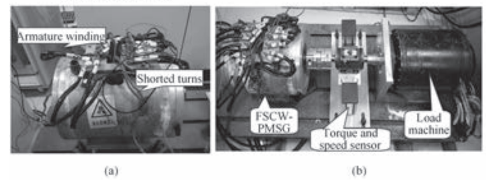

Fig.7. The prototype and experiment platform. (a) The 24-slot, 16-pole PMSG prototype. (b) The experiment platform.

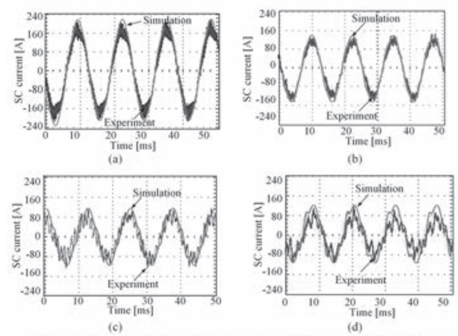

Fig. 8. SC current plots under different i_d. (a) SC currrent at i_d =0A. (b) SC currrent at i_d =-90A. (c) SC currrent at i_d =-120A. (d) SC currrent at i_d =-150A.

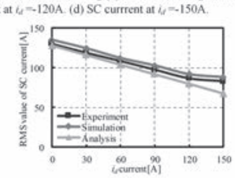

Fig.9. The RMS value of the SC current under different i_d.

3:45

DH-08. Design and Performance Assessments of a Surface-mounted Permanent-magnet Vernier Motor for Exoskeleton System Application.

C. Liu[1], K. Yang[1], Z. Cai[1], P. Shih[1] and C. Hwang[2]
1. Department of Electrical Engineering, National Sun Yat-Sen University, Kaohsuing, Taiwan; 2. Department of Electrical Engineering, Feng Chia University, Taichung, Taiwan

Introduction: By appropriately adjusting the induced back electromagnetic forces on the stator windings, similar to those of a magnetic-geared motor, extra torque components can be generated from a surface-mounted permanent-magnet Vernier motor (VM) [1]. Since the joint parts of an exoskeleton system are generally equipped with appropriate motor-gear sets to provide the desired driven torques, the costs of these incorporated mechanical components can greatly be reduced with smaller gears ratios. With its relatively larger torque output, as long as the output speeds of the motor-gear set can still meet operational specifications, the VM will thus offer a competitive alternative for such applications. Following the same physical and operational constraints, an optimized VM (Opt. VM) capable of generating twice the torque output of an existing commercial VM (Ref. VM) that is commonly adopted on the exoskeleton system will thus be expected. By setting adequate design objectives and adopting the Taguchi's methodology, from the results calculated by thorough finite element analyses (FEA), the designed Opt. VM will be constructed and the related experimental measurements will be supplied to validate the design adequacies. The Scheme: Based on the related design concepts as discussed in [2], with proper selections of the VM parameters for optimizations, the air-gap flux density distributions of the Opt. VM and the Ref. VM are shown in Fig. 1(a). These two VMs, all have 18 stator slots and 12 rotor pole pairs, as illustrated in Fig. 1(b), and the larger flux densities of the Opt. VM compared with those of the Ref. VM at the designed harmonic orders are evident. To provide better comparisons for application assessments, the detailed performance indices of these two VMs are described by a radar chart as shown in Fig. 1(c). Clearly, at the same material costs and external physical volumes, the Opt. VM can exhibit its superiorities than those of the Ref. VM within the specified operational ranges of the exoskeleton system. The Results: The constructed laboratory Opt. VM is shown in Fig. 2(a), and the comparison results about the torque-speed characteristics among the Ref. VM and the Opt. VM are illustrated in Fig. 2(b). It is obvious that the output torques can almost be doubled from the designed Opt. VM at the lower speed range, with the sacrifices of about 1/2 of the rated and maximum speed levels than those of the Ref. VM. However, from the standard operational specifications, an exoskeleton system must be capable of rotating $\pi/2$ mechanically in 2.5 s to comply the desired stand-up operation, which indicates the standard operational speed is 6.0 rpm. This confirms that by equipping the Opt. VM with a 50:1 gears set, which is only halved the ratio of the one equipped by the Ref. VM will be sufficient enough for the objective exoskeleton system application.

[1] B. Kim and T. A. Lipo, "Operation and design principles of a PM Vernier motor," *IEEE Trans. Ind. Appl.*, vol. 50, no. 6, Nov./Dec. 2014, pp. 3656-3663. [2] S. Hyoseok, N. Niguchi, and K. Hirata, "Characteristic analysis of surface permanent-magnet Vernier motor according to pole ratio and winding pole number," *IEEE Trans. Magn.*, vol. 53, no. 11, Nov. 2017, Art. ID 8211104.

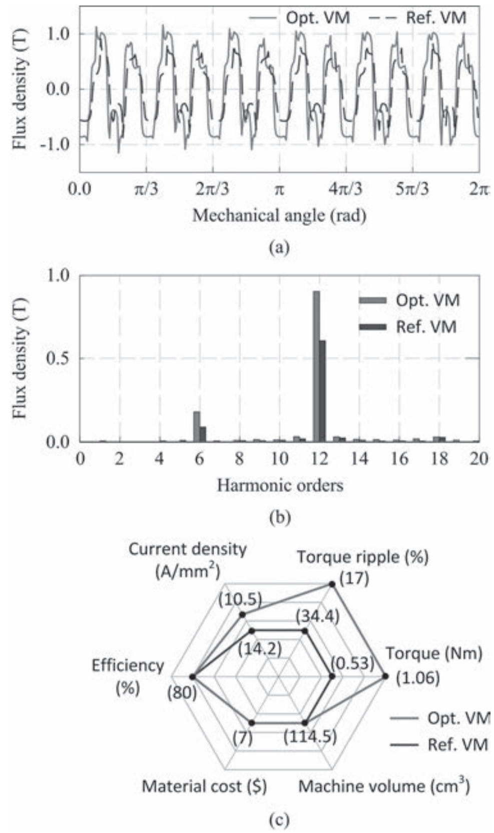

Fig. 1. Performance evaluations of the two Vernier motors. (a) Air-gap flux density distributions. (b) Comparisons of harmonic terms. (c) The performance radar chart.

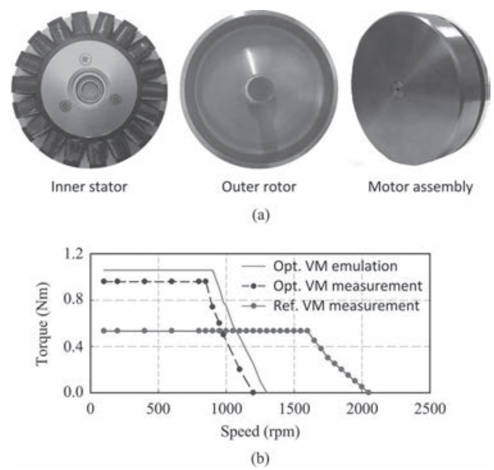

Fig. 2. System experimental verifications. (a) Laboratory prototype of the Opt. VM. (b) The emulated and measured torque-speed characteristics.

WEDNESDAY AFTERNOON, 25 APRIL 2018 ORCHID I-II, 4:00 TO 6:00

Session PL

PLENARY

Sara Majetich, Chair
Carnegie Mellon University, Pittsburgh, PA, United States

INVITED PAPER

5:00

PL-01. Spintronics Nanodevices.

H. Ohno[1,2]
1. Laboratory for Nanoelectronics and Spintronics, Research Institute of Electrical Communication, Tohoku University, Sendai, Japan; 2. Center for Spintronics Integrated Systems, Tohoku University, Sendai, Japan

Development of spintronics nonvolatile nanodevices and their integration with CMOS circuits are critical to realize standby power free, low-power consumption, yet high performance integrated circuits for Internet-of-Things (IoT), high performance computing and artificial intelligence. Endurance and low supply-voltage operation make these spintronics device capable of being used in the place of current volatile working memories such as DRAM and SRAM [1] and beyond. Magnetic tunnel junction (MTJ), a two-terminal nonvolatile spintronic device that can scale down to 20 nm with the perpendicular-easy-axis CoFeB-MgO system [2, 3], is the device most widely employed for such a purpose. I will review the development of MTJs, and discuss about its ultimate scalability beyond 10 nm by showing MTJs with current induced switching and high thermal stability in the range of 4-8 nm [4]. I will then describe the work on three-terminal devices that separate the write current path from the read current path. Here I focus on devices that utilize spin-orbit torque arising from structures involving heavy metals as well as from antiferromagnets [5-9]; the latter is shown to operate as analog memory suitable for neuromorphic applications [10]. Work supported in part by the ImPACT Program of CSTI, the R & D for Next-Generation Information Technology of MEXT, Grant-in-Aid for Specially Promoted Research (17H06093) and the FIRST Program.

[1] H. Ohno, International Electron Device Meeting (IEDM) (invited) 9.4.1 (2010). [2] S. Ikeda, *et al. Nature Materials,* 9, 721 (2010). [3] H. Sato, *et al.* IEDM 2013 and *Appl. Phys. Lett.* 105, 062403 (2014). [4] K. Watanabe, *et al. Nature Communications,* to appear (2018). [5] M. Yamanouchi, *et al. Appl. Phys. Lett.* 102, 212408 (2013). [6] C. Zhang, *et al. Appl. Phys. Lett.* 107, 012401 (2015). [7] S. Fukami *et al. Nature Nanotechnology* doi:10.1028/nnano2016.29 (2016). [8] S. Fukami *et al.* 2016 *Symp. on VLSI Tech.*, T06-5 (2016). [9] S. Fukami *et al. Nature Materials* 15, 535 (2016); doi:10.1038/nmat4566. [10] W. A. Borders *et al.*, *Appl. Phys. Express* 10, 013007 (2017).

THURSDAY MORNING, 26 APRIL 2018 ORCHID I, 9:00 TO 12:00

Session EA

SYMPOSIUM ON NOVEL HARD MAGNETIC MATERIALS AND THEIR APPLICATIONS

Jinbo Yang, Chair
Peking University, Beijing, China

INVITED PAPERS

9:00

EA-01. Heavy rare earth free, free rare earth and rare earth free magnets - vision and reality.

O. Gutfleisch[1] and K. Skokov[1]
1. Material Science, TU Darmstadt, Darmstadt, Germany

It is commonly understood that among the intermetallic phases used for permanent magnets, practically none can fully realize its potential based on the intrinsic magnetic properties. We discuss different reasons leading to this limitation, known as the Brown paradox, and discuss some possible ways of overcoming it. We look into Dy- and Tb-less grain boundary diffused magnets and the scope for the complete elimination of the heavy rare earth elements. Then we compare the intrinsic magnetic properties of (Nd1-xCex-)2(Fe1-yCoy)14B single crystals with the extrinsic characteristics of sintered and hot compacted magnets, so-called rare earth balance magnets, made from the very same alloys. Finally, assessing RE-free materials, our results obtained on Mn- and Co-based RE-free single crystals are compared with the hard magnetic properties of Mn-based permanent magnets.

[1] O. Gutfleisch, M. A. Willard, E. Brück, C. H. Chen, S. G. Sankar, and J. P. Liu, Magnetic materials and devices for the 21st century: stronger, lighter, and more energy efficient. Adv. Mater. 23 (2011) 82. [2] K. Löwe, D. Benke, C. Kübel, T. Lienig, K.P. Skokov, O. Gutfleisch, Grain boundary diffusion of different rare earth elements in Nd-Fe-B sintered magnets by experiment and FEM simulation, Acta Materialia 124 (2017) 421. [3] M.D. Kuz'min, K.P. Skokov, H. Jian, I. Radulov, O. Gutfleisch, Towards high-performance permanent magnets without rare earths, J. Phys. Condens. Matter 26 (2014) 064205. [4] A. Edstrom, M. Werwinski, D. Iusan, J. Rusz, O. Eriksson, K.P. Skokov, I.A. Radulov, S. Ener, M.D. Kuz'min, J. Hong, M. Fries, D. Yu Karpenkov, O. Gutfleisch, P. Toson, J. Fidler, Effect of doping by 5d elements on magnetic properties of (Fe1−xCox)2B alloys, Phys. Rev. B 92 (2015) 174413. [5] M. Dürrschnabel, M. Yi, K. Uestuener, M. Liesegang, M. Katter, H.-J. Kleebe, B. Xu, O. Gutfleisch, L. Molina-Luna, Atomic structure and domain wall pinning in samarium -cobalt based permanent magnets, Nature Communications 8:54 (2017), DOI: 10.1038/s41467-017-00059-9. [6] K. P. Skokov and O. Gutfleisch, Heavy rare earth free, free rare earth and rare earth free magnets - vision and reality, Scripta Materialia, Invited View Point paper, accepted.

9:30

EA-02. $Fe_{16}N_2$: from a 40-year mystery of magnetic materials to one of promises for rare-earth-free magnets.

J. Wang[1,2], Y. Jiang[1], M.A. Mehedi[2], J. Liu[1], Y. Wu[3] and B. Ma[1]
1. Electrical and Computer Engineering, University of Minnesota, Minneapolis, MN, United States; 2. Chemical Engineering and Materials Science, University of Minnesota, Minneapolis, MN, United States; 3. Niron Magnetics, Minneapolis, MN, United States

ABSTRACT $Fe_{16}N_2$ is one of the most promising rare-earth-free magnet candidates with high magnetic energy product. Iron nitride magnet is of great interest as a magnetic material for applications at relatively low temperature (<150 ^oC) ranging from magnets in hard disk drives for data storage and in all kinds of electrical motors, wind turbines, and other power generation machines. A perspective review on our research work on bulk $Fe_{16}N_2$ compound permanent magnet in past years is presented on the aspects of material processing and magnetic characterizations. Specifically, we will introduce and discuss our effort to prepare bulk $Fe_{16}N_2$ compound permanent magnet by using three different approaches, including an ion implantation method, a ball milling method and a strained-wire method. A feasibility of free-standing iron nitride foils with magnetic energy product up to 20 MGOe was successfully demonstrated based on an ion implantation method. Based on our theoretical and experimental progress, we believe that $Fe_{16}N_2$ compound permanent magnet is currently in an accelerating step to be an alternative magnet candidate. TECHNICAL RESULTS AND DISCUSSION During past decades, several permanent magnet materials were discovered, especially those based on rare-earth intermetallic compounds [1,2,3]. The key figure of merit of permanent magnets is the energy product $(BH)_{max}$. Figure 1 lists the development in the maximum magnetic energy product $(BH)_{max}$ at room temperature of market-available hard magnetic materials so far [4] and our predicted value for iron nitride magnet. It is interesting to note that this value, starting from 1MGOe for steels discovered during the early part of last century, increasing to 3MGOe for ferrites, and finally that peaks at 56MGOe for neodymium-iron-boron magnets during the past twenty years. However, new magnets with more abundant and less economically-limited and environmentally-restricted elements is highly demanded to supplement rare earth magnets [3]. At the same time, the saturation magnetization of rare earth magnets may not be high enough to satisfy the requirements for the applications of electric machines. One of basic function of permanent magnets used in electric vehicles and wind turbines is to provide magnetic flux. This function requires a higher saturation magnetization as well as an appropriate coercivity to against self-demagnetization. The most ideal permanent magnet should have the following features: (1) be composed by abundant and environment friendly elements; (2) large saturation magnetization; (3) large energy product; (4) reasonable high coercivity; $(BH)_{max}$ has doubled every 12 years during the 20th century mainly with the progress due to improvements in coercivity [4]. Next generation permanent magnet would be expected with a higher remanent magnetization while with a reasonable coercivity. $Fe_{16}N_2$ has been viewed as a controversial material or mystery before 2000. We have started to work on this material since 2003. Besides reporting a systematic experimental study on $Fe_{16}N_2$ thin films and confirmed its giant saturation magnetization and large anisotropy constant [5], we proposed a "cluster + atom" model based on the first-principles calculation to explain the giant saturation magnetization of $Fe_{16}N_2$ [6]. This model is supported by the discovery of partially localized 3d electrons in $Fe_{16}N_2$ [5]. After those validations, $Fe_{16}N_2$, with a magnetic flux density as high as 2.9T and an anisotropy constant up to 1.0-1.8 MJ/m^3 [7] has been expected to be one of possible rare-earth-free magnet candidates. Moreover, $Fe_{16}N_2$ has combined features of low cost with most redundant elements on earth, environment-friendly and theoretically two times higher energy product than the current market available rare earth magnets, as shown in Fig. 1. In this paper, we introduce three approaches, including an ion implantation approach, a strained-wire method and a ball milling method, which we developed in past six years, for the synthesis of bulk $Fe_{16}N_2$ magnets. By using a nitrogen ion implantation approach [8], we successfully synthesized free-standing $Fe_{16}N_2$ foils with a coercivity of up to 1910 Oe and a magnetic energy product of up to 20 MGOe at room temperature. An integrated synthesis technique was developed, including a direct foil-substrate bonding step, an ion implantation step and a two-step post-annealing process. With the tunable capability of the ion implantation fluence and energy, a microstructure with grain size 25-30 nm is constructed on the FeN foil sample with the implantation fluence of 5×10^{17} /cm^2. To the best of our knowledge, this could be the first experimental evidence of the existence of a giant saturation magnetization, an obviously large coercivity with a magnetic energy product of up to 20 MGOe in a bulk-type FeN magnet sample. Ball milling is one of the other approaches to prepare the $Fe_{16}N_2$ powder [9]. Shock compaction using a gas gun was used to compact the powder into a dense disk shape. We experimentally demonstrated that the volume ratio of the $Fe_{16}N_2$ phase is 70% and that it is stable under shock compaction, without obvious phase decomposition. This approach presents the possibility of mass producing bulk permanent magnets using $Fe_{16}N_2$ with enhanced magnetic properties. Furthermore, we proposed and demonstrated a novel synthesis method for bulk anisotropic $Fe_{16}N_2$ magnet, named as the "strained wire method" [10]. Based on this method, an anisotropic bulk iron nitride magnet with 9 MGOe was achieved for the first time.

[1] O.Gutfleisch, M.A.Willard, E. Brück, C.H.Chen, S.G.Sankar and J.Ping Liu, Magnetic Materials and Devices for the 21st Century: Stronger, Lighter, and More Energy Efficient, Adv.Mater.23(2011) 821-842 [2]L.H. Lewis, F. Jimenez-Villacorta, J., Perspectives on Permanent Magnetic Materials for Energy Conversion and Power Generation, Metallurgical and Materials Transactions A, Physical Metallurgy and Materials Science, 41A(2012) [3]M.J.Kramer, R.W.McCallum, I.A.Anderson, S.Constantinides, J., Prospects for Non-Rare Earth Permanent Magnets for Traction Motors and Generators, Journal of Meta, 64(2012) 752-763 [4] J. M. D. Coey, Advances in Magnetics - Hard Magnetic Materials: a Perspective, IEEE Trans. Magn. 47(2011) 4671 [5] J-P Wang, N. Ji, X. Liu, Y. Xu, C.Sánchez-Hanke, F.M.F. de Groot, Lawrence F.Allard and Edgar Lara-Curzio, J., Fabrication of $Fe_{16}N_2$ Films by Sputtering Process and Experimental Investigation of Origin of Giant Saturation Magnetization in $Fe_{16}N_2$, IEEE Transactions on Magnetics, 48(2012) 1710-1717 [6] N.Ji, X Liu and J-P Wang, J., Theory of giant saturation magnetization in $Fe_{16}N_2$: role of partial localization in ferromagnetism of 3d transition metals, New Journal of Physics, 12(2010) 063032 [7] N.Ji, M.S.Osofsky, V.Lauter, L.F.Allard, X.Li, K.L.Jensen, H.Ambaye, E. Lara-Curzio and J.P Wang, Perpendicular magnetic anisotropic and high spin-polarization ratio in epitaxial Fe-N thin films, Phys,Rev.B84(2011) 245310 & X. Li, et al, to be submitted [8] Y.F. Jiang, M Mehedi, E. Fu, Y. Wang, L.F.Allard and J.P.Wang, J., Synthesis of $Fe_{16}N_2$ compound Free-standing Foils with 20 MGOe Magnetic Energy Products by Nitrogen Ion-Implantation, Nature *Scientific Reports 6*(2016)6:25436 [9] Y.F. Jiang, J.Liu, P.K. Suri, G.Kennedy, N.N. Thadhani, D.J.Flannigan and J.P.Wang, J., Preparation of Fe16N2 Magnet via a Ball Milling and Shock Compaction Approach. *Advanced Engineering Materials*(2015).DOI: 10.1002/ adem.201500455 [10]Y.F.Jiang, V.Dabade, L.F.Allard, Edgar Lara-Curzio, R.James, J.P.Wang, Synthesis of Bulk Fe16N2 Anisotropic Magnet by a Strained Wire Method, *Physical Review Applied,* 6 (2016), 024013

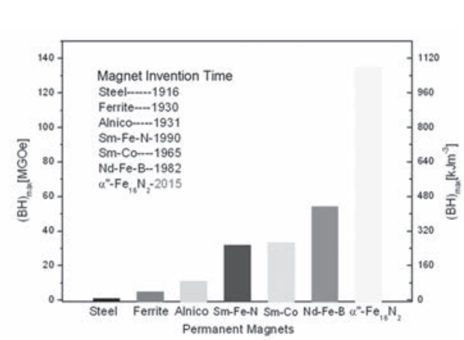

Fig.1 Development and prediction of the energy density (BH)max at room temperature of permanent magnets; Energy product of Fe16N2 was predicted based on the best Bs, Br and projected coercivity;

10:00

EA-03. Rare earth permanent magnets with ultimate hard magnetic properties.

K. Hono[1,2]
1. Elements Strategy Initiative Center for Magnetic Materials, National Institute for Materials Science (NIMS), Tsukuba, Japan; 2. Research Center for Magnetic and Spintronic Materials, National Institute for Materials Science (NIMS), Tsukuba, Japan

There has been much research interest during the past decade to attain high coercivity in Nd-Fe-B magnets without using heavy rare earth (HRE) elements. Now that the supply of rare earth elements has been stabilized, the renewed goal is how to achieve the highest permanent magnetic properties with a balanced use of rare earth elements. In this talk, we will present an overview on our recent progresses on the development of high-coercivity Dy-free Nd-Fe-B magnets that were carried out at NIMS in collaboration with many industrial partners. Thereafter, we will discuss how to achieve ultimate permanent magnet properties by adding trace amounts of HRE to the Nd-Fe-B system. To obtain better understandings of the microstructure-coercivity relationships, we have investigated the microstructures of experimental magnets with wide ranges of coercivities that varied depending on chemical compositions, processing routes and post-manufacturing heat treatments. The microstructure and magnetic domain observations have been carried out using aberration-corrected STEM, atom probe tomography (APT), magneto-optical Kerr microscopy and finite element micromagnetic simulations. We found that the intergranular phase parallel to the c-planes are mostly crystalline with a higher Nd concentration in contrast to the phase lying parallel to the c-axis that contains higher Fe content with an amorphous structure in both sintered and hot-deformed magnets. Micromagnetic simulations suggest that the reduction of magnetization in the latter phase is critical for enhancing the coercivity. Based on these new experimental findings together with our detailed characterization results of the intergranular phases in Nd-Fe-B magnets, we propose a method to increase the coercivity of Nd-Fe-B magnets while maintaining high remanence. Lastly, we will discuss the possibility of industrially viable high-performance magnets other than the Nd-Fe-B system. This talk includes results obtained in collaboration with industrial collaborators including TOYOTA, Toyota Central Research Lab. Intermetallics, YSM and Daido Steel conducted under JST's Collaborative Research Based on Industrial Demand projects.

10:30

EA-04. Recent developments in melt-spun Nd-Fe-B bonded magnets for automotive applications.

Z. Chen[1], W. Zhao[1], N.K. Sheth[1], A. Meerani[1] and J. Herchenroeder[1]
1. Magnequench Technology Center, Neo Performance Materials (S) Pte Ltd, Singapore, Singapore

In recent years, there has been a significant increasing use of Nd-Fe-B permanent magnetic powders and its bonded magnets in the mobility/automotive applications. High performance bonded magnets helps in achieving smaller, lighter and more efficient motors leading to green and efficient vehicles. This also brings new challenges for bonded Nd-Fe-B magnets with requirement of higher mechanical strength, better thermal stability and improved corrosion resistance due to harsh working environment. In this talk, we will review Magnequench's comprehensive efforts with case studies to promote spreading applications of bonded Nd-Fe-B magnets into the automotive industry. These include the development of higher-performance melt-spun Nd-Fe-B powders with more uniform microstructure, development of novel compounds for making bonded Nd-Fe-B magnets with higher mechanical strength, better aging and improved corrosion resistance, and novel design of magnet and magnetizing fixture leading to the optimal use of the magnet.

11:00

EA-05. Effects of Cerium on Magnetic Properties of Sintered R-Fe-B Permanent Magnets.

X. Rao[1], E. Niu[1], F. Du[1] and B. Hu[1]
1. Zhong Ke San Huan Research, Beijing, China

As an element in Lanthanide, Cerium has the highest reserve in global rare earth resources (up to 40 ~ 50 % of total RE). To make the best use of Ce will improve the balance of rare-earth applications. Originating from the mixed valence characteristics of Ce ions in rare-earth transition compounds, its physical and chemical properties usually deviate from the trend of whole RE family. Ce exists in $Ce_2Fe_{14}B$ almost as Ce^{4+} ion. The lack of 4f electron leads Ce^{4+} to make no contribution to magnetism, especially the magneto-crystalline anisotropy. Small ion radius shrinks the Fe-Fe distances and consequently decreases the exchange interaction of Fe sub-lattice, which makes $Ce_2Fe_{14}B$ have lower Curie temperature T_C than other $R_2Fe_{14}B$ compounds. The T_C of $Ce_2Fe_{14}B$ is 422 K which is 164 K less than $Nd_2Fe_{14}B$. J_s is 1.17 T, 0.43 T less than $Nd_2Fe_{14}B$. The anisotropic field μ_0H_a is 3.6T, only 47% of $Nd_2Fe_{14}B$. In addition to decreasing the intrinsic magnetic properties in $Ce_2Fe_{14}B$, Ce also makes heavy damage on the coercivity of sintered Ce-Fe-B magnet. Because the conventional powder metallurgic procedure is in favor of forming $CeFe_2$ Laves phase instead of Ce-rich phase that magnetically decouple $Ce_2Fe_{14}B$ grains. Even so, $Ce_2Fe_{14}B$ still has comparable J_s to that of $SmCo_5$ and reasonable μ_0H_a for permanent magnet development. To add La, the RE element with the largest ion radius, is possible to improve the intrinsic magnetic properties of $(La_xCe_{1-x})_2Fe_{14}B$ [1]. The lattice parameters increase linearly with Ce content x which gives a = 0.8763 + 0.0033x (nm) and c = 1.2135 + 0.0114x (nm). As a result, T_C do increase linearly with T_C = 427.4 + 59.0x (K). Unfortunately the J_s at the temperature of 5K do not indicate the same increase with lattice expansion and keeps approximately a constant of 1.51 T. The practical way of preparing Ce-contained permanent magnet is to let Ce replace Nd to its upper limit. Rapidly quenching routine is straight forward to get rid of the necessity of Ce-rich phase. As shown in Fig.1 [2], even though all the permanent magnetic parameters drop linearly with Ce content x, isotropic $[(Nd_{0.75}Pr_{0.25})_{1-x}Ce_x]_{11.65}Fe_{82.75}B_{5.6}$ powder can still realize reasonable H_{cJ} and $(BH)_{max}$ for certain applications. For example, B_r = 8.54 kG, H_{cJ} = 9.4 kOe and $(BH)_{max}$ = 14.8 MGOe when Ce replaces Nd-Pr by 20 at% (x=0.2). At x=0.5, H_{cJ} keeps about 6.8 kOe with $(BH)_{max}$ of 11.6 MGOe. And the B_r is 7.82 kG. T_C at this composition is reasonably high as 509 K. In preparation of sintered magnets containing Ce, dual-alloy or dual main-phase techniques are usually applied. With Ce-rich/Nd-lean alloy and Nd-rich/Ce-lean alloy as starting materials, sintered (Ce,Nd)-Fe-B magnet is commercialized with high ratio of performance to cost. The key point is to let plenty of Nd-rich phase magnetically decouple $(Ce,Nd)_2Fe_{14}B$ grains. As shown in Table 1 [3], by mixing strip casted Nd-Fe-B and (Ce-Nd)-Fe-B alloy powder with different ratio, the sintered magnet with 45wt% Ce and 55wt% Nd in total rare earth composition gives B_r = 12.4 kG, H_{cJ} = 6.2 kOe and $(BH)_{max}$ = 33.4 MGOe. At Ce of 20wt%, the correspondent parameters are 13.7 kG, 12.0 kOe and 45.0 MGOe, which is good enough to many applications. The melting points of R-rich phase decrease with Ce composition. This implies that sintering temperature for high Ce-containing magnet can be lower than low Ce-containing magnet. Another example is to directly use misch-metal (MM) as raw material [4]. The typical composition of MM is La 27.06 wt%, Ce 51.46 wt%, Pr 5.22 wt%, and Nd 16.16 wt%. When MM to total RE ratio is 21.5%, B_r = 12.09 kG, H_{cJ} = 10.70 kOe and $(BH)_{max}$ = 34.04 MGOe. For magnet only with MM, H_{cJ} is as low as 0.46 kOe. $(BH)_{max}$ is just 2.40 MGOe. Microstructure observation shows that RFe_2 grains, in which Ce is the main component of R, distribute in triangle junction area formed by neighbor $R_2Fe_{14}B$grains. The lack of inter-granular R-rich phase is responsible for low H_{cJ} in sintered MM-Fe-B magnet.

[1] C. D. Fuerst, T. W. Capehart, F. E. Pinkerton, J. F. Herbst, *J. Magn. Magn. Mater.*, 139, 359-363 (1995) [2] Z. M. Chen, Y. K. Lim, D. Brown, *IEEE Trans. Magn.*, 51, 2102104 (2015) [3] M. G. Zhu, W. Li, J. D. Wang et. al.,*IEEE Trans. Magn.*, 50, 1000104 (2014) [4] E. Niu, Z. A. Chen, G. A. Chen et al., *J. Appl. Phys.*, 115, 113912 (2014)

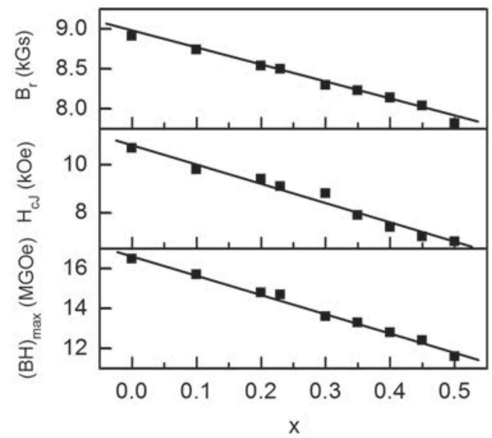

Fig. 1. Magnetic parameters of rapidly quenched $[(Nd_{0.75}Pr_{0.25})_{1-x}Ce_{x}]_{11.65}Fe_{82.75}B_{5.6}$ at RT [2]

x (wt%)	B_r (kG)	H_{cJ} (kOe)	$(BH)_{max}$ (MGOe)	H_k/H_{cJ}	T_C (°C)	Melting point of R-rich phase (°C)
0	14.2	13.1	48.1	0.80	315	455
10	14.0	12.2	46.6	0.87	306	433
15	13.8	11.4	45.6	0.95	294	422
20	13.7	12.0	45.0	0.90	293	419
30	13.6	9.3	43.3	0.93		
45	12.4	6.2	33.4	0.90		

Table 1 Magnetic properties of sintered $(Nd_{100-x}Ce_x)_{30}(Fe, TM)_{69}B_1$ (wt%) by dual main-phase technique [3]

11:30

EA-06. The advances of high-performance permanent magnets by microstructure designing.

W. Cui[1]
1. Northeastern University, Shenyang, China

Since discovered in 1983, Nd-Fe-B magnets have been developed for more than 35 years and its applications have been widened greatly1. The theoretical μ0Ha was predicted to be 7.5 T and (BH)max to be 512 kJ/m3. However, the coercivity of commercialized Nd-Fe-B permanent magnets was still be of ~1.5T, which inhibits its wide applications in hybrid/electric motors and wind powder generators. A general approach is to add heavy rare-earth (HRE) Tb or Dy to enhanced the μ0Ha and subsequent coercivity. Due to scarcity of HRE, many efforts were paid to reduce the addition or get rid of HRE. In a modeled Ta(50 nm)/Nd15Fe75B10(100 nm)/Ta(10nm) single-layer (SL) thin film system, Nd(20nm), Nd70Cu30(20 nm), Nd80Ag20(20nm) layers were diffusion-processed (DPed) into Nd-Fe-B layer. The ambient coercivity is greatly increased from 1.4 T in SL film to ~ 3 T after diffusion process with good squareness(as seen in Fig.1a). The microstructure observation shows the columnar shapes with c-axis perpendicular to substrates. The in-plane view TEM shows that the grains sizes in diffusion-processed films are more refined compared with that of SL film(as seen in Fig.1b-e). And Nd-rich grain boundaries (GBs) are observed, which is the microstructural reason for increased coercivity2. By using diffusion process, the coercivities of Ce-contained Nd-Fe-B magnets was also investigated. Many efforts had been paid to explore hard/soft-magnetic nanocomposite with high-performance. However, the experimental results are far behind such a theoretical prediction. The major challenge is to modify the interface between hard/soft-magnetic phase. Between Nd-Fe-B and F2Co soft-magnetic phase, a Ta(1nm) spacer layer was deposited. And a supereme (BH) max of 486 kJ/m3 and the coercivity of 1.38 T have been obtained as seen in Fig.2a.3 From cross-sectional TEM image, Nd2Fe14B grain was covered by a thin Nd-rich layer. Both Nd2Fe14B grain and soft-magnetic Fe phase were observed without contacting with each other(as seen from Fig.2b-d). Due to the existence of spacer layer, the interfacial coupling cannot be explained by the conventional exchange coupling mechanism. By tuning the thickness of spacer layer, the coercivity, demagnetization process and recoil curves had been analyzed. It was found that the exchange coupling was dominated when Ta spacer layer was less than 2 nm while dipolar coupling became dominated when Ta layer was thicker than 2 nm. Further semi-quantitative dependence between coupling energy and thickness of Ta spacer layer was established4. The dipolar coupling is related with the configuration of magnetic moments. By using quasi-epitaxial growing Sm(Co,Cu)5 films onto Cr-buffered MgO[110] substrate and Ru-buffered Al2O3[001] substrates, the easy axis of Sm(Co,Cu)5 phase can be tuned along either in-plane direction or out-of-plane direction, which provides the opportunity to study the coupling geometry effects on the magnetic properties of Sm(Co,Cu)5/Fe2Co bilayer films. Further TEM observations showed the high-density stacking faults caused by slipping within c-plane of Sm(Co,Cu)5 phase. The crystallographic relationshipe between SmCo3, Sm2Co7 and SmCo5 was caused by periodic slipping within c-plane.5

1.M. Sagawa et al, IEEE Magn. Mag. 20 (1984) 1584; 2.W. B. Cui et al Acta Mater. 59 7768 (2011) 3.W. B. Cui et al Adv. Mater., 24 6530 (2012) 4.W. B. Cui et al Acta Mater. 84 405 (2015) 5.W. B. Cui et al Acta Mater.107 49(2016)

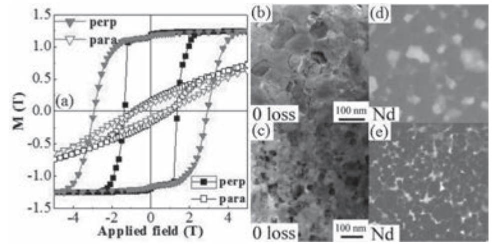

Fig. 1. (a) The hysteresis loops of single-layer film (black) and diffusion-processed film (red) along two directions. The in-plane view of (b) single-layer film and (c) diffusion-processed film along with corresponding Nd-loss image (d and e).

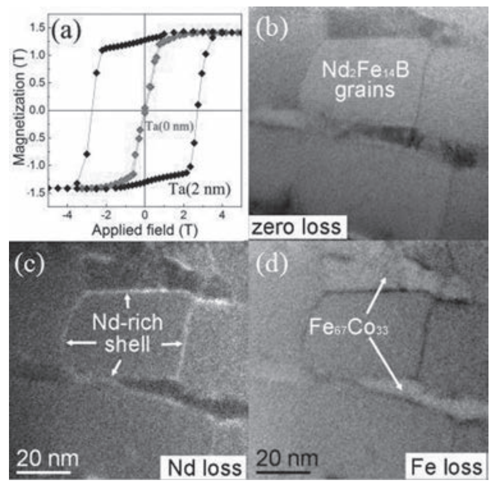

Fig. 2. (a) Hystersis loops of Ta(50 nm)/HM(50 nm)/Ta(x nm)/Fe (5 nm)/Ta(20 nm) bilayer films (x = 0 and 2 nm). (b) Bright-field image of Ta(50 nm)/[HM/Ta(1 nm)/Fe65Co35(10 nm)/Ta(1 nm)]14/HM/Ta(20 nm) and its (c) Nd-loss and (d) Fe-loss image

THURSDAY MORNING, 26 APRIL 2018 ORCHID III, 9:00 TO 12:00

Session EB
MAGNETO-ELASTIC AND MAGNETO-OPTIC MATERIALS

Victorino Franco, Chair
University of Sevilla, Sevilla, Spain

CONTRIBUTED PAPERS

9:00

EB-01. Polymer-based magnetoelectric materials: from fundamentals to applications.

P. Martins[1] and S. Lanceros-Mendez[2,3]
1. Physics, University of Minho, Braga, Portugal; 2. BCMaterials, Leioa, Spain; 3. Ikerbasque, Basque Foundation for Science, Bilbao, Spain

Developing new smart materials and exploring their applicability has been in focus in the field of materials, sensors, actuators and biomedical applications. Smart and functional polymers are taking advantage on the understanding and control of their physico-chemical properties leading to a suitable tailoring of processability, shape control and performance[1,2]. In particular, magnetic devices have become an essential measuring/actuation tool in a range of application areas including biomedicine, multimedia, automobile and military, just to mention some of them, being the magnetoelectric (ME) effect increasingly considered as an attractive alternative for magnetic field sensing/actuation, able to sense/induce static and dynamic magnetic fields[3]. In contrast with ceramic-based ME composites, polymer-based ME composites can be easily fabricated by conventional low temperature processing into a variety of forms, such as thin sheets or molded shapes and can exhibit improved mechanical properties, meeting the latest magnetic sensing market demands[4,5]. This work reports on the development of novel composites based on the understanding of the magnetoelectric coupling as well as on the development of magnetic sensors, magnetic actuators, energy harvesters and biomedical applications, not only understanding and optimizing their magnetoelectric coupling, but also demonstrating their practical characteristics as technological devices. Thus, sensors are developed based on PVDF/Metglas and PVDF-TrFE/$CoFe_2O_4$(CFO) composites (Figure 1a,b) and the ME coefficient (Figure 1c,d), full scale input (FS), hysteresis, sensitivity, linearity and resolution of the materials will be demonstrated and discussed. Further, the main characteristics and potential applicability of polymer composites based on isotropic and anisotropic magnetostrictive magnetic nanoparticles within a piezoelectric polymer will be introduced. This work provides an overview of the frontline research of this fascinating research field and will present the open questions and open needs to reach full applicability of the novel materials[6]. Acknowledgements The authors thank the FCT- Fundação para a Ciência e Tecnologia- for financial support in the framework of the Strategic Funding UID/FIS/04650/2013 and under project PTDC/EEI-SII/5582/2014. P.M also support from FCT (SFRH/BPD/96227/20130 grants). Financial support from the Spanish Ministry of Economy and Competitiveness (MINECO) through the project MAT2016-76039-C4-3-R (AEI/FEDER, UE) (including the FEDER financial support) and from the Basque Government Industry Department under the ELKARTEK Program is also acknowledged.

1. Undre, S. B.; Pandya, S. R.; Kumar, V.; Singh, M. "Dendrimers as smart materials for developing the various applications in the field of biomedical sciences", Advanced Materials Letters 2016, 7, 502-516. 2. Li, S.; Tiwari, A.; Prabaharan, M.; Aryal, S. Smart polymer materials for biomedical applications, 2011. 3. Zong, Y.; Zheng, T.; Martins, P.; Lanceros-Mendez, S.; Yue, Z.; Higgins, M. J. "Cellulose-based magnetoelectric composites", Nature Communications 2017, 8. 4. Martins, P.; Lopes, A. C.; Lanceros-Mendez, S. "Electroactive phases of poly(vinylidene fluoride): Determination, processing and applications", Progress in Polymer Science 2014, 39, 683-706. 5. Martins, P.; Kolen'Ko, Y. V.; Rivas, J.; Lanceros-Mendez, S. "Tailored Magnetic and Magnetoelectric Responses of Polymer-Based Composites", ACS Applied Materials and Interfaces 2015, 7, 15017-15022. 6. Lanceros-MÃ©ndez, S.; Martins, P. Magnetoelectric Polymer-Based Composites: Fundamentals and Applications; Wiley, 2017.

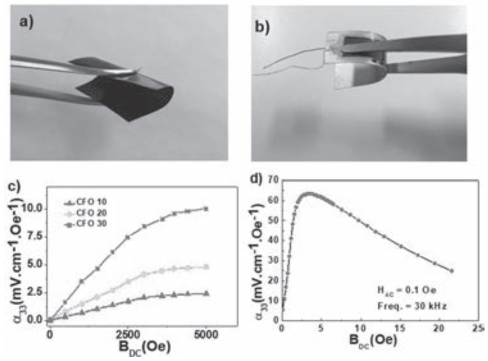

Fig. 1. a) PVDF-TrFE/CFO composite photograph. b) PVDF/Metglas photograph. c) ME response on PVDF-TrFE/CFO composite. d) ME response on PVDF/Metglas laminated composite.

9:15

EB-02. MR Elastomers for Energy Harvesting System.

G. Diguet[1], G. Sebald[1], M. Nakano[2,1] and M. Lallart[3]
1. ELyTMaX UMI 3757. International Joint Unit, Tohoku University, CNRS, Université de Lyon, Tohoku University, Sendai, Japan; 2. Intelligent Fluid Control Systems Laboratory, Institute of Fluid Science, Tohoku University, Sendai, Japan; 3. LGEF EA682, Université de Lyon, INSA-Lyon, Lyon Villeurbanne, France

MREs (Magneto-Rheological Elastomers) are composite materials based on magnetic particles dispersion within a non-magnetic and elastic soft matrix. Combination of these two properties leads to classifying these materials as smart materials using the conversion between the magnetic energy and elastic energy; one property is tunable through the second one. Such MREs were studied for the magnetically tuned stiffness, better known as ΔG effect corresponding to an increase of the elastic modulus G_0 of the composite as a magnetic field is acting on the particles [1]. Here, we study this material for generating electricity [2]. For this purpose, a magnetic circuit with an excitation coil and a search coil are used. A DC flux is generated by the excitation coil (a permanent magnet can also be used). Along with the magnetic circuit, a MRE which can be sheared is placed. The search coil will detect a varying magnetic flux Φ due to the effect of the MRE under shear. Experimental evidences and models can be found in the papers [2-3]. In this study, we used COMSOL® to simulate the pure shear effect on the magnetic properties of a magnetic particle and a representative composite at different magnetic field. At the particle level, assuming that the particle is a homogeneous sphere (with the demagnetizing factor N=1/3 and magnetic saturation $\mu_0 M_{p\_sat}$=2.14 T) placed in a non-magnetic medium where a magnetic field H_a exists, the particle magnetization M_p at low field is $M_p = 3H_a$. In the case of anisotropic MRE, where the composite was cured under an applied magnetic induction field, the particles form chain-like structures. The field H_a is the superposition of two contributions: the external field H_0 (along z-axis) and the field due to other particles in the chain H_p, so that $H_a = H_0 + H_p$. In this case, the field generated by other particles depends on the inter-particles distance as seen in Fig1. As the particles are getting farther, the field chain H_p is getting weaker. In a pure shear of the chain, the field H_p will change in direction and strength and consequently the particle induction magnetic state will also change as seen in Fig.2. For a representative composite cell with a filling factor of 30%, the saturation is 510000 A/m. At low shear ($dy/2a$=0.1) the particles are magnetically saturated by a magnetic induction field around B_0=0.5 T whereas at relatively high shear ($dy/2a$=1.3) the particles are magnetically saturated around B_0=0.8 T which is the usual saturating field of an isolated (non-interacting) ferromagnetic sphere. As the composite is sheared, the average volume of the representative composite cell induction is decreased to the non-interacting position. Moreover, as the inter-particles distance dz is reduced, the change ΔB is larger. This is this change of induction ΔB which can be converted into electricity.

[1] YC Li, JC Li, WH Li, H. Du. (2014) A state-of-the-art review on magnetorheological elastomer devices. Smart Material Structure 23:123001 [2] M. Lallart, G. Sebald, G. Diguet, J-Y. Cavaille, M. Nakano (2017) Anisotropic magnetorheological elastomers for mechanical to electrical energy conversion. Journal of Applied Physics 122, 103902 [3] G. Sebald, M. Nakano, M. Lallart, T. Tian, G. Diguet, J-Y. Cavaille (2017) Energy conversion in magneto-rheological elastomers. Science and Technology of Advanced Materials, 18:1, 766-778.[1] YC Li, JC Li, WH Li, H. Du. (2014) A state-of-the-art review on magnetorheological elastomer devices. Smart Material Structure 23:123001

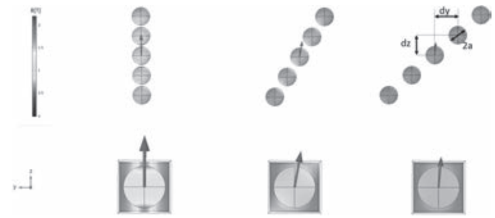

Fig. 1. Induction in chain of particle (top) and in a representative composite (*30* %vol.) cell (bottom) at different shear. Red arrow represents the particle induction vector.

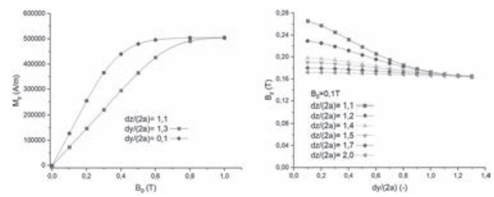

Fig. 2. Representative composite cell magnetization (z-component) versus applied field and representative composite cell magnetic induction (z-component) versus shear strain.

9:30

EB-03. Dynamic Characterization of a Magnetostrictive-based Sensor for Fast Force Profile Detection.

V. Apicella[1], C.S. Clemente[1], D. Davino[1], D. Leone[1] and C. Visone[1]
1. Department of Engineering, University of Sannio, Benevento, Italy

Force detection in mechanical systems is a task of great interest in several technological applications and hence the development of new force sensors able to operate without undergoing measurement alterations due to electromagnetic disturbances, focused the attention of both industry and research in last years. Attention is so focused on new materials able to exploit the simplest transduction principle, in order to guarantee the easiest sensor design and, at the same time, show good durability properties that allows the sensor to be employed in the widest application range. These features make *Galfenol,* an *Fe-Ga* alloy, a suitable candidate for the development of force sensors. In [1], a new methodology based on the anisotropy energy measurement has been exploited with the aim of estimate the stress state of a Galfenol sample if subjected to external compressive forces. Since the procedure makes use of the well-known *quasi-static* magnetic characteristic of the magnetostrictive material, it has proved to be effective only if slow varying force profiles are applied to the sensing device. Actually, there are lots of applications which require the detection of forces with high rate of variation. In limit cases, the detection of impulse-like forces, i.e. crashes, would also be required. A remarkable example is represented by automotive applications, such as crash sensors for air-bag actuation systems, [2]. It is clear that, when fast force profiles are of concern, the procedure described in [1] is not appropriate, since it neglects any dynamic effect that can appear into the material for fast input variations, [3], as, for example, magnetic diffusion phenomena, [4, 5]. In this work, a dynamic characterization of a Galfenol cylindrical sample of *30 mm* length and *5 mm* diameter is carried out, with the aim of develop a magnetostrictive force sensor able to detect and measure fast inputs, up to the crash limit. As often proposed in literature, for example in [6], the idea is to use a *Hammerstein-like* system which assumes the splitting of the nonlinear static characteristic and hence to identify the dynamic contribution to the whole magneto-mechanical sample response. The starting point is represented by the *quasi-static* Galfenol characteristic, shown in Figure 1. In particular the figure shows the *Flux Density, B,* with respect to the external applied compressive stress, σ. Different curves are represented for different values of the magnetic bias field. These curves could be used to measure a slow varying force profile, by a proper modeling of the rate-independent memory effect. Conversely, if fast input forces are applied to the specimen, the dynamic behavior can be taken into account and modeled through the exploitation of the *Hammerstein system* sketched in Figure 2. The first block refers to the above described *quasi-static* characteristic of the material. At this stage the hysteresis is neglected and, as a consequence, Π[σ] is a non-linear function without memory. The second block describes a *linear dynamic* system and *G(s)* is its transfer function in the *Laplace* domain. The first block, Π[σ], could be identified by a suitable quasi-static measurements set, while the linear dynamic subsystem *G(s)* is identified by standard methods, from experimental data collected in dynamic conditions. This preliminarily requires the compensation of the nonlinear static part of the system accomplished through the construction of the inverse (or compensator) of Π[σ] operator. It is also important noting that, as described in [7], a special attention must be paid to the bias value which modifies the working point on the static characteristic which could affect the entire identification procedure. Finally, once the whole response of the specimen has been completely described, arbitrary force profiles can be applied to the sample in order to validate the proposed model.

[1] Apicella, V., Clemente, C. S., Davino, D., & Visone, C. (2017). Experimental evaluation of external and built-in stress in Galfenol rods. *Physica B: Condensed Matter*. [2] Chan, C. Y. (2002). A treatise on crash sensing for automotive air bag systems. *IEEE/ASME transactions on mechatronics*, *7*(2), 220-234. [3] Scheidler, J. J., Asnani, V. M., & Dapino, M. J. (2016). Frequency-dependent, dynamic sensing properties of polycrystalline Galfenol (Fe81. 6Ga18. 4). *Journal of Applied Physics*, *119*(24), 244902. [4] Scheidler, J. J., & Dapino, M. J. (2016). Mechanically induced magnetic diffusion in cylindrical magnetoelastic materials. *Journal of Magnetism and Magnetic Materials*, *397*, 233-239. [5] Davino, D., Giustiniani, A., Visone, C., & Zamboni, W. (2012). Stress-induced eddy currents in magnetostrictive energy harvesting devices. *IEEE Transactions on Magnetics*, *48*(1), 18-25. [6] Guo, Y., Mao, J., & Zhou, K. (2012, August). Rate-dependent modeling and control of GMA based on Hammerstein model with Preisach operator. In *Mechatronics and Automation (ICMA), 2012 International Conference on* (pp. 343-347). IEEE. [7] Butcher, M., Giustiniani, A., & Masi, A. (2016). On the identification of Hammerstein systems in the presence of an input hysteretic nonlinearity with nonlocal memory: Piezoelectric actuators–an experimental case study. *Physica B: Condensed Matter*, *486*, 101-105.

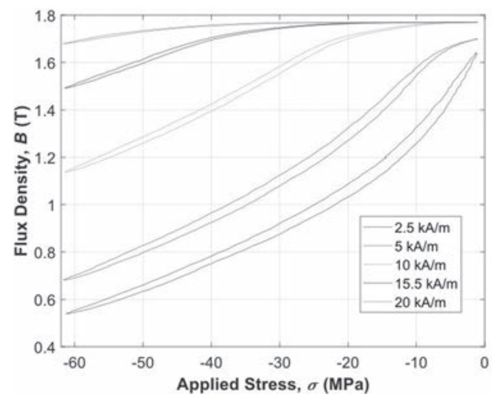

Fig. 1. Static magneto-mechanical characteristic of the Galfenol rod. Magnetic induction with respect to the stress applied with slow rate of variation is shown for different values of the bias magnetic field.

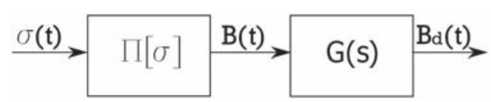

Fig. 2. Block diagram of the Hammerstain-like system exploited to model the dynamic behavior of the magnetostrictive sample. σ(t) is the applied stress, while B(t) is the quasi-static response of the specimen, obtained through the constitutive relation Π[σ]. G(s) is the transfer function of the second block which allows to take into account the dynamic behavior of the system. Finally, $B_d(t)$ is the overall system response.

9:45

EB-04. Effect of substrate temperature driven magnetic anisotropies on the magnetostrictive behaviour of Tb-Fe-Co thin films.

U. K[1,2], A. Talapatra[3], *A. Chelvane*[1], J. Mohanty[3] and J. V[2]
1. Defence Metallurgical Research Laboratory, Hyderabad, India;
2. Physics, National Institute of Technology Warangal, Warangal, India;
3. Physics, Indian Institute of Technology Hyderabad, Kandi, Sangareddy, India

Rare earth transition metal based alloy thin films exhibit giant magnetostriction owing to the large magnetic anisotropy arising from the rare earth sub-lattice. Elaborate studies carried out on these films have shown that Tb-Fe-Co based thin films are promising candidates for magnetostrictive applications as their magnetic anisotropy and thermal stabilities are large [1,2]. Tb-Fe-Co magnetic phase diagram shows that films with compositions $Tb_{10}(Fe,Co)_{90}$ and $Tb_{50}(Fe,Co)_{50}$ exhibit strong in-plane (IP) magnetic anisotropy which is an important mandate for realizing high magnetostriction [3,4]. Recent studies carried out on $Tb_{10}(Fe,Co)_{90}$ films have shown that presence of competing IP and out-of-plane (OOP) magnetic anisotropies has been found to be detrimental for magnetostriction [4]. Hence, there is an interest to explore the magnetic properties of $Tb_{50}(Fe,Co)_{50}$ films. It has also reported recently, that a considerable improvement in the magnetostriction has been obtained for thin films processed with in-situ substrate heating during thin film deposition [5]. In this context, a study has been planned to investigate the magnetic and magnetostrictive behaviour of $Tb_{50}(Fe,Co)_{50}$ films grown with different substrate temperatures. $Tb_{50}(Fe,Co)_{50}$ films were grown on Si <100> substrates by dc magnetron sputtering employing an alloy target. Prior to deposition a base vacuum of 1 x 10^{-8} torr has been achieved in the sputtering chamber. During deposition films were grown with different substrate temperatures (T_s) *viz*., 30, 300, 400, 450, 500 and 550^o C. Deposition parameters such as sputtering power (50 W) and gas pressure (5 m.torr) were kept constant for all the depositions. Structural and microstructural investigations were carried out using X-ray diffraction (XRD) and scanning electron microscopy (SEM) respectively. Simultaneous atomic and magnetic force microscopy (AFM/MFM) studies were carried out for the as-deposited and films processed with various T_s to observe the topography and magnetic domains. IP and OOP magnetization curves were traced upto maximum magnetic field of 15 kOe. IP magnetostriction measurements were measured using a homemade optical setup. The thickness of the as-deposited and films processed with different substrate temperatures are found to be ~150 nm. Structural studies showed that the as-deposited Tb-Fe-Co film is amorphous in nature. Upon increase in T_s, formation of $Tb_2(Fe,Co)_{17}$ phase could be noticed. Surface roughness estimated from AFM studies indicated an increase in the surface roughness with increase in T_s. SEM studies exhibited a globular kind of surface morphology whose sizes increased with increase in T_s owing to the growth of Fe-Co grains. Magnetization studies showed an IP magnetic anisotropy for the as-deposited film with low coercivity. With increase in T_s, a spin reorientation transition (SRT) from IP to OOP direction (SRT1) could be noticed (Fig. 1). Accordingly, the OOP coercivity was found to increase with increase in T_s. With subsequent increase in T_s (> 450^o C) the film undergoes one more SRT from OOP to IP direction (SRT2) (Fig. 2). The possible reason for SRT1 could be attributed to the magnetoelastic anisotropy arising due to the interfacial stresses developed in the film owing to the difference in the thermal expansion co-efficient between the film and interface [6]. The large formation of randomly distributed $Tb_2(Fe,Co)_{17}$ phase induces SRT2 at higher T_s. MFM image of as-deposited film indicate weak domain contrast with no identifiable domain pattern. However, with increase in T_s the OOP magnetic contrast is found to be enhanced (Fig. 1). The magnetic phase difference (MPD) which is a figure of merit to quantify the strength of OOP magnetic components show a considerable increase with increase in T_s upto 400^o C (Fig. 2). With subsequent increase in T_s the MPD decreases. Finally, the film grown at 550^o C shows a weak domain contrast devoid of any domain pattern. The microscopy results further confirms the SRT transitions observed from magnetization studies. Magnetostriction estimated from tip deflection measurement has been found to decrease marginally with increase in T_s upto 300^o C. Films deposited with higher substrate temperatures such as 400 and 450^o C show small change in magnetostriction owing to strong OOP magnetic anisotropy [4]. With subsequent increase in T_s, the magnetostriction was found to increase considerably. The possible reason for the increase in magnetostriction at higher substrate temperatures (> 450^o C) can be attributed to the formation of crystalline $Tb_2(Fe,Co)_{17}$ with enhanced grain sizes and relaxation of residual stresses. Based on the structural, microstructural (surface and magnetic), magnetization and magnetostriction studies a strong correlation between magnetic anisotropy and magnetostriction has been established.

1. du Tremolet de Lachiesserise, E., Magnetostriction: Theory and Applications of Magnetoelasticity (CRC press, Boca Raton (USA), 1993). 2. Danh, T.M., N.H. Due, H.N. Thanh and J. Teillet, Magnetic, Mossbauer and magnetostrictive studies of amorphous Tb(Fe,Co)1.5 films. J. Appl. Phys., 87 (2000) 7208. 3. K. Uma Devi, J. Arout Chelvane, Himalay Basumatary, M. Ramudu, S.V. Kamat, V. Jayalakshmi, J. Magn. Magn. Mater., 418 (2016)163. 4. K. Umadevi, A. Talapatra, J. Arout Chelvane, Mithun Palit, J. Mohanty, and V. Jayalakshmi, J. Appl. Phys., 122 (2017) 065108 5. HimalayBasumatary, J. AroutChelvane, D.V. Sridhara Rao, S.V. Kamat, and R. Ranjan, J. Magn. Magn. Mater.384 (2015) 58 6. Liuniu Tong, Peng Deng, Xian-Mei He, Tingting Li, Thin Solid Films, 562 (2014) 543

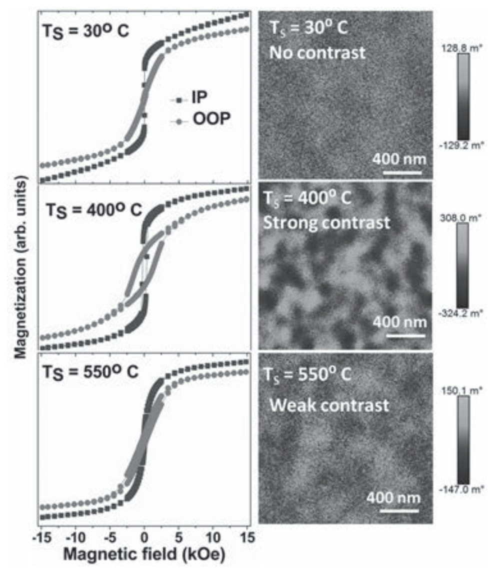

Fig. 1. Magnetization curves and MFM images of Tb-Fe-Co films grown with different substrate temperatures.

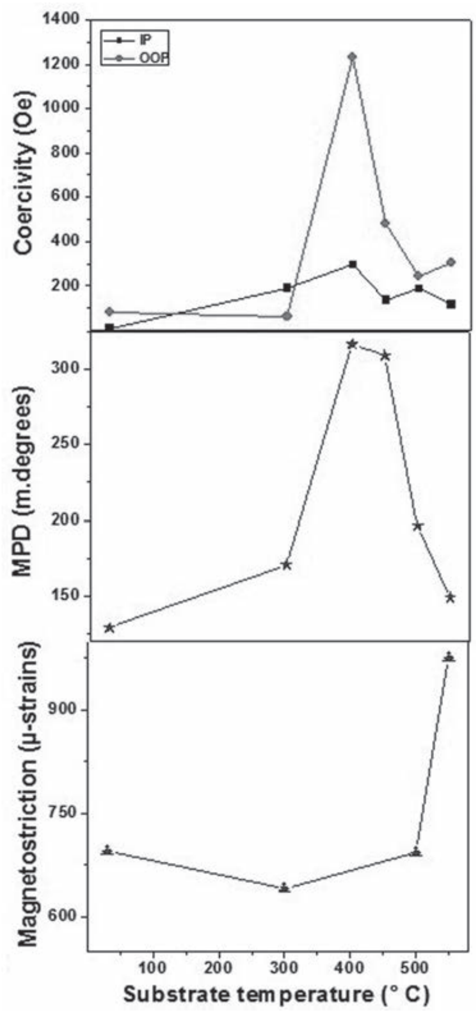

Fig. 2. Variation of coercivity, magnetic phase contrast and magnetostriction with substrate temperature for Tb-Fe-Co films.

10:00

EB-05. Investigating the magnetization process of Ni-Mn-Ga films with different types of microstructure.

F. Casoli[1], S. Fabbrici[1], M. Takhsha Ghahfarokhi[1], L. Nasi[1], R. Cabassi[1], G. Varvaro[2], F. Celegato[3], P. Tiberto[3] and *F. Albertini*[1]
1. IMEM-CNR, Parma, Italy; 2. ISM-CNR, Roma, Italy; 3. INRIM, Torino, Italy

Magnetic shape memory materials display multifunctional properties (e.g. magnetomechanical, magnetocaloric, magnetoreisistive) arising from the presence of a martensitic transformation and magnetic states [1]. Low-dimensional materials, mainly thin films, have recently attracted much interest for their possible integration in micro/nanosystems for the realization of new-concept devices (e.g. microactuators, energy harvesters, solid-state microrefrigerators) [2]. Microstructure engineering is crucial for the optimization of their functional behaviour, where twin variant configuration plays a major role. The intimate link between magnetic and structural degrees of freedom and the hierarchical twin-within-twin martensitic structure makes epitaxial films and nanostructures a unique platform for the precise control of the structural and magnetic configuration from the atomic to the macroscale We have shown that in epitaxial thin films the magnetic and structural properties can be optimized at the different length-scales by an appropriate choice of substrates/underlayers, thickness and growth parameters [3, 4]. In addition, we have found that lateral confinement in patterned thin films in able to strongly influence the twin variants configuration [5]. In the present paper we will mainly focus on the relation between the film microstructure and magnetization processes by performing micromagnetic simuations. Ni–Mn–Ga thin films of thickness ranging from 75 to 200 nm were epitaxially grown in the temperature range T=200-400 °C by rf sputtering on a 50 nm on MgO (001) and Cr/MgO(100) changing sputtering rate and applied stress at the substrate during growth. Thermal treatments in the same T range were done after growth also in presence of applied stress along selected substrate crystallographic directions. The films were deposited from a target of composition $Ni_{49.3}Mn_{27.8}Ga_{22.9}$ (at%) and show a monoclinic martensitic structure at RT. Their characterization was carried out by different techniques, thus realizing a multi-scale structural and magnetic study. The sample microstructure was studied by means of Scanning Electron Microscopy in conventional and backscattered mode. The microstructure at the nano and atomic scale was investigated by Scanning Transmission Electron Microscopy (STEM), high resolution TEM imaging and Electron Diffraction. X-ray diffraction was collected using a diffractometer equipped with a solid-state Si(Li) Peltier detector and an environmental chamber. Atomic Force and Magnetic Force Microscopy were performed to correlate the magnetization patterns and the magnetic domain structure to the microstructural pattern. A thorough magnetic study was performed in the temperature range 4-300 K by means of Alternated Gradient Force, SQUID and Vectorial Vibrating Sample magnetometry. By applying T and stress to the substrate during and after growth, a variety of martensitic patterns (i.e. orientation and spatial organization of the martensitic twin variants) can been obtained for epitaxial thin films of different thickness, giving rise to peculiar magnetization processes. Metamagnetic processes characterized by magnetization jumps of variable intensity along different crystallographic directions have been found and correlated with the orientation and spatial organization of the martensitic twin variants. The micromagnetic simulations demonstrate that magnetization jumps, typically attributed to the magnetically induced reorientation of twin variants, similarly to what occurs in bulk materials, can have a purely magnetic origin and can take place in the first quadrant of the (M,H) diagram, with variable intensity (Figure 1). The results of the simulations have been compared with a detailed experimental investigation realized by magnetometry and vectorial magnetometry: we have measured magnetization curves along different directions of the substrate crystal, simultaneously recording parallel and transverse components of magnetization

[1].M. Acet, et al., Handbook of Magnetic Materials vol. 19, Elsevier, Amsterdam, 2001. [2] A. Backen et al., Adv. Eng. Mat. 14,(2012) 696. [3] P. Ranzieri et al., Acta Mater. 61 (2013) 263. [4] P. Ranzieri et al., Adv. Mater. 32, (2015) 4760. [5] M. Campanini er al., (under review, Nature Communications)

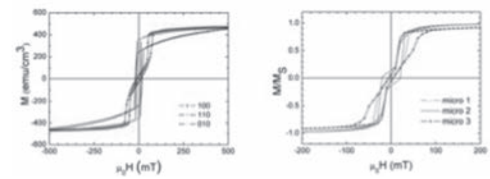

Fig. 1. XLeft Experimental hysteresis curves along different substrate directions for NiMnGa thin film of 200 nm grown on Cr/MgO(100). Right: Hysteresis curves simulated for different types of microstructures.

10:15

EB-06. Magnetostrictive Behaviors of fcc-Co Single-Crystal Films under Rotating Magnetic Fields.

T. Kawai[1], K. Serizawa[1], M. Ohtake[2] and M. Futamoto[1]
1. Chuo Univ., Tokyo, Japan; 2. Kogakuin University, Tokyo, Japan

Introduction Meta-stable fcc-Co structure has been stabilized in thin films prepared by molecular beam epitaxy or by sputter deposition[1] and much interest is paid for their magnetic properties in comparison to those of stable hcp-Co structure. The magnetic anisotropy of fcc-Co film has been already reported[2]. However, there is no systematic study on magnetostriction. In this study, fcc-Co single crystal films with three major planes of (100), (110), and (111) were prepared and the magnetostrictive behaviors were investigated under rotating magnetic fields up to 1.2 kOe. The experimental results were analyzed by using a coherent rotation model of magnetization under applied magnetic fields. Experimental procedures Co films with 500 nm thickness were deposited on MgO(001) and MgO(110) single-crystal substrates with under layers of Pd and Cu and on Al_2O_3(0001) single-crystal substrate directly using an UHV RF magnetron sputtering system at a substrate temperature of 300 °C for MgO and 150 °C for Al_2O_3 substrates[3]. The film structure was analyzed by RHEED and XRD. The film structures were confirmed to be fcc(001), fcc(110), and fcc(111) single-crystal respectively. Magnetostriction was measured by using a cantilever method under rotating magnetic fields up to 1.2 kOe. Magnetostriction observation directions were along [100] and [110] for (001) and (110) films and along [112] for (111) film. Assuming a coherent rotation of magnetization, the magnetostrictive behaviors were analyzed. Results and discussion Figure 1 shows the magnetostrictive behaviors measured for fcc-Co films with different orientations measured under a magnetic field at 1 kOe. For the (001) film, the output waveform is triangle along [100], which is the hard magnetization axis, and bathtub-like along [110], which is the easy magnetization axis. The experimental results reflect four-fold in-plane anisotropy. On the other hand, the output waveforms for the (110) film are different from those of (001) film, even though the observation directions are similar. The output waveform is sinusoidal for the (111) film. The experimental results were analyzed by using a coherent rotation model of magnetization. The behaviors for (001) film show good agreement with the calculated results assuming a four-fold in-plane magnetocrystalline nisotropy, whose easy magnetization axis is along <110> and hard axis along <100>. Under the condition, the magnetization tends to keep the direction along the easy magnetization direction under rotating magnetic filed. The results for (110) film along <100> is similar to the calculation showed in the Fig. 1 (d) assuming the uni-axial anisotropy, where the easy axis is along <100>. In the (110) plane, the anisotropy due to hetero-epitaxial growth is considered to be dominant. For the (111) film, the magnetic property is almost isotropic because K_1 can be neglected in the plane. Therefore, the magnetization rotates simultaneously with applied rotating magnetic fields and the output looks like sinusoidal as expected. The magnetostriction constants, λ_{100} and λ_{111}, are respectively estimated to be 90×10^{-6} and -40×10^{-6}. The large positive value of l_{100} is consistent with those of fcc Co-Ni alloys[4] and also consistent with that of the first-principle calculation[5].

[1] D. Weller, G. R. Harp, R. F. C. Farrow, A. Cebollada, and J. Sticht, *Phys. Rev. Lett.*, 72, 2097 (1994). [2] M. J. M. Pires, A. A. C. Cotta, M. D. Martins, A. M. A. Silva, and W. A. A. Macedo, *J. Magn. Magn. Mater.*, 333, 789 (2011). [3] M. Ohtake, O. Yabuhara, J. Higuchi, and M. Futamoto, *J. Appl. Phys*., 109, 07C105 (2011). [4] S. Ishio, T. Kobayashi, H. Saito, S. Sugawara, and S. Kadowaki, *J. Magn. Magn. Mater.*, 164, 208 (1996). [5] R. Q. Wu, L. J. Chen, A. Shick, and A. J. Freeman, *J. Magn. Magn. Mater.*, 177-181, 1216 (1998).

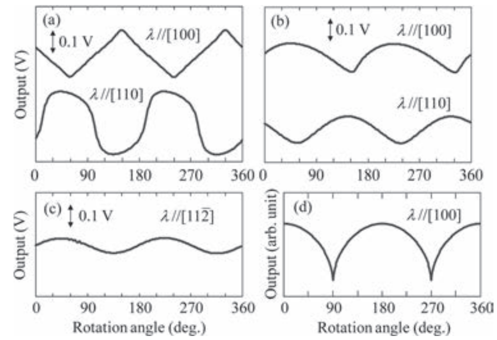

Fig. 1. Magnetostrictive behaviors measured for single-crystal fcc-Co films with (a) (001), (b) (110), and (c) (111) orientations under a rotating magnetic field at 1 kOe. The calculated output for (110) orientation assuming the uni-axial anisotropy shows in (d).

10:30

EB-07. Microstructure and elastocaloric effect in as-undercooled $Pd_{59.3}In_{23.2}Fe_{17.5}$ magnetic shape memory alloys.

Q. Shen[1] and J. Liu[1]
1. Key laboratory of Magnetic Materials and Devices, Ningbo Institute of Material Technology and Engineering, Ningbo, China

Based on the reversible martensitic transformation (MT) induced by uniaxial stress accompanying a large latent heat release/absorption, the research on elastocaloric effect (eCE) refrigeration has been rapidly developed due to the relatively simple design of cooling systems. Shape memory alloys (SMAs) undergoing a diffusionless MT exhibit large eCE owing to a stress driven MT from cubic austenite to a lower symmetric martensitic phase [1]. The outstanding superelastic behavior, good ductility and metamagnetic transformation suggest Pd-In-Fe magnetic SMAs as a great candidate of eCE. From the previous report [2], the MT temperatures of Pd-In-Fe alloys are sensitive to the Pd content. In addition, the annealing at high temperature of 1473 K for 24 h is required to obtain a homogeneous microstructure. The high undercooling solidification treatment has been proposed to refine grains and increase the MT temperatures, as well as to directly obtain the chemically homogenized samples [3]. In this study, we have prepared $Pd_{59.3}In_{23.2}Fe_{17.5}$ alloys by undercooling process upon a degree of 170 K below the liquid temperature. Microstructure was observed by Scanning Electron Microscopy (SEM) and transmission electron microscopy (TEM) and eCE was investigated by universal testing machine with a K-type thermocouple. Fig. 1 shows the SEM backscattered image and TEM microstructure of as-cast and as-undercooled $Pd_{59.3}In_{23.2}Fe_{17.5}$ alloys, respectively. For the as-cast sample, typical dendritic morphology is observed (a), whereas homogeneous austenitic phase at room temperature is obtained by annealing at 1473 K, indicating it transforms below room temperature (~ 250 K). In contrast, a 2*M* martensitic structure with typical microtwins at room temperature can be seen in (b) for the as-undercooled sample. The appearance of martensitic phase in the as-undercooled sample is ascribed to the large recalescence inducing residual internal stress. Fig. 2 shows adiabatic temperature change (ΔT) as a function of temperature of the as-undercooled sample when loading the stress of 154 MPa in the temperature range of 312 - 361 K. As the loading stress is up to 500 MPa, there is no MT recorded for the as-cast sample with dendritic structure, and thus the ΔT is negligible. The value of ΔT is 2.1 K at 312 K as the sample still contains a part of martensitic phase. With increasing temperature, the ΔT starts to increase up to 2.8 K until 326 K due to the larger fraction of austenite phase. Then ΔT decreases with further increasing the initial temperature as the critical stress to induce MT becomes higher and correspondingly the transformation fraction is smaller. The temperature window is as wide as 50 K. Our results indicate that the highly undercooled $Pd_{59.3}In_{23.2}Fe_{17.5}$ alloy is promising to be a new magnetic SMA with large eCE and easy to be prepared.

[1] L. Manosa and A. Planes, Advanced Materials, (29) 2017 1603607. [2] H. Ishikaw, Y. Sutou, et al., Applied Physics Letters, (90) 2007 261906. [3] W. Sun, X.H. Xu, et al., Journal of Applied Physics, (117) 2014 163909.

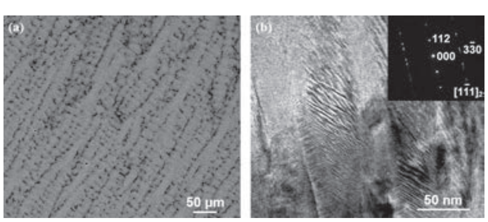

Fig. 1. (a) SEM backscattered image of as-cast $Pd_{59.3}In_{23.2}Fe_{17.5}$ at room temperature. (b) TEM bright-field image and electron diffraction patterns (the inset) taken from the as-undercooled $Pd_{59.3}In_{23.2}Fe_{17.5}$ at room temperature.

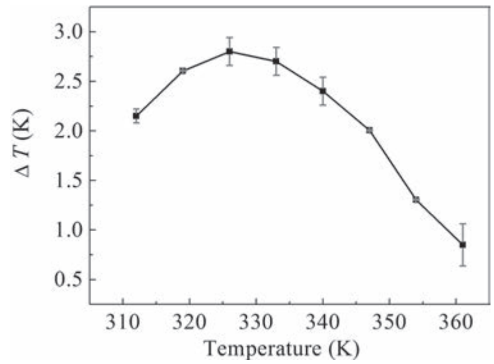

Fig. 2. ΔT as a function of temperature when loading the stress of 154 MPa in the temperature range of 312 - 361 K for the as-undercooled alloy.

10:45

EB-08. FDTD simulation of enhanced Faraday effect in plasmonic composite structures with rectangularly arranged Au particles.

J. Schlipf[1,2], Y. Itabashi[1], T. Goto[1], H. Takagi[1], P.B. Lim[1], Y. Nakamura[1], I.A. Fischer[2], J. Schulze[2], H. Uchida[1] and M. Inoue[1]
1. Toyohashi University of Technology, Toyohashi, Japan; 2. Institut für Halbleitertechnik, University of Stuttgart, Stuttgart, Germany

1. Introduction Magneto-optical (MO) effects enable non-reciprocal optical components like optical circulators and isolators as well as a magneto-optical spatial light modulator with switching speeds superior to a digital micromirror and a liquid crystal device. To develop a magneto-optical device with high performance, it is desirable to use materials with large rotation angles and small extinction coefficients. In other approaches introduction of nanostructures, magnetophotonic crystals [1] and localized surface plasmon resonance (LSPR) [2] has been shown to provide enhancement of the Faraday effect for distinct wavelengths. This work shows how rectangular arrays of gold (Au) particles embedded into thin films of bismuth-substituted yttrium iron garnet (Bi:YIG) offer different phenomena in comparison with the square arrays previously studied [3] [4] [5]. This enhancement of Faraday rotation was first observed in samples fabricated and characterized experimentally [6]. 2. Simulation approach Our finite-difference time-domain (FDTD) simulations focus on a periodic array of spherical Au particles embedded into a film of Bi:YIG on a fused quartz substrate, as shown in figure 1. The structure uses a rectangular unit cell with a width of 200 nm and a depth of 200 to 300 nm. A diameter of 120 nm was chosen for the Au particles. The dimensions are chosen this way to observe the enhancement of the Faraday effect, as similar to previous experimental samples [6]. The magnetic field is oriented perpendicular to the surface. Large rotation of several tens of degrees of linearly polarized light incident at an angle of 45° between the x and Y axes of the unit cell is mainly caused by the structure effect of the rectangular array of Au particles. To determine the Faraday rotation (FR), it is necessary to remove this structure effect from the results through simulations for both positive and negative magnetic fields, which is the same procedure as the conventional measurement method of Faraday rotation angle. 3. Results and Discussion From components of the electrical field of the transmitted light, it was observed that this large rotation can be attributed to different transmission minima for the x- and y- polarized components of the field. Figure 2 shows FR and transmission of a 200 by 250 nm array after removal of the effects mentioned above. While enhanced FRs were observed for distinct structure geometries for incident polarizations of 0° and 90°, transmissivity minima coincident with the Faraday rotation maxima were caused by the excitation of surface plasmon resonance for the polarized incident light waves in x- and y-directions. However, for diagonally polarized incident light at 45°, the FR maximum does not coincide with any minima, which is not observed in the square arranged particles. At 45° the peak in FR occurs at the wavelength where the structure-induced polarization rotation becomes zero. FDTD simulations with varied Bi:YIG layer thickness and particle spacing in y-direction were performed in search of the optimum geometry. Taking into account the transmission as well through computing a figure of merit as the product of the absolute value of the FR and the square root of the transmission is a well-established method to gauge the utility of magneto-optical materials and devices. There appears to be a specific Bi:YIG layer thickness for each y-direction array spacing where significant Faraday rotation enhancement happens, which can be attributed to coupling of the plasmon and waveguide modes of the structure. The wavelength where this maximum enhancement occurs was found to increase linearly with the y-direction particle spacing when the Bi:YIG layer thickness is chosen optimally. A Bi:YIG layer thickness of 160 nm and a particle spacing of 260 nm in y-direction appeared to provide the highest figure of merit, and thus seem favorable for experiments. 4. Conclusion The extraordinary enhancement of the Faraday effect in thin garnet films through rectangular Au particle arrays, as previously observed experimentally, has been thoroughly examined and visualized by simulation. The non-square geometry can help overcoming the spectral coincidence of high magneto-optical response and low transmissivity, known as a major problem in the efforts to achieve high-performance, thin MO devices through utilization of LSPR. Experimental analysis based the ideal geometric parameters determined by simulation is ongoing in order to corroborate the simulation results as well as prior experiments. Acknowledgement: This work was partially supported by JSPS KAKENHI (Nos. 17K06349, 26220902), and Program for Advancing Strategic International Networks to Accelerate the Circulation of Talented Researchers No. R2802. The authors would like to thank the Japan Student Service Organization for financial support through its Short-term Student Exchange Support Program.

[1] M. Inoue, A. V. Baryshev, A. B. Khanikaev, M. E. Dokukin, K. H. Jung, J. Heo, H. Takagi, H. Uchida, P. B. Lim, and J. Kim, "Magnetophotonic materials and their applications," IEICE Trans. Electron. E91-C, 1630–1638, 2008. [2] H. Uchida, Y Mizutani, Y Nakai, A A Fedyanin and M Inoue, Garnet composite films with Au particles fabricated by repetitive formation for enhancement of Faraday effect, J. Phys. D: Appl. Phys. 44, 064014-1-7, 2011. [3] A. B. Khanikaev, A. V. Baryshev, A. A. Fedyanin, A. B. Granovsky and M. Inoue, "Anomalous Faraday Effect of a system with extraordinary optical transmittance," OPTICS EXPRESS, vol. 15, no. 11, pp. 6612-6622, 2007. [4] A. V. Baryshev, H. Uchida and M. Inoue, "Peculiarities of plasmon-modified magneto-optical response of gold-garnet structures," J. Opt. Soc. Am. B, vol. 30, no. 9, pp. 2371-2376, 2013. [5] E. Almpanis, P.-A. Pantazopoulos, N. Papanikolaou, V. Yannopapas and N. Stefanou, "Metal-nanoparticle arrays on a magnetic garnet film for tunable plasmon-enhanced Faraday rotation," Journal of the Optical Society of America B, vol. 33, no. 12, pp. 2609-2616, 2016. [6] H. Uchida, Y. Mizutani, J. Schlipf, A. Baryshev, T. Goto, H. Takagi, Y. Nakamura, I. A. Fischer, J. Schulze, M. Inoue, to be published.

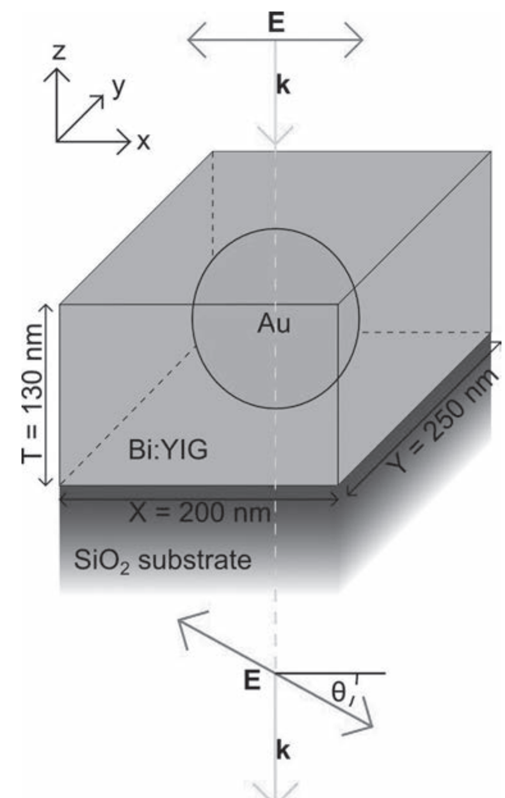

Fig. 1. Simulation model, for the propagation of light through the Au particle arrays. The model has periodicity in the x and y directions.

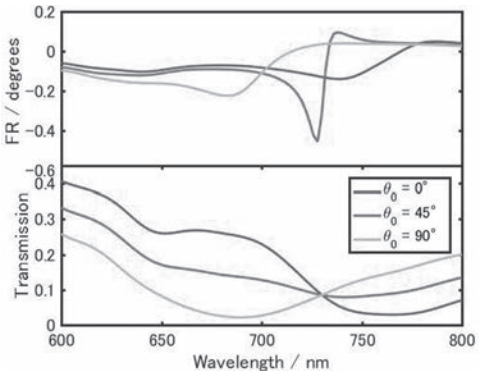

Fig. 2. Faraday rotation (FR) and relative transmission through a thin film with a 200 by 250 nm Au particle array, depending on the incident angle θ_0.

11:00

EB-09. Helicity dependent photovoltaic conversion at nonmagnetic interface with inversion asymmetry.

F.V. Auvray[1], J. Puebla[2], M. Xu[1] and Y. Otani[1,2]
1. Advanced Materials Science, The University of Tokyo, Kashiwa, Japan; 2. CEMS, RIKEN, Wako, Japan

Generation and manipulation of spin (angular momentum) is an important step in developing spintronics devices. One priority is to combine and convert spin information in current electronic technologies, such as charge current, voltage or light. Especially, optical generation of spin current or spin-polarized charge current has attracted attention for contemporary spintronics, aiming at efficient energy conversion with spin information. Splitting the electron band by spin-orbit interactions allows creation of photocurrent by injection of circularly polarized light. Signature of the photocurrent appears under illumination of circularly polarized light and reverses its direction when the polarization is changed to opposite direction due to the Circular Photogalvanic effect (CPGE) [1]. This effect has been already studied in many materials such as topological insulator, Rashba bulk and semi-conductor quantum wells. Our work focuses on the optical characterization of the interface between Copper(Cu) and Bismuth Oxide(Bi_2O_3). Interestingly, recent works done with electrical spin pumping experiment [2] and characterization using MOKE system [3] showed that Cu/Bi_2O_3 interface present Rashba-like spin orbit interaction. Here, we demonstrate a new functionality of a spinphotovoltaic converter at room temperature at an all-nonmagnetic interface, in visible range energies occurring at Cu/Bi_2O_3 interface. The oblique incidence dependence at two distinct laser energies, reflects independent signatures for spin-photovoltage excited above and below the optical transition of Bi_2O_3. This interface is formed between a 30 nm thick Cu layer and 20 nm thick Bi_2O_3, these thicknesses are selected to avoid interaction with the Si/SiO_2 substrate and the excitation light. The texture of the Cu layer at the interface reflects preferential (111) orientation while our Bi_2O_3 layer is amorphous in alpha-phase which is the most stable phase at room temperature with an expected energy band gap E_g=2.85 eV. Our light excitation are continuous wave lasers at energies of 1.15eV, 1.96 eV, and 3.05 eV. The photon polarisation is controlled by a linear polariser and a quarter wave plate mounted on a rotator. As the workfunction of Cu (4.45 eV) is lower than the workfunction of Bi_2O_3 (4.92 eV), it forms a Ohmic junction. In figure 1, we show a typical result of our helicity dependent photovoltaic measurement, obtained with an excitation laser energy of 1.96eV. Changing contributions of polarized light due to the rotation of the quarter wave plate leads to periodic modulation in photovoltage with a periodicity of 90 deg. Photovoltage peaks have different amplitudes, showing periodically two different values. This asymmetry comes from the circularly polarised light modulation. From this asymmetry, at a laser energy of 3.05eV at 1mW, we estimated the spin current by taking the voltage due to circular polarisation from fitting and obtained $J_s = 1.3*10^7$ A/m^2 which is comparable with spin current generated by spin pumping experiments [2] but significatively better than previous report on Pt/GaAs [4]. An other interesting result is showed Figure 2 and represents the dependence of the circularly polarised voltage V_C on the angle of incidence, for a laser energy of 1.96eV and power of 50uW. In contrast to previous experiment, the energy of the laser does not excite the direct optical transition of Bi_2O_3. The photovoltage excited by 1.96eV laser can be attributed to metal induced gap states at our Cu/Bi_2O_3 interface. At metal/semiconductor interface, the electron wavefunction of the metallic side penetrates into the forbidden gap creating the so-called metal induced gap states (MIGS) and presence of MIGS states have been observed in metallic interfaces with both semiconductor and insulator [5]. Regarding these results, we discuss the conversion process. Photovoltaic conversion efficiency is mainly determined by two factors, efficiency in optical absorption and efficiency in carrier disassociation (electron-hole). At the Cu/Bi_2O_3 interface, the lack of inversion symmetry induces spin orbit interaction of Rashba type. Recent reports [6-7] showed reduced carrier recombination due to the appearance of Rashba spin orbit coupling, enhancing the carrier disassociation in perovskites. Our study reflects the relevance of selecting appropriate engineering of heterojunctions. In conclusion, we showed the photovoltaic conversion with helicity dependence at Cu/Bi_2O_3 interface at visible energies where solar spectrum peaks. Due to the increase number of interfaces with spatial broken symmetry, we expect that the present work motivates further studies, advancing conversion efficiencies and further understanding.

[1] S. D. Ganichev et al., *Spin dependent photocurrents in quantum well structures induced by FIR radiation, Proc. of 26th Int. Conf. of Infrared and Millimeter Waves, eds. O. Portugal and J. Leotin, 4-19 (2002)* [2] S. Karube et al., *Experimental observation of spin-to-charge current conversion at non-magnetic metal/Bi2O3 interfaces,* Applied Physics Express 9 033001 (2016) *[3]* J. Puebla et al. *Direct optical observation of spin accumulation at nonmagnetic metal/oxide interface* Appl. Phys. Lett. 111, 092402 (2017) [4] K. Ando et al., *Photoinduced inverse spin-Hall effect: Conversion of light-polarization information into electric voltage,* Appl. Phys. Lett. 96, 082502 (2010) [5] M. Kiguchi et al., *Metal-Induced Gap states at well defined alkali-halide/metal interfaces*, Phys. rev. Lett. 90, 196803 (2003) [6] T. Etienne et al., *Dynamical origin of the Rashba effect in organohalide Lead perovskites: A key to suppressed carrier recombination in perovskite solar cells*, J. Phys Chem. C., 119 (12) 66966702 (2015) [7] F. Zheng et al., *Rashba spin - orbit coupling enhanced carrier lifetime in CH3NH3Pbl3*, Nano Lett., 15 (12), (2015)

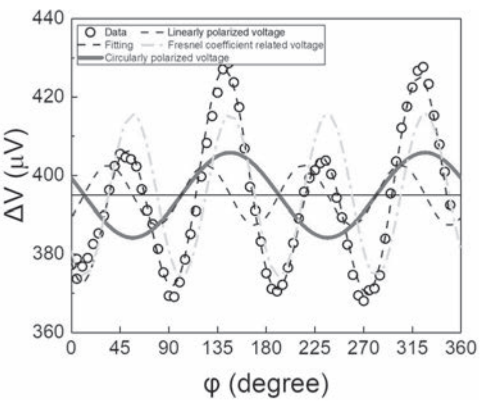

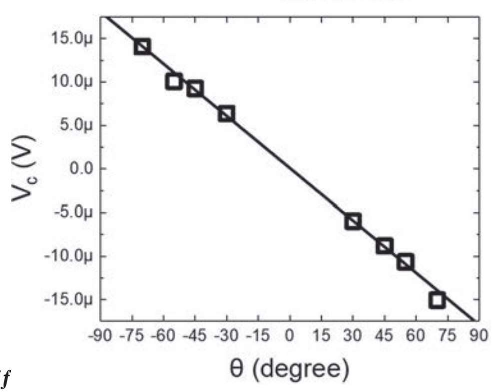

ff

Fig. 2. Incident angle θ dependence of the circular voltage at 1.96eV energy laser.

11:15

EB-10. Broadband Magneto-Optical Response of Magnetoplasmonic Quasicrystals.

A. Kalish[2,1], R. Komarov[2], M. Kozhaev[1,3], V. Achanta[4], S. Dagesyan[2], A. Shaposhnikov[5], V. Berzhansky[5], A. Zvezdin[1,3] and V. Belotelov[1,2]
1. Russian Quantum Center, Skolkovo, Russian Federation; 2. Faculty of Physics, Lomonosov Moscow State University, Moscow, Russian Federation; 3. Prokhorov General Physics Institute of Russian Academy of Sciences, Moscow, Russian Federation; 4. Tata Institute of Fundamental Research, Mumbai, India; 5. V.I. Vernadsky Crimean Federal University, Simferopol, Russian Federation

Resent research has demonstrated the enhancement of magneto-optical effects in structured media. In particular, the attention has been paid to plasmonic crystals which are periodic structures supporting surface plasmon polaritons. It was demonstrated that the transverse Kerr effect and the Faraday effect are resonantly enhanced in magnetoplasmonic crystals, and also novel promising effects arise, namely the longitudinal intensity effect [1-3]. As a rule, these effects are of resonant nature, due to their relation to the excitation of eigenmodes, which leads to narrow spectral range of magneto-optical response. In the present work, we propose and demonstrate an approach for forming a broadband magneto-optical response using one-dimensional magnetoplasmonic quasicrystals. Plasmonic quasicrystalline structures offer advances in their optical response over their periodic counterparts, such as broadband and polarization-independent optical transmittance [4]. The considered 1D magnetoplasmonic quasicrystalline structure is formed by a metallic quasicrystal grating on top of the smooth magnetic dielectric layer on a substrate. The sequence of metal stripes and air slits of the grating can be described by symbols ‘1’ and ‘0’. Our structure is based on the 1D binary Fibonacci sequence, where ‘0’ is substituted by ‘010’. The metal grating of the experimentally studied samples is made of 80-nm-thick gold layer. The air slit width corresponding to single ‘0’ in the binary sequence is 80 nm and the metal stripes width corresponding to single ‘1’ in sequence is 600 nm. The magnetic dielectric is bismuth substituted iron-garnet of composition $Bi_{1.5}Gd_{1.5}Fe_{4.5}Al_{0.5}O_{12}$. The thickness of the magnetic film was made rather small, 80 nm, to exclude the waveguide modes excitation in the considered frequency range, so only surface plasmon polaritons (SPPs) can be excited. Spectrum of the SPPs excited by the incident light in a plasmonic grating structure is determined by the reciprocal lattice vectors which enter the phase matching condition. The numerical calculation of the Fourier transform of the quasicrystalline pattern reveals that the reciprocal lattice for the quasicrystal is discrete and it is far denser compared to the periodic-crystal’s one. In particular, it is non-equidistant. For example, the studied structure possesses reciprocal vectors equal to 15.39, 16.76 and 19.01 μm^{-1}, while the corresponding periodic structure has only reciprocal vector of 18.48 μm^{-1} in this spectral range. The excitation of the SPPs in plasmonic structures with magnetic materials is accompanied by the resonant enhancement of the Transverse magneto-optical Kerr effect (TMOKE). Experimentally measured TMOKE spectrum for the magnetoplasmonic quasicrystal is shown in Fig. 1, together with calculated SPP dispersion curves. It is far richer than the one for the corresponding periodic structure. Apart from the first pair of resonances at around λ=820 nm (for small incidence angles) that is quite similar to the resonances for the periodic structure, two other additional pairs appear at around λ=890 nm and λ=950 nm corresponding to the reciprocal vectors of 16.76 and 15.39 μm^{-1}. It demonstrates that the magneto-optical response of plasmonic quasicrystals is broadband, contrary to single narrow resonances in the case of periodic structures. It makes the proposed structures very promising for numerous nanophotonics applications including optical sensing, control of light, all-optical control of magnetization etc. Additionally, TMOKE spectroscopy is an efficient tool for investigation of the peculiarities of plasmonic quasicrystals. The multiplicity of the excited plasmonic modes attracts attention also because they possess different values of the penetration depth. Estimations show that for the plasmonic resonances shown in Fig.3a the SPP penetration depth in the magnetic dielectric varies approximately from 70 to 100 nm. This fact opens new possibilities for manipulation of the optical near field, 3D sensing, control of the inverse magneto-optical effects and optically-induced magnetization. Quasicrystalline structures provide designable reciprocal lattice, i.e. the set of reciprocal vectors and therefore, dispersion of eigenmodes, by means of adjusting geometrical parameters. In particular, plasmonic quasicrystals offer designable spectrum of magneto-optical response for light modulation, which is prosperous for parallel light information processing at several frequencies. Furthermore, the plasmonic quasicrystals are prosperous for achieving other broadband magneto-optical effects related to the excitation of eigenmodes. If the structure supports waveguide modes then there are many resonances for TE and TM modes with the resonant wavelengths close to each other. This condition is favorable for the enhancement of the Faraday effect and the longitudinal intensity effect, as the TE-TM conversion is the most effective. The work is supported by the Russian Presidential Grant MK-2047.2017.2.

1. V. I. Belotelov, I. A. Akimov, M. Pohl, V. A. Kotov, S. Kasture, A. S. Vengurlekar, Achanta Venu Gopal, D. R. Yakovlev, A. K. Zvezdin, and M. Bayer. Enhanced magneto-optical effects in magnetoplasmonic crystals. Nature Nanotechnology 6, 370–376 (2011). 2. J.Y. Chin, T. Steinle, T. Wehlus, D. Dregely, T. Weiss, V. Belotelov, B. Stritzker and H. Giessen. Nonreciprocal plasmonics enables giant enhancement of thin-film Faraday rotation. Nature Communications 4, 1599 (2013). 3. V. I. Belotelov, L. E. Kreilkamp, I. A. Akimov, A. N. Kalish, D. A. Bykov, S. Kasture, V. J. Yallapragada, Venu Gopal Achanta, A. M. Grishin, S. I. Khartsev, M. Nur-E-Alam, M. Vasiliev, L. L. Doskolovich, D. R. Yakovlev, K. Alameh, A. K. Zvezdin, and M. Bayer. Plasmon-mediated magneto-optical transparency. Nature communications 4, 2128 (2013). 4. S. Kasture, A. P. Ravishankar, V. J. Yallapragada, R. Patil, N. V. Valappil, G. Mulay, and V. G. Achanta. Plasmonic quasicrystals with broadband transmission enhancement. Scientific Reports 4, 5257 (2014).

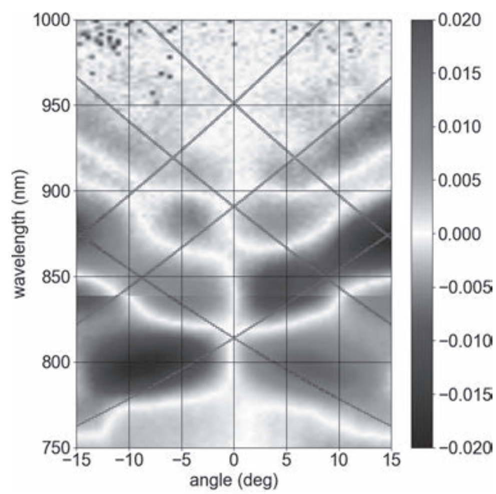

Fig. 1. The dependence of the TMOKE on the wavelength and the incident angle for the magnetoplasmonic quasicrystal. Green lines show the calculated dispersion curves for the surface plasmon polaritons.

11:30

EB-11. Investigation of amorphous $SmFe_2$ thin films with giant negative magnetostriction and perpendicular magnetic anisotropy.

M. Tomita[1], Y. Ishitani[1], S. Ishiyama[1], *Y. Takamura*[1] and S. Nakagawa[1]
1. Electrical and Electronic Engineering, Tokyo Institute of Technology, Tokyo, Japan

Further reduction of the consumption energy for the magnetization switching of a free layer of magnetic tunnel junctions (MTJs) is required in a spin transfer torque magnetoresistive random access memory (STT-MRAM). Using ferromagnetic materials with small magnetic anisotropy for the free layer can reduce the consumption energy but it will also cause the loss of thermal stability. Our group has proposed strain-assisted magnetization reversal (SAMR) using inverse magnetostriction (IMS) MTJs to reduce magnetic anisotropy only during the switching [1]. The proposed IMS-MTJs consist of an MTJ with a magnetostrictive material for the free layer and a piezoelectric material surrounding the MTJ pillar to apply pressure to the free layer effectively. Since lowering magnetic anisotropy caused by the inverse magnetostrictive effect, which results in a reduction of the switching current, occurs only while magnetization switching, thermal stability of the free layer will be kept. Ferromagnetic materials for the free layer of IMS-MTJs are required to have both a large, negative magnetostriction constant λ and perpendicular magnetic anisotropy (PMA). $SmFe_2$ is promising as such materials since $SmFe_2$ is well-known materials with large negative magnetostriction constant [2]. In addition, $SmFe_2$ films are expected to have PMA since some amorphous rare earth transition metal (RE-TM) alloys have been reported to show PMA [3]. In this paper, we systematically investigated magnetic anisotropy and magnetostriction of sputtered $SmFe_2$ thin films, and found that amorphous $SmFe_2$ films showed PMA and large, negative λ. All the films were prepared with a facing targets sputtering system. The stack structure was quartz-substrate/W (20nm)/Sm-Fe (100nm)/W (10nm). The substrate temperature T_S during sputtering varied from RT to 400°C. The post annealing temperature T_A also varied from 300°C to 600°C. The chemical composition of deposited Sm-Fe film was determined to be 1.05:2 by inductively coupled plasma-optical emission spectrometer (ICP-OES). X-ray diffraction (XRD) analysis showed that all of the fabricated $SmFe_2$ thin films had amorphous structure. Figure 1(a) shows *M*-*H* curves for a $Sm_{1.05}Fe_2$ film formed at T_S = 200°C and post-annealed at T_A = 500°C measured by vibrating sample magnetometer (VSM) with perpendicular and in-plane magnetic fields, clearly indicating that the $Sm_{1.05}Fe_2$ film had PMA. ΔK, difference between perpendicular and in-plane magnetic anisotropy energy density, was determined to be 0.17 Merg/cc. Figure 2(b) shows ΔK of the $Sm_{1.05}Fe_2$ thin films with various T_S and T_A. PMA were observed only in the $Sm_{1.05}Fe_2$ films formed at low T_S and annealed at high T_A. One of the origin of this PMA in the amorphous $Sm_{1.05}Fe_2$ films could be anisotropic, short range order similar to other amorphous RE-TM alloys [4]. Then, IMS effect of the $Sm_{1.05}Fe_2$ thin film with T_S = 200°C and T_A = 500°C exhibiting PMA were analyzed. Pressures were applied to the sample by sandwiching it with two sample holders having the same curvature radius. In this experiment, a 0.03-mm thick quartz substrate was used to prevent it from cracking while bending. Figure 2(a) shows the demagnetization curves in the first quadrant under various applied pressures. The sample qualitatively exhibited negative λ as magnetization energy reduced (the demagnetization curve shifted in the upward direction) by compressive stress and increased by tensile stress. The change, $\Delta K_{|\sigma|}$, of the magnetization energy density of the $Sm_{1.05}Fe_2$ film by stress was quantitatively evaluated from the demagnetization curves. Figure 2(b) shows $\Delta K_{|\sigma|}$ as a function of induced stress. The slope is equivalent in -3λ and λ was determined to be -920 ppm. From these results, we concluded that the $Sm_{1.05}Fe_2$ film formed at T_S = 200°C and T_A = 500°C exhibited both PMA (ΔK = 0.17 Merg/cc) and large, negative magnetostriction ($\lambda = -920$ ppm). In conclusion, we found that $Sm_{1.05}Fe_2$ thin films formed at low T_S and annealed at high T_A showed PMA. One of the possible origins of this PMA is the anisotropic, short range order of Sm and Fe atoms. The $Sm_{1.05}Fe_2$ film with T_S = 200°C and T_A = 500°C exhibiting PMA also showed large, negative magnetostriction $\lambda = -920$ ppm. This result indicates that $Sm_{1.05}Fe_2$ thin films are promising as the free layer of IMS-MTJ for ultra-low energy STT-MRAMs.

[1] Y. Takamura, Y. Shuto, S. Yamamoto, H. Funakubo, M. K. Kurosawa, S. Nakagawa, and S. Sugahara, "Inverse-magnetostriction-induced switching current reduction of STT-MTJs and its application for low-voltage MRAM," *Solid-State Electronics*, vol. 128, pp. 194-199, Feb. 2017. [2] H. Samata, N, Fujiwara, Y. Nagata, T. Uchida, and M. D. Lan, "Magnetic anisotropy and magnetostriction of $SmFe_2$ crystal," *Journal of Magnetism and Magnetic materials*, vol. 195, no. 2, pp. 376-383, May 1999. [3] R. Hasegawa, R. J. Gambino, J. J. Cuomo, and J. F. Ziegler, "Effect of thermal annealing and ion radiation on the coercivity of amorphous Gd-Co films," *Journal of Applied Physics*, vol. 45, no. 9, pp. 4036-4040, Apr. 1974. [4] V. G. Harris, K. D. Aylesworth, B. N. Das, W. T. Elam, and N. C. Koon, "Structural origins of magnetic anisotropy in sputtered amorphous Tb-Fe films," *Physical Review Letters*, vol. 69, no. 13, Sep. 1992.

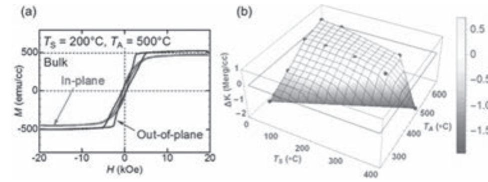

Fig. 1. (a) *M* – *H* loops of a Sm-Fe thin film formed at T_S = 200°C and annealed at T_A = 500°C.
(b) T_S and T_A dependence of ΔK for Sm-Fe thin films.

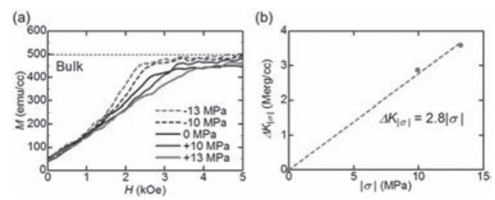

Fig. 2. (a) Demagnetization curves with various applied pressures for the $Sm_{1.05}Fe_2$ thin film with T_S = 200°C and T_A = 500°C.
(b) The change of magnetization energy density, $\Delta K_{|\sigma|}$, as a function of induced stress $|\sigma|$.

11:45

EB-12. Smart Shape Memory Actuator based on Monocrystalline Ni_2FeGa glass-coded microwire.

L. Frolova[1], T. Ryba[2], P. Diko[3], V. Kavecansky[3], J. Kravcak[4], Z. Vargova[5] and *R. Varga*[1,2]
1. Cond. Matt. Phys., Inst. Phys., Fac. Sci., UPJS, Kosice, Slovakia; 2. RVmagnetics a.s., Hodkovce, Slovakia; 3. Inst. Exp. Phys., SAS, Kosice, Slovakia; 4. Dept. Phys., FEEI TUKE, Kosice, Slovakia; 5. Dept. Inorg. Chem., Inst. Chem.,Fac. Sci., UPJS, Kosice, Slovakia

Shape memory alloys (SMAs) are a group of metallic alloys that recover to their original form after deformation. Shape memory effect (SME) is characterized by diffusion-less transition between two phases: austenite and martensite [1]. Up to date, the Heusler alloy with chemical composition Ni-Mn-Ga (near to stoichiometry 2:1:1) is one of the prototype of SMA [2]. This alloy is known for its large recoverable deformation up to 12% strain and high-frequency response (up to 1 kHz) induced by magnetic or mechanical loadings. However, in spite of its remarkable properties, Ni_2MnGa has some drawbacks originating from the loss of Mn, relatively low Curie and martensitic transformation temperatures etc. [3]. Therefore, it is necessary to develop new alloy systems to overcome such a disadvantage. Alternatively, Ni_2FeGa alloy have been proposed as promising magnetic shape memory alloy. Taylor-Ulitovsky method for production of glass-coated microwires allows easy production of few kilometres of high quality monocrystalline wire along entire length with well oriented crystallographic axis. It is shown that such wire is characterized by temperature induced shape memory effect accompanied by ~2% reversible strain. As a result of different anisotropy of both low- and high- temperature phase, such strain is accompanied by huge variation of permeability. In the given contribution we show how magnetic parameters must be adjusted in order to achieve up to 1600% change of permeability due to the phase transition. Such variation allows us to control straining very precisely, which transforms the microwires into the SMART shape memory actuators. This work was supported by APVV-16-0079.

[1] J. M. Jani, et al., *Materials and Design* 56 (2014) 1078. [2] M. Siewert, et al., *Adv. Eng. Mater.* 14 (2012) 530. [3] Q. Peng, et al., *Scripta Materialia* 127 (2017) 49.

THURSDAY MORNING, 26 APRIL 2018 ORCHID IV, 9:00 TO 12:00

Session EC

GMR, TMR, AND MULTIFERROIC MATERIALS

Liang Liu, Co-Chair
National University of Singapore, Singapore
Hao Wu, Co-Chair
University of California at Los Angeles, Los Angeles, CA, United States

INVITED PAPER

9:00

EC-01. Very large voltage-controlled magnetic anisotropy and extremely reliable voltage-induced switching.

T. Nozaki[1], A. Koziol-Rachwal[1,2], M. Tsujikawa[3], Y. Shiota[1], T. Yamamoto[1], T. Ikeura[1], X. Xu[5], T. Ohkubo[5], T. Tsukahara[4], S. Miwa[4], M. Suzuki[6], H. Imamura[1], S. Tamaru[1], H. Kubota[1], A. Fukushima[1], K. Hono[5], M. Shirai[3], Y. Suzuki[1,4] and S. Yuasa[1]
1. Spintronics Research Center, National Institute of Advanced Industrial Science and Technology (AIST), Tsukuba, Japan; 2. Faculty of Physics and Applied Computer Science, AGH University of Science and Technology, Al. Mickiewicza 30, 30-059, Poland; 3. Research Institute of Electrical Communication, Tohoku University, Sendai, Japan; 4. Graduate School of Engineering Science, Osaka University, Toyonaka, Japan; 5. Research Center for Magnetic and Spintronic Materials, National Institute for Materials Science (NIMS), Tsukuba, Japan; 6. Japan Synchrotron Radiation Research Institute (JASRI), Sayo, Japan

Voltage-controlled magnetic anisotropy (VCMA) effect is drawing attention as a promising approach for low-power spin manipulation in future spintronic devices [1,2]. Purely electronic VCMA effect originates from several mechanisms, such as the electric-field induced change in electronic occupation states [2] and induction of magnetic dipole moment [3], at the interface between ultrathin ferromagnetic metal and dielectric layers. Successful application of VCMA effect in MgO-based magnetic tunnel junctions (MTJs) [4] realized voltage-induced dynamic magnetization switching [5-7] and exhibited the feasibility of voltage-controlled spintronic devices, such as voltage-torque MRAM. For the voltage-induced dynamic magnetization switching, we need to eliminate the perpendicular magnetic anisotropy (PMA) energy to induce precessional dynamics of magnetization around an applied in-plane magnetic field. Since the higher PMA is required for smaller element to keep sufficient thermal stability, more efficient VCMA coefficient is demanded to show the scalability of voltage-torque MRAM. For example, target values are estimated to be 300 fJ/Vm for cache memory and 1000 fJ/Vm for main memory applications [8, 9], however the demonstrated VCMA effect with high speed response is limited to be about 100 fJ/Vm in practical MTJ devices [10, 11]. First principles calculations predict that utilization of large spin-orbit constant in 4*d* and 5*d* transition metals is effective to enhance the VCMA effect, for example by inserting a heavy metal monolayer at the Fe/MgO interface [12]. Stimulated by this expectation, we developed a new technique of heavy metal iridium (Ir) doping in the ultrathin Fe layer to achieve large VCMA coefficient exceeding 300 fJ/Vm [9]. Fully epitaxial MTJs consisting of Cr(30 nm)/ultrathin Fe(t_{Fe})/Ir doping layer(t_{Ir})/MgO(2.5 nm)/Fe (10 nm)/Ta/Ru were deposited on MgO(001) substrates by a combination of molecular beam epitaxy and sputtering techniques. The ultrathin Ir doping layer, ranging from $0 \leqq t_{Ir} \leqq 0.15$ nm, was inserted between the Fe and MgO layers. However, as shown in Fig. 1(a), we found that Ir atoms were dispersed uniformly into the Fe layer through the interdiffusion during the post-annealing process for the MgO layer. Figure 1(b) shows an example of polar MOKE hysteresis curves for the 1 nm-thick Fe layer with t_{Ir}=0.1 nm (red) and without doping (black). Clear transition of magnetic easy axis from the in-plane to the out-of-plane direction was induced by Ir doping. By evaluating the Fe thickness dependence of PMA, very large intrinsic interfacial PMA energy, $K_{i,0}$ of 3.7 mJ/m^2 was confirmed for the case of t_{Ir}=0.05 nm. Figure 2(a) shows bias voltage dependence of normalized TMR curves for the MTJ with t_{Fe}=0.77 and t_{Ir}=0.05 nm measured under in-plane magnetic field. Due to the orthogonal magnetization configuration for out-of-plane magnetized free layer and in-plane magnetized reference layer (top Fe) at the remanent state, saturation property in the tunneling resistance under the in-plane magnetic field application reflects the effective PMA of the free layer. Clear shifts in the saturation field were observed depending on the amplitude of the applied bias voltages. The estimated PMA change is summarized in Fig. 2(b) as a function of applied electric field. We obtained large VCMA coefficient of 320 fJ/Vm [9]. High speed response was also confirmed by voltage-induced FMR excitation. First principles calculations revealed that dispersed Ir atoms having proximity induced magnetism play a significant role to enhancing the interfacial PMA and VCMA effect. Electric-field induced modification in magnetic anisotropy energy mainly originates from the majority spin Ir-5*d* states and its amplitude can be 5-10 times larger than that of Fe atoms. Since we still have numerous choices of 4*d* and 5*d* elements, materials engineering using heavy metal doping has enourmous possibilities for further improvement in both interfacial PMA and VCMA properties. In the presentation, we'll also introduce recent effort to reduce the write error rate in voltage-induced dynamic magnetization switching [13, 14] and discuss future challenges to develop the voltage-torque MRAM. This work was supported by the ImPACT Program of the Council for Science, Technology and Innovation (Cabinet Office, Government of Japan).

[1] M. Weisheit *et al. Science* 315, 349 (2007). [2] T. Maruyama *et al. Nat. Nanotechnol.* 4, 158 (2009). [3] S. Miwa *et al. Nat. Commun.* 8, 15848 (2017). [4] T. Nozaki *et al. Appl. Phys. Lett.* 96, 022506 (2010). [5] Y. Shiota *et al. Nat. Mater.* 11, 39 (2012). [6] S. Kanai *et al. Appl. Phys. Lett.* 101, 122403 (2012). [7] C. Grezes *et al. AIP Adv.* 6, 075014 (2016). [8] P. Khalili Amiri *et al. IEEE Trans. Magn.* 51, 3401507 (2015) [9] T. Nozaki *et al. NPG Asia Mater.* 9, e451 (2017). [10] W. Skowronski *et al. Appl. Phys. Exp.* 8, 053003 (2015). [11] X. Li *et al. Appl. Phys. Lett.* 110, 052401 (2017). [12] K. Nakamura *et al. J. Magn. Magn. Mater.* 429, 214 (2017). [13] Y. Shiota *et al. Appl. Phys. Exp.* 9, 013001 (2016). [14] Y. Shiota *et al. Appl. Phys. Lett.* 111, 022408 (2017).

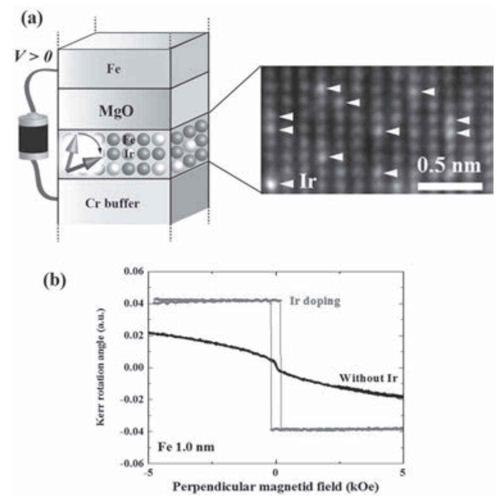

Fig. 1. (a) Schematic illustration of voltage-controlled MTJ device and HAADEF STEM image of the Ir-doped ultrathin Fe free layer. (b) Comparison of polar MOKE hysteresis curves of 1 nm-thick Fe with Ir doping (red) and without doping (black).

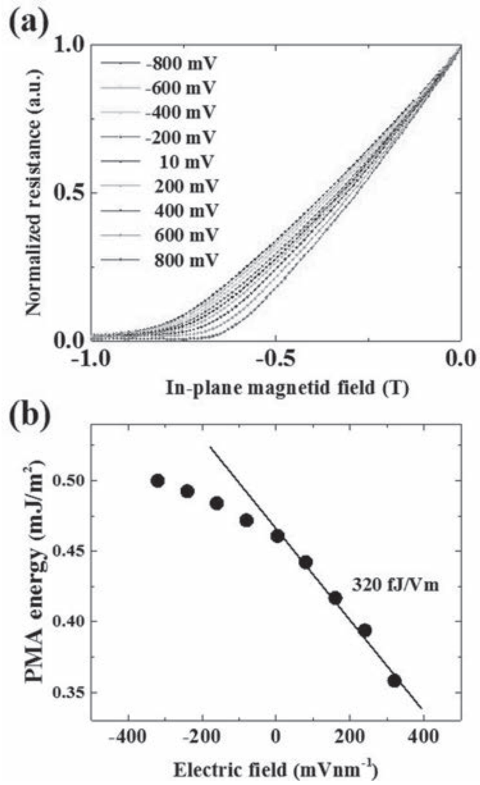

Fig. 2. VCMA properties of the MTJ with an Ir-doped ultrathin Fe free layer; (a) bias voltage dependence of normalized TMR curves measured under in-plane magnetic fields and (b) applied electric-field dependence of PMA energy.

CONTRIBUTED PAPERS

9:30

EC-02. Flexible MgO-based Magnetic Tunnel Junctions on Silicon Substrate.

S. Amara[1], G. A. Torres Sevilla[1], I. Ivanov[1], J. Gerhard[2], S. Jaiswal[2,3], H. Muhammad Mustafa[1], M. Kläui[2] and J. Kosel[1]
1. CEMSE, King Abdullah University of Science and Technology (KAUST), Thuwal, Saudi Arabia; 2. Institut für Physik, Johannes Gutenberg Universität Mainz, Mainz, Germany; 3. Singulus Technologies AG, Kahl am Main, Germany

Flexible electronic devices are emerging in many areas, providing novel features and creating new applications [1]. Due to their ubiquitous utilization, flexible magnetic sensors [2] play a critical part in this development. In particular, magnetic tunnel junctions (MTJs) are of great interest, because of advantages like low power consumption or high sensitivity. We report the development of flexible MTJs on a silicon substrate fabricated by a low-cost batch process [3]. Thereby, conventionally fabricated MTJ devices are transformed into flexible ones by thinning down the silicon wafer from 500 μm to 5 μm. This process leads to thin, bendable silicon devices, while maintaining their original performance. The fabrication process steps are shown in figure 1a to e. The MTJs were fabricated by standard multilayer magnetic stack deposition with an MgO tunnel barrier of 1.6 nm thickness. After backside etching of the wafer the thickness of the substrate was reduced to 5 mm as shown in the inset of figure 1f. The resulting flexible MTJ films are extremely bendable with a diameter down to 500 mm (figure 1f). The magnetic properties and magneto-transport properties of the flexible MTJs were the same as those of the rigid ones. The TMR ratio was tested under different bending conditions (figure 2a) and no degradation was found as shown in figure 2b. The reliability of the flexible MTJs was evaluated by exposing them to periodic strain cycles. To this end, an MTJ sample was mounted to an elastomeric support, which was repetitively stressed moving it from a flat state to a tensile state and visa-versa. Figure 2c shows that even after 1000 cycles, the TMR ratio showed no relevant differences (figure 2c). The presented method enables fabricating silicon devices without comprising any of their performance characteristics like cost/yield advantage or integration density. Entire devices can be fabricated prior to thinning, benefiting from standard batch processes without introducing any constraint in design, thermal budgets or fabrication methods. Therefore, these flexible silicon-based MTJs are a crucial contribution on the way to integrated state-of-the-art flexible magnetoelectronics. The maturity of silicon fabrication techniques makes the flexible MTJ sensors on silicon semiconductor substrates the natural choice for very large integration of high-performance electronic applications on flexible substrates.

T. Sekitani, H. Nakajima, H. Maeda, T. Fukushima, T. Aida, K. Hata, T. Someya, Stretchable active-matrix organic light-emitting diode display using printable elastic conductors. *Nat. Mater.* 2009, *8*, 494. M.Melzer, D.Makarov, A.Calvimontes, D.Karnaushenko, S.Baunack, R.Kaltofen, Y.Mei, and O.G. Schmidt. Stretchable Magnetoelectronics. Nano Lett., 2011, 11 (6). Galo A. Torres Sevilla, Mohamed T. Ghoneim, Hossain Fahad, Jhonathan P. Rojas, Aftab M. Hussain, and Muhammad Mustafa Hussain, Flexible Nanoscale High-Performance FinFETs, ACS Nano, 8 (10), 9850–9856 (2014).

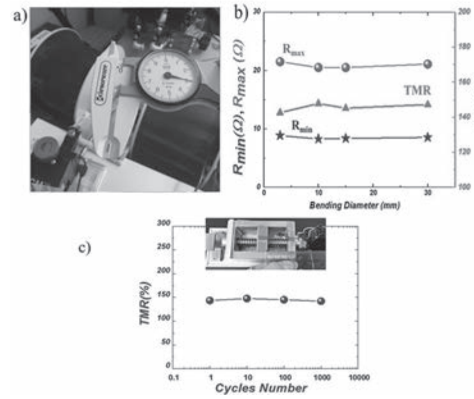

Fig. 1. (a) A flexible MTJ sensor mounted on top of a cylinder with 3 mm in diameter (tensile strain). (b) Resistance in the parallel state (R_{min}) and antiparallel state (R_{max}) of the magnetic layers, as well as TMR ratios for positive bending diameters from 30 mm to 3 mm. The junction size is 1×1.2 μm² and the RA product is about 10 Ωμm². (c) TMR ratio versus cycles of tensile strain. The inset shows the experimental setup, used to repetitively apply the strain.

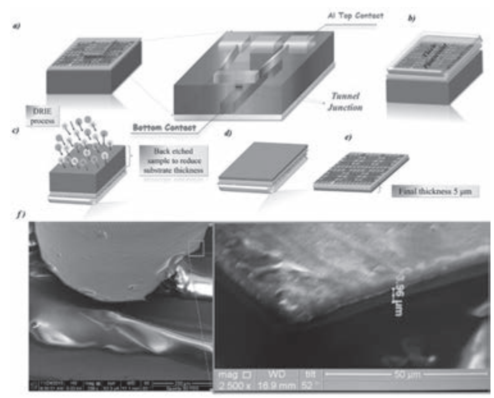

Fig. 2. Fabrication process flow: (a) MTJ devices fabricated on Si (500 mm) substrate with a $Si0_2$ (300 nm) passivation layer; (b) Photoresist coating to protect the device during the subsequent back etching process; (c) Back etching of the substrate by deep reactive ion etching; (d) MTJ devices on flexible silicon substrate with 3-5 μm thickness; and (e) photoresist removal. f) SEM image of MTJ stack after back etching of the Si substrate showing the final thickness.

9:45

EC-03. Tunneling anisotropic magnetoresistance driven by magnetic phase transition.

X. Chen[1], C. Song[1], J. Feng[2], X. Zhong[1] and F. Pan[1]
1. Tsinghua University, Beijing, China; 2. Institute of Physics, Chinese Academy of Sciences, Beijing, China

The independent control of two magnetic electrodes and spin-coherent transport in magnetic tunneling junctions (MTJs) are strictly required for tunneling magnetoresistance (TMR), while MTJs with only one ferromagnetic electrode exhibit tunneling anisotropic magnetoresistance (TAMR) [1] dependent on the anisotropic density of states and no room temperature performance so far. Apparently, during the ferromagnetic switching for the tunneling effect, only the magnetization direction is changed, where no modulation of intrinsic magnetism is involved, irrespective of one or two magnetic electrodes. Now the interest is whether there exists an elegant approach via the manipulation of the intrinsic magnetic ground state to manipulate the spin transport, which would provide an alternative opportunity to obtain tunneling magnetoresistance and make the tunneling behavior more designable. CsCl-ordered FeRh (a'-FeRh) films, show a first order phase transition from antiferromagnetic (AFM) to ferromagnetic (FM) order, which can be driven by temperature or magnetic field above room temperature [2]. Such an AFM–FM transition means a strong variation of magnetic ground state accompanied by a large DOS variation at the Fermi level. Thus, it would be fundamentally transformative if the magnetic phase transition of a'-FeRh was used to drive the tunneling effect. Basically, the AFM–FM transition itself is associated with an obvious change of resistance, but the current-in-plane geometry is not capable for implementing high density storage, thus demanding the experimental exploitation of MTJs structure with current-perpendicular-to-plane geometry as the basis of memories with a cross bar structure. Furthermore, considering the low lattice misfit between MgO and a'-FeRh, a MgO (001) substrate is commonly chosen for the deposition of epitaxial a'-FeRh, while epitaxial growth of MgO tunneling barrier is highly expected on the top of a'-FeRh bottom electrode, which would be beneficial for achieving sizeable tunneling effect. We demonstrate an a'-FeRh magnetic phase transition TAMR (PT-TAMR) with the ratio up to 20% at room temperature in MTJs with only one a'-FeRh magnetic electrode, and the polarity and magnitude of PT-TAMR are profoundly dependent on the design of the a'-FeRh/MgO interface [3].

[1] Y. Y. Wang, C. Song, B. Cui, G. Y. Wang, F. Zeng, and F. Pan, Phys. Rev. Lett. 109, 137201 (2012). [2] M. Jiang, X. Z. Chen, X. J. Zhou, B. Cui, Y. N. Yan, H. Q. Wu, F. Pan, and C. Song, Appl. Phys. Lett. 108, 202404 (2016). [3] X. Z. Chen, J. F. Feng, Z. C. Wang, J. Zhang, X. Y. Zhong, C. Song, L. Jin, B. Zhang, F. Li, M. Jiang, Y. Z. Tan, X. J. Zhou, G. Y. Shi, X. F. Zhou, X. D. Han, S. C. Mao, Y. H. Chen, X. F. Han, and F. Pan, Nature Commun. 8, 449 (2017).

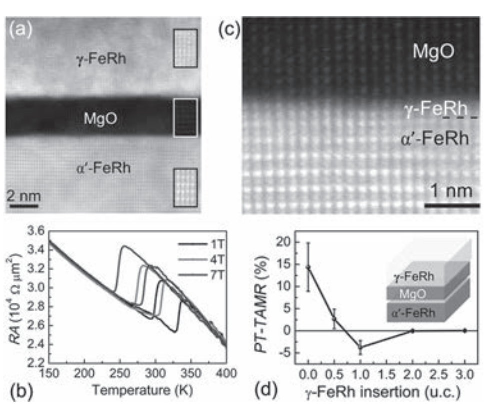

INVITED PAPER

10:00

EC-04. Ionic liquid gating control of magnetism in ultrathin magnetic multilayers.

M. Liu[1] and Z. Zhou[1]
1. Electronic Materials Research Laboratory, Key Laboratory of the Ministry of Education & International Center for Dielectric Research, Xi'an Jiaotong University, Xi'an, China

One of the central challenges in realizing magnetoelectric (ME) devices lies in finding a deterministic way to modulate magnetism in integrated circuits with a circuit-operation voltage [1-4]. Ionic liquid (IL) gating on magnetic thin films with abundant electronic, chemical and magnetic interactions at the interface has become an emerging technology for controlling magnetism in a fast, compact and energy-efficient way. [5-7] Compared with conventional strain effect dominated piezo/ferroelectric layer multiferroics, IL gating method has advantages like small gating voltage (V_g<5 V), easy-to-integration and compatibility with varied substrates such as Si, flexible substrates etc. In additional, unlike the oxide structures require a high temperature to overcome the oxidation energy barrier, the IL gating control process can be operated at room temperature, suitable for applications in room temperature environment. Here, we will summarize our recent progresses of IL gating control of magnetism in varied magnetic heterostructures, including: 1) IL gating of ultrathin Co magnetic film as the first demonstration of quantitatively determination of spatial magnetic anisotropy;[8] 2) IL gating of perpendicular magnetic anisotropy structure (Co/Pt) with record high >1500 Oe ferromagnetic resonance field shift as well as a reversible in-plane and out-of-plane anisotropy switching; 3) IL gating of spinel ferrite (Fe O) with 600 Oe FMR field switching with great reversibility and voltage controlled phase transition; 4) IL gating of spin-orbital coupling that leads to ~1400 Oe FMR field tunability with the greatest ME coupling figure of merit in ferrites: ΔH /ΔH ~30; As thus, the IL gating process, proven to be a truly powerful and compatible gating method, enables giant ME tunability in different heterostructures and provides a tremendous potential in next generation of voltage-tunable spintronics/electronics.

1. M. Liu, Z. Y. Zhou, T. X. Nan, B. M. Howe, G. J. Brown, N. X. Sun, Advanced Materials, 25 (10), 1435 (2013) 2. M. Liu, B. M. Howe, L. Grazulis, K. Mahalingam, T. X. Nan, N. X. Sun, G. J. Brown, Advanced Materials, 25 (35), 4886 (2013) 3. B. Peng, Z. Zhou, T. Nan, G. Dong, M. Feng, Q. Yang, X. Wang, S. Zhao, D. Xian, and Z.-D. Jiang. W. Ren, Z-G Ye, M. Liu, ACS nano, DOI: 10.1021/acsnano.7b01547 (2017) 4. M. Zhu, Z. Zhou, B. Peng, S. Zhao, Y. Zhang, G. Niu, W. Ren, Z.G. Ye, Y. Liu, and M. Liu. Advanced Functional Materials, 27 1605598. (2017) 5. S. Zhao, Z. Zhou, B. Peng, M. Zhu, M. Feng, Q. Yang, Y. Yan, W. Ren, Z.G. Ye, and Y. Liu. M. Liu, Advanced Materials, DOI: 10.1002/adma.201606478 (2017) 6. M. Weisheit, S. Faehler, A. Marty, Y. Souche, C. Poinsignon, and D. Givord. Science, 315(5810): p. 349-351. (2007) 7. Y. Yamada, K. Ueno, T. Fukumura, H.T. Yuan, H. Shimotani, Y. Iwasa, L. Gu, S. Tsukimoto, Y. Ikuhara, and M. Kawasaki,. Science,. 332(6033): p. 291-296.(2011) 8. T. Fujimoto, and K. Awaga. Physical Chemistry Chemical Physics, 15(23): p. 8983-9006. (2013)

CONTRIBUTED PAPERS

10:30

EC-05. Tailoring magnetic properties of giant magnetoresistance spin-valves by inserting ultrathin noble metals between pinned and pinning layers.

S. Kim[1], J. Choi[2] and S. Lim[1]
1. Materials Science and Engineering, Korea University, Seoul, The Republic of Korea; 2. Center for Spintronics Research, Korea Institute of Science and Technology, Seoul, The Republic of Korea

In this study, the interlayer exchange coupling field (H_{int}) in giant magnetoresistance spin valves (GMR SVs) is manipulated by inserting an ultrathin noble metal spacer between pinned and pinning layers. Among many noble metals, Cu and Pt are used as a single or dual spacer layer, with the spacer thickness varied from 1 to 8 Å in steps of 1 Å. Figures 1 and 2 show in-plane MR-H curves measured along the easy and hard directions, respectively (MR and H are the magnetoresistance and applied magnetic field, respectively). It is seen from the results that there is a large change in H_{int}, the maximum GMR ratio, and the low field sensitivity depending on the type and thickness of the spacer layer. For example, an H_{int} value of 5.3 Oe observed in the sample without the spacer is dramatically reduced to 0.25 Oe after inserting a Pt/Cu dual spacer. This reduction mainly results from the increase in the switching field from anti-parallel to parallel state. It is noted that the switching field from parallel to anti-parallel state remains nearly unchanged. The increase in the maximum GMR ratio is approximately 10%, probably owing to the specular scattering at the interfaces between noble metal and its adjacent layers [1]. The low field sensitivity, an important parameter in magnetic sensor applications, is dominantly affected by H_{int}; for example, a decrease in H_{int} from 5.3 to 0.5 Oe with the insertion of the Cu/Pt dual spacer results in a significant improvement of the sensitivity from 6.01 to 12.01 mV/ mA×Oe. In summary, with the insertion of a spacer between the pinned and pinning layers, it is possible to control the H_{int} value and hence the performance of GMR sensors such as biosensors and oscillation detectors for microelectromechanical systems (MEMS) [2]. This work was supported by the Technology Innovation Program [10054578, Development of Core Technology for 9-axis Smart Motion Sensor] funded by the Ministry of Trade, Industry & Energy (MOTIE), Korea. *Presenting author: Si Nyeon Kim, e-mail: smurff1@korea.ac.kr

[1] W. F. Egelhoff, Jr., P. J. Chen, C. J. Powell, M. D. Stiles, and R. D. McMichael, J. H. Judy, K. Takano, A. E. Berkowitz, and J. M. Daughton, *IEEE Trans. Magn.* 33, 3580 (1997). [2] João Valadeiro, Susana Cardoso, Rita Macedo, Andre Guedes, João Gaspar, and Paulo P. Freitas, *Micromachines* 7, 88 (2016).

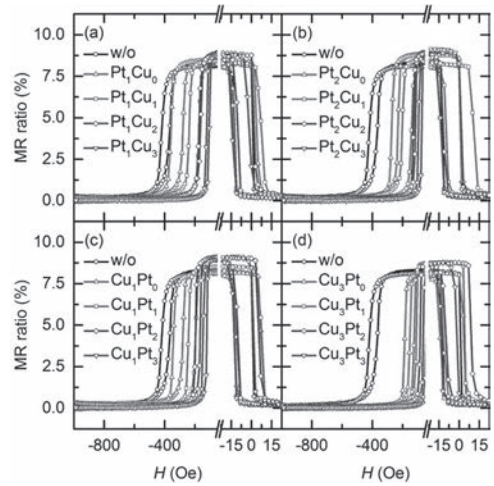

Fig. 1. In-plane MR-*H* curves along easy direction for GMR SVs with spacer of noble metals. The numbers in the subscript denote the layer thickness in Å.

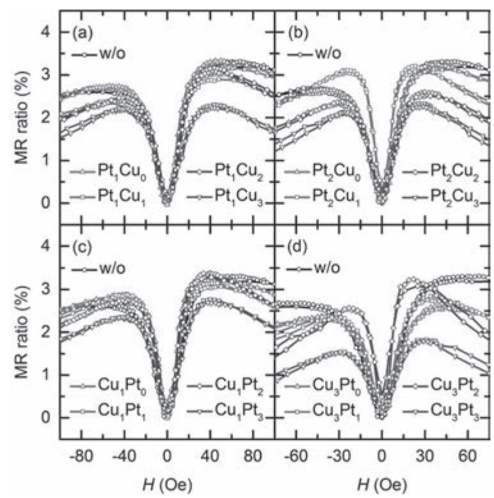

Fig. 2. In-plane MR-*H* curves along hard direction for GMR SVs with spacer of noble metals. The numbers in the subscript denote the layer thickness in Å.

10:45

EC-06. Giant magnetoresistance effects in interface-tailored current-perpendicular-to-plane type junctions using Heusler alloy electrodes.

T. Kubota[1,2], Y. Ina[1], Z. Wen[1,2] and K. Takanashi[1,2]
1. Institute for Materials Research, Tohoku University, Sendai, Japan;
2. Center for Spintronics Research Network, Tohoku University, Sendai, Japan

Current-perpendicular-to-plane (CPP) giant magnetoresistance (GMR) junctions are of interest for potential application to magnetic sensor elements. Half-metallic Heusler alloys are a promising class of materials for realizing a large MR ratio and an areal resistance change (ΔRA) for CPP-junctions. Interfacial properties are crucial for the value of MR ratio because the interfacial spin-scattering plays an important role for CPP-GMR as well as the bulk contribution according to a theoretical model [1]. To modify the interface contribution to CPP-GMR, ultrathin inserts have been studied for the Heusler layer/spacer interfaces to tailor the interfaces. According to previous papers [2, 3], either ultrathin non-magnetic inserts or ferromagnetic inserts drastically changed an MR ratio. Previously we reported the development of CPP-GMR junctions with an $L1_2$-type Ag_3Mg ordered alloy spacer and half-metallic $Co_2Fe_{0.4}Mn_{0.6}Si$ (CFMS) electrodes, which exhibited an enhanced MR ratio and ΔRA of 63% and 25 mΩ μm^2 at room temperature [4]. To realize a higher output for the CPP-GMR, the interface tailoring effect between $L1_2$-Ag_3Mg and CFMS has been investigated in this study. Layered film samples were deposited onto MgO (100) single crystalline substrates by using an ultra-high vacuum magnetron sputtering system (base pressure < 1 × 10^{-7} Pa). The materials for the insert were Mg or Fe with the thickness, $t_{\mathrm{Mg\ or\ Fe}}$, in the range of 0 to 0.60 nm in 0.15 nm increments. The stacking structure of the samples was MgO substrate | Cr (20) | Ag (40) | CFMS (20) | Mg or Fe ($t_{\mathrm{Mg\ or\ Fe}}$) | Ag_3Mg (5) | Mg or Fe ($t_{\mathrm{Mg\ or\ Fe}}$) | CFMS (7) | Ag (2) | Au (5), unit in nanometer. The deposition temperature was room temperature for all layers, and *in situ* post annealing was carried out at 650°C and 550°C after the depositions of Cr layer and CFMS layer, respectively. The crystal structure of surface of the upper CFMS layer was characterized by reflection high energy electron diffraction (RHEED). CPP-GMR effects were measured by a four-probe method at room temperature. For the insert thickness dependence of CPP-GMR, the bias current density, J, was set so small that the applied bias voltage was about 1 mV for the parallel magnetization configuration. The J dependence of the output voltage, ΔV for the CPP-GMR junction was also investigated. Figure 1 shows RHEED images of the upper CFMS surface for the layered film with t_{Mg} = 0.60 nm. Streak patterns are clearly observed for both azimuths of CFMS[100] (Fig. 1(a)) and CFMS[110] (Fig. 1(b)). In addition, superlattice streaks of the $L2_1$ phase are also observed for CFMS[110] azimuth, which are pointed by white markers. All other RHEED images with different inserts showed similar features. These results suggest that the epitaxial growth and the $L2_1$ phase of CFMS layer are maintained for all the samples using Mg or Fe inserts with thicknesses up to 0.60 nm. Figure 2 shows the insert thickness dependence of MR ratio and ΔV. ΔV is defined as $\Delta V = (R_{\mathrm{AP}} - R_{\mathrm{P}}) \times |I_{\mathrm{bias}}|$, where R_{AP}, R_{P}, and I_{bias} are the junction resistance at antiparallel configuration, that at parallel configuration, and applied bias current, respectively. For both insert materials, the MR ratio decreases with the thickness of the insert. On the other hand, ΔV is nearly independent of t_{Mg} and t_{Fe} up to the thicknesses of 0.60 nm and 0.45 nm, respectively. The critical current density, J_c, for the spin-transfer-torque (STT) effect was also evaluated by the shape of MR curves. With increasing the insert thickness, J_c increased slightly. These results imply that the fluctuation of magnetization suppressed because of the suppressed STT effect at a high bias J, which resulted in relatively large ΔV. The suppression of STT can contribute for reducing the noise in sensor devices, which is an attractive feature of the junctions with inserts. In summary, the interface tailoring effects for CPP-GMR junctions were investigated using Mg or Fe inserts. Although the MR ratio at low bias J decreased with the thickness of inserts, ΔV was nearly independent of the inserts' thickness. The relatively large ΔV was possibly caused by the suppressed STT effect for the junctions with the inserts, which is favorable from a view point of reducing STT-noise. This work was partially supported by Grant-in-Aid for Scientific Research(S), Grant No. 25220910, from the Japan Society for the Promotion of Science, and Advanced Storage Research Consortium (ASRC). This work was a part of a cooperative program (Grant No. 17G0409) of the CRDAM-IMR, Tohoku University.

[1] T. Valet and A. Fert, Phys. Rev. B 48, 7099 (1993). [2] J. Jung *et al*., Appl. Phys. Lett. 108, 102408 (2016). [3] M. Inoue *et al*., Appl. Phys. Lett. 111, 082403 (2017). [4] T. Kubota *et al*., Phys. Rev. Materials 1, 044402 (2017).

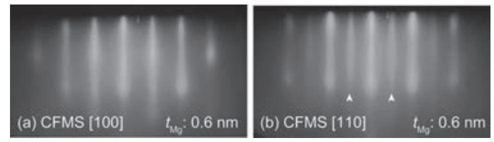

Fig. 1. RHEED images for the surface of upper $Co_2Fe_{0.4}Mn_{0.6}Si$ layer with the 0.6-nm-thick Mg inserts. (a) CFMS[100] azimuth, (b) CFMS[110] azimuth.

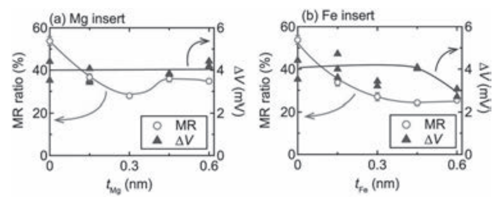

Fig. 2. The insert thickness dependence of MR ratio and the device output, ΔV for the CPP-GMR junctions. Insert materials are (a) Mg and (b) Fe.

11:00

EC-07. Perpendicular Anistropy in $Co_2FeAl_{0.5}Si_{0.5}$ for CPP-GMR devices.

W.J. Frost[1], M. Samiepour[1] and *A. Hirohata*[1]
1. Department of Electronic Engineering, University of York, York, United Kingdom

Heusler alloys have signicant potential for application in giant magnetoresistance (GMR) and tunelling magnetoressitance (TMR) devices [1]. However for the next generation of devices with a current-perpendicular-to-plane (CPP) geometry it would be required that the Heusler alloys were grown with perpendicular anisotropy. For perpendicular anisotropy to be achieved it is required that a significant anisotropy be generated to meet the condition such that $K > 2\pi M_S^2$. This then requires films with a high degree of crystallisation. In general the crystallisation of Heusler alloy films requires annealing at relatively high temperatures T>300°C. In this work we describe the fabrication of Heusler alloys based on $Co_2FeAl_{0.5}Si_{0.5}$ on substrates heated to modest temperatures which nonetheless result in films exhibiting significant perpendicular anisotropy and coercivities of over 1 kOe. Previous work has shown that perpendicular anisotropy can be induced in Heusler alloys using a vanadium or tungsten seed layer deposited at 400°C [2]. The coercivity of the films is highly dependent on layer thickness and as such spin valve structures are easily constructed. In this work modest substrate temperatures T_S < 75°C have been used prior to deposition. Samples with the structure Si/W(10nm)/$Co_2FeAl_{0.5}Si_{0.5}$(12.5nm)/W(1.2nm)/$Co_2FeAl_{0.5}Si_{0.5}$(2.5nm)/Ru(3nm) were used as a basic spin valve structure. As shown in fig. 1 even the modest values of TS > 45°C lead to a partially crystallised tungsten seed layer, with a weakly crystallised $Co_2FeAl_{0.5}Si_{0.5}$ layer. Nonetheless these samples had a significant coercivity out-of-plane of up to 500 Oe. The crystallisation was enhanced by T_S being increased to 60°C. With increasing crystallisation the tungsten reflection also relaxes towards the bulk position. The increasing crystallisation is matched by a large increase in the coercivity out-of-plane up to 1 kOe. This is caused by the increase in the grain size of the films from 3.5nm to 8 nm. The nature of the magnetic reversal also changes. At low values of T_S the switching is characteristic of a film with strong intergranular coupling, with a sharp reversal at a nucleation field H_n. The presence of the intergranular exchange field is confirmed by DCD and time-dependence measurements, which gave an effective activation volume V_{eff} = 30nm. The value of the H_n increases with the crystallinity of the film. However so too does the rotation in the film, reaching almost $0.5M_S$ before H_n is reached. This is partly due to the increasing grain size. However, this is also due to an increase in the perpendicular anisotropy in the films overcoming the intergranular coupling. However, no layer thickness dependent coercivity was observed, with only one nucleation in the hysteresis loop. In order to improve the spin valve properties of the film a silver barrier layer was used instead with a thicker top $Co_2FeAl_{0.5}Si_{0.5}$ layer to improve the signal. An optimised 3nm layer of silver was found for production of CPP-GMR devices giving a device structure of Si/W(10nm)/$Co_2FeAl_{0.5}Si_{0.5}$(12.5nm)/Ag(3nm)/$Co_2FeAl_{0.5}Si_{0.5}$(5nm)/Ru(3nm) deposited at 70°C. Figure 2 shows an example of a CPP-GMR measurement of a pillar with dimensions (150 x 100) nm. The observed ΔRA is very small at around 0.03% but a sharp and distinct switch was observed. The GMR ratio will be improved by further optimising layer thickness and deposition temperatures. In this work we have shown that perpendicular anisotropy can be induced in $Co_2FeAl_{0.5}Si_{0.5}$ with modest substrate temperatures. Furthermorewe have shown that the anisotropy is strongly dependent upon the crystallisation of a tungsten seed layer and the grain size. Finally, these Heusler alloys layers can be incorporated into CPP-GMR devices operated out of plane, with a small but distinct GMR. The authors would like to acknowledge Kevin O'Grady, University of York for fruitful discussion and Seagate Technology, Derry for their support.

[1] Atsufumi Hirohata and Koki Takanashi, *Future perspectives for spintronic devices*, J. Phys. D. Appl. Phys. 47 (2014), no. 19, 193001. [2] W. Frost and A. Hirohata, *Perpendicular anisotropy in heusler alloy layers induced by a V seed layer*, IEEE Trans. Magn. 52 (2016), no. 7, 2-5.

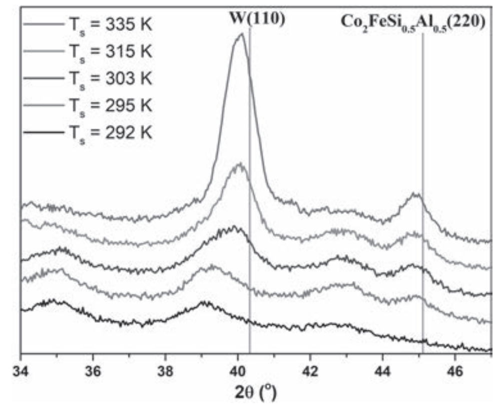

Fig. 1. θ/2θ scans of Heusler alloy films on a 10 nm Tungsten seed layer with increasing substrate temperature.

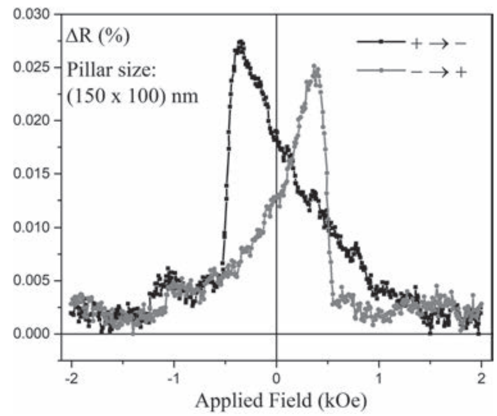

Fig. 2. Out-of-plane GMR measurement on a (150 x 100) nm pillar based on $Co_2FeAl_{0.5}Si_{0.5}$.

11:15

EC-08. Mn-composition dependence of strength of bi-quadratic interlayer exchange coupling in Co_2MnSi-based pseudo spin-valves.

M. Inoue[1], D. Mouri[1], K. Inubushi[2], K. Nakada[2], M. Yamamoto[1] and T. Uemura[1]
1. Division of Electronics for Informatics, Hokkaido University, Sapporo, Japan; 2. Technical Center, TDK Corporation, Ichikawa, Japan

Co-based Heusler alloy thin films are promising ferromagnetic electrode materials for spintronic devices, including magnetic tunnel junctions (MTJs) [1-4] and current-perpendicular-to-plane (CPP) giant magnetoresistance (GMR) devices [5-11], and for spin injection into semiconductors [12,13]. We have shown that harmful defects in Heusler alloy thin films of Co_2MnSi (CMS), $Co_2(Mn,Fe)Si$ (CMFS), and Co_2MnGe (CMG) can be suppressed by appropriately controlling the film composition; *i.e.*, Co_{Mn} antisites detrimental to half-metallicity can be suppressed and half-metallicity was enhanced by preparing CMS and CMFS thin films with a Mn-rich composition [1-5]. In light of these findings, we have demonstrated giant tunneling magnetoresistance ratios of 1995% at 4.2 K and 354% at 290 K for CMS/MgO MTJs [3] and up to 2610% at 4.2 K and 429% at 290 K for CMFS/MgO MTJs [4]. Moreover, we have observed an increase in the magnetoresistance (MR) ratio with increasing Mn composition in CMS-based CPP spin valves, and demonstrated that Mn-rich CMS is highly effective in GMR devices, as it is in MTJs [5]. However, the MR ratio decreased as the temperature decreased in a certain low temperature region [5]. A similar decrease in the MR ratio at low temperatures was previously reported for other CPP-GMR devices based on CMS, CMG, and CMFS [6-9], and its origin is still an open question. Goripati *et al*. reported that the decrease in the MR ratio at low temperatures was alleviated by spin transfer torque (STT) switching, and suggested that the origin of the reduction of MR ratio is the presence of a bi-quadratic interlayer exchange coupling (90° coupling) between the upper and lower ferromagnetic layers [6]. Thus, it is important to investigate the strength of the 90° coupling systematically to fully utilize the half-metallicity of Mn-rich CMS in GMR devices. The purpose of this study was to clarify how the strength of the 90° coupling changes with the Mn composition, α, in $Co_2Mn_\alpha Si$ electrodes. To do this, we fabricated CPP pseudo spin valves (PSVs) having CMS electrodes with various Mn compositions, α, and an Ag spacer, and investigated the influence of α on the MR characteristics and STT properties. The fabricated CPP-PSV layer structure was as follows: (from the substrate side) MgO buffer (10 nm)/CoFe (10)/Ag (100)/CoFe (10)/CMS lower electrode (10)/Ag spacer (5)/CMS upper electrode (3)/Ru cap (5) with various Mn compositions, α, in $Co_2Mn_\alpha Si_{0.82}$ electrodes ranging from $\alpha = 0.62$ to 1.40, grown on MgO(001) substrates. The preparation procedure of the CMS electrodes with various values of α was the same as the one for the CMS/MgO MTJs [1-4] and the CMS-based CPP spin valves [5]. Just after deposition of the upper electrode, the layer structure was *in-situ* annealed at 550°C. We fabricated CPP-PSVs with the junction sizes ranging from 26 × 50 nm to 320 × 525 nm by electron beam lithography and Ar ion milling. The MR curve and STT curve were measured using a dc four-probe method by sweeping the magnetic field (H) and bias current, respectively. Both measurements were done at room temperature. Figure 1(a) and 1(b) compares the MR curve and STT curve for CPP-PSVs with Mn compositions of (a) $\alpha = 0.62$ and (b) $\alpha = 1.40$. Clear MR characteristics with a hysteretic nature were obtained for both devices. Since the anti-parallel (AP) state appears around $H = 0$ without bistability, an anti-ferromagnetic coupling intrinsically existed. There were also clear changes in resistance due to switching of the magnetization configuration between the parallel (P) and AP states driven by the STT. The resistance in the AP state obtained by STT ($R_{AP}^{(STT)}$) was larger than that for the AP state obtained by the magnetic field sweep ($R_{AP}^{(Mag)}$) in all devices. This indicates that the AP state was not perfectly formed by sweeping the magnetic field due to the presence of the 90° coupling and that the STT brought the magnetization configuration more closely to the perfect AP state. Figure 2 shows the ratio of $R_{AP}^{(STT)}$ and $R_{AP}^{(Mag)}$ as a function of the Mn composition, α. The ratio increases as the Mn composition increases, indicating that the strength of the 90° coupling increases with increasing Mn composition. In summary, we investigated the influence of the Mn composition on the strength of the 90° coupling in CMS-based CPP-SVs through evaluating the MR characteristics and STT properties, and found that the strength of the 90° coupling increases with increasing Mn composition. This indicates that the Mn involved in the CMS/Ag/CMS trilayer structure plays a critical role in regard to the presence of the 90° coupling. These findings help to clarify the origin of the interlayer exchange coupling. This work was partly supported by the Japan Society for the Promotion of Science (KAKENHI: Grant Number, 17H03225).

[1] T. Ishikawa *et al.*, Appl. Phys. Lett. 95, 232512 (2009). [2] M. Yamamoto *et al.*, J. Phys.: Condens. Matter. 22, 164212 (2010). [3] H.-x. Liu *et al.*, Appl. Phys. Lett. 101, 132418 (2012). [4] H.-x. Liu *et al.*, J. Phys. D: Appl. Phys. 48, 164001 (2015). [5] M. Inoue *et al.*, Appl. Phys. Lett. 111, 082403 (2017). [6] H. S. Goripati *et al.*, J. Appl. Phys. 110, 123914 (2011). [7] T. Furubayashi *et al.*, J. Appl. Phys. 107, 113917 (2010). [8] Y. Sakuraba *et al.*, J. Phys. D: Appl. Phys. 44, 064009 (2011). [9] M. J. Carey *et al.*, J. Appl. Phys. 109, 093912 (2011). [10] J. W. Jung *et al.*, Appl. Phys. Lett. 108, 102408 (2016). [11] S. Li *et al.*, Appl. Phys. Lett. 108, 122404 (2016). [12] Y. Ebina *et al.*, Appl. Phys. Lett. 104, 172405 (2014). [13] T. Uemura *et al.*, Phys. Rev. B. 91, 140410(R) (2015).

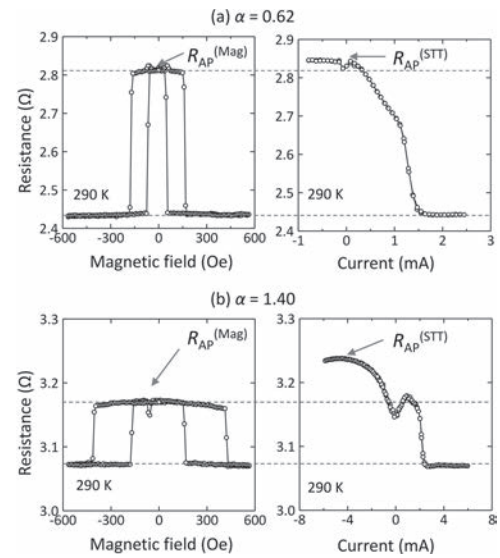

Fig. 1. Comparison of MR curve and STT curve for CPP-PSVs with Mn compositions, α, in $Co_2Mn_\alpha Si_{0.82}$ of (a) $\alpha = 0.62$ and (b) $\alpha = 1.40$.

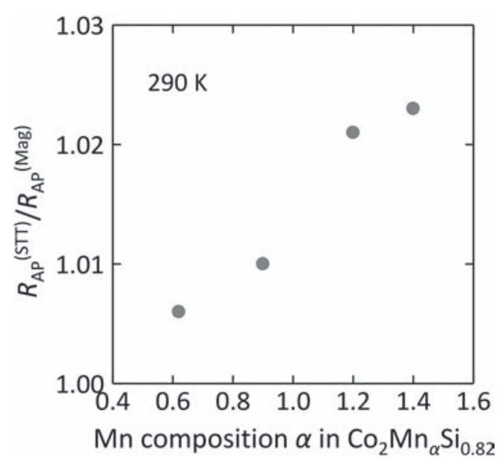

Fig. 2. Ratio of $R_{AP}^{(STT)}$ and $R_{AP}^{(Mag)}$ as a function of Mn composition, α, in $Co_2Mn_\alpha Si_{0.82}$, where $R_{AP}^{(STT)}$ and $R_{AP}^{(Mag)}$ are, respectively, the resistance for AP state obtained by STT switching and that obtained by sweeping the magnetic field, respectively. The ratio increases as Mn composition increases.

INVITED PAPER

11:30

EC-09. Control ferromagnets all electrically at room temperature without external magnetic field.

K. Wang[1]
1. Institute of Semiconductors, Chinese Academy of Sciences, Beijing, China

Electrically control the spin state in solids is the core of spintronics. We investigated the spin Hall effect control the magnetization switching in heavy metal/ferromagnet/heavy metal multilayers and also piezo voltages control the magnetization switching of heusler ally Co2FeAl. By design the device structrue, we demonstrate a strong damping-like torque from the spin Hall effect and unmeasurable field-like torque from Rashba effect. The spin-orbit effective fields due to the spin Hall effect were investigated quantitatively and were found to be consistent with the switching effective fields after accounting for the switching current reduction due to thermal fluctuations from the current pulse[1]. The spin-orbit torque switching controllablly in above structures have to have the assistant of the external magnetic field. Without breaking the symmetry of the structure of the thin film, we realize the deterministic magnetization switching in a hybrid ferromagnetic/ferroelectric structure with Pt/Co/Ni/Co/Pt layers on PMN-PT substrate. The effective magnetic field can be reversed by changing the direction of the applied electric field on the PMN-PT substrate, which fully replaces the controllability function of the external magnetic field[2]. We also investigated the planar Hall effect devices based on the tunability of the planar Hall resistance in ferromagnetic Co_2FeAl devices solely by piezo voltages, which can largely reduce the energy consumption. The room temperature magnetic NOT and NOR gates have been demonstrated based on the Co_2FeAl planar Hall effect devices without external magnetic field[3].

[1] Meiyin Yang, Kaiming Cai, Hailang Ju, Kevin William Edmonds, Guang Yang, Shuai Liu, Baohe Li2, Bao Zhang, Yu Sheng, Shouguo Wang, Yang Ji & Kaiyou Wang, *Scientific Reports*, 6 (2016)20778. [2] Kaiming Cai, Meiyin Yang, Hailang Ju, Sumei Wang, Yang Ji, Baohe Li, Kevin William Edmonds, Yu Sheng, Bao Zhang, Nan Zhang, Shuai Liu, Houzhi Zheng and Kaiyou Wang, *Nature Materials* (in Press). [3] Bao Zhang, Kang-Kang Meng, Mei-Yin Yang, K. W. Edmonds, Hao Zhang, Kai-Ming Cai1, Yu Sheng, Nan Zhang, Yang Ji, Jian-Hua Zhao, Hou-Zhi Zheng & Kai-You Wang, *Scientific Reports*, 6 (2016)28458.

THURSDAY MORNING, 26 APRIL 2018 PEONY IV, 9:00 TO 12:00

Session ED
SPIN-ORBITRONICS III

Shunsuke Fukami, Co-Chair
Tohoku University, Sendai, Japan
Xuepeng Qiu, Co-Chair
Tongji University, Shanghai, China

CONTRIBUTED PAPERS

9:00

ED-01. Hybrid strain-mediated spin-orbit torque switching for magnetic memory.

Q. Wang[4], J. Domann[1], G. Yu[2,3], H. Wu[3], A. Barra[4], K. Wang[3] and G.P. Carman[4]
1. Department of Biomedical Engineering and Mechanics, Virginia Tech, Blacksburg, VA, United States; 2. Institute of Physics, Chinese Academy of Sciences, Beijing, China; 3. Department of Electrical and Computer Engineering, University of California, Los Angeles, CA, United States; 4. Department of Mechanical and Aerospace Engineering, University of California, Los Angeles, CA, United States

Spin-orbit torque (SOT) represents an energy efficient method to control magnetization in magnetic memory devices. However, deterministically switching perpendicular memory bits requires the application of an additional effective bias field for breaking lateral symmetry. Here we present a new perpendicular switching method of using voltage induced strain coupled with SOT. The strain-induced magnetoelastic anisotropy breaks the lateral symmetry which provides deterministic control of perpendicular magnetization. A finite element model and a macrospin model are used to numerically simulate the strain-mediated SOT switching mechanism. Experimental tests are being conducted to validate the models predictions. Fig. 1a shows the magnetoelastic/heavy metal/piezoelectric heterostructure simulated in the finite element model. The magnetic element is a CoFeB disk with a 50 nm diameter and a 1.5 nm thickness. Underneath the CoFeB disk, there is a thin (< 10 nm) heavy metal (e.g., Ta) strip with the SOT current applied 45° from the *y* axis. At t = 0, a ±0.5 V voltage is applied to the two top electrodes while a current density of 5×10^7 A/cm^2 is applied to the heavy metal strip. Both voltage/current inputs are removed at t = 2 ns. The simulation results shown in Fig. 1b clearly demonstrates that the switching direction ('up' or 'down') is dictated by the voltage polarity (positive or negative) applied to the piezoelectric layer. Removing the voltage/current any time after 0.2ns produces successful perpendicular switching corresponding to 5 GHz write frequency. Fig. 2 shows the results from parametric studies using the macrospin model to investigate the impact of strain amplitude, current density, and relative orientation of strain/current. Fig. 2a illustrates the principal strain directions and defines the relative orientation angle θ. For simplicity, producing a biaxial strain defined by. Fig. 2b illustrates the four different types of magnetic state that are possible. The first parametric study consists of 2,601 cases that varies the magnitude of the biaxial strain and the current density with fixed SOT orientation as θ = 45°. Fig. 2c shows the switching phase diagram with the four separate regions corresponding to the four magnetic states shown in Fig. 3b. The successful switching cases (region I) are further examined in Fig. 3d. The m_z amplitude at t = 2 ns is illustrated in color for each case. Switching initiates when the biaxial strain is as low as. As the strain increases, the threshold current (i.e., the minimum current that enables switching) decreases. In other words, a tradeoff exists between the threshold strain and threshold current. Fig. 2e shows the switching phase diagram for the second parametric study, which consists of an additional 2,061 cases with fixed biaxial strain while varying θ and current density. Only three types of magnetic states (type I, II, and III) are discovered, i.e. the magnetic oscillation (type IV) is absent due to the relatively small strains investigated. Fig. 2f further examines all the successful switching cases (region I). The results show that switching is absent when the current is parallel (θ = 0°) or perpendicular (θ = 90°) to the magnetoelastic field (i.e., *y* axis). This feature can be explained using symmetry analysis (not shown here). It is also interesting to note that the dashed cut-lines in Figs. 3d and 3f have similar profiles because they both represent switching behaviors as a function of current density for a fixed current direction θ = 45° and a fixed biaxial strain. In conclusion, the simulation results from the finite element model and the macrospin model show that the strain-induced magnetoelastic anisotropy can break lateral symmetry and produce field free deterministic perpendicular switching in SOT devices. The switching is field-free, fast, and deterministic. Using the uniaxial anisotropy to break the in-plane symmetry opens a new genre of field-free deterministic perpendicular switching in SOT devices and paves the way for next-generation non-volatile memory.

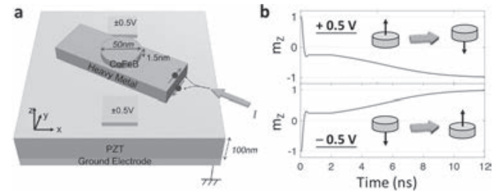

Fig. 1. Finite element simulation: model setup and results. (a) Schematic illustration of the simulated structure and the direction of applied current. (b) Finite element model results of strain-mediated SOT switching for different voltage polarities (positive or negative). The voltage/current application and removal are identified as the blue and red portions of the response, respectively. For +0.5V applied voltage, the final magnetic state is down. For –0.5V applied voltage, the final state is up.

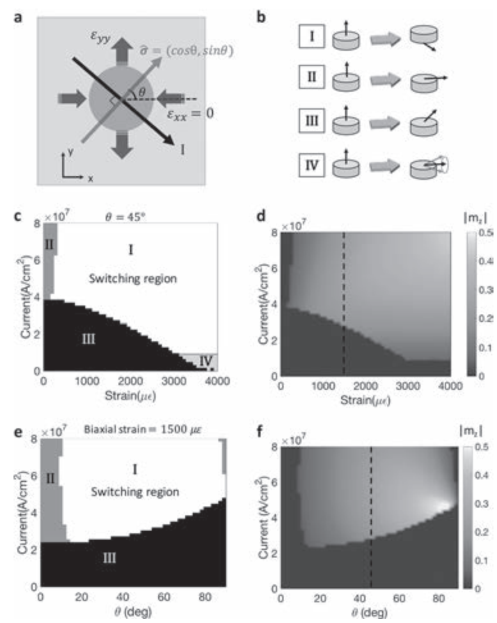

Fig. 2. Switching phase diagrams drawn from the parametric studies using macrospin model. (a) Definition of θ and in-plane principal strain directions. (b) Illustrations for different switching behaviors at t = 2 ns found in the simulations, which correspond to region I, II, III, and IV, respectively in following figures. (c) Switching phase diagram for fixed θ = 45° with varying biaxial strain and current density. (d) Amplitude of m_z after switching for cases in the region I in b. (e) Switching phase diagram for fixed biaxial strain with varying θ and current densities. (f) Amplitude of m_z after switching for cases in the region I in e.

9:15

ED-02. Switching of exchange-coupled perpendicular magnetized layers driven by spin orbital torque with low power consumption.

S. Wang[1] and J. Luo[1]
1. Institute of Microelectronics, UCAS, Beijing, China

Extensive experiments have been devoted to study the deterministic switching of perpendicularly magnetized layers in heavy metal/ferromagnet devices driven by spin orbital torque by the spin Hall effect [1-4]. A perpendicular magnetized layer has been proved to be successfully and deterministically switched under certain circumstances experimentally and theoretically [5-8]. To obtain high perpendicular anisotropy, the thickness of the film needs to be sufficiently small (<1nm). To resist the thermal fluctuations during operation, we proposed a multilayer structure including exchange-coupled perpendicularly magnetized layers to switch at relatively low currents and maintain thermal stability, inspired by the ECC media in HDD systems [9]. Without loss of generality, we simply used an in-plane field along the charge current direction (y) to describe the effective field to break the symmetry of rotation in response to the spin orbital torque in our simulation. Fig.1(a) illustrates our design: the bottom magnetic layer is softer ($K_1<K_2$) and is relatively vulnerable to the reversal torque. We used typical magnetic parameters for each layer: the saturation magnetization M_{s1}=1200 emu/cm^3 and M_{s2}=800emu/cm^3, and the effective anisotropy constants K_1=0.5×10^6 erg/cm^3 and K_2=2×10^6 erg/cm^3. We assume only the bottom magnetic layer is subject to the spin orbital torque as the torque originates from spin orbit interaction. Without any applied currents the multilayer relaxes to its equilibrium state and the average magnetization is slightly tilted towards y axis (about 12°). In the switching process, the softer magnetic layer tends to reverse first and the harder layer follows driven by the exchange interaction. The critical spin current density is 5MA/cm^2. Our new structure provides a way to design and optimize the spintronic device.

[1] I. M. Miron, K. Garello, G. Gaudin, P. J. Zermatten, M. V. Costache, S. Auffret, *et al.*, "Perpendicular switching of a single ferromagnetic layer induced by in-plane current injection," *Nature,* vol. 476, pp. 189-194, Aug 11 2011. [2] L. Q. Liu, C. F. Pai, Y. Li, H. W. Tseng, D. C. Ralph, and R. A. Buhrman, "Spin-Torque Switching with the Giant Spin Hall Effect of Tantalum," *Science,* vol. 336, pp. 555-558, May 4 2012. [3] K. Ando, S. Takahashi, K. Harii, K. Sasage, J. Ieda, S. Maekawa, *et al.*, "Electric manipulation of spin relaxation using the spin Hall effect," *Physical Review Letters,* vol. 101, p. 036601, Jul 18 2008. [4] T. Suzuki, S. Fukami, N. Ishiwata, M. Yamanouchi, S. Ikeda, N. Kasai, *et al.*, "Current-induced effective field in perpendicularly magnetized Ta/CoFeB/MgO wire," *Applied Physics Letters,* vol. 98, p. 142505, Apr 4 2011. [5] K. Cai, M. Yang, H. Ju, S. Wang, Y. Ji, B. Li, *et al.*, "Electric field control of deterministic current-induced magnetization switching in a hybrid ferromagnetic/ferroelectric structure," *Nature Materials,* 2017. [6] S. Wang, M. Yang, and C. Zhao, "Deterministic switching of perpendicularly magnetic layers by spin orbital torque through stray field engineering," submitted. [7] S. Fukami, C. L. Zhang, S. DuttaGupta, A. Kurenkov, and H. Ohno, "Magnetization switching by spin-orbit torque in an antiferromagnet-ferromagnet bilayer system," *Nature Materials,* vol. 15, pp. 535-542, May 2016. [8] L. Q. Liu, O. J. Lee, T. J. Gudmundsen, D. C. Ralph, and R. A. Buhrman, "Current-Induced Switching of Perpendicularly Magnetized Magnetic Layers Using Spin Torque from the Spin Hall Effect," *Physical Review Letters,* vol. 109, p. 096602, Aug 29 2012. [9] R. H. Victora and X. Shen, "Composite Media for Perpendicular Magnetic Recording," *IEEE TRANSACTIONS ON MAGNETICS,* vol. 41, pp. 537-542.

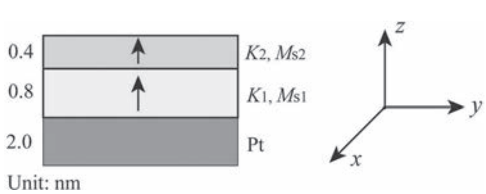

Fig. 1. Schematics of our design

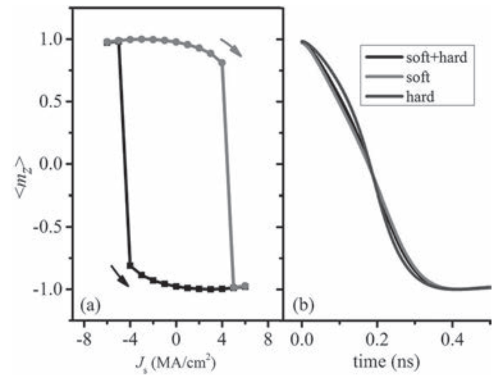

Fig. 2. The switching loop and trajectories of the exchange-coupled layers. To simplify, we refer to the top and bottom magnetic layer as hard and soft layers, respectively

INVITED PAPER

9:30

ED-03. Spin orbit torque via interfacial oxidation in magnetic heterostructures.

X. Qiu[1] and H. Yang[2]
1. Department of Physics Science and Engineering, Tongji University, Shanghai, China; 2. Department of Electrical and Computer Engineering, National University of Singapore, Singapore

Realizing energy efficient SOT devices essentially relies on the magnitude of SOT. On the other hand, constructing multifunctional spin logic and memory devices requires an enhanced control of SOT. Here, we report on the manipulation of the sign and magnitude of SOT via interfacial oxidation in Pt/CoFeB/MgO heterostructures. As the oxygen level in the CoFeB layer goes above a threshold level, SOT suddenly reverses its direction while its magnitude remains roughly invariant. As the Pt is strong against oxidation which is further confirmed by the X-ray photoelectron spectroscopy (XPS) measurements, the sign reversal of SOT via oxygen manipulation cannot be explained by the spin Hall theory and instead it suggests the important role of interface Rashba effect in SOT generation in HM/FM heterostructures. [1] To examine the proportion of SHE and Rashba effect contributions, the samples with varied Pt thickness (t_{Pt}) are studied. The variation of t_{Pt} enables the tuning of the proportion between SHE and Rashba effect based SOTs. H_{SHE} = 155.1 Oe and H_{Rashba} = -143.8 Oe are obtained from the analysis, showing SOT originated from SHE and Rashba effects are of comparable magnitude but opposite in sign in the magnetic heterostructures with oxygen incorporation.[2]

[1] X. P. Qiu *et al.*, Nature Nanotechnology 10, 333 (2015) [2] X. P. Qiu *et al.*, accepted for Advanced Materials (2017)

CONTRIBUTED PAPERS

10:00

ED-04. Spin Hall magnetoresistance in Co / transparent-conductive-oxide bilayers.

S. Isogami[2] and M. Hayashi[1,2]
1. The University of Tokyo, Tokyo, Japan; 2. Research Center for Magnetic and Spintronic Materials, National Institute for Materials Science (NIMS), Tsukuba, Japan

Introduction : Spin Hall magnetoresistance (SMR) in metallic bilayers [1-5] and heterostructures consisting of ferromagnetic insulator (FI) / heavy metal (HM) [6-8] are widely studied, moreover, the experimental results can be explained by theoretical models that invoke spin accumulation at the FI / HM interfaces [9-11]. To extend the previous pioneering works to the case of heterostructures with the other spin Hall materials and to survey their potentials, we newly focus on the In_2O_3 based transparent-conductive-oxide such as In-W-O (IWO) in this study. It was reported that thin film transistors (TFTs) were achieved when the IWO was used as an active channel semiconductor in the TFTs [12-14]. The transport and output properties of the IWO-TFTs demonstrate both the high stability and high field-effect, therefore, the IWO is considered beneficial to future application products in addition to the conventional TFT with e.g. amorphous In-Ga-Zn-O (IGZO) [15,16]. On the other hand, it is still unknown that the doped W atoms with strong spin-orbit interaction would induce spin Hall effect in IWO films. The present study is intended to confirm the spin Hall effect in the IWO by measuring the SMR for Co / IWO heterostructures. Experimental procedure : The heterostructures, capping layer / Co (3 nm) / IWO (t_{IWO} = 4, 6, 8, 10 nm) / thermally oxidized Si substrate, were fabricated using a magnetron sputtering machine at room temperature. To prevent crystal growth and reduce surface roughness of the IWO, oxygen additive sputtering with 0.5 % O_2 and Ar mixture gas was performed in the IWO film deposition. A metal mask was used to produce Hall bar samples with dimensions of L = 1.2 mm and W = 0.8 mm. The longitudinal resistance (R_{xx}) was measured with DC bias current of 5 μA using PPMS at room temperature while scanning magnetic field (H) from - 6 T to 6 T. The SMR ratio was defined as the R_{xx} change at H = 4 T, namely, [R_{xx} (H_y = 4 T) - R_{xx} (H_z = 4 T)] / R_{xx} (H_z = 4 T). The sheet electric conductance was defined as the product of conductivity and film thickness. Results and discussion : Figure 1 shows the typical SMR curves in which the H were applied in H_x, H_y and H_z directions. For the SMR curve with H_z (shown by open circles), convex downward behavior was observed up to $|H_z|$ = 2 T, which corresponds to the magnetic saturation of the 3-nm-thick Co film in H_z direction, then monotonic decrease was observed. Unlike the case with H_z, the dip patterns were observed at H_x and H_y = 0 T (shown by solid triangles and circles). Therefore, it was found that the 3-nm-thick Co film involved in-plane magnetization. The different R_{xx} at H_y and H_z = 4 T could be attributed to the spin accumulation at the interface that strongly depends on the adjacent Co magnetization. Resultant SMR ratio was estimated to be - 0.12 %. Figure 2(a) and 2(b) show the t_{IWO} dependences of the SMR ratio and the sheet electric conductance, respectively. As for Fig. 2(b), the sheet electirc conductance exhibited slight variation with t_{IWO}, around 0.003 Ω^{-1}. The solid line shows calculation results assuming the parallel circuit of the Co and IWO layers, which agreed well with the data points using ρ_{IWO} = 11800 μΩcm and ρ_{Co} = 90 μΩcm. Note that the value of 10-nm-thick IWO film obtained in another experiment was adopted to the ρ_{IWO}. While further investigation might be necessary, the fitting parameter of ρ_{Co} on the IWO layer was increased compared with that of bulk Co. Fig. 2(b) revealed significantly weak t_{IWO} dependence, which can be attributed to that ρ_{IWO} was over 100 times higher compared with ρ_{Co}. As for Fig. 2(a), calculation was conducted based on the extended SMR model that can account for the spin absorption in metallic interfaces [4], because electric conduction is expected in both the Co and IWO layers. The results revealed that the spin diffusion length of IWO (λ_{IWO}) = 1.5 nm and minimum limit of spin Hall angle (θ_{SH}) = 0.57, which led us to conclude that the presence of spin Hall effect in the Co / IWO heterostructure was confirmed. To clarify such the spin Hall mechanisms involved, further discussion on the microstructure at the interface as well as transport properties of IWO will be presented at the conference.

[1] J. C. Rojas-Sanchez, *et al*., Phys. Rev. Lett. 112, 106602 (2014). [2] J. Liu, *et al.*, Appl. Phys. Lett. 107, 232408 (2015). [3] C. O. Avci, *et al.*, Nat. Phys. 11, 570 (2015). [4] J. Kim, *et al*., Phys. Rev. Lett. 116, 097201 (2016). [5] L. Wang, *et al*., Phys. Rev. Lett. 116, 196602 (2016). [6] M. Weiler, *et al*., Phys. Rev. Lett. 108, 106602 (2012). [7] S. Y. Huang, *et al*., Phys. Rev. Lett. 109, 107204 (2012). [8] C. Hahn, *et al*., Phys. Rev. B 87, 174417 (2013). [9] H. Nakayama, *et al*., Phys. Rev. Lett. 110, 206601 (2013). [10] M. Althammer, *et al*., Phys. Rev. B 87, 224401 (2013). [11] Y. Chen, *et al*., Phys. Rev. B 87, 144411 (2013). [12] S. Aikawa, *et al*., Appl. Phys. Lett. 102, 102101 (2013). [13] T. Kizu, *et al*., Appl. Phys. Lett. 104, 152103 (2014). [14] T. Kizu, *et al*., J. Appl. Phys. 118, 125702 (2015). [15] H.J. Yoon, *et al*., J. Electrochem. Soc. 139, 3229 (1992). [16] M. Kim, *et al*., Appl. Phys. Lett. 90, 212114 (2007). [17] J.Y. Kwon, *et al*., Electron Mater. Lett. 7, 1 (2011).

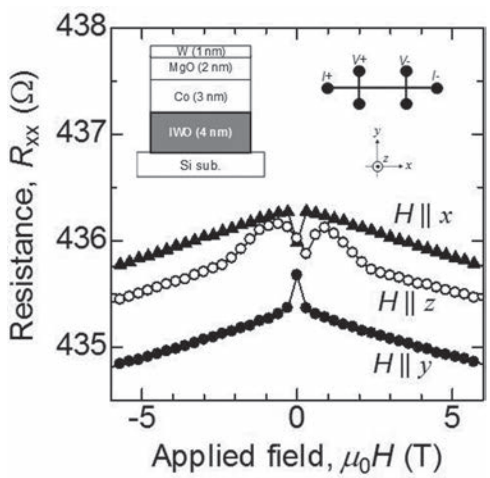

Fig. 1. Spin-Hall magnetoresistance (SMR) as functions of applied magnetic fields (H_x, H_y and H_z) for the Co (3 nm) / IWO (4 nm) heterostructure. Insets show the stacking structure and the measurement configuration in the Hall bar.

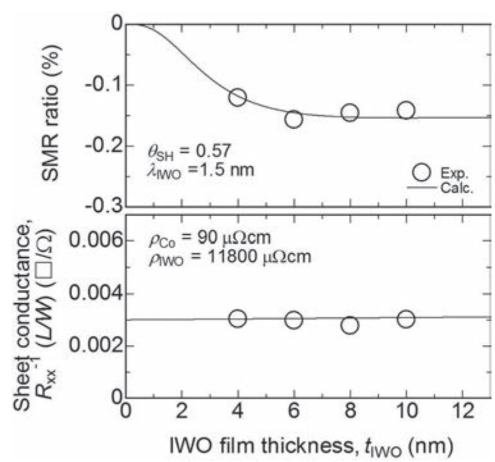

Fig. 2. (a) Spin-Hall magnetoresistance (SMR) ratio and (b) sheet conductance as a funtion of IWO film thickness (t_{IWO}) for the Co (3 nm) / IWO (t_{IWO} = 4, 6, 8, 10 nm) heterostructure. Open circles and solid lines correspond to the experimantal data and calclated results, respectively. Parameters used in the calculation are shown on each panel.

10:15

ED-05. Direct optical observation of spin accumulation at nonmagnetic metal / oxide interface.

J. Puebla[1], F.V. Auvray[2], M. Xu[2], B. Rana[1], K. Kondou[1] and Y. Otani[1,2]
1. CEMS, RIKEN, Wako, Japan; 2. The University of Tokyo, Kashiwa, Japan

We report the direct observation of uniform in-plane spin accumulation at room temperature by magneto optical Kerr effect, at the interface formed between nonmagnetic metal (Cu, Ag) and oxide (Bi_2O_3). Recent reports show spin to charge conversion at these interfaces suggesting the presence of Rashba like spin orbit coupling (SOC). The formation of spin accumulation is the result of current induced spin polarization at our interfaces (direct Rashba–Edelstein effect), without external magnetic field or proximity to ferromagnetic materials. We observe opposite orientation of spin accumulation at Cu/Bi_2O_3 and Ag/Bi_2O_3 interfaces reflecting their opposite sign of Rashba SOC (Rashba parameter). Moreover, estimation of spin accumulation from values of Rashba parameters obtained by independent spin pumping measurements, agrees well with the difference in amplitude of our normalized Kerr signals for Cu/Bi_2O_3 and Ag/Bi_2O_3 interfaces. Uniform in-plane spin accumulation due to Rashba-Edelstein effect can be applied for spin filter devices and efficient driving force for magnetization switching.

Appl. Phys. Lett. 111, 092402 (2017); doi: 10.1063/1.4990113

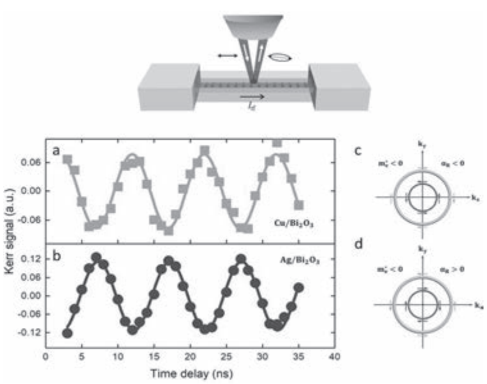

10:30

ED-06. Enhancement of Spin Orbit Torques by Oxygen Implantation.

J. Nath[1,2], A.V. Trifu[1,2], S. Auffret[1,2], G. Gaudin[1,2] and I. Miron[1,2]
1. SPINTEC/CEA/CNRS, Grenoble, France; 2. Université Grenoble Alpes, Grenoble, France

A diversified demand stemming primarily from consumer products and Internet of Things (IoT) devices has led to a spurt in the growth of the memory industry in the past decade. This has also led to a faster adoption of Non-Volatile Memory (NVM) technologies such as Magnetic Random Access Memories (MRAM). MRAMs are high-speed, low-power and non-volatile spintronic memories. It uses the Tunneling Magneto-Resistance (TMR) mechanism for the read out of the memory bit and can use either the Spin-Transfer Torque (STT) or the Spin-Orbit Torque (SOT) mechanism for the write operation. In SOT-MRAM, the write current is injected in the plane of the magnetic bit, decoupling the read and write paths. This leads to a lower current flowing through the oxide tunnel barrier, slowing the oxide aging and enhancing the overall endurance of the bit. Furthermore, this also enables the use of a tunnel barrier with a higher Resistance Area (RA) product, leading to a lower read disturb and hence increased reliability. SOT-MRAMs typically use a tri-layer structure with inversion asymmetry. A current injected in to the heavy metal (HM) layer with high Spin Orbit Coupling (SOC) gives rise to various torques, namely the Field-Like (FL) torque and the Damping-Like (DL) torque. These torques act on the magnetization of the adjacent Ferro-Magnetic (FM) layer in order to switch it during the write operation [1-2]. They originate from two distinct mechanisms – the Spin Hall Effect (SHE), which is a bulk effect and the Inverse Spin Galvanic Effect (ISGE), which is an interfacial effect. The efficiency of these torques determine the write energy. It also determines the size of the switching transistor and correspondingly the overall memory density. Hence it is vital to determine the contributions of these two effects. One of the ways of ascertaining this is by oxidizing the HM layer to determine the bulk and interfacial contributions. The presence of interfacial oxygen at a cobalt-metal oxide interface can lead to an increased asymmetric band splitting of the Co 3*d* bands [3]. This can induce a Perpendicular Magnetic Anisotropy (PMA), and has been widely studied in the development of perpendicular Magnetic Tunnel Junctions (pMTJ) [3-4]. However, the role of oxygen on SOTs is only starting to be explored experimentally [5-7]. Here we present the enhancement of DL torques by oxygen implantation of the FM/HM interface in a Ta/Cu/Co/Pt hetero-structure. Figure 1 shows the DL field corresponding to the top platinum thickness. As the platinum thickness is reduced, a higher concentration of oxygen atoms reach the Co/Pt interface. Up to a certain reduction in Pt thickness, we see no significant variation of the DL torques. However when the amount of oxygen present at the interface crosses a certain threshold, we see a sharp increase in the DL torques. This signifies a dominant interfacial effect in our samples. Further, in the sample with a thinner Cu layer, we notice this increase to be even higher as less current is shunted through the Cu layer. Such an enhancement of torques could lead to a lower write current, and thereby higher energy efficiency and bit density of SOT-MRAMs. This increase in DL torques has also been observed to correspond to an increase in PMA, which determines the thermal stability of pMTJs. Hence, the oxidation of the FM/HM interface appears as a valuable tool in the development of SOT-MRAMs for longer retention times and a net reduction in write energy.

[1] Miron, I. M. *et al.*, *Nature* 476, 189, 2011 [2] Liu, L. *et al.*, *Science* 336, 555, 2012 [3] Manchon, A. *et al., Journal of Applied Physics* 104, 043914, 2008 [4] Monso, S. *et al., Applied Physics Letters* 80, 4157, 2002 [5] Demasius, K.-U. *et al., Nature Communications* 7, 10644, 2016 [6] An, H. *et al., Nature Communications* 7, 13069, 2016 [7] Qui, X. *et al., Nature Nanotechnology* 10, 333, 2015

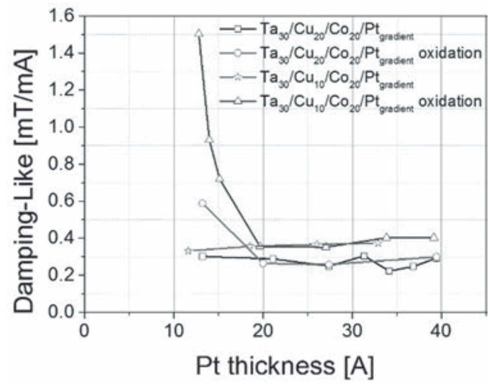

Fig. 1. Increase in Damping-Like effective field per unit current applied, with platinum thickness. The oxidized samples are represented by the blue and the red curves, while the un-oxidized samples by the black and the green curves. The platinum thickness is inversely proportional to the amount of oxygen at the Co/Pt interface.

10:45

ED-07. Reliable Estimation of TaB Spin Hall Angle by Incorporating the Interfacial Transparency and Isolating Inverse Spin Hall Effect in ST-FMR Analysis.

A. Tiwari[1], H. Yoda[1], Y. Kato[1], K. Koi[1], M. Ishikawa[1], S. Oikawa[1], Y. Saito[2], T. Inokuchi[1], N. Shimomura[1], M. Shimizu[1], S. Shirotori[1], A. Buyandalai[1], H. Sugiyama[1], Y. Ohsawa[1] and A. Kurobe[1]
1. Corporate Research and Development, Toshiba Corporation, Kawasaki, Japan; 2. Center for Innovative Integrated Electronic System, Tohoku University, Sendai, Japan

The requirement of low power consumption, high speed, high endurance for emerging next generation universal memory, a three terminal (separate read/write terminals) spin-orbit-torque (SOT) based non-volatile memory (SOT-MRAM) devices have been gaining much interests than two-terminal spin-transfer-torque MRAM (STT-MRAM) due to its improved magnetization switching, exploiting the spin Hall effect (SHE) mechanism [1-6]. The free layer of SOT-MRAM devices, consists of heavy metal (HM)/ferromagnet metal (FM) bilayer structure, essentially rely on two factors, first the magnitude of SOT from HM which is proportional to spin Hall angle (SHA), and the second is the effective damping constant (α_{eff}) of FM in FM/HM bilayer structure. Since the switching current in SOT-MRAM using in-plane magnetization of magnetic tunnel junction (i-MTJ) is inversely proportional to HM's SHA and directly proportional to FM's α_{eff}, we need to search for HM materials with high SHA and at the same time with low α_{eff} of FM for HM/FM bilayer structure combination. Previously, we have shown the excellent magnetization switching behavior of SOT-MRAM using $Ta_{50}B_{50}$ (HM), and evaluated its SHA by spin Hall magnetoresistance (SMR) measurement [7]. However, analysis of SHA based on SMR assume a simple drift-diffusion model and as for estimation of the effective damping constant, SMR cannot be applied. In this study, the spin-transfer ferromagnetic resonance (ST-FMR) method was used to evaluate both SHA of $Ta_{50}B_{50}$ (HM) and α_{eff} of $Co_{40}Fe_{40}B_{20}$ (FM) for $Ta_{50}B_{50}$ (*t* nm)/$Co_{40}Fe_{40}B_{20}$ (4 nm) bilayer structure. The ST-FMR mixed-signal can be fitted by the combination of symmetrical and asymmetrical components by $V_{Total} = V_{Sym} + V_{Asym}$, where V_{Total} is total mixed signal, V_{Sym} is total symmetrical signal due to spin current, and V_{Asym} is total asymmetrical component due to charge current. The ST-FMR signal, its fitting and extracted each individual components are shown in Fig. 1 (a). The SHA evaluation is not straightforward, since other parameters/mechanisms, which are taking place simultaneously, have to be taken into account. At ferromagnetic resonance two phenomenons are taking place concurrently, the SHE from HM to FM and spin pumping (SP) from FM to HM. The SP induced spin current is converted back to charge current in HM through the inverse spin Hall effect (ISHE) which is reflected in symmetrical ST-FMR voltage signal and can be represented by $V_{Sym} = V_{ST\text{-}FMR} + V_{ISHE}$. In order to remove the SP influence or considering contribution only from SHE i.e. $V_{ST\text{-}FMR}$, the ratio of $V_{ST\text{-}FMR}$ to V_{Sym} defined by η, is crucial and can be expressed as $\eta = V_{ST\text{-}FMR}/ V_{Sym} = V_{ST\text{-}FMR}/ (V_{ST\text{-}FMR} + V_{ISHE})$. This ratio η is very important, since both SHE and ISHE have the same angle dependence (due to similar mechanism), it is very difficult to isolate them, as suggested by other groups too [8, 9]. In addition, the influence of transparency *T* at $Ta_{50}B_{50}/Co_{40}Fe_{40}B_{20}$ interface has to be taken into account for reliable SHA estimation [9, 10]. The transparency, which controls the spin trasnmittance at interface, is related to spin mixing conductance at the HM/FM interface. The spin mixing conductance was calculated from the enhancement of damping constant ($\Delta\alpha$) of FM due to spin pumping from its intrinsic value (α_0). The real value of SHA can be calculated by incorporating interface transparency *T* and isolating the ISHE (V_{ISHE}) contribution from V_{Sym}, that is η. These contributions are incorporated by mathematically multiplying *T* and η to conventional SHA $\Theta_{SH(r)} = \eta T\, \Theta_{SH(m)}$, where $\Theta_{SH(r)}$ is the real value of SHA while $\Theta_{SH(m)}$ is the observed value of SHA estimated by typical approach. In the observed SHA value, neither SHE contributions were separated nor was interface transparency considered, which leads to the overestimation of SHA. The values η, *T* and ηT are shown as a function of $Ta_{50}B_{50}$ layer thickness in Fig. 1 (b). As it is clear that the ratio η decreases systematically with $Ta_{50}B_{50}$ layer thickness, however the interface transparency *T* increases steeply and then saturates at around 2.5 nm. Their product ηT shows initial enhancement and after peak, a systematic decrease is observed. It is obvious that at lower $Ta_{50}B_{50}$ thickness, interface transparency controls whereas at higher thickness the $V_{ST\text{-}FMR}$ contribution dominates. In the Fig. 1 (c), each individual symmetrical components are shown, which is required for reliable SHA estimation. The dependency of $\Theta_{SH(r)}$ on $Ta_{50}B_{50}$ layer thickness is illustrated in Fig. 1(d). By considering only SHE contribution and interface transparency we are able to evaluate the real value of SHA. This SHA value is nearly consistent with the derived SHA from separately fabricated SMR devices [7]. In conclusion, we have successfully estimated the SHA (-0.18) of $Ta_{50}B_{50}$ by isolating SHE contribution from total ST-FMR signal combined with transparency at $Co_{40}Fe_{40}B_{20}/Ta_{50}B_{50}$ interface. Additionally, we were able to achieve desired low damping constant (α_{eff}) ≈ 0.008 for $Co_{40}Fe_{40}B_{20}/Ta_{50}B_{50}$ bilayer which is also crucial factor for realizing low switching current for future SOT-MRAM applications. This work was partly supported by the ImPACT Program of the Council of Science, Technology and Innovation (Cabinet Office, Government of Japan).

[1] D. Apalkov *et al.*, Proc. IEEE 104, 1796 (2016) [2] H. Yoda *et al.*, IEDM Tech. Dig., 2761 (2016) [3] S. Shirotori *et al.*, IEEE Trans. Magn. 53, 3401104 (2017) [4] T. Inokuchi *et al.*, Appl. Phys. Lett. 110, 252404 (2017) [5] S. A. Wolf *et al.*, Science 294, 1488 (2001) [6] C. -F. Pai *et al.*, Appl. Phys. Lett. 104, 082407 (2014) [7] Y. Kato *et al.*, MMM Conf. Nov. 2017 (AE-07) [8] K. Kondou *et al.*, Appl. Phys. Exp. 9, 023002 (2016) [9] A. Kumar *et al.*, Phys. Rev. B 95, 064406 (2017) [10] W. Zhang *et al.*, Nat. Phys. 11, 496 (2015)

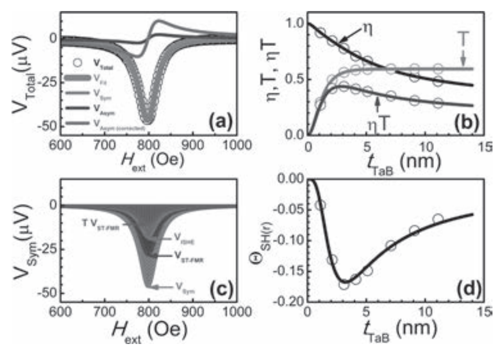

Fig. 1. (a) The ST-FMR spectra, it's fitting and extracted individual components, (b) the ratio of ST-FMR symmetrical signal to total symmetrical signal η, interface transparency *T* and their product η*T* (c) individual symmetrical components of spin signal (d) real spin Hall angle $\Theta_{SH(r)}$ of $Ta_{50}B_{50}$ HM layer.

11:00

ED-08. Spin-orbit-torque switching in an exchange-biased ferromagnetic system.

P. Lin[1], M. Tsai[1], K. Huang[1], H. Lin[2] and C. Lai[1]
1. Department of Materials Science and Engineering, National Tsing Hua University, Hsinchu, Taiwan; 2. Department of Physics, National Tsing Hua University, Hsinchu, Taiwan

With a fast writing speed and less disturbance for the insulating barrier, the spin-orbit torque (SOT) switching is regarded as a promising writing method for next-generation magnetic random-access memory (MRAM). All of magnetization switching by SOT is performed for ferromagnetic (FM) layers with uniaxial anisotropy, that is, the switching occurs between two degenerate energy states. Therefore, the thermal stability to have good data retention while scaling down has been a critical challenge. Here, we demonstrate that the perpendicular magnetization of a ferromagnetic (FM) Co layer with a perpendicular exchange bias (EB) can be switched by the spin-orbit torque when passing current pulses through the underlayer Pt layer. Not only the Co magnetization is switched, but the direction of the EB, established between Co and antiferromagnetic (AFM) IrMn, is simultaneously switched. Due to the existence of the EB, the FM possesses a uni-directional anisotropy and FM magnetization is in its universal minima state. The current-pulse-induced magnetization switching by SOT, accompanying the change of EB direction, can significantly relieve the concern of thermal stability because there is only one stable state at zero field with unidirectional anisotropy so the thermal stability is greatly enhanced. Furthermore, the spin-orbit torque mechanism provides an innovative method to control the exchange bias by electrical means, which enables us to realize the new switching mechanism of highly stable perpendicular memory cells. We prepare the sample by dc sputtering. The perpendicular EB exists in the as-deposited Ta (2.5)/Pt (2)/Co (1.2)/IrMn (8)/Pt (4)/Ta (2.5) stacks (in nm). The magnetic properties are verified by the vibrating sample magnetometer (VSM). Then, the specimens are patterned from the as-deposited films into 5μm×10μm single wire with current pulses running along the x-axis as shown in Figure 1(a). We applied the current pulses with the duration of 10 μs through the single wire in the presence of an in-plane magnetic field (Hx=300 Oe) and measured the SOT switching by the focused polar magneto-optical Kerr effect (FMOKE). As shown in Figure 1(b), when the current density surpasses the threshold Jc, the magnetization exhibits a sharp transition due to the spin-orbit torque. To further examine the magnetic property after the SOT switching, as shown in Figure 1(c)(d), we measured the out-of-plane hysteresis loop (no current flowing now) and found the direction of EB changed along with the FM magnetization switching. That is, in the Pt/Co/IrMn tri-layer structure, the SOT not only flips the magnetization but also changes the EB accordingly. It is rather remarkable that, with the insertion of the IrMn layer, the SOT switching between states with unidirectional anisotropy is achieved. We then further explore to verified (1) the dominate spin current source is from the bottom Pt layer and (2) Joule heating effect cannot explain the change of the direction of exchange bias alone. For the first one, we fabricate the devices with different IrMn thickness. From the SOT switching polarity (Figure 2(a)), the dominant spin current source is from bottom Pt for IrMn≥2nm. As for the second one, we first measure the blocking temperature (T_B) for the device. The T_B is about 150°C. The device temperature at critical switching current density is estimated to be about 90°C from the temperature-dependent resistance (Figure 2(b)), which is much lower than the blocking temperature. Thus, the thermal fluctuations associated with Joule heating is not sufficient to explain the observed EB shifts induced by current pulses. We believe the SOT may also disturb the interfacial spins between FM and AFM, leading to the change of EB direction by current pulses. In conclusion, we demonstrated that SOT can not only switch FM magnetization but also change the EB direction simultaneously. This finding provides an innovative method to redefine EB via electrical means and enhances the thermal stability tremendously. With further investigation and optimization along this direction, the current-pulse-induced EB shall have significant impacts on the SOT-MRAM and other spintronics devices.

arXiv:1706.01639

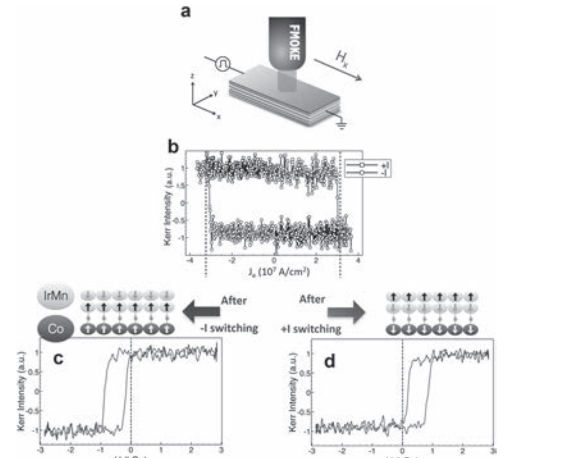

Fig. 1. SOT switching curves and the current-pulse-induced EB.(a) Experimental setup for measuring the SOT switching curves by FMOKE.(b) The SOT switching curve under the Hx=300 Oe for t_{IrMn}=8 nm. (c)(d) The negative pulses (red line) reverse the magnetization from negative to positive and shift the easy axis loop to the left. The opposite behavior can be observed when we apply the positive pulses (blue line) through the wire.

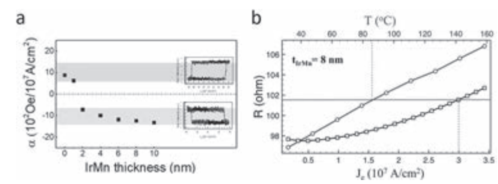

Fig. 2. (a) The SOT switching polarity is changed when IrMn^2nm. α is defined as the anisotropy field divided by threshold switching current density (b) Resistance for IrMn=8 nm at different temperatures and applied current densities. The red line represents the current-density threshold in SOT switching and the extracted temperature due to joule heating is about 90°C.

11:15

ED-09. Enhanced spin orbit torques in Pt/Co/Pt films with inserting Ru layers.

Y. Wu[1], K. Meng[1], Y. Wu[1], J. Chen[1], J. Miao[1], X. Xu[1] and Y. Jiang[1]
1. Materials Science and Engineering institute, University of Science and Technology Beijing, Beijing, China

Spin orbit torque (SOT) has attracted much attention and interest as it provides a new way to manipulate the magnetization of ferromagnetic metal (FM) in heavy metal (HM)/FM heterostructures by electrical current instead of external magnetic field.[1-2] Various approach for getting lower switching current density and higher switching efficiency have been reported in recent years, such as improving chemical ordering, oxygen incorporation, controlling composition of FM alloys. These published works mostly focused on enhancing spin current originated from either the SHE or the interfacial Rashba effect, and we will focus on how to enhance the spin current absorption in the FM layer. In recent years, Ru has attracted great attention due to its significant role in enhancing giant magnetoresistance and substantial reduction of critical current for magnetization switching in a vertical spin valve.[3] In this work, we attempt to modulate the switching current density and SOT efficiency in the Pt/Co/Pt films via a Ru insertion. Figure 1(a) and (b) show the spin current originate from the charge current in the Pt/Co/Pt and Pt/Co/Ru/Pt multilayers, respectively. After inserting a Ru layer, the majority spins of the polarized spin current flowing to the Co layer in the top Pt layer will be reflected at the Ru/Pt interface,[3] whereas the minority spins are easily absorbed in the Ru. In this case, the spin accumulation at the top and bottom interface of the Co layer have uniform spin polarization, which can theoretically enhance the overall torques exerting on the magnetization of the Co layer. Figure 1(c) and (d) show the magnetic field H dependence of the out-of-plane magnetization M and the anomalous hall resistance R_H at room temperature for the two multilayers, respectively. The reduced saturation magnetization of the multilayer with a Ru layer insertion can also contribute to the reduction of the critical current, which are shown in the Figure 2(a) and (b). The non-adiabatic harmonic Hall voltage measurements with external sweeping magnetic field along the longitudinal and transversal of the hall-bar were carried out at room temperature to quantitatively determine the strength of the spin orbit effective field. The results of the first and second harmonic voltage with the out-of-plane magnetization component $M_Z>0$ and $M_Z<0$ are shown in the Figure 2(c) and (d) respectively. According to the harmonic voltage measurement, we have calculated the damping-like torque H_D to be 41.66 Oe per 10^7 A/cm^2 and 49.04 Oe per 10^7 A/cm^2 in the Pt/Co/Pt and Pt/Co/Ru/Pt multilayers, respectively. The field-like torque H_F in the Pt/Co/Pt and Pt/Co/Ru/Pt multilayers is 8.91 Oe per 10^7 A/cm^2 and 30.49 Oe per 10^7 A/cm^2, respectively. The more evident change happened in the H_F, which is larger in Pt/Co/Ru/Pt multilayers than that in the Pt/Co/Pt multilayers. The result has proved our supposition that the Ru insertion can enhance the SOT.

I. M. Miron, K. Garello, G. Gaudin, P. J. Zermatten, M. V. Costache, S. Auffret, S. Bandiera, B. Rodmacq, A. Schuhl, and P. Gambardella, Nature 476, 189 (2011). K. K. Meng, J. Miao, X. G. Xu, Y. Wu, X. P. Zhao, J. H. Zhao, and Y. Jiang, PHY. REV. B 94, 214413 (2016). Y. JIANG, T. NOZAKI, S. ABE, T. OCHIAI, A. HIROHATA, N. TEZUKA and K. INOMATA, Nature Materials 3, 361–364 (2004).

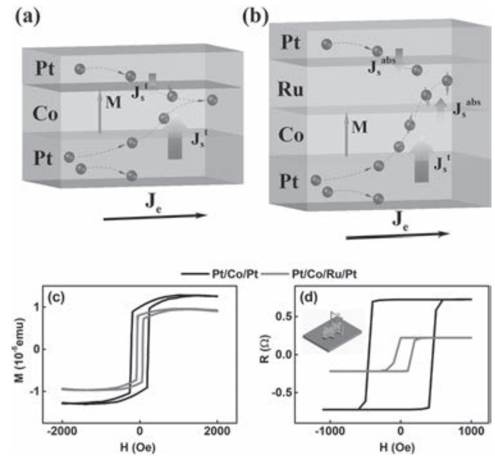

Fig. 1. The geometric relation between the flow of electrons and accumulated spins in the multilayers of Pt/Co/Pt/ (a) and Pt/Co/Ru/Pt (b). (c) The out-of-plane magnetization M. (d) The anomalous hall resistance RH for the two multilayers as a function of the magnetic field H.

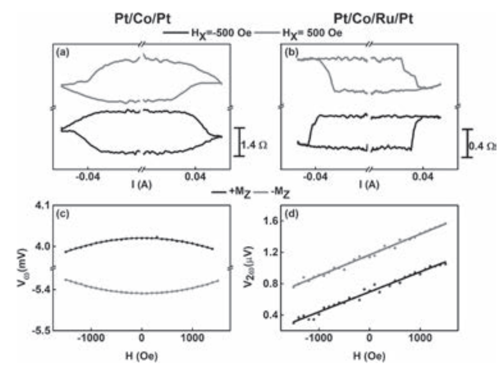

Fig. 2. R_H as a function of pulsed current of Pt/Co/Pt/ (a) and Pt/Co/Ru/Pt (b). (c) and (d) The first and second harmonic voltage against small external fields.

11:30

ED-10. Harmonic measurement of current induced spin-orbit torques in high-resistivity-W/CoFeB/MgO.

Y. Takeuchi[1], C. Zhang[1], A. Okada[1], H. Sato[1], S. Fukami[1] and H. Ohno[1]
1. Tohoku University, Sendai, Japan

Spin-orbit torque (SOT) is induced by an in-plane current flowing in heterostructures with broken inversion symmetry, e.g., a tri-layer system consisting of heavy metal/ ferromagnetic metal/ oxide. Because the SOT can bring about magnetization reversal in ferromagnetic layers [1-3] without applying much stress to the barrier layer in magnetic tunnel junctions (MTJs), it has attracted great attention as a new ingredient for the writing scheme of nonvolatile spintronics memory or logic. SOT is generated by a spin accumulation due to the spin Hall effect and/or the Rashba-Edelstein effect, and is known to have two components with different symmetries, i.e., Slonczewski-like (SL) and field-like (FL) torques. The strength of SOT is characterized by dimension-less spin-torque efficiencies ξ_{SL}, ξ_{FL} that represent conversion ratio from the charge current to SL and FL components of SOT, respectively. We here note that ξ_{SL} corresponds to the spin Hall angle in case that the SOT originates from the spin Hall effect. Large ξ_{SL} is desirable for low-power switching. FL torque was also revealed to effectively reduce the switching current [4], but could cause switch-back events according to recent studies [5]. β-W is one of the promising candidates for the heavy metal material owing to its large ξ_{SL} = -0.2 ~ -0.5 [6-8]. Since an increase in ξ_{SL} with W resistivity ρ_W in the range of 100-300 μΩcm has been reported in previous works [7,8], larger ξ_{SL} is expected be obtained in W with higher ρ_W. On the other hand, FL torque of the systems with W has not been well investigated yet. Here we study both components of the SOT in CoFeB/MgO stacks on high-resistivity (470 μΩcm) W underlayers with various thicknesses t_W. We find a very high ξ_{SL} exceeding 1, relatively small ξ_{FL}, and different t_W dependence of ξ_{SL} and ξ_{FL}. The stacks of W(t_W)/ CoFeB(1.8)/ MgO/ Ta(1) are prepared on thermally oxidized Si substrates by dc/rf magnetron sputtering, where the numbers in parentheses are nominal thickness in nanometer. The films are processed into Hall bar devices with a channel of 10×50 μm^2. The Effective fields of SL and FL components of SOTs, H_{SL} and H_{FL}, are determined by an extended harmonic Hall resistance measurement, which is capable of excluding artifacts originating from the anomalous Nernst and spin Seebeck effects [9]. Figure 1 shows the sheet conductance versus t_W for W(t_W)/ Ru(1) blanket films. The linear relation indicates that ρ_W is almost constant in the studied range (t_W = 2–10 nm) and the slope gives ρ_W = 470±28 μΩcm. This is the highest value of W resistivity reported so far. A similar measurement is conducted for CoFeB layer and the resistivity of CoFeB is obtained to be 142±4 μΩcm. We then perform the harmonic measurement using Hall devices to evaluate SOT. 10-Hz AC current is applied to the Hall bar and harmonic Hall voltages are measured by lock-in amplifier while rotating an external magnetic field H_{ext} in the film plane. Figures 2(a) and (b), respectively, show a typical first (R_ω) and second ($R_{2\omega}$) harmonic Hall resistances as a function of the azimuthal angle ϕ of the field. Note that R_ω reflects the planar Hall resistance and $R_{2\omega}$ reflects the current-induced effective fields. H_{SL} and H_{FL}, respectively, are obtained by fitting H_{ext} dependence of cosϕ and 2cos³ϕ - cosϕ contributions in $R_{2\omega}$-ϕ curves [9, 10]. $\mu_0 H_{SL,\,FL}$ as a function of J_W are summarized in Figure 2(c) and (d) (μ_0: permeability of vacuum), where J_W is the current density flowing in W layer determined from the resistivity and thickness of W and CoFeB layers. We obtain ξ_{SL} = -1.03±0.05, ξ_{FL} = -0.12±0.01 for t_W = 6 nm by using an expression $\xi_{SL(FL)} = (2eH_{SL(FL)}M_St)/(h\_barJ_W)$, where e is electron charge, M_St is magnetic moment per unit area, and h_bar is the Dirac constant. The obtained ξ_{SL} is much higher than any previous reports on tri-layer systems except for those with topological insulators. We also confirm ξ_{SL} = -0.15 when we use a device with low resistivity W (ρ_W = 150 μΩcm), in agreement with previous works [6,8]. ξ_{FL} is one order of magnitude smaller than ξ_{SL}. The relatively low ξ_{FL} is also consistent with an implication in our previous work [8] and is contrasting to the perpendicular magnetized systems with Ta [4] and Pt [11] underlayers. In addition, we also investigate t_W dependence of ξ_{SL} and ξ_{FL}, which show contrasting trend. The former is well described by a drift-diffusion model [2], suggesting its origin in the spin Hall effect, whereas the latter does not show clear dependence on t_W, suggesting its origin in interfacial effects. In summary, we evaluate SOTs in high-resistivity-W/CoFeB/MgO heterostructures by the extended harmonic Hall techniques and the structure exhibits a large ξ_{SL} of -1.03±0.05 and relatively small ξ_{FL} = -0.12±0.01. Our results suggest that the heterostructures using high-resistivity-W as a heavy metal layer can offer a low power switching and have a potential for MTJ devices. This work was partly supported by ImPACT Program of CSTI, JST-OPERA, and GP-Spin of Tohoku Univ.

[1] I. M. Miron, *et al.*, Nature 476, 189-193 (2011). [2] L. Liu, *et al.*, Science 336, 555-558 (2012). [3] S. Fukami *et al*., Nat. Nanotechnol. 11, 621 (2016). [4] C. Zhang, *et al*., Appl. Phys. Lett. 107, 012401 (2015). [5] J. Yoon, *et al*., Science Adv. 3, e1603099 (2017). [6] C.-F. Pai *et al*., Appl. Phys. Lett. 101, 122404 (2012). [7] K. -U. Demasius *et al*., Nat. Commun. 7, 10644 (2016). [8] C. Zhang *et al*., Appl. Phys. Lett. 109, 192405 (2016). [9] C. O. Avci, *et al*., Phys. Rev. B 90, 224427 (2014). [10] Y.-C. Lau, *et al*., Jpn. J. Appl. Phys. 56, 0802B5 (2017). [11] K. Garello, *et al*., Nat. Nanotechnol. 8, 587 (2013).

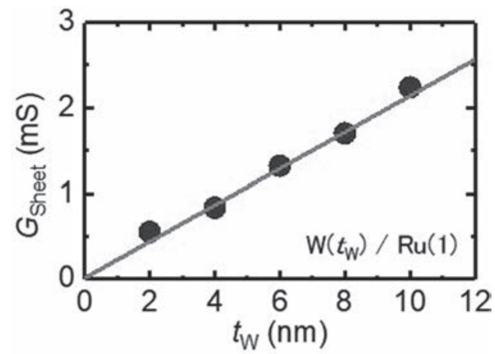

Fig. 1. W thickness t_W dependence of sheet conductance G_{Sheet}.

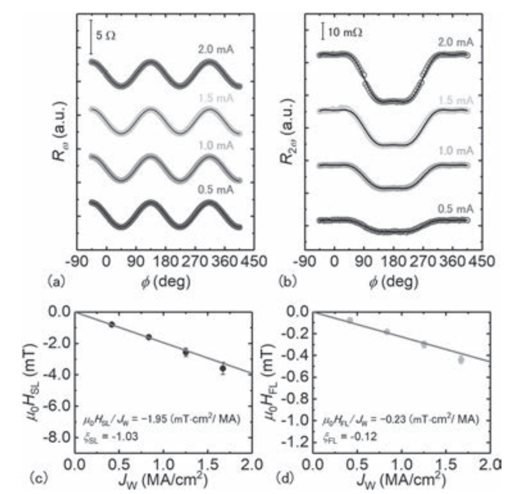

Fig. 2. (a) First and (b) second harmonic Hal resistance as a function of ϕ for various AC current amplitudes. (c) H_{SL} and (d) H_{FL} versus current density J_W flowing in W layer.

11:45

ED-11. Enhancement of Spin-Orbit Torques through Material Engineering: The Role of Boron.

Y. Du[1], P. Chen[1], B. Yang[1], P. Lin[1], G. Guo[2] and C. Lai[1]
1. Department of Materials Science and Engineering, National Tsing Hua University, Hsinchu, Taiwan; 2. Department of Physics, National Taiwan University, Taipei, Taiwan

The conversion of charge current into pure spin current based on the spin Hall effect provides a new way of spin injection and manipulation in novel spintronic architectures. The seeking for materials with large spin Hall angle (SHA) values is important for both scientific interest and device applications. Compared to a rather small value in GaAs when it was first observed a decade ago, much larger SHAs have been observed in heavy metals such as Pt, Ta and W [1,2]. Ta and W have the benefits such as the economic advantage as well as the largest SHA reported to date. However, the Joule heating due to the rather high resistivity of both β-W and β-Ta becomes of a great concern for the applications, combined with the excessive challenges in achieving a stable β form of W and Ta. Pt possesses low resistivity and high stability, but the high cost and the rather small spin diffusion length hinders its further development in this field. With a similar structure to Pt, but a much larger spin diffusion length [3], Pd has anomalously small SHA values reported, and has little been explored. Understanding the underlying mechanism plays an important role in the enhancement of SHA in different materials. It could be of intrinsic origin connected with the band structure or device geometry, or extrinsic origin due to impurities [4,5]. As a common element and doping source in a spintronic device/structure, the role of boron in the enhancement of spin Hall effect is largely unexplored, when discussed into the mechanisms involved. Here we report a giant enhancement of SHA in palladium through boron engineering. We measure a large SHA of 0.16 in palladium, with perpendicular magnetic anisotropy in the Pd/CoFeB-based structure compared to the Pd/CoFe-based structure (SHA=0.02). Combined with theoretical calculations, it is found that both intrinsic and extrinsic spin Hall effects have been significantly enhanced through the introduction of boron. The incorporation of boron in the thin films results in significant microscopic and electronic changes in the Pd host metal. Our result provides a further understanding of the spin Hall effect in metals, leading to a new exploration of material engineering for large SHA sources. Together with high conductivity and long spin diffusion length, this work makes Pd a promising candidate for spintronic devices with magnetization switching by current pulse injection. The film stacks Pd(5 nm)/$Co_{40}Fe_{40}B_{20}$(1 nm)/MgO(2 nm)/Ta(5 nm) and Pd(5 nm)/$Co_{50}Fe_{50}$(1 nm)/MgO(2 nm)/Ta(5 nm) are sputtered on thermally oxidized Si substrates. The stacks are patterned into Hall bar devices using photolithography (Fig. 1a and 1b). Fig. 1c and 1d shows the longitudinal and transverse effective field as a function of the injected current density for the CoFeB-based sample, with the magnitude of the former about three times larger than that of the latter, indicating a strong Slonczewski-like torque. Based on the data, the SHA determined is 0.16. It is the largest SHA reported so far for Pd based PMA structures. Fig. 1f shows the magnetization switching loop measured by the magneto-optical Kerr effect (MOKE) from a 5 μm×20 μm device. To explore the possible origins, we carry out synchrotron X-ray photoelectron spectroscopy (XPS) study of the samples for depth profiling. Fig. 2 shows that the introduction of B results in a highly pure metallic Pd state, as well as a high concentration of metallic contents of Co and Fe in the Pd layer for the CoFeB based sample, which is strikingly different to that observed in the CoFe based sample. The consumption of oxygen by B, leads to the highly metallic Pd state as well as reduced Co/Fe oxidation in Pd. We perform *ab initio* calculations of spin Hall conductivity (SHC) of B-, Fe- and Co-doped palladium as well as pure palladium metal based on the density functional theory. The calculated SHCs for pure Pd, B_1Pd_{31}, Fe_1Pd_{31} and Co_1Pd_{31} are 2852, 1818, 3114 and 3758 (h/2e)(S/cm), respectively. Interestingly, doping Pd with ~3% B reduces the SHC by ~36%. In contrast, doping Pd with ~3% Co (Fe) increases the SHC by ~32% (~9%). Pure palladium metal has a large SHC which is further enhanced by substitutional Fe- and Co-doping. The experimental results comply well with the theoretical modelling.

[1] A. Hoffmann, *IEEE Trans. Magn.* 49, 5172 (2013). [2] K.-U. Demasius *et al., Nat. Commun.* 7, 10644 (2016). [3] A. Ghosh et al., *Phys. Rev. Appl.* 7, 014004 (2017). [4] G.-Y. Guo et al., *Phys. Rev. Lett.* 100, 096401 (2008). [5] M. Gradhand et al., *Phys. Rev. Lett.* 104, 186403 (2010).

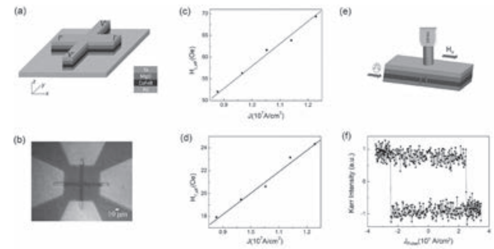

Fig. 1. (a) Schematic diagram of the multilayer structure and electrical measurement setup. (b) Optical microscope image of a fabricated Hall device with electrodes. (c, d) Dependence of longitudinal and transverse effective fields on AC current density after the planar Hall effect (PHE) correction. (e) Schematic diagram of the MOKE setup for the measurement of switching of a device. An external magnetic field *H*x is applied parallel to the current direction. (f) Pulsed current/voltage spin-orbit torque switching: pulse length = 50 ns, *H*x = 5 mT.

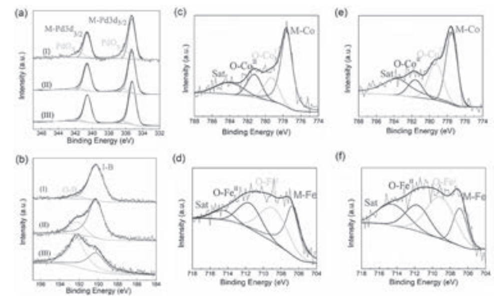

Fig. 2. XPS spectra for CoFeB and CoFe based samples. (a, b) Evolution of the Pd 3d and B 1s XPS spectra as a function of sputtering times (time I to III stands for continuous Ar^+ sputtering at different time points, and time (III) is the longest) for CoFeB-sample. The metallic Pd is labeled M-Pd. The two B peaks are the oxidic B (O-B) and the intermediate B (I-B). No metallic B is shown. (c, d) Co $2p_{3/2}$ and Fe $2p_{3/2}$ XPS spectra in the deep Pd layer for CoFeB-sample. (e, f) Co $2p_{3/2}$ and Fe $2p_{3/2}$ XPS spectra in the deep Pd layer for CoFe-sample. The metallic Co and Fe are labeled M-Co and M-Fe, respectively. The oxidic peaks are labeled with O-Co^{I}, O-Co^{II}, O-Fe^{I} and O-Fe^{II}, respectively. "Sat" represents satellite peaks.

THURSDAY MORNING, 26 APRIL 2018 ROSELLE II, 9:00 TO 12:00

Session EE

SYMPOSIUM ON RECENT ADVANCES AND FUTURE CHALLENGES OF COMPUTATIONAL MAGNETICS

Jan Sykulski, Chair
University of Southampton, Southampton, United Kingdom

INVITED PAPERS

9:00

EE-01. Steady state solution of periodically excited nonlinear eddy current problems.

O. Biro[1] and G. Koczka[2]
1. TU Graz, Graz, Austria; 2. Siemens AG Österreich – Transformers Weiz, Weiz, Austria

Abstract In many cases the steady state periodic solution of eddy current problems with periodic excitation is needed only. If the problem is linear, it is straightforward to obtain this solution either in the frequency domain applying harmonic balance techniques or in the time domain using discrete Fourier transforms. For nonlinear problems, this cannot be done, since the harmonics are all coupled. Using a fixed-point method to solve the nonlinear equations, however, enables using harmonic balance or discrete Fourier transforms within each nonlinear iteration. The method is described in the presentation and examples of its application are given. Introduction The most straightforward method of solving nonlinear electromagnetic field problems in the time domain by the method of finite elements (FEM) is using time-stepping techniques. This requires the solution of a large nonlinear equation system at each time step and is, therefore, very time consuming, especially if a three-dimensional problem is being treated. If the excitations are non-periodic or if, in case of periodic excitations, the transient solution is required, one cannot avoid time-stepping. In many cases however, the excitations of the problem are periodic, and it is only the steady-state periodic solution which is needed. Then, it is wasteful to step through several periods to achieve this by the "brute force" method [1] of time stepping. A successful method to avoid stepping through several periods in such a case is the time-periodic finite element method introduced in [2]. To accelerate the originally slow convergence of the method a singular-decomposition technique has been introduced in [3] and it has even been parallelized in [4]. A time domain technique using the fixed-point method to decouple the time steps has been introduced in [5] and applied to two-dimensional eddy current problems described by a single component vector potential. The optimal choice of the fixed point permeability for such problems has been presented in [6] both in the time domain and using harmonic balance principles. The method has been applied to three-dimensional problems in terms of a magnetic vector potential and an electric scalar potential (A,V-A formulation) in [7] and, employing a current vector potential and a magnetic scalar potential (T,Φ-Φ formulation), in [8] and [9]. In contrast to the time-periodic finite element method, the periodicity condition is directly present in the formulation instead of being satisfied iteratively. The aim of this work is to present a review of the fixed-point based method and to show its application to industrial problems. A detailed version has been published in [10]. Summary of the method The problem is formulated in terms of vector and scalar potentials approximated by edge and node based finite element basis functions. The application of Galerkin techniques leads to a large, nonlinear system of ordinary differential equations in the time domain. The excitations are assumed to be time-periodic and the steady state periodic solution is of interest only. This is represented either in the frequency domain as a finite Fourier series or in the time domain as a set of discrete time values within one period for each finite element degree of freedom. The former approach is the (continuous) harmonic balance method and, in the latter one, discrete Fourier transformation will be shown to lead to a discrete harmonic balance method. Due to the nonlinearity, all harmonics, both continuous and discrete, are coupled to each other, so the size of the equation system is the number of harmonics times the number of degrees of freedom. In the time domain approach, the number of discrete harmonics is equal to the number of the time values within one period. The harmonics would be decoupled if the problem were linear, therefore, a special nonlinear iteration technique, the fixed-point method is used to linearise the equations by selecting a time-independent permeability distribution, the so called fixed-point permeability in each nonlinear iteration step. This leads to uncoupled harmonics within these steps resulting in two advantages. One is that each harmonic is obtained by solving a system of algebraic equations with only as many unknowns as there are finite element degrees of freedom. A second benefit is that these systems are independent of each other and can be solved in parallel. The appropriate selection of the fixed point permeability accelerates the convergence of the nonlinear iteration. The applications presented concern the simulation of the steady state of large power transformers with time-harmonic excitations. In addition to taking account of the nonsinusoidal time variation of the electromagnetic field due to saturation, direct current bias in the magnetizing currents can also be allowed for.

[1] R. Albanese, E. Coccorese, R. Martone, G. Miano, G. Rubinacci, Periodic solutions of nonlinear eddy current problems in three-dimensional geometries, IEEE Trans. Magn. 28 (1992) 1118-1121. [2] T. Hara, T. Naito and J. Umoto, Time-periodic finite element method for nonlinear diffusion equations, IEEE Trans. Magn. 21 (1985) 2261-2264. [3] Y. Takahashi, T. Tokumasu, A. Kameari, H. Kaimori, M. Fujita, T. Iwashita, S. Wakao, Convergence acceleration of time-periodic electromagnetic field analysis by the singularity decomposition-explicit error correction method, IEEE Trans. Magn. 46 (2010) 2947-2950. [4] Y. Takahashi, T. Iwashita, H. Nakashima, T. Tokumasu, M. Fujita, S. Wakao, K. Fujiwara, Y. Ishihara, Parallel time-periodic finite-element method for steady-state analysis of rotating machines, IEEE Trans. Magn. 48 (2012) 1019-1022. [5] O. Bíró, K. Preis, An efficient time domain method for nonlinear periodic eddy current problems, IEEE Trans. Magn. 42 (2006) 695–698. [6] G. Koczka, S. Ausserhofer, O. Bíró, K. Preis, Optimal convergence of the fixed-point method for nonlinear eddy current problems, IEEE Trans. Magn. 45 (2009) 948-951. [7] G. Koczka, S. Ausserhofer, O. Bíró, K. Preis, Optimal fixed-point method for solving 3D nonlinear periodic eddy current problems, COMPEL 28 (2009) 1059-1067. [8] G. Koczka, O. Bíró, Fixed-point method for solving nonlinear periodic eddy current problems with T,Φ-Φ formulation, COMPEL 29 (2010) 1444-1452. [9] O. Bíró, G. Koczka, K. Preis, Fast time-domain finite element analysis of 3D nonlinear time-periodic eddy current problems with T,Φ-Φ formulation, IEEE Trans. Magn. 47 (2011) 1170-1173. [10] O. Bíró, G. Koczka, K. Preis, Finite element solution of nonlinear eddy current problems with periodic excitation and its industrial applications, Appl. Num. Math. 79, (2014) 3 - 17..

9:30

EE-02. Advanced soft- and hard-magnetic material models for the numerical simulation of electrical machines.

K. Hameyer[1], S. Steentjes[1], N. Leuning[1], G. Bravendiek[1] and S. Elfgen[1]
1. IEM, RWTH Aachen University, Aachen, Germany

The development of energy-efficient electrical machines requires an accurate knowledge of the soft- and hard-magnetic material behavior already in the design stage. Accurate numerical models are required which offer the ability of better understanding and modelling in an appropriate accuracy. With such model properties on the one hand accurate simulations can be performed and on the other hand the best possible material choice for a particular application, i.e. for an electrical machine, can be done. The soft-magnetic material constitutes the magnetic core of an electrical machine and its properties. On that account, the accurate prediction of iron losses of soft-magnetic materials for various frequencies and magnetic flux densities, i.e., arbitrary magnetic field waveforms, is eminent for the design of electrical machines [1]. For this purpose different phenomenological iron-loss models were proposed, which describe the loss-generating effects, i.e., hysteresis, non-local eddy currents and anomalous eddy currents. Most of these suffer from poor accuracy for not considering the effect of high frequencies and high material utilization as well as the material degradation due to the magneto-elastic coupling [2,3,5]. This paper presents a comparison of common iron-loss models. The IEM-formula used, resolves the limitation by introducing a high-order term of the magnetic flux density and considers the alteration of material-dependent loss-parameters due to the magneto-elastic coupling [3]. The knowledge of the magnetic property deterioration due to induced residual stress occurring during the manufacturing or operation of the electrical machine is indispensable for the contemporary design. It has been widely ascertained that processing of electrical steel laminations significantly alters the magnetic properties of the electrical steel [2-6]. Cutting induces plastic deformation and residual stress in the laminations. Due to their strong sensitivity to mechanical stress, the magnetic properties are locally degraded near the cut edge. The extent of the degradation depends substantially on the process characteristics, i.e., the cutting procedure and cutting parameters in combination with material properties, such as mechanical strength and grain size [4-6]. In [7] a continuous material model for an efficient numerical model of the local magnetization was introduced. By replacing numerically expensive sliced models, the continuous model (CM) is independent of the discretization and converges in the case of coarse meshes to the sliced model [7]. Measured single-sheet specimens are used to identify the different model parameters. In Fig. 1 results on hysteresis loss distribution are presented. The vital advantage of the proposed CM is that properties depend only on the distance to the cut edge. For improved estimation of penetration depth and mechanical stress distribution, novel experimental procedures are utilized [8] and mechanical simulations are evaluated [6] to further advance the cut-edge model. Permanent magnets are central to the electromagnetic energy conversion process in permanent-magnet synchronous and flux-switching machines. In order to design the magnetic circuit and a magnetizing circuit for post-assembly magnetization as well as to analyze the resistance to being demagnetized during the simulation of electrical machines, it is indispensable to describe the magnetization behavior of the permanent magnets accurately. However, due to the complex interplay of the non-linear and hysteretic magnetization behavior and the magnetic anisotropy, it is a complex problem. Commonly, simplified models are used, which are based on empirical and phenomenological approaches. These describe the major loop of the permanent magnets only. However, the magnetization state of the permanent magnet depends on the magnetic and thermic history, i.e., it is indispensable to account for minor loops or incompletely magnetized permanent magnets. In this paper, a pragmatic methodology to replicate the hysteresis of permanent magnets is presented, which uses first-order return curves and the magnetization behavior starting from the virgin state for model-parameter identification [10]. Efficient parametric models with low additional computational effort are perfectly suited for the finite-element analysis. Starting from these advanced models of soft- and hard-magnetic materials, a methodology for selecting the optimal steel grade during the design-stage of electrical machines in due consideration of the application-specific requirements on torque-speed operating points, i.e., all have to meet the requirements of the same driving cycle, is presented [1]. This allows one to study the effect of different electrical steel grades on the operational characteristics along the torque-speed map [11]. In order to determine the efficiency of each combination of machine topology and lamination type, the iron-loss model with material degradation is used in combination with a machine simulation scheme of the entire operating range of the machine. In the light of this, this paper will give an overview on the current modeling approaches applied at the Institute of Electrical Machines (IEM) for soft- and hard-magnetic materials in the simulation of rotating electrical machines.

[1] A. Ruf, S. Steentjes, G. von Pfingsten, T. Grosse, and K. Hameyer, ‘Requirements on Soft Magnetic Materials for Electric Traction Motors’, Conf. Proc. 7th international Conference on Magnetism and Metallurgy, WMM'16, 2016. [2] J. Karthaus, S. Steentjes, N. Leuning, and K. Hameyer, ‘Effect of mechanical stress on different iron loss components up to high frequencies and magnetic flux densities,’ COMPEL, vol. 36, no. 3, pp. 580-592, 2017. [3] S. Steentjes, G. von Pfingsten, and K. Hameyer, ‘An Application-Oriented Approach for Consideration of Material Degradation Effects Due to Cutting on Iron Losses and Magnetizability,’ IEEE Transactions on Magnetics, vol. 50, no. 11, pp. 7027804, 2014. [4] M. Emura, F. J. G. Landgraf, W. Ross, and J. R. Barreta, ‘The influence of cutting technique on the magnetic properties of electrical steels’, Journal of Magnetism and Magnetic Materials, vol. 254–255, no. Supplement C, pp. 358–360, Jan. 2003. [5] N. Leuning, S. Steentjes, K. Hameyer, M. Schulte, and W. Bleck, ’Effect of Material Processing and Imposed Mechanical Stress on the Magnetic, Mechanical, and Microstructural Properties of High-Silicon Electrical Steel’, steel research int., vol. 87, no. 12, pp. 1638-1647, 2016. [6] H. A. Weiss, N. Leuning, S. Steentjes, K. Hameyer, T. Andorfer, S. Jenner, W. Volk, ‘Influence of shear cutting parameters on the electromagnetic properties of non-oriented electrical steel sheets’, Journal of Magnetism and Magnetic Materials, vol. 421, no. Supplement C, pp. 250–259, Jan. 2017. [7] S. Elfgen, S. Steentjes, S. Böhmer, D. Franck, and K. Hameyer, ‘Continuous Local Material Model for Cut Edge Effects in Soft Magnetic Materials’, IEEE Transactions on Magnetics, vol. 52, no. 5, pp. 1–4, May 2016. [8] H. A. Weiss, S. Vogt, A. Backs, T. Neuwirth, W. Volk, K. Hameyer, S. Steentjes, N. Leuning, M. Schulz, P. Böni, ’Targeted Local Stress Imprint in Electrical Steel as Means of Improving the Energy Efficiency,’ Conf. Proc. 4th International conference on X-ray and Neutron Phase Imaging with Gratings XNPIG2017, Zurich Switzerland, 2017. [9] S. Elfgen, S. Steentjes, S. Böhmer, D. Franck and K. Hameyer, ‘Influences of Material Degradation Due to Laser Cutting on the Operating Behavior of PMSM Using a Continuous Local Material Model,’ IEEE Transactions on Industry Applications, vol. 53, no. 3, pp. 1978-1984, May-June 2017. [10] G. Glehn, S. Steentjes, and K. Hameyer, ‘Pulsed-Field Magnetometer Measurements and Pragmatic Hysteresis Modeling of Rare-Earth Permanent Magnets,’ IEEE Transactions on Magnetics, vol. PP, no. 99, pp. 1-4, 2018. [11] www.iem.rwth-aachen.de

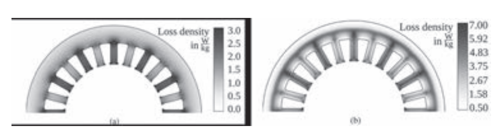

10:00

EE-03. Modern Finite-Element Discretization Techniques for Electromagnetic Field Simulation.

H. De Gersem[1] and S. Schöps[1]
1. Technische Universitaet Darmstadt, Darmstadt, Germany

Today, Finite-element (FE) analysis is one of the main workhouses in design procedures for electrical devices. 2D cartesian, 2D axisymmetric and 3D FE simulation have become standard and are embedded in almost all professional design packages. The performance of FE analysis needs to keep pace with the increasing complexity of contemporary devices and with new designer needs such as e.g. parameter studies, uncertainty quantification and optimization. Only part of the envisioned performance increase is to be expected from hardware improvement. The remainder part is guaranteed from recent advances in field modeling and field discretization methods. This paper gives an overview about recent developments in the domain of electromagnetic field simulation. Contemporary designs consist of multiple components which interact as a system. Often, simulations of the different components are not sufficient for a complete characterization of the device. Moreover, failing to model the interactions may lead to a suboptimal or even wrong design. In a cascadic approach, the component field models are reduced to surrogate models (e.g. a circuit model) and put together in a later design phase. In a co-simulation approach, the components are simulated, each with their own appropriate simulation platform, and data are exchanged at synchronization points and time instants. A proper co-simulation needs waveform relaxation, which in turn needs to be checked for convergence [1]. In a few cases, a full strong coupling is indispensable. Co-simulation approaches allow to select different spatial discretization techniques for different parts of the overall model, e.g. a field solver for the electric machine and a circuit solver for the power converter. The necessary field-circuit coupling is carried out along so-called winding functions [2]. Also for complicated winding types (e.g. foil windings), appropriate coupling or homogenization techniques exist [3,4,5]. Many contemporary problems suffer from multiple spatial scales, e.g. when large devices suffer from eddy-current effects with small skin depths or when the macroscopic material behavior can only be predicted from microscale models. Then multiscale models [6,7] or homogenization techniques [8] are applied. The case where one part of the model needs a fine spatial resolution, whereas in other parts a coarse resolution will do, fits in this class of problems as well. The paper shows impressive results for dealing with small-scale eddy-current effects in magnetic brakes [9], machine windings [10] and ferromagnetic lamination stacks [11], and for dealing with highly accurate field solutions in the aperture of a Stern-Gerlach magnet [12,13,14]. Many designs feature geometric symmetries. These are typically exploited in FE analysis by choosing for a 2D cartesian or 2D axisymmetric solver, thereby saving more than one order in magnitude for the computation time. A more exotic symmetry is radial symmetry as occurring in e.g. axial-flux machines [15] and induction-heating devices [16]. More frequently, however, one encounters designs where only parts feature a certain symmetry or where the symmetry is disturbed by a few items or by asymmetric excitations or boundary conditions. For e.g. a pallet heating device [17], an inductive sensor for artificial lenses [18] and a high-accurate current sensor [19], the paper will show how dedicated FE discretization methods enable 3D FE simulation outperforming standard 3D FE analysis tools by orders of magnitude.

[1] S. Schöps, H. De Gersem, A. Bartel, "Higher-order co-simulation of field-circuit coupled eddy-current problems", IEEE Transactions on Magnetics, Vol. 48, No. 2, February 2012, pp. 535-538. [2] S. Schöps, H. De Gersem, T. Weiland, "Winding functions in transient magnetoquasistatic field-circuit coupled simulations", COMPEL, Vol. 32, No. 6, 2013, pp. 2063-2083. [3] H. De Gersem, K. Hameyer, "A finite element model for foil winding simulation", IEEE Transactions on Magnetics, Vol. 37, No. 5, September 2001, pp. 3427-3432. [4] P. Dular, C. Geuzaine, "Spatially dependent global quantities associated with 2-d and 3-d magnetic vector potential formulations for foil winding modeling", IEEE Transactions on Magnetics, Vol. 38, No. 2, March 2002, pp. 633-636. [5] R. Sabariego, P. Dular, J. Gyselinck, "Time-domain homogenization of windings in 3-D finite element models", IEEE Transactions on Magnetics, Vol. 44, No. 6, June 2008, pp. 1302-1305. [6] L. Daniel, M. Rekik, O. Hubert, "A multiscale model for magneto-elastic behaviour including hysteresis effects," Arch. Appl. Mech., 84(9–11), pp. 1307–1323, 2014. [7] D. Vanoost, S. Steentjes, J. Peuteman, H. De Gersem, D. Pissoort, K. Hameyer, "Multiscale and macroscopic modeling of magneto-elastic behavior of soft magnetic steel sheets", International Journal of Numerical Modelling Electronic Networks, Devices and Fields, 2017, e2255. [8] I. Niyonzima, R. V. Sabariego, P. Dular, C. Geuzaine, "Finite element computational homogenization of nonlinear multiscale materials in magnetostatics", IEEE Transactions on Magnetics, Vol. 48, No. 2, February 2012, pp. 587-590. [9] H. De Gersem, "Combined spectral-element, finite-element discretization for magnetic-brake simulation", IEEE Transactions on Magnetics, Vol. 46, No. 8, August 2010, pp. 3520-3523. [10] H. De Gersem, O. Henze, T. Weiland, A. Binder, "Simulation of wave propagation effects in machine windings", COMPEL, Vol. 29 No. 1, 2010, pp. 23-38. [11] H. De Gersem, S. Vanaverbeke, G. Samaey, "Three-dimensional—two-dimensional coupled model for eddy currents in laminated iron cores", IEEE Transactions on Magnetics, Vol. 48, No. 2, February 2012, pp. 815-818. [12] H. De Gersem, B. Masschaele, T. Roggen, E. Janssens, T.T. Nguyen, "Improved field post-processing for a Stern-Gerlach magnetic deflection magnet", International Journal of Numerical Modelling Electronic Networks, Devices and Fields, Vol. 201, No. 27, pp. 472-484. [13] A. Pels, Z. Bontinck, J. Corno, H. De Gersem, S. Schöps, "Optimization of a Stern-Gerlach magnet by magnetic field-circuit coupling and isogeometric analysis", IEEE Transactions on Magnetics, Vol. 51, No. 12, July 2015, article number 7209907. [14] U. Römer, S. Schöps, H. De Gersem, "A defect corrected finite element approach for the accurate evaluation of magnetic fields on unstructured grids", Journal of Computational Physics, Vol. 335, 2017, 688-699. [15] D. Vanoost, H. De Gersem, J. Peuteman, G. Gielen, D. Pissoort, "Two-dimensional magnetostatic finite-element simulation for devices with a radial symmetry", IEEE Transactions on Magnetics, Vol. 50, No. 5, May 2014, paper no. 7400204. [16] D. Vanoost, H. De Gersem, J. Peuteman, G. Gielen, D. Pissoort, "Finite-element discretisation of the eddy-current term in a 2D solver for radially symmetric models", International Journal of Numerical Modelling: Electronic Networks, Devices and Fields, Vol. 201, No. 27, pp. 505–516, 2013. [17] L.A.M. D'Angelo, H. De Gersem, "Quasi-3D finite-element method for simulating cylindrical induction-heating devices", submitted to IEEE Journal on Multiscale and Multiphysics Computational Techniques. [18] D. Doornaert, C. Glorieux, H. De Gersem, R. Puers, W. Spileers, J. Blanckaert, "Quasi-3-D finite-element method for cylindrically symmetric models with small eccentricities", IEEE Transactions on Magnetics, Vol. 52, No. 3, March 2016, paper 7401404. [19] H. De Gersem, N. Marsic, W.F.O. Müller, F. Kurian, T. Sieber, M. Schwickert, "Finite-element simulation of the performance of a superconducting meander structure shielding for a cryogenic current comparator", Nuclear Instruments and Methods in Physics Research A, Vol. 840, 2016, pp. 77-86.

10:30

EE-04. Advanced constitutive laws for computational magnetics: The case of magneto-mechanical behaviour.

L. Daniel[1]
1. GeePs-CentraleSupelec, Gif sur Yvette, France

Abstract – Ferromagnetic materials in electromagnetic devices are subjected to multiaxial stress states. Stress significantly affects the material behaviour, and appropriate modelling tools are required to describe this coupling effect. Multiscale approaches for magneto-elastic behaviour can provide a useful description of the complex interaction between magneto-mechanical loading and material response. However, these models are not easily implementable into numerical simulations. This paper gives a brief overview of different strategies to extract information from multiscale approaches so as to use them in standard numerical tools for the design of electromagnetic devices.

It is known for long that mechanical stress state significantly influences the magnetic and magneto-mechanical behaviour of ferromagnetic materials [1]. The different stages required in the manufacturing of electrical machines and electromagnetic devices, as well as the operational conditions, generate a variety of mechanical stress states in the ferromagnetic materials used in their fabrication. These mechanical loadings usually have a detrimental effect on the material behaviour and hence on the device performance [2-4]. It is then highly desirable that the designer of electromagnetic devices can have access to constitutive equations representative for the magneto-mechanical behaviour of ferromagnetic materials. The stress being described by a second order tensor (six independent components), and the magnetic field by a vector (three independent components), it is easy to understand that the possible combinations for the magneto-mechanical loading are huge. Many experimental and numerical studies are restricted to 1D configurations considering uniaxial stress (usually tensile) applied in the direction parallel to the magnetic field. Although these studies are very useful to explore the mechanisms of magneto-mechanical coupling, they obviously need to be generalised in order to cover the practical configurations encountered in most real devices. The problem seems too complex to be described by macroscopic phenomenological approaches, as often used in the modelling of – uncoupled – magnetic behaviour. A variety of approaches have been developed to describe and understand magneto-mechanical coupling effects, based on different levels of approximations. Among them, multiscale approaches (MSA [5-11]) appear particularly promising to capture the complexity of magneto-elastic behaviour. These approaches are based on an energetic description of the magneto-elastic equilibrium at the magnetic domain scale combined to a statistic description of the average magnetic domain distribution. A main strength of MSA is that they can naturally deal with heterogeneous and anisotropic materials. They also naturally introduce the multiaxiality of magneto-mechanical loadings (3D stress state and any relative orientation between stress and magnetic field). Some of the MSA can also consider hysteresis effects. However MSA remain usually too complex to be easily implemented into numerical analysis tools for the design of electromagnetic systems. Hence modelling strategies are required to take benefit from the output of MSA while keeping the numerical burden acceptable. A first idea is to use MSA as a "numerical testing machine" and consider it as a tool to identify the material parameters of macroscopic models. Indeed, macroscopic constitutive models, notably those based on thermodynamic approaches [12-15], are capable of tackling the multiaxility of magneto-mechanical effects. However they are more reliable if the modelling parameters are obtained from more complex configurations than simple uniaxial magneto-elastic tests. An option is to develop multiaxial experimental setups [16-19], but the use of MSA is an alternative path. The modelling parameters of MSA can usually be identified on simple experimental tests due to their univocal physical meaning. MSA can then be used to perform ''numerical tests" in any loading condition suitable for the identification of macroscopic model parameters. Another strategy is to derive simplified models from full MSA, usually neglecting the effects of material heterogeneity [20-22]. The multiaxial feature of MSA is preserved, and the constitutive equations can incorporate anisotropy [22,23] or hysteresis effects [21,24]. Such approaches have been shown to be efficient to describe the behaviour of simple test structures [25], transformers [22,26] or electrical machines under magneto-mechanical loading [23,24]. The simplest – but also less accurate - strategy is probably to use the concept of equivalent stress [27,28] or equivalent strain [29]. An equivalent stress is a uniaxial stress that – applied in the direction parallel to the magnetic field – would have the same effect as the real multiaxial stress existing in the structure. Heterogeneity and initial anisotropy effects are neglected, but it is a simplified way to take into account the multiaxiality of stress in electromagnetic structures without developing fully multiaxial magneto-mechanical numerical tools. This approach has been applied successfully to evaluate the potentiality of smart materials to perform flux weakening in electrical machines [30] or to analyse the effect of stress on the losses in electrical machines [31].

[1] R. M. Bozorth, Ferromagnetism, Van Norstand, 1951. [2] F. Ossart, E. Hug, O. Hubert, C. Buvat, R. Billardon, "Effect of punching on electrical steels: Experimental and numerical coupled analysis," IEEE Trans. Magn., 36(5), pp. 3137–3140, 2000. [3] K. Fujisaki, R. Hirayama, T. Kawachi, S. Satou, C. Kaidou, M. Yabumoto, T. Kubota, "Motor core iron loss analysis evaluating shrink fitting and stamping by finite-element method," IEEE Trans. Magn., 43(5), pp. 1950–1954, 2007. [4] M. Hofmann, H. Naumoski, U. Herr, H.G. Herzog, "Magnetic properties of electrical steel sheets in respect of cutting: Micromagnetic analysis and macromagnetic modeling," IEEE Trans. Magn., 52(2), 2000114, 2016. [5] N. Buiron, L. Hirsinger, R. Billardon, "A multiscale model for magneto-elastic couplings", J. Phys. IV, 9, pp. 187, 1999. [6] W.D. Armstrong, "A directional magnetization potential based model of magnetoelastic hysteresis," J. Appl. Phys., 91, pp.2202, 2002. [7] L. Daniel, O. Hubert, N. Buiron, R. Billardon, "Reversible magnetoelastic behavior: A multiscale approach," J. Mech. Phys. Solids, 56, pp. 1018-1042, 2008. [8] L. Daniel, N. Galopin, "A constitutive law for magnetostrictive materials and its application to Terfenol-D single and polycrystals", Eur. Phys. J. Appl. Phys., 42, pp.153–159, 2008. [9] A. van den Berg, L. Dupré, B. Van de Wiele, G. Crevecoeur, "A Mesoscopic Hysteresis Model Based on the Unconstrained Minimization of the Gibbs Free Energy", IEEE Trans. Magn., 46, pp. 220-224, 2010. [10] L. Daniel, M. Rekik, O. Hubert, "A multiscale model for magneto-elastic behaviour including hysteresis effects," Arch. Appl. Mech., 84(9–11), pp. 1307–1323, 2014. [11] D. Vanoost, S. Steentjes, J. Peuteman, G. Gielen, H. De Gersem, D. Pissoort, K. Hameyer, "Magnetic hysteresis at the domain scale of a multi-scale material model for magneto-elastic behaviour,", J. Magn. Magn. Mater., 414, pp.168-179, 2016. [12] L. Hirsinger, G. Barbier, C. Gourdin, R. Billardon, "Application of the internal variable formalism to the modelling of magnetoelasticity", in Mech Electromagn Mater Struct 19, pp. 54-67, J.Y. Yang and G.A Maugin (Eds), IOS Press, 2000. [13] K. Azoum, M. Besbes, F. Bouillault, T. Ueno, "Modeling of magnetostrictive phenomena. Application in magnetic force control", Eur. Phys. J. Appl. Phys., 36, pp. 43-47, 2006. [14] K. Fonteyn, A. Belahcen, R. Kouhia, P. Rasilo, A. Arkkio, "FEM for directly coupled magneto-mechanical phenomena in electrical machines", IEEE Trans. Magn., 46(8), pp. 2923–2926, 2010. [15] P. Rasilo, D. Singh, U. Aydin, F. Martin, R. Kouhia, A. Belahcen, A. Arkkio, "Modeling of Hysteresis Losses in Ferromagnetic Laminations Under Mechanical Stress", IEEE Trans. Magn., 52(3), 7300204, 2016. [16] J. Pearson, P.T. Squire, M.G. Maylin, J.G. Gore, "Apparatus for magnetic measurements under biaxial stress," IEEE Trans. Magn., 36(5), pp. 3599–3601, 2000. [17] Y. Kai, Y. Tsuchida, T. Todaka, M. Enokizono, "Influence of biaxial stress on vector magnetic properties and 2-D magnetostriction of a nonoriented electrical steel sheet under alternating magnetic flux conditions," IEEE Trans. Magn., 50(4), 6100204, 2014. [18] M. Rekik, O. Hubert, L. Daniel, "Influence of a multiaxial stress on the reversible and irreversible magnetic behaviour of a 3%Si-Fe alloy," Int. J. Appl. Electromagn. Mech., 44(3–4), pp. 301–315, Mar. 2014. [19] U. Aydin, P. Rasilo, D. Singh, A. Lehikoinen, A. Belahcen, A. Arkkio, Coupled Magneto-Mechanical Analysis of Iron Sheets Under Biaxial Stress IEEE Trans. Magn., 52(3), 2000804, 2016. [20] L. Daniel, "An analytical model for the effect of multiaxial stress on the magnetic susceptibility of ferromagnetic materials," IEEE Trans. Magn., 49(5), pp. 2037–2040, 2013. [21] L. Daniel, O. Hubert, M. Rekik, "A simplified 3D constitutive law for magneto-mechanical behaviour", IEEE Trans. Magn., 51(3), 7300704, 2015. [22] S.S. Mbengue, N. Buiron, V. Lanfranchi, "Macroscopic modeling of anisotropic magnetostriction and magnetization

in soft ferromagnetic materials", J. Magn. Magn. Mater., 404, pp. 74-78, 2016. [23] L. Bernard, X. Mininger, L. Daniel, G. Krebs, F. Bouillault, M. Gabsi, "Effect of stress on switched reluctance motors: A magneto-elastic finite-element approach based on multiscale constitutive laws", IEEE Trans. Magn., 47(9), pp. 2171–2178, 2011. [24] L. Bernard, L. Daniel, "Effect of stress on magnetic hysteresis losses in a switched reluctance motor: application to stator and rotor shrink fitting", IEEE Trans. Magn., 51(9), 7002513, 2015. [25] D. Vanoost, S. Steentjes, H. De Gersem, J. Peuteman, G. Gielen, D. Pissoort, K. Hameyer, "Embedding a Magnetoelastic Material Model in a Coupled Magnetomechanical Finite-Element Solver", IEEE Trans. Magn., 51(11), 7403204, 2015. [26] M. Liu, O. Hubert, X. Mininger, F. Bouillault, L. Bernard, "Homogenized Magnetoelastic Behavior Model for the Computation of Strain Due to Magnetostriction in Transformers", IEEE Trans. Magn., 52(2), 8000212, 2016. [27] L. Daniel, O. Hubert, "Equivalent stress criteria for the effect of stress on magnetic behavior", IEEE Trans. Magn., 46(8), pp. 3089-3092, 2010. [28] O. Hubert, L. Daniel, "Energetical and multiscale approaches for the definition of an equivalent stress for magneto-elastic couplings", J. Magn. Magn. Mater., 323(13), pp. 1766-1781, 2011. [29] L. Daniel, "An equivalent strain approach for magneto-elastic couplings", IEEE Trans. Magn., 53(6), 2001204, 2017. [30] G. Krebs, L. Daniel, "Giant magnetostrictive materials for field weakening: a modeling approach", IEEE Trans. Magn., 48(9), pp. 2488-2494, 2012. [31] K. Yamazaki, H. Takeuchi, "Impact of Mechanical Stress on Characteristics of Interior Permanent Magnet Synchronous Motors", IEEE Trans. Ind. Appl., 53(2), pp. 963-970, 2017.

11:00

EE-05. High Resolution Modeling of Magnetic Field Exposure Scenarios in the Vicinity of Inductive Wireless Power Transfer Systems.

M. Clemens[1], M. Zang[1], M. Alsayegh[2] and B. Schmuelling[2]
1. Chair of Electromagnetic Theory, University of Wuppertal, Wuppertal, Germany; 2. E-Mobility Research Group, University of Wuppertal, Wuppertal, Germany

The increasing development and commercialization of electric and hybrid electric vehicles includes the challenge of enabling an efficient and comfortable charging process of a car‘s battery. A promising solution for this purpose is provided by the use of inductive power transfer (IPT) technologies for a contactless charging with an electric power in the order of several kW [1]. A current driven charging coil (primary coil) is positioned on the floor below the car and coupled via an airgap with a secondary coil attached to the bottom of the car. IPT systems generate magneto-quasistatic fields with frequencies from 80 up to 140 kHz. A person positioned inside or near the car, however, will also be exposed to these magnetic fields. Exposure related changes of the electric field strength inside the human body can lead to stimulations of nerve and muscle tissues. Therefore, limits for the volume-averaged body-internal electric strength are proposed by the International Commission on Non-Ionizing Radiation Protection (ICNIRP) [2]. Investigations of the human exposure to magneto-quasistatic fields require the use of high-resolution numerical simulation techniques such as the Finite-Difference Time Domain (FDTD) method. Complex geometries of conductive and/or permeable sheets contained in the IPT system and the car body as well as anatomical body phantoms have to be considered in exposure simulations. Also, potential misalignments between the IPT system’s coils might have an influence on the exposure and need to be taken into account. A high-resolution discretization of such scenarios within commercially available eddy current solvers is often unfeasible as it requires the solution of very high-dimensional and extremely ill-conditioned algebraic systems of equations. As an alternative, three two-step methods have been introduced in [3] and [4] making use of domain decomposition approaches enabling a division of the exposure scenario into two domains: the source area including the influence of shielding geometries and the area occupied by the exposed body. These three two-step methods – the Coupled Scaled-Frequency (SF-)FDTD method, the Co-Simulation SF-FDTD method and the Co-Simulation Scalar-Potential Finite Difference (SPFD) method – are used here for a high-resolution modeling of magneto-quasistatic exposure scenarios including realistic models of various IPT systems, the car and the human body. With the application of the two-step methods a reduction of the memory demands and the simulation time is achieved in comparison to a monolithic application of the SF-FDTD method and the simulations can be performed on a standard computer workstation. Figure 1 a) shows an exposure scenario where a human body model (body phantom Duke [5]) is positioned beside a car model with an IPT system positioned below the car. For an improvement of the coupling between the IPT‘s coils, optimization analyses are conducted using an FEM-based magneto-quasistatic field solver included in the software ANSYS Maxwell 3D [6]. Here, different geometry designs are compared to each other regarding an optimization of the coupling coefficient and a reduction of the magnetic leakage fields, coincidentally. The optimized model geometries of different IPT systems are used in exposure analyses carried out with the abovementioned two-step methods. In a first step, the magnetic source field simulation is performed with the software CST Microwave Studio (MWS) [7]. The simulation model includes the IPT system and the car body sheets, but not the human body model, since its interaction with the magnetic source field is negligible. Source field simulations are also carried out considering lateral misalignment of the IPT system’s coils and different values for the thickness of the car body sheets for an analysis of a consequential variation of the leakage fields – and thus the exposure of the human body. Figure 1 b) shows the magnetic flux density in a cross section of the car and in the center of the IPT system with the designated position of the human body model indicated. In a second step, the exposure of the human body is calculated, i.e., the exposure-related distribution of the body-internal electric field strengths, using the previously calculated source fields. Within the two-step SF-FDTD methods this second step is also carried out using CST MWS or, alternatively, using the software Sim4Life [8], whereas within the Co-Simulation SPFD method a discrete Poisson equation is solved using a preconditioned conjugate gradient solver. A high flexibility is achieved by the use of the Co-Simulation SPFD method (as well as with the Co-Sim SF-FDTD method), since the magnetic source field simulation can be computed using any magnetic field simulation tool. Figure 1 c) shows the electric field strength in the median plane of the human body voxel model. The maximum voxel-averaged electric field strength is evaluated for each scenario to analyze the influence of each configuration (different IPT systems, coil misalignments and car body sheet thicknesses) on the exposure and for an exposure assessment according to the ICNIRP guidelines.

[1] S. Li and C. C. Mi, Wireless Power Transfer for Electric Vehicle Applications, IEEE Journal of Emerging and Selected Topics in Power Electronics, vol. 3, no. 1, pp. 4 – 17, 2015. [2] ICNIRP – International Commission on Non-Ionizing Radiation Protection: Guidelines for limiting exposure to time-varying electric and magnetic fields (1 Hz-100 kHz), Health Physics, vol. 99, no. 6, pp. 818 – 836, 2010. [3] M. Zang, M. Clemens, C. Cimala, J. Streckert, and B. Schmülling, Simulation of Inductive Power Transfer Systems Exposing a Human Body With Two-Step Scaled-Frequency FDTD Methods, IEEE Transactions on Magnetics, vol. 53, no. 6, pp. 1 – 4, 2017. [4] M. Zang, C. Cimala, M. Clemens, J. Dutiné, T. Timm, and B. Schmuelling, A Co-Simulation Scalar-Potential Finite Difference Method for the Numerical Analysis of Human Exposure to Magneto-Quasi-Static Fields, IEEE Transactions on Magnetics, vol. 53, no. 6, pp. 1 – 4, 2017. [5] A. Christ, W. Kainz, E. G. Hahn, et al., The virtual family - development of surface-based anatomical models of two adults and two children for dosimetric simulations, Phys. Med. Biol., vol. 55, no. 2, pp. N23 – N38, 2010. [6] ANSYS, Inc., Suite 501, 2855 Telegraph Avenue, Berkeley CA 94705, USA. [7] CST AG, Bad Nauheimer Straße 19, D-64289 Darmstadt, Germany. [8] ZMT Zurich MedTech AG, Zeughausstraße 43, CH-8004 Zurich, Switzerland.

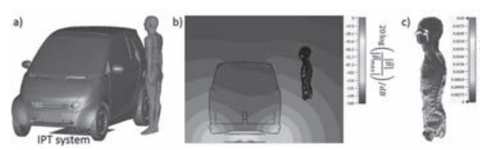

Fig. 1. a) Exposure scenario including an IPT system positioned below a car model and a human body voxel model standing beside the car, b) Magnetic source field of the IPT system in a cross section of the car and with the indication of the designated position of the human body model, c) Body-internal electric field strength in the median plane of the human body model

11:30

EE-06. Design and Optimisation of Magnetic Devices.

D. Lowther[1]
1. Elec and Comp Eng, McGill University, Montreal, QC, Canada

Magnetic devices are found in applications ranging from power generation and electric vehicles to domestic equipment and industrial processes. The design of these devices has become more complex as the requirements become more demanding [1]. Frequently, a designer is expected to generate more output from a smaller frame size, lower the production cost and increase the overall efficiency as well as producing more versatile devices driven by power electronic systems capable of generating variable frequency and voltage excitations. The problem is beyond the conventional multi-physics analysis and is truly multi-domain where the physics of the device and its coupling with the drive system have to be considered together, [2]. Finding a design which can meet the specifications is an optimisation process and, in most situations it is now a multi-objective, multi-domain problem. In addition, manufacturing processes can introduce tolerances on many of the parameters which can have a significant effect on the device performance [3]. Thus, the design finally chosen should be robust, i.e. insensitive to small parameter changes, [4]. Computer simulation of magnetic devices can now provide the designer with advanced multi-physics representations, [5], which can model the magnetic, mechanical, thermal and acoustic performance and can couple to the power electronics drive. However, such systems, particularly in three-dimensions and driven with pulse-width modulation excitations, involve significant amounts of computational effort and solutions can take of the order of hours. Recent advances in multi-objective optimization using stochastic algorithms, [6], when combined with the concept of robustness [7], [8] have provided a possible solution to the design problem. However, such systems often need thousands of solutions during the search process and this is currently infeasible using full multi-domain simulations. In the early stages of the design process, it is unnecessary to consider the full virtual simulation since the shape of the design space is controlled by a few critical factors such as the dimensions of the magnetic flux paths, the excitation windings, etc. In many devices, the influence of these parameters can be studied through two-dimensional field simulations which can generate performance characteristics including the local losses needed for efficiency. While much faster than three-dimensional systems, such analyses can still be too slow for the initial stages of an optimization process. To avoid this computational bottleneck, optimizers can estimate the effect of parameter variations through the use of a surrogate model – typically a response surface. This can be generated iteratively through approaches such as Kriging [9], [10] or prior to the optimization process through the use of a high performance computer system. In the latter approach, the data generated can be used to predict the information needed by the optimizer, [11]. Once a likely solution to the design problem is found, the system can automatically move towards a full, multi-domain simulation of the prototype solution. The presentation will consider the current state of reduced order and surrogate modeling, including robustness issues, for the optimization of magnetic devices.

1. J.R.Hendershot, T.J.E.Miller, "The Design of Brushless Permanent-Magnet Machines", Motor Design Books LLC, Florida, U.S.A., 2010. 2. Lowther, D.A., "The Development of Industrially-Relevant Computational Electromagnetics Based Design Tools," IEEE Transactions on Magnetics, v. 49, 5, 2013, pp. 2375-2380. 3. Mac, D., Clenet, S., Bedek, K., Chevallier, L., Korecki, J., Moreau, O. & Thomas, P.., "Influence of Uncertainties on the B (H) Curves on the Flux Linkage of a Turboalternator", International Journal of Numerical Modelling: Electronic Networks, Devices and Fields, v. 27, 2014, pp. 385-399. 4. Salimi, A., Lowther, D.A., "On the Role of Robustness in Multi-Objective Robust Optimization in the Design of Electromagnetic Devices," Proceedings of the International Conference on the Computation of Electromagnetic Fields (COMPUMAG) 2015, Montreal, Quebec, Canada, June 28 to July 2, 2015, paper PB4-15, 2 pages 5. Lowther, D.A., "The Inclusion of Coupled Problems and High Performance Computing in the Design of Electromagnetic Devices", Proceedings of HES-16 International Conference on Heating by Electromagnetic Sources, Padova, Italy, May 2016. 6. Di Barba, P. "Multiobjective Shape Design in Electricity and Magnetism", Springer, 2010. 7. Li, M., Silva, R., Guimaraes, F. and Lowther, D. "A New Robust Dominance Criterion for Multiobjective Optimization", IEEE Transactions on Magnetics, v. 51, 2015, pp. 1-4. 8. Deb, K. and Gupta, H. "Introducing Robustness in Multi-Objective Optimization", Evolutionary Computation, 14, 2006, pp. 463-494. 9. Lebensztajn, L., Marretto, C. A. R., Costa, M. C. & Coulomb, J. L.., "Kriging: a Useful Tool for Electromagnetic Device Optimization", IEEE Transactions on Magnetics, v. 40, 2004, pp.1196-1199. 10. Li, Y., Xiao, S., Rotaru, M, Sykulski, J., "A Kriging-Based Optimization Approach for Large Data Sets Exploiting Points Aggregation Techniques", IEEE Transactions on Magnetics, v. 53, 6, 2017, Art. Seq. No. 7001704, 11. Ghorbanian, V., Lowther, D.A., "A Statistical Solution to Efficiently Optimize the Design of an Inverter-fed Permanent Magnet Motor," IEEE Trans on Industry Applications, DOI 10.1109/TIA.2017.2726968, 2017.

THURSDAY MORNING, 26 APRIL 2018 PEONY I, 9:00 TO 12:00

Session EF
ENERGY ASSISTED RECORDING

Yuepeng Zhang, Chair
Argonne National Laboratory, Argonne, WI, United States

CONTRIBUTED PAPERS

9:00

EF-01. Micromagnetics of FePt-$L1_0$ Media with Thermally Insulating Magnetic Grain Boundaries.

J. Zhu[1] and Y. Qin[1]
1. Data Storage Systems Center, Carnegie Mellon University, Pittsburgh, PA, United States

In heat assisted magnetic recording (HAMR), grain-to-grain Curie temperature variation presents a practical limit to grain size reduction hence, the scaling of recording area density capability (ADC), for the advancement of granular FePt-$L1_0$ media[1][2]. At small grain sizes, a reduction of grain size yields an increase of surface-to-volume ratio, thereby, a reduction of Curie temperature [3]. The resulting grain size dependence of Curie temperature gives rise to the cause of the Curie temperature variation due to unavoidable grain size distributions with today's film fabrication technique. Aiming at this grand challenge, a recent experimental study has shown a potentially practical solution by successfully fabricating granular FePt-$L1_0$ media with thermally insulating magnetic grain boundaries [4]. In this paper, we present a systematic modeling study on the micromagnetic recording characteristics of such media. In the study, both the FePt-$L1_0$ grain core and a thin layer of ferromagnetic grain boundaries are meshed and modeled using dynamic Landau-Lifshitz-Bloch (LLB) equations. The room temperature anisotropy field of the FePt core is assumed to be H_k=80 kOe and zero magnetocrystalline anisotropy is assumed for the soft magnetic grain boundary material. Gaussian geometric thermal profile is assumed along with realistic media motion are used to simulate practical recording process. Figure 1(a) shows the M_s(T) curves for both the FePt grain core and the insulating magnetic grain boundary material assumed. Note that the assumed magnetic grain boundary has a Curie temperature significantly higher than that of the FePt core. For all the results presented in this digest, the diameter of the FePt core is assumed to be 6nm with 1nm thick magnetic grain boundary. The modeling simulation shows that the ferromagnetic grain boundary provide significant assist in the magnetization process of the FePt grain core during recording. With the grain boundary coupled to the FePt core, the magnetization process of the core becomes significantly more deterministic. Figure 1(b) shows the switching probability of the FePt grain core as a function of recording field amplitude with the medium moving at a speed of 15 m/s and a spatial thermal gradient of 8 K/nm. The case "Not Coupled" indicating no exchange coupling between the grain boundary and the FePt core is plotted for comparison. With the magnetic grain boundary exchange coupled to the core, full saturation recording can be reached at lower field values in comparison with the case of non-magnetic grain boundaries. The effect is even more enhanced for smaller size of FePt grain cores, which will be presented in the full paper. Please note the "Not Coupled" case is essentially the same as the case with non-magnetic grain boundaries. Figures 2(a) and 2(b) show the writing of a transition when the head field direction is reversed (black dashed lines). The case with the exchange-coupled grain boundary and FePt core shows more rapid and better defined magnetization switching with the magnetizations of the core and grain boundary switching together. Whereas for the case that the core and grain boundary are not coupled, the switching of the FePt core is much more gradual with noticeably fluctuations. Also note that the grain boundary actually magnetizes a little faster than the FePt core does. In summary, the magnetic grain boundary exchange coupled to the FePt core provides significant assistance to the magnetization process of the FePt core during recording, both in heat assisted magnetization process and in transition magnetization process with field reversal. Therefore, it is important for the Curie temperature of the grain boundary material to be higher than that of the FePt core for the obvious reasons. The level of grain boundary magnetization at the recording temperature is important and the higher the magnetization level, the more enhanced assisting effect will be during recording. It is also important to note that the exchange coupling between the grain boundaries of adjacent grains needs to be minimized in practice. The experimental study has shown that this objective could be achieved in practice [4]. In conclusion, granular FePt media with a thin layer of soft magnetic grain boundaries that are exchange coupled to the FePt cores not only can suppress or eliminate grain-to-grain Curie temperature variation, but also can assist the magnetization process, especially for small size grains, during recording in HAMR. The more deterministic magnetization processes helps to suppress thermal-induced transition jitter during recording process, consequently enhancing the scalability of both the linear recording density capability and the overall ADC.

[1] R. Acharya et al, "Heat Assisted Magnetic Recording Media: Challenges and Recent Developments," Paper D3, TMRC 2014, Berkeley (2014). [2] H. Li, and J.-G. Zhu, "The role of media property distribution in HAMR SNR," IEEE Trans. Magn., 49(7), 3568-3571 (2013). [3] C. Rong et al, Adv. Mater. 2006, 18, 2984-2988. [4] Bing Zhou, B. Varapasad, D. E. Laughlin, and J.-G. Zhu, "Magnetic oxide added to grain boundary materials for L10 HAMR mdia," Paper EE06, MMM Conference 2017, Pittsburgh (2017).

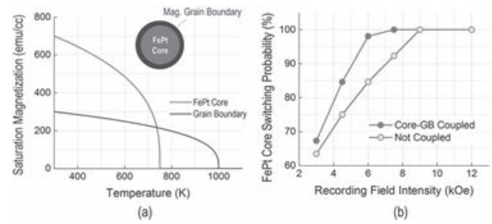

Fig. 1. (a) Saturation magnetization vs. temperature curves used for the micromagnetic simulations. Both grain core and grain boundaries are meshed with space-filling polygons of approximately 1x1 nm^2 area. The height of each mesh is the same as the height of the grain at 6 nm. (b) Calculated FePt core switching probability as function of recording field amplitude for the case with grain boundary and core are exchange coupled (Left) and the case that are not coupled (Right).

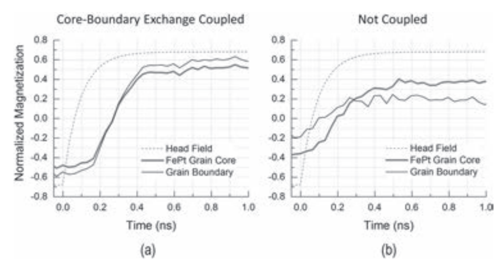

Fig. 2. (a) Calculated switching dynamics for the case of exchange coupled grain boundary and FePt core (Left) and the case that they are not coupled (Right) which is essentially the same as FePt grain with non-magnetic grain boundaries.

9:15

EF-02. Sources and Impact of Media Thermal Fluctuations in Heat Assisted Magnetic Recording.

P. Jubert[1] and C. Papusoi[1]
1. Western Digital, San Jose, CA, United States

Heat assisted magnetic recording (HAMR) is being developed to achieve recording densities well beyond 1 Tb/in^2. The technology uses a laser-coupled near-field transducer (NFT) to locally heat the recording layer, made of small high-anisotropy FePt grains, such that the grains' magnetization freezes in the direction of the head write field while the temperature cools just below their Curie temperature. Given the inherent variations of grains position, size and properties, the recording performance also relies on having a large temperature gradient at the freezing location. The temperature gradient requirement effectively replaces the field gradient requirement in conventional magnetic recording. The heat is provided by the local absorption of the laser light under the NFT and the resulting temperature profile stems from the medium thermal transport properties. As a result, both the optical characteristics and the thermal transport properties of the medium stack need to be properly designed. In addition, it has been shown that grain-to-grain temperature fluctuations can significantly contribute to transition jitter and limit HAMR performance [1, 2]. It is therefore important to identify all potential sources of temperature fluctuations and to evaluate their relative impact to HAMR performance. This work aims at understanding and quantifying the effect of spatial variations of the light absorption and spatial variations of the medium stack thermal properties on HAMR. Optical and thermal modeling is carried out to calculate temperature profiles in a simplified HAMR medium stack as a function of in-plane variations in the medium properties. The medium stack comprises a 5-nm-thick overcoat, a 10-nm-thick recording layer, a 5-nm-thick thermally resistive layer, a 100-nm-thick heatsink layer, and a glass substrate. To comprehend the relative contribution of each medium property, the spatial variations are first simplified to sinusoidal modulations with varying amplitude and period. These lead to sinusoidal variations of the location of the freezing point or sinusoidal transition jitter, whose amplitude δx_{max} is evaluated systematically for different optical absorption modulations and modulations of the thermal conductivities at each layer and interface. The main sources to transition jitter are found to be fluctuations of the absorption and of the thermal properties in the recording layer, in the thermally resistive layer and to a lesser extent in the overcoat. Absorption and thermal property fluctuations in the heatsink have significantly smaller impact on transition jitter. For all cases, δx_{max}, is proportional to the amplitude of the source fluctuation. δx_{max} is also strongly affected by the length scale of the source fluctuation. This is illustrated in Fig. 1, which shows δx_{max} as a function of the period for modulations of the optical absorption in the recording layer and for modulations of the effective thermal resistance between the recording layer and the heatsink. The trends at long periods are quantitatively understood with 1D heat flow considerations, while the reduction at low periods is explained by in-plane heat spreading in the HAMR stack. In addition, we note that contrary to what previous reports may suggest [1, 2], temperature fluctuations are quite different from the intrinsic Curie temperature fluctuations. The temperature fluctuations are proportional to the input laser power, which is also proportional to the downtrack thermal gradient. As illustrated in the Fig. 1, increasing thermal gradient does not reduce δx_{max}; the transition jitter associated with grain-to-grain temperature fluctuations does not improve with increasing the thermal gradients. The effect of roughness at the interfaces of the HAMR medium stack is also investigated. Roughness is source of combined optical absorption and thermal property spatial fluctuations. Interface roughness results similarly in grain-to-grain temperature fluctuations and therefore in sizeable transition jitter. The amplitude of the jitter is found to scale with the amplitude of the interface roughness and to also depend on the length scale of the roughness.

1) J.G. Zhu, and H. Li, "Signal-to-noise ratio impact of grain-to-grain heating variation in heat assisted magnetic recording", *J. Appl. Phys.* vol. 115, 17B747, (2014) 2) J.G. Zhu, and H. Li, "SNR Impact of Noise by Different Origins in FePt-L10 HAMR Media", *IEEE Trans Magn*. vol. 51, n. 4, pp. 3200407, (2015)

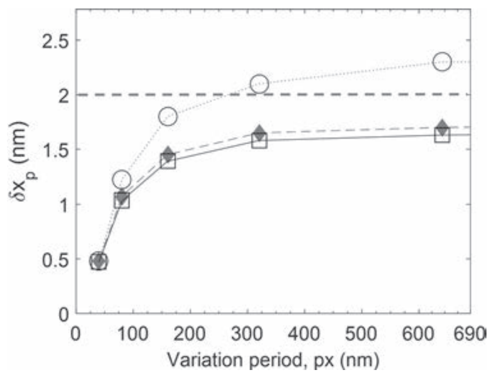

Fig. 1. Transition jitter peak amplitude as a function of the period of a sinusoidal spatial variation of (blue dots) the optical absorption in the recording layer and (black squares and red diamonds) the effective thermal resistance between the recording layer and the heatsink. The amplitude of the modulation is +/-10% around the average value of optical absorption or effective thermal resistance. The heatsink thermal conductivity is (blue dots, black squares) 45 W/mK or (red diamonds) 90 W/mK.

9:30

EF-03. A Split Pole and Gap-NFT Write Head Design for Transition Curvature Reduction in Heat Assisted Magnetic Recording.

C. Chow[1] and J.A. Bain[1]
1. Electrical and Computer Engineering, Carnegie Mellon University, Pittsburgh, PA, United States

Transition curvature poses a significant challenge to areal density capability in heat assisted magnetic recording (HAMR). Potential solutions include curvature correction through cross track (XT) write field gradient [1, 2] and engineering a flatter thermal contour using a crown-shaped near field transducer (NFT) [3]. We propose a head design aimed at curvature correction through XT magnetic field gradients using a split pole and with the potential for thermal contour flattening due to its gap NFT design. Our focus here will be an examination of the XT field profile. We use a finite element method (FEM) in COMSOL to model the final 100 nm of the pole/NFT tip in this work to assess how to get thermal and magnetic profiles close enough in the downtrack direction without excessive power absorption in the pole. A tapered low index dielectric separator (LIS) inserted between the NFT and the write poles is the key innovation to accomplish this proximity and is the focus of the analysis herein. Our write head design, shown in Fig. 1a, consists of split write poles which are magnetically driven in the same direction. The magnetic gap between these poles creates a XT field gradient inside the recording media. A gap-NFT, similar to that suggested in [4], is formed by a layer of Au on both poles, with the point of smallest separation between the Au layers being termed the optical gap. In simulation, we excite the surface plasmon mode confined in the optical gap, which propagates from the feed position to the air bearing surface (ABS). The optical feed structure to launch this mode is an important consideration in this design but is beyond the present analysis. Fig. 1b shows the reference media stack layers used in our model, including the magnetostatic boundary conditions. Media properties are taken from the 2015 ASTC reference media stack, except that the lubricant, head overcoat, and media overcoat layers are combined into a single air gap layer. The write poles are modeled to be FeCo and have a saturation magnetization of 2.4 T. They are driven to saturation at the distance of 100 nm from the ABS. A soft underlayer (SUL) beneath the heatsink layer in the media is modelled by a zero magnetic potential. For a 35 nm wide magnetic gap, we can achieve a difference of 2 kOe between the minimum and maximum write field in the XT direction inside the recording media. The temperature profile of the hotspot is computed through optical and thermal modelling with a free space wavelength λ_{fs} = 800 nm. The NFT material is assumed to be nanoscale Au (n = 0.2 - 5j, k_{th} = 100 Wm^{-1}K^{-1}), while the high index core is composed of SiN (n = 2, kth = 1 Wm^{-1}K^{-1}), and the low index cladding is SiO2 (n = 1.5, k_{th} = 1 Wm^{-1}K^{-1}). The pole material is assumed to have a combination of properties of Fe and Co (n = 2.8 – 4j, k_{th} = 80 Wm^{-1}K^{-1}). An LIS is inserted between the optical gap and the magnetic gap to reduce absorption in the poles due to proximity to the NFT and confine light to the optical gap. The LIS between the NFT and the poles provides optical isolation (reducing loss) which is desirable, but also increases the downtrack separation between the thermal and magnetic profiles, which is undesirable. We resolve this conflict by introducing a taper to the LIS with a thin section near the ABS to bring the write fields closer to the optical gap at the ABS without incurring the loss associated with a thin LIS over the entre pole tip. Fig 2a shows a side view of the taper. We hold total length constant at 100 nm and the length of the thin section near the ABS at 20 nm. The taper length and thick LIS input length are allowed to vary (producing different taper angles, as noted in the figure). Fig. 2b shows the ratio of power absorbed by the medium to total power absorbed by head and medium as a function of taper length, with both of the untapered cases shown for comparison. Fig 2c shows the location of the field profile relative to the hotspot for the two untapered cases and a representative tapered case. Together these figures show that the thick (35 nm) untapered LIS case gives the best efficiency of power delivered to the medium (31%) but creates a XT field gradient that is too far from the hotspot to be useful in curvature correction. Conversely, the thin (10 nm) untapered LIS gets good overlap of the hotspot and the magnetic field, but reduces power delivery efficiency by almost a factor of 3 down to 13%. The tapered LIS is a good compromise between the two untapered cases. It is able to achieve a field gradient sufficiently close to the hotspot to match the 10 nm thin LIS case, but it does so with a much more desirable power delivery efficiency of 25% for all taper lengths.

[1] Qin, Yuwei, Hai Li, and Jian-Gang Zhu. "Curvature-Eliminating Head Field and Track Edge Characteristics in Heat-Assisted Magnetic Recording." *IEEE Transactions on Magnetics* 53, no. 11 (November 2017): 1–4. https://doi.org/10.1109/TMAG.2017.2707804. [2] Zhu, Jian-Gang Jimmy, and Hai Li. "Correcting Transition Curvature in Heat-Assisted Magnetic Recording." *IEEE Transactions on Magnetics* 53, no. 2 (February 2017): 1–7. https://doi.org/10.1109/TMAG.2016.2614836. [3]Li, Zhongyang, Weibin Chen, Chris Rea, Martin G. Blaber, Nan Zhou, Hua Zhou, and Huaqing Yin. "Head and Media Design for Curvature Reduction in Heat-Assisted Magnetic Recording." *IEEE Transactions on Magnetics* 53, no. 10 (October 2017): 1–4. https://doi.org/10.1109/TMAG.2017.2732940. [4]Rea, Chris, Werner Scholz, Lina Cao, Chubing Peng, Martin Blaber, Julius Hohfeld, Weibin Chen, et al. "Heat Assisted Magnetic Recording Performance and Integration Challenges." edited by Ryuichi Katayama and Thomas D. Milster, 92010K, 2014. https://doi.org/10.1117/12.2064537.

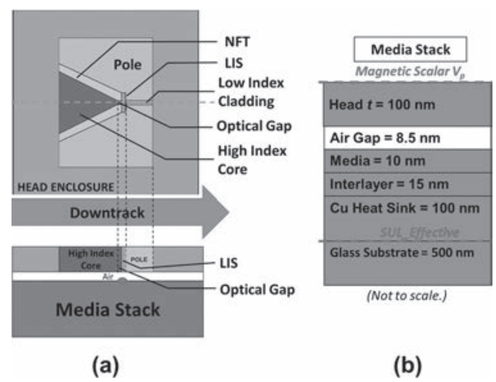

Fig. 1. (a) Schematic of split pole-gap NFT write head design. b) Reference media stack layers and thicknesses.

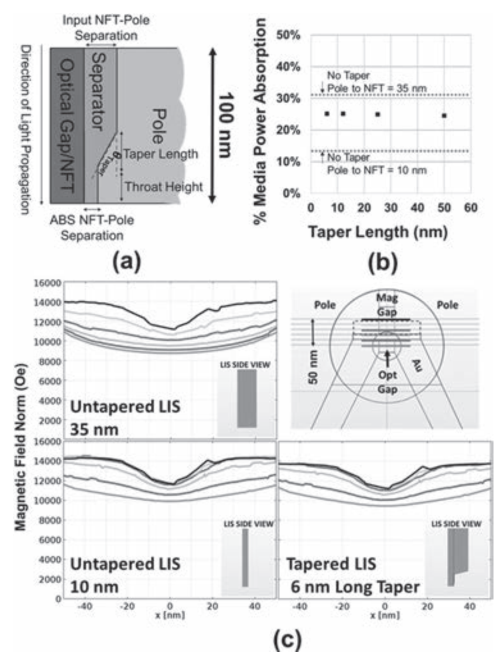

Fig. 2. (a) Side view of LIS showing taper geometry. (b) Power absorbed in media layer as percent of total power absorbed in media and in write head. (c) Magnetic write field norm in recording media at five downtrack positions near optical gap for 35 nm untapered LIS, 10 nm untapered LIS, and a typical tapered LIS.

9:45

EF-04. Design of field generating layer in all-in-plane spin-torque-oscillator.

H. Sepehri-Amin[1], C. Abert[2], D. Suess[2] and K. Hono[1]
1. Research Center for Magnetic and Spintronic Materials, National Institute for Materials Science, Tsukuba, Japan; 2. Christian Doppler Laboratory, Advanced Magnetic Sensing and Materials, University of Vienna, 1090, Vienna, Austria

Microwave assisted magnetic recording (MAMR) is a promising technology to overcome the stagnated areal density increase of hard disk drives. However, its most essential part, spin-torque-oscillator (STO), has not been realized. The STO device for MAMR should have a size of 30-40 nm and be able to generate large $\mu_0 H_{ac} > 0.1$ T with a frequency over 20 GHz at a small current density $J<1.0\times10^8$ A/cm^2 [1]. In addition, large oscillation cone angle of free layer is desired to maximize the $\mu_0 H_{ac}$. Such a device has not been realized experimentally due to the lack of fundamental understandings on the desired materials and structure of the STO. We have recently demonstrated experimentally that mag-flip spin-torque-oscillator (STO) consisting of out-of-plane magnetized spin injecting layer (SIL) and in-plane magnetized field generating layer (FGL) with a diameter of 30-40 nm that can oscillate with resonance frequency of 21 -25.5 GHz and produced an ac magnetic field of 0.15 T [2,3]. However, the main disadvantage of the mag-flip STO device is its large thickness due to the need for ~10 nm out-of-plane magnetized FePt. In addition, the required bias current density of oscillation of mag-flip STO device is over 4.3×10^8 A/cm^2 that needs to be substantially educed for real application [3]. In order to reduce the total thickness of a STO device, in this work we propose all-in-plane STO device consisting in-plane magnetization SIL and FGL. In this study, we will show how design of materials in all-in-plane STO can lead to a STO that can generate large $\mu_0 H_{ac}$ with a frequency over 20 GHz in a small bias current density for MAMR. We employed a micromagnetic simulation code, *magnum.fe*, which solves the coupled dynamics of magnetization (*m*) and spin accumulations (*s*) simultaneously using the time dependent 3D spin diffusion equations and the Landau-Lifshitz-Gilbert (LLG) equation, respectively [4]. This will allow us to directly simulate the effect of locally varying spin accumulations on the magnetization dynamics. Based on the micromagnetic simulations, we propose desired spin polarization and saturation magnetization of FGL so that all-in-plane STO device can generate large $\mu_0 H_{ac}$ with a frequency over 20 GHz in a small bias current density. Figure 1 (a) shows our designed all-in-plane mag-flip STO device consisting a 3-nm-thick SIL and 14-nm-thick FGL separated by a 5-nm-thick Ag layer. An external magnetic field of 1 T is applied to saturate the magnetization of the SIL and FGL out-of-plane and electrons are pumped from bottom to top, and due to the reflection of electrons from FGL/Ag, the SIL switches and transmitted down-spin electrons lead to oscillation of FGL. Unlike the conventional mag-flip STO device, we found that the spin polarization of FGL play a very important role in J_c required for switching of SIL and OOP oscillation of FGL. As shown in Fig. 1, by increase of spin polarization of FGL, J_c can be substantially reduced. The underlying mechanism is shown in Fig. 2 (a). Fig. 2 (a) shows the STO device and 3D spin accumulation in Z direction in the model when all the layers are magnetized OOP under 1 T external magnetic field. Distribution of S_z from SIL toward FGL for different spin polarization of FGL is shown in Fig. 2 (a). It was found that by increase of β^{FGL}, we get more reflected negative spins from FGL/Ag interface that will be beneficial for switching of SIL and OOP oscillation of FGL, resulting in smaller J_c. However, highly spin-polarized materials such as Heusler alloys have limited saturation magnetization of below ~ 1.3 T. In order to increase the ac-field generated by STO, it is necessary to increase the saturation magnetization of FGL. In order to gain large spin polarization of FGL combined with large saturation magnetization in FGL, we propose all-in-plane STO with dual FGL as shown in Fig. 2 (b). By use of this model, we can gain large spin accumulation in SIL that is beneficial for the magnetization switching of SIL and second layer of FGL can have a large saturation magnetization with lower spin polarization desired for large ac magnetic field out-put of device. Acknowledgement: This work was supported by Grant-in-Aids for Young Scientific Research B (17K14802).

[1] Takeo A. *et al*., Intermag Conference 2014 (AD-02). 2] Bosu S. *et al.,* Appl. Phys. Lett. 108,072403 (2016). [3] Bosu S. *et al.,* Appl. Phys. Lett. 108,072403 (2017). [4] Abert C. *et al*., Sci. Rep. 5, 14855 (2015).

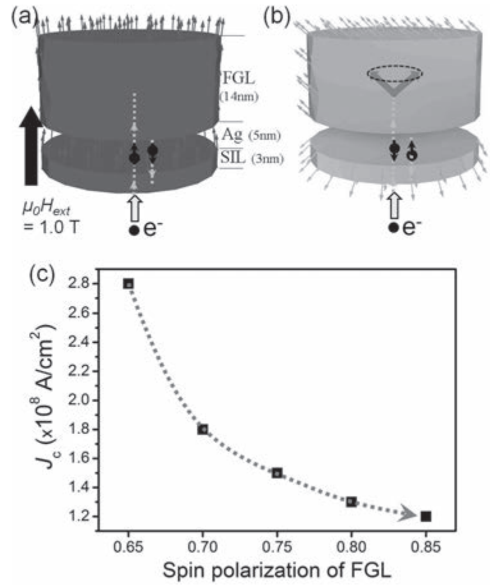

Fig. 1. (a) and (b) Schematic illustration of all-in-plane mag-flip STO and OOP oscillation of FGL while magnetization of SIL is switched, (b) calculated critical current density for switching of SIL and OOP oscillation of FGL versus spin polarization of FGL.

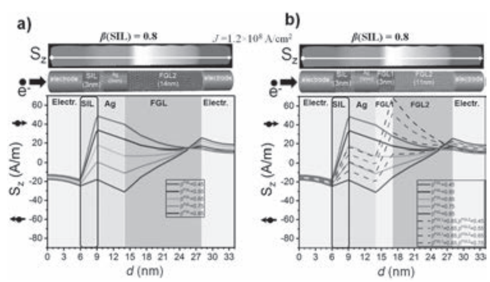

Fig. 2. All-in-plane mag-flip STO device magnetized OOP upon applying 1T external magnetic field and spin accumulation in Z direction (S_z) for J = 1.2 × 10^8 A/cm^2 calculated line contour of S_Z from SIL toward FGL for different spin polarization of FGL for all-in-plane STO with (a) one FGL and (b) dual FGL.

INVITED PAPERS

10:00

EF-05. Magnetization Switching of a Co/Pt-Multilayer Perpendicular Nanomagnet Assisted by a Microwave Field with Time-Varying Frequency. ***(Invited)***

H. Suto[1], T. Kanao[1], T. Nagasawa[1], K. Mizushima[1] and R. Sato[1]
1. Corporate Research & Development Center, Toshiba Corporation, Kawasaki, Japan

Microwave-assisted magnetization switching (MAS) has been studied as a candidate write method in next-generation high-density magnetic recording [1-3]. Although large switching field reduction by MAS has been theoretically and experimentally demonstrated, generating a large microwave field from a write head is a key challenge in developing MAS-based drives. In addition, the microwave field amplitude required for MAS will increase as the media anisotropy increases for further increasing recording density. One way to realize MAS by a smaller microwave field is to utilize a varying-frequency (VF) microwave field. Because the resonance frequency of a perpendicular nanomagnet is not constant and decreases as the magnetization excitation evolves, applying a VF microwave field that follows the resonance frequency can induce larger magnetization excitation and enhance the MAS effect [4-8]. In this presentation, we experimentally study MAS of a Co/Pt perpendicular nanomagnet by applying a VF microwave field. The microwave field is generated by introducing a microwave signal to a waveguide fabricated near the nanomagnet. Figure 1(a) and 1(b) show the waveforms of microwave signals used to generate a constant-frequency (CF) and VF microwave field. The frequency of the CF microwave field is 12 GHz, and that of the VF microwave field changes from 12 to 0.02 GHz in a 10-ns time period. The frequency is confirmed by estimating the instantaneous frequency from the zero-cross intervals of the waveforms [Figs. 1(c) and 1(d)]. Figure 2(a) shows the result of CF-MAS. The switching field decreases as the microwave field frequency increases and abruptly increases at the critical frequency, which is typical MAS behavior. Figure 2 (b) shows the switching field of VF-MAS as a function of the start frequency of the VF microwave field. The end frequency is fixed to 0.02 GHz. Similar to CF-MAS, the switching field decreases as the start frequency increases and continues to decrease when the start frequency exceeds the critical frequency. The switching field, thus, becomes smaller than that for CF-MAS, showing that the MAS effect is enhanced. As further increasing the start frequency, the switching field abruptly increases and becomes almost the same as the minimum switching field of CF-MAS, which indicates the following. When the start frequency becomes too high, the frequency change rate becomes so fast that the magnetization cannot follow the frequency change, and the enhancement of MAS disappears. In this case, MAS occurs in the same manner as CF-MAS when the frequency decreases to the frequency at which CF-MAS occurs. The MAS behavior in a VF microwave field is qualitatively explained by the theory based on the macrospin model [9]. This work is supported by Strategic Promotion of Innovative Research and Development from Japan Science and Technology Agency, JST.

[1] C. Thirion, W. Wernsdorfer, and D. Mailly, Nature Mater. 2, 524 (2003). [2] J.-G. Zhu, X. Zhu, and Y. Tang, IEEE Trans. Magn. 44, 125 (2008). [3] S. Okamoto, N. Kikuchi, M. Furuta, O. Kitakami, and T. Shimatsu, J. Phys. D: Appl. Phys. 48, 353001 (2015). [4] K. Rivkin and J. B. Ketterson, Appl. Phys. Lett. 89, 252507 (2006). [5] S. Okamoto, N. Kikuchi, and O. Kitakami, Appl. Phys. Lett. 93, 142501 (2008). [6] Z, Wang and M. Wu, J. Appl. Phys. 105, 093903 (2009). [7] T. Taniguchi, Appl. Phys. Express 8, 083004 (2015). [8] K. Kudo, H. Suto, T. Nagasawa, K. Mizushima, and R. Sato, Appl. Phys. Express 8, 103001 (2015). [9] H. Suto, T. Kanao, T. Nagasawa, K. Mizushima, and R. Sato, submitted to Phys. Rev. Applied.

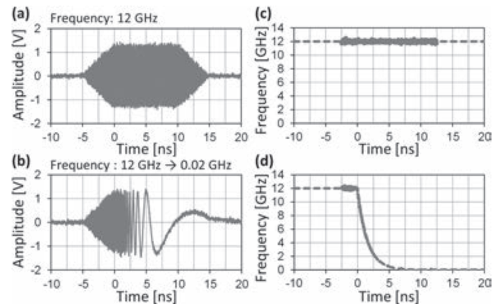

Fig. 1. (a) and (b) Waveform of CF and VF microwave signals. (c) and (d) Instantaneous microwave field frequency estimated from the zero-cross intervals of the waveform in (a) and (b).

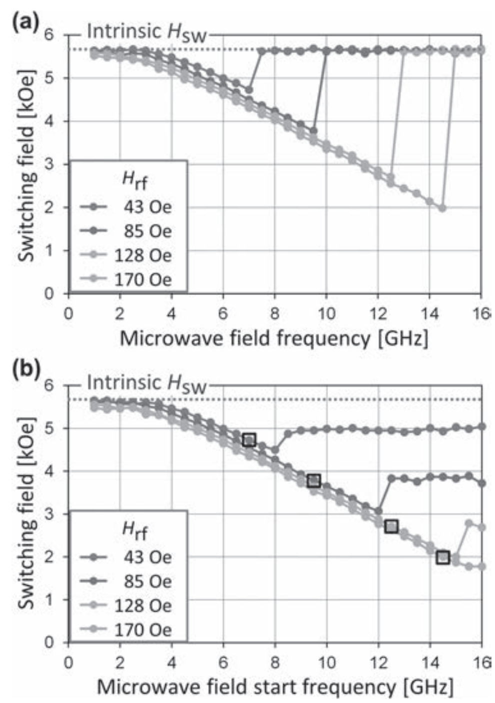

Fig. 2. (a) Switching field versus microwave field frequency for CF-MAS. (b) Switching field versus microwave field start frequency for VF-MAS. Squares show the critical frequency and the corresponding switching field in (a).

10:30

EF-06. Heat Assisted Magnetic Recording – Next Generation Mass Storage Technology.

G. Ju[1], J. Thiele[1], Y. Peng[1], T. Klemmer[1], Y. Ding[1], Y. Kubota[1], A.Q. Wu[1], X. Zhu[1], E.K. Chang[1], L. Gao[1], F. Zavaliche[1], P. Huang[1], H. Amini[1], S.D. Granz[2], C.J. Rea[3], J. Qiu[3], H. Yin[3], M.A. Seigler[3], T. Rausch[2], Y. Chen[3], E. Gage[3], S. Hwang[1] and M.E. Re[1]
1. Seagate Technology, Fremont, CA, United States; 2. Seagate Technology, Shakopee, MN, United States; 3. Seagate Technology, Bloomington, MN, United States

Magnetic hard disk drives (HDDs) store over 90% of the world's digital data enabling the internet and economical access to data to power everything from social media to self-driving cars. Heat assisted magnetic recording (HAMR) is being developed as the next recording system for HDDs. HAMR will bring profound changes to the HDD components and architecture, incorporating laser diodes in an innovative plasmonic light delivery system into the recording heads, and novel nano-magnetic materials and layer architectures in the recording media [1]. Seagate demonstrated the promise of HAMR with a 1 -2 Tb/in^2 areal density demonstration [2,3] and the subsequent demonstration of a fully functional drive with more than 1000 write power-on hours [4, 5]. The significant progresses have been enabled by breakthroughs in media and head technology together with drive integration. With continuing development efforts in reliability and data density HAMR will serve the demand for economical hard disk drive storage solutions for the world's ever growing data. As announced in a recent blog, Seagate is now shipping HAMR units to select customers for integration tests, and will start shipping commercial HAMR products to key customers by the end of 2018 [6]. This paper will cover the key enablers for HAMR technology to support both high areal density and linear density, which will be critical for bringing a new "S" curve for the magnetic recording industry. It will also be discussed about the challenges and breakthroughs in fundamental magnetic properties for the recording layer and near field optical transducers, to support the extension of HAMR to around 4-5 Tbit/in^2.

1. W. A. Challener et al., "Heat-assisted magnetic recording by a near-field transducer with efficient optical energy transfer," Nature Photon.,vol.3, pp. 220–224, Mar. 2009. 2. A. Q. Wu et al., "HAMR areal density demonstration of 1+ Tbpsi on spinstand," IEEE Trans. Magn., vol. 49, no. 2, pp. 779–782, Feb. 2013. 3. S. Granz, W. Z. Zhu, C. Rea, G. Ju, J. U. Thiele, T. Rausch, and E. Gage, Digest of TMRC2017, August 2 – 4, 2017, Tsukuba, Japan. 4. T. Rausch et al., "Recording performance of a pulsed HAMR architecture," IEEE Trans. Magn., vol. 51, no. 4, Apr. 2015, Art. ID. 3000405 5. T. Rausch et al., "HAMR drive performance and integration challenges," IEEE Trans. Magn., vol. 49, no. 2, pp. 730–733, Feb. 2013. 6. M. E. Re, http://blog.seagate.com/intelligent/hamr-next-leap-forward-now/, Oct. 2017

CONTRIBUTED PAPERS

11:00

EF-07. Spin torque oscillator with in-plane magnetized spin-injection layer for microwave assisted magnetic recording.

W. Zhou[1], H. Sepehri-Amin[1], Y. Sakuraba[1], S. Kasai[1], S. Bosu[1] and K. Hono[1]
1. Research Center for Magnetic and Spintronic Materials, National Institute for Materials Science (NIMS), Tsukuba, Japan

Introduction: Energy assisted recording technologies have become indispensable for maintaining the continuous increase of the recording density of the hard disk drives. One of the promising candidates is the microwave assisted magnetic recording (MAMR). It allows us to record information on media with high magnetic anisotropy, by applying an additional ac magnetic field (h_{ac}) to induce the precessional motion of magnetic moments, which results in magnetization switching under a much smaller write head field. One critical component for MAMR is the spin torque oscillator (STO) that can generate large h_{ac}. The STO device consists of a perpendicularly magnetized spin-injection layer (SIL) and an in-plane field generating layer (FGL), mag-flip STO, was originally proposed for MAMR. [1] Previous studies using this design have shown the out-of-plane precession (OPP) mode of FGL for the generation of h_{ac}. [2, 3] However, some of the specifications of the STO device, *e.g.*, required currents, frequency and amplitude of h_{ac}, still do not fulfill the requirement for MAMR. Recently, another design for a STO device using an in-plane magnetized SIL with negligible magnetic anisotropy was proposed [4]. During the operation of the STO device, the trailing gap field is applied perpendicularly to the device to align the magnetization of SIL and FGL. As electrons flow from SIL to FGL, the spin torque scattered from FGL reverses the magnetization of SIL opposite to the trailing gap field, then an anti-damping torque can be applied to FGL to induce the OPP mode. In this study, we investigated the behavior of the STO device having an in-plane SIL with both experiment and micromagnetic simulation. We focused on the influence of the material of SIL to understand the SIL material parameters dependence on magnetization oscillation dynamics in FGL. Experimental procedures: The STO devices were microfabricated from epitaxial thin films grown on MgO (100) single crystalline substrates using magnetron sputtering. The stacking structures of the thin films were MgO (100) subs. // Cr (10 nm)/Ag (100 nm)/SIL (3 nm)/Ag (3 nm)/FGL (7 nm)/ Ag (5 nm)/Ru (8 nm), where full Heusler alloy $Co_2Fe(Al_{0.5}Si_{0.5})$ (CFAS) or $Fe_{67}Co_{33}$ (FeCo) were used as SIL while FeCo was used for FGL. Since CFAS has a half-metallic nature, it is interesting to compare the oscillation properties of STO with CFAS-SIL and FeCo-SIL to understand the effect of spin-polarization (β). Using electron-beam lithography and Ar ion milling, STO devices having a circular-shape pillar with the diameter of 100 nm were microfabricated. For characterization of the STO devices, electrical transport measurements were performed using a DC four-probe method. The STO devices were connected to a source meter and a nanovolt meter while placed in a Physical Properties Measurement System for field (H) and temperature control. Micromagnetic simulation was carried out using *magnum.fe*, [5] which can calculate the coupled dynamics of magnetization and the spin accumulation simultaneously. A 30 nm-diameter circular pillar with 3 nm SIL, 5 nm spacer and 14 nm FGL was modeled and calculated. Results: Under low current of 0.1 mA, the devices with SIL of CFAS and FeCo showed ordinary MR curves under perpendicular H, with MR ratio of 5.7% and 4.0%, respectively. Under large current above around 8 mA with electrons flowed from SIL to FGL, a clear increase of resistance into an intermediate resistance state (IRS) was observed for both devices under large H, where both SIL and FGL were aligned toward the direction of H under low current. The IRS was observed under positive and negative H, and expanded on both sides towards high and low H when the current increased (Fig. 1 (a)); however, the IRS was not observed when electrons flowed from FGL to SIL. Such behavior was qualitatively reproduced by micromagnetic simulation, which showed that the IRS was due to the reversal of SIL, while FGL underwent the OPP mode. Using micromagnetic simulation, we also investigated the influence of β of SIL, which showed higher β led to higher current for reaching IRS. To verify this, we carried out the electrical transport measurements at 10 K. The MR ratio of the device with SIL of CFAS increased up to 10.4%, which is attributable to the increase of β of CFAS. On the other hand, no IRS was observed until the current was increased up to around 18 mA (Fig. 1 (b)). This result is consistent with simulation, suggesting that materials with lower β as SIL lead to lower critical current density for SIL magnetization reversal.

[1] J. G. Zhu, X. Zhu, and Y. Tang, *IEEE Trans. Magn.* 44, 125 (2008). [2] S. Bosu, H. Sepehri-Amin, Y. Sakuraba, M. Hayashi, C. Abert, D. Suess, T. Schrefl, and K. Hono, *Appl. Phys. Lett.* 108, 072403 (2016). [3] S. Bosu, H. Sepehri-Amin, Y. Sakuraba, S. Kasai, M. Hayashi, and K. Hono, *Appl. Phys. Lett.* 110, 142403 (2017). [4] J. G. Zhu, 2016 Joint MMM-Intermag, AB11. [5] C. Abert, M. Ruggeri, F. Bruckner, C. Vogler, G. Hrkac, D. Praetorius, and D. Suess, *Sci. Rep.* 5, 14855 (2015).

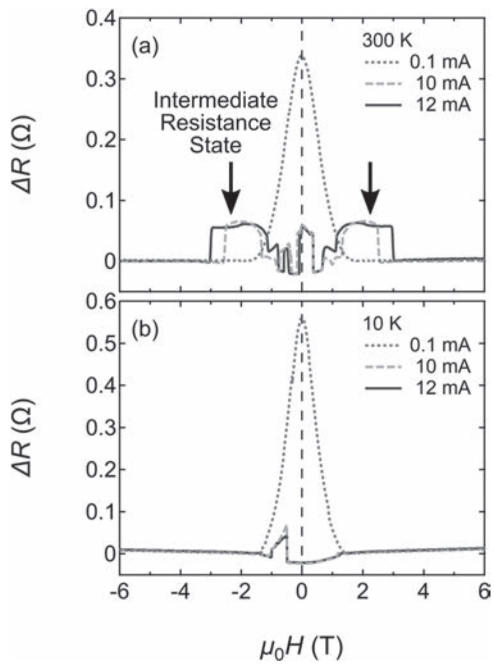

Fig. 1. MR curves of the STO device with CFAS-SIL (a) at 300 K, and (b) at 10 K. The black arrows indicate the emergence of the intermediate resistance state corresponding to the SIL magnetization reversal.

11:15

EF-08. Systemic Evaluation of Microwave Assisted Magnetic Recording.

Z. Liu[1], P. Huang[2], S. Hernandez[1], G. Ju[2], T. Rausch[1] and E. Gage[1]
1. Seagate Technology, Shakopee, MN, United States; 2. Seagate Technology, Fremont, CA, United States

Microwave Assisted Magnetic Recording (MAMR) is a type of energy assisted recording technology that uses microwaves to assist in the recording process. This allows for the use of high anisotropy media to maintain good thermal stability at high areal densities [1]. In MAMR, a spin torque oscillator (STO) is placed between the main pole and trailing shield to generate a magnetic field at microwave frequencies. The magnetic recording trilemma [2] is overcome by reducing the coercive field of the media via this microwave field, thereby aiding in the switching of media grains. Appropriate media stack configurations for MAMR and STO optimization have been investigated by both analytical theory and micromagnetic simulation [3], [4], [5]. In this paper, MAMR performance is evaluated on a reference design using our MAMR micro-magnetic model and the results are reported using EWSNR metrics [6]. In this study, we compare performance metrics for MAMR with other recording technologies such as Perpendicular Magnetic Recording (PMR) and Heat Assisted Magnetic Recording (HAMR). Recording media dynamics are modeled using the Landau-Lifshitz-Gilbert (LLG) equation for PMR and MAMR, and utilizing the renormalized LLG method for HAMR [7]. The DC magnetic write field is a current generation PMR writer design with 55 nm physical pole width and 1.0 T peak field strength. The STO stack has an optimized geometry that applies a 3D circularly polarized AC field to the media. STO field strength (~0.1Hk) and oscillating frequency (~35 GHz) are determined by the magnetic properties of the field generation layer (FGL) and the magnitude of the injected spin current. The magnetic head to media spacing (HMS) is fixed at 6.0 nm and head velocity is modeled to be 20 m/s. For MAMR, single layer media with varying anisotropy are considered. The PMR ECC multilayer media model, which is calibrated based on current PMR products, contains multiple magnetic layers and non-magnetic break layers that provide optimal exchange coupling. The HAMR media is a single layer $L1_0$ FePt media with a Curie temperature distribution of 3% and anisotropy field distribution of 10%. The down track thermal gradient used in the HAMR model is around 8K/nm, which is consistent with common near field transducer designs. The average media grain size is around 8.0 nm with 17% grain size distribution. A magnetoresistive reader with 30 nm width is used for obtaining the play back signal. Magnetic information is encoded using pseudo random bit sequences (PRBS), which mimic real user data. Figure 1 shows a comparison between PMR, HAMR and MAMR with thick free layer designs in terms of common performance metrics. Ensemble waveform analysis is used to calculate the total spatial SNR, the breakdown between transition and remanence SNR contributions, and the channel bit density (CBD) [6]. Bit error rate (BER) is calculated using a pattern dependent Viterbi detector [8]. The use of an NFT in HAMR allows the recording of much narrower tracks than PMR, with similar CBD and reasonable SNR and BER. In general, MAMR exhibits a large CBD, which may be related to intersymbol interference and track edge erasure caused by the demagnetization field. This high CBD results in much worse BER than both HAMR and PMR at all track width and linear density combinations considered. For the same ADC (shown in the last two table items in figure 1), SNR and BER are much better when the linear density is higher and the track width is larger. Since track edge demagnetization effects seem to have such a large effect in MAMR, this data suggests MAMR should aim to increase ADC via higher linear density and lower track density. For thick free layers, multi domains and multi-scattering contributions to electron's propagation can greatly deteriorate STO performance. Therefore, SNR versus recording media Hk for MAMR with thin free layer designs below 15 nm and STO width of 40 nm is shown in Figure 2. The figure suggests an optimal for MAMR media of around 25 kOe. MAMR SNR degradation at 20 kOe is due to erasure effects for low Hk material [9]. For high anisotropy media ~30 kOe, the transition SNR is reasonable (around 12 dB), but remanence noise is high, causing a 2 dB loss in total SNR.

[1] J.-G. Zhu, X. Zhu, and Y. Tang, "Microwave assisted magnetic recording," IEEE Trans. Magn., vol. 44, no. 1, pp. 125-131 (2008). [2] H. J. Richter, "The Transition from Longitudinal to Perpendicular Recording," J. Phys. D: Appl. Phys. 40 (2007). [3] S. Okamoto, M. Igarashi, N. Kikuhi, and O. Kitakami, "Microwave assisted switching mechanism and its stable switching limit," J. Appl. Phys. 107, 123914 (2010). [4] K. Rivkin, M. Benakli, N. Tabat and H. Yin, "Physical principles of microwave assisted magnetic recording," J. Appl. Phys. 115, 214312 (2014). [5] M. Mallary, K. Srinivasan, G. Bertero, D. Wolf, C. Kaiser et. al. "Head and media challenges for 3Tb/in^2 microwave-assisted magnetic recording," IEEE Trans. Magn. vol. 50, no. 7 (2014). [6] S. Hernandez, P-L. Lu, P. Krivosik, P.-W. Huang, W. Eppler, T. Rausch, and E. Gage, "Using Ensemble Waveform Analysis to Compare Heat Assisted Magnetic Recording Characteristics of Modeled and Measured Signals," IEEE Trans. Magn., vol. 52 (2016). [7] R. H. Victora and P.-W. Huang, "Simulation of heat-assisted magnetic recording using renormalized media cells," IEEE Trans. Magn., vol. 49, no. 2 (2013). [8] A. Kavcic and J.M.F. Moura, "The Viterbi Algorithm and Markov Noise Memory", IEEE Trans. Inf. Theory, vol. 46, no. 1 (2000) [9] X. Bai and J.-G. Zhu, "Medium stack optimization for microwave-assisted magnetic recording," IEEE Trans. Magn., vol. 53, no. 11 (2017).

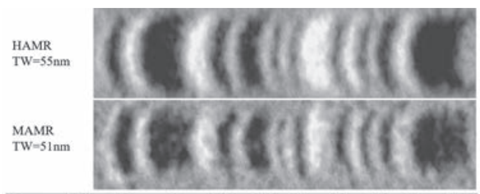

System	Media Hk (kOe)	STO width (nm)	FL Thickness (nm)	KFCI	TW (nm)	SNR (dB)	tSNR (dB)	rSNR (dB)	CBD	BER
PMR-ECC	16	--	--	2540	75	13.7	14.1	18.1	2.40	-2.35
HAMR-FePt	60	--	--	2540	55	11.3	11.7	15.2	2.30	-1.88
MAMR	20	40	20	2540	75	8.11	8.28	10.6	2.96	-1.01
MAMR	25	40	20	2540	65	11.2	11.5	13.3	2.73	-1.39
MAMR	30	45	20	3000	51	10.8	11.1	12.5	2.69	-1.18
MAMR	30	35	30	2540	42	9.23	10.6	10.8	--	-1.29

Fig. 1. systemic performance of PMR, HAMR and MAMR

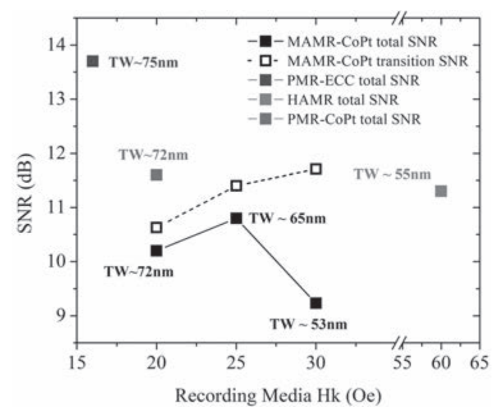

Fig. 2. SNR comparison between MAMR (thin free layer design ~15 nm), PMR and HAMR.

THURSDAY MORNING, 26 APRIL 2018 PEONY III, 9:00 TO 12:00

Session EG

SHIELDING, ELECTROMAGNETIC COMPATIBILITY, MOTORS AND GENERATORS I

Shunsuke Ohashi, Chair
Kansai University, Osaka, Japan

CONTRIBUTED PAPERS

9:15

EG-02. Fast Surrogate-Assisted Design of Multilayered Magnetic Shields.

H. Chen[1,2], Y. Du[2] and Q. Cheng[1]
1. Department of Electrical and Electronic Engineering, Southern University of Science and Technology, Shenzhen, China; 2. Department of Building Service Engineering, The Hong Kong Polytechnic University, Hong Kong, Hong Kong

Abstract — This paper presents a surrogate-assisted optimization process to design multilayer magnetic shields. The method builds the surrogate of the original problem to reduce the time consuming 3D calculation. Response surface approximation (RSA) is applied to construct a surrogate from a physics-based model. Evaluation time of the surrogate is negligible. The optimum design found by the surrogate is then refined using space mapping technique to give the location of the optimum design of the original model. The method is applied to optimize a double shield to demonstrate its efficiency. *Index Terms— magnetic shielding; surrogate; space mapping*. I. Introduction Planar multilayer shield is superior than the single-layer counterpart of equal thickness. Although the calculation of the shielding effectiveness of multilayered structures has been widely investigated, the problem of designing such shielding structures is not well addressed. Meanwhile, the high ratio of width to thickness of a planar shield leads to dense mesh in the calculation. The optimization process will be time consuming due to the fundamental challenge of the high computational cost of high-fidelity simulations on such 3D structures. Therefore, we present a surrogate based optimization (SBO) [1] to accelerate the design process of the planar multilayer shields. Its biggest advantage is the fact that because the surrogate embeds system-specific knowledge, usually a small number of high-fidelity simulations are sufficient to configure a reliable optimization. For demonstration of its efficiency, this approach is developed to optimize a double shield with aluminum and iron materials. II.Design Optimization Methodology The multilayered shield design problem R_f, here we call it a "fine model", can be formulated as a non-linear minimization problem of the form x_f = arg min $U(R_f(x))$ where U is a given objective function. $R_f : X_f \rightarrow R^m$, $X_f \subseteq R^n$, denotes the response vector of the fine model, x are designable variables. is the optimal solution to be determined. To accelerate the optimization process, an approximated physics-based "coarse model" R_c is constructed in the first step, where $R_c : X_c \rightarrow R^m$, $X_c \subseteq R^n$, denote the coarse model response vector. Thus, the optimization problem is approximated by x_c = arg min $U(R_c(x))$ However, it is still relatively expensive. Therefore, Instead of optimizing the coarse model directly, we built its surrogate for optimization. The process can be described as $x_c \approx x^{(i+1)}$ = arg min $U(s^i(x))$ where $x^{(i)}$, i = 0, 1,..., is a sequence of approximate solutions to the original problem, $s^{(i)}$ is the surrogate at the ith iteration. Response surface approximation (RSA) model (q) is then employed to build the surrogate. Its evaluation time is negligible. Obtained optimal design $x^{(i+1)}$ gives a good approximation of the location of the coarse model optimum. However, in order to include the unavoidable misalignment between and, the RSA model (surrogate) needs to be further refined using space mapping [2]. $q^{(i)}(x) = A^{(i)}R_c(B^{(i)}x+c)+d^{(i)}$ Thus, the surrogate is updated by solving. The optimum of the fine model then can be obtained using the updated surrogate. III.Numerical Simulation Results Consider a planar double shield with total thickness of 5 mm as shown in Fig. 1. The shield is composed of plates of aluminum and iron with thicknesses of d_1 and d_2, respectively. Both plates have the dimensions of 2 m × 2 m. A rectangular loop source is located 200 mm below the shield. The source loop carries a current of I_{rms} = 200 A and f = 50 Hz. The measured lines at the height of 300 mm above the shield. The design aims to find the optimal shield with the lowest magnetic field in the shielding area. The design variables are $x = [d_1, d_2]^T$ with the constrains $d_1 + d_2 \leqq 5$ mm. The fine model R_f is simulated in 3D ANSOFT MAXWELL. The coarse model R_c is also simulated in the same software, while, in a 2D solution. It is obvious that 2D simulation is more efficient while less accurate than 3D solution. The optimum of the surrogate = $[2.3, 1.1]^T$ was obtained using 24 evaluations of coarse model. The refined design = $[1.8, 1.0]^T$ was obtained by the refinement using SM. Only one evaluation of the fine model is needed through the whole process. In order to show the advantages of the proposed optimization procedure, the shield was designed with R_f directly using pattern search. However, direct optimization of the find model failed without finding the optimum. Acknowledgment The work was supported by grants from the RGC of HKSAR, No. 152038/15E, and NSF of China, No. 61471258.

[1] A. I. J. Forrester, A. Sbester, and A. J. Keane, *Engineering design via surrogate modelling: a practical guide*. John Wiley & Sons, 2008. [2] Q. S. Cheng, S. Koziel, and J. W. Bandler, "Simplified space-mapping approach to enhancement of microwave device models," *International Journal of RF and Microwave Computer-Aided Engineering,* vol. 16, no. 5, pp. 518-535, 2006.

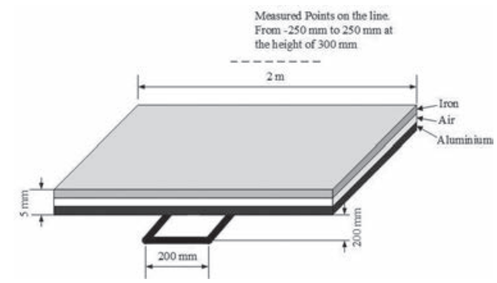

Fig. 1. Configuration of the simulated multilayer shield.

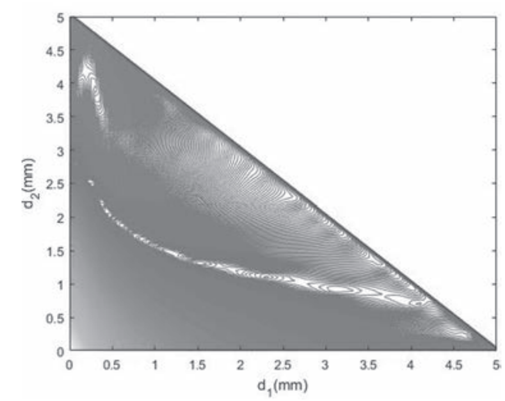

Fig. 2. The contour plot of the location of the minimum magnetic flux verse plate thickness for coarse model.

9:30

EG-03. Research on Common Mode Current and Electromagnetic Radiation in PWM Motor System.

F. Niu[1,2], S. Cao[1], X. Huang[2], J. Zhang[2], J. Ma[2], K. Li[1] and Y. Fang[2]
1. School of Electrical Engineering, Hebei University of Technology, Tianjin, China; 2. College of Electrical Engineering, Zhejiang University, Hangzhou, China

I. INTRODUCTION In recent years, the switching performance of power devices have improved significantly, and the switching frequency of power inverter in pulse width modulated (PWM) motor system becomes higher and higher. As a result, the electromagnetic interference (EMI) problem in PWM motor system becomes more and more serious. In PWM motor system, EMI can be divided into two main parts: common mode current (CMC) and electromagnetic radiation (EMR). CMC is mainly caused by the large du/dt of common mode voltage (CMV) during inverter switching transition which will charge and discharge the distributed capacitance in motor system. The high frequency CMC will further generate EMR which is distributed around motor system. The CMC and EMR have long been known to cause a variety of problems. In order to reduce the CMC and EMR in motor system, lots of research work have been done in hardware topology modification and software control strategy optimization [1]-[5]. But very few papers have focused on the amplitude-frequency characteristic research of CMC and EMR. In this paper, the generation mechanism of CMC and EMR is illustrated, and the main influencing factors of CMC and EMR are theoretically analyzed and experimentally verified, which lays theoretical foundation for the CMC and EMR suppression in PWM motor system. II. GENERATION MECHANISM AND INFLUENCING FACTORS OF CMC AND EMR In PWM motor system, the outputted CMV of inverter is equal to the mean value of three-phase instantaneous voltage. For a two-level three-phase inverter, there are eight candidate vectors and the corresponding CMV are different. The CMV caused by zero vectors are higher than caused by active vectors, which is the reason why some papers propose nonzero vector PWM method to reduce CMV and CMC. The variation of CMV can charge and discharge the distributed capacitance, which results in the CMC and its complexity flowing paths. The RMS value of CMC can be roughly calculated according to the voltage-current equation of equivalent capacitance in motor system, and the value of CMC is related to three main factors: the value of equivalent capacitance, the DC bus voltage and the switching frequency of inverter. 1. The value of equivalent capacitance The capacitance impedance is inversely proportional to the capacitance value and the frequency of passed signal. So, the larger the capacitance value, the greater the CMC flowing through. In addition, under the same capacitance, the high frequency components of CMV are easier to pass through because of the corresponding smaller impedance, which result in that CMC contains lots of high frequency components. 2. The DC bus voltage According to the capacitance voltage-current equation, the CMC flow through distributed capacitance is proportional to the changing rate of CMV during a single switching operation of power device. In general, the duration of switch on or off of power device can be considered as fixed as several microseconds. So, the CMC passing through distributed capacitance is indirectly related to the value of DC bus voltage. 3. The switching frequency of inverter There is a certain amount of CMC passing through distributed capacitance in a single switching operation of power device. So, the RMS value of CMC in a certain duration is decided by the number of switching operations of power devices which is equivalent to the switching frequency of inverter. Theoretically speaking, the higher the switching frequency, the greater the CMC RMS value. The high frequency and high amplitude CMC can generate strong EMR. Within a certain distance, the motor system can be treated as a lumped parameter circuit, and the intensity of EMR can be approximated calculated by Biot-Savart law. In addition, according to the principle of equivalent circuit, the flowing path of CMC can be represented as an RLC circuit, the series resonant frequency of equivalent RLC circuit changes with the variation of distributed capacitance in motor system. III. EXPERIMENTAL RESULTS A PWM motor system experimental platform is built to test the CMC and EMR, and Capacitance with different values are artificially added between phase line and ground to simulate distributed capacitance. The CMC is measured by a leakage current sensor and the EMR is measured by a spectrum analyzer with built-in omnidirectional antenna. Fig. 1 is the CMC experimental waveforms under various values of the three main influencing factors. Fig. 2 is the experimental results of CMC, EMR and resonant frequency under various values of main influencing factors. It can be obviously seen from Fig. 1 and Fig. 2 that, the RMS values of CMC and EMR changes with the variation of DC bus voltage, switching frequency of inverter and distributed capacitance. The fitting curves of CMC and EMR RMS values shown in Fig. 2 further reveals that the RMS values of CMC and EMR change linearly with the variation of these three main influencing factors. In addition, the resonant frequency of CMC flowing path also changes with the variation of distributed capacitance as shown in Fig. 2(d), which are same with the calculation results of equation (5). In general, the experimental results are consistent with the above theoretical analysis, which verifies the correctness of theoretical analysis. Because of space limitation, more theoretical analysis and experimental results will be included in the full paper.

[1] X. J. Pei, "Research of conducted electromagnetic interference in PWM inverter," *Huazhong University of Science & Technology*, Sep. 2004. [2] D. Han, W. Lee, S. L. Li, B. Sarlioglu, "New method for common mode voltage cancellation in motor drives: Concept, realization, and asymmetry influence," *IEEE Trans. Power Electron.*, vol. 33, no. 2, pp. 1188-1201, Feb. 2018. [3] H. Akagi, R. Kondo, "A transformerless hybrid active filter using a three-level pulse width modulation (PWM) converter for a medium-voltage motor drive[J]," *IEEE Trans. Power Electron.*, vol. 27, no. 8, pp. 42-48, Aug. 2012. [4] O. Magdun, A. Binder, "High-frequency induction machine modeling for common mode current and bearing voltage calculation," *IEEE Trans. Ind. Appl.*, vol. 50, no. 3, pp. 1780-1790, Oct. 2013. [5] C. T. Morris, D. Han, B. Sarlioglu, "Reduction of common mode voltage and conducted EMI through three-phase inverter topology," *IEEE Trans. Power Electron.*, vol. 32, no. 3, pp. 1720-1724, Mar. 2017.

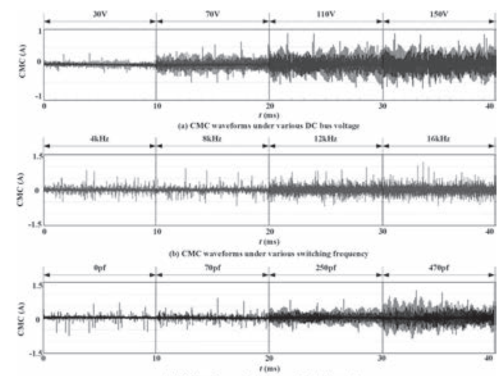

Fig. 1. CMC waveforms under various values of main influencing factors.

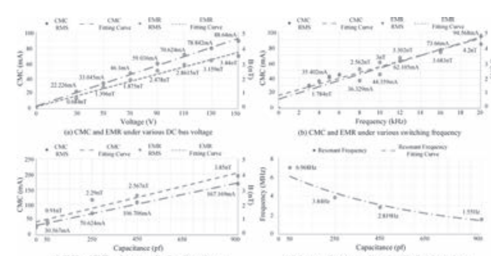

Fig. 2. CMC, EMR and resonant frequency under various values of main influencing factors.

9:45

EG-04. Dual Mode Dual Stator Wound Rotor Synchronous Machine for Variable Speed Applications.

A. Hussain[1], M. Ayub[1], T. Yazdan[1] and B. Kwon[1]
1. Electronic Systems Engineering, Hanyang University, South Korea, Ansan, The Republic of Korea

1. Introduction Electric vehicles and hybrid electric vehicles are being developed as a means to extenuate the environmental concerns. Permanent magnet (PM) machines have been used for such applications due to their high torque density, robust structure and no need for an external excitation system. However, the limited supply and increasing price of PM material create a need to search the alternative solutions such as the brushless wound rotor synchronous machines (BL-WRSM). Several brushless topologies for WRSMs have been presented in [1-3]. In [1] and [2], the brushless operation of WRSM is achieved by utilizing sub-harmonic and third harmonic components of stator MMF, respectively. In [3], the sub-harmonic component of stator MMF is generated by dividing the stator winding into two sets of series connected windings, which are then supplied through a single inverter. In the brushless topologies, the stator current is the only source of excitation and the field current is induced from the harmonic component of MMF. When the machine operates below the rated speed, the induction process slows down and the magnitude of the field current is gradually decreased with the decrease in the speed of the machine. Therefore, the torque in the constant torque region cannot be maintained constant by the BL-WRSM. However, at or above the rated speed these machines work properly. In this paper, a dual mode dual stator wound rotor synchronous machine (DMDS-WRSM) for variable speed applications is proposed. Through the dual mode (DM) machine operation, the constant torque and the constant power are achieved in the constant torque and constant power region, respectively. However, the dual stator design has been chosen to improve the torque density of the machine as compared to the torque density of the single stator BL-WRSM presented in [3]. A 2-D finite element analysis is performed to validate the proposed DMDS-WRSM. 2. Proposed Topology and Operation Principle The topology for the proposed machine is shown in Fig.1(a). The winding of each stator is divided into two sets of series connected windings; winding ABC and a centrally tapped winding XYZ and both the windings have an equal number of turns. The winding of inner and outer stator is connected in series and supplied through a single inverter. The winding XYZ is tapped at the center point by using switches. There are two separate windings on the rotor i.e. harmonic winding and the field winding. Both windings are connected through a bridge rectifier mounted on the rotor periphery. The field winding is also connected to the slip rings so that it can be supplied through the external dc voltage source when needed. There are two modes of operation of the proposed topology as shown in Fig. 1(b) and 1(c). In mode-I: the switches S1 to S4 are in open state and the three-phase sinusoidal current is supplied to the stator winding through the inverter. The field winding is connected to the external dc supply by closing the switch S5. In this mode, the proposed topology is operating as a brushed WRSM. Mode-I is proposed to achieve the constant torque in the constant torque region. In mode-II, the proposed topology is operating as a BL-WRSM. The switches S1 and S3 are closed to tap the winding XYZ at the center point, such that the number of turns in winding XYZ becomes half compared to that of winding ABC. On the other hand, switch S4 is closed to connect the field winding in parallel with the harmonic winding through a bridge rectifier. Meanwhile, the switch S5 is opened to disconnect the field winding from the external dc supply. The difference in the number of the turns in both windings is responsible for the generation of the sub-harmonic component of stator MMF (SH-MMF). This SH-MMF induces the voltages in the harmonic winding, which is then rectified to supply the dc current to the field winding of the machine. The proposed topology is verified by designing an 8-pole, 48-slot machine. It has two stators and a sandwiched rotor. An 8-pole, double layer distributed winding is configured on both the stators. Both the stators have two windings; winding ABC and winding XYZ and these windings are connected in series. The machine model and winding configuration are shown in Fig. 1(d). Two separate windings are placed on the rotor; harmonic winding and field winding. The harmonic winding has 4 poles, while the field winding has 8 poles. The 4-pole SH-MMF generated in the airgap couples with the 4-pole harmonic winding and induces the voltages accordingly. 3. Simulation Analysis 2-D finite element analysis is performed on 8-pole 48-slot machine shown in Fig. 1(d). Fig. 1(e) shows the torque of the mode-I operation. The Fig. 2(a) shows the induced current in the harmonic winding and the rectified current in the field winding, during the mode-II. The average torque in mode-II of the proposed topology is shown in Fig. 2(b). The proposed topology is suitable for variable speed application due to its DM operation and it exhibits 20.24% higher torque density as compared to the BL-WRSM proposed in [3]. However, the use of switches makes this topology complex compared to the existing topologies. Figure 2(c) summarizes the performance comparison of the proposed DMDS-WRSM with the conventional WRSM. Detailed analysis of the proposed topology will be presented in the full paper.

[1] Qasim Ali, Thomas A. Lipo, Kwon, Byung-il "Design and Analysis of a Novel Brushless Wound Rotor Synchronous Machine*" IEEE Trans. on Magn.,vol. 51, no. 11, Nov. 2015, Art. ID 8109804* [2] G. Jawad, Q. Ali, T. A. Lipo and B. I. Kwon, "Novel Brushless Wound Rotor Synchronous Machine with Zero-Sequence Third-Harmonic Field Excitation," in *IEEE Transactions on Magnetics*, vol. 52, no. 7, pp. 1-4, July 2016 [3] Hussain Asif, and Kwon, Byung-il "A new brushless wound rotor synchronous machine using a special stator winding arrangement." Electrical Engineering (2017): 1-8

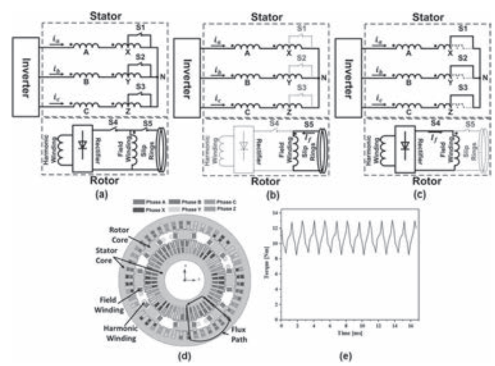

Fig. 1. (a) Proposed topology (b) Mode-I (c) Mode-II (d) DMDS-WRSM structure (e) Torque in mode-I operation

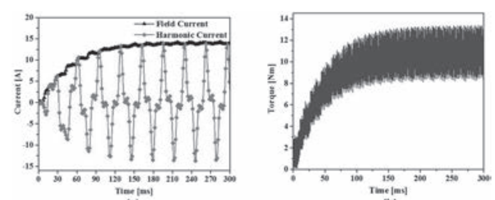

Table 1 Performance comparison

Parameter	Conventional WRSM		Proposed DMDS-WRSM	
	Brushed WRSM	BL-WRSM	Brushed WRSM	BL-WRSM
Torque, Nm	7.88	7.83	9.88	9.82
Torque ripple, %	16.9	18.2	43.5	49.5
Torque density, Nm/kg	2.6	2.58	3.28	3.26

(c)

Fig. 2. (a) Induced rotor currents in mode-II (b) Torque in mode-II operation (c) Performance comparison

10:00

EG-05. Radial Force and Vibration Calculation for Modular Permanent Magnet Synchronous Machine with Symmetrical and Asymmetrical Open-circuit Faults.

Y. Pei[1], Z. Song[1], *F. Chai*[1] and Y. Li[1]
1. Harbin Institute of Technology, Harbin, China

I. INTRODUCTION The vibration characteristic of Permanent Magnet Synchronous Machines (PMSMs) has become a research hotspot in recent years especially for those applied in demanding working situations with respect to fault tolerance [1, 2]. To reduce the possibility of failures, fault-tolerant topology such as modular three-phase structure is widely used [3]. For modular three-phase PMSM, there are special fault conditions such as symmetrical and asymmetrical open-circuit faults. Obviously, they will have a negative impact on the motor's vibration characteristic with additional harmonics and unbalanced magnetic pull to be significant due to structural and electrical asymmetries. Researches on this problem are quite limited. In this paper, the theoretical analysis of the air-gap magnetic field and radial force density under open-circuit fault is presented based on the modification of armature magnetomotive force (MMF). The simulation results under symmetrical and asymmetrical open-circuit faults by Finite Element Analysis (FEA) verify the theoretical ones. Multi-physics model for the stator system is built to determine the inherent properties and vibration characteristics. The investigations help analyze and mitigate the modular machine's vibration dealing with fault conditions in the engineering practice. II. THEORETICAL ANALYSIS The air-gap radial force, which is the main source of electromagnetic vibration, can be obtained from the air-gap magnetic fields. The difference of air-gap magnetic fields between normal and open-circuit fault conditions starts from the stator armature MMF. Suppose phase A winding is open. The resulting armature MMF harmonic of the three-phase winding can be expressed as (1). $f_v(\alpha, t) = F_{v1}\cos(\omega t\text{-}vp\alpha) + F_{v2}\cos(\omega t\text{+}vp\alpha)$ (1) For the harmonic orders $v = 6k+3 = 3, 9, 15,...$, $F_{v1} = F_{v2} = -F_{\Phi v}/2$; for the harmonic orders $v = 6k+1 = 1, 7, 13,...$, $F_{v1} = F_{\Phi v}$, $F_{v2} = -F_{\Phi v}/2$; for the harmonic orders $v = 6k-1 = 5, 11, 17,...$, $F_{v1} = -F_{\Phi v}/2$, $F_{v2} = F_{\Phi v}$. Here, $F_{\Phi v}$ is the magnitude of vth single-phase MMF; ω is the current angular frequency; α is the electrical degree. Note that there are no even harmonic orders in the MMF. To simplify the calculation, we consider only the average and the first tooth harmonic components of the air-gap permeance. Then the magnetic field and the radial force density along the air-gap can be derived according to the Maxwell stress tensor theory. During open-circuit condition, additional harmonic orders are (0,2*f*) generated by the armature magnetic fields, (2*p*, 0*f*) and (Z-2*p*, 0*f*) generated by the interaction of armature and PM fields. III. FEA SIMULATION The simulation results of the air-gap magnetic fields and the radial force density are obtained based on a 16p24s modular PMSM with four individual units. As is illustrated in Fig. 1, when two individual phase windings in non-adjacent units are open, it is called symmetrical fault; when two windings in adjacent units are open, it is called the asymmetrical fault. The radial force density distribution of the faulty unit is consistent with theoretical analysis. The radial force density harmonic contents under the two open faults are quite different, which is shown in Fig. 2. Secondary harmonics with frequencies of 0 and 2*f* appear in both the two fault conditions, and the low-order harmonic components of asymmetrical fault tend to be concentrated, while those of symmetrical fault tend to be dispersive. IV. VIBRATION CHARACTERISTICS Through 3-D model of stator system in structural field, including stator core, concentrated windings and frame, the inherent properties of the stator system can be analyzed through modal analysis. We take several test nodes on the frame circumference to get the instantaneous acceleration waveform and frequency response. The frequencies of acceleration peaks in the low frequency band mainly appear at 2*f* = 533Hz and 6*f* = 1600Hz. Open-circuit fault enlarges the acceleration amplitudes and asymmetrical fault makes the distribution more unbalanced. V. CONCLUSION This paper investigates the radial force and vibration for modular three-phase PMSM under symmetrical and asymmetrical open-circuit faults. The expressions of the MMF, air-gap magnetic fields and radial force density under open-circuit fault are first derived theoretically. The FEA simulation compares the radial force density under the two fault conditions. The results agree well with theoretical analysis. Acceleration response at low frequency band especially 2*f* is quite severe and asymmetrical fault makes the radial acceleration distribution more unbalanced.

[1] Han S H, Jahns T M, Zhu Z Q. Analysis of rotor core eddy-current losses in interior permanent-magnet synchronous machines[J]. IEEE Transactions on Industry Applications, 2010, 46(1): 196-205. [2] Foo G H B, Zhang X, Vilathgamuwa D M. A sensor fault detection and isolation method in interior permanent-magnet synchronous motor drives based on an extended Kalman filter[J]. IEEE Transactions on Industrial Electronics, 2013, 60(8): 3485-3495. [3] Ouyang W, Lipo T A. Modular permanent magnet machine with fault tolerant capability[C]. Applied Power Electronics Conference and Exposition, 2009. APEC 2009. Twenty-Fourth Annual IEEE. IEEE, 2009: 930-937.

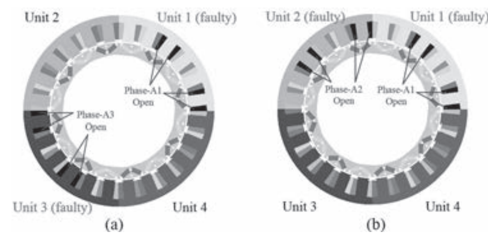

Fig. 1. Open-circuit fault conditions of modular PMSM (a) symmetrical; (b) asymmetrical.

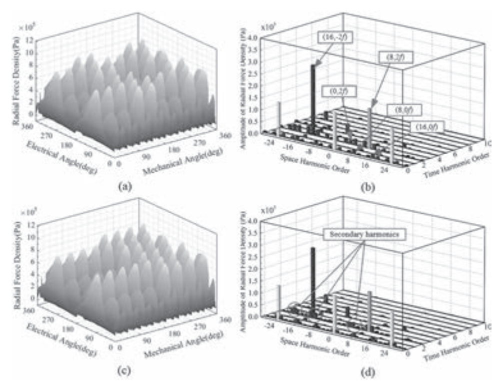

Fig. 2. Radial force density and harmonic analysis (a) waveform under symmetrical fault; (b) harmonics under symmetrical fault; (c) waveform under asymmetrical fault; (d) harmonics under asymmetrical fault.

10:15

EG-06. Weighted Average Efficiency Optimization for Permanent Magnet Synchronous Generators Used in Hybrid Electric Special Vehicles.

J. Gao[1], *L. Dai*[1] and W. Zhang[2]
1. College of Electrical and Information Engineering, Hunan University, Changsha, China; 2. Department of Electronic and Electrical Engineering, Changsha University, Changsha, China

I. Introduction In recent years, permanent magnet synchronous generators (PMSG) have been widely used in hybrid electric special vehicles (HESV) due to their high efficiency, power density and reliability [1]-[6]. But the output power of PMSG for HESV (H-PMSG) changes in a wide range with the different operating environment, such as normal driving, climbing and accelerating [1]. Therefore, the traditional rated efficiency (RE) optimization method (OM) for PMSG can no longer work well in this application. The efficiency optimization for PMSG has been discussed in many literatures. The efficiency characteristics of H-PMSG were analyzed under varied conditions [2]. In [3], the losses and efficiency in wide speed range for H-PMSG and switched reluctance generator were compared. The rotor structure of H-PMSG was optimized by Response Surface Methodology to reduce the vibration and noise under rated load [4]. The efficiency under rated load of H-PMSG were optimized by Particle Swarm Algorithm and Genetic Algorithm separately in [5] and [6]. This paper presents a new efficiency OM for H-PMSG with the weighted average efficiency (WAE) of the varied load ratios. The load ratio rule for H-PMSG in a driving cycle is investigated, and then the weighted coefficients for each load ratio (100%, 75%, 50% and 25%) are determined according to the operation time with the varied load ratios. Finally the optimization design by the genetic algorithm aiming at the weighted average efficiency is developed. Comparing with the traditional efficiency OM based on the rated load, the proposed method has significantly improved the global efficiency of H-PMSG and the overall fuel efficiency of HESV in the driving cycle. II. Model and Optimization The dimensions of the active parts can be obtained from the conventional magnetic circuit laws, which have been estimated to be sufficient for a preliminary generator design [7]. In this section, the analytic formulas for air-gap flux density B_g, no-load voltage E_0, stator currents I_1, losses p and efficiency η are deduced, which are made up of the analytic model of H-PMSG. In order to simplify the optimization process and save computation time, four typical load ratios of 100%, 75%, 50% and 25% are selected to match the whole load ratios in a drive period (an hour) of H-PMSG by the least square method. Therefore, the WAE for the four typical load ratios is defined as $\eta_{wa}=\alpha_1\eta_1+\alpha_2\eta_2+\alpha_3\eta_3+\alpha_4\eta_4/(\alpha_1+\alpha_2+\alpha_3+\alpha_4)$ (1) where η_1, η_2, η_3, and η_4 are the efficiency due to 100%, 75%, 50% and 25% load ratios separately, α_1, α_2, α_3 and α_4 are the weighted coefficients for the four typical load ratios. Seven variables are chosen to vary within a certain range, including the stator inner diameter, length of core, slot height, slot width, yoke height, length of air gap and PM thickness. The following constraints are used in the optimization program. The air-gap flux density is set to be 0.7-1.0*T*; the current density is limited to 5-7 A/mm^2; the current loading is limited to 60-70 *kA*/*m* due to the water cooling, and the slot filling factor is limited to 75%. The genetic algorithm is used for solving the efficiency optimization problems for H-PMSG. The objective function to maximize the WAE is as following maximize $\eta_{wa}(X)$ (2) where X is a vector of the optimal design variables. The feasibility of the design is guaranteed by adding a penalty to the objective function due to constraint violations. In each generation of the genetic algorithm, according to individual fitness value (i.e. the value of the objective function), referring to the transformation method of natural genetics to choose the individuals, the new individuals will be more adaptable to the environment than the original individuals, and then run over when the decision condition of the algorithm program is satisfied, Fig. 1(a) shows the block diagram of WAE optimization. III. Results and Prototype Verification A 500-*kW* H-PMSG with a constant speed of 4200 *r*/*min* has been chosen to demonstrate the developed electromagnetic design and the optimization models. The four weighted coefficients α_1, α_2, α_3 and α_4 are set to be 0.23, 0.32, 0.3 and 0.15 due to the actual operation conditions. It can be seen from Fig. 1(b) that the efficiency with WAE-OM are improved by 2.01%, 2.5% and 2.35% on 25%, 50% and 75% load ratios comparing to that with RE-OM, and is only decreased by 0.37% on full load ratio. The calculated input energy with WAE-OM is 340.9 *kWh*, which is reduced by 1.4% comparing to that of 345.8 *kWh* with RE-OM. Fig. 1 (c) shows that the active material weight with WAE-OM is 13.1% lower than that with RE-OM. In order to verify the results of the optimization, the prototype of 500kW-4200 *r*/*min* is manufactured. The experiment platform is shown in Fig. 2 (a). The prototype is dragged by an 800kW induction motor controlled on the constant rated speed, and the output power is consumed by a water resistance. The experimental and design efficiency on 25%, 50%, 75% and 100% load ratios of the prototype are shown in Fig. 2 (b), which shows that the experimental results are agreed well with those of the optimization design.

[1] K. T. Chau, C. C. Chan, and L. Chunhua, “Overview of permanent-magnet brushless drives for electric and hybrid electric vehicles,” *IEEE Trans*. *Ind*. *Electron*., vol. 55, no. 6, Jun. 2008, pp. 2246-2257. [2] Jorge O. Estima, Antonio J. Marques Cardoso, “Efficiency Analysis of Drive Train Topologies Applied to Electric/Hybrid Vehicles “ *IEEE Trans. Vehic. Tech.*, vol. 61, no. 3, Mar 2012, pp.1021-1031. [3] Katsuhiko Urase, Kyohei Kiyota, Hiroya Sugimoto, Akira Chiba, “Energy Efficiency of SR and IPM Generators for Hybrid Electric Vehicle,” *IEEE Trans. Ind. App.,* vol. 51, no. 4, 2015, pp.2874-2883. [4] Jae-Woo Jung, Sang-Ho Lee, et al, “Reduction Design of Vibration and Noise in IPMSM Type Integrated Starter and Generator for HEV,” *IEEE Trans. on Magn.*, vol. 46, no. 6, 2010, pp.2454-2457. [5] Tao Wang, Qingfeng Wang, “Optimization Design of a Permanent Magnet Synchronous Generator for a Potential Energy Recovery System, “ *IEEE Trans*. *Energy*. *Convers*., vol. 27, no. 4, 2012, pp.856-863. [6] Andreas Schmidhofer, Peter Pisek, et al, “Design aspects of low cost electric machines used for highly integrated starter-Generator Systems, “ 2013 World Electric Vehicle Symposium and Exhibition (EVS27), 2013, pp.1-7. [7]A. Grauers, “Design of direct-driven permanent-magnet generators for wind turbines, “ Ph.D. dissertation, Chalmers Univ. Technol., Goteborg, Sweden, 1996.

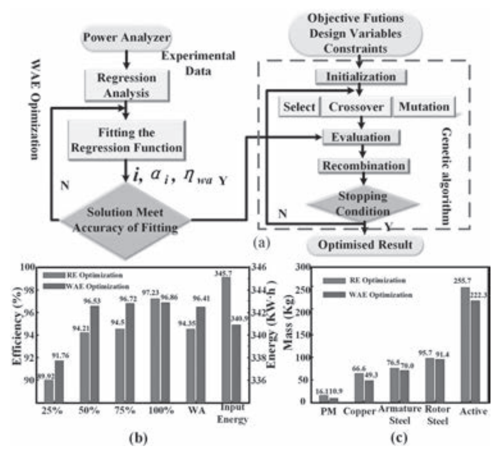

Fig. 1. WEA optimization process and results (a) Block diagram of WAE optimization (b) Comparison of efficiency optimization (c) Comparison of active material weight

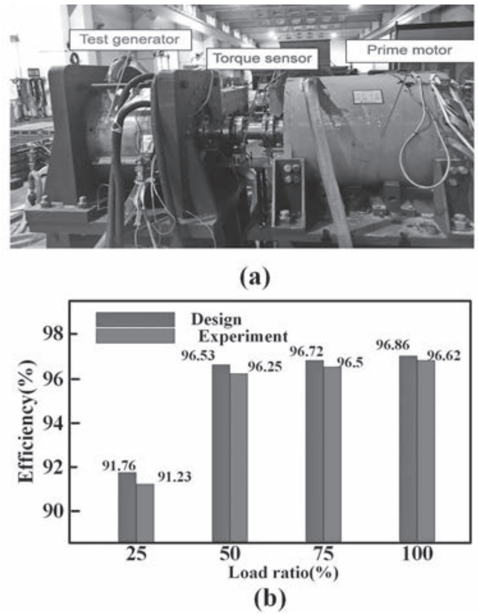

Fig. 2. Experiment of prototype (a) Experiment platform (b) Comparison of experimental and optimization efficiency

10:30

EG-07. Modeling Induction Motors under Mixed Radial-Axial Asymmetry of Air Gap Produced by Oil Whirl in a Sleeve Bearing.

M. Ojaghi[1] and R. Akhondi[1]
1. Electrical Engineering, University of Zanjan, Zanjan, The Islamic Republic of Iran

I. Introduction Squirrel cage induction motors (SCIMs) are widely used in modern industry due to their various merits; however, some faults may lead to their deterioration and economical losses. Several studies show that 40–50% of the motor failures are related to the bearing defects caused by many factors [1]. The SCIM bearings are of two main categories: rolling element bearings and sleeve bearings. Oil whirl fault (OWF) is a common faulty mode in the sleeve bearings and if not early detected and removed, leads to serious damage of the bearing [2-4]. The OWF usually happens in one bearing of the SCIM and introduces time-dependent mixed radial-axial asymmetry to the air gap distribution. This paper offers an analytical model for the SCIM with OWF in one of its sleeve bearings. Multiple coupled circuit model (MCCM) along with 2-D modified winding function theory (MWFT) are used for this purpose. The modeling and simulation results are in agreement with corresponding experimental results and show some harmonic components in the self-inductances of the stator windings. The most efficient harmonic is selected as the OWF index by further analysis performed using simulation under different fault severities, load levels and voltage unbalance conditions. II. Modeling Procedure Dynamic equations governing MCCM for Y-connected SCIMs are well defined in previous references [5]. Various self/mutual inductances of the SCIM are the main parameters of the equations. Due to rigid construction of the rotor, by happening oil whirl in a sleeve bearing, the OWF components will linearly change along the axial coordinate (z-axis) as follows: $OW_x(z) = (OW_x / L)z$ (1) $OW_y(z) = (OW_y / L)z$ (2) where OW_x and OW_y are the x and y components of the shaft vibration magnitude produced in the bearing location by the fault [2] and L is the distance between the two bearings of the motor. Using (1)-(2) and considering little inherent eccentricity as well, the coordinates of the rotor shaft center (C_x and Cy) versus the bearing center are determined as follows [2]: $C_x(\theta_r,z) = SE_x+DE\cos(\theta_r)+OW_x(z)\cos(k_{ow}\theta_r+\pi/6)$ (3) $C_y(\theta_r,z) = SE_y+DE\sin(\theta_r)+OW_y(z)\sin(k_{ow}\theta_r)$ (4) where k_{OW} is the oil whirl frequency ratio that is usually between 0.42 and 0.48 [3-4], θ_r is the rotor position angle, SE_x and SE_y are the inherent static eccentricity components in the x and y directions and DE is the inherent dynamic eccentricity degree. Then, the coordinates are changed to the polar form and used to define the air gap distribution function as follows: $R_c(\theta_r,z) = \sqrt{[C_x(\theta_r,z)^2 + C_y(\theta_r,z)^2]}$ (5) $\theta_c(\theta_r,z) = \tan^{-1}[C_y(\theta_r,z) / C_x(\theta_r,z)]$ (6) $g(\theta_s,\theta_r,z) = g_0 - R_c(\theta_r,z)\cos[\theta_s - \theta_c(\theta_r,z)]$ (7) where R_c and θ_c are the coordinates in the polar form, θ_s is the angle in the stator reference, $g(\theta_s,\theta_r, z)$ is the air gap distribution function and g_0 is the uniform air gap length in healthy condition. Using 2-D MWFT with this air gap function and ignoring the air gap mean radius variations, the mutual inductance between any x and y circuits of the SCIM is expressed as follows [5]: $L_{yx}(\theta_r) = \mu_0 r \iint[n_y(\theta_s,\theta_r) M_x(\theta_s,\theta_r,z) / g(\theta_s,\theta_r,z)]d\theta_s dz$ (8) where the inner and outer integrals are performed from 0 to 2π and along the stack length, respectuvely, $M_x(\theta_s,\theta_r,z)$ denotes 2-D modified winding function of circuit x, $n_y(\theta_s,\theta_r)$ denotes the turn function of circuit y, μ_0 is the air permeability and r is the air gap mean radius. Self-inductance of the circuit x is calculated by putting y=x in (8). Numerical techniques are used to solve the dynamic equations, where (8) is used to update the inductances values by varying the rotor position. III. Simulation Results A 510kW, 6kV, 50Hz, 2-pole SCIM is simulated under the healthy and OWF conditions. The simulation results, in accordance to the corresponding experimental results, approve the presence of the related harmonics in the stator line current due to the OWF [2]. However, the stator inductance fluctuation could be a more reliable index for the fault [6]. Fig. 1 shows time variation of the self-inductance of a stator phase winding (L_{aa}) during the motor startup in the healthy and OWF conditions. Inherent eccentricity is included in both cases. As seen, L_{aa} fluctuates slightly in the healthy condition due to the inherent eccentricity, while the OWF increases the magnitude and distorts the shape of the fluctuation. Fast Fourier transformation is applied to the time trend of L_{aa} during steady-state operation of the SCIM to show its harmonic content. Fig. 2 shows the attained results. As seen, in the healthy condition, L_{aa} includes a constant component at zero frequency and two harmonics at f_r (49.6 Hz) and $2f_r$ (99.2 Hz) frequencies produced by the inherent eccentricity (f_r is the rotor speed) [6]. The spectrum for the OWF condition includes new harmonics at $k_{ow}f_r$, $2k_{ow}f_r$ and $(1\pm k_{ow})f_r$ frequencies. Using an analytical approach, it is shown that the harmonics are introduced in the inductances by the air gap function (6). Therefore, the presence of $k_{ow}f_r$, $2k_{ow}f_r$ and $(1\pm k_{ow})f_r$ harmonics in the L_{aa} spectrum indicates the occurrence of the OWF. However, more detailed analysis show that $k_{ow}f_r$ harmonic is more robust against the load change and the voltage unbalance, while its magnitude is the highest and its frequency is the least, so, this harmonic is a more reliable index for diagnosing the OWF.

[1] J. Morales, and E. Hernandez, "Multiple-fault diagnosis in induction motors through support vector machine classification at variable operating conditions", Electr. Eng, pp. 12-23, 2016. [2] M. Ojaghi, and N. Yazdandoost, "Oil-whirl fault modeling, simulation, and detection in sleeve bearings of squirrel cage induction motors," IEEE Trans. Energy Conversion, vol. 30, no. 4, pp. 1537-1545, Dec 2015. [3] G. Oliver, "An introduction to oil whirl and oil whip," A Quarterly Publication from Turbo Components & Engineering, vol. 3, no. 2, 2001. [4] C. C. Fan, J. W. Syu, M. C. Pan, and W. C. Tsao, "Study of start-up vibration response for oil whirl, oil whip and dry whip," Mechanical Systems and Signal Processing, vol. 25, no. 8, pp. 3102-3115, 2011. [5] M. Ojaghi, and M. Mohammadi, "Unified modeling technique for axially uniform and non-uniform eccentricity faults in three-phase squirrel cage induction motors," IEEE Trans. Industrial Electronics, Accepted to be published. [6] J. Faiz, and M. Ojaghi, "Stator inductance fluctuation of induction motor as an eccentricity fault index," IEEE Trans. on Magnetics, vol. 47, no 6, pp. 1775-1785, Jun 2011.

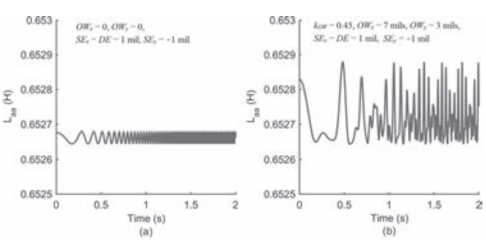

Fig. 1. Variation of L_{aa} with time during startup of the SCIM for: a) Healthy case with inherent eccentricity, b) OWF case with inherent eccentricity

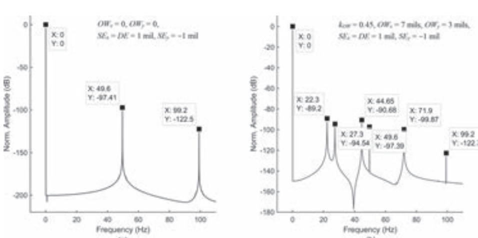

Fig. 2. Normalized spectra of L_{aa} for: a) Healthy SCIM with inherent eccentricity, b) SCIM with OWF and inherent eccentricity

10:45

EG-08. PM Vernier Machine with Multiple Working Harmonics and Enhanced Flux Modulation Effect.

T. Zou[1], D. Li[1] and *R. Qu*[1]
1. School of Electrical and Electronic Engineering, Huazhong University of Science & Technology, Wuhan, China

I. Introduction With ever improving performance of rare earth permanent magnet (PM) material, PM machines have been widely used. In recent years, PM vernier (PMV) machines have gained increasing attentions due to their inherently high torque density [1-2], and have become promising candidates in low speed, high power applications such as wind power and ship propulsion. Researches on PMV machines have been mainly focused on proposing novel topologies [3-6], evaluating performances [7-8] and establishing analytical theories [9]. For non-overlapping winding PMV machines, it has been found that through changing the flux modulation pole (FMP) pitch, i.e., configuring non-uniformly distributed FMPs, additional working field harmonics can be introduced [10]. Based on this research work, a novel spoke type PMV machine with multiple working harmonics and enhanced flux modulation effect is further proposed in this paper. Section II will be devoted to introduction of the machine topology and working principle. In Section III, the production of multiple working airgap field harmonics involved torque production will be analyzed, and an enhanced flux modulation effect will be introduced for the fisrt time. Finally, in the full paper, electromagnetic performances of the proposed machine will be further investigated and compared with several existing PMV machine topologies to demonstrate its superiority in torque density. Experimental test results on several prototypes will also be provided. II. Machine Topology and Configuration Basically, the rotor pole pair number P_r, stator pole pair number P_s and FMP number P_f of a PMV machine should satisfy $P_f=nZ=P_r \pm P_s$ where Z is the stator slot number for embedding windings. Pole ratio (PR), defined as P_r/P_s, is a special design parameter for PMV machines. Generally, the higher PR is, the stronger flux modulation effect and higher torque density it will be. The exploded view of the proposed PMV machine is shown in Fig. 1(b). This machine is constructed with a spoke type PM rotor and a stator wound with non-overlapping windings. It can be seen that the stator is designed with auxiliary teeth, which work as FMPs. More specifically, the pitch angle θ of FMPs connected to one main tooth is set unequal to the slot opening angle. Essentially, the proposed machine topology is developed from a regular spoke-type PMV machine with uniformly distributed FMPs as illustrated in Fig. 1(a). The parameter k is defined as flux modulator pitch ratio and calculated as $k=\theta/(2\pi/P_f)$. The slot-pole combination of the proposed machine is carefully chosen, i.e., $Z=6$, $P_f=18$ and $P_r=14$. Then, P_s is supposed to be 4 and PR=3.5. III. Operation Principle of Multiple Field Harmonics with Enhanced Flux Modulation Effect Due to the existence of FMPs, the airgap field of a PMV machine cannot directly couple the stator windings. In order to reveal the nature of the proposed machine, a corresponding integrated magnetic geared (MG) machine is designed for evaluation, as shown in Fig. 2. When the additional outer airgap gets infinitely small, the two machines in Fig. 2 will become exactly equivalent. Field evaluation in the outer airgap of the MG machine can give a better insight into the harmonics which are actually involved in back-EMF and torque production of a PMV machine. Essentially, the variation of the flux modulator pitch k changes the airgap permeance distribution and enriches the permeance harmonics. Then, the main produced flux density harmonics including the newly induced ones are summarized in Table II. All these harmonics are with the same spatial electrical angular speed, and can induce back EMF with exactly the same frequency. The FEA-obtained outer airgap flux density harmonics for k=1.0 and 1.2 are illustrated in Fig. 3. It can be clearly seen that the 2^{nd}, 8^{th}, 10^{th}, 16^{th}, and 20^{th} harmonics are newly produced flux density terms for the proposed PMV machine, while the originally existed 4^{th} and 14^{th} harmonics are weakened. Fig. 4 gives the fundamental back-EMF contribution of these field harmonics. It can be seen that for the regular case with k=1, the back-EMF is induced by only the 4^{th}, 14^{th} and 22^{th} harmonics, in which the 22^{th} harmonic actually weakens the fundamental back-EMF. Nevertheless, for the proposed PMV machine with k=1.2, there are multiple harmonics which work together for the back-EMF production. With the same PM usage, the total back-EMF is increased significantly by ~40% compared with the regular case. Among these newly produced harmonics, it is interesting to find that the lowest harmonic order has been changed from 4 to 2. Since the winding pole pair number P_s is decided by the lowest order of working harmonics, it has been reduced to 2, and the pole ratio is in fact doubled to 7. Hence, the flux modulation effect has been enhanced compared with that in [10]. It will be verified in the full paper taht this newly found enhanced flux modulation effect can boost the torque capability of PMV machine much more significantly than that in [10]. IV. Conclusion In this paper, a spoke type, non-overlapping winding PMV machine with multiple working flux density harmonics and enhanced flux modulation effect has been proposed. The proposed PMV machine is supposed capable of improving the torque density by ~50% compared with its regular counterpart. The detailed comparison between the proposed machine and corresponding counterparts will be given in the full paper through both FEA and experimental results, and the advantage of the proposed machine will be verified.

[1] A. Toba and T. A. Lipo, "Generic torque-maximizing design methodology of surface permanent-magnet vernier machine," *IEEE Trans. Ind. Appl.*, vol. 36, no. 6, pp. 1539–1546, Nov. 2000. [2] A. Ishizaki, et al., "Theory and optimum design of PM vernier motor," in *Proc. IEE Int. Conf. Electrical Machines and Drives '95*, 1995, pp. 208–212. [3] W. Zhao, X. Sun, J. Ji and G. Liu, "Design and analysis of new vernier permanent-magnet machine with improved torque capability," *IEEE Trans. Appl. Supercond.*, vol. 26, no. 4, pp. 1-5, June 2016. [4] J. Li, K. T. Chau, J. Z. Jiang, C. Liu and W. Li, "A new efficient Permanent-Magnet Vernier Machine for Wind Power Generation," *IEEE Trans. Magn.*, vol. 46, no. 6, pp. 1475-1478, June 2010. [5] S. Niu, S. L. Ho, W. Fu, and L. Wang, "Quantitative comparison of novel vernier permanent magnet machines," *IEEE Trans. Magn.*, vol. 46, no. 6, pp. 2032–2035, Jun. 2005. [6] D. Li, R. Qu and Z. Zhu, "Comparison of Halbach and Dual-Side Vernier Permanent Magnet Machines," *IEEE Trans. Magn.*, vol. 50, no. 2, pp. 801-804, Feb. 2014. [7] X. Li, K. T. Chau, M. Cheng, B. Kim and R. D. Lorenz, "Performance analysis of a flux-concentrating field-modulated permanent-magnet machine for direct-drive applications," *IEEE Trans. Magn.*, vol. 51, no. 5, pp. 1-11, May 2015. [8] C. Liu, K. T. Chau, J. Zhong, W. Li and F. Li, "Quantitative comparison of double-stator permanent magnet vernier machines with and without HTS bulks," *IEEE Trans. Appl. Supercond.*, vol. 22, no. 3, pp. 5202405, June 2012. [9] D. Li, R. Qu, J. Li, L. Wu and W. Xu, "Analysis of torque capability and quality in vernier permanent magnet machines," *IEEE Trans. Ind. Appl.*, vol. 52, no. 1, pp. 125-135. [10] T. Zou, D. Li, R. Qu, D. Jiang, and J. Li, "Advanced high torque density PM vernier machine with multi working harmonics", *IEEE Trans. Ind. Appl.*, accepted, 2017.

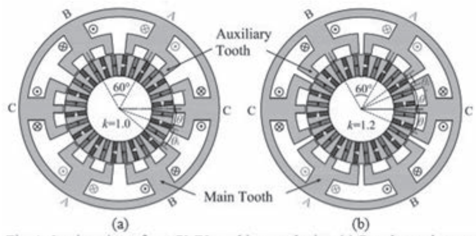

Fig. 1. Section view of two PMV machine topologies. (a) Regular spoke type PMV machine. (b) The proposed PMV machine.

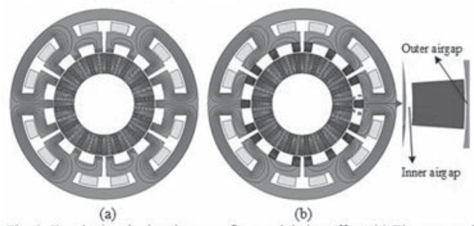

Fig. 2. Topologies sharing the same flux modulation effect. (a) The proposed PMV machine. (b) Corresponding MG machine.

TABLE I
Parameters of the MG Machine

Item	Value
Stator outer diameter	124mm
Inner airgap diameter	67.2mm
Inner airgap length	0.8mm
Outer airgap length	0.2mm
PM thickness	2.6mm
FMP thickness	6.0mm
FMP width ratio	0.4

TABLE II
Working Flux Density Harmonics

Pole pairs	Speed	Frequency
P_r=14	Ω_r	$\Omega_r \times P_r$
$\lvert P_r \pm iP_f \rvert$=4, 22, 30, 38…	$\frac{P_r\Omega_r}{P_r \pm iP_f}$	$\Omega_r \times P_r$
$\lvert P_r \pm iZ \rvert$=2, 8, 10, 16, 20, 26…	$\frac{P_r\Omega_r}{P_r \pm iZ}$	$\Omega_r \times P_r$

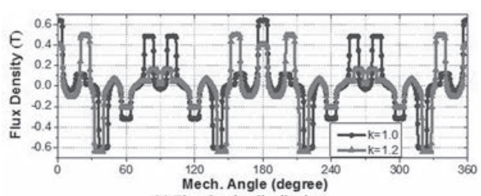

(a) Flux density distributions.

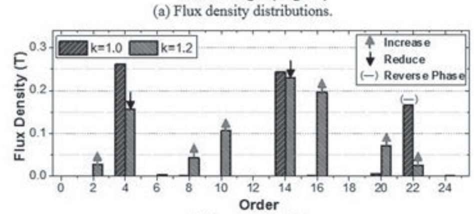

(b) Spectra of FFT.

Fig. 3. Outer airgap field comparison of the MG machines with k=1.0 and 1.2.

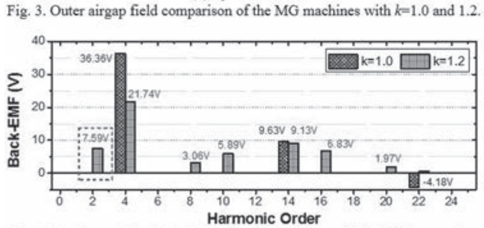

Fig. 4. Fundamental back-EMF contributions of the multiple field harmonics.

11:00

EG-09. Design and Analysis of A Novel PMSM with Single Stator and Contra-rotating Rotors.

D. Luo[1], *X. Su*[1], J. Gao[1], R. He[1] and S. Huang[1]
1. College of Electrical and Information Engineering, Hunan University, Changsha, China

INTRODUCTION Nowadays, dual-rotor motor is drawing more and more attention for wide application in drive for underwater and electric vehicles, as well as wind power generation due to the double mechanical port. Various types of dual-rotor motors have been studied in previous articles. The anti-directional-twin-rotary motor with a stator and a rotor is discussed [1]-[2].In [3], the four-quadrant transducer(4QT), consisting of two combined radial flux machines, one double rotor machine and one conventional machine, is presented for HEV applications. Professor Hoeijmakers put forward the electric variable transmission, which use the PMs to take place the winding of intermediate rotor of the 4QT [4]. In this paper, a novel dual-rotor motor -disk-type Single Stator Contra-rotating Rotors PMSM- is presented to improve machine efficiency and boost the torque density. The design principle and back electromotive force (EMF) characteristic are studied to validate the feasibility and evaluate the performance by means of 3D FEM and experiments taken from a machine prototype. Consequently, the results validates the correctness of design principle and shows good operating performances of the motor. DESIGN PRINCEPLE AND OPERATING CHARACTERISTIC ANALYSIS The principle of the motor is briefly introduced for better understanding this paper. The motor is mainly composed of one stator and two same rotors, all of them having a disk form. Dual rotors, which are mechanically independent, are set on the opposite side of the stator co-axially shown in Fig. 1a through a simplified 3D model. The most innovative part is that the stator windings is characteristic in a toroidal fashion as shown in Fig.1a. The windings terminal connection mode of one pole pair is shown in Fig.1c, which lead to the windings of rotor1 and rotor2 indicated by solid lines and dashed lines respectively. Hence, a pair of opposite rotating magnetic fields will be produced on both sides of the stator. The referential basis of magnetic circuit design is obtained by analyzing magnetic circuit variation. Compared with TORUS-NS PMSM [5], the motor's magnetic circuit of 3D FEM always changes from NN parallel magnetic circuit [6] to NS series [7]. Since the stator core of NN magnetic circuit is thicker than NS, the motor shall be designed according to NN magnetic circuit. The motor can be simply designed single stator single rotor structure, because dual rotors are symmetry with segmentation of the central plane stator core. In consideration of practical application, the main parameters is given in the Fig1.c. The detail will be presented in the full article. In view of the complexity of 3D analytical modeling and the accuracy of 2D simplified modeling [8-9], an approximate analytical formula from the simplified 2D model [10] has been applied to the motor to validate the feasibility of the motor. The influence of the dual rotors position variations on total back EMF should be considered to evaluate the performance of the motor through 3D FEM. Due to the structure of the motor, the total EMF of the motor can be deduced to be the sum of the dual rotors EMF. If the loads of dual rotors are balanced, the EMF waveforms is indicated in Fig.2b-c. It is suggested that the waveforms of dual rotors EMF are almost synchronous, thereby total EMF waveform is sinusoid with little harmonic, which is revealed that the motor with balanced load performances well. Considering the unbalanced case, Fig.2d intuitively shows peak value and phase variation of the total back EMF versus the absolute difference of dual rotors position angle through a line graph. It is provided that the peak total EMF decreases and the phase increases as the absolute difference of dual rotors position angle grows, which presents the distortion of total EMF waveform increases in the process. The fact indicated that the ripple will appear in the waveforms of speeds and torques when loads of dual rotors are unequal. PROTOTYPE VALIDATION AND EXPERIMENT RESULT The experiment was made to validate the machine operating principle using a constructed machine prototype. Fig.2a shows the physical picture of the motor prototype. To apply loads of dual rotors separately, the prototype's outer shafts are at two sides of the machine. Fig.2b-c presents the dual rotors EMF waveforms of 3D FEM and experiment results with rated loads, which are almost the same. The result is indicated that the ratio of the differences of EMF peak value are within 4% among the two situation. Therefore the correctness of prototype design is validated, and the motor performances with balanced loads are excellent to put into application. In the asynchronous case, the total EMF of the motor has a degree of distortion discussed in the paper. Thus, rotors' synchronous control strategy on a condition of the unbalanced load should be explored from the existing methods, which is very meaningful for drive of underwater vehicles. The specific solving of prototype machine parameter and operating characteristic analysis will be proposed in detail in the full article.

[1] Kawamura A., Hoshi N., Tae Woong K., et al. Analysis of anti-directional-twin-rotary motor drive characteristics for electric vehicles. IEEE Transactions on Industrial Electronics, 1997, 44(1): 64-70 [2] Clarke J., Connor G., Grant A., et al. Contra-rotating Marine Current Turbines: Single Point Tethered Floating System Stability and Performance. In: Proceedings of the 8th European Wave and Tidal Energy Conference. Uppsala, Sweden. 2009 [3] Nordlund E., Sadarangani C. The four-quadrant energy transducer. In: Proceedings of the 37th IAS Annual Meeting Conference on Industry Applications. Pittsburgh, PA, USA,2002 [4] Nordlund E., Eriksson S. Test and verification of a four-quadrant transducer for HEV applications. In:Proceedings of the 2005 IEEE Conference on Vehicle Power and Propulsion.2005, 37-41 [5] Spooner E., Chalmers B. J. 'TORUS': a slotless, toroidal-stator, permanent-magnet generator. IEE Proceedings B: Electric Power Applications, 1992, 139(6): 497-506 [6] Aydin M., Huang S., Lipo T. A. Axial Flux Permanent Magnet Disc Machines: A Review. Symposium on Power Electronics, Electrical Drives, Automation, and Motion, 2004 [7] Kahourzade S., Mahmoudi A., Hew Wooi P., et al. A Comprehensive Review ofAxial-Flux Permanent-Magnet Machines. Electrical and Computer Engineering, Canadian Journal of, 2014, 37(1): 19-33 [8] Nasar S. A., Xiong G. Determination of the field of a permanent-magnet disk machine using the concept of magnetic charge. IEEE Transactions on Magnetics, 1988, 24(3): 2038-2044 [9] Gair S., Canova A., Eastham J. F., et al. A new 2D FEM analysis of a disc machine with offset rotor. In: Proceedings of the International Conference on Power Electronics, Drives and Energy Systems for Industrial Growth. New Delhi, 1996, 617 - 621 [10] Virtic P., Pis, X030c, et al. Torque Analysis of an Axial Flux PermanentMagnet Synchronous Machine by Using Analytical Magnetic Field Calculation. IEEE Transactions on Magnetics, 2009, 45(3): 1036-1039

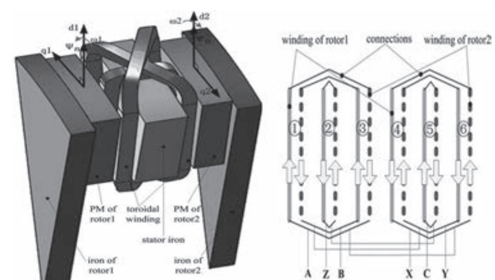

a b

Rating speed	600rpm
Rating frequency	80Hz
Rating torque	17.5N.m
Peak total EFM	100V
Number of poles	16
Air gap peak flux density	0.6T
Core inner diameter	156mm
Core outer diameter	240mm
Core axial thickness	12mm
PM diameter	8mm
Number of turns per phase	480
Number of coils	48
Number of turns per coil	6 turns ×5 layers

c

Fig. 1. (a) Simplified 3D model of the motor;(b) Winding diagram of one pole pair;(c)The main parameters of the motor

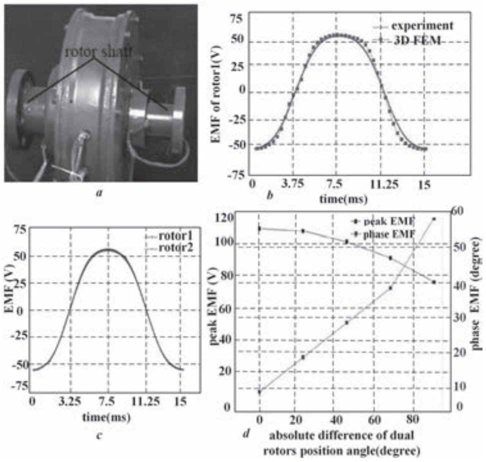

Fig. 2. (a) Real figure of the prototype which has outer shafts on two sides;(b) The EMF waveforms of rotor1 versus time;(c) Dual rotors EMF waveform in experiments versus time (d)Peak and phase of total EMF versus the absolute difference of dual rotors' position angles

11:15

EG-10. Characteristics Verification of a Novel Motor with Two Controllable Rotors.

H. Suzuki[1], K. Hirata[1], N. Niguchi[1] and A. Kohara[1]
1. Graduate School of Engineering, Osaka University, Suita, Japan

1. Introduction The electrification of automobiles has been gaining momentum recently, and more and more automobiles are being fitted with electric motors and their inverters. In order to reduce the space of the motors and inverters, a motor with two controllable rotors was proposed [1-2]. This motor has two rotors and one stator. The two rotors can be independently controlled using 3- and 6-phase superimposed currents created by a 6-phase inverter. One rotor is driven by a 3-phase current and the other is driven by a 6-phase current. However, this motor has problems such as low heat dissipation and complicated support structure of the stator because the stator is sandwiched between the two rotors. In order to solve these problems, a motor with its stator on the outside of its rotors was proposed [3]. This motor has also two rotors and one stator, and the two rotors can be independently controlled using 3- and 6-phase superimposed currents. However, this motor has also a problem of a complicated support structure of the middle rotor. Therefore, we proposed a novel motor with two controllable rotors to solve above problems [4]. In this paper, 3D-FEM analysis coupled with vector control is conducted in order to verify that the two rotors can be independently controlled. 2. Structure and Operational Principle Fig. 1 shows the proposed motor with two controllable rotors. The proposed motor has two rotors and one stator as shown in Fig. 1. The 3-phase and 6-phase rotors have 12 and 6 poles, respectively, and the common stator has 18 slots with concentrated windings. This motor has a high heat dissipation because the stator is located outside. The two rotors can be easily supported because the two rotors are axially located with each other and the 6-phase rotor shaft is mounted in the 3-phase rotor shaft through bearings. The 3- and 6-phase rotors are driven as 3- and 6-phase permanent magnet synchronous motors, respectively, by using superimposed currents created by a 6-phase inverter, where the 3- and 6-phase currents do not interfere with each other [1]. 3. FEM Analysis 3D-FEM analysis coupled with vector control is conducted in order to verify that the two rotors can be independently controlled. In the analysis, a DC voltage of 12 V is used for 3- and 6-phase drives. The torque and rotation speed when the 3-phase rotor is rotated under a load of 2.4 Nm and the 3-phase voltage is applied is shown in Fig. 2, where the initial rotation speed of the 3-phase rotor is 660 rpm, and the 6-phase rotor is free. Similarly, the torque and rotation speed when the 6-phase rotor is rotated under a load of 1.2 Nm and the 6-phase voltage is applied is shown in Fig. 3, where the initial rotation speed of the 6-phase rotor is 660 rpm, and the 3-phase rotor is free. From Figs. 2 and 3, the driving current does not create any rotation torques on the free rotor. The torque and rotation speed when the 3- and 6-phase rotor are rotated under loads of 2.4 and1.2 Nm, respectively, and the superimposed voltage is applied are shown in Fig. 4, where the initial rotation speed of both rotors is 660 rpm. From Fig. 4, it is verified that the two rotors can be independently controlled because the both rotors are driven at a different rotation speed from each other. 4. Conclusion In this paper, 3D-FEM analysis coupled with vector control is conducted in order to verify that the two rotors can be independently controlled. From the analysis results, the driving current not create any rotation torques on the free rotor, and the two rotors can be independently controlled. In the final paper, the computed N-T curves of both rotors and the experimental results of a prototype will be shown.

[1] M. Arimitsu, Y. Naruse, Y. Minagawa, M. Nakano, and T. Inoue,"Characteristics of a Coaxial Motor Driven",SAE TECHNICAL PAPER SERIES,2005-01-3755 (2005) 1-9 [2] N. Tan, M. Arimitsu,Y. Naruse,J. Watanabe, "Cooling Performance Design for Super Motor and Its Experimental Validation", The International Power Electronics Conference, (2005) 1482-1488 [3] N. Niguchi, K. Hirata, A. Miyagawa, and Y. Sakaidani, "A Novel Motor with Two Controllable Output Shafts Using Superimposed Current", Proceedings of IEEE International Magnetics Conference, Dresden, FQ-5, pp.2328-2329, 2014.05 [4] H. Suzuki, K. Hirata, N. Niguchi, E. Morimoto, and A. Kohara, "Characteristics Analysis of a Novel Motor with Two Controllable Rotors Employing 3-D FEM", International Conference on the Computation of Electromagnetic Fields, Daejeon, PD-A5-3, 2017.06

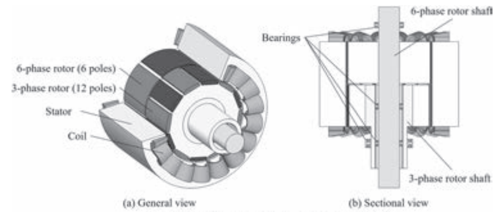

Fig. 1. Our proposed motor with two controllable rotors.

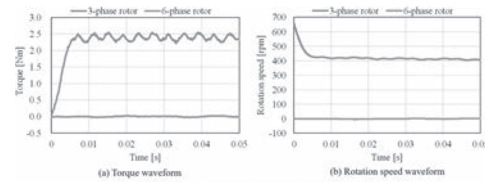

Fig. 2. Analysis result when the 3-phase rotor is driven.

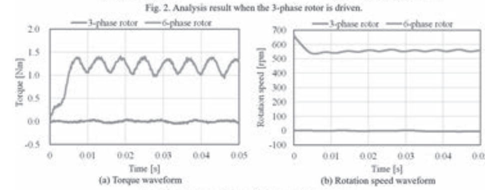

Fig. 3. Analysis result when the 6-phase rotor is driven.

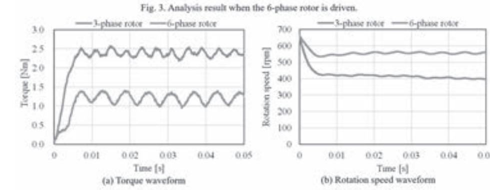

Fig. 4. Analysis result when the both rotors are driven.

11:30

EG-11. A New Structure of Stator Pole to Reduce Torque Ripple and Acoustic Noise in Switched Reluctance Motor.

M. Babaei[1] and A. Ahmarinejad[1]
1. Electrical Engineering Department, Yadegare Imam Khomeini (RAH) Shahr-e-Rey Branch, Islamic Azad University, Tehran, The Islamic Republic of Iran

Abstract—Radial forces are the main source of acoustic noise in Switched Reluctance Motors (SRMs). This paper presents new pole tip shape of SRMs for decreasing the torque ripple and reduces radial forces. By using time-stepping finite element analysis (TSFEA), this new structure is simulated numerically in case of single-phase and multiphase excitations to obtain electromagnetic torque characteristic of the motor. Then radial force that affected on stator of the motor calculated precisely from a new analytic proposed method. Simulation results show the high ability of the proposed structure to reduce the two main drawbacks of the motor. I. *Electromagnetic torque Calculation* An 8/6 SRM with new stator pole shape is simulated in Flux2d FE software for TSFEA. Rotor and stator pole angle are 23 and 21 degrees and motor rotates at 1500 rpm. Fig. 1 (a), shows the pieces of iron between stator poles. These pieces reduce the effect of salient structure of stator. Torque ripple is defined as the difference between maximum and minimum instantaneous torque dividing to average torque, as: Torque ripple=$(T_{ins}(max)-T_{ins}(min))/T_{ave}$ (1) Torque profile in normal form and new structures with various widths of iron pieces are shown in Fig. 1(b). Iron pieces widths in three models are 2, 2.5 and 3mm. As seen from Fig. 1(b), the average output torque and torque ripple of proposed structures decreased. Results are presented in Table 1. II. *Radial and tangential force calculation* The magnetic flux passes across the air gap in an approximate radial direction producing radial forces on stator and rotor, resulting in magnetic noise and vibration [1]-[3]. Assume that iron is infinitely permeable and has zero reluctance. The air gap flux density is given as: $B_g(\theta,l_g,i)=\phi/Lr\theta=\mu_0H_g=\mu_0T_{ph}i/l_g$ (2) and $T_{ph}i=l_g\phi/\mu_0rL\theta$ (3) where θ is the stator and rotor overlap angle, l_g is air gap length, consider equal to 0.35mm and r is the rotor radius that equal to 39.35mm. Also L, T_{ph}, i, H_g and ϕ are stach length, number of winding turns in one phase, winding current, magnetic field intensity in air gap and flux, respectively. The incremental electrical input energy is: $dW_e=id(T_{ph}\phi)=T_{ph}id\phi= (l_g\phi/\mu_0rL\theta)d\phi$ (4) and the stored energy in magnetic field is given by: $W_s=(l_gLr\theta/2\mu_0)Bg^2(\theta,l_g,i)=l_g\phi^2/2\mu_0Lr\theta$ (5) energy balance equation neglecting losses is: $dW_e=dW_m+dW_s$ (6) where dW_m is the incremental mechanical energy. To compute tangential force that is in direction of rotor pole arc and is a function of the varying rotor position, the incremental field energy is obtained from (7) as: $dW_s=-(l_g\phi^2/2\mu_0Lr\theta^2)d\theta+(l_g\phi/\mu_0Lr\theta)d\phi$ (7) Substituting (4) and (7) in (6), the incremental mechanical energy is obtained as: $dW_m= (l_g\phi^2/2\mu_0Lr\theta^2)d\theta$ (8) From the tangential torque that known as electromagnetic torque is obtained as: $T_e=dW_m/d\theta=(l_grL/2\mu_0)\ Bg^2(\theta,l_g,i)$ (9) Tangential force is obtained by dividing the tangential torque by the radius of the rotor pole, yielding: $F_t=T_e/r= (l_gL/2\mu_0)\ Bg^2(\theta,l_g,i)$ (10) Similarly, the normal force which is the radial force in the direction of the air gap is obtained as: $F_n=dW_m/dl_g=-(rL\theta/2\mu_0)\ Bg^2(\theta,l_g,i)$ (11) The ratio between tangential and radial force is: $F_n/F_t=-r\theta/l_g$ (12) Substituting (10) to (12), the radial force from electromagnetic torque is obtained as: $F_n=-T_e\theta/l_g$ (13) The rotor angle is equal to one phase conduction angle in terms of rotor and stator pole is given as: $\theta=4\pi/P_sP_r$ (14) where P_s and P_r are the number of stator and rotor poles. The radial force multiple times that of the tangential force in electrical machine. In SRMs, radial component of the force is the main source of radial vibration and acoustic noise. From TSFEA, electromagnetic torque obtained by single-phase excitation at unaligned to aligned position and the radial force can be calculated from (13) with considering nonlinearity. Fig. 1(c) showed the radial force of normal and proposed structures in one phase excitation from unaligned to aligned position of rotor and stator poles. According to this figure, radial force decreases and so acoustic noise will be reduced. III. *Conclusion* This paper presents the new pole shape of switched reluctance machine for decreasing the torque ripple and acoustic noise. This new structure of 8/6 SRM implemented by Flux2d for TSFEA. Multiphase excitations are used for obtaining actual and accurate electromagnetic torque performance such as average torque and torque ripple. It is shown that the proposed new structure will be able to decrease the torque ripple from 53% to 20%. For calculating radial force single-phase excitation is used. Radial force calculated from unaligned to aligned position with use the nonlinear electromagnetic torque characteristic and the analytical formula. Comparison between radial force characteristics shown that the new structure reduced the average and maximum force on stator. Therefore, acoustic noise will be reduced.

[1] G. J. Li, X. Y. Ma, G. W. Jewell, and Z. Q. Zhu "Influence of Conduction Angles on Single-Layer Switched Reluctance Machines," IEEE Transactions on Magnetics, Volume: 52, Issue: 12, Dec. 2016. [2] D. S. Mihic, M. V. Terzic, and S. N. Vukosavic, "A New Nonlinear Analytical Model of the SRM with Included Multiphase Coupling," IEEE Transactions on Energy Conversion, Volume: 32, Issue: 4, Dec. 2017 [3] J. T. Shi, and Z. Q. Zhu "Analysis of Novel Multi-Tooth Variable Flux Reluctance Machines With Different Stator and Rotor Pole Combinations," IEEE Transactions on Magnetics, Volume: 51, Issue: 5, May 2015.

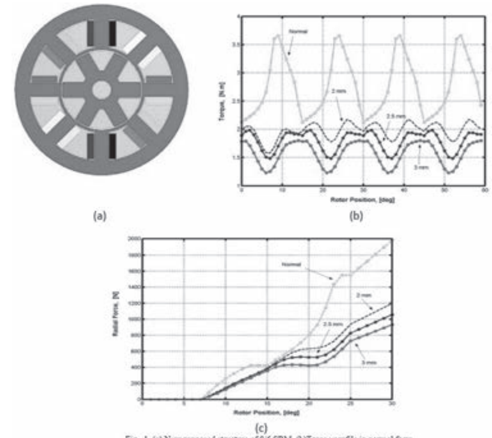

Fig. 1. (a) New proposed structure of 8/6 SRM, (b)Torque profile in normal form and proposed new structure, iron pieces widths in three models are 2, 2.5 and 3mm, and (c) Radial force in normal form and proposed structure.

Table 1. Results of the FEA

	Normal	*2mm iron*	*2.5mm iron*	*3mm iron*
T_{max}	3.7	2.2	2	1.8
T_{min}	2.2	1.8	1.5	1.25
T_{avg}	2.8	2	1.8	1.6
Torque Ripple	53%	20%	27%	34%

THURSDAY MORNING, 26 APRIL 2018 PEONY II, 9:00 TO 12:00

Session EH
MAGNETIC SEMICONDUCTORS AND OXIDES

Chen Ge, Chair
Institute of Physics, Chinese Academy of Sciences, Beijing, China

INVITED PAPER

9:00

EH-01. Giant Magnetoelectric Effects in Multiferroic Hexaferrites.

Y. Sun[1], K. Zhai[1], J. Shen[1], D. Shang[1] and Y. Chai[1]
1. Institute of Physics, Chinese Academy of Sciences, Beijing, China

Multiferroics materials with coupled magnetic and electric orders have attracted tremendous research interest because of their potential in constructing next-generation multifunctional devices. The application of single-phase multiferroics is currently limited by their usually small magnetoelectric (ME) effects. Therefore, a major challenge for single-phase multiferroics is to explore new mechanisms that will significantly improve the ME coefficients. Hexaferrites with various tunable conical magnetic structures are among the most promising multiferroic materials for realizing large ME effects at low magnetic fields because the electric polarization is directly induced by magnetic ordering. Kimura et al. first reported magnetic-field-induced ferroelectricity in the Y-type hexaferrite $Ba_{0.5}Sr_{1.5}Zn_2Fe_{12}O_{22}$ [1]. Later, Ishiwata et al. demonstrated low magnetic field reversal of electric polarization in the Y-type hexaferrite $Ba_2Mg_2Fe_{12}O_{22}$ [2]. These discoveries have triggered considerable studies on hexaferrites. Here we report the realization of giant magnetoelectric effects in a Y-type hexaferrite $Ba_{0.4}Sr_{1.6}Mg_2Fe_{12}O_{22}$, which exhibits record-breaking direct and converse ME coefficients and a large electric-field-reversed magnetization at 10 K [3]. A systematic study in the Y-type hexaferrite $Ba_{2-x}Sr_xMg_2Fe_{12}O_{22}$ family with magnetization, spin-induced ferroelectricity and neutron diffraction measurements reveals that tuning the transverse spin cone symmetry is an effective route to enhance the ME effects in hexaferrites. Besides, we demonstrate a new type of nonvolatile memory device based on a single-phase multiferroic Z-type hexaferrite $Sr_3Co_2Fe_{24}O_{41}$ which exhibits nonlinear ME effects even at room temperature [4]. The principle of the memory is to store binary information by employing the states (magnitude and sign) of the ME coefficients, instead of using magnetization, electric polarization, and resistance [5,6]. Such kind of memory device using single-phase multiferroics pave a pathway towards practical applications of spin-driven multiferroics.

[1] T. Kimura, et al. Electric polarization rotation in a helimagnet with long-wavelength magnetic structures. Phys. Rev. Lett. 94, 137201 (2005). [2] S. Ishiwata, et al. Low-magnetic-field control of electric polarization vector in a helimagnet. Science 319, 1643 (2008). [3] K. Zhai, et al., Giant magnetoelectric effects achieved by tuning spin cone symmetry in Y-type hexaferrites, Nat. Commun. 8, 519. (2017). [4] K. Zhai, et al., Room-Temperature Nonvolatile Memory Based on a Single-Phase Multiferroic Hexaferrite, Adv. Fun. Mater. 1705771 (2018). [5] J. Shen, et al., Nonvolatile Memory Based on Nonlinear Magnetoelectric Effects, Phys. Rev. Applied 6, 021001 (2016). [6] J. Shen, et al., Nonvolatile Multilevel Memory and Boolean Logic Gates Based on a Single Ni/[Pb($Mg_{1/3}Nb_{2/3}$)O_3]$_{0.7}$[$PbTiO_3$]$_{0.3}$/Ni Heterostructure, Phys. Rev. Applied 6, 064028 (2016).

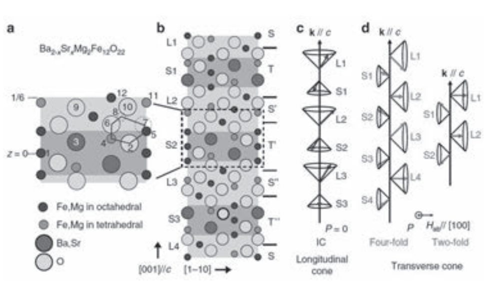

Fig. 1. The crystal structure and conical magnetic structures of Y-type hexaferrites.

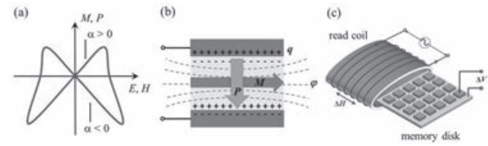

Fig. 1. The principle of a nonvolatile memory based on nonlinear magnetoelectric effects.

CONTRIBUTED PAPERS

9:30

EH-02. The atomic-scale magnetism of Cr-doped Bi2Se3 topological insulators.

W. Liu[1], D. West[2], L. He[3], S. Zhang[2], Y. Xu[4], R. Zhang[5] and K. Wang[3]
1. Department of Electronics Engineering, Royal Holloway Universtiy of London, Egham, United Kingdom; 2. Department of Physics, Rensselaer Polytechnic Institute, Troy, NY, United States; 3. Department of Electrical Engineering, University of California Los Angeles, LA, CA, United States; 4. Electronics Department, University of York, York, United Kingdom; 5. Nanjing Unversity, Nanjing, China

Three-dimensional topological insulators (TIs) are insulating bulk materials that carry a conducting surface state, arising from the intrinsically strong spin-orbital coupling (SOC) in the bulk band structure protected by time-reversal symmetry (TRS). While such unique systems offer nontrivial surface states that can be utilized to perform dissipationless spin transport, it is equally important to break the TRS of TIs to realize novel physical phenomena like quantum anomalous Hall (QAH) effect. [1-3] Within the growing family of TIs, ferromagnetism has been reported in V-, Cr-, and Mn-doped single crystals of Sb2Te3 [4] and Fe- and Mn-doped single crystals of Bi2Te3. [5] Both ferro- [6] and antiferromagnetism [7] have been reported in Cr-doped Bi2Se3, [10] and for Fe- doped Bi2Se3 observations are rather controversial. [8-9] So far, evidence for the detailed spin and orbital ordering of magnetically doped TIs are inconclusive. [1-8] In this regards, the synchrony-based X-ray absorption (XAS) / X-ray magnetic circularly dichroism (XMCD) technique can be an ideal tool as a valence-, site-, and symmetry-specific probe. Although XAS/XMCD has been intensively utilized in the determination of the impurity magnetism of diluted magnetic semiconductors (DMSs), to apply it to the 3d-metal-doped TIs emerged only very recently. [4-5] Here, we present a comprehensive study of the spin (mspin) and orbital (morb) magnetic moment of a prototype magnetic TI, i.e. Bi2Cr2- xSe3, in its ultrathin limit that is expected to give rise to QAH effect. The 10 nm Bi1.94Cr0.06Se3 thin film used in this study was grown by molecular beam epitaxy (MBE), whose ferromagnetism at low temperatures has been investigated by angular resolved photoemission spectroscopy (ARPES) and magnetotransport measurement as published elsewhere. [11] The XAS/XMCD experiments at the L2,3 Cr absorption edges were performed at the beamline I10 of the UK National Synchrotron Radiation Laboratory. XAS was performed at 3 K by total electron yield (TEY) in Faraday geometry and XMCD was taken as the difference spectrum by flipping the X-ray helicity at fixed magnetic field of 10 kOe. As presented in Fig.1., significant multiplet structure at each spin-orbit component of the 2p core was obtained, suggesting a mixed valance state of Cr and the peak asymmetry features of the dichroism point to a predominant contribution of trivalent Cr cations to the magnetization. By applying sum rules on the integrated XMCD and total XAS spectra,[10] we obtained a remarkable mspin = (1.54 ± 0.2) μB/Cr and a small negative morb = (-0.05 ± 0.02) μB/Cr at 3 K. The sum-rules derived value is considerably reduced from the Hund's rule value of 3 μB for the spin moment of substitutional Cr3+ onto Bi sites and that promoted us to investigate the possible scenarios. Simulations were performed based on first-principles density functional theory (DFT) within the Perdew-Burke- Ernzerhof generalized gradient approximation (GGA) and the SOC was included. The layered structure of Bi2Se3 allows the Cr dopants not only to enter the host substitutionally, but also in the van der Waals gap between the layers interstitially. Under the given growth conditions, the formation energies (ΔH) at various lattice positions including interstitial (CrI) and substitutional sites with Cr replacing Bi (CrBi), and Se (CrSe), as well as that of larger defect complexes containing pairs of Cr-atoms, such as the CrBi - CrSe and CrBi - CrI were calculated, as presented in Fig.2. In agreement with the ponieering reports by Zhang et al., [8] we also found that Bi substitutional sites are more stable than interstitial sites for Cr impurities. However, the CrBi - CrI bonding can significantly alter ΔH, leaving the (CrBi - CrI)3+ complex an energetically equally favorable defect. While both CrBi0 and CrI3+ have a magnetic moments of ~3 μB/atom, the CrBi-CrI pair is antiferromagnetic in nature with a nearly vanishing magnetic moment. Such spontenous coexsitance of ferro- and antiferromagnetic Cr in Bi2-xCrxSe3 can explain the observed suppressed magnetic moment and those reported by Haazen et al. [12] and Collins-McIntyre et al. [13]ours who consistently obtained magnetic moments of less that 2 μB/atom using different techniques. To summarize, we have presented a symmetric study of the mspin and morb of the Bi2Cr2-xSe3 thin film combining the XAS/XMCD and DFT methods. We quantitatively addressed the magnetic moment of Cr in the Bi2Cr2-xSe3 TI thin film and the results were well reproduced by DFT caculations. Our work provides valuable information of the fundemental quantities of the magnetic TI systems and has strong implications for the research of the interplay of magnetism with the topological states of matters.

[1] Chang, C.-Z. et al. Science 2013, 340, 167. [2] Liu, C.-X. et al. Phys. Rev. Lett. 2008, 101, 146802. [3] Yu, R. et al. Science 2010, 329, 61. [4] Dyck, J. et al. Phys. Rev. B 2005, 71, 115214. [5] Hor, Y. S. et al. Phys. Rev. B 2010, 81, 195203. [6] Haazen, P. P. J. et al. Appl. Phys. Lett. 2012, 100, 082404. [7] Choi, Y. H et al. J. Appl. Phys. 2011, 109, 07E312. [8] Zhang, J.-M. et al. Phys. Rev. Lett. 2012, 109, 266405. [9] Vobornik, I. et al. Nano Lett. 2011, 11, 4079–4082. [10] Liu, W. et al. Nano Lett. 2014, DOI: 10.1021/nl504480g. [11] He, L. et al. status solidi - Rapid Res. Lett. 2013, 7, 50. [12] Zhang, D. et al. Phys. Rev. B 2012, 86, 205127. [13] Collins-McIntyre, L. J. et al. Europhysics Lett. 2014, 107, 57009.

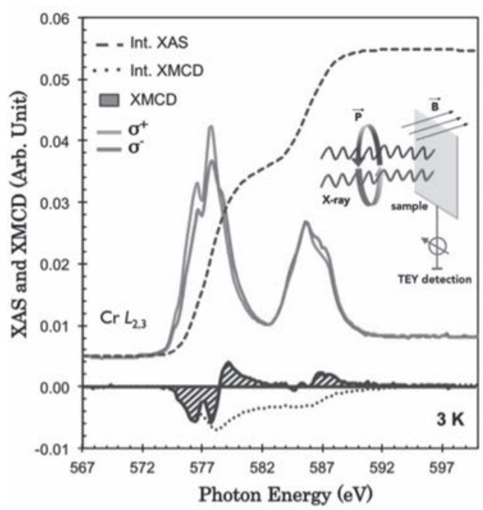

Fig. 1. Typical pair of XAS and XMCD spectra of the Bi1.94Cr0.06Se3 thin film. Insert: the experimental configuration.

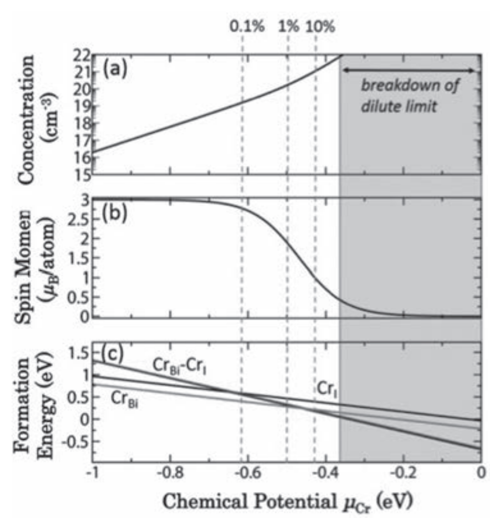

Fig. 2. The DFT calculated (a) Cr concentration, (b) average magnetic moment, and (c) ΔH of the three predominant Cr defects, respectively, against the chemical potential.

9:45

EH-03. Role of R^{3+} ion on structural and magnetic properties of R_2NiMnO_6 double perovskites.

M. Nasir[1], S. Ayaz[2] and S. Sen[1,2]
1. Physics, IIT Indore, INDORE, India; 2. MEMS, IIT Indore, Indore, India

Double perovskites R_2NiMnO_6 (R = La, Pr, Tb) are ferromagnetic semiconductors that have received significant scientific attention[1, 2] because of their high magnetic Curie temperature which can be tuned by varying the size of rare-earth ions. From structural aspects, these systems adopt two different structures depending on the B-site ordering of Ni and Mn cations. A random distribution of B-site ions results in an orthorhombic *Pbnm* symmetry. While, an alternate regular arrangement leads to a monoclinic $P2_1/n$ symmetry[3, 4]. The replacement of La^{3+} by a smaller rare-earth ions modify the crystal structure which in turn influence magnetic properties. This is associated with the change of B-O-B' bond angles and exchange interactions. So by tuning their magnetic and electrical properties, these materials can be useful for variety of spintronic industry applications. Compared to La_2NiMnO_6, other R_2NiMnO_6 perovskites are relatively less studied. It is generally known that the entire series of R_2NiMnO_6 are ferromagnetic with Curie temperatures smaller than that of La_2NiMnO_6. Structure property relationship for R_2NiMnO_6 is not fully established. In the present work, R_2NiMnO_6 (R = La, Pr, Tb) perovskites have been prepared by means of a sol-gel assisted combustion method followed by high temperature sintering. R_2NiMnO_6 series has been examined by X-ray diffraction (XRD), magnetic measurements, and synchrotron based X-ray absorption near edge spectroscopy (XANES). Rietveld refinement was carried out using *FullProf* software with $P2_1/n$ space group as starting structural model. In all cases the crystal structure is defined in the monoclinic $P2_1/n$ space group, with an almost complete order between Ni^{2+} and Mn^{4+} ions. XANES measurements were employed at Ni and Mn K-edges to elucidate the oxidation sates of Ni and Mn ions which play an important role in magnetism [Figure 1]. XANES results are in well agreement with XRD data. Further, magnetic measurements show that there is a reduction in Curie temperature with smaller crystal radii of R^{3+} [Figure 2]. The Curie temperature is decreased to 104 K form 264 K with replacement of La^{3+} by Tb^{3+}. Infact, Curie temperature of R_2NiMnO_6 series is a linear function of the crystal radii of R. Thus, ferromagnetic ordering temperature of the R_2NiMnO_6 can be better correlated with the radius of R^{3+} atoms than with the average Ni– O–Mn angle. Our results which are presented here provide a detailed insight into the role of R^{3+} ions on the magnetic properties of the series.

1. W. Z. Yang, X. Q. Liu, H. J. Zhao, Y. Q. Lin and X. M. Chen, Journal of Applied Physics 112 (6), 064104 (2012). 2. D. C. Kakarla, K. M. Jyothinagaram, A. K. Das and V. Adyam, Journal of the American Ceramic Society 97 (9), 2858-2866 (2014). 3. R. J. Booth, R. Fillman, H. Whitaker, A. Nag, R. M. Tiwari, K. V. Ramanujachary, J. Gopalakrishnan and S. E. Lofland, Materials Research Bulletin 44 (7), 1559-1564 (2009). 4. H. J. Zhao, X. Q. Liu, X. M. Chen and L. Bellaiche, Physical Review B 90 (19), 195147 (2014).

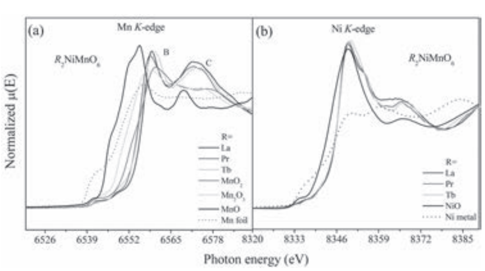

Fig. 1. Normalized XANES spectra ((μ) vs E) at (a) Ni K-edge and (b) Mn K-edge of the R_2NiMnO_6 double perovskites compared with reference samples.

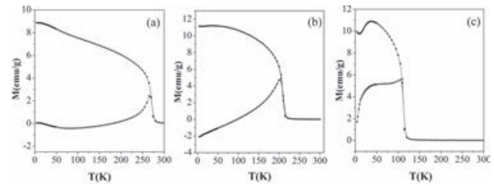

Fig. 2. Temperature dependent magnetisation (M-T) curves for (a) La_2NiMnO_6 (b) Pr_2NiMnO_6 (c), and Tb_2NiMnO_6 double perovskites. A change in TC is obsrved as La^{3+} is replaced by Pr^{3+} and Tb^{3+}.

10:00

EH-04. Enhancing the low-field magnetoresistance by ac current excitation in $La_{0.7}Sr_{0.3}MnO_3$.

P. Kumar[1], U. Chadhuri[1] and *R. Mahendiran*[1]
1. Physics Department, 2 Science Drive 3, National University of Singapore, Singapore

Among the oxides possessing perovksite (ABO_3) structure, $La_{0.7}Sr_{0.3}MnO_3$ is widely known because it is a rare example of ferromagnetic metal with ferromagnetic transition above room temperature (T_C = 382 K) and exhibits colossal negative magnetoresistance (-$\Delta R/R \approx$ 50-60 % in a dc magnetic field of 6 Tesla) near T_C.[1,2] However, the dc magnetoresistance (measured with direct current passing through the sample) is small in low magnetic fields, typically less than 1% in H = 1 kOe. Surprisingly, magnetoresistance of this compound in response to an alternating current driving current through the sample or exposing the sample to an oscillating magnetic field has been overlooked so far except by a few researchers[3]. Few years ago, we reported [4] that the resistive component of the ac impedance (Z = R+iX) of a bulk $La_{0.7}Sr_{0.3}MnO_3$ sample showed a remarkable decrease (ΔR/R(H= 0) ~ 45 % for f = 1 MHz, where f is the frequency of alternating current through the sample) in a dc magnetic field of 1 kOe at room temperature. Here, we extend the frequency of measurement from 1 MHz to 3GHz. We measured both resistive (R) and reactive (X) components of the ac impedance using a shorted-coaxial cable and an Agilent Impedance Analyzer (model E4991A RF) $R(H)$ shows a single peak centered around H = 0 for 1 < f < 30 MHz but it transforms into a dip at H = 0 accompanied by double peaks at H = $\pm H_p$ for higher frequencies. The position of the double peak shifts towards higher field with increasing frequency. Ac magnetoresistance changes sign from positive to negative with increasing frequency ($\Delta R/R$ = -0.07%, -20.2%, and +27.5%) for f = 1, 50 MHz and 3 GHz, respectively. The transition from a single to double peak is also seen in $X(H)$ with additional features developing near zero field for f > 2 GHz. We suggest that transverse magnetic permeability and ferromagnetic resonance govern the high frequency magnetotransport in this oxide. Our findings indicate that this ferromagnetic manganite could be used for sensing low magnetic field by properly exploiting its high frequency magnetic property. Our simple experimental technique can be also used to study magnetization dynamics in metallic ferromagnets Acknowledgement: R. M. acknowledges the Ministry of Education, Singapore for supporting this research through Tier 2 grant (R144-000-381-112 and R144-000-373-112)

[1] Y. Tokura in "Colossal Magnetoresistive Oxides", Gorden and Breach Science Publishes, Singapore(2000). [2] A. Gupta, G. Q. Cong, G. Xiao, P. R. Duncombe, R. leccouer, P. Troilloid, Y. Y. Wang, V. P. Dravid and J. Z. Sun, Phys. REv. B 54, R15629 (1996). [3] Jifan Hu and Honwei Qin, J. Magn. Magn. Mater. 234, 419 (2001); S. E. Lofland, V. Ray, P. H. Kim, S. D. Tyagi, M. Mukovskii, and A.M. Balbashov, J. Appl. Phys. 80, 3592 (1996). [4] A. Rebello, V. B. Naik and R. Mahendiran, J. Appl. Phys. 106, 073905 (2009).

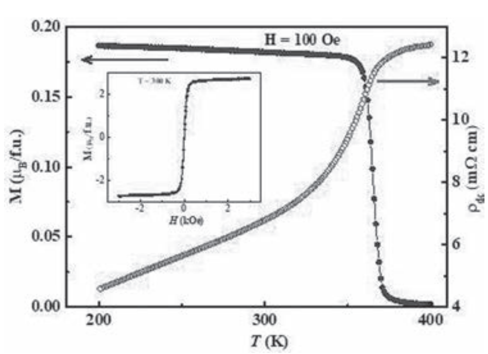

Fig. 1. Temperature dependence of dc resistivity (ρ) in zero magnetic field (right y-axis) and magnetization (M) measured in a magnetic field of 100 Oe (left y-axis). Inset: Magnetization isotherm at room temperature.

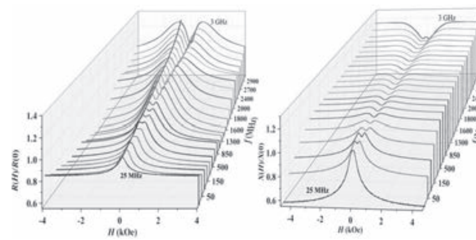

Fig. 2. (left) Magnetic field dependence of magnetoresistance, ΔR/R(0), and (right) magnetoreactance, ΔX/X(0), for varying frequency (*f*) of current excitation.

10:15

EH-05. Suppression of charge and antiferromagnetic ordering in Ru substituted $Bi_{0.5}Ca_{0.5}MnO_3$ probed by electrical, magnetic and thermoelectric transport.

M. Kumari[1], A. Chanda[1] and R. Mahendiran[1]
1. Physics, National University of Singapore, Singapore

Half-doped manganites of general formula $R_{0.5}A_{0.5}MnO_3$ (R = rare-earth, A= alkaline earths) are known to undergo charge ordering (ordering of electrons and holes in a regular pattern) and e_g-orbital ordering.[1] These systems are normally antiferromagnetic insulators at low temperatures and charge ordering occurs in the paramagnetic state, well below room temperature (T_{CO} = 240 K-270 K for various rare earth ions).[2] However, Bi based systems *i.e.,* $Bi_{0.5}A_{0.5}MnO_3$ (A = Ca and Sr) show some interesting peculiarities that differ from the general behavior of previously studied rare-earth based manganites. For instance, these systems show a charge ordering far above room temperature (T_{CO} = 325 K for Ca and 550 K for Sr system).[3-4]. The charge ordering in these systems is reported to be so robust that remains stable even at fields as high as 60 T. Also, the substitution at Mn-site with other transition metal ions (Cr^{3+} or Ni^{2+}) fails to induce a ferromagnetic metallic state.[5] In this work, we are demonstrating that a systematic substitution of Ru at Mn site in $Bi_{0.5}A_{0.5}MnO_3$ samples suppress the charge-ordering and transforms the antiferromagnetic insulating ground state into ferromagnetic conducting state even in the absence of an external magnetic field. Here, we report the magnetization, electrical resistivity and thermopower in $Bi_{0.5}Ca_{0.5}Mn_{1-x}Ru_xO_3$ (x = 0.00, 0.01, 0.03 and 0.05) system for the first time. In pure $Bi_{0.5}Ca_{0.5}MnO_3$ (x = 0), on cooling from 400 K, charge ordering takes place at $T= T_{CO}$ ~325 K and on further lowering the temperature, an antiferromagnetic ordering of Mn-spins takes place, showing a second peak at T_N~130 K. In 5% Ru doped sample (x = 0.05), both the charge and antiferromagnetic ordering are suppressed and the magnetic moment increases gradually below CO temperature for this sample. Resistivity decreases with increasing Ru content and falls by two orders of magnitude for x = 0.05 in comparison to the pure compound. Thermopower increases gradually and shows a temperature independent behaviour above 230 K due to polaronic conduction. We will discuss the connection between magnetism, electrical resistivity, magneresistance and thermopower as a function of Ru content in this series.

[1]Y. Tomioka, A. Asamitsu, H. Kuwara, Y. Moritomo, and Y. Tokura, Phys. Rev. B 53, R1689 (1996). [2]G. Subias, J. Garcia, P. Beran, M. Nevrriva, M. C. Sanchez, and J. L. Garcia-Munoz, Phys. Rev. B 73, 205107 (2006). [3]P. Amirzadeh, H. Ahmadvand, P. Kameli, B. Aslibeiki, H. Salamati, A. G. Gamzatov, A. M. Aliev, and I. K. Kamilov, J. Appl. Phys. 113, 123904 (2013). [4]T. Kimura, Y. Tomioka, R. Kumai, Y. Okimoto, and Y. Tokura, Phys. Rev. Lett. 89, 3940 (1999). [5]C. M. Xiong, J. R. Sun, R. W. Li, S. Y. Zhang, T. Y. Zhao, and B. G. Shen, J. Appl. Phys. 95, 1336 (2004).

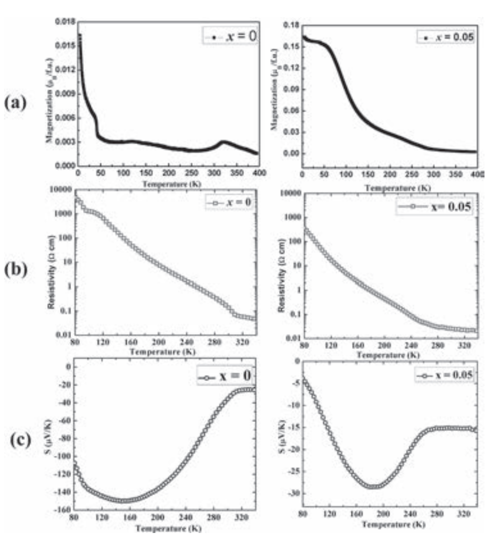

10:30

EH-06. Anisotropic Electronic Transport Properties in Low-Temperature Phase Fe_3O_4 Epitaxial Films.

X. Liu[1], *W. Mi*[1], Q. Zhang[2] and X. Zhang[2]
1. Department of Applied Physics, Tianjin University, Tianjin, China;
2. PSE Division, King Abdullah University of Science and Technology (KAUST), Thuwal, Saudi Arabia

Magnetite (Fe_3O_4) has attracted tremendous attention due to its unique electrical and magnetic properties including high Curie temperature (~858 K), large net magnetic moment (~4 μ_B/f.u.) and theoretical -100% spin polarization. As the first known phase transition in oxides accompanied with charge ordering, Verwey transition at 125 K (T_V) in Fe_3O_4 is being actively investigated. At T_V, physical properties of Fe_3O_4 show distinct changes where conductivity and magnetization show abrupt decrease and the specific heat shows an anomalous maximum.[1] Although the Verwey transition has been found nearly eighty years, the underlying physics of Verwey transition is still unclear. The detailed electronic transport properties around T_V are rarely, especially the anisotropy magnetoresistance (AMR). AMR is considered as a consequence of spin-orbital interaction in magnets and has relation with the easy axis. In Fe_3O_4, the easy axis undergoes a transition from <111> to (001) as temperature cools down to 130 K where the cubic magnetocrystalline anisotropy (MCA) transforms to a uniaxial one.[2] In previous studies AMR of Fe_3O_4 films shows fourfold symmetry below T_V which is contradictory to the uniaxial MCA. This work investigated the detailed structural properties and AMR across T_V based on high quality Fe_3O_4(100)/MgO(100) and Fe_3O_4(111)/Al_2O_3(0001) films. The configuration of sample, current and magnetic field is shown in Fig. 1(a). In Fe_3O_4(100) film, the symmetry of AMR shows a fourfold to twofold transition as the temperature cools below T_V. At temperature $T<T_V$-15 K, the twofold AMR gradually evolves to a fourfold one. Considering the sharp Verwey transition in our Fe_3O_4 sample, the evolvement of AMR has no correlation with the charge ordering. Then, the novel microstructure of trimeron[3] inspires us. The distribution of in-plane trimeron in monoclinic Fe_3O_4(100) and (111) samples are compared together with their AMR curves as shown in Figs. 1(b) and 1(c). It is found that the AMR shows maximum when external magnetic field is parallel to trimeron. The evolvement of fourfold symmetry in Fe_3O_4(100) film below T_V may also have relation with the formation of trimeron. From this perspective, the temperature gap between Verwey transition and lattice distortion detected by Raman spectroscopy is easy to understand. So, two significant outcomes of the analysis are (a) the Verwey transition contains two steps including the formation of charge ordering together with cubic-monoclinic transition at temperature just below T_V and the formation of trimerons at a lower temperature, (b) the fourfold symmetry of AMR in Fe_3O_4 below T_V derives from the in-plane trimerons. Although the fourfold AMR has been found for many years, the mechanism is not clear yet. Our work not only explains the anomalous magnetotransport behavior in monoclinic Fe_3O_4 but also looks into the Verwey transition at temperature just below T_V, which push forward the understanding of Verwey transition in structural and electronic aspects. This work is supported by National Natural Science Foundation of China (51671142, U1632152), Key Project of Natural Science Foundation of Tianjin (16JCZDJC37300).

[1] F. Walz, J. Phys.: Condens. Matter 14, R285 (2002). [2] L. R. Bickford Jr, Phys. Rev. 78, 449 (1950). [3] M. S. Senn, J. P. Wright, and J. P. Attfield, Nature 481, 173 (2012).

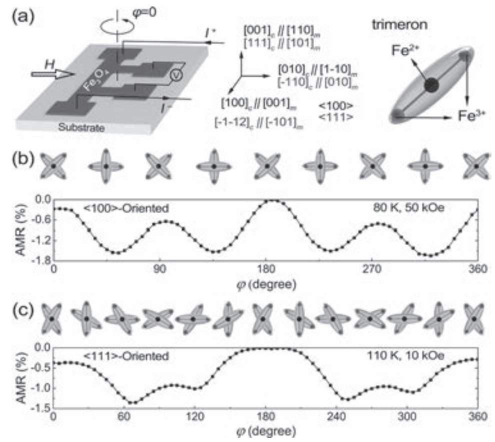

Fig. 1. (a) Configuration of sample, current and magnetic field throughout the AMR measurements. (b) and (c) AMR in Fe_3O_4(100) and (111) films with correspondent distribution of in-plane trimeron.

10:45

EH-07. Effect of $CaCO_3$ and V_2O_5 on the microstructure and magnetic property of MnZn ferrites.

G. Wu[1], Z. Yu[1], Z. Tang[2], K. Sun[1], R. Guo[1], X. Zou[1], X. Jiang[1] and Z. Lan[1]
1. University of Electronic Science and Technology of China, Chengdu, China; 2. China Aerospace Components Engineering Center, Beijing, China

Manganese-zinc (MnZn) ferrites have been widely applied in convertors and switching mode power supplies, on account of its high saturation magnetic induction B_s, initial permeability μ_i and low core losses P_L [1-3]. With the development of miniaturization and integration of electronic devices, the application frequency of MnZn ferrite core has been raised from tens of kilohertz to several megahertz (2~4MHz). Thus, MnZn ferrites with low core losses especially at high frequency (~3MHz) are urgently demanded. Aiming at this goal, many efforts have been done to investigate the factors that may influence core losses, such as the main compositions, fabrication processes of powders and additives [4-6]. K. Praveena [4] et al investigated the effect of Zn^{2+} content on the core losses for $Mn_{1-x}Zn_xFe_2O_4$ and found that optimized Zn^{2+} content could reduce the core losses from 358kW/m^3 (x=0) to 163kW/m^3 (x=0.9) at 1MHz. Haining Ji [5] et al studied the effect of second milling time on the loss characteristics of MnZn ferrites. The results showed that when the second milling time is 2h, the core losses achieved its minimum value of 430kW/m^3 at 100kHz and 200mT. A low-loss MnZn ferrite material DMR508, sintered in precisely controlled oxygen partial, has been developed through optimized additives of CaO, SiO_2, Nb_2O_5, TiO_2 and ZrO_2 [6]. The core losses of this material were only 200kW/m^3 at 3MHz and 10mT. To sum up, it is a feasible way to unify these factors harmoniously for the realization of even lower losses at 3MHz. In this work, $Mn_{0.67}Zn_{0.21}Fe_{2.12}O_4$ ferrites doped with $CaCO_3$ (0~0.3wt%) and V_2O_5 (0~0.03wt%) have been prepared by solid-state reaction method, and ultra-low core losses at 3MHz 10mT and 30mT were achieved through the combinative doping of $CaCO_3$ and V_2O_5, as well as other additives (TiO_2, Co_2O_3 and SnO_2). The effect of $CaCO_3$ and V_2O_5 on the microstructure and electromagnetic properties of MnZn ferrites have been investigated in detail, such as initial permeability μ_i, saturation magnetic induction B_s, coercivity H_c and resistivity ρ. In addition, based on core losses separation method, the core losses mechanism has been discussed. Core losses are divided into three parts: hysteresis loss P_h, eddy current loss P_e and residual loss P_r through following equation: $P_L/f = K_hB^3+K_eB^2f/\rho+P_r/f$ (1), where K_h and K_e are constants, B is the magnetic flux density, f is the frequency and ρ is the resistivity. In view of the relationship curve between P_L/f and f, P_h/f, P_e/f and P_r/f could be obtained from the interception part, slope of linear part and nonlinear part, respectively. The SEM micrographs of MnZn ferrites are shown in Fig. 1. Remarkably, the average grain size decreased with the increase of $CaCO_3$ content via the refinement grain growth as shown in Fig. 1(a)-(b). Besides, small and even grains were obtained with 0.1wt% $CaCO_3$ and 0.01wt% V_2O_5 co-doping in Fig. 1(c). Fig. 2(a) shows the P_L variation of MnZn ferrites with different $CaCO_3$ contents at room temperature. With the increase of $CaCO_3$ content, the core losses at 3MHz 10mT and 30mT showed a tendency of decreasing then increasing with the minimum of 56kW/m^3 and 859kW/m^3 for 0.1wt% $CaCO_3$ doping. Furthermore, on the basis of 0.1wt% $CaCO_3$ doping, the core losses were furtherly reduced with 0.01wt% V_2O_5 doping. The core losses at 3MHz 10mT and 30mT were only 33kW/m^3 and 598kW/m^3, respectively, as shown in Fig. 2(b). The excellent properties of MnZn ferrite core with ultra-low core losses make it a candidate for the application of high frequency of 3MHz.

[1] M.A. Ahmed, K.E. Rady, M.S. Shams, Enhancement of electric and magnetic properties of Mn-Zn ferrite by Ni-Ti ions substitution, J. Alloys Compd., 622 (2015) 269-275. [2] J. Töpfer, A. Angermann, Complex additive systems for Mn-Zn ferrites with low power loss, J. Appl. Phys., 117 (2015) 17A504 [3] Dong Liu, Xiaping Chen, Yao Ying, Ling Zhang, Wangchang Li, Liqiang Jiang, Shenlei Che, MnZn power ferrite with high Bs and low core loss, Ceram. Int., 42 (2016) 9152-9156. [4] K. Praveena, Hsiao-Wen Chen, Hsiang-Lin Liu, K Sadhana, S.R. Murthy, Enhanced magnetic domain relaxation frequency and low core losses in Zn^{2+} substituted manganese ferrites potential for high frequency applications, J. Magn. Magn. Mater., 420 (2016) 129-142. [5] H. N. Ji, Z. W. Lan, Z. Y. Xu, H. W. Zhang, J. X. Yu, M. Q. Li, Effects of second milling time on temperature dependence and improved Steinmetz parameters of low loss MnZn power ferrites, IEEE Trans. Magn., 24 (2014) 1-4. [6] Yapi Liu, Shijin He, Development of high DC-bias Mn-Zn ferrite working at frequency higher than 3MHz, J. Alloys Compd., 489 (2010) 523-529.

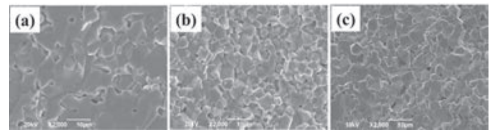

Fig. 1. SEM micrographs of MnZn ferrite cores: (a) with 0.0wt% $CaCO_3$+0.03wt% V_2O_5, (b) with 0.1wt% $CaCO_3$+0.03wt% V_2O_5 and (c) with 0.1wt% $CaCO_3$+0.01wt% V_2O_5.

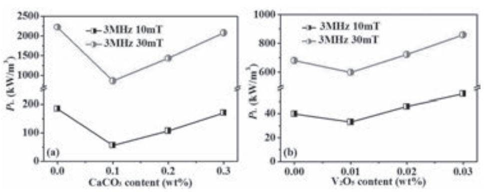

Fig. 2. The P_L variation with (a) $CaCO_3$ and (b) V_2O_5 contents for MnZn ferrite core at room temperature.

11:00

EH-08. Magnetically driven insulating behavior in monoclinic antiferromagnetic Ni-Mn-In Heusler alloys.

H. Yang[1,2], B. Wang[1,2] and R. Li[1,2]
1. Key Laboratory of Magnetic Materials and Devices, Ningbo Institute of Materials Technology and Engineering, Chinese Academy of Sciences, Ningbo, China; 2. Laboratory of Magnetic Materials and Application Technology, Ningbo Institute of Materials Technology and Engineering, Chinese Academy of Sciences, Ningbo, China

In solid state matters, the electrons are confined in a potential that is constructed by atomic networks. As electrons have both charge and spin characters, the potential can be separated into charge potential and spin potential. In most cases, the charge potential plays a decisive role in determining the electronic structures in solids [1]. However, in some cases, the spin potential cannot be ignored, as it could split the electronic structure into two spin dependent channel and result in spin-polarized conducting electrons. A unique case has been pointed out by J. C. Slater in the 1950s [2], where he suggested that in certain antiferromagnets, an insulator could be purely induced by spin potential. In recent years, it has been suggested that some 5d transition-metal oxides could be Slater-type insulators. However, their insulating nature as being Slater-type or Mott type has been frequently debated [3-6]. Therefore, it is still unclear if there are purely magnetically driven insulating behaviors. Here we report an anomalous insulating behavior in the monoclinic $Ni_{50}Mn_{50-x}In_x$ bulk alloys. The alloys show low resistivity (~ 10^{-4} Ω cm) and high carrier density (~ 10^{22} per cm^3) that are comparable to those of common alloys, yet, an insulating behavior was identified. The insulating behavior was found in the doping range of roughly $10 < x < 16$ [Fig. 1]. By comparing the electrical transportation with magnetism, a correlation between antiferromagnetic order and the insulating behavior is revealed: both the high temperature paramagnetic phase and the low temperature super-spin glass phase are metallic, and the insulating behavior is observed when long range AFM order is established [Fig. 2]. Furthermore, applying magnetic fields tend to destroy the AFM state, thus the temperatures at which MIT occurs (Tp) increase as the applied magnetic field is increased. Neutron results indicate that in our case, the spin order doubles the lattice periodicity no longer holds, manifesting that the alloys do not belong to Slater-type insulator. Our results indicate that the insulating behavior could be ascribed to certain peculiar spin dependent scattering process.

1. M. Imada, A. Fujimori, Y. Tokura, et al. Rev. Mod. Phys. 70, 1039 (1998). 2. J. C. Slater, Phys. Rev. 82, 538 (1951). 3. Y. G. Shi, Y. F. Guo, et al. Phys. Rev. B 80, 161104(R) (2009). 4. S. Calder, V. O. Garlea, et al. Phys. Rev. Lett. 108, 257209 (2012). 5. M. Kim, B. H. Kim & B. I. Min, Phys. Rev. B 93, 195135 (2016). 6. B. Kim, et al. Phys. Rev. B 94, 241113 (2016).

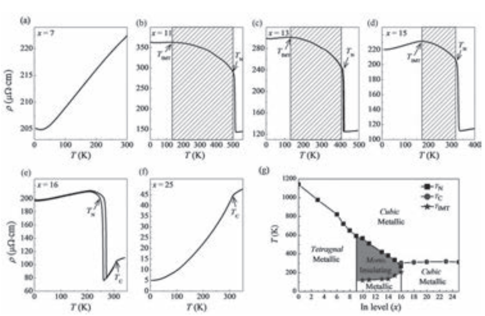

Fig. 1. (a) - (f) Transportation properties of the investigated $Ni_{50}Mn_{50-x}In_x$ alloys. The insulating region has been marked by hatched area. (g) Phase diagram of the investigated Ni-Mn-In system. The crystal structures and corresponding transportation behaviors have been indicated. The red region shows area where insulating behavior shows up.

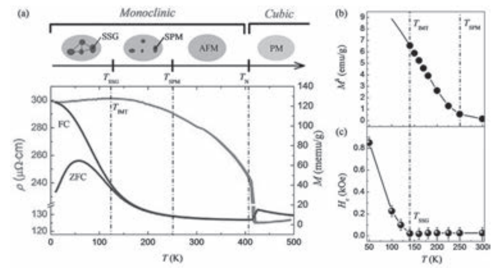

Fig. 2. Correspondence between electrical and magnetic properties of In13. (a) Temperature dependent magnetization and resistivity of In13 alloy. (b) and (c) Temperature dependence of (b) the saturated magnetization of SPM phase and (c) coercivity of In13 alloy.

11:15

EH-09. Valley polarized tunneling through magnetic and electrical barriers in Weyl semimetals.

C. Yesilyurt[1], Z. Siu[1], S. Tan[1], G. Liang[1] and M.B. Jalil[1]
1. Electrical and Computer Engineering, National University of Singapore, Singapore

Recently, valley polarized tunneling has been predicted in Weyl semimetals with tilted energy dispersion in the presence of magnetic and electrical barriers [1]. It has been shown that Weyl electrons that encounter an electrical potential barrier experience a valley dependent transverse momentum shift, which originates from the coupling of the tilted energy dispersion and electrical potential difference. Despite the electrons being valley-polarized in angle-space, the contribution of each valley to the total conductance remains constant. Additional magnetic barrier breaks the angular transmission symmetry and leads to valley dependent conductance at the barrier interface. Here, we delve deeper into the physics of magnetic barrier structure and provide a detailed quantitative analysis based on more realistic model. We focus on the simplest Weyl semimetal case, where two Weyl fermions emerge with opposite chirality, and reversed tilt vector, whose low energy characteristics can be described by $H_{K,K'} = \eta h(v_F k.\sigma + w.k)$, where the σ is the vector of Pauli matrices in three dimensions, w is the tilt vector, $\eta = \pm 1$ and represents the chirality of the Weyl node. The system consists of a one-dimensional rectangular electrical potential [Fig. 1 (b)], and magnetic gauge potential [Fig. 1 (c)] induced by the ferromagnetic layer deposited on the Weyl semimetal, as illustrated in Fig. 1 (a). The ferromagnetic layer induces two asymmetric spike-like magnetic fields at the interface of the barrier as shown in Fig. 1 (c). The realistic magnetic field profile can be analytically described by $B_{z(x)}$ that is plotted in Fig. 2 (a), where the *z* is the distance along *z*-direction [2]. The strongest magnetic field strength $B_{max(z)}$ (i.e., the peak value of $B_{z(x)}$) is experienced by electrons at the Weyl semimetal region that is closest to the top ferromagnetic layer. $B_{max(z)}$ decreases along *z*, and the field profile spreads out over wider extent in *x*. We note that the integral of $B_{z(x)}$ over *x* is constant at all depth *z* even though the peak value of $B_{z(x)}$ reduces along *z* [i.e., shown in Fig. 2 (c)]. Therefore, the magnetic gauge profiles at different depths exhibit similar characteristics, such that the maximum height of the gauge potential is independent of the field variations along *z* [i.e., shown in Fig. 2 (b)]. We perform numerical calculations by considering tunneling conductance of Weyl electrons and dividing the whole device into short segments where the magnetic gauge potential is spatially varying along *x*. The valley dependent conductance profiles are shown in Fig. 2 (d), which exhibit almost the same characteristic at different depths *z*. Our results revealed that the valley-dependent conductance profile is mostly determined by the maximum point of the magnetic gauge potential, and not sensitive to field variations along the transmission direction, as well as the direction along the B-field.

[1] C. Yesilyurt, Z. B. Siu, S. G. Tan, G. Liang, S. A. Yang, and M. B. A. Jalil, arXiv:1705.07067 (2017). [2] T. Vančura, T. Ihn, S. Broderick, K. Ensslin, W. Wegscheider, and M. Bichler, Phys. Rev. B 62, 5074 (2000).

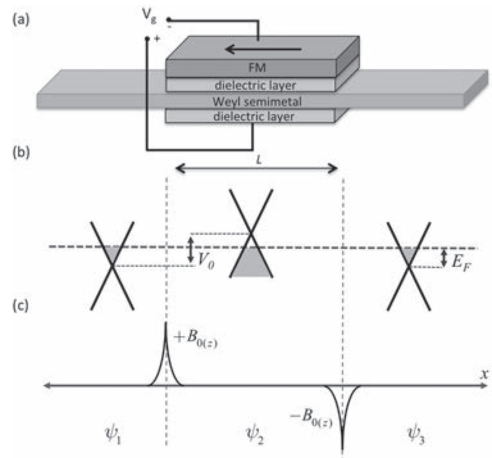

Fig. 1. Weyl semimetal with one-dimensional rectangular, square electrical potential (b) and magnetic barrier (c) induced by ferromagnetic (FM) layer deposited on the central region of the p-n-p junction.

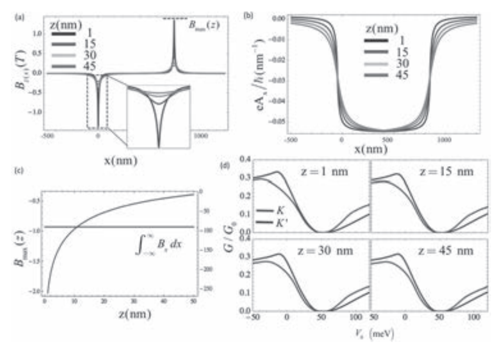

Fig. 2. Realistic magnetic barrier configuration. (a) shows magnetic field profile with two asymmetric peaks, induced at the edges of the ferromagnetic layer shown in Fig. 1. Different colors represent the field profile at different points in the z-direction. (b) shows the shift of the k_y due to the gauge potential $A_{(x)}$ induced by the magnetic fields shown in (a). The maximum magnetic field strength $B_{max(z)}$ shown in (a) reduces with increasing distance along *z*, of which characteristic calculated for continuous distance in (c), while the integration of the magnetic field over *x* is constant as shown at the right axis in (c). Since the maximum height of the $A_{(x)}$ does not depend on the field profile, the valley resolved conductance shows very similar profiles at varying depth of the device, as shown in (d).

11:30

EH-10. Nucleation and annihilation of skyrmions in spin gapless semiconductor Mn_2CoAl.

S. Granville[1,2], B. Ludbrook[1,2], G. Dubuis[1,2], A. Puichaud[1,2] and B.J. Ruck[1,2]
1. Victoria University of Wellington, Lower Hutt, New Zealand;
2. MacDiarmid Institute for Advanced Materials and Nanotechnology, Wellington, New Zealand

Magnetic skyrmions are topologically protected spin textures with great technological potential for high-density, low-power electronics in the form of magnetic storage as well as for magnonic devices [1]. The time-varying magnetic field experienced by an electron passing through a topologically non-trivial spin texture such as a skyrmion generates an emergent magnetic field that in turn exerts an additional Lorentz force on the electron [2]. This appears as an additional transverse voltage in the Hall effect, known as the topological Hall effect, allowing skyrmions to be detected electrically. A class of magnetic materials that is particularly interesting for a wide range of magnetoelectronic technologies are the Heusler alloys - many are ferromagnetic with high Curie temperatures and highly spin polarized band structures [3]. However, there have been very few efforts to explore the possible use of Heusler alloys for stabilising skyrmions at room temperature [4-6] – a critical aspect for developing a practical skyrmionic device. Recently, we have shown that perpendicularly magnetised thin films of Heusler alloy Mn_2CoAl show the electrical characteristics of skyrmions up to ambient temperature [7]. Thin films were grown by DC magnetron sputtering as multilayer stacks in the sequence MgO(2)/Mn_2CoAl(t)/Pd(2.5), where the number in parentheses is the nominal layer thickness in nanometres and t=1.3-2.6 nm. Samples were grown at ambient temperature and post-growth annealed in-situ for 1 hour at 300 °C in such a way as to induce a perpendicular magnetic anisotropy [8,9]. Hall effect measurements were made on samples patterned into Hall bars using photolithography and dry etching or lift-off, and on unpatterned samples in a Van der Pauw geometry. Figure 1 shows Hall resistivity measurements for a trilayer at different temperatures. On top of the typical anomalous Hall effect signal seen for magnetic materials, the topological Hall effect is clearly seen as a peak, appearing near the coercive field. At 3 K, where the anomalous Hall effect dominates, the topological Hall effect persists as a shoulder in (a) and (b). The topological Hall effect peaks are clearer at higher temperatures as shown in (c) and (d), indicating skyrmions exist to above 275 K. In Figure 2, we demonstrate a novel method to explore the magnetisation and skyrmion nucleation processes by studying minor loops of the Hall effect. The measurements were done at 225 K where both anomalous and topological Hall effect components are obvious. The full field sweep starts at +300 Oe, above the saturation field of the topological and anomalous Hall effects, is swept to the desired negative field and back to positive saturation at +300 Oe. This minor loop, explained with cartoons, implies that opposite skyrmion polarities can coexist in a carefully conditioned sample. The sweep to negative field is stopped just at the start of the rise in Hall resistivity (position 4) showing that the film magnetization is being reversed and some skyrmions are being annihilated. Upon sweeping the field in the positive direction, the Hall resistivity is more negative than the saturation value reached at large positive fields. This is a clear sign that, during the up sweep through zero field, some skyrmions still exist in the film. Between positions 4 and 5 there is a positive contribution to the Hall resistivity that comes from the nucleation of opposite polarity skyrmions, taking the total Hall value back to that of the positive saturated state. Conclusions: We have shown the topological Hall effect in ultrathin layers of Heusler alloy Mn_2CoAl, implying the existence of skyrmions to ~ 280 K. As shown by Hall effect minor loops, we can controllably nucleate and annihilate skyrmions of opposite polarity as well as induce a state where skyrmions of both polarities coexist.

[1] A. Fert, N. Reyren and V. Cros, Nat. Rev. Mater. 2, 17031 (2017). [2] N. Nagaosa, X. Z. Yu and Y. Tokura, Philos. Trans. A. Math. Phys. Eng. Sci. 370, 5806 (2012). [3] T. Graf, T, C. Felser and S. S. Parkin, Prog. Solid State Chem. 39, 1 (2011). [4] K. G. Rana, O. Meshcheriakova, J. Kubler, B, Ernst, J. Karel, R. Hillebrand, E. Pippel. P. Werner, A. K. Nayak and C. Felser, New J. Phys. 18, 085007 (2016). [5] A. K. Nayak, V. Kumar, T. Ma, P. Werner, E. Pippel, R. Sahoo, F. Damay, U. K. Rößler, C. Felser and S. S. P. Parkin, Nature, 548, 561 (2017). [6] S. Husain, N. Sisodia, A. K. Chaurasiya, A. Kumar, S. Akanse, A. Barman, P. K. Mudulli, P. Svedlindh and S. Chaudhary, arXiv:1703.10224 (2017). [7] B. M. Ludbrook, G. Dubuis, A.-H. Puichaud, B. J. Ruck and S. Granville, Sci. Rep. 7, 13620 (2017) [8] B. M. Ludbrook, B. J. Ruck and S. Granville, J. Appl. Phys. 120, 13905 (2016). [9] B. M. Ludbrook, B. J. Ruck and S. Granville, Appl. Phys. Lett. 110, 62408 (2017).

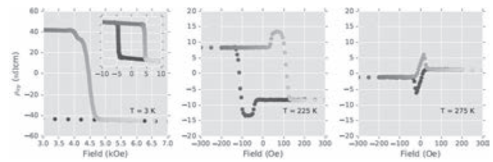

Fig. 1. Temperature range of the topological Hall effect in a trilayer with a compensation temperature of 270 K. The Heusler is 1.5 nm thick.

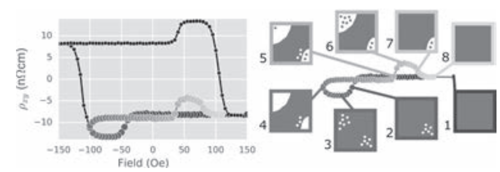

Fig. 2. Minor loop of a skyrmion-containing trilayer. The colour represents the sweep direction from blue to green.

11:45

EH-11. Anomalous Hall effect in a wide range of conductivity in Co_2FeSi Heusler-alloy thin films.

B.K. Hazra[1], S.N. Kaul[1], S. Srinath[1], M. Raja[2], R. Rawat[3] and A. Lakhani[3]
1. School of Physics, University of Hyderabad, Hyderabad, India;
2. Defence Metallurgical Research Laboratory, Hyderabad, India;
3. UGC-DAE Consortium for Scientific Research, Indore, India

Co_2FeSi thin films with different disorder states are prepared in order to tune the longitudinal resistivity (ρ_{xx}) in a wide range and investigate the scaling with anomalous Hall resistivity (ρ_{xy}). The thin films of 50 nm thickness are grown on Si (111) substrate using ultra-high vacuum dc magnetron sputtering at different substrate temperature ranging from room temperature (RT) to 600°C. The films, deposited at RT, 200°C are amorphous in nature, crystallinity improved with increase in deposition temperature. A2, B2 disorder is found in the films deposited at 450°C and 550°C respectively. 'Zero-field resistivity', ρ_{xx} (*T, H=0 Oe*), and 'in-field resistivity', ρ_{xx} (*T, H=80 Oe*), of all the thin films go through a minimum at a temperature, T_{min} and exhibit a metallic behaviour for $T > T_{min}$ as shown in fig. 1. T_{min} is maximum for the RT samples with the value of 115 K and systematically decreases with increase in deposition temperature. T_{min} is lowest (~ 12 K) for the most ordered film (550°C). In crystalline film enhanced electron-electron interaction (EEI) is the responsible mechanism for the resistivity minima wherein diffusons and weak localization give rise to resistivity minima in amorphous films. Temperature dependence of Hall resistivity isotherms are shown in fig.2 for the RT film. At any temperature, anomalous Hall resistivity (ρ_{xy}) is maximum for the RT deposited film and lowest for the ordered film (550°C). Like longitudinal resistivity, low temperature upturn is observed in Hall resistivity for the RT, 200 and 300 films [inset of fig. 2 for RT film]. In the amorphous films, upturn at low temperature is observed in ρ_{xy}, suggesting that effect of diffusons reflect in anomalous Hall resistivity ρ_{xy}. The effect of EEI is absent in ρ_{xy} for the crystalline samples, resulting no upturn in ρ_{xy} at low temperature [1]. In clean region ($10^4 < \sigma_{xx} < 10^6$ S/cm, σ_{xx} = longitudinal conductivity) side jump plays major role for the scattering mechanism of ρ_{xy} along with skew and intrinsic contributions [2]. In amorphous films (dirty region, $\sigma_{xx} < 10^4$ S/cm), anomalous Hall coefficient (R_A) scales with intrinsic resistivity, ρ_{xxT}, only when ρ_{xx} and ρ_{xy} are corrected for quantum correction of diffusons.

1. Binoy Krishna Hazra, S. N. Kaul, S. Srinath, M. Manivel Raja, R. Rawat, Archana Lakhani; *Physical Review* B 96, 184434 (2017). 2. T. Miyasato et al., Phys. Rev. Lett. 99, 086602 (2007).

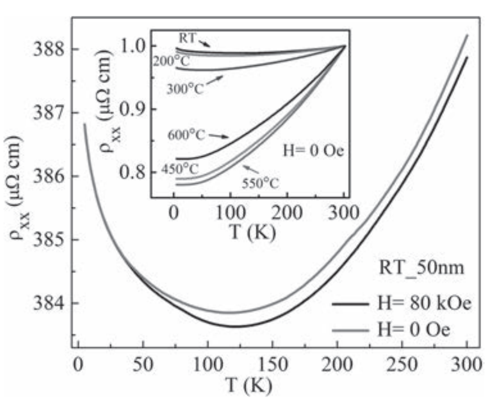

Fig. 1. Temperature dependence of zero-field and in-field longitudinal resistivity for the 50 nm Co_2FeSi thin film deposited at RT. Inset shows the normalized resistivity for the films grown at different substrate temperatures.

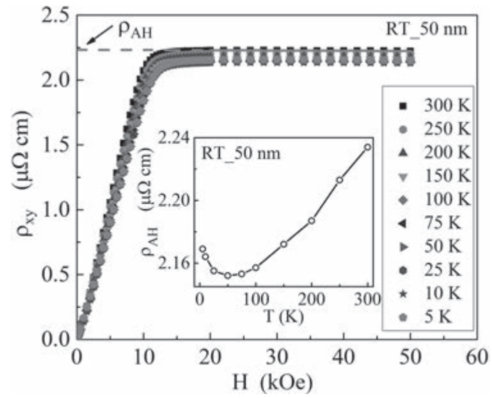

Fig. 2. Hall resistivity as a function of magnetic field measured at different temperatures for the Co_2FeSi film deposited at RT. Inset shows the observed upturn in anomalous Hall resistivity at low temperatures.

THURSDAY MORNING, 26 APRIL 2018 ORCHID II, 9:00 TO 12:00

Session EI
MAGNETIC THERAPIES AND NANOMEDICINE II

Irving Weinberg, Chair
Weinberg Medical Physics, Bethesda, MD, United States

INVITED PAPER

9:00

EI-01. Magnetic Nanoparticles for Theranostics. ***(Invited)***

Y. Ichiyanagi[1], H. Takeuchi[1], K. Fujiwara[1], T. Ide[1] and A. Oshima[1]
1. Yokohama National University, Yokohama, Japan

Magnetic nanoparticles have attracted attention for biomedical applications. One of the author reported original preparation method of magnetic nanoparticles (MNPs), and the way of functionalization by amino-silane coupling procedure [1]. We tried to introduce these functional particles into the living cells, and these particles were localized by the external magnetic field. Then cancer cell selective NPs were further developed by conjugating with folic acid [2]. We have also suggested that these magnetic nanoparticles can be utilized in biomedical applications, such as hyperthermia treatment [3] or MRI agent [4], for producing functional magnetic nanoparticles. These magnetic nanoparticles are expected as agents for future theranostics, namely, performing therapy and diagnostics simultaneously [5]. Effective heat dissipation for magnetic hyperthermia treatment in AC field depends on the magnetic relaxation parameters. Several kinds of ferrite NPs were prepared and AC magnetic measurements were performed in order to improve heating effect of MNPs for hyperthermia treatment. The relationship between imaginary part of AC magnetic susceptibility χ" and increase in temperature in the AC field was estimated. The particle size and composition of the samples were varied and examined. Fig.1 shows temperature dependence of imaginary part of AC magnetic susceptibility χ" for various particle size of $Co_{0.3}Fe_{2.7}O_4$ nanoparticles in a 1 Oe, 100 Hz field. The temperature rise of this sample upon an alternative field was measured, and it was found that the temperature increased by about 20 K under AC frequency of 15 kHz and field of 210 Oe. From the result of the temperature increase rate, heat dissipation was evaluated quantitatively according to Néel relaxation theory. An AC field was found to cause an increase in temperature, with the 7.5 nm particles exhibiting the highest temperature increase as expected. Therefore, finally *in vitro* experiments to study the hyperthermia effects of $Co_{0.3}Fe_{2.7}O_4$ particles on cancerous cells were carried out. Drastic effect of magnetic hyperthermia was observed. (Fig.2) Imaging methods are one of the effective tools for diagnostics. Specifically, magnetic resonance imaging (MRI) and mass spectrometric imaging (MSI) [6], and MNPs can be used to improve these imaging methods. Currently, main components of γ-Fe_2O_3 and Fe_3O_4 have been used for MRI contrast agents to emphasize the relaxation time of T_2 in the clinical scene. We synthesized Co-ferrite nanoparticles surrounded by amorphous SiO_2, and the relationship between these MR relaxivity and physical properties was investigated by spin echo sequence. The T_2 relaxation curves of $CoFe_2O_4 \cdot nSiO_2$ (n = 1,3,6 and removed Si) and other sample γ-Fe_2O_3, Fe_3O_4 and agarose for comparison were measured. These samples also had larger R_2 compared with conventional materials such as γ-Fe_2O_3, Fe_3O_4 and background. The parameters of T2 and R2 varied depending on only Si composition even same metal compositions, same particle size. It is considered that distance between nanoparticle and proton would be increased as the thickness of SiO_2 shell increased. Furthermore, dispersibility of nanoparticles was improved under the influence of negative charge carried SiO_2 layer. Magnetic particle imaging (MPI) and CT (X-ray tomography) imaging using our particles are in progress. Our metal oxide nanoparticles and their hybrid materials with organic compounds are anticipated to find use in the area of multifunctional nanomedicine such as magnetic hyperthermia and MRI contrast agents, called "Theranostics"

[1] Yuko Ichiyanagi, Shinji Moritake, Shu Taira, Mitustoshi Setou, *J. Magn. Magn. Mater.* 310 (2007) 2877 [2] S. Taira, S. Moritake, Y. Kai, T. Hatanaka, Y. Ichiyanagi and M. Setou, *eJ. Surf. Sci. Nanotech.*, 5 (2007) 23. [3] Takaya Kondo, Kazumasa Mori, Masaya Hachisu, Takahiro Yamazaki, Daiki Okamoto, Masatoshi Watanabe, Kohsuke Gonda, Hiroshi Tada, Yoh Hamada, Mayumi Takano, Noriaki Ohuchi, and Yuko Ichiyanagi J. Appl. Phys. 117 (2015) 17D157. [4] N. Sakai, L. Zhu, A. Kurokawa, H. Takeuchi, S. Yano, T. Yanoh, N. Wada, S. Taira, Y. Hosokai, A. Usui, Y. Machida, H. Saito and Y. Ichiyanagi, *J. Phys. Conf. Ser.* 352 (2012) 012008 [5] S. C. Wu, Y. J. Chen, H. C. Wang, M. Y. Chou, T. Y. Chang, S. S. Yuan, C. Y. Chen, M. F. Hou, J. T. A. Hsu and Y. M. Wang, *Theranostics* 6 (2016) 118. [6] S. Morimoto, T. Ishikawa, K. Hyodo, T. Yamazaki, S. Taira, K. Tsuneyama, and Y. Ichiyanagi, *Surf. Interface Anal.* 48 (2016) 1127.

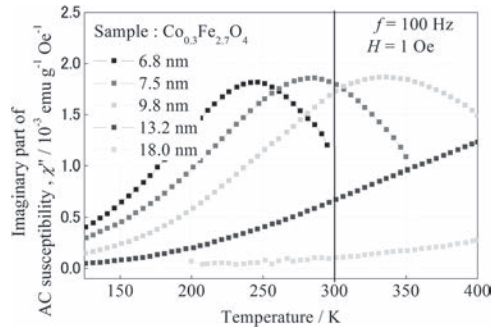

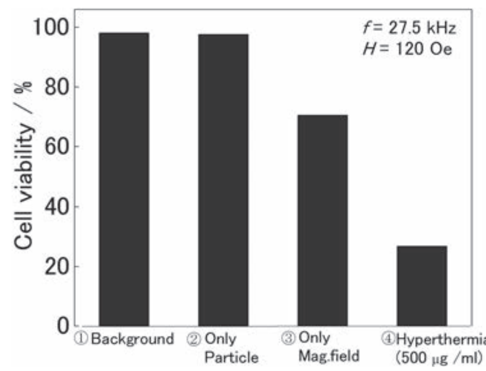

CONTRIBUTED PAPERS

9:30

EI-02. Magneto-photothermal effects of pegylated superparamagnetic iron-oxide nanoparticles for multimodal cancer therapy.

S.A. Shah[1,2], M. Hashmi[3], K. Javed[2], N. Ahmad[4] and M. Arshad[5]
1. Materials Science & Engineering, University of Washington, Seattle WA, USA, Seattle, WA, United States; 2. Physics, Forman Christian College (University), Lahore, Pakistan; 3. Superior University, Lahore, Pakistan; 4. Physics, International Islamic University, Lahore, Pakistan; 5. National Center for Physics, Islamabad, Pakistan

Magnetite (Fe_3O_4) is a favorite material to be used in biomedical applications owing to its remarkable magnetic properties and suitable biocompatibility & biodegradability. It has been widely studies as a material of choice for magnetic hyperthermia therapy, controlled drug delivery, magnetic separation and as a magnetic resonance imaging contrast agent [1-2]. Under an oscillating magnetic field magnetite nanoparticles generate heat due to Néel losses and Brownian rotations in physiological fluids [3]. Magnetite nanoparticles also respond to certain visible light wavelengths near infrared region and are excited upon irradiation. During de-excitation it releases extra energy into molecular vibration modes that transform into thermal energy [4]. Current study is about combining the magnetic hyperthermia and photothermal therapies into a single bimodal system for cancer therapy. The synthesized magnetite nanoparticles were superparamagnetic having appropriate colloidal stability due to being coated with polyethylene glycol. Cell viability and cytotoxicity were studied on HeLa cells using MTT assay and proteome apoptosis kit. They were subjected to an oscillating magnetic field of 375 kHz & 170 Oe for hyperthermia. For photothermal therapy, the system was irradiated with a laser emitting 808 nm wavelength which is a near infrared regime in electromagnetic spectrum. The two treatments were performed separately as well as in combination and the combined treatment was multifold more effective in treating the cancer cells as compared to separate sessions.

[1] K.M. Krishnan, *IEEE Trans. Magn. 46*, 2523 (2010). [2] S.A. Shah, K.M. Krishnan, et al., *Phys. Rev. B, 92*, 094438 (2015). [3] S.A. Shah, et al., *Mater. Chem. Phys, 137*, 365 (2012). [4] M. Chu, Y. Shao, et al., *Biomaterials, 34*, 4078 (2013).

9:45

EI-03. Properties of Permalloy nanodiscs in magnetic vortex state and magneto-mechanical treatment of cancer cells.

M. Goiriena-Goikoetxea[1,2], I. Orue[3], K. Guslienko[4], E. Berganza[5], M. Jaafar[5], A. Asenjo[5], D. Muñoz[6], A. Muela[6,7] and *A. García-Arribas*[2,7]
1. Electrical Engineering and Computer Science, University of California, Berkeley, CA, United States; 2. Departamento de Electricidad y Electrónica, Universidad del País Vasco, UPV/EHU, Leioa, Spain; 3. SGIKER Medidas Magnéticas, Universidad del País Vasco, UPV/EHU, Leioa, Spain; 4. IKERBASQUE and Depto. de Física de Materiales, Universidad del País Vasco, UPV/EHU, San Sebastián, Spain; 5. Instituto de Ciencia de Materiales de Madrid, CSIC, Cantoblanco, Spain; 6. Depto. de Inmunología, Microbiología y Parasitología, Universidad del País Vasco, UPV/EHU, Leioa, Spain; 7. Basque Center for Materials, Applications and Nanostructures, BCMaterials, Leioa, Spain

Magnetic dots in vortex state have been intensively studied due to their attractive properties for emerging multidisciplinary applications such as magnetic information storage, spintronics and biomedicine. In the vortex ground state, the magnetic moments are curled in the dot plane and only at the center the core of the vortex points perpendicularly to the plane. This configuration gives rise to a characteristic magnetic behavior as a function of the in-plane applied magnetic field, displaying hysteresis loops with no remanence or coercive field and open lobes at high field [1]. Apart from the intrinsic interest that this peculiar magnetic structure offers from a fundamental point of view, some appealing applications for this type of particles have been proposed, such as the magneto-mechanical actuation for cancer cell destruction [2]. This therapy employs disc-shaped particles with vortex magnetic configuration that, under an low amplitude (about 10 mT) and low frequency (tens of Hertz) AC fields, are made to oscillate, hitting and damaging the integrity of cancer cells to which they were attached. Since this actuation does not imply heat generation, in principle, the magneto-mechanical actuation avoids the risk of damaging the surrounding healthy tissue as it can occur in magnetic hyperthermia. Additionally, it is thought that the magneto-mechanical actuation leads to the apoptosis of the cells instead of the necrotic pathway caused by heating, avoiding cell-leakage in the surrounding extracellular environment and inflammatory reactions caused by necrosis [3]. In this work, we present the results obtained in Permalloy circular dots fabricated by hole mask colloidal lithography (HCL) with diameters ranging from 60 to 140 nm, and different thicknesses from 20 to 60 nm. HCL is a bottom-up fabrication technique that basically uses a monolayer of self-assembled polystyrene nanospheres to create a template of holes in a polymer film deposited over a substrate. The holes are filled with sputtered Permalloy and the polymeric template removed to produce a dense pattern of dots on the substrate [4]. For their use in the *in vitro* experiments, the nanostructures are prepared on top of a sacrificial layer that is later removed to release the discs. In this case, the discs are prepared with a thin (4 nm) gold layer on both sides. The nanodiscs on the substrate are magnetically characterized by SQUID and MOKE magnetometries, and Magnetic Force Microscopy (MFM). Additional micromagnetic simulations and analytic calculations have been performed to clarify the magnetization configuration in the dots with different diameter to thickness ratios [5]. In the dots with a diameter of 140 nm, the MFM images reveal that the vortex core occupies about half the size of the dots. This vortex core diameter is approximately equal to the dot diameter for the smaller dots (60 nm). Micromagnetic calculations confirms that, in this case, the size of the core can be even greater that the dot size. Nevertheless, this does not prevent the existence of a clear magnetic vortex behavior as demonstrated by the measured hysteresis loops. The suitability of nanodiscs for cancer cell treatment using the magneto-mechanical actuation is evaluated using lung carcinoma cells for the *in vitro* experiments. For comparing with previous studies, we simultaneously perform the experiments using Permalloy discs with a diameter of 2 μm fabricated by photolithography. The internalization process in cancer cells, along with the cytotoxic effect, and the influence of a low magnetic field on the viability of the cells are studied. We observe that the discs do not disrupt the viability of the cells, but they seem to inhibit their proliferation. The application of an alternating magnetic field to produce the magneto-mechanical actuation seems to have a scarce impact on the cell viability when using large discs (2 um in diameter) but, with the use of nanodiscs, the destroyed cell rate is increased to 30 % among the cells that have internalized discs. Figure 2 show an example of cell death by the treatment. We must stress that these results are obtained in a small number of experiments, and that we have used manual counting of cells under the microscopy (no cytometers used). In any case, although the percentages may not be statistically sound, the results prove the ability of the nanodiscs to produce irreparable changes in cancer cell integrity. Acknowledgements This work was supported by the Spanish Government under Project MAT2014-55049-C2-R and by the Basque Government under the Micro4Fab Project (KK-2016/00030). K. G. acknowledges support by IKERBASQUE (Basque Foundation for Science) and by Spanish MINECO grant FIS2016-78591-C3-3-R.

[1] K. Y. Guslienko, *et al. Phys. Rev. B* 65 (2002) 024414. [2] D-H. Kim, *et al. Nature* Mat. 9 (2010) 165. [3] J. Vakkila and M. T. Lotze, *Nature Reviews Immunology*, 4 (2004) 641. [4] M. Goiriena-Goikoetxea, *et al*. *Nanotechnology* 27 (2016) 175302. [5] M. Goiriena-Goikoetxea, *et al. Nanoscale* 9 (2017) 11269.

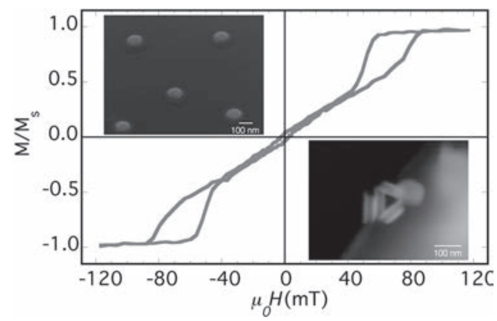

Fig. 1. Hysteresis loop of the nanodiscs with 140 nm diameter and 50 nm thick, displaying a typical vortex behaviour. Upper left inset: SEM image of these discs as prepared on the substrate. Bottom right inset: Nanodiscs detached from the substrate and covered with gold as they are used in the *in vitro* experiments.

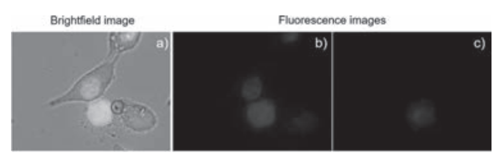

Fig. 2. Microscope images of lung carcinoma cells incubated with Permalloy nanodiscs (140 nm diameter, 50 nm thick, covered with gold), 4 h after the application of an alternating magnetic field of 10 mT and 10 Hz for 30 min. *a*) Brightfield image of the cells. The cell that has internalized nanodiscs is marked in red. *b*) NucBlue live stain marks all cells in the field. *c*) Propidium Iodine stain marks only dead cells. Only the cell that contains nanodiscs has been destroyed by the magneto-mechanical action of the discs.

INVITED PAPER

10:00

EI-04. In silico testing of clinical magnetic hyperthermia: progresses and future directions. *(Invited)*

I. Rubia-Rodríguez[1], H. Verdaguer[2], T. Macarulla[2] and *D. Ortega Ponce*[1]
1. IMDEA Nanoscience, Madrid, Spain; 2. Medical Oncology, Vall d'Hebron University Hospital, Barcelona, Spain

Computer simulations (*in silico*) have helped in vitro and in vivo experiments to develop new therapies in medicine, reducing time and costs to produce the tests. In the particular case of healthcare, in silico trials can predict the effectiveness of a treatment and optimize it to get the best benefit/risk ratio. In turn, this improvement will allow for adjusting the treatment to each patient following into high-performance, precision therapies. Magnetic hyperthermia is one of the nanotechnology-driven cancer treatments benefiting from computer simulations as the prime component of its planning platform [1]. When addressing localised tumours, magnetic hyperthermia relies on the intratumoral injection of magnetic nanoparticles that are excited by an external alternating magnetic field. The nanoparticles then release heat through hysteresis losses, eventually killing tumour cells. Magnetic hyperthermia has already been trialled in clinical settings as coadjuvant to chemotherapy and radiotherapy to successfully treat several types of tumours [2-3]. The specialised instrumental development is moving forward, and commercial systems are being deployed throughout Europe and USA [4]; nevertheless, research on safety, dosimetry, and treatment planning does not progress to the same pace. The therapy has to be adapted to each patient and tumour as well as to the evolution of the tumour along the process. Due to the complexity in programming the therapy plan for each patient, we intend to achieve a semiautomatic means to get the optimum number and placement of injections points of the nanoparticles into the tumour. The present work encompasses results obtained by jointly considering both the tumour vasculature and nanoparticle distribution inside a virtual tumour model (Fig. 1a) when simulating the power deposition in tissues. The resulting temperature distributions (Fig. 1b) generated by changing the vasculature branching and the nanoparticle distribution are discussed. In addition, in this presentation we report on our dedicated research program aimed to accelerate the pre-clinical and clinical testing of MH based on *in silico* methods.

[1] "Fundamentals and advances in magnetic hyperthermia", E. Périgo, G. Hemery, O. Sandre, D. Ortega, E. Garaio, F. Plazaola and F. J. Teran Applied Physics Reviews 2 (2015) 041302 [2] "Clinical hyperthermia of prostate cancer using magnetic nanoparticles: presentation of a new interstitial technique", M. Johannsen et al., Int. J. Hyperthermia 21, 637 (2005); "Morbidity and Quality of Life During Thermotherapy Using Magnetic Nanoparticles in Locally Recurrent Prostate Cancer: Results of a Prospective Phase I Trial", M. Johannsen et al., Int. J. Hyperthermia 23, 315 (2007); "Magnetic hyperthermia", D. Ortega and Q. A. Pankhurst, in Nanoscience: Vol. 1: Nanostructures through Chemistry (2013, RSC) p. 60. [3] http://www.nocanther-project.eu. This NoCanTher project has received funding from the European Union's Horizon 2020 research and innovation programme under grant agreement No 685795. [4] www.magforce.de

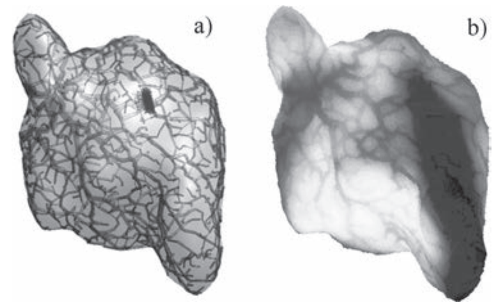

Fig. 1. a) Physical model of a real pancreatic tumour showing the modelled vasculature and the injected magnetic nanoparticles, and b) calculated temperature distribution during a therapy session.

CONTRIBUTED PAPERS

10:30

EI-05. Magnetic hysteresis, cellular uptake and cytoxicity of submicron magnetic nanodisks for biomedical applications.

P. Tiberto[1], G. Barrera[1], F. Celegato[1], M. Coisson[1], C. Divieto[1] and M. Sassi[1]
1. INRIM, Torino, Italy

Progress in nanotechnology-based fabrication process have boosted the quest to exploit magnetic nanostructures in nanomedicine (i.e. magnetic resonance imaging, controlled target-drug delivery and magnetic hyperthermia). High-aspect ratio nanoparticles (i.e. nanodisks) allow an easy remote vehiculation by magnetic fields and limit agglomeration as they display high saturation magnetisation and zero remanence values [1]. Au-layers allow an easy functionalisation for target controlled released. Magnetic $Ni_{80}Fe_{20}$ nanodisks (30 nm thickness and diameter ranging in the interval 200 – 650 nm) having disc shape have been fabricated and directly coated by a Au layer by means of a bottom-up self-assembling nanolithography process assisted by polystyrene nanospheres [2]. The room-temperature magnetic behavior of the two systems dispersed in liquid is reported in Fig. 1a (disks diameter having diameter 650 nm). In both cases, the typical shape of magnetization vortex nucleation is observed. In fact, the loops exhibit a magnetic remanence close to zero and an almost linear behaviour at low fields followed by an increase of hysteresis at fields preceding the magnetic saturation. In particular, the low-field reversible linear behaviour corresponds to the movement of magnetic vortex perpendicular to the applied field across the nanodisk In addition, the Au-layer is seen not substantially alter the magnetic behavior being the annihilation and nucleation vortex field practically the same for the two systems. Despite their multifunctionality, two major issues prevent the application of magnetic nanostructures in nanomedicine as biocompatibility and cellular uptake for submicron nanoparticles. To this aim, in-vitro toxicity assessment of the nanodisks will be here discussed together with the evaluation of cellular uptake. To assess the cell viability, PT-45 cells (human lung cancer) have been exposed to varying concentrations of nanodisks with and without the protective gold layer (from 0.12 to 58 μg/ml) in order to investigate their cytotoxicity. Generally, a considerable fraction of cells remains alive and proliferate at all nanodisks concentration. The metabolic activity value is similar to the one obtained in absence of magnetic nanoparticles. As expected, lower cytotoxicity has been observed over time when cells were exposed to Au- covered nanodisks compared with bare nanodisks Electron microscopy images have been acquired with a FEI Inspect-F scanning electron microscope (SEM) equipped with three different detectors: secondary electrons (SE), backscattered electrons (BSE) and transmitted electrons (STEM). The results are reported in Fig. 1 b, c and d after dispersing 58 μg/ml in PT-45 cells. After careful washing they were transferred to a TEM holey carbon grid. The combination of the three different detectors allows, by comparing the images, to clearly distinguish le presence of several nanodisks in the cells or in their membrane. The effectiveness of the washing procedure is demonstrated by the fact that there no nanodisks can be observed neither on the holey carbon structure nor on the copper grid. The remaining nanodisks have therefore become part of the cells, having adhered to their membrane or having being internalised making magnetic submicron nanodisks good and realistic candidate for application in nanomedicine and theranostics.

[1] D.H. Kim, Nat Mater., 9, 165 (2010) [2] G. Barrera et al., Inter. Focus, 17B304 (2016)

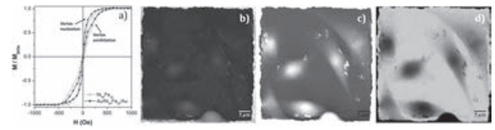

Fig. 1. (a) Room-temperature magnetisation loops of free standing nanodisks dispersed in deionized water (green circles and blue triangles for bare and Au-coated $Ni_{80}Fe_{20}$ disks respectively); (b) Electron microscopy images (secondary electrons) of PT45 cancer cell in which Au-coated $Ni_{80}Fe_{20}$ disks (650 nm) have been dispersed; (c) Same as in (b) for backscattered electrons and (d) Same as in (b) for transmitted electrons (STEM)

10:45

EI-06. Fe-Cr-Nb-B magnetic nanoparticles - a good solution for cancer cell destruction by magneto-mechanical effect.

H. Chiriac[1], E. Radu[1,2], M. Tibu[1], D. Herea[1], L. Labusca[1] and N. Lupu[1]
1. National Institute of Research and Development for Technical Physics, 47 Mangeron Boulevard, 700050 Iasi, Romania, Iasi, Romania; 2. Physics, Alexandru Ioan Cuza University of Iasi, Iasi, Romania

Magnetic particles (MPs) were found useful in different cancer treatment applications such as magnetic hyperthermia, magnetic controlled delivery and release of antitumoral drugs at the targeted site of a tumour [1-3]. Lately, cancer cell destruction techniques involving the movement of magnetic particles in alternative magnetic fields (MFs) came to the fore [4, 5]. Once the destruction effect of moving MPs on cancer cells was demonstrated, researches focused on the study of magnetic materials appropriate for this application and their magnetic properties in order to achieve a larger mechanic torque of MPs under the alternative MFs action. In this work, we aimed to find proper MPs for this type of application – MPs that can be produced by a controllable process in a large amount without involving costly technologies. For this experiments we used a new type of particles developed by us, with the nominal composition Fe79.7-xETMxNb0.3B20 (ETM = Cr, Ti, Mn; x = 12÷20 at.%), which exhibit high saturation magnetization, characteristic that leads to an increased magnetic torque and force of action on cellular membrane and high magnetic susceptibility that make the actuation of the particles possible even in low magnetic fields and low Curie temperature. These particles are suitable for self-controlled hyperthermia application [6], and were obtained by high energy ball milling of FeCrNbB amorphous ribbons prepared by rapid quenching from the melt. The size of the particles is ranging between 20 – 200 nm, depending on the milling conditions and they present a particular non-spherical and irregular shape which leads to an improved amplitude of the movement in the rotating alternative MFs caused by the shape anisotropy. We have applied linear and rotating alternative magnetic fields and studied the influence of the intensity of the field, its frequency, and the time of exposure on cellular viability. The MPs were dispersed in calcium gluconate prior adding in cell culture media. In order to set up the experiments, we designed a system consisting of four coils placed in cross which can be supplied either to produce a MFs variable in time providing a high gradient moving from one coil to another or to produce a rotating MFs and a special electronic system which allows us setting of the MFs intensity, its frequency and the time of exposure. In the centre of the coils system there is a space of about 20 cm^3 where the MFs is uniform, where cell culture plates containing cells to be studied can be placed. A device which allows temperature variation can be inserted in order to modify and maintain the desired temperature of the cell plates. We have first evaluated the cytotoxicity of the FeCrNbB ferrofluid for concentrations of MPs in cell culture media ranging between 0.5 – 5 mg/ml and we observed that there is no cytotoxic effect even at high concentration rates such as 5 mg/ml. A systematic experimental setup was then performed by analysing one by one the parameters involved in the MFs– cells – MPs interaction, such as frequency and intensity of the field, time of exposure and magnetic particle concentration. We have observed that the concentration of MPs in cell culture media, when the cells are exposed in rotating magnetic field, has an important influence on cellular viability, as shown in figure 1. The higher concentration of MPs is, the lower the viability of cells after treatment becomes, reaching 14% cellular viability at a concentration of 5 mg/ml for a time of treatment of 10 minutes and a field intensity of 1 mT. The influence of time of exposure on cellular viability was also tested by applying the rotating MFs for 5, 10, 15 and 20 minutes on osteosarcoma cells, at a field intensity of 1 mT and a frequency of 20 Hz. The results show that, when we increase the time of cells exposure in MFs cellular viability is decreasing sharply. Following the same experimental setup we have tested the influence of field intensity and its frequency and observed that in both cases the cellular viability decreases with the increase of the frequency or of the field, but only to specific values. In an additional experiment, we sought to check if a simultaneous overlapping of hyperthermia treatment with rotating magnetic fields could boost the cytotoxicity. The heating effect was induced by a laboratory-made incubation system with the walls heated by water recirculated by a thermostated bath. Temperature of the cell culture well was raised from 37°C to about 46°C and the magneto-mechanical treatment was applied for 3 minutes from the moment temperature reached 45°C in the well. The results showed that the viability of osteosarcoma cells was reduced to about 80% when a conventional hyperthermic regime was applied and decreased to 73 % when hyperthermia was conjugated with rotating magnetic field. While the applied treatments were efficient for killing the human cancer cells, normal cells (fibroblasts) were not affected by the hyperthermia or rotating MFs combined with hyperthermia. Acknowledgments: 3MAP NUCLEU Programme 2018

[1] Reddy, L.H., Arias, J.L., Nicolas, J., Couvreur, P. Magnetic nanoparticles: design and characterization, toxicity and biocompatibility, pharmaceutical and biomedical applications. Chem. Rev.112 (11), 5818–5878 (2012). [2] Oliveira, H. et al. Magnetic field triggered drug release from polymersomes for cancer therapeutics. Journal of Controlled Release 169, 165–170 (2013). [3] Garaio, E. et al. Specific absorption rate dependence on temperature in magnetic field hyperthermia measured by dynamic hysteresis losses (acmagnetometry). Nanotechnology 26, 015704 (2015). [4] Kim, D. H. et al. Biofunctionalized magnetic-vortex microdiscs for targeted cancer-cell destruction. Nature Materials 9, 165–171 (2010). [5] Cheng, D., Li, X., Zhang, G. & Shi, H. Morphological effect of oscillating magnetic nanoparticles in killing tumor cells. Nanoscale Research Letters 9, 195 (2014). [6] Chiriac et al., Low TC Fe-Cr-Nb-B glassy submicron powders for hyperthermia applications J Appl Phys 115, 17B520 (2014)

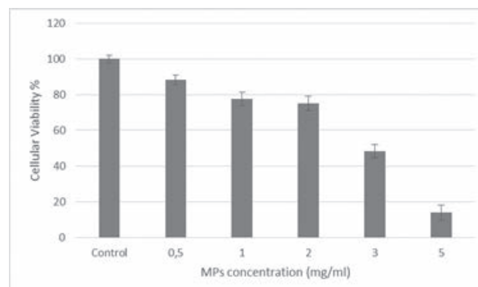

Fig. 1. Cellular viability of osteosarcoma cells with concentration of ferrofluid in cell culture media, after the exposure in an alternative magnetic field

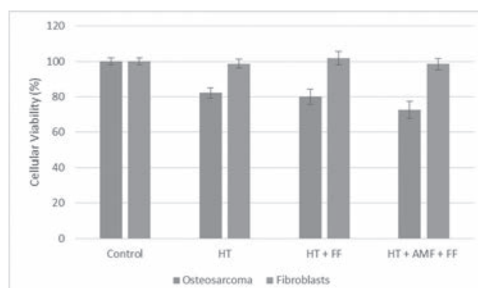

Fig. 2. Cellular viability of osteosarcoma cells with concentration of ferrofluid in cell culture media, after the exposure in an alternative MFs of 1mT at 20 Hz. (HT – cells exposed to hyperthermia, HT+FF – cells loaded with ferrofluid and exposed to hyperthermia, HT + AMF + FF – cells loaded with ferrofluid and exposed to hyperthermia)

11:00

EI-07. Twin Coil Design Considerations for Depth and Focality in Transcranial Magnetic Stimulation.

S. Chang[1], X. Wei[1], Z. Zhang[1], S. Li[1], J. Wang[1] and G. Yi[1]
1. School of Electrical and Information Engineering, Tianjin University, Tianjin, China

INTRODUCTION As a non-invasive stimulation treatment, the transcranial magnetic stimulation (TMS) utilizes the magnetic pulses to modulate neural activities via the induced electric field inside brain. The corresponding stimulation depth and focality determines the locus of activation in the brain, which is the most technical concern for the design of stimulating coils of TMS systems. Previous studies have shown that the twin coil can offer an enhanced stimulation performance, whereas the relationship between electric field spatial features and twin coil geometry has nearly unexplored before. Accordingly, this paper carries out a comprehensive analysis for the impact of the coil size and the angle on the stimulation depth and focality, which aims to provide theoretical basis on the optimal design and contribution of twin coils for TMS researchers and clinicians. METHODS The exemplified model are set up based on the finite element method, where the human head is modelled as a homogeneous sphere with the 170 mm diameter and the isotropic conductivity of 0.33 S/m. The distance between the stimulation coil and the surface of the head is 5 mm. In order to reveal the impact of the coil size and angle on the stimulation performance, as depicted in Fig. 1(a), the coil diameter and the opening angle are adjusted from 102 mm to 162 mm and from 60° to 180°, respectively. Fig. 1(b) shows the corresponding distribution of twin-coil-induced electric field on the surface of the human brain. By choosing the depth and the focality as the performance indicators of TMS systems, the penetration of the electric field can be quantified as the half-value depth ($d_{1/2}$). It is the distance between the head surface and the deepest position with the half value of the maximum electric field strength. In addition, denote the half-value volume as $V_{1/2}$, which is the volume of area where the strength of the electric field is stronger than the half of the maximum value. Besides, the focality is quantified by the tangential spread ($S_{1/2}$), which is the ratio of the half-value volume to the half-value depth, namely $S_{1/2}=V_{1/2}/d_{1/2}$. RESULTS As shown in Fig. 2(a), the exemplified twin coils with the diameter of 102mm, 122mm, 142mm and 162mm have the maximum electric field half-value depth $d_{1/2}$ when the opening angle is 100°, 120°, 140°, and 160°, respectively. Fig. 2 graphically shows that $d_{1/2}$ has a peak value along with the increases of the opening angle, while the electric field spread $S_{1/2}$ increases monotonically with respect to the opening angle. In addition, Fig 2(c) depicts the electric field $S_{1/2}$-$d_{1/2}$ locus with the coil size and opening angle change. The corresponding deepest half-value depth values of exemplified four twin coils are 23.7mm, 26.3mm, 29.6mm and 31.5mm, respectively. When $d_{1/2}$=29.6 mm, the values of $S_{1/2}$ of 142-mm coil and 162-mm coil are 188cm^2 and 151 cm^2. It shows that the coil size determines the maximum half-value depth value, namely the larger coil the deeper half-value depth. Furthermore, for the identical stimulation half-value depth, the increased size of the simulation coil can also enhance the electric field focality. Thus, the optimal design of the coil size can offer salient advantages of the depth and the focality of the induced electric field, thus effectively improve the stimulation performance for TMS systems. CONCLUSION This paper carried out a comprehensive analysis on the impact of the coil size and the opening angle of twin coils on the stimulation depth and the focality. According to the computational simulation, the main result can be summarize as: (i) there is a deepest stimulation depth when the opening angle is adjusted, (ii) the coil size limits the maximum stimulation depth, (iii) the large coil has salient advantages of the depth and the focality. The presented results shows significant meanings for researchers and clinicians to design or configure the optimal twin coil for TMS systems. Besides, the detailed parameters, theoretical analysis, simulated results, and experiment results will be presented in the full manuscript.

[1] Z. D. Deng, S. H. Lisanby, and A. V. Peterchev, "Electric field depth-focality tradeoff in transcranial magnetic stimulation: simulation comparison of 50 coil designs," *Brain Stimulation*, vol. 6, no. 1, pp. 1-13, 2013.

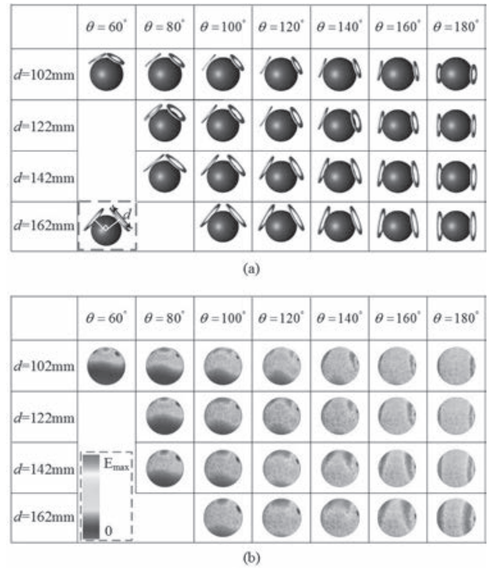

Fig. 1. Simulated results: (a) testing scheme; (b) distribution of induced electric field on head surface.

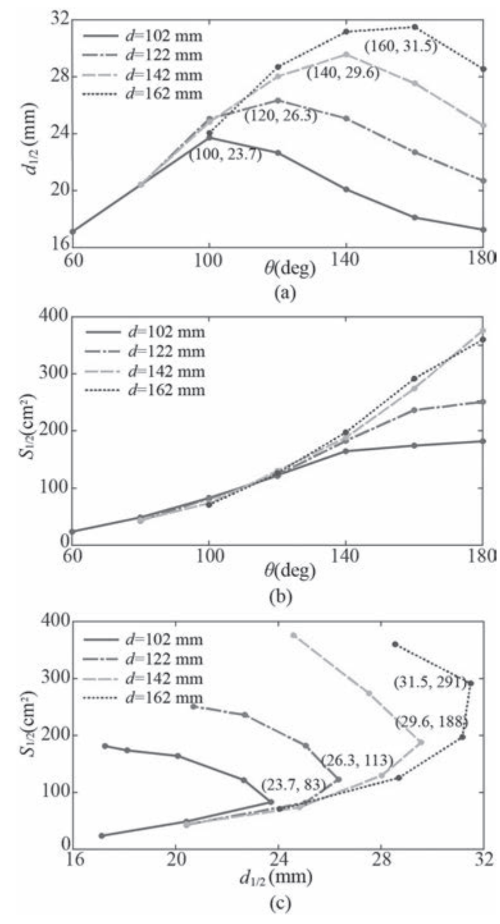

Fig. 2. Comparative analysis: (a) depth of electric field $d_{1/2}$; (b) electric field spread $S_{1/2}$; (c) locus of $S_{1/2}$ vs $d_{1/2}$.

11:15

EI-08. Development of Angular Coil for Transcranial Magnetic Stimulation.

M.A. Yedeas[1], Y. Kawasaki[2], S. Liu[1], J. Gu[1], Y. Saitoh[3] and M. Sekino[1]
1. Department of Electrical Engineering and Information Systems, Graduate School of Engineering, The University of Tokyo, Tokyo, Japan; 2. Department of Bioengineering, Graduate School of Engineering, The University of Tokyo, Tokyo, Japan; 3. Department of Neuromodulation and Neurosurgery, Graduate School of Medicine, Osaka University, Osaka, Japan

Recent studies show that transcranial magnetic stimulation (TMS) is effective for the treatment of neurological and psychiatric diseases, however, the therapeutic effect varies significantly among patients. The distribution of the electric fields induced by TMS is affected by individual variability in the shape of the human head and by the targeted area of the brain, thus, the efficiency of the existing magnetic stimulators or coils varies considerably among patients because of their fixed geometries. Moreover, all existing coils are subjected to a depth focality tradeoff limiting their use to narrow area of TMS application. In this study, we try to create a universal coil with a variable geometry by employing figure-of-eight coil with bending wings, as shown in Figure 1. A novel rotary mechanism is proposed to realize this coil and we name it as Angular coil or Acoil. In numerical simulations with a human brain model, we found that its optimal angular degree is markedly different between not only subjects but also stimulation positions. We define the efficiency of the coils by the value of the induced eddy current density in the targeted area of the brain for the same driving current intensity. Numerical simulations through scalar potential finite difference (SPFD) method were conducted on a conductive sphere model to study the depth and focality characteristics of the stimulation induced by Acoil for bending angles ranging from 90 to 180 (figure of eight coil configuration) degrees. Then, using the same numerical method on real brain models constructed from MR images of 5 healthy human subjects, we measured the induced eddy current in the motor cortex left hand, foot and face areas by the Acoil for different bending angles. The positions of the coil were defined by medical doctors using a neuronavigation system. For the study of the coil stimulation characteristics. we calculated the magnetic flux density for different distances from the center of the coil revealed that by bending the coil, we could obtain a stronger magnetic field with a higher field penetration and the highest values were obtained in the case of 90 degrees bending which is the most acute angle for this study. We found through the study on the conductive sphere model that for a range of 30 degrees bending from a figure of eight coil configuration (180 degrees), we could obtain a focused stimulation with a higher efficiency the more we bend the coil. For bending angles ranging from 120 to 150 degrees, the stimulation was deeper and more efficient but much less focalized compared to figure eight-coil. Thus, we could conclude that the bending angle that had the best depth-focality tradeoff for the case of Acoil was 150 degrees. Finally, for 90 to 120 bending angles, The stimulation was neither deep nor focalized because the angle becomes largely acute so we are obliged to elevate considerably the coil center from the sphere surface to avoid the penetration of the wings in the model, losing the efficiency of the coil. The results with brain models show that the efficiency of the stimulation varies considerably among the subjects and for the different brain areas, as shown in Figure 2. However, because of the variable geometry of the Acoil, we could adapt its shape to obtain the most efficient stimulation defining the best bending angle in each case, with an increase in efficiency of an average 30% compared to baseline figure of eight coil for all the cases. Furthermore, we found that the stimulation is the most efficient for the bending angles for which the coil fits the head geometry and has a maximum contact with the scalp. In fact, we demonstrated through the study of the stimulation characteristic that Acoil can be used to provide efficient focused stimulations and deep stimulations depending on the bending angle covering a wide area of TMS applications (nTMS, dTMS, rTMS among others).

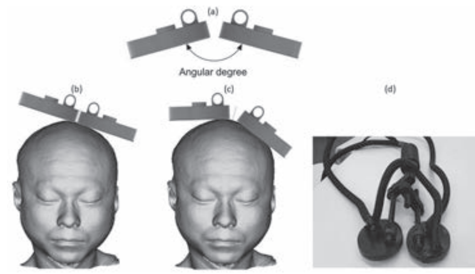

Fig. 1. (a) Acoil model. (b) Head model constructed form MR mages and Acoil with 180 degrees bending angle in the position defined by medical doctors for the stimulation of the foot area of the brain. (c) Same head model and Acoil with 140 degrees bending angle. (d) Prototype of Acoil.

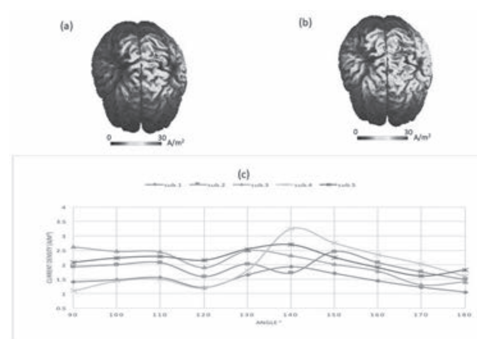

Fig. 2. Study of the efficiency of Acoil for the stimulation of the foot area of the brain for different bending angles considering 5 human subjects. (a) Distribution of the eddy current induced in subject 4 brain after the stimulation by Acoil with 180 degrees angle. (b) Distribution of the eddy current induced in subject 4 brain after the stimulation by Acoil with 140 degrees angle which is the most efficient bending angle for the stimulation of subject 4 foot area. (c) Evolution of the eddy current density induced by Acoil for different bending angles in the foot areas of 5 human subjects brains. From this graph, we can conclude that the most efficient angle for subject 4 is 140 degrees.

11:30

EI-09. Flexibility of Micro-magnetic Flagella in the Presence of an Oscillating Field.

Y. Li[1] and C. Yen[1]
1. Department of Mechanical and Aerospace Engineering, National Defense University, Taoyuan, Taiwan

Magnetic microbeads have recently been the subject of much study because of their potential applications in microfluidic systems which facilitate mixing[1], labeling[2], separation[3] and transport[4] in lab-on-a-chip devices. It has been proposed that rotating superparamagnetic beads chains can enhance the mixing efficiency in microfluidic devices[5] and the magnetic micro-bead chain that is subjected to an oscillating field can be used to design a micro-swimmer[6]. To manipulate the micro-beads chain swimming in the low-Reynolds number environment, various magnetic actuation methods have been employed to obtain the higher propulsive efficiency for the locomotion in the viscous fluid. A flexible flagellum is arguably the simplest mechanism to duplicate as it is a one-dimensional structure. However, a challenge to create the stable planar beating motion for propulsion generation is to fabricate the magnetic flagellum simultaneously flexible and stable structure at a microscale. In order to effectively use an oscillating magnetic flagellum as a tail of a microswimmer, the measurement of the bending rigidity for the flexible micro-chains is essential. In this study, the curvatures and the bending rigidity of distorted chains with different lengths subjected to an external field with various controlling parameters (such as the field intensity and frequency) were probed to evaluate the flexibility of the magnetic flagellum. The magnetic flagellum is obtained by combining the self-assembling ability of micro-sized superparamagnetic particles composed the iron oxide magnetite (Fe_3O_4) embedded in polystyrene microspheres suspended in distilled water. Properties of the commercially available micro-beads are density ρ=1500 kg/m^3, diameter $d = 4.5$ μm, initial magnetic susceptibility $\chi = 1.6$, and without magnetic hysteresis or remanence, which could be magnetized under an applying external field and completely demagnetized when the field is removed. Firstly, the magnetic beads magnetized by a homogeneous static field H_d tended to aggregate and form the linear flagellum, and a dynamical sinusoidal field H_y with a maximum amplitude H_p and an adjustable frequency f, that is, $H_y = H_p \sin(2\pi ft)$, were then applied in a direction perpendicular to H_d. Thus, the planar beating motion is created to form the dynamic flexible flagellum. In order to accurately obtain the chain flexibility and bending rigidity, we model the waggling chains as continuous elastic flagella and analytically derive their curvatures as a function of magnetic field strength. The maximum dimensionless curvature (denoted as C_{max}) of the chain is given as $C_{max}=d/R$, R represents the flagellum's radius of curvature. The bending rigidity κ of the waggling chain is measured from the S-shape of the chain by using the equation given as[4]: $C_{max}=(Bd/4)(\pi/3\kappa\mu_0)^{0.5}$ Where the μ_0 represents the vacuum permeability, B is the overall magnetic field strength. Figure 1 shows the most significant deformed shapes for the flexible flagella of various lengths subjected to the increasing field strength. It can be seen that all the chains bend to S-shape for all values of applying field strength, and the deformation increases slightly with an increase in the perpendicular dynamic field intensity H_p for each flagellum. On the other hand, the influences of flagellum strengths are not consistent. By examining figure 1 carefully, we found the increase of the length doesn't enhance the deformation significantly. On the contrary, the longer length as flagellum consisting of 16 particles (denoted as P16) behaves more insignificant S-shape than the counterpart of the P15 chain because of the more significant constraint from the stronger hydrodynamic drag acting on a longer chain. The further inspection of the interesting finding can be done by the examination of figure 2, which shows the geometrical relation between the flagellum's radius of curvature R and the diameter d of the magnetic bead. It can be seen that for all lengths of flagella the maximum curvature of the flagellum increases linearly with the intensity of the applied field. In addition, the value of C_{max} of the flagellum firstly gets higher then declines with the increase of the length, which indicates the magnetic flagellum subjected to an oscillating field would have the most flexible structure at the certain length. The further discussions are shown in full paper demonstrating the effects of the other controlling parameters on C_{max} and the bending rigidity κ.

[1] S. L. Biswal and A. P. Gast, *Anal. Chem.*, 76(2004), 6448-6455. [2] J. Kolosnjaj-Tabi, C. Wilhelm, O. Clément and F. Gazeau, *J. Nanobiotechnology,* 11(2013), 1 [3]N. Minc, C. Fütterer, K. D. Dorfman, A. Bancaud, C. Gosse, C. Goubault, and J. L. Viovy, *Anal. Chem.,* 76(2004), 3770-3776. [4] R. Dreyfus, J. Baudry, M. L. Roper, M. Fermigier, H. A. Stone and J. Bibette, *Nature*, 437(2005), 862-865. [5] R. J. S. Derks, A. Dietzel, R. Wimberger-Friedl and M. W. J. Prins, *Microfluid. Nanofluid.,*3(2007), 141–149. [6]K. E. Peyer, L. Zhang, and B. J. Nelson. *Nanoscale*, *5* (2013), 1259-1272.

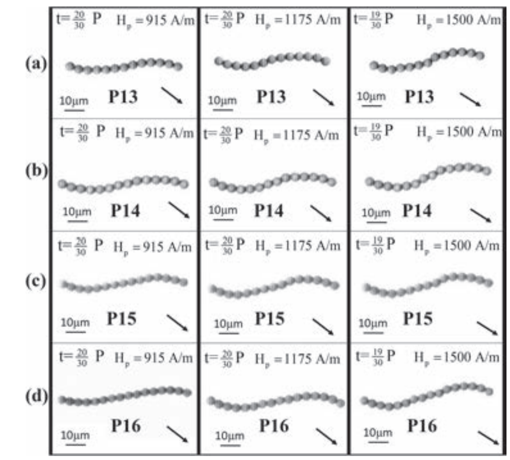

Fig. 1. The most significant deformed snapshots of the waggling flagellum comprising (a)13, (b)14, (c)15, and (d)16 particles (denoted as P13, P14, P15,and P16, respectively) in a field configuration of H_d =1450 (A/m), and the various H_p = 915(A/m), 1175(A/m) and 1500(A/m) with f = 1 Hz.

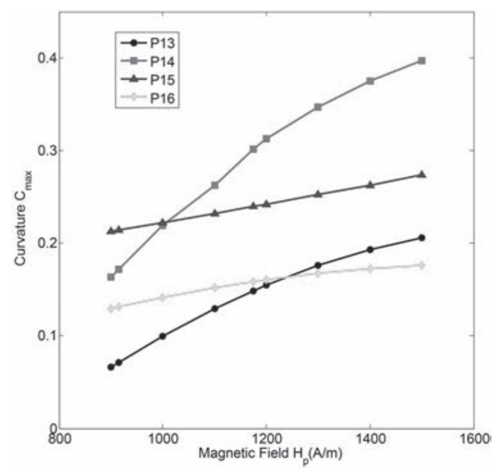

Fig. 2. Maximum dimensionless curvatures (C_{max}=d/R) as a function of the magnetic field intensity for different lengths of the flexible flagella shown in figure1.

11:45

EI-10. Novel Electromagnetic Targeting System for Navigating Surgery in Endobronchoscopy.

C. Chen[1], C. Lin[1,2], Y. Cheng[1], T. Chung[1], C. Chang[1], S. Tsai[1], J. Chen[1] and X. Lin[1]
1. National Chiao Tung University, Hsinchu, Taiwan; 2. National Taiwan University Hospital, Taipei, Taiwan

I. INTRODUCTION Nowadays, lung cancer is one of common cancers around the world. To increase the survival rate of the patient, early diagnosis is necessary. To achieve this, bronchoscopists usually use endobronchial ultrasound for navigating surgery in endobronchoscopy. However, because the bronchoscopist has to continuously re-navigate/re-target the bronchoscope to collect specimens from the same tumor, the whole navigating/targeting process has to be repeated many times in one surgery. Due to this, navigating/targeting the bronchoscope to correct/same tumor is still a time-consuming process. Therefore, a more accurately tumor-targeting approach is needed to significantly save time in navigating surgery. To address this issue, recently researchers combined electromagnetic (magnetic-sensor-based) targeting technology with conventional endobronchial ultrasound as a hybrid targeting approach to achieve a more accurate real-time tumor-targeting in endobronchoscopy [1]. However, when comparing conventional bronchoscopes, the bronchoscope with magnetic sensor is more expensive and less compatible. Thus, a cheaper and compatible electromagnetic targeting technology is required. Recently, some researchers demonstrated electromagnetic-induction/magnetic-interaction approaches to target distal screw-hole in intramedullary interlocking-nail surgery [2]-[5]. We think that these targeting approaches can be modified to develop as a new, cheaper, and compatible electromagnetic targeting technology for general endobronchoscopy. Hence, in this paper, we demonstrate the electromagnetic targeting system for endobronchoscopy. II. DESIGN The system is illustrated in figure 1(a). The system consists of an emitting electromagnets-array, a receiving electromagnets-array, a 2D model of bronchial tree, and a high-permeable silicon-steel collar fixed on an endobronchoscopic guide sheath. The targeting principle of the system is shown in figure 1 (b)(c). As shown in figure 1(b), an AC current is applied to the emitting electromagnets-array to produce AC magnetic flux. Consequently, the magnetic flux is received by the receiving electromagnets-array. Due to the electromagnetic-induction, each receiving electromagnet produces a corresponding voltage output. When the guide sheath with the collar travels through the air gap between the emitting and receiving electromagnets no. 1, the collar concentrates the magnetic flux and thereby the magnetic flux received by the receiving electromagnet no. 1 is increased. Thus, the voltage output of receiving electromagnet no. 1 is increased. However, at this moment, the magnetic flux in the other air gaps is not concentrated. Thus, the voltage outputs of the other receiving electromagnets are not changed. By analyzing these voltage changes of receiving electromagnets, the location of the collar/guide-sheath is targeted. III. FABRICATION Figure 1(d) shows fabrication result of the system. We used AWG 25 enameled wires and silicon-steel stack to fabricate an electromagnet. 12 electromagnets are arranged on a print-circuit-board as the emitting electromagnets-array (note: same fabrication-process for the receiving electromagnets-array). The 2D model of bronchial tree is produced from PMMA plate by laser machining. We used aluminum extrusion beams and PMMA plates to fabricate the mechanical frame. The silicon-steel collar is attached on the guild sheath. Finally, we assembled the electromagnets-arrays, 2D model, mechanical frame, and emitting/receiving-electronics (i.e., switches, function generator, and lock-in amplifier) as the system. IV. TESTING AND RESULTS The testing procedure, shown in figure 2(a), is guiding the guide sheath (silicon-steel collar) to insert into right primary bronchus and sequentially travels above the receiving electromagnet no. 2, 7, and 12. While the sheath/collar is traveling, we use the lock-in amplifier with the switch to sequentially measure voltage output of each receiving electromagnet. The voltage outputs are shown in figure 2(b)-(d). When the collar is above the electromagnet no. 2, the voltage output of the electromagnet no. 2 becomes relatively large. When the collar travels away from electromagnet no. 2 toward no. 7, the voltage output of the electromagnet no. 2 and 7 gradually decreases and increases, respectively. When the collar is above the electromagnet no. 7, the voltage outputs of electromagnet number 7 is relatively large. Similarly, the change of voltage output of the electromagnet no. 12 is similar as the electromagnet no. 7. By analyzing the changes of the voltage outputs of the electromagnets, the location of the collar (with the guide sheath) in the 2D model of bronchial tree is successfully targeted. V. CONCLUSION We demonstrated a novel electromagnetic targeting system for navigating surgery in endobronchoscopy. Experimental results show that the system successfully targeted the guide sheath traveling in bronchial-tree model. This means the system can navigate the bronchoscope and forceps for surgery. In the future, we will continuously improve the system and apply the system to clinical test. VI. ACKNOWLEDGEMENT Chin-Chung Chen and Chin-Kai Lin are equal contribution (co-first author). All authors thank the support provided by the Taiwan Ministry of Science and Technology (No. 105-2628-E-009-001-MY2).

[1] H. Sorder, E. F. Hofstad, T. Amundsen, T. Lango, J.B.L. Bakeng, and H. O. Leira, "A multimodal image guiding system for navigated ultrasound bronchoscope (EBUS): a human feasibility study", *PLos One*, vol. 12, no. 2, e0171841, Feb., 2017. [2] T. H. Wong, T. K. Chung, T. W. Liu, H. J. Chu, W. Y. Hsu, P. C. Yeh, C. C. Chen, M. S. Lee, and Y. S. Yang, "Electromagnetic/magnetic-coupled targeting system for screw-hole locating in intramedullary interlocking-nail surgery", *IEEE Sen. J.*, vol. 14, no. 12, pp. 4402-4410, Dec., 2014. [3] T. K. Chung, H. J. Chu, T. H. Wong, W. Y. Hsu, M. S. Lee, W. T. Lo, and C.Y. Tseng, "An electromagnetic-induction approach for screw-hole targeting in interlocking-nail surgery", *IEEE Sen. Conf.*, Taipei, Taiwan, pp. 1704-1707, Oct., 2013. [4] T. K. Chung, H. J. Chu, T. H. Wong, Y. W. Cheng, W. Y. Hsu, and M. S. Lee, "Electromagnetic coil/inductance-based nondestructive methods for locating distal screw-holes of an intramedullary interlocking-nail", *in Proc. SPIE.*, vol. 8695, pp. 86952, Apr., 2013. [5] T. H. Wong, M. S. Lee, S. Y. Wu, W. Y. Hsu, T. K. Chung, C. P. Wu, P. J. Hsu, Y. S. Yang, "Novel passive two-stage magnetic targeting devices for distal locking of interlocking nails", *J. of Healthc. Eng.*, vol. 2017, pp. 3619403, Aug., 2017.

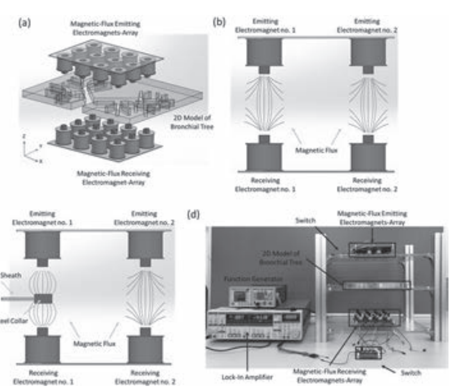

Fig. 1. Targeting system: (a) illustration, (b)(c) targeting principle, (d) photograph.

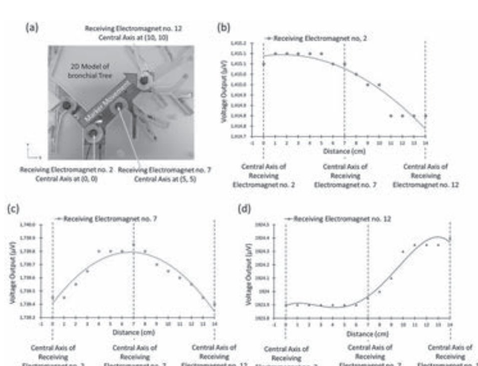

Fig. 2. (a) Testing procedure, (b)(c)(d) Experimental results of targeting system.

Session EP
EXCHANGE COUPLING, SUPERCONDUCTIVITY AND ELECTRONIC STRUCTURE I
(Poster Session)

Xiaolin Wang, Chair
University of Wollongong, Wollongong, NSW, Australia

EP-01. Thickness dependence of spin polarization in Co_2FeAl thin films.

X. Zhang[1], L. He[1], Y. Xu[1,2] and W. Liu[2]
1. Nanjing Unversity, Nanjing, China; 2. University of York, York, United Kingdom

Half-metallic ferromagnets (HMFs) have only one spin channel for conduction at the Fermi level, while they have a band gap at the other spin channel. Therefore, in principle this kind of material has 100% spin polarization for high efficient spin dependent transport, which is perfect for spin injection, spin filtering, and spin transfer torque devices. We have studied the half-metallic Co_2FeAl thin films with different thicknesses epitaxially grown on GaAs (001) by molecular beam epitaxy. The magnetic properties and spin polarization of the films were investigated by *in-situ* magneto-optic Kerr effect (MOKE) measurement and spin-resolved angle-resolved photoemission spectroscopy (spin-ARPES), respectively. We have found that the films possess an in-plane uniaxial anisotropy with the easy axis of [-1 1 0]. Along the easy axis, the field dependent MOKE signals of various thicknesses are presented in Fig. 1a. Square hysteresis loops can be observed. As the film thickness increases, both MOKE intensity and the coercivity increases. The coercivity saturates after the film thickness is beyond 4 uc. The magnetization of all the films demonstrates a linear relationship with the thickness and a kink at 4 uc (Fig. 1), above which it reaches the bulk value of 1000 emu/cm^3. For the film thickness below 4 uc, a linear relationship cross zero suggests that there are no magnetic dead layers. The magnetization and coercivity imply that the films thicker than 4 uc are bulk-like, while films thinner than 4 uc are mostly affected by the interface. The magnitude of spin polarization of ferromagnetic materials is a key property for their application in spintronic devices, especially at room temperature. To investigate the spin polarization of the Co_2FeAl films, samples were transferred under ultra-high vacuum to the ARPES chamber upon the growth is finished. Figure 2 exhibits the representative spin-resolved photoemission spectra and the corresponding spin polarization at room temperature. A broad peak at ~1.0 eV in Fig. 2a comes from the combination of Co and Fe's 3d electronic states. As shown in Fig. 2b-2e, the spin polarization of Co_2FeAl films exhibits a peak at the Fermi energy (E_F), then decreases slowly with the binding energy increasing, and reaches zero beyond 1 eV. A high spin polarization of ~ 65% has been observed for the Co_2FeAl film of 21 uc (Fig. 2), for the first time in this system. As the thickness decreases, the spin polarization stays roughly constant until it drops down to 37% at 2.5 uc. For the film of 2.5 uc, the peak value is much lower than the thicker films, and also the spin polarization goes to a negative value at higher binding energies, suggesting the swap of spin direction of the majority and the minority band. The strong attenuation of the spin polarization at 2.5 uc may be due to the interface bonding or the site disorder, resulting the spin polarization much less than the bulk. Both the *in-situ* MOKE and *in-situ* spin-resolved ARPES indicate that the Co_2FeAl films is suitable for the fabrication of MTJs after about 4-6 uc. Our results show that the intrinsic spin polarization is still rather high and doesn't limit the TMR value. It is the interface, where the sharp decrease of spin polarization happens, that leads to a relatively smaller TMR in the epitaxial Co_2FeAl based MTJ.

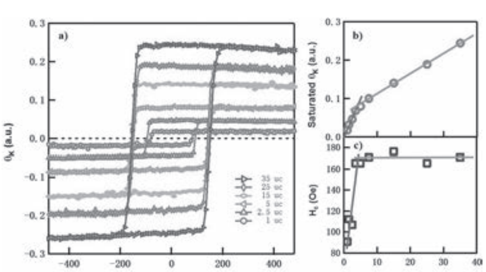

Fig. 1. Thickness-dependent *in-situ* MOKE measurements of the Co_2FeAl films. (a) In-plane magnetization measured at 300 K along [-1 1 0] (easy axis direction) by a longitudinal-mode MOKE set up. Both thickness dependent (b) Kerr rotation & (c) coercive field estimated from (a) show a turning point at ~ 4 uc.

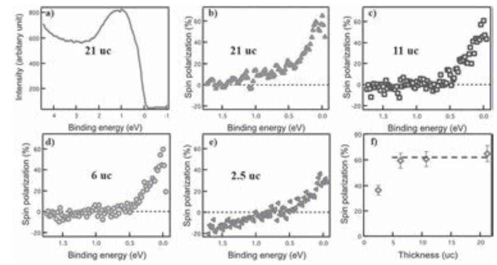

Fig. 2. *In situ* spin-resolved ARPES measurements. (a) Spin-resolved photoemission spectra of the 21-uc-thick Co_2FeAl film, probed by 21.2 eV photons at 300 K. (b)-(e) Spin polarizations of Co_2FeAl films with thicknesses of 21 uc, 11 uc, 6 uc and 2.5 uc, respectively. (f) Spin polarizations at the Fermi level versus film thicknesses. It is almost constant of 60 - 65% with film thicknesses more than 6 uc, and it then decreases to 37% at 2.5 uc.

EP-02. Levitation Force Computation of HTS/PM system by H-formulation.

W. Chen[1], J. Shi[1] and Y. Xu[1]
1. Huazhong University of Science & Technology, Wuhan, China

Abstract—This paper presents a model to predict the electromagnetic behavior of HTS/PM system which based on finite element method and H-formulation combining with E-J characteristics and J-B relationship. And the model is suitable for axial symmetric problems. The axial levitation force of the HTS/PM system is calculated considering the nonlinear and anisotropic properties of HTS bulks. In order to validate the model, experimental results of the system are obtained and compared with simulation results. The comparison shows experimental and simulation results match well. Keywords— HTS/PM system; H-formulation; levitation force; finite element method I. Introduction The superconducting magnetic levitation system has great advantages due to its passive levitation stability comparing to permanent and active magnetic levitation system. Hence, it has lots of applications such as flywheel energy storage system, motor, maglev vehicles [1-3] etc. And the system usually consists of HTS bulks and permanent magnets (PM). Besides, it's important to be able to predict its electromagnetic behavior in order to optimize its performance in the processing of designing the superconducting magnetic levitation system. But it's difficult to predict the electromagnetic behavior of SMB because of inhomogeneous, nonlinear and anisotropic properties of HTS bulks. So in order to explore the levitation properties of the system, a model is presented to predict its electromagnetic behavior combining with E-J characteristics and J-B relationship of the HTS bulk. This model is suitable for 2-D axial symmetry system, but the hysteresis effect is not considered for the sake of the simplification. The computation is based on finite element method and H-formulation which is evaluated by COMSOL Multiphysics. II. The H-Formulation The Maxwell equations can describe macroscopic electromagnetic phenomena. And the H-formulation can be obtained from Maxwell equation. Besides, H-formulation can be applied to the entire region and only has one variable *H*. Meanwhile, in 2-D axial symmetry problem, the variable *H* only has 2 components *Hr* and *Hz*. The electromagnetic behavior of HTS bulk can be represented by E-J power law relationship, KIM model for J-B relationship and linear B-H relationship [4]. And the levitation force between HTS and PM can be obtained by Lorentz force equation. III. Modelling and Computation of HTS/PM System A. HTS/PM System Model Fig.1(a) presents the HTS/PM system which consist of a cylindrical permanent magnet above a HTS bulk. The magnet and HTS bulk are made of rare earth material and melt textured yttrium barium copper oxide (YBCO) respectively. According to Fig.1(a), the corresponding 2-D model can be obtained due to the symmetry of the system, which shows in Fig.1(b). More importantly, the 2-D model can reduce the computation time comparing to its 3-D counterpart without accuracy loss. B. Computation of the Levitation force The levitation force computation of HTS/PM system is based on finite element method combining with the H-formulation. And the simulation process is implemented by COMSOL Multiphysics. In this paper, we focus on the 2-D symmetry model, and only the movement along the z-axis is considered. And the computation is to simulate the process of experiment scenario of levitation force measurement. In the initial position, the HTS bulk and PM are coaxial with a fixed gap and the HTS bulk is cooled at 77K in zero field condition. After that, the PM is brought down to the HTS bulk until reaching the previously fixed minimum gap. Then the PM is brought back to the initial position. When the gap between HTS and PM varies, during the movement, the HTS bulk generates induced persistent current to resist the movement, hence the levitation force can be calculated by using Lorentz force equation. IV. Simulation Results To evaluate the interaction between HTS bulk and PM, the simulation is carried out by COMSOL Multiphysics. The simulation result of axial levitation force is shown in Fig.2(a). In order to verify the accuracy of the simulation result, the comparison of the simulation result and its experiment counterpart [5] is shown in Fig.2(b). From Fig. 2(b), the simulation and experiment results match well, especially when PM approaches HTS bulk, hence the simulation verifies the validity and accuracy of the model. V. Conclusions This paper presents a model to predict the electromagnetic behavior of HTS/PM system which based on finite element method and H-formulation combining with E-J characteristics and J-B relationship. In the meantime, the levitation force alone the z-axis is calculated. The comparison of simulation and experiment results matches well. Meanwhile, the results verifies the accuracy and validity of the model.

[1] S Mukoyama, K Nakao, H Sakamoto, "Development of Superconducting Magnetic Bearing for 300 kW Flywheel Energy Storage System, "IEEE Transactions on Applied Superconductivity, vol. 27, no. 4, pp. 1-4, June 2017. [2] Berger K, Boufatah F, Linares R, et al, "Solar Electric Motor on Superconducting Bearings: Design and Tests in Liquid Nitrogen, "IEEE Transactions on Applied Superconductivity, vol. 27, no. 4, pp. 1-5, June 2017. [3] Deng Z, Li J, Zhang W, et al. "High-Temperature Superconducting Magnetic Levitation Vehicles: Dynamic Characteristics While Running on a Ring Test Line, "IEEE Vehicular Technology Magazine, vol. 12, no. 3, pp. 95-102, Sept. 2017. [4] Ruizalonso, D, T. Coombs, and A. M. Campbell. "Computer modelling of high-temperature superconductors using an A V formulation," Superconductor Science & Technology 17.5(2004):S305-S310 (6). [5] Ruizalonso, D, T. A. Coombs, and A. M. Campbell. "Numerical solutions to the critical state in a magnet high temperature superconductor interaction, "Superconductor Science & Technology 18.2(2005):S209.

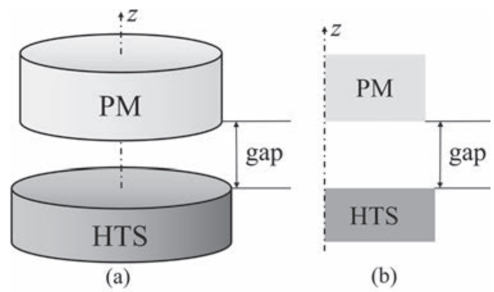

Fig.1 The schematic of HTS/PM system model

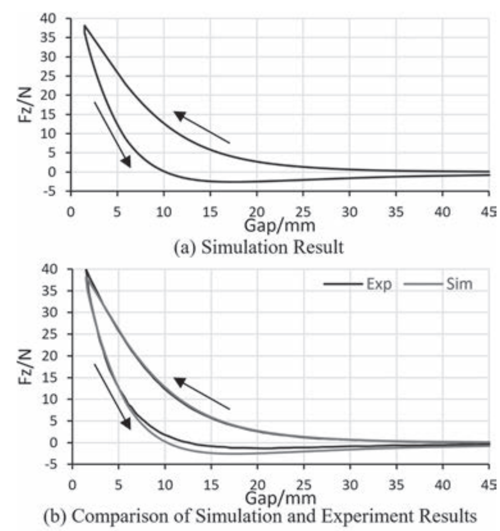

Fig.2 Levitation force-gap relationship

EP-03. Key features of the magnetic and magnetoelectric properties of rare-earth langasite $Ho_{0.09}La_{2.91}Ga_5SiO_{14}$.

N. Kostyuchenko[1,2], A. Mukhin[3], A. Pimenov[2], L. Weymann[2] and A. Zvezdin[1,3]

1. Moscow Institute of Physics and Technology (State University), Moscow, Russian Federation; 2. Institut für Festkörperphysik, Technische Universität Wien, Vienna, Austria; 3. A. M. Prokhorov General Physics Institute of Russian Academy of Sciences, Moscow, Russia, Moscow, Russian Federation

In this study, we investigate both experimentally and theoretically the holmium doped rare-earth langasite $Ho_{0.09}La_{2.91}Ga_5SiO_{14}$. The magnetic and magnetoelectric behavior in single crystalline $Ho_{0.09}La_{2.91}Ga_5SiO_{14}$ along the main crystallographic directions has been studied in broad magnetic field and temperature ranges. To explain the observed properties we applied a theoretical approach successfully used previously for rare-earth borates [1-4]. Here we extend the quantum theory of magnetoelectric effect in rare-earth langasites to the holmium doped compound. From the comparison to the experiment we evaluate the parameters of the crystal field and of the magnetoelectric Hamiltonian. Both magnetic and magnetoelectric properties of the Ho-doped langasite can be successfully explained by the suggested model. Figure 1: Experimental (solid lines) magnetization curves along two crystallographic axes in $Ho_{0.09}La_{2.91}Ga_5SiO_{14}$ as compared to the theoretical model (dotted lines). Supported by RFBR, pr. No. 15-02-08509 and by the Austrian Science Funds (W1243, I 2816-N27, I1648-N27).

1) A. I. Popov, D. I. Plokhov, and A. K. Zvezdin, Phys. Rev. B, 86, (2012). 2) A. I. Popov, D. I. Plokhov, and A. K. Zvezdin, Phys. Rev. B, 87, 024413 (2013). 3) N.V. Kostyuchenko, A.I. Popov, A.K. Zvezdin. SSP. 54, is. 8, 1493 (2012). 4) A. M. Kadomtseva, Yu. F. Popov, G. P. Vorob'ev, N. V. Kostyuchenko, A. I. Popov, A. A. Mukhin, V. Yu. Ivanov, L. N. Bezmaternykh, I. A. Gudim, V. L. Temerov, A. P. Pyatakov and A. K. Zvezdin. Phys. Rev. B 89, 014418 (2014).

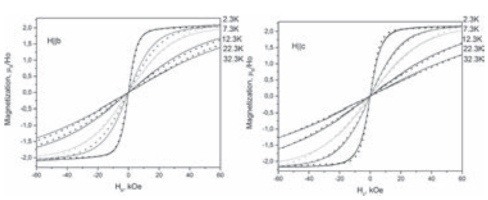

Fig. 1. Experimental (solid lines) magnetization curves along two crystallographic axes in $Ho_{0.09}La_{2.91}Ga_5SiO_{14}$ as compared to the theoretical model (dotted lines).

EP-04. Anomalous magnetic and Electrical properties of $Fe_2V_{2-x}Al_x$ (x=0-1) alloys.

S. Hari[1] and V. Srinivas[1]
1. Department of Physics, IIT Madras, Chennai, India

Intriguing correlated electronic structure is revealed when vanadium is substituted in place of iron in ferromagnetic DO_3-Fe_3Al intermetallic alloy and transforms it into a Fe_2VAl Heusler alloy with $L2_1$ crystal structure. This particular composition exhibits nonmagnetic semi-metallic character [1], [2]. Both DFT calculations and experiments revealed the existence of pseudogap or gap ranging up to 0.5 eV. The origin of the gap and the role of hybridization in these alloys is still debated[3]. These studies reveal that the vanadium reduces the moment, yet the role of aluminium in altering the electronic properties is still need to be investigated. Therefore, in the present investigation, we have studied the structural and magnetic properties of $Fe_2V_{2-x}Al_x$ alloys with x varying from 0 to1 to unravel the role of Al in Fe_2VAl which is known to be exhibiting the features similar to that of equiatomic FeV. Alloy ingots were synthesized by arc melting the elemental constituents and subsequent annealing at 1273 K for 3 days. From X-Ray Diffraction studies it is observed that x=0 composition (FeV) stabilized in σ-phase, while a mixed phase (σ+cubic) is obtained for x=0.2. It is observed that as the Al-composition varies from 0.4 to 1 it exhibits a cubic phase. DC magnetic measurements were performed for all samples, which revealed that the magnetic character decreases with Al concentration. The extreme compositions (well ordered) of this series namely, FeV (with σ-phase) and Fe_2VAl ($L2_1$-phase) are found to be paramagnetic down to lowest temperature. The temperature dependence of magnetization curves shown in Fig.1 for composition x=0.2 suggest ferromagnetic character with Curie temperature (T_c) close to 240 K and for x=0.4 with T_c~ 130K, while the compositions x=0.8, 1 exhibit nonmagnetic behavior down to 5K (Fig.1). The magnetic isotherms of these compositions exhibit anomalous magnetic character i.e., exhibit higher coercivity at 300K compared to 5K (except for Fe_2VAl), with lower saturation magnetization. The existence of hysteresis behavior above T_c indicates the possibility of the presence of ferromagnetic clusters in intermediate compositions. Analysis of magnetic data suggests that disorder plays a significant role in addition to the composition. To see whether the magnetic anomalies affect the electrical transport, we carried out electrical resistivity measurements in the low temperature range, shown in Fig.2. The electrical resistivity shows a positive temperature coefficient of resistivity (TCR) for x=0 to x=0.8 and the resistivity at temperatures below 250K decreases with Al concentration which indicates the presence of Al improves the metallic nature of these samples. But the sample with highest Al concentration i.e Fe_2VAl shows negative TCR which also exhibits high values of resistivity compared to other compositions of the series. This kind of behavior can be attributed to band structure formed due to structural disorder in samples, x=0.2, 0.4, 0.8, and pseudo band gap formed in Fe_2VAl near Fermi level[4], [5]. From above studies, it is quite evident that the material going from metallic state to semi-metallic state with a small variation in Al concentration. The resistivity increased by two orders of magnitude from $Fe_2V_{1.2}Al_{0.8}$ to Fe_2VAl, whereas both the samples were paramagnetic down to 5K. An inflection point in resistivity curve near the magnetic transition temperature T_c is observed, which suggests a correlation between transport and magnetic properties. These magnetic and electrical transport anomalies show even non-magnetic aluminum plays a significant role in electronic properties and will be discussed in detail.

[1] Y. Nishino, M. Kato, and S. Asano, "Semiconductorlike Behavior of Electrical Resistivity in Heusler-type Fe_2VAl Compound," *Phys. Rev. Lett.*, vol. 79, no. 10, pp. 1909–1912, 1997. [2] H. Okamura, J. Kawahara, T. Nanba, S. Kimura, K. Soda, U. Mizutani, Y. Nishino, M. Kato, I. Shimoyama, H. Miura, K. Fukui, K. Nakagawa, H. Nakagawa, and T. Kinoshita, "Pseudogap formation in the intermetallic compounds $(Fe_{1-x}V_x)_3Al$," *Phys. Rev. Lett.*, vol. 84, no. 16, pp. 3674–3677, 2000. [3] O. Kristanovski, R. Richter, I. Krivenko, A. I. Lichtenstein, and F. Lechermann, "Quantum many-body intermetallics: Phase stability of Fe_3Al and small-gap formation in Fe_2VAl," *Phys. Rev. B*, vol. 95, no. 4, p. 45114, 2017. [4] Y. Nishino, "Electroni structure and transport properties of pseudogap system Fe_2VAl," *Mater. Trans.*, vol. 42, no. 6, pp. 902–910, 2001. [5] Ch.Venkatesh, V. Srinivas, V. V. Rao, S. K. Srivastava, and P. Sudheer Babu, "Effect of site disorder on the electronic properties of Fe_2VAl Heusler alloy," *J. Alloys Compd.*, vol. 577, pp. 417–425, 2013.

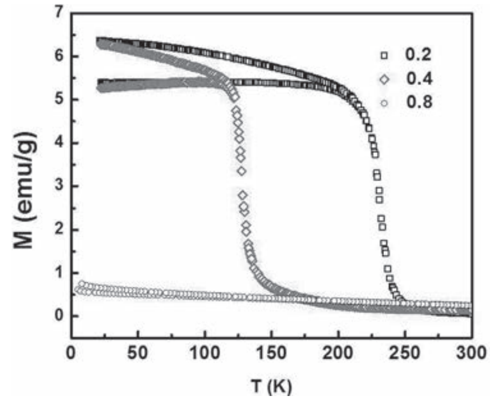

Fig.1. Magnetization as a function of temperature of $Fe_2V_{2-x}Al_x$ alloys.

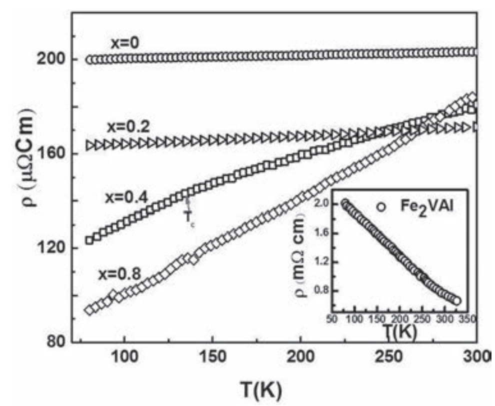

Fig.2 Temperature variation of resistivity of $Fe_2V_{2-x}Al_x$ alloys, inset-resistivity of Fe_2VAl

EP-05. Spinterface Properties and Magnetic Coupling of Tris(8-hydroxyquinoline)iron(III) on Cobalt Surface.

L. Yu[1], J. Lin[1,2], Y. Lai[1], H. Shiu[1] and Y. Hsu[1]
1. National Synchrotron Radiation Research Center, Hsinchu, Taiwan;
2. Program for Science and Technology of Accelerator Light Source, National Chiao Tung Universoty, Hsinchu, Taiwan

Tris(8-hydroxyquinoline)aluminium (Alq_3) has been successfully sandwiched between two ferromagnetic electrodes as a buffer layer in organic spin-valve (OSV) devices to exhibit prominent magnetoresistance (MR) values [1]. Compare with inorganic spintronics, organic/molecular spintronics use the chemical versatility of molecules to own charming properties, such as paramagnetic behaviour of metal ions, and tuneable electronic structure [2-8]. The tris(8-hydroxyquinoline)iron(III) (Feq_3) containing the paramagnetic iron centre has the similar structure with Alq_3, that implies that Feq_3 has the potential for promising organic/molecular spintronics. Here we report that Feq_3 was synthesized and deposited on cobalt for investigating the electronic and magnetic interplay between Feq_3 and ferromagnetic Co surface. Feq_3 was synthesized by the recipe described as bellow. Iron(III) chloride (367 mg, 2.3 mmol) and 8-hydroxyquinoline (1.09 g, 6.9 mmol) were dissolved in 80 ml methanol. The solution was then heated to reflux for 20 minutes. Triethylamine (698 mg, 6.9 mmol) was added, and the resulting mixture was heated for 20 minutes. The deep green crystal Feq_3 was precipitated and filtered (842 mg, 75%). All thin films were fabricated and characterized under ultra-high vacuum (UHV) conditions without air exposure to avoid surface contamination during deposition and spectroscopy measurements. The Co/Feq_3 film was evaporated on Si(100)/Au near 295 K. The Co and Feq_3 films were sequentially deposited in two separate deposition chambers which are also detached from the analysis chamber. After complete fabrication, samples were transferred to the analysis chamber for x-ray photoelectron spectroscopy (XPS), near-edge x-ray absorption fine structure spectroscopy (NEXAFS). The powder x-ray diffraction were measured to identify the crystalline structure. The chemical states, electronic structures and magnetic properties were recorded at beam lines (BL) 09A2 U5 for spectroscopy, 17A for powder x-ray diffraction and 11A Dragon for XMCD at National Synchrotron Radiation Research Center (NSRRC) in Taiwan. XPS was used to examine the interfacial chemical and electronic properties at Co/Feq_3 interface. At the bottom contact interface for Feq_3 atop Co surafce, three N peak features are observed at binding energy (BE) 399.8, 398.8 and 397.5 eV for a sub-monolayer of Feq_3 adsorbed on Co. The BE at 399.8 eV is corresponding to the molecular state, the lower BE at 398.8 eV and 397.5 eV are attributed to the hybridized states of N atoms in Feq_3 with underneath Co. On the other hand, the O peak features of the Co/Feq_3 interface express negative shift in the low coverage of Feq_3, but shift back to the position of molecular state in high coverage of Feq_3, that implied the oxygen atoms in Feq_3 are also involved in the hybridization with Co. The XPS results indicate that the interface interaction between Feq_3 and cobalt is similar to Alq_3 on Co [9-10]. The nitrogen atoms of pyridyl ring and oxygen atoms of phenoxide ring in Feq_3 show strong hybridization with cobalt by XPS. The chemical states and electronic structure of central iron are also influenced by thermal evaporation and the hybridization. Two absorption peaks of Fe *L*3-edge at 709.2 and 710.8 eV corresponding to iron(II) and iron(III), respectively are observed for 10 nm Feq_3 adsorbed on Au. Nevertheless, a sub-monolayer of Feq_3 adsorbed on Co only shows the iron(II) absorption peak at 709.2 eV. The iron(III) of Feq_3 was reduced to iron(II) when sub-monolayer Feq_3 deposited on Co. XMCD spectra reveal the magnetic interaction between Fe ion and Co in the Co/Feq_3 interface as depicted in Fig. 1. The Au/Feq_3 film shows slight XMCD dichorism at Fe *L*3-edge in Fig. 1(a), meaning the intrinsic paramagnetism of Fe ion in Feq_3 is observed in the magnetic field [11-12]. However, in Fig. 1(b), the more evident XMCD dichorism is obtained when a sub-monolayer of Feq_3 deposited on Co, and the negative dichroism is found in Co *L*3-edge as well (Fig. 1(c)). As a result, the spin-polarization of Fe ion is enhanced by the magnetic coupling with Co. The magnetic hysteresis loops of XMCD measured at the Fe and Co *L3*-edge in the sample of Co/Feq_3 is depicted in Fig. 1(d). The same magnetization direction and coercivity (H_c) are found in the MH loops that corresponding to the ferromagnetic interaction between Feq_3 and Co. Feq3 containing the paramagnetic metal center was synthesized and deposited on Co surface. The interfacial characterization of nitrogen and oxygen in Feq3 on Co display similar behaviour to Alq3 on Co that all show strong hybridization with Co. The chemical states and electronic structure of central iron are also strongly influenced by the interfacial hybridization. Measurements of XMCD at Fe and Co L-edge illustrate that central iron metal of Feq3 exhibiting apparent spin-polarization after contact with cobalt that is the ferromagnetic interaction between central iron ion and cobalt.

[1] Z.H. Xiong, D. Wu, Z.V. Vardeny, J. Shi, Nature 427, 821-824 (2004). [2] S. Sanvito, Chem. Soc. Rev. 40, 3336 (2011). [3] S. Sanvito, Nat. Mater. 10, 484 (2011). [4] A. Lodi Rizzini, C. Krull, T. Balashov, J. J. Kavich, A. Mugarza, P. S. Miedema, P. K. Thakur, V. Sessi, S. Klyatskaya, M. Ruben, S. Stepanow, and P. Gambardella, Phys. Rev. Lett. 107, 177205 (2011). [5] T. Miyamachi, M. Gruber, V. Davesne, M. Bowen, S. Boukari, L. Joly, F. Scheurer, G. Rogez, T. K.Yamada, P. Ohresser, E. Beaurepaire, and W. Wulfhekel, Nat. Commun. 3, 938 (2012). [6] M. Warner, S. Din, I. S. Tupitsyn, G. W. Morley, A. M. Stoneham, J. A. Gardener, Z. Wu, A. J. Fisher, S. Heutz, C. W. M. Kay, and G. Aeppli, Nature 503, 504 (2013). [7] Y.-J. Hsu, Y.-L. Lai, C.-H. Chen, Y.-C. Lin, H.-Y. Chien, J.-H. Wang, T.-N. Lam, Y.-L. Chan, D.-H. Wei, H.-J. Lin, C.-T. Chen, J. Phys. Chme. Lett. 4, 310 (2013). [8] T.-N. Lam, Y.-L. Huang, K.-C. Weng, Y.-L. Lai, M.-W. Lin, Y.-H. Chu, H.-J. Lin, C.-C. Kaun, D.-H. Wei, Y.-C. Tseng, Y.-J. Hsu, J. Mater. Chem. C 5, 9128 (2017). [9] T.-N. Lam, Y.-L. Lai, C.-H. Chen, P.-H. Chen, D.-H. Wei, H.-J. Lin, C. T. Chen, J.-T. Sheu, Y.-J. Hsu, appl. Surf. Sci. 354, 90 (2015). [10] T.-N. Lam, Y.-L. Lai, C.-H. Chen, P.-H. Chen, Y.-L. Chan, D.-H. Wei, H.-J. Lin, C. T. Chen, J.-H. Wang, J.-T. Sheu, Y.-J. Hsu, Phys. Rev. B 91, 041204(R) (2015). [11] B. Li, J.-P. Zhang, X.-Y. Zhang, J.-M. Tian, G.-L. Huang, Inorg. Chim. Acta 366, 241 (2011). [12] Z.-Y. Pang, L. Lin, F.-G. Wang, S.-J. Fang, Y. Dai,S.-H. Han, Appl. Phys. Lett. 99, 153306 (2011).

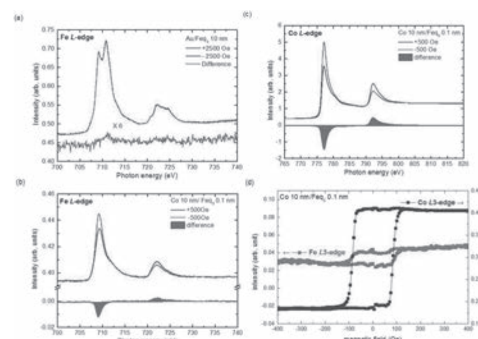

Fig. 1. Magnetic properties of Feq_3 thin film and Feq_3 on Co. Fe *L*-edge XAS/XMCD (a) 10 nm Feq_3 thin-film on Au surface. (b) 0.1 nm Feq_3 deposited on Co surface. Co *L*-edge XASXMCD (c) 0.1 nm Feq_3 deposited on Co surface. (d) Magnetic hysteresis loop of XMCD measured at the Fe and Co *L*3-edge in Co(10 nm)/ Feq_3(0.1 nm).

EP-06. Observation of superconductivity in $LaNiO_3/La_{0.7}Sr_{0.3}MnO_3$ superlattice.

G. Zhou[1], Z. Quan[1] and X. Xu[1]
1. Shanxi Normal University, Linfen, China

School of Chemistry and Materials Science, Key Laboratory of Magnetic Molecules and Magnetic Information Materials, Ministry of Education, Shanxi Normal University, Linfen 041004, China Atomic scale control of the hetero-interfaces in transition metal oxides has attracted significant attention due to the possibility of observing novel phenomena[1,2]. The cuprate- and ferrite-based interfacial superconductors have been investigated extensively, while the research of nickelate-based heterostructure is quite rare[3,4]. Recently Chaloupka and Khaliullin theoretically predicted that antiferromagnetism and high temperature superconductivity (SC) may be stabilized in LNO-based superlattices[5]. However, the superconductivity state in LNO-based heterostructure has not yet been experimentally reported. In this work, we investigate the properties of a superlattice (SL) composed of an ultrathin $LaNiO_3$ layer, with a ferromagnetic insulating $La_{0.7}Sr_{0.3}MnO_3$ (LSMO) layer. Zero resistance and Meissner effect are observed by resistive and magnetic measurements on the superlattice, which gives experimental indication of superconductivity in new kinds of superconductors. X-ray linear dichroism causes the NiO_2 planes to develop electron occupied x^2-y^2 orbital order similar to a cuprate-based superconductor. Our findings demonstrate that artificial interface engineering is a useful way to realize novel physical phenomena, such as superconductivity. Typical x-ray diffraction scans through (002) symmetric reflections of the LNO/LSMO superlattice are shown in Fig. 1a. The main peak of the superlattice and satellite peaks of SL-1 and SL+1 are observed, suggesting sharp interfaces in this superlattice. The coherent epitaxial growth and the absence of secondary phases or dislocations in LNO/LSMO superlattice are both confirmed by high resolution high-angle annular dark field scanning transmission electron microscopy, as shown in Fig. 1b. Because the A site is similar to the superlattice, and the atomic number of B site is contrasted in this image, the LNO layers appear brighter than the LSMO layers The high quality epitaxial $[(LNO)_2/(LSMO)_3]_{20}$ superlattice was measured with a current of $5E10^{-3}$ mA in a Van der Pauw geometry. In order to directly observe the superconducting property at low temperatures, the temperature dependence of resistivity was measured, as shown in the inset of Fig. 2a. The superlattice displays metallic behavior with the temperature below 10 K and the resistivity abruptly drops around 3.7 K, clearly indicating superconductivity. To further verify the superlattice nature of the observed superconductivity, we measure the magnetic susceptibility (χ) as a function of temperature at magnetic field (H) strength of 10 Oe. As shown in Fig. 2b, the zero field cooled (ZFC) and field cooled (FC) susceptibility are essentially temperature independent at low temperatures. A sharp drop of magnetic susceptibility is observed for both ZFC and FC processes, indicating that the magnetic onset of superconductivity appears around 3.5 K, which is the same as the zero-resistivity temperature. Further confirmation of superconductivity in the superlattice is shown in the inset of Fig. 2b, displaying the typical magnetic hysteresis curve for a superconductor at 2 K after zero-field cooled process. The characteristic M-H loop indicates that the present superlattice is a superconductor of the second kind with a lower critical field of 50 Oe. The work was supported by National Key R&D Program of China (No. 2017YFB0405703), NSFC (Nos. 61434002, 51571136, 11274214), and the Special Funds of Sanjin Scholars Program.

1. Hwang, H. Y., et al., *Nat. Mater.,* 2012, 11, 103-113. 2. Bozovic, I., et al., *Nat. Phys.,* 2014, 10, 892-895. 3. Wu, M. K., et al., *Phys. Rev. Lett.,* 1987, 58, 908-910. 4. Wang, Q. K., et al., *Chin. Phys. Lett.,* 2012, 29, 037402. 5. Chaloupka, J., et al., *Phys. Rev. Lett.,* 2008, 100, 016404.

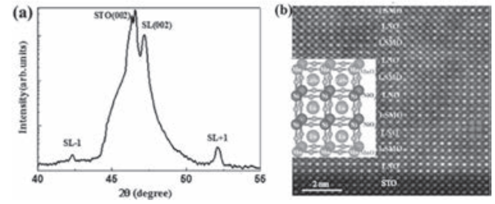

Fig. 1. (a) XRD pattern and (b) High-angle annular dark field scanning transmission electron microscope image of $LaNiO_3/La_{0.7}Sr_{0.3}MnO_3$ superlattice.

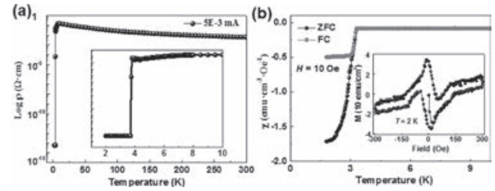

Fig. 2. (a) Temperature dependence of electrical resistivity for LSMO/ LNO superlattice between 300 and 2 K with a detecting current of $5E10^{-3}$ mA. (b) Magnetic susceptibility (χ) of SL is measured in zero field cooling (black circles) and field cooling (red circles) processes at a magnetic field of 10 Oe.

EP-07. Enhanced Spin Ordering Temperature in Ultrathin FeTe Films Grown on a Topological Insulator.

J. Warmuth[1], U. Singh[1], L. Cornils[1], A. Kamlapure[1], P. Hofmann[2], J. Wiebe[1] and R. Wiesendanger[1]

1. Institute of Applied Physics, University of Hamburg, Hamburg, Germany; 2. Department of Physics and Astronomy, Aarhus University, Aarhus, Denmark

The closely related interplay between magnetism and superconductivity has been an intriguing phenomenon in high-T_C superconductors for several decades and was heavily explored in the case of bulk single crystals. Superconductivity in bulk Fe based materials, similar to cuprates, emerges upon the suppression of the magnetic order in the parent compounds via doping, signifying an intimate relation between magnetism and superconductivity [1, 2, 3]. The parent compound FeTe of the high-T_C Fe-chalcogenide family exhibits a bi-collinear antiferromagnetic (AFM) diagonal double-stripe (DDS) order [4,5,6]. Recently, it was shown that ultrathin films of Fe-based superconductors can have transition temperatures approaching the highest values that have been reported for cuprates, which boosted the interest in these materials even further. However, an understanding of the relevant mechanisms on the atomic scale, in particular, related to the spin degree of freedom, is still lacking and calls for an in-depth investigation of the phase transitions in these systems. A real-space visualization of spin-dependent phenomena on the atomic scale independence of the doping and temperature can thus provide a new dimension towards an understanding of high-T_C superconductivity. A suitable technique for this purpose is spin-polarized scanning tunneling microscopy (SP-STM) which has widely been utilized in studying magnetic nanostructures and spin-dependent phenomena of metallic materials on the atomic scale [7]. While superconductivity in chalcogenide materials such as $Fe_{1+y}Te_xSe_{1-x}$ has been extensively investigated by spin-averaging STM in the past few years [8,9,10], there are only a few results using SP-STM for these materials [11,12,13,14,15]. The DDS spin order in the parent compound $Fe_{1+y}Te$, emerging around the Néel temperature (T_N~65K) from the paramagnetic state [5,6,16,17,18], has been recently confirmed by SP-STM at low temperatures (T) [11,12,13,15]. In the regime of low excess Fe content y, T_N generally strongly increases with decreasing y [16], with reported maximum values of T_N of 72K [17,18], which is limited by the lowest achievable values of y=0.02 in conventional bulk crystal growth [19]. Here, the successful growth of well-defined one and two unit cell (UC) thin FeTe films of high stoichiometric quality on the topological insulator Bi_2Te_3 is demonstrated. The sample surface after the growth procedure probed by STM is displayed in Fig. 1 (a). The line profile in (b) plots the height information along the line in (a) and illustrates the corresponding sample composition. Since the investigated FeTe thin films do not exhibit any excess Fe, they are an ideal model system to study the pure stoichiometric composition of $Fe_{1+y}Te$ (y=0). On this system, we performed the first atomic-scale real-space observation of the evolution of spin order of the parent compound of a Fe-based superconductor with temperature. The spin order on the FeTe films persists up to temperatures which are higher than the transition temperature reported for bulk $Fe_{1+y}Te$ with lowest possible excess Fe content y. The STM images displayed in Fig. 2 (a,c,e,g) show the surface of one UC thin FeTe islands within the temperature range from 30K to 78K. The AFM DDS spin order is clearly visible in the STM images (a,c,e) as a bi-collinear surface modulation along the crystallographic axes a (red arrow) up to 73K. Further evidence gives the corresponding Fourier peaks associated with the DDS order marked in the fast Fourier transformations (FFTs) displayed in Fig. 2 (b,d,f). At 78K, in Fig. 2 (f), the atomic lattice is clearly visible, but the DDS order has vanished in accordance to the lack of Fourier spots in the corresponding FFT shown in (g). For two UC thin FeTe islands, the SP-STM investigation reveals the DDS order even up to 79K. The enhanced spin order stability is assigned to a strongly decreased y with respect to the lowest values achievable in bulk crystal growth, and effects due to the interface between the FeTe and the topological insulator substrate. The result is relevant for understanding the recent observation of a coexistence of superconducting correlations and spin-order at the interface of the two materials [14] and highlights the significance of magnetism and interfacial doping in the realm of unconventional superconductivity. This work is submitted for publication in a peer-reviewed journal and available as a preprint [20].

[1] D. Scalapino, Rev. Mod. Phys. 84, 1383 (2012). [2] D. C. Johnston, Advances in Physics 59, 803 (2010) [3] Y. Mizuguchi, et al. J. Phys. Soc. Jpn. 79, 102001 (2010). [4] J. Wen, et al. Phys.: Condens. Matter 22, 203203 (2010). [5] W. Bao, et al. Phys. Rev. Lett. 102, 247001 (2009). [6] S. Li, C. de la Cruz, et al. Phys. Rev. B 79, 054503 (2009). [7] R. Wiesendanger, Rev. Mod. Phys. 81, 1495 (2009). [8] U. R. Singh, et al. Phys. Rev. B 88, 155124 (2013). [9] T. Hanaguri, et al. Science 328, 474 (2010). [10] J. E. Hoffman, Rep. Prog. Phys. 74, 124513 (2011). [11] M. Enayat, et al. Science 345, 653 (2014). [12] U. R. Singh et al. Phys. Rev. B 91, 161111(R) (2015). [13] A. Sugimoto, et al. Phys. Rev. B 90, 224503 (2014). [14] S. Manna, et al. Nat. Comms. 8, 14074 (2017). [15] T. Hänke, et al. Nat. Comms. 8, 13939 (2017). [16] C. Koz, et al. Phys. Rev. B 88, 094509 (2013). [17] T. J. Liu, et al. Phys. Rev. B 80, 174509 (2009). [18] T. Machida, et al. Physica C 484, 19 (2013). [19] Z. K. Liu, et al. Phys. Rev. Lett. 110, 1–5 (2013) [20] U.R. Singh, et al. *arXiv* 1711.10406 (2017)

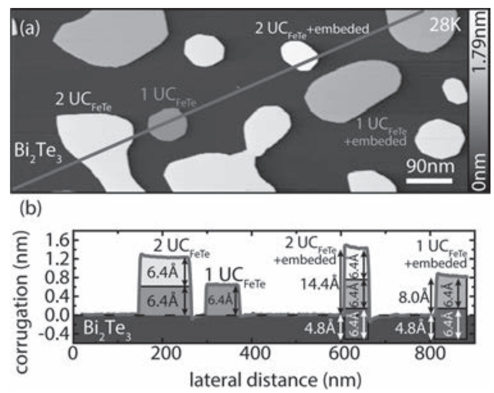

Fig. 1. Overview of FeTe thin films on Bi_2Te_3. (a) Constant-current STM image showing the surface after the growth procedure. FeTe islands of different apparent heights and sizes have formed. (b) Line profile showing the height information along the solid blue line in (a). The composition of the FeTe islands is illustrated matching the colors in (a). Tunneling parameters: (a) V_s=100mV, I_t=40pA.

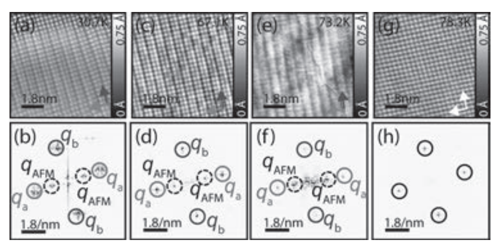

Fig. 2. Temperature dependence of the AFM order in 1UC thin FeTe films. (a,c,e,g) Constant-current STM images of 1UC thin FeTe islands in the temperature range from 30.7K to 78.3K. (b,d,f,h) The FFT maps of the corresponding STM topographies. The Bragg peaks related to the atomic lattice are marked by solid circles and dashed circles mark Fourier peaks associated with the AFM order observed up to 73.2K. Tunneling parameters: (a) V_s=-40mV, I_t=8.2nA; (c) V_s=20mV, I_t=2nA; (e) V_s=60mV, I_t=2nA; (g) V_s=25mV, I_t=3.5nA.

EP-08. The long-range exchange bias in ultrathin paramagnetic $LaNiO_3$-based heterostructure.

X. Xu[1], G. Zhou[1] and Z. Quan[1]
1. Shanxi Normal University, Linfen, China

With the rapid development of synthesis techniques, it has become possible to control transition metal oxide heterostructures by manipulating atomic flatness.[1] In the nickelate family, $LaNiO_3$ (LNO), is an exception since it exhibits metallic paramagnetic behavior over all temperatures.[2] Recently, the antiferromagnetic (AFM) state in ultrathin LNO layers has been theoretically predicted.[3] However, as far as we know, this has not yet been experimentally realized. The long-range exchange bias effect[4], where a non-magnetic material is inserted into ferromagnetic/AFM heterostructure, is a useful way to exclude the contribution of exchange bias by the interfacial coupling between Ni and Mn ions.[5,6] In this work, high quality LNO/STO(n)/LSMO superlattices are grown using a pulse laser deposition system. Both the exchange bias and coercive fields decrease monotonically with the spacer thickness. The role of antiferromagnetic behavior in the ultrathin LNO layer is essential for understanding the behavior of this exchange bias system. Hopefully, this work reveals new perspectives for simplifying the behavior of confusing systems. Fig. 1a shows the configuration of the investigated LNO/STO(n)/LSMO superlattices, which consists of a non-magnetic STO layer. The STO layer changed from 1 u.c. to 7 u.c. and inserted in every interface between the LNO and LSMO layers. Typical x-ray diffraction patterns measured with Cu-K_α radiation around the (002) STO Bragg peak of the investigated specimens are shown in Fig. 1b. Satellite peaks SL+1 and SL+2 are observed, indicating smooth interfaces in the LNO/STO/LSMO superlattices.[25] To support of the claims of coherent and epitaxial heterostructure growth and the absence of secondary phases, an atomically resolved high-angle annular dark field scanning transmission electron microscopy image of the LNO(2)/STO(2)/LSMO(5) superlattice is shown in Figure 1c. The good layering with atomically flat interfaces is readily identified from this image. Typical in-plane magnetic loops at 5 K in the LNO(2)/LSMO(5) superlattice after positive field cooling (FC) and negative field cooling processes are shown in Figure 2a. In this field-cooling magnetic loop, the exchange field and coercivity are 603 Oe and 1999 Oe, respectively.[8] In Figure 2b, the H_{EB} and H_C decrease to 230 Oe and 1181 Oe for the LNO(2)/STO(2)/LSMO(5), respectively. In Figure 2c, when the thickness of the inserted STO spacer layer is 6 u.c., the negative coercive field and positive coercive field values after the ±5 kOe FC procedures are consistent with each other. This indicates that the exchange bias effect is absent. The dependence of the exchange bias field and coercivity on the LNO/STO(n)/LSMO system STO spacer layer thickness is shown in Figure 2d. As the spacer layer thickness increases, the exchange bias field decreases monotonically and smoothly. At a maximum thickness of 6 u.c., the exchange coupling vanishes. According to these magnetic measurements, long-range exchange coupling can be confirmed in the LNO/STO(n)/LSMO system. The work was supported by National Key R&D Program of China (No. 2017YFB0405703), NSFC (Nos. 61434002, 51571136, 11274214), and the Special Funds of Sanjin Scholars Program.

1. Biswas, A., et al., *Prog. Surf. Sci.,* 2017, 92, 117-141. 2. Sreedhar, K., et al., *Phys. Rev. B,* 1992, 46, 6382. 3. Chaloupka, J., et al., *Phys. Rev. Lett.,* 2008, 100, 016404. 4 Gokemeijer, N. J., et al., *Phys. Rev. Lett.,* 1997, 79, 4270-4273. 5. Gibert, M., et al., *Nat. Mater.,* 2012, 11, 195-198. 6. Zhou G. W., et al., *ACS Appl. Mater. Interfaces,* 2017, 9, 3156-3160.

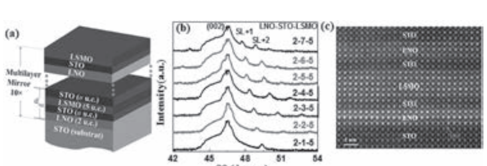

Fig. 1. (a) Schematic view of epitaxial LNO/STO(n)/LSMO superlattices on (001)-oriented $SrTiO_3$ substrates. (b) XRD patterns for a series of LNO/STO(n)/LSMO superlattices. (c) Atomically resolved HAADF-STEM image for the (2-2-5) superlattice.

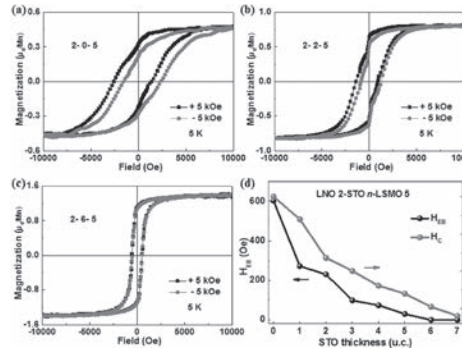

Fig. 2. (a)-(c) Magnetic hysteresis loops at 5 K after ±5 kOe field-cooling process for LNO(2)/LSMO(5), LNO(2)/STO(2)/LSMO(5), and LNO(2)/STO(6)/LSMO(5) superlattices. (d) Exchange bias field and coercivity as a function of STO spacer layer thickness for LNO/STO(n)/LSMO superlattices.

EP-09. Comparative magnetic properties of Ag/Fe bilayer and nano-dot arrays.

B. Alkadour[2], W. Chuang[1], S. Ciou[3], J. Wu[3], P. Manna[2], *K. Lin*[1] and J. van Lierop[2]

1. National Chung Hsing University, Taichung, Taiwan; 2. University of Manitoba, Winnipeg, MB, Canada; 3. National Changhua University of Education, Changhua, Taiwan

Nanostructured materials consisting of metal and magnetic layers have been studied widely in order to obtain enhanced magneto-optical effects- a research activity known as magneto-plasmonics [1]. In this study, the magnetic properties of nano-dot arrays and thin films were investigated. The Ag (~ 30 nm)/Fe (~ 50 nm) bilayers were prepared on amorphous SiO_2 substrates by using a dual ion-beam sputtering deposition technique [2]. Ag/Fe nano-dot arrays (diameter ~ 200 nm, center-to-center distance ~ 400 nm) were fabricated by using electron beam lithography and followed by Ar-ion etching techniques [3]. Continuous Ag/Fe thin film exhibits a smooth surface with an average roughness of R_a ~ 0.9 nm, as measured by atomic force microscopy, and grain sizes ranged from ~ 10 to ~15 nm, as characterized by transmission electron microscopy. Grazing incidence x-ray diffraction identified that both Fe and Ag of the reference Ag/Fe bilayer were crystallized in their fcc phase (space group: F*m*-3*m*), and the lattice parameters are 4.16 and 4.31 Å for Ag and Fe, respectively. The reference Ag/Fe thin film exhibits soft magnetic properties with a coercivity (H_c) of ~ 20 Oe. By contrast, the Ag/Fe nano-dot arrays present half of that H_c at 300 K, with H_c (T) increasing with cooling (H_c~ 100 Oe at 2 K). In addition, asymmetric hysteresis loops observed at temperatures below 100 K signify different domain reversal modes and their associated energetics in positive and negative fields, in contrast to the reference film that presents symmetric hysteresis loops. The impact of magnetic coupling between dots (Fig. 1) is also observable from the difference in the temperature dependent DC susceptibilities of the reference film and the nano-dot arrays (e.g. $\Delta\chi_{FC-ZFC}$ (T > 50 K) = 0 for the film and $\Delta\chi_{FC-ZFC}$ (T > 50 K) ~ 10^{-5} emu for the nano-dot arrays). Numerical simulations analysis will be used to elucidate the nature and strength of different coupling energies. Research was supported by MOST of Taiwan and NSERC of Canada.

[1] R. Sachan et al., Nanotechnology 23, 275604 (2012). [2] R. D. Desautels et al., Appl. Phys. Lett. 108, 172410 (2016). [3] N. Ou et al., IEEE Trans. Magn. 45, 4027 (2009).

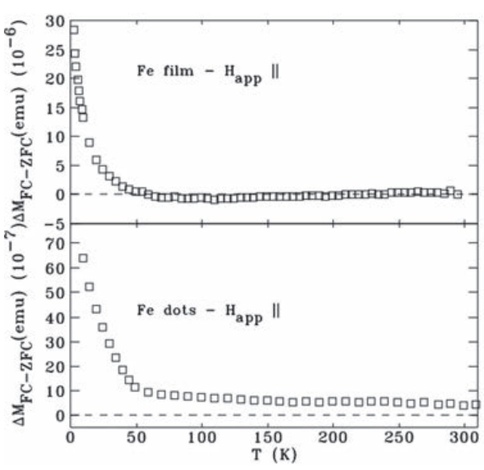

Fig. 1. The magnetic coupling between nano-dot arrays (cf. continuous Fe films), as characterized by the difference in temperature dependent magnetization between field-cooled (FC) and zero-field cooled (ZFC) processes.

EP-10. Exchange bias induced asymmetry in the magnetization reversal process of Fe/GaAs/GaMnAs hybrid structure.

s. Lee[1,2], S. Choi[2], S. Bac[2], K. Lee[2], J. Chang[2], S. Choi[2], P. Chongthanaphisut[2], S. Lee[2], M. Dobrowolska[3], X. Liu[3] and J. Furdyna[3]
1. Korea Institute of Science and Technology, Seoul, The Republic of Korea; 2. physics, Korea University, SEOUL, The Republic of Korea; 3. physics, University of Notre Dame, Notre dame, IN, United States

Magnetization reversal process of a Fe/GaAs/GaMnAs hybrid structure has been investigated by using planar Hall resistance (PHR) measurement. The transitions of magnetization in the Fe and GaMnAs layers are clearly observed as abrupt change in the PHR value during the magnetization reversal process. Interestingly, the hysteresis observed in the field scan PHR measurement with low sensing current of 0.5 mA at temperature of 3 K was asymmetric indicating presence of additional effective field. The asymmetry in the PHR hysteresis, however, becomes weaken as the current increases and it disappears at 3.36 mA of current. The asymmetry in the PHR hysteresis of the Fe/GaAs/GaMnAs structure was assigned to the exchange bias effect arising from the antiferromagnetic FeO, which forms on the surface of Fe layer by oxidation. The exchange bias effect of FeO on Fe film is known to be very sensitive to the temperature and it appears only very low temperature below 20 K.[1] The disappearance of asymmetry in the PHR hysteresis with increasing current is due to the Joule heating effect that increases the sample temperature up to 52 K at 3.36 mA.[2] The magnetization reversal process of the Fe/GaAs/GaMnAs hybrid structure was carefully analyzed by considering such exchange bias effect on the Fe layer.

1. S. Choi, T. Yoo, S. Khym, S. Lee, X. Liu and J. K. Furdyna, Appl. Phys. Lett. 101 (13) (2012). 2. S. Lee, T. Yoo, S. K. Bac, S. Choi, H. Lee, S. Lee, X. Y. Liu, M. Dobrowolska and J. K. Furdyna, Sci Rep-Uk 7 (2017).

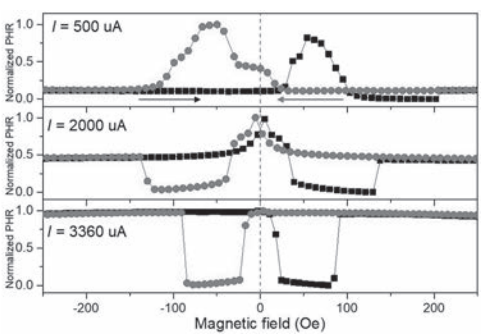

Fig. 1. Field scans of planar Hall resistance (PHR) obtained for three different currents at a magnetic field applied along ϕ_H = 70°

EP-11. Giant perpendicular exchange bias in a sub-nanometer inverted $(Co/Pt)_n/Co/IrMn$ structure.

J. Feng[1], H. Wei[1], H. Liu[1], X. Zhang[2], Y. Ren[3], X. Li[3], J. Wang[4] and X. Han[1]
1. Institute of Physics, Chinese Academy of Sciences, Beijing, China; 2. Department of Physics and Quantum Theory Project, University of Florida, Gainesville, FL 32611, American Samoa; 3. Institute of Nuclear Physics and Chemistry, China Academy of Engineering Physics, Mianyang, 621999, China; 4. The Center for Micromagnetics and Information Technologies (MINT) and Department of Electrical and Computer Engineering, University of Minnesota, 200 Union St SE, Minneapolis, Minnesota 55455, MN, United States

The phenomenon of exchange coupling has become major research area since its discovery [1] and was extensively studied in various ferrromagnet (FM) - antiferromagnet (AFM) systems in the presence of spintronics [2-4], which usually occurs in a FM/AFM bilayer [1-4]. A large exchange bias field (H_{ex}) at room temperature is preferred, but perpendicular magnetic anisotropy is found to be more desirable due to a high thermal stability for various spintronic devices. In our work [5], we report a giant perpendicular exchange bias H_{ex}^{per} exhibited in the *R-H* curves of an inverted $(Co/Pt)_n$/Co/IrMn multilayer and an inverted $(Co/Pt)_n/Co/Cu/(Co/Pt)_4$/Co /IrMn spin valve structure, in which the Pt layers are only 1/4 nm in thickness and less than Co layers. H_{ex}^{per} has an unusual linear scaling with the repetition n+1 of the $(Co/Pt)_n$/Co free layer, with its maximum value near the order of 1000 Oe for n+1 = 9. The in-plane exchange bias H_{ex}^{in} is almost constant. The origin of exchange bias in inverted spin valve structure is due to Co/IrMn interfacial magnetic coupling in inverted $(Co/ Pt)_4$/Co/IrMn reference layer, which is magnified by the exchange coupling between the interface Co layer and the multilayer $(Co/ Pt)_n$ (n = 4 for the spin valve structures) in the reference stack. As shown Figure 1, giant conventional and pseudo H_{ex}^{per} in the perpendicular inverted $(Co/Pt)_n$/Co spin valves enhances their roles in perpendicular spintronic devices.

[1] W.H. Meiklejohn, C.P. Bean, New magnetic anisotropy, Phys. Rev. 102, 1413(1956). [2] R. L. Stamps, Mechanisms for exchange bias, J. Phys. D: Appl. Phys. 33, R247 (2000). [3] J. Nogués, Ivan K. Schuller, Exchange bias, J. Mag. Mag. Mat. 192, 203(1999). [4] J. Nogués, J. Sort, V. Langlais, V. Skumryev, S. Suriñach, J.S. Muñoz, M.D. Baró, Exchange bias in nanostructures, Phys. Reports 422, 65 (2005). [5] J. F. Feng, H. F. Liu, H. X. Wei, X.-G. Zhang, Y. Ren, X. X. Li, Y. Wang, J. P. Wang, X. F. Han, Giant perpendicular exchange bias in a subnanometer inverted (Co/Pt)n/Co/IrMn structure, Phys. Rev. Appl. 7 (2017) 054005.

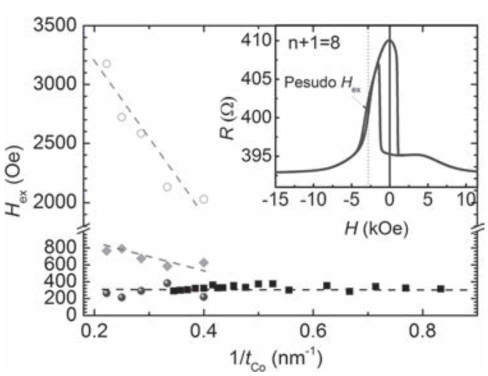

Fig. 1. Dependence of conventional and pseudo H_{ex}^{per} (diamonds and open triangles) on inverse thickness of the Co free layer in $(Co/Pt)_n/Co/Cu/(Co/Pt)_4$/Co/IrMn spin valves, and conventional H_{ex}^{in} (solid triangles and solid squares) in $(Co/Pt)_n/Co/Cu/(Co/Pt)_4$/Co/IrMn and $Co/Cu/(Co/Pt)_4$/Co/IrMn spin valves. Inset shows the perpendicular *R - H* curve for $(Co/Pt)_8/Co/Cu/(Co/Pt)_4$/Co/IrMn spin valve, where the pseudo H_{ex}^{per} is defined.

EP-12. Tunable exchange bias field, damping, and misalignment anisotropies of FeCo/IrMn multilayers tailored by MgO-dilution in antiferromagnets.

Z. Zhang[1], Z. Xu[1], F. Hu[1], E. Liu[1] and F. Xu[1]
1. Nanjing University of Science and Technology, School of Materials Science and Engineering, Nanjing, China

Exchange bias has long been the focus of scientific attention due to its tremendous applications in various spintronics devices although underlying physics of the misalignment anisotropies and dynamic magnetization relaxation still remain unclear.[1] Herein, we investigate the exchange bias field, noncollinear magnetic anisotropies and unidirectional damping in a series of $[Fe_{70}Co_{30}/(Ir_{25}Mn_{75})_{1-x}(MgO)_x]_3$ multilayer exchange bias system with nonmagnetic MgO-dilution in the antiferromagnetic. Fig. 1(a)-(g) shows the in-plane angular dependent resonance field in diluted-AFM $[Fe_{70}Co_{30}/(Ir_{25}Mn_{75})_{1-x}(MgO)_x]_3$ (x £ 0.09) exchange bias multilayers by using the following expression:[2] $H_{res}= H_0-H_{eb}\cos(\phi_H)-H_k\cos2(\phi_H-\beta)$ where H_0 is the angular-independent, isotropic term. H_{res}, H_{eb}, and H_k denote the resonance, exchange-bias, and in-plane uniaxial anisotropy fields, respectively. ϕ_H, β is respectively the azimuthal angle of the external magnetic field applied in the film plane and misalignment angle between unidirectional anisotropy and the uniaxial anisotropy. We plot the doping concentration dependence x of fitted misalignment angle β in Fig. 1(h). β first decreases at small doping concentration (x<0.019) from 5° to 1° then increases up to 15° at high doping concentration (x=0.09). And the fitted exchange bias field H_{eb} is shown in Fig.2 (a). H_{eb} first increases from 185 Oe to 300 Oe at low doping concentration (x<0.019) then decreases to 80 Oe at high doping concentration. The enhancement of H_{eb} has been successfully interpreted by the domain state theory.[3] It is favored by the doping of nonmagnetic impurities and gives rise to the increase of excess magnetization, thereby increases the H_{eb}. For the higher dilution concentrations, the AFM bonds will be broken by the excess impurities. It leads to the connectivity loss of the AFM spin lattice and thus the decrease of H_{eb}. Hence, the H_{eb} of an exchange bias system with diluted AFM layers is determined by the competition between the dilution induced additional net magnetization and the decrease of connectivities in the AFM lattice. We notice that the misalignment angle β shows exactly opposite variation trend to that of H_{eb}, suggesting the noncollinear magnetic anisotropy in the diluted-AFM exchange bias multilayers may be related to the dilution in the AFM layers. Small nonmagnetic dilution will be in favor of the formation of volume domain wall. The driving force for the domain formation is a statistical imbalance of the number of impurities of the two antiferromagnetic sublattices within the dilution region. The imbalance leads to a net magnetization within that region which couples to the external field. During the spin reversal of the region, a domain wall will be created to lower the energy of the system. The necessary energy increase due to the formation of a domain wall can be minimized if the domain wall passes preferentially through nonmagnetic defects at a minimum cost of exchange energy. The domain wall may increase the AFM anisotropy thus β decreases. For larger dilution, it leads to the connectivity loss of the AFM spin lattice and isolated spin clusters appears which do not contribute to AFM anisotropy on longer-time scales leading to a increase of β. In Fig. 2(b), we show the in-plane angular dependence of effective Gilbert damping α for all samples. A cosine dependence of on the in-plane angle was observed, indicating that the dissipation rate depends upon the projection of the magnetization along the bias field. Our study reveals a misalignment of unidirectional and uniaxial anisotropy in the exchange bias system, and the misalignment angle β can be quantified by in-plane angular dependent FMR measurements. We are able to show that misalignment angle can be effectively tuned by the dilution concentration, which is in part caused by the change of AF anisotropy caused by dilution. Also, a very strong unidirectional magnetization relaxation in this system has been observed. The result is beneficial for the understanding of the dilution effect and EB mechanism, and it will contribute to the realization of high-speed spintronics devices with low-energy consumptions.

1. Jamileh Beik Mohammadi, Joshua Michael Jones, Soumalya Paul, Behrouz Khodadadi, Claudia K. A. Mewes, Tim Mewes, and Christian Kaiser.Phys. Rev. B. 95, 064414 (2017). 2. Hyeok-Cheol Choi and Chun-Yeol You, Phys. Rev. B. 81, 224410 (2010). 3. R. Urban, B. Heinrich, G. Woltersdorf, et al, Phys. Rev. B. 65, 020402 (2001).

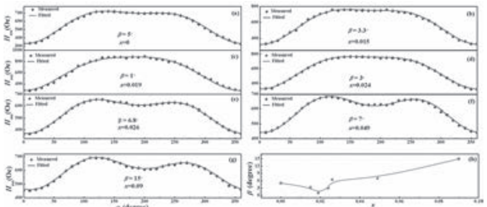

Fig. 1. (a)-(g) In-plane angular dependence of the resonance field H_{res} in $[Fe_{70}Co_{30}/(Ir_{25}Mn_{75})_{1-x}(MgO)_x]_3$ as a function of nonmagnetic MgO doping concentration. The doping concentration x dependence of misalignment angle β are shown in (h).

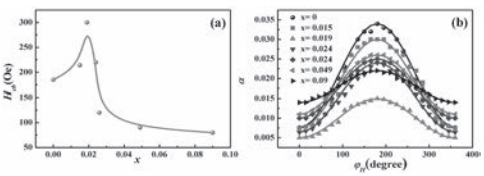

Fig. 2. (a) The doping concentration x dependence of exchange bias $H_{eb.}$ (b) In-plane angular dependencies of the effective Gilbert damping α as as a function of nonmagnetic MgO doping concentration x, the line is a cosine fit to the data.

EP-13. Exchange Bias in $LaMnO_3$ film Induced by Electron Beam Irradiation.

M. Xue[1], X. Chen[2], H. Chen[3], S. Ding[1], Y. Lai[1], L. Zha[1], Y. Men[4], Z. Xu[4], X. Kong[4], L. Han[4], K. Li[1], Z. Shao[1], G. Qiao[1], X. Li[1], Y. Zhang[1], H. Zhao[1], X. Wen[1], W. Yang[1], H. Du[1], J. Han[1], Y. Yang[1], S. Liu[1], C. Wang[1] and J. Yang[1]

1. Peking University, Beijing, China; 2. University of Nebraska-Lincoln, Lincoln, GA, United States; 3. University of International Business and Economics, Beijing, China; 4. Chinese Academy of Sciences, Beijing, China

Exchange Bias in $LaMnO_3$ film Induced by Electron Beam Irradiation Mingzhu Xue [a], Xuegang Chen [d], Hao Chen [e], Shilei Ding [a], Youfang Lai [a], Liang Zha [a], Yong Men [f], Zhuang Xu [f], Xiangdong Kong [f], Li Han [f], Kun Li [a], Zhuyin Shao [a], Guanyi Qiao [a], Xin Li [a], Yinfeng Zhang [a], Hui Zhao [a], Xin Wen [a], Wenyun Yang [a], Honglin Du [a], Jingzhi Han [a], Yingchang Yang [a], Shunquan Liu [a], Changsheng Wang [a] and Jinbo Yang [a, b, c*] [a] State Key Laboratory for Mesoscopic Physics, School of Physics, Peking University, Beijing 100871, P.R. China [b] Collaborative Innovation Center of Quantum Matter, Beijing, 100871, P.R. China [c] Beijing Key Laboratory for Magneto-electric Materials and Devices, Beijing 100871, P. R. China [d] Department of Physics and Astronomy & Nebraska Center for Materials and Nanoscience, University of Nebraska-Lincoln, Lincoln, NE 68588-0299, USA [e] Institute of International Economy, University of International Business and Economics, Beijing 100029, P. R. China [f] Department of Micro-nano Fabrication Technology, Institute of Electrical Engineering, Chinese Academy of Sciences, Beijing 100190, P.R. China Perovskite transition-metal oxide $LaMnO_3$ has been studied extensively due to its interesting physical properties. Bulk $LaMnO_3$ is an A-type antiferromagnetic insulator and is typically found to be ferromagnetic and semiconducting from various doping. Besides, even without extrinsic doping, $LaMnO_3$ itself has very rich phases induced by its nonstoichiometry [1]. For example, as-grown $LaMnO_3$ films usually exhibit ferromagnetism rather than antiferromagnetism, because the cation vacancies derived from oxygen nonstoichiometry lead to a mixed valence state for Mn ions. Ferromagnetic double-exchange and antiferromagnetic super-exchange interaction compete in the as-grown $LaMnO_3$ films. The exchange bias (EB) effect is observed in systems exhibiting the exchange interaction at the interface between a ferromagnetic material and an antiferromagnet, ferrimagnet, or a spin glass [2, 3, 4]. It has been widely used in spintronic devices, such as giant magneto resistance (GMR) read heads and magnetic random access memory (MRAM) [2, 5]. The EB effect was mostly found in the heterogeneous interface between two separately materials [6]. However, the electronic phase separation (PS) in mixed-valence manganites, namely the coexistence of FM metal and AFM insulator, provides a unique opportunity to construct a "homo-interface" in a chemically uniform material, which may exhibit exchange bias effect and metal-insulator transition [7]. In this paper, we reported the exchange bias effect in the $LaMnO_3$ film by using electron beam irradiation technology, which can provide not only thermal effect but also reduction characteristics to control the Mn valance state. $LaMnO_3$ films (13 nm) were first fabricated on $SrTiO_3$ (001) substrates by pulsed laser deposition technique (PLD), and the as-grown films were treated by electron beam irradiation process (the EBI films). The X-ray diffraction (Figure 1(a)) shows that the as-grown $LaMnO_3$ films and the EBI films all present only the (00*l*) peaks, confirming that all samples were grown epitaxially oriented with respect to the substrate. Figure 1(b) indicates that the EBI film shows a pronounced peak with an increased *c*-axis lattice constant which can be explained by the valence state of the Mn ions. The dominant mechanism for ferromagnetism in as-grown $LaMnO_3$ films is the ferromagnetic double-exchange interaction induced by the mixed valence of Mn^{3+}-Mn^{4+}. After electron beam irradiation process, Mn^{4+} transformed into Mn^{3+} partly owing to reduction characteristics, which corresponds to the increase of *c*-axis lattice constant. Fig 2(a) shows the magnetic moments as the function of temperature, and figure 2(b) exhibits magnetization versus applied magnetic field at 10 K. The Curie temperature (T_C) of the EBI films is lower than the Curie temperature of the as-grown films, and the magnetic moments also decrease in lower temperature. In particular, figure 2(b) shows that the EBI film exhibits unexpected exchange bias in 10 K. As the amount of the Mn^{3+} ions in EBI films increases, the antiferromagnetic super-exchange interaction becomes stronger and meanwhile the ferromagnetic double-exchange interaction is weakened. Therefore, the Curie temperature (T_C) and the magnetic moments all decrease in EBI films. Besides, with the amount of the Mn^{3+} ions in EBI films increasing, the exchange coupling between the ferromagnetic phases and the antiferromagnetic phases enhanced, which induce the exchange bias in EBI films. This explanation also corresponds to the XRD results.

[1]. Ritter C, Ibarra M R, De Teresa J M, *et al*. Physical Review B Condensed Matter. 56, 8902 (1997). [2]. Nogues J, Schuller I K. J. Magn. Magn. Mater. 192, 203 (1999). [3]. Ch B, Polisetty S, He X, *et al*. Physical Review Letters. 96, 067201 (2006). [4]. Ali M, Adie P, Marrows C H, *et al*. Nature Material. 6, 70 (2007). [5]. Sando D, Agbelele A, Rahmedov D, *et al*. Nature Materials. 12, 641 (2013). [6]. Gibert M, Zubko P, Scherwitzl R, *et al*. Nature Materials. 11, 195 (2012). [7]. Peng J J, Song C, Cui B, *et al*. Phys. rev. b. 89, 130 (2014).

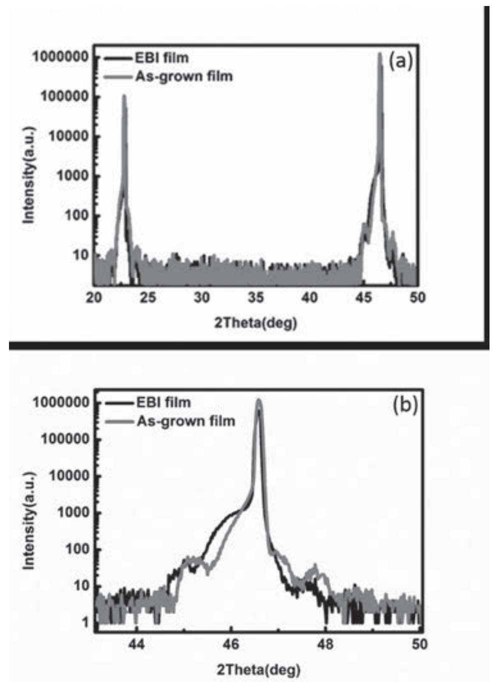

Fig. 1. (a) XRD θ-2θ scans and (b) θ-2θ patterns near (002) peaks for as-grown and EBI $LaMnO_3$ films grown on $SrTiO_3$ (001) substrate.

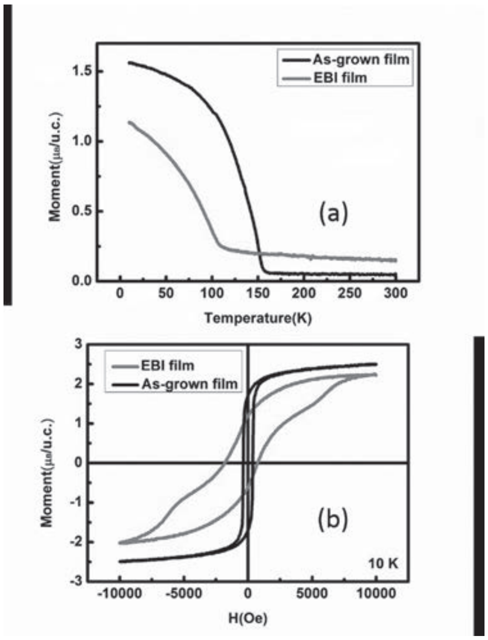

Fig. 2. (a) The temperature - dependent magnetization (5000 Oe, field cooled) (b) hysteresis loops (10 K) of as-grown and EBI $LaMnO_3$ films.

EP-14. Perpendicular exchange bias effect in CoFeB/Pt/MnIr multilayers.

w. Li[1], J. Yan[1], Y. Lu[1], *S. Lou*[1], Z. Zhang[2], X. Zhang[1] and Q. Jin[1,2]
1. State Key Laboratory of Precision Spectroscopy, East China Normal University, Shanghai, China; 2. Department of Optical Science and Engineering, Fudan University, Shanghai, China

The exchange bias effect is investigated in CoFeB / MnIr multilayers system with perpendicular magnetic anisotropy. An interlayer of Pt (0.5nm) between CoFeB and MnIr layer enhanced both the perpendicular anisotropy and the exchange bias. Both the exchange bias and the coercivity field depend on the thickness of the MnIr layer, the largest exchange bias field of 201.7 Oe was obtained in a 5nm MnIr thickness samples which had been annealed at 573 K in external magnetic field. The exchange bias becomes weaker when the thickness of the Cu or Pd underlayer increases in [Pd / CoFeB]$_4$ / MnIr multilayer system. The Gilbert damping constant obtained from the Kerr effect (TR-MOKE) measurement increases as the thickness of Cu or Pd underlayer increases. However, in the pump-probe measurement, the exchange bias fields decreased before the Kerr signal starts change and restored when the change of the Kerr signal reaches its maxima, the total time of this process is about 1 ps. The loss of the exchange bias is probably attributed to the electron temperature. The relation between the exchange bias and the Gilbert damping constant is detail discussed.

1. H. N. Fuke, K. Saito, Y. Kamiguchi, H. Iwasaki, and M. Sahashi, J. Appl. Phys. 81, 4004 (1997). 2. D. Lacour, J. A. Katine, N. Smith, M. J. Carey, and J. R. Childress, Appl. Phys. Lett. 85, 4681 (2004). 3. G. Malinowski, K. C. Kuiper, R. Lavrijsen, H. J. M. Swagten, and B. Koopmans, Appl. Phys. Lett. 94, 102501 (2009). 4. S. Iihama, S. Mizukami, H. Naganuma, M. Oogane, Y. Ando, and T. Miyazaki, Phys. Rev. B 89, 174416 (2014). 5. H. S. Song, K. D. Lee, J. W. Sohn, S. H. Yang, S. P. P. Stuart, C. Y. You, and S. C. Shin, Appl. Phys. Lett. 103, 022406 (2013). 6. S. Mizukami, S. Iihama, N. Inami, T. Hiratsuka, G. Kim, H. Naganuma, M. Oogane, and Y. Ando, Appl. Phys. Lett. 98, 052501 (2011).

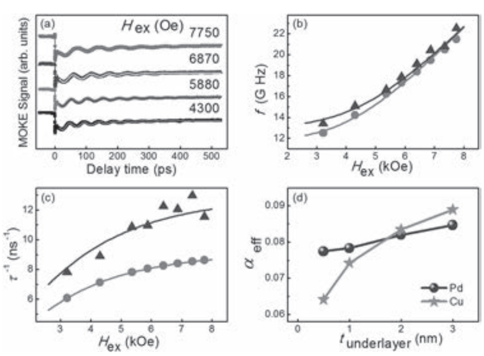

Fig. 1. (a) The laser-induced magnetization dynamic Kerr signals and the fitting curves for [Pd(1.5)/CoFeB(0.4)]$_4$/MnIr(0) with H_{ex} = 4300~7750 Oe and external magnetic field-sample plane angle θ=17°. (b) and (c) display the magnetic field dependences of magnetization precession frequency and decay time fitted from the laser-induced magnetization dynamic Kerr signals. (d) shows the Gilbert damping as a function of the thickness of Cu and Pd underlayer.

EP-15. Vectorial mapping of exchange anisotropy in [NiFe/FeMn] bilayers through angular resonant absorption curves.

D. Adams[1,2], P. Kern[3] and L. Spinu[1,2]
1. Advanced Materials Research Institute, University of New Orleans, New Orleans, LA, United States; 2. Physics, University of New Orleans, New Orleans, LA, United States; 3. Fisica, Universidade Federal de Santa Maria, Santa Maria, Brazil

The interfacial coupling between ferromagnetic and antiferromagnetic thin films displays noticeable features such as an enhancement of the coercivity and an offset of the magnetic hysteresis loop from zero, known as exchange bias field (H_{EB}). Since its discovery [1], the phenomenon of exchange bias has been studied thoroughly, although a complete connection between the static and dynamic properties of exchange-biased systems is still lacking [2]. In this study, a series of [NiFe/FeMn] bilayer films with varying thicknesses (t_{AF}) of the antiferromagnetic layers (3 nm ≤ t_{AF}≤ 15 nm) and constant thickness of the ferromagnet (50 nm) were deposited on silicon (100) substrates through magnetron sputtering. The exchange bias properties in these samples were evaluated through angular-dependent ferromagnetic resonance (FMR) measurements conducted at room temperature in the plane of the sample. The saturation fields were determined through the major hysteresis loop. It has been shown that the switching peaks obtained through reversible susceptibility measurements performed for different orientations of the applied magnetic field can be used to construct a critical curve [3]. In this work, the high frequency properties of the material were studied in a way reminiscent of this static critical curve, as has been done for other systems [4]. The microwave absorption of the exchange bias systems was investigated through vector network analyzer ferromagnetic resonance (VNA-FMR) spectroscopy. The sample was coupled to the signal line of a coplanar waveguide, which was connected to the VNA. The dc magnetic field was created in the plane of the sample by an electromagnet on a rotation stage capable of 360° rotation. For a fixed frequency, the S_{21} transmission coefficient was recorded as a function of applied field for different orientations of the applied field with respect to exchange bias axis to construct a dynamic critical curve for different frequencies. This therefore gives a fingerprint of the high frequencies properties of the sample. Analogous to the static critical curve, H_{EB} can be determined from the opposite branches of a single dynamic critical curve. Noncolinear anisotropy axes were observed for t_{AF} ≥ 6 nm. The magnitude and direction of exchange anisotropy can be determined using this dynamic critical curve. Our results show a reasonable agreement between the value of H_{EB} obtained through static measurements as well as other FMR studies for these samples including broadband and X-band measurements.

1. Meiklejohn, W.H. and C.P. Bean, *New Magnetic Anisotropy.* Physical Review, 1957. 105(3): p. 904-913. 2. Khanal, S., et al., *Exchange bias in (FeNi/IrMn)n multilayer films evaluated by static and dynamic techniques.* Journal of Physics D-Applied Physics, 2014. 47(25): p. 8. 3. Spinu, L., et al., *Vectorial mapping of exchange anisotropy in IrMn/FeCo multilayers using the reversible susceptibility tensor.* Physical Review B, 2003. 68(22): p. 4. 4. Cimpoesu, D., et al., *Angular resonant absorption curves in magnetic nanowire arrays.* Applied Physics Letters, 2013. 102(23).

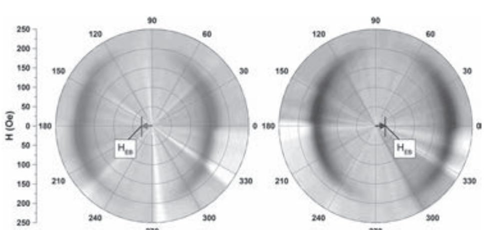

Fig. 1. Experimentally determined dynamic curves for t_{AF} = 15 nm and FMR frequency f = 4 GHz

EP-16. Extraordinary Optical Transmission of sub-wavelegth metallic grating with mirror symmetric cavities.

Y. Qi[1], H. Gong[1] and X. Zhang[1]
1. College of Physics and Electronic Engineering, Northwest Normal University, Lanzhou, China

I. INTRODUCTION The extraordinary optical transmission (EOT) of light through nanostructured metallic films with sub-wavelength metallic grating has got a lot of researchers attention attracted who work in the areas of nanooptics and plasmonic applications[1] Many research shows that the EOT phenomenon of the metal sub-wavelength slit array is mainly due to the resonance coupling of the incident wave with the SPPs excited by the free electron oscillation of the metal surface. SPPs was found to be responsible for enhanced transmission[2,3]. At the same time, it was found that the EOT phenomenon is also affected by LSP resonance within the metal slit[4]. Both of which play an important role in the generation of EOT phenomena, but only when the two energy is similar, it is most conducive to enhanced transmission[5]. In addition, the study also found that the spectrum of the EOT caused by the main role of LSP is narrow and its application is limited[6]. Therefore, it is significant to study the broadband enhanced optical transmission caused by non-LSP. In 2011, G.Subramania et al. Designed a rectangular array of connected holes, and found that the structure can achieve a non-resonant wide band enhanced transmission[7]; then in 2012, Shen HH and others use the transmission line theory to design a wedge-shaped slit grating structure from the entrance to the exit port, whose the characteristic impedance is gradually changed. The resonant condition of the FP cavity is destroyed, and the enhanced transmission of the non - resonant wide band is realized[8]. In 2013, Qin Yan designed the embedded rectangular cavity wedge-shaped metal slit array, which further promoted the enhanced projection of the metal sub-wavelength slit[9]. In 2016, Xiao Gongli et al proposed an array of symmetrical rectangular cavity wedge-shaped metal slit array. Dimensional structure is extended to three-dimensional structure, on the basis of improving the transmittance, while achieving a short wavelength range transmission band gap and long wavelength range of transmittance[10]. However, the study found that, in some cases, the wedge-shaped slit has a better transmission than the straight slit, so there was less research on the study of the straight-slit EOT phenomenon of the embedded mirror symmetric rectangular cavity. So we present a novel periodic sub-wavelength metallic grating on the silica substrate. This is compound structure of the rectangular metallic slit embedded with mirror symmetric rectangular cavity, as shown in figure 1a, and with finite difference time domain (FDTD) method simulation. The effects of length, width and position of embedded rectangular cavities on transmission property of metallic slits array were studied. The result shown that the grating not only can achieve higher transmission efficiency, but also the band gap can be adjusted through change the geometric parameter of the structure. Meanwhile it has enhanced optical transmission in long-wavelength range and showing double peaks, the transmission efficiency can reach even over 99%. We find that the transmission properties of the proposed grating strongly depend on the geometric parameters including the period. The transmission spectra can be manipulated by tuning the parameters of the structure. II. Modeling and Simulation The structure was characterized by the thickness h, the period P, the slit width W, the rectangular cavity width a, the rectangular cavity depth b, the distance between two rectangular cavities d, and the rectangular wall thickness c. the thickness of silica substrate was 100nm. The metal film material was silver, Both electrolytes in Metal slits and rectangular cavities are air, the perfectly matched layers (PML) boundary condition was used in the Z direction, and the period boundary condition was used in the X direction and Y direction. The light source was set to a plane wave placed on the upper surface of the silver film at 200 nm incident normally onto the metallic slit array from the air side. As shown in fig 2d, we can clearly observed that enhanced optical transmission in long-wavelength range and showing double peaks, the transmission efficiency can reach even over 99% at l=. Furthermore, the full width at half maximum (FWHM,T>50%) is over. To understand the physical mechanism of the optical properties observed above, the normalized electric field intensity distributions in the yoz plane at corresponding peak and trough wavelength as shown in fig 2 a b and c.

1) Ebbesen, T. W., Lezec, H. J., Ghaemi, H. F., Thio, T., & Wolff, P. A. Extraordinary optical transmission through sub-wavelength hole arrays. Nature,391(12): 667-669. (1998). 2) Wang Y K, Qin Y, Zhang Z Y. Broadband Extraordinary Optical Transmission Through Gold Diamond-Shaped Nanohole Arrays[J]. IEEE Photonics Journal, 6(4):1-8, (2014). 3) Huang F, Yang H, Li S, et al. Tunable Unidirectional Coupling of Surface Plasmon Polaritons Utilizing a V-Shaped Slot Nanoantenna Column[J]. Plasmonics, 10(6):1825-1831, (2015). 4) Najiminaini M, Vasefi F, Kaminska B, et al. A Three-Dimensional Plasmonic Nanostructure with Extraordinary Optical Transmission[J]. Plasmonics, 8(2):217-224, (2013). 5) Nie J, Li H Q, Liu W. Robust Broadband Optical Transmission Realized in a Dual-Metallic-Grating Structure[J]. IEEE Photonics Journal, 6(4):1-8, (2014). 6) Jia S, Wu Y, Wang X, et al. A Subwavelength Focusing Structure Composite of Nanoscale Metallic Slits Array With Patterned Dielectric Substrate[J]. IEEE Photonics Journal, 6(1):1-8., (2014). 7) Subramania G, Foteinopoulou S, Brener I. Nonresonant broadband funneling of light via ultrasubwavelength channels.[J]. Physical Review Letters, 107(16):163902, (2011). 8) Shen H, Maes B. Enhanced optical transmission through tapered metallic gratings[J]. Applied Physics Letters, 100(24):667, (2012). 9) Qin Y. Cao W, Zhang Z Enhanced optical transmission through metallic slits embedded with rectangular cavities[J]. Acta Physica Sinica, 62(12):127302-464, (2013). 10) Xiao G, Zheng L, Wang B, Broadband enhanced transmission through wedge-shape metallic slits array embedded with mirror symmetric rectangular cavities[J] Semiconductor Optoelectronics, 37(4):505-509, (2016)

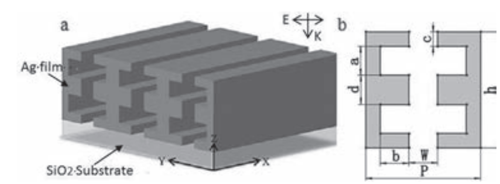

Fig. 1. Schematic drawing of the metallic grating with mirror symmetric rectangular cavities along with Two-dimensional profile dimensions.

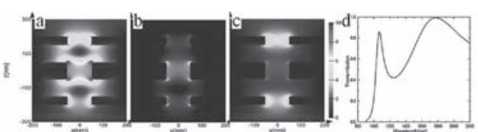

Fig. 2. Electric field intensity distribution and Optical Transmission Spectrum of our proposed structure with P=400nm, c=50nm, h=400nm, W=100nm,a=b=d=100nm. (a) l=1070nm, (b) l=1248nm, (c) l=1374nm. (d) Optical Transmission Spectrum

Session EQ
FERRITE MATERIALS AND APPLICATIONS
(Poster Session)

Haizhong Guo, Chair
Zhengzhou University, Zhengzhou City, China

EQ-01. Ferromagnetic resonance linewidth and magnetic property of cobalt-substituted NiCuZn ferrites.

K. Li[1], K. Sun[1], C. Chen[2], X. Liu[2], R. Guo[1], H. Liu[1], Z. Yu[1], X. Jiang[1] and Z. Lan[1]

1. University of Electronic Science and Technology of China, Chendu, China; 2. Global Energy Interconnection Research Institute, Beijing, China

NiCuZn ferrites have important application in the microwave magnetic devices. The energy cost, reliability and working range of these devices mainly depends on the ferromagnetic resonance (FMR) linewidth (ΔH) of ferrite materials [1]. Therefore, the study about the contribution of FMR linewidth of NiCuZn ferrites is significant and meaningful. The polycrystalline ferrites $Ni_{0.5-x}Cu_{0.12}Zn_{0.4}Co_xFe_{1.98}O_4$-δ with different cobalt-substituted contents (x=0.000~0.015) have been synthetized via the solid-state reaction method. All samples exhibit single phase of cubic spinel structure. The lattice parameter (a) increases while the amount of cobalt substitution increases. The main reason for this phenomenon is that Co^{2+} ions intend to occupy the position of Ni^{2+} ions on the octahedral site (B sublattice) and Co^{2+} ion (0.78 Å) has a larger radius than Ni^{2+} ion (0.74 Å) [2]. As the amount of cobalt substitution increases, both grain size and porosity rise. Meanwhile, remanence ratio (B_r/B_s) increases and the saturation magnetization (M_s) has little change. The ΔH of polycrystalline ferrites is the sum of three parts [3]: (1) the anisotropy linewidth broadening (ΔH_a), (2) the porosity linewidth broadening (ΔH_p) and (3) the intrinsic linewidth broadening (ΔH_i). However, ΔH_i can be ignored in polycrystalline ferrites owing to their less value that is smaller than 1 kA/m. Meanwhile, ΔH_a and ΔH_p are attributed to magnetocrystalline anisotropy constant (K_1) and porosity, respectively. Based on the law of approach to saturation, the magnetocrystalline anisotropy constant (K_1) of samples have been calculated and the results are shown in Fig. 1, the sign change of K_1 was caused by positive K_1 value of Co^{2+} ions. The addition of cobalt compensates the negative K_1 value of NiCuZn ferrites. While the amount of cobalt substitution is 0.003, the K_1 represents the minimum absolute value of 1.77kJ/m^3. With the previous data of K_1 and porosity, an approximate calculation for the separation of ΔH has been done by adopting dipolar narrowing theory [4]. As shown by the calculated results (see in Fig. 2), the porosity linewidth broadening contribution (ΔH_p) is larger than the anisotropy linewidth broadening (ΔH_a). Thus, the uniform and dense microstructure is effective to reduce the ferromagnetic resonance linewidth. Far more important is that proper amount of cobalt substitution can reduce the value of anisotropy linewidth broadening.

[1] J. D. Adam, L. E. Davis, G. F. Dionne, E. F. Schloemann, S. N. Stitzer, Ferrite devices and materials, IEEE Trans. Microw. Theory Tech., 50 (2002) 721-737. [2] A. M. Kumar, P. A. Rao, M. C. Varma, G. S. Choudary, K. H. Rao, Cation distribution in $Co_{0.7}Me_{0.3}Fe_2O_4$, J. Mod. Phys., 2 (2011) 1083-1087. [3] P. Söschmann, Separation of anisotropy and porosity contributions to inhomogeneous broadened FMR linewidth in polycrystalline YIG, IEEE Trans. Magn., 11 (1975) 1247-1249. [4] M. Sparks, Ferromagnetic resonance porosity linewidth theory in polycrystalline insulators, J. Appl. Phys., 36 (1965) 1570-1573.

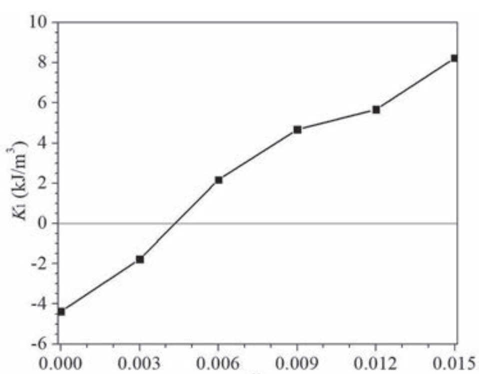

Fig. 1. The magnetocrystalline anisotropy constant of $Ni_{0.50-x}Cu_{0.12}Zn_{0.34}Co_xFe_{1.98}O_{4-\delta}$ ferrites with different amounts of cobalt substitution

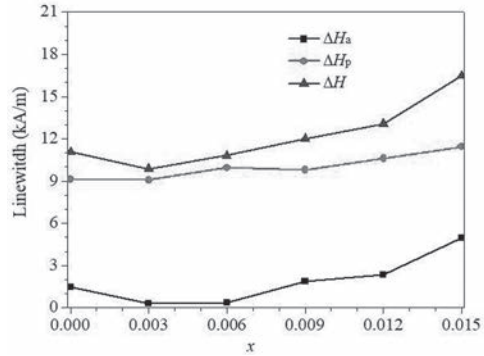

Fig. 2. The ΔH_a, ΔH_p and ΔH of $Ni_{0.50-x}Cu_{0.12}Zn_{0.34}Co_xFe_{1.98}O_{4-\delta}$ ferrites with different amounts of cobalt substitution.

EQ-02. Fabrication of Magnetic Ultrafine Particles-Insulator Composite Film Using the LbL Assisted Composite Plating Method.

N. Fujita[1], M. Takeuchi[1], Y. Watanabe[1], N. Matsumoto[2] and H. Muto[2]
1. Electrical Engineering, National Institute of Technology, Nara College, Yamatokoriyama, Japan; 2. Electrical and Electronic Information Engineering, Toyohashi University of Technology, Toyohashi, Japan

Magnetic ultrafine particles-insulator composite films including Fe-Ni ultrafine particles and insulating epoxy films used for electromagnetic wave absorbing films were synthesized by a newly developed electrochemical method termed the “LbL assisted composite plating method”. The reaction solution containing 40 ml / L water-solve epoxy resin prepared by NIPPON PAINT Co., LTD and 0-3 g / L Fe-Ni ultrafine particles 60 nm in diameter manufactured by the Nilaco corporation were used for film fabrication. Cu substrates and Ti / Pt plates were used as the cathode and anode, respectively. Epoxy films were deposited by the following schemes: $O_2 + 2H_2O + 4e^- \rightarrow 4OH^-$ $(Resin)_3NH^+ + OH^- \rightarrow (Resin)_3N + H_2O$ In LbL assisted composite plating, charged Fe-Ni ultrafine particles are attracted to the cathode by electrostatic force simultaneously with insulator epoxy film electrodeposition. LbL treatment was performed using 1 wt.% PSS (Poly (sodium 4-styrenesulfonate)) and 0.5 mM NaCl solution, and 1 wt.% PDDA (poly (diallyl dimethyl ammonium chloride)) and 0.5 mM NaCl solution. Fe-Ni ultrafine particles were alternately immersed in PSS solution and PDDA solution. In water Fe-Ni ultrafine particles before LbL treatment have 20 mV zeta potential. After immersion in PSS solution, Fe-Ni ultrafine particles have -40 mV zeta potential, and after immersion in PDDA solution, Fe-Ni zeta potential increases to 60 mV. This increase of zeta potential means that the amount of charged electrons on the ultrafine particles surface were increased through a layer by layer structure of cationic and anionic polyelectrolytes formed on the particles. The Fe-Ni ultrafine particles not treated with LbL precipitated in the reaction solution within 30 minutes, while the particles subjected to the LbL treatment were stable in the reaction solution over 16 days. Figure 1 shows the particle size distribution of Fe-Ni ultrafine particles with LbL treatment and without LbL treatment in water. The peak diameters of the distribution curves with LbL treatment and without LbL treatment were 35 nm and 52 nm, respectively. LbL treatment using PSS and PDDA were effective for increasing the charging electrons on Fe-Ni ultrafine particles and for enhancing the dispersibility of ultrafine particles in the reaction solution. At electrophoresis of only Fe-Ni ultrafine particles without epoxy film on Cu substrate, the 4.3-fold increase in the mass of deposited particles with LbL treatment was observed compared with no LbL treatment, as a result of the increase of charging electrons on Fe-Ni particles. Electrodeposition of Fe-Ni ultrafine particle-epoxy composite films was conducted under a constant current density of 4 mA / cm^2, and 5-minute deposition time using the LbL assisted composite plating method. The film thickness was measured from the cross-section SEM image of the films. The film thickness of the deposited film prepared from the reaction solution containing 3 g / L Fe-Ni fine particles without LbL treatment is about 30μm, whereas that prepared from the reaction solution containing 3 g / L Fe-Ni particles with LbL treatment is about 80 μm. From the EDX mapping image of the film prepared using Fe-Ni particles without LbL treatment, the agglomerates of Fe-Ni particles were observed. On the other hand, there are no agglomerates in the film prepared using Fe-Ni particles with LbL treatment. These aggregates of Fe-Ni particles not treated with LbL were generated due to less electron charging on the particle surface than particles having LbL treatment, and act as the growth inhibiter of the epoxy film. Therefore, the film thickness of the films prepared using Fe-Ni particles not treated with LbL was less than that of the film prepared using Fe-Ni particles having LbL treatment. Figure 2 shows the Fe-Ni content in the films dependence on the concentration of Fe-Ni ultrafine particles in the reaction solution. The Fe-Ni content in the films increased in proportion to the Fe-Ni concentration in the reaction solution. Using LbL treatment, the Fe-Ni content in the films increased 1.6 times compared to that without LbL treatment. Over 22 vol. % Fe-Ni ultrafine particles included in epoxy films were successfully obtained using LbL assisted composite plating from the 3 g / L Fe-Ni content reaction solution. The experimental results clearly show the dispersibility in the reaction solution could be greatly improved using LbL treatment for Fe-Ni ultrafine particles, and Fe-Ni ultrafine particles uniformly dispersed in epoxy film could be fabricated using our newly developed electrochemical method.

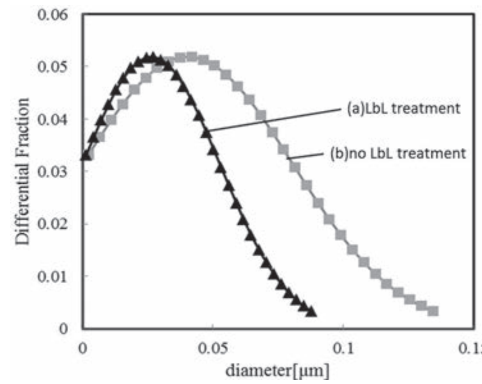

Fig. 1. Particle size distribution of Fe-Ni ultrafine particles in the water. (a)LbL treatment, (b)no LbL treatment.

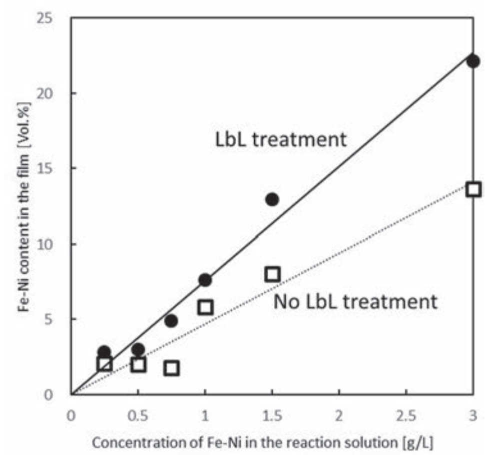

Fig. 2. Fe-Ni content in the films dependence on the concentration of Fe-Ni ultrafine particles in the reaction solution.

EQ-03. A Rotational Hysteresis Model of the Soft Magnetic Composite Material.

N. Duan[1], W. Xu[2], Y. Li[3], S. Wang[1] and J. Zhu[4]
1. Xi'an Jiaotong University, Xi'an, China; 2. State Grid Shaanxi Electric Power Company Economic Research Institute, Xi'an, China; 3. Hebei University of Technology, Tianjin, China; 4. University of Technology Sydney, Sydney, NSW, Australia

I.Introduction Modeling the rotational magnetic hysteresis phenomenon based on the physical mechanism is particularly challenging for magnetic research [1, 2]. Among various approaches proposed, a typical one is the Stoner-Wohlfarth (S-W) model, which has been investigated for many decades primarily due to its strong appeal to physical intuition and vectorial nature. The S-W model assumes that a magnetic material is composed of a great number of single-domain particles with uniaxial crystal anisotropy. This assumption, however, is inconsistent with the phenomena in cubic textured magnetic materials which have biaxial anisotropy in each crystal plane. Also, the numerical implementation is very inconvenient for its incorporation in magnetic field analysis software packages. Many improvements and extensions have been presented based on the conventional S-W model. The asteroid rule was introduced to directly determine the orientation of magnetization based on the graphical interpretation. However, these phenomena-based methods are lack of physical background and difficult to directly apply in the practical engineering calculation. In this paper, in the framework of biaxial operator and wind-rose method, the magnetic properties of a soft magnetic composite under rotational magnetization are predicted and compared with the experimental results. II.Model Description Most magnetic materials are polycrystalline, composed of microscopic crystalline grains. In the ferromagnetic material, such as iron, each crystal lattice has multi-easy-axes and multi-hard-axes [3]. In this paper, magnetization process in the (100) plane, which has two easy axes, is studied. Similar to the determination method of S-W particle, the stable orientation of the magnetization vector in the crystal structure can be obtained by minimizing the energy of the elemental operator. Thus the wind-rose curve, which with two orthogonal easy axes and two orthogonal hard axes and separates the regions with different energy minimum, can be determined. With this wind–rose curve, graphical interpretation can be given for the magnetization process of this biaxial elemental operator. In this H_x-H_y plane, four regions can be separated by the wind–rose curve, and different region corresponding to different number of the energy minima exists, as shown in Fig.1 [4]. The determination of the actual energy minimum is related to the magnetization history. When the magnetic field applies inside the wind–rose shape, with the increase of magnetic field, four, three and two energy minima may exist corresponding to different magnetic field magnitudes. When the magnetic field applies outside the wind–rose curve, the magnetization only has one stable orientation as there is only one energy minimum. When the loci of the rotational magnetic field is outside the wind-rose curve, the magnetization rotates with the magnetic field. The magnetic field and the magnetization cross simultaneously the easy axes and the hard axes, but elsewhere the magnetization is shifted more or less forward or backward depending on the orientation of magnetic field. III.Numerical Implementation To simulate the magnetic properties of different materials by this model, the different distribution functions and parameters are needed. Each magnetic material has an optimal distribution function and parameters, which deliver the best results. This model utilizes the concept of distribution function density in order to consider the interaction field and the coercive force of each elemental operator, which is similar to the method in the traditional Preisach model. The implementation of the Preisach model can be used for reference. In the Preisach model, the distribution can be produced by combing some well-known continuous statistical distributions, such as Gaussian-Cauchy distribution, Gaussian-Lognormal distribution, Cauchy-Lognormal distribution [5]. IV. Experimental Verification To verify the proposed model, the magnetic hysteresis of a soft magnetic composite material, SOMALOY 500, under rotational excitations has been simulated and compared with the experimental results. In the measurement process, the magnetic materials always be controlled to work under the circularly rotational flux B, hence, to verify the introduced method, the corresponding magnetic field should be predicted and measured, respectively [6]. Fig.2 shows the comparison of a series of B and H loci while the magnetic flux densities with magnitudes of 0.3, 0.6, 0.9, 1.2, 1.5 T at 50Hz. As shown, the simulated results agree well with the experiment results in both major and minor rotational hysteresis loops under different rotational magnetization. V.Conclusion In this paper, the rotational magnetic properties have been presented based on the elemental operator and wind-rose method. By adopting the concept of distribution function in Preisach model, the effects of the elemental operators can be integrated to simulate the magnetic hysteresis phenomenon. It has shown that this method features strong physical background, easy software implementation, and acceptable precision.

[1] L. Dupré and J. Melkebeek, "Electromagnetic hysteresis modelling: from material science to finite element analysis of devices," ICS-Newsletter, vol. 10, pp. 4-15, 2003. [2] E Cardelli, "A general hysteresis operator for the modeling of vector fields," IEEE Trans. Magn., vol. 47, no.8, pp. 2056-2067, Aug.2011. [3] G. Bertotti, Hysteresis in magnetism: for physicists, materials scientists, and engineers, New York: Academic, 1998, pp. 235-236. [4] J. M. Coey, Magnetism and magnetic materials, Cambridge University Press, New York, 2010 [5] P. Pruksanubal, A. Binner and K. H. Gonschorek, "Determination of distribution functions and parameters for the Preisach hysteresis model," Proc. 17th Int. Zurich Symp. EMC-Zurich, 2006, pp. 258-261. [6] Y. J. Li, Y. F. Li, et al., "Magnetic anisotropic properties measurement and analysis of the soft magnetic composite materials," IEEE Trans. Appl. Supercond., vol. 24, no. 5, pp. 1-4, Aug. 2014.

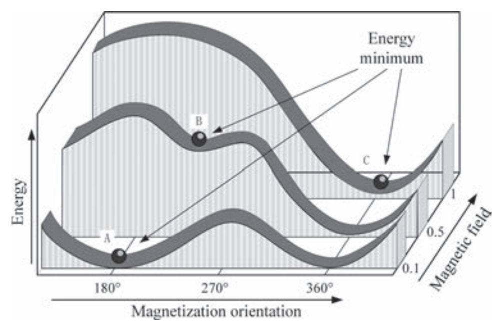

Fig. 1. The stable orientation of the magnetization and the corresponding energy minimum of the elemental operator

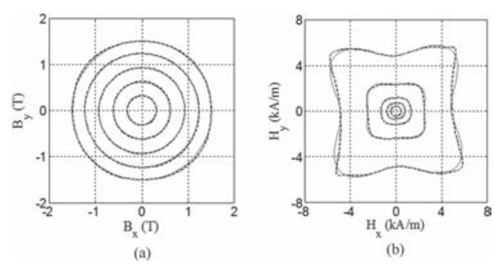

Fig. 2. Comparison of simulated (red) and experimental results (blue) about the loci of (a) B and (b) H of SOMALOY 500 under rotational magnetization

EQ-04. Influence of Al doping on the magnetic and magnetodielectric properties of $GaFeO_3$ nanoparticles.

T. Han[1], Z. Tu[1], Y. Huang[1] and Y. Su[1]
1. Department of Applied Physics, National University of Kaohsiung, Kaohsiung, Taiwan

1. Background- Recently, magnetoelectric (ME) gallium ferrite ($GaFeO_3$, denoted as GFO), which exhibits ferrimagnetism and piezoelectricity, has gained a considerable attention from the scientific community in the context of multiferroics [1,2]. Site-disorder in GFO is reported to be induced by adopting different preparation conditions and methods, such as quenching, ball milling, and chemical routes, which are shown to affect the magnetic properties significantly [3,4]. In addition, all the metal cations in GFO are trivalent, similar to those of rare earth orthoferrites which enhance their magnetic property for isovalent substitution. Acharya et al. [5] reported that magnetization of $LaFeO_3$ was highly enhanced by doping with Al^{3+} ions. Furthermore, the doping of Al^{3+} ions in GFO will be isovalent substitution because of which there will be no charge imbalance. In this work, therefore, we prepare a series of $Ga_{1-x}Al_xFeO_3$ (GAFOx, $0 \le x \le 0.5$) nanoparticles by a modified Pechini method to systematically study the effect of Al doping on their structural, magnetic, and magnetodielectric (MD) properties. In particular, the simultaneous enhancement of magnetization, magnetic transition temperature, and MD effect of the Al-doped GFO samples will be quite interesting for applications in electronic and memory devices. *2. Experimental Methods*- The $Ga_{1-x}Al_xFeO_3$ (GAFOx, $0 \le x \le 0.5$) nanoparticles were synthesized through a modified Pechini method using nitrates as starting materials. First, stoichiometric amounts of gallium nitrate, iron nitrate, and aluminum nitrate were dissolved in distilled water. And then, citric acid ($C_6H_8O_7$) in a 1:1 molar ratio, with respect to the metal nitrates, was added to the solution as a complexant. The mixture was dried 120 ^oC to form a gel, and then the obtained gel was burned until the combustion process was completed. Finally, the precursory powders were reground and sintered at 800 ^oC for 2 h. The crystalline structure and the phase purity of the samples were examined with a typical x-ray diffraction (XRD) system of Cu K_a radiation. The temperature- and field-dependent magnetizations were measured with a Quantum Design superconducting quantum interference device (SQUID) magnetometer. For the magnetodielectric measurements, the powders were pressed into the disk (5 mm in diameter and 1 mm in thickness) under a pressure of 1.5 GPa and then coated with 100 nm thick silver layers on both the top and the bottom sides of the disk as electrodes. A capacitance bridge (Agilent E4980A Precision LCR meter) hooked to a probe station was used. The dielectric constant of the samples was measured in absence and presence of magnetic field at RT. *3. Results*- Based on the standard reference, all the observed XRD patterns of the GAFOx nanoparticles can be indexed on the basis of an orthorhombic unit cell of space group, $Pc2_1n$, suggesting that all samples are pure phases without any impurity. The mean particles sizes of the GAFOx nanoparticles are around 28 nm. The fact that the value of lattice parameters *a*, *b*, and *c* of GAFOx nanoparticles decrease systematically with increasing Al-context (x) implies that the Al-ions do replace the Ga-ions. The magnetic characterization indicates that with increasing Al-content, up to 0.5, the ferrimagnetic transition temperature (T_C) increases from 310 to 350 K, as shown in the Fig.1. The magnetic hysteresis curves measured below T_C exhibit two-phase-like magnetic behavior consisting of soft and hard magnetic phases. The results could be explained by the site-disorder of the cations in GAFOx. In addition, the magnetization has been enhanced due to doping of Al^{3+} in GFO compared to that of the pristine sample. The cause of magnetic enhancement could be explained from the modification exchange interaction due to the substitution of smaller size cations of Al^{3+} in place of relatively larger size cations of Ga^{3+}. In GFO, Fe^{3+}-ions have a distorted octahedral local environment and the distortion is manifested as a tilting of the octahedron from the direction of the *c*-axis. Actually, this distortion arises due to the change in the bond length and bond angle introduced in the change in cation distribution of different cations among different crystallography sites. Owing to site-disorder, an anti-symmetric exchange interaction acts between Fe^{3+} pairs, and this would lead to a spin-canted magnetism with enhancement of magnetization in Al-doped GFO samples. The change in dielectric constant with the applied magnetic field is one of the important ways to study the ME coupling effect. In each GAFOx sample, the dielectric constant is strongly perturbed by the external magnetic field. It is to be noted that the value of MD increases in the doped samples for different applied magnetic fields. The values of MD for GAFOx samples are higher than that observed for bulk GFO. Furthermore, the simultaneous enhancement of magnetization and MD coupling effect in Al-doped samples are prominent candidates for the applications of RT multiferroic devices.

[1] D. Khomskii, *Physics* 2 (2009) 20. [2] K. F. Wang, J. M. Liu, and Z. F. Ren, *Adv. Phys.* 58 (2009) 321. [3] M. B. Mohamed, A. Senyshyn, H. Ehrenberg, and H. Fuess, *J. Alloys Compd.* 492 (2010) L20. [4] S. Mukherjee, V. Ranjan, R. Gupta, and A. Garg, *Solid State Commun.*152 (2012) 1181. [5] S. Acharya, A. K. Deb, D. Das, P. K. Chakrabarti, *Mater. Lett.* 65 (2011) 1280.

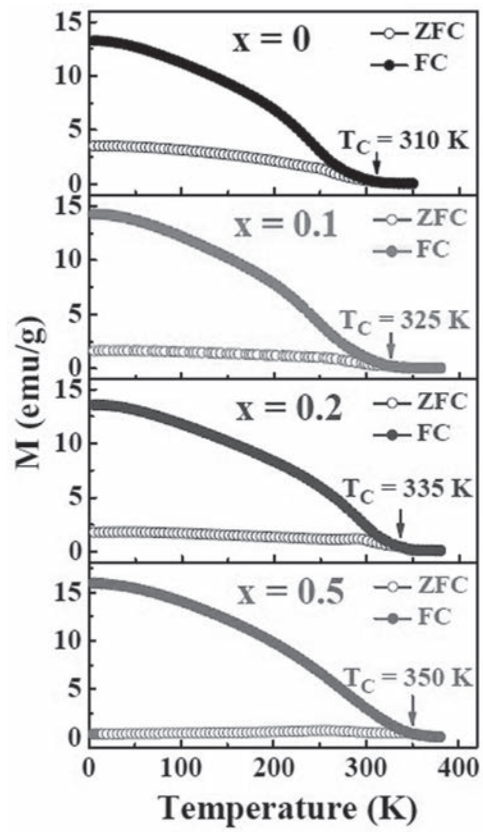

Fig. 1. Temperature-dependent magnetization for GAFOx samples.

EQ-05. Analysis of magnetic properties of electrical steel sheets under the coupling of temperature and pressure.

L. Xiao[1], G. Yu[1], J. Zou[1], Y. Xu[1], H. Lan[1], M. Wang[1] and F. Gao[1]
1. Harbin Institute of Technology, Harbin, China

Abstract—This paper not only reveals the influence of coupled temperature and pressure on the magnetic properties of electrical steel sheets, but also analyzes the influence of the pressure direction perpendicular or parallel to the magnetic field lines on the measurement results. 1. Introduction Almost all motor designs need to be validated by using the finite element method (FEM), especially for motors operating in high temperature and pressure environments. However, if the analysis uses the magnetic properties of the electrical steel sheets measured under the normal environment (0.1MPa and 30K) [1, 2] or only a single environmental variable (temperature or pressure), there will be a significant difference between the results obtained by the finite element analysis software and the experimental results. The main reason for the difference is that the magnetic properties of electrical steel sheets are different under different environments. However, most of literatures only analyze the effect of temperature or stress on the magnetic properties. Therefore, in order to design a motor that can operate in high temperature and high pressure environment for a long time, it is necessary to know the magnetic characteristics of electrical steel sheets used. In this paper, the magnetic properties of electrical steel sheets under different temperatures and pressures are determined by ring specimen [2, 3] and laminated specimen [4]. The changes of magnetic properties with the changes of temperature and pressure were discussed in detail. By comparing the measurement results of the two specimens, the change of the magnetic properties under the Cartesian coordinate system when the pressure is perpendicular or parallel to the magnetic field lines is analyzed. There are only vertical cases in the ring specimen, while the lamination specimen contains the vertical and the parallel cases. 2. Measurement specimens Fig.1 shows two measurement specimens for measuring the magnetic properties of electrical steel sheets under high temperature and high pressure, and the specimens are cut from the same product lot number. The measured magnetic properties are different when compressive stresses are applied to the specimen in the rolling and transverse directions, respectively. However, when the stress is greater than -50 MPa, the difference in magnetic characteristics measured in these two directions will become smaller [4]. Therefore, in order to reduce the difference in the magnetic measurement due to the rolling direction and the transverse direction, when the ring specimen and the laminated specimen are stacked and glued, the rolling direction and the transverse direction specimen are alternately placed. 3. Measurement results and discussion The variation of the measurement results is consistent with the reported data measured under the influence of the finite axial stress. This result shows that the effect of pressure (equivalent to infinite axial stress) on magnetic properties under normal conditions is similar to the effect of finite axial stress. By comparing the measurement results of the two specimens, the effect of the relationship between the pressure direction and the magnetic field direction on the magnetic properties can be found, as shown in Fig.2. In the Cartesian coordinate system, the direction of the pressure perpendicular to the magnetic field has a greater effect on the magnetic properties than both the vertical and the parallel ones. This indicates that the direction of the pressure perpendicular magnetic field makes the magnetic properties of the electrical steel sheet deteriorate more than the parallel existence. However, when the direction of pressure is perpendicular to the direction of the magnetic field, the effect of different pressures on the magnetic properties is small, especially on the core loss. 4. Error analysis In addition to accidental factors, there are two main factors that lead to errors. The main factor is determining the cross-section ofcoil. Another factor is that whencoil is wound, a certain amount of mechanical stress may appear in the specimens, which may have an impact on the measurement results. 5. Conclusion The magnetic properties of the electrical steel sheets (DW460-50) were measured at different temperatures and pressures using a ring specimen and a laminated specimen. By comparing the measurement results of the ring specimen and the laminated specimen, the influence of the relationship between the pressure direction and the magnetic field line on the magnetic properties can be analyzed. In contrast to the lamination specimen, the ring specimen under high pressure has larger iron loss and smaller relative permeability. In the Cartesian coordinate system, the pressure exerted by the ring pattern is always perpendicular to the magnetic field lines, whereas in the laminated specimen, some of the pressure is parallel to the magnetic field lines. This shows that the magnetic properties of the electrical steel sheet under high pressure are indeed affected by the relationship between the pressure direction and the magnetic field lines. When the direction of pressure perpendicular to the magnetic field lines, the greater the impact of pressure, resulting in increased magnetic deterioration. However, different pressure values have less effect on magnetic properties.

[1] S. E. Zirka, Y. I. Moroz, P. Marketos, A. J. Moses, and D. C. Jiles. "Measurement and Modeling of B-H Loops and Losses of High Silicon Nonoriented Steels," IEEE Trans. Magn. Vol. 42, no. 10, pp. 3177-3179, 2006. [2] A. Abou-Elyazied Abdallh, P. Sergeant, G. Crevecoeur, etc. "Magnetic Material Identification in Geometries With Non-Uniform Electromagnetic Fields Using Global and Local Magnetic measurement," IEEE Trans. Magn. Vol. 45, no. 10, pp. 4157-4160, 2009. [3] Norio Takahashi, Masayuki Morishita, Daisuke Miyagi, and Masanori Nakano. "Examination of Magnetic Propertis of Magnetic Materials at High temperature Using a Ring Specimen," IEEE Trans. Magn. Vol. 46, no. 2, pp. 548-551, 2010. [4] Daisuke Miyagi, Kohei Miki, Masanori Nakano, and Norio Takahashi. "Influence of Compressive Stress on Magnetic Properties of Laminated Electrical Steel Sheets," IEEE Trans. Magn. Vol. 46, no. 2, pp. 318-321, 2010.

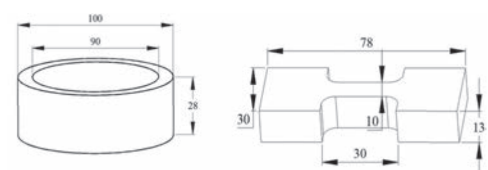

(a) The dimension of ring specimen (a) The dimension of ring specimen

Fig.1 The ring specimen and laminated specimen

Fig. 1. The ring specimen and laminated specimen

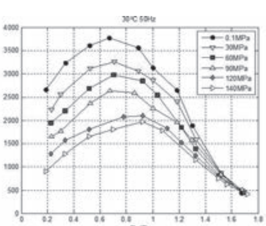

(a) Relative permeability of laminated specimen at 303.15K

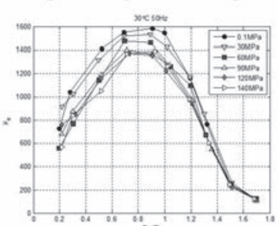

(a) Relative permeability of ring specimen at 303.15K

Fig.2 Measurement results of laminated specimen and ring specimen at 303.15K with excitation current frequency of 50 Hz

Fig. 2. Measurement results of laminated specimen and ring specimen at 303.15K with excitation current frequency of 50Hz

EQ-06. Influence of In-plane Stress on 1D Magnetic Property of Silicon Steel.

J. Chen[1], D. Wang[1], Y. Jiang[1], X. Teng[1] and X. Zhang[1]
1. Naval University of Engineering, Wuhan, China

1 Introduction Silicon steel(FeSi) is the core material for conducting magnetic field in magnetic device such as electrical motors and transformers, which can be classified into grain-oriented(GO) and non-oriented steel(NGO). Due to shrink fitting or some incorrect installation, the influence of the compressive and tensile stresses on the magnetization exists more or less in electrical motors and transformers[1-2]. Recently, there are research articles about the measured stress dependent magnetic property[3-12], but physical mechanism of stress effect is seldom reported. This paper aims to quantify the stress effect on each of loss components of silicon steel, which is helpful for proposing a stress-dependent iron loss model based on loss separation theory. 2 Magnetic measurement In order to measure magnetic properties of FeSi steel sheet under in-plane tensile and compressive stress, a special single sheet tester was designed, shown in Fig. 1. The specimen used is the strip of 300mm(L)×30mm(W), whose middle region is chosen as the effective zone, where B coil is wound to inspect the induced EMF signal. Considering the magnetic potential drop is small enough in the compared with specimen, magnetic field strength of specimen is obtained based on Ampere's law. The mechanical part of the system allows both compressive and tensile stress up to 150 MPa. The key point of this design is to make sure that applied stress evenly distribute over the sheet specimen. Although collets may not apply ideal uniform force along width of specimen. Saint-Venant's principle points out that for a system of forces statically equivalent to zero force and zero couple, strains are of negligible magnitude at distances which are large compared with linear dimension of the part[13]. Fig. 2(a) shows the ideal case, that stress is evenly distributed along the length of specimen if both collets apply ideal uniform pull. Fig. 2(b) and (c) show two non-ideal cases of collets applying concentration pull, except the area close to the collets, stress distribution in other parts of specimen are always uniform, not influenced by end effect caused by collets. Based on facts above, designed test platform is effective and can be used to investigate stress effect on magnetic property of silicon steel. 3 AC Magnetic Measurement Result Fig. 3 shows the effect of stress on measured hysteresis loop at 50Hz from 0.1T to 1.7T, with the step of 0.1T. The tensile and compressive loading varies from -30 to 150MPa. It is obvious that elastic deformation affects the shape of the hysteresis loops and such magnetic properties index as coercivity, remanence, and permeability. Compared with hysteresis loop of unloaded specimen, shape of loop with compressive stress changed tremendously, even becoming S-shaped in first quadrant of B-H plane. It is obvious that at typical rated working point of 1.7T nearby, the in-plane stress influences GO steel more than NGO. While both the NGO and GO silicon steel is more influenced by compressive stress, which indicates that compressive stress is harmful and should be get rid of during the duty period of electromagnetic devices. From Fig. 3(a), the greater the compressive stress is applied on GO steel, the worse magnetization property it turns out to be, while tensile stress even advances the permeability, a 50MPa tensile stress can achieve a better permeability than 100MPa and 150MPa, which needs an in-depth study. From Fig. 3(b), unlike GO steel, tensile stress doesn't advance permeability of NGO steel, which indicates a different physical mechanism from GO steel. It is interesting that iron loss varies little when tensile stress increases from 50MPa to 150MPa, which indicates that tensile stress effect on GO steel exists a limit. 4 Stress-dependent iron loss separation According to loss separation principle, iron loss can be divided into static and dynamic loss. Static loss is known as hysteretic loss, which is related to energy consumed when domain wall moves and rotates. Dynamic loss is composed of classic eddy current loss and excess loss[14]. To find out root cause of iron loss's variation with in-plane stress, we have studied its effect on each of loss components, respectively. Ballistic method is adopted to measure the static hysteresis loop and loss with no eddy current involved. Fig. 5 shows the DC static hysteresis loss result versus magnetic induction B_m. The result of pure magnetic test also indicates compressive stress is harmful to magnetic property. Classic eddy current loss originates from electrical resistivity. To measure the DC resistivity of silicon steel sheet with in-plane stress applied, insulation system of experimental setup shown in Fig. 1 was upgraded. There is no more electrical contact and metallic parts except collets, winding and collets. Therefore, both collets at the end of specimen are also used as the electrodes to inject the DC current. Test was implemented by four wire method. DC conduction simulation shows that electrical equipotential line in the middle area of specimen is parallel to width direction. It is shown that stress influences the electrical resistivity significantly, which was seldom reported. With static hysteresis loss and resistivity of specimen, excess loss component is calculated by subtracting hysteresis and classic eddy current loss components from iron loss at various frequencies. So we can obtain the influence of stress on each loss components. Now, the data analysis is being done, due to the length of digest, the measured result and analysis will be given in full paper.

[1] L. Bernard and L. Daniel, Effect of Stress on Magnetic Hysteresis Losses in a Switched Reluctance Motor: Application to Stator and Rotor Shrink Fitting, IEEE Transactions on Magnetics 51 (2015) 1-13. [2] S. K. Shekhawat, V. Basavaraj, V. D. Hiwarkar, A. Ingle, K. G. Suresh and I. Samajdar, Degradation of Magnetic Properties in Transformer Steel: Role of Prior Elastic Deformation, IEEE Transactions on Magnetics 50 (2014) 1-12. [3] A. J. Moses and H. Rahmatizadeh, Effects of stress on iron loss and flux distribution of an induction motor stator core, Magnetics, IEEE Transactions on 25 (1989) 4003-4005. [4] D. Singh, P. Rasilo, F. Martin, A. Belahcen and A. Arkkio, "Effect of Mechanical Stress on Excess Loss of Electrical Steel Sheets," IEEE Transactions on Magnetics, vol. 51, no. 11, pp. 1001204, 2015. [5] P. Rasilo, D. Singh, U. Aydin, F. Martin, R. Kouhia, A. Belahcen and A. Arkkio, Modeling of Hysteresis Losses in Ferromagnetic Laminations Under Mechanical Stress, IEEE Transactions on Magnetics 52 (2016) 1-4. [6] D. Atherton and D. Jiles, Effects of stress on the magnetization of steel, IEEE Transactions on Magnetics 19 (1983) 2021-2023. [7] R. Fischell, Effects of transverse compressional stress on magnetic laminations, Transactions of the American Institute of Electrical Engineers, Part I: Communication and Electronics 74 (1955) 190-193. [8] M. X. Xu, Z. H. Chen, M. Q. Xu and T. Q. You, Discussion of modified Jiles-Atherton model including dislocations and plastic strain, International Journal of Applied Electromagnetics and Mechanics 47 (2015) 61-73. [9] M. J. Sablik, T. Yonamine and F. J. G. Landgraf, Modeling plastic deformation effects in steel on hysteresis loops with the same maximum flux density, IEEE Transactions on Magnetics 40 (2004) 3219-3226. [10] J. Makar and B. Tanner, The effect of plastic deformation and residual stress on the permeability and magnetostriction of steels, Journal of Magnetism and Magnetic Materials 222 (2000) 291-304. [11] O. Hubert and S. Lazreg, Multidomain Modeling of the Influence of Plastic Deformation on the Magnetic Behavior, IEEE Transactions on Magnetics 48 (2012) 1277-1280. [12] N. Leuning, S. Steentjes, M. Schulte, W. Bleck and K. Hameyer, Effect of elastic and plastic tensile mechanical loading on the magnetic properties of NGO electrical steel, Journal of Magnetism and Magnetic Materials 417 (2016) 42-48. [13] Information on http://en.wikipedia.org/wiki/Saint-Venant's_principle [14] G. Bertotti and M. Pasquale, Physical interpretation of induction and frequency dependence of power losses in soft magnetic materials, IEEE Transactions on Magnetics 28 (1992) 2787-2789.

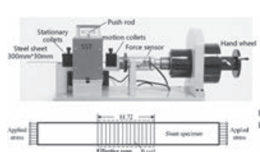

Fig. 1. Magnetic property test rig for silicon steel sheet with in-plane stress

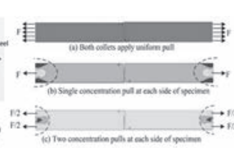

Fig. 2. Simulated stress distribution over the specimen

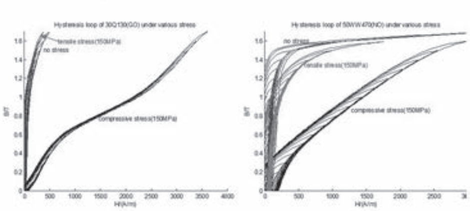

(a) GO Steel (b) NGO steel

Fig. 3. Hysteresis loop of silicon steel with applied tensile and compressive stress(50Hz)

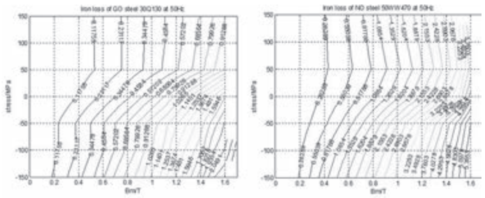

(a) GO steel at 50Hz (b) NGO steel at 50Hz

Fig. 4. Iron loss properties of FeSi steel under various stress

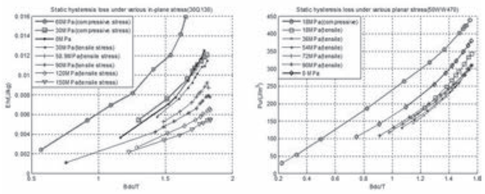

(a) GO steel (b) NGO steel

Fig. 5. Quasi-static hysteresis properties of FeSi steel under various stress

EQ-07. Voltage Control of Two-Magnon Scattering in MnZn Ferrite thin film.

W. Hou[1], Z. Zhou[1] and M. Liu[1]
1. Xi'an Jiaotong University, Xi'an, China

Recently, the magnetic-piezoelectric heterostructures show great potential for the next-generation of compact, lightweight, and energy-efficient RF/microwave devices [1-3]. The voltage applied to the piezoelectric layer produces a mechanical deformation that couples to the magnetic layer, and thus induces a change in the magnetic anisotropy and a shift in the resonance field for the ferromagnet. Large voltage-induced effective ferromagnetic resonance (FMR) field has been demonstrated in multiferroic composites such as YIG/PZT, FeGaB/PZN-PT, Fe_3O_4/PMN-PT [4-6]. Nevertheless, great efforts have been made to discover novel mechanisms and achieve tremendous magneotoelectric (ME) coupling effects. In this work, we established a bilayer $Mn_{0.8}Zn_{0.2}Fe_2O_4$ (MZFO)/PMN-PT multiferroic heterostructure (Fig. 1a). The external bias magnetic field (H) was applied along the in-plane and out-of-plane directions of the MZFO film, respectively. The FMR field (H_r) shift shows strong dependence with H field direction (Fig. 1b). We found a giant ferromagnetic resonance (FMR) field shift of 653 Oe took place at the critical angle of 30^o rather than the in-plane [100] direction, along which the maximum ME effect usually occurs. A giant ME tunability enhancement of ~1800 % was determined. We related this significant ME coupling strength improvement to the voltage control of spin dynamics, specifically, two-magnon scattering (TMS) mechanism. TMS is an extrinsic magnetic damping mechanism that scatter the k=0 magnons excited by FMR into degenerate states of magnons having wave vectors k≠0 [7-8], offering a framework for voltage control of spin dynamics and further increase the ME interactions. This demonstrating provides an alternative route for novel integrated multiferroic materials and energy-efficient electronic/spintronic devices devices.

[1]. J.-M. Hu, L.-Q. Chen, and C.-W. Nan, Adv. Mater. 28 (1), 15-39 (2016). [2]. H. Ohno, D. Chiba, F. Matsukura, T. Omiya, E. Abe, T. Dietl, Y. Ohno, and K. Ohtani, Nature 408 (6815) 944-946 (2000). [3]. D. Chiba, S. Fukami, K. Shimamura, N. Ishiwata, K. Kobayashi, and T. Ono, Nat. Mater. 10 (11), 853 (2011). [4]. M. I. Bichurin, V. M. Petrov, and Y. V. Kiliba, Phys. Rev. B 66, 134404 (2002) [5] J. Lou, M. Liu, D. Reed, Y. Ren and N. X. Sun, Adv. Mater. 21 (46) 4711-4715 (2009) [6] M. Liu, O. Obi, J. Lou, Y. Chen, Z. Cai, S. Stoute, M. Espanol, M. Lew, X. Situ, K.S. Ziemer, V. G. Harris and N. X. Sun, Adv. Funct. Mater. 19 (11) 1826-1831 (2009) [7] A. K. Srivastava, M. J. Hurben, M. A. Wittenauer, P. Kabos, C. E. Patton, R. Ramesh, P. C. Dorsey and D. B. Chrisey, J. Appl. Phys. 85(11) 7838-7848 (1999). [8] M. Körner, K. Lenz, R. A. Gallardo, M. Fritzsche, A. Mücklich, S. Facsko, J. Lindner, P. Landeros, and J. Fassbender, Physical Review B 88 (5) 054405 (2013)

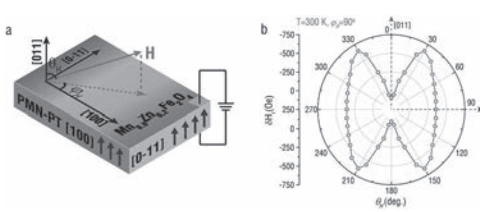

Fig. 1. (a) Schematic of the sample under E-field for angular dependence of FMR measurements; Magnetic field is rotating within the (100) plane or (0-11) plane; (b) Angular dependence of FMR field shifts within the (0-11) plane at 300 K.

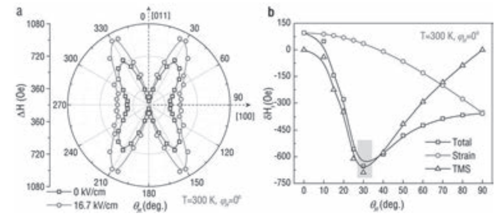

Fig. 2. (a) Angular dependence of FMR linewidth within the (0-11) plane at 300 K; (b) Angular dependence of FMR field shifts within the (0-11) plane at 300 K.

EQ-08. Numerical Modeling on *B-H* Characteristics of Fe-Based Soft Magnetic Composites Considering Saturation.

D. Zhang[1], W. Guan[1], M. Yang[1], Y. Gao[2] and K. Muramatsu[2]
1. School of Electrical Engineering, Wuhan University, Wuhan, China;
2. Department of Electrical and Electronic Engineering, Saga University, Saga, Japan

I.Introduction Soft magnetic composites (SMCs) are magnetic materials composed of ferromagnetic powder particles surrounded by electrical insulations. These composite materials have several advantages compared with commercial laminated steel cores, which are traditionally widely used in electric machines [1-2]. At low frequency applications, the advantage of three-dimensional (3D) isotropic magnetic characteristics, and flexible machine design and assembly of SMCs is preferred for axial gap motors which need 3D magnetic design. At medium and high frequency regions, the advantage of low iron loss due to small particle size in SMCs is preferred for transformer and reactors for harmonics suppression etc. With potential wide applications of SMC materials expected in the future, this paper introduces a method to model the *B-H* characteristics of Fe-based SMC immersed in air, Fe_3O_4, and Ferrites until the pure iron particles are deep saturated. The effective permeability of magnetic composites is derived through nonlinear magnetic field analysis based on energy homogenization technique under the assumption that the structure of the magnetic composite is periodic and the particle is sphere. The obtained effective *B-H* curves are compared and analytical expressions for them are presented. II.Energy Equivalent Homogenization Method A.Analysis Models and Conditions Fig.1(a) shows the analyzed periodic 3D SMC material model, which includes pure iron particles surrounded by background materials: air,Fe_3O_4, or MnZn Ferrites. Here, it is assumed that the particles are distributed inside the model evenly and the cell holds structural isotropy. The calculated region consists 27 pure iron particles with a diameter of 50 micrometers and the volume fraction of the pure iron particles varies with the distance between two particles. The SMC material model is regarded as a homogeneous magnetic solid one with the effective permeability as shown in Fig. 1 (b). The original and the homogenized models have equivalent magnetic energy when they are imposed under the same uniform magnetic field. B.Magnetic Field Analysis 3D nonlinear magnetostatic field analysis using the magnetic vector potential *A* is carried out. The uniform magnetic field is imposed through the Dirichilet boundary conditions until the pure iron particles reaches saturation. The initial *B-H* curve for the pure iron particle is nonlinear .The relative permeability of Fe3O4 is set as 5 and that of Ferrite is 2000. C.Homogenization Method The effective permeability is defined on the basis of magnetic energy equivalence in the two models [3]. The magnetic energies in the original and homogeneous models are calculated as follows. $E_{origin}=\sum(B^{\wedge 2}_{ie}/u_{ie})$ (1) $E_{hom}=B^{\wedge 2}_{imp}/u_{eff}$ (2) where B_{ie} and m_{ie} represent the flux density and permeability in each element *ie* in the original model, *K* is the total element number in the original model, the magnetic field, B_{imp} is the imposed flux density. By equalize the energies in the original and homogeneous models, the effective permeability can be expressed as follows. $u_{eff}=B^{\wedge 2}_{imp}/(\sum(B^{\wedge 2}_{ie}/u_{ie}))$ (3) III. Results and Discussions The obtained effective *B-H* curves for the pure iron particles immersed in air and Fe3O4 versus different volume fraction of iron particles will be shown in full paper. The obtained effective permeabilities versus different volume fraction of iron particles for the pure iron particles immersed in air and Fe3O4 at 5000A/m is shown in Fig.2. The comparison with the famous analytical Ollendorff homogenization formula [4] as shown in (4) is also shown. It shows that discrepancy exists between the numerical results and the analytical equations. $u_{eff}=\eta(u_t-u_b)/(N(1-\eta)(u_t-u_b)+u_b)$ (4) where m_b represents the permeability in the background material, m_t represents the permeability of the particles, *h* is the volume fraction, and *N* is constant. Therefore, the analytical homogenization formula is modified according to the numerical results as follows. $u_{eff}=\eta(u_t-u_b)/(N(1-\eta)(u_t-u_b)+u_b)+u_b$ (5) The comparison between the original analytical and the modified formula is shown in Fig. 2. The discrepancy can be about 5% reduced by using the modified analytical equation. Furthermore, the modified formula is applied to the situation that the iron particles are at deep saturation state. Hence the effective permeabilities versus different volume fraction of iron particles for the pure iron particles immersed in air, Fe3O4, and Ferrite are obtained at 15000A/m, which will be shown in full paper. The discrepancy can be about 10%, 15%, and much reduced by using the modified analytical equation, respectively. IV.Conclusion With potential wide applications of SMC materials expected in the future, this paper introduced a method to model the effective *B-H* characteristics of Fe-based SMC immersed in air, Fe3O4, and Ferrites until the pure iron particles are deep saturated based on the homogenization technique. The obtained effective permeability are compared with an original analytical formula and an improved analytical formula is proposed according to the numerical results. And the results by using the improved formula shows better agreement with the numerical results.

[1] G. Zhao, C. Wu, and M. Yan, “Fe-Based Soft Magnetic Composites With High Bs and Low Core Loss by Acidic Bluing Coating,” *IEEE Trans. on Magnetics*, vol. 51, no. 11, #2002904, 2015. [2] L. Ferrarisa, E. Pošković, and F. Franchini, “New Soft Magnetic Composites for electromagnetic applications with improved mechanical properties,” *AIP Advances*, vol. 6, no. 5, 2015. [3] H. Waki, H. Igarashi, and T. Honma, “Analysis of magnetic shielding effect of layered shields based on homogenization,” *IEEE Trans. on Magnetics*, vol. 42, no. 4, pp. 847-850, 2006. [4] F. Ollendorff, “Magnetstatik der Massekerne”, Arch. f. Electrotechnik, Vol. 25, pp. 436-447, 1931.

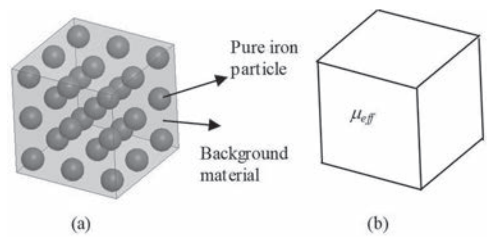

Fig. 1. (a)The analyzed period 3D SMC model and its (b) homogeneous model.

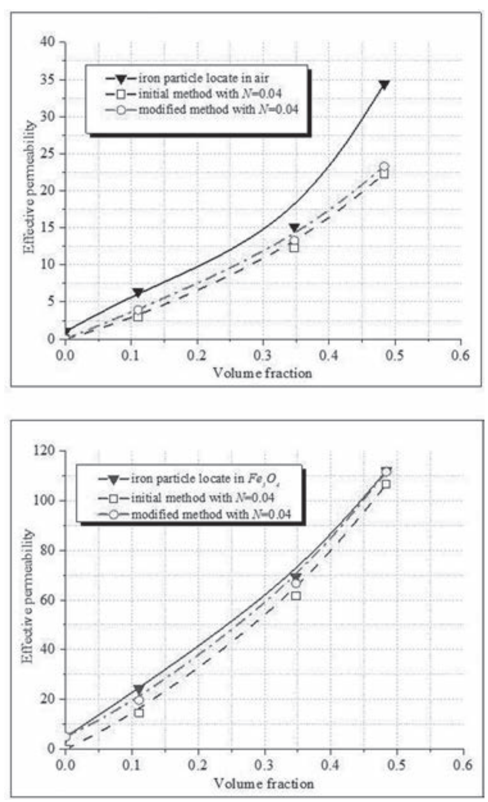

Fig. 2. Comparison of effective permeability between the numerical analysis, original analytical and the modified formula of particles immersed in air and Fe_3O_4.

EQ-09. Systematic Experimental and Simulation Studies of Dimensional Resonance in Mn-Zn Ferrite Toroidal Cores.

H. Kawano[1], H. Oshima[1], K. Shimizu[2], A. Furuya[2], Y. Uehara[2], J. Kato[3], M. Kitaoka[3] and K. Hakamata[3]

1. Fujitsu Laboratories Ltd., Atsugi, Japan; 2. Fujitsu Limited, Kawasaki, Japan; 3. FDK Corporation, Kosai, Japan

I. INTRODUCTION Mn-Zn ferrite cores have been used in inductors and transformers in the power supply because of their high permeability and low loss at low frequency below a few hundred kHz. Recently, they are also expected to be driven at up to a few MHz for downsizing of the power supply. The loss per unit volume in Mn-Zn ferrite cores at high frequency depends on their core size because of the dimensional resonance that occurs at a frequency of a few MHz, which is induced by charge accumulation at high-resistive grain boundaries in low-resistive ceramics (the dielectric effect). In the usage of Mn-Zn ferrite cores at high frequency, therefore, accurate estimation of core loss requires consideration of the dimensional resonance effect. Some of the authors proposed an analytical method for core loss with consideration of the dielectric effect and confirmed effectiveness of the method by comparison with the experiment using commercial Mn-Zn ferrite toroidal cores [1]. However, the difference between the measured and calculated losses was about 20% at maximum. The reason could be that simple cylindrical approximation was used in the calculation although the cores have toroidal shape with rectangular cross sections. Simulation by a finite element method (FEM) will be more effective to accurately analyze loss in cores with complex shapes. In this paper, we prepared a series of Mn-Zn ferrite toroidal cores with different dimensions, and measured frequency dependence of the magnetic permeability and core loss. We then performed magnetic simulation for comparison by applying the FEM with a model considering the dielectric effect to the core models with real shapes. We show excellent agreement between our experimental results and model calculations: the observed systematic variations of the magnetic properties can be fully explained by the dimensional resonance effect. II. MEASUREMENT AND SIMULATION To observe the dimensional resonance effect without any influence of other factors such as inhomogeneity of material and residual stress in the manufacturing process, we prepared five samples of as-sintered Mn-Zn ferrite toroidal cores with different sizes but the same material, whose outer diameters are from 60 mm to 15 mm (LL, L, M, S, and SS). Complex permeability of the cores was measured at room temperature (RT) using the network analyzer, E5061B (Keysight Technologies Inc.), with the input power of –10 dBm, which corresponds to the excitation by the magnitude of magnetic flux density (Bm) of less than 1 mT. Core loss was also measured at RT with the excitation by Bm of 2.5 mT. For frequencies below 1 MHz, we used the B-H analyzer, SY-8219 (Iwatsu Electric Co. Ltd.). At over 1 MHz, we used our precise loss measurement system which utilizes electrical resonance with the capacitors connected in series to the core [2]. We analyzed the dimensional resonance effect by magnetic simulation based on the FEM with a model considering the dielectric effect, which was formulated by dealing with the capacitive performance at high-resistive grain boundaries in low-resistive Mn-Zn ferrite ceramics as the equivalent RC circuit [1, 3]. A linear relationship between the magnetic flux density and the magnetic field was assumed and the hysteresis loss was ignored. III. EXPERIMENTAL AND NUMERICAL RESULTS Figure 1 shows frequency dependence of measured and simulated complex permeability in the five Mn-Zn ferrite toroidal cores with different sizes. In the experiment, systematic variation of the permeability depending on the core size was observed. The simulation well reproduced the experiment. These results indicate that the experimental variation comes from the dimensional resonance effect in Mn-Zn ferrite cores and that all the samples were produced quite homogeneously. It should be noted that such size-dependence cannot be observed in high-resistive Ni-Zn ferrite cores with similar dimensions, which suggests that the dielectric effect at grain boundaries plays an important role in the dimensional resonance. Figure 2 exhibits frequency dependence of measured and simulated core loss in the five Mn-Zn ferrite toroidal cores with different sizes. The experimental results were again in good agreement with the simulation. In the previous work [1], the difference between the measurement and the analytic calculation was about 20% at maximum, and the slopes of the frequency dependence slightly diverged. In the simulation with the FEM, however, the difference was improved to be less than 10%, and the slopes showed good agreement as shown in Fig. 2. Such improvement would become larger when the core shapes are more complicated. Simulation with the FEM, therefore, would be quite important for accurate loss estimation at high frequency for cores with realistic core designs.

[1] A. Furuya, Y. Uehara, K. Shimizu, J. Fujisaki, T. Ataka, T. Tanaka, and H. Oshima: Magnetic field analysis for dimensional resonance in Mn-Zn ferrite toroidal core and comparison with permeability measurement, (IEEE Trans. Magn. 53 (2017) 7301004) [2] M. Mu, Q. Li, D. J. Gilham, F. C. Lee, and K. D. T. Ngo: New core loss measurement method for high-frequency magnetic materials, (IEEE Trans. Power Electron. 29 (2014) 4374-4381) [3] F. Fiorillo, C. Beatrice, O. Bottauscio, and E. Carmi: Eddy-current losses in Mn-Zn ferrites, (IEEE Trans. Magn. 50 (2014) 6300109)

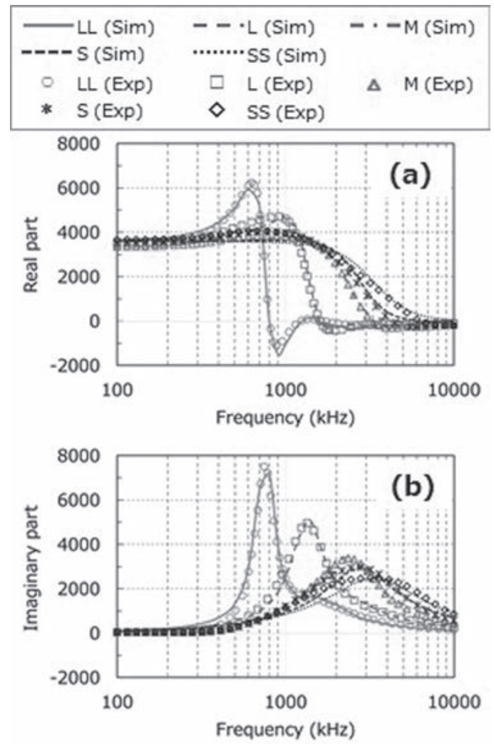

Fig. 1. Frequency dependence of measured and simulated complex permeability in Mn-Zn ferrite toroidal cores with different sizes. (a) Real part. (b) Imaginary part. Simulation (Sim) is represented by the solid or the dashed lines. Experiment (Exp) is represented by open symbols.

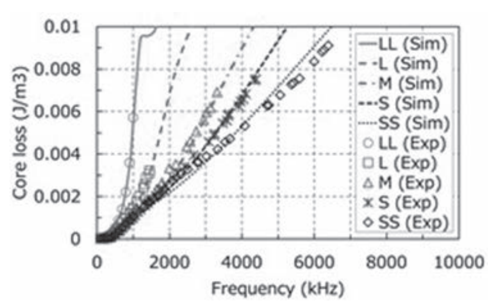

Fig. 2. Frequency dependence of measured and simulated core losses in Mn-Zn ferrite toroidal cores with different sizes. Magnitude of magnetic flux density is 2.5 mT.

EQ-10. Gel-casting Hexagonal Ferrites for High Density and Low Loss Microwave Devices.

J. Adams[1], A.S. Sokolov[1] and V. Harris[1]
1. Electrical & Computer Engineering, Northeastern University, Medway, MA, United States

In this work, a high density hexagonal ferrite is processed and characterized using a unique gel-casting process and organic chemicals. The gel-casting processing method is a colloidal technique that provides a short forming time, while also having a high green body density and the ability to create complex shapes due to low shrinkage and cracking effects. The hexagonal ferrites used were M-type hexaferrites, chosen for their excellent applications in self biased RF, microwave, and mm-wave devices. It is well known that magnetic microwave devices rely on low ferromagnetic resonance (FMR) linewidths to achieve low loss and high performance of RF devices. Furthermore, the FMR of a ferrite is directly related to the density of the material. Therefore, in order to achieve a low loss polycrystalline magnetic material, achieving high density is of paramount importance. Typical maximum densities in polycrystalline hexaferrites is 90% of theoretical [5]. In this work, we approach 98% of theoretical density by use of gel-casting processing methods, and anticipate low FMR losses. In addition to the aforementioned benefits of lower FMR linewidths via higher densities, this process is very beneficial to self-biased hexaferrites. The use of self-biased hexaferrites at low enough FMR frequencies for device operation less than K band requires the modification of crystal structure with cation substitutions. This decreases the magnetocrystalline anisotropy field that is intrinsic to the hexaferrite structure and chemistry. While this is effective in reducing FMR, it also complicates the processing of textured compacts for the use as self-biased materials. These compacts are typically formed under the application of magnetic fields while simultaneously applying uniaxial mechanical pressure. However, this mechanical pressure imparts stress on the particles and often results in difficulties in achieving high remnant magnetization. Using the gel-casting method described herein, it is anticipated that this will improve both density and magnetic remanence. Gel-casting is a process by which a slurry of powders, water and water-soluble organic monomers are polymerized to form parts using inexpensive plastic molds. Following the green body formation, drying, burn out and sintering finish the process. This is a generic process that can be used with numerous types of ceramic powders, and has recently been successful with Alumina powders [3]. A similar process is slip casting, however gel-casting provides much more homogenous densities. Additionally, the very small percentage of organic components makes the removal during burnout far less dramatic. In this work, a water-soluble alternating co-polymer of isobutylene and maleic anhydride called ISOBAM was used. This is chemical is very beneficial because it uses one organic component that acts as a binder and dispersant at very low concentrations. Other works have shown the use of ISOBAM produces dense green bodies at high solid loading of up to 80% by volume, with low added organic content (i.e., <1 wt% of ceramic powder), and minimal shrinkage and cracking [3]. The gelling mechanism of ISOBAM is credited to surface interactions between ceramic particles and the long chains of polymer that wrap around the particles and interact with each other, creating an elastomer network of intramolecular interactions [3]. This paper is represents the first known use of ISOBAM for gel-casting of magnetic ferrites. The processing of samples for this digest is described as follows. High purity Barium M Type hexaferrite ($BaFe_{12}O_{19}$, Alfa Aesar) powders were obtained and the morphology of these powders were examined with a scanning electron microscope (SEM). An average particle size of 1 micrometer was observed. A solution of ISOBAM was made and then mixed with the hexaferrite material. The resulting solution was then dispensed into molds and dried at low temperatures for 24-48 hours. The final stage of processing consisted of sintering the samples. This processed was used to create cylinders with a radius of 4mm and a height of 5mm before drying. Twelve samples were made consisting of ISOBAM concentrations of 0.25%, 0.50%, 0.75% and 1.00% ISOBAM concentrations (with respect to the ferrite mass) and with 60%, 70% and 80% percent mass loading. Samples were analyzed with two independent methods to verify their densities. The first method was the use of an analytical balance and Pycnometer to determine the density. The second method used the analytical balance and a vibrating sample magnetometer (VSM) to determine the density through the known theoretical magnetization saturation values of pure Barium M type hexaferrites. The theoretical maximum value of M_s is 72 emu/g [4]. A plot showing various values of M_s, as a percentage of the theoretical maximum, for each sample is appended at the end of this digest. As can be seen, extremely high densities were attained near 98%. This data was corroborated, as mentioned previously, with pycnometer measurements and is within 1.15% on average. Also, the morphology of the highest density sample was observed with an SEM and is appended at the end of this digest.

[1] R. Gilissen, "Gelcasting, a near net shape technique," *Materials and Design*, vol. 21, pp. 251-257, 2000. [2] V. Harris, "Consequences of magnetic anisotropy in realizing practical microwave hexaferrite devices," *Journal of Magnetism and Magnetic Materials*, vol. 324, pp. 3393–3397, 2012. [3] C. Moorehead, "Characterization of Novel Gel-Casting System to Make Complex-Shaped Aluminum Oxide (Al2O3) Parts," US Army Research Laboratory, Aberdeen Proving Ground, MD, Rep. ARL-TR-7620, 2016. [4] R. Pullar, "Hexagonal ferrites: A review of the synthesis, properties and applications of hexaferrite ceramics," *Progress in Materials Science*, vol. 57, pp. 1191–1334, 2012. [5] J. Yang, "Recent developments in gelcasting of ceramics," *Journal of the European Ceramic Society*, vol. 31, pp. 2569–2591, 2011

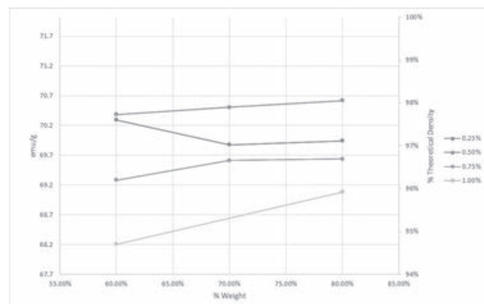

Fig. 1. Plot of magnetization in emu/g (left axis) and % theoretical density (right axis) vs solids loading percent

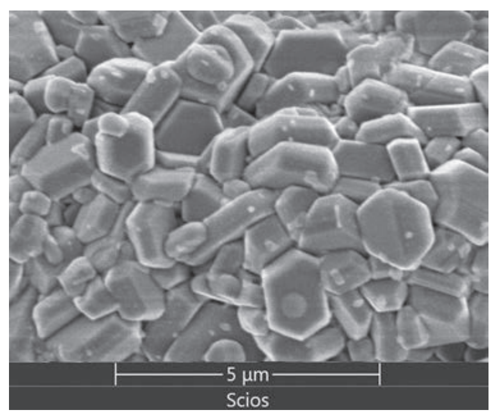

Fig. 2. Scanning Electron Microscopy image showing high particle density

EQ-11. Correlation of calcination temperature and flux doping on the microstructure and magnetic properties of low-temperature-fired NiCuZn ferrites.

H. Su[1], *Q. Luo*[1], Y. Jing[1], Y. Li[1], H. Zhang[1] and X. Tang[1]
1. University of Electronic Science and Technology of China, Chengdu, China

Multilayer chip inductors (MLCIs) play important roles in advanced electronic products, such as cellular phones, computers, video cameras etc. Currently, MLCIs are mainly prepared by low-temperature-fired NiCuZn ferrites because these ferrites have relatively low sintering temperature, high resistivity and good performance at high frequencies. The magnetic properties of NiCuZn ferrites are sensitive to their microstructures. Preparation conditions, such as calcination temperature and sintering curves, and doping schemes influence the microstructure of NiCuZn ferrites. For low-temperature-fired NiCuZn ferrites used in MLCIs, fluxes are the most important dopants because they can reduce the sintering temperature of NiCuZn ferrites to around 900 °C and obtain a dense microstructure and good magnetic properties. The effects of flux dopants on the microstructure of NiCuZn ferrites are correlated with ferrite preparation process, especially calcination and sintering temperature. However, studies of correlative influences of preparation process and flux dopants on the microstructure of low-temperature-fired NiCuZn ferrites have been seldom reported in literature. In this study, the correlative influences of calcination temperature and Bi_2O_3 doping content on the microstructure and magnetic properties of the low-temperature-fired NiCuZn ferrites were investigated. For ferrites with relatively low calcination temperatures, such as 750 °C and 850 °C, Bi_2O_3 doping easily triggered inhomogeneous grain growth. Controlling the flux amount to lower than the 'critical' value, which triggered abnormal grain growth, was preferred to obtain good magnetic properties. For ferrites with relatively high calcination temperatures, such as 950 °C and 1050 °C, flux doping was not prone to stimulating abnormal grain growth. Thus, the optimum doping content could be added when the highest sintered density was detected. With excessive Bi_2O_3 concentrations, low-temperature-calcined ferrites could produce homogeneous microstructures with a relatively large average grain size. By contrast, high-temperature-calcined ferrites could form homogeneous microstructures with a relatively small average size, which favoured a high Q-factor and was more favourable for high frequency applications.

[1] J Murbe, J Topfer, Ni-Cu-Zn ferrites for low temperature firing. Effects of powder morphology and Bi_2O_3 addition on microstructure and permeability, J. Electroceram., 16 (2006) 199-205. [2] Wenting Yang, Xiaoli Tang, Huaiwu Zhang, Hua Su, Effects of Li_2CO_3 addition on the microstructure and magnetic properties of low-temperature-fired NiCuZn ferrites, Ceram. Int., 42 (2016) 14609-14613. [3] Jianhua Zhu, Chenxin Ouyang, Shumin Xiao, Yongyi Gao, Microwave sintering versus conventional sintering of NiCuZn ferrites. Part I: Densification evolution, J. Magn. Magn. Mater., 407 (2016) 308-313.

EQ-12. Mn-Zn ferrite thin films with anomalously large magnetic moments.

P. Rajagiri[1], B. Sahu[1], N. Venkataramani[2], *S. Prasad*[1] and R. Krishnan[3]
1. Physics, Indian Institute of Technology Bombay, Mumbai, India;
2. Department of Metallurgical Engineering and Materials Science, Indian Institute of Technology Bombay, Mumbai, India; 3. Retired scientists, CNRS/Universite de Versailles-St-Quentin, Versailles, France

Ferrites order ferrimagnetically through superexchange interaction mediated by an anion, which generally results in lower magnetization than ferromagnetic metals. An increase in the magnetization of ferrites is required for applications [1]. Recently we have reported a possibility to obtain higher magnetization in some of the ferrites in their nanocrystalline thin film form [1-3]. The bulk saturation magnetization of $MnFe_2O_4$ is ~ 7.0 kG (~ 4.6 μ_B) at 0 K which is the highest among binary ferrites [4]. This value can be increased further by Zn substitution [4]. The largest reported value of magnetization obtained in $Mn_{1-x}Zn_xFe_2O_4$ (MZF) is 10.8 kG (~ 7.1 μ_B) for x = 0.5 at 0 K [5]. Further increase of x in MZF system results in a decrease in the magnetic moment due to the weakening of superexchange interaction between A and B sites, which causes canting of magnetic moments on the B sites [3,5]. Here, we present a systematic study of pulse laser deposited (PLD) nanocrystalline MZF ($0.1 \le x \le 0.8$) films with an attempt to increase the magnetic moment higher than bulk. The single phase MZF PLD targets were prepared in our laboratory using the ceramic method in presence of Ar environment (based on Ellingham diagram). MZF thin films were deposited on an amorphous quartz substrate by PLD using Nd:YAG laser. Before starting the deposition, the PLD chamber was evacuated to a base pressure of 4.6×10^{-6} mbar. Thin films were deposited at T_S = 650 °C for 30 minutes in Ar environment at a pressure of 0.16 mbar. All the observed XRD peaks of the films could be indexed to spinel phase. The M-H loops were measured at 10 K and 300 K. The ferromagnetic resonance (FMR) spectra of the films were recorded at 300 K. The thickness of the films were measured using FEG-SEM and were observed to vary between 60 – 85 nm. The diamagnetic contribution of the substrate was subtracted before arriving at the final M-H loops. The spontaneous magnetization ($4\pi M_S$) of the films was estimated by linearly extrapolating the high field part (30 – 50 kOe) of M-H loops to the zero field, similar to our earlier work [1-3]. The average grain sizes of the films estimated from Scherrer's formula varies in the range ~ 30 – ~ 38 nm with no systematic variation as a function of x. Figures 1 (a) and (b) show $4\pi M_S$ values of the bulk and thin film of MZF measured at 300 K and 10 K respectively. As seen from these figures, the bulk $4\pi M_S$ values at 300 K do not show any significant variation between x = 0.1 to x = 0.4. However, for x > 0.4 the $4\pi M_S$ values decrease with increase in x and becomes paramagnetic for x = 0.8. The maximum value of $4\pi M_S$ obtained at 300 K was ~ 5.2 kG for x = 0.2. The bulk $4\pi M_S$ values at 10 K, on the other hand, initially increase from ~ 7.6 kG for x = 0.1 to ~ 10.9 kG for x = 0.5 and then show a monotonous decrease until ~ 1.8 kG for x = 0.8. The maximum magnetization observed at 10 K was 10.9 kG for x = 0.5. These $4\pi M_S$ values are in close agreement with standard reported values [5]. We see from figures 1 (a) and (b) that the value of $4\pi M_S$ for the thin film shows a very different behavior than bulk. At 300 K, we note a small drop in $4\pi M_S$ from 4.3 kG for x = 0.1 to 3.9 kG for x = 0.3. However, for larger values of x, the magnetization rises again and reaches a maximum value of ~ 6.1 kG for x = 0.7. This value is higher than bulk $4\pi M_S$ for the same value of x by 7.5 times. The thin film $4\pi M_S$ values become higher than bulk for $x \ge 0.4$. At 10 K, the $4\pi M_S$ values of the films show an overall increase from 5.5 kG for x = 0.1 to 9.2 kG for x = 0.7 and then drops to ~ 8.0 kG for x = 0.8. The $4\pi M_S$ values of the films become higher than bulk only for x > 0.6. The resonance field values of FMR spectra were used in Kittel's equation to estimate the $4\pi M_{eff}$ values. These values have also been shown in figure 1 (a) to compare with the $4\pi M_S$ values measured using VSM. We see that the $4\pi M_{eff}$ shows a similar trend as $4\pi M_S$ even though $4\pi M_{eff}$ values are generally higher. Such higher values of $4\pi M_{eff}$ in comparison to $4\pi M_S$ are often seen [6] and could be because of multiple reasons, one of which could be the presence of an anisotropy due to stresses [7]. The largest value of $4\pi M_S$ (~ 9.2 kG) observed by us for x = 0.7 is highest among all MZF thin films. Similar largest magnetization value was also reported for x = 0.7 in $Co_{1-x}Zn_xFe_2O_4$ ($0.1 \le x \le 0.7$) thin films and was 8.1 kG [3], while the bulk value there was 6.2 kG. The magnetic moment values in Bohr magnetons (μ_B) of bulk and thin films are listed in Table 1. The XRD densities of the films were used to convert $4\pi M_S$ of the films to μ_B as the actual density or mass was not known. Hence the actual magnetic moment values of the films given in the Table are underestimates. Thin film deposition techniques induce a different cation distribution in spinel ferrite thin film compared to its corresponding bulk distribution [8]. Higher than bulk magnetic moment in MZF thin films [refer to Table 1] can be understood on the basis of cation distribution in thin films. Due to quenching, the Zn^{2+} enters both on A and B-sites. A decrease in spin canting is resulted from strengthening of A-B exchange interaction when less number of Zn^{2+} occupying the A-sites. Also the presence of Zn^{2+} ions on B-sites would reduce B-B interaction making canting weaker [3]. This would result in an increase of net magnetic moment of the films compared to bulk even at higher Zn.

1. R. Prabhu et. al., J. Phys. Commun. 1 (2017) 035010 2. B.N. Sahu et. al., IEEE Trans. Magn. 51 (2015) 1 3. R. Prabhu et. al., J. Magn. Magn. Mater. 448 (2018) 192 4. S. Chikazumi C. D. Graham. *Physics of Ferromagnetism*. Oxford University Press Inc, New York (1997) 5. J. Smith and H. P. J. Wijn. *Ferrites*. Philips Tech Library. Clever-Hume Press Ltd, Netherlands (1959). 6. B. Bhoi et. al., IEEE Trans. Magn. 49 (2013) 990 7. M Sultan et.al., J. Phys.: Conference Series 200 (2010) 072090 8. S. Nakashima et.al., J. Phys.:Condens. Matter 17 (2004) 137

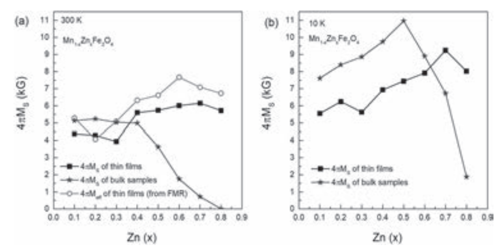

Fig. 1. The $4\pi M_S$ values of bulk and thin films of MZF at (a) 300 K and (b) 10 K

$Mn_{1-x}Zn_xFe_2O_4$	Magnetic moment at 300 K (μ_B)		Magnetic moment at 10 K (μ_B)	
	Bulk	Thin film	Bulk	Thin film
x = 0.1	3.41	2.89	5.06	3.67
x = 0.2	3.49	2.85	5.60	4.14
x = 0.3	3.34	2.57	5.87	3.68
x = 0.4	3.31	3.68	6.47	4.55
x = 0.5	2.37	3.71	7.18	4.81
x = 0.6	1.16	3.90	5.87	5.14
x = 0.7	0.48	4.01	4.41	6.03
x = 0.8	0.01	3.68	1.23	5.16

Table: 1 Magnetic moment in μ_B at 300 K and 10 K of MZF

EQ-13. Ion diffusion and microwave electromagnetic characteristics of LiZn/NiCuZn ferrites.

R. Guo[1], K. Sun[1], X. Liu[2], C. Chen[2], Z. Yu[1], X. Jiang[1], C. Wu[1], W. Wang[1], G. Wu[1], Y. Liu[1], H. Liu[1] and Z. Lan[1]
1. State Key Laboratory of Electronic Thin Films and Integrated Devices, University of Electronic Science and Technology of China, Chengdu, China; 2. Global Energy Interconnection Research Institute, Beijing, China

Both LiZn and NiCuZn ferrites are excellent microwave magnetic materials and have been extensively used in various high frequency and power micro/millimeter-wave devices [1]. With regard to LiZn ferrites, one have wide range of saturation magnetization M_s at room temperature, high Curie temperature T_c, low sensitivity of remanence B_r to stress, rectangular hysteresis loop and low fabrication cost [2]. Compared with LiZn ferrites, NiCuZn ferrites have lower ferromagnetic resonance (FMR) linewidth ΔH, however, one have relative lower T_c [3]. In order to meet the requirements of low insertion loss, high temperature stability, miniaturization and lightening of micro/millimeter-wave devices, it is an opportunity to explore an effective composite means to deal with the contradiction between the FMR linewidth ΔH and T_c for LiZn and NiCuZn ferrites. Here $Li_{0.35}Zn_{0.30}Fe_{2.21}O_{4-}\delta$ and $Ni_{0.52}Zn_{0.40}Cu_{0.10}Fe_{1.98}O_4$ ferrite have been fabricated by conventional ceramic process, respectively, and LiZn and NiCuZn powders were mixed together with 0.1wt% Bi_2O_3 and NiCuZn mass percent from 0wt% to 100wt% to prepare LiZn/NiCuZn ferrites with sintering temperature T_s from 800 to 1200°C. The ion diffusion and microwave electromagnetic characteristics of LiZn/NiCuZn ferrites have been investigated in detail. Fig. 1 shows Ni element atomic percent contents for the LiZn/NiCuZn ferrites with different NiCuZn ferrites contents from 20 to 80wt% for the sintering temperature from 800 to 1200°C. Considering a certain composition of LiZn/NiCuZn ferrite, dozens of grains in random region have been chosen to measure the Ni element atomic percent contents by means of EDS. The Ni element randomly distributes in different grains at the low sintering temperature, especially, when the sintering temperature is 800°C. The detected minimum and maximum of Ni element atomic percent contents keep on a rise with the increase of NiCuZn contents in LiZn/NiCuZn ferrites at T_s=800°C. However, the Ni element atomic percent contents show a convergence trend with the increase of sintering temperature and tends to be a stable state beyond T_s=1020°C, meanwhile, the stable state Ni element atomic percent contents at T_s=1200°C increases from 4.3 to 14.3 corresponding to the increase of NiCuZn ferrites contents from 20 to 80wt% in LiZn/NiCuZn ferrites. When the sintering temperature is 800°C, due to the melting point 825°C of Bi_2O_3, the Ni ion diffusion mechanism would be solid phase transfer, which causes its contents be randomly distributed. But the liquid layer of Bi_2O_3 would promote the solid state reaction when the sintering temperature beyond 825°C, and the Ni ion diffusion would be easier so that Ni element contents exhibit a convergence trend, which reflects the LiZn/NiCuZn ferrites be homogeneous mass. FMR linewidth (ΔH) spectra has been measured and fitted by Lorentz model for LiZn/NiCuZn ferrites with sintering temperature of 1200°C in Fig. 2, and the Lorentz fitting curve coincides well with the experimental data, which is consistent with previous relevant illumination [4]. ΔH monotonously decreases with the increase of NiCuZn contents. ΔH of polycrystalline ferrite consists of single crystal or intrinsic linewidth ΔH_i, the crystalline anisotropy and porosity induced line broadening contributions ΔH_a and ΔH_p, respectively. Because of the large crystalline anisotropy and porosity linewidth contributions, the small ΔH_i part (on the order of few Oe from single crystal [5]) could be neglected. Thus, ΔH is affected mainly by ΔH_a and ΔH_p.

[1] V. G. Harris, A. Geiler, Y. Chen, et al. Recent advances in processing and applications of microwave ferrites[J]. J. Magn. Magn. Mater., 321(2009) 2035-2047. [2]F. Xu, Y. L. Liao, D. N. Zhang, et al. Synthesis of highly uniform and compact lithium zinc ferrite ceramics via an efficient low temperature approach[J]. Inorg. Chem., 56 (2017) 4512-4520. [3]K. Sun, Z. Y. Pu, Y. Yang, et al. Rietveld refinement, microstructure and ferromagnetic resonance linewidth of iron-deficiency NiCuZn ferrites[J]. J. Alloys Compd., 681(2016) 139-145. [4]Y. L. Liao, F. Xu, D. N. Zhang, et al. Magnetic properties and microstructure of low temperature sintered LiZnMnTi ferrites doped with Li_2CO_3-B_2O_3-Bi_2O_3-SiO_2 glasses[J]. J. Alloys Compd., 680(2016) 729-734. [5]E. G. Spencer, D. A. Lepore, J. W. Nielsen. Measurements on lithium ferrite crystals having near zero defect concentrations[J]. J. Appl. Phys., 39(1968) 732-733.

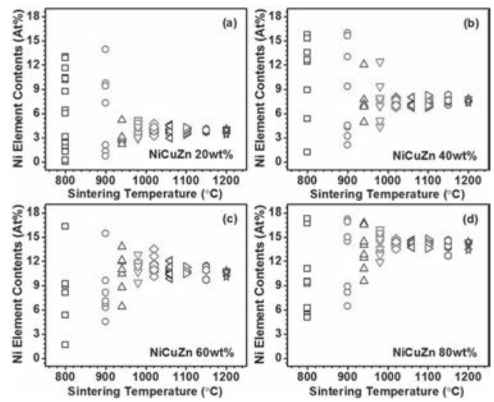

Fig. 1. Ni element contents as a function of sintering temperature for LiZn/NiCuZn ferrites with (a) 20wt% NiCuZn, (b) 40wt% NiCuZn, (c) 60wt% NiCuZn, and (d) 80wt% NiCuZn.

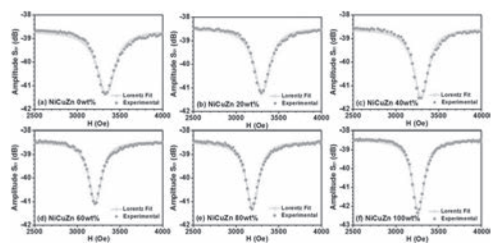

Fig. 2. Ferromagnetic resonance (FMR) linewidth ΔH spectra of LiZn/NiCuZn ferrites sintered at 1200°C with (a) 0wt% NiCuZn, (b) 20wt% NiCuZn, (c) 40wt% NiCuZn, (d) 60wt% NiCuZn, (e) 80wt% NiCuZn and (f) 100wt% NiCuZn.

EQ-14. Withdrawn

EQ-15. Fabrication of Fe-Ga Alloy Particle based Magnetorheological Fluid and Its Viscoelastic Characteristics.

H. Choi[1], S. Kwon[1], S. Na[2] and A.B. Flatau[2]

1. Dept. of Polymer Science and Engineering, Inha UNiversity, Incheon, The Republic of Korea; 2. Department of Aerospace Engineering, University of Maryland, College Park, MD, United States

I. INTRODUCTION Magnetic stimuli-responsive magnetorheological (MR) fluids composed of magnetic particles dispersed in non-magnetic carrier fluids have been extensively investigated as smart and intelligent magnetic materials due to their reversible and rapid changes when an external magnetic field is applied [1] along with their industrial applications such as damper, shock absorber and polishing devices [3]. They are distinctive with their dramatic change in rheological properties such as yield stress and dynamic moduli [2]. Among the many magnetic particles available, carbonyl iron microspheres have been widely used as magnetizable particles for MR fluids due to their high magnetic permeability, soft magnetic property and common availability [4]. As for a new MR material, we introduce iron–gallium (Fe-Ga) alloy particles, in which the Fe-Ga alloy (Fe_{100-x} Ga_x where $5 < x < 35$) is commonly known as Galfenol, a rare-earth free magneto-strictive alloy [5] with a high Curie temperature and corrosion resistance. The raw materials used to produce Fe-Ga alloys are relatively inexpensive, thus making Galfenol have great promise as an engineering material for myriad sensing, actuating, and energy harvesting devices [6]. In this study, we prepared Fe-Ga alloy particle-based MR fluid to investigate its MR characteristics using a rotational rheometer with a magnetic field supply device. II. EXPERIMENT Soft magnetic Fe-Ga alloy particles were fabricated using the Fe-Ga alloy materials (Eterma Products Inc.) consisted of melting elemental Ga with pure iron. They were chill-casted into an ingot form through an induction melting technique, and the ingot was then enclosed in a stainless steel can and sealed to prevent an oxidation. The Galfenol flakes were prepared through a conventional rolling and texture annealing process using Fe-Ga alloy ingot. The MR fluid was then prepared by dispersing Fe-Ga alloy flake-typed particles in silicone oil (50 cSt, Shin-Etsu, Japan) with a weight fraction of 30%. Morphology of the Fe-Ga particles was confirmed using scanning electron microscopy (SEM), while their crystal structure and magnetic property were confirmed by X-ray diffraction (XRD) and vibration sample magnetometer (VSM), respectively. The MR properties of the Fe-Ga alloy based MR fluid were measured via the rotational rheometer (MCR 300, Anton Paar, Germany) equipped with a parallel-plate geometry (PP20, gap distance of 1 mm) and a magnetic field supply device (MRD 180). The steady shear test was applied at shear rates ranging from 0.1 to 200 s^{-1} under a range of magnetic fields, while viscoelastic properties of the Galfenol based MR fluid was also investigated by strain amplitude sweep and angular frequency sweep tests. III. RESULT AND DISCUSSION As shown in Fig. 1, SEM image of the Galfenol particles exhibit approximately 50 μm of particle size with the thickness of 1 μm. From the SEM image, we can confirm that the Galfenol particles show a flake structure. In addition, the Galfenol particles were almost soft-magnetic with their saturation magnetization value of 174 emu/g, measured from VSM data. Figure 2 represents shear stress curve as a function of shear rate for Galfenol based MR fluid under four different external magnetic field strengths ranging from 0 to 343 kA/m. Without an external magnetic field, the MR fluid behaves as like a Newtonian fluid. However, when the magnetic field was applied, the Galfenol based MR fluid exhibited typical Bingham fluid-like behavior because the particles form chain-like structures via magnetic dipole-dipole interaction between the adjacent particles. Furthermore, the plateau shear stress region on a broad shear rate range could be explained by reconstitution of the destructed chain-like structure. The extent of the shear stress increased depending on the magnetic field strength at a whole shear rate range. Based on these rheological data, an attempt was made to fit the flow curves using the Bingham model Eq. which is one of the most widely used models for traditional MR suspension systems, as follows: $\tau = \tau_y + \eta_0$ where τ_y and τ are the dynamic yield stress and shear stress, respectively, and η_0 is the shear viscosity at high shear rate. The solid lines in Fig. 2 for Galfenol based MR suspension were obtained from the above mentioned equation and demonstrate a deviation from the experimental data. Furthermore, to obtain τ_y of the MR fluid from the flow curves, we extrapolated the corresponding shear stress in Fig. 2 to a zero-shear rate. The dynamic yield stress also increased with increasing magnetic field strength and the τ_y was dependent on the magnetic field strength (H) as follows: $\tau_y \alpha H^{\alpha}$. Based on VSM results of Galfenol particles, the slope (α) of Galfenol based MR fluid was proportional to $H^{1.5}$ at low magnetic field strengths [7]. However, as the magnetic field strength increases, the Galfenol particles become easily saturated and the slope of Galfenol based MR fluid decreases to 1. From this study, Galfenol particles showed their typical MR characteristics for the first time.

1) R. Tao, "Super-strong magnetorheological fluids", *J. Phys: Condens. Matter* 13, R979-R999 (2001). 2)S. G. Sherman, N. M. Wereley, "Effect of particle size distribution on chain structures in magnetorheological fluids", *IEEE Trans. Magn*. 49, 3430-3433 (2013). 3) L. H. Zong, X. L. Gong, S. H. Xuan, C. Y. Guo, "Semi-active H infinity control of high-speed railway vehicle suspension with magnetorheological damper", *Vehicle Syst. Dyn.* 51(5), 600-626 (2013). 4) B. J. Park, K. H. Song, H. J. Choi, "Magnetic carbonyl iron nanoparticle based magnetorheological suspension and its characteristics", *Mater. Lett.* 63, 1350-1352 (2009). 5) J. B. Restorff, M. Wun-Fogle, K. B. Hathaway, A. E. Clark, T. A. Lograsso, G. Petculescu, "Tetragonal magnetostriction and magnetoelastic coupling in Fe-Al, Fe-Ga, Fe-Ge, Fe-Si, Fe-Ga-Al, and Fe-Ga-Ge alloys," *J. Appl. Phys.* 111, 023905 (2012). 6) J. Atulasimha, A. B. Flatau, "A review of magnetostrictive iron–gallium alloys". *Smart Mater. Struct.*, 20, 043001 (2011). 7)H. S. Chae, S. D. Kim, S. H. Piao, H. J. Choi, "Core-shell structured $Fe_3O_4@SiO_2$ nanoparticles fabricated by sol–gel method and their magnetorheology", *Colloid Polym. Sci.* 294, 647-655 (2016).

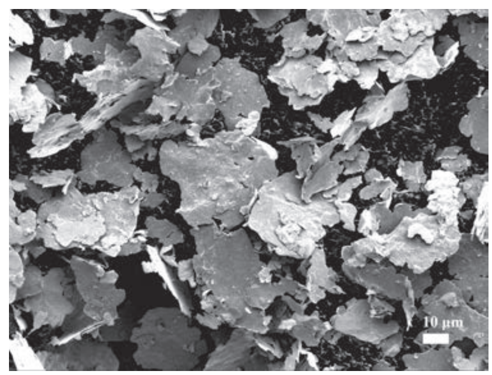

Fig. 1. SEM image of Galfenol particles

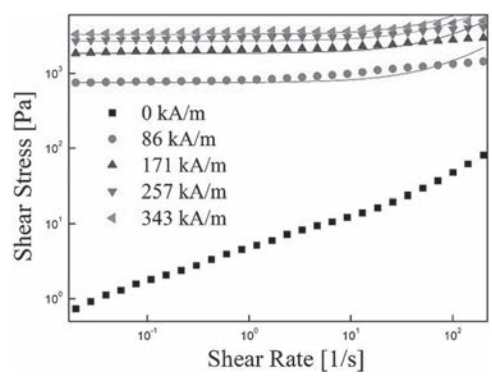

Fig. 2. Shear stress curves of Galfenol particle based MR suspension at different magnetic field strengths

THURSDAY MORNING, 26 APRIL 2018 SIMPOR/ROSELLE BALLROOM, 8:30 TO 11:30

Session ER
MAGNETIC BEARINGS, AND LEVITATION
(Poster Session)

Myounggyu D Noh, Co-Chair
Chungnam National University, Daejeon, The Republic of Korea
Jang-Young Choi, Co-Chair
Chungnam National University, Daejeon, The Republic of Korea

ER-01. Study of characteristics on stability of the yoke equipped magnetic rotor in the HTS Magnetic Bearing.

T. Arai[1], T. Minami[1], S. Hiraoka[1] and S. Ohashi[1]
1. Electrical and Electronic Engineering, Kansai University, Suita, Japan

Pinning effect of the high temperature superconductor (HTS) is introduced to realize magnetic levitation without gap control [1], [2]. Applications for the contact less magnetic bearing system [2] have been developed. For example, there is application to a flywheel electric power storage device. The rotor is supported by pinning effect of the HTS with contact less and control less. The conventional rotor has two magnetic poles [3] [4]. The flux use of the rotor is inefficient. The system consists of the stator and the rotor in this paper. The stator generates the rotating magnetic field. The induced current is generated in the rotor by this rotating magnetic field. The rotor is rotated by the induced current and the rotating magnetic field using the principle of the induction motor. It consists of the iron equipped magnet and the aluminum. In the iron equipped magnet, the yoke covers the permanent magnet in order to increase the linkage flux on the HTS. The aluminum is installed around the iron equipped magnet in order to generate rotational torque. But, the rotating magnetic field affects the magnetic field in the iron equipped magnet. The flux inside the iron equipped magnet is disturbed. Therefore, the iron is installed as a shield and it is defined as the magnetic shield. It is used to guide the rotating magnetic field to the outside without getting inside the iron equipped magnet. Thus, the air gap and the magnetic shield are attached between the iron equipped magnet and the aluminum. As a result, the influence of the rotating magnetic field in the iron equipped magnet becomes small. Fig.1 shows the structure of the iron equipped magnetic rotor. The yoke is installed around the permanent magnet to increase the linkage flux on the HTS. The aluminum is installed as the secondary of the induction motor. The induced current is generated in the aluminum by the rotating magnetic field. The air gap and the magnetic shield are attached between the iron equipped magnet and the aluminum to suppress the magnetic disturbance by the stator. The levitation gap between the upper surface of the HTS and the lower surface of the rotor is 10 mm. The air gap between the stator and the aluminum is 2 mm. The width of the air gap is defined as W_{Air}, and the width of the magnetic shield is defined as W_{shield}. The turn of the stator coil is 300 turns, and it is distributed winding of 6 poles. The Three Dimensional Finite Element Method (3D FEM) analysis is carried out to calculate the flux density and the torque. The flux density is calculated at the boundary between the air gap and the yoke. The torque is calculated in the shield part and the aluminum part. The width of the air gap and the width of the shield are changed in this analysis. However, the total width of the air gap and the shield is 10 mm. The analysis is performed using the 3D FEM software JMAG Designer. The analysis conditions are coil current 4 A, frequency 60 Hz and sliding 0.01 in the stator. Figs.2 shows the analysis result of the flux density distribution at the boundary between the air gap and the yoke, and the analysis result of the torque. From Figs.2 (a), the flux of the iron equipped magnet is disturbed by the rotating magnetic field in the non-shield type. Then, the models with the shield are considered. (W_{Air}, W_{shield}) = (5, 5) is defined as the large shield type. (W_{Air}, W_{shield}) = (7, 3) is defined as the small shield type. The influence decreases by enlarging the width of the air gap. This is because the magnetic resistance between the shield and the iron equipped magnet is increased by enlarging the width of the air gap. From Figs.2 (b), average torque T is calculated at steady state. The torque is 0.0381 Nm in the large shield type, 0.0371 Nm in the small shield type. There is little difference. Thus, we designed the iron equipped magnetic rotor under the condition of the small shield type. The characteristics of the iron equipped magnetic rotor are studied. The linkage flux on the HTS is calculated by the 3D FEM analysis. The levitation force and the restoring force are improved because the linkage flux on the HTS increases. Thus, the pinning force is improved in the iron equipped magnetic rotor. The iron equipped magnetic rotor is suppressed the horizontal vibration at the resonance state because the restoring force is improved. Thus, the proposed model uses flux from the permanent magnet effectively.

[1] F. C. Moon, "Superconducting levitation", John Wiley & Sons, New York, 1994. [2] J. Hull, M. Murakami, "Applications of bulk high-temperature Superconductors", Proc. of IEEE, vol.92, 2004, pp1705-1718. [3] R. Sugiyama, K. Oguni, S. Ohashi, "Study on the Levitation and Restoring Force Characteristics of the Improved HTS-permanent Magnet Hybrid Magnetic Bearing", *Physics Procedia* vol.58, 2013, pp282-285. [4] K. Emoto, R. Sugiyama, S. Takagi, S. Ohashi, "Improvement of the rotational characteristics in the HTSC-permanent magnet hybrid bearing using ring shaped magnet", Physica C Vol.494, 2012, pp235-241. [5] T. Minami, S. Sakai, S. Ohashi, "Improvement of Stability against Vibration at the Mechanical Resonance in Attractive type HTS- Permanent Hybrid Magnet Bearing.", 2016 IEEE Region 10 Conference (TENCON), 2016, 16657805, pp3294-3297.

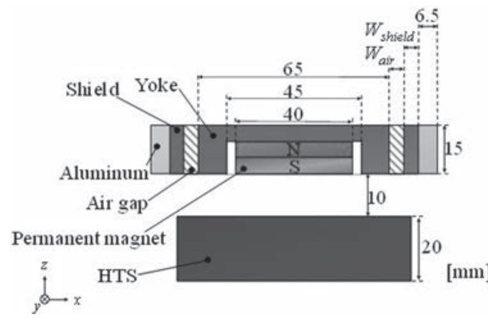

Fig. 1. Experimental device.

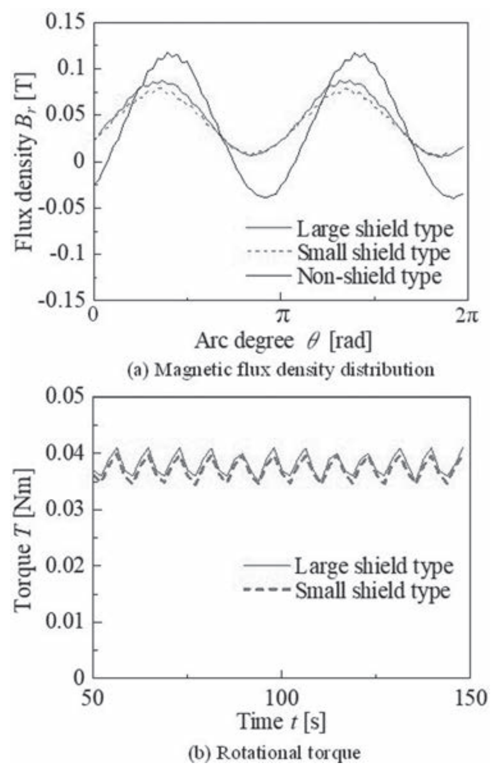

Fig. 2. Analysis result.

ER-02. A Proposal of Noncontact Baton-pass System for a Thin Steel Plate Based on Magnetic Levitation Technique.

Y. Sudo[1], Y. Arita[1], M. Yamada[1] and T. Nakagawa[1]
1. Electrical and Electronic Engineering, Tokyo City University, Setagaya, Japan

1. Introduction Thin steel plates widely used for many industrial products have mainly been conveyed on rollers or by suckers in workspaces. However, for such contact types of conveyance method, there is a problem that quality deterioration by scratches or pressed marks occurs on steel plate-surfaces. In order to resolve this problem, adoption of magnetic levitation techniques can be effective in a conveyance system for steel plates. For this reason, other institutions are studying such a system intensively ([1], [2] and [3]). Our laboratory has already succeeded in stable levitation and noncontact conveyance for thin steel plates ([4]). As the next stage, we aim at the realization of noncontact baton-pass system, in which electromagnets hand a levitating steel plate to the adjoined electromagnets without any contacts. If such a motion is realized, it will be utilized as "branching mechanism" in a conveyance lane for steel plates. Moreover, if the motions of baton-pass are repeated, the levitating steel plates can continue to proceed along the conveyance lane. In this paper, we will propose an interesting baton-pass mechanism for a thin steel plate. In addition, we will show the successful experimental results when the thin steel plate is handed to the adjoined electromagnets without any contacts. 2. Structure and Control Method of Magnetic Levitation System Our magnetic levitation system for steel plates consists of six electromagnets, six gap sensors, four sideslip sensors, and LabVIEW-PXI (DSP with A/D and D/A converters). Basically, the steel plate can levitate by four electromagnets, four gap sensors, two sideslip sensors, and LabVIEW-PXI as proposed in our original paper ([5]). In this study, we deal with the apparatus structure shown in Fig. 1(a), in order to verify experimentally that the thin steel plate can be handed to the adjoined electromagnets without any contacts. As for the levitation control in our series of studies, we have designed the controller for each independent motion mode of the steel plate, based on "Optimal control theory". On the other hand, as for the guidance control in our series of studies, we have adopted an idea of tilting the steel plate. This idea is very interesting, because we don't need any actuators for guidance control. That is, a levitating steel plate is tilted so as to obtain the guidance-force, as shown in Fig. 1(b). (As for the detail, refer to [5]) 3. Proposal of Noncontact Baton-Pass System and Experimental Verification Figure 2(a) shows a flow in the baton-pass process of the levitating steel plate that moves to the adjacent electromagnets without any contacts. First, as the step1, the steel plate is levitated stably. Second, as the step2, it is tilted by regulating the attractive force of the front and rear electromagnets and is proceeded to the adjacent electromagnets. As the step3, the levitating steel plate is grasped by the adjacent electromagnets without any contacts. As the step4, the levitating steel plate is tilted inversely to stop itself. Finally, as the step5, the steel plate keeps stable levitation. Figure 2(b) shows the photos captured from the movie taken when the thin steel plate is handed to the adjoined electromagnets, corresponded to each step in Fig.2(a). As a result, we succeeded in realization of noncontact baton-pass system, in which electromagnets hand a levitating steel plate to the adjoined electromagnets without any contacts.

[1] H. Hayashiya, H. Ohsaki, E. Masada, "Non-contacting conveyance of a steel plate using electromagnetic force by transverse flux linear motors," IEEJ Trans, Vol. 120-D, No.7, 2000 pp. 928-933 [2] Y. Oshinoya and S. Hasegawa, "Control of electromagnetic levitation transport of flexible steel plate," Proc. of IPEC, ISBN: 978-1-4244-5394-8, June 2010, pp.284-288p, Sapporo. [3] H. Hayashiya, N. Araki, J.E. Paddison, H. Ohsaki, E. Masada"Magnetic levitation of a flexible steel plate with a vibration suppressing magnet," IEEE Trans. on Magnetics, Vol.32, Issue.5, 3686-3689p, September 2017 [4] O. Suzuki, T. Nakagawa, "Study of Magnetic Levitation for a 0.18-mm thick Steel Plate by Adopting Twisting-mode Control" IEEE Trans. on Magnetics, Vol. 51, No. 11, 4p-length, Nov. 2015 [5] T. Nakagawa and M. Hama, "Magnetic Levitation Control of a Thin Steel Plate by Means of Gap Length Correction Commands", Electrical Engineering in Japan, Vol. 135, No.2, 2001, (Translated from Transaction of IEEJ, Vol. 120-D, No.4, April 2000, pp. 489-494)

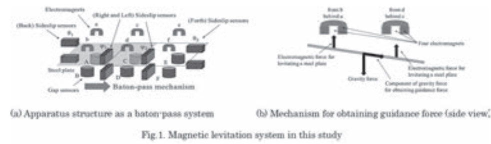

Fig. 1. Magnetic levitation system in this paper

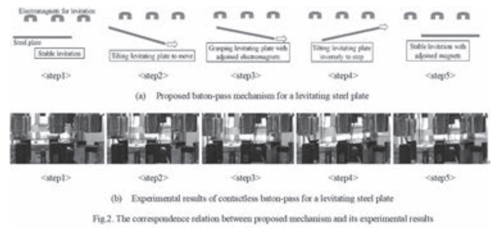

Fig. 2. The correspondence relation between proposed mechanism and its experimental results

ER-03. A study on Optimal Operating Point of Linear Induction Motor considering Normal Force and Efficiency in MAGLEV Vehicle.

J. Lim[2], J. Jeong[1] and D. Park[2]
1. Electrical Engineering, Chung Nam National University, Daejeon, The Republic of Korea; 2. Magnetic Levitation and Linear Drive, Korea Institute of Machinery & Materials (KIMM), Daejeon, The Republic of Korea

Introduction This paper deals with the analysis of the optimal operating point of linear induction motor(LIM) which is used in magnetic levitation trains. LINIMO of Japan and ECOBEE of Korea have been developed as the urban maglev of 110km / h class, and have successfully operated commercial operation. China is developing three routes independently and some have begun commercial operation. All of the developed low speed maglev trains use LIM as propulsion system. The secondary of LIM is advantageous in that the production cost of the line is low and the maintenance cost is significantly lower than other systems. In the rotating induction machine, the dq-axis-based vector control is widely used. The LIM as the magnetic levitation propulsion system, however, the applied voltage and the frequency are the main control variables for scalar control. In detail, a constant slip frequency control has been used to stabilize the levitation of the Maglev. The constant slip frequency has a constant normal force on the levitation system regardless of the speed at the maximum thrust control [1]. However, in actual train operation, various thrust are required to operate at various speeds. The normal force of the LIM is also proportional to the current command of the demanded thrust. While the train is under operation, the maximum vertical force of the LIM will only occur at the maximum thrust point. Although the constant slip frequency control is advantageous in terms of normal force, it operates in a region with low operation efficiency due to the characteristics of the LIM. Therefore, variable slip control has been applied as an effective method to improve the operation efficiency. Propulsion system spends the largest portion of the power consumption of maglev trains, and improvement of the propulsion efficiency has been continuously required in order to achieve the higher operating efficiency of the entire system. In addition, the propulsion efficiency of an actual vehicle may fluctuate by 5 to 10 depending on the operating conditions. In order to increase the propulsion efficiency of the LIM, it is important to operate in a low slip frequency region. As noted earlier, lowering the slip causes a higher attraction force. Therefore, interference with the levitation system should be considered for low sleep frequency domain operation. Main Body The thrust due to speed and slip is shown in Fig. 1. In the constant thrust region, the applied voltage and frequency rise with the speed based on the fixed slip frequency. In the constant power region, the driving frequency increases with the speed to create thrust. In the figure, three additional lines are drawn, which denote constant slip frequency operation (red line), maximum thrust operation (blue line), and maximum efficiency operation (green line). In the case of the constant slip frequency control, as the speed increases, the slip at the operating point decreases, and thus it can operate in a relatively high efficiency region at high speed operation. At low speeds, the slip of the operating point is large due to the fixed slip frequency, so it operates in low thrust and efficiency regions. Therefore, when the vehicle is operated in the low slip region within the maximum normal force of the LIM, a higher driving efficiency can be achieved. The thrust, efficiency and the attraction force of the LIM according to the operation slip are shown in Fig. 2. For a semi-high speed maglev vehicle, the LIM is designed to meet the maximum thrust of 4 kN at a rated speed of 90 km/h and a slip frequency of 12.5Hz. However, due to the nature of the LIM as a means of transportation, a thrust command of 4 kN is not always required at a speed of 90 km/h. The driving force of the LIM is defined as an acceleration pattern determined according to the train 's driving pattern. When the propulsion command is 50% of the thrust, the voltage and current are reduced to 50%, and the normal force of the LIM is also reduced. Applying a low slip frequency to maintain a constant normal force, the LIM can be operated with the slip frequency down to 10.5 Hz. It can be defined as a constant normal force control. When driving at a slip frequency of 10.5 Hz for a command of 50% at a speed of 90 km/h, the efficiency is 63%, which is 5% higher than the efficiency of 58% when the motor is driven at a slip frequency of 12.5 Hz. Conclusion In this paper, by analyzing the characteristics of LIM used in magnetic levitation trains, the thrust and normal force for velocity and slip were analyzed, and a constant normal force control method was proposed to suggest a high efficiency driving scenario for the same normal force. In the final paper, we will present a comparison of driving scenarios and efficiency for the proposed driving method.

[1] Lu, Qinfen, Yanxin Li, Yunyue Ye, and Z. Q. Zhu. "Investigation of forces in linear induction motor under different slip frequency for low-speed maglev application." *IEEE Transactions on energy conversion* vol. 28, no. 1, pp. 145-153, 2013.

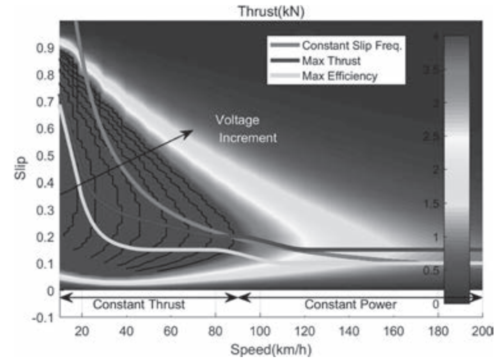

Fig. 1. Thrust map and slip control strategies

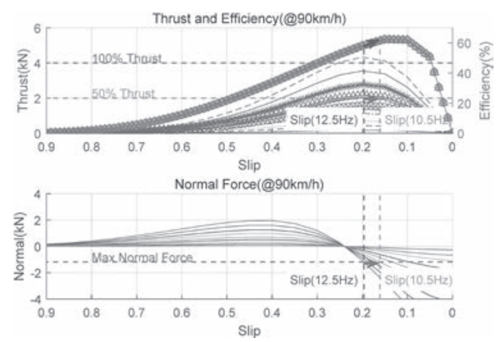

Fig. 2. Thrust and Normal force according to applied voltage and slip(@90km/h)

ER-04. Improvement of damping factor on the lateral guideway displacement by using weight-reduced damper coil on superconducting magnetically levitation bogie.

R. Nakakita[1], E. Shin[1], T. Takeuchi[1] and S. Ohashi[1]
1. Electrical and Electronic Engineering, Kansai University, Suita, Japan

Superconducting magnetically levitated transportation system has been developed in Japan since 1962 [1-2]. Results of numerical simulations show that the damping factor of the EDS system is small. Therefore, the damper coils are installed in front of the SC coils to increase damping factor. The damper coils are used to increase damping of the EDS system against oscillation of the bogie, but the energy loss is larger because of the weight of the damper coil [3-6]. Therefore, by changing the shape of the conventional coil, its weight and the energy loss is reduced. The number of operation types of the damper coil is two. One is the passive mode, and the other is the semi-active mode. In the passive mode, the damper coils are used just as the short circuit coils. The effect of the conventional damper coils is larger than that of the weight-reduced damper coils in this mode, and damping factor becomes larger than without the conventional damper coils. However, this system may generate unnecessary damper coil current because of the discrepancy of the phase of the damping current and the oscillation velocity generated by the self-inductance of the damper coils. The effect of the conventional damper coil becomes large in this mode. In the semi-active mode, the IGBT which also has a part to protect the circuits from large current is installed, and damper coils are switched according to the oscillation velocity of the bogie and the magnetic force generated by the damper coils. When the switch is ON, the damper coils are short circuited, and OFF, open circuited and resistances are inserted to the circuits. The effect of the weight-reduced damper coil becomes large in this mode. In Japan, ground condition is not good, so the guideway displacement may occur by earthquakes and it is important to estimate effects of the guideway. When the bogie passes the lateral displacement, rolling angle occurs at the same time, and just after this, the levitation force changes and it induces vertical displacement, pitching angle and yawing angle. In this study, simulations when the conventional damper coils and the weight-reduced damper coils pass the lateral displacement $y = 0.01$ m are shown. Fig.1 shows the shape and position of the weight-reduced damper coil. The levitation force is generated by the SC coils attached to the bogie. The eight-figure null-flux connection is used for the levitation coils on the ground. When the bogie passes the center of the eight-figure coils, the levitation force is generated to the bogie. The current induced in the levitation coils is calculated. EDS system has an air-coil system and modeled as electric circuits. The mutual inductance between the SC coils and levitation coils is calculated from the electric circuit equations and in order to solve the electric circuit equations, the current of the levitation coils is calculated. Also, the motion of the bogie is calculated from the motion equations. By repeating these procedures, the transient motion of the bogie is given. Runge-Kutta method is used to solve these equations [7]. Running simulations of the conventional damper coils and the weight-reduced damper coils in the semi-active mode are studied. The bogie moves to the running direction at the constant velocity $v = 120$ m/sec. The bogie passes the lateral displacement $y = 0.01$ m at the time $t = 0.6$ sec. Fig.2(a) shows the lateral displacement and Fig.2(b) the rolling angle. In the lateral displacement, the maximum oscillation of the weight-reduced coils is smaller than that of the conventional damper coils. Thus, 1.804% improvement is seen. Also, the convergence time of the weight-reduced damper coils is shorter than that of the conventional damper coils. Thus, 59.02% improvement is seen. In both the maximum oscillation and the convergence time, improvements are seen. In the rolling angle, the maximum oscillation of the weight-reduced coils is smaller than that of the conventional damper coils. Thus, 5.333% improvement is seen. Also, the convergence time of the weight-reduced damper coils is shorter than that of the conventional damper coils. Thus, 57.40% improvement is seen. In both the maximum oscillation and the convergence time, improvements are seen. In conclusion, improvements in the lateral displacement and rolling angle are seen when the weight-reduced damper coils pass the lateral guideway displacement in the semi-active mode compared with the conventional damper coils. Especially in the convergence time, drastic improvement is seen.

S.Ohashi and N.Ueda, "Influence of the Damper Coil System on the Levitation Characteristics in the Superconducting Magnetically Levitated System is Case of SC Coil Quenching", *IEEE Trans. on Magnetics* vol.50, No.11, 8300304, 2014 A.Seki, J.Kitano and S.Miyamoto, "Dynamics of the bogie of a maglev system with guideway irregularities", *IEEE Trans. on Magnetics* vol.32, No.5, pp5043-5045, 1996 S.Ohashi, "Effect of the Damper Coils on the Rotational Motion of the Superconducting Magnetically Levitated Bogie", *IEEE Trans. on Magnetics* vol.36, No.5, pp3680-3682, 2000. S.Ohashi, "Effect of the Active Damper Coils of the Superconducting Magnetically Levitated Bogie in Case of Acceleration", *IEEE Trans. on Magnetics* vol.44, No.11, pp4163-4166, 2008. S.Ohashi and T.Ueshima, "Control Method of the Semi-Active Damper Coil System in the Superconducting Magnetically Levitated Bogie Against Vertical and Pitching Oscillation", *IEEE Trans. on Magnetics* vol.48, No.11, pp4542-4544, 2012..

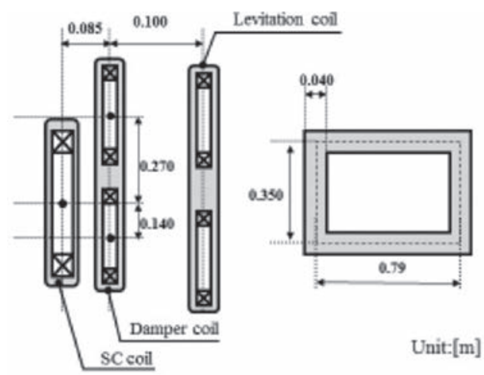

Fig. 1. Shape and position of the weight-reduced damper coil

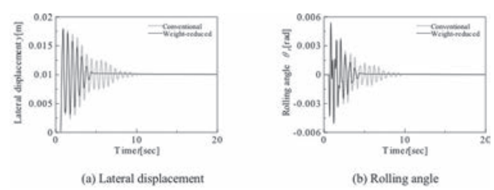

Fig. 2. Lateral displacement and rolling angle

ER-05. A Novel Bearingless Switched Reluctance Machine with Axial Split Phase Inner Stator Permanent Magnet Structure.

Z. Zhu[1,2], Y. Jiang[2] and Y. Sun[1]
1. School of Electric Power Engineering, Nanjing Institute of Technology, NANJING, China; 2. School of Electrical and Engineering, Southeast University, NANJING, China

INTRODUCTION: Flywheel energy storage system (FESS) is a kind of physical energy storage device for electromechanical energy conversion. In order to simplify the system structure and improve the critical speed, magnetic levitation electric machines that combine magnetic bearing and electric machine are applied in FESS [1]. Bearingless switched reluctance machine (BSRM) fully preserves the excellent characteristics of switched reluctance motor, and improves the high speed performance and operation efficiency by active control of its own radial force. Introducing the BSRM into FESS, the system volume and loss could be greatly reduced, suspension performance could be improved, and critical speed and power density could be increased. BSRM is one of the ideal choices for flywheel suspension support and energy conversion [2]. There are serious electromagnetic coupling between torque winding and suspension winding of the traditional 12/8 poles type BSRM, which lead to the difficulty of controlling [3]. In this paper, a novel BSRM with axial split phase inner stator permanent magnet (PM) structure is proposed to cancel the electromagnetic coupling between torque winding and suspension winding. Meanwhile the power density of the BSRM is improved due to the PM bias magnetic field for suspension. TOPOLOGY: Fig. 1 shows the structure of the BSRM with axial split phase inner stator PM structure, where outer rotor is combined with the flywheel directly to improve the axial utilization ratio, reduce the volume of the whole system, and increase the specific capacity and specific power of the flywheel energy storage system. The proposed BSRM could been seen as combination of two single-phase 12/12 poles type BSRM along axial direction, and the angle difference of their rotors is q_r. As shown in Fig. 1(a), There are two kinds of stator poles with different tooth width in the stator, namely suspension pole (wide tooth) and torque pole (narrow tooth), respectively. They are used to assemble suspension winding and torque winding, respectively. There are magnetic isolation sleeves between suspension poles and torque poles. Then the physical decoupling of the magnetic circuits of the torque pole (Y_{ma}) and the suspension pole (Y_{sa}) is realized, as shown in Fig. 1(b). There is PM between two stators to provide the bias magnetic field for suspension pole. Then a larger suspension force could be produced by smaller current input to suspension winding, and the power density of the BSRM could be improved. As the existence of magnetic isolation sleeve, the PM flux (Y_{PM}) will not cross through the torque winding as shown in Fig. 1(b). Then PM flux will do not impact on the torque control, and the main circuit and control method are the same as the traditional two phase switched reluctance machine. FINITE ELEMENT ANALYSIS: In order to verify the effectiveness of the proposed BSRM, its electromagnetic field is analyzed by the finite element method (FEM), and the results are shown in Fig. 2. Fig. 2(a) shows the distribution of magnetic field in the proposed BSRM without currents input to the torque winding and suspension winding. It can be seen that the PM flux only crosses through the suspension windings and rotor, and there is not PM flux cross through the torque winding. Fig. 2(b) shows the distribution of magnetic field in the proposed BSRM where currents input to the torque winding and suspension winding. It can be seen that the magnetic flux generated by torque winding and suspension winding cross the torque poles and suspension poles respectively, and the physical decoupling are realized. If the current is inputted to two suspension windings in series on y-axis, the magnetic fields of two airgaps on y-axis are strengthen and weaken according to the direction of current, respectively, and the suspension force will be generated. Fig. 2(c) and Fig. 2(d) show the decoupling characteristics of suspension winding and torque winding. When 2A current is input to the torque windings, if the current input to suspension windings changes among 0A and 4A, the variation of torque is small, as shown in Fig. 2(c). When 1.5A current is input to the suspension windings, if the current input to torque windings changes among 0A and 4A, the variation of suspension force is small, as shown in Fig. 2(d). So the coupling of the torque wingding and suspension winding is weak, and the torque and suspension force could be controlled separately. CONCLUSIONS: In this paper, a novel BSRM with axial split phase inner stator PM structure is proposed to realize the physical decoupling of the torque winding and suspension winding, and improve the power density of the BSRM. The topology and operation principles of the proposed BSRM are introduced. Moreover, the electromagnetic characteristics, such as torque, suspension force and decoupling are analyzed by FEM to verify the performance superiority.

[1] M. Ooshima, S. Kobayashi, and H. Tanaka. "Magnetic suspension performance of a bearingless motor/generator for flywheel energy storage systems." *IEEE Power and Energy Society General Meeting*. pp. 1-4, 2010. [2] Y. Yuan, Y. Sun, and Y. Huang. "Design and analysis of bearingless flywheel motor specially for flywheel energy storage." *IET electronics letters*, vol. 52, no. 1, pp. 66-68, 2016 [3] M. Takemoto, H. Suzuki, and A. Chiba, et al. "Improved analysis of a bearingless switched reluctance motor." *IEEE Trans on Industry Application*, vol. 37, no. 1, pp. 26-34, 2001.

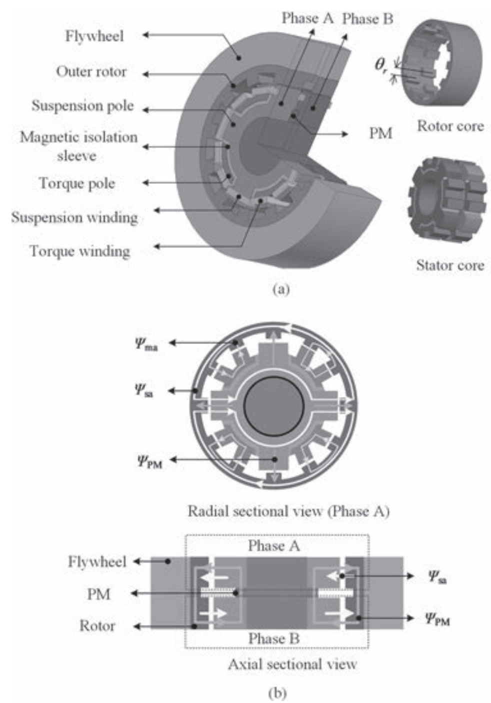

Fig. 1. BSRM with axial split phase inner stator PM structure. (a) Structure of the proposed BSRM; (b) Sectional view and magnetic circuit.

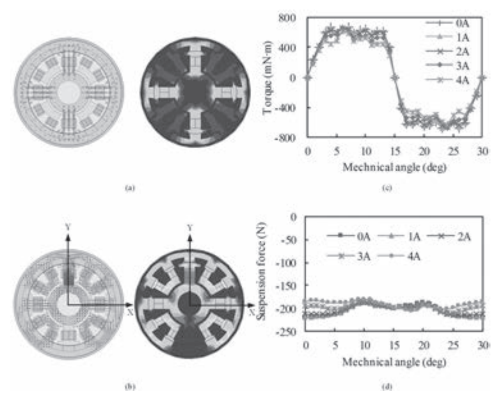

Fig. 2. Dcoupling characteristics of the proposed BSRM. (a) Distribution of magnetic field without current input to torque windings or suspension windings; (b) Distribution of magnetic field with crrent input to suspension windings of Y-axis and torque windings; (c) Influence of current input to suspension windings on torque; (b) Influence of current input to torque windings on suspension force.

ER-06. Analysis of a Multi-Phase Bearingless PMSM With Double-Winding Based on MMF.

Y. Qin[1] and H. Zhu[1]
1. Jiangsu University, Zhenjiang, China

I. INTRODUCTION Bearingless motors have wide application prospects in high-purity and high-speed areas for the virtues of no wear and lubrication [1]. And, multi-phase motors have higher torque density, lower torque ripple and superior fault-tolerant operation when compared with three-phase motors [2]. So, the multi-phase bearingless motors combining the advantages of bearingless and multi-phase motors have better performances and higher reliability. Compared with the integer-slot concentrated-winding (ISCW) topology, the multi-phase fractional-slot concentrated-winding (FSCW) bearingless permanent magnet synchronous motor (BPMSM) has higher torque density and smaller torque ripple [3]. However, the air gap magnetomotive force (MMF) harmonic distribution in the FSCW BPMSM is quite complex, which will interact with each other to affect the suspension force, so, they must be emphasized and quantified. Hence, a five-phase 10-slot/8-pole (10/8) FSCW BPMSM is proposed in this paper. The principle of the suspension force is elaborated based on the armature and rotor MMF harmonic distribution. And the new general mathematical model of armature MMF is first established in detail based on the winding function method which verified by the finite element analysis (FEA). In addition, the mathematical model of the suspension force is derived based on the Maxwell tensor method. For comparison, a 10-slot/2-pole integer-slot concentrated-winding (ISCW) BPMSM with the same size of outer stator is designed, and the torque and suspension force of the two motors are computed, compared and analyzed. Finally, the dynamic experiments on a prototype are developed to validate the analyses. II. THE MMF OF ARMATURE AND ROTOR There are two groups of armature winding on the stator slot, one is for torque driving (pole pair P_M is 4) and another is for self-suspension (pole pair P_B is 3), as shown in fig.1 (a). The armature MMF is a function of the spatial windings distribution and the phase current, so it generated by suspension force current can be given by $f_s=\sum\sum\sum N_v I_s \cos v[\alpha-\theta(j-1)]*\sin m[\omega t-\theta P_B(j-1)]=5F_{mv}\sin(v\alpha\pm m\omega t)$, $v\pm mP_B=10k$ (k=0,1,2, …) (1) where $\theta = 2\pi/5$, $F_{mv} = N_v I_{sm}$, v and m are the space and current harmonic order. The armature MMF produced by the mth suspension force and torque current has $10k \pm mP_B$ and $10k \pm mP_M$ (k is an integer which makes v as positive integer) harmonic components, respectively. Such as 3rd, 7th, 13th... and 4th, 6th, 14th... generated by suspension force and torque fundamental current, respectively. The rotor MMF will mainly contain the fundamental (4th) components when the surface-mounted permanent magnets (SMPMs) on the rotor are optimized into sine-shape. III. PRINCIPLE OF SUSPENSION FORCE Fig.1 (b) shows that the air gap MMFs can be basically equivalent into 2 types: one is the synthesis $MMF_{r,t,4}$ generated by the 4th rotor and armature MMF, and another is the 3rd armature $MMF_{s,3}$ generated by the suspension force current. The balance of $MMF_{r,t,4}$ is broken by the $MMF_{s,3}$, which produces a constant suspension force $F_{3,4}$. Besides, the amplitude of 6th armature $MMF_{t,4}$ is only 1.5% of the $MMF_{r,t,4}$, so the suspension force $F_{6,7}$, $F_{13,14}$ and etc. can be negligible in this paper. The radial suspension force is the resultant force of controllable suspension force F_c and unilateral magnetic force F_u. In the case of rotor eccentricity, and according to the Maxwell stress tensor method, the x- and y-axis components of the resultant radial suspension force F_x and F_y can be expressed as $F_x=F_c+F_u=k_m(i_f i_{sd}+i_M i_{sq})+ k_e x$, $k_m=5\mu_0 lrN_1N_2k_mk_b/(2\pi\delta_0^2P_BP_M)$, $k_e=25\mu_0 lrN_1^2k_m^2i_{Mf}^2/(2\pi\delta_0^3P_M^2)$ (2) where N_{mf} and N_s are the turn numbers of equivalent torque windings and suspension force windings, respectively; k_{mw} and k_{bw} are the fundamental winding distribution coefficient of torque and suspension force windings, respectively; l and r represent the stator inner diameter and motor length, respectively. It can be seen from (2) that the controllable suspension force is linear with the suspension force current in unsaturated state. And, the unilateral magnetic force is linear with the eccentric displacement in a small range. So the rotor can be effectively pulled back to the center by controlling the suspension force current. IV. SIMULATION AND EXPERIMENTAL For comparison, a 10/2 ISCW BPMSM with the same size of outer stator is designed, the comparison results are shown in Fig. 2 at the same armature current. When the motor speed is 3000 rpm, the average torque and torque ripple of the five-phase 10/8 FSCW BPMSM are 4 times and 34% of the 10/2 ISCW BPMSM, respectively. And the average controllable suspension force and its ripple of the former are 101.5% and 88.7% of the latter which is in accordance with the mathematical mode. Note that the five-phase 10/8 FSCW BPMSM is easy to realize the stability control because of its suspension force ripple is smaller than the 10/2 ISCW BPMSM. At last, a prototype of the five-phase 10/8 FSCW BPMSM is designed and experiment to verify the feasibility of the proposed motor. V. CONCLUSION The five-phase BPMSM has higher torque density and lower torque ripple when compared to the traditional three-phase BPMSM. Besides, the performance of FSCW topology is superior to ISCW topology. And with the capability of the fault-tolerant performance, the proposed motor will have a wide prospect in the future.

H. Q. Zhu and H. Li, "Magnetic field equivalent current analysis-based radial force control for bearingless permanent magnet synchronous motors," *Energies*, 8(6) 4920-4942, (2015). J. Huang, B. N. Li, H. B. Jiang, *et al*, "Analysis and Control of Multiphase Permanent-Magnet Bearingless Motor With a Single Set of Half-Coiled Winding", *IEEE Trans. Ind. Electron.,* 61(7) 3137-3145, (2014). A. M. EL-Refaie, "Fractional-Slot Concentrated-Windings Synchronous Permanent Magnet Machines: Opportunities and Challenges", *IEEE Trans. Ind. Electron.,* 57(1) 107-121, (2010).

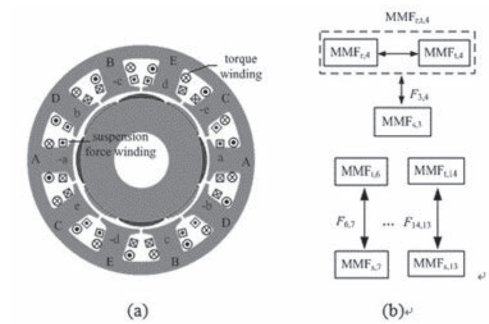

Fig. 1. (a) Structure of the five-phase 10/8 FSCW BPMSM (b) Interaction of air gap MMF between armature and rotor

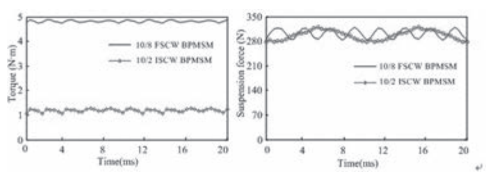

Fig. 2. Torque and suspension force comparison between the two motors

ER-07. Design and Control of Radial Homopolar Hybrid Magnetic Bearing.

A. Roshanzamir[1] and B. Kwon[1]

1. Electronic Systems Engineering, Hanyang University, Ansan-si, The Republic of Korea

1. Introduction Now a day the magnetic bearing system used in vacuum technology, machine tools, turbomachinery, artificial heart system etc. The use of magnetic bearing is rising day by day because of some advantages compared to mechanical bearing such as control capability, contactless, long life and has no lubrication [1,2]. In spite of the fact that the magnetic bearing has much superiority, it can make some weaknesses such as hysteresis loss, needing bias current and back up bearing to protect the rotor [3]. Magnetic bearings are categorized into three main structures such as Passive Magnetic Bearing(PMB), Active Magnetic Bearing(AMB) and the last but not the least is Hybrid Magnetic bearing(HMB). [4]. PMBs levitate rotor by using permanent magnets which mostly use as the backup bearing or axial bearing. Radial Magnetic bearings are classified by Heteropolar and Homopolar configurations. The Heteropolar Magnetic bearings have more applications because of easy produced and low cost, but if we need more efficiency Homopolar configuration must be used. The hysteresis loss, eddy current loss, rotational loss, and field variation can be reduced by using homopolar configuration bearings. HMBs use a permanent magnet to generate bias flux and electromagnet to control the flux to reduce copper loss and price of power amplifier [3,5]. In control point of view magnetic bearing is difficult to control because the system is nonlinear, time variant, multi input-multi output, and strongly unstable that's why we must use the robust controller. [6,7]. This paper proposed a new Radial Homopolar Hybrid Magnetic Bering(RHHMB). In conventional HMB used a permanent magnet to provide bias flux but they need backup bearing to protect the rotor. The proposed RHHMB uses the permanent magnet to generate bias flux and make system safe. Therefore, by using this topology the system does not need the radial backup bearing that causes decrease the size and the weight of the system. Some losses such as hysteresis loss can be reduced because of the Homopolar forming as well, it makes the system more stable and robustness especially in high-speed applications. In the homopolar model, the polarity of the magnetic field is the same as rotor rotating to reduce the hysteresis loss. In this paper, we will consider in radial suspension system by finding the mathematical formulation and design Sliding Mode Controller(SMC) for rotor position control. 2. Topology and working principle The new Radial Homopolar Hybrid Magnetic Bearing(RHHMB) is shown in figure 1. Top view of the RHHMB that shown in Figure1_a, illustrates that the system has four pairs of electromagnets and four pairs of permanent magnets which can produce magnetic force separately. Four pairs of permanent magnet used as radial backup bearing and bias flux generator. On the other hand, four pairs of the electromagnet can make control flux to levitate the rotor if the system has the disturbance. Sketch view in figure1_b can be shown the homopolar configuration and magnetic flux of the poles. If the system has disturbance in direction the air gap in the same axis will be decreased and magnetic force will be increased on the opposite side air gap and magnetic force will be increased and decreased respectively, on that time control flux will be provided by electromagnets to counteract the variation of magnetic force and keep the rotor in the central position. Each pair of permanent magnets make attractive force independently, regarding angle between each pair in the normal condition without disturbance all forces counteract each other therefore rotor place in the central position, the total force calculates $F_{x,y}=(F_1+F_2)-(F_3+F_4)$ where $F_{1\sim4}$ are first, second, third, and fourth pair of permanent magnet respectively. So, it can be used as radial backup bearing and can generate bias flux for radial axis as well. Both permanent magnet and electromagnet always generate the magnetic field in the same polarity as rotor rotating which can reduce hysteresis loss. 3. Mathematical Modelling & Control Design The mathematical formulation of the system is found by using the equivalent circuit of the system. Assume that the rotor moves in x-direction so: $F_x=(\mu_o A_{go})/2\ [N^2\ ((i_p^2/(L_{go}-x)^2 - (i_p)^2/(L_{go}+x)^2) + (\sqrt{2}\ (f_m^2)/(L_{go}-\sqrt{2}/2\ x)^2 + (\sqrt{2}\ (f_m)^2)/(L_{go}+\sqrt{2}/2\ x)^2]$ (1) Where F_x is the magnetic force in the x-direction, F_m is the magnetomotive force, x is displacement, μ_o, A_{go}, i_p, L_{go}, and N are vacuum permeability, cross-section area, control current, air gap and number of turn respectively. By using Taylor series for linearization: $F_{tot}=K_r\ X+K_i\ i_p$ (2) Since that the magnetic bearing is nonlinear system and inherently unstable we should design a robust nonlinear control system. In this paper, Sliding Mode Controller(SMC) has used the controller for the RHHMB system which is four degrees of freedom. We suppose that the system in vertical condition and has two RHHMB as upper and lower bearings. Rotor displacement by using SMC for the system is shown in figure 2.

[1] Schweitzer, Gerhard, Alfons Traxler, and Hannes Bleuler. Magnetlager: Grundlagen, Eigenschaften und Anwendungen berührungsfreier, elektromagnetischer Lager.Springer-Verlag,2013. [2] Yoon, S. Y. "Control of Surge in Centrifugal Compressors by Active Magnetic Bearings, Advances in Industrial Control." (2013). [3] Bleuler, Hannes, et al. Magnetic bearings: theory, design, and application to rotating machinery. Springer Science & Business Media, 2009. [4] Xie, Zhiyi Huangqiu Zhu, and Yukun Sun. "Structure and control of AC-DC three-degree-of-freedom hybrid magnetic bearing." Electrical Machines and Systems, 2005. ICEMS 2005. Proceedings of the Eighth International Conference on. Vol. 3. IEEE, 2005. [5] Zhang, Weiyu, and Huangqiu Zhu. "Control system design for a five-degree-of-freedom electrospindle supported with AC hybrid magnetic bearings." IEEE/ASME Transactions on Mechatronics 20.5 (2015): 2525-2537. [6] Slotine, Jean-Jacques E., and Weiping Li. Applied nonlinear control. Vol. 199. No. 1. Englewood Cliffs, NJ: Prentice hall,1991. [7] Lin, F-J., S-Y. Chen, and M-S. Huang. "Intelligent double integral sliding-mode control for five-degree-of-freedom active magnetic bearing system. " IET control Theory & applications5.11 (2011): 1287-1303.

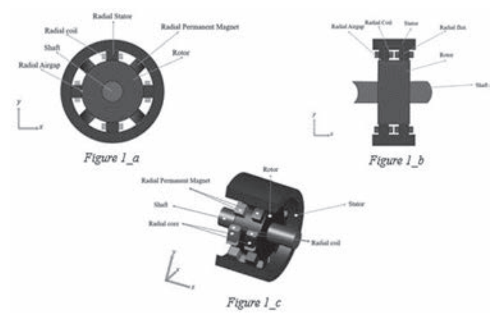

Fig. 1. Proposed RHHMB a)top view b)Scetck view c)3D model

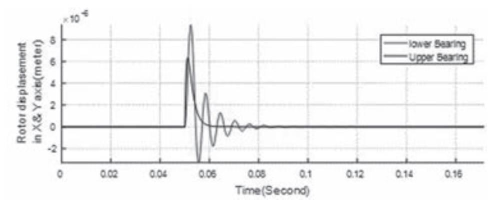

Fig. 2. Rotor displacement in radial position with 100N disturbance of proposed RHHMB

ER-08. Study on propulsion force characteristics by improving distance between the coils and excitation method in permanent magnet-HTS hybrid magnetically levitated conveyance system.

T. Inui[1], Y. Takaki[1], H. Sasaki[1] and S. Ohashi[1]
1. Electrical and Electronic Engineering, Kansai University, Suita, Japan

Conventional conveyance systems using wheels and belt conveyors occur friction and wear at the contact portions. And vibration, noise and dust occur. In order to solve these problems, a noncontact conveyance system has been developed. In this research, a permanent magnet repulsion levitation system and superconducting magnetic levitation system are adopted. The permanent magnet repulsion levitation system cause a large levitating force at the loading part. Superconducting magnetic levitation system cause a stable levitation at the carrier body. There is no influence of large load weight on the levitation of the carrier because the loading part and the carrier body are connected by the linear way. The carrier moves above the magnetic rail. The coils are installed on magnetic rail, and the magnetic field gradient is generated by the exciting coils. The carrier is propelled by the magnetic field gradient. By increasing the flux of the coil behind the HTS in the propulsion direction and reducing the flux of the HTS in the propulsion direction, magnetic field gradient is generated and the carrier propels. The coil pitch is optimized and propulsion force is examined by adding the exciting coils [1] ~ [4]. Fig.1 shows the experimental device. The change of the magnetic field gradient is analyzed when changing the coil pitch by 5mm in the range of 25~50mm with the magnetic analysis software JMAG-Designer. Also, the propulsion force is measured. Experimental condition is as follows; current of the coil I=2.0A and levitation gap g=23mm. The propulsion force is measured at interval of 5mm in the range of -25~25mm. The center of the two coils is defined as x=0. The propulsion force is measured by the load cell installed in front of the carrier. From the analytical result, when the coil pitch is changed, the position of peak value of the flux density due to the magnetization and demagnetization on the magnetic rail changes, but the crest value of the magnetic field gradient is not changed. In the range of coil pitch 40~50mm, the excitation coils are separated. The flat section is formed between the positive peak value and the negative one in the magnetic gradient field. Thus, in the z-axis direction, the surface flux density of the HTS is the strongest at the center. Fig.2 (a) shows the average value and the maximum value of the propulsion force at each the coil pitch. At the coil pitch 50mm, both the average propulsion force and the maximum propulsion force are largest. As a result, the optimum value of the coil pitch under the HTS is 50mm. Center of the HTS keeps the largest flux from HTS. The coils are arranged on the magnetic rail at the coil pitch 50mm, as the diameter of the coil used in this research is 22mm, only the odd number coil in Fig.1 (b) will be installed. Thus, the excitation switching interval becomes large. Thus, as shown in Fig.1 (b), coils are installed at intervals of 25mm. At first, No.1 coil and No.3 coil in Fig.1 (b) are excited. Next, their excitation is stopped, and No.2 coil and No.4 coil are excited. Then their excitation is stopped, and No.3 coil and No.5 coil are excited. In this way, the coils to be excited are switched, and coil pitch 50mm is realized. Next, the case of exciting the coil between the two excited coils is considered. No.1 coil shown in Fig.1 (b) is magnetized, No.2 and No.3 coils are demagnetized. The flux density in the y-axis direction at that time is analyzed with the magnetic analysis software JMAG-Designer. In the range of x=-20~20, the flux density in the y-axis direction in three excitation coil case is smaller than that in two excitation coil case. As the magnetic rail is composed of Halbach array, the y-axis direction flux density is strong on the magnetic rail. Therefore, the change of the flux due to the excitation of the coil tends to occur in the y-axis direction. The propulsion force is compared when exciting two coils at intervals of 50mm with the propulsion force when three coils are excited at intervals of 25mm. No.1 coil in Fig.1 (b) is magnetized, No.2 and No.3 coils are demagnetized. The load weight 0, 19.6, 39.2, and 58.8N is placed on the carrier. Fig.2 (b) shows the maximum propulsion force for each load weight. Larger propulsion force is given when No.1, No.2 and No.3 coil in Fig.1 (b) are excited at all load weight. This is because the range of the magnetic field gradient is increased by adding a coil to be excited. In the case of three coils excitation, as the change of flux density in the y-axis direction is large, it is necessary to consider the magnetic gradient field in the y-axis direction. In the case of two coils excitation, it is suitable to install the coils at intervals of 50mm so as to catch the center of the HTS. In addition, in the case of three coils excitation the propulsion force increases by generating a gradient in the flux density in the y-axis direction.

[1] F. C. Moon, Superconducting levitation, John Wiley & Sons, New York, 1994. [2] J. Hull, M. Murakami, "Applications of bulk high-temperature Superconductors", *Proc. of IEEE*, vol.92, 2004, pp1705-1718. [3] S. Ohashi, D. Dodo, "Influence of the Propulsion System on the Levitation Characteristics of the HTSC-Permanent Magnet Hybrid Magnetically Levitated System", *IEEE Transactions on Applied. Superconductivity*. vol.17, no.2, 2007, pp2083-2086. [4] Y. Takaki, T. Sumida, S. Ohashi, "Improvement of Velocity Control in the Permanent Magnet-HTS Hybrid Magnetically Levitated Conveyance System", *IEEE Region 10 Conference (TENCON)*, 2016, pp3105-3108

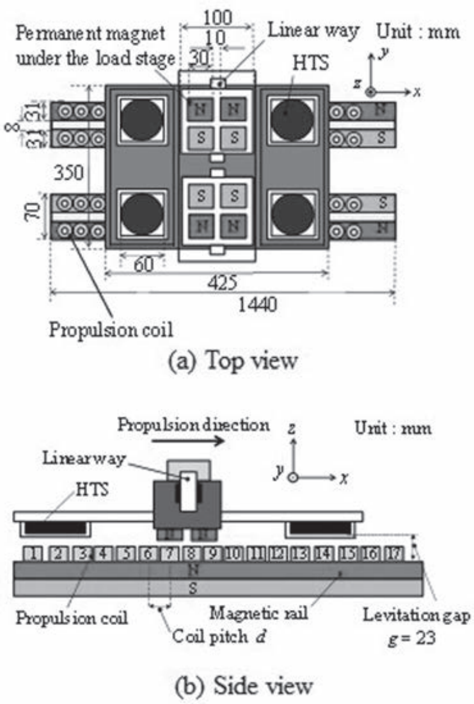

Fig. 1. The experimental device

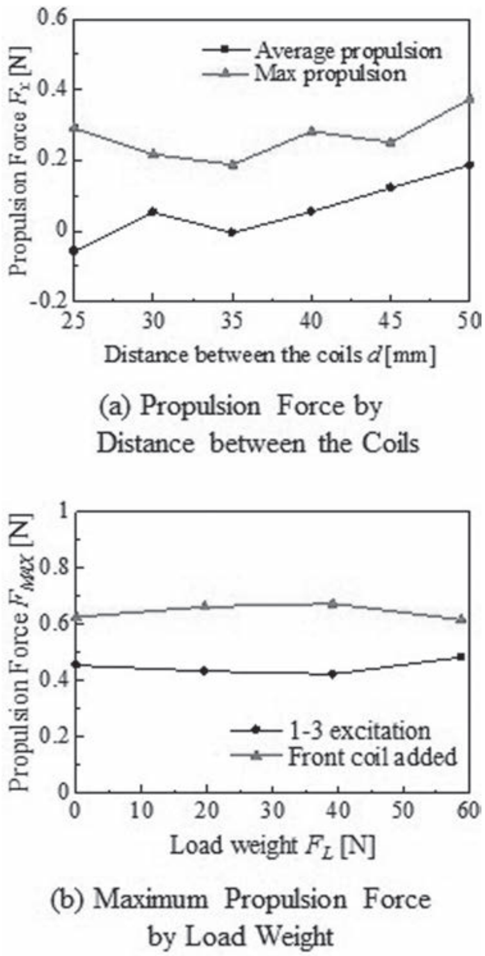

(a) Propulsion Force by Distance between the Coils

(b) Maximum Propulsion Force by Load Weight

Fig. 2. Results

ER-09. Novel Heteropolar Hybrid Radial Magnetic Bearing with Double-Layer Stator for Flywheel Energy Storage System.

W. Xu[1], R. Zhu[1], C. Ye[1] and J. Zhu[2]
1. School of electrical and Electronic Engineering, Huazhong University of Science and Technology, Wuhan, China; 2. Faculty of Engineering and Information Technology, University of Technology Sydney, Sydney, NSW, Australia

Abstract—In this paper, one novel heteropolar radial hybrid magnetic bearing (HRHMB) with double-layer stator is proposed for flywheel energy storage system (FESS). Firstly, its topology and working principle are introduced in details. Then, some main dimension parameters are optimized to improve its suspension performance based on the equivalent magnetic circuit (EMC) and three-dimension finite element analysis (3-D FEA). Finally, the comparison of main performance indexes between the proposed HRHMB and conventional one under the same constraints is made, such as displacement stiffness, current stiffness and iron loss. It indicates that the novel HRHMB has smaller displacement stiffness, larger current stiffness and lower rotor iron loss, which is more suitable for high-speed FESS. *Index Terms*—Heteropolar radial hybrid magnetic bearing (HRHMB), double-layer stator, flywheel energy storage system (FESS), equivalent magnetic circuit (EMC), three-dimension finite element analysis (3-D FEA). I.Introduction Traditional heteropolar radial hybrid magnetic bearing (HRHMB) with eight poles has been widely applied in high-speed applications, such as flywheel energy storage system (FESS), because of its simple structure, low power loss, high critical speed, *etc*. [1]. However, this topology suffers large displacement stiffness, magnetic coupling, and non-negligible rotor iron loss, which are harmful to its stable suspension and cooling [2]. With the development of magnetic bearing technology, many studies in the new structures of HRHMB have been conducted to improve its performances. Recently, one HRHMB with only four active magnetic poles, which has less alternating frequency of magnetic field and low power loss, has been studied in [3]. However, the introducing of second air gap in X-axis would increase the needed control current and thus reduce its current stiffness. To overcome these drawbacks, one novel HRHMB with double-layer stator is proposed in this paper, whose pole number is reduced from eight to four without introducing the second air gap. Such improvement could reduce the displacement stiffness, rotor iron loss, and magnetic coupling, while the control flux and current are unaffected. Thus, the novel HRHMB is especially suitable for high-speed and low-loss situations, such as the FESS. II.Configuration and Working Principle The configuration of the proposed HRHMB is shown in Fig. 1. From this figure, it can be seen that the stator consists of two parts, namely, X (upper) and Y (lower) stators. Each layer of the stator includes two poles, which is distributed in one dimension. Meanwhile, each pole is wounded by a coil, which is used to produce the control flux. Four permanent magnets (PMs) are located between X and Y stator teeth, and X and Y stators are separated by PMs and PM ring. The bias-flux consists of two parts: one part is closed through PMs, X and Y stator teeth, air gap and rotor, while another part is closed through PM ring, X and Y stator, air gap and rotor. And the control-flux is closed through X/Y stator, air gap and rotor respectively. For limited space, more details will be given in the full paper. III.Electromagnetic Optimization In this section, some refinement specifications for the proposed HRHMB are given. Moreover, the HRHMB are optimized to improve its suspension performance based on EMC and 3-D FEA. More details will be given in the full text. IV.Performance Comparison A.Displacement Stiffness and Current Stiffness The force-displacement and force-current curves for both machines are shown in Fig. 2(a) and Fig. 2(b). From this figure, the stiffness is obtained by calculating the slope of curve. Compared with the conventional HRHMB, the displacement stiffness for novel HRHMB can be reduced from 1.36 to 0.87 N/μm and the current stiffness for novel HRHMB can be increased from 179.2 to 218.5 N/A with the equal coil turns. B.Iron Losses Reducing iron losses is vital to FESS, especially while it is in standby state frequently. As shown in Fig. 2(c) and Fig. 2(d), the rotor iron losses distribution under no load for the two HRHMBs are analyzed at rated speed 20,000 rpm. It can be seen that the rotor iron loss is nearly distributed around the edge of the magnetic pole where magnetic field occurs fluctuation. Besides, the rotor iron losses for Fig. 2(c) and Fig. 2(d) are calculated to be 22 and 5.9 W, respectively. Compared with conventional HRHMB, the rotor iron losses of the novel HRHMB are reduced to 26.8%. V.Conclusion In this paper, one novel HRHMB with double-layer stator has been proposed. In comparison with conventional eight-pole HRHMB, the novel HRHMB with double-layer stator exhibits several merits, as summarized below: 1) In the novel HRHMB, the displacement stiffness (k_d=0.87 N/μm) can be reduced to 64% from that of the conventional HRHMB. In addition, its current stiffness (k_i=218.5 N/A) can be enhanced by 21.9% due to the large area of the magnetic pole. 2) The alternating frequency of bias magnetic flux of the novel HRHMB is decreased from 8 to 4 times, which would greatly reduce the rotor iron loss.

[1] Y. Okada, H. Koyanayi, and K. Kakihara, "New concept of miracle magnetic bearings," in *Proc. 9th Int. Symp. Magnetic Bearings*, Lexington, KY, Aug. 2004, pp. 89–95. [2] G. Schweitzer and E. Maslen, *Magnetic Bearings-Theory, Design, and Application to Rotating Machinery*. Berlin, Germany: Springer Verlag, 2009. [3] R. Z. Zhu, W. Xu, C. Y. Ye, and J. G. Zhu, "Novel heteropolar radial hybrid magnetic bearing with low rotor core loss," *IEEE Trans. Magn*., vol. 53, no. 11, Nov. 2017, Art. ID. 8210305.

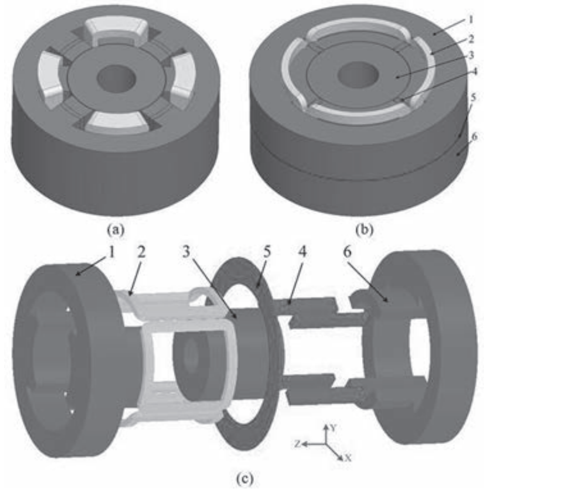

Fig. 1. Structures for magnetic bearings. (a). Conventional HRHMB. (b). Novel HRHMB. (c). Exploded view of the novel HRHMB components. 1-X stator (upper stator), 2-control coil, 3-rotor, 4-permanent magnet, 5-permanent magnet ring, 6-Y stator (lower stator).

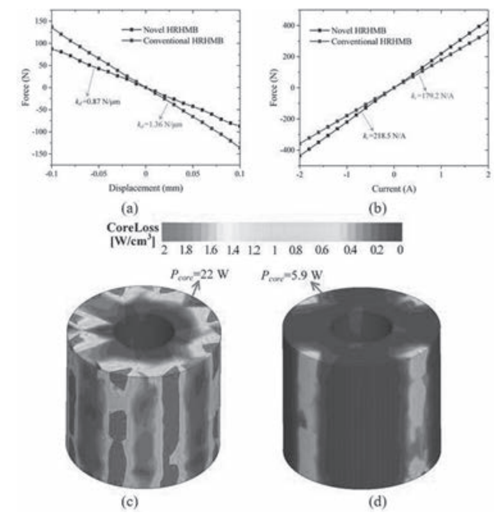

Fig. 2. Performance comparison for two HRHMBs. (a). Force-displacement curves. (b). Force-current curves. (c). Rotor iron loss for conventional HRHMB. (d). Rotor iron loss for novel HRHMB.

ER-10. Exploration of a floating magnet rotor in diamagnetic levitation system.

K. Zhang[1], *Y. Su*[1], J. Gao[1], Z. Duan[2] and J. Ding[1]

1. School of Mechanical Engineering, Zhengzhou University, Zhengzhou, China; 2. School of Physical Engineering, Zhengzhou university, Zhengzhou, China

Abstract: This paper presents a floating magnet rotor with a toothed shape in diamagnetic levitation system. The floating rotor is levitated between two pyrolytic graphite sheets to allow for friction-free rotation. The rotor has a special shape with three notches which are evenly distributed on circle direction. The revolution of the rotor is demonstrated by applying a pulsing airflow with a mechatronics cylinder, showing pulse actuation with the minimum speed of 8 r/min. The promising results suggest potential applications of the mechanism toward frictionless sensors and actuators INTRODUCTION: In 1939, the diamagnetic levitation was firstly realized by Braunbek[1] with the levitation of small pieces of graphite and bismuth in a non-uniform strong electromagnetic field. At present, the diamagnetism of the pyrolytic graphite [2] is the strongest of all materials. In a diamagnetic levitation system, the levitated object does not contact with any bodies. In other words, the levitated object is free-friction when the object moves, which is the most valuable point of the diamagnetic levitation system. Diamagnetic levitation system can be used by for sensors [3], actuators[4] and energy harvester[5]. Clara[6] presented an advanced device based on a diamagnetically stabilized levitated permanent magnet for viscosity and density measurements. Gao and Zhang[7] proposed a novel bistable vibration energy harvester using the diamagnetic levitation mechanism. In this paper, a diamagnetic levitation system with a specially shaped rotor was studied. STRUCTURE OF THE DIAMAGNETIC LEVITATION SYSTEM: The diamagnetic levitation system consists of a shell, a lifting magnet (type N35), two pyrolytic graphite (PG) sheets and a floating magnet rotor (type N35) with three teeth, as shown in Fig. 1(a). The rotor has a special shape with three notches which are evenly distributed on circle direction, as shown in Fig. 1(b). The rotor is freely levitated between the two pyrolytic graphite sheets. The gap spacing produced by the levitation serves essentially as an air bearing of the rotor. Because the lifting magnet is cylindrical, the magnetic field distribution is horizontally symmetrical. In this magnetic field, the rotor will be reached to the center position automatically. Two flow-guiding holes are set on the wall of the shell, one is the air inlet, and the other one is the air outlet. The height of the two holes is equal to the levitation height of the rotor. When the airflow enters the cavity through the air inlet, the rotor will be driven by the airflow and rotate around the centerline of the lifting magnet. EXPERIMENT: To explore the rotational behavior of the levitation rotor, a simple experiment was implemented. In the experiment, a 10 ml syringe was used as an air pump, and the syringe piston was fixed on the tip end of the shaft of a mechatronics cylinder (SCN5, Dyadic systems co., Ltd) which consists of a rotary-linear motion transfer mechanism, a stepper motor, an encoder, and a servo controller. By controlling the mechatronics cylinder, the shaft can do the reciprocating linear motion. So pulse airflow will be produced by the syringe. A hose with an inner diameter of 1.5mm was attached to the syringe. One end of the hose positioned close to the rotor. The stroke of the reciprocating linear motion of the shaft was set to 60mm. With the reciprocating linear motion of the syringe piston, the rotor will be driven by airflow. The speed of the rotor was measured with a laser speed sensor (ERS-1, Expert Technology Co., Ltd). The relationship between the velocity of the syringe piston (v) and the rotating speed of the rotor (ω) is shown in Fig. 2. When v is smaller than 50mm/s, the rotor cannot be driven; when v is approximately 50mm/s, the rotor simply waggled between the two graphite sheets without producing rotational motions; When v is larger than 50mm/s, the rotor is driven to rotate. If the airflow is continuous, the rotor can be driven by a smaller flowrate. When v is approximately 450mm/s, the increment of the speeds of the floating rotor gradually reduced. Since the maximum velocity of the mechatronics cylinder is 450 mm/s, only 9 groups of data tested were obtained. CONCLUSIONS: The basic actuating mechanism of a magnet rotor diamagnetically levitated was explored in this paper. The feasibility of the floating magnet rotor was verified, and the rotation characteristic of the floating rotor was studied by experiment. The minimum speed of the rotor was 8 r/min when the velocity of the mechatronics cylinder was 50mm/s, which is the minimum velocity that can drive the rotor to rotate. In the future, some more accurate experiments with continuous airflow and a high precision flowmeter will be carried out to further understand the characteristics of the floating magnet rotor. The floating rotor in diamagnetic levitation system can be used as sensors and actuators. This work is supported by the National Natural Science Foundation of China under grant no.51475436 and the Henan Province Key Project on Science and Technologies under grant no.152102210042.

[1] W.Braunbek,Z. PhyS.,112,764 (1939). [2] D.B. Fischbach, Phys. Rev., 123, 1613(1961). [3] Y. Shimokawa, Y. Matsuura and T. Hirano, Rev. Sci. Instrum. 87, 12510 (2016). [4] W. Hilber, B. Jakoby, IEEE Sens. J., 13,2785 (2013). [5] Y. Su, K. Zhang and Z. Ye, Int. J. Appl. Electrom.,55,113 (2017). [6] S. Clara, H. Antlinger, and A. Abdallah, Sensor. Actuat. A: Phys., 248, 46 (2016). [7] Q. Gao, W. Zhang, and H.Zou,IEEE T. Magn, 53,1 (2017).

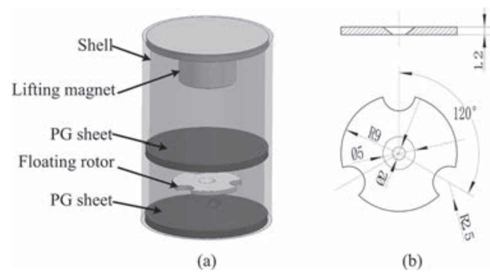

Fig. 1. (a) Structure of the diamagnetic levitation system, and (b) Schematic of the floating magnet rotor

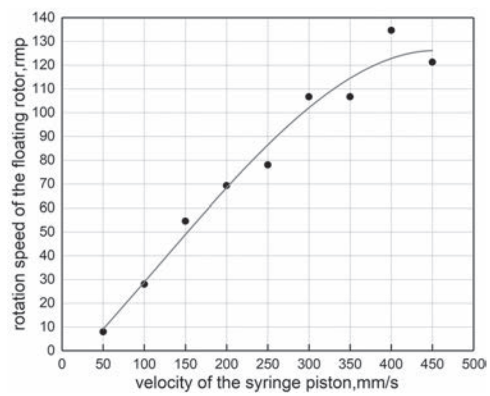

Fig. 2. Relationship between the velocity of the syringe piston and the speed of the rotor

ER-11. Design and analysis of a centripetal force type-magnetic bearing for a flywheel battery system.

W. Zhang[1], L. Cheng[1] and H. Yang[1]
1. Jiangsu University, Zhenjiang, China

Introduction Flywheel battery, as a new energy storage device in recent years, it has the characteristics of high current charge-discharge capability, very short charging-discharging time, good environment adaptation, high energy conversion efficiency and long cycle life[1-2]. Flywheel battery technology is relatively mature after years of development, including the applications in electric vehicle systems. For a vehicular magnetically flywheel battery, the gyroscopic effect can be caused by the different driving conditions and the road conditions of the vehicle. Therefore, the flywheel battery has very strict requirements for bearings. The most popular magnetic bearings today are the magnetic bearings with cylinder structures, which have many industrial applications [3-4]. However, an inevitable unbalanced magnetic pull parallel (The pull can be considered as a disturbance force) to the axis of the rotor will be produced when the rotor is deflected. The disturbance force and the resultant disturbance torque to the rotor will accelerate the gyroscopic effect and it is very bad for the stability control of the flywheel battery. In this paper, a novel centripetal force type magnetic bearing (CFT-MB) for a flywheel battery system is proposed. Whether the rotor is shifted or deflected, the magnetic force will point to the centre of the rotor because of the centripetal force, which can substantially reduce the interference force and torque. New Topology As shown in Figure 1, the CFT-MB is a radial magnetic bearing(2 DOF CFT-MB) and it is made up of two mirror symmetrical stators with three poles, six radial control coils, a rotor, some aluminum rings or blocks for flux-insulation (an outer aluminum ring, a inner aluminum ring, three central aluminum blocks), and three permanent magnets. The overall topology of the CFT-MB is a section body of structure of spherical. There are three spherical envelopes in a bearing. They are shell envelope, poles envelope and rotor envelope. Six stator poles are spherical structure and their spherical points are coincided, which constitutes a spherical envelope. The spherical rotor is located in the in the centre of the spherical envelope formed by the stator magnetic poles. The center of the rotor is coincident with the centre of the spherical enveloping surface formed by the stator poles, which forms the spherical gas gap between them. Stators and rotor are made of stacked silicon steel sheets. There are three pieces of non-complete axial-magnetized permanent magnets distributed on the circumference within 120 degrees due to the spherical envelopes. Each piece of permanent magnet is sandwiched between two mirror symmetrical poles. The three central aluminum blocks are also distributed on the circumference within 120 degrees, which is a complementary way of placement with permanent magnet to make a full ring. The material of permanent magnet is Neodymium-iron-boron (Nd-Fe-B). Results In order to verify the proposed flywheel, the finite element method is used to analyze the electromagnetic characteristics of the proposed magnetic bearing. As shown in Fig.2, when the rotor reaches its displacement of 0.05mm in x direction and rotation of 0.5 degrees around the x axis, the interference torque of the cylindrical magnetic bearing-rotor is -3.5047mN.m, the interference torque of spherical magnetic bearing-rotor is –1.59830mN.m. The interference torque produced by cylindrical magnetic bearing-rotor is as much as 2.2 times of that of spherical magnetic bearing-rotor for the complex motion. The magnetic pull of the cylindrical magnetic bearing-rotor is as much as 3.5 times of that of spherical magnetic bearing-rotor for the complex motion. The tests results have shown that the final stationary values of magnetic pull and even torque of the CFT-MB are far more advanced than that of the cylindrical magnetic bearing-rotor, which show the superior performance of the CFT-MB.

[1]X. Zhang, J. Q. Yang, "A robust flywheel energy storage system discharge strategy for wide speed range operation," IEEE Trans. Ind. Electron., vol. 64, no.10, pp.7862-7873, Apr. 2017. [2]J. Q. Tang, Z. J. Liu, B. Peng, et al, "Control of rotor's vernier-gimballing for a magnetically suspended flywheel," IEEE Trans. Ind. Electron., vol.64, no.4, pp.2972-2981, Dec. 2017. [3]W. Y. Zhang, H. Q. Zhu, "Radial magnetic bearings: an overview," Results Phys., vol. 7: pp.3756-3766, 2017. [4]W. Y. Zhang, H. Q. Zhu, Z. B. Yang, et al, "Nonlinear model analysis and "switching model" of AC-DC three-degree of freedom hybrid magnetic bearing," IEEE/ASME Trans. Mechatronics,vol.21,no.2,pp.1102-1115, Aug. 2016.

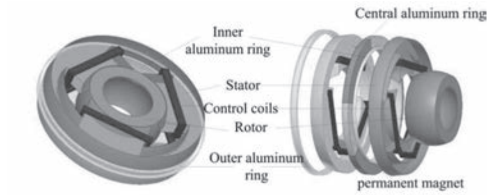

Fig. 1. Assembling structure and exploded view of CFT-MB components

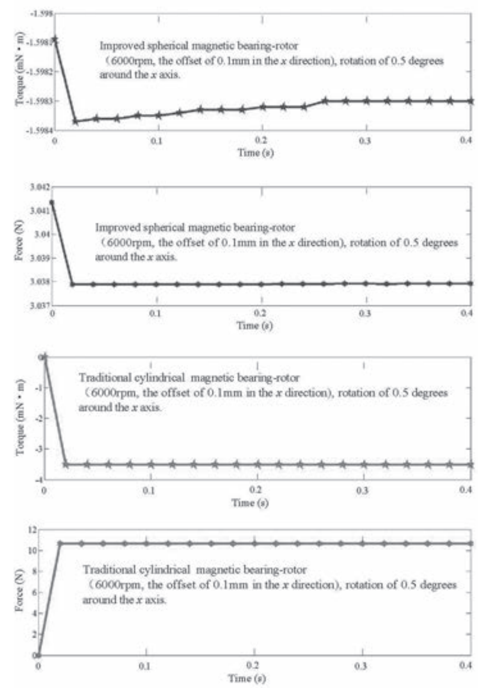

Fig. 2. Torque and force analysis on complex motion

ER-12. Proposal of New Superconducting Magnetic Bearing Using High Tc Superconducting Bulk and Coil.

M. Komori[1], K. Yamanaka[1], K. Asami[1] and N. Sakai[1]
1. Kyushu Institute of Technology, Kitakyushu, Japan

1. INTRODUCTION Recently, magnetic levitation techniques have been developed for various fields such as energy storage flywheels[1] and magnetically levitated vehicles[2]. The magnetic levitation techniques are very useful because of friction free, energy-loss free, etc. Thus, there are many reports about levitation techniques using high critical temperature (*T*c) superconducting magnetic bearings (SMBs) [3]-[5]. SMBs are composed of superconducting (SC) bulk and permanent magnet (PM). These SMBs are based on pinning forces between SC bulk and PM. In this paper, new SMBs composed of SC bulk, SC coil and PM are proposed. *2. SC BEARING AND EXPERIMENTAL METHOD* *2.1 SC bearings* In this paper, we propose two types SC bearings Type-I and Type-II. Both SC bearings are composed of SC bulk, SC coil and PM. The levitation is performed using pinning force between SC bulk and PM. The schematic illustration of the SC bearing Type-I is shown in Fig.1-1. A neodymium (NdFeB) PM with a diameter of 27 mm and a thickness of 3.4 mm is used. The SC bulk ($Dy_1Ba_2Cu_3O_X$, J_c=3 $\times 10^8$ A/m^2 at 77 K and 1.0 T) is 44 mm in diameter and 7.5 mm in thickness. The yttrium type SC coil (I_c=150A) is 35mm in inner diameter, 38mm in outer diameter and 5mm in thickness with four turns. *2.2 Experiment method* After the PM is put on a mechanical support, the SC bulk and the SC coil are field-cooled using liquid nitrogen. Then, the PM is levitated by pinning force after the mechanical support is removed. In order to study the levitation characteristics by pinning force, impulse responses for the levitated PM are performed in the vertical direction as shown in Fig.1-2. Impulse forces are applied to the PM using a small hammer (D1.8mm xL33.5mm, 0.73g) made of brass. Then, damped free vibrations of levitated PM are measured using a laser displacement sensor. Supposing that the SC bearing is represented by a mechanical model with a spring and a damper, stiffness *k* and damping coefficient *c* are calculated using impulse responses. *3. EXPERIMENTAL RESULTS AND DISCUSSIONS* In the experiments, the SC bearing with SC coil is compared with the SC bearing without SC coil. The distance between SC bulk and PM is changed in the range of 7mm, 8mm, 9mm. At each distance, impulse responses for the SC bearing without SC coil are performed, and the results are shown in Fig.1-4. The displacement amplitude for each distance of 7mm, 8mm, 9mm decreases gradually as the time increases. Especially, It is found that the displacement amplitude at a distance 7mm decays to zero within 2.0s. Impulse responses for the SC bearing with SC coil are shown in Fig.1-5. The displacement amplitude for each distance of 7mm, 8mm, 9mm decreases rapidly. Especially, the amplitude at a distance 7mm decays to zero within 0.3s. The damping for the SC bearing with SC coil in Fig.1-5 is larger than that in Fig.1-4. Stiffness and damping coefficient are calculated using the damped free vibration curves in Figs.1-4 and 1-5. Fig.2-1 shows the relationships between (a) stiffness and distance and between (b) damping coefficient and distance for three cases. In the figures, white circle, black circle and triangle show SC bearing without coil, SC bearing with coil and coil effect, respectively. The coil effect means the difference between SC bearing without coil and SC bearing with coil. Fig.2-1(a) shows that the stiffness with coil and that without coil decrease as distance increases. The coil effect on damping coefficient is not so large. Fig.2-1(b) shows that the damping coefficient with coil and that without coil is almost constant as the distance increases. Thus the coil effect on damping coefficient is not so large. As a result, the SC bearing Type-I is not effective on the damping coefficient. As shown in Fig.2-2 the SC bearing Type-II is proposed to compare with the SC bearing Type-I. The SC bearing Type-II is composed of a SC bulk with 24 mm in diameter and 10 mm in thickness, a SC coil and a PM. The SC coil and the PM are the same as the SC bearing Type-I. Impulse responses for the SC bearing Type-II are performed in the range of 7 mm, 8 mm and 9 mm. The experimental method is the same as that for the SC bearing Type-I. The experimental results for the SC bearing Type-II show the relationships between (a) stiffness and distance and between (b) damping coefficient and distance as shown in Fig.2-3. In the figures, white circle, black circle and triangle show SC bearing without coil, SC bearing with coil and coil effect, respectively. Fig.2-3(a) shows that the stiffness with coil and that without coil decreases as distance increases. The coil effect (triangle) on stiffness is rather large compared with Fig.2-1(a). Fig.2-3(b) shows that the damping coefficients with coil and that without coil decrease as the distance increases. The damping coefficient with coil is very larger than that without coil. As a result, the SC bearing Type-II is more effective on the damping coefficient than the SC bearing Type-I. *4. CONCLUSION* In order to compare the SC bearings Type-I and Type-II, impulse responses are performed. Then, damped free vibration curves for impulse responses are observed. The SC coil is effective for the SC bearings Type-II. The damping coefficient for the SC bearing Type-II is larger than the Type-I. From the experimental results, both stiffness and damping coefficient for the SC bearing Type-II are improved compared with the Type-I.

[1] K. Murakami, M. Komori and H. Mitsuda, Flywheel Energy Storage System Using Permanent Magnetic Bearing and Superconducting Magnetic Bearing, IEEE Transactions on Applied Superconductivity, vol. 17, pp. 2146 - 2149, 2007. [2] M. Yamaji, H. Nakashima, Superconducting Magnet for Magnetically Levitated Vehicle, Procs of the 1st International Symposium on Superconductivity (ISS '88), (August, 1988, Nagoya) pp. 71-76 [3] Moon F. C, Chang P. -Z. High-speed rotation of magnets on high Tc superconducting bearings. Applied Physics Letters, vol.56, no.4, pp.397-399, 1990 [4] Komori M, Kitamura T. A new type of Superconducting journal bearing using high Tc superconductors. Cryogenics, vol.32, no.7, pp. 628-633, 1992. [5] J. R. Hull, T. M. Mulcahy, K. L. Uherka, R. G. Abboud, Low rotational drag in high-temperature superconducting bearings

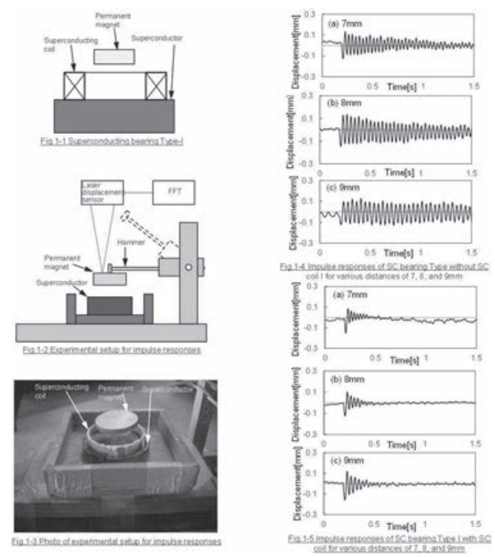

Fig. 1. The figure consists of Fig.1-1, Fig.1-2, Fig.1-3, Fig.1-4, Fig.1-5.

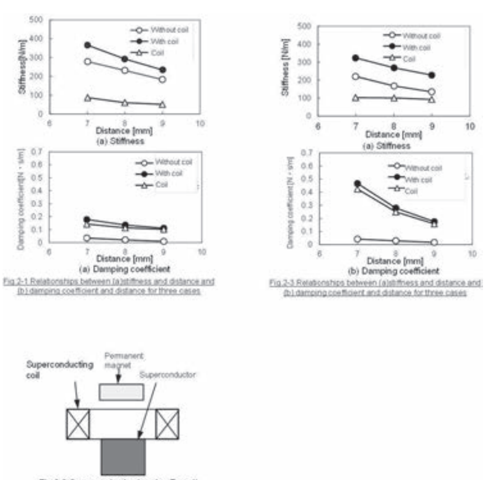

Fig. 2. The figure consists of Fig. 2. -1, Fig. 2. -2, Fig. 2. -3.

ER-13. Design and Analysis of a Magnetic Levitation Voice Coil Actuator for Multi-Degree-of-Freedom High-Precision Positioning System.

Y. Zhou[1], B. Kou[1], H. Zhang[1], F. Xing[1] and X. Yang[1]

1. School of Electrical Engineering and Automation, Harbin Institute of Technology, Harbin, China

I. INTRODUCTION Multi-degree-of-freedom high-precision positioning system (MHPS) is one of the key technologies in many advanced industrial applications [1-2]. In general, the MHPS can be realized by three solutions: stacking linear actuators, planar actuators [3-4], and combining coarse positioning module (CPM) and fine positioning module (FPM) [5-11]. Benefiting from the two-module structure, the third solution becomes a widely adopted scheme, which can simultaneously satisfy the requirements of long stroke and high accuracy. Among various FPMs, the magnetic levitation fine positioning module (MLFPM) is considered to be the state of the art because of its feature of no mechanical contact. In the MLFPM, a stage that integrates multiple actuators and sensors is often adopted, in which the actuator is an electromagnet [7-8], or a voice coil actuator (VCA) [9-11]. As a key component, the performance of actuators strongly determines the MLFPM's positioning ability. Compared with single-degree-of-freedom applications, the MLFPM has special technical requirements for the actuators because of its multi-degree-of-freedom motion. When an actuator works in multi-degree-of-freedom, not only its output force in the driven direction will be influenced by the movements in the other directions, but also it will produce parasitic force and torque in the other directions, which will reduce the MLFPM's performance and increase the control system's complexity [12]. Therefore, the actuators used in MLFPMs should be specially designed to be able to output a force which is independent from position, and it is named as force uniformity here. In this paper, we put forward a novel magnetic levitation voice coil actuator using rhombus magnet array (RMA-MLVCA). With the specially designed magnet array, the proposed RMA-MLVCA has the advantage of excellent force uniformity, which makes it suitable for multi-degree-of-freedom applications. II. BASIC STRUCTURE AND OPERATING PRINCIPLE The proposed RMA-MLVCA consists of two components, i.e., stator, and mover, as shown in Fig. 1(a). The stator consists of two rectangular stator coils and a stator frame. The mover consists of a rhombus magnet array and a mover frame. The rhombus magnet array consists of four cubic mover magnets which are arranged on the four edges of a rhombus, and the magnetization of mover magnets are shown as arrows in Fig. 1(b). The RMA-MLVCA works based on the Lorenz force law. When the mover moves around the initial position, the horizontal component of the magnetic field generated by the magnet array interacts with the current in the stator coils, by which the force and torque will be produced. The difference between the RMA-MLVCA and conventional VCAs is that the magnetic field in the RMA-MLVCA is a cluster of hyperbolas. This is the most important reason why the RMA-MLVCA can achieve excellent force uniformity, and it is discussed in Section III. In addition, the MLFPM's load stage will be levitated and positioned using at least six RMA-MLVCAs, as shown in Fig. 1(c). To determine the force and torque of the RMA-MLVCA, the magnetic flux density distribution is required. Considering the six-degree-of-freedom motion, a global coordinate system and four local coordinate systems are defined first. Then, the magnetic field generated by one mover magnet is derived in the corresponding local coordinate system with an equivalent current model, as shown in Fig. 1(d) and converted to the expression in the global coordinate system. Finally, the force and torque can be calculated with Lorenz's force law. III. FINITE ELEMENT ANALYSIS Considering the six-degree-of-freedom motion, a three-dimensional finite element model (3-D FEM) is employed for accurate consideration of the complex magnetic field distribution and asymmetry caused by motion. The six-degree-of-freedom force and torque characteristics are analyzed, as shown in Fig. 2. Then, in order to find a useful optimized method for future design process, the influence of fundamental parameters are also analyzed. IV. EXPERIMENTAL VERIFICATION To validate the performance of the RMA-MLVCA, experiments are conducted on a prototype. The test platform for measuring force characteristics of the RMA-MLVCA is composed of a three-degree-of-freedom position adjuster, a force sensor, a high-precision multimeter and a support, as shown in Fig. 1 (e). Then, the characteristics of the RMA-MLVCA are compared with conventional VCAs. V. CONCLUSION In this paper, a novel RMA-MLVCA has been investigated. The equations of magnetic flux density, electromagnetic force and torque are deduced based on an equivalent current model. Then, its six-degree-of-freedom force and torque characteristics, as well as the influence of structural parameters on force density and uniformity are analyzed by 3-D FEA. To verify the analysis, a prototype has been built and tested. The results show that the RMA-MLVCA possesses the advantage of excellent force uniformity, and is suitable for multi-degree-of-freedom applications.

[1] Rust H P, Buisset J, Schweizer E K, et al. High precision mechanical approach mechanism for a low temperature scanning tunneling microscope[J]. Review of scientific instruments, 1997, 68(1): 129-132. [2]Pohl D W. Some design criteria in scanning tunneling microscopy[J]. IBM Journal of Research and Development, 1986, 30(4): 417-427. [3] Kim W, Trumper D L. High-precision magnetic levitation stage for photolithography[J]. Precision Engineering, 1998, 22(2): 66-77. [4] Ueda Y, Ohsaki H. A planar actuator with a small mover traveling over large yaw and translational displacements[J]. IEEE Transactions on Magnetics, 2008, 44(5): 609-616. [5] Fung R F, Hsu Y L, Huang M S. System identification of a dual-stage XY precision positioning table[J]. Precision Engineering, 2009, 33(1): 71-80. [6] Zheng J, Su W, Fu M. Dual-stage actuator control design using a doubly coprime factorization approach[J]. IEEE/ASME Transactions on Mechatronics, 2010, 15(3): 339-348. [7] Kuo S K, Menq C H. Modeling and control of a six-axis precision motion control stage[J]. IEEE/ASME transactions on Mechatronics, 2005, 10(1): 50-59. [8] Shan X, Kuo S K, Zhang J, et al. Ultra precision motion control of a multiple degrees of freedom magnetic suspension stage[J]. IEEE/ASME Transactions on mechatronics, 2002, 7(1): 67-78. [9] Choi Y M, Gweon D G. A high-precision dual-servo stage using Halbach linear active magnetic bearings[J]. IEEE/ASME Transactions on Mechatronics, 2011, 16(5): 925-931. [10] Hazelton A, Ebihara A, Novak W. Wafer stage with magnetic bearings: U.S. Patent Application 10/272,930[P]. 2002-10-18. [11] Verma S, Shakir H, Kim W J. Novel electromagnetic actuation scheme for multiaxis nanopositioning[J]. IEEE transactions on magnetics, 2006, 42(8): 2052-2062. [12] Vrijsen N H, Jansen J W, Lomonova E A. Comparison of linear voice coil and reluctance actuators for high-precision applications[C]// Power Electronics and Motion Control Conference (EPE/PEMC), 2010 14th International. IEEE, 2010: S3-29-S3-36.

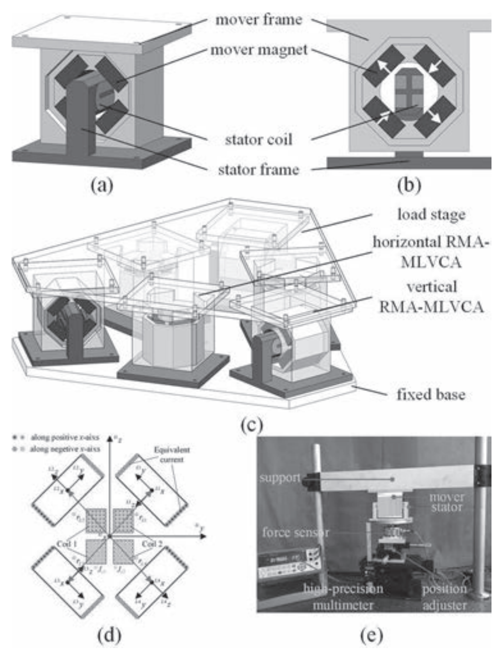

Fig. 1. Structure and model of the RMA-MLVCA and MLFPM. (a) 3-D view of RMA-MLVCA. (b) Sectional view of RMA-MLVCA. (c) 3-D view of MLFPM using six RMA-MLVCAs. (d) Equivalent current model.(e) Test platform.

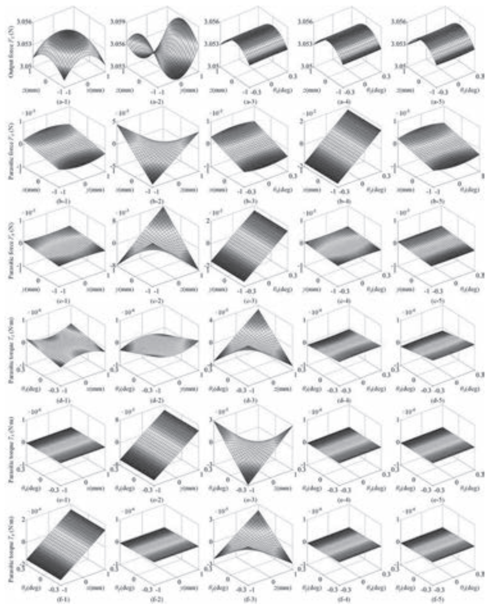

Fig. 2. Force and torque characteristics of the RMA-MLVCA. (a) Output force Fz. (b) Parasitic force Fx. (c) Parasitic force Fy. (d) Parasitic torque Tz. (e) Parasitic torque Tx. (f) Parasitic torque Ty.

ER-14. Radial Suspension Forces Modeling for Bearingless Flus-Switching Permant Magnet Motor.

C. Zhao[1] and H. Zhu[1]
1. Jiangsu University, Zhenjiang, China

I. INTRODUCTION Bearingless permanent magnet (PM) motors have advantages of high efficiency, high power density, and no wear, no lubricant and maintenance-free because a magnetic bearing function is magnetically integrated into a conventional motor, the bearingless PM motor is a competitive candidate for high power density [1]. However, the conventional bearingless PM motors usually suffer from the problems of mechanical integrity and thermal instability due to their PMs located in the rotor, which lead to a discount of the maximum electric loading performance. In order to realize stable control of suspending of the BFSPM motor, it is essential to establish a precise mathematical model of radial suspension force [2]. By using the Lorentz force, the analytical radial suspension force and torque equations for parallel magnetized magnets have been derived. As show in Fig. 1, by feeding a suitable current into suspension force windings, the balance and symmetry of rotating magnetic field produced by the torque windings in the motor airgap can be disturbed. In other words, the magnetic fields in some partial areas of the airgap are enhanced and those in the corresponding symmetrical areas can be weakened due to the contribution of suspension current. Thus, the radial resultant force, namely suspension force can be produced in the direction with the enhanced magnetic field. Based on the operation principle of the BFSPM motor in [3], the relative mathematical models have been constructed, including the permeance of airgap, the magnetic motive force (MMF) of torque windings, the MMF of suspension force windings and the MMF of PMs. Then, based on the theory of Maxwell stress tensor, the mathematical models of radial suspension force are derived. And the validity of the mathematical model is proved by finite element analysis (FEA) predictions. It can be concluded that the mathematical model of radial suspension force can reflect the radial suspension force correctly as shown in Fig. 2. The specific derivational process of mathematical model will be shown in the full paper. II. MOTOR STRUCTURE AND OPERATION PRINCIPLE The configuration of the proposed motor is very similar with that of the traditional FSPM motor which adopts a three-phase 12/10-pole (12-stator-teeth and 10-rotor-poles) configuration. The key difference is that there are two sets of windings wound around the stator teeth, namely torque windings and suspension force windings. ϕ_f is generated by the PMs sandwiched in the stator. The suspension magnetic flux ϕ_s generates when *Y-axis* suspension force winding current is excited. When forward current I_1~I_6 flows through relevant suspension force windings, the direction of flux ϕ_s is shown in Fig. 1. The flux density in the top air gap is increased due to the direction of ϕ_f is the same as ϕ_s. Oppositely, the flux density in the bottom air gap is decreased since direction ofϕ_f is opposite to that of ϕ_s. So the flux density in bottom airgap would be reduced while the flux in top airgap enhanced, the radial suspension force generated as shown in Fig. 2. Naturally, this superimposed magnetic field results in the radial suspension force F_y acting on the rotor toward the positive direction in the *Y-axis*. A radial suspension force toward the negative direction in the *Y-axis* can be produced with a negative current. III. MATHEMATICAL MODEL For the proposed BFSPM motor, radial suspension force is generated by the flux density in the air-gap as well as torque, so the air-gap flux density should be calculated. The permeances can be given as: $\Lambda_{srk=}\ \Lambda_0+\Lambda_1\cos(N_r\theta_{0sr}+(5\text{-}2k)N_r\pi/N_s)$, (k=1,2,3,4) (1) where θ_{0sr} is the relative position between the rotor and stator. The maximum flux linkage is obtained when a rotor tooth is aligned with the *d-axis,* i.e., $\theta_{0sr} = \pi/2Nr$. N_r is the rotor tooth number. The air-gap flux density MMF should be composed of three components: the MMF of torque windings $F_{T,}$ the MMF of PMs F_{mag} and the MMF of suspension force windings F_s, The air-gap flux density can be written as: $B_{srk}=(F_T+F_{mag}+F_s)\Lambda_{srk}$, (k=1,2,3,4) (2) The radial suspension force of the BFSPM motor acting on the rotor can be calculated by using the theory of Maxwell stress tensor: $dF_{srk}(\theta)= B_{srk}(\theta,t)^2dS/2\mu_0=B_{srk}(\theta,t)^2lr/2\mu_0d\theta$ (3) where *r* is the outer radius of the rotor, *l* is the stack length of the motor. V. CONCLUSION The calculation results are verified by FEA, and a series of comparisons between the FEA computed and calculated values are conducted, and the results indicate that the calculated values closely agree with FEA results.

[1]X. D. Sun, L. Chen, and Z. B. Yang, "Overview of bearingless permanent magent synchronous motors," *IEEE Trans. Ind. Electron.*, vol. 60, no. 2, pp. 5528-5538, 2013. [2]M. Takemoto, A. Chiba, H.Akagi, and T. Fukao, "Radial force and torque of a bearingless switched reluctance motor operating in aregion of magnetic saturation," *IEEE Trans. Ind. Appl.*, vol.40, no. 1, pp. 103-112, 2004. [3]C. Y. Zhao, H. Q Zhu, "Decoupling analysis of a novel bearingless flux-switching permanent magnet motor," *AIP Advances*, vol. 7, no. 5, Mar. 2017, Art. No. 056733.

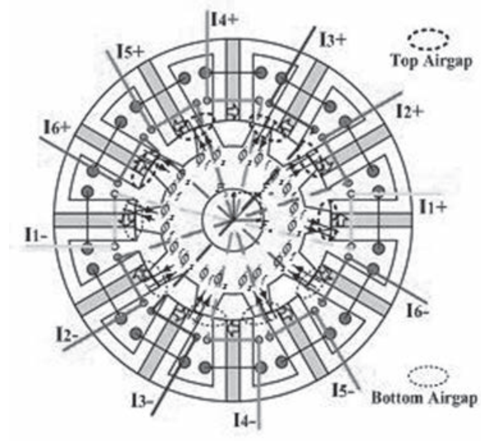

Fig. 1. Operation principle of the BFSPM motor.

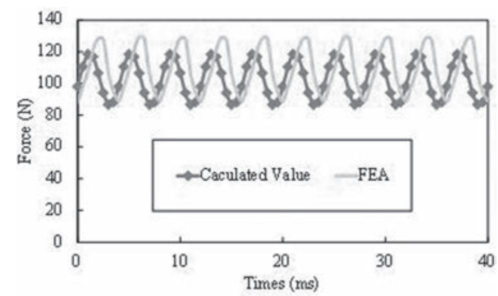

Fig. 2. Radial suspension force of FEA vs mathematical model.

ER-15. Multi-Optimal Design of Novel Bearingless Switched Reluctance Motor Based on Atifical Bee Colony Particle Swarm Optimizer.

Y. Sun[1] and *Z. Binbin*[2]
1. School of Automation, Nanjing University of Science and Technology, Nanjing, China; 2. School of Electrical and Information Engineering, Jiangsu University, Zhenjiang, China

INTRODUCTION: In recent decades, bearingless switched reluctance motors (BSRMs) have been proposed [1]. However, few researchers focused on the optimal design of the BSRMs [2-4]. In this paper, the multi-objective optimal design of BSRMs is investigated [5-6]. At first, an analytical design model is derived from the mathematical model of the BSRMs. An initial design is calculated by the analytical design model. Then, the objective functions, constraints, and decision variables are also determined. Corresponding sensitivity analysis of the decision variables such as stator yoke,rotor yoke ,stator pole arc and rotor diameter is implemented. Then, a novel multi-objective atifical bee colony particle swarm optimizer (ABC-PSO) is presented. The proposed ABC-PSO is applied for the optimal design of BSRMs to increase the radial force and efficiency. The electromagnetic performance is compared with the initial design and verified by the FEM. Verification results show that the optimal design of BSRMs based on the analytical design model and the proposed MOGPSO is feasible and effective. PROPOSED MULTI-OBJECTIVE Atifical Bee Colony Particle Swarm Optimizer: The PSO has been proposed and developed in recent decade. The Pareto dominance is used to determine the dominated or non-dominated solutions in all particles, and all non-dominated particles are filtered and stored in a repository during iteration. In order to avoid the particles falling into local optimums, a moderate mutation operator was utilized at the beginning of the search. However, with the iteration process, fewer particles are affected by the mutation. This phenomenon may lead to particles trapping into local optimums in the later period of iteration and cannot reach more accurate Pareto front. Hence, the conventional PSO may be not suitable for the multi-objective optimization of the BSRM in this paper. An improvement of ABC-PSO is investigated, and the ABC-PSO is proposed. The ABC-PSO combines atifical bee colony mechanism with the particle swarm optimizer, which can obtain the global Pareto front and avoid converging to the local optimal solutions. OPTIMIZATION OF BSRM: After the validation of the proposed ABC-PSO, it is applied to optimize the BSRM. The optimization variables include stator yoke,rotor yoke ,stator pole arc and rotor diameter, which to enhance efficiency and increase radial force. It is regarded motor's fixed shape as constrained condition. The fig.1 (a) shows the design variables of novel BSRM. Fig1 (b) shows relations between radial force and stator pole arc at different stator yokes. Fig1 (c) shows relations between radial force and stator yokes at different rotor yokes. Fig1 (d) shows relations between radial force and rotor yokes at different rotor diameter. As shown in fig.1, it is complicit to optimize motor. RESULTS: we should provide multiple objectives in line with above requirements: we expect efficiency and levitated force to be larger, but BSRM's fixed shape to be changeless. Fig.2 (a) shows the BSRM's efficiency optimization results with different single variable. Fig2 (b) shows efficiency optimization results with different variables. Fig2 (c) shows multi-objective optimization results with different variables. Fig2 (d) shows the magnetic flux density by 3-D finite element analysis, it can be seen that the proposed ABC-PSO is particularly suitable for solving disconnected, non-uniformly distributed optimization problem.

[1] Morrison, Carlos R., Mark W. Siebert, and Eric J. Ho. "Electromagnetic forces in a hybrid magnetic-bearing switched-reluctance motor." *IEEE Transactions on Magnetics*44.12 (2008): 4626-4638. [2] Raminosoa, Tsarafidy, et al. "Design and optimization of a switched reluctance motor driving a compressor for a PEM fuel-cell system for automotive applications." *IEEE Transactions on Industrial Electronics* 57.9 (2010): 2988-2997. [3] BAI, Feng-xian, Yu-huai SHAO, and Jian-zhong SUN. "OPTIMIZATION DESIGN OF POLE SHAPE OF SRM BY USING INTELLIGENT SIMULATED ANNEALING ALGORITHM [J]." *Proceedings of the Csee* 1 (2003): 027. [4] Liu, Zeyuan, et al. "Optimal design of a bearingless switched reluctance motor." *Applied Superconductivity and Electromagnetic Devices, 2009. ASEMD 2009. International Conference on*. IEEE, 2009. [5] Liu, Xu, and Bangcheng Han. "The multiobjective optimal design of a two-degree-of-freedom hybrid magnetic bearing." *IEEE Transactions on Magnetics* 50.9 (2014): 1-14. [6] Zhang, Jingwei, et al. "Multi-Objective Optimal Design of Bearingless Switched Reluctance Motor Based on Multi-Objective Genetic Particle Swarm Optimizer." *IEEE Transactions on Magnetics* (2017).

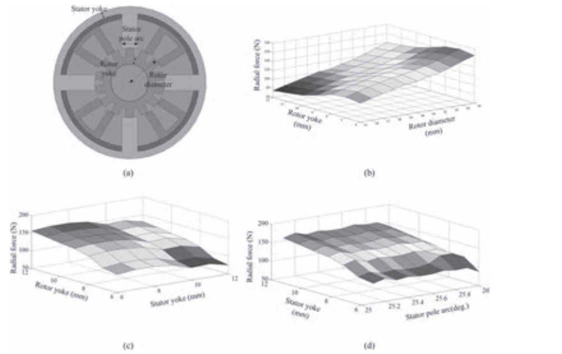

Fig. 1. Relations between design variables of novel BSRM. (a) Design variables of novel BSRM. (b) Relations between radial force and stator pole arc at different stator yokes. (c) Relations between radial force and stator yokes at different rotor yokes. (d) Relations between radial force and rotor yokes at different rotor diameter.

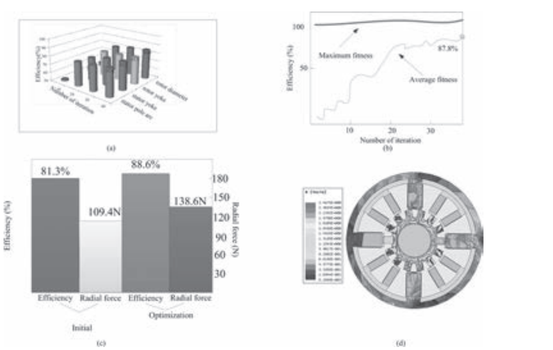

Fig. 2. Optimization results. (a) Efficiency optimization results with different single variable. (b) Multi-objective optimization results with different variables. (c) Radial force multi-objective optimization results with different variables. (d) The magnetic flux density.

THURSDAY MORNING, 26 APRIL 2018 SIMPOR/ROSELLE BALLROOM, 8:30 TO 11:30

Session ES
MAGNETIC GEARS
(Poster Session)

Byungtaek Kim, Chair
Kunsan National University, Gunsan, The Republic of Korea

ES-01. Comparison of the Magnetic Field and Torque Characteristics for Axial Magnetic Gears with Various Permanent Magnet arrays.

X. Liu[1], Y. Zhou[1], D. Wan[1] and Z. Chen[2]

1. College of Electrical and Information Engineering, Hunan University, Changsha, China; 2. Department of Energy Technology, Aalborg University, Aalborg, Denmark

INTRODUCTION Magnetic gears (MGs) could offer some distinct advantages over mechanical gears, such as no lubrication, no maintenance, low acoustic noise, high reliability, long lifetime and inherent overload protection [1-2]. They are particularly attractive for those applications desiring a high speed reduction ratio, such as electric vehicles [3] and wind turbines [4]. Most of the previous work on magnetic gears has focused on the radial field topology because axial magnetic gears (AMGs) are difficult in construction. However, AMGs show superiority in applications requiring hermetic isolation and high torque density. In according to the various arrays of permanent magnets (PMs), the AMG could be classified as the conventional axial field magnetic gear (AFMG), the axial flux focusing magnetic gear (AFFMG) [5], and the axial magnetic gear with Halbach permanent magnet arrays (HAMG) [6]. In this paper, the magnetic field and torque characteristics of the above three AMGs are compared basing on 3D FEM simulation. In addition, the advantages and disadvantages of the three AMGs will be discussed based on 3D finite element analysis. TOPOLOGIES OF THREE AMGs The topologies of three AMGs are shown in Fig. 1. All the three AMGs are composed of three parts, namely, the high-speed rotor, the low-speed rotor and the modulation ring sandwiched between the two rotors. The difference of the three topologies lies in the magnetization modes of PMs. The PMs of the AFMG are magnetized along the axial direction. The AFFMG consists of PMs magnetized along the azimuthal direction. The HAMG has different orientations of PM pieces. For the HAMG, the numbers of PMs per pole on the high-speed rotor and the low-speed rotor are equal to 3 and 2, respectively. For the three topologies, the numbers of pole pairs on two rotors are respectively 4 and 13 and the number of the modulator pieces is 17. In order to carry out a fair comparison, the same radius of 70 mm and axial length of 45.5 mm are applied for all the three topologies. Magnetic HARMONICS ANALYSIS In order to clarify the torque transmission abilities of the three AMGs, the axial spatial harmonic components of the magnetic field of the three AMGs are firstly studied. Fig. 2(a), Fig. 2(b) and Fig. 2(c) show the axial spatial harmonic components in the air gap adjacent to high-speed rotors of three AMGs. According to the PM pole pairs on the high speed and low speed rotors, the harmonic components with 4, 13, 21, 30, 38 and 47 pole pairs are effective harmonics which may contribute to torque transmission. These effective harmonics match well with the major harmonics in the harmonic spectrum shown in Fig. 2(a), Fig. 2(b) and Fig. 2(c). The harmonic components shown in Fig. 2(c) with 12, 20, 29 and 36 pole pairs are decreased which may cause torque ripples and iron losses compared with Fig. 2(a) and Fig. 2(b). The axial spatial harmonic components in the air gap adjacent to low-speed rotors of three topologies are shown in Fig. 2(d), Fig. 2(e) and Fig. 2(f). The harmonic components with 4, 13, 21, 30, 38 and 47 pole pairs are effective harmonics contributing to torque transmission in the air gap adjacent to low-speed rotors. These effective harmonics match with the major harmonics in the harmonic spectrum shown in Fig. 2(d), Fig. 2(e) and Fig. 2(f). The 13th harmonic components shown in Fig. 2(e) and Fig. 2(f) are significantly improved compared with Fig. 2(d). Compared with Fig. 2(d) and Fig. 2(e), the harmonic components shown in Fig. 2(f) that are the source of torque ripples and arouse iron losses in the ferromagnetic modulator pole-pieces are suppressed. TORQUE TRANSMISSION The maximum static torques of the AFMG, AFFMG and HAMG are 47.5 Nm, 55.2 Nm and 55.5 Nm, respectively. Compared the AFMG, the maximum static torque of the other two topologies has a growth of 17%. However, the PM consumption of the AFFMG is only 87.5% of that of the other two topologies, which implies a higher torque/cost ratio for the AFFMG. CONCLUSION The 3D FEM simulation results show that the HAMG could offer lower torque ripple and higher effective magnetic harmonics than the AFMG and the AFFMG. Both the HAMG and the AFFMG could offer 17% higher output torque than the AFMG. The AFFMG may achieve highest permanent magnet utilization. The specific comparison on the magnetic field and torque characteristics of the three AMGs and the 3D FEM simulation results will be presented in detail in the full paper.

[1] K. Atallah and D. Howe, "A novel high-performance magnetic gear," *IEEE Trans. Magn*., vol. 37, no. 4, pp. 2844–2846, Jul. 2001. [2] K. Atallah and S. D. Calverley et al., "Design, analysis and realisation of a high-performance magnetic gear," in *Proc. IEE Proc.-Electr. Power Appl.*, 2004, vol. 151, pp. 135–143. [3] K. T. Chau, D. Zhang, J. Z. Jiang, C. Liu, and Y. J. Zhang, "Design of a magnetic-geared outer-rotor permanent-magnet brushless motor for electric vehicles," *IEEE Trans. Mag.*, vol. 43, no. 6, pp. 2504–2506, Jun. 2007. [4] L. Jian, K. T. Chau, and J. Z. Jiang, "A magnetic-geared outer-rotor permanent-magnet brushless machine for wind power generation," *IEEE Trans. Ind. Appl.*, vol. 45, no. 3, pp. 945–962, May/Jun. 2009. [5] V. M. Acharya, J. Z. Bird, and M. Calvin, "A Flux Focusing Axial Magnetic Gear," *IEEE TRANSACTIONS ON MAGNETICS*, vol. 49, no. 7, pp. 4092-4095, July 2013. [6] M. Johnson, M. C. Gardner, and H. A. Toliyat, "Analysis of axial field magnetic gears with Halbach arrays," *Electric Machines & Drives Conference* IEEE, 2016:108-114.

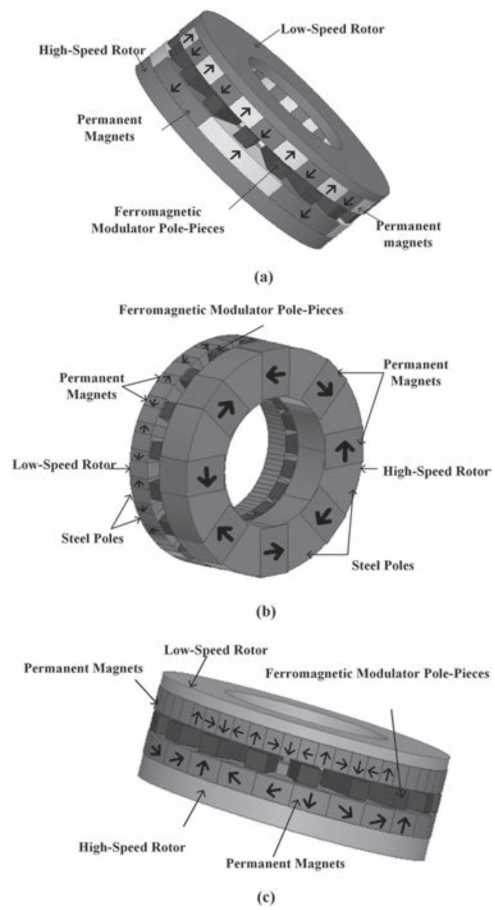

Fig. 1. Topologies of the AMGs. (a) AFMG. (b) AFFMG. (c) HAMG.

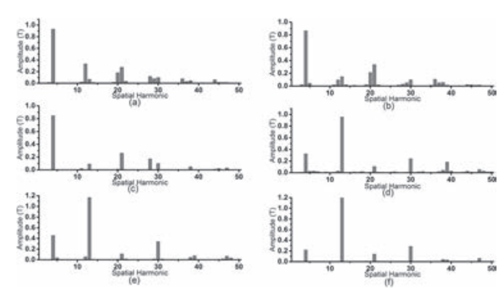

Fig. 2. Axial harmonic spectra in the air gap adjacent to high-speed rotor of the AMGs. (a) AFMG. (b) AFFMG. (c) HAMG. Axial harmonic spectra in the air gap adjacent to low-speed rotor of the AMGs. (d) AFMG. (e) AFFMG. (f) AHAMG.

ES-02. Investigation of the Torsion and Vibration Characteristics of a Dual-Flux-Modulator Coaxial Magnetic Gear.

X. Liu[1], Y. Zhao[1], Z. Chen[2], D. Luo[1] and S. Huang[1]

1. College of Electrical and Information Engineering, Hunan University, Changsha, China; 2. Department of Energy Technology, Aalborg University, Aalborg, Denmark

I.Introduction Coaxial magnetic gear (CMG) is a promising power transmission device, which could realize non-contact torque and speed transmission by the interaction of the modulated magnetic fields in the air-gaps [1]. The CMG takes the advantages of low friction loss, minimum acoustic noise and no maintenance. The dual-flux-modulator coaxial magnetic gear (DFM-CMG) presented in [2] shows a higher torque capability, comparing to other CMGs. However, the DFM-CMG works like a torsion spring and the torsional stiffness of the conventional CMG is lower than that of the mechanical gearboxes [3]. Although the steady-state performance of the DFM-CMG has been studied by using the analytical model method and finite-element method (FEM) [2], the torsion properties and vibration characteristics of the CMG has not yet been studied in depth [4]. Moreover, the DFM-CMG has the drawbacks of vibration caused by electromagnetic force (EMF) generated by the interaction between the pole-pieces of the auxiliary flux modulator and the two rotors compared with conventional CMGs, which will affect the overall vibration performance significantly. Motivated by this, the presented research mainly focuses on the torsion properties and vibration characteristics of the DFM-CMG. In this paper, firstly, electromagnetic finite-element (FE) model and analytical model of the DFM-CMG are developed to analyze the torsion properties. Then, the torsion properties of a DFM-CMG prototype are tested to validate the simulation results. Finally, a multi-physics simulation model is established to calculate the radial displacement caused by the EMF and the vibration characteristics of the DFM-CMG. II.Modeling and torsional performance of the DFM-CMG Fig. 1(a) shows the topology of the DFM-CMG. The DFM-CMG employs surface-mounted permanent magnets (PMs) on the inner rotor but adopts spoke-type PMs on the outer rotor. A stationary auxiliary flux modulator is introduced in the outermost layer of the DFM-CMG [2]. The studied DFM-CMG in this paper has 4 pole-pairs for the inner rotor (p_{in}) and 26 pole-pairs for the outer rotor (p_{out}), which has a theoretical gear ratio of 6.5. The magnetic torque exerted on the inner are calculated by Maxwell 3-D static magnetic solver. The calculated static pull-out torque on the inner rotor is 30Nm. Afterwards, an analytical torsional model of the DFM-CMG is established. In the torsion properties model, the outer rotor was locked to standstill, while the inner rotor was connected to sudden application of a load torque. Fig. 1(b) shows a photograph of the test rig for the torsion properties measurement, where the relative angular position was measured by an encoder. The initial torque is fixed to 10.7Nm and the total moment of inertia J with inner rotor, rod and load is 0.405kgm^2. The torsion properties of the inner rotor could be estimated by calculating the developed model. Fig. 2(a) and (b) present simulation and experimental load angle of the inner rotor under a sudden load of 5Nm at t=0s. As could be seen, the end load angle θ obtained from simulation and experiment reaches a value of 6.95° and 6.92°, respectively. This discrepancy is due to the resolution of the encoder and the compromises made on the structure design. Moreover, the simulated oscillation period T=0.38s agrees well with the experimental results of T=0.37s as shown in Fig. 2(a) and (b). In the torsion properties analysis, two of the most important parameters are the torsional stiffness K and coefficient of damping B. The K and B of the inner rotor in experiment are K=116Nm/rad and B=2.36Nms/rad that are very close to the simulation results K=120Nm/rad and B=2.4Nms/rad, respectively. III.EMF and vibration characteristics of the DFM-CMG In the DFM-CMG, the inner rotor and main flux modulator are very similar to those of conventional CMG. However, the spoke-type pole-shoes and the auxiliary flux modulator are relatively unique. Firstly, the multi-physics models for EMF, structural displacement and vibration are developed by using the software ANSYS Workbench. Then, the flux densities in the three air gaps are obtained by Maxwell 2-D transient magnetic solver. The Maxwell stress tensor method is used to calculate the EMF [5]. Fig. 2(c) and (d) present the transient distribution EMF acting on each pole-piece of auxiliary flux modulator and their time harmonic spectra at no load and rated load, respectively, when the speeds of inner rotor and outer are 650rpm and -100rpm. The average radial forces for each pole-shoe of the auxiliary flux modulator are 316N and 201N at no load and rated load conditions. The first largest frequency of the EMF is $2\mu p_{in} f_{in}$=86.67Hz (f_{in} is the frequency of the inter rotor and μ=1, 2,...). Finally, the distribution of the EMF obtained from the electromagnetic model is loaded to the surface of the auxiliary flux modulator and spoke-type pole-shoes in the 3-D structural FE model of the DFM-CMG. Modal superposition method is adopted to calculate the vibration by using the software ANSYS Workbench. The detailed analyses on the structural vibration characteristics of the spoke-type pole-shoes and the auxiliary flux modulator under different operation conditions, will be presented in the full paper.

[1] K. Atallah and D. Howe, “A novel high-performance magnetic gear,” *IEEE Trans. Magn.,* vol. 37, no. 4, pp. 2844- 2846, Jul. 2001. [2] Xiaoxu Zhang, Xiao Liu, and Zhe Chen, “A Novel Dual-Flux-Modulator Coaxial Magnetic Gear for High Torque Capability,” *IEEE Trans. Energy Convers.,* to be published. [3] P. Rasmussen, T. Andersen, F. Jorgensen, and O. Nielsen, “Development of a high-performance magnetic gear,” *IEEE Trans. Ind. Appl.,* vol. 41,no. 3, pp. 764–770, May/Jun. 2005. [4] G. Cooke and K. Atallah. “‘Pseudo’ Direct Drive Electrical machines with alternative winding configurations,” *IEEE Trans. Magn.,* vol. 53, no. 11, Nov. 2017, Art. ID 8111608. [5] R. Islam and I. Husain, “Analytical model for predicting noise and vibration in permanent-magnet synchronous motors,” *IEEE Trans. Ind. Appl.,* vol. 46, no. 6, pp. 2346–2354, Nov./Dec. 2010.

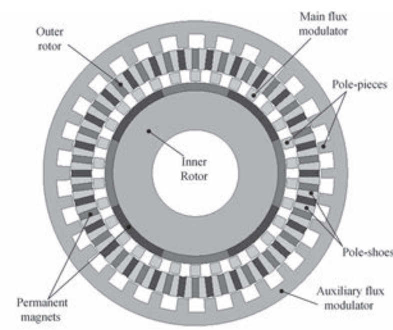

(a)

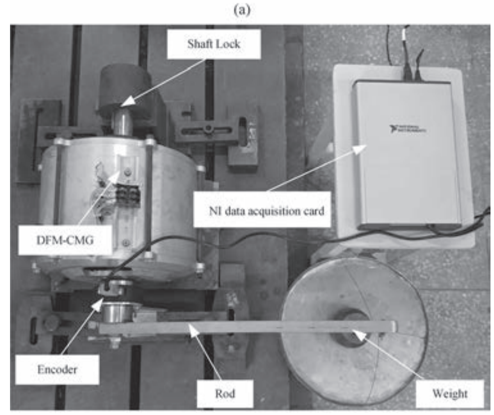

(b)

Fig. 1. (a) Topology of the DFM-CMG. (b) Photo of experimental setup for the torsion properties (top view).

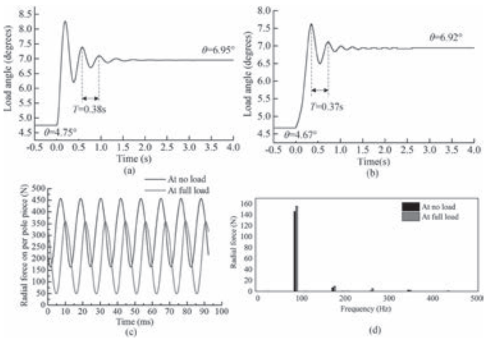

Fig. 2. Load angle oscillations: (a) Simulation results and (b) experimental results. Radial EMF on each pole-piece of auxiliary flux modulator: (c) Transient distribution and (d) time harmonic spectra.

ES-03. Torque Parameter Characteristics of Non-contact Magnetic Coupling considering Rotor Volumetric Modeling.

J. Park[1,2], K. Lee[1], S. Lee[1] and S. Jung[2]
1. Korea Institute of Industrial Technology, Gwangju, The Republic of Korea; 2. School of Electronics and Electrical Engineering, Sungkyunkwan University, Gwangju, The Republic of Korea

Magnetic couplings that transmit torque without mechanical contact are widely used in underwater electrical machines. It is advantageous to increase the reliability of the underwater structure and to reduce the maintenance cost by utilizing the air gap between the inner rotor and outer rotor. However, most commercial magnetic couplings are larger in size than their capacities. Magnetic coupling is a major component that affects the size of underwater electrical system, and research on miniaturization and weight reduction is needed. The structure of the magnetic coupling is classified into a radial flux type and an axial flux type. In the case of an underwater electric propellant, the radial magnetic flux type is more advantageous because the magnetic coupling and the propeller are integrated. In addition, the radial magnetic flux type ensures sufficient air gap and torque for waterproof structure inside the underwater electrical system. Magnetic couplings of radial flux type have been studied to derive torque characteristics with analytical magnetic field calculations [1-2]. In this study, we derive the torque by calculating the relationship between the inner rotor and the outer rotor as parameters by using the electromagnetic transfer relation method. Through the derived equation, the torque per rotor volume of the magnetic coupling is calculated and the rotor volume design is presented according to the relation of rotation speed, torque and output power. The volume design results using the torque parameters were confirmed to be similar to those of the finite element analysis results. Finally, the magnetic couplings of 2[kW] output power were fabricated to reflect the volume design results and the validity of rotor volume modeling was verified through testing. Fig. 1(a) shows the structure of a magnetic coupling used in an underwater electric propulsion system. It has a structure of 8 poles in radial flux type, the inner rotor is connected to the gear and the outer rotor is integrated with the propeller. The magnetization and the magnetic vector potential are calculated as the boundary condition of the material region by applying the electromagnetic transfer relation and the magnetic flux density of the air gap region is derived. The torque of the rotor was calculated using the Maxwell stress tensor and the volume design modeling parameter were derived. The main components of the parameters are rotor diameter, lamination, air gap and material properties of permanent magnet. Rotor volume modeling is performed by torque per rotor volume considering rotation speed and output power. Fig. 2(a) shows the rotor volume modeling curve using the torque per rotor volume. Volume curves of the air gap [3mm, 5mm. 7mm] and torque [10Nm, 15Nm, 20Nm] were presented by volumetric modeling according to the rotational speed and output power characteristic of the magnetic coupling. Smaller air gaps and smaller torques confirm that the size is smaller and the volume of the magnetic coupling is optimized using design parameters and volume curves. Next, magnetic coupling was designed through volume modeling and output power characteristics were compared through finite element analysis. Fig. 2(b) shows a photograph of the evaluation system of the magnetic coupling. The magnetic coupling was fabricated to reflect the rotor volume modeling results and the dynamo evaluation system was constructed. The servo motor is connected to the inner rotor of the magnetic coupling and rated at rated speed. The outer rotor was connected to the hysteresis brake to evaluate the load characteristics. It is confirmed that the design results and test results of volume modeling are similar. At the end of this study, we modeled the volume of magnetic coupling by deriving the torque per rotor volume through an analytical method. The volume of the magnetic coupling can be optimized using parameters such as rotor diameter, stack length, air gap, rotating speed, output torque. Furthermore, the size of the underwater electrical system can be further reduced in size and weight by optimizing volume modeling of the magnetic coupling.

[1] Jang-Young Choi, Hyeon-Jae Shin, Seok-Myeong Jang, Sung-Ho Lee, "Torque Analysis and Measurements of Cylindrical Air-Gap Synchronous Permanent Magnet Couplings Based on Analytical Magnetic Field Calculations" IEEE Trans. Magn., Vol. 49, No. 7, pp3921-3924, July 2013.

[2] Kang Li; Jonathan Z. Bird; Vedanadam M. Acharya, "Ideal Radial Permanent Magnet Coupling Torque Density Analysis" IEEE Trans. Magn., Vol. 53, No. 6, pp8106304, June 2017.

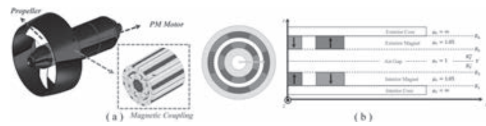

Fig. 1. (a) Structure of magnetic coupling for underwater electrical system (b) Polar coordinate transformation system for analytical methods of magnetic coupling

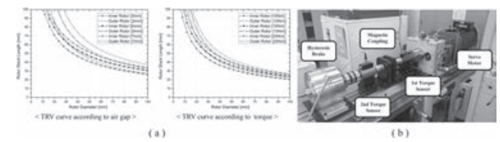

Fig. 2. (a) Volumetric modeling curve with air gap and output power (b) Magnetic coupling test configuration

ES-04. Withdrawn

ES-05. Modeling and Transmission Characteristics Analysis of Dual-Mechanical-Port Magnet-Geared Machine Using Control Block Diagrams.

C. Chen[1] and *M. Tsai*[1]
1. Mechanical Engineering Department, National Cheng Kung University, Tainan, Taiwan

I. Introduction The dual-mechanical-port magnet-geared machine (DMPMGM) has gained great research interest due to the development of the electronically controlled continuously variable transmission (E-CVT) in hybrid electric vehicles. The analysis for transmission characteristics, including torque and speed relationships between input and output ports, plays a crucial fundamental role in extending control applications. This study aims to propose a simple and intuitive approach to analyze the DMPMGM from the view of control engineering [1]. Both the kinematic and dynamic characteristics are represented with the block diagram descriptions. The concepts of feedforward and feedback loops are employed to illustrate the transmission interactions between DMPMGM rotors. The modeling method in this study conveniently integrates into an E-CVT control system. The feasibility of the proposed approach is verified by the corresponding simulation results with the finite element analysis-based method. II. Model Description and Simulation The non-contacting transmission of a DMPMGM is realized by the magnetic flux modulations. The induced polarized poles are generated at inner and outer air-gaps to transmit mechanical power. This study proposes a new concept, by which a DMPMGM would have a full structural correspondence with its mechanical planetary gear as shown in Fig. 1. The inner/outer PM rotors and the modulator correspond to the sun gear, ring gear, and the carrier, respectively. It should be noted that the virtual PM rotors are considered as the magnetic planet gears. The block diagram description of the DMPMGM is then obtained as shown in Fig. 2(a). The pole-pair numbers of the inner and outer PM rotors are n and p, respectively. The pole-piece number of the modulating ring rotor is q. J and B denote the moment of inertia and damping coefficient. The subscripts of OPM, IPM, Ind, and Mod separately indicate the outer, inner, and virtual PM rotors, and the modulator. ω and T are the angular velocity and torque imposed on the rotor. θ_{DO} and θ_{DI} are defined as the angular displacement differences between the virtual and real PM rotors. Moreover, T_{CI} and T_{CO} are the peak values of magnetic coupling torques in the inner and outer air-gaps, respectively. In the proposed block diagram description in Fig. 2(a), the transmission interactions of the DMPMGM can be easily illustrated for the multi-port or single input/single output transmission modes. The kinematic characteristics of DMPMGM can also be obtained from the description in Fig. 2. Consider that the inner and outer PM rotors are utilized as the main driving and regulating inputs. The modulator is the output port. The kinematic torque and speed relationships are given as shown in Fig. 2(b) without any power loss for the kinematic analysis. In this transmission mode, the regulating input ω_{OPM} has a positive effect of speeding up the output ω_{Mod}. Moreover, a negative feedback loop exists in this transmission mode such that the outer PM rotor brings the other transmission path to compensate for the speed difference between ω_{IPM} and ω_{Mod} via its own rotary speed ω_{OPM}. Distinct from the speed transmission, the torque between the PM rotors and the DMPMGM modulator are transmitted via the feedforward loop, which gives the additional acceleration path and strengthens the torque response. Based on the simulation results in Fig. 2(c), the E-CVT application is realized by the DMPMGM such that the required speed and torque assistance can be generated for different operation conditions. Furthermore, the multi-port transmission mode of DMPMGM is simulated by the proposed approach as shown in Fig. 2(d), where T_{IPM}=10Nm and T_{OPM}=5Nm are applied as the main driving and regulating torques, respectively. Note that the dynamic responses of the three rotors based on the proposed approach are all close to the simulation results from the FEM in ANSYS Maxwell. The verification of the proposed block diagram description shows the accuracy of the kinematic and dynamic analysis of the DMPMGM, which is much more intuitive and simpler than the FEA-based method. III. Conclusion This study has proposed a block diagram description for the DMPMGM in the view of control engineering. The concepts of feedforward and feedback control loops are employed to illustrate the speed and torque transmission between the input and output ports. The kinematic and dynamic relationships of the DMPMGM based on the proposed block diagram technique are consistent with the FEA-based method [2]. A new transmission description of magnetic planet gear is also proposed in this study to characterize the internal power interaction between DMPMGM rotors. This approach places the DMPMGM in full structural correspondence with the mechanical planetary gear. Moreover, this study provides the analysis convenience for more advanced control applications, by which the control system can be designed directly based on the block diagram description of DMPMGM.

[1] C. L. Chen, and M. C. Tsai, "Torque Control of Power-Assisted Bike via Planetary Gear Mechanism," *International Conf. on Electrical Machines and Systems (ICEMS)*, pp. 1-5, Oct. 2017. [2] J. Bai, P. Zheng, C. Tong, Z. Song, and Q. Zhao, "Characteristic Analysis and Verification of the Magnetic-Field-Modulated Brushless Double-Rotor Machine," *IEEE Trans. on Industrial Electronics*, vol. 62, no. 7, pp. 4023-4033, Jul. 2015.

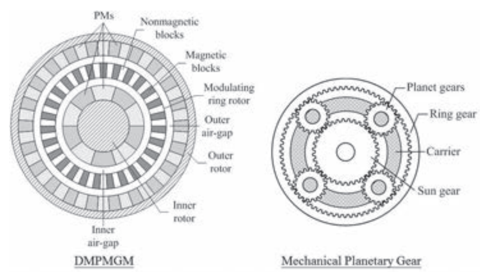

Fig. 1. Structures of DMPMGM and planetary gear

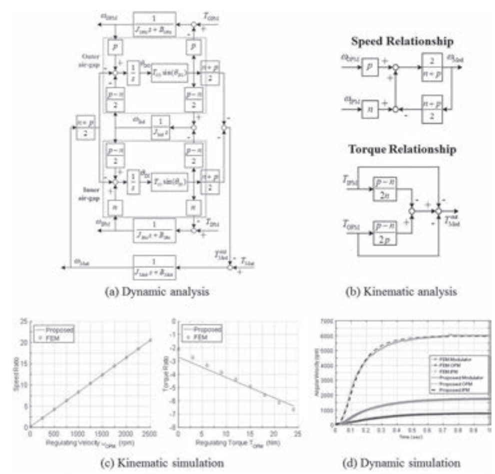

Fig. 2. DMPMGM in block diagram descriptions and its simulation results

ES-06. Analytical and Experimental Study for Electromagnetic Performance Analysis of Magnetic Geared Permanent Magnet Machines.

K. Shin[1], H. Cho[3], D. You[2] and J. Choi[1]

1. Dept. of Electrical Engineering, Chungnam National University, Daejeon, The Republic of Korea; 2. Dept. of Fire Safety Engineering, Chungnam Provincial Cheongyang College, Chungnam, The Republic of Korea; 3. Dept. of Electric, Electronic and Comm. Eng. Edu., Chungnam National University, Daejeon, The Republic of Korea

Low-speed high-torque machines are being increasingly used in various applications such as electric vehicles, wind-power generation, electric vessels, industrial robots, and home appliances, because they can offer direct-drive operation, which avoids the inconveniences of mechanical gearboxes [1]. The magnetic geared permanent magnet (MGPM) machine, which works similar to an electrical machine coupled with a coaxial magnetic gear, can be used as a substitute for direct drive systems and mechanical gears [2]. The MGPM machine is gaining interest owing to its significant features, such as reduced acoustic noise, maintenance-free operation, improved reliability, precise peak torque transmission capability, and inherent overload protection. In addition, an MGPM machine can further reduce the overall size and weight, compared to the simple combination of gear and electric motor. Despite these advantages, it is difficult to gain insight into the influence of the design parameters on the electromagnetic performance of MGPM machine. Analytical methods are useful for the first evaluation of machine performances and for design optimization, because continuous derivatives, which are obtained from the analytical solutions, are required during most optimization methods. Detailed knowledge about the magnetic field distribution in an air gap is vital for the design and optimization of permanent magnet (PM) machines, especially MGPM machines. Although numerical tools such as the finite element (FE) method offer precise field prediction, they can provide neither a closed-form solution nor physical insight. In recent years, much progress has been made in the analytical modeling of PM machines. The corresponding analysis is generally based on magnetic circuit methods in which only the fundamental component is considered, while the harmonic components are ignored [3]. Alternatively, a few viable analytical methods have been proposed for magnetic gears and other PM machines [4], [5]. Fourier analysis is used to obtain the solutions of Laplace and Poisson equations that represent the field behavior in each analysis region. The validity of the proposed analytical approach was verified by comparing the calculated results with those obtained from the FE results. In this paper, an analytical modeling based on Fourier analysis is proposed to compute the electromagnetic performance of MGPM machines. Fig. 1 (a) shows the configuration of the MGPM machines. As seen in Fig. 1 (b), the entire domain of the field problem is divided into six subdomains: Region I and II (air-gap subdomain); Region III (PM subdomain); Regions b (b = 1, 2,…, N_s) (N_s air subdomains); Regions i (i = 1, 2,…, Q) (Q stator slots-opening subdomains); and Regions j (j = 1, 2,…, Q) (Q stator slots subdomains). The subdomains I, II, and III have annular shapes and the subdomains b, i, and j have non-periodic shapes. By using the separation of variables technique, we obtained the analytical solutions to Poisson's equations in the PM and slot subdomains (magnetization or current density regions), and Laplace's equation in the slot-opening, air, and air-gap subdomains. The governing equation in all subdomains can be solved, and the field distribution can be obtained by applying the boundary conditions on the interfaces between the subdomains [6]. Based on these solutions, the electromagnetic performance can also be determined analytically. The magnetic field and the electromagnetic performance obtained using the analytical method were compared with those obtained using the FE analysis, and the comparison validates the analytical methods presented in this paper, as shown in Fig. 2. Using the analytical solution, a design method, which includes outstanding operating characteristics (wide operating range and low torque ripple), is proposed in this paper, according to the selected pole-slot combination and the gear ratio. Specific illustrations of the analyses and the experimental results will be presented later on in the full paper. ACKNOWLEDGMENTS This work was supported by the Basic Research Laboratory (BRL) of the National Research Foundation (NRF-2017R1A4A1015744) funded by the Korean government.

[1] L. Jian, W. Gong, G. Xu, J. Liang, W. Zhao, "Integrated magnetic-geared machine with sandwiched armature stator for low-speed large-torque applications", IEEE Trans. Magn., vol. 48, no. 11, pp. 4184-4187, Nov. 2012. [2] K. Atallah, J. Rens, S. Mezani, D. Howe, "A novel pseudo direct-drive brushless permanent magnet machine", IEEE Trans. Magn., vol. 44, no. 11, pp. 4349-4352, Nov. 2008. [3] P. M. Tlali, S. Gerber, and R.-J. Wang, "Optimal Design of an Outer-Stator Magnetically Geared Permanent Magnet Machine," vol. 52, no. 2, 8100610, Feb. 2016. [4] L. Jian and K. T. Chau, "A coaxial magnetic gear with Halbach permanent-magnet arrays," IEEE Trans. Energy Convers., vol. 25, no. 2, pp. 319–328, Jun. 2010. [5] T. Lubin, S. Mezani, and A. Rezzoug, "2-D exact analytical model for surface-mounted permanent-magnet motors with semi-closed slots," IEEE Trans. Magn., vol. 47, no. 2, pp. 479–492, Feb. 2011. [6] B. L. J. Gysen, K. J. Meessen, J. J. H. Paulides, and E. A. Lomonova, "General formulation of the electromagnetic field distribution in machines and devices using Fourier analysis," IEEE Trans. Magn., vol. 46, no. 1, pp.39-51, 2010.

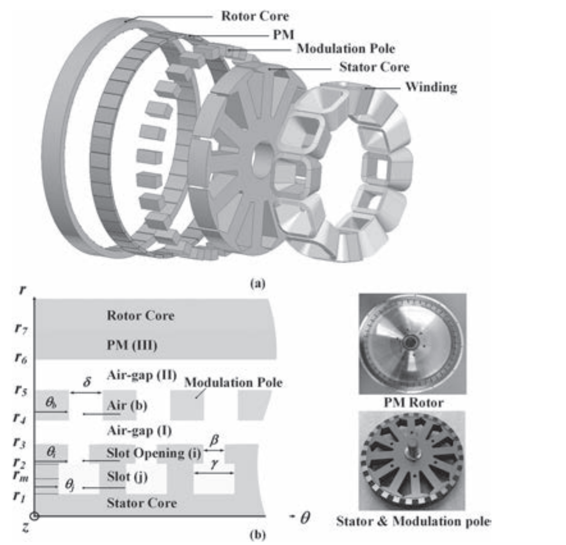

Fig. 1. Structure of MGPM machine: (a) FE model; (b) analytical and prototype model.

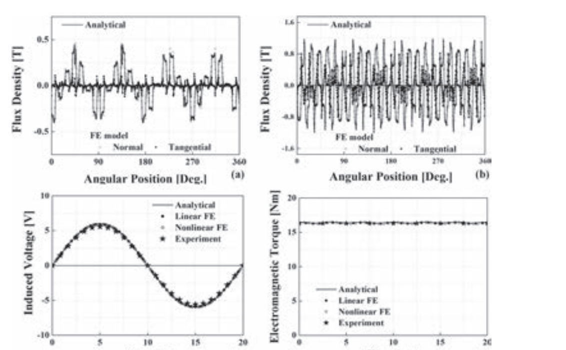

Fig. 2. Comparison between analytical, FE, and experimental results: (a) flux density at the inner air gap; (b) flux density at the outer air gap; (c) back EMF; and (d) electromagnetic torque.

ES-07. Design of Doubly Fed Magnetic Geared Motor Considering Inherent Characteristics.

H. Shin[1] and J. Chang[1]
1. Electrical engineering, University of Dong-A, Busan, The Republic of Korea

As shown in Fig. 1(a), the doubly fed magnetic geared motor (DFMGM) has the 3-phase AC winding in both the inner and outer windings, and the modulating pieces, which modulate the winding flux, are used as the output rotor [1]-[2]. The speed of the output rotor is determined by the frequencies of the inner and outer windings, and the ratio of output rotor speed to the frequency of each winding is defined by the numbers of pole of winding and the modulating piece. At this operating principle, the variation of the frequencies in the inner and outer windings has no effect on the average torque of the output rotor, and it only changes the speed of the output rotor. Thus, the speed of the output rotor can be adjusted by both of the frequencies of inner and outer windings without the torque variation, and hence, the DFMGM has the wide constant torque region compared to the magnetic geared motor with single AC winding [4]-[8]. In addition, the DFMGM has much wider field-weakening region because it can directly adjust the field flux by handling the amplitude of the winding current, and due to the high torque by the magnetic gearing effect, the DFMGM can be applied in the traction system including the electric vehicles. Unlike the general synchronous motor, the DFMGM has the operating principle by the magnetic gearing effect and the excitation structure by two windings, and the frequencies in the inner and outer windings are individually controlled. Hence, some important characteristics should be considered when the DFMGM is designed. Firstly, the flux modulation characteristics in the inner and outer windings should be separately analyzed. The modulated magnetic fields by the inner and outer windings are different in the amplitude of the working harmonic and the order of the space harmonics. Due to these difference, the back-EMFs of the inner and outer windings have different characteristic each other. Fig. 1(b) shows the time harmonic spectra of the no-load back-EMF with 360Hz in each winding, when the excitation winding and the output rotor operate at 0Hz and the 1,662rpm, respectively. The fundamental component of no-load back-EMF in the outer winding is 40% smaller than that of inner winding, and the total harmonic distortions (THDs) of 2.4% and 4.5% are produced in the inner and outer windings, respectively. Secondly, the characteristic variation according to the frequency condition in the inner and outer windings should be considered. Fig. 1(c) shows the time harmonic spectra of the no-load back-EMF with 360Hz in each winding, when the excitation winding and the output rotor operate at 180Hz and the 2,492rpm, respectively. Compared with the case of the excitation frequency with 0Hz in Fig. 1(b), the fundamental component of the no-load back-EMF in the inner winding is decreased by 4.5%, and in the outer winding, it is increased by 3.8%. But, the THDs are 19.4% and 24.5% in the inner and outer windings, respectively, and these are considerably higher than those of the case of the excitation frequency with 0Hz. It means that the characteristics are varied by the conditions of the frequency of the excitation winding and the speed of the output rotor. Finally, the characteristics according to the winding MMF should be investigated. Fig. 2(a) and Fig. 2(b) show the variations of the amplitude of the no-load back-EMF and the output torque according to the winding MMF, respectively. The no-load back EMF of inner winding are increased as the MMF of the outer winding is getting bigger, while the increment of the no-load back EMF of the outer winding is gradual when the MMF of inner winding is increased. Furthermore, as shown in Fig. 2(b), the torque distribution by the variation of the inner and outer winding MMFs is not symmetric because the torque variations according to the winding MMF are different in each winding. Based on these characteristics, in this paper, the design process of the DFMGM, considering the flux modulation characteristics and the performance variation according to the frequency condition and the winding MMF in the inner and outer windings, is presented. First of all, based on the torque characteristics according to the winding MMF, the MMFs in the inner and outer windings, which are to produce the target torque, are determined. Secondly, the characteristics of the no-load back-EMF in each winding are analyzed, and the maximum frequencies of each winding in the constant torque region are selected. And then, the no-load back-EMF at the maximum frequency and whether the DFMGM can be operated at the maximum speed or not, are checked. Based on these performances, each winding is assigned as the armature and field windings. Finally, the total losses and the efficiencies at the main operating points are examined, and the whole process is repeated if the efficiencies at the main operating points are lower than the target efficiencies. By the systematic approach considering the inherent characteristics, the novel design process of the DFMGM is presented, and the possibility to apply the DFMGM to the traction system is proven.

[1] X. Guo, S. Wu, W. Fu, Y. Liu, Y. Wang, and P. Zeng, "Control of a dual-stator flux-modulated motor for electric vehicles," Energies, vol. 9, no. 7, Jul. 2016. [2] Y. Chen, W. Fu, and X. Weng, "A concept of general flux-modulated electric machines based on a unified theory and its application to developing a novel doubly-fed dual-stator motor," IEEE Trans. Ind. Electron., vol. 64, no. 12, pp. 9914-9923, Dec. 2017. [3] K. Atallah, S. D. Calverley, and D. Howe, "Design, analysis and realization of a high-performance magnetic gear," IEE Proc-Electr. Power Appl., vol. 151, pp. 135-143, Mar. 2004. [4] L. L. Wang, J. X. Shen, Y. Wang, and K. Wang, "A novel magnetic-geared outer-rotor permanent-magnet brushless motor," in Proc. PEMD, Apr. 2008. [5] Y. Fan, H. Jiang, M. Cheng, and Y. Wang, "An improved magnetic-geared permanent magnet in-wheel motor for electric vehicles," in Proc. VPPC, pp. 1-5, Sept. 2010. [6] Y. Fan, L. Gu, Y. Luo, X. Han and M. Cheng, "Investigation of a new flux-modulated permanent magnet brushless motor for EVs," Hindawi the scientific world journal, vol. 2014, Apr. 2014. [7] J. Bai, P. Zheng, C. Tong, Z. Song, and Q. Zhao, "Characteristics analysis and verification of the magnetic-field-modulated brushless double-rotor machine," IEEE Trans. Ind. Elec., vol. 62, no. 7, pp. 4023-4033, Jul. 2015. [8] J. Bai, P. Zheng, L. Cheng, S. Zhang, J. Liu, and Z. Liu, "A new magnetic-field-modulated brushless double-rotor machine," IEEE Trans. Magn., vol. 51, no. 11, Nov. 2015.

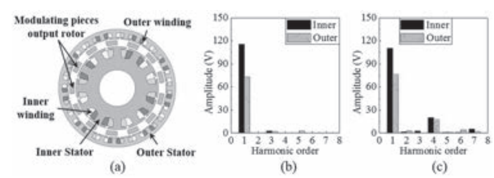

Fig. 1. Doubly Fed Magnetic Geared Motor: (a) Basic structure, (b) Time harmonic spectra of no-load back-EMF when the excitation frequency and the output rotor operate at 0Hz and 1662rpm, respectively, (c) Time harmonic spectra of no-load back-EMF when the excitation frequency and the output rotor operate at 180Hz and 2492rpm, respectively.

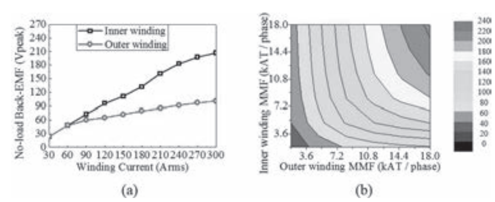

Fig. 2. Characteristics according to the variation of the winding MMF: (a) Amplitude of no-load back-EMF, (b) Output torque.

ES-08. Analysis on Torque Characteristics of Magnetic-Geared Machine with Sandwiched Armature Stator according to Pole Pair Combination.

D. Kang[1], J. Song[1], D. Kim[1], Y. Kim[2] and S. Jung[1]
1. Electronic, Electrical & Computer Engineering, Sungkyunkwan University, Suwon, The Republic of Korea; 2. Department of Electronical Engineering, Chosun University, Gwangju, The Republic of Korea

I Introduction Magnetic geared Machine (MGM) have gained importance in recent years for low speed large torque (LSLT) applications, such as wind power generation, traction drives and industrial robot arms [1]. Chau and Atallah have introduced MGM, which is combination of the magnetic gear (MG) and the permanent magnet (PM) type motor. The idea regarding MGM was further developed into two different topologies, which are outer armature stator (OAS) and inner armature stator (IAS), respectively [2], [3]. As the pole-pair combination has direct effects on the machine performance of MGM, it has been studied in many literatures for OAS-MGM and IAS MGM [4]-[7]. The sandwiched armature stator MGM (SAS-MGM), which is one of the recently proposed MGM topologies, utilizes not only the magnetic gearing effect from inner rotor torque, but also the vernier effect generated by stator compared to other types of MGM, as shown in Fig. 1. [8]-[10] However, the pole-pair combination of SAS-MGM is anticipated to follow that of the conventional MG, OAS-MGM, and IAS-MGM, indicating that additional research is required to derive proper pole-pair combinations to maximize the torque density of the SAS-MGM. In this paper, we analyzed the torque characteristics of SAS-MGM according to the various combinations of the outer rotor and armature pole pairs, to derive which pole-pair combination is more suitable for SAS-MGM. Then, we have proposed the SAS-MGM design of high torque density with proper pole-pair combination. II. OPERATING PRINCIPLE The magnetic gearing effect and the Vernier effect are theoretically identical. However, there are some differences in terms of source of the magnetic flux, which are modulated by the pole pieces. The main flux source of the magnetic gearing effect is generated from an internal rotor that rotates at high speed, and that of the Vernier effect comes from the stator armature winding. The number of pole-pair in the space harmonic flux density distribution produced by high and low speed rotor PM, is given by $p_{m,k} = \left| mp + kN_m \right|$, $m=1,3,5,\ldots$ $k=0,\pm1,\pm2,\pm3,\ldots$ (1) Where p is the number of pole-pairs on PM rotor and the N_m is the number of modulation ring. The speed of the flux density space harmonics is $\omega_{m,k}=mp/(mp+kN_m)\,\omega_r$ *(2)* Where ω_r is the speed of the PM rotor. Due to the effect of modulation ring, the rotating speed of the space harmonics of the flux density is not equal to that of the high speed PM rotor. Consequently, the number of modulator ring, as well as the high and low speed rotor pole-pair number should follow (3), in order to employ the magnetic gearing effect and the Vernier Effect. $N_m= p_{HS}+ p_{LS}$ (3) Where p_{HS} and p_{LS} are the number of high and low speed PM rotor pole pair, respectively. The operating principle of the SAS-MGM can be described by separating the machine into two PM motors and a magnetic gear. The first PM motor is of the high speed rotor and armature winding current, as the second PM motor is a Vernier motor, which is of the modulated armature winding and the low speed outer rotor. The high and low speed rotor, and the modulator forms magnetic gear that provides additional torque to the low speed rotor using the magnetic gearing effect. Under high current density conditions, core of the high speed rotor is magnetically saturated, limiting the magnetic gearing effect, which generates additional torque by means of the Vernier effect. [10] Due to the distinct configuration of the SAS-MGM, the effective air gap length is shorter than that of the OAS-MGM and IAS-MGM, which emphasizes use of the Vernier effect. III COMBINATION OF ROTOR AND STATOR POLE PAIRS Considering the manufacturing constraints, the gear ratio is selected between 3.2 and 12.5 with combination of P_{HS}=2,3,4,5 and 27, 24, 21 as given in Table I, as p_{LS} is calculated by means of (3). The torque characteristics of the pole pair combinations are analyzed, which is amplified by the gear ratio of the machine that significantly increases its torque density. In other perspective, the requisite input torque for its operation is determined by the gear ratio of the machine. The slope of the torque curve according to the gear ratio has inflection point, while the torque of Vernier effect has different inflection point. The combination of these two inflection points will result in optimal combination of SAS-MGM, which is designed based on the parameters of Table II. In the manuscript, the torque characteristics variation due to combinations of rotor pole pair ratio will be described and the torque-curve of optimal design model will be addressed.

[1] Razzell, Anthony G., and John JA Cullen. "Compact electrical machine." U.S. Patent No. 6,794,781. 21 Sep. 2004. [2] K. T. Chau, D. Zhang, J. Z. Jiang, C. Liu, and Y. Zhang, "Design of a magnetic-geared outer-rotor permanent-magnet brushless motor for electric vehicles," *IEEE Trans. Magn.*, vol. 43, no. 6, pp. 2504–2506, 2007. [3] K. Atallah, J. Rens, S. Mezani, and D. Howe, "A novel 'pseudo' direct-drive brushless permanent magnet machine," *IEEE Trans. Magn.*, vol. 44, no. 11 PART 2, pp. 4349–4352, 2008. [4] L. L. Wang, J. X. Shen, P. C. K. Luk, W. Z. Fei, C. F. Wang, and H. Hao, "Development of a magnetic-geared permanent-magnet brushless motor," *IEEE Trans. Magn.*, vol. 45, no. 10, pp. 4578–4581, 2009. [5] D. J. Evans and Z. Q. Zhu, "Optimal torque matching of a magnetic gear within a permanent magnet machine," *2011 IEEE Int. Electr. Mach. Drives Conf. IEMDC 2011*, no. Im, pp. 995–1000, 2011. [6] P. M. Tlali, S. Gerber, and R. J. Wang, "Optimal Design of an Outer-Stator Magnetically Geared Permanent Magnet Machine," *IEEE Trans. Magn.*, vol. 52, no. 2, 2016. [7] N. W. Frank and H. A. Toliyat, "Gearing ratios of a magnetic gear for wind turbines," *2009 IEEE Int. Electr. Mach. Drives Conf. IEMDC '09*, pp. 1224–1230, 2009. [8] L. Jian, W. Gong, G. Xu, J. Liang, and W. Zhao, "Integrated magnetic-geared machine with sandwiched armature stator for low-speed large-torque applications," *IEEE Trans. Magn.*, vol. 48, no. 11, pp. 4184–4187, 2012. [9] Z. Deng, L. Jian, G. Peng, Y. Shi, and J. Wei, "Modeling of Magnetic-Geared Permanent Magnet Machines with Sandwiched Armature Stator," *2016 IEEE Veh. Power Propuls. Conf. VPPC 2016 - Proc.*, 2016. [10] Y. Shi, J. Wei, and L. Jian, "Parallel-Path Power Flows in Magnetic-Geared Permanent Magnet Machines with Sandwiched Armature Stator," vol. 3, no. 1, 2017.

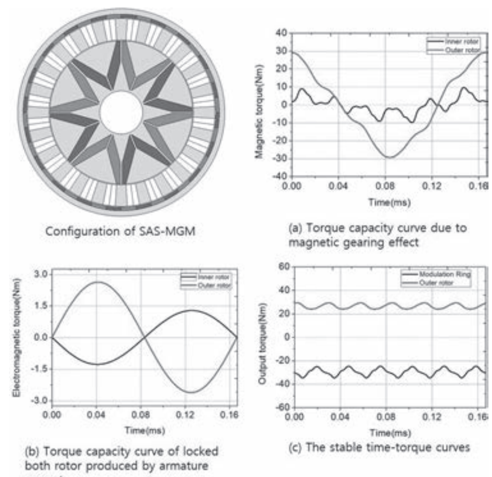

Fig. 1. Configuration and torque capacity

P_{HS}	P_{LS}	N_m	Gear ratio
4	50	27	12.5
	44	24	11
	38	21	9.5
6	48	27	8
	42	24	7
	34	21	5.67
8	32	27	6.5
	40	24	5
	52	21	4
10	32	27	4.4
	38	24	3.8
	44	21	3.2

Table I. The combination of pole-pairs

Parameter	Value	단위
Outer rotor Diameter	170	mm
Air Gap	0.7	mm
Split ratio	0.7	
Rated Speed	20	rpm

Table II. Specification of proposed SAS-MGM

Fig. 2. The Combination of Pole-pairs and the required specification

ES-09. Efficiency Improvement of Magnetic-Geared Motor by Open-Slot and Interior Permanent Magnet Structure.

K. Nakamura[1], T. Kadomatsu[1] and Y. Hane[1]
1. Graduate School of Engineering, Tohoku University, Sendai, Japan

Magnetic gears can transmit torque without any mechanical contacts. Hence, they have low vibration, no wear and fatigue, which offer maintenance-free operation. Various kinds of magnetic gears have been introduced in previous papers and patents. Among them, a flux-modulated type magnetic gear, which consists of an inner and outer rotor with surface–mounted permanent magnets, and ferromagnetic stationary parts which are called pole–pieces, is attracting interest since the torque density is higher than the other magnetic gears [1]. Furthermore, torque generation principles of a magnetic gear and a conventional permanent magnet (PM) motor are the same, hence both can be magnetically combined (not mechanically), which offers reduction of size, weight, the number of parts, and the cost. Several papers report torque increase of the magnetic-geared motors [2], [3], however the reports on efficiency improvement are few [4]. This paper describes the efficiency improvement of the magnetic-geared motor. First, a proposed magnetic-geared motor with open-slot stator and interior permanent magnet (IPM) rotor is compared to a conventional one in terms of efficiency. Next, it is demonstrated that a prototype magnetic-geared motor has high efficiency as designed. Fig. 1(a) shows configuration of a conventional magnetic-geared motor. The inside part of the magnetic-geared motor is an outer-rotor type PM motor, while the outside one is a flux-modulated type magnetic gear. As shown in the figure, the outer-rotor of the PM motor and the inner rotor of the magnetic gear are shared each other. Fig. 1(b) shows a proposed magnetic-geared motor. Basic configurations of both motors are the same, but the shared-rotor of the proposed motor has IPM structure, thereby eddy current loss of the magnets can be reduced. In addition, the number of parts and cost are expected to be reduced. Furthermore, the stator has the open-slot structure, which increases winding space factor. Although the open-slot structure causes large cogging and ripple of torque in general, the proposed motor employs 9-slot and 8-pole combination and the pole number of inner rotor and pole-pieces of the magnetic gear are chosen 8 and 27 so that the least common multiple of both number becomes large. Fig. 1(c) indicates the comparison of efficiency calculated by three-dimensional finite element method (3D-FEM). The figure reveals that the efficiency of the proposed magnetic-geared motor is higher than that of the conventional one, and reaches 90%. Based on the above results, a trial magnetic-geared motor was prototyped. Fig. 2(a) shows an experimental setup of the prototype magnetic-geared motor. Fig. 2(b) indicates the current density versus torque characteristics. It is understood that the proposed magnetic-geared motor has the good characteristics as designed. Fig. 2(c) represents the efficiency of the prototype machine. The measured maximum efficiency is about 85%, which is smaller than that of the calculated one because mechanical loss cannot be taken into account in 3D-FEM. A part of this work was supported by JSPS KAKENHI Grant-in-Aid for Scientific Research (b), Grant Number 16H04310.

[1] K. Atallah and D. Howe, "A Novel High-Performance Magnetic Gear", IEEE Trans. Magn. Vol. 37, No. 4, pp. 2844-2846 (2001). [2] K. Atallah, S. Calverley, R. Clark, J. Rens, and D. Howe, "A New PM Machine Topology for Low-Speed, High Torque Drives". Proceedings of the 2008 International Conference on Electrical Machines (ICEM). [3] K. Nakamura, K. Akimoto, T. Takemae, and O. Ichinokura, "Basic Characteristics of In-Wheel Magnetic-geared Motors", Journal of the Magnetics Society of Japan, Vol. 39, No. 1, pp. 29-32 (2015) [4] T. V. Frandsen and P. O. Rasmussen, "Loss Investigation of Motor Integrated Permanent Magnet Gear", Proceedings of the 17th International Conference on Electrical Machines and Systems (ICEMS), pp. 2673-2679 (2014).

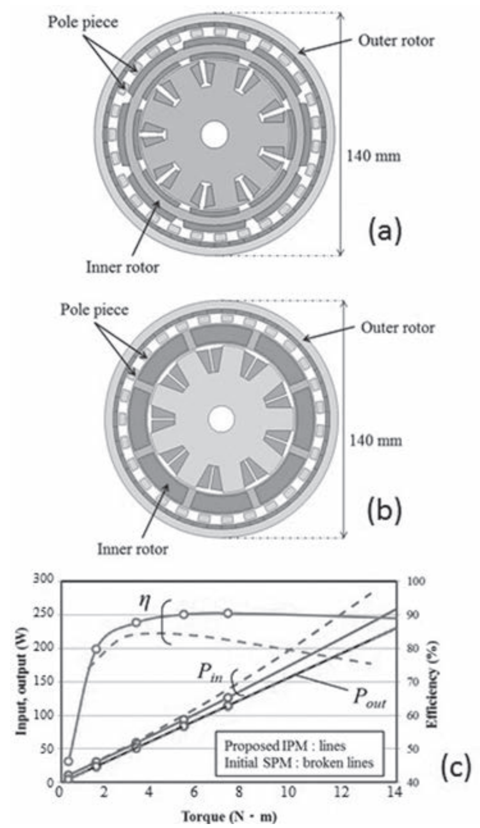

Fig. 1. Basic configurations of a conventional and proposed magnetic-geared motors and comparison of efficiency calculated by 3D-FEM.

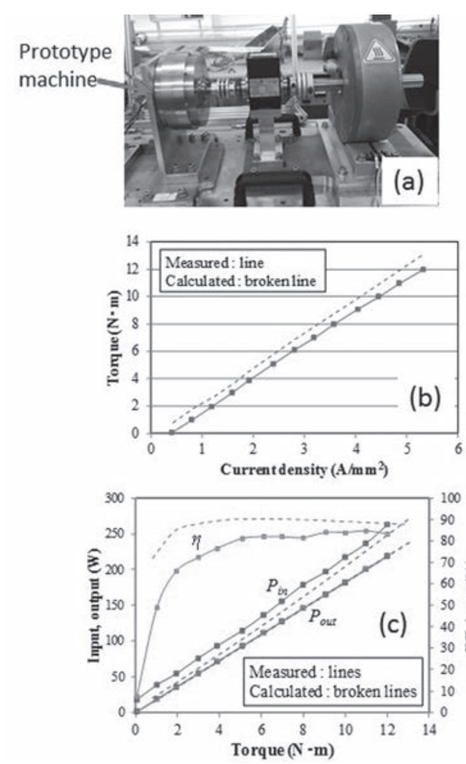

Fig. 2. Prototype magnetic-geared motor and its measured torque and efficiency characteristics.

ES-10. Comparative Study on the Characteristics of Magnetic-geared Permanent Magnet Synchronous Motor for Electric Vehicles according to Gear Ratio Variation.

C. Park[1] and G. Jeong[2]
1. Korea National University of Transportation, Uiwang-si, The Republic of Korea; 2. Hanyang University, Seoul, The Republic of Korea

1. Intoduction Conventional driving system of hybrid electric vehicle (HEV) or electric vehicle(EV) are composed of traction motor, mechanical or magnetic reduction gear, and wheels, so that the structure of the driving system is complicated and there is a limit in reducing the size and weight of each component. In addition, the conventional driving system has problems of increase in maintenance cost due to transmission oil leakage and tooth wear of the ruction gear, and low efficiency due to additional power loss by the mechanical gear. Therefore, it is necessary to develop a new technology that can increase the output power density and maintainability of the conventional system in a driving system for HEV or EV. Currently, research on magnetic gears to replace mechanical reduction gears is being carried out variously all over the world [1]-[3]. Japan conducted a comparative analysis of the fuel consumption in LEXUS IS300h hybrid electric vehicle with a mechanical reduction gear and a traction motor, and with a magnetic split and traction motor. The use of magnetic gears has reduced fuel consumption by up to 3.6%, which has proven the superiority of magnetic geared system over mechanical reduction system [4], [5]. Fig. 1 demonstrates the structure of an MG-PMSM system as opposed to a conventional driving system. In this paper, the design technique of the MG-PMSM is first studied for the application of the MG-PMSM structurally integrated with magnetic gear and PMSM to the electric vehicle driving system. In addition, a small-scale MG-PMSM model is designed and characteristic analysis were conducted using an electromagnetic FEM tool. *2. Design and analysis* Unlike conventional traction motors, the MG-PMSM presented in this study features a dual-rotor structure in which the outer and inner rotors rotate at different speeds. Generally, the inner rotor has a high-speed, low-torque characteristic, while its outer counterpart functions in low-speed, high-torque conditions [6]-[8]. Therefore, when the MG-PMSM is applied in a driving system for electric vehicles, the wheels should be directly linked to the outer rotor, with its low-speed and high-torque qualities. This study presents an additional process that allows for the simultaneous design of pole-pieces consisting of a low-speed outer rotor, which is based on the PMSM design process for inner rotors that apply the loading distribution method commonly used in traction motors for electric vehicles. In this paper, a basic design was performed to establish MG-PMSM models for electric vehicles. The pole number of the permanent magnet of the inner rotor of the MG-PMSM was set to 4. The gear ratio in a typical gear reducer for electric vehicles ranges from 3 to 8 [1]. In this study, the gear ratio was restricted to 5:1 or less in consideration of the production viability of the MG-PMSM miniatures, where the rated torque and rotational speed of the low-speed rotor was set to 12 Nm and 800 rpm, respectively. Table I shows the design criteria for the 1kW-class MG-PMSM. In compliance with the established criteria, models 30-7(Model A), 42-9 (Model B) and 54-11 (Model C) were designed, where the pairs of numbers, 30-7, 42-9 and 54-11, indicate the slot number followed by the number of pole-pieces of the stator. A final version of the designed models was established for the 1kW-class MG-PMSM based on the geometric data of the determined stator and rotors, as summarized in Table II. Fig. 2 shows the cross section of the basic 1kW-class MG-PMSM models designed in this study. This study analyzes the electromagnetic characteristics of three MG-PMSM Models, which were designed using the 2D-FEA (Finite Element Analysis) tool. The Back-EMF and the magnetic flux density of the MG-PMSM at the inner and outer air gaps were analyzed in the no-load and full-load conditions. In addition, the cogging and rated torque analysis of the MG-PMSM models were analyzed in the no-load and full-load conditions. Table III summarizes the characteristics of the electromagnetic parameters of the 1kW-class MG-PMSM models. *3. Conclusions* In this study, the design technique of the MG-PMSM for electric vehicles was examined in the application of the MG-PMSM being structurally integrated with a magnetic gear to the electric vehicle driving system. In designing the MG-PMSM models, this study presents an additional process that allows for the simultaneous design of pole-pieces consisting of the low-speed outer rotor, which is based on the PMSM design process for inner-rotors that apply the loading distribution method, commonly used in traction motors for electric vehicles. A comparative analysis of the three 1kW-class MG-PMSM models, in terms of electromagnetic properties, was performed to assess their general performance. 3 models showed performance levels that met the design requirements, while Model B had better torque performance than Model A and C. Yet, the magnetic flux density of both models was distributed asymmetrically at the air gaps and the core of the stator, and less than 90 percent of the torque was delivered to the inner rotor. Our follow-up study will develop an improved model in which an even number of pole-pieces is included in the outer rotor so that the magnetic flux density is distributed symmetrically at the air gaps and the core of the 1kW-class MG-PMSM, as well as optimizing pole-piece designs to improve the efficiency of torque delivery.

[1] L. Sun, M. Cheng, H. Jia, "Analysis of a novel magnetic-geared dual-rotor motor with complementary structure," *IEEE Transaction on Industrial Electronics*, vol.62, no.11, pp.6737-6747, 2015. [2] K. T. Chau, D. Zhang, J. Z. Jiang, C. Liu, Y. Zhang, "Design of a magnetic-geared outer-rotor permanent-magnet brushless motor for electric vehicles," *IEEE Transaction on Magnetics*, vol.43, no.6, pp.2504-2506, 2007. [3] K. Atallah, S. D. Calverley, D. Howe, "Design, analysis and realization of a high-performance magnetic gear, *IEE Proceedings- Electric Power Applications*, vol. 151, no. 2, pp.135-143, 2004. [4] N. Niguchi, K. Hirata, "Cogging Torque Characteristics of a Magnetic-Geared Motor, *Electrical Engineering in Japan*, vol. 185, no. 2, pp.40-50, 2013. [5] M. Taha, D. Greenwood, "PM material selection guide for IPMSM," *2016 XXII International Conference on Electrical Machines (ICEM)*, 2016. [6] K. H. Shin, H. I. Park, H. W. Cho, K. H. Choi, J. Y. Choi, "Analytical Prediction for Electromagnetic Performance of Magnetic-Geared Permanent Magnet Machine based on Space Harmonic Method," *KIEE Summer Conference 2016*, pp.837-838, 2016. [7] G. S. Park, S. Y. Jung, Y. J. Kim, "Transfer Torque and Power Density Characteristic Analysis according to Combination of Rotor Poles for Magnetic Gear," *KIEE Summer Conference 2015*, pp.760-761, 2015. [8] S. A. Hong, J. Y. Choi, "Comparison and Torque Analysis for Magnetic Gear with Parallel/Halbach Magnetized PMs according to Design Parameters," *Journal of the Korean Magnetics Society*, vol. 24, no. 5, pp.152-159, 2014.

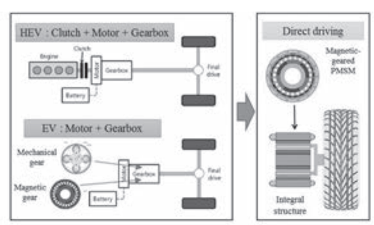

Fig. 1. Conventional driving system and MG-PMSM system for EV

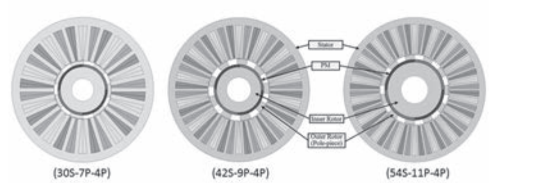

Fig. 2. Design models of the 1kW-class MG-PMSM

TABLE I : Design criteria for 1kW-Class MG-PMSM

Specification	Value
Gear Ratio	Under 1:5
Rated Speed of Outer Rotor	800 RPM
Rated Torque of Outer Rotor	12 Nm
Output Power of Outer Rotor	1 kW
DC Link Voltage	Under 150 V
Phase / PM Poles	3 / 4
Current Density	4.5 A_{rms}/mm^2
Operation Temp.	150 ℃
Core / Magnet Material	S08 / $SmCo_5$

TABLE II : Design results of 1kW-Class MG-PMSM

Dimension	Value		
	30S-7P-4P	42S-9P-4P	54S-11P-4P
Rated Speed / Torque of Inner Rotor	2000 rpm / 3.5 Nm	2800 rpm / 3.43 Nm	3600 RPM / 2.67 Nm
DC-Link Voltage / Voltage Limit (SVPWM)	120 V_{dc} / 69 V_{peak}	120 V_{dc} / 69 V_{peak}	100 V_{dc} / 57.7 V_{peak}
Phase Rated Current	6.5 A_{peak}	6.5 A_{peak}	5.0 A_{peak}
Slots of stator / Pole Pieces	30 / 7	42 / 9	54 / 11
Outer Dia. of Stator	190 mm	183.8 mm	170 mm
Outer / Inner Dia. of Inner Rotor	60 mm / 30 mm	58 mm / 31.9 mm	65 mm / 32.5 mm
Stack Length / Thickness of PM	100 mm / 3 mm	100 mm / 3 mm	120 mm / 3 mm
Inner / Outer Airgap	0.5 / 0.5 mm	0.5 / 0.5 mm	0.5 / 0.5 mm
Thickness / Angle of Pole-piece	4.5 mm / 25.7 °	7 mm / 20.3 °	5 mm /16.4 °

TABLE III : Electromagnetic characteristic analysis results of the 1kW-Class MG-PMSM models

Dimension	Value		
	30S-7P-4P	42S-9P-4P	54S-11P-4P
Back EMF (No-load/Full-load)	27.7 V_{peak} / 68.1 V_{peak}	29.2 V_{peak} / 61.3 V_{peak}	28.3 V_{peak} / 54.9 V_{peak}
Average Airgap B_r per pole (No-load)	Inner 0.67 / Outer 0.38 T	Inner 0.67 / Outer 0.39 T	Inner 0.64 / Outer 0.43 T
Average Airgap B_r per pole (Full-load)	Inner 0.64 / Outer 0.43 T	Inner 0.65 / Outer 0.37 T	Inner 0.63 / Outer 0.42 T
Cogging Torque of Inner/Outer Rotor	2.6 / 2.6 Nm_{ptop}	0.95 / 1.07 Nm_{ptop}	2.70 / 2.82 Nm_{ptop}
Rated Torque of Inner/Outer Rotor	3.8 / 12.6 Nm	3.20 / 12.6 Nm	2.32 / 12.3 Nm

ES-11. Comparative Study and Analysis of Two Different Types of Coaxial Magnetic Gears Considering Magnetic Losses and Magnet Volume.

J. Lee[1], T. Bang[1], K. Shin[1], S. Cho[1] and J. Choi[1]
1. Dept. of Electrical Engineering, Chungnam National Universtiy, Daejeon, The Republic of Korea

A gear is a mechanical device that transfers rotational force or power through the engagement of its teeth on the primary and secondary sides. Currently, gears are used in many industries, including automotive systems, conveyors, consumer electronics, and rotating machineries [1]. Mechanical gears that are normally used are mainly made of metal materials. Gears have mechanical friction due to physical contact and have many problems, such as noise, vibration, and dust. Another disadvantage is that the life of a system is shortened because its gear is worn or damaged when the system is overloaded. To overcome these problems, maintenance work with lubricants is necessary [2]. In recent years, magnetic gears using permanent magnets have being studied as alternatives to mechanical gears. The structure of the magnetic gear has a permanent magnet attached to the inner and outer rotors, and transmits the rotational force or power in a noncontact manner (without physical contact) using the force of attraction of the permanent magnet. Further, noncontact driving can compensate for the disadvantages of mechanical gears, such as noise and vibration, and does not require maintenance. Moreover, it has the advantage that it can be used semi-permanently because the gear is not worn or damaged by slip when overloaded [3]. However, due to China's export restrictions on rare earth recently, the prices of rare earth elements are unstable and have problems with price fluctuations. Due to these problems, various structures that are useful in minimizing the use of permanent magnets have been studied recently. In this paper, the characteristics of surface-mounted coaxial magnetic gear (SMCMG) and consequent pole coaxial magnetic gear (CPCMG) were analyzed. The SMCMG model has a structure in which permanent magnets are attached to the inner and outer sides, and a fixed iron core is located between them [4]. Figure 1 shows the structure and prototype of a magnetic gear. The CPCMG structure is similar to that of SMCMG; however, it has a structure using inner and outer permanent magnets with only N poles [5]. The gear ratio of a magnetic gear can be calculated by the number of poles of the inner and outer permanent magnets. For CPCMG, the pole pitch of the inner and outer permanent magnets was changed, and the optimum pole pitch with the maximum torque was selected. Further, CPCMG uses only N pole for permanent magnets, resulting in a lower pull-out torque characteristic than that of SMCMG. Therefore, the stack length of the CPCMG is increased by about 1.5 times and the torque is designed to be the same as that of the SMCMG. Thus, when the two types meet the same 7.75 gear ratio and torque characteristics, the total amount and weight of the used permanent magnets and the loss characteristics of each gear were analyzed. When the same torque is satisfied, the characteristics analysis result of SMCMG shows 0.947 kg of permanent magnet used and 0.941 kg used for CPCMG. The total weight of the magnetic gear was 3.794 kg for SMCMG and 5.82 kg for CPCMG. For CPCMG, as the axial length increases, the permanent magnet usage decreases as compared to that for SMCMG; however, its total weight increases. The torque characteristic analysis result shows that the torque total harmonic distortion (THD) was not significantly different for both CPCMG and SMCMG. However, the torque ripple characteristics are larger in CPCMG than in SMCMG. As per the loss analysis, the SMCMG uses more permanent magnets than the CPCMG, resulting in more eddy current losses being generated than the CPCMG. However, the CPCMG uses more steel core. Therefore, the core loss is lower in SMCMG than in CPCMG. In this paper, a comparative study and analysis of two different types of coaxial magnetic gears were performed. As per the analysis, the stack length of the CPCMG must increase in order to satisfy the condition of having the same torque characteristic as that of the SMCMG. In the ripple characteristics, SMCMG is advantageous; however, in terms of efficiency, CPCMG is more effective. Therefore, we have completed the analysis to select the most suitable and efficient coaxial magnetic gear for the use conditions. More detailed analysis results will be explained in the final paper. Acknowledgment This work was supported by the Basic Research Laboratory (BRL) of the National Research Foundation (NRF-2017R1A4A1015744) funded by the Korean government.

[1] H. Rashidi and D. Pishdad, "Integrated Multispeed Magnetic Gears: A Novel Approach to Design of Magnetic Transmission Systems," IEEE Transactions on Magnetics, vol. 51, no. 4, Apr. 2015. [2] M. Fukuoka, K. Nakamura, and O. Ichinokura, "Dynamic Analysis of Planetary-Type Magnetic Gear Based on Reluctance Network Analysis," IEEE Transactions on Magnetics, vol. 47, no. 10, Oct. 2011. [3] T. V. Frandsen, L. Mathe, N. I. Berg, R. K. Holm, T. N. Matzen, P. O. Rasmussen, and K. K. Jensen, "Motor Integrated Permanent Magnet Gear in a Battery Electrical Vehicle," IEEE Transactions on Industry Applications, vol. 51, no. 2, Mar./Apr. 2015. [4] W. N. Fu and L. Li, "Optimal Design of Magnetic Gears With a General Pattern of Permanent Magnet Arrangement," IEEE Transactions on Applied Superconductivity, vol. 26, no. 7, Oct. 2016. [5] J. X. Shen, H. Y. Lim, H. Hao, and M. J. Jin, "A Coaxial Magnetic Gear With Consequent-Pole Rotors," IEEE Transactions on Energy Conversion, vol. 32, no. 1, Mar. 2017.

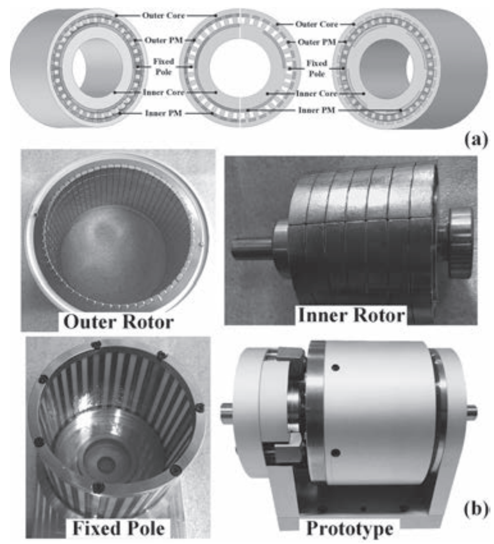

Fig. 1. Coaxial magnetic gear. (a) Structure of a magnetic gear (b) Prototype and parts

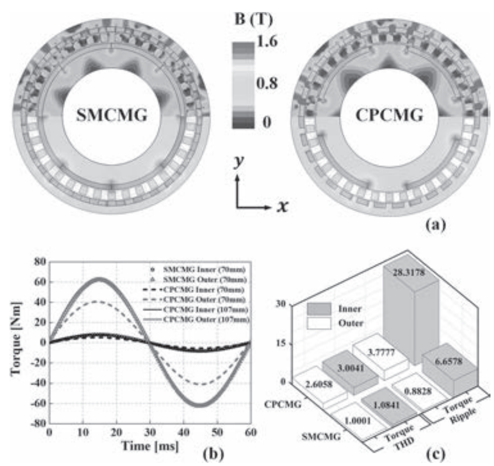

Fig. 2. Characteristics of two different types of coaxial magnetic gears. (a) Magnetic flux density distribution and flux line (b) Torque characteristics (c) Torque THD and torque ripple

ES-12. Comparative Study of Axial Flux Magnetically Geared Machine with Conventional Axial Flux YASA Machine.

M.F. Khatab[1], Z. Zhu[1], H. Li[1] and Y. Liu[1]
1. The University of Sheffield, Sheffield, United Kingdom

I. Introduction Magnetic gears (MGs) have recently been proposed to replace conventional mechanical gears in various electromechanical systems. MGs have competitive torque transmission capability compared with their mechanical counterpart [1]. Moreover, by integrating an MG into a conventional PM machine, a magnetically geared machine has emerged, greatly broadening the machine topology. It always has the merits of high torque density and reduced overall size in comparison with conventional PM machine axially combined with MGs [2]. In general, the same as conventional machines, magnetically geared machines can be considered by their flux orientations, i.e. radial and axial flux machines. Axial flux permanent magnet (AFPM) machines have unique advantages over radial flux PM (RFPM) machines, such as high torque density, low rotor losses, and high efficiency. Among various AFPM machines, the yokeless and segmented armature (YASA) machine has shown to exhibit superior performance. The machine has a unique design in which the stator is formed by separated segments with windings, and moreover, two identical surface mounted PM rotors are axially located on both stator sides [3]. Based on YASA machine, a new axial flux magnetically geared machine for power split applications has been presented in [4]. The presented machine essentially has the same stator structure as the conventional YASA machine. However, by employing different rotor pole pairs in the YASA machine, a new axial flux magnetically geared machine can be created. In this study, the axial flux magnetically geared machine and the conventional YASA machine with the same volume will be comparatively studied. Individual optimizations have been carried out to maximize the average torque of two machines. Moreover, the machine performance at no load and on load will be compared. II. Machine structure and principle of operation In the full paper, the compared machine dimensions and parameters, as well as the principle of operation, will be fully described. The axial flux magnetically geared machine structure is shown in Fig. 1(a). The machine consists of 12 stationary ferromagnetic iron pieces equipped with concentrated windings and located between two surface mounted PM rotors with different poles and rotate at different speeds. By assuming high-speed rotor (HSR) of 10 poles and low-speed rotor (LSR) of 14 poles, the torque can be transferred between both rotors due to the MG effect. On the other hand, YASA machine shown in Fig. 1(b) also has 12 stator pole numbers sandwiched between two identical 14 poles surface mounted PM rotors which are physically connected to each other. The torque of the axial flux magnetically geared machine consists of two parts: the MG torque which is a function of the relative angle between HSR and LSR and electromagnetic torque produced by the interaction between winding armature reaction flux harmonics and PMs flux harmonics of each rotor. The machine MG torque is calculated at maximum relative angle between HSR and LSR. It has been stated that maximum torque can be transferred between HSR and LSR when the angle between both rotors is 90 elec. Deg. [5]. Moreover, by considering that the LSR torque is the output which is connected to the drive shaft and the HSR is connected to the external prime-mover, the total torque of the LSR is increased by the armature reaction torque produced by the applied current. III. Performance comparison of axial flux magnetically geared with conventional YASA machine In the full paper, with the aid of 3D-finite element analysis (FEA), the axial flux magnetically geared machine and YASA machine will be analysed and compared with the same machine outer diameter, axial length and copper loss. A comparison between the MG torque performance (no-load) and the torque at rated current (on-load) of the axial flux magnetically geared machine with YASA machine torque is illustrated in Fig.2. It is obvious that magnetically geared machine has higher output torque exerted by LSR due to the MG effect of about 5.2 Nm. Moreover, the torque can be increased by armature reaction to reach just below 7 Nm. Both are higher than YASA machine torque of 3.2 Nm. It clearly shows that higher torque density can be obtained by the magnetically geared machines compared with the conventional PM machines. IV. Conclusion In this study, the proposed axial flux magnetically geared machine and the conventional YASA machine have been designed with the aid of 3D-FEA. Their machine no-load and on-load performances have been analysed and compared. Simulation results show that a significantly higher torque density can be obtained compared with YASA machine. Moreover, more performance aspects at no-load and full load will be given in details and compared in the full papers, together with the measured results.

[1] K. Atallah and D. Howe, "A novel high-performance magnetic gear," *IEEE Trans. on Magn.*, vol. 37, no.4, pp. 2844-2846, Jul. 2001. [2] L. L. Wang, J. X. Shen, P. C. K. Luk, W. Z. Fei, C. F. Wang, and H. Hao, "Development of a magnetic-geared permanent-magnet brushless motor," *IEEE Trans. on Magn.*, vol. 45, no.10, pp. 4578-4581, 2009. [3] W. Fei, P. Luk, and K. Jinupun, "A new axial flux permanent magnet segmented-armature-torus machine for in-wheel direct drive applications", *IEEE Power Elect. Specialists Conf., PESC,* 2008, pp. 2197-2202. [4] Z. Q. Zhu, M. F. H. Khatab, H. Y. Li, and Y. Liu, "A novel axial flux magnetically geared machine for power split application", *Twelfth Int.Conf. Ecolo. Vehicles and Renewable Energies (EVER)*, 2017, pp. 1-8. [5] N. W. Frank and H. A. Toliyat, "Gearing ratios of a magnetic gear for wind turbines," *in Proc. IEEE int. Elec. Mach. Drives Conf.*, 2009, pp. 1224-1230.

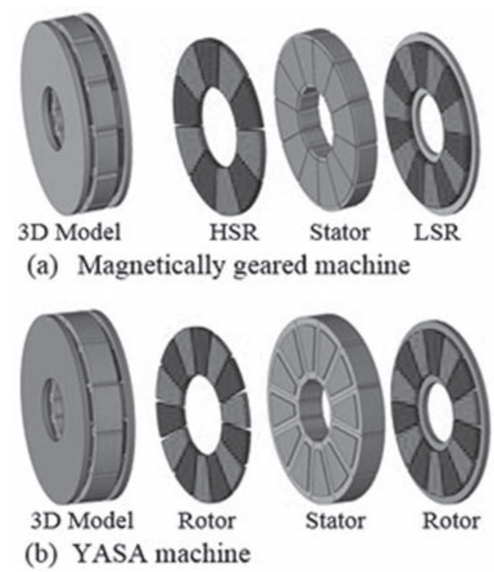

Fig. 1. Machine configurations.

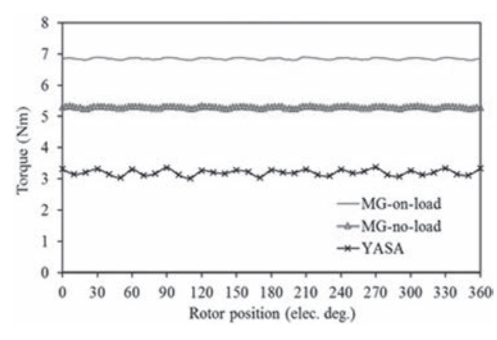

Fig. 2. Comparison of torque performance.

ES-13. Design of Marine Current Power Generation System Based on a Magnetic Gear.

N. Feng[2,1], H. Yu[1], X. Liu[1] and R. Guo[1]
1. School of Electrical Engineering, Southeast University, Nanjing, China;
2. School of information and electrical engineering, Ludong University, Yantai, China

1. introduction This paper presents the design and analysis of a marine current power generation system (MCPGS) for capturing energy from marine current. In this paper, a magnetic gear will be presented for an MCPGS application. The marine current turbine (MCT) blade speed is amplified by a magnetic gear (MG) and then converted into electrical energy for supplying the loads by a permanent magnet synchronous generator (PMSG). The main features of the MCPGS based on the MG will be described. The technological solution could lead to a feasible marine-current-power future scenario. 2. MCPGS 2.1 Design of MG The MG consists of the outer armature (stator) and the inner armature (high-speed rotor) carrying PM arrays with different numbers of poles and the intermediate low-speed rotor having a set of annular ferromagnetic pole pieces. The torque and speed transformation between the two rotors can be transmitted by the modulation effect of magnetic field of the ferromagnetic pole pieces, so as to generate the appropriate space harmonic with the same pole-pairs as the other permanent magnet armature. The MG is designed with 3 pole pairs PMs in the inner armature and 22 pole pairs PMs in the outer armature. Between inner armature and outer armature locates 25 ferromagnetic pole-pieces, which modulate space harmonic flux distribution. The magnetic field distribution under no-load is depicted in Fig.1 (a). The radial flux densities in the inner and outer air gap are shown in Fig1. (b) and Fig1. (c), respectively. It is worth mentioning that the 3th and 22th space harmonic components are the most dominant ones. It can be seen that the ferromagnetic segments modulate the appropriate harmonic components having the same number of pole-pairs as the PMs of the other armature. If the outer armature is kept stationary, the inner armature and ferromagnetic ring have the same rotation direction. The gear ratio between inner armature and the ferromagnetic ring is followed: $G_r=n_s/p_{1=25/3=8.33.}$ 2.2 Fundamental CONFIGURATION of MCPGS The MCPGS unit consists of four-blade MCT, a MG, a three-phase PMSG, and a power converter that is used for converting generated energy to be stored in the battery. The MG with a single-input shaft and a single-output shaft is specially designed and manufactured to couple the output rotor shaft of the designed MCT to the input rotor shaft of the employed PMSG. The gear ratio of 8.33 is designed for the MG in order to increase the low rotational speed of the MCT (around 26 rpm) to the required rotational speed of the PMSG (around 220 rpm). The output terminals of the PMSG are connected to a load through power converters with appropriate control. 3.Design of Test Bench For the performance tests of MG, the MG is to couple the output shaft of the three-phase drive motor on low-speed side to the input shaft of the load PMSG on high-speed side, as shown in Fig.2(a). In this scheme, the drive motor on the low-speed side is geared up by a MG and then converted into voltage by a PMSG.The performance of MG is analyzed in the test bench. Because of processing precision of parts, mechanical assembling accuracy and measurement error, compared to simulation results of static torque, there was a fall of 20 percent in the test results. When the ferromagnetic rings and the inner armature rotate at rated speed (26 rpm and 220 rpm) respectively, the steady torque characteristics are obtained. The inner armature test torque is T_1 = 10 Nm, and the outer armature test torque is T_2 =71 Nm. With the parameters of MG, the peak torque of the ferromagnetic ring is 81 Nm, giving an active region torque density of 79 Nm/L. 4. MCPGS Test The experimental conditions are as follows: a water depth of 0.6-0.7 meters and the current speed of 0.4-0.5m/s. The blade diameter of the MCT is 0.6 m. Due to the limitations of experimental conditions, four MCTs are cascaded so as to obtain the bigger drive torque. The marine current generation device is presented in Fig. 2(b). The rated voltage and rated speed of the PMSG are 12V and 220 rpm, respectively. The no-load EMF of the MCPGS is 9.8V at the current speed of 0.4 m/s in test tank. For the load of 10 ohm, the peak voltages of the MCPGS at different current speed are presented. Typically, when the speed of ferromagnetic ring and the inner armature is 22.7rmp and 190rmp respectively, the peak voltage is 7.09V.The output voltage of the MCPGS shows a linear relationship for rotational speed of MG. 5.Conclusion This paper presents a MCPGS consists of a PMSG driven by a MCT with an accelerated diffuser through a MG. We shall describe the main features of the MCPGS based on the MG.The proposed MCPGS equipped with an accelerated diffuser can capture the kinetic energy of marine currents efficiently and improve the system efficiency. The high-performance MG is designed for a low speed ocean generation application and adopted to improve the system reliability. The technological solution could lead to a feasible scheme for MCPGS in the future.

[1] EUREC Agency. The future for renewable energy: prospects and directions. London, UK: James & James Ltd.; 1996. [2] Bahaj AS, Myers LE. Fundamentals applicable to the utilisation of marine current turbines for energy production. Renew Energy 2003; 28: 2205–11. [3] CENEX Project. Marine current energy extraction. Report JOU2-CT93-0355, IT-Power, Tecnomare, ENEL, University of Patras; 1996. [4] F.L. Ponta, P.M. Jacovkis, “Marine-current power generation by diffuser-augmented floating hydro-turbines,” Renew. Energy, vol. 33, no. 4, pp. 665–673, Arp. 2008. [5] I. G. Bryden and S. J. Couch, “ME1—Marine energy extraction: Tidal resource analysis,” Renew. Energy, vol. 31, no. 2, pp. 133–139, Feb. 2006. [6] A. S. Bahaj and L. Myers, “Analytical estimates of the energy yield potential from the Alderney Race Channel Islands using marine current energy converters,” Renew. Energy, vol. 29, no. 12, pp. 1931–1945, Oct. 2004. [7] S. Bahaj, A. F. Molland, J. R. Chaplin, and W. M. J. Batten, “Power and thrust measurements of marine current turbines under various hydrodynamic flow conditions in a cavitation tunnel and a towing tank,” Renew. Energy, vol. 32, no. 3, pp. 407–426, Mar. 2007. [8] Peter Omand Rasmussen, Torben Ole Andersen, Frank T. Jorgensen, and Orla Nielsen. Development of a High-Performance magnetic gear [J].IEEE Transactions on Industry Applications, 2005, 41(3):764-770. [9] K. Atallah, S.D. Calverley, and D Howe. Design, analysis and realization of a high-performance magnetic gear [J]. IEE Pro.-Electr. Power Appl. 2004, 151(2):135–143. [10] L. Jian, K. T. Chau, Y. Gong, J. Z. Jiang, C. Yu, and W. Li. Comparison of coaxial magnetic gears with different topologies[J].IEEE Trans. Magn., 2009, 45(10):4526–4529. [11] Thierry Lubin, Smail Mezani, Abderrezak Rezzoug, Analytical computation of the magnetic field distribution in a magnetic gear [J]. IEEE Trans. Magn., 2010, 46(7): 2611–2621.

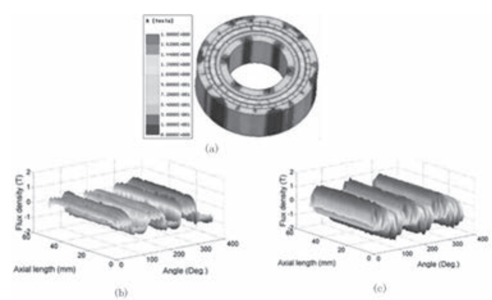

Fig. 1 (a)Magnetic field distribution of magnetic gear at no load. (b)Flux density in inner air gap of magnetic gear. (c) Flux density in outer air gap of magnetic gear.

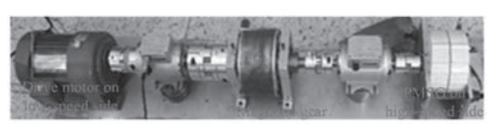

(a)Test beach

(b)MCPGS
Fig.2 Actual conditions on the test field

ES-14. Analysis of Doubly Fed Magnetic Geared Motor with Maximum Efficiency Operation by Individual Frequency Control.

H. Shin[1] and J. Chang[1]
1. Electrical engineering, University of Dong-A, Busan, The Republic of Korea

As shown in Fig. 1 (a), unlike the general synchronous machine, the magnetic geared motor has the modulating pieces which modulate the winding flux and the permanent magnets (PMs) flux, respectively. The winding flux of the magnetic geared motor is changed into the magnetic field with the high number of poles by the magnetic gearing effect, and they are synchronized with the PM flux [1]. Thus, the speed of the output rotor is reduced by the ratio of the pole number between the winding and the PMs, and the output torque is increased by the same ration. Due to these characteristics, many researches of the magnetic geared motor have been focused on the low-speed, high-torque applications, and the efforts to replace with the magnetic geared motor to the power transmission of the electric vehicle (EV), which consists of the synchronous machine and the mechanical gear box, have been continued [2]-[4]. But, the narrow field-weakening region by the PM excitation and the problems for unstable supply and price by the usage of rare-earth magnet are regarded as the shortcomings in the traction applications including the EVs. Meanwhile, as shown in Fig. 1(b), recently, the doubly fed magnetic geared motor (DFMGM), which is done the 3-phase windings in both the inner and outer stators, is proposed [5]-[6]. The speed of the modulating pieces output rotor is adjusted by the individual frequency control in the inner and outer windings. Fig. 1(c) shows the example for the speed-torque curve of the DFMGM with the division of operating region by the individual frequency control. While the frequency of the outer winding is fixed at 0 Hz corresponding to the DC operation, the frequency of the inner winding is increased until the base speed I, $\omega_{base\ I}$. And then, the frequency of the outer winding is increased until the base speed II, $\omega_{base\ II}$, without variation of the frequency of the inner winding. Thus, the frequency range and inverter power of each winding can be reduced because the operating region of the DFMGM is divided into two sub-regions according to the selection of the frequency range of the inner and outer windings. Moreover, the field-weakening region of the DFMGM can be considerably extended thanks to the field flux which can be adjusted by the winding current. With these characteristics of DFMGM, it is very important to determine the frequency ranges of the inner and outer windings and roles of each winding as a part of field and armature by considering the iron loss and the efficiency. Fig. 2 shows the iron loss map and the efficiency map for the difference in the two cases which have different frequency range each other. In the case I, the inner and outer windings have the maximum frequencies of 180Hz and 360Hz, respectively. In contrast, in the case II, the maximum frequencies of the inner and outer windings are 360Hz and 180Hz, respectively. The current of the inner winding is adjusted when the current of the outer winding is fixed, and as mentioned above, the frequency of the inner winding is increased until the maximum value, and then the frequency of the outer winding reaches the maximum value. As shown in Fig. 2(a), in the high-torque region, the case II, which the frequency range of the inner winding is wider than that of the outer winding, has the bigger iron loss than that of the case I. However, in the low-torque region, the case I, which the frequency range of the outer winding is wider than that of the inner winding, has the larger iron loss than that of the case II. It means that, in the constant torque region, the frequency ranges of the inner and outer winding, which has the advantage in the iron loss, are different according to the amplitude of the current of the armature winding. Besides, as shown in Fig. 2 (b), there is 4% or more efficiency difference between the case I and II in the low-torque region. Based on these characteristics, the DFMGM can operate at each point with the maximum efficiency by the individual frequency control in the inner and outer windings when the operating point is changed according to the driving conditions in EVs. Furthermore, the overall efficiency in the traction system can be increased by the frequency combination map of inner and outer windings with the maximum efficiency for the whole operating region. To do the task of the efficiency maximization for the whole operating region by the individual frequency control and the frequency mapping, firstly, the iron losses at the inner core, outer core, and the modulating pieces are presented according to the frequency variations in the inner and outer windings. In addition to this, the effect of the space harmonic components of the air-gap flux density on each ferromagnetic material is separately investigated. Secondly, the iron loss maps and the efficiency maps according to the frequency map are drawn, and the causes of the difference between the maps are analyzed. Finally, the maximum efficiency map for the whole operating region is obtained.

[1] K. Atallah, S. D. Calverley, and D. Howe, "Design, analysis and realization of a high-performance magnetic gear," IEE Proc-Electr. Power Appl., vol. 151, pp. 135-143, Mar. 2004. [2] L. L. Wang, J. X. Shen, Y. Wang, and K. Wang, "A novel magnetic-geared outer-rotor permanent-magnet brushless motor," in Proc. PEMD, Apr. 2008. [3] Y. Fan, H. Jiang, M. Cheng, and Y. Wang, "An improved magnetic-geared permanent magnet in-wheel motor for electric vehicles," in Proc. VPPC, pp. 1-5, Sept. 2010. [4] Y. Fan, L. Gu, Y. Luo, X. Han and M. Cheng, "Investigation of a new flux-modulated permanent magnet brushless motor for EVs," Hindawi the scientific world journal, vol. 2014, Apr. 2014. [5] X. Guo, S. Wu, W. Fu, Y. Liu, Y. Wang, and P. Zeng, "Control of a dual-stator flux-modulated motor for electric vehicles," Energies, vol. 9, no. 7, Jul. 2016. [6] Y. Chen, W. Fu, and X. Weng, "A concept of general flux-modulated electric machines based on a unified theory and its application to developing a novel doubly-fed dual-stator motor," IEEE Trans. Ind. Electron., vol. 64, no. 12, pp. 9914-9923, Dec. 2017.

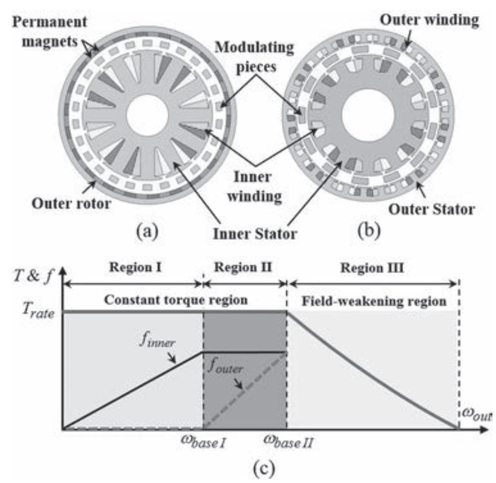

Fig. 1. Basic structure: (a) Magnetic geared machine, (b) Doubly Fed Magnetic Geared Machine (DFMGM), (c) Speed-Torque curve of DFMGM

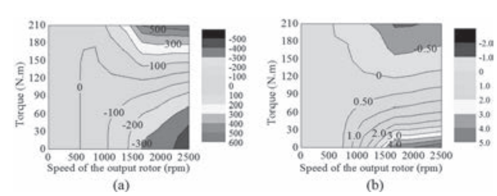

Fig. 2. Characteristics difference between the case I and II in the constant torque region: (a) Iron loss, (b) Efficiency.

ES-15. Performance Evaluation of Magnetic Lead Screws Equipped with Segmented Arc Magnets Instead of Helical Ones.

F. Gao[1], Q. Wang[1] and J. Zou[1]
1. Department of Electrical Engineering, Harbin Institute of Technology, Harbin, China

I. Introduction Recently, there has been growing interest in the magnetic lead screw (MLS). Integrated with the permanent magnet (PM) rotational machine, the MLS has brought an electromagnetic linear actuator with high thrust force density into reality [1]. Generally, there are three types of MLS, i.e., PM-type, reluctance type and inductor type, among which the PM lead screws exhibit much higher force densities than the other two and are becoming the focus of research interest. In the PM lead screw, the helical PMs are key components. Since it's quite hard to manufacture the ideal helical PM poles, the PM was obtained by cutting the arc magnet with the same arc angle in [2] and [3]. The number of required PMs were decreased significantly and the characteristic of thrust force and torque had a better approximation with the ideal one. However, it still has a larger error with the ideal helical PM. Furthermore, it's noticed that almost all investigations had regarded the thrust force and torque as the assessment indicator of the approximation technology, and the gear ratio wasn't taken into account. As will be highlighted in the paper that the gear ratio is the fundamental indicator for a motion transmission. This paper proposes a novel PM reshaping method. Segmented arc magnets are adopted to replace the ideal helical PMs. For the MLS equipped with the resultant PMs, the performance is evaluated and analyzed compared with the ideal one, and the effect of magnetization on the performance is investigated. Finally, additional consideration on the fabrication of MLS is presented as well. II. Principle of approximation for helical PMs A MLS is shown in Fig. 1 (a), where helical PMs with radial magnetization are mounted on the inner surface of nut and outer surface of screw, respectively. Limited to the current processing technic of sintered NdFeB PMs, helical PMs are difficult to be obtained. One popular approach to approximate the helical PM segment is to cut the arc magnet with the same arc angle. An ideal helical PM segment and the approximated one by cutting method are shown in Fig. 1 (b). It's observed that the side surfaces of helical PM are identical rectangles, whereas the corresponding are skewed into different parallelograms, which causes mismatches on the side surfaces during assembling. Fig. 1 (c) and (d) depicts the geometry of the cut PM segment with different arc angle scope, δ is the angle of reference plane versus the side surface. A bigger error will occur when the arc angle are greater than $\pi/2$. To avoid this situation, some limits are made. With the geometry of PM segments, the cutting angle is derived. There're four combinations of nut and screw to be selected, and the best combination is verified by three-dimensional (3-D) finite element method (FEM). III. Performance Optimization The PM segment is optimized from the aspects of reference angle, arc angle and magnetization. The reference angle affects the resultant shape of PM segment, whereas the thrust force and torque of MLS by different reference angles are almost overlapped totally. Therefore, the gear ratio is investigated as shown in Fig. 2 (a), and the steady gear ratio is preferred. Fig. 2 (b) shows the difference of axial component with the helical PM. Obviously, a smaller arc angle leads to a closer shape to the helical PM and a better performance of MLS. However, it needs a balance between the number of PM segments and the performance of MLS. Fig. 2 (c) shows the torque of MLS with the PM segment magnetized radially and in parallel. Evidently, there are lower thrust force and torque when magnetized in parallel. Furthermore, the PM segments with parallel magnetization result in a distorted torque curve, which may cause instability problems during the transmission. IV. Additional consideration As stated in this paper, the helical PM poles are assembled by approximated PM segments. There will exist magnetic force to prevent the PM segments of same polarity from getting close, which make it hard to assemble the MLS. To make the fabrication of the MLS simpler, dovetail bulge and groove are set up on the side surface of the PM segment as shown in Fig. 2 (d). In this way, the PM segments will snuggle closer to each other compulsively. More detailed analysis and results will be presented in the full paper.

[1] J. Wang, K. Atallah, and W. Wang, "Analysis of a magnetic screw for high force density linear electromagnetic actuators," *IEEE Trans. Magn.*, vol. 47, no. 10, pp. 4477–4480, Oct. 2011. [2] K. Lu, Y. Xia, W. Wu and L. Zhang, "New helical-shape magnetic pole design for magnetic lead screw enabling structure simplification," *IEEE Trans. Magn.*, vol. 51, no. 11, Nov. 2015, Art. ID: 8204404. [3] Z. Ling, J. Ji, J. Wang, and W. Zhao, "Design optimization and test of a radially magnetized magnetic screw with discretized PMs," *IEEE Trans. Ind. Electron.*, to be published.

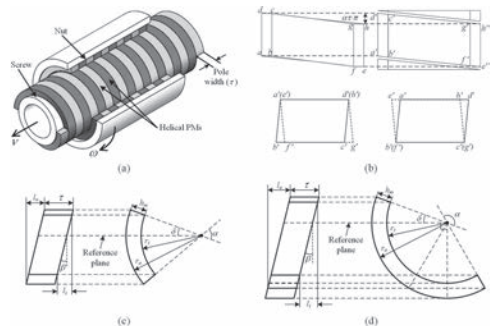

Fig. 1. (a) Schematic of a MLS. (b) Cutting method. (c) Geometry of cut PM segment ($\alpha<\pi/2$). (d) Geometry of cut PM segment ($\pi/2<\alpha<\pi$).

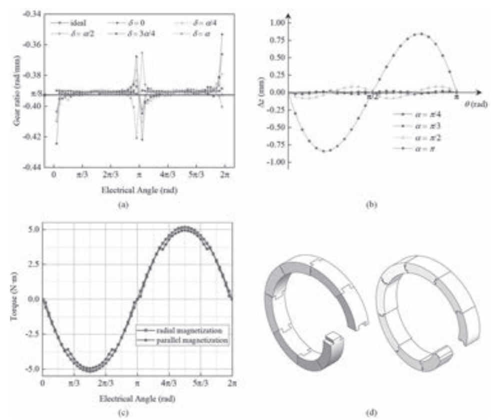

Fig. 2. (a) Comparison of gear ratio with different reference angle. (b) Difference of axial component from the helical PM. (c) Comparison of torque with different magnetization. (d) PM segments with dovetail bulge and groove.

Session ET
MAGNETISATION DYNAMICS II
(Poster Session)

Jiangwei Cao, Chair
Lanzhou Univercity, Lanzhou, China

ET-01. Unravelling the effects associated with ferromagnetic dynamics in non-magnet/ferromagnet metallic multilayers.

O. Gladii[1], L. Frangou[1], *G. Forestier*[1], S. Auffret[1], U. Ebels[1], S. Gambarelli[2] and V. Baltz[1]
1. SPINTEC (Univ. Grenoble Alpes / CNRS / INAC-CEA / GINP), Grenoble, France; 2. SYMMES (Univ. Grenoble Alpes / CNRS / INAC-CEA), Grenoble, France

In physical systems, out-of-equilibrium vibration dynamics is governed by numerous parameters, like local anisotropy and coupling. In practice, dynamics is most often driven by resonance. Resonance experiments are therefore powerful to characterize physical systems to an extent which depends on how well it is possible to disentangle the effects associated with dynamics. In non-magnet/ferromagnet metallic multilayers for example, the physical properties related to the ferromagnet (e.g. saturation magnetization, anisotropy, damping), to the non-magnetic metal (e.g. spin penetration length, relaxation mechanisms, eddy currents) and to the interface (e.g. spin filtering, roughness) can be recorded through measurements of ferromagnetic resonance spectra (e.g. absorption vs. magnetic field for a fixed frequency) and determination of their position, linewidth, and symmetry [1]. In this work we investigated experimentally the ferromagnetic resonance response of a 8-nm-thick NiFe film sandwiched between two conductive Cu layers, the whole stack being sputter-deposited on thermally-oxidized silicon substrates (Si/SiO_2). We compared the changes induced by varying the thicknesses of either the buffer- or the capping-layer of Cu [Fig. 1(a)], in an attempt to disentangle and characterize the different effects associated with ferromagnetic dynamics. The spectra measurements were carried out by using a coplanar waveguide setup [Fig. 1(a)]. Through measurements of the spectra linewidths we observed a non-monotonous dependence of Gilbert damping with Cu buffer-layer thickness. We attribute such a behavior to the possible non-monotonous changes in Cu/NiFe interface properties. It is actually known that Cu wets poorly on SiO_2 compared to NiFe on SiO_2 and NiFe on Cu. In addition, roughness creates spatially inhomogeneous stray fields that results in strong incoherent dephasing of the spin current injected from the NiFe to the Cu, and thus leads to damping enhancement [2]. In this regards, varying the capping layer thickness has virtually no influence on damping. We observed that the spectra position is also influenced by the buffer-layer thickness. It gradually reduces as a likely consequence of gradual NiFe surface-anisotropy enhancement for thicker buffer-layer [3]. Most interestingly, we detected that a spectrum asymmetry gradually build up when the Cu layer thickness increases [Fig. 1(b)]. The amplitude of this effect is independent on the buffer or capping nature of the Cu layer, in contrast to its sign. Such a behavior reveals the non-negligible impact of eddy currents circulating in the conductive Cu layers. A scenario involving eddy currents generated directly by the microwave excitation cannot readily explain the sign change observed here between capping and buffer layer [4]. We rather consider that the oscillation of the NiFe magnetization generates a time varying out-of-plane magnetic flux that creates eddy currents in the plane of the surrounding Cu layers. In return, the eddy currents generate a feedback rf magnetic field that contributes to the dephasing of the NiFe magnetization dynamics. This dephasing translates into an absorption-dispersion admixture ($\chi=(\chi+i\chi)e^{i}\Phi$) and gives rise to the asymmetry of the NiFe resonance lineshape. In this scenario, the feedback rf magnetic fields of the top and bottom Cu layers are then naturally in antiphase to one another. We acknowledge the financial support of ANR [Grant Number ANR-15-CE24-0015-01] and KAUST [Grant Number OSR-2015-CRG4-2626].

[1] W. E. Bailey, chapter 4 in 'Introduction to Magnetic Random Access Memories', IEEE Press, R. B. Goldfarb, B. Dieny, and K.-J. Lee, eds. (2017) [2] Y. Tserkovnyak, A. Brataas, G. E. W. Bauer, and B. I. Halperin, Rev. Mod. Phys. 77, 1375 (2005) [3] G. C. Bailey and C. Vittoria, Phys. Rev. B 8, 3247 (1973) [4] V. Flovik, F. Maci, A. D. Kent, and E. Wahlström, J. Appl. Phys. 117, 143902 (2015)

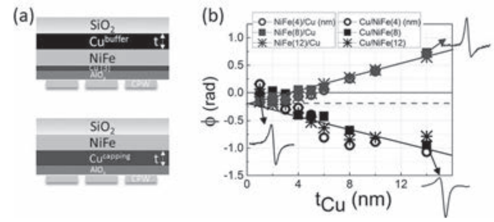

Fig. 1. (a) Schematic representation of the coplanar waveguide (CPW) – ferromagnetic resonance experiment. The sample is placed face down on the waveguide. (b) Dependence of spectrum dephasing/asymmetry (Φ) on capping (blue, positive panel) and buffer (black, negative panel) Cu layer thickness. The dashed red line indicates the reference dephasing of the experimental setup.

ET-02. Temperature dependence of spin-torque driven ferromagnetic resonance in MgO-based magnetic tunnel junction with a perpendicularly free layer.

X. Wang[1], J. Feng[1], P. Guo[1], H. Wei[1], B. Fang[2], Z. Zeng[2] and *X. Han*[1]
1. State Key Lab of Magnetism, Institute of Physics, Beijing, China;
2. Institute of Nano-tech and Nano-bionics, Chinese Academy of Sciences, Suzhou, China

Recently, magnetic tunnel junctions (MTJs) with a perpendicular magnetic anisotropy in combination of high tunnel magnetoresistance and high thermal stability were demonstrated to be a promising candidate for spin-torque (ST) magnetic random access memory, or ST nano-scaled oscillators. In such systems, the perpendicular anisotropy plays an important role in determining the magnetization dynamics. Here, We report the temperature dependence of the ST driven ferromagnetic resonance in MgO-based MTJ nanopillars with a perpendicularly free layer and an in-plane reference layer. From the evolution of the resonance frequency with magnetic field, we clearly identify the free-layer resonance mode and reference-layer mode. For the reference layer, we demonstrate a monotonic increase in resonance frequency and the effective damping with decreasing temperature, which suggests the saturated magnetization of the reference layer is dominant. However, for the free layer, the frequency and damping exhibit almost no change with temperature, indicating that the perpendicular magnetic anisotropy plays an important role in magnetization dynamics of the free layer[1]. The related parameters, such as the effective $\mu_0 M_s$ of in-plane reference layer, (H_k-4$\pi\mu_0 M_s$) cosϕ of the perpendicular free layer, and the damping factor of both free and reference layers, have been obtained in the temperature range from 300 K to 100 K. The values of $\mu_0 M_s$ and (H_k-4$\pi\mu_0 M_s$) cosϕ at 300 K are 1.66 Tesla and 180 Oe, while the effective damping factors of both free and reference layers at 300 K are 0.0057 and 0.01, respectively. The effective damping factor of the reference layer shows normal temperature dependence, while that of the free layer remains almost unchangeable with temperature due to the suppressed Hk and $\mu_0 M_s$ when the free layer remains in-plane. From our work, one may find MgO MTJ stack with a perpendicular free layer and an in-plane reference layer is good candidate for studying the microwave oscillation at high frequency using the ST-FMR effect.

[1] X. Wang, J. F. Feng, P. Guo, H. X. Wei, X. F. Han, B. Fang, Z. M. Zeng. *J. Magn. Magn. Mater.* 443, 239 (2017).

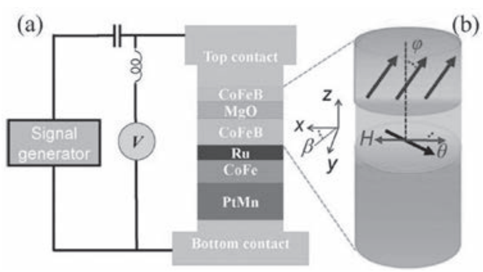

Fig. 1. (a) The schematic ST-FMR circuit setup and cross-sectional view of the MTJ structure. (b) The magnetic configurations of free and reference layers when applying an in - plane magnetic field H. The *x*- *y*-, and *z*-axes and the angles ϕ, θ, and β are defined, which are the angle ϕ of the free layer deviating from z-axis, θ between the reference layer and the field direction, and β between the reference and free layers.

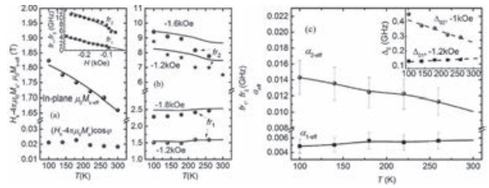

Fig. 2. The temperature dependence of (a) fitted in-plane effectiveμ0Ms-eff and perpendicular (H_k-4$\pi\mu_0 M_s$)cosϕ and (b) resonance frequencies of free and reference layers at different fields. The insert in (a) shows the field dependence of oscillation frequencies f_{r1} and f_{r2} at 100 K. The solid lines in (a) and in the insert are the fitted results and the solid lines in (b) are the calculated results. (c) The temperature dependence of the effective damping factor of free ($\alpha_{1\text{-eff}}$) and reference ($\alpha_{2\text{-eff}}$) layers. The insert shows the fitted linewidth of free (Δ_{01}) and reference (Δ_{01}), which are taken at -1.2 kOe and -1 kOe. The solid and dash lines are guide to eye.

ET-03. Role of intersublattice coupling in current-induced spin torque in Rashba antiferromagnet.

C. Ho[1] and M.B. Jalil[1]
1. Department of Electrical and Computer Engineering, National University of Singapore, Singapore

We investigate the spin-orbit torque in Rashba antiferromagnet (AFM). The model AFM composes of two square sublattices with magnetizations m_1 and m_2 (Fig. 1) [1,2]. The intersublattice electron dynamics is described by the hopping energy *t,* and Rashba coupling α_{Ri} is sublattice-dependent. In linear response theory, the spin-torque acting on m_i is derived as $T^i=\Delta J_{dd}$ $(m_i \times m_{j\neq i}) + m_i \times H_i$, where the first term represents the modified AFM exchange coupling between m_1 and m_2 with additional strength ΔJ_{dd}, the second term is the current induced torque with $H_i \propto \alpha_{Ri}(z\times j_e)$. Firstly, we show that ΔJ_{dd} is induced by the intersubllatice electron dynamics. As shown in Fig. 2a, when the hopping is small, ΔJ_{dd} increases with *t* and reaches its maximum ΔJ_{max}=$2J_{sd}/3\sqrt{3}$ at $t=\sqrt{2}\ J_{sd}$ (red circle), where J_{sd} is the *sd* coupling. However, when $t\geq\sqrt{2}J_{sd}$, the modulation becomes diminishing. To explain this trend, we can consider the exchange time scale which is $\tau_{sd}\sim 1/J_{sd}$, and the inter-sublattice hopping time scale $\tau_{hop}\sim 1/t$. When $t<J_{sd}$,i.e., $\tau_{sd}<\tau_{hop}$, adiabatic condition can be applied, which allows the angular momentum carried by the electron can be adiabatically transferred between m_1 to m_2, and ΔJ_{dd} is scaled with the hopping rate, i.e., $\Delta J_{dd}\sim t$. However, when $t>J_{sd}$, which means $\tau_{sd}>\tau_{hop}$, the angular momentum transfer would be less effective due to the relaxation, similar to strong spin-flip effect, thus resulting in the diminishing trend as shown. Second, the torque fields acting on m_1 and m_2 are staggered for α_{R1}=-α_{R2} as shown in Fig. 2b. Moreover, the magnitude of the torque fields are reduced as a result of the intersublattice electron dynamics. Indeed, opposite Rashba fields induced opposite spin polarizations in each sublattices, and that can cancel each others through the intersublattice dynamics, thus reduces the torque fields.

[1] Zeleznÿ, J., et al., Phys. Rev. Lett, 113 157201 (2014). [2]Yuta Yamane, Jun'ichi Ieda, Jairo Sinova, Phys. Rev. B 94, 054409 (2016).

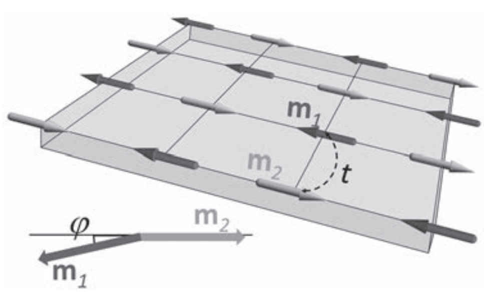

Fig. 1. Model square AFM lattice. m_1 and m_2 are the magnetizations, t is the intersublattice electron dynamics.

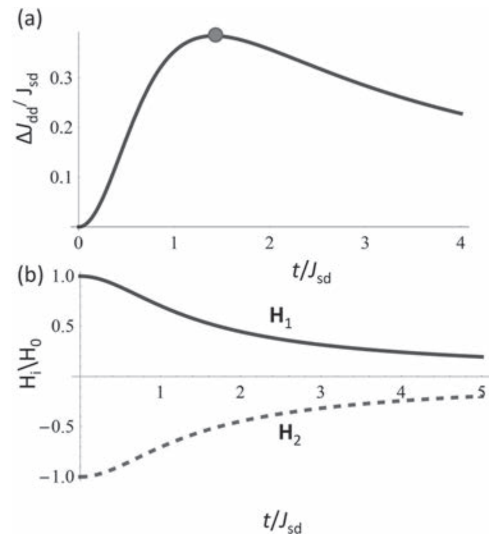

Fig. 2. (a) Modified AFM coupling as a function of hopping energy *t*, the red circle shows the maximum value. (b) Torque fields acting on m_1 and m_2 for α_{R1}=-α_{R2}, the magnitudes diminish at large t.

ET-04. Quasi-oscillating transition between magnetic states in Pt/Co/Ir/Co/Pt/GaAs spin valves.

G. L'vova[1,2], R. Morgunov[1,2], T. Fache[3] and S. Mangin[3]
1. 1 Institute of Problems of Chemical Physics, Chernogolovka, Russian Federation; 2. Tambov State Technical University, Tambov, Russian Federation; 3. Institut Jean Lamour, Nancy, France

The multilayered heterostructures attract great attention due to the Giant Magneto Resistance (GMR) applications in spintronics, since they can be used as biomedical sensors. An understanding of the origin of magnetic relaxation in large sized structures will allow an acceleration of the sensor switching to develop optimal conditions of the sensor exploration. Analysis of magnetic relaxation in the multilayered Pt/Co/Ir/Co/Pt/GaAs system is subject of our work. The time dependence of the magnetic moment M(t) was recorded by SQUID magnetometer in the magnetic fields corresponding to the transition fields between four stable states (Fig. 1). Fig.1. Sketch of Pt/Co/Ir/Co/Pt/GaAs. The states M_2, M_3 and M_4 correspond to the parallel and antiparallel mutual orientations of the magnetization vectors of the free and hard Co layers. Fig. 2. Time dependence of the quasi-oscillating relaxation of the magnetic moment M(t) recorded in the sample at T=100 K for sample Pt(3.2nm)/Co(0.7nm)/Ir(1.4nm)/Co(1nm)/Pt(3.2nm). The dependences were recorded in the fields corresponding to the $M_2 \rightarrow M_4$ transition fields. MOKE images of the surface magnetization accompanying similar transition at 300 K are shown in the insertions. In the Pt/Co/Ir/Co/Pt/GaAs heterostructure, an inverse magnetic relaxation (opposite to the external magnetic field direction) is observed. This process starts from M_2 initial metastable state, passes through M_4 transient metastable state and finalizes in M_3 stable state (Fig. 2). The stability of these magnetic states can be understood as a competition between the anisotropy energy, the interlayer exchange coupling and the Zeeman energies providing the sequence of the spin valve switching in external magnetic field [1]. Transition MOKE pictures illustrate spreading of the M_4 state corresponding to magnetic moments of the both magnetic layers aligned along the external field. The fact that dipolar field of state M_2 favors M_4 state instead of M_3: at 10 minutes (Fig.2), there is no more state M_2. State M_3 is energetically favored due to antiferromagnetic exchange between ferromagnetic layers. Final equilibrium state of the system is M_3 that is reached by tilting of the magnetic moment of the free Co layer. This $M_4 \rightarrow M_3$ transition leads to the final system state corresponding to the dark MOKE image (see insert in Fig.2). Thus, we have found an unusual quasi-oscillating mode of the transition between stable magnetic states of the bilayer system with perpendicular anisotropy. The work was supported by Ministry of Education and Science of the Russian Federation (grant 3.1992.2017/4.6)

[1] Morgunov R., Hamadeh A., Fache T., Lvova G., Koplak O., Talantsev A., Mangin S, Magnetic field and temperature control over Pt/Co/Ir/Co/Pt multistate magnetic logic device, Superlattices and Microstructures, 104, (2017) 509–517.

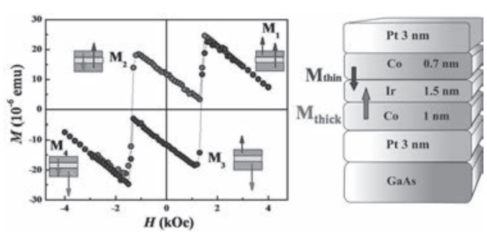

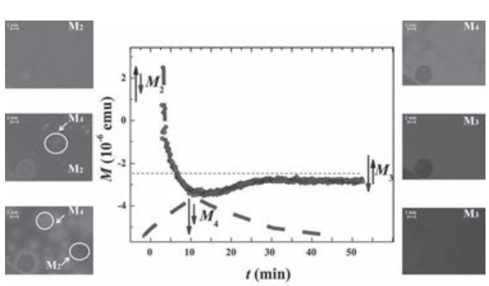

ET-05. Exchange coupling induced giant damping enhancement in $Y_3Fe_5O_{12}$/ $Co_2FeAl_{0.5}Si_{0.5}$ bilayers.

M. Li[1], L. Jin[1], Y. Rao[1], H. Zhang[1], C. Hong[1], Z. Zhong[1] and Q. Yang[1]
1. University of Electronic Science and Technology of China, Chengdu, China

The spin pumping effect induced Gilbert damping enhancement in $Y_3Fe_5O_{12}$(YIG)/heavy mental bilayers has been intensively investigated. $Co_2FeAl_{0.5}Si_{0.5}$ (CFAS) is a promising ferromagnetic material in spintronics devices due to its high spin polarization and low Gilbert damping. We studied the microwave dynamic magnetizations in YIG/CFAS bilayers by combining vector network analyzer ferromagnetic resonance (VNA-FMR) and revealed a giant damping enhancement about five times compared that of YIG/Pt bilayers. This phenomenon was attributed to both the exchange coupling effect and spin pumping effect. By inserting a 10nm Cu spacer, the direct exchange coupling can be excluded. A spin mixing conductance of $7.75\times10^{18}m^{-2}$ generated by spin pumping was obtained. The study provides an effective approach to tailor the damping in magnetic thin films.

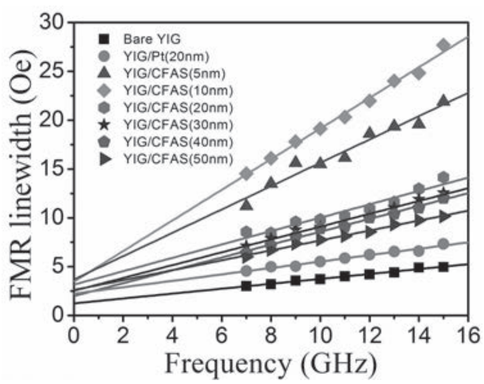

Fig. 1. The FMR line width ΔH as a function of microwave frequency for bare YIG, YIG/Pt(20nm), and YIG/CFAS.

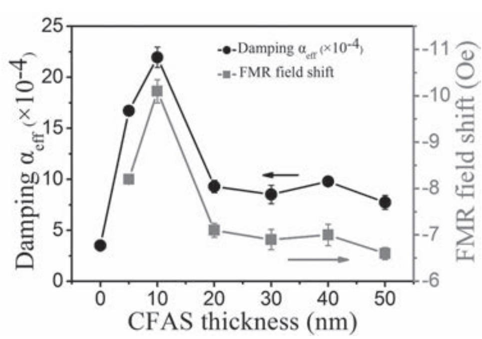

Fig. 2. The damping α_{eff} and the FMR field shift as a function of the CFAS thickness.

ET-06. Threshold field of Resonance Frequency in Permalloy Films with stripe domains.

L. Pan[1], C. Zhao[1], X. Cheng[1], D. Cao[2], J. Wang[1,3] and *Q. Liu*[1]
1. Key Laboratory for Magnetic and Magnetic Materials of the Ministry of Education, Lanzhou Univercity, Lanzhou, China; 2. College of Physics, Qingdao University, Qingdao, China; 3. Key Laboratory of Special Function Materials and Structure Design of the Ministry of Education, Lanzhou Univercity, LAnzhou, China

I. INTRODUCTION Recently, more and more interests focus on the stripe domain structure of magnetic films due to their tunable microwave properties, which are useful for microwave signal processing devices, including inductor, resonator, phase shifters, and filter. The magnetic films with stripe domain overcome the restraint in devices of uniaxial anisotropy films, such as in-plane orientation dependence on magnetic device applications. What's the more, the stripe domain films show different resonance modes when the direction of stripes is parallel or perpendicular to the microwave magnetic field, namely acoustic mode and optic mode [1-3]. In this work, we fabricated the permalloy film with stripe domain with in-plane anisotropy induced by oblique sputtering with oblique incidence angles were set at 31^o, 34^o, 36^o, 40^o and 42^o, respectively. Then we find the samples reveal unlike microwave responses at acoustic mode when the direction of stripe domain along the easy magnetization axis (EA) [0-configuration] or hard magnetization axis (HA) [1-configuration] of samples. It's interesting to note that the resonance frequencies keep constant firstly, and then flips to a higher value suddenly when it reaches to a turn-on applied field at 1-configuration. Maybe it can be used for special microwave devices. II. RESULTS AND DISSCUSION The zero-field magnetic permeability spectra and MFM images of film with oblique sputtering angle of 31^o were shown in Fig. 1. We can find the permeability spectra show different resonance modes. In the case of 0-configuration, the domain width is about 315 nm, which is smaller than that of 388 nm of the 1-configuration measured by MFM images. When the direction of in-plane anisotropy field and stripe domain is inconsistent, the magnetic moments deflect to the in-plane anisotropy field with a small angle. So the magnetic domain is wider. Fig.2 shows magnetic permeability spectra of imaginary part under sweeping field from 0 to 180 Oe at (a) 0-configuration and (b) 1-configuration of film with oblique sputtering angle of 31^o. In the case of 1-configuration, the resonance frequency increases with applied magnetic field, which is agreement with Kittle's equation. However, the resonance frequencies keep a constant, and suddenly jump to another value when the magnetic field reaches to a threshold value (Turn-on field). Turn-on field (H_{on}) as a function with different oblique sputtering angles was shown in Fig. 2(c). It is found that the oblique sputtering angle increases, in-plane anisotropy filed increases, H_{on} increases as well. This is due to the in-plane anisotropy increases, the magnetic reoriented field of the stripe domains increases. Fig. 1 Zero-field magnetic permeability spectrum and MFM images at (a-b) 0-configuration and (c-d) 1-configuration of film with oblique sputtering angle of 31^o. Fig. 2 Magnetic permeability spectra of imaginary part under applied magnetic field from 0 to 180 Oe in the case of (a) 0-configuration and (b) 1-configuration of film with oblique sputtering angle of 31^o. (c) Turn-on field as a function with different oblique sputtering angles.

[1] U. Ebels, L. Buda, K. Ounadjela, and P. E. Wigen, "Ferromagnetic resonance excitation of two-dimensional wall structures in magnetic stripe domains," *Phys. Rev. B,* vol. 63, no. 17, pp. 174437, 04/13/, 2001. [2] N. Vukadinovic, M. Labrune, J. B. Youssef, A. Marty, J. C. Toussaint, and H. Le Gall, "Ferromagnetic resonance spectra in a weak stripe domain structure," *Phys. Rev. B,* vol. 65, no. 5, pp. 054403, 12/27/, 2001. [3] J. Wei, Z. Zhu, H. Feng, J. Du, Q. Liu, and J. Wang, "Top-down control of dynamic anisotropy in permalloy thin films with stripe domains," *Journal of Physics D: Applied Physics,* vol. 48, no. 46, pp. 465001, 2015.

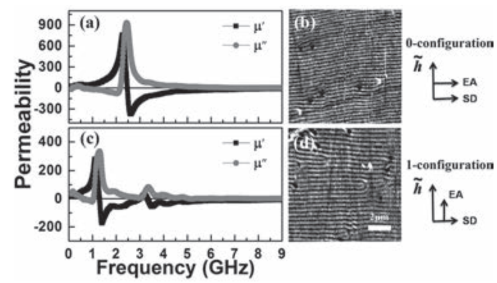

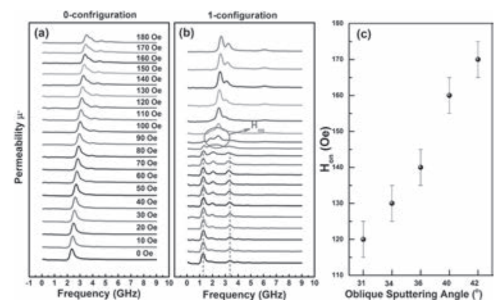

ET-07. Effect of absorption of hydrogen on the linewidth of the ferromagnetic resonance response of Co/Pd bilayer films.

T. Schefer[1,2] and *M. Kostylev*[1]
1. University of Western Australia, Perth, WA, Australia; 2. University of Basel, Basel, Switzerland

Hydrogen is expected to play a major role as a future energy carrier, ultimately replacing fossil fuels[1]. However, due to its high flammability it is mandatory to have control over its concentration and confinement at any stage of usage. Recently the magnetic hydrogen gas sensor (mHGS) has been proposed[2]. It relies on the shift of the ferromagnetic resonance (FMR) frequency or field in thin ferromagnetic (FM)/palladium (Pd) bilayer films upon absorption of hydrogen gas (H_2) by the Pd capping layer. This shift has been assigned to a change in the interface perpendicular magnetic anisotropy (PMA) due to changes to electron orbitals at the interface. While this sensing principle allows detecting H_2 over a wide sensing range[3], the amplitude of the FMR peak is inherently small due to the small thickness of the FM layer. Additionally to the shift in the resonance position H_{res}, an increase in the FMR amplitude as well as a decrease in FMR linewidth ΔH are always observed in the experiment. In this work, we try to separate the impact of H_2 on the resonance shift from the H_2-induced linewidth narrowing by varying the FM (Cobalt, Co) layer thickness t over a broad range. The Co layer is sandwiched between 10 nm of tantalum (Ta, seed layer) and 10 nm of Pd (capping layer). The stacks with varying t (t = 3, 5, 7, 10, 20, 30, 40, 50, 60, 70, 80 nm) were sputtered onto preheated (200°C) Si <100> wafers, where Ta and Pd were sputtered with dc magnetron sputtering and Co with RF sputtering. The differential broadband stripline FMR spectroscopy[4] measurements were taken employing an airtight chamber through which either nitrogen (N_2) or H_2 flowed with a constant flow rate of 800 SCCM. The recorded raw FMR traces were fitted with the real part of the first derivative of the complex Lorentz function, which gave us H_{res} and ΔH: $V=\mathrm{Re}(-A/(H-H_{res}+i\Delta H)^2)$. Here, V is the Lock-in amplifier signal, A the amplitude of the complex-valued Lorentz function and H the applied magnetic field. Fig. 1 demonstrates the obtained results. One sees that for thinner films, the change in H_{res} is well fitted with the $1/t$ dependence. This dependence is consistent with a reduction in the interface PMA with an increase in t. For the thicker films the behaviour is more complicated. The linewidth ΔH does not change significantly for the thinner films in the presence of H_2, while it decreases by over 20 % for 50 nm+ Co layers. This leads to a differential FMR amplitude change of over 50 %. This change can be used to sense H_2 with high concentration resolution over an impressive concentration range, as will be shown in our presentation. Fig. 2 displays an exemplary result of our concentration resolved measurements. The data presented in this figure were collected for the sample with t=70 nm. To enable this, we measured a time resolved differential FMR spectra at different H_2 concentrations. The external magnetic field and the microwave frequency are hold constant during the whole process and measurements of the FMR absorption amplitude are taken every few seconds. For the trace in fig. 2, the sample is exposed to three different concentrations (10, 25, 50 %) of H_2 sequentially. One sees that the absorption amplitudes for the three different concentrations are well distinguishable and that the signal recovers to its original level after evacuation of H_2 from the sample environment. This result demonstrates that monitoring the amplitude of the FMR response of 50 nm+ Ta/Co/Pd films in the presence of H_2 represents an alternative concept of an mHGS. It is characterised by a high sensitivity to H_2 concentration and much larger output FMR signal than for the sensing method which employs thinner Co layers and exploits the FMR peak shift for sensing. Potentially, the much larger FMR amplitude will considerably simplify signal processing electronics for future mHGS.

1. Marbán, G. & Valdés-Solís, T. Towards the hydrogen economy? *Int. J. Hydrog. Energy* 32, 1625–1637 (2007). 2. Chang, C. S., Kostylev, M. & Ivanov, E. Metallic Spintronic Thin Film as a Hydrogen Sensor. *Appl. Phys. Lett.* 102, 142405 (2013). 3. Lueng, C., Metaxas, P. J., Sushruth, M. & Kostylev, M. Adjustable Sensitivity for Hydrogen Gas Sensing Using Perpendicular-to-Plane Ferromagnetic Resonance in Pd/Co Bi-Layer Films. *Int. J. Hydrog. Energy* 42, 3407–3414 (2017). 4. Lueng, C., Metaxas, P. J. & Kostylev, M. Pd/Co Bi-Layer Films for Microwave-Frequency Hydrogen Gas Sensing Applications. in *Optoelectronic and Microelectronic Materials & Devices (COMMAD), 2014 Conference On* 27–29 (IEEE, 2014).

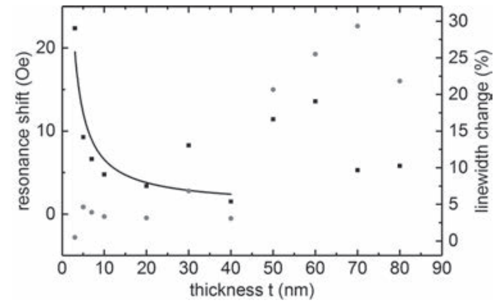

Fig. 1. Black squares (left axis): the resonance shift vs the thickness. Red dots: the relative linewidth change in % (right axis). Solid line: 1/*t* fit to black squares for 3nm<*t*<40nm.

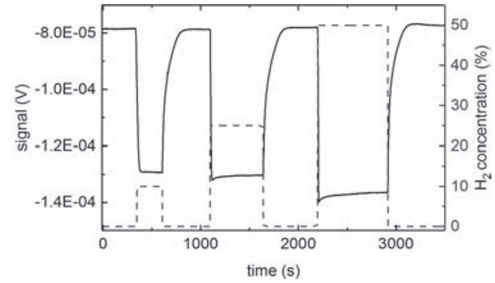

Fig. 2. Time resolved FMR trace taken for the 70 nm Co stack (black solid line, left-hand axis). The H_2 concentrations are 10 %, 25 %, 50 % (blue dashed line, right-hand axis).

ET-08. Angle-dependent static and dynamic magnetic properties of B2 ordered Co_2FeSi film.

Z. Xu[1], Z. Zhang[1], X. Li[1], J. Tang[1], F. Hu[1], E. Liu[1] and F. Xu[1]
1. School of Materials Science and Engineering, Nanjing University of Science and Technology, Nanjing, China

Co_2FeSi (CFS) Heusler alloy has attracted tremendous scientific attention in the emerging spintronics field, such as spin torque nano-oscillators, spin wave propagation and magnonics, due to the high saturation magnetic moment, high Curie temperature and low Gilbert damping [1]. In this work, we demonstrate angle dependence of static and dynamic properties of B2 ordered CFS thin film. The 60 nm thick CFS film was deposited on MgO (001) substrates by RF magnetron sputtering with a 3-inch CFS alloy disk as the target at room temperature. After growth, the stacks were *in situ* annealed for 1 hour in vacuum at 400 ^{o}C. The X-ray diffraction shows that the CFS film forms B2 structure. Figure 1(a) shows the in-plane measured M-H loops along the easy and hard axis. The high squareness of easy-axis M-H loop with full remanence was obtained. The extracted saturation magnetization (M_s) is 1205 emu/cm^3, which is smaller than the bulk value for B2 ordered CFS. The in-plane measurement azimuthal angel dependence of remnant magnetization ratio (M_r/M_s) for CFS film is shown in the inset of Fig. 1(a). The relationship, which can be well described by a cosine function, shows a two-fold symmetry, confirming an in-plane uniaxial magnetic anisotropy in the film. To investigate the magnetization reversal mechanism, the in-plane measurement azimuthal angel dependence of easy-axis coercivity (H_c) is shown in Fig. 1(b). It can be well fitted with Stoner-Wohlfarth model when the field orientation is close to the hard axis, showing the magnetization reversal is dominated by coherent rotation. When the field orientation is close to the easy axis, it is not fitted well with Stoner-Wohlfarth model, since the magnetization reversal is partially controlled by the domain-wall depinning according to Kondorsky model. The H_c value attains ~10 Oe for all angles, suggesting a soft-magnetic behavior similar to other Heusler alloys. The film was subjected to an in-plane microwave field *h* at various frequencies between 2 and 14 GHz, and an in-plane magnetic field *H* was applied perpendicular to *h* and swept from 0 to 2000 Oe. In the inset of Fig. 1(c), a typical spectrum measured at 12 GHz is given. It is notable that two resonance modes were observed in the spectrum. One appears at about H_{res}=1.0 kOe, and is identified as the fundamental FMR mode, which is characterized by a uniform magnetization precession through the film thickness. The other weak resonance, which is observed at the lower field, can be considered as the first exchange-dominatedperpendicular standing spin wave (PSSW) mode. The PSSW mode has a non-zero wave vector pointing perpendicularly to the thin-film plane and a thickness dependent spin-wave amplitude and phase. The typical field dependence of the FMR and PSSW modes at various frequencies for 60 nm CFS thin film is shown in Fig. 1(c). The magnetic anisotropy, H_k, extracted from the FMR mode, agrees well with that estimated from M-H loops. Exchange stiffness *A* can thus be extracted from the PSSW mode. In order to evaluate the damping factor, we also performed FMR measurements between 2 to 14 GHz. The frequency dependences of the FMR linewidth with the external field along in-plane easy and hard axes, are depicted in Fig. 1(d). The obtained values of Gilbert damping and inhomogeneous broading are 6.7×10^{-3}, 5.1×10^{-3} and 11.45 Oe, 24.29 Oe for easy and hard axes, respectively. The CFS film was then examined by in-plane angle-dependent FMR measurements at 8 GHz. The angular dependence of the resonance field is show in the inset of Fig. 1(d). The uniaxial anisotropy is clearly observed from this figure, agreeing well with that estimated from M-H loops.

[1] F. J. Yang, Y. Sakuraba, S. Kokado, Y. Kota, A. Sakuma, and K. Takanashi, Phys. Rev. B 86, 020409(R) (2012)

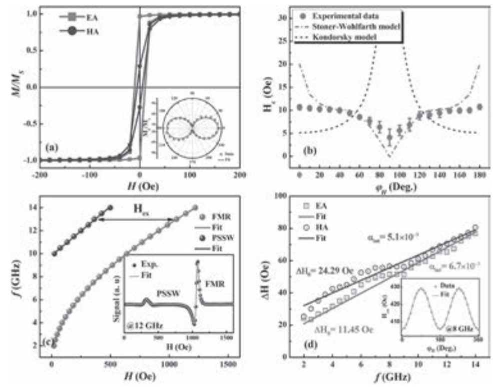

Fig. 1. (a) Hysteresis loops along easy and hard axes of CFS film. The inset in (a) shows measurement angular dependence of remanence ratio (M_r/M_s) (b) Angular dependence of coercivity. (c) Measurement frequency versus the resonance fields of PSSW and FMR modes. The inset in (c) shows typical ferromagnetic resonance (FMR) absorption derivative spectra at 12 GHz. (d) Frequency dependence of the FMR linewidth for CFS film along the easy and hard axes. The inset in (d) shows the angular dependence of FMR resonance field at 8 GHz.

ET-09. Voltage control of two magnon scattering and an enhanced ME coupling in multiferroic heterostructures.

X. Xue[1], *Z. Zhou*[1] and M. Liu[1]
1. Xi'an Jiaotong University, Xi'an, China

Driven by growing demands of fast, compact, and energy-efficient devices based on multiferroic systems, great efforts have been making to discover novel mechanisms and achieve tremendous magneotoelectric (ME) coupling effects. Electric field control of dynamic spin interactions is promising to break through the limitation of the magnetostatic interaction based ME effect. In this work, electric field control of the two-magnon scattering (TMS) effect has been demonstrated in $Ni_{0.5}Zn_{0.5}Fe_2O_4$ (NZFO)/Pb($Mn_{2/3}Nb_{1/3}$)-$PbTiO_3$ (PMN-PT) (001) multiferroic heterostructure. The angular dependence of ferromagnetic resonance (FMR) measurement has been performed by the electron paramagnetic resonance spectrometer. As shown in Fig. 1a and b, a large electric field modulation of magnetic anisotropy (-347 Oe) and FMR linewidth (275 Oe) is achieved at the TMS angle of θ_H=60°. Particularly, the TMS intensity is increased by 14.5% at room temperature. The TMS effect is an extrinsic magnetic damping mechanism that scatter the k=0 magnons excited by FMR into degenerate states of magnons having wave vectors $k\neq0$, offering a framework for voltage control of spin dynamics and further increase the ME interactions. The present work provides a promising paradigm for next generation voltage tunable electronic/spintronic devices such as RF/microwave devices, memories and spin wave logic devices.

[1] Rodrigo Arias, D. L. Mills, *Phys. Rev. B* 1999, 60, 7395. [2] M. Liu, Z. Zhou, T. Nan, B. M. Howe, G. J. Brown, N. X. Sun, Adv. Mater. 2013, 25, 1435. [3] Z. Zhou, M. Trassin, Y. Gao, Y. Gao, D. Qiu, K. Ashraf, T. Nan, X. Yang, S.R. Bowden, D.T. Pierce, M.D. Stiles, J. Unguris, M. Liu, B. M. Howe, G. J. Brown, S. Salahuddin, R. Ramesh, N. X. Sun, *Nat. Commun.* 2015, 6, 6082.

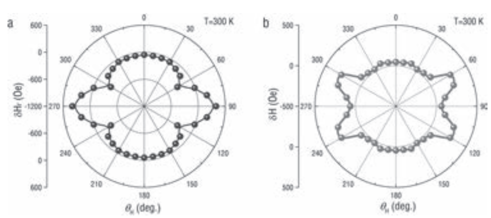

ET-10. Magnetic anisotropy and damping constant in CoFeB/Ir and CoFeB/Ru systems.

M. Belmeguenai[1], D. Apalkov[2], M. Gabor[3], F. Zighem[1], G. Feng[2] and X. Tang[2]
1. LSPM, Université Paris 13, Villetaneuse, France; 2. New Memory Technology Lab, Samsung Semiconductor Inc, San Jose, CA, United States; 3. Center for Superconductivity, Spintronics and Surface Science, Technical University of Cluj-Napoca, Cluj-Napoca, Romania

Thin systems incorporating heavy metal/ferromagnet (HM/FM) stacks are currently under intensive research due to their potential applications in the field of spintronics. Indeed, various novel spin-related effects and phenomena could occur in these structures such as spin Hall [1] and inverse spin Hall effects [2], spin orbit torques [3] and interfacial Dzyaloshinskii-Moriya interaction (iDMI) [4]. In addition to the magnetic anisotropy, the damping constant is an important magnetic parameter in such structures as it determines the magnetization dynamics such as the speed of the magnetization switching. Therefore, the aim of this work is to use micro stripe ferromagnetic resonance (MSFMR) to investigate the Gilbert damping constant and the magnetic anisotropy as a function of the thickness of the CoFeB capped with Ir or Ru, where a special attention is given to the annealing temperature. For this, $Co_{20}Fe_{60}B_{20}$ thin films of different thicknesses have been sputtered on thermally oxide Si substrates and capped with 8 nm thick Ir or Ru layers. Both as grown films and samples annealed at 400°C are considered here. Vibrating sample magnetometer has been used to measure the CoFeB thickness dependence of the saturation magnetic moment per unit area in order to straightforwardly determine the magnetization at saturation (M_s) and the magnetic dead layer thickness (t_d). t_d are found to be 0.76 nm and 1.53 nm for the as deposited CoFeB/Ru and CoFeB/Ir, respectively. The magnetic dead layer is mainly due to intermixing at the interface of CoFeB with the capping layer. The larger magnetization value (M_s=1115±50 emu/cm^3) of CoFeB/Ir compared to that of CoFeB/Ru (M_s=930±50 emu/cm^3) is most likely due to the proximity induced magnetization in Ir. This corresponds to a change in film magnetization of 19% which is in good agreement with the reported values for Ir/Co [5] systems. Both M_s and t_d increase for films annealed at 400°C. The obtained values are 1185±50 emu/cm^3 (1110±50 emu/cm^3) and 2.93 nm (1.62 nm) for CoFeB/Ir (CoFeB/Ru). MSFMR measurements revealed that these systems present small in-plane uniaxial anisotropy with the magnetization easy axis direction depends on the sample. While the in-plane anisotropy field for the as grown films does not show a clear behavior versus the CoFeB thickness, clear linear behavior of this field versus the reciprocal CoFeB effective thickness can be observed for the annealed samples. This field decreases for samples annealed at 400°C and it is higher for CoFeB films capped with Ru with respected to those capped with Ir. Moreover, the effective magnetization varies linearly with the inverse effective thickness of CoFeB due to the perpendicular interface anisotropy. This surface anisotropy constant which was estimated to be 0.84 erg/cm^2 and 0.89 erg/cm^2 for the as deposited CoFeB films capped with Ir or Ru, respectively reinforces the perpendicular easy axis. It increases (decreases) slightly (drastically) for films annealed at 400°C and capped with Ir (Ru). The corresponding values for the annealed Ir and Ru capped films are found to be 1.07 erg/cm^2 and 0.57 erg/cm^2, respectively. Note also the existence of a high negative perpendicular anisotropy (reinforcing the in-plane easy axis), especially for the as deposited CoFeB/Ru films. This volume anisotropy decreases drastically from -1.83 $\times10^6$ erg/cm^3 (-0.6 $\times10^6$ erg/cm^3) to -0.4 $\times10^6$ erg/cm^3 (-0.21 $\times10^6$ erg/cm^3) when the CoFeB/Ru (CoFeB/Ir) are annealed at 400°C. MSFMR has also been used to investigate the CoFeB thickness dependence of damping parameter. For this, the field peak to peak linewidth has been measured as function of the driven frequency for an in-plane magnetic field applied along the direction giving the minimal linewidth. This direction is obtained from the investigation of the angular dependence of field linewidth for each sample. The obtained results revealed that the damping coefficient increases linearly with the reciprocal effective thickness of CoFeB most probably due to spin pumping. By considering that the total damping is given by $\alpha= \alpha_{CFB}+\alpha_{pump}$, where is the Gilbert damping of the bulk CoFeB and α_{pump} is the damping introduced by spin pumping effect due to Ir or Ru, the fitted data gives α_{CFB}=0.0027 and α_{CFB}=0.0013. The spin pumping contribution to the damping α_{pump} allowed determining the effective spin mixing of CoFeB/Ru and CoFeB/Ir estimated to be 12.93 nm^{-2} and 29.3 nm^{-2}, respectively. Note the higher value for CoFeB/Ir compared to that of CoFeB/Ru due to the higher spin orbit coupling of Ir. Moreover and in contrast to α_{CFB}, the spin mixing conductance increases for the annealed films at 400°C (the obtained values are 22.4 nm^{-2} and 43.85 nm^{-2} for CoFeB/Ru and CoFeB/Ir, respectively) traducing the enhancement of the spin pumping efficiency of the annealed films.

[1] S. O. Valenzuela and M. Tinkham, Nature 442, 176-179 (2006). [2] L. K. Werake, B. A. Ruzicka, and H. Zhao, Phys. Rev. Lett. 106, 107205 (2011). [3] S. Woo, M. Mann, A. J. Tan, L. Caretta, and G. S. D. Beach, Appl. Phys. Lett. 105, 212404 (2014). [4] M. Belmeguenai, J-P. Adam, Y. Roussigné, S. Eimer, T. Devolder, J-V. Kim, S. M. Chérif, A. Stashkevich, and A. Thiaville, Phys. Rev. B 91, 180405(R) (2015). [5] K.-S. Ryu, S.-H. Yang, L. Thomas, and S. S. P. Parkin, Nat. Commun. 5, 3910 (2014).

ET-11. Detection sensitivity exceeding 10^5 mV/mW in spin-torque diode.

B. Fang[1], J.L. Cai[1], P. Khalili Amiri[2], G. Finocchio[3] and Z. Zeng[1]
1. Suzhou Institute of Nano-tech and Nano-bionics, Chinese Academy of Sciences, Suzhou, China; 2. Department of Physics and Astronomy, University of California, Los Angeles, CA, United States; 3. Department of Mathematical and Computer Sciences, Physical Sciences and Earth Sciences, University of Messina, Messina, Italy

Magnetization dynamics induced by spin transfer torque (STT) in nanoscale magnetic structures result in a range of interesting phenomena, including magnetization switching, microwave oscillations, and the spin-torque diode (STD) effect. The STD effect can be used for the development of a new kind of microwave detectors [1]. Previous studies have demonstrated the STD microwave detectors have the potential to overcome the theoretical performance limits of their semiconductor counterparts at room temperature. For examples, Miwa et al reported a detection sensitivity of 1,2000 mV/mW by controlling their magnetization-potential profiles in magnetic tunnel junctions [2]. In our previous work [3], we have demonstrated a detection sensitivity of over 7×10^4 mV/mW in magnetic tunnel junction with perpendicularly magnetized free layer and in-plane magnetized reference layer at zero external magnetic field. The enhanced detection sensitivity is ascribed to the large-amplitude out-of-plane precession when the injection locking occurs due to the simultaneous application of d.c. and microwave currents. In this study, we investigated the effect of the perpendicular magnetic anisotropy (PMA) on the detection properties of STD. We found that the PMA at the interface of the CoFeB free layer with the MgO tunnel barrier is critical to improve the orbit of magnetization precession. At proper condition, by applying simultaneously a d.c. bias current to a STD, microwave emission induced by spin-torque is locked to an external microwave signal, leading to a drastically enhanced detection sensitivity in the locking regime. The optimized STD exhibited the detection sensitivity of 2.1×10^5 mV/mW in absence of the external magnetic fields, which is the highest sensitivity from a STD reported to date. The results suggest that the STD with injection locking technique is promising for next generation microwave detectors.

[1] A .A .Tulapurkar et al, Nature 438, 339 (2005). [2] S. Miwa et al, Nat. Mater.13,50–56 (2014). [3]B. Fang et al, Nat. Comm.7,11259 (2016).

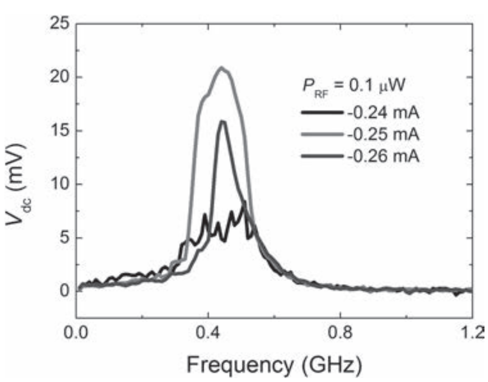

Fig. 1. The RF detection voltage (V_{dc}) as a function of the RF input frequency in the absence of magnetic field and under different d.c. bias current. The RF input power (P_{RF}) is 0.1 μW

ET-12. Proximity effect induced enhanced spin pumping in Py/Gd at room temperature.

R. Bansal[1], N. Chowdhury[1] and P.K. Muduli[1]
1. Physics, Indian Institute of Technology, New Delhi, Delhi, India

Investigating the damping processes and the behavior of dynamic magnetic properties in ferromagnetic (FM) thin films has been an important key towards design and fabrication of different microwave and magnetic recording devices. Damping in a magnetic material can be enhanced due to spin pumping, in which magnetization precession in the FM layer produces a spin current that flows into the adjacent non-magnetic (NM) layer[1-2]. It is an interfacial effect and plays an important role in thin films. A recent theoretical work predicted that magnetic relaxation can be significantly enhanced when spin pumping is performed into a ferromagnet near Curie temperature (T_C) due to the fluctuation enhancement of the spin conductance across the interface [3]. This was qualitatively confirmed by Khodadadi *et al.* [4] in Py/Gd system at low temperature. Here, we discuss the relaxation mechanism in Py/Gd structure by means of broadband ferromagnetic resonance (FMR) technique at room temperature. We show that a portion of the Gd layer at the interface becomes ferromagnetically ordered at room temperature and become antiferromagnetically (AFM) coupled to the Py due to the magnetic proximity effect (MPE). The ordered Gd at the interface of Py/Gd acts as a spin sink and contributes to the increase in spin pumping. In this work, we performed FMR measurement on two series of samples consisting of Py (15nm)/Gd (*t*) and Py (15 nm)/Al (*t*), where *t* is the varying thickness of material from 0 to 16 nm. Py/Gd films were designed to study proximity induced magnetization in Gd due to neighboring Py. A series of Py/Al reference samples were used to distinguish proximity induced effect in Py/Gd films from other interface-related effects due to long spin diffusion length of Al compared to Gd. FMR measurements were carried out using a co-planner waveguide (CPW) based FMR set-up in the frequency range of 3-17 GHz. The raw FMR spectra were fitted using a derivative of Lorentzian line shape to determine the resonance field (H_R) and line-width (ΔH). Fig.1 shows the FMR spectra for Py/Gd samples at a fixed frequency of 10 GHz. The inset shows Gd-caused FMR resonance field shift (H_{shift}) as a function of t_{Gd}. This change in H_{shift} with t_{Gd} can be attributed to the MPE. The observed negative H_{shift} indicate a reduction of effective magnetization of the Py layer due to AFM coupling between the Py and the ordered interfacial Gd layer. We found that M_{eff} decreases with increase in t_{Gd} due to the AFM coupling between Py and ordered portion of the Gd layer. To further confirm that this is caused due to the MPE, not from other interfacial effects, we performed similar FMR measurements in a series of Py/Al samples. We did not observe any decrease of magnetization in Py/Al samples as shown in the inset of fig. 2(a). In these samples, the behavior of M_{eff} with t_{Al} is almost constant, indicating the absence of AFM coupling. The effective Gilbert damping parameter (α_{eff}) increases significantly with increase in t_{Gd} as shown in Fig.2 (b). An increase of 63.5% is observed in α_{eff} for Py/Gd bilayers as compared to Py alone. The inset of Fig. 2(b) shows the behavior of α_{eff} with t_{Al} for which we did not find significant enhancement of α_{eff}. We will show that a major contribution of this enhancement is due to the spin pumping effect into the ordered ferromagnet Gd layer which is near it's Curie temperature. This provides a qualitative confirmation of a recent theoretical prediction of spin sinking enhancement in this situation.

[1] Y.Tserkovnyak et.al. "Spin pumping and magnetization dynamics in metallic multilayers", Phys. Rev. B 66, 224403(2002). [2] Y. Tserkovnyak, "Enhanced Gilbert Damping in Thin Ferromagnetic Films", Phys. Rev. Lett. 88, 117601 (2002). [3] Y. Ohnuma et.al. "Enhanced dc spin pumping into a fluctuating ferromagnet near T_C " Phys. Rev.B 89, 174417 (2014). [4] B. Khodadadi et.al. "Enhanced spin pumping near a magnetic ordering transition "Phys. Rev. B 96, 054436 (2017).

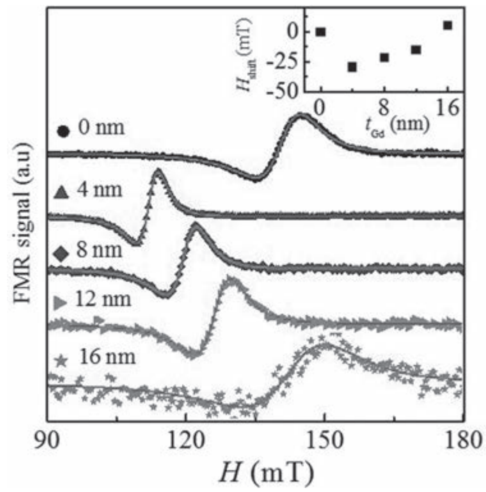

Fig. 1. FMR spectra at a fixed frequency of 10 GHz for Py/Gd samples with varying t_{Gd}. Symbols represent the experimental data while solid lines are the fit. The inset shows H_{shift} as a function of t_{Gd}.

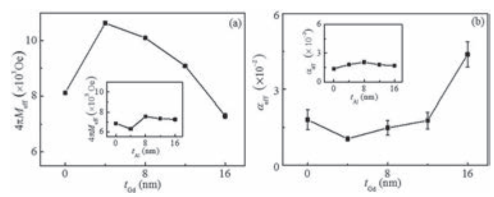

Fig. 2. (a) Effective magnetization (M_{eff}) versus Gd thickness. For comparison, the inset shows the variation of M_{eff} with Al thickness. (b) Effective damping (α_{eff}) as a function of Gd thickness. Inset shows behavior of α_{eff} with Al thickness.

ET-13. Bias Field Tunable Spin Configuration and Spin Dynamics in Arrays of $Ni_{80}Fe_{20}$ Nano-Cross Structures.

K. Adhikari[1], S. Choudhury[1], S. Barman[2], Y. Otani[3] and *A. Barman*[1]
1. S. N. Bose National Centre for Basic Sciences, Kolkata, India; 2. Institute of Engineering & Management, Management House, Kolkata, India; 3. Institute for Solid State Physics, University of Tokyo, Riken, Japan

1. Introduction Recently attractions in nanomagnetism[1] is triggered by their fundamental physics as well as their huge potential applications in various fields of nanotechnology such as magnetic storage, memory, sensors, logic and communication devices. Bi-stable ferromagnetic cross-shaped nanoelements showed complex spin configurations[2] and subsequent report[3] proposed application of ferromagnetic cross-shaped elements as reconfigurable spin-based logic devices using spin-wave (SW) scattering and interference. The above results open a door for application of ferromagnetic cross structures as a building block of the above-mentioned devices, and hence, investigation of the static and dynamic magnetic properties of this structure with its size, inter-element interaction and variation of bias magnetic field strength and in-plane orientation has become very important. 2. Results and discussions Here, we report a systematic study of SW dynamics in $Ni_{80}Fe_{20}$ (Py) nano-crosses with varying arm lengths (200 nm $\leq L \leq$ 600 nm) while keeping edge to edge separation (S = 150 nm) fixed, fabricated by a combination of e-beam lithography and e-beam evaporation and measured using broadband ferromagnetic resonance technique. We have rigorously investigated bias field strength (H) and in-plane orientation (θ) dependent evolution of static spin configuration and magnetization dynamics in Py nano-cross[4] arrays of varying size (L). The bias field dependent ferromagnetic resonance (FMR) spectra for the nano-cross arrays with L = 600 nm and 500 nm at θ = 0° respectively are shown in Figures 1(b)-1(c) and surface plot with θ = 15° for L = 600 nm is shown in Figure 1(a). We have observed a remarkable variation in the SW dynamics with H which is also modified with size of nano-crosses including mode softening, mode splitting, mode crossover and mode merging. Particularly, SW mode softening strongly depends on the external bias field orientation. We also demonstrate that the mode splitting, mode crossover, mode merging and number of modes can be easily tuned by changing the applied bias field direction, which is further modified with size of the nano-cross element also. To understand the experimental results, we have performed micromagnetic simulations using OOMMF software, which reproduced the experimental results very well. Further, we simulated phase profiles of different SW modes using a home built code, from where we have characterized the observed SW modes. In Figures 1(e)-1(f) it is shown that how lowest frequency branch gets modified with the increase in bias fields. Here *n, m* corresponds to quantization number for backward volume mode and Damon-Eshbach mode, respectively. To understand the dynamics further, we have numerically calculated the magnetostatic field distributions in the nano-cross arrays (Fig. 1(g)). Line scan of this field reveals that with the decrease in arm length (L), the inter-cross interaction field as well as the internal field decrease monotonically as plotted in Figs. 1(h)-1(i). 3. Conclusions In summary, we investigated bias field strength and orientation dependent evolution of static magnetic configuration and magnetization dynamics in $Ni_{80}Fe_{20}$ nano-cross arrays of varying cross size using broadband ferromagnetic resonance technique. We observed a strong variation in the number of spin-wave (SW) modes and mode frequencies (f) with bias field magnitude (H) as well as in-plane orientation (θ). Simulated static spin configurations and SW mode profiles explain the rich variation of the SW spectra, including mode softening, mode crossover, mode splitting and mode merging. Such variation of SW spectra is further modified by the size of the nano-cross. Calculated magnetostatic field distributions supported the above observations and revealed the non-collective nature of the dynamics in closely packed nano-cross structures. The latter is useful for their possible applications in magnetic storage, logic and communication devices. We gratefully acknowledge the financial support from S. N. Bose National Centre for Basic Sciences (Grant no. SNB/AB/12-13/96) and Department of Science and Technology, Government of India (Grant No.SR/NM/NS-09/2011(G)).

1. R. Skomskii, J. Phys.: Condens. Matter 15, R841 (2003). 2. K. Machida, et al, J. Magn. Magn. Mater. 290, 779 (2005). 3. K. Nanayakkara, et al, J. Appl. Phys. 118, 163904 (2015). 4. K. Adhikari, et al, J. Appl. Phys. 121, 043909 (2017).

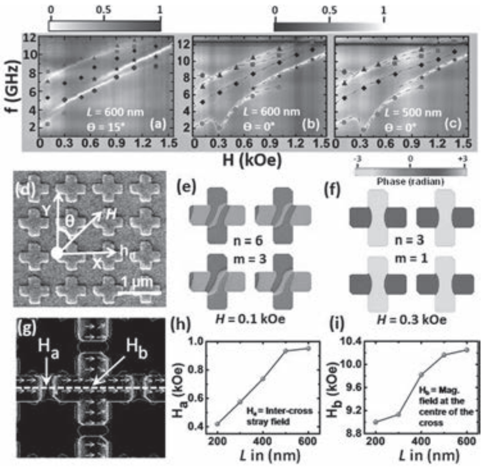

Fig. 1. Surface plot of the bias field dependent FMR spectra for the nano-cross with arm length (L) of 600 nm (a) θ = 15°, (b) θ = 0° and (c) for L = 500 nm at θ = 0°, respectively. (d) Scanning electron micrographs of $Ni_{80}Fe_{20}$ nano-cross arrays with L = 600 nm. Simulated mode frequencies are shown by filled symbols, while the dotted lines are guide to eye. (e)-(f) Spatial distribution of simulated phase profiles corresponding to lowest frequency branch at two different H values for L = 600 nm. (g) Contour plots of the simulated magnetostatic field distribution for L = 600 nm and H = 0.6 kOe. Linescans are taken along the white dotted lines. (h) Inter-cross stray field and (i) effective magnetic field at the centre of the cross for different L values.

ET-14. Losses Modeling Based on Domain Wall Processes and Validation Considering Rotational Excitation of Electrical Steel Sheets.

J. Li[1], Q. Yang[2,3], S. Wang[1] and Y. Li[2]
1. State Key Laboratory of Control and Simulation of Power System and Generation Equipments, Tsinghua University, Beijing, China; 2. State Key Laboratory of Reliability and Intelligence of Electrical Equipment, Hebei University of Technology, Tianjin, China; 3. Municipal Key Laboratory of Advanced Technology of Electrical Engineering and Energy, Tianjin Polytechnic University, Tianjin, China

Abstract Body: On the basis of damping principle of vibration, the domain wall processes is investigated and modeled at low-to-medium frequencies in electrical steel sheets. Due to the energy dissipation chiefly descends from a micro-vortex current caused by domain wall motion, the coupled Landau-Lifshitz-Gilbert (LLG) and Maxwell electromagnetic diffusion equations are thus considered to describe the high-frequency characteristics. The overall core losses are eventually deduced in terms of separate contributions by domain wall processes and classical eddy current. Moreover, the calculation model can be extended to rotational excitation pattern. Hence, taking the typical electrical steel sheets as example, the novel core losses calculation model is analysed and compared with the total alternating core losses supplied by electrical steel sheets manufacturers and the 3-D rotating experimental core losses of sheets specimens which are carried out by using a 3-D magnetic properties testing system, and also achieve some beneficial conclusions. 1. Since the domain wall processes is essentially the magnetic moment rotation, then domain wall motion can be interpreted by solving LLG equation, that is [1, 2]: $\partial J/\partial t = -\chi J\times[H_{eff}+(\alpha/J_s)J\times H_{eff}]$, $|J| = J_s$ (1) where, $J = \mu_0 M$ represents the magnetic polarization vector inside the domain, M is the magnetization vector, μ_0 is the permeability of vacuum, $\chi = |e|/m_e = 1.76\times10^{11}$ $T^{-1}s^{-1}$ is the absolute value of the electron gyromagnetic ratio [3]; H_{eff} represents the overall effective field, which affects on the magnetic moments; $\alpha = \eta J_s$ is the qualitative dimensionless damping constant (Landau-Lifshitz damping coefficient), η is the damping coefficient of domain wall motion, J_s is the saturation polarization. The first term on the right side of Eq. (1) describes the magnetic moment precession around the effective field direction, while the second term is the damping motion towards the effective field. 2. As regard to the right sheet with the walls in Fig. 1, in effect of the high-frequency excitation field H, the wall moves to make on both sides of the domains contraction and expansion. Now, by applying Maxwell electromagnetic diffusion equation: $\partial^2 H_{vor}/\partial y^2 = \sigma\mu_0[\partial(M+H_{vor}+H)/\partial t]$ (2) where, σ is the electrical conductivity of magnetic materials and the vortex current field H_{vor} is directed to y-axis. At this point, such a response can be described in general terms by the solution of the coupled LLG (Eq. (1)) and Maxwell electromagnetic diffusion (Eq. (2)) equations. 3. According to the above derivation, the overall core losses per unit mass of electrical steel sheets are eventually deduced in terms of separate contributions by classical eddy current and domain wall processes, as follows: $P_{cl} = P_{cel}+\bar{P}_{mel} = (\sigma\pi^2 d^2/3\rho)f^2(B_m)^2+(\sigma\pi^2 d^2/4\rho)f^2(B_m)^2=(7\sigma\pi^2 d^2/12\rho)f^2(B_m)^2$ [W/kg] (3) where, P_{cl} is the overall core losses per unit mass of electrical steel sheets; P_{cel} is the classical eddy current loss per unit mass; $\bar{P}_{mel}$ is the mean micro-vortex current losses per unit mass; d is the thickness of the magnetic sheet; ρ is the mass density of magnetic materials; f is the excitation frequency; B_m is the peak flux density. 4. In order to validate the precision of the calculation model, the total alternating core losses supplied by electrical steel sheets manufacturers are used to compare with the calculation of Eq. (3), including cold-rolled GO electrical steel, NO electrical steel and hot-rolled electrical steel over wide range of excitation frequency [4, 5]. In addition, the model can be extended to rotational excitation pattern, so the 3-D rotational experimental core losses of typical electrical steel sheets carried out by using a 3-D magnetic properties testing system are also considered in the validity of the calculation model [6, 7]. The typical comparison result is shown in Fig. 2. Conclusion: Based on the basic equation of Micromagnetism (LLG equation), the vibration analysis of micro domain wall processes is carried on by applying excitation field at low-to-medium frequencies in combination with the field intensity spatial distribution of magnetic dipoles in this paper. By coupling Maxwell electromagnetic diffusion equations, the high-frequency micro-vortex current losses due to domain wall motion are deduced. Consequently, the calculation model of overall core losses are developed ultimately by means of the separate contributions of domain wall processes and classical eddy current. Precision and validity of the model are testified by several kinds of typical electrical steel sheets, including their alternating and 3-D rotational core losses. The modelling method of mean micro-vortex current losses and the characteristics analysis of the total core losses calculation model are helpful to engineering application. In addition, the investigation is a very important problem in the research field of Micro-magnetism and Magnetization Dynamics. This study can not only reveal the intrinsic characteristics of electrical steel sheets, but also provide reference for exploring origins of the core losses in magnetic materials in practice.

[1] L. D. Landau and E. M. Lifshitz. *Vol. 8 of Course of Theoretical Physics: Electrodynamics of Continuous Media*[M]. UK, Oxford: Pergamon Press, 1984. [2] T. L. Gilbert. A lagrangian formulation of gyro-magnetic equation of the magnetization field[J]. *Phys. Rev.*, 1955, no. 100, pp. 1243. [3] O. Bottauscio, F. Fiorillo, C. Beatrice, *et al.* Modeling high-frequency magnetic losses in transverse anisotropy amorphous ribbons[J]. *IEEE Trans. Magn.*, 2015, vol. 51, no. 3, pp. 2800304. [4] QWG (GG) 02-2010. WUSTEEL Cold-Rolled GO Electrical Steel. [5] Q/BQB 480-2009. BAOSTEEL Cold-Rolled NO Electrical Steel. [6] Y. J. Li, Q. X. Yang, J. G. Zhu, *et al*. Design and analysis of a novel 3-D magnetization structure for laminated silicon steel[J]. *IEEE Trans. Magn.*, 2014, vol. 50, no. 2, pp. 7009504. [7] J. S. Li, Q. X. Yang, Y. J. Li, *et al*. Anomalous loss modeling and validation of magnetic materials in electrical engineering[J]. *IEEE Trans. Appl. Supercon*, 2016, vol. 26, no.4, pp. 8800105.

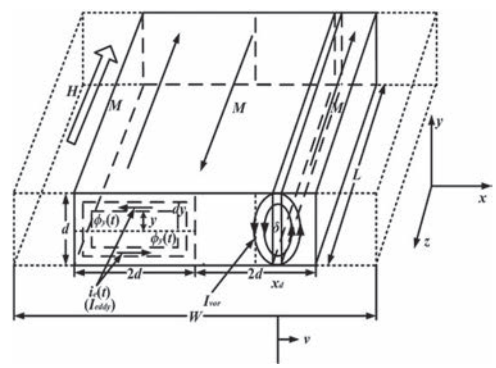

Fig. 1. Physical mechanism model of the classical eddy current loss production and the domain wall motion energy dissipation.

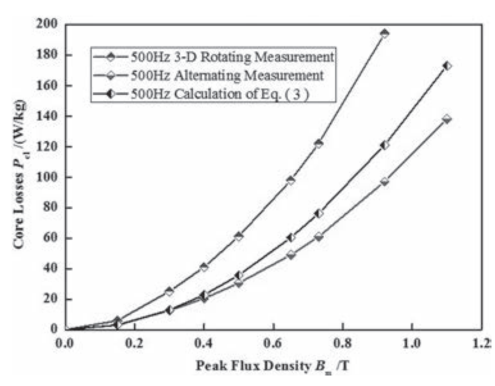

Fig. 2. Comparisons among the 3-D rotational and alternating measurements and calculation of Eq. (3) for SOMALOY™500 (500Hz).

ET-15. Withdrawn

ET-16. Switching of Skyrmion chirality by local heating.

Y. Nakatani[1], K. Yamada[2] and A. Hirohata[3]
1. University of Electro-Communications, Chofu, Japan; 2. Gifu University, Gifu, Japan; 3. University of York, York, United Kingdom

A magnetic Skyrmion is a chiral structure appearing in a magnetic thin film with Dzyaloshinskii-Moriya interaction (DMI) [1-4]. Because of its small size and the small threshold current for motion, it is expected to be used as an information carrier for a magnetic storage system [5-7]. The methods to manipulate the Skyrmion, nucleation, annihilation, switching of the core direction, motion, by external field, spin-polarized current and the others have been proposed. In this paper, we propose a method to switch the chirality of the Skyrmion by a pulse heat spot, and study it by simulation. The micromagnetic model was used and the motion of the magnetization in the thin film was calculated using the Landau-Lifshitz-Gilbert equation. The thin film model possessed dimensions of $256\times256\times1.4$ nm^3, and was further divided into rectangular prisms with dimensions of $0.5\times0.5\times1.4$ nm^3. Typical material parameters for perpendicularly-magnetized CoFeB thin films were used. These were a saturation magnetization M_s = 1600 emu/cm^3, a gyromagnetic ratio γ= 1.76×10^7rad/(s Oe), an exchange stiffness constant A = 3.1×10^{-6} erg/cm, an uniaxial anisotropy constant K_u = 16.2 Merg/cm^3, the Gilbert damping constant α = 0.1, and the DMI constant D = 0.6 erg/cm^2. Two types of Skyrmions with clock wise (CW) and counter clock wise (CCW) chirality were used as the initial states. In the simulation, a pulse heat spot with Gaussian shape was applied. The σ of the head spot (σ_h) was varied from 5 to 50 nm. The room temperature and the maximum temperature of the heat spot were set to be 300 and 550 K. The rise and fall time of the heat spot was assumed to be zero. The pulse length of the heat spot (t_p) was varied from 0.2 to 3.0 ns. Simulation was continued for 10 ns after to cut the pulse. The material parameters M_s, K_u, A, and D of each prisms were decreased as temperature was increased. Figure 1 shows the simulated time-resolved chirality switching by a heat spot. The CCW Skyrmion (fig. 1(a)) expands by the heat spot keeping the magnetization direction (fig. 1(b)). The Skyrmion shrinks after to cut the pulse, the magnetization rotates to the crock wise direction, and the CW Skyrmion appears (fig. 1(c)). The CW Skyrmion (fig. 1(d)) expands slightly by the heat spot, however the magnetization rotates to the counter clock wise direction (fig. 1(e)). The magnetization keeps to rotate to the same direction after to cut the pulse, and the CCW Skyrmion appears (fig. 1(f)). The Skyrmion breathes by these operations especially with large and long pulse. It annihilates with large breathing when it shrinks. Figure 2 show the diagram plotting the switching, not switching and annihilating of the Skyrmion structure on σ_h and t_p for CCW (fig. 2(a)) and CW (fig. 2(b)) Skyrmions. They show that there are conditions to switch both Skyrmions and there are also conditions to switch only one type of Skyrmions. The chirality of the Skyrmion can be specified by using the latter conditions. We investigate the switching of Skyrmion chirality dependence on the pulse heat spotσ_h and the pulse heat time t_p. It is found that there are the optimized conditions for Skyrmion chirality to be controlled, and that the changing of magnetization structure in Skyrmion during the pulse heating is different dependence on the initial Skyrmion chiral state.

[1] T. H. R. Skyrme, *Nucl. Phys*. 31, 556 (1962). [2] S. Muhlbauer *et al.*, *Science* 323 (5916), 915 (2009). [3] X. Z. Yu *et al.*, *Nature* 465 (7300), 901 (2010). [4] S. Seki *et al.*, *Science* 336 (6078), 198 (2012). [5] F. Jonitz *et al.*, *Science* 330 (6011), 1648 (2010). [6] X. Z. Yu *et al.*, *Nat. Commun.* 3, 988 (2012). [7] A. Fert *et al.*, *Nat. Nanotechnol* 8 (3), 152 (2013).

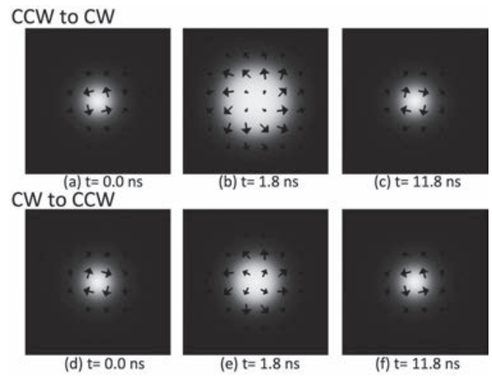

Fig. 1. Simulated time-resolved chirality switching by a pulse heat spot (σ_h = 25 nm, t_p = 1.8 ns) (a) to (c) CCW to CW, (d) to (f) CW to CCW. A side of a square is 256 nm.

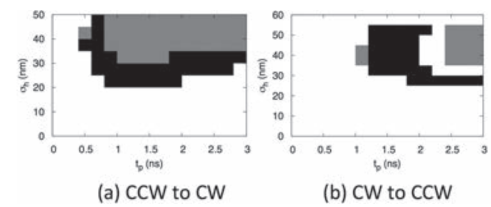

Fig. 2. Diagram plotting the switching (black), not switching (white) and annihilating (gray) of the Skyrmion structure on σ_h and t_p. (a) CCW to CW case, (b) CW to CCW case.

Session EU
MICROMAGNETICS I
(Poster Session)

Zhuo Bin Siu, Chair
National University of Singapore, Singapore

EU-01. Magnetic properties of $L1_0$ FePt thin film influenced by strains stemmed from the polarization of PMN-PT substrate.

L. Liu[1], C. Hu[2], Y. Xu[1] and W. Rao[1]
1. Department of Materials Physics, and IEMM, Nanjing University of Information Science and Technology, Nanjing, China; 2. College of Materials Science and Engineering, Liaocheng University, Liaocheng, China

I. INTRODUCTION The perpendicular magnetic anisotropy(PMA) depending on structural domain orientation is vital to the performance of magnetic devices based on the $L1_0$ FePt thin films. In general, the out-of-plane ordered structural domains(OPOSDs) are desired in devices. However, the maximal volume of the OPOSDs can only reach 76 % [1]. One of the ways to increase the volume of OPOSDs is to change the strain states between the thin film and substrate. Experimental results [1, 2] showed that the large lattice mismatch between the thin films and substrates can cause tensile stress to the thin films, resulting in a large volume of OPOSDs and large PMA. Nevertheless, the experimental work [21] showed that the coercivities increase with the increase of the compressive strain in the thin film deposited on PMN-PT substrate. II. SIMULATION METHOD Phase field method is a powerful tool to simulate the magnetic properties in magnetic materials [4], In this work, based on the work [3], especially considering the role of magnetoelastic energy, the effect of the compressive strains on the PMA, magnetic domains evolution, in the $L1_0$ FePt thin film were studied in details by using the phase field model. III. RESULTS Fig. 1 shows the effect of compressive strain on the magnetic hysteresis loops and magnetic coercivities of the $L1_0$ FePt thin film. The area D in magnetic hysteresis of the $L1_0$ FePt thin film in Fig. 1(a) is enlarged shown in Fig. 1(b), which show that the magnetic coercivities increase with the decrease of compressive strains. Fig. 2 shows the magnetic domain structures corresponding to the point A, B, C, D, E, and F in the simulated hysteresis loops of the $L1_0$ FePt thin film with the strain of -0.06% in Fig. 1(a). The evolution of magnetic domain structure of the $L1_0$ FePt thin film under this strain shows that the magnetization changes from [001] single domain to multidomain and then from multidomain change to single magnetic domain at the reversible magnetization processes. The magnetic energies variations will be analyzed in future studies.

1) H. Ho, J. X. Zhu, A. Kulovits, David E. Laughlin, and J. G. Zhu, "Quantitative transmission electron microscopy analysis of multi-variant grains in present $L1_0$-FePt based heat assisted magnetic recording media", *J. Appl. Phys.* 116 193510 (2014). 2) K. F. Dong, H. H. Li, and J. S. Chen, "Lattice mismatch-induced evolution of microstructural properties in FePt Films", *J. Appl. Phys.* 113, 233904 (2013). 3) M. F. Liu, L. Hao, T. L. Jin, J. W. Cao, J. M. Bai, D. P. Wu, Y. Wang, and F. L. Wei, " Electric-field manipulation of coercivity in FePt/Pb$(Mg_{1/3}Nb_{2/3})O_3$–$PbTiO_3$ heterostructures investigated by anomalous Hall effect measurement ", *Applied Physics Express* 8 063006 (2015). 4) J. M. Hu, C. G. Duan, C. W. Nan, L. Q. Chen, "Understanding and designing magnetoelectric heterostructures guided by computation: progresses, remaining questions, and perspectives", *npj Comput. Mater.* 3 18 (2017).

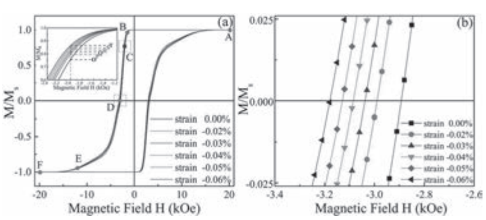

Fig. 1. (a) Simulated magnetic hysteresis loops and (b) the enlargement of area D in the hysteresis loops of the $L1_0$ FePt(3 nm) thin film with different compressive strains.

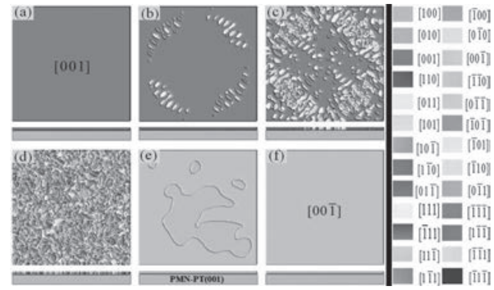

Fig. 2. Simulated magnetic domain structures (a), (b), (c), (d), (e) and (f) corresponding to the point A, B, C, D, E and F in the hysteresis loops of the $L1_0$ FePt(3 nm) thin film when the compressive strain is -0.06%. The upper part is plan-view image and the lower part is cross-section image in each of figure.

EU-02. Voltage controlled spin torque nano-oscillator based on magnetic skyrmion.

C. Song[1], C. Jin[1], H. Xia[1], J. Wang[1], J. Wang[1,2] and Q. Liu[1]
1. Key Laboratory for Magnetism and Magnetic Materials of the Ministry of Education, Lanzhou University, Lanzhou, China; 2. Key Laboratory for Special Function Materials and Structural Design of the Ministry of Education, Lanzhou University, Lanzhou, China

Magnetic skyrmions are topologically protected stable magnetization configurations, which exhibit to be a promising candidate for future memory and logic devices[1-4], due to their its topological stability, small size and low driving current[5-7]. One of the potential applications of skyrmion is nanocontact spin transfer nano-oscillators (STNOs)[8-9]. In this work, we propose a voltage controlled magnetic skyrmion STNO by using micromagnetic simulations. Here, a ring shaped voltage controlled magnetic anisotropy (VCMA) gate is applied on the skyrmion based STNO. It is found that the skyrmion size can be increased or decreased by applying a negative or positive electric field in the ring. Furthermore, the skyrmion dynamics can also be effectively modulated with applying ring-shaped VCMA gate. By tnning the current density, ring-shaped VCMA gate position and VCMA effect of the ring, the oscillarion frequency varies in a large range. This unconventional manipulation of magnetic skyrmions in STNOs allows a robust way of controlling frequency of skyrmions oscillator, and provides a new path to skyrmions based STNOs. Figure 1 depicts a schematic diagram of skyrmion based STNO device with a VCMA gate (white ring), which consists of free layer, a non-ferromagnetic space layer and a fixed layer. At the top and bottom of this device, there are two point-contact electrodes to ensure the spin polarized current flowing locally and perpendicularly, the radius of point-contact electrode is 10 nm. The ring shaped VCMA gate is applied on the free layer, and the spin polarization takes the form in the out-of-plane magnetized fixed layer along –*z*-direction. The magnetic free layer is assumed to be an ultrathin film with perpendicular magnetic anisotropy (PMA) and interfacial Dzyaloshinskii–Moriya interaction (DMI). Magnetic skyrmion is in the center of the free layer as a ground state, and it is gyrotropic in the free layer under the spin-polarized current. Figure 2 shows the oscillation frequency as a function of r for different K_{uv}. The skyrmion oscillation frequency is 430 MHz without VCMA effect in the nanodisk, which is represented by the black line in figure 2. When applying a current, the skyrmion reaches a steady motion and r_o is about 16 nm, and the radius r_s is about 10 nm in the rotation for all the cases. With applying a negative electric field, the PMA of the ring K_{uv} is reduced to 0.72×10^6 J/m^3, the frequency is still 430 MHz at $r = 15$ nm. While it reaches to 20.39 GHz at $r = 20$ nm. The inset shows the corresponding magnetization distribuions in this case. It indicates that the skyrmion is pinned with the edge of skyrmion expanding to the VCMA-gated region, and the inner magnetizations of skyrmion (red region) keep a steady precession under spin-polarized current. Increasing r to 25 nm, the oscillation frequency is 515 MHz, and it decreases to 475 MHz at $r = 30$ nm. It is noteworthy that the oscillation frequency decreases to a minimum value 335 MHz when $r = 35$ nm, and it is close to 430 MHz when $r = 40$ nm and 45 nm. When K_{uv} increases to 0.76×10^6 J/m^3, the frequency reaches a maximum at $r = 25$ nm with the value of 475 MHz, and a minimum at $r = 35$ nm with the value of 380 MHz. However, when applying a positive electric field with increasing to 0.84×10^6 J/m^3, the frequency decreases to 395 MHz with $r = 25$ nm, and then increases to the maximum 480 MHz at $r = 35$ nm. In the case of $K_{uv} = 0.88 \times 10^6$ J/m^3, the oscillation frequency reaches a minimum 360 MHz at $r = 25$ nm, and a maxmimum 525 MHz at $r = 35$ nm.

1) Fert A, Cros V and Sampaio J 2013 “Skyrmions on the track” *Nat. Nanotechnol.* 8 152–6 2) Tomasello R, Martinez E, Zivieri R, Torres L, Carpentieri M and Finocchio G 2014 “A strategy for the design of skyrmion racetrack memories” *Sci. Rep.* 4 6784 3) Zhang X, Zhou Y, Ezawa M, Zhao G P and Zhao W 2015 “Magnetic skyrmion transistor: skyrmion motion in a voltage-gated nanotrack” *Sci. Rep.* 5 11369 4) Zhang X, Ezawa M and Zhou Y 2015 “Magnetic skyrmion logic gates: conversion, duplication and merging of skyrmions” *Sci. Rep.* 5 9400 5) Sampaio J, Cros V, Rohart S, Thiaville A and Fert A 2013 “Nucleation, stability and current-induced motion of isolated magnetic skyrmions in nanostructures” *Nat. Nanotechnol.* 8 839–44 6) Hrabec A, Sampaio J, Belmeguenai M, Gross I, Weil R, Chérif S M, Stachkevitch A, Jacques V, Thiaville A and Rohart S 2016 “Current-induced skyrmion generation and dynamics in symmetric bilayers” *arXiv* 1611.00647 7) Fert A, Cros V and Sampaio J 2013 ”Skyrmions on the track“ *Nat. Nanotechnol.* 8 152–6 8) Zhang S, Wang J, Zheng Q, Zhu Q, Liu X, Chen S, Jin C, Liu Q, Jia C and Xue D 2015 “Current-induced magnetic skyrmions oscillator” *New J. Phys.* 17 23061 9) Garcia-Sanchez F, Sampaio J, Reyren N, Cros V and Kim JV 2016 “A skyrmion-based spin-torque nano-oscillator” New J. Phys., vol. 18, 075011

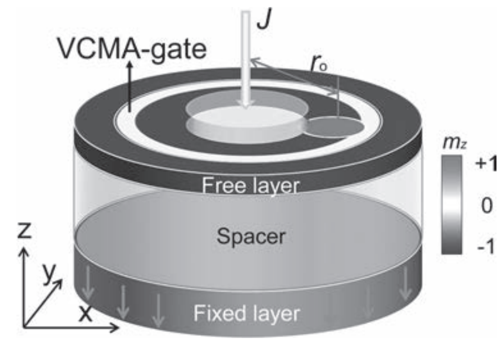

Fig. 1. Schematic of a STNO based on skyrmion with a ring-shaped VCMA gate.

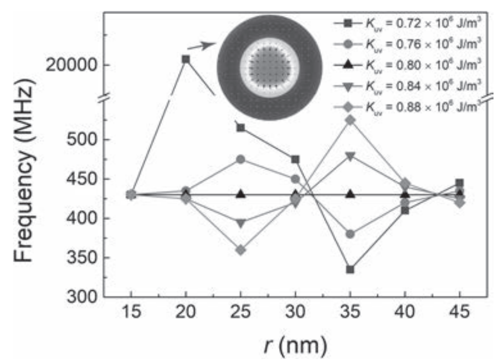

Fig. 2. The oscillation frequency as a function of r and K_{uv}. The inset shows the magnetization distributions of the nanodisk, where the skyrmion expands to the ring-shaped VCMA gate.

EU-03. Effects of Anisotropy Field and easy axis dispersions on squareness ratio for HDDR-processed NdFeB powders.

F. Akagi[1], T. Shirai[1] and R. Kariya[1]
1. Kogakuin Univ., Shinjuku-ku, Japan

I. INTRODUCTION NdFeB magnetic powders that are produced by a hydrogenation decomposition desorption recombination (HDDR) process consist of small grains with highly anisotropic energy [1-3]. Therefore, HDDR-processed NdFeB magnet powders are expected to have a high squareness ratio and high coercivity (H_c) to obtain the high maximum energy product ($BH_{\max}$) that is required in highly efficient motors of hybrid or electric vehicles. The squareness ratio is defined as the value of the magnetic field at 90% of the remanent magnetization divided by H_c. However, the squareness ratio is much lower than the expected value of 1.0, and the H_c is lower than a third of the average anisotropy fields. A previous study using a micromagnetic simulator has shown that when an anisotropy field (H_k) dispersion of grains was assumed to be a Gaussian distribution with a coefficient variation ($\sigma H_k/\langle H_k\rangle$) of 30%, the squareness ratio corresponded with an experimental value [4]. However, Nishio et al. showed that the H_k of a single crystal was 7600 kA/m [5]. Therefore, when the $\sigma H_k/\langle H_k\rangle$ is 30%, the $\langle H_k\rangle + 3\sigma H_k$ is unrealistically higher than the H_k of a single crystal. In this study, the H_k dispersion of the grains was assumed to be a horizontally flipped lognormal distribution, and the effects of the H_k dispersion of the grains on the squareness ratio were investigated by using a micromagnetic simulator. Moreover, Nishio et al. showed that an easy axis (c-axis) inclination angle was distributed within ±20° [6], so we also investigated the effects of the c-axis dispersion on the squareness ratio. II. CALCULATION METHOD AND MODEL We calculated the time change of magnetization for each grain using an EXAMAG LLG simulator [7]. The Landau-Lifshitz-Gilbert equation shown below was calculated by using the finite element method (FEM): $dM/dt = -\gamma(M\times H_{eff}) + \alpha/M_s(M\times dM/dt)$, (1) where M is magnetization, t is time, γ is the gyromagnetic ratio, H_{eff} is the effective field (which is the sum of the applied, static, anisotropy, and exchange fields), α is the damping constant, and M_s is the saturation magnetization. The calculation model of the NdFeB powder contained 64 grains, and each grain was a cube with a side length of 40 nm, including cube cells with a side length of 2 nm. The grain boundaries were 2 nm wide and the deterioration layers of the grain surfaces were also 2 nm wide [4]. The saturation magnetization (M_s) of the main phase was 1.61 T. The average H_k ($\langle H_k\rangle$) was 5000 or 6077 kA/m, and the coefficient variation of H_k ($\sigma H_k/\langle H_k\rangle$) was changed from 0 to 30%. The exchange stiffness constant was 1.0×10^{-11} J/m. The grain boundaries were assumed to be made from non-magnetic or soft magnetic materials. In the case of soft magnetic material, the M_s was 0.805 T, the H_k was 1 kA/m, and the exchange stiffness constant was 6.25×10^{-12} J/m. The H_k of the deterioration layer was 10% of the main-phase grain, and the M_s was the same as that of the main phase. The c-axis followed a Gaussian distribution with a standard deviation from 0 to 30°. III. RESULTS AND DISCUSSIONS Figure 1 shows the $\sigma H_k/\langle H_k\rangle$ dependence of the squareness ratio for the non-magnetic grain boundaries. As seen from this graph, there was only a small difference between the average H_ks of 5000 and 6077 kA/m, and each squareness ratio decreased with increasing $\sigma H_k/\langle H_k\rangle$. When the $\sigma H_k/\langle H_k\rangle$ was about 27%, the squareness ratio was close to the experimental value. Figure 2 shows the standard deviation of the c-axis dependence of the squareness ratio. The squareness ratio for the soft magnetic grain boundaries was substantially independent of the standard deviation of the c-axis and was far from the experimental value. This is because the magnetizations for the soft magnetic grain boundaries reversed rapidly due to a magnetic domain wall motion between the grains and the grain boundaries. On the other hand, the squareness ratio of the non-magnetic grain boundaries was much lower than that of the soft magnetic grain boundaries. The squareness ratio for the non-magnetic grain boundaries decreased and was close to the experimental value with increasing standard deviation of the c-axis. Therefore, the non-magnetic grain boundaries led to a low squareness ratio. However, Nd-enriched grain boundaries and grain boundaries comprised of ferromagnetic elements were experimentally observed [8]. As a result, some grain boundaries might be soft magnetic materials, and others might be non-magnetic materials that pin the magnetization reversal. In comparison, the squareness ratio of the non-magnetic boundaries was larger than the experimental value, although the standard variation was up to 30°. Therefore, the low squareness ratio cannot be explained by only the c-axis dispersion. The results show that both the H_k dispersion and the c-axis dispersion affect the squareness ratio. IV. CONCLUSION We investigated the effects of the H_k and the easy axis dispersions of the grains on the squareness ratio using a micromagnetic simulator. It resulted that both dispersions affected the squareness ratio, and the average H_k hardly contributed to the squareness ratio. It was also found that the non-magnetic grain boundaries led to a low squareness ratio. ACKNOWLEDGMENTS We thank Dr. Mishima of Aichi Steel Corporation for his advice on experimentally bonded magnets.

[1] R. GAO and J. ZHANG, “Demagnetization Process and Coercivity for Anisotropic HDDR NdFeB Bonded Magnets”, J. Mater. Sci. Technol., Vol. 16 No. 4, 445-446 (2000). [2] T. Nishiuchi, S. Hirosawa, M. Nakamura, M. Kakimoto, T. Kawabayashi, H. Araki, and Y. Shirai, “Relationship between Coercivity and Microstructural Changes During DR Treatment in the HDDR-processed Nd-Fe-Co-B Alloy”, IEEJ Trans. on Electrical and Electronic Engineering, Vol. 3, 390-393 (2008). [3] Y. Honkura, Proceeding of 19th International Workshop on Rare Earth Permanent Magnets and Their Application, Beijing, CHINA 2006, 231 (2006). [4] F. Akagi, and Y. Ishii, “Effects of anisotropy field dispersion and grain boundary on corecivity and squareness ratio for HDDR-processed NdFeB powders”, AIP Advances 8, 056201 (2018); http://doi,org/10.1063/1.5005047. [5] H. Nishio, H. Taguchi, S. Hashimoto, K.Yajima, A. Fukuno, and H. Yamamoto, “A comparison of magnetic anisotropy constants and anisotropy fields of permanent magnets determined by various measuring methods”, J. Phys. D, Appl. Phys. 29, 2240-2245 (1996). [6] H. Nishio, T. Tayu, H. Ono, M. Shimada, and H. Yamamoto, “Anisotropy Distribution of Nd-Fe-B Magnet Powder Prepared by the HDDR Process”, JMSJ. MAG, Vol. 29, No. 2, 105-110 (2005). [7] http://www.fujitsu.com/global/abount/resources/news/press-releases/ (12/18/2017). [8] W. F. Li, To. Ohkubo, K. Hono, T. Nishiuchi, and S. Hirosawa, “Coercivity mechanism of hydrogenation disproportionation desorption recombination processed Nd-Fe-B based magnets”, Appl. Phys. Lett., 93, 052505 (2008).

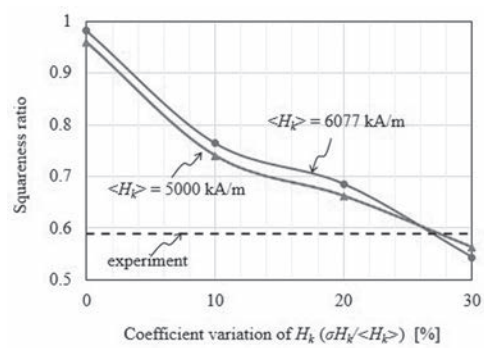

Fig. 1. $\sigma H_k/\langle H_k\rangle$ dependence of squareness ratio.

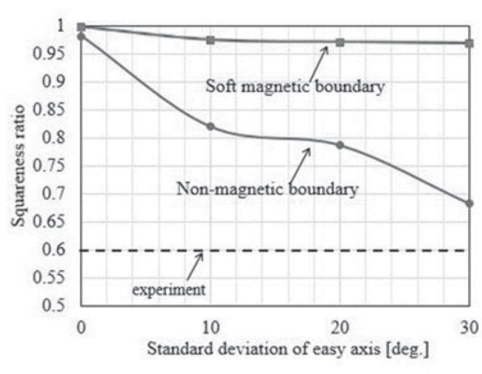

Fig. 2. Standard deviation of easy axis dependence of squareness ratio.

EU-04. Numerical analysis of write current reduction in magnetic tri-layer strucutre with low-Tc interlayer for MRAM.

Y. Kayama[1], K. Machida[1], S. Greaves[2], Y. Sonobe[3] and Y. Nakatani[1]
1. University of Electro-Communications, Chofu, Japan; 2. RIEC, Tohoku University, Sendai, Japan; 3. Samsung Research Institute of Japan, Yokohama, Japan

Introduction Spin-transfer torque (STT) magnetic random access memory (MRAM) with perpendicular anisotropy is expected to replace dynamic random access memory (DRAM) in high density nonvolatile memory applications. To realise high density MRAM, the write current has to be reduced while keeping high thermal stability $\Delta=K_uV/k_BT$[1]. Bi-layer structures, such as a magnetically hard-soft composite structure with Joule heating (EcC) [2], have been proposed to achieve these aims. Structures with three or more layers, such as the graded magnetic anisotropy medium structure [3], have been used for high density magnetic recording, and their application to MRAM has also been proposed to improve the switching efficiency. Recently, Zhang et al. [4] suggested that a tri-layer with a low Currie temperature (Tc) magnetic interlayer sandwiched between two hard magnetic layers could be used as a hybrid free layer (HFL) to solve the dilemma between writability and retention in MRAM. We previously proposed a new tri-layer with a low-Tc, hard magnetic interlayer between magnetically soft and hard layers, which has the possibility to be graded. In this work, we use numerical simulations with a Landau-Lifshitz-Bloch (LLB) model to analyze the switching characteristics of the new tri-layer and show that it has advantages over EcC in MRAM applications. The Model In our simulations, the micromagnetic simulator described in [5] was used. In this simulator, a Landau-Lifshitz-Bloch (LLB) model [6] with a Slonczewski STT term [7] was implemented to calculate STT-induced magnetization switching characteristics such as the switching probability, switching time and thermal stability factor. The model also takes account of the increase in temperature due to Joule heating during switching operations. The device diameter was fixed at 20 nm and the total thickness of the new tri-layer was 4 nm. As shown in fig. 1(a), the EcC structure consisted of two layers: one soft layer (2nm) and one hard layer (2nm), while the new tri-layer structure consisted of three layers: one soft layer (1nm), one low-Tc, hard interlayer (1nm), and a high-Tc, hard layer (2nm). The key material parameters of the structures are shown in fig. 1(b). The magnetic anisotropy K_u for each structure was chosen to satisfy $\Delta=60$ at room temperature. The same damping constant α, exchange stiffness A_{ex}, and interlayer exchange coupling A_{iec} were used for all structures. In our simulations, the magnetization evolution was calculated for 20 ns. Fig. 1(c) shows the write current I_c and temperature profile due to Joule heating [5]. The write current I_c was applied for 10 ns and was assumed to be uniform inside the structures. For the temperature profile, the device temperature increased for 1 ns with a temperature rise proportional to I_c^2, then remained constant for 9 ns, and finally decreased to the initial temperature over a period of 5 ns. Results Fig 2.(a) shows the write current I_c [υA] dependence of the switching probabilities at room temperature for the EcC and the new tri-layer structures. As shown in the figure, a smaller I_c can switch the magnetization in the new tri-layer when compared with the EcC structure. To demonstrate this current reduction more qualitatively, the critical switching current I_{c0} was estimated by fitting the inverse of the switching time $1/T_{sw}$ [1/nsec] and linearly extrapolating to the x-axis, as shown in Fig 2.(b). As shown in the table in fig. 2(b), the new tri-layer can reduce I_{c0} by 10% when compared with the EcC structure. The magnetic anisotropy of the second layer in the new tri-layer becomes smaller than that of the third layer due to Joule heating when the write current exceeds I_{c0}. The reduction in switching current may be considered to be partly caused by this faster reduction of magnetic anisotropy in the second layer. In this work, we compared the switching performance of EcC and the new tri-layer structure using a LLB model, and showed that the new tri-layer had a better switching performance. It is concluded that the new tri-layer is a more promising approach to reduce the write current while keeping the thermal stability. The tri-layer structures can realise various structures, such as graded anisotropy, to further improve the switching characteristics because they have a larger number of degrees of freedom for the magnetic properties. In the presentation we will discuss the temperature dependence of the switching probability and optimisation of the magnetic properties of the new tri-layer structure, and the effect of thermally assisted graded anisotropy on the write current reduction.

[1]. Apalkov, D., Dieny, B., & Slaughter, J. M. (2016). Magnetoresistive Random Access Memory. Proceedings of the IEEE, 104(10), 1796-1830. [2]. Yulaev, I., et al. "Spin-transfer-torque reversal in perpendicular anisotropy spin valves with composite free layers." Applied Physics Letters 99.13 (2011): 132502. [3]. Suess, D., et al. "Exchange-coupled perpendicular media." Journal of Magnetism and Magnetic Materials 321.6 (2009): 545-554. [4]. Zhao, W., Kimura, T., Kato, T., Oshima, D., Sonobe, Y., Kawato, Y., Iwata, S., Hybrid memory layer with low Curie temperature CoPd/Pd multilayer for high-density magnetic random access memory cells, submitted to Intermag 2018 [5]. Machida, Ken, Yoshiaki Sonobe, and Yoshinobu Nakatani. "Numerical study on a novel Curie temperature controlled hybrid thermo-magnetic structure for magnetic random access memories." IEEE Transactions on Magnetics 53.11 (2017): 1-5 [6]. Garanin, Dmitry A. "Fokker-Planck and Landau-Lifshitz-Bloch equations for classical ferromagnets." Physical Review B 55.5 (1997): 3050. Evans, Richard Francis L., et al. "Stochastic form of the Landau-Lifshitz-Bloch equation." Physical Review B 85.1 (2012): 014433. [7]. Slonczewski, J. C. "Currents, torques, and polarization factors in magnetic tunnel junctions." Physical Review B 71.2 (2005): 024411.

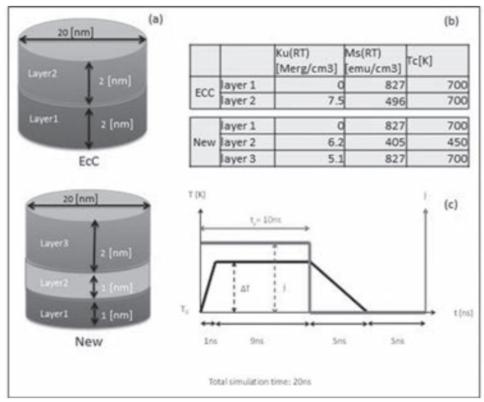

		Ku(RT) [Merg/cm3]	Ms(RT) [emu/cm3]	Tc[K]
ECC	layer 1	0	827	700
	layer 2	7.5	496	700
New	layer 1	0	827	700
	layer 2	6.2	405	450
	layer 3	5.1	827	700

Fig. 1. (a) schematic of EcC and new HFL, (b) material parameters of EcC and new HFL, (c) schematic of write current and temperature profile from [5].

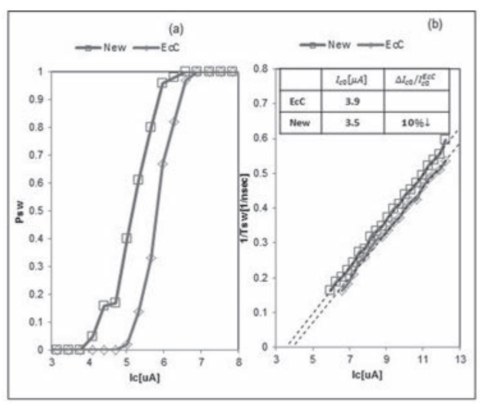

	$I_{c0}[\mu A]$	$\Delta I_{c0}/I_{c0}^{EcC}$
EcC	3.9	
New	3.5	10%↓

Fig. 2. (a) switching probabilities and (b) inverse of switching times and critical current densities at room temperature.

EU-05. Multiscale Modeling of Magnetic Distribution in a Magnetic Core of high-frequency transformer.

H. Li[1], *S. Wang*[1] and J. Zhu[2]

1. Xi'an Jiaotong University, Xi'an, China; 2. The University of technology, Sydney, Sydney, NSW, Australia

I. INTRODUCTION The discretization of the micro-structure of ribbon magnetic cores and laminated iron cores, i.e. by finite element method, would lead to a prohibitively large systems of equation. It is a huge difficulty for the modern computer to solve, even for the supercomputers. Surely, it is far away from being a routine task for engineers in the design and analysis of electrical devices. To overcome this unpleasant fact, homogenization methods have been developed. In 2003, Dular adopted FEM combined with the homogenization method to study a 3D magnetic field and the eddy currents in laminated stacks were taken into account[1]. Gyselinck presented a novel time-domain homogenization technique for laminated iron cores in three-dimensional (3-D) FE models for linear and nonlinear problems, respectively[2],[3]. However, the homogenization method is external equivalent. More often, it is desirable to capture the small-scale effect on the large scales, like the eddy currents, and magnetic distribution in the laminations for loss calculation. In order to capture the effects on the small scale, some researchers proposed their solutions. Duan proposed an improved extended finite element method (XFEM) for modeling electromagnetic devices with multiple nearby geometrical interfaces and discontinuities in electric fields [4], [5]. Meanwhile, Hollaus developed a 'multiscale finite element method' for the 2D, and 3D eddy current problem in iron laminates [6], [7]. The mesh is independent of the geometries for the XFEM and the multiscale finite element proposed by Hollaus. In a word, these methods are homogenization techniques relying on analytical expression or asymptotic expansions of fields, and mixed formulas based on finite element method. In this paper, we aimed to capture the magnetic distribution in the small scale of a ribbon magnetic cores through another multiscale finite element method (MsFEM) which is totally different from the one proposed by Hollaus. This MsFEM is first proposed by Hou for the elliptic problems in composite materials and porous media [8]. The magnetic distribution in each ribbon and the gaps between ribbons will be obtained. Hence, it is no longer to use some assumptions to get the losses since magnetic field is finely calculated. Observation on each single ribbon is possible for engineers. II. MATHEMATICAL MODEL The main idea of MsFEM is to construct finite element basis functions which capture the small scale information within each macro element. The small scale information is then brought to the large scales through the coupling of the global stiffness matrix. Thus, the effects of small scale on the large scale is captured. Like the XFEM, the mesh is independent of the geometries of the models, and several materials are might contained in each macro element. Compared to other multiscale modeling methods, basis function of MsFEM is numerical type basis function, which means that we do not have to find the expression of a numerical basis function, it is a more general method. What is more, MsFEM could be implemented based on the commercial simulation software packages. It is more flexible. In general, there are three major steps for MsFEM's implementation: basis function construction, global formulation, and downscaling analysis. Basis function construction is obtained by solving the local boundary problem with certain specified boundary conditions. The governing equations for the static magnetic field of the simulation model shown in Fig.1., Fig.1. (a)Simulation model, (b) and its mesh schematic diagram The specified boundary conditions for macro element E along x direction of Γ_1 is shown in (2). III. CONCLUSSION By adopting the MsFEM, the magnetic distribution in the each ribbon and the gap between the ribbons could be finely computed. We believe that it is much useful for loss calculation of the ribbon magnetic cores of high frequency transformer and iron cores of power transformers' design and performance analysis. Hence, methods resorting to some assumptions will be no longer needed for losses calculation.

[1] P. Dular, J. Gyselinck, C. Geuzaine, N. Sadowski, and J. P. A. Bastos, "A 3-D magnetic vector potential formulation taking eddy currents in lamination stacks into account," *IEEE Trans. Magn.*, vol. 39, no. 3 I, pp. 1424–1427, 2003. [2] J. Gyselinck, R. V. Sabariego, and P. Dular, "A nonlinear time-domain homogenization technique for laminated iron cores in three-dimensional finite-element models," *IEEE Trans. Magn.*, vol. 42, no. 4, pp. 763–766, 2006. [3] Gyselinck, J, and P. Dular. "A time-domain homogenization technique for laminated iron cores in 3-D finite-element models." IEEE Transactions on Magnetics 40.2(2004):856-859. [4] Duan, Nana, et al. "An Improved XFEM With Multiple High-Order Enrichment Functions and Low-Order Meshing Elements for Field Analysis of Electromagnetic Devices With Multiple Nearby Geometrical Interfaces." IEEE Transactions on Magnetics 51.3(2015):1-4. [5] Xu, Weijie, et al. "Extended Finite-Element Method for Weak Discontinuities in Electric Fields." IEEE Transactions on Applied Superconductivity 26.7(2016):1-5.

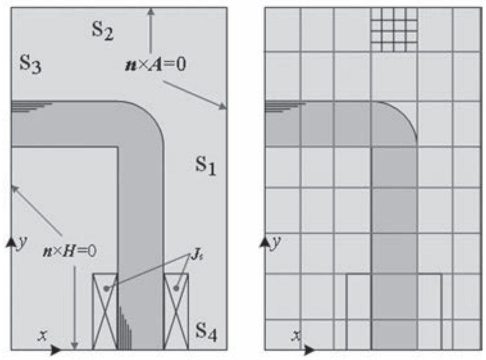

Fig. 1. (a)Simulation model, (b) and its mesh schematic diagram

$$\begin{cases} \dfrac{\partial}{\partial x}\left(\mu \dfrac{\partial A_z}{\partial x}\right) + \dfrac{\partial}{\partial y}\left(\mu \dfrac{\partial A_z}{\partial y}\right) = J_s \\ \boldsymbol{n} \times \boldsymbol{A} = \boldsymbol{0} \quad \text{on } \mathrm{s}_1, \mathrm{s}_2 \\ \boldsymbol{n} \times \boldsymbol{H} = \boldsymbol{0} \quad \text{on } \mathrm{s}_3, \mathrm{s}_4 \end{cases} \tag{1}$$

$$\phi_i^E(x)\Big|_{\Gamma_1} = \int_x^{x_m} \frac{\mathrm{d}\xi}{\mu(\xi)} \Big/ \int_{x_i}^{x_m} \frac{\mathrm{d}\xi}{\mu(\xi)} \tag{2}$$

EU-06. The effect of easy axis deviations on the magnetic property of Co nanowire.

Y. Peng[1], M. Yue[1], H. Li[1], Y. Li[1], C. Li[1], H. Xu[1] and Q. Wu[1]
1. College of Materials Science and Engineering, Beijing University of Technology, Beijing, China

I. INTRODUCTION The 3d transition metals such as iron, cobalt, and their alloys bear high saturation magnetization (M_s) and high Curie temperatures (T_C), which are necessary for the giant energy product and good thermal stability, respectively. For the nanowire of 3d transition metals, such as Co nanowires, the effective anisotropy field can be as much as 16.5 kOe by combining the shape anisotropy and magnetocrystalline anisotropy. However, such high coercivity has never been achieved, because there are much defects and the easy axis deviation from the length direction for the nanowires. Therefore, in this study, we investigate the influence of the defects and deviation of easy axis on the coercivity and magnetization reversal process via 3D micromagnetic simulations. II. METHOD The micromagnetic simulation on Cobalt nanowire is performed by OOMMF (the Object Oriented Micromagnetic Framework) which is based on the Landau-Lifhitz-Gilbert (LLG) dynamic equation [1]. The size of simulated mode is considered as a 10 nm × 10 nm × 200 nm prism. The error of the simulated results between the prismatic models and cylindrical is not more than 5% [2]. The magnetocrystalline easy axis deviates from the applied field H with the angle β, while the easy axis deviation of the defects is β_2. Based on the finite difference method of OOMMF, the nanowire has been divided into 1 nm × 1 nm × 1 nm cells. In the simulation process, a small angle of 0.6° between the applied field and the easy axis has been utilized to break the non-stable equilibrium states which would produce an overly large coercivity [3, 4]. III. RUSULTS AND DISSUSION The hysteresis loops of the nanowires with different easy axis deviation β are quite different as shown in Fig.1. The nanowire with β = 0° shows the good squareness and high coercivity of 12.15 kOe. The coercivity and remanence decreases linearly with the β increases. Meanwhile, the squareness of the hysteresis loops has been destroyed rapidly. The relationship between the coercivity and β is consistent with the results of coherent rotation[5]. The magnetization distribution also shown that the magnetization reversal mode is quasi-coherent rotation that the magnetic reversal nucleation is easy to occur at both the ends. Besides, we also calculated the magnetization process of Co nanowire with defects. Here, we just consider the situation that the easy axes of the defects deviate from the length direction. Fig. 2 shows the simulated hysteresis loops of nanowires with the defect in the middle and ends, respectively. For the nanowire with the defect in the middle, as $\beta_2 \leq 60°$,the defect has no effect on the coercivity of the nanowire. When β_2 is as large as 90°, the coercivity decreases from 10.7 kOe to 8.86 kOe. For the nanowire with the defect in the ends, as shown in Fig. 2(b), the coercivity decrease monotonously with the increase of β_2. IV. CONCLUSION The demagnetization process of a Co nanowire have been investigated with the easy axis deviation from the nanowire direction. As β inceases, the coercivity and remanence decrease gradually, which lead to the reduction of the maximum energy products. Besides, the defects occurring at different position also have effects on the magnetic property of Co nanowire. The nanowires is more sensitive to the defects in the ends than in the middle because the magnetization rotation starts from the ends of the nanowire. Thus, to obtained high coercivity permanent nanowire materials, we must ensure that the easy axis orient in the length direction and reduce the defects, especially reduce the defects in the ends of the nanowire.

[1] M. J. Donahue, D. G. Porter, OOMMF User's Guide, Version 1.0. NISTIR 6376, National Institute of Standards and Technology, Gaithersburg, MD,1999. [2] A. Leon, J. G. Zhu, A. B. James, J. Appl. Phys. 87(9):5538-5540 (2000) [3] X. C. Zhang, G. P. Zhao, J. Xia, M. Yue, X. H. Yuan, L. H. Xie, Chin. Phys. B 23 097504 (2014). [4] H. orster, N.Bertram, X.Wang, R.Dittrich, T.Schrefl, J. Magn. Magn. Mater. 267 69–79 (2003). [5] L. Sun, Y. Hao, C. L. Chien, P. C. Seaeson. IBM J. RES. &DEV. VOL 49 NO.1 (2005).

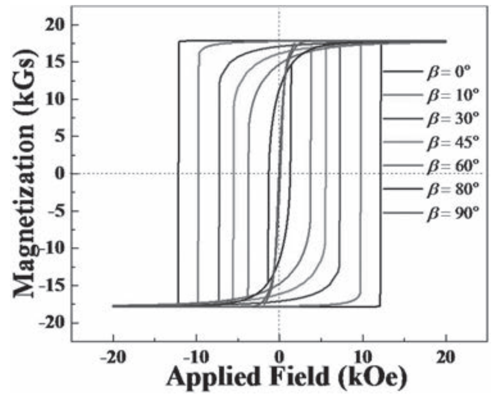

Fig. 1. The hysteresis loops with the different easy axis deviation angle β.

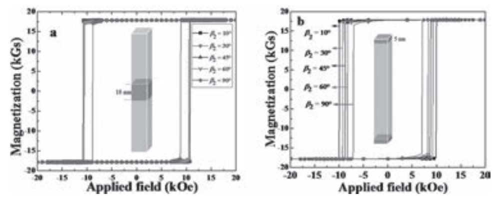

Fig. 2. The hysteresis loops with partial easy axis deviation in the ends (a) and middle (b) of the Co nanowire.

EU-08. An optimal design of an electromagnetic actuator for targeting magnetic micro/nano-carriers in a desired region.

T. Le[1] and *J. Yoon*[1]
1. School of Integrated technology, Gwangju Institutue of Science and Technology, Gwangju, The Republic of Korea

I. INTRODUCTION Magnetic drug targeting (MDT) is a technique for transporting magnetic nanoparticles (MNPs) to, and concentrating them in, a desired location [1, 2]. MDT can increase the concentration of drugs in the desired region inside a body, therefore reduce the side effects of drugs in the rest of body. The focusing function of micro/nano-particles into a target region is prerequisite for the success of the MDT. However, a static magnetic field is unable to focus micro/nanoparticles [3]. To overcome this limitation, a new scheme using ferromagnetic rods and fast magnetic pulses was introduced in [4]. Our group also introduced a novel electromagnetic actuation scheme for concentrating spherical nano particles (SNPs), which are being extensively utilized in biomedical fields [5]. However, the targeting actuator requires a compact design with fast targeting efficiency. In this paper, the optimal design of the suggested actuation system for focusing micro/nano-particles is studied. Since maximizing the magnetic gradient within the workspace of the actuator can enhance the efficiency of the targeting and the capacity of device is limited in fact, the magnetic gradient is selected to be optimized to focus nanoparticles on a specified surface. The configuration and specifications of the optimized design for the actuator are presented, and its performance was examined through simulations in the COM-SOL™ Multiphysics software. II. Actuation scheme for Focusing Field Two independent actuation coils (ACC) can be oppositely placed, as shown in Fig. 1(a). By adjusting the distance of the two ACCs and/or changing the current of coils, a focusing region between two free field point (FFP) locations can be generated on the *x*-axis. The proposed scheme can focus the SNPs in the *x*-axis. We propose a focusing scheme for a surface region by combining two focusing actuators for line segment. The *x*- and *y*-axis coils will be operated alternately with the time function (TF) of the currents shown in Fig. 1(b). By applying TF, the SNPs can be pushed from the four sides of the surface region and concentrated into a target surface region. The SNPs will be focused on the *x*-axis and *y*-axis; the SNPs tend to emerge toward both sides of the *z*-axis. Thus, to focus on one side of the surface region, the particle sample should be placed on one side (positive or negative) of the *z*-axis. III. Design and optimal system The proposed system consists of 8 separate circular coils as Fig 2(a). To investigate the influence of coil parameters on the magnetic field, the simulations are performed using the COMSOL Multiphysics software. To simplify the simulations and data analysis, one pair coil is considered for optimization in this paper. The structural parameters of the coils are shown in Fig. 2(a). In the simulations, the coil width w_1, w_2, coil height h_1, h_2, and wire diameter d_w are assumed to be independent parameters. To minimize the size and use one cooling system for both coils, the internal diameter d_i, d_o was fixed as 30 mm which are enough space for a frame and cooling systems, and the edge distance between two coils d_c equals h_1. The width of focusing region *wsp* was fixed as 30 mm which can cover a mouse brain for drug targeting. The relations between these design parameters and the independent variables were as follows: $d_0 = d_i = 30$ mm; $h_1 = 20 \div 140$ mm; $w_1 = 20 \div 140$mm; $h_2 = 20 \div 140$ mm; $w_2 = 20 \div 140$ mm; $d_c = h_1$; $wsp = 30$ mm; $d_w = \{0.32;0.4;0.51;0.64;0.81;1.02\}$ mm; The wire turns of the coil can be calculated as: $T_j = kw_jh_j/d_w^2$ where k is the winding factor (k=0.85÷0.95) and j = 1, 2 is corresponding to the inner and outer coils. The objective function is the average value of magnetic field gradient $\nabla H_x(h_1,w_1,h_2,w_2,I_1,I_2)$ in the area $-wsp/2 \le x \le 0$; $-wsp/2 \le y \le wsp/2$; *Design constraint 1*: For generating the focusing region *wsp* * *wsp*. The constraint assures a pushing force. The constraint is identical to the right focusing region. $\nabla H_x > 0$ with $-wsp/2 \le x < 0$ and $-wsp/2 \le y \le wsp/2$; $\nabla H_x = 0$ with $(x,y)=0$; $\nabla H_x < 0$ with $0 < x \le wsp/2$ and $-wsp/2 \le y \le wsp/2$. *Design constraint 2:* For power, voltage and current conditions of the proposed DC supply (AMETEK SGA 600/17, 10 kW). $0 < P_j \le 10$ kW; $0 < V_j \le 600$ V; $0 \le I_j \le 17$ A where the P, V, and I are the power DC, voltage, and current of the coil, respectively. The optimal problem is solved by using the COMSOL Optimization module. The coordinate search method is utilized as an optimization method to maximize the objective function [6]. The final optimal result can be obtained at d_w = 1.02 mm with the highest objective function.

IV. Simulation Results The optimized actuator can generate a focusing area with 3*3 cm, which was not possible from the original design [5]. A cylinder-shaped container (height 1 cm and radius 1.5 cm) was initially used for the simulations of targeting, as shown in Fig 2(b)(c)(d). The container was filled with blood environment [5]. The SNPs diameter is 1000 nm. In the simulation, 2000 particles of 1000 nm diameter are distributed uniformly in the cylinder. Their trajectories according to the magnetic force were captured after 1200 s with f = 0.01 Hz ($T_x = T_y$). The optimized actuator can concentrate SNPs into the center of the desired surface region (0.4*0.4 cm) as shown in Fig. 2 (d) with an acceptable targeting time for drug delivery.

[1] J. Bar, R. S. Herbst, and A. Onn, "Targeted drug delivery strategies to treat lung metastasis," *Expert opinion on drug delivery,* vol. 6, pp. 1003-1016, 2009. [2] V. P. Torchilin, "Passive and active drug targeting: drug delivery to tumors as an example," in *Drug delivery*, ed: Springer, 2010, pp. 3-53. [3] S. Earnshaw, "On the nature of the molecular forces which regulate the constitution of the luminiferous ether," *Trans. Camb. Phil. Soc,* vol. 7, pp. 97-112, 1842. [4] A. Nacev, I. Weinberg, P. Stepanov, S. Kupfer, L. Mair, M. Urdaneta*, et al.*, "Dynamic inversion enables external magnets to concentrate ferromagnetic rods to a central target," *Nano letters,* vol. 15, pp. 359-364, 2014. [5] T.-A. Le, X. Zhang, A. K. Hoshiar, M. O. Kim, and J. Yoon, "Simulation studies of a novel electromagnetic actuation scheme for focusing magnetic micro/nano-carriers into a deep target region," *AIP Advances,* vol. 7, p. 056724, 2017. [6] A. R. Conn, K. Scheinberg, and L. N. Vicente, *Introduction to derivative-free optimization*: SIAM, 2009.

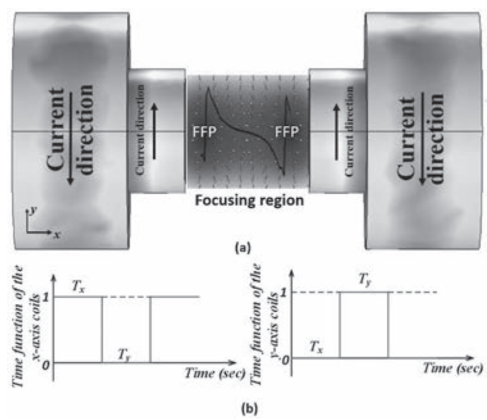

Fig. 1. (a) The focusing scheme for line segment. The black curve is a magnetic gradient along the x-axis. The arrow shows the direction of the magnetic gradient. (b) TF function of the focusing scheme.

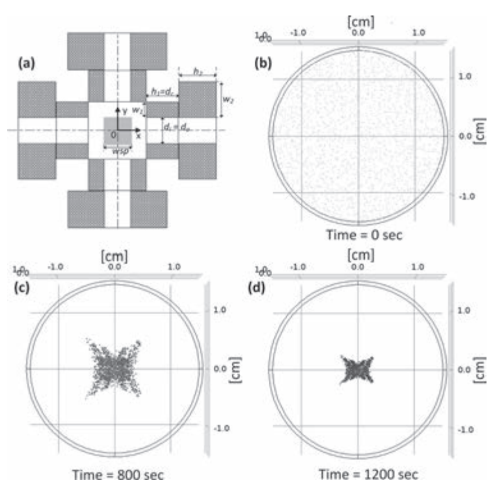

Fig. 2. (a) Structural parameters of the coils. (b)(c)(d) Simulation result.

EU-09. AC Loss Database Built with Numerical Multi-scale Model and Status Prediction of a 150 kJ SMES.

Z. Zhang[1]
1. State Key Laboratory of Advanced Electromagnetic Engineering and Technology, School of Electrical and Electronic Engineering, Huazhong University of Science and Technology, Wuhan, China

Abstract—In the process of dynamic power compensation of superconducting magnetic energy storage system (SMES), AC loss is produced inevitably, which will influence the thermal stability of the SMES. In this paper, we firstly use a fast-numerical model, multi-scale model, to analyze the AC loss of a 150 kJ high temperature superconducting (HTS) SMES, and arrange the AC loss under different working conditions into a database. Then, based on the AC loss database, we build a neural network model to provide a real-time prediction of AC loss and thus to adjust the cooling power accordingly. This AC loss data base and neural network system will help keep the SMES magnet thermally stable and prevent the SMES from overload working condition. *Index Terms*—AC loss database, multi-scale model, neural network model, SMES magnet I. Introduction AC loss is one major heat source in the SMES magnet which has great influence on the dynamic thermal stability. However, AC loss calculation of large-scale HTS SMES is a very challenging task, especially in working condition for power compensation when the current load is irregular and unpredictable. The multi-scale model can dramatically speed up the AC loss calculation and verified to have relatively good accuracy. So, the multi-scale model is particularly suitable for building an AC loss database. In this paper, we firstly introduce the modeling methodology of the multi-scale model for AC loss calculation of a 150 kJ HTS SMES magnet. and calculate the AC loss of the magnet under several working conditions, including a series of maximum power working conditions and a series of dynamic power compensation working conditions. Secondly, all these AC losses are arranged into a database, which is used train the neural network model. Thirdly, we use a specific maximum power output working condition to test the accuracy of the neural network model. II. Multi-scale Model and AC Loss Database The 150 kJ SMES magnet was wound with the two types of HTS wires, the BSCCO tape and the YBCO tape. The magnet consists of 12 BSCCO double-pancake coils and 6 YBCO double-pancake coils. Due to the critical current characteristic of the two tapes, the BSCCO coils are divided equally into two groups, placed at the ends of the magnet, and 6 YBCO coils are placed in the middle. The main idea of multi-scale model is described in detail in [1], [2]. The multi-scale model is featured with high calculation speed and low computation complexity. It is suitable for AC loss calculation of large-scale HTS magnet especially when the current load of the SMES magnet is complex. We use the iteration method in the multi-scale model for background field estimation. The diagram of the multi-scale model is shown in Fig. 1. The 150 kJ HTS SMES system is developed in authors' laboratory [3] and its maximum power is 100 kW. AC loss is calculated under two series of working conditions, one is the maximum power working condition where the initial current of the magnet varies from 0.2 I_c to 0.8 I_c, the other is the dynamic power compensation working condition where the SMES is used to stabilize the output power fluctuation of the hydropower station. All these AC loss curves are arranged into a database. III. Neural Network Model Neural network is widely used in nonlinear system for its good function approximation ability, and dynamic NARX neural network can accurately model the time domain problem. The neural network model is suitable for predicting the AC loss of the HTS magnet, which is nonlinear and dynamic [4]. The steps of the neural network model are as follows. (1) Set the exchange power P_{SMES} and the initial current load I_0 of the SMES as the input variable, and the AC loss as the output variable. (2) Use the AC loss database to train the neural network model, and obtain an optimized weight coefficient W. (3) When the training is done, test the accuracy of the neural network model with a certain power compensation working condition. IV. Results and Discussion With the neural network model, we can predict the AC loss of the HTS magnet rapidly and adjust the cooling power accordingly, and thus to keep the thermal stability and prevent the magnet from overload working condition. To test the neural network model, we charge the magnet to I_0 = 150 A and set the exchange power to ± 100 kW. Each power command is maintained for 10 ms. AC loss calculated with H-formulation model, multi-scale model and neural network model is shown in Fig. 2. The multi-scale model speeds up AC loss calculation by 15 to 20 times and restrict the error under 10%. Based on the AC loss database, the neural network model provides a real-time calculation result, which has similar accuracy with the multi-scale model.

[1] Quéval L, Ohsaki H. "AC Losses of a Grid-Connected Superconducting Wind Turbine Generator," *IEEE Trans. Appl. Supercond.*, vol. 23, no. 3, Jun.2013, Art. no. 5201905. [2] Quéval L, Zermeño V M R, Grilli F. "Numerical models for AC loss calculation in large-scale applications of HTS coated conductors," *Supercond. Sci. Technol.*, vol. 29, no. 2, 2016, Art. no. 024007. [3] L. Ren et al., "Development of a Movable HTS SMES System," *IEEE Trans. Appl. Supercond.*, vol. 25, no. 4, Aug. 2015, Art. no. 5701109. [4] Leclerc J et al. "Artificial neural networks for AC losses prediction in superconducting round filaments," *Supercond. Sci. Technol.*, vol. 29, no. 6, Apr. 2016, Art. no. 065008.

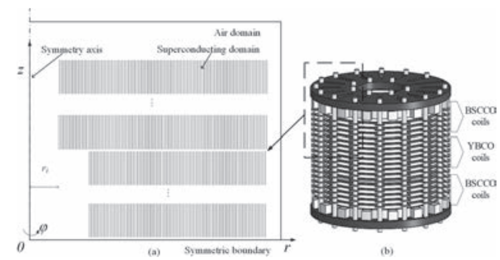

Fig. 1. (a) Diagram of the coil sub-model of the multi-scale model. (b) Structure of the HTS SMES magnet.

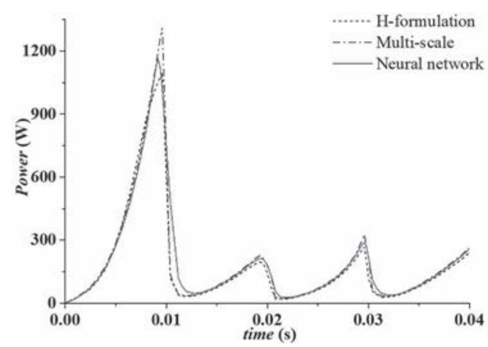

Fig. 2. AC loss calculated with different model in maximum power output working condition

EU-10. Analytical functions of magnetization curves for high magnetic permeability materials.

M. Mirzaei[1] and P. Ripka[1]
1. Czech Technical University, Prague, Czechia

In this paper, a combined rational and power functions are used to represent magnetization and *B-H* curves of high magnetic permeability ferromagnetic materials. The proposed functions cover wide range of magnetic flux density values, *B* and magnetic field strength values, *H* from very low values of magnetic fields to highly saturated magnetic fields. High magnetic permeability materials have numerous industrial applications such as magnetic sensors, high efficiency transformers, magnetic recording heads and magnetic shields [1]. Analytical representations of the *B-H* curve of magnetic materials are used for magnetic modeling, numerical analysis and design process. It gives apparent and fast picture of maximum magnetic relative permeability and magnetic saturation without *B-H* data table. Several publications have shown different analytical functions for *B-H* curve modeling such as rational function [2] and [3]. The modeled magnetic materials were silicon steel laminations and solid irons and steels in [2] - [4], which have small magnetic permeability especially at low magnetic fields. Rational functions and power functions are combined for modeling of very high permeability *B-H* curves. In order to calculate analytical functions for *B-H* curve, magnetization parameter, *J* versus magnetic field strength is represented by the proposed function: $J = B-\mu_0 H$ and *J* is constant when $H\rightarrow\infty$. The main difficulty to find analytical function for *B-H* curve or *J-H* curve of high permeability material is very sharp changing of relative magnetic permeability at very low magnetic fields. It is problematical to use conventional rational functions or conventional power functions. The proposed function is as following: $F(x)=(a.x^b+ c.\ x^d+ e.\ x^f)/(1+ a'.\ x^b+ c'.x^d+ e'.x^f)$ (1) where, *x* is variable and *a*, *a*', *b*, *c*, *c*', *d*, *e*, *e*', *f* are the function constants which are calculated by the curve fitting process. Large difference between magnetic field strength, *H* at maximum permeability point and magnetic field strength at high saturation points creates complexities to calculate function constants. In order to overcome this problem and improve curve fitting performance, powers of J^m and H^n are used for curve fitting instead of *J* and *H*. The parameters *m* and *n* are positive numbers, which are mostly less than 1. H^n and J^m are variable *x* and function *F*(*x*) in (1), respectively: $J^m=(a.(H^n)^b+ c.(H^n)^d+ e.(H^n)^f)/(1+ a'.(H^n)^b+ c'.(H^n)^d+ e'.(H^n)^f)$ (2) Three high magnetic permeability materials are chosen from [5] and [6] and curve fitting method is used [7] to calculate the function constants. The results of calculation are shown in Fig. 1 - Fig. 2. It is shown that the proposed functions correctly model *B-H* curve of high permeability materials. - The normalized rms error of *B* and μ_r for Moly permalloy are 0.27 and 0.55, respectively. - The normalized rms error of *B* and μ_r for Supermalloy are 0.28 and 1.55, respectively. - The normalized rms error of *B* and μ_r for Mumetal are 0.20 and 0.64, respectively. The calculated errors between *B-H* data [5] and curve fitting function results confirm high precision of the proposed method. 1- The calculated function constants for Moly Permalloy - *a*=-2.679, *a*'=-0.8315, *b*=28, *c*=2.758, *c*'=0.9487, *d*=27.74, *e*=0.08104, *e*'=0.09077, *f*=39.48, *m*=0.56, *n*=0.07 2- The calculated function for Supermalloy - *a*=17.37, *a*'=19.92, *b*=85.01, *c*=0.52, *c*'=0.2364, *d*=11.73, *e*=0.8789, *e*'=6.982, *f*=73.74, *m*=0.56, *n*=0.07 3- The calculated function for Mumetal - *a*=0.04578, *a*'=0.0576, *b*=33.42, *c*=0.617, *c*'=0.469, *d*=15.65, *e*=-0.3419, *e*'=-0.3305, *f*=22.79, *m*=0.56, *n*=0.07

[1] Pavel Ripka, "Magnetic Sensors and Magnetometers", Jan 2001, Artech House Publishers [2] G. F. T. Widger, "Representation of magnetization curves over extensive range by rational-fraction approximations", Proc. Inst. Elect. Eng., vol. 116, no. 1, pp. 156-160, Jan. 1969. [3]Patrick Diez andJ. P. Webb, "A Rational Approach to B – H Curve Representation", IEEE Transactions on Magnetics, Year: 2016, Volume: 52, Issue: 3 [4] Patrick Diez, "Symmetric Invertible B – H Curves Using Piecewise Linear Rationals", IEEE Transactions on Magnetics, Year: 2017, Volume: 53, Issue: 6 [5] http://www.femm.info/wiki/Documentation/ [6] Metals Handbook, Volume 1, American Society for Metals, 1966 [7] https://www.mathworks.com/products/curvefitting.html

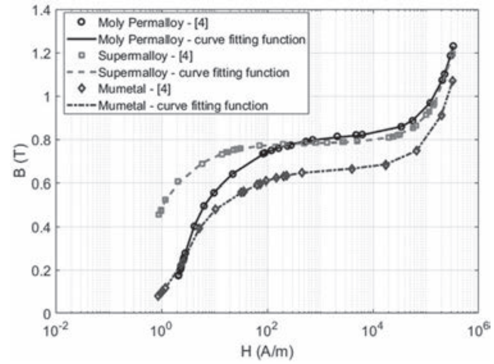

Fig. 1. The curve fitting for *B-H* curve

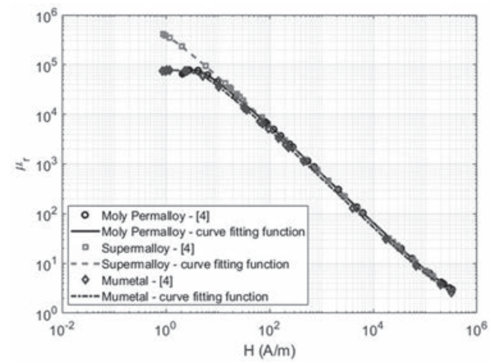

Fig. 2. The curve fitting for μ_r-*H* curve

EU-11. Size effect on the magnetic behavior of rapidly solidified cylindrical amorphous nanowires.

C. Rotarescu[1], H. Chiriac[1], N. Lupu[1] and *T.A. Ovari*[1]
1. National Institute of Research and Development for Technical Physics, Iasi, Romania

Results on the influence of sample dimensions, specifically nanowire length, L, and diameter, D, on the magnetization processes taking place in cylindrical amorphous nanowires prepared by rapid quenching from the melt are reported. Nanowires with various compositions - $(Co_{0.94}Fe_{0.06})_{72.5}Si_{12.5}B_{15}$ and $Fe_{77.5}Si_{7.5}B_{15}$ - have been investigated in order to correlate their magnetic behavior with the dimensions, mainly to reveal the role played by the large aspect ratio of these novel nanowires, which can exhibit significant lengths, in their overall magnetic behavior. The approach taken was to simulate first the axial hysteresis loops of amorphous nanowires with different lengths, whilst keeping their diameter constant. The simulations have been performed in the micromagnetic approximation employing finite element discretization. This method allowed us to perform a unique study of the magnetization reversal process within this new type of cylindrical nanowires, starting from a fully saturated state ($+M_S$) with the nucleation of a domain with reverse magnetization, continuing with the depinning and propagation of the newly formed 180° domain wall until it reaches the opposite end of the nanowire, which is again fully saturated in the opposite direction ($-M_S$). The usual inductive hysteresis loops (experimental) are bypassing nucleation, since there already are end domains with reversed magnetization due to demagnetization, and magnetization reversal only consists in the depinning and propagation of the preexistent 180° domain wall. The results of micromagnetic simulations, illustrated in Figure 1 for the case of $(Co_{0.94}Fe_{0.06})_{72.5}Si_{12.5}B_{15}$ amorphous nanowire samples, which exhibit nearly zero magnetostriction, reveal the fact that the remanence to saturation ratio M_R/M_S increases with the nanowire length to diameter ratio L/D. This dependence shows directly the critical effect of shape anisotropy, which also increases with the L/D ratio (aspect ratio). The relatively large coercivity of the calculated high-field loops is the result of the magnetization reversal mechanism described above, which begins with the nucleation of a reverse domain, requiring thus a quite large applied field. The inset of Figure 1 shows the region near the switching field for every value of the sample length. From the results illustrated in the inset, one can clearly observe that the remanence to saturation ratio (M_R/M_S) varies monotonically with the sample length, showing that it is easier to nucleate domains with reversed magnetization in the shorter samples. In order to thoroughly understand the mechanisms of magnetization reversal, the visualization of the orientation of the magnetic moments within the sample at various stages is extremely helpful. Figure 2 shows the orientations of the magnetic moments for an amorphous nanowire sample with 2.7 mm in length and the diameter of 90 nm at various stages of the hysteresis loop. Magnetic moments are represented by red arrows when pointing in the direction of the applied field and by blue arrows when pointing in the opposite direction. The magnetization reversal process begins from both ends of the nanowire, with a small delay, the two domain walls propagating towards the middle of the wire. Here, the two domain walls collide, canceling out each other. Such behavior has been previously emphasized experimentally in the case of thicker amorphous glass-coated microwires subjected to large applied fields [1]. We have also simulated the axial hysteresis loops for amorphous nanowires with various diameters, whilst keeping a constant sample length. The results confirm that M_R/M_S increases with L/D. The same result has been also confirmed experimentally, by means of inductive hysteresis loop measurements. Thus, shape anisotropy and the demagnetizing field play a key role in the magnetic behavior of rapidly solidified nanowires. Moreover, the correlation between the simulated loops and the experimental ones allows us to get a deeper insight into the magnetization reversal mechanism, and to analyze the two separate stages of axial magnetization switching, i.e. the nucleation of new domains with reversed magnetization, as indicated by the variation of the remanence to saturation ratio with the nanowire dimensions, and the propagation of the domain wall between the newly nucleated domains or pre-existent end domains and the rest of the nanowire, as shown by the changes in the value of the experimental switching field. The results are key for understanding and controlling the magnetization processes in these novel nanowires, with important application possibilities in new miniaturized sensing devices. Thus, it is possible to tailor a nanowire's anisotropy and magnetic characteristics (switching field, remanence, coercivity) by changing its dimensions (diameter and/or length).

Acknowledgement - Work supported by the Romanian Ministry of Research and Innovation (MCI) under the 3MAP NUCLEU Program (2018).

[1] T.-A. Óvári, M. Tibu, H. Chiriac, IEEE Trans Magn. 47 2838 (2011).

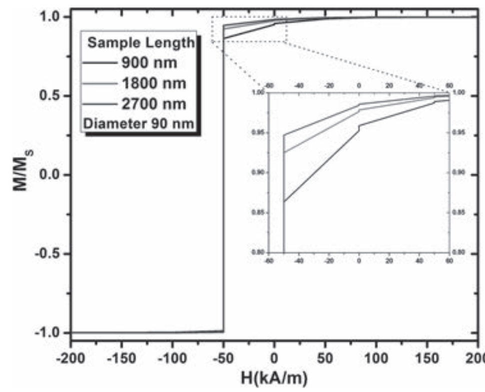

Fig. 1. Micromagnetic simulations of the hysteresis loops for cylindrical amorphous nanowires with the diameter of 90 nm and various sample lengths.

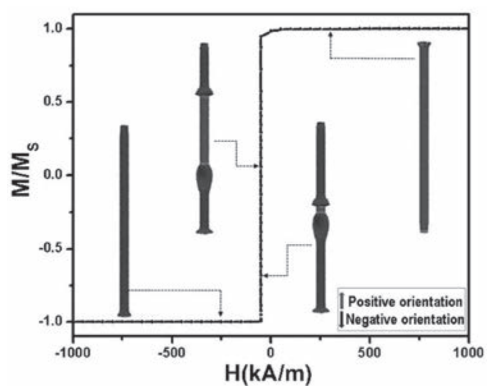

Fig. 2. Orientation of magnetic moments for an amorphous nanowire with the length of 2.7 mm and the diameter of 90 nm at different stages of the magnetization reversal process.

THURSDAY MORNING, 26 APRIL 2018 SIMPOR/ROSELLE BALLROOM, 8:30 TO 11:30

Session EV
MICROSCOPY, IMAGING AND CHARACTERIZATION III
(Poster Session)

Haifeng Du, Co-Chair
High Magnetic Field Laboratory of Chinese Academy of Sciences, Hefei, China
Yonggang Zhao, Co-Chair
Tsinghua University, Beijing, China

EV-01. High resolution magnetic field energy imaging of the magnetic recording head by A-MFM with superparamagnetic tip.

P. Kumar[1], Y. Suzuki[1], Y. Cao[2], S. Yoshimura[1] and *H. Saito*[1]
1. Graduate School of Engineering Science, Akita University, Akita City, Japan; 2. Regional Innovation Center, Akita University, Akita City, Japan

To achieve high magnetic recording density, the magnetic recording head of the hard disk drive is the key element [1]. Therefore, the quantification of spatial variation in recording head's magnetic field and field gradient is very important and provide useful information to the design goals, which is critical for the development of new recording heads [2]. In this regard, magnetic force microscopy (MFM) is recognized as one of the most widely used technique for imaging the stray magnetic field distribution at the microscopic level with high lateral resolution [3]. In literature, there are few investigation reported in order to improve the MFM performance for measurement of the stray magnetic field from the recording head [3, 4]. However, despite the impressive performance and widespread use of the MFM, there are important probe-related limitations that need to be overcome to realize its full potential. From the MFM images it is not easy to demonstrate the magnetic field distribution because of artifacts due to shape, size, and tip hysteresis [1]. To conquer these limitations in MFM images, the superparamagnetic (SP) tip is an attractive candidate due to no hysteresis over wide operating field range that results in MFM images without tip memory effects [5]. Motivates by these backgrounds, here we have fabricated 100 nm high performance Co-GdO$_x$ SP tip and demonstrated the magnetic field energy observation from the magnetic recording head by using Co-GdO$_x$ SP tip and self-developed alternating magnetic field microscopy (A-MFM) [5]. In A-MFM, AC magnetic field is used to change MFM tip moment periodically. The interaction between the tip moment and magnetic field from head causes the change of effective spring constant of a cantilever. Frequency modulated (FM) cantilever oscillation occurs in accordance with the following equations; $m(d^2z(t)/dt^2)+m\gamma(dz(t)/dt)+(k_0+k_{eff}\cos(\omega t))z(t) = F_0 \cos(\omega_0 t)$, (1) Here the cantilever oscillates in the z direction. In narrow-band FM, the intensity of the side-band spectra is proportional to the derivative of AC magnetic force and magnetic field detection is achieved by the following equation, $k_{eff} = \partial F_z(t)/\partial z$. When the change of effective spring constant is smaller than the intrinsic spring constant ($k_{eff} \ll k_0$) narrow-band FM with one pair of side-band spectra occurs in the following equation, $z(t) = (F_0/m\gamma\omega_0) \sin(\omega_0 t+\Delta\theta) + (F_0 k_{eff}/(2(m\gamma\omega_0)^2) (\cos((\omega_0+\omega)t+\Delta\theta) + \cos((\omega_0-\omega)t+\Delta\theta))$, (2) The, A-MFM signal is obtained by a lock-in amplifier using frequency demodulated output of a PLL. The concept of high-resolution magnetic field energy imaging technique is demonstrated by high initial susceptibility ($\chi_i = 5.15 \times 10^{-7}$ H/m) Co-GdO$_x$ SP tip for perpendicular magnetic recording (PMR) head. The magnetic moment of the SP tip m_{tip} is parallel to head magnetic field and is proportional to its strength i.e. ($m_{tip} = \chi H$) and each grain behave as the magnetic dipole. the magnetic force on dipole type Co-GdO$_x$ SP tip can be expressed by taking integral over tip volume as, $F_z(t) = \partial/\partial z(\int m_{tip}(t)\bullet H(t)dV) = \partial/\partial z(\int \chi H(t)\bullet H(t)dV) = \chi \int(\partial(H(t))^2/\partial z)\, dV$, (3) Therefore, magnetic field energy $(H(t))^2$ is measured by the SP tip. The distribution of magnetic energy gradient from the PMR head is imaged by 100 nm Co-GdO$_x$ SP tip and compared with the magnetic field imaging by 20 nm FePt-MgO hard magnetic (HM) tip (coercivity (H_c) ~15 kOe and magnetization (M_s) ~ 680 emu/cm^3). Figure 1(a) shows the A-MFM amplitude image measured on magnetic recording head by Co-GdO$_x$ SP tip. The dotted line in Fig. 1(a) indicates the actual topographic (Physical) size of the main pole and trailing shield of the recording head. Further, the line profile measured from the amplitude image of Co-GdO$_x$ SP tip is shown in Fig. 1(b). Here, the FWHM of the A-MFM amplitude peak (Fig. 1(b)) measured for the Co-GdO$_x$ SP tip is 77 nm, clearly indicate the higher resolution for the Co-GdO$_x$ SP tip. Fourier analysis of the A-MFM amplitude image revealed that the spatial resolution of 13 nm is achived by Co-GdO$_x$ SP tip which is higher than the state of-the-art FePt-MgO HM tip of 17 nm resolution in the present study and the other MFM tips reported in literature. The Co-GdO$_x$ SP tip consists of nano-size superparamagnetic Co particles surrounded by the non-magnetic GdO$_x$. The physical model for the Co-GdO$_x$ SP tip is shown in the Fig. 1(d). The magnetic moment of each grain in the Co-GdO$_x$ SP tip depends on the strength of magnetic field, results in inhomogeneous magnetic charges distributed along the tip volume as shown in Fig 1(d). Therefore the tip volume near the tip end mainly contributes to the magnetic field energy imaging as shown in Fig. 1(d). The transfer function of the Co-GdO$_x$ SP tip against a single magnetic charge source located at the origin (x, y, z) = (0, 0, 0) is given by considering as dipole for the SP tip. $\int\chi(\partial^2(H_{AC}(\approx 0, \approx 0, z))^2/\partial z^2)\, dV = \int((5\chi)/(4(\pi\mu_0)^2))\,(1/z^6)\, dV$. From this transfer function equations, it is clear that magnetic field energy imaging by SP tip is more dependent on the tip sample separation distance ($1/z^6$) as compared to the magnetic field imaging ($1/z^3$). Thus the fabricated Co-GdO$_x$ SP tip opens an opportunity for the development of advanced high-resolution magnetic energy based imaging methods and development of the high-resolution MFM tips.

[1] W. Lu, Z. Li, K. Hatakeyama, G. Egawa, S. Yoshimura and H. Saito, High resolution magnetic imaging of perpendicular magnetic recording head using frequency-modulated magnetic force microscopy with a hard magnetic tip. Appl. Phys. Lett. 96 (2010) 143104. [2]S. Li, E. Lin, Z. George, D. Terrill, H. Mendez, J. Santucci and D. Yie, Method for characterizing magnetic footprints of perpendicular magnetic writer head, J. Appl. Phys. 115 (2014) 17B733. [3] F. Liu, S. Li, D. Bai, J. Wang, Z. Li, D. Han, T. Pan and S. Mao, Characteristics of magnetic force microscopy magnetic on high moment perpendicular magnetic recording writers with high coercivity probes, J. Appl. Phys. 111 (2012) 07E346. [4] S. Tanaka, Y. Azuma and Y. Majima, Secondary resonance magnetic force microscopy, J. Appl. Phys. 111 (2012) 084312. [5] P. Kumar, Y. Suzuki, Y. Cao, S. Yoshimura and H. Saito, High resolution magnetic field energy imaging of the magnetic recording head by A-MFM with Co-GdO$_x$ super-paramagnetic tip, Appl. Phys. Lett. 111 (2017) 183105.

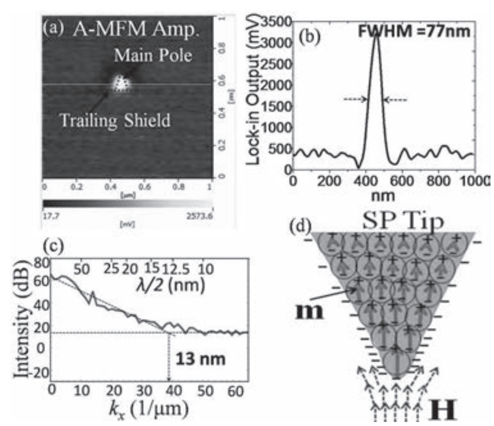

Fig. 1. (a) A-MFM amplitude image of the main pole by Co-GdO$_x$ SP tip, (b) line profile on the amplitude image (white line in (a)), (c) the spatial resolution result of the A-MFM image by using Co-GdO$_x$ SP tip (d)) SP tip (magnetic dipole) behavior in the head magnetic field.

EV-02. Rotatable magnetic anisotropy in Fe-based thin films with stripe domains by Field-Dependent Magnetic Force Microscopy.

P. Tiberto[1], G. Barrera[1], F. Celegato[1], M. Cialone[2], M. Coisson[1] and P. Rizzi[2]
1. INRIM, Torino, Italy; 2. Chemistry, Università di Torino, Torino, Italy

Fe-based thin films are characterised by critical thickness above which the in-plane magnetisation is replaced by a dense stripe domain configuration [1], originating from internal stresses quenched during film growth that can be progressively released by means of relaxation thermal treatments. Such systems are generally characterised by a transcritical, in-plane hysteresis loop shape and an in-plane component of the stripe magnetisation that can be aligned to any direction in the film plane, provided that a strong enough in-plane magnetic field is applied (rotatable anisotropy). Stripe domain rotation have been studied in the two Fe-based compositions being characterised by different anisotropy values: a) $Fe_{70}Pd_{30}$ with different thickness (50-600 nm) deposited by electrodeposition on Si(100)//Si02//Cr//Au substrate; b) $Fe_{78}B_9Si_{13}$ sputtered on Si substrate (thickness ranging from 100 to 800 nm). Both alloys display stripe domain structure above a critical thickness originated by quenched stresses at the magnetic film/substrate interface. Critical thickness values are different for the two Fe-based compositions and this can be ascribed to the different deposition tecniques exploited. As an example, room-temperature hysteresis loop of a $Fe_{70}Pd_{30}$ sample having thickness higher than 300 nm measured by means of a vibrating sample magnetometer (VSM) is shown in Fig. 1a. The typical fingerprint of a transcritical loop is visible. In the inset, the corresponding MFM image at the magnetic remanence is reported showing that the magnetisation of the film is organised into parallel stripes alternately tilted upwards and downwards. By exploiting a recently developed field-dependent MFM technique [2,3] coupled with a novel analysis of the acquired data, we have been able to investigate the orientation of the magnetisation in the stripes as a function of the applied field, and their rotation towards saturation. The field evolution of the stripes for increasing field values is followed by applying a magnetic field perpendicular to stripe orientation (horizontal direction). The intensity of the magnetic field applied during the acquisition of MFM images following the procedure described in [2,3] is shown in Fig. 1b. Conversely, the field-dependent MFM image of the same sample during application of an in-plane field along the horizontal direction in Fig.1c. After a threshold field, the MFM contrast changes indicating that the stripes, initially orthogonal to the scan direction of the tip, rotate along the field direction, resulting parallel to the scan direction. The rotation field turns out to be connected with the change of slope in the transcritical loop indicating its link with the perpendicular magnetic anisotropy that is also progressively reduced. For both Fe-based compositions, the detailed field evolution of the magnetisation in the stripes is investigated by direct comparison of vector measurements made by VSM and field-dependent MFM, as a function of the magnetic anisotropy. The origin of the threshold field, whose amplitude is independent on the field direction in the sample plane, is discussed as well to rule out the role of the two deposition techniques inducing microstructure characterised by different stress.

[1] M. Coïsson, F. Celegato, E. Olivetti, P. Tiberto, F. Vinai, M. Baricco, J. Appl. Phys. 104 (2008) 033902. [2] M. Coïsson, G. Barrera, F. Celegato, E. Enrico, A. Manzin, E.S. Olivetti, P. Tiberto, F. Vinai, J. Phys. D: Appl. Phys. 47 (2014) 325003. [3] M. Coïsson, G. Barrera, F. Celegato, P. Tiberto submitted to Sci. Rep.

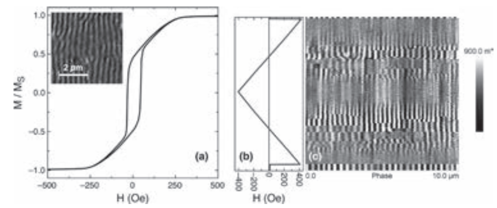

Fig. 1. (a) In-plane hysteresis loops of electrodeposited FePd thin film: in the inset MFM image acquired at the magnetic remanence after application of an in-plane saturating field along the vertical direction. (b) Intensity of the magnetic field applied during the acquisition of (c). (c) Field-dependent MFM image of the same sample during application of an in-plane field along the horizontal direction.

EV-03. Observation of superconducting vortices and vortex clusters in S/F hybrids.

C. Di Giorgio[1,2], F. Bobba[1], D. D'Agostino[1], S.A. Moore[2], I. Maria[2], G. Karapetrov[3], N. Valentyn[4], V. Yefremenko[4] and *A. Cucolo*[1]
1. Physics, Universita' degli studi di Salerno, Fisciano, Italy; 2. Physics, Temple University, Philadelphia, PA, United States; 3. Physics, Drexel University, Philadelphia, PA, United States; 4. Material Science Division, Argonne National Laboratory, Chicago, IL, United States

Abstract— Resistive dissipation in superconductors is a direct consequence of vortex motion, that causes a reduction of transport efficiency, limits the coherence times for quantum computation, and generally introduces noise. Such unwanted effects can be limited by adding vortex pinning (structural or magnetic) into the superconductor. Here, we will be focusing on the magnetic pinning exerted on vortices by a ferromagnetic layer, in superconductor/ferromagnet (S/F) heterostructures only magnetically coupled, where F is in the magnetic-stripe regime (the magnetization alternates its direction by crossing adjacent domains). We used low temperature magnetic force microscopy (MFM) to image both ferromagnetic domains and superconducting vortices in Nb/Py (Permallloy-$Ni_{80}Fe_{20}$) heterostructures. By tuning Nb and Py thickness, we observed spontaneous formation of vortices in Nb thin films, due to the magnetic stray field coming from Py itself, as well as clusters of vortices when in presence of magnetic domain bifurcations. Our findings suggest that stripe magnetic topology is useful to minimize vortex motion and enhance the critical current value, by pinning vortices and organizing them in ordered chains along the stripes. Moreover, vortex confinement and jamming, producing clusters, are eventually induced in presence of defects in magnetic domain arrangement. Many of the potential applications of superconductors in electronic devices demand high current densities with minimal losses, requiring a mandatory pinning of vortices. In the last decade several studies have focused on the influence of different types of pinning centers on the dynamics of superconducting vortices [1-7]. Among them, magnetic pinning in magnetically coupled S/F heterostructures, appears to be stronger than other mechanisms [4,8]. Particularly, an enhanced pinning has been reported due to vortex coupling with ordered magnetic structures, such as stripes and dots [9-11]. Nevertheless, unconventional vortex configurations such as vortex chains, vortex clusters as well as multi-vortex and giant vortex phases can also be induced by a strong magnetic or geometric confinement potential [12-16]. In this work, we used low-temperature MFM to investigate S/F heterostructures composed of Py as the magnetic material and Nb as the superconductor, with several Py and Nb thickness, separated by a thin SiO_2 insulating layer to prohibit proximity effects. A thick Py film presents peculiar arrangement of magnetic domains, made by stripes with canted magnetization vectors, mainly oriented along the film plane, but with small alternating up-and-down out-of-plane components. Moreover, its Curie temperature T_C is much greater than the superconducting critical temperature T_S, ensuring a field cooling of Nb in a spatially nonuniform magnetic field, giving place to vortices with opposite polarities, namely Vortices and Antivortices (V and AV). We investigated the conditions for nucleation of spontaneous V-AV structures as a function of thickness of superconducting films as well as magnetic domain width. We compared our results with those of existing theoretical models and provided an estimate of the threshold of the local out-of-plane component of the magnetization for different Py film thickness. In this sense, the MFM imaging of spontaneous V-AV in Nb/Py bilayers, for different Nb and Py thickness, is also proposed as an indirect but quantitative method to estimate the out-of-plane magnetization value of our F layers. Moreover, the periodic out-of-plane stray field coming out from Py surface plays the role of magnetic cofinement potential for vortices, forcing those to align in chains along the domains (Fig. (a)). When in presence of intrinsic topological defects of the magnetic template, called *bifurcations*, we found a peculiar distribution of superconducting vortices. In such cases, we demonstrated that a bifurcation can naturally lead to unusual vortex distribution, and eventually to the formation of vortex clusters, without any need of invasively engineering the shape of the sample via lithography or self-assembly (Fig. (b)). MFM measurements clearly show that a bifurcation, where two magnetic stripe domains converge and coalesce in a single one, leads to a local enhancement of the out-of-plane stray field. As imaged by MFM, this enhancement induces vortex clusters. We infer that such a phenomenon can be also explained by taking into account the role of the bifurcation magnetic topology. Indeed, while each vortex inside an infinite chain would feel the same net repulsive force, which leads to a constant intervortex distance, an unbalanced force is felt by vortices close to magnetic channel interruptions (stripe endpoint or bifurcation core). For instance, the vortex at the stripe endpoint feels a long-range repulsive interaction due to the semi-infinite vortex chain on one side, while on the other side only the Lorentz force would keep it away from the domain wall. In such a case a reduction of the inter-vortex distance close to the magnetic stripe endpoint is expected. The bifurcation topology indirectly affects the vortex distribution at the nearest neighbour domains as well. Indeed, our experimental results show that hexagonal vortex lattice is achieved at the matching field [19] wherever the stripes are straight and regular, as expected. On the other hand, around the dislocations the inter-vortex distance is affected by the stripe curvature, leading to a modulation of the vortex-vortex spacing.

[1] Otani, Y., Pannetier, B., Nozieres, J. P. & Givord, D. *J. Magn. Magn. Mater.* 126, 622–625 (1993). [2] Baert, M., Metlushko, V. V., Jonckheere, R., Moschalkov, V. V. & Bruynseraede, Y. *Phys. Rev. Lett.* 74, 3269–3272 (1995). [3] Martin, J. I., Velez, M., Hoffman, A., Schuller, I. K. & Vicent, J. L. *Phys. Rev. Lett.* 83, 1022–1025 (1999). [4] Milošević, M. V. & Peeters, F. M.. *Phys. Rev. B* 68, 094510-1–094510-12 (2003). [5] Karapetrov, G., Fedor, J., Iavarone, M., Rosenmann, V. & Kwok, W. K. *Phys. Rev. Lett.* 95, 167002-1–167002-4 (2005). [6] Silhanek, A. V. *et al. Phys. Rev. B* 76, 100502-1–100502-4 (2007). [7] Gomez, A. *et al. Supercond. Sci. Technol.* 26, 085018-1–085018-8 (2013). [8] Carneiro, G. *Phys. Rev. B* 69, 214504-1–214504-12 (2004). [9] Bulaevskii, L. N., Chudnovsky, E. M. & Maley, M. P. *Appl. Phys. Lett*. 76, 2594–2596 (2000). [10] Vlasko-Vlasov, V. *et al. Phys. Rev. B* 77, 134518-1–134518-7 (2008). [11] Vlasko-Vlasov, V. *et al. Phys. Rev. B* 85, 064505-1–0645015-15 (2012). [12] Tanaka, K., Robel, I. & Janko, B. *PNAS* 998, 5233–5236 (2002). [13] Lyuksyutov, I. F. & Pokrovsky, V. L. *Advances in Physics* 541, 67–136 (2005). [14] Zhang, L. F., Covaci, L., Milosevic, M. V., Berdiyorov, G. R. & Peeters, F. M. *Phys. Rev. B* 88, 144501-1–144501-13 (2013). [15] Cieplak, M. Z. *et al. Phys. Rev. B* 87, 014519-1–014519-13 (2013). [16] Cren, T., Fokin, D., Debontridder, F., Dubost, V. & Roditchev, D. *Phys. Rev. Lett.* 102, 127005-1–127005-4 (2009). [17] Buzdin, A. I. *Rev. Mod. Phys.* 77, 935–976 (2005). [18] Zhang, T. *et al. Nat. Phys.* 6, 104–108 (2010). [19] Tinkham, M. "Introduction to Superconductivity", 2nd edition, McGrow-Hill, Inc. (1996).

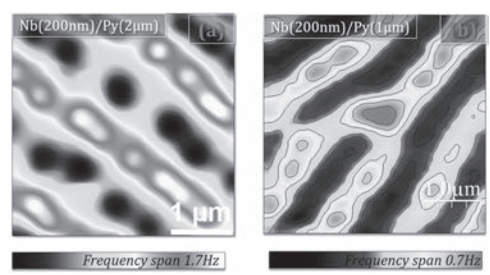

EV-04. Resolution enhancement of magneto-optical Kerr images using modern image processing algorithms.

N. Gorn[2], *I. Soldatov*[1], R. Schäfer[1,3] and D. Berkov[2]
1. Institute for Metallic Materials, Leibniz Institute for Solid State and Materials Research (IFW) Dresden, Dresden, Germany; 2. General Numerics Research Lab, Jena, Germany; 3. Institute for Materials Science, Technical University Dresden, Dresden, Germany

The imaging of small magnetic microstructures, such as chiral skyrmions or magnetic bubbles, is of current interest in spintronic and spin-orbitronic research. If such an object is smaller than the optical resolution limit, direct observation demands sophisticated imaging techniques based on electron-, x-ray spectro-, or scanning probe microscopy, all of them with limitations in the expense and complexity of the method or limitations in their dynamic capabilities. Magneto-optical Kerr microscopy, on the other hand, is an in-house technique that offers high versatility without restrictions in dynamic imaging, field compatibility etc.. Recently the method was applied to the imaging of micron-sized "skyrmionic" bubble domains in metallic film systems [Jiang2015, Jiang2017]. Skyrmion research, however, aims at objects smaller than 100 nm in size, which is well below the resolution limit of Kerr microscopy that can be estimated to be about 180 nm at best according to the Abbe criterion. In this contribution we present a methodology for the processing of magneto-optical images, which allows simultaneously to suppress the noise and to enhance the resolution of domain images beyond the mentioned limit, thus making Kerr microscopy attractive for skyrmion research. We start with the determination of the point spread function (PSF) for the specific m/o setup, because despite the existence of so-called blind deconvolution methods (see, e.g., [Caron2002]), the knowledge of this function strongly increases the deconvolution quality. To measure the width of a PSF, we fit a line scan across a domain wall (DW) image obtained on a NeFeB sample. Due to the high magnetocrystalline anisotropy of this material, the DW width is well below 5 nm, so that this wall can be considered to be infinitely thin from the Kerr microscopy 'point of view'. For this reason, fitting of the magneto-optical profile along the corresponding line cut using an error function, we can directly extract the PSF width of the given Kerr setup. For the processing of the image of interest (as an example, see panel (a) in Fig. 1), we first apply the Wiener filter $W(k) = H^{*}(k)/(|H(k)|^2 + K(f))$ with a Fourier transform of the convolution kernel $H(k)$ evaluated using the obtained PSF width (see above). The frequency-dependent function $K(f)$, representing the noise-to-signal ratio, can in principle be extracted from standardized magneto-optical images, but in this study it is held constant; its value is adjusted to avoid an excessive noise amplification arising for too small values of this threshold. The result of this operation is a deconvolved image without white noise, but with clearly seen artificial features (Fig. 1b); this image is then passed to the next step. Finally, the wavelet denoising [Gonzalez2008, Neelamani2004] is applied. After comparing various wavelet types, we have found that best results are obtained using the so called Haar wavelet system [Porwik2004], as this system is best suited to approximate the images with sharp domain boundaries often encountered in magneto-optics. The appropriate choice of the decomposition level by the wavelet transform allows to reduce the noise level of the image significantly without losing its fine details (Fig. 1c). Test results obtained on artificial images and results obtained on various types of domain structures in real magnetic samples (Fig. 2), which demonstrate a substantial resolution improvement of our Kerr microscopy technique, are presented.

[Caron2002] J.N. Caron, N.M. Namazi, C.J. Rollins, Noniterative blind data restoration by use of an extracted filter function, Appl. Opt. 41 (2002) 6884 [Gonzalez2008] R. Gonzalez, R. Woods, Digital Image Processing, Pearson Prentice Hall, 2008 [Jiang2015] W. Jiang et al.: Blowing magnetic skyrmion bubbles. Science 349 (6245), 283-286 (2015) [Jiang2017] W. Jiang et al.: Direct observation of the skyrmion Hall effect. Nature Phys. 13, 162 (2017) [Neelamani2004] R. Neelamani, H. Choi, and R. Baraniuk, ForWaRD: Fourier-Wavelet Regularized Deconvolution for Ill-Conditioned Systems, IEEE Trans. Signal Proc. 52 (2004) 418 [Porwik2004] P. Porwik, A. Lisowska, The Haar–Wavelet Transform in Digital Image Processing: Its Status and Achievements, Machine Graphics & Vision, 13 (2004) 79

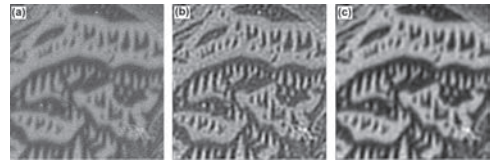

Fig. 1. (a) Raw image of magnetic domains in FeSi, (b) resolution enhancement (sharper domain boundaries) and removal of the white noise after applying the Wiener filter and (c) elimination of artificial image features appearing after Wiener filtering by wavelet processing

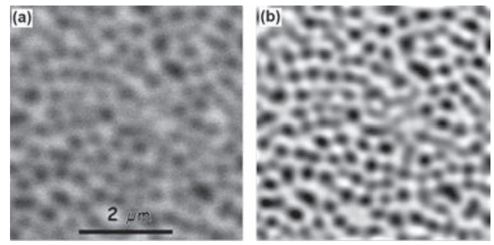

Fig. 2. Kerr image of nano-sized bubble-kyrmion hybrid domains in a multilayer Ta(2nm)[Pt(1.5nm)/Co(1nm)/Ir(1nm)]$_8$Pt(15nm) (a) before and (b) after the image processing as described in the text (sample courtesy of S. te Velthuis and A. Hoffmann, Argonne National Laboratory, USA)

EV-05. Machine-Learning Assisted X-Ray Spectroscopy for High-Throughput Characterization of Magnetic Materials.

T. Ueno[1], H. Hino[2] and K. Ono[3]
1. Quantum Beam Science Research Directorate, National Institutes for Quantum and Radiological Science and Technology, Sayo, Japan; 2. Department of Computer Science, University of Tsukuba, Tsukuba, Japan; 3. Institute of Materials Structure Science, High Energy Accelerator Research Organization, Tsukuba, Japan

X-ray spectroscopy is one of the essential experimental methods in materials science to probe electronic structures of materials. As a derived method, X-ray magnetic circular dichroism (XMCD) spectroscopy is frequently used to investigate microscopic magnetic properties of magnetic materials. In these days, we have revealed that adaptive design of an XMCD experiment by a Gaussian process (GP) modeling, one of a machine-learning technique, can improve the efficiency of a measurement [1,2]. In that study, we supposed an ideal experimental condition that measurement data does not include noise. GP modeling predicted spectra by learning of experimental data points. We revealed that magnetic moments with required accuracy could be evaluated from predicted spectra. Convergence of the measurement was determined by the values of the magnetic moments. In this study, we applied GP modeling to X-ray absorption spectra (XAS) with various signal-to-noise (S/N) ratios to develop general versatility of the GP modeling of X-ray spectroscopy. Convergence of the measurement was determined by similarity measure between the GP-predicted XAS and simulated XAS. X-ray absorption spectra were simulated using CTM4XAS [3]. Sm $M_{4,5}$ XAS were calculated for Sm^{3+} ion. Total data points were set to 201 that is similar to typical XAS experiments. Gaussian process modeling was performed using a DiceKriging package for R [4]. Adaptive design of XAS experiment was implemented as follows. (1) 20 data points were extrapolated from an XAS spectrum as initial data points. (2) Predicted XAS spectra and its variance were calculated by GP modeling with the learning of initial data points. (3) Energy point of the maximum variance σ was chosen as a next data point to measure. (4) Gaussian process modeling predicted an XAS spectra again including new data point. (3) and (4) repeated 500 times by permitting multiple measurements on same energy points. Furthermore, we investigated another strategy that including a prior distribution to improve the efficiency of adaptive design of the experiment. The inclusion of prior distribution means that one can use prior knowledge about general view of a spectrum, i.e., energy ranges, peak positions and so on in an actual situation. In this study, the prior distribution was set to the noiseless XAS. Prior distribution was considered in (3); thus, the energy point with the maximum $\sigma + k \times prior$ was chosen as a data point to measure. This prior increase preference of sampling around peaks. Coefficient k was set to 0.05 in the present study. A similarity between GP-predicted XAS and noiseless XAS was evaluated to determine convergence of measurement and prediction. We used Pearson correlation coefficient (PCC), a similarity metric robust for noisy XAS, as a similarity measure [5]. Pearson correlation coefficient takes a value between +1 and -1. In the present study, the more similar the GP-predicted XAS to the noiseless XAS, the more approaching the PCC value to +1. Figure 1 shows simulated X-ray absorption spectra of Sm^{3+} with different levels of signal-to-noise (S/N) ratio. Gaussian noise is artificially added to the noiseless XAS. The S/N ratio is defined as a ratio between an M_5 peak intensity and a square root of a variance of a Gaussian distribution. Figure 2(a) shows the similarity between GP-predicted XAS and simulated-noiseless XAS versus number of measurements. Circles and lines represent results for without and with a prior distribution, respectively. For results without the prior distribution (full circles in Fig. 2), high S/N spectra (i.e., S/N = 1000, 200, and 100) converges with fewer numbers of measurements as an overall trend. In particular, similarity for S/N = 1000 and 200 converges to almost 1 in below 100 measurements. On the other hand, similarity for S/N = 20 converges to almost 0.98 with about 300 measurements. Similarity for S/N = 10 does not converge in the present result. For results with the prior distribution (lines in Fig. 2), similarities for S/N = 1000, 200, 100, and 20 become closer to 1 with much fewer measurement as compared to the results without the prior distribution. In particular for high S/N spectra (S/N = 1000, 200, and 100) converges less than 50 measurements as shown in Fig. 2(b). These results indicate the GP-predicted XAS spectra with fewer data points are very similar to the "true" spectrum with 201 data points (noiseless XAS in Fig. 1). The method is reliable for XAS with S/N larger than 100 with including the prior distribution in the range of the present study. In conclusion, we investigated the application of the GP modeling and similarity measure to improve the efficiency of XAS experiments. The results indicate that the GP modeling for XAS experiment is useful to decrease data points to be measured. Moreover, the efficiency of the GP modeling is improved by including the prior distribution in adaptive sampling. The present method reduces experimental costs and realizes high-throughput characterization of magnetic materials.

[1] T. Ueno, H. Hino, A. Hashimoto, Y. Takeichi, and K. Ono, IEEE International Conference on Magnetics (INTERMAG2017), GE-07, Dublin, Ireland (2017). [2] T. Ueno, H. Hino, A. Hashimoto, Y. Takeichi, M. Sawada, and K. Ono, npj Comput. Mater., *In press*. [3] E. Stavitski and F. M. F. de Groot, Micron 41, 687 (2010). [4] O. Roustant, D. Ginsbourger, and Y. Deville, J. Stat. Softw. 51, 1 (2012). [5] Y. Suzuki, M. Kotsugi, H. Hino and K. Ono, *Submitted*.

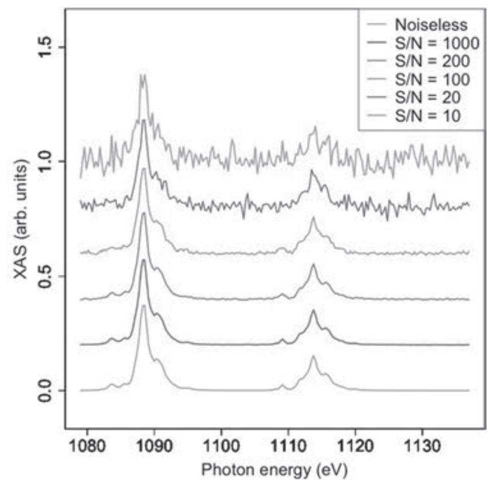

Fig. 1. Simulated X-ray absorption spectra of Sm^{3+} with different levels of signal-to-noise (S/N) ratio. The S/N ratio is defined as a ratio between an M_5 peak intensity and a square root of a variance of a Gaussian distribution.

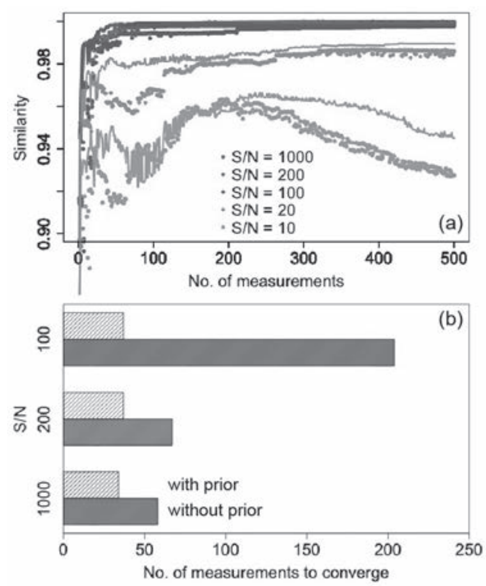

Fig. 2. (a) Similarity between GP-predicted XAS and simulated-noiseless XAS versus number of measurements. Circles and lines represent results for without and with a prior distribution, respectively. (b) No. of measurements to converge for S/N = 1000, 200, and 100 without and with the prior distribution.

EV-06. Revealing complex magnetic order in nanostructure patterns via nuclear X-ray scattering.

K. Schlage[1], D. Erb[1,2], L. Bocklage[1,3], H. Wille[1], L. Dzemiantsova[1,3], G. Meier[3,4], R. Rüffer[5] and R. Roehlsberger[1,3]
1. Deutsches Elektronen-Synchrotron (DESY), Hamburg, Germany; 2. Helmholtz-Zentrum Dresden-Rossendorf, Dresden, Germany; 3. The Hamburg Centre for Ultrafast Imaging, Hamburg, Germany; 4. Max Planck Institute for the Structure and Dynamics of Matter, Hamburg, Germany; 5. European Synchrotron Radiation Facility, Grenoble, France

Determining magnetic properties of nanostructured materials is a key issue for designing functional nano-devices for information storage, sensor technology, or medical diagnostics. Recent development of new magnetic nanopatterns raised the need for advanced tools to quantify lateral heterogeneous magnetization states. Addressing this demand, we have introduced two new X-ray scattering approaches, namely nuclear grazing incidence small angle scattering [1] and nuclear surface diffraction [2]. Both techniques employ resonant off-specular scattering to allow for a unique insight into complex lateral magnetization states of nanopatterned systems. In the last decades, various synchrotron based X-ray scattering techniques have proven to be essential for nanoscopic magnetic characterization of ultra-thin films and multilayers. Experiments benefitted from the high sensitivity of polarized X-rays to magnetic moment orientations and their relatively large penetration depth. Recently, a new field of research has emerged, which focusses on the lateral magnetization state of nanopatterns like spin ice and skyrmion lattices or magnetic nanostructure arrays with tilted or curved surface morphology. Their heterogeneous magnetization state within the sample plane hinders a characterization with X-rays via specular scattering which yields integral magnetic information only. We developed two new scattering approaches, which overcome this limitation and allow disentangling of magnetic contributions from selected parts of magnetic nanopatterns. In the first experiment we demonstrated how the resonant analogue of the widely applied grazing incidence small angle X-ray scattering (GISAXS) can be used to disentangle nanomagnetic information from a sample with facetted surface morphology. For this purpose, we sputter-deposited iron at non-normal incidence onto a nanofacetted sapphire template to form a continuous magnetic film with periodically varying thickness (Fig. 1). Performing non-resonant GISAXS on this sample in-situ allows to precisely follow the structural growth of the nanostructured film. Thickness oscillations with decreasing period become visible during deposition along the two scattering rods oriented perpendicular to both facet nanosurfaces. To correlate this structural information with the nanomagnetic state of the sample we additionally recorded the time dependent nuclear resonant scattering (NRS) signal of iron in the same GISAXS configuration (Fig. 1b). To separately extract the magnetic signal from both types of nanostripes we did not collect the NRS signal along the specular scattering direction but on both scattering rods. This allowed us to follow the evolution of magnetic order in the nanostripes during the deposition run. In subsequent magnetic field cycles we found an unexpected heterogeneous nanomagnetic behavior: The magnetic moments in the thinner nanostripes tend to follow the external magnetic field much stronger than the thicker ones and show a different magnetic hysteretic behavior in general (Fig. 1b, bottom). This observation on the nanoscale became only possible using this new resonant GISAXS approach which can be generally applied to magnetic nanopatterns with 3D morphology. In the second experiment we applied nuclear resonant surface diffraction as a new technique for the characterization of lateral magnetic order in magnetic nanopatterns. For this purpose, we fabricated a custom-made permalloy nanograting, which was intended to undergo a ferromagnetic-antiferromagnetic transition upon field cycling. The non-resonant scattering signal in the GISAXS configuration shows a diffraction pattern from which the morphology of the nanograting was determined with sub-nanometre precision. To be sensitive to the lateral magnetization state we collected the nuclear resonant diffraction pattern via horizontal line scans (Fig. 2b). It turned out that during magnetic reversal strong pure magnetic superstructure peaks (red arrows) are formed, which are caused by an antiferromagnetic superstructure in the grating with a lateral correlation length of twice the structural one. The angular position, relative strength and field-dependent intensity of these superstructure peaks enabled us to precisely study the nanoscale magnetic reversal. The experiment thus successfully demonstrated that nuclear surface diffraction is technically feasible and could offer a completely new insight into a wide range of nanomagnetic sample systems.

[1] Disentangling magnetic order on nanostructured surfaces, D. Erb, K. Schlage, L. Bocklage, R. Hübner, D. Geza Merkel, R. Rüffer, H.-C. Wille, R. Röhlsberger, Phys. Rev. Materials 1, 023001 (2017) [2] Nuclear Resonant Surface Diffraction of Synchrotron Radiation, K. Schlage, L. Dzemiantsova, L. Bocklage, H.-C. Wille, M. Pues, G. Meier, and Ralf Röhlsberger, Phys. Rev. Lett. 118, 237204 (2017)

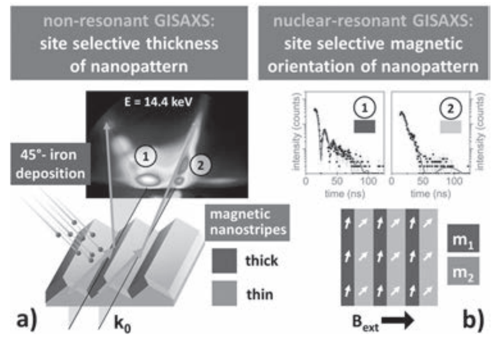

Fig. 1. Nuclear resonant GISAXS is applied to monitor the formation of a magnetic nanopattern with periodically varying thickness. (a) Conventional, non-resonant GISAXS allows to follow the growth of both types of nanostripes via detection of diffuse thickness oscillations along scattering rods. (b) Nuclear resonant time spectra detected at both GISAXS scattering rods (position 1 and 2) allow to precisely disentangle their heterogeneous magnetic moment orientations during growth and subsequent field dependent reversal.

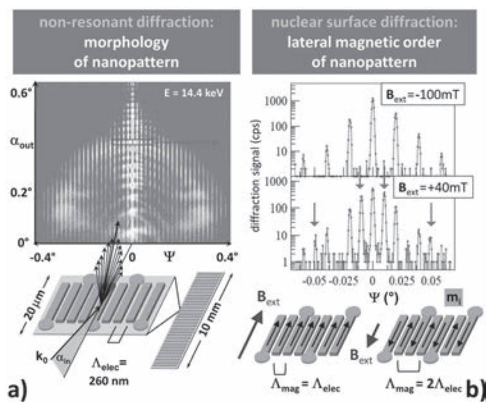

Fig. 2. (a) Non-resonant surface diffraction on a grating of magnetic nanostripes results in formation of a scattering pattern from which the morphology of the nanostructure can be determined with sub-nanometre precision. (b) Nuclear resonant surface diffraction is in addition sensitive to the lateral magnetic ordering in the grating. During field-dependent reversal of this nanograting, pure nuclear superstructure peaks (red arrows) appear, which identify a ferromagnetic-antiferromagnetic transition on the nanoscale.

EV-07. Spin-orbit torque magnetometry by wide-field magneto-optical Kerr effect.

T. Tsai[1] and C. Pai[1]
1. Materials Science and Engineering, National Taiwan University, Taoyuan City, Taiwan

Magneto-optical Kerr effect (MOKE) is an efficient approach to probe surface magnetization in thin film samples. Here we present a wide-field MOKE technique that adopts a Köhler illumination scheme to characterize the current-induced spin-orbit torques (SOTs) in micron-sized and unpatterned magnetic heterostructures with perpendicular magnetic anisotropy. Through a current-induced hysteresis loop shift analysis, we quantify the SOT efficiency of Ta-based heterostructures to be ξ_{DL}=0.08. We also find that the estimated SOT efficiencies strongly depend on the probing area-of-interests for Hall-cross devices. This issue can be resolved by considering the shunting of current in devices with Hall-cross geometry. The proposed wide-field MOKE approach therefore provides an instant and direct characterization of SOT, without the need of any further interpretation on electrical signals.

[1] I. M. Miron, K. Garello, G. Gaudin, P. J. Zermatten, M. V., Costache, Stéphane Auffret, Sebastien Bandiera, Bernard Rodmacq, Alain Schuhl, and P. Gambardella, Nature 476, 189 (2011). [2] L. Q. Liu, C.-F. Pai, Y. Li, H. W. Tseng, D. C. Ralph, and R. A. Buhrman, Science 336, 555 (2012). [3] A. Brataas, A. D. Kent, and H. Ohno, Nat. Mater. 11, 372 (2012). [4] J. A. Katine, F. J. Albert, R. A. Buhrman, E. B. Myers, and D. C. Ralph, Phys. Rev. Lett. 84, 3149 (2000). [5] E. B. Myers, D. C. Ralph, J. A. Katine, R. N. Louie, and R. A. Buhrman, Science 285, 867 (1999). [6] D. C. Worledge, G. Hu, D. W. Abraham, J. Z. Sun, P. L. Trouilloud, J. Nowak, S. Brown, M. C. Gaidis, E. J. O'Sullivan, and R. P. Robertazzi, Appl. Phys. Lett. 98, 022501 (2011). [7] L. Q. Liu, T. Moriyama, D. C. Ralph, and R. A. Buhrman, Phys. Rev. Lett. 106, 036601 (2011). [8] U. H. Pi, K. W. Kim, J. Y. Bae, S. C. Lee, Y. J. Cho, K. S. Kim, and S. Seo, Appl. Phys. Lett. 97, 162507 (2010). [9] J. Kim, J. Sinha, M. Hayashi, M. Yamanouchi, S. Fukami, T. Suzuki, S. Mitani, and H. Ohno, Nat. Mater. 12, 240 (2013). [10] K. Garello, I. M. Miron, C. O. Avci, F. Freimuth, Y. Mokrousov, S. Blugel, S. Auffret, O. Boulle, G. Gaudin, and P. Gambardella, Nat. Nanotechnol. 8, 587 (2013). [11] M. Weiler, M. Althammer, M. Schreier, J. Lotze, M. Pernpeintner, S. Meyer, H. Huebl, R. Gross, A. Kamra, J. Xiao, Y. T. Chen, H. J. Jiao, G. E. W. Bauer, and S. T. B. Goennenwein, Phys. Rev. Lett. 111, 176601 (2013). [12] S. Cho, S. H. C. Baek, K. D. Lee, Y. Jo, and B. G. Park, Sci. Rep. 5, 14668 (2015). [13] J. Kim, P. Sheng, S. Takahashi, S. Mitani, and M. Hayashi, Phys. Rev. Lett. 116, 097201 (2016). [14] C. O. Avci, K. Garello, A. Ghosh, M. Gabureac, S. F. Alvarado, and P. Gambardella, Nat. Phys. 11, 570 (2015). [15] S. Emori, E. Martinez, K. J. Lee, H. W. Lee, U. Bauer, S. M. Ahn, P. Agrawal, D. C. Bono, and G. S. D. Beach, Phys. Rev. B 90, 184427 (2014). [16] C.-F. Pai, M. Mann, A. J. Tan, and G. S. D. Beach, Phys. Rev. B 93, 144409 (2016). [17] T. Y. Chen, C. T. Wu, H. W. Yen, and C. F. Pai, Phys. Rev. B 96, 104434 (2017). [18] K. Ueda, M. Mann, C.-F. Pai, A.-J. Tan, and G. S. D. Beach, Appl. Phys. Lett. 109, 232403 (2016). [19] J. H. Han, A. Richardella, S. A. Siddiqui, J. Finley, N. Samarth, and L. Q. Liu, Phys. Rev. Lett. 119, 077702 (2017). [20] X. Fan, H. Celik, J. Wu, C. Y. Ni, K. J. Lee, V. O. Lorenz, and J. Q. Xiao, Nat. Commun. 5, 3042 (2014). [21] M. Montazeri, P. Upadhyaya, M. C. Onbasli, G. Q. Yu, K. L. Wong, M. R. Lang, Y. B. Fan, X. Li, P. K. Amiri, R. N. Schwartz, C. A. Ross, and K. L. Wang, Nat. Commun. 6, 8958 (2015). [22] X. Fan, A. R. Mellnik, W. R. Wang, N. Reynolds, T. Wang, H. Celik, V. O. Lorenz, D. C. Ralph, and J. Q. Xiao, Appl. Phys. Lett. 109, 122406 (2016). [23] S. Mondal, S. Choudhury, N. Jha, A. Ganguly, J. Sinha, and A. Barman, Phys. Rev. B 96, 054414 (2017). [24] T.-Y. Chen, T.-C. Chuang, S.-Y. Huang, H.-W. Yen, and C.-F. Pai, Phys. Rev. Applied 8, 044005 (2017). [25] For programs please see: https://github.com/ctwxdd/pySOT. [26] M. Ali, Ph. D. Thesis, The University of Sheffield (1999). [27] O. J. Lee, L. Q. Liu, C. F. Pai, Y. Li, H. W. Tseng, P. G. Gowtham, J. P. Park, D. C. Ralph, and R. A. Buhrman, Phys. Rev. B 89, 024418 (2014). [28] A. Thiaville, S. Rohart, E. Jue, V. Cros, and A. Fert, Europhys. Lett. 100, 57002 (2012).

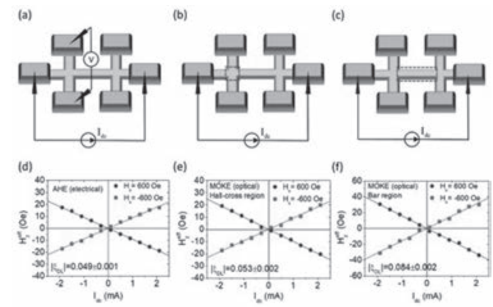

Fig. 1. Schematic illustrations of DL-SOT effective field measurements through (a) electrical and (b, c) optical approaches on a Ta(4)/CoFeB(1.4)/Hf(0.5)/MgO(2) Hall-cross device. The red dashed boxes in (b) and (c) represent the MOKE detection areas-of-interest, namely the Hall-cross region and the bar region, respectively. (d, e, f) as functions of for Oe under different measurement schemes.

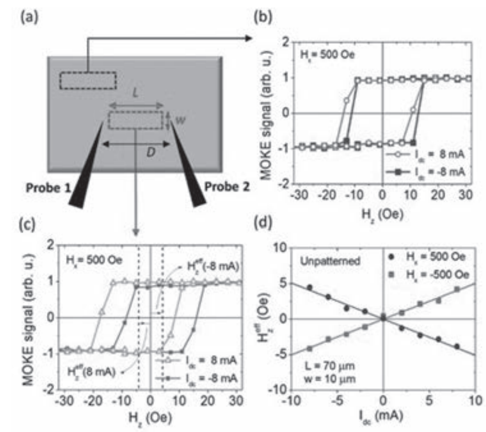

Fig. 2. (a) Schematics (top view) of tungsten probes configuration for measuring SOT effective field in a Ta(4)/CoFeB(1.4)/Hf(0.5)/MgO(2) unpatterned film. The two dashed boxes represent two different probing areas. w and L represent the width and the length of the probing area, respectively. D is the distance between two probe tips. Optically-detected hysteresis loops for I_{dc} =±8mA and H_x=500Oe from the probing area (b) away from the region with strong current flow and (c) within the strong current flow region. (d) H_z^{eff} of the unpatterned Ta-based heterostructure as functions of I_{dc} for H_x=±500Oe.

EV-08. Combined FORC and Kerr Microscopy Domain Analysis.

I. Soldatov[2], J. Garcia[2], A. Volegov[3], P. Dhagat[4], A. Jander[4] and R. Schäfer[2,1]

1. Institute for Materials Science, TU Dresden, Dresden, Germany; 2. Institute for Metallic Materials, Leibniz Institute for Solid State and Materials Research (IFW) Dresden, Dresden, Germany; 3. Institute of Natural Science, Ural Federal University, Ekaterinburg, Russian Federation; 4. School of EECS, Oregon State University, Corvallis, OR, United States

In recent years, the First-Order Reversal Curve (FORC) method has gained increasing interest for exploring magnetic phenomena in natural and synthetic multicomponent magnetic materials, such as interaction and coupling phenomena in particle and film systems [Roberts2014]. The method consists of the measurement of minor hysteresis curves, starting by saturating the sample, decreasing the field to a reversal field, then sweeping the field back to saturation in regular field steps. This process is repeated for many values of the reversal field, yielding a series of FORCs. The FORC distribution function [Mayergoyz1986] is then obtained by the calculation of a second-order mixed derivative of the output variable with respect to the reversal and measuring field values. The interpretation of FORC plots has been historically based on the classical Preisach model, in which hysteresis is assumed to be associated with a collection of single square irreversible curves, called mathematical hysterons. The connection between hysterons and the physically relevant reversal events governing the FORC plots, such as switching by domain wall motion or rotational processes, is often non-trivial and needs refined models in order to evaluate such diagrams. FORCs are commonly measured by vibrating sample-, SQUID- or alternating gradient magnetometry. All these methods suffer from being time consuming with FORC acquisition times well above one day if a high field resolution is required. Recently, it was shown that MOKE (Magneto-Optical Kerr Effect) magnetometry can significantly reduce the measurement time by keeping a high field resolution [Gräfe2014]. In this presentation, we extend this method by implementing MOKE-based FORC magnetometry in a wide-field Kerr microscope. The Kerr image intensity of selectable areas on the sample is used as magnetization signal [Soldatov2017]. At the same time the magnetic domains along each FORC can be recorded, allowing to directly see the relevant magnetization process that is responsible for the curve. The benefit of supporting FORC analysis by domain imaging was already appreciated previously, see e.g. [Beron2012, Ma2014, Gräfe2016]. In those studies, however, the imaging and FORC experiments were performed in different setups. Our approach of in-situ measurement and imaging in the same setup provides the possibility to understand both, the FORC distribution and the magnetization processes, thus offering the prospect to propose realistic models for complex magnetization reversal mechanisms. In our presentation we will show combined experiments on interacting (see figure) and isolated thin film elements, magnetic film systems with perpendicular anisotropy and extended specimens such as amorphous ribbons.

[Beron2012] F. Beron et al., J. Magn Magn. Mat. 324, 1601 (2012) [Gräfe2014] J. Gräfe, M. Schmidt, P. Audehm, G. Schütz, E. Goering, Rev. Sc. Instr. 85, 023901 (2014) [Gräfe2016] J. Gräfe et al., Phys. Rev. B 93, 014406 (2016) [Ma2014] L. Ma et al., J. Appl. Phys. 116, 033922 (2014) [Mayergoyz1986] I.D. Mayergoyz, Physical Review Letters 56 (1986) 1518 [Roberts2014] A. P. Roberts, D. Heslop, X. Zhao, C. R. Pike, Rev. Geophys. 52, 557 (2014) [Soldatov2017] I. Soldatov and R. Schäfer, J. Appl. Phys. 122, 153906 (2017)

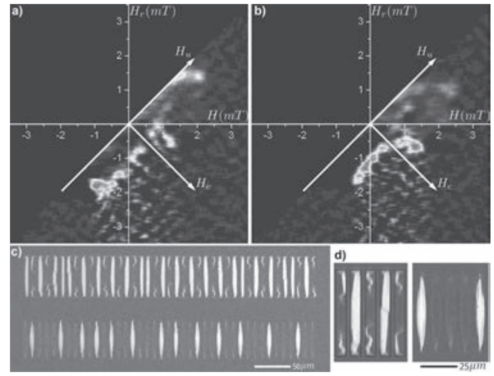

Fig. 1. FORC diagrams of interacting Permalloy elements of rectangular (a) and pointed (b) shapes with a thickness of 240 nm. The Kerr image in (c) shows typical domain states of both types of elements along one of the FORCs at zero field. Whereas the pointed elements (lower row) appear completely saturated before and after switching, at the blunt ends of the rectangular structures (upper row) closure domains are formed. They reduce the stray field, which is reflected in subtle differences in the FORC plots. Image (d) shows a magnified view of some of the elements. The FORCs were measured on the whole row of each element type.

EV-09. Improvement of the measurement method of rock magnetic properties based on the scanning SQUID microscope with an in-situ magnetization/demagnetization field.

J. Du[1,2], Q. Wang[1] and *T. Song*[1,2]
1. Institute of Electrical Engineering, Chinese Academy of Science, Beijing, China; 2. University of the Chinese Academy of Sciences, Beijing, China

The magnetic properties of geological samples provide significant information about the Earth, which can reflect the evolution of the continent and the oceans [1, 2]. A scanning SQUID microscope with an in-situ magnetization/demagnetization field (Fig1) had been developed by us [3], which can obtain not only the distribution of the magnetic field but also the remanent curves of a wafer sample at each point. In this paper, we developed an improved method to measure the remanent curves of rock magnetic properties. The remanent curves at each point can characterize the magnetic properties of the samples. But selecting all the points on the sample for measurement would consume a lot of time; randomly selecting some points to measure would lose important information. For the above problems, we proposed a measurement method to choose the characteristic point. At first, we mapped the distribution of magnetic field of a wafer sample which need to be measured, and the extreme points in the distribution of magnetic field were obtained by the contour map of magnetic field. Because the extreme value of the magnetic field generally appears above the position of the magnetic particles, and the field value in the vicinity of the magnetic particles is gradually reduced, we selected the extreme points in each area as the points to measure the remanent curves which are marked with red solid circle in the Fig. 2. Then the sample moving platform could move the sample to place the point to be measured below the probe. Based on the magnetization/demagnetization field the remanent curves were obtained. Using the method, the magnetic properties of geological samples could be rapidly measured. Relative to the random selection and all selection, this method of selecting points to be measured based on the distribution of magnetic field can save measuring time without losing feature information. This work was supported by the National Science & Technology Support Program of the Ministry of Science and Technology of China (2015BAI01B07).

[1] Sato, M., S. Yamamoto, Y. Yamamoto, Y. Okada, M. Ohno, H. Tsunakawa, and S. Maruyama, Rock-magnetic properties of single zircon crystals sampled from the Tanzawa tonalitic pluton, central Japan, Earth Planets Space 67 (2015) 150. [2] Oda, H., A. Usui, I. Miyagi, M. Joshima, B.P. Weiss, C. Shantz, L.E. Fong, K.K. McBride, R. Harder, and F.J. Baudenbacher, Ultrafine-scale magnetostratigraphy of marine ferromanganese crust, Geology 39 (3) (2011) 227-230. [3] Liu, X.H., J.W. Du, Z. Wei, and T. Song, Research on the In Situ Magnetization and Demagnetization System for Scanning SQUID Microscopy, IEEE Trans. Magn. 51 (11) (2015) 6502704.

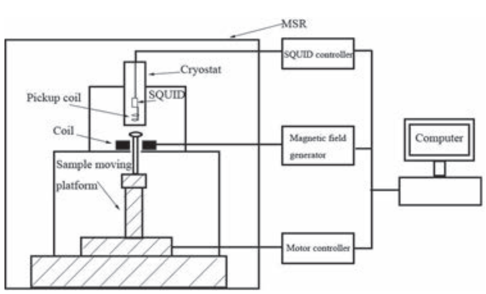

Fig. 1. The schematic of the system.

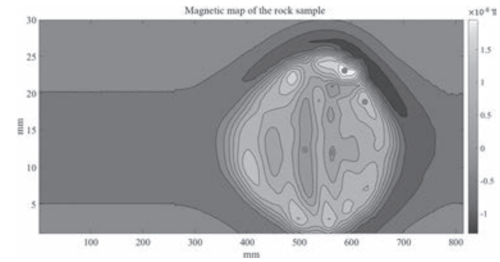

Fig. 2. The measured magnetic map of a sample and the points to be measured.

EV-10. Implementation of 16-channel AMR sensor array for quantitative mapping of two-dimension current distribution.

G. Huang[1] and *J. Jeng*[1]
1. Mechanical Engineering, National Kaohsiung University of Applied Sciences, KAOHSIUNG, Taiwan

In recent years, the development of system-on a-chip (SoC) magnetic sensors makes it possible to mass-produce the miniature vector magnetometers with stable quality, e.g. Hall Effect and anisotropic magnetoresistance (AMR) magnetometers [1]-[3]. For applications in quantitative magnetic source imaging, it is necessary to map the field distribution with high accuracy. The traditional field scanner employs a single magnetometer [4],[5], which may take hours to map the magnetic field at a high spatial resolution. The multi-channel magnetic imaging system based on linear array of AMR sensors [2] can achieve a higher scanning efficiency. However, the feature size of 10 mm for the sensor made the center-to-center distance between sensors as large as 15 mm, which limits the achievable spatial resolution. In addition, the sensor operation requires external driving and analog-to-digital circuits, which results in high complexity and high total cost when the number of channels are increased. In this work, we investigated a magnetic source imaging system based on a 16-element array of SoC AMR sensors to reduce the complexity in system construction. The magnetic field was mapped in a one-way scan and the current distribution was subsequently obtained within one second by using the calculation program to solve the magnetic inverse problem. The accuracy of current amplitude was analyzed and the parameters affecting the spatial resolution were discussed. The 16-element sensor array consists of the IST8308 AMR vector magnetometers from iSentek Inc. [3]. The maximum dynamic range is ±500 μT and the maximum data rate is 200 Sa/s in the high sensitivity mode. The small package size of 3 mm for the sensor reduces the center-to-center distance of adjacent sensors to 6 mm. The total length of the 16-element sensor array is 90 mm. The sensors communicate with the Arduino Nano microcontroller unit via I^2C interface. The real-time data are transmitted via a Bluetooth Module to a desktop computer for processing and display. The object under test was moved during scanning with an X-Y scanning stage of 0.002-mm resolution. The scanning time is only 20 seconds for a 100-mm scanning range, which covers an area of 90 mm×100 mm. To probe the accuracy for current mapping, a pair of anti-parallel long straight conductors of known current is used as the specimen. The experiment was conducted at three different heights of 2.5, 3.5, and 4.5 mm at various current of 0.25, 0.5, 0.75, and 1 A. After each adjustment of height changes, the map of background magnetic field was recorded for subtraction from the observed field distribution. The size of raw field data is 16×256 points. Before the current-inversion calculation, the size of measured field data is expanded to 256×256 points, as shown in Fig. 1a, by linear interpolation between the data points taken by adjacent sensors. The typical field map for z = 2.5 mm and current of 0.5A different is shown in Figure 1a. The algorithm used for retrieving the current distribution is the Fourier transform [4], for which the source current density was solved by assuming that the distribution is periodic on the same plane of constant height [4],[5]. The calculated current density distribution, as shown in Figure 1b, is obtained by using the Fourier algorithm as follows [5]: $j_x(k_x, k_y)=-(2*i/(u_0*d))*(k_y/k)*(e\wedge(k*z))*b_z(k_x, k_y, z)$ and $j_y(k_x, k_y)=(2*i/(u_0*d))*(k_x/k)*(e\wedge(k*z))*b_z(k_x, k_y, z)$. Figure 2 shows the retrieved current magnitude along the long conductors carrying a current of 0.5 A. The data are taken on the sensing planes of different heights. It is found that the full width at half maximum of current trace is about 3.9 mm and 3.1 mm respectively for the top (forward) and bottom (backward) conductors. The current amplitudes in Fig. 2 are calculated by definite integral from the current density distribution in Figure 1b. The current amplitudes observed by our system at three different heights were close to source amplitude of 0.5A with the error within 4-6%. Moreover, at the same height, the calculated current values of two long straight conductors were similar with a non-uniformity less than 3%. The results indicated that, by using our non-contact field mapping and source current calculation method, the current density as well as the current amplitude could be determined quantitatively at high efficiency. The Fourier algorithm is currently restricted by several conditions. It can only solve the problem of the two-dimensional inverse problem, which excludes the cases with a tilt sensing plane and three-dimensional current distribution. Further work to include the inversion algorithm, e.g. minimum norm estimation, which is compatible with three- dimensional current distribution, will help improve the quality of source current mapping. The developed magnetic source imaging system is useful for detection of current leakages and shorts of printed circuit [6]. This work is supported by the Ministry of Science and Technology of Taiwan under Grant No. MOST 106-2221-E-151-025.

[1] J. Pascal, D. Vogel, S. Knecht, M. Vescovo, L. Hébrard, "Three-dimensional Magnetic Camera for the Characterization of Magnetic Manipulation Instrumentation Systems for Electrophysiology Procedures", EMBEC & NBC 2017, pp 410-413 [2] J. A. Leyva-Cruz, E. S. Ferreira, M. S. R. Miltão, A. V. Andrade-Neto, A. S. Alves, J. C. Estrada, and M. E. Cano "Reconstruction of magnetic source images using the Wiener filter and a multichannel magnetic imaging system", Review of Scientific Instruments 85, 074701 (2014). [3] IST8303 AMR sensor, iSentek Inc. (accessed Dec. 26, 2017), http://www.isentek.com/zhtw/index.php [4] B. J. Roth, N. G. Sepulveda, J. P. Wikswo Jr., "Using a magnetometer to image a two dimensional current distribution," *J. Appl. Phys*., vol. 65, pp.361-372, 1989. [5] F. C. Wellstood, J. Matthews and S. Chatraphorn, "Ultimate limits to magnetic imaging," in *IEEE Transactions on Applied Superconductivity*, vol. 13, no. 2, pp. 258-260, June 2003 [6] L. A. Knauss, A. Orozco and S. I. Woods, "Advances in magnetic-based current imaging for high resistance defects and sub-micron resolution," Proceedings of the 11th International Symposium on the Physical and Failure Analysis of Integrated Circuits. IPFA 2004 (IEEE Cat. No.04TH8743), 2004, pp. 267-270.

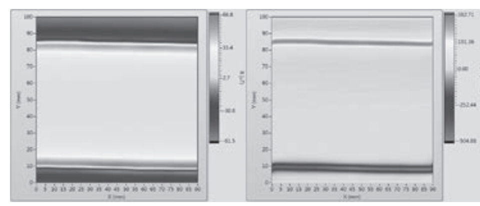

Fig. 1. a. Distribution of z-axis magnetic-field component for a pair of anti-parallel long straight conductors. The sensing plane is at height of z = 2.5 mm from the specimen and the current is 0.5 A. b. Distribution of current density calculated from the data of Fig 1a by using Fourier transform algorithm.

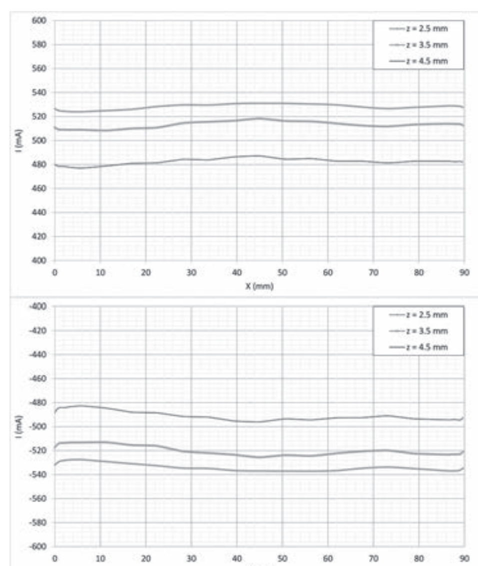

Fig. 2. Current magnitude distribution along the *x*-axis obtained at the sensing plane z = 2.5, 3.5, and 4.5 mm for the forward (top) and backward (bottom) conductors.

EV-11. Magnetic control of guanine-vesicle hybrid and its possible application in live cell imaging.

A. Mootha[1], K. Suzuki[3] and M. Iwasaka[1]
1. Research institute of Nanodevice ad Biosystems, Hiroshima University, Higashihiroshimashi, Japan; 3. Kanagawa University, Hiratsuka, Japan

The ability to visualize the biological processes in real time rather than observing it at discrete point of times has a promising potential application in observing tissue regeneration. The prospects of live cell imaging is increasing to observe changes in anatomy during cell differentiation, studying the cell signaling- molecular analysis of cell processes, sensing transgene activity and therapeutic applications including targeted drug delivery. Studying these cells in real time helps us to record invaluable data whose knowledge holds great importance in understanding several aspects of cell functions at both microscopic and macroscopic level. Ability to trace cells in real time requires cell labeling using suitable markers (that may be injected or Endocytose) which tremendously improves cell visualization. Various cell labeling techniques have been attempted successfully in the past for live cell imaging. Some procedures targeted to label the cells directly, whereas it is also possible to view cell functions by tracing labeled giant vesicles made of double lipid layers endocytosed in living cells. Using photonic crystals which have brilliant light reflective properties that respond rapidly to magnetic field has never been tried before. Guanine crystals are optical nanoparticles present abundantly in the scales of fish skin and other color changing animals. These guanine crystals respond rapidly to light and align parallel to an applied magnetic field. We have observed that the optical and magnetic properties of synthetically available guanine nanoparticles behave similarly to biogenic guanine crystals. Our target was to encapsulate synthetically available guanine nano-particles inside giant vesicles and subject them to strong light source and magnetic field. Figure 1 shows bilayer lipid giant vesicles encapsulated with guanine nanoparticles. Under dark field microscopy, we observed that a cluster of guanine particles accumulated and were encapsulated into the giant vesicles successfully. When this giant vesicle was subjected to an external light source, guanine nanoparticles shine brilliantly and reflect light in a direction opposite to the light source, and magnetic field caused flickering of guanine nanoparticle. Additionally, this strong illumination of the flickering guanine nanoparticles in turn caused strong illumination of the giant vesicle itself into which they lay encapsulated, making it look like an iridosome similar to those found in natural cells in skin of color changing animals. These brilliantly illuminated giant vesicles marked with encapsulated guanine nanoparticles can be entirely endocytosed into living cells. Further, the location of the cells carrying giant vesicle-guanine nanoparticle complex could possibly be traced with MRI to track the exact real-time location of the cell; thus holding a promising potential application for live cell imaging to study changes in cell anatomy during tissue regeneration and wound healing around dental implants. Moreover, visualizing the response of tissues around the dental implant to invading bacteria could be studied. This work was supported by JST-CREST "Advanced core technology for creation and practical utilization of innovative properties and functions based upon optics and photonics (Grant number: JPMJCR16N1).

Russell E. Jacobs, Cyrus Papan, Seth Ruffins, J. Michael Tyszka, Scott E. Fraser. MRI: volumetric imaging for vital imaging and atlas construction. Nature Reviews Molecular Cell Biology October 2003 pages 10 to16

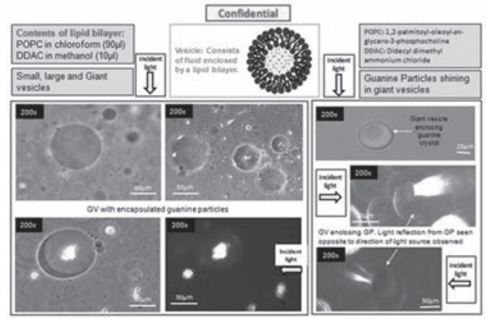

Fig. 1. Under dark field microscopy with an external light source, the encapsulated guanine nanoparticles into giant vesicles resulted in brilliant illumination of giant vesicle. Additionally, it can be noted that the flickering guanine nanoparticle in the vesicle reflected bright light in a direction opposite to the light source and caused bright illumination of the giant vesicle like an iridosome.

EV-12. Modifying coercivity via growth rate on domain wall pinning (001) FePd thin film.

C. Hsiao[1], H. Chang[2] and *C. Ouyang*[1]
1. Materials science and engineering, National Tsing Hua University, Hsinchu, Taiwan; 2. National Chung Cheng University, Chia-Yi, Taiwan

Perpendicular magnetic anisotropy (001) oriented FePd films epitaxially grown on MgO(100) substrates(as shown in Fig.1) with high order parameters(S=0.94) and large out-of-plane coercivity have been demonstrated. Stacking faults induced by strain relaxation are closely related to out-of-plane coercivity ($H_{c,\wedge}$) of FePd films prepared at various temperatures through examining all defects related to coercivity variations based on statistical simulations. Through climbing dissociation of total dislocation, the stacking fault densities($r_{S.F.}$) are promoted(as shown in Fig.2), resulting in distinguished promotion in out-of-plane coercivity. $H_{c,\wedge}$ drops significantly via raising or decreasing growth rate, indicating $r_{S.F.}$ is affected strongly by deposition parameters. This result suggests the coercivity can be manipulated via controlling stacking fault density in FePd film, which may pave a way for future magnetic devices.

C.H. Hsiao *et al.*, "Domain wall pinning on strain relaxation defects (stacking faults) in nanoscale FePd (001)/MgO thin films", Appl. Phys. Lett., vol. 107, pp. 1407.1-5, Oct. 2015.

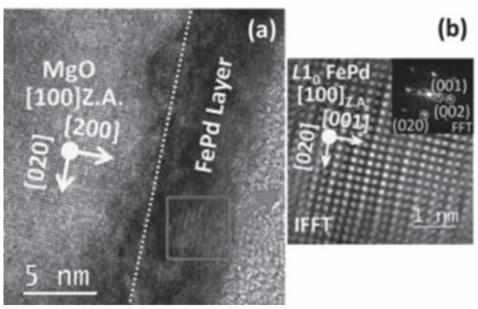

Fig. 1. micrographs of FePd film prepared at 600^{o}c (a)cross sectional HRTEM image,
(b)IFFT image of red rectangular area in (a)

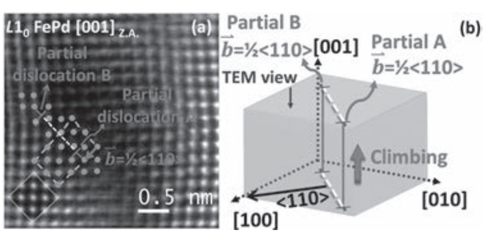

Fig. 2. FePd films prepared at 700^{o}C (a) HAADF image with a simulation, (b)cartoon scheme of stacking fault and partial dislocation showing climbing phenomenon of (a)

EV-13. Design and Simulation of a Double Tuned RF Coil for ^{1}H and ^{31}P MR imaging at 7T.

F. Du[1,2], S. Liu[1], N. Li[1,2], Y. Dou[2], X. Zhang[3,4] and Y. Li[2]
1. Department of Biomedical Engineering, Chongqing University of Technology, Chongqing, China; 2. Lauterbur Research Center for Biomedical Imaging, Shenzhen Institutes of Advanced Technology, Chinese Academy of Sciences, Shenzhen, China; 3. Department of Radiology and Biomedical Imaging, University of California, San Francisco, San Francisco, CA, United States; 4. UCSF/UC Berkeley Joint Graduate Group in Bioengineering, San Francisco, CA, United States

Abstract: The research on the performance of ultra-high magnetic field radio frequency (RF) coils is one of the main aspects in the research of ultra-high field magnetic resonance imaging (MRI)system. In this paper, a ^{1}H /^{31}P dual-tuned multi-channel RF coil for the ultrahigh magnetic field 7T MRI was proposed. The performance of the proposed coil is evaluated by using numerical co-simulation approach. The result demonstrates the feasibility of the proposed double-tuned RF coil in the applications of 1H/31P ultrahigh magnetic field. 1.INTRODUCTION The improvement of RF coil performance is the most challenging topic in ultrahigh field MRI, particularly in the heteronuclear MRI where double nuclei are often involved. It is important to study the performance of ^{1}H /^{31}P double tuned RF coils to study metabolism of living systems[1]. In multi-channel dual-tuned RF coils, a technical challenge is to achieve sufficient electromagnetic coupling between adjacent channels and between non-adjacent channels[2]. In this work, we propose to design an 8-channel dual-tuned coil for ^{1}H/^{31}P imaging at 7T. The dual-tuned RF circuit of the dual-tuned coil can make it difficult to obtain optimal tuning and matching with high efficiency at both frequencies. The field distribution and tuning/matching conditions of the RF coil are modeled separately by EM and RF simulation[3].Through simulation, EM fields and SAR can be investigated to ensure imaging quality and patient safety[4]. Therefore, in this work, we used field-circuit co-simulation to model and field analyze dual-tuned coils[5] to evaluate the performance of the proposed dual-tuned RF coil imaging. The parameters evaluated coils performance include the homogeneity for B1+ field and specific absorption rate(SAR) value. 2. METHOD The 4-channel by 4-channel double-tuned coil design was used to image ^{1}H with a four-channel dipole array and ^{31}P with a four-channel Loop array. Sufficient decoupling of adjacent channel was achieved by using loop-overlapping approach. The dipole coils were placed in the center of the loop coils to minimize the coupling between the two coils [6]. The diagram of the double tuned structure is shown in Figure1(a). The loop size was 180×168 mm. The line width was 6 mm, and dipole size was 240×8 mm. The coil conductor was made of copper wire. The overlapping area of adjacent loops was 34.7 mm. The length of the single-side adapted dipole antenna was 117 mm, the distance between the two sides is 6 mm, placed in the center of the loop coil. These coils surrounded a cylinder with an outer diameter of 185 mm. The load was a cylindrical saline phantom with a diameter of 150 mm and a length of 200 mm. Its permittivity was 78, permeability was 0.99, conductivity was 0.6 S/m. The present study was modeled using a commercial CST software (Computer Simulation Technology, Darmstadt, Germany) and laboratory matrix codes were used to analyze and calculate B1+ field data and SAR derived from CST.The coil was modeled in a microwave studio (MWS). In joint simulation, all lumped elements were replaced by discrete excitation ports with impedance of 50Ω instead of the integrated elements on each of the loop coils. Other parameters were set in accordance with those of electromagnetic field simulation. As shown in Figure1(b). The number of mesh cells was about 510000 and boundary conditions were set to be omnidirectional. With time-domain solver, the steady-state accuracy limit was set to -40dB.The coil was tuned by changing the capacitance and inductance in RF circuit and combining individual B1+ fields based on tuning data for the external port to obtain the B1+ field. Since the four-channel coil was cylindrically shaped, four-channel orthogonal excitation was achieved during the emission mode. Therefore, the on-field phase was set to 0°, 90°,180°, and 270°in turn. When calculating the B1+ field results, the received power field was normalized to 1w. SAR post-processing results were normalized to 1W of input power. A graph of SAR was calculated using the average of 10g. The local SAR value (average of any 10 g tissue SAR) generated by the RF signal in the MRI system cannot exceed 10W/Kg. B1+ field uniformity calculated as follows: B1+homogeneity=($B1+_{Max}$ -$B1+_{Max}$)/(2×B1+Average) 3. RESULT The SAR distribution of ^{1}H and ^{31}P in xz plane are shown in Fig.2(a)and(b), respectively. The B1+ distribution of ^{1}H and ^{31}P in xz plane are shown in(c)and(d). In the center of interest area, distributions of B1+ and SAR show a desired pattern with high intensity B1+ and weak SAR, ensuring sensitive yet safe imaging acquisition. B1+ field distribution is symmetrical and uniform. B1+homogeneity of ^{31}P is 0.6, B1+homogeneity of ^{1}H is 0.65. Therefore, the proposed double-tuned coil design is feasible for ^{1}H/^{31}P imaging applications at the ultrahigh field of 7T. 4.DISCUSSION From the simulation results, the proposed ^{1}H /^{31}P double tuned multi-channel RF coil design for the UHF MRI system has good performance. This coil design method should be a feasible and efficient technique in designing high frequency double-tuned RF coil arrays for heteronuclear metabolic MR imaging at ultrahigh fields. However, the coupling between non-adjacent channels needs to be further improved. To address this issue, one possible solution would be the use of the magnetic wall or ICE decoupling technique[7].

[1] P. B. Roemer, W. A. Edelstein, C. E. Hayes, S. P. Souza, and O. M. Mueller,"The NMR Phased-Array," Magn.Reson.Med., vol.16,no.2,pp.192-225,2010. [2]Hani A F M, Kumar D, Malik A S."Performance evaluation of dual tuned knee coil ($_{23}$Na/^{1}H) for articular cartilage imaging on 1.5Tesla MRI,"IEEE Trans. Magn.,PP.357-361.2012. [3] M. Kozlov and R. Turner, "Fast MRI coil analysis based on 3-D electromagnetic and RF circuit co-simulation,"J. Magn. Reson., vol. 200,no.1, pp.147–152,2009. [4]C.M.Collins and M. B. Smith, "Calculations of B1 distribution, SNR,257 and SAR for a surface coil adjacent to an anatomically-accurate human 258 body model,"Magn.Reson.Med.,vol.45,no.4,pp.692–699,2001. [5]N.Li,S.Liu,X. Hu,et al."Electromagnetic Field and Radio Frequency Circuit Co-Simulation for Magnetic Resonance Imaging Dual-Tuned Radio Frequency Coils,"IEEE Trans. Magn.,PP:1-4,2017. [6]Rutledge O,Kwak T,Cao P,et al."Design and test of a double-nuclear RF coil for (1)H MRI and (13)C MRSI at 7T,"J. Magn. Reson.,vol,267.no.15,2016. [7]Y. Li, Z. Xie, and Y. Pang, D. Vigneron and X. Zhang, "ICE Decoupling Technique for RF Coil Array Designs," Medical, vol.38,no.7, pp.4086-4093, 2011.

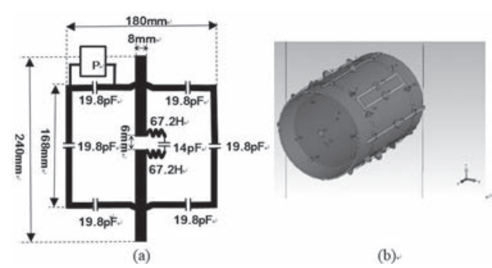

Fig. 1. (a) Dipole and Loop coil Schematic, "P" represents the Discrete Port, and (b) RF coil simulation model and saline phantom(the blue section)

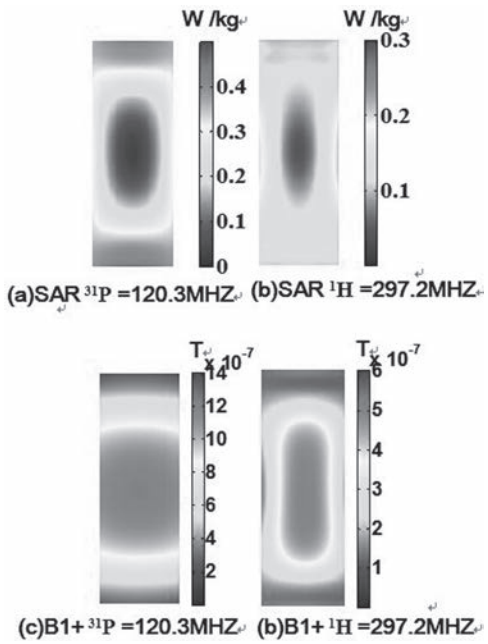

Fig. 2. (a)-(b)SAR distribution maps of $^{31}P/^{1}H$, and(c)-(d)B1+field distribution of $^{31}P/^{1}H$.

EV-14. Effect of synthesis method on particle size and magnetic and structural properties of Co-Ni ferrites.

S. Sharmin[1], M. Kishimoto[1], E. Kita[1], H. Latiff[1] and H. Yanagihara[1]
1. Applied Physics, University of Tsukuba, Nagareyama, Japan

Introduction Spinel type ferrites are considered to be key materials for advancement in electronics, magnetic data storage, ferrofluid technology and many bio-inspired applications. Their magnetic properties, such as anisotropy, coercive force, and saturation magnetization are affected by various factors such as particle size and shape, crystal structure, and composition [1]. Co-Ni spinel ferrite particles have been studied mainly for the purpose of increasing saturation magnetization, even though the coercive force showed a tendency to decrease with the substitution of Ni. In the present study we have discussed the magnetic properties, Mössbauer parameters, particle sizes and cation distribution in Co-Ni spinel ferrites synthesized via a succession of chemical co-precipitation, hydrothermal treatment, and etching in hydrochloric acid (HCl). Experiment Co-Ni spinel ferrite nanoparticles were synthesized through the following processes. First, 0.02 mole of $FeCl_3$, 0.005 mole of $CoCl_2$, and 0.003 mole of $NiCl_2$ were dissolved in 20 mL of water, to obtain a 2.5 times molar ratio of Fe^{3+} against ($Co^{2+} + Ni^{2+}$). The solution containing Fe^{3+}, Co^{2+} and Ni^{2+} was added to an aqueous solution of 0.228 mole of NaOH to prepare the co-precipitant while stirring at room temperature. Then, the suspension containing the co-precipitant composed of Fe^{3+}, Co^{2+} and Ni^{2+} ions was treated hydrothermally using an autoclave at 180 °C for 2 h to grow Co-Ni spinel ferrite particles. After the hydrothermal treatment, the suspension containing Co-Ni spinel ferrite particles was washed with pure water until a neutral pH was reached. The suspension containing hydrothermally treated particles was then furthermore divided into several parts with equal volume, and each suspension was etched in 40 mL of HCl solutions diluted with water at concentrations from 2.0 to 6.0 mole/L for 2 h. The dimensions of the synthesized materials was examined by transmission electron microscopy (TEM). The Mossbauer spectra were collected at room temperature and at helium temperature (4.2K) using a constant acceleration Mossbauer spectrometer. The samples produced by chemical co-precipitation and hydrothermal treatment are denoted by AP and HT respectively, while the samples produced as a result of etching are indicated by ET2 (HCl solution 2.0 mole/L), ET4 (4.0 mole/L), and ET6 (6.0 mole/L). The magnetic properties were measured using a vibrating sample magnetometer (VSM) under a maximum magnetic field of 1353 kA/m (17000 Oe). Results and Discussion TEM images showed that the co-precipitant (AP) consists of fine particles of a few nanometers in size. When the co-precipitant was hydrothermally treated (HT), there was remarkable particle growth of the co-precipitant to almost cubic shape approximately 30–40 nm in size. A large quantity of fine particles were also present. However, after etching, the fine particles were almost all removed. Figures 1(a), (b) and (c) show the M-H curves of the co-precipitant, hydrothermally treated co-precipitant particles and the ET4 sample respectively. Table 1 shows the saturation magnetization (M_s) and coercive force (H_c) obtained. (Co-Ni) Fe_2O_4 can be described as a cubic close-packed arrangement of oxygen ions with Co, Ni and Fe^{3+} ions at two crystallographic sites. The analysis of room temperature Mössbauer spectra of the samples indicates that it comprises two subspectra; one for tetrahedral (A) site and the other for octahedral (B) site. On the premise that all of the Fe^{3+}, Co^{2+}, and Ni^{2+} metal ions, with the molar ratio 20:5:3, were used to form the spinel ferrite and that Co^{2+} and Ni^{2+} ions (M^{2+}) preferentially occupy B-sites while Fe^{3+} occupies the A-site, the composition should be $Fe^{3+}_{1.0}(Co^{2+}_{0.526}Ni^{2+}_{0.316}Fe^{3+}_{1.105\Delta 0.053})O_4$. Here, $_\Delta$ indicates vacancy. From room temperature Mössbauer spectra, we found that the nanosized AP sample is partly paramagnetic at room temperature, as evidenced by a central quadrupole doublet attributed to the superparamagnetic relaxation effect of nanometer-sized particles which is observed when relaxation time becomes significantly less than the Mössbauer effect observation time i.e. ~99 ns. The effects of superparamagnetic relaxation were offset by reducing the sample temperature to 4.2 K. The Mössbauer parameters (hyperfine field, H_{eff}, isomer shift, IS, and relative area) for the AP, HT, ET2 and ET4 samples at liquid He temperature are given in Table 1. We see that the ratio A/B changes as particle size is increased indicating that the cation distribution is changed as a result of the size and synthesis method. The ratio A/B is almost 1 in ET samples. Summary: Co-Ni spinel ferrite particles were synthesized via chemical co-precipitation, hydrothermal treatment, and etching in HCL solutions. A maximum coercive force of 519 kA/m and saturation magnetization of 60.4 Am^2/kg was obtained by after etching in HCl with a concentration of 4.0 mole/L.From the Mossbauer data, we can conclude that there are no Fe^{2+} ions as the obtained ISs are close to the typical value for Fe^{3+} ions, 0.36 mm/s. The reduction in particle size and the defects introduced in particles by etching are expected to have contributed to the high coercive force exceeding 500 kA/m.

1. S. K. Gore, S. S. Jadhav, V. V. Jadhav, S. M. Patange, M. Naushad, R. S. Mane and K. H. Kim, Scientific Reports 7 (2017).

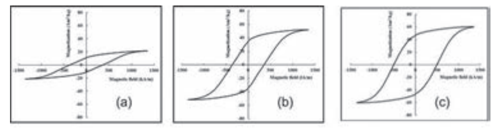

Fig. 1. Hysteresis loops of AP, HT and ET4 samples

Sample (He)	H_{eff} (T)		Isomer shift (mm/s)*		Area (%)		M□ (Am^2/kg)	H_c (kA/m)
	A	B	A	B	A	B		
AP	52.7	55.9	0.31	0.38	60	40	21.5	367
HT	53.3	56.3	0.29	0.38	54	46	52.0	358
ET2	53.2	56.3	0.29	0.38	51	49	60.6	446
ET4	53.8	56.7	0.29	0.39	50	50	60.4	519

Table 1. Mössbauer parameters measured at He temperature (4.2 K) and magnetic properties at 300K

EV-15. Effect of Sputtered Flux Direction on Damping Properties in Magnetic Bilayers.

S. Nayak[1], S. Mallick[1], B.B. Singh[1] and *S. Bedanta*[1]
1. LNMM, School of Physical Sciences, NISER, Bhubaneswar, India

The magnetic hard/soft bilayers have been studied widely due to high saturation magnetization (M_s) and magnetic anisotropy compared to its constituent layers [1]. These bilayers with high energy product $(BH)_{max}$ value have the application in various devices, permanent magnets, etc [2-6]. The material with high magnetic anisotropy has the application in high density recording devices [7]. Therefore, various deposition methodologies and conditions have been utilized to tune the value of magnetic anisotropy [8]. In addition, the materials with lower damping constant value have been studied for its application in spin-transfer switching devices [9]. Various deposition parameters and fabrication methodologies are being used to tune the value of damping constant. In magnetic bilayers, the interface roughness has a strong role in tuning the magnetic properties. We have fabricated Co (soft)/ $Co_{40}Fe_{40}B_{20}$ (hard) magnetic bilayers in UHV deposition system with oblique angle of deposition which induces uniaxial magnetic anisotropy. We have chosen the position of the targets in our deposition system in such a way that the plane of projection of the sputtered atoms of the individual layers on the substrate is perpendicular to each other. This geometry is termed as perpendicular configuration. Again, we rotated the substrate by 90° after depositing the first magnetic layer such that the direction of deposition of both magnetic layers becomes parallel to each other. This geometry is termed as parallel configuration. With these deposition methodologies, we tuned the value of magnetic anisotropy and damping constant. Table 1 shows the sample structure of all the magnetic layers with the deposition configuration and coercive field (H_C). The domain imaging and damping constant have been probed with magneto-optic Kerr effect (MOKE) based microscopy and ferromagnetic resonance (FMR) method. Due to direct exchange interaction between the individual layers, the magnetic domains found in the magnetic bilayers have the cumulative effect of the individual layers. Fig. 1 shows the magnetic domains of all the magnetic layers. The modification of line width and resonance magnetic field value in the magnetic bilayers indicates the existence of coupling between the individual layers. By fitting the experimental data shown in fig. 2 (a), we can get the value of damping constant. By fitting Kittel equation with experimental shown in fig. 2 (b), the magnetic properties like effective magnetization $4\pi M_{\mathrm{eff}}$ and anisotropy field value H_k are extracted. We found magnetic bilayer deposited in parallel configuration has lower damping constant value than the bilayer deposited in perpendicular configuration. The study of controlling the anisotropy, damping and reversal of the magnetic bilayers by varying the deposition geometry may have significant implications in future spintronics applications.

E E *et al*. 1998 *Appl. Phys. Lett.* 72, 380 Fullerton E. E. Fullerton *et al., J. Magn. Magn. Mat.* 200, 392 (1999) Jiang J S *et al*. 1998 *J. Appl. Phys*. 83, 6238 Davies J E *et al*. 2005 *Appl. Phys. Lett.* 86, 262503 Fullerton E E 1998 *Phys. Rev. B* 58, 18 Hellwig O et al. 2000 Phys. Rev. B 62, 17 Y. Fukuma *et al., J. Appl. Phys.* 106, 076101 (2009) N. Chowdhury and S. Bedanta *AIP Adv.* 4, 027104 (2014) A. Conca *et al., J. Appl. Phys.* 113, 213909 (2013)

Table 1. Sample structure, the deposition configuration, H_C along EA and HA of all the samples.

Sample	Sample structure	Deposition configuration	H_C(EA) (mT)	H_C(HA) (mT)
S1	Si (100)/Ta (3 nm)/Co (10 nm)/Ta (3 nm)	--	2.73	0.80
S2	Si (100)/Ta (3 nm)/CFB (10 nm)/Ta (3 nm)	--	8.89	0.34
S3	Si (100)/Ta (3 nm)/CFB (10 nm)/Co (10 nm)/Ta (3 nm)	CFB || Co	4.79	1.35
S4	Si (100)/Ta (3 nm)/CFB (10 nm)/Co (10 nm)/Ta (3 nm)	CFB ⊥ Co	7.53	2.79

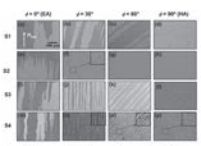

Figure 1. Magnetic domain images along $\phi = 0°$ (EA), 30°, 60° and 90° (HA) for the samples S1 to S4 taken in longitudinal mode at room temperature. The insets in (f), (n), (o), and (p) are the zoom-in view of the area marked in the respective images.

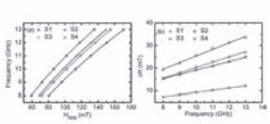

Figure 2. (a) Resonance field (H_{res}) vs frequency plot, (b) line width (ΔH) vs frequency plot for the samples.

THURSDAY MORNING, 26 APRIL 2018 SIMPOR/ROSELLE BALLROOM, 8:30 TO 11:30

Session EW
SENSORS: NEW SENSING PRINCIPLES
(Poster Session)

Jai Lin Tsai, Chair
National Chung Hsing University, Taichung, Taiwan

EW-01. Hall effect spintronics for gas detection.

A. Gerber[1] and G. Kopnov[1]
1. School of Physics, Tel Aviv University, Tel Aviv, Israel

Reliable detection of hazardous gases has become a major issue due to the more stringent environmental and safety regulations worldwide. Solid state conductometric gas sensors present a high potential for the applications where use of conventional analytical systems such as gas chromatography or optical detection is prohibitively expensive or impossible. Operation of such sensors is based on a change of electric conductivity when exposed to an atmosphere containing specific reagents, due to charge transfer between the sensor material and the adsorbed species. An important disadvantage of such sensors is the lack of chemical selectivity and sensitivity to humidity. Sensing materials are typically sensitive to more than one chemical species and show cross-sensitivity when different reactive gases are present simultaneously in the atmosphere. When the only parameter measured by the sensor is the change of resistance one cannot discriminate between different gases and their concentrations that can generate the measured signal. We present a new concept of magnetic gas sensors that will be able to solve the problem of cross-sensitivity by monitoring two independent parameters sensitive to the target gases: resistance and magnetization. The detection is based on the spintronics phenomenon of the Extraordinary Hall effect (EHE). Feasibility of the approach was demonstrated by detecting low concentration hydrogen using thin CoPd films as the sensor material. The Hall effect sensitivity of the optimized samples exceeds 240% per 10^4 ppm at hydrogen concentrations below 0.5% in the hydrogen/nitrogen atmosphere, which is more than two orders of magnitude higher than the sensitivity of the conductance detection.

1. A. Gerber, G. Kopnov, and M. Karpovski, Appl. Phys. Lett. 111, 143505 (2017).

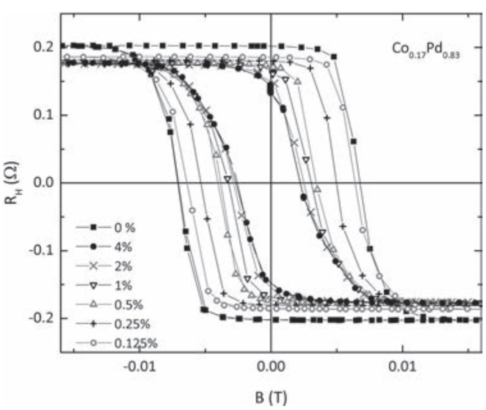

Fig. 1. EHE resistance hysteresis loops in H_2/N_2 atmosphere with different hydrogen concentrations (0%, 0.125%, 0.25%, 0.5%, 1%, 2% and 4%).

EW-02. Design of a Hall-Effect Current Sensor using Integrated Magnetic Concentrator and Magnetic Shield.

H. Hwang[1], J. Cho[1], Y. Choo[1], C. Kim[1] and C. Lee[1]
1. Electrical and Computer Engineering, Pusan National University, Pusan, The Republic of Korea

Eco-friendly vehicles consist of a motor, an inverter, and a battery, and high current flows through all of the components. In order to ensure the efficiency and safety of a vehicle, there is a need for a high-performance current sensor capable of monitoring the status of instantaneous current in real time. In general, a Hall-effect sensor, a shunt resistor, and a current transformer are widely used as a current sensor. A shunt resistor causes several critical problems such as insulation breakdown and significant power dissipation, and in case of a current transformer as an indirect measurement, a non-sinusoidal waveform is distorted. A Hall-effect sensor overcomes the disadvantages of a shunt resistor and a current transformer, but big ferromagnetic core in a Hall-effect sensor is needed to avoid magnetic saturation in measuring high current. Recently, a Hall-effect current sensor with an integrated magnetic concentrator (IMC) has been developed for solving the disadvantages of the three conventional sensors by inserting a thin soft magnetic material into an integrated circuit chip instead of ferromagnetic core. The remove of ferromagnetic core makes an IMC sensor more compact at high current. However, because an IMC Hall-effect current sensor is sensitive to external magnetic field, a ferromagnetic shield outside the current sensor is employed to ensure the linearity and accuracy of current measurement, and the design of a shield plays an important role in determining the size of an IMC Hall-effect current sensor [1-4]. In this paper, how to minimize a magnetic shield is proposed in an IMC current sensor suitable for eco-friendly vehicles. In Fig. 1(a), a commercial IMC Hall-effect sensor having a U-shaped shield is given, and the sensor is designed under the condition of 600 amperes in current. Because a concentrator starts to be magnetically saturated at 25 milli Tesla in an integrated circuit chip, flux density around the chip must be maintained under 25 milli Tesla in designing a shield. As shown in Fig. 1(a), an IMC current sensor has the width of 30 millimeters in its U-shaped shield targeted at 600 amperes in current, but the shield of a proposed IMC sensor in Fig. 1(b) is significantly reduced due to the enclosure of the shield to have better prevention of external magnetic field. The optimization of magnetic reluctance in the enclosed shield plays a critical role in volume reduction, and a step-by-step design procedure will be detailed in the final paper. In designing the shield, it is important to consider four key performances such as shield magnetic saturation, flux density around a sensing chip, shielding factor, and error rate caused by skin effect in a bus bar. An experimental design method is employed to meet the four performances in optimizing the enclosed shield. Fig. 2 shows the simulation result of the proposed IMC Hall-effect current sensor having an enclosed shield, and it is verified that all the given specifications are satisfied at current level of 600 amperes. As a result, compared to a commercial IMC sensor with a U-shaped shield, approximately 84% of size is reduced in the proposed structure under the same current condition.

[1] Imamura, M., Nakahara, M., Yamaguchi, T., & Tamura, S. (1998). Analysis of magnetic fields due to three-phase bus bar currents for the design of an optical current transformer. IEEE transactions on magnetics, 34(4), 2274-2279. Mohammad, Mizanoor Rahman, Kyung-Tae Kim, and Jin Hur. "Design and analysis of a spoke type motor with segmented pushing permanent magnet for concentrating air-gap flux density." *Magnetics, IEEE Transactions on* 49.5 (2013): 2397-2400. [2] Imamura, M., & Tokubuchi, M. (1996). Magnetic field analysis for the optical current-transformer used for three-phase bus-bars arranged longitudinally. IEEE Transactions on Magnetics, 32(5), 4962-4964. [3] Popovic, R. E., Randjelovic, Z., & Manic, D. (2001). Integrated Hall-effect magnetic sensors. Sensors and Actuators A: Physical, 91(1), 46-50.

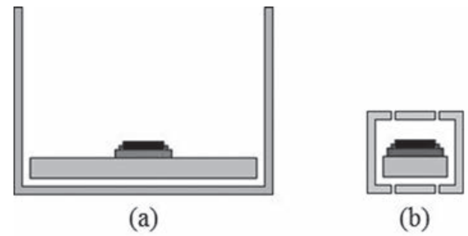

Fig. 1. Cross-sectional view of an IMC Hall-effect current sensor designed under the condition of 600A in current, (a) U-shaped shield, (b) enclosed shield.

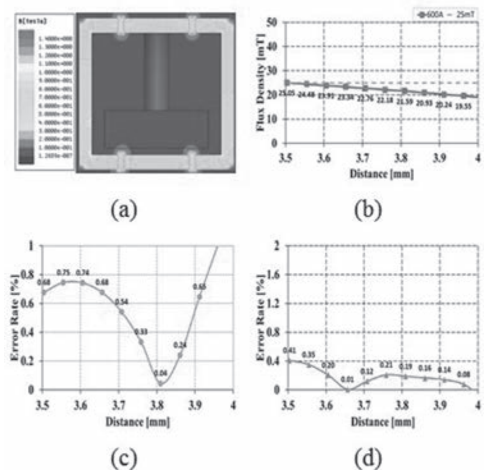

Fig. 2. Simulation results for the four considerations of an IMC Hall-effect current sensor in the proposed shield, (a) saturation level in the shield, (b) flux density around a sensing chip, (c) external magnetic shielding factor, (d) error rate due to skin effect.

EW-03. Magnetoimpedance strain gage sensors on FeNi alloys.

E. Fernandez Martin[1], I. Orue[3], J. Feuchtwanger[2] and A. García-Arribas[2,1]
1. BCMaterials, Leioa, Spain; 2. Electricity and electronics, University of the Basque Country (UPV/EHU), Leioa, Spain; 3. SGIKER Magnetic Measurements, University of the Basque Country (UPV/EHU)), Leioa, Spain

I- Introduction The magneto-impedance (MI) effect accounts for the large change of the electrical impedance experienced by soft magnetic materials when a magnetic field modifies its magnetic permeability by external agents, such as magnetic field, stress or temperature. Due to the skin effect, there is a limited penetration of the electromagnetic field associated with an alternating current flowing through the material. The skin effect reduces the effective cross section available for the ac current to flow and consequently the impedance depends on the external agents. In previous studies, we have systematically optimized the preparation conditions, structure and combination of shape and induced anisotropies to enhance the MI ratios and sensitivities on $Ni_{80}Fe_{20}$ multilayers [1-3]. In this work, we explore the route of using MI as strain gage sensors depositing them onto flexible substrates. This option has already been marginally explored [4-6], but not in materials with relative large magnetostrictive coefficient as $Fe_{60}Ni_{40}$ [7] and reasonable MI ratios. II- Structure and preparation of multilayered samples Sputtered Iron-Nickel based thin films lose their magnetic softness when the thickness is increased above the critical one (typically about 200 nm) [1,7]. Iron-Nickel films below that limit display excellent magnetic properties with slight differences below 100 nm films [2]. If nanometric non-magnetic spacers are inserted between two consecutive magnetic layers, thicker magnetically soft multilayer structures can be obtained [3]. We have therefore selected the $[Fe_{100-x}Ni_x(100\ nm)/Ti(6\ nm)]_2/Cu(200\ nm)/[Ti(6\ nm)/Fe_{100-x}Ni_x(100\ nm)]_2$ multilayered structure for fabrication of two series of the samples, with x=80 and 40. The two sets of samples were prepared using metallic masks during the sputtering to obtain elongated stripe shaped samples of 10 mm long and 0.5 mm wide. Square Cu pads were deposited at the stripe's ends for electrical contacts. For comparison, the samples were deposited simultaneously on Silicon, Cyclic olefin copolymer (COC) and Kapton® polyimide film. The samples were prepared by DC sputtering under a magnetic field oriented in a transverse direction to the stripe length inducing a transverse magnetic anisotropy. Being this field 250 Oe for $Fe_{20}Ni_{80}$ and 500 Oe for $Fe_{60}Ni_{40}$. III- Measurements and results Samples were magnetically characterized by measuring the hysteresis loops with a Vibrating Sample Magnetometer (VSM). Figure 1 shows the typical hysteresis loops, displaying a well define transverse magnetic anisotropy of 5 Oe, but with larger coercivity in the samples deposited onto flexible substrates. The impedance was extracted from the reflection coefficient measured using a network analyzer. To determine the stress-impedance characteristics of the MI material deposited onto the flexible substrates, a custom sample holder was designed as described in [4,5]. The samples are glued to a miscrsotrip line together with a commercial resistive strain gage, closely situated to the sample and experiencing the same deformation. At the same time that the stress is applied, the hysteresis loops is measured using the magneto-optical Kerr effect (MOKE) while measuring the impedance as function of the applied magnetic field. As shown in figure 2, the sample deposited onto Silicon shows a maximum MI ratio, calculated for the absolute value of the impedance Z as MI(%) = 100x $(Z-Z_{min})/Z_{min}$, of 80% at 70 MHz and a sensitivity, defined as the derivative of the MI ratio, of 25 %/Oe.

[1] A. V. Svalov et al., "Structure and magnetic properties of thin permalloy films near the "transcritical" state", IEEE Trans. on Mag., 46(2), 333–336, (2010). [2] E. Fernández et al., "GMI in nanostructured FeNi/Ti multilayers with different thicknesses of the magnetic layers" IEEE Trans. on Mag., 49(1), 18–21, (2013). [3] A. V. Svalov, et al., "FeNi-based magnetoimpedance multilayers: Tailoring of the softness by magnetic spacers", Appl. Phys. Lett, 100(16), 162410, (2012). [4] Bodong Li, et al., "Flexible magnetoimpedance sensor", Journal of Magnetism and Magnetic Materials, Volume 378, pp. 495-505, 2015. [5] A. García-Arribas et al., "Thin-Film Magnetoimpedance Structures Onto Flexible Substrates as Deformation Sensors," IEEE Transactions on Magnetics, vol. 53, no. 4, pp. 1-5, (2017). [6] G. Buettel, et al., "Micromachined silicon cantilevers with integrated high-frequency magnetoimpedance sensors for simultaneous strain and magnetic field detection", Applied Physics Letters, 111(23), 232401, 2017 [7] J. G. Kim, et al., "Magnetic properties of sputtered soft magnetic Fe–Ni films with an uniaxial anisotropy", Thin Solid Films, 440(1), 54-59, (2003).

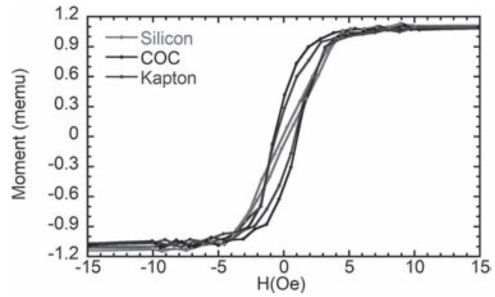

Fig. 1. VSM hysteresis loop of $Fe_{20}Ni_{80}$ deposited onto Silicon, COC and Kapton

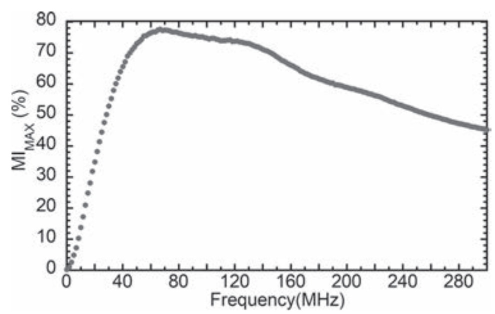

Fig. 2. Maximum MI ratio of $Fe_{80}Ni_{20}$ deposited on Silicon as a function of the frequency.

EW-04. Magnetic non-destructive materials characterization of non-ferromagnetic materials using magnetic susceptibility.

B. Gupta[1,2], B. Ducharne[1], G. Sebald[2] and T. Uchimoto[2]
1. INSA LYON, Laboratoire de Génie Electrique et Ferroélectricité, Villeurbanne, France; 2. ELyTMaX, Sendaï, Japan

Abstract All materials interact with an external magnetic field to some extent quantified by the magnetic susceptibility c. There is a correlation between local c value and local anomalies of material composition, deformation and stress, which makes it interesting to explore related sensor principles with a potential for NDT application. This contribution however concerns a modification over the magnetic force based sensor for laterally resolved susceptibility measurement and demonstrates the possible range of NDT applications on different non-ferromagnetic material samples. This sensor however eliminates the use of cantilever to avoid possible vibrations in the industrial environment. Keywords: non-destructive testing, magnetic force, magnetic susceptibility, paramagnetism, diamagnetism 1. Introduction Micromagnetic materials characterization is a well-known field of non-destructive evaluation and testing (NDE/NDT). It is based on the interaction of magnetic domain walls (Bloch walls) with microstructure, which is similar to the interaction of dislocations with microstructure [1 – 3]. Every material interacts with a magnetic field to some extent, depending on its internal composition and structure. The interactions which define the material's behavior in a magnetic field take place on the micro- and nanometer scale and are partially quantum mechanical in nature. The magnetic susceptibility c describes how a material interacts with an external magnetic field. It has been verified before that a correlation exists between micro- or electromagnetic and mechanical properties in para- and diamagnetic materials as well [4]. Previously, a magnetic force sensor developed [4][5] has shown promising potential in characterizing the materials like composites, plastics and many other non-ferromagnetic materials. Since, luxury car makers and aerospace industry are using more and more composites in manufacturing, it becomes very important to have a method to control the quality check, e.g., adhesion between two composites. However, one major drawback of this approach [4] was the use of cantilever which is not very useful when it comes to industrial test conditions which are more prone to vibrations. Hence, a new modification is proposed in this contribution in which the experimental set-up is changed entirely and a diaphragm is used instead of a cantilever. This system shows more stability and is less prone to vibrations. As an added advantage, the cost of the entire set-up is also reduced. 2. Experimental set-up and results Previously, a capacitive distance sensor was used in order to determine the deflection of a cantilever carrying a sensing magnet [4]. In the new proposed method, the authors use a plastic film thick enough to hold the sensing magnet with one layer of reflector on top for the laser sensor to sense the displacement (Figure 1). The sheet used to hold the sensing magnet is polyvinylidene fluoride (PVDF) in order to be strong enough to hold the magnet and at the same time thin enough to sense some stretching due to the force on the magnet when exposed to the material under test. The thickness of the diaphragm used in this set-up is 500 microns. The laser sensor used in this method is an MTI instruments device whose resolution is 0.5 μm/mV. The output voltage change of the laser sensor electronics when the sensing magnet is approaching a material is proportional to the displacement of the magnet. When investigating practical materials such as plastics or aluminium, the deflections are so small that the distance between sample and magnet changes to very small extent. In this case, the deflection (or voltage change) is almost proportional to the susceptibility of the material. The output of the laser sensor is calibrated in terms of force. Figure 2 depicts the initial results with aluminium and graphite sample over varied distances. Many other non-ferromagnetic materials characterization will be presented in the extended version of this article to verify the efficiency of the sensor. Figure 1: Experimental set-up schematic Figure 2: Initial results 3. Conclusions In this study a new experimental set-up is proposed for the characterization of the non-ferromagnetic materials non-destructively. A diaphragm is used to avoid any vibrations which are a major possibility in the industrial testing conditions. Additionally, the cost of the sensor is also reduced to make it easily available for the industry. In the extended version of the article, many different non-ferromagnetic materials will be characterized and imaged as per their magnetic susceptibility.

[1] R.M. Bozorth, Ferromagnetism, Van Nordstrand, Princeton, 1951. [2] B.D. Cullity, Introduction to magnetic materials, Addison-Wesley, 1972. [3] D.C. Jiles, Introduction to magnetism and magnetic materials, Chapman and Hall, 1991. [4] B. Gupta, K.Szielasko, J. Non-destructive Evaluation, Springer, pp. 35-41, 2016. [5] K. Szielasko, M. Amiri, B. Ducharne, B. Gupta, Magnetic Susceptibiliy as a new approach towards characterization and testing of para-and diamagnetic materials, proceeding of 18th International Symposium on Applied Electromagnetics and Mechanics (ISEM), 2017.

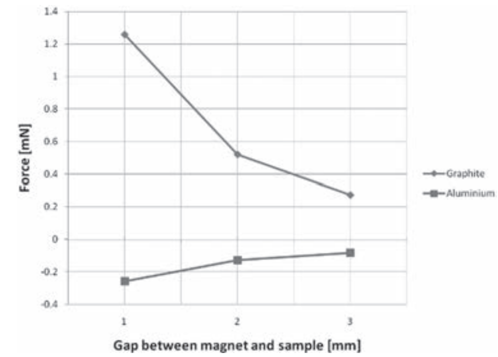

Fig. 2. Initial results

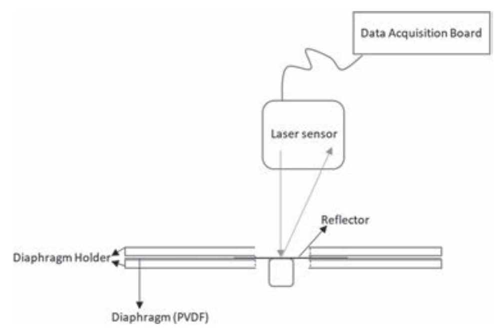

Fig. 1. Experimental set-up schematic

EW-05. Low noise fundamental mode orthogonal fluxgate (FM-OFG) magnetometer built with an amorphous ribbon core.

I. Sasada[1]
1. Sasada Magnetics & Sensors Laboratory, Fukuoka, Japan

Room temperature operating magnetometers able to detect a few pT magnetic field would play a crucial role in such areas as bio-magnetic field detection and very tiny ferromagnetic contaminats detection in battery production lines. We have already reported fundamental mode orthogonal fluxgate having a noise density ~3 pT/√Hz at 1 Hz using a Co-based amorphous wire (made by Unitika) core sensor head [1]. However, the supply of the amorphous wire is limited. In this paper, we present that the narrow amorphous ribbon core is an alternative to the wire core if the dc bias current for the fundamental mode operation [2] is properly adjusted. In a particular case of as-cast Metglas 2714A ribbon of 1 mm width, the dc bias current elevated to 200 mA, which is to be 40 mA for the wire core sensor head, reduces the noise down to a few pT/√Hz. In the experiment, we made several sensor heads listed in Table I using the above mentioned ribbon. A 1 mm width ribbon which is made by slitting a wider sample is bent in a U-shape or more likely in a hair-pin shape and inserted into a cylindrical pickup coil of length 30 mm, bore diameter of 2 mm and having 500 turn copper winding. The driving and signal processing electronics used is the one developed for the wire core sensor head. The only difference is that an adopter circuit is inserted between the ribbon core sensor head and the driving electronics to supply a large dc bias current from the battery and to moderately (≈2x) amplify the ac excitation current; the ac excitation current for ribbon core sensor heads is 24 mArms while that for wire core one is 12 mArms. The driving frequency is 100 kHz and the magnetometer is configured to operate in a closed loop (feedback) using a 10 kΩ feedback resistor. The sensitivity increases slightly with increase in length of the core, because the demagnetization effect becomes smaller for longer cores. The sensitivity of the magnetometer with the wire core sensor head is about one half of that of the magnetometer with the ribbon core sensor head because the number of turns of the pickup coil used for the wire core is 1000. It should be noted that the sensitivity of the closed loop system is R/n [V/A/m] where R is the feedback resistance and n is the winding density per meter of the pickup coil. The noise spectral density of the magnetometer was measured by placing the sensor head in a five shell cylindrical shield and by using an FFT analyzer (Stanford Research Systems SR780). Results are listed in Table I from which we can conclude that the noise level obtained with a ribbon core sensor head is comparable to that obtained with a wire core sensor head. Fig. 1 shows the noise spectral density of the ribbon core sensor head R19 for three different dc bias currents. It is interesting to see that the noise level is dramatically reduced by increasing the dc bias current. This is probably related to the nature of the as-cast Metglas 2714A ribbon such that weak magnetic anisotropies are distributed randomly in the ribbon plane. It is also interesting to compare the magnetic field produced by the dc bias current at surfaces of the ribbon core and of the wire core. For the wire core, the radius is about 60 μm and the bias current is 40 mA, hence the magnetic field is about 106 A/m. For the ribbon core, because the thickness (<20 μm) is negligible compared to the width (1 mm), the magnetic field at the surface of the ribbon is quite uniform along the width direction, hence the magnetic field can be calculated by dividing the current (220 mA) by the peripheral length which is twice the width, yielding 110 A/m which is similar to the one for the wire. One may expect that necessary dc bias current can be reduced by making the width of the ribbon narrower. A very weak magnetic field of rectangular waveform of 15 pT in peak-to-peak is well detected with a short averaging. Details on the adapter circuit will be explained.

[1] Hikaru Karo and Ichiro Sasadaa, "Magnetocardiogram measured by fundamental mode orthogonal fluxgate array", J. Appl. Phys. Vol.117, 17B322 (2015) [2] I. Sasada: "Orthogonal fluxgate mechanism operated with dc biased excitation", J. Appl. Phys., Vol.91, No.10, pp.7789-7791 (2002)

Sample name	Length of core [mm]	Sensitivity [V/μT]	@1 Hz pT/Sqrt[Hz]	@10 Hz pT/Sqrt[Hz]
R16	45	0.57	5.2	1.9
R17	50	0.61	4.9	2.0
R19	35	0.53	5.7	2.6
R20	40	0.54	5.6	2.1
wire	45	0.29	2.4	1.2

Table I Comparison of noise spectral densities at 10 Hz and 1 Hz between ribbon core sensor heads and a wire core sensor head

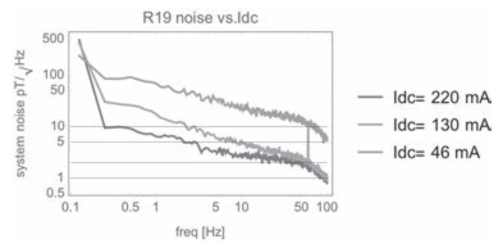

Fig. 1. Dependence of the noise spectral density on the bias current for the ribbon core sensor head R19. Noise spectral density plot at the top is for Idc=46 mA, that at the middle for Idc=130 mA and that at the bottom for Idc=220 mA.

EW-06. Accuracy Analysis of Sensing Coils in 2D Magnetic Properties Measurement.

X. Ding[1] and S. Ren[1]
1. Beihang University, Beijing, China

It has long been recognized that the rotating magnetic flux appears in electrical machine cores and leads to considerable power loss [1]. Beisides, the magnetic properties of electrical steel sheet are affected by stress because of produce process and external environment. The alternating and rotating magnetic properties have been invesgated widely [2-6]. However, there is a lack of research on two-dimensional magnetic properties of electrical steel sheet under laminated direction stress, and few mature measurement apparatus has been proposed. In the two-dimensional magnetic properties measurement considering laminated direction stress, the traditional micro-holes method[7], novel needle probe method[8] and H-coils could not be employed, since the B- and H- sensing part is restricted to destruction due to mechanical stress. While a novel sensing structure with cubic specimen is designed for three-dimensional magnetic properties measurement [9], which could be expanded to two-dimensional properties measurement considering laminated direction stress. Whereas the accuracy of the novel sensing structure has not been emphasized. Therefore, the sensing structure with cubic specimen is designed for two-dimensional properties measurement considering laminated direction stress, and the accuracy of the sensing is analyzed in detail. The two-dimensional magnetic properties measuring apparatus considering laminated direction mechanical stress is illustrated in Fig.1(a). The overall apparatus is composed of stress loading part, closed magnetic circuits, support and pedestal. As the amplitude, frequency and phase of X- and Y-direction currents controlled, the vector *B* along arbitrary direction in magnetization plane XOY could be induced in specimen. And the stress along Z-direction which is parallel to laminated direction of electrical steel sheets specimen, is exerted by rotating the handle wheel. The sensing coils for *B* and *H* are attached to the surfaces of cubic specimen, as shown in Fig.1(b). In order to enhance the magnetic field in cubic specimen, the gap in which the *B* and *H* sensing coils are placed needs to be reduced. Hence, the *B* coils made of four layers PCB (Printed circuit board) is employed, and the *H* coils are wound around the PCB, as shown in Fig 1(c). However, in the measurement of two-dimensional magnetic properties, the normal component H_n of magnetic field strength in sensing coils regions is considerable, which could lead to measuring error of *H*, as shown in Fig.1 (d). Therefore, a modified *H* coil made of four layers PCB is proposed in this paper. Fig.1(e) and (f) illustrate the PCB diagram as well as the product of modified *H* coil respectively. Since the projection of the conductors of each coil are coincided perfectly, the equivalent closed loop whose area is perpendicular to Hn is eliminated. Consequently, the modified *H* coils just examine the tangential component H_t of *H* on the boundary which between the specimen and gap. The thickness of *H* sensing coil is 1mm, and the thickness of the overall sensing structure for *B* and *H* is less than 2mm. The accuracy of the sensing coils in the apparatus is validated by both FEM and experiment. In the FEM analysis of closed magnetic circuits, the currents which present 5A amplitude, 50Hz frequency and 90 degree phase difference are set to the exciting coils. The distribution of B_x and B_y components both in specimen and *B* sensing coils regions are shown in Fig.2(a). Each component of the vector *B* is homogeneous in specimen, and equal to the counterpart in *B* sensing coils regions. In the same way, the H_x and H_y components in specimen and *H* sensing coils regions are also examined. Fig.2(b) shows the H_x and H_y components in specimen and *H* sensing coils regions. It indicates that each component of *H* in specimen is homogeneous, and the same as the counterpart in *H* sensing coils regions. The modified *H* sensing coils are also validated by the experiment. As the exciting current shows the same phase of magnetic field in the gap, the phase of Hx-coils induced voltage presents 90 degree ahead of the X-direction exciting current. However, the phase difference of original Hx coils induced voltage and X-direction current is 21.3 degree, as shown in Fig.2(c). The obtained voltage of original H_x coils contains considerable induced voltage which influenced by Y-direction current. Fig.2 (c) also shows the induced voltage of modified H_x coils. The phase difference between X- direction current and induced voltage is 90 degree. Thus, the modified H_x coils could not affected by Y-direction magnetic field. For further validation of *B* and *H* sensing structure in this paper, plenty of measuring experiments of different types of steel sheet would be conducted, applying both Epstein frame measuring system, which acts as the standard measuring method of one-dimensional magnetic properties of magnetic meterial, and the measuring apparatus in the full paper.

[1] J. Zhu, and V. Ramsden, “ Improved Formulations for Rotational Core Losses in Rotating Electrical Machines,” IEEE Trans. on Magnetics, vol. 34, no. 4, pp. 2234-2242, 1998. [2] D. Miyagi, K. Miki, M. Nakano, and N. Takahashi, “ Influence of Compressive Stress on Magnetic Properties of Laminated Electrical Steel Sheets,” IEEE Trans. on Magnetics, vol. 46, no. 2, pp. 318-321, 2010. [3] D. Miyagi, Y. Aoki, M. Nakano, and N. Takahashi, “ Effect of Compressive Stress in Thickness Direction on Iron Losses of Nonoriented Electrical Steel Sheet,” IEEE Trans. on Magnetics, vol. 46, no. 6, pp. 2040-2043, 2010. [4] M. Kawabe, T. Nomiyama, A. Shiozaki, M. Mimura, N. Takahashi, and M. Nakano, “ Magnetic Properties of Particular Shape Specimen of Nonoriented Electrical Steel Sheet Under Compressive Stress in Thickness Direction,” IEEE Trans. on Magnetics, vol. 48, no. 11, pp. 3462-3465, 2012. [5] N. Takahashi, T. Imahashi, M. Nakano, D. Miyagi, T. Arakawa, H. Nakai, and S. Tajima, “ Method for Measuring the Magnetic Properties of High-Density Magnetic Composites Under Compressive Stress,” IEEE Trans. on Magnetics, vol. 43, no. 6, pp. 2749-2751, 2007. [6] Y. Kai, T. Tsuchida, T. Todaka, and M. Enokizono, “ Influence of Stress on Vector Magnetic Property Under Rotating Magnetic Flux Conditions,” IEEE Trans. on Magnetics, vol. 48, no. 4, pp. 1421-1424, 2012. [7] S. Tumanski, “ Induction coil sensors—a review,” Meas. Sci. Technol, vol. 18, no. 3 pp. 31-46, 2007. [8] M. Ishida, K. Senda, A. Honda, and M. Komatsubara, “ Localized Magnetic Properties in Grain-Oriented Electrical Steel Measured by Needle Probe Method,” Electrical Engineering in Japan, vol. 126, no. 4, pp. 1-11, 1999. [9] Y. Li, Q. Yang, J. Zhu, and Y. Guo, “ Magnetic Properties Measurement of Soft Magnetic Composite Materials Over Wide Range of Excitation Frequency,” IEEE Transactions on, vol. 48, no. 1, pp. 88-97, 2012.

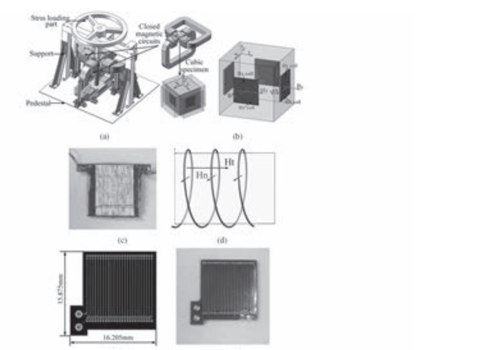

Fig.1 Two-dimensional magnetic properties measuring apparatus: (a) The overall apparatus; (b) The sensing structure for ***B*** and ***H***; (c) The original ***H*** sensing coil; (d) The magnetic field strength that the ***H*** sensing coil detected; (e) The PCB diagram and (f) the product of modified ***H*** sensing coil.

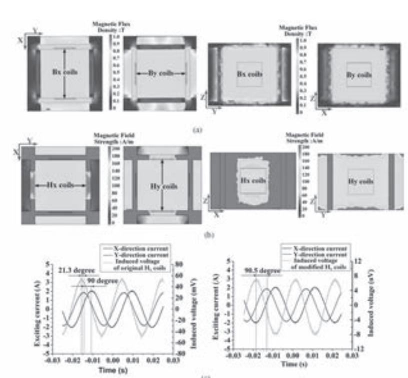

Fig.2 The results of FEM analysis and experiments: (a) The distribution of B_x and B_y components within ***B*** sensing coils regions; (b) The distribution of H_x and H_y components within ***H*** sensing coils regions; (c)The two directions exciting currents and the induced voltage of H_x coils.

EW-07. Magnetic Properties and Detection Methods of the Metal Wear Particles under Harmonic Magnetic Field.

R. Jia[1], B. Ma[1], C. Zheng[1], L. Wang[2] and Q. Du[1]
1. Beijing Institute of Technology, Beijing, China; 2. Beijing Information Science and Technology University, Beijing, China

1.Introduction The wear particles, as the production of abrasion, not only involve rich information of device-wearing but also will lead to further failure of equipment. According to the statistics, more than 75% failures of mechanical equipment were caused by the abrasion or wear particles[1]. Consequently that analyzing particles mixed in lubricating oil in real time appears particularly importance,and the inductive wear particles detection sensor has been widely studied and concerned due to its advantages of simple structure, good temperature stability and anti-interference ability. In order to guarantee the wear particle detection sensor both can detect ferromagnetic and non-ferromagnetic particles, this type of sensor often adopt alternating magnetic field. The field frequency covers an extremely wide range. S.P.Wang established a kind of particle detection sensor based on the static magnetic field, which only effective for ferromagnetic particles. The MetalScan system adopted 107Khz, Du Li et[2-4] fabricated a microfluidic device for metal particle detection in lubrication oil, which fluidic channel with dimension of 250μm×500μm and the excitation frequency was range of 1 and 3MHz. It is known that the magnetic field disturbances caused by metal particles, when debris through the sensor, is closely related to the field frequency. Researchers often adopt the static magnetization model to approximately analyze the effect of the ferromagnetic particles on the magnetic field and ignore the Eddy current effect in the particle, but with the increase of the field frequency the eddy current effect will show more significance. 2.Magnetic properties of wear particles The excitation signal of three-coil abrasive detection sensor is generally sinusoidal AC power supply, so the internal magnetic field of the sensor is alternating. The metal wear debris in alternating magnetic fields will produce eddy currents effect and affect the external magnetic field. The influence of metal sphere particle on the magnetic field in the sensor should satisfy the equation:$\sigma(\partial A/\partial t)+\nabla\times(1/\mu\nabla\times A)=0$, Where: A is the vector magnetic potential,μis the permeability of material,σis conductivity. Under harmonic magnetic field, the vector magnetic potential A can be described as $A=Ae^{-j\omega t}$which makes $\partial A/\partial t=j\omega A$, so the governing equation can be expressed as$\sigma j\omega A+\nabla\times(1/\mu\nabla\times A)=0$. In the cartesian coordinate, the magnetic orientation of the sensor oscillates along the X axis, so the vector magnetic potential outside of the particle is:$A=[A_x,A_y,A_z]=[0,0,B.y]\cos(\omega t)$, Where B is peak value of the local magnetic induction intensity at the position of particle; When calculate the distribution of magnetic field inside and around the particle, some boundary conditions should also be satisfied as follows. The equations (2) (3) describe the continuity of magnetic potential at the inside and outside surfaces of the sphere wear particles, and the equations (4) is the infinite boundary condition. 3.Validation of the model To verify the validation of the model, the magnetic property of iron particles in static magnetic field is calculated by both of the analytical solution and the numerical solution. We calculated the magnetic field distribution around the particle by the numerical method under the circumstance of $B_0=0.035T$,the magnetic induction intensity along the X and Z axes are presented in Fig.3. It shows that the distribution of magnetic field in the particle is equally distributed, and the magnetic induction intensity in the particle is B_{inner}=0.1047T, which agrees perfect with the analytical solution and validates the solution of the harmonic magnetic field model. 4.Magnetic properties of iron particles under harmonic field For the wear particle detection sensor, the frequency of the magnetic field generally ranges from 80 kHz to 3 MHz, so the magnetic properties of iron particle under the magnetic field of different frequencies were simulated. In this case, the radius of the particle was set to 0.125mm, and the frequency of magnetic field was set 0Hz, 100 Hz,1kHz,10kHz and 100 kHz respectively. The magnetic flux intensity distribution inside and around of the particle at different circumstance is shown at the Fig.4. It illustrates that when the exciting frequency is lower than 1 kHz, the eddy current in the particle can be ignored, the magnetic field distribution can be approximately estimated by static model, and with the increase of the exciting frequency, the magnetic field in the particle gradually weaken to 0, and the magnetic flux intensity at the surface of the particle along the direction of the initial magnetic field shows a maximum(0.5129T when f_0=100kHz) which is much larger than background magnetic field(0.035T). 5.The influence on sensor coil of particles The change of the local induced electromotive force caused by wear particles lead to the variation of magnetic flux of the through the sensor coil. In the studies[5, 6], the variation of magnetic flux of the through the sensor coil is estimated by the equation$\Delta\phi=N\iint\Delta B ds$, where N is the turns of coil. However the change of the induced electromotive force caused by wear particles only occurs at local position, so this calculation method over-estimated the inductance change of the coil resulted from the wear particle; especially on the occasion of the length of coil *l* is greatly larger than the diameter of particle. To precisely estimate the influence on sensor coil of wear particle, The total change of magnetic flux of the sensor coil caused by wear particle $\Delta\phi=\int\gamma\iint\Delta B ds dl$.

[1] Wu Y, Zhang H, Zeng L, et al. Determination of metal particles in oil using a microfluidic chip-based inductive sensor[J]. INSTRUMENTATION SCIENCE & TECHNOLOGY, 2016,44(3):259-269. [2] Du L, Zhe J. A high throughput inductive pulse sensor for online oil debris monitoring[J]. TRIBOLOGY INTERNATIONAL, 2011,44(2):175-179. [3] Li Du X Z Y H. Improving sensitivity of an inductive pulse sensor for detection of metallic wear debris in lubricants using parallel LC resonance method[EB/OL]. [4] Du L J Z. Real-time monitoring of wear debris in lubrication oil using a microfluidic inductive Coulter counting device[EB/OL]. [5] Hong H and Liang M 2008 A fractional calculus technique for on-line detection of oil debris. MEAS SCI TECHNOL. 19 055703. [6] Vutha A K, Davaji B, Lee C H and Walker G M 2014 A microfluidic device for thermal particle detection. Microfluidics & Nanofluidics. 17 871-878.

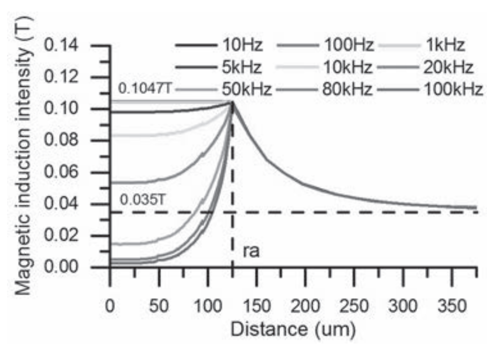

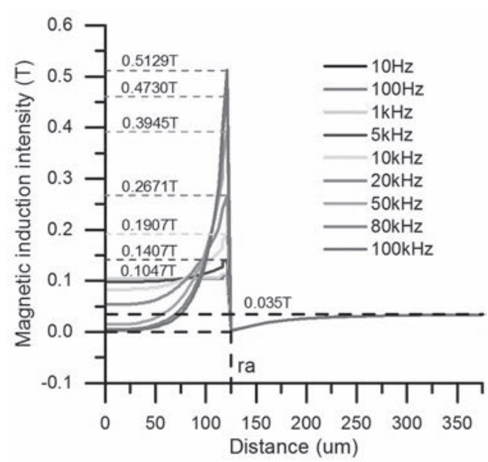

EW-08. Graphene-Co Nanoparticle Composites: Sensor Applications.

c.g. ünlü[1], A. Tekgül[3,4], M. Acet[2], M. Ak[1] and M. Farle[2]
1. Department of Chemistry, Pamukkale University, Denizli, Turkey; 2. Department of Physics, Duisburg-Essen University, Duisburg, Germany; 3. Department of Physics, Akdeniz University, Antalya, Turkey; 4. Department of Physics, Uludag University, Bursa, Turkey

Graphene based two dimensional carbon nanostructures that is characterized by exceptional biological, electrical, electrochemical, mechanical, optical and structural properties. To detect a wide variety of targets including biomolecule, chemical, electronical, and even living cells, graphene has a particularly great potential for use in sensors. Despite its recent discovery, graphene has already demonstrated its superiority to the well-established carbon nanotube in terms of electrocatalytic activity and conductivity. For electrochemical sensor applications, graphene is a promising material due to its large electrochemical window. Similarly, for electronic sensor such as field-effect transistor, graphene offers high carrier mobility and has low noise for better detection [1]. The properties of graphene based sensors could be tuned by incorporating magnetic nanoparticle to be formed as graphene-nanoparticle hybrid structure. Functionalized with different nanoparticle in order to enhance their individual properties to bring additionally advantages for the sensing application. Bio-compatibility property of graphene based sensors provides the promising candidate in the bio-sensor application. Their flexibility, easy integration and high precision gain new advantage than the other sensor systems in the biological systems. In this perspective, we present the sensing application of graphene-Co nanoparticle hybrid structure. In these systems, graphene sheets were prepared by chemical vapour deposition (CVD). Graphene is growth to be 0.1 mm thick, 2×2 cm^2 Cu-foils of 99.8 % purity were used as metallic catalyser. Copper foils were pre-cleaned by acetone, isopropanol and deionized water for 10 min in an ultrasonic cleaner. Then, it was placed into a furnace. The furnace was evacuated to 10^{-6} Torr and pre-heated to 1000°C with flowing H_2 at 100sccm for 30 min. This pre-heating and annealing process for Cu is targeted to create graphene seeds for growth. After annealing, CH_4 gas is let into the chamber at 30 sccm flow for 30 min. The chamber pressure was kept at 9×10^2 Torr while holding the Cu-substrate at 1000°C during the growth of the graphene. Finally, the Cu-foil covered with graphene was quickly cooled to room temperature. The large-area graphene ($2\times2cm^2$) prepared on the Cu foils was transferred onto FTO substrates. To be able to carry out the transfer, graphene on Cu foil was covered homogeneously with PMMA (Poly methyl methacrylate) solution with a spin-coater rotating at 4000 rpm for 40 s. Then, the sample was floated onto $Fe(NO_3)_3 9H_2O$ for a day in order substrate etched. The remaining graphene with PMMA was transferred onto the FTO substrate. After the PMMA solution was removed by acetone, we were able to complete transferring the pure single layer graphene onto the FTO substrate. Primary and sintered Co nanoparticles were prepared by the inert-gas condensation method based on DC-magnetron sputtering in a gas-flow of Ar and He [2, 3]. The primary nanoparticles are produced without in-flight annealing whereas the sintered particles are subjected to in flight heat treatment. The liquid nitrogen cooled nucleation chamber hosts the Co targets. The total gas pressure was maintained at 0.5 mbar. After nucleation and growth, the particles undergo in-flight annealing in a sintering furnace at 1000 K. The particles were deposited on standard carbon coated copper TEM grids held at liquid nitrogen temperature and Graphene/FTO substrate. The morphological and structural properties and the composition of the deposited particles and graphene were investigated ex-situ by using Raman Spectroscopy, High Resolution Electron Microscopy (HRTEM) and Energy Dispersive X-ray Spectroscopy (EDX). Furthermore, the magnetic properties of the samples were investigated by Magnetic Properties Measurement System (MPMS). Analytical and electrochemical performance of the samples were investigated with Iviumstat potentiostat-galvanostat.

[1] Yin, P. T., Kim, T-H., Choi, J-W., Lee, K-B. *Phys. Chem. Phys.* 2013, 15, 12785. [2] C. G. Ünlü, Z. Li, M. Acet, M. Farle, *Cryst. Res. Tech*. 2016, *51*, 333. [3] C. G. Ünlü, M. Acet, A. Tekgül, M. Farle, S. Atakan, J. Lidner. *Cryst. Res. Tech*. 2017, 1700149.

EW-09. Force sensors based on magnetic amorphous wires.

C. Hlenschi[1,2], S. Corodeanu[1], *H. Chiriac*[1] and N. Lupu[1]
1. National Institute of Research and Development for Technical Physics, Iasi, Romania; 2. Alexandru Ioan Cuza University, Iasi, Romania

The very convenient soft magnetic properties of the amorphous magnetic wires, that originate in the combination of the magnetic structure and cylindrical symmetry [1-3], and the high sensitivity to stress of their magnetic properties recommends them for a large number of applications, mainly as sensors and actuators [3-5]. A new type of sensor with high capability to measure applied forces is proposed by this paper. The sensing element consists of a $Co_{68.18}Fe_{4.32}Si_{12.5}B_{15}$ amorphous micro wire with100 μm in diameter and 12 mm in length, around which was wound a two layer coil with 200 turns using enameled 0.04 mm copper wire. The sensitive element is mounted circumferentially between two elastic tubes having around 7 mm in diameter and 5 mm in length (Figure 1). This attaching mode assure a pretension of the sensitive element, by bending it around the tube, and possibility to tailor the sensitivity and force measuring range by using tubes with different diameter and elasticity. For the presented results we used a latex tube with 7 mm external diameter and 2 mm wall thickness as inner tube and a heat shrinking tube around, to fix the sensitive element (Figure 1). The operating principle of the sensor is based on the variation of the coil impedance due to magnetic core permeability modification when the stress induced by bending is changing. The sensor coil is connected in series with a 470 Ω resistor, to limit the current trough the sensor coil at peak values smallest than 1 mA, and powered, using a sinusoidal signal. The drop voltage at the coil terminals is processed by a specific electronic device and correlated with the applied force by calibration. The coil excitation frequency was chosen at 160 kHz in order to obtain a good balance between the amplitude of the coil drop voltage and force sensitivity. At low frequencies the output signal is low due to small coil impedance (3.7 Ω in DC) and requires strong amplification while at to higher frequencies the coil signal is higher but the sensing element response to stress is less sensitive due to wire permeability decrease. At a frequency of 160 kHz the impedance of the sensor is approximately 75 ohm. The change of the applied force modifies the wire curvature, stress and permeability and consequently the drop voltage amplitude at the coil terminals. An analogical device was built to extract the amplitude of the coil signal, to filter and amplify the signals and to provide offset correction. In the first stage, the pick-up signal is amplified using a low noise operational amplifier to obtain a signal with higher amplitude. Then the signal is applied to a precision rectifier and the positive components of the signal are selected. To extract the force related signal, the signal from the previous step is passed through a low pass filter to remove the AC component which is coming from the excitation. In the last stage of analogue processing the offset is removed and the signal is filtered and amplified to get rid of hi frequency noise and to obtain a reasonable voltage value for output. To trace the compressive force versus output voltage characteristic we build a test device consisting of a non-magnetic metal frame and a vertical piston witch have at top end a tray and at the bottom the force sensor which is pressed under the action of weights placed on tray. The applied force was calculated as product between loaded weight and gravitational acceleration (9.81 m/s^2). The sensor voltage was measured using a voltmeter and the measured voltage values where plotted for each applied force. When the compressive force is applied (referred as positive values) the elastic tube is compressing and become elliptic with the center of the sensing element perpendicular to the major axis. In this case the stress induced in the sensing element is increasing, permeability of the wire is decreasing and consequently the output voltage is decreasing (Figure 2). If a tensile force is applied the elastic tube is also deforming and become elliptic with the center of the sensing element perpendicular to the minor axis. In this case stress on which the sensing element is subjected decrease, permeability of the wire is increasing and consequently the output voltage is increasing. The applying of tensile force is similar wit the case of compressive force on the sensor rotated with 90 degree. The dependence of output voltage versus compressive force shows a linear dependence for a wide range of applied force values (Figure 2). The sensitivity of the force sensor for the given configuration was 1.24 V/N and the force range up to 1N. The new developed force sensor can be easily adapted for specific applications such as medical devices and instrumentation (robotic surgery, tweezers for manipulating fragile objects) or other devices which requires force feedback. Acknowledgment – Work supported by the Nucleu Programme (Project PN 16 37 01 02)

[1] H. Chiriac, S. Corodeanu, M Tibu, and T. -A. Óvári, J. Appl. Phys., Vol. 101, 2007. [2] H. Chiriac, T. A. Óvári, M. Takajo, J. Yamasaki, and A. Zhukov, Mater. Res. Soc. Symp. Proc. vol. 674, pp. U7.7.1.–U7.7.6., 2001. [3] M. Vázquez, Physica B, vol. 299, pp. 302–313, 2001. [4] A. Zhukov, J. Mag. Mag. Mater., vol. 242–245, pp. 216–223, 2002. [5] C. Hlenschi, S. Corodeanu, H. Chiriac, IEEE Trans. Mag., Vol. 49, No. 1, Pp. 117 – 119, 2013.

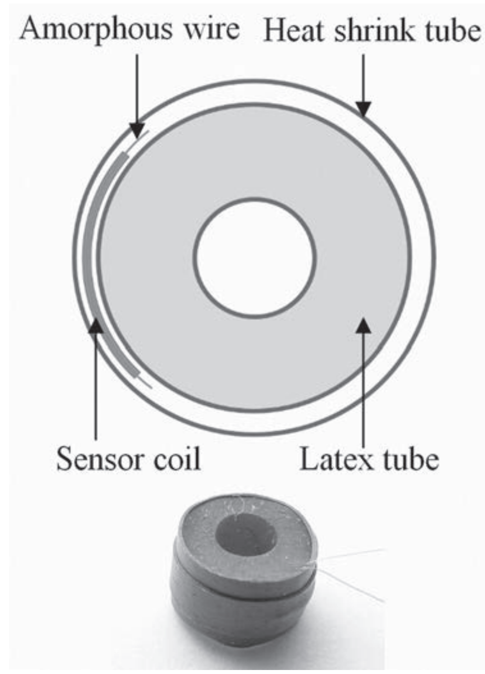

Fig. 1. Force sensor design and picture.

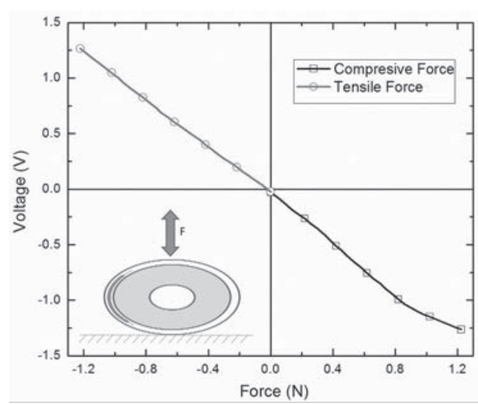

Fig. 2. Sensor response to external applied force for insert indicated configuration.

EW-10. Rotating magnetoelectric sensor for DC magnetic field measurement.

Y. Ren[1], J. Ouyang[1], X. Wu[1], W. Wang[1], J. Liang[1], S. Chen[1] and X. Yang[1]
1. School of Optics and electronic information, Huazhong University of Science and Technology, Wuhan, China

The magnetoelectric sensor has the advantages of high sensitivity, low noise and simple preparation process. It has great application prospects in weak magnetic field detection such as geomagnetic field, biomagnetic field and so on. What's more, the resolution of detection for low-frequency AC magnetic field can reach pT magnitude[1]. Because the piezoelectric material will produce a continuous output only when it is in a periodic vibration. so it needs to use modulation technology when measuring the statics magnetic field. The modulation techniques commonly used today are AC modulation and electric field modulation[2~3].But now, a new modulation method will be introduced in this paper, that is what referred to as rotation modulation. As shown in Fig.1(a), the component of the measured direct current projection on the shaft is a sinusoidal signal whose frequency is equal to the frequency of rotation, thus, we can measure constant magnetic field directly. More exciting, we may apply the rotation to MEMS structure to achieve miniaturization and integration. The test platform shown in Fig.1(b) is consist of rotation system and measurement system. Rotation system inclueds a ultrasonic motor and a fixture used for installing the magnetoelectric sensor and induction coil providing DC bias. The measurement system is composed of Signal Generator, Regulated DC Power Supply, Spectrum Analyzer, Magnetic Shield Tube. The magnetoelectric sensor used in the experiment was composed of Metglas/PZT/Metglas, which top layer and bottom layer are composed of two-layers of magnetostrictive Metglas. In order to obtain the best bias magnetic field, we firstly design a series of experiments with linearly increasing bias DC field at 2Hz(because the maximum rotation frequency of ultrasonic motor is 2Hz). Fig.2(a) shows that the optimal DC bias is about 8Oe. Then our group has tested the ME output voltage of magnetoelectric sensor with 10Oe measured DC field providing by coil, and the four groups experiments had been processed under condition of statics or rotation at three different speeds shown in Fig.2(b). There are three spikes whose value far greater than other's, and their position is just corresponding to the frequency of rotation. Fig.2(c) has shown almost linear change between ME voltage and the measured DC field. Thus, it can be conclued that the proposed modulation method is really effective. In these experiments, our team have used coils to ensure the DC bias can be controlled accurately. The next step we will use ferromagnet for bias. Using the proposed modulation method can realize high-precision DC magnetic field measurement like AC modulation and electric field modulation after enchancing ME out voltage through the selection of magnetic composite materials, the optimization of the rotating structure and the using of charge amplifier.

[1] Wang Y, Gray D, Berry D, et al. An extremely low equivalent magnetic noise magnetoelectric sensor[J]. Advanced Materials, 2011, 23(35): 4111-4114. [2] Petrie J, Viehland D, Gray D, et al. Enhancing the sensitivity of magnetoelectric sensors by increasing the operating frequency[J]. Journal of Applied Physics, 2011, 110(12): 124506. [3] Hayes P, Salzer S, Reermann J, et al. Electrically modulated magnetoelectric sensors[J]. Applied Physics Letters, 2016, 108(18): 182902.

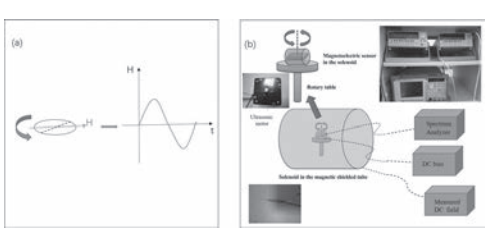

Fig. 1. (a)Simple schematic diagram of rotation modulation, (b) schematic diagram of measuring system

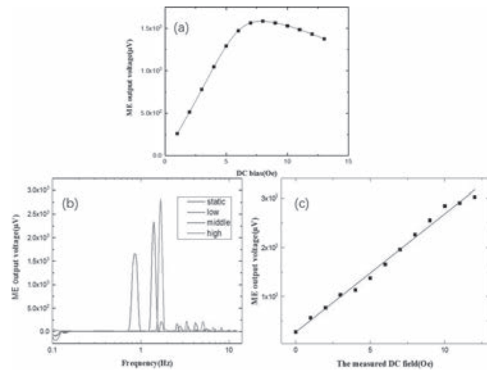

Fig. 2. (a)The ME output voltage with the DC bias magnetic field changes(b)ME response under condition of statics or rotation with low, middle, high speeds (c) The linear change between ME voltage and the measured DC field

EW-11. Development of the Technique for Measuring the Magnetic Flux in the Motor Core under Operating Conditions.

Y. Maeda[1], S. Urata[1] and H. Nakai[1]
1. Toyota Central R&D Labs., Inc., Nagakute, Japan

The increasing need for EV, PHV and HV has led to an intense research and development in the field of high efficiency motors. In order to develop the high efficiency motors, we have to evaluate magnetic properties of the core materials that consider the influences of manufacturing processes and actual motor operating conditions accurately. It is useful to develop designing techniques that can consider those evaluated properties accurately. The evaluations are carried out with a single sheet specimen by simulating stress [1], rotating magnetic field [2], direct flux superimposition [3] and so on, because emphasis is placed on their simplicity and versatility of the measurement. However, evaluations with a single sheet specimen have problems because they can't evaluate actual magnetic phenomena occurred in the motor core under operating conditions completely. In order to solve these problems, we have examined some techniques to visualize magnetic phenomena occurred in the motor core. In this paper, we introduce the newly developed technique to measure the magnetic flux flow in the motor core. In order to measure the magnetic flux in the motor core, the magnetic flux sensor that does not disturb the magnetic flux flow and has electric noise tolerance in operating motor is required. Newly developed three directional (radial, circumferential, and axial direction of the motor core) thin magnetic flux sensor to locate in the motor core is shown in Fig.1. This sensor consists of two-layered flexible printed board. Thickness of the sensor is about 170μm, thinner than an electrical steel sheet. Therefore, the sensor is able to set easily between the steel sheets without additional modification of the motor core. The magnetic flux in the radial direction and circumferential direction are measured by the needle probe method [4], which does not require any hole-drillings for measuring. The flux in the radial direction can be calculated by measuring the induced voltage between r_1 and r_2, the one in the circumferential direction can be calculated by the induced voltage between θ_1 and θ_2. The magnetic flux in the axial direction is calculated by measuring the induced voltage of the square search coil located on the flexible printed board. In order to make the higher tolerance for electric noise depending on the leakage flux, we constructed twisted pair line by using through holes in the two-layered circuit board, as a lead line connected to the sensor and the terminal point. Then, measurement results with developed sensors and magnetic field analyses results under the motor operating condition are compared. The magnetic flux density loci comparisons at the local area on the tooth in the stator core are shown in Fig.2. The solid line means measured results. The dotted line means analyses results. According to Fig.2, the measured magnetic flux density at the tip part of the teeth has elliptical locus. And the calculated result at the same position has alternating locus. Occurrence factors of the difference between measurement and analyses are considered as follows: (1) influence depending on an anisotropic of the magnetic material, (2)influence depending on manufacturing process such as form shaping, sheet lamination, coil winding. Analyses results ignore the influence (1) and (2), on the other hand, measurement results reflect them all. In other words, the proposed measurement technique can grasp the behavior of the magnetic flux flow, which is not able to grasp by analyses results. In conclusion, the newly developed measurement technique can measure the magnetic flux flow in motor core under operating condition, and visualize the behavior of the magnetic flux flow which cannot be considered by calculation. In the future, we will evaluate the magnetic properties of the motor core in detail by using developed technique.

[1] A.J. Moses, D. Davie, "Influence of compressive stress on magnetic properties of commercial", IEEE Trans. Magn. Vol.16, No. 2, pp454-460 (1980) [2] J. Sievert, "Two-dimensional magnetic measurements", PRZEGLAD ELEKTROTECHNICZNY, ISSN 0033-2097, R.87, No.9b (2011) [3] D. Miyagi; T. Yoshida; M. Nakano; N. Takahashi, "Development of Measuring Equipment of DC-Biased Magnetic Properties Using Open-Type Single-Sheet Tester", IEEE Trans. Magn., Vol.42, Issue 10 (2006) [4] T.Yamaguchi, M.Imamura, K.Senda, M.Ishida, K.Sato, A.Honda, T.Yamamoto, "Analytical Evaluation of the Accuracy of Localized Magnetic Flux Measurement by the Stylus Probe Method", T.IEE Japan, Vol,115-A, No.1 (1995)

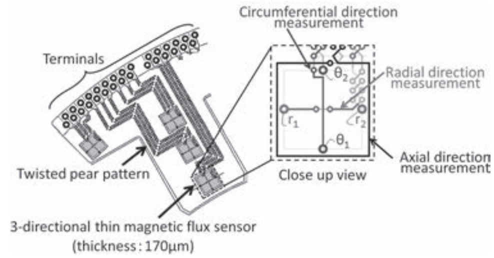

Fig. 1. Three directional thin magnetic flux sensors located in the motor core.

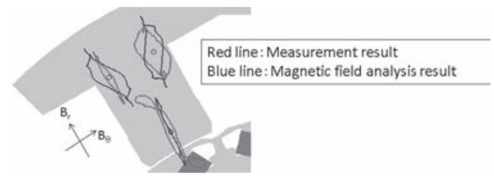

Fig. 2. The magnetic flux density loci comparisons at the local area on the teeth in the stator core.

EW-12. The perceptually-inspired model of tactile texture sensor based on the inverse magnetostrictive effect.

L. Wan[1] and B. Wang[1]
1. Hebei University of Technology, Tianjin, China

With the development of online shopping and intelligent industry, tactile perception has become the focus of attention and research. This sensitive texture detection of human is realized by characteristics of skin structure and several kinds of highly sensitive tactile capacitors in skin. The surface texture characteristic is regarded to be important information to evaluate and recognize the object. Tactile sensors are necessary to mimic the human touch sensing ability in many areas, such as virtual environment, e-commerce, robotic telemanipulation, and so on. Most of tactile sensors are based on piezoresistive or capacitive principles. They can provide some tactile or touch information, which includes weight, stiffness, elasticity and friction. At present, the cost-effective measurement of fine geometric texture is still a challenging task because the nonvisual texture sensors are relatively difficult to be design. The magnetostrictive material has the characteristics of small saturated magnetic field, good ductility and high tensile strength, so that it can withstand a variety of mechanical loads, such as pressure, tension and impact. The inverse-magnetostriction effect indicates that the permeability of a magnetostrictive material can be changed by an external impact. Therefore, the tactile sensor can be designed, based on the inverse-magnetostrictive effect. However, the relationship between the output voltage and the external impact is still unclear on the tactile sensor, based on the inverse-magnetostrictive effect, and the theoretical model of the output voltage for the tactile sensor has not been founded. Therefore it is necessary to investigate the perceptually-inspired model of the tactile sensor based on the inverse-magnetostrictive effect. At the same time, the perceptually-inspired model can also predict surface texture and classification by mimicking the active texture perception process of a human finger. In this paper, the model of the output voltage for tactile texture sensor has been founded and the relationship between the output voltage and the contacted object texture has been determined, according to the inverse magnetostrictive effect, the flexure mode, the Jiles-Atherton model, and the signal processing theory. The output voltage is relative with the bias magnetic field, the positive force and the information of the object texture, which is dependent on the height, the width and the total number (the period) of the surface ridge in the fixed length in addition to the Galfenol material parameters and the detecting coil. The output voltage of the tactile texture sensor is caused by the change of magnetic induction in Galfenol material. When the tactile texture sensor contacts the moving object, the deflection of Galfenol sheet moves up and down with the characteristics of the surface texture, then the magnetic domains will rotate. The rotation of magnetic domains will lead to the change of magnetic induction. The magnetic induction is mainly determined by the effective magnetic field and the magnetization of Galfenol material. Based on the trajectory by probe, the deflection signal of tactile texture sensor can be represented by the step sequence in the digital signal system. The sequence function is mainly determined by the height, the number of the texture ridge. The relationship between the output voltage and the texture parameters of the object is founded. The model of the output voltage of the tactile texture sensor can be used for the classification and imperfect testing of the object. From the experimental results in Fig.1, the tactile sensor move up and down as the height of ridge and spatial period of fabric when the tactile sensor contacts with the fabric surface with the speed of 3cm/s. The output voltage in Fig.1 (a) and (e) are mostly between 5mv and 10mv, but the period of the voltage wave is relatively longer in Fig.1 (a). The peak of the output voltage in Fig.1 (b) is obviously the largest, which is more than 10mv. Both voltage amplitude in Fig.1 (c) and (d) are mostly below 5mv, but their average voltage and period are different. Therefore, we speculate that the output voltage can represent the surface texture of the object. According to the results above, two conditions can be obtained on the tactile texture sensor: the surface texture has a large effect on the output voltage of the tactile texture sensor. The tactile texture sensor can complete the classification of fabrics. This work was supported by the Natural Science Foundation of Hebei Province No. E2017202035, and national natural Science foundation of China No. 51777053.

[1] Kentaro Noda, Kiyoshi Matsumoto, Isao Shimoyama, Skin-type tactile sensor using standing piezoresistive cantilever for micro structure detection, IEEE SENSORS 2010 Conference, 978-1-4244-8168-2/10. [2] ThiagoEustaqioAlvesde, Ana-Maria Cretu, and Emil M.Petriu. "Multimodal bio-inspired tactile sensing module", IEEE Sensors journal, vol.17, No.11, June 1.2017. [3]Qi Jiang, Longhai Xiang, "Design and experimental research on small-structures of tactile sensor array unit based on fiber bragg grating", IEEE sensors journal, Vol.17, No.7, Apr.2017

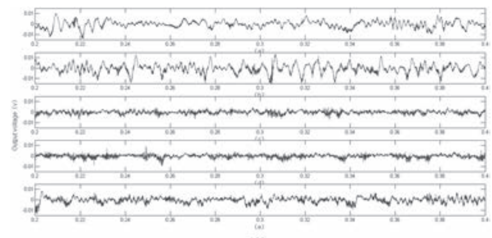

Fig. 1. The experimental output voltage versus different fabric under the contact pressure of 1N and the speed of 3cm/s, (a) Denim fabric, (b) Silk fabric, (c) Soft silk fabric, (d) Medical gauze fabric, (e) Cotton fabric

EW-13. A magnetoresistive sensor based on the elasticity of domain walls.

X. Zhang[2,3], N. Vernier[3], Z. Cao[2,1], Q. Leng[2], A. Cao[1,2], D. Ravelosona[3] and W. Zhao[1,2]

1. Fert Beijing Institute, School of Electronic and Information Engineering, Beihang University, Beijing, China; 2. Beihang-Goertek Joint Microelectronics Institute, Qingdao Research Institute, Beihang University, Qingdao, China; 3. Center for nanoscience and nanotechnology, Université Paris-Sud, Orsay, France

Magnetic sensors based on the magnetoresistance effects (MR sensors for short, e.g. GMR sensors and TMR sensors) have a promising application prospect due to their excellent sensitivity[1] and advantages in terms of the integration. The traditional MR sensors detect the magnetic field based on the deviation of the magnetization direction from the easy axis in the free layer (FL). However, competition between higher sensitivity and larger measuring range remains a problem. For the MR sensor with an in-plane anisotropy in the FL, the strength of anisotropy, which determines the measuring range and the sensitivity, can be tuned via manipulating the geometry of the device[2]. However, for MR sensor with perpendicular anisotropy, the measuring range is determined by the property of the multi-layer stack[3] and cannot be tuned via the geometry of devices. Here, we propose a novel mechanism for the design of MR sensors: probing the perpendicular field by detecting the expansion of the elastic magnetic Domain Wall (DW) in the FL of a spin valve or a magnetic tunnel junction. Fig. 1 shows the structure of the structure of the proposed device. The FL of two or more MTJs are connected via wire bridges while the pinned layer of MTJs are isolated. Free layers have a PMA and magnetizations of pinned layers are perpendicularly initialized on the same direction. The response of the magnetization in the FL of the device versus external fields was simulated, as shown in Fig. 2. Before working, opposite current pulses should be applied so that the magnetization of the free layer of two adjacent MTJs are initialized to opposite directions via the spin transfer torque. A DW will be created in the bridge. When the device is put in an external field H_{ext}, the DW will be moved in either of the two directions, depending on the direction of the external field. When the DW arrives at the connection between the bridge and one of the FL, it will be pinned, since the further expansion means a larger DW surface and thus a raised DW surface energy γ, as demonstrated in our previous experiments. In equilibrium, the DW will be of a circular arc shape and the radius can be given as follows[4], $R=\gamma/[\mu_0 M_S(H_d+H_{ext})]$ Here, M_S is the saturation magnetization. The demagnetizing field H_d is determined by the magnetic state and the structure of the device, varying with H_{ext}. Other parameters are all intrinsic. Therefore, the radius of the DW arc is solely dependent on H_{ext}. The expansion of the DW leads to a change of the magnetoresistance. In this way, the external field is quantified through the resistance of the MTJ. After the external field is removed, DW can come back to the bridge owing to its elasticity. Further simulations show that the device proposed shows a good performance on the measurement of the direct or alternating field. The advantage of the proposed sensor is: the device with larger size has a better sensitivity but the measuring range is relatively small; vice versa. Various devices with different size and geometry, thus with different performance (e.g. measuring range, sensitivity etc.) can be fabricated in the same chip. No modulation of the intrinsic properties of the film, such as the PMA, is required. Therefore, magnetic sensors based on the elasticity of DWs promise a higher integration level and a better performance[5].

[1] T. J. Moran and E. D. Dahlberg, “Magnetoresistive sensor for weak magnetic fields,” *Appl. Phys. Lett.*, vol. 70, no. 14, pp. 1894–1896, 1997. [2] Y. Lu *et al.*, “Shape-anisotropy-controlled magnetoresistive response in magnetic tunnel junctions,” *Appl. Phys. Lett.*, vol. 70, no. 19, pp. 2610–2612, 1997. [3] Z. M. Zeng, P. Khalili Amiri, J. A. Katine, J. Langer, K. L. Wang, and H. W. Jiang, “Nanoscale magnetic tunnel junction sensors with perpendicular anisotropy sensing layer,” *Appl. Phys. Lett.*, vol. 101, no. 6, p. 62412, 2012. [4] X. Zhang, N. Vernier, W. Zhao, H. Yu, L. Vila, and D. Ravelosona, “Direct observation of domain wall surface tension by deflating or inflating a magnetic bubble,” *arXiv*, 2017. https://aps.arxiv.org/abs/1708.06719 [5] X. Zhang et al. “Magnetoresistive sensors based on the elasticity of domain walls”, arXiv (2018)

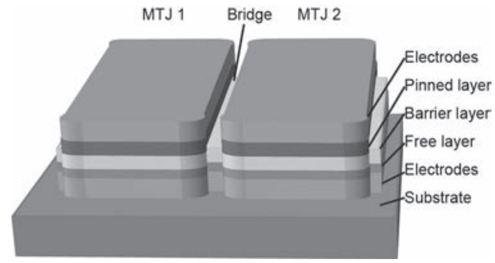

Fig. 1. Structure of a sensor device proposed based on the elasticity of the DW. Two MTJs are connected via a bridge while the pinned layer and the upper electrodes are isolated.

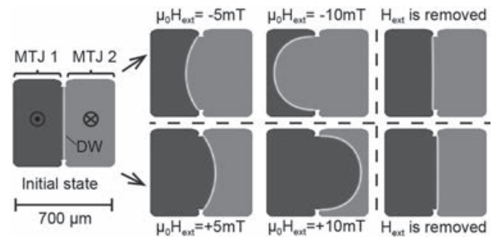

Fig. 2. DW states in the free layer of two coupled MTJs: First, DW was set in the middle of the bridge of the device. Then an external perpendicular field of -5 mT (+5 mT), -10 mT (+10 mT) was applied and the stable state of the DW was snapshotted, respectively. At last, the external field was removed and the DW returned to the bridge due to its elasticity.

EW-14. Determination of the strain-impedance gauge factor of Si-cantilever-based giant magnetoimpedance sensors.

G. Büttel[1], J. Joppich[1] and U. Hartmann[1]
1. Institute of Experimental Physics, Saarland University, Saarbrücken, Germany

Magnetoresistive sensors are currently widely investigated for flexible electronics and strain-sensing applications by employing magnetostrictive materials in GMR, TMR and giant magnetoimpedance (GMI) devices [1-3]. A true comparison of the three underlying effects for strain detection was so far not possible, because GMI strain sensors have so far been reported only on low-quality polymer substrates or Si wafers. Deposition on strongly bendable Si-cantilevers has only been reported very recently [4]. In this report a fabrication process and its effect on the magnetic and transport properties of GMI sensors integrated onto Si cantilevers are discussed. A strong change of permeability and therefore an impedance change is induced by the dry etching plasma processes needed to release the cantilevers from a 20 µm thick Si membrane. It softens the sensors magnetically. The downsizing of the GMI strain sensor required to deposit it on a cantilever allows accurate finite element simulations of induced stress/strain in the magnetostrictive layers ($Ni_{82}Fe_{18}$). As a result the strain-impedance gauge factor could be determined to be almost 200 at an ac current frequency of 2 GHz (Fig. 1). In consideration of the small dimensions, the consequently small magnetic field sensitivity and the low maximum GMI ratio of this device and due to the low-magnetostrictive NiFe employed in multilayer system, much higher strain gauge factors are assumed to be possible for GMI sensors. They could even surpass TMR strain-gauge factors. In addition, the highest strain gauge factor of the present device was measured in the ferromagnetic resonance regime. GMI ratios beyond 500% have already been reported for bigger NiFe multilayer GMI field sensors in the skin-effect regime and when magnetization rotation is the dominating reversal mechanism in the low-field regime. In the present case, complex domain-wall annihilations and creations dominate the reversal in the low-field regime and even lead to domain-wall resonances (DWR) in a distinct frequency regime. This could be proven by magneto-optical widefield microscopy and corresponding micromagnetic simulations of the magnetization dynamics. By optimizing the NiFe ratio of the sputtering target and the deposition parameters a nearly zero magnetostriction ($Ni_{80}Fe_{20}$) was realized for the sensor material. In contrast to low-magnetostrictive $Ni_{82}Fe_{18}$ (Fig. 2) the effective anisotropy field is not changing when applying compressive and tensile strain. This proves that even for thin film NiFe, which has been microstructured by means of lithography and which contains thin Ti spacer layers to bypass the critical thickness of emerging stripe domains, nearly zero magnetostriction can be reached. Therefore, ultraflexible GMI magnetic field sensors can be fabricated without the need of employing materials with high spin polarization and a high magnetostriction such as Co and Fe alloys, which are often deposited in TMR and GMR sensors. Additionally, no high-quality MgO or Al_2O_3 interfaces are necessary. In conclusion we show that thin-film GMI sensors have a very promising but not completely known potential on flexible substrates. Further optimization of the geometry is necessary and especially highly permeable materials with higher magnetostriction coefficient than that of NiFe ought to be investigated to analyze their full potential for strain or hybrid magnetic field and strain detection.

[1] A. Tavassolizadeh et al., Appl. Phys. Lett. 102(15), 153104 (2013) [2] A. Garcia-Arribas et al., IEEE Trans. Magn. 53, 2000605 (2017). [3] D. Karnaushenko et al., Adv. Mater. *27*(42), 6582 (2015) [4] G. Buettel et al., Appl. Phys. Lett. 111, 232401 (2017)

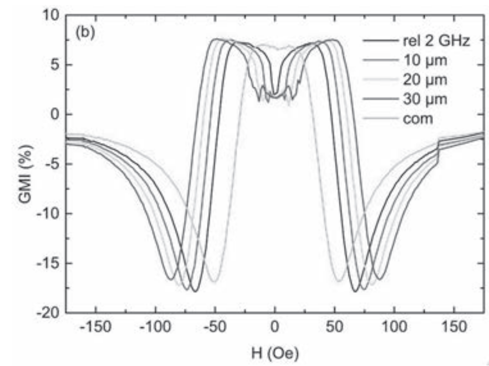

Fig. 1. Transport measurement for the cantilever in the relaxed (rel) and in a 10, 20, 30 µm tensely and 30 µm compressively (com) deflected state at an ac current frequency of 2 GHz in the FMR regime.

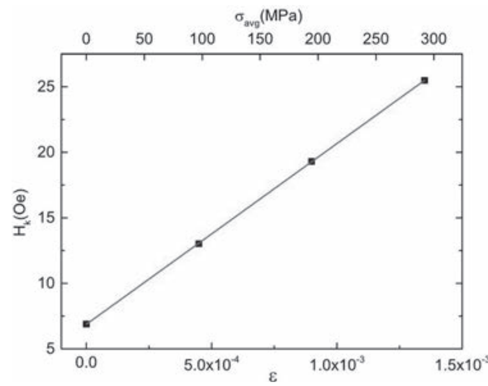

Fig. 2. Change of the effective anisotropy field under tensile stress/strain. The data was deduced from the shift of the peaks of the GMI curve in the skin-effect regime at an ac current frequency of 0.3 GHz.

EW-15. MgO-based Magnetoresistive Biosensor for Magnetically labeled Cells Detection.

S. Amara[1], R. Bu[2], M. Alawein[1] and H. Fariborzi[1]
1. CEMSE, King Abdullah University of Science and Technology (KAUST), Thuwal, Saudi Arabia; 2. Computer School of Physics. Shandong University, Jinan, China

Since the discovery of the giant magnetoresistance (GMR), many spintronic devices have been developed and used in various applications such as information storage and automotive industry. Nowadays, increasing research in the field of spintronics and its application in the development of magnetoresistive (MR) biomolecular and biomedical platforms is giving rise to a new family of biomedical sensors [1-3]. Magnetic tunnel junctions (MTJ), based on MgO barriers, are promising magnetic field sensor solutions in the framework of electronic components integration and miniaturization. MgO-based MTJs show superior sensitivity for the detection of small magnetic fields needed in many industrial and biomedical applications. MgO-based MR sensors have been integrated for biological applications, such as biochips. The concept, explained in [4] and [5], relies on the capability of the sensor for detection of the fringe field generated by magnetized nano/microparticles attached to biomolecules. In this work, we aim to implement MgO-based MR biosensors for measurement of the flux of magnetically labeled cells. As a representative schematic, the biochip in figure 1.a shows different components of the MR biosensor. Figure 1.b illustrates the concept with superparamagnetic beads. As shown, a magnetic bead above the sensor will be magnetized by the magnetic field generated by the current in the gold strip. The stray field of the bead can be sensed by the magnetic field sensor, if the magnetic bead is within its sensing space. When a larger number of magnetic beads labeling the cells are mobilized inside the micro-tube, a larger signal will be observed. We should mention that the manipulation of these particles and biomolecules requires handling fluidic samples. Moreover, the labeling particles should be handled under minimum aggregation, preferably in a paramagnetic state. We designed and fabricated MgO-based MR sensors presented in figure 2.a. Each sensor consists of 1200 elliptic 16*8 mm^2 pillars in series. MTJ multilayer films were deposited using a magnetron sputtering system (Singulus Rotaris) on thermally oxidized Si wafers. The MTJ stack used in this study had the following layer structure: (thicknesses in nanometers) Si/SiO2/ (3) Ru / (8) Ta / (3) Ru / (8) Ta / (3) Ru / (8) $MnIr_{20}$ / (2.3) $Co_{70}Fe_{30}$ / (0.85) Ru / (2.4) $Co_{60}Fe_{20}B_{20}$ (ferromagnetic pinned layer)/ (1.53) MgO / (1.45) $Co_{60}Fe_{20}B_{20}$ (magnetic free layer)/ (3) Ru / (8) Ta. MTJ stack was patterned into micron-sized elliptical devices using standard optical lithography and ion milling. A 150-nm-thick gold layer was deposited over the junction area and patterned into low-resistance electrical contacts for each MTJ. After patterning, the samples were annealed at 360 °C for 2 h at 1.10^{-6} Torr in an applied field of 8 kOe. The magnetoresistance properties of the MR sensors were measured at room temperature in air by a conventional DC four-probe method and current driven Helmholtz coils controlled with LabView. Figure 2.d shows the transfer curve of one of MR sensor. The results prove that the proposed MR sensor has great sensitivity and has linear response in the range of [-5 Oe -5 Oe]. In this work we propose a new design for MgO-based MTJ magnetoresistive biosensor and demonstrate its functionality for detection of magnetically labelled cells. More experiments are in progress to fully optimize and characterize the proposed device.

J. Germano, V. Martins, F. Cardoso, T. Almeida, L. Sousa, P. Freitas and M. Piedade, Sensors, 2009, 9, 4119–4137. B. M. de Boer, J. A. H. M. Kahlman, T. P. G. H. Jansen, H. Duric and J. Veen, Biosens. Bioelectron., 2007, 22, 2366–2370 R. S. Gaster, D. A. Hall and S. X. Wang, Lab Chip, 2011, 11, 950–956. P. P. Freitas et al., "Spintronic platforms for biomedical applications," Lab-on-Chip, vol. 12, no. 3, pp. 546–557, 2012. G. Li, S. X. Wang, and S. Shouheng, "Model and experiment of detecting multiple magnetic nanoparticles as biomolecular labels by spin valve sensors," IEEE Trans. Magn., vol. 40, pp. 3000–3002, 2004.

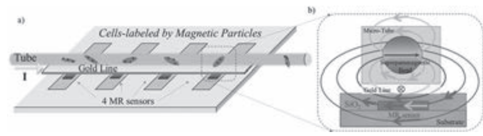

Fig. 1. (a) Magnetic biosensor system consisting of 4 MR sensors. Each sensor is composed of 1200 MTJ pillars, a gold strip that conducts current, and a micro tube for labeled cells. The MTJ sensor is underneath the gold strip; (b) Zoom-in of one of local TMR sensors: The current in the gold strip generates a magnetic field, which magnetizes the superparamagnetic bead labeling the cell. The stray field of the magnetic bead is detected by the MTJ. The blue lines represent the current-generated magnetic field with the black arrows on the lines pointing along the direction of the magnetic field. The orange lines represent the stray field of the magnetic bead with the orange arrows on the lines pointing along the direction of the stray field. The blue arrow inside of the magnetic bead represents the direction of the bead's magnetization.

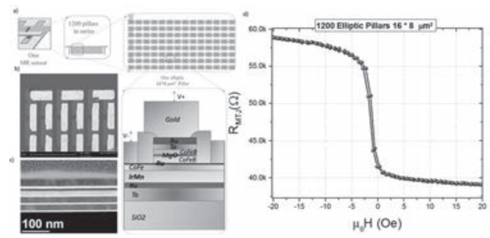

Fig. 2. (a) Zoom in of one MR sensor shows schematic image of an array of 1200 MTJ pillars in series, (b) SEM image of the serial MTJ pillars. (c) Scanning Transmission Electron Microscopy image (TEM) image of the MTJ multilayers. (d) Device transfer curve.

EW-16. Detection of magnetic nanoparticles by variation of magnetization dynamics of Co/Ni multilayer.

Y. Otaki[1], *T. Kato*[1], S. Okamoto[2], N. Kikuchi[2], D. Oshima[3], S. Iwata[3] and O. Kitakami[2]

1. Department of Electronics, Nagoya University, Nagoya, Japan; 2. Institute of Multidisciplinary Research for Advanced Materials, Tohoku University, Sendai, Japan; 3. Institute of Materials and Systems for Sustainability, Nagoya University, Nagoya, Japan

Biosensor technology to detect specific biomolecules such as protein and DNA has the potential to provide fast and accurate diagnosis of cancer and diabetes. Bio-functionalized magnetic nanoparticles are known to be sensitive and cost-efficient for labeling specific biomolecules, and the use of magnetic nanoparticles are also attractive for drug delivery by magnetic field gradient and heating therapy by alternating magnetic field. We consider spin wave biosensor to detect magnetic nanoparticles with high sensitivity, and in this paper we report the detection of Fe_3O_4 nanoparticles by the variation of magnetization dynamics of Co/Ni multilayers. Co/Ni multilayer is known to exhibit large perpendicular anisotropy [1] which is useful to create large field gradient at the surface by forming the maze domain structure, and the large field gradient was used to capture the Fe_3O_4 nanoparticles dispersed in liquid. Moreover, low Gilbert damping is reported in Co/Ni multilayers [2] which will be effective to detect the variation of magnetization dynamics by the adsorption of Fe_3O_4. In this experiments, we used water-based liquid containing 0.003 mol/L Fe_3O_4 nanoparticles with average diameter of 10 nm. The magnetization dynamics of Co/Ni multilayers were measured by vector network analyzer - ferromagnetic resonance (VNA-FMR) technique under static field of H_{dc} = 2 – 10 kOe along the film normal direction. Figure 1 shows (a) atomic force microscope (AFM) and (b) magnetic force microscope (MFM) images of Ta (2) / [Co (0.29) / Ni (0.71)]$_{10}$ / Ta (30) / SiO_2 substrate (thickness in nm) after adsorbing of Fe_3O_4 nanoparticles. Before adsorbing nanoparticles, the multilayer was demagnetized to form the maze domain structure as shown in Fig. 1 (b). In Fig. 1 (a), the adsorbed Fe_3O_4 nanoparticles were clearly seen as bright contrast, and the shape of the bright region is well consistent with the maze domain structure seen in Fig. 1 (b). This means that the large field gradient produced on the surface of Co/Ni multilayer effectively capture the nanoparticles dispersed in the liquid. Figure 2 (a) shows the applied field dependence of resonance frequency f_r of Ta buffered [Co (0.29 nm) / Ni (0.71 nm)]$_{10}$ multilayers with and without magnetic nanoparticles. The anisotropy field H_k of the Co/Ni multilayer estimated from Fig. 2 (a) was 2.6 kOe, and it increased to 3.7 kOe by adsorbing magnetic nanoparticles. Figure 2 (b) shows the dependence of full-width-half-maximum (FWHM) Δf_{50} of the resonance curve on the resonance frequency f_r. Anisotropy field dispersion ΔH_k and damping α were estimated from y-intercept and slope of the linear fits, respectively, and both were found to increase by adsorbing the nanoparticles. Similar results were also confirmed for Pt buffered Co/Ni multilayers. These results suggest the adsorption of Fe_3O_4 nanoparticles significantly modifies the magnetization dynamics of Co/Ni multilayer, and the Co/Ni is considered as a candidate material for spin wave sensors to capture and detect biomolecules.

[1] G. H. O. Daalderop *et al*., Phys. Rev. Lett., 68, 682 (1992). [2] T. Kato *et al*., IEEE Trans. Magn., 47, 3036 (2011).

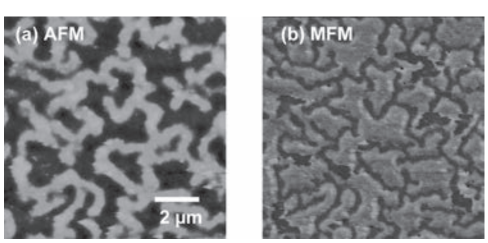

Fig. 1. (a) AFM and (b) MFM images of Ta buffered [Co (0.29 nm) / Ni (0.71 nm)]$_{10}$ multilayer after adsorbing of Fe_3O_4 nanoparticles. Before adsorbing nanoparticles, the multilayer was demagnetized to form the maze domain structure.

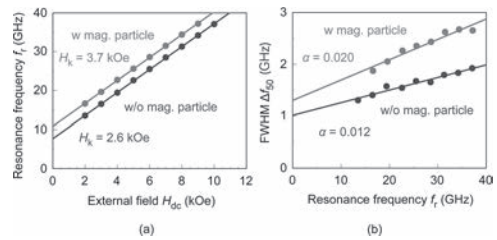

Fig. 2. (a) H_{dc} dependence of resonance frequency f_r and (b) f_r dependence of resonance line width Δf_{50} of Ta buffered [Co (0.29 nm) / Ni (0.71 nm)]$_{10}$ multilayers with and without magnetic nanoparticles.

THURSDAY AFTERNOON, 26 APRIL 2018 ORCHID I, 2:00 TO 5:00

Session FA
SYMPOSIUM ON TOPOLOGICAL AND COLLECTIVE MAGNETIC PHENOMENA

Anjan Soumyanarayanan, Co-Chair
Data Storage Institute, Singapore, Singapore
Fusheng Ma, Co-Chair
Nanyang Technological University, Singapore, Singapore

INVITED PAPERS

2:00

FA-01. Topology of magnonic bands: From chiral edge modes to spin superfluidity.

Y. Tserkovnyak[1]
1. Physics and Astronomy, UCLA, Los Angeles, CA, United States

Topological contrast in magnetic materials can lead to robust gapless modes, as dictated by an appropriate bulk-edge correspondence. I will discuss our recent proposal for engineering such an (chiral) edge mode in the coupled dynamics of magnetic solitons in a honeycomb lattice [1]. The existence of the chiral magnonic edge can be understood by mapping the system to the Haldane model for an electronic system. Extending the topological magnon-band arguments, we propose an emergent spin superfluidity in classes of rather mundane easy-axis magnets (both ferro- and antiferromagnetic), at their domain boundaries. We thereby suggest to utilize such domain walls for the establishment and manipulation of robust spin transport in magnetic insulators. The spin superfluidity at a topological boundary, furthermore, turns out to have several emergent topological properties that are absent in conventional superfluids. In particular, the phase-unwinding slips create and destroy skyrmions to obey the conservation of the total skyrmion number, which allows to use a domain wall as a generator and detector thereof.

[1] S. K. Kim and Y. Tserkovnyak, Physical Review Letters 119 (2017) 077204 [2] S. K. Kim and Y. Tserkovnyak, Physical Review Letters 119 (2017) 047202

2:30

FA-02. Topological Magnon Materials.

I. Mertig[1,2], A. Mook[1] and J. Henk[1]
1. Physics, Martin-Luther-Universität Halle-Wittenberg, Halle, Germany;
2. Max Planck Institute for Microstructure Physics, Halle, Germany

Topology has conquered the field of condensed matter physics with the discovery of the quantum Hall effect. Since then the zoo of topological materials is steadily increasing. In this talk, I demonstrate how to realize different topological phases with magnons: the magnon pendants to topological insulators [1] as well as Weyl [2] and nodal-line semimetals are presented [3]. Magnon bulk spectra are characterized by topological invariants, dictating special surface properties. For instance, the bulk bands of topological magnon insulators (TMIs) carry nonzero Chern numbers, causing topological magnon edge states that revolve unidirectionally the sample [1]. Magnon Weyl semimetals possess zero-dimensional band degeneracies acting as source and sink of Berry curvature; at their surface they feature "magnon arcs" connecting the surface projections of Weyl points [2]. Magnon nodal-line semimetals exhibit one-dimensional band degeneracies, i. e., closed loops in reciprocal space. Surface projections of these nodal lines host "drumhead" surface states whose details depend strongly on the surface termination [3]. Similar to the electronic case, nonzero Berry curvature causes transverse transport, that is, magnon Hall effects [1]. I show how these effects can be quantified by classical spin dynamics simulations of the TMI Cu(1,3-benzenedicarboxylate) [4] and a skyrmionic TMI [5].

[1] H. Katsura et al., Phys. Rev. Lett. 104, 066403 (2010); Y. Onose et al., Science 329, 297 (2010); R. Matsumoto et al., Phys. Rev. Lett. 106, 197202 (2011); L. Zhang et al., Phys. Rev. B 87, 144101 (2013); A. Mook et al., Phys. Rev. B 89, 134409 (2014); A. Mook et al., Phys. Rev. B 90, 024412 (2014) [2] F.-Y. Li et al., Nature Commun. 7, 12691 (2016); A. Mook et al., Phys. Rev. Lett. 177, 157204 (2016) [3] A. Mook et al., Phys. Rev. B 95, 014418 (2017) [4] Chisnell et al., Phys. Rev. Lett. 115, 147201 (2015); Hirschberger et al., Phys. Rev. Lett. 115, 106603 (2015); A. Mook et al., Phys. Rev. B 94, 174444 (2016) [5] A. Mook et al., Phys. Rev. B 95, 020401(R) (2017)

3:00

FA-03. Quantum anomalous Hall effect and topological Hall effect in magnetic topological insulators.

Y. Wang[1]
1. Tsinghua University, Beijing, China

The interplay between the nontrivial topology and broken time reversal symmetry in topological insulator (TI) can lead to exotic quantum phenomenon such as the quantum anomalous Hall effect. However, there are still many open questions regarding the mechanism of magnetic order and magneto transport in TI. In this talk, we present transport studies on magnetically doped TI thin films grown by molecular beam epitaxy. We found a variety of interesting transport phenomena by varying the magnetic dopants, film thickness, applied electric field, and device geometries. In Cr doped Bi2(Se,Te)3 near a topological quantum critical point, we found a gate-tuned ferromagnetic to paramagnetic phase transition. We propose that the most likely mechanism is the Stark effect induced electronic energy level shift, which causes a topological quantum phase transition followed by magnetic phase transition. In Mn doped Bi2Te3, we observe pronounced topological Hall effect only at a specific film thickness at the dimensional crossover regime. We propose that this is due to the coupling between the top and bottom surface states, which stabilizes the magnetic skyrmion structure. More recently, we construct a bilayer structure consisting of two magnetic topological insulator films with different coercivity. By using a moderate magnetic field, we can drive the system from a quantum anomalous Hall phase with chiral edge states to a synthetic quantum spin Hall phase with helical edge states.

1. Zuocheng Zhang et al., “Magnetic quantum phase transition in Cr-doped Bi2(SexTe1-x)3 driven by the Stark effect “, Nature Nanotechnology 12, 953 (2017) 2. Chang Liu et al., “Dimensional Crossover-Induced Topological Hall Effect in a Magnetic Topological Insulator”, Physical Review Letters 119, 176809 (2017)

3:30

FA-04. Mixed semimetals for magnetization and momentum space topology control.

J. Hanke[1], C. Niu[1], F. Freimuth[1], G. Bihlmayer[1], S. Bluegel[1] and *Y. Mokrousov*[1]
1. IAS-1, Forschungszentrum Julich, Juelich, Germany

The topological properties of magnets, encoded in the reciprocal space distribution of the Berry phase, have caused a revolution in our understanding of their transport and response properties. By focusing on two-dimensional spin-orbit-gapped ferromagnetic materials, we uncover the richness of their topological phase diagrams as a function of the magnetization direction and its magnitude. We further uncover that the phase transitions between various topological states, which manifests in an emergence of topological metallic features in the electronic structure, can be best understood by referring to the topology of the "mixed" space of k-vectors and magnetization direction. We show that non-trivial topological features such as mixed Weyl points and mixed nodal lines not only give rise to complex topological phases in the k-space of two-dimensional magnetic materials, but also manifest in "singular" magnetic properties. Namely, we predict that in 2D magnetic systems with non-trivial mixed topologies the strength of orbital magnetism and magneto-electric response, as manifested e.g. in the magnitude of the current-induced spin-orbit torques and Dzyaloshinskii-Moriya interaction, can exceed significantly that of conventional metallic magnets. Given that the direction of the magnetization in complex spin-orbit ferromagnets can be efficiently controlled by spin-orbit torques, our findings open new perspectives in low-dissipation control of magnetization and topological phases in low-dimensional magnetic materials. This work was supported by the DFG under Grant No. MO 1731/5-1 and SPP 1666, by the EU Horizon 2020 research and innovation programme under grant agreement number 665095 (FET-Open project MAGicSky), and by the DFG through the Collaborative Research Center SFB 1238.

[1] Garello et al., Nature Nanotech. 8, 587 (2013) [2] F. Freimuth, S. Blugel and Y. Mokrousov, J. Phys.: Cond. Mat. 26, 104202 (2014) [3] J.-P. Hanke, F. Freimuth, C. Niu, S. Blugel and Y. Mokrousov, Nature Comm. 8, 1479 (2017)

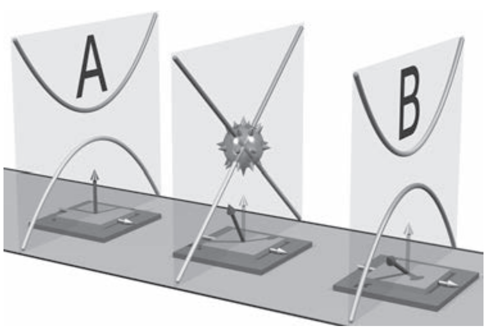

Fig. 1. In mixed Weyl semimetals, the presence of metallic points in the mixed space of the k-vectors and magnetization direction can be utilized for generating strong anti-damping spin-orbit torques, which provide an efficient tool for low-dissipation switching between different topological phases in reciprocal space.

4:00

FA-05. Topological bands and topological phase transitions in electronic and magnonic systems.

S. Murakami[1,2]
1. Department of Physics, Tokyo Institute of Technology, Tokyo, Japan;
2. TIES, Tokyo Institute of Technology, Tokyo, Japan

In electronic systems, various interesting phenomena such as spin Hall effect and topological insulators originate from Berry curvature of Bloch wave-functions. We theoretically study analogous phenomena for magnons (spin waves). We propose that the dipolar interaction gives rise to nonzero Berry curvature [1-3]. In a thin-film ferromagnet in a long-wavelength regime, we can calculate the Berry curvature for each magnonic band, and only when the magnetic field is out-of-plane, the Berry curvature is nonzero. When the exchange coupling is included, the magnonic bands are modified, and there appear a number of band anticrossing points. Around such an anti-crossing point, the Berry curvature is enhanced. This Berry curvature gives rise to thermal Hall effect of magnons [1,2], and it also gives rise to a shift of wavepackets in reflection or refraction [3]. Furthermore, in analogy to the quantum Hall effect for electrons, we can design topological magnon band structure. By introducing artificial spatial periodicity into the magnet, for example by fabricating nanostructures with two different magnets in a periodic structure or by making a periodic array of nanomagnets, we theoretically propose emergence of topological edge modes, analogous to those in electronic quantum Hall effect. The edge modes are chiral, and propagate along the edge of the magnet in one way. We call this a topological magnonic crystal [4,5]. As a related subject, we also have been studying topological phase transitions. It leads to the notion of topological semimetals in the context of electronic band structures. In particular, in the Weyl semimetal [6,7], which is an example of topological semimetals, the band structure has nondegenerate 3D Dirac cones in the bulk. We show that in a transition between topological and ordinary insulators, the Weyl semimetal phase necessarily appears, for any inversion-asymmetric crystals [6,8]. This transition from an insulator to the Weyl semimetal is realized for example in tellurium (Te). At high pressure the band gap of Te decreases and it runs into a Weyl semimetal phase, as shown by our ab initio calculation [9]. As various examples show, transitions between different topological phases with a gap are universal, and they depend only on dimensionality and symmetry. For example in three dimensions with broken inversion or time-reversal symmetry, such topological phase transitions usually accompany a topological semimetallic phase between them. This topological evolution of band structure applies to magnon band structures as well.

[1] R. Matsumoto and S. Murakami, Phys. Rev. Lett. 106, 197202 (2011); Phys. Rev. B 84, 184406 (2011). [2] R. Matsumoto, R. Shindou, and S. Murakami, Phys. Rev. B 89, 054420 (2014). [3] A. Okamoto, S. Murakami, Phys. Rev. B 96, 174437 (2017); S. Murakami and A. Okamoto, J. Phys. Soc. Jpn. 86, 011010 (2017). [4] R. Shindou, R. Matsumoto, S. Murakami, and J. Ohe, Phys. Rev. B 87, 174427 (2013). [5] R. Shindou, J. Ohe, R. Matsumoto, S. Murakami, and E. Saitoh, Phys. Rev. B 87, 174402 (2013). [6] S. Murakami, New J. Phys. 9, 356 (2007); S. Murakami and S. Kuga, Phys. Rev. B 78, 165313 (2008). [7] X. Wan, A. M. Turner, A. Vishwanath, S. Y. Savrasov, Phys. Rev. B 83, 205101 (2011). [8] S. Murakami, M. Hirayama, R. Okugawa, S. Ishibashi, T. Miyake, Sci. Adv. 3, e1602680 (2017). [9] M. Hirayama, R. Okugawa, S. Ishibashi, S. Murakami, and T. Miyake, Phys. Rev. Lett. 114, 206401 (2015).

4:30

FA-06. Magnonic Topological Materials and Devices.

X. Wang[1,2] and X. Wang[3,1]
1. Physics, The Hong Kong University of Science and Technology, Kowloon, China; 2. HKUST Shenzhen Research Institute, Shenzhen, China; 3. University of Electronic Science and Technology of China, Chengdu, China

Topological matters have attracted enormous attention in recent years because of their interesting and exotic properties. One such property is the existence of unidirectional and topologically protected surface/edge states that are robust against internal and external perturbations. The study was initially exclusive for electron systems and was believed to be a quantum phenomenon. It is now known that the topological states can exist in classical mechanics and photonics. Topological states can also exist in magnetic materials govern both by quantum mechanics at the zero temperature and by classical magnetization dynamics at finite temperatures. In fact, topological states do not depend on the detail of their underlying dynamics, whether it is Newtonian mechanics for vibrations or Maxwellian equations for lights, or Schrodinger/Dirac equations for electrons. So far, the important ingredients are the collective modes form inverted bands with gap in the bulk. Magnetic materials are highly correlated spin systems that do not respect the time-reversal symmetry. The low-energy excitations of magnetic materials are spin waves whose quanta are magnons. In the ambient temperature that is far below the Curie temperature, the magnetization dynamics of real magnetic material shall be govern by the Landau- Landau-Lifshitz-Gilbert (LLG) equation. Like electronic materials that can be topologically nontrivial, magnetic materials govern by the LLG equation can also be topologically nontrivial with topologically protected edge spin waves. Unlike the normal spin waves that are very sensitive to the system changes and geometry, these edge spin waves are robust against internal and external perturbations such as geometry changes and spin wave frequency change. Therefore, the magnetic topological matter is of fundamental interest and technologically useful in magnonics. We will see several examples of magnonic topological materials, including pyrochlore [1] and stacked honeycomb [2] ferromagnets as Weyl magnons, as well as perpendicularly magnetized two-dimensional films with Dzyaloshinskii-Moriya and/or pseudodipolar interactions as generic magnonic insulators [3,4]. The edge spin waves in these magnonic materials are robust against perturbations. Interesting functional magnonic devices called beamsplitter and interferometer can be made out of a domain wall in a strip. It is shown that an in-coming spin wave beam along one edge splits into two spin wave beams propagating along two opposite directions on the other edge after passing through a domain wall. This work was supported by National Natural Science Foundation of China (Grant No. 11374249) and Hong Kong RGC (Grant No. 16301115 and 16301816).

1) "Magnonic Weyl semimetal and chiral anomaly in pyrochlore ferromagnets", Ying Su, X.S. Wang, and X.R. Wang, Phys. Rev. B 95 (22), 224403 (2017). 2) "Chiral anomaly of Weyl magnons in stacked honeycomb ferromagnets, Ying Su and X. R. Wang, Phys. Rev. B 96, 104437 (2017). 3) "Topologically protected unidirectional edge spin waves and beam splitter", X.S. Wang, Ying Su, and X.R. Wang, Phys. Rev. B 95 (1), 014435 (2017) 4) "Reconfigurable topological spin wave beamsplitters and interferometers", X. S. Wang, H. W. Zhang, and X. R. Wang, arXiv:1706.09548

THURSDAY AFTERNOON, 26 APRIL 2018 ORCHID III, 2:00 TO 5:00

Session FB
HARD MAGNETIC MATERIALS AND PROCESSING I

Alberto Bollero, Chair
IMDEA Nanoscience, Madrid, Spain

CONTRIBUTED PAPERS

2:00

FB-01. Remanence enhancement melt-spun *Nitroquench* $Sm_2Fe_{17}N_3$.

M. Coey[1], P.S. Stamenov[1], M. Venkatesan[1], S.B. Porter[1] and T. Iriyama[2]
1. School of Physics, Trinity College Dublin, Dublin, Ireland; 2. Daido Electronics Company, Nagoya, Japan

The discovery of the interstitial rare earth nitride $Sm_2Fe_{17}N_3$ came about seven years after the discovery of the rare earth iron boride $Nd_2Fe_{14}B$ [1,2], and the nitride initially seemed to offer intrinsic magnetic properties that were superior (Curie temperature T_C, magnetocrystalline anisotropy K_1) or comparable (spontaneous magnetization M_s) to those of its illustrious predecessor. However, the promise of the new material to seriously challenge $Nd_2Fe_{14}B$ was not realized. The 2:17 nitride powder, prepared by a low-temperature gas-phase interstitial modification process proved difficult to orient and worse still, it lost its nitrogen at the temperatures needed to process dense sintered magnets [3]. Attempts at explosive compaction [4] or spark sintering [5] failed to yield material with good enough coercivity. Nevertheless, work continued in Japan and China to develop a coercive powder that could be used for bonded magnets. An early realization was zinc-bonded $Sm_2Fe_{17}N_3$ [6] with an energy product of 84 kJm^3 but a rather low coercivity of 480 kAm^{-1}, less than 5 % of the anisotropy field ($H_a = 2K_1/M_s \approx 11$ MAm^{-1}). The anisotropy field of $Nd_2Fe_{14}B$ is significantly less (6 MAm^{-1}) yet several decades of intensive development have led to higher values and continuous improvements of the coercivity, even in unsubstituted material. Historical experience with permanent magnets shows that a long period of materials development is needed to arrive at the best composition and processing conditions tfor a microstructure that allows the hard magnetism to be optimized. Coercivities of about 25% of the anisotropy field are utimately achieved. Here we compare the magnetic properties of melt-spun material. Our *Nitroquench* powder, produced by Daido Steel, was in the form of flakes 10 μm thick and up to 100 μm in diameter. A crystallite size of approximately 15 nm deduced from Scherrer broadening of the X-ray reflections. Composition was checked by EDX microprobe analysis. Hysteresis loops have been measured in applied fields of up to 14 T, at room temperature and at 4 K.The material exhibits a room-temperature coercivity of 690 kAm^{-1}after saturation in 14 T, with a remanence of 700 kAm^{-1} in zero applied field and an extrapolated saturation magnetization of 1230 kAm^{-1}. The remanence ratio M_r/M_s of 63% when the remanence is corrected to zero internal field, is reflected in a preferred orientation seen in the X-ray powder diffraction patterns and in ^{57}Fe Mössbauer spectra of magnetized powder. Spectra obtained after saturation of an immobilized powder absorber either in-plane or perpendicular to the sample plane exhibit distinctly different relative intensities of the $\Delta M = 0$ absorption lines. The maximum energy product for the powder, assuming full density, is 162 kJm^{-3}. The remanence enhancement is attributed to fact that the nanocrystallite size is not much greater than the exchange length. Melt-spun Sm-Fe-N powder has superior corrosion resistance and thermal stability compared to melt-spun Nd-Fe-B. The *Nitroquench* powder may be used to produce polymer-bonded magnets with an energy product in excess of 100 kJm^{-3}.

[1] J M D Coey and Sun Hong, J Magn Magn Mater 87 L251-254 (1990) [2] T. Iriyama et al, IEEE Trans. Magn., 28 2326 (1992) [3] R. Skomski, Ch 4 in *Rare-Earth Iron Permenent Magnets* (J. M. D. Coey editor) Clarendon Press, Oxford 1995 [4] W. Kaszuwara et al, J. Mater. Sci; Materials in Electronics 9, 17 (1998) [5] T. Saito, J. Magn. Magn. Mater 369 184 (2014) [6] Y Otani et al, J Appl Phys 69 6735-6737 (1991)

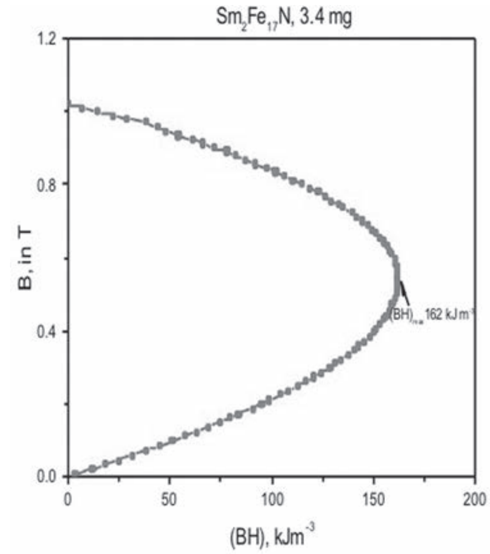

Fig. 1. Energy product of *Nitroquench* powder at room temperature. The measured magnetization is expressed as that of the fully dense material.

2:15

FB-02. Preparation and characterization of phenol formaldehyde bonded Nd-Fe-B magnets with high strength and heat resistance.

W. Xi[1], W. Liu[1], *M. Yue*[1], D. Zhang[1], Q. Lu[1], H. Zhang[1], Q. Wu[1] and Y. Li[1]
1. College of Materials Science and Engineering, Beijing University of Technology, Beijing, China

I. INTRODUCTION Bonded Nd-Fe-B magnets are widely used in the fields of electrical appliances, automation equipment and automobile due to their stable magnetic properties, and easy processing into smaller [1-3]. However, the use of epoxy (EP) bonded magnets is limited because of poor mechanical properties and low heat resistance of epoxy. In this work, phenol formaldehyde resin (PF) was considered as a binder for NdFeB magnets because PF has high temperature resistance properties and excellent bonding properties. The magnetic properties, mechanical properties and fracture morphology were investigated. The results show that PF can endow high temperature resistance and excellent mechanical properties to the material. II. EXPERIMENTS PF/NdFeB bonded magnets were prepared by compression molding. First, NdFeB powders and PF were pre-mixed to get uniform mixture. Then, the mixture was transferred into a mold to moulded and densified with isostatic pressing. Finally, the magnets were obtained by curing in the oven. The magnetic properties of PF/NdFeB bonded magnets at 20^{o}C and 200^{o}C were tested by B-H hysteresis loop tracer. The compressive strength was measured by electronic tensile testing machine. The fracture surface observation and composition analysis for crushed magnets was performed on the Scanning Electron Microscope (SEM) with the Energy Dispersive X-ray (EDX). III. RESULTS AND DISCUSSIONS In Fig.1(a), Br, Hcj and (BH)max of 2.5 wt.% PF/NdFeB magnets can reach 6.659kG, 9.569kOe and 9.573MGOe respectively at room temperature. The results are close to 2.5 wt.%EP/NdFeB magnets data of the same process, and this means that PF binder has no effect on magnetic properties during the preparation of Nd-Fe-B bonded magnets. The magnetic properties of NdFeB will decrease with the increased of temperature. From our previous work, EP/NdFeB magnetic data were not obtained because epoxy can't keep the original shape of magnet at 200^{o}C. While PF/NdFeB magnets the magnets still has usable magnetic properties at 200^{o}C in this work. The reason is that the main chain of PF binder molecule containing rigid structure, which can form the strong cross-linking network structure with high temperature resistance during the curing process. Therefore, the bonded magnets can keep the shape and usable magnetic properties at 200^{o}C. While the magnetic properties are satisfied, the mechanical properties are important factors for the application. Fig.1(b) shows that with the increasing of binder content, the compressive strength of PF/NdFeB magnets were increased effectively. The compressive strength of 4 wt.% PF/NdFeB increased to 253.6MPa, which was 15 times higher than EP/NdFeB magnets. In order to further disclose the mechanism of compressive strength enhancement, SEM photos and EDX analysis of fracture surface morphology were obtained from 4 wt.% PF/NdFeB, and it was illustrated in Fig.2(a-g). Fig.2(a) shows that the morphology of facture surface is very smooth, this suggests that the magnet has higher compactness. To further explore PF how to work with magnetic powders, the facture surface was investigated by EDX analysis. We have carried out line and point scanning for randomly selected gaps in Fig.2(b), according to the elements distribution, the results shows that PF binder can be enriched in the gaps of magnetic powders from Fig.2(c-d). In sum, the mechanism of compressive strength enhancement can be inferred according to the discussed results. On the one hand, liquid PF binder can endow magnetic powder better liquidity to obtain higher compact magnets in the process of molding. More importantly, the main chain of PF binder molecule containing rigid structure (benzene ring), it can form the hard cross-linking network structure in the gaps of magnetic powders to combine tightly during the high temperature curing process. Two mechanisms of action can effectively increase the mechanical properties. IV. CONCLUSIONS The binder PF was applied in NdFeB bonded magnets. The magnetic properties, mechanical properties and fracture morphology have been investigated. We also researched the reason of the high temperature resistance and the mechanism of compressive strength enhancement by SEM-EDX analysis. PF as a kind of excellent binder can increase the working temperature and the compressive strength of NdFeB bonded magnets obviously. Therefore, it would have a wide application prospect. ACKNOWLEDGEMENT This work was supported by the National Natural Science Foundation of China (Nos. 51331003 and 51371002).

[1] Z. Q. Wang, J. He, Appl. Mech. Mater., 345, 218-222 (2013). [2] M. I. Qadeer, S. J. Savage, U. W. Gedde, M. S. Hedenqvist, J. Mater. Sci., 49, 7529-7538 (2014). [3] L. Kelhar, J. Zavašnik, P. McGuiness, S. Kobe, J. Magn. Magn. Mater., 419, 171-175 (2016).

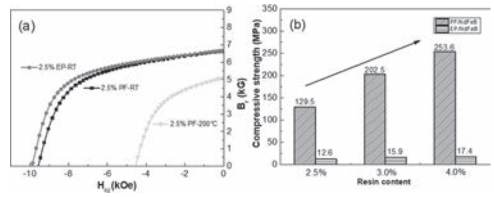

Fig. 1. Demagnetization curves at 20^{o}C and 200^{o}C bonded NdFeB magnets with 2.5wt.% PF and 2.5wt.% EP (a) and compressive strength data (b) of bonded NdFeB magnets with different phenolic resin content

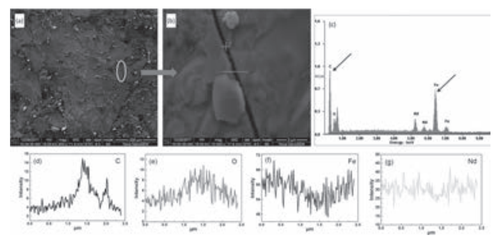

Fig. 2. Analysis of fracture surface morphology by SEM-EDX. (a) Fracture morphology. (b) EDX analysis of one area in picture (a). (c) The element content of line scan and point scan. (d-g) The EDX results of concentration elements distribution of C, O, Nd and Fe.

2:30

FB-03. Effects of initial alloy on microstructure and magnetic properties during hot-deformation of Nd-Fe-B HDDR powder.

J. Lee[1], J. Yoo[1,2], Y. Baek[1], D. Lee[2] and H. Kwon[3]
1. Korea Institute of Materials Science, Changwon, The Republic of Korea; 2. Pusan National University, Pusan, The Republic of Korea; 3. Pukyong National University, Pusan, The Republic of Korea

High coercive Nd-Fe-B magnets are indispensable materials to traction motors in hybrid and electric vehicles. However, substitution of heavy rare earth element (HRE) such as Dy or Tb for Nd has been necessary for high coercive Nd-Fe-B magnets despite the critical problem of supply and demand with HRE. Therefore, HRE-lean and/or HRE-free high coercive Nd-Fe-B magnets have drawn a great attention to solve HRE resource problem in the automotive industry [1]. To achieve high coercivity with reducing HRE, the control of microstructures, such as grain size and grain boundary, is of significant importance. Melt-spinning and hydrogenation–disproportionation–desorption–recombination (HDDR) are known as quite suitable method to decrease grain size down to the single domain size (~250nm). It addition, hot-deformation is known as a useful method to obtain anisotropic magnets with magnetic powders produced by these methods. On the other hand, the coercivity of hot-deformed Nd-Fe-B magnets was too low to be used for motors of hybrid and electric vehicles even though they had submicron grain size. It is because of the presence of crystallographic defects, low anisotropic energy at the grain surface, and exchange coupling between neighboring grains, which could be improved by grain boundary diffusion process (GBDP) with HRE compounds or non-magnetic materials. However, the GBDP of ultrafine grained materials produced with melt-spun powders should be done at a temperature, lower than about 700 °C. The GBDP above 700 °C could induce remarkable grain growth and low coercivity. On the other hands, HDDR powder has relatively large grains about 250~400 nm compared to melt-spun powders, so the grain growth does not occur at temperature up to about 850 °C. Therefore, it can be expected that hot-deformed magnets produced with HDDR powder have an advantage for subsequent GBDP compared to that of the melt-spun powder. However, there were only a few studies examining the hot-deformation behavior of HDDR powders and the reported magnetic properties were relatively poor. On the other hand, numbers of research reveal that rare earth-rich phase is critical factor to the texture formation during the hot-deformation process. So, it is expected that the microstructure of initial alloy could effect on the deformation behavior during hot-deformation process. Therefore, in this study, effect of initial alloy on microstructure and magnetic properties during hot-deformation of Nd-Fe-B HDDR powder was investigated. Alloy with composition of $Nd_{12.5}Fe_{bal}Ga_{0.3}Nb_{0.2}B_{6.4}$ prepared by strip-casting process was used as a starting material. The alloy was subjected to HDDR process after pre-annealing (SC-HT) at 1100 °C for 12 hours or without pre-annealing (SC). Produced HDDR powders were then hot-pressed at 700 °Cunder 400 MPa in a vacuum. The cylindrical compact with 7 mm in diameter and 6 mm in height were then die-upsetted at 800 °C with deformation degree of ε= 1.5 and deformation rate of ε'=~0.01 s^{-1}. Figure 1 shows magnetic properties and microstructure of each initial HDDR powder. The remanence of the powders is similar. However, their coercivity is diffenent about 1 kOe. This could be attributed to that the SC_HT HDDR powder have non-uniform and discontinuous Nd-rich phase distribution in grain boundary which can decrease coercivity by magnetic coupling between neighbor grains although it is not clear from SEM image as shown in Fig. 1 (b) and (c). Figure 2 shows demagnetization curve ((Fig. 2 (a)) and microstructure of hot-deformed magnets which is deformed using SC_HDDR powder (Fig. 2 (b)) and SC_HT (Fig.2 (c)), respectively. The remanence of hot-deformed magnet with SC_HT HDDR powder is lower than that with SC_HDDR powder. The difference in the remenance could be attributed to the fact that the distribution of the Nd-rich phase of the grain boundary may be affected by the hot deformation behavior which could be confirmed from Fig. 2 (b) and (c). This non-uniformed Nd-rich phase of grain boundary can make it difficult to grain boundary sliding during the hot-deformation process, which induce poor grain alignment and low remanence. Based upon these results, effect of initial alloy on microstructure and magnetic properties during hot-deformation of Nd-Fe-B HDDR powder will be discussed. Fig. 1. Demagnetization curve (a) of obtained HDDR powders and FESEM images of SC_ HDDR powder (b) and SC_HT HDDR powder. Fig. 2. Demagnetization curve (a) of hot-deformed magnet and FESEM images of hot-deformed magnet with SC_HDDR powder (b) and hot-deformed magnet with SC-HT HDDR powder (c).

[1] K. Hono and H. Sepehri-Amin, Scr. Mater.67, 530 (2012).

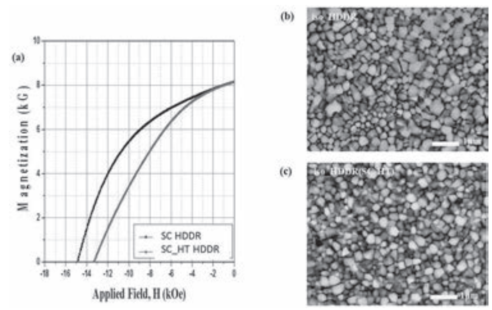

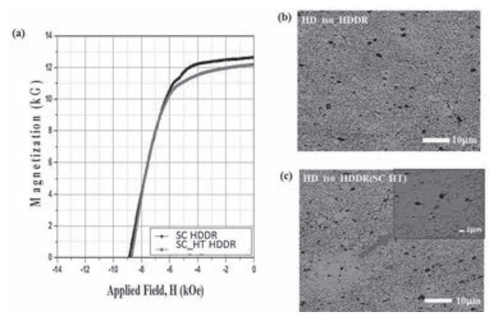

2:45

FB-04. Comparison of two Magnetizing Fixture Designs to Achieve Radial Magnetization Profile for Isotropic Bonded Neo Magnets.

R.C. Angara[1], K.W. Hsu[1], P.J. Villar[1] and N.K. Sheth[1]
1. R&D Magnequench, Magnequench Neo Powders Pte Ltd, Singapore, Singapore

The requirement of stringent environment and fuel efficiency target on automotive demand the use of lighter, smaller and efficient motors. The advantages like higher magnetic properties than ferrite, near net shape magnet production, and no use of heavy rare earth elements makes the use of bonded neo magnet in an automotive accessory motors very attractive. The isotropic nature of bonded neo magnets offers a feasibility to obtain wide range of magnetization profiles. The magnetization of the magnet influences the air-gap flux distribution and hence the motor performance[1]. The performance of permanent magnet motors using isotropic bonded neo magnet can be improved by optimizing the air-gap flux profile using magnetization. Based on the magnet circumference touching the motor air-gap and the desired magnetization profile, an appropriate magnetization fixture needs to be designed. In an external rotor permanent magnet brushless (PMBL) DC motor and brushed DC motors, the inner circumference of the magnet touches the airgap and hence the magnet is magnetized using an inner-only fixture which has magnetization coils next to the inner circumference of the magnet. When the radial magnetization is desired, a double sided magnetization can also be used to magnetize bonded neo ring magnets[2]. The use of double sided magnetization helps in enhancing the motor performance[3]. To ensure that the bonded neo magnet is fully saturated a minimum magnetizing field of around 3T is to be generated throughout the magnet thickness[4]. Considering this required magnetizing field, a fixture each offering inner-only and inner-outer magnetization (double sided magnetization) is designed using Finite element analysis (FEA) to achieve the radial magnetization. The simulation based results on the performance comparison of two fixtures is summarized. Figure 1 shows the simulated mid airgap flux density when magnet is magnetized with inner-only and inner-outer magnetizing fixtures. From this figure it is observed that, compared to inner-only fixture, the inner-outer fixture results in flat topped radial wave shape of flux density. Both designed fixtures are fabricated and the measured performance is used to validate the simulation results. It is observed that the peak magnetizing current and the energy required to achieve the magnet saturation in an inner-outer fixture is 19.8% and 26.5% less respectively compared to inner only fixture. The reduction in peak magnetizing current and magnetization energy requirement will lead to reduced thermal stress and improved fixture reliability. It will also help in reducing the magnetization cycle time due to better heat dissipation in inner-outer fixture. During magnetization of the magnet, the effectiveness of the inner-outer fixture depends highly on the alignment of the inner and outer magnetization coils. The alignment and hence the performance of the fixture is influenced by the fabrication tolerances[5]. Even a small misalignment between the coils on either side of the magnet will result in flux waveform distortion and reduction in magnetic flux. Considering the manufacturing tolerances, the effect of the various misalignment angles between the inner and outer magnetization coils on the magnet flux is arrived at using the FEA based simulation. The magnetization result is also measured by creating various misalignments between the inner and outer magnetization coils in the fabricated inner-outer magnetization fixture. Table I gives the measured magnet flux integral for various misalignment angles. It is observed from Table I that the ±2° mechanical misalignment between the coils will not result in significant change in magnet flux and higher misalignment angles will result in considerable reduction of flux per pole. It is also observed that the misalignment effect is symmetric about the aligned position and higher degree of misalignment causes drooping wave shape on one side and a hump on the other side in any given pole depending on the direction of misalignment.

[1] Seok-Myeong Jang, Han-Wook Cho, Sung-Ho Lee, Hyun-Sup Yang, and Yeon-Ho Jeong, "The influence of magnetization pattern on the rotor losses of permanent magnet high-speed machines," *IEEE Trans. Magnetics*, vol 40, no 4, Jul. 2004. [2] C. D. Riley, G. W. Jewell, and D. Howe, "Design of impulse magnetizing fixtures for the radial homopolar magnetization of isotropic NdFeB ring magnets," *IEEE Trans. Magnetics*, vol 36, no 5, Sep. 2000. [3] Jaenam Bae, Seung-Joo Kim, Sung-Chul Go, Hyung-Woo, Yon-Do Chun, Cheol-Jick Ree, and Ju Lee, "Novel configuration of the magnetizing fixture for a brushless permanent-magnet motor," *IEEE Trans. Magnetics*, vol 45, no 6, Jun. 2009. [4] Nimitkumar K. Sheth, Raghu C. S. Babu Angara, "Effect of partial saturation of bonded neo magnet on the automotive accessory motor," in *AIP Advances*, vol 7, issue 5, 2016. [5] C. J. Lee, C. I. Lee, and G. H. Jang, "Source and Reduction of Uneven Magnetization of the Permanent Magnet of a HDD Spindle Motor," *IEEE Trans. Magnetics*, vol 47, no 7, Jul. 2011.

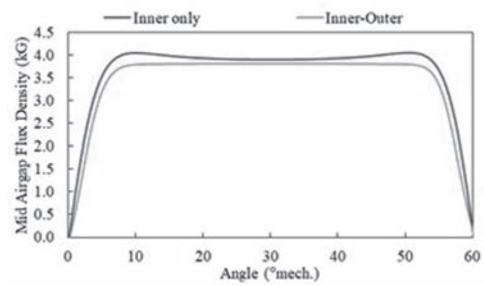

Fig. 1. Simulated mid airgap flux

Position	Misalignment Angle	Magnet flux integral (kG-°mech)	Change in integral
1	5°	166.55	-3.8%
2	3°	168.49	-2.7%
3	1.5°	172.68	-0.3%
4	0°	173.17	0%
5	-1°	172.99	-0.1%
6	-2°	172.35	-0.5%

TABLE I Magnet Flux Integral at Various Misalignment Positions Between Inner and Outer Magnetization Coils

3:00

FB-05. Desirable Measurement on Accurate Hysteresis Curve for Large Nd-Fe-B Sintered Magnets at Elevated Temperatures.

H. Nishio[1,2] and K. Machida[1]
1. Division of Applied Chemistry, Osaka University, Suita, Japan;
2. Research Institute for Measurement of Magnetic Materials, Yokohama, Japan

1. Introduction Nd–Fe–B sintered magnets have excellent intrinsic coercivity (H_{cJ}). They are widely used in motor generators and electric power steering and compressor motors for electric vehicles. Hence, it is very important to determine with accuracy the magnetic properties of magnets at elevated temperatures. To provide an accurate hysteresis curve in large Nd-Fe-B sintered magnets with high H_{cJ} at elevated temperatures, we compared the magnetization curves obtained from the following methods: superconducting magnet-based vibrating sample magnetometer (SCM-VSM) and the hysteresis graph (HG) which is widely used [1]. Attention was paid to the values of the differential susceptibility (dJ/dH) near H_{cJ} related to the squareness ratio (H_k/H_{cJ}) and the distribution of nucleation fields, where H and H_k are the magnetic and knee fields, respectively [1], [2]. 2. Experiment The samples with different shapes were machined from the same Nd-Fe-B sintered magnet block. To prevent the effects of machining on the magnetic properties, we used $S/V \leq 1.0$ mm^{-1}, where S and V are the surface area and volume, respectively [3]. The cylindrical samples used for the HG method had a diameter (D) of 10 mm and lengths (L) of 7, 14, and 21 mm ($S/V = 0.5 – 0.69$ mm^{-1}). We prepared a cube of $L = 7.1$ mm, then, a spherical sample with a D of 7 mm ($S/V = 0.86$ mm^{-1}) was prepared using the two-pipe method for the SCM-VSM measurement [4]. To remove the deteriorated surface layer of approximately 8 μm, all processed samples were chemically etched in 3% HNO_3 solution for 1 min. H_{cJ} of the Nd-Fe-B sintered magnet samples A and B were 1.2 and 2.7 MA/m, respectively. The samples were magnetized with a maximum magnetic field (H_m) of 8.0 MA/m in the case of SCM-VSM. Hybrid twisted superfine wires composed of NbTi and Nb_3Sn were used for the cryogen-free solenoid coil superconducting magnet (SCM). This is very suitable for the control of H precisely because of very small screening-current-induced field related to unstable central field of the SCM [5]. The HG measurements were performed according to the IEC 60404-5 and JISC 2501 standards [1], [6], [7]. The technique in the fixture of heated sub-pole pieces has been generally applied for the HG method at elevated temperatures over the past years [8]. In this study, a large electromagnet (H_m of 2.7 MA/m) was employed with a fixture of 80-mm diameter heated Fe-Co main pole pieces. This represents an improvement relative to the former techniques as follows. This has the advantage that the condition of the air-gap between the face of the test specimen and the pole piece can be considered independent of the sample temperatures. 3. Results and Discussion In the measured curves obtained from the HG method, the magnetization distortion in H values up to 1.0–1.3, 1.1–1.5, and 1.4–1.8 MA/m was shown clearly for samples with L = 7, 14, and 21 mm, respectively. The magnetization distortion was closely related to the values of H_m, L, and saturation magnetization (J_s) as has been previously found in our study [2]. On the contrary, the magnetization distortion did not appear at all in the SCM-VSM method. The value of dJ/dH near H_{cJ} increased linearly as the temperature increased for the magnet A with a lower H_{cJ} regardless of measuring method. On the other hand, these obtained from the HG method (in all cases of L/D) increased rapidly as the temperature increased for the magnet B with a higher H_{cJ} at temperatures below 373 K (Fig. 1). The measured values almost agreed well at temperatures above 423 K in all cases of measurements, where H_{cJ} and J_s above 423 K were considerably decreased relative to the values below 323 K. The value of H_k/H_{cJ} for the magnet B with a higher H_{cJ} obtained from the SCM-VSM method gradually decreased and these obtained from the HG method at temperatures below 373 K increased rapidly as the temperature increased (Fig. 2). However, these agreed well at temperatures above 423 K in both methods. The effect of the distortion of magnetic flux distribution was decreased at temperatures above 423 K in the HG method. This is caused by the deterioration of H_{cJ} and J_s as the case of dJ/dH near H_{cJ} mentioned above. For the magnet A with a lower H_{cJ}, H_k/H_{cJ} decreased as temperature increased in all cases of measurements. The value obtained from the HG method deteriorated in the order of decreases in L/D above 373 K. It is caused by the distortion of magnetic flux distribution in the HG method. In the HG method, greater L/D led to easier uniform magnetization of cylindrical magnets, causing larger L/D to improve dJ/dH near H_{cJ} and H_k/H_{cJ}. However, the magnetization distortion did not appear at all in the SCM-VSM method at elevated temperatures and thus we could measure the values of dJ/dH near H_{cJ} and H_k/H_{cJ} as well as the magnetization curve exactly.

[1] H. Nishio, K. Machida, and K. Ozaki "More accurate hysteresis curve for large Nd-Fe-B sintered magnets employing a superconducting magnet-based vibrating sample magnetometer," IEEE Trans. Magn., vol. 53, no.4, pp. 6000306, April 2017. [2] H. Nishio, "Accurate measurement of magnetic properties of Nd-Fe-B sintered magnets with high coercivity," IEEE Trans. Magn., vol. 48, no.12, pp. 4779–4785, Dec. 2012. [3] H. Nishio, H.Yamamoto, M. Nagakura, and M. Uehara, "Effects of machining on magnetic properties of Nd-Fe-B system sintered magnets," IEEE Trans. Magn., vol. 26, no.1, pp. 257–261, Jan. 1990. [4] J. Durand, "Making sphere of crystals with anisotropy of hardness," Rev. Sci. Instrum. vol. 30, p. 840, 1959. [5] Y. Yanagisawa, H. Nakagome, D. Uglietti, T. Kiyoshi, R. Hu, T. Takematsu, T. Takao, M. Takahashi, and H. Maeda, "Effect of YBCO Shape on the Screening-Current-Induced Magnetic Field Intensity, " *IEEE Trans. Appl. Superconduct.*, vol. 20, pp.744-747, June 2010. [6] Magnetic materials–Part 5: Permanent magnet (magnetically hard) materials-methods of measurement of magnetic properties, IEC standard publication 60404-5 Ed. 3.0, April 2015, Geneva: IEC central office. [7] Methods of test for permanent magnet, Japanese industrial standard JISC2501, 1998, Tokyo: Japanese industrial standards committee. [8] R. M. W. Strnat, "Practical method of demagnetization curve testing on hard PM materials at low and elevated temperatures," in Proc. 10 th Int. Workshop on Rare-Earth Magnets and Their Application, Kyoto, Japan, 1989, pp.91-100.

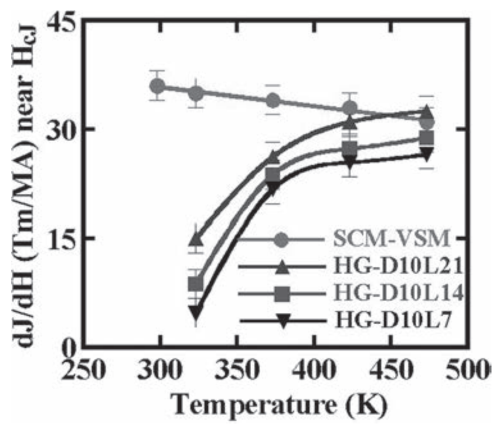

Fig. 1. Temperature dependence of differential susceptibility near coercivity for sample B.

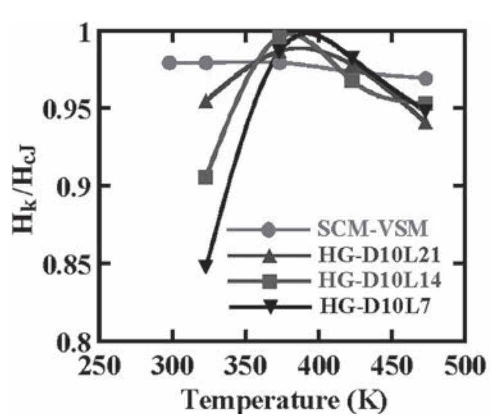

Fig. 2. Temperature dependence of squareness ratio for sample B.

3:15

FB-06. High performance magnetic properties of CoFe2O4 nanoparticles for rare earth free permanent magnet applications.

Y. Kumar[1] and P.M. Shirage[1,2]
1. Metallurgy Engineering and Materials Science, Indian institute of Technology Indore, Indore, India; 2. Discipline of Physics, Indian Institute of Technology Indore, Indore, India

High performance magnetic properties of $CoFe_2O_4$ nanoparticles for rare earth free permanent magnet applications Yogendra Kumar[1], and Parasharam M. Shirage[1, 2] 1. *Discipline of Metallurgy Engineering and Materials Science, Indian Institute of Technology Indore, Simrol, Indore-453552, India* 2. *Discipline of Physics, Indian Institute of Technology Indore, Simrol, Indore-453552, India* pmshirage@iiti.ac.in, yogendra.iitp@gmail.com In the recent decades, rare earth (RE) materials based permanent magnets have great scientific and technological attention because of their large number of applications in modern technologies such as high-density magnetic-recording media, electronic devices, and hybrid electric vehicles [1]. On the other hand, nowadays risk of supply of RE materials have increased because of natural exhaustion, social, and environmental serious concerns about their mining process [2]. Furthermore, extraction of rare-earth materials produce the large volume of toxic reagents and contaminate the water sources. Based on the USGS reports, demand of rare earth based permanent magnets increasing per year in global market [3]. The rapidly growing demands of permanent magnets in the global market and a limited supply of raw materials, diverting the attention of the researcher towards a viable alternative to these rare earth based permanent magnets. Nevertheless, it is a consensus among the scientific community that complete substitution of RE based magnets in all existing technological applications is not a long term plausible option due to high-performance magnetic properties of $SmCo_5$ and $Nd_2Fe_{12}B$ phase [2]. Therefore, there is a high demand of suitable materials for permanent magnets which led to wide demands of a low-grade rare earth based magnets in some industry application [4]. Cobalt ferrites nanostructured have been point out as a promising alternative to rare earth based permanent magnets due to its higher saturation magnetization and coercivity [5]. To achieve this goal, we studied the magnetic properties such as the saturation magnetization (M_s) remanent magnetization (M_r) and coercivity (H_c) of a series of cube shaped cobalt ferrite NPs with different size. Figure 1 (a) shows the X-ray diffraction patterns of the series of as-prepared cobalt ferrite nanoparticles, which are in well agreement with the inverse spinel cubic crystal structure of ferrites. Fig 1 (b) exhibits the TEM images of cubic shaped NPs with 34 nm particle size. M (H) loops of CF NPs at room temperature shown in Fig. 2 (a), which exhibit that M_s increases consistently as a function of particle size up to saturation point. We observed the M_s of 62.40 emu/g for CF-1 NPs, whereas 93.45 emu/g for CF-6 NPs. H_c exhibits the non-monotonous behaviour with the particle size as shown in Fig 2 (a). H_c at 10 K and at room temperature observe 16921Oe and 3229 Oe CF-4 NPs. Decrease of H_c at larger particle size may be due to expected crossover from single domain to multi-domain behaviour with increases particle size. H_c increases with size up to single domain limit, where the magnetization reverses its orientation through a uniform coherent rotation of all spins. From analysis of M_s, M_r and H_c, we extract the energy product (BH_{max}) at low and room temperature. A higher value of $(BH)_{max}$ of 2.53 MGOe obtained for CF-4 NPs at room temperature shown in Fig 2 (b), which is the highest reported to date in literature for cobalt ferrite NPs. The highest $(BH)_{max}$ product exhibits the potentiality of cobalt ferrite NPs in permanent magnet applications.

[1]M. Sugimoto, *J. Am. Ceram. Soc.*, 2004, 82, 269-280. [2] E. Alonso, A. M. Sherman, T. J. Wallington, M. P. Everson, F. R. Field, R. Roth and R. E. Kirchain, Environ. Sci. Technol., 2012, 46, 3406–3414. [3] U.S.G.S. Minerals information. Mineral Yearbook and Mineral Commodity Summary. [4] M. A. Willard, E. Bruck, C. H. Chen, S. G. Sankar, and J. Ping Liu, Adv. Mater. 23, 821–842 (2011). [5]. Yogendra Kumar and Parasharam M. Shirage, J Mater Sci (2017) 52:4840–4851

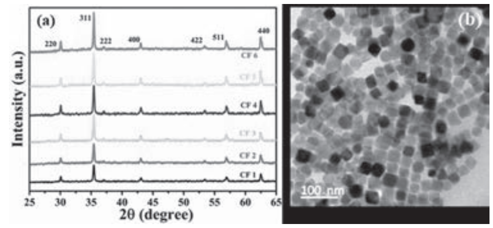

Fig. 1. (a) XRD patterns for a series of cobalt ferrite NPs, and (b) TEM images of the as-prepared CF-4 NPs.

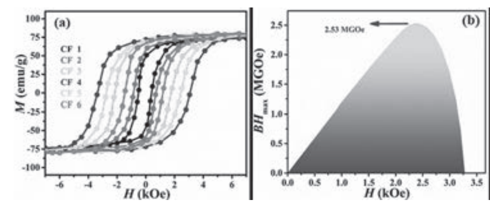

Fig. 2. (a) Hysteresis loops at room temperature of a series of $CoFe_2O_4$ NPs, and (b)
$(BH)_{max}$ energy product at room temperature of CF=4 NPs.

3:30

FB-07. 3-D Magnetic Field Analysis of a Permanent Magnet Spherical Actuator Using Spherical Harmonics.

X. Li[1,2], J. Liu[1] and W. Chen[1]
1. School of Automation Science and Electrical Engineering, Beihang University, Beijing, China; 2. Department of Materials and Production, Aalborg University, Aalborg, Denmark

I. INTRODUCTION With the rapid development of multi-DOF precision devices applied for complex movement, integration of multi-DOF motors has attached more and more attention. Conventionally, the implementation of multi-axis motion is realized by connecting several single-axis actuators in parallel or in series. However, this leads to a significant increase in complexity of the mechanical structure, bulkiness of the volume, and deterioration of the dynamic performance. Permanent magnet spherical actuator (PMSA) is a type of electromagnetic device similar to human joints which can realize multi-DOF rotations in a single joint. Due to its advantages of compact structure, high energy density, low inertia moment and rapid response, PMSAs show extensive application prospect in areas like satellite attitude control [1][2], medical apparatus, robotic applications [3]. To design efficient PMSMs for applications, a high torque density is a beneficial factor that should be taken into account. According to the Lorentz force law, the torque density generated by the PMSA is related to the magnetic field distribution of the rotor permanent magnets (PMs) in the air gap. Among various numerical methods, finite element analysis (FEA) is a widely used modeling tool to analyze the 3D magnetic field and to optimize the actuator design. However, FEA is very time-consuming, and analytical models are needed. Spherical harmonic (SH) analysis [4] is an analytical solution which has been put forward in various spherical motors. The spherical harmonic model can be expressed as a closed-form function by a finite space harmonics, and then the specific distribution of permanent magnetic field can be obtained based on suitable boundary conditions [5]. In this paper, an analytical model of the 3-D magnetic flux density is solved by the magnetic scalar potential equation in the spherical coordinate system using spherical harmonics. Verification of the magnetic field distribution surrounding the rotor is also carried out by a finite element software Maxwell. Afterwards, the design of the proposed PM array is analyzed using the analytical model. II. DESIGN AND WORKING PRINCIPLE A CAD model of the proposed PMSA is shown in Fig. 1. Figure 1 (a) and (b) show that the rotor with eight PMs surrounded in a ring is housed in a spherically shaped stator with three-layer individually activated coils. The rotor can generate continuous spinning motion about its output shaft, and incline about its equatorial plane to a position that the axis of a PM pole and the coil are aligned. The maximum tilting angle is ±15°. The structure of the rotor PM array is described in Fig. 1 (c). The eight PMs are uniformly distributed around the rotor equator with the alternative variation of the N pole and S pole. Conventionally, the magnets are shaped as cylinder or dihedral cone. Herein, the shell-shape PM is adopted. Compared with the cylindrical PM, the shell-shape PM decreases the interspace between the adjacent poles considerably, and has smaller moment of inertia than the dihedral cone PM. III. OPERATING PRINCIPLE OF THE PROPOSED SPHERICAL ACTUATOR According to the magnetic field distribution, space can be divided into four zones, PM, rotor core, air region outside the rotor and inside the rotor core. For each region, the magnetic field distribution is established, which is used to solve the general solution to Laplace equations. Using the method of separation of variables, the expression of the scale magnetic potential is solved by the boundary conditions and the spherical harmonic functions. The torque generated by the interaction between the PMs and the stator coils mainly depends on the radial component of magnetic field in the air gap, so only the spatial distribution of radial magnetic flux density in the air gap is calculated. (The detailed model will be introduced in the final paper.) IV. VERIFICATION OF THE ANALYTICAL MODEL In Fig. 2 (a), the fundamental component of B_r varies in the form of a cosine-like wave along θ and ϕ. There are four positive peak points and four negative peak points around the equator, which are in accordance with the four pairs of poles array. In order to validate the results of the analytical model, a numerical method is used. A finite element model built in the environment of Ansoft Maxwell is introduced to verify the analytical results. The analytical results are compared with FE results, which show the variation of radial magnetic flux density along the ϕ-direction at r=55.5mm, θ=90° (Fig.2 (b)) and r=55.5mm, θ=80° (Fig.2 (c)), respectively. It can be seen that the analytical model and FEM are in good agreement, thus, the analytical model can be used for further structural optimization design of PMSA. In addition, to obtain the optimal design of the rotor efficiently, several related configuration parameters used in the analytical model, such as spherical angle, radial thickness, and material of rotor core, are analyzed in this paper. V. CONCLUSION In this paper, an analytical model using spherical harmonics has been developed for analyzing the proposed rotor PM array of spherical motor and the 3-D solution of the spatial magnetic flux density is obtained. By comparing with the numerical FEA, the spherical harmonics is validated as an effective method with advantages of with reasonable accuracy and rapid computation, which has already been used to optimize the PM array design of the spherical actuator.

[1] L. Rossini, S. Mingard, A. Boletis, E. Forzani, E. Onillon, Y. Perriard, "Rotor design optimization for a reaction sphere Actuator," *IEEE Trans. Ind. Appl.*, vol. 50, no. 3, pp. 1706 - 1716, 2014. [2] M. Strumik, R. Wawrzaszek, M. Banaszkiewicz, K. Seweryn, M. Sidz, E. Onillon, L. Rossini, "Analytical model of eddy currents in a reaction sphere actuator," *IEEE Trans. Magn.*, vol.50, no.6 Jun. 2014. [3] D. Kang, J. Lee, "Analysis of electric machine characteristics for robot eyes using analytical electromagnetic field computation method,." *IEEE Trans. Magn.*, vol. 50, no. 2, Feb. 2014. [4] C. X, H. Li, T. Shi, "3-D magnetic field and torque analysis of a novel Halback array permanent-magnet spherical motor," *IEEE Trans. Magn.*, vol. 44, no. 8, pp. 2016-2020, Aug. 2008. [5]B. van Ninhuijs, T. E. Motoasca, E. A. Lomonova, "Accurate analytical computation of magnetic flux density of spherical permanent magnet arrays," in *Proc. IEEE Int. Conf. Electr. Mach. (ICEM)*, Sep. 2012, pp. 2746-2751.

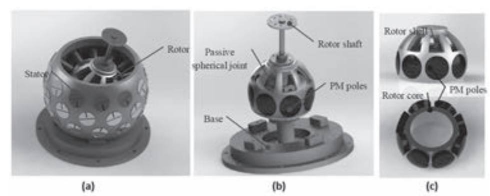

Fig. 1. CAD model of PMSA

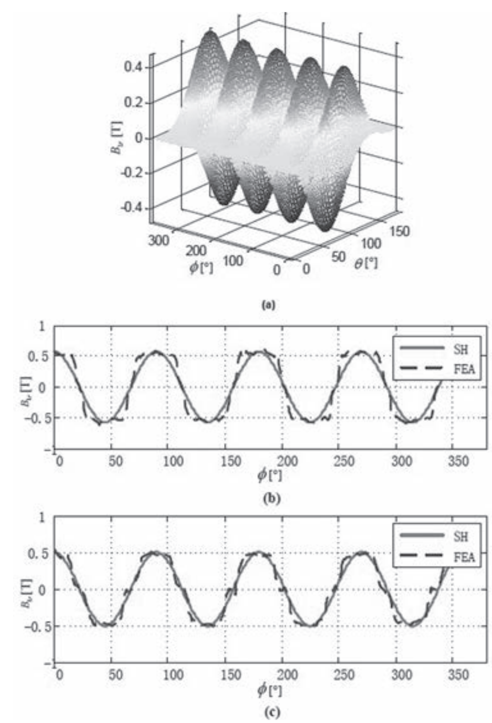

Fig. 2. Radial component of magnetic field distribution

3:45

FB-08. Influence of Soft Magnetic Material type in Fixture Components on the Magnetization of Bonded Neo Magnet and Motor Performance.

R.C. Angara[1], K.W. Hsu[1], P.J. Villar[1] and N.K. Sheth[1]
1. R&D Magnequench, Magnequench Neo Powders Pte Ltd, Singapore, Singapore

The advantages like higher magnetic properties than ferrite, near net shape magnet production, and no use of heavy rare earth elements makes the bonded neo magnet very attractive in motors used for automotive accessory, home appliance and office automation. The isotropic nature of bonded neo magnets offers a feasibility to obtain wide range of magnetization profiles. The magnetization of the magnet influences the air-gap flux distribution and hence the motor performance[1]. Magnetizing fixture comprising of copper coils embedded in soft magnetic material is used to magnetize the magnet. When radial magnetization profile is desired, a back iron made up of soft magnetic material is also used to reduce the amount of magnetizing energy needed to saturate the magnet. Laminated steel is the preferred material for the magnetizing fixture as well as back iron. We have observed that at times solid steel is used in place of laminated steel. This paper presents the effects of using solid steel in place of laminated steel on the magnetization and motor performance. A magnetizing fixture is designed using the 2-D finite element analysis (FEA). The designed fixture is fabricated with fixture core and back iron made of laminated steel (LCLB). The magnetization performance of the designed fixture is evaluated using 2-D FEA and validated by performing magnetization of the magnets. To evaluate the influence of solid steel as a soft magnetic material two more combinations; (i) fixture core is of laminated steel but the back iron is of solid steel (LCSB) and (iii) both fixture core and back iron made of solid steel (SCSB) are simulated and evaluated. To ensure the full saturation in a bonded neo magnet a magnetizing field of 3T is desired through the thickness of the magnet[2]. From the simulation it is observed that to achieve 3T magnetizing field for LCLB combination the magnetizing energy required is 5.44 kJ. The required energy increases to 34.02 kJ and 68.28 kJ for LCSB and SCSB combinations respectively. The increase in energy is due to the generation of eddy currents in solid steel components which counteract the applied field, reducing the available field for magnetization. The energy needed to achieve full magnet saturation in LCSB and SCSB combination exceeds the capability of most of the commercially available magnetizers also the increase in magnetization energy requirement will lead to higher thermal stress and reduced fixture reliability. Based on the capability of the available magnetizer we applied up to 6 kJ for LCSB and SCSB combinations. We have also measured the corresponding applied field at the back of the magnet as 1.6 T and 1.4 T respectively. The less than desired applied field led to the partial saturation of the magnet. Figure 1 shows the measured mid airgap closed circuit flux density waveforms for magnets magnetized using various combinations. From this figure it is observed that the use of solid steel component makes the airgap flux density waveform less radial. The flux integral is reduced by 11% and 6.6% for LCSB and SCSB combinations compared to LCLB combination. The magnets magnetized using various combinations are assembled in a motor for performance measurement, the results of which are summarized in Table I. The presence of solid steel component during magnetization leads to partial magnetization of the magnet, resulting in higher no-load speed and lower stall torque. It is also observed that the motor with the magnets magnetized using LCSB and SCSB combinations has 64% and 60% lower cogging torque compared to LCLB combination. This is due to partial magnetization and hence lower flux offered by the magnets from these combinations.

[1] Seok-Myeong Jang, Han-Wook Cho, Sung-Ho Lee, Hyun-Sup Yang, and Yeon-Ho Jeong, "The influence of magnetization pattern on the rotor losses of permanent magnet high-speed machines," IEEE Trans. Magnetics, vol 40, no 4, Jul. 2004. [2] Nimitkumar K. Sheth, Raghu C. S. Babu Angara, "Effect of partial saturation of bonded neo magnet on the automotive accessory motor," in AIP Advances, vol 7, issue 5, 2016.

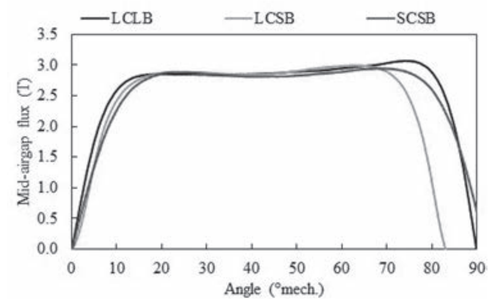

Fig. 1. Measured closed circuit mid airgap flux density

Fixture component combination	No-load speed (rpm)	Back-emf at 3300 rpm (V)	Stall torque (mN-m)	Peak-peak cogging torque (mN-m)
LCLB	5062	8.53	329	69.9
LCSB	5435	7.82	297	25.2
SCSB	5220	8.20	313	27.9

TABLE I Effect of Magnetization Fixture on Motor Performance

4:00

FB-09. A hybrid coercivity mechanism for exchange-coupled nanocomposite permanent magnets.

G. Zhao[1]
1. Physics, Sichuan Normal University, Chengdu, China

Hard/soft permanent magnets have been a subject of continuous interests in the past two decades due mainly to their potential in achieving giant energy products as well as their rich variety of magnetic behaviors, *e.g.*, exchange-spring in the response of the applied field[1-4]. Recently the applications have been extended to the area of data storage as exchange-coupled composite (ECC) media has been found to own various advantages over the traditional longitudinal and perpendicular recoding media[5]. Although there are some limitations, micormagnetics is still the most important theoretical tool to elucidate the reversal mechanism, to predict the magnetic behaviors and to provide clues on how to improve the magnetic properties of nanocomposite permanent magnets[6-8]. In this work, we propose a hybrid coercivity mechanism for exchane coupled hard-soft permanent magnets, which incorporates elemnts of both the traditional nucleation and pinning mechanisms based on our micromagnetic calculation. Our proposed coercivity mechanism and calculated results agree very well with available experimental results, especially the recent reported high energy products achieved in NdFeB[9] and SmCo[10] based hard/soft multilayers. Careful comparison and contrast with other numerical and analytical micromagnetic methods have been done, where the virtues and weakness are classified and discussed, with salient deviations between experiment and theory listed and analyzed. A critical assessment on how to reach a satisfactory micromagnetic theory will be made. The focus of the comparison and contrast is on the thin film system, where the thickness of the layers can be controlled precisely so that the calculated results can be compared directly with available experimental data. Spin distributions and microscopic hysteresis loops are important references on whether a calculation is reliable, along with the well-known macroscopic hysteresis loops. Based on the calculations, magnetic phase diagrams, nucleation modes and coercivity diagrams as well as their size effects are summarized. The influences of various microstructure structures, such as defects, easy axis distributions and interface qualities on the hysteresis loops are evaluated. These issues help to digest the outstanding deviations between the observed and calculated energy products in composite magnets. This paradox is closely linked to the more famous and widely existed coercivity paradox proposed by Brown in 1940s. The proposed coercivity mechanism and modeling techniques are ready to be extended to single-phased permanent magnets and ECC system. Further, they shed light on the micromagnetic calculations of the antiferromagnet-ferromagnet bilayers, where exchange bias and exchange springs have some common underlying physics. This work is supported by Natural Science Foundation of China (51771127, 51571126, 51772004)

1. E. F. Kneller and R. Hawig, Exchange-spring magnet: A new material principle for permanent magnets. *IEEE Trans. Magn.* 27, 3588 (1991). 2. R. Skomski and J. M. D. Coey, Giant energy product in nanostructured two-phase magnets. *Phys. Rev. B* 48, 15812 (1993). 3. H. Zeng, J. Li, J. P. Liu, Z. L. Wang, and S. Sun. Exchange-coupled nanocomposite magnets by nanoparticle self-assembly. Nature, 420: 395-398, (2002). 4. X. Li, L. Lou, W. Song, G. Huang, F. Hou, Q. Zhang, H. T. Zhang, J. Xiao, B. Wen, and X. Zhang. Novel bimorphological anisotropic bulk nanocomposite materials with high energy products. Adv. Mater., 29(16): 1606430, (2017). 5. F. Wang, J. Zhang, J. Zhang, C. L. Wang, Z. F. Wang, H. Zeng, M. G. Zhang, and X. H. Xu, Graded/soft/graded exchange-coupled thin films fabricated by [FePt/C]5/Fe/[C/FePt]5 multilayer deposition and post-annealing. *Applied Surface Science* 271, 390 (2013) 6. G. P. Zhao and X. L. Wang, Nucleation, pinning, and coercivity in magnetic nanosystems: An analytical micromagnetic approach. *Phys. Rev. B* 74, 012409 (2006). 7. G. P. Zhao, M. G. Zhao, H. S. Lim, Y. P. Feng and C. K. Ong, From nucleation to coercivity. *Appl. Phys. Lett.* 87, 162513 (2005). 8. G. P. Zhao, X. L. Wang, Chun Yang, L. H. Xie, and G. Zhou, Self-pinning: Dominant coercivity mechanism in exchange-coupled permanent/composite magnets. *J. Appl. Phys.* 101, 09K102 (2007). 9. W. B. Cui, Y. K. Takahashi, and K. Hono, Correction: $Nd_2Fe_{14}B$/FeCo anisotropic nanocomposite films with a large maximum energy product. *Adv. Mater.* 24, 6530 (2012). 10.S. Sawatzki, R. Heller, C. Mickel, M. Seifert, L. Shultz, and V. Neu, Largely enhanced energy density in epitaxial $SmCo_5$/Fe/$SmCo_5$ exchange spring trilayers. *J. Appl. Phys.* 109, 123922 (2011).

4:15

FB-10. The corrosion behavior with sintered (Ce,Nd)-Fe-B in the presence of pressurised vapour.

X. Shi[1], M. Zhu[1], D. Zhou[1], *L. Song*[1], Y. Fang[1] and W. Li[1]
1. Division of Functional Materials, Central Iron & Steel Research Institute, Beijing, China

Introduction Sintered neodymium-iron-boron (Nd-Fe-B) magnets have become the most widely used as the high energy product [1]. Recently, Cerium, is used to substitute Nd in $Nd_2Fe_{14}B$ for reducing the cost. The double main phase (DMP) methods, sintering the mixture of Ce-free and Ce-containing Re-Fe-B powders, is taken to synthesize the (Ce, Nd)-Fe-B magnets. The method can realize the adjustment of the composition and combination of main phases, and reach the fine magnetic properties [2-3]. The corrosion of the magnets, which is an important material selection criterion in practical application, is affected by the microstructures and composition [4]. In this paper, the microstructures and corrosion of $(Ce_xNd_{1-x})_{30}Fe_{bal}B$ (x=0.15, 0.3, 0.5, wt.%) named as Ce15, Ce30, Ce50 were studied. The commercial Ce-free magnet with energy product 45MGOe named as N45 is used as the reference magnet. The corrosion was tested in pressurised vapour atmosphere, which enables the electrochemical reaction and facilitates the transfer of the water molecules through the magnet. Key words : Ce, sintered Nd-Fe-B, microstructure, galvanic corrosion Experimental Procedure The DMP magnets $(Ce_xNd_{1-x})_{30}Fe_{bal}B$ were prepared with mixture of $Nd_{30}Fe_{bal}B_1$ (wt.%) and $Ce_{15}Nd_{15}Fe_{bal}B_1$ (wt.%) powders. The magnets $(Ce_xNd_{1-x})_{30}Fe_{bal}B$ were sintered and annealed at temperatures between 400°C and 600°C without the traditional high temperature annealing around 900°C. The reference magnets have the same energy product with Ce15. The samples were put in an autoclave at 120°C, 1.2Mpa, 100% RH with the size of 15mm×15mm×4mm for the corrosion testing. The inductively coupled plasma (ICP) mass spectrometry is used for measuring element composition of the magnets by PerkinElmer optima 2100 DV. The back scattered electron (BSE) images and element distribution (EDS) maps of the polished sample surfaces and the corrosion surfaces were carried out by Phenom ProX. Results and discussion Fig. 1 presented the microstructures of magnets. The dark contrast with highest volume fraction corresponds to the magnetic $Re_2Fe_{14}B$ grains and the bright one refers to the Re-rich phase around magnetic phase. The single area of Re-rich phase in N45 (Fig.1a) is largest, and the magnetic particle is not isolated by the Re-rich phase. The distribution of the Re-rich phase in Ce15 (Fig.1b) is relatively scattered. The network structure of Re-rich phase is formed in Ce30 and Ce50 (Fig.1c and Fig.1d), and the structure is efficient to improve coercivity by blocking interaction of the magnetic phase. The EDS maps show the distribution of elements with the same area in the magnets. In Ce15 and Ce30, some of magnetic phase is Ce-free while some magnetic particles contain high content Ce. Ce exists in all the Re-rich phase of Ce15. Some of Re-rich phases contain high Ce while some of Re-rich phases contain low Ce in Ce30 and Ce50. Besides, it is clearly that the concentration of Nd and O elements is high while Fe and Ce is low in Re-rich phase, which means that O prefers to combine with Nd in Ce30 and Ce50. The uneven distribution of Ce is caused by solidification process in the Re-rich phase of the Ce30 and Ce50. Ce performs better infiltration than Nd to the magnetic phase, so Ce is easier to solidity on the surface of the magnetic particle than Nd. That may be also the reason that Nd prefer to combine with O. The corrosion morphology of samples is observed (Fig.2). The corrosion morphology of N45 (Fig.2a) represents pitting. The pitting occurs when the potential difference is small between the magnetic phase and Re-rich phase, the existence of Co and Al decreases the potential difference which makes pitting easier. The appearance of Ce15 (Fig.2b) performs discontinuous pits. The grain boundary phase is small and scattered, the grain boundary phase dissolves as the anode, so the corrosion channel is difficult to form further corrosion depth. The corrosion morphology of Ce30 and Ce50 is different from N45 and Ce15, the corrosion form is that the magnetic phase is corroded while the Re-rich phase keeps intact. Larger magnification image of corrosion morphology and element distribution of special area were taken of Ce30 and Ce50. Re-rich phase located in grain boundary is corroded, lager area of the Re-rich phase is clear and distinguishable in Ce30. In the Ce50, the magnetic phases present corrosion, the Re-rich phases almost have no missing. So untraditional galvanic corrosion that Re-rich phases refer to cathode and the Re-Fe-B main phases refer to anode appear in Ce30 and Ce50. Conclusion The effects of Ce on the microstructure and corrosion of sintered (Ce,Nd)-Fe-B permanent magnets were investigated. Taken together, we found that: 1. Some of the magnetic phases contain Ce while some of the magnetic phase doesn't contain Ce in the dual-main-phase magnet. 2. All the Re-rich phase contains Ce in the Ce15 magnets. However, the distribution Nd and Ce is uneven in different Re-rich phase of Ce30 and Ce50. The uneven distribution is caused by the fine wettability of Ce. 3. The magnetic phase is corroded as the anode and the grain boundary phase keep intact as cathode in the samples of Ce30 and Ce50. The shift of anode and cathode between the magnetic phase and Re-rich phase is due to the compact microstructure.

[1] M. Sagawa, S. Fujimura, H. Yamamoto, Y. Matsuura, K. Hiraga, IEEE Trans. Magn. Vol.20, pp.1584-1589,1984. [2] M.G. Zhu, W. Li, J.D. Wang, L.Y. Zheng, Y.F. Li, K. Zhang,H.B. Feng, and T. Liu, IEEE. Trans. Magn., Vol.50, pp.1-4, 2014,. [3] Y.J Zhang, T.Y Ma, J.Y Jin, J.T Li, C Wu, B.G Shen, M Yan, Acta Mater. Vol.128 pp. 22-30, 2017. [4] L. J. Yang, M. X. Bi, J. J. Jiang, X. F. Ding, M. G. Zhu, W. Li, Z. S. Lv, Z. L Song, J. Magn. Magn. Mater. Vol.432, pp:181, 2017.

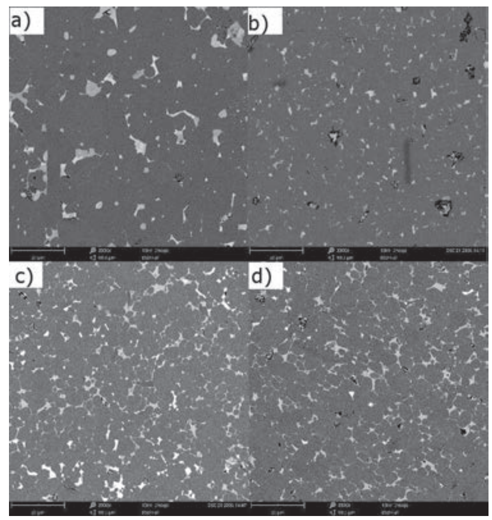

Fig. 1. The back scattered electron (BSE) images of magnets a) N45 b) Ce15 c) Ce30 d) Ce50

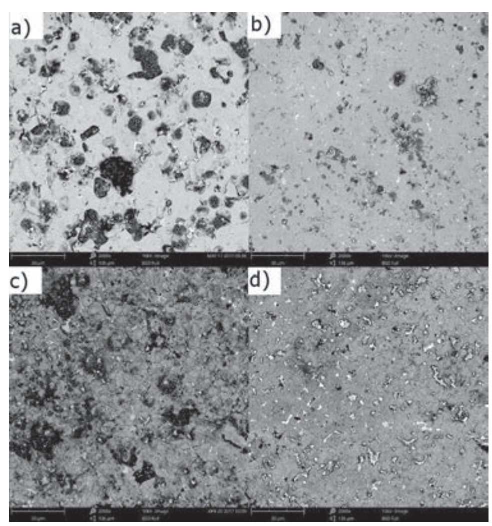

Fig. 2. BSE images for corrosion morphology with accelerated corrosion time for 60h a) N45 b) Ce15 c) Ce30 d) Ce50

4:30

FB-11. Element-specific characterization of Co:FePt nanocomposite magnet films.

F. Wilhelm[1], V. Dupuis[2], D. Le Roy[2], N. Dempsey[3] and A. Rogalev[1]
1. ESRF, Grenoble, France; 2. Institut Lumière Matière, Villeurbanne, France; 3. Institut Néel, Grenoble, France

Nanocomposite magnets consisting of a mixture of a hard magnetic material and a high saturation magnetization ferromagnet are promising systems to overpass performances of the best permanent magnets. Theoretical descriptions of nanocomposite magnets [1] revealed the necessity of confining a soft magnetic material in clusters of typically less than 10 nm. Yet standard fabrication processes do not permit to produce such microstructures in a controllable manner. In this context a cluster-dedicated synthesis could permit to realize model films to experimentally explore underlying mechanisms that govern magnet performances in such nanocomposite magnets [2]. We have been able to synthesize Co:FePt nanocomposite films by combining low energy cluster beam deposition (LECBD) technique and e-beam evaporation. To separately adjust size, composition and concentration, Co:FePt nanocomposite were prepared from low energy cluster beam deposition technique (LECBD) of mass-selected Co clusters preformed in gas phase, in-situ embedded in hard L10-FePt matrix independently produced by alternative electron gun evaporation on substrate. Doing so, the soft phase is restricted to clusters of nanometer size, selected from 2 to 8 nm while the volume fraction of nanoclusters in L10-FePt matrix was varied up to 30%. Here we report on results of standard structural (e.g. XRD, SEM, TEM) and magnetic characterizations (SQUID magnetometry, MFM) performed on these nanocomposite samples. A typical XRD pattern of nanocomposite on Si substrate is reproduced on a left panel of Fig. 1. An anomalously intense (001) reflection with respect to (110) peak is a signature of a certain texture of the L10-FePt film. A strong magnetic coupling is between FePt and Co clusters could be inferred from SQUID magnetization curves on nanocomposite when compared with the results obtained from superparamagnetic Co clusters in an inert carbon matrix and from a pure FePt film (see right panel on Fig.1). Macroscopic characterization was complemented with more sophisticated element selective approaches, i.e. X-ray natural linear dichroism (XLD) and X-ray magnetic circular dichoism (XMCD) spectroscopies at the K-edges of Fe and Co. We have concentrated on Co:FePt nanocomposite with Co nanoclusters of 6 nm size embedded in L10-FePt matrix. Firstly, a high degree of texture in composite films is confirmed on microscopic level. Secondly, XLD signals at both Co and Fe sites are found to be nearly identical in amplitude and spectral shape. The latter is nearly identical to those measured on a pure L10-ordered FePt film. This observation is a very indication that the Co clusters do not keep fcc structure as expected but rather adopt a tetragonal L10 structure. Microscopic magnetic characterization with XMCD has revealed that Co magnetic moments are aligned ferromagnetically with Fe moments in the L10-FePt matrix. Moreover, both are exhibiting the same magnetization curves that demonstrates that the Co:FePt nanocomposite behaves like a single magnetic phase material. Funding by the ANR-SHAMAN (ANR-16-CE09-0019) is acknowledged.

[1]Skomski R. and Coey J. M. D. Giant energy product in nanostructured two-phase magnets. Phys. Rev. B 48, 15812–15816 (1993). [2] Balasubramanian B., Mukherjee P., Skomski R., Manchanda P., Das B. and Sellmyer D. J. Magnetic nanostructuring and overcoming Brown's paradox to realize extraordinary high temperature energy products. Scientific reports 4, 6265 (2014).

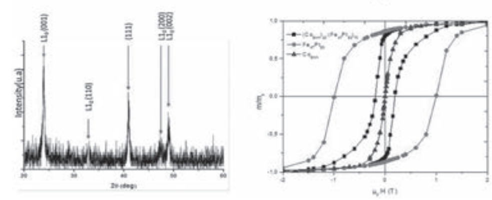

Fig. 1. Evidence of L10 phase from X-ray diffraction obtained on annealed FePt thin film of 30 nm in thickness deposited in Si wafer (left). Hysteresis loops at 300K obtained for Co clusters of 6 nm in diameter with size dispersion < 10 % embedded in carbon matrix (blue) and for FePt Films upon annealing without (red) and with (black) identical Co Nanoparticles with 30% volume concentration (right.)

4:45

FB-12. Effect of residue hydrogen content on microstructure and magnetic properties of $Sm(Co_{bal}Fe_{0.28}Cu_{0.053}Zr_{0.02})_{7.84}$.

C. Zhang[1], Z. Liu[1], L. Liu[1], T. Li[1], R. Chen[1], D. Lee[2] and A. Yan[1]
1. Key Laboratory of Magnetic Materials and Devices, Ningbo Institute of Industrial Technology, Chinese Academy of Sciences, Ningbo, China; 2. University of Dayton, Dayton, OH, United States

Hydrogen decrepitation (HD) has been widely used in Nd-Fe-B magnets preparation[1]. Traditional 2:17 type Sm-Co alloys have very harsh hydrogen absorption conditions. Recently, our group reports that 2:17 type Sm-Co alloys with high iron content shows excellent ability to absorb hydrogen and the HD has been applied in the magnets preparation[2]. HD utilizes two steps (absorption and release)[3] and if the hydrogen does not need to release, it could be much shorter time for HD process. However, the effect of residue hydrogen to the microstructure and magnetic properties remains unknown in iron-rich 2:17-type Sm-Co magnets. Therefore, it is meaningful to systematically investigate the effect of residue hydrogen in iron-rich 2:17-type Sm-Co magnets. The nominally $Sm(Co_{bal}Fe_{0.28}Cu_{0.053}Zr_{0.02})_{7.84}$ magnets were prepared by traditional metallurgy route. The as-cast alloys were pre-crushed by HD technology. The HD powders with different hydrogen content (25 ppm, 715 ppm, 1512 ppm) were prepared through changing dehydrogenation time (240 min, 20 min, 0 min). The green bodies were sintered at 1200°C for 30min, and then homogenized at 1175°C for 3h, followed by a rapid cooling step to room temperature. The subsequent isothermal aging was at 830°C for 16h, followed by slow cooling to 400°C and finally rapid cooling to room temperature. Fig. 1 shows demagnetization curves of the magnets A (25 ppm), B (715 ppm) and C (1512 ppm) at the room temperature. The remanence doesn't change with the residue hydrogen content. However, the intrinsic coercivity is improved from 24.03 kOe to 26.37 kOe as the residual hydrogen content increases from 25ppm to 1512ppm. Interestingly, the squareness also increases from 0.56 to 0.63. Fig. 2(a-c) show the BSE images of aged magnets. Obviously, the average grain size of magnet A is smaller than B and C. The average grain sizes of magnet A, B and C are 49μm, 53μm and 59μm, respectively, which means the residual hydrogen content can promote the average grain size. Fig. 2(d-f) show the TEM-BF image with c-axis within image plane and corresponding Fresnel Lorentz images for magnet A at the grain boundaries. The regions near grain boundary shows indistinct cell boundaries and less lamellar phase (Fig. 2d). The lamellar phases provide diffusion paths for rapid segregation of Cu atoms to cell boundaries[4]. Therefore, less lamellar phase may lead to indistinct cell boundary phase and less Cu content in cell boundary. In addition, minor grain boundary phase with many stripes can be also observed, as is shown in Fig. 2e (over focus) and Fig. 2f (under focus). Because domain walls (white arrows) pass through the grain boundary phase, it should be magnetic phase. These two regions act as easy points for the occurrence of reversal magnetic domains. Therefore, a reduced amount of grain boundary phase results in less weak pinning points, and as a result, the intrinsic coercivity and the squareness are improved. Furthermore, cell structures and lamellar phase are comprehensively investigated.

[1] P. J. McGuiness, and I. R. Harris, "The use of hydrogen in the production and characterization of NdFeB magnets," *Journal of Applied Physics,* vol. 64, no. 10, pp. 5308-5310, 1988. [2] M. Li, Z. Liu, L. Liu, H. W. Zhang, R. J. Chen, X. C. Liu, D. Lee, and A. R. Yan, "Effect of Fe and Annealing Treatment on Hydrogenation Behavior of $Sm(Co_{bal}Fe_xCu\ Zr_{0.068(0.034)})_{7.33}$ (x = 0.237, 0.251, 0.265) Alloys," *Ieee Transactions on Magnetics,* vol. 50, no. 11, pp. 4, Nov, 2014. [3] S. Guo, Q. Y. Zhou, R. J. Chen, D. Lee, and A. R. Yan, "Microstructure and magnetic properties of sintered Nd–Fe–B magnets with high hydrogen content," *Journal of Applied Physics,* vol. 109, no. 7, pp. 07A734, 2011. [4] Y. Horiuchi, M. Hagiwara, M. Endo, N. Sanada, and S. Sakurada, "Influence of intermediate-heat treatment on the structure and magnetic properties of iron-rich Sm(CoFeCuZr)Z sintered magnets," *Journal of Applied Physics,* vol. 117, no. 17, pp. 17C704, 2015.

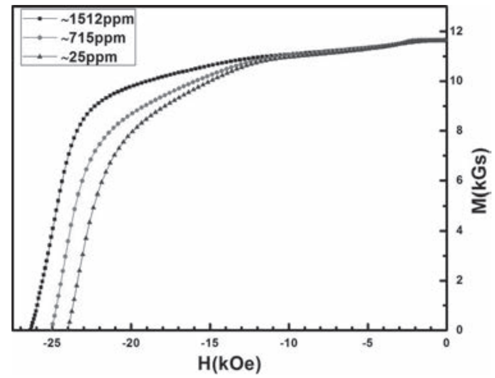

Fig. 1. The demagnetization curves of the magnets A, B and C at the room temperature.

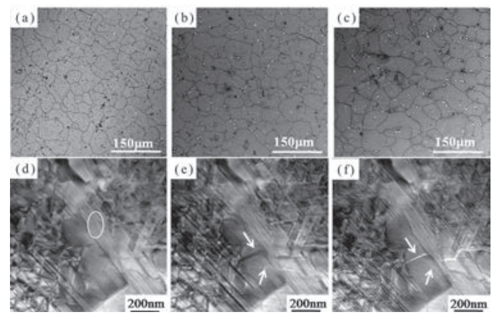

Fig. 2. The BSE images of aged magnets prepared by powder with different residual hydrogen content. (a) Magnets A, (b) Magnets B, (c) Magnets C. The TEM-BF image for magnet A at the grain boundaries with c-axis within image plane (d) and corresponding Fresnel Lorentz images (e, f).

THURSDAY AFTERNOON, 26 APRIL 2018 ORCHID IV, 2:00 TO 5:00

Session FC

TMR, VCMA AND SWITCHING

Caihua Wan, Chair
Institute of Physics, Chinese Academy of Sciences, Beijing, China

CONTRIBUTED PAPERS

2:00

FC-01. Voltage-driven precessional switching at zero bias magnetic field in a conically magnetized free layer.

R. Matsumoto[1], T. Nozaki[1], S. Yuasa[1] and H. Imamura[1]
1. Spintronics Research Center, National Institute of Advanced Industrial Science and Technology (AIST), Tsukuba, Japan

Voltage-driven magnetization switching [1] at zero bias magnetic field has become one of the key requirements in developing voltage-controlled magnetoresistive random access memory (MRAM). In a conventional magnetic tunnel junction (MTJ) with a perpendicular magnetization, however, voltage-driven magnetization switching has been demonstrated under a bias magnetic field having in-plane (IP) component [2-4]. Instead of bias magnetic field, the IP component of the shape anisotropy field, H_k, is being often used for controlling the magnetization. Finite H_k is commonly obtained in a ferromagnet having an elliptic-cylinder shape. In the case of a perpendicularly magnetized free layer, on the other hand, the shape anisotropy field cannot move the magnetization from an equilibrium state because H_k is zero at $(m_x, m_y, m_z) = (0, 0, \pm 1)$ where m_x and m_y (m_z) are IP (perpendicular) components of the unit magnetization vector (m) of the free layer (see Fig. 1(a)). Tilting the magnetization from the perpendicular direction is also necessary for the switching of the free layer magnetization. To tilt the magnetization, we propose the use of a cone state. Cone state is the magnetization state (see Fig. 1(b)) where the tilted magnetization is stabilized by the competition between the first- and the second-order magnetic anisotropy energies, $K_{1,\mathrm{eff}}$ and K_{u2} [5, 6]. Here $K_{1,\mathrm{eff}}$ is the effective anisotropy constant, where demagnetization energy is subtracted from the first-order anisotropy constant (K_{u1}). In this study [7], the voltage-driven precessional switching in a conically magnetized free layer having an elliptic cylinder shape is theoretically analyzed in order to derive analytical expressions of the conditions for the precessional switching at zero bias magnetic field. The MTJ we assume is illustrated in Fig. 1(a). The axis x is parallel to the major axis of the ellipse. The conditions for the precessional switching is analyzed using the following dimensionless energy density, $\varepsilon = (1/2)(N_x m_x^2 + N_y m_y^2 + N_z m_z^2) + \kappa_1(1 - m_z^2) + \kappa_2(1 - m_z^2)^2$. Here $\kappa_1 = K_{u1}/(\mu_0 M_s^2)$ and $\kappa_2 = K_{u2}/(\mu_0 M_s^2)$. μ_0 is the vacuum permeability, and M_s is the saturation magnetization of the free layer. The demagnetization coefficients, N_x, N_y, and N_z are assumed to satisfy $N_z \gg N_y > N_x$. Although our analysis can be applied to a general situation, it is easier to understand the benefit by showing specific examples. Accordingly, following parameters are assumed: M_s = 1400 kA/m, the volume of the free layer is $50 \times 20 \times \pi \times 1$ nm^3, $K_{u1}^{(0)}$ = 1067 kJ/m^3, $K_{1,\mathrm{eff}}^{(0)} = K_{u1}^{(0)} - (1/2)\mu_0 M_s^2(N_z - N_x)$ = -80 kJ/m^3, $K_{u2}^{(0)}$ =150 kJ/m^3, $m_z^{(0)}$ = 0.856, and the thermal stability factor at 300 K is 61.2. Hereafter the superscript "(0)" indicates the quantities at zero bias voltage. The direction of $m^{(0)}$ is indicated by an open circle in Fig. 2(a). Voltage-driven dynamics in the free layer is analyzed with the contour curve of ε including $m^{(0)}$ on the Bloch sphere shown in Fig. 2(a). When $(\kappa_{1,\mathrm{eff}}(=K_{1,\mathrm{eff}}/(\mu_0 M_s^2)), \kappa_2) = (-0.040, 0.025)$ at a finite voltage, for example, the contour curve extends from the upper hemisphere to the lower hemisphere as shown in Fig. 2(a). It enables the voltage-driven precessional switching. The switching in the free layer is confirmed by the calculations using the Landau-Lifshitz-Gilbert equation, $\mathrm{d}m/\mathrm{d}t = -\gamma_0\, m \times H_{\mathrm{eff}} + \alpha\, m \times \mathrm{d}m/\mathrm{d}t$, as shown in Fig. 2(a). Here t is time, γ_0 is the gyromagnetic ratio, α is the Gilbert damping constant being $\alpha = 0.005$, and H_{eff} is the effective magnetic field defined as $H_{\mathrm{eff}} = -M_s \nabla\varepsilon$. Starting from $m_z^{(0)} > 0$, m switches to the lower hemisphere moving along the contour curve of ε including $m^{(0)}$. It indicates that voltage-driven precessional switching at zero bias magnetic field is possible in a conically magnetized free layer with the elliptic-cylinder shape and that the trajectory can be analyzed by the contour curve of ε. The analyzed conditions for the precessional switching at zero bias magnetic field are shown as a $\kappa_{1,\mathrm{eff}}$ - κ_2 phase diagram in Fig. 2(b). The shade region indicates the switching region. The switching region is analytically expressed as follows. At $\kappa_{1,\mathrm{eff}} < \kappa_{1,\mathrm{eff}}^{(i)}$, $\{-\kappa_{1,\mathrm{eff}} - [-\kappa_{1,\mathrm{eff}}(N_y - N_x) - (1/4)(N_y - N_x)^2]^{1/2}\}/[2(1 - Z^{(0)})] < \kappa_2 < -\xi\,\kappa_{1,\mathrm{eff}}$. At $\kappa_{1,\mathrm{eff}}^{(i)} \le \kappa_{1,\mathrm{eff}} < 0$, $-\xi\,\kappa_{1,\mathrm{eff}} - \eta < \kappa_2 < -\xi\,\kappa_{1,\mathrm{eff}}$. At $\kappa_{1,\mathrm{eff}} \ge 0$, $-\xi\,\kappa_{1,\mathrm{eff}} - \eta < \kappa_2 < -(\kappa_2^{(0)}/\kappa_{1,\mathrm{eff}}^{(0)})\,\kappa_{1,\mathrm{eff}}$. Here, $\kappa_{1,\mathrm{eff}}^{(i)}$ is $\kappa_{1,\mathrm{eff}}$ of the point (i) in Fig. 2(b) being $\kappa_{1,\mathrm{eff}}^{(i)} = -(N_y - N_x)[2 - 2Z^{(0)} + (Z^{(0)})^2]/[2(Z^{(0)})^2]$, $Z^{(0)} = (m_z^{(0)})^2$, $\xi = 1/(2 - Z^{(0)})$, and $\eta = \xi(N_y - N_x)/(2Z^{(0)})$. The results provide a practical guide to design the bias-field-free voltage-controlled MRAM, which simplifies the device structure and reduces the fabrication cost. This work was partly supported by the ImPACT Program of the Council for Science, Technology and Innovation and JSPS KAKENHI Grant Number 16K17509.

[1] Y. Shiota et al., *Nat. Mater.*, 11, 39 (2012). [2] S. Kanai et al., *Appl. Phys. Lett.*, 101, 122403 (2012). [3] Y. Shiota et al., *Appl. Phys. Express*, 9, 013001 (2015). [4] C. Grezes et al., *Appl. Phys. Lett.*, 108, 012403 (2016). [5] D. Apalkov and W. Butler, US Patent 8,780,665 (2014). [6] R. Matsumoto et al., *Appl. Phys. Express*, 8, 063007 (2015). [7] R. Matsumoto et al., accepted in *Phys. Rev. Applied*.

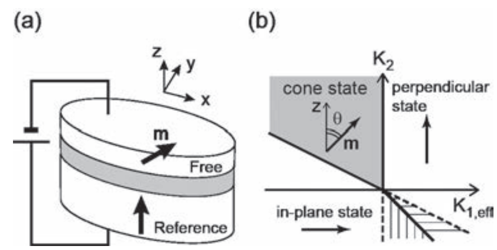

Fig. 1. (a) MTJ with elliptic cylinder shape and definitions of Cartesian coordinates (x, y, z). (b) Phase diagram of magnetic film with uniaxial anisotropy constants, $K_{1,\mathrm{eff}}$ and K_{u2}, at equilibrium state. The shaded area represents the cone-state phase, where the film is conically magnetized with polar angle, θ. The bistable regions are hatched.

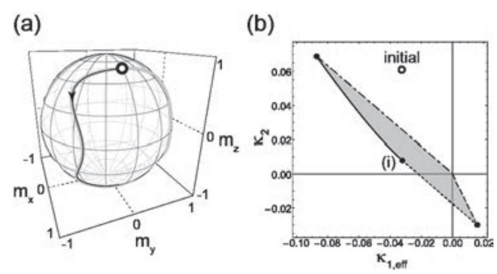

Fig. 2. (a) Contour curve of ε including $m^{(0)}$ (thick gray curve) and simulated trajectory of m (thin black curve) for $0 \le t \le 0.56$ ns on the Bloch sphere. (b) Phase diagram in $\kappa_{1,\mathrm{eff}}$ - κ_2 space. The switching region is indicated by shade. Open circle represents anisotropy constants at initial state, ($\kappa_{1,\mathrm{eff}}^{(0)}$, $\kappa_2^{(0)}$).

2:15

FC-02. Field-Free Switching of Perpendicular Magnetization through Voltage-Gated Spin Hall Effect.

S. Peng[1,2], W. Kang[1], X. Li[2], H. Zhang[1], Z. Wang[1], Y. Zhang[1], K. Wang[2] and W. Zhao[1]
1. Fert Beijing Institute, BDBC, School of Electronic and Information Engineering, Beihang University, Beijing, China; 2. Department of Electrical Engineering, University of California, Los Angeles, CA, United States

Magnetic random access memory (MRAM) is becoming a mainstream memory due to its non-volatility, unlimited endurance, and low power consumption.[1,2] One of the key challenges for MRAMs is to efficiently manipulate the magnetization of the free layer. Recent studies demonstrate that data writing can be achieved by spin Hall effect (SHE), in which an in-plane charge current flowing in a nonmagnetic layer generates a vertical spin current, leading to the magnetization reversal of the adjacent magnetic layer.[3] Voltage-controlled magnetic anisotropy (VCMA) is another promising method for low-power write operations.[4] It enables reducing the interfacial perpendicular magnetic anisotropy (PMA) by applying a voltage, thus lowering or even eliminating the energy barrier during switching. With a combination of the SHE and VCMA effect, it is feasible to decrease the critical SHE switching current by applying a gate voltage.[5-7] However, an external magnetic field is commonly needed for switching of perpendicularly magnetized tunnel junctions (pMTJs) with SHE.[8] Recently, field-free switching of perpendicular magnetization was reported in the IrMn/CoFeB/MgO structure, where the antiferromagnetic material IrMn provides an exchange bias and the SHE at the same time.[9-10] Nevertheless, the VCMA effect in the IrMn/CoFeB/MgO structure has never been reported. Consequently, it is essential to investigate the VCMA in the IrMn/CoFeB/MgO-based pMTJs and to study the voltage-gated SHE switching in this structure. In this paper, we first studied the VCMA effect in the IrMn/CoFeB/MgO structure. The films consisting of IrMn(5nm)/$Co_{40}Fe_{40}B_{20}$(1.05nm)/MgO(2.5nm)/Al_2O_3(5nm) were deposited on thermally oxidized Si substrate using magnetron sputtering, followed by annealing at 150°C for 30 minutes in vacuum (<10^{-7} Torr). Subsequently, the films were patterned into Hall bar devices with dimension of 20 μm × 130 μm. Figure 1(a) presents the anomalous Hall resistance under an in-plane magnetic field. When a gate voltage is applied, the interfacial PMA is changed due to the VCMA effect, leading to variations of the anomalous Hall resistance, as clearly shown in the right inset of the Fig. 1(a). Using the method reported in Ref. 11, we acquire the electric field dependence of the interfacial anisotropy constant, as shown in Fig. 1(b). From the slope of the linearly fitting, we obtain a VCMA coefficient of 39 fJ/Vm for the IrMn/CoFeB/MgO structure, which is comparable with that of Ta/CoFeB/MgO structure.[12] Figure 2(a) illustrates the voltage-gated SHE switching of the IrMn/CoFeB/MgO-based pMTJ device. With the aid of an exchange bias generated by the IrMn layer, field-free magnetization switching can be achieved by flowing an in-plane charge current in the IrMn layer. In addition, when a gate voltage is applied, the energy barrier for magnetization reversal can be reduced due to the VCMA effect, as shown in Fig. 2(b). Consequently, the critical SHE switching current can be controlled by the gate voltage. Micromagnetic studies are performed to study the voltage-gated SHE switching. Figure 2(cd) present the results. When no gate voltage is applied, field-free switching is observed, but a large SHE current of 45 MA/cm^2 is required. When a gate voltage of 1.5 V is applied, the critical switching current drops to 4.5 MA/cm^2, which is 10-folds decreasing. These results verify that a gate voltage can be used to effectively modulate the SHE-driven switching. A spintronics memory array with multiple MTJs located on a single IrMn strip is proposed and evaluated with hybrid pMTJ/CMOS circuit simulations. During switching, a bidirectional current is applied in the IrMn strip, combined with a voltage above the MTJs for addressing. It is worth noticing that all MTJs on a single IrMn strip share two driving transistors and can be switched simultaneously, leading to high density and fast speed. Moreover, the energy dissipation is much lower than that of conventional SHE-driven switching. In summary, we experimentally investigated the VCMA effect in the IrMn/CoFeB/MgO structure and obtained a VCMA coefficient of 39 fJ/Vm, which is comparable with that of Ta/CoFeB/MgO structure. Field-free switching of perpendicular magnetization is demonstrated with the aid of an exchange bias generated by the antiferromagnetic IrMn layer. Moreover, when a gate voltage of 1.5 V is applied, the critical switching current can be reduced by 10 times due to the VCMA effect. A spintronics memory array based on this pMTJ was proposed and evaluated by hybrid pMTJ/CMOS circuit simulations. The results demonstrated that reliable and fast-speed write operations can be achieved by the voltage-gated SHE. We believe our work may promote the development of high-density and low-power spintronics memories with pMTJs.

[1] D. Kent and D. C. Worledge, "A new spin on magnetic memories," *Nat. Nanotechnol.*, vol. 10, no. 3, pp. 187–191, 2015. [2] S. Peng *et al.*, "Giant interfacial perpendicular magnetic anisotropy in MgO/CoFe/capping layer structure," *Appl. Phys. Lett.*, vol. 110, p. 072403, 2017. [3] L. Liu, C.-F. Pai, Y. Li, H. W. Tseng, D. C. Ralph, and R. a Buhrman, "Spin-torque switching with the giant spin Hall effect of tantalum," *Science*, vol. 336, no. 6081, pp. 555–558, May 2012. [4] W.-G. Wang, M. Li, S. Hageman, and C. L. Chien, "Electric-field-assisted switching in magnetic tunnel junctions," *Nat. Mater.*, vol. 11, no. 1, pp. 64–68, 2012. [5] L. Liu, C.-F. Pai, R. D.C., and R. A. Buhrman, "Gate voltage modulation of spin-Hall-torque-driven magnetic switching," *arXiv*:1209.0962, 2012. [6] T. Inokuchi *et al.*, "Improved read disturb and write error rates in voltage-control spintronics memory (VoCSM) by controlling energy barrier height," *Appl. Phys. Lett.*, vol. 110, no. 25, p. 252404, 2017. [7] H. Zhang, W. Kang, L. Wang, K. L. Wang, and W. Zhao, "Stateful Reconfigurable Logic via a Single-Voltage-Gated Spin Hall-Effect Driven Magnetic Tunnel Junction in a Spintronic Memory," *IEEE Trans. Electron Devices*, vol. 64, no. 10, pp. 4295–4301, 2017. [8] L. Liu, O. J. Lee, T. J. Gudmundsen, D. C. Ralph, and R. A. Buhrman, "Current-induced switching of perpendicularly magnetized magnetic layers using spin torque from the spin hall effect," *Phys. Rev. Lett.*, vol. 109, no. 9, p. 096602, 2012. [9] Y.-W. Oh *et al.*, "Field-free switching of perpendicular magnetization through spin–orbit torque in antiferromagnet/ferromagnet/oxide structures," *Nat. Nanotechnol.*, vol. 11, no. 10, pp. 878–884, 2016. [10] W. Zhang *et al.*, "Giant facet-dependent spin-orbit torque and spin Hall conductivity in the triangular antiferromagnet IrMn3," *Sci. Adv.*, vol. 2, no. 9, p. e1600759, 2016. [11] X. Li *et al.*, "Thermally stable voltage-controlled perpendicular magnetic anisotropy in Mo|CoFeB|MgO structures," *Appl. Phys. Lett.*, vol. 107, no. 14, p. 142403, 2015. [12] J. G. Alzate *et al.*, "Temperature dependence of the voltage-controlled perpendicular anisotropy in nanoscale MgO|CoFeB|Ta magnetic tunnel junctions," *Appl. Phys. Lett.*, vol. 104, no. 11, p. 112410, 2014.

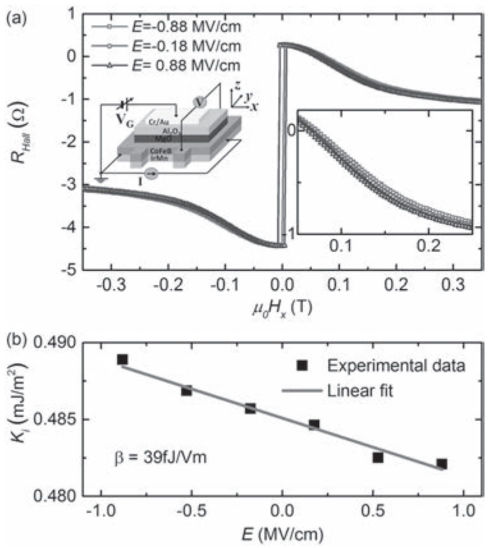

Fig. 1. (a) Anomalous Hall resistance (R_{Hall}) of the IrMn/CoFeB/MgO structure under an in-plane magnetic field ($\mu_0 H_x$) and a gate electric field (E). The left inset illustrates the Hall bar structure in the measurements. The right inset shows an amplification of the figure with 0.05T<$\mu_0 H_x$<0.25T. (b) Interfacial anisotropy constant (K_i) as a function of the electric field (E) in the MgO layer.

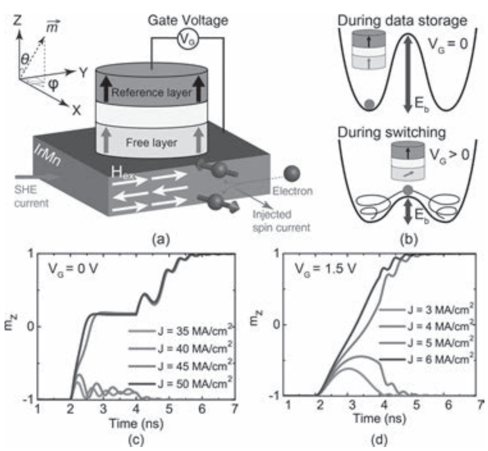

Fig. 2. (a) (b) Schematic of (a) the IrMn/CoFeB/MgO-based pMTJ device and (b) the effect of a gate voltage (V_G) on the energy barrier (E_b). (c) (d) Perpendicular component of the magnetization (m_z) under different SHE currents combined with (c) V_G=0V and (d) V_G=1.5V.

2:30

FC-03. Atomic layer number dependence of voltage-controlled magnetic anisotropy in Cr/Fe/$MgAl_2O_4$ heterostructure.

Q. Xiang[1,2], H. Sukegawa[1], M. Al-Mahdawi[1], M. Belmoubarik[1], S. Kasai[1], Y. Sakuraba[1], S. Mitani[1,2] and K. Hono[1,2]
1. Research Center for Magnetic and Spintronic Materials, National Institute for Materials Science (NIMS), Tsukuba City, Japan; 2. Graduate School of Pure and Applied Sciences, University of Tsukuba, Tsukuba, Japan

Perpendicular magnetic anisotropy (PMA) and its voltage control in magnetic heterostructures [1] are expected to be the key to achieve low-power consumption spintronic devices such as voltage-torque magnetoresistive random access memories (MRAMs). For actual high-density memory applications, large interface PMA energy density (K_i) and voltage-controlled magnetic anisotropy (VCMA) coefficient (β), e.g., K_i > 2-3 mJ/m^2 and β > 1000 fJ/Vm, are needed. In order to achieve such a large VCMA effect, exploring the origin of the VCMA effect using ideal PMA heterostructures without any interfacial defects is indispensable. Recently, large PMA energies were reported in lattice-matched Fe/$MgAl_2O_4$ [2] and Co_2FeAl/$MgAl_2O_4$ heterostructures [3]. Also, the Cr/Fe/Oxide layered structure is well-known to form quantum well (QW) states of majority spin electrons in the Fe layer, since there is no Δ_1 states near the Fermi level in metallic Cr. Note that Cr can be regarded as a "potential barrier" for Δ_1 electrons. The formed QWs can modulate the coherent tunneling behavior referred as spin dependent resonant tunneling (SDRT) effect, where the tunneling conductance enhances at specific resonant bias voltages due to different QW width, namely effective Fe thickness [4]. Associated with QW-SDRT effect, the VCMA is likely to be anomalously modulated. Hence, in this study, we focused on the Cr/ultrathin-Fe/$MgAl_2O_4$ epitaxial interfaces to achieve high K_i and β and investigate the possible influnence of QW-SDRT effect on VCMA. We report that only a monolayer thickness difference has a significant impact on the PMA energy and VCMA effect. Magnetic tunnel junction (MTJ) stacks of Cr buffer (30)/Fe (t_{Fe})/$MgAl_2O_4$ (2)/$Co_{20}Fe_{60}B_{20}$ (5)/Ru (10) (unit in nm) were epitaxially grown on an MgO(001) substrate by electron-beam evaporation, where t_{Fe} = 0.70, 0.84, 0.98 nm and correspond to 5, 6, 7 atomic layers, respectively. The top 5-nm CoFeB is the reference layer with in-plane magnetization for evaluating the VCMA effect of the bottom Fe layer. The Cr, Fe, $MgAl_2O_4$, and CoFeB layers were post-annealed to improve their crystallinity and flatness. Magnetic properties were investigated using a vibrating sample magnetometer incorporated with superconducting quantum interference device (SQUID). After microfabrication (5×10 mm scale), magnetotransport properties of the MTJs were characterized by a Physical Property Measurement System (PPMS) at room temperature. The positive bias was defined with respect to CoFeB (electron tunneling from the bottom to top electrode). Figure 1 shows the typical in-plane magnetization curves for the MTJ stacks with different Fe thicknesses. It was found that the 5- and 6-ML Fe layers had perpendicular magnetization. Areal PMA energy density $K_{eff} \times t_{Fe}$ for the 5-ML (6-ML) Fe sample was determined to be 0.85 mJ/m^2 (0.77 mJ/m^2). We investigated the bias voltage dependence of $K_{eff} \times t_{Fe}$ for the 5- and 6-ML Fe samples using normalized tunnel magnetoresistance ratios as functions of both bias voltage and in-plane magnetic field. As clearly seen in Fig. 2, a strong SDRT effect is confirmed as significant enhancement of conductance at resonant voltages around ± 0.5V for the 5-ML sample (around 0 V for 6-ML sample). The resonant voltages agree well with those of the theoretical calculation [4]. Importantly, the areal PMA energy, $K_{eff} \times t_{Fe}$ values for the both samples behave similar with bias dependence of conductance, demonstrating strong Fe atomic layer number dependence. The underneath mechanism of the QW-SDRT modulation on VCMA is unclear, nevertheless, the modulated density of states of ultrathin Fe and the interface resonant states may play important roles. This work was partly supported by the ImPACT Program of Council for Science, Technology and Innovation, Japan.

[1] T. Maruyama, *et al*. Nat. Nanotech. 4, 158 (2009). [2] J.W. Koo *et al*., Phys. Status Solidi RRL 8, 841 (2014). [3] H. Sukegawa *et al*., Appl. Phys. Lett. 110, 112403 (2017). [4] Z. Lu *et al*., Phys. Rev. Lett. 94, 207210 (2005)

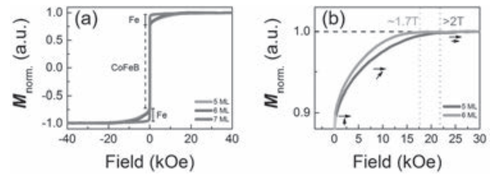

Fig. 1. a) Normalized magnetizations as a function of in-plane magnetic fields for ultrathin-Fe/$MgAl_2O_4$/CoFeB MTJs with 5-7 ML thick Fe; b) inplane component from ultrathin-Fe layer

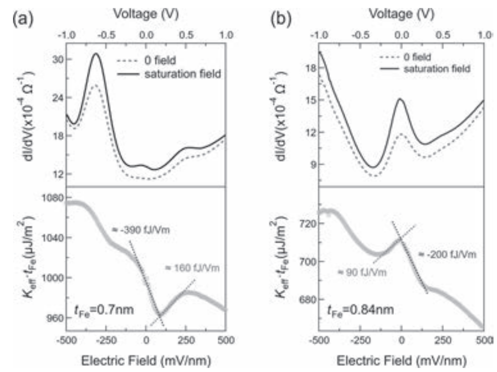

Fig. 2. dI/dV spectra and VCMA curves of a) 0.7nm (5-ML) Fe sample and b) 0.84nm (6-ML) Fe sample. dI/dV spectra indicate different QWs of different t_{Fe} samples, guide line(dot line) in VCMA curves indicate different local VCMA coefficients(slope) with differrent QWs.

2:45

FC-04. The lower bound of the write error rate of a voltage-torque MRAM.

H. Imamura[1] and R. Matsumoto[1]
1. Spintronics RC, AIST, Tsukuba, Japan

Spin manipulation by voltage controlled magnetic anisotropy (VCMA) in a thin ferromagnetic film has attracted much attention as a key phenomenon for low power spintronics memory called "voltage-torque magnetoresistive random access memory (VT-MRAM)" [1-7]. In the VT-MRAM the information is stored by the direction of magnetic moments in a perpendiculary magnetized recording layer, and an in-plane magnetic field is applied to the memory cells. Application of the voltage pulse eliminates the MA and induces the precessional motion of the magnetic moments around the external magnetic field. If the voltage is turned off at one-half period of the precession the magnetization switching completes. It was shown that an MgO-based magnetic tunnel junction is a powerful candidate for a memory cell of the VT-MRAM because of the fast (less than 1 ns) switching time as well as of the low (order of 10^{-5}) write error rate (WER) [7]. For practical application, however, the WER of less than 10^{-9} is necessary. The thermal distribution of the equailibrium state and switching trajectory are the main origins of the WER. The dependence of the WER on the material parameters such as the anisotropy constant (K) and the Gilbert damping constant (α) has been studied by solving the Langevin equations [6,7]. It was predicted that the WER decreases with decrease of α and/or with increase of K. Although the Langevin equation based numerical studies are useful to calculate the statistical properties, it is very difficult to estimate the practical value of the WER because of the huge computational cost. For example, in order to evaluate the WER less than 10^{-9} enormous amount of trials more than 10^{10} are required. In this paper we performed the Fokker-Planck (FP) equation based analysis [8] of the WER. The FP equation is a differential equation for the probability distribution function and can be solved analytically under appropriate assumptions. The macro-spin model is employed to represent the dynamics of the magnetization in the recording layer. The direction of the magnetization is expressed by the unit vector m=($\sin\theta\cos\phi$, $\sin\theta\sin\phi$, $\cos\theta$), where θ and ϕ are the polar and azimuthal angles, respectively. We assume that the easy axis of the MA is the z-axis, and the MA vanishes during the voltage pulse. The magnetic field (H) is applied to the positive x-direction during the voltage pulse. The initial state is assumed to distribute around $\theta=0$ because of the thermal agitation field. Since the thermal stability factor (Δ) of VT-MRAM should be larger than 60 the distribution function of the initial state can be well approximated by the Gaussian distribution on the upper hemisphere. During the voltage pulse the magnetization precesses around the x-axis with the frequency of $f=\gamma H/[2\pi(1+\alpha^2)]$. Introducing $\mu=\cos(\theta-2\pi f t)$ the FP equation during the voltage pulse is given by $\partial F(\mu,\tau)/\partial\tau=\partial/\partial\mu[(1-\mu^2)\partial F(\mu,\tau)/\partial\mu]$, where $\tau=[\alpha/(1+\alpha^2)][(\gamma k_B T)/(\mu_0 M_s V)]t$ is the dimensionless time. Here γ is the gyromagnetic ratio, k_B is the Boltzmann constant, T is temperature, μ_0 is the vacuum permeability, M_s is the saturation magnetization, and V is the volume of the recording layer. This FP equation can be solved by using the Legendre polynomial expansion. The WER is estimated by setting pulse width (τ_p) to the half period of the precession and integrating $F(\mu, \tau_p)$ on the uppre hemisphere. Figure 1 shows the Δ-dependence of WER for various values of τ_p. For all values of Δ the WER decreases with decease of τ_p, which means the WER decreases with increase of H. From the definition of τ one can see that WER decreases with decreasing (increasing) α and/or T (M_s and/or V). Assuming that $M_s = 10^6$ A/m, T = 300 K, V = $\pi\times15^2\times2$ nm^3, the value of τ_p = 0.02 corresponds to the pulse width of 0.78 ns. For all values of τ_p the WER is a decreasing function of Δ. It should be noted that the decreasing rate of WER decreases with increase of Δ, which implies that the WER remains finite in the limit of $\Delta\to\infty$. The analytical expression of the lower bound of the WER, $\lim_{\Delta\to\infty}$ WER, can be calculated by setting the initial distribution to be a delta function. After some algebra we obtain $\lim_{\Delta\to\infty} \mathrm{WER} = 1/2 - \Sigma_{n=1}^{\infty} \{(2n+1)/[2(n+1)]\, P_{n-1}(0) \exp[-n(n+1)\tau_p]\}$, where $P_{n-1}(0)$ is the (n-1)-th Legendre function. Figure 2 shows the lower bound of the WER as a function of τ_p. The circles indices WER at τ_p = 0.02, 0.04, 0.06, 0.08, and 0.1. The results show that in order to achieve the WER less than 10^{-9} τ_p should be less than 0.03. The authors would like to thank T. Nozaki and S. Yuasa for valuable discussions. This work was partly supported by the ImPACT Program of the Council for Science, Technology and Innovation and JSPS KAKENHI Grant Number 16K17509.

[1] M. Weisheit, S. Fahler, A. Marty, Y. Souche, C. Poinsignon, and D. Givord, Science 315 (5810), 349 (2007). [2] T. Maruyama, Y. Shiota, T. Nozaki, K. Ohta, N. Toda, M. Mizuguchi, A. A. Tulapurkar, T. Shinjo, M. Shiraishi, S. Mizukami, Y. Ando, and Y. Suzuki, Nat Nanotechnol 4 (3), 158 (2009). [3] T. Nozaki, Y. Shiota, M. Shiraishi, T. Shinjo, and Y. Suzuki, Applied Physics Letters 96 (2), 022506 (2010). [4] S. Kanai, M. Yamanouchi, S. Ikeda, Y. Nakatani, F. Matsukura, and H. Ohno, Applied Physics Letters 101 (12), 122403 (2012). [5] H. Noguchi, Ikegami, K., Abe, K., Fujita, S., Shiota, Y., Nozaki, T., Yuasa, S., Suzuki, Y., IEEE Tech. Dig. IEDM, 27.5 (2016). [6] Y. Shiota, T. Nozaki, S. Tamaru, K. Yakushiji, H. Kubota, A. Fukushima, S. Yuasa, and Y. Suzuki, Applied Physics Express 9 (1), 013001 (2016). [7] Y. Shiota, T. Nozaki, S. Tamaru, K. Yakushiji, H. Kubota, A. Fukushima, S. Yuasa, and Y. Suzuki, Applied Physics Letters 111 (2), 022408 (2017). [8] W. F. Brown, Physical Review 130, 1677 (1963).

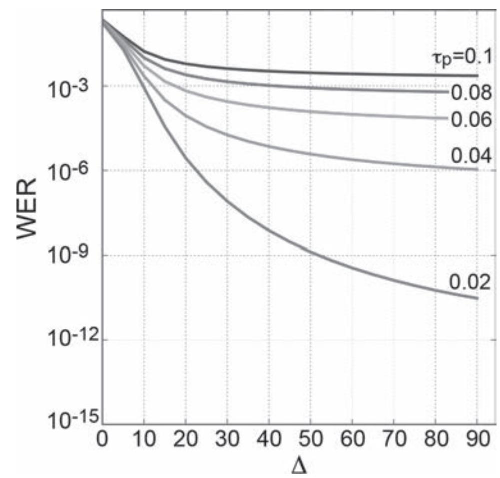

Fig. 1. WER is plotted as a function of Δ for τ_p=0.02, 0.04, 0.06, 0.08, and 0.1.

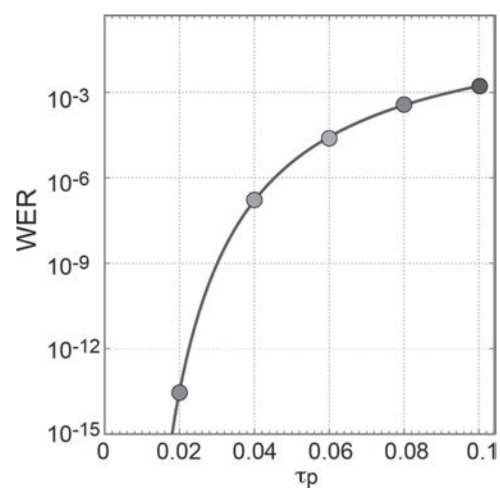

Fig. 2. WER in the limit of $\Delta \to \infty$ is plotted as a function of τ_p. The values at τ_p = 0.02, 0.04, 0.06, 0.08, and 0.1 are indicated by the circles.

3:00

FC-05. Study of voltage-controlled perpendicular magnetic anisotropy in Ta/FeB/MgO and W/FeB/MgO nanowires by the Hall effect measurements.

V. Zayets[1], T. Nozaki[1], A. Fukushima[1] and S. Yuasa[1]
1. Spintronics Center, National Institute of Advanced Industrial Science and Technology (AIST), Tsukuba, Japan

Voltage-controlled perpendicular magnetic anisotropy (PMA) is a recently-found effect, which may be used in MRAM and all-metal transistor[1] applications as a magnetization-switching mechanism. Conventionally the strength of the voltage-controlled PMA effect is measured in a MTJ, which electrodes are magnetized perpendicularly each other[2]. The angle between magnetization of electrodes is evaluated from the magneto-resistance at different applied voltages. From this data the strength of the voltage-controlled PMA is estimated. The second method is the measurement of the dependence of the coercive field on a gate voltage[3-5]. The second method is the direct measurement the voltage-controlled PMA effect and it can reveal different interesting features of the effect. However, the magnetization switching is thermo-activated process and the required high-precission measurement of the coercive field is difficult. Therefore, the measurements of the voltage-dependence of the coercive field have been reported only for the cases when the change of the coercive field is substantial. It is the case when the sample temperature is near the Curie temperature[3] or the change of the coercive field is larger than 100 Oe[4] or when the easy axes of the sample is near the transition from in-plane to out-plane direction[5]. We have developed a method of a precise measurement of the coercive field. Main merit of this method is that it is able to detect even very small changes of the coercive field. Therefore, the magnitude of the voltage-controlled PMA effect can be measured in a variety of different samples of different structure and of different magnitude of the voltage-controlled PMA. The coercive field is measured by measuring Hall angle in a pulsed magnetic field. The precise value of the coercive field was evaluated from two sets of the measurements. In the first measurement, the magnetic pulse of a gradually-increased amplitude was applied and the switching field was measured. In the second measurement, the magnetic pulse of constant amplitude was applied and the switching probability was measured. A sufficient number of those two combined measurements and a statistical analysis were used to evaluate the coercive field. Details of the proposed method will be described at conference site. The precession of measured coercive field was better than 1 Oe. We have studied the voltage-controlled PMA effect in Ta(2)/FeB(1.1)/MgO, W(3)/FeB(1.1)/MgO, Ta(2)/FeB(0.5)/W(0.8)/FeB(0.5)/MgO and W(3)/ $(FeB/W)_n$ /FeB(0.2)/MgO multilayers. The width of fabricated nanowires was 100, 200, 400 and 1000 nm. A pair of 80-nm-wide Hall nanoprobes was connected to the middle of nanowire. A thick 6-nm MgO gate oxide and Ta(1)/Ru(5) gate electrode were used (Fig. 1(a)). All studied samples show the increase of the coercive field under a negative gate voltage and the decrease of the coercive field under a positive gate voltage (See Fig.1(b)). The polarity of the voltage-controlled PMA effect is the same as when it was measured by another method[2]. Additionally to change of the coercive field, there is a small change of the Hall angle. The Hall angle increases at a negative gate voltage and decreases at a positive gate voltage. Figure 2(a) shows coercive field of Ta(2)/FeB(0.5)/W(0.8)/FeB(0.5)/MgO 400-nm-wide nanowire as a function of the gate voltage. In the measurement range, the dependence is linear. The magnitude of the voltage-controlled PMA is 11 Oe per 1 V or 1.8 Oe/(V/nm). All fabricated samples shows the magnitude of the voltage-controlled PMA effect in the range between 5 and 11 Oe / V. Figure 2(b) shows the Hall angle as a function of the gate voltage for the same nanowire. The change is about 5 mdeg per 1 V of gate voltage or 2.5% per 1 V. Additionally, there is a hysteresis loop. The CV-measurements indicate that the hysteresis loop might be due to the deep defects in the thick MgO gate oxide. The defects in the MgO gate oxide might be due to a low annealing temperature of our samples (~200^0 C). Figure 2(c) shows the magnetization switching probability as a function of an external magnetic field. The switching probability is clearly distinguished at different gate voltages. A feature, which is substantially different for all our studied samples, is the value of the Hall angle. The Hall angle in the Ta(2)/FeB(1.1)/MgO was the largest (1200 mdeg). The Hall angle decreases to 30-50 mdeg, when the number of the W/FeB interfaces increases. It is known[6] that the polarity of the Anomalous Hall effect is opposite for electrons and holes. The measurements of the ordinary Hall effect and anomalous Hall effect is a standard method[6] to determine the type of conductivity in a metal and to estimate the position of the Fermi level. The study the dependence of the magnitude of the voltage-controlled PMA effect on the conductivity type (the Hall angle) will be reported at the conference site.

[1] V. Zayets, T. Nozaki, A. Fukushima, S. Yuasa, Japanese patent application 2017-001433. [2] T. Nozaki *et al.*, Phys. Rev. Applied 5, 044006 (2016). [3] D. Chiba *et al.*, Nature Mat. 10, 853 (2011). [4] H. Meng *et al.*, APL 105, 042410 (2014). [5] M. Endo *et al.*, APL 96, 212503 (2010). [6] Colin M. Hurd "The Hall effect in metals and alloys", Plenum Press, 1972

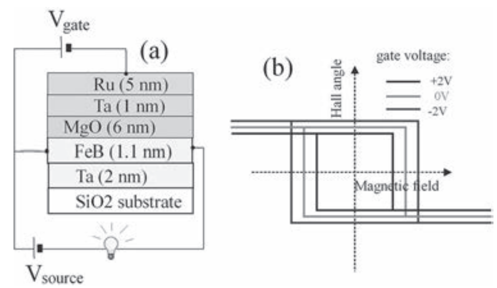

Fig. 1. (a) FeB/Ta nanowire with MgO gate oxide and Ta/Ru gate electrode. (b) Hall angle as function of magnetic field for different gate voltage (schematic). Under a negative gate voltage both the coercive field and the Hall angle increase.

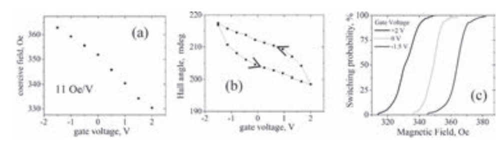

Fig. 2. Coercive field of Ta(2)/FeB(0.5)/W(0.8)/FeB(0.5)/MgO nanowire as a function of gate voltage which measured with 1000-ms-long magnetic pulses. Each point was evaluated from measured 300 loops. (b) Hall angle of the nanowire as function of gate voltage. (c) Switching probability from magnetization-up to magnetization-down direction as a function of external perpendicular magnetic field. Data was obtained from measured 300 loops.

3:15

FC-06. Electric-field effect on the exchange stiffness in CoFeB/MgO stacks.

N. Ichikawa[1], *T. Dohi*[1], A. Okada[1], H. Sato[1,2], S. Fukami[1,2] and H. Ohno[1,2]
1. RIEC, Tohoku University, Sendai, Japan; 2. CSIS, Tohoku University, Sendai, Japan

Exchange stiffness plays a crucial role in determining the performance of various magnetic and spintronic devices. For nanoscale magnetic tunnel junctions, which are the heart of nonvolatile spintronics memory devices, exchange stiffness governs the magnetization reversal mode and determines the thermal stability factor with an incoherent reversal.[1,2)] For other devices utilizing domain wall or skyrmion,[3,4)] size and stability of such magnetic solitons also depend on the exchange stiffness.[5)] To access the physics of magnetic parameters like the exchange stiffness in terms of electronic structures, application of electric field often provides a useful insight.[6)] Recently, electric-field effect on the exchange stiffness constant A_S was observed in a magnetic domain structure[7,8)] and spin-wave resonance.[9)] In addition, first-principles calculation predicts that the electric field could modulate the exchange stiffness.[10,11)] In this study, we investigate the electric-field effect on A_S of CoFeB/MgO stacks, a key building block of nonvolatile spintronics devices. A_S is evaluated from an observation of domain structure and an analytical model[12)] describing the relation between the domain period D_P and A_S. The stacks, Ta/ CoFeB (t_{CoFeB} = 1.18 - 1.25 nm)/ MgO (2 nm)/ Al_2O_3 (5 nm), are deposited by dc/rf magnetron sputtering on thermally oxidized Si substrate, and are annealed at 350°C for 1 h. Subsequently, they are processed into a capacitor structure to apply electric fields. Indium tin oxide (30 nm) is deposited and patterned into a transparent top electrode. Positive gate voltage V_G is defined in a direction where electrons are accumulated at CoFeB/MgO interface. The applied V_G of +10V corresponds to an electric field of approximately 0.2 V/nm. Magnetic anisotropy with electric field is first determined from ferromagnetic resonance. Electric-field dependence of effective anisotropy field H_K^{eff} for each t_{CoFeB} is shown in Fig. 1. Sign of H_K^{eff} is positive for all samples, indicating a perpendicular easy axis. H_K^{eff} varies almost linearly with the applied electric field for all the thicknesses. Closer look at the slope reveals that the electric-field effect slightly increases with decreasing t_{CoFeB} as observed in a previous work,[13)] which is accounted for by a screening effect where the electric field penetrates only into sub-nanometer region near the interface. Domain structure under electric field for the same samples is then observed by magneto-optical polar-Kerr-effect microscope. The details of measurement and analysis procedure are described in Ref. 8. Kerr microscope images of the domain structure are taken after ac-demagnetization (Fig. 2(a)). To analyze the structure, we conduct image processing by two-dimensional fast Fourier transform (2D-FFT). This process yields a circular-shape pattern as shown in Fig. 2(b), indicating in-plane isotropic domain structure. The inverse of distance from center in the 2D-FFT pattern represents the distance in real space and D_P is defined as the distance for the peak. Figures 2(c) – (f) show electric-field dependence of D_P for the samples with different t_{CoFeB}. Interestingly, the electric-field modulation of D_P shows non-linear behavior for all t_{CoFeB} unlike the case for H_K^{eff} that varied almost linearly with the electric field (Fig. 1). Note that the variation in D_P in a small electric field region ($|E| <\sim \pm 0.1$ V/nm) is consistent with our previous work,[8)] whereas non-linear response of D_P to the electric field observed in larger region ($|E| >\sim \pm 0.2$ V/nm) has not been reported so far. We finally quantify the electric field effect on A_S using an analytical model that describes the relation between A_S, H_K^{eff}, M_S, and D_P in thin films whose thickness is much smaller than D_P.[12)] Here, spontaneous magnetization M_S is assumed to be unchanged with the electric field because the expected number of electrons accumulated/depleted under $E = \pm 0.3$ V/nm is estimated to be only about 0.008 per a Fe(Co) atom, which is too small to observe sizable change in M_S according to the Slater-Pauling curve.[8)] The analysis with the obtained electric-field dependence of H_K^{eff} (Fig. 1) and D_P (Fig. 2) reveals that A_S shows non-linear response to the electric field and the direction of response depends on the magnitude of the applied electric field. Such a non-monotonic variation in A_S implies that the A_S of CoFeB/MgO is governed by more than two factors, such as p-d hybridization[10,11)] and itinerant 3d band,[14)] which is expected to have an opposite response to the electric field. These results offer significant insight into the understanding of the exchange stiffness in ultrathin magnetic systems and engineering of spintronics devices operated under electric fields. We thank M. Tsujikawa and M. Shirai for fruitful discussion. This work was supported in part by JST-OPERA, JSPS KAKENHI 16J05455, and GP-Spin of Tohoku Univ.

1) S. Ikeda *et al*., Nat. Mater. 9, 721 (2010). 2) H. Sato *et al*., Appl. Phys Lett. 99, 042501 (2011). 3) S. S. P. Parkin *et al*., Science 320, 190 (2008). 4) A. Fert *et al*., Nat. Nanotechnol. 8, 152 (2013). 5) M. Heide *et al*., Phys. Rev. B 78, 140403 (2008). 6) H. Ohno et al., Nature 408, 944 (2000). 7) F. Ando *et al*., Appl. Phys. Lett. 109, 022401 (2016). 8) T. Dohi *et al*., AIP Adv. 6, 075017 (2016). 9) T. Dohi *et al*., Appl. Phys. Lett. 111, 027403 (2017). 10) M. Oba *et al*., Phys. Rev. Lett. 114, 107202 (2015). 11) A-M. Pradipto *et al*., Phys. Rev. B 96, 014425 (2017). 12) A. L. Sukstanskii *et al*., J. Magn. Magn. Mater. 169, 31 (1997). 13) M. Endo *et al*., Appl. Phys. Lett. 96, 212503 (2010). 14) C. Takahashi *et al*., J. Phys.: Condens. Matter. 19, 365233 (2007).

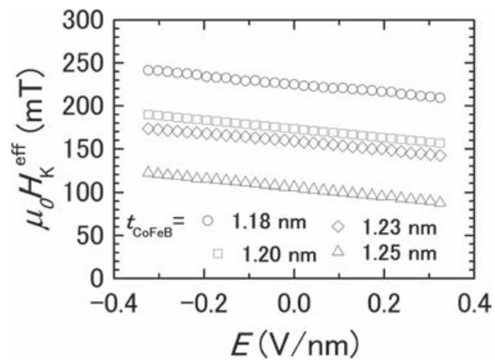

Fig. 1. Electric field E dependence of effective $\mu_0 H_K^{eff}$ for different CoFeB thicknesses t_{CoFeB}.

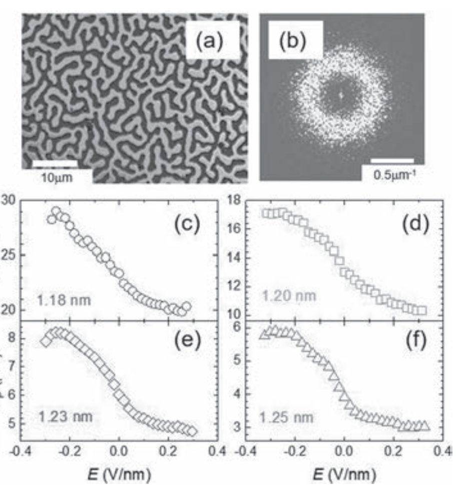

Fig. 2. (a) Typical domain image and (b) its 2D-FFT pattern. (c)–(f) Electric-field E effect on domain period D_P for each t_{CoFeB}.

3:30

FC-07. Voltage-Controlled Magnetic Tunnel Junctions for Processing-In-Memory Implementation.

L. Wang[1,2], K. Wang[1], F. Ebrahimi[2], X. Li[2], Y. Huang[1], C. Zhao[3], K. Wang[2] and W. Zhao[1]
1. Beihang University, Beijing, China; 2. UCLA, LA, CA, United States; 3. Institute of Microelectronics, Chinese Academy of Sciences, Beijing, China

Data transport between the processor and the memory in conventional von-Neumann architecture results in huge power consumption (power wall) and performance degradation (memory wall), known as the von-Neumann bottleneck, which becomes increasingly challenging in current big-data era [1]. Previous studies have shown that moving data is even much more expensive than computing itself [2]. Memory-centric processing-in-memory (PIM) paradigm has been considered as an effective way to address such a data transport bottleneck and maintain the data locality by embedding computation capability into the memory. On the road towards implementing such a promising architecture, finding a novel memory that is able to support dense data storage and logic processing capability is the key step. Unfortunately, until now, such promising studies cannot render practical prototype designs owing to the incompatibility of the state-of-the-art logic and memory technologies within the same die. Recently, the emergence of nonvolatile memories, such as resistive random access memory, phase change memory, and magnetic RAM (MRAM), provide great potential as candidates for PIM implementation. The earliest attempt is based on the material implication with resistive devices [3], which can form a complete Boolean logic set, however, relies on lengthy iteration processes for some certain logic functions. On the other hand, PIM studies based on spintronic devices, e.g., magnetic tunnel junctions (MTJs), have also been widely reported in literature [4]. In comparison with resistive devices, spintronic devices generally can allow for higher endurance, higher speed, and lower power consumption for PIM implementation. In this abstract, we report a voltage-controlled MTJ device, which is a potential candidate for efficient PIM implementation. We fabricated 60/80 nm MTJ devices and characterized at room temperature. The utilization of a voltage (via voltage-controlled magnetic anisotropy, VCMA) instead of a current for MTJ switching is promising to achieve ultralow-power memory and PIM by significantly reducing Joule heating. As shown in Fig. 1(b), the magnetic field for magnetization switching of the MTJ device can be tuned by V_b, which can be exploited for stateful logic operations. The key idea is to program the magnetization or resistance state (denoted as logic value, R) of the MTJ based on the configuration of V_b and H_{ex} (denoted as two logic inputs, p and q). In our experimental demonstration, we set R_{ap} and R_p denote logical value "1" and "0", respectively. Further, we set two V_b, i.e., V_H = +1.0 V and V_L = - 1.0V, denote the logical values "1" and "0" of input p, respectively. Accordingly, we can obtain four critical H_{ex}, denoted as H_1, H_2, H_3, and H_4, respectively, under V_H and V_L for MTJ magnetization switching operations, as shown in Fig. 1(c). In this configuration, we choose H_H and H_L to denote the logical values "0" and "1" for input q, respectively. In practice, the magnetic field can be generated via a current line similar to that in the field-driven toggle-MRAM. In a practical memory chip, the translation between the logical signals and the physical signals can be automatically performed via a peripheral circuity, just like the operations for a regular memory. In the following, we present the experimental demonstration of the Boolean logic functions with our fabricated VCMA-MTJ device. Furthermore, typical stateful Boolean logic functions, e.g., "OR", "AND" and "NXOR", were experimentally demonstrated with the MTJ device, as shown in Fig.2. Based on the above configuration, the final logic state of the MTJ can be transited as diagram in Fig. 1(d). Arbitrary combination logic functions can be realized in two steps: initializing and programming. An additional read step is required to readout the logic output that is in-situ stored in the MTJ (or memory cell). Our work opens up a new way for PIM implementation in spintronic memories.

[R1] G. Koo, et al., in *ACM/IEEE. MICRO-50*, 2017, pp. 219-231. [R2] J. Ahn, et al., in *ACM/IEEE. ISCA*, 2015, pp. 336-348. [R3] E. Linn, et al., *Nanotech*, 23(30), pp. 305205. 2012. [R4] Z. Chowdhury, et al., *IEEE Computer Archi Lett.*, pp(99), p. 1-1, 2017.

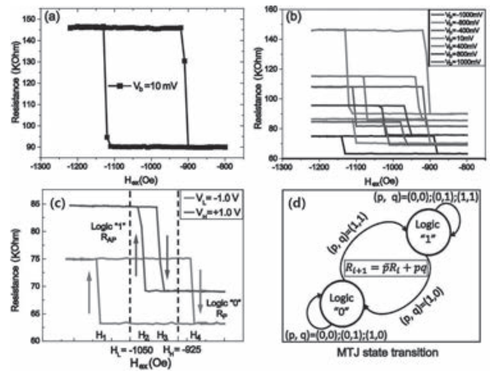

Fig. 1. Measured R-H curve with sweeping out-of-plane magnetic field of the fabricated VCMA-MTJ device, (a) under V_b = 10 mV; (b) under various V_b; (c) Measured R-H curve with Hex under V_b = - 1.0 V and +1.0 V; (d) State transition diagram of the MTJ device.

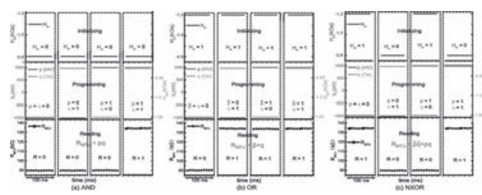

Fig. 2. Experimental demonstration of the typical Boolean logic functions with the fabricated MTJ device; (a) "AND", (b) "OR", and (c) "NXOR", respectively.

3:45

FC-08. Ultrafast random number generator based on voltage-controlled switching.

A. Fukushima[1], T. Yamamoto[1], T. Nozaki[1], K. Yakushiji[1], H. Kubota[1] and S. Yuasa[1]
1. Spintronics Research Center, National Institute of Advanced Industrial Science and Technology (AIST), Tsukuba, Japan

Random number generator is one of the key elements of security devices. We have developed a new type of random number generator (RNG) based on spin torque switching in small magnetic tunnel junctions (MTJs), named spin dice [1]. Setting the pulse current to switch an MTJ with the switching probability of 50%, the switching results are unpredictable and can therefore be used as an ideal entropy source of random number generator. In our previous study [1], we generated random numbers from an MTJ by the verbose procedure using a pair of the initial pulse and the excite pulse to obtain the same initial state and the same switching probability. Consequently, the speed of random number generation was limited to about several hundred Mbit/sec. Later, a modified version of spin dice with enhanced generation speed was proposed, where two different current pulses are applied depending on the parallel or antiparallel magnetic state, and both current pulses switch the MTJ by 50% [2]. Spin dice using a random telegraph noise type switching in a super-paramagnetic tunnel junction was also proposed as RNG with lower power consumption [3]. Recently, the voltage-controlled switching in perpendicular magnetic tunnel junctions (p-MTJ) has been attracting considerable attentions due to its high switching speed and ultra-low power consumption. We have studied the mechanism of the voltage-controlled switching events [4], where the switching probability oscillatory varies as the function of the voltage pulse width in nanosecond regime. With an appropriate pulse width, the voltage-controlled switching can yield the switching probability of 50% and therefore be used as a new type of entropy source for spin dice. Furthermore, the circuit concept of RNG based on voltage-controlled switching in an MTJ has already proposed [5]. Here, we experimentally demonstrate random number generation using voltage-controlled switching in p-MTJ. The p-MTJ has the bottom-free and top-pinned structure. The p-MTJ film was deposited on a thermally oxidized Si substrate with a thick bottom Cu lead electrode at room temperature. The film stack was [substrate/ bottom electrode/ Ta(5)/ $Co_{24}Fe_{56}B_{20}$(1.1)/ MgO(1.4)/ $Co_8Fe_{72}B_{20}$(1.4)/ W(0.3)/ Co(0.5)/ synthetic antiferromagnetic layer (CoPt/ Ru/CoPt)/ capping layer], where numbers in parentheses are the thicknesses in nm. The MgO thickness was adjusted to have the resistance-area (RA) product about 1 kΩμm^2. After the deposition, the film was annealed at 250 degrees C for 1 hour and then was fabricated into circular junctions with about 80 nm diameter (the resistance of the p-MTJ is about 200 kΩ) using a conventional microfabrication process. The switching probability (P_{sw}) of the p-MTJ was measured at room temperature using the experimental setup shown in Fig. 1. The external magnetic field (H) of 900 Oe with the polar angle θ of 80 degrees was applied to the p-MTJ to slightly tilt the free-layer magnetization from perpendicular direction. Voltage pulses with the duration time t_{pulse} were generated by a pulse generator and were fed into the p-MTJ through the rf port of a bias tee. To sense the tunneling magnetoresistance effect, the p-MTJ was biased at about 30 mV by a dc voltage source through a 1 MΩ resister. The magnetization configuration of p-MTJ, either parallel (P) or antiparallel (AP), was measured by the voltage across p-MTJ using a real-time oscilloscope. P_{sw} depends on the voltage pulse amplitude and t_{pulse}. We choose the voltage amplitude of 1.26V, which was the highest possible voltage below a breakdown voltage, to obtain the fast magnetization switching. Figure 2(a) shows the t_{pulse} dependence of P_{sw}, where P_{sw} varies oscillatory as a function of t_{pulse}. The t_{pulse} of 0.36 ns was chosen to generate random numbers from the switching results of P to AP switching, because P_{sw} was too sensitive to t_{pulse} to control at the shorter pulse range (t_{pulse} < 0.2 ns). Output voltage of the MTJ after switching trials is shown in Fig. 2(b), and its histogram is shown in Fig. 2(c). The unbalance between P and AP peaks in Fig.2(c) is due to a slightly higher switching probability (> 0.5) from AP to P state. By setting the intervals between the voltage pulses to 10 ns t_{pulse}, the speed of random number generation speed can be up to 100 Mbit/sec, which is 2 orders of magnitude faster than the previous spin dice. Moreover, the voltage-controlled spin dice is suited for the parallel processing with a large number of MTJs because each MTJ consumes a very small power. The voltage-controlled switching in p-MTJs will be one of the promising candidates for a ultrafast physical random number generator. This work was funded by ImPACT Program of Council for Science, Technology and Innovation (Cabinet Office, Government of Japan).

[1] A. Fukushima *et al.*, Appl. Phys. Express 7, 083001 (2014). [2] W. H. Choi *et al*., 2014 IEDM, 12.5.1 (2014). [3] D. Vodenicarevic *et al*., Physical Review Applied 8 (5): 054045 (2017). [4] Y. Shiota *et al.*, Appl. Phys. Lett. 111, 022408 (2017). [5] H. Lee *et al.*, AIP Advances 7, 055934 (2017).

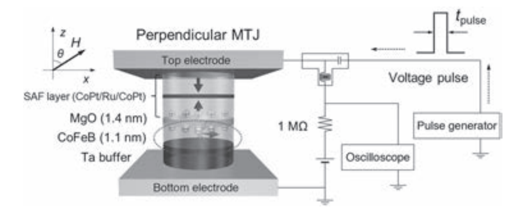

Fig. 1. Measurement setup for random number generation using a p-MTJ.

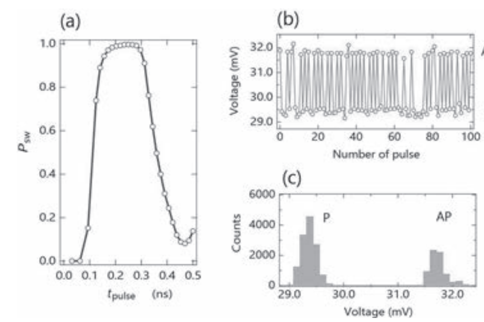

Fig. 2. Characteristics of voltage-controlled switching in a p-MTJ at V_{pulse} = 1.26 V. (a) The t_{pulse} dependence of switching probability (P_{sw}) from AP to P state. (b) Output voltage of MTJ after voltage-controlled switching events measured by a real-time oscilloscope at t_{pulse} = 0.36 ns, where P_{sw} = 0.503, and (c) histogram of the output voltage. The two peaks correspond to P and AP states.

4:00

FC-09. Withdrawn

4:15

FC-10. Effect of insertion layer on the properties of Mn_2Ru_xGa in magnetic tunnel junctions.

A. Titova[1,2], C. Fowley[1], Y. Lau[3], D. Betto[3], N. Thiyagarajah[3], G. Atcheson[3], C. Xu[1], M. Coey[3], P.S. Stamenov[3], K. Rode[3], J. Lindner[1], J. Fassbender[1,2] and A. Deac[1]
1. Institute of Ion Beam Physics and Materials Research, Helmholtz - Zentrum Dresden - Rossendorf, Dresden, Germany; 2. Institute for Physics of Solids, Technische Universität Dresden, Dresden, Germany; 3. AMBER and School of Physics, Trinity College Dublin, Dublin, Ireland

The choice of proper materials for magnetic tunnel junctions (MTJs) for storage and communication applications (like MRAM or spin-transfer-torque nano-oscillators (STNOs)) is always an issue. On the one hand, the magnetic layers should exhibit as little stray field as possible and be mostly insensitive to the external magnetic field. On another hand, in order to maximize the tunneling magnetoresistance (TMR) ratio, these materials should provide high spin polarization, or even ideally possess half-metallic properties. An option which satisfies both criteria are the compensated half-metallic ferrimagnets (CHFMs) — a class of materials predicted in 1995 by van Leuken and de Groot [1]. CHFMs are materials which behave as antiferromagnets (AFMs) with respect to external magnetic fields, since the magnetic moments of the two sublattices compensate, while simultaneously exhibiting half-metal behavior from the point of view of magnetotransport. Experimentally, the first identified zero-moment half-metal was Mn_2Ru_xGa (MRG) in 2014 [2]. It was already known that Mn-based Heusler compounds possess huge uniaxial anisotropy fields (exceeding tens of teslas [3]); this, together with their vanishing magnetization, lead to resonance frequencies of several hundred GHz in such materials [4,5], making them very attractive candidates for STNOs in the sub-THz range [6]. Such devices, due to the much higher bandwidth accessible, are expected to open the way for remote hospitals, 3-D remote meetings and much more. Earlier MRG studies have already shown that these materials exhibit tunable magnetic properties. Indeed, the compensation temperature varies between 2 and 450K, depending on the Ru concentration [2]. They also yield giant spontaneous Hall angle (7.7%) [7]. MRG has also been successfully integrated into perpendicular MRG/MgO/CoFeB MTJs, with low-bias TMR reaching up to 40 % at 10 K and 7 % at 300 K [8]. As the low value of TMR was attributed to diffusion of Mn atoms inside the MgO barrier, here, we investigate the effect of different insertion layers introduced between MRG and MgO on the magnetic properties and transport of MTJs. Mn_2Ru_xGa (23)/insertion layer(t)/MgO(1.7)/CoFeB(1)/Ta(0.3)/CoFeB(0.9)MgO(0.7)/Ta(3)/Ru(4) multilayers were deposited using a "Shamrock" fully automated sputter deposition tool (thickness given in nm). Mn_2Ru_xGa was grown by co-sputtering from a Mn_2Ga and a Ru target. Different MRG compositions ($Mn_2Ru_{1.1}Ga$, $Mn_2Ru_{0.9}Ga$, $Mn_2Ru_{0.75}Ga$, and $Mn_2Ru_{0.65}Ga$) have been obtained by varying the sputtering power of Mn_2Ga while keeping the sputtering power of Ru constant. Changing Ru concentration in MRG allows adjusting the compensation temperature T_{comp} from 2 to 450 K. We fabricated MTJs without insertion layers, as well as stacks with Ta (0.3 nm, 0.6 nm, 0.9 nm) and Al (0.3 nm, 0.6 nm, 0.9 nm) insertion layers. The switching properties of MTJs were analyzed through magnetotransport measurements as a function of applied bias voltage at room temperature. Al 0.6 nm acts as the best diffusion barrier. Magnetic properties of the multi-layers were characterized by the quantum design superconducting quantum interference device (SQUID) with a maximal applied field of 7n T at the range of temperatures from 60 K to 300 T. The magnetometry data was extracted from the typical out-of-plane hysteresis loop of the investigated MTJs (Fig.1). As the magnetic field is swept from +7 T to – 7 T, the magnetic moment of CoFeB starts to rotate first and switches close to 0 T. The sharp jump observed at -0.4 T is attributed to the reversal of MRG magnetization. With conducting the same measurements at different temperatures, it is possible to detect the compensation temperature of MRG, which will lead to a decrease of its magnetic moment and a divergence of the coercive field. The temperature with zero magnetic moment and extremely high H_c corresponds to the compensation point of MRG (the grey area in the Fig.2). In Fig.2 the temperature dependence of magnetic properties of MTJs with the same MRG composition, but different diffusion barriers, is presented. For different insertion layers, T_{comp} can shift over a large range, showing that the choice of insertion layer can have a dramatic effect on the properties of MRG. For instance, in MTJs with no insertion layer 100 K < T_{comp} < 160 K; the shift to the higher temperatures is observed for Ta 0.3 nm insertion (140 K < T_{comp} < 200 K), and to the lower temperatures with Al 0.6 nm insertion (T_{comp} < 120 K). Moreover, we demonstrate that T_{comp} can also be altered by post-annealing, as a 20 K shift is observed after annealing at 325°C for 1 hour. Mn_2Ru_xGa integrated into MTJs demonstrates a low magnetic moment, high coercivity, and thereby high immunity to the applied magnetic field over a broad temperature range (60 K – 300 K). At the same time, these MTJs show TMR even at the compensation temperature [10], highlighting a fundamental difference between an AFM and a CHFM. All these make MRG extremely attractive for spintronics applications, and for the excitation of magnetic resonances in STNOs. Part of this work was carried out under the EU Project TRANSPIRE - DLV-737038.

[1] H. van Leuken and R. A. de Groot, *Phys. Rev. Lett*. 74, 1171 (1995). [2] H. Kurt *et al*., *Phys. Rev. Lett.* 112, 027201 (2014). [3] C. Fowley *et al., J. Phys. D: Appl. Phys.,* 48 164006 (2015). [4] N. Awari *et al., Appl. Phys. Lett.* 109, 032403 (2016) [5] S. Mizukami *et al., Phys. Rev. Lett.* 106, 117201 (2011) [6] A. M. Deac *et al., Nature Physics* 4, 803 (2008). [7] N. Thiyagarajah *et al.*, *Appl. Phys. Lett.* 106, 122402 (2015). [8] K. Borisov *et al*., *Appl. Phys. Lett.* 108, 192407 (2016).

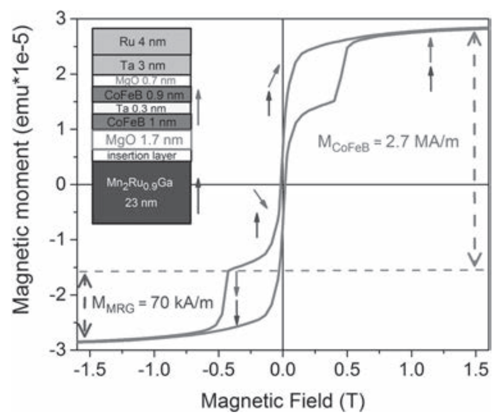

Fig. 1. Out-of-plane hysteresis loop of $Mn_2Ru_{0.9}Ga$/MgO/CoFeB MTJ at 80K with Ta 0.3 nm insertion layer.

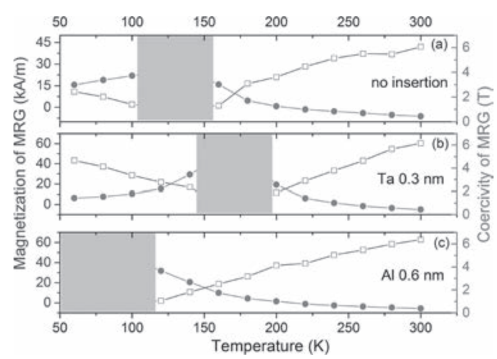

Fig. 2. Temperature dependence of magnetization (blue) and coercive field (red) on $Mn_2Ru_{0.75}Ga$-based MTJs without any diffusion barrier (a), with Ta 0.3 nm (b) and Al 0.6 nm (c) insertion layer.

4:30

FC-11. Current-induced magnetization switching in atom-thick tungsten engineered perpendicular magnetic tunnel junctions with large tunneling magnetoresistance.

M. Wang[1], W. Cai[1], *K. Cao*[1], J. Zhou[1], J. Wrona[2], S. Peng[1], H. Yang[1], J. Wei[1], W. Kang[1], Y. Zhang[1], J. Langer[2], B. Ocker[2], A. Fert[1,3] and W. Zhao[1]
1. Fert Beijing Institute, BDBC, and School of Electronic and Information Engineering, Beihang University, HaiDian District, China; 2. Singulus Technologies, Kahl am Main, Germany; 3. Unité Mixte de Physique, CNRS, Thales, Univ. Paris-Sud, Université Paris-Saclay, Palaiseau, France

Perpendicular magnetic tunnel junctions (p-MTJs) based on MgO/CoFeB structures are drawing attention as their excellent thermal stability, scaling potential, and power dissipation are significant for the study of spin-transfer torque magnetic random access memories (STT-MRAMs) [1]. In particular, p-MTJs with a MgO/CoFeB/heavy metal structure have been thoroughly studied for their enhanced perpendicular anisotropy that originates from both MgO/CoFeB and CoFeB/heavy metal interfaces [2], bringing a reasonable magnetoresistance ratio (TMR) and STT switching threshold current density (*Jc*). Moreover, p-MTJs with a double MgO/CoFeB interfaces free layer, have been shown to have a considerably better thermal stability factor (Δ) and *Jc* compared to that of p-MTJs with a single interface [3]. However, it is still challenging to realize both a large TMR and a low junction resistance in p-MTJ nanopillars that can perform current-induced magnetization switching. In this work, the bottom-pinned p-MTJ stack with atom-thick W layers and double MgO/CoFeB interfaces are patterned into nanopillars to demonstrate the current-induced magnetization switching, which present a large TMR of 249%, a resistance area product as low as 7.0 $\Omega\mu m^2$ and relatively low *Jc* at room temperature (Fig. 1). Furthermore, by using the first-principle calculation, we find that atom-thick W layers can induce resonant tunnelling transmission that are more efficient than Ta layer, providing a comprehensive explanation to the origin for this large TMR [4]. Besides, the robustness of W layers against high temperature diffusion can avoid TMR degradation during annealing (Fig. 2). We expect that this work can contribute to the research and development of STT-MRAMs.

[1] S. Ikeda et al. *Nat. Mater.* 9, 721–724 (2010). [2] S. Z. Peng et al. *Appl. Phys. Lett.* 110, 072403 (2017). [3] T. Devolder et al. *Phys. Rev. B* 93, 224432 (2016). [4] J. Q. Zhou et al. *Appl. Phys. Lett.* 109, 242403 (2016).

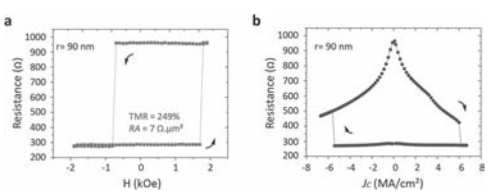

Fig. 1. Magnetoresistance and STT measurements for p-MTJ (*r* = 90 nm) at room temperature. (a) magnetoresistance as a function of out-of-plane magnetic field; and (b) STT switching measured by DC current sweep. Arrows show the perpendicular magnetization transitions from AP to P states or the opposite situation.

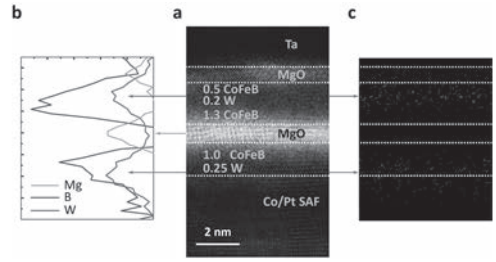

Fig. 2. Cs-corrected TEM and EELS results. (a) Cs-corrected TEM image that profiles the crystallization. The p-MTJ stack was annealed at 390 °C. (b) EELS intensities of Mg, B, and W. Arrows show the positions of the same layer in the two figures. (c) EDS mapping of the p-MTJ stack, where W is in red.

4:45

FC-12. Highly (001)-textured $MgAl_2O_4$-based magnetic tunnel junctions with large magnetoresistance over 240%.

I. Tiar[1], *H. Sukegawa*[1], X. Xu[1], M. Belmoubarik[1], H. Lee[1], S. Kasai[1] and K. Hono[1]
1. Research Center for Magnetic and Spintronic Materials, National Institute for Materials Science (NIMS), Tsukuba, Japan

Recently, $MgAl_2O_4$ spinel-based oxides (Mg-Al-O) have been investigated as alternatives to MgO for barrier materials in a magnetic tunnel junction (MTJ) [1]. Tunnel magnetoresistance (TMR) ratios over 300% at room temperature (RT) were observed in epitaxial Mg-Al-O based MTJs due to the coherent tunneling mechanism [1,2]. Nevertheless, polycrystalline Mg-Al-O based MTJs in combination with CoFeB electrodes failed to show a large TMR ratio due to the absence of (001) texture in Mg-Al-O grown on amorphous CoFeB [3]. Therefore, achieving highly (001) textured Mg-Al-O on CoFeB is critical in realizing industrially viable polycrystalline spinel-based MTJs. Here we report (001) textured Mg-Al-O barriers realized through the use of CoFe/MgO insertion between Mg-Al-O and CoFeB [4]. The insertion worked as an effective templating layer in order to obtain a highly textured Mg-Al-O(001) barrier. Large TMR ratios exceeding 240% at RT were obtained in the polycrystalline CoFeB/Mg-Al-O/CoFeB MTJs. Pseudo-spin-valve type MTJ stacks of Si/SiO_2 substrate/Ta (5)/Ru (10)/Ta (5)/$Co_{20}Fe_{60}B_{20}$ (CoFeB) (5)/$Co_{75}Fe_{25}$ (CoFe) (1)/MgO (t_{MgO} = 0-0.7)/Mg-Al-O (1.2)/CoFeB (3)/Ta (5)/Ru (5), (thickness in nm) were prepared using RF/DC magnetron sputtering system at RT (base pressure ~ $1x10^{-6}$ Pa). The Mg-Al-O layer was RF-sputtered [5] from two different sintered targets with the Mg-Al compositions of Mg-rich Mg_2Al-O_x and Al-rich $MgAl_2-O_x$. The stacks were patterned into elliptical pillars (200x400 nm^2) using electron-beam lithography, photolithography, and Ar-ion etching. The MTJs were then post-annealed at 500°C. Magnetotransport measurements were performed at RT by DC 4-probe method under in-plane magnetic fields. For microstructural analysis, high resolution scanning transmission electron microscopy (STEM) imaging was performed using an FEI G2 80-200 Titan transmission electron microscope equipped with an aberration probe corrector. Figures 1 shows the cross-sectional bright-field STEM image of an $MgAl_2-O_x$ MTJ stack with t_{MgO} = 0.7 nm. The grain-to-grain epitaxy of CoFe(B)/Mg-Al-O/CoFe(B) with the (001) orientation was observed. Therefore, the CoFe/MgO insertion effectively promotes the crystallization of Mg-Al-O. Additionally, the MgO/$MgAl_2-O_x$ bilayer was confirmed to transform into a single barrier layer. No misfit dislocations are observed within the Mg-Al-O grain. Therefore, the structural prerequisite for the coherent tunneling was fulfilled. The formation of the uniform Mg-Al-O barrier, i.e., a CoFeB/Mg-Al-O/CoFeB(001) structure, is very likely to reduce the lattice mismatch with CoFeB-based electrodes. Figure 2 shows the TMR ratio (upper panel) and resistance-area-product (*RA*) (lower panel) as a function of t_{MgO} for Mg-rich Mg_2Al-O_x and Al-rich $MgAl_2-O_x$ MTJs. The trend of ln(*RA*) versus t_{MgO} for the Mg_2Al-O_x MTJs is almost linear, suggesting that the MgO/Mg_2Al-O_x bilayer forms a physically single barrier for a wide t_{MgO} range. The TMR ratio increases with increasing t_{MgO}, and a large TMR ratio up to 242% is achieved (see the inset of Fig. 2). This significant TMR enhancement can be attributed to the Δ_1 symmetry filtering effect by the coherent tunneling through the barrier. For the $MgAl_2$-O MTJs, the non-linear In(*RA*) regime and much smaller TMR ratios are observed for t_{MgO} < 0.3 nm due to a loss of the (001) texture. Therefore, the MgO insertion and Mg-Al compositional optimization are important to obtain a (001) textured Mg-Al-O barrier. Further enhancement of TMR ratio can be expected through fine tuning of elemental composition and process optimization. This study demonstrates the industrially viability of polycrystalline spinel-based barriers for spintronic devices with a large TMR signal output. This work was partly supported by the ImPACT Program of Council for Science, Technology and Innovation, Japan, and JSPS KAKENHI Grant 16H03852.

[1]H. Sukegawa, Y. Miura, S. Muramoto, S. Mitani, T. Niizeki, T. Ohkubo, K. Abe, M. Shirai, K. Inomata, and K. Hono, Phys. Rev. B 86, 184401 (2012). [2]T. Scheike, H. Sukegawa, K. Inomata, T. Ohkubo, K. Hono, and S. Mitani, Appl. Phys. Express 9, 053004 (2016). [3]B. Tao, D. Li, H. Liu, H. Wei, J. F. Feng, S. Wang, and X. F. Han, IEEE Trans. Magn. 50, 4401004 (2014). [4]Ikhtiar, Hiroaki Sukegawa, Xiandong Xu, Mohamed Belmoubarik, Hwachol Lee, Shinya Kasai, and Kazuhiro Hono, Appl. Phys. Lett., in-press (doi: 10.1063/1.5013076) [5]M. Belmoubarik, H. Sukegawa, T. Ohkubo, S. Mitani, and K. Hono, Appl. Phys. Lett. 108, 132404 (2016).

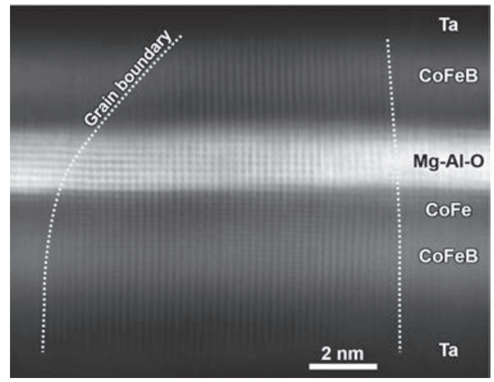

Fig. 1. Cross-sectional STEM image of the stack with CoFeB/CoFe/MgO (0.7 nm)/$MgAl_2-O_x$ (1.2 nm)/CoFeB structure.

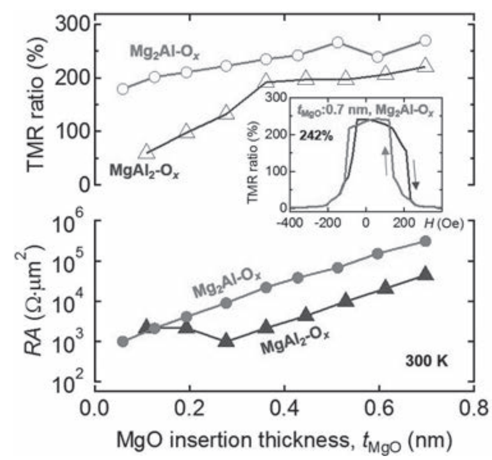

Fig. 2. TMR ratio (upper panel) and *RA* (lower panel) as a function of t_{MgO} of MTJs with 1.2 nm thick Mg_2Al-O_x and $MgAl_2-O_x$ barriers. The inset show the TMR-magnetic field (*H*) curve for Mg_2Al-O_x and t_{MgO} = 0.38 nm.

THURSDAY AFTERNOON, 26 APRIL 2018 PEONY IV, 2:00 TO 5:00

Session FD
MAGNETO-CALORIC MATERIALS I

Ramanathan Mahendiran, Co-Chair
National University of Singapore, Singapore
R. Nirmala, Co-Chair
IIT Madras, IIT Madras, India

CONTRIBUTED PAPERS

2:00

FD-01. Finding the separation between first- and second-order phase transitions in $La(Fe,Ni,Si)_{13}$ magnetocaloric materials.

L.M. Moreno-Ramírez[1], J. Law[1], C. Romero-Muñiz[2], *V. Franco*[1], A. Conde[1], F. Maccari[3], I.A. Radulov[3], K. Skokov[3] and O. Gutfleisch[3]
1. University of Sevilla, Sevilla, Spain; 2. Universidad Autónoma de Madrid, Madrid, Spain; 3. TU Darmstadt, Darmstadt, Germany

Magnetocaloric (MC) materials have the potential to renew the basis of refrigeration technologies for the next years. To date (and since first commercial devices in 1927), refrigerators operate by expansion/compression of gases in a closed circuit where the condensation/evaporation produces wasted heating/the cooling of a load. The main disadvantages of such devices are their usage of non-environmental-friendly gases (e.g. ozone depletion) and low energy efficiency. Conversely, magnetic refrigerator using magnetocaloric materials addresses these issues by utilizing solids of non-contaminating refrigerants and their prototypes show a larger energetic efficiency. In this case, the MC material replaces those gases and the expansion/compression is replaced by the application/removal of a magnetic field. The largest reversible temperature variation of a material submitted to a variable magnetic field in adiabatic conditions (ΔT_S) occurs near the temperature of a magnetic or magnetostructural phase transition. These phase transitions can be classified as first order (FOPT) or second order ones (SOPT) according to the Ehrenfest classification. Therefore, the MC characterization is not only useful from a technological point of view but can also be used to extract information about the phase transition. It has been demonstrated that assuming a power law expression for the field dependence of the magnetic entropy change (ΔS_T), taking the form $\Delta S_T(T,H)=a(T)\Delta H^{n(T,H)}$. The values of the exponent n at the transition temperature (T_{trans}) are related with the critical exponents of a SOPT as $n=1+(1-1/\beta)/\delta$, where the exponents β and δ give the temperature dependence of M at zero field and the field dependence of M at T_{trans}, respectively. For materials with long range interactions the values of $n(T_{trans})$ in SOPT are typically close to those using the critical exponents for mean field model (0.67). On the other hand, for short range interactions, the typical values are close to Heisenberg or 3D-Ising models (0.63 and 0.57, respectively). For the $n(T_{trans})$ of SOPT there exists a lower limit that corresponds to the case where the material transits from a SOPT to a FOPT character, this point is called the critical point of the second order phase transition. The value at that point is 0.4 according to the critical exponents obtained from theoretical considerations. For FOPT, even if there is no critical region, the field dependence of ΔS_T in the high field range leads to n values lower than 0.4. Therefore, a clear criterion exits to identify the change from SOPT to FOPT according to the values of $n(T_{trans})$. One of the most promising families of magnetocaloric materials are LaFeSi alloys. These alloys show a magnetic FOPT that implies a large magnetocaloric response. Hydrogenation of the samples shifts the transition temperature from ≈200 K to temperatures close to room temperature, to facilitate their applications in devices. However, some issues have to be solved before commercialization: its cyclic stability needs to be improved and thermal hysteresis is to be minimized. Different dopants can be used to tune properties such as T_{trans}, the MC response and hysteresis. In this work, we study the magnetocaloric properties of LaFeSi alloys doped with Ni ($LaFe_{11.6-x}Ni_xSi_1$ with x=0, 0.1, 0.2, 0.3 and 0.4). Microstructural characterization (BSE and XRD) shows a high percentage of $LaFe_{13}$ phase in the alloys. EDX analysis confirms the desired nominal compositions. Magnetocaloric characterization has been performed by indirect measurements of ΔS_T (from magnetization measurements) and direct measurements of ΔT_S (dedicated device built in TU Darmstadt). Figure 1 shows how the temperature dependence of ΔT_S is modified by the addition of Ni. The criterion to distinguish the order of the phase transition from the value of the exponent of the field dependence of ΔS_T has been applied (Figure 2). This procedure allows us to estimate the composition for which the transition is in the critical point of the second-order phase transition (sample with x=0.21), also shown in Figure 2. DFT calculations have been performed in order to explain the role of Ni atoms in $LaFe_{13}$ phase, showing a good agreement with experimental data. This work was supported by MINECO and EU FEDER (project MAT2013-45165-P), AEI/FEDER-UE (project MAT-2016-77265-R), the PAI of the Regional Government of Andalucía, the Deutscher Akademischer Austauschdienst DAAD (Award A/13/09434). L. M. Moreno-Ramírez acknowledges a FPU fellowship from the Spanish MECD. O.G., I.R., and K.S. would like to acknowledge funding by the DFG in the framework of the priority program "Ferroic Cooling" (SPP1599).

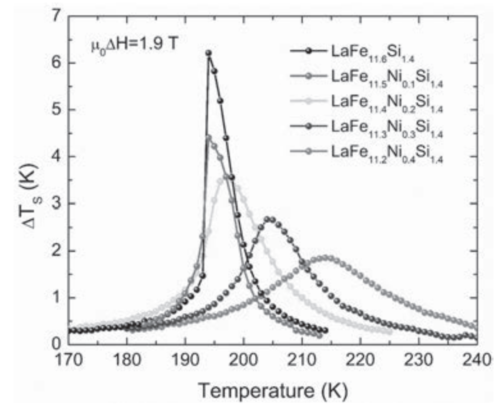

Fig. 1. Temperature dependence of the adiabatic temperature change for the set of $La(Fe,Ni,Si)_{13}$ samples.

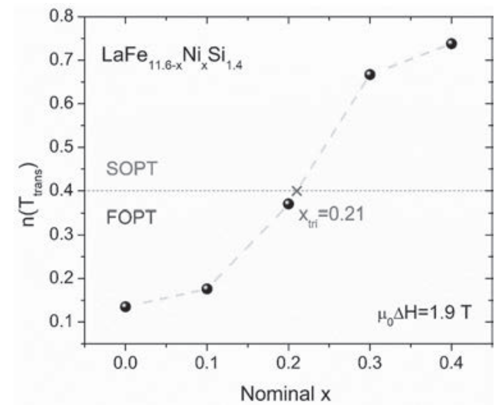

Fig. 2. Values of the field dependence exponent $n(T_{trans})$ for the set of $La(Fe,Ni,Si)_{13}$ samples.

2:15

FD-02. Magnetocaloric effect in melt-spun rare earth high entropy alloy YGdTbDyHo.

N. R[1], A. Sankar[1], A. Chelvane[2], A. Morozkin[3], A.K. Nigam[4], S. Quezado[5] and S.K. Malik[5]
1. Physics, Indian Institute of Technology Madras, Chennai, India; 2. DMRL, Hyderabad, India; 3. Lomonosov Moscow State University, Moscow, Russian Federation; 4. TIFR, Mumbai, India; 5. UFRN, Natal, Brazil

In the last decade, high entropy alloys (HEA) have emerged as novel materials for various applications with superior mechanical and corrosion resistance properties. These generally contain five or more major principal elements in nearly equimolar ratio and the formation and stability of the alloy phase is determined by Gibb's free energy of mixing. Recently, a rare earth high entropy alloy, namely, YGdTbDyHo, has been found to crystallize in single phase, in Mg-type hexagonal close packed structure [1]. This particular system is considered very special because it is formed on a hcp lattice of near zero-distortion but with a huge chemical disorder thus possessing a dual nature of a metallic glass on an ordered lattice. In addition, this alloy presents a very complex, magnetic field-temperature phase diagram and promises to be a potential material for magnetocaloric applications [2, 3]. Since melt-spinning technique is known to yield a highly crystalline giant magnetocaloric materials such as $La(Fe, Si)_{13}$ with superior magnetic and magnetocaloric properties [4], the YGdTbDyHo HEA has been prepared by this rapid solidification process and studied. Melt-spinning leads to texture effects in the sample. The room temperature X-ray diffraction data confirm the hcp structure and the formation of preferred crystal orientation in the melt-spun sample of YGdTbDyHo alloy. The intensity of Bragg reflection (0 0 2) is found to get greatly enhanced in the melt-spun ribbon of YGdTbDyHo. The sample composition has been confirmed using EDAX analysis. The arc-melted and melt-spun samples of YGdTbDyHo show an antiferromagnetic cusp around 178 K and 176 K in their magnetization vs temperature data obtained in 5 kOe field. Both samples develop ferromagnetic interactions at low temperatures. The field-cooled magnetization data shows thermal hysteresis around this first order AFM-FM transition. The thermal hysteresis is more pronounced in the field-cooled magnetization data of the melt-spun sample and that could be related to the enhanced anisotropy. Field dependent magnetization (M-H) data at 2 K and 5 K display a metamagnetic transition in both samples with a tendency to saturate in high fields. The isothermal magnetic entropy change (ΔS_m) close to T_N has been calculated from the M-H data. The maximum isothermal magnetic entropy change, ΔS_m^{max}, is ~6.3 J/kg K and ~6 J/kg K for the arc-melted and melt-spun YGdTbDyHo alloy for 50 kOe field change, near T_N [Fig. 1a-b]. The sluggish nature of the magnetic transition in this high entropy alloy system leads to a broad spread of magnetic entropy over a large range of temperatures and hence the relative cooling power values are reasonable. Small positive DS_m values are observed for small field changes signify the underlying antiferromagnetic interactions present in this system. These values gradually change to show normal magnetocaloric effect as the system undergoes metamagnetic transition into a ferromagnetic state. Thus rare earth based high entropy alloys offer a novel test bed for the study of competing RKKY interactions and also provide a possibility to build alternative magnetocaloric materials.

1. M. Feuerbacher, M. Heidelmann and C. Thomas, Mat. Res. Lett. 3 (2014) 1. 2. J. Luznik, P. Kozelj, S. Vrtnik, A. Jelen, Z. Jaglicic, A. Meden, M. Feuerbacher and J. Dolinsek, Phys. Rev. B 92 (2015) 224201 3. Y. Yuan, Y. Wu, X. Tong, H. Zhang, H. Wang, X. J. Liu, L. Ma, H. L. Suo and Z. P. Lu, Acta Materialia 125 (2017) 481 4. J. Lyubina, R. Schäfer, N. Martin, L. Schultz and O. Gutfleisch, Adv. Mater. 22 (2010) 3735

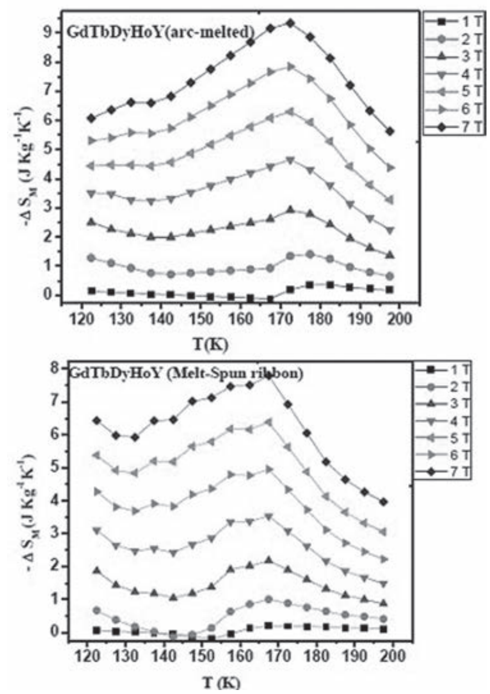

Fig. 1. Isothermal magnetic entropy change vs temperature of the arc-melted and melt-spun high entropy alloy YGdTbDyHo, for field changes up to 7 Tesla.

2:30

FD-03. Pressure-Dependent Magnetic Transition Temperatures in Magnetocaloric High Entropy Alloys.

A.E. Perrin[1], S. Mccall[3], M. Sorescu[2], D. Laughlin[1] and M. McHenry[1]
1. Materials Science and Engineering, Carnegie Mellon University, Pittsburgh, PA, United States; 2. Physics, Duquesne University, Pittsburgh, PA, United States; 3. Lawrence Livermore National Lab, Livermore, CA, United States

We present x-ray diffraction and SQUID magnetometry measurements taken under various applied pressures that demonstrate the shift in magnetic transition temperatures in the magnetocaloric high entropy alloy system FeCoNiCuMn. Bulk samples of equiatomic and near-equiatomic FeCoNiCuMn are produced via arc melting and melt spinning, a process in which molten ingots are rapidly quenched on a spinning wheel, producing powder and flakes of sample with a metastable, single phase face-centered cubic crystal structure. Our previous work identified this alloy system as a viable material for use in magnetocaloric applications due to the ease with which the Curie temperature of the alloys can be tuned with small (~1%) compositional changes, as well as the relatively large saturation magnetization of the alloys within the system with Curie temperatures at room temperature. [1] The random distribution of atoms on the crystal lattice lead to distributed exchange interactions, which broadens the change in magnetic entropy in the temperature range above and below the Curie temperature, increasing the refrigeration capacity of these alloys. We have characterized the nature of these exchange interactions using Mössbauer spectroscopy and found that the hyperfine field distributions of these alloys (fig. 1) are made up of several distinct, discrete peaks which we suggest are evidence of individual pairwise interactions between the three ferromagnetic components in these alloys (Fe, Co and Ni) [2]. The presence of discrete pairwise exchange interactions can be used to better understand the magnetic behavior of these alloys under applied pressure. M(T) curves measured after zero field cooling samples in a pressure cell show that the ferromagnetic to paramagnetic transition temperature decreases with increasing applied pressure, likely due to the smaller lattice spacing that forces atoms closer together, which favors antiferromagnetic exchange. X-ray diffraction of equiatomic FeCoNiCuMn under up to 9GPa of applied pressure show a shift in the lattice parameter of the FCC crystal structure from 3.615 Angstroms to 3.602 Angstroms over the applied pressure range of 0GPa to 9GPa, a 1% decrease in total cell volume, but no changes in phase stability or crystal structure are seen. The Bethe-Slater curve shows the empirical relationship between lattice spacing and exchange energy in magnetic elements, and the average exchange energy estimated by the lattice spacing of our alloys with applied pressure increases as well, suggesting that the Curie temperature of the alloy should get larger with pressure. However, the experimental ferromagnetic to paramagnetic transition temperature decreases with increasing applied pressure, likely due to the discrete pairwise antiferromagnetic interactions Mn-Mn and Mn-Fe, which are favored with decreased atomic spacing. We analyze the observed transitions using the Ehrenfest equations, supplemented with heat capacity data previously measured for these samples. [3] The M(T) curves measured after zero field cooling samples also reveal an antiferromagnetic to ferromagnetic phase transition at low temperatures that is not seen during field cooling due to the coupling of moments in the ferromagnetic phase (fig. 2). This transition is not observed to change with applied pressure. Additionally, we found that compositional tuning of these alloys, which has been used to shift the Curie temperatures in the range of 265K to 400K, does not influence the antiferromagnetic to ferromagnetic transition temperature, and this transition is not observed at all for FeCoNiCuAg, a high entropy alloy in which antiferromagnetic Mn is replaced with diluent noble metal Ag. This indicates that this magnetic behavior arises entirely from the presence of Mn-Mn or Mn-Fe interactions, ruling out the possibility that there are contributions from Fe-Fe antiferromagnetic interactions.

[1] Kurniawan M., Perrin, A., Xu, P., Keylin, V., McHenry, M. (2016). "Curie Temperature Engineering in High Entropy Alloys (HEAs) for Magnetocaloric Applications". *IEEE Magnetics Letters, PP*(99). http://dx.doi.org/10.1109/LMAG.2016.2592462 [2] Perrin, A., Sorescu, M., Burton, M.T., Laughlin, D.E., McHenry, M. (2017). "The Role of Compositional Tuning of the Distributed Exchange on Magnetocaloric Properties of High-Entropy Alloys". JOM, 1047-4838 (8). http:https://doi.org/10.1007/s11837-017-2523-3 [3] Sakarya, Serdar. "Magnetic Properties of Uranium Based Ferromagnetic Superconductors."*Magnetic Properties of Uranium Based Ferromagnetic Superconductors*, Delft University Press, 2007, pp. 99–108.

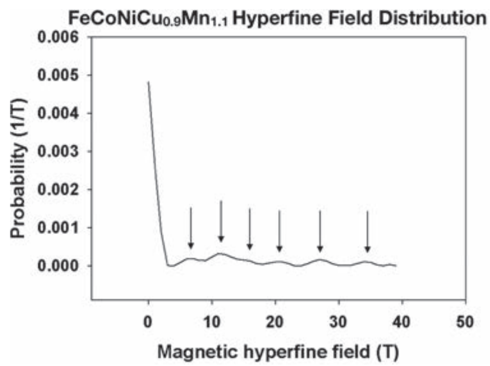

Fig. 1. Hyperfine field distribution of FeCoNiCuMn, displaying distinct peaks (emphasized with arrows) suggestive of discrete pairwise exchange interactions.

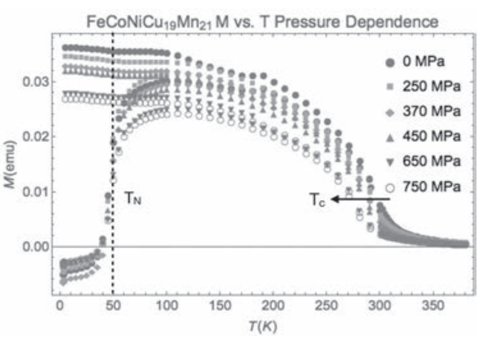

Fig. 2. Magnetization versus temperature curves for sample undergoing applied pressures from 0GPa to 1GPa, measured from 1K to 400K. Zero field cooling before measurements reveals an antiferromagnetic to ferromagnetic transition at 50K (T_N) which is not pressure dependent. T_C denotes the Curie temperature of the sample, which decreases linearly with applied pressure.

2:45

FD-04. Magnetocaloric Behavior of $Fe_{75-x}Mn_xAl_{25}$ Alloys for Near Room Temperature Cooling.

V.K. Sharma[1], V. Chaudhary[1] and R.V. Ramanujan[1]
1. School of Materials Science and Engineering, Nanyang Technological University, Singapore, Singapore

Abstract Magnetic cooling is an energy efficient and environmentally friendly thermal management technology. We report the magnetocaloric properties of low cost, high relative cooling power $Fe_{75-x}Mn_xAl_{25}$ ($12.5 \leq x \leq 20$) alloys with tunable Curie temperatures. A second order magnetic phase transition with negligible magnetic and thermal hysteresis was observed. $Fe_{60}Mn_{15}Al_{25}$ and $Fe_{57.5}M_{17.5}Al_{25}$ exhibited high values of relative cooling power i.e. 395 Jkg^{-1} and 430 Jkg^{-1} and Curie temperatures near room temperature, making such alloys technologically attractive. The low cost, easy availability and established manufacturing technology make these alloys attractive candidate materials for magnetic cooling applications. *Introduction* Global warming, climate change and the impact of ozone layer depleting chemicals necessitate alternatives to conventional gas compression based technology. Magnetic cooling offers significantly higher energy efficiency and no harmful gas emissions[1]. Recently many leading companies, like BASF, Haier and Astronautics Corporation of America have shown considerable interest in developing magnetic cooling systems and a commercial wine cooler has been developed[2]. Magnetic cooling is based on the magnetocaloric effect (MCE) which is manifested in the magnetocaloric material (MCM) by a heating or cooling effect due to the application or removal of an external magnetic field[3]. Figures-of-merit include isothermal magnetic entropy change ($-\Delta S_m$) and relative cooling power (RCP)[4]. Although rare earth (RE) metal based alloys show high $-\Delta S_m$ values the high processing cost, geographical limitations in availability and poor corrosion resistance makes these materials less suitable for commercial applications[5]. Several low cost first order transition materials exhibit "giant" MCE cost but they suffer from thermal hysteresis and narrow operating temperature range, which degrades the performance of device[6]. On the other hand, Fe based transition metal alloys are easily available, low cost, exhibit second order transitions (hence negligible hysteresis) and offer Curie temperature (Tc) tuning over a broad temperature range[7]. We explore the magnetocaloric properties in Fe-Al based alloys as they are commercially proven materials due to their low cost, excellent oxidation resistance, superior mechanical properties and established manufacturing techniques[8]. The high Tc of Fe_3Al composition was reduced to near room temperature by substitution of Fe by Mn without compromising on the magnetization values of Fe_3Al. We report for the first time the magnetocaloric properties of $Fe_{75-x}Mn_xAl_{25}$ alloys. *Experimental* Buttons with nominal compositions of $Fe_{75-x}Mn_xAl_{25}$ (x = 12.5, 15, 17.5 and 20) were prepared from high purity (~ 99%) elemental Fe, Mn and Al in an arc melter (Edmund Buhler, MAM-1) under Ar gas atmosphere and further annealed at 1000 ˚C for 48 h to achieve homogenization. The MCE properties were investigated by a Physical Property Measurement System (PPMS) unit, (EC-II, QD, USA) with a VSM head. *Results and discussion* Temperature dependent magnetization measurements at 1 kOe from 400 K to 10 K were performed to determine the Tc and magnetization values. 15 % and 17.5 % Mn addition in $Fe_{75-x}Mn_xAl_{25}$ yielded Tc values near room temperature, i.e., 305 K and 265 K respectively (Fig. 1). This reduction of Tc by addition of Mn can be explained by antiferromagnetic ordering of Mn in Fe-Al. As the Mn content increased, the effective exchange integral decreased, leading to more antiferromagnetic coupling[9]. A similar decrease in Tc upon Mn addition was observed in other iron based MCM[10]. For MCE property evaluation, field dependent isothermal magnetization curves were recorded from 10 K to 400 K at temperature intervals of 5K. The $-\Delta S_m$ was calculated using Maxwell's equation, for a range of magnetic field strengths (ΔH = 1 to 5 T). The behavior of $-\Delta S_m$ with magnetic field (Fig. 2(B)) showed a linear change in $-\Delta S_m$ values for both 15 % Mn and 17.5%Mn samples suggesting the absence of magnetic inhomogenities. The highest value of $-\Delta S_m$ was 1.07 $Jkg^{-1}K^{-1}$ at 5 T for 17.5%Mn. RCP is another important performance metric that quantifies the amount of heat that can be transferred from the hot end to the cold end during operation of a cooling cycle. It can be expressed as where is the temperature span at full width of half maximum. RCP values of 430 Jkg^{-1} and 395 Jkg^{-1} were observed for 17.5%Mn and 15 % Mn samples at 5 T (Fig. 2(A)). These value are higher than $Co_{71}Mo_9P_{14}B_6$ metallic glasses which showed $-\Delta S_m$ of 0.96 $Jkg^{-1}K^{-1}$ and RCP of 70.5 Jkg^{-1} and high entropy alloys like $NiFeCoCrPd_{0.25}$ which showed $-\Delta S_m$ of 0.9 $Jkg^{-1}K^{-1}$ and RCP of 215 Jkg^{-1} at 5 T [11, 12]. *Conclusions* The magnetocaloric properties of $Fe_{75-x}Mn_xAl_{25}$ alloys were explored for the first time. They exhibited high RCP values as well as Curie temperatures at desired values near room temperature for x = 15 and 17.5 alloys. The low cost, established manufacturing techniques, good corrosion and oxidation resistance and negligible hysteresis makes these alloys attractive for magnetic cooling. *Acknowledgement* This research is supported by grants from the National Research Foundation, Prime Minister's Office, Singapore under its Campus of Research Excellence and Technological Enterprise (CREATE) programme.

[1] N. A. Zarkevich, D. D. Johnson, and V. K. Pecharsky, "High-throughput search for caloric materials: the CaloriCool approach," *Journal of Physics D: Applied Physics,* 2017. [2] V. Franco, J. S. Blázquez, J. Ipus, J. Y. Law, L. M. Moreno-Ramírez, and A. Conde, "Magnetocaloric effect: from materials research to refrigeration devices," *Progress in Materials Science*, 2017. [3] V. K. Pecharsky and K. A. Gschneidner, "Advanced magnetocaloric materials: What does the future hold?," *International Journal of Refrigeration,* vol. 29, pp. 1239-1249, 2006. [4] V. Franco, J. Blázquez, J. Ipus, J. Law, L. Moreno-Ramírez, and A. Conde, "Magnetocaloric effect: from materials research to refrigeration devices," *Progress in Materials Science,* 2017. [5] V. K. Pecharsky and K. A. Gschneidner Jr, "Giant magnetocaloric effect in Gd 5 (Si 2 Ge 2)," *Physical review letters,* vol. 78, p. 4494, 1997. [6] K. A. GschneidnerJr, V. Pecharsky, and A. Tsokol, "Recent developments in magnetocaloric materials," *Reports on progress in physics,* vol. 68, p. 1479, 2005. [7] V. Chaudhary and R. Ramanujan, "Magnetocaloric Properties of Fe-Ni-Cr Nanoparticles for Active Cooling," *Scientific Reports,* vol. 6, 35156, 2016. [8] V. Sharma, D. M. Repaka, V. Chaudhary, and R. Ramanujan, "Enhanced magnetocaloric properties and critical behavior of (Fe0. 72Cr0. 28) 3Al alloys for near room temperature cooling," *Journal of Physics D: Applied Physics,* vol. 50, p. 145001, 2017. [9] D. Guo, Y. Yuan, and K. Chan, "The effect of different minor additions on the magneto-caloric effect of FeZrB metallic ribbons near room temperature," *Journal of Magnetism and Magnetic Materials,* vol. 446, pp. 12-17, 2018. [10] V. Chaudhary and R. V. Ramanujan, "Magnetic and structural properties of high relative cooling power (Fe70Ni30)92Mn8magnetocaloric nanoparticles," *Journal of Physics D: Applied Physics,* vol. 48, p. 305003, 2015. [11] C. Liu, Q. Li, J. Huo, W. Yang, L. Chang, C. Chang, *et al.*, "Near room-temperature magnetocaloric effect of Co-based bulk metallic glass," *Journal of Magnetism and Magnetic Materials,* vol. 446, pp. 162-165, 2018. [12] D. D. Belyea, M. Lucas, E. Michel, J. Horwath, and C. W. Miller, "Tunable magnetocaloric effect in transition metal alloys," *Scientific reports,* vol. 5, 2015.

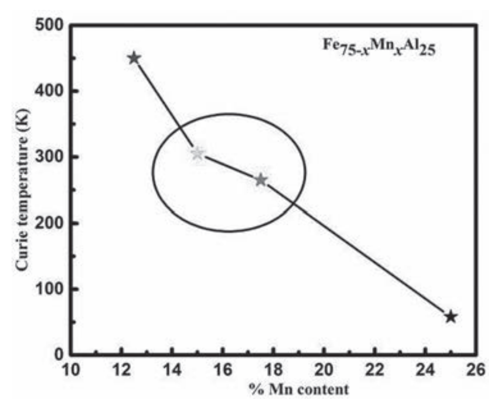

Fig. 1. Tc versus % Mn content in $Fe_{75-x}Mn_xAl_{25}$ alloys.

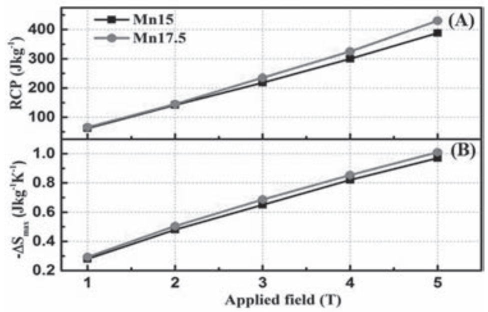

Fig. 2. Field dependence of (A) RCP and (B) ($-\Delta S_m$) for Mn 15% and Mn 17.5% in $Fe_{75-x}Mn_xAl_{25}$ alloys.

3:00

FD-05. Magnetocaloric effect in diluted magnetic ferroelectric: $Ba_{0.6}Eu_{0.4}TiO_3$.

K. Rubi[1] and *R. Mahendiran*[1]
1. Physics, National University of Singapore, Singapore

Magnetic refrigeration is an emerging technology based on magnetic solids that act as a refrigerants by magnetocaloric effect(MCE). Magnetic refrigeration makes use of the fact paramagnetic and ferromagnetic materials heat up upon increasing external magnetic field in an isothermal process and cool below the starting temperature when the external magnetic field is removed adiabatically. Many studies have devoted to Gd- based intermetallics, Heusler magnetic alloys, Mn-based oxides, MnAs based compounds and rare earth free $(LaFe)Si_{13}$, MnPSi[1,2,3,4] Although major thrust is to find cheaper and reliable materials for room temperature magnetic cooling, high performance materials are also needed for cryogenic magnetic refrigeration particularly for temperatures between 1 K and 20 K - the temperature range where hydrogen gas/fuel can be converted into liquid form. In this work, we report the occurrence of a large magnetocaloric effect in ferroelectric material doped with a magnetic element for the first time. We have measured the magnetization, heat capacity and magnetization isotherms in $Ba_{0.6}Eu_{0.4}TiO_3$. Seven unpaired 4f electrons associated with Eu^{2+} ion order antiferomagnetically below 5.6 K in $EuTiO_3$ [5]. The substitution of Ba^{2+} for Eu^{2+} dilutes magnetic interactions between 4f ions on neighboring Eu^{2+} sites. Our magnetization data indicates that $Ba_{0.6}Eu_{0.4}TiO_3$ is paramagnetic down to 2 K in zero field but the application of a 5 T magnetic field at 2 K saturates the 4f spins. Magnetic entropy change (ΔS_m) was calculated from M-H isotherms and adiabatic temperature change (ΔT_{ad}) was estimated from the zero field heat capacity and $\Delta S_{m.}$ We found ΔS_m = 25 J/Kg.K at 2K and ΔT_{ad} = 16.5 K at 5 K for a field change of 5 T. This is the highest adiabatic temperature change found in a diluted magnetic oxide for temperatures above 1 K.

[1] K.A.Gschneidner,Jr.,V. K.Percharsky, and A. O. Tsokol, Rep. Prog. Phys.68,1479 (2005) [2] E. Bruck, J. Phys. D.38, R381 (2005) [3]A. Smith, C. R. H. Bahl, R. Bjork, K. Engelbrecht, K. P. Neilsen, and N. Pyrds, Adv. Energy Materials,2, 1288 (2012) [4]M. F.. J, Boejie, P. Roy, F. Guillou, H. Yibole, X. F. Miao, L. Caron, D. Banerjee, N. H. van Dijik, R. A. de Groot, and E. Bruck, Chem. Mater. 28, 4901 (2016) [5] A. Midya, P. Mandal, Km. Rubi, C. Ruofan, J.S. Wang, R. Mahendiran G. Larusso, and M. Evangilisti, Phys. Rev. B 93, 094422 (2016)

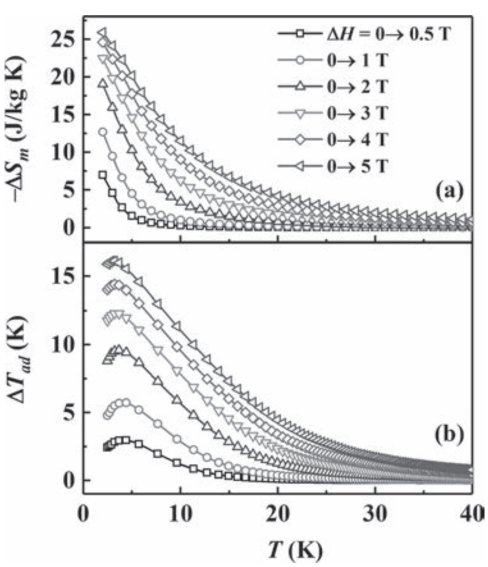

Fig. 1. Temperature dependence of (a) magnetic entropy change (ΔS_m) and (b) adiabatic temperature change (ΔT_{ad}) for variations of magnetic field (ΔH) from 0 to H Tesla.

3:15

FD-06. $Gd_5(Si,Ge)_4$ nanoparticles produced by pulsed laser deposition.

V.M. Andrade[1], N. Checca[2], J. Belo[3], B. Almeida[4], M.S. Reis[2,5], A. Pereira[1] and J. Araujo[1]
1. Department of Physics and Astronomy, IFIMUP-IN, Porto, Portugal; 2. Departamento de Física, Instituto de Física da Universidade Federal Fluminense, Rio de Janeiro, Brazil; 3. Department of Physics and CICECO, Aveiro University - CICECO, Aveiro, Portugal; 4. Physics Department, Minho University, Braga, Portugal; 5. Physics Department, Aveiro University - I3N, Aveiro, Portugal

Since the discovery of the Giant Magnetocaloric Effect (GMCE) near room temperature on $Gd_5Si_2Ge_2$ by Pecharsky and Gschneidner in 1997 [1], the $Gd_5(Si_{1-x}Ge_x)_4$ alloys have been intensively studied for magnetic refrigeration (MR) application. The magnetic entropy change of $Gd_5Si_2Ge_2$ is 25% higher than the observed in pure Gd – that is the reference material for MR at room temperature. The thorough $Gd_5(Si_{1-x}Ge_x)_4$ research performed so far revealed many other important properties, such as giant magnetoresistance and colossal magnetostriction (CMS) [2,3]. The interplay between magnetic and structural behavior in these system leads to an extreme sensitivity to variation of external (e.g., temperature, magnetic field and pressure) and internal (e. g. stoichiometry, dimensionality and doping) parameters. Such features makes these materials very promising for a wide range of applications such as MR at room temperature, actuator/sensors and energy harvesting. Few reports are dedicated to the study of the $Gd_5(Si_xGe_{1-x})_4$ system in a reduced dimensionality, such as thin films and nanoparticles. A recent work performed by our team have successfully obtained $Gd_5Si_{1.3}Ge_{2.7}$ granular thin film, ~790 nm thick, using the femtosecond pulsed laser ablation technique, but still with a significant amount of an unknown phase and a wide size distribution [4]. Through Synchrotron X-ray Diffraction collected in the [150,250] K range, we have shown that the obtained thin film presents a giant thermal expansion of 8000 ppm, showing its potential for sensing/actuating applications. Although femtosecond pulsed laser ablation proved to be a good technique to obtain these films without oxidation issues, it is an expensive and irreproducible method that does not guarantee a continuous surface or a homogeneous distribution. Thus, a more conventional and accessible nanosecond pulsed laser deposition was chosen to produce these metal nanoparticles (NPs). For such purposes, $Gd_5(Si_{1-x}Ge_x)_4$ with x = 0.55 and 0.6 bulk targets were chosen since they present a stable orthorhombic Gd_5Si_4-type [O(I)] structure across the magnetic transition at 301 K and 307 K, respectively [1]. The targets were produced by tri-arc melting and ablated by an Excimer KrF laser with 248 nm of wavelength, pulse duration of 20 ns with a repetition of 10 Hz and maximum energy of 550 mJ. In order to prevent oxidation issues, the chamber was pumped several times down to a base pressure of 10^{-6} Torr. For the deposition, Argon was used as the inert gas in a continuous flux in a constant pressure of 1 Torr inside the chamber and the substrates were positioned 1 cm away from the target. Two types of substrates were used to collect the nanoparticles: *i)* carbon coated grids for HR-TEM imaging and *ii)* Si (001) substrate for magnetic measurements. The TEM micrographs obtained for all samples have revealed that NPs produced by PLD present an average particle size below ~30 nm and good crystalline features. As can be seen in Fig. 1(a) for x = 0.55 composition, particles present a continuous crystalline morphology with a broad particle size distribution. An amplified image allows the observation of the interplanar distances, as shown on the inset of Fig.1(a), that correspond to the observed peaks on the X-ray diffraction patterns (not shown) and is related with the (231) plane of the O(I) phase. Magnetic results confirm that there is no changes on the Curie temperature (T_C) in relation with the bulk targets, as highlighted in Fig. 1(b) for each sample. On the inset of Fig. 1(b), it is possible to observe that the systems do not reach saturation at 5 K. By extrapolating the M vs. 1/H curve we obtain that the saturation magnetization are approximately 3.3 μ_B/Gd^{3+}, 50% less than the targets, surely associated with the particle size confinement [6]. Thereby, we can conclude that the nanosecond PLD successfully produce dispersed crystalline nanoparticles of $Gd_5(Si_{1-x}Ge_x)_4$ family compounds. This technique allows the formation of NPs with particles size under 30 nm without loss on the stoichiometry of the targets, since there is no change on the T_C [6]. Notwithstanding, there is a reduction on the saturation magnetization at low temperature as a consequence of dimensionality confinement.

[1] V. K. Pecharsky and K. A: Schneidner Jr., *Phys. Rev. Lett.* 78, 4494 (1997); [2] L. Morellon, *et. al.,* Phys. Rev. B 58, R14721(R) (1998); [3] A. Guiguère, et al., *Physical Review Letters* 83, 2262 (1999); [4] R. L. Hadimani, *et. al., Appl. Phys. Lett.* 106, 032402 (2015); [5] J. D. Moore, et al., *Applied Physics Letters* 88.7, 072501 (2006); [6] V. M. Andrade, et al., *Materials Chemistry and Physics* 172, 20 (2016).

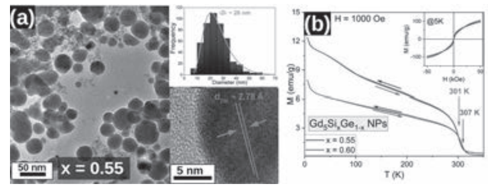

3:30

FD-07. Influence of overlapping transitions on the MCE response of a series of $Ni_{0.49-x}Mn_{0.36+x}In_{0.15}$ Heusler alloys.

J. Law[1], V. Franco[1], A. Conde[1] and A. Giri[2]
1. Condensed Matter Physics, Sevilla University, Sevilla, Spain;
2. Weapons and Materials Research Directorate, US Army Research Laboratory, Aberdeen, MD, United States

Metamagnetic NiMn-based Heusler alloys are one of the promising rare-earth-free magnetocaloric materials due to their attractive large magnetocaloric effect (MCE) arising from their first order phase transition (FOPT). Both austenitic and martensitic states of $Ni_{0.50}Mn_{0.5-y}In_y$ are ferromagnetic for composition of $0.15 \leq y \leq 0.16$ [1, 2]. For $Ni_{0.50}Mn_{0.34}In_{0.16}$, it exhibits an inverse MCE of ~12 J kg^{-1} K^{-1} at 190 K, which is far away from room temperature [2]. On the other hand, for y=0.15 in $Ni_{0.50-z}Mn_{0.5+z}In_{0.15}$, its field-induced martensitic transformation shifts to 285 K[3]. Most efforts in optimizing the performance of this alloy series have been dedicated to compositional studies and mainly reported only the temperature range of its inverse MCE due to the interest in giant MCE for practical applications. However, these ferromagnetic alloys exhibit at least three temperature-induced phase transitions: a low temperature ferromagnetic-paramagnetic (FM-PM) transition followed by a first order martensitic structural transition at higher temperatures and the FM-PM transition of high temperature austenitic phase. In this work, we aim to study, in a broad temperature range, the influence of these three overlapping transitions on the field dependence of MCE in $Ni_{0.49-x}Mn_{0.36+x}In_{0.15}$. Fig 1(a) shows the magnetization vs. temperature (*M(T))* data of $Ni_{48.1}Mn_{36.5}In_{15}$ which reveals that it exhibits three phase transitions occurring at different temperatures as observed from the $\partial M/\partial T$ slopes. The first one corresponds to the Curie transition of the martensitic phase, producing a small gradual decrease of *M* in the range of T<225 K. The steep increase of *M* observed within 225 K < T ≤ 260 K corresponds to the martensite-austenite transition, which occurs before the T_C of the martensite phase. At higher temperatures, a gradual decrease of $\partial M/\partial T$ is observed. These are in agreement with the 3D MCE (magnetic entropy change, ΔS_M) plot shown in Fig 1(b) whereby two direct MCE and an inverse MCE are observed. A small direct MCE is observed at low temperatures up to ~220 K, followed by a large inverse MCE at higher temperatures up to ~268 K due to the subsequent competing phase transitions followed by a direct MCE peak. While the martensitic-austenitic transition does not significantly overlap with the Curie transition of the austenite, the direct MCE of that FM-PM transition exhibits a magnitude of the same order of that of the inverse MCE (7.13 J kg^{-1}K^{-1} versus -2.83 J kg^{-1}K^{-1} respectively). However, the low temperature direct MCE is rather diminished due to the overlapping of its Curie transition and the martensitic transition, whereby the martensite phase disappears before its T_C. Fig 2 shows that the variant electron/atom (e/a) ratio (due to alteration of Ni/Mn ratio) shifts the different magnetic phase transitions in the $Ni_{49+x}Mn_{36-x}In_{15}$ alloys. With increasing e/a ratio, the T_{pk} of 1st direct MCE (1st transition), inverse MCE (2nd transition) and direct MCE at higher temperatures (3rd transition) regimes exhibit an increase, increase and decrease respectively. The T_{pk} of the inverse MCE agree with the temperature at which the austenite phase begins to form, as observed from DSC data. For both 2nd and 3rd transitions, it can be observed that both exhibit similar trends of increased T_{pk} for e/a ratio ≥7.86, indicating their phase competition, which also affected the visibility of their peaks as shown in the inset of Fig 2 (their peak ΔS_M remain rather small for e/a ratio ≥7.86). Hence, the peak ΔS_M values of the 2nd and 3rd transitions are comparable (i.e. same order of magnitude) when their temperatures are well separated, as observed for e/a ratio ≤7.84. Although it is previously found that the entropy change of the phase transition from DSC data correlates well with the e/a ratio[4], there is no direct correlation between the ΔS_M of the martensitic transition and the e/a ratio partly due to this overlap. The previously described behavior for $Ni_{48.1}Mn_{36.5}In_{15}$ agrees well with the observed trend of exponent *n* (as in $\Delta S_M \propto H^n$ [5]) controlling the field dependence of MCE. For its first transition, *n* gradually decreases from *n*~1 and abruptly increases as the sign of ΔS_M switches at the FOPT (2nd transition). For the 3rd transition, the typical *n* behavior for a second order phase transition is observed and the main features of the field dependence of each transition are essentially maintained.

This work was supported by MINECO and EU FEDER (project MAT2013-45165-P), AEI/FEDER-UE (project MAT-2016-77265-R) and the PAI of the Regional Government of Andalucía.

1. Krenke, T., Acet, M., Wassermann, E. F., Moya, X., Mañosa, L., Planes, A., "*Ferromagnetism in the austenitic and martensitic states of Ni–Mn–In alloys*," Physical Review B 73(17), 174413 (2006). 2. Krenke, T., Duman, E., Acet, M., Wassermann, E. F., Moya, X., Mañosa, L., Planes, A., Suard, E., Ouladdiaf, B., "*Magnetic superelasticity and inverse magnetocaloric effect in Ni-Mn-In*," Physical Review B 75(10), 104414 (2007). 3. Gao, B., Hu, F. X., Shen, J., Wang, J., Sun, J. R., Shen, B. G., "*Tuning the magnetic entropy change of $Ni_{50-x}Mn_{35+x}In_{15}$ alloys by varying the Mn content*," Journal of Applied Physics 105(8), 083902 (2009). 4. Zhou, L., Mehta, A., Giri, A., Cho, K., Sohn, Y., "*Martensitic transformation and mechanical properties of $Ni_{49+x}Mn_{36-x}In_{15}$ (x=0, 0.5, 1.0, 1.5 and 2.0) alloys*," Materials Science and Engineering: A 646, 57-65 (2015). 5. Franco V., Blázquez J. S., Conde A., "*Field dependence of the magnetocaloric effect in materials with a second order phase transitions: A master curve for the magnetic entropy chance*," Applied Physics Letters 89, 222512 (2006)

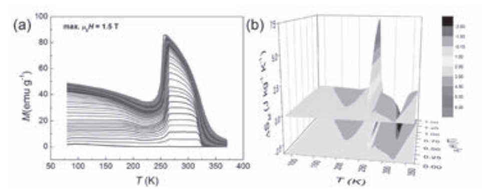

Fig. 1. $Ni_{48.1}Mn_{36.5}In_{15}$: (a) its *M*(*T*) data ; (b) ΔS_M as a function of temperature for applied fields up to 1.5 T. For guide to the eye, the colormap is also projected as bottom contour in the 3D plot.

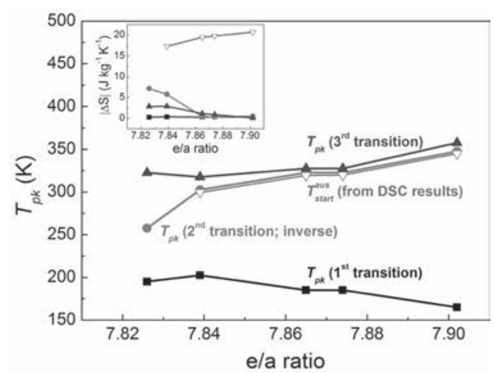

Fig. 2. Influence of e/a ratio of $Ni_{49+x}Mn_{36-x}In_{15}$ on its transition temperatures (Main) and entropy change (inset) in various phase transitions for $\mu_0 H$ = 1.5 T. T_{pk} in this case denotes the temperature of the peak $|\Delta S_M|$ values.

3:45

FD-08. Magnetocaloric effect in MnNiSi-Fe_2Ge and MnNiSi-Fe-Sn alloys.

D. Kamble[1,2] and R.V. Ramanujan[1,2]

1. Materials Science and Engineering, Nanyang Technological University, Singapore, Singapore; 2. Singapore-HUJ Alliance for Research and Enterprise (SHARE), Nanomaterials for Energy and Energy-Water Nexus (NEW), Campus for Research Excellence and Technological Enterprise (CREATE), Singapore, Singapore

INTRODUCTION The near room temperature magnetocaloric effect (MCE) of MnNiSi based alloys is of current interest in magnetocaloric cooling applications [1]. MnNiSi is a ferromagnetic alloy with a Curie temperature (Tc) of 620 K [2], it exhibits a structural transition from orthorhombic to hexagonal above 1200 K [3]. Single element substitution has been found to be unable to decrease T_c to near room temperature, therefore 2 element substitution is necessary to obtain magnetostructural coupling near room temperature [4] [5]. A magnetostructural transition near room temperature is observed in $(MnNiSi)_{1-x}(Fe_2Ge)_x$ (x = 0.32 to 0.36) and $Mn_{0.45}Fe_{0.55}NiSi_{1-y}Sn_y$ (y = 0.12 to 0.18) alloys. A high temperature paramagnetic hexagonal phase which is converted to a low temperature ferromagnetic orthorhombic phase. Fe_2Ge stabilizes the hexagonal phase of MnNiSi to create a Curie temperature window (CTW) near the room temperature. In $Mn_{0.45}Fe_{0.55}NiSi$, it has been observed that the T_c could only be decreased to 438K. The Sn composition was varied from 0.12 to 0.18 to further reduce T_c to near room temperature values. Sn also reduces the cost of the material. EXPERIMENTAL PROCEDURE Polycrystalline $(MnNiSi)_{1-x}(Fe_2Ge)_x$ (x = 0.32 to 0.36) and $Mn_{0.45}Fe_{0.55}NiSi_{1-y}Sn_y$ (y = 0.12 to 0.18) alloys were synthesized from the elements using arc melting. The mass of the elements was selected on the basis of the nominal composition. Arc melting was carried out several times to ensure homogeneity. For $(MnNiSi)_{1-x}(Fe_2Ge)_x$, no heat treatment was conducted. For $Mn_{0.45}Fe_{0.55}NiSi_{1-y}Sn_y$ (y = 0.12 to 0.18) alloys, heat cycling was performed by subjecting it to 2 cycles of heating above the transition temperature and cooling using liquid nitrogen to eliminate the "virgin effect" [6,7]. RESULTS AND DISCUSSIONS 1. $(MnNiSi)_{1-x}(Fe_2Ge)_x$ alloys XRD analysis was carried out of samples at room temperature, the results showed peaks corresponding to the hexagonal structure for x = 0.34, 0.35 and 0.36, indicating that the structural transition temperature (T_t) was below room temperature. The orthorhombic structure was observed for x = 0.32 and 0.33, indicating T_t higher than room temperature. The observed values of T_t from the DSC analysis were 199K, 237K, 285K, 313K and 352K during cooling and 216K, 262K, 301K, 328K and 367 K during heating for x = 0.32 to 0.36 respectively. Thermal hysteresis of ~15 K was observed between heating and cooling cycles, which is a characteristic of a first order magnetocaloric material. Magnetic measurements showed Tc values of 200K, 238K, 276K, 315K, 350K during cooling and 218K, 259K, 301K, 331K, 363K during heating for x = 0.32, 0.33, 0.34, 0.35 and 0.36 respectively. The coupling between the magnetic and the structural transformation gave rise to a giant magnetocaloric effect for all the compositions studied. The entropy, calculated using Maxwells relation, large values of 47.3, 54.1, 57.6, 55.2 and 53.5 J $kg^{-1}K^{-1}$ (ΔH = 5T) for x = 0.32, 0.33, 0.34, 0.35 and 0.36, respectively were obtained. The relative cooling power (RCP) values were 376, 332, 342, 480 and 312 J kg^{-1} for x = 0.32, 0.33, 0.34, 0.35 and 0.36 respectively. A summary of the magnetic measurements are shown in Fig 1. 2. Results for $Mn_{0.45}Fe_{0.55}NiSi_{1-y}Sn_y$ alloys Room temperature XRD Analysis of the $Mn_{0.45}Fe_{0.55}NiSi_{1-y}Sn_y$ alloys showed an increase in the intensity of hexagonal peaks and diminution of the orthorhombic peaks when y was increased from 0.12 to 0.18, suggesting a change in T_t occurring by varying the Sn content. DSC analysis showed structural transformation peaks at 382K, 355K and 325K during heating and 325K, 295K and 260K during cooling for y = 0.12, 0.14 and 0.16. However, there was no DSC peak observed for alloy with y = 0.18. This suggested that the first order transformation is limited to Sn compositions below y = 0.16. Magnetic measurements showed T_c of 352K, 330K, 290K and 255K during heating and 343K, 315K, 260K and 225K during cooling for y = 0.12, 0.14, 0.16 and 0.18 respectively. The hysteresis was 9K and 15 K for y = 0.12 and 0.14, respectively and ~30K for y = 0.16 and 0.18. The M-H measurements were performed using the loop process [8] and the entropy was calculated using Maxwells equation was 7.5, 8.6, 3.7 and 1.8 J $kg^{-1}K^{-1}$ (ΔH = 5T) and the RCP values were found to be 165, 95, 204 and 252 J kg^{-1} for y = 0.12, 0.14, 0.16 and 0.18, respectively. A summary of the magnetic measurements are shown in Fig 2. A comparison of magnetocaloric properties of the two alloys shows high entropy, easy synthesis and better magnetostructural tunability for $(MnNiSi)_{1-x}(Fe_2Ge)_x$ alloys whereas $Mn_{0.45}Fe_{0.55}NiSi_{1-y}Sn_y$, being a Ge-free alloy, can be useful for low cost applications operating near room temperature.

[1] A.. Tishin,. Spichkin, Y. I., The Magnetocaloric Effect and its Applications, Institute of Physics Publishing, Bristol (UK), 2003. [2] V. Johnson, C.G. Frederick, Magnetic and crystallographic properties of ternary manganese silicides with ordered Co2P structure, Phys. Status Solidi. 20 (1973) 331–335. [3] H. Fjellvåg, A.F. Andresen, On the Crystal Structure and Magnetic Properties of MnNiGe, J. Magn. Magn. Mater. 50 (1985) 291–297. [4] E. Liu, W. Wang, L. Feng, W. Zhu, G. Li, J. Chen, H. Zhang, G. Wu, C. Jiang, H. Xu, F. de Boer, Stable magnetostructural coupling with tunable magnetoresponsive effects in hexagonal ferromagnets., Nat. Commun. 3 (2012) 873. [5] Y. Li, Z.Y. Wei, E.K. Liu, G.D. Liu, H.Z. Luo, X.K. Xi, W.H. Wang, G.H. Wu, Coupled Magnetic and Structural Transitions in Fe-Doped MnNiSi Compounds, IEEE Trans. Magn. 51 (2015) 4–7. [6] O. Tegus, Bao Li-Hong, Song Lin, Phase transitions and magnetocaloric effects in Phase transitions and magnetocaloric effects in intermetallic compounds MnFe X (X = P, As, Si, Ge), Chin. Phys. B. 22 (2013) 37506. [7] M. Fries, L. Pfeuffer, E. Bruder, T. Gottschall, S. Ener, K.P. Skokov, O. Gutfleisch, V.B. Diop, T. Grob, Microstructural and magnetic properties of Mn-Fe-P-Si (Fe2P-type) magnetocaloric compounds, Acta Mater. 132 (2017) 222–229. [8] L. Caron, Z.Q. Ou, T.T. Nguyen, D.T.C. Thanh, O. Tegus, E. Bruck, On the determination of the magnetic entropy change in materials with first-order transitions, J. Magn. Magn. Mater. 321 (2009) 3559–3566.

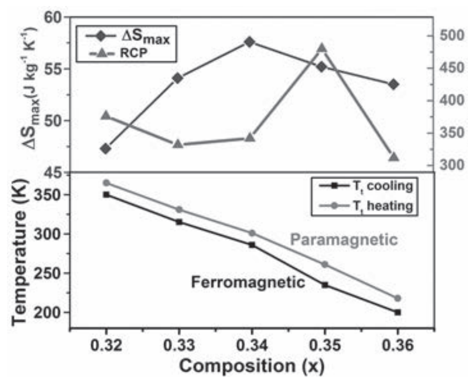

Fig. 1. Magnetostructural transition temperature during heating and cooling, ΔS_{max} and RCP v/s alloy composition x in $(MnNiSi)_{1-x}(Fe_2Ge)_x$ alloys

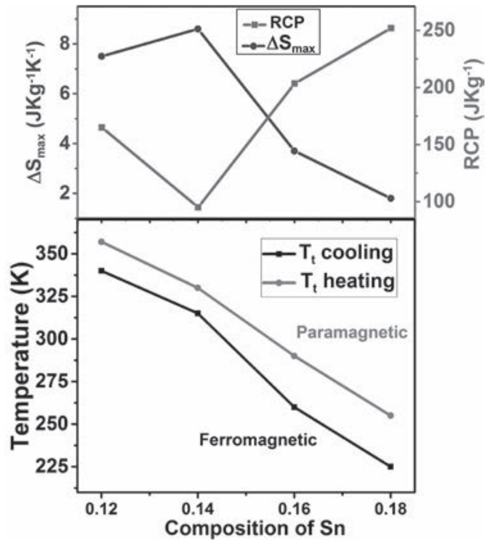

Fig. 2. Magnetostructural transition temperature during heating and cooling, ΔS_{max} and RCP v/s alloy composition y in $Mn_{0.45}Fe_{0.55}NiSi_{1-y}Sn_y$ alloys

4:00

FD-09. Entropy Change and Hysteresis Losses in $Ni_{45}Co_5Mn_{(37-x)}In_{(13+x)}$ Alloy Family.

M. Ghahremani[1], A. Aslani[2], M. Hosseinnia[3], L.H. Bennett[2] and E. Della Torre[2]
1. Computer Science, Mathematics, and Engineering, Shepherd University, Shepherdstown, WV, United States; 2. Electrical and Computer Engineering, The George Washington University, Washington, DC, United States; 3. Beatson Institute, University of Glasgow, Glasgow, United Kingdom

The use of Maxwell equations to calculate the entropy change (ΔS) in materials that have a first-order phase transition (FOPT) has been questioned as they are only valid at thermal equilibrium [1,2]. Though, it has been recently shown that this artifact can be minimized after using appropriate protocol for the measurements [3]. The hysteresis losses and magnetocaloric effect of $Ni_{45}Co_5Mn_{(37-x)}In_{(13+x)}$ alloy have been studied in this work. The ingots were prepared by vacuum arc melting technique under an argon atmosphere and were annealed at 900 C for 24 h followed by water quenching. The heating and cooling isothermal magnetizations, M(H), were measured up to 1.5 T and 5 T at a temperature range of 240 K to 338 K. During the heating process the temperature was raised from 240 K to 338 K and at each discrete temperature point, the M(H) was measured. The reverse procedure was carried in the cooling process. The area between the ascending and descending loops of the field-dependent magnetization curves of the $Ni_{45}Co_5Mn_{37}In_{13}$ alloy was calculated for both heating and cooling processes at different temperatures and is shown in Fig. 1. These areas are interpreted as the magnetic hysteresis losses at different temperatures. The results reveal that under 1.5 T applied magnetic field, the heating process has significantly higher hysteresis compared to the cooling process. Both for the cooling and heating processes, the hysteresis losses are negligible up to 310 K. Though, after 314 K the hysteresis losses are considerable for the heating process, yet negligible for the cooling process. Furthermore, as shown in Fig. 1, by increasing the applied magnetic field up to 5 T, the hysteresis loss curve is shifted to the lower temperatures compared to the ones at 1.5 T. As depicted in this figure the maximum hysteresis losses at 5 T occurs at 312 K, whereas for 1.5 T the peak befalls at 318 K. By interpreting these results we can determine the temperature regions which indirect MCE measurements via Maxwell's and thermodynamic equations will produce the highest discrepancy with the direct MCE measurements. These areas are shown in Fig. 1, for the 1.5 T field (blue shaded temperature region) and the 5 T filed (red shaded temperature region). For instance, the indirect MCE measurements within 316 K to 322 K should be taken with caution for the heating process under 1.5 T. For the 5 T magnetic field this region falls within the temperature range of 307 K to 316 K. To study the magnetocaloric effect of $Ni_{45}Co_5Mn_{(37-x)}In_{(13+x)}$ alloy family (x=0, 0.4) the isofield temperature-dependent magnetization curves, M(T), were derived from isothermal magnetization loops for both ascending and descending magnetic fields, and the entropy changes (ΔS) were derived and are shown in Fig. 2. This figure reveals three distinct results as follow. Firstly, for $Ni_{45}Co_5Mn_{37}In_{13}$ sample, the peak of the entropy change curve under 5 T applied field occurs at 308 K in the descending curve and at 314 K in the ascending curve, whereas for the 1.5 T filed these peaks happen at 318 K and 320 K, respectively. This emphasizes the fact that the variation of the maximum applied magnetic field within same stoichiometry composition can very well change the critical temperature at which the peak of the entropy change curves occur. So when synthesizing the magnetocaloric materials, one should consider the maximum applied magnetic field in which the magnetic refrigeration system will be operational. Secondly, even a small change in the stoichiometry composition of a material can significantly change the material's critical temperatures. As shown in Fig. 2, the critical temperature of the $Ni_{45}Co_5Mn_{36.6}In_{13.4}$ has been shifted by about 36 K to lower temperatures compared to the $Ni_{45}Co_5Mn_{37}In_{13}$. This suggests that material with high MCE at temperatures out of room temperature can be customized by changing their stoichiometry in order to shift their high MCE toward desirable temperatures. This is promising especially in finding suitable refrigerants for room temperature magnetic refrigeration systems. Thirdly, it is observed that the entropy change curves of $Ni_{45}Co_5Mn_{36.6}In_{13.4}$ are broader than the ones for $Ni_{45}Co_5Mn_{37}In_{13}$. Relative cooling power (*RCP*) is given by $RCP=-\Delta S_M(T,H) \times \delta T_{FWHM}$, where ΔS_M is the refrigerant's isothermal magnetic entropy change and δT_{FWHM} is the full-width-at-half-maximum of the peak of magnetic entropy. Therefore, the *RCP* of the $Ni_{45}Co_5Mn_{36.6}In_{13.4}$ sample is higher than the one for $Ni_{45}Co_5Mn_{37}In_{13}$ sample. This leads to obtaining a higher refrigeration capacity in a magnetic refrigeration system. In summary, the results of this research are very promising in synthesizing high-performance magnetocaloric materials that can be used to develop practical room temperature magnetic refrigeration systems.

[1] I. Rodionov, Y. Koshkidko, J. Cwik, *et.al.*, *JETP Letters*, Vol. 101, No. 6, 385-389 (2015). [2] B. Kaeswurm, V. Franco, K. Skokov, O. Gutfleisch, *J. Magn. Magn. Mater*. 406:259–265 (2016). [3] V. Franco, Lake Shore Cryotronics: application note. https://www.lakeshore.com/products/Vibrating-Sample-Magnetometer/Pages/MCE.aspx.

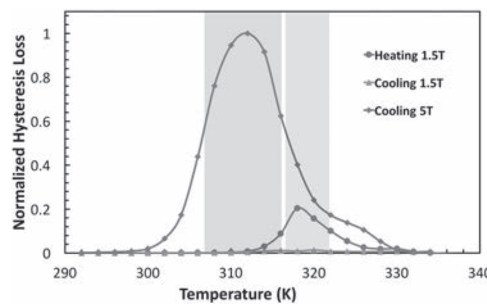

Fig. 1. The area between the ascending and descending M(H) loops (known as hysteresis loss) of $Ni_{45}Co_5Mn_{37}In_{13}$ under 1.5 T and 5 T applied fields for heating and cooling processes. The red and blue shaded regions show the temperature range in which the maximum discrepancy between direct and indirect MCE measurements occurs for 5 T and 1.5 T, respectively.

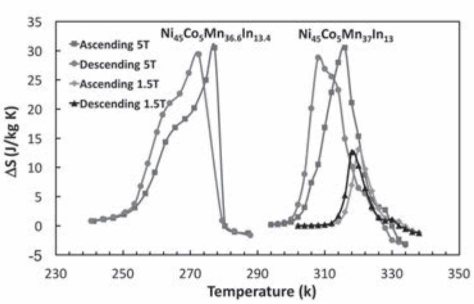

Fig. 2. The entropy change of $Ni_{45}Co_5Mn_{(37-x)}In_{(13+x)}$ under 1.5 T and 5 T. The measurements for $Ni_{45}Co_5Mn_{37}In_{13}$ were performed during heating process under 1.5 T and cooling process under 5 T. For the $Ni_{45}Co_5Mn_{36.6}In_{13.4}$ sample measurement was performed during cooling process under 5 T.

4:15

FD-10. Low field and large magnetocaloric effect in Ni-Mn-Sn (Fe-B) alloys.

K. Srikanti[1], R. V.V[1], G. Anusha[1] and G. Raghavan[1]
1. CAEM, International Advanced Research Centre for Powder Metallurgy, Chennai, India

Ni-Mn based ferromagnetic shape memory alloys (FSMAs) received lot of attention by virtue of their giant magnetocaloric effect and have application potential for magnetic refrigeration. They are very cheap and environmental friendly [1-5]. These alloys undergo a first-order magnetic transition from a high moment phase (austenite) to a low moment phase (martensite) with decreasing temperature, associated with the sharp changes of magnetization, leading to large magnetoresistance, giant magnetocaloric effects, and magnetic-field-induced strain. Most of these properties are attributed to their first order martensitic transition (MT), which can be tuned by changing the chemical composition, elemental doping and substitution [6-8]. In this work we investigate the structural, magnetic and magnetocaloric properties of Ni-Mn-Sn-Fe-B alloy. Fe_2B has been added with an intention to increase the magnetization. Experimental $Ni_{43}Mn_{46}Sn_{11}$ $(Fe_2B)_{0.5}$ was prepared by arc-melting the raw materials in a cold copper crucible under the argon atmosphere protection. For better homogeneity the sample was melted four times and consequently annealed in evacuated quartz tube at 1123 K for 72 hours and quenched in liquid nitrogen. The room temperature structure of the alloys was identified employing powder X-ray diffraction (XRD) using Cu Kα radiation. A Rigaku make diffractometer was used for this purpose. The austenite and martensite transition temperatures were determined by differential scanning calorimetry (DSC, Netzsch) at a heating and cooling rate of 10 K/min. The magnetization measurements were carried out using a vibration sample magnetometer (Microsense, Model EZ9) equipped with a magnetic field of 2T. Figure 1 (a) shows the room temperature XRD pattern of the $Ni_{43}Mn_{46}Sn_{11}$ $(Fe_2B)_{0.5}$ alloys. The XRD patterns of the parent alloy exhibits the cubic Heusler L_{21}-type structure at room temperature representing the austenite phase. The structural transformation temperatures of the alloy was determined from the DSC curves recorded during heating and cooling cycles (Fig. 1 (b)). A well-defined endothermic peak appears in the martensite (M) to austenite (A) phase transformation during heating while an exothermic peak observed in the austenite to martensite phase transformation during cooling. These alloys display both first-order structural transformation associated with martensitic transition and a second-order magnetic transition (small peak—change in base line) corresponding to the Curie temperature of the austenite phase ($T_{A C}$) as evident in Fig. 1 (b). Figure 1 (c) shows the temperature dependence of magnetization (*M-T* curve) for the alloy taken in the presence of 500 Oe during heating. The alloy undergo a structural transition from martensite phase to austenite phase at *As* denoted by a sudden jump in the magnetization. The structural transition occurs around 200 K, which is far below the T_{AC}. The transition temperatures *As*, *Af*, and T_{AC} determined from the thermomagnetic curves are in close agreement with the results obtained from the DSC thermograms in these alloys. The magnetic entropy (delta S_M) as a function of temperature in the magnetic field up to 2T was calculated from isothermal magnetization curves with increase in temperatures at an interval of 2 K in the vicinity of martensite transition (shown in Fig 1 (d)) using the Maxwell relation. It is observed from Fig 1 (d) that there is a sudden change in magnetization from 202 K to 204 K and around 206 K, a metamagnetic transition is observed which is attributed to the onset of magnetic field induced structural transition from martensite phase with lower magnetization to austenite phase with higher magnetization. Figure 1 (e) shows the variation of magnetic entropy with temperature. A huge positive delta S_M of 17 J/Kg-K has been observed around 203 K at a low field of 2 T. The magnetic entropy found in this work is higher than that of the values reported in the literature [9-11]. The reason for such a huge magnetocaloric effect is due to the strong magnetostructural coupling due to Fe-B addition.The variation of concentration of Fe-B and its effect on martensite transition and magnetic entropy is in progress. Conclusion We have studied the effect of Fe-B addition in Ni-Mn-Sn alloy. This alloy shows a DS_M of 17 J/Kg-K has been observed around 203 K at a low field of 2 T. The huge magnetocaloric effect found in this alloy makes it promising for fundamental studies as well as for magnetic refrigeration applications.

R. Kainuma, Y. Imano, W. Ito, Y. Sutou, H. Morito, S. Okamoto, O. Kitakami, K. Oikawa, A. Fujita, T. Kanomata, K. Ishida, Nature (London) 439 (2006) 957. T. Krenke, E. Duman, M. Acet, E.F. Wassermann, X. Moya, L. Manosa, A. Planes, Nat. Mater. 4 (2005) 450. N.V.R. Rao, R. Gopalan, V. Chandrasekaran, K.G. Suresh, Appl. Phys. A 99 (2010) 265. D. Pal, K. Mandal, J. Phys. D Appl. Phys 43 (2010) 455002. R. Sahoo, A.K. Nayak, K.G. Suresh, A.K. Nigam, J. Magn. Magn. Mater. 324 (2012) 1267. T. Krenke, M. Acet, E.F. Wassermann, X. Moya, L. Manosa, A. Planes, Phys. Rev. B 72 (2005) 014412. M. Khan, I. Dubenki, S. Stadler, N. Ali, J. Appl. Phys. 97 (2005) 10M304. M. Khan, I. Dubenki, S. Stadler, N. Ali, J. Phys.: Condens. Matter 16(2004) 5259. Z.D. Han, D.H. Wang, C.L. Zhang, S.L. Tang, B.X. Gu, Y.W. Du, Appl. Phys. Lett. 89 (2006) 182507. Z.D. Han, D.H. Wang, C.L. Zhang, B.X. Gu, Y.W. Du, Appl. Phys. Lett.90 (2007) 042507. H.C. Xuan, D.H. Wang, C.L. Zhang, Z.D. Han, H.S. Liu, B.X. Gu, Y.W. Du Solid State Communications 142 (2007) 591

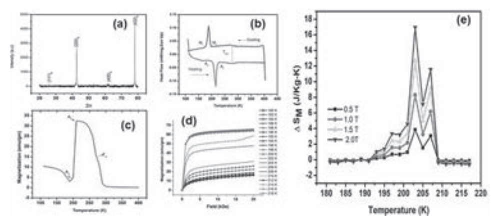

Fig. 1. (a) XRD pattern, (b) DSC curves,(c) M-T curve while heating (d) Isothermal magnetization curves (e) Magnetic entropy at different fields of $Ni_{43}Mn_{46}Sn_{11}$ $(Fe_2B)_{0.5}$ alloy

4:30

FD-11. Thermal stability, magnetic and magnetocaloric properties of $Gd_{55}Co_{35}M_{10}$ (M=Si, Zr and Nb) amorphous alloys.

X. Zhong[1], X. Huang[1], D. Jiao[1], H. Zhang[1], W. Qiu[1], Z. Liu[1] and R.V. Ramanujan[2,3]
1. School of Materials Science and Engineering, South China University of Technology, Guangzhou, China; 2. School of Materials Science and Engineering, Nanyang Technological University, Singapore, Singapore; 3. Singapore-HUJ Alliance for Research and Enterprise (SHARE), Nanomaterials for Energy and Energy-Water Nexus (NEW), Campus for Research Excellence and Technological Enterprise (CREATE), Singapore, Singapore

Abstract: The relatively high reduced glass transition temperature (T_{x1}/T_m > 0.60) and low melting point (T_m) resulted in excellent glass forming ability of $Gd_{55}Co_{35}M_{10}$ (M=Si, Zr and Nb) alloys. The Curie temperatures (T_C) for M=Si, Zr and Nb alloys were 166, 148 and 173 K, respectively. Under an applied field change of 2 T, the maximum values of magnetic entropy change $(-\Delta S_M)^{max}$ for $Gd_{55}Co_{35}Si_{10}$, $Gd_{55}Co_{35}Zr_{10}$ and $Gd_{55}Co_{35}Nb_{10}$ were 2.86, 4.28 and 4.05 $Jkg^{-1}K^{-1}$, while the values of refrigerant capacity (RC) were found to be 154, 274 and 174 Jkg^{-1}, respectively. The values of RC for $Gd_{55}Co_{35}M_{10}$ (M=Si, Zr and Nb) amorphous alloys are comparable to or larger than that of the well-known MCM crystalline alloy $LaFe_{11.6}Si_{1.4}$. With good thermal stability, large RC and a considerable magnetic entropy change, $Gd_{55}Co_{35}M_{10}$ (M=Si, Zr and Nb) amorphous alloys can be potentially used as magnetic cooling materials working in the temperature range of 150-175K, e.g., as part of a gas liquefaction process. Introduction: Magnetic refrigeration (MR) based on the magnetocaloric effect (MCE) is a promising energy efficient, green, condensed state technology, which can potentially replace conventional technology based on gas compression/expansion cycles [1-2]. Amorphous alloys have advantages such as negligible magnetic and thermal hysteresis, tailorable ordering temperature, high thermal stability, high electrical resistivity, high corrosion resistance, and good mechanical properties [3]. Among these, Gd-based alloys have recently attracted intensive interest because they are very useful for sub-room temperature magnetic refrigeration [4-7]. There are few reports on the influence of non-ferromagnetic elements Si, Zr and Nb substitution on the MCE of ternary Gd-based $Gd_{55}Co_{35}M_{10}$ (M=Si, Zr and Nb) amorphous alloys. In this work, the magnetic properties and magnetocaloric effects (MCEs) of ternary Gd-based $Gd_{55}Co_{35}M_{10}$ (M=Si, Zr and Nb) amorphous alloys are investigated. Experimental: $Gd_{55}Co_{35}M_{10}$ alloys with M=Si, Zr and Nb were firstly prepared from mixtures of high purity Gd(>99.98wt.%), Co(99.98wt.%), Si(>99.99wt.%), Zr(>99.5wt.%) and Nb(>99.5wt.%) by arc melting in argon atmosphere. Melting was performed four times to ensure composition homogeneity, weight loss was less than 0.5wt.%. Ribbons of these samples were obtained by the single roller melt spinning technique with a copper wheel velocity of 50 m/s in a purified argon atmosphere. The width and thickness of the ribbons were about 1 mm and 15 μm, respectively. X-ray diffraction (XRD) measurements were performed at room temperature using a Philips X'pert Pro MPD X diffractometer with Cu Kα radiation. The thermal stability was analyzed by differential scanning calorimetry using a NETZSCH–STA449C calorimeter at a heating rate of 20 K/min under argon atmosphere to study crystallization behavior. The values of onset crystallization temperature T_x were determined from the DSC traces with an accuracy of ±1K. Magnetic measurements were carried out using a Quantum Design Physical Property Measurement System (model PPMS-9) with the field direction in the plane of the ribbons, therefore the demagnetization factor was neglected. The magnetocaloric properties of the materials were calculated by the indirect-measurement method from the M–H curves. Results: The onset crystallization temperatures (T_{x1}) are 620, 568 and 555 K for $Gd_{55}Co_{35}M_{10}$ alloys with M=Si, Zr and Nb, respectively, which implies that these amorphous ribbons are stable at room temperature. The thermal properties of these amorphous alloys are summarized in Table 1. The T_{x1}/T_m can be understood as the reduced glass transition temperature (T_g/T_m) of these alloys. Relatively high T_{x1}/T_m and small T_m make $Gd_{55}Co_{35}M_{10}$ (M=Si, Zr and Nb) alloys possess excellent glass forming ability. Fig.1 shows the magnetic entropy change as a function of temperature for $Gd_{55}Co_{35}M_{10}$ (M=Si, Zr and Nb) amorphous alloys at a maximum magnetic field change from 0 to 2T. All three $(-\Delta S_M)$–T curves exhibit a typical λ-shape, indicating that the magnetic transition near the T_C of the $Gd_{55}Co_{35}M_{10}$ (M=Si, Zr and Nb) amorphous alloys is a second-order phase transition. For an applied field change of 2T, the maximum values of magnetic entropy change $(-\Delta S_M)^{max}$ for $Gd_{55}Co_{35}Si_{10}$, $Gd_{55}Co_{35}Zr_{10}$, and $Gd_{55}Co_{35}Nb_{10}$ are 2.86, 4.28, and 4.05 $Jkg^{-1}K^{-1}$, respectively. These values are much higher than those of $Gd_{55}Co_{20}Fe_5Al_{20}$ BMG alloy (2.24 $Jkg^{-1}K^{-1}$ at 20 kOe) [8], $Gd_{55}Co_{35}Fe_{10}$ (1.72 $Jkg^{-1}K^{-1}$ at 2T) [6] and $Gd_{65}Fe_{20}Al_{15-x}B_x$ glassy ribbons [9]. Conclusion: Good thermal stability, large relative cooling power (RC) and considerable magnetic entropy change make $Gd_{55}Co_{35}M_{10}$ (M=Si, Zr and Nb) amorphous alloys attractive candidates for magnetic refrigerant applications.

[1] K. A. Gschneidner Jr, V. K. Pecharsky. Inter. J. Refri. 2008, 31(6):945-961. [2] *V. Franco, J.S. Blázquez, J.J. Ipus, et al. Prog. Mater. Sci. 2018, 93:112-232.* [3] *Q. Y. Dong, B. G. Shen, J. Chen, et al.* J. Appl. Phys. 2009, 105: 053908. [4] *X. C. Zhong, P. F. Tang, Z. W. Liu, et al. J. Appl. Phys. 2012, 111: 07A919.* [5] *J. X. Min, X. C. Zhong, Z. W. Liu, et al. J. Alloys Compd. 2014, 606: 50-54.* [6] *X. C. Zhong, X. W. Huang, X. Y. Shen, et al. J. Alloys. Compd. 2016, 682: 476-480* [7] X. Y. Shen, X. C. Zhong, X. W. Huang, et al. J. Phys. D Appl. Phys. 2017, 50: 035005. [8] *C. L. Jo, L. Xia, D. Ding, et al. J. Alloys. Compd. 2008, 458: 18-21.* [9] *Y. K. Fang*, C. H. Lai, C. C. Hsieh, et al. J. Appl. Phys. 2009,107: 09A901.

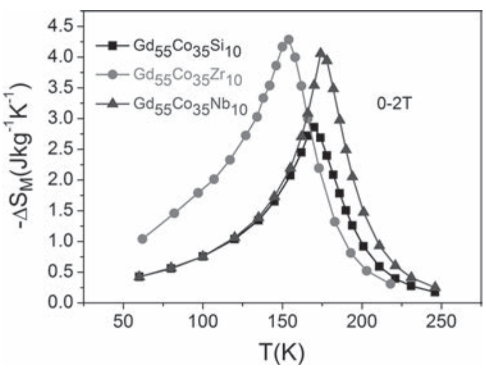

Fig. 1. Magnetic entropy changes as a function of temperature for $Gd_{55}Co_{35}M_{10}$ (M=Si, Zr and Nb) amorphous alloys.

Alloys	T_{x1} (K)	T_C (K)	$\Delta T=T_{x1}-T_C$ (K)	T_m (K)	$\Delta T_m=T_m-T_{x1}$ (K)	T_{x1}/T_m
$Gd_{55}Co_{35}Si_{10}$	620	166	454	921	301	0.67
$Gd_{55}Co_{35}Zr_{10}$	568	148	420	925	357	0.61
$Gd_{55}Co_{35}Nb_{10}$	555	173	382	924	369	0.60

Table 1 Values of the onset crystallization temperature (T_{x1}), Curie temperature (T_C), melting temperature (T_m), stabilizing temperature region (ΔT), and reduced crystallization temperature (T_{x1}/T_m) of $Gd_{55}Co_{35}Si_{10}$, $Gd_{55}Co_{35}Zr_{10}$ and $Gd_{55}Co_{35}Nb_{10}$ amorphous alloys.

4:45

FD-12. Table-like Magnetocaloric Effect in $Ho_{36}Co_{48}Al_{16}$ Multiphase Alloy.

E.A. Balfour[1], Y. Shang[1], Y. Cao[1], *H. Fu*[1], A.A. El-Gendy[2] and R.L. Hadimani[3]

1. Applied Physics, School of Physical Electronics, University of Electronic Science and Technology of China, Chengdu, China; 2. Department of Physics, University of Texas at El Paso, El Paso, TX, United States; 3. Department of Mechanical and Nuclear Engineering, Virginia Commonwealth University, Richmond, VA, United States

I. INTRODUCTION Magnetocaloric effect (MCE) has recently gained wide attention in both fundamental research [1, 2], and application in magnetic refrigeration (MR) systems. It is promising as an efficiently competitive technology for the replacement of the potentially environmentally risky gas compression/expansion refrigeration [3-5]. Ericsson cycle implementation of MR is one of the most suitable thermodynamic cycles for enhanced performance. However, its requirement that magnetic entropy change ($-\Delta S_M$) of the magnetic refrigerant is constant (table-like MCE) over the operating temperature range severely limits the availability of appropriate magnetocaloric materials (MCMs). The search for MCMs with such property is a daunting challenge. Some proposed research approach include multilayered and powder composite mixtures but the low density of powder composites significantly deteriorates the magnitude of $-\Delta S_M$. Moreover, the lifespan of sintered or glued layer refrigerants is shortened by repeated differential expansion and contraction at the interfaces. Single bulk multiphase alloys with table-like feature could be a solution to overcoming the issues associated with layered and ex-situ composite mixtures. However, the challenge of identifying such alloy systems with temperature independent $-\Delta S_M$ or improved refrigerant capacity (*RC*) can be overwhelming. Their discovery is strictly dictated by the nature of the related phase diagrams. Several Ho(Co, Al)-based binary and quasi-binary crystalline alloys are known to have good magnetocaloric properties. Therefore, we examine the Ho-Co-Al system to identify a suitable multiphase region for study in expectation of a single bulk multi-crystalline alloy that exhibits table-like MCE. In particular, $HoCo_2$, HoCoAl, and Ho_2Co_2Al compounds have good magnetocaloric properties [6-8]. Consequently a carefully selected region of the Ho-Co-Al system, bounded by the three compounds and expected to contain all three phases, was studied. Results show that the title multiphase alloy, which comprises the $HoCo_2$, HoCoAl, and Ho_2Co_2Al main phases, exhibits table-like MCE. The effect of interatomic substitution on the magnetic properties of relevant phases and its contributions to the attainment of the table-like MCE and *RC* are discussed in detail. II. EXPERIMENTAL DETAILS Stoichiometric proportions of Ho, Co and Al all of purities 99.99 wt.% were arc melted in a water cooled crucible under Ti-gettered argon environment. The sample was flipped over and re-melted three times to enhance homogeneity while minimizing weight loss. Powder X-ray diffraction (XRD) data was collected at room temperature for phase characterization. Rietica software was used for Rietveld refinement for the crystal structure and phase composition analysis. Magnetization measurements were performed with a superconducting quantum interference device (SQUID) magnetometer. III. RESULTS AND DISCUSSIONS The four sets of vertical bars (blue) of Rietveld refinement shown in Fig. 1 correspond to the HoCoAl, Ho_2Co_2Al, $HoCo_2$ main phases and trace amount of Ho_2O_3, respectively from top to bottom. Lattice parameters and EDS analysis indicate that Al substitution for Co occurs in the $HoCo_2$ phase while the HoCoAl phase has higher Co content than the Co:Al ratio for equiatomic HoCoAl. Temperature dependence of magnetization under field cooled (FC) condition shows a broad transition, which is beneficial for obtaining table-like MCE. Maximum magnetization of isotherms reaches 172 emu/g at 7 K under applied field of 50 kOe. Small magnetic hysteresis is observed at 7 K but disappears with increasing temperature and is not visibly evident from 13 K. Again, no step-like magnetization could be seen for all the measured isotherms. It indicates that the first-order metamagnetic transition associated with $HoCo_2$ and its low Al-substituted counterparts is absent. The order of magnetic phase transitions in the $Ho(Co_{1-x}Al_x)_2$ alloys changes from first-order to second-order for x > 0.06 [9]. Therefore, the suppressed hysteresis and absence of the first-order transition are attributed to the high content of Al in the $HoCo_2$ phase. Table-like MCE is attained for the studied alloy under different applied field changes (ΔH) as shown in Fig. 2. The $-\Delta S_M$ platforms become flatter with decreasing field. When ΔH = 5 T, the magnitude of the platform is about 8.5 J/kg K, which is among the highest known for MCMs with table-like MCE. The plateau spreads over the temperature range from 20 K to 50 K. At the decreased field of 2 T, $-\Delta S_M$ = 2.9 J/kg K and spands from 20 K to 57 K. In addition, large *RC* of 525 J/kg and 180 J/kg are obtained for the ΔH = 5 T and 2 T, respectively. IV. CONCLUSIONS The single bulk multiphase $Ho_{36}Co_{48}A_{16}$ alloy with three main crystalline phases, HoCoAl, Ho_2Co_2Al and $HoCo_2$ has been prepared and its magnetic and magnetocaloric properties studied. The well distributed transition temperatures and accompanying $-\Delta S_M$ result in table-like MCE with magnitude of 8.5 J/kg K under ΔH = 5 T. The large magnitude of the table-like MCE and its relatively wide temperature span of up to about 40 K, coupled with its large *RC* of 525 J/K under ΔH = 5 T make the alloy a competitively good candidate for MR using Ericsson cycle and suitable for use with permanent magnets at 2 T. ACKNOWLEDGEMENT This work was supported by the National Natural Science Foundation of China [Grant No. 51271049 and 51750110501]

REFERENCES [1] O. Tegus, E. Brück, L. Zhang, Dagula, K. H. J. Buschow, F. R. de Boer, Magnetic-phase transitions and magnetocaloric effects, Phy. B 319 (2002) 174–192. [2] V. K. Pecharsky, K. A. Gschneidner Jr., Magnetocaloric effect and magnetic refrigeration, J. Mag. Mag. Mat. 200 (1999) 44-56. [3] K. A. Gschneidner Jr ., V. K. Pecharsky, Rare Earths and Magnetic Refrigeration, J. Rar. Ear. 24 (2006) 641-647. [4] V. K. Pecharsky, K. A. Gschneidner Jr., Advanced magnetocaloric materials: What does the future hold? Int. J. Ref. 29 (2006) 1239-1249. [5] M.-H. Phan, S.-C. Yu, Review of the magnetocaloric effect in manganite materials, J. Magn. Magn. Mat.er 308 (2007) 325-340. [6] M. Balli, D. Fruchart, D. Gignoux, The influence of gadolinium on magnetism and magnetocaloric properties of $HoCo_2$ alloy, J. Alloy. Compd. 455, (2008) 73-76. [7] X. X. Zhang, F. W. Wang, G. H. Wen, Magnetic entropy change in RCoAl (R = Gd, Tb, Dy, and Ho) compounds: candidate materials for providing magnetic refrigeration in the temperature range 10 K to 100 K, J. Phys.: Condens. Matter 13, (2001) L747-L752. [8] E. A. Balfour, Y. F. Shang, H. Fu, Ahmed A. El-Gendy, R. L. Hadimani, Y. Luo, Suppression of impurity phases and the study of magnetic and magnetocaloric properties of Ho_2Co_2Al intermetallic compound, J. Magn. Magn. Mater. 443, (2017) 79-84. [9] T. I. Ivanova, S. A. Nikitin, G. A. Tskhadadze, Yu. S. Koshkid'ko, W. Suski, W. Iwasieczko, D. Badurski, Magnetic, transport and magnetocaloric properties in the Laves phase intermetallic Ho(Co1-xAlx)2 compounds, J. Alloy. Compd. 592, (2014) 271-276.

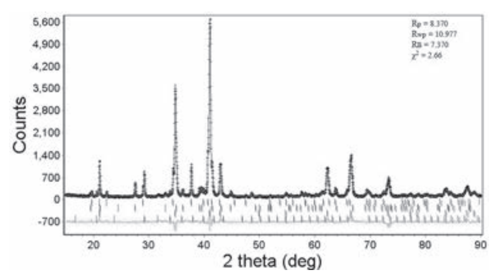

Fig. 1. Rietveld refinement profile of $Ho_{36}Co_{48}Al_{16}$ multiphase alloy

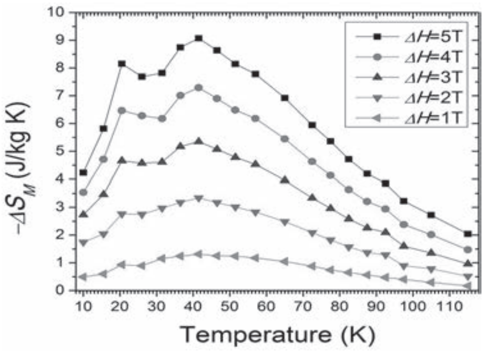

Fig. 2. $-\Delta S_M$ **of the** $Ho_{36}Co_{48}Al_{16}$ **multiphase alloy for** ΔH **= 1 T, 2 T, 3 T, 4 T, and 5 T**

THURSDAY AFTERNOON, 26 APRIL 2018 ROSELLE II, 2:00 TO 5:00

Session FE

PATTERNED FILMS AND ELEMENTS

Olivier Fruchart, Chair
Univ. Grenoble Alpes, CNRS, CEA, Grenoble, France

CONTRIBUTED PAPERS

2:00

FE-01. Peculiarities of disorder-induced ferromagnetism phenomena in $Fe_{60}Al_{40}$ films on a local scale.

A. Smekhova[1], E. La Torre[2], T. Szyjka[2], B. Eggert[2], B. Cöster[2], K. Ollefs[2,3], D. Walecki[2], S. Salamon[2], R. Bali[4], J. Lindner[4], F. Wilhelm[3], A. Rogalev[3], E. Weschke[5], D. Többens[5], R. Banerjee[6], B. Sanyal[6], C. Schmitz-Antoniak[1] and H. Wende[2]
1. PGI-6, FZ Juelich, Berlin, Germany; 2. University of Duisburg-Essen and CENIDE, Duisburg, Germany; 3. ESRF, Grenoble, France; 4. HZDR, Dresden, Germany; 5. HZB (BESSY II), Berlin, Germany; 6. Uppsala University, Uppsala, Sweden

Thin films of Fe-rich transition metal aluminide $Fe_{60}Al_{40}$ (at. %) are very promising for implementation in modern technology due to a possibility of having tailored magnetic properties. Being weakly ferromagnetic at room temperature in the chemically ordered B2 phase, $Fe_{60}Al_{40}$ films can be reversibly transformed into the ferromagnetic chemically disordered A2 phase with much higher magnetization in a well controlled way by means of ion irradiation. Prior studies point on important influence of created chemical disorder on static and dynamic magnetic properties of $Fe_{60}Al_{40}$ films while achievements in magnetic patterning and studies of magnetization reversal have shown their perspective for further use in spin-transport devices [1–3]. Detailed studies performed on a local scale can clarify hidden mechanisms of disorder induced ferromagnetism phenomena in $Fe_{60}Al_{40}$ films via understanding the influence of the local surrounding and features of Fe-Al hybridization on the magnetic properties. In our work, element-specific X-ray absorption spectroscopy (EXAFS, XANES, and XMCD) in hard- and soft energy ranges together with synchrotron-based XRD (SR-XRD) have been applied to probe the local rearrangements and related magnetic and electronic properties of Fe and Al atoms in bare $Fe_{60}Al_{40}$ thin films of 40 nm thickness through the order-disorder (B2 → A2) phase transition initiated by 20keV Ne^+ ion irradiation with low fluences (~10^{14} ions cm^{-2}). Extended X-ray absorption fine structure (EXAFS) spectra recorded at the Fe and Al K edges at room temperature (RT) and low temperature of 5K (LT) and SR-XRD have shown significant changes in the local environment of Fe and Al absorbers before and after the irradiation. In the course of the transition a number of Fe-Fe nearest-neighbors grew from 3.47(7) up to 5.0(1) for the ordered B2 and the fully disordered A2 phases, correspondingly, and ~1% of the unit cell volume expansion was found. Distinct changes of Fe and Al coordination due to disordering resulted in increased Fe 3d spin and 4p orbital polarizations and characteristic changes in electronic structure of Al atoms as was demonstrated by RT XMCD at the Fe $L_{2,3}$ and Fe K edges as well as LT XANES at the Al K edge, respectively [4,5]. A unique possibility to probe the magnetism of 3d states by hard X-rays has been realized by recording the XMCD signal at ~ 60eV above the Fe K edge where so-called magnetic multi-electronic excitations (MEE, secondary processes) are present [6,7]. The analysis of MEE peak amplitude and its integrated intensity has revealed similar tendencies in their changes with fluence as for 3d effective spin and 3d orbital magnetic moments obtained from XMCD spectra at the Fe $L_{2,3}$ edges, respectively. Moreover, this analysis points towards increased localization of Fe 3d states in A2 phases created by fluencies of $(0.75 - 6) \times 10^{14}$ ions cm^{-2}. Element-specific hysteresis loops (ESHL) recorded by XMCD either at the Fe K or L_3 absorption edges have confirmed the preferential in-plane magnetic anisotropy of irradiated films; the variations in coercive fields depending on temperature and irradiation fluence have been checked by ESHL at the Fe L_3 edge. The specific shoulder related to hybridization effects between Fe and Al has been uncovered with the help of *in-situ* hydrogen plasma treatment. It has been also illustrated that the reduction of the top oxide layer leads to increase or decrease of Fe 3d spin magnetic moments in the surface region depending on the time of treatment. This suggests that the use of a capping layer could either protect the films from continuous uncontrolled oxidation or further increase the macroscopic magnetization of films that is much more favorable for technological applications. A theory support was provided by self-consistent DFT calculations using the VASP program package applied to relaxed model systems. A clear variation of local configurations in B2 and A2 phases followed by sizable changes in Fe and Al magnetic moments has been found. The work was partially funded by Helmholtz Association (Young Investigator's Group "Borderline Magnetism", VH-NG-1031). The authors thank the ESRF (ID12 beamline) and HZB-BESSY II (UE46_PGM-1 and KMC-2 beamlines) for provision of synchrotron radiation facilities and allocation of synchrotron radiation; Swedish National Infrastructure for Computing (SNIC) is acknowledged for providing high performance supercomputing time.

[1] J. Fassbender, M. O. Liedke, T. Strache, *et al.*, Phys. Rev. B, 77 (2008) 174430. [2] R. Bali, S. Wintz, F. Meutzner, *et al.*, Nanoletters, 14 (2014) 435-441. [3] N. Tahir, R. Gieniusz, A. Maziewski, *et al.*, IEEE Transactions on Magnetics 50, 1 (2014). [4] E. La Torre, A. Smekhova, C. Schmitz-Antoniak, *et al.*, to be submitted. [5] A. Smekhova, E. La Torre, C. Schmitz-Antoniak, *et al.*, to be submitted. [6] N. Kawamura, H. Maruyama, K. Kobayashi, *et al.*, J. Phys. Soc. J., 68 (1999) 923. [7] N. Kawamura, T. Yamamoto, H. Maruyama, *et al.*, J. Synch. Rad. 8 (2001) 410.

2:15

FE-02. Anomalous Nernst and Hall Effects in $Co_x(MgO)_{1-x}$ Granular Thin Films.

P. Sheng[1] and M. Mizuguchi[1,2]
1. Institute for Materials Research, Tohoku University, Sendai, Japan;
2. CREST, Japan Science and Technology Agency, Kawaguchi, Japan

From the discovery of the spin Seebeck effect, many researches in spin caloritronics have been reported. Significant roles of anomalous Nernst effect (ANE) in spin caloritronics regarding not only physical aspect but also application to thermoelectric devices are now recognized. ANE is the thermal analogue of anomalous Hall effect (AHE). So far ANE in metallic multilayers attracts a lot of interest due to the enhancement of ANE [1-3]. On the other hand, giant AHE is observed in ferromagnetic-insulator (FM-I) granular films, such as $Fe_{1-x}(SiO_2)_x$ [4]. In strongly disordered systems such as granular films, the mechanism of longitudinal and anomalous Hall transports are not simple [4,5]. To understand ANE in nano-structured systems further, it is interesting to investigate ANE in FM-I nano composite granular films. Here we systematically study the electrical and thermal transport properties in $Co_x(MgO)_{1-x}$ granular films with Co volume fractions (x) changes. The films with different x were fabricated by co-sputtering method on MgO substrates at RT by changing the sputtering powers for Co and MgO targets. Thickness of all the films is 100 nm. In the electrical measurement, the longitudinal (R_{xx}) and transverse resistance (R_{xy}) decrease with increasing x. In addition, the AHE angle (ρ_{xy}/ρ_{xx}) increases with x increases, it shows maximum value for pure Co film. On the otherhand, for the thermal measurement, the longitudinal (Seebeck) voltage and transverse (ANE) voltage increase with increasing x. Interestingly, ANE angle (S_{xy}/S_{xx}) nonmonotonically changes with x increases. It shows maximum value when large amount of Co is included in MgO matrix, which is 1.9 times larger than that of pure Co. It means that significant enhancement of ANE angle can be obtained in $Co_x(MgO)_{1-x}$ films compared with pure Co. ANE angel can be tuned through changing the amount of Co into MgO. The comparison between ANE and AHE will be discussed in detail. Our results provide a new way to enhance ANE angle and it is helpful for realizing the applications of ANE-based devices. Acknowledgements This work was supported by JST CREST Grant Number JPMJCR1524, Japan. We would like to thank H. Sharma, K. Takanashi and T. Seki for their help in experiments.

[1] Y. Sakuraba, K. Hasegawa, M. Mizuguchi1, T. Kubota, S. Mizukami, T. Miyazaki and K. Takanashi, Appl. Phys. Express 6, 033003 (2013). [2] K. Uchida, T. Kikkawa, T. Seki, T. Oyake, J. Shiomi, Z. Qiu, K. Takanashi, and E. Saitoh, Phys. Rev. B 92, 094414 (2015). [3] C. Fang, C. H. Wan, Z. H. Yuan, L. Huang, X. Zhang, H. Wu, Q. T. Zhang, and X. F. Han, Phys. Rev. B 93, 054420 (2016). [4] W. J. Xu, B. Zhang, Q. X. Wang, W. B. Mi, Z. Wang, W. Li, R. H. Yu, and X. X. Zhang, Phys. Rev. B 83, 205311 (2011). [5] Z. Qin, X. D. Liu, and Z. Q. Li, J. Appl. Phys. 111, 083919 (2012).

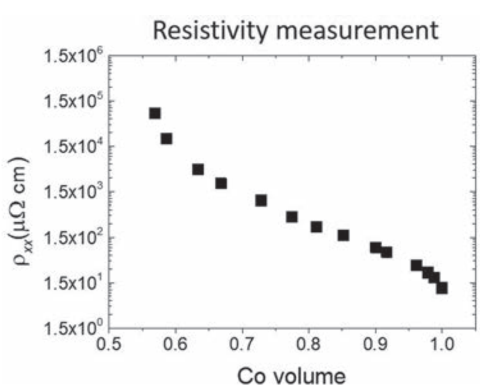

Fig. 1. Resistivity of $Co_x(MgO)_{1-x}$ granular thin films

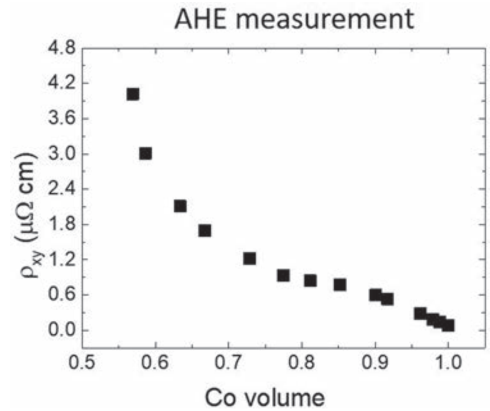

Fig. 2. Anomalous Hall resistivity of $Co_x(MgO)_{1-x}$ granular thin films

2:30

FE-03. ***Zero Field Cooled Exchange Bias Effect in Nano-Crystalline Mg-Ferrite Thin Film.***

H. Roy Dakua[1,2], N. Venkataramani[3] and S. Prasad[4]
1. physics, Indian Institute of Technology, Mumbai, India; 2. physics, National University of Singapore, Singapore; 3. Metallurgical Engineering and Materials Science, Indian Institute of Technology, Mumbai, India; 4. physics, Indian Institute of Technology, Mumbai, India

The applicability of Exchange Bias (EB) effect systems in magnetic devices, such as data storage devices, spin valve devices and voltage control magnetic devices is the main motivation of the research in this topic[1-5]. So far, many EB systems have been studied such as Ferromagnetic (FM)-Antiferromagnetic (AFM), FM-Spin Glass (SG) and Ferrimagnetic (FIM)-AFM heterostructures[1, 6, 7]. These systems show EB shift in the M-H loop as a result of field cooling through the Néel temperature or glass transition temperature of the AFM or SG phase. Apart from the Conventional Exchange Bias (CEB) effect, Wang *et al.* had reported an unusual exchange bias effect in the $Ni_{50}Mn_{50-x}In_x$ (x = 11-15) bulk alloy in 2011[8]. Here, unlike the CEB systems, this material showed a large exchange bias in the M-H loops even in the zero field cooled (ZFC) sample. Subsequently, Nayak *et. al.* had reported ZFC EB effect in bulk Heusler alloy Mn_2PtGa [9]. Recently, some other groups have also reported ZFC EB effect in bulk Ni-Mn-Sn, $Ni_{50}Mn_{36}Co_4Sn_{10}$ and $La_{2-x}Sr_xCoMnO_6$[10-12]. All these studies have broadly pointed out that a unidirectional anisotropy is introduced to the FM state during the initial magnetization process which caused the ZFC EB in the system. In this paper, we report Zero Field Cooled (ZFC) Exchange Bias (EB) effect in nanocrystalline Mg-ferrite thin film. The film of this material was deposited on amorphous quartz substrate using pulsed laser ablation technique. The deposition was carried out in oxygen atmosphere at a pressure 0.16 mbar at the 500^0C substrate temperature using a Nd-YaG pulsed laser. The thickness of the film was ~135 nm. This film was ex-situ annealed at 250^0C for 2 hours. The crystal structure, elemental purity, and the microstructural properties of the film was studied using X-ray Diffraction (XRD), X-ray Photoelectron Spectroscopy (XPS), Atomic Force Microscopy (AFM) and Scanning Electron Microscopy (SEM). These studies confirm that the film is nanocrystalline $MgFe_2O_4$. The magnetic properties of the film was studied using Vibrating Sample Magnetometer (VSM). Figure 1 shows enlarged view of ZFC M-H loop of the film, measured at 10 K by sweeping the magnetic field from 0 Oe → +50 kOe → -50 kOe → +50 kOe. In the inset of figure 1 we show full M-H loop within the field range ± 50 kOe. The spontaneous magnetization of the thin film (~160 emu/cc at 10 K) is comparable to that of the bulk Mg-ferrite. The ZFC M-H loop of our film is asymmetric and shifted along the negative field axis. This shift indicates the presence of ZFC EB effect in the film. The exchange bias field (H_E) of the film is defined as $H_E = |H_{C1}+H_{C2}|/2$; where H_{C1} and H_{C2} are the lower and upper cut-off fields. The highest value of ZFC H_E obtained by us in this Mg-ferrite thin film, is ~230 Oe at 10 K. This value is higher than the reported value of ZFC H_E (H_E ~ 120 Oe at 10) in heterostructure thin films by Murthy *et. al.*;[13]. The ZFC H_E our film is comparable to that of the bulk $Ni_{50}Mn_{50-x}In_x$ (H_E ~200 Oe for ±50 kOe field sweep at 10 K for x = 11, 12, 14, 12, 14, 15) reported by Wang *et. al.*;[8]. Figure 2 shows the variation of the ZFC EB field (H_E) with temperature. The highest value of H_E ~230 Oe was obtained at 10 K. The ZFC EB field (H_E) decreased with increasing temperature and tends to be zero as the ZFC M-H loop become symmetric at high temperature (T > 70 K). We have also measured the low temperature M-H loop after Field Cooling (FC) with 50 kOe magnetic field. The 50 kOe FC M-H loop shows a much lower H_E (~110 Oe at 10 K) as compared to the ZFC M-H loop. A decrease in the FC EB field compare to the ZFC EB field was also reported by Wang *et. al.*[10]. The FC EB field of our film decreased with increasing temperature and tends to be zero as the FC M-H loops become symmetric for T > 70 K. The 10 K FC H_E value of our film is comparable to the FC H_E of Ni-Mn-Sn and the Conventional Exchange Bias (CEB) H_E of the $(MnZnFe)_3O_4$ thin films[14]. Alaan *et. al.* and Venzke *et. al.* have observed CEB effect in ferrite thin films and it was attributed to the presence of disordered region (namely, AFM or SG) in the boundary of the FIM crystallites[14, 15]. Similarly, our Mg-ferrite thin film may also contain disordered regions in the FIM nanocrystalline boundary. The coexistence of disordered regions and the FIM phase could lead to the observed Zero Field Cooled (ZFC) Exchange Bias (EB) effect in the film. The details of this ZFC EB effect will be presented in the paper.

[1] M. Kiwi, Journal of Magnetism and Magnetic Materials 234, 584 (2001). [2] R. Stamps, Journal of Physics D: Applied Physics 33, R247 (2000). [3] S. Gider, B.-U. Runge, A. Marley, and S. Parkin, Science 281, 797 (1998). [4] B. Park, et al., Nature materials 10, 347 (2011). [5] S. M. Wu, S. A. Cybart, P. Yu, M. D. Rossell, J. X. Zhang, R. Ramesh, and R. C. Dynes, Nat Mater 9, 756 (2010). [6] D. Kavich, J. Dickerson, S. Mahajan, S. Hasan, and J.-H. Park, Physical Review B 78, 174414 (2008). [7] M. Ali, P. Adie, C. H. Marrows, D. Greig, B. J. Hickey, and R. L. Stamps, Nature Materials 6, 70 (2007). [8] B. Wang, Y. Liu, P. Ren, B. Xia, K. Ruan, J. Yi, J. Ding, X. Li, and L. Wang, Physical review letters 106, 077203 (2011). [9] A. Nayak, M. Nicklas, S. Chadov, C. Shekhar, Y. Skourski, J. Winterlik, and C. Felser, Physical review letters 110, 127204 (2013). [10] B. Wang, Y. Liu, B. Xia, P. Ren, and L. Wang, Journal of Applied Physics 111, 043912 (2012). [11] P. Liao, et al., Applied Physics Letters 104, 092410 (2014). [12] J. K. Murthy, K. Chandrasekhar, H. Wu, H. Yang, J. Lin, and A. Venimadhav, Journal of Physics: Condensed Matter 28, 086003 (2016). [13] J. K. Murthy and P. A. Kumar, Scientific Reports 7, 6919 (2017). [14] U. Alaan, G. Sreenivasulu, K. Yu, C. Jenkins, P. Shafer, E. Arenholz, G. Srinivasan, and Y. Suzuki, Journal of Magnetism and Magnetic Materials 405, 129 (2016). [15] S. Venzke, et al., Journal of materials research 11, 1187 (1996).

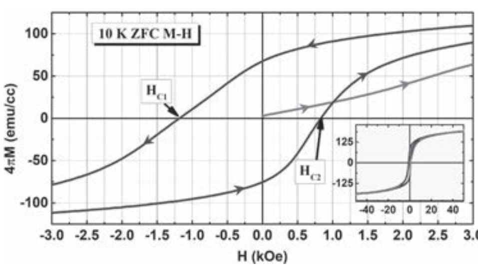

Fig. 1. Zoomed view of Zero Field Cooled (ZFC) M-H loop, measured at 10 K. The red curve shows the initial magnetization. The arrow indicates the field sweep direction. The inset of the figure represent the full range (± 50 kOe) M-H loop.

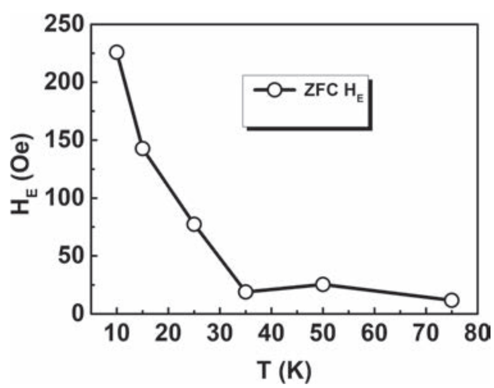

Fig. 2. Temperature dependence of ZFC EB Field (H_E)

2:45

FE-04. Growth and Characterisation of Antiferromagnetic Polycrystalline Mn_3Ga and Mn_3Ge Films.

H. Wu[1], L. Sudoh[2], R. Xu[3], W. Si[3], T. Takahashi[2], C.A. Vaz[4], J. Kim[1], G. Vallejo-Fernandez[1] and *A. Hirohata*[1]
1. university of york, YORK, United Kingdom; 2. Nagaoka University of Technology, Nagaoka, Japan; 3. City University of Hong Kong, Hong Kong, Hong Kong; 4. Paul Scherrer Institute, Villigen, Switzerland

Antiferromagnetic spintronics has been recently investigated intensively in the view of realising a new device without suffering from the cross-talks between cells due to no net magnetic moment for example. Such a study requires the development of a new antiferromagnetic materials with (i) room temperature (RT) antiferromagnetism, (ii) large (out-of-plane) anisotropy and (iii) large grain volume in a thin-film form. One of the candidates to satisfy these criteria is a Heusler alloy [1]. In this study, we have grown polycrystalline hexagonal $D0_{19}$-Mn_3Ga and $D0_{22}$-Mn_3Ge films using sputtering and characterised their magnetic and structural properties systematically. Polycrystalline binary Heusler alloy Mn_3Ga and Mn_3Ge films were grown on thermally oxidised Si(001) substrates by high-target utilisation sputtering system (HiTUS). A seed layer of Ta (5 nm)/Pt (35 nm) was used as it promotes a Mn_3Ga(0002) crystalline orientation as reported by Kurt *et al.* [2]. A Mn_3Ga layer was then deposited with varying the thickness between 3 and 20 nm, followed by the deposition of a ferromagnetic $Co_{0.6}Fe_{0.4}$ layer (3.3 nm) and a Ta capping layer (5 nm). All the layers were deposited at RT and the films were not annealed during and after the deposition to maintain their well-defined interfaces. Polycrystalline Mn_3Ge films were grown using the same stack structure as Mn_3Ga. The Mn_3Ge layer thickness was varied between 3-100 nm. For the Mn_3Ga films, XRD intensities confirms that all films are in their $D0_{19}$ phase. The 100 nm Mn_3Ge films annealed at 500 show the Mn_3Ge(222) peak, indicating that the increase in film thickness reduces the hexagonal crystallisation strain-induced by the seed layer. The corresponding magnetisation curves for Mn_3Ga are shown in Fig. 1(a). The 6-nm-thick Mn_3Ga film shows the largest exchange bias of 430 Oe at 120K. By increasing the Mn_3Ga thickness, the exchange bias is found to decrease, which agrees with the crystallisation degree. PEEM measures the Mn_3Ga films shows that there is magnetic contrast in both CoFe and Mn_3Ga layers which indicates that the CoFe layer polarises a part of the Mn atoms at the interface. The blocking temperature of these samples were then measured using the York Protocol [3] as shown in Fig. 1(b). Here, the magnetisation curves were taken at 100K after thermally activating at elevating temperatures between 100K and 350K in the presence of a negative saturating field of 20 kOe. Figure 1(b) plots all the exchange bias values measured after thermally activating at elevating temperatures. For the 6-nm-thick film, the blocking temperature is determined to be 225K. The blocking temperature is again found to decrease with increasing the Mn_3Ga thickness. The grain size of the Mn_3Ga was measured using transmission electron microscope, the mean grain size is 13.2 nm hence the magneto-crystalline anisotropy was determined to be. These results confirm that the hexagonal binary Heusler alloys can exhibit a reasonable magnetic anisotropy and the corresponding exchange bias. By further optimising the growth conditions and the compositions, the polycrystalline binary Heusler alloy films can exhibit RT antiferromagnetism, which can be be used in antiferromagnetic spintronics.

1. C. Felser and A. Hirohata, *Heusler Alloys* (Springer, Berlin, 2016). 2. H. Kurt *et al.*, *Phys. Status Solidi B* 248, 2338 (2011). 3. K. O'Grady, *J. Magn. Magn. Mater.* 322, 883 (2010).

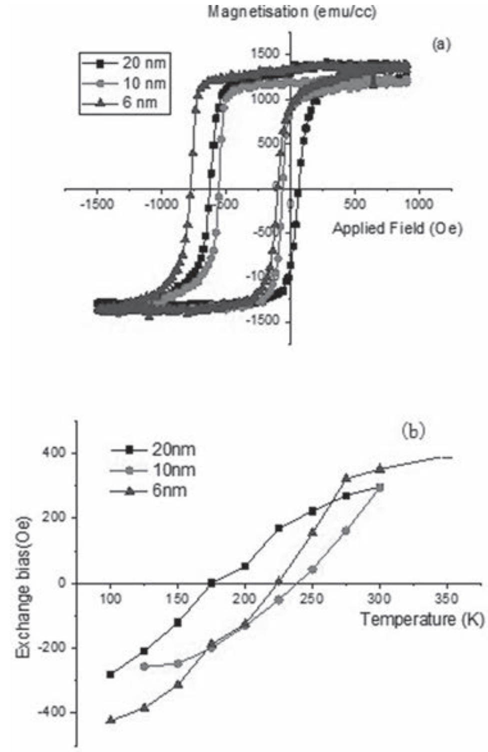

Fig. 1. (a) Magnetisation curves for the polycrystalline Mn_3Ga films with their thicknesses of 6 (triangle symbols), 10 (circles) and 20 nm (squares) measured at 120K. (b) Temperature dependence of exchange bias measured for the Mn_3Ga films with their thickness of 6, 10 and 20 nm.

INVITED PAPER

3:00

FE-05. Emergent dynamic chirality in a thermally driven artificial spin ratchet.

S. Gliga[1]
1. Physics and Astronomy, University of Glasgow, Glasgow, United Kingdom

The study of emergent phenomena in two-dimensional artificial spin ices is presently the focus of intense research. Artificial spin ices are composed of geometrically frustrated arrangements of lithographically patterned single-domain nanomagnets and have so far mainly been used to investigate fundamental aspects of the physics of frustration [1-8]. Recently, it has become clear that artificial spin ice has the potential to become a class of functional material with technological applications. I will present a spin ice based active material – consisting in a repeating pattern of chiral units (shown in Figure 1) – in which energy is converted into unidirectional dynamics, thus functioning like a ratchet [9]. Measurements combining photoemission electron microscopy (PEEM) with X-ray magnetic circular dichroism (XMCD) show that following saturation by an external field, thermal relaxation proceeds through the rotation of the average magnetization in a unique sense (Figure 2). Throughout the evolution, the rotation of the net vertex magnetization (sketched in the gray inset of Figure 2) starts at the edges of the array and propagates towards its center. The rotation continues until the magnetization in the array has mostly rotated by 180 degrees with respect to the initial state, and is approximately aligned with a weak applied bias field. Our micromagnetic simulations demonstrate that this emergent chiral behavior is driven by the topology of the magnetostatic field at the boundaries of the nanomagnet array, resulting in an asymmetric energy landscape. This opens the possibility of implementing a Brownian ratchet [10], which may find applications in nanomotors, actuators or memory cells. I will also discuss other routes towards applications that aim to combine artificial spin ice lattices, which were found to display localized spectral features based on topological defects [11-12], and magnonics, in which propagating spin waves in patterned magnetic thin films are manipulated [13], potentially leading to the creation of metamaterials for spin waves [14]. Finally, I will discuss perspectives for functionalizing artificial spin ices in three dimensions in light of recent experimental advances in magnetic x-ray based nanotomography [15]. SG is funded by the European Union's Horizon 2020 research and innovation programme under the Marie Sklodowska-Curie grant agreement No. 708674.

[1] R. F. Wang, *et al*., Nature 439, 303306 (2006) [2] L. J. Heyderman, R. L. Stamps, J. Phys. Condens. Matter 25, 363201 (2013) [3] M. J. Morrison, T. R. Nelson, C. Nisoli, New J. Phys. 15, 045009 (2013) [4] E. Mengotti, *et al*., Nat. Phys. 7, 6874 (2010) [5] E. Y. Vedmedenko, Phys. Rev. Lett. 116, 077202 (2016) [6] I. Gilbert, *et al*., Nat. Phys. 10, 670675 (2014). [7] A. Farhan, *et al*., Nat. Commun. 7, 12635 (2016) [8] W. R. Branford, S. Ladak, D. E. Read, K. Zeissler, L. F. Cohen, Science 335, 15971600 (2012) [9] S. Gliga, G. Hrkac, C. Donnelly, J. Büchi, A. Kleibert, J. Cui, A. Farhan, E. Kirk, R. V. Chopdekar, Y. Masaki, N. S. Bingham, A. Scholl, R. L. Stamps, L. J. Heyderman, Nat. Mater. 16, 1106 (2017) [10] S. T. Bramwell, Nat. Mater. 16, 1053 (2017) [11] S. Gliga, A. Kákay, R. Hertel, O. G. Heinonen, PRL 110, 117205 (2013) [12] S. Gliga, A. Kákay, L. J. Heyderman, R. Hertel, O. G. Heinonen, Phys. Rev. B 92, 060413(R) (2015) [13] M. Krawczyk, D. Grundler, J. Phys.: Condens. Matter 26, 123202 (2014) [14] E. Iacocca, S. Gliga, R. L. Stamps, O. Heinonen, Phys. Rev. B 93, 134420 (2016) [15] C. Donnelly, M. Guizar-Sicairos, V. Scagnoli, S. Gliga, M. Holler, J. Raabe, L. J. Heyderman, Nature 547, 328 (2017)

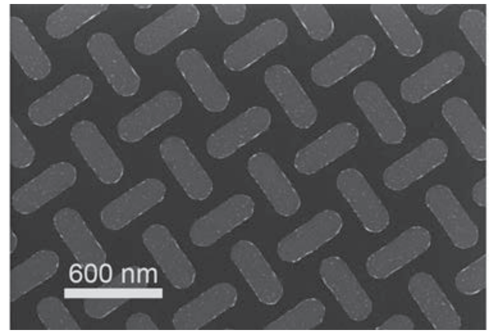

Fig. 1. Scanning electron microscopy image of a region of the investigated system.

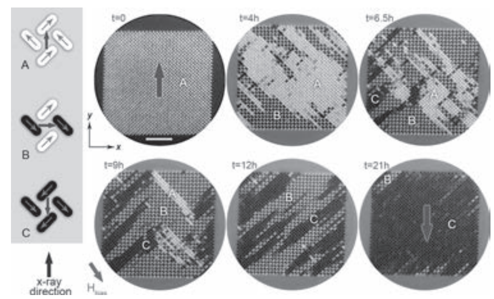

Fig. 2. Thermally-activated evolution of the system following saturation by an external magnetic field along the x-ray direction (+y axis). The schematic evolution of the magnetization at an individual vertex is sketched in the gray box. The the white or black colour, respectively, indicates the direction of the magnetization *M* toward the positive or negative y axis. The thin orange arrows represent the magnetization within the nanomagnets while the net magnetization at each individual vertex is indicated by the large brown arrows. The thermal relaxation at room temperature takes place stepwise via a clockwise rotation of the net magnetization by 90 degrees from state A (after saturation) to state B. When the system is heated above room temperature in the presence of a weak bias field, the average magnetization can locally rotate further to state C. On the right of the figure, the experimentally-measured evolution using XMCD-PEEM over a period of 21 hours is shown, indicating the regions in states A, B and C.

CONTRIBUTED PAPERS

3:30

FE-06. Long-range multi-modal ordering in artificial spin ice.

R. Puttock[1,2], V. Neu[3], A. Manzin[4], F. Garcia-Sanchez[4], A. Fernandez-Scarioni[5], V. Antonov[2] and *O. Kazakova*[1]
1. Quantum Science, National Physical Laboratory, Teddington, United Kingdom; 2. Department of Physics, Royal Holloway University of London, Egham, United Kingdom; 3. Leibniz Institute for Solid State and Materials Research (IFW) Dresden, Dresden, Germany; 4. Istituto Nazionale di Ricerca Metrologica, Turin, Italy; 5. Physikalisch-Technische Bundesanstalt, Braunschweig, Germany

Artificial spin ice (ASI) are arrays of nanoislands (NIs), composed of in-plane ferromagnetic material, which are magnetically frustrated due to the intrinsic geometric ordering. Each NI can be regarded as two opposing out-of-plane Ising-spins and the ASI conforms into macro-ordered magnetic patterns to minimise the net-energy at each geometric junction. ASI are thermally stable, yet susceptible to external agitation into many magnetic metastable (MMS) states. Thus, they are primed for applications in high-density magnetic memory, reconfigurable magnonics, and logic devices [1]. In this work we use Magnetic Force Microscopy (MFM) to map the stray-field distributions emanating from ASIs with high resolution (<10nm). As a standard MFM image is a convolution of the sample's magnetic properties and the probe's imaging property, to obtain true stray field values the image needs to be corrected for the latter contribution. We use a fast-Fourier transform based procedure to calibrate the probe through its tip-transfer function (TTF) (Fig. 1a) [2], [3]. By convolving the TTF with magnetisation models of the ASI in its different MMS states, we can access the real magnetic field values for ASI and confirm the methodology's validity. Both ASI presented are 100×100μm^2 arrays of NIs (380×100nm) composed of [Py(25nm)/Pt(2nm)]. Design ASI-1 is adapted from [4] (Fig. 1b, left); whereas the ASI-2 is a new design (Fig. 1b, right) comprised of three vertex-junctions [symbols X, Y and λ] (Fig. 1c). Despite their different 2D geometries, the MMS states for both ASIs can be characterised into the same "types" from their four-fold Ising-spin groupings [5] (Fig. 1d), making them directly comparable. To create the different states, we apply in-plane magnetic fields, then image with MFM at remanence. In Fig. 1e (top), uniform low-energy MMS states [type I (left) and type II (right) for ASI-1 and ASI-2, respectively] are generated by vertical demagnetisation (vDM). The bottom two images demonstrate other MMS states: ASI-1 still has a uniform macro-order (type III) configuration (left); and ASI-2 is in a reoccurring complex state, type {II, III, III, II} (right). This unique long-range multi-modal ordering may have important applications in logic devices [4]. We studied the breakdown of long-range ordering in ASI-2 by applying large magnetic fields along the NI hard axis, creating double-domain (DD) states. Fig. 2a-e shows the change in MMS order under increasing horizontal field. Fig. 2f and g are histograms summarising the frequency of different internal magnetic configurations in a 10×10 μm^2 area. Fig. 2 a-b demonstrate mono- and multi-modal ordering as in Fig. 1e (right). By applying larger horizontal field, the system becomes disordered (Fig. 2c), as seen by a small number of individual NIs that break down into DD states. We have classified the DD vertex junctions as "perturbation" in the histograms. Fig. 2f demonstrates the small degree of perturbations in the Y and λ configurations and the total stability in the X-shaped configuration. By further increasing the horizontal field, more of the NIs break into DDs (Fig. 2d), and other junction-types appear, to minimise the global energy. Finally, we apply the same high field in the opposite direction (Fig. 2e), to further agitate the system. In the histogram (Fig. 2f), only the perpendicular NIs are seen to be perturbed, the diagonal NIs magnetically switch to maintain their mono-domain state (i.e. crosses are reversed type II). We also consider the pairs of parallel NIs (Fig. 2g). Whilst some NIs perpendicular to the applied field break down into the DD states in high fields, some configurations are flipping into anti-parallel (AP) states to avoid perturbation. As AP states are more energetically favourable to the parallel equivalent, their frequency increases with disrupting field, and higher fields are required to break AP NIs into DD states; they also give rise to the alternative junction types highlighted in Fig 2f. To summarise, we have introduced a new ASI configuration, which possesses both mono- and multi-modal long-range ordering and have studied its switching behaviour in the presence of strong magnetic fields. Furthermore, quantitative values of the ASI stray field are addressed by calibration of the MFM probe using the TTF approach. The modelling results match the experimental measurements, outlining the reliability of the methodology used.

[1] C. Marrows, "Experimental Studies of Artificial Spin Ice," *arXiv*, pp. 1–24, Nov. 2016. [2] R. Puttock, H. Corte-Leon, V. Neu, D. Cox, A. Manzin, V. Antonov, P. Vavassori, and O. Kazakova, "V-Shaped Domain Wall Probes for Calibrated Magnetic Force Microscopy," *IEEE Trans. Magn.*, vol. 53, pp. 1–5, Nov. 2017. [3] P. J. a. van Schendel, H. J. Hug, B. Stiefel, S. Martin, and H.-J. Güntherodt, "A method for the calibration of magnetic force microscopy tips," *J. Appl. Phys.*, vol. 88, p. 435, 2000. [4] Y.-L. Wang, Z.-L. Xiao, A. Snezhko, J. Xu, L. E. Ocola, R. Divan, J. E. Pearson, G. W. Crabtree, and W.-K. Kwok, "Rewritable artificial magnetic charge ice," *Science*, vol. 352, pp. 962–966, May 2016. [5] J. Drisko, T. Marsh, and J. Cumings, "Topological frustration of artificial spin ice," *Nat. Commun.*, vol. 8, May 2016, p. 14009, Jan. 2017.

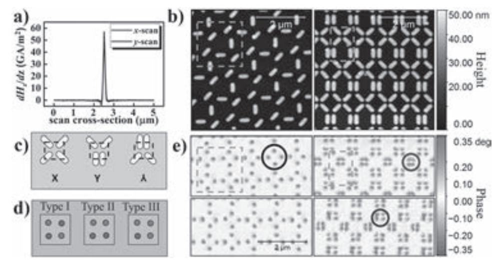

Fig. 1. (a) Cross-sectional plot of TTF from the MFM probe. (b) AFM image of ASI-1 (*left*) and ASI-2 (*right*) with unit-cell outlined (green). (c) Schematic of different junctions present in ASI-2 [cross, upsilon and reverse-upsilon (left to right)]. (d) Schematic depicting different MMS states in the two ASI patterns, red and blue dots correspond to Ising-spins pointing along the *z*-axis in opposite directions. (e) MFM images of MMS configurations for ASI-1 (*left*) and ASI-2 (*right*) at remanence: *top*: low energy [type I and II] uniform macro-ordering (ASI-1 and ASI-2 respectively); *bottom* higher energy uniform and complex (ASI-1 and ASI-2 respectively) MMS states. Examples of type I, II, III MMS states are circled (black, red and blue, respectively).

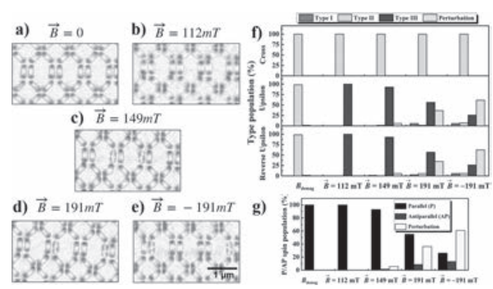

Fig. 2. Zoomed MFM images of ASI-2 at remanence after applying horizontal magnetic fields highlighting regions of interest (a-e). NI topography is outlined for ease of comparison (green lines). Histograms characterising the MMS junctions: cross, upsilon and reverse-upsilon (f) and double-parallel islands (g) at different applied fields for 10×10 μm^2 scan area.

3:45

FE-07. Phase domain development in nanopatterned FeRh islands.

R.C. Temple[1], T.P. Almeida[2], J. Massey[1], K. Fallon[2], S. Morley[1,3], F. Maccherozzi[4], S. Dhesi[4], T.A. Moore[1] and *C.H. Marrows*[1]
1. School of Physics and Astronomy, University of Leeds, Leeds, United Kingdom; 2. School of Physics and Astronomy, University of Glasgow, Glasgow, United Kingdom; 3. Physics Department, University of California, Santa Cruz, Santa Cruz, CA, United States; 4. Surfaces and Interfaces, Diamond Light Source Ltd, Didcot, United Kingdom

The B2-ordered equiatomic alloy FeRh has a magnetostructural phase transition at an unusually high temperature of approximately 370 K [1]. This is a first-order transition from an antiferromagnetic (AF) state to a ferromagnetic (FM) state and is accompanied by a 1% uniform volume expansion of the crystal lattice. The transition temperature can be manipulated through magnetic field [2], strain [3,4], chemical doping [5] and spin-polarised currents [6]. Due to this remarkably rich flexibility this material has been extensively investigated in recent years for its potential for technological applications in heat-assisted memory recording [7], memory resistors [8] and magnetocalorics [9]. Most of these potential applications will require thin film material patterned on the nanoscale. The properties of the transition are relatively well understood for bulk forms of FeRh but when it is confined to lower dimensions complications to this picture arise. While there have been many have investigations of sheet film FeRh, few studies have looked at the effects of lateral confinement of the FeRh layer. Electronic transport in FeRh nanowires has been seen to show large supercooling effects and a highly asymmetric transition between heating and cooling [10]. Nevertheless, a resistance measurement averages over the whole sample with no spatial resolution. Due to the first order nature of the transition, the AF and FM phases can coexist in the same sample. Previous successful magnetic imaging of the transition has been done using x-ray photo-emission microscopy (XPEEM) and it has been shown that the transition obeys the expected behaviour of nucleation and growth of FM regions in an AF matrix [11,12]. Lorentz microscopy has also recently been employed [13]. Those studies were all on sheet film samples: here we use XPEEM to image FeRh samples which have been nanopatterned to various length scales well above and close to the typical size for a nucleated FM domain. Previous studies have not imaged the transition in a confined structure. In this work, the antiferromagnetic to ferromagnetic phase transition in nanopatterned islands of FeRh was studied using XPEEM with XMCD contrast. This technique images the ferromagnetic phase regions with contrast arising from the projection of the magnetisation onto the soft x-ray beam direction. The islands were squares with dimensions varying between 5 and 0.5 microns. These were patterned from an FeRh film, sputtered onto MgO with a NiAl buffer layer, using electron beam lithography with a hard mask and Ar ion milling as the pattern transfer method. Quantitative analysis of the magnetically sensitive dichroism images show that the phase domain development in larger structures proceeds in three distinct nucleation, growth, and coarsening stages. Images from a 5 micron square island are shown in Figure 1(a) for both cooling and heating cycles. The material within about 200 nm of the patterned edge has a transition temperature that is lower than the centre of the island, remaining ferromagnetic order for about 20 K below the point at which FM order in the centre collapses. FM order is also restored in this edge region first on warming with a fine, submicron-scale FM domain structure. Such an FM domain structure then also nucleates and grows throughout the island before coarsening into micron-scale domains when it fills the island. Magnetic vector maps of selected stages of this process are shown in Figure 1(c) and (d). The magnetisation of the island as a whole can be determined from the sum of the absolute XMCD contrast, and is plotted in Figure 1(b). This shows a downward shift of approximately 20K with respect to the transition temperature in the unpatterned film. In 0.5 micron square islands, which are smaller than the typical final domain size, the transition temperature was found to be reduced by 30 K. This is because they are small enough to be entirely edge with no centre. The reduction in transition temperature is caused by side wall damage during the mask transfer process. This common problem in nanofabrication will need to be addressed in FeRh which is highly sensitive to rearrangement of the crystalline order.

[1] L. H. Lewis, C. H. Marrows, and S. Langridge, J. Phys. D: Appl. Phys. 49, 323002 (2016). [2] S. Maat, J.-U. Thiele, and E. E. Fullerton, Phys. Rev. B 72, 214432 (2005). [3] Z. Q. Liu, L. Li, Z. Gai, J. D. Clarkson, S. L. Hsu, A. T. Wong, L. S. Fan, M. W. Lin, C. M. Rouleau, T. Z. Ward, H. N. Lee, A. S. Sefat, H. M. Christen, and R. Ramesh, Phys. Rev. Lett. 116, 097203 (2016). [4] R. O. Cherifi, V. Ivanovskaya, L. C. Phillips, A. Zobelli, I. C. Infante, E. Jacquet, V. Garcia, S. Fusil, P. R. Briddon, N. Guiblin, A. Mougin, A. A. Unal, F. Kronast, S. Valencia, B. Dkhil, A. Barthelemy, and M. Bibes, Nat. Mater. 13, 345 (2014). [5] R. Barua, F. Jimenez-Villacorta, J. E. Shield, D. Heiman, and L. H. Lewis, J. Appl. Phys. 113, 17B523 (2013). [6] I. Suzuki, T. Naito, M. Itoh, and T. Taniyama, Appl. Phys. Lett. 107, 082408 (2015). [7] J.-U. Thiele, S. Maat, and E. E. Fullerton, Appl. Phys. Lett. 82, 2859 (2003). [8] X. Marti, I. Fina, C. Frontera, J. Liu, P. Wadley, Q. He, R. J. Paull, J. D. Clarkson, J. Kudrnovsky, I. Turek, J. Kunes, D. Yi, J.-H. Chu, C. T. Nelson, L. You, E. Arenholz, S. Salahuddin, J. Fontcuberta, T. Jungwirth, and R. Ramesh, Nat. Mater. 13, 367 (2014). [9] Y. Liu, L. C. Phillips, R. Mattana, M. Bibes, A. Barthelemy, and B. Dkhil, Nat. Commun. 7, 11614 (2016). [10] V. Uhlir, J. A. Arregi, and E. E. Fullerton, Nat. Commun. 7, 13113 (2016). arXiv:1605.06823. [11] C. Baldasseroni, C. Bordel, A. X. Gray, A. M. Kaiser, F. Kronast, J. Herrero-Albillos, C. M. Schneider, C. S. Fadley, and F. Hellman, Appl. Phys. Lett. 100, 262401 (2012). [12] C. J. Kinane, M. Loving, M. A. de Vries, R. Fan, T. R. Charlton, J. S. Claydon, D. A. Arena, F. Maccherozzi, S. S. Dhesi, D. Heiman, C. H. Marrows, L. H. Lewis, and S. Langridge, New J. Phys. 16, 113073 (2014). [13] T. P. Almeida, R. Temple, J. Massey, K. Fallon, D. McGrouther, T. Moore, C. H. Marrows, and S. McVitie, Sci. Rep. 7, 17835 (2017).

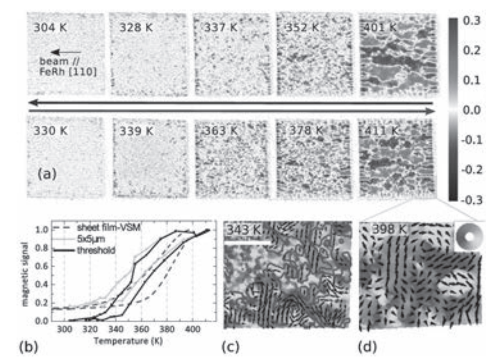

Fig. 1. XMCD PEEM imaging of a 5 micron × 5 micron square island. (a) magnetic dichroism images shown as a function of temperature during the cooling process (upper) and the heating process (lower). The beam and crystal directions are shown in the top left image. (b) The integrated absolute XMCD signal as a function of temperature in comparison to magnetometry measurements. Both signals are normalised to the saturation value. The thresholded XMCD signal is also shown, where pixels with an absolute XMCD signal smaller than 0.03 are not counted. (c) and (d) Vector magnetisation maps of the bottom right portion of the island. The colour represents the vector direction indicated in the colour wheel. The inset scale bar on (c) is 0.5 micron.

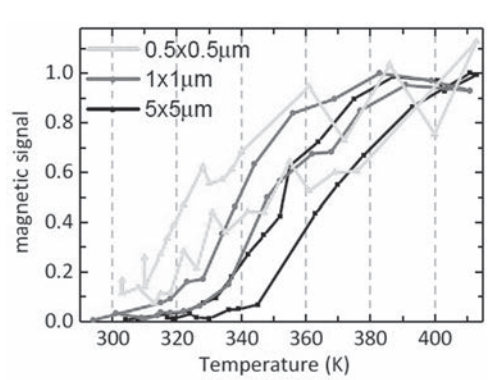

Fig. 2. The average absolute dichroism signal plotted vs. temperature for three island sizes. For the smaller two sizes an average signal over four FeRh islands have been plotted.

INVITED PAPER

4:00

FE-08. Nonlinear Response of Patterned Ferromagnets with Spin Vortex Ground State.

M.P. Nikitin[1,2], A.V. Orlov[3], I. Sokolov[2], A. Minakov[3], P.I. Nikitin[3], J. Ding[1], S.D. Bader[1], E.A. Rozhkova[4] and *V. Novosad*[1]
1. Materials Science Division, Argonne National Laboratory, Argonne, IL, United States; 2. Moscow Institute of Physics and Technology (State University), Dolgoprydny, Russian Federation; 3. Prokhorov General Physics Institute, Moscow, Russian Federation; 4. Center for Nanoscale Materials, Argonne National Laboratory, Argonne, IL, United States

Geometrically confined magnetic particles due to their unique response to external magnetic fields find a variety of applications, including magnetic guidance, heat and drug delivery, magneto-mechanical actuation, and contrast enhancement. Highly sensitive detection and imaging techniques based on *nonlinear properties* of nanomagnets were recently proposed as innovative methods applicable in complex, often opaque, biological systems [1,2]. Here we report on enhancement of the detection capability using optical-lithography-defined, ferromagnetic iron-nickel alloy disk-shaped particles. These materials are known to possess a vortex ground state which is characterized by an in-plane curling spin configuration with zero net magnetization in remanece (Fig. 1). The detection mechanism is based the nonlinear magnetic response of the sample subjected to a two-component alternating magnetic field with different amplitudes and frequencies f_1 and f_2, with output signal detected at a frequency $f = mf_1 \pm nf_2$ [1]. During the measurements, the 3x 3 mm^2 sample of 1.5 um FeNi disks was slowly translated through the pick-up coil. As expected, the signal changes continuously when the sample is displaced and reaches a maximum value when the sample is located in the center of the measurement cell. The highest signal-to-noise ratio (SNR) in these measurements was achieved for 30-nm-thick disks. Specifically, as few as 87 particles which amounts to 39.4 pg of permalloy or a magnetic moment of 3.5x10^{-9} emu (3.5x10^{-12} Am^2) could be readily detected against the background noise. This limit of detection is at least an order-of-magnitude better than data published thus far for conventional superparamagnetic particles. To validate our initial findings in a biological system, we performed a series of *in vivo* studies. For this purpose, the 1.5-µm-diameter disks were lifted off the wafer and re-suspended in phosphate buffered saline (PBS) resulting in a concentration of ~2 x 10^9 disks per 1 ml, following the procedures reported elsewhere [3,4]. The *in-vivo* experimental setup was configured to include a detector coil generating the excitation (*ac*) field, and a larger coil that provides an external bias (*dc*) field, see photograph shown in the Fig. 2 (left). The magnetic disks suspended in PBS solution were injected retro-orbitally (that is via the ophthalmic venous sinus) into the blood flow of the animal. The anesthetized animal was placed inside the pick-up coil, which quantified the magnetic content passing through the animal's tail veins and arteries. Figure 2 (right) shows that right after injection the magnetic signal quickly raises as the disks reach the tail blood vessels to the maximum concentration, and then exponentially declines as the disks get cleared by the reticulo-endothelial system. The disks were cleared from the blood stream within <10 min. Interestingly, when an external *dc* magnetic field (of ~15 Oe) was applied in addition to the to the detector's *ac* field one minute after the disks injection, the kinetics of the particles' clearance remained the same, while the signal remarkably increased, and then abruptly decreased upon turning the field off. Both processes can be fitted with exponents having the same decay constant, which suggest that the magnetic particle removal rate is not affected by spatially uniform *dc* magnetic fields. Such responsiveness of the signal produced by the disks readily allows discrimination of the vortex labels from conventional isotropic ones, thereby providing an opportunity to multiplex magnetic labels for various *in vivo* applications and *in vitro* assays. In summary, we show that an irreversible transition between a strongly non-collinear (vortex) and single domain states, driven by an alternating magnetic field translates into a nonlinear magnetic response that enables ultrasensitive detection of these particles. The sensitivity of ~ 3.5 x 10^{-9} emu, which is equivalent to ~39 pg of magnetic material is demonstrated at room temperature for arrays of patterned disks. We also show that unbound disks re-suspended in aqueous buffer can be successfully detected and quantified in real-time when administrated into a live animal allowing for tracing their biodistribution. Use of nanoscale ferromagnetic particles with engineered nonlinear properties opens prospects for further enhancing sensitivity, scalability and tunability of noise-free magnetic tag detection in high-background environments for various applications spanning from biosensing and medical imaging to anti-counterfeiting technologies.

[1] Nikitin, P. I.; Vetoshko, P. M.; Ksenevich, T. I., New type of biosensor based on magnetic nanoparticle detection. *J Magn Magn Mater* 2007, *311* (1), 445-449. [2] Krishnan, K. M., Biomedical Nanomagnetics: A Spin Through Possibilities in Imaging, Diagnostics, and Therapy. *Ieee T Magn* 2010, *46* (7), 2523-2558. [3] Vitol, E. A.; Novosad, V.; Rozhkova, E. A., Multifunctional Ferromagnetic Disks for Modulating Cell Function. *IEEE Trans Magn* 2012, *48* (11), 3269-3274. [4] Kim, D. H.; Rozhkova, E. A.; Ulasov, I. V.; Bader, S. D.; Rajh, T.; Lesniak, M. S.; Novosad, V., Biofunctionalized magnetic-vortex microdiscs for targeted cancer-cell destruction. *Nat Mater* 2010, *9* (2), 165-171.

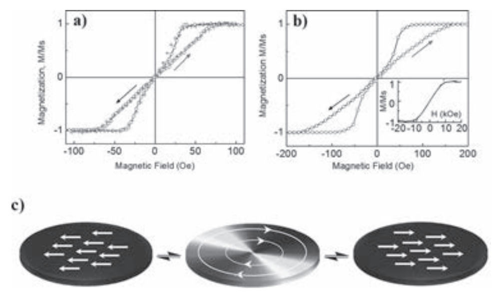

Fig. 1. An in plane hysteresis loops for arrays of permalloy microdisks of 1.5-µm diameter for thickness *h* = 20 nm (a), and 40 nm (b). Normalized magnetization curve *M*(*H*) with no hysteresis in the magnetic field perpendicular to the disk plane is shown in the inset. (c) In remanence the samples possess no net magnetic moment, which is indicative of the spin vortex state (central image). In the saturated state the vortices annihilate and the sample becomes uniformly magnetized.

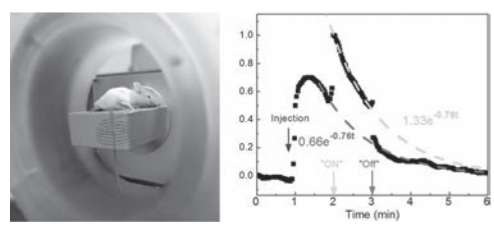

Fig. 2.
(*Left*) Experimental setup for the study of blood-circulation kinetics of the magnetic disks *in vivo*. The disks are injected retro-orbitally and detected in real time as they pass through the veins and arteries of the animal's tail.
(*Right*) Representative blood circulation kinetics of the magnetic disks in mice: injection, distribution within the blood volume and clearance. Please note modulation of the response of the magnetic disks by the external *dc* field in blood flow *in vivo.*

CONTRIBUTED PAPERS

4:30

FE-09. Interpreting FORC diagrams beyond the Preisach model: an experimental permalloy micro array investigation.

F. Gross[1], S. Ilse[1], G. Schütz[1], *J. Gräfe*[1] and E. Goering[1]
1. Modern Magnetic Systems, Max Planck Institute for Intelligent Systems, Stuttgart, Germany

First-order reversal curves (FORC) are a powerful tool that is increasingly used in material science and nano-magnetism research [1-4]. Besides its utility for fingerprinting magnetic systems, it can distinguish between different components in a complex magnetic system without the need for a laterally resolving magnetometer [5]. Furthermore, quantitative information about the intrinsic coercivities and interaction fields between magnetic particles can be extracted from FORC measurements. Unfortunately, the interpretation of a FORC diagram as a Preisach distribution is not straight forward as most real system violate the Mayergoyz criteria [6], *i.e.* congruency and wiping-out. In these cases, the interpretation of the peaks in a FORC diagram needs to rely on additional tools like magnetic microscopy [1, 2]. Thus, it would be desirable to extend the interpretability of FORC diagrams beyond the limits set by the Mayergoyz criteria [3, 4]. Here, we systematically design artificial multi-component systems that purposely violates the congruency criterion to gain insights into the interpretability of FORC diagrams of such systems. These systems are made up of 150 μm long Permalloy (Py, $Ni_{80}Fe_{20}$) stripes that are structured by photo lithography and arranged into micro arrays (*cf.* inset in Figure 1). The coercivity of these stripes is tuned by their width (10 – 50 μm), the interaction strength by their spacing (10 – 30 μm). Thus, we are able to specifically determine the coercive and interaction fields of these well-defined systems. Subsequently, FORCs are measured with a customized *Durham Magneto Optics NanoMOKE3* magnetometer. This allows fast acquisition of high resolution FORC diagrams [5], thus, enabling us to systematically investigate a large number of samples. Additionally, 250.000 local hysteresis loops with a spatial resolution of 5 μm are measured per sample to gain an independent measure of the spatial distribution of coercive and interaction fields. Such a comparison between FORC diagram and the spatial coercivity distribution is shown in Figure 1. The two coercivities of the wide (1 Oe) and narrow (3 Oe) stripes are reflected in the FORC diagram. However, an additional peak-dip feature (marked as A in Figure 1) appears in the FORC diagram that cannot be individually attributed to a magnetic element in the system. Looking into the magnetization configuration during each minor loop, it becomes evident that this peak-dip feature is a consequence of the wide stripes (smaller coercivity) to reverse their magnetization at different applied fields when the initial magnetization is aligned parallel or anti-parallel to the narrow stripes (larger coercivity). This additional signal in the FORC diagram arises purely from the interaction when the system violates the Mayergoyz criteria. More precisely the interaction field, between narrow and wide stripes, which switch at different fields respectively. Following the evolution of this interaction peak while tuning the interaction strength of the system, a clear change in the peak size and position is observed. Figure 2 shows the integral of the interaction peak in dependence of the stripe spacing, which governs the interaction strength. As the interaction strength decreases, the peaks' integrated FORC density also decreases. Finally, the peak vanishes when the interaction strength is sufficiently decreased and the system fulfils the Mayergoyz criteria again (not shown in Figure 2). Thus, it can be deduced that here the integrated FORC density of the peak is also a quantitative measure for the interaction strength. We have used a systematic study of artificial micromagnet arrays that intentionally violate the Mayergoyz criteria, to investigate FORC diagrams beyond the Preisach interpretation of discrete hysterons. The combination of magnetic microscopy and fast FORC measurements to get to independent measures of coercive and switching field distributions allowed us to reliably interpret these FORC diagrams. Thereby, we identified an interaction peak that arises from the strong interaction of magnetic elements in the system. When such an interaction peak occurs, it is a mere manifestation of an interaction field. With this knowledge, interaction peaks in FORC diagrams of unknown system like NdFeB magnets can be interpreted. This opens up a pathway to fully interpreting FORC diagrams and elevating FORC beyond mere fingerprinting.

1. Gräfe, J., et al., *Combined first-order reversal curve and x-ray microscopy investigation of magnetization reversal mechanisms in hexagonal antidot lattices.* Physical Review B, 2016. 93(1): p. 014406. 2. Gräfe, J., et al., *Geometric control of the magnetization reversal in antidot lattices with perpendicular magnetic anisotropy.* Physical Review B, 2016. 93(10): p. 104421. 3. Dobrotă, C.-I. and A. Stancu, *What does a first-order reversal curve diagram really mean? A study case: Array of ferromagnetic nanowires.* Journal of Applied Physics, 2013. 113(4): p. -. 4. Pike, C.R., et al., *First-order reversal curve diagram analysis of a perpendicular nickel nanopillar array.* Physical Review B, 2005. 71(13): p. 134407. 5. Gräfe, J., et al., *Application of magneto-optical Kerr effect to first-order reversal curve measurements.* Review of Scientific Instruments, 2014. 85(2): p. 023901. 6. Mayergoyz, I.D., *Mathematical Models of Hysteresis.* Physical Review Letters, 1986. 56(15): p. 1518-1521.

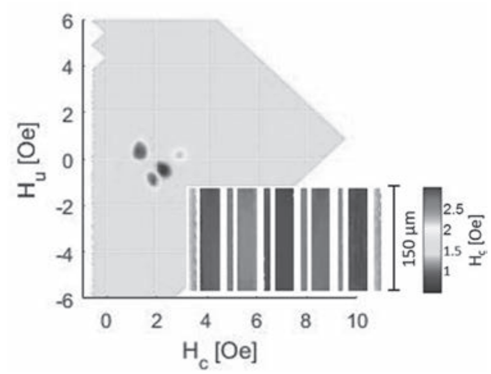

Fig. 1. FORC diagram of an array of Py microstripes, showing an interaction peak-dip feature (marked as A), and coercivity map calculated from local hysteresis loops (inset).

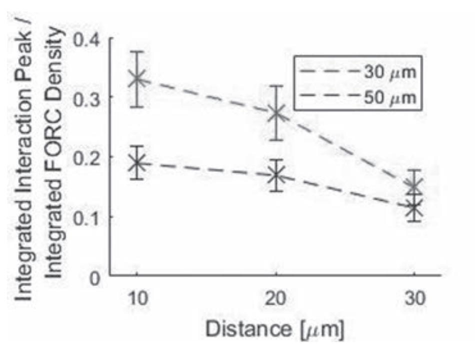

Fig. 2. Integrated FORC density of the interaction peak in dependence of the distance between Py microstripes, i.e. interaction strength.

4:45

FE-10. Ion Irradiation Induced Cobalt/Cobalt Oxide Heterostructures: From Materials to Devices.

D. Hilliard[1,2], O. Yildirim[1,3], C. Fowley[1], S. Arekapudi[2], H. Cansever[1,4], R. Böttger[1], G. Hlawacek[1], O. Hellwig[2], J. Lindner[1], J. Fassbender[1,4] and A. Deac[1]
1. Institute of Ion Beam Physics and Materials Research, Helmholtz-Zentrum Dresden-Rossendorf, Dresden, Germany; 2. Institute of Physics, Chemnitz University of Technology, Chemnitz, Germany; 3. Empa-Swiss Federal Laboratories for Materials Science and Technology, Dübendorf, Switzerland; 4. Institute of Physics of Solids, Dresden University of Technology, Dresden, Germany

The demand on high data transfer and storage capacities requires smaller devices to transmit or save data. Forming well-defined ferromagnetic and electrically conducting volumes within a non-magnetic and insulating matrix in the dimensions of several nanometers can pave a way to the production of such small devices. It has been demonstrated that the reduction of oxygen in Co_3O_4/Pd multilayers is possible via local proton irradiation resulting in ferromagnetic and conducting Co embedded in a nonmagnetic and insulating Co_3O_4 matrix [1]. However, the physical mechanism behind the ion irradiation-induced oxide reduction was not addressed clearly. There are two possible mechanisms suggested to play a role behind this oxide reduction. The first one is the chemical reduction of oxygen by reacting with implanted H^+ ions, while the second possible mechanism is atomic displacements induced by ion irradiation. To address this issue, we analysed cobalt oxide thin films after irradiation with H^+ and Ne^+ ions at different doses. The irradiation parameters for Ne^+ were chosen to give the same displacements per atom (dpa) as that of H^+ which is required to reduce cobalt oxide. We also confined irradiated areas on the films in the range of microns to sub-micron, in order to ascertain the lateral distribution of oxygen after irradiation. We prepared single layer films of CoO (6-12nm) and Co_3O_4 (10nm) capped with Pt protection layers. Broad-beam H^+ irradiations were performed at 0.3 keV for ion doses ranging from 10^{15} to 10^{17} ions/cm^2 on unpatterned films. After irradiation the films were characterized structurally and magnetically and compared to un-irradiated films. Extended films showed approximately 7% of the Co bulk metal saturation magnetization (M_S) after irradiation at a dose of 5 x 10^{16} ions/cm^2 (fig. 1a inset). The increase is more pronounced with Co_3O_4 than CoO (fig. 1a). A sample was also prepared with a striped irradiation mask of 40 μm pitch. These films showed a higher magnetization after irradiation at lower doses as compared to unpatterned films, 0.14 MA/m for a dose of 10^{16} ions/cm^2 (striped) as opposed to 0.025 MA/m (extended) for a dose of 10^{17} ions/cm^2. Figure 1 (b) shows the effect of stripe width (0.5, 5, 10, 20 μm) on the resulting magnetization after H^+ irradiation at the same energy with a dose of 10^{17} ions/cm^2. No clear correlation between stripe width and M_S was seen in either oxide phase for stripes down to 0.5 μm. However, the CoO sample with 0.5 μm stripes and a thinner oxide thickness of 6 nm (gold line) as opposed to 12 nm exhibited larger M_S after irradiation, indicating oxygen displacements occur in the first few nanometers of the oxide. We also performed 5 keV Ne^+ irradiations with the helium-ion microscope (HIM) varying the ion dose from 10^{14} to 10^{16} ions/cm^2. After Ne^+ irradiations magnetic force microscopy (MFM) images were taken along with a topography image in the remnant state (fig. 2). Starting from the ion dose of 5x10^{14} ions/cm^2, a magnetic contrast could be observed by MFM, suggesting that oxygen atoms were successfully removed locally by reducing paramagnetic CoO to ferromagnetic Co. The formation of topographical bubbles was observed upon increasing the ion dose from 10^{15} ions/cm^2 to 10^{16} ions/cm^2. The lateral and horizontal sizes of the observed bubbles show a clear dependence on the ion dose with a narrow size distribution. In conclusion, our results show that, oxygen removal by means of H^+ irradiation is more efficient in Co_3O_4 films as opposed to CoO. Additionally, although there is little dependence of the resulting M_s on the pitch of the stripes (in the range of 0.5 - 20 μm), the use of a stripe mask has a more pronounced effect on the oxygen removal process as compared to the irradiations on extended films. Therefore, the physical mechanism behind the ion-irradiation induced oxide reduction process cannot purely be a chemical reaction between oxygen and hydrogen. As an outlook, the lateral size and spacing of the ferromagnetic regions generated by H^+ irradiation is only limited by the resolution of EBL. This method and the successful formation of ferromagnetic regions upon Ne^+ irradiation using the HIM can be exploited to print smaller, closer and synchronized contacts for nanocontact spin torque oscillators. Acknowledgements This work is supported by the Helmholtz Young Investigator Initiative Grant No. VH-N6-1048. Support by the Nanofabrication Facilities Rossendorf at the IBC is gratefully acknowledged (Dr. Artur Erbe, Bernd Scheumann). Support by the Structural Characterization Facilities Rossendorf at the IBC is gratefully acknowledged (Andrea Scholz, Dr. Rene Hübner).

[1] S. Kim, S. Lee, J. Ko, J. Son, M. Kim, S. Kang, and J. Hong. Nature Nanotechnology, 7:567, 2012.

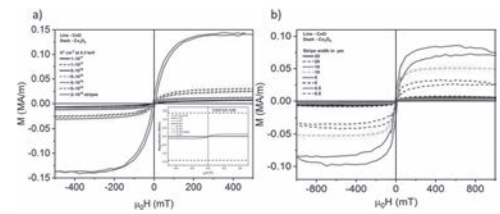

Fig. 1. a): M-H curves of unpatterned CoO and Co_3O_4 films irradiated with H^+ at different doses, a sample with a striped irradiation mask (gold line) is shown for comparison. The mask consists of periodic stripes which are 20 μm in width. Inset of a): Measured M-H curves compared to the M_s of bulk-Co, horizontal dashed line. b): M-H curves of patterned CoO and Co_3O_4 films, the line width and spacing is varied from 0.5 – 20 μm.

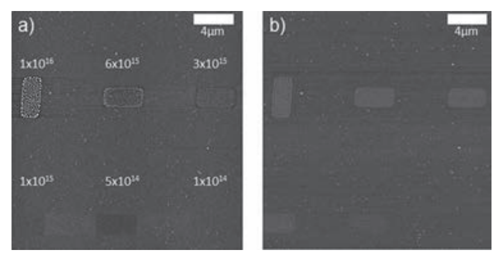

Fig. 2. a) AFM image of CoO irradiated locally with Ne^+, the regions are labelled by dose. b) Corresponding MFM image showing increasing magnetic phase contrast with ion dose. The formation of topographical bubbles is evident in both images and the lateral dimensions of the bubbles show a clear dependency on dose.

Session FF

SPIN WAVES I

Olivier Klein, Co-Chair
CEA-SPINTEC, Grenoble, France
Mathias Kläui, Co-Chair
Universität Mainz, Mainz, Germany

CONTRIBUTED PAPERS

2:00

FF-01. All-electrical detection of spin-wave interference in CoFeB waveguides.

G. Talmelli[1,2], T. Devolder[3], M. Heyns[1], I.P. Radu[1], C. Adelmann[1] and *F. Ciubotaru*[1]
1. IMEC, Leuven, Belgium; 2. Department of Materials Engineering, KU Leuven, Leuven, Belgium; 3. Centre de Nanosciences et de Nanotechnologies, Université Paris-Sud, Orsay, France

Spintronic devices based on spin waves are promising alternatives to the CMOS technology and have high potential for power and area reduction per computing throughput[1,2]. The information can be encoded in either the amplitude or the phase of the wave, while the logic operation is based on the interference of spin waves, which is a keystone for the realization of logic gates. Different logic systems based on spin waves have been proposed e.g. Mach Zender interferometers[3], magnonic transistors[4], or spin wave majority gates[1] (SWMGs). The SWMG is the most promising concept since it posesses a higher expressive power with respect to e.g. NAND or NOR gates and thus may reduce circuit complexity. The basic functionality of a such device has already been proved at a mm scale using YIG[5] films, while the device scalability to micro- and nanometer dimensions was demonstrated by micromagnetic simulations[6,7]. However, these SWMG devices are based on a "trident" shape, which leads to issues due to spin wave reflection at the bending area[6] and a difficult implementation in scaled CMOS technology due to lithography limitations. In this work, we investigate the spin wave interference in micron-sized ferromagnetic waveguides using a sequential "in-line" layout of input and output antennas (Fig. 1(a)). The waveguide consisted of a 4 μm wide and ~ 40 μm long CoFeB stripe of 30 nm thickness. The waveguide was covered with 40 nm of SiN for electric isolation. Spin waves were excited by the Oersted field produced by RF currents flowing through U-shaped antennas and detected by a single wire antenna (see Fig. 1(a)). The antennas were 500 nm wide and made of 100 nm of Au patterned by electron-beam lithography and lift-off. This design provided a very low direct electromagnetic parasitic coupling between neighboring input antennas, as well as between the input and output antennas, as shown both by experiments and electromagnetic simulations[8]. Furthermore, electromagnetic simulations of the Oersted field distribution have shown that the U-shaped antennas can excite spin waves with wavelengths down to 700 nm. To study spin wave interference, the magnetic waveguide was magnetized by applying a transverse magnetic bias field (Damon–Eshbach configuration) and the spin wave transmission was measured by a vector network analyzer. Initial experiments determined the propagation characteristics of spin waves emitted from each of the three input antennas towards the output antenna. A typical frequency-field dependence of the S_{21} parameter from input I_1 towards output O (corresponding to a spin wave propagation distance of 4.8 μm) is shown in Fig. 1(b). It can be seen that the device allowed a wide operating frequency range between 3 GHz and 22 GHz depending on the external applied field. For a given magnetic field, the spin wave transmission signal existed only above a certain frequency and stayed detectable within a frequency transmission band of width Δf. The dispersion relations calculated using parameters extracted from experiments (see Fig.1 (c)) indicated that the lower threshold frequency matched well the ferromagnetic resonance frequency. The upper limit was given by the maximum wavenumber of the spin wave that antenna could excite (k_{max} ~ 8.9 rad/μm). Further experiments were aimed to study the interference of the spin waves generated simultaneously by multiple input antennas. Microwave currents with the same frequency were applied to all three inputs and the output signal was studied as a function of the input frequency, bias field, and relative phase difference between the input signals. For a given set of field-frequency parameters, an oscillatory signal was detected by varying the phase of the input signals corresponding to the constructive or destructive interference of the three generated spin waves. For example, Fig. 1(d) shows the detected signal for a phase rotation of the signal at the input I_1 up to 720 degrees, while I_2 and I_3 were kept in-phase. The position of the maxima/minima could be tuned by varying the applied frequency, which changed the spin wave wavelength and thus modified the interference pattern. In conclusion we succesfully measured interference in CoFeB waveguides by employing an all-electrical detection method using a sequential in-line antenna arrangement. This represents the first step towards the experimental demonstration of (sub-)micrometer spin wave line majority gates with a scalable geometry, overcoming spin wave reflection issues in bent regions of trident designs.

1. A. Khitun and K. Wang, J. Appl. Phys. 110, 034306 (2011). 2. Radu et al., Proc. IEEE IEDM (2015). 3. T. Schneider et al., APL 92, 022505 (2008). 4. Chumak et al., Nature Comm. Vol. 5 No. 4700 (2014). 5. T. Fisher et al., APL 110, 152401 (2017). 6. S. Klinger et al., APL 105, 152410 (2014). 7. O. Zogragfos et al., AIP Advances 7 (5), 056020 (2017). 8. The simulations were performed using "ANSYS HFSS: High Frequency Electromagnetic Field Simulation" software.

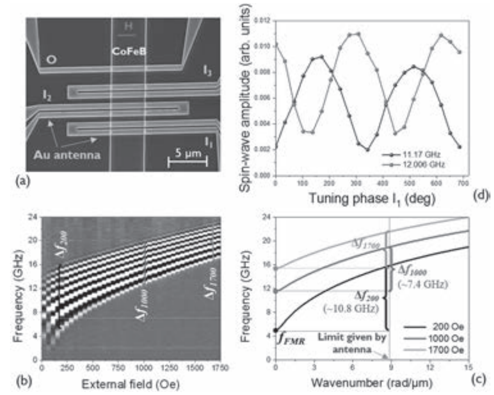

Fig. 1. (a) Scanning electron micrograph of a device consisting of a 4 μm wide CoFeB stripe with 3 U-shaped antennas (I1, I2, I3), used to generate spin waves, and a wire antenna (O) used for detection. (b) Field dependence of the forward transmission signal between I1 and O. Light blue color corresponds to a zero spin-wave transmission, while the dark blue and the white stands for propagating spin waves. (c) Spin wave dispersion relations calculated analytically for 3 values of the applied magnetic field. The frequency range is delimited by FMR frequency and the maximum spin wave wavevector that can be excited by the U-shaped antenna I1. (d) Spin-wave signal detected at the output when I1, I2 and I3 are simultaneously powered at the same frequency (11.17 GHz - blue curve; 12.006 GHz - red curve) as a function of the relative phase at input I1 (I2 and I3 are in-phase). The maxima and minima correspond to the constructive and destructive interference of the three generated spin waves.

2:15

FF-02. Voltage-controlled reconfigurable spin wave nanochannels and logic devices.

B. Rana[1] and Y. Otani[1,2]
1. Center for Emergent Matter Science, RIKEN, Wako, Japan; 2. Institute for Solid State Physics, The University of Tokyo, Kashiwa, Japan

Spin waves (SWs) i.e. collective precessional motion of localized magnetic moments in ferromagnetic thin films may be used as potential information carrier in future non-volatile spintronics devices with lower power consumption. Quanta of SWs are known as magnons. Following this a new sub-field of spintronics called 'magnonics' [1] is rapidly evolving. One of the essential tasks for successful implementation of SWs in future magnonics devices is guiding SWs through reconfigurable nanochannels (NCs), formed on a waveguide (WG), to send them to a desired position. This is generally done by geometrically patterning the WGs into a stripe [2]. However, the SW path can't be further manipulated in this case, which is essential for reprogrammable magnonic devices [3]. Several reports also show SW channeling by using internal demagnetizing field [2,4], ferromagnetic domain wall [5] and SW caustics [6,7]. In practical magnonic devices, we need to selectively control a number of closely spaced spin wave nanochannels (SWNCs) simultaneously, which is very difficult to execute by using all the methods mentioned above. Moreover, the NC with any arbitrary pattern can't be realized by above means. An immediate solution to this problem could be recently discovered voltage-controlled magnetic anisotropy (VCMA), which allow us to tune interfacial perpendicular magnetic anisotropy (PMA) of an ultrathin 3d-ferromagnet by voltage i.e. electric field [8,9] without flow of charge current. Moreover, the localized nature of VCMA is suitable for nanoscale magnonic devices. We propose reconfigurable NCs generated by electric field i.e. voltage-controlled magnetic anisotropy (VCMA) in an ultrathin ferromagnetic WG for SW propagation. We perform micromagnetic simulations by using Object Oriented Micromagnetic Frameworks (OOMMF) [10] to demonstrate the confinement of exchange dominated magnetostatic forward volume like spin waves (MSFVW) in NCs by VCMA. We choose a 1.3 nm ultrathin Co20Fe60B20 (CoFeB) film with width w (100 nm, 200 nm & 800 nm) and length L (2 μm) as a model WG for simulation. Practically NCs can be formed by placing a top gate electrode on the WG and applying voltage across gate electrode and WG (Fig. 1a). The applied voltage creates a sharp potential well (i.e. channel) of PMA on the WG, underneath the gate electrode, with dimension same as gate electrode. We demonstrate that the NCs, with width down to few tens of nanometer (Fig. 1b), can be configured either into straight or curved structure (Fig. 1c) on an extended SW waveguide. Our results show that either a single NC or any combinations of a number of NCs can be easily configured by VCMA for simultaneous propagation of SWs either with same or different wavevectors (Fig. 1d) according to our needs. Furthermore, we demonstrate logic operation of voltage-controlled magnonic XNOR and universal NAND gate formed by using Mach-Zehnder interferometer based on geometrically structured WGs. Our results show that universal NAND gate can be developed even by using voltage-controlled reconfigurable NCs (Fig. 2). These voltage-controlled logic devices are more suitable for nanoscale devices due to the localized nature of electric field unlike previously reported charge current induced Oersted field controlled logic devices [11]. We also propose voltage-controlled reconfigurable SW switch for development of multiplexer and demultiplexer. We find that the NCs and logic devices, developed by using ultrathin ferromagnetic film with PMA, can even be functioning in absence of external bias magnetic field reducing power consumption to a great extent. Our results are a step towards the development of all-voltage-controlled low power nanoscale magnonic devices.

[1] V. V. Kruglyak, S. O. Demokritov, and D. Grundler, *J. Phys. D: Appl. Phys.* 43, 260301 (2010). [2] V. E. Demidov, S. O. Demokritov, K. Rott, P. Krzysteczko, and G. Reiss, *Appl. Phys. Lett.* 92, 232503 (2008). [3] A. Khitun, M. Bao, and K. L. Wang, *IEEE Trans. Magn.* 44, 2141 (2008). [4] V. E. Demidov, J. Jersch, S. O. Demokritov, K. Rott, P. Krzysteczko, and G. Reiss, *Phys. Rev. B* 79, 054417 (2009). [5] K. Wagner, A. Kákay, K. Schultheiss, A. Henschke, T. Sebastian, and H. Schultheiss, *Nat. Nanotech.* 11, 432 (2016). [6] T. Schneider, A. A. Serga, A. V. Chumak, C. W. Sandweg, S. Trudel, S. Wolff, M. P. Kostylev, V. S. Tiberkevich, A. N. Slavin, and B. Hillebrands, *Phys. Rev. Lett.* 104, 197203 (2010). [7] T. Sebastian, T. Brächer, P. Pirro, A. A. Serga, B. Hillebrands, T. Kubota, H. Naganuma, M. Oogane, and Y. Ando, *Phys. Rev. Lett.* 110, 067201 (2013). [8] K. Miura, S. Yabuuchi, M. Yamada, M. Ichimura, B. Rana, S. Ogawa, H. Takahashi, Y. Fukuma, and Y. Otani, *Sci. Rep.* 7, 42511 (2017). [9] T. Maruyama, Y. Shiota, T. Nozaki, K. Ohta, N. Toda, M. Mizuguchi, A. A. Tulapurkar, T. Shinjo, M. Shiraishi, S. Mizukami, Y. Ando, and Y. Suzuki, *Nat. Nanotech.* 4, 158 (2009). [10] M. J. Donahue and D. G. Porter, OOMMF User's Guide, Version 1.0, Interagency Report NISTIR 6376, National Institute of Standards and Technology, Gaithersburg, MD (Sept 1999), http://math.nist.gov/oommf/. [11] K.-S. Lee and S.-K. Kim, *J. Appl. Phys.* 104, 053909 (2008).

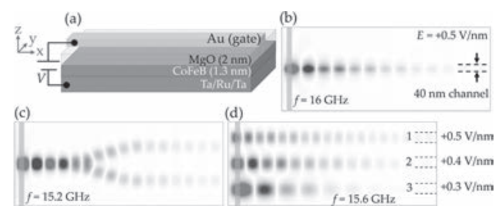

Fig. 1. (a) Schematic diagram of a practical SW device for confinement of propagating SWs within a NC formed by VCMA. Voltage is applied across top metal gate electrode and WG. (b) Simulated spatial maps of dynamic magnetization demonstrate the SW confinement in 40 nm straight channel formed by applying +0.5 V/nm electric field through top gate electrode. (c) Snapshots of dynamic magnetization show the SW (f = 15.2 GHz) confinement in a curve shaped NC. (d) Spatial maps of dynamic magnetization show that SWs in different NCs can be simultaneously sent and configured with different wavelength i.e. wavevector by VCMA.

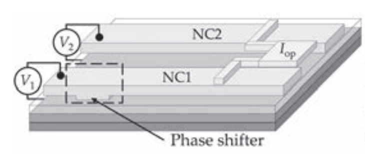

Input		Output
V_1	V_2	I_{op}
0	0	1
1	0	1
0	1	1
1	1	0

Fig. 2. Schematic diagram shows the device structure of a voltage-controlled universal NAND gate consists of two parallel NCs (NC1 and NC2) with dimension 2 μm (L) × 200 nm (d), formed by applying voltage across two top gate electrodes. A phase shifter with dimension 300 nm × 200 nm is formed on top of NC1 at x = 300 nm for adding 2π/3 phase to the SWs in NC1 with respect to the SWs in NC2. This phase shifter is designed by reducing the thickness of the dielectric (MgO) layer in 300 nm × 200 nm rectangular area by physical ion etching before depositing gate electrodes. The truth table for NAND gate is also shown on the right hand side.

2:30

FF-03. Spin wave interference in vortex stacks.

C. Behncke[1,2], C.F. Adolff[1,2], N. Lenzing[1], M. Hänze[3,4], B. Schulte[4], M. Weigand[5] and G. Meier[2,4]
1. Institute of Applied Physics, University of Hamburg, Hamburg, Germany; 2. The Hamburg Centre for Ultrafast Imaging, Hamburg, Germany; 3. Max Planck Institute for Solid State Research, Stuttgart, Germany; 4. Max Planck Institute for the Structure and Dynamics of Matter, Hamburg, Germany; 5. Max Planck Institute for Intelligent Systems, Stuttgart, Germany

Spin waves are promising candidates as a building block for future electronic devices. Having full control over the spin waves is fundamental for the realization of such devices. Interference phenomena of spin waves can be used to localize the information at distinct points in space [1]. Recently it has been shown that stacked vortex structures are efficient emitters of spin waves with tunable wavelengths [2]. We investigate spin wave interferences in merged vortex stacks by scanning transmission x-ray microscopy (STXM) at the MAXYMUS microscope of the BESSY II synchrotron in Berlin, Germany and micromagnetic simulations. The magnetic vortex state forms in ferromagnetic nanodisks of suitable geometry. The magnetization curls in the plane around the vortex core in the center region where the magnetization points out-of-plane [3]. The vortex is described by two state parameters: the polarization *p* of the magnetization in the core region pointing either up or down, and the circularity *c*, the sense of the in-plane magnetization curling either clockwise or counterclockwise. A stack of two vortices can serve as spin wave emitter with tunable wavelengths [2,4]. For the emission of spin waves with small wavelengths the circularities of the upper and lower disks have to be aligned antiparallel. The propagation direction of the spin waves hereby depends on the absolute orientation of the two circularities [2]. We investigate a stack of two merged disks in the vortex state. Each layer of the stack contains two vortices leading to an overall number of four vortices in the structure (see Fig. 1). For the excitation of spin waves the structures are placed upon a coplanar waveguide. A high-frequency current sent through the waveguide leads to a unidirectional high-frequency magnetic field H_{rf} that excites the magnetization dynamics (Fig. 1(a)). The disks are merged and therefore exchange coupled [5] with an overlap o = 300 nm and have a radius r = 800 nm (Fig. 1(b)). The stacks consist of permalloy ($Ni_{80}Fe_{20}$) layers that are separated and covered by silicon layers (Fig. 1(c)) [6]. In Fig. 2(a) a snapshot of an exemplary STXM measurement is shown, where the black and white contrast corresponds to the *z* component of the altering magnetization. The vortices are excited with a high frequency magnetic field H_{rf} with a frequency of 5 GHz. The vortices in the left stack emit outwards propagating spin waves with a wavelength of 120 nm. The vortices on the right side emit spin waves that propagate inwards with the same wavelength. It is observed that the amplitude of these spin waves varies in the structure. On the left side a cone-like region with high-amplitude spin waves is surrounded by a low-amplitude region. The spin wave dynamics can be explained by comparison with micromagnetic simulations [7]. Figure 2(b) depicts a snapshot of a micromagnetic simulation where the structure is excited with a frequency of 6 GHz. In the simulation the vortices on the left emit outwards propagation spin waves, while the vortices in the right stack emit inwards propagating spin waves. The spin waves interfere with each other leading to an interference pattern similar to the measurement. The ground state magnetization configuration of this simulation is illustrated in Fig. 2 (c,d). The observed spin wave dynamics correspond to a diamond magnetization configuration. The vortices on the left and right side have opposing circularities as well as the upper and lower vortices. The polarizations of the upper and lower vortices differ as well (Fig. 2 (d)). As the propagation direction of the vortices depends on the absolute orientation of the circularities in a stack, inwards and outwards propagating spin waves are observed. The inwards propagating spin waves result from spin wave modes with long wavelengths that are non-reciprocally reflected at the edges of the structure [2]. It is thus possible to directly observe spin wave interference in two merged stacks of vortices. Due to the interference, the amplitude of the spin waves varies in the structure with distinct areas of low and high spin wave amplitudes. This is an important feature for the use of vortices as spin wave emitters in e.g. spin wave based signal-processing devices. A cascade of the investigated structure could serve as an efficient way to carry information in such a device.

[1] K. Vogt, F. Y. Fradin, J. E. Pearson, T. Sebastian, S. D. Bader, B. Hillebrands, A. Hoffmann, and H. Schultheiss. Realization of a spin-wave multiplexer. *Nat. Commun.* 5, 3727 (2014). [2] S. Wintz, V. Tiberkevich, M. Weigand, J. Raabe, J. Lindner, A. Erbe, A. Slavin, and J. Fassbender. Magnetic vortex cores as tunable spin-wave emitters. *Nat. Nanotech.* 11, 948 (2016). [3] T. Shinjo, T. Okuno, R. Hassdorf, K. Shigeto, and T. Ono. Magnetic Vortex Core Observation in Circular Dots of Permalloy. *Science* 289, 930 (2000). [4] M. Kammerer, M. Weigand, M. Curcic, M. Noske, M. Sproll, A. Vansteenkiste, B. Van Waeyenberge, H. Stoll, G. Woltersdorf, C. H. Back, and G. Schuetz. Magnetic vortex core reversal by excitation of spin waves. *Nat. Commun.* 2, 279 (2011). [5] S. Jain, V. Novosad, F. Y. Fradin, J. E. Pearson, V. Tiberkevich, A. N. Slavin, and S. D. Bader. From chaos to selective ordering of vortex cores in interacting mesomagnets. *Nat. Commun.* 3, 1330 (2012). [6] M. Hänze, C. F. Adolff, S. Velten, M. Weigand, and G. Meier. Two-body problem of core-region coupled magnetic vortex stacks. *Phys. Rev. B* 93, 054411 (2016). [7] Micromagnum. *http://micromagnum.informatik.uni-hamburg.de/*

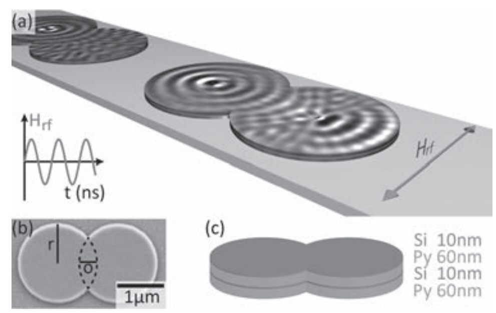

Fig. 1. (a) Schematic representation of the investigated vortex system. The black and white contrast on the structures are exemplary simulations of the spin wave dynamics. The inset shows the high-frequency field used to excite the spin wave dynamics. (b) Scanning electron micrograph of the investigated sample. (c) Schematic representation of the vortex structure consisting of two permalloy layers separated and covered by silicon layers.

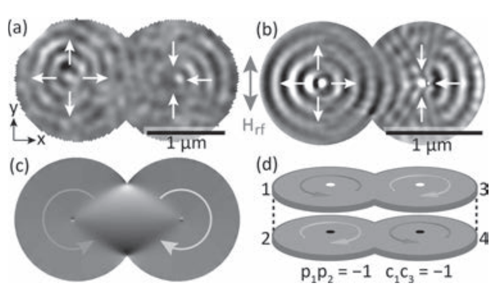

Fig. 2. (a) Normalized STXM data of the investigated structure for an excitation with a frequency of 5 GHz. The black and white contrast shows the *z* component of the magnetization M_z. The white arrows show the propagation direction of the spin waves. (b) Normalized micromagnetic simulations of the spin wave emission for an excitation with a frequency of 6 GHz. (c) Micromagnetic simulation of the ground-state magnetization-configuration corresponding to the dynamics shown in (b). The blue and yellow arrows represent the in-plane magnetization of the upper vortices, i.e. a circularity of *c*=+1 and *c*=-1, respectively. (d) Schematic of the *c,p* configurations in the simulation, where the arrows depict the circularities and the black and white dots the polarizations of the vortices.

2:45

FF-04. Protected Chiral Spin-Wave Modes for Backscattering-Immune Magnonic Transport.

M. Mohseni[1], T. Brächer[1], Q. Wang[1], D.A. Bozhko[1], B. Hillebrands[1] and P. Pirro[1]
1. Physics, TU Kaiserslautern, Kaiserslautern, Germany

Protected transport of energy and information as an emerging realm of research and technology has gained a tremendous amount of interest during the last decade [1-2]. Indeed, one of the biggest challenges in reducing the level of energy consumption and increasing the efficiency of information technology devices arises from various mechanisms of energy loss and signal distortion. Among them, defects, disorders and inhomogeneities that are induced inside or at the surfaces of the used materials, e.g., during the fabrication processes, play an important role. This motivated, inter alia, many contributions to the field of topological states of matter because topology opens the possibility to create protected and unidirectional transport [1-4]. In this contribution, we study the protection of spin waves and their quanta, the magnons, which are the low energy excitations of the spin ensemble of a magnetically ordered system. They are considered as a promising counterpart of electrons, photons and phonons to serve as information carriers in future wave-based data processing devices [5,6]. This stimulated a lot of theoretical works on the potential topological protection of spin waves in different systems like, e.g., magnonic crystals have been proposed to host topological spin wave bands [7-9]. Nevertheless, protected transport is still a great challenge since most of the proposed systems obtain their protection from Dzyaloshinskii-Moriya interaction or strongly inhomogeneous magnetic ground states which are properties that are hard to realize experimentally. Here, we demonstrate that backscattering-immune spin-wave modes exist even in simple thin film systems which have homogeneous magnetic parameters and feature no DMI. By micromagnetic simulations, we investigate the transmission of different spin-wave modes in YIG films of varying thickness after scattering of the waves by different kinds of defects and inhomogeneities. In particular, we show that chiral waves known as Magneto Static Surface Waves (MSSW, compare sketch in Fig 1a) whose reciprocity is broken because of the symmetry-breaking part of the dynamic dipole-dipole interaction with respect to the inversion of the propagation direction [7, 10] can be robust against even large inhomogeneities and defects. As an example, Figure 1b shows the micromagnetically calculated band structure of spin waves propagating perpendicular to the static field in a film of Yttrium Iron Garnet (YIG) with thickness d =100 nm. Here, the protection of MSSW against scattering is particularly strong since the MSSW frequency (red curve) is located in the band gap of the volume modes (black curve) which is opened due to the quantized exchange energy. Figure 2 compares the transmission for a topographical defect of height h for this band structure (red squares) with the case of MSSW in thicker films (d =1000nm, yellow triangles) and the Backward Volume Magneto Static Waves (BVMSW, blue circles) for the same film thickness d =100nm. It is apparent that the MSSW in the thinner film is robust against defects up to 40% of the film thickness whereas the other modes undergo strong scattering. Similar trends have been observed for inhomogeneities of the effective magnetic field and saturation magnetization. The observed protected spin waves open the possibility for designing highly efficient magnonic elements. From a more general point of view, the strong protection related to the interplay of dipole-dipole and exchange interaction should stimulate further investigation of the topology of these waves.

[1] Pedram Roushan, et al, "Topological surface states protected from backscattering by chiral spin texture" *Nature* 460, 1106–1109 (2009) [2] M. C. Rechtsman, et al, "Photonic Floquet topological insulators", *Nature* 496, 196–200 (2013) [3] M. Z. Hasan, et al, "Colloquium: Topological insulators", *Rev. Mod. Phys*. 82, 3045 (2010) [4] X.-L. Qi, et al, "Topological insulators and superconductors", *Rev. Mod. Phys*. 83, 1057 (2011) [5] A. V. Chumak, V. I. Vasyuchka, A. A. Serga, B. Hillebrands, "Magnon spintronics", *Nature Physics* 11, 453–461 (2015) [6] D. Sander, et al., The 2017 Magnetism Roadmap, *J. Phys. D Appl. Phys*. 50, 363001 (2017). [7] R. Shindou, R. Matsumoto, S. Murakami, J. Ohe, "Topological chiral magnonic edge mode in a magnonic crystal", *Phys. Rev. B* 87, 174427 (2013) [8] A. Roldán-Molina, A. S. Nunez, J. Fernández-Rossier, "Topological spin waves in the atomic-scale magnetic skyrmion crystal", *New J. Phys*. 18, 045015 (2016) [9] X. S. Wang, Ying Su, and X. R. Wang, "Topologically protected unidirectional edge spin waves and beam splitter", *Phys. Rev. B* 95, 014435 (2017) [10] I. Lisenkov, et al., "Spin-wave edge modes in finite arrays of dipolarly coupled magnetic nanopillars", *Phys. Rev. B* 90, 104417 (2014)

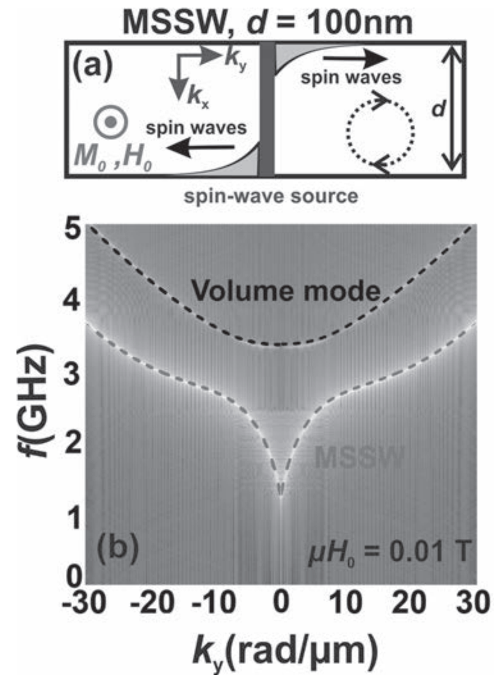

Fig. 1. Spin-wave band structure in a 100 nm thick YIG film

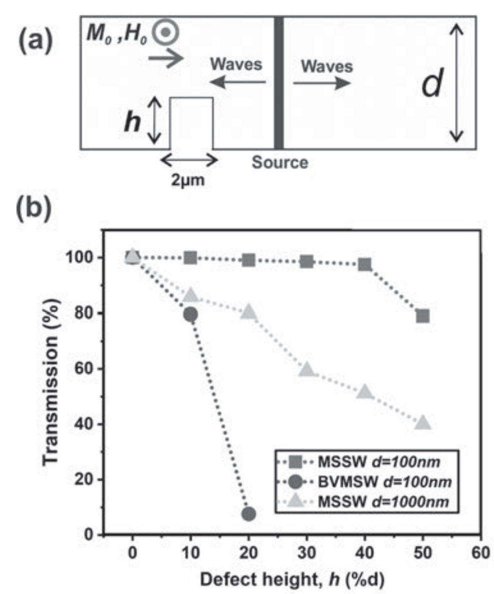

Fig. 2. Transmission of different spin-wave modes through a topographical defect.

3:00

FF-05. Excitation of Coherent Heterosymmetric Spin Waves with Ultrashort Wavelengths.

G. Dieterle[3], J. Förster[3], H. Stoll[3], A.S. Semisalova[2], S. Finizio[1], A. Gangwar[4], M. Weigand[3], M. Noske[3], M. Fähnle[3], I. Bykova[3], D.A. Bozhko[5], H.Y. Musiienko-Shmarova[5], V.S. Tiberkevich[6], A.N. Slavin[6], C. Back[4], J. Raabe[1], G. Schütz[3] and *S. Wintz*[1,2]
1. Paul Scherrer Institut, Villigen PSI, Switzerland; 2. Helmholtz-Zentrum Dresden-Rossendorf, Dresden, Germany; 3. Max Planck Institute for Intelligent Systems, Stuttgart, Germany; 4. Universität Regensburg, Regensburg, Germany; 5. Technische Universität Kaiserslautern, Kaiserslautern, Germany; 6. Oakland University, Rochester, MI, United States

The investigation of spin-wave phenomena, also referred to as magnonics, plays an important role in present magnetism research [1]. This holds true, in particular, as spin waves are seen as signal carriers for future spintronic information and communication technology devices, with a high potential for further device miniaturization and reduced power consumption. Yet a successful implementation of magnonic technology will require the usage of spin waves with nanoscale wavelengths. So far, spin-wave excitation was mainly realized either by patterned transducers with sizes of the order of the desired wavelengths (current striplines or point-contacts) or by parametric pumping via a spatially uniform double-frequency microwave signal [1-3], where both concepts suffer from severe scaling problems to achieve a local excitation of ultrashort waves. Recently, however, novel spin-wave excitation mechanisms were found [4-7], which overcome the minimum excitable wavelength limit imposed by the smallest patterning size. In particular, one of those methods utilizes the translation of layered topological magnetic defects, i.e. the gyration of coupled spin vortex cores, to locally generate short wavelength propagating spin waves in a controlled way (cf. Fig. 1) [7]. In this contribution we will show that the vortex core driven excitation mechanism discovered in a highly specific trilayer system earlier [7] can be generalized to that of a plain magnetic film, in our case a $Ni_{81}Fe_{19}$ layer with 80 nm thickness [8]. The resulting spin waves were directly imaged by means of time-resolved scanning transmission x-ray microscopy (cf. Fig. 2). Here, a 7.4 GHz excitation led to the emission of concentric spiraling spin waves with ~140 nm wavelength. Furthermore, it was found that the emitted wavelength can be efficiently tuned by the excitation frequency in the range between 5 GHz and 10 GHz, resulting in ultrashort wavelengths of ~80 nm for the highest frequencies. Remarkably, at the given frequencies, the spin waves observed exhibit much shorter wavelengths than those expected for the common Damon-Eshbach mode that is characterized by a propagation perpendicular to the equillibrium in-plane magnetization and a quasi-uniform precession amplitude over the film thickness. By means of analytic calculations based on earlier predictions [9] we identified the emitted spin waves to belong to the first higher order mode of the Damon-Eshbach geometry, which is known to be antisymmetric in amplitude over the film thickness (bearing a precessional node in both dynamic components) for the case of ferromagnetic resonance -or equivalently- for infinite spin-wave wavelengths. In contrast to the latter, our calculations show that for the short wavelengths observed in our experiment, multi-mode hybridisation leads to a heterosymmetric spin-wave thickness profile with a node only in one of the dynamic magnetization components. This peculiar profile coincides with a cross-sectional line of pure linear magnetic oscillation as well as of regions with reversed (anti-Larmor) magnetization precession sense.

[1] A. V. Chumak et al., Nat. Phys. 11, 453 (2015). [2] M. Madami et al., Nat. Nanotech. 6, 635 (2011). [3] A. G. Gurevich and G. A. Melkov, Magnetization Oscillations and Waves. New York CRC, 1996. [4] H. Yu et al., Nat. Commun. 4, 2702 (2013). [5] Wiele, B. V. et al., Sci. Rep. 6, 21330 (2016). [6] N. J. Whitehead et al., Phys. Rev. B 96, 064415 (2017). [7] S. Wintz et al., Nat Nanotech. 11, 948 (2016). [8] G. Dieterle et al., arXiv:1712.00681 (2017). [9] B. A. Kalinikos and A. N. Slavin, J. Phys. C: Solid State Phys. 19, 7013 (1986).

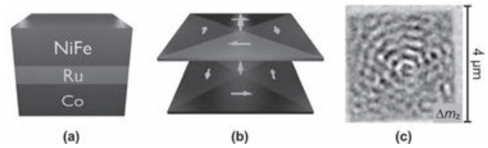

Fig. 1. Spin-wave emission from magnetic vortex cores, from [4]. (a) Trilayer with two ferromagnetic layers (Co and $Ni_{81}Fe_{19}$) separated by a Ru layer (schematics). (b) Spin vortex pair with antiferromagnetic in-plane circulations and parallel perpendicular cores (schematics). (c) Spin-wave emission for 1 GHz alternating magnetic field excitation as measured by time-resolved scanning transmission x-ray microscopy.

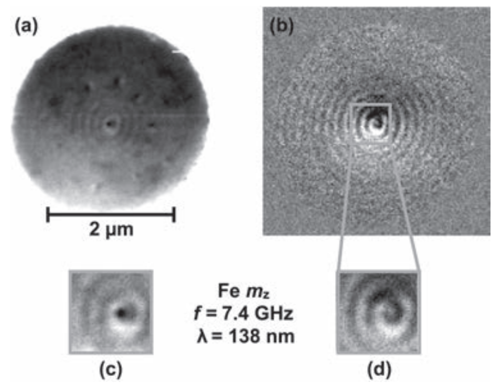

Fig. 2. Ultrashort spin-wave emission from a magnetic vortex core in a single 80 nm thick $Ni_{81}Fe_{19}$ disk in response to a 7.4 GHz magnetic field excitation as measured by time-resolved scanning transmission x-ray microscopy. (a) and (c) absolute contrast, (b) and (d) normalized magnetic contrast.

3:15

FF-06. Direct observation of sub-100 nm spin wave propagation in magnonic wave-guides.

N.A. Träger[1], P. Gruszecki[2], F. Lisiecki[3], J. Förster[1], M. Weigand[1], P. Kuswik[3,4], J. Dubowik[3], G. Schütz[1], M. Krawczyk[2] and *J. Gräfe*[1]
1. Modern Magnetic Systems, Max Planck Institute for Intelligent Systems, Stuttgart, Germany; 2. Faculty of Physics, Adam Mickiewicz University, Poznan, Poland; 3. Institute of Molecular Physics, Polish Academy of Sciences, Poznan, Poland; 4. Centre for Advanced Technology, Adam Mickiewicz University, Poznan, Poland

In magnonics research, capabilities of data processing mediated by spin waves are of current interest for beyond-CMOS data processing technologies, promising non-Boolean computing algorithms or majority gates substituting several tens of CMOS transistors and making this an exciting candidate for next level computing [1-3]. Furthermore, due to the short wavelength of magnons at technological relevant radio frequencies, smaller structural elements and, thus, miniaturization of various devices will be possible [4]. However, for magnonic logic operations, reliable spin wave guides are indispensable. Here, we use scanning transmission x-ray microscopy (STXM, MAXYMUS@BESSY II) with magnetic contrast and a spatial and temporal resolution of 18 nm and 35 ps respectively to investigate such wave-guides. These were structured in 50 nm thin Py stripes with a width of 350, 700 or 1400 nm and a length of 11 μm. A coplanar waveguide (Cr/Cu/Al) was deposited on top to allow RF excitation of spin waves in the structures (*cf.* Fig. 1 for a schematic sketch and a microscopy image). After time-domain STXM acquisition of the magnetization movie under RF excitation, a temporal Fourier transformation is performed to gain the spatial distribution of the spin wave amplitude and phase. This is shown exemplary in Fig. 2(a) for a 1400 nm wide Py stripe under CW excitation at 4.6 GHz and in an external field of 15 mT applied parallel to the long axis of the wave-guide (BV configuration). One can clearly observe that highly directed spin waves emerge from the edges of the wave-guide [5]. Due to the emission from both edges, a standing wave forms along the Py stripe. To quantify the spin-wave properties a spatial Fourier transformation was performed to derive the k-space distribution of the wave vectors, which is shown in Fig. 2(b). Here, two components stand out beside the DC peak in the center showing that these microstructures act as multimode wave-guide. The first spin-wave modes has a wave vector $k_1 = 4.7\ \mu m^{-1}$, which corresponds to a wavelength of $\lambda_1 = 210$ nm, and a second mode with a k-vector $k_2 = 10.5\ \mu m^{-1}$ is visible. Thus, we are able to microscopically observe a spin-wave with a wavelength of $\lambda_2 = 95$ nm and experimentally break through the 100 nm limit. Furthermore, we have performed a systematic variation of excitation frequency and applied external field for the different wave-guide widths. By varying these parameters, the wavelength as well as the propagation direction are tuned, indicating also diagonal and curved propagating of spin-waves that resembles the propagation of light in a graded-index fiber. Additionally, we recreated a data transmission scenario by using a Burst excitation scheme, *i.e.* four periods of RF excitation followed by a free decay time. Thereby, simultaneously excited multiple modes are carried by the Py wave-guide. They are interleaving without disrupting each other, further confirming the multimode properties of the wave-guide. Surprisingly, these modes did not disperse in frequency during the decay time making this system an ideal candidate for data transmission. In summary, we have directly observed sub-100 nm spin waves in a Py wave-guide by time-resolved STXM. The simple wave-guides were found to be able to non-dispersively carry multiple modes simultaneously. Thus, they are ideal candidates for magnon based data transmission between logic elements and provide a promising basis for future technology developments.

1. Chumak, A.V., et al., *Magnon spintronics.* Nat Phys, 2015. 11(6): p. 453-461. 2. Kruglyak, V.V., S.O. Demokritov, and D. Grundler, *Magnonics.* Journal of Physics D: Applied Physics, 2010. 43(26): p. 264001. 3. Krawczyk, M. and D. Grundler, *Review and prospects of magnonic crystals and devices with reprogrammable band structure.* Journal of Physics: Condensed Matter, 2014. 26(12): p. 123202. 4. Yu, H., et al., *Approaching soft X-ray wavelengths in nanomagnet-based microwave technology.* Nature Communications, 2016. 7: p. 11255. 5. Mushenok, F.B., et al., *Broadband conversion of microwaves into propagating spin waves in patterned magnetic structures.* Applied Physics Letters, 2017. 111(4): p. 042404.

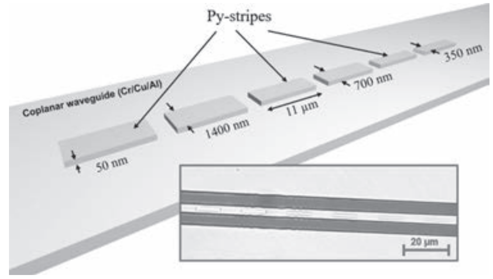

Fig. 1. Sketch of the sample with different Py stripes (yellow) on top of a coplanar waveguide (grey). The red box shows the microscopic image of the magnonic structures.

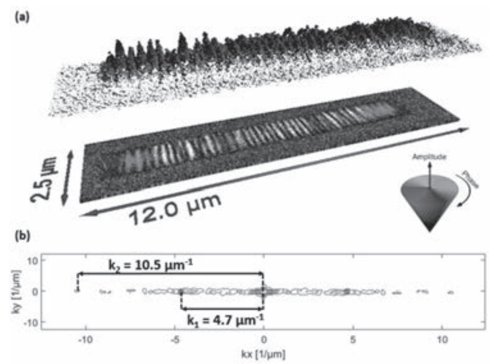

Fig. 2. (a) Frequency image of a STXM measurement (1.4 μm Py stripe) with information on amplitude and phase represented by the colour code. Standing spin-wave structures are clearly visible within the Py stripe. The three-dimensional image emphasizes the appearance of standing spin waves. (b) K-space of the frequency image. K-vectors emerge next to the DC-peak with k-values up to 10.5 μm-1 revealing a spin-wave wavelength of 95 nm.

3:30

FF-07. Long Distance Lateral Spin Transport in Antiferromagnetic Insulators.

R. Lebrun[1], A. Ross[1,2], A. Qaiumzadeh[3], S. Bender[4], L. Baldrati[1], J. Cramer[1,2], O. Gomonay[1], J. Sinova[1], R. Duine[5], A. Brataas[3] and M. Kläui[1,2]
1. Johannes Gutenberg University, Mainz, Germany; 2. Graduate School of Excellence Materials Science in Mainz, Mainz, Germany; 3. Norges teknisk-naturvitenskaplige universitet (NTNO), Trondheim, Norway; 4. University of California, Los Angeles, CA, United States; 5. Utrecht University, Utrecht, Netherlands

Spintronics based devices have found broad applications, for instance in sensors and in storage as read-heads of hard disk drives. Device prototypes, exploiting the effect of spin-torque, are anticipated to enhance the functionalities of Boolean logic circuits by integrating logic and memory functions. Despite successes, devices utilising ferromagnetic materials and spin-polarised charge currents have a number of drawbacks; parasitic magnetic stray fields, intrinsically low characteristic frequencies, and large magnetic damping and ohmic losses that respectively limit density integration and operation speed, and increases power consumption. The two key challenges are thus to design devices that remove stray fields and charge transport. Theoretically it was predicted that pure spin currents could be generated, transported and employed in antiferromagnetic insulators to enable such new devices[1–3]. However experimentally, only a few systems have been investigated, most relying on coupled ferromagnet(FM)/antiferromagnet (AFM) layers[4–7]. A key limiting factor for the transport of a spin-current in insulating antiferromagnets has been the reported spin-diffusion length of only a few nanometers and spin currents mediated by evanescent waves when generated by spin-pumping[5–7] or the spin Seebeck effect in adjacent ferromagnets[8]. Here, we demonstrate for the first time spin transport in insulating antiferromagnets over micrometer distances, which is 2-3 orders of magnitude larger than what has been previously reported when using a ferromagnet for spin injection. We obtain unprecedented long-distance spin transport by injecting spin currents from Pt contacts into selected single crystal antiferromagnets and thus open antiferromagnetic insulator systems to novel spintronics devices. In our study, we employ a non-local geometries (see Fig. 1) to study high frequency magnon propagation in an antiferromagnetic insulator. Our devices consist of platinum (Pt) strips, deposited on different 3d insulating antiferromagnetic compounds like the prototypical antiferromagnet NiO[4,9], in which ultralow magnetic damping has been reported ($\alpha < 5.10^{-4}$). When we apply a direct current in a platinum stripe, we inject magnons by both the spin Hall effect (SHE) and ohmic heating of the injector, generating magnons via the spin Seebeck effect (SSE) in the AFMI, and detect their cumulative propagation via the inverse SHE in a non-local Pt stripe. We can ascribe the first harmonic signal of the recorded voltage (linear term) to the spin transport signal and the second harmonic (quadratic term) to the thermal signal. We apply an in-plane field and note that the first harmonic voltage (see Fig. 1.i), related to the spin conductance, presents a maximum at the spin-flop reorientation, whilst the second harmonic signal, related to the spin Seebeck coefficient, is linear with the applied magnetic field (see Fig. 1.ii). In contrast to the conventional behaviour in ferromagnets[10], our spin transport signal displays a 90 degree shift whilst still displaying the characteristic π-periodicity previously observed as the field is rotated in-plane relative to the applied current direction. However, we observe an angular dependence identical to the ferromagnetic case for the thermal signal indicating different origins of the two signals. The transport signal is dependent upon the relative orientation of the Neel vector and injected spin accumulation whilst the thermal signal depends on the degeneracy of the magnon modes. Based on the geometry of our system, we also unambiguously distinguish long-distance transport based on equilibrium (Bose-Einstein condensate) or non-equilibrium magnons. The underlying physical mechanisms in our experiments allows us to observe the persistence of the two signals for distances larger than a micron, i.e more than two orders of magnitude larger than previous reports in antiferromagnetic thin films (see Fig. 2). Those results demonstrate the possibility of propagating long distance magnons in antiferromagnetic insulators, opening the way to spin-electronics devices with antiferromagnets.

1. Gomonay, E. V. & Loktev, V. M. Spintronics of antiferromagnetic systems (Review Article). *Low Temp. Phys.* 40, 17–35 (2014). 2. Jungwirth, T., Marti, X., Wadley, P. & Wunderlich, J. Antiferromagnetic spintronics. *Nat. Nanotechnol.* 11, 231–241 (2016). 3. MacDonald, A. H. & Tsoi, M. Antiferromagnetic metal spintronics. *Philos. Trans. R. Soc. Math. Phys. Eng. Sci.* 369, 3098–3114 (2011). 4. Zhang, W. *et al.* Spin Hall Effects in Metallic Antiferromagnets. *Phys. Rev. Lett.* 113, 196602 (2014). 5. Wang, H., Du, C., Hammel, P. C. & Yang, F. Antiferromagnonic Spin Transport from YFeO3 into NiO. *Phys. Rev. Lett.* 113, 097202 (2014). 6. Hahn, C. *et al.* Conduction of spin currents through insulating antiferromagnetic oxides. *EPL Europhys. Lett.* 108, 57005 (2014). 7. Frangou, L. *et al.* Enhanced Spin Pumping Efficiency in Antiferromagnetic IrMn Thin Films around the Magnetic Phase Transition. *Phys. Rev. Lett.* 116, 077203 (2016). 8. Prakash, A., Brangham, J., Yang, F. & Heremans, J. P. Spin Seebeck effect through antiferromagnetic NiO. *Phys. Rev. B* 94, 014427 (2016). 9. Baldrati, L. *et al.* Negative spin Hall magnetoresistance in epitaxial antiferromagnetic NiO(001)/Pt thin films. *ArXiv170900910 Cond-Mat* (2017). 10. Cornelissen, L *et al.* Long-distance transport of magnon spin information in a magnetic insulator at room temperature, *Nat. Phys.* 11, 1022–1026 (2015)

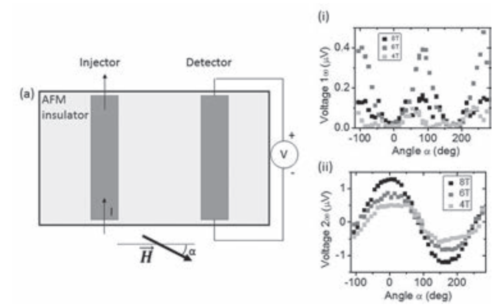

Fig. 1. (a) Schema of the experimental setup. (i) When applying a current in the injecting platinum stripe, the spin Hall Effect induces a spin accumulation oriented perpendicular to the bar, which can generates propagating magnons when the Neel vector has the appropriate symmetry. Those magnons are then detected at the 1st harmonic of the signal by ISHE. Below 6T, the direction of the Neel vector is pinned along the platinum stripes. The optimal orientation of the Neel vector is obtained at the spin-flop field, around 6T, for a magnetic field applied along the platinum stripes. (i) When applying a current in the injecting platinum stripe, a thermal gradient is also generated perpendicular to the magnons. Thermal magnons are excited by the Spin-Seebeck when an applied magnetic field lifts the degeneracy of the magnon modes. (i) Those propagating magnons are detected by ISHE at the 2nd harmonic ($\propto I^2$) when the magnetic field lifts the degeneracy of the magnon modes.

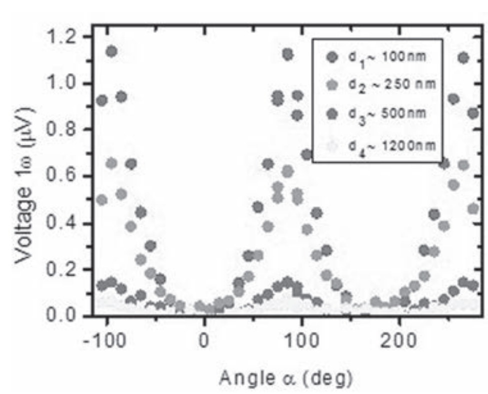

Fig. 2. Angular dependence of the 1st harmonic signal, corresponding to the propagated magnons generated by the spin-accumulation in the injecting platinum stripe, for four different distances (from 100 nm to 1.2 µm).

3:45

FF-08. Variable effective magnetization and spin wave velocity in low magnetic damping metallic multilayers.

J.M. Shaw[1], E.R. Edwards[1], T. Silva[1] and H. Nembach[1,2]
1. Quantum Electromagnetics Division, NIST, Boulder, CO, United States;
2. JILA, University of Colorado, Boulder, CO, United States

We used broadband ferromagnetic resonance spectroscopy and Brillouin light scattering to measure the damping, effective magnetization, and spin-wave velocity in multilayer metallic samples that exhibit exceptionally low values of the damping parameter. We show that we are able to vary the effective magnetization from 2.6 T to values approaching 1 T while maintaining a total damping parameter of approximately 0.002 for a 20 nm film. This is achieved by careful choice of the layers in the multilayer stack that intrinsically are low damping materials and/or minimize spin-pumping contributions. Some proposals for alternative computation technologies are based on the generation, interaction, and propagation of spin excitations. Such proposals ultimately rely on the such spin excitations having long lifetimes and therefore low values of the damping parameter. The recent discovery of simple metallic CoFe systems that exhibit ultra-low damping show promise since these systems have trivial fabrication constraints relative to half-metallic and insulating low damping materials. [1] However, the CoFe system also has an exceptionally high magnetic moment since it lies at the peak of the Slater-Pauling curve. A high effective magnetization ($\mu_0 M_{eff}$) can be beneficial by providing high spinwave velocities for magnonic structures. In fact, it is conceivable that even higher spinwave velocities and therefore high values of $\mu_0 M_{eff}$ may be desired. [2] On the other hand, the high values of $\mu_0 M_{eff}$ may be prohibitive in system that require the magnetization to be arbitrarily oriented. Therefore, tunability of $\mu_0 M_{eff}$ would be desired while at the same time maintaining the low magnetic damping properties. Such tunability is a challenge since we have previously shown that in the case of CoFe, changing alloy composition rapidly increases the density of states at the Fermi energy, thereby increasing the damping. [3] An alternative approach is to vary $\mu_0 M_{eff}$ through multilayer and interfacial effects, which typically exploits the phenomenon of interfacial anisotropy. In this case, $\mu_0 M_{eff}$ can straightforwardly be tuned by varying the thicknesses of the layers in the multilayer stack.[4] However, careful choice of the materials in the multilayer or superlatice is needed to maintain a low damping parameter. [5,6] We have found that superlattice structures composed of alternating layers of $Co_{25}Fe_{75}$ with Cu and $Co_{90}Fe_{10}$ can be used, while maintaining a total damping parameter of approximately 0.002. In order to increase $\mu_0 M_{eff}$, the use of $Co_{25}Fe_{75}/Co_{90}Fe_{10}$ structure was used, which has a negative value of the interfacial anisotropy (favoring an in-plane magnetization). Figure 1 shows that $\mu_0 M_{eff}$ can be increased from 2.3 T to 2.6 T by decreasing the bilayer thickness. Also shown is the damping parameter which is scattered around a value of approximately 0.002. In contrast, the use of $Co_{25}Fe_{75}$/Cu superlattice structures can be used to decrease $\mu_0 M_{eff}$ since the interfacial anisotropy is positive (favors an out-of-plane magnetization). Figure 2 shows that the use of Cu in the multilayer stack can reduce $\mu_0 M_{eff}$ from approximately 2.3 T to almost 1 T before the damping parameter begins to increase significantly. Finally, the spinwave group velocities were measured with wavevector-dependent Brillouin light scattering (BLS). Figure 3 is an example of the measured spinwave velocities as a function of the wavevector. We find that the spinwave velocities vary with the effective magnetization as expected. These results open up new approaches to achieve low magnetic damping while maintaining the ability to vary other static and dynamic magnetic properties.

[1] M. A. W. Schoen, D. Thonig, M. L. Schneider, T. J. Silva, H. T. Nembach, O. Eriksson, O. Karis, and J. M. Shaw, Nat. Phys. 12, 839 (2016). [2] V. V. Kruglyak, S. O. Demokritov, and D. Grundler, J Phys D 43, 264001 (2010). [3] M. A. W. Schoen, J. Lucassen, H. T. Nembach, B. Koopmans, T. J. Silva, C. H. Back, and J. M. Shaw, Phys. Rev. B 95, 134411 (2017). [4] B. N. Engel, C. D. England, R. A. Van Leeuwen, M. H. Wiedmann, and C. M. Falco, Phys. Rev. Lett. 67, 1910 (1991). [5] J. M. Shaw, H. T. Nembach, and T. J. Silva, Appl. Phys. Lett. 99, 012503 (2011). [6] J. M. Shaw, H. T. Nembach, and T. J. Silva, Phys. Rev. B 85, 054412 (2012).

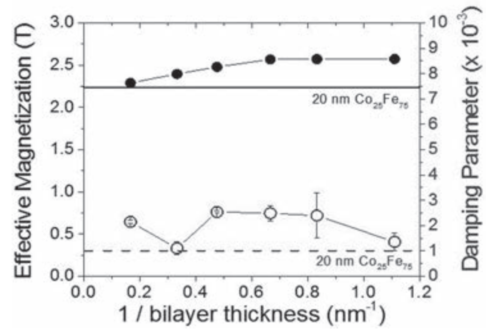

Fig. 1. The effective magnetization (black) and damping parameter (blue) as a function of the reciprocal $Co_{25}Fe_{75}$ thickness in a $Co_{25}Fe_{75}$/$Co_{90}Fe_{10}$ superlattice structure.

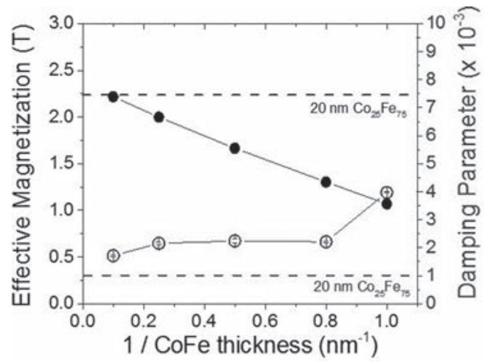

Fig. 2. The effective magnetization (black) and damping parameter (blue) as a function of the reciprocal $Co_{25}Fe_{75}$ thickness in a $Co_{25}Fe_{75}$/Cu superlattice structure.

4:00

FF-09. Finite Speed of Propagation of Spin Waves in the Inertial Regime.

C. Serpico[2], M. d'Aquino[1], V. Scalera[2] and M. Lo Bue[3]
1. Dipartimento di Ingegneria, Università degli Studi di Napoli "Parthenope", Napoli, Italy; 2. DIETI, University of Naples Federico II, Naples, Italy; 3. SATIE, CNRS, ENS Paris-Saclay, Université Paris-Saclay, Cachan, France

In this work, we discuss small wavelengths, exchange interaction dominated, spin waves in a ferromagnetic media which oscillate in the THz frequency range. This type of spin excitations is of considerable interest in the area of ultrafast (subpicosecond) magnetization dynamics [1],[2]. In this respect, it has been pointed out that ultrafast magnetization dynamics can be considerably affected by inertial effects. This idea was proposed originally in the framework of nonequilibrium thermodynamics [3], and later discussed by other authors from a more fundamental point of view [4], [5]. In this work, we discuss inertial effects in connection with the issue of speed of propagation of spin-waves. In the first part of the discussion, we consider usual spin waves analysis in a uniaxial ferromagnetic media subject to a constant external field in the limit when the magnetostatic field is negligible with respect to the exchange field. The exchange field, as it is usually done, is taken proportional to the Laplacian of the magnetization vector field. In these conditions, the equation governing spin wave oscillations can be transformed into a Schroedinger equation which can be analytically solved. This leads to the fact that spin-waves perturbation propagate with infinite speed. More specifically, if we solve the Schroedinger equation with an initial condition such that the wave function is zero outside a certain finite region, at any arbitrarily small time after, the wave function is different from zero anywhere in space. This fact leads us naturally to question about relativistic consistency of the model. In this respect, it is evident that the usual spin waves theory includes approximations which leads to the neglecting of fast phenomena which are normally not relevant for the range of physical situations to be analyzed. The situation is similar to the use of quasi-static Maxwell Equations in which fast dynamics connected to the propagation of electromagnetic waves are negligible due to the fact that the system under consideration is small with respect to the wavelength of the electromagnetic radiation. In the area of ultrafast magnetization dynamics, for magnetization dynamics in the THz frequency range, it might be important to understand in which sense the usual model of exchange dominated spin waves is a low frequency approximation of a more general model. In comparison with the electromagnetic field theory, the situation is less clear because we do not have currently a well accepted theory for high-frequency spin-wave propagation. In general terms, the theory could be modified in two respects. First, one could modify the expression of the exchange field in terms of magnetization vector fields, given the fact that the Laplacian operator is only a low wavelength approximation of a more general linear operator. Second, one could consider the fact that usual Larmor precessional dynamic equation is a low frequency limit of a more general equation. In this work, we explore this second possibility considering inertial terms in the equation governing spin waves dynamics. In the last part of the work, we derive the dispersion relation in the inertial regime which consists of two branches as represented in Fig.1. On the basis of this dispersion relation, we are able to prove that this generalization of spin dynamics equation leads to a finite speed of propagation of spin waves, and thus it removes the inconsistency of the usual theory. We conclude our contribution by showing that the maximum speed of propagation of the spin waves in the inertial regime is given by the formula $u=l_{ex}/\tau_I$, where l_{ex} is the exchange length of the media, and τ_I is a time constant related to the intertial effect (which has been estimated to be in the picosecond range [3]).

[1] E. Beaurepaire, J.-C. Merle, A. Daunois, and J.-Y. Bigot, Phys. Rev. Lett. 76, 4250 (1996). [2] A. Kirilyuk, A. V. Kimel, and Th. Rasing, Rev. Mod. Phys. 82, 2731 (2010). [3] M. C. Ciornei, J. M. Rubi, and J. E.Wegrowe, Phys. Rev. B 83, 020410 (2011). [4] T. Kikuchi and G. Tatara, Phys. Rev. B 92, 184410 (2015). [5] R. Mondal, M. Berritta, A. K. Nandy, and P. M. Oppeneer, Phys. Rev. B 96, 024425 (2017)

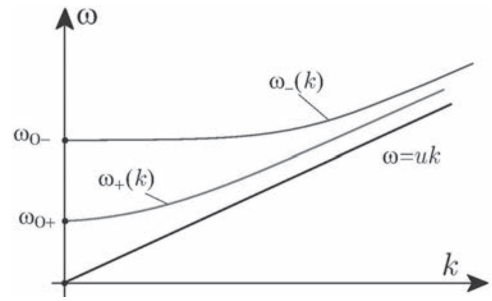

Fig. 1. Angular frequency ω versus wave vectors k for the two branches of the dispersion relation. The values ω_{0+} and ω_{0-} are the frequencies associated with spatially uniform oscillations. The quantity u is the maximum speed of propagation of spin waves.

4:15

FF-10. The general Boltzmann method for magnon transport with full scattering process.

Y. Li[1], T. Liu[1], W. Wang[1] and *J. Zhang*[1]
1. School of Physics, Tongji University, Shanghai, China

Information transport with the spin degree of freedom was adapted to revive electronic devices. In particular, magnon, the flow of quantized excitations of the spin system have been considered as the ideal carrier because of its excellent transport characters. Ferromagnetic insulators (FMIs) was most promising material for magnon devices to generate, process, and transport spin information over long distances[1]. Some phenomena explored in insulating spintronics include spin pumping, the spin Seebeck effect, the spin Peltier effect, magnon drag effect, and magnon spin transport (MST)[2-6]. While, a precise magnon transport picture in FMIs thin film was still demanded. A novel complete picture of magnon transport in FMIs was builded with a new Boltzmann equation which combined magnon, phonon and spin-polarized electron system together. In three magnons scattering, we found the N-process scattering which due to dipole-dipole interaction, dominated the decay dynamics of magnon group. To conduct N-process scattering, a new spatial dependent magnon draft field U was introduced, which was describing collective local motion field in magnon. We also found N-process scattering is the physical origin that why coherence magnons can transfer to thermal magnons in FI relaxation process. With those effects, we proposed a new method try to modify generation, amplification and controlling of magnon transport and the conversion to other particles (phonon). In our state of art Boltzmann equation, we analyses three-magnon scattering with a new spatial dependent magnon interaction field U, and construct the effective magnon temperature. We also find that three-magnon scattering causes at least two physical effects. First, it takes part in the thermal conductivity adjustment as anther heat carrier in addition to phonon. Second, it is also the physical origin that why coherence magnons can transfer to thermal magnons in FI relaxation process. Beside we also fund nonlinear effect of magnon in transport length(see attach figure). With those two effects, we find a brand new method to effectively generate, amplify and control magnon transport and the conversion with other particles. Furthermore, three-magnons scattering engender a novel collective dynamic of magnon, which is the extending of global decay length of spin information. In this framework, we also provide the methods to adjust the magnon distribution, with applying the gradient magnetic field and temperature field. This work was supported by NSFC

[1] Cornelissen, L. J., Liu, J., Duine, R. A., Youssef, J. B. & van Wees, B. J. Nature Physics 11, 1022-1026(2015). [2] Zhang, S. S. & Zhang, S. PhysRevLett.109.096603 (2012). [3] Tianyu Liu, G. Vignale, and Michael E. Flatté, Phys. Rev. Lett. 116, 237202 (2016) [4] Steven S.-L. Zhang and Shufeng Zhang, Phys. Rev. Lett. 109, 096603 (2012) [5] Li, J., et al. Nat. Comm. 7: 10858. (2016). [6] L. J. Cornelissen, K. J. H. Peters, and B. J. van Wees, Phys. Rev B 94, 014412 (2016) Corresponding should send to: zhang@tongji.edu.cn

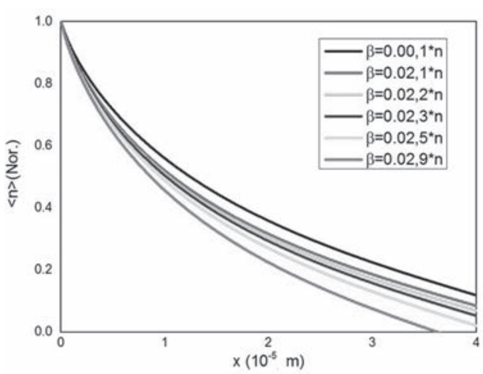

Fig. 1. The Nonlinear effect in magnon transport, With increasing density number of magnon(from 1n to 9n), the transport length of magnon decreasing (from red to purple line).

4:30

FF-11. Bose-Einstein Condensation of Quasi-Particles in a Dynamically Cooled System.

T. Brächer[1], M. Schneider[1], V. Lauer[1], P. Pirro[1], O. Serga[1], B. Heinz[1], Q. Wang[1], H. Musiienko-Shmarova[1], T. Meyer[1], F. Heussner[1], S. Keller[1], B. Lägel[1], T. Löber[1], V.S. Tiberkevich[2], A.N. Slavin[2], C. Dubs[3], B. Hillebrands[1] and A. Chumak[1]
1. Physics, TU Kaiserslautern, Kaiserslautern, Germany; 2. Oakland University, Rochester, MI, United States; 3. INNOVENT e.V. Technologieentwicklung, Jena, Germany

Bose Einstein condensation (BEC) is an ensemble of (quasi-)particles occupying a single state in momentum space. BECs have not only been observed in clouds of ultracold atoms but also the BEC of different bosonic quasi-particles like exciton polartions [1] and magnons [2,3], the quanta of spin wave excitation, have been experimentally reported. This has opened up a manifold of research directions and allows for the realization of coherent macroscopic states in a solid state material at room temperature. Recent advances like the observation of room-temperature magnonic supercurrents are just one example [4] for the rich physics of quasi-particle BEC. Here, we report on a fundamentally new way to create such a quasi-particle BEC using magnons in the ferromagnetic insulator yttrium iron garnet (YIG) as a model system. In previous realizations of quasi-particle BECs, a large number of 'hot' quasi-particles has been injected into the respective quasi-particle system either by microwave pumping (magnons) or, for instance, by optical pumping (polaritons). In our experiment, we demonstrate that the interaction of magnons with the phonon bath can provide a very simple way to achieve a magnon BEC at room temperature: By cooling down a previously heated nanostructure made of YIG in contact with Pt and Au heat sinks on a time-scale that lies below the lifetime of dipolar magnons, a non-equilibrium state is induced in the magnon subsystem. Using time-resolved Brillouin light scattering spectroscopy, we demonstrate that this results in the formation of a magnon BEC manifesting itself by a large magnon intensity at the bottom of the spectrum during the cooling of the magnetic structure. In my presentation, I will reveal the influence of the heating time and the achieved maximum temperature. I will demonstrate that a high cooling rate on the order of 20 K/ns is crucial for the realization of the quasi-particle BEC. This research has been supported by the ERC Starting Grant 678309 Magnon-Circuits, the ERC Advanced Grant 694709 Supermagnonics, and by the Deutsche Forschungsgemeinschaft (DU 1427/2-1).

[1] H. Deng, H. Haug, Y. Yamamoto, *Exciton-polariton Bose-Einstein condensation*, Rev. Mod. Phys. 82, 1490 (2010) [2] S. O. Demokritov, V. E. Demidov, O. Dzyapko, G. A. Melkov, A. A. Serga, B. Hillebrands, and A. N. Slavin, *Bose-Einstein condensation of quasi-equilibrium magnons at room temperature under pumping*, Nature 443, 430 (2006) [3] A. A. Serga, V. S. Tiberkevich, C. W. Sandweg, V. I. Vasyuchka, D. A. Bozhko, A. V. Chumak, T. Neumann, B. Obry, G. A. Melkov, A. N. Slavin, and B. Hillebrands, *Bose–Einstein condensation in an ultra-hot gas of pumped magnons*, Nat. Commun. 5:3452 (2014) [4] D. A. Bozhko, A. A. Serga, P. Clausen, V. I. Vasyuchka, F. Heussner, G. A. Melkov, A. Pomyalov, V. S. L'vov, and B. Hillebrands, *Supercurrent in a room-temperature Bose–Einstein magnon condensate*, Nature Physics 12, 1057 (2016)

4:45

FF-12. A Magneto-elastic Correlator Using Acoustic Wave Pumping of Spin Waves.

I. Lisenkov[1], M. Hansen[1], J. Davies[2], P. Dhagat[1] and *A. Jander*[1]
1. Electrical Engineering and Computer Science, Oregon State University, Corvallis, OR, United States; 2. NVE Corporation, Minneapolis, MN, United States

The group velocity of both acoustic waves and spin waves in crystals are orders of magnitude less than those of electromagnetic waves. As a result, complex analog signal processing tasks that span multiple periods of a signal can be implemented more compactly with acoustic or spin waves than with electromagnetic waves. Acoustic wave devices have thus become common in RF communications circuits, realizing complex linear filter functions in a compact and efficient manner. Although spin-wave-based devices could, in principle, perform many of the same functions as acoustic wave devices, the much higher losses and non-linear effects have limited the practical application of spin wave signal processors. However, we propose that for *nonlinear* signal processing functions, such as signal correlation, the combination of acoustic and spin wave signals in a single device may prove advantageous. We have developed a magneto-elastic device that exploits the nonlinear interactions between acoustic waves and spin waves to implement a microwave signal correlator. The device, illustrated schematically in Fig. 1a, uses an acoustic wave signal generated by a piezoelectric transducer to parametrically pump [1-3] a signal spin wave launched into a thin-film yttrium-iron-garnet (YIG) waveguide by an antenna. The resulting idler spin wave is picked up by an output antenna. The frequencies of the three waves are related $f_p = f_s + f_i$. In our experiments, the acoustic pump signal is at a frequency of f_p=2.4 GHz while the signal and idler spin wave frequencies, f_s and f_i, are a few MHz above and below 1.2 GHz. It can be shown that if the microwave input signal and pump signal are modulated with signals S(t) and P(t) respectively, the generated idler signal is modulated by the combination of the two signals as $I(t)=\int_0^{t_o} S(2\tau-t)P(\tau)\, d\tau$, thus implementing a signal correlator. The correlation time window, t_o, depends on the length of time that the spin wave transits the pumping region. The correlation signal processing is used to increase the signal-to-noise ratio of weak signals in a presence of an interference. In our proposed scheme the weak signal is used to generate spin-waves via the input spin-wave transducer, while the “reference” code is applied to the pumping acoustic transducer. We created a theoretical formalism, which allows us to predict the characteristics of the output idler signal taking into account the features of the magneto-elastic parametric interactions, magnetic damping and the non-linearities in spin-waves associated with the pumping process. As an example we calculate the distribution of the spin-wave amplitude under the transducer for two orthogonal Walsh codes, while the pumping signal is modulated with one these codes. Fig. 2a demonstrate the distribution of two “signal” spin-waves, while Fig.2b shows the corresponding two “idler” spin-waves under the influence of the the pumping signal. Our simulations show, that i) the output idler power is enhanced when the signal spin-wave code matches the reference and suppressed otherwise, ii) the non-linearity introduced by a relative high pumping amplitude does not spoil the correlation process, and iii) the spin-wave damping does not spoil the correlation processing. We have fabricated such a device, and sample results of its operation with a continuous pump are shown in Fig. 1b. The input microwave pulse of duration t_s = 30 ns on the signal channel generates an idler pulse that appears after some delay at the output. Since the pump is continuous, the output spans a time $t_s + t_o$, where t_o is approximately 200 ns, the time required for the pulse to traverse the 2 mm long device. We are currently implementing the ability to modulate the pump signal as well, so that the convolution of two signals, such as in Fig 2, can be demonstrated. Such a signal correlator could be used to great advantage at the input to a code division multiple access (CDMA) communications receiver, such as a cellular telephone, to de-correlate the incoming code sequence in the analog domain. Shifting this function to the analog domain could result in significant power savings and may improve the receiver’s resilience to interfering signals.

[1] P. Chowdhury, A. Jander, and P. Dhagat, *“Nondegenerate Parametric Pumping of Spin Waves by Acoustic Waves,”* IEEE Magnetics Letters, v. 8, 3108204, (2017); doi: 10.1109/LMAG.2017.2737962. [2] P. Chowdhury, P. Dhagat, and A. Jander, *“Parametric Amplification of Spin Waves Using Bulk Acoustic Waves,”* IEEE Transactions on Magnetics, v. 51, no. 11, 1300904, (2015); doi: 10.1109/TMAG.2015.2445791. [3] I. Lisenkov, P. Dhagat and A. Jander, *“Inhomogeneous Parametric Pumping of Spin-waves by Acoustic Waves in an Yttrium-iron-garnet Film”*, presented at the IEEE International Magnetics Conference, Dublin, Ireland, Apr. 2017.

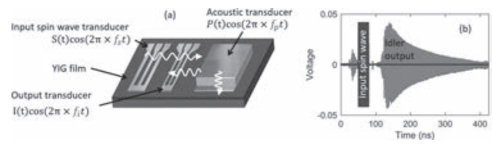

Fig. 1. (a) Illustration of the magneto-elastic correlator. (b) Experimental results showing generation of a parametrically generated idler pulse from an input signal pulse.

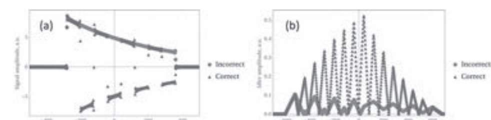

Fig. 2. (a) Input modulated signal spin-waves modulated with orthogonal Walsh codes. (b) Output idler signals after application of a pumping signal modulated with one of the Walsh codes.

THURSDAY AFTERNOON, 26 APRIL 2018 PEONY III, 2:00 TO 5:00

Session FG

MAGNETIC BEARINGS, GEARS AND LEVITATION

Mochimitsu Komori, Co-Chair
Kyushu Institute of Technology, Kitakyushu, Japan
Will Robertson, Co-Chair
Adelaide University, The University of Adelaide, SA, Australia

CONTRIBUTED PAPERS

2:00

FG-01. Design and Analysis of a Hybrid Stator Permanent Magnet Biased Bearingless Switched Reluctance Motor.

Y. Yuan[1], Y. Sun[1], Y. Huang[1], J. Yan[2] and F. Yang[1]
1. School of Electrical and Information Engineering, Jiangsu University, Zhenjiang, China; 2. School of Automation, Nanjing University of Science and Technology, Nanjing, China

Introduction: High integration, low loss and high-reliability are the main development trends of flywheel battery [1]. Magnetic bearings (MB) [2] with several advantages, such as eliminating of a lubrication system, friction-free operation and low power consumption can be promoted in various practical industrial applications, especially in flywheel batteries. The structure of MB is similar to that of the switched reluctance stator (SRM) [3]. Thus, the bearingless technology can be applied to SRM to extent its high-speed limitation. The bearingless SRM (BSRM) [4] rotates and levitates simultaneously by integrating magnetic levitation winding into the stator of a motor. However, one common problem in these existing structures [5-7] is that there is strong coupling between torque and radial force. Moreover, the copper loss and temperature rise of windings are also a problem that cannot be ignored [8]. Thus, this study presents the first prototype of a hybrid stator permanent magnet biased (HSPMB) BSRM with the advantages of weak coupling and low power consumption. The structure, operation principle and main electromagnetic characteristics of the HSPMB BSRM are analyzed. The proposed motor exhibits the following advantages: 1) High integration. The proposed motor can realize energy conversion and two degrees of freedom(2-DOF) radial suspension through the torque and suspension systems, correspondingly. 2) Low loss. The biased flux is provided by the permanent magnet which leaves out the extra biased winding correspondingly. 3) Weak coupling. Self-decoupling is realized between the torque and the suspension systems according to the structural design. 4) Favorable controllability. The suspension force is only related to the current and has no relation to the rotor position, thereby increasing controllability. New Machine: The structure of the proposed bearingless motor is illustrated in Fig. 1. Fig. 1(a) presents the HSPMB BSRM, which mainly consists of a outer stator with twelve poles, a rotor with eight poles and a hybrid inner stator. The windings with condition current i_{TA} on the poles of the outer stator can produce rotational torque. The configuration of torque winding in *A* phase of the outer stator is drawn as an example. Fig. 1(b) presents the structure of the inner stator, which consists of a left inner stator with four poles, a permanent magnet (PMR) and a right inner stator with four poles. The biased flux for generating a suspending force is provided by the PMR with axial magnetization and forms a closed loop through the left inner stator poles, the rotor and the right stator poles. As shown in Fig. 1(c), the winding with condition currents i_{RFy} and i_{LFy} on the poles of the hybrid inner stator can produce 2-DOF suspension forces and the configuration of it in the *y* direction is drawn as an example. Fig. 1(d) depicts the control magnetic flux and biased flux paths. By adjusting the directions of the control flux Φ_{RFy} and Φ_{LFy} to superposing or reducing the biased flux Φ_m, the suspension force can be produced in 2-DOF. Main Electromagnetic Characteristics: Fig. 2 depicts the main electromagnetic characteristics of the TSPMB BSRM. Fig. 2(a) presents the distribution of biased flux and the value and of air-gap flux density. It can been seen that the biased flux distributes in the rotor and hybrid inner stator symmetrically and evenly, and the value of the inner stator air-gap flux density is approximately 0.5 T. As shown in Fig. 2(b), the air-gap flux density in the *y* positive direction decreases with the increase in the current value when i_{LFy} and i_{RFy} are conducted with 2 A, 2.5 A, 3 A, and 3.5 A. Therefore, the air-gap magnetic flux density can be regulated by controlling the magnitude and direction of the suspension current, and the required suspension force can then be generated. Fig. 2(c) and Fig. 2(d) present the values of suspension force and torque. Fig. 2(c) demonstrates the values of suspension force with i_{LFy} and i_{RFy}= 2 A, 2.5 A, 3 A, and 3.5 A in the *y* direction. The values of the suspension force are approximately 34 N with 2 A, 42 N with 2.5 A, 49 N with 3 A, and 54 N with 3.5 A conduction. The suspension force value in the *y* direction is approximately linear with the value of suspension current. This analysis denotes that the controllability of the magnitude of radial suspension forces in the 2-DOF direction can be achieved by adjusting the suspension force winding current magnitude. Fig. 2(d) depicts the torque values when the rotor rotates at a 2π mechanical angle with different suspension current operations. The maximum torque value is approximately 0.003 Nm which can be ignored when the suspension system is conducted in the *y* direction. Thus, the self-decoupling is realized between the torque and the suspension systems.

[1] Y. Yuan, Y. Sun and Y. Huang, “Radial force dynamic current compensation method of single winding bearingless flywheel motor,” IET Power Electronics, vol.8, no.7, pp. 1224-1229, 2015. [2] Z. Su, D. Wang, J. Chen, X. Zhang and L. Wu, “Improving Operational Performance of Magnetically Suspended Flywheel With PM-Biased Magnetic Bearings Using Adaptive Resonant Controller and Nonlinear Compensation Method,” IEEE Transactions on Magnetics, vol.26, no.7, pp. 1-5, 2016. [3] C. Morrison, M. Siebert and E. Ho, “Electromagnetic Forces in a Hybrid Magnetic-Bearing Switched-Reluctance Motor,” IEEE Transactions on Magnetics, vol. 44, no.12, pp. 4626-4638, 2008. [4] M. Takemoto, A. Chiba and H. Akagi, “Radial force and torque of a bearingless switched reluctance motor operating in a region of magnetic saturation,” IEEE Transaction on Industry Applications, vol.40, no. 1, pp.103-112, 2004. [5] Y. Yuan, Y. Sun and Y. Huang, “Accurate mathematical model of bearingless flywheel motor based on Maxwell tensor method,” Electronics Letters, vol.52, no.11, pp. 950-952, 2016. [6] L. Chen and W. Hofmann, “Design procedure of bearingless high speed switched reluctance motors,” Int. Symp. on Power Electronics Electrical Drives Automation and Motion, Pisa, Italy, pp. 1442-1447, June 2010. [7] X. Cao, J. Zhou and C. Liu, “Advanced Control Method for Single-Winding Bearingless Switched Reluctance Motor to Reduce Torque Ripple and Radial Displacement,” IEEE Transactions on Energy Conversion, pp. 1533-1543, 2017. [8] H. Wang, Y. Wang and X. Liu, “Design of novel bearingless switched reluctance motor,” IET Electric Power Application, vol.6, no.12, pp. 73-81, 2012.

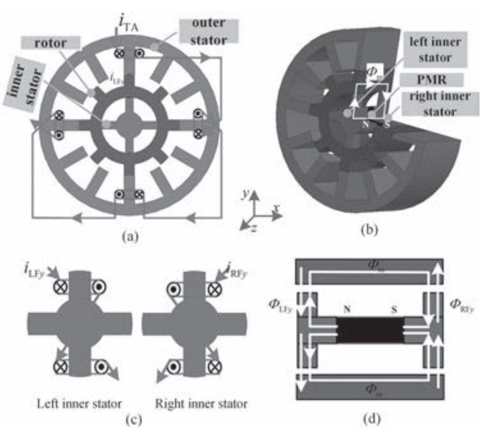

Fig. 1. Structure of HSPMB BSRM. (a) Basic structure. (b) Biased flux. (c) Winding configuration of hybrid inner stator. (d) Control flux.

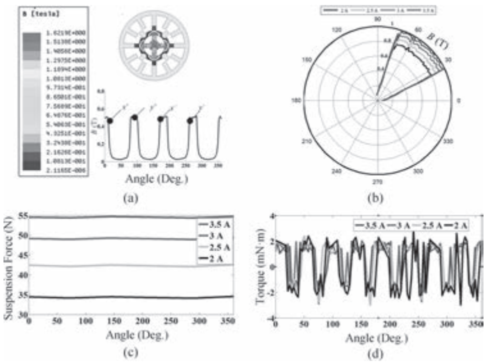

Fig. 2. Main electromagnetic characteristics. (a) Static air-gap flux density of the hybrid inner stator. (b) Air-gap flux density of the inner stator with different current values in the *y* negative direction. (c) Values of suspension force. (d) Values of torque.

2:15

FG-02. Weight reduction of the damper coils in the superconducting magnetically levitated bogie.

S. Ohashi[1]
1. Electrical and Electric Engineering, Kansai University, Osaka, Japan

A Superconducting magnetically levitated (Maglev) transportation system has been developed in Japan. Fig .1 shows a cross section of the system. The null flux eight figure levitation coils are set on the ground[1][2]. And Superconducting (SC) coils that are used for both secondary of the linear synchronous motor and the levitation magnet are installed on the side of the bogie. This system which is based on the side wall electrodynamic suspension (EDS), keeps the air-gap length at about 100 mm. When the bogie passes below the center of the levitation coil, current is induced on the levitation coils, and its value depends on vertical position and velocity of the SC coils on the train. Interaction between this current and flux of the magnet, levitation force is generated. Although the EDS system has the advantage of stable levitation without active control, results of the numerical simulation show that the damping factor of the levitation system is small. Thus additional damper system has been proposed to increase damping of the system against oscillation of the bogie. Although the mechanical dampers are installed between the bogie and the cabin, the primary damping factor is needed. As the train runs with levitation, it is impossible to install the mechanical damper for the primary one. The damper coils are installed in front of the SC coils. From the results of the three-dimensional running simulation, it is shown that the damper coils works effectively[3]. The specifications of the damper coils are decided by the damping effect against the natural vertical oscillation of the bogie. The weight of the conventional damper coils is heavy. So weight reduction of the damper coils is needed. In this paper reduction of the damper coil weight is studied. The weight reduction damper coils are introduced. And its damping characteristics are shown by the numerical analysis. Levitation force is generated by passing the SC coils on the bogie. The eight-figure null-flux connection is used for the levitation coil on the ground. If the bogie passes under the center of the eight-figure coils, levitation force is generated. We use virtual displacement method to calculate levitation force. Current induced in the levitation coils is calculated as follows [4]; the EDS system is given as an air-core coil system, and modeled as electric circuits. Mutual inductance between SC coils and levitation ones are calculated, and the electric circuit equations are given. Then solving the electric circuit equations, we can calculate the current of the levitation coils. The motion of the bogie is calculated by putting these electromagnetic forces. Iterating these procedures, the transient motion of the bogie is given. We use Eular method to solve differential equations. In the conventional system, weight of the damper coils reaches about 2.5% of the bogie. It affects motion of the bogie. Also, increment of the total weight of the bogie changes levitation gap of the train. So it is important to reduce the weight of the damper coils. They are set in front of the SC coils. Two damper coils are installed for each SC coil. Change of the linkage flux generates electromotive force on the damper coils. Then interaction between the current of the damper coils and flux of the levitation coil causes electromagnetic force. This force acts to decrease vibration of the bogie. Same as the calculation for the levitation force, we regard the SC coils, the levitation coils and damper coils system as electric circuits. Then the current induced in the damper coils is given. As one bogie has eight SC coils, sixteen damper coils are set for one bogie. Reduction of the damper coils weight are studied. Target weight of the damper coil is half as much as the conventional one. The diameter of the coil is fixed at 4 mm, and number of turn is 2. Then width and height of the coil is changed as parameters. These parameters are defined as follows; energy consumed in them is calculated when the bogie oscillates vertically at natural oscillation. The damper coils that energy takes maximum is defined as the optimal one. Fig.2 shows dependence of the energy on the height of the coil. The negative value means the damper coils absorb the vibration energy. As shown in Fig.2, the energy takes maximum value at coil height = 0.35 m. (The width of the coil is defined automatically from the weight of the damper coil). Running simulations with the weight reduction have been undertaken. The weight of the reduction model becomes half as that of the conventional one. This means size of the damper coils becomes small, and effect of the damper coil should decrease. The number of operation type of the damper coil is two. One is the passive mode, and the other is semi-active one. In the passive mode, the damper coils are used just as the short circuit coil. The effect of the conventional damper coil becomes large in this mode. In the semi-active mode, the switching device are installed, and damper coils are switched depends on the vibration velocity of the bogie and current of the coil. When the switch is ON, the damper coils are short circuited, and OFF, open circuited. In this semi-active mode, oscillation of the bogie converges faster than that by the conventional one.

S.Ohashi, K.Higashi, H.Ohsaki and E.Masada, “Running Simulation of the Superconductive Magnetically Levitated System”, in Proceedings of EPE'95, 1995, vol.3, pp650-655. J.L He, D.M.Rote and H.T.Coffey, “Electrodynamic Force of the Cross-Connected Figure-Eight Null-Flux Coil Suspension system”, in Proceedings of the 13th International Conference on Magnetically Levitated Systems and Linear Drives (Maglev'93, U.S.A.), 1993, pp.64-70. S.Ohashi, “Effect of the Active Damper Coils of the Superconducting Magnetically Levitated Bogie in Case of Acceleration”, *IEEE Trans. on Magnetics* vol.44, No.11, pp4163-4166, 2008. S.Ohashi and N.Ueda, “Influence of the Damper Coil System on the Levitation Characteristics in the Superconducting Magnetically Levitated System in Case of SC Coil Quenching”, *IEEE Trans. on Magnetics* vol.50, No.11, 8300304, 2014.

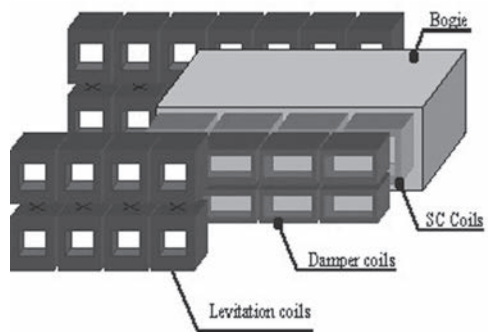

Fig. 1. Coil arrangement of the Maglev system

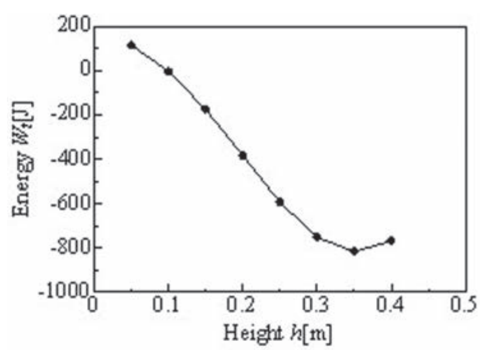

Fig. 2. Dependence of the energy on the height of the levitation coil

2:30

FG-03. Analysis of a Coaxial Magnetic Gear without Rotor Iron Yoke.

E. Göbl[1], G. Jungmayr[2], E. Marth[1] and W. Amrhein[1]
1. Johannes Kepler University, Linz, Austria; 2. Linz Center of Mechatronics GmbH, Linz, Austria

Abstract—This paper deals with the analysis and optimization of radial, coaxial magnetic gears. Multi-objective optimizations of the modulator shape of two magnetic gears with and without outer rotor iron yoke will be presented and discussed. To guarantee comparable results, equal start geometries, optimization parameters, objectives and constraints are considered. After the optimization process the geometries of the two gears show different optimal modulator shapes and therefore different flux and force distributions. The optimized gear without yoke will then be analysed in more detail. It achieves a comparable torque capability in comparison with the optimal gear with yoke but reduces losses by 70% estimated by 2D FEM Calculations. *I. Introduction* In recent years the interest in contactless torque transmission is growing and a lot of research and publications were conducted in the field of magnetic gears and magnetic geared drives. Present motor-gear solutions are in most of the cases electrical drives combined with mechanical gears to transform the high speed side of the motor to the *low speed/high torque* side of the application. When low speeds and high torques are required a Direct Drive can be a good solution, but with the disadvantage of lower efficiencies and bulky structures. The combination of a high speed motor and an efficient gear can give a rise to system power densities and reduce the space of the whole configuration [1]. At the moment mechanical gears are limiting the use of high speed motors as input speed source [2]. Magnetic gears show many advantages in comparison with mechanical gears. The biggest advantage is the contactless transmission. Due to friction, maintenance costs in mechanical gears are quite high and are reducing the lifetime of a gearbox drastically. A lot of research focuses on the topology presented in Fig.1, which is a combination of an inner rotor with few pole pairs p_1, a flux modulator and an outer rotor with a high number of pole pairs p_3. Fig.1 shows the topologies of the presented gears with the pole pair numbers p_1=1 and p_3=17 and the modulator teeth n_2=18 and different modulator geometries. The rotational speeds are presented by $\omega_1=\omega_h$, $\omega_2=\omega_l$ and $\omega_3=0$ (Index l and h represent the low and high speed side). In the last years many topologies and variations were investigated ([3], [4], [5], [6] and [7]) to improve the torque transmission capabitity. Although a lot of papers were published since the key publication in 2004 [8] just few papers picked a high speed pole pair number p_1 of 1 [9] and in general there are not many publications that focus on magnetic gears in combination with motor speeds beyond 10.000 rpm [1]. *A. Modulation Effect and Gear Ratio* High input speeds $\omega_h=\omega_1$ require a high gear ratio G_r to adjust the motor speed to low speed ω_l applications. In magnetic gears with modulation effect the equation $n_2=p_1+p_3$ has to be satisfied. When the outer rotor is stationary the ratio results in $G_r=\omega_h/\omega_l=\omega_2/\omega_1=-n_2/p_1$}.The detailed derivationof these equationes and all necessary relations can be found in [8]. A low pole pair number p_1 and a high number n_2 of modulator teeth result in a high gear ratio. In contrast to previously set up prototypes higher motor speeds can be transfomed to the necessary application *speed/torque* due to the higher ratio. *II. Influence of Modulator Geometry* The conventional gear G_1 with iron as outer rotor yoke material shows the highest losses in the back iron yoke of rotor 3. In order to reduce these losses the outer rotor back iron is set to vacuum in a second gear configuration G_2. This section will describe the optimization of the gears and it will be introduced with the description of the start geometry, followed by the optimization parameters, objectives and constraints. Besides high torque, also low losses, low ripple and low flux density in the gear surrounding are requirements. The optimized gears (G_1, G_2) will be analysed and then the influence of the different modulator shapes on the force and torque generation at G_1 and G_2 will be presented. *III. Outlook* The introduction briefly explains the chosen topology. A more detailed description will be given in the full paper. Especially the reduction of losses by equal torque generation capabilities of the gear without rotor yoke (G_2) is of particular interest and requires further analysis of the gear characteristics. Finally, the conclusion of the paper will summarize the results and give an outlook on future work and developments.

[1] K. Aiso and K. Akatsu, "A novel reluctance magnetic gear for high speed motor," in 2016 IEEE Energy Conversion Congress and Exposition (ECCE), 2016, pp. 1–7. [2] F. Wang and S. Wang, "Failure diagnosis of high speed gear," in Proceedings of 2011 International Conference on Fluid Power and Mechatronics, 2011, pp. 878–883. [3] P. O. Rasmussen, T. O. Andersen, F. T. Jorgensen, and O. Nielsen, "Development of a high-performance magnetic gear," IEEE Transactions on Industry Applications, vol. 41, no. 3, pp. 764–770, 2005. [4] K. Uppalapati and J. Bird, "A flux focusing ferrite magnetic gear," in 6th IET International Conference on Power Electronics, Machines and Drives (PEMD 2012), 2012, pp. 1–6. [5] J. X. Shen, H. Y. Li, H. Hao, M. J. Jin, and Y. C. Wang, "Topologies and performance study of a variety of coaxial magnetic gears," IET Electric Power Applications, vol. 11, no. 7, pp. 1160–1168, 2017. [6] J. Rens, K. Atallah, S. D. Calverley, and D. Howe, "A novel magnetic harmonic gear," IEEE Transactions on Industry Applications, vol. 46, no. 1, pp. 206–212, 2010. [7] K. Davey, T. Hutson, L. McDonald, and G. Hutson, "The design and construction of cycloidal magnetic gears," in 2017 IEEE International Electric Machines and Drives Conference (IEMDC), 2017, pp. 1–6. [8] K. Atallah, S. D. Calverley, and D. Howe, "Design, analysis and realisation of a high-performance magnetic gear," IEE Proceedings - Electric Power Applications, vol. 151, no. 2, pp. 135–143, 2004. [9] G. Jungmayr, J. Loeffler, B. Winter, F. Jeske, and W. Amrhein, "Magnetic gear: Radial force, cogging torque, skewing, and optimization," IEEE Transactions on Industry Applications, vol. 52, no. 5, pp. 3822–3830, 2016.

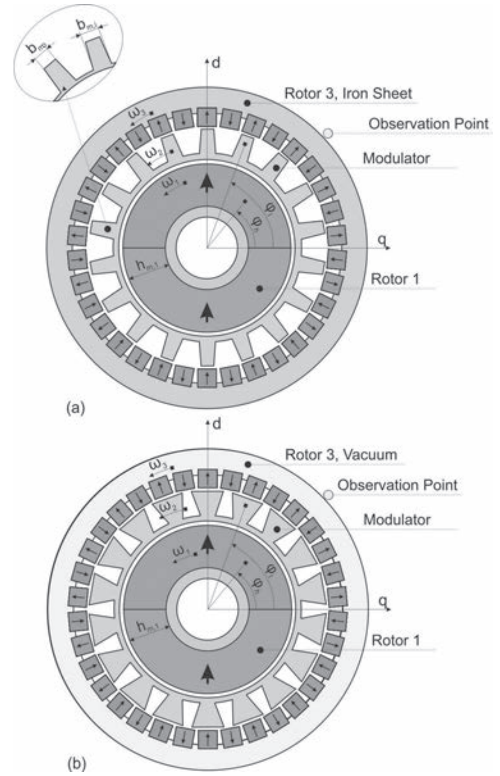

Fig. 1. Magnetic Gears G_1 (a) and G_2 (b) with different modulator shapes.

2:45

FG-04. Investigating the Performance of a Halbach Rotor Magnetic Gearbox with 3-D Printed Structural Components.

D.H. Wong[1] and *J.Z. Bird*[1]
1. Portland State University, Portland, OR, United States

INTRODUCTION A popular approach to achieving robotic actuation is to use a high-speed motor connected to a rotary gearbox [1]. Mechanical gearboxes with volumetric torque densities in excess of 300 Nm/L are achievable [2, 3]. However, mechanical gearboxes need regular servicing and lubrication. Some gearing systems are not back-drivable and most offer limited compliance capabilities. The mechanical gearing system can also often be noisy. The main alternative to the use of a gearbox is to use a direct-drive (DD) permanent magnet (PM) motor. The use of the DD-PM motor removes the reliability concerns with regard to the mechanical gearbox failures and maintenance needs. DD-PM motors can also be designed to be quiet in operation. However, the torque density of a DD-PM motor is thermally limited (by current) and therefore a PM motor does not normally achieve volume torque densities greater than 50Nm/L [4] and mass torque densities higher than 6Nm/kg [5]. Hydraulic and pneumatic actuators are capable of creating extremely high force densities. Mass torque densities in the range of 96Nm/kg [5] have been reported. However their dependence on non-portable pressure supplies limits their range of application. Hydraulic and pneumatic actuators are typically also only efficient over a limited operating range [5]. Review articles [1, 5] discuss other actuator technologies such as shape memory actuators and engineered muscle tissue actuators. However most newly proposed actuators operate with low efficiency [1, 6]. A robot actuator that could combine the features of high efficiency, high torque density and high reliability would be most desirable. Recently a number of authors have proposed that a magnetic gearbox (MG) could potentially meet these requirements [7, 8]. A MG uses a contactless mechanism for speed amplification. Initial MG designs tried to mimic their mechanical counterparts [9, 10] however such approaches only resulted in a fraction of the magnetic fields being utilized for torque production. In 2004 Atallah showed that the coaxial MG shown in Fig. 1 could operate with a torque density of up to 100Nm/L. This is approximately twice the peak torque density of a DD generator [11]. The speed relationship for the coaxial MG is $\omega_1 = (n_2/p_1)\omega_1 - (p_3/p_1)\omega_3$ [11], where the subscripts denote rotor number. If the outer rotor is held stationary the speed ratio will be $\omega_1 = (n_2/p_1)\omega_2 = G_{12}\omega_2$ where G_{12} is the gear ratio. Along with not needing gear lubrication and offering the ability to potentially increase efficiency a MG offers unique features such as inherent overload protection. A number of authors have proposed using a Halbach magnetic rotor [12, 13] to improve the MG torque density [14-16]. However, the Halbach rotor is difficult to fabricate. Recently a 3-D printed housing for a Halbach rotor was presented by Laimer [17] for a motor application. Laimer design however, required support bridges to be placed between magnet segments and this then greatly reduces the air-gap field. In this paper a new 3-D printed Halbach rotor retaining structure is presented and the Halbach rotor MG is optimized for peak mass and volumetric torque density. The Halbach rotors do not need ferromagnetic material and since only the central modulation rotor is required to be made of ferromagnetic material it is shown that the 3-D printed MG structure can have a high mass torque density. MAGNETIC GEARBOX ANALYSIS The Halbach typology being investigated is shown in Fig. 2. Table I shows the fixed geometric MG parameters. The pole pair combination selected is (p_1, n_2, p_3)=(3,17,14). This pole combination gives a gear ratio of G_{12}=5.67. As both p_1 and n_2 are prime numbers the torque ripple is low. The outer radii and axial length of the MG have been fixed at r_{o3} = 60mm and d=75mm respectively. The three radial parameters that were varied are shown in Table II and defined in Fig. 3. These three radial length parameters have the largest impact on the torque density. Note that since the outer radii was fixed at r_{o3} = 60mm when the modulation length l_2 is changed the outer rotor radii length r_{i3} is also changed (since $r_{i3} = r_{o1} + l_2$). The volumetric torque density and mass torque density for each design was computed. The torque density trade-off plot is shown in Fig. 4. A clear trade-off between maximizing mass torque density (design A) and volumetric torque density (design B) is apparent. The design parameters for the peak torque density designs are shown in Table III. Also shown is a trade-off design, design C, in which both a relatively high mass and volumetric torque density is obtained. Design C was chosen to construct. The impact of axial length on torque density is shown in Fig. 4. The 3-D design approaches that of the 2-D design as axial length increases. The axial length of 75mm was selected as this achieves a high torque density. 3-D PRINTED ROTOR STRUCTURE The mechanical design utilizes 3-D printed parts. The design object was to fabricate a mechanical structural design in which the entire MG could be assembled first without any magnets. Following this magnets could be inserted. Such a design approach can be achieved by using 3-D printing. The 3-D printed structural part drawings are shown in Fig. 6. The modulation rotor is shown in Fig. 7. The full paper will present the experimental testing results as well as provide much more design drawing details [18] on the 3-D printed design approach.

[1] A. J. Veale and S. Q. Xie, “Towards compliant and wearable robotic orthoses: A review of current and emerging actuator technologies,” *Medical Engineering and Physics* vol. 38, no. pp. 317–325, 2016. [2] Sm-Cyclo Speed Reducers and Gearmotors, Series 4000, Sumitomo Machinary Corporation of America, Catalog # 04.401.50.009. [3] *Nabtesco Cycloidal Gearbox*. Available: http://www.nabtescomotioncontrol.com/products/ [4] T. J. E. Miller, *Brushless Permanent-Magnet and Reluctance Motor Drives*: Oxford University Press, 1989. [5] J. M. Hollerbach, I. W. Hunter, and J. Ballantyne, “A comparative analysis of actuator technologies for robotics,” in *Robotics Review 2*, ed: MIT Press Cambridge, MA, USA, 1992. [6] J. M. Jani, M. Leary, A. Subic, and M. A. Gibson, “A review of shape memory alloy research, applications and opportunities,” *Materials and Design*, vol. 56, no. pp. 1078 - 1113, 2014. [7] H. Komiyama and Y. Uchimura, “Contactless magnetic gear for robot control application,” *Elect. Eng. Japan*, vol. 184, no. 4, pp. 389-396, Apr. 2013. [8] G. Puchhammer, “Magnetic gearing versus conventional gearing in actuators for aerospace applications,” in *The 42nd Aerospace Mechanism Symposium*, Greenbelt, MD, USA, 2014, pp. 175-182. [9] C. G. Armstrong, “Power transmitting device,” USA Patent 687,292, 1901. [10] H. T. Faus, “Magnet gearing,” USA Patent 2,243,555, 1941. [11] K. Atallah, S. D. Calverley, and D. Howe, “Design, analysis and realisation of a high-performance magnetic gear,” *IEE Proc.-Electr. Power Appl.*, vol. 151, no. 2, pp. 135-143, 2004. [12] K. Halbach, “Design of permanent multipole magnets with oriented rare earth cobalt material,” *Nucl Instr. and Meth.*, vol. 187, no. pp. 1-10, 1980. [13] H. A. Shute, J. C. Mallinson, D. T. Wilton, and D. J. Mapps, “One-sided fluxes in planar, cylindrical, and spherical magnetized structures,” *IEEE. Trans. Magn.*, vol. 36, no. 2, pp. 440-451, 2000. [14] L. Jian, K. T. Chau, Y. Gong, J. Z. Jiang, C. Yu, and W. Li, “Comparison of coaxial magnetic gears with different topologies,” *IEEE Trans. Magn.*, vol. 45, no. 10, pp. 4526-4529, 2009. [15] L. Jian and K. T. Chau, “A Coaxial Magnetic Gear With Halbach Permanent-Magnet Arrays,” *IEEE Trans. Energy Conv.*, vol. 25, no. 2, pp. 319-328, 2010. [16] A. Penzkofer and K. Atallah, “Magnetic Gears for High Torque Applications,” *IEEE Trans. Magn.*, vol. 50, no. 11, p. Article#: 8104704 2014. [17] C. Laimer. (2017). Available: https://www.youtube.com/watch?v=YsSm65DAcCg [18] J. Bird, H. Y. Wong, A Halbach rotor magnetic gearbox using a 3-D printed structural support, US Provisional Patent, submitted 2018.

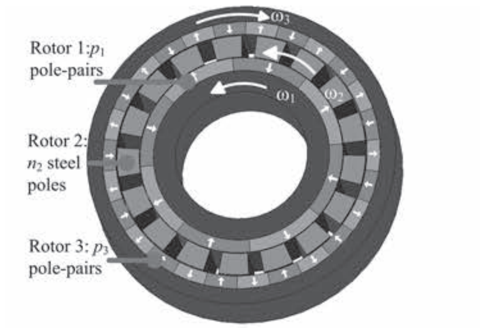

Fig. 1. A coaxial magnetic gearbox using surface PMs. p_1=4 pole-pairs, n_2=17 steel poles and p_3=13 pole-pairs on outer rotor.

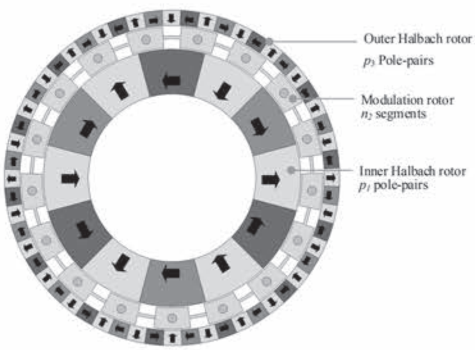

Fig 2. Cross-sectional view of the 5.67:1 Halbach rotor magnetic gearbox. The inner rotor as p_1=3 pole-pairs, the outer rotor has p_3=14 pole-pairs and there are n_2 =17 ferromagnetic segments.

TABLE I.
HALBACH MAGNETIC GEARBOX FIXED GEOMETRIC PARAMETERS

Description		Value	Unit
Inner rotor	Pole pairs, p_1	3	-
	Angular span, θ_1	$\pi/(2p_1)$	radians
Modulation rotor	Inner radius, r_{i2}	44.5	mm
	Outer radius, r_{o2}	52.5	mm
	Pole pairs, n_2	17	-
	Angular span, θ_2	$\pi/(n_2)$	radians
Outer rotor	Outer radius, r_{o3}	60	mm
	Pole pairs, p_3	14	-
	Angular span, θ_3	$\pi/(2p_3)$	radians
Axial stack length, d		75	mm
Airgaps		0.5	mm

TABLE II
GEOMETRIC PARAMETER SWEEP VARIABLES

Parameter	Sweep range [mm]
Inner rotor inner radii, r_{i1}	8, 2... 30
Inner rotor outer radii, r_{o1}	30, 32… 50
Modulation rotor radial length, l_2	2.5, 3…8 9,10…13

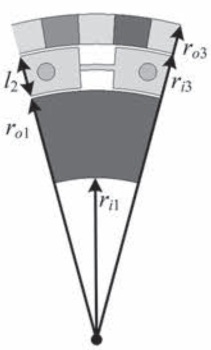

Fig 3. Parameter definition

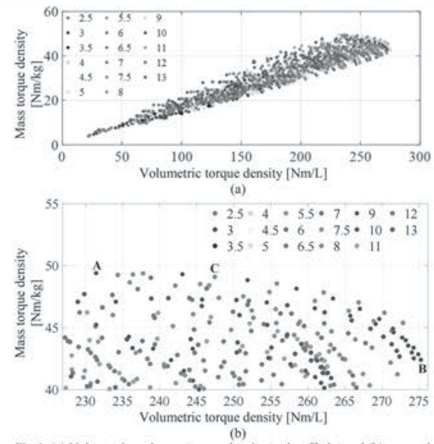

Fig 4. (a) Volumetric and mass torque density trade-off plot and (b) zoomed in view. The legend shows the different modulation rotor length, l_2 values. Design A has the highest mass toque density, Design B has the highest volumetric torque density and Design C has the best trade-off between maximizing mass and volumetric torque density.

TABLE III
DESIGN CHOICES

Parameter	Maximum torque density		Trade-off design (C)	Unit
	Mass (A)	Volume (B)		
Inner rotor inner radii, r_{i1}	30	18	26	mm
Inner rotor outer radii, r_{o1}	46	44	44	mm
Modulator radial length, l_2	7.5	8	8	mm
Inner radii of outer rotor	54.5	53	53	mm
Peak torque	201.7	231.5	217.0	Nm
Volumetric torque density	237.8	272.9	255.8	Nm/L
Mass torque density	49.4	45.4	45.5	Nm/kg

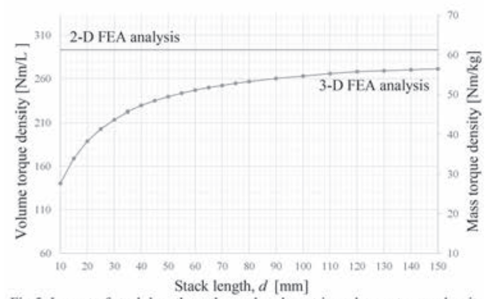

Fig 5. Impact of stack length on the peak volumetric and mass torque density for design A

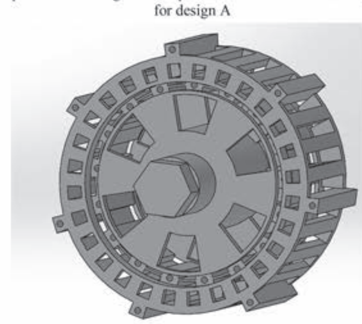

Fig. 6 The 3-D printed parts being used for the assembly of the magnetic gear

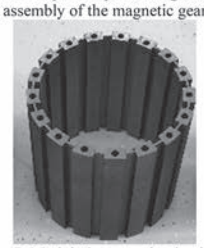

Fig. 7. Modulation rotor laminations

3:00

FG-05. A Disc-type Contra-rotating Permanent Magnet Synchronous Motor for Marine Electrical Propulsion System.

Z. Rao[1], S. Huang[1] and C. Luo[1]
1. College of Electrical and Information Engineering, Hunan University, Changsha, China

I Introduction The contra-rotating propeller (CRP) has the ability of keeping the navigation posture of the ships and recovering energy from the circumferential flow of its main propeller [1], which can raise the efficiency of propulsion system by 15%. Thus it is widely used in the electrical propulsion system of torpedoes and unmanned underwater vehicles. A double-rotor DC motor, whose stator and rotor can move in opposite direction to drive CRP, has two sets of brushes and slip rings. So the reliability and torque density are relatively low. A radial-flux PMSM with two contra-rotating rotors is presented in [2-3]. However, the output torque of one rotor is not the same as that of the other one, which poses a great challenge for motor control. A novel disc type contra-rotating motor (DTCRM)is proposed in this paper to solve the above problem. The 3-D FEA is used for modeling of the DTCRM. The two prototypes are built and the preliminary measurements of the torque and no-load output voltage are done. II Structure and Operating Principle As shown in Fig.1(a-b), the stator of DTCRM sandwiched between two PM disc rotors has a slotless toroidally wound strip-iron core and the armature coils wound in a toroidal cross fashion. And the two PM rotors are coaxially connected by CRP. The DTCRM can be regarded as an integration of two identical disc type motors being connected together, which are characterized by sharing a common winding in series. Since the two working surfaces of the stator are both fully utilized, the DTCRM has a higher torque-to-weight. The end windings are quite short, which leads to lower copper loss and higher efficiency for this topology. As shown in Fig.1 (c), the phases A and B have an opposite spatial displacement against the phase C, and thereby two synchronous contra-rotating magnetic fields(CRMF) will exist in annual air gaps if the stator winding is fed by a symmetric three-phase current. The two synchronous CRMF interact with the field generated by the magnets, then the two rotors move towards opposite direction with the same speed. III Analysis Of The DTCRM To obtain the characteristic of output torque of the two rotors, a transient-magnetic 3-D FEA with one rotor position leading the other one by 0°, 22.5°, 45°, 67.5° and 90° deg in electric angle is investigated. In these cases, the phase angle of the currents is set to such a value that the rotor with lagging position produces a maximum torque. As shown in Fig.2(a), owing to the slotless structure of the stator core, the output torque ripples of the two rotors are relatively small and the average torques of the two rotors are almost the same (20.5N.m) when they are the same position (0°). With the leading angle getting bigger, the torque of the leading rotor decreases. Its value approaches to zero when the leading angle reaches 90° deg. However, the torques of the lagging rotor are basically the same, as shown in the lower part of Fig.2(a). To acquire the relationship between the amplitude of back-EMF and the position of the two rotors, a transient-magnetic analyses of the 3-D FEA model with different rotor positions is performed. As illustrated in the Fig.2 (b), the blue lines represent the total back-EMF waveforms with one rotor position leading the other one by 22.5°, 45°and 90° deg in electric angle, respectively. The amplitude of back-EMF decreases with the growth of the leading angle, especially in 90°deg. The peak of the three-phase no-load back-EMF has a slight deviation owing to the different end length of the winding.

[1] F. Caricchi, F. Crescimbini, and E. Santini, "Basic principle and designcriteria of axial-flux PM machines having counterrotating rotors," IEEE Trans. Ind. Appl., vol. 31, no. 5, pp. 1062-1068, 1995. [2] M. Ranlof, and U. Lundin, "Finite element analysis of a permanent magnet machine with two contra-rotating rotors," Electric Power Components and Systems, vol. 37, pp. 1334–1347, 2009. [3] M. Ranlof, G. Connor, and U. Lundin, "Simulation of a radial flux Permanent magnet generator with tow contra–rotating rotors," in International Conference on Electrical Machines, Uppsala, Sweden,2008.

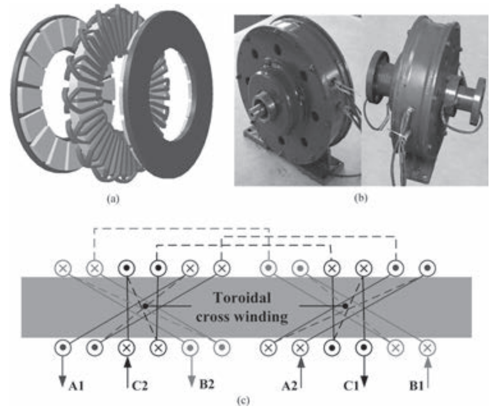

Fig. 1. (a) Construction of the DTCRM, (b) Two prototypes, (c) Stator winding arrangement.

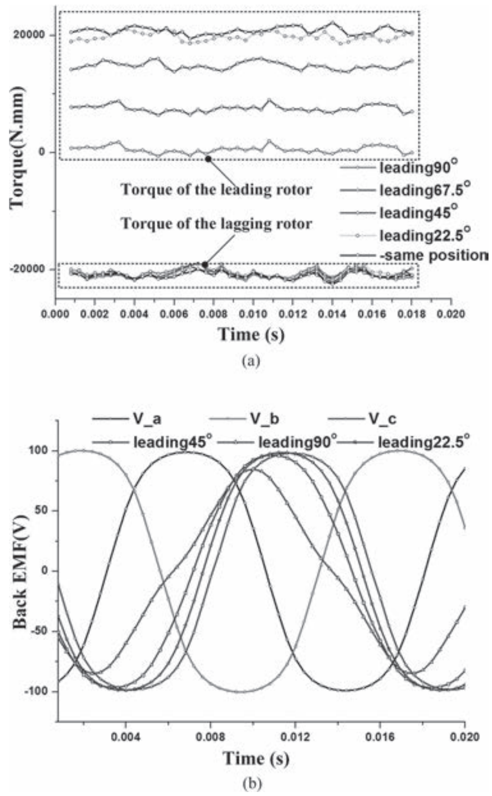

Fig. 2. (a) Output torques of the two rotors, (b) Three-phase back-EMF.

3:15

FG-06. Comparative Analysis of a Coaxial Magnetic Gearbox with a Flux Concentration Halbach Rotor and Consequent Pole Rotor Typology.

D.H. Wong[1], S. Modaresahmadi[2], *J.Z. Bird*[1] and W. Williams[2]
1. Portland State University, Portland, OR, United States; 2. University of North Carolina at Charlotte, Charlotte, NC, United States

INTRODUCTION By utilizing magnetic field space modulation magnetic gearboxes (MGs) are able to create speed amplification without any physical contact [1-3]. An example of a flux-focusing coaxial MG is illustrated in Fig. 1. This coaxial MG consists of an inner rotor 1 that contains $p_1 = 4$ pole-pairs an outer rotor 3 with p_3 =13 pole-pairs and a central ferromagnetic segment central rotor 2 that consists of $n_2 = 17$ pieces. The n_2 ferromagnetic segments serve to modulate the inner and outer rotor magnetic fields. In order to create the highest level of field coupling between the inner and outer rotors the number of ferromagnetic segments must be chosen to satisfy n_2=p_1+p_3. With this condition satisfied the rotor angular velocity relationship between each rotor is w_2p_2=w_3p_3+$w_1p_1$where the subscript denotes rotor number. If the outer rotor is fixed (ω_3 = 0) the torque will be maximized and the gearing ratio will be w1=Gw_2 where G = n_2/p_1. For the example MG shown in Fig. 1 the gear ratio is G=4.25. In order to try to increase the torque density of a MG a range of different coaxial type rotor typologies have recently been investigated [4-14]. Along with the flux focusing MG design two other coaxial radial type MG rotor typologies that have been shown to create high torque density are the flux concentration Halbach rotor typology [15] and the consequent pole triple-PM rotor MG typology [16]. In this paper, these two design typologies are compared for the first time. The objective is to provide an idealized comparative analysis of the two competing typologies and then present the experimental design and testing of the best design. ROTOR DESIGN ANALYSIS The pole combinations for both designs was selected to give a gear ratio of G = 7.5. The outer diameter and stack length was held fixed at 110mm and 75mm respectively. The fixed geometric and material properties for both designs are summarized in Table I. The flux concentration and consequent pole MG design typologies are shown in Fig. 2 and Fig. 3. Note that the consequent pole MG has a flux concentration inner rotor and consequent pole outer and central rotor. This typology increased torque. The pole combinations used for both designs are given in Table II. The consequent pole design is unique in that the slots can be used to create torque as well as the magnets. This is because $p_3 = n_3$ and $p_2 = n_2$. As an example, the inner rotor magnet poles (p_1=4) will be modulated by the n_2 = 30 ferromagnetic segments and therefore interact with the outer rotor pole pairs since p_3=n_2-p_1=26. At the same time the modulation rotor's p_2=30 pole pairs can be modulated by the outer rotor n_3=26 ferromagnetic slots to give $p_1 = p_2 - n_3$ = 4 pole pairs. In contrast the flux concentration MG typology cannot create torque interactions through the outer rotor slot numbers since $p_3 \neq n_3$. In order to provide a fair comparison between both typologies the outer rotor number of slots n_3 was kept the same. To enable the gear ratio to be equal for both typologies this then meant that the inner rotor pole pair number had to be different. This is shown in Table II. PARAMETER ANALYSIS Three key parameters were identified that have the greatest impact on the MG designs. These three radial parameters are shown in Table III. The slot width for both designs were kept equal with the magnet width. Fig. 4 and Fig. 5 show the volumetric and mass torque density values for each parameter design. It can be noted that the flux concentration MG can achieve a significantly higher torque density than the consequent pole MG typology. Table IV summarizes the design value and performance metrics. It can be noted that the the flux concentration MG was able to achieve an active region torque density that is twice that of the consequent pole design. It should be noted that higher torque densities for the consequent pole design could be achieve when using a larger outer diameter. However, for small diameter applications the authors was not able to achieve a high torque density. CONSTRUCTION The flux concentration design was further refined by adding bolt support as shown in Fig 6. The torque ripple for this design was shown to be low (0.13% at peak torque) as shown in Fig 7. Unlike the design in [15] bridges are used on the outer rotor so as to enable the magnets to be inserted more easily. The assembly rods on the outer diameter are made of non-magnetic material. This creates a flux barrier for the leakage flux. The leakage through the bridges as well as the effect of the flux barrier is clearly evident in Fig 8. The use of a 75mm axial length will decrease the torque. Using 3-D FEA the torque is shown to decrease to 107Nm (151Nm/L) from 121Nm (170Nm/L). The assembly drawing for this new type of flux concentration design is shown in Fig. 9. The full paper will present the experimental testing results for this new type of flux concentration MG as well as efficiency analysis.

[1] K. Atallah, S. D. Calverley, and D. Howe, "Design, analysis and realisation of a high-performance magnetic gear," *IEE Proc.-Electr. Power Appl.*, vol. 151, no. 2, pp. 135-143, 2004. [2] K. Atallah and D.Howe, "A Novel High-Performance Magnetic Gear," *IEEE Trans. Magn.*, vol. 37, no. 4, pp. 2844 - 2846 2001. [3] T. B. Martin, "Magnetic Transmission," USA Patent 3,378,710, 1968. [4] N. Niguchi and K. Hirata, "Cogging torque analysis of magnetic gear," *IEEE Trans. Ind. Elec.*, vol. 59, no. 5, pp. 2189-2197, May 2012. [5] L. Bronn, R.-J. Wang, and M. J. Kamper, "Development of a shutter type magnetic gear " in *Proc. 19th Southern African Univ. Power Eng. Conf.*, Johannesburg, 2010. [6] P. O. Rasmussen, T. O. Andersen, F. T. Jorgensen, and O. Nielsen, "Development of a high-performance magnetic gear," *IEEE Trans. Ind. Appl.*, vol. 41, no. 3, pp. 764-770, 2005. [7] N. W. Frank and H. A. Toliyat, "Analysis of the concentric planetary magnetic gear with strengthened stator and interior permanent magnet inner rotor," *IEEE Trans. Ind. Appl.*, vol. 47, no. 4, pp. 1652-1660, July 2011. [8] L. Shah, A. Cruden, and B. W. Williams, "A variable speed magnetic gear box using contra-rotating input shafts," *IEEE Trans. Mag.*, vol. 47, no. 2, pp. 431-438, 2011. [9] L. Jian, K. T. Chau, Y. Gong, J. Z. Jiang, C. Yu, and W. Li, "Comparison of coaxial magnetic gears with different topologies," *IEEE Trans. Magn.*, vol. 45, no. 10, pp. 4526-4529, 2009. [10] X. Liu, K. T. Chau, J. Z. Jiang, and C. Yu, "Design and analysis of interior-magnet outer-rotor concentric magnetic gears," *Jour. Appl. Physics*, vol. 105, no. pp. 07F101-07F103, 2009. [11] J. Bird, "Flux focusing magnetic gear assembly using ferrite magnets or the like," USA Patent, Publication No.: WO/2013/052516, Publication Date 11/04/2013 [12] K. K. Uppalapati, W. Bomela, J. Bird, M. Calvin, and J. Wright, "Experimental Evaluation of Low Speed Flux Focusing Magnetic Gears," *Submitted to IEEE Trans. Ind. Appl.*, no., Sept. 16-20th 2013. [13] K. K. Uppalapati, W. Bomela, J. Bird, M. Calvin, and J. Wright, "Construction of a low speed flux focusing magnetic gear," in *5th IEEE Energy Conversion Congress & Exposition,*, Denver, CO, USA, 2013. [14] V. M. Acharya, M. D. Calvin, and J. Z. Bird, "A low torque ripple flux focusing axial magnetic gear," presented at the 7th IET Inter. Conf. Power Elect. Mach. Drives, Manchester, UK, 2014. [15] D. Som, K. Li, J. Kadel, J. Wright, S. Modaresahmadi, J. Z. Bird*, et al.*, "Analysis and Testing of a Coaxial Magnetic Gearbox With Flux Concentration Halbach Rotors," *IEEE Trans. Magn.*, vol. 53, no. 11, p. Article # 8112206, 2017. [16] S. Peng, W. N. Fu, and S. L. Ho, "A Novel High Torque-Density Triple-Permanent-Magnet-Excited Magnetic Gear," *IEEE Trans. Magn.*, vol. 50, no. 11, p. Article # 8001704, 2014.

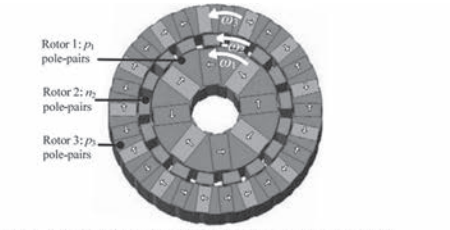

Fig. 1. Cross-sectional view of a 4.25:1 flux focusing magnetic gearbox. The inner rotor as p_1=4 pole-pairs, the outer rotor has p_3=13 pole-pairs and there are n_2 =17 ferromagnetic segments on the central rotor

TABLE I.
FIXED MAGNETIC GEARBOX PARAMETERS

Gear ratio	7.5
Nd-Fe-B magnet grade	N40
Laminated rotor steel grade	M19
Stack length, d	75 mm
Active region outer diameter, r_{o3}	110 mm
Airgap between rotors	0.5mm
Magnet retaining lips	1mm

TABLE II.
MAGNETIC GEARBOX CONFIGURATION

Description		Flux concentration	Consequent pole
Inner rotor	Pole pairs, p_1	2	4
	Slots, n_1	4	8
Modulation rotor	Pole pairs, p_2	-	30
	Slots, n_2	15	30
Outer rotor	Pole pairs, p_3	13	26
	Slots, n_3	26	26

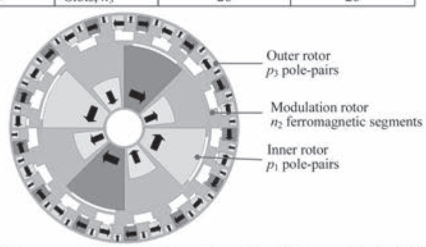

Fig. 2. Flux concentration magnetic gearbox with a 7.5:1 gear ratio. Lamination bridges are used on each rotor to minimize part count. The pole combination is given by $(p_1, n_2, p_3) = (2, 15, 13)$

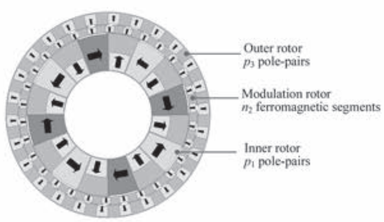

Fig. 3. Consequence pole MG design with a triple PM rotor typology. A 7.5:1 gear ratio. Lamination bridges are used on each rotor to minimize part

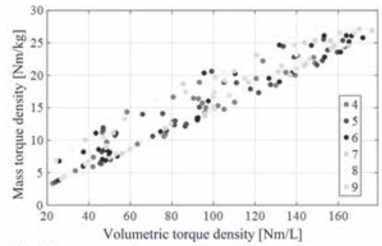

Fig.4 Flux concentration magnetic gearbox geometry sweep results.

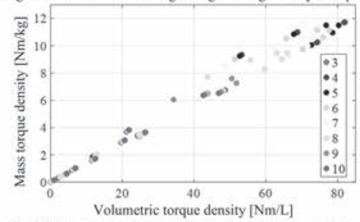

Fig 5. Consequent pole magnetic gearbox geometry sweep results.

TABLE I.
GEOMETRY SWEEP PARAMETERS

Parameter	Sweep range [mm]
Inner rotor inner radius, r_{i1}	5, 10. . 30
Inner rotor outer radius, r_{o1}	10, 15.. 40
Modulation rotor radial length, l_2	3, 4.. 10

TABLE II.
SUMMARY OF HIGHEST TORQUE DENSITY DESIGNS

Parameter	Flux concentration	Consequent pole	Units
Inner rotor inner radii, r_{i1}	10	15	mm
Inner rotor outer radii, r_{o1}	35	40	mm
Modulator radial length, l_2	7	3	mm
Inner radii of outer rotor	45	44.5	mm
Peak torque	130.4	61.2	Nm
Volumetric torque density	176.5	82.9	Nm/L
Mass torque density	26.9	11.8	Nm/kg

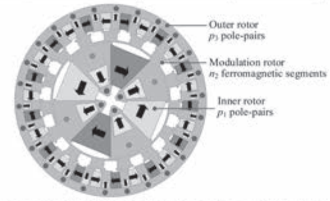

Fig 6. Flux concentration Halbach magnetic gearbox with supporting rods added. Support rods on outer rotor and inner radii or inner rotor are made of non-magnetic 316 stainless steel (blue color). Support rods on outer radii side of inner rotor (pink in color) are made of magnetic 416 stainless steel.

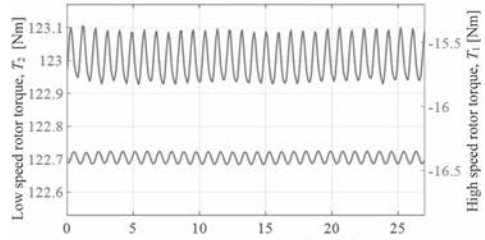

Fig 7. Torque on both the high speed and low speed rotors

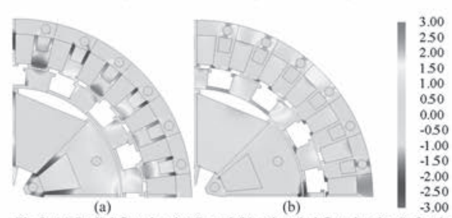

Fig 8. (a) Radial flux density B_r and (b) azimuthal flux density B_θ for the flux concentration Halbach design with reduced B_r values

Fig. 9. Mechanical assembly drawing for the flux concentration design.

3:30

FG-07. A Novel Design Philosophy for Low-Stiffness Magnetic Levitation Gravity Compensation.

H. Zhang[1], Y. Zhou[1], B. Kou[1] and Z. Zhu[2]
1. Harbin Institute of Technology, Harbin, China; 2. University of Sheffield, Sheffield, United Kingdom

I. Introduction This paper presents a novel design philosophy by which the low stiffness performance for the magnetic levitation gravity compensation can be obtained easily. Generally, the absolute levitation is desired in many ultra-precision positioning systems, because the vibration disturbance can be effectively isolated. However, it is very difficult to obtain the low stiffness performance due to the serious nonlinearity of the passive force between two permanent magnets [1-4]. The proposed design method is based on the principle of stiffness counteraction. The magnetic levitation gravity compensator in this paper is combined with two passive units whose stiffness curves are just the opposite, so the resultant stiffness is low enough while the two levitation forces are superimposed. II. Topology and Principle The configuration of the proposed magnetic levitation gravity compensator (MLGC) is shown in Fig. 1(a). The passive levitation force is produced by the interaction between the mover PM rings and the stator PM ring. The active levitation force is produced by the interaction between the mover PM rings and the circumferential current. To realize a low passive levitation force stiffness, the concept of stiffness counteraction is adopted in the proposed MLGC. Actually, the proposed MLGC in Fig. 1 is composed of two passive magnetic levitation units that share the same stator PM ring, as shown in Fig. 1(b) and 1(c). The passive levitation force characteristic curves for the two units are shown in Fig. 1(d). For Unit A, the passive levitation force has a maximum value in the symmetrical position. On the contrary, there is a minimum value for Unit B in the same position. Therefore, the stiffness characteristics for the two units are just the opposite, so the resultant stiffness in theory could be very low, as shown in Fig. 1(e). III. Model Discussion Fig. 2(a) shows the magnetic field intensity produced by a magnetic ring with radial magnetization. Considering the volume integral operation, the charge model is more complex if the volume charge is not zero. Furthermore, multiple integrals, e.g. quadruple or quintuple integral, is also required when calculating the force, which is time consuming. Therefore, the equivalent current method is more suitable for modeling the cylindrical MLGC, in which the PM ring with radial magnetization is contained. Additionally, the errors due to some common assumptions should be considered when modeling the MLGC. To make a quantitative analysis, the MLGC is compared with a linear PM synchronous machine. Fig. 2(b) shows the average points of the PMs in MLGC and in linear machine. The average working points in linear machine are obviously higher than the ones in MLGC. Therefore, the average working point needs to be considered when calculating the magnetic field and the levitation force of MLGC. IV. Design and Optimization To reduce the passive levitation force stiffness as much as possible, two approximate opposite stiffness characteristics are required. From the characteristic curves (not given in the digest due to figure limits), the air-gap length (g) is the most important parameter for Unit A, which strongly impact the maximum stiffness. When the air-gap length of Unit A varies from 5mm to 15mm, the maximum stiffness changes from 2648 N/m to -109 N/m. Compared with g, other parameters contribute less influence on the maximum stiffness. However, the passive levitation force is strongly impacted by other parameters. The force level of Unit B is higher than the one of Unit A at the same air-gap length. The design flow chart for the MLGC is shown in Fig. 2(c), which consists of two blocks. The first block is based on the ideal equivalent current model. The function of the first block is to obtain the approximate parameters quickly. The second block is based on the finite element simulation in which the ideal mathematical model is improved, the zero-stiffness position is adjusted and the accurate values for all parameters are determined. V. Conclusion In this paper, a novel design philosophy for low-stiffness magnetic levitation gravity compensation is proposed. Based on the design philosophy, a new magnetic levitation gravity compensator is put forward, analyzed and designed. Compared with previous topologies, the superiorities of the new MLGC are as follows, (1) Based on the principle of counteraction, the zero-stiffness performance within the effective stroke can be theoretically obtained. (2) The stiffness for each passive levitation unit is not strictly limited. The resultant low stiffness can be obtained, as long as two stiffness characteristics counteract with each other. In other words, the design flexibility is greatly improved. (3) There is only one radially magnetized PM ring, which is difficult to process and very expensive. In addition, the active levitation force density can be improved, because the size of the radially magnetized PM ring is relatively large and close enough to coil in the proposed MLGC. (4) The space for the coil frame is large enough due to the single-layer air gap, which is beneficial for the cooling design.

[1] W. Robertson, B. Cazzolato, and A. Zander, "A multipole array magnetic springs," IEEE Trans. Magn., vol. 41, no. 10, pp. 3826–3828, Oct. 2005. [2] S. A. J. Hol, E. Lomonova, and A.J.A. Vandenput, "Design of a magnetic gravity compensation system," Precision Eng., vol. 30, no. 3, pp. 265–273, Jul. 2006. [3] Y. M. Choi, M. G. Lee, D. G. Gweon, and J. Jeong, "A new magnetic bearing using Halbach magnet arrays for a magnetic levitation stage," Rev. Sci. Instrum., vol. 80, no. 4, pp. 045106-1–045106-9, Apr. 2009. [4] He Zhang, Baoquan Kou, Yinxi Jin, and Hailin Zhang, "Modeling and analysis of a new cylindrical magnetic levitation gravity compensator with low stiffness for the 6-DOF fine stage," IEEE Trans. Ind. Electron., vol. 62, no. 6, pp. 3629–3639, Jun. 2015.

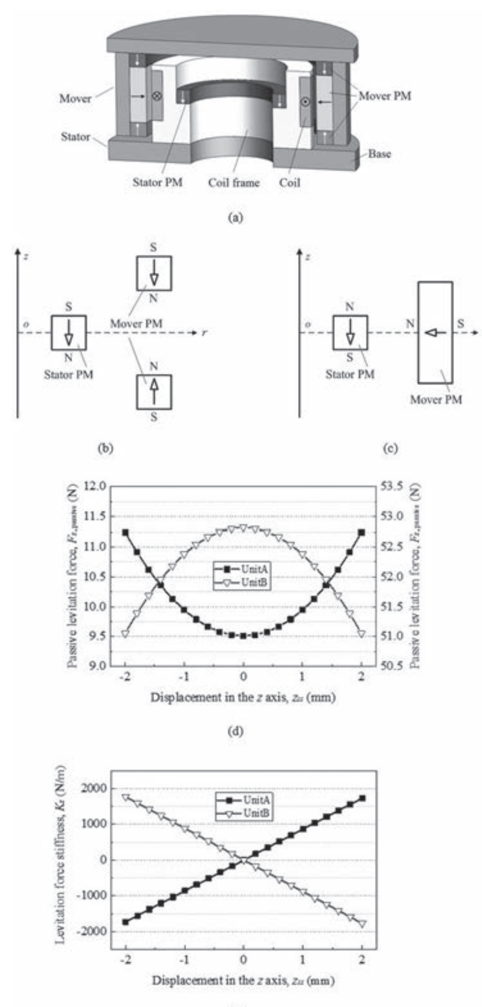

Fig. 1. Configuration and performance of the novel magnetic levitation gravity compensator. (a) 3-D sectional view. (b) Unit A. (c) Unit B. (d) Passive levitation force curves. (e) Passive levitation force stiffness curves.

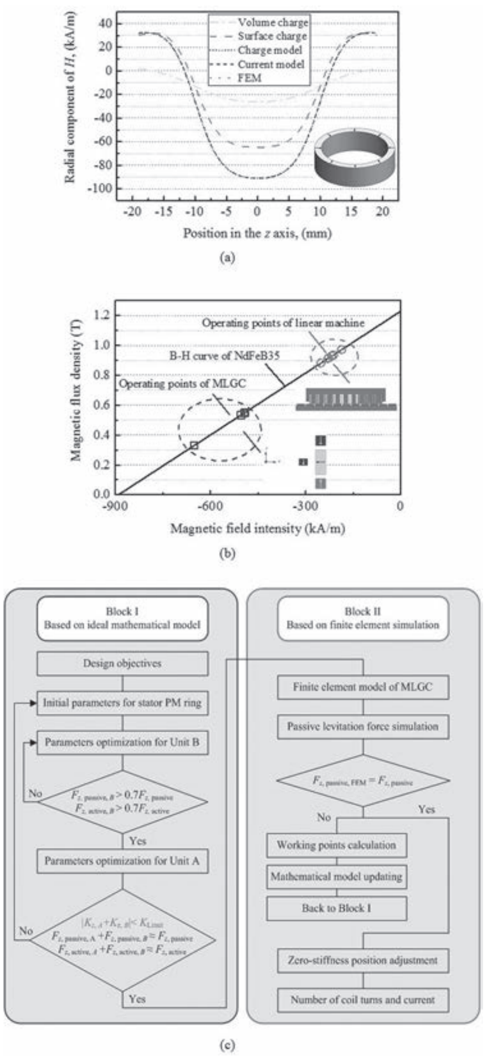

Fig. 2. Modeling and design method. (a) Magnetic field intensity of the magnetic ring with radial magnetization. (b) The average points of the PMs in MLGC and in linear PM synchronous machine. (c) Design flow chart.

3:45

FG-08. Design of a Novel Halbach-Array Permanent Magnet Motor for Electric Submersible Pumps.

S.F. Rabbi[1] and M. Rahman[2]
1. Electrical and Computer Engineering, Memorial University of Newfoundland, St. John's, NL, Canada; 2. Electrical and Computer Engineering, Memorial University of Newfoundland, St. John's, NL, Canada

Electric submersible pumps (ESPs) are widely used as downhole artificial lift devices in oil and gas production units for improved oil recovery [1]. An ESP is a motor/pump configuration comprised of multi-stage impellers driven by an electric ac motor. Since the inception of ESPs, squirrel-cage rotor induction motors have been the de-factor standard in ESP drive systems. The diameter of an ESP motor is restricted by the outside diameter of the casing which is between 4 and 10 inches [2]. Submersible motors have a small outer diameter and a long axial length to meet the required torque demand. In the case of ESPs, these motors are modular in nature and comprised of multiple rotors. The multi-rotor assembly is supported by intermediate bearings between consecutive rotors [2]. There are two types of most widely used submersible induction motors: IM5 and IM10 [2]. Each of the rotors in IM5 and IM10 are rated as 5-HP and 10-HP, respectively. However, submersible motors operate in a hostile environment and experience severe temperature, high pressure and the presence of debris. Due to its long axial length, submersible motors are often subjected to severe torsional vibration resulting in mechanical failures such as broken rotor bars, shaft breakdowns and bearing failures [2]-[4]. Brushless permanent magnet motors (PMMs) have been recently introduced in the market for use in ESPs which provides better efficiency, smaller dimensions, wide operating range, lower heat generation and superior performance than same size submersible IMs [2],[5]-[6]. Due to the limitation in thermal stability, high power brushless PMMs are typically designed to fit inside a large diameter casing to provide better cooling and avoid saturation [2]. In offshore oil and gas, drilling is expensive and sometimes it is not feasible to drill a well wide enough that can accommodate the brushless PM submersible motor. Thus, submersible induction motors are still the de-facto standard for high power ESPs. In recent years, due to the advancement in rare earth permanent magnet materials, neodymium-boron-iron (Nd-B-Fe) magnets with the addition of dysprosium can handle temperature up to 200^0C [7]. The significant progress in polarization of sintered magnets have made it possible to achieve various types of magnetization in the rotor magnets including radial, parallel, continuous ring and halbach-arrray [8]-[11]. This paper presents the design of a novel permanent magnet submersible motor that is more compact and light-weight than the existing ESP motors. Fig. 1a illustrates the axial view of a 3-phase 6-pole 12 kW/rotor prototype permanent magnet submersible motor. The outer diameter of the stator is 95 mm. The axial length of the stator is 600 mm. The stator is equipped with an integral slot distributed winding. Its back-iron is made of low loss laminated steel with a saturation flux density higher than 2.0 T. The thickness of the lamination is 0.1mm. The stator is skewed to reduce the torque ripple. The length of the airgap is selected as 1 mm. Fig. 1b illustrates the distribution of magnetic flux density inside the motor. The rotor contains a cylindrical ring made of rare earth permanent magnetic material. The ring is magnetized as a continuous halbach array that intensifying the field outside of the cylinder towards the air-gap while minimizing the magnetic field inside the cylindrical ring. Due to this special polarization of the magnets, the motor requires less/no back iron in the rotor. Thus, the motor becomes more compact and light-weight. It also allows more room for the stator windings and return back-iron. The halbach-array arrangement provides more torque per unit rotor length than the available brushless dc permanent magnet submersible motors. It also reduces the outer diameter of the stator, making the motor more slimmer to be able to fit inside offshore subsea wells. Figs. 2a and 2b show performances of the prototype submersible permanent magnet motor. The input dc voltage is considered 400 V. The maximum AC line current is 40 A (rms). This limits the peak current density of the stator windings to 4 A/mm^2. The efficiency and power factor maps of the motor with one rotor are displayed in Figs. 2a and 2b, respectively. The control strategy for the motor is selected as the maximum torque per amp control. The rated speed for the motor is 4000 rpm. The maximum operating speed of the motor is 5500 rpm. The operating zone for the motor is shown in Fig. 2a. The motor is capable to operate with a high efficiency (>96%) over the entire operating region. The efficiency reaches to its peak when the motor is running at a speed over 3000 rpm with a load torque between 50% of the rated torque and rated torque. The motor can operate at the constant torque mode with a rotor speed up to 4250 rpm. It operates in the constant power mode when the speed becomes higher than 4250 rpm. The power factor is over 0.95 in the entire operating zone, and it remains high over a wide range of the load torque. Thus, the designed permanent magnet submersible motor can be driven efficiently with a high power factor for ESP systems. In comparison to the existing 4-inch submersible permanent magnet motors, the proposed motor has higher efficiency, higher torque density, more than 50% shorter in length and has a very high power quality.

1. O. J. Romero and A. Hupp, "Subsea electrical submersible pump significance in petroleum offshore production," *ASME Journal of Energy Resources Technology,* vol. 136, no. 1, pp. 012902, September 2014 2. T. R. Brinner, R. H. McCoy and T. Kopecky, "Induction versus permanent-magnet motors for electric submersible pump field and laboratory comparisons," *IEEE Transactions on Industry Applications,* vol. 50, no.1, pp. 174-181, January 2014 3. C. Di, X. Bao, H. Wang, Q. Lv and Y. He, "Modeling and analysis of unbalanced magnetic pull in cage induction motors with curved dynamic eccentricity", *IEEE Transactions on Magnetics*, Vol. 51, No. 8, pp. 8106507, August 2015. 4. Y. Fang, X. Bao, Q. lv, X. Cheng and Y. He, "Analysis of Electromagnetic Force Distribution on End Winding of Electrical Submersible Motor During Starting Transient Operation", *IEEE Transactions on Magnetics*, Vol. 49, No. 10, pp. 5341 - 5345, October 2013 5. V. Pavlenko, "Permanent magnet synchronous motor (PMSM)-new type of drives for submersible oil pumps", in *proceeding of the 2008 SPE Russian Oil & Gas Technical Conference and Exhibition*, Moscow, Russia, October 28-30, 2008. 6. J. Liu, T. A. Nondahl, P. B. Schmidt, S. Royak and T. M. Rowan, "Generalized stability control for open loop operation of motor drives", *IEEE Transactions on Industry Applications,* vol. 53, no.3, pp. 2517 – 2525, May/June 2017. 7. M. P. Thompson, E. Chang, A. Foto, J. G. Citron-Rivera, D. Haddad, R. Waldo and F. E. Pinkerton, "Grain-Boundary-Diffused magnets: the challenges in obtaining reliable and representative BH curves for electromagnetic motor design", *IEEE Electrification Magazine*, vol. 5, no. 1, pp. 19-27, March 2017. 8. Y. Sheng, et. al., "Design of Novel Shaftless Pump-Jet Propulsor for Multi-Purpose Long-Range and High-Speed Autonomous Underwater Vehicle", *IEEE Transactions on Magnetics*, vol. 52, no. 7, pp. 7403304, July 2016. 9. L. Yang, S. L. Ho, W. N. Fu and W. Li, "Design optimization of a permanent magnet motor derived from a general magnetization pattern", *IEEE Transactions on Magnetics*, vol. 51, no. 11, pp. 7209704, Nov. 2015. 10. S. F. Rabbi and M. A. Rahman, "Equivalent Circuit Modeling of a Hysteresis Interior Permanent Magnet Motor for Electric Submersible Pumps", *IEEE Transactions on Magnetics*, Vol. 52, No. 7, pp. 1-4, July 2016. 11. S. F. Rabbi, P. Zhou and M. A. Rahman, "Design and Performance Analysis of a Self-Start Radial Flux Hysteresis Interior Permanent Magnet Motor", *IEEE Transactions on Magnetics*, Vol. 53, No. 11, pp. 1-4, November 2017.

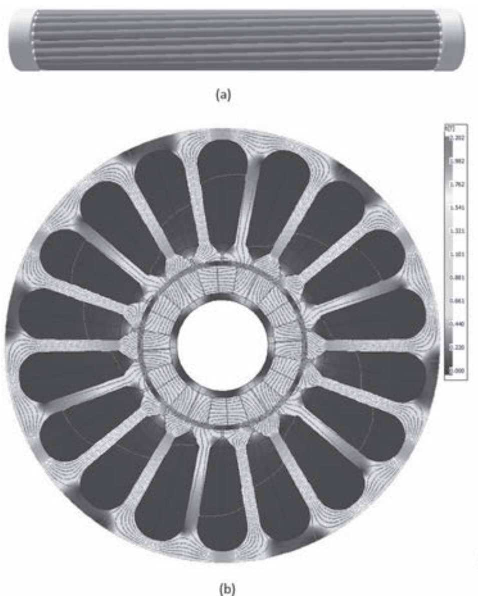

Fig. 1. (a) Axial view of the motor and (b) Flux density distribution inside the motor.

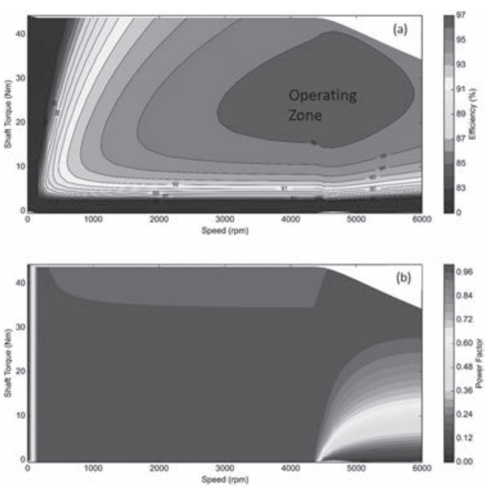

Fig. 2. (a) Efficiency contour of the motor and (b) Power factor map of the motor.

4:00

FG-09. Modeling and Analysis of Suspension Force of a New Bearingless Reluctance Machine with Independent DC Bias Winding.

L. Yu[1], Z. Zhang[1], Y. Shi[1] and W. Lu[1]
1. Department of Electrical Engineering, Nanjing University of Aeronautics and Astronautics, Nanjing, China

I.INTRODUCTION The bearingless switched reluctance machine (BSRM), free from the mechanical bearings, has advantage of the robust structure, and is suitable for operating in the harsh environment [1]. However, the torque control is tightly coupled with the suspension force control, and the operating point of the BSRM has to be selected to be in compromise between torque and suspension force, which reduces the power density. Meanwhile, the suspension windings are energized by turns according to the conducting phases, thus the BSRM faces the challenge of high-frequency suspension current control in high-speed operation. The rotor angular position detection is indispensable for feedback to the suspension force controller. With an independent field winding in stator, which functions as a dc bias winding, the bearingless doubly salient electro-magnetic machine (BDSEM) exhibits decoupling characteristics. The suspension force control can be independent of rotor angular position detection which increases the reliability [2], [3]. In this paper, the suspension characteristics of BDSEM are analyzed. A prototype BDSEM and controller are developed, and the experimental results are given to verify the analysis. II.CONFIGURATION AND OPERATION PRINCIPLE *A.Configuration* Fig. 1 shows the configuration of the proposed BDSEM. It has the advantages of robust structure. The three phase armature windings W_{ma}, W_{mb}, W_{mc}, are wound around every stator pole. A set of independent dc bias winding W_{dc} wound across three stator poles consists of four coils connected in series. It provides the magnetic flux which is the basis of torque generation and also the basis of suspension force generation. The suspension windings W_{sx} and W_{sy} consist of two coils each. *B.Suspension Force Generation* When the rotor angle is 0^o as shown in Fig. 2 (a), the dominant bias flux ψ_b is generated by the bias current I_{dc}, and the suspension flux ψ_{sy} generated by the suspension current I_{sy} is superimposed upon it. The air gap flux density in the upper half is increased, while the flux density in the bottom half is decreased as shown in Fig. 3. The suspension force is generated along the positive *Y*-axis. The positive suspension force is also generated along the *Y*-axis when the rotor angle is 22.5^o, as shown in Fig. 2 (b). The direction of the suspension force is independent of the rotor angle. III.PERFORMANCE ANALYSIS *A.Mathematical Model* Fig. 4 shows the magnetic equivalent circuit (MEC) model of the BDSEM, neglecting the magnetic saturation. $2N_{dc}I_{dc}$ is the magnetomotive force (MMF) of dc bias winding, $N_{sx}I_{sx}$, $N_{sy}I_{sy}$ are the MMF of suspension windings. N_mI_{ma}, N_mI_{mb}, and N_mI_{mc} are the MMF of armature windings. G_1,…, G_{12} are the permeance of air gap. The standard angle control (SAC) method is adopted to produce the torque [4], and the magnitude of the phase current is I_m. When the rotor angle is $0^o \le \theta_r < 15^o$, the air gap flux density B_1 corresponding to G_1 is described by Eq.1, where μ_0 is the vacuum permeability, and L_{gap} is the air gap length. The suspension force is described by Eq.2, where L is the core length and R is the rotor radius. The composition of the force along the X- and Y-axis is described by Eq.3. The total suspension force is obtained by Eq.4. The corresponding coefficients are shown in Eq.5 to Eq.9. *B.Suspension Force Characteristics* Fig. 5 shows the *Y*-axis suspension force predicted both by the mathematical model and the finite element method (FEM). The suspension force is almost held constant in different rotor position. Thus the angular position feedback to the suspension force controller is not required. The suspension force control is significantly simplified, particularly in the high speed operation of the BDSEM. The results predicted by mathematical model agree well with FEM. The self-inductance of the suspension winding changes slightly as shown in Fig.6. The mutual-inductance among the suspension and armature windings is almost zero. IV.EXPERIMENTAL RESULTS A prototype BDSEM and its suspension current controller are designed and developed to verify the suspension characteristics. The experiments are conducted as shown in Fig.7. The *Y*-axis suspension force is linearly increased with increase of the suspension current I_{sy} as shown in Fig.8, considering the rotor gravity. The experimental results agree well with the results predicted FEM. When the bias current is increased appropriately, the suspension force is increased with the same suspension current. Fig.9 shows the waveforms of the suspension current and radial displacement. V.Conclusion In this paper, the new BDSEM is proposed and implemented. The suspension characteristics are investigated. The mathematical model of suspension force is deduced. The suspension force is independent of the rotor position and the suspension force control is simplified, particularly for high speed operation. The experimental results verify that the rotor can be levitated steadily with the different dc bias current.

[1]M. Takemoto, H. Suzuki, A. Chiba, T. Fukao and M. A. Rahman, "Improved analysis of a bearingless switched reluctance motor," *IEEE Transactions on Industry Applications*, vol. 37, no. 1, pp. 26-34, Jan/Feb 2001. [2]Li Yu, Zhuoran Zhang, Wenjing Lu and Yuke Shi, "Influence of rotor pole width on suspension performance of a new bearingless doubly salient electro-magnetic machine," *IEEE Workshop on Electrical Machines Design, Control and Diagnosis (WEMDCD)*, Nottingham, 2017, pp. 101-106. [3]W. Lu, Z. Zhang, L. Yu and Y. Shi, "Influence of the armature current on suspension characteristics of a new bearingless doubly salient electro-magnetic motor," *IEEE Transportation Electrification Conference and Expo, Asia-Pacific (ITEC Asia-Pacific)*, Harbin, 2017, pp. 1-5. [4] Y. Wang, Z. Zhang, R. Liang, W. Yuan and Y. Yan, "Torque Density Improvement of Doubly Salient Electromagnetic Machine With Asymmetric Current Control," *IEEE Transactions on Industrial Electronics*, vol. 63, no. 12, pp. 7434-7443, Dec. 2016.

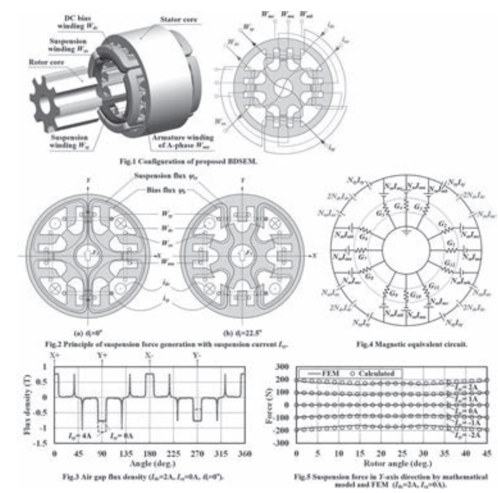

Fig. 1.

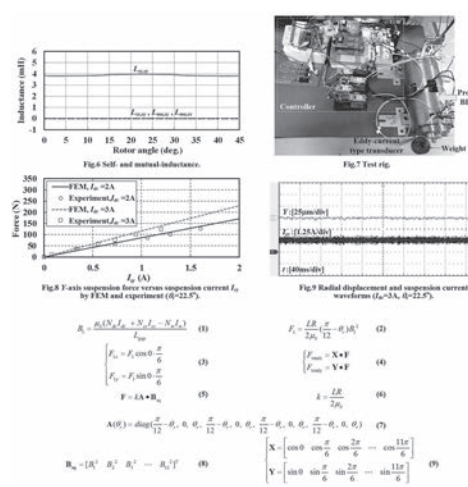

Fig. 2.

4:15

FG-10. The influences of lever arm on the stability of a quasi-zero stiffness magnetic levitation vibration isolation system.

N. Kamaruzaman[1], M. Ghayesh[1], B. Cazzolato[1], A. Zander[1] and W. Robertson[1]
1. School of Mechanical Engineering, The University of Adelaide, Adelaide, SA, Australia

Stable quasi-zero stiffness (QZS) magnetic levitation is a key to isolating ultra-low frequency vibration [1]. QZS systems are defined by nonlinear force-displacement relationships in which the operating position is at or near points of zero stiffness. While Earnshaw's theorem [2] governs the stability of a magnetic levitation system in the translational directions, no such theory has been deduced for the rotational degree-of-freedom (DOF). Due to cross-axis coupling, total elimination of active controllers for contactless stable operation is not possible [3]. However, it is anticipated that the system would be less dependent upon the controllers as the number of unstable DOF is minimised. A method to improve the passive stability of the system in the rotational DOF without adding significant stiffness in the translational DOF is by introducing lever arm [4]. Figure 1(a) shows the schematic of the proposed QZS magnetic spring system. The lever arm is a function of the fixed, normalised vertical gap *e* between the levitating magnets, and the normalised horizontal gap *p* between the side-by-side bottom magnets. A single plane constraint was imposed for the analysis of the static behavior of the system with varying horizontal gap *p*. Using the MATLAB© function created by Robertson [4] based on the analytical force expression of Akoun and Yonnet [5], the resultant force exerted on the levitating assembly was computed as the superposition of forces between the attractive and repulsive magnet pairs. Consequently, using a small angle approximation of magnet rotation [3], the moment around the out-of-plane axis was calculated as the cross product of the force and the lever arm. Typically, a QZS magnetic spring system has a quadratic-like force-displacement curve in which the minimum force value corresponding to the QZS position is obtained when the levitating assembly is operated midway between the top and bottom fixed magnets [6]. However, with non-zero horizontal gap *p*, the QZS position shifts towards the bottom fixed magnets, and the load bearing force depreciates (Figure 1(b)) due to the loss of some magnetic interactions between the magnets on opposite side. Investigation into the stability of the out-of-plane and horizontal direction due to the vertical displacement suggests that *p* has little effects on the translational stability of the system, particularly upon operating within close proximity to the QZS position. This ensures that there is no reduction in the range of isolation frequency for the translational DOFs. In contrast, Figure 2 highlights that the rotational stability improves significantly with the lever arm especially for negative vertical displacement. However, with greater stability, the rotational resonance frequency increases and thus, decreases the range of frequency over which vibration attenuation occurs. Therefore, appropriate level of stability must be chosen based on the system requirement. The analyses presented so far considered the centre of mass of the levitating assembly as the centre of rotation. It is assumed that the mass of the rod linking the levitating magnets is negligible, and the levitating magnets are point mass. In practice however, it may be difficult to place the payload at the exact geometric centre of the levitating assembly, especially involving irregular shapes. To examine the effects of non-centred payload position (the pink cube in Figure 1(a) represents the payload) on the rotational stability of the system due to the vertical displacement, the rotational natural frequency versus load force were plotted for different payload position. It is seen that with a relatively small payload position offset (only in the horizontal direction), the rotational DOF remains stable for non-zero horizontal gap *p*. However, as the offset increases to a certain value, even with large *p*, rotational instability appears for positive vertical displacement. As the levitating assembly moves upward, the repulsion force decreases, resulting in a reduction of the moment. Furthermore, with large payload position offset, the centre of rotation is shifted further away from the geometric centre of the levitating assembly, which causes large imbalance between the system clockwise moment and that of the counter-clockwise. In conclusion, the addition of lever arm provides stability in the rotational DOF without deterring the realisation of QZS characteristics in the translational axes. Dynamic analysis will emphasise on identifying the influences of the lever arm on the cross-axis coupling to provide a complete picture of the planar stability of the system.

[1] W. Robertson, M. R. F. Kidner, B. Cazzolato, and A. Zander, "Theoretical design parameters for a quasi-zero stiffness magnetic spring for vibration isolation," *Journal of Sound and Vibration,* vol. 326, pp. 88-103, 2009. [2] R. Bassani, "Earnshaw (1805–1888) and passive magnetic levitation," *Meccanica,* vol. 41, pp. 375-389, 2006. [3] W. Robertson, B. Cazzolato, and A. Zander, "Theoretical analysis of a non-contact spring with inclined permanent magnets for load-independent resonance frequency," *Journal of Sound and Vibration,* vol. 331, pp. 1331-1341, 2012. [4] W. Robertson, "Modelling and design of magnetic levitation systems for vibration isolation," Doctor of Philosophy Thesis, School of Mechanical Engineering, The University of Adelaide, 2013. [5] G. Akoun and J. P. Yonnet, "3D analytical calculation of the forces exerted between two cuboidal magnets," *IEEE Transactions on Magnetics,* vol. 20, pp. 1962-1964, 1984. [6] T. Zhu, "Six degrees of freedom active vibration isolation using quasi-zero stiffness magnetic levitation," Doctor of Philospohy Thesis, School of Mechanical Engineering, The University of Adelaide, 2013.

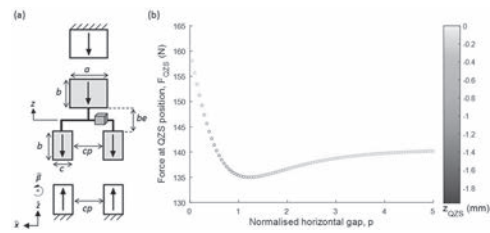

Fig. 1. (a) Schematic of a quasi-zero stiffness magnetic spring system. The top magnets have the size ratio of *b*/*a* = 0.4, while the width *c* of the bottom magnets equals *a*/2. Bold arrows denote direction of magnetisation. The pink cube represents the payload with a slight position offset from the centre of mass of the levitating assembly. (b) Force at QZS position versus the normalised horizontal gap *p*. The vertical QZS position z_{QZS} changes with *p*.

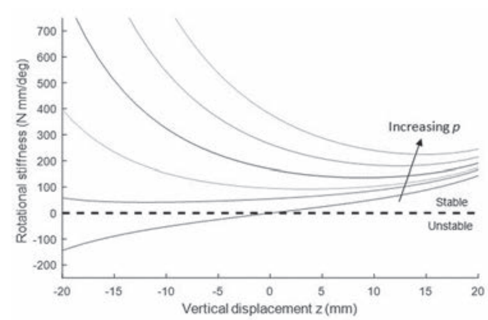

Fig. 2. Rotational stiffness due to vertical displacement for normalised horizontal gap *p* from 0 to 5. The levitating assembly was assumed to be horizontally-centred with zero payload position offset.

4:30

FG-11. Design and Analysis of a Double Stator Halbach Permanent Magnet Bearingless Brushless DC Motor.

Y. Yuan[1], Y. Sun[2], F. Yang[1] and Y. Huang[1]
1. School of Electrical and Information Engineering, Jiangsu University, Zhenjiang, China; 2. School of Power Engineering, Nanjing Institute of Technology, Nsnjing, China

Introduction: High integration, low loss and high-reliability are the main development trends of flywheel energy storage [1]. Magnetic bearings (MB) [2] with several advantages, such as eliminating of a lubrication system, friction-free operation and low power consumption can be promoted in various practical industrial applications, especially in flywheel batteries. Brushless DC motor is widely used because of its high efficiency and simple control. The bearingless brushless DC motor (BBLDC) has the advantages of the above advantages, while it has the characteristics of small friction loss [3]. The problem of strong coupling between the magnetic field and the torque magnetic field can be solved by the double stator bearingless brushless DC motor (DS-BBLDC) [4]. Halbach permanent magnet structures are suitable for use in permanent magnet motors because they enhance the unidirectional magnetic field [5]-[6]. Thus, this study presents the first prototype of a Double Stator Halbach Permanent Magnet (DSHPM) BBLDC with the advantages of weak coupling and simple control. The structure, operation principle and main electromagnetic characteristics of the DSHPM BBLDC are analyzed. The proposed motor exhibits the following advantages: 1) High integration. The motor can not only realize the problem of energy conversion, but also realize two degrees of freedom (2-DOF) suspension control. 2) Low loss. The biased flux is provided by the permanent magnet which leaves out the extra biased winding correspondingly. 3) Weak coupling. The application of halbach structure can make motor rotor yoke adopt non-magnetic material to completely isolate torque system and suspension system. 4) Favorable controllability. The dual-stator structure of the torque system and suspension system separately control, to achieve a simplified control. New Machine: The structure of DS-HAL-BBLDC is shown in Fig.1. As shown in Fig.1(a), the DS-HAL-BBLDC is primarily made of an inner stator, the permanent magnets of halbach, a rotor and an outer stator. The rotor consists of three layers. The halbach permanent magnets can produce an inward magnetic field. So the rotor is divided into two layers. The inner layer is a magnetic isolating material used to isolate the torque magnetic field and the suspended magnetic field. The outer layer provides the magnetic path of the silicon steel sheet for the suspended magnetic field. The inner stator and the permanent magnet consist of an 8 pole 12 slot brushless DC motor, which is the torque system. A suspension subsystem is composed of the two outer stators with four poles structure and the rotor outer layer. The suspension system can produce 2-DOF suspension. The bias magnetic path provided by the outer stator permanent magnet is shown in fig.1(b). Fig.1(c) shows the torque system of a phase winding connection. The windings are arranged in a centralized manner, with the other two similar. Fig.1(d) shows the control of magnetic circuit. Taking the y-direction magnetic circuit as an example, starting from one pole to the other pole via the stator yoke and forming a closed loop through the rotor from the other pole Main Electromagnetic Characteristics: The operation mechanism of the motor is verified as shown in Fig.2. The static magnetic density of the motor is shown as shown in Fig.2(a). It can be seen that the magnetic field is evenly distributed on the outer stator and the reloaded outer layer. Fig.2(b) changes in suspension force when the motor suspension current is 0A to 4A. The suspension force increases linearly with the increase of current, which proves that the motor can produce a stable suspension force. Fig.2(c) and (d) are the air magnetic density of the y positive direction and the y negative direction respectively. With the increase of current, the magnetic density in the positive direction of y increases and the magnetic density in the negative direction of y decreases. It is that prove the magnetic field generated by the suspension coil has good controllability.

[1] Y. Yuan, Y. Sun and Y. Huang, "Radial force dynamic current compensation method of single winding bearingless flywheel motor," IET POWER ELECTRNICS, vol.8, no.7, pp. 1224-1229, 2015. [2] Z. Su, D. Wang, J. Chen, X. Zhang and L. Wu, "Improving Operational Performance of Magnetically Suspended Flywheel With PM-Biased Magnetic Bearings Using Adaptive Resonant Controller and Nonlinear Compensation Method," IEEE Transactions on Magnetics, vol.26, no.7, pp. 1-5, 2016. [3] M. Ooshima, C. Takeuchi, "Magnetic Suspension Performance of a Bearingless Brushless DC Motor for Small Liquid Pumps." IEEE Transactions on Industry Applications, vol.47, no.1, pp.72-78, 2011. [4] Y. Qin, H. Zhu, C. Zhao, "Design and Analysis of Five-Phase Double-Stator Bearingless Brushless DC Motor," Vehicle Power and Propulsion Conference. IEEE, pp.1-6, 2016. [5] Q. Z. Zhu, D. Howe, "Halbach permanent magnet machines and applications: a review," IEE Proceedings - Electric Power Applications, Vol.148, No.4, pp.299-308, 2001. [6] P. R. Praveen, H. M. Ravichandran and S. T. V. Achari, "A Novel Slotless Halbach-Array Permanent-Magnet Brushless DC Motor for Spacecraft Applications," IEEE Transactions on Industrial Electronics, Vol.59, no.9, pp.3553-3560, 2012.

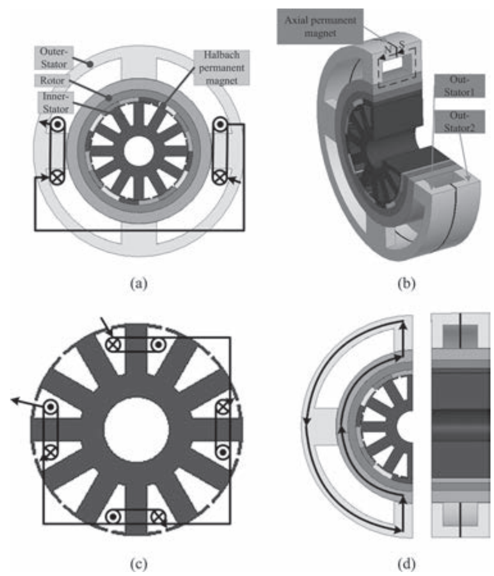

Fig. 1. Structure of HSPMB BSRM. (a) Basic structure. (b) Biased flux. (c) Winding configuration of hybrid inner stator. (d) Control flux.

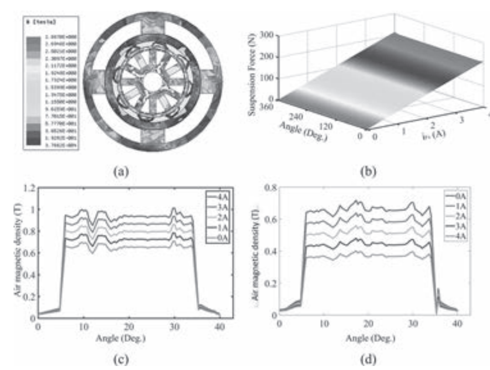

Fig. 2. Main electromagnetic characteristics. (a) Static magnetic density distribution. (b) Values of suspension force. (c) Air-gap flux density of the outer stator with different current values in the *y* positive direction. (d) Air-gap flux density of the outer stator with different current values in the *y* negative direction.

THURSDAY AFTERNOON, 26 APRIL 2018 PEONY II, 2:00 TO 5:00

Session FH

ANALYSIS AND OPTIMISATION OF ELECTRICAL MACHINES I

Chunhua Liu, Co-Chair
City University of Hong Kong, Hong Kong, Hong Kong
Li Zhu, Co-Chair
Shanghai Jiao Tong University, Shanghai, China

CONTRIBUTED PAPERS

2:00

FH-01. Development of a Radial Flux Permanent Magnet Machine with an Amorphous Metal Stator Core.

W. Tong[1], R. Sun[1], S. Wu[1] and R. Tang[1]
1. School of Electrical Engineering, Shenyang University of Technology, Shenyang, China

With the aggravation of the energy crisis, increasingly prominent of the environment issues, techniques to improve electrical machine efficiency continue to be explored. Employing low core loss materials instead of traditional counterparts becomes a valuable way to improve motor efficiency. Amorphous metal has features of extremely low core losses due to its high resistivity and only one twentieth the thickness of the conventional silicon steel sheet (SSS). Amorphous metal has already been shown to reduce core losses dramatically in power transformers [1] as well as in high frequency axial flux motors [2-3]. For radial flux motors, the related research achievements are relatively few, mainly due to the limited physical sizes and manufacturing difficulties of amorphous metal. In order to further promote the application of amorphous metal in electrical machines, radial flux motors should be further investigated. In this paper, a series of typical fabrication processes are adopted to develop a stack amorphous metal stator core (AMSC) for a 2.1kW, 4000 rpm radial flux permanent magnet motor (RFPMM), and the configurations of the stator core and motor prototype are shown in Fig. 1. In order to quantify the magnetization and AC loss characteristics of the AMSC, an experiment is conducted on the AMSC under different supply frequencies according to the standard of IEC 60404-6. The working principle of the experimental model is similar to an electromagnetic transformer. Two sets of winding are wound on the stator core for excitation and flux detection, and the magnetic flux alternates along the stator yoke. In this experiment, the excitation current is kept sinusoidal. On the basis of the experimental system, the magnetization and AC loss characteristics of the stack AMSC are obtained, as shown in Fig. 2. As a comparison, the magnetic performances of typical W270-35 type SSS are given in Fig. 2. It can be seen from the figure that the magnetization curves of the AMSC and SSS are almost the same when B is below 0.8T. Within this range, the permeability of AMSC is a little bit higher than that of W270-35. However, a contrary tendency of the permeability is obtained when B is above 0.8T. The saturation flux density of AMSC is about 1.4T, which is much lower than that of conventional SSS material. The core loss of the AMSC is much smaller than that of conventional SSS material. This result also demonstrates that the magnetic performance of amorphous magnetic material is sensitive to the externally applied stress. In order to demonstrate the advantages of amorphous metal permanent magnet motors over conventional silicon steel permanent magnet motors, two RFPMMs with the same dimensions but different stator core materials are analyzed, manufactured and tested in different conditions. The permanent magnets of the two motors are mounted on the surface of the rotor core, and shaped to make the air gap flux density waveform approach to sine wave. A search coil is placed in the top of the slot for each motor. 3-D finite element method is adopted to analyze the no-load flux density distribution of both motors. According to the calculation results, the flux density of stator teeth in amorphous metal permanent magnet motor is a little bit lower than that in conventional motor. The induced back EMF in the test coils is calculated and compared with the experimental results. In order to identify the difference of the no load iron loss of the two motors, the 3-D finite element method is introduced to analyze the no-load loss distributions of the two motors under both sinusoidal supply and converter supply conditions. The relationships between the no load iron losses and the rotation speeds of the two motors are also investigated. To verify the accuracy of the calculation results and to demonstrate the advantages of amorphous metal permanent magnet motors over conventional SSS permanent magnet motors, the no load loss test is proceeded for both of the motors. The results illustrate that the simulation results are in good agreement with the test results, and the RFPMM with an AMSC has a characteristic of extremely low no-load iron loss, relative to the conventional SSS motor.

[1] L. A. Johnson, E. P. Cornell, D. J. Bailey and S. M. Hegyi, "Application of low loss amorphous metals in motors and transformers," *IEEE Trans. Powe. Appa. Syst.*, vol. 101, no. 7, pp. 2109-2114, Jul. 1982. [2] Ertugrul N, Hasegawa R, Soong W L, Gayler J, Kloeden S, and Kahourzade S, "A novel tapered rotating electrical machine topology utilizing cut amorphous magnetic material," *IEEE Trans. Magn*, vol. 51, no. 7, 8106006, Jul. 2015. [3] Z. Wang, Y. Enomoto, R. Masaki, K. Souma, H. Itabashi and S. Tanigawa, "Development of a high speed motor using amorphous metal cores," in *Jeju.* ICPE *Conf.*, 2011, pp. 1940-1945

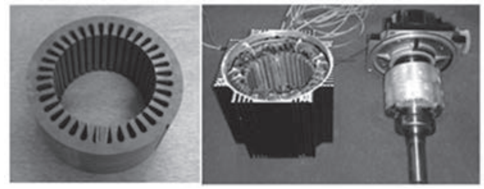

Fig. 1. Configurations of the amorphous metal stator core and the permanent magnet motor prototype

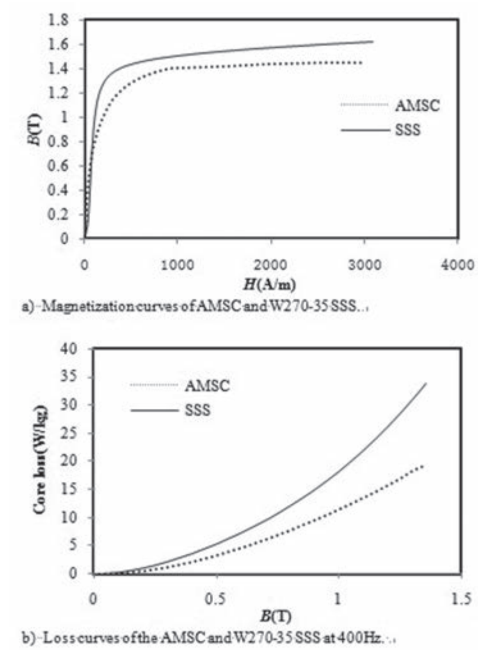

Fig. 2. Magnetization curves and loss curves of the AMSC

2:15

FH-02. Optimal Design of a Novel Five-phase SPM Machine with Electronic Pole-Changing Effects.

J. Gong[1], T. Tong[1] and N. Bracikowski[2]
1. School of Electrical Engineering, Shandong University, Jinan, China;
2. IREENA Laboratory, Nantes University, Saint Nazaire, France

I. Introduction Multiphase machines have been widely used in critical applications, such as marine applications, where high density of torque with high quality and fault tolerant capability are required [1]. Thanks to vector control and injection of non-sinusoidal currents, permanent magnet (PM) machines with high number of phases can obtain the same torque density as the three-phase DC brushless machines, moreover with lower torque pulsation [2]. Another important property of multiphase machines is the fault tolerant, due to the more degree of freedom of control [3]. The reason is that, referring to classical wye-coupled three phase machines, which possess the minimum number of independent currents for achieving a rotating field in normal condition, multiphase machines have more degree of freedom than the minimum necessary, thus allowing a rotating field even with one opened phase. Moreover, with injection of high order harmonics of current, an electronic pole-changing effects can be obtained, e.g. the p pair of poles with fundamental current and $3p$ ones with the third harmonic current. The appropriate polarity can be selected regarding the load demand in transient or steady state by changing the levels of first and third harmonics of current, which can also take into account the inverter rating and efficiency or torque quality requirements. Then the flux weakening is no more than the unique solution when maximum voltage is reached and the speed range can be extended by switching between different pole polarities. In order to achieve such property, the multiphase machine should develop the torque with equal share by each first and third harmonic of current and electromotive forces (EMF). In this case, a real degree of freedom for the control can be achieved. An Interior PM five-phase machine is proposed in [4], which has demonstrated this valuable property using different control strategies. In this paper, a novel five-phase surface-mounted PM (SPM) machine with pole-changing effects is investigated. Its specificity is to be able to develop torques of comparable values under three kinds of supply: with only first, third or both first and third sinusoidal currents, due to first (E_1) and third (E_3) harmonic of comparable EMF values. In order to achieve such objective, the configuration of fractional-slot concentrated winding is firstly investigated; Secondly, the shape of magnets is optimized in order to adapt the selected winding configuration; Thirdly, the speed-torque characteristics of whole speed range is investigated through MTPA control strategy and compared to a classical sinusoidal three-phase SPM machine. II. Main Design Consideration A. Winding Configuration Selection As the winding is one of the most complex parts of the process in a classical machine, fractional slot concentrated winding (FSCW) with simple and short end-winding is more and more popular in industry applications, especially for hybrid vehicles where the compactness, high efficiency and easy manufacturing are required. In this part, two criteria are used to make selection of FSCW configuration: 1) the winding factors of both fundamental and third harmonic, and 2) the eddy current losses in the rotor. In order to design a double-polarity five-phase machine, a compromise for the choice of different slot/pole combinations must be achieved by considering a sufficiently high winding factors for both the first harmonic and the third harmonic. The 20-slot/8-pole of 5-phase winding configuration is chosen for the reason with the fundamental winding factor K_{w1}=0.588 and the third harmonic winding factor K_{w3}=0.958, moreover the slot per pole per phase (S_{pp}) is 0.5 which presents low amplitude harmonics and subharmonics of magneto-motive force (MMF), with a consequently low level of eddy current losses [5]. The MMF distribution and its harmonic analysis is presented in Fig. 1, with the injections of both first and third harmonic currents. This machine has 4 pairs of poles with first harmonic current injection and 3×4 pairs of poles with third harmonic current injection. Therefore, an electronic pole-changing effect can be obtained if the machine operates at low speed with 3×4 pairs of poles and 4 pairs of poles at high speed by taking into account the inverter rating, the efficiency and the output torque. B. Rotor structure adaptation A particular trapezoidal magnet shape is determined in order to enhance the contribution of the third harmonic flux density, with a consequently the boost of torque under the third harmonic current supply. Fig. 2(a) shows the machine topology with optimized magnet shape and Fig. 2(b)-(c) shows the no-load back EMF and its harmonic analysis calculated using FEM. As a result, the back EMF of 3rd harmonic is widely increased compared to a sinusoidal machine. For a given rms value of current, Fig. 2(d) shows the output torque with MTPA control strategy under three kinds of current supply: with only the first, the third and both the first and the third sinusoidal. It is proved that the injection of third harmonic current can not only boost the output torque, but also allow changing the polarity of the machine, with a consequently the expansion of the speed range. The detail design consideration will be presented in the full paper, and a comparison of speed-range operation with a sinusoidal machine of the same ratings will also be covered.

[1] F. Barrero, M. J. Duran, "Recent Advances in the Design, Modeling and Control of Multiphase Machines—Part 1," IEEE Transactions on Industrial Electronics, Vol. 63, No. 3, pp. 449-458, January 2016. [2] K. Wang, Z. Q. Zhu, G. Ombach, "Torque Enhancement of Surface-mounted Permanent Magnet Machine Using Third-Order Harmonic," IEEE Transactions on Magnetics, Vol. 50, No. 3, March 2014. [3] C. Tong, F. Wu, P. Zheng, B. Yu, Y. Sui, L. Cheng, "Investigation of Magnetically Isolated Multiphase Modular Permanent-Magnet Synchronous Machinery Series for Wheel-Driving Electric Vehicles," IEEE Transactions on Magnetics, Vol. 50, No. 11, November 2014. [4] H. Zahr, J. Gong, E. Semail, F. Sciuller, "Comparison of Optimized Control Strategies of a High-Speed Traction Machine with Five Phases and Bi-harmonic Electromotive Force,"Energies, Vol. 9, No. 12, December 2016. [5] B. Aslan, E. Semail, J. Legranger, "General Analytical Model of Magnet Average Eddy-Current Volume Losses for Comparison of Multiphase PM Machines with Concentrated Winding," IEEE Transactions on Energy Conversion, Vol. 29, No. 1, March 2014.

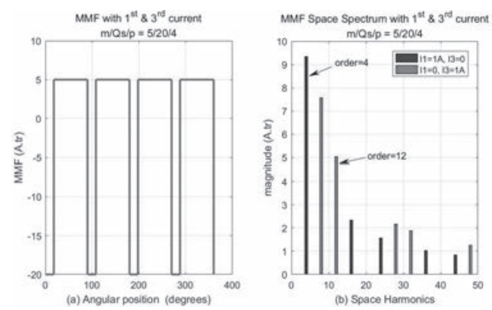

Fig. 1. 20/8/5 winding with (a)MMF distribution and (b)harmonics analysis

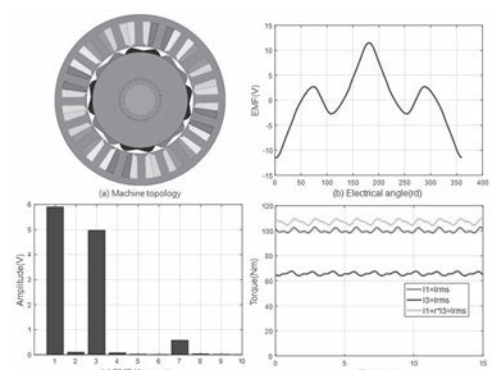

Fig. 2. (a)Machine topology (b)No-load EMF (c)EMF harmonic (d) Output torque under three kinds of supply

2:30

FH-03. Analysis and Control of the Permanent Magnet Synchronous Motor with Auxiliary Modular Design.

H. Lin[2], *F. Zhao*[1] and B. Kwon[3]
1. Harbin Institute of Technology Shenzhen Graduate School, Shenzhen, China; 2. Chang'an University, Xi'an, China; 3. Hanyang University, Ansan, The Republic of Korea

I. Introduction U-shape core permanent magnet synchronous motor (PMSM) has the features of small size, simple and robust construction, generally working in the low power and low cost industry applications [1], [2]. Due to the simple structure and the self-starting ability, single-phase PMSM with U-shape core got more attentions in early research and application, however, its development was limited by motor large torque ripple and low efficiency. As one effective way to solve the problem, the PMSM with auxiliary modular design comes out [2], which can obtain a smooth operation feature with shifted magnets array and supply the opportunity for fault tolerant control. Based on the two-phase PMSM with auxiliary modular design, the motor mathematical model and the fault tolerant control configuration are presented in this paper to illustrate motor characteristics and achieve the fault-tolerant ability. Finally, the motor prototype is tested and the experimental results are used to verify the proposed steady operation and the fault-tolerant strategy. II. Motor configuration and control strategy The configuration of the two-phase PMSM with auxiliary modular design is shown in Fig. 1. The proposed motor is designed as a combination of two normal single-phase PMSMs parallel arranged, sharing one shaft of the rotor. Two pairs of ferrite magnets are placed with 90 electrical degrees shifted, and the stator coils wound on two U-shape cores are designed as two independent phases with minor mutual inductance. When two stator windings are fed by two independent voltage sources with 90 degree phase shift, the flux linkage and MMF in the stator cores are alternately produced when rotor rotates. When the MMF is generated in the stator cores by two phase stator currents alternately, the motor obtains a constant electromagnetic torque which is the sum torque of two phases. As a kind of motor modular design, this PMSM with auxiliary modular requires good replaceability and fault tolerant ability during different operation conditions. Therefore, two H-Bridge inverters are used to feed current into two windings of the PMSM respectively. If one phase winding or H-bridge inverter falls in fault, the fault diagnosis and fault-tolerant control method can be used to remove the fault module and drive immediately. That means the motor can work continually by the left modules. A drive block with the fault-tolerant ability is illustrated for the PMSM as in Fig. 1. Fault-tolerant scheme can be automatically selected by a fault detection switch, which acts following the signal from the fault diagnosis circuit in the inverter. During the steady operation, a control scheme with the two-phase space vector modulation technique is used to drive the motor by an eight-switch inverter including two H-bridge inverters as in a conventional two-phase motor [3]. One speed PI controller and two current PI controllers are used to regulate the rotor speed and winding current, respectively. When one H-bridge inverter or one winding fault occurs, the system can still work by the other stator and H-bridge inverter, as well as a simple sinusoid PWM scheme with one speed PI controller. The fault-tolerant control flowchart is presented in detailed as in Fig. 2. The system starts from the mode of speed open loop, the system begins to work under a series steps of speed and position calculation, speed PI regulator, voltage and current sampling and fault tolerant operation. Generally, the system operates on the healthy mode of Clark and Park transformation, current PI regulators, inverse Park transformation and two-phase SVPWM. If any winding falls into fault, the system turns to the fault mode of reference voltage generation and one-phase PWM. In the healthy mode, a two-phase SVPWM scheme is used in the system to achieve a constant switching frequency and a low torque ripple. While in the fault mode, only the traditional single-phase PWM scheme is used for the drive in order to get a continual working ability of motor. The experimental responses of speed, rotor position and currents of two phase windings are achieved in Fig. 3 to illustrate the steady operation process and the fault-tolerant operation of the system. In the paper, the DC-link voltage of the inverter is set to 310V. The reference speed of the motor is set to 300rpm with no load. The PWM switching frequency is set to 20kHz. There is a good dynamic and steady performance of the speed, rotor position, as well as the currents of phase A and phase B. In the steady operation, the rotor speed and two phase currents have a steady and smooth waveform. As in Fig. 3(a), the motor continues working at 300rpm within 0.2second after the fault of phase A winding occurs. Fig. 3(b) shows the steady operation again after fault, where this PMSM operates as the single-phase PMSM with only phase B working. It shows that the proposed drive can achieve a good fault-tolerant ability with the proposed scheme in this PMSM with auxiliary modular design.

[1] M. Fazil, K. R. Rajagopal, "A novel air-gap profile of single-phase permanent-magnet brushless dc motor for starting torque improvement and cogging torque reduction," *IEEE Transactions on Magnetics*, vol. 46, no. 11, pp. 3928-3932, Nov. 2010. [2] F. Zhao, T. A. Lipo, B. I. Kwon, "A Novel Two-Phase Permanent Magnet Synchronous Motor Modeling for Torque Ripple Minimization," *IEEE Transactions on Magnetics*, vol. 49, no. 5, pp. 2355-2358, May 2013. [3] H. Lin, B. I. Kwon, "Space-vector PWM Techniques for a Two-Phase Permanent Magnet Synchronous Motor Considering a Reduction in Switching Losses," *Journal of Electrical Engineering Technology*, Vol. 10, No. 3, pp. 295-303, 2015.

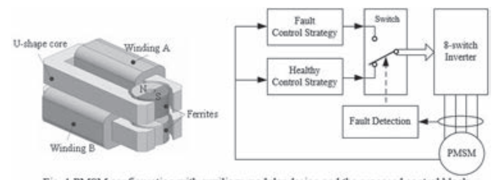

Fig. 1 PMSM configuration with auxiliary modular design and the proposed control block

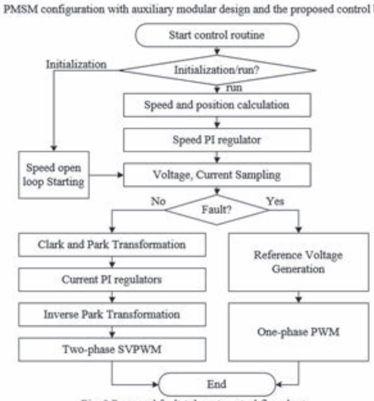

Fig. 2 Proposed fault-tolerant control flowchart

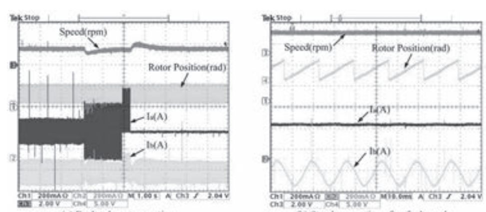

(a) Fault tolerant operation (b) Steady operation after fault mode
Fig. 3 Experimental results in the PMSM with auxiliary modular design

2:45

FH-04. Experimental Results and Parameter Identification of a Permanent Magnet Assisted Synchronous Reluctance Machine with a Ribless Rotor.

M. Zimmermann[1], A. Lange[1] and B. Piepenbreier[1]
1. Institute of Electrical Drives and Machines, University of Erlangen-Nuremberg, Erlangen, Germany

1.) Introduction Synchronous Reluctance Machines attracted a lot of interest in the past decades because of the simple rotor manufacturing and low costs. However, this machine type suffers from a low power factor and the design is sensitive to torque ripple. Furthermore, the mechanical limits have to be considered carefully. In general, this machine type is not used in high speed applications because the increasing rib thickness influence strongly the electromagnetic behaviour of the machine. Sensorless control strategies are often focused on the full exploitation of the allowed operating area of the machine. Nowadays there is an increasing demand for variable speed drives. The omission of a position sensor provides a smaller machine size, reliability and lower costs. A common approach is to use the Back-EMF to detect the rotor position. This approach fails at low speed. A remedy are signal injection methods which are well known. The magnetic anisotropy (saliency) is needed to get information of the rotor position. This paper addresses the previously described problems in the following way: The machine design is introduced. By using ferrite magnets the low power factor of a SynRM can be increased. These magnets are low-priced, corrosion- and temperature-resistant. The machine design is also focussing on a saliency in all current operating points. A ribless approach, which was introduced by Villet [1], is used and extended by an glass fiber-reinforced sleeve to ensure mechanical stability. The rotor design was supported by Finite Element Analysis (FEA). A identification of the flux linkages and the inductances will be provided to compare it to the FEA results. Furthermore, the saliency and a efficiency will be evaluated. *2.) Machine Design* The idea of a ribless rotor is surveyed. This rotor design has two advantages for the PMaSynRM which was not researched sufficiently yet. A part of the PM-flux is not short-circuited along the ribs. The utilisation of the permanent magnets is higher. A ribless design provide less leakage. Especially, L_q is influenced by the ribs. In a SynRM the ribs have a strong influence on the inductances. These tend to be strongly current-dependent [5]. A saturation of these ribs enables the desired anisotropy of the machine. For the PMaSynRM the saturation of the ribs is provided due to the permanent magnets and the current. However, both aspects do not lead to a optimal machine design with respect to utilisation or saliency at low currents. The ribs have to be adjusted to withstand the desired speed. A mechanical-electromagnetic trade-off has to be found. The design of high-speed machines is limited because larger ribs cause a huge impact. The first manufacturing step for this design is to insert the magnets in the flux barriers of the bonded lamination stack. Non-corrosion ferrites are advantageous here. Afterwards the rotor will be filled and cast by glass fiber/ epoxy resin. The ribs are removed by milling. Finally, the unstable rotor structure is protected by an glass fiber sleeve to withstand speeds up n_{max} = 3000 rpm. However, the rotor sleeve enlarge the electromagnetic air gap and lower the d-inductance. Though a good magnetic anisotropy can be achieved. A cross-section of the rotor is illustrated in the Figures. The electromagnetic design is described in [9]. *3.1) Measurement routine* The device under test is operated in current control mode with an industrial converter using a conventional field oriented control. The speed was kept constant with a DC-load machine (speed control). For one operation point the measurement data is sampled ten periods of the fundamental frequency with f_s = 8 kHz. Afterwards the data is averaged. The temperature-dependent stator resistance is considered for the determination. The temperature in the machine is measured with the help of three PT1000 temperatures sensors. The end-winding temperature is taken for further calculation. The voltages are the control signals and are not measured directly. A compensation of the inverter voltage errors are implemented similar to [13]. The voltage errors are caused by non-ideal switching, forward voltage drop due to power electronics an on delay time to prevent DC-link short circuiting. *3.2) Parameter Identification* The equations will be given in the full paper. The result is illustrated in the Figures. A strong magnetic anistropy is visible. *3.3) Differential Saliency Analysis via Rotating Test Signal* Test signal injection is a common used technique for sensorless control at low or zero speed. A rotating voltage testsignal is superimposed on the fundamental voltage signals at the output of the PI-controllers. The current response of a rotating voltage testsignal gives an excellent visual representation of the machine saliency. In a salient machine the current response ideally depicts an ellipsis in the dq-reference frame. The centre of the ellipses is the fundamental current operating point. The more formed the ellipsis are, the higher is the saliency. A circular current response means L_{dd}=L_{qq}. When the orientation of the ellipsis is not vertical, an impact of cross-coupling is visible. Measurements show nearly equal ellipsis. No saliency loss over the whole current range is visible. Moreover, the ellipsis are almost vertical due to nearly no cross-coupling. The highlighted red rectangle is the operating area of SynRMs, where usually a loss of saliency occurs.

[1] W. Villet, “Critical evaluation and application of position sensorless control techniques for reluctance synchronous machines,” Thesis, 2014. [2] N. Bianchi and S. Bolognani, “Influence of rotor geometry of an interior pm motor on sensorless control feasibility,” in Fourtieth IAS Annual Meeting. Conference Record of the 2005 Industry Applications Conference, 2005., vol. 4, Conference Proceedings, pp. 2553–2560 Vol. 4. [3] J. Cordier, P. Landsmann, and R. Kennel, “The influence of magnetic hysteresis on hf injection based inductance calculation,” in 2011 IEEE Energy Conversion Congress and Exposition, Conference Proceedings, pp. 638–645. [4] I. Hahn, “Differential magnetic anisotropy - prerequisite for rotor position detection of pm-synchronous machines with signal injection methods,” in 2010 First Symposium on Sensorless Control for Electrical Drives, Conference Proceedings, pp. 40–49. [5] M. Kamper and W. Villet, “Design of a reluctance synchronous machine for saliency based position sensorless control at zero reference current,” p. 6, 2013. [6] D. Mingardi, M. Morandin, S. Bolognani, and N. Bianchi, “On the proprieties of the differential cross-saturation inductance in synchronous machines,” IEEE Transactions on Industry Applications, vol. 53, no. 2, pp. 991–1000, 2017. [7] R. Leuzzi, P. Cagnetta, S. Ferrari, P. Pescetto, G. Pellegrino, and F. Cupertino, “Analysis of overload and sensorless control capability of pm-assisted synchronous reluctance machines,” in 2017 IEEE Workshop on Electrical Machines Design, Control and Diagnosis (WEMDCD), Conference Proceedings, pp. 172–178. [8] M. Palmieri, M. Perta, F. Cupertino, and G. Pellegrino, “High-speed scalability of synchronous reluctance machines considering different lamination materials,” in IECON 2014 - 40th Annual Conference of the IEEE Industrial Electronics Society, Conference Proceedings, pp. 614–620. [9] M. Zimmermann and B. Piepenbreier, “Design of a permanent magnet assisted synchronous reluctance machine enhanced for saliency based sensorless control,” in 2017 IEEE International Electric Machines and Drives Conference (IEMDC), Conference Proceedings, pp. 1–7. [10] F. Brasas and J. Germishuizen, “Determination of equivalent circuit parameters of a direct drive wind power generator,” in 2012 XXth International Conference on Electrical Machines, Conference Proceedings, pp. 201–206. [11] J. Reill, Lagegeberlose Regelung fr ein accelerometergesttztes, hochdynamisches Roboterantriebssystem mit permanenterregtem Synchronmotor, 2010. [12] A. Rambetius, Lagegeberlose Regelung der elektrisch erregten Synchronmaschine fr den Einsatz in Elektrofahrzeugen, 2015. [13] M. Seilmeier, C.Wolz, and B. Piepenbreier, “Modelling and model based compensation of non-ideal characteristics of two-level voltage source inverters for drive control application,” in 2011 1st International Electric Drives Production Conference, Conference Proceedings, pp. 17–22. [14] J. Richter, A. Dollinger, and M. Doppelbauer, “Iron loss and parameter measurement of permanent magnet synchronous machines,” in Electrical Machines (ICEM), 2014 International Conference on, Conference Proceedings, pp. 1635–1641. [15] M. Seilmeier and B. Piepenbreier, “Identification of steady-state inductances of pmsm using polynomial representations of the flux surfaces,” in Industrial Electronics Society, IECON 2013 - 39th Annual Conference of the IEEE, Conference Proceedings, pp. 2899–2904.

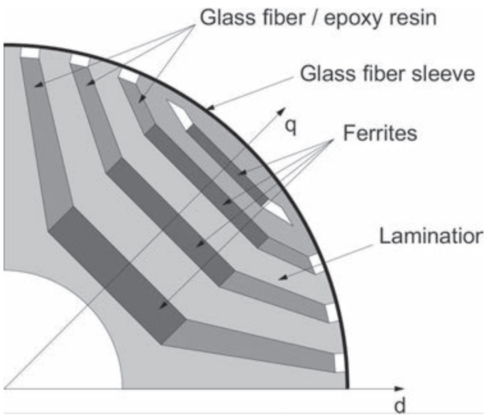

Fig. 1. Proposed ribless rotor design

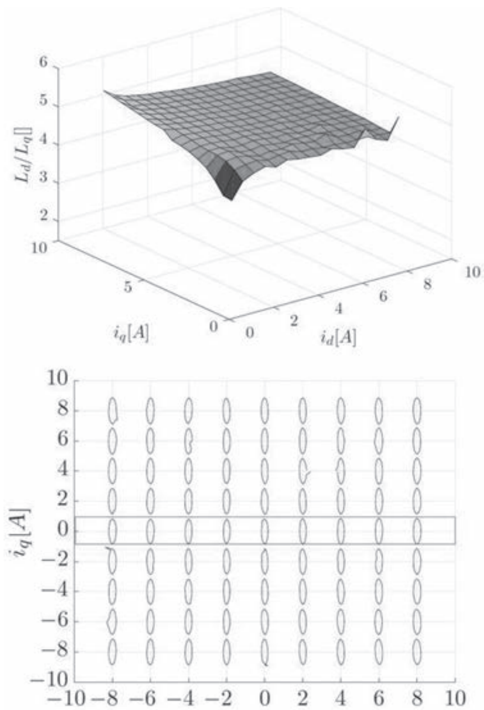

Fig. 2. 1.) Absolute magnetic saliency L_d/L_q
2.) Differential magnetic saliency: Current response to rotating testsignal

INVITED PAPER

3:00

FH-05. Magnetic materials and technologies enabling an even brighter future for electrical machines.

P. Upadhyay[1]
1. US Corporate Research, ABB Inc., Raleigh, NC, United States

About 50% of the total energy on Earth is utilized through electromagnetic devices. Transformers, for the long distance power transmission and energy distribution, large AC motors and low voltage (LV) motors, for energy generation and utilization are the major electric power equipment driving today's technologies. The presentation will review past innovations and developments, as well as remaining major technical challenges in motors, generators, and transformers. The discussion on market needs and present snapshots will provide essential driving factors for the research community for the future technology developments. The cost and performance factors and the evolution of relevant industrial standards, government regulations, and their impacts on associated technologies will be discussed. Introduction: The major form of the energy consumption is by means of electricity. About 50% of the energy used on Earth is utilized through electromagnetic devices. Motors, generators, and transformers have been commercial products for over a century. These electromagnetic power products play a vital role in energy transformations from non-electric forms to electricity, in short and long distance transmissions, and final utilization and energy conversion for the end use. The historical development indicates that for power generation and transmission (large AC generators and power transformers), no major technology revolution has occurred. The transformer stepped core technology used in the 1950s is still a base technology with life expectancy of more than 50 years and having continuous duty operation. Costumers of power product companies still demand conventional synchronous generators across the globe. However, the technology in the energy utilization market has evolved significantly over the past 100 years. 65% of total electricity at industrial sites is consumed by electric motors and distribution transformers, which are majorly influenced by political, economic, social and technology revolutions. *Market needs:* The global electrical energy demand is predicted to be at about 5 percent compound annual growth rate (CAGR) which includes about 4.2 percent increase in the motor market. Unlike consumer products like cellphones and computers, the power product industry demands lower cost and higher performance. The power range of the motors and transformers vary from a few watts for fractional horse power machines to hundreds of MW. *Past innovation, trends in machines and role of magnetic materials* The magnetic material evaluation has gradually reduced the size of the induction motor as shown in Hitachi's motor technology evolution over a hundred years. This indicates that materials having higher magnetic saturation and lower magnetic losses can be deployed to both motor and transformer products. ABB's wound core transformers using amorphous metal (AM) core material drastically reduces core losses by 20%, and magnetizing current to $1/10^{th}$ versus the stepped cores enables the US Department of Energy to implement higher efficiency standards. Magnetic material such as soft magnetic composites and AM also enables deployment of axial flux, transverse flux or conical gap machines for direct drive applications to replace conventional induction motors (IM) and permanent magnet (PM) motors. The capital cost for the PM machines represents only 10% of the total life cycle operational costs of the motor. The increased cost of rare-earth magnets and challenges in supply chain in certain global regions also restricts the PM machine to be accepted for high efficiency needs set up by regulation. Recycling of the magnets will further improve acceptance of PM motors in the global market. With present material technologies and optimized designs, IM can achieve up to IE4 efficiency standard for medium and large powers. That exaggerates the demand for PM machine technology to grow and it may cover 25% of the world motor market by 2020. Reliable motors with a high efficiency level ensure the lowest life cycle costs. European Commission predicts that the efficiency of EU's motor systems could be improved 20-30% by 2020. Standardization initiatives have resulted in the harmonization of energy-efficient requirements, testing methods and certification schemes in the electric motor markets. More than 90% of the motor market is supplied through Synchronous, DC, Induction and PM machine topologies. PM assisted Synchronous reluctance machines (SynRM) is another alternative using low cost ferrite magnets to enables higher power factor at a competitive cost and footprint for some industrial applications in fan, pump, HVAC and marine propulsions. Transverse flux (TFM), axial-flux, homo-polar (HPM), flux switching (FSM), flux reversal (FRM), switched Reluctance (SRM), spoke type flux focusing (SFM), spherical, linear, conical gap, oscillatory generator, hysteresis and stepper motors are some interesting and promising machine topologies investigated in academia and industries for niche market segments where cost is not a primary consideration. *Conclusions:* The motor technology is matured over more than 100 years. Induction motors, synchronous motors and PM motors are key topologies accepted globally. Recycling of the magnets will further improve acceptance of PM motors in the global market. The innovative steps in magnetic material development not only supports conventional technologies but also enables new motor and transformer topologies which improves performance and reduces size and total ownership cost.

[1] Historical Evolution of Motor Technology, Hiroyuki Mikami, Kazumasa Ide, Yukiaki Shimizu, Masaharu Senoo, Hideaki Seki, Hitachi Review, Vol. 60, No. 1, Year: 2011, Pages: 39 – 45. [2] Beyond Induction Motors—Technology Trends to Move Up Efficiency, Aníbal T. de Almeida; Fernando J. T. E. Ferreira; Ge Baoming, IEEE Transactions on Industry Applications, Vol:50, Issue: 3, Year: 2014, Pages: 2103 – 2114. [3] Soft Magnetic Material Status and Trends in Electric Machines, Andreas Krings, Aldo Boglietti, Andrea Cavagnino, and Steve Sprague, IEEE Transaction on Industrial Electronics, Vol.64, No.3, March 2017, Pages: 2405 - 2414 [4] Barriers and incentives policies to high-efficiency motors and drives market penetration, M. Benhaddadi; G. Olivier, 2008 International Symposium on Power Electronics, Electrical Drives, Automation and Motion (SPEEDAM 2008), Year: 2008, Pages: 1161 – 1164, [5] Electric motor standards, ecodesign and global market transformation, Anibal T. de Almeida; Fernando J. T. E. Ferreira; Joao A. C. Fong; Conrad U. Brunner, 2008 IEEE/IAS Industrial and Commercial Power Systems Technical Conference, Year: 2008, Pages: 1 - 9 [6] Technical and Economical Considerations on Super High-Efficiency Three-Phase Motors, Aníbal T. De Almeida; Fernando J. T. E. Ferreira; André Quintino Duarte, IEEE Transactions on Industry Applications, Vol: 50, Issue: 2, Year: 2014, Pages: 1274 – 1285 [7] REE Recovery from End-of-Life NdFeB Permanent Magnet Scrap: A Critical Review, Yongxiang Yang, Allan Walton, Richard Sheridan, Konrad Güth, Roland Gauß, Oliver Gutfleisch, Matthias Buchert, Britt-Marie Steenari, et al. Journal of Sustainable Metallurgy, Vol. 3, No. 1, Springer 2017, Pages: 122 – 149

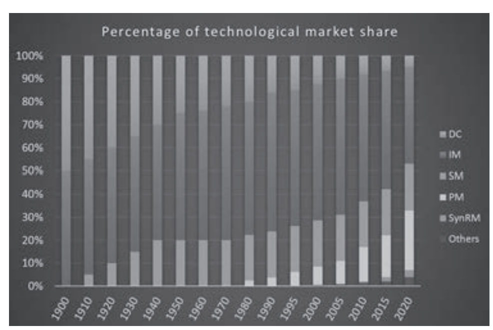

Fig. 1. Market share by various rotating machines

CONTRIBUTED PAPERS

3:30

FH-06. Analysis of a Novel Double-sided Dual-PM Hybrid-excitation Switched-flux Linear machine.

Z. Zeng[1] and Q. Lu[1]
1. College of Electrical Engineering, Zhejiang University, Hangzhou, China

Introduction: Hybrid-excitation switched-flux linear machine (HESFLM) has been studied increasingly due to the advantages of high force density, flexible flux controllability, robust secondary, etc. Existing HEFSLM structures have excitation winding, armature winding, and PMs entirely accommodated on the single-primary [1], [2]. Consequently, both flux-regulation capability and PM force density are restricted. In order to solve the aforementioned problem, this paper proposes a novel double-sided dual-PM HESFLM (DSDP-HESFLM) featuring dual-PM and double-sided primaries, hence both excitation and armature windings can be separately amounted with corresponding slot areas augmented simultaneously [3-5]. As a result, electromagnetic performances can be improved effectively. Based on 2-D finite-element (FE) analysis, the operating principles of the proposed machine from both generator- and motor-oriented perspectives are systematically investigated, and then its electromagnetic performances are studied. Topology and Operation Principle: Fig. 1(a) shows the topology of the proposed 6-slot/7-pole (6s/7p) DSDP-HESFLM. Apparently, the primary is partitioned into two asymmetrical parts and concentrated non-overlapping armature and field windings can be observed. Moreover, armature-PM is sandwiched between two U-shaped steel lamination while field-PM is inset in the field teeth. It is worth mentioning that magnetization direction of armature-PM is parallel to moving direction, while that of field-PM is perpendicular to moving direction. Besides, magnetization direction of two adjacent field-PMs and their middle armature-PM should resemble clockwise or anti-clockwise to make armature flux-linkage caused by armature-PM and field-PM the same polarity. Actually, the proposed machine can be taken as a combination of double-sided HEFSLM with armature-PM and field-PM, respectively. Fig. 1(c) shows the operation principle of the proposed machine from generator-oriented perspective, which is based on flux-switching mechanism. Namely, armature coil PM flux changes periodically with secondary position, where an electrical circle corresponds to a secondary-pitch movement. Hence, brushless AC operation is also suitable for the proposed machine. Alternatively, the operation principle from the perspective of motor-oriented, emphasizing the interaction of PM and armature reaction fields, can be illustrated in Fig. 1(d) and (e). As is shown, the modulation of salient secondary pole to both PM and armature reaction source MMFs produces lots of harmonics. Specifically, apart from source PM MMF harmonics with pole-pair number $(2i-1)P_{PM}$, where i=1,2,3..., new dominant PM flux-density harmonic components with pole-pair number of 2, 4, 10, 16 ($|(2i-1)P_{PM}\pm jN_s|$, j=1, i=1,2) are also produced. Similarly, apart from source armature reaction MMF harmonics with pole-pair number, dominant new-emerging flux-density harmonics are also produced with pole-pair number 3, 5, 9, 11 ($|2k\pm jN_s|$, k=1,2, j=1). In other words, after the modulation effect of secondary poles, stable thrust force can be generated by the interaction of PM and armature reaction flux-density harmonics with same speed and pole-pair number, which is called magnetic-gearing effect [6], [7]. Feasible slot/pole combinations of DSDP-HESFLM can be 6s/4p, 6s/5p, 6s/7p and 6s/8p, among which 6s/5p and 6s/7p structures exhibit larger winding coefficient. Furthermore, 6s/7p has relatively large thrust force constant compared with its 6s/5p counterpart. Hence, it is reasonable to choose 6s/7p as the optimal slot/pole combination. Electromagnetic Performance Investigation: For the globally optimized 6s/7p DSDP-HESFLM, electromagnetic performances are comprehensively investigated. As is shown in Fig. 2(a) and (b), *d*-axis flux-linkage can be easily adjusted by field current, and its DC components can be adjusted from 75.38% to 116.66%. The detent force is shown in Fig. 2(c), indicating it mainly derives from end effect. Besides, force waveform under rated condition is shown in Fig. 2(d), and corresponding PM force density is 1.38N/cm^2, which is high for hybrid-excitation linear machine. Flexible average force regulation capability by armature copper loss or field current can be also observed in Fig. 2(e). As shown in Fig. 2(f), relatively smooth inductances can be observed, which benefits smooth output force. Conclusion: A novel DSDP-HESFLM has been proposed and its operation principles are analyzed from both generator- and motor-oriented perspectives, which demonstrates that it also operates on magnetic–gearing effect. Then, electromagnetic performances are investigated, showing the proposed machine exhibits good flux-adjusting capability and high PM force density.

[1] J. T. Chen, Z. Q. Zhu, S. Iwasaki and R. P. Deodhar, "A Novel Hybrid-Excited Switched-Flux Brushless AC Machine for EV/HEV Applications," in IEEE Transactions on Vehicular Technology, vol. 60, no. 4, pp. 1365-1373, May 2011. [2] C. C. Hwang, P. L. Li and C. T. Liu, "Design and Analysis of a Novel Hybrid Excited Linear Flux Switching Permanent Magnet Motor," in IEEE Transactions on Magnetics, vol. 48, no. 11, pp. 2969-2972, Nov. 2012. [3] Z. Q. Zhu, A. L. Shuraiji and Q. F. Lu, "Comparative Study of Novel Tubular Partitioned Stator Permanent Magnet Machines," in IEEE Transactions on Magnetics, vol. 52, no. 1, pp. 1-7, Jan. 2016. [4] A. L. Shuraiji, Z. Q. Zhu and Q. F. Lu, "A Novel Partitioned Stator Flux Reversal Permanent Magnet Linear Machine," in IEEE Transactions on Magnetics, vol. 52, no. 1, pp. 1-6, Jan. 2016. [5] H. Hua, Z. Q. Zhu and H. Zhan, "Novel Consequent-Pole Hybrid Excited Machine With Separated Excitation Stator," in IEEE Transactions on Industrial Electronics, vol. 63, no. 8, pp. 4718-4728, Aug. 2016. [6] Z. Wu, Z. Q. Zhu and H. Zhan, "Comparative Analysis of Partitioned Stator Flux Reversal PM Machine and Magnetically Geared Machine Operating in Stator-PM and Rotor-PM Modes," in IEEE Transactions on Energy Conversion, vol. 32, no. 3, pp. 903-917, Sept. 2017. [7] Z. Z. Wu and Z. Q. Zhu, "Analysis of Air-Gap Field Modulation and Magnetic Gearing Effects in Switched Flux Permanent Magnet Machines," in IEEE Transactions on Magnetics, vol. 51, no. 5, pp. 1-12, May 2015.

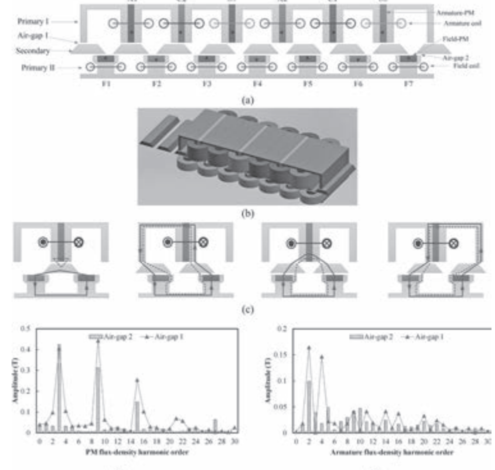

Fig. 1. (a) Topology of proposed DSDP-HFSFLM. (b) 3D view of the DSDP-HEFSLM. (c) Operating principle from generator-oriented perspective under only PM excitation. (d) PM flux-density spectra. (e) Armature reaction flux-density spectra.

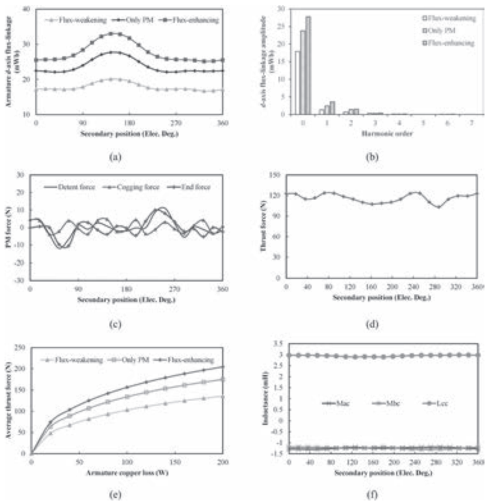

Fig. 2. (a) *d*-axis flux-linkage under three typical excitation conditions. (b) Spectra of *d*-axis flux-linkage. (c) Detent force separation. (d) Rated thrust force waveform. (e) Average thrust force versus armature copper loss. (f) Inductances.

3:45

FH-07. Study of efficiency characteristics of Interior Permanent Magnet Synchronous Motors.

S. Feng[1], W. Jiang[1], Z. Zhang[1], J. Zhang[1], Y. Li[2] and Y. Wang[1]
1. Department of Electrical Engineering, Nanjing University of Aeronautics and Astronautics, Nanjing, China; 2. Nanjing YueBoo Power System Co.,Ltd, Nanjing, China

I.Introduction Interior Permanent Magnet (IPM) synchronous motor configuration is preferred in electric vehicle (EV) traction system. Efficiency map is a common tool to describe the performance of a traction motor [1]. For each operating point (torque and speed), the excitation (current amplitude and angle) must be defined to evaluate its efficiency. If brute force method is applied to search for current excitations, the process of developing the efficiency map for an IPM machine can be time consuming. In this study, the relationships between operating points and corresponding optimal current excitations are summarized. Therefore, the process of searching for the optimal current excitations can be simplified. A script in ANSYS Maxwell has been developed to find the current excitations for optimal operating condition automatically. The efficiency performance of an IPM motor can be evaluated using finite element (FE) method with the optimal current excitations, and the efficiency map can be obtained rapidly. The effectiveness of the proposed method was validated by comparing efficiency maps created based on FE analysis results and experimental results of an IPM machine. II.IPM machine analysis A 70kW 8-pole/48-slot IPM machine for EV traction has been studied. Maximum torque per ampere (MTPA) and flux weakening (FW) are used as control strategies. As Fig.1 shows, for any given current amplitude, torque is a function of current angle (Gamma), which suggests there is only one optimal current excitation for the IPM machine to produce certain torque at a speed. In the figures below, torque is denoted as T; amplitude and angle of the current excitation are denoted as Ipeak and Gamma respectively. For the optimal current excitations of operating points at a certain speed, some conclusions have been drawn: (1)The relationship between torque and current amplitude for optimal operating condition is near linear regardless of speed, as shown in Fig.2. (2)The relationship between torque and current angle for optimal operating condition can be well fitted by a cubic polynomial if speed is below a certain value. As the speed exceeds the value, the relationship is no longer monotonic, as shown in Fig.3. III. Automatic calculation of optimal current excitations A method to simplify the search process of current excitations for optimal operating condition has been summarized with a script written in ANSYS Maxwell. Operating steps of the script are as follows: (1)Set a revolution speed and a series of typical current values in ANSYS Maxwell. Analyze corresponding current angle for optimal operating condition with step searching. (2)Call MATLAB. Fit the T-Ipeak curve of optimal excitations with a linear function and fit the T-Gamma curve with a cubic function. An exemplary fitting process in MATLAB is shown in Fig.4. (3)Process and record the data of other several typical speeds with steps (1)(2). Obtain the characteristic data of optimal current excitations at each speed and record them in a document package. (4) For an arbitrary torque at a certain speed, the corresponding current amplitude and angle can be obtained immediately by solving the recorded fitted equations reversely. If T-Gamma curve is not monotonic at this speed, the current amplitude still can be calculated with the fitted T-Ipeak function, whereas the current angle will be found by step searching. Newton interpolation will be adopted if the characteristic data of optimal current excitations at the required speed have not been analyzed before. The time of searching for the current excitations is shortened significantly. Select a certain amount of operating points and calculate the efficiency of each operating case. Then, the efficiency map can be obtained. IV.Experiment and Verification A prototype IPM machine for EV traction was designed and fabricated. The experiment bench has been established as shown in Fig.5. MTPA and FW are adopted control strategies. Several current excitations for optimal operating condition of the IPM machine were calculated with the script and with brute force method respectively. Corresponding T-Ipeak curves and T-Gamma curves are compared as shown in Fig.6 and Fig.7. The results prove the feasibility of automatic calculation with script. The efficiency map obtained through experiment is shown in Fig.8 a). In the simulation, more than 100 optimal current excitations were automatically calculated by script. Efficiency of every corresponding operating point was calculated and the efficiency map is shown in Fig.8 b). The good correspondence between two efficiency maps proves the accuracy of automatic calculation with the script. V.Conclusion A study has been conducted to simplify the steps of searching for the optimal current excitations of IPM machines. The rules between operating points and corresponding optimal current excitations have been summarized. A method to simplify search process of optimal current excitations was proposed and a script for ANSYS Maxwell has been developed. The excitations for optimal operating points at lower speed can be calculated rapidly through fitting, function solving and interpolation. For the operating points at higher speed, the optimal current amplitude can be obtained by solving fitting functions, the corresponding current angle will be searched with step searching. The automatic calculation reduces the search time of optimal current excitations and accelerate the procedure for creating the efficiency map significantly. In addition, the effectiveness of this method is validated with experiments.

[1]Williamson S S, Emadi A, Rajashekara K. Comprehensive Efficiency Modeling of Electric Traction Motor Drives for Hybrid Electric Vehicle Propulsion Applications[J]. IEEE Transactions on Vehicular Technology, 2007, 56(4):1561-1572. [2] Zhu Z Q, Howe D. Electrical Machines and Drives for Electric, Hybrid, and Fuel Cell Vehicles[J]. Proceedings of the IEEE, 2007, 95(4):746-765. [3] Williamson S, Lukic M, Emadi A. Comprehensive drive train efficiency analysis of hybrid electric and fuel cell vehicles based on motor-controller efficiency modeling[J]. IEEE Transactions on Power Electronics, 2006, 21(3):730-740. [4] Dlala E, Solveson M, Stanton S, et al. Efficiency map simulations for an interior PM motor with experimental comparison and investigation of magnet size reduction[C]// Electric Machines & Drives Conference. IEEE, 2013:23-29. [5] Novak M, Novak J, Novak Z, et al. Efficiency mapping of a 100 kW PMSM for traction applications[C]// IEEE, International Symposium on Industrial Electronics. IEEE, 2017:290-295. [6] Burress T A, Coomer C L, Campbell S L, et al. Evaluation of the 2007 Toyota Camry Hybrid Syneregy Drive System[J]. Fuel Efficiency, 2008.

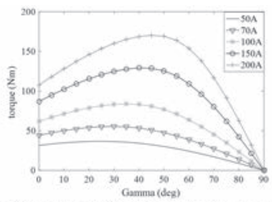

Fig. 1 Variation of the IPM machine's torque with stator current angle

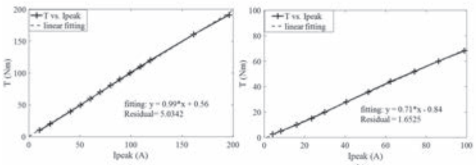

a) b)

Fig. 2 Relationship between torque (T) and current amplitude (Ipeak) of the current excitations for optimal operating condition a)1000r/min b)7000r/min

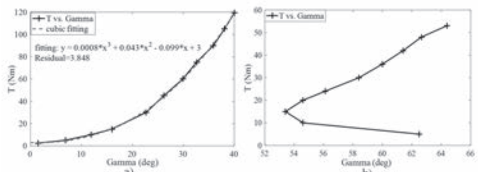

a) b)

Fig. 3 Relationship between torque (T) and current angle (Gamma) of the current excitations for optimal operating condition a)4000r/min b)9000r/min

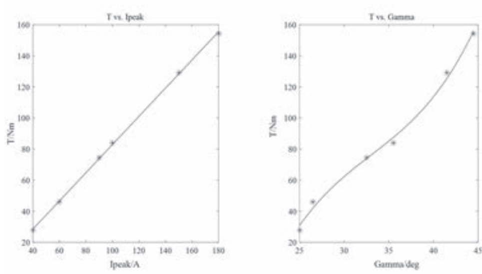

Fig4. Automatic fitting process in MATLAB at 3000r/min

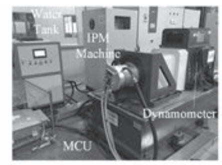

Fig.5 Experiment bench

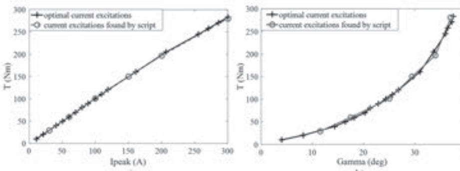

a) b)

Fig.6 Comparison of optimal current excitations found with brute force method and script respectively at 1000r/min

a)T-Ipeak curve b) T-Gamma curve

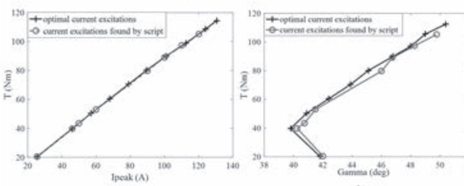

a) b)

Fig.7 Comparison of optimal excitations found with brute force method and script respectively at 5000r/min

a)T-Ipeak curve b) T-Gamma curve

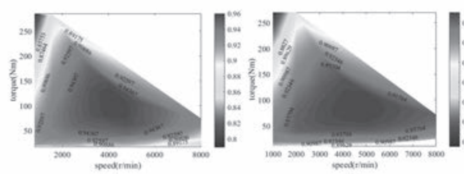

a) b)

Fig.8 Efficiency maps of the prototype IPM machine
a) experimental results b) cases calculated by the script

4:00

FH-08. Consequent Pole Hybrid Brushless Wound Rotor Synchronous Machine.

A. Hussain[1] and B. Kwon[1]
1. Electronic Systems Engineering, Hanyang University, South Korea, Ansan, The Republic of Korea

1. Introduction Several brushless topologies for wound rotor synchronous machines (WRSMs) have been presented in recent years to replace the brushes and slip-ring assembly in conventional WRSMs [1-4]. The brushless operation of the WRSM presents these machines as an alternative to the permanent magnet synchronous machines (PMSMs) because of their low cost and competitive performance as compared to the PMSMs. However, the drawback of the brushless wound rotor synchronous machines (BL-WRSMs) is their low starting torque because of the absence of the excitation source on their rotor. Although, the BL-WRSM achieves the rated torque at the base speed but low starting torque under the base speed makes these machines less suitable for variable speed applications. A PM assisted BL-WRSM was presented in [5] to overcome the problem of the low starting torque and to provide better performance under full-load conditions. However, the presence of the PM on each pole increases the cost of the machine. Moreover, the leakage flux is increased in PM assisted machines. These issues can be resolved by the consequent pole (CP) machines [6]. In this paper, a consequent pole hybrid brushless wound rotor synchronous machine (CPH-BL-WRSM) is proposed to overcome the problem of low starting torque, and to reduce the PM usage as compared to the PM assisted machines. A 2-D finite element analysis is performed to validate the proposed CPH-BL-WRSM and its performance is compared with the existing BL-WRSM and PM assisted BL-WRSM. 2. Proposed machine configuration and Operation Principle The single inverter fed brushless excitation topology applied to the proposed CPH-BL-WRSM is shown in Fig. 1(a). In this brushless topology, the sub-harmonic component of stator magneto-motive force (MMF) is generated and utilized to excite the rotor field winding as discussed in [4]. The proposed CPH-BL-WRSM with windings and PMs on the alternate poles of the rotor helps the machine with smooth startup without any external aid. Initially, the proposed machine will start as the consequent pole permanent magnet synchronous machine because there will be no induced current in the harmonic winding. Therefore, at the startup, the excitation flux is provided by the PMs only for the torque production. With the increase of the speed, the current is induced in the harmonic winding which is then rectified and supplied to the rotor field winding. At this stage, the machine operates as the CPH-BL-WRSM with the flux from both the PMs and rotor field windings. The configuration of the 2-D models of the existing PM assisted BL-WRSM and proposed 8-pole, 48-slot CPH-BL-WRSM are shown in Fig. 1(b) and Fig. 1(c) respectively. The proposed machine is designed such that its outer dimensions, rated power, rated speed and other specifications are same as the existing BL-WRSM [4] and the PM assisted BL-WRSM [5]. The stator and rotor winding configuration is kept same as the winding configuration shown in Fig. 1(a). For the fair comparison, both rotors were optimized using the Kriging method based Latin hypercube sampling and a genetic algorithm. The detailed optimization process will be explained in the full paper. Finally, the proposed CPH-BL-WRSM was manufactured to verify the operation of the machine. The stator and rotor of the prototype are shown in Fig. 1(d) and Fig. 1(e) respectively. 3. Simulation Analysis 2-D finite element analysis is performed to analyze the performance of the proposed CPH-BL-WRSM and existing BL-WRSM and PM-assisted BL-WRSM. Fig. 2(a) shows the back-EMF comparison of the machines compared in this paper. It can be observed that the back-EMF of the proposed machine is 34.5% and 9.5% higher as compared to the back-EMF of the existing BL-WRSM and PM-assisted BL-WRSM respectively. Fig. 2(b) shows the comparison of the induced current in the field winding. The torque comparison is shown in Fig. 2(c). The proposed CPH-BL-WRSM exhibits 11% higher torque than that of the existing BL-WRSM and 9.5% higher torque than that of the PM assisted BL-WRSM with 44.6% less PM usage. The overall performance comparison of both machines is summarized in Fig. 2(d). It is observed that the proposed CPH-BL-WRSM exhibits high starting torque, high torque density with less PM usage. Detailed simulation analysis of both machines will be presented in full paper. Finally, the prototype of the proposed CPH-BL-WRSM will be experimented to validate the brushless operation and verify the simulation analysis.

[1] F. Yao, Q. An, X. Gao, L. Sun, and T. A. Lipo, "Principle of Operation and Performance of a Synchronous Machine Employing a New Harmonic Excitation Scheme," in *IEEE Transactions on Industry Applications*, vol. 51, no. 5, pp. 3890-3898, Sept.-Oct. 2015. [2] Qasim Ali, Thomas A. Lipo, Kwon, Byung-il "Design and Analysis of a Novel Brushless Wound Rotor Synchronous Machine*" IEEE Trans. on Magn.,*vol. 51, no. 11, Nov. 2015 [3] G. Jawad, Q. Ali, T. A. Lipo and B. I. Kwon, "Novel Brushless Wound Rotor Synchronous Machine with Zero-Sequence Third-Harmonic Field Excitation," in *IEEE Transactions on Magnetics*, vol. 52, no. 7, pp. 1-4, July 2016 [4] Hussain Asif, and Kwon, Byung-il "A new brushless wound rotor synchronous machine using a special stator winding arrangement." Electrical Engineering (2017): 1-8 [5] Ali, Q., Atiq, S., Lipo, T. A., & Kwon, B. I. (2016). PM Assisted, Brushless Wound Rotor Synchronous Machine. *Journal of Magnetics,* 21(3), 399-404. [6] Li, Dawei, Ronghai Qu, Jian Li, and Wei Xu. "Design of consequent pole, toroidal winding, outer rotor vernier permanent magnet machines." In *Energy Conversion Congress and Exposition (ECCE), 2014 IEEE*, pp. 2342-2349. IEEE, 2014.

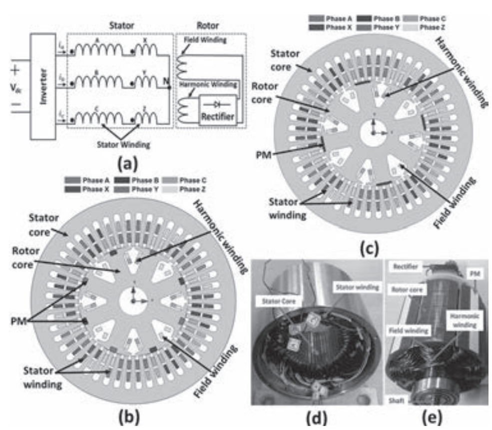

Fig. 1. (a) Single inverter fed brushless topology, (b) PM assisted BL-WRSM, (c) Proposed CPH-BL-WRSM (d) stator of prototype and (e) consequent pole hybrid rotor of prototype

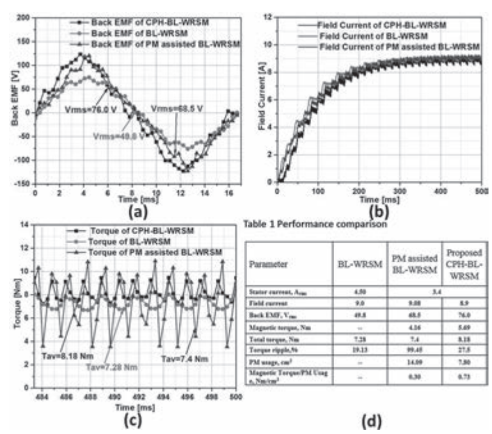

Parameter	BL-WRSM	PM assisted BL-WRSM	Proposed CPH-BL-WRSM
Stator current, A_{rms}	4.50	3.4	
Field current	9.0	9.08	8.9
Back EMF, V_{rms}	49.8	68.5	76.0
Magnetic torque, Nm	--	4.16	5.69
Total torque, Nm	7.28	7.4	8.18
Torque ripple,%	19.13	99.45	27.5
PM usage, cm^3	--	14.09	7.80
Magnetic Torque/PM Usage, Nm/cm^3	--	0.30	0.73

Fig. 2. 2-D FEM analysis (a) Back EMF comparison (b) Induced field current comparison (c) Torque comparison (d) Performance comparison

4:15

FH-09. An Innovative Dual-Rotor Axial-Gap Flux Switching Permanent Magnet Machine Topology with Hybrid Excitation.

E. Yildiriz[1], M. Gulec[2] and M. Aydin[2]
1. Electrical and Electronics Engineering, Duzce University, Düzce, Turkey; 2. Mechatronic Engineering, Kocaeli University, Kocaeli, Turkey

I. INTRODUCTION Flux-switching machines (FSM) have attracted a lot of attention by researchers over the last decade due to their high torque density and sinusoidal back-EMF in addition to robust, magnetless and cost effective rotors. The theory of flux switching can be applied to axial, radial, linear and transverse flux machines. Axial-flux machines in general have advantages such as short axial length, better heat dissipation and high efficiency compared with radial-flux machines [4]. Furthermore, flux switching machines proposed in the literature so far are mostly radial-flux structures [1, 2]. A limited number of FSM papers deal with axial gap flux switching topologies due to difficulties in the design and analyses in 3-dimensional space [3-5]. In this study, a new double-rotor-single-stator, axial-gap, flux switching permanent magnet (PM) synchronous (AGFSPM) machine with hybrid excitation is proposed for the first time in literature. The proposed hybrid-excited AGFSPM machine combines the advantages of PM machine and the wound-rotor synchronous machine. II. OPERATION PRINCIPLE, ANALYSIS AND EXPERIMENTAL RESULTS *A.Structure and Operating Principles* The proposed AGFSPM motor has double-rotor-single-stator with 12-slot 10-pole configuration with hybrid excitation. The structure of the AGFSPM is displayed in Figure 1. AC windings are placed in the slots openings on both sides of the stator core. DC windings, on the other hand, are placed inside the stator core in a back-to-back (or toroidal) manner in order to ease the stator manufacturing. Permanent magnets are placed in the slot openings in a consecutive manner so as to help the flux reverse the polarity as the DC winding is energized. When the rotor pole and the stator tooth are in full alignment as in Figure 2a, the flux is switched. Thus, the flux passing through the air gap encircles the phase-A windings. When there is no excitation current, some of the magnet flux passes through the air gap and some passes through the stator yoke short-circuiting the magnetic circuit. If a sufficient amount of positive DC current is applied (Figure 2c), the magnetic flux generated by the excitation current together with all of the magnet flux will also pass through the motor airgap for energy conversion. When the rotor pole reaches at the next stator tooth, the flux direction passing through the airgap is reversed as illustrated in Figure 2b when MMF is 0 AT and Figure 2d when MMF is 1100 AT. *B.Optimization of Design Parameters and 3D Finite Element Analyses* To design of the flux switching machine, the number of stator slots and rotor poles, shape and width of the poles, slots and magnets are critical parameters of the AGFSPM motor [6]. Electrical output power of such disc motor can be expressed as $P_{out} = (2m/T)\int e(t)i(t)d(t)$ (1) $P_{out} = mE_{max}I_{max}$ (2) $P_{out} = ((\sqrt{2}\pi^2)/240)A_sB_{g\,max}\,K_dK_f(P_r/P_s)D_on(1+\lambda)/2[(\pi/4)D_o^2(1-\lambda^2)-P_rL_{pm}W_{pm}]$ (3) The main parameters of the proposed designed AGFSPM machine are given in Table 1.3D modeling of the proposed AGFSPM has been made according to Table1. Figure 3 shows mesh profile and flux distributions for positive MMF. *C. Prototype Motor and Experimental Results* The picture of the prototype AGFSPM motor, stator with both AC and DC windings and magnetless rotor are all illustrated in Figure 4. The test results and the comparison with the FEA will be provided in the final version of the paper. III. CONCLUSION In this paper, a new axial-gap, flux switching PM machine with AC and DC hybrid excitation is proposed. Motor principles, initial design equations, some 3D FEA results are provided. Proof-of-concept motor is manufactured based on the design and experimental work has started. Detailed results and comparison between the FEA and test data will be provided in the final version of the paper.

1- Z. Q. Zhu, "Switched flux permanent magnet machines — Innovation continues," 2011 International Conference on Electrical Machines and Systems, Beijing, 2011, pp. 1-10. 2- Z. Xu, S. Xie and P. Mao, "Analytical Design of Flux-Switching Hybrid Excitation Machine by a Nonlinear Magnetic Circuit Method," in IEEE Transactions on Magnetics, vol. 49, no. 6, pp. 3002-3008, June 2013. 3- L. Hao, M. Lin, X. Zhao and H. Luo, "Analysis and optimization of EMF waveform of a novel axial field flux-switching permanent magnet machine," 2011 International Conference on Electrical Machines and Systems, Beijing, 2011, pp. 1-6. 4- L. Hao, M. Lin, W. Li, H. Luo, X. Fu and P. Jin, "Novel Dual-Rotor Axial Field Flux-Switching Permanent Magnet Machine," in IEEE Transactions on Magnetics, vol. 48, no. 11, pp. 4232-4235, Nov. 2012. 5-X. Liu, Y. Diao, C. Zhang, D. Chen, L. Zuo and L. Yi, "Design optimization of an axial flux-switching hybrid excitation synchronous machine at no-load," in IET Electric Power Applications, vol. 8, no. 9, pp. 342-348, 11 2014. 6- W. Zhang, X. Liang, M. Lin, L. Hao and N. Li, "Design and Analysis of Novel Hybrid-Excited Axial Field Flux-Switching Permanent Magnet Machines," in IEEE Transactions on Applied Superconductivity, vol. 26, no. 4, pp. 1-5, June 2016.

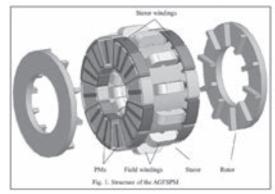

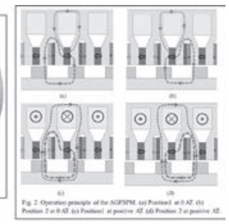

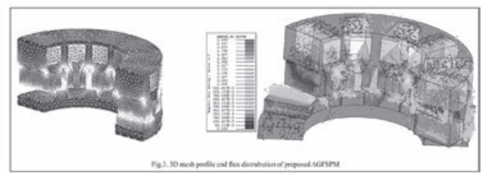

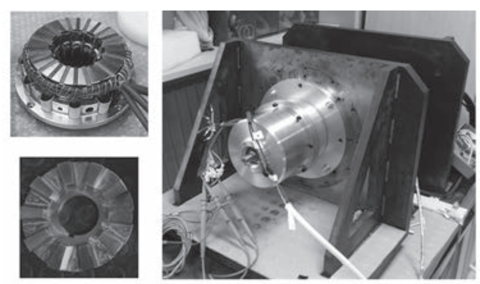

Fig. 4. Prototype of the hybrid excitation dual-rotor AGFSPM

Table 1. Main Parameters of the Hybrid Excited AGFSPM

Parameter	Value
Number of phase	3
Nember of turn per phase	360
Rated speed (r/min)	750
Stator outer diameter (mm)	126
Stator inner diameter (mm)	72
Number of stator slots	12
Number of poles	10
Magnet Width (deg)	7,5°
Pole Width(deg)	15,5°
Air-gap length (mm)	1

4:30

FH-10. Design of a ▽+U shape Interior PM Machines for Electric Vehicle Applications.

M. Sheng[1]
1. Nanjing University of Aeronautics and Astronautics, Nanjing, China

I. Introduction Interior permanent magnet (IPM) machines are widely used in electric vehicle (EV) applications because of outstanding performance characteristics such as the wide constant-power speed range, high power density, and low magnet eddy-current loss [1], [2]. A parameterized finite-element analysis model is adopted to optimize the pole-arc to pole-pitch ratios to maximize the fundamental air-gap flux density (model I) and minimize its total harmonic distortion (model II). The torque density, torque ripple, *d*- and *q*-axis inductances, iron losses, power, and efficiency are analyzed and compared of the two models. II. Main Body Fig. 1 shows the core loss density and the iron loss segregation of two ▽+U shape IPM machines, where V_{am} is the amplitude of phase voltage, I_{em} is the amplitude of the phase current. The ▽+U shape IPM machine with maximize the fundamental air-gap flux density is model I, the ▽+U shape IPM machine with minimum THD of air-gap flux density is model II. The rated power of the machines is 48 kW, and the maximum speed of the machines is 12000 r/min. The core loss density at the stator teeth of model I is significantly higher than the model II, the rotor core loss densities of the two models are almost the same. The eddy current loss is larger than hysteresis, and the stator eddy current and hysteresis loss of the model II are significantly lower than that of the model I. The PM eddy current losses of the two models are almost the same. At 12000 r/min, the total iron loss of the model I is 1636.6 W, and model II is 1089 W which reduced 50 % than the model I. The *d*- and *q*-axis inductances and the saliency ratio ρ of the two models under the limitation of inverter voltage are investigated. A prototype IPM machine with model II is manufactured to verify the results of the analysis. Fig. 2(a) shows the photographs of the rotor. The measured EMF of the prototype machine are shown in Fig. 2(b). The FEA predicted and measured torques, and efficiencies of model II are shown in 2(c), and exhibit good agreement. III. Conclusion This paper proposed a ▽+U shape IPM machine for electric vehicle applications. A parameterized finite-element analysis model is adopted to optimize the pole-arc to pole-pitch ratios to maximize the fundamental air-gap flux density and minimize its total harmonic distortion. The ▽+U shape IPM machine with minimized THD of air-gap flux density can reduce the torque ripple and iron losses with only slight reduction of the average torque. Finally, the prototype ▽+U shape IPM machine with the minimum THD of air-gap flux density is fabricated, and the experiments are presented to verify the results of FEAs.

[1] Qi Li, Tao Fan, and Xuhui Wen, "Characterization of Iron Loss for Integral-Slot Interior Permanent Magnet Synchronous Machine During Flux Weakening," *IEEE Trans. Magn*., vol. 53, no. 5, May. 2017, Art. no. 8101308.

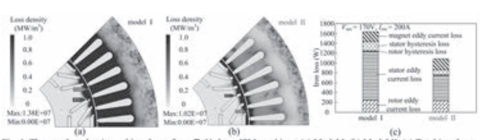

Fig. 1. The core loss density and iron loss of two ▽+U shape IPM machines. (a) Model I. (b) Model II. (c) Total iron loss.

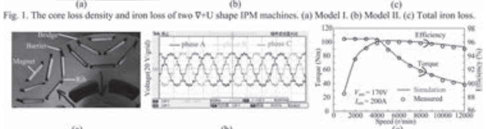

Fig. 2. The rotor, simulated and tested results of EMF, torque, and efficiency. (a) Photographs of rotor. (b) Measured EMF. (c) Simulated and measured torque, and efficiency.

4:45

FH-11. Optimal Design and Experimental Test of Surface-Mounted Permanent Magnet Motors with Cost-Effective Magnet Utilization to Suppress Torque Pulsations.

W. Zhao[1], H. Shen[1], W. Chai[2], X. Wang[1] and B. Kwon[2]
1. School of Electrical Engineering, Shandong University, Jinan, China; 2. Department of Electronic Systems Engineering, Hanyang University, Ansan, The Republic of Korea

I. Introduction The surface-mounted permanent magnet (SPM) motors with NdFeB magnets, offering high torque density and high efficiency, have been widely applied to various domestic and industrial applications [1]. However, the adoption of NdFeB magnets not only brings high torque density, but also leads to high torque pulsations and high magnet cost. The approaches to suppress torque pulsations in SPM motors have been heavily investigated through drive control or motor design methods [2], [3]. In particular, the suppression of cogging torque has received great attention along with numerous methods, such as skewing [4], auxiliary slots [5], teeth notching [6], and slot-opening shifting [7], etc. However, most of the methods to suppress cogging torque may not result in low torque ripple due to the effects of armature reaction fields. Hence, the approaches to suppress both cogging torque and torque ripple simultaneously are more desired. It is well known that the magnet flux density distribution has a significant effect on torque performance. Accordingly, extensive magnet shaping methods, such as magnet pole shape optimization [8] and sinusoidal magnet poles [9], have been reported to obtain a sinusoidal magnet flux density distribution, thus to reduce torque pulsations. However, these reported methods inevitably lead to manufacturing difficulty and performance degradation. Regarding to the magnet cost saving, the approaches by using ferrite magnets, or hybrid ferrite and NdFeB magnets are investigated, but generally neglecting the issues on torque pulsations [10]. In this paper, an optimal design is proposed for the SPM motor to reduce the cogging torque and toque ripple, and save the magnet cost using multi-grade NdFeB and ferrite magnets. Based on a conventional SPM motor with single-grade NdFeB magnets, the proposed SPM motor is designed with three-grade NdFeB and ferrite magnets, and then optimized to further reduce torque pulsations and save the magnet cost by maintaining the high average torque using the Kriging method and a genetic algorithm. All the motor characteristics are first predicted using the finite element method (FEM) at the same operating conditions. Then the experimental test is performed for the optimized model to validate the optimal design and analysis results. II. Modeling, Optimal Design, and FEM Analysis Results The conventional SPM motor with arched magnet shape is referred as the basic model as shown in Fig. 1 (a). The rotor is mounted with single-grade NdFeB magnets (0.5 T) with radially magnetized direction. Theoretically, the basic model produces a rectangular airgap flux density waveform, which contains extensive harmonics as shown in Fig. 1(b). The proposed SPM motor exhibits the feature of multi-grade magnets as shown in Fig. 2(a). Ideally, a sinusoidal airgap flux density can be obtained when the remanence of magnets varies in a sinusoidal manner diminished from the middle piece as shown in Fig. 2(b). To avoid excessive manufacturing difficulty and cost, the proposed model herein adopts two-grade NdFeB magnets (1-0.67 T and 2-0.61 T) and one-grade ferrite magnet (3-0.375 T). To obtain the superior performance with the limited magnet pieces, the proposed model is optimized by the Kriging method and a genetic algorithm by selecting the angular width of the magnets as the design variables. The cogging torques are compared in Fig. 3. The proposed and optimized model can highly reduce the cogging torque, while the optimized model reduce the cogging torque by 68.4%, as compared to the basic model. Fig. 4 compares the electromagnetic torques, which indicates that the proposed and optimized models exhibit not only lower torque ripple, which is reduced by 46.1% in the optimized model, but also higher average torque when compared to the basic model. Although the proposed and optimized models adopt better grade of NdFeB magnets, their magnet costs are much lower than the basic model due to the utilization of low-cost ferrite magnets and low-volume NdFeB magnets. The magnet cost of the optimized model is decreased by 39.7%, when compared to that of the basic model, as listed in Table I. III. Experimental Test The optimized model is manufactured for experiments to verify the analysis results as shown in Fig. 5. Fig. 6 shows the comparison of the simulated and measured phase back EMFs at 600 rpm, and Fig. 7 displays the corresponding harmonic analysis. The results indicate that the measured back-EMF waveform agrees well with the simulated result, whereas there exists a discrepancy around the peak points and fundamental values because of the distorted radial magnetization attributing to the relatively small angular width of NdFeB magnet "2". Therefore, the simulated and measured cogging torques exhibit good accordance in waveforms, but with a slight difference in peak-to-peak values, as revealed in Fig. 8. IV. Conclusion This paper has proposed an optimal design for a SPM motor to reduce cogging torque and torque ripple, as well as the magnet cost by using multi-grade NdFeB and ferrite magnets. The results obtained by the FEM show that the optimized model obtained through the Kriging method and genetic algorithm has greatly reduced cogging torque by 68.4%, torque ripple by 46.1%, and magnet cost by 39.7%, as well as the increased average torque when compared to the basic model. Finally, the experimental results have validated the optimal design and analysis results, which sufficiently demonstrated the effectiveness of the proposed SPM motor in terms of minimization of torque pulsations.

[1] D. G. Dorrell, M. F. Hsieh, M. Popescu, L. Evans, D. A. Staton, and V. Grout, "A review of the design issues and techniques for radial-flux brushless surface and internal rare-earth permanent-magnet motors," *IEEE Trans. Ind. Electron*., vol. 58, no. 9, pp. 3741-3757, Sep. 2011. [2] Z. Q. Zhu, Y. Liu, and D. Howe, "Minimizing the influence of cogging torque on vibration of PM brushless machines by direct torque control," *IEEE Trans. Magn*., vol. 42, no. 10, pp. 3512-3514, Oct. 2006. [3] N. Bianchi and S. Bolognani, "Design techniques for reducing the cogging torque in surface-mounted PM motors," *IEEE Trans. Ind. Appl*., vol. 38, no. 5, pp. 1259-1265, Sep./Oct. 2002. [4] J. C. Urresty, J. R. Riba, L. Romeral, and A. Garcia, "A simple 2-D finite-element geometry for analyzing surface-mounted synchronous machines with skewed rotor magnets," *IEEE Trans. Magn*., vol. 46, no. 11, pp. 3948-3954, Nov. 2010. [5] C. Xia, Z. Chen, T. Shi, and H. Wang, "Cogging torque modeling and analyzing for surface-mounted permanent magnet machines with auxiliary slots," *IEEE Trans. Magn*., vol. 49, no. 9, pp. 5112-5123, Sep. 2013. [6] C. S. Koh and J.-S. Seol, "New cogging torque reduction method for brushless permanent-magnet motors," *IEEE Trans. Magn*., vol. 39, no. 6, pp. 3503-3506, Nov. 2003. [7] T. Liu, S. Huang, J. Gao, and K. Lu, "Cogging torque reduction by slot-opening shift for permanent magnet machines," *IEEE Trans. Magn*., vol. 49, no. 7, pp. 4028-4031, Jul. 2013. [8] N. Chen, S. L. Ho, and W. N. Fu, "Optimization of permanent magnet surface shapes of electric motors for minimization of cogging torque using FEM," *IEEE Trans. Magn*., vol. 46, no. 6, pp. 2478–2481, Jun. 2010. [9] W. Zhao, T. A. Lipo, and B.-I. Kwon, "Material-efficient permanent magnet shape for torque pulsation minimization in SPM motors for automotive applications," *IEEE Trans. Ind. Electron*., vol. 61, no. 10, pp. 5779-5787, Oct. 2014. [10] Q. Chen, G. Liu, W. Zhao, M. Shao, and Z. Liu, "Design and analysis of the new high reliability motors with hybrid permanent magnet material," *IEEE Trans. Magn.*, vol. 50, no. 12, Art. no. 8207010, Dec. 2014.

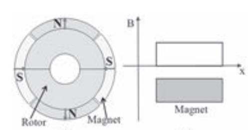

Fig. 1 Basic model and design schematic diagram

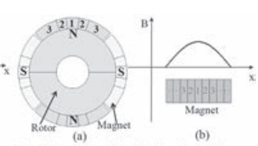

Fig. 2 Proposed model and design schematic diagram

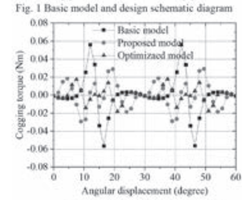

Fig. 3 Cogging torques by the FEM

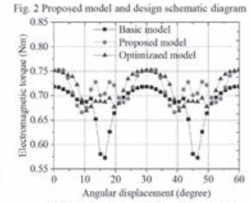

Fig. 4 Electromagnetic torques by the FEM

Table I Analysis results by the FEM

Item	Unit	Basic	Prop.	Opti.
Cogging torque	Nm	0.114	0.059	0.036
Torque	Nm	0.683	0.715	0.716
Torque ripple	%	21.38	12.21	11.53
Magnet cost	$	5.82	3.61	3.51

Fig. 5 Manufactured prototype motor

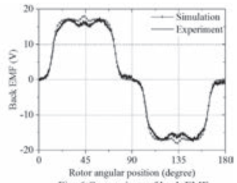

Fig. 6 Comparison of back EMFs

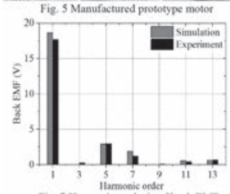

Fig. 7 Harmonic analysis of back EMFs

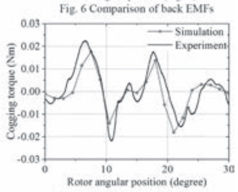

Fig. 8 Comparison of cogging torques

Session FI
FUNDAMENTAL PROPERTIES AND COOPERATIVE PHENOMENA II

Solveig Felton, Chair
Queen's University Belfast, Belfast, United Kingdom

CONTRIBUTED PAPERS

2:00

FI-01. Recovery of long-range magnetic order by Rh substitution in spin glass compound $Mn_{0.7}Fe_{0.3}NiGe$.

S. Samatham[1], A.K. Patel[1] and K. Suresh[1]
1. Department of Physics, Indian Institute of Technology Bombay, Mumbai, India

Introduction Heusler alloys have continued to be on the frontline research for their multi-functional properties such as shape memory effect, large magnetocaloric effect, exchange bias, negative thermal expansion, spintronics, spin-filters etc. Some of these are reported to show complex magnetic behavior with various magnetic ground states such as ferromagnetic, antiferromagnetic, ferromagnetic, coexistence of two magnetic phases, short-range order such as spin-glass, magnetic glass and re-entrant spin glass. Though, many potential compounds have resulted from the interchanging of 3d-transition metals, recently heavy metal (Rh and Pt) based Heusler compounds haven been reported to be good fertile for the technological applications by showing large spontaneous exchange bias [1] and skyrmion characteristics [2]. In the present paper, we discuss the properties of $Mn_{0.7}Fe_{0.3}NiGe$ in which Rh is doped for Fe. We present the combined results of structural, dc-magnetization and ac-susceptibility measurements. In particular, the evolution of long-rang magnetic order with increase of Rh concentration for Fe and manifestation of short-range magnetic correlations are addressed. Experimental Techniques Polycrystalline $Mn_{0.7}Fe_{0.3-x}Rh_xNiGe$ with nominal compositions of x = 0.1, 0.2 and 0.3 are prepared by arc melting the constituent elements (of at least 4N purity) in Argon gas flow-environment. Room temperature X-ray diffraction patterns are recorded using powder specimens using Cu-K_α radiation. Magnetization as a function of temperature and magnetic field is measured using 7 T-SQUID-Vibrating Sample Magnetometer down to 2K and in fields up to 70 kOe. Results and discussion $Mn_{0.7}Fe_{0.3}NiGe$ is a derived compound from MnNiGe [3] (Fe doped for Mn) which undergoes a structural transition from TiNiSi-type orthorhombic to Ni_2In-type hexagonal at a particular concentration [4]. Figure 1(a) shows the temperature dependent magnetization $M(T)$ measured from 2-300 K in 100 Oe for nominal compositions with x = 0, 0.1, 0.2 and 0.3 of $Mn_{0.7}Fe_{0.3-x}Rh_{x}NiGe$. A finite difference between zero-field cooled (ZFC) (hallow symbols) and field-cooled warming (FCW) (solid red-line) curves is evident for all the compounds. However, $Mn_{0.7}Fe_{0.3}NiGe$ shows spin-glass transition (T_g) below 82.8 K which is in agreement with the literature [4]. T_g values for $Mn_{0.7}Fe_{0.2}Rh_{0.1}NiGe$ and $Mn_{0.7}Fe_{0.1}Rh_{0.2}NiGe$ are 66.0 K and 61.05 K respectively. On the other hand $Mn_{0.7}Rh_{0.3}NiGe$ orders ferromagnetically below $T_C \sim 120$ K. A cursory look at temperature dependent magnetization of $Mn_{0.7}Fe_{0.3-x}Rh_xNiGe$, from Fig. 1(a) and (b), reveals that Rh substitution in place of Fe recovers the long-range magnetic order which is a second order phase transition from paramagnetic to ferromagnetic within austenite phase. Magnetization isotherms from -70 to 70 kOe are shown in Fig. 1(b) measured at 2 K. Magnetization shows non-saturating behavior for x = 0, 0.1 and 0.2, as expected for spin-glass compounds while x = 0.3 saturates above 13 kOe with 2.18 μ_B/f.u. Under a magnetic field of 70 kOe, magnetization is found to decrease for x = 0.1 and 0.2 as compared to x = 0 with an exceptionally sudden increase for x = 0.3. Shown in Fig. 2 is the expanded-view of low-field isothermal magnetization curves of $Mn_{0.7}Fe_{0.3-x}Rh_{x}NiGe$ measured after cooling the specimen to 2 K in 0 kOe. Commonly, it is noticed that $M(H)$ of spin-glass compounds x = 0, 0.1 and 0.2 is asymmetric around H = 0 kOe, indicating the exchange bias (EB) behavior. However, the ordered compound $Mn_{0.7}Rh_{0.3}NiGe$ does not show hysteretic behavior. Coercive magnetic field (H_{Coerc}) and EB (H_{EB}) are estimated as $H_{Coerc} = (H_2-H_1)/2$ and $H_{EB} = -(H_2+H_1)/2$ where H_1 and H_2 are the zero-magnetization points on negative and positive field axes. H_{Coerc} and spontaneous H_{EB} are found to increase with Rh substitution. Conclusion In the full paper, we discuss the effect of heavy 4d-metal Rh substitution on the spin glass behavior of $Mn_{0.7}Fe_{0.3}NiGe$ using the combined results of X-ray diffraction, dc-magnetization and ac-susceptibility measurements. At room temperature, all the compounds are found to crystallize in Ni_2In-type hexagonal austenite structure. The austenite high-temperature paramagnetic to low-temperature spin-glass-like transition is observed for x = 0, 0.1 and 0.2. A long-range ferromagnetic ordering is achieved upon complete replacement of Fe by Rh. Importantly, the spin-glass compounds are observed to show spontaneous exchange bias i.e., in zero-field cooled mode.

[1] A. K. Nayak et al., Nature Materials 14, 679 (2015) [2] A. K. Nayak et al., Nature 548, 561 (2017) [3] H. Fjellvag et al., J. Magn. Magn. Mater. 50, 291 (2015) [4] E. Liu et al., Nature Communications 3, 873 (2012)

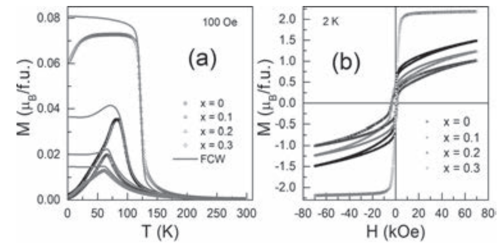

Fig. 1. (a) Temperature dependent magnetization $M(T)$ of $Mn_{0.7}Fe_{0.3-x}Rh_{x}NiGe$ with x = 0, 0.1, 0.2 and 0.3, measured in ZFC and FCW protocols. $M(T)$ of x = 0, 0.1 and 0.2 resemble spin-glass-like behaviour whereas x = 0.3 shows a typical ferromagnetic transition below 120 K. (b) Magnetic field dependence of magnetization of $Mn_{0.7}Fe_{0.3-x}Rh_xNiGe$ measured isothermally at 2 K. Non-saturation along with hysteretic behaviour for x = 0, 0.1 and 0.2 indicate the spin-glass-like nature as suggested by $M(T)$. x = 0.3 is a ferromagnet with saturation magnetization of about 2.18 μ_B/f.u.

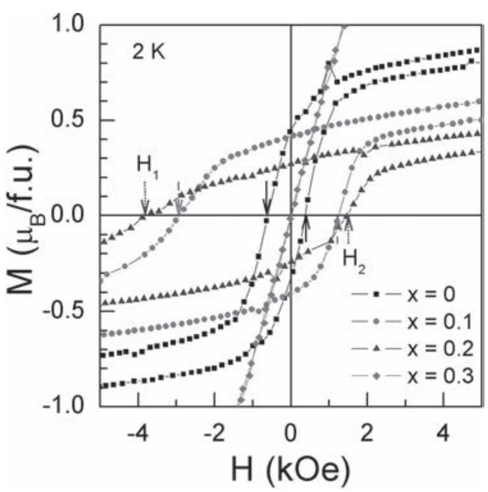

Fig. 2. Expanded low-field $M(H)$ of $Mn_{0.7}Fe_{0.3-x}Rh_xNiGe$. H_1 and H_2 are the zero-magnetization points on negative and positive field axes. ZFC/spontaneous exchange bias is about 117.6, 835.5 and 897.9 Oe respectively for x = 0, 0.1 and 0.2.

2:15

FI-02. Magnetization dynamics of weakly interacting sub-100 nm square artificial spin ices.

J. Porro Azpiazu[1,2], S. Morley[3,4], D. Alba Venero[1], R. Macêdo[5], M. Rosamond[3], R.L. Stamps[5], C.H. Marrows[3] and S. Langridge[1]
1. ISIS, the Neutron and Muon Source, Rutherford Appleton Laboratory, Didcot, United Kingdom; 2. BCMaterials, the Basque Center for Materials, Applications and Nanostructures, Leioa, Spain; 3. School of Physics and Astronomy, University of Leeds, Leeds, United Kingdom; 4. Department of Physics, University of California, Santa Cruz, Santa Cruz, CA, United States; 5. School of Physics and Astronomy, University of Glasgow, Glasgow, United Kingdom

Artificial Spin Ice (ASI), consisting of a two dimensional array of nanoscale magnetic elements [1], provides a fascinating opportunity to observe the physics of out of equilibrium systems. Initial studies concentrated on the static, frozen state, whilst more recent studies have accessed the out-of-equilibrium dynamic, fluctuating state [2, 3, 4]. This opens up exciting possibilities such as the observation of systems exploring their energy landscape through monopole quasiparticle creation, potentially leading to ASI magnetricity, and to directly observe unconventional phase transitions. In this work [5] we have measured and analysed the magnetic relaxation of thermally active ASI systems by means of SQUID magnetometry. We fabricated and measured square Artificial Spin Ice samples formed by nanoimagnets made of Permalloy ($Ni_{80}Fe_{20}$) with lateral dimensions of 68nm x 22nm, with two different thicknesses: 5nm and 6nm, and three different lattice spacings: 138nm, 175nm and 208nm, forming a total of six samples. We have investigated the effect of the interaction strength on the magnetization dynamics at different temperatures in the range where the nanomagnets are thermally active and have observed that they follow an Arrhenius-type Nèel-Brown behaviour. An unexpected negative correlation of the average blocking temperature with the interaction strength is also observed, which is supported by Monte Carlo simulations. The magnetization relaxation measurements show faster relaxation for more strongly coupled nanoelements with similar dimensions. The analysis of the stretching exponents obtained from the measurements suggest 1-D chain-like magnetization dynamics. This indicates that the nature of the interactions between nanoelements lowers the dimensionality of the ASI from 2-D to 1-D. Finally, we present a way to quantify the effective interaction energy of a square ASI system, and compare it to the interaction energy calculated from a simple dipole model and also to the magnetostatic energy computed with micromagnetic simulations.

[1] R. F. Wang et al. *Nature* 439, 303 (2006) [2] A. Farhan et al., *PRL* 111, 057204 (2013) [3] J. M. Porro et al., *New J. Phys.* 15, 055012 (2013) [4] S. Zhang et al., *Nature* 500, 553 (2013) [5] J. M. Porro et al, *arXiv preprint*, arXiv:1710.03018 (2017)

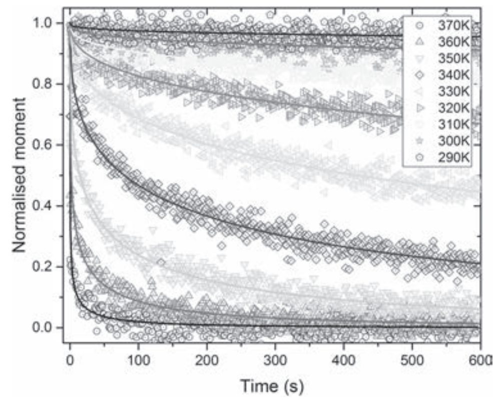

Fig. 1. Measurements of the magnetization relaxation dynamics of one of the samples studied. Each scatter plot corresponds to the measurement of the time evolution of the magnetic moment of the sample at a fixed temperature. The moment is normalised to the magnetic moment of the lowest temperature measured (frozen sample). The superimposed lines correspond to the stretched exponential model fitted to the data to extract the relaxation time and the stretching exponent.

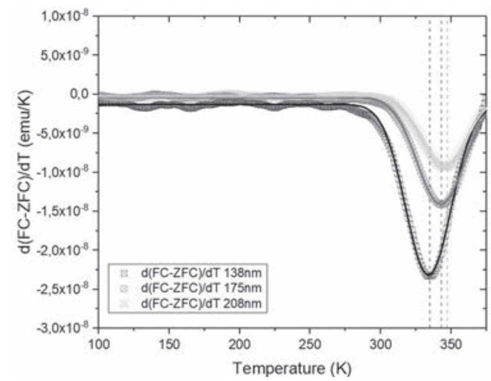

Fig. 2. Plots of the derivative of the difference between the Field Cooling (FC) and the Zero Field Cooling (ZFC) curves measured for three of the samples with different lattice spacings (138nm, 175nm and 208nm) studied (similar nanoisland volumes). The position of the peak indicates the average blocking temperature of each sample. The trend observed in the peak positions indicates that the average blocking temperature decreases with the interaction strength.

2:30

FI-03. Electron Accumulation and Emergent Magnetism in LaMnO3/ SrTiO3 Heterostructures.

Z. Liu[1]
1. School of Materials Science & Engineering, Beihang University, Beijing, China

Emergent phenomena at polar-nonpolar oxide interfaces have been studied intensely in pursuit of next-generation oxide electronics and spintronics. Here we report the disentanglement of critical thicknesses for electron reconstruction and the emergence of ferromagnetism in polar-mismatched $LaMnO_3$/$SrTiO_3$ (001) heterostructures. Using a combination of element-specific x-ray absorption spectroscopy and dichroism, and first-principles calculations, interfacial electron accumulation, and ferromagnetism have been observed *within* the polar, antiferromagnetic insulator $LaMnO_3$. Our results show that the critical thickness for the onset of electron accumulation is as thin as 2 unit cells (UC), significantly thinner than the observed critical thickness for ferromagnetism of 5 UC. The absence of ferromagnetism below 5 UC is likely induced by electron overaccumulation. In turn, by controlling the doping of the $LaMnO_3$, we are able to neutralize the excessive electrons from the polar mismatch in ultrathin $LaMnO_3$ films and thus enable ferromagnetism in films as thin as 3 UC, extending the limits of our ability to synthesize and tailor emergent phenomena at interfaces and demonstrating manipulation of the electronic and magnetic structures of materials at the shortest length scales.

Z. Chen *et al*. Electron Accumulation and Emergent Magnetism in $LaMnO_3$/$SrTiO_3$ Heterostructures. *Phys. Rev. Lett.* 119, 156801 (2017).

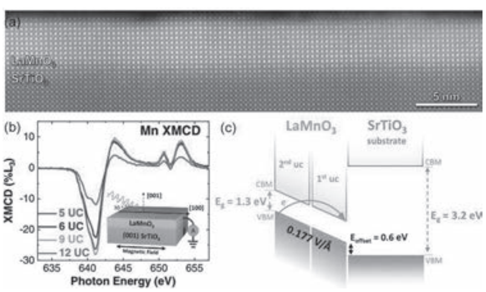

Fig. 1. Emerging ferromagnetism and interfacial electron accumulation in $LaMnO_3$/$SrTiO_3$ (LMO/STO) heterostructures. (a) TEM image of a 12-unit-cell LMO/STO heterostructure. (b) X-ray magnetic circular dichroism spectra of the Mn L_3 edge for different LMO/STO heterostructures. (c) Schematic for the polar-field-induced electron transfer *within* the LMO layer.

2:45

FI-04. Complex Magnetic Structure of Tb_3Ni.

S. Goswami[1], P. Babu[1] and R. Rawat[2]
1. Magnetism, UGC-DAE Consortum for Scientific Research, Mumbai Centre, Mumbai, India; 2. UGC-DAE Consortium for Scientific research, Indore, India

Rare-earth rich intermetallic compounds of the type R_3T (R = rare earth, T = transition metal) received much less attention although rare-earth (RE) intermetallic compounds in general have been well studied. This is because R_3T compounds, which crystallize in orthorhombic Fe_3C type structure exhibit complex magnetic behavior.[1] A number of magnetic transitions as function of temperature and sometimes magnetic field have been observed in these compounds. In this study, one such compound, Tb_3Ni, is explored to unravel its complex magnetic behavior. Tb_3Ni is prepared by arc melting in Ar atmosphere and studied by dc magnetization, specific heat and neutron diffraction techniques. Magnetization results show Tb_3Ni orders magnetically below ~77K and the 'zero-field cooled' (ZFC) and 'Field Cooled' (FC) magnetization curves show (Fig.1) large bifurcation below 75K or so. ZFC exhibits two consecutive peaks at around ~ 77K and ~ 53K before rapidly falling towards low magnetization as T is decreased. It again shows a sharp peak at ~ 3K and it falls rapidly as 2K is reached. On other hand, FC curve continues to increase as T is lowered and 3K peak is observed in FC curve also. Curie-Wiess analysis of inverse susceptibility obtained from ZFC curve above T_C yields an effective paramagnetic moment of μ_{eff} = 4.75 μB /atom and θ_P = 88K. The effective paramagnetic moment turns out to be much less than the free ion moment of Tb^{3+}. The virgin magnetic isotherms measured at some selected temperatures show metamagnetic transition for T < 65K. The behavior of critical field at which this metamagnetic like transition takes place is different for T < 45K and for 50K < T < 65K, clearly indicating spin reorientation around 50K. M-H loops suggest that a strong anisotropy is present in the compound in the lower temperature region which is reported earlier also.[2] Magnetic saturation was not observed up to highest field of 9T that could be because of canted spin like structure in the compound. All these results are indicative of presence of a complex magnetic order. The measured MH isotherms between 2 to 120K are used to obtaine magnetocaloric effect (MCE) using the standard equation generally used. The magnetic entropy change thus derived is shown in the inset of Fig.1 at different magnetic field intervals. We found the maximum value of change in magnetic entropy is ~6.9 J/Kg-K for the maximum field change of 9T at T = 60K. To understand magnetic structure more clearly, temperature dependent neutron diffraction (ND) data was collected. As the sample is cooled below 100K, peak starts developing at low angles and becomes extremely intense shown in Fig.2. In addition to this peak, there are few other peaks denoted by '*' in Fig.2 which also develop as T is lowered. At the same time some peaks already present and represent crystalline structure also grow in intensity indicating ferromagnetic like order. These features, i.e. appearance of new diffraction peaks and increase intensities of existing peaks reflects presence of antiferromagnetic (AFM) and ferromagnetic (FM) orders simultaneously. This can arise when magnetic structure is not-collinear, then spin components in certain direction are aligned antiparallel giving rise AFM character and aligned parallel in certain other direction giving FM character. The AFM character at low temperature (2K) is so strong that it cannot be suppressed even by 7T magnetic field as seen infield neutron diffraction data at 2K. However, at 50K this AFM peak could be suppressed by 7T field. Specific heat measured as function of temperature at different fields is shown in the inset of Fig.2. Specific heat (Cp) data shows a sharp peak at ~ 52K which is consistent with the corresponding magnetic transition. However, Cp data does not exhibit any noticeable features at other temperatures as seen in ZFC magnetization. This is not surprising as Cp comprises of large non-magnetic electronic and phononic contributions apart from magnetic part. The sharp feature in Cp gets suppressed with external magnetic field (up to 3T). The low temperature zero field C_P data was analyzed in terms of the expression $C_P/T = \gamma + \beta T^2$ to extract the Sommerfeld's coefficient, γ, and Debye Temperature Θ_D from β. The values of γ ~ 71 mJ/mol-K_2 obtained from Cp data for Tb_3Ni is much large than that for isostructural compound of Tb_3Co for which γ ~ 45 mJ/mol-K2.[3] Similarly Debye Temperature Θ_D = 111K is slightly lower than that expect for these type compounds (150 to 200 K). This is because of crystal field effects at very low temperatures makes estimation of accurate Debye temperature difficulty. [4] Magnetic, specific heat and neutron diffraction studies indicate that Tb_3Ni has a dominant AFM order at low temperatures but the magnetic structure is non-collinear type. It exhibits two spin re-orientation transitions at ~3K and ~50K. Strong anisotropy in the compound is reflected in these studies. The moderate value of MCE is quite lower than the isostructural compound Tb3Co that may be because of strong anisotropy present in the compound.[5]

[1]. O.A.W. Strydom, L. Alberts, J. Less-Common Met., 22(4), (1970), 511-515. [2].D. Gignoux, J. C. Gomez-Sal, D. Paccard, Soild State Commun., 44(5), (1982), 695-700. [3]. J C B Monteiro, G.A. Lombardi, R.D. dos Reis, H.E. Freitas, L.P. Cardoso, A.M. Mansanares, F.G. Gandra, Physica B, 503, (2016), 64 [4]. N.V. Tristan, K. Nenkov, K. Skokov, T. Palewski, Physica B, 344, (2004) 462-469. [5]. B.Li, J. Du, W. J. Ren, W. J. Hu, Q. Zhang, D. Li, and Z. D. Zhang, Phys. Lett. A, 92, (2008), 242504.

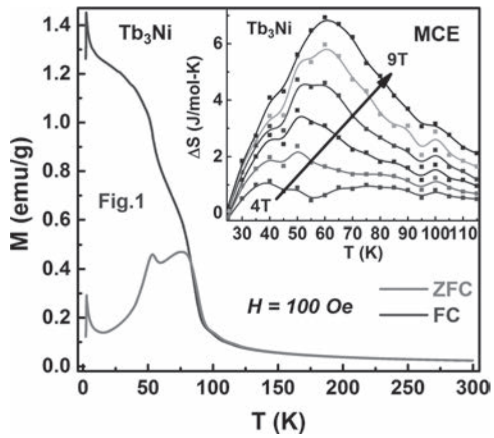

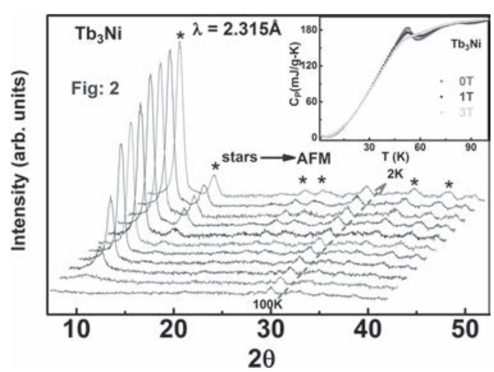

3:00

FI-05. Universal magnetic behavior of $Ni_2Mn_{1-x}Fe_xIn$ (x = 0.0 and 0.1) through magnetization, magnetocaloric and magnetoresistnace scaling methods.

A.K. Patel[1], S. Samatham[1] and K. Suresh[1]
1. Department of Physics, Indian Institute of Technology Bombay, Mumbai, India

Introduction Ever since the discovery of Heusler alloys, these have been continuously claiming prominent place in condensed matter research for their rich properties [1, 2]. One of the interesting aspects of these alloys is the giant magnetocaloric effect (MCE), suitable for magnetic refrigeration for room temperature (RT) applications. There have been numerous compounds identified and investigated for the large MCE at RT, based on rare-earth elements [3]. However, Huesler alloys also provide nearly same order of MCE values, but these are more cost effective. The large MCE is due to the first order magneto-structural transition. Therefore, there is an ample scope to search for good MCE materials within the Heusler family with different combinations of 3d and 4d elements. Nevertheless, apart from the technological view point, it is important and crucial to understand the underlying physics of these compounds in terms of magnetic interactions. Although some of these exhibit second order phase transition from paramagnetic to ferromagnetic state, universality class and origin of magnetic interactions are not still clear. Towards this end, we have made an attempt to unravel the spin interaction and universality class of Fe doped Ni_2MnIn compounds with the help of a novel magneto-entropic scaling. Experimental Technique Polycrystalline $Ni_2Mn_{1-x}Fe_xIn$ (x = 0.0 and 0.1) alloys were prepared by arc melting technique with stoichiometric ratios having at least 4N purity of each element. Room temperature X-ray diffraction (XRD) patterns were recorded on the powder specimens of as-prepared alloys using Cu-K_α radiation. Structural details were obtained using Rietveld refinement using FullProf suite. Magnetization as a function of temperature and field was measured using Vibrating Sample Magnetometer. Resistivity was measured using standard four-probe method down to 5 K with the help of Physical Property Measurement System (QD, USA). Results and Discussion Figure 1(a) shows the room temperature XRD of $Ni_2Mn_{1-x}Fe_xIn$ (x = 0.0 and 0.1) along with Rietveld refinement. The compounds are found to be phase pure and crystallize in cubic structure with space group Fm-3m. The estimated lattice parameters are 6.059 and 5.056 Å respectively. Inverse susceptibility is fitted with Curie-Weiss law, $\chi^{-1} = (T-\theta_{CW})/C$ where C is the Curie constant, to estimate the Curie-Weiss temperature (θ_{CW}) and the effective magnetic moment (μ_{eff}). The fits are shown in the Fig. 1(b). θ_{CW} values for x = 0.0 and = 0.1 are 321 and 332 K while μ_{eff} = 5.04 and 5.82 μ_B respectively. For x = 0.0, in order to estimate the magnetocaloric effect in terms of the change in magnetic entropy, isothermal magnetization curves are measured near magnetic transition T_C at a regular temperature interval of 1 K. The estimated magnetic entropy change is shown in the Fig. 2(a). The maximum magnetic entropy change is found to be 4.2 J.Kg^{-1}.K^{-1} at 50 kOe near 312 K. So as to understand the magnetic interactions, the commonly suggested method is to evaluate the critical exponents near transition temperature. The slope of the Arrott's plot (M^2 vs H/M) is used to identify the type (positive for second order and negative for first order) of phase transition [4]. Here, we have implemented magnetocaloric method [5] to evaluate the critical exponents, as shown in the Fig. 2(b) and (c). Thus obtained critical exponents are $\beta \sim$ 0.28, $\gamma \sim 2.24$ and $\delta \sim 8.06$. Primarily, it is understood from the exponents that x = 0.0 does not specifically belong to any common universality class but may be close to the tricritical mean-field universality class (β = 0.25, γ = 1.0 and δ = 5.0) [6] with slightly higher values of γ and δ. Using these critical exponents as initial guess, we will evaluate the more accurate exponents using modified Arrott's plot (MAP), Kouvel Fisher (KF) methods. In addition, we also perform the similar scaling using magnetoresistance (MR). Finally, the universal scaling of the isothermal magnetization curves and magnetic-entropy will be carried out below and above T_C to unravel the normalization of spin interaction, thereby unveiling the type and range (short or long) of magnetic interactions. Conclusion In the full paper, we mainly explore the type and range of spin interactions of $Ni_2Mn_{1-x}Fe_xIn$ (x = 0.0 and 0.1) with the help of MAP, KF, MCE and MR methods. The ambiguity over the association of first order phase transition near T_C will be explored. The universal scaling by various methods will definitely be helpful to understand the spin interactions. Similar methods will be employed for x = 0.1 and the results will be compared with those of x = 0.0.

[1] Kainuma et al., Nature 439, 957 (2006) [2] Nayak et al., Phys. Rev. Lett. 110, 127204 (2013) [3] Pacharsky et al., Phys. Rev. Lett. 78, 4494 (1997) [4] S. K. Banerjee, Phys. Lett. 12, 16 (1964) [5] Franco et al., J. Phys.: Condens. Matter 20, 285207 (2008) [6] K. Huang, *Statistical Mechanics* (Wiley, New York, 2nd Ed., 1987)

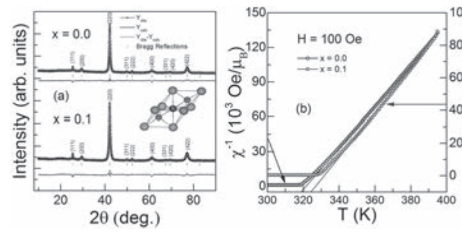

Fig. 1. (a) Room temperature X-ray diffraction patterns for $Ni_2Mn_{1-x}Fe_xIn$ (x = 0.0 and 0.1). The compounds are found to be phase pure and crystallize in Cubic structure with space group Fm-3m. Inset shows the schematic of unit cell showing Ni, Mn and In positions. (b) Inverse susceptibility versus temperature in 100 Oe.

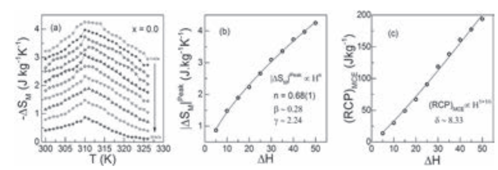

Fig. 2. (a) Magnetic entropy change at few representative magnetic fields. (b) and (c) Evaluation of critical exponents as per Franco et al. [5].

3:15

FI-06. Signature of a Griffiths phase in layered canted antiferromagnet Sr_2IrO_4.

A. Rathi[2], P. Rout[1], S. Perween[2], R. Singh[3], A. Gupta[2], R. Pant[2] and G. Basheed[2]
1. CSIR-National Physical Laboratory (NPL), New Delhi, India, New Delhi, India; 2. AcSIR, CSIR-National Physical Laboratory (NPL) Campus, New Delhi, India; 3. Indian Institute of Science Education and Research (IISER), Bhopal, India

The 5d layered iridate Sr_2IrO_4 has been greatly acknowledged recently, after the pioneering experiments [1] claiming spin-orbital Mott state and isotropic 2D quantum pseudospin-1/2 Heisenberg AFM excitations, despite weak electronic correlations and large spin-orbit interaction, respectively in 5d systems. Nevertheless, these unconventional observations make SIO analogous to the novel 3d layered high-T_C superconducting (HTSC) cuprates. This led to a theoretical prediction of HTSC in doped-Sr_2IrO_4 [2]; however, recent studies introduce new complexities and alternatively suggest Slater gap [3] and anisotropic 2D XY interactions through critical exponent study [4]. Nevertheless, recently observed HTSC signatures in surface-doped Sr_2IrO_4 [5] recommend reinvestigation of the system. More surprisingly, the magnetic correlations between j = ½ spins even persist in paramagnetic (PM) state [6], which suggest the existence of short-range magnetic clusters in a PM matrix, leading to a Griffiths singularity [7]. In this study, we report the signatures of non-analytic Griffiths phase (GP) in 5d Sr_2IrO_4 and further correlate its unconventional insulating nature with GP above T_N. The temperature-dependent dc magnetization, M (T) shows the magnetic ordering at $T_N \sim 221$ K, in close agreement with the earlier study [4]. The Curie-Weiss (CW) fit in high-temperature range unexpectedly give larger $\mu_{eff} = 0.72\ \mu_B$ than the theoretical value of 0.57 μ_B with $J_{eff} = 1/2$ and $g_J = 2/3$. More importantly, the $1/\chi$ (T) is not fully described by CW behavior down to T_N, but shows negative downturn at much higher temperature, $T_G \sim 285$ K [Fig. 1]. These observations suggest the presence of short-range AFM ordering (or equivalently, finite spin-canted clusters sustained by a strong basal-plane anisotropy) in microscopically phase-separated regions much above the expected bulk T_N. This is a signature of Griffiths singularity, which is further supported by power-law behavior of low-field (100 Oe) inverse magnetic susceptibility, $1/\chi$ (T) α $(T/T_N^R - 1)^{1-\lambda}$ [8] with less-than-unit power exponent, $\lambda = 0.24(1)$ above the magnetic ordering temperature T_N when $T_N < T \leq T_G \sim 285$ K [see inset (a) in Figure 1]. The presence of GP has been associated with the partially irregular sequence of IrO6 octahedral rotation in alternate layers in real samples [9], in contrary to clockwise and anticlockwise rotation in an ordered structure. This can lead to the formation of finite size clusters with local distribution of short-range magnetic interactions. Apart from these, another striking feature in Sr_2IrO_4 is the competition between intralayer canted AFM (in ab-plane) and interlayer AFM (along c-axis) interactions which can stabilize and largely enhance Griffiths phase-like effects, as reported in other systems [10]. The non-analytic nature of GP [7] results in unique critical exponent, $\beta = 0.75(1)$ from modified Arrott plot (MAP) method [11] [see inset (b) in Figure 1], in corroboration with magneto-caloric study. More importantly, the Bray model [7] in GP regime yields a reliable critical exponent, $\beta = 0.19$ (1) [see Figure 1], which falls between that expected for 2D Ising and 2D XY interactions [Table-I], and indicates highly anisotropic 2D XY interactions (XYh_4 universality class) [12]. Finally, the GP signatures in Sr_2IrO_4 suggest the onset of gap formation (from short-range AFM ordering) above the expected bulk T_N, which explains the pseudo-gap above T_N, bad metallic behavior in PM state and continuous nature of "Slater" metal-to-insulator (MIT) transition, as observed in earlier studies [3]. Table 1: Comparison of obtained critical exponents of Sr_2IrO_4 from Modified Arrott plot (MAP) and Griffiths phase (GP) analysis with earlier reported values and different theoretical models. Material/Model Reference Method β γ δ Sr_2IrO_4 This Work MAP 0.75(1) 1.49(2) 2.98(4) Sr_2IrO_4 This Work GP 0.19(1) - - Sr_2IrO_4 [4] ND 0.18 - - Sr_2IrO_4 [4] μSR 0.20 - - 3D Heisenberg [11] Theory 0.365 1.386 4.8 2D XY [12] Theory 0.23 - - 2D Ising [12] Theory 0.125 1.75 15.0

1. B. J. Kim et. al., Science 323, 1329 (2009); J. Kim et. al., Phys. Rev. Lett. 108, 177003 (2012). 2. Z. Y. Meng et. al., Phys. Rev. Lett. 113, 177003 (2014). 3. Q. Li et. al., Sci. Rep. 3, 3073 (2013); A. Yamasaki et. al., Phys. Rev. B 89, 121111(R) (2014). 4. F. Ye et. al., Phys. Rev. B 87, 140406 (2013); M. Miyazaki et. al., Phys. Rev. B 91, 155113 (2015). 5. Y. K. Kim et. al., Nat. Phys. 12, 37 (2016). 6. S. Fujiyama et. al., Phys. Rev. Lett. 108, 247212 (2012); H. Gretarsson et. al., Phys. Rev. Lett. 116, 136401 (2016). 7. R. B. Griffiths, Phys. Rev. Lett. 23, 17 (1969), A. J. Bray, Phys. Rev. Lett. 59, 586 (1987); A. J. Bray et. al., Phys. Rev. B 40, 6980 (1989). 8. A. H. Castro Neto et. al., Phys. Rev. Lett. 81, 3531 (1998). 9. Q. Huang et. al., J. Solid State Chem. 112, 355 (1994). 10. J. Burgy et. al., Phys. Rev. Lett. 87, 277202 (2001); C. Magen et. al., Phys. Rev. Lett. 96, 167201 (2006). 11. A. Arrott et. al., Phys. Rev. Lett. 19, 786 (1967); S. N. Kaul, J. Magn. Magn. Mater. 53, 5 (1985). 12. A. Taroni et. al., J. Phys.: Condens. Matter 20, 275233 (2008).

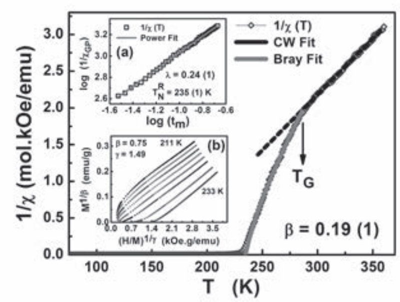

Fig. 1. The temperature dependence of inverse magnetic susceptibility at 100 Oe with Bray and Curie-Weiss fits in Griffiths and paramagnetic phase regimes, respectively. The inset (a) shows the $1/\chi_{GP}$ (T) versus $t_m = (T - T_N^R)/ T_N^R$ plot on log scale with power-law fit. The inset (b) shows the Modified Arrott plot (MAP) with β = 0.75 and γ = 1.49 for temperatures around T_C.

3:30

FI-07. Modulation of spin dynamics across metal to insulator transitions in hybrid heterostructures.

M. Zhu[1], Z. Zhou[1], W. Ren[1] and M. Liu[1]
1. Xi'an Jiaotong University, Xi'an, China

Novel functionalities can be achieved in nanostructured materials in proximity with other dissimilar materials. An interesting possibility along these composite heterostructures is offered by ferromagnets in proximity to materials that undergo a metal insulator transition (MIT) and structural phase transition (SPT). In this study, the electron spin resonance (ESR) and spin switching behaviors of ferromagnetic films have been modulated by the proximity to the VO_2 films that undergo a metal to insulator transition (MIT), accompanying with structural phase transition and sharp resistance changes. On one hand, in the VO_2/FeCoB/Ta composite heterostructures, the modulation mechanism for the MIT of VO_2 films induced ESR changes in the FeCoB thin films with different thicknesses has been explored, in which the temperature effect and MIT effect may alternately take the leading role as the thickness varying. On the other hand, in the VO_2/Ta/$(Co/Pt)_3$/Pt/Ta composite heterostructures, the perpendicular magnetic anisotropy (PMA) in the $(Co/Pt)_3$ multilayers can be reoriented by temperature driven MIT in the coupled VO_2 films, leading to the magnetic easy axis of multilayers switching from out-of-plane to in-plane direction, as well as the spin reorientation in the $(Co/Pt)_3$ multilayers. This opens up an avenue for the modulation of spin dynamics in the composite heterostructures, and produces more possibilities of novel functionalities for the spintronics devices.

1. J. de la. Venta, S. Wang, J. G. Ramirez, I. K. Schuller, Control of magnetism across metal to insulator transitions *Appl. Phys. Lett.* 102, 122404 (2013). 2. J. G. Ramírez, J. de la Venta, S. Wang, T. Saerbeck, A. C. Basaran, X. Batlle, I. K. Schuller, Collective mode splitting in hybrid heterostructures, *Phys. Rev. B* 93, 214113 (2016).

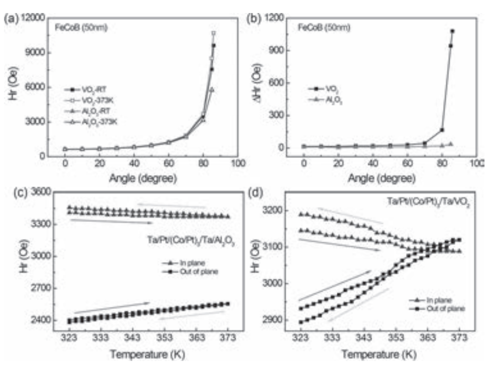

3:45

FI-08. Alternating spin chain compound $AgVOAsO_4$ probed by ^{75}As NMR.

N.A. Koodacadavan[1]
1. Physics, Indian Institute of Science Education and Research, Thiruvananthapuram, India

We performed ^{75}As NMR measurements on a polycrystalline sample of spin-1/2 alternating spin chain Heisenberg antiferromagnet $AgVOAsO_4$. Since the ^{75}As nucleus (nuclear spin $I = 3/2$) is coupled to the magnetic spin V^{4+} via hyperfine coupling, we can extract, understand and investigate the low-lying excitations of the V^{4+} spins by measuring ^{75}As NMR spectra, the NMR shift, and the spin-lattice relaxation rate $1/T_1$. From the fit of ^{75}As NMR spectra, the quadrupole frequency was found to be $v_Q = 6.29$ MHz. The spectral shape remains almost intact over the whole measured temperature range, thus ruling out the possibility of any lattice distortion. The temperature-dependent NMR shift *K(T)*, which is a direct measure of the intrinsic spin susceptibility, and hence free from impurity contributions unambiguously establishes the the spin-1/2 alternating-chain nature of $AgVOAsO_4$. When there is random distribution of defect spins (which would result in a paramagnetic upturn at low temperatures in $\chi(T)$), this paramagnetism broadens the NMR line but without contributing to the NMR shift. Thus, one can precisely estimate the magnetic parameters such as the exchange couplings and the spin gap by analyzing *K(T)* instead of $\chi(T)$. From the analysis of *K(T)*, magnetic exchange parameters were estimated as follows: the leading exchange $J/k_B = 38.4$ K and the alternation ratio $\alpha = J'/J = 0.69$. At low temperatures, the exponential decrease in *K(T)* confirms the presence of the spin gap and implies that the Curie-like upturn observed in $\chi(T)$ was extrinsic in nature and possibly arising from defects in the polycrystalline sample. The transferred hyperfine coupling between the ^{75}As nucleus and V^{4+} spins obtained by comparing the NMR shift with the bulk susceptibility amounts to $A_{hf} = 3.3$ Tμ_B. Below 10 K, both *K(T)* and $1/T_1$(T) enter an activated regime. Its detailed analysis reveals the predominance of 3D correlations triggered by sizable interchain couplings. One can also estimate the spin gap by analyzing the temperature-dependent spin-lattice relaxation rate $1/T_1$. The ^{75}As spin-lattice relaxation time T_1 was measured at the field corresponding to the highest peak position. The recovery of the longitudinal magnetization at different temperatures after a group of saturation pulses was fitted by the following double-exponential function. From the $1/T_1$ data, we estimate the first critical field $H_{c1} = 10$ T, in agreement with the magnetization data. The low-temperature part of *K(T)* yields the spin gap of 6K, which is slightly higher than 4.2 K expected at 6.8 T. The effect of interchain couplings on the low-temperature activated behavior of *K(T)* and the spin-lattice relaxation rate $1/T_1$ is identified.

1. N. Ahmed *et al.,* Alternating spin chain compound $AgVOAsO_4$ probed by ^{75}As NMR, Physical Review B 96, 224423 (2017). 2. Alexander A. Tsirlin *et al.,* Frustrated couplings between alternating spin-1/2 chains in $AgVOAsO_4$, Physical Review B 83, 144412 (2011).

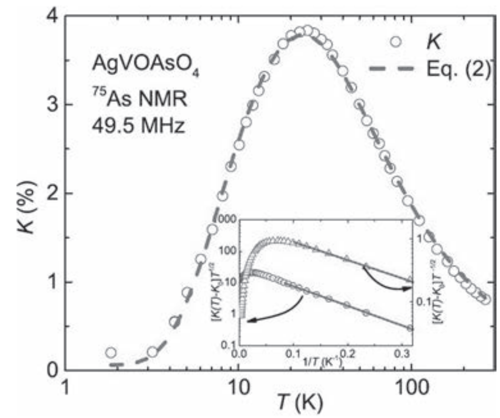

Fig. 1. The temperature dependent ^{75}As NMR shift *K* as a function of temperature *T*. The dashed red line is the fit of *K* by the equation $K(T)=K_0+A_{hf}\,\chi_{spin}(T)/N_A$, $\chi_{spin}(T)$ is the intrinsic spin susceptibility of the spin-1/2 Heisenberg alternating spin chain model. Inset: $(K-K_0)T^{1/2}$ vs $1/T$ and $(K-K_0)T^{-1/2}$ vs $1/T$ along the left and right y axes, respectively. The solid lines indicate the activation laws $(K-K_0)T^{1/2} \propto \exp(-\Delta^{K1D}/T)$ with $\Delta^{K1D}/k_B \approx 14$ K, and $(K-K_0)T^{-1/2} \propto \exp(-\Delta^{K3D}/T)$ with $\Delta^{K3D}/k_B \approx 6$ K, respectively.

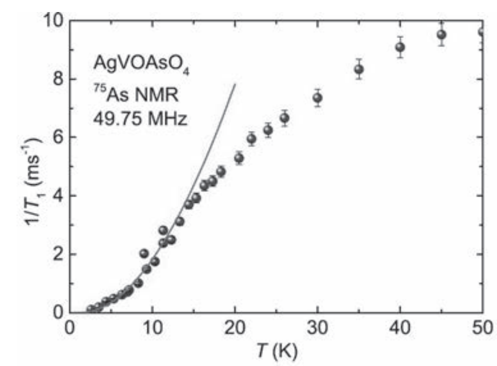

Fig. 2. $1/T_1$ as a function of temperature. The solid line is the fit using the equation $1/T1 \propto T^{\alpha 0}\exp[g\mu_B(H-H_{c1})/k_BT]$. This activated behaviour is due 3D magnon excitations that are gapped below the critical field of gap closing H_{c1}. The exponent α_0 depends on the effective dimension of the magnon dispersion.

INVITED PAPER

4:00

FI-09. Suppression of the double exchange in 4d-5d transition metal compounds. *(Invited)*

S. Streltsov[1] and D. Khomskii[2]
1. Institute of Metal physics, Ekaterinburg, Russian Federation;
2. University of Cologne, Cologne, Germany

The 4d and 5d transition metal compounds attracts nowadays considerable attention due to their specific properties, such as large covalency, strong spin-orbit coupling, the possibility to observe topological effects, etc. Magnetic ordering in these systems often displays strong suppression of magnetic moments, becoming (much) less than the nominal ones. One usually explains this by single-site effects: possible role of spin-orbit interaction, with orbital contribution opposite to the spin one, or by strong hybridization with ligands e.g. oxygens. We show that there exist in such system an intersite mechanism which, in particular, can lead to suppression or at least strong reduction of magnetism: the orbital-selective formation of covalent bonds (molecular orbitals) between metal ions, leading to “exclusion” of corresponding electrons from magnetic subsystem [1]. Especially spectacular are these effects in the situation with noninteger electron occupation, in which case this mechanism leads to suppression of the famous double exchange – the main mechanism of ferromagnetism in transition metals and compounds, including well-known colossal magnetoresistance manganites [2]. We demonstrate this novel mechanism by analytical and numerical model calculations, and show by ab-initio calculation that it explains magnetic behavior of several materials, including Nb2O2F3 and Ba5AlIr2O11[3]. Interplay of covalent bond formation and spin-orbit coupling is also discussed. Special attention will be paid to Ba3CeIr2O9, for which recent neutron and RIXS experiments demonstrates strong reduction of magnetic moments on Ir [4]. Our results thus demonstrate that the strong intersite interaction, typical for 4d and 5d compounds, may invalidate the standard single-site starting point for considering magnetism, and can lead to qualitatively different behavior. More specifically, they also show yet one more unexpected effect in the rich field of orbital physics.

[1] S.V. Streltsov and D.I. Khomskii Phys. Rev. B 89, 161112(R) (2014) [2] S.V. Streltsov and D.I. Khomskii Proceedings of the National Academy of Science 113, 10491 (2016) [3] S.V. Streltsov, G. Cao, D.I. Khomskii Phys. Rev. B 96, 014434 (2017) [4] A. Revelli, M. Moretti Sala, G. Monaco, P. Becker, L. Bohat.y, M. Hermanns, T. Koethe, N. Borgwardt, R. German, T. Frohlich, P. Warzanowski, T. Lorenz, S.V. Streltsov, P.H.M. van Loosdrecht, D.I. Khomskii, J. van den Brink, and M. Gruninger to be published

CONTRIBUTED PAPERS

4:30

FI-10. Topological magnons and excitons.

R. Shindou[1]
1. Physics, Peking University, Beijing, China

Topological phases have been explored in various fields in condensed matter physics such as semiconductor physics, correlated electron systems, photonics and phononics. This leads to the recent foundation of emerging materials such as topological insulators, topological superconductors/superfluid, topological photonic crystals and topological phononic crystals. In this talk, I review our past works on magnonic analog of integer quantum Hall states (quantum magnon Hall) [1-3,5], where robust spin wave propagation along chiral topological edge modes may enable novel fault-tolerant spintronic devices. I will first introduce the topological integer in the context of the Landau-Lifshitz equation, and argue how the non-zero topological integer guarantees the existence of chiral magnon modes [1,2]. Then I will review material realizations of our ideas with band-calculations results based on a Landau-Lifshitz equation and micromagnetic simulations results [1-3]. I will also discuss a chiral topological exciton in Chern band insulator [4], and localization effect and thermal magnon Hall conductivity in disordered quantum magnon Hall systems [5].

[1] R. Shindou, R. Matsumoto, S. Murakami, J-i. Ohe, Phys. Rev. B 87, 174427 (2013) [2] R. Shindou, J-i Ohe, R. Matsumoto, S Murakami, E. Saitoh, Phys. Rev. B 87, 174402 (2013) [3] R. Shindou and J-i. Ohe, Phys. Rev. B 89, 054412 (2014). [4] K. Chen and R. Shindou, Phys. Rev. B 96, 161101(R) (2017). [5] B. Xu, T. Ohtsuki and R. Shindou, Phys. Rev. B 94, 220403(R) (2016).

4:45

FI-11. Interface Effects on Coercivity and Training in Exchange Bias Systems.

J. Gompertz[1], R. Carpenter[2], S.A. Cavill[1,3], G. Vallejo-Fernandez[1] and *K. O'Grady*[1]
1. Department of Physics, University of York, Heslington, York, UK, YO10 5DD, York, United Kingdom; 2. Seagate Technology, Springtown Industrial Estate, Londonderry, United Kingdom; 3. Diamond Light Source Ltd, Harwell Science and Innovation Campus, Fermi Ave, Didcot, United Kingdom

Since the discovery of exchange bias in 1956 the origin of phenomena associated with the effect was unknown until the publication of what is known as the York Model of Exchange Bias in 2010 [1]. This work showed that the key to understanding the effect is the thermal stability of the AF grains in a sputtered film. The orientation of the AF order can be changed via the influence of the exchange field from the F layer when the sample is heated. The analysis of the loop shift via the York Model has enabled both the film thickness and lateral grain size dependence of the loop shift to be determined once the grain size distribution is known to high resolution. The calculated values are shown together with the results for the grain diameter dependence in Figure 1a, and the thickness dependence in Figure 1b. However there is still an ongoing lack of knowledge concerning the behaviour of atoms at the interface between the F and AF layers. At the interface there are competing interactions between AF and F order. However it is known that the interface spins order ferromagnetically because of the setting field dependence of the loop shift during the field annealing process [2]. There is also evidence of interface spin freezing resulting in an enhanced loop shift at low (<50K) temperatures and of the ability in a trilayer F/AF/F stack to order the interfaces independently of the order in the AF layer [1]. The influence of the interfaces on key parameters such as the observed coercivity, defined as the half loop width, and other effects such as training in which the initial measured loop after field annealing and subsequent loops are not identical, has also not been established. It is a conundrum that the coercivity of an exchange bias system can be as high as 1kOe whereas the coercivity of the F layer is typically 100Oe. This coercivity can occur in fields of several kOe. Furthermore if measurements are undertaken at low temperature then the grains in the AF layer will be completely stable against reorientation. Hence the observed coercivity of the F layer is not related to the properties of the F layer, nor can it be attributed to changes in the AF layer. Hence any observed coercivity must come from changes in the orientation of the interface spins. Given that the interface spins can be aligned in fields of the order of 10 to 20kOe, it is clear that these are not single spin effects but rather the behaviour of clusters of spins similar to those which were found to occur in spin glass systems. Hence the coercivity must be associated with irreversibility in the moment orientation of the interface spin clusters as the hysteresis loop is traversed. Hence the origin of the coercivity can thereby be explained. The phenomenon of training must for the same reasons, be an interface effect. In this case there must be a different process that occurs on field cooling to that which occurs after the first reversal of the F layer. This is analogous to the difference between a TRM and an IRM process as was commonly found in the case of spin glass systems [3]. Figure 2 shows the variation of the coercivity (H_C) and the training effect (H_T) with temperature over a range from room temperature to below 2K. The sample structure was Si/Ta (2)/Ru (2)/IrMn (10)/CoFe (5)/Ru (5) (thickness in nm). The results are quite remarkable and unexpected. Figure 2 shows that there must be some entities at the interface that are stable against thermal activation at room temperature. This implies that they must be small particles with a significant anisotropy presumably deriving from coupling to the grains in the AF layer. In all probability they would be of a similar diameter to the AF grains. However given that the variation of the coercivity continues at temperatures down as low as 2K this would indicate that there are also extremely small entities at the interface possibly down to a few or even single spins. Hence this implies that there is a very wide distribution of energy barriers at the interface regardless of its origin. In the presentation the nature of this distribution will be discussed as will the mechanisms by which the distribution gives rise to the observed phenomena.

[1] O'Grady K, Fernandez-Outon L E and Vallejo-Fernandez G; J. Magn. Magn. Mater. 322 (2010) p883 – 89. [2] Fernandez-Outon L E, O'Grady K, Oh S, Zhou M, and Pakala M; IEEE: Transactions on Magnetics, vol. 44 no. 11, (2008). [3] Tholence J, Tournier R; Journal de Physique Colloques, (1974), 35 (C4), pp.C4-299C4-235.

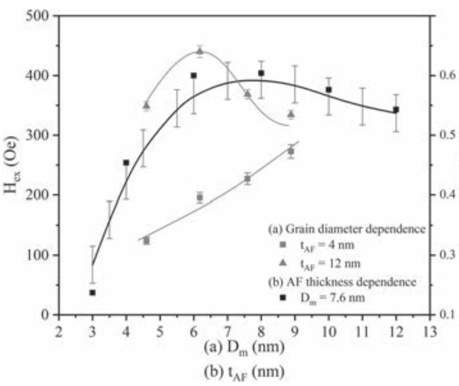

Fig. 1. The film thickness and lateral grain size dependence of the loop shift.

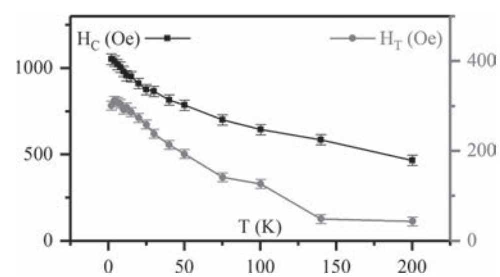

Fig. 2. The variation in coercivity and the training effect with temperature.

Session FP
CIRCUIT ANALYSIS OF TRANSFORMERS
(Poster Session)

Arokiaswami Alphones, Co-Chair
NTU, Singapore, Singapore
Tetsuya Ueda, Co-Chair
Kyoto Institute of Technology, Kyoto, Japan

FP-01. Effect of annealing on magnetic and mechanical behavior of NANOPERM-type alloys.

M. Hasiak[1] and A. Laszcz[1]
1. Wroclaw University of Science and Technology, Wroclaw, Poland

NANOPERM-type metallic glasses [1, 2] are still attractive candidates for variety of practical applications, because of their unique magnetic [3, 4] as well as mechanical properties [5]. Their annealing above crystallization temperature induces partial crystallization that is characterized by formation of α-Fe grains with typical sizes of up to tens of nanometers. Soft magnetic properties and mechanical properties of such nanocrystalline materials can be tailored not only with the aid of their chemical composition, but also by controlling the size the nanocrystalline grains created by heat treatment of amorphous precursor, their morphology, and structural composition. In order to understand magnetic and mechanical properties of NANOPERM-type alloys it is necessary to understand their microstructure and physical consequences of transformation from amorphous to nanocrystaline state. It is well known that structural changes demonstrate themselves also via macroscopic magnetic and mechanical parameters such as temperature dependence of magnetization, Curie temperature, AC and DC hysteresis loops as well as microhardness. We have studied a NANOPERM-type Fe76Mo8Cu1B15 alloy in form of ribbon 0.025 mm thick and 10 mm wide, produced by a rapid quenching method, with emphasis upon its magnetic and mechanical properties. All measurements were performed for the sample in the as-quenched state and after annealing at 837 K for 30 min. (above the primary crystalization temperature i.e. 723 K). Microstructure of the samples was studied by X-ray diffraction and AFM/LFM investigations. Temperature evolution of DC magnetization measured under zero-field cooling conditions using amorphous and nanocrystalline samples with different amounts of nanocrystalline grains was performed in temperature range from 50 K up to 400 K. In addition, DC hysteresis loops were also taken with the help of a VersaLab system (Quantum Design). Room tempertaure AC soft magnetic properties versus frequency and maximum induction were studied for toroidal samples by a hysteresisgraph (AMH-50K-S, Laboratorio ElletroFisico Engineering) at frequency up to 20 kHz. The Steinmetz coefficients for the amorphous and nanocrystaline alloys were calculated in the frequency range 50 Hz - 20 kHz. Mechanical characterization of investigated materials was performed by nanoindentation tests with respect to Oliver-Pharr method for maximum load of 250 mN. Sample of the Fe76Mo8Cu1B15 alloy in the as-quenched state was fully amorphous, which was confirmed by a broad halo in X-ray diffraction pattern and absence of visible precipitates on AFM/LFM images recorded in contact mode. The peaks present in X-ray diffraction pattern confirm two-phase behaviour of annealed material. It was also seen in measurements of microhardnesas for different regions in samples. The average values of hardness obtained for the amorphous matrix and nanocrystalline bcc grains are equal to 1221 HV and 1600 HV, respectively. The magnetic behavior described by DC hysteresis loops for the Fe76Mo8Cu1B15 alloy in the as-quenched state and after annealing at 837 K for 30 min. measured in the temperature range 200-400 K presented in Fig. 1 show a completely different behavior. The Curie temperature of the amorphous alloy equals 313 K, whereas for the annealed sample the higher value of the Curie point due to the nanocrystalline α-Fe phase was observed. For designing process and simulation of inductive elements (e.g. transformers, chokes) the AC magnetic characteristics are very important. Fig. 2 shows core losses as a function of maximum induction for the Fe76Mo8Cu1B15 alloy. It is seen that nanocrystalline material with low core losses in wide range of frequency and Curie point above 400 K (Fig. 1) is excellent candidate for high temperature and frequency soft magnetic material. Moreover, the Steinmetz coefficients K and α [6] calculated for the nanocrystalline Fe76Mo8Cu1B15 alloy increase from 0.0381 to 0.5840 and from 1.71 to 2.42, respectively for with frequency range 500 Hz - 20 kHz.

1. K. Suzuki, A. Makino, A. Inoue, T. Masumoto, J. Appl. Phys. 70, 6232 (1991). 2. C. Gomez-Polo, D. Holzer, M. Multigner, E. Navarro, P. Agudo, A. Hernando, M. Vazquez, H. Sassik, R. Grossinger, Phys. Rev. B 53, 3392 (1996). 3. M.E. McHencry, M.A. Willard, D.E. Laughlin, Prog. Mater. Sci. 44, 291 (1999). 4. M. Hasiak, M. Miglierini, IEEE Trans. Magn. 51, 2000804 (2015). 5. C.A. Shuch, T.C. Hufnagel, U. Ramamurty, Acta Mater. 55, 4067 (2007). 6. M. Hasiak, M. Miglierini, M. Lukiewski, A. Laszcz, M. Bujdos, AIP Advances, 8, 56116 (2018)

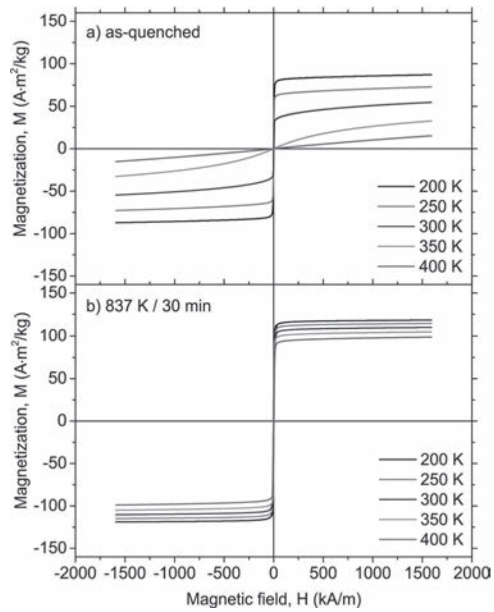

Fig. 1. DC hysteresis loops for the Fe76Mo8Cu1B15 alloy in the as-quenched state and after annealing at 837 K for 30 min. measured at the indicated temperatures.

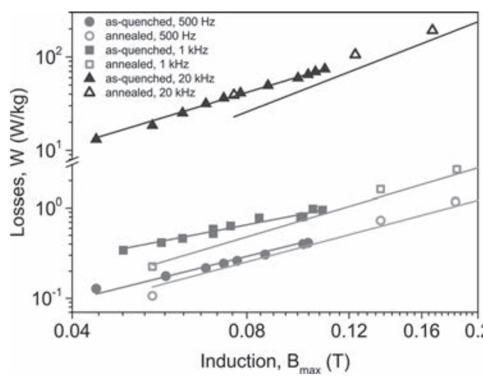

Fig. 2. AC core losses versus maximum induction for the Fe76Mo8Cu1B15 alloy in the as-quenched state and after annealing at 837 K for 30 min. recorded at room temperature at frequency f = 500 Hz, 1 kHz and 20 kHz .

FP-02. Magnetic Force Analysis in a Gapped-Core Reactor Model under Harmonic Magnetizations by Efficient Frequency-Domain Decomposition.

X. Zhao[1], Z. Jin[1], Z. Cheng[2], B. Forghani[3], L. Li[1] and H. Zhang[1]
1. North China Electric Power University, Baoding, China; 2. Institute of Power Transmission and Transformation Technology, Baoding, China; 3. Infolytica Corporation, Montreal, QC, Canada

I. Introduction As key electrical devices, large reactors and converter transformers play an important role in the operation of ultra high voltage direct current (UHVDC) transmission [1]. Meanwhile, the existence of rich harmonics in the exciting current or driving voltage leads to distorted flux densities in the saturated iron core. Consequently the magnetic force due to the leakage flux not only exhibits special spectrum in the frequency domain but also threatens the normal operation of electrical devices e.g. vibration and deformation of windings [2-3]. Therefore it is important to investigate the influence of magnetic force on iron core and windings when electrical devices such as reactors work under harmonic magnetizations. The time-stepping method starting from arbitrary initial value is usually used for the computation of time-periodic nonlinear problems. However, the main drawback is that many periods are required to be stepped through for steady state solution, especially when a much larger time constant exists in the nonlinear system to be analyzed. Numerical methods in time domain and frequency domain have been presented and developed to solve the steady state nonlinear magnetic field efficiently [4-5] by combining the fixed point technique with the finite element method. In this paper, the harmonic-balance system of equations is established first by approximating all time-periodic variables by complex series. Thereupon, decomposition of the system of equations is achieved according to diagonal dominant characteristic of the reluctivity matrix so that harmonic solutions can be decoupled and computed separately and in parallel. This method is used to compute the magnetic force in a gapped-core model under harmonic magnetizations based on the harmonic solutions of magnetic field. II.Decomposition Scheme in Frequency-Domain The two-dimensional nonlinear magnetic field can be formulated as follows by using the magnetic vector potential A, $\nabla\times v\nabla\times A+\sigma\partial A/\partial t=J$(1) where J is the impressed current density, σ and v are the conductivity and reluctivity, respectively. Owing to the time periodicity of the electromagnetic field under harmonic excitations, periodic variables such as current density J, magnetic vector potential A and reluctivity v can be represented by a summation of trigonometric function, $W(\mathrm{t})=\sum W_n e^{jn\omega t}$ (2) $W_f=[W_0,W_{-1},W_{-2},\ldots,W_{-Nh},W_{Nh}]$(3) where W can be replaced by J, A and v. N_h is the total number of harmonics truncated in computation and ω is the angular frequency. W_n is the n-th component in frequency domain. W_f is the spectrum of the periodic variable W. Actually the time-domain multiplication of magnetic vector potential A and reluctivity v in (1) is equivalent to the frequency-domain convolution of the two variables, therefore a new system of equations in the frequency domain can be obtained, as follows, by using the harmonic-balance theory, $M(\sigma,H)A_f+S(D)A_f=K_f$(4) where M is the mass matrix and S the stiffness matrix. H and D are, respectively, the harmonic matrix and the reluctivity matrix. K_f is related to spatial distribution of the impressed current density. A_f is the vector potential in frequency domain. The convolution product term including v_0, which is dc component of reluctivity, is often dominant, therefore the other terms can be assumed as locally constant and moved to the right-hand side. Consequently, a new decomposed harmonic-balance system of equations can be obtained to decouple harmonic solutions, $[\mathrm{j}n\omega M(\sigma)+\mathrm{S}(v_0)]A_{f,n}=F_{f,n}+K_{f,n}$(5) where $A_{f,m}$ and $J_{f,n}$ are the m-th harmonic solution of magnetic vector potential and n-th harmonic vector of impressed current density. $F_{f,n}$ is obtained from the convolution product of reluctivity and vector potential in harmonic domain. The decomposed system of equations can be solved separately and in parallel. Meanwhile only N_h+1 equations in (5) are required to be solved due to the conjugate symmetry of the harmonic solutions. III.Gapped Iron Core and Experiment A gapped-core reactor model made of grain-oriented silicon steel sheet (B30P105) produced by Baosteel is used in experiment for comparison of magnetic forces when the model is magnetized by sinusoidal and harmonic excitation. Fig.1 shows the gapped laminated core and the experimental setup. IV. Computation and Results A gapped-core reactor model is used for the computation of the nonlinear magnetic field and the corresponding magnetic nodal force [6]. A sinusoidal exciting current of 50 Hz is applied to make the model operate in nonlinear region. Variations of reluctivity in nonlinear iteration are shown in Fig. 1. One node on the interface between the iron core and the air gap is selected to compare the calculated magnetic nodal forces (F_y) by the proposed method in this paper and the time-stepping method in MagNet, Infolytica, which is shown in Fig. 2. V.Conclusion An efficient frequency-domain decomposition method is presented to analyze the magnetic force resulted from harmonic magnetizations. Comparison of computed magnetic nodal forces by the proposed method and the time-stepping method shows good consistency, which proves the accuracy of the decomposition method in the frequency domain. VI.Acknowledgement This work is supported by the National Natural Science Foundation of China (Grand No. 51777073,51577066), and by the Natural Science Foundation of Hebei Province (Grand No. E2017502061), and by the National Key Research and Development Program of China(Grant No. 2017YFB0902703).

[1] Z. Cheng, N. Takahashi, and B. Forghani, et al, *Electromagnetic and Thermal Field Modeling and Application in Electrical Engineering*. Beijing: Science Press, 2009, pp. 4-14. [2] Y. Gao, K. Muramatsu, K. Fujiwara, Y. Ishihara, S. Fukuchi and T. Takahata, “Vibration analysis of a reactor driven by an inverter power supply considering electromagnetism and magnetostriction,” *IEEE Trans. Magn.*, vol.45, no.10, pp. 4789-4792, Oct. 2009. [3] Y. Gao, K. Muramatsu, M. J. Hatim, K. Fujiwara, Y. Ishihara, S. Fukuchi and T. Takahata, “Design of a reactor driven by inverter power supply to reduce the noise considering electromagnetism and magnetostriction,” *IEEE Trans. Magn.*, vol.46, no.6, pp. 2179-2182, Jun. 2010. [4] E. Dlala, A. Belahcen and A. Arkkio, “A fast fixed-point method for solving magnetic field problems in media of hsyteresis,” *IEEE Trans. Magn.*, vol.44, no.6, pp. 1214-1217, Jun. 2008. [5] O. Biro and K. Preis, “An efficient time domain method for nonlinear periodic eddy current problems,” *IEEE Trans. Magn.,* vol.42, no.4, pp. 695-698, Apr. 2006. [6] A. Kameari, “Local force calculation in 3D FEM with edge elements” *Int. J. of Applied Electromagnetics in Materials,* vol.3, pp. 231-240, 1993.

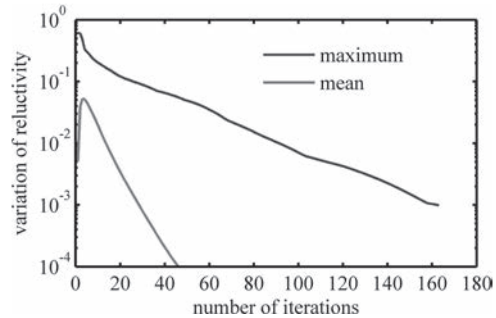

Fig. 1. Variation of reluctivity with nonlinear iterative steps

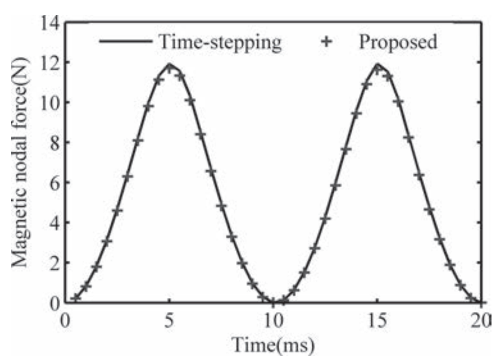

Fig. 2. Comparison of computed magnetic nodal force

FP-03. Investigation into the Effect of Yoke Pressed Structure on Electromagnetic Performance of Transformer.

X. Yan[1], Z. Peng[2], Y. Kang[3], X. Yu[4], Z. Ren[1] and Y. Zhang[1]

1. Shenyang University of Technology, Shenyang, China; 2. Shaoyang University, Shaoyang, China; 3. TEBA Shenyang Transformer Group Co. Ltd., Shenyang, China; 4. Shandong Power Equipment Co. Ltd., Jinan, China

I. Introduction With the increment of transformer capacity, the physical dimension of transformer will be larger and larger. With consideration of transportation limitation, to ensure the transformer capacity, it is feasible to reduce transformer size in large capacity transformer design[1][2]. The yoke-pressed transformer is a kind of special structure, in which widths of widest steel sheets of iron yoke are pressed for height reduction of the transformer. Consequently, the smallest steel sheets are enlarged to keep a constant core cross-section area. The structure variation of transformer core definitely results in variation of electromagnetic performance of transformer. However, the manufacturers still design this type of transformer according to conventional structure. Moreover, it is hard to find researches on electromagnetic performance analysis of transformer resulted from yoke pressed structure. In this paper, four different yoke structures representing different pressing level have been constructed. The corresponding electromagnetic performances have been investigated and discussed through numerical experiments. II. Yoke structures with different pressing levels To research the change of magnetic field distribution in the transformer core in different yoke pressed level, four different yoke structures have been built as shown in Fig.1. Model 1: Normal iron core transformer (no yoke pressed) Model 2: DSP-241000 kVA /500kV transformer product with pressed yoke Model 3: Transformer with yoke further pressed based on model 2 Model 4: Transformer with yoke completely pressed to rectangle Due to symmetry, half transformer configuration has been constructed for finite element analysis for all models. Besides different yoke structures, the configuration and parameters of four transformer models are same. The data of yoke for four models are shown in Table.1. The pressing rate is calculated by dividing the width difference by the width of the widest steel sheet of model 1, in which the width difference is the difference between the width of the widest steel sheet of model 1 and that of other model. III. Electromagnetic performance analysis For the above model transformers, the primary windings are excited with the same rating voltage while the secondary windings are open-circuit. With the field-circuit coupled FEM, the magnetic field in the iron core and excitation current can be obtained. The magnetic circuit of yoke pressed transformer is built to analyze the change of magnetic field in different yoke structures. From Fig.2, it can be seen that even with a same cross-section area and same yoke length for four models, the magnetic field distribution in the iron core have been changed in different level with different pressing rate. The magnetic field distribution in the iron core is not uniform any more once the yoke structure has been reconstructed. The changes in core column and yoke section are opposite, and the changes in the widest and the smallest steel sheets regions are different for core column and yoke. With the enhancing of yoke pressed level, the flux density in the widest sheets region of yoke is increased, while the flux density is decreased in the smallest sheets region of yoke. For the core column, the changes of flux density in corresponding regions are opposite to yoke. The flux density in different regions of four models are shown in Table.2. Furthermore, the magnitude of excitation current is getting bigger and bigger, while the distortion of current waveform becomes worse with the increment of pressing rate. Detailed analysis will be presented in extended paper. IV. Conclusion For the transformer with pressed yoke structure, the widths of steel sheets in different regions of yoke have been modified to keep the cross section area constant in manufacturing process. Generally, it should be no effect on magnetic flux due to same area and length for the magnetic circuit. However, the flux distribution in iron core is not uniform any more once the yoke structure has been reconstructed. The magnetic field distribution in different regions should be researched systematically.

[1] Zhang Yanli, Liu Liang, Kang Yahua, et al. Study on Main Magnetic Field in Iron Core of a Yoke -Pressing Configuration Transformer. Advanced Materials Research, vol. 614-615, pp.1210-1213, 2013. [2] Kang Yahua, Bai Baodong, Xin Zhaohui, et al. Analysis of magnetic field and loss of the large disintegration transformer. pp.851-854, ICEMS2013.

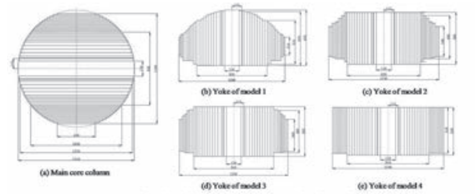

Fig.1 The configuration schematic diagrams of core column and yokes

Table 1 The data of yoke for four models

Transformer Model	Effective cross section area of yoke(cm²)	The width of the widest steel sheets of yoke(mm)	The width of the smallest steel sheets of yoke(mm)	Pressing rate
Model 1	6481.54	655	210	0%
Model 2	6481.54	590	340	10%
Model 3	6481.54	565	360	14%
Model 4	6481.54	530	510	19%

Table.2 Flux density in different regions

Transformer Model	Flux Density(T)			
	Core Column		Side-Yoke	
	The widest sheets region	The smallest sheets region	The widest sheets region	The smallest sheets region
Model 1	1.68618	1.70618	1.69895	1.68808
Model 2	1.60585	1.73665	1.73489	1.46645
Model 3	1.53975	1.79777	1.76387	1.40418
Model 4	1.53571	1.81561	1.78549	1.30401

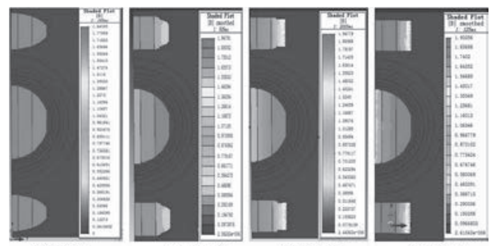

Fig.2 The flux density distribution in core column and side-yoke for four transformer models

FP-04. A Switched-capacitorless Energy-encrypted Transmitter for Roadway-charging Electric Vehicles.

W. Liu[1], K. Chau[1], C. Lee[2], C. Jiang[1] and W. Han[1]
1. The University of Hong Kong, Hong Kong, Hong Kong; 2. Massachusetts Institute of Technology, Boston, MA, United States

I. INTRODUCTION Due to cleanliness, convenience and high efficiency, wireless power transfer (WPT) technology has been extensively and deeply investigated. In recent years, energy encryption has drawn researchers' attention to satisfy practical requirements of security and reliability in the theme of intelligent transportation and smart city. Especially for roadway-charging electric vehicles (EVs), the use of energy encryption can guarantee the transmitted energy being effectively harvested by the authorized receptors instead of being secretly stolen by the unauthorized ones. Recently, a chaotic encryption strategy based on switched capacitor arrays has been proposed to realize energy security in WPT systems [1, 2]. However, because of the need of discretely adjusting the resonant capacitance and hence the operating frequency, this encryption scheme suffers from the drawbacks of limited energy-transferred channels, high voltage stress across switches and relatively low flexibility. In addition, a generic encryption model based on certificate-less cryptography has been developed to improve the energy security performance for WPT systems [3], but its computational complexity and time involved seriously restrain from dynamically encrypting the operating frequency. Meanwhile, a traditional series-to-series (SS) topology with fixed values of resonant inductance and capacitance has been identified to exhibit a selective characteristic for multiple loads when operating at the selected receptor's resonant frequency [4]. This mechanism can be newly extended to derive an energy-encrypted transmitter without using a switched-capacitor array for multiple energy receptors such as roadway-charging EVs. Consequently, in this paper, a switched-capacitorless energy-encrypted transmitter is proposed for roadway-charging EVs. Moreover, a two-dimension chaotic frequency-and-duration encryption (FDE) algorithm is proposed to improve the security performance while maintaining relatively high efficiency. II.METHODOLOGY The proposed FDE-WPT system without using a switched-capacitor array in the transmitter is shown in Fig. 1(a). The switched-capacitorless transmitter is firstly introduced to the energy-encrypted WPT system, which can offer the definite merit of continuously and flexibly regulating the operating frequency. When the receptors in the *m*-th channel are authorized, no matter the transmitter operates at resonance or not, the corresponding efficiency can be derived out. It indicates that the primary coil inductance and the matched resonant capacitance have no influence on its operating efficiency. Although the primary coil internal resistance leads to extra power loss, because of the enhanced mutual inductance by the ferromagnetic spokes as shown in Fig. 1(b), the power loss in the primary coil can be effectively suppressed and even insignificant. Thus, the proposed system takes the advantage of lower transmitter's power loss over the energy-encrypted SS WPT system with switched-capacitor arrays. Data interaction based on wireless communication facilitates the encryption and decision-making unit to achieve maximum efficiency band trace (MEBT), which provides a secure frequency band to ensure relatively high efficiency in the authorized receptor. Then, a two-dimension chaotic encryption technique is adopted to generate the encrypted frequency and its active duration sequences, namely, the security key. Furthermore, hysteresis control and high-frequency pulse modulation (HFPM) are employed to realize pulse density modulation (PDM). The output voltages of both the authorized and unauthorized receptors and the two-dimension FDE security key are shown in Fig. 2(a). Only the authorized receptor with knowledge of the security key can readily decrypt the encrypted energy, while, due to the lack of security key, the unauthorized ones fail to pick up any energy. Hence, it confirms that the proposed FDE and switched-capacitorless transmitter can effectively enforce the energy security. Additionally, the efficiency and output power versus the operating frequency are plotted in Fig. 2(b). Although the efficiency will decrease when the operating frequency is adjacent to the unauthorized receptors' resonant frequency, the proposed MEBT and FDE can dynamically generate a new sequence of secure energy-transferred channels to guarantee high-efficiency operation, always higher than 90.75%. Finally, an experimental prototype has been constructed and tested to further verify the feasibility of the proposed FDE-WPT system. More experimental results will be given in the full paper. II.CONCLUSION A switched-capacitorless energy-encrypted transmitter, incorporated with two-dimension FDE technology, has been proposed and implemented for roadway-charging EVs. To prevent the energy from being illegally harvested by the unauthorized receptors, the proposed two-dimension chaotic FDE technology generates a well-defended key to improve the security performance while retaining high efficiency. Theoretical analysis, numerical simulation and experimental results will be given to verify the feasibility of the proposed FDE-WPT system. This work was supported by a grant (Project No. 17204317) from the Hong Kong Research Grants Council, Hong Kong Special Administrative Region, China.

[1] Z. Zhang, K.T. Chau, C. Liu, C. Qiu and F. Lin, "An efficient wireless power transfer system with security considerations for electric vehicle applications," *J. Appl. Phys.*, vol. 115, no. 17, paper no. 17A328, pp. 1-3, May 2014. [2] Z. Zhang, K. T. Chau, C. Qiu, and C. Liu, "Energy encryption for wireless power transfer," *IEEE Trans. Power Electron.*, vol. 30, no. 9, pp. 5237-5246, Sep. 2015. [3] E. Ahene, M. Ofori-Oduro, and B. Agyemang, "Secure energy encryption for wireless power transfer," in *Proc. IEEE Int. Advance computing Conf.*, Jan. 5-7, 2017, pp. 199-204. [4] Y. Zhang, T. Lu, Z. Zhao, F. He, K. Chen and L. Yuan, "Selective wireless power transfer to multiple loads using receivers of different resonant frequencies," *IEEE Trans. Power Electron.*, vol. 30, no. 11, pp. 6001-6005, Nov. 2015.

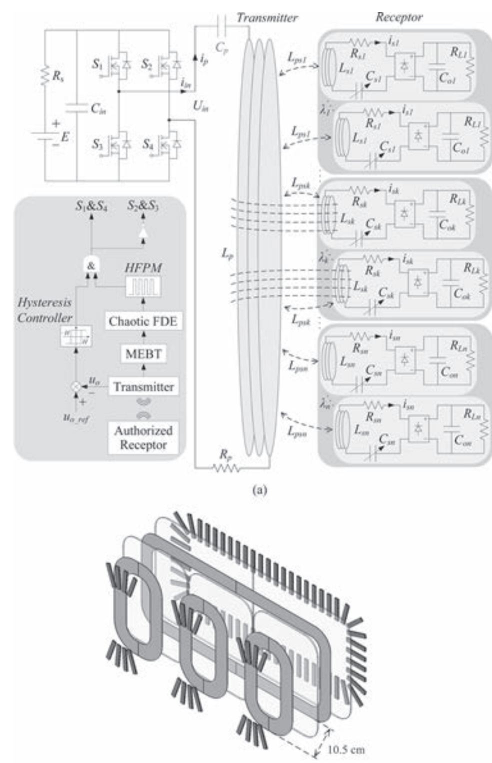

Fig. 1. Proposed FDE-WPT system without using switched-capacitor array in transmitter. (a) Topology and control. (b) Geometries.

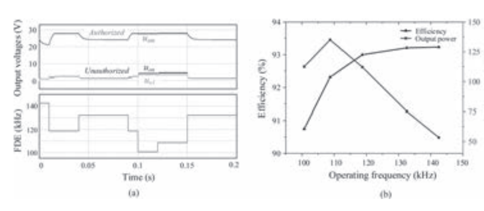

Fig. 2. Waveforms of proposed FDE-WPT system. (a) Output voltages and FDE security key. (b) Efficiency and output power.

FP-05. Reduction of an Eddy Current Losses in Metallic Support of an Underground Power Cable.

H. Song[1], S. IM[1] and G. Park[1]
1. Department of Electrical and Computer Engineering, Pusan National University, Busan, The Republic of Korea

1. Introduction Underground power cable was adopted for the enhancement of the aesthetic the city, the convenience of the citizens and the development of urbanization. To operate this power cable, a metallic supporting of the power cable is necessary. The metallic supporting structure of the power cable was installed at 1.5 m intervals. This structure supports a three-phase AC power cable running 24 hours a day. This metallic supporting structure of the power cable can be classified into angle, hanger, and cleat. Especially, Cleat is the closest to the power cable and the material of the cleat has both conductivity and permeability. [1]. it has conductivity and generates eddy current. The eddy current loss continues to the thermal loss and may cause metal structure damage [2][3]. In addition, it should be predictable because it can cause heat generation. However, there is not enough research on structure metallic supporting of power cable. This paper analyzes the distribution of eddy currents in power cable supporting structure, and estimate the loss through distribution. Also, a method for reducing the eddy current generated in the metallic structure of the power cable is proposed. The method proposed in this paper is not a method to block the eddy current path, which is a conventional eddy current reduction method. This paper proposes a method to reduce the eddy current by reducing the magnetic field which causes eddy currents. This is applied to the metallic supporting of power cable, and the simulation shows how to reduce the eddy current. 2. Eddy current loss distribution The analytical conditions for the structures supporting underground power cables are the same as the actual operating conditions. Since 3-phase AC is used, it was analyzed at 1.157A, 60Hz. Among the structures, especially the cleats with conductivity and permeability, the material contains Al and has a conductivity of 2.06 and a permeability of 1000. There are two major types of arrays: triangular arrays and horizontal arrays. In Figure 1 (a), It is an array of underground power cable which is operated. but in this paper, the triangular array is analyzed. the triangular array is modeled in three dimensions. In (b), the mesh of the Cleat portion is shown in all models. the loss of the eddy current will mainly deal with the occurrence in Cleat. Eddy current distribution occurs at the cleat portion supporting of power cable. while the three-phase ac current flows. The value of the eddy current increases near the cable where a large amount of current flows. In this part, the loss of the eddy current is remarkably generated in the inside and outside. The reddest point of the cleat is the largest part of the eddy current and its value is 0.41 A/mm2. 3. Reduction of eddy current loss There are two main types of eddy current reduction. First, cut off the path of the eddy current. The eddy current can be reduced by blocking the path of the eddy current. By blocking the direction in which the eddy current flows, it is possible to reduce the eddy current by dispersing the direction in which the eddy current flows in two directions. Second, reduce the size of the magnetic field. The current generates a magnetic field, the magnetic field generates an induced electromotive force, and the induced electromotive force generates an eddy current. At this time, if the magnitude of the magnetic field generated by the current is reduced, the magnitude of the eddy current eventually generated is also reduced. Considering the method of reducing the eddy currents flowing in the cleat in the triangular array, it was predicted that the eddy current loss would be reduced by blocking the path of the largest eddy current. Figure 2 (a) shows the eddy current distribution of the cleat. The eddy current distribution of the cleats was larger than the inside of the cleats, and the patterns of eddy currents occurred inside and outside the cleats, respectively. In Fig. 2 (b), full-slit is applied to the side where the eddy current distribution is large, and the eddy current path is blocked. Comparing Fig. 2 (a) and (b), eddy current distribution is noticeably reduced. However, one side of Cleat was cut out of one structure, so mechanical strength was not considered sufficiently. 4. Comparison of iron loss The distribution of eddy currents in the cleat, which is a metallic structure supporting underground power cable, is analyzed. In addition, a reduction scheme was proposed to reduce the eddy currents generated in the cleats. When the maximum value of the eddy current was compared, about 59.5% eddy current loss was reduced. 5. Conclusion Eddy currents occur because of the conductivity and permeability of metal structures that support 24-hour cables. To prevent such accidents, the eddy currents flowing through the metal structure must be cut off. It is possible to reduce the eddy current by blocking the eddy current path which is a method of blocking the eddy current. There are many ways to cut off the eddy current path, but it is necessary to adopt a method considering mechanical strength and balance among them.

[1] P. A. Hargreaves, B. C. Mecrow and R. Hall, "Calculation of Iron Loss in Electrical Generators Using Finite-Element Analysis," in IEEE Transactions on Industry Applications, vol. 48, no. 5, pp. 1460-1466, Sept.-Oct. 2012. [2] D. Miyagi, N. Maeda, Y. Ozeki, K. Miki and N. Takahashi, "Estimation of Iron Loss in Motor Core With Shrink Fitting Using FEM Analysis," in IEEE Transactions on Magnetics, vol. 45, no. 3, pp. 1704-1707, March 2009. [3] M. S. Lim, J. H. Kim and J. P. Hong, "Experimental Characterization of the Slinky-Laminated Core and Iron Loss Analysis of Electrical Machine," in IEEE Transactions on Magnetics, vol. 51, no. 11, pp. 1-4, Nov. 2015. [4] M. Oka, T. Ogasawara, N. Kawano and M. Enokizono, "Estimation of Suppressed Iron Loss by Stress-Relief Annealing in an Actual Induction Motor Stator Core by Using the Excitation Inner Core Method," in IEEE Transactions on Magnetics, vol. 50, no. 11, pp. 1-4, Nov. 2014.

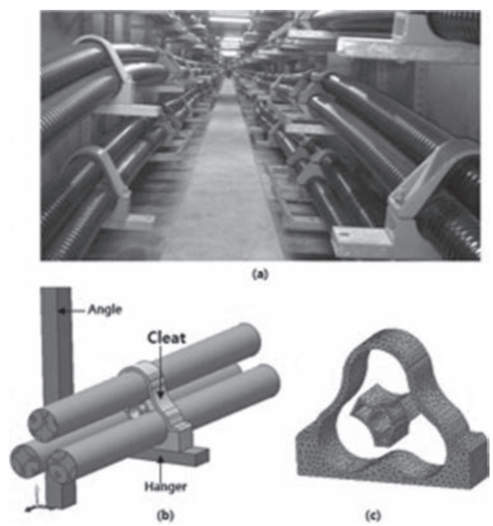

Fig. 1. Structure of Underground Power Cable. (a) Horizontal arrangement of installed underground power cables. (b) Three-dimensional modeling of triangular array of underground power cable. (c) Metallic cleat supporting underground power cables mesh.

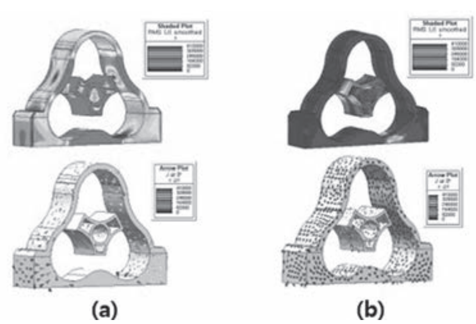

Fig. 2. Eddy current reduction effect. (a) Original model- Distribution of eddy currents in underground power cable cleats. (b) Full-Slit model- eddy current reduction of cleat.

FP-06. Calculation of AC Resistance in a Multi-strand Coil Considering Proximity Effect with Eddy Current Induced Magnetic Fields.

D. Um[1] and G. Park[1]
1. School of Electrical and Computer Engineering, Pusan National University, Busan, The Republic of Korea

I. Introduction Recently, the interest in high-frequency applications such as wireless power transfer(WPT), induction heaters, high speed motors and high-frequency transformers is increasing. At these high frequency systems, the large amount of losses due to the eddy currents occurs, leading to an increase in the equivalent resistance. To prevent this adverse effect, multi-strand coils are used. Moreover, it is important to calculate the exact resistance of multi-strand coils. Therefore, the understanding of effects by the eddy currents should be necessarily conducted. The conventional methods to calculate ac resistance are studied by Dowell, Ferreira and many other authors [1]-[2]. The Dowell's method calculated the resistance by setting the foil conductor equivalent to the high aspect ratio windings [3]. In this method, the exact solution can be calculated when the conductors are closely packed. However, this method increases the error when the aspect ratio is not really high and the coil distance is far apart. Some papers clarify the weakness and limitations of the Dowell's method [4]. The Ferreira's method can be solved by Maxwell's equation in the cylindrical coordinates [5]. The exact solution of round conductors can be provided. Some papers calculate the resistance of multi-strand coils using Ferreira's method [6]. However, this method considering only a single conductor makes error when the conductors are closely packed. In this paper, the Ferreira's method is used to derive a formula for the ac resistance of multi-strand coils. The results suggest a correction factor that describes mutual effects by analyzing analytical considerations on the losses by the eddy currents and using FEA. The final equation can be changed to a closed form formula that can be used by finding local minima for coil optimization. II. Eddy Current Analysis by Using Maxwell's Equation In general circular conductor, the Maxwell's equation in the cylindrical coordinates can be used to obtain the internal and external magnetic fields of the coil and the current density distribution inside the coil as shown in equation (1). $rot(rot\ \mathrm{H})+\mathrm{j}k^2\mathrm{H}=0,\ \mathrm{k}=(\omega\mu_0\sigma)^{1/2}$ (1) The solution of the skin effect can be obtained by solving above equation with the source current and no external magnetic field. The solution of the proximity effect can be represented by considering the external magnetic field [7]. The total loss in equation (2) can be calculated juts by adding these solutions due to the orthogonal relationship. $P=I^2k/(4\pi\sigma r_0)\Psi_1(kr_0)-2\pi k r_0 H^2/\sigma\Psi_2(kr_0)$ (2) where I is the source current, is the conductivity of a conductor, r_0 is a radius of the conductor, H is external magnetic fields, Ψ_1 and Ψ_2 are forms of kelvin function [8]. However, the distributed coil, not a single coil makes the results different. As shown in equation (3), it can be seen that external magnetic field is affected within the effective range due to the magnetic field induced by the eddy currents. $\mathrm{H}^*=\mathrm{H}_0(\mathrm{r}_0/\mathrm{r})^{1/2}\mathrm{J}_2(\mathrm{j}^{3/2}k\mathrm{r}_0)/\mathrm{J}_0(\mathrm{j}^{3/2}k\mathrm{r}_0)$ (3) The magnetic field induced by the eddy currents is represented by the function of distance from a conductor and normalized frequency, which is the ratio of the radius of a strand to conventional skin depth. On the surface of the conductor, the ratio of induced to applied magnetic fields can be only a function of normalized frequency, and it is assumed to reflection factor, F. With putting proper correction factors, the exact resistance calculation can be conducted. The details will be discussed in the next chapter. III. Calculate Correction Factor Using FEA As shown in Fig.1, the analysis of two independent alignments parallel to the magnetic field, and perpendicular to the magnetic field of coils is carried out by using FEA. The magnetic field generated by the eddy currents in parallel alignments shields the applied magnetic field evenly, not locally. In contrast, the magnetic field generated by the eddy currents in perpendicular alignments locally shields the applied magnetic field inside alignments and it leads to the difference of current density distribution among layers. In Fig.2, (a) shows simulation model for parallel alignments by setting boundary conditions. From FEA results, the correction factor of parallel alignments, X is defined as the ratio of losses considering mutual effects to losses of single conductor, shown in equation (4). $\mathrm{X}=1-p(\Delta/\mathrm{r}_0)F(\mathrm{r}_0/\delta)$ (4) where p is a function of the ratio of spacing, Δ to a radius of coils. The correction factor in the perpendicular direction can be obtained in the same method as we put correction factor, Y. Finally, two results are combined by setting weighting values, w in equation (5) and these will be covered in the full paper. $\Delta R_{prox}=(-w\mathrm{X}+(w-1)\mathrm{Y})2\pi k\mathrm{r}_0(H/I)^{1/2}/\sigma\Psi_2(k\mathrm{r}_0)$ (5) IV. Conclusion To find the coil resistance in an alternating magnetic field, the losses in the coil must be calculated accurately. The proximity effect with the conventional single conductor solution does not reflect the shielding effect among the coils, so that the results are overestimated. In this paper, the losses occurring among the coils are analyzed with respect to the magnetic field direction. Finally, two correction factors considering mutual effects are proposed and the results are reflected well by setting proper weight between these two factors.

[1] D. Dai, X. Zhang, and J. Wang, "Calculation of AC resistance for stranded single-core power cable conductors," IEEE Trans. Magn., vol. 50, no. 11, Nov. 2014, Art. ID 6301104. [2] N. Xi and C. R. Sullivan, "An improved calculations of proximity-effect loss in high-frequency windings of round conductors," in Proc. 34t Annu. EEE PESC, 2003, pp. 853–860. [3] L. Dowell, "Effects of eddy currents in transformer windings," Proc. Inst. Elect. Eng., pt. B, vol. 113, no. 8, pp. 1387–1394, Aug. 1966. [4] F. Robert, "A theoretical discussion about the layer copper factor used in winding losses calculation," IEEE Trans. Magn., vol. 38, no. 5, pp. 3177–3179, Sept. 2002. [5] J. Ferreira, "Analytical computation of ac resistance of round and rectangular litz wire windings," in Proc. Inst. Elect. Eng., Part B, Jan. 1992, vol. 139, no. 1, pp. 21–25P. [6] Jesús Acero, Member, IEEE, Rafael Alonso, José M. Burdío, Member, IEEE, Luis A. Barragán, and Diego Puyal, "Frequency-Dependent Resistance in Litz-Wire Planar Windings for Domestic Induction Heating Appliances," IEEE Trans. Power Electron., vol. 21, no. 4, pp. 856–866, Jul. 2006. [7] J. Acero, R. Alonso, L. A. Barragan, and J. M. Burdio, "Magnetic vector potential based model for eddy-current loss calculation in round-wire planar windings," IEEE Trans. Magn., vol. 42, no. 9, pp. 2152–2158, Sep. 2006. [8] F. Tourkhani and P. Viarouge, "Accurate analytical model of winding losses in round litz wire windings," IEEE Trans. Magn., vol. 37, no. 1, pp. 538–543, Jan. 2001.

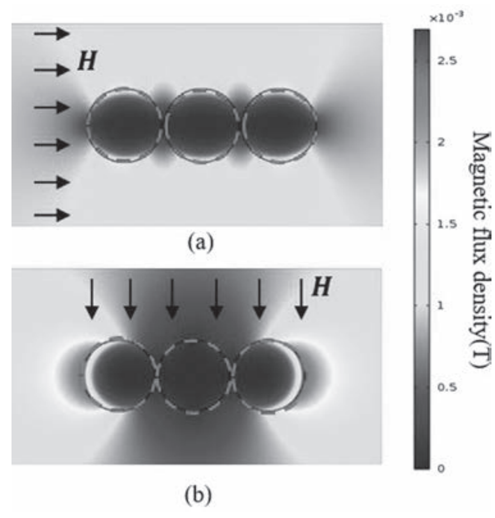

Fig. 1. The magnetic field distribution with resepct to coil alignment direction. (a) parallel alignments (b) perpendicular alignments.

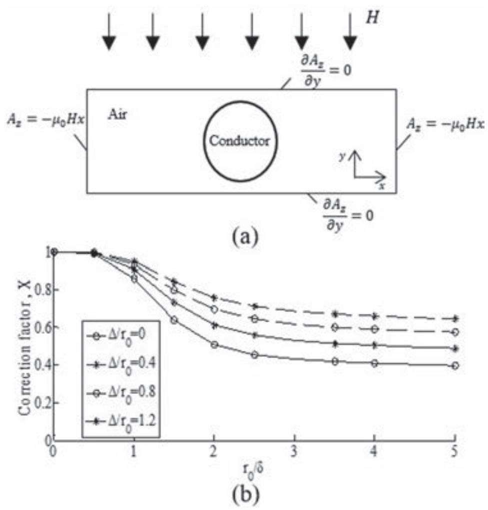

Fig. 2. The frequency response with FEA results. (a)Simulation model and boundary conditions (b) Correction factor X with respect to Δ/r_0.

FP-07. Copper Loss Reduction of Planar Transformer Using Magnetic Cap and Plate.

T. Yamamoto[1], Y. Bu[1] and T. Mizuno[1]
1. Shinshu university, Nagano, Japan

INTRODUCTION A switched mode power supply is used to provide stable DC power to the electrical apparatus. The DC-DC converter in the power supply should have high efficiency and power density. To reduce the size of this converter, it is necessary to increase the switching frequency. However, the power losses in such a converter are observed to increase to an increase in the switching frequency. The losses that are observed in the converters are attributed to the transformer and circuit losses. It is observed that reducing the switching loss of the circuits requires soft switching using SiC and GaN power semiconductors, because SiC and GaN exhibit a considerably lower electrical loss than that exhibited by conventional Si. Moreover, it is necessary to reduce the copper and iron losses to improve the efficiency of the transformers [1]–[3]. The planar transformer uses a rectangular wire as the winding wire for its coil. This type of transformer exhibits a small volume because the space factor of the coil is observed to be high. To reduce the copper loss in a planar transformer, we suggest the production of a transformer based on a novel structure that uses a magnetic cap and plate. This structure can reduce the AC resistance that is caused by the skin and proximity effects. In this study, we additionally investigate an LLC resonant converter using a planar transformer having a magnetic cap and plate. STRUCTURE OF PLANAR TRANSFORMER WITH MAGNETIC CAP AND PLATE Figure 1 shows the structure of a planar transformer with a magnetic cap and plate. This transformer is used in an LLC resonant converter. The magnetic cap cover both the side surfaces of the coil in the core, and the magnetic plate is sandwiched between the primary and secondary side coils. The magnetic cap and plate can reduce the copper loss due to the skin and proximity effects, because these components can reduce the magnetic flux that pass an end of the winding wire. The thicknesses of the magnetic cap and plate were evaluated using finite element method analysis. Magnetic cap and plate is the silicon sheet which is mixed amorphous alloy powder. The mean diameter of the amorphous powder grains is 2.56 μm. The core shape of transformer is EERS, and the core material is metal composite core [4]. IMPEDANCE CHARACTERISTICS OF PLANAR TRANSFORMER WITH MAGNETIC CAP AND PLATE Figure 2 shows the resistance vs. frequency characteristics of the primary side coil when the secondary side coil is short-circuited. The impedance characteristics that are exhibited by a planar transformer for an LLC resonant converter were evaluated using an impedance analyzer (Agilent, 4294A). Further, when the secondary side coil was short-circuited, we measured the resistance to simulate the operating conditions of an LLC converter. When the S1 coil was short-circuited at a frequency of 5 MHz, the resistance of the primary coil was observed to be 177.1 and 189.7 mΩ for a structure with and without a magnetic cap and plate, respectively. Thus, the resistance of a structure with a magnetic cap and plate was observed to be lower that of a structure without a magnetic cap and plate by 6.6%. Further, when the S2 coil was short-circuited, the resistance of the primary coil was observed to be 189.4 and 218.9 mΩ for a structure with and without a magnetic cap and plate, respectively. Thus, the resistance of a structure with a magnetic cap and plate was observed to be lower than that of the structure without a magnetic cap and plate by 13.4%. This reason was the reduction of the resistance due to the skin effect and proximity effect when magnetic cap and plate was applied. LLC RESONANT CONVERTER USING PLANAR TRANSFORMER WITH MAGNETIC CAP AND PLATE The primary side of the LLC resonant converter was the inverter of a half bridge. We used a GaN FET as the switching FET. The secondary side was connected to a rectification circuit. Further, we measured the efficiencies of the input and output powers of the LLC resonant converter. The switching frequency of the converter is 5 MHz. At an output power of 50 W, the efficiencies of the converter were observed to be 82.5% and 81.7%, respectively, while using a planar transformer with and without a magnetic cap and plate. Thus, the efficiency was improved by 0.8% by using magnetic cap and plate. This was attributed to the reduction of resistance owing to the proximity effect when magnetic cap and plate was applied. CONCLUSIONS We investigated an LLC resonant converter using a planar transformer that contained a magnetic cap and plate. At a frequency of 5 MHz, application of a magnetic cap and plate reduced the resistance of a planar transformer by up to 13.4%. Furthermore, in the LLC converter with the output power of 50 W, efficiency was improved by 0.8% by applying the magnetic cap and plate. This was attributed to the reduced resistance owing to the skin and proximity effects when a magnetic cap and plate were incorporated into the structure. From the aforementioned results, it can be inferred that incorporating a magnetic cap and plate into the structure were useful to improve the efficiency of the MHz driving converter that uses a planar transformer. For future studies, we intend to investigate the improvement in efficiency of the MHz driving converter that uses a planar transformer, which is incorporated with a magnetic cap and plate.

[1] T Mizuno, S Enoki, T Asahina, T Suzuki, M Noda, and H Shinagawa, IEEE Transactions on Magnetics., Vol. 43, No.6, pp. 2654-2656 (2007). [2] H Shinagawa, T Suzuki, M Noda, Y Shimura, S Enoki, and T Mizuno, IEEE Transactions on Magnetics., Vol. 45, No.9, pp. 3251-3259 (2009). [3] T Fujiwara, and R Tahara, IEEE Translation Journal on Magnetics in Japan., Vol. 8, No.11 pp.795-800 (1993). [4] K Sugimura, D Shibamoto, N Yabu, T Yamamoto, M Sonehara, T Sato, T Mizuno and H Mizusaki, IEEE Transactions on Magnetics., Vol. 53, No.11, 2801406 (2017).

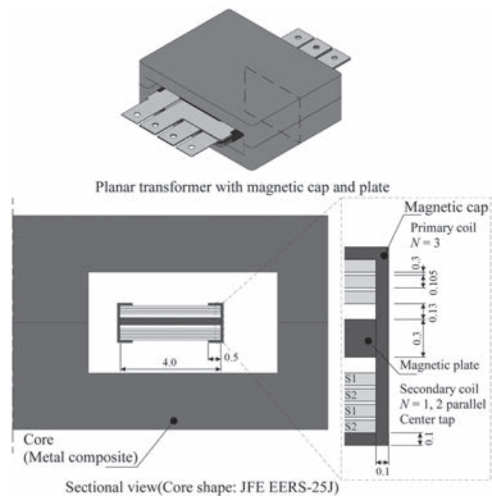

Fig. 1. Structure of a planar transformer with a magnetic cap and plate (unit: mm).

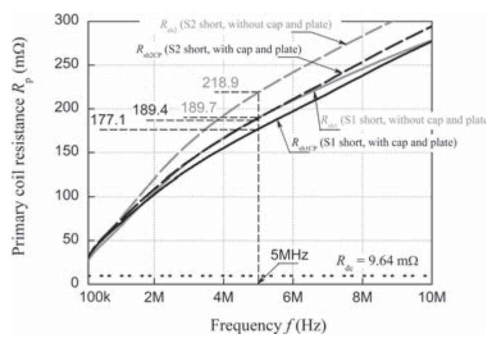

Fig. 2. Primary side coil resistance vs. frequency characteristics of planar transformer (Secondary side: short).

FP-08. Determination Approach for the Parameters of Equivalent Circuit Model of Deep Saturated Three-phase Integrative Transformers.

Y. Wang[1], Y. Shangguan[1] and J. Yuan[1]
1. Dept. of Electrical Engineering, Tsinghua University, Beijing, China

Abstract Based on the analysis of the defects of the traditional methods for determining the equivalent circuit parameters of three-phase integrated transformers by single-phase excitation, an expression method of equivalent circuit parameters and their determination approach based on three-phase simultaneous excitation are presented in this paper. The parameters are expressed in terms of the excitation source phase, and the value of parameters is determined by calculating the reluctance of core segments based on the FEM simulations. Then the electric circuit parameters are obtained by converting the magnetic circuit into the electric circuit. This kind of electric circuit model is suitable for analyzing the problems of deep saturation of transformers and the concerning power grid problems. 1. Introduction Each circuit element in the equivalent circuit derived from the magnetic circuit has a definite physical meaning, but the circuit model has a complicated topology and a large number of elements. How to determine the parameters is the difficulty for all researchers [1]. The former scholars only applied the excitation in single phase and used the information of the port measurement to determine the circuit parameters [2]. It is suitable for analyzing the steady state operation of the transformer, but is not suitable to analyze the deep saturation state. The single-phase excitation method did not fully consider the coupling between phases, and it cannot accurately describe the nonlinear parameters. The purpose of this paper is to study the equivalent circuit of saturated transformers based on three-phase simultaneous excitations. 2. Defects in the method of determining parameters by single-phase excitation When the transformer works at a linear state, the influence between the three phases can be neglected [3]. However, when the iron core is deeply saturated, the phase-to-phase coupling becomes significant due to the severe nonlinearity of the core material. Moreover, the saturation degree of the iron core varies greatly at different phase points of three-phase sinusoidal excitation. So it can be predicted that the equivalent circuit parameters of the transformer will vary with the phase of excitation source. The calculated parameters based on single-phase excitation cannot reflect these characteristics. 3. The expression method and determination approach of parameters based on three-phase simultaneous excitation The non-linear inductance parameters are expressed in terms of the excitation source phase. It means that the circuit model will have a set of parameters for each phase of the sinusoidal excitation. The value of parameters is determined by calculating the reluctance of core segments based on the numerical simulations [4]. This kind of determination approach is not limited by the number of parameters, and the equivalent circuit topology can be modeled more complete, as shown in Figure 1. Numerical simulations based on three-phase simultaneous excitations are carried out by using the coupled circuit-FEM method. Symmetrical three-phase voltage excitations are applied to the three windings, and the phase α of the central phase is taken as a control parameter. By observing the electromagnetic field distribution at each phase, we can determine the values of the inductance at this phase. Then, by changing the amplitude of the excitation voltage for each phase, we will obtain a series of inductances and finally the phase-dependent nonlinear inductances can be obtained. 4. Parameter calculation examples and the difference between single-phase and three-phase excitation A 50MVA three-phase transformer is taken as an example to analyze the phase-dependent nonlinear inductances. By increasing the amplitude of the sinusoidal voltage excitation at the transformer winding port, the saturation of the transformer core is gradually aggravated. Table 1 compares the inductance of the central leg determined by single-phase and three-phase excitations when the phase α of the central phase is equal to $\pi/6$. When the excitation voltage is 31.25kV, the flux density in the central leg is about 1.8T and the core is not yet deeply saturated, the difference of the inductance value between the three-phase and the single-phase excitation is very small, it is about 1%. However, as the core is saturated more and more seriously, the difference increases. When the excitation voltage is 62.5kV, the flux density is about 3.26T, and the difference increases to about 12%. Taking into account the closing process and the influence of remanence, the flux density in the transformer core may reach nearly 2.5 times the rated one, and the error caused by single-phase excitation cannot be ignored. In addition, the errors of all the parameters of the equivalent circuit will accumulate, which makes the circuit parameters obtained by single-phase excitation more unreliable. 5. Conclusion The error of equivalent circuit parameters determined by single-phase excitation cannot be ignored when the core operates at deep saturation state. Three-phase simultaneous excitation is required to determine the equivalent circuit parameters. The duality derived complicated equivalent circuit model with phase-dependent nonlinear parameters is more suitable to analyze the deep saturation state of the transformer.

[1] Martinez, J.A. and Mork, B.A. (2005), "Transformer Modeling for Low-and Mid-Frequency Transients-A Review", *IEEE Transactions on Power Delivery*, Vol.20 No.2, pp. 1625~1632. [2] Mork, B.A., de León, F. and Ishchenko, D. (2007), "Hybrid Transformer Model for Transient Simulation—Part I: Development and Parameters", *IEEE Transactions on Power Delivery*, Vol.22 No.1, pp. 248-255. [3]Mork, B.A., de León, F. and Ishchenko, D. (2007), "Hybrid Transformer Model for Transient Simulation—Part II: Laboratory Measurements and Benchmarking", *IEEE Transactions on Power Delivery*, Vol.22 No.1, pp. 248-255. [4] Wang, Y., Yuan, J. (2017), "Calculation Approach of Reluctance in the Magnetic Circuit of Transformer Employed to Convert into Equivalent Electric Circuit", *18th International Symposium on Electromagnetic Fields in Mechatronics, Electrical and Electronic Engineering,* Lodz, Poland, 2017.

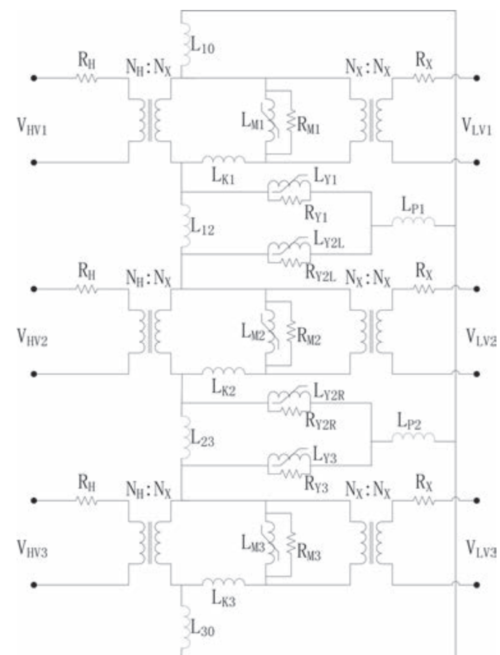

Fig. 1. Equivalent circuit model of three-phase integrative transformer derived from the magnetic circuit

Excitation voltage (kV)	30	31.25	32.5	33.75	37.5
L_{M2} (H),three-phase excitation	753.1	219.5	38.2	15.2	2.76
L_{M2} (H),single-phase excitation	751.1	216.7	36.8	14.4	2.62
Excitation voltage (kV)	40	45	50	62.5	
L_{M2} (H),three-phase excitation	1.88	1.21	0.94	0.66	
L_{M2} (H),single-phase excitation	1.78	1.14	0.88	0.58	

Table 1 Nonlinear inductance of the central leg with three-phase simultaneous excitation and single-phase excitation

FP-09. Research on Split-Core Reactor Vibration Reduction Method Based on Magnetostrictive Effect.

L. Zhu[1], R. Sha[1], X. Zhang[1], B. Wang[1] and T. Han[1]
1. Key Laboratory of Advanced Electrical En, Tianjin Polytechnic University, Tianjin, China

I. INTRODUCTION The reactor is an important power equipment in the transmission and transmission system, which plays many different roles in the power system. As a typical reactor structure, the split-core reactor can reduce the residual magnetism and effectively control the inductance. In recent years, it has developed rapidly and has been widely used. The vibration noise generated by the power equipment in operation not only affects its normal operation and service life, but also produces audible noise and other environmental problems [1]. How to reduce its vibration noise effectively has become an urgent problem for manufacturers and power departments. Accurate measurement of magnetization and magnetostrictive properties of silicon steel is the basis for the study of reactor noise and vibration. Lieven Vandevelde, a Belgian scholar, puts forward the method of calculating the deformation of an object due to maxwell and magnetostrictive force by means of finite element analysis [2]. GaoYanhui, Japan, Kazyhiro Muramatsu USES the relationship between the node displacement, the magnetostrictive stress of the node and the distance between the node and the center point to calculate the vibration displacement of the iron core of the reactor [3]. In the literature [4], the British scholar Annable Shahaj proposed using magnetic twin chips to control the magnetostriction on the stator teeth of the motor, and the magnetostrictive force components were offset by the magnetostrictive force. Manufacturers often compression core column and base structure, such as the increase of rubber vibration isolator between ontology and body and improve the air gap materials and other methods of reducing the electromagnetic vibration in the reactor from the vibration mechanism of reactor vibration noise research is less. Calculating the magnitude and distribution of electromagnetic vibrations is necessary for designing reactors with lower vibration noise. Based on the measurement results of the magnetization and magnetostrictive properties of orientation silicon steel and non-oriented silicon steel, the model of three-dimensional split-core reactor is established. Based on the inherent magnetostrictive properties of oriented and non-oriented silicon steel sheets, a new type of iron core with alternating core-column structure consisting of oriented silicon steel sheet and non-oriented silicon steel sheet was proposed. Numerical calculation of magnetic field, stress field and vibration displacement of reactor under ordinary structure and new structure, the results show that the method has a certain damping effect. II. EXPERIMENT MEASUREMENT As shown in Fig.1(a), the magnetostrictive measuring device MST500, which is produced by German BROCKHAUS, is used to measure the magnetostriction characteristics of the non-oriented and oriented silicon steel sheet. Fig.1(b) shows the butterfly curves along the rolling direction of a set of 50WW470 non-oriented silicon steel and 30JG130 oriented silicon steel in Fig.1(c) measured at different peak magnetic flux densities. With the increase of magnetic flux density, the area of the magnetostrictive return ring increases, and each ring is symmetric around the origin. The elongation of the samples corresponds to the magnetostriction of the positive value, while the negative magnetostriction means that the sample has undergone a contraction deformation. In short, the “wing” quadrant of the butterfly curve shows the scaling changes of the samples [5]. It can be clearly seen that the non-oriented silicon steel sheet 50WW470 magnetostrictive curve is mainly manifested as the elongation deformation of the silicon steel sheet, and the orientation of the silicon steel sheet 30JG130 magnetostrictive curve is mainly shown as the contraction deformation. III. SIMULATION ANALYSIS When the reactor is running normally, there is a alternating electromagnetic field in the magnetic circuit formed by the core. The differential equations of magnetic field in the core of the reactor can be written as: $B=\mu_0^{-1}\mu_r^{-1}H=\nabla\times A$(1) The mathematical model of magnetostriction is usually described by linear pressure magnetic equations. The elastic deformation of the material and the magnetic strain equation caused by the external magnetic field can be written: $\varepsilon=\sigma/E_y^{H}+dH$ (2) $B=d\sigma+\mu^{\sigma}H$ (3) A single-phase 220V split-core reactor is chosen as the research object. The simulation model of the split-core reactor is shown in Fig.2(a). In analysis and calculation of deformation caused by magnetostriction of split-core reactor, need the magnetostriction model combined with finite element calculation, calculation to simulate reactor actual place state, to fix the bottom of the physical model as constraints. As shown in Fig.2, Simulation of the split-core reactor core structure vibration test point displacement change, under transient conditions, compared with the ordinary reactor structure, the vibration displacement of the split-core reactor test points in the new structure is significantly reduced.

[1] Lihua Zhu, Qingxin Yang, Rongge Yan, et al. Research on Vibration and Noise of Power Transformer Cores Including Magnetostriction Effects[J]. Transactions of China Electrotechnical Society, 2013,(04):1-6. [2] Hilgert T., Vandevelde L., Melkebeek J. Comparison of Magnetostriction Models for Use in Calculations of Vibrations in Magnetic Cores[J]. IEEE Transactions on Magnetics, 2008, 44(6): 874-877. [3] Gao Yanhui, Muramatsu Kazuhiro, Hatim Muhd Juzail, et al. Design of a Reactor Driven by Inverter Power Supply to Reduce the Noise Considering Electromagnetism and Magnetostriction[J]. IEEE Transactions on Magnetics, 2010, 46(6): 2179-2182. [4] Shahaj Annabel, Garvey Seamus D. A Possible Method for Magnetostrictive Reduction of Vibration in Large Electrical Machines[J]. IEEE Transactions on Magnetics, 2011, 47(2): 374-385. [5] Yanli Zhang, Jiayin Wang, Baodong Bai, et al. Influence Analysis of DC Biased Magnetic Field on Magnetostrictive Characteristics of Silicon Steel Sheet[J]. Proceeding of the CSEE, 2016,(15):4299-4307.

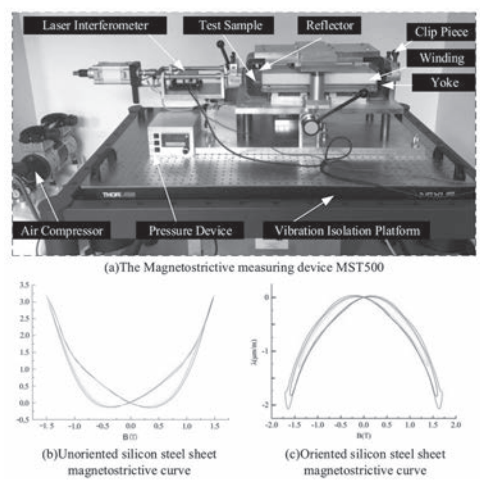

Fig. 1. Magnetostrictive measuring devices and experimental curves

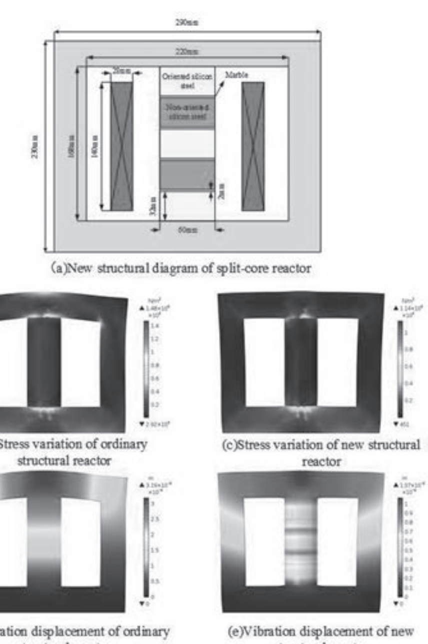

Fig. 2. Structure design and vibration simulation of the split-core reactor

FP-10. Research on Transformer Inductance Parameter Calculation Model for High Frequency Characteristic Analysis.

X.M. Zi[1], *G. Jian*[1] and Z. Ying[1]

1. Nanjing University of Aeronautics and Astronautics, Nanjing, China

Abstract — This paper considers the core nonlinear material, the weak magnetic effect of core eddy current and the diamagnetic effect of non-measured coil load operation under the condition of high-frequency transformer. A magnetic field model suitable for the calculation of inductance parameters in high-frequency applications such as transformer lightning shock wave process analysis and frequency response analysis is proposed. The influence of the magnetic conductivity of the core on the high-frequency inductance parameters is analyzed under the load condition. The parameters of a three-split transformer were measured and compared with the calculated results to verify the validity of the proposed model. 1.Introduction Power transformers include core, winding and insulating materials. The high frequency characteristic model can be represented by the equivalent circuit of resistance, capacitance, self-inductance and mutual inductance. The transformer winding have their own electrical and magnetic properties for each turn of the winding, line or segment such as loss, inductance and capacitance..The high frequency equivalence model of transformer can be obtained by grouping the basic unit of transformer. For the actual analysis of the issue, the establishment of high-frequency transformer equivalent model is accurate mainly depends on two aspects. Firstly, the calculation of total parameters in the basic unit is accurate:the total parameters include inductance, mutual inductance, capacitance, resistance and so on. The calculation method of capacitance and resistance is mature, but the calculation of inductance and mutual inductance is the most tedious and difficult to calculate accurately. This is mainly due to the non-test coil is short-circuit and other constraints, the physical definition of inductance and mutual inductance is not clear, resulting in a variety of inductance calculation method. Unfortunately, these calculations are not uniform in the inductance calculation. Secondly, the equivalent of the core flux characteristics is reasonable:the equivalent model does not directly reflect the core, but the core permeability nonlinear and frequency-dependent characteristics will affect the internal magnetic field distribution transformer, and makes the equivalent inductance and mutual inductance calculation results in the model are affected. Research now seen in more than 10 kHz frequency can ignore the core permeability. Based on this assumption, the calculation of inductance and mutual inductance is simplified, but at the same time, the frequency response of the equivalent model is not continuous. That is, the model based on characteristics of magnetic conductivity will not be suitable for medium and low frequency operation. In order to study the core nonlinear material and the weak magnetic effect of core eddy current from the mechanism, this paper analyzed the law of the relative permeability of the silicon steel sheet under different frequencies based on the core non-linear eddy current magnetic field model. Based on this, the coupling analysis model of the high-frequency inductance in the load condition is proposed. The inductance and mutual inductance of the unit under different operating frequencies are calculated. The experimental results verify the effectiveness of the proposed model. 2.Analysis model of nonlinear and frequency-dependent characteristics of core Analysis of core equivalent permeability with frequency is shown in Fig.1(a). Select 30Q120 silicon steel sheet and analyze the corresponding variation of relative permeability of silicon steel plate at different frequencies by calculating the nonlinear vortex field of the core (shown in Fig.1(b)). It can be seen that when the relative permeability is above 500 kHz, the magnitude is small, and the corresponding magnetic characteristics of different magnetic working points in high frequency are different. The study also revealed that the inductance of coil inductance affected by magnetic conductivity is associated with both the excitation frequency and the magnitude of the excitation. 3. Calculation model of the inductance of the load conditions Fig.2 shows the magnetic field - circuit coupling analysis model of high frequency inductance calculation under load conditions. Based on the frequency-dependent curves of the magnetic permeability of the core material calculated above, by changing the relative permeability of the core to equalize the frequency of the magnetic field, then the self-inductance and mutual inductance of each coil unit under different frequencies are obtained. Conventional finite element method for computing the inductance Parameter in transformers cannot take into account the diamagnetic effect of non-measured coil load operation. To address this issue, a novel field-circuit coupled calculation method is proposed, in which the electromagnetic field based on the coupled A-Emf formulation and circuit equations are solved simultaneously. The formulation for the new method is derived in detail and the *U*r-*f* curve of the iron core materials are included to consider the effect of iron core frequency dependent. 4.Analysis of the calculation results This paper selects a 2500kVA three-split transformer as an example, and the calculation results of the unit self-inductance and mutual inductance corresponding to different frequencies are analyzed. The detailed calculation method and the influence factors will be seen in the full paper.

[1]Xin Liu; Chenyang Ti; Guishu Liang Wide-band modelling and transient analysis of the multi-conductor transmission lines system considering the frequency-dependent parameters based on the fractional calculus theory[J]. IET Generation, Transmission & Distribution, 2016, 10(13): 3374-3384. [2]J. Wang, H. Y. Lin, Y. K. Huang, et al. Numerical analysis of 3D eddy current fields in laminated media under various frequencies[J], IEEE Transactions on

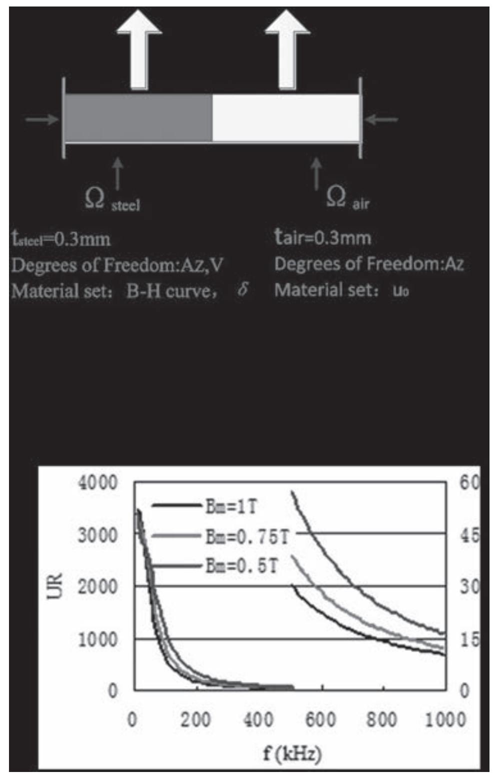

Fig. 1. (a)Analysis model of the equivalent permeability of iron core with frequency-dependent
(b)Core μ_R-f curve

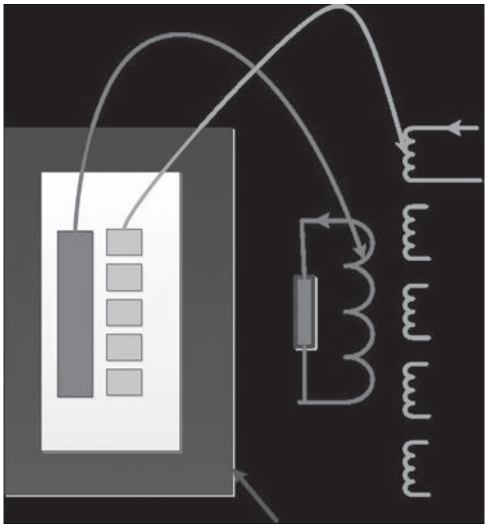

Fig. 2. Analysis model

FP-11. Inverse Updating Method of High-frequency Equivalent Circuit Model in Transformer for Winding Deformation Diagnosis.

H. Zhang[1], *S. Wang*[2], S. Wang[2] and S. Wang[2]
1. Hubei Universitie of Arts and Science, Xiangyang, China; 2. Xi'an Jiaotong University, Xi'an, China

I. INTRODUCTION Transformer is one of the most essential equipment in the electric systems, which plays the role of electromagnetic energy conversion and transmission. Statistically, winding deformation produced by huge and dynamical electromagnetic forces under short-circuit fault is one of the most serious problem which may make the transformer fault. In practice, the transformer is like to be a black-box. It is very hard to diagnose the winding deformation accurately by using the present approaches [1], such as the Correlation Coefficient Method (CCM). During the frequency response analysis (FRA) studies, the equivalent circuit model of transformer is usually used to solve the forward problem [2], as shown in Fig.1, but how to determine the increments of equivalent electromagnetic parameters, such as the inductance, capacitance and resistance, is an important inverse problem. The diagnosis of winding deformation for transformer is a typical inverse problem. This paper proposes a novel method for diagnosing winding deformation in transformer more accurately and intuitively, based on Equivalent Circuit Model Updating (ECMU) at a high-frequency range (10Hz ~10MHz). In fact, the ECMUM is an inverse method to determine the electromagnetic parameters states under FRA excitation. It is a challenge to find a unique and accurate solution during inverse updating operation. In our study, thanks to the ECMU and frequency selection, the certainty and qualitative relationship between FRA error data and electromagnetic parameter increments of transformer equivalent circuit model can be determined easily. Also, the maximum approximate unique solution can be obtained exactly. II. Derivation of Inverse Updating equations Similar to the vibrating equations in structural dynamic system [3], the dynamic governing equations in the circuit system can be given as: (1) where, *L*, *R* and *C* are the parameter matrixes of inductance, resistance and capacitance. Under harmonic excitation $u(t)$, the dynamic stiffness matrix of circuit system in frequency domain can be obtained as:(2) where, ω and *j* are the frequency in rad/s and imaginary unit, respectively. In this study, absolute sensitivity of FRF with respect to the *i*th parameter Φ is used and defined as: (3) where, $H(\omega)$ is the frequency response function (FRF). After calculating all the sensitivity at each frequency, the sensitivity matrix can be constructed. Finally, the model updating equation can be obtained as: (4) Here, *S* is the sensitivity matrix; ΔΦ is the updating parameter vector, and ε is the output residual vector. Then, the updating problem in (4) can be solved by [3]: (5) The updated parameters are can be determined iteratively by solving (5), until the residual, ε, becomes sufficiently small. III. Verification and Results Fig. 2 shows the model updating results of FRF error after two iterations. Table I presents the comparison results between the 1st and 2nd updating (*DP* is the updating precision). It can be seen that the updating algorithm has a high efficiency. Also, the parameter increments determined by solving model updated equations iteratively can qualitatively reflect the frequency response errors which are produced by winding faults. According to the parameter increments, we can estimate the transformer winding deformations much more intuitively and accurately. Besides, it is found that the updating precision can be improved by iteratively updating, where the residual of FRF may become sufficiently small.

[1]G. Eduardo, A. Guillermo, G. Carlos, "Current Status and Future Trends in Frequency-Response Analysis with a Transformer in Service", *IEEE Trans. Power Del.,* 28(2) 1024–1031, (2013). [2]H. Zhang, S. Wang, D. Yuan, et al, "Double-ladder Circuit Model of Transformer Winding for Frequency Response Analysis Considering Frequency-dependent Losses", *IEEE Trans. Magn.,* 51(11): 8402304, (2015). [3]K. Kwon, R. Lin. "Frequency selection method for FRF-based model updating". Journal of Sound and Vibration, 2004, 285–306.

$$L\ddot{q}(t)+R\dot{q}(t)+Cq(t)=u(t) \quad (1) \qquad G(\omega)=-\omega^2 L+j\omega R+C \quad (2)$$

$$S_{\phi}^{H(\omega)}=-H(\omega)\frac{\partial G(\omega)}{\partial \phi}H(\omega) \quad (3) \qquad S\Delta\phi=\varepsilon \quad (4) \qquad \Delta\phi=[S]^{+}\varepsilon \quad (5)$$

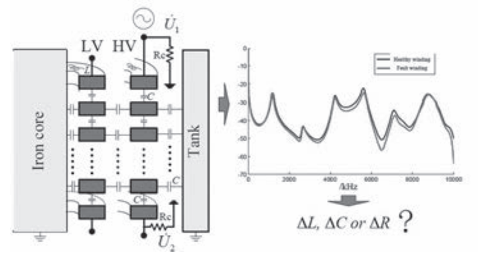

Fig. 1. Inverse problem in winding deformation diagnosis of transformer using FRA

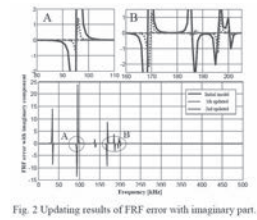

Table I Comparison results.

Parameter	Simulated	Updated	*DP*
Cgh4	-10%	-10.08%	99.2%
Cgh5	-2%	-2.00%	100%
Cgh7	-3%	-2.98%	99.3%
Csh2	-5%	-4.95%	99.0%
Csh3	+5%	5.18%	96.4%

Fig. 2. Updating results of FRF error with imaginary part.

FP-12. The Integration of Energy-saving Transformer Possessing Variable Impedance.

S. Wang[1], S. Wang[1], y.h. He[1,2], m.N. Zhang[1] and S. Wang[1]
1. Xi'an Jiaotong University, Xi'an, China; 2. State Grid Yulin Electric Power Company, Yulin, China

1 INTRODUCTION The safety of power transformer was seriously impacted by the short-circuit current with the level of power load continuing to rise [1]. Accordingly, the fault current levels may exceed the rated breaking capacities of existing circuit breakers, which will impose a heavy burden on the transformer, even cause unstable operation of the power system [2]. Therefore, it is significant to take effective measures for the purpose of limiting short-circuit current to a reasonable and low level. At present, high-impedance transformer and current-limiting device are most common methods of limiting short-circuit current[3]. However, high leakage reactance of high-impedance transformer will cause the energy loss, volume increase and bus voltage fluctuation under normal circumstances. In addition, the large amount of maintenance and high economic costs are the defects of different fault current limiter. Hence, the integration of high-speed switching current-limiting device and power transformer design is presented in this paper, the impedance of the autonomic regulation, achieve low loss, low voltage loss. The current limiting device, which composed of current-limiting reactor, capacitor and high-speed switch in parallel, is in series with the high-voltage winding of transformer, as shown in Fig 1(a). Variable impedance transformer will be the integration of transformer and current-limiting reactor design, and current-limiting reactor needs to be switched by high-speed switch controlled. Current-limiting reactor is short circuit by high-speed switch in normal working condition, and the loss and impedance of transformer is not increased. Different from normal working condition, the current-limiting reactor is connected with the system while high-speed switch is open when short-circuit fault of power system occurs, to improve the impedance of transformer and limit the short-circuit current. Based on the analysis, the self-regulation of impedance which variable impedance transformer possessing can reduce reactive loss of power system; improve the quality of the power grid. 2 DESIGN OF CURRENT-LIMITING REACTOR To realize the integration of high-speed switching current limiting device and transformer design, the current-limiting reactor is in series with the high-voltage winding of transformer. Taking a transformer rated 110/38.5/10.5kV and 63000kVA as an example, current-limiting reactor is connected to the system, when the three-phase short-circuit fault occurs at the location of the termination of medium-voltage winding. The indicator of short-circuit current is limited to the below 60% of the original short-circuit current. The reactance of current-limiting reactor which is required to limit the fault current can be expressed as follows in governing equation (1) shown in Fig.1(b). Taking magnetic shielding measures to prevent electromagnetic effects of current-limiting reactor from the original transformer, the coils of current-limiting reactor are placed within the aluminum tube. The reactance value of current-limiting coils is reduced considering the effect of eddy current of aluminum tube. In order to weaken the demagnetization effect of aluminum tube while ensuring the shielding effect, determining reasonable the spacing between aluminum tube and coils of reactor is particularly critical. Varying the spacing between aluminum tube and coils, Fig.1 (c) shows the reactance value changing with spacing. Eventually determine the spacing is 100 mm and the reactance value of 14.53 Ω in eddy current field, satisfies the requirement of current limit. 3 THE STRUCTURE AND PERFORMANCE OF VARIABLE IMPEDANCE TRANSFORMER Compared with the conventional transformer, high speed switch and air-core current-limiting reactor is known as rapid current limiting device which is placed in high voltage bushing of transformer, as shown in Fig.1 (d), constituted the so-called variable impedance transformer possessing energy-saving and cost-reducing. The windings of transformer is placed in the transformer tank which is filled with transformer oil and put high speed switch, current-limiting reactor and the module of control and protection in the aluminum tube, filled with SF6 gas. Oil tank and aluminum tube are connected through basin-type insulator of 220 kV. Therefore the benefits in economy and society are remarkable and its extending foreground is roomy. Fig.2 shows the current-limiting ability of variable impedance transformer. The short-circuit current medium-voltage winding is reduced by 42.14% when current-limiting reactor is connected to the system. Therefore the adjustable reactive power, the favorable current limiting effect, easy modification, convenient maintenance and considerably reduce the impact, shown in Fig.3(a) and (b), are the significantly superiority of variable impedance. In addition, the benefits in economy and society are remarkable and its extending foreground is roomy. Reliability analysis and life prediction of variable impedance transformer are also conducted in this paper. Compared with conventional transformers, the variable impedance transformer has higher reliability and longer service life.

[1]Z. Haijun, Y. Bin, X. Weijie, W. Shuhong, W. Guolin, H. Youpeng, and Z. Iingyin, "Dynamic Deformation Analysis of Power Transformer Windings in Short-Circuit Fault by FEM," IEEE Transactions on Applied Superconductivity, vol. 24, pp.502-510, (2014). [2]G. Chaffey and T. C. Green, "Directional current breaking capacity requirements for HVDC circuit breakers," *2015 IEEE Energy Conversion Congress and Exposition (ECCE)*, Montreal, pp. 5371-5377, (2015). [3]N. Hayakawa, H. Kojima, M. Hanai and H. Okubo, "Progress in Development of Superconducting Fault Current Limiting Transformer (SFCLT)," *IEEE Transactions on Applied Superconductivity*, 21(3) 1397-1400, (2011).

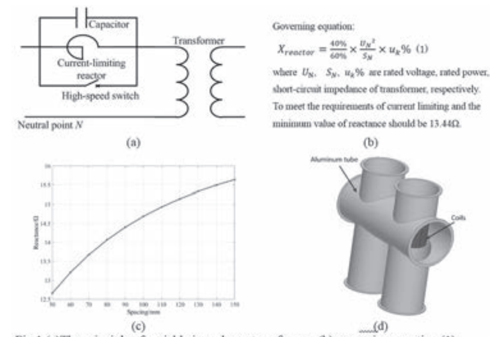

Fig.1 (a)The principle of variable impedance transformer, (b) governing equation (1), (c) reactance value of current-limiting reactor, (d) structure of current limiting device.

Fig. 1. (a)The principle of variable impedance transformer, (b) governing equation (1), (c) reactance value of current-limiting reactor, (d) structure of current limiting device.

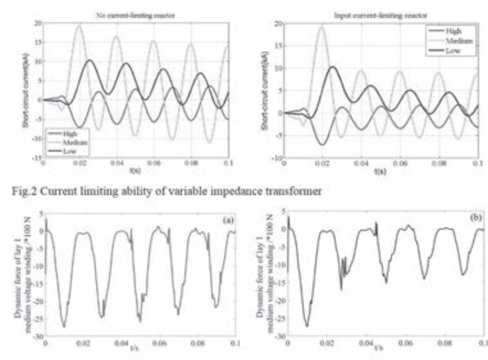

Fig.2 Current limiting ability of variable impedance transformer
Fig.3 Transient dynamic force (a) No current-limiting reactor (b) Inputting current-limiting reactor
Fig.2 Current limiting ability of variable impedance transformer and Fig.3 Transient dynamic force (a) No current-limiting reactor (b) Inputting current-limiting reactor.

Fig. 2. Current limiting ability of variable impedance transformer and Fig.3 Transient dynamic force (a) No current-limiting reactor (b) Inputting current-limiting reactor.

FP-13. Analysis of a Novel Three-Coil Wireless Power Transfer System Applied in Biomedical Devices.

X. Zhang[1], L. Wang[2] and X. Zhang[1]
1. Tianjin Normal University, Tianjin, China; 2. Chinese Academy of Medical Science & Peking Union Medical College Institute of Biomedical Engineering, Tianjin, China

Since the concept of wireless power transfer has been proposed and implemented by Tesla over a hundred years ago, it has obtained lots of breakthroughs and applied in many potential fields especially in implantable biomedical devices [1-2]. The implantable biomedical devices are surgically introduces into the human body to rebuild body function, achieve a better quality of life, and expand longevity. With the development of microelectronics, biotechnology, and materials, the industry of implantable biomedical devices grows up quickly. The researches show that in America 8% to 10% of the people have experienced an implantable medical device, while in industrialized countries 5% to 6% of population have consumption demand in implantable medical devices. How to provide a constant power supply, for implantable medical devices, becomes a restricted problem. In order to guarantee the implanted medical devices to work normally, the energy storage or harvesting components should be included in these devices. In the traditional implantable medical devices, there are two ways to provide power for the devices. The common method is the implantable batteries are used to be as a power supply, and the other method is to transfer the power in vitro to the devices with the lead wires through the skin. For implantable batteries, their lifetime, size and toxic composition will lead to potential hazard to the patients. The transcutaneous wires, as well, will bring infection and reliability problems. In order to address above problems, the technology of wireless power transfer is used in the biomedical devices. The system has two parts in which one part including power supply and the transmitter coil is placed outside the patients' body, and the other part including the receiver coil is placed in the patients' body. For this system, the receiver coil should be limited as small as possible and the power transfer efficiency should be as high as possible. Different from the traditional two-coil wireless power transfer system, a novel three-coil system is proposed in this paper. In the novel system, there are two rectangular transmitter coils and one circular receiver coil. To obtain the maximum power transfer efficiency, the system is optimal designed according to the following step as shown in Fig. 1. Firstly, the size and the geometry of the receiver coil are determined. A circular coil with a radius of 10mm is chosen as the receiver coil. Secondly, the distribution of the magnetic field generated by the rectangular coil is analyzed based on the Biot-Savart's law. Then the relationship between the distance and the magnetic field intensity will be obtained and expressed as a formula according to the analysis result. Finally, the above formula is chosen as the optimization constrains and the power transfer efficiency is chosen as the optimization objective function. After the optimal designing, the optimal parameters of the transmitter coils are obtained and verified through the experimental system as shown in Fig. 2. The power transfer distance is about 30cm, and the power received by the receiver coil can achieve about 5W. The detailed results will be given in the full paper.

[1] H. Zhang, F. Lu, H. Hofmann, W. Liu and C. C. Mi, "A four-plate compact capacitive coupler design and LCL-compensated topology for capacitive power transfer in electric vehicle charging application," *IEEE Transactions on Power Electronics*, vol. 31, no. 12, pp. 8541-8551, Dec. 2016. [2] D. R. Smith, V. R. Gowda, O. Yurduseven, S. Larouche, G. Lipworth, Y. Urzhumov, and M. S. Reynolds, "An analysis of beamed wireless power transfer in the Fresnel zone using a dynamic, metasurface aperture" J. Appl. Phys. 121, 014901 (2017).

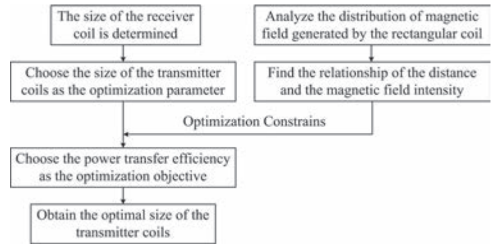

Fig. 1. The flowchart of the optimal design.

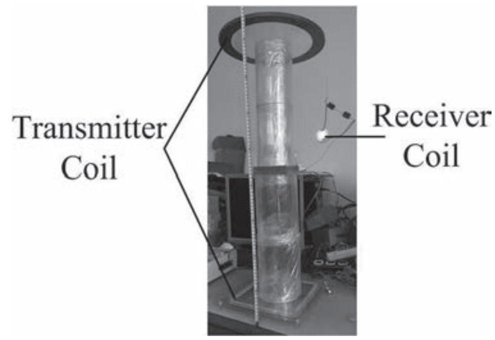

Fig. 2. A novel three-coil wireless power transfer system.

Session FQ
HARD MAGNETIC MATERIALS AND MOTOR APPLICATIONS
(Poster Session)

Mi-Ching Tsai, Chair
National Cheng Kung University, Tainan, Taiwan

FQ-01. Reduced magnetic respone of Dy doped $CoFe_2O_4$ nanoparticles.

H. Kumar[1]
1. H.A.S.(Physics), Rajkiya Engineering College Bijnor India, Bijnor, India

Reduced magnetic respone of Dy doped $CoFe_2O_4$ nanoparticles Hemaunt Kumar[a,b], R.C. Srivastava[b], Jitendra Pal Singh[c], R. K. Patel[d], Keun Hwa Che[c] [a]Rajkiya Engineering College, Bijnor, Uttar Pradesh, India [b]Department of Physics, Govind Ballabh Pant University of Agriculture and Technology, Pantnagar, Uttarakhand 263145, India [c]Advanced Analysis Canter, Korea Institute of Science and Technology, Seoul 02792, Republic of Korea [d] Department of Physics, Jai Narayan Vyas University, Jodhpur, India Corresponding Author: hvatsal@gmail.com Rare earth ferrites brings tremendous opportunity for researchers to develop a relationship among rare earth concentration and magnetic behaviour. In the present work, effect of Dy doping on the magnetic response is discussed by using Mossbauer spectroscopy and magnetic measurments using vibrating sample magnetometer. Dy doped $CoFe_2O_4$ nanoparticles of crystallite size 22 nm were synthesized using metal nitrates and citic acid by heating precursor at 500^{o}C [1]. X-ray diffraction (XRD) studies reveal presence of pure spinel phase in pure $CoFe_2O_4$ nanoparticles. Crystalline phase do not influenced by the Dy doping, however, onset of poor crystallinity was observed as Dy concentration increases from 0.05 to 0.15. Raman spectroscopic measurments corroborates the results obtained from XRD studies. The values of crystallite size are 22±2, 16±2, 13±1 and 11±1 nm for Dy concentration of 0.0, 0.05, 0.10 and 0.15. Magnetic hysteresis curves measured for these nanoparticles exhbit ferrimagnetic behavior. Saturation magnetization, remanent magnetization, coercivity and anisotropy constant decreases with increases of Dy doping (Table 1). To get insight of underlying mechansim of magnetic response of Dy doped ferrite, measurments to proble local structre are perfromed at room temperature. Mössbauer spectroscopy measurments reveal presence of Fe^{3+} in high spin state as corroborated from isomer shift values. This behavior of Fe ions are furhter confirment by Fe *L*-edge near edge X-ray absorption fine structure measurments. Pre-edge spectral features modifies with Dy doping reflecting the modification of metal-oxygen hybridization as Dy incorpotes into the spinel lattice. With Dy doping cation redistribution occurs among tetrahedral and octahedral stie of spinel lattice. Thus, there two factors which influences magnetic response of ferrite systems- (1) Dy doping induced cation redistribtuion and (2) Dy doping induced reduction of crystallite size. If magnetic moment is calculation on the basis of cation redistribution, magnetic moment remain almost same, however, experimentally magnetic moment reduces almost 50% to its initial value. Another factor which affects the magnetic behavior is crystallite size. Thus, reduction of magnetization with Dy concentration is associated with cation redistribtuion and reduction of particle size.

FQ-02. A Study on Optimal Design for Direct Drive Submerged Pump Actuator.

Y. KIM[1], Q. Yan[1], *D. Ryu*[1] and J. Lee[1]
1. Hanbat National University, Daejeon, The Republic of Korea

This paper deals with the characteristic analysis & optimum design criteria of Permanent Magnet Assisted Synchronous Reluctance Motor (PMA-SynRM) for power improvement. The focus of this paper is through torque density and d, q-axis inductance according to flux barrier shape. The proposed procedure allows the definition of the rotor magnet & flux barrier shape, dimensions starting from an existing motor or a preliminary design according to the rated wattage. The performance of a synchronous reluctance motor (SynRM) in terms of torque and power factor depends on the two-axis inductance L_d and L_q of the machine. The large difference of L_d - L_q and L_d / L_q ratio are good for the machine's properties. Therefore, Considerable attention has been paid in the past to improve rotor design of SynRM[1]-[3] as shown in Fig 1. By adding a proper quantity of permanent magnets the torque density and power factor of SynRM can be greatly increased. It is called Permanent Magnet Assisted Synchronous Reluctance Motor (PMA-SynRM). And it is important to select an appropriate combination of design parameters to enhance more torque density than an existing PMA-SynRM. In this paper, finite element analysis for a PMA-SynRM is presented and the d-q axis inductance, torque characteristics analysis are performed. Comparisons are given with inductance and torque characteristics of normal Synchronous reluctance motor and those according to quantity of residual flux density (0T, 0.4T) in PMA-SynRM, respectively. And then, it is confirmed that the PMA-SynRM results in high output power performance through numerical analysis data. The focus of this paper is to find design solutions through the comparison of torque density and d-q axis inductance, especially torque ripple of PMA-SynRM according to the rotor magnet and flux barrier shape, dimensions variations under each rated wattage condition (1HP–7 HP) corresponding to the rotor diameters (66.82, 71.4, 84.95, 92.1, 101, 109.1 mm preliminary design). Coupled finite elements analysis (FEA) and Response surface Methodology (RSM) have been used to evaluate design solutions [4]-[7] as shown in Fig 2. A normal synchronous reluctance motor runs at a somewhat poorer power factor than the induction motor. This problem can be alleviated by inserting permanent magnets between rotor segments. For a PMA-SynRM, the L_d and L_q axis inductances affect performance in terms of torque and power factor; in our case the optimization has been oriented on the maximization of their difference (L_d-L_q) and minimization of torque ripple (objective function) The RSM seeks to find a relationship between design variables and responses through statistical fitting methods, which are based on observed data from a system. The response is generally obtained from either real experimentation or computer simulations. Therefore finite element analysis (FEA) is performed to obtain the data of SynRM in this paper. There are many experimental designs for the creation of response surface. In this paper the central composite design (CCD) is chosen to estimate the interactions of design variables and curvature properties of response surfaces in a number of repeated experiments. A method of optimum design related to the torque density and torque ripple of PMA-SynRM according to the flux barrier number, and especially, rotor diameter has been proposed. For rapid design, an automatic pre-process including an automatic ACAD file drawing and mesh generation with regard to the stator and rotor shape variations has been developed. Starting from an existing design, the best design solution is selected, and it is confirmed repeatedly that the flux barrier number, can be a fixed value related to the rotor diameter, whether PMASynRM or SynRM.

[1] J. H. Lee, J. C. Kim, D. S. Hyun, "Effect of Magnet on Ld and Lq Inductance of Permanent Magnet Assisted Synchronous Reluctance Motor", IEEE Transaction on Magnetics, Vol. 35, No. 5, pp. 1199-1202, May 1999. [2] J. H. Lee, D. S. Hyun, "Hysteresis Analysis for Permanent Magnet Assisted Synchronous Reluctance Motor by Coupled FEM & Preisach Modelling", IEEE Transaction on Magnetics, Vol. 35, No. 5, pp. 1203-1206, May 1999. [3] Y. J. Jang, J. H. Lee, "Characteristic Analysis of Permanent Magnet-assisted Synchronous Reluctance Motor for High Power Application", Journal of Applied Physics, Vol.97, No.10, 10Q503, May, 2005. [4] R. P. Tomas, Statistical methods for Quality Improvement. New York: Wiley, 2000. [5] J.T. Li, Z.J. Liu, M.A. Jabbar, X.K. Gao: Design optimization for cogging torque minimization using response surface methodology, IEEE Transactions on Magnetics, Vol 40, No 2, 2004, pp.1176-1179. [6] S. J. Park, S. J. Jeon, J. H. Lee, "Optimum design criteria for a synchronous reluctance motor with concentrated winding using response surface methodology", Journal of Applied Physics, vol.99, issue 8, April, 2006. [7] J. M. Park, S. I. Kim, J. P. Hong, J. H. Lee, "Rotor design on Torque Ripple Reduction for a synchronous reluctance motor with concentrated winding using response surface methodology", IEEE Transactions on Magnetics, vol. 42, No. 10, pp.3479-3481. Oct. 2006.

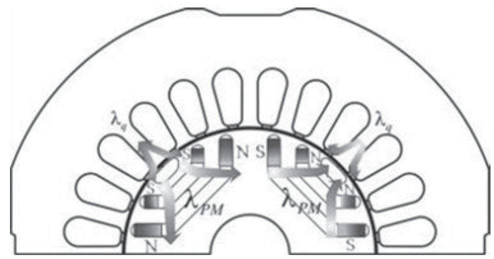

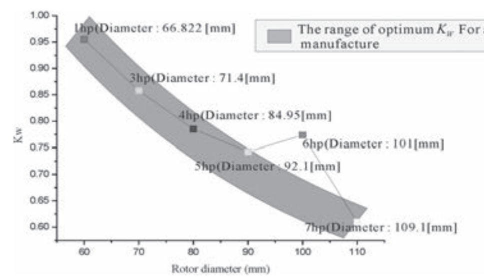

FQ-03. Analytical Method for 3-D Overhang Effect of Surface-Mounted Permanent-Magnet Motor Using Conformal Mapping.

Y. Ko[1], J. Song[1], M. Seo[1], Y. Kim[2] and S. Jung[1]
1. Sungkyunkwan University, Suwon, The Republic of Korea; 2. Chosun University, Gwangju, The Republic of Korea

Introduction: In various industrial applications, the overhang structure is often applied to improve the power density by concentrating the magnetic flux at the end part of the stator. The magnet overhang is usually used for small motors such as engine cooling fan to increase the power density. However, 3-D finite element method(FEM) is requisitely conducted to take the precise overhang effect into account. Although accurate analysis results are provided, the 3-D computation time is inevitably longer than 2-D analysis. Therefore, we propose the well-established analytical method applying conformal mapping(CM), so it is possible to consider the overhang effect and significantly save the computation time. The overhang effect has been reflected through the approximation 2-D FEM by changing the remanence flux density, B_r, of the permanent magnet(PM) according to the overhang length of the 3-D structure [1],[2]. Also, it is essential that 3-D analysis is conducted. Magnetic equivalent circuit(MEC), one of analytical methods, takes into account the overhang effect using the effective air-gap length between the overhang part and stator core [3],[4]. When applying MEC, the radial component of no-load air-gap flux density, B_R, is calculated, but it is difficult to estimate the tangential component of no-load air-gap flux density, B_{th}. Therefore, it is hard to compute the cogging torque, calculated by the combination of B_R and B_{th}. In most papers, considering the overhang effect, the 2-D analysis has been carried out by increasing the average of the air-gap magnetic flux density corresponding to the entire stator length or changing PM B_r corresponding to the overhang length. In this paper, we propose the analytical method for considering 3-D overhang effect using the two type CMs, x-y plane CM and x-z plane CM. The x-y plane CM is based on 2-D no-load magnetic flux density, which is the conventional CM, and the x-z plane CM is related to no-load magnetic flux density of overhang structure along to z-axis. For the validity of the proposed method, the no-load analysis, cogging torque and EMF, is computed via B_R and B_{th} from CMs and the result can be compared with 3-D FEM. Overhang Effect: It is requisite to predict the appropriate overhang length at the motor design stage. As the overhang length increases, the power density is not linearly improved. After the limit overhang length, L_{lim}, the leakage flux of PM occurs. Therefore, as the overhang length increases, it is necessary to estimate the change of the air-gap flux density and calculate the L_{lim}. The overhang effect is greatly related to the end layer of the stator along to the z-axis. Especially, the overhang effect is insufficient in the center layer. The total stator can be divided into two layers, applied layer and non-applied layer, based on the influence of the overhang effect. It is also important to calculate the boundary point between the applied layer and non-applied layer to conduct the exact overhang effect. This point is called as the non-overhang effect length, $L_{non\text{-}OH}$. Fig. 1(a) shows the x-z plane cross-section overhang structure including the leakage magnetic flux part of PM. Fig. 1(b) shows the air-gap flux densities for each points of the layers. The leakage flux part has a long effective air-gap length between the magnet and the stator so the air-gap flux density is small. In this paper, the overhang effect is predicted though the overhang function, f_{OH}, that is derived from the x-z plane CM. No-load Field distribution: The conformal transformation is a significantly useful method for the analytical solution of Laplacian field with boundaries. The x-y plane CM is used to transform the stator slot model into the stator slotless model. After the process, the x-y plane CM result is the complex relative air-gap permeance, λ^*, of the relation between slot model and slotless model. It consists of the real and imaginary components. Based on λ^*, the no-load magnetic flux density of the slot model is written as [5] $B_{slot}=B_{slotless}\ \lambda^*$ (1) where $B_{slotless}$ is the no-load magnetic flux density of the slotless model. The x-y plane CM is calculated without overhang structure. The proposed x-z plane CM transforms the overhang model into the non-overhang model. In this case, the real component of λ^* is contributed to overhang effect. Therefore, f_{OH} is the real component of λ^*. Thanks to the x-y plane CM, the maximum f_{OH}, L_{lit} and L_{non_OH} for each overhang length can be founded. Fig.2 (a) shows x-y plane CM and x-z plane CM configurations. f_{OH} is a function that gradually increases with respect to 1 when moving from the center line to the stator end layer along the z-axis. Fig. 2 (b) shows overhang function along the z-axis. The no-load air-gap magnetic flux density considering overhang effect, $B_{overhang}$, is calculated by the combination of B_{slot} and f_{OH} and is written as $B_{overhang}(z)=B_{slot}f_{OH}(z)$. (2) If the overhang length changes, the $B_{overhang}$ can be obtained by performing only the x-z plane CM associated with f_{OH} again. Without 3-D FEM analysis, no-load cogging torque and EMF can be computed by using no-load air-gap magnetic flux density, consists of radial and tangential components, for each element stack length. The results, air-gap magnetic flux density, cogging torque and EMF, of the proposed method can be verified to compare the 3-D FEM results. Also, the method is applied to other size and pole-slot combination to verify the proposed x-z plane CM.

[1] Ki-Chan Kim and Ju Lee, "The dynamic analysis of a spoke-type permanent magnet generator with large overhang," *IEEE Trans. Magn*, vol. 41, no. 10, pp. 3805-3807, Oct. 2005. [2] J. Y. Song, J. H. Lee, Y. J. Kim and S. Y. Jung, "Computational Method of Effective Remanence Flux Density to Consider PM Overhang Effect for Spoke-Type PM Motor With 2-D Analysis Using Magnetic Energy," in *IEEE Trans. Magn*, vol. 52, no. 3, pp. 1-4, March 2016. [3] H. K. Yeo, D. K. Lim, D. K. Woo, J. S. Ro and H. K. Jung, "Magnetic Equivalent Circuit Model Considering Overhang Structure of a Surface-Mounted Permanent-Magnet Motor*," IEEE Trans. Magn*, vol. 51, no. 3, pp. 1-4, March 2015. [4] J. M. Seo, I. S. Jung, H. K. Jung and J. S. Ro, "Analysis of Overhang Effect for a Surface-Mounted Permanent Magnet Machine Using a Lumped Magnetic Circuit Model," *IEEE Trans. Magn*, vol. 50, no. 5, pp. 1-7, May 2014. [5] D. Zarko, D. Ban and T. A. Lipo, "Analytical Solution for Electromagnetic Torque in Surface Permanent-Magnet Motors Using Conformal Mapping," in *IEEE Trans. Magn*, vol. 45, no. 7, pp. 2943-2954, July 2009. [6] A. Hanic, D. Zarko and Z. Hanic, "A Novel Method for No-Load Magnetic Field Analysis of Saturated Surface Permanent-Magnet Machines Using Conformal Mapping and Magnetic Equivalent Circuits," in *IEEE Trans. Energy Conversion*, vol. 31, no. 2, pp. 740-749, June 2016.

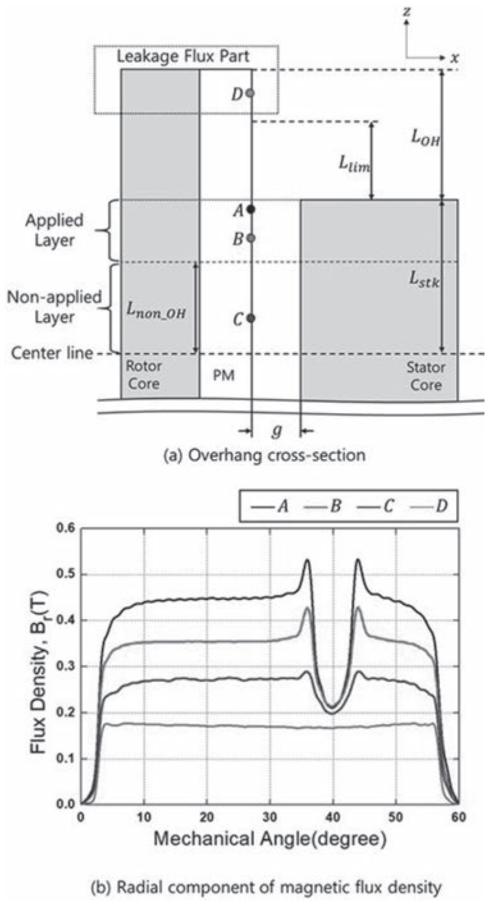

Fig. 1. Overhang Effect

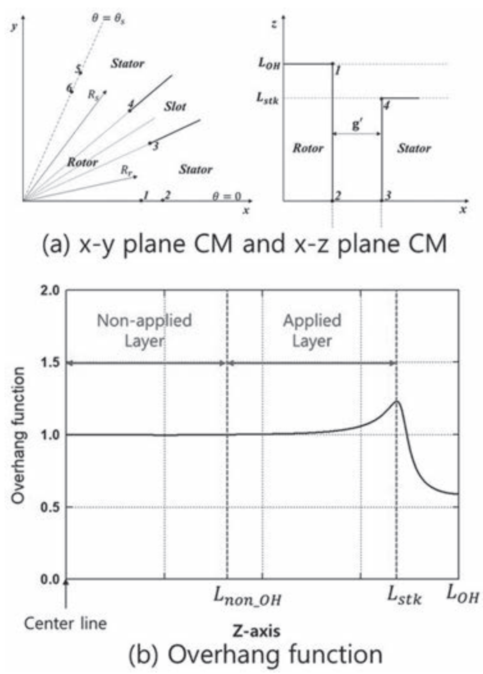

Fig. 2. CM configurations and overhang function

FQ-04. Investigation of flux adjustment capability in hybrid excited switching flux permanent magnet machines.

X. Liu[1,2], S. Wang[1,2] and D. Dong[1,2]

1. State Key Laboratory of Reliability and Intelligence of Electrical Equipment, Hebei University of Technology, Tianjin, China; 2. School of Electrical Engineering, Hebei University of Technology, Tianjin, China

Permanent magnet (PM) excited machines have been applied in many applications, such as automotive, aerospace, industrial automation and renewable energy. However, due to the poor flux-weakening performance of PM machine, the concept of hybrid excited machines, which employ both dc filed windings and PMs to generate field flux, has been developed. Recently, in order to improve the flux-weakening capability of switching flux permanent magnet (SFPM) machines, the hybrid excited SFPM (HESFPM) machines, which adopt double salient stator and rotor structure, have been developed [1][2]. With the help of dc field windings, the air-gap flux density can be either enhanced or weakened. Fig.1 (a) and (b) show two types of 12/10 hybrid excited SFPM machines, respectively. Compared with the conventional SFPM machine, in HESFPM-1 partial permanent magnets (PMs) are replaced by dc field windings. However, in HESFPM-2, the dc field windings are added on the outside of conventional SFPM machine together with an extra outer ring structure. Compared with HESFPM-1, which has limited space for the dc field windings, much larger slot area can be used for dc field windings in HESFPM-2, which increase the flexibility of dc field windings design. By defining the ratio of dc slot area to ac slot area in Eq. (1), γ_s, the influence of dc slot area on the flux adjustment capability can be investigated. $Y_s=S_{dc}/S_{ac}$ where S_{dc} refers to the stator slot area filled by dc windings, whereas S_{ac} refers to the stator slot area filled by armature windings. The principle of flux regulation of two types 12/10 HESFPM machines is illustrated in Fig.2. In order to evaluate the flux adjustment capability, the coefficient is defined by: $K_f=(\Psi_{max}-\Psi_{min})/\Psi_{pm}=\Delta\Psi/\Psi_{pm}$ where Ψ_{pm}, Ψ_{max}, Ψ_{min} represent the amplitude of PM flux-linkage, enhanced flux-linkage and weakened flux-linkage with maximum positive and negative dc current, respectively. Fig. 3(a) shows the flux adjustment coefficient against the ratio of dc slot area to ac slot area. Due to the much larger γ_s in HESFPM-2, the flux adjustment coefficient can reach to 0.161, which is twice of that in HESFPM-1, whose flux adjustment coefficient is 0.0877. In terms of electromagnetic torque, Fig. 3 (b), compared with HESFPM-1 with optimized γ_s, larger torque adjustment can also be obtained in HESFPM-2. Thus, the flux weakening performance of HESFPM-2 will be better than HESFPM-1. However, with the optimal ratio of dc slot area to ac slot area, HESFPM-1 can produce higher torque than HESFPM-2, as shown in Table I. In the full paper, the flux weakening performance will also be compared between the two types of the hybrid excited machine together with the validation of the prototype machine.

[1] W. Hua, Z. Q. Zhu, M. Cheng, Y. Pang, and D. Howe, "Comparison of flux-switching and doubly-salient permanent magnet brushless machines,'' in *Proc. ICEMS2005*, September 2005, pp. 165-170. [2] Z. Q. Zhu, Y. Pang, D. Howe, S. Iwasaki, R. Deodhar, and A. Pride, "Analysis of electromagnetic performance of flux-switching permanent-magnet machines by nonlinear adaptive lumped parameter magnetic circuit model," *IEEE Trans. Magn.*, vol. 41, no. 11, pp. 4277- 4287, Nov. 2005. [3] Y. Amara, L. Vido, M. Gabsi, E. Hoang, M. Lecrivain, and F. Chabot, "Hybrid excitation synchronous machines: Energy efficient solution for vehicle propulsion," in *Proc. IEEE Vehicle Power and Propulsion Conf. (VPPC2006)*, Sep. 6–8, 2006, pp. 1–6. [4] Richard L. Owen, Z. Q. Zhu, Geraint W. Jewell, "Hybrid-excited flux-switching permanent-magnet machines with iron flux bridges" *IEEE Trans. Magn.*, vol. 46, no. 6, pp. 1726 - 1729, June 2010.

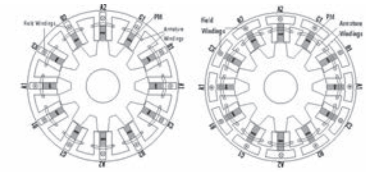

(a) HESFPM-1 (b) HESFPM-2

Fig.1 Machine topologies of two hybrid excited switching flux permanent magnet machines

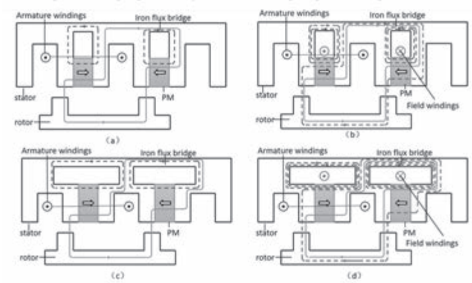

Fig.2 Flux-regulation principle of the HESFPM-1, HESFPM-2

Table I Performance comparison between HESFPM-1 and HESFPM-2 (optimized).

Machines	Excitation	Average Torque (Nm)	Flux-linkage Amplitude (Wb)	k_f	Ratio of dc slot area to ac slot area, γ_s
HESFPM-1	I_{dc}=-5A/mm^2	1.494	0.008615	0.0877	0.27
	I_{dc}=0A/mm^2	1.599	0.009013		
	I_{dc}=5A/mm^2	1.704	0.009405		
HESFPM-2	I_{dc}=-5A/mm^2	1.160	0.007264	0.1607	1.41
	I_{dc}=0A/mm^2	1.271	0.007890		
	I_{dc}=5A/mm^2	1.387	0.008532		

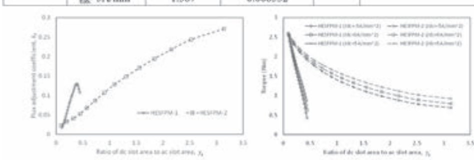

(a) Flux adjustment coefficient (b) Torque -

Fig.3 Comparison of flux adjustment and torque between HESFPM-1 and HESFPM-2.

FQ-05. Multi-Objective Design Optimization of A New Cost Effective Axial Flux Permanent Magnet Assisted Eddy Current Brake.

M. Gulec[1] and M. Aydin[1]
1. Mechatronics Engineering, Kocaeli University, Kocaeli, Turkey

Eddy current brakes (ECB) are used in various areas such as electric vehicles, high-speed trains, elevators, gym products and domestic applications [1-2]. ECB have numerous topologies such as radial or axial flux paths and rotational or linear type alternatives [2-4]. The aim of all topologies is to generate retarding force or torque in the moving conductive part. Owing to Faraday's law of induction, altering magnetic fields occurred from windings or permanent magnets (PM) create the circular fields and these fields cause eddy currents. In general, most ECB in the literature and in the market consist of only DC windings. Nowadays, this conventional ECB structures have not been used as frequently as before due to rapid development in the field of ECB and demand in electrical applications. PM assisted ECB are promising area of research future for the future applications due to benefits in control and high-efficiency structure [5-8]. However, accomplishing the optimum design parameters is vital for PM assisted ECB. In this paper, a novel axial flux (AF) PM assisted ECB is designed and optimized by multi-objective particle swarm optimization (MO-PSO) based on a non-linear magnetic reluctance network modeling. The proposed AFPM-ECB has a single-rotor and single-stator configuration. Magnets are placed to slot openings so that closed slot structure is obtained in order to improve the braking torque characteristics. In addition, it can be clearly said that the same braking torque can be achieved by less excitation with the proposed AFPM-ECB compared to traditional ECB. The proposed AFPM-ECB structure is illustrated in Fig. 1. PM magnetizations and excitation coils are also provided in the figure. Before the running the MO-PSO, an accurate analytical model should be developed. In this paper, a non-linear magnetic reluctance network modeling is used to calculate the air gap flux density profile and the magnetic field in the conductive region. Magnetic reluctance network model is illustrated in Fig. 2. The globally convergence Newton-Raphson based on back-tracking method is used in the non-linear magnetic network modelling. The general braking torque equation derived from Lenz Law related to the calculation of the current density in the conductive region is used in the MO-PSO and the flowchart of the non-linear magnetic model is given in Figure 3. In MO-PSO, three cost functions, 'braking torque', 'PM weight' and 'total ampere-turn', are described to determine the 3-dimensional Pareto front curve. The number of 500 populations and repository are used in the MO-PSO and the best design point is selected reference by 3D Pareto front curve (Fig. 4). The results show that total ampere-turns in proposed AFPM-ECB is reduced as half compared to conventional ECB which has same rated braking torque. In addition, 25% of reduction in weight is achieved by proposed AFPM-ECB. Detail explanations of non-linear magnetic modelling and MO-PSO with 3D-FEA validation will be provided in the final version of the paper.

[1] B. Lequesne, L. Buyun, T.W. Nehl, "Eddy-current machines with permanent magnets and solid rotors", *IEEE Trans. on Ind. Appl.*, vol. 33, no. 5, pp. 1289-1294, 1997. [2] R. Yazdanpanah, M. Mirsalim, "Hybrid electromagnetic brakes: Design and performance evaluation," *IEEE Trans. on Energy Con.*, vol. 30, no. 1, pp. 60-69, 2015. [3] S. E. Gay, M. Ehsani, "Parametric analysis of eddy-current brake performance by 3-D finite-element analysis," *IEEE Trans. on Magnetics*, vol. 45, no. 2, pp. 319-328, 2006. [4] K. Baoquan, J. Yinxi, Z. He, Z. Lu, Z. Hailin, "Analysis and design of hybrid excitation linear eddy current brake", *IEEE Trans. on Energy Conv.*, vol. 39, no. 2, pp. 496-506, 2014. [5] H. Shin, J. Choi, H. Cho, S. Jang, "Analytical torque calculations and experimental testing of permanent magnet axial eddy current brake", *IEEE Trans. on Magn.*, vol. 49, no. 7, pp. 4152-4155, 2013. [6] Y. Lezhi, L. Desheng, M. Yuanjing, J. Jiao, "Design and performance of a water-cooled permanent magnet retarder for heavy vehicles," *IEEE Trans. on Energy Conversion,* vol. 26, no. 3, pp. 953-958, 2011. [7] M. Gulec, E. Yolacan, M. Aydin, "Design, analysis and real time dynamic torque control of single-rotor-single-stator axial flux eddy current brake," *IET Elect. Power Appl.*, vol. 10, no. 9, pp. 869-876, 2016. [8] M. Gulec, M. Aydin, "Modelling and analysis of a new axial flux permanent magnet biased eddy current brake," *in Proc. of International Conference on Electrical Machines*, pp. 459-465, 2016

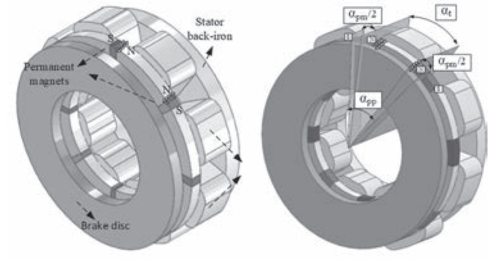

Figure 1. Proposed AFPM-ECB structure

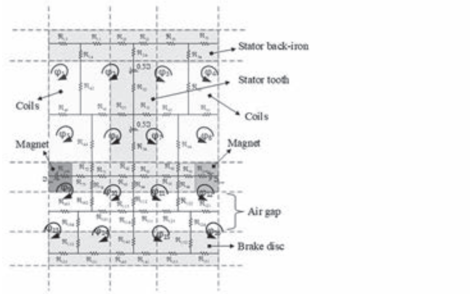

Figure 2. Symmetry magnetic reluctance network modelling of proposed AFPM-ECB

Fig. 1. and Fig. 2.

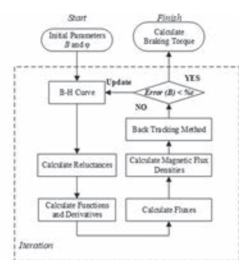

Figure 3. Flowchart of the non-linear magnetic reluctance network modelling

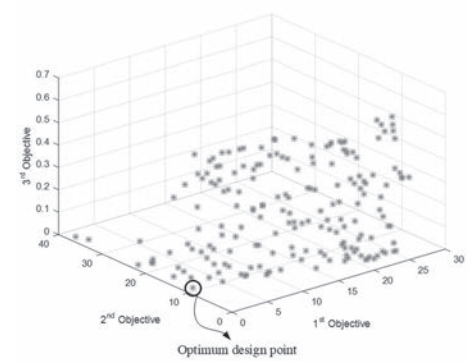

Figure 4. 3D Pareto front curve of proposed AFPM-ECB

Fig. 3. and Fig. 4

FQ-06. The Influence of Magnetization on Modular Spoke-type Permanent-Magnet Machine for In-Wheel Traction Applications.

H. Zhang[1] and *W. Hua*[1]
1. School of Electrical Engineering, Southeast University, Nanjing, China

Abstract—The main purposes of this paper consist of two parts: Firstly, the geometric topology of novel modular spoke-type permanent-magnet (MSTPM) machines with different magnetization modes are introduced. Secondly, based on magnetic field modulation (MFM) analysis and finite element method (FEM), the influence of magnetization on MSTPM machines are investigated with respect to field harmonic, combination of slots and poles, winding factor, back electromotive force (EMF), inductance, eletromagnetic torque, and so on. A prototype machine is manufactured to verify the MFM and FEM predicted results. I. Introduction and Topology As shown in Fig. 1, modular spoke-type permanent-magnet (MSTPM) machines are inspired from flux-switching permanent-magnet (FSPM) machines by moving the sandwiched structure from the stator to the rotor to solve the space competition in stators. It has been found that MSTPM machines have better over-load capability and higher efficiency than FSPM machines [1], and stronger flux-weakening capability and superior high-speed performance than SPM machines [2]. Hence, the MSTPM machine is certainly a good choice for in-wheel traction applications where low speed and high torque are required. In [3], the operation principle of MSTPM machines is analyzed based on magnetic field modulation (MFM), and the back-EMF of MSTPM machines is discussed in [4]. However, there is no research covering the MSTPM machines under different magnetization modes and the corresponding influences on performances. Hence, this paper will introduce MSTPM machines with different magnetization and investigate the influence of magnetization based on MFM and finite element method (FEM). More details will be given in the full paper. II. Analysis and Verification Two magnetization modes of MSTPM machines are illustrated in Fig. 2. The Mode I (MI) is that two adjacent magnets have the same magnetization direction; the Mode II (MII) is that two adjacent magnets are magnetized in reversal directions. As shown in Fig. 3, MSTPM machines with different magnetization modes have different permanent-magnet magneto motive force (PM-MMF) waveforms. Hence, for MI MSTPM machine, the PM-MMF can be expressed by formula (1). For MII MSTPM machine, the PM-MMF can be expressed by formula (2). The θ_{rt} and θ_{pm} are the arc width of rotor tooth and magnet, respectively, and f_{pm} is PM magnetic potential. According to the PM-MMF function, it is found that the number of magnet N_{pm} in MII MSTPM machines must be an even number. However, this constraint does not exist in MI MSTPM machines. Based on the Fourier analysis of the PM-MMF function, the working fundamental field harmonic of MI MSTPM machines and MII MSTPM machines can be calculated by formula (3) and (4). The h_1 is the filed harmonic which induces the fundamental back-EMF. Formula (3) and (4) is suitable for MI and MII MSTPM machines, respectively. Hence, the field harmonic which induces the *k*-th back-EMF harmonic can be calculated by formula (5). To verify the above analysis, field harmonics of two MI and MII MSTPM machines with 26 pieces of magnets are analyzed and compared based on PM-MMF function and FEM. Fig. 4 shows the field harmonic spectrums of MI and MII MSTPM machines according to analytical and FEM results. It can be found that there is a good agreement between analytical and FE results. The 26th and 13rd field harmonics are the main working harmonic of MI and MII MSTPM machines with 26 pieces of magnets, respectively, according to analytical and FE results. Besides, there is a considerable 39th field harmonic which is related to the 3rd EMF harmonic in MII MSTPM machines with 26 pieces of magnets, and the MI MSTPM machines however do not have such high field harmonic. This phenomenon will lead to the discussion of combination of slot and pole, winding factor, electromagnetic torque, core loss, and so on, which are key indexes of in-wheel traction machine design and will be displayed with details in the full paper. To verify the analytical and FE investigation, a prototyped MI MSTPM machine as shown in Fig. 5 was manufactured and tested, whose key parameters are listed in Table I. In Fig. 6, the predicted and tested phase to phase (line) back-EMF waveforms @480r/min (the rated speed) are illustrated. It can be found that the tested fundamental frequency is the same as the FEM one, which verifies the correctness of analytical and FEM results. More experimental details will be given in the full paper.

[1] H. L. Zhang, and W. Hua, "A novel outer-rotor-permanent-magnet flux-switching machine for in-wheel light traction," in Proc. IEEE-IECON, Florence, Italy, Oct. 2016, pp. 6633-6638. [2] H. L. Zhang, W. Hua, and X. K. Zhu, "Design of novel modular-spoke-type permanent magnet machines," in Proc. IEEE-IEMDC, Miami, USA, May 2017. [3] P. Su, W. Hua, Z. Z. Wu, P. Han, and M. Cheng, "Analysis of the operation principle for rotor-permanent-magnet flux-switching machines," IEEE Trans. Ind. Electron., vol.65, no.2, pp.1062-1073, Feb. 2018. [4] H. L. Zhang, W. Hua, and G. Zhang, "Analysis of back-EMF waveform of a novel outer-rotor-permanent-magnet flux-switching machine," IEEE Trans. Magn., vol.53, no.6, Jun. 2017. Article #:8105004.

$$F_{pm}(\theta)=\begin{cases}0 & 0\le\theta<\theta_{rt}\\ f_{pm} & \theta_{rt}\le\theta<\theta_{rt}+\theta_{pm}\\ 0 & \theta_{rt}+\theta_{pm}\le\theta<2\theta_{rt}+\theta_{pm}\\ -f_{pm} & 2\theta_{rt}+\theta_{pm}\le\theta<2\theta_{rt}+2\theta_{pm}\end{cases}\quad(1)$$

$$h_1=N_{pm}\quad(3)$$

$$F_{pm}(\theta)=\begin{cases}0 & 0\le\theta<\theta_{rt}\\ -f_{pm} & \theta_{rt}\le\theta<\theta_{rt}+\theta_{pm}\\ 0 & \theta_{rt}+\theta_{pm}\le\theta<2\theta_{rt}+\theta_{pm}\\ f_{pm} & 2\theta_{rt}+\theta_{pm}\le\theta<2\theta_{rt}+2\theta_{pm}\\ 0 & 2\theta_{rt}+2\theta_{pm}\le\theta<3\theta_{rt}+2\theta_{pm}\\ f_{pm} & 3\theta_{rt}+2\theta_{pm}\le\theta<3\theta_{rt}+3\theta_{pm}\\ 0 & 3\theta_{rt}+3\theta_{pm}\le\theta<4\theta_{rt}+3\theta_{pm}\\ -f_{pm} & 4\theta_{rt}+3\theta_{pm}\le\theta<4\theta_{rt}+4\theta_{pm}\end{cases}\quad(2)$$

$$h_1=\frac{N_{pm}}{2}\quad(4)$$

$$h_k=k\times h_1\quad(5)$$

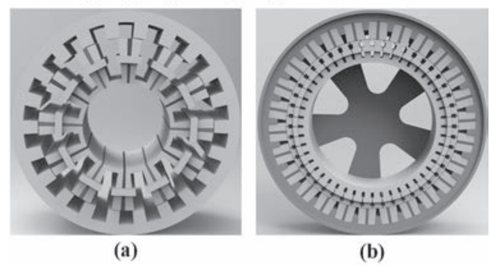

Fig. 1. Topologies of FSPM and MSTPM machines. (a) FSPM machine. (b) MSTPM machine.

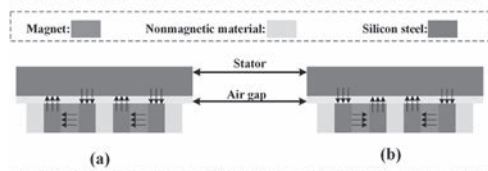

Fig. 2. Two magnetization modes in MSTPM machines. (a) MI MSTPM machines. (b) MII MSTPM machines.

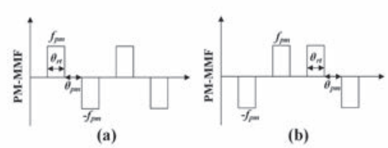

Fig. 3. The PM-MMF waveforms of MSTPM machines with different magnetization. (a) MI MSTPM machines. (b) MII MSTPM machines.

TABLE I

Parameters of MSTPM Machine

Parameter	Value
Slot number	48
Magnet number	26
Magnet material	NdFeB35
Outer radius	138mm
Airgap length	0.5mm
Stack length	45mm

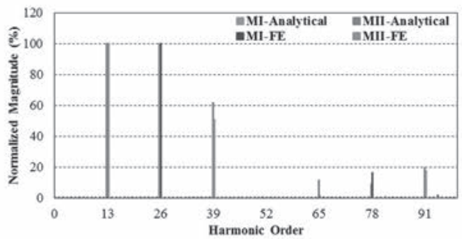

Fig. 4. Field harmonic spectrums of MSTPM machines with different magnetization.

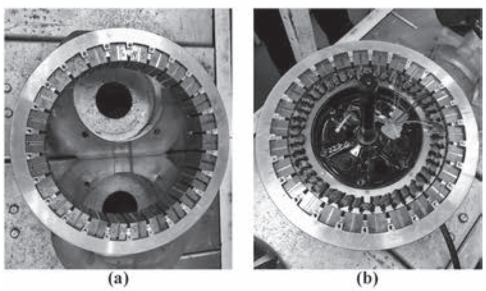

Fig. 5. The prototype MSTPM machine. (a) Rotor. (b) Rotor and stator.

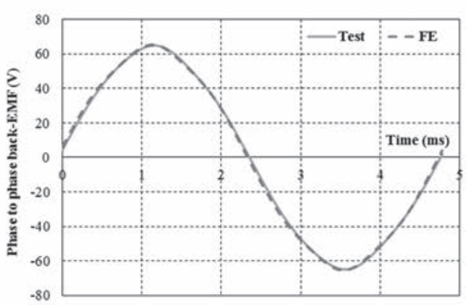

Fig. 6. Predicted and tested phase to phase back-EMF of MI MSTPM machine with 26 magnets @480r/min.

FQ-07. Proposal of Maxwell Stress Tensor for Local Force Calculation in Magnetic Body.

M.K. Ghosh[1], Y. Gao[1], H. Dozono[1], K. Muramatsu[1], W. Guan[2], J. Yuan[2], C. Tian[2] and B. Chen[2]
1. Department of Electrical & Electronic Engineering, Saga University, Sagacity, Japan; 2. Department of Electrical & Electronic Engineering, Wuhan University, Wuhan, China

1. Introduction To investigate the noise reduction of an electrical machine, the deformation and vibration of the cores are evaluated by using the coupled magnetic and mechanical analyses [1]. In these analyses, the local force calculated by using the flux distribution obtained from the magnetic field analysis is required in the mechanical analysis. In the local force calculation [2], the Maxwell stress tensor is usually used. The Maxwell stress tensors are often represented by the Minkowski and Chu models with linear and nonlinear energy expressions, respectively. In the nonlinear magnetic field analysis, the volume forces, which move the magnetic bodies, obtained from both models coincide with each other, whereas their local forces, which deform the magnetic bodies, are different. Therefore, more investigation is required to clarify the suitable expression of the Maxwell stress tensor. In this paper, to clarify the proper expression of the Maxwell stress tensor for the local force calculation of a nonlinear magnetic body, the Maxwell stress tensors are derived from the Fleming's left hand rule because the volume current density can be used to determine the magnetization in the nonlinear magnetic body. As a result, a new Maxwell stress tensor is derived. The surface force obtained from the new Maxwell stress tensor is compared with those obtained from the ordinary Minkowski and Chu models, and the equivalent magnetizing current method [3] to show the effectiveness and validity of the proposed Maxwell stress tensor. 2. Derivation of the Proposed Maxwell Stress Tensor The magnetization of the magnetic body can be expressed by using volume current density. So, the local force in the magnetic body can be calculated by using the total current density J_t, which is not only the magnetizing current density J_m but also conductive current density J_c, such as eddy current, in free space with permeability μ_0. In this case, for example, the x component f_x of the force density is calculated by using the Fleming's left hand rule in free space with permeability μ_0 as follows: $f_x=(J_t\times B)_x+(B_x/\mu_0)\ \mathrm{div}B=(1/\mu_0)[\partial\{1/2\ (B_x^2-B_y^2-B_z^2)\}/\partial x+\partial(B_xB_y)/\partial y+\partial(B_xB_z)/\partial z]$ where B is the flux density. The second term, which is zero, in the first equation on the right hand side is added to derive the Maxwell stress tensor. Finally, the following Maxwell stress tensor T^p can be obtained: $T^p_{ij}=(\mu/\mu_0)\{H_iB_j-\delta_{ij}(1/2)H\bullet B)\}$ where i, j denotes x, y, and z components. δ is the Kronecker's delta. H is the magnetic field intensity in the magnetic body defined by $B=\mu H$ (μ: permeability). In the Maxwell stress tensor T^m of the Minkowski model, μ/μ_0 on the right hand side is 1. Moreover, in the Maxwell stress tensor T^c of the Chu model, the nonlinear energy expression is used in the second term on the right hand side. In the volume force calculation, the volume force obtained from T^p coincides with those obtained from T^m and T^c. However, the local forces are different with each other as shown in the next section. 3. Comparison of Maxwell Stress Tensor in Local Force Calculation Various Maxwell stress tensors T^p, T^m, and T^c described in Section 2 are compared by using a simple nonlinear magnetostatic model shown in Fig. 1. The core (JIS C 2552-2014: 35A300), which is infinite in y and z directions, is placed in the air and the uniform flux density B_{ty} of 1T is imposed in y direction. The x-component f_{sx} of the surface force density on surface A-B is calculated by using T^p, T^m, and T^c. To clarify the proper Maxwell stress tensor, the equivalent magnetizing current method [3], in which the uniform magnetization in the magnetic body is replaced by the equivalent magnetizing current on the surface, is also used. The surface forces f_{sx} obtained by using the Maxwell stress tensors and the equivalent magnetizing current method are shown in Table I. The f_{sx} obtained from the proposed Maxwell stress tensor T^p is much different from those obtained from T^m and T^c. Moreover, f_{sx} by T^p coincides with the equivalent magnetizing current method. So, it can be concluded that the Maxwell stress tensor T^p proposed in this paper should be used for the local force calculation of the nonlinear magnetic body.

[1] Y. Gao, et al., *IEEE Trans. Magn.*, vol. 46, no. 6, pp. 2179-2182, 2010. [2] A. Kameari, *International Journal of Applied Electromagnetics in Material*, vol. 3, pp. 231-240, 1993. [3] T. Kabashima, et al., *IEEE Trans. Magn.*, vol. 24, no. 1, pp. 451-454, 1988.

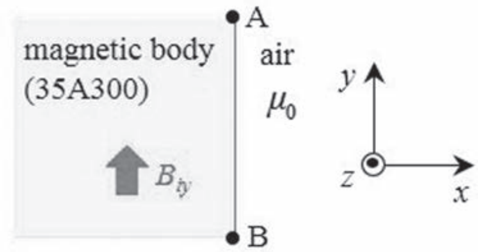

Fig. 1. Verification model.

Maxwell stress tensor			Equivalent current method
Proposed T^p	Minkowski T^m	Chu T^c	
397888	66	75	397888

TABLE I COMPARISON OF SURFACE FORCE DENSITY f_{sx} [N/m²] ON SURFACE A-B

FQ-08. Coercivity enhancement of Nd-Ce-Fe-B sintered magnets by the grain boundary diffusion process using Nd-Al-Cu alloys.

Q. Zhou[1], R. Tang[1], F. Xiao[1] and Z. Liu[2]
1. GuangDong Research Institute of Rare Metals, Guangzhou, China;
2. School of Materials Science and Engineering, South China University of Technology, Guangzhou, China

1 Introduction Nd-Fe-B based sintered magnets have a wide range of applications in energy efficient technologies such as traction motors of hybrid electric vehicles and wind generators [1]. In general, Nd-Fe-B based sintered magnets have a large amount of rare earth elements, such as Nd, Pr and Dy. From an economic point of view, new type of magnets incorporating light rare earth elements such as La and Ce into Nd-Fe-B based sintered magnets has stimulated considerable research efforts due to the analogous structure recently [2]. However, magnets incorporated with Ce exhibit much deteriorated magnetic properties due to the inferior intrinsic magnetic properties of $Ce_2Fe_{14}B$, which saturation magnetization, ambient anisotropic field and Curie temperature were reported to be 1.17 T, 2.6 T and 152°C, respectively [3]. Many efforts had been paid to improve the performance. One well-known method to increase the coercivity of sintered magnets is to refine the grain boundary (GB) structure and chemistry through grain boundary diffusion (GBD) [4, 5]. Previous investigations have demonstrated that the coercivity of Ce-based magnets is enhanced by diffusion process with minor amounts of $Nd_{70}Cu_{30}$ and $Nd_{80}Ag_{20}$ [6]. In this work, we investigated the microstructure of Nd-Ce-Fe-B sintered magnets and the eutectic grain boundary diffusion process using Nd-Al-Cu in order to comprehend the origin of the coercivity enhancement by the Nd-Al-Cu diffusion process. 2 Experimental As Nd-Ce-Fe-B sintered magnets with a nominal composition of $(Nd, Ce)_{31.5}Fe_{bal}B_1$ (wt. %) were fabricated by the conventional powder metallurgy method. The magnets were cut into a cube shape with an edge of 10 mm and a height of 4 mm. $Nd_{80}Al_{10}Cu_{10}$ alloy ribbons as a diffusion source were prepared by the melt spinning technique using the high vacuum quenching system. In the diffusion process, the Nd-Ce-Fe-B sintered magnets were covered by the $Nd_{80}Al_{10}Cu_{10}$ alloy ribbons. And the subsequent diffusion process was carried out at 800°C for 1h and subsequent 580°C for 5 h in a vacuum furnace. 3 Results and discussion Fig. 1 shows the demagnetization curves at 300 K for Nd-Ce-Fe-B magnets before and after diffusion treatment. After diffusion process, the coercivity is substantially enhanced from ~0.86 T to ~1.27 T, while the remanent magnetization decreased slightly from ~1.03 T to ~1.02 T. The changes in the magnetic properties were usually related with the microstructure evolution. Fig. 2 shows back-scattered electron(BSE) images and mapping images of the diffusion-processed sample with the *c*-axis in the plane for magnets. The selected analysis peaks for the elemental maps are Nd, Ce, Fe, Cu, and Al, respectively. As shown in Fig. 2a, the dark gray region indicates the $Nd_2Fe_{14}B$ matrix phases (matrix phase), and the brightly imaged regions correspond to the so-called "Nd-rich phases". It is obviously shown that the Nd-rich layers become continuous, distinct and smooth after the diffusion process. These Nd-rich phases are believed to be non-ferromagnetic based on the low Fe concentration, which would be beneficial to the exchange decoupling between $Nd_2Fe_{14}B$ grains [7]. The Nd-rich shell in the $Nd_2Fe_{14}B$ phase was selectively formed at certain $Nd_2Fe_{14}B$/Nd-rich phase interfaces, as indicated by arrows in the Fig. 2a. SEM-EDS mapping images of the diffusion-processed sample are shown in Figs. 2b-2f. It is found that most of the intergranular phases are depleted of Fe and enriched with Nd and Ce, which are similar to those of commercial sintered magnets. It is surprising to find that Cu and Al are also enriched in these Nd-rich phases in the diffusion-processed magnet. It claimed that certain Cu addition promotes the formation of the C-Nd_2O_3 phase during annealing, which was attributed to the high coercivity [8]. On the other hand, although the distribution of Al element is inhomogeneous, it indicated that the eutectic decomposition in the intergranular phase into Al-lean regions and the modified wettability of boundary phase through Al is also advantageous for coercivity. This is probably the reason for the enhancement of coercivity of the diffusion-processed magnet. 4 Conclusions In summary, the phase constitution and magnetic properties were investigated in Nd-Ce-Fe-B sintered magnets by the grain boundary diffusion process using Nd-Al-Cu alloys. The coercivity of Nd-Ce-Fe-B sintered magnet was substantially increased from ~0.86 T to ~1.27 T while smaller degradation of remanence. The detailed microstructure characterization has shown the formation of Nd-rich core/shell microstructure and the distribution of intergranular phases. The coercivity enhancement in this work can be attributed to be the microstructure evolution during the Nd-Al-Cu eutectic grain boundary diffusion process. Finally, these investigations could serve as a reference for the grain boundary diffusion on the Ce-based magnets with moderate performances.

[1] O. Gutfleisch, M. A. Willard, E. Brück, C. H. Chen, S. Sankar, and J. P. Liu, "Magnetic materials and devices for the 21st century: stronger, lighter, and more energy efficient," *Advanced materials,* vol. 23, no. 7, pp. 821-842, 2011. [2] J. Jin, T. Ma, Y. Zhang, G. Bai, and M. Yan, "Chemically Inhomogeneous RE-Fe-B Permanent Magnets with High Figure of Merit: Solution to Global Rare Earth Criticality," *Scientific Reports,* vol. 6, pp. 32200-8, 2016. [3] S. Hirosawa, Y. Matsuura, H. Yamamoto, S. Fujimura, M. Sagawa, and H. Yamauchi, "Single Crystal Measurements of Anisotropy Constants of R2Fe14B (R= Y, Ce, Pr, Nd, Gd, Tb, Dy and Ho)," *Japanese journal of applied physics,* vol. 24, no. 10A, pp. L803-L805, 1985. [4] Q. Zhou, Z. W. Liu, X. C. Zhong, and G. Q. Zhang, "Properties improvement and structural optimization of sintered NdFeB magnets by non-rare earth compound grain boundary diffusion," *Materials & Design,* vol. 86, pp. 114-120, 2015. [5] X. Tang, H. Sepehri-Amin, T. Ohkubo, M. Yano, M. Ito, A. Kato, N. Sakuma, T. Shoji, T. Schrefl, and K. Hono, "Coercivity enhancement of hot-deformed Ce-Fe-B magnets by grain boundary infiltration of Nd-Cu eutectic alloy," *Acta Materialia*, pp. 884-895, 2017. [6] W. Cui, Tongbo Zhang, Xiaoqian Zhou, D. Yu, Q. Wang, X. Zhao, W. Liu, and Z. Zhang, "Enhanced coercivity and grain boundary chemistry in diffusion-processed Ce13Fe79B8 ribbons," *Materials Letters,* vol. 191, pp. 210-213, 2017. [7] A. Sakuma, T. Suzuki, T. Furuuchi, T. Shima, and K. Hono, "Magnetism of Nd–Fe films as a model of grain boundary phase in Nd–Fe–B permanent magnets," *Applied Physics Express,* vol. 9, no. 1, pp. 013002-4, 2016. [8] T.-H. Kim, S.-R. Lee, M.-W. Lee, T.-S. Jang, J. W. Kim, Y. D. Kim, and H.-J. Kim, "Dependence of magnetic, phase-transformation and microstructural characteristics on the Cu content of Nd–Fe–B sintered magnet," *Acta Materialia,* vol. 66, pp. 12-21, 2014.

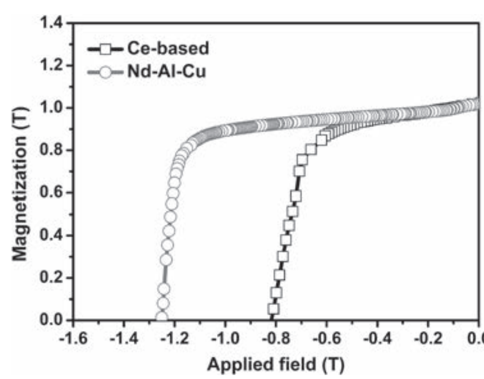

Fig. 1. The demagnetization curves at 300 K for Nd-Ce-Fe-B magnets before and after diffusion treatment.

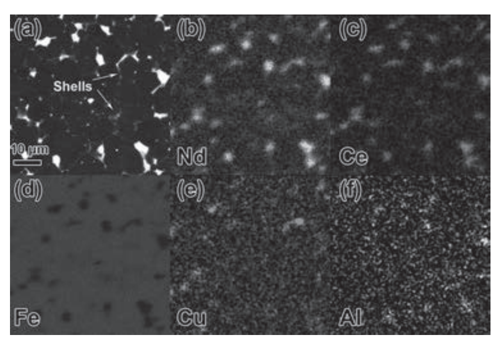

Fig. 2. BSE image and mapping images of the diffusion-processed sample. The selected analysis peaks for the elemental maps are Nd, Ce, Fe, Cu, and Al, respectively.

FQ-09. An Improved Analysis Method of Irreversible Demagnetization for Single-Phase Line Start Permanent Magnet Motor.

J. Jung[1], B. Lee[2], M. Lim[1] and J. Hong[3]
1. Hyundai Mobis, Yongin, The Republic of Korea; 2. Korea Automotive Technology Institute, Daegu, The Republic of Korea; 3. Hanyang University, Seoul, The Republic of Korea

I. Introduction Single-phase induction motors (IM), which do not require power electronics switching devices and position sensors, are more economical and higher maintenance than electric motors powered by additional inverters [1]. Therefore, it is generalized to the driving motor for home appliances operated by commercial single phase power grid. However, the motor has vibration due to the unbalanced rotating magnetic field generated by the main winding and the auxiliary winding [2]. It also has problems such as difficulty in improving efficiency due to loss of conductor bar. A line-start permanent magnet (LSPM) has been developed in which a conductor bar and a permanent magnet (PM) are inserted at the same time to compensate the disadvantage of the single-phase induction motor. The LSPM is possible to line-start and can operate at the synchronous speed in steady state by magnetic torque and reluctance torque. Therefore, unlike general PM motor, position sensor for starting and operation is unnecessary. Consequently, LSPM motor provides lower production cost than general PM motors and higher efficiency than general induction motors. However, when the LSPM is started, a large inrush current flows, which can result in irreversible demagnetization in the PM [3]. Generally the irreversible demagnetization of PM is occured by the operating point in B-H or M-H curve of PM when only primary part is excited. The LSPM is started by the magnetic flux generated by the induction current of the secondary conductor. Fortunately, the induction current of the secondary conductor reduces the reactive magnetic field that affects the PM. Therefore, general demagnetization analysis leads to the over estimation of magnetic field acting on PM, and results in excessive PM usage. In this paper, a demagnetization analysis method considering the current of the secondary conductor of the LSPM motor is discussed. II. Analysis Method This paper deals with analysis methods of demagnetization of LSPM motor. Conventional method is general demagnetization analysis method and process of conventional method is shown in Fig. 1 (a). Initially, no-load back EMF is estimated. Then, magneto-static field analysis is conducted with maximum current flowing through primary conductor. At this point, the maximum current value can be found by examining the slip variation. In this method, induced current in the secondary conductor is ignored. When the operating point of PM is below its knee point, the residual flux density of the PM is renewed. Finally, with renewed flux density of the PM elements, no-load back-EMF is calculated. By comparing no-load back-EMF before and after demagnetization field, demagnetization ratio of PM is determined. The proposed irreversible demagnetization analysis method for LSPM is distinguished from conventional analysis method which is only considering primary current. The proposed demagnetization analysis method is shown in Fig. 1 (b). Firstly, the currents of the primary and secondary conductors are obtained through the transient analysis based on the voltage source. Then calculated currents by transient analysis which is flowing through primary and secondary conductors are applied to irreversible demagnetization analysis in every rotor position considering not only nonlinear characteristic of the core but also that of the PM on the B-H curve. In the next, determination whether PM is irreversibly demagnetized or not can be made with identical process of conventional method. III. Results and Discussion Demagnetization analysis and experiments were carried out to verify the proposed analysis method. DC current was applied to the motor to verify the conventional analysis method. On the other hand, in order to verify the proposed analysis method that reflects the actual phenomenon, AC current is applied to the test motor. As shown in Table I, the results of the no-load back EMF analysis before the demagnetization experiment is the same for both analysis methods. On the other hand, as a result of examining the demagnetization ratio of the conventional analysis methods, it has a demagnetization ratio of 7.7 % based on the experimental value. In the conventional analysis method which does not consider the secondary current, the analysis itself is verified through the demagnetization experiment. As a result of the demagnetization analysis using both the primary and secondary currents, the demagnetization ratio was 0%. When the design of the LSPM is performed by using the conventional demagnetization analysis method, it is possible to overestimate the grade or usage of the PM. The proposed analysis method is expected to be useful for the optimization of the grade selection and the usage of the PM in the design of the LSPM motor.

[1] T. J. E. Miller, “Single-Phase Permanent-Magnet Motor Analysis”, *IEEE Trans. on Ind. Appl.*, vol. IA-21, no. 4, May/June 1985. [2] H. Nam, K. H. Ha, J. J. Lee, J. P. Hong, and G. H. Kang, “A study on iron loss analysis method considering the harmonics of the flux density waveform using iron loss curves tested on Epstein samples,” *IEEE Trans. on Magn.*, vol. 39, pp. 1472–1475, May 2003. [3] G. H. Kang, J. Hur, H. Nam, J. P. Hong, and G. T. Kim, “Analysis of Irreversible Magnet Demagnetization in Line-Start Motors based on Finite Element Method,” *IEEE Trans. on Magn.*, vol. 39, no. 3, pp. 1488-1491, May 2003.

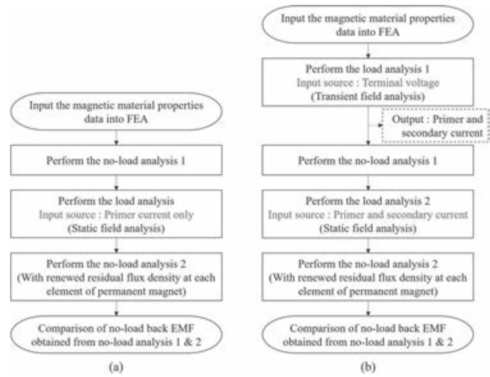

Fig. 1. Demagnetization analysis process. (a) Conventional analysis method (b) Proposed analysis method

Method / Results	FEA results		Experimental results	
	Conventional method	Proposed method	Conventional method	Proposed method
Back EMF before demagnetization [Vrms]	81.99	81.99	78.42	78.42
Back EMF after demagnetization [Vrms]	74.77	81.99	72.35	78.41
Demagnetization ratio [%]	8.80	0.00	7.74	0.00

Table I. Comparision of analysis and experimental results between conventional method and proposed method.

FQ-10. Demagnetization and Permanent-Magnet Minimization Analyses of Less-Rare-Earth Interior Permanent-Magnet Synchronous Machines Used for Electric Vehicles.

W. Wang[1], *P. Zheng*[1,2], M. Wang[1], Y. Liu[1] and Z. Fu[1]
1. Department of Electrical Engineering, Harbin Institute of Technology, Harbin, China; 2. State Key Laboratory of Robotics and System, Harbin Institute of Technology, Harbin, China

I. Introduction Rare-earth permanent magnet synchronous machines (RE-PMSMs) are widely used in electric vehicles (EVs) due to their characteristics of high efficiency, high torque density and high power factor. While the dramatic price fluctuations of the rare-earth permanent magnets (PMs) have been restricted the application of RE-PMSMs. Hence, the less-rare-earth interior permanent magnet synchronous machines (LRE-IPMSMs), which combine the features of high electromagnetic performance as well as low cost, have attracted increasing attention in recent years [1]. The anti-demagnetization ability of the LRE-IPMSMs is crucial to the machine safety [2]. In [3], the tapered flux barriers are adopted to improve the anti-demagnetization ability of the LRE-IPMSMs. In [4], a practical analytical approach is proposed to express the direct link between the PM thickness and the demagnetization limit. In addition, the PM minimization is also a significant issue for the LRE-IPMSMs as it is crucial to decrease the machine cost. In [5], an analytical procedure is proposed to reduce the PM quantity in the LRE-IPMSMs without affecting the torque versus speed performance. In this paper, the demagnetization equivalent magnetic circuit (EMC) model of the investigated LRE-IPMSM is established and the effects of structure parameters on the PM flux density are investigated. The PM minimization design of the LRE-IPMSMs is obtained on the premise of no side effect on the machine output toque and anti-demagnetization ability. II. Demagnetization EMC Model The rare-earth PM material used in the investigated LRE-IPMSM is N35UH and the demagnetization curve of N35UH at 150 degrees Celsius (with margin) is shown in Figure 1a. When the demagnetization current is fed, the PM demagnetization condition is examined by comparing the knee point flux density (B_k in Figure 1a) and the PM flux density. In the demagnetization EMC model, the bridge is equivalent to be a magnetomotive force (MMF) (F_{Br_Dei}) and a serial-connected reluctance (R_{Br_Dei}) because the magnetization curve of silicon steel is an approximate straight line in saturation area as shown in Figure 1b [5]. The demagnetization EMC model of the investigated LRE-IPMSM is shown in Figure 1c and it is rewritten as Figure 1d shows. In the demagnetization EMC model, R_{g_Dei} and R_{Ba_Dei} are the air gap reluctance and flux barrier reluctance, respectively; Φ_{Dei} is the segmental demagnetization flux that flows through R_{g_Dei}, as shown in Figure 1d; R_δ is the leakage reluctance; F_{S_Dei} is the MMF producing by the stator current; F_{PMi} and R_{PMi} are the equivalent MMF and reluctance of PM, respectively. III. Effects of Structure Parameters on the PM Flux Density The stator current is the rated current (371A) when the effects of structure parameters on the PM flux density are investigated. Figures 2a-2c show the variations of the PM flux density (B_{PMi}) with respect to the PM width (b_{PMi}), which are calculated by the EMC method and finite-element analysis (FEA). As can be seen, when a certain PM is widened, the flux density of this PM decreases. Besides, the flux densities of the other two PMs increase as a certain PM is widened. The effects of the PM thickness, the flux barrier thickness and the flux barrier span angle as well as the bridge width on the PM flux density are also investigated, which will be given in the following full text. IV. PM Minimization Analysis The PM minimization is obtained on the premise of no side effect on the machine output toque and anti-demagnetization ability. The output torque of LRE-IPMSMs is consisted of PM torque and reluctance torque. As a small quantity of the PM is normally employed in the LRE-IPMSMs, hence the effect of the PM shape on the reluctance torque is neglected when the PM minimization is investigated. In other words, the PM quantity is minimized with providing the targeted PM torque, i.e., the targeted no-load flux. The PM minimization design of the LRE-IPMSMs is obtained by the no-load EMC analysis. Then, the performances and parameters (including the reluctance torque, the PM torque, the anti-demagnetization ability and the PM volume, etc.) of the preliminary and PM minimization machine designs are compared and analyzed. The detailed analyses and results will be given in the full text. V. Conclusion In this paper, the demagnetization EMC model of the investigated LRE-IPMSM is established. Then, the effects of structure parameters, such as the PM width, the PM thickness, the flux barrier thickness, the flux barrier span angle and the bridge width, on the PM flux density are investigated, respectively. It can be found that widening the PM can decrease the corresponding PM flux density slightly and thickening the PM can increase the corresponding PM flux density obviously. After that, the PM minimization analysis of the LRE-IPMSMs is studied on the premise of no side effect on the machine output toque and anti-demagnetization ability. Finally, the performances and parameters of the preliminary and PM minimization machine designs are compared and analyzed in detail.

[1] A.Vagati, B.Boazzo, P.Guglielmi and G.Pellegrino,IEEE Trans. Ind. Appl.,50, 1768-1779.(2014) [2] M.Degano, E.Carraro and N.Bianchi,IEEE Trans. Ind. Appl.,51, 4383-4391.(2015) [3] S.Morimoto, S.Ooi, Y.Inoue and M.Sanada, IEEE Trans. Ind. Electron.,61, 5749-5756.(2014) [4] N.Bianchi and H.ahmoud, IEEE Trans. Energy Convers.,31, 800-809.(2016) [5] P.Guglielmi, B.Boazzo, E.Armando, G.Pellegrino and A.Vagati,IEEE Trans. Ind. Appl.,49, 31-41.(2013)

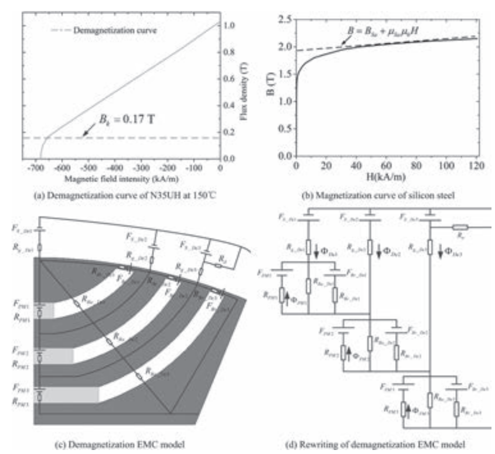

Fig. 1. (a) Demagnetization curve of N35UH; (b) Magnetization curve of silicon steel; (c) and (d) Demagnetization EMC model

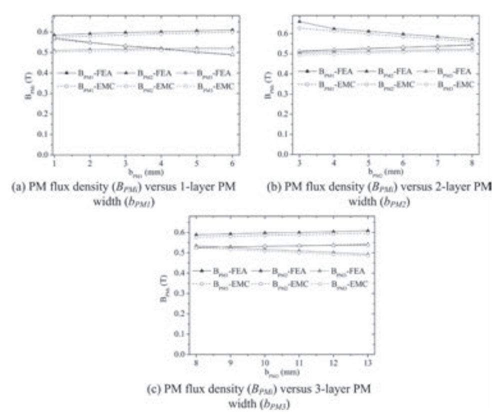

Fig. 2. PM flux density (B_{PMi}) versus *i*-layer PM width (b_{PMi})

FQ-11. Structural and magnetic ordering in MnBi nanoclusters produced in a low energy cluster beam deposition system.

D. Le Roy[1], F. Orlandini-Keller[2], J. Jacquot[3], N. Blanchard[1], N. Dempsey[2] and V. Dupuis[1]
1. Institut Lumière Matière, Villeurbanne, France; 2. Institut Néel CNRS, Grenoble, France; 3. CEA, Grenoble, France

MnBi has attracted much interest within the past decade for its potential use in rare-earth free magnets. When stabilized in the so-called low temperature phase, MnBi exhibits an intriguing magnetic behavior with an unusual positive-dependence of anisotropy constant on temperature, reaching a maximum of 2.2 $MJ.m^{-3}$ at 490 K [1]. However there is a lack of experimental investigation of the thermal stability of single domain MnBi nanomagnets. On the other hand, two magnetic phase nanocomposites, made of a fine mixture of nanosized grains with respectively high magnetization and high anisotropy, are good candidates to build high performance magnets [2]. In the context of limiting the amount of critical elements like heavy lanthanides, using MnBi is an attractive alternative. In this study we put the focus on structural and magnetic properties of MnBi nanosized grains. MnBi nanoclusters, with a mean size of 5 nm, were produced by gas aggregation in a low energy cluster beam deposition system. They were deposited on silicon substrate and protected with an amorphous carbon layer. We investigated their structure in a transmission electron microscope and by X-ray diffraction, and their magnetic response in a superconducting quantum interference device (SQUID) magnetometer. In this study, we focused on the onset of magnetic ordering after annealing at various temperatures, ranging from 250°C to 500°C. In the as-deposited state, MnBi clusters, with nearly equiatomic composition, present a low degree of crystallinity. They show a linear and positive response to an applied magnetic field, with relatively large magnetic moment. The magnetic moment is inversely proportional to temperature, as expected from a Curie law of paramagnetism. This paramagnetic response contrasts with a recent report on as-prepared MnBi 10-nm clusters made by sputtering [3]. This absence of ferromagnetic response at 10 K shows a low degree of MnBi chemical ordering. We found that their magnetism evolves drastically with annealing conditions, as shown by the temperature dependence of the magnetic moment measured under an external field of 10 kOe, displayed on Fig.1. After annealing at the relatively low temperature of 250°C for 20 minutes, the magnetic moment measured under a field of 10 kOe becomes nearly constant between 10 K and 300 K. The onset of ferromagnetic (or ferrimagnetic) ordering in the MnBi nanoclusters would lead to a superparamagnetic response, that follows the Curie law, provided the elementary magnetic moment does not change within the considered temperature range. Therefore, our findings would be consistent with a superparamagnetic state of MnBi nanoclusters only if the magnetic moment increases with temperature. Fitting with a Langevin function the magnetic response suggests that the magnetic moment hold by elementary magnetic volumes increases by a factor of 5 from 10 to 300 K. Interestingly, annealing at a temperature ranging between 300°C and 400°C leads to the formation of a ferromagnetic phase that exhibit relatively large switching fields, up to 25 kOe, but a relatively low thermal stability as the moment drops below 100 K. We will discuss the evolution of structural and magnetic properties upon annealing conditions, notably considering finite size effects.

[1] Chen, T., and Stutis, W. E., IEEE Trans. Magn. (1974) 10, 581 [2] Kneller, E. F., and Harwig, R., IEEE Trans. Magn. (1991) 27, 3588 [3] Mukherjee, P., Balamurugan, B., Shield, J. E., and Sellmyer, D., RSC Adv. (2016) 6, 92765-92770

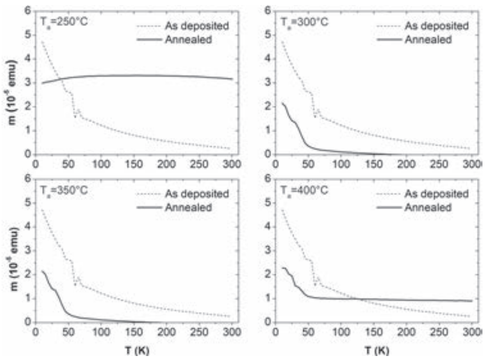

Fig. 1. Temperature dependence of magnetization at an applied field of 10 kOe, for a film of MnBi nanoclusters in the as deposited state (black dashed line), or annealed at 250°C (top left), 300°C (top right), 350°C (bottom left), and 400°C (bottom right).

FQ-12. Novel Permanent Magnet Design and Materials Structures.

Y. Zhang[1] and *K. Gao*[1]
1. Argonne National Laboratory, North Oaks, MN, United States

Permanent magnets (PMs) are one of the earliest functional magnetic materials. Nowadays, they are used in wide and diverse applications. The demand of PMs increases rapidly, in particular for the applications related to hybrid and electric vehicles, direct-drive wind turbines, and many other energy-efficient appliances [1]. The $Nd_2Fe_{14}B$-based magnets, one of the earliest discovered PMs, are well-known for their high magnetic moment and high energy density. The magnetic properties of NdFeB magnets, such as coercivity (H_c) and energy product $(BH)_{max}$, can be further improved by doping heavy rare-earth elements such as Tb and Dy [2]. A number of other permanent magnetic materials, such as SmCo and MnBi, were explored after NdFeB and utilized for the energy related applications [3, 4]. Additional efforts were made to search for new PM materials with reduced consumption of heavy rare-earth elements. It is also desired to have PM materials that work efficiently at elevated temperatures [1, 5]. Recent progress on magnetic materials design, particularly on thin film based magnetic data storage media, demonstrated an exchange-spring mechanism between the relatively hard and soft magnetic layers [6, 7]. This concept was also applied to the development of high energy density PMs [8, 9]. Despite some success in thin film materials, the application of exchange coupling approach to bulk PMs was hindered by a significant technical challenge – a rapid reduction of H_c with the increase of soft phase volume percentage [6, 7], making it difficult to find an optimal design configuration. Micromagnetic simulation indicated that the reduction of H_c was originated from the rotation of the soft phase magnetization, which lowers the energy barrier of magnetization reversal in the exchange-coupled materials (see Fig 1a) [6]. Although there have been tremendous efforts on exploring new PMs and improving PMs energy product, the usage of PMs magnetic flux is not very efficient in many cases. Because most PMs have a high magnetic moment, the surface magnetic charges push the magnetic flux (B) away from the surface normal direction as a result of magnetostatic coupling (see Fig. 2). A rapid decay of the magnetic flux with distance away from a PM surface is often observed ($B \propto 1/d^2$). For applications such as power generation, such drop of magnetic flux density over distance greatly reduces magnets and devices efficiency. Here we propose a PM structure that addresses this issue. Our design can be understood from Fig. 2, where a weakly exchange coupled or exchange decoupled hybrid PM structure is illustrated. The top and bottom sections of the PMs are made from magnetic materials with a high magnetic anisotropy H_k and a relatively smaller magnetization M_s, while the middle section of the PM consists of a relative low H_k and a high M_s magnetic material. The high H_K/M_s ratio of the surface magnetic materials enables a high out of plane component of the surface magnetization, which facilitates a larger magnetic flux out of the hybrid magnet surface. The middle-section of the magnet, due to a smaller demagnetizing field within the magnet body, can be made of magnetic materials with a smaller H_k. In this hybrid PM, the interaction between the surface and body materials is not necessary to be strongly exchange coupled. The thickness of different layers and the exchange coupling between different layers can be varied based on different application needs. Compared to conventional PMs, this hybrid PM structure has many advantages. It has a higher surface magnetic flux density and lower cost. The high grade PMs are only used at surface section of the magnets. The main body of the magnets are made from less expensive PMs. Modeling and calculation indicates that this hybrid structure can improve magnet efficiency by more than 10% without introducing more cost. The other advantage is the flexibility in materials selection. Depending on applications, the choice of materials for the surface and body section of PM can have many options. In high temperature applications the hybrid PM can show a less negative or even positive temperature coefficient with the properly chosen surface and center materials, as illustrated in Fig. 1b. More detailed examples and measurements have been achieved and the results are consistent with the theoretical predictions [6, 7].

[1] R.W. McCallum, L.H. Lewis, R. Skomski, M.J. Kramer, and I.E. Anderson, "Practical Aspects of Modern and Future Permanent Magnets", Annu. Rev. Mater. Res. 44, 451 (2014). [2] O. Gutfleisch, M. A. Willard, et al., "Magnetic Materials and Devices for the 21st Century: Stronger, Lighter, and More Energy Efficient", Adv. Mater. 23, 821-842 (2010). [3] A. E. Ray and K. J. Strnat, "Research and Development of Rare Earth Transition Metal Alloys as Permanent Magnet Materials", Technical Report AFML-TR-72-202 (AD-750746), 1972. [4] N. V. Rama Rao, A. M. Gabay, W. F. Li and G. C. Hadjipanayis, "Nanostructured bulk MnBi magnets fabricated by hot compaction of cryomilled powders", J. Phys. D: Appl. Phys. 46, 265001 (2014). [5] T.G. Woodcock, Y. Zhang, et al., "Understanding the microstructure and coercivity of high performance NdFeB-based magnets", *Scripta Materialia* 67, 536-541 (2012). [6] K. Z. Gao and J. Fernandez-de-Castro, "Energy Surface Model and Magnetization Switching for Exchange Coupled Magnetic Particles", J. Appl. Phys., 99, 08K503 (2006). [7] K. Z. Gao, J. Fernandez-de-Castro and H. N. Bertram, "Micromagnetic study of the switching fields in polycrystalline magnetic thin-film media", IEEE Trans. Magn. 41, 11 (2004). [8] E.F. Kneller, R. Hawig, "The exchange-spring magnet: a new material principle for permanent magnets", IEEE Trans. Magn. Vol 27, Is. 4, 3588-3600, (1981). [9] Eric E. Fullerton, J. Samuel Jiang, "Structure and magnetic properties of exchange-spring Sm–Co/Co superlattices", Appl. Phys. Lett. 72, 380 (1998).

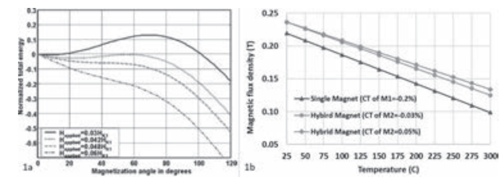

Fig. 1a. Total energy versus the magnetization angle of the soft particles under an external applied magnetic field that has 10° angle from the grain's anisotropy direction. The magnitude of the applied fields is 0.03, 0.042, 0.048 and 0.06 times of the anisotropy field H_{k1}. The saturation magnetization and volume of the soft phase (phase 2) is 5 times and 2 times of the hard phase (phase 1), i.e., $Ms_2 = 5Ms_1$ and $V_2 = 2V_1$. 1b. The magnetic flux density versus temperature curves of a conventional PM (made from material M1) and hybrid PMs (made from materials M1 and M2). Due to a smaller temperature coefficient (CT) of M2 than M1, the magnetic flux of the hybrid PMs is higher than the conventional PM at each temperature.

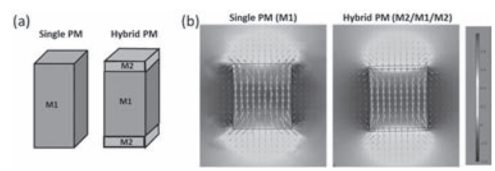

Fig. 2. (a) Schematic drawings of a conventional PM (left) and hybrid PM (right). The surface section of the hybrid PM can be made from different materials and processes than the middle-section of the PM. The top and bottom surface of the hybrid PM can also be different materials. (b) Static magnetic simulation of the magnetic field distribution (amplitude and orientation) within and out of the magnets for the single and hybrid PMs illustrated in (a).

THURSDAY AFTERNOON, 26 APRIL 2018 SIMPOR/ROSELLE BALLROOM, 1:30 TO 4:30

Session FR

MAGNETIC FLUIDS AND ORGANIC MAGNETIC MATERIALS II
(Poster Session)

Mei Fang, Chair
Central South University, Changsha, China

FR-02. Reversible Control of Intrinsic Spins by Guest Molecules in a Layered Ferrimagnetic Metal-Organic Framework.

J. Zhang[1], W. Kosaka[1] and H. Miyasaka[1]
1. Institute for Materials Research, Tohoku University, Sendai, Japan

Reversible magnetic change in response to external stimuli is one of the desired functionalities in molecular magnetic materials. It could be more favorable that the magnetic change is induced by changes of intrinsic spins than that only by structural changes, because the magnetic change could become more drastically. In this study, we demonstrate a reversible magnetic change closely associated with electronic state modulations, as well as structural modulations, in the target material, which is achieved by a solvation/desolvation cycle (i.e., sponge behavior) of the material. The compound is a D_2A-type layered magnet, $[\{Ru_2(O_2CPh\text{-}2,3,5\text{-}Cl_3)_4\}_2(TCNQMe_2)]$-4DCM (1; 2,3,5-$Cl_3PhCO_2^-$ = 2,3,5-trichlorobenzoate; $TCNQMe_2$ = 2,5-dimethyl-7,7,8,8-tetracyanoquinodimethane, DCM = dichloromethane), synthesized by the reaction of $[Ru_2(O_2CPh\text{-}2,3,5\text{-}Cl_3)_4]$ ($[Ru_2^{II,II}]$) acting as an electron-donor (D) and $TCNQMe_2$ as an electron-acceptor (A). Compound 1 has a one-electron transferred charge ordered state with a $[\{Ru_2^{II,II}\}$–$TCNQMe_2^-$–$\{Ru_2^{II,III}\}^+]$ (1e-I) formula (inset of Figure 1). Strong intralayer antiferromagnetic couplings between $[Ru_2^{II,II}]$ with $S = 1$ or $[Ru_2^{II,III}]^+$ with $S = 3/2$ and $TCNQMe_2^-$ with $S = 1/2$, as well as ferromagnetic interlayer interactions, induce long-range ferrimagnetic ordering at $T_c = 101$ K (Figure 1). The interstitial DCM molecules are located in void spaces between layers, which are gradually eliminated under vacuum at 80°C to form a solvent-free compound (1-dry) without loss of crystallinity. The electronic state of 1-dry is thermally fluctuated via a fully electron transferred state at high temperatures to eventually be a charge-disproportionate disordered state with a $[\{Ru_2\}^{0.5+}$–$TCNQMe_2^{1.5-}$–$\{Ru_2^{II,III}\}^+]$ (1.5e-I) [1] formula as the ground state (inset of Figure 1). The T_c in 1-dry is 34 K (Figure 1) because of the presence of diamagnetic $TCNQMe_2^{2-}$ that weakens super-exchange coupling over the framework. A large T_c variation with $T_c \approx 70$ K is switchable, which is achieved by charge state modulations accompanied with a subtle structural modification in a solvation/desolvation treatment.

[1] H. Fukunaga, et al., *Chem. Commun.* 51, 7795 (2015).

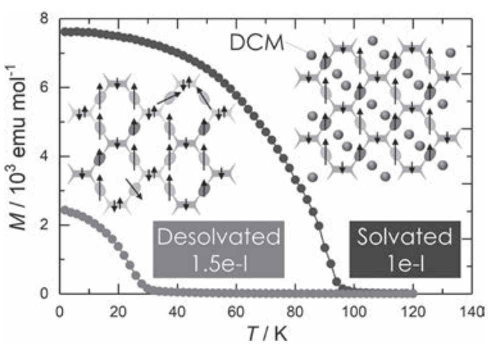

Fig. 1. Temperature dependence of molar magnetic susceptibility for solvated phase 1 (blue curve) and desolvated phase 1-dry (red curve) in an applied dc field of 100 Oe; inset shows the schematic representations of the electronic state in the present $[\{Ru_2\}_2(TCNQ)]$ system (D_2A system).

FR-03. Magnetorheology of Core-Shell Structured Mesoporous Fe_3O_4@$mSiO_2$ Nanoparticle Added Carbonyl Iron Dispersion.

W. Han[1] and H. Choi[1]

1. Polymer Science and Engineering, Inha University, Incheon, The Republic of Korea

I. INTRODUCTION Magnetorheological (MR) fluids, which are composed of micron or sub-micron sized soft-magnetic particles and nonmagnetic fluids, possess tunable and reversible ability to be transformed from a liquid-like to a solid-like state under an applied magnetic field [1, 2]. In the absence of an external magnetic field, MR fluids exhibit a free-flowing state, similar to the behavior presented by Newtonian fluids. However, with the application of a magnetic field strength, their rheological properties can instantly be changed as a result of building up chain-like structure of dispersed magnetic particles under a magnetic field due to magnetic polarization interaction, and this phenomenon has great potential in designing diverse high performance engineering products including vehicle shock absorber, active damper system, torque transducer and MR polishing equipment [3, 4]. Generally, high yield stress and low apparent viscosity without magnetic field as well as good stability and durability have become very crucial factors for the MR fluid application. Among the diverse magnetic materials, soft magnetic carbonyl iron (CI) particles have been regarded as the most attractive materials for MR fluids because of their controllable magnetization and high saturation magnetization; however, the density mismatch between CI particles and the surrounding oil could easily cause sedimentation issues. Therefore, numerous methods have been explored to improve these problems [5, 6]. In this study, we synthesized core-shell structured mesoporous Fe_3O_4@$mSiO_2$ nanoparticles by a surfactant-based sol–gel approach, and then adopted them as an additive for the CI based MR fluid to improve both suspension stability and MR performance. Rheological properties of both pure CI and CI/ Fe_3O_4@$mSiO_2$ nanoparticle based MR fluids for various magnetic field strengths were investigated via rational and oscillatory tests using a rotational rheometer. A profile of sedimentation ratio as a function of time was also recorded to evaluate the effect of mesoporous Fe_3O_4@$mSiO_2$ nanoparticles on sedimentation. II. EXPERIMENT Initially, Fe_3O_4 nanoparticles were synthesized by a solvo-thermal method. The mesoporous-silica-coated Fe_3O_4 magnetic nanoparticles were then prepared by a surfactant-based sol–gel approach. Briefly, 1 g of Fe_3O_4 and 5 g of cetyl trimethylammonium bromide were uniformly dispersed in deionized water by ultrasonic treatment for 30 min. Second, the solution prepared in the first step was added into 900 mL of a 1.0 mM sodium hydroxide aqueous solution and subjected to ultrasonication for 20 min. After stirring the resulting mixture at 60 °C for 30 min, a tetraethyl orthosilicate/ethanol (1/4, v/v) solution (25 mL) was added dropwise, followed by stirring for 3 min. The obtained mixture was then kept for 12 h at 60 °C. The Fe_3O_4@CTAB/SiO_2 nanoparticles were collected and washed several times with ethanol and DI water. Finally, the mesoporous SiO_2 shell was formed by calcination at 550 °C for 5 h to remove the CTAB embedded in the silica layer. Soft magnetic CI micro-spherical particles were dispersed in a silicone oil (1000 cSt) to prepare the MR fluid system. Two different MR fluids with and without mesoporous Fe_3O_4@$mSiO_2$ nanoparticles in the CI suspension were fabricated. The two systems have same particle concentration of CI at 50 wt%, while the one was added with the mesoporous Fe_3O_4@$mSiO_2$ additive (0.1 wt% in the MR fluid). The transmission electron microscopy (TEM) (Philips CM200) was employed to observe the surface morphologies of the magnetic particles before and after coating. A vibrating sample magnetometer (VSM, DMS 1660) was used to examine the magnetic characteristics over a broad magnetic field range. The MR behaviors of the prepared MR fluids were conducted by using a rotational rheometer (MCR 300, Anton PAAR, Germany) equipped with a MR device (MRD 180). III. RESULT AND DISCUSSION Figure 1 shows TEM images of the different stages of products. Primarily, nearly monodisperse spheres with a mean diameter of about 230 nm were observed for pure Fe_3O_4 nanoparticles (Fig.1a). As shown in Fig. 1b, the core–shell structure of Fe_3O_4@CTAB/SiO_2 nanoparticles was successfully formed, where a silica shell with a thickness of approximately 22 nm was uniformly coated on the Fe_3O_4 dark core. After the removal of the CTAB template, the silica shell in the mesoporous Fe_3O_4@$mSiO_2$ nanoparticles exhibited a clear mesoporous structure, with a thickness of approximately 15 nm (Fig.1c). As for their MR performance, Fig. 2a and 2b represent shear stresses as a function of shear rate and three different yield stresses for CI based MR fluids with and without Fe_3O_4@$mSiO_2$ nanoparticle additive under various external magnetic field strengths ranging from 0 to 342 kA/m, respectively. The CI/ Fe_3O_4@$mSiO_2$ additive based MR fluid exhibits higher shear stress and yield stresses than those of pure CI based MR fluid. This is thought to come from both novel increased magnetic interactions with magnetic Fe_3O_4@$mSiO_2$ from the increased magnetic property and the typical extra gap-filling additive effect of the Fe_3O_4@$mSiO_2$ nanoparticles, forming a stronger column structure. Sedimentation was also observed to be improved for the additive system.

1. J. de Vicente, D.J. Klingenberg, R. Hidalgo-Alvarez, "Magnetorheological fluids: a review," *Soft Matter* 7, 3701–3710, (2011). 2. M. Cvek, M. Mrlik, M. Ilcikova, T. Plachy, M. Sedlacik, J. Mosnacek, V. Pavlinek, "A facile controllable coating of carbonyl iron particles with poly(glycidyl methacrylate methacrylate): a tool for adjusting MR response and stability properties," *J. Mater. Chem*. C3, 4646–4656, (2015). 3. I. Bica, Y. D. Liu, H. J. Choi, "Physical characteristics of magnetorheological suspensions and their applications," *J. Ind. Eng. Chem.* 19, 394–406, (2013). 4. A. Sidpara, V.K. Jain, "Rheological properties and their correlation with surface finish quality in MR fluid-based finishing process," *Machining Sci. Tech.* 18, 367–385, (2014). 5. A.J.F. Bombard, M. Knobel, M.R. Alcantara, "Phosphate coating on the surface of carbonyl iron powder and its effect in magnetorheological suspensions," *Int. J. Mod. Phys. B* 21, 4858–4867, (2007). 6. M. Ashtiani, S.H. Hashemabadi, A. Ghaffari, "A review on the magnetorheological fluid preparation and stabilization," *J. Magn. Magn. Mater*. 374, 716–730, (2015).

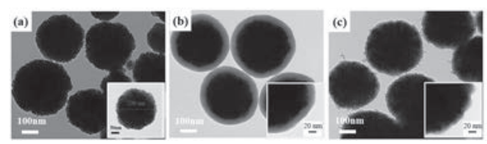

Fig. 1. TEM image of Fe_3O_4 particles (a), Fe_3O_4@CTAB/SiO_2 nanoparticles (b) and mesoporous Fe_3O_4@$mSiO_2$ nanoparticles (c).

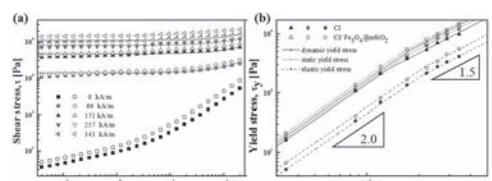

Fig. 2. Shear stress vs. shear rate (a), and comparison of yield stresses (b) for CI (closed symbol) and CI/Fe_3O_4@$mSiO_2$ (open symbol) based MR fluids at different magnetic field strengths.

FR-01. Effect of Fe_3O_4/sepiolite Nanocomposite Additive on Carbonyl Iron Based Magnetorheological Fluid.

Y. Dong[1], S. Piao[1] and H. Choi[1]

1. Polymer Science and Engineering, Inha University, Incheon, The Republic of Korea

I. INTRODUCTION Magnetorheological (MR) fluids are considered to be a kind of intelligent materials, which are suspensions of magnetically particles disperse in non-magnetic carrier liquids, such as, aqueous, silicone oil, mineral oil and so on [1], [2]. Because their rheological behaviors are strongly influenced by the presence of external magnetic field, the shear viscosity and yield stress of MR fluids can be controlled by applied magnetic field with their fast response time of only a few tens of milliseconds. Therefore, controllable MR fluids have been widely developed in many applications, such as, polishing, haptic device, vehicle dynamics and so on [3], [4]. Among the candidates of MR materials, carbonyl iron (CI) particles are considered to be an excellent one owing to its high saturation magnetization, spherical shape and suitable particle size, and have been widely researched. While the high density of CI particles always causes heavy sedimentation problem, which is a particularly adverse factor for industrial application, recently, many researchers have been using magnetic iron oxide particles as additives and it has been proven that they can enhance both the sedimentation stability and MR characteristics of MR fluids [5]. In this work, we synthesized Fe_3O_4/sepiolite magnetic nanocomposites via a chemical co-precipitation method, and introduced these particles as additives of CI MR fluid. We anticipated that the additives can impede the immediate contact of CI particles and then improve the dispersion stability of the pristine CI based MR fluid. Furthermore, the particles also were expected to occupy the interspace of the chain structure of CI particles and then enhance the MR properties of the CI MR fluid. II. EXPERIMENT The Fe_3O_4/sepiolite nanoparticles were synthesized as previously reported [6], in which 3.1 g ferric chloride and 0.5 g sepiolite were added in 50 mL distilled water and sonicated at 40 Celsius for 1 h. The homogeneous suspension was then transferred into a reactor, and the solution with 2.4 g ferrous sulfate heptahydrate dissolved in 50 mL distilled water was added into the reactor and stirred at 60 Celsius for 30min. The 10 mL ammonium hydroxide solution was added dropwise and reaction for 1 h with vigorous stirring. After being aged for 2 h, the product was washed with distilled water, collected via magnetic separation and dried for 12 h. The CI based MR fluid was prepared by dispersing 50 wt% of CI particles in the silicone oil. The CI-Fe_3O_4/sepiolite based MR fluid was prepared with same CI particle concentration of CI MR fluid, while added 0.1 wt% of Fe_3O_4/sepiolite nanoparticles as an additive. The morphology of Fe_3O_4/sepiolite added in CI particles was examined by scanning electron microscopy (SEM) (SU-8010, Hitachi, Japan) and the MR characteristics of both two MR fluids were measured by using a rotational rheometer (Physica MCR 300, Anton Parr, Germany) under various magnetic field strengths. III. RESULTS AND DISCUSSION The SEM images of synthesized Fe_3O_4/sepiolite nanocomposites, CI and CI-Fe_3O_4/sepiolite mixture are shown in Fig. 1 (a), (b) and (c), respectively. In Fig. 1 (a), it is evident that the Fe_3O_4 grows on the surface of nanosized sepiolite. As shown in Fig. 1 (b), CI exhibits spherical shape with a diameter about 4. After adding the Fe_3O_4/sepiolite in CI particles, it can be confirmed that the nanosized Fe_3O_4/sepiolite particles attached on the surface of microsized CI particles and occupy the free spaces between the CI particles (Fig. 1 (c)). Therefore, we could predict that the sedimentation stability and MR characteristics of the CI-Fe_3O_4/sepiolite MR fluid compare with the pure CI MR fluid will be improved. The flow curves of the CI MR fluid and CI-Fe_3O_4/sepiolite MR fluid were investigated with controlled shear rate mode under various magnetic field strengths, ranging from 0 to 342 kA/m. Figure 2 shows the shear stress of two kinds of MR fluid as a function of shear rate via a log-log scale. Both two kinds of MR fluid behave like a Newtonian fluid with the absence of magnetic field, while when the magnetic fields is applied, for each magnetic field strength, they show an obvious yield stress, which exhibits typical Bingham fluid behavior, indicating the formation of chain structures by induced magnetic dipole-dipole interactions between particles [7]. The shear stress shows dramatic increase with increasing magnetic field strength, which because the interactions between particles increases with increasing external magnetic field strength and the stronger magnetic polarization interaction between particles give rise to the stronger particle chains. In addition, at high magnetic field strength, both two MR fluids hold plateau shear stress region in the whole shear rate range, due to the fact that magnetic field induced magnetic force is stronger than the flow induced hydrodynamic force. When the chain structures are disrupted by the shear flow, they will reformed quickly by the strong magnetic force. More importantly, CI-Fe_3O_4/sepiolite MR fluid shows higher shear stress values than pure CI MR fluid at every magnetic field strength, which proves that the presence of additives make chain structures stronger.

1) S.H. Kwon, B. Sim, H.J. Choi, "Magnetorheological Characteristics of Nano-Sized Iron Oxide Coated Polyaniline Composites", *IEEE Trans. Magn.*, 52, 1-4 (2016). 2) A.J.F. Bombard, M. Knobel, M.R. AlcÂNtara, "Phosphate coating on the surface of carbonyl iron powder and its effect in magnetorheological suspensions", *Int. J. Mod. Phys. B*, 21, 4858-4867 (2007). 3) N. Kobayashi, K. Kawase, S. Sato, T. Nakagawa, "Experimental verification of effects in an emergency stop by installation of magnetorheological fluid damper to an elevator", *IEEE Trans. Magn.*, 53, 1-4 (2017). 4) B. Liu, W.H. Li, P.B. Kosasih, X.Z. Zhang, "Development of an MR-brake-based haptic device", *Smart Mater. Struct.*, 15, 1960 (2006). 5) A. Hajalilou, S.A. Mazlan, S.T. Shila, "Magnetic carbonyl iron suspension with Ni-Zn ferrite additive and its magnetorheological properties", *Mater. Lett.*, 181, 196-199 (2016). 6) Y.Z. Dong, S.H. Piao, H.J. Choi, "Fe_3O_4/sepiolite magnetic composite particles and their magneto-responsive characteristics", *Colloid Polym. Sci.*, DOI: 10.1007/s00396-017-4221-7 (2018). 7) I.G. Kim, K.H. Song, B.O. Park, B.I. Choi, H.J. Choi, "Nano-sized Fe soft-magnetic particle and its magnetorheology", *Colloid Polym. Sci.*, 289, 79-83 (2011).

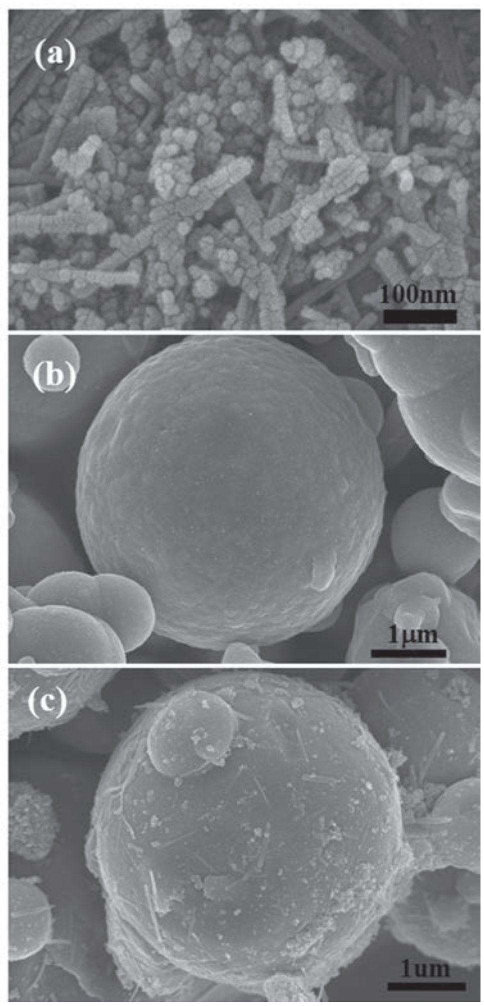

Fig. 1. SEM images of Fe_3O_4/sepiolite nanocomposites (a), pure CI particles (b) and Fe_3O_4/sepiolite added in CI particles (c)

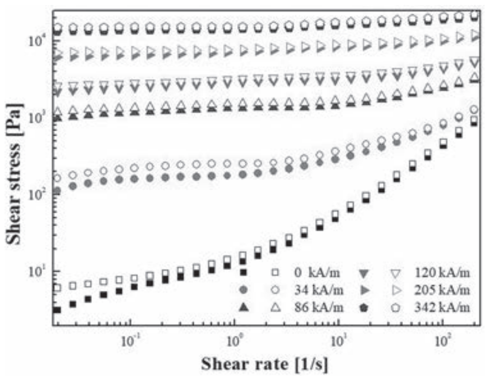

Fig. 2. Shear stress for CI (closed) and CI-Fe_3O_4/sepiolite (open) based MR fluid vs. shear rate

FR-04. Synthesis of Organic-inorganic Poly(diphenylamine)/magnetite Composite Particles and Their Magnetorheological Response.

Y. Dong[1] and H. Choi[1]

1. Polymer Science and Engineering, Inha University, Incheon, The Republic of Korea

I. INTRODUCTION Organic-inorganic smart composites have been extensively studied for their ability to integrate the structure and properties of both organic and inorganic components. Recently, poly(diphenylamine) (PDPA) has attracted much attention in many fields because of its good mechanical properties, special electrochemical properties, low density and ease of synthesis [1], [2], while magnetite (Fe_3O_4) has been widely used in magnetorheological (MR) fluid due to its super-paramagnetic properties [3]. MR fluid usually composed of magnetic particles dispersed in non-magnetic carrier medium is considered as a kind of intelligent materials, which can transform quickly (milliseconds) from a liquid-like state to a solid-like state with dramatic increase of shear stress, shear viscosity, and dynamic modulus by applying external magnetic field [4]. On the other hand, when the external electric field is removed, it returns to the fluid-like state again. Because of its regulable rheological properties, MR fluids are thought to have great potential in many industrial fields. However, the large density difference between the particles and the carrier medium often leads to serious sedimentation problems, which limits its development in engineering [5]. In this work, we synthesized the organic-inorganic PDPA/Fe_3O_4 magnetic composites by a simple route, and applied them in the MR fluid. The PDPA/Fe_3O_4 based MR fluid exhibited pronounced MR characteristics, in addition, the sedimentation stability was improved beneficial from the relatively low density of PDPA/Fe_3O_4 particles. II. EXPERIMENT Firstly, the PDPA was prepared by a chemical oxidative polymerization process as suggested [6], in which 6.00 g diphenylamine monomer (99.0% purity, Sigma-Aldrich) was dissolved in 150 mL ethanol (95.0% purity, Samchun Pure Chemical Co.) over a few minutes of intensive magnetic stirring then transformed into the 500 mL three-neck glass reactor and 120 mL of 3 M hydrochloric acid (HCl, Junsei Chemical Co.) aqueous solution was added. The mixture was maintained at 5 °C under continuous stirring. A solution of 3.01 g ammonium persulfate (APS, >98.0% purity, Daejung Chemicals & Metals Co.) dissolved in 15 mL of 3 M HCl was added dropwise to the mixture. After stirring for additional 16 h, the reaction mixture was collected and washed several times with ethanol and water. The precipitate was dried in a vacuum oven at 60 °C overnight. Then, the PDPA/Fe_3O_4 composites were fabricated by as-synthesized PDPA. 1.00 g PDPA powder was dispersed in a 100 mL mixture of ethanol and distilled water with volume fraction of 1:1 and transfered to a 250 mL three-neck glass reactor with intensive stirring. 5.40 g ferric chloride hexahydrate (97.0% purity, Sigma-Aldrich) and 1.39 g ferrous sulfate heptahydrate (99.0% purity, Sigma-Aldrich) were dissolved in 20 mL distilled water respectively and added in the reactor. The reaction mixture was heated to 60 °C. 10 mL ammonia solution (NH_3: 28.0~30.0% (m/m), Junsei chemical Co.) was added dropwise and continued stirring for 2 h. The final black precipitate was collected by magnetic separation and dried at 60 °C for 12 h. The MR fluid based on PDPA/Fe_3O_4 composites was prepared by dispersing PDPA/Fe_3O_4 composites in silicone oil (100 cSt, KF-96, Shin-Etsu, Japan) with particle concentration of 15 vol%. The microstructures of the PDPA and PDPA/Fe_3O_4 were investigated by the transmission electron microscopy (TEM, CM-220, Phillips, U.S.A.) and the MR characteristics of PDPA/Fe_3O_4 based MR fluid were measured by the rotational rheometer (MCR 300, Physica-Paar, Germany) under various magnetic field strengths. III. RESULT AND DISCUSSION Figure 1 shows the TEM images of PDPA (Fig. 1(a), 1(b)) and PDPA/Fe_3O_4 composites (Fig. 1(c), 1(d)). Both PDPA and PDPA/Fe_3O_4 show irregular shapes and the spherical Fe_3O_4 particles with diameter about 10-20 nm can be observed distinctly in the partial enlargement (inset in Fig. 1(d)) of PDPA/Fe_3O_4. Figure 2 shows the shear stress for PDPA/Fe_3O_4 based MR fluid as a function of shear rate ranging from 0.01-200 1/s under various magnetic field strengths (0-274 kA/m) on a log-log scale. The shear stress shows dramatic increase when the external magnetic field is applied and increases with increasing magnetic field strengths, which indicate that as the magnetic field strength increases, the magnetic field-induced attractive interactions between particles increase, resulting in a stronger chain structure. The solid lines in Fig. 2 were drawn for the Herschel-Bulkley (HB) model [7], which can be shown as: $\tau=\tau_y+K\gamma^n$ where τ is the shear stress, τ_y represents the dynamic yield stress, γ is the shear rate, K and n represent the consistency index and power-law exponent, respectively. As shown, the shear stress curves for PDPA/Fe_3O_4 based MR fluid under external magnetic field are in agreement with the HB model. In addition, the yield stress obtained from Fig. 2 was further investigated as a function of input magnetic field strength based on a power-law relationship.

1) M. Baibarac, I. Baltog, S. Frunza, A. Magrez, D. Schur, S. Yu. Zaginaichenko, "Single-walled carbon nanotubes functionalized with polydiphenylamine as active materials for applications in the supercapacitors field", *Diamond Related Mater.* 32, 72-82 (2013). 2) T. Permpool, A. Sirivat, and D. Aussawasathien, "Polydiphenylamine/zeolite Y composite as a sensor material for chemical vapors", *Sensors Actuators B: Chem.* 220, 91-100 (2015). 3) X. Ruan, L. Pei, S. Xuan, Q. Yan, X. Gong, "The rheological responds of the superparamagnetic fluid based on Fe3O4 hollow nanospheres", *J. Magn. Magn. Mater.* 429, 1-10 (2017). 4) J. E. Kim, H. J. Choi, "Magnetic Carbonyl Iron Particle Dispersed in Viscoelastic Fluid and Its Magnetorheological Property", *IEEE Trans. Magn.* 47, 3173-3176 (2011). 5) M. Mrlik, M. Ilcikova, M. Sedlacik, J. Mosnacek, P. Peer, P. Filip, "Cholesteryl-coated carbonyl iron particles with improved anti-corrosion stability and their viscoelastic behavior under magnetic field", *Colloid Polym. Sci.* 292, 2137–2143 (2014). 6) M. H. Kim, D. H. Bae, H. J. Choi, Y. S. Seo, "Synthesis of semiconducting poly(diphenylamine) particles and analysis of their electrorheological properties", *Polymer* 119, 40-49 (2017). 7) N. M. Wereley, "Nondimensional Herschel—Bulkley Analysis of Magnetorheological and Electrorheological Dampers", *J. Intelligent Mater. Syst. Struct.* 19, 257-268 (2007).

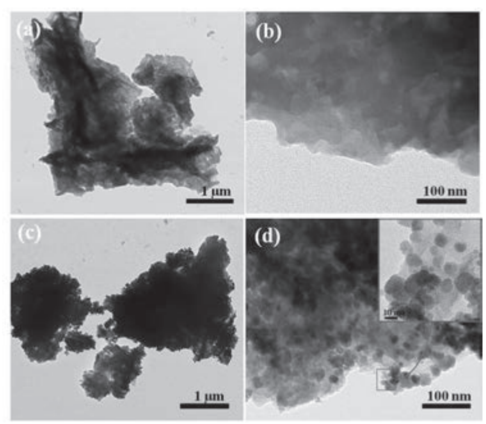

Fig. 1. TEM images of (a), (b) PDPA and (c), (d) PDPA/Fe_3O_4 composite. (Inset shows the partial enlargement of PDPA/Fe_3O_4)

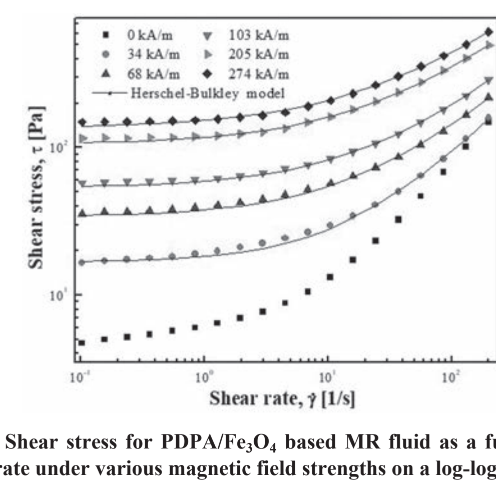

Fig. 2. Shear stress for PDPA/Fe_3O_4 based MR fluid as a function of shear rate under various magnetic field strengths on a log-log scale

FR-05. Synthesis and Viscoelastic Behavior of Non-stoichiometric Inverse Spinel Ferrite Nanoparticle Suspension with Controlled Morphology and Enhanced Magnetization.

J. Han[1], W. Han[1], C. Gao[1], Y. Dong[1] and *H. Choi*[1]
1. Dept. of Polymer Science and Engineering, Inha UNiversity, Incheon, The Republic of Korea

Magnetorheological (MR) fluid, an active field-responsive colloidal suspension in which magnetic particles are dispersed in an insulating fluid, becomes one of the most promising smart advanced materials. It has a characteristic of reversible and fast phase transition from a liquid-like to a solid-like state depending on the presence or absence of magnetic field [1]. Based on these characteristics, MR fluids are used widely in engineering applications, especially in a mechanical areas such as haptic devices, active dampers, clutches and MR polishing devices [1]. Various spinel ferrite-based magnetic particles, such as magnetite and hematite (γ-Fe_2O_3), have drawn an attention in engineering applications in addition to MR suspensions as an alternative to widely adopted carbonyl iron (CI) microspheres because of their lower density than CI [1]. On the other hand, commonly used spinel ferrites have a relatively low saturation magnetization which strongly affects their MR behavior [2]. Consequently, the ferrite materials generally exhibit poorer MR performance than CI. As a solution, we applied a method of doping non-magnetism metal cations in inverse spinel structure to improve the low magnetization of Fe_3O_4. In the inverse spinel structure, the A^{2+} cations occupy the octahedral site, whereas the half of B^{3+} cations occupy the tetrahedral site, written as $B^{3+}{}_{tetra}[A^{2+}B^{3+}]_{octa}O_4$ [3]. Fe_3O_4 can be expressed by the following structural formula: $Fe^{3+}{}_{tetra}[Fe^{2+}Fe^{3+}]_{octa}O_4$ as inverse spinel structure. In two sites of spinel structure, doping of metal cation changes the cation distribution, and this distribution also affects magnetic property [4]. The metal dopant influences the interaction between tetrahedral site and octahedral site, which finally improves the magnetic property [5]. Among divalent metal cations, Zn^{2+} cation has non-magnetism and prefers to occupy the tetrahedral site. The structural formula of the Zn-doped ferrite can be expressed as $Zn_d{}^{2+}Fe_{1-d}{}^{3+}[Fe_{1-d}{}^{2+}Fe_{1+d}{}^{3+}]O_4$. The addition of Zn^{2+} cation induces a decrease of magnetic moment of tetrahedral site and as a result increase the total magnetic moment [6]. In this study, to improve MR performance through enhanced magnetization and controlled morphology, we synthesized non-stoichiometric $Zn_{0.417}Fe_{2.583}O_4$ nanoparticles via thermal decomposition process and adopted them as for MR fluid expecting more robust chain-like structure than normal ferrites [7]. II. EXPERIMENT Iron acetylacetonate [$Fe(C_5H_7O_2)_3$] (12 mmol) and zinc acetylacetonate hydrate [$Zn(C_5H_7O_2)_2H_2O$] (8 mmol) were initially dissolved in benzyl ether (20 ml). Subsequently, oleic acid (28 mmol) was added to the above solution mixture as a surfactant that controls the morphology and prevents agglomeration between particles. The mixture was heated to 120 degC for 30 min to evaporate the traces of water included in the precursor, and then to 280 degC under reflux using a condenser for 30 min. After that, the reactor was cooled to room temperature and the brown-black precipitates were obtained using filtration and centrifuge. The obtained product was washed three times with hexane, and dried in a vacuum oven at 60 degC for 12 h. To analyze the MR behavior, the MR fluid was fabricated by dispersing the particles (5 vol%) in silicone oil. Morphology of the synthesized particles was tested using transmission electron microscopy (TEM), and rheological characteristics of the MR fluid was inspected using a rotational rheometer in a parallel-plate geometry with an external magneto-cell. III. RESULT AND DISCUSSION Figure 1 presents TEM image exhibiting the polyhedral structure with truncated octahedron-like form with approximately 150 to 200 nm size. MR fluids with non-spherical angulated particles are expected to develop denser chain structure and strengthen the particles packing under magnetic field, because when forming a chain-like structure, a face-to-face contact occurs rather than a point-to-point contact. Dynamic oscillation test was performed to analyse viscoelastic characteristics of MR fluid. The strain amplitude sweep test was performed before the frequency sweep test under presence of magnetic field to confirm linear viscoelastic region of storage (G') and loss modulus (G''), as shown in Fig. 2(a) in a strain amplitude range of 0.001 to 70 % and the fixed frequency at 1 Hz. As the magnetic field strength increased, G' and the difference between G' and G'' increased, demonstrating that the characteristics of solid-like structure with elasticity were revealed more clearly. In addition, we selected strain amplitude value of 0.005 % to apply frequency sweep test in the linear viscoelastic region where the storage modulus became plateau. Fig. 2(b) shows G'(ω) and G''(ω) as a function of angular frequency at constant strain amplitude value of 0.005 %. Without a magnetic field, both moduli show a tendency of increase with angular frequency possessing a liquid-like behavior. On the other hand, with a magnetic field, high and constant moduli were observed in the same frequency range. This shows that the MR fluid was transformed from viscous to elastic characteristic as the magnetic field was applied, confirming that the elasticity increases with the strength of the magnetic field for this MR fluid.

1) J. Sutrisno, A. Purwanto, S. A. Mazlan, "Recent progress on magnetorheological solids: materials, fabrication, testing, and applications", *Adv. Eng. Mater*. 17, 563-597 (2015). 2) S. P. Rwei, H. Y. Lee, S. D. Yoo, L. Y. Wang, J. G. Lin, "Magnetorheological characteristics of aqueous suspensions that contain Fe3O4 nanoparticles", *Colloid Polym. Sci.* 283, 1253-1258 (2005). 3) D. S. Mathew, R. S. Juang, "An overview of the structure and magnetism of spinel ferrite nanoparticles and their synthesis in microemulsions", *Chem. Eng. J.* 129, 51-65 (2007). 4) J. E. Galindo, A. H. Adair, C. E. Botez, V. C. Flores, D. B. Baques, L. F. Cobas, J. A. Matutes-Aquino, "Zn-doping effect on the energy barrier to magnetization reversal in superparamagnetic nickel ferrite nanoparticles", *Appl. Phys. A* 87, 743-747 (2007). Y. Yang, X. Liu, Y. Yang, W. Xiao, Z. Li, D. Xue, J. Ding, "Synthesis of nonstoichiometric zinc ferrite nanoparticles with extraordinary room temperature magnetism and their diverse applications" *J. Mater. Chem. C* 1, 2875-2885 (2013). D. Makovec, A. Kodre, I. Arcon, M. Drofenik, "Structure of manganese zinc ferrite spinel nanoparticles prepared with co-precipitation in reversed microemulsions" *J. Nanoparticle Res.* 11, 1145-1158 (2009). H. S. Jung, H. J. Choi, "Hydrothermal fabrication of octahedral-shaped Fe3O4 nanoparticles and their magnetorheological response" *J. Appl. Phys.* 117, 17E708 (2015).

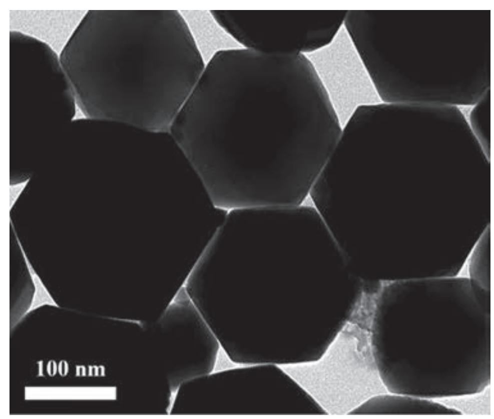

Fig. 1. TEM image of truncated octahedral $Zn_{0.417}Fe_{2.583}O_4$ nanoparticles

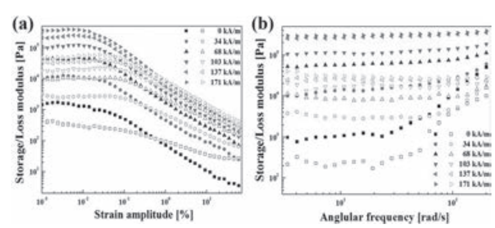

Fig. 2. Strain amplitude (a) and angular frequency sweep tests (b) with G' (closed) and G'' (open) for $Zn_{0.417}Fe_{2.583}O_4$-based MR fluid under various magnetic field strengths

FR-06. Effect of Magnetic Nanoparticle Additive on Viscoelastic Behaviors of Carbonyl Iron-based Magnetorheological Suspension.

C. Gao[1], Q. Lu[1] and H. Choi[1]
1. Polymer Science and Engineering, Inha University, Incheon, The Republic of Korea

I. INTRODUCTION Magnetorheological (MR) fluids which are smart colloidal suspensions of magnetic particles dispersed in non-magnetic fluids, are capable of being solid-like under applied magnetic fields, while being liquid-like without a magnetic field [1]. Their rheological properties such as yield stress and shear viscosity can reversibly and quickly be changed as a result of dispersed magnetic particles building up a chain-like structure under a magnetic field [2]. Without magnetic field, the MR fluid behaves like a Newtonian fluid, recovering to a free-flowing liquid state [3]. These phenomena of MR fluids imply a huge potentials in designing diverse high-performance engineering products including active damper system, torque transducer, and MR polishing equipment [4]. Among various magnetic materials, carbonyl iron (CI) particles have been adopted as a superior candidate for MR fluids in both scientific investigation and industrial applications, due to their high saturation magnetization, controllable magnetic property, and appropriate particle size. However, the large density mismatch between CI particles and medium oil leads to a serious sedimentation drawback, thus, obstructing smooth operation of the MR devices. Therefore, many strategies have been explored to solve this problem, such as coating polymer layers on CI particles to decrease the particle density. However, as one of the effective and fastest methods, the introduction of additives has been found to improve the dispersion stability by occupying the interspaces between the CI particles. Addition of various additives such as organoclay, magnetic nanoparticles have been reported to enhance the MR properties. In this study, the additive magnetic Fe_3O_4/polystyrene (PS) composites were synthesized via a Shirasu porous glass (SPG) membrane emulsification technique and added to the CI based MR fluids [5]. The SPG method was adopted for achieving a narrow size distribution of the product. Here, we used the composites as an additive not only to increase the MR behaviors but also to improve the stability of MR fluids relative to CI particles based MR fluid. Rheological properties of both pure CI and CI- Fe_3O_4/PS additive based MR fluids were investigated via steady shear tests under different external magnetic field strengths. II. EXPERIMENT Firstly, preparation of hydrophobically coated magnetite nanoparticles, in which the Fe_3O_4 nanoparticles were synthesized through the coprecipitation method. $FeCl_3{\cdot}6H_2O$ and $Fe_2SO_4{\cdot}7H_2O$ were dissolved in de-ionized (Di) water while stirring under a N_2 atmosphere. After heating the solution to 80 °C, $NH_3{\cdot}H_2O$ was added followed by the addition of oleic acid for the hydrophobic modification of Fe_3O_4. The temperature was maintained at 80 °C for 3 h to obtain the ferrofluid. Then, preparation of magnetic miniemulsion and styrene macroemulsion, the ferrofluid was added to an aqueous solution of sodium dodecyl sulfate and the resulting mixture was treated with an ultrasonifier for 15 min in an ice bath. In order to obtain styrene droplets with a uniform size, SPG was employed. Styrene and hexadecane were mixed and loaded into a tank for forming the dispersion phase. SDS was dissolved in DI water for forming the continuous phase and then N_2 pressure (35 kPa) was applied to obtain monodisperse styrene droplets. Subsequently, the synthesis of Fe_3O_4/PS nanocomposites, where both the emulsions were mixed in a three-neck-flask to which KPS was added. The solution was stirred for 30 min at 250 rpm under a N_2 atmosphere. The reactor was heated to 80 C and the reaction was carried out for 24 h. The Fe_3O_4/PS nanoparticles produced were washed with ethanol and were collected by using a magnet. Finally, two systems with and without additives in the MR suspension were prepared, where both pristine CI (50 wt %) with and without Fe_3O_4/PS additive (0.1 wt %) were dispersed in silicone oil (1000 cSt). III. RESULT AND DISCUSSION Figure 1 shows TEM image and DLS data of morphology and size distribution of the Fe_3O_4/PS composite particles. We can confirm that the Fe_3O_4 nanoparticles were successfully embedded into the PS particles by emulsion polymerization, which were suffused uniformly and almost perfectly in the PS particles. The diameter of the particles varied from 40 to 310 nm and had an average value of 127 nm. Figure 2 shows flow curves of MR characteristics of two different systems, CI and CI-Fe_3O_4/PS based MR fluids to examine the effect of additives. Typical MR characteristics of shear stress were measured as a function of applied shear rate in different magnetic field strengths ranging from 0 to 342 kA/m. When the magnetic field is absent, the shear stress linearly increases almost with increasing the shear rate, following a Newtonian fluid-like behavior of a typical dilute suspension. When the external magnetic field is present, both MR fluids exhibited a Bingham behavior, representing the formation of the stable chain structures of the magnetized particles [6]. We found that regardless of the external magnetic field, the MR properties of the CI-Fe_3O_4/PS suspension showed higher shear stress than that of pure CI based MR suspension, being attributed to the magnetic response of the added Fe_3O_4/PS composites with the magnetic field.

1) J. Noh, C. M. Yoon, Y. K. Kim, J. Jang, "High performance asymmetric supercapacitor twisted from carbon fiber/MnO_2 and carbon fiber/MoO_3", *Carbon* 116, 470-478 (2017). 2) S. G. Sherman, N. M. Wereley, "Effect of particle size distribution on chain structures in magnetorheological fluids", *IEEE Trans. Magn*. 49, 3430-3433 (2013). 3) M. Mrlik, M. Sedlacik, V. Pavlinek, P. Bazant, P. Saha, P. Peer, P. Filip, "synthesis and magnetorheological characteristics of ribbon-like, polypyrrole-coated carbonyl iron suspensions under oscillatory shear," *J. Appl. Polym. Sci.* 128, 2977–2982 (2013). 4) I. Bica, Y. D. Liu, H. J. Choi, "Physical characteristics of magnetorheological suspensions and their applications," *J. Ind. Eng. Chem*. 19, 394–406 (2013). 5) C. Y. Gao, M. W. Kim, D. H. Bae, Y. Z. Dong, S. H. Piao, H. J. Choi, "Fe3O4 nanoparticle-embedded polystyrene composite particles fabricated via a Shirasu porous glass membrane technique and their magnetorheology", *Polymer* 125, 21-29 (2017). 6) J. E. Kim, H. J. Choi, "Magnetic Carbonyl Iron Particle Dispersed in Viscoelastic Fluid and Its Magnetorheological Property", *IEEE Trans. Magn.* 47, 3173-3176 (2011).

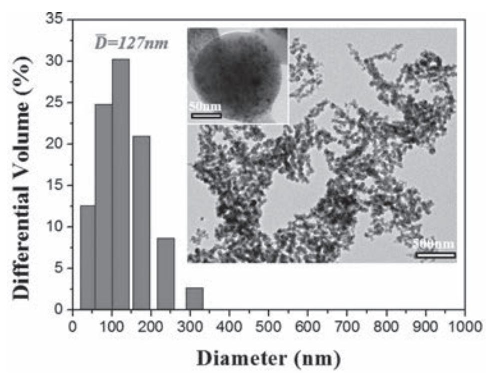

Fig. 1. TEM images and size distribution of Fe_3O_4/PS composites analysed by dynamic light scattering (DLS)

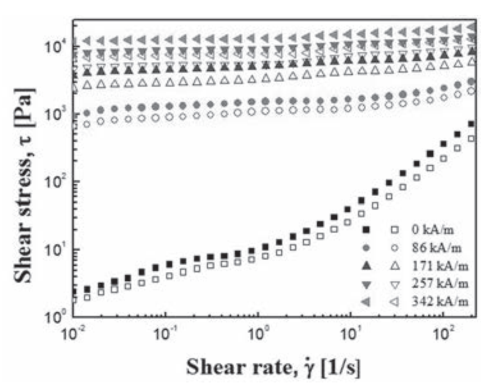

Fig. 2. Flow curve for CI (open) and CI-Fe_3O_4/PS (closed) MR fluid under various magnetic field strengths: Shear stress as a function of the shear rate

FR-07. Experimental Verification of Effectiveness of Magnetorheological Fluid Damper fixed to an Elevator in Case of Earthquake.

K. Kawase[1], N. Kobayashi[1], M. Yamada[1] and T. Nakagawa[1]
1. Faculty of Engineering, Tokyo City University, Tmazutsumi, Japan

I. Introduction In countries where the economy is growing rapidly, many skyscrapers are being built one after another. For such skyscrapers, high-speed and safe elevators are essential as transportation means. Therefore, we have proposed an elevator with magnetorheological fluid (i.e., MRF) dampers to improve the safety of passengers ([1]). For supplying safe elevators, we have to consider various dangerous factors, such as natural disasters, accidents and so on. If a disastrous earthquake occurs, an elevator works an earthquake-sensing system and stops at a nearest floor to evacuate the passengers. However, in reality, it often happens that passengers are shut into the elevator for a few minutes or more. During the earthquake, the passengers feel fear or may be conscious of death. In this paper, we would like to verify whether the proposed MRF damper can absorb strong vibrations of elevator caused by an earthquake, and would like to confirm the effectiveness of MRF damper by using our experimental simulator. II. Structure and Characteristics of Our MRF Damper Fig. 1(a) shows the structure and the specification of the MRF damper. Our MRF damper is composed of a cylinder filled with magneto rheological fluid, a coil winded around the cylinder, and a piston. As for the magnetorheological fluid, Fig. 1(b) shows the states of a change in viscosity depending on whether magnetic field is applied or not. Thus, we can control the equivalent damping coefficient C (Ns/m) of the MRF damper in real time, by regulating the coil current for making magnetic field ([2]). Fig. 1(c) shows the damping coefficient C (Ns/m) of our MRF damper to the coil currents (0 (A) ~ 1.0 (A)), by adopting "temperature" as parameter. As shown in this figure, we have confirmed that the characteristics of MRF damper are linear to the coil current and invariable in the fluid-temperature (10 (°C) ~ 40 (°C)) that is close to "room-temperature". III. Experimental Verification *1) Evaluated variables* We have advanced this study to build the damper system which can absorb strong vibrations of an elevator during earthquake. Fig. 2(a) shows the acceleration of the disastrous earthquake occurred in Kumamoto prefecture. In order to evaluate the effectiveness of our damper system, we evaluate the acceleration of elevator, from two kinds of variables; (i) the root mean squared value a_{rms} (m/s^2) in the earthquake-period having the acceleration value 0.25 (m/s^2) or more and (ii) the vibration-energy-consumptions E_d (J) performed by using our MRF damper. *2) Designing of controller and system formation* The controller of the proposed MRF damper-system is designed by using the nonlinear control theory with Hamilton Jacobi Inequality ([3]). On the other hand, based on the actual seismic wave shown in Fig. 2(a), our experiment-simulator remakes this wave to another one that will be directly input to the elevator. This remade vibration is input to the mass-body in our experiment simulator corresponding to an actual elevator-cage via out MRF damper in real time. *3) Experimental Results* In this chapter, we would like to verify the vibration damping-characteristics of an elevator for three cases, such as a conventional elevator, an elevator with passive MRF damper and an elevator with controlled MRF damper, where "passive MRF damper" means that it has constant damping coefficient with the constant coil current and "controlled MRF damper" means that its damping coefficient is controlled by the coil current as explained in II. Fig. 2(b) shows the acceleration characteristics of the elevator, under the condition of full passengers and 150 (m) long wire for hanging the elevator cage. From Fig.2 (b), we can obtain that a_{rms} (m/s^2) is reduced by 40 (%) in case of the controlled MRF damper and 33 (%) in case of the passive MRF damper, compared to the case of the conventional elevator. In addition, from Fig.2 (c), we can confirm that the vibration-energy consumptions E_d (J) performed by the controlled MRF damper increased by 42 (%) from that performed by the passive MRF damper. IV. Conclusions These experimental results indicate that the proposed MRF damper, especially the controlled MRF damper can absorb strong vibrations. In conclusion, we confirmed by experiments that the proposed elevator has effectiveness at occurrence of an earthquake.

[1] Takato Uchida, Shunsuke Sato and Toshiko Nakagawa "A Proposal of Control Method for an Elevator Emergency Stop Device with a Magnetic Rheological Fluid Damper", IEEE Transaction on Magnetics, Vol.50, No.11, 4600404(4p-length), ISSN 0018-9464, Nov. 2014. [2] Naoki Kovayashi, Keisuke Kawase, Shunsuke Sato and Toshiko Nakagawa "Experimental Verification of Effects in an Emergency Stop by Installation of Magnetorheological Fluid Damper to an Elevator", IEEE Transaction on Magnetics, Vol.53, No.11, ISSN 0018-9464, Nov. 2017. [3] A. J. van der Schaft, "On a state space approach to nonlinear H-infinity control," System and Control Letters 16, p.1-8, 1991.

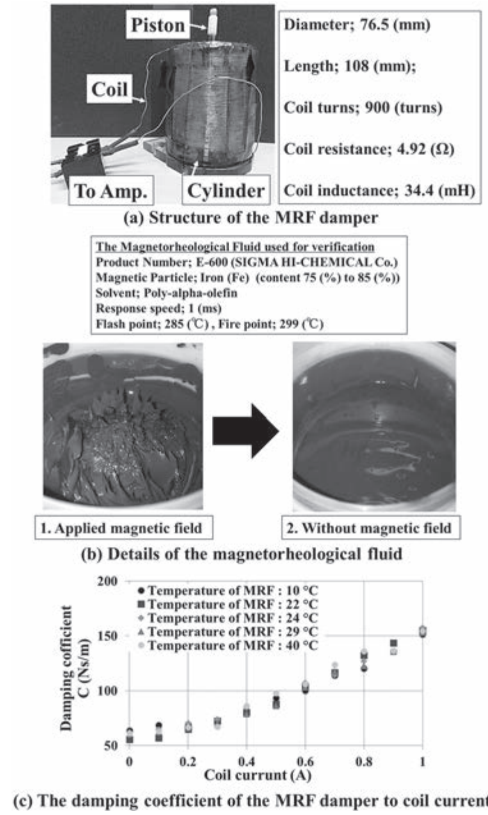

Fig. 1. Characteristic of our MRF damper

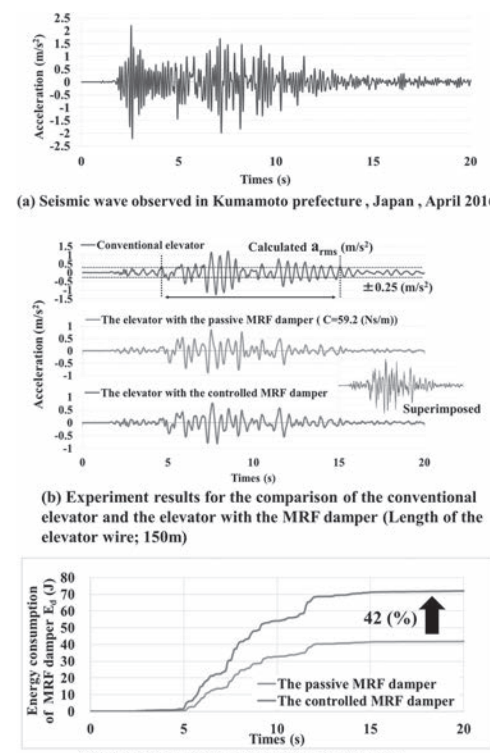

Fig. 2. Verification of effectiveness of our MRF damper

FR-08. Characterization of Output Torque of a Permanent Magnet-based MRF Clutch with a Field Blocking Mechanism.

M.A. Fernández[1], J. Chang[1] and C. Huang[1]
1. Power Mechanical Engineering, National Tsing Hua University, Hsinchu, Taiwan

Introduction Although it is not an impossible task, previous work [1-2] on magnetorheological fluid (MRF) clutches has proved that the prediction of the torque transmission capacity is not a straight forward process. The prior MRF clutch presented in [3] also showed a big discrepancy between expected torque capacity of the clutch and actual measured torque. In this work, a new MRF clutch has been proposed and fabricated, with the expectation that its torque transmission capacity would be larger, as the clutch itself is also larger. This new clutch is a cylinder-based clutch with four MRF layers, which uses permanent magnets, but uses a steel cylinder which vary the magnetic field by covering the magnets. With the use of simulations and mathematical models, study of the MRF clutch is presented in this paper on how accurately the output torque can be modelled. Magnetostatic simulation The clutch with its MRF layers and with the field-blocking steel cylinder at several different positions were simulated using ANSYS Maxwell. Since the datasheet of the used MRF shows that for weaker fields the relation between the magnetic field and the yield stress is nearly linear, the average magnetic field of each layer was used to calculate the yield stress at that particular layer. Mathematical model The mathematical model used in [3] was used again in this paper, except that the torque due to rotational forces was not taken into account. Since the magnetic field was averaged across each layer, the yield stress will be constant across a layer, and the torque equation was reduced to simply multiplying the average yield stress of the layer by its radius and area. This process was repeated for each of the four layers and then the four values summed together. The results from these calculations can be seen in Fig. 1. Fluid simulation Simulations were also performed in ANSYS Fluent in order to confirm the mathematical model. For these simulations, the Herschel-Bulkley viscosity model was used, with $n = 1$ in order for it to represent a Bingham-type fluid. Again, the yield stress for each layer was chosen based on the same procedure as in the mathematical model, using the average magnetic field in each layer. The inner wall of each layer was set to rotate at low angular velocity of 0.1 *rads/s* in order to reduce its effects on the torque transmission. The results from these simulations are seen in Fig. 1. Experimental procedure The first set of tests performed on the new clutch showed a torque transmission capability similar to that of the previous clutch. These test were performed by having a DC motor drive the input of the clutch while the output was static and pressing down on a force gage. The force gage measurements were recorded and used to calculated the torque. Several measurements were carried out with the field blocking cylinder at different positions in order to discover its effect on the output torque. This first set of tests were performed early in the development of the clutch and did not take into account the effect of angular velocity. The second set of tests repeated the measurements made before, but this time the angular velocity of the input stage was set at 2.09 *rad/s*. The third set of tests followed the same procedure as the second set of tests, and in addition some tests were made to test the effects of angular velocity in the torque. Results The first set of test was carried out after the clutch was built and before any simulation. The results from this first set of tests are seen in Figure 1. After the simulations and the calculations based on the mathematical model were performed, big discrepancies between them and the experimental results were found. Since the simulations and the mathematical model agree on their result, it was decided to reevaluate the experimental set up. More MRF was added to the clutch through a screw hole, not originally designed for this purpose. The addition of this extra MRF proved effective in raising the torque transmission capability of the clutch as seen in Fig. 1, where an increase of at least 67% is seen. This value is still lower than the expected value, therefore, it was decided to dissemble the clutch and modify it to make the filling of MRF easier and more effective. After this, the third set of tests were carried out, whose results are seen in Fig. 1. It was found the torque only increased at most by 13%, which indicates that the discrepancy seen before is not completely due to lack of MRF in the clutch. Thus, further refinement of the models and simulations have to be done. As for the effects of angular velocity in the torque transmission capability, the results can be seen in Fig. 2. Here it can be seen that the addition of MRF to the clutch reduces the slope of the angular velocity-torque relationship. The slope after magnets were added back, however, reaches a value similar as when the magnets were not present. Further study of this phenomena will be done.

[1] W. Li, P. Yadmellat and M. R. Kermani, "Linear torque actuation using FPGA-controlled Magneto-Rheological actuators," *2014 IEEE International Conference on Robotics and Automation (ICRA)*, Hong Kong, 2014, pp. 1060-1065. [2] N. Najmaei, A. Asadian, M. R. Kermani and R. V. Patel, "Magneto-Rheological actuators for haptic devices: Design, modeling, control, and validation of a prototype clutch," *2015 IEEE International Conference on Robotics and Automation (ICRA)*, Seattle, WA, 2015, pp. 207-212. [3] M. A. Fernández and J. Y. Chang, "Development of magnetorheological fluid clutch for robotic arm applications," *2016 IEEE 14th International Workshop on Advanced Motion Control (AMC)*, Auckland, 2016, pp. 510-515.

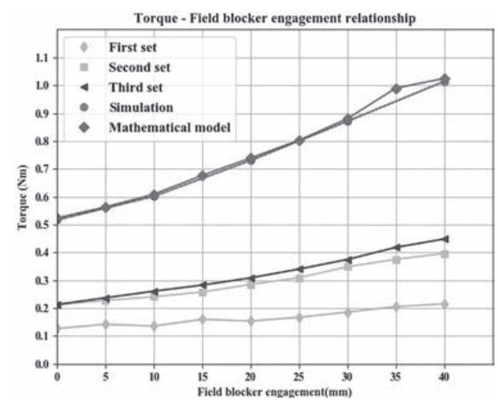

Fig. 1. Torque versus field blocker engagement relationship. The three sets of torque versus field blocker engagement tests carried out are shown, along with the predicted torque output according to simulations and the mathematical model.

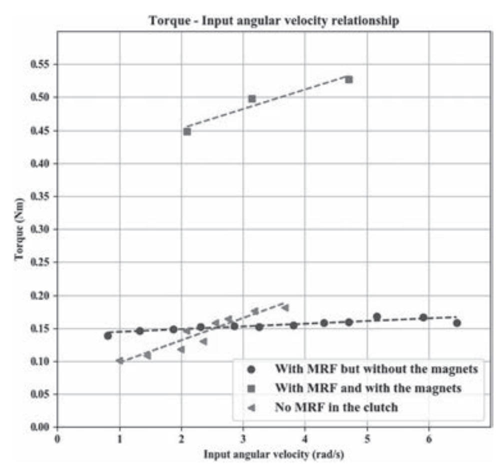

Fig. 2. Torque versus input angular velocity relationship. The blue plot is the torque when the clutch is empty. The green plot is the torque when the clutch has MRF but no magnets. The red plot is when the clutch has MRF and the magnets.

FR-09. Phenomenological magnetic hysteresis model of a polymer matrix filled with magnetic particles.

Z. Xiang[1], B. Gupta[1], M. Le[1], G. Coativy[1] and *B. Ducharne*[1]
1. INSA LYON, Laboratoire de Génie Electrique et Ferroélectricité, Villeurbanne, France

ABSTRACT Based on experimental results and finite element method (FEM) simulations, a magnetic lump model of a 3D printed polymer matrix filled with magnetic particles is proposed in this article. Due to the intrinsically dielectric nature of the polymer and since the percolation threshold is not reached even for a high percentage of particles the tested sample shows a high resistivity. This property implies a significant limitation of the formation of the so-called "macroscopic" eddy currents. Taking into account this characteristic, the proposed model is limited to microscopic eddy currents (mainly related to the movement of the walls of magnetic domains). This approach is validated by simulation/measurement comparisons over a wide frequency band of excitation. KEYWORDS magnetic polymer matrix, magnetic hysteresis, frequency dependence, electromagnetic modeling. MAIN TEXT The use of 3D printing for rapid tooling and manufacturing is a very promising technique to manufacture components with complex geometries with the help of computer designing. Due to the mechanical properties and limited application of printed pure polymer parts, there is a critical need to develop printable polymer composites with high performance. 3D printing offers many advantages in the fabrication of composites, including high precision, cost effectiveness and customized geometry. 3D printable materials based on polymer matrices filled with magnetic particles, also called composite materials, are of high interest as they can provide solution for many industrial applications: damage sensing and self-healing [1], thermoplastic induction welding [2], magnetic core for inductors or electric transformers [3]. According to the targeted application, the focus can switch from the ability to drive the magnetic flux (electric inductor) to the local distribution of Joule losses, i.e. localized variations of temperature (thermoplastic welding). In ferromagnetic materials, magnetic losses appear as soon as a tested sample is exposed to a time-varying magnetic excitation field. These magnetic losses have two origins: _ The so-called "microscopic" eddy currents originate from the interactions between the walls of the magnetic domains and the microstructure during the magnetization of the sample. The so-called "macroscopic" eddy currents linked to the diffusion equation [4] of the magnetic field and are strongly dependent on the physical properties of the material (conductivity and permeability). The frequency dependence of these two contributions is different. It is legitimate to assume that when a polymer matrix is filled with a significant percentage of ferromagnetic particles, these properties observable in a ferromagnetic materials will continue to exist to some extent. In this study the composite used is PLA – Rustable Magnetic Iron filament (1.75 mm diameter) consisting of a polylactic acid (PLA) polymer matrix and a particulate phase of 40 wt% iron. This percentage of particles issufficiently weak to avoid the percolation threshold and if the particle distribution is homogeneous, each particle will be electrically insulated (this property will be confirmed by microscopic study in the extended version of the article). This electrical insulation will prevent the macroscopic eddy current formation, and consequently the ferromagnetic losses will be limited to the domain wall motions resulting in the microscopic eddy currents. In [4][5] a simple formulation is proposed to consider Joule variations in a ferromagnetic material when the material's electrical conductivity is weak and the dynamic contribution is mainly based on microscopic eddy currents: equation (1) Here, f^{-1}_{static} is the quasi-static contribution of hysteresis, which in a ferromagnetic material can be provided by the classic Preisach or Jiles-Atherton models. ρ.dB/dt is the dynamic contribution (dynamic losses) and ρ, a constant which depends on the geometry and on the nature of the material. For the polymer composite considered in this study, this formulation can still be used but the high percentage of non-ferromagnetic polymer in the composite highly limits the level of induction. Non-linear behavior (saturation) under magnetic excitation for this kind of material is just inconceivable. f^{-1}_{static} is replaced then by a linear function $\mu_0.\mu_r$. A finite element method simulation has been run for the determination of this relative permeability (figure 1). Fig. 1. Magnetic induction distribution in a magnetic polymer composite homogeneously filled with magnetic particles. In the extended version of the article, a detailed experimental set-up will be illustrated used for the validation of the model. Large number of comparison simulations/experimental results will be shown and the influence of the size, the shape and the distribution of the particle will be studied extensively.

[1] A.S. Ahmed, R.V. Ramanujan, "Magnetic field triggered multicycle damage sensing and self healing",Scientific Reports, 2015. [2] T. Bayerl, M. Duhovic, P. Mitschang, D. Bhattacharyya, "The heating of polymer composites by electromagnetic induction – A review", Composites: Part A, vol. 57, pp. 27-40, 2014. [3] L.M. Bollig, P.J. Hilpisch, G.S. Mowry, B.B. Nelson, Cheeseman, "3D printed magnetic polymer composite transformers", J. of Mag. and Mag. Mat, vol. 442, pp. 97-101, 2017. [4] M. A. Raulet, B. Ducharne, J.P. Masson, and G. Bayada, "The magnetic field diffusion equation including dynamic hysteresis: a linear formulation of the problem", IEEE Trans. on Mag., vol. 40, n° 2, pp. 872 – 875, 2004. [5] B. Gupta, B. Ducharne, G. Sebald and T. Uchimoto, "Magnetic lump model for the hysteresis frequency dependence of a polymer matrix", proceeding of the 21st international conference on the Computation of Electromagnetic Fields COMPUMAG, 2017.

$$\rho.\frac{dB(t)}{dt} = H_{dyn}(t) - f^{-1}_{static}(B(t)) \quad (1)$$

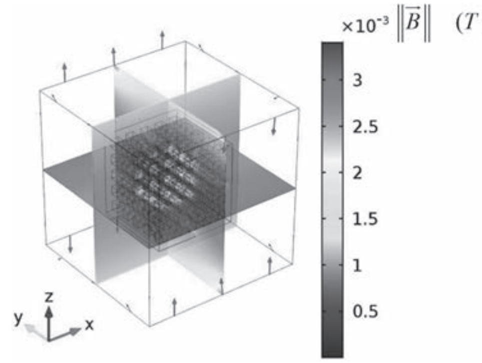

Fig. 1. Magnetic induction distribution in a magnetic polymer composite homogeneously filled with magnetic particles.

FR-10. Magnetically controlled light manipulating properties of biogenic and synthetic guanine crystals.

H. Kashiwagi[1], M. Iwasaka[2], H. Asada[3], T. Koyanagi[3] and K. Kishimoto[3]
1. Graduate School of AdSM, Hiroshima University, Higashihiroshima, Japan; 2. RNBS, Hiroshima University, Higashihiroshima, Japan; 3. Graduate School of Science and Technology for Innovation, Yamaguchi University, Ube, Japan

Ultra structural photonic properties of biogenic crystals derived from various animals have been studied in recent years with an aim toward developing biomedical optical instruments and microelectronic mechanical system (MEMS) elements. These crystals play significant roles as biological reflectors and in forming structural color (i.e. silvery shine, iridescent luster) on skin surface and scales by the effective use of ambient light [1]-[2]. Mainly derived from fish, guanine crystals in particular have specific light reflecting and light concentrating properties [3]-[5], together with very high refractive indices (n = 1.83), and are promising for the future. It has been shown that micro crystals exhibit magnetic orientation along the direction of a magnetic field due to the highly directional dependency of diamagnetic susceptibility [6]-[10]. In an early study we found that biogenic guanine crystals suspended in water display rotational alignment within a few seconds under several hundreds tesla, thus efficiently switching the direction of reflected light. Subsequently we have focused on developing remote control micro manipulation techniques using magnetic fields that noninvasively affect crystal alignment inside a material. As of yet, however, biogenic crystal capabilities (i.e. uniformly generated platelets, highly efficient reflection/refraction, nano/submicron sizing) have not been realized. Recently chemically synthesized guanine crystals have become commercially available. In the present study we sought to compare the diamagnetic, light propagation, reflection and structural color properties of several types of synthetic guanine crystals supplied by different companies (Wako Pure Chemical Industries, Sigma-Aldrich, Tokyo Chemical Industry). Crystals further crushed by mechanical alloy milling (MAM) were also examined. Suspensions were prepared by collecting supernatants after centrifugation for various lengths of time. Suspensions of guanine crystals derived from goldfish (*Carassius auratus*) were also prepared. Prior to centrifugation, single frequency ultrasonic cleaning was performed for various lengths of time up to 18 hrs in order to break down the guanine crystals into smaller pieces. Magnetic response properties and light reflection dependence of the various submicron through several-micron sized crystals obtained were evaluated by real-time microscopy and high-resolution spectroscopic measurement, with and without magnetic field application. Suspensions, a halogen light source, a charge-coupled device (CCD) microscope and the optical fiber of a spectrometer were placed between the electromagnets. The incident light angle was set at 60°. Guanine crystal behavior was observed from directly above under dark field illumination. Light incidence direction, magnetic field, and the observation/detection were orthogonally directed in the experimental equipment. Results of this study indicate that the synthetic guanine crystals supplied by Wako show a more significant increase in reflective properties under magnetic exposure than do the crystals of other suppliers. Centrifugation time proved to be a significant factor in determining optimum conditions for collecting microcrystals with high diamagnetic properties. Synthetic guanine crystals crushed by MAM and fractured biogenic crystals showed a decrease in light reflection compared with intact crystals. Time-series reflection spectrometry analysis quantitatively confirmed the CCD microscope results, and the variations in light reflection under a magnetic field were duplicated in a number of trials. The light condensing efficiency of goldfish-derived crystals increased by approximately 100 % under a magnetic field, and this held true even though the crystals were thoroughly fractured. Synthetic guanine crystals, on the other hand, showed limited increases of up to 30 %. Furthermore, it was noted that reflection was slightly higher for longer wavelengths than for shorter wavelengths in each crystal examined. Diamagnetic anisotropic energy was also estimated for the various synthetic and biogenic crystals under a magnetic field. In conclusion, it was found that microscopic crystals produced by conventional synthetic processes used in chemical engineering do display diamagnetic orientation properties and light reflection abilities such as those seen in biogenic crystals. A more detailed examination of the physical properties of microcrystals may lead to various biomedical applications, such as optical elements and harmless, eco-friendly convectional tracers to replace radioactive isotopes in micro fluidic systems. It is also hopeful that a bio-inspired light condensing device might be applied to highly sensitive biosensors for use in evaluating human cellular activity. This work was supported by JST-CREST "Advanced core technology for creation and practical utilization of innovative properties and functions based upon optics and photonics (Grant number: JPMJCR16N1)."

[1] S. Yoshioka, B. Matsuhana, S. Tanaka, Y. Inouye, N. Oshima, and S. Kinoshita, J R Soc Interface. 8, 56 (2011). [2] Avital Levy-Lior, Boaz Pokroy, Berta Levavi-Sivan, Leslie Leiserowitz, Steve Weiner and Lia Addadi, Cryst. Growth Des. 8, 507 (2008). [3] T. M. Jordan, J. C. Partridge & N. W. Roberts, Nature Photonics 6, 759 (2012). [4] Shulei Zhao, Parrish Clawson Brady, Meng Gao, Robert Ian Etheredge, George W. Kattawar, Molly E. Cummings, J R Soc Interface. 12, 20141390 (2015). [5] Parrish C. Brady, Kort A. Travis, Tara Maginnis, and Molly E. Cummings, PNAS 110, 9764 (2013). [6] Masakazu Iwasaka, Yuito Miyashita, Yuri Mizukawa, Kentaro Suzuki, Taro Toyota and Tadashi Sugawara, Applied Physics Express 6, 037002 (2013). [7] M. Iwasaka, J. Appl. Phys. 107, 09B314 (2010). [8] Y. Mizukawa, M. Iwasaka, IEEE Transactions on Magnetics 49, 3480 (2013). [9] M. Iwasaka, Y. Mizukawa, Langmuir 29, 4328 (2013). [10] Masakazu Iwasaka, Yuri Mizukawa, and Nicholas W. Roberts, Langmuir 32, 180 (2016).

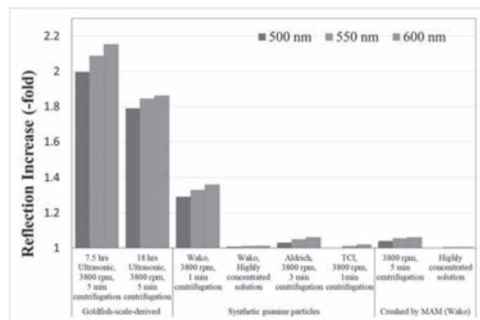

Fig. 1. Increase in reflection of biogenic and synthesized guanine crystals under a magnetic field

FR-11. Cr and Fe substitution effects on magnetic properties and phase stabilities in tetragonal Mn_3(Ga,Ge).

H. Okada[1], K. Moriya[1] and M. Doi[1]
1. Tohoku Gakuin University, Tagajo, Japan

Tetragonal Mn-based compounds have attracted much attention due to their functional properties. Among them, Mn_3Ga and Mn_3Ge with $D0_{22}$-type ($TiAl_3$-type) structure have been expected to be candidates for new spintronic and permanent magnet materials [1,2], because these compounds exhibit high uniaxial magnetic anisotropy despite 3d transition metal compounds and high Curie temperature. The compounds show a ferrimagnetic state with a small net magnetization, arising from an antiferromagnetic interaction between magnetic moments on two different crystallographic Mn_I and Mn_{II} sites (2b and 4d sites, respectively). It is known that off-stoichiometric composition stabilizes the $D0_{22}$ structure. The $D0_{22}$ phase of Mn-Ga alloy is synthesized with Mn-deficient composition $Mn_{3-x}Ga$, whereas Mn-rich composition $Mn_{3+x}Ge$ is required for obtaining the $D0_{22}$ single phase of Mn-Ge alloys. Recently, we reported that the $D0_{22}$ structure without the deficient and excess Mn atoms is synthesized in $Mn_3Ga_{1-x}Ge_x$ [3]. Theoretical investigations predicted that the exchange interaction between the two Mn sites is sensitive to the atomic ordering and the off-stoichiometry [4,5]. On the other hand, structural stability and magnetic property of the tetragonal phase in substitution systems strongly depend on a number of the valence electron of the compounds [6]. Therefore, in order to clarify the magnetic properties and phase stabilities of the Mn-based compound with the $D0_{22}$ structure, it is needed to control the number of the valence electron in the samples. In this work, we have investigated the magnetic properties and phase stabilities of the Cr-substituted, Fe-substituted and (Cr,Fe)-substituted $Mn_3Ga_{0.5}Ge_{0.5}$. Polycrystalline samples of $Mn_{3-x}Cr_xGa_{0.5}Ge_{0.5}$, $Mn_{3-x}Fe_xGa_{0.5}Ge_{0.5}$ and $Mn_{3-x}Cr_{x/2}Fe_{x/2}Ga_{0.5}Ge_{0.5}$ were synthesized by arc-melting method. The ingots were annealed at 1073 K for a week, and then heated at 673 K for a week. Structural properties were investigated by powder X-ray diffraction (XRD) experiments at room temperature. Phase stabilities of the $D0_{22}$ phase were determined by differential scanning calorimetric (DSC) measurements. The magnetization measurements were carried out using vibrating sample magnetometer. The hyperfine magnetic structure was characterized on the basis of the conventional ^{57}Fe Mössbauer effect. The single phase of the $D0_{22}$ phase were confirmed up to $x = 0.2$ for $Mn_{3-x}Fe_xGa_{0.5}Ge_{0.5}$ and $Mn_{3-x}Cr_{x/2}Fe_{x/2}Ga_{0.5}Ge_{0.5}$ and up to $x = 0.1$ for $Mn_{3-x}Cr_xGa_{0.5}Ge_{0.5}$, respectively. In the Cr-substituted system, lattice constant *a* increases and lattice constant *c* decreases with increasing the Cr content, resulting in a suppression of tetragonality (*c*/*a*). On the other hand, the Fe substitution leads to a decrease in lattice constant *a* and an increase in the lattice constant *c*. As shown in Fig. 1, a transition temperature T_{22} from the $D0_{22}$ phase to hexagonal $D0_{19}$ phase slightly increases with increasing Cr content, although the T_{22} decreases in the Fe and (Cr,Fe) substitution systems. These results indicate that a thermal stability of the $D0_{22}$ phase is influenced by the structural properties such as lattice parameters and site occupation rather than the number of valence electron. Magnetization of the Cr substitution system increases with increasing Cr content, although that of the Fe substitution system decreases with increasing Fe content. According to previous report of neutron diffraction measurement [7], magnetic moments of Mn atoms are estimated to be -3.07 m_B at the Mn_I site and 2.08 m_B at the Mn_{II} site for Mn_3Ga. Our results of Mössbauer spectroscopy reveal that the Fe atoms occupy the Mn_{II} site with extremely lower hyperfine filed, resulting in the decrease in the magnetization. On the other hand, it seems that the nonmagnetic Cr atoms occupy the Mn_I sites, leading to the increase in the magnetization. Therefore, the site preference of the substitution elements is important role for the magnetic properties of the substitution systems with the $D0_{22}$ structure.

[1] B. Balke et al. Appl. Phys. Lett. 90, 152504 (2007). [2] J. M. D. Coey J. Phys.: Condens. Matter 26, 064211 (2014). [3] H. Okada et al., IEEE Trans. Mag. 53, 1000506 (2017) [4] D. Kim et al., Phys. Rev. B 90, 144413 (2014). [5] S. Khmelevskyi et al., Phys. Rev. B 93, 184404 (2016). [6] V. Alijani et al., Appl. Phys. Lett. 99, 222510 (2011). [7] K. Rode et al., Phys. Rev. B 87, 184429 (2013).

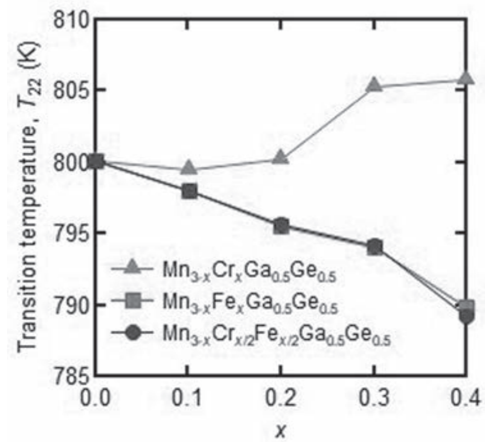

Fig. 1. Composition dependence of transition temperature T_{22} from the $D0_{22}$ to the $D0_{19}$ phases.

FR-12. Fabrication of biogenic guanine crystal/ferromagnetic film hybrid plate for micro-optical MEMS.

T. Sogame[1], K. Deguchi[1], M. Inoue[1], T. Kimura[1], E. Muneyama[1], K. Kishimoto[1], T. Koyanagi[1], H. Asada[1] and M. Iwasaka[2]
1. Graduate School of Sci. & Tech. for Innov., Yamaguchi University, Ube, Japan; 2. RNBS, Hiroshima University, Higashihiroshima, Japan

Bio-photonic crystals in fish and so on have attracted much attention due to their unique biological nano-sturcture. Guanine crystals of fish scales are the thin plate having the interesting properties such as high reflection and optical biaxiality. It has been demonstrated that the magnetic field controls the light reflection intensity from the guanine crystal plates[1], [2]. This reflection anisotropy is generated by a diamagnetic orientation of the guanine crystal with the magnetic filed more than 100 mT (goldfish guanine case). From the viewpoint of optical devices application, the reduction of magnetic field amplitude is effective. In this study, we have prepared a hybrid thin film consisting of diamagnetic guanine crystal plates and soft ferromagnetic material, and demonstrated that the hybridization enables to orient the guanine plate with the magnetic field of several mT. A ferromagnetic thin film was developed by sputtering method. After the chamber was evacuated to a pressure below 5×10^{-7} Pa, the sputtering was carried out with DC power of 50 W at sputter gas pressures of 0.53 Pa in an Ar gas atmosphere. A permalloy film with a thickness of 5-30 nm was formed on the dried surface of the stacked biogenic guanine crystal plates considering the typical thickness of guanine plates of goldfish is around 100 nm. Figure 1(a) shows the SEM image of guanine crystal plate after depositing the permalloy film of 5 nm in thickness. The permalloy entirely covers the guanine crystal surface but the edge of guanine plate is clearly seen. Next, the hybrid plate has been detached from the substrate and the dynamic behavior under the magnetic field has been investigated. Figure 1(b)-(d) shows optical microscope images of the hybrid plate having the 5-nm-thick permalloy film under the magnetic field generated by a three-axis Helmholtz coil. The hybrid plate still tends to float in water. When the rotating field of x-y plane is applied, the hybrid plate rotates according to the magnetic field as shown in Fig.1 (b) and (c), and the reflected light from the plate can be confirmed. When z-direction field is applied, hybrid plate easily stands up (see Fig.1 (d)) unlike pure guanine crystal which is oriented so that the long axis of guanine plate takes orthogonal to the magnetic field due to the gravity[2]. In the pure guanine case, it has been reported that more than 2 T magnetic field is needed to make the guanine crystal stand up against the gravity[3]. These hybrid plate motions arise from the strong shape anisotropy of permally film which fixes the magnetization direction parallel to the long axis direction of guanine plate due to the elongated shape. Critical magnetic field amplitudes for controlling the plate motion, which are 0.6 mT for in-plane motion and 3 mT for standing up, drastically decrease compared to the diamagnetic orientation of the pure guanine crystal. This work was supported by JST-CREST "Advanced core technology for creation and practical utilization of innovative properties and functions based upon optics and photonics (Grant number: JPMJCR16N1)".

[1] M. Iwasaka and Y. Mizukawa, Langmuir, 29, 4328-4334(2013). [2] M. Iwasaka et al., Appl. Phys. Express, 6, 037002(2013). [3] T. Chikashige and M. Iwasaka, AIP Advances, 8, 056704(2018).

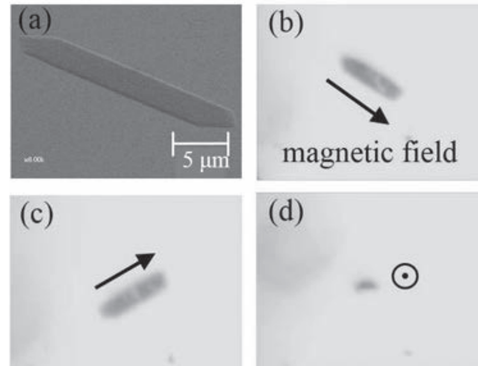

Fig. 1. (a) SEM image of guanine crystal plate after depositing the permalloy film of 5 nm in thickness and (b)-(d) optical microscope images of guanine crystal/permalloy hybrid plate motion under magnetic field.

FR-13. Magnetic Field Analysis and Optimization Design of Magneticrheological Fluid Brake.

N. Yan[1], W. Li[1] and B. Zhang[1]
1. Shenyang University of Technology, Shenyang, China

I.Introduction Magnetorheological fluid braking system utilizes the mechanical and magnetic properties of the magnetorheological fluid to provide accurate and fast braking response and realize the precise braking of the vehicle. The core of the magnetorheological fluid brake system design is to realize braking torque in the shortest possible time, the less braking torque and no residual. The performance is better than one of the conventional vehicle brake.[1] One of the key points of the design of magnetic fluid brake system is the design of magnetic field generator and the design of magnetic field optimization. The viscosity of the magnetorheological fluid under the influence of the external magnetic field is obviously changed. When the magnetic field reaches a certain range, the fluid loses its fluidity and shows obvious resistance to shear. There is no known numerical calculation model of magneto-rheological hydraulic force, which leads to no basis for the optimization of magnetic field for improving brake mechanics characteristics.[2-3] This paper presents the design and optimization process of the magnetic field of magnetic rheological fluid brake. The power law model is introduced, and the relationship between torque and magnetic induction intensity is obtained by the fitting of experimental data. So the optimization of magnetic field can be carried out smoothly. The electromagnetic design scheme of the magnetic field of brake with different structure is given. The finite element method is used to analyze and optimize. Then the magnetic circuit design was made for brake. As much as possible to meet the needs of the car. II.Numerical calculation model of magnetorheological fluid force The viscosity, shear stress and yield stress of magnetic fluid under different magnetic field strength were tested experimentally. The research objects used in the study were MRF-50 magnetic fluid. The test equipment is an Anton Paar rheometer. The viscosity of the liquid under zero magnetic field is small without considering the subsidence of the magnetorheological fluid. The relationship between shear rate and viscosity can be obtained. With the increase of magnetic field, the shear rate and viscosity meet the relationship. A power law model is introduced to characterize the relationship between shear stress and magnetic induction intensity. III.Design and optimization of magnetic field in generator Magnetic field translocation design requires a strong and uniform magnetic field in a limited volume. This part of the work includes, electromagnetic distribution simulation for different structure brakes, optimization brake thickness and magnetic ring thickness, increasing the strength of the surface magnetic field as much as possible, take into account the amount of magnetorheological fluid. Because the permeability of magnetorheological fluid is lower than that of the shell, it is possible to have low magnetic induction strength. Therefore, it is difficult to design the work. IV.Design of magnetic circuit in brake Considering the leakage and magnetic circuit saturation, the brake needs to be designed in a reasonable way. Design assumptions include: axisymmetric structure, ignoring the bearing's influence on the magnetic circuit, nonlinear permeability, ignoring outer shell magnetic leakage. The design steps are: 1) The shear stress is determined by the maximum torque of the car. 2) The induction strength of working face is obtained by substituting power law model. 3) The working face magnetic flux is estimated. 4) The relation between magnetic resistance and structural dimension is deduced. 5) The magnetic circuit model is derived. 6) The coil and brake sizes are optimized. The finite element simulation model of brake is established after the design, and the design torque is verified. V.Conclusion In this paper, a power law model is introduced to simulate the experimental data. The magnetic field analysis method can play a good role in the magnetic field of magnetic fluid transfer and brake design. An example of finite element analysis of magnetic field in generator and the design of magnetic circuit in brake is given.

[1] Ma L, Yu L. Design, Testing and Analysis of a Novel Multiple-Disc Magnetorheological Braking Applied in Vehicles[C]. SAE Technical Paper, 2015, doi:10.4271/2015-01-0724. [2] Phuong-Bac Nguyen and Seung-Bok Choi. A new approach to magnetic circuit analysis and its application to the optimal design of a bi-directional magnetorheological brake[J]. Inha University, Korea,2011.6. [3] R Russo and M Terzo,Design of an adaptive control for a magnetorheological fluid brake with model parameters depending on temperature and speed[J]. University of Naples 'Federico II', Italy, 2011.9.

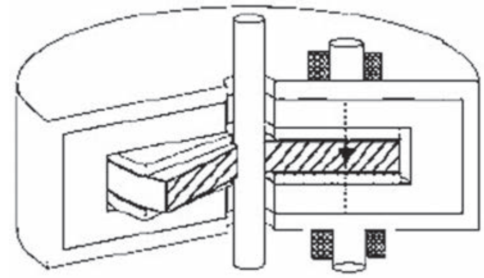

Fig. 1. Brake model

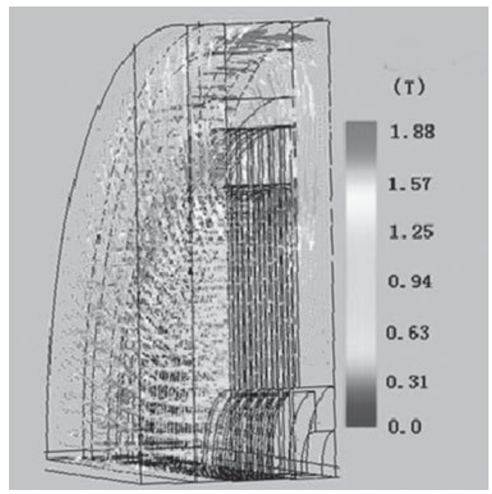

Fig. 1. Distribution of magnetic field

FR-14. A Permanent Magnet-Excited Magneto-rheological Fluid Brake Manipulated by Mechanical Magnetic Shield.

P. Lee[1] and J. Chang[1]
1. Power Mechanical Engineering, National Tsing Hua University, Hsinchu, Taiwan

In this paper we proposed a magneto-rheological fluid (MRF) brake manipulated by moving magnetic shield in which magnetic field is generated by permanent magnet (PM). With this movable shield mechanism as a switch, the magnetic field and the corresponding braking torque can be controlled continuously within small space. Furthermore, by changing the edge angle of the shield, the toque-displacement response can be modified. The size of the device is 270mm in diameter and 100mm in length. The estimated torque is 300Nm when excited by high strength NdFeB PMs, thus is suitable for rotary table of machining tool. A MRF is a smart material that consists of micro-sized magnetic particles dispersed in a carrier fluid such as oil. Without external magnetic field it appears as normal viscous fluid. With external magnetic field the magnetized particles link as chains that restrict the movement of the fluid, hence make the MRF resistive to shear force. This reaction is reversible and responses in several tens of millisecond [1-2]. Many devices such as damper, brake, etc. employed the MRF effect such that their properties can be controlled by changing magnetic fields [3-5]. In MRF brake/clutch the MRF fills the working gap between the fixed stator and the movable rotor, thus the shear stress formed between them and the resulting braking torque can be manipulated by changing magnetic fields [6]. The major two ways to produce magnetic field are electromagnet (EM) and PM. Excited by EM, relation of braking torque and magnetic field with MRF is explored [7] leading to automobile applications [8]. Although EM is easier for controlling the devices, it requires larger space and continuous electric supplement than PM to provide the same magnetic field strength, worsen by high power consumption leading to heat generation and fail-safe power failure issues. On the other hand, although PM is of high magnetic field and compact in size, and no heat and power consumption, the magnetic field control is much difficult. A PM excited MRF clutch in which the transmitted torque can be switched by moving the magnet is studied in [9-10]. In this paper a MRF brake module with mechanical movable shields as magnetic field switches is proposed. This device is designed for brake module of a rotary table for machining tool system. By moving blocks of ferromagnetism steel as magnetic shields, the magnetic field of PMs can be continuously controlled, similar to magnetic stands in which magnetic flux is confined within an iron case when the knob is turned off and vice versa. In this research we adopted this principle by using steel structure as shields. As shown in Fig.1 a pair of PMs is on the both sides of a typical disk type MRF brake module. Each magnet is encircled by two fixed steel shields and two movable ones. The 2D magnetic field of cross section of the device is simulated by Ansoft with 3D model built by this view revolving about the center axis. When the movable shields are closed, the magnets are encircled and thus no outward magnetic flux. When the shields are opened magnetic flux emits and magnetizes the MRF. Then braking torque is produced gradually in response to the opening displacement of the movable shields. Base on the resulting magnetic field the shear force can be obtain, and the braking torque is then calculated by integrating the shear force about its revolving axis. The outer diameter of the brake module is set to be 270mm for dimension restriction, the inner/outer diameters of PMs are 174/218mm and thickness is 24mm. A shield structure of 5mm in thickness is sufficient for magnetic shield purpose, and a displacement of 7mm between on and off states is enough for magnetic switch function. To separate the movable and fixed shields, an optimal edge angle is expected to alleviate the magnetic force between the movable and fixed shields such that the shields could be slip-out by smaller shear force rather than pull out directly by stronger normal force. Relationship of braking torque vs. displacement of movable shields for different edge angles is studied with results shown in Fig.2. The toque-displacement response varies by angle variation. When the edge angels are 0~45°, the curves increase rapidly and different angles result in similar effects. At angles above 45° the torque response rates decrease and become nearly linear to the displacement at the angle between 75~80° within the designed displacement range. For angles more than 80° the rates further decrease and when close to extreme value 90°, where almost no torque is observed for displacements less than 2mm, thus is not suitable for this design. The results indicated that braking torque can be manipulated by giving shield displacement as input and the torque response can be specified by shield edge angle. For manufacture consideration we adopted 60° for the first prototype. An infinite displacement of the moving shield results in a braking torque of 337.4Nm. When opening to 7mm, the resulting torque is 299.5Nm. This indicates that 90% of torque range can be controlled by moving these shields within 7mm. After proper mechanism designed for controlling the movable shields, the proposed MRF brake module will be manufactured and its performance result will be evaluated.

[1] M. Kciuk, R. Turczyn, "Properties and Application of magnetorheological fluids", *Journal of Achievements in Materials and Manufacturing Engineering*, 18, 2006. [2] A.G. Olabi and A. Grunwald, "Design and application of magneto-rheological fluid", *Materials and Design*, 28, pp. 2658-2664, 2007. [3] Mark R. Jolly, Jonathan W. Bender, and J. David Carlson, "Properties and applications of commercial magnetorheological fluids", *Journal of Intelligent Material System and Structures*, 10, 1999. [4] J.Wang, G Meng, "Magnetorheological fluid devices: principles, characteristics and applications in mechanical engineering", *Proc. Instn. Mech. Engrs.*, 215, 2001. [5] Deepak Baranwal, and T.S. Deshmukh, "MR-fluid technology and its application-a review", *International Journal of Emerging Technology and Advanced Engineering*, 2012. [6] J. Huang, J.Q.Zhang, Y.Yang, Y.Q.Wei, "Analysis and design of cylindrical magneto-rheological fluid brake", *Journal of Materials Processing Technology*, 129, pp.559-562, 2002. [7] W. Li and H. Du, "Design and experimental evaluation of a magnetorheological brake," *International Journal of Advanced Manufacturing Technology*, pp. 508-515, 2003. [8] K. Karakoc and E. J. Park, "Design considerations for an automotive magnetorheological brake," *Mechatronics*, 18, pp. 1-14, 2008. [9] Francesco Bucchi, Paola Forte, Francesco Frendo, "Experimental characterization of a permanent magnet magnetorheological clutch for automotive applications", *ASME 2012 11th Biennial Conference on Engineering Systems Design and Analysis*, 4, pp. 345-355, 2012. [10] Francesco Bucchi, Paola Forte, Francesco Frendo, A.Musolino, and R.Rizzo, "A fail-safe magnetorheological clutch excited by permanent magnets for the disengagement of automotive auxiliaries", *Journal of Intelligent Material Systems and Structures*, 25, pp.2102-2114, 2014.

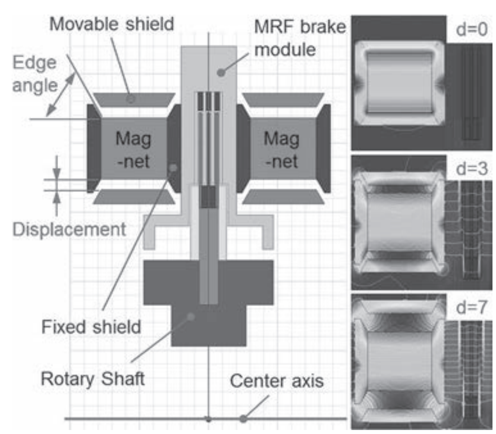

Fig. 1. MRF Brake module and magnetic field change as magnetic shields move.

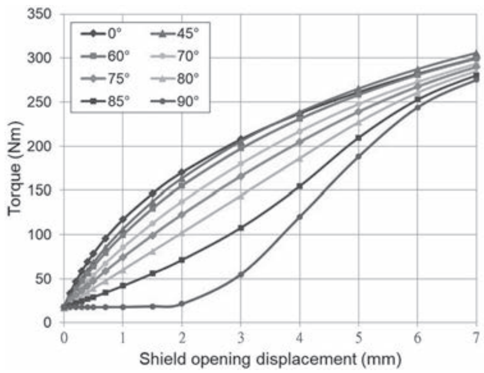

Fig. 2. Braking torque calculated as different edge angle of shield.

FR-15. Fe_3O_4@Angelica Sinensis Polysaccharides Nanoparticles for Magnetic Resonance Imaging.

X. Xu[1], K. Wang[1], Y. Li[1], Y. Wang[2], J. Wang[2] and Y. Jiang[1]
1. School of Materials Science and Engineering, University of Science and Technology Beijing, Beijing, China; 2. Department of molecular imaging, Peking Union Medical College Hospital, Chinese Academy of Medical Sciences, Beijing, China

The superparamagnetic Fe_3O_4 nanoparticles (NPs) are potential magnetic resonance imaging (MRI) contrast agents.[1] Unfortunately, the exposed Fe_3O_4 NPs have poor solubility and biocompatibility. Therefore, the surface of the Fe_3O_4 NPs needs to be suitably engineered to acquire improved biocompatibility.[2] Angelica sinensis polysaccharides (ASP) are one of the most important component in the roots of angelica, a common traditional Chinese medicine, and possess good water solubility, biocompatibility and the function of increasing hemoglobin.[3] Therefore, it is reasonable to expect the Fe_3O_4@ASP core-shell nanoparticles to have the function of both MRI contrast agents and increasing hemoglobin. In this work, we report our study on the Fe_3O_4@ASP NPs synthesized using a two step approach involving hydrothermal synthesis and consequence esterification. As shown in the TEM image in Figure 1a, the Fe_3O_4@ASP NPs are dispersed spherical with a diameter of about 12 nm. However, the dynamic light scattering (DLS) (Fig. 1b) results in a mean size of about 24.3 nm. Since the molecular composition of ASP contains C, H, O and N elements, which are light elements and invisible in TEM, the DLS result demonstrates the existence of the ASP shell wrapped on the surface of Fe_3O_4 NPs, supported by the results of saturation magnetization decreasing and the FT-IR spectra changes after ASP wrapping shown in Fig. 1c and 1d. Moreover, the Fe_3O_4@ASP NPs take on a outstanding superparamagnetic property, water solubility and stability even after ASP wrapping. Cytotoxicity assessment in Hela cells proved the good biocompatibility and low toxicity of the Fe_3O_4@ASP NPs. The Fe_3O_4@ASP NPs suspension was characterized by MRI. As shown in Fig. 2a, the T_2* signal intensity decreased significantly with increasing Fe concentration. The transverse relaxivity (r_2*) of the Fe_3O_4@ASP NPs are calculated to be 363 $mM^{-1}s^{-1}$, which indicates the Fe_3O_4@ASP NPs to be a promising contrast agents for MRI applications. Fig. 2c presents the T_2 weighted image of mice, and shows no obvious damage in the observed organs after 30 days intragastric administration, which demonstrates the safety of Fe_3O_4@ASP NPs as MRI contrast agents. The study of Fe_3O_4@ASP NPs presents a possibility to design functional nanocomposites using purified natural component from Chinese medicine for biologic applications.

[1] Lin L S, Cong Z X, Cao J B, et al. Multifunctional Fe_3O_4@polydopamine core–shell nanocomposites for intracellular mRNA detection and imaging-guided photothermal therapy. ACS nano, 2014, 8(4): 3876-3883. [2] Scialabba C, Puleio R, Peddis D, et al. Folate targeted coated SPIONs as efficient tool for MRI. Nano Research, 2017, 10(9): 3212-3227. [3] Ji P, Wei Y, Sun H, et al. Metabolomics research on the hepatoprotective effect of Angelica sinensis polysaccharides through gas chromatography–mass spectrometry. Journal of Chromatography B, 2014, 973: 45-54.

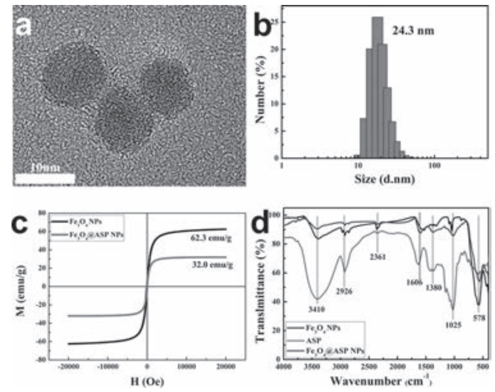

Fig. 1. TEM image (a) and hydrodynamic profiles (b) of the Fe_3O_4@ASP NPs. Magnetization curve of the Fe_3O_4@ASP NPs (c). FT-IR spectra of the Fe_3O_4 NPs, ASP and Fe_3O_4@ASP NPs (d).

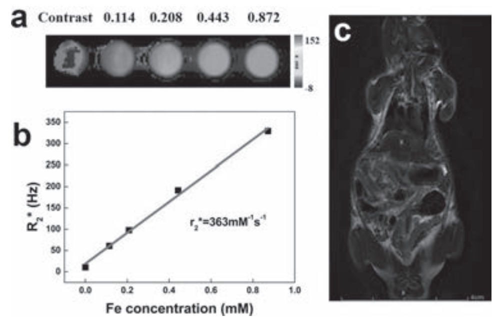

Fig. 2. T_2* images (a) and relaxivity curve (b) of the Fe_3O_4 @ASP NPs. T_2 weighted image of the mice after 30 days intragastric administration.

FR-16. Micro optical-interference-plate featuring highly efficient dia-magnetic rotation of biogenic crystals.

T. Sogame[1], E. Muneyama[1], M. Inoue[1], T. Kimura[1], K. Kishimoto[1], T. Koyanagi[1], *H. Asada*[1] and M. Iwasaka[2]
1. Graduate School of Sci. & Tech. for Innov., Yamaguchi Univesity, Ube, Japan; 2. RNBS, Hiroshima University, Higashihiroshima, Japan

Optical interference, which enhances or reduces intensity of light propagating, is very important for many kinds of shape analysis methods. It will be available to detect a morphology change in micro- to nano-scale by using optical interference when we can obtain a new optical material from the animal kingdom. This paper focused on the light interference in biogenic guanine crystals which is derived from fish skin/scale. So far, it has been reported that two cross-stacked guanine crystals show stripe patterns which are produced by the optical interference between guanine crystals[1]. In this study, we have found that a very clear moiré effect pattern is generated on a single guanine crystal plate combining with the mirror surface substrate. The observation system is consisted with telecentric lens and coaxial vertical illumination using blue LED. Guanine crystals in water are set on a mirror polishing Si substrate. Figure 1(a) shows the optical image of guanine crystal plates in water using our observation system. It can be clearly seen that homogeneous light and shade stripe patterns are observed on the plates when the surface of the guanine plates are parallel to the Si substrate reflecting that their very flat surface morphology. By contrast, when the guanine crystals in water are set on the substrates having the diffused reflection surface such as the black vinyl tape and Teflon plate, the light and shade stripe pattern is not observed on the single guanine crystal but observed on two cross-stacked crystals as reported before (Fig.1(b)). These results suggest that moiré pattern on the guanine crystal plate is perturbed or disappears when the substance or the defect which changes the reflective state of the light exists under the crystal plate. Next, we have investigated the response of guanine crystal to the magnetic field by using the moiré pattern to determine that the guanine plate is parallel to the substrate. Furthermore, it makes possible to estimate the quite small angle between the guanine crystals and substrate surface from the pattern period of moiré stripes measured by optical observation system. The time dependences of the ratio of guanine crystals oriented in the horizontal magnetic field direction are measured by changing the magnetic field amplitude as shown in Fig.2. The experimental procedure is as follows: First, the horizontal magnetic field of 500 mT is applied and guanine crystals are aligned as the long axis of the guanine plate is parallel to the field (step A). Next, the vertical magnetic field of 200 mT is applied in order to align guanine crystals as the long axis of guanine plate is orthogonal to the field and the moiré pattern disappear (step B) [2]. From this state, the horizontal magnetic field which is orthogonal to the first horizontal filed is applied and moiré patterns appear again (step C). As shown in the figure, the guanine crystal plates quickly oriented to the horizontal direction with the magnetic field of 350 mT or more. This suggests that the magnetic field operates moiré pattern switching which is effective to obtain a reference signal. The dependence of orientation time of guanine crystal upon the angle between the long axis of guanine plate and horizontal magnetic field and the tilt angle dependence of reflection brightness from the guanine plate will also be presented. This work was supported by JST-CREST "Advanced core technology for creation and practical utilization of innovative properties and functions based upon optics and photonics (Grant number: JPMJCR16N1)".

[1] M. Iwasaka and Y. Mizukawa, Langmuir, 29, 4328-4334(2013). [2] M. Iwasaka et al., Appl. Phys. Express, 6, 037002(2013).

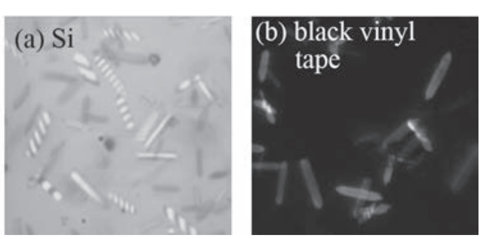

Fig. 1. Optical images of guanine crystal plates in water on (a) Si substrate and (b) black vinyl tape.

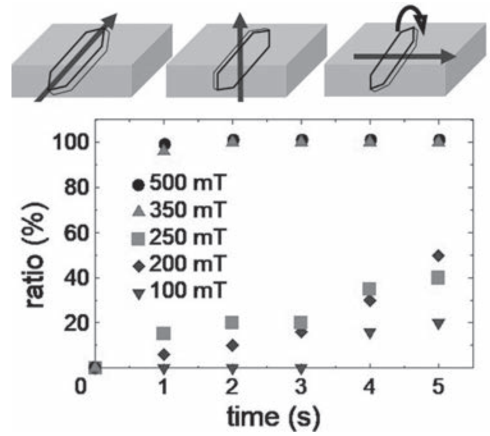

Fig. 2. Time dependences of guanine crystal ratio oriented in horizontal magnetic field direction.

Session FS
MAGNETO-ELASTIC MATERIALS
(Poster Session)

Rastislav Varga, Chair
Faculty of Sciences, UPJS, Kosice, Slovakia

FS-01. Structural Dynamic Modeling and Optimization for Vibration Control of a Composite Cantilever with Magnetostrictive Shunt Damper.

J. Zheng[1], S. Cao[1] and R. Pan[1]
1. Hebei University of Technology, Tianjin, China

Structural vibrations can cause excessive noise and damage. Piezoelectric, electromagnetic and magnetostrictive (e.g., Terfenol-D, Galfenol) transducers can convert unwanted vibration into electrical energy, thus they can be used as energy harvesters for powering other devices and as shunt dampers for vibration control. The vibration control method using the dampers with shunt circuits becomes more attractive because such lightweight devices do not cause high load effects and require little or no power supply. To increase broadband damping, it is necessary to establish an accurate structural dynamic model of the dampers and optimize parameters of the shunt circuits, which have been extensively studied in vibration control of piezoelectric and electromagnetic shunt dampers [1]-[4]. Recently, magnetostrictive shunt dampers [5]-[9] begin to receive attention. The experimental results show that the dampers can effectively suppress vibration [5]-[7] and the attenuation of transmissibility of 5–15 dB occurs in the wide frequency range from 400 to 800 Hz [5]. Different expressions and models of the dampers are also presented. The electrical energy loss expressions [8] of a damper with shunt resistance Rs and parallel shunt resistance-capacitance (Rs-Cs) circuits are derived by a purely electrical model. Based on the linear piezomagnetic equations, the storage modulus and loss factor expressions [5] of a damper with negative inductance Ls are derived, a damper's electromechanical linear model [9] is established, and general analytical expressions for storage modulus and loss factor [9] of the damper with Rs, Ls and series Rs-Cs circuits are derived. However, the above expressions and models are limited because they neglect structural dynamic behaviors of the devices. Although a dynamic compliance model [9] of a vibrating structure is presented, the validity of the model is not proven. A structural dynamic linear model [7] of a composite cantilever with magnetostrictive shunt damper is established. However, three key model parameters [7] are not related to conventional magnetostrictive properties, thus have to be experimentally determined. A generalized structural dynamic model and optimization for vibration control using the magnetostrictive shunt damper have not been reported. In this paper, the structural dynamic modeling framework of a composite cantilever with the magnetostrictive shunt damper is studied. Based on the structural dynamic equilibrium theory, the linear piezomagnetic equations, the law of electromagnetic induction and the circuit theory, the actuation and sensing equations are established to describe the dynamic behaviors of the mechanical-magneto-electro coupled system. The transmissibility, the effective mechanical-mechanical-electro coupled coefficient, the effective storage stiffness and the loss factor of the system are derived from the proposed model. The stability for the system with Rs, Cs and series Rs-Cs circuits are analyzed. The optimal tuning ratio fopt, the optimal electrical damping ratio ζeopt (the corresponding optimal resistance Rsopt and optimal capacitance Csopt) of the series Rs-Cs circuit are obtained by using H2 optimization criteria to minimize the RMS value of transmissibility. The results calculated by the proposed model for the damper are shown in Fig.1 and Fig.2. In Fig.1, comparisons between the calculated and measured results show that the proposed model can accurately describe the transmissibility frequency response curves of the system with positive resistance Rs and positive capacitance Cs, and can predict the changing laws of the resonant frequency and the peak transmissibility with Rs and Cs. Fig.2 (a) shows that to ensure a better damping performance, Rs should have a limitation of [–60Ω,100Ω] under the stability condition Rs≥–Rc (Rc =460Ω is the inherent resistance of the damper's coil [7]). In Fig.2(b), we can discuss the effects of different electrical damping rations of the series Rs-Cs circuit on the transmissibility. Fig.2(c) shows the damping ration of the peak transmissibility under the series Rs-Cs circuit with optimal resistance Rsopt =55Ω and optimal capacitance Csopt=10μF reaches 90.89%, which is higher than 70.44% under Cs circuit with optimal capacitance Csopt=5μF, and 53.29% under Rs circuit with optimal resistances Rsopt=[–60Ω,100Ω]. The proposed model has clear physical meaning, and can describe the vibration control behaviors of the magnetostrictive shunt damper, thus has very strong practicability.

[1]K. Yamada, H. Matsuhisa, H. Utsuno, and K. Sawada, "Optimum tuning of series and parallel LR circuits for passive vibration suppression using piezoelectric elements," J. Sound Vib., vol. 329, no.24, 5036–5057,2010. [2] O. Thomas, J. Ducarne, and J-F Deü, "Performance of piezoelectric shunts for vibration reduction," Smart Mater. Struct., vol.21, no.1, pp. 015008-1–015008-16, 2012. [3]B. Yan, X. Zhang, and H. Niu, "Design and test of a novel isolator with negative resistance electromagnetic shunt," Smart Mater. Struct., vol.21, no.3, pp. 035003-1–035003-9, 2012. [4]X. Tang, Y. Liu, W. Cui, and L. Zuo, " Analytical solutions to H2 and H∞ optimizations of resonant shunted electromagnetic tuned mass damper and vibration energy harvester," ASME J. Vib. Acoust., vol. 138, no. 1, pp. 011018-1–011018-8, 2016. [5] E. Fukada, M. Date, and K. Sekigawa, "Vibration control by magnetostrictive actuator coupled with negative inductance circuits Japan, "Jpn. J. Appl. Phys., vol.42, no.11, pp.7124 –7128,2003. [6] D. Davino, A. Giustiniani, C. Visone, and Amr Adly, "Experimental analysis of vibrations damping due to magnetostrictive based energy harvesting," J. Appl. Phys., vol.109, pp.07E509-1 –07E509-3,2011. [7]J.H. Yoo, A. Murray, and A. B. Flatau, " Evaluation of magnetostrictive shunt damper performance using iron (Fe)-gallium (Ga) alloy, " Proc. SPIE, vol. 9057, pp. 90573I-1 –90573I -7, 2014. [8]Z. Deng, V. M. Asnani, and M. J. Dapino, "Magnetostrictive vibration damper and energy harvester for rotating machinery," Proc. SPIE, vol. 9433, pp. 94330C-1–94330C-11, 2015. [9]J.J. Scheidler and V. M. Asnani, "Validated linear dynamic model of electrically-shunted magnetostrictive transducers with application to structural vibration control, "Smart Mater. Struct., vol.26, no.3, pp. 035057-1–035057-17,2017.

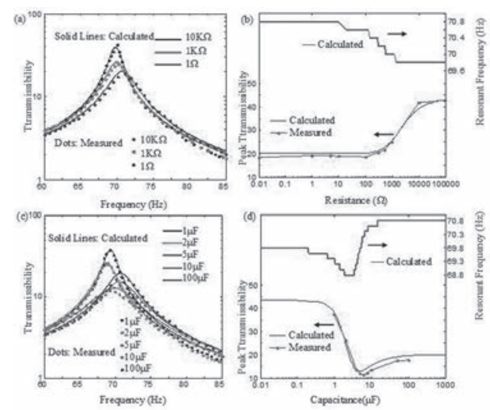

Fig. 1. Calculated and measured curves of the system: (a) Transmissibility versus frequency, and (b) Peak transmissibility and resonant frequency versus positive resistance under Rs circuit. (c) Transmissibility versus frequency, and (d) Peak transmissibility and resonant frequency versus capacitance under Cs circuit. Measured results from [7].

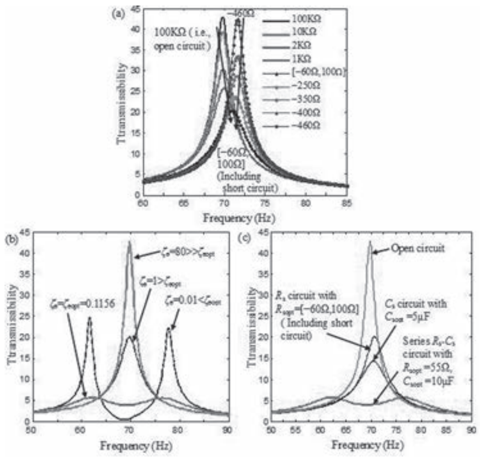

Fig. 2. Calculated curves of the system: (a) Transmissibility versus frequency under Rs circuit with different resistances. (b) Transmissibility versus frequency under series Rs-Cs circuit with the optimal tuning ratio fopt =0.9839, the optimal electrical damping ration ζeopt =0.1156 (the corresponding optimal resistance Rsopt =55Ω and optimal capacitance Csopt=10μF), and other damping rations ζe: 80,1 and 0.01. (c) Comparisons of transmissibility versus frequency under open circuit, Rs circuit with optimal resistances Rsopt=[–60Ω,100Ω], Cs circuit with optimal capacitance Csopt=5μF, series Rs-Cs circuit with optimal resistance Rsopt =55Ω and optimal capacitance Csopt=10μF.

FS-02. Determination of stress-coefficient of magnetoelastic anisotropy in flexible amorphous CoFeB film by anisotropic magnetoresistance.

X. Wen[1,2], B. Wang[1,2] and R. Li[1,2]

1. CAS Key Laboratory of Magnetic Materials and Devices, Ningbo Institute of Materials Technology and Engineering, Chinese Academy of Sciences, Ningbo, China; 2. Zhejiang Province Key Laboratory of Magnetic Materials and Application Technology, Ningbo Institute of Materials Technology and Engineering, Chinese Academy of Sciences, Ningbo, China

Flexible magnetic device is one of the indispensable flexible devices. However, the deformation of the magnetic devices will change the magnetic anisotropy of magnetic materials,[1-3] which will decrease the performance of the devices. A determination of the stress-coefficient of magnetoelastic anisotropy in a magnetic thin film is crucially important not only to the fundamental understanding of the magnetoelastic anisotropy but also to the design and fabrication of novel flexible magnetic devices.[4,5] Magnetic anisotropic constants can be obtained by ferromagnetic resonance (FMR), rotational magneto-optic Kerr effect (ROT-MOKE) magnetotransport measurements *et al*. Among them, anisotropic magnetoresistance (AMR) measurements have been proven to be a simple and effective probe to determine the anisotropy energies in magnetic films. Here, we determined the stress-coefficient of magnetoelastic anisotropy of CoFeB amorphous film by using AMR. The CoFeB films were deposited on the flexible polyvinylidene fluoride (PVDF) substrate with anisotropic thermal expansion coefficient. The uniaxial stress is applied on the films by changing the temperature of PVDF substrate [Fig. 1(a)], resulting in the changing of the magnetic anisotropy of CoFeB amorphous film [Fig. 1(b)-(d)]. On the basis of AMR curves, the angle between the magnetization and magnetic field, and hence the normalized magnetic torque can be derived [Fig. 2(a)-(b)]. Finally, the magnetic anisotropy constants can be precisely obtained by fitting the normalized magnetic toque curves [Fig. 2(c)]. Then, the stress-coefficient of magnetoelastic anisotropy in the amorphous CoFeB film was obtained by fitting the magnetic anisotropy constants in different stress states [Fig. 2(d)]. Our work suggests that the extremely sensitive AMR can provide the detailed contributions of stress-induced magnetic anisotropy constants in flexible magnetic thin films.[6]

1. Zhenhua Tang, Baomin Wang, Run-Wei Li *et al*, Appl. Phys. Lett. 105, 103504 (2014) 2. Yiwei Liu, Baomin Wang, Run-Wei Li *et al*, Sci. Rep. 4, 6615 (2014) 3. Ping Sheng, Baomin Wang, Run-Wei Li *et al*, J. Semiconduct. (Mini Review, in press) 4. Xinyu Qiao, Baomin Wang, Run-Wei Li *et al*, Appl. Phys. Lett. 111, 132405 (2017) 5. Xinyu Qiao, Baomin Wang, Run-Wei Li *et al*, AIP Adv. 6, 056106 (2016) 6. Xingcheng Wen, Baomin Wang, Run-Wei Li *et al*, Appl. Phys. Lett. 111, 142403 (2017)

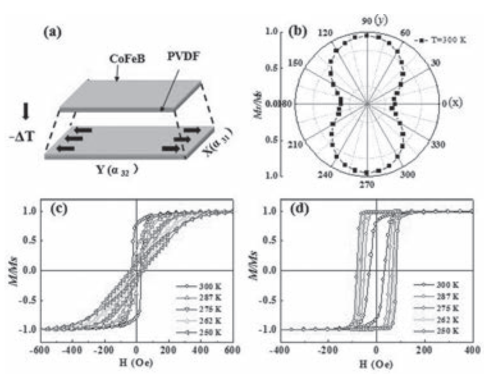

Fig. 1. (a) Schematic view of the PVDF/CoFeB when temperature change. The characteristics for CoFeB/PVDF:(b)angular dependence of normalized Mr/Ms at room temperature, (c) and (d) M-H along x and y direction under different temperature.

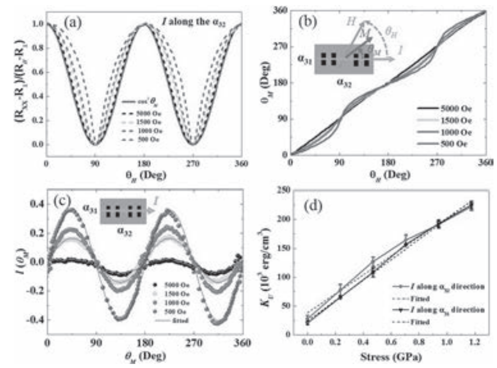

Fig. 2. The in-plane AMR curves at different fields and the correlation between θ_H and θ_M along the x direction at 250 K. Angular dependence of the in-plane AMR (a), and the correlation between θ_H and θ_M at different fields (b). (c) Normalized magnetic torque curves at different fields along the x direction at 250 K, the solid lines are fitting curves. (d) The fitted magnetic anisotropy of Ku as a function of temperature along different directions.

FS-03. Modeling and analysis of bistable Galfenol cantilever energy harvester with dynamic elastic magnifier.

S. Cao[1], L. Liu[1] and J. Zheng[1]
1. Hebei University of Technology, Tianjin, China

The magnetostrictive (e.g., Terfenol-D, Galfenol) [1]-[6] and piezoelectric (PZT)[7]-[10] cantilever energy harvesters (CEHs) can replace batteries, and have wide applications in monitors, wireless sensors, and implantable devices, etc. Galfenol, with low brittleness and high tensile strength, is more suitable for bending-mode energy harvesting than Terfenol-D and PZT. However, the performance prediction of Galfenol CEHs is complicated because the devices exhibits nonlinear mechanical- magnetic-electric coupled (NMMEC) behaviors. Moreover, traditional CEHs have bigger electrical output only at resonance. In order to improve traditional CEHs' output performance, a elastic base [7], a dynamic magnifier [8], a bistable CEH [9] and a bistable CEH with an elastic magnifier [10] are introduced to PZT CEHs. Recently, three configurations of Galfenol bistable CEHs (BCEHs) using magnetic attractive force [4], buckled beam [5] and magnetic repulsion force[6] have been proposed to enhance the CEHs' low-frequency broadband performances. The measured results show that half bandwidth of the BCEH using magnetic attractive force between magnets is 1.2 times larger than the traditional CEH without magnets [4], and the frequency bandwidth of a BCEH can be improved from 1.5 Hz to 10.5 Hz by manually adjusting the buckling force [5]. Moreover, different models for Galfenol CEHs are presented, including lumped parameter uncoupled model [2], lumped parameter coupled model [6], finite element uncoupled model [1], finite element coupled model [5] and distributed parameter coupled model [3]. However, it is difficult to maintain the BCEH oscillation in a high-orbit state because the ambient vibration level cannot provide adequate velocity for BCEHs to overcome the potential well barrier. Thus, the BCEH has a lower net available power density than the traditional CEHs [5], and the BCEH has a lower peak open-circuit root mean square (RMS) voltage than the traditional CEHs [6].The performances of a bistable Galfenol cantilever energy harvester with dynamic elastic magnifier have not been reported. In order to maintain the Galfenol BCEH [6] oscillation in a high-orbit state, a new structure combining the BCEH [6] with an dynamic elastic magnifier (DEM), which is called BCEH+DEM, is studied in this paper. The DEM consisting of a mass, a damper and a spring element is added between the BCEH [6] and the base to magnify the base vibration level or acceleration and provide a high excitation level for BCEH so as to jump from low-energy orbit to high-energy orbit. The whole system is subjected to a base acceleration excitation. Based on the structural dynamic equilibrium theory, the piezomagnetic equations, the law of electromagnetic induction and the circuit theory, a 2-degree-of-freedom (2DOF) nonlinear lumped-parameter dynamic model of the BCEH+DEM configuration is derived to exhibit the large-amplitude oscillation behaviors. Then, we can further get the dimensionless dynamic model and determine the model's parameters. The model can be solved to calculate the time-domain and frequency-domain characteristics of the system. When the base excitation acceleration amplitude is 2g and frequency is 100Hz, the output voltage, displacement, velocity and Pioncare map of the BCEH+DEM are compared with those without an DEM (i.e. BCEH [6]), as shown in Fig.1.In Fig.1(d), the red curve represents the high-energy orbit of BCEH+DEM and it oscillates in a large-amplitude periodic motion with output displacement 2.156mm and velocity 400mm/s. The low-energy orbit of the BCEH is shown with blue curve and it shows that the BCEH oscillates in a low-amplitude periodic motion with output displacement 0.33mm and velocity 144.7mm/s. It is clear from Fig.1(a) that the output open-circuit peak voltage of the BCEH is only 0.038V and the output open-circuit peak voltage of BCEH+DEM reaches 1.246V, which is about 32 times higher than that of the BCEH. It is verified that the validity of the proposed BCEH+DEM.

[1]B. Rezaeealam, T. Ueno, and S. Yamada, "Finite element analysis of galfenol unimorph vibration energy harvester," IEEE Trans. Magn., vol. 48, no. 11, pp. 3977–3980, Nov. 2012. [2]J. -H. Yoo and A. B. Flatau, "A bending-mode galfenol electric power harvester," J. Intell. Mater. Syst. Stru., vol. 23, no. 6, pp. 647–654, 2012. [3]S. Cao, J. Zheng, Y. Guo, Q. Li, J. Sang, B. Wang, and R. Yan, "Dynamic characteristics of Galfenol cantilever energy harvester," IEEE Trans. Magn., vol.51, no.3, pp. 8201304-1–8201304 -4, 2015. [4]S. Furumachi and T. Ueno, "Wide operation frequency band magnetostrictive vibration power generator using nonlinear spring constant by permanent magnet," Proc. SPIE, Smart Materials and Nondestructive Evaluation for Energy Systems, 9806, 98060X,2016. [5]Z. Deng and M. J. Dapino, "Influence of electrical impedance and mechanical bistability on Galfenol-based unimorph harvesters," J. Intell. Mater. Syst. Stru., vol. 28, no.3, pp. 1–11, 2016. [6]S. Cao, S. Sun, J. Zheng, B. Wang, L. Wan, R. Pan, R. Zhao, and C. Zhang, "Modeling and analysis of Galfenol cantilever vibration energy harvester with nonlinear magnetic force, " AIP Advances, vol.8, no.5, 056718-1–056718-5, 2018. [7]W. Li, T. S. Liu, and C. C. Hsiao, "A miniature generator using piezoelectric bender with elastic base," Mechatronics, vol.21, pp.1183-1189,2011. [8]O. Aldraihem and A. Baz, "Energy Harvester with a Dynamic Magnifier," J. Intell. Mater. Syst. Stru., vol.22, no.6, pp.521-530,2011. [9]A. Erturk and D.J. Inman, "Broadband piezoelectric power generation on high-energy orbits of the bistable Duffing oscillator with electromechanical coupling," J. Sound Vib., vol. 330, no.10, pp. 2339–2353, 2011. [10]G. Wang and W. Liao, "A bistable piezoelectric oscillator with an elastic magnifier for energy harvesting enhancement," J. Intell. Mater. Syst. Stru., vol.28, no.3, pp.1-16,2016.

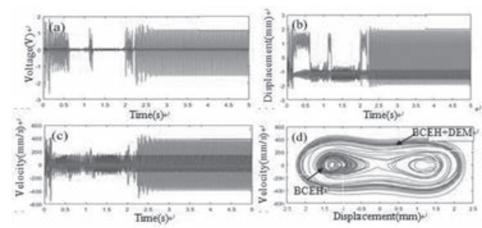

Fig. 1. (a) Open-circuit voltage, (b) displacement, (c) velocity and (d) Pioncare map of BCEH+DEM (red curve) and BCEH(blue curve) under acceleration a(t)=a0sin(2π100t), a0=2g.

FS-04. Balancing negative and positive expansion effect in dual-phase $La(Fe,Si)_{13}$/α-Fe composite with improved mechanical property.

J. Wang[1]
1. School of Materials Science and Engineering, Nanjing University of Science and Technology, Nanjing, China

Most materials exhibit a positive coefficient of thermal expansion (CTE), which leads to expanded lattices with temperature increases due to the population of higher energy levels of anharmonic lattice vibrations. However, small amount of materials contract upon heating and this phenomenon is called negative thermal expansion (NTE).Up to the present time, NTE has been observed in the well-known ZrW_2O_8 family of materials [1-3], MnCoGe-based alloys [4,5], $PbTiO_3$-based compounds [6,7], ScF_3-based compounds [8],$(Bi,La)NiO_3$ [9] and antiperovskite manganese nitrides [10-12]. $NaZn_{13}$-type $La(Fe,Si)_{13}$-based alloys are widely known to exhibit large negative thermal expansion during the magnetic transition. However, zero thermal expansion, which is more promising towards the utilization, has been rarely reported. Here, we introduce α-Fe phase naturally to compensate the negative thermal expansion of 1:13 phase, and thus achieve zero thermal expansion in $La(Fe,Si)_{13}$/α-Fe composite. It is notable that the sample with x=0 breaks itself during the magnetic transition for its poor mechanical property. In this case, it cannot be machined into regular shapes for the measurement of thermal expansion. Therefore, the average CTEs of the rest 4 samples are measured in this paper. The curves of ΔL/L are shown in Fig 1. Here, the reference temperature is 300 K and the average CTE is calculated by ΔL/(L×ΔT). NTE is observed in the samples with x=4 and 6. The average CTEs of samples with x=4 and 6 reach -9.54×10-6 K^{-1} (278-304 K) and -6.25×10-6 K^{-1} (270-291 K). With the increase of extra Fe in ingredient, a large amount of α-Fe phase appears and distributes in the 1:13 phase. NTE of 1:13 phase is offset by the PTE of α-Fe phase. An extremely low CTE of -6.55×10^{-7} K^{-1} between 261 K and 282 K is obtained in sample with x=8, leading to the establishment of ZTE. Besides the low CTE, good mechanical property is another crucial prerequisite for ZTE or NTE materials. La(Fe,Si)13-based alloys with main 1:13 phase is typical brittle. In this experiment, the cuboid sample used for thermal expansion and stress-strain measurements are processed by diamond wire-sawing. During the machining process, the sample with x=0 will break itself into some small bulks (right inset of Fig. 2, the small bulks are carefully polished for the microstructure observation on SEM), while the other sample are strong enough to be processed (left inset of Fig. 2). This indirectly proves that the increase of additional α-Fe phase can improve the mechanical property. With increasing x, the values of largest yield compressive stress are sharply enhanced to 864, 900, 970 and 1004 MPa for x=4, 6, 8 and 10, respectively (see Fig. 2). The improved mechanical property is highly related with the existence of α-Fe phase. It is known that most brittle intermetallics display intrinsic weakness of grain boundaries and insufficient number of slip systems [13,14]. Therefore, the applied stress will easily broke the weaker links between grains and leads to intergranular fractures. However, this situation will greatly changes when introducing a secondary ductile phase. In this experiment, the distributed ductile α-Fe phase is helpful to prevent the movement and slipping of dislocation, thus hinder the cracks propagation along the weak grain boundaries and enhance the mechanical property. On the other hand, additional Fe atoms suppress the formation of La-rich phase, which is detrimental to the mechanical and corrosion properties. It also contributes to the improved mechanical property. In summary, we successfully fabricate dual-phase La(Fe,Si)13/α-Fe composite. The microstructures, magnetic properties, thermal expansion and mechanical properties of samples are investigated. With the increase of extra Fe in ingredient, a large amount of α-Fe phase appears and distributes in the 1:13 phase. NTE of 1:13 phase is offset by the PTE of α-Fe phase. An extremely low CTE of -6.55×10-7 K-1 between 261 K and 282 K is obtained in sample with x=8, leading to the establishment of ZTE. Additionally, as a reinforcing factor, α-Fe phase is helpful to prevent the movement and slipping of dislocation, thus enhancing the mechanical property. Based on these improvement, ZTE and improved mechanical property are achieved simultaneously in La(Fe,Si)13/α-Fe composite.

[1]T.A. Mary, J.S.O. Evans, T. Vogt, et al., Negative thermal expansion from 0.3 to 1050 Kelvin in ZrW_2O_8. Science 272 (1996) 90-92. [2]J.S.O. Evans, P.A. Hanson, R.M. Ibberson, et al., Low-temperature oxygen migration and negative thermal expansion in $ZrW_{2-x}Mo_xO_8$. J. Am. Chem. Soc. 122 (2000) 8694-8699. [3]J.S.O. Evans, Z. Hu, J.D. Jorgensen, et al., Compressibility, phase transitions, and oxygen migration in zirconium tungstate, ZrW_2O_8. Science 275 (1997) 61-65. [4]Y.Y. Zhao, F.X. Hu, L.F. Bao, et al., Giant negative thermal expansion in bonded MnCoGe-based compounds with Ni_2In-type hexagonal structure. J. Am. Chem. Soc. 137 (2015) 1746-1749. [5]J.C. Lin, P. Tong, K. Zhang, et al., Colossal negative thermal expansion with an extended temperature interval covering room temperature in fine-powdered $Mn_{0.98}CoGe$. Appl. Phys. Lett. 109 (2016) 241903. [6]J. Chen, X.R. Xing, G.R. Liu, et al., Structure and negative thermal expansion in the $PbTiO_3$-$BiFeO_3$ system. Appl. Phys. Lett. 89 (2006) 101914. [7]J. Chen, X.R. Xing, C. Sun, et al., Zero thermal expansion in $PbTiO_3$-based perovskites. J. Am. Chem. Soc. 130 (2008) 1144-1145. [8]B.K. Greve, K.L. Martin, P.L. Lee, et al., Pronounced negative thermal expansion from a simple structure: cubic ScF_3. J. Am. Chem. Soc. 132 (2010) 15496-15498. [9]M. Azuma, W. Chen, H. Seki, et al., Colossal negative thermal expansion in $BiNiO_3$ induced by intermetallic charge transfer. Nat. Commun, 2 (2011) 347. [10] K. Takenaka, H. Takagi, Giant negative thermal expansion in Ge-doped anti-perovskite manganese nitrides. Appl. Phys. Lett. 87 (2005) 261902. [11]S. Iikubo, K. Kodama, K. Takenaka, et al., Local lattice distortion in the giant negative thermal expansion material $Mn_3Cu_{1-x}Ge_xN$. Phys. Rev. Lett. 101 (2008) 205901. [12]S.H. Deng, Y. Sun, H. Wu, et al., Invar-like behavior of antiperovskite $Mn_{3+x}Ni_{1-x}N$ compounds. Chem. Mater. 27 (2015) 2495-2501. [13]C.T. Liu, J.O. Stiegler, Ductile ordered intermetallic alloys. Science 226 (1984) 636-642. [14]Z. Yang, D.Y. Cong, X.M. Sun, et al., Enhanced cyclability of elastocaloric effect in boron-microalloyed Ni-Mn-In magnetic shape memory alloys. Acta Mater. 127 (2017) 33-42.

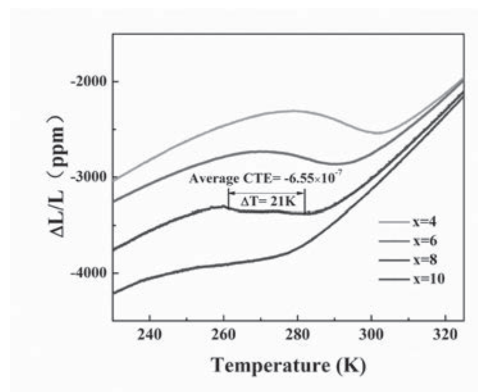

Fig. 1. Temperature dependence of linear thermal expansions (ΔL/L) (the reference temperature is 300 K) for samples with x=4, 6, 8, 10.

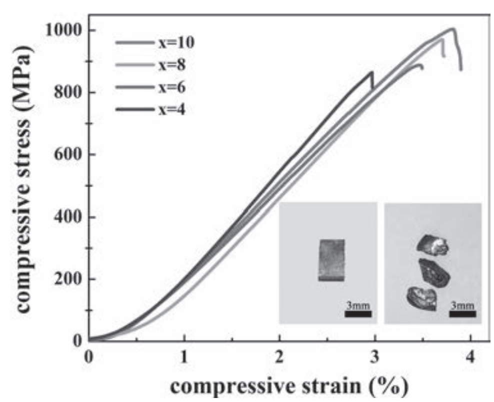

Fig. 2. The compression strain-stress curves of samples with x=4, 6, 8, 10 at room temperature. Inset: the processed cuboid sample (left) and the broken sample with x=0 (right).

FS-05. Magneto-mechanical Optimization and Analysis of a Magnetostrictive Cantilever Beam for Energy Harvesting.

V. Apicella[1], C.S. Clemente[1], D. Davino[1], *D. Leone*[1] and C. Visone[1]
1. engineering, University of Sannio, Benevento, Italy

The requirement of self-powered stand-alone sensors or wireless sensor networks (WSN) with a "fit and forget" paradigm, that is, without the need of batteries, seems to have attracted the interest of technological research in last years. Activity in development of devices, Known as Energy Harvesters, able to transform ambient energy into a kind of usable energy were boosted. Among this quite large set of solutions, those able to transform mechanical vibrations into electric power and referred to as Kinetic Energy Harvesters (KEH) are among the most known and studied, [1]. Such special set of self powered systems found a noteworthy interest in the health monitoring of civil structures or in automotive or railway applications, where, in the latter, the KEH potentialities have been identified for low cost self power sensors in freight railway wagons, [2]. Among them, one solution is represented by the cantilever configuration exploiting magnetostrictive materials, [3], based on Fe-Ga (Galfenol) alloys, showing interesting mechanical and magnetostrictive properties, [4]. Vibrations energy spectrums are complex and usually distributed over a quite large frequency range, while, conversely, cantilever KEH work in a relatively narrow band and this requires both modelling and experimental effort in order to provide an "optimal" system tuning. In this paper as a first step, different configurations employing one or more Fe-Ga strips over an Al substrate have been developed and tested through the analysis of a converted RMS power vs. frequency in order to detect the geometric and physical parameters affecting resonance frequency, bandwidth and converted power by Villari effect, [2]. The selected cantilever is implemented by bonding two single Galfenol strips 120X15X0,3 mm to a 120X15X2 mm Aluminium foil. The latter guarantees a better mechanical resistance to cyclic loads and provides a larger stiffness yielding to a consequent increase of the resonance frequency. The device has been equipped by a 300 turns coil, as it can be observed in Fig. 1. Experimental tests were performed with an electrodynamic shaker (Fig. 2a) in the *50-200 Hz* frequency interval with sinusoidal acceleration in the *1-4 g* amplitude range [5]. The excitation level has been detected by a reference accelerometer, while the beam bending is measured by a strain gauge based system. The effect of a resistive load on the RMS converted power is shown in Fig. 2b) where the power response with different resistive loads and 4g acceleration is shown. The best result of 305mW is achivied with a 9,9 W. The low energy conversion required the design of a suitable magnets set in order to supply a sufficient magnetic bias to the active material with the aim to increase the converted power [6]. In order to increase the flux captured by the coil, two magnets were attached to the structure [7]. The field generated by two magnets was measured spanning from 43 kA/m on the upper strip down to 3 kA/m on the lower strip. In Fig. 2c) the effect of the magnetic bias on the RMS converted power is shown. However, it should be outlined that the applied bias is the result of an optimization procedure since, as known, high magnetic biases pushes the material towards saturation and energy conversion is no longer observed [6]. Considering the importance of the bias, tests were carried out by varying the number of magnets (Fig. 2d). In this case it is important to evaluate the position of the magnet on the beam as it influences the resonance frequency and the magnetoelatic coupling [8]. These results seem quite encouraging, due to the relatively high converted energy (37mW) and the simple device structure. However, a thorough and accurate modelling analysis in connection to the experimental data, in order to quantitatively show the dependence of the converted power on geometric and physical parameters will be discussed in the full paper.

[1] S. P. Beeby, M. J.Tudor, N. M. White. Energy harvesting vibration sources for micro-systems applications. Measurement Science and Technology, 2006, 17(12):175-195. [2] M. Balato, L. Costanzo and M. Vitelli, MPPT in Wireless Sensor Nodes Supply Systems Based on Electromagnetic Vibration Harvesters for Freight Wagons Applications, IEEE Transactions on Industrial Electronics, vol. 64, no. 5, pp. 3576-3586, May 2017, doi: 10.1109/TIE.2016.2644605. [3] G. Engdahl, Handbook of Giant Magnetostrictive Materials, Academic Press. [4] J. H. Yoo, A. B. Flatau, A bending mode galfenol electric power harvester- Journal of Intelligent Material Systems and Structures 23(6) 647–654. [5] S. Cao, J. Zheng, Y. Guo, Q. Li, J. Sang, B. Wang, and R. Yan, Dynamic Characteristics of Galfenol Cantilever Energy Harvester- IEEE Transactions On Magnetics, Vol. 51, No. 3, March 2015. [6] D. Davino, A. Giustiniani, and C. Visone, Analysis of a magnetostrictive power harvesting device with hysteretic characteristics, Journal of Applied Physics, 105, 7, pp.07A939, (2009). [7] T. Ueno and S. Yamada, Performance of Energy Harvester Using Iron–Gallium Alloy in Free Vibration - IEEE Transactions On Magnetics, Vol. 47, No. 10, October 2011. [8] Z. Deng and M. J. Dapino, Modeling and design of Galfenol unimorph energy harvesters - Smart Materials and Structures, Volume 24, Number 12.

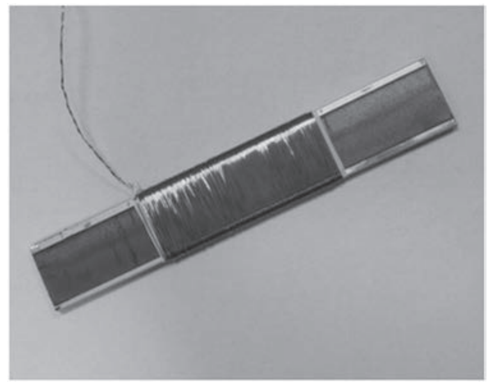

Fig. 1. Magnetostrictive cantilever beam device

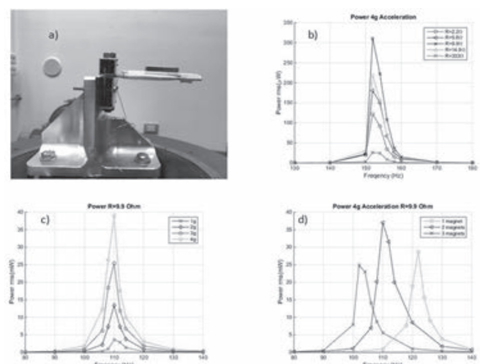

Fig. 2. a) Magnetostrictive cantilever beam attached to the head of the shaker.

Fig. 2. b) RMS power vs. frequency, with no magnetic bias for different electric loads.

Fig. 2. c) RMS power when a magnetic bias is provided by 2 Nd-Fe-B magnets.

Fig. 2. d) RMS power when a magnetic bias is provided by varying magnets.

FS-06. Magnetoelastic Coupling Effect on Magnetization in FeGa Film Induced by Surface Acoustic Waves.

C. Zhao[1], L. Pan[1], X. Li[1], Q. Liu[1] and *J. Wang*[1]
1. Key Laboratory for Magnetic and Magnetic Materials of the Ministry of Education, Lanzhou University, Lanzhou 730000, People's Republic of China, Lanzhou University, Lanzhou, China

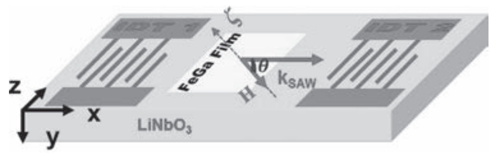

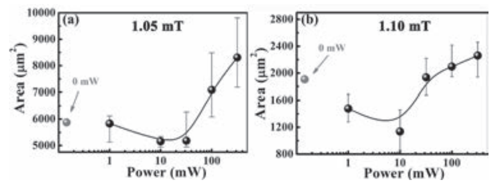

Surface Acoustic Waves (SAW) devices are attracting increasing interests for their low power consumption, miniaturization, and low-damping to spin wave propagation [1-3]. SAW also can be used to switch magnetization directions in ferromagnetic films by applying a voltage instead of an external magnetic field [4-12], which result in fast magnetization changes in the thin film. In this work, SAW is generated by interdigitated transducers (IDT) on a NbLiO3 piezoelectric substrate, as shown in figure 1. The finger width and a spacing of the IDT was set as 5.5 μm and 5μm, respectively, which is expected to launch SAW with wavelength of 21 μm. Actually, the foundational frequency of SAW has been characterised as about 170 MHz by using VNA with the time domain function. We combine magneto-optical Kerr effect (MOKE) to investigate the propagation of SAW in the magnetic FeGa film, and magnetoelastic coupling effect on magnetization in FeGa film induced by SAW was investigated. In order to confirm the influence of SAW on magnetization process of the FeGa film, MOKE image of magnetic domain was measured and the area of magnetic domain has been calculated to characterize the magnetization process quantificationally, as shown in figure 2. We can find that the input driving power of SAW has an optimal value (about 10 - 15 dBm and with the relationship of Y(dBm)=10lg(X(mW)/1(mW)))), and the magnetization process will be hindered above the optimal value. Image captions Fig. 1 Schematic illustration of the SAW device with 50 nm FeGa rectangle film. There are two IDTs in the device, and the input IDT1 connection to port 1 of VNA is used to generate SAW, and IDT2 connection to port 2 of VNA is used to detect SAW. The LiNbO3 crystalline cut and SAW propagation direction k_{SAW} are along x-axis, which ensure that the maximum strain (stretching strain and compressing strain) amplitude is along the direction of propagation. The effective field due to magnetoelastic coupling effect can be given as,$h_\sigma=(3\lambda_s\sigma)/(\mu_0 M_s)$, where σ is the external stress induced by SAW, is the unit vector in the direction of the external stress. Fig. 2 Area of magnetic domain as a function of driving power *P* at a certain field: (a) H= 1.05 mT, (b) H= 1.10 mT. Before each measurement, the FeGa film is saturated along the axis of ζ at a field of 2.5 mT. After the external field H is reverse and increasing gradually form zero, and the magnetic moments switch from ζ axis to –ζ axis. The area of magnetic domain can be calculated to characterize the magnetization process quantificationally.

[1] M. Weiler, L. Dreher, C. Heeg, H. Huebl, R. Gross, M. S. Brandt, and S. T. Goennenwein, Physical review letters 106 (11), 117601 (2011). [2] X. Li, D. Labanowski, S. Salahuddin, and C. S. Lynch, Journal of Applied Physics 122 (4), 043904 (2017). [3] P. Chowdhury, P. Dhagat and A. Jander, IEEE Transactions on Magnetics, 51 (11), 1-4 (2015). [4] W. Li, B. Buford, A. Jander and P. Dhagat, IEEE Transactions on Magnetics, 50 (3), 37-40 (2014). [5] S. Davis, J. A. Borchers, B. B. Maranville, and S. Adenwalla, Journal of Applied Physics 117 (6), 063904 (2015). [6] V. Sampath, N. D'Souza, G. M. Atkinson, S. Bandyopadhyay and J. Atulasimha, Applied Physics Letters 109 (10), 102403 (2016). [7] L. Thevenard, I. S. Camara, S. Majrab, M. Bernard, P. Rovillain, A. Lemaître, C. Gourdon and J. Y. Duquesne, Physical Review B 93 (13) (2016). [8]J. Tejada, E. M. Chudnovsky, R. Zarzuela, N. Statuto, J. Calvo-de la Rosa, P. V. Santos, and A. Hernández-Mínguez, EPL (Europhysics Letters) 118 (3), 37005 (2017). [9] S. Davis, A. Baruth, and S. Adenwalla, Applied Physics Letters 97 (23), 232507 (2010). [10] V. Sampath, N. D'Souza, D. Bhattacharya, G. M. Atkinson, S. Bandyopadhyay, and J. Atulasimha, Nano letters 16 (9), 5681 (2016). [11] L. Thevenard, J. Y. Duquesne, E. Peronne, H. J. von Bardeleben, H. Jaffres, S. Ruttala, J. M. George, A. Lemaître, and C. Gourdon, Physical Review B 87 (14) (2013). [12] E. M. Chudnovsky and R. Jaafar, Physical Review Applied 5 (3) (2016).

FS-07. Mössbauer investigation of magnetostrictive $Fe_{83}Ga_{17}$ with trace rare-earth doping.

P.S. Stamenov[1], Y. He[2], C. Jiang[2] and *M. Coey*[1]
1. School of Physics, Trinity College Dublin, Dublin, Ireland; 2. School of Materials Science and Engineering, Beihang University, Beijing, China

Fe-Ga alloys (Galfenol) are known to exhibit an unusually large magnetostriction, of order 320 ppm, which is attributed to the presence of nanoscale tetragonal Ga-rich $L6_0$ inclusions embedded in the bcc A2 Fe-rich matrix solid solution. The tetragonal axis in a particular nanoinclusion is determined by the orientation of nearest-neighbour Ga-Ga pairs. The distribution of these axes parallel to the three {100} directions means that the maximum magnetostriction can be achieved in a single crystal when the magnetic field is applied parallel to any cube edge. More recently it has been shown that traces of rare-earth atoms, ≈ 0.1 at. %, which can be incorporated into these alloys when they are rapidly cooled, can greatly increase the magnetostriction by a factor of 2 – 3 [1-3]. The mode of action of the trace dopants has yet to be determined. Here we employ Mössbauer spectroscopy in an attempt to gain some insight into the location and mode of action of the trace rare earth dopants. The samples were produced by melt spinning. Precursor ingots of $Fe_{83}Ga_{17}M_x$, with M = La, Nd, Sm, Tb and Tm and x = 0, 0.05 or 0.25 were first prepared from 4N pure Fe and Ga by arc melting under argon four times and annealed at 1000°C in Ar to ensure homogeneity. The ingots were then melt spun on a copper wheel with a surface velocity of 20 ms^{-1}, to obtain ribbons about 50 μm thick, and 5 mm wide. Transverse magnetostriction was measured by the strain gauge method in the direction of the ribbon length, with the field applied perpendicular to the plane of the ribbon. A field of up to 2 T was used to saturate the magnetization. Mössbauer spectra were obtained at room temperature in a conventional constant acceleration spectrometer with a source of ^{57}Co in Rh. The spectrum of undoped $Fe_{83}Ga_{17}$ is shown in Figure 1, together with associated fit to six hyperfine components [3]. It is composed of two main broad overlapping components with hyperfine fields of 31.2 and 26.9 T, associated with iron in the A2 phase with 0 or 1 Ga neighbours [3-5]. They constitute 87 % of the total spectral area, and their ratio is 66:34, compared to a ratio 37:63 expected for a purely random distribution of Ga in the bcc phase. The Ga concentration in A2 on this basis should be 4.8 %, and the remainder is therefore Ga-rich. We identify two minor components with the tetragonal nanoinclusions, which make up 4.8 % of the total volume. One typical example of a doped sample, with 0.5 % La is shown in Figure 2. The sum of the spectra of iron with 0 and I Ga neighbours again represents 87 % of the total area, but the ratio to rises to 68:32, and the amount of iron in the tetragonal nanoinclusions rises to 5.6 % of the total. These are small changes, but they are observed systematically in spectra with five different rare earth dopants. We can therefore conclude that the rare earths serve to increase the volume of nanoinclusions in the sample, and they increase the amount of Ga present in the nanoinclusions. A second conclusion from the data is that there is no significant difference between the 0.05 % and 0.25 % doping, when they are measured for the same dopant. This shows that the solubility limit for the rare earth in these melt-spun ribbons is below 0.05 %. The conclusions are consistent with electron microscopy observations. We consider that the rare-earth dopant is probably initially incorporated into the nanoinclusions and it enhances their tetragonality up to the metastable solubility limit, which is less than 0.05 %. Beyond that, there is no further effect and the rare earth probably precipitates out in a 2:17 or 1:2 phase. In this way we can understand the strong influence of very small amounts of rare earth doping on the magnetostriction of $Fe_{83}Ga_{17}$.

[1] W. Wu *et al*, Appl. Phys. Lett. 103 262403 (2013) [2] T. Y. Jin *et al*, Scr. Mater. 74 100 (2014) [3] Yangkun He *et al*, Acta Materialia 109 177 (2016) [4] R. A. Dunlap *et al,* J. Magn. Magn. Mater. 305 315 (2006) [5] N. J. Mellors *et al,* J. Magn. Magn. Mater. 325 3817 (2012)

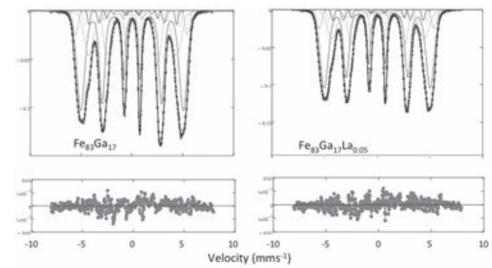

Fig. 1. Mössbauer spectrum of a melt spun ribbon of $Fe_{83}Ga_{17}$ (left) and $Fe_{83}Ga_{17}La_{0.05}$ (right). The six components of the fits are illustrated, and the residual spectra which show the quality of the fits.

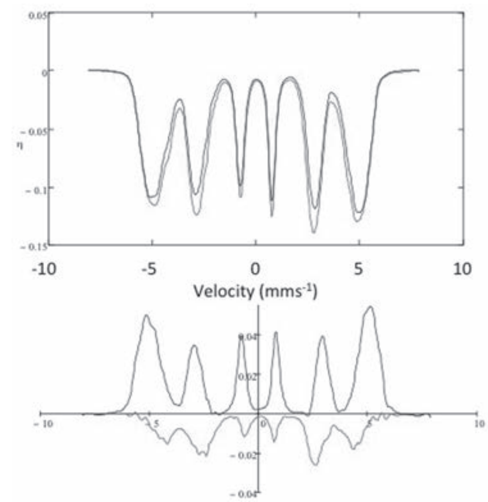

Fig. 2. Mössbauer spectrum of a melt spun ribbon of $Fe_{83}Ga_{17}$ (left) and $Fe_{83}Ga_{17}La_{0.05}$ (right). The six components of the fits are illustrated, and the residual spectra which show the quality of the fits.

FS-08. High Frequency Vibration Model with Electromagnetic-Mechanical-Thermal Multi-Field Coupled Effects for Giant Magnetostrictive Transducer.

Y. Li[1], *W. Huang*[1], B. Wang[1], C. Gao[1], X. Wu[1] and Y. Xu[1]
1. State Key Laboratory of Reliability and Intelligence of Electrical Equipment, Hebei University of Technology, Tianjin, China

Terfenol-D is a kind of magnetostrictive material that couples magnetic and mechanical energy. It exhibits giant magnetostriction (~1600ppm), giant energy density (25kJ/m^3) and broad bandwidth (~30kHz). It is the core component of giant magnetostrictive transducer (GMT) which has been widely used in the field of ultra-precision machining, precision fluid control and underwater exploration. These applications require GMT to work in a high frequency excitation state. However, when the GMT operates at high frequency magnetic field, hysteresis loss, eddy current loss and Joule's heat energy lead to serious temperature rise. The temperature of Terfenol-D rod can reach above 120°C without a cooling device. The temperature rise of Terfenol-D rod seriously affects the output properties of GMT. So, it is necessary for GMT to analyze vibration model with electromagnetic-mechanical-thermal multi-field coupled effects at high frequency. A time-dependent nonlinear electromagnetic-mechanical-thermal multi-field coupled high frequency vibration model for GMT is established based on Jiles-Atherton model, Armstrong model, Maxwell's equations, Newton's law and Fourier's heat transfer equation. Firstly, the temperature-dependent Terfenol-D dynamic magnetization model is established by a hybrid Jiles-Atherton/Armstrong magnetization model. It includes two parts: numerical integration of the function for anhysteretic magnetization in anisotropic Terfenol-D material; solving of ordinary differential equation for calculating *dM/dH*. The magnetization can be calculated for uniaxial anisotropy Terfenol-D rods when they are subjected to an external magnetic field and stress. The implementation of this algorithm is made in MATLAB. Secondly, a 3-D simulation of the whole GMT working process is programmed using commercial finite element software COMSOL Multiphysics. In order to realize the real-time temperature dependence material properties, the calculated magnetization curve at different temperature of the Terfenol-D is introduced into COMSOL by calling MATLAB files. In this method, the proposed model considers the compositive effect of magnetic, stress and temperature. It also describes the influence of pinning loss, eddy current loss and the magnetocrstalline anisotropy. In order to verify the vibration model, the vibration characteristics of the Terfenol-D rod and the output rod of GMT are measured by means of the test platform, as shown in Fig.1. Combined with the typical application of GMT in underwater acoustic frequency bands, a GMT is designed and fabricated. Its resonant frequency is 6400Hz. The GMT consists of two Terfenol-D rods with 15 mm in diameter and 102 mm in length, two drive coils, disc spring, adjusting nut, output rod, magnetic yoke and shell. Meanwhile, a new temperature control device of high flowing velocity double cavity cooling cycle system is designed. It includes the circulating oil cooler, mass flowmeter and double cooling cavity. The Terfenol-D rod is surrounded by exciting and bias coils. The magnetic circuit is closed through an annular magnetic yoke. Disc spring and adjusting nut allow the Terfenol-D to be placed under a variable prestress. The GMT is cooled by a turbulent cooling medium flow in an internal double cavity cooling channel. The cooling channel is formed between coil skeleton and Terfenol-D rod, coil skeleton and external magnetic yoke where the temperature rise of the transducer is most serious. The cooling medium is dimethyl silicone oil. It is compression refrigeration by circulating oil cooler. Then it flows from the inlet of cooling channel to outlet. The flowing velocity of cooling cycle system can be as high as 20 L/min. The temperature of GMT is controlled to below 22.3 °C. Fig.2a shows the relationship between the amplitude of output displacement and frequency in the conditions of 800 N prestress, 2 A excitation current and 5 A bias current. When f<6400Hz, the amplitude of the output displacement increases with increasing frequencies; When f=6400Hz, the output amplitude reaches the maximum value, the amplitude reaches 49 μm; When f>6400Hz, the amplitude of the output displacement decreases with frequency increases. It can be seen that the measured resonant frequency is 6400 Hz. Therefore, the driving frequency has a great influence on the output displacement. A real-time vibration acceleration of the Terfenol-D rod at 6400 Hz is shown in Fig. 2b. The measured vibration acceleration is 20 m/s^2. The mechanisms of the output acceleration, stress and displacement at the different excitation amplitudes and frequencies have been analyzed. The vibration characteristics of GMT will be tested under conditions of variable temperatures. This research can provide theoretical guidance for design and precise controlling of magnetostrictive devices at high frequency.

[1] B. Cullity and C. Graham, "Introduction to magnetic materials," Addison-Wesley Pub. Co., 1972. [2] D. C. Jiles, "Modelling the effects of eddy current losses on frequency dependent hysteresis in electrically conducting media," IEEE T. Magn., vol. 30, pp. 4326-4328. Nov. 1994. [3] E. Fallah and V. Badeli. "A new approach for modeling of hysteresis in 2-D time-transient analysis of eddy current using FEM," IEEE T. Magn., vol. 53, no. 7, pp. 1-14, Jul. 2017. [4] W. Huang, Y. Li, and L. Weng, "Multifield coupling model with dynamic losses for giant magnetostrictive transducer," IEEE T. Appl. Supercon., vol. 26, no.4, pp. 1-5, Jun. 2016. [5] Y. Zhu and J. Liang. "Theoretical and experimental investigations of the temperature and thermal deformation of a giant magnetostrictive actuator," Sensor Actuat. A Phys., vol. 218, pp. 167-178 Oct. 2014.

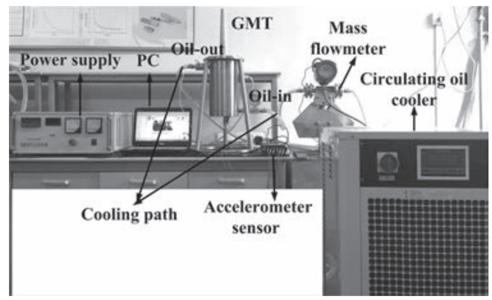

Fig. 1. Measurement system.

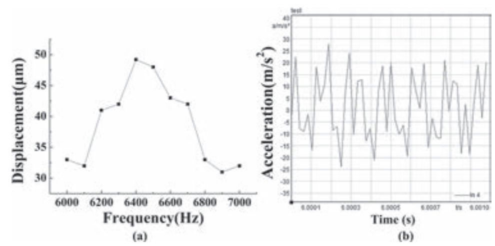

Fig. 2. (a) Frequency dependence of output displacement. (b) Vibration acceleration of the Terfenol-D rod at 6400 Hz.

FS-09. Concurrent inverse effects of magnetostriction and electrostrictionin magnetoelectric layered structures.

B. Zadov[2], *M. Auslender*[1] and E. Liverts[3]

1. Electrical and Computer Engineering, Ben Gurion University of the Negev, Beer Sheba, Israel; 2. Electrical and Computer Engineering, Ben Gurion University of the Negev, Beer Sheba, Israel; 3. Department of Mechanical Engineering, Ben Gurion University of the Negev, Beer Sheba, Israel

The structures comprising intermittently bonded (laminated or deposited) magnetostrictive and piezoelectric layers attract a keen interest in sensor applications since they exhibit strong strain-mediated magnetoelectric (ME) coupling [1]. The bonding compliance exerts hidden stresses on the structure's layers that cause changes in their properties at *no* mechanical load. We termed such effects in the ME structures concurrent *inverse effects of magnetostriction and electrostriction* (IEME), similarly to inverse effect of magnetostriction in ferromagnetic magnetostrictive materials [2], where it means a change in the magnetic anisotropy, and so the magnetization curve under external stresses. We studied theoretically and experimentally IEME for a laterally wide bi/tri-layer ME structure. Our theory is based on minimization of the total energy including bare elastic [3], magnetic-anisotropy and magneto-elastic energies [4] under the strains matching and zero-mean traction conditions at the layers interfaces and facets, respectively. Unlike the previous theories [4, 5], our theory involves also the *shear* strain and traction. We predicted IEME of the following types: (i) a latent-stress induced magnetic anisotropy unnoted previously [5, 6]; (ii) a decrease of the ME coupling coefficient [5] *below* the values obtained previously [5, 6], which may make a slipping correction factor [6] to be redundant; (iii) a decrease of the dielectric permittivity of the piezoelectric layer(s) larger than in the previous theories [5, 6]. Our materials were Alfa Aesar 99.95% purity polycrystalline Ni foil and APC-844 ceramic lead zinc titanate (PZT). Two 20x20mm^2 area samples with 0.5 mm thick Ni and 0.83 mm thick laminates were used for the magnetostriction measurements, and a pair of 5x2 mm^2 area samples with 0.25 mm thick Ni and 0.58 mm thick laminates, for the magnetization measurements. The magnetostriction was measured with Vishay Micro-Measurements two-axis SR-4 strain gauges. The room temperature magnetization curves were obtained with a Physical Properties Measurement System (PPMS) machine. The type (i) IEME is seen in Figs.1 and 2 which show the magnetization and strain curves of the above Ni layer and the Ni/PZT laminate, respectively. A notable decrease of the initial susceptibility and magnetic saturation lag in the laminate, compared to the bare Ni layer is observed in Fig.1 and similar effects for the magnetostriction in Fig.2. Except reduction of the ME coefficient α, as compared to the Harshe et. results [5], we predicted a shift of the magnetic bias of the α maximum abou twice that predicted from differential magnetostriction of the standalon Ni layer ~ 68 Oe, see in Fig.2, as assumed in previous theories [5, 6]. Our theoretical results on all above noted IEME agree well with the expriment.

1. W. Eerenstein, N. D. Mathur, J. F. Scott, *Nature*, 442, 759-765 (2006) 2. R. M. Bozorth, *Ferromagnetism*, D. Van Nostrand Company, Inc., Princeton, NJ, 1951; S. Chikazumi, *Physics of Ferromagnetism*, Oxford University Press Inc., NY, 1997. 3. L.D. Landau, E.M. Lifshitz, *Electrodynamics of Continuous Media*, Pergamon Press, Oxford, 1960. 4. L.D. Landau, E.M. Lifshitz, *Theory of Elasticity*, Pergamon Press, Oxford, 1970. 5. G. Harshe, J. O. Dougherty, R.E. Newnham, *Int. J. Appl. Electromagn. Mater.*, 4, 145-159 (1993). 6. M.I. Bichurin, V.M. Petrov, G. Srinivasan, *J. Appl. Phys.*, 92 7681-7683 (2002).

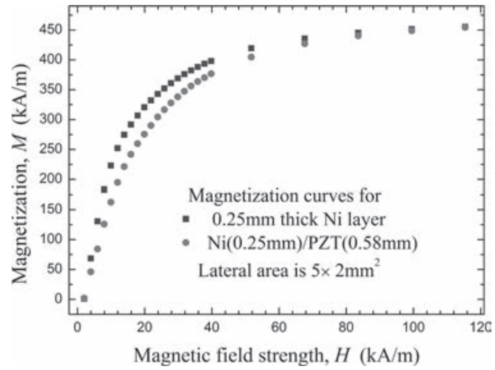

Fig. 1. Magnetization curves of the Ni/PZT laminate and standalone Ni layer obtained as described in the text

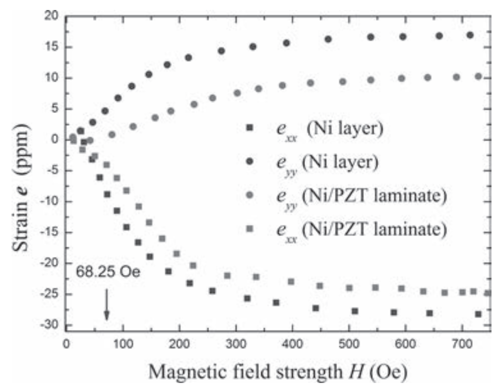

Fig. 2. Lateral magnetostriction curves of Ni/PZT laminate and standalone Ni layer as described in the text. Arrow shows magnetic bias for maximum ME coefficient in previous theory

FS-10. Experimental and Calculating Analysis of High Frequency Magnetic Energy Losses for Terfenol-D Magnetostrictive Material.

W. Huang[1], C. Gao[1], B. Wang[1] and Y. Li[1]
1. Hebei University of Technology, Tianjin, China

Magnetostrictive terbium-iron-dysprosium alloys (Terfenol-D) exhibit strong coupling between magnetic and mechanical energies. Terfenol-D generates giant magnetostriction (~1600 ppm) combined with a large energy coupling factor (0.75) and fast dynamic response (20 kHz). Hence, Terfenol-D is widely used in dynamic applications such as sonar transducers, ultrasonic devices, linear motors, and micropumps and microvalves[1]. These applications require Terfenol-D working under high frequency excitation conditions. At present, the study of experimental and calculating analysis of high frequency magnetic energy Losses for Terfenol-D magnetostrictive material mainly focuses on low frequency excitation[2-3]. The traditional losses are divided into hysteresis losses and eddy current losses. The currently available core losses calculation formulae do not take the impacts of frequency and flux density on the loss coefficients into account at high frequency and high flux density[4]. These are only suitable for low frequency excitation conditions. Therefore, it is necessary to deduce high frequency magnetic energy losses calculation formulae[5]. In this paper, Several Terfenol-D samples were made into square annular sheets. They were tested with different thickness, different types and different magnetization direction. The values of magnetic energy losses were measured to investigate its variation under different driving magnetic field and different magnetic density. Based on a great deal of experimental data, we proposed an improved losses calculation formula, which can reflect the hysteresis losses, eddy current losses, anomalous losses and losses coefficient. The formula also takes the influence of eddy current skin effect and the dynamic hysteresis loop into consideration. The results show that the losses calculated by the proposed formulae have a good consistency with the measured data. The proposed method can improve the computation accuracy obviously, and reduce the maximum error from 30% to 10%. The results of the calculation and experiments show that: 1. For the Terfenol-D samples, high frequency magnetic energy losses are measured, as shown in Fig. 1. When the frequency is 5kHz, the losses increase from 2.742 to 218.322W / Kg as the flux density varies from 0.01to 0.13T. The losses increase 79.62 times. When the flux density is 0.05T, the losses increase from 8.138 to 319.428W/Kg as the frequency is from 1kHz to 20kHz. The losses increase 39.25 times. The results show that: the losses will increase rapidly with the increasing frequency. Moreover high flux density has great impact on the losses of Terfenol-D. 2. The separation losses are obtained when the flux density is 0.05T according to experimental data and the calculation formula, as shown in Fig. 2. When the frequency increases from 1kHz to 20kHz, the eddy current losses increase from 0.27W/Kg to 117.51W/Kg. More calculating results show that the proportion of hysteresis and eddy current losses are higher, and the anomalous losses are relatively lower. The proportion of hysteresis losses decrease slowly with the increasing of frequency. And the proportions of the eddy current losses increase more quickly than the proportion of anomalous losses. This variation tendency can be explained by the theoretical calculation. Hysteresis losses and eddy current losses are mainly influenced by Bm2, anomalous losses is mainly affected by Bm3/2. The trend of calculating result is consistent with that of the experimental one. Under a given flux density, the eddy current losses change with f 2, and the hysteresis changes with f, meanwhile the anomalous losses are affected by f 3/2. So the eddy current losses change the fastest. The total magnetic losses show the trend of numerical increase and accelerated growth.

[1]Zhu Y, Li Y, A hysteresis nonlinear model of giant magnetostrictive transducer[J].. Journal of Intelligent Material Systems and Structures, 2015, 26(16): 2242-2255. [2]Yu chuan Zhu, Liang Ji. Theoretical and experimental investigations of the temperature andthermal deformation of a giant magnetostrictive actuator[J]. Sensors and Actuators A: Physical.,2014, 18:167–178. [3] Li Y J, Yang Q X, Zhu J G, et al. Magnetic properties measurement of soft magnetic composite materials over wide range of excitation frequency[J]. IEEE Transactions on Industry Applications, 2012, 48(1):88-97. [4] Li J S, Yang Q X, Li Y J, et al. Improved Calculation Formula of Core Losses for Laminated Silicon Steels at High Frequency and High Flux Density[J]. High Voltage Engineering, 2016, 42(3): 994-1002. [5] Tu J Z, Zhang J, Bu G Q, et al. Analysis of the sending-side system instability caused by multiple HVDC commutation failure[J]. CSEE Journal of Power and Energy Systems, 2015, 1(4): 37-44.

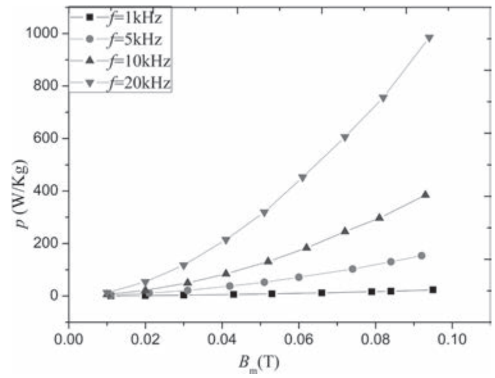

Fig. 1. The loss of magnetostriction materials vs flux density

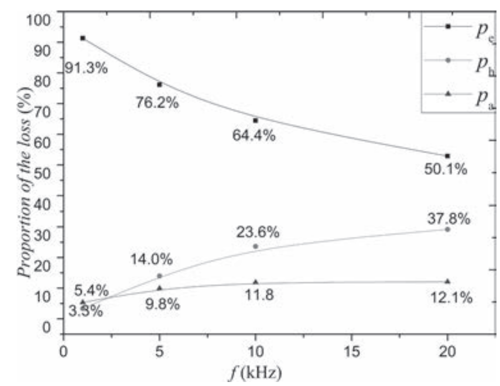

Fig. 2. The proportion of losses vs frequency.

FS-11. Magnetoelectric surface acoustic wave characteristics of the ScAlN/FeGa heterostructure with negative Poisson's ratio.

J. Jiang[1] and *F. Bai*[1]
1. State Key Laboratory of Electronic Thin Films and Integrated Devices, University of Electronic Science and Technology of China, Chengdu, China

Magnetoelectric (ME) heterostructures of magnetostrictive/piezoelectric laminates and films contains enormous opportunities in spintronic memory, gyromagnetic-field sensor, transformer, energy harvester, electrical field tunable RF/microwave devices, etc. Recently, the traditional static and dynamic ME effects have been extended to high frequency ME effects,[1] such as electrical field induced ferromagnetic resonance frequency shift and magnetic field induced acoustic resonance frequency shift of surface acoustic wave (SAW) [2] or bulk acoustic wave (BAW) [3]. The former is related to the magnetic anisotropy of the magnetic layer mediated by piezoelectric stress or ferroelectric domain transformation, and has very important applications in tunable RF/microwave devices. The later can be attributed to the piezoelectricity and elastic anisotropy of the piezoelectric layer alternated by magnetoelastic modulus (ΔE) effect, and can be used in ultra sensitive DC magnetic field detection and NEMS antenna. [3-4] In current work, we have investigated the magnetoelectric SAW characteristics of a novel piezoelectric/magnetostrictive heterostructure, i.e. ScAlN/FeGa laminates. Sc doping in AlN can result in more than 400% increase in piezoelectric constant. [5] Galfenol ($Fe_{1-x}Ga_x$ with $12<x<33$) alloys has giant magnetostriction up to 400 ppm under a low driven field between 150 and 250 Oe. Of particular interest is that Galfenol is also auxetic in the <110>{100} direction. A negative Poisson ratio of as low as -0.7 has been reported under either elastic load or magnetic field. [6,7] Fig. 1 (a) and (b) shows the magnetic field dependent modulus of $Fe_{81.7}Ga_{18.3}$ along the <100>{100} direction and <110>{100} direction, measured by a mechanical resonance/antiresonance method. As can be seen in Fig. 1(a), a giant ΔE about 25% and a maximum dE/dH close to 600 MPa/Oe were obtained in the <100>{100} direction. Due to the higher elastic modulus, the ΔE effect along the <110>{100} direction is only ~3%, and the corresponding $(dE/dH)_{max}$ is 80 MPa/Oe (Fig. 1b). Fig.2(a) shows the phase velocity dispersion of the ScAlN/(100) $Fe_{81.7}Ga_{18.3}$ half space calculated by a scattering matrix method.[2] The SAW was designed to propagate along the [110] direction. As can be seen, only the basic Rayleigh mode was found due to the softening of the ScAlN layer by the FeGa substrate with the lower modulus. The phase velocity increases smoothly from 3009 m/s to 3296 m/s with increasing f^*H_{ScAlN} up to 1.58 GHz*μm. But then the curve is broken between 1.58 and 4.6 GHz*μm, indicating that even the basic Rayleigh wave mode cannot be excited. In this sense, there is a cutoff modulus for metallic magnetostrictive substrate, which sets an upper limit on the product of piezoelectric layer thickness and the SAW center frequency. For example, the upper limit of f^*H_{AlN} for AlN/FeSiB heterostructure is only 0.18 GHz*μm, since the lowest Young's modulus of FeSiB is ~60 GPa upon applying magnetic field. This is why the [100] direction was not selected for SAW design, even that the ΔE effect is very large. However, due to the contribution of negative Poisson's ratio, Galfenol alloys with high Ga concentration all have very large f*HScAlN greater than 0.9 GHz*μm, even though the modulus $Fe_{81.7}Ga_{18.3}$ of is as low as 68 GPa, as shown in Fig. 2(b). Note that the modulus and Poisson's ratio data come from Ref. [6]. Finally, we have deposited highly c-axis oriented $Sc_{0.29}Al_{0.71}N$ film on a polished $Fe_{81.7}Ga_{18.3}$ alloy with a 50nm-thickness Ti buffer layer. The full width at half maxiumu of the (002) rocking curve is 3.6°. A one-port SAW resonator was then patterned on the ScAlN surface via a lift-off photolithography techniques. The measured wavelength was 15.76 μm. The characterization of the SAW resonator was performed by measuring S_{11} parameters as a function of frequency using a vector network analyzer (Agilent N5230A) and a microwave micro-prober. It was found that the resonance frequency f_r appeared at 208.87~218.75 MHz, corresponding to a phase velocity in the range of 3292~3448 m/s.

[1] Srinivasan G. Annu. Rev. Mater. Res. 40, 153 (2010) [2] L. Huang, Q. Q. Lv, Z. Z. Zhong, H. W. Zhang, F. M. Bai, AIP Advances 6, 015103 (2016) [3] T. X. Nan, Y. Hui, M. Rinaldi, and N. X. Sun, Sci. Rep. 3, 1985 (2013). [4] T. X. Nan, H. Lin, Y. Gao et al. Nature Commun. 8, 296 (2017) [5] M. Akiyama, T. Kamohara, A. Teshigahara, Y. Takeuchi, N. Kawahara, Adv. Mater. 21, 593 (2009) [6] R.A. Kellogg, A.M. Russell, T.A. Lograsso, A.B. Flatau, A.E. Clark, M. Wun-Fogle, Act. Mater. 52, 5043-5050 (2004) [7] G. Raghunath, A. B. Flatau, H. Wang, and R. Wu, Phys. Status Solidi B, 253, 1440-1448 (2016)

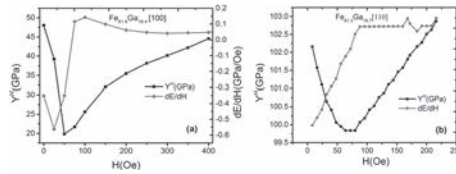

Fig. 1. Magnetic field dependent modulus of $Fe_{81.7}Ga_{18.3}$ along (a) the <100>{100} direction and (b) the <110>{100} direction.

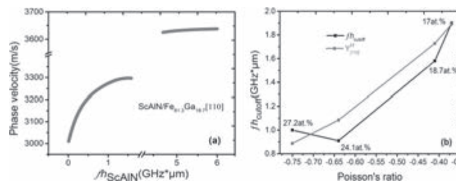

Fig. 2. (a) Phase velocity dispersion of ScAlN/(100)FeGa heterostructure with SAW propagating along the [110] direction, and (b) the upper limit of *fH_{ScAlN} on $Fe_{1-x}Ga_x$ with different x and Poisson's ratio.**

FS-12. Tuning ferromagnetic properties of $LaMnO_3$ thin films by oxygen vacancies and strain.

Y. Liu[1], H. Wong[1], K. Lam[1], C. Mak[1] and *C. Leung*[1]
1. Department of Applied Physics, The Hong Kong Polytechnic University, Hong Kong, Hong Kong

The compound of $LaMnO_3$ (LMO) is an archetypal manganite for investigating the interface coupling when adjoining with other complex oxides [1-3]. Although showing an A-type antiferromagnetic (AFM) insulating ground state in bulk [4], LMO thin films in heterostructures tend to exhibit ferromagnetic (FM) behavior [1-3]. This unexpected FM behavior has gained renewed interests recently [5-8]. In this work, we fabricate a series of LMO thin films on $SrTiO_3$ (STO) substrates with different oxygen pressures (P_{O2}) from 0.2 to 200 mTorr and systematically studied their magnetic properties. LMO/STO films deposited at low P_{O2} (20 mTorr or below) show obvious enhancement of coercive field (HC) that can reach up to 30 times that of LMO film deposited at 200 mTorr (Fig. 1(a)). On the other hand, exchange bias effect is observed in LMO/STO samples with $P_{O2} \leq 20$ mTorr (Fig. 1(b)). H_C and H_{EB} decrease with rising measurement temperature, and H_{EB} vanishes at the blocking temperature (T_B, about 60 K). Fig. 1(c) shows dependence of H_C and H_{EB} on P_{O2}. Obviously, HC and HEB show similar variation with PO2, such that HC and HEB firstly increase with decreasing PO2 and then remain constant. On the other hand, we deposited the LMO films on different substrates [$LaAlO_3$ (LAO), $(LaAlO_3)_{0.3}(Sr_2AlTaO_6)_{0.7}$, STO and $KTaO_3$] at 20 mTorr, to investigate the strain effect in FM properties of LMO film grown on low oxygen pressure. X-ray diffraction measurements indicate LMO films shows epitaxial growth but with strongly tensile, weakly tensile, more weakly tensile, and strongly compressive strains, respectively (Fig. 2(a)). Fig. 2(b) exhibits the field cooling *M-T* curves of LMO films upon cooling field, both the measured and cooled field are 1 kOe. The saturation magnetization of LMO films under strong compressive or tensile strains are much smaller below 100 K, and the magnetization of LMO/LSAT is slight smaller than that of LMO/STO. Fig. 2(c) depicts the hysteresis loops of LMO films on different substrates (hence strain states) at 3 K. All the samples were field cooled in a 2 T external field from 300 K to 3 K. It can be seen that the *M-H* loops of highly-stressed LMO films (with LAO, LSAT and KTO) are much narrower than that deposited on STO, and only in LMO/STO do H_C enhancement and the "kinked" behavior in *M-H* loop prevail. The temperature dependence of magnetization for LMO films deposited at 20 mTorr is consistent with the strain state of LMO films on different substrates. When the LMO film is slightly strained it shows robust ferromagnetic behavior, and the compressive or tensile strain will result in the progressive reduction of magnetization in LMO film. Theoretical investigated on the LMO films also indicated that a large cooperative coupling of Jahn-Teller distortion to oxygen-octahedron rotations has a significant effect on its magnetic property, which can be manipulated by the epitaxial strain [9]. Our results confirm the magnetic properties of LMO thin film are closely related to the deposited oxygen pressure and substrate, and the enhanced coercive field and exchange bias are attributed to the competition between different magnetic phases induced by oxygen vacancies and strain-induced Jahn-Teller effect. This work was supported by the National Natural Science Foundation of China (Grant No. 51502129), the Hong Kong Research Grant Council (PolyU 153015/14P) and The Hong Kong Polytechnic University (1-ZE25, 1-ZVGH).

[1] S. Smadici, P. Abbamonte, A. Bhattacharya, X. Zhai, B. Jiang, A. Rusydi, J. N. Eckstein, S. D. Bader, and J. M. Zuo, Phys. Rev. Lett. 99, 196404 (2007). [2] J. Garcia-Barriocanal, F. Y. Bruno, A. Rivera-Calzada, Z. Sefrioui, N. M. Nemes, M. Garcia-Hernandez, J. Rubio-Zuazo, G. R. Castro, M. Varela, S. J. Pennycook, C. Leon, and J. Santamaria, Adv. Mater. 22, 627 (2010). [3] J. Garcia-Barriocanal, J. C. Cezar, F. Y. Bruno, P. Thakur, N. B. Brookes, C. Utfeld, A. Rivera-Calzada, S. R. Giblin, J. W. Taylor, J. A. Duffy, S. B. Dugdale, T. Nakamura, K. Kodama, C. Leon, S. Okamoto, and J. Santamaria, Nat. Commun. 1, 82 (2010). [4] E. O. Wollan and W. C. Koehler, Phys. Rev. 100, 545 (1955). [5] H. S. Kim and H. M. Christen, Journal of physics. Condensed matter : an Institute of Physics journal 22, 146007 (2010). [6] A. Gupta, T. R. McGuire, P. R. Duncombe, M. Rupp, J. Z. Sun, W. J. Gallagher, and G. Xiao, Appl. Phys. Lett. 67, 3494 (1995). [7] T. R. McGuire, A. Gupta, P. R. Duncombe, M. Rupp, J. Z. Sun, R. B. Laibowitz, W. J. Gallagher, and G. Xiao, J. Appl. Phys. 79, 4549 (1996). [8] W. S. Choi, Z. Marton, S. Y. Jang, S. J. Moon, B. C. Jeon, J. H. Shin, S. S. A. Seo, T. W. Noh, K. Myung-Whun, H. N. Lee, and Y. S. Lee, J. Phys. D: Appl. Phys. 42, 165401 (2009). [9] J. H. Lee, K. T. Delaney, E. Bousquet, N. A. Spaldin, and K. M. Rabe, Phys. Rev. B 88, 174426 (2013)

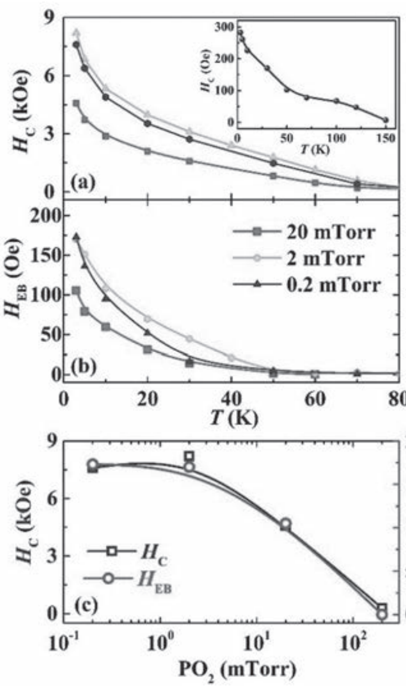

Fig. 1. (a) Temperature dependence of H_C of LMO thin films deposited at 200 mTorr (inset), 20 mTorr (red squares), 2 mTorr (green triangles) and 0.2mTorr (blue circles). (b) H_{EB} as a function of temperature with different P_{O2}. (c) The deposited oxygen pressure P_{O2} dependence of H_C and H_{EB}.

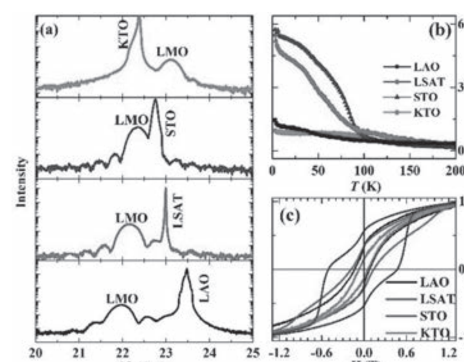

Fig. 2. (a) X-ray diffraction *q-2q* scans of LMO films on LAO, LSAT, STO and KTO. (b) Field-cooled magnetization vs. temperature for LMO films. Both the field cooling and measuring fields were 1 kOe. (c) Magnetic hysteresis loops of LMO/LAO, LMO/LSAT, LMO/STO and LMO/KTO films at 3 K.

Session FT
MODELLING OF MACHINES II
(Poster Session)

Ronghai Qu, Chair
Huazhong University of Science and Technology, Wuhan, China

FT-01. Analysis and Measurements of Interior Permanent Magnet Motor Based on Equivalent Magnetic Circuit Method.

T. Bang[1], K. Shin[1], J. Lee[1], C. Han[1], H. Cho[1] and J. Choi[1]
1. Chungnam National University, Daejon, The Republic of Korea

Recently, with the expansion of the DIY industry worldwide, the development of lithium ion battery manufacturing technology has accelerated the trend of lightweight and miniaturized power tools, and the share of portable power tools having special functions is gradually increasing in the electric tool industry. As the market share of such portable power tools has increased and international metal prices have continued to rise sharply, conventional DC motors have been replaced by high-speed permanent magnet motors with high output and efficiency in the power tool industry for mass production. This paper presents the magnetic field analysis of an interior permanent magnet (IPM) motor conducted by the equivalent magnetic circuit (EMC) method and consuming a small amount of computational time. The IPM motor has a specific rotor shape with embedded permanent magnets as shown Fig 1. (a). Magnetic saturation is generated by the permanent magnets and the rotor shape, which affects the magnetic flux density distribution in the air-gap of the IPM motor and its characteristic. The simplified analysis model for the EMC analysis is presented in Fig 1. (b). This study analyzed the magnetic field characteristic of the IPM motor by using an EMC, which was designed with consideration of the magnetic saturation in the bridge region. The EMC is shown in Fig. 1. (c), and the concept for considering the magnetic saturation in the bridge region is shown in Fig 1. (d). The validity of the analysis method was verified through a comparison of the finite-element method (FEM) analysis results. Fig. 2 (a) shows a prototype which was designed and fabricated based on the EMC method considering the bridge region magnetic saturation. The measurement system for the validation of the analysis method is shown in Fig 2(b). The results obtained by measurement, the EMC method, and FEM analysis were compared, and the validity of the analysis method was demonstrated, as shown in Figs 2. (c), (d). The results are discussed in detail in the full paper. This work was supported by the Basic Research Laboratory (BRL) of the National Research Foundation (NRF-2017R1A4A1015744) funded by the Korean government.

[1] W. H. Kim, K. C. Kim, S. J. Kim, D. W. Kang, S. C. Go, H. W. Lee, Y. D. Chun, and J. Lee, "A Study on the Optimal Ro16tor Design of LSPM Considering the Starting Torque and Efficiency," IEEE Tran. Magn., vol. 45, no. 3, pp. 1808-1811, Feb. 2005. [2] R. Dutta, M. F. Rahman, and L. Chong, "Winding Inductances of an Interior Permanent Magnet Machine With Fractional Slot Concentrated Winding," IEEE Trans. Magn., vol. 48, no. 12, pp. 4842–4849, Dec. 2012. [3] N. Bianchi, S. Bolognani, and F. Luise, "Analysis and design of a PM Brushless Motor for high-speed operations," IEEE Trans. Energy Convers., vol. 20, no. 3, pp. 629-637, Sep. 2014. [4] J. Azzouzi, G. Barakat, and B. Dakyo, "Quasi-3-D analytical modelling of the magnetic field of an axial flux permanent-magnet synchronous machine," IEEE Trans. Energy Convers., vol. 20, no. 4, pp. 746–752, 2005. [5] S. M. Jang, J. Y. Chio, H. W. Cho, and S. H. Lee, "Thrust analysis and measurements of tubular linear actuator with cylindrical Halbach array," IEEE Trans. Magn, vol. 41, pp. 2028–2031, May 2005

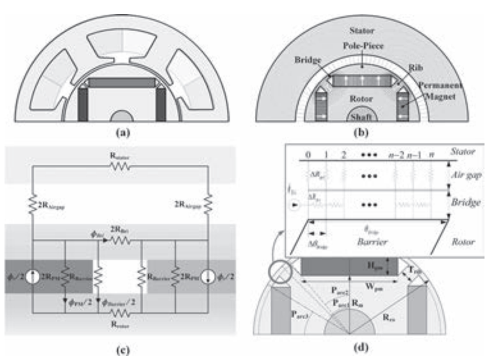

Fig. 1. Analysis model: (a) actual model of the IPM motor, (b) the analysis model of EMC, (c) EMC, and (d) bridge-region magnetic circuit.

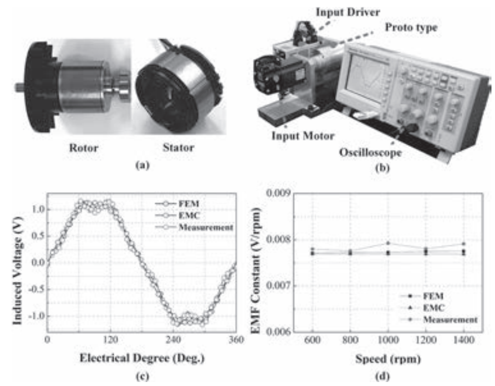

Fig. 2. Measurement model and results: (a) manufactured model (b) the measurement system of back EMF. (c) Comparison of the back EMF results and (d) comparison of the back EMF constant results.

FT-02. Coupled Finite Element Analysis of Magnetic and Thermal Fields Using Adaptive Single-Mesh Method.

W. Chen[1] and Z. Li[2]
1. Key Laboratory of Low-Voltage Apparatus Intellectual Technology of Zhejiang, Wenzhou University, Wenzhou, China; 2. College of Electrical Engineering, Zhejiang University, Hangzhou, China

Abstract: This paper proposes a coupled finite element analysis of magnetic and thermal fields using object-oriented and adaptive single-mesh methods. A fine mesh is built for both magnetic and thermal analysis to avoid errors of data transfer and mesh reconstruction. An adaptive meshing method based on master-slave definition is employed to simplify the origin mesh into magnetic and thermal mesh according to their field characteristics. Object-oriented method is used for a flexible customization in programming architecture. A permanent magnet machine is introduced to test the proposed coupled analysis method. I. Introduction Recently, requirements of high power density and compact structure have been claimed for electric machines with extensive applications of military, transportation, aeronautics and astronautics, etc. Thermal analysis has become a key factor which affects the system reliability in machine design and optimization process. Lumped parameters, finite element analysis (FEA), and computational fluid dynamics have been widely used for thermal analysis. Normally, losses in machines are calculated by magnetic analysis using FEA and then imported as heat sources into the foregoing thermal analysis models [1-2]. Various researches have proved that FEA can achieve transient reasonable results for magnetic and thermal analysis with an acceptable efficiency using adaptive method, shape optimization, etc. [1-4]. However, there is still lots of problems during coupled analysis using commercial FEA software, such as massive computing effort, customized settings, iron loss calculation under non-sinusoidal magnetization, errors by data transfer and mesh reconstruction, etc. [5-6] According to the characteristics of field distribution, the meshing requirements of magnetic and thermal analysis can be quite different. This paper proposes an adaptive single-mesh method for coupled FEA. Firstly, a relatively fine mesh is built for both magnetic and thermal analysis to avoid errors by data transfer and mesh reconstruction. Then, an adaptive meshing based on master-slave method is employed to reduce matrix order for non-linear transient iterative calculation process. Moreover, object-oriented method is applied to optimize the programming architecture for flexible customization in coupled analysis [7]. Finally, numerical results are obtained using proposed method with low computing effort. II. Coupled FEA Method Finite element variational equations of thermal field based on Galerkin method was employed. During the non-linear transient analysis, cubic spline interpolation was used to describe the non-linear permeability of silicon steels, and Newton iterative method was used to gain approximate solutions of non-linear equations. Object-oriented method was employed to built a programming architecture, including data classes of model data and computing data. The model data consisted of elements, nodes, material properties, boundary conditions, excitations, etc. The computing data was comprised of matrixes and vector results. For the coupled FEA, a fine mesh of triangular elements was built, from which both magnetic mesh and thermal mesh could be converted with some elimination. According to the original mesh, zero order approximate solution of the magnetic field was calculated and posteriori errors was then estimated according to the distribution. An adaptive meshing was applied to simplify the original mesh by eliminating internal nodes which satisfied error verification requirements. A diagram of master-slave definition is illustrated in Fig. 1. Node 5 was defined as a slave node when Eqn. (1) was satisfied. The solution of node 5 could be described as a function of its master nodes 2 and 3 in Eqn. (2). $\mathrm{abs}(A_5-(m_{25}*A_2+m_{35}*A_3))<\xi$ (1) $A_5= m_{25}*A_2+m_{35}*A_3$ (2) where A_i denoted the magnetic vector potential of node i. m_{jk} denoted the influence weight coefficient of node j on node k. ξ denoted the upper limit of specified error. The magnetic mesh was reconstructed from the original mesh by eliminating all salve nodes from the computing matrixes. Based on this magnetic mesh, results of master nodes could be gained and then applied for calculation of slave nodes. Area-weighted losses were gained using loss models in all elements of the original mesh. Similar to the magnetic analysis process, zero order approximate solution of the thermal field based on the original mesh was obtained, followed by a simplified thermal mesh using the master-slave method. Thus, coupled FEA was achieved using an adaptive single-mesh method to avoid errors of data transfer and mesh reconstruction. III. Results and Conclusions A classical permanent magnet machine was introduced to test the proposed coupled FEA method. 2-D analysis was carried out and results were presented in Fig. 2 using software GID. Despite the massive computing efforts of zero order solution based on the original fine mesh, the cost of the non-linear transient process was reduced by 8% using the master-slave method. More results along with more details about the programming architecture and loss models will be presented in the full version of the manuscript.

[1] Lihong Mo, Xiaoyong Zhu, Tao Zhang, Li Quan, Yeqin Wang, and Juan Huang, "Temperature Rise Calculation of a Flux-Switching Permanent-Magnet Double-Rotor Machine Using Electromagnetic-Thermal Coupling Analysis", IEEE Trans. Magn., 2017. [2] Gan Zhang, Wei Hua, Ming Cheng, Bangfu Zhang, and Xibin Guo, "Coupled Magnetic-Thermal Fields Analysis of Water Cooling Flux-Switching Permanent Magnet Motors by an Axially Segmented Model", IEEE Trans. Magn., vol. 53, no. 6, Jun. 2017. [3] Lingshu Lin, Weiqun Yuan, Ying Zhao, Zhizeng Wang, and Ping Yan, "Thermal Analysis on Electromagnetic Launcher Under Transient Conditions", IEEE Trans. Plasma Sci., vol. 45, no. 7, Jul. 2017. [4] Katsumi Yamazaki and Yuji Kanou, "Shape Optimization of Rotating Machines Using Time-Stepping Adaptive Finite Element Method", IEEE Trans. Magn., vol. 46, no. 8, Aug. 2010. [5] W. N. Fu and S. L. Ho, "Elimination of Nonphysical Solutions and Implementation of Adaptive Step Size Algorithm in Time-Stepping Finite-Element Method for Magnetic Field-Circuit-Motion Coupled Problems", IEEE Trans. Magn., vol. 46, no. 1, Jan. 2010. [6] Yanpu Zhao, S. L. Ho, and W.N. Fu, "A Novel Adaptive Mesh Finite Element Method for Nonlinear Magnetic Field Analysis", IEEE Trans. Magn., vol. 49, no. 5, May 2013. [7] G.R. Miller, "An Object-Oriented Approach to Structural Analysis and Design", Computers & Structures, vol. 40, no. 1, pp. 75-82, 1991.

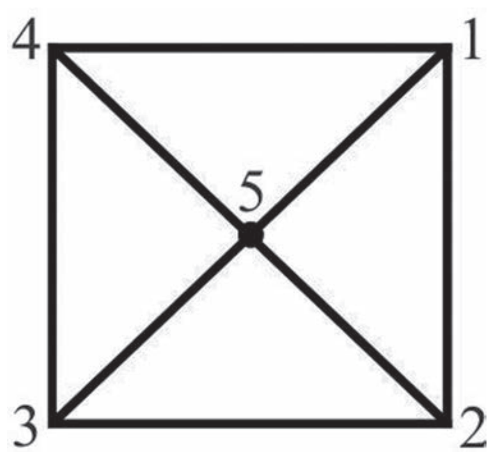

Fig. 1. Diagram of master-slave definition for adaptive meshing.

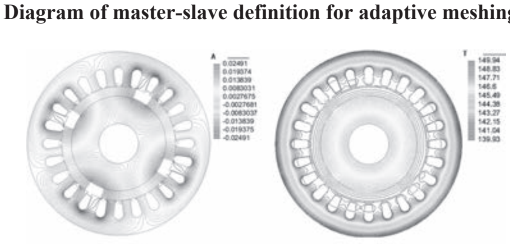

Fig. 2. Results of the proposed coupled FEA. (a) Magnetic field distribution of transient analysis. (b) Temperature distribution.

FT-03. Theoretical and Experimental Analysis of Transverse Flux Linear Machines Using Mutually Coupled Windings for High Force Density.

J. Du[1,2], Q. Liu[1], Y. Long[1] and D. Yai[1]
1. State Key Laboratory of Electrical Insulation and Power Equipment, Xi'an Jiaotong University, Xi'an, China; 2. Aviation Industry Corporation of Qing'an Group, Xi'an, China

Abstract :This paper presents an analysis method for a double salient linear machine with transverse flux for high force density. By employing mutually coupled windings, the utilizations of the magnetic and electric circuits are increased as well as the airgap flux density. The effects of tooth pitches of the translator and stator on the force output under a constant volume have been explored based on a rapidly simplified circuitry. Moreover, the electromagnetic features of the proposed machine are simulated and compared with that from 3-D finite element method including the waveforms of magnetic fluxes, inductances, and induced voltages. The correctness of the proposed analysis method is also confirmed by experimental results. I. Introduction The transverse flux machines are comparative candidates with axial flux ones requiring high force density within the restricted space of system[1,2], especially for linear drive industries like rail transportation systems[3], aviation actuator systems[4] and aircraft launch systems[5]. The transverse flux linear machine system gets rid of the intermediately transmission mechanisms and decouples the electrical loading and magnetic loading to obtain a higher force density. In this paper, a double-salient cylindrical linear machine with transverse fluxes (DLMTF) is proposed to enhance the airgap flux by mutually coupled windings in a constant volume of the motor. Based on the 3-D magnetic field distributions, a 2-D analysis approach is proposed to effectively calculate the magnetodynamic performances. Moreover, the design method to maximize the force-density is presented and verified by simulation and experimental results. II. Magnetostatic and magnetodynamic Analysis The structure of the proposed DLMTF is shown in Fig. 1. It has 8 poles in the radial directions and combination of 6/4 poles in the axialdirections. The stator and translator core are double salient and laminated along the axial directions perpendicular to each flux path. Every two phases of integrated coil windings are inserted into the slot of the one united translator block. The two phases of integrated windings in one translator block can maximize the mutual inductance and increase the utilizations of magnetic circuits. Furthermore, the copper loss can be effectively reduced due to the decreases of the end-coil parts. A. Analysis of DLMTF To obtain an accurate electromagnetic analysis of the proposed DLMTF with 3-D magnetic flus paths, a 3-D numerical analysis method should be adopted. However, the 3-D analysis is time consuming in the initial design stage. Therefore, a simplified circuitry shown in Fig. 2 is proposed considering the axial symmetry of the DLMTF machine. In the proposed circuitry, magnetic fluxes from the magnetomotive force of the PM and translator currents flow radially across the airgap, link coils on the translator block and shape complete loops over the aligned or unaligned poles. B. Analysis of DLMTF and drive system To identify the magnetic properties of the DLMTF, the magnetic circuit model combining with the external circuit is given in Fig. 2. Each branch in the asymmetrical half-bridge converter includes the corresponding resistance and inductance. The inductance is calculated from the magnetic circuit model. According to the circuitry, the field distributions, the inductance, induced voltage, flux and force varying with translator positions can be calculated and verified by the 3-D FEM. III. Design improvements of high force density From the proposed circuitry, it can be seen that the field morphology is similar to the transverse switched reluctance machine but much higher airgap flux in a constant volume due to the mutual inductances. As shown in Fig. 1, the translator and stator has available space for teeth extensions in the radial and axial directions under a certain volume of the machine, which lead to increased fluxes for every magnetic loop. However, the increased tooth pitch of the translator and stator will decrease the window area in the axial direction and limit the electrical loading due to the translator current. In addition, the teeth pitch has significant effects on the flux varying with translator positions. Therefore, teeth pitches of the translator and stator have major influences on the power-density. In order to obtain a high force density design, the reluctances of each component in the magnetic circuit in Fig. 2 are expressed by the tooth pitch and the relationship between the force and the teeth pitch is deduced and verified by 3-D FEM. IV. Experiment and discussion To verify the accuracy of the simulated results, a DLMTF prototype is manufactured and the test bench is set up. At different translator positions and saturation conditions, the flux, induced voltage and inductance can be measured and compared with the simulation results. V. Conclusions A transverse flux double salient linear machine is proposed and analyzed by using an accurate and rapid circuitry in this paper. According to the simplified analysis method, tooth pitches of the translator and stator give different force output under a certain volume. And a design with the higher force density is given based on the deduced relationship between the force and tooth pitches. The validity of the proposed analysis method, the properties of a prototype are measured in the laboratory and compared with the simulation results. In full papers, an extended analysis and experimental results will be illustrated in detail.

[1]J. M. Seo, J. S. Ro, S. H. Rhyu, I. S. Jung, and H. K. Jung, "Novel hybrid radial and axial flux permanent-magnet machine using integrated windings for high-power density," *IEEE Trans. on Magnetics*, vol. 51, no. 3, pp. 1-4, Mar. 2015. [2]E. Kurt, H. Gor, and M. Demirtas, "Theoretical and experimental analyses of a single phase permanent magnet generator (PMG) with multiple cores having axial and radial directed fluxes," *Energy Conversion and Management*, vol. 77, pp. 163-172, Jan. 2014. [3] G. Patterson, T. Koseki, and Y. Aoyama, "Simple modeling and prototype experiments for a new high-thrust low-speed permanent-magnet disk motor," *IEEE Trans. on Industry Applications*, vol. 47, no. 1, pp. 65-71, Jan. 2011. [4]Q. Wang, Y. Xu, Y. Li, and J. Zou, "Design criteria, modeling, and verification of tubular transverse flux machines for force-to-current ratio improvement in direct drive applications," *IEEE Trans. on Magnetics*, vol. 52, no. 7, pp. 1-1, Jul. 2016. [5]M. Zhao, and J. Zou, "The thrust characteristic investigation of transverse flux tubular linear machine for electromagnetic launcher," IEEE Trans. on Plasma Science, vol. 39, no. 3, pp. 925-930, Mar. 2011.

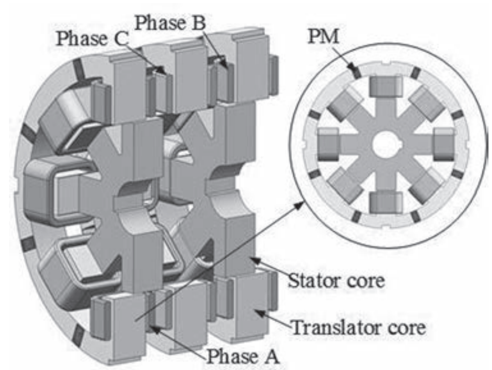

Fig. 1. Structure of the proposed DLMTF

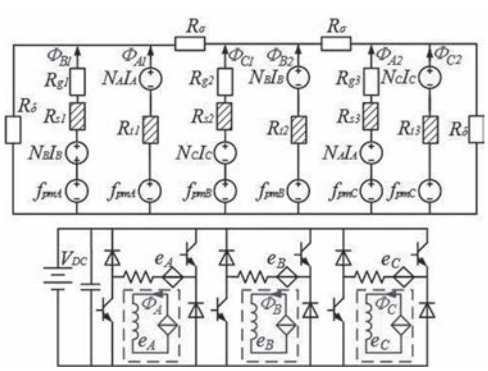

Fig. 2. Simplified circuitry of the proposed DLMTR and drive

FT-04. Electromagnetic Analysis of a Balanced Armature Receiver Considering Fringing Flux Effect by Lumped Parameter Method.

D. Xu[1,2], Y. Jiang[2] and S. Hwang[2]

1. School of Mechanical Engineering and Automation, Shanghai University, Shanghai, China; 2. Mechanical Engineering, Pusan National University, Busan, The Republic of Korea

1. Introduction With the increasing market demand for balanced armature (BA) receivers due to their small size and premium performance, an effective analysis method with high accuracy is required to design BA receivers. Jensen et al. [1, 2] investigated the distributions of nonlinear magnetic characteristics, such as the cogging force, force factor, inductance and speedance, by lumped parameters method (LPM) while treating the relative permeability of soft magnetic materials as infinite to disregard the reluctance of soft magnetic materials. Xu et al. [3, 4] improved upon the study of Jensen by considering the reluctance of soft magnetic materials with nonlinear relative permeability of soft magnetic materials, and verified the analysis results by finite element method (FEM). However, both Xu and Jensen only considered the magnetic flux follows the particular intended path in the magnetic circuit, and did not consider the effect of fringing flux, flux leakage and magnetic refraction flux. The comparison of nonlinear magnetic characteristics with Jensen's method, Xu's method and FEM in [3, 4] states that the results of Xu's method are much improved from those of Jensen's research, but there is still a gap needs to be improved in the situation of large current and large vibration displacement, which is caused by the influence of ignored fringing flux, flux leakage and magnetic refraction flux on the saturation of soft magnetic materials. Even though the electromagnetic analysis of Xu et al. [5, 6] by 3D FEM is more accurate, significant time is required in the analysis. The fringing flux [7] is generated in the air gaps in the magnetic circuit of a BA receiver, where the magnetic flux lines repel each other and bulge outward when passing through. Thus, the cross-sectional area and the effective length of air gap are increased, and the total flux in air gap is changed. As a result, the flux linkage passing through the armature calculated by the flux of air gap is also affected. Therefore, the distributions of the nonlinear magnetic characteristics calculated by the flux density of air gap and the flux linkage passing through the armature are influenced by the fringing flux effect. 2. Analysis method In previous research [3, 4], only the reluctances of permanent magnet (PM), air gap, armature and magnet housing are considered, the equivalent 2D modeling of magnetic circuit is shown in Figure 1 (a) and the equivalent magnetic circuit (EMC) is presented as Figure 2. Except for considering the fringing flux effect, two improvements are also completed in this study compared with previous research [3]: one is that one more part of reluctance on the armature arm is added, the other is that two different nonlinear material properties are used for armature and magnet housing. The flux line distribution at equilibrium position without current is depicted in Figure 1 (b), and the Figure 1 (b) depicts that the fringing flux areas generated in the air gaps are different on the right and left side because of the influence of the armature on the left side. Therefore, four reluctances of fringing volume are considered, as shown in Figure 1 (a). The ratio of the mean width of the cross-sectional length to the air gap [7] on the left and right are defined as "a" and "b", and the ratio of the mean MPL of the fringing flux to the air gap [7] on the left and right are defined as "c" and "d". Thus, the mean width and length of fringing flux on each side is shown in Figure 1 (b), and the EMC of the modeling considering fringing flux is added as pink color in Figure 2. Magnetic equations can be obtained by Kirchhoff's current law and Kirchhoff's voltage law with eight nodes and three loops. The flux density and flux can be obtained by solving those equations, and then the total force acting on armature and the induced back EMF can be calculated. Finally, in the same manner as [3, 4], equations of the nonlinear magnetic characteristics can be obtained, and the distributions in variation of vibration position and current can be obtained by iterations with under-relaxed Newton-Raphson method. The distributions obtained by the previous research method [3, 4], the improved method considering fringing flux effect in this study and 2D FEM used to verify the results will be compared and presented in the full paper. It can be predicted that the distributions of nonlinear magnetic characteristics are much more close to those obtained by FEM when considering fringing flux. 3. Conclusion This study presents the effect of fringing flux on the distributions of nonlinear magnetic characteristics of a balanced armature receiver by lumped parameter method. The nonlinear magnetic characteristics can be established by solving the nonlinear equations obtained from the equivalent magnetic circuit. The distributions of the nonlinear magnetic characteristics in variation of vibration position and current could be obtained by iterations with under-relaxed Newton-Raphson method. Compared with the distributions without considering fringing flux, the distributions considering fringing flux will be much more close to those obtained by 2D finite element method. Therefore, the analysis method in this study could provide valuable information with high accuracy and save significant simulation time in electromagnetic analysis of balanced armature receivers.

[1] J. Jensen, F. T. Agerkvist, and J. M. Harte,"Nonlinear time-domain modeling of balanced-armature receivers," *Journal of the Audio Engineering Society*, vol. 59, no. 3, pp. 91–101, 2011. [2] Jensen, J. "Nonlinear Distortion Mechanisms and Efficiency of Miniature Balanced-Armature Loudspeakers". Diss. Ph. D. thesis, Technical University of Denmark, Kgs. Lyngby, Denmark, 2014. [3] Xu, Dan-Ping, et al. "Electromagnetic Analysis of the Nonlinear Magnetic Circuit in a Balanced Armature Receiver Considering the Reluctances of Soft Magnetic material," under review. [4] Xu, Dan-Ping, "Analysis of a Balanced Armature Receiver Performances Considering Eddy Current, and Electromagnetic, Mechanical and Acoustic Coupling Effects," Dissertation of Ph.D., Pusan National University, February 2018. [5] Xu, Dan-Ping, Lu, H. W., Jiang, Y. W., Kim, H. K., Kwon, J. H., & Hwang, S. M. "Analysis of Sound Pressure Level of a Balanced Armature Receiver Considering Coupling Effects." *IEEE Access* (2017). [6] Xu, Dan-Ping, Jiang, Jiang, Y. W., Kwon, J. H., & Hwang, S. M. "Analysis of the Effects of Electromagnetic Circuit Variables on Sound Pressure Level and Total Harmonic Distortion in a Balanced Armature Receiver." *IEEE Transactions on Magnetics* (2017). [7] Kazimierczuk, Marian K. *High-frequency magnetic components*. John Wiley & Sons, 2009.

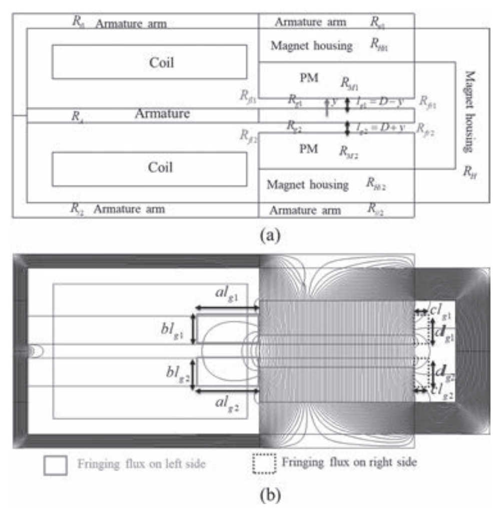

Fig. 1. (a) Modeling of a BA receiver (b) Flux line distribution of a BA receiver at equilibrium position without current.

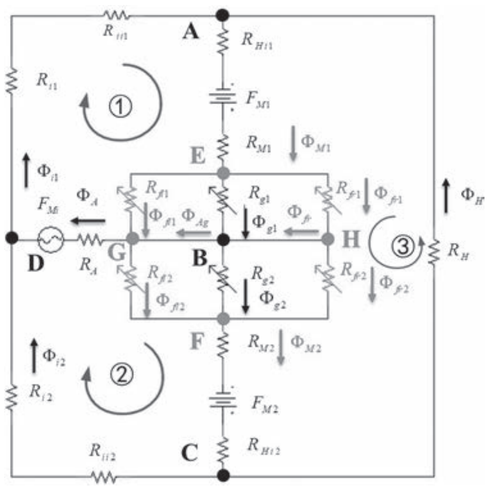

Fig. 2. The equivalent magnetic circuit of a BA receiver considering fringing flux.

FT-05. Iron loss characteristics of a nanocrystalline ring excited by Si-IGBT and GaN-FET inverters.

A. Yao[1], *T. Sugimoto*[1] and K. Fujisaki[1]
1. Department of Engineering, Toyota Technological Institute, Nagoya, Japan

INTRODUCTION Pulse-width-modulation (PWM) inverters are often utilized in motor drive system, which has motor cores made of magnetic materials. Recently, many studies have shown that iron losses in the magnetic core magnetized by PWM inverters are increased by the higher harmonic components superimposed in current and voltage waveforms [1-12]. In order to reduce iron losses of the motor core, some studies have focused on novel materials, namely, nanocrystalline magnetic materials (NMM) [13] that offer low iron losses compared to conventional non-oriented (NO) silicon steel [14, 15]. Therefore, it is important to understand iron loss properties of the NMM core under the PWM inverter excitation. However, there has been no report on iron loss properties of the NMM core excited by PWM inverters with different semiconductors. Power semiconductor is a main component of inverter circuit. Recently, next-generation semiconductors such as Silicon Carbide (SiC) or Gallium Nitride (GaN) have been studied. Such new material semiconductors allow us to have advantages of high-voltage and high-temperature operation, low on-resistance and fast switching. Recently, we have shown that there are influences of power semiconductor characteristics on iron loss properties of NO materials [16]. Therefore, the next phase is to correctly understand the influence of PWM inverters with conventional and next generation semiconductors in NMM core. This study focuses on an evaluation of iron losses of NMM excited by different PWM inverters using conventional and next generation semiconductors. To do this, we examine the iron loss characteristics as a function of carrier frequency of the NMM ring excited by two PWM inverters using Si-insulated gate bipolar transistor (IGBT) and GaN-field effect transistor (FET). RING CORE AND ITS MEASURMENT SYSTEM In this study, we examine iron loss properties of a ring specimen made of NMM under a single phase PWM inverter. Fig. 1 shows a schematic of the ring specimen and its measurement setup. This ring specimen is excited by two kinds of full bridge inverters; The first inverter is constructed with four GaN-FETs (DGF6010, Sanken Electric Corporation) and the second inverter consists of four Si-IGBTs (PM75RSA060, Mitsubishi Electric Semiconductor). The first (second) inverter is called GaN-FET inverter (Si-IGBT inverter) from here on. The ring specimen made of NMM is impregnated with acrylic resin. The stacking factor of the NMM core is 0.91. The iron losses of the ring specimen W can be calculated by $W = f_0\int H dB/\rho$, where ρ is the density of the magnetic sheet, $H = N_1I/L$ is the magnetic field intensity, and $B = \int V\, dt \,/\, N_2S$ is the magnetic flux density. Here I is the current through core, N_1 (= 264) is the number of turns of the exciting coil, L (= 0.36 m) is the average magnetic path length, V is the B-coil voltage, N_2 (= 264) is the number of turns of B-coils, and S (= 87.5 mm^2) is the cross-sectional area of the core. In the following experiments, a fundamental frequency f_0, a modulation index, and a switching dead time are set to 50 Hz, 0.5, and 3500 ns, respectively. The maximum magnetic flux density B_m of the ring is adjusted by tuning the applied voltage V_{dc} and set to 1.0 T. The ring tests are performed at carrier frequencies f_c of 1, 4, 8, 12, 16, and 20 kHz. See Ref. 5 for details of the ring measurements. RESULTS AND DISCUSSION Fig. 2 (a) shows the iron loss properties with respect to the carrier frequency of the Si-IGBTand GaN-FET-inverter-excited NMM ring. The iron losses under Si-IGBT inverter excitation are almost a constant value. The NMM ring tests under GaN-FET inverter excitation at high carrier frequency (*e.g.* f_c = 20 kHz) show drastically large iron loss compared with that excited by Si-IGBT inverter. The iron loss properties of NMM ring under Si-IGBT and GaN-FET inverter excitations have the different tendency. Figs. 2(b) and (c) show the *B-H* curves of the NMM ring under Si-IGBT and GaN-FET inverter excitations at f_c = 1 kHz. In the NMM ring under GaN-FET inverter excitation, ringing noises of the magnetic field intensity occur due to the high speed switching of GaN-FET. It is thought that the iron losses in the GaN-FET-inverter-fed ring rise with increasing carrier frequency because the number of times of ringing increases. In other words, the iron loss properties of NMM ring depend strongly on power semiconductor characteristics. CONCLUSIONS We for the first time examined iron loss properties of the NMM core excited by the PWM inverter with different semiconductors. The iron losses of the NMM ring under GaN-FET inverter excitation increased with increasing carrier frequency owing to the ringing noises. However, the iron losses based on the Si-IGBT-inverter-fed NMM ring test were an almost constant value. The iron loss properties of NMM ring depended strongly on power semiconductor characteristics. These results open the way to further research in low loss reduction in magnetic material core based on semiconductor characteristics.

[1] M. Kawabe, T. Nomiyama, A. Shiozaki, H. Kaihara, N. Takahashi, and M. Nakano, Behavior of minor loop and iron loss under constant voltage type PWM inverter excitation, IEEE Transactions on Magnetics, 48 (11), 3458–3461 (2012). [2] K. Fujisaki and S. Liu, Magnetic hysteresis curve influenced by power-semiconductor characteristics in pulse- width-modulation inverter, Journal of Applied Physics, 115 (17), 17A321 (2014). [3] S. Odawara, K. Fujisaki, and F. Ikeda, Proposing a numerical method for evaluating the effects of both magnetic properties and power semiconductor properties under inverter excitation, IEEE Transactions on Magnetics, 50 (11), 1–4 (2014). [4] T. Taitoda, Y. Takahashi, and K. Fujiwara, Iron loss estimation method for a general hysteresis loop with minor loops, IEEE Transactions on Magnetics, 51 (11), 1–4 (2015). [5] A. Yao, K. Tsukada, S. Odawara, K. Fujisaki, Y. Shindo, N. Yoshikawa, and T. Yoshitake, PWM inverter-excited iron loss characteristics of a reactor core, AIP Advances, 7 (5), 056618 (2017). [6] A. Boglietti, P. Ferraris, M. Lazzari, and M. Pastorelli, Influence of modulation techniques on iron losses with single phase dc/ac converters, IEEE Transactions on Magnetics, 32 (5), 4884–4886 (1996). [7] A. Boglietti, P. Ferraris, M. Lazzari, and F. Profumo, Iron losses in magnetic materials with six-step and PWM inverter supply (induction motors), IEEE Transactions on Magnetics, 27 (6), 5334–5336 (1991). [8] A. Boglietti, P. Ferraris, M. Lazzari, and M. Pastorelli, Change of the iron losses with the switching supply frequency in soft magnetic materials supplied by PWM inverter, IEEE Transactions on Magnetics, 31 (6), 4250– 4252 (1995). [9] W. A. Roshen, Magnetic losses for non-sinusoidal waveforms found in ac motors, IEEE transactions on power electronics, 21 (4), 1138–1141 (2006). [10] W. A. Roshen, A practical, accurate and very general core loss model for nonsinusoidal waveforms, IEEE Transactions on Power Electronics, 22 (1), 30–40 (2007). [11] A. Yao, T. Sugimoto, S. Odawara, and K. Fujisaki, Core losses of a permanent magnet synchronous motor with an amorphous stator core under inverter and sinusoidal excitations, AIP Advances, 8 (5), 056804 (2017). [12] A. Yao and K. Fujisaki, Iron loss characteristics under pwm inverter excitation at high ambient temperatures, The 11th International Symposium on Linear Drives for Industry Applications (LDIA2017), 1–3 (2017). [13] Y. Yoshizawa and K. Yamauchi, Fe-based soft magnetic alloys composed of ultrafine grain structure, Materials Transactions, JIM, 31 (4), 307–314 (1990). [14] N. Nishiyama, K. Tanimoto, and A. Makino, Outstanding efficiency in energy conversion for electric motors constructed by nanocrystalline soft magnetic alloy "nanomet® " cores, AIP Advances, 6 (5), 055925 (2016). [15] N. Denis, M. Inoue, K. Fujisaki, H. Itabashi, and T. Yano, Iron loss reduction of permanent magnet synchronous motor by use of stator core made of nanocrystalline magnetic material, IEEE Transactions on Magnetics, (2017). [16] A. Yao, K. Tsukada, and K. Fujisaki, Iron loss properties of an amorphous ring excited by different inverters, IEEJ Transactions on Industry Applications (submitted).
ACKNOWLEDGMENT This work was partly supported by the New Energy and Industrial Technology Development Organization (NEDO), ISIJ Research Promotion Grant 2017, the JSPS KAKENHI 16H07320, the Ministry of Education, Culture, Sports, Science and Technology Program, Japan, for private universities, and Sanken Electric Corporation.

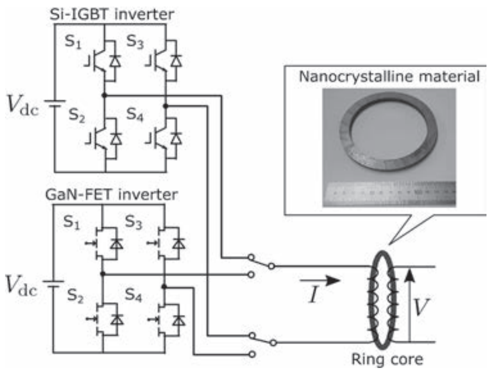

Fig. 1. Schematic of a NMM ring specimen and its measurement setup. The ring core is excited by either Si-IGBT or GaN-FET inverters.

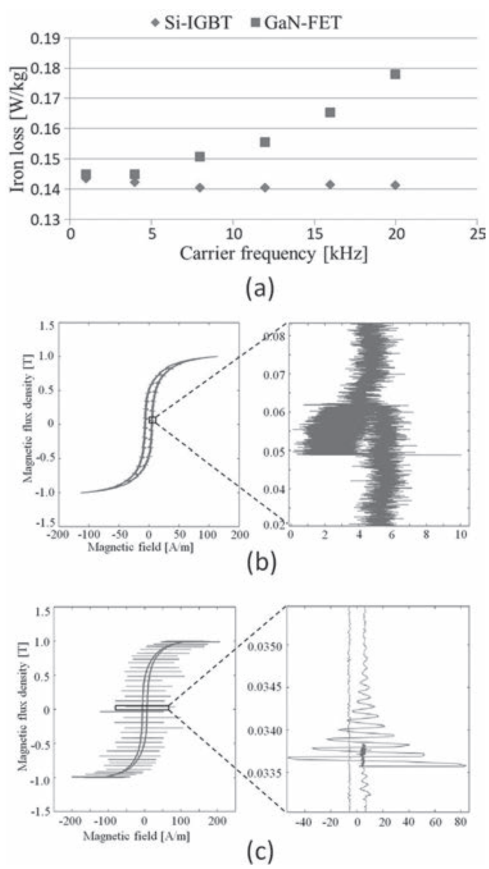

Fig. 2. (a) Iron loss properties as a function of carrier frequency. (b) Hysteresis loops of the NMM ring excited by Si-IGBT inverter (c) Hysteresis loops under GaN-FET inverter excitation.

FT-06. Analysis of Vibration of a Dual-stator Hybrid Excitation Permanent Magnet Motor for Electric Vehicles.

Y. Fan[1], Z. Wu[1] and C. Tan[1]
1. School of Electrical Engineering, Southeast University, Nanjing, China

INTRODUCTION The Permanent magnet synchronous motor (PMSM) has been broadly applied in electric vehicles due to its high efficiency, high power/torque density, low cogging torque and the ability of fault tolerance[1]. However, both in the integral-slot and fractional-slot motors, the electromagnetic vibration and noise issue, as one of the parasitic effects, has been paid much attention in low noise applications[2]. Furthermore, the vibration and noise levels have been the indexes to evaluate the performance of PMSM for electric vehicles. The conventional permanent magnet motor has the disadvantage that the excitation magnetic field can't be adjusted. Generally, the field weakening operation can be achieved by applying a flux-weakening current in the d-axis. While, the capacity of flux-weakening is limited and there is a risk of demagnetization of permanent magnets. Thus, a dual-stator hybrid excitation permanent magnet (DSHEPM) motor is proposed to realize the field regulation. The vibration of motor is attributed to the electromagnetic forces acting upon the stator and rotor, which are induced by the air-gap magnetic field[3]. Compared with the conventional permanent magnet motor, the DSHEPM motor can operate in a variety of working states, such as increasing magnetization, weakening magnetization and no excitation. Therefore, the air gap magnetic field is relatively complex. Both the electromagnetic force generated under different working states and the electromagnetic vibration characteristics caused by the electromagnetic force are different. Thus, it is necessary to analyze the vibration characteristics produced by the motor, which can provide guidance for the effective suppression of the vibration of the motor. AIR-GAP FLUX DENSITY ANALYSIS To obtain the air gap flux distribution under different operating modes of the motor, the finite element analysis model of the DSHEPM motor is established by the commercial finite element software Ansys. The rotor structure of the DSHEPM motor is composed of 12 permanent magnetic poles and 6 iron core poles. The rotor core pole is aligned with the d axis of the inner stator excitation magnetic field as the motor operates normally. The electromagnetic field can be adjusted by energizing the field winding, and the magnetic field can be enhanced or weakened by changing the direction of the excitation magnetic field. The air-gap flux distribution under different operating modes was shown in Fig. 1. In addition, the motor output torque can be adjusted by changing the q-axis component of the excitation magnetic field. Through the FFT analysis of air-gap flux density harmonics, the frequency domain characteristics of air-gap flux density harmonics can be obtained. ELECTROMAGNETIC FORCE ANALYSIS The electromagnetic forces are the main causes of the electromagnetic vibration in electric motors. As the vibration of motor is mainly delivered from the stator teeth to the case, and the tangential component of the electromagnetic force is very small compared with the radial component, thus the tangential electromagnetic force can be neglected. Based on the Maxwell stress tensor method, the radial electromagnetic force density can be calculated. The radial force density, which occurs from the air-gap magnetic field, is function of time and space. To accurately locate the dominant force harmonics which contribute most to the vibration and noise of the motor with the different excitation modes of the field windings. The 2D FFT is used to decompose electromagnetic force wave in the time domain and space domain. Fig. 2 shows the temporal and spatial decompositions of the radial electromagnetic force density of the motor at four different excitation modes. In Fig. 2 (a) (b) (c) the armature winding is open circuit. In Fig.2 (d) the armature winding and the excitation winding are powered, and the excitation winding is positive excitation. The electromagnetic force harmonics are influenced by the armature magnetic field and the excitation magnetic field. ELECTROMAGNETIC VIBRATION ANALYSIS A multi-physics model is established to analyze the vibration of the DSHEPM motor under different operation modes. The coupling considered in this model is the coupling of magnetic and vibrational systems, which is weak and unidirectional. Using the interpolation method, the electromagnetic force is transferred from electromagnetic mesh to structural mesh, and the vibration of case is calculated through the mode superposition method. The vibration displacement and velocity of the motor case are obtained, and the vibration peaks of motor are influenced by the electromagnetic force harmonics. CONCLUSION In this paper, the vibration level in dual-stator hybrid excitation permanent magnet motor with different operation modes are discussed based on the multi-physics model. The radial force is decomposed with 2D FFT to explain the vibration peaks induced by the dominant force harmonics. The study of this paper can be used to suppress the vibration and noise of the DSHEPM motor.

[1] L. Zhu, S. Z. Jiang, Z. Q. Zhu, and C. C. Chan, "Analytical modeling of open-circuit air-gap field distributions in multisegment and multilayer interior permanent-magnet machines," *IEEE Trans. Magn.*, vol. 45, no. 1, pp. 124-135, Aug. 2009. [2] F. Lin, S. Zuo, X. Wu, "Electromagnetic vibration and noise analysis of permanent magnet synchronous motor with different slot-pole combinations," TET Electric Power Applications, vol. 10, no. 9, pp. 900-908, Jul. 2016 [3] W. Ling, P. Luk, W. Fei, "Analytical investigation of sideband electromagnetic vibration in integral-slot PMSM drive with SVPWM technique," *IEEE Trans. Power Electron*., vol. 32, no. 2, pp. 4785-4795, Jun. 2017.

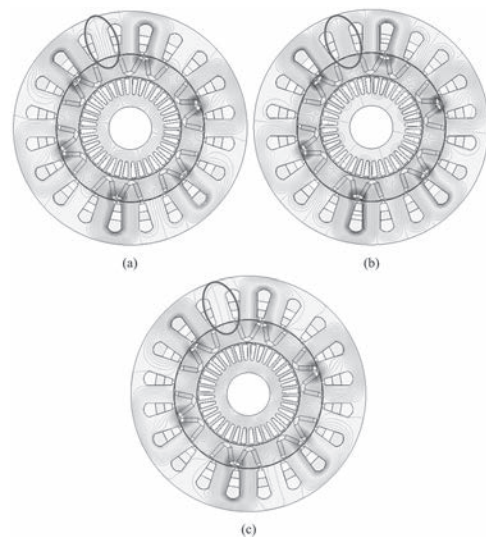

Fig. 1. Flux distributions of DSHEPM motor. (a) No excitation (b) Positive excitation (c) Negative excitation

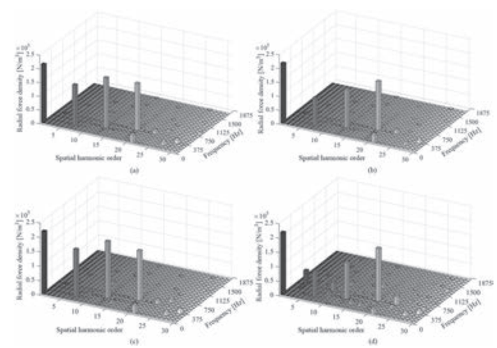

Fig. 2. The temporal and spatial decomposition of the radial electromagnetic force density (a) No excitation (b) Positive excitation (c) Negative excitation (d) Both windings powered and excitation winding positive excitation

FT-07. Thermal Effects on Magnetic Noise and Vibrations of Synchronous Motors.

I. Ibrahim[1], H. Mohammadi[1], V. Ghorbanian[1] and *D. Lowther*[1]
1. Elec and Comp Eng, McGill University, Montreal, QC, Canada

ABSTRACT This paper investigates the influence of temperature on vibrations and the acoustic field of electric machines using finite-element simulations. To predict magnetic noise, the process is multi-physical in nature. First, an electromagnetic model is simulated to calculate the magnetic pressure in the air gap as the speed and temperature of the motor changes. The magnetic forces are then loaded into the structural model to study the dynamic response of the stator. Next, this response connects to an acoustic model to translate the vibrations at the stator surface into sound. Therefore, the main contribution of this work is the inclusion of thermal effects in acoustic noise calculations. It also attempts to establish a relationship between temperature and loudness by exploring a design space of an interior permanent-magnet motor, from which new design rules may be determined.
INTRODUCTION The electric machine is one of the major contributors to noise pollution. Prolonged exposure to industrial machines without safety equipment, can pose serious health risks. Therefore, in design and operation, noise is a crucial performance index. The sources of machine noise can be grouped into four: aerodynamic, electronic, magnetic and mechanical [1]. Usually, for small and medium-sized motors (below 15kW), magnetic noise is the most essential component of the global noise [2]. Magnetic noise is caused by the presence of magnetic pressure in the air gap. The force acts on the stator tooth and cause vibratory resonances. This is what propagates in the ambient air as acoustic noise. To study acoustic noise, an understanding of the dynamic behavior of the stator is a prerequisite. This can be achieved through modal analysis. This step computes the natural frequencies of the stator and their mode shapes. Natural frequencies depend on the design parameters, material properties, DOF constraints and the fixture [3]. Heat, according to [4], is the 'biggest killer' of electric motors. Even a rise of 10 degrees C above the thermal limit of the motor can shorten its life by half [5]. Therefore, thermal effects cannot be ignored in machine performance analysis. Previous works [2], [6], [7] have extensively explored the vibro-acoustic domain of electric machines. Unfortunately, thermal effects from the acoustic perspective were not given prominence in these studies. There has been a lack of publications considering the fully coupled magneto-thermal-vibration-acoustic problem related to electrical machine design. The goal of this paper, therefore, is to consider the influence of temperature on the acoustic performance of the electric machine. Also, the variations in noise levels obtained from the simulation of a wide range of design examples for geometric variations of the motor model will be used to extract new design rules relating to the thermal-acoustic performance of the devices. In this digest, some relevant aspects of the full paper are emphasized, along with a sample case study to demonstrate the importance of the work. METHODOLOGY Infolytica's interoperable FE software MotorSolve and MagNet [8] are used to build and simulate high-fidelity electromagnetic models to extract the magnetic field solutions. Temperature-dependent BH curves are used as part of a fully coupled magnetic-thermal analysis. The radial pressure wave, P_r, at any angle,θ, along the airgap is calculated from the Maxwell stress tensor given in [2]. The magnetic forces derived a FFT decomposition of the pressure wave are mapped onto the structural mesh. The FEA solver for structural simulations NX Nastran [9] is used for modal analysis. Modal analysis is vital because it calculates the natural frequencies that resonate with the exciting forces to trigger vibrations in the stator structure. These frequencies are extracted over a range of temperatures using temperature-dependent material properties of iron and copper. This is achieved by updating the material properties at each iterative step. The vibrations are calculated by modal superposition of magnetic forces and modal parameters in the frequency domain. This is performed for several design samples of our motor model over a range of speed sweeps. Varying the rotor speed and the winding excitation frequency in a synchronous motor helps account for the electromagnetic harmonics in the vibration analysis. Finally, the vibrations data computed at the stator surface is fed into an acoustic model to estimate the sound power levels at each speed step of the sample. The Figure 1 summarizes the simulation process. PRELIMINARY RESULTS Initial results from studying one sample of a 4pole/12slot IPM motor are presented in Figure 2. In Figure 2 (a), modal analysis reveals a massive reduction in the natural frequencies at 20 degrees C and 100 degrees C. Only modes 1-6 are shown. In Figure 2 (b), the average sound pressure levels are 58.1dB and 62.8dB for 20 degrees C and 100 degrees C respectively. The variance in noise levels is substantial even though only the first 10 modes were considered, this value is expected to increase as the number of modes increases and the results will be given in the full paper. All modes within the audible frequency range (20Hz—20kHz), will be superposed in the full version. Furthermore, more design variations will be studied to extract design knowledge about the thermal effects on magnetic noise and vibrations of synchronous motors.

P. Vijayraghavan and R. Krishnan, "Noise in electric machines: A review," *IEEE Trans. Ind. Appl,* vol. 5, pp. 1007-1013, Sep./Oct. 1999. R. Islam, I. Husain, "Analytical model for predicting noise and vibration in permanent-magnet synchronous motors," *IEEE Trans. Ind. Appl,* vol. 46, no. 6, pp. 2346-2354, Dec. 2010. J. F. Gieras, C. Wang, and J. C. Lai, *Noise of Polyphase Electric Motors*, CRC Press, 2005. S. M. A. Nawazish, A. Hanif, and A. Qadeer, "Review in Thermal Effects on the Performance of Electric Motors," in *Intl. Conf. Intell. Syst. Eng.*, 2016. B. Venkataraman, B. Godsey, W. Premerlani, E. Shulman, M. Thakur, and R. Midence, "Fundamental of motor thermal model and its application in motor protection," in *Proc. 58th Annu. Conf. for Protective Relay Engineers,* pp. 127-142, Jul. 2005. C. Lin, and B. Fahimi, "Prediction of Acoustic Noise in Switched Reluctance Motor Drives," *IEEE Trans. Energy Convers.,* vol. 29, no. 1, pp. 250-258, Mar. 2014. F. L. M. Dos Santos, J. Anthonis, F. Naclerio, J. J. C. Gyselinck, H. Van der Auweraer, "Multiphysics NVH Modeling: Simulation of Switched Reluctance Motor for an Electric Vehicle," *IEEE Trans. Ind. Electron.,* vol. 61, no. 1, pp. 469-476, Jan. 2014 *MagNet&MotorSolve*. Infolytica Corp., 2017. [Online]. Available: http://infolytica.com.[Accessed: 19-Dec-2017] *NX Nastran (v.11). Siemens PLM., 2017. [Online]. Available: https://www.plm.automation.siemens.com/en/products/simcenter/nastran.[Accessed: 20-Dec-2017]*

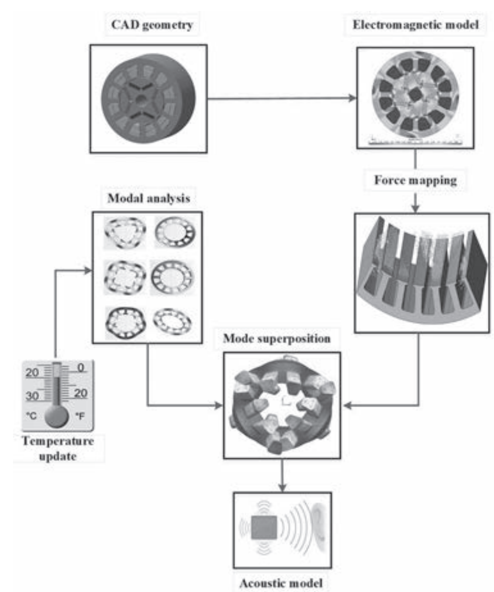

Fig. 1. Calculation flowchart of vibration and noise.

Mode	1	2	3	4	5	6
20°C [Hz]	6961	7368	9480	10260	11063	11474
100°C [Hz]	5155	5256	6511	6858	7294	7501
%Δf	25.9	28.7	31.3	33.2	34.1	34.6

(a)

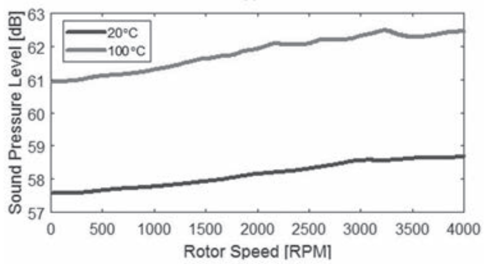

(b)

Fig. 2. Thermal effects on (a) modal analysis results, (b) noise levels.

FT-08. Improvement of efficiency and vibration noise characteristics depending on excitation waveform of a brushless DC motor.

S. Noguchi[1]
1. Motor Drive Laboratory, Tokyo City University, Setagaya-ku, Japan

I. Introduction A structure of BLDC motor is similar to PMSM, so its characteristics are different by slot combinations [1]. Especially in 10poles-12slots BLDC motor, the back EMF waveform is pretty close to sine-wave and the cogging torque is smallest than any other slot combinations. Therefore, 10poles-12slots BLDC is superior as AC servo motor by sine-wave excitation. However, using the motor as a BLDC motor by square-wave excitation leads its efficiency, torque ripple, and noise characteristics worse than sine-wave excitation. Although, it is known that adjusting excitation angle and excitation phase can make these characteristics improvements [2]-[4]. In this paper, assumes to use the 10poles-12slots motor as a BLDC motor by square-wave excitation, we examined experimentally the changes of efficiency, vibration, and noise by adjusting excitation waveform, excitation angle, and excitation phase. II. Extension of Excitation Angle in Square-wave Excitation In order to drive a BLDC motor easily, 120 degree square-wave excitation is commonly used as simple BLDC motor driving method. However, 120 degree square-wave excitation leads the motor efficiency, torque ripple, and noise characteristics worse than sine-wave excitation. Therefore, we improved the motor efficiency by extending excitation angle in a direction of ahead and advancing current phase practically. In this experiments, we extended the excitation angles from 120 degree to 135 degree, 150 degree, and 165 degree. Then we compared the motor efficiency with each excitation angles. Also in this experiments, we use 10poles-12slots BLDC motor whose output is 30W. III. Efficiency Comparison of Each Excitation Waveform In this examination, applied voltage was fixed at constant voltage when the motor drives at 2500rpm(rated speed) and 0.12Nm load(rated). Then, we compared efficiencies with each excitation waveform. Fig.1(a),(b) shows the efficiency and loss characteristics of 120degree, 135degree, 150degree, 165degree, and sine wave excitation. From fig.1(a), the maximum efficiency is 69.0% of sine-wave excitation, but the second highest efficiency is 67.6% of 150 degree square-wave excitation, and it is increased about 3% from 120 degree square-wave excitation. Same as efficiency characteristics, from loss characteristics shown in fig.1(b), the minimum loss is 11.8W of sine-wave excitation, but the second smallest loss is 13.5W of 150 degree square-wave excitation, and it is decreased from 120 degree square-wave excitation. Therefore, as with the sine-wave excitation, it was confirmed to be able to improve the efficiency by using square-wave excitation which used hall sensors and counters. IV. Torque and Noise Comparison of Each Excitation Waveform In this examination, the motor drives at 300rpm or 600rpm and 0.12Nm load(rated). Then, we compared torque and noise characteristics with each excitation waveform. Fig.2(a), (b) shows torque characteristics of 120degree excitation and 150degree excitation, and fig.2(c), (d) shows noise characteristics of 120degree excitation and 150degree excitation. From fig.2(a), (b), 150degree excitation makes current waveform similar to sine wave compare than 120degree excitation current waveform, and torque ripple rate of 150degree excitation is decreased to 57.2% from 81.7% of 120degree excitation ripple rate. Also from fig.2(a), (b), at the range of 4kHz which clearly seen as noise easily, noise level of 150degree excitation is decreased to -72dB from -66dB of 120degree excitation noise level. Therefore, it is found that torque characteristics and noise characteristics are able to improve by extension of excitation angle. V. Conclusion In this paper, it is confirmed that using 150degree excitation leads improvement of drive characteristics like efficiency, loss, vibration and noise from characteristics of 120degree excitation for BLDC motor drive. Also, in torque characteristics, it is found that applying pseudo sine-wave excitation (improvement 150 degree excitation) can further improve the torque characteristics (will be shown in full paper). Consequently, we think the 150 degree square-wave excitation is suited for easy way to improve BLDC motor drive characteristics because 150 degree excitation is able to construct easily by using hall sensors and counters.

[1]M. Yoneda, H. Dohmeki: "Novel Selection of the Slot/Pole Ratio of the PMSM for Auxiliary Automobile", 41st IAS Annual Meeting., Vol. 1, pp.8-13, 2006. [2]S. Noguchi, K. Suzuki, and H. Dohmeki, "The efficiency comparison by exciting angle of the square-wave brushless DC motor" The 23th MAGDA conference. Takamatsu, OS3-07, pp. 319-324, Dec. 2014. [3] M. Miyamasu, K. Akatsu, "Efficiency Comparison between Brushless DC Motor and Brushless AC Motor Considering Driving Method and Machine Design", Annu. Conf. IEEE Ind. Electron. Soc., Vol.37th, Vol.2, pp.1830-1835, 2011. [4]H. Jounokuchi, M. Moriyama, H. Inayama, "High efficient control of brushless motor by optimizing phase angle and conduction angle," IEEJ rotating machinary workshop material, Vol.RM-04, No.161-178, pp.27-32, 2004.

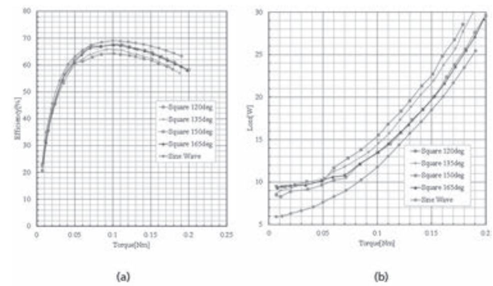

Fig. 1. The efficiency and loss characteristics of each excitation waveform. (2500rpm, 0.12Nm rated load)
(a) efficiency comparison (b)loss comparison

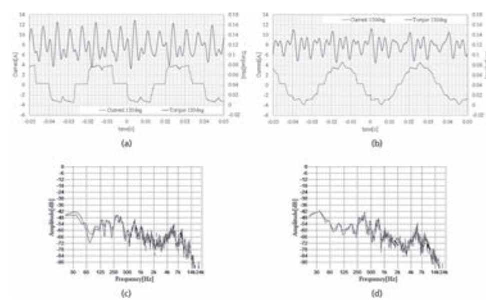

Fig. 2. Torque and noise characteristics of each excitation waveform. (a)Torque characteristics of 120degree excitation(300rpm, 0.12Nm rated load) (b)Torque characteristics of 150degree excitation(300rpm, 0.12Nm rated load) (c)Noise characteristics of 120degree excitation(600rpm, 0.12Nm rated load) (d)Noise characteristics of 150degree excitation(300rpm, 0.12Nm rated load)

FT-09. Analysis and Comparison on Motor Core Losses with Si-IGBT and SiC-MOSFET Inverter Excitations.

G. Nguyen[1], S. Odawara[2], K. Fujisaki[3], F. Iwamoto[4], T. Yamada[4] and T. Sasaya[4]
1. Research Center for Smart Vehicles, Toyota Technological Institute, Nagoya, Japan; 2. Kitami Institute of Technology, Kitami, Japan; 3. Electromagnetic Energy System Laboratory, Toyota Technological Institute, Nagoya, Japan; 4. Advanced Research and Innovation Div. 3, DENSO CORPORATION, Aichi, Japan

I. INTRODUCTION In recent years, the silicon carbide (SiC) power semiconductors have been evaluated and proven to provide the superior overall performance for power-electronic converters and electric vehicles as compared to the silicon (Si) power semiconductors [1-4]. According to [2], the SiC-MOSFET switching device was assessed to offer the better efficiency and power density for a DC-AC inverter and DC-DC converter than the Si-IGBT switching device. Most of those studies focused on evaluation of losses in inverter and power-electronic converters. However, inverter and its power devices need to be also evaluated in the core loss of interior permanent magnet synchronous motor (IPMSM), because inverters are reported to have influence on the iron core loss characteristics [5,6]. Authors in [5] showed that an inverter with low on-voltage power semiconductors has about 10-20% smaller iron loss than the one with high on-voltage power semiconductors. In our previous work [6], we carefully considered iron loss characteristics of electrical steel sheet with the Si-IGBT and SiC-MOSFET inverter excitations. The SiC-MOSFET inverter with low on-voltage has smaller iron loss than the Si-IGBT inverter with high on-voltage; this is a material evaluation of magnetic body. So as the next step, motor core loss should be carefully assesses by three-phase inverters using the Si-IGBT and SiC-MOSFET power devices. This paper investigates core loss characteristics of the IPMSM with the Si-IGBT and SiC-MOSFET inverter excitations. Models of two three-phase inverters are developed to excite the motor, where its parameters are referred from an experimental IPMSM in our laboratory. The first inverter uses the Si-IGBT devices, and the second inverter uses the SiC-MOSFET devices. The two inverters are controlled by PWM method with a low carrier frequency of 1 kHz and a fixed DC-link voltage; the motor is operated with a low rotational speed of 750 rpm and in load operational case. In computational analysis, motor core losses with the two inverters are compared and evaluated on both time and frequency domains; waveforms of stator phase voltage of the motor with the two inverters are also examined to demonstrate efficacy of the two inverters. In addition, the magnetic flux density and distribution contours of motor core losses are analyzed. II. STRUCTURES OF Si-IGBT AND SiC-MOSFET INVERTER EXCITATIONS FOR IPMSM In this research, structures of the Si-IGBT and SiC-MOSFET inverter excitations for the IPMSM are presented in Fig. 1 panels (a) and (b), respectively. Moreover, the voltage-current characteristics of the Si-IGBT, SiC-MOSFET power devices and their built-in diodes are described in Fig. 1 panel (c). In this subfigure, where the current is smaller than 100 A, the drop voltages of the SiC-MOSFET devices are noticeably smaller than the one of the Si-IGBT device. III. COMPUTATIONAL METHOD IN SIMULATION The total core loss of the IPMSM can be calculated as expressed in (1). $P_{core} = P_{3\Phi} - R_s(I_u^2 + I_v^2 + I_w^2) - P_f - \omega T$ (1) Where P_{core} : total core loss of IPMSM, $P_{3\Phi}$: total input active electrical power, R_s : phase resistance (measured in DC condition), 0.6 Ω, I_u, I_v, I_w : phase currents in rms, P_f : IPMSM and encoder mechanical losses, 0.628 W, ω : rotational speed of IPMSM, 750 rpm, T : output torque. The stator and rotor are made of a non-oriented material, named as 35H300, and the permanent magnet in the rotor is sintered NdFeB. The nominal power of the motor is 400 W. The analysis software used for simulation is JMAG. The operational parameters for the PWM inverter are as follows; the fixed DC-link voltage is V_{dc} = 100 V, the fundamental frequency is f_0 = 50 Hz, the carrier frequency is f_C = 1 kHz, the dead-time of inverter is 3500 ns, and the torque in the load test case is fixed as T = 1 Nm. IV. COMPUTATIONAL RESULTS The total core losses of IPMSM with the Si-IGBT and SiC-MOSFET inverter excitations are P_{core} = 4.1 W and 3.99 W, respectively; the reduction value of motor core loss is about 2.76%. The waveforms of phase voltage V_{un} with the two excitations are presented in Fig. 2 panel (a); and the expanded waveforms around the value of 0 V are depicted in Fig. 2 panel (b). From the time t = 0.002 s to 0.008 s, the phase voltage with Si-IGBT inverter has the bias value of -1 V to -0.7 V; meanwhile, the phase voltage with SiC-MOSFET inverter has the much smaller bias value of -0.3 V to 0.3 V, which is symmetric around the value of 0 V. This helps the SiC-MOSFET inverter can mitigate the total core loss of IPMSM. V. CONCLUSION This study has presented analysis and evaluation on total core loss of the IPMSM with the Si-IGBT and SiC-MOSFET inverter excitations. Numerical simulation results demonstrated that the SiC-MOSFET inverter excitation is slightly better in reducing the motor core loss as compared to the Si-IGBT inverter excitation. The FFT analysis of motor core loss in frequency domain also confirmed the advantages of the SiC-MOSFET inverter excitation. In future work, we are going to soon develop a testbed for evaluating the core loss of an experimental IPMSM with the SiC-MOSFET inverter. Detailed comparison between experimental results and the computational analysis in simulation will be conducted and shown in the full version of this abstract.

[1] "Application Considerations for Silicon Carbide MOSFETs," available at: https://www.wolfspeed.com/downloads/dl/file/id/821/product/194 (accessed on 5 January 2018). [2] J. Biela, M. Schweizer, S. Waffler, and J. W. Kolar, "SiC versus Si—Evaluation of Potentials for Performance Improvement of Inverter and DC–DC Converter Systems by SiC Power Semiconductors," *IEEE Trans. on Industrial Electronics*, vol. 58, no. 7, pp. 995-1006, July 2011. [3] E. Gurpinar, and A. Castellazzi, "Single-Phase T-Type Inverter Performance Benchmark Using Si IGBTs, SiC MOSFETs and GaN HEMTs," *IEEE Transactions on Power Electronics*, vol. 31, no. 10, pp. 7148-7160, October 2016. [4] X. Dinga, M. Dua, T. Zhoua, H. Guoa, C. Zhangb, and F. Chen, "Comprehensive Comparison Between Sic-Mosfets and Si-Igbts Based Electric Vehicle Traction Systems under Low Speed and Light Load," *Proceedings of The Applied Energy Symposium and Summit 2015: Low carbon cities and urban energy systems,* pp. 991-997, June 2016. [5] D. Kyamoari, and K. Fujisaki, "Influence of power semiconductor on-voltage on iron loss of inverter-fed," *Proceedings of 10th International Conference on Power Electronics and Drive Systems*, pp. 840-845, April 2013. [6] S. Odawara, D. Kayamori, and K. Fujisaki, "Iron Loss Characteristics of Electrical Steel Sheet under Inverter Excitation by Using Semiconductor with Extremely Low On-voltage Property," *IEEJ Transactions on Industry Applications*, vol. 134, no. 7, pp. 649-655, 2014 (in Japanese).

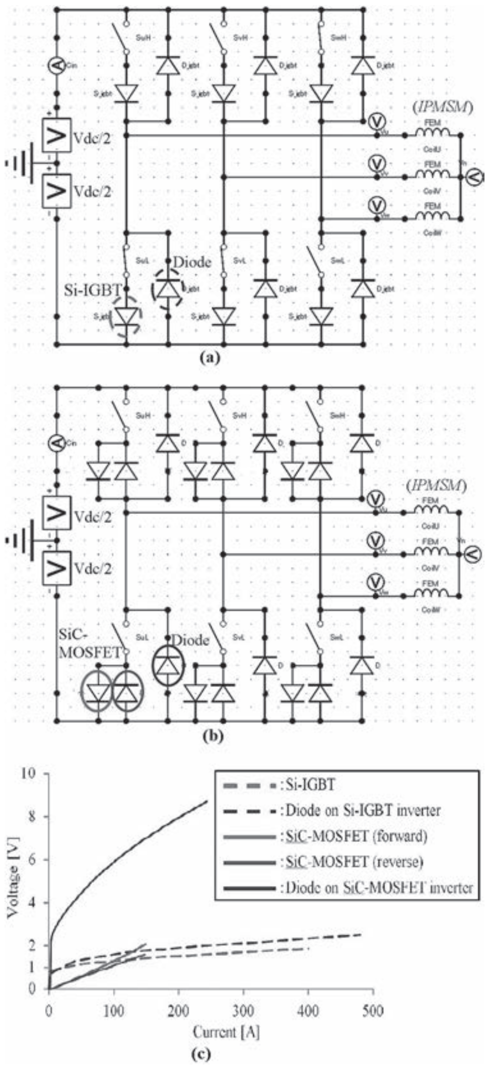

Fig. 1. (a) Structure of Si-IGBT inverter excitation; (b) Structure of SiC-MOSFET inverter excitation; (c) Characteristics of Si-IGBT and SiC-MOSFET devices.

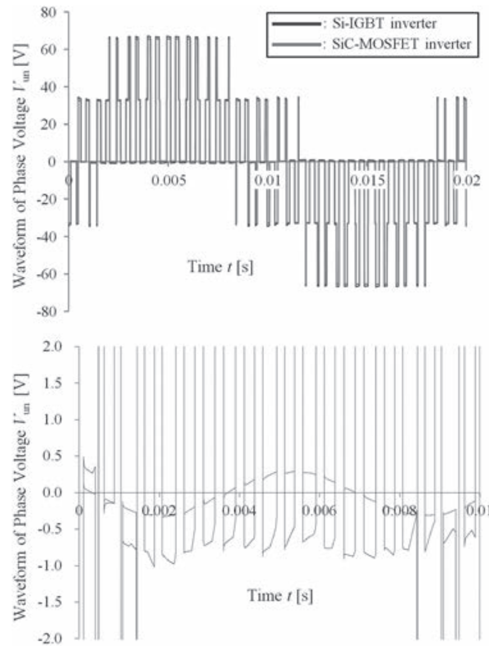

Fig. 2. (a) Waveforms of phase voltage with the two inverter excitations; (b) Expanded waveforms of phase voltage around the value of 0 V.

FT-10. Modeling Magnetic Holding Forces of Permanent Magnet Wheels.

M.D. Noh[1], J. Kim[1] and Y. Park[1]
1. Mechatronics Engineering, Chungnam Natl Univ, Daejeon, The Republic of Korea

Wall-climbing robots have been developed for many applications such as reactor-vessel inspection robot [1], welding robot [2], or pipe inspection robot [3]. To maintain the robot position on inclined surfaces, two mechanisms are typically used: pneumatic suction or magnetic wheel. For irregular ferromagnetic surfaces, magnetic wheel is the only option. The first step in designing a magnetic wheel is to determine the size of the wheel and the magnetic source. Past efforts to design a magnetic wheel include a rule-of-thumb approach [4] and finite-element analyses (FEA) [1-2]. In most cases, the rule-of-thumb method results in a bulky design due to safety factors. Finite-element calculations take very long time for design iterations or optimizations especially for the inherently three-dimensional wheel geometry. Therefore, a simple yet accurate model to estimate the holding force of a magnetic wheel would greatly expedite the design process. If necessary, complicated three-dimensional FEA can be performed at the final stage of design validations. This paper presents a model for magnetic holding forces of permanent magnet wheels. The paper also shows how to use 2D FEA for approximating the 3D analysis. Figure 1(a) shows the schematic of a magnetic wheel. It consists of two ferromagnetic disks joined by a permanent magnet (PM). To increase traction force, a ring-shaped flexible tire surrounds the PM. To model the holding force of the wheel, it is necessary to estimate the reluctances seen by PM and the magnetic flux density along the surface of the wheel. If the disk and the surface is highly permeable, it is reasonable to assume that the flux lines are perpendicular to the surfaces. Then, the shortest path from the perimeter of the disk to the holding surface would follow a circular pattern, as evident from the results of FEA shown in Figure 1(b). If the coordinate system and the parameters are defined as in Figure 1(c), the center of this circular path is on the x-axis. From the geometric relationships, the radius of the path can be expressed as $\rho=\{R(1-\cos\theta)+d\}/\sin\theta$. Thus, the differential permeance at the angle θ is (1) $dP_g = \mu_0\, w\, R\, d\theta / r\theta$ where w is the axial width of the disk. The total permeance can be obtained by integrating this differential permeance as (2) $P_g = 2 \int \mu_0\, w \sin\theta\, d\theta / \theta\, (1-\cos\theta+d/R)$ The integration is from 0 to θ_m, the angle limit where the flux density falls off below a negligible value. Once the air gap perneance is estimated, the air gap reluctance, R_g is simply its inverse. The MMF applied to the air gap between the disk and the holding surface can then be obtained as (3) $F_m = H_c\, l_m\, R_g / (R_m+R_g)$ where R_m is the PM reluctance, H_c the coercivity of PM and l_m is the axial length of PM. Using the Ampere's law, the magnetic flux density at the angle θ can be expressed as (4) $B_g = \mu_0\, F_m / r\theta$ Using the Maxwell stress tensor, the holding force can be expressed as (5) $Fy = (1/\mu_0) \int B_g^2 \cos\theta\, w\, R\, d\theta$ The integration is again from 0 to θ_m. The validation of the force model may require a 3D FEA at much computational cost. In this paper, we propose an equivalent 2D FEA that can greatly reduce the analysis time. Shown in Figure 2(a) is the 2D rendering of the magnetic wheel. The size of PM is adjusted so that it produces the same MMF. Since the ferromagnetic material (pure iron in our case) has very high permeability, it contributes little in determining the magnetic field. As long as the flux lines with respect to the holding surface are similar, the 2D FEA would produce approximately the same forces as the 3D FEA of the magnetic wheel. Figure 2(b) shows the comparison between the results of FEA and the force model proposed in this paper. The parameters of magnetic wheel are as follows: wheel radius R = 30 mm, wheel thickness w = 10 mm, PM axial length l_m = 10 mm, The coercivity of PM, H_c is 8800 kA/m (NdFeB32), PM radius is 8 mm. The integration limit in eq. (2) and (5) is 60 deg. The results display the usefulness and limitations of the force model. First, the model predicts about the same force range that FEA calculates. If needed, the material properties of core can be adjusted so that the the predictions by the model matches better with the FEA calculations. Even the current results are very useful for the initial design of the wheel, where we need to determine the size of the wheel and PM. The actual wheel would produce higher holding forces that the design predicts. Using the force model, a design optimization can be carried out, size the force variation predicted by the model matches well with FEA. The limitations of the model is that since it assumes essentially infinite permeability of core, the predictions will be erroneous when magnetic saturation occurs. Even in that case, the model can be useful, since it is possible to determine whether the wheel is saturated or not. It would help the designers to avoid highly saturated designs such as [1-2]. Acknowledgement This work was supported by the Korea Institute of Energy Technology Evaluation and Planning (KETEP) and the Ministry of Trade, Industry & Energy (MOTIE) of the Republic of Korea (No. 20171520101780)

[1] S.-C. Han, J. Kim and H.-C. Yi, "A novel design of permanent magnet wheel with induction pin for mobile robot," Int. J. Pre. Eng. Manufac., Vol. 10, pp. 143-146, 2009. [2] M. Wu, et. al., " New mechanism to pass obstacles for magnetic climbing robots with high payload, using only one motor for force-changing and wheel-lifting," Industrial Robot: An International Journal, Vol. 38, pp. 372-380, 2011. [3] F. Tache, et. al., "Magnebike: a magnetic wheeled robot with high mobility for inspecting complex-shaped structures," Journal of Field Robotics, Vol. 26, pp. 453-476, 2009. [4] Z. Xu and P. Ma, "A wall-climbing robot for labelling scale of oil tank's volume," Robotica, Vol. 20, pp. 209-212, 2002.

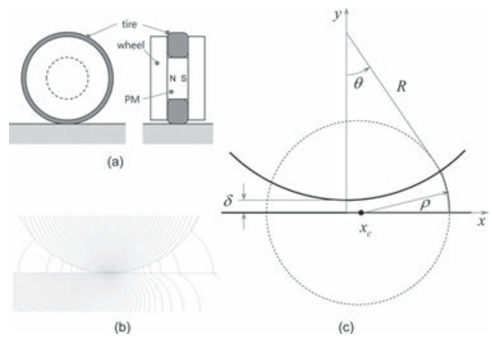

Fig. 1. (a) Schematic of magnetic wheel (b) Flux lines aross the air gap between the wheel disk and the holding surface (c) Coordinate and design parameters

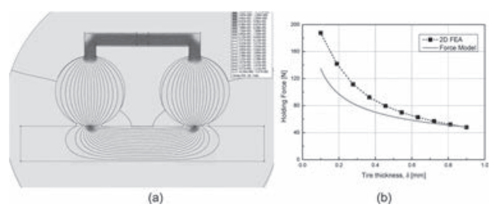

Fig. 2. (a) FEA of 2D equivalent of magnetic wheel (b) Comparison between results of FEA and force model

FT-11. Analytical Modeling and Experimental Verification for Electromagnetic Analysis of Tubular Linear Synchronous Machines with Axially Magnetized Permanent Magnets accounting for Flux-Passing Iron Pole.

K. Shin[1], H. Cho[2], D. You[3] and J. Choi[1]

1. Dept. of Electrical Engineering, Chungnam National University, Daejeon, The Republic of Korea; 2. Dept. of Electric, Electronic and Comm. Eng. Edu., Chungnam National University, Daejeon, The Republic of Korea; 3. Dept. of Fire Safety Engineering, Chungnam Provincial Cheongyang College, Chungnam, The Republic of Korea

Recently, tubular linear synchronous machines (TLSMs) are increasingly being employed in industries ranging from transportation, manufacturing, and office automation to material processing, health care, and generation systems owing to their high force density, high bandwidth, virtually zero attraction force, and the absence of end windings [1]. An axially magnetized permanent magnet (AMPM) topology can be produced at lower costs because its PMs are easily magnetized [2]. Therefore, an AMPM topology is suitable for TLSM and this paper deals with TLSM with AMPMs, as shown in Fig. 1. As is well known that the detailed knowledge of the magnetic field distribution in air gap is vitally important for design and optimization of permanent magnet machines, especially for TLSM with AMPMs. Although numerical tools, such as finite element method (FEM), are able to offer precisely field prediction, they can provide neither closed-form solution nor physical insight. Analytical methods are useful for the first evaluation of machine performances and for design optimization since continuous derivatives, which are issued from the analytical solutions, are required during most optimization methods. However, it is difficult to gain insight into the influence of the design parameters on the machine performance of TLSMs with AMPMs through analytical solutions due to magnetically complex outer PM mover structures. Therefore, this paper presents an analytical modeling and experimental study for electromagnetic analysis of a TLSM with AMPMs, accounting for the flux passing iron pole. As shown in Fig. 1(a), the analytical field domains are divided into five regions: air (I, III, V), slotless winding (II), and PMs (i) regions. The analytical model provides a description of the magnetic flux density distribution and accounts for flux passing iron pole. The governing equation in all subdomains can be solved, and the field distribution can be obtained by applying the boundary conditions on the interfaces between the subdomains [3]. The magnetic field and the electromagnetic performance obtained by the analytical method were compared with those obtained by FEM and experimental measurement of prototype (as shown in Fig. 1(b)); the comparison validates the analytical methods presented in this paper. The analytical results for the magnetic field are in good agreement with the FE analysis results, as shown in Fig. 2(a) and 2(b). For slotless coil subdomain, the computation of the flux linkage using the method of winding function theory is not suitable. Instead, the method based on the Stokes theorem using the vector potential in the slotless coil region is used. The back-EMF is calculated by the derivative of the flux linkage with respect to time. Based on analytical solution, equivalent circuit parameters, such as the back-EMF and inductance can be obtained analytically. The generating characteristics are derived with the equivalent circuit method. As shown in Fig. 2(c) ~ 2(f), the analytical predictions are compared with the measured data in order to confirm the validity of the methods proposed in this paper. The analytical solutions allow the prediction of the back-EMF, the inductance, and generating characteristics in closed forms. In turn, these facilitate the characterization of the machines and provide a basis for comparative studies, design optimization, system dynamic modeling and simulations, and control development. The analytical modeling, analysis results, discussions, and measurements of the TLSM with AMPMs will be presented in more detail in the final paper. ACKNOWLEDGMENTS This work was supported by the Basic Research Laboratory (BRL) of the National Research Foundation (NRF-2017R1A4A1015744) funded by the Korean government.

[1] B. L. J. Gysen, E. A. Lomonova, J. J. H. Paulides, A. J. A. Vandenput, "Analytical and numerical techniques for solving Laplace and Poisson equations in a tubular permanent-magnet actuator: Part I. Semi-analytical framework", IEEE Trans. Magn., vol. 44, no. 7, pp. 1751-1759, Jul. 2008. [2] M.-G. Park, J.-Y. Choi, H.-J. Shin, K. Lee, K. Hong, "Electromagnetic analysis and experimental testing of a tubular linear synchronous machine with a double-sided axially magnetized permanent magnet mover and coreless stator windings by using semi analytical techniques", IEEE Trans. Magn., vol. 50, no. 11, Nov. 2014. [3] B. L. J. Gysen, K. J. Meessen, J. J. H. Paulides, E. A. Lomonova, "General formulation of the electromagnetic field distribution in machines and devices using Fourier analysis", IEEE Trans. Magn., vol. 46, no. 1, pp. 39-52, Jan. 2010.

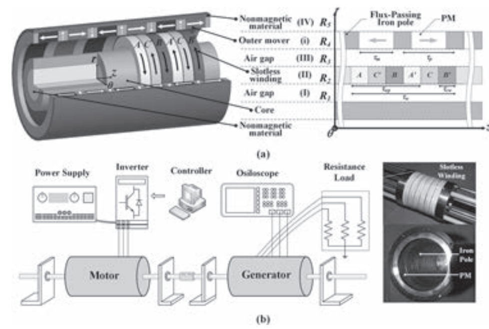

Fig. 1. Schematic of TLSM with AMPMs: (a) TLSM with the AMPM topology and an analytical model; (b) experimental setup and manufactured model.

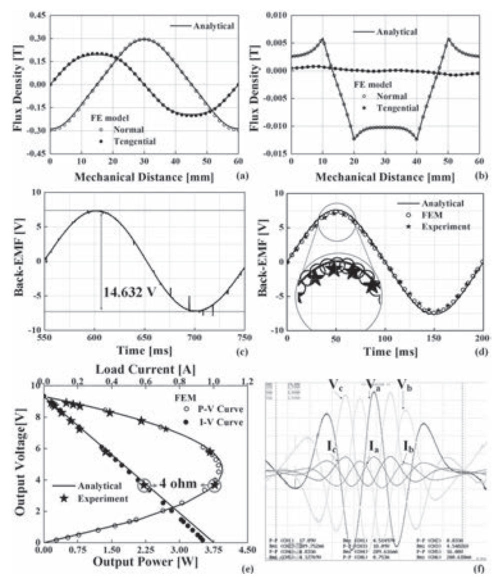

Fig. 2. Comparison among analytical, FEM and experimental results: (a) flux density due to PMs, (b) flux density due to coils, (c) measurement of back-EMF, (d) back-EMF at fixed speed, (e) Generating characteristics analysis: P–V and I–V curves with measurements, and (f) measured voltage and load current at R_{load} = 4 ohm.

FT-12. A Nonlinear Permanent Magnet Working Point Migration Model and its Application to Simulation of a Polarized Magnetic System.

J. You[1,2], X. Liao[1], R. Wang[1], *H. Liang*[1] and J. Sykulski[2]
1. School of Electrical Engineering and Automation, Harbin Institute of Technology, Harbin, China; 2. Electronics and Computer Science, University of Southampton, Southampton, United Kingdom

Abstract: The paper addresses the issue of the working point migration in non-linear permanent magnets (PM). Starting from the considerations of energy, a novel working-point migration model (WPM) is proposed which can be incorporated into a magnetic equivalent circuit (MEC). The static characteristic of a bistable polarized magnetic system (BPMS), as used in actuators, is calculated using the magnetic circuit method based on the WPM, while a finite element model (FEM) is also derived. The WPM based MEC model yields reasonable results, compared with FEM, of the latching force but with much faster calculation speeds. Furthermore, the working-point state of the PM is clearly illustrated. The test system of the BPMS prototype is established. It is shown that the WPM model provides accurate prediction of static characteristics of an electromagnetic system. I. The Model Magnets such as AlNiCo are widely used in polarized magnetic systems due to their stable structure, high Curie point, simple manufacturing and low cost. However, they suffer from what is known as the working point migration (WPM) phenomenon. Even under special conditions (e.g. coil overcurrent) a reverse magnetization will occur. The phenomenon is quite complex and there exist no reliable simulation methods. An inverse hysteresis model based on spline approximation [1] achieves good accuracy but the calculation is cumbersome. A linear approximate hysteresis model of AlNiCo [2] allowed transient calculation of a PM motor, but the model is somewhat inflexible. A hysteresis model [3] based on a support vector machine (SVM) approach used statistical learning theory and structural risk minimization principle. In this paper, a non-linear WPM model based on affine transformation is established, relying on the demagnetization curve model, the recoil line model and affine transformation hysteresis loop model. Shown in Fig. 1a, the initial working point is located at Q_0, and the working point migration can be calculated by the demagnetization curve model, depicted by the black line. If after demagnetizing the working point migrates to $Q_{1,}$ then a new working point when magnetized will follow the recoil line shown by the green line. However, assume the PM is demagnetized further to reach Q_2 below the H-axis, implying reverse magnetization. Now the working point migrates along a minor hysteresis loop, shown in blue. This migration can be calculated using an affine transformation model, where a minor hysteresis loop can be transformed from the major loop as a new demagnetization curve. By combining the demagnetization curve model and the recoil line model in the minor hysteresis loop, the resultant working point can be established. II. Application of the WPM Model to a Polarized Magnetic System The structure of the system is shown in Fig. 1b, where the top PM is AlNiCo5 and the lower is NdFeB. Soft magnetic components are made of DT4E. The working principle is described graphically with the black and red dashed lines depicting the magnetic flux of the magnets and the electromagnet, respectively. With the coil excited for forward movement, in the lower air gap the fluxes due to the PM and the electromagnet are in opposition, resulting in a decrease of the downward magnetic force. In the upper air gap, on the other hand, the two fluxes act in the same direction resulting in an increase of the upward force. Consequently, the armature is pulled up by the upward net force. Conversely, with a reverse coil current, the armature is pulled down by the downward net force. Applying the WPM model results in the equivalent magnetic circuit of Fig. 1c. Using the WPM model and previous (or initial) working point, the temporary PM working point is calculated. Then the force and branch fluxes are calculated using the equivalent magnetic circuit. Next, the temporary PM working point is fixed according to the WPM model and the branch magnetic flux. The calculating process is repeated iteratively until the final working point and the force can be calculated. A prototype was built and measurements taken. Results of the calculations and experiments are shown in Fig. 2. III. Conclusion It has been demonstrated that the magnetic circuit model based on the proposed working-point migration model enables accurate and very fast calculations of the performance – in particular the magnetic force – of a polarized magnetic system. Thanks to reasonable accuracy and short computing times, this model can be used for robust design optimization.

[1] S. E. Zirka, Y. I. Moroz, R. G. Harrison and N. Chiesa, "Inverse Hysteresis Models for Transient Simulation," in IEEE Transactions on Power Delivery, vol. 29, no. 2, pp. 552-559, April 2014. [2] C. Yu, S. Niu, S. L. Ho, W. Fu and L. Li, "Hysteresis Modeling in Transient Analysis of Electric Motors With AlNiCo Magnets," in IEEE Transactions on Magnetics, vol. 51, no. 3, pp. 1-4, March 2015. [3] S. Zhang, M. Wang, P. Zheng, G. Qiao, F. Liu and L. Gan, "An Easy-to-Implement Hysteresis Model Identification Method Based on Support Vector Regression," in IEEE Transactions on Magnetics, vol. 53, no. 11, pp. 1-4, Nov. 2017.

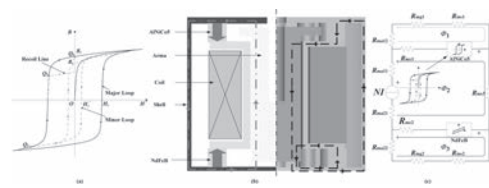

Fig. 1. (a) The nonlinear WPM model, (b) The structure and working principle of the BPMS, (c) MEC of the BPMS.

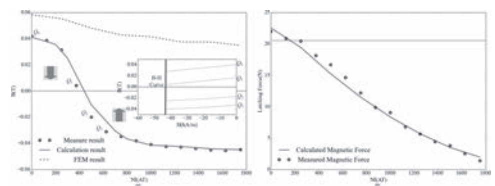

Fig. 2. Comparison of the results (a) flux density at the top of the magnet, (b) magnetic force.

FT-13. Analysis of Multi-phase and Multi-layer Factional-Slot Concentrated-Winding on PM Eddy Current Loss Considering Axial Segmentation and Load Operation.

Q. Chen[1], D. Liang[1], S. Jia[1] and X. Wan[1]
1. Xi'an Jiaotong University, Xi'an, China

1. Abstract: The PMs eddy-current loss of the 12-slot 10-pole machine with multiphase and multilayer windings are mainly investigated using the 3-D finite element analysis (FEA) in this paper. PMs eddy-current losses considering axial segmentation of PM is also analyzed. It is demonstrated that dual-three-phase four-layer (DTP-FL) winding layout has minimum value of the PM eddy current loss with segmentation number N=4. DTP-FL winding layout has smaller magnitude of high-order MMF harmonics. PMs eddy-current paths are divided into smaller loops, which increase the effective resistance. Finally, the average torque and torque ripple changing with multiphase, multilayer and axial segmentation are obtained.2. Introduction: Surface-mounted permanent magnet synchronous machine (SPMSM) with fractional-slot concentrated-winding (FSCW) has many attractive advantages, which can reduce the magnitude of the high-order harmonic potential, tooth harmonic potential and pulsating magnetic field. However, FSCW of SPMSM includes a large amounts of the magnetomotive force (MMF) high-order harmonics, which induce the eddy-current losses in the permanent magnets (PMs). Therefore, it is necessary for high frequency applications to investigate the multiphase and multilayer winding in order to analyse their harmonic distribution and decrease the eddy current losses in the PMs to avoid its demagnetization. A. Masmoudi et al [1] considered the impact of the axial and circumferential segmentation of the surface mounted 12-slot 10pole PM ma-chine on PM eddy current loss by 3-D finite element analysis. A comparative studies are made considering the results yielded by 2-D and 3-D FEA and their analytical model with and without considering the end effect. G. Choi et al [2] presented a new method by introducing flux barriers into the rotor back in order to reduce the rotor eddy current losses for the FSCW of PMSM with single layer layout. C.F.Wang et al [3] comparatively analysed sur-face mounted PM (SPM) and interior PM (IPM) rotor eddy current loss. The influence of the ro-tor protecting sleeve material and thickness, axi-al segmental sleeves, and short circuit rings around each magnet are particularly investigated. W. Jara et al [4] presented a novel interior axial flux PMSM by introducing steel lamination and PM circumferential segmentation. PM eddy cur-rent losses reduce obviously with steel lamination thickness and segmentation number in circumferential direction.3. Target Models Stator winding layout of SPMSM are general-ly classified into several categories as shown in Fig.1 stator (a) three-phase single-layer (TP-SL) winding layout ; stator (b) three-phase double-layer (TP-DL) winding layout ; stator (c) dual-three-phase double-layer (DTP-DL) winding layout; stator (d) three-phase four-layer (TP-FL) winding layout; stator (e) dual-three-phase double-layer (DTP-DL) winding layout. Rotor adopts surface-mounted structure, and axial segmentation of PM is shown in Fig.1.rotor (a, b, c, d). The stator outer diameter is 186 mm, the stator inner diameter is 130mm and the stack lengths in axial direction is 124 mm for the SPMSM. The remanence, relative permeability and conductivity of PM are 1.25T, 1.05 and 6.67e5 (Simens/m) respectively. 4. Results Eddy current loss in PMs for different segments number in axial direction and winding layout are different under load condition. It because that different winding layout have different winding coefficient and harmonic MMF, which is significantly affect PM eddy current loss. The loss in PMs can be calculated from the eddy current density integral by considering the effects of eddy currents in the 3-D transient magnetic field analysis as shown in Fig.2 (a, b, c, d). Winding MMF harmonic amplitude of five winding layout for 12-slot 10-pole is shown in Fig.2.(e). For example, PM eddy current losses of the DTP-FL winding layout is obtained in two electric cycle, in Fig.2 (f). A general trend of the PM eddy current loss reduce obviously with axial segmentation number increasing based on the analysis above mentioned five winding layout in Fig.2(g). However, PM eddy current loss of two segments is greater than that of the unsegmented PM from TP-SL to TP-FL winding layout. Eddy current density of two segments PM are also greater than that of unsegmented PM. Therefore, PM segmentation should avoid this segment number. PM eddy current loss have downward trend for the specified segmentation number from TP-SL to DTP-FL in sequence, similarly, PM losses reduce with segmentation number increasing, which are shown in Fig.13. 5. Conclusion The paper established a 3-D SPMSM model that takes the multiphase winding, multilayer winding and PM axial segmentation into ac-count dedicated to the analysis of the eddy cur-rent loss in PMs using the 3-D FEA. It has been found that DTP-FL winding layout has mini-mum value of the PM eddy current loss for the specified segmentation number. When axial segmentation number is four, PM eddy current loss is reduced to 74.2W. Finally, the average torque and torque ripple changing with multiphase, multi-layer and axial segmentation are analyzed. Although DTP-FL has small PM losses, a part of average torque is sacrificed compared with other winding layout.

[1] A. Masmoudi and A. Masmoudi, "3-D analytical model with the end effect dedicated to the prediction of PM eddy-current loss in FSPMMs," IEEE Trans. Magn., vol. 51, no. 4, Apr 2015, Art. ID 8103711. [2] G. Choi and T. M. Jahns, "Reduction of eddy-current losses in fractional-slot concentrated-winding synchronous PM machines," IEEE Trans. Magn., vol. 52, no. 7, May 2016, Art. ID 8105904. [3] C. F. Wang, M. J. Jin and J. X. Shen et al, "A permanent magnet integrated starter generator for electric vehicle onboard range extender application," IEEE Trans. Magn., vol. 48, no. 4, pp.1625-1628, Apr 2012. [4] W. Jara, P. Lindh and J. A. Tapia et al, "Rotor eddy-current losses reduction in an axial flux permanent-magnet machine, " IEEE Trans. Ind. Electron., vol. 53, no. 3, pp. 4729–4736, Aug. 2016.

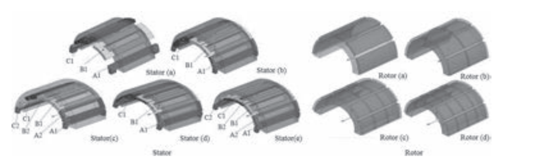

Fig. 1. Multiphase and mulilayer model of SPMSM

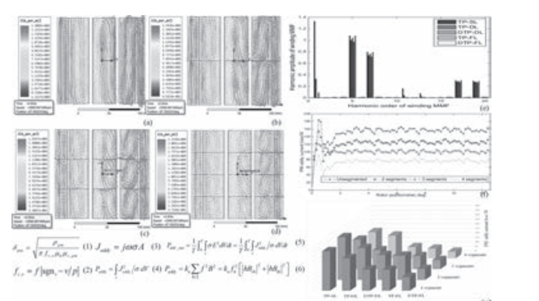

Fig. 2. Eddy-current density,eddy-current loss and multiphase-multilayer winding

FT-14. A study on the analytical methods for demagnetization characteristics of FEM-based permanent magnet synchronous motor.

G. Jeong[1], *D. Jung*[1], H. Kim[1] and W. Kim[2]
1. Electrical Engineering, Hanyang university, Seoul, The Republic of Korea; 2. Gachon University, Seognam-si, The Republic of Korea

1.Introduction Interior permanent magnet synchronous motor, used in this study is a high-capacity traction motor for railway veicles and has a totally-enclosed structure to prevent dust, foreign materials, etc during operation as it is placed at the bottom of railway vehicles [1]. This totally-enclosed structure is vulnerable to temperature because the cycle of heat is not good. The high-capacity traction motor for railway vehicles requires a high weight to output ratio and to increase the weight to output ratio, rare-earth neodymium permanent magnet with high energy density should be used, but are characterized by high-temperature demagnetization [2]. Also, high current may flow due to failure in power converter and it may produce a big reverse magnetic field and be demagnetized by the reverse magnetic field. Demagnetization characteristics caused by such high- temperature demagnetization and reverse magnetization are characterized by permanent demagnetization as a new demagnetization curve called as recoil line is generated. Therefore, the purpose of this study is to propose a demagnetization analytical methods considering recoil line based on FEM. It sets up an analysis scenario to drive motor based on demagnetization characteristics by considering recoil line and predicts the demagnetization of permanent magnet. And it examines the effects of output based on predicted demagnetization characteristics. Through the performance test, the proposed analytical methods is proved. 2.IPMSM for traction railway vehicles a.IPMSM design model Fig. 1 shows the IPMSM designed to the design point and winding is selected as distributed winding by considering sinusoidal gap flux density, and the numb of slot per pole/phase is selected as 3 by considering the effects of harmonic wave and then finally the combination of 6 poles and 54 slots is selected. 3.Analytical methods for demagnetization characteristics of FEM-based a.Demagnetization characteristics analysis considering recoil line Fig. 2 shows analysis scenario. Analysis was performed per cycle (for three cycles in total). Section T1 was for no-load driving, section T2 for 100% or 200% load, and section T3 for counter electromotive force demagnetized during no-load. 200% load is a condition for reverse magnetic field. Temperature is a totally-enclosed condition vulnerable to heat and 180°c is set as the worst condition for insulation design. Fig. 3 is a result of demagnetization analysis of N38UH, and the peak value is reduced by approx. 2.7% in case of 100% load and by approx. 53% in case of 200% load. In conclusion, much of permanent magnet was demagnetized at the temperature of 180°c in case of 200% load. The result was obtained that N38UH has a big influence on the performance of electric motor due to high temperature and reverse magnetic field. Therefore, materials are changed to obtain the reliability of rotor prior to reanalysis. Material is selected as Sm2Co17 that is lower than residual magnetic flux density of N38UH, but strong in high temperature. Fig. 4 is an analysis result, and the peak value was reduced by approx. 0.4% in case of 100% load and by approx. 1.3% in case of 200% load. Therefore, the reliability of rotor was obtained because the peak value of the demagnetized counter electromotive force was reduced by approx. 1.3% max. 4.Final prototype model a.Test product and performance test As speed-specific test, performance test was conducted up to 3,200 rpm within the allowable range because high-velocity section test is inevitable due to lack of IGBT switch capacity of power converter that is held and it can be seen in Fig. 5. Fig. 5 compares speed-torque characteristics between performance test and analysis result of IPMSM and the errors are 0.22% min. and 5.75% max. The reason why such an error occurs is that error factor increases because in case of analysis using the electromagnetic field finite element method, it does not consider machine loss and stray load loss and in case of performance test, machine losses such as frictional loss and wind loss gradually increases with the increasing speed. 5.Conclusion This study examined the study of analytical methods for demagnetization characteristics of FEM-based permanent magnet synchronous motor. The high-capacity interior permanent magnet synchronous motor for traction railway vehicles required the weight to output ratio greatly and used neodymium permanent magnet with high energy density. However, it had a disadvantage in that it was vulnerable to high temperature and might cause reverse magnetic field because high current might flow due to failure in power converter. In this case, neodymium permanent magnet may be permanently demagnetized by high temperature and reverse magnetic field. Therefore, this study proposes how to analyze the demagnetization characteristics by considering recoil line FEM-based, carries out an analysis, and conducts design to obtain the reliability of rotor. By using this proposed method, the reliability of rotor was obtained, test prototype was manufactured, and the validity of this study was verified through performance test.

[1] C.B. Park, J.H. Kim, J.H. Lee, "Thermal Characteristic Analysis of IPMSM for Traction Considering a Driving Pattern of Urban Railway Vehicles", *The transactions of the Korean Institute of Electrical Engineers 63(3),* pp. 431-436, 2014. [2] Ki-Doek Lee, Hyung-Woo Lee, Ju Lee, Won-Ho Kim, "Analysis of Motor Performance According to the Inductance Design of IPMSM", *IEEE Trans on Magnetics*, Vol. 51, No. 3. Article. 8201204, 2015.

Fig. 1. IPMSM model for traction railway vehicles

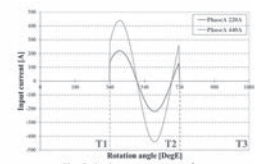

Fig. 2. A-phase current waveform

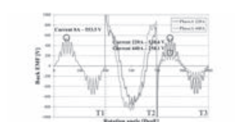

Fig. 3. Demagnetization analysis result of N38UH (220A, 440A, 180℃)

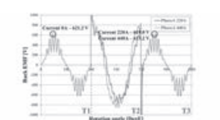

Fig. 4. Demagnetization analysis result of Sm2Co17 (220A, 440A, 180℃)

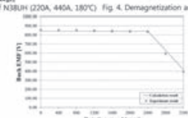

Fig. 5. Comparison of torque characteristic between performance test and analysis result

FT-15. Determination of Solenoid Coil Size for Resonance-Based Magnetically Coupled Wireless Power Transfer with Rated Distance.

H. Song[1] and Q. Xu[1]

1. Key Laboratory of Image Processing and Intelligent Control of Education Ministry, Department of Control Science and Engineering, Huazhong University of Science and Technology, Wuhan, China

ABSTRACT In this paper, the relationship between the distance with the best efficiency and the size of the coil for WiTricity system has been investigated. An equation with the coil radius and transmission distance is derived by lumped circuit theory and empirical parameter formulas. It shows a good agreement among our numeric results, finite element simulations, and experimental data. INTRODUCTION Recently, several wireless power transfer (WPT) techniques have been investigated. Microwave power transfer systems are able to transmit power with an efficiency of over 90%. But they are limited by the need for high alignment. Inductive coupling techniques are extensively used in the near-field applications. Though many novel smartphones have already featured inductive charging, these products still suffer from the distance restrictions. In 2007, MIT researchers proposed a new WPT technique called 'WiTricity' using strongly coupled magnetic resonances [1]. Coupled-mode theory and lumped circuit theory are the most popular methods used by researchers to analyze the system and optimize the designs [1, 2]. It has been proved that these two theories can be consistent with each other [3]. Many efforts have been made to optimize the coil design and to determine the relations between system efficiency and different variables [4]-[7]. However, the relation between transmission distance and the smallest coil size with the best power transfer is still unclear. Using lumped circuit theory and empirical formulas, this paper answers this question and the results are in agreement with simulations and experiments. METHODOLOGY In this paper, the system is modeled by lumped circuit theory. Firstly, each part of the circuit can be modeled as a combination of resistance, inductance, and capacitance. Secondly, the mutual inductions between the coils need to be considered. Since the couplings between any two distant coils are too weak to have an effect on the circuit, we considered only three pairs of coils. The coupling coefficients between drive loop, Tx coil, Rx coil and load loop are represented as k_{12}, k_{23}, and k_{34} respectively. Thirdly, four equations can be obtained by Kirchhoff's voltage law. This WiTricity system can be considered as a two-port network (that one port fed by the source as the input, and the other feeding the load as the output). The power transfer can be represented in terms of linear magnitude scattering parameters ($|S_{21}|$). These four equations can be solved simultaneously for the voltage across the load resistance that can be used to compute the equivalent S_{21} scattering parameter when the resistance of the load and the source are well matched [8, 9]. When we plot S_{21} magnitude as the function of frequency and the transmitter-to-receiver coupling coefficient k_{23}, frequency splitting can be clearly observed as the value of k_{23} is increased. Frequency splitting occurs when the system works in the over coupled regime and the two coils are strongly coupled. The two frequencies will converge at f_0 which is the self-resonant frequency of the coil when the system works at the "critically coupled" state corresponding to a critical coupling coefficient k_{cr}. In practical situations, the working frequency of a system is usually fixed so that the self-resonant frequency f_0 is often chosen to be the frequency of the source. Therefore, the distance between Tx coil and Rx coil corresponding to the critical coupling coefficient is the most suitable transmission distance for a given system. It is worth noting that only parameter k_{23} is related to the distance d between transmitter and receiver coils. Other parameters including resistance, inductance, and capacitance are related to the material and the structure of coil. To determine the relation between the transmission distance and the radius of the coil, the parameters a and N are treated as constants. Using empirical formulas [10, 11], the circuit parameters can be evaluated by the coil's radius and then be substituted into the equations. An equation with d and r can be obtained from the simultaneous equations, wherefore the optimal coil size can be computed with rated distance. SIMULATION AND EXPERIMENT The High Frequency Structure Simulator (HFSS) software (ANSYS Corporation, Canonsburg, PA, USA) is used to simulate the S_{21} parameter for different coil radius and at different distances. The critical transmission distance was measured for different coil sizes. In Fig. 1, it shows that the experimental results well meet the numerical solution from the derived equation. DISCUSSION This paper investigates the key question for coil designing that what is the smallest coil size with the best efficiency when the working distance is given. Lumped circuit theory and empirical formulas are used to establish a relation between the transmission distance and the critical coil radius. This result shows great agreement among numeric solutions, finite element simulations, and experimental data. Though our work only investigates the helix structure coils, the method using lumped circuit theory and empirical formulas likely extends to coils with other structures such as planar spiral coils. Meanwhile, more experiments remain to be done.

[1] A. Kurs, A. Karalis, R. Moffatt, J. D. Joannopoulos, P. Fisher, and M. Soljacic, "Wireless power transfer via strongly coupled magnetic resonances," Science, vol. 317, no. 5834, pp. 83–86, Jul. 2007. [2] A. Sample, D. Meyer and J. Smith, "Analysis, Experimental Results, and Range Adaptation of Magnetically Coupled Resonators for Wireless Power Transfer, " Industrial Electronics, IEEE, vol. 58, no. 2, pp. 544-554, Mar. 2011. [3] E. Bou, E. Alarcon, J. Gutierrez, "A comparison of analytical models for resonant inductive coupling wireless power transfer," in "PIERS 2012: Progress in Electromagnetics Research Symposium: proceedings: Moscow, Russia: August 19-23, 2012". Moscow: The Electromagnetics Academy, 2012, pp. 689-693. [4] C. Zhu, K. Liu, C. Yu, R. Ma, and H. Cheng, "Simulation and experimental analysis on wireless energy transfer based on magnetic resonances," in Proc. IEEE VPPC, Sep. 2008, pp. 1–4. [5] Z. N. Low, R. Chinga, R. Tseng, and J. Lin, "Design and test of a high-power high-efficiency loosely coupled planar wireless power transfer system," IEEE Trans. Ind. Electron., vol. 56, no. 5, pp. 1801–1812, May 2009. [6] Y.-H. Kim, S.-Y. Kang, M.-L. Lee, B.-G. Yu, and T. Zyung, "Optimization of wireless power transmission through resonant coupling," in Proc. CPE, May 2009, pp. 426–431. [7] A. K. RamRakhyani, S. Mirabbasi and M. Chiao, "Design and Optimization of Resonance-Based Efficient Wireless Power Delivery Systems for Biomedical Implants," in IEEE Transactions on Biomedical Circuits and Systems, vol. 5, no. 1, pp. 48-63, Feb. 2011. [8] R. Mongia, RF and Microwave Coupled-Line Circuits. Norwood, MA: Artech House, 2007. [9] J. Chen, Feedback Networks: Theory and Circuit Application. Singapore: World Scientific, 2007. [10] C. Zierhofer and E. Hochmair, "Geometric approach for coupling enhancement of magnetically coupled coils," IEEE Trans. Biomed. Eng., vol. 43, no. 7, pp. 708–714, Jul. 1996. [11] E. Rosa and L. Cohen, "Formulæ and tables for the calculation of mutual and self-inductance," Government Printing Office, Washington, DC, 1908

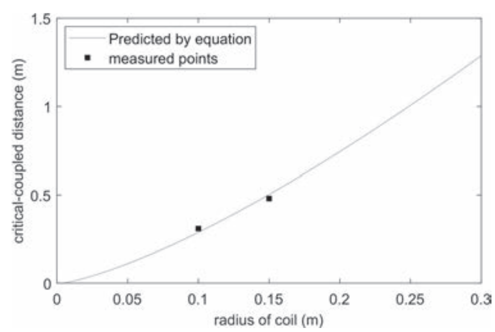

Fig. 1. Relation between critical-coupled transmission distance and coil radius predicted by the equation, along with experimentally measured points. (All other parameters are given as follows: f=13.56MHz, a=0.0015m, N=10, R_1=50Ω, M_{12}=0.637μH.)

FT-16. Adagrad Algorithm based Optimal Slot-pole Selection for Reduced Inductance Harmonics in Concentrated Wound Multiphase PMSM.

H. Dhulipati[1], E. Ghosh[1], S. Mukundan[1], J. Tjong[1] and N. C. Kar[1]
1. University of Windsor, Windsor, ON, Canada

Motivation: Fractional slot concentrated windings (FSCW) permanent magnet synchronous machines (PMSM) have high content of space harmonics in the magnetomotive force (MMF) due to which the harmonic inductance is much larger than the magnetizing inductance [1]. These inductance harmonics lead to high torque ripple and low power factor. In case of FSCW, the coils are full pitched and cannot be chorded like in distributed windings to reduce inductance harmonics and also a suitable rotor structure have small impact on reduction of these harmonics. However, the space harmonic content in the FSCW PMSM vary significantly with the choice of slot-pole combination. Thus, the inductance harmonics can be modeled and minimized using an optimal choice of machine phases (m), stator slot numbers (S) and rotor poles (P). *State of the art*: [2] has presented the selection of slot, pole and phase numbers for reducing harmonic leakage inductance specifically for single layer CW PMSM. In [3], a detailed procedure for slot-pole selection based on inductances for single and double layer windings are provided. However, these are restricted for odd phase numbers and the selection process is time consuming. In this paper, the impact of winding layers, phase belt, slots, poles, and phase numbers on inductance harmonics has been studied. Further, an Adapative gradient (Adagrad) algorithm based approach is implemented to optimally select these parameters with little prior knowledge about the structural data. *Methodology*: MMF for a FSCW PMSM can be analyzed using stator slot star approach [3] or winding function theory [4]. In this paper, winding function method has been adapted to calculate the harmonic winding factors in the MMF and using this, the inductance harmonics are computed. Adagrad algorithm shown in Fig. 1(a) is implemented for optimally selecting slot, pole and phase numbers. This algorithm is a stochastic gradient descent with varying learning rate for every parameter unlike the standard algorithms that gives one global learning rate. Learning rate determines the size of steps the algorithm takes to reach a local minimum [5]. Adagrad algorithm performs larger updates for infrequent data sets and smaller updates for frequent parameters. This feature is well suited for sparse data such as large set of varying slot, pole and phase numbers. Initially, input data sets for slot, pole and phase numbers are provided as shown in step 1 for i number of iterations. Based on denominator of slot per pole per phase (spp), a space harmonic range (h) is defined for calculating the winding factor harmonics as in step 2. The phase belt (α) for a particular spp is calculated as in step 3. Further, using the values of phase belt and space harmonic range, the harmonic winding factors for single layer and double layer winding configurations are calculated using (1) and (2) respectively. The objective function (f) in step 4, which is to be minimized, is described in terms of inductance harmonic coefficient (ϕ) and harmonic winding factors for single and double layer configurations. In order to comprehensively obtain the slot-pole combination, it has been assumed that the inner stator diameter (D_{in}), air-gap length (l_g), stack length (L_{st}) and number of turns per coil (N_c) are one per unit for all the FSCW PMSM. *Results*: The best solution sets obtained from adagrad algorithm for all the phase numbers are shown in Fig 1(b) for double layer winding configuration. A sample solution set for three and six-phase FSCW PMSM with double layer winding configuration having least inductance harmonic coefficients is chosen from the solution sets and is presented in Fig. 2(a). Electromagnetic models for these solution sets are developed and the self-inductance harmonics obtained from FEA for 3- and 6-phase configurations are shown in Figs. 2(b) and (c) respectively. It has been observed that the self-inductance harmonic trend obtained from FEA and the proposed algorithm are in close agreement. Detailed modelling of self and mutual inductance harmonics, validation of best solution sets obtained for all the phase numbers with single layer and double layer winding configurations and analysis of MMF harmonics for these solutions will be provided in full paper.

[1] G. Dajaku, W. Xie, and D. Gerling, "Reduction of low space harmonics for the fractional slot concentrated windings using a novel stator design," *IEEE Trans. Magn.*, vol. 50, no. 5, 2014. [2] A. J. Mitcham, G. Antonopoulos and J. J. A. Cullen, "Favourable slot and pole number combinations for fault-tolerant PM machines," *IEE Proc. Electr. Power Appl.*, vol. 151, no. 5, pp. 520-525, 2004. [3] N. Bianchi and M. Dai Pre, "Use of the star of slots in designing fractional-slot single-layer synchronous motors", *IEE Proc. Electr. Power Appl*., vol.153, no. 3, pp. 459–466, 2006. [4] T. A. Lipo, *Introduction to AC Machine Design*, 3rd ed. Madison, WI, USA: Univ. Wisconsin–Madison, pp. 65, 70, 79–80, 2009. [5] A. T. Hadgu, A. Nigam and E. Diaz-Aviles, "Large-scale learning with Adagrad on Spark," *IEEE International Conference on Big Data,* Santa Clara, CA, pp. 2828-2830, 2015.

ALGORITHM:

Step 1: Define training set for 1<*i*<*n*
$w_i \in \{m_i, S_i, P_i\} \in R^d$
$m_i = \{3,4,5,6,9\}$
$S_i, P_i \in 2k, k = 1,2,\ldots 25$

Step 2: Generate harmonic range for winding factor
$spp = S_i / P_i m_i = a/b$
$\left.\begin{array}{l} b: odd \\ h = \pm P_i/b\,(2m_i k+1) \\ b: even \\ h = \pm P_i/b\,(2m_i k+2) \end{array}\right\} k = 0,1,2,\ldots$

Step 3: Calculate phase belt
$if\ S_i = (2k \pm 1)m_i : k = 0,1,2..$
$\alpha_i = 360/m_i$
$else$
$\alpha_i = 180/m_i$

Step 4: Define objective function
$\varphi = 1.52e-06\left(N_c^2 D_{in} L_{st} / g_0 P_i\right)$

$$\left.\begin{array}{l} f_1(w_i) = \varphi/i \sum_{i=1}^{n} K_{wh\_SL}(w_i) \\ K_{wh\_SL}(w_i) = \sum_{h=1}^{\infty} \dfrac{\sinh \alpha_i}{2spp\,\sin\left(h\alpha_i / 2spp\right)} \end{array}\right\} (1)$$

$$\left.\begin{array}{l} f_2(w_i) = \varphi/i \sum_{i=1}^{n} K_{wh\_DL}(w_i) \\ K_{wh\_DL}(w_i) = K_{wh\_SL}(w_i) \sum_{h=1}^{\infty} \cos\left(h\alpha_i / 2P_i spp\right) \end{array}\right\} (2)$$

Step 5: Initialize learning rate >0, weights w_{ij}=0 for iterations i
Step 6: Compute, aggregate and update gradient, $g_{t,i}^2 = \sum_{t'=1}^{t} g_{t',i}^2$
Step 7: Update weights,
$w_{t+1,i} = w_{t,i} - \dfrac{\eta_0}{\beta + \sqrt{\sum_{i=1}^{t} g_{t,i}^2}} g_{t,i}$
Step 8: Repeat Step 5-7 for 1<t<*i*+1;
Step 9: Return *w*

(a)

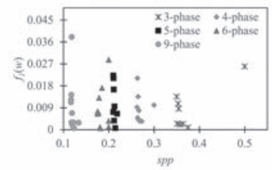

(b)

Fig.1. Adagrad algorithm procedure and the outputs obtained. (a) Detailed proposed methodology for optimal selection of slots, poles and phase numbers for FSCW PMSM using adagrad algorithm. (b) Best solution sets satisfying the objective function for varying *spp* for all the phase numbers in double layer FSCW PMSM.

Three phase PMSM				
SPC	Poles	Slots	α	φ
#1	16	18	60	0.0023
#2	28	30	120	0.0053
#3	22	24	60	0.0079
Six phase PMSM				
#1	28	30	30	0.0025
#2	22	24	30	0.0033
#3	30	36	30	0.0064

(a)

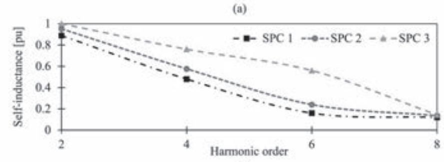

(b)

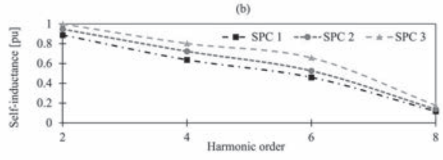

(c)

Fig.2. Validation of sample set of best solutions of SPC obtained from Adagrad algorithm using FEA. (a) Sample of best SPC for three and six phase configurations for double layer FSCW PMSM. (b) Validation of self-inductance harmonics for three phase sample slot-pole using FEA. (c) Validation of self-inductance harmonics for six phase sample slot-pole using FEA.

THURSDAY AFTERNOON, 26 APRIL 2018 SIMPOR/ROSELLE BALLROOM, 1:30 TO 4:30

Session FU
MODELLING OF MACHINES III
(Poster Session)

Johannes Paulides, Chair
AE-Group, Sprang-Capelle, Netherlands

FU-01. Performance Analysis of Squirrel Cage Induction Motors under Broken Rotor Bar and Stator Interturn Fault Conditions Using Analytical Modeling.

M. Ojaghi[1], M. Sabouri[1] and J. Faiz[2]

1. Electrical Engineering, University of Zanjan, Zanjan, The Islamic Republic of Iran; 2. University of Tehran, Tehran, The Islamic Republic of Iran

I.INTRODUCTION Three phase squirrel cage induction motors (SCIMs) have found wide applications in industry. Condition monitoring for early detection of the faults in the SCIMs can involve many advantages including: - Preventing the motor from major damages and the related costly and long-term repairs. - Avoiding unexpected stop of the production line. - Reducing wasted products. Alerting the incipient fault type and extent can increase the benefits attained from using the condition monitoring systems. Among the SCIM faults are the stator winding interturn (SWI) short-circuit fault and the broken rotor bar (BRB) fault. These faults have various effects on the motor performance and may be rooted in each other, so, they may be present at the same time in a SCIM [1]. This paper applies multiple coupled circuit modeling (MCCM) along with the modified winding function theory to achieve an analytic model for the SCIMs under the SWI and BRB faults presenting simultaneously or individually with variable degrees. The magnetic saturation effect is included in the model by applying appropriate air gap function. Simulation results show that the well-known indices for the BRB fault in the stator current spectrum are also produced by the SWI fault. Analytical study approves the simulation results. This fact may cause the condition monitoring systems alarming presence of BRB fault instead of SWI fault or vice-versa. How to discriminate between the faults is the other aim of this paper. II.SCIM Model with SWI and BRB Faults MCCM can be applied to model SCIMs under the SWI faults. For this purpose, the shorted turns of the faulty phase in the stator are considered as the 4-th winding of the stator whose terminals have been shorted. Differential voltage equation is written for the 4-th winding, too, and added to the set of differential equations governing MCCM of the SCIM [2]. Assuming the shorted turns to be in the same coil of the stator winding, the model can be made flexible to encounter variable number of shorted turns, i.e. the SWI fault severity. By the event of breaking any bar of the rotor, its current diminishes to zero. To model this faulty condition, the resistance of the broken bar can be increased sufficiently in the model. This way, the faulty condition is introduced to the model without changing the number of the rotor meshes, and this approach facilitates flexible modeling with variable number of the broken rotor bars. The proposed SWI fault and BRB fault modeling techniques can be applied at the same time to achieve a flexible model for the mixed fault condition. When simulation, the faults severities, i.e. the number of the broken rotor bars and the number of the shorted stator turns, should be introduced to the model, first. Individual faults are simulated by entering zero for the severity of the other fault and the healthy condition is simulated by entering zero for the severities of both the faults. III.Inductances Calculation by Including Magnetic Saturation Effect Modified winding function theory yields the following expression for calculating the SCIM various self-/mutual-inductances at different rotor and air gap flux positions [3]: $L_{yx} = \mu_0 rl \int g^{-1} n_x N_y \, d\phi$ (1) The integration should be performed from 0 to 2π, where x and y are representing any stator phase or rotor mesh, L_{yx} is the mutual inductance between the x and y circuits, n_x and N_y are the turn function and the modified winding function of the x and y circuits, μ_0 is the air magnetic permeability, r is the air gap mean radius, l is the stack length, ϕ is the angle in the stator reference and g^{-1} is the inverse of the fictitious air gap function under magnetic saturation effect [4], which is defined as follows [3]: $g = g'[1-\rho\cos(2P(\phi - \phi_f))]$ (2) where ϕ_f is the angular position of a zero-crossing point of the air gap flux density, P is the pole pairs and g' and ρ are defined by the following expressions: $g' = 3k_s g_0 / (k_s+2)$ (3) $\rho = 2(k_s-1) / 3k_s$ (4) where k_s is the saturation factor [4]. IV.Simulation Results Using the proposed modeling technique, an industrial 1.1kW, 380V, 50Hz, 4-ploe SCIM is simulated under mixed and individual SWI and BRB faults as well as the healthy conditions. Fig. 1 show the stator current spectra obtained by simulation under various conditions. As seen, the BRB fault causes sideband harmonics around fundamental current whose frequencies are determined using (5) with k=1. $f_{BRB} = \left|(1\pm 2ks)\, f_s\right|$ (5) where s is the slip, f_s is the fundamental frequency and k=1,2,3,…. These sidebands are the well-known indices for diagnosing the BRB faults. However, the same sideband harmonics are also present in the spectrum corresponding to the SWI fault condition. The SWI fault can produce harmonic components in the stator currents whose frequencies are determined by following expression [5]: $f_{SWI} = \left|[m \pm n(1-s)/P]\, f_s\right|$ (6) where n=1,2,3,…, m=1,3,5,…. Putting n=4 and m=1 and 3 in (6), yields the same harmonic frequencies as (5) yields with k=1. In addition, the spectrum corresponding to the SWI fault shows the harmonics whose frequencies are obtained using (5) with k=2 and 3. In fact, these frequencies are attained from (6) by proper setting of the n and m values. This study shows that the stator current harmonics, which have been known as the main indices for the BRB faults, are also produced by the SWI faults. This fact was noticed when both the faulty conditions studied at the same time. The authors will offer a technique for discriminating the faults in the full paper.

[1]. S. E. Zouzou, M. Sahraoui, A. Ghoggal, and S. Guedidi, “Detection of inter-turn short-circuit and broken rotor bars in induction motors using the Partial Relative Indexes: Application on the MCSA,” in Proc. ICEM 2010, pp. 1 – 6, Sept. 2010. [2]. M. Ojaghi, M.Sabouri and J. Faiz, “Diagnosis methods for stator winding faults in three-phase squirrel-cage induction motors”, Int. Trans. Electr. Energ. Syst., pp, 891–912, Jun. 2013. [3]. M. Ojaghi and J. Faiz, “Extension to multiple coupled circuit modeling of induction machines to include variable degrees of saturation effects”, IEEE Trans. Magn., vol. 44, no. 11, pp. 4053-4056, Nov. 2008. [4]. J. C. Moreira and T. A. Lipo, “Modeling of saturated ac machines including air gap flux harmonic components”, IEEE Trans. Ind. Appl., vol. 28, no. 2, pp. 343–349, Mar./Apr. 1992. [5] H. Douglas, P. Pillay, and P. Barendse, “The detection of interturn stator faults in doubly-fed induction generators,” in Proc. IAS Annual Meeting 2005, vol. 2, pp. 1097 – 1102, Oct. 2005.

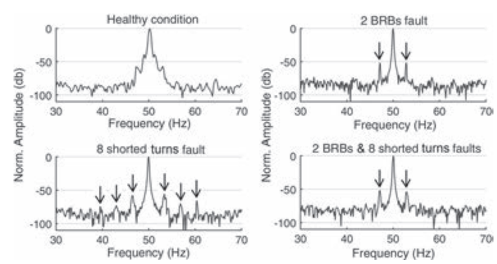

Fig. 1. Normalized spectra for the stator line current

FU-02. Hybrid analytical modeling of saturated electromagnetic devices: Integration of Fourier modeling and magnetic equivalent circuits.

J. Bao[1], B. Gysen[1] and E. Lomonova[1]
1. Eindhoven University of Technology, Eindhoven, Netherlands

Modeling of the electromagnetic field distribution is vitally important in the design and optimization process of electromagnetic devices. In recent years, several advanced methods are being researched, e.g. Fourier modeling, charge modeling, Schwarz–Christoffel conformal mapping, boundary element method, etc [1]. Among these, Fourier modeling is particularly interesting for structures with periodicity, however, the drawback is the unavailability of including geometric details (regions smaller than the full periodicity) made of high-permeable material, e.g. slot shapes [2]-[3]. In [3], a hybrid analytical modeling (HAM) technique that integrates Fourier modeling and meshed magnetic equivalent circuit (MEC) is introduced to model complex structures in Cartesian coordinate system. It provides promising results under the assumption of linear material properties, however, such assumption is not often sufficient during the design of electromagnetic devices. Therefore, this paper further investigates the HAM technique to include nonlinear materials for saturated electromagnetic devices. To present the diverse applicability of the proposed method, it is applied to two electromagnetic examples, one in Cartesian coordinate system with permanent magnet excitation (geometry shown in Fig. 1(a)), and the other one in polar coordinate system with current excitation (geometry shown in Fig. 1(b)). Only 2D solutions are discussed in this paper, however, it could be extended to 3D modeling [4]. In the examples, periodicities are respectively applied in x- or θ-directions, while regions are divided in y- or r-directions. Only the airgap and outer air regions are modeled using Fourier expressions since Fourier modeling divides the geometry in periodical regions with homogeneous permeability and does not allow to model local saturation. The meshed MEC, on the other hand, is used for regions with nonlinear permeability (such as stator and rotor), since each mesh element has its unique permeability and hence, is able to take saturation into account. Inside Fourier and MEC regions, the expression of magnetic field is derived by solving the magnetostatic Maxwell equations. Each mesh-based element in MEC regions contains the information of dimension, permeability and magnetic source as presented in Fig. 1(c). In elements that represent soft magnetic materials, the permeability and magnetic source are defined by a locally linearized B-H characteristic in terms of differential permeability and remanent magnetic flux density, and are updated by an iterative approach [1]. The elements representing permanent magnets and coils have magnetomotive (MMF) sources related to magnetization and current. Particularly, the distribution of current-related MMF sources has to fulfill the Ampere's law [5]. Between Fourier and MEC regions, boundary conditions are given such that continuity of magnetic field is ensured, i.e., consistent normal flux density and tangential magnetic intensity in both spatial frequency and space domains [3]. Details of model formulations, iterative algorithm and field solutions will be discussed in the full paper. The results calculated by this modeling technique are validated by finite element analysis (FEA). Excellent agreement is achieved in both examples as can be observed in the flux density waveforms in Fig. 2(a) and Fig. 2(b), respectively. Additionally, the flux density waveforms when a linear B-H curve would be applied for the iron materials are shown as reference. The HAM technique has several advantages with respect to FEA. It has the potential to be faster than FEA since Fourier regions are not meshed, while for the airgap, a high mesh density is required in FEA to obtain an accurate flux density distribution. Additionally, since the expression of the magnetic field in the airgap is obtained analytically, force and torque calculations are straightforward and fast since the Maxwell stress tensor can be solved analytically. Furthermore, it offers the advantage of fast dimension and topology sweeping without redrawing geometries, therefore is able to simplify and accelerate the design and optimization procedures for saturated electromagnetic devices, resulting in a new computational and design framework. Future research will focus on implementation for different motor topologies, improvement of meshing and iterative algorithms to reduce computation time, and derivation of inductance and iron losses, etc.

[1] R. L. J. Sprangers, J. J. H. Paulides, B. L. J. Gysen and E. A. Lomonova, "Magnetic saturation in semi-analytical harmonic modeling for electric machine analysis", IEEE Transactions on Magnetics, vol. 52, no. 2, pp. 1-10, 2016. [2] B. L. J. Gysen, K. J. Meessen, J. J. H. Paulides and E. A. Lomonova, "General formulation of the electromagnetic field distribution in machines and devices using Fourier analysis", IEEE Transactions on Magnetics, vol. 46, no. 1, pp. 39-52, 2010. [3] K. J. W. Pluk, J. W. Jansen and E. A. Lomonova, "Hybrid analytical modeling: Fourier modeling combined with mesh-based magnetic equivalent circuits", IEEE Transactions on Magnetics, vol. 51, no. 8, pp. 1-10, 2015. [4] K. J. W. Pluk, J. W. Jansen and E. A. Lomonova, "3-D Hybrid Analytical Modeling: 3-D Fourier Modeling Combined With Mesh-Based 3-D Magnetic Equivalent Circuits", IEEE Transactions on Magnetics, vol. 51, no. 8, pp. 1-10, 2015. [5] S. Ouagued, Y. Amara and G. Barakat, "Comparison of hybrid analytical modelling and reluctance network modelling for pre-design purposes"", Mathematics and Computers in Simulation, vol. 130, pp. 3-21, 2016.

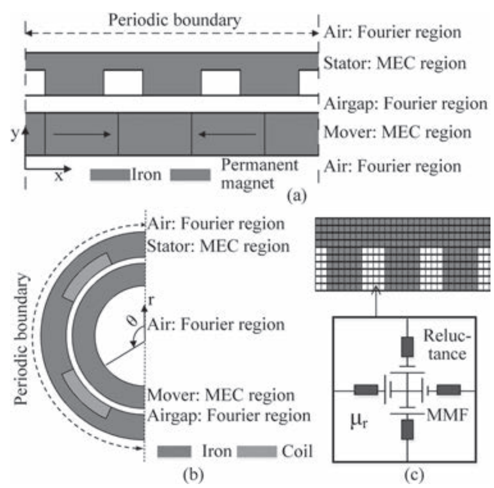

Fig. 1. (a) Geometry of the example in Cartesian coordinate system, (b) geometry of the example in polar coordinate system and (c) schematic graphs of a meshed MEC region and a mesh element.

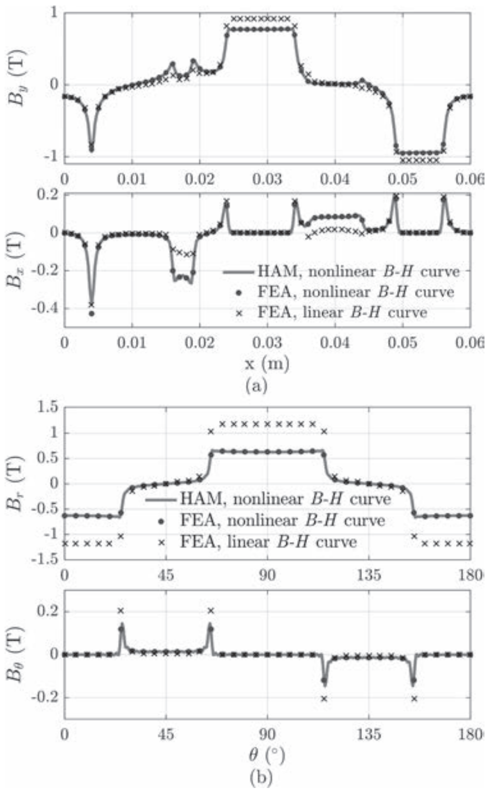

Fig. 2. (a) Normal and tangential components of the flux density distribution at center of the airgap in Fig. 1(a) and (b) radial and tangential components of the flux density distribution at center of the airgap in Fig. 1(b).

FU-03. Convergence Analysis of SEM and FEM to an analytical field distribution in the airgap.

M. Curti[1], J. Jansen[1] and E. Lomonova[1]
1. Electrical Engineering, Eindhoven University of Technology, Eindhoven, Netherlands

1. Introduction The optimisation routines and the validation models for the Electrical Machines (EM) are often based on Finite Element Method (FEM) models. However, their computation time is manifestly high, and are often replaced by semi-analytical models, which approximate the essential performance of EM with reduced computational cost. Therefore, the trade-off between the model accuracy and the size of the problem leads to the appropriate choice of the modelling technique [1]. Recently, Spectral Element Method (SEM) which uses higher order mesh elements compared to FEM, has been implemented for EM [2]. The latter benefits from higher convergence rate, resulting in a smaller size of the problem. Therefore, SEM is considered a potential option for building low-cost EM models. However, complex EM geometries are challenging for any technique, limiting their accuracy by the high aspect ratio and shapes with sharp corners. Consequently, the performance analysis must be thoroughly checked before making the choice. In this paper, the performance analysis of both SEM and FEM is discussed. An analytical solution for the magnetic field is used for the reference which is generated by the Harmonic Model (HM) [3] using a finite number of harmonics. 2. Analytical Model of the airgap field In the Fig. 1. an equivalent EM geometry is presented. Where only the airgap field is modelled, the sources from the rotor and the stator slots are mapped in the current sheets. This technique is commonly used to simplify EM models [4]. In this paper, the later is used to obtain an analytical solution for the EM. Following the transformations, the geometry has two boundary conditions: $H_t\,|_{rs}=j_s$ *(1)* $H_t\,|_{rr}=j_r$ *(2)* where, H_t is the tangential component of the magnetic field strength, j is the current density distribution on the interfaces and r_r and r_s are the outer radius of the rotor and inner radius of the stator, respectively. Given that, the current sheets are approximated by a finite number of harmonics. The solution for the Laplace equation in polar coordinate systems for the magnetic vector potential is: $A_z=\Sigma_n^{Q}(a_{z1n}sin(\omega_n\theta) + a_{z2n}cos(\omega_n\theta))$ *(3)* where $a_{z1n}=c_{1n}(r/r_p)^{\omega_n}+c_{2n}(r/r_p)^{-\omega_n}$ and $a_{z2n}=c_{3n}(r/r_p)^{\omega_n}+c_{4n}(r/r_p)^{-\omega_n}$ with the spatial harmonics ω_n, scaling constant r_p, unknowns $c_{1\text{-}4n}$, and number of harmonics Q. The close form of H_t is obtained from eq. (3) and is used to force the Neumann boundary conditions on the rotor and the stator sides of the airgap. Following [3], the unknowns can be solved for each harmonic separately, $c_{1n}=((r_p/r_r)^{\omega+1}a_{ns}-(r_p/r_s)^{\omega_n+1}a_{ns})/\delta_n$ *(4)* $c_{2n}=((r_r/r_p)^{\omega-1}a_{ns}-(r_s/r_p)^{\omega_n-1}a_{ns})/\delta_n$ *(5)* $c_{3n}=((r_p/r_r)^{\omega+1}b_{ns}-(r_p/r_s)^{\omega_n+1}b_{ns})/\delta_n$ *(6)* $c_{4n}=((r_r/r_p)^{\omega-1}b_{ns}-(r_s/r_p)^{\omega_n-1}b_{ns})/\delta_n$ *(7)* where, $\delta_n=\omega_n(-(r_r/r_p)^{\omega-1}(r_s/r_p)^{-\omega_n-1}+(r_s/r_p)^{\omega-1}(r_r/r_p)^{-\omega_n-1})$, *(8)* a_n and b_n are the Fourier coefficients of the current density distribution along the interfaces. 3. Numerical approximation To generate an analytical solution from section 2, it is considered that a limited number of harmonics Q equal to 60 are enough to get the distribution of the current sheets. The same amount of source harmonics are injected in the boundary conditions of SEM and FEM models. By increasing the accuracy of the methods, the convergence is evaluated with the respect to their degrees of freedom (dof). 3.A. Finite element method The numerical approximation by FEM is implemented in FLUX2D [5], where, the second order triangular mesh elements are used. The mesh density is generated by homogeneously enforcing the number of line elements on the rotor and stator lines. No relaxation is applied in the airgap region, so that a homogeneous mesh distribution is obtained, which is important to capture the field in the airgap, containing most of the energy in a rotating EM. 3.B.Spectral element method The major difference of SEM with the respect to FEM is the distinctive features of the mesh elements used to discretize the geometry. Unlike FEM, SEM implementation from this paper uses quadrilateral mesh elements where the solution is approximated with high order Legendre polynomials giving the possibility to choose between fewer high order elements (p refinement), or more elements with a lower degree of polynomials (h and r refinement) [6]. It should be noted that quadrilateral elements can have curved boundaries, which allow a more precise approximation of the geometrical features of the model. Moreover, the arrangement of the orthogonal Legendre basis offers a fast convergence of the error giving a more stable approximation and fewer dof for similar accuracy compared to FEM [7]. 4. Results In the Fig. 2. the overlap of SEM, FEM and analytical solution of the tangential and radial component of the magnetic field in the middle of the airgap is shown. The convergence plot from the Fig. 2c. shows that, for an increased accuracy, SEM approximation gives a better performance compared to FEM. Reaching 3500 dof, SEM reaches round off errors while FEM has a limited accuracy. 5. Conclusion In this paper, the FEM and SEM model is compared with an analytical solution in the airgap of an EM. It can be seen that the solution approximated by SEM gives higher accuracy, as a consequence, SEM becomes an efficient technique for modelling EM. In the full paper, detailed performance analysis of SEM and FEM will be presented.

[1] K. Ramakrishnan, M. Curti, D. Zarko, G. Mastinu, J. J. H. Paulides, and E. A. Lomonova, "Comparative Analysis of Various Methods for Modelling Permanent Magnet Machines," *IET Electr. Power Appl.*, Jan. 2017. [2] M. Curti, J. J. H. Paulides, and E. A. Lomonova, "Magnetic Modeling of a Linear Synchronous Machine with the Spectral Element Method," *IEEE Trans. Magn.*, vol. 53, no. 11, 2017. [3] B. L. J. Gysen, K. J. Meessen, J. J. H. Paulides, and E. A. Lomonova, "General Formulation of the Electromagnetic Field Distribution in Machines and Devices Using Fourier Analysis," *Magn. IEEE Trans.*, vol. 46, no. 1, pp. 39–52, Jan. 2010. [4] Z. Q. Zhu, D. Howe, E. Bolte, and B. Ackermann, "Instantaneous magnetic field distribution in brushless permanent magnet DC motors. I. Open-circuit field," *IEEE Trans. Magn.*, vol. 29, no. 1, pp. 124–135, Jan. 1993. [5] Altair Engineering Inc, *Altair FLUX2D User's Guide*. United States of America, 2017. [6] J. P. Boyd, *Chebyshev and Fourier spectral methods*. Springer-Verlag, 1989. [7] D. A. Kopriva, *Implementing Spectral Methods for Partial Differential Equations*. Springer, 2009.

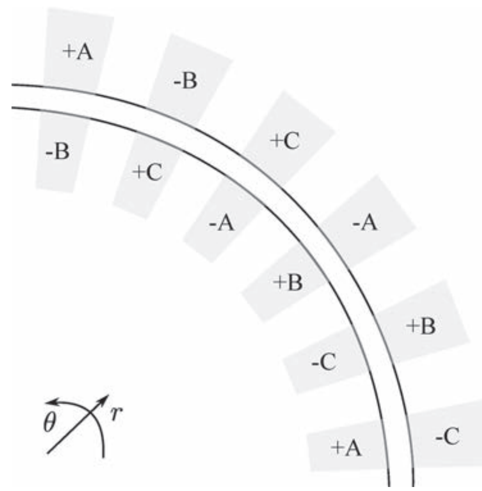

Fig. 1. Equivalent geometry of a rotating electrical machine

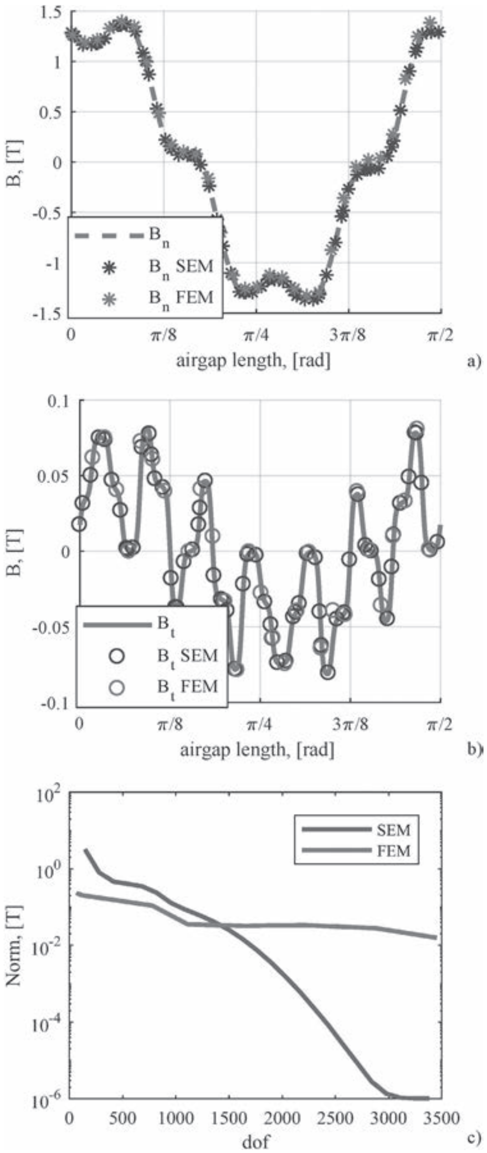

Fig. 2. Magnetic flux density in the middle of the airgap: a) Normal component b) tangential component and c) Convergence towards the analytical solution.

FU-04. Reduction of Stator Core Loss in Interior PM Machines for Electric Vehicle Applications.

Y. Hu[1] and *S. Zhu*[1]
1. Nanjing University of Aeronautics and Astronautics, Nanjing, China

I. Introduction Interior permanent magnet (IPM) machines are very attractive for the electric vehicle (EV) traction applications due to its excellent performance such as high torque density, high power density, and wide constant power speed range [1]. Stator core losses are the main component of power loss in the Interior permanent magnet (IPM) machines under high speed operation. They depend essentially on the flux-density waveform of stator core which are influenced by the rotor magnetomotive force [2]. Therefore, reduce the harmonics of air-gap density is an important issue of IPM machine design. II. Main Body Fig. 1 shows magnet configurations and there air-gap flux density of four IPM machines, where ap1-ap3 are the pole-arc to pole-pitch ratio of PMs. The single layered IPM machine is model I, the single-layered IPM machine with shaping is model II, the two-layered IPM machine is model III, and the three-layered IPM machine is model IV. It can be seen that the air-gap field distribution of model IV is closer to sinusoidal waveform. The rated power of the machines is 48 kW, the continuous rated current (rated load) is 200 A, the maximum speed of the machines is 12000 r/min. A prototype IPM machine with model IV is manufactured to verify the effects of core loss. Fig. 2(a) shows the photographs of the stator and rotor. The FEA predicted core losses density distributions of four IPM machines on 12000 r/min are analyzed and compared. In order to clear show the flux-density waveform and its harmonics of stator core and rotor core, the flux-density waveform and its harmonics of stator teeth are added. Fig. 2(b) shows the spectral components of stator teeth flux density and core loss. It can be seen that, the 3th, 5th, 7th harmonics of model I are significantly higher than the other machines. The 9th harmonics of model III are higher than the other machines. The 13th, 15th harmonics of model IV are higher than the other machines, and the model IV has the lowest stator teeth flux density and core loss. The simulated and measured total iron loss of the prototype machine are shown in Fig. 2(c). In general, good agreement of FEA and experimental results. III. Conclusion This paper has analyzed and compared the core loss of four Interior PM machines for electric vehicle applications. The major conclusions derived from the results of analysis and experiments are summarized as follows. [1] The shaping of single-layered IPM machine can reduce the stator core loss due to the harmonics of air-gap density can be reduced. [2] Increase the rotor magnet layer number of IPM can effectively reduce the stator core loss but also increase the manufacturability compared with the single-layered machines.

[1] Yinye Yang, Sandra M. Castano, Rong Yang. et al., "Design and Comparison of Interior Permanent Magnet Motor Topologies for Traction Applications," IEEE Trans. Transp. Electrif., vol. 3, no. 1, pp. 86-97, Mar. 2017. [2] Chun Tang, Wen L. Soong, Thomas M. Jahns and Nesimi Ertugrul, "Analysis of Iron Loss in Interior PM Machines With Distributed Windings Under Deep Field Weakening," IEEE Trans. Ind. Appl., vol. 51, no. 5, pp. 3761-3772, Sep./Oct. 2015.

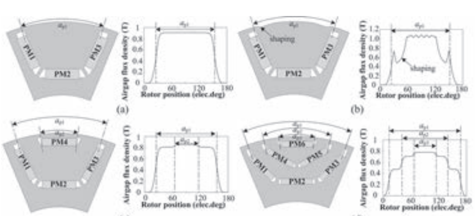

Fig. 1. The structure and air-gap density of four IPM machines. (a) Model I. (b) Model II. (c) Model III. (d) Model IV.

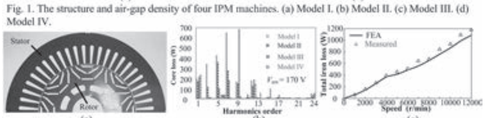

Fig. 2. Photographs of stator and rotor, FEA calculated and tested results of core losses. (a) Photographs of stator and rotor. (b) Spectral components of core losses at 12000 r/min. (c) FEA calculated and tested total iron loss at different speeds.

FU-05. Vector Magnetic Characteristic Analysis of Induction Motor Considering Harmonic Wave by Slip Motion.

M. Enokizono[1] and N. Kunihiro[2]
1. Vector Magnetic Characteristic Technical Laboratory, Usa-city, Japan;
2. Oita University, Oita, Japan

Induction motors are widely used in houses and factories. Furthermore, it is noticed as a motor for EV. Improvement of their efficiency of even one percentage would result in a great energy savings. On the other hand, it is well known that the magnetic field intensity *H* is not parallel to the magnetic flux density *B* in soft magnetic materials under two-directional excitation. This property is called the two-dimensional vector magnetic property. We have proposed the dynamic E & S modeling for numerical simulation, which is able to express precisely the two-dimensional vector magnetic property and enabled the analysis taking account of the magnetic anisotropy and non-linearity [1, 2]. In this paper, results of magnetic characteristic analysis of an induction motor core by using the finite element method taking account of the two-dimensional vector magnetic properties are reported. In this method we can obtain directly the iron loss distributions in the stator core with the direct calculation from hysteresis loops obtained at each finite element. In the analysis, we propose a new method to consider harmonic components based on slip motion. The load characteristics depending on slip under harmonic magnetic field are made clear by vector magnetic characteristic analysis considering vector magnetic characteristics. Analytical Results and Discussion Generally, the waveforms of the magnetic flux density and the magnetic field intensity in the stator yoke of the induction motors include secondly slot harmonic components. Figure.1. shows the loci of *B* at each point as an example. As shown in Fig.1. loci of *B* had distortion, and the distortion was very large at the tooth top. The influence of the secondly slot harmonic was very small at the core back part. From these results, it was shown that not only the magnetic flux density but also the magnetic field intensity was distorted. Moreover, it can be concluded that the magnetic flux and field intensity waveforms include about 20% of the harmonic components in the maximum at the tooth top parts near the air gap. Then, it was understood that the largest number of harmonic was changed depending on slip. The tendency is well known as a slot ripple depending on the number of secondly slot and relative velocity. Inclusion of number of harmonic is similar, however the amplitudes are little different. As results, it can be said that the relationship between *B* and *H* should be understood as a vector property. Figure.2. shows BH loops in x-direction when slip = 0.5 at point A indicated in the Fig. 1. Induction motor has three kinds of coordinate system, which are static coordinate, rotational exciting coordinate and slip coordinate. Therefore the hysteresis loop is not closed in the period. Firstly, it is understood that BH loops close within few periods according to slip as shown in Fig. 2, though this is a only characteristic of an induction motor (have a slip). In a word, when the iron loss of the induction motor is evaluated, it is necessary to know the lowest common multiple of the rotating magnetic field and the rotor rotation to obtain the closed. The core loss of induction motor can be obtained by equation (this equation will be shown on full paper). Where, N is the order of considering component, T_{LCM} is period of exciting waveform of the lowest common multiple, ρ is core material density. When slip is 0.5, T_{LCM} is 2.

[1]M.Enokizono and S. Urata, "Dynamic Vector Magneto-Hysteretic E&S Model and Magnetic Characteristic Analysis", CONPUMAG07, Aachen in Germany, 2007. [2]S.Urata, T.Todaka, M.Enokizono, and H.Simoji, "Magnetic field analysis considering two dimensional vector magnetic properties of distorted magnetic condition" Institute of Electrical Engineers, Mag-05-106, 2005.

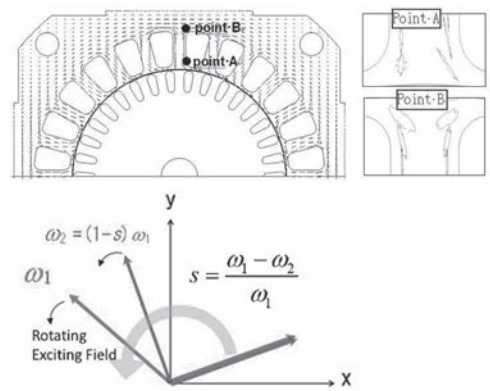

Fig. 1. Loci of magnetic flux density vector *B*

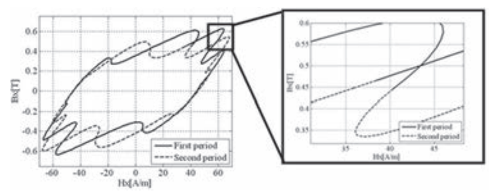

Fig. 2. BH loops in x-direction at point A (Slip = 0.5)

FU-06. Elimination of Unipolar Leakage Flux in Consequent-Pole PM Machines by Employing Novel Pole Sequence.

J. Li[1], *K. Wang*[1] and C. Liu[1]
1. Electrical Engineering, Nanjing University of Aeronautics and Astronautics, Nanjing, China

I. Introduction Many permanent magnet (PM) machines have employed rare-earth magnets such as NdFeB as magnetic potential source owing to its high energy density, which can obtain high efficiency and high torque density [1]. However, the one of their drawbacks is the high production cost, which results from the shortage and unstable supply of rare-earth materials around the world [2]. In order to improve the PM utilization ratio, the consequent-pole PM (CPM) machine is proposed and investigated in recent years. These reported literature indicates that consequent-pole structure in both rotor-PM machines [3] and stator-PM machines [4] has a great potential to reduce the cost. However, due to the magnetic unbalance, the unipolar leakage flux exists in the end region of the CPM machine. It can lead to the magnetization of the mechanical components such as the shaft, bearing and screws, and even poses threats to the reliability and safety of the machine system. In this paper, a novel CPM machine with N-iron-N-iron-N-S-iron-S-iron-S sequences is proposed to eliminate the unipolar leakage flux. Besides, the tangential magnetized PMs are embedded to the rotor of the novel CPM machine, i.e., hybrid-pole PM (HPM) machine, further improving the PM utilization ratio and output torque. Both finite element (FE) analyses and experiment are used to investigate these machines. II. Machine Topologies The 9-slot/10-pole PM machine with double-layer non-overlapping winding is employed to investigate the electromagnetic performance of the conventional and proposed machines. Fig. 1 (a) shows the conventional CPM (CPM1) machine, whilst Figs. 1 (b) and (c) show the proposed CPM (CPM2) machine and HPM machine, respectively. Fig. 1 (d) shows the prototyped HPM rotor. All these machines have the same stator, stack length and airgap length. The PM-arc ratio α_p ($\alpha_p = \theta_m p/2p$, where θ_m is the PM arc and p is the number of pole-pair) of the CPM1 machine is optimized for maximizing the output torque, and it equals to 0.65. The N-S in the pole-sequences of the proposed machines is adjoining, and thus the PM-arc ratio α_p is fixed by 0.5. In addition, the thickness of the tangential magnetized PM in the HPM machine is optimized and equals to 2mm. It should be noted that the magnetized direction of all the PMs in the CPM1 machine is uniform, whilst the PMs of the proposed CPM2 and HPM machines have opposite magnetized direction, which is preferred for the elimination of the unipolar leakage flux, as will be shown later. III. Elimination of Unipolar Leakage Flux Figs. 2 and 3 show the 3D FE predicted flux density distributions at the surface of the end shaft for all the investigated machines. It is up to 0.008T within the axial length of 10mm for the CPM1 machine. However, the peak flux density is 0.002T within the axial length of 10mm for the CPM2 machine, which is much lower than that for the CPM1 machine. Apparently, the HPM machine has higher flux density of the end shaft than the CPM2 machine due to the assisted flux provided by the tangential magnetized PMs. It should be noted that the polarity of the leakage flux in the end shaft of the CPM2 machine is opposite to that in the HPM machine. This is due to the fact that the tangential magnetized PMs in the HPM machine can be regarded as the flux barriers, which changes the leakage flux path, as shown in Fig. 2 (c). More importantly, the leakage flux in the end of the CPM1 machine is unipolar, as shown in Fig. 3 (a). However, in the proposed CPM2 and HPM machines, the unipolar leakage flux does not exists and replaced by the bipolar one, as shown in Figs. 3 (b) and (c). Therefore, the magnetization of the mechanical components in the end of the proposed machines can be effectively reduced. Fig. 4 shows the measured flux density at 30 mm of the end shaft of the HPM machine, which agrees with FE predicted one. The detailed analysis and experimental results will be presented in the full paper.

[1]D. G. Dorrell, M.-F. Hsieh, M. Popescu, L. Evans, D. A. Staton, and V. Grout, "A review of the design issues and techniques for radial-flux brushless surface and internal rare-earth permanent magnet motors," *IEEE Trans. Ind. Electron.*, vol. 58, no. 9, pp. 3741–3757, Sep. 2011. [2]I. Boldea, L. N. Tutelea, L. Parsa, and D. Dorrell, "Automotive electric propulsion systems with reduced or no permanent magnets: An overview," *IEEE Trans. Ind. Electron.*, vol. 61, no. 10, pp. 5696–5711, Oct. 2014. [3]S. U. Chung, J. W. Kim, Y. D. Chun, B. C. Woo, and D. K. Hong, "Fractional slot concentrated winding permanent magnet synchronous machine with consequent pole rotor for low speed direct drive," *IEEE Trans. Magn.*, vol. 48, no. 11, pp. 2965–2968, Nov. 2012. [4]Z. Z. Wu and Z. Q. Zhu, "Comparative analysis of end effect in partitioned stator flux reversal machines having surface-mounted and consequent pole permanent magnets," *IEEE Trans. Magn.*,vol. 52, no. 7, Jul. 2016, Art. ID 8103904. [5]X. Ge, Z. Q. Zhu, J. B. Li, and J. T. Chen, "A spoke-type IPM machine with novel alternate airspace barriers and reduction of unipolar leakage flux by step-staggered rotor," *IEEE Trans. Ind. Appl.*, vol. 52, no.6, pp. 4789-4797, Nov./Dec. 2016. [6]Z. Q. Zhu, H. Hua, Adam Pride, Rajesh Deodhar, Toshinori Sasaki, "Analysis and reduction of unipolar leakage flux in series hybrid permanent magnet variable flux memory machines," *IEEE Trans. Magn.*, vol. 53, no. 11, Nov. 2017, Art. ID 2500604.

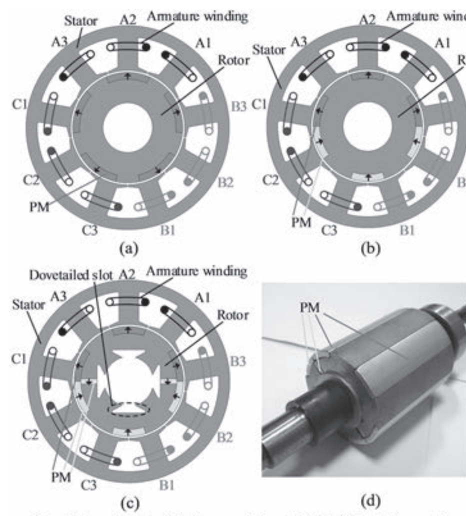

Fig. 1. Topologies. (a) Conventional CPM (CPM1) machine. (b) Proposed CPM (CPM2) machine. (c) Proposed HPM machine. (d) Prototyped HPM rotor.

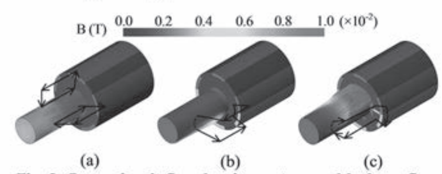

Fig. 2. Open-circuit flux density vectors and leakage flux path on end. (a) CPM1. (b) CPM2. (c) HPM.

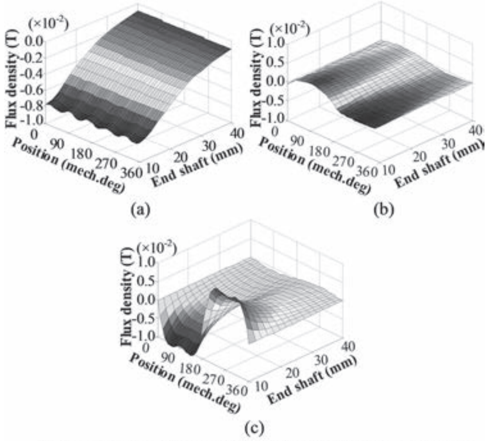

Fig. 3. Flux density of end shaft surface at different shaft position. (a) CPM1. (b) CPM2. (c) HPM.

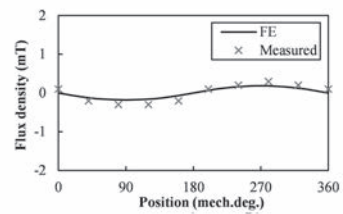

Fig. 4. Comparison of FE predicted and measured flux density of end shaft (30mm).

FU-07. Indirect Analytical Method for Electromagnetic Performances Analysis of V-shaped Interior Permanent Magnet Synchronous Machine.

L. Xu[2] and M. Lin[1]
1. Southeast University, Nanjing, China; 2. School of Electrical and Information Engineering, Jiangsu University, Zhenjiang, China

In this paper, an indirect analytical method is presented to analysis and optimize the electromagnetic performances, such as air-gap flux density, back EMF, cogging torque, and torque, of the V-shaped Interior permanent magnet (PM) synchronous Machine (IPMSM). The new method provides an indirect calculation model of the V-shaped IPMSM, by transferring the rotor into an equivalent linear one in the Cartesian coordinate system. Based on a proposed magnetic field curvature factor, the magnetic field distribution of the motor is initially analyzed using the magnetic scalar potential. The Maxwell stress tensor method with Schwarz–Christoffel (SC) transformation is subsequently utilized to analyze the magnetic field in detail and predict the torque performances of the V-shaped IPMSM accurately. The magnetic field and torque performances obtained by the analytical method are compared with those obtained from finite element analysis (FEA). The analytical predictions are compared with the measured results in order to confirm the validity of the methods. II. Electromagnetic Analysis of the V-shaped IPMSM A.V-shaped IPMSM Configuration A 9-slot-6-pole motor with V-shaped interior PMs is instanced, and this motor adopts concentrated windings. The parameters of the IPMSM is shown in Table I. The model of the motor is shown in Fig. 1(a). B.Analysis Model For establishing the analytical model, the motor shown in Fig. 1(a) is cut along the axial and flattened as shown in Fig. 1(b). The rotor is divided into three parts which named Region II, Region III-1, and Region III-2 respectively. Region II is the PM region. The Region III-1 and Region III-2 are the rotor iron core region. In order to further simplify the analytical model, the model shown in Fig. 1(b) can be equivalent to the one as shown in Fig. 2. Region I is the stator region, and Region IV is the armature current sheet. Thus, the V-shaped PMs are equivalent to two parts, and the air-gap flux can be calculated separately. Based on the some assumptions, the air-gap flux density in open circuit can be deduced by solving the Maxwell and Laplace's equations in the two parts, and the SC transformation is utilized to calculate the slot effects. The Matlab SC Toolbox is used to draw the real slot shape. Moreover, considering the armature winding current effect, the Laplace's equation is solved again, and the fractional slot windings are assumed as thin wires. In terms of the Maxwell stress tensor method, the rotary cogging torque and torque can be indicated. C.Curvature Factor The curvature factor k_q, which has been proposed as a modifying function in [1], is defined as the ratio of the analytical flux densities in 2-D parallel magnetization PM array to in 2-D radial magnetization linear PM array by $k_q = B_{rq} / B_l$ III. Results and Discussion Based on the analysis in Section II, the electromagnetic performances including air-gap flux density, back-EMF, cogging torque, and torque are given, and they are compared with that obtained by FEM in this section. The air-gap flux density is shown in Fig. 3. Furthermore, the prototype of the V-shaped IPMSM is constructed as shown in Fig. 4, and the experiments are done. IV. Conclusion Based on the equivalent model, the analytical method with curvature factor is presented for the electromagnetic performances investigation of the V-shaped IPMSM in this paper. Both of the FEM and experimental results verified the correctness of the analytical method.

[1] Z. P. Xia, Z. Q. Zhu, and D. Howe, "Simplified analytical model for predicting magnetic field distribution in tubular linear PM motors with surface-mounted magnets," presented at the 4th Int. Symp. Linear Drives for Ind. Appl., Birmingham, U.K., 2003. [2] Z. Q. Zhu and D. Howe, "Analytical prediction of the cogging torque in radial-field permanent magnet brushless motors," IEEE Trans. Magn., vol. 28, no. 2, pp. 1080–1083, Mar. 1992. [3] A. Rahideh and T. Korakianitis, "Analytical open-circuit magnetic field distribution of slotless brushless permanent-magnet machines with rotor eccentricity," IEEE Trans. Magn., vol. 47, no. 12, pp. 4791–4808, Dec. 2011. [4] T. Wang and Z. Zhou, "Analytical solution of magnetic field distribution in brushless permanent magnet machines with rotor axis deflection," IEEE Trans. Magn., vol. 51, no. 4, Oct. 2014, Art. ID 8202606.

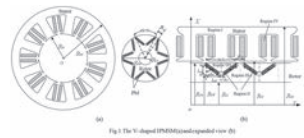

TABLE I
PARAMETERS OF THE V-SHAPED IPMSM

Item	Value	Item	Value
Rated Output Power / kW	0.72	Rated Torque / Nm	1.8
Rated Speed / r·min⁻¹	3600	Rated Voltage / V	220
Outer Diameter / mm	100	axial length / mm	45

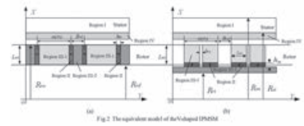

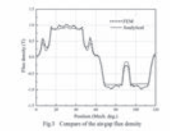

FU-08. Improved E&S Model for Core Loss Calculation of Brushless Doubly Fed Machine with Hybrid Rotor.

F. Zhang[1], Y. Wang[1] and S. Yu[1]
1. School of Electrical Engineering, Shenyang University of Technology, Shenyang, China

Brushless doubly fed machine (BDFM), is a new type of machine with special structure, shows promising features for the field of variable frequency speed regulation and wind power generation due to its inherent characteristics, which has the advantages of reliable operation, adjustable power factor, lower operation and maintenance costs as well as requiring a smaller capacity converter [1]-[2]. Since core loss has an important effect on efficiency and temperature distribution, it is vital to accurately calculate such component in an optimal design procedure. Furthermore, rotor core loss is also a significant factor which can affect the performance characteristics of BDFM due to the complex magnetic field distribution and relatively high value of slip. Specifically, a novel hybrid rotor structure which is combined with magnetic barrier and assisted cage has better coupling ability than the commonly used rotor structures such as cage rotor and reluctance rotor is presented but it also increases the difficulty of core loss calculation. E&S model is a vector magnetic hysteresis property model [3]-[4], in which H (magnetic field intensity) is dependent not only on B (magnetic flux density) but also on time derivative of B. Increase of core loss when the phase difference between B and H occurs, is well expressed in this method, while the conventional analysis was not able to consider the phase difference between B and H. Furthermore, the total core loss including both alternating and rotational losses can be directly calculated from the fundamental terms of obtained B_x, B_y, H_x and H_y without other fitting data, which can improve the core loss computation accuracy of BDFM with hybrid rotor in contrast with conventional core models. In this paper, an improved E&S model based on a 2-D rotational magnetic property analysis for core loss of BDFM with hybrid rotor is proposed by considering the high-order harmonic magnetic field. The finite element analysis model of BDFM with hybrid rotor is established. The core loss calculation results are compared with the simulation results to verify the correctness and feasibility of the proposed E&S model. Fig. 1 shows the finite element model, hybrid rotor of prototype and special points distribution diagram of BDFM with hybrid rotor. As shown in Fig. 1 (a)-(b), the cage bars are added on the non-magnetic layer of the radial magnetic barrier rotor, and the cage bars are respectively divided into concentric cage bar and common cage bar. There are two kinds of rotating magnetic fields with different poles and frequencies in the air-gap of BDFM, which renders that the air-gap magnetic density harmonic contents are rich and the magnetic properties of each part of core are different. According to the basic principle, structure characteristics and magnetic field distribution of BDFM with hybrid rotor, some special points of stator and rotor are analyzed and calculated. The relationship between B vector and H vector, and the relationship between the waveform of B_x, B_y and the waveform of H_x, H_y, obtained by the combination of the improved E&S model and finite element analysis, is shown in Fig. 1 (c), which is seen that the phase between B and H is different. The improved E&S model can consider higher order harmonic magnetic field than the conventional E&S model. As shown in Fig. 2 (a), the stator and rotor core loss calculation process of BDFM with hybrid rotor is described by the flow diagram. The datum of B_x, B_y, H_x, H_y are obtained by the combination of the improved E&S model and finite element method, and all order harmonic of B_x, B_y, H_x, H_y are computed by fourier series expansion. Therefore, the total core loss of BDFM with hybrid rotor can be calculated by the formula in the flow diagram, where, ρ is the magnetic material density, T is the period, m is the amount of the special points, n is the harmonic order, and M_i is the mass. In addition, in order to verify the accuracy of the core loss calculation, the 2-D finite element model of BDFM with hybrid rotor is established, and the simulation results are shown in Fig. 2 (b). The validity and feasibility of the improved E&S model is verified by comparing with the simulation results. In addition, the full paper will present the detailed calculation procedure and analysis.

[1] Mohammad Naser Hashemnia, Farzad Tahami, and Estanis Oyarbide, “Investigation of core loss effect on steady-state characteristics of inverter fed brushless doubly fed machines,” *IEEE Trans. Energy Convers.*, vol. 29, no. 3, pp. 57-64, Mar. 2014. [2] Hamed Gorginpour, Hashem Oraee, and Ehsan Abdi, “Calculation of core and stray load losses in brushless doubly fed induction generators,” *IEEE Trans. Ind. Electron.*, vol. 61, no. 7, pp. 3167-3177, Jul. 2014. [3] Masato Enokizono, “Vector magneto-hysteresis E&S model and magnetic characteristic analysis,” *IEEE Trans. Magn.*, vol. 42, no. 4, pp. 915-918, Apr. 2006. [4] Y. Zhang, Y. H. Eum, D. Xie, and C. S. Koh, “An improved engineering model of vector magnetic properties of grain-oriented electrical steels,” *IEEE Trans. Magn.*, vol. 44, no. 11, pp. 3181-3184, Nov. 2008.

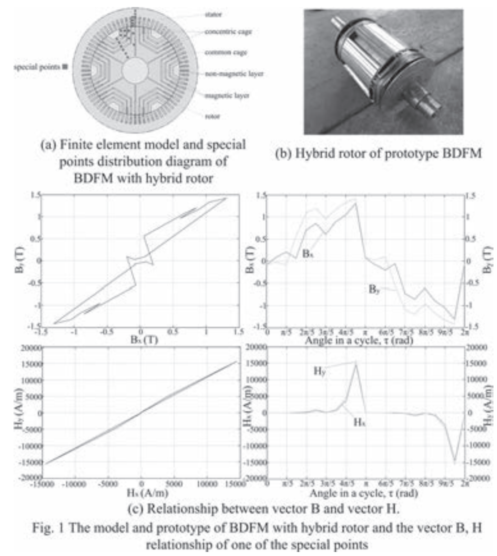

Fig. 1. The model and prototype of BDFM with hybrid rotor and the vector B, H relationship of one of the special points

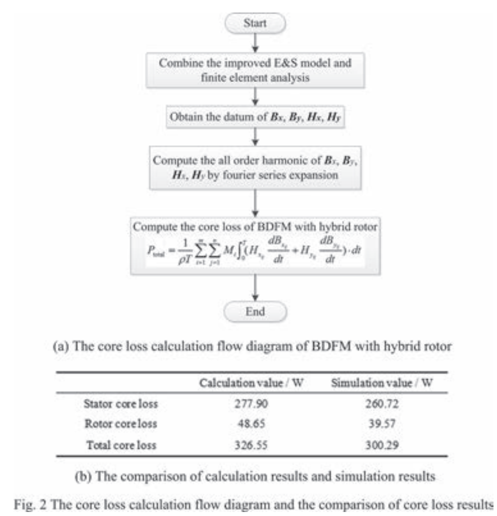

	Calculation value / W	Simulation value / W
Stator core loss	277.90	260.72
Rotor core loss	48.65	39.57
Total core loss	326.55	300.29

Fig. 2. The core loss calculation flow diagram and the comparison of core loss results

FU-09. About Accuracy and Influence of the Pole Coverage for Eddy Current Losses within Permanent Magnets of Electrical Machines.

E. Schmidt[1] and M. Kaltenbacher[2]
1. Institute of Energy Systems and Electrical Drives, Vienna University of Technology, Vienna, Austria; 2. Institute of Mechanics and Mechatronics, Vienna University of Technology, Vienna, Austria

Abstract In particular with surface mounted permanent magnets, eddy current losses within the magnets are one of the most significant portion of losses in permanent magnet exited synchronous machines. These losses are generated by asynchronous components of the air-gap field caused by either higher harmonic waves or higher time harmonics. On one hand, there is no interaction of the various harmonics with regard to these losses. On the other hand, the pole coverage shows a significant impact on these losses. Thus, detailed numerical analyses with various higher order formulations are carried out in order to show aspects of the accuracy of these eddy current losses, too. Introduction The precalculation of eddy current losses arising in surface mounted permanent magnets caused by sub- and superharmonics harmonics of the air-gap field is a matter of particular interest with the design process of permanent magnet excited electrical machines. On one hand by using very fast evaluation methods for the standard design procedures, on the other hand by using highly accurate calculation methods for reference purposes \cite{Wang09,Etem12}. These eddy current losses may always lead to an excessive partial heating and subsequently can cause the magnets to get partially or even fully demagnetised \cite{Elre10,Wang10,Okit12}. As shown with the full paper, both planar and cylindrical arrangements are described with only few parameters, such as air-gap, ratio of pole pitch and air-gap, ratio of magnet height and air-gap as well as the pole coverage as ratio of magnet width and pole pitch. In order to compare the various approximation orders of the finite element analyses and their influence on the accuracy of the numerically obtained results, an analytical calculation will be used for the reference results. In addition, various pole coverages with their effects on the eddy current losses are discussed by these numerical analyses. A surface current sheet in axial direction K_z(x,t) at the inner stator boundary perpendicular to the cross section of the conducting region as K_z(x,t) = \hat{K}_z \Re (exp{j om t} exp{-j nu pi x/tau_p}) can cover for any harmonics generated from either the stator currents, the slotting as well as the saturation. Therein, om = 2 pi f denotes the exciting circular frequency with respect to the moving region, nu the harmonic order and -1 <= x/tau_p <= 1 being the region of two pole pitches along the circumferential direction, respectively. Referring to the total eddy current losses, there is no interaction between waves with different harmonic orders as well as different frequencies. General numerical results All analyses carried out with different high order approximation functions utilise an identical discretisation with the minimum skin depth as approximately the half of the mesh size in radial direction and the mininum wave length as approximately 7.5 times the mesh size in circumferential direction. Obviously and as included with the full paper, the total eddy current losses are quite similar between both arrangements with a deviation in the range +-5% only. With a ratio of wave length to skin depth <<1, the power losses versus frequency increase with a power of 2. On the other hand with a ratio of wave length to skin depth >>1, the power losses versus frequency increase with a power of 0.5 only. However with very low ordinal numbers, there is a transitional region where the power losses are rather constant. Accuracy of the numerical results The relative error eps = Power_{FEA} / Power_{Ana} - 1 between the power losses of finite element and analytical analyses with different approximation orders is shown in Fig.1 and Fig.2. Thus, the usage of 3rd or even higher order elements is strongly suggested for evaluating such eddy current losses. In particular with 3D meshes, the possibility of generating a relatively coarse mesh within the conducting regions shows explicit advantages against a dense mesh with 2nd order elements. Influence of the pole coverage The finite element calculations very easily allow to encounter for the influence of various pole coverages on the eddy current losses, too. With regard to a practical point of view with planar and cylindrical arrangements, the pole coverages as of 5/6, 3/4 and 2/3 are concerned in more detail. Obviously and as shown with the full paper, the pole coverage only affects the power losses of the lower harmonics while the power losses of the higher harmonics are directly proportional to the value of the pole coverage. Conclusion The paper discusses the numerical evaluation of eddy current losses in surface mounted permanent magnets of electrical machines. Planar and cylindrical arrangements are compared against their results by using identical geometry parameters and various pole coverages. Additionally, the finite element analyses utilise different approximation orders with hierarchic shape functions in order to validate the accuracy of the eddy current losses.

Wang J., Papini F., Chin R., Arshad W.M., Lendenmann H.: "Computationally Efficient Approaches for Evaluation of Rotor Eddy Current Loss in Permanent Magnet Brushless Machines". Proceedings of the International Conference on Electrical Machines and Systems, ICEMS, Tokyo (Japan), 2009. Etemadrezaei M., Wolmarans J.J., Polinder H., Ferreira, J.A.: "Precise Calculation and Optimization of Rotor Eddy Current Losses in High Speed Permanent Magnet Machines". Proceedings of the International Conference on Electrical Machines, ICEM. Marseille (France), 2012. El-Refaie A.M.: "Fractional Slot Concentrated Windings Synchronous Permanent Magnet Machines: Opportunities and Challenges". IEEE Transactions on Industrial Electronics, Vol. 57, No. 1, January 2010. Wang J., Atallah K., Chin R., Arshad W.M., Lendenmann H.: "Rotor Eddy Current Loss in Permanent Magnet Brushless AC Machines". IEEE Transactions on Magnetics, Vol. 46, No. 7, July 2010. Okitsu T., Matsuhashi D., Yanhui Gao, Muramatsu K.: "Coupled 2-D and 3-D Eddy Current Analyses for Evaluating Eddy Current Losses of a Permanent Magnet in Surface Permanent Magnet Motors". IEEE Transactions on Magnetics, Vol. 48, No. 11, November 2012.

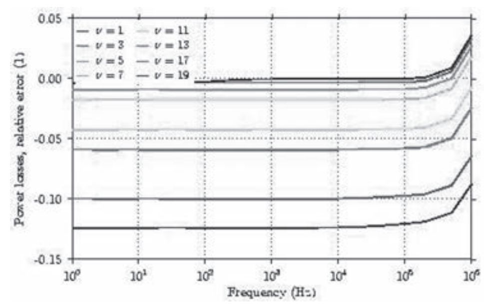

Fig. 1. Relative error of power losses, planar arrangement, pole coverage 1, order p=2.

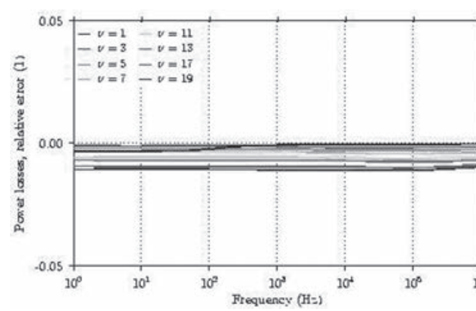

Fig. 2. Relative error of power losses, planar arrangement, pole coverage 1, order p=3.

FU-10. Non-conforming finite element method to simulate eddy currents due to motion using the T,Φ-Φ formulation.

G. Wallinger[1] and O. Biro[1]
1. Institute of Fundamentals and Theory in Electrical Engineering, Graz University of Technology, Graz, Austria

Abstract: The non-conforming meshing approach, which is based on interpolation techniques, is used to carry out a time transient simulation of a two pole asynchronous machine with a squirrel cage rotor at constant rated speed. This newly revisited approach uses 2nd order node-based hexahedral elements and represents an alternative to computational demanding methods like the use of Lagrange multipliers and mortaring methods. 1. Introduction The analysis of electromagnetic devices, especially electrical machines is an expensive task starting with finite element (FE) modeling of the machine and ending with time consuming computations. These tasks get even more costly, if a three dimensional model is taken into account. In terms of classical finite element modeling, the procedure of discretization and time transient computation to take rotor movement into account is even more demanding. To overcome this problem of exhaustive pre-processing and enormous computational costs, it is favorable to allow two meshes of separable domains to become non-conforming with hanging nodes on a defined sliding surface. This enables modeling of two independent FE meshes, one for the fixed and another one for the moving domain, respectively. The most popular and successfully implemented methods are the use of Lagrange multipliers as well as the mortaring method with both techniques imposing the essential interface conditions weakly at the sliding surface. The resulting system matrix in case of the latter method is symmetric and positive definite, whereas the use of Lagrange multipliers introduces additional degrees of freedom which leads to an ill-conditioned and non-positive definite matrix [1]-[6]. Furthermore, most current computational tools introduce a magnetic vector potential to describe the fields. This leads to high computational costs, since it results in a large number of degrees of freedom and the use of edge elements is mandatory. When analyzing electrical machines, the sliding surface can be naturally selected in the air gap of the machine. Hence, using a magnetic scalar potential in non-conducting regions e.g. the air gap and a current vector potential in conducting regions enables the sliding interface to connect scalar potential degrees of freedom. This also reduces the number of unknowns and thus computational costs will decrease. We have shown earlier [7]-[9] that the non-conforming meshing method based on interpolation techniques can be used to take account of the relative motion between a fixed domain and a moving domain by coupling the scalar potential associated with nodes of the moving domain with those of the fixed domain applying a master slave principle. This paper presents the analysis of a standard two pole asynchronous machine with a squirrel cage rotor [10] with eddy currents due to motion taken into account. In a first step, a time transient analysis of the machine driven by voltage sources is performed at constant rated speed of the rotor. 2. Numerical method The current vector potential T is used in the conductors carrying eddy currents and a reduced magnetic scalar potential F in the non-conducting domain. The description of the voltage excitation results in additional equations. The governing equations are obtained by applying Galerkin techniques as well as the interpolation method of [7]-[9] to Faraday's law and the Gaussian law of magnetism. 3. Finite Element Model The finite element model consists of two independent meshes of the fixed stator domain and the moving rotor domain, respectively. These meshes lead to an overall mesh with about *60 000,* 2nd order node-based hexahedral elements. As a starting point, the computations are performed using a quasi 2D model, i. e. a 3D geometrical model of the machine consisting of only one mesh layer in axial direction. The model consists of *48* stator teeth and *40* rotor teeth and linear material properties are assumed. Figure 1 shows the model, stator winding as well as the rotor bars, and provides a detailed view of the mesh in the air gap region. 4. Preliminary Results The results are obtained for voltage driven sources with the winding of the phases in a star-connection. The time resolution chosen is 15 time steps per electrical period at a frequency *f=50* Hz. Figure 2 shows the computed eddy current density of the stator winding and rotor bars at a certain time instant. Comparisons with results obtained by mortar techniques will also be provided. 5. Conclusion The proposed non-conforming meshing approach is found to be an adequate alternative method to the use of Lagrange multipliers or mortaring techniques. It will be shown in the final version that the method leads to adequate results when simulating the startup of the investigated asynchronous machine.

[1] D. Rodger, H. Lai and P. Leonard, "Coupled elements for problems involving movement," IEEE. Trans. Magn., vol. 26, no. 2, pp. 548-550, Mar 1990. [2] H. Lai, D. Rodger and P. Leonard, "Coupling meshes in 3d problems involving movements," IEEE. Trans. Magn., vol. 28, no. 2, pp. 1732-1734,Mar 1992. [3] C. Golovanov, J. L. Coulomb, Y. Marechal and G. Meunier, "3D mesh connection techniques applied to movement simulation," IEEE. Trans. Magn., vol. 34, pp. 3359-3362, Sep 1998 [4] B. F. Belgacem and Y. Maday, "The mortar element method for three dimensional finite elements," RAIRO-Modelisation mathematique et analyse numerique, vol. 31. Jg., Nr. 2, pp. 289-302, 1997 [5] R. Becker, P. Hansbo and R. Stenberg, "A finite element method for domain decomposition with non-matching grids," ESAIM: Mathematical Modelling and Numerical Analysis, vol. 37, pp. 209-225, 2003 [6] R. Stenberg, "On some techniques for approximating boundary conditions in the finite element method", Journal of Computational and applied Mathematics, vol. 63, pp. 139-148, 1995 [7] G. J. Wallinger, O. Biro, "A coupling method for nonconforming meshes in the 3D FEM analysis of static fields," 16th IGTE symposium on Numerical Field Calculation in Electrical Engineering, digest, pp.54, 2014. [8] G. J. Wallinger, and O. Biro, "3D FEM analysis of static fields for non-conforming meshes with 2nd order node-based elements," IEEE Transactions on Magnetics, vol. 52, 2016, 1-4. [9] G. J. Wallinger and O. Bíró, "Comparison of two formulations taking account of 3D motion induced eddy currents," *2016 IEEE Conference on Electromagnetic Field Computation (CEFC)*, Miami, FL, 2016, pp. 1-1. [10] P. Ponomarev, L. Aarniovuori and J. Keränen, "Selection of optimal slice count for multislice analysis of skewed induction motors," *IECON 2017 - 43rd Annual Conference of the IEEE Industrial Electronics Society*, Beijing, China, 2017, pp. 2149-2153.

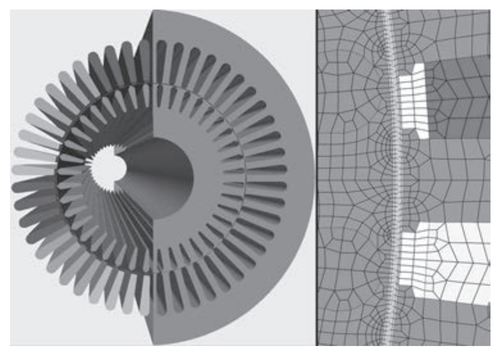

Fig. 1. Model of the two pole asynchronous machine, the stator winding and the rotor bars. A detailed view shows the two independent meshes of the stator and rotor domain. The two meshes are allowed to become non-conforming at the defined sliding surface at the middle of the air gap.

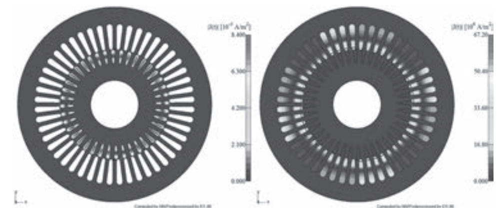

Fig. 2. Preliminary results obtained for a time resolution of 15 steps per electrical period, with stator excitation by voltage sources. The current density of the stator winding and rotor bars are shown.

FU-11. Analytical Method of the Cogging Torque in External Rotor Single-phase BLDC Motors applied Tapered Air-gap with notches.

D. Kim[1,2], *Y. Park*[1,2] and K. Woo[3]

1. Electrical Control Engineering, Sunchon National University, Suncheon, The Republic of Korea; 2. Green Energy Laboratory, Sunchon National University, Suncheon, The Republic of Korea; 3. Pukyong National University, Busan, The Republic of Korea

I. Introduction The conventional methods for reducing the cogging torque of single-phase BLDC motors include the length change of the air-gap, PM asymmetry arrangement, skew of the stator or rotor and shape change of the stator teeth. Some papers reported reduction in the cogging torque for single-phase BLDC motors by varying the air-gap profile, considering the tapered teeth [1-4]. We reduced the cogging torque by applying method to variation of air gap, considering manufacturing and cost aspects[5]. The most accurate style among the other techniques for analyzing the cogging torque is to use finite element analysis(FEA), however this method has the disadvantage in which modeling is actually executed by user also the analysis takes a long period of time [6]. Therefore, it is important to understand trends in the initial design of BLDC motors. Analytical method can be used to obtain proper accuracy and quick analysis results. These studies are being conducted to improve the accuracy and algorithm simplification of shape [7]. This paper presents an analytical method when applied tapered air-gap with notches for cogging torque analysis for single-phase BLDC motor. In order to calculate the magnetic flux density, the asymmetric slot function was applied to express the tapered air gap and was tested for the analysis of the cogging torque. We proposed analytical method technique with asymmetric slot function in stator and analysis about cogging torque in motor with notches. Finally, the proposed analytical method technique was confirmed by cogging torque characteristic of 2D FEA. II. Cogging Torque of Single-phase BLDC Motor This paper used the 120[W] class single-phase BLDC motor with an eight-pole/eight-slot structure. Because in the case of a single phase, the ratio of the number of poles to the number of slots should be 1:1. In consideration of securing the winding space and effectiveness must be in the accordance with the design requirements. Also, the outer diameter was 94 [mm], and stator teeth has designed asymmetric that length of both ends as g1 and g2 of figure1 and it applied two notches on stator teeth. III. Cogging Torque Calculation Cogging torque is occurred inevitably, due to the torque interaction between the permanent magnets of the rotor and the stator slots of a permanent magnet machine. Also, that is one of the causes of noise and vibration, so that the more precision motor should be designed considering cogging torque. In order to establish analytical solutions for the field distributions, the following assumptions are made: - the permeability of iron is infinite - the slot openings have rectangular shape and are infinitely deep - the relative permeability of the permanent magnet is unity The cogging torque is the amount of energy variation according to the amount of rotor rotation that can be expressed the following: $T_{cog} = -(\Delta W(\alpha)/\Delta\alpha)$ ------------ (1) where W is the magnetic energy of the machine and α is the rotational angle of the rotor. For surface permanent magnet type of BLDC, most of the energy change occurs in the air-gap portion. Therefore, the energy in the air-gap must be considered when calculating the cogging torque. For surface permanent magnet type of BLDC, most of the energy change occurs in the air-gap portion. The air-gap energy for the external rotor motor of cogging torque can be expressed as (3) by differentiating the air-gap energy gained from (1) according to (2) with the rotation angle of the rotor. $W(\alpha) = (L_s/4\mu_0)(R_m^2-R_s^2)\{\int_0^{2\pi}\sum B_{nNL}G_{nNL}\cos({}_nN_L(\theta+\alpha))\cos({}_nN_L\theta)d\theta)\} = (L_s/4\mu_0)(R_m^2-R_s^2)\sum B_{nNL}G_{nNL}\cos({}_nN_L\alpha)$ ------------ (2) $T(\alpha) = (L_s\pi/4\mu_0)(R_m^2-R_s^2)\sum B_{nNL}G_{nNL}\sin({}_nN_L\alpha)$ ------------ (3) where B, G, R_m and R_s are the flux density, relative air-gap permeance function, inner radius of the rotor and inner radius of the stator, respectively. Also, where N_p is the number of rotor poles, N_s is the number of stator slots, B_{nNL} is the Fourier coefficients of the flux density function, and G_{nNs} is the Fourier coefficients of the relative air-gap permeance function. L_s is the stack height and N_L is the least common multiple(LCM) of N_p and N_s. According to (3), the cogging torque can be reduced by changing B_{nNL}, G_{nNL}, and N_L. Thus, Cogging torque can be reduced through effectual applied notches. The analytical field solution is found by combining the field solution in the slot less air gap developed by Zhu et al[8, 9]. This paper is calculated by combining the stator teeth function $B(\theta,\alpha)$ for eq(4) and figure2. $\int Rs(\theta)d\theta=Rs-\{g1+((g2/a)\int a(\theta)d\theta)\}$ ------------ (4) that shows magnetic flux density is calculated by applying the stator function according to [9]. When $np \neq 1$ and External Rotor, $Rr = Rs + g + hm$ and hm is radial thickness. Fig.2 comparison cogging torque between the analytical method of Equation (2), FEM and experiment for model applied asymmetric air-gap. The period and magnitude of the cogging torque of analytical method were similar to the results of FEA and experiment. IV. Conclusion The properties of the proposed cogging torque analytical method were verified experiment. The cogging torque meter with a 0.001% RPM accuracy was made by SUGAWARA in Japan. The period and magnitude of the cogging torque were similar to the results of FEA and experiment. More details on additional results will be presented in the INTERMAG2018.

[1] B.-I. Kwon, B.-Y. Yang, S.-C. Park, and Y.-S. Jin, "Novel topology of unequalair-gapinasingle-phase brushless dc motor," IEEETrans. Magn., vol. 37, no. 5, pp. 3723–3726, Sep. 2001. [2] Der-Ray Huang, Tai-Fa Ying, Shyn-Jier Wang, and Chi-mou Zhou, "Cogging torque reduction of a single-phase brushless DC motor", IEEE TRANSACTIONS ON MAGNETICS, vol. 34, no. 4, pp.2075-2077, 1998. [3] A. Hamler and B. Hribernik, "Impact of shape of stator pole of one phasebrushless motor on cogging torque", IEEE Transactions on Magnetics, Vol. 32, No. 3, pp. 1545 – 1548, MAY 1096. [4] D.R. Huang, C.Y. Fan, S.J. Wang, H.P. Pan, T.F. Ying, C.M. Chao and Eric G. Lean, "A new type single-phase spindle motor for HDD and DVD", IEEE Transactions on Magnetics, Vol. 35, No. 2, pp. 839-844, MARCH 1999. [5] Young-Un Park, Ju-Hee Cho, Dae-kyong Kim, Cogging Torque Reduction of Single-Phase Brushless DC Motor With a Tapered Air-Gap Using Optimizing Notch Size and Position, IEEE Transactions on Industry Applications, 51 (2015) 4455-4462. [6] Der-Ray Huang, Tai-Fa Ying, Shyn-Jier Wang, and Chi-mou Zhou, "Cogging torque reduction of a single-phase brushless DC motor", IEEE TRANSACTIONS ON MAGNETICS, vol. 34, no. 4, pp.2075-2077, 1998. [7] S. Ahmed, P. Lefley, "Study of the impact of asymmetrical stator pole arc on the cogging torque for single phase Permanent Magnet BLDC Motor", EPECS Conference, pp.1-4, 2009. [8] Z. Q. Zhu, D. Howe, and C. C. Chan, "Improved Analytical Model for Predicting the Magnetic Field Distribution in Brushless Permanent-Magnet Machines," IEEE Transactions on Magnetics, vol. 38, no. 1, pp. 229-238, 2001. [9] Z. Q. Zhu, D. Howe, E. Bolte, and B. Ackermann, "Instantaneous Magnetic Field Distribution in Brushless Permanent Magnet DC Motors, Part I: Open-Circuit Field," IEEE Transactions on Magnetics, vol. 29, no. 1, pp. 124-135, 1993.

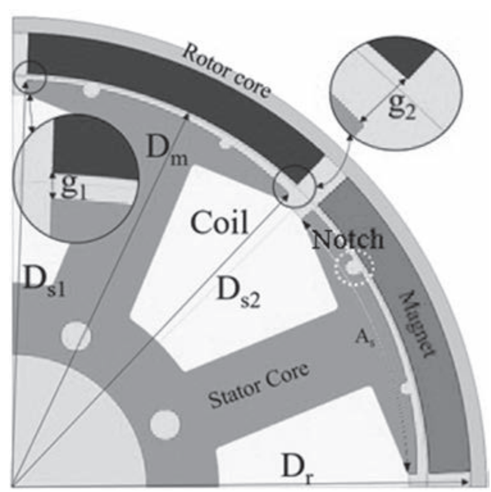

Fig. 1. Analysis Model

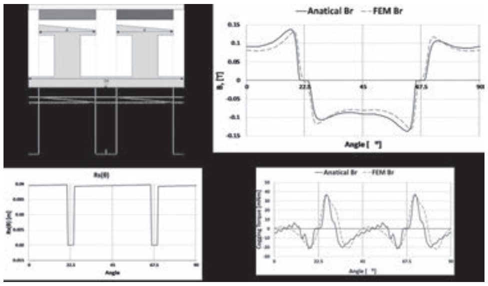

Fig. 2. Shape of asymmetric stator and results
(a) Stator shape and permeance function (b) applied stator function
(c) magnetic flux density of Slotted type (d) Result of cogging torque

FU-12. Two-Level Surrogate-Assisted Differential Evolution Multi-objective Optimization of Electric Machines Using 3D Finite Element Analysis (FEA).

N. Taran[1], D. Ionel[1] and *D.G. Dorrell*[2]

1. Electrical and Computer Engineering, University of Kentucky, Lexington, KY, United States; 2. Discipline of Electrical, Electronics and Computer Engineering, University of KwaZulu-Natal, Durban, South Africa

Introduction Many parameters are considered in electric machine design and an optimization algorithm can be used. These usually need thousands of design evaluations before meeting the termination criterion. Time consuming 3D finite element analyses (FEAs) are not tenable although machines with 3D flux paths, such as axial flux and transverse flux, cannot be accurately evaluated with 2D models. One solution is to use surrogate models rather than 3D FEA; however, the accuracy of surrogate models reduces for a large and nonlinear search space. Another solution can utilize algorithms that find the global optima with a minimum number of design evaluations. A combination of these two solutions is proposed here. *Optimization Algorithm* The proposed approach has an exterior level evolutionary algorithm, replacing the mutation with an interior level complete differential evolution (DE) optimization. The exterior loop uses expensive FEAs while interior loop uses cheap surrogate models. The first generation of exterior loop parent designs are estimated Pareto and, in fact, very close to the actual Pareto front (non-dominated designs). The two-level evaluation of Pareto designs results in an efficient exploration and exploitation approach so that the global optima can be located within the first few generations, depending on the surrogate model accuracy. The surrogate model is a Gaussian process prediction, known as universal kriging in geostatistics [1]. The algorithm does not solely rely on estimated values; it has a dynamic sample pool that stops increasing in size once the estimation error is sufficiently small and gradually improves the kriging model resolution only around the Pareto designs. This achieves accurate final results with self-adjustment of the sample pool for different problems, avoiding unnecessary expensive evaluations and faster convergence. Multi-objective optimization sets a maximum number of function evaluations or maximum number of generations as the termination criterion. For algorithms that quickly converge to the optima, this criterion can produce many dispensable generations; it is vital to avoid this for more expensive functions. Here, a hybrid stopping criterion is used. Negligible improvement in the tips and middle point of the Pareto front for a few consecutive generations will satisfy the third stopping criterion. Meeting any of these criteria stops the algorithm. Fig 1 gives a flowchart for the algorithm. *Algorithm Validation and Machine Design Examples* The new optimization algorithm was implemented and validated using the test function DTLZ2 [2]. This is capable of assessing the algorithm for problems with different complexity levels, i.e., number of optimization variables and objectives. Tests with one to three objective functions, each with four to twelve variables, were studied. The results show that even for high numbers of variables, the proposed two-level algorithm outperforms the conventional method. For complex problems with more than 3 objectives and 12 variables, the sample pool construction needs almost as many function calls as the total number of evaluations in the conventional DE algorithm. Hence, their performance is comparable. Two practical implementations of the optimization algorithm are developed here. These are for an axial flux permanent magnet (AFPM) machine. Two different arrangements are considered: a multi-disc coreless machine with two stators and a commercially available motor with a single-rotor single-stator topology [3]. The objectives are to minimize the total loss and active mass under rated operational conditions. The number of variables are four for the coreless machine and six for the conventional machine. The Pareto front obtained from conventional multi-objective DE (MODE) and two-level surrogate assisted algorithm (SAMODE) are presented. *Discussion and Conclusions* A two-level surrogate assisted DE based optimization is proposed for electric machine design with 3D FEA. The results (Fig 2) show that the algorithm outperforms conventional methods with less than half the number of design evaluations. If the kriging model is sufficiently accurate, the number of generations of the exterior loop remains low. Comparing the Pareto fronts for the different examples, the conventional algorithm terminates prematurely and needs a tighter stopping criterion. This is because the total number of function calls in two-level optimization is the sum of interior loop (cheap) and exterior loop (expensive) function evaluations which will be orders of magnitude more than that of the conventional algorithm. Increased number of evaluated designs means a wider search for each generation, hence faster convergence towards optimum designs. It can be noted is that the two-level algorithm constructs a high-quality kriging model for designs close to Pareto. Therefore, the gap between designs in the Pareto can be easily filled using the kriging model. For the conventional algorithm, the only way to have a fuller Pareto front is to increase the population of each generation, which requires even more expensive FEA simulations be run.

[1] C. E. Rasmussen and C. K. I. Williams, "Gaussian Processes for Machine Learning", MIT Press, 2006. [2] K. Deb, L. Thiele, M. Laumanns and E. Zitzler, "Scalable multi-objective optimization test problems," *Evolutionary Computation, 2002. CEC '02. Proceedings of the 2002 Congress on*, Honolulu, HI, 2002, pp. 825-830. [3] N. Taran, V. Rallabandi, D. M. Ionel and G. Heins, "A comparative study of coreless and conventional axial flux permanent magnet synchronous machines for low and high speed operation," *2017 IEEE Energy Conversion Congress and Exposition (ECCE)*, Cincinnati, OH, 2017, pp. 321-327.

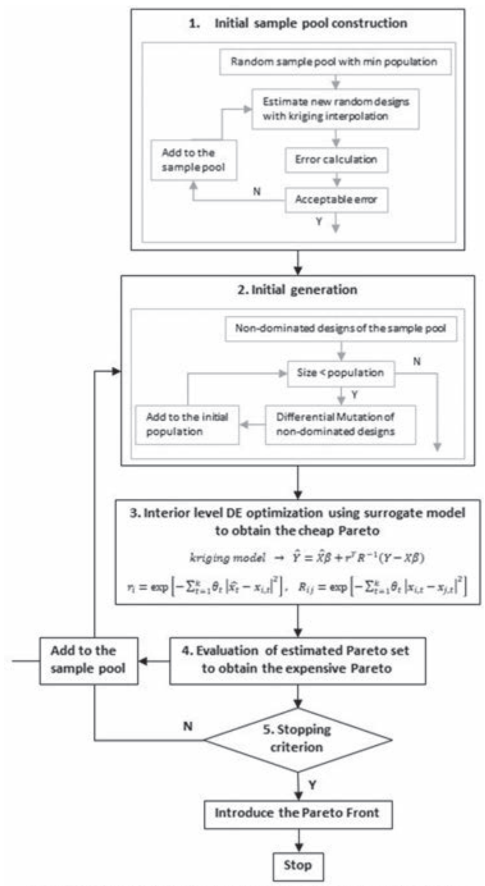

Fig. 1. The flowchart of the proposed two level surrogate assisted optimization algorithm.

Fig. 1.

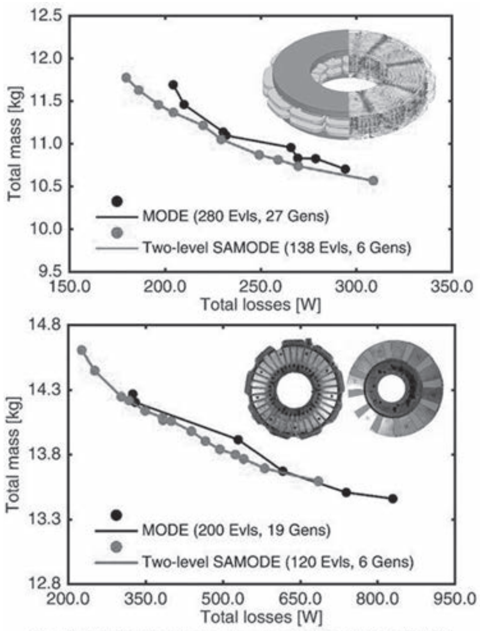

Fig. 2. Pareto fronts for the example coreless AFPM design study and 3D FEA model (top) and prototype optimization of a conventional AFPM.

Fig. 2.

FU-13. Comparison of Various Constraints in 3-D Adaptive Degrees-of-Freedom Finite Element Method.

Y. Zhang[1], S. Ho[1] and W. Fu[1]
1. Department of Electrical Engineering, The Hong Kong Polytechnic University, Hong Kong, Hong Kong

In this paper, the 3-D application of a novel adaptive degrees-of-freedom (DoFs) finite element method (FEM) is presented with different categories of constraints. Performance of this novel method is compared with the conventional h-refinement adaptive finite element (AFEM). Moreover, various constraints are investigated to balance the efficiency and the accuracy. A preliminary study on the constraint constructed with shape function of polyhedron is conducted. I. Introduction Adaptive finite element methods (AFEMs) have been widely applied in electromagnetic device design and analysis. The major purpose of AFEMs is to obtain solutions, which have a uniform error distribution over the entire domain, for practical problems. There are two key technologies used in the adaptive method, the error estimator and the mesh adaptive method [1]. According to the mesh adaptive method, the AFEMs are classified into three categories: h-refinement method, p-refinement method and r-refinement method. The h-refinement method [2, 3], which changes the number and size of elements, is a popular one and is adopted in many commercial and opensource software packages [4, 5]. Recently, adaptive degrees-of-freedom (DoFs) FEM is proposed as a novel AFEM [6, 7]. Through this method, explicit elimination of nodes is replaced by imposing constraints on DoFs of these nodes. The symmetry characteristic of the stiffness matrix is maintained, while the size of the global equations is reduced. In [6, 7], a formulation of two master DoFs is employed for 2-D problems, which is validated with several examples. In this paper, this method is extended to 3-D application. Meanwhile, constraints of different number of master DoFs are investigated to find a balance between efficiency and accuracy. Further estimation on the performance of the adaptive DoFs FEM is conducted through comparisons with the conventional AFEM. II. Methodology Constraints are linear or nonlinear formulations involving one or several DoFs, which are classified into slave DoFs and master DoFs. These formulations are used to eliminate and recover variables in the preprocessor and postprocessor. The stiffness equations are modified before global assembly in the form given by $Ku=f$ *to* $T^{T}KTu'=T^{T}f$ Although the dimensions of these three matrixes are increased in the element level, the size of global stiffness equations is reduced by the number of constraints. The sparseness of the stiffness matrix is decreased, which requires more memory space. The increment of nonzero entries of stiffness matrix is determined by the number of master DoFs used in constraints. New correlations between DoFs are introduced to the mesh mathematically and corresponding geometric links may not exist. However, more master DoFs could increase the accuracy of the constraints. The gradients of field along different directions are unknown, then it may be difficult to find two master DoFs to represent one slave DoF accurately. The extreme scheme is regard all the nodes, which share edges with the slave node, as master nodes. And shape function of the polyhedron [8] involving all the master nodes is employed as the constraint. For this scheme, the number of master DoFs in one constraint is uncertain and is larger than ten under some circumstances. A simple scheme is to employ two master DoFs in a liner manner. Because of the insufficient knowledge of field distribution, the choice of master DoFs is blindness to some extent. Then choosing the most adjacent nodes to the slave node is reasonable and easily implemented. Despite of the number of master DoFs, the mesh is not coarsened, i.e. the quality of mesh is maintained. For traditional AFEM, slave nodes are eliminated explicitly. The performance of this novel method can be evaluated through comparison with that of the traditional method in terms of memory requirement, computation time and accuracy. III. Numerical Results A preliminary study of the constraints is conducted on a cylinder shape domain, which is meshed with tetrahedron element. Then several nodes are randomly chosen and regarded as slave nodes. The number of their master nodes ranges from nine to seventeen. Based on the shape function of polyhedron and the coordinates of slave nodes, linear constraints for each slave node is conducted. The sum of the coefficients of each constraint formulation equals to one. Detailed information of two slave nodes with fewest and most master nodes are shown in Fig. 1 with the master node Id and corresponding coefficient. It can be found that the correlations between slave node and master nodes are roughly uniform. Reducing the number of master nodes may result in large sacrifice on accuracy. IV. Conclusion The application of a novel ADoF FEM in 3-D problems is investigated in this paper, and the performance of this method is compared with that of the traditional AFEM. One type of constraint is tested in the preliminary study. Detailed information about the evaluation of different categories of constraints will be reported in the full paper.

[1] Z. J. Cendes and D. N. Shenton, "Adaptive Mesh Refinement in the Finite-Element Computation of Magnetic-Fields," *IEEE Trans. Magn.*, vol. 21, no. 5, pp. 1811-1816, 1985. [2] Raizer, G. Meunier, and J. L. Coulomb, "An approach for automatic adaptive mesh refinement in finite element computation of magnetic fields," *IEEE Trans. Magn.*, vol. 25, no. 4, pp. 2965–2967, Jul. 1989. [3] J. F. Remacle, C. Geuzaine, P. Dular, H. Hedia, and W. Legros, "Error estimation based on a new principle of projection and reconstruction,"*IEEE Trans. Magn.*, vol. 34, no. 5, pp. 3264–3267, Sep. 1998. [4] Infolytica. [Online]. Available: https://www.infolytica.com/ [5] ANSYS. [Online]. Available: http://www.ansys.com [6] Y. P. Zhao, S. L. Ho, and W. N. Fu, "A Novel Adaptive Mesh Finite Element Method for Nonlinear Magnetic Field Analysis," *IEEE Trans. Magn.*, vol. 49, no. 5, pp. 1777-1780, May 2013. [7] Y. P. Zhao, S. L. Ho, and W. N. Fu, "An Adaptive Degrees-of-Freedom Finite-Element Method for Transient Magnetic Field Analysis," *IEEE Trans. Magn.*, vol. 49, no. 12, pp. 5724-5729, Dec 2013. [8] M. Wicke, M. Botsch, and M. Gross, "A finite element method on convex polyhedra," *Comput. Graph. Forum*, vol. 26, no. 3, pp. 355-364, 2007.

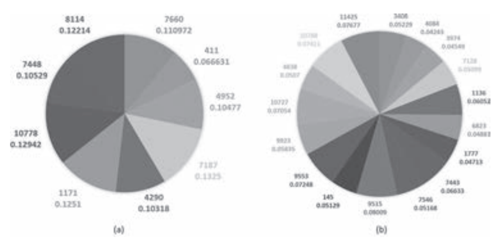

Fig. 1. Constraints of two slave nodes with fewest and most master nodes.

FU-14. Finite-element Method with Topological Data Structure Mesh for Optimization of Electrical Device.

X. Liu[1] and *W. Fu*[1]
1. Electrical Engineering, The Hong Kong Polytechnic University, Hong Kong, Hong Kong

Abstract–This work applied the finite-element method (FEM) with topological data structures to the optimization of electrical devices. A generic modifiable graph data structure is built according to the graph-theoretic foundation for these data structures. The employed topological FEM avoids rebuilding of the mesh in traditional FEM method while geometrical variations happen. The effectiveness of the algorithm which can save computer storage and working time when applied to successive optimization is verified by numerical example. Comparison of the topological FEM with traditional FEM on storage load and working time is shown in this work. I. Introduction The commonly used node element mesh contains a set of elements which corresponds with a set of node impact. Since this data structure lacks of topological information, it is not enough in an adaptive analysis environment [1]. Abstract topological entities on which relay a type of model can be manifested by topological data structures. For 2D models, a face of an element in a 2D mesh usually corresponds to face, edge and vertex. In order to consider a topological representation sufficiently, the data structure must contain enough information which retrieve all adjacency relationships among its topological entities and it should capable of preventing errors or ambiguities [2]. In computational science, one problem is to develope methods for the problems on domains which contain one or several objects which may have time-dependent geometry structure [3]. In this case, the regeneration of mesh at each time step will cost dramatic amount of computing time and storage. One of the approaches for this type of problems is to employ a novel mesh structure which can make the regeneration much efficient and economical. In this paper, modifiable array data structures for topology FEM mesh is employed, and it is applied in the optimization of electrical device which contains geometrical deformation. Numerical test is executed to prove the methodology is practical. II. Conforming of FEM mesh Finite element mesh is consisted by *m*-entities whose closures are one of the following types: (1) point (d=0); (2) line (d=1); (3) triangle (d=2); (4) tetrahedron (d=3). The fields of the FEM are defined as piecewise functions composed of basis functions. They are controlled by a finite set of degrees of freedom which are attached to mesh entities. Therefore, a mechanism is required for connecting degrees of freedom with mesh entities. The graph structure is developed as in Fig. 1(a) and it is used to represent a mesh topology graph, and the example of graph structure layout is shown as Fig. 1(b). While vertices point to one adjacent element, implementations of elements and vertices are represented with three adjacency relations: elements point, adjacent elements and vertices. A modifiable structure is the GRUMMP system which is developed by [4]. This structure clearly explains the vertices, sides and elements. The adjacencies which are from elements to sides, sides to vertices, and vertices to sides are always stored. III. Structure of Arrays for Geometrical Deformation Problem In the process of optimization, the geometrical position of an object may be modified. This process can be decomposed to two steps: removing and adding. Removing an object can create a hole at some arbitrary index. If the indices cannot be changed, then the holes must be remained. These holes will be tracked by using a free list, or list of available space and this means new variable array along with those of the objects will be created. To remove an object, the resulting hole will be simply added as the first hole in the free list. Adding an object first needs to check whether there are holes in the free list. If hole exist then the first hole is used as space for the object, and it will be removed from the free list. Otherwise the object should be added at the end and a geometric growth of all arrays may be triggered at the same time. A helpful layout diagram of modifiable object arrays is shown as Fig. 1(c). IV. Optimization procedure Sizing and shape optimization of the optimal design problems is of paramount importance. In the process of optimization, FEM for field computation is widely used in order to get parameters, including design parameters that can be computed by static field analysis and transient field analysis. In this paper, genetic algorithm (GA) is employed for the optimal design problem. V. Numerical Examples An optimal shape design problem is solved using the topological FEM with the graph structure mesh and the GA. The direct current (DC) magnet device is shown in Fig. 2(a). The pole shape AB is to be optimized. It is to generate a magnetic flux density as uniform as possible in the observation line CD. For this problem, the design variables are taken to be $\{x_0, y_0, r_0\}$ as shown in Fig. 2(a). The constraint conditions are shown as Fig. 2(b). The optimization result is shown as Fig. 2(c). And the comparison of the topological FEM with traditional FEM is shown as Fig. 2(d). VI. Conclusion The validation shows that it is capable of the proposed method to reach an accurate result. The numerical example shows that the algorithm the working load of the optimization with topological FEM is significantly reduced compare to the optimization with traditional FEM. The computing time of FEM simulations is shortened and the optimization process is accelerated while the accuracy of it is still ensured.

[1] B. MW and S. MS, "A general topology-based mesh data structure," International Journal for Numerical Methods in Engineering, vol. 40, pp. 1573–1596, 1997. [2] W. K, "Topological structures for geometric modeling," Ph.D. Thesis, vol. Rensselaer Polytechnic Institute, p. New York, 1986. [3] W. N. F., S. L. Ho, and H. C. Wong, "Generation and rotation of 3-D finite element mesh for skewed rotor induction motors using extrusion technique," IEEE Transactions on Magnetics, vol. 35, pp. 1266-1269, 1999. [4] Ollivier-Gooch, "GRUMMP --- Generation and Refinement of Unstructured, Mixed-Element Meshes in Parallel," http://tetra.mech.ubc.ca/GRUMMP/.

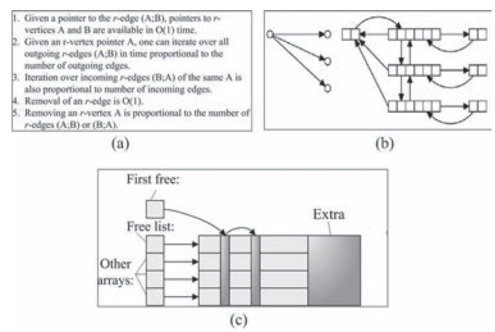

Fig. 1. The runtime properties and the schematics

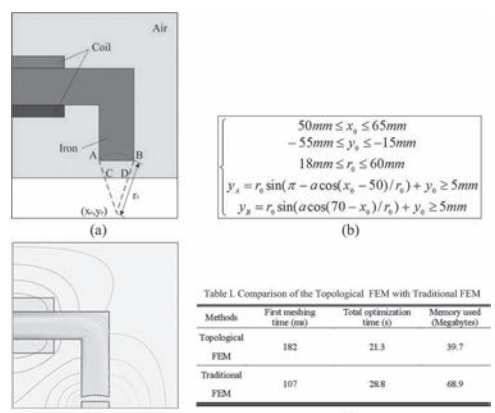

Table I. Comparison of the Topological FEM with Traditional FEM

Methods	First meshing time (ms)	Total optimization time (s)	Memory used (Megabytes)
Topological FEM	182	21.3	39.7
Traditional FEM	107	28.8	68.9

Fig. 2. Numerical example and the simulation results

FU-15. An equivalent circuit model for predicting core losses of a claw pole permanent magnet motor with molded soft magnetic composite core.

X. Ba[1,2], C. Zhang[1], Y. Guo[2] and J. Zhu[2]
1. Beijing Institute of Technology, BeiJing, China; 2. University of Technology, Sydney, Sydney, NSW, Australia

1.Introduction Soft magnetic composite (SMC) materials and SMC electromagnetic devices have attracted strong research interest in the past decades due to its unique properties, such as isotropic magnetic and thermal properties and low eddy current loss[1-2]. Compared to the laminated steels commonly used in electrical machines, SMC ones have core losses comparable to the copper losses[3]. Therefore, effective and accurate prediction of core losses is crucial for design and optimization of high-performance motors, especially for those with new materials and nonconventional topology and complex structures and three-dimensional (3D) magnetic fluxes. As shown in figure1, the three phases of the motor are stacked axially with an angular shift of 120^o electrical from each other. Each stator phase has a single coil (not shown in the figure for clarity) around an SMC core, which is molded in two halves. The outer rotor comprises a tube of mild steel with an array of magnets for each phase mounted on the inner surface. Mild steel is used for the rotor because the flux density in the yoke is almost constant. 2.Modelling of core losses Core losses is crucial for high-speed motor because the core losses is the dominant component of power loss due to high operating frequency[4]. The local flux density patterns within a claw pole permanent magnet motor are quite complex, with flux density locus at one position can be alternating (1D), two dimensional (2D) or even 3D rotating with purely circular or elliptical patterns[5]. For alternating core loss modelling, a standard practice is to separate the loss into three components: hysteresis, eddy current and anomalous losses, i.e. $P_a=C_{ha}fB^h+C_{ea}(fB)^2+C_{aa}(fB)^{1.5}$, where B is the peak value of flux density, f the frequency, and C_{ha}, h, C_{ea}, and C_{aa} are the loss coefficients. Similarly, the specific core loss with a circular rotating flux vector B can also be separated into three components as $P_r=P_{hr}+C_{er}(fB)^2+C_{ar}(fB)^{1.5}$, where C_{er} and C_{ar} are coefficients for the rotational eddy current and anomalous loss components, and P_{hr} is the rotational hysteresis loss and it was proposed by a formulation: $P_{hr}/f=a_1[1/s/(a_2+1/s)^2+a_3^2-(1/(2-s)/(a_2+1/(2-s))^2+a_3^2)]$ where $s=1-B/Bs*sqrt(1-1/(a_2^2+a_3^2))$ More generally, the flux density loci in 3D flux machines may be elliptical, characterised by major and minor axes B_{maj} and B_{min}, with ratio $R_B=B_{min}/B_{maj}$, with alternating ($R_B=0$) and circular ($R_B=1$) patterns as limiting cases. The core loss with an elliptical rotating flux density can be predicted from the alternating and purely circular formulations as: $P_t=R_BP_r+(1-R_B)^2P_a$, where P_r and P_a are the core losses with a circular B and an alternating B with $B_{maj}=B_p$, respectively, and B_p the peak value of the alternating B[6-7]. 3.Equivalent circuit for predicting core losses in steady-state conditions The motor is assumed to operate in the optimum brushless DC mode. When running in synchronous mode, the claw pole motor's steady-state performance including core losses can be predicted by the equivalent circuit model as shown in Fig. 2. Where E_1 is the root-mean-squared(RMS) value of induced back EMF, R_1 is the stator winding resistance, ω_1 is the angular frequency, $L_{1\sigma}$ is the leakage inductance of the phase winding, and L_1 is the synchronous inductance of the phase winding, which equals the self inductance of a phase winding plus half the mutual inductance between two phase windings. All these parameters have been obtained in the electromagnetic design. Particularly, R_{c1} is the core loss resistance, and it can be expressed by: $R_{c1}=V_1^2/P_t$ 4.Experimental validation To measure the core loss of the claw pole PM machine, a calibrated dc motor is used as a prime mover. At no-load and connected to the tested machine, the power fed into the dc motor is measured. The difference gives the sum of the core loss and mechanical loss of the tested machine. The mechanical loss of the PM machine is measured by replacing the SMC stator with a wood tube (to imitate the windage) and then repeating the previous procedure. The core loss is obtained by subtracting the mechanical loss from the sum of the core loss and mechanical loss. 5.Conclusion The comparison between the calculated core loss using equivalent core-loss resistance and measured core loss in a claw pole permanent magnet SMC machine shows that the proposed equivalent circuit model and calculation method are practical.

1 'The latest development in soft magnetic composite technology'. Reports of H.ogan.as AB, Sweden, 1997-2005. Available at http://www.hoganas.com, see News then SMC update 2 Jack, A.G.: 'Experience with the use of soft magnetic composites in electrical machines'. Int. Conf. Electrical Machines, Istanbul, Turkey, 1998, pp. 1441–1448 3. Guo, Y.G., Zhu, J.G., Zhong, J.J., and Wu, W.: 'Core losses in claw pole permanent magnet machines with soft magnetic composite stators', IEEE Trans. Magn., 2003, 39, (5), pp. 3199–3201 4. Guo, Y.G., Zhu, J.G., Watterson, P. A., and Wu, W.: 'Comparative study of 3-D flux electrical machines with soft magnetic composite core', IEEE Trans. Ind. Appl., 2003, 39, (6), pp. 1696–1703 5. Y. G. Guo, J. G. Zhu, J. J. Zhong, P. A. Watterson, and W. Wu, "An improved method for predicting magnetic power losses in SMC electrical machines," *Int. J. Applied Electromagnetics and Mechanics*, Vol. 19, pp. 75-78, 2004. 6. J.G. Zhu, J.J. Zhong, V.S. Ramsden, and Y.G. Guo, Power losses of composite soft magnetic materials under two dimensional excitations, Journal of Applied Physics, USA, Vol.85, No.8, April 1999, pp.4403-4405. 7. J.G. Zhu and V.S. Ramsden, Improved formulations for rotational core losses in rotating electrical machines, IEEE Transactions on Magnetics, Vol.34, No.4, July 1998, pp. 2234-2242.

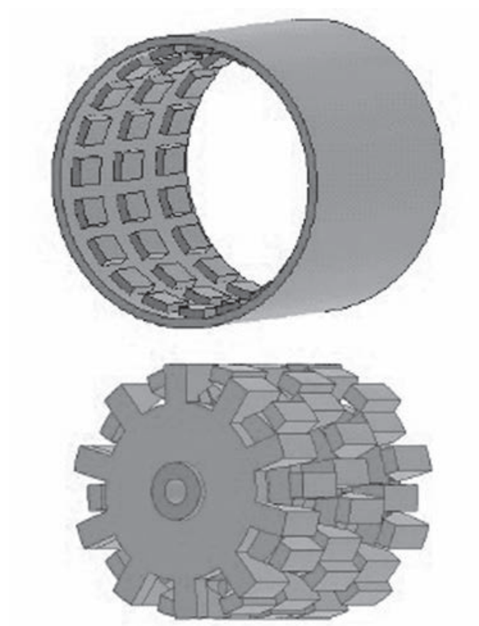

Fig. 1. Magnetically relevant parts of the claw pole SMC motor

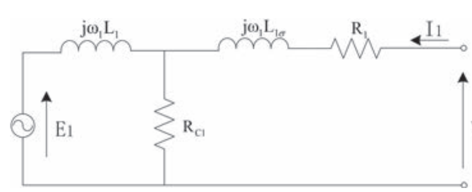

Fig. 2. Equivalent circuit including core losses

FU-16. Finite-element models for foil windings with an improved resolution of the electric field distribution.

H. De Gersem[1]
1. Technische Universitaet Darmstadt, Darmstadt, Germany

Foil winding are sometimes preferred over wire windings because of their favorable electric and thermal properties. Foil windings, however, feature a very particular eddy-current effect, i.e., the current gathers at the foil tips and may there cause substantial thermal problems. As the operating frequency increases, the skin depth gets smaller and an accurate consideration of this particular eddy-current effect in an overall finite-element model of e.g. a transformer or an inductor featuring several foil windings gets cumbersome. In [1] and [2], dedicated finite-element models for foil windings have been proposed. These models avoid to resolve the individual turns of the winding in the finite-element mesh which would make the overall model prohibitively large. Instead, the electric field is modeled such that it is experiences the resistive voltage drop along the winding, the insulating voltage drop perpendicular to the foil and remains constant in the third direction by an additional set of finite-element basis functions. These models, however, turned out to be quite heavy because they necessitate an interpolation between two independent finite-element meshes and because of large dense matrix blocks in the system of equations. In this paper, the mesh interpolation problem is alleviated by a better choice of the finite-element basis functions for discretizing the electric field strength. Based on Legendre polynomials, a basis can be provided which allows an interpolation without the necessity to intersect mesh elements. The overall procedure also leads to smaller dense matrix blocks in the systems of equations. The paper illustrates the improvements by comparing the original models proposed in [1] and [2] with the new technique proposed here, according to the convergence of the finite-element discretization error and according to the computational efficiency.

[1] H. De Gersem, K. Hameyer, "A finite element model for foil winding simulation", IEEE Transactions on Magnetics, Vol. 37, No. 5, September 2001, pp. 3427-3432. [2] P. Dular, C. Geuzaine, "Spatially dependent global quantities associated with 2-d and 3-d magnetic vector potential formulations for foil winding modeling", IEEE Transactions on Magnetics, Vol. 38, No. 2, March 2002, pp. 633-636.

THURSDAY AFTERNOON, 26 APRIL 2018 SIMPOR/ROSELLE BALLROOM, 1:30 TO 4:30

Session FV
SPIN WAVES AND OPTICAL MAGNETISATION SWITCHING
(Poster Session)

Kaiyou Wang, Chair
Institute of Semiconductors, Chinese Academy of Sciences, Beijing, China

FV-01. Excitation of spin waves by pure spin current.

B. Divinskiy[1], V.E. Demidov[1], S.O. Demokritov[1] and S. Urazhdin[2]
1. University of Muenster, Muenster, Germany; 2. Emory University, Atlanta, GA, United States

Downscaling poses a number of new challenges for the implementation of magnonic devices. In particular, the traditional inductive method for spin wave excitation becomes inefficient at nanoscale due to the increasing requirements for the power density, the unavoidable limitations imposed on the wavelength of the excited waves by the geometry of the inductive antennae, and the difficulty of the impedance matching of the latter. An alternative approach to the excitation of spin waves can be based on the spin-transfer torque (STT) mechanism, which provides the ability to directly convert dc electrical currents into microwave-frequency spin waves on nanoscale. Unfortunately, the limitations of the geometry of traditional STT devices operating with spin-polarized electric currents place significant constraints on their compatibility with magnonic devices. By contrast, a significant geometric flexibility can be achieved in the STT devices operated by pure spin currents generated either by the spin Hall effect or by the nonlocal spin injection (NLSI). Indeed, excitation of propagating spin waves by pure spin currents generated by the NLSI mechanism has been recently demonstrated, providing a simple and flexible route compatible with magnonic devices. The ability of a spin-wave source to generate short wave packets is particularly important for the practical implementations of high-speed integrated magnonic circuits. The performance of the traditional inductive excitation technique is very limited in this respect, since the externally generated microwave signal has to be pulse-modulated by semiconductor switches, which are generally characterized by a relatively low power efficiency, and on-off times of at least several nanoseconds. The fastest spin-wave excitation rate demonstrated so far was achieved by utilizing ultra-short laser pulses. However, this approach requires a high-power femtosecond optical source, and therefore has significant technological limitations. Here, we use the time- and space-resolved micro-focus Brillouin light scattering spectroscopy to study the temporal characteristics of the NLSI-based mechanism for the excitation of propagating spin waves. The studied magnonic devices consist of a vertical NLSI spin valve based on a 60 nm diameter nanocontact dynamically coupled to a spin-wave waveguide formed by a 20 nm-thick and 500 nm-wide Py strip fabricated on top of the CoFe(8 nm)/Cu(20nm)/Py(5 nm) trilayer, and terminated at the distance of 150 nm from the nanocontact. Pure spin current, produced due to the spin accumulation in Cu layer above the nanocontact, flows into the active Py layer, exerting STT on its magnetization that results in the compensation of the magnetic damping. When damping is completely compensated by the spin current, the magnetization of the Py layer exhibits microwave-frequency auto-oscillations in the area above the nanocontact. These localized oscillations are then transformed into spin waves propagating in the Py waveguide. By applying the driving dc current in the form of short pulses, we show that the NLSI mechanism is sufficiently fast to enable generation of short spin-wave packets with the duration down to 2 ns, close to the best results achieved by using optical-pulse excitation. Moreover, we find that the intense spin-wave packets generated by the pure spin current experience a nonlinear compression while propagating in the magnonic nano-waveguides, which further reduces their temporal width. A similar mechanism is responsible for the formation of nonlinear spin-wave solitons. It allows one to compensate for the dispersive broadening of spin-wave packets by engineering the nonlinear characteristics of magnonic transmission lines, resulting in improved information flow capacity. Our findings clearly demonstrate the unique benefits of NLSI oscillators as nanocale sources of short spin-wave packets for the implementation of high-speed magnonic devices. We believe that our results should stimulate further developments in magnonics, and bring this area of research closer to the real-world applications.

V. E. Demidov, et al., Sci. Rep. 5, 8578 (2015). V. E. Demidov, et al., Appl. Phys. Lett. 107, 202402 (2015). V. E. Demidov, et al., Nat. Commun. 7, 10446 (2016). S. Urazhdin, et al., Appl. Phys. Lett. 109, 162402 (2016). B. Divinskiy, et al., Appl. Phys. Lett. 109, 252401 (2016). V. E. Demidov, et al., Phys. Rep. 673, 1 (2017).

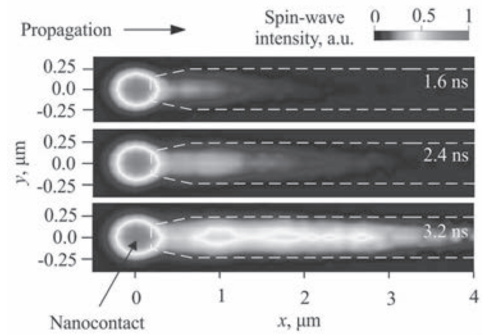

Fig. 1. Measured maps of the spin-wave intensity recorded at delays of 1.6, 2.4 and 3.2 ns with respect to the start of the driving current pulse, as labeled. The temporal width of the spin-wave packet is 2.1 ns and its center frequency is 8 GHz. Dashed lines indicate the contour of the nano-waveguide.

FV-02. Spin wave coupling in strain-tuned magnonic waveguide and reconfigurable magnonic crystals.

A.V. Sadovnikov[1,2], A. Grachev[1], S. Sheshukova[1], Y. Sharaevsky[1], A. Serdobintsev[1] and S. Nikitov[1,2]

1. Nonlinear Physics, Saratov State University, Saratov, Russian Federation; 2. Kotel'nikov Institute of Radioengineering and Electronics, Russian Academy of Sciences, Moscow, Russian Federation

The formation and development of concepts of magnonics, the field of research based on the use of elementary quanta of magnetic excitations (magnons) and spin waves as carriers of information signals, will allow us to develop a new generation of devices and devices for data transmission and processing operating at microwave frequencies with characteristics that could not be obtained earlier[1,2]. Finite-width microstructures based on yttrium iron garnet (YIG) films are key elements of "magnonic networks," which are widely used in planar devices for signal processing, where information is transferred by means of spin waves and logical operations are implemented according to the principles of spin-wave interference [3,4]. The variation of the working frequency range under the action of a magnetic field for magnonics devices [5] operates much slower and requires a higher energy than that under the action of an electric field. The use of piezoelectric layers in lateral topologies of magnetic microstructures makes it possible to significantly expand the functionality of these microstructures owing to the possibility of creating controlled waveguide channels [6,7]. Here we report on numerical and experimental study of the dynamics of spin waves propagating in a magnonic microwaveguide with a piezoelectric layer. Figure 1 schematically shows the structure, consisting of a magnonic waveguide formed by the CW laser patterning from a YIG film with a thickness of 7.7 μm on a gallium-gadolinium garnet substrate. The piezoelectric layer of lead zirconate-titanate (PZT) is placed on the magnonic waveguide. The structure is placed in a static magnetic field H = 1100 Oe, directed along the short axis of the magnonic waveguide for effective excitation of surface magnetostatic waves (MSSW). 150 nm thick electrodes of chromium were deposited on the surface of the piezoelectric layer (on the side where the YIG film is bonded) using a laser cutting method on this side a system of "counter pins" was formed to improve the interaction with the magnonic waveguide. Positive and negative voltage values are applied to the electrodes, as shown in Fig. 1. 250 nm thick electrodes of chromium are deposited on the top of the piezoelectric layer. We use the finite-element method (FEM) to find the strain produced in the YIG film by the PZT layer and then we compute the internal magnetic field profile in the magnetic layer. Figure 2 shows the internal magnetic field profile in the case of positive and negative electric field values. By the means of microwave vector network analyzer and Brillouin light scattering (BLS) technique (by scanning the probing light spot over the MC surface) we demonstrate the electric field induced forbidden gap formation in the SW transmission. Magnetic tuning can be performed through the variation of a bias magnetic field, while electric tuning is possible due to control of the properties of PZT layer through the variation of an applied electric field.

[1] S. O. Demokritov, Spin Wave Confinement: Propagating Waves (2nd Edition) (Pan Stanford Publishing Pte. Ltd, 2017). [2] V. V. Kruglyak, S. O. Demokritov, and D. Grundler, J. Phys. D: Appl. Phys. 43, 264001 (2010). [3] A. V. Chumak, V. I. Vasyuchka, A. A. Serga, and B. Hillebrands, Nat Phys 11, 453–461 (2015) [4] A. V. Sadovnikov, C. S. Davies, V. V. Kruglyak, D. V. Romanenko, S. V. Grishin, E. N. Beginin, Y. P. Sharaevskii, and S. A. // Phys. Rev. B 96, 060401(R) (2017) [5] A. V. Sadovnikov, A. A. Grachev, E. N. Beginin, S. E. Sheshukova, Y. P. Sharaevskii, and S. A. Nikitov, Phys. Rev. Applied 7, 014013 (2017). [6] A.V. Sadovnikov, S.A. Odintsov, E.N. Beginin, S.E. Sheshukova, Yu.P. Sharaevskii, S.A. Nikitov // IEEE Transactions on Magnetics.2017. Vol. 53 Issue 11. Pp. 1-4. [7] A.V. Sadovnikov, A.A. Grachev, E.N. Beginin, S.E. Sheshukova, Yu.P. Sharaevskii, A.A. Serdobintsev, D.M. Mitin, S.A. Nikitov // IEEE Transactions on Magnetics.2017. Vol. 53 Issue 11. Pp. 1-4.

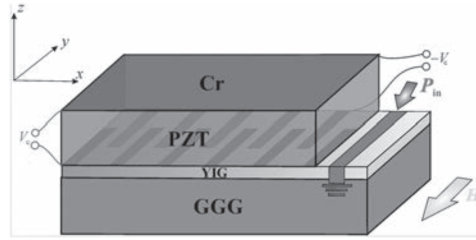

Fig. 1. The schematic of the strain tuned magnonic waveguide.

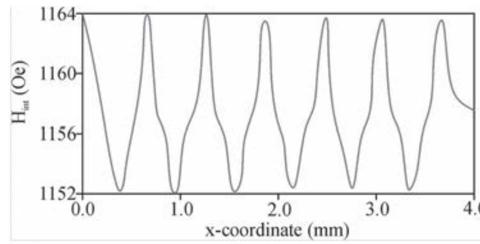

Fig. 2. The internal magnetic field profile $H_{int}(x)$ transformation as a result of the variation of the static electric field E.

FV-03. Spin wave propagation in sputter-deposited YIG nanometer films.

Y. Shiota[1], S. Kasukawa[1], T. Moriyama[1] and T. Ono[1,2]

1. Institute for Chemical Research, Kyoto University, Uji, Japan; 2. Center for Spintronics Research Network, Osaka University, Toyonaka, Japan

Yttrium iron garnet ($Y_3Fe_5O_{12}$, YIG) is well-known material with an extremely small magnetic damping, $\alpha = \sim 10^{-5}$ in bulk, which is two orders of magnitude smaller than that in ferromagnetic metals. The growing demands for YIG-based spintronics have led to the development of YIG thin films with a nanometer thickness range [1, 2]. Recently, magnonics has been attracted considerable interests for the transmission, storage and processing of the information using propagating spin waves [3]. To miniaturize the magnonic devices, it is necessary to reduce the thickness of YIG films for a shorter wavelength. For high quality YIG nanometer films, it has been reported that the YIG thin films by pulsed laser deposition (PLD) show the relatively low damping constant of 2.3×10^{-4} for 20 nm thickness [1]. From the view point of a broad utility and industry, the sputtering growth is better than PLD. In this study we investigate the spin wave propagation in sputter-deposited YIG nanometer films, and characterize the YIG thickness dependence of the several parameters, such as magnetic damping constant, spin wave group velocity and nonreciprocity. The YIG thin films were grown on 0.5-mm-thick single crystal gallium gadolinium garget (GGG) substrates with (111) orientation by RF magnetron sputtering. During the deposition, the substrate was kept at room temperature, the argon pressure and sputtering power was 0.06 Pa and 150 W, respectively. The films were annealed at 900 °C for 8 h in the air. We varied YIG film thickness from 20 nm to 50 nm. Using electron-beam lithography and Ar ion-milling technique, the films were patterned into a circular shape with 10-μm-diameter for ferromagnetic resonance (FMR) measurement and a rectangular shape with 50-μm-width for the spin wave measurement. After patterning the YIG films, an insulating layer of 30 nm SiO_2 was deposited on the entire surface. Finally, microwave antennas were deposited for the FMR and spin wave measurement. First, we evaluate the magnetic damping constant α from FMR measurement using a vector network analyzer. Figure 1 (a) shows the FMR linewidth as a function of resonance frequency. α was extracted from the slope of the linear fits to the data. As shown in Fig. 1(b), the α value decreases with increasing the thickness and we obtained lowest value of $\alpha = 1.3 \times 10^{-3}$ in 50-nm-thick YIG, which is slightly larger than the reported values for sputter-deposited YIG thin films [2]. While we need further optimization of the sputtering condition and/or annealing process to reduce α, it should be noted that the obtained α in this study is significantly smaller than that of ferromagnetic metallic films with similar thickness. Second, the propagating spin wave spectroscopy was performed under the in-plane magnetic field to excite the magnetostatic surface spin wave (MSSW) mode. Figure 2(a) shows the group velocity of spin wave estimated from the oscillation period in transmission spectra. It was about 1.1 km/s in 50-nm-thick YIG waveguide under 14 mT. We found that the spin wave group velocity decreases with increasing the magnetic field and decreasing the film thickness. The group velocity v_g can be calculated from the spin wave dispersion $\omega(k)$ as defined $v_g = d\omega(k)/dk$, which nicely reproduces the experimental results. By comparing the signal intensity, the nonreciprocity defined as A_{12}/A_{21} was also estimated, where A_{12} and A_{21} denote the signal intensity of S_{12} and S_{21}, respectively. The unity value indicates the reciprocal characteristics. In our experiment, the nonreciprocity is mainly caused by x- and z-components of microwave magnetic field [4]. As shown in Fig. 2(b), the nonreciprocity increases with increasing magnetic field and we obtained the largest nonreciprocity of 0.1 at 85 mT. This This nonreciprocity is much more significant than that in ferromagnetic metals [4], which is attributed to the smaller saturation magnetization of YIG than that in ferromagnetic metals.

[1] O. d'Allivy Kelly *et al., Appl. Phys. Lett.* 103, 082408 (2013) [2] H. Chang *et al., IEEE Magn. Lett.* 5, 670104 (2014) [3] A. V. Chumak *et al., Nat. Phys.* 11, 453-461 (2015) [4] V.E. Demidov *et al., Appl. Phys. Lett.* 95, 112509 (2009)

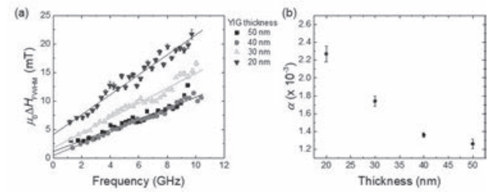

Fig. 1. (a) FMR line width as a function of frequency. (b) YIG thickness dependence of magnetic damping constant α.

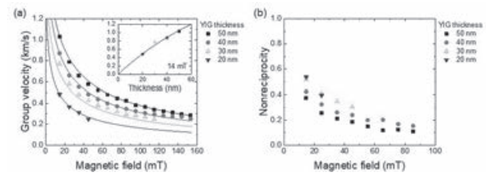

Fig. 2. (a) Spin wave group velocity as a function of magnetic field. Inset shows the YIG thickness dependence of the group velocity. The lines represent the calculated curve from theoretical equation. (b) Nonreciprocity as a function of magnetic field.

FV-04. Suppression of spin-wave transport in antiferromagnets.

J. Ohe[1] and N. Arakawa[1]
1. Department of Physics, Toho University, Funabashi, Japan

Manipulation of the spin-wave is an important task for the spintronics field. Especially, the unidirectional propagating spin-wave is used as a carrier of spin currents or heat currents. It is pointed out that the interference effect of the spin-wave in the Mach-Zender type magnonic circuit gives the NOR gate in the new type of spintronics logistic devices. The other interference effect has been well studied in terms of the Anderson localization that causes the suppression of the electron conductivity in the low dimensional electron gas system. The weak localization effect is occurred in the electron wave function because the time reversal symmetry is conserved. By applying the magnetic field, the time reversal symmetry is lifted and it causes the negative magneto-resistance. For magnetic systems, the time reversal symmetry is broken when the magnetization has an ordered configuration such as a ferromagnetic phase. It means that the spin wave in ferromagnetic systems has no localization effect. However, the time reversal symmetry is conserved when the system has an anti-ferromagnetic order. The localization effect on the spin-wave may affect the thermal conductivity and open a new type of spin wave transport in mesoscopic regime. In this report, we investigate theoretically the weak localization effect of the spin-wave in the disordered antiferromagnetic systems. We calculate the thermal conductivity in classical Heisenberg model by using the diagram technique and found the suppression of the spin wave transport.[1,2] We also calculate the magnetization dynamics using the micromagnetic simulation. The wave packet dynamics shows the strong coherent back scattering [3] during the propagation through antiferromagnetic systems. We prepare the initial wave packet with a certain averaged wavenumber k_0 in antiferromagnetic system. After time evolution, the intensity of the spin wave with the negative value $-k_0$ becomes large as shown in Fig.1. The peak value of the coherent back scattering is larger than that obtained by the ferromagnetic systems. The thermal transport via the spin wave is also suppressed and the possibility of the experimental set up is investigated.

[1] N. Arakawa and J. -i. Ohe, Phys. Rev. B 96, 214404 (2017). [2] N. Arakawa and J. -i. Ohe, arXiv:1710.03445. [3] M. Evers, C. A. Müller, and U. Nowak, Phys. Rev. B 92, 014411 (2015).

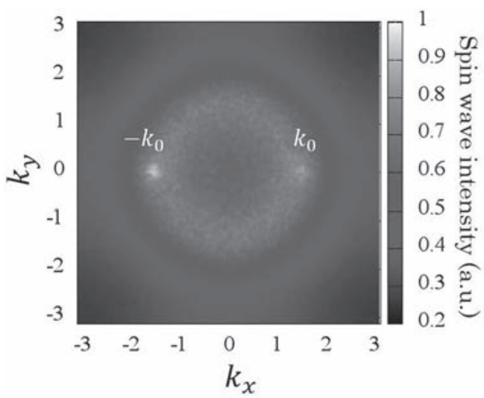

Fig. 1. Spin wave intensity after time evolution of antiferromagnets. Initial wave packet with the wave numver k_0 is strongly refrected with negative wave number $-k_0$.

FV-05. Antiferromagnetic magnonic crystals with alternating Dzyaloshinskii-Moriya interaction.

S. Lee[1] and K. Lee[1]
1. Korea Univ., Seoul, The Republic of Korea

1. Introduction The collective excitation of magnetic moments in magnetic material is named spin-wave (magnon). The spin wave logic devices have been extensively investigated in "magnon spintronics"[1-5], because spin-wave frequency can cover conventional GHz range electronic devices and also can have THz frequencies in antiferromagnet. Moreover spin-wave devices have attractive feature in energy consumption because the spin-wave devices, do not involve electron transport, can avoid Joule heating and thus it is appropriate for low power computing. The antiferromagnetic materials are regarded as proper for magnonic medium. Because the antiferromagnetic materials can have THz frequency with higher spin-wave group velocity. Furthermore, recent works showed that spin-wave devices with antiferromagnetic materials could be performed as spin wave field-effect transistor [3] and polarizer/retarder [4]. Recently, in ferromagnetic materials, magnonic crystals with alternating Dzyaloshinskii-Moriya interaction show large tunability of spin-wave band gap [5]. In this work, based on micromagnetics, we demonstrate sub-THz spin-wave band gap in antiferromagnetic magnonic crystals with alternating Dzyaloshinskii-Moriya interaction. 2. Model In our system, the magnetic free energy density W is given by $W=(1/2)[A(d_x n)^2 - D(x)e_y.(n \times d_x n) - K_u(n.e_y)^2]$ where A is the exchange stiffness constant, $n=(m_1-m_2)/2$ is the staggered order, $D(x)$ is the interfacial DMI constant as function of position x and K is the anisotropy constant. In this work, based on equation of motion for magnetic moments in antiferromagnetic materials, we obtain boundary condition at the boundary between two different DMI constant regions. With this boundary condition, we can obtain reflectance and transmittance of spin-wave and establish dispersion relations in this system with Bloch's theorem. Also to verifying our analytic solution, we performed micromagnetic simulation in 1-D antiferromagnetic system with 1) DMI step and 2) magnonic crystals with alternating DMI constant. In this simulation we use following parameters: the atomic lattice parameter is 0.3 nm, the exchange stiffness constant A is -1×10^{-6} erg/cm, the anisotropy constant K_u is 1×10^6 erg/cm^3, the magnetic moments is 800 emu/cm^3, the Gilbert damping parameter α is 0.001 and we fixed DMI constant in region 1. D_1 as 0 erg/cm^2 and varying D_2 with -2~2 erg/cm^2. 3. Result and Discussion Figure 1 a) shows spin-wave transmittance as a function of DMI constant in region 2 (D_2). The lines are obtained from the analytic solution with boundary condition and symbols are obtained from the micromagnetic simulations. The circle symbols correspond to circular polarized spin-wave and star symbols correspond to linear polarized spin-wave. Here we find that the spin-wave transmittance could be larger than 1 and results from both cases have reasonable agreements regardless of spin-wave polarization. Figure 1 b) shows constructed bands in antiferromagnetic magnonic crystals with alternating DMI constant. Here we plot spin-wave forbidden gap(black) and allow bands(white) as DMI constant in region 2 (D_2). The black(white) regions are calculated from analytical dispersion relation in magnonic crystals. The Symbols are obtain from micromagnetic simulations. Likewise results for spin wave transmittance (Fig. 1. a)), the analytical solution and numerical results are well matched and the spin-wave polarization does not affect to the results. From Fig. 1. b), we find that for D_2= 2 erg/cm^2 the spin-wave band gap opens up to 0.1 THz. 4. Summary We propose antiferromagnetic magnonic crystal with alternating DMI and investigate its property based on micromagnetic simulation. Also, compared with ferromagnetic materials, the large band gap can opens in this system. Moreover, since the DMI constant can be modulated by external electric field, the spin-wave band gap also has tunability with electric fields. Thus these results show that the antiferromagnetic magnonic crystal also can be one of candidates for magnon transistor like modulating electron transport in semiconductor transistors by electric field.

1. B. Lenk, H. Ulrichs, F. Garbs, and M. Münzenberg, Phys. Rep. 507, 107 (2011). 2. A. V. Chumak, V. I. Vasyushka, A. A. Serga, and B. Hillebrands, Nat. Phys. 11, 453 (2015). 3. Ran Cheng, Matthew W. Daniels, Jian-Gang Zhu and Di Xiao Sci. Rep. 6,24223 (2016) 4. Jin Lan, Weichao Yu and Jiang Xiao, Nat. Comm. 8, 178 (2017) 5. S.-J. Lee, J.-H. Moon, H.-W. Lee and K.-J. Lee, Phys. Rev. B 96, 184433 (2017)

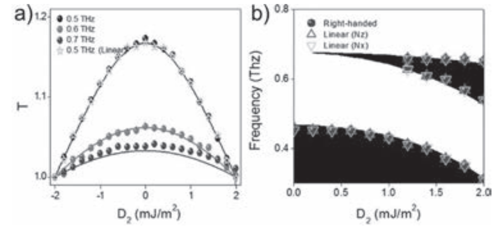

Fig. 2. a) The spin-wave transmittance in DM-step as a function of D_2. b) The spin-wave forbidden gap and allowed bands in magnonic crystals as a function of D_2

FV-06. Motion of a skyrmionium driven by spin wave.

M. Shen[1], Y. zhang[1], J. Ouyang[1], X. Yang[1] and L. You[1]
1. School of Optical and Electronic Information, Huazhong University of Science and Technology, Wuhan, China

A skyrmionium is composed of two skyrmions with opposite skyrmion numbers and different sizes in the same track. In recent years, the motion of a skyrmionium driven by spin-polarized current has been investigated. However, the motion of a skyrmionium driven by a spin wave has not been reported. In this paper, we report our work concerning the numerical analysis of spin wave-driven motion of a skyrmionium in a nanotrack. The results show that the motion of a skyrmionium was significantly influenced by varying the frequency and amplitude of the AC magnetic field for exciting a spin wave, the distance between the spin wave source and the skyrmionium, and the damping coefficient of the ferromagnetic track. We found skyrmionium deformation during its initial motion process, but its shape could be recovered as it moved farther away from the spin wave source. Additionally, a series of velocity peaks were observed in the frequency range between 25 GHz and 175 GHz. When compared to a skyrmion, the skyrmionium could be driven by a spin wave to move in a wider frequency range at a higher velocity, which offers the skyrmionium potential application in wide-frequency spintronic devices.

1.W. Jiang, X. Zhang, G. Yu, W. Zhang, X. Wang, M. B. Jungfleisch, J. E. Pearson, X. Cheng, O. Heinonen, K. L. Wang, Y. Zhou, A. Hoffmann, and S. G. E. te Velthuis, Nat. Phys. 13, 162 (2017). 2.X. Zhang, Y. Zhou, and M. Ezawa, Nat. Commun. 7, 10293 (2016). 3.X.Zhang, J. Xia, Y. Zhou, D. Wang, X. Liu, W. Zhao, and M. Ezawa, Phys. Rev. B 94, 094420 (2016). 4. S.-M. Seo, H.-W. Lee, H. Kohno, and K.-J. Lee, Appl. Phys. Lett. 98, 012514 (2011).

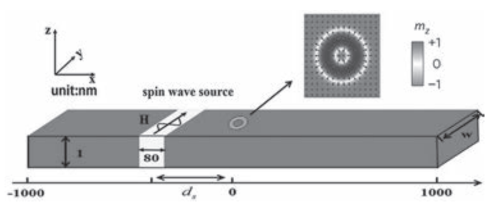

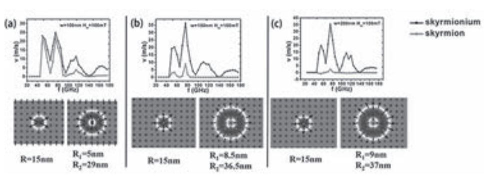

FV-07. Bose-Einstein condensation of magnons in confined systems studied by micromagnetic simulations.

M. Mohseni[1], T. Brächer[1], Q. Wang[1], O. Serga[1], B. Hillebrands[1] and P. Pirro[1]
1. Physics, TU Kaiserslautern, Kaiserslautern, Germany

Magnonics studies the utilization of spin waves in magnetic materials for applications like wave based information processing and logic. Spin waves and their quanta, the magnons, are a type of quasi particles which belongs to the family of bosons, and can be considered as the low energy excitations of the spin ensemble of a magnetically ordered system. Magnons carry a quantized amount of energy and momentum, and due to their bosonic nature, they can occupy a single energy state at the same time, e.g. form a Bose-Einstein Condensate (BEC) [1] at room temperature. Since the first observation of this macroscopic quantum state in 2006, numerous studies have been performed to explore the rich physics of the magnon BEC and the novel dynamics that can emerge in a BEC, like supercurrents [2] or condensation in ultra-hot gases [3]. However, these experimental studies have been restricted to BEC formation in bulk samples and the theoretical description has been performed using effective theories and not by the full solution of the Landau-Lifshitz-Gilbert equation. Here, we present a micromagnetic study of the possibility of the formation of a magnon BEC in magnetic microstructures. We use the finite difference code Mumax 3.0 [4] to solve the full LLG including Gilbert damping in micron sized rectangular waveguides made of Permalloy (Py) and Yttrium Iron Garnet (YIG). By specifically designing the band structure and the excitation source, we show that the magnons occupy the lowest energy level in the systems which can be explained in favor of a BEC formation in the case of YIG and by asymmetric parallel pumping in case of Py. Fig. 1a shows the frequency spectrum close to the band bottom of a 500 nm wide Py waveguide magnetized along its long axis and driven by a localized, high power microwave source at f_p = 16.5 GHz which is used to parametrically inject magnons [5]. The dispersion relation of the first waveguide mode calculated based on [6] is displayed in Fig. 1b. The injected magnons directly occupy the mode at f_{BEC} = 7.75 GHz and a secondary mode f_{sec} =8.95 GHz, without populating the mode at $f_p/2$. It can be seen that f_{BEC} corresponds to the BEC point which is the band bottom of the first waveguide width mode. This asymmetric parallel pumping, which populates directly the BEC point, is possible due to the localized pumping source and it is favored due to the vanishing radiation losses at this spectral point (vanishing group velocity). In contrast to the Py case, the observation of the formation of a magnon BEC by nonlinear magnon scattering is possible in YIG. Fig. 2 shows the band structure of a 500 nm wide YIG waveguide also magnetized along its long axis and driven by a localized excitation source at f_p = 10 GHz. Due to multi-magnon scattering processes which occur in the system when the excitation power is high enough, magnons condense at the global minimum and form a BEC. We found that after switching off the excitation, the magnon population at the BEC point further increases whereas the directly injected magnons decay. This confirms that the redistribution of magnon energy via scattering processes, which is facilitated by the long life time of the magnons in YIG, is the underlying mechanism of the BEC formation in this case.

[1] "Bose-Einstein condensation of quasi-equilibrium magnons at room temperature under pumping", S. O. Demokritov, V. E. Demidov, O. Dzyapko, G. A. Melkov, A. A. Serga, B. Hillebrands, A. N. Slavin, *Nature* 443 (7110), 430-433 [2] "Supercurrent in a room-temperature Bose-Einstein magnon condensate", D. A. Bozhko, A. A. Serga, P. Clausen, V. I. Vasyuchka, F. Heussner, G. A. Melkov, A. Pomyalov, V. S. L'vov, B. Hillebrands, *Nature Physics* 12, 1057–1062 (2016) [3] "Bose–Einstein condensation in an ultra-hot gas of pumped magnons", A. A. Serga, V. S. Tiberkevich, C. W. Sandweg, V. I. Vasyuchka, D. A. Bozhko, A. V. Chumak, T. Neumann, B. Obry, G. A. Melkov, A. N. Slavin, and B. Hillebrands, *Nature Communications* 5, 3452 (2014) [4] "The design and verification of mumax3", A. Vansteenkiste, J. Leliaert, M Dvornik, M. Helsen, F. Garcia-Sanchez, and B. V. Waeyenberge, *AIP Advances* 4, 107133 (2014). [5] "Parallel pumping for magnon spintronics: Amplification and manipulation of magnon spin currents on the micron-scale", T. Brächer, P. Pirro, and B. Hillebrands, *Physics Reports* 699, 1 (2017). [6] "Theory of dipole-exchange spin wave spectrum for ferromagnetic films with mixed exchange boundary conditions", B.A. Kalinikos and A. Slavin, *Journal of Physics C: Solid State Physics* 19, 7013 (1986).

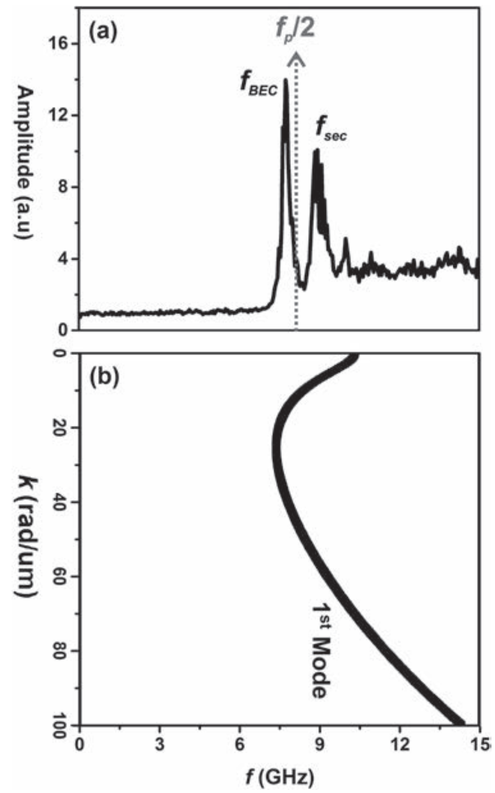

Fig. 1. a) Frequency spectrum of the system driven at f_p = 16.5 GHz exhibiting two populated modes, b) Dispersion relation of the waveguide displays the first width mode of the system.

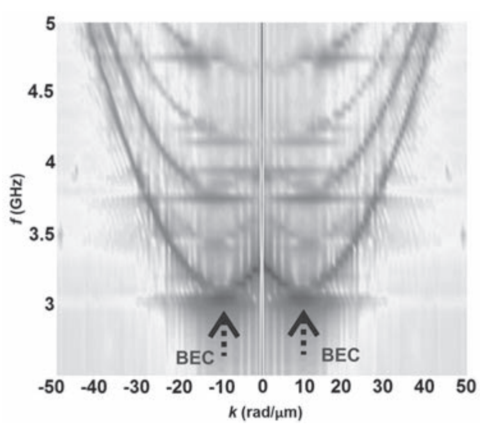

Fig. 2. Band structure close to the BEC point of a YIG waveguide driven by a localized source at f_p = 10 GHz (outside the depicted spectral area). The formed magnon BEC is indicated by arrows.

FV-08. Phase locking, intermittency and chaos, of an array of magnonic crystal cavities driven by spin torque nano oscillators.

N. Kumar[1] and A. Prabhakar[1]
1. Electrical Engineering, IIT Madras, Chennai, India

Magnonic crystals created by an array of periodically arranged holes on a thin ferromagnetic film show frequency bandgaps in their spin wave spectrum. By removing a few holes, or anti-dots, from the array, we are able to create magnonic crystal cavities (MCCs) where spin waves of a particular wavelength are resonant. By adding a nano-contact and driving spin polarized current, or a spin torque nano-contact oscillator (STNO) to each cavity, we are able to simulate a gain element within that cavity. The combination of gain and a resonant cavity, lead to the creation of a SWASER, whose optical analogue is the commonly used LASER. We have previously reported how a MCC can be designed to generate a narrow linewidth spin wave excitation [1]. The aim of the present work is to demonstrate how arrays of these cavities can be arranged to transfer power, in phase, to an adjacent magnonic crystal waveguide (MCW). The radius of the anti-dot and the lattice constant of the magnonic crystal are 40 nm and 150 nm, respectively. The full geometry consists of 49 x 49 unit cells, and the MCW was created by removing one row of anti-dots. The MCCs were placed on either side of the MCW, again separated by one row of anti-dots. Each MCC was created by removing 3 anti-dots, and a STNO placed at the center of the MCC. We work with the magnetic properties of permalloy, assume a damping constant of 0.01, and apply a static external field along the direction of the MCW. The simulation data was probed in a region of the MCW and saved every 10 ps, with sufficient resolution to observed spin wave oscillations up to 50 GHz. Other aspects of the simulation methodology have been previously reported [1]. The locations of the MCCs, relative to each other and the adjacent waveguide, are restricted by the very nature of the peridocity of the underlyig lattice. We use the GPU accelerated parallel micromagnetic solver, MuMax [2], to study the performance of different numbers of MCCs, and observe that the coupling between cavities can cause a loss of resonant spin wave precession. However, this can be mitigated by changing the spin polarized current that drives the spin torque within each cavity. We find that it is possible to lock adjacent cavities using 20% lower spin polarized currents, as compared to a single cavity. The same (lower) spin polarized current when applied to a single cavity requires a much longer time to drive the spin waves into resonance, as shown in Figure 1. Our studies thus establish one means to scale the spin wave power that can be generated using spin polarized current pumping into nano-contacts. This has immense practical significance, as it has been thus far difficult to use arrays of nano-contacts to generate sufficent spin wave amplitudes that can be used in RF devices. Changing the spin polarized current in the STNO allows us to tune the wavelength of the SWs in the cavity, and find the correct phase locking between cavities. However, we must be cautious to report that in the process of scaling to arrays of SWASERs, we have observed the onset of intermittency and chaos in the SW oscillations that are reminiscent of similar phenomena in LASERs [3]. These nonlinear phenomena have been traditionally observed in SW propagation in magnetic films [4]. However, we believe that these are the first observations, albeit through simulations, of the possible onset of these nonlinearities in coupled SWASER cavities.

[1] N Kumar, A Prabhakar, Resonant spin wave excitations in a magnonic crystal cavity, J. of Magn. and Magn. Mat., 2017 (online) [2] A. Vansteenkiste et al, The design and verification of mumax3", AIP Advances 4, 107133, 2014. [3] G. E. James, E. M. Harrell, and R. Roy, Intermittency and Chaos in Intracavity Doubled Lasers. in: J. H. Eberly, L. Mandel, E. Wolf (eds) Coherence and Quantum Optics VI. Springer, Boston, MA, 1989 [4] M. G. Cottam, Linear and Nonlinear Spin Waves in Magnetic Films and Superlattices, World Scientific, 1994.

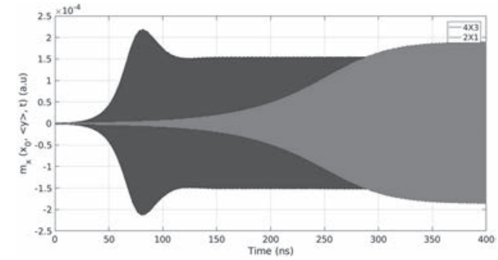

Fig. 1. Resonant oscillations emanating from an array of seven STNO-MCCs evanesnently coupled on the broadside to a MCW (blue). Superimposed (red) are the resonant oscillations from a single STNO-MCC, which exhibit a significantly longer rise time for the spin wave amplitudes to reach steady state.

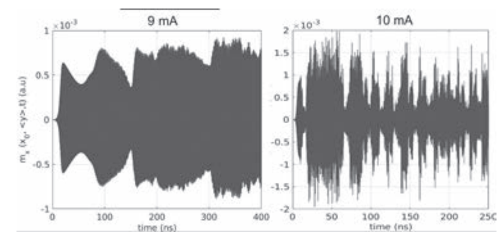

Fig. 2. Onset of intermittency and chaos, observed in the time series of the average magnetization in the magnonic crystal waveguide. The MCW was evanescently coupled to the MCCs, that were in turn pumped by STNOs. The two plots are at two different spin polarized currents, 9mA and 10mA, driving the STNOs.

FV-09. Excitation of spin waves with controllable wavelength and spectrum by femtosecond laser pulses.

I.V. Savochkin[1], M. Jäckl[2], V. Belotelov[1,3], I. Akimov[2,4], M. Kozhaev[1,5], D. Sylgacheva[3,1], A. Chernov[1,5], A. Shaposhnikov[6], A. Prokopov[6], V. Berzhansky[6], D. Yakovlev[2,4], A. Zvezdin[1,5] and M. Bayer[2,4]
1. Russian Quantum Center, Moscow, Russian Federation; 2. TU Dortmund, Dortmund, Germany; 3. Lomonosov Moscow State University, Moscow, Russian Federation; 4. Ioffe Institute, St. Petersburg, Russian Federation; 5. Prokhorov General Physics Institute, Moscow, Russian Federation; 6. Vernadsky Crimean Federal University, Simferopol, Russian Federation

Excitation of spin waves (SW) and their detection in magnetic materials can be accomplished all-optically by the femtosecond laser pulses using the pump-probe technique [1, 2]. However, usually broad spectrum of optically excited magnons hides the microscopic spin dynamics and results in fast decay of the magnetization precession. In this work we identify a novel feature of the periodic optical excitation of SWs. In particular, we excited magnetization of the sample with a sequence of circularly polarized pulses (Fig 1) at high repetition rate so that interval between pulses was shorter than the decay time of the oscillations, which provides a collective phenomenon. SWs of the frequencies multiple to the laser pulse repetition rate are mostly supported while SWs of the frequencies that are semi-integer multiples to the laser pulse repetition rate become suppressed. As a result, SWs are generated in a specific narrow range of wavenumbers. Furthermore, modifying laser pulse repetition rate or value of the external magnetic field provides significant level of SW wavelength tunability. In our particular case, we have chosen a magnetic film with such magnetic parameters and thickness that allow to change SW wavelength by about 20 times from 15 μm to 290 μm with just tiny modification of the external magnetic field by a few percent. This work was financially supported by Russian Science Foundation (Project No. 17-72-20260).

[1] M. van Kampen, C. Jozsa, J.T. Kohlhepp, P. LeClair, L. Lagae, W.J.M. de Jonge, B. Koopmans, *Phys. Rev. Lett.*, 88 (2002) 227201. [2] T. Satoh, Y. Terui, R. Moriya, B.A. Ivanov, K. Ando, E. Saitoh, T. Shimura, K. Kuroda, *Nature Photon.*, 6 (2012) 662-666. [3] L.P. Pitaevskii, *J. Exptl. Theoret. Phys.*, 39 (1960) 1450-1458. [4] J.P. van der Ziel, P.S Pershan, L.D. Malmstrom, *Phys. Rev. Lett.*, 15 (1965) 190-193.

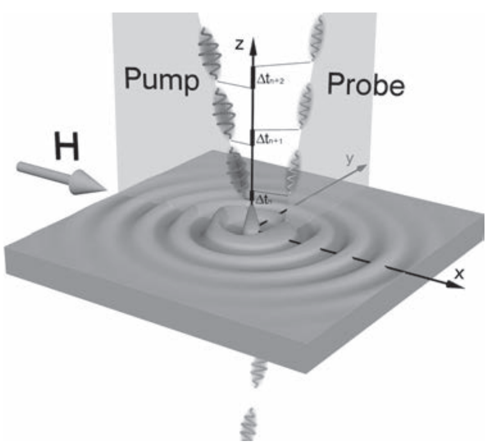

Fig. 1. Scheme of the pump-probe experiment: magnetization dynamics is excited by circularly polarized pump pulses via inverse Faraday effect [3, 4] and is observed by the variation of the Faraday angle of the linearly polarized probe pulses propagating through the sample at some time delay with respect to the pump pulses. The external magnetic field H is applied in-plane of the sample using electromagnet.

FV-10. Mechanism of Magnetic Orientation Reversal Induced by Ultrafast Laser.

Y. Zou[1], H. Wang[1], Z. Zeng[1], T. Huang[1], Y. Xiao[1], W. Cheng[3], K. Wang[2] and C. Xie[1]
1. Wuhan National Laboratory for Optoelectronics, Huazhong University of Science & Technology, Wuhan, China; 2. School of Physics, Huazhong University of Science & Technology, Wuhan, China; 3. School of Optical and Electronic Information, Huazhong University of Science & Technology, Wuhan, China

Although a phenomenological description, the inverse Faraday effect (IFE) is generally adopted for all optical magnetic switching (AOS) study, and has been successfully incorporated into the dynamics of AOS. The origin of IFE has been investigated theoretically by Pitaevskii[1], and predictions made by the study have been proved by experiments in 1966[2]. However, the effective field of IFE is deduced within the nanosecond time scale, which means the approximations valid in nanosecond scale are not quite suitable for femtosecond scenario. Further, the ~10-times mismatch between the duration of IFE in magnetic materials and the width of the incident laser pulse remains an open question for magnetic materials which exhibit AOS[3]. We investigate the process of AOS with quantum mechanical descriptions. The interactions between the incident femtosecond laser and magnetic materials are attributed to Rashba effect and stimulated Raman scattering (SRC): the incident femtosecond laser breaks the space inversion symmetry and splits the energy band of the electrons of magnetic material into two due to Rashba effect, which in turn maintains a quasi-stationary state for SRC (The three level system is depicted in Fig.1). The fine energy structure is spin dependent, so each sub-band is exclusive for spin up or spin down. The adiabatic transition of the states of electrons among the fine energy bands and the excited state gives rise of the spin direction switching, which switches the orientation of the magnetization of the material. The process discussed above can be described by Rabi model[4]. Simulation carried on this model shows that by tuning the center frequency of the incident femtosecond laser regarding the energy gap of the ground state and the excited state, the spin flip could be realized, results are shown in Figure 2. The further investigation will be focused on the details of decay rate for the two sub-bands.

1 Pitaevskii, L. Electric forces in a transparent dispersive medium. *Sov. Phys. JETP* 12, 1008-1013 (1961). 2 Van der Ziel, J., Pershan, P. & Malmstrom, L. Optically-induced magnetization resulting from the inverse Faraday effect. *Physical Review Letters* 15, 190 (1965). 3 Huang, T., Wang, H., Cheng, W., Zou, Y. & Xie, C. Critical switching fluence of L10-FePt nanoparticles with practical size to ultrafast all-optical polarization switching. *EPL (Europhysics Letters)* 118, 67006 (2017). 4 Shore, B. W. *Manipulating quantum structures using laser pulses*. (Cambridge University Press, 2011).

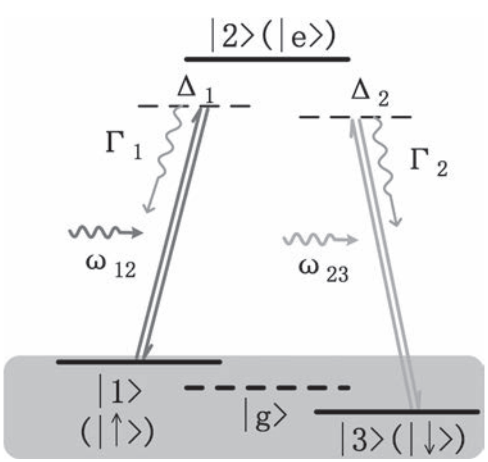

Fig. 1. The schematic diagram of Λ three-level system. The ground state is split into two fine energy band, caused by Rashba effect, in the ming blue background. |1> and |3> is spin up or down respectively, it dependents on the polarization of incident light.

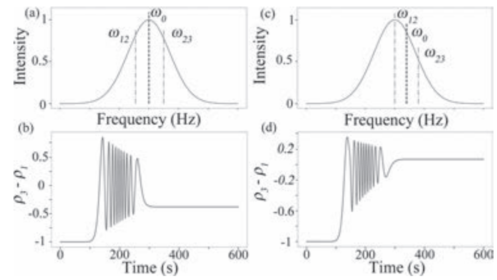

Fig. 2. The transition of electron influenced by the relation between the center frequency of laser and ω_0.

FV-11. Hybrid characteristic of multi-shot circularly polarized laser pulses for magnetization switching process in $L1_0$-FePt nanoparticles.

Y. Xiao[1], H. Wang[2], T. Huang[1], Y. Zou[1], Z. Zeng[1], K. Wang[1] and C. Xie[1]
1. Wuhan National Laboratory for Optoelectronics, Huazhong University of Science & Technology, Wuhan, China; 2. Wuhan National Laboratory for Optoelectronics, Huazhong University of Science & Technology, Wuhan, China

All-optical magnetic switching (AOS) observed on some materials provides a potential recording option due to its ultra-short recording-time [1]. In most studies, it is attributed to inverse Faraday effect (IFE) that circularly polarized laser will induce an opto-magnetic field [2, 3] or magnetic circular dichroism (MCD) that one magnetization orientation will absorb more energy than another [4, 5]. L10-FePt is a promising candidate for high density magnetic recording due to its high perpendicular anisotropy [6] whose magnetization is fixed out of plane either up or down. However, the mechanism about AOS on FePt is still under debate. In our research, we show that it benefits from both IFE and MCD. Taking both the thermal effect and the induced opto-magnetic field into account, we calculate the switching probability of L10-FePt nanoparticles for a single laser pulse with different opto-magnetic fields by atomistic level simulation [7], as shown in Fig. 1(a-d). We consider the effect of multi-shot pulses by an accumulative model, assuming that the switching probability after each shot is identical. Fig. 1(f) shows the normalized net magnetisation variation with different MCD ratios when the opto-magnetic field induced by left circularly laser pulse (σ-) is -0.1 Tesla. Obviously, when the MCD ratio is 2%, the final magnetisation is in agreement with the experiment result of Lambert et al. that the magnetization induced by circularly polarized laser is ~10 to 20% of saturation magnetization [8]. This MCD ratio is reasonable for FePt [5, 9]. Fig. 2(a-c) show the final magnetisation over multiple linearly (L), left (σ-) and right (σ+) circularly laser pulses respectively with different initial magnetization states, which verify that AOS is helicity-dependent but independent of the initial state. Fig. 2(d) shows the magnetisation variation over laser fluence with different opto-magnetic fields. Applying an external magnetic field 0.03 Tesla when the opto-magnetic field is -0.1 Tesla, the corresponding effective magnetic field is -0.07 Tesla. In this case, the net magnetisation roughly equals to 0 at a wide laser fluence range, which is qualitatively consistent with the results of Lambert et al. that a 700 Oe field could eliminate the all-optical switching. In addition, when the opto-magnetic fields are ±0.4 Tesla, there will be a deterministic switching that the final magnetization is greater 90% of the saturation magnetization. Taking the opto-magnetic field -0.4T as example, the net magnetisation after multiple laser pulses is shown in Fig. 2(e), and the fastest deterministic switching occurs at 34 mJ/cm2 after 34 left circularly laser pulses. Although our simulation is simplified, these results demonstrate the possibility of reaching deterministic all-optical magnetic recording by optimizing the parameters presented above.

[1] V. Mizrahi, M. Saifi, M. Andrejco, K. DeLong and G. Stegeman. Optics Letters. 14, 1140-1142(1989). [2] J. Van der Ziel, P. Pershan and L. Malmstrom. Physical Review Letters. 15, 190(1965). [3] C. Stanciu, F. Hansteen, A. Kimel, A. Kirilyuk, A. Tsukamoto, A. Itoh and T. Rasing. Physical review letters. 99, 047601(2007). [4] J. Gorchon, Y. Yang and J. Bokor. Physical Review B. 94, 020409(2016). [5] Y. Takahashi, R. Medapalli, S. Kasai, J. Wang, K. Ishioka, S. Wee, O. Hellwig, K. Hono and E. Fullerton. Physical Review Applied. 6, 054004(2016). [6] B. Zhang and W. Soffa. IEEE Transactions on Magnetics. 26, 1388-1390(1990). [7] J. Barker, R. F. L. Evans, R. W. Chantrell, D. Hinzke and U. Nowak. Applied Physics Letters. 97, 192504(2010). [8] C.-H. Lambert, S. Mangin, B. C. S. Varaprasad, Y. Takahashi, M. Hehn, M. Cinchetti, G. Malinowski, K. Hono, Y. Fainman and M. Aeschlimann. Science. 345, 1337-1340(2014). [9] K. Sato, A. Mizusawa, K. Ishida, T. Seki, T. Shima and K. Takanashi. Transactions of the Magnetics Society of Japan. 4, 297-300(2004).

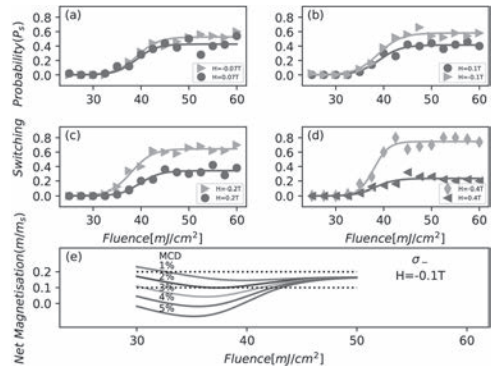

Fig. 1. The switching probability with different opto-magnetic field (a)±007 Tesla, (b)±0.1 Tesla, (c)±0.2 Tesla and (d)±0.4 Tesla. (e) The normalized net magnetisation variation over laser fluence with different MCD ratios when the opto-magnetic field is -0.1Tesla induced by left circularly laser pulse.

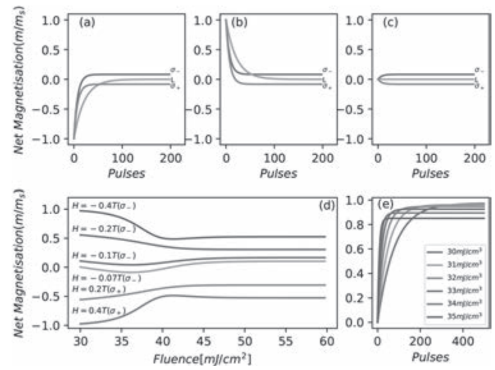

Fig. 2. The net magnetisation evolution over a sequence of laser pulses with different polarization starting from (a) spin-up state, (b) spin-down state and (c) demagnetized state. (d) The magnetisation evolution over laser fluence with different opto-magnetic fields. (e) The magnetisation evolution with the increasing number of laser pulses at certain laser fluence when the opto-magnetic field is -0.4 Tesla.

FV-12. Roles of heating and helicity in ultrafast all-optical magnetization switching in TbFeCo.

X. Lu[1,2], X. Zou[1], D. Hinzke[3], T. Liu[4], T. Cheng[8], J. Wu[1,2], T. Ostler[5,6], J. Cai[4], U. Nowak[3], R.W. Chantrell[1], Y. Zhai[7] and Y. Xu[2,8]
1. Department of Physics, University of York, York, United Kingdom; 2. York-Nanjing International Joint Center in Spintronics, Nanjing University, Nanjing, China; 3. Department of Physics, University of Konstanz, Konstanz, Germany; 4. Institute of Physics, Chinese Academy of Sciences, Beijing, China; 5. Computing, Engineering and Sciences, Sheffield Hallam University, Sheffield, United Kingdom; 6. Département de Physique, L'Université de Liège, Liège, Belgium; 7. Department of Physics, Southeast University, Nanjing, China; 8. Department of Electronics, University of York, York, United Kingdom

Since the magnetization was demonstrated to be reversed by a femtosecond laser pulse without any external magnetic field, this all-optical switching (AOS) has been extensively studied in recent years. All-optical manipulation of magnetism becomes attractive due to its potential technological applications. AOS in the ferrimagnetic GdFeCo alloy, the initially investigated material for AOS, is demonstrated to be a pure laser-induced thermal effect via a transient ferromagnetic-like state. Very recently, ultrafast electronic heat currents have been shown experimentally to be sufficient to switch the magnetization in GdFeCo, which further verifies the thermal origin of AOS in GdFeCo. Consequently, AOS in GdFeCo is independent to the circular helicity of laser pulses, which is named as helicity-independent AOS (HI-AOS). To explore the roles of the thermal effect and laser helicity in HD-AOS and the time scales in this process, we used the ultrafast laser pump-probe technique, also known as time-resolved magneto-Kerr effect measurement, to measure the transient magnetization change after single laser pulse irradiation in TbFeCo. The transient reflectivity change is also monitored in the same time. TbFeCo is a very similar ferrimagnet compared to GdFeCo in so much as the Tb sublattice is antiferromagnetically coupled with the FeCo sublattice. However, because of the large difference between the spin-orbit coupling of Tb and Gd, Gd- and Tb-based alloys show different ultrafast spin dynamics as well as a distinct switching mechanisms. Also, with a large coercive field, TbFeCo is suitable for magnetic recording applications. Using time-resolved magneto-optical Kerr effect (TR-MOKE) method, helicity-dependent all-optical magnetization switching (HD-AOS) is observed in ferrimagnetic TbFeCo films. The thermal effect and opto-magneto effects are separately justified after single circularly polarized laser pulse. The integral evolution of this ultrafast switching is characterized on different time scales and the defined magnetization reversal time of 460 fs is the fastest ever observed. Combining the heat effect and inverse Faraday effect (IFE), micromagnetic simulations based on a single macro-spin model are performed that reproduce HD-AOS following a linear reversal mechanism. In summary, the HD-AOS is unambiguously demonstrated in TbFeCo film by one single circularly polarized laser pulse. The thermal and opto-magnetic effects are seen to have different time scales, respectively. High pump fluences are required for the effect of the laser helicity, which is consistent with other reported works. Besides, the reflectivity change relaxation time is quite small in our measurements so the effect of accumulative heat should not play a role. The interplay between laser heating and helicity is stimulated by a single laser pulse. The integral evolution using the TR-MOKE method including the time points when it comes peak electron temperature, fully demagnetized state, magnetization switching triggered and a new magnetization direction is defined. Furthermore, from the sub-picosecond time domain evolution of HD-AOS, the observed magnetic switching time in 460 fs is the fastest among the reported times. On the other hand, this sub-picosecond switching is reproduced using a single macro-spin model based on the stochastic Landau-Lifschitz-Bloch equation, confirming the linear reversal mechanism without spin precession in the all-optically induced magnetization switching. Also, the simulation suggests that heating the electrons system to a critical temperature may play an important role in this kind of magnetization reversal. Above all, the finding of the ultrafast helicity-dependent all-optical magnetization switching in a high anisotropy system triggered by single laser pulse brings all-optical magnetic recording a major step close to the high data rate and high data density applications.

[1]T. A. Ostler *et al.*, Nature communications 3, 666 (2012). [2]S. Mangin *et al.*, Nature materials 13, 286 (2014). [3]C. Stanciu, F. Hansteen, A. Kimel, A. Kirilyuk, A. Tsukamoto, A. Itoh, and T. Rasing, Physical Review Letters 99, 047601 (2007).

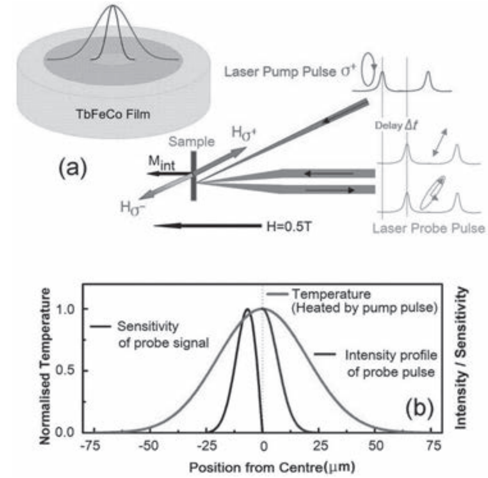

Fig. 1. (a) a schematic diagram of the experimental set-up with a bias field H = 0.5 T. $H_{\sigma+}$ represents the opto-magnetic field of the pump pulse of σ+ polarization (red line) via the IFE. The direction of $H_{\sigma-}$ would switch by 180°. (b) the normalized radial sensitivity of Kerr rotation (only left half shown for clarity) and temperature distribution across the pump spot together with the intensity profile of the probe spot (only right half shown for clarity).

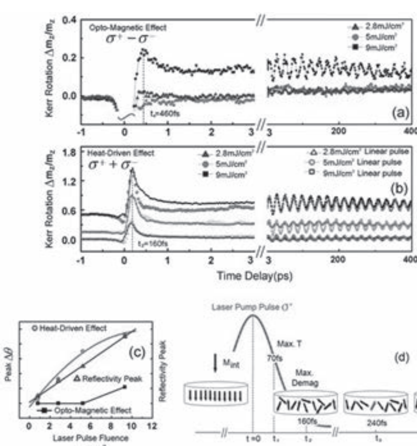

Fig. 2. (a) shows the difference between the time domain under σ^+ and σ^- pump pulses. (b) The three solid curves show the sum of the time domain data under σ^+ and σ^- pump pulses. The hollowed curves are time domain responses excited by the linearly polarized laser pulse at the same pump fluences. (c) The peak amplitude of the heat-driven effect (red circles), of the reflectivity (blue crosses), and of the opto-magnetic effect (black dots) at a delay time of 460 fs as a function of the pump fluence. (d) Shows a schematic diagram on ultrafast process induced at 9 mJ/cm² pump fluence.

FV-13. Femtosecond laser heating induced ultrafast magnetization reversal in TbCo films with different electron-phonon coupling interaction.

W. Cheng[1,2], Y. Wang[1], Z. Liu[1], Y. Hui[2], H. Wang[2], J. Chen[2], Y. Hao[1] and X. Miao[1,2]

1. School of Optical and Electronic Information, Huazhong University of Science and Technology, Wuhan, China; 2. Wuhan National Research Center for Optoelectronics, Huazhong University of Science and Technology, Wuhan, China

TbCo alloy films possess ferrimagnetic structure and high perpendicular anisotropy and have been proven to rapidly reverse their magnetic moments irradiated with an ultra-short pulse laser, which have the potential to use as all optical switching media [1-2]. In this paper, we have adopted a two-temperature model [3] and a general theoretical framework [4] to calculate the temperatures of the electron gas (T_e) and the phonon (T_p) and the magnetization dynamics of $Tb_{26}Co_{74}$ films, respectively, and found that electron-phonon coupling factor (G) plays a significant influence on the T_e and magnetization reversal dynamics of TbCo films. In our simulation, the laser wavelength and pulse width, laser fluence are 560 nm, 100 fs and 15 J/m^2, respectively. The G values vary from 1 to 10×10^{17} W/m^3. K. Fig 1 shows the time evolution of T_e and T_p. T_e rapidly increases to the peak temperature within about 0.3ps and then decreases with different rates until reaching the same value as T_p. TbCo films with a smaller G have a higher peak temperature of T_e and exhibit a slower cooling rate, and thus experience a longer heat exchange time between the electron gas and phonon. Fig 2 presents the computed time-resolved magnetization dynamics of Co- and Tb- sublattices. When G is just 1×10^{17} W/m^3. K, only the rapid demagnetization process occurs in Co- and Tb- sublattices and no magnetization reversal is observed due to the higher T_e and slower cooling rate. As G continues to increase, the demagnetization time of Co- sublattice rises slowly, but the initial reversal time of Co- sublattice drops gradually from 1.27ps to 0.66ps, which is attributed to the decreasing T_e and the increasing cooling rate of electron gas. Moreover, Tb- sublattice delays to reverse its magnetic moment with the increase of G perhaps owing to the lower T_e and the slower demagnetization of Tb- sublattice. Furthermore, although Co- and Tb- sublattices both generate magnetization reversal, the total magnetization reversal of $Tb_{26}Co_{74}$ films does not occur within the timescale of 5ps and will happen after a relatively longer recovery of magnetic moments of Tb- sublattice. ACKNOWLEDGMENTS This work was supported by the National Natural Science Foundation of China (Grant Nos. 61432007 and 61672246) and the Fundamental Research Funds for the Central Universities, HUST (Grant No. 2016YXMS204).

[1] S. Alebrand, M. Gottwald, M. Hehn, et al. Applied Physics Letters, 101, 162408 (2012). [2] W.M Cheng, X. Li, H.W. Wang, et al. Laser induced ultrafast magnetization reversal in TbCo film. AIP Advances, 7, 056018 (2017). [3] J.K. Chen, D.Y. Tzou, J.E. Beraun. International Journal of Heat and Mass Transfer, 49,307-316(2006). [4] J. H. Mentink, J. Hellsvik, D. V. Afanasiev, et al. Physical review letters, 108, 057202(2012).

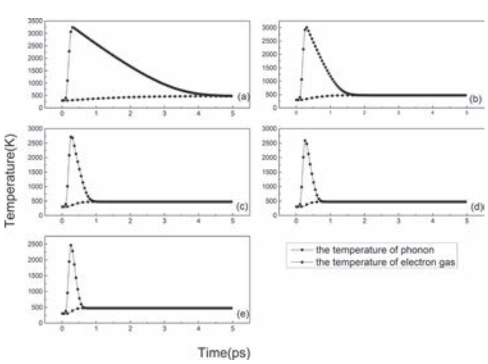

Fig. 1. Time evolution of T_e and T_p of TbCo films with different G values (a)1×10^{17} (b) 3×10^{17}, (c) 6×10^{17}, (d) 8×10^{17}, (e) 10×10^{17} W/m^3.K

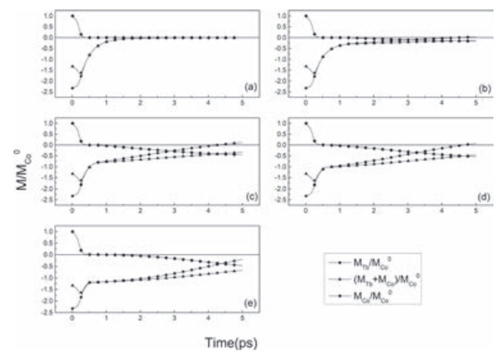

Fig. 2. Computed time-resolved dynamics of the magnetization of Co- and Tb- sublattices with different G values (a)1×10^{17} (b) 3×10^{17}, (c) 6×10^{17}, (d) 8×10^{17}, (e) 10×10^{17} W/m^3.K

FV-14. Photonic orbital angular momentum transfer and magnetic skyrmion rotation.

W. Yang[1], H. Yang[1], Y. Cao[1] and *P. Yan*[1]
1. Microelectronics and Solid-State Electronics, University of Electronic Science and Technology of China, Chengdu, China

Magnetic skyrmions are chiral quasiparticles that show promise for future spintronic applications such as skyrmion racetrack memories and logic devices because of their topological stability, small size (typically ~ 3 - 500 nm), and ultralow threshold force to drive their motion. On the other hand, the ability of light to carry and deliver orbital angular momentum (OAM) in the form of optical vortices has attracted a lot of interest. In this work, we predict a photonic OAM transfer effect, by studying the dynamics of magnetic skyrmions subject to Laguerre-Gaussian optical vortices, which manifests a rotational motion of the skyrmionic quasiparticle around the beam axis. The topological charge of the optical vortex determines both the magnitude and the handedness of the rotation velocity of skyrmions. In our proposal, the twisted light beam acts as an optical tweezer to enable us displacing skyrmions over large-scale defects in magnetic films to avoid being captured.

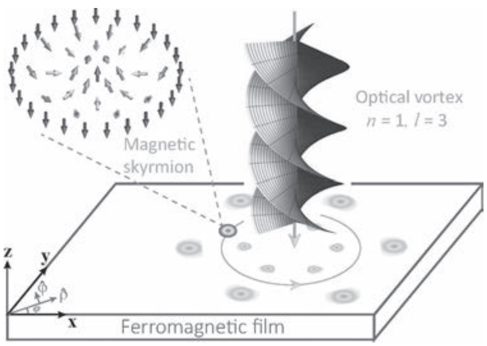

Fig. 1. Schematic of the rotational motion of a Néel skyrmion in a thin ferromagnetic film driven by an optical vortex with radial index n = 1 and OAM l = 3. The solid circle with a red core represents the skyrmion. The flower-like pattern (pink and blue spots) sketches the induced magnetization profile by the optical vortex field shinning on the magnetic film. In the main text, the origin of Cartesian coordinates coincides with the beam center, while it does not in the figure for clarity.

FV-15. Dependency of Spin Pumping on Seed and Capping Layers in Co Ultrathin Films.

B.B. Singh[1], S. Jena[1] and *S. Bedanta*[1]
1. Physical sciences, National Institute of science education and research, Bhubaneswar, India

Generation of pure spin current and its effect on the switching of the magnetization by spin transfer torque via spin orbital torque has been subject of major research in last one decade. Switching of magnetization by current at lower current density is required for fast processing and low power consumption devices. The potential applications of pure spin current are in spintronics/spin-orbitronics [1-4], spin torque- oscillator [5], magnetic random memory devices [6], magnonics [6] etc. Pure spin current is produced by asymmetric scattering of the two electrons with opposite spin angular momentum in the presence of spin orbit coupling at the interface which is known as spin Hall effect [1-3]. Ferromagnetic resonance (FMR) is widely used technique to excite the spins by microwave frequency. The excitations of spin in ferromagnetic (FM) layer and their dissipation into a paramagnetic heavy metal (NM) are called "spin pumping" [7]. The understanding of magnetic dynamics dissipation in the material is very important to get sustainable spin current. The interfaces are very important for creating pure spin current and its dissipation. In order to understand the effect of seed and capping layers on spin pumping dynamics we fabricated the multilayer structure *Seed layer/Co/Capping layer.* The seed layer and capping layers are the combination of heavy metals like Ta, Pt, and Au. The samples are deposited at room temperature in a high vacuum system (Mantis Deposition Ltd., UK) having base pressure better than 5.0×10^{-7} mbar. The Ta, Cu, and Co layers are deposited by dc sputtering. While Pt and Au thin films are prepared by rf sputtering and electron beam evaporation, respectively. We deposited the multilayers Ta(3)/HM^T/Co(3)/HM^B/Ta(3) (nm) on Si(100) substrate in which HM^T and HM^B stands for heavy metal for top and bottom layers, respectively as shown in Figure 1. We measured the samples using ferromagnetic resonance spectroscopy (FMR) [8]. The FMR data were fitted with Kittel's equation to extract the values of damping constant and g-factor. A strong dependence of seed and capping layers on spin pumping has been observed. The value of damping constant (α) is found to be relatively large i.e. 0.0326±0.0008 for the Ta(3)/Pt(3)/Co(3) /Pt(3)/Ta(3) (nm) multilayer structure, while it is 0.0104±0.0003 for Ta(3)/Co(3)/Ta(3) (nm). Increase in α is observed due to Pt layer that works as a good sink for spins due to high spin orbit coupling. In addition, we evaluated the effective spin conductance $= 5.82 \pm 0.08 \times 10^{18}$ m^{-2} for the structure Ta(3)/Pt(3)/Co(3)/Pt(3)/Ta(3) (nm) as a result of the enhancement in α relative to its bulk value (Table I).

(1) J. E. Hirsch, Spin Hall Effect. *Phys. Rev. Lett.* 1999, *83* (9), 1834–1837. (2) T. Kuschel *et al., Nat. Nanotechnol.* 2015, *10* (1), 22–24. (3) J. Sinova *et al., Rev. Mod. Phys.* 2015, *87* (4), 1213–1260. (4) F. Hellman *et al,. Rev. Mod. Phys.* 2017, *89,* 025006. (5) D. Ciudad, *Nat. Mater.* 2016, *15* (2), 127–127. (6) A. D. Kent, *et al., Nat. Nanotechnol.* 2015, *10* (3), 187–191. (7) Y. Tserkovnyak *et al., Rev. Mod. Phys.* 2005, *77* (4), 1375–1421. (8) B. B. Singh *et al.*, J. Phys. D- Appl. Phys. 2017, 50, 345001.

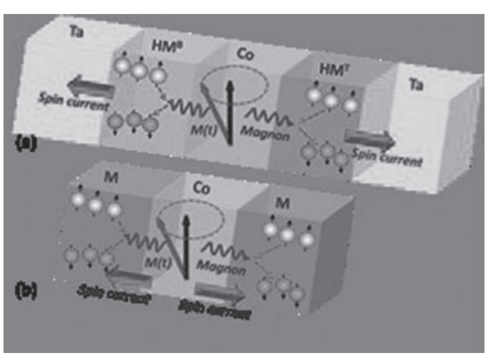

Fig. 1. Schematic of spin current generation in multilayer structure (a) and tri-layer structure (b).

Table 1: Effective spin mixing conductance values for sample S1 to S7

Sample	Sample details (In parenthesis thickness is in nm)	Effective spin mixing conductance ($g^{\uparrow\downarrow}$) ($\times 10^{18}$ m^{-2})
S1	Si/Ta(3)/Pt(3)/Co(3)/Pt(3)/Ta(3)	5.82±0.08
S2	Si/Ta(3)/Au(3)/Co(3)/Au(3)/Ta(3)	1.56±0.04
S3	Si/Ta(3)/Au(3)/Co(3)/Pt(3)/Ta(3)	3.53±0.05
S4	Si/Ta(3)/Pt(3)/Co(3)/Au(3)/Ta(3)	3.67±0.05
S5	Si/Ta(3)/Co(3)/Ta(3)	0.20±0.01
S6	Si/Cu(3)/Co(3)/Cu(3)	0.01±0.001
S7	Si/Pt(3)/Co(3)/Pt(3)	2.82±0.08

THURSDAY AFTERNOON, 26 APRIL 2018 SIMPOR/ROSELLE BALLROOM, 1:30 TO 4:30

Session FW
TRANSFORMERS AND INDUCTORS: MODELLING II
(Poster Session)

Makoto Sonehara, Co-Chair
Shinshu University, Nagano, Japan
Zhen Zhang, Co-Chair
Tianjin University, Tianjin, China

FW-01. A Magnetic Integration Structure of Hybrid Distribution Transformer.

Y. Liu[1], D. Liang[1], M. Zhang[1], Y. Liang[1], X. Wan[1], Q. Chen[1], S. Wang[1] and S. Wang[1]
1. Xi'an Jiaotong University, Xi'an, China

Abstract: Hybrid distribution transformer (HDT) is significant for the intelligence of the power network due to its powerful controllability. In this paper, a three-phase circuit scheme of HDT is presented. To reduce the number of discrete magnetics and make high efficient use of the magnetic material, a magnetic integration structure of HDT (MIHDT) is proposed, which is realized by creating the adjustable magnetic circuit, setting up the common magnetic circuit and shifting windings' phase. In this way, the large numbers of discrete magnetics in HDT are integrated together. Furthermore, the magnetic density of MIHDT is analyzed and the inductance matrix is calculated by 3-D Finite Element Method, and then the model of MIHDT based on the inductance matrix is established. Finally, the correctness of IMHDT is verified. 1 Introduction HDT is a novel transformer that combines the conventional distribution transformer with the PWM convertors, which is quite useful for the construction of the future intelligent distribution power network. [1-3] presents several topologies of HDT based on the DC-AC convertors, and discuss various issues on HDT, such as the reactive power compensation, high efficient design, and capacity calculation. Compared with the conventional distribution transformer, HDT is much more controllable, but which contains large numbers of discrete magnetics, such as the main transformer, isolation transformer and the output inductances of convertors. Obviously, a system constructed with discrete magnetics will be complex and the total volume and electromagnetic capacity of HDT will be quite large, which can't make the most of the magnetic material, therefore, it is significant to design the integrated structure for HDT. The magnetic-integration techniques has been widely used in the optimization design of the convertors used in the low and medium power application [4,5], but which has not been used in the design of the magnetic integration HDT (MIHDT). The design principle of MIHDT is integrating the discrete magnetics together under the precondition of inheriting the original functions of HDT. In this paper, a MIHDT based on the above design principle is presented, and the magnetic field is analyzed by 3-D Finite Element Method, then the mathematical model based on the inductance matrix of MIHDT is established, and the simulation results verifies the correctness of MIHDT finally. 2 Basic working principle of HDT Fig.1 (a) shows the three-phase circuit scheme of HDT proposed in this paper, T_1 and T_2 are the main and isolation transformer respectively. CV_t and CV_p are two convertors shared a common DC-bus. T_1 contains W_1(W_{1a}, W_{1b}, W_{1c}. same as the other windings), W_2, W_3 in each phase, Where, W_3 is the auxiliary winding. T_2 consists of W_4 and W_5 in each phase. CV_p and CV_t are connected to W_3 and W_4 through the output inductance L_p and L_t respectively. The basic working principle of HDT is that: CV_p and CV_t can be controlled as controllable current and voltage source, thus the grid current i_s and load voltage u_2 can be compensated to be sinusoidal, symmetrical and steady in real time. 3 Magnetic integration structure of HDT HDT shown as Fig.1(a) usually contains the following discrete magnetics: T_1, T_2, L_p and L_t. Where, T_1 is usually a three-limb concentric-type transformer, and T_2 can be a three-phase four-frame shell-type transformer, L_p and L_t should be 6 separated inductances. The MIHDT presented in this paper is shown as Fig.1(b), which is a shown as 3-D Finite Element model. Where, W_1, W_2 and W_3 are concentric windings wrapped around the core limb of T_1 in each phase, the arranging sequence of which is W_2, W_1, and W_3 from the inside of the core limb to the outside. W_4 and W_5 are pancake windings folding around the core frame of T_2 in each phase. T_1 and T_2 are integrated together by sharing the common iron yoke. The adjustable iron cores for leakage flux of T_1 are set between W_1 and W_3, while the which of T_2 are set between W_4 and W_5. Furthermore, the windings of T_2 are arranged by phase shifting, which can avoid the superposition of the flux amplitudes of T_1 and T_2 in same phase, thus, the cross-sectional area of common iron yoke can be reduced prominently. 4 Simulation and analysis The flux density of iron core is shown in Fig.2(a), which indicates that iron core of MIHDT is not saturated, and the flux density in the common iron yoke is less than the superposition of the flux density of each limb due to phase shifting. Fig.2(b) compares the flux density between W_1 and W_3 of phase A when the iron core for leakage flux exists or not, which indicates that the iron core for leakage flux will increase the leakage flux greatly, and then will increase the leakage inductance of W_1 and W_3 (shown as l_{k13} in Fig.2(b)). In this way, L_p can be replaced by the leakage inductance and be integrated into the transformer equivalently. Based on the model shown in Fig.1(b), the inductance matrix of MIHDT can be calculated, regarding the matrix as the equivalent circuit of MIHDT and according to the control strategy of PWM convertor, the control system of MIHDT can be established in MATLAB. Fig.2(c) shows the compensating effect of i_s and u_2, which indicates that MIHDT can also compensate the i_s and u_2 to be sinusoidal, symmetric, stable, and unity power factor as HDT.

[1] J. Burkard, J. Biela "Evaluation of topologies and optimal design of a hybrid distribution transformer", *2015 17th European Conference on Power Electronics and Applications (EPE'15 ECCE-Europe)*, pp. 1-10, (2015). [2] M. A. Radi, M. Darwish. "Var control considerations for the design of hybrid distribution transformers", *11th IET International Conference on AC and DC Power* Transmission, pp. 1-9, (2015). [3] J. Burkard, J. Biela. "Protection of hybrid transformers in the distribution grid", *2016 18th European Conference on Power Electronics and Applications (EPE'16 ECCE Europe)*, pp. 1-10, (2016). [4] B. Bai, Z. Chen and D. Chen. "DC bias elimination and integrated magnetic technology in Power Transformer". *IEEE Transactions on magnetics*, vol. 51, no. 11, Nov. 2015, Art. ID 8401304. [5] C. W. Park, S. K. Han. "Design of an integrated magnetics structure for LLC resonant converter". *IECON 2017-43rd Annual Conference of the IEEE Industrial Electronics Society*, pp. 1888-1893, (2017).

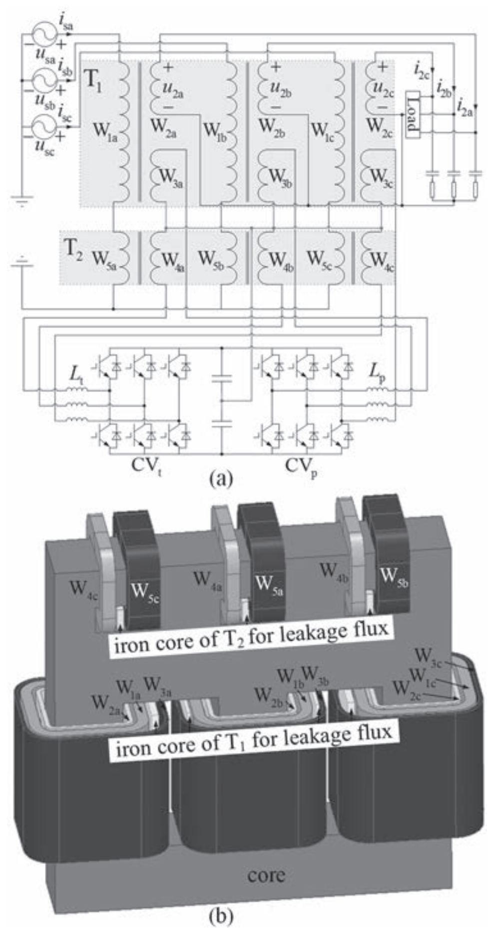

Fig. 1. (a) Circuit scheme of HDT, (b) Magnetic integration Structure of HDT

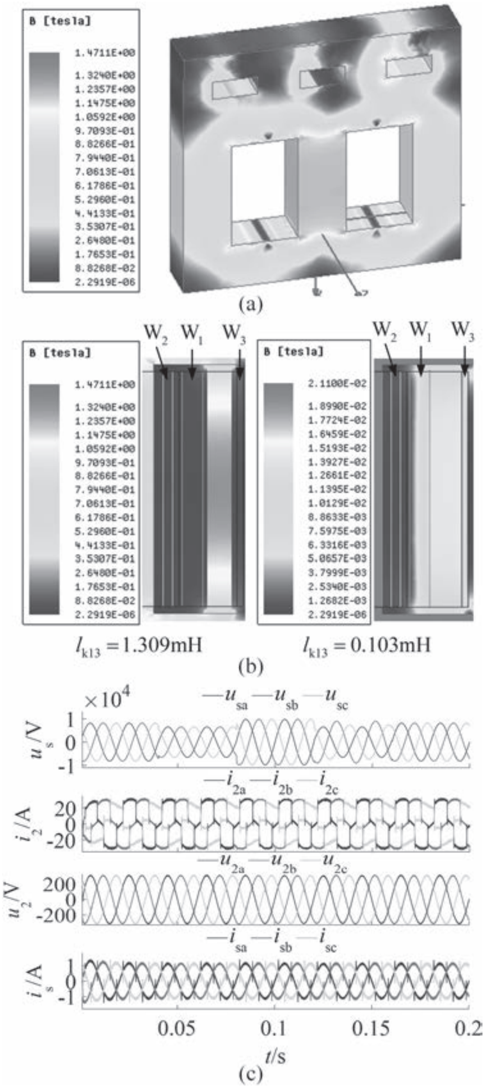

Fig. 2. (a) Flux density of iron core, (b) Flux density between W_1 and W_3 in phase A, (c) Compensating results

FW-02. Analytical and FEM Calculation of Electrical Parameters of Carbon Steel Pipelines for DEH systems.

A. Chen[1], A. Nysveen[1], M. Høyer-Hansen[2] and J. Lervik[2]
1. Electrical power engineering, Norwegian University of Science and Technology, Trondheim, Norway; 2. SINTEF Energy Research, Trondheim, Norway

Introduction Direct Electrical Heating (DEH) is a flow assurance technology developed for subsea process to safeguard well stream through production pipelines to topside process platform or shore, where the magnetic production pipelines directly conduct one-phase AC current to generate heat to prevent the oil from formatting hydrates or wax. The heating source is the conductive power and hysteresis power losses in the pipelines. The required power is supplied from topside via a power cable. Comparing to conventional chemistry treatment, this method is more cost-efficient and environmentally friendly. All currently implemented DEHs operates at 50/60Hz. To further improve the effectiveness of a DEH-system, consequently reducing the cable size and the corresponding installation cost, higher operation frequency and high magnetic permeability material such as carbon steel for the pipeline is preferable. Operating at higher frequencies, the hysteresis power in carbon steel pipeline becomes considerable and have to be taken into account for evaluating the electrical parameters of the pipeline, which is essential for dimensioning power system in a DEH design. These parameters are not available from pipe manufactures, since the pipes are not originally designed for this purpose. This paper presents how to analytically evaluate the electrical parameters of the pipeline based on experimentally measured properties of the material sample. The hysteresis power loss has been considered as the power from an equivalent resistance. The analytical results are verified by FEM simulations. *Electrical parameters of the pipeline* The production pipeline in a DEH system is an active conductor in the electric circuit, and both conductive power and hysteresis power losses in the pipeline contribute to the heating. For a DEH system design, the total power can be considered as the active power from the pipeline resistance. Therefore, the calculated pipeline resistance R_p includes the pipeline conductive resistance R_c and an equivalent resistance R_h representing the hysteresis power loss. The inductance of the pipeline L_p consists of the pipeline internal inductance L_{in} and the external inductance L_{ex} introduced by the field from the power cable. *Current distribution due to skin effect* The current distribution in the production pipeline due to skin effect is governed by Maxwell equations. In the discussed case of conducting a large current of 1500A, the displacement current in the pipeline is negligible, therefore the current density is determined by (1) $\nabla^2 J = j\omega\mu\sigma J$ (1) In carbon steel material, the magnetic permeability μ is a non-linear function of magnetic field. Including such a function, equation (1) becomes too complicated to be analytically solved. Moreover, both μ and conductivity σ vary with temperature. To simplify the problem for the analytical study, following assumptions have been made: ■ Constant room temperature ■ Neglect proximity effect from the cable ■ Homogeneity of σ over the pipe. ■ Constant effective permeability:the effective permeability is obtained by curve fit tool in MATLAB based on the measured BH curve. In the investigated frequency range of 50-200Hz, the penetration depths into the pipeline are less than 1.7 mm,much less than the wall thickness of 18.3mm. It is therefore applicable to consider the current distribution in the pipeline similar to a plane analysis. The internal resistance and inductance are respectively evaluated by (2) and (3). $R_c=\sqrt{(\mu\omega/2\sigma)}/(2\pi r_o)$ (2) $L_{in}=\sqrt{(\mu\omega/2\sigma)}/(2\omega\pi r_o)$ (3) The external inductance between the cable and pipe is determined by (4) $L_{ex}=(\mu_0/2\pi)\ ln(D/r_o)$ (4) where r_o is the outer diameter of the pipe, and D is the distance between the cable and pipe. *Hysteresis power loss and equivalent resistance* The hysteresis power loss P_{hys} is evaluated by integrating the hysteresis energy over the pipeline volume and multiplying frequency f and mass density ρ as: $P_{hys}=2\pi\rho f \int r E_{hys} dr$ (5) The hysteresis energy E_{hys} is the area enclosed by hysteresis loop of B-H curve at DC condition, and it is material dependent and determined by the maximum flux density B_{max}, but independent of frequency. The relation between E_{hys} and B_{max} is experimentally obtained by measuring a rod made of the pipe, and it can be expressed by (6) $E_{hys}=0.285B_{max}^{1.55}$ (6) The B_{max} distribution in the pipeline can be derived based on (1) with peak input current, and Fig. (1) shows the analytical calculated B_{max} distribution in the pipeline with constant current 1500A at 50, 100, 150 and 200 Hz, respectively. Then the equivalent resistance for the hysteresis power is $R_h= P_{hys}/I_{in}^2$. To verify the analytical results, FEM simulation is performed, and Fig.2 shows the comparison of the analytical calculated R_p, L_p, R_c and R_h to those from the FEM simulation. *Conclusion* The paper has presented an analytical modeling for evaluating electrical parameters of the pipeline in DEH system, and the calculated resistance includes an equivalent resistance representing the hysteresis power loss, which is derived based on experimentally measured hysteresis loop energy at DC condition. It shows that the hysteresis power loss in carbon steel pipeline contributes around one third of the total power loss. FEM simulation are carried out to verify the analytical results. The results match each other satisfactorily. More detailed information will be given in the final paper.

[1] Arne Nysveen, Harald Kullbotten, Jens Kristian Lervik, Atle Harald Børnes, Martin Høyer-Hansen and Jarle J. Bremnes, Direct Electrical Heating of Subsea Pipelines—Technology Development and Operating Experience", IEEE Transactions on Industry Applications, VOL. 43.NO:1 Jan/Feb. 2007. [2] Simon Ramo, John R. Whinnery, Theodore Van Duzer, "Fields and Waves in Communication Electronics" 2rd edition, ISBN 0-471-81103-3, John Willy & sons, 1984. [3] V. T. Morgen, "The current Distribution, Resistance and Internal Inductance of Linear Power System Conductors-A review of Explicit Equations", IEEE Trans. Power Del., Vol.28 NO.3, pp. 1252-1262, Jul. 2013. [4] V.T Morgan, Bo Zhang and R.D. Findlay, "Effects of temperature and tensile stress on the magnetic properties of a steel core from an ACSR conductor", IEEE Trans. Power Del. Vol. 11 No.4, pp1907-1913 Oct. 1996. [5] A. Mekjian and M. Sosnowski, "Calculation of alternating current losses in steel pipes containing power cables," IEEE Trans. Power App. Syst., vol. PAS-102, no. 2, pp. 382–388, Feb. 1983. [6] Wael Moutassem and George J. Anders, "Calculation of the eddy current and hysteresis losses in sheathed cables inside a steel pipe", IEEE Trans. Power Del. VOL.25, NO.4, pp2054-2063, Oct. 2010. [7] Howard Johnson, and Martin Graham, "High-Speed Signal Propagation: advance black magic" ISBN 0-13-084408-X, 2003, Pearson Education. Inc. [8] H. B. Dwight, "A precise method of calculation of skin effect in isolated tubes," AIEE Trans., vol. 42, pp. 827–831, 1923. [9] V. T. Morgan, R. D. Findlay, and S. Derrah, "New formula to calculate the skin effect in isolated tubular conductors at low frequencies," Proc. Inst. Elect. Eng., Sci. Meas. Technol., vol. 147, no. 4, pp. 169–171,2000. [10] K. Kawasaki, M. Inami, and T. Ishikawa, "Theoretical considerations on eddy current losses in non-magnetic and magnetic pipes for power transmission systems", presented at the IEEE Summer Power Meeting, Minneapolis, MN, 1980, Paper 80 SM54–7-0.

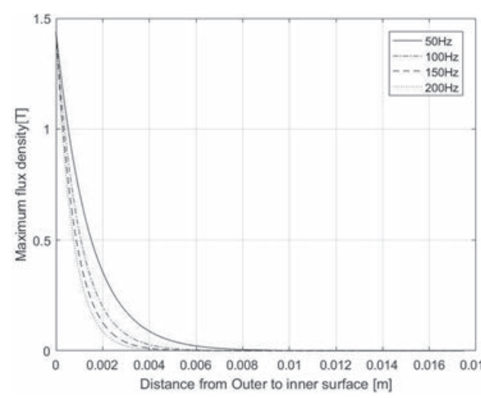

Fig. 1. B_{max} distribution along the depth into the pipeline as function of frequency

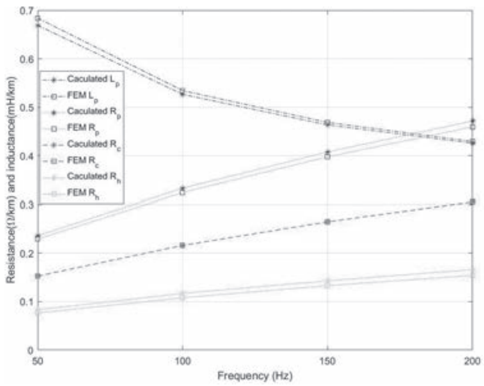

Fig. 2. Comparison of resistance and inductance as function of frequency with FEM simulation results.

FW-03. Calculation method of armature commutation coil inductance in universal motor.

H. Jun[1], H. Kim[1], *S. Oh*[1] and W. Kim[2]
1. Electric Engineering Department, Hanyang University, Seoul, The Republic of Korea; 2. Energy IT department, Gachon University, Seongnam, The Republic of Korea

Universal motors are now widely applied to household appliances and tools because of their advantages of high starting torque and high speed operation without additional power conversion device in a commercial power supply. However, there is a serious drawback that arc discharge and electromagnetic interference problems may occur due to the mechanical commutation method. In motor design, it is better to avoid such problem, but it is difficult to accurately predict the mechanical commutation characteristics through conventional FEM analysis. Currently, when designing a universal motor, the design is being carried out through existing design experience and trial and error. If a reliable mathematical commutation model is developed, the brush commutation characteristics can be predicted and reflected in the motor design process. To create a commutation model of a universal motor, the inductance of the armature coil must be mathematically expressed in order to establish the voltage equation in the commutation coil. In particular, the commutation coil can be viewed as a short-circuited coil through the brush. Finding the commutation coil current can be seen as a process of finding the equilibrium solution of the first-order differential equation in the RL circuit without input power when ignoring the EMF voltage. Therefore, it is necessary to accurately predict the inductance of an armature single coil to make a reliable commutation model. To understand the commutation phenomenon occurring in the commutating coil, information on the inductance term associated with the armature single coil is needed. These include self-inductance, leakage inductance, and mutual inductance with field coil of the armature single coil as shown in figure 1 (a). Assuming that the center of the field core of the universal motor is the d axis, and the axis separated 90 degrees from the d axis is the q axis, The calculation result of the magnetic flux, permeance, and inductance components obtained from the d and q axis magnetomotive force components can be obtained from the simplified design parameter of the universal motor as shown in figure 1 (b). The magnetomotive force is calculated from the magnitude of the armature input current and the number of coil turns, and the total flux magnitude can be calculated. In the process of calculating the total flux linkage when the magnetic flux component links the coil, the permeance and the inductance value can be separately calculated. In this process, the position of the brush and the width of the stator core are the most important design parameters. To calculate inductance of an armature single coil accurately, the coil pitch angle should be considered. Through this, the leakage magnetic flux component of the commutating coil can be accurately considered. In this study, it was confirmed that magnetic flux leakage through the stator core exists when considering the coil pitch angles of the armature single coil, and reflected in the inductance calculation process. In this process, mathematically calculation result of the armature coil inductance using the design parameter of the example universal motor model is compared with the inductance calculated from the magnetic flux distribution obtained by the FEM analysis. And it was confirmed that the proposed inductance calculation method in this study is reasonable. Finally, the inductance calculated through above method was used to decide the coil current in the commutation period by solving the voltage equation, and compared with the test results as shown in figure 2.

[1] Y. Niwa, Y. Akiyama, "Propositions for the analysis of commutation phenomenon and the modeling of universal motors based on introducing the state function method into FEM electromagnetic field analysis", IEEE Energy Conversion Congress and Exposition, Sept. 20-24. 2009. [2] T. Fujii, "Study of universal motors with lag angle brushes", IEEE Power Engineering Review, Vol. Per-2, Issue.6, Jun. 1982. [3] T. Matsuda, T. Moriyama, N. Konda, Y. Suzuki, Y. Hashimoto, "Method for analyzing the commutation in small universal motors", IEE Proceedings-Electric Power Applications, Vol. 142, Issue. 2, Mar. 1995. [4] M. Willing, T.J.E. Miller, I. Corral, "A brush model for detailed commutation analysis of universal motors", 2012 International Conference on Electrical Machines (ICEM), Sept. 2-5. 2012. [5] R.H. Wang, R.T. Walter, "Modeling of universal motor performance and brush commutation using finite element computed inductance and resistance matrices", IEEE Transactions on Energy Conversion, Vol. 15, No. 3, Sept. 2000. [6] G. Mizaeva, "Mathematical model for brush current density estimation based on known field distribution in the interpolar space", Austrian Mining Technology Conference, Oct. 2-4. 2007. [7] G.C.R. Sincero, J. Cros, P. Viarouge, "Arc models for simulation of brush motor commutation", IEEE Transactions on Magnetics, Vo. 44, No. 6, Jun. 2008. [8] K. Sawa, T. Shigemori, "Characteristics of carbon flat commutator with condenser for arc quenching", 22nd International Conference on Electrical Contacts, Oct. 2004.

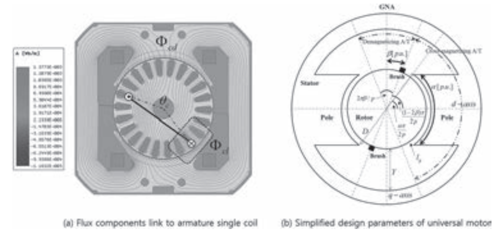

Fig. 1. (a) Flux components link to armature single coil
(b) Simplified design parameters of universal motor

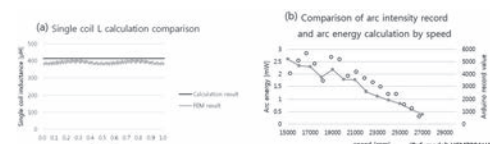

Fig. 2. (a) Silgle coil inductance calculation comparison
(b) Comparison of arc intensity record and arc energy calculation by speed

FW-04. Study the Effect of Inductor Nonlinear Behavior on the LCL Three Phase Grid- Connected Inverter.

S. Jiang[1], *Y. Liu*[1], H. Wang[1], G. Wang[1], J. Peng[1] and Y. Liu[2]
1. College of Mechatronics and Control Engineering, Shenzhen University, Shenzhen, China; 2. School of Electrical and Electronic Engineering, Nanyang Technological University, Singapore, Singapore

1.Introduction With the development of renewable energy, grid-connected inverter technology has become an important research area [1-3]. Compared with the traditional L or LC filter, LCL filter is widely used in the grid-connected inverter due to its harmonic attenuation performance and system stability. According to the IEEE 519-STD as shown in [4] that the grid current harmonic order higher than 35 times must be less than 0.3% and the total harmonic distortion (THD) should be lower than 5%. LCL filter is a third-order circuit which is selected based on the grid current quality requirements. However, according to the electromagnetic analysis, the filtering inductor value will not be constant but display a nonlinear relationship between magnetic field and magnetization [5-7]. The inductor nonlinear behavior is usually ignored in the LCL filter design, but the magnetic characteristics of the inductance would obviously affect the resonant frequency of LCL filter and underestimate the parameters of filter design [8]. 2.LCL filter design and inductor nonlinearity modeling Fig. 1 shows the LCL type grid connected inverter system with the controller and inductor nonlinearity. The output LCL filter is a necessary part for the harmonic limit requirement in the grid connected system [9-11]. L_i is the inverter side inductor, C_f is the filtering capacitor, L_g is the grid side inductor, V_i is the inverter side voltage and V_g is the grid side voltage. Design filtering inductors having inductance L, which carries maximum current I_{max} without saturating. The copper and core loss must be dissipated through the surface of magnetic core. From the theory of electromagnetism [12], the inductance of a coil is defined as the relationship between magnetic strength and flux density. The inductor model can be built with a controlled current source, an integrator for the flux, a divide unit and a look-up table which stores the B-H mapping of Fe-Si-Al. Inductor nonlinearity consideration would improve the accuracy and efficiency of filter parameters design. 3.Controller design and analysis According to previous analysis, it is necessary to adopt an active damping method to suppress the resonance peak [13]. If adding a damping resistor in filtering capacitor branch, the proportional gain must be chosen to a small value. When the proportional gain is increased, the partial poles would be distributed in the right half of the S-plane, resulting in poor system stability. The inverer side current i_i is used as the inner loop that wouldn't improve the system stability significantly. Hence, the capacitor current i_c is used as the inner loop control loop to further improve the control performance of the system. The closed-loop transfer function of the double-loop controller is a typical fourth-order system, it is difficult to obtain accurate parameters, so the pole assignment method is used to calculate the parameters. Using the output current i_g as the outer control loop and the capacitor current i_c as the inner control loop. The double closed-loop active damping method makes the system more stable compare with other control methods [14]. Simulation and experiment results The simulation of LCL three - phase grid - connected inverter is carried out based on Matlab/Simulink with the consideration of inductor nonlinearity. The grid phase voltage V_g is 220 V/50 Hz, the DC-link voltage V_{dc} is 750 V, the switching frequency f_s is 15 kHz and the rated power P is 5 kW. In order to analyze the effect of taking the nonlinear feature of inductor, the grid current harmonic distortion analysis is analyzed to evaluate the LCL filter design. The grid-connected inverter system with the inductor nonlinearity consideration is simulated, it can be found that the THD is acceptable but grid current harmonic distortion over 35 order is larger than 0.3%. Thus it is essential to take nonlinearity of inductor into consideration in order to improve the accuracy of LCL filter design. In term of the above analysis and the magnetic nonlinearity of inductor, two larger inductors 4 mH and 2 mH are selected to replace the original 3 mH and 1.5 mH inductors in the experiment. The experiment set-up and its results considering the nonlinearity of inductor is shown in Fig.2. It can be seen that the total harmonic distortion of the grid side current is reduced to 2.49% and the harmonic distortion at switching frequency is below 0.3%. Compared with the system model without taking the nonlinearity of the inductor, the design accuracy and efficiency has been improved obviously. 5.Conclusion In this paper, LCL there-phase grid-connected inverter with double close loop control is analyzed in detail. Also the nonlinear characteristics of filtering inductors is analyzed and modelled based on the B-H curve of Fe-Si-Al. The parameters of LCL filter without inductor nonlinearity consideration is underestimated and harmonic distortion is not compatible with the standard. Considering the nonlinearity of the inductor could improve the accuracy of the LCL filter design that have been verified in the simulation and experiment results.

[1] Z. Zou, Z. Wang, and M. Cheng, "Modeling, analysis, and design of multifunction grid-interfaced inverters with output LCL filter," *Power Electronics, IEEE Transactions on,* vol. 29, pp. 3830-3839, 2014. [2] X. Wang, X. Ruan, S. Liu, and C. K. Tse, "Full feedforward of grid voltage for grid-connected inverter with LCL filter to suppress current distortion due to grid voltage harmonics," *Power Electronics, IEEE Transactions on,* vol. 25, pp. 3119-3127, 2010. [3] W. Wu, Y. Sun, M. Huang, X. Wang, H. Wang, F. Blaabjerg, *et al.*, "A Robust Passive Damping Method for LLCL-Filter-Based Grid-Tied Inverters to Minimize the Effect of Grid Harmonic Voltages," *Power Electronics, IEEE Transactions on,* vol. 29, pp. 3279-3289, 2014. [4] "IEEE Recommended Practice and Requirements for Harmonic Control in Electric Power Systems," pp. 1-29, 2014. [5] H. Q. Li, Q. F. Li, X. B. Xu, T. B. Lu, J. J. Zhang, and L. Li, "A Modified Method for Jiles-Atherton Hysteresis Model and Its Application in Numerical Simulation of Devices Involving Magnetic Materials," *IEEE Transactions on Magnetics,* vol. 47, pp. 1094-1097, May 2011. [6] P. R. Wilson, J. N. Ross, and A. D. Brown, "Optimizing the Jiles-Atherton model of hysteresis by a genetic algorithm," *IEEE Transactions on Magnetics,* vol. 37, pp. 989-993, 2001. [7] R. A. Mastromauro, M. Liserre, and A. D. Aquila, "Study of the effects of inductor nonlinear behavior on the performance of current controllers for single-phase PV grid converters," *Industrial Electronics, IEEE Transactions on,* vol. 55, pp. 2043-2052, 2008. [8] Z. W. Liu, A. Abou-Alfotouh, and M. Wilkowski, "Nonlinear Inductor Modeling for Power Converter," *2012 Twenty-Seventh Annual Ieee Applied Power Electronics Conference and Exposition (Apec),* pp. 1868-1871, 2012. [9] Z. Xin, X. Wang, P. C. Loh, and F. Blaabjerg, "Grid-Current-Feedback Control for LCL-Filtered Grid Converters With Enhanced Stability," *IEEE Transactions on Power Electronics,* vol. 32, pp. 3216-3228, 2017. [10] X. Jinbang, Y. Jun, Y. Jie, Z. Zhixiong, and S. Anwen, "An LTCL Filter for Three-Phase Grid-Connected Converters," *Power Electronics, IEEE Transactions on,* vol. 29, pp. 4322-4338, 2014. [11] X. Wang, F. Blaabjerg, and P. C. Loh, "Virtual RC damping of LCL-filtered voltage source converters with extended selective harmonic compensation," *IEEE Transactions on Power Electronics,* vol. 30, pp. 4726-4737, 2015. [12] A. Andersson, "Electromagnetism in terms of quantum measurements," *Journal of Mathematical Physics,* vol. 57, Dec 2016. [13] M. Huang, X. Wang, P. C. Loh, and F. Blaabjerg, "Active damping of LLCL-filter resonance based on LC-trap voltage or current feedback," *IEEE Transactions on Power Electronics,* vol. 31, pp. 2337-2346, 2016. [14] Y. Liu, D. Jin, H. Wang, G. Wang, J. Peng, and Y. Shan, "Magnetic components design of LCL filter in the grid connected power converter," in *IEEE International Future Energy Electronics Conference and Ecce Asia*, 2017, pp. 1189-1193.

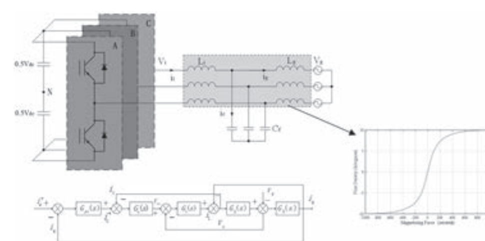

Fig. 1. LCL three phase grid-connected inverter

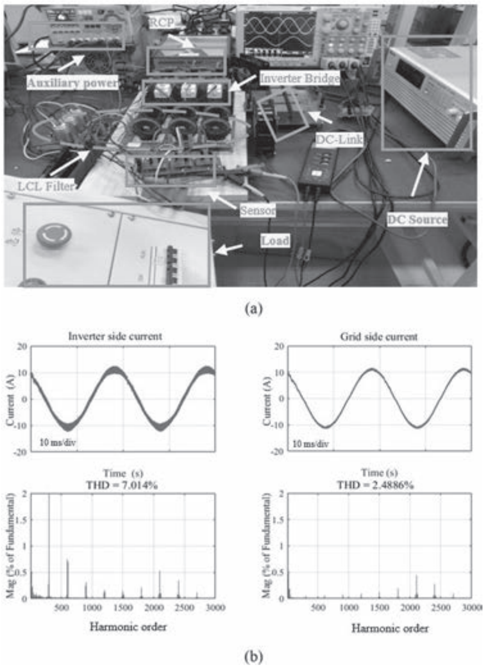

Fig. 2. Experiment, (a), set-up, (b) harmonic distortion of inverter and grid side currents

FW-05. Prediction of Stray Loss in Transformer Wall Shunt due to Leakage Magnetic Flux.

K. Park[1], S. Hahn[1] and H. Ahn[2]
1. Electrical Engineering, Dong-A University, BUSAN, The Republic of Korea; 2. R&D Center, Power & Industrial Systems Performance Group, Hyosung Corporation, Changwon, The Republic of Korea

1. Introduction Recently, energy problems such as depletion of resources have been emerging and electric power demand has been increasing. As a result, discussions on ways to improve the efficiency of the existing power system have been continuously posed. The problem of improving the efficiency of the power system is much more economical to improve the existing system efficiency than to replace the existing built and installed power equipment in a completely new form. Therefore, accurate loss analysis is needed to improve the efficiency. Transformer losses are largely divided into load loss and no-load loss. Load loss is the sum of eddy current loss and stray loss. The no-load loss is the sum of the hysteresis loss and the eddy current loss. The total loss of the transformer accounts for about 10% to 15% of no-load loss and about 85% to 90% of load loss, and the stray loss generated in the transformer structure part accounts for about 10 to 40% of the total load loss. In order to improve the transformer efficiency, many researches have been conducted to reduce the stray loss generated in the structure[1]. A common method is to using a magnetic wall shunt for the transformer tank. Most of them researches, however, rely on analysis using commercial tools[2]. The results from these methods are not accurate. In addition, it is very difficult to measure the stray load generated in the transformer structure through testing. Therefore, accurate loss calculation must precede loss reduction. In this paper, the stray loss predicate in the wall shunt of the transformer due to the leakage flux. To verify the validity of the analysis, proto-types were manufactured and tested. The manufactured proto-type consists of two exciting coils and a laminated magnetic steel plate. The magnetic flux density of the magnetic steel plate was measured using a search coil. The validity of the analysis was verified by comparing the measured magnetic flux density value with the analyzed value. The stray loss was then predicted using the comparative flux density. 2. Stray Loss Analysis 2.1 Skin Effect The skin effect is the effect that the high frequency current flows on the conductor surface and attenuates toward the center. This skin effect should be considered in order to accurately calculate the eddy currents generated in the transformer structure. The eddy current density and skin depth considering the skin effect can be expressed as the following equation[3]. $J_e=J_o \times e$^$(d/\delta\}$, $\delta=1/\sqrt{\pi f\mu\sigma}$ Where δ is skin depth [m] and f is frequency [Hz]. 2.2 Stray Loss The power loss in the wall shunt of the transformer is caused by the leakage flux. This power loss is called stray loss. The leakage flux, frequency, conductivity and permeability determine the stray loss. The stray loss considering the skin depth can be expressed[3]. $P = \iint_s \sqrt{(\omega\mu/2\sigma)}(H_0^2/\ 2)ds$ Where ω is angular frequency [rad / s] and s is area [m^2]. 3. Result and Discussion In this paper, we predicted stray loss in transformer wall shunt due to leakage flux. The magnetic flux density of the manufactured proto-type was measured using a search coil. The proto-type is shown in Fig 1. In order to analyze the effect of leakage flux on the wall shunt, the measurement was made according to the change of the current direction in the excitation coil. Also, the validity of the analysis was verified by comparing the measured value with the analyzed value. The stray loss was predicted using the verified magnetic flux density. The 3-D magnetic flux density distribution and 2-D magnetic field distribution is shown in Fig 2. The magnetic flux density was measured by changing the number of laminations of magnetic steel plate. These results confirm the validity of the analysis and are expected to be applicable to future stray loss prediction of power transformers. The results of analyzing the measured magnetic flux density values by changing the number of laminations of magnetic steel plate are expected to be economically advantageous because it is possible to optimize the technology for the loss reduction in the transformer tank.

[1] Masood Moghaddami, Arif I. Sarwat, and Francisco de Leon, Fellow, IEEE, “Reduction of Stray Loss in Power Transformers Using Horizontal Magnetic Wall shunt” IEEE TRANSACTIONS ON MAGNETICS, VOL. 53, NO. 2, FEBRUARY 2017 [2] O. Biro, G. Koczka, G. Leber, K. Preis, and B. Wagner, “Finite element analysis of three-phase three-limb power transformers under dc bias,” IEEE Trans. Magn., vol. 50, no. 2, pp. 565–568, Feb. 2014. [3] Robert M. Del Vecchio, “Transformer Design Principles: With Application to Core-Form Power Transformers”, CRC Press, 2010.

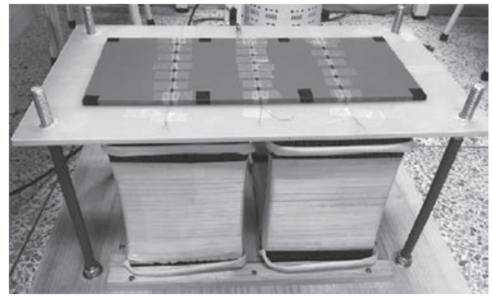

Fig. 1. Proto-Tyep Model

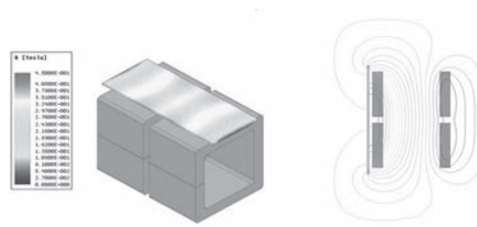

Fig. 2. (a) Magnetic flux density (b) Magnetic field distribution
Fig 2. Case 1 : Proto-Type Analysis (same Current direction)

FW-06. A Novel Multi-unit Out-rotor Homopolar Inductor Machine for Flywheel Energy Storage System.

J. Yang[1], C. Ye[1], X. Liang[1], F. Xiong[1] and W. Xu[1]
1. State Key Laboratory of Advanced Electromagnetic Engineering and Technology (AEET), School of Electrical and Electronic Engineering (SEEE), Huazhong University of Science and Technology, Wuhan, China

Abstract— Homopolar inductor machine (HIM) has been widely applied in the field of flywheel energy storage system (FESS). However, conventional HIM suffers from the low power and torque density due to its unipolar air-gap flux density. To solve this problem, a novel multi-unit out-rotor HIM (MOHIM) with bipolar air-gap flux density is proposed. First, the structure and operation principle of MOHIM are illustrated. To simplify analysis, MOHIM is divided into unit machines (UMs) based on the equivalent magnetic circuit. The back-EMF, flux density and output torque of MOHIM and UM are respectively compared, which proves the effectiveness of UM. Finally, the performance of MOHIM is investigated by three-dimension finite element analysis (3-D FEA), which indicates that this machine is a good candidate for the application of FESS. Keywords-Homopolar inductor machine (HIM); multi-unit out-rotor HIM (MOHIM); bipolar air-gap flux density; unit machine (UM). I.Introduction Homopolar inductor machine (HIM) has good applications in the field of flywheel energy storage due to its merits of robust rotor structure, brushless exciting, high-speed operation, and so on. Continuous free-wheeling losses of HIM caused by magnetizing flux could be significantly reduced by cutting off the field current, especially in a long-term standby state [1]. While HIM would suffer from the low power and torque density due to its unipolar air-gap flux density [2]. To solve this problem, a novel multi-unit out-rotor HIM (MOHIM) with bipolar air-gap flux density is proposed in this work. II.Structure and Operation Principle Structure of the proposed MOHIM is shown in Fig. 1(a) and (b). As drawing here, the rotor of MOHIM consists of two parts: a non-magnetic conductive rotor sleeve and (m+1) segments rotor cores. The salient iron poles of adjacent segments rotor cores are differed π electrical degree from each other. m segments laminated stator cores are set on a back-iron and evenly placed in the axial direction. (m+1) field coils encircle the back-iron and are sandwiched by the stator cores. The dc current directions of all field windings are the same. The magnetizing flux paths of MOHIM are shown in Fig.1(b). In this paper, m is equal to 3. III. Performance of MOHIM A.Equivalent magnetic circuit of MOHIM Fig.2(a) shows the equivalent magnetic circuit (EMC) of MOHIM, where Rsn and Rrn are the reluctances of stator and rotor, respectively; Rσn is the reluctance of air-gap; Rln is the leakage reluctance between two salient iron poles; Nf is the number of field winding and If is the excitation current. It can be obtained that the MOHIM can be divided into three unit machines(UMs)through the analysis of EMC, as shown in Fig. 2(b). The performance of MOHIM could be predicted by analyzing UM. B.Performance of MOHIM Fig.2 (c) shows the flux density distribution of UM and that of air-gaps I,II and III of MOHIM in Fig.1(b). It can be found that the air-gap flux density distributions of MOHIM are bipolar and are the same. Besides, the air-gap flux density waveforms obtained by UM and MOHIM are good agreement. Fig. 2(d) shows the back-EMF of MOHIM and UM when the rotation speed is 10,000r/min. It can be found the back-EMF of MOHIM can be well predicted by UM. Comparing the output torque waveforms presented in Fig. 2(e), it indicates that the results obtained by UM agree well with that of MOHIM. IV. Conclusion A MOHIM with bipolar air-gap flux density is proposed in this paper. The analysis process of MOHIM divided into UMs is investigated based on the EMC. The performance of MOHIM can be well predicted by UM. More detailed analysis and results will be given in the following full paper.

[1] P. Tsao, M. Senesky, and S.R. Sanders, "An integrated flywheel energy storage system with homopolar inductor motor/generator and highfrequency drive," *IEEE Trans. Ind. Appl.*, vol. 39, no. 6, pp. 1710–1725, Nov./Dec. 2003. [2] E. Severson, R. Nilssen, T. Undeland, and N. Mohan, "Magnetic equivalent circuit modeling of the ac homopolar machine for flywheel energy storage," *IEEE Trans. Energy Convers.*, vol. 30,no. 4, pp. 1670–1678, Dec. 2015.

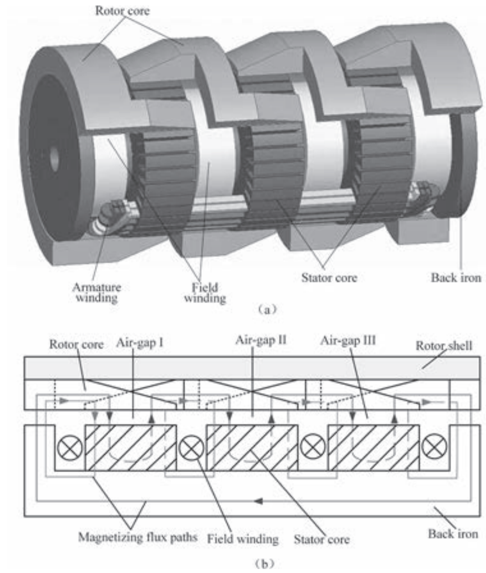

Fig. 1. MOHIM. (a) Topology. (b) Magnetizing flux paths.

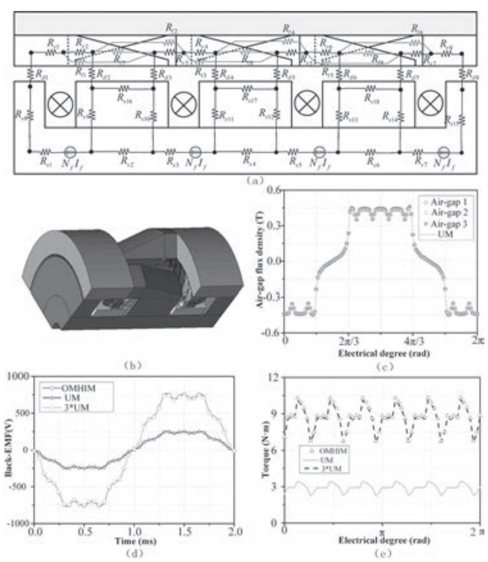

Fig. 2. (a) EMC. (b) UM. (c)Air-gap flux density waveforms. (d) Back-EMF of one phase. (e) Out-put torque.

FW-07. Fabrication and development of miniaturized efficient power converters using ultra-soft magnetic ribbons.

H. Ahmadian Baghbaderani[1], D.J. Cronin[1], P. McCloskey[1], S. Kulkarni[1], Z. Pavlovic[1], A. Masood[1], K. Ackland[2], P. Stamenov[2] and C. O'Mathuna[1]
1. Stategic Programs, Tyndall National Institute, Cork, Ireland; 2. School of Physics, Trinity College, Dublin, Ireland

 I. Abstract Advances in power conversion technologies have highlighted the need for development of new class of magnetic components (inductors, transformers etc) with lower footprint and higher efficiency. Presently, the sizes of these magnetic components have been limited due to the use of low flux density ferrite as a core material. In this paper, the assembly and working of an amorphous ribbon transformer with low loss performance as a replacement for ferrite based ones were studied. The minimum amount of power loss of the material was measured as <750 kW/m^3 at 100 kHz. The paper also shows the significant reduction in the footprint of the fabricated inductor. II. Introduction A key metric for an inductor and transformer is their magnetic material power loss performance. Presently, ferrites, iron powder and tape wound cores are primarily used for power applications. However, the low flux density of ferrites (0.3-0.4 T) requires considerable cross-sectional area in many deployments [1]. As the major size, weight, and cost drivers of electrical components are converters, using alternative materials with higher flux density can result in smaller, lighter and cheaper electrical components. In this study, the assembly and characterization of a magnetic transformer, using ultra-low loss soft magnetic ribbon core were presented. III. Low loss Magnetic Material The master Co-based, soft magnetic alloy was prepared by arc-melting of pure elements Co, Fe, B and Si in a highly pure argon atmosphere. The ingots were re-melted in quartz tubes by induction heating. Structure analysis of the samples was carried out by X-ray diffraction (XRD) method using Cu-Kα radiation (λ=1.54 Å). The absence of crystalline peaks confirms the amorphous structure of the in-situ ribbons. Therefore, a novel 8-12 μm thick Co-based amorphous ribbon was developed. This thickness is much lower than the thickness of Vitrovac, Vitroperm from Vacuumschmelze, Toshiba MT series etc causing reduction in the eddy current losses at high frequencies. A detailed review of high flux density ribbon materials was presented in previous works from the authors [2, 3]. Based on B-H loop tracer and in-plane magnetic hysteresis loops measurements, the coercivity of the ribbon was measured to be about 0.1 A/m which implies the ultra-soft magnetic properties of the ribbons as a result of near-zero magnetostriction of Co-based amorphous alloy. Additionally, the saturation flux density of the ribbons was more than 1 T which can be considered as an acceptable amount for high frequency applications. Amorphous structure of ribbons results in 150 mΩ as their resistivity. The AC loss measurement was performed over a number of frequencies, 100 kHz to 500 kHz, and various signal amplitudes. The ribbons were wound on the 150 μm sticky tapes to make 30 windings in total around a straw and two arrays of copper wire used to make two 25 turns which one of them considered as primary and the other one as secondary coil. The detail of the instrument and equivalent circuit for loss measurement is published in our previous studies [4, 1, 5]. Power loss density in the material which was extracted from the respective hysteresis loops and plotted logarithmically (Fig. 1), increases with applied AC flux density, B_{AC}, and frequency values which was expected due to rise in eddy current and hysteresis loss. It is well understood that as the operating frequency (f) increases, the eddy-current loss (P_{LE} α f^2) increases more sharply than the hysteresis loss (P_{LH} α f) and the total core energy loss becomes dominant at f > 100 kHz [4]. IV. Conclusion This paper describes development of low loss magnetic transformers for high efficiency dc-dc converter. The transformer uses laminated amorphous magnetic ribbons as core materials. The footprint of the fabricated transformer was more than 68% smaller than the commercial equivalent which can be considered as the lighter and smaller transformer compared to the Ferrite ones.

[1] S. Kulkarni, N. Wang, Z. Pavlovic, D. Li, P. McCloskey, G. Ypung, C. Ó Mathúna, Low loss thin film magnetics for high frequency power supplies. 16th European Conference on Power Electronics and Applications, Lappeenranta, 2014. [2] A. Masood, K. Ackland, P. Stamenov, P. McCloskey, C. Ó Mathúna, S. Kulkarni, Novel Rapid-Quenched Soft Magnetic Amorphous Thin Film Materials Using High Glass Forming Elements for Ultra-Low Electrical Losses. A Meeting of the Materials Research Society, Phoenix, 2017. [3] A. Masood, K. Ackland, P. Stamenov, P. McCloskey, C. Ó Mathúna, S. Kulkarni, High performance melt-spun CoFeBSi-based soft magnetic alloys. in Magnetism and Magnetic Materials, Pittsburgh, 2017. [4] S. Kulkarni, D. Li, N. Wang, S. Roy, C. Ó Mathúna, G. Young, P. McCloskey4, Low Loss Magnetic Thin Films for Off-Line Power Conversion. IEEE Transactions on Magnetics, VOL. 50, NO. 4, 2014.

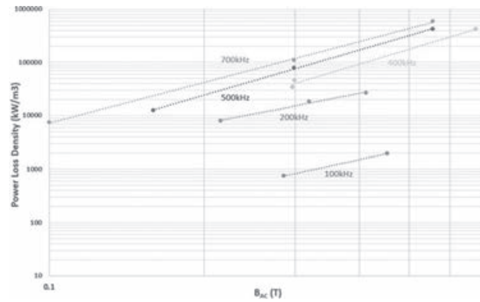

Fig. 1. Plot of power loss density as a function of magnetic saturation flux density in different frequencies.

FW-08. Prediction of Heating Power in Magnetic Pipe Conducting Large AC Current with High Frequencies Up to 200Hz.

A. Chen[1], A. Nysveen[1], J. Lervik[2] and M. Høyer-Hansen[2]
1. Electrical power engineering, Norwegian University of Science and Technology, Trondheim, Norway; 2. SINTEF energy, Trondheim, Norway

In direct electrical heating system (DEHs), which is developed for subsea process to safeguard well stream through pipelines to topside process platform or shore, the production pipeline is also acts as an active conductor conducting large AC current to generate heat. The heating source is conductive and hysteresis power losses in the pipe. Currently, the all implemented DEHs operate at 50Hz. There is a potential to further improve the heating capacity of the DEHs by operating the system at higher frequency so that the same power can be achieved at lower current. Consequently, the cross-session of the power cable can be reduced. Furthermore, operation in higher frequency directly results in better system utilization and less AC corrosion of the pipeline. This will further reduce the installation and operational cost and increase the system lifetime. For DEHs design it is critical to predict the heating power as function of input current and frequency so that proper frequency and current can be selected correspondingly. This paper analytically evaluate the heating power as functions of current and frequency based on experimentally measured material properties such as mass density, conductivity, B-H curve and hysteresis B-H loop energy. To verify the analytical results, both FEM simulation and prototype test are performed. *Current distribution* Comparing to the conducting current in the carbon steel pipe, generally in several hundred amperes, the displacement current is the pipe is negligible. The current distribution in the pipe is therefore determined by $\nabla^2 J=j\omega\mu\sigma J$ (1) The permeability of carbon steel is a nonlinear function of magnetic fields. To solve the problem analytically, it is common to assume an effective constant permeability uniformly over the pipe and this will be discussed later in detail. The solution of (1) for an isolated thick tubular conductor can be derived as $P_R=k_R I_{rms}^2\sqrt{(\mu f)}$ *(2) where* $k_R=1/(2r_o\sqrt{(\pi\sigma)})$ *(3) Hysteresis power loss* Due to the varied electric field produced by the AC current in the pipe, magnetic field in the pipe also varies, which causes hysteresis loss that is part of the heating power. The dissipated hysteresis energy per unit volume (or weight) in one cycle is the area enclosed by the hysteresis loop of B-H curve. The area and shape of the B-H loop is dependent on maximum magnetic field. This hysteresis B-H loop of the pipe is measured at laboratory in DC condition (< 0.003Hz) to eliminate the influence from eddy current loss. So the hysteresis energy is independent of frequency. Hysteresis energy in a magnetic material is usually expressed as a function of the maximum flux density B_{max} $E_{hys}=k_h B_{max}^{k_p}$ (4) where k_h and k_p are material dependent constants, and k_p as "Steinmetz coefficient" is generally near to 1.6. The hysteresis power in unit length can be evaluated by integrating the hysteresis energy over the pipe volume and multiplying frequency f and mass density ρ as $P_{hys}=2\pi\rho f\int rE_{hys}dr$ (5) Based (1) and (5), the hysteresis power in the pipe can be derived and finally expressed as $P_{hys}=k_c I_{rms} k_p \mu^{(k_p-0.5)}\sqrt{f}$ *(6) where* $k_c=2r_o k_h\rho\sqrt{(\pi/\sigma)}/(k_p(\sqrt{2}\pi r_o)^{k_p})$ *(7) Effective permeability* As given in (2) and (6), both the conductive and hysteresis powers are a function of effective permeabililty in addition to frequency and input current, so the effective permeability should satisfy following two conditions: 1) The effective permeability should be acceptable for both conductive and hysteresis power loss calculations. 2) The effective permeability should be obtainable based on the measured permeability and the input current of the pipe. An effective permeability as function of input current has been derived here and the result is shown in Fig.(1), where the effective constant relative permeability used for the analytical calculation is plotted as function of the maximum magnetic flied that is determined by the input peak current. *Result verification* To verify the result, both FEM simulation and prototype test are carried out for a specific case, a 12" carbon steel pipe having tube thickness of 17.1mm where the current varies between 300 and 1000 A, and the frequency between 50 to 200Hz. A rod example is made of the pipe for measuring the properties. The results are expressed as resistance per km ($R=P/I_{rms}^2$) and presented in Fig.(2) *Conclusion* An analytical method to predict the heating power in magnetic pipe is derived, in which the heating power is expressed in terms of operating frequency and input current. Effective permeability for the analytical calculation is also derived based on measured B-H curve of the magnetic material and its value is determined by the peak input current. The analytical results are compared with FEM simulation and prototype test, and they match each other satisfactorily. More detail will be presented in final paper, including proximity effect.

[1] Arne Nysveen, Hrald Kullbotten, Jens Kristian Lervik, Atle Harald Børnes, Martin Høyer-Hansen and Jarle J. Bremnes, Direct Electrical Heating of Subsea Pipelines—Technology Development and Operating Experience", IEEE Transactions on Industry Applications, VOL. 43.NO:1 Jan/Feb. 2007. [2] Simon Ramo, John R. Whinnery, Theodore Van Duzer, "Fields and Waves in Communication Electronics" 2nd edition, ISBN 0-471-81103-3, John Willy & sons, 1984 [3] Howard Johnson, and Martin Graham, "High-Speed Signal Propagation: advance black magic" ISBN 0-13-084408-X, 2003, Pearson Education. Inc [4]H. B. Dwight, "A precise method of calculation of skin effect in isolated tubes," AIEE Trans, vol. 42, pp. 827–831, 1923. [5] T. Morgan, R. D. Findlay, and S. Derrah, "New formula to calculate the skin effect in isolated tubular conductors at low frequencies," Inst. Elect. Eng., Sci. Meas. Technol vol. 147, no. 4, pp. 169–171. [6] Kawasaki, M. Inami, and T. Ishikawa, "Theoretical considerations on eddy current losses in non-magnetic and magnetic pipes for power transmission systems", presented at the IEEE Summer Power Meeting, Minneapolis, MN, 1980, Paper 80 SM54–7-0. [7] K. Zakrzewski and F. Pietras, "Method of calculating the electromagnetic field and Power losses in ferromagnetic materials, taking into account magnetic hysteresis", Proc. IEE, Vol, 118, Nio:11 November 1971 [8] Bruce C. W. McGee and Fred E. Vermeulen, " Power losses in steel pipe delivering very large currents2, IEEE Trans. Power Del.VOL. 17 No.1 pp25-72, Jan.2002. [9] Wael Moutassem and George J. Anders, " Calculation of the eddy current and hysteresis losses in sheathed cables inside a steel pipe", IEEE Trans. Power Del. VOL.25, NO.4, pp2054-2063, Oct. 2010 [10] A. Mekjian and M. Sosnowski, "Calculation of alternating current losses in steel pipes containing power cables," IEEE Trans. Power App. Syst., vol. PAS-102, no. 2, pp. 382–388, Feb. 1983 [11] .P. Steimetz, "On the law of hysteresis", Proc. IEEE, Vol.72, No, 2, pp 197-221,Feb.1984.

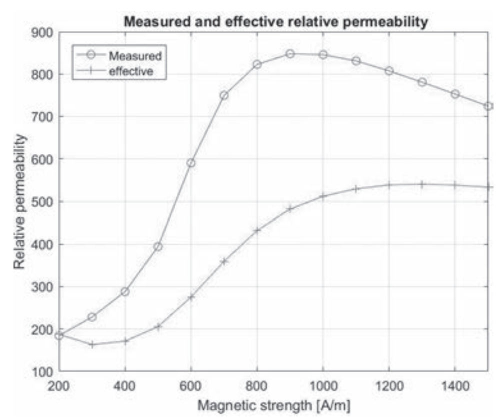

Fig. 1. Measured relative permeabilily and effective relative permeabilily in carbon steel

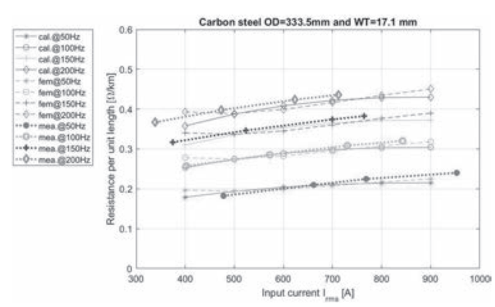

Fig. 2. Comparison of analytical calulated, FEM simulated and measured power loss in terms of resistance as function of input current in the carbon steel pipeline.

FW-09. A Novel Three Limb Topology of a Saturated Core Fault Current Limiter in HVDC System.

H. Zhou[1], J. Yuan[1], L. Wei[1,2], P. Gan[1], F. Chen[1], Y. Zhong[1], C. Tian[1], B. Chen[1], Y. Gao[3] and K. Muramatsu[3]
1. School of Electrical and Engineering, Wuhan University, Wuhan, China; 2. Department of Electrical Engineering, Graduate School of Engineering, Kyoto University, Kyoto, Japan; 3. Department of Electrical and Electronic Engineering, Saga University, Saga, Japan

I. Introduction In order to protect high voltage direct current(HVDC) system from destructive damage caused by large DC fault current, a HVDC system saturable core type fault current limiter(DCSFCL) is proposed previously. However, through principle investigation and simulation analysis of DCSFCL, coil inductance of DCSFCL do not have a large changing rate (CR) when a fault occurs, so clipping performance of it will not be quite satisfying. In order to increase CR and improve clipping performance of original DCSFCL, further improvements need to be carried out. In this digest, a modified three limb structure of DCSFCL(TSFCL) is proposed and equivalent magnetic and electric circuit are analyzed. Simulations carried out on ANSYS shows that clipping performance is improved by a large scale. II. Basic Principle Analysis Previous deduction and design shows that a fixed inductance value is required in normal state so that proposed DCSFCL can replace normal smoothing reactor. Besides, inductance value of DCSFCL depends on total magnetic resistance of the flux path and among those different parts that form the core, PM account for the major proportion. However, when normal inductance value is designed to be constant, those changing parts of the core that desaturate from saturation state define the CR of DC coil's inductance value when a fault occurs. In that case, once CR rises, DC coil's inductance value will rise simultaneously and therefore, fault current will be restricted more efficiently. Thus, if somehow the magnetic resistance of changing parts increase and even account for the main part in total magnetic resistance, CR will increase and the clipping performance will be enhanced. Based on deductions mentioned above, a novel TSFCL is proposed and Fig.1 illustrates original topology of DCSFCL, TSFCL and its equivalent electric and magnetic circuits, respectively. Based on previous works[1,2], another PM limb is added into the original topology to "force" the flux flows through center limb. After analyzing those two circuits and applying Faraday's law of electromagnetic induction and the constitutive relationship between voltage and inductance, inductance value of TSFCL can be derived: $L_{fcl}=(N_{dc}^2)/[R_e+2R_{u1}+(2R_c+R_a)(2R_m+2R_{u2}+2R_{u3}+R_y)/(2R_c+R_a+2R_m+2R_{u2}+2R_{u3}+R_y)]$, where N_{dc} is number of DC coil. R_e, R_c, R_y, R_u, R_a, R_m are the magnetic resistance of left limb, center limb, right limb, left yoke, center PM and upper yoke PM, respectively. By inserting this center limb, flux generated by DC coil is inclined to flow through this center limb instead of original PM path due to obvious difference in magnetic resistance between these two paths. Hence, proposed new topology makes the CR increases in the premise of normal inductance value. Besides, the cross-sectional area of the center limb can be designed to be larger than yoke, thus further increase the proportion of saturated parts and render the CR of inductance value rise more when fault occurs. In that case, fault current can be restricted more efficiently. III. Simulation Study To verify our deductions, simulation using ANSYS is performed and comparison studies are carried out. Fig.2(a), (b) and (c) show flux density distribution of TSFCL and its inductance value variation. It is obvious that normally, left limb, upper and downer yoke stays in critical saturation state and the presented inductance of DC coil is exactly 300mH owing to the structure design. When a fault occurs(t=0.02s), limb and yoke of proposed TSFCL desaturate very fast and make inductance value of DC coil rises immediately. From Fig.2(c) and (d), it is obvious that compared with former proposed DCSFCL, the new three limb structure has 19.5% rise in fault state inductance value, i.e., from 0.82H to 0.98H. As for the fault current limiting performance compared with fixed 300mH smoothing reactor, traditional DCSFCL makes fault current drop for 28% in less than 5ms. This number, on the contrary, goes straight up to 41.2% for the proposed new TSFCL. Therefore, proposed new structure is more efficient. IV. Conclusion In this digest, a novel three limb structure saturable core fault current limiter for HVDC system is proposed. Working principle is analyzed and simulations are carried out. Comparative study shows that proposed TSFCL has about 20% increase in clipping performance than traditional DCSFCL and over 40% increase than normal smoothing reactor. Considering that length of center PM is quite important to CR and final clipping performance of TSFCL, different PM length and related optimization study will be carried out soon. Detailed information and investigation will be shown in the full paper.

[1] J. Yuan, Y. Zhong, Y. Lei, C. Tian, W. Guan, Y. Gao, K. Muramatsu and B. Chen, "A novel hybrid saturated core fault current limiter topology considering permanent magnet stability and performance," *IEEE Trans. Magn.*, vol. 53, no. 6, Jun. 2017, Art. no. 8400304.

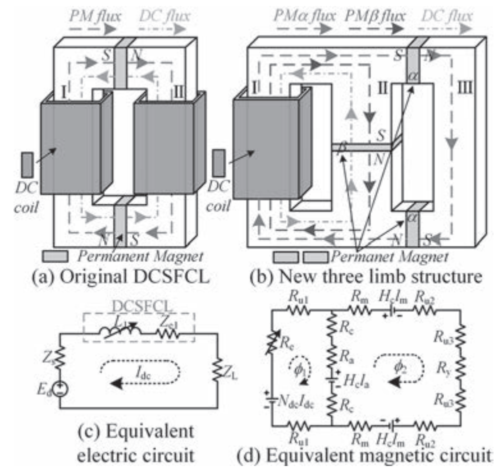

Fig. 1. Basic configuration and equivalent circuits

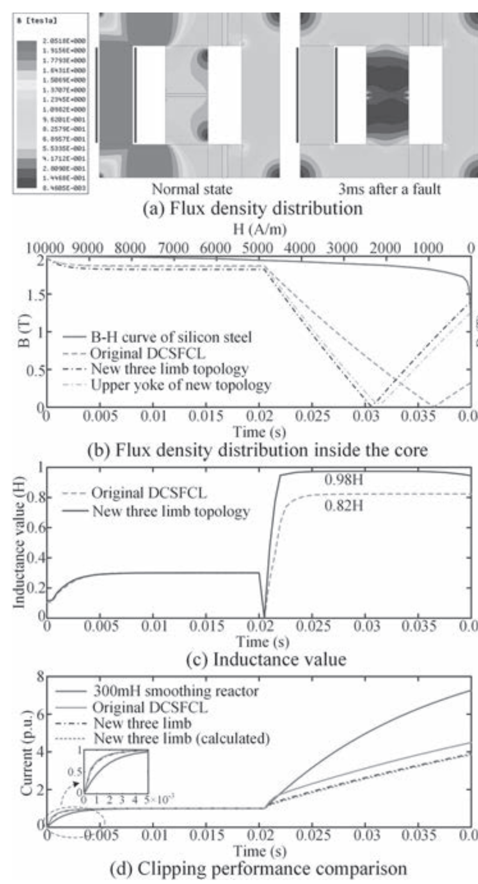

Fig. 2. Simulation and comparative study

FW-10. New Equivalent Circuit Model of UHVDC Converter Transformer Winding for the Calculation of Transient Potential Distribution.

s. He[1], C. Li[1], Y. Liu[1], Z. Zhao[1], J. Deng[2], J. Li[1] and H. Qian[2]
1. electrical engineering, xi'an jiaotong university, Xi'an, China;
2. Maintenance and Test Center of EHV Power Transmission Company, China Soutern Power Grid, Guangzhou, China

1 INTRODUCTION Power transformers especially UHVDC converter transformers, need not only to bear the working voltage, but also to have the ability to withstand a certain degree of overvoltage, such as lightning, operation overvoltage, and very fast transient overvoltage (VFTO) which is characterized by a fast rise time of several nanoseconds and an oscillating waveform caused by switch operation in Gas-insulated substation. In order to study the propagation of the transient overvoltage on the transformer windings, a model is needed which is able to simulate the transient potential distribution along the transformer winding. Obviously, an accurate computational model of transformer winding for potential distribution analysis under impulse voltage is very important for the design of transformer interturn insulation especially for large capacity transformers such as UHVDC converter transformers. Quite a lot of research have been done to seek an appropriate transient computational model for transformer windings. Two basic physical methods have been obtained. They are multiconductor transmission line models and equivalent circuit models. For the multiconductor transmission line model, the transformer winding is represented by distributed parameters, but the losses caused by hysteresis, eddy current and proximity effect cannot be modeled. On the contrary, the equivalent circuit model can take saturation and losses caused by the core into account, but always assumming that the influence of magnetic core is negligible at frequencies higher than 10kHz,which is not always valid in practice. Lightning impulse or VFTO waveforms usually contain abundant frequency components higher than 10kHz. To obtain a more accurate model and also to provide a wide-band frequency response, in this paper, a new equivalent circuit representation of UHVDC converter transformer winding is given taking into consideration of comprehensive frequency characteristic of core lamination stack. 2. Equivalent Circuit Model and Calculation of its Parameters A. Effective Permeability of Core Lamination Stack Considering the skin effect and saturation effect of the core lamination stack, the effective permeability of the core is obtained through the finite element method. The loss of the core is performed as a reduced permeability, then the law of permeability varies with frequency is acquired. B. Parameters Calculation The equivalent capacitance and the interturn capacitance between the continuous winding pancakes are calculated by the plate capacitor formula. The frequency dependent parameters such as the self-inductance and mutual inductance of the winding are calculated using the equivalent permeability of the core lamination stack, and the conductor resistance is calculated considering the skin effect. C. Establishment of the Equivalent Circuit Model According to the structure parameters of the UHVDC converter transformer, and taking two pancakes as one unit, the equivalent circuit of the winding is established by using the calculated resistance, inductance and capacitance parameters. The equivalent circuit of two units is shown in fig.1. Each unit consists of a capacitance branch between the core (grounded) and winding, a inductance and a resistance series branch, N-1 interturn capacitances, N-1 capacitances between pancakes (where N is the number of turns of one pancake). For UHVDC converter transformers there are usually more than one windings as the fig.1 shows, and there are coupling inductances and capacitance between the conductors of the two windings. Note that the resistance and inductance parameters mentioned above are functions of frequency. So the problem is difficult to solve with ATP or PSPICE. It is efficient to use MATLAB's powerful matrix calculation capability to solve the problem, and the potential distribution of the windings under transient overvoltage is obtained. 3. Results and discussion The equivalent circuit model is realized in MATLAB, taking lightning overvoltage for an example, and the propagation of voltage and the transient potential distribution in the winding are studied carefully. The potential distribution of the winding is presented in fig.2. The detailed results will be shown in full text. 4. Conclusion This paper has proposed an equivalent circuit for modelling the UHCDC transformer winding (especially inserted capacitance continuous winding) to study the potential distribution property. Considering the eddy current and skin effect which are variable with frequency, the inductance and resistance parameters of the model vary with the frequency, respectively. Using MATLAB programming to solve the voltage equation of the equivalent circuit to obtain the potential distribution properties of the windings, the new proposed model may provide more accurate winding potential distribution prediction for transformer interturn insulation design.

[1] Jäschke C, Schegner P. Computing the Coupling Resistances in High-Current Instrument Transformers Considering Skin and Proximity Effect[J]. IEEE Transactions on Magnetics, 2017, 53(11):1-7. [2] Preis K, Renhart W, Rabel A, et al. Transient Behavior of Large Transformer Windings Taking Capacitances and Eddy Currents Into Account[J]. IEEE Transactions on Magnetics, 2017, PP(99):1-4. [3] Popov M, Lou V D S, Ren P P S, et al. Analysis of Very Fast Transients in Layer-Type Transformer Windings[J]. IEEE Transactions on Power Delivery, 2006, 22(1):238-247.

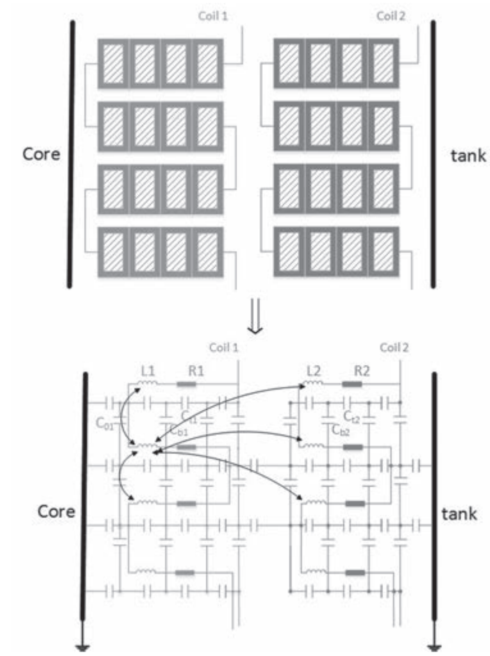

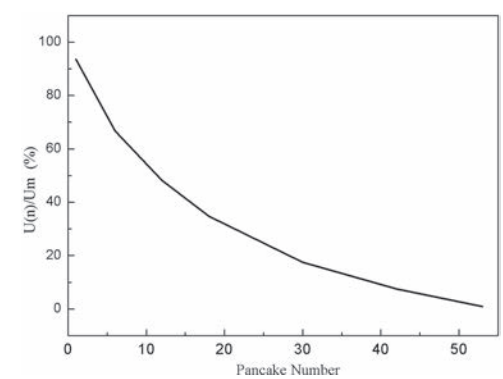

FW-11. Dynamic Transformer Core Model Based on the Inverse Three-component Preisach Model.

W. Sima[1], *D. Peng*[1], M. Yang[1], M. Zou[1] and Y. Liu[1]
1. Chongqing University, Chongqing, China

Transformer is one of the crucial equipment in power systems. A precise transformer model is very essential for most of the electromagnetic transient studies. Iron core, the most complicated part of a transformer, may have different hysteresis trajectories, and be saturated when suffering variety of excitations. For transformer modeling, the hysteresis of the iron core is one of the most complicated phenomena to be accurately modeled because it is a nonlinear, history- and frequency-dependent phenomenon. The classical Preisach model is one of the most practical methods to model the hysteresis of ferromagnetic materials due to its good history-dependent wiping-out and congruency properties. The most important point of the Preisach theory is that the magnetic field in the ferromagnetic material can be considered as a set of elementary hysteresis loops, which have only two states, $+B_S$ and $-B_S$. Despite the physical meaning of Preisach theory is not clear, the classical Preisach model (CPM) is widely used for modeling hysteresis phenomenon. In the application of power system transients, the voltage U and the current I are the most common variables that can be accurately measured in the filed. The flux Φ is obtained by the integration of U. In most of the EMTP platforms, the Φ-I curve is the priority to model the iron core hysteresis. Therefore, this paper presents the hysteresis characteristic of a transformer core by Φ and I. Compared with the current, the voltage is much easier to be measured and more accurate in power systems. Therefore, the flux linkage is more suitable to be the input variable of a model than the current. Moreover, the integration of U can avoid the oscillation of calculation. So it is necessary to build the inverse Preisach model denoted by I-Φ expression. The I-Φ Preisach plane is shown in Fig.1. It also reveals the variation trend of plane under the different direction of flux linkage. Considering the conveniences of the applications, the distribution function of I-Φ Preisach model is determined by quasi-static sinusoidal loops, which is easy to be generated. The center cycle method is utilized here to identify the Preisach distribution function (PDF). The Preisach plane is discretized to uniform cells by the method. According to the principle of the method, the distribution function of the cell is determined by the difference of the flux linkages of two adjacent curves in the same current. Therefore, although the data is easy to acquire, the accuracy requirement of the measured data is high. By assuming the symmetry of the PDF, the computation is reduced to half. The determination result can calculate the current from the flux linkage accurately. The static Preisach model can predict the major hysteresis loop as well as any symmetrical or asymmetrical minor loops at zero frequency. However, in power systems, flux linkage in a transient is a complex waveform containing various frequency components. Therefore, the exciting current I depends not only on the magnitude of the flux linkage, but also on the magnetization frequency and hence on the voltage which represents the differential of the flux linkage. In this situation, a simple three-component dynamic hysteresis model can be used to represent the transformer core. In the composite model, the total current is decomposed into the hysteresis component I_h(t), classical eddy-current component I_{ec}(t), and excess component I_{exc}(t). The inverse Preisach model is applied here to depict the static hysteresis current I_h(t). $I_{ec}(t)$ can be given by the well-known formula $I_{ec}(t)=v(t)lk_{ec}/(N^2S)$. l and S is the equivalent length and the cross section of the magnetic circuit, respectively, and can be calculated from IEC 60205:2016. The constant $k_{ec}=d^2/(12\rho)$ is determined by the lamination thickness and resistivity of the core material. The excess component $Iexc(t)$ can be acquired by $Iexc(t)=\delta|v(t)|^{\alpha}lkec/(N^{\alpha+1}S^{\alpha})$. δ is the direction coefficient of v(t). G(Φ) and α are usually obtained from fitting the measured dynamic loops. When the dynamic loops are obtained, the measured Φ is used to calculate I_h, and the measured V is used to calculate I_{ec}. The last component Iexc was acquired by the function G(Φ) and α. They are obtained by minimizing the deviation of the calculated dynamic loop from the experimental loop using the nonlinear optimization algorithm. The dynamic inverse Preisach model was tested on a two-winding transformer. The calculated dynamic hysteresis loops are compared with the measured loops. In order to demonstrate the frequency dependence of the model, different frequencies are chosen, they are 25Hz, 50Hz, 60Hz, 100Hz, respectively. The primary current and the secondary voltage waveforms are obtained from the transformer simulation studies and also the laboratory test results corresponding to the no-load steady state. The results demonstrate that the proposed model coincides with the measurements in the acceptable engineering accuracy. It shows that the dynamic hysteresis model can accurately simulate the dynamic magnetization of the transformer core in a certain frequency range.

[1] Zirka S E, Moroz Y I, Marketos P, et al. Generalization of the Classical Method for Calculating Dynamic Hysteresis Loops in Grain-Oriented Electrical Steels[J]. IEEE Transactions on Magnetics, 2008, 44(9):2113-2126.

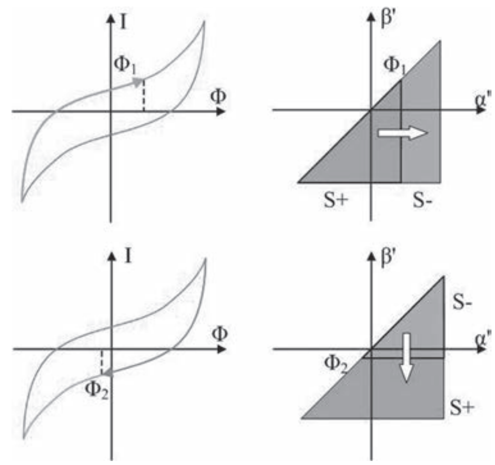

Fig. 1. I-Φ Preisach plane under different magnetization processes

FW-12. An Analytical and Numerical Hybrid Model for Static Characteristics of a Interior Permanent Magnet Machine.

P. Jin[1], Y. Guo[1] and Y. Zhu[1]

1. School of Energy and Electrical Engineering, Hohai University, Nanjing, China

I.Introduction Recently, permanent magnet (PM) machine having high dynamic performance, good power/mass ratio, and simple structure has been proposed [1]. A number of numerical techniques are used to analyze its performance while some pure analytical modeling with magnetic scalar potential are also employed [2-4]. However, on one side numerical techniques such as the Finite Element (FE) Method are time-consuming and less insightful when looking into the influence of design parameters upon the machine's behavior. On the other entire analytical methods just can be used in limited topologies, such as surface PM machine, but ineffectively for general topologies like interior PM machine,. This paper presents an analytical and numerical hybrid model for static characteristics of an interior PM machine. II.Analytical and Numerical Hybird Model II-A.Interior PM Machine As shown in Fig. 1, the interior PM machine prototype has a tubular rotor, in which there are alternately polarized iron poles along the *q*-direction, and a stator with distributed windings. Region I ($R_m \le r \le R_s$) is air region and region II ($R_r \le r \le R_m$) is rotor region with the PMs and iron poles. In the 2D model, the end effects are not taken into account; the PMs have a linear demagnetization characteristic, and are fully magnetized in the direction of magnetization. II-B.Field Distribution on the surface of the rotor A knowledge of the magnetic field distribution on the air region produced by the rotor is fundamental to establishing an accurate model of the PM machine for design optimization and dynamic modeling. In region I, the static magnetic field is governed by the Laplace equation only and the boundary on the stator's inner surface where $r=R_s$ is of the Dirichlet boundary condition. In order to obtain the magnetic field distributions in the other boundary where $r=R_m$, a simplified partial 2D FE model contained rotor and stator without coils will be established. The nonlinear magnetic field of the machine which can be treated as static field and analyzed by ignoring the eddy current, satisfies the governing equation (1) (equations and functions are all given in Fig. 2) and boundary conditions functions (2), where S_Ω is the outer boundary of the solution domain. A is the magnetic vector potential. H_c is the residual flux intensity of PM. By using the FE method, flux density $B_S(\theta, r)$ in the different points of the rotor's surface where $r=R_m$ can be calculated by equation (3) where B_{rS} and $B_{\theta S}$ are *r*- and θ-direction flux density components respectively. By using the discrete Fourier transform, B_{rS} and $B_{\theta S}$ which are calculated by the FE model, are decomposed into the equation (4) where ν=np; C_{rkn} and $C_{\theta kn}$, are the *n*th harmonic coefficients of the Fourier Transform. II-C.Field Distribution in the air region In the polar coordinate system, based on the magnetic scalar potential (MSP) ϕ, the magnetic field intensity components can be expressed by equations (5) where ϕ is governed by the Laplace equation in the air region as equation (6) whose general solution is equation (7) and boundary conditions can be expressed by equation (8). By solving the Laplace equation in region I subject to former boundary conditions, the Fourier expansions of the flux density components in the *r*- and θ-direction in region I in the polar coordinate system can be given. The electromagnetic torque of the machine can be subsequently predicted by the hybrid method. III.Verification by Integrated FE model To verify the correctness of the analytical solutions, we calculated magnetic field of the interior PM machine using an integrated FE model. The meshed elements are triangular-shaped and the free mesh algorithm is imposed. The predicted flux densities along the r-direction in an electrical period of the tubular rotor and along the q-direction with different methods are compared. Some excellent agreements verify the validity of the hybrid model. The electromagnetic torque and the flux linkage of the stator winding are subsequently derived and validated by the integrated FE model in the full paper. IV.Acknowledgment This work was jointly supported by the NSFC (51407061) and the NSF of Jiangsu Province (BK20140854).

[1] Z. S. Du, T. A. Lipo, "Torque performance comparison between a ferrite magnet vernier motor and an industrial interior permanent magnet machine," IEEE transactions on industry applications, vol. 53, no. 3, pp. 2088-2097, May/June 2017. [2] X. Ge, Z. Q. Zhu, G. Kemp, et al, "Optimal step-skew methods for cogging torque reduction accounting for three-dimensional effect of interior permanent magnet machines," IEEE transactions on energy conversion, vol. 32, no. 1, pp. 222-232, March 2017. [3] S. Yang, S. M. Yang, and J. H. Hu, "Design consideration on the square-wave voltage injection for sensorless drive of interior permanent-magnet machines" IEEE transactions on industrial electronics, vol. 64, no. 1, pp. 159-168, January 2017. [4] S. G. Min and B. Sarlioglu, "Analytical calculation of back emf waveform for linear pm motors in slotted and slotless structures," IEEE transactions on magnetics, vol. 53, no. 12, pp. 8112910:1-10, December 2017.

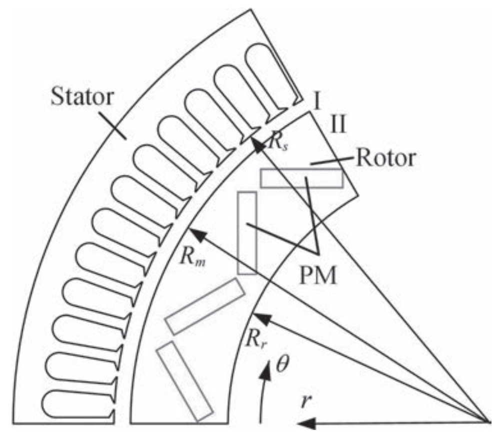

Fig. 1. Cutaway view of the interior PM machine.

$$\frac{1}{\mu}\nabla\times\mathbf{A}-\nabla\frac{1}{\mu_e}\nabla\cdot\mathbf{A}=\begin{cases}0 & \text{Region I}\\ \nabla\times\mathbf{H}_c & \text{Region II}\end{cases} \quad (1)$$

$$\left.\begin{aligned}\mathbf{A}\times \mathrm{n}=0\\ \nabla\cdot\mathbf{A}=0\end{aligned}\right\} \quad (2)$$

$$\vec{B}_S(\theta)=B_{rS}(\theta,z)\vec{r}+B_{\theta S}(\theta,z)\vec{\theta} \quad (3)$$

$$\begin{cases}B_{rS}=\sum_{n=1,3,5\cdots}^{\infty}C_{rn}\sin(np\theta)\\ B_{\theta S}=\sum_{n=1,3,5\cdots}^{\infty}C_{\theta n}\sin(np\theta)\end{cases} \quad (4)$$

$$H_r=-\frac{\partial\varphi}{\partial r},\quad H_\theta=-\frac{1}{r}\frac{\partial\varphi}{\partial\theta} \quad (5)$$

$$\frac{\partial^2\varphi}{\partial r^2}+\frac{1}{r}\frac{\partial\varphi}{\partial r}+\frac{1}{r^2}\frac{\partial^2\varphi}{\partial\theta^2}=0 \quad (6)$$

$$\phi_1(r,\theta)=\sum_{n=1,3,5\cdots}^{\infty}(A_n r^{np}+B_n r^{-np})\cos np\theta \quad (7)$$

$$\begin{cases}H_r(r,\theta)|_{R_s}=0\\ \vec{B}(r,\theta)|_{R_m}=\vec{B}_S(\theta)\end{cases} \quad (8)$$

Fig. 2. Equations and functions.

FW-13. AC Loss Analysis of a Flux-coupling type Superconducting Fault Current Limiter.

S. Yan[1], Y. Tang[1], L. Ren[1] and Z. Wang[1]
1. Hua Zhong University of Science and Technology, Wuhan, China

I. Introduction Large short-current level has a severe impact on the transient stability, operational life of electrical equipment and leads to other unforeseen troubles in the power systems[1]. A flux-coupling type SFCL (FC-SFCL), which has the advantages of low steady-state impedance, easily adjustable current-limiting impedance ratio, and helping with system reclosing, is developed. An improved AC loss calculation model for the SFCL is studied and a scheme to reduce the AC loss is proposed. II. Principle and structure The FC-SFCL [2],[3]with a pair of HTS parallel windings is developed here. The limiter is based on disconnecting coupling windings for current-limiting, which has a low steady impedance at normal state and higher limiting one after fault. Fig. 1(a) shows the basic structure of the FC-SFCL, the current-limiting unit is made of two HTS windings W_1 and W_2 carrying current in opposite directions. It is installed in series with the power system, which can be divided into three operating conditions: normal condition (the system operates normally with S_1 closed), fault condition (fault happens before opening S_1), and limiting condition (after opening S_1, the limiter acts). The layer winding with a 2G Super Power SCS 4050 4-mm wide YBCO tape is used for the two windings. To reduce the total length of the tape and increase inductance of the single winding, an iron core made by silicon steel sheet, 30Q120, is chosen to manufacture the magnet shown in Fig.1 (b). Due to air gaps in the core column and yokes, the inductance value is stable and large iron core volume can be avoided. III. An AC loss calculation model Due to the larger leakage flux and greater fault current impulsion on the online HTS winding after disconnecting, AC losses will increase rapidly and lead to the reduction of thermal stability. An improved AC loss calculation model is used to analysis the influences of different winding structures on losses and current distribution. A 10 kV / 500 A FC-SFCL single prototype with windings wound on the iron-core with air gap is regarded as a calculation sample. The method of modeling local tapes in detail is used to improve the speed of calculation. However, the non-linearity of the iron core permeability leads to poor convergence and large time consumption. This problem can be solved rapidly by a formula using the pre-defined Magnetic Field (mf) module in Comsol Multiphysics. The permeability of the core region in the PDE module is transmitted from the mf module. Integral constraints are used to impose an explicit transport current in each superconducting conductor. The two modules, PDE and mf, are fully coupled and simultaneously solved [4],[5]. IV. Improved method and result The superconducting winding of the SFCL is made of two cross-connection sub-modules in series, which adopt the layer-wound structure, as shown in Fig. 2 (a)(b). Each HTS winding is made of 3×n tapes in parallel, with 3 tapes arrayed in the z direction and n tapes arranged along the r direction. Model I is with 3×6 tapes in parallel for each winding, and Model II is with 3×7 tapes in parallel for winding 2 and 3×5 tapes for winding 1. They have the same total parallel numbers. Fig. 2(c) shows the currents and AC loss in two windings in the two Models. There is no quench on the windings. The changes of current and magnetic field lead to large AC loss and uneven magnetic distribution on the two windings. In Model I, the AC loss of winding 2 is large after decoupled for the low I_c margin. In addition, inductive AC loss on winding 1 is also great. In Model II, the total AC loss obtains remarkable improvements and magnetic field distribution becomes more uniform. While the current in each tape of winding 1 is higher than that of winding 2, AC loss of winding 1 is also larger than that of winding 2 in fault condition. After decoupling, AC loss of winding 2 is still larger than that of winding 1, but compared with Model I, AC loss in winding 1 is minished due to the reduction of the number of parallel tapes, and AC loss in winding 2 has also reduced because of the increasing critical current margin with adding the parallel tapes. The scheme of adding the parallel number of winding 2 and reducing that of winding 1 is reasonable for improving the SFCL performance. V. Conclusion This work studies an AC loss calculation method for a Flux-coupling SFCL with an iron core. The non-linearity of the iron core permeability leads to poor convergence and large time consumption. An improved AC loss calculation model is used to analysis the influences of different winding structures on losses and current distribution. Then a scheme to reduce losses is proposed. Through adjusting the parallel numbers of the two windings, the losses characteristic has significant improvements, with losses on each winding balancing, total losses declining, and magnetic field distribution uniform. Acknowledgment This work was supported in part by the Science and Technology Project of Hubei Electric Power Company (SGCC) under Grant SGTYHT/16-JS-198 and Natural Science Foundation of Hubei Province 2016 (2016CFA075).

[1] H. S. Ruiz, X. Zhang, and T. A. Coombs, "Resistive-Type Superconducting Fault Current Limiters: Concepts, Materials, and Numerical Modeling," *IEEE Trans. Appl. Superconduct.*, vol. 25, no. 3, pp. 1-5, Jun. 2015. [2] L. Chen et al., "Current limiting characteristics of a novel flux-coupling type superconducting fault current limiter," *IEEE Trans. Appl. Superconduct.*, vol. 20, no 3, pp 1143-1146, Jun. 2010. [3] S. N. Yan, et al, "Simulation analysis and experimental tests of a small-scale flux-coupling type superconducting fault current limiter," *IEEE Trans. Appl. Supercond.*, vol. 27, no. 4, Jun. 2017, Art. no. 5600205. [4] L. Quéval, V. M. R. Zermeño, F. Grilli, "Numerical models for ac loss calculation in large-scale applications of HTS coated conductors," *Supercond. Sci. Tech.*, vol. 29, no. 2, 2016, Art. no. 024007. [5] Quéval L, Ohsaki H, "AC losses of a grid-connected superconducting wind turbine generator," *IEEE Trans. Appl. Supercond.*, vol. 23, no. 3, Jun. 2013, Art. no. 5201905.

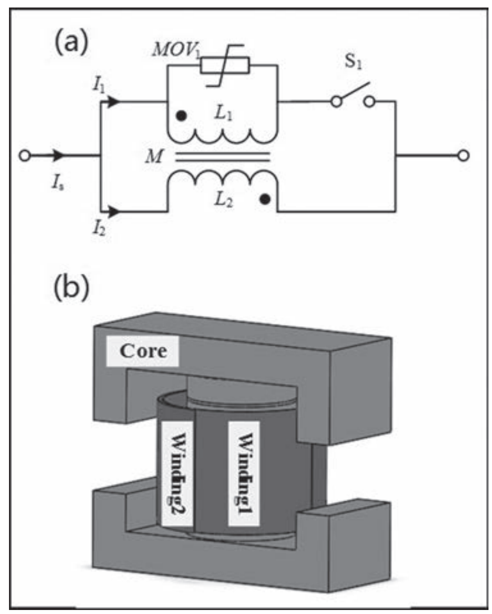

Fig. 1. The structure of the FC-SFCL. (a)Basic topology. (b)Specific Structure.

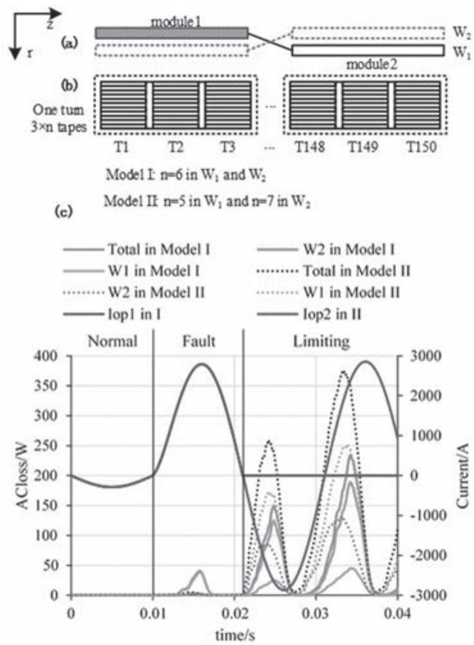

Fig. 2. (a)(b)The structure of the HTS windings. (c) Current and AC loss waveforms.

THURSDAY EVENING, 26 APRIL 2018 ORCHID I, 5:30 TO 7:00

Session YA
PANEL DISCUSSION: THE FUTURE OF MEMORY TECHNOLOGIES

Jingsheng Chen, Chair
National University of Singapore, Singapore

FRIDAY MORNING, 27 APRIL 2018 ORCHID I, 9:00 TO 12:00

Session GA
SYMPOSIUM ON THE PRESENT AND FUTURE OF STT-MRAM

Hyunsoo Yang, Chair
National University of Singapore, Singapore

INVITED PAPERS

9:00

GA-01. Highly Manufacturable Embedded STT-MRAM Technology.

K. Nam[1]
1. Samsung Electronics, Hawsung-City, The Republic of Korea

STT-MRAM (spin transfer torque-Magnetic random access memory) has a wide range of potential for its various applications as a versatile device and deserves attention on the perspective of manufacturing embedded device with non-volatility, high speed and excellent reliability. Furthermore, embedded STT-MRAM has an excellent extendibility that can easily plug into various CMOS platform from 28 LPP to extending 28/22 FD-SOI and beyond. Recently, as a tipping point of MRAM product, several companies have commenced with eMRAM development from several years ago and some of companies are embarking on eMRAM business to make it. In the meanwhile, we demonstrated eMRAM using perpendicular STT-MRAM with 28nm logic process and successfully fabricated as mass production level [1]. However, for mass production of eMRAM, there are still lots of issues to overcome such as optimal MTJ stack with a wide read/write operation margin, integration-induced damage, robust MTJ stack with standing 400C BEOL process. In this presentation, we will show the recent progress in the commercialization of embedded MRAM and discuss the key factors influencing the mass product that should be stably handled. STT-MRAM integration is quite difficult to control due to inherently structural vulnerability such as very thin MgO barrier, laminated magnetic/non-magnetic multi-layer and sensitive heat properties, etc, which can cause an unwanted short failure, electrical and magnetic distribution and properties degradation. Perpendicular MTJ stack consisting of CoFeB/MgO has been developed to achieve higher TMR, low switching current and strong retention. Each feature strongly interdigitate with each of parameters, for example, large thermal stability is prerequisite to long retention time, but there is a trade-off between retention and switching current. Therefore large switching current can help it gain a higher retention, but it is inevitable to impinge the write fail. Those kinds of relationships can be alleviated by optimizing MTJ stack and process integration. Fig.1 shows the retention time vs switching current in terms of the improved MTJ stack and process. Retention time is approximately 5 times higher than that of before at similar switching current range by optimizing process, which means that efficiency (Δ/I_{sw} : Δ thermal stability, Isw switching current) factor corresponding to the feature of MTJ stack is significantly improved with other properties intact. Here, efficiency can be defined as a relationship with retention and switching current of MTJ cell, which is considerably hard to break between both since they have physically strong dependency. Thus, it is more important to find the optimum sweet spot of retention and switching current of MTJ cell in the light of the improving thermal stability while maintaining switching current and it can be found not merely by optimizing MTJ stack but also by specializing integration scheme without any compromising structural integrity. Fig.2 indicates the dependence of MTJ degradation on various patterning process. MTJ degradation and MTJ short fail during the process involving MTJ patterning has been unavoidably accompanied so far, due to thin MgO barrier and multiple metallic layers as mentioned above. By adopting IBE (ion beam etching) process for MTJ patterning, we were able to reach MTJ short fail below 1ppm level and simultaneously to lower the propensity of MTJ degradation. For minimizing the integration-induced damage, we additionally tweaked IBE parameters such as power, angle, etching sequences and consequently could obtain the significant improvement of MTJ degradation as shown in Fig. 2. With process optimization, we were able to achieve the scalability technology for MTJ cell shrink and it has become possible to improve manufacturing technology and close to mass production. In the presentation, Key technologies and feasibility for highly manufacturable eMRAM would be discussed more detail.

[1] J. Song et al., “Highly functional and reliable 8MbSTT-MRAM embedded in 28nm logic” in Proc. IEEE International Electron Devices Meeting, Dec. 2016, pp. 27.2.1-27.2.4

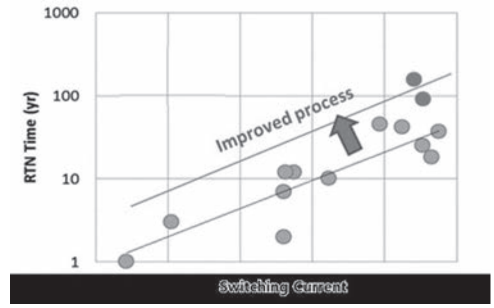

Fig. 1. Retention time vs switching current after full integration with respect to the process. Retention time is improved by improving process while maintain switching current

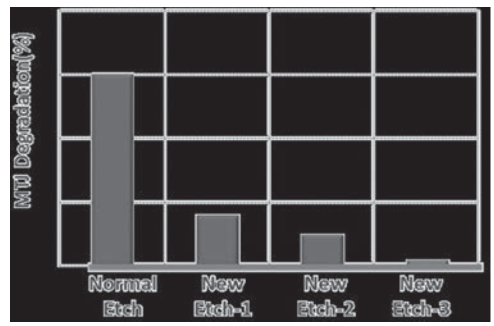

Fig. 2. MTJ degradation(%) trend according to damage-less pattering process. With optimizing etching process, MTJ degradation is remarkably reduced

9:30

GA-02. Embedded MRAM for Next-Generation Microcontroller Platform.

K. Lee[1], S. Noh[1], V.B. Naik[1], J. Kwon[1], J. Lim[1], S. K[1], B. Behin-aein[1], K. Yamane[1], D. Zeng[1], K. Gan[1], H. Yang[1], N. Thiyagarajah[1], S. Jang[1], L. Goh[1], R. Chao[1], N. Chung[1], T. Wee[1], T. Ling[1], J. Wong[1] and S. Woo[1]
1. TD, GLOBALFOUNDRIES Singapore, Singapore

Embedded Flash (eFlash) technology has been the dominant embedded non-volatile memory (eNVM) solution for microcontroller (MCU) products, primarily used for data and code storage. The latest eFlash technology has reached 28 nm for product level and is a few generations behind the most advanced logic technology. Scaling down eFlash below 28 nm has been demonstrated [1], however it is becoming increasingly difficult to integrate conventional floating-gate-based eFlash technology with advanced CMOS logic process features (e.g. HKMG, FinFET). This scalability challenge has driven industry to actively explore emerging eNVM technologies. Embedded MRAM (eMRAM) has been considered one of the most promising emerging eNVM technologies due to fast write speed and high endurance. This unique feature makes eMRAM capable of replacing eFlash, SRAM and other miscellaneous memory blocks in MCU, which may eventually improve overall cost, power and performance at the system level beyond brute-force device scaling [2]. In addition, increasing demands for low-power MCU, particularly in the automotive sector and emerging MCU markets, make eMRAM more attractive than power-hungry eFlash. Since the first chip-level demonstration of spin-transfer-torque MRAM in 2005 [3], we have observed tremendous progress in eMRAM technology, fueled by continuous improvements in magnetic tunnel junction (MTJ) processes. However, there are still remaining challenges to establish eMRAM as an eNVM platform for a variety of memory blocks in MCU products. Multiple flavors of eMRAM bitcells and magnetic tunnel junction (MTJ) film stacks need to be developed and validated to cover a range of system specifications in the consumer, industrial and automotive sectors. In this work, we present eMRAM technology fully integrated into 2x-nm CMOS logic platforms and show the status of eMRAM technology as a next-generation MCU platform. Key challenges for enabling MRAM-based MCU products are also discussed in terms of reliability and scalability.

[1] S. Tsuda *et al*., “First demonstration of FinFET split-gate MONOS for high-speed and highly-reliable embedded flash in 16/14nm-node and beyond,” *2016 International Electron Devices Meeting (IEDM)*, 2016, pp. 11.1.1-11.1.4. [2] K. Lee, J. J. Kan and S. H. Kang, “Unified embedded non-volatile memory for emerging mobile markets,” *2014 IEEE/ACM International Symposium on Low Power Electronics and Design (ISLPED)*, 2014, pp. 131-136. [3] M. Hosomi *et al*., “A novel nonvolatile memory with spin torque transfer magnetization switching: spin-ram,” *IEEE InternationalElectron Devices Meeting, 2005. IEDM Technical Digest.*, 2005, pp. 459-462.

10:00

GA-03. STT-MRAM for embedded memory applications from eNVM to Last Level Cache.

L. Thomas[1], G. Jan[1], Y. Lee[1], H. Liu[1], J. Zhu[1], S. Le[1], S. Serrano-Guisan[1], J. Iwata-Harms[1], R. Tong[1], S. Patel[1], V. Sundar[1], D. Shen[1], J. Haq[1], Y. Yang[1], R. He[1], Z. Teng[1], V. Lam[1], P. Liu[1], H. Fukuzawa[1], Y. Wang[1], T. Zhong[1] and P. Wang[1]
1. TDK-Headway Technologies, Inc., Milpitas, CA, United States

Perpendicular Spin-Transfer-Torque Magnetic Random Access Memories (pSTT-MRAMs) combine fast read/write, low voltage operation, low power consumption, non-volatility and quasi-infinite endurance. Moreover, owing to STT physics used for writing bits, Magnetic Tunnel Junction (MTJ) devices at the heart of the technology can be tailored to emphasize low current/high speed, data retention and/or high operation temperature, depending on the specific application. This versatility makes pSTT-MRAM an ideal candidate for next generation "universal" embedded memory, potentially capable of replacing technologies spanning from embedded Non Volatile Memory (eNVM) to working memory and Last Level Cache (LLC). However, for pSTT-MRAM to fulfill its promises and emerge as a mainstream embedded memory, the technology must both satisfy stringent technical requirements and demonstrate its competitiveness compared to established alternatives. In this presentation, we will discuss recent advances that have overcome major technical hurdles and demonstrated the viability of pSTT-MRAM technology for mass production. Compatibility to CMOS processes is a prerequisite for most embedded applications. Standard back-end-of-line (BEOL) CMOS processes such as low-k dielectric deposition or forming gas annealing are performed at 400°C. Thus, the MTJ stack must withstand this temperature for an extended period of time. Exactly how long depends on the number of metal layers following the fabrication of pSTT-MRAM. For high-density applications, for which the memory is embedded just above the logic level, where lithographic features are the smallest, the total time at 400°C may exceed 3 hours. Submitting a multilayered MTJ stack comprising many atomically thin layers to such a thermal treatment leads to detrimental effects such as recrystallization and grain growth, which can impact the roughness and microstructure of the stack, as well as elemental diffusion within each layer and between layers. Moreover, BEOL 400°C processes must take place after patterning the MTJ stack. Thus, sidewall damage, etch residues and encapsulation materials also play a major role, the more so at advanced lithography nodes, for which devices smaller than 30nm will likely be needed. Solving these problems requires thorough engineering of not only the MTJ stack constituting layers, but also of the top and bottom electrodes and encapsulation materials, as well as process conditions. Since we first reported 400°C compatibility in 2013 [1,2], significant progress has been made, as shown by our recent demonstration of perpendicular magnetic anisotropy (PMA) exceeding 10 kOe for sub-30nm devices submitted to 2.5 hours annealing after patterning [3]. Adoption of pSTT-MRAM as an alternative to eflash for eNVM applications poses specific challenges. For example, for practical as well as cost considerations, the memory must be programmed before the chips are packaged and soldered to a printed circuit board. The soldering process uses reflow soldering for a total of 90 seconds at 260°C. Thus, pSTT-MRAM must retain data during solder reflow with a low error rate [4]. This is particularly challenging because the thermal stability factor Δ, which determines data retention, decreases rapidly with increasing temperature. Indeed, since $\Delta = E_B/k_BT$ (where k_B is the Boltzmann constant, T the absolute temperature and E_B the energy barrier separating parallel and antiparallel states), increasing temperature from 25°C to 260°C has a twofold effect. First, the denominator increases, reducing Δ by almost half. Second, E_B is a function of the PMA of the free layer of the MTJ, which is also strongly temperature dependent. We have shown that this combined effect leads to an almost linear decrease of Δ over a wide range of temperatures, with a variation coefficient as high as 0.45 per degree for standard MTJ stacks [5, 6]. To account for such a rapid decrease, extremely high values of Δ would be needed at room temperature. However, since STT write current is also proportional to Δ, such devices would be extremely hard to write. To solve this challenge and qualify pSTT-MRAM for reflow soldering, we have designed a MTJ stack with high PMA and low Δ temperature coefficient. As shown in Fig. 1, all 30 chip tested pass reflow qualification without compromising write performance [4, 7]. pSTT-MRAM technology is also an attractive alternative to SRAM at advanced nodes for LLC applications. Indeed, the 1Transistor-1MTJ STT-MRAM cell is much more compact than the standard 6 transistors SRAM cell. Even though L1 and L2 cache memories operate at rates beyond today's pSTT-MRAM capabilities, LLC cache is within reach if write speeds below 10 ns can be achieved. As shown in Fig. 2, full array switching is achieved on a 10 Mb test chip without ECC for write pulses as short as 3 ns [8]. It should be emphasized that pSTT-MRAM is the only emerging non-volatile memory capable of such nanosecond write speed. Moreover, we have reported recently sub-30nm devices with PMA fields exceeding 10 kOe [3], promising excellent data retention beyond 1X lithography nodes.

[1] L. Thomas *et al*, J. Appl. Phys. 115, 172615 (2014). [2] G. Jan *et al*, Dig. Tech. Pap., Symp. VLSI Technology, 2014, p. 42. [3] L. Thomas *et al*., Tech. Dig. - Int. Electron Devices Meet. 2017, 38.4. [4] M. C. Shih *et al*., Dig. Tech. Pap., Symp. VLSI Technology, 2016, p. 114. [5] L. Thomas, G. Jan, S. Le and P.-K Wang, App. Phys. Lett. 106, 162402 (2015). [6] L. Thomas *et al*., Tech. Dig. - Int. Electron Devices Meet. 2015, p 672. [7] C. Y. Wang *et al*., Tech. Dig. - Int. Electron Devices Meet. 2017, 21.1. [8] G. Jan *et al*., Dig. Tech. Pap., Symp. VLSI Technology, 2016, p. 18.

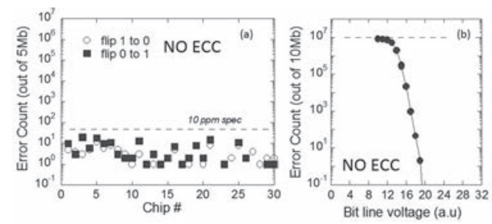

Fig. 1. (a) Bit Error Count (BEC) measured on 30 10Mb chips fabricated in our backend facility, after simulated reflow soldering (90 seconds bake at 260°C). Chips are initialized in two 5 Mb blocks of logic 0 and 1 (b) Example of BEC as a function of bit line voltage for one of the chips shown in (a), using 250ns write pulses. All bits are written without error.

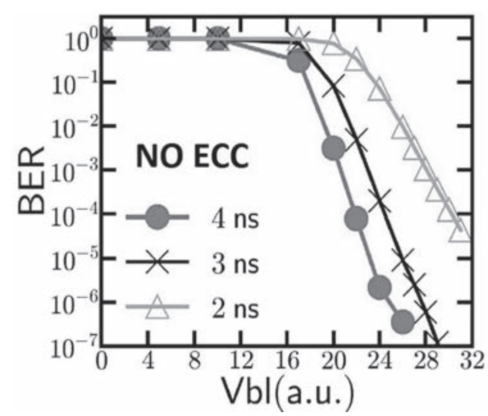

Fig. 2. Bit Error Rate as a function of bit line voltage Vbl for a 10 Mb chip.

10:30

GA-04. High Performance pMTJ with Ir as RKKY and PMA enhancing Layer.

Y. Huai[1]
1. Avalanche Technology, Fremont, CA, United States

I. INTRODUCTION After decades of research and development, the long sought-after STT-MRAM technology is now entering the mass production phase.[1] High performance perpendicular magnetic tunnel junction (pMTJ) with large TMR and thin total stack thickness is critical for high yield STT-MRAM production. A TMR ratio of over 200% after the high temperature BEOL processing of 400 °C and a total stack thickness of less than 10 nm are required.[2] The former is critical for large sensing margin and the latter is important for etching and integration yield. Thin reference layer with low magnetic moment and strong perpendicular magnetic anisotropy (PMA) is key to improved TMR and reduced total thickness of the full pMTJ stack. II. pMTJ WITH Co/Ir INTERFACIAL ANISOTROPY For the conventional pMTJ design, Ru has been considered as the best RKKY material. However, interface engineering is difficult for Ru at high annealing temperature, partly due to the complete solubility of Ru in Co up to 420 °C. In addition, owing to the lack of perpendicular anisotropy at Co/Ru interface, thin reference layer MTJ design using Ru as RKKY layer is often plagued by the weak anisotropy of the reference layer. In this talk, we will present results that demonstrate both strong interfacial PMA and perpendicular Ruderman-Kittel-Kasuya-Yosida (RKKY) exchange interaction in the Co/Ir system. Figure 1(a) shows the structure of pMTJ that incorporates Ir as the RKKY layer. The total MTJ film stack is only 8.6 nm thick. Figure 1(b) shows the VSM loop after 30 min and 150 min annealing at 400 °C, respectively. The magnetic performance is stable with high RKKY field after extended hours of annealing, which may be partly attributed to the low solubility of Ir in Co up to 1000 °C.[3] Figure 1(c) shows the CIPT measurement after annealing at 400 °C for 30 min and 150 min, respectively. The TMR results are shown in Figures 1(d) and 1(e). The combination of the additional high PMA at the Ir/Co interface and the conventional CoFeB/MgO interface in the Ir/Co/Mo/CoFeB/MgO reference layer results in the full film pMTJ attaining a TMR ratio of over 210%. In addition, there is almost no degradation of TMR after long hours annealing. III. DEVICE PERFORMANCE To further evaluate Ir based pMTJ device performance, test chips incorporating the advanced pMTJ design were fabricated from wafers processed through BEOL at temperatures of up to 400 °C. The MTJ devices have a diameter of 55 nm and a pitch of 130 nm, which allows the STT-MRAM to have a capacity beyond 1 Gb. The pMTJ has a RA value of 10 $\Omega\mu m^2$. The final device TMR ratio is over 210%, which is comparable to the full film level CIPT measurement, suggesting little, if any, degradation owing to the BEOL process. We also obtained an Hc larger than 2k Oe, a Vc around 550 mV with a conventional tri-layer free layer structure shown in Figure 1(a). In addition, we performed 400 °C annealing for 150 min at device level. Almost no degradation of MTJ performance is observed. These results demonstrate Ir/Co system can have large TMR, high spin transfer efficiency, and superior thermal stability, which are suitable for high density and high performance STT-MRAM application.

1) "STT-MRAM TO MASS PRODUCTION", (Invited) The 3rd ImPACT International Symposium on Spintronic Memory, Circuit and Storage, Qatar Science Computer Hall, Aobayama Campus, Tohoku University, September 23-25, 2017. 2) "Perpendicular magnetic tunnel junction with thin CoFeB/Ta/Co/Pd/Co reference layer," Applied Physics Letters 105 (19), 192403(1)-192403(5), 2014 3) T. B. Massalski, H. Okamoto, P. R. Subramanian, and L. Kacprak: in Binary Alloy Diagrams (ASM International, Materials Park, OH, USA, 1990) 2nd ed.

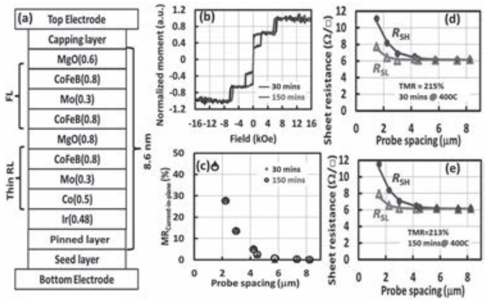

Fig. 1. (a) Schematic of pMTJ structure for film study with bottom and top CIPT electrodes. (b) M-H loops of the pMTJ film annealed at 400 °C for 30 min and 150 min. (c) Magnetoresistance ratio as a function of the probe spacing. (d) Measured (symbol) and fitted (line) RSL and RSH of the pMTJ films annealed at 400 °C for 30 min as a function of the probe spacing. (e) Measured (symbol) and fitted (line) RSL and RSH of the pMTJ films annealed at 400 °C for 150 min as a function of the probe spacing.

11:00

GA-05. Advances in three-terminal spin-orbit torque MRAM devices.

R. Buhrman[1]
1. Cornell University, Ithaca, NY, United States

With the successful development of STT-MRAM and its progression into commercial products, the question arises as to whether the strong spin-orbit torques (SOT) resulting from the spin Hall effect (SHE) [1,2] can provide utility by improving some of the performance parameters of magnetic memory devices, hence broadening the scope of spin-torque applications. In a SOT device the transverse spin current generated in a heavy metal layer results in damping-like and field-like torques being exerted on an adjacent ferromagnetic (FM) free layer of a nanoscale magnetic tunnel junction (MTJ) in a three-terminal configuration (3T-MTJ) [3]. While SOT devices certainly have a larger footprint than two-terminal STT-MRAM, they could be capable of a much shorter write time, and due to the separate read and write channels may offer additional advantages with respect to faster read-out without read disturbance, and lower write energy. Currently there are two distinct implementations of SOT devices, the first where the MTJ electrodes are perpendicularly magnetized (PM), and the second where the electrodes are in-plane magnetized (IPM). In the former case the magnetic reversal is driven by the effective field(s) of the SOT, which at least in principle could result in very high-speed performance. In the ideal situation, the free layer behaves as a single domain and the reversal is quasi-ballistic, but unless the MTJ is very small it is more likely to be the case that the reversal proceeds by the nucleation of a sub-volume domain, with that domain then being expanded by the effective field of the anti-damping torque acting on the domain walls against the pinning field [4]. In either situation a small in-plane bias field, or its functional equivalent, is required; in the first instance to break the symmetry, or in the second instance to overcome the DMI imposed chirality on the domain wall. A number of approaches have been identified to deal with this bias field requirement, but that is not the main concern with PM SOT devices. Instead the issue is the very high current (density) levels required to drive the effective-field reversal of a nanoscale, thermally stable free layer due to the limited efficiency by which even the best SHE materials to date can generate an interfacial effective field. At present the required current densities in the SH channel of PM devices are $\geq 1.4 \times 10^8$ A/cm^2 [5], which is equivalent to current levels >> than can be readily supplied by a scaled CMOS transistor. Even at those current density levels low write error rate switching with ns scale pulses has yet to be demonstrated, due in part at least to heating and thermal fluctuation effects [4,6]. For IPM SOT devices the reversal is driven by antidamping excitation and the expectation has been that fast, 1 ns, highly reliable anti-damping switching would not be achievable, based largely on previous experience with IPM STT-MRAM devices and on macrospin calculations. Recently we have shown that 3T-MTJs devices can exhibit characteristic pulse switching times of ≤ 0.5 ns, considerably faster than expected from rigid domain modeling, with no indication of an "incubation delay," and with a critical current density of $\approx 5 \times 10^6$ A/cm^2. This approach is also capable of yielding reliable switching in the short pulse regime with the best results to date being write error rates (WER) $\approx 10^{-6}$ with 2ns pulses as shown in Fig.1b [7]. There are a number of factors that combine to yield these results. First with respect to switching speed, as indicated by micromagnetic modeling the spin-torque driven reversal does not appear to proceed uniformly but non-uniformly with reversal beginning at one end of the FL structure and then sweeping across the ellipse. Second, the in-plane (effective) magnetic field generated by the Oersted effect and/or by the field-like torque effect will, if the sign is correct, act to help suppress the formation of localized magnetic inhomogeneities during the reversal process, speeding the reversal and apparently reducing reversal errors [8]. The low switching currents are the result of the development of SHE materials with high (> 20%) damping-like spin torque efficiency, beta-W and several different Pt alloys, in combination with the use of atomic and sub-atomic Hf layers to (a) passivate the HM/FM interface, reducing the effective damping, and (b) to controllably enhance the interfacial magnetic anisotropy energy density of the FM/MgO interface thereby lowering the effective demagnetization field of the FL to 2 kOe or less for FL thicknesses of ≈ 2 nm; both of which directly reduce the required pulse switching current [7]. In this presentation I will discuss the factors involved in obtaining this level of performance from IPM SOT devices, summarize our latest results with respect to switching current, speed and WER, and discuss pathways that might lead to further enhancements in SOT device performance.

[1] I. M. Miron, K. Garello, G. Gaudin, P.-J. Zermatten, M. V Costache, S. Auffret, S. Bandiera, B. Rodmacq, A. Schuhl, and P. Gambardella, Nature 476, 189 (2011). [2] L. Liu, O. J. Lee, T. J. Gudmundsen, D. C. Ralph, and R. A. Buhrman, Phys. Rev. Lett. 109, 96602 (2012). [3] L. Liu, C.-F. Pai, Y. Li, H. W. Tseng, D. C. Ralph, and R. A. Buhrman, Science 336, 555 (2012) [4] O. J. Lee, L. Q. Liu, C. F. Pai, Y. Li, H. W. Tseng, P. G. Gowtham, J. P. Park, D. C. Ralph, R. A. Buhrman, Phys Rev B 89, 024418 (2014). [5] S. Fukami and H. Ohno, Jpn. J. Appl. Phys 56, 0802A1 (2017). [6] J. Park, G. E. Rowlands, O. J. Lee, D. C. Ralph, R. A. Buhrman, Appl. Phys Lett 105, 102404 (2014) [7] Shengjie Shi, Yongxi Ou, S. V. Aradhya, D. C. Ralph, and R. A. Buhrman, Physical Review Applied, in press (arXiv:1710.06391) [8] S. V. Aradhya, G. E. Rowlands, J. Oh, D. C. Ralph, and R. A. Buhrman, Nano Lett. 16, 5987 (2016)

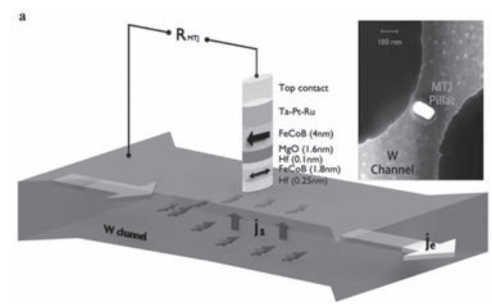

Fig. 1. A schematic for an IPM 3T-MTJ device is shown in Fig. 1a, with the inset showing an SEM image of a representative nanopillar on a W channel.

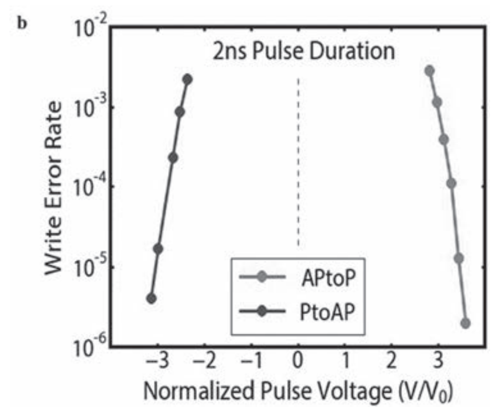

Fig. 2. Write error rate (WER) results for a W-based 3-T MTJ SOT device

11:30

GA-06. The Pursuit of Saving Energy Consumption of Memory Systems by MRAMs, from STT-MRAM to Voltage-Control Spintronics Memory (VoCSM).

H. Yoda[1], N. Shimomura[1], Y. Ohsawa[1], Y. Kato[1], S. Shirotori[1], m. shimizu[1], K. Koi[1], T. Inokuchi[1], H. Sugiyama[1], S. Oikawa[1], B. Altansargai[1], M. Ishikawa[1], A. Tiwari[1] and A. Kurobe[1]
1. R&D Center, Toshiba Corporation, Kawasaki, Japan

I. INTRODUCTION MRAM has been developed since 1980s until now with several ups and downs. The ultimate purpose is to realize non-volatile working memories to save energy consumption of conventional volatile working memories such as SRAM and DRAM. However all of non-volatile memories including MRAM have been facing a dilemma of non-volatility and high energy consumption in their active mode because non-volatility has led to large writing-energy consumption, E_w. As a result, they have been used as data storages and none of them overcame the historical dilemma for busy applications. This is the one of the reasons why MRAM has not had big markets so far. Recently, the possibilities of overcoming the dilemma were demonstrated by both STT-MRAM and VoCSM [1], [2]. STT has better maturity but less room for further improvement. On the other hands, VoCSM has poor maturity but better potentials in terms of higher writing efficiency and better endurance [3]. In this talk, STT technologies and VoCSM technologies is reviewed with respect to saving energy consumption and remaining issues for VoCSM will be discussed at the conference. II. POSSIBILITY OF SMALL CRITICAL SWITCHING ENERGY PER BIT, e_{csw}, OF VoCSM Critical switching current for VoCSM with voltage, V, applied is given by the equation (1) [3]. $I_{csw}(VoCSM) = 8\pi e\alpha^*_{eff}/h\theta_{SH}\times\Delta E_{sw}(V)\times t_{SH}/w_f$ (1) Here, α^*_{eff}, e, h, θ_{SH}, ΔE_{sw}, t_{SH}, w_f are the effective damping constant, charge of an electron, Plank's constant, the spin-Hall angle(spin polarization), the switching energy-barrier, the thickness of a storage-layer, and the width of the storage-layer, respectively. In this case, the width of spin-Hall electrode is assumed to be the same as w_f, i.e. MTJs are self-aligned with the electrode. An example of voltage dependence of critical switching current density is shown in Fig.1. If negative voltage is applied, I_{csw} is reduced to less than half of spin-Hall switching current, I_{csw} with no voltage applied. The VoCSM-writing can be addressed as voltage-assisted spin-Hall writing. Small I_{csw} of 37μA at write pulse-width of 20nsec. was successfully demonstrated due to high efficiency of spin-Hall writing and combined voltage-assist [4]. The value of the I_{csw} is almost the same as that for STT-writing, even though the size of MTJ for VoCSM-writing (~50nm×150nm) is much larger than that of STT-writing(30nmø). Critical switching energy per bit for VoCSM-writing, $e_{csw}(VoCSM)$, is the product of I_{csw}, write pulse-width (t_p), and voltage across the spin-Hall electrode. It is roughly given by the equations (2), assuming the spin-Hall electrode has square in-plane shape. $e_{csw}(VoCSM) = \{8\pi e\alpha^*_{eff}/h\theta_{SH}\times\Delta E_{sw}(V)\times t_{SH}/w_f\}^2\times t_p\times R_{sh}$ (2) Here, R_{sh} is the sheet resistance of spin-Hall electrode with the typical value of 200-400Ω. Similarly, critical switching current for STT-MRAM is given by the equation (3) [3]. $I_{csw}(STT) = 8\pi e\alpha_{eff}/h\, g(\theta)\times\Delta E_{sw}$ (3) Here, α_{eff} and $g(\theta)$ are the effective damping constant and the spin polarization. And critical switching energy per bit for STT-writing, $e_{csw}(STT)$, is given by the equation(4). $e_{csw}(STT) = \{8\pi e\alpha_{eff}/h\, g(\theta)\times\Delta E_{sw}\}^2\times t_p\times R_{MTJ}$ (4) Here, R_{MTJ} is the resistance of MTJ with a typical value of 10kΩ. Fig.2 shows reduction trend of the e_{csw}s for STT-writing and VoCSM-writing. Even though the maturity of VoCSM is poor, the smallest e_{csw}s of about 100fJ/bit have been demonstrated by VoCSM. III. PRACTICALLY UNLIMITED ENDURANCE of VoCSM In VoCSM, write-current flows in the spin-Hall electrode made of heavy metal such as Ta having high melting temperature. Due to this, unlimited endurance of 1E+13 was demonstrated even at write pulse-width of 5nsec. [3]. V. CONCLUSION Both non-volatility and low energy consumption have been proved to coexist in VoCSM. Further, VoCSM cell has practical unlimited endurance of 1E+13. VoCSM also has a future reduction potential of I_{csw} by the factor of t_{SH}/w_f. Therefore, it is concluded that VoCSM has a potential to solve the historical dilemma of non-volatility and high energy consumption even for busy applications. ACKNOWLEDGMENT This work was partly supported by the ImPACT Program of the Council for Science, Technology and Innovation (Cabinet Office, Government of Japan).

[1] H. Yoda, *et al.*, "The Progresses of MRAM as a Memory to Save Energy Consumption and Its Potential for Further Reduction," 2015 Symposium on VLSI Technology, T104-105 [2] H. Yoda, *et al.*, "Voltage-Control Spintronics Memory (VoCSM) Having Potentials of Ultra-Low Energy-Consumption and High-Density," *Digests of 62th IEDM*, 27.6 (2016) [3] H. Yoda, *et al.*, "VOLTAGE-CONTROL SPINTRONICS MEMORY HAVING POTENTIALS FOR HIGH-DENSITY AND HIGH-SPEED APPLICATIONS," to be published, presented at TMRC2017, http://www.nims.go.jp/mmu/tmrc2017/att/F1.pdf [4] Y. Ohsawa, *et al.*, "Ultra-high-efficient Writing in Voltage-Control Spintronics Memory (VoCSM); the Most Promising Embedded Memory for Deep Learning." to be presented at EDTM2018

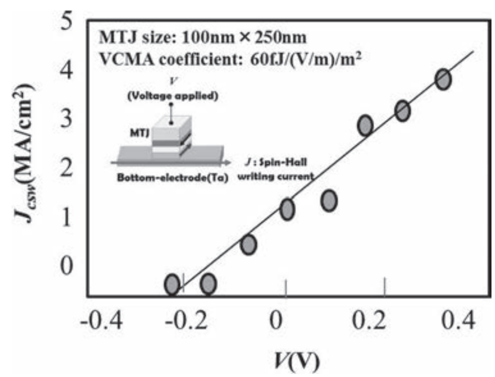

Fig. 1. Fundamental writing feature of VoCSM cells, voltage dependence of critical switching current-density [2].

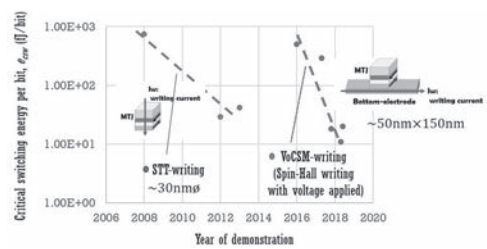

Fig. 2. Reduction trend of critical switching energy per bit, e_{csw}s, for STT-writing and VoCSM writing. For STT-writing, resistance of MTJ is assumed 10kΩ.

FRIDAY MORNING, 27 APRIL 2018 ORCHID III, 9:00 TO 12:00

Session GB
NANOSTRUCTURED HARD MAGNETIC MATERIALS

Chih-huang Lai, Chair
National Tsing Hua University, HsinChu, Taiwan

CONTRIBUTED PAPERS

9:00

GB-01. Multicomponent nanostructured Nd-Fe-B permanent magnets prepared by Spark Plasma Sintering technique.

T. Tomše[1,2], L.M. Scherf[3], J. Jaćimović[3], J. Dubois[1,2] and S. Kobe[1,2]
1. Department for Nanostructured Materials, Jožef Stefan Institute, Ljubljana, Slovenia; 2. Jožef Stefan International Postgraduate School, Ljubljana, Slovenia; 3. ABB Corporate Research Center, Baden-Daettwil, Switzerland

Rapidly solidified nanostructured Nd-Fe-B melt spun ribbons have unique magnetic properties not obtainable with the conventional powder metallurgy. Due to the grain size that is of the order of the single-domain size, the room temperature coercivity is much higher than the values of sintered magnets with similar composition, where the grains are a couple of orders of magnitude larger. This works even in the case without the addition of the critical heavy rare earth (HRE = Dy or Tb) elements. The temperature coefficient of coercivity is smaller, which effectively increases the performance of the magnet at high temperature. Some applications like traction motors for electric vehicles and electric power steering motors require magnets with high coercive force, since the operating temperatures are high and magnets are exposed to large demagnetizing fields. The standard approach is to use magnets with homogeneously distributed Dy or Tb in order to prevent the overall reversal of magnetization. HREs increase the magnetocrystalline anisotropy of the hard magnetic $Nd_2Fe_{14}B$ phase. Since the magnetic moments of the HRE atoms couple antiparallel to the moments of Fe atoms, the remanent magnetization is reduced consequently. We present a new strategy to achieve the resource efficiency and to minimize the loss of the magnetic flux density without degrading the performance of the magnet [1]. A magnet with locally different magnetic properties (multicomponent magnet) can be used in applications where only certain parts of the specimen experience strong demagnetizing fields and significant increase in temperature. We employed "Spark Plasma Sintering" (SPS) approach to prepare a dense nanostructured multicomponent magnet containing a high-coercivity region. For this purpose, a HRE-free nanostructured powder was used in combination with a Dy-containing powder. We showed that this type of magnets can be manufactured in a single step by stacking both powders in the desired manner while avoiding mixing. Alternatively, individual single component magnets with different magnetic properties are prepared in the first SPS step. Afterwards, the respective parts are placed together and condensed into a single magnet body in a second SPS step. The grain growth during the SPS consolidation was supressed and the magnetic properties of the respective Nd-Fe-B powders were preserved in the multicomponent magnet. Information on the specimen's local magnetic properties was obtained by cutting the two-part magnet in half and measuring the individual parts separately with a closed-loop permeameter (Figure 1). Short manufacture time and low consolidation temperature of the SPS process inhibit the diffusion of Dy into the Dy-free region of the magnet. SEM and EDX analysis of the interface between both parts of the multicomponent specimen revealed that the microstructural characteristics and chemical compositions of the respective parts were comparable to the single component magnets prepared from the individual powders, which corresponded with the results of the magnetic characterization. In summary, magnets with locally different magnetic properties were prepared from the nanostructured melt-spun ribbons with the SPS approach. Alternatively, the SPS technique can be used to consolidate other types of Nd-Fe-B powders into dense magnets, including highly anisotropic jet-milled powders, at significantly lower temperatures than conventional sintering.

R. Simon, J. Jacimovic, D. Tremelling, F. Greuter, E. Johansson and T. Tomse, *Magnet having regions of different magnetic properties and method for forming such a magnet*. 2017, Google Patents.

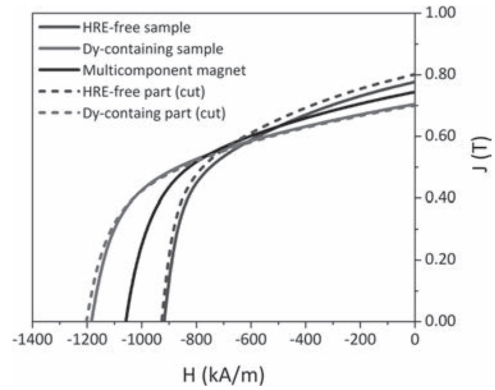

Fig. 1. Demagnetization curves of the multicomponent magnet, single component samples prepared from the HRE-free and Dy-containing powders and individual parts (HRE-free and Dy-containing) obtained by cutting the multicomponent magnet in half. Curves were recorded at 120 °C.

9:15

GB-02. Ultra thin films of $L1_0$-MnAl on GaAs (001): tuning the properties of the Mn-Ga-As-Al interphase.

C. Navío[1], M. Villanueva[1], E. Céspedes[1], F. Mompean[2], M. García-Hernández[2], J. Camarero[3,1] and A. Bollero[1]
1. Division of Permanent Magnets and Applications, IMDEA Nanoscience, Madrid, Spain; 2. Instituto de Ciencia de Materiales de Madrid, ICMM-CSIC, Madrid, Spain; 3. Condensed Matter Physics, Universidad Autónoma de Madrid, Madrid, Spain

In the last years, the scientific community is making a great effort on developing new combinations of materials to overcome the problem on the scarcity of certain elements. For this purpose, the use of the ferromagnetic Manganese-based alloys has been proposed for certain applications as rare earth free permanent magnets, due to their well-known high magnetic anisotropy constants [1, 2, 3]. In particular, the $L1_0$-MnAl (or τ-MnAl) is the only ferromagnetic phase of the Mn-Al phase diagram. This phase has been widely studied showing that the growth of this material on different semiconductors enhances the potential applications on the fields of spintronics, ultra high-density recording media and non-volatile magnetoresistive random access memory [2, 4, 5]. In this study, ultra thin films of MnAl have been grown on GaAs (001) by MBE (Molecular Beam Epitaxy) with thickness varying from 1 to 5 nm and without any buffer layer. XPS (X ray Photoelectron Spectroscopy) and LEED (Low Energy Electron Diffraction) were performed *in situ* in order to characterize the chemical states and the arrangement of the surface atoms. In order to prevent from ambient oxidation, a protective capping layer of Ta was deposited before the sample was withdrawn from ultra high vacuum and magnetic and structural characterization was done *ex situ* by SQUID magnetometry and XRD, respectively. In this work, well-oriented ultra thin films of $L1_0$-MnAl with coercivities over 8 kOe have been obtained. The X Ray Diffraction measurements show the main reflections of the $L1_0$-MnAl phase in register with the substrate orientation, as it was expected for the epitaxial growth. This result is correlated with the magnetic properties, where it is found that there is a strong magnetic anisotropy with all the magnetization pointing out of the film surface. The use of a GaAs (001) substrate has allowed the simultaneous formation of a ferromagnetic interphase of Mn-Ga-As-Al which contribution competes with the MnAl one and can be tuned by the experimental growth conditions. Thanks to the surface analysis techniques available *in situ* in the MBE chamber, it was possible to discriminate the signal coming from the interphase compound (Figure 1-a) [6]. Further experiments of growth of only Al or only Mn on the GaAs (001) at the same experimental conditions of the previous $L1_0$-MnAl films, played the role of simulated interphase compounds and contributed to the understanding of the magnetic contribution of the interphase to the magnetic properties (Figure 1-b) of this multicomponent system. Acknowledgments Research supported by MINECO-M-era.Net Programme: NEXMAG (PCIN-2015-126), MINECO through ENMA project (MAT2014-56955-R); and Comunidad de Madrid: NANOFRONTMAG (S2013/MIT-2850). E.C. acknowledges MINECO for the Formación Posdoctoral (JdC) program (FPDI-2013). MDEA Nanociencia acknowledges support from the 'Severo Ochoa' Programme for Centres of Excellence in R&D (MINECO, Grant SEV-2016-0686).

[1] J. Coey, *Journal of Physics: Condensed Matter*, vol. 26, no. 6, p. 064211, 2014. [2] R. L. Stamps, S. Breitkreutz, J. Åkerman, A. V. Chumak, Y. Otani, G. E. Bauer, J.-U. Thiele, M. Bowen, S. A. Majetich, M. Kläui *et al.*, *Journal of Physics D: Applied Physics*, vol. 47, no. 33, p. 333001, 2014. [3] E.Céspedes, M.Villanueva, C.Navío, F.J.Mompeán, M.García-Hernández, A.Inchausti, P.Pedraz, M.R.Osorio, J.Camarero and A.Bollero. Journal of Alloys and Compounds, Volume 729, 30 December 2017, Pages 1156-1164 [4] W. Van Roy, J. De Boeck, H. Bender, C. Bruynseraede, A. Van Esch, and G. Borghs, *Journal of applied physics*, vol. 78, no. 1, pp. 398–404, 1995. [5] T. Sands, J. Harbison, M. Leadbeater, S. Allen Jr, G. Hull, R. Ramesh, and V. Keramidas, *Applied physics letters*, vol. 57, no. 24, pp. 2609–2611, 1990. [6] C. Navío, M. Villanueva, E. Céspedes, F. Mompeán, M. García-Hernández, J. Camarero, and A. Bollero. Submitted for publication.

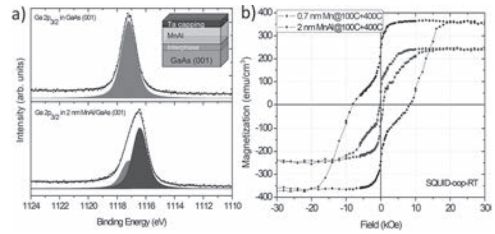

Fig. 1. a) XPS core levels of the substrate before and after the growth of 2 nm of $L1_0$-MnAl on GaAs (001). b) Out-of-plane (oop) hysteresis loops measured by SQUID at room temperature (RT) for a 2 nm film of $L1_0$-MnAl on GaAs (001) and a 0.7 nm film of Mn growth on GaAs (001) under the same experimental conditions: the substrate is kept at 100 °C during the growth followed by post-annealing at 400 °C.

9:30

GB-03. Mechanochemical synthesis of Dy substituted $Nd_2(Fe,Co)_{14}B$ magnetic nanoparticles.

Y. Zhong[1], V. Chaudhary[2], H. Parmar[2], X. Tan[1] and R.V. Ramanujan[1]
1. School of Materials Science and Engineering, Nanyang Technological University, Singapore, Singapore; 2. Rolls-Royce@NTU Corporate Lab, Nanyang Technological University, Singapore, Singapore

Abstract We report the synthesis of the Dy substituted $(Nd_{0.9}Dy_{0.1})_2(Fe,Co)_{14}B$ nanoparticles with a coercivity value of 10.4 kOe, by a "green" and low cost mechanochemical technique. The properties of these $(Nd_{0.9}Dy_{0.1})_2(Fe,Co)_{14}B$ nanoparticles can be improved by magnetic alignment. The remanence (M_r) tripled after alignment, with an average misalignment angle of 34.2°. The thermal coefficient of remanence (α) is -0.12%, comparable to the room temperature value of commercial Nd-Fe-B magnets. Introduction High performance permanent magnets are extensively used in many applications, e.g., energy generation and conversion systems [1, 2]. Recently, the quest to develop novel processing routes to produce improved magnets has become urgent [2]. Nd-Fe-B based permanent magnets have attracted enormous attention due to their superior magnetic properties. However, applications of Nd-Fe-B magnets at elevated temperatures is limited by their Curie temperature and strong temperature dependence of magnetocrystalline anisotropy [3]. Co substitution for Fe can increase the Curie temperature [4-6], while Dy substitution of Nd can extend the operating temperature range [7]. Conventional physical synthesis of Nd-Fe-B magnets are associated with high cost and limited control, while most chemical synthesising methods have limited magnetic properties and poor scalability [8, 9]. In previous work, we successfully produced $Nd_2(Fe,Co)_{14}B$ nanoparticles with relatively good magnetic properties through a "green", low cost mechanochemical technique [10]. To further improve magnetic properties, Dy-substituted $(Nd_{0.9}Dy_{0.1})_2(Fe,Co)_{14}B$ nanoparticles by the mechanochemical method was prepared. Experimental Details $(Nd_{0.9}Dy_{0.1})_2(Fe,Co)_{14}B$ nanoparticles were prepared through processing a mixture of commercially available Nd_2O_3, Dy_2O_3, Fe_2O_3, CoO, B_2O_3, CaO (99.9% Sigma Aldrich) powders and Ca granules (99.9%, ~ 6 mesh, Sigma Aldrich) via the mechanochemical ball milling process. Excess 50wt% of Nd_2O_3 and 100wt% of Ca granules were added to ensure full reaction. All precursors were milled with a Fritch Pulverisette-7 planetary ball mill under Ar atmosphere, at 500 rpm for 6 h, with a ball to powder ratio of 14:1. The milled powder samples were collected in Ar atmosphere and pressed into a pellet. The pellet was then heat treated in a vacuum furnace (~10^{-5} torr) at 850°C for 90 min, followed by washing in NH_4Cl/methanol solution to remove the by-product. The structure and phase were determined by X-ray diffraction (XRD) using a Bruker D8 X-ray diffractometer (CuKα radiation). The magnetic properties measurements were performed by using the PPMS (EverCool-II, Quantum Design). For alignment, a small amount of sample was sonicated within an adhesive and then dried and aligned on a glass slide under 1.8 T uniform magnetic field. Results and discussions Figure 1 shows the room temperature hysteresis loop for the aligned $(Nd_{0.9}Dy_{0.1})_2(Fe,Co)_{14}B$ nanoparticles measured // and $\perp$to the c-axis, respectively. A high coercivity of 10.4 kOe is observed $\perp$to the c-axis. The M-H loops // and$\perp$to the c-axis are substantially different. The magnetic nanoparticles can be crystallographically aligned and their properties are highly sensitive to magnetic alignment. After alignment, the M_r value increases drastically from 1.1 memu for the $\perp$ samples to 3.9 memu for the // samples. The average misalignment angle ϕ (ϕ=arctan((2$M_r^{\perp}$)/($M_r^{//}$))) is calculated to be 34.2°, comparable to the angle range (20° – 47°) of aligned $SmCo_5$ nanoparticles prepared by surfactant assisted ball milling [11]. Figure 2 shows the temperature dependent magnetic hysteresis loop for the aligned $(Nd_{0.9}Dy_{0.1})_2(Fe,Co)_{14}B$ nanoparticles measured // to c-axis. The thermal stability was studied. The thermal coefficient of remanence (α) and thermal coefficient of coercivity (β) in the temperature range of 100 to 400 K was found to be -0.12% and -0.31%, respectively. The thermal coefficient of remanence improved considerably after alignment. Typically, Nd-Fe-B magnets have a thermal coefficient of remanence of -0.12% [7]. Our aligned particles shows comparable thermal stability as commercial Nd-Fe-B magnets. Conclusions Dy substituted $(Nd_{0.9}Dy_{0.1})_2(Fe,Co)_{14}B$ nanoparticles with a coercivity of 10.4 kOe was successfully synthesized by a "green" and low cost mechanochemical process. The properties of these nanoparticles were highly sensitive to magnetic alignment, with an average misalignment angle of 34.2°. The thermal stability of these nanoparticles was comparable to those of commercial Nd-Fe-B magnets.

[1] N. Poudyal and J. P. Liu, "Advances in nanostructured permanent magnets research," Journal of Physics D: Applied Physics, vol. 46, pp. 043001, 2012. [2] O. Gutfleisch, M. A. Willard, E. Brück, C. H. Chen, S. Sankar, and J. P. Liu, "Magnetic materials and devices for the 21st century: stronger, lighter, and more energy efficient," Advanced materials, vol. 23, pp. 821-842, 2011. [3] E. Burzo, "Permanent magnets based on R-Fe-B and R-Fe-C alloys," Reports on Progress in Physics, vol. 61, pp. 1099, 1998. [4] C. B. Rong, D. Wang, V. Van Nguyen, M. Daniil, M. A. Willard, Y. Zhang, et al., "Effect of selective Co addition on magnetic properties of Nd2 (FeCo) 14B/α-Fe nanocomposite magnets," Journal of Physics D: Applied Physics, vol. 46, p. 045001, 2013. [5] X. Tan, H. Parmar, Y. Zhong, V. Chaudhary, and R. V. Ramanujan, "Microwave Based Chemical Synthesis of Co alloyed NdFeB Hard Magnetic powders," IEEE Magnetics Letters, vol.8, pp.5508805, 2017. [6] H. Parmar, T. Xiao, V. Chaudhary, Y. Zhong, and R. V. Ramanujan, "High energy product chemically synthesized exchange coupled Nd2Fe14B/α-Fe magnetic powders," *Nanoscale*, vol.9, pp. 13956, 2017. [7] L. Yu, J. Zhang, S. Hu, Z. Han, and M. Yan, "Production for high thermal stability NdFeB magnets," Journal of Magnetism and Magnetic Materials, vol. 320, pp. 1427-1430, 2008. [8] V. Swaminathan, P. K. Deheri, S. D. Bhame, and R. V. Ramanujan, "Novel microwave assisted chemical synthesis of $Nd_2Fe_{14}B$ hard magnetic nanoparticles," Nanoscale, vol. 5, pp. 2718-2725, 2013. [9] S. Shukla, A. Banas, and R. V. Ramanujan, "Atomistic mechanism of cyclic phase transitions in Nd–Fe–B based intermetallics," Intermetallics, vol. 19, pp. 1265-1273, 8// 2011. [10] Y. Zhong, V. Chaudhary, X. Tan, H. Parmar, and R. V. Ramanujan, "Mechanochemical synthesis of high coercivity Nd2(Fe,Co)14B magnetic particles," Nanoscale, vol. 9, pp. 18651, 2017. [11] C.-b. Rong, V. V. Nguyen, and J. P. Liu, "Anisotropic nanostructured magnets by magnetic-field-assisted processing," Journal of Applied Physics, vol. 107, p. 09A717, 2010.

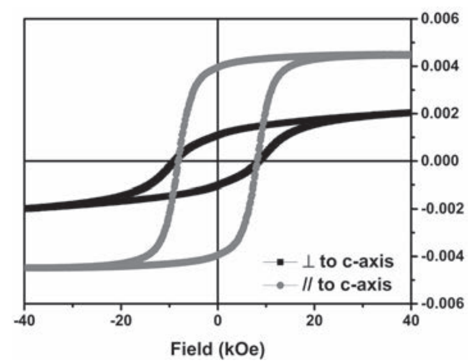

Fig. 1. Room temperature M-H loop of aligned $(Nd_{0.9}Dy_{0.1})$2(Fe,Co)14B nanoparticles measured // and ⊥ to c-axis direction.

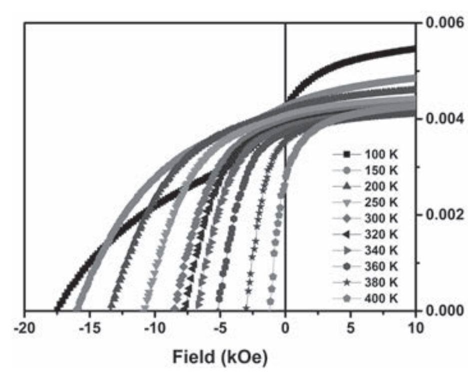

Fig. 2. Demagnetization curves of M-H loops from 100 K to 400 K for aligned $(Nd_{0.9}Dy_{0.1})_2(Fe,Co)_{14}B$ nanoparticles measured // to c-axis.

9:45

GB-04. Large improvement in magnetic properties of hot deformed HREE-free Nd-Fe-B magnets using the rapid heating technique of the powder.

Y. Nakazawa[1], R. Kato[1], Y. Shintani[1] and H. Shimizu[1]
1. Honda R&D Co., Ltd. Automobile R&D Center, Haga-machi, Haga-gun, Japan

1. BACKGROUND AND GOAL The traction motors of electric vehicles generally use neodymium sintered magnets, with heavy rare-earth elements, which are added to increase heat resistance. Honda and Daido Steel have succeeded in making the traction motor without heavy rare-earth elements by using hot-deformed neodymium magnets that have high heat-resistance potential, and by modifying the motor design [1]. Meanwhile, higher traction-motor performance is increasingly demanded, which calls for further enhancing of the magnetic properties employed in traction motors while still keeping them heavy rare-earth element-free. The goal of this study was to enhance the properties of hot-deformed magnets, hence the authors focused on the coarse grain presence within the microstructure of these magnets, investigated the coarsening mechanism, and verified a method to suppress coarsening by rapid heat treatment of the raw powder. 2. EXPERIMENTAL METHOD $Nd_{10.5}Pr_{3.5}Fe_{77.1}Co_{2.5}B_{5.7}Ga_{0.7}$ (at%) composition alloy ribbons were obtained by using single roller melt spinning. Then the ribbons were crushed into powder. Hot-deformed magnets were made by hot-pressing the raw material powder at 650°C to mold it into a solid that was then compression formed at 700°C to 750°C. Transmission electron microscopy (TEM) and scanning electron microscopy (SEM) were used to observe the structure, and a superconducting type of vibrating-sample magnetometer (VSM) was used to measure the magnetic properties. The free-fall type heat-treatment furnace was used to rapidly heat treat the raw material powder at 700°C in an argon atmosphere in order to suppress crystal grain coarsening. 3. RESULTS AND DISCUSSION A. Coarsening Mechanism The crystal grain coarsening of hot-deformed magnets occurs at the powder interface. The reason of this coarsening is considered to be related to the powder. Therefore, we studied behavior of crystal grain growth in the powder heated at 600°C and 700°C in an argon atmosphere and investigated where crystal grain coarsening occurred in the powder. Fig. 1 shows the microstructure of the raw-powder before and after heat treatment. The raw-powder structure before the heat treatment is in an amorphous state. In contrast, the raw-powder structure after heat treatment at 600°C has $Nd_2Fe_{14}B$ crystalized in the center area. However the roller contact surface side crystalizes into Nd_2O_3 and α-Fe, and the amorphous phase also remains between the surface and the interior, resulting in a heterogeneous microstructure. In addition, the raw-powder structure after heat treatment at 700°C exhibited crystal grain coarsening on the single roller contact surface side, indicating that the coarsening occurred in the same manner as that after hot-deformation. Therefore, crystal grain coarsening of hot-deformed magnet is assumed to occur on the roller contact surface side of the powder due to heterogeneity of the crystallization and growth processes of the structures within the raw powder. B. Method to Suppress Coarsening Based on the coarsening mechanism described above, $Nd_2Fe_{14}B$ crystal grain coarsening is considered to originate in the primary crystals NdOx and α-Fe and the amorphous phase. Therefore, a method of controlling the crystallization process of the raw-powder structure was investigated. It is reported that in Nd-Fe-B type amorphous alloys with a low Nd content, α-Fe crystallizes even at temperatures of 500°C or less, but $Nd_2Fe_{14}B$ crystallization starts at around 600°C. Therefore, to suppress α-Fe crystallization and increase the $Nd_2Fe_{14}B$ crystallization, this study focused on the heating rate of annealing in order to reach to the $Nd_2Fe_{14}B$ crystallization temperature in a short time. The induction heating and lamp heating are generally used as annealing methods with rapid heating rate. However, both of these methods have poor temperature uniformity and have difficulty in scale-up, hence they are not suitable for heat treatment of powder. Therefore, we selected the free-fall type heat treatment method. In this method, the raw powder falls freely from the top of a stainless steel pipe with a heated length of approximately 6 m. As a result of using this method, the powder was heated instantly during the few seconds of free fall and a heating rate of 10^3 to 10^4°C/min was realized. The free-fall type annealing heat treatment method continuously heats small quantities of powder, thus heating can be performed rapidly while providing thermal uniformity and continuous treatment can also be performed to enable mass treatment. Fig. 2 shows SEM images comparing the structures of a hot-deformed magnet using conventional powder and a hot-deformed magnet made using powder with the rapid heat treatment method. The addition of rapid heat treatment to the raw material powder suppresses crystal grain coarsening at the powder interface and realizes a homogeneous and refined structure. The magnetic properties of the conventional magnet were M_r = 1.33 T, H_{cj} = 1584 kA/m, and H_k = 1470 kA/m. In contrast, the addition of rapid heat treatment suppressed the coarsening and enhanced the respective magnetic properties to M_r = 1.40 T, H_{cj} = 1614 kA/m, and H_k =1536 kA/m. The paper and scheduled presentation will provide a detailed report of the coarsening mechanism and the method used to suppress coarsening.

[1] H. Shimizu, R. Kato, Y. Nakazawa, A. Hattori, K. Hioki and T. Oikawa, "Heavy Rare Earth-free Hot-deformed Magnet for Traction Motor" *Honda Technical Review,* Vol.28 No.2, 2016, 85-89.

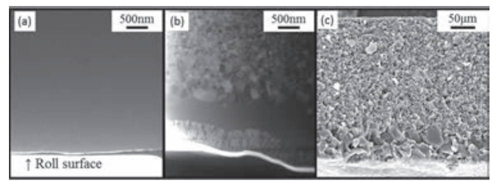

Fig. 1. Microstructure of raw material powder
(a) As-spun, (b) After heat treatment at 600°C, (c) After heat treatment at 700°C

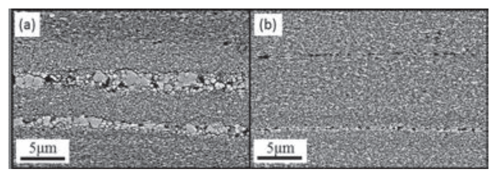

Fig. 2. (a) Microstructure in a conventional hot-deformed magnet, (b) Microstructure in a hot-deformed magnet with rapid heat treatment

10:00

GB-05. Sustainability In The Production Of Sr-ferrite Magnets: Understanding Microstructure-Magnetic Correlation Translates To A Successful Recycling Case In Industry.

A. Bollero[1], J. Rial[1], M. Villanueva[1], A. Seoane[2], J. Almunia[2] and R. Altimira[2]
1. Permanent Magnets and Applications, IMDEA Nanoscience, Madrid, Spain; 2. Ingeniería Magnética Aplicada, IMA S.L., Barcelona, Spain

Ferrites are the most widely used permanent magnets throughout the world [1,2]. They are used in low field and low power applications, high-frequency systems, biotechnology... Based on the high demand of these magnets, recycling of the residues generated in the manufacturing process is beneficial from an environmental point of view but also economically to reduce costs at the magnet company while additionally guarantying sustainability by closing the loop in production line. Despite the large amount of ferrites waste generated during manufacturing, there is a lack of studies dealing with the possibility of recycling Sr-ferrite (SF) waste. There are only studies dealing with the possibility of recycling the elemental constituents from different sources, but not the SF material after completion of magnets manufacturing. A successful recycling procedure for the SF residues produced in the manufacturing process of ferrite magnets will be explained in detail. The aim of this study is to establish a proper correlation between morphological, microstructural and magnetic properties in SF and make use of this understanding to develop a method that can be easily and cost-efficiently implemented in a permanent magnets manufacturing plant. Highlights from this study are: (i) The recycling process makes use of the facilities already existing in the company. (ii) The parameters comprising the recycling process are comparable to those used in the processing of the SF commercial powder. (iii) The magnetic quality of the recycled material is by far superior to that of the starting brand new material, resulting in a more competitive product. The prices of both the constituent elements and the processing route are very low for ferrites by comparison with those of rare earth-based magnets. Based on this, recovery and recycling of the residues generated during the manufacturing process might be interesting only from an environmental point of view but prohibitive in terms of implementation costs for a company. However, a recovery and recycling process fulfilling the attained requirements listed as highlights of this study has guaranteed straightforward implementation in production with no economical looses but gain. Residues used in this study were collected in the permanent magnet factory from a line of cutting machines used to shape ferrite magnets. The residue consisted of moisture comprising Sr-ferrite ($SrFe_{12}O_{19}$) powder, water and coolant fluid. In this study the residues were dried in air at 250°C for 1 h for removal of organic components (see Fig. 1(a)). Calcination in air at 1000°C was carried out straightforward on the wet residues in an industrial muffle to modify their properties. SEM images shown in Fig. 1 prove the particle size refinement and homogenization induced by the cutting process, when comparing the dried SF residue (Figs. 1(b)) and the starting commercial powder (Fig. 1(c)). Application of the calcination process to the commercial SF powder results in an increased coercivity of 1.8 kOe (Fig. 2(a)), proving the possibility of quality enhancement already in the case of the starting material. More striking is the effect of calcination on the residues, which results in a recycled SF powder with a large coercivity of 3.3 kOe, i.e. well beyond the increased value (1.5 kOe) achieved through exclusively drying of the residue and more than 3.5 times larger than that of the brand new commercial SF powder acquired by the company (Fig. 2(b)). It will be shown that the improvement in magnetic properties is the result of an efficient nanostructuration and homogenization of the powder through processing and subsequent heat treatment [3]. Moreover, and for the aim of properties comparison, brand new SF powders, identical to those used to fabricate the magnets, were milled by application of a self-developed surfactant-assisted rapid-milling method [3-5]. This comparison proves the fundamental importance of microstructure refinement on the enhancement of permanent magnet properties in SF. Consequently, a recycling procedure for the Sr-ferrite residues produced in the manufacturing process of ferrite magnets has been developed, resulting in a ferrite powder with coercivity and remanence values superior to those of the starting commercial material. The developed process guarantees sustainability by demonstrating a recycling method that can be cost-efficiently implemented in a permanent magnet manufacturing plant. *Acknowledgements* This research has been supported by EU-FP7 NANOPYME Project (No. 310516), MINECO through ENMA (MAT2014-56955-R), EUIN2017-88502 and from the Regional Government of Madrid through NANOFRONTMAG project (Ref. S2013/MIT-2850). IMDEA Nanociencia acknowledges support from the ‘Severo Ochoa’ Programme for Centres of Excellence in R&D (MINECO, Grant SEV-2016-0686).

[1] S. Constantinides, Market Outlook for Ferrite, Rare Earth and Other Permanent Magnets: 2015 to 2025, *Magnetics Conference* 2016. [2] A. Goldman, *Modern Ferrite Technology*, 2nd ed.; Springer: New York, 2006. [3] A. Bollero, J. Rial, M. Villanueva, K.M. Golasinski, A. Seoane, J. Almunia, and R. Altimira, *ACS Sustainable Chem. Eng.* 5, 3243-3249 (2017). [4] F. J. Pedrosa, J. Rial, K. M. Golasinski, M. N. Guzik, A. Quesada, J. F. Fernandez, S. Deledda, J. Camarero and A. Bollero, *Appl. Phys. Lett.* 109, 223105 (2016). [5] F. J. Pedrosa, J. Rial, K. M. Golasinski, M. Rodriguez-Osorio, G. Salas, D. Granados, J. Camarero and A. Bollero, *RSC Adv.* 6, 87282 (2016).

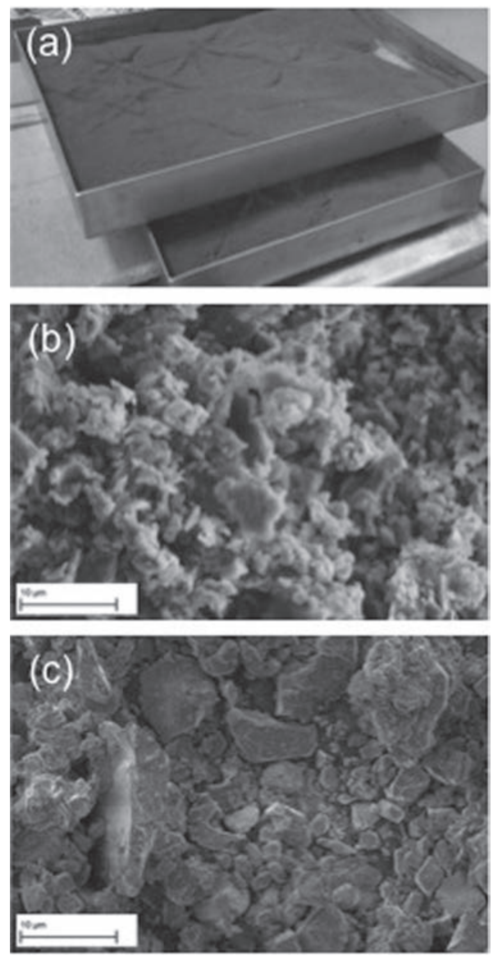

Fig. 1. (a) Image of dried SF residue (amount used: 50 kg). SEM images of (b) residue after drying process, and (c) commercial SF. Scale bar: 10 μm.

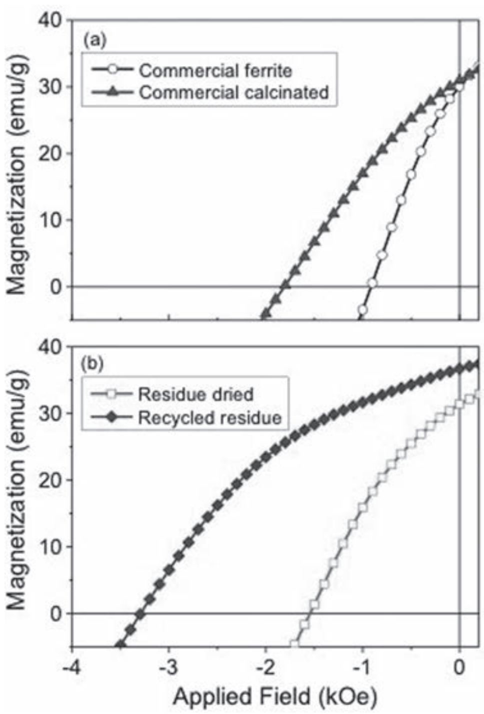

Fig. 2. Room temperature second quadrant hysteresis loops measured for (a) commercial SF (circles) and same powder after calcination process (triangles); (b) SF residue after drying (square) and recycling (diamonds).

10:15

GB-06. Effects of Hot Pressing Temperature on Magnetic Properties of Hot Pressed Nanocrystalline Nd-Fe-B Magnets.

Z. Jing[1], *Z. Guo*[1], M. Li[1], M. Zhu[1] and W. Li[1]
1. Central Iron & Steel Research Institute, Division of Functional Materials, Beijing, China

Introduction The hot deformation technique is an important method for fabricating nanocrystalline anisotropic Nd-Fe-B bulk magnets [1]. This technique consists of two steps, namely hot pressing and hot deformation. The magnetic properties of hot deformed magnets are determined not only by the process route of hot deformation but also by the status of hot pressed magnets [2-4]. As the precursor of hot deformation, the hot pressed magnet plays a very important role in determining the magnetic properties of the final hot deformed magnets. Therefore, it is necessary to explore the factors impacting the hot pressed magnets, which will contribute to preparing high performance hot deformed magnets. In this paper, the effects of hot pressing temperature on magnetic properties of hot pressed nanocrystalline magnets have been discussed by analyzing the magnetic properties, phase composition, and microstructure. Experimental Procedure The starting melt-spun powders with a nominal composition of $(Nd,Pr)_{29}Fe_{bal}Co_4Ga_{0.42}B_{0.92}$(wt.%) were hot pressed in vacuum at different temperature (450 °C, 500 °C, 550 °C, 600 °C and 650 °C) under 500 MPa for 70s to obtain nanocrystalline isotropic bulk magnets. The hot pressed magnets prepared at 450 °C, 500 °C, 550 °C, 600 °C and 650 °C were denoted as HP450, HP500, HP550, HP600 and HP650, respectively. Magnetic properties of the magnets were measured on a physical property measurement system (PPMS) without demagnetization correction. Phase composition and microstructure were identified by X-ray diffraction (XRD), simultaneous thermal analyzer (STA) and transmission electron microscope (TEM). Results and discussion The densities of the magnets increase from 7.04g/cm^3 to 7.60 g/cm^3 with the hot pressing temperature increasing from 450 °C to 650 °C. The results of magnetic measurement show that the coercivity increases from 15.15 kOe to 20.42 kOe with the temperature increasing from 450 °C to 650 °C, while the remanence increases when the temperature is lower than 600 °C, then decreases with the temperature further increasing to 650 °C. The best magnetic properties with coercivity of 17.29 kOe, remanence of 8.25 kGs and energy product of 17.69 MGOe are obtained at 600 °C. Figure 1 shows the initial magnetization curves and hysteresis loops of hot pressed magnets prepared at different temperature. For the magnets prepared below 600 °C, from the initial magnetization curves it can be seen when the field is low, the magetization increases slowly, and then increases sharply after the applied field exceeding a critical field(H_p), which can be interpreted by the pinning of the domain walls. The values of H_p increases with the temperature increasing from 450 °C to 600 °C. Two steps occur on the initial magnetization curve of the HP650 magnet, the magnetization increases fast when the field is lower than 7000 Oe, which are different from that of the magnets prepared below 600 °C. The critical field (H_p) of HP650 magnet increases further compared with that of HP600 magnet. The demagnetization curve of the HP650 sample contains a shoulder localized in the second quadrant, which results from the decoupling between the soft phase and the hard phase. Figure 2 shows the δM curves of hot pressed magnets prepared at different temperature. δM curves indicate when the applied field is low, the exchange-coupling interaction of neighboring grains is dominant, and the magnetostatic interaction increases with the field increasing and only one positive peak can be observed on the δM curve for the magnets prepared at the temperature not higher than 600 °C. Two positive peaks can be seen on the δM curve for the HP650 magnet. The first peak near 7000 Oe is corresponding to the first step on the initial magnetization curve of HP650 magnet, resulting from the exchange-coupling interaction of the soft and hard phase, and the second peak near the coercivity of HP650 magnet is attributed to the exchange-coupling of neighboring $Nd_2Fe_{14}B$ grains. XRD results show when the temperature is less 600 °C, the magnets are composed of single $Nd_2Fe_{14}B$ phase, while in the HP650 magnet the soft magnetic phase formed is $NdFe_2$. The peak occurred on the TG curve at 778 °C is due to the Curie transition of $NdFe_2$. TEM reveals that the grains in all the hot pressed magnets are equiaxed and the grain size is less than 150 nm. Conclusion In summary, the effects of hot pressing temperature on magnetic properties of hot pressed nanocrystalline Nd-Fe-B magnets have been investigated. The coercivity of the magnets increases with the temperature increasing, while the remanence increases when the temperature is lower than 600 °C, then decreases with the temperature further increasing to 650 °C. There are two steps on the initial magnetization curve as well as two positive peaks on the δM curve for the HP650 magnet, which are different from that of the magnets prepared at the temperature not higher than 600 °C The first step and peak occurred near 7000 Oe due to the exchange-coupling interaction of soft and hard phase. XRD results indicate in the HP650 magnet the soft phase formed is $NdFe_2$, resulting in the change in magnetization behavior of the HP650 magnet. TEM reveals that the grains in all the hot pressed magnets are equiaxed and the grain size is less than 150 nm. The grain size increases with the temperature increasing.

[1] R.W. Lee, Appl. Phys. Lett., vol.46, pp.790-791, 1985. [2] X. Tang, R. Chen, W. Yin, J. Wang, X. Tang, D. Lee, A. Yan, vol.623, pp. 386-392, 2015 [3] Y.H. Hou, Y.L. Wang, Y.L. Huang, Y. Wang, S. Li, S.C. Ma, Z.W. Liu, D.C. Zeng, L.Z. Zhao, Z.C. Zhong, Acta Mater. vol.115, pp. 385-391, 2016 [4]. T.T. Sasaki, T. Ohkubo, Y. Takada, T. Sato, A. Kato, Y. Kaneko, K. Hono, Scr. Mater. vol. 113, pp.218-221, 2016

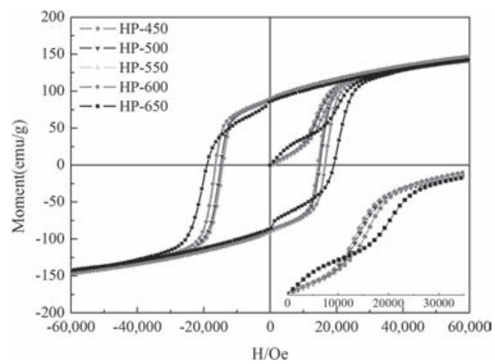

Fig. 1. Initial magnetization curves and hysteresis loops of hot pressed magnets prepared at different temperature

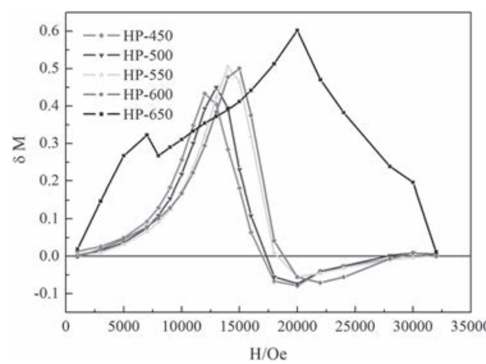

Fig. 2. δM curves of hot pressed magnets prepared at different temperature

10:30

GB-07. Withdrawn

10:45

GB-08. Structural Evolution and Magnetic Properties of Bulk MnAl-C Prepared by High Pressure Compaction of Gas-atomized Powders.

P. Si[1,2], H. Qian[1], J. Park[1], C. Choi[1], S. Han[1] and H. Ge[2]
1. Korea Institute of Materials Science, Changwon, The Republic of Korea; 2. China Jiliang University, Hangzhou, China

The ferromagnetic Mn-Al system has been studied for more than one century since 1908 [1]. The report on the metastable tetragonal ferromagnetic Mn-Al with about 54 at.% manganese in 1958 had attracted intensive research work to optimize the materials and to understand the phase transformation mechanisms in Mn-Al [2-5]. However, the research on MnAl was soon interrupted by the discovery of Nd-Fe-B. Recently the ferromagnetic τ-phase MnAl is attracting increasing research interests for its potential in plugging the gap between Nd-Fe-B and ferrites [6-8]. Various techniques such as hot extrusion, backpressure equal channel angular extrusion, hot deformation, hot compaction, spark plasma sintering, and microwave sintering have been employed to make bulk MnAl magnets in the previous work [9,10]. The precursors for hot extrusion and deformation are usually bulk materials while the precursors for the other methods are milled powders, which usually shows a higher coercivity and lower magnetization than that of the bulk. When the powders were consolidated in bulk magnets, both magnetization and coercivity would be decreased. The previous methods to make bulk samples usually involve high temperature processes that may result in a partial decomposition of the τ-phase, and thus a reduced magnetization. In this work, nanocrystalline MnAl-C bulk magnets were prepared by pressing the τ-phase gas-atomized micro-powders under high pressures and at low temperatures. The as prepared gas-atomized powders were mainly composed of ε-phase and a small fraction of γ_2-phase. The phase transformation temperature of the ε-MnAl-C to τ-phase were determined by using magnetization measurements. The triggering temperature for massive phase transformation of the ε-MnAl-C gas atomized powders is around 720 K. The phase transformation accomplished at temperatures above 806 K. The gas-atomized powers are spherical in shape with size ranges from several to 10 micrometers, as shown in Fig.1. Bulk nanocrystalline MnAl-C magnets were prepared from the gas atomized powders by using high pressure compaction, which results in a severe deformation of the spherical micro-powders and thus the grain size of the τ-phase was refined in the bulk materials, as shown in Fig.2. The compacted bulk materials show an enhanced coercivity and a higher magnetic performance to that of the powders. The structure, phase transformation, and magnetic properties of the powders and bulk samples were studied systematically.

[1] G. Hindrichs, Z. Anorg. Chem. 59 (1908) 414-449. [2] H. Kono, J. Phys. Soc. Jpn. 13 (1958) 1444-1451. [3] A. J. J. Koch, P. Hokkeling, M. G. Van der Steeg, and K. J. de Vos, J. Appl. Phys. 31 (1960) 75S-77S. [4] T. Ohtani, N. Kato, S. Kojima, K. Kojima, Y. Sakamoto, I. Konno, M. Tsukahara, and T. Kubo, IEEE Trans. Magn. MAG-13 (1977) 1328-1330. [5] J. J. van den Broek, H. Donkersloot, G. van Tendeloo, J. van Landuyt, Acta Metall. 27 (1979) 1497-1504. [6] P. Müllner, B. E. Bürgler, H. Heinrich, A. S. Sologubenko, G. Kostorz, Philos. Mag. Lett. 82 (2002) 71-79. [7] F.Bittner, L.Schultz, T.G.Woodcock, Acta Mater. 101 (2015) 48-54. [8] W. Lu, J. Niu, T. Wang, K. Xia, Z. Xiang, Y. Song, H. Zhang, S. Yoshimura, H. Saito, J. Alloys Compd. 675 (2016) 163-167. [9] R. Madugundo, O. K. Alkan, G. C. Hadjipanayis, AIP Adv. 6 (2016) 056009. [10] J. Thielsch, F. Bittner, T. G. Woodcock, J. Magn. Magn. Mater. 426 (2017) 25-31.

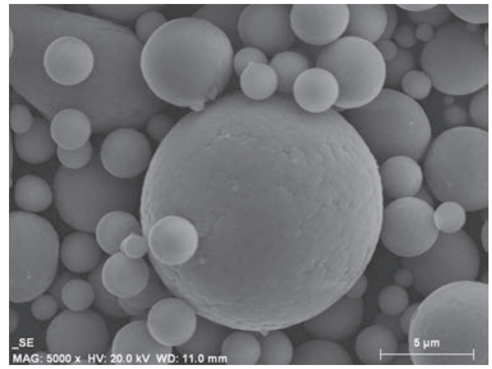

Fig. 1. SEM images of the MnAlC gas atomized powders

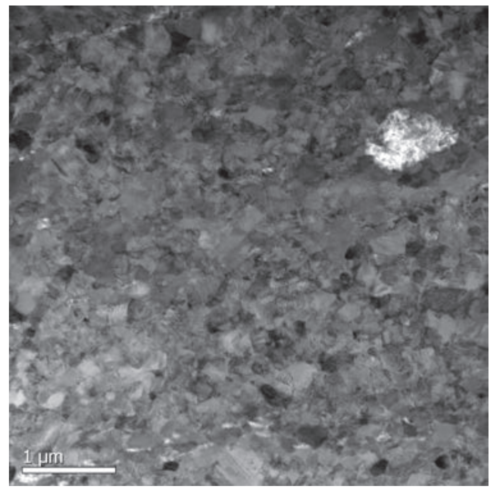

Fig. 2. TEM images of the bulk MnAl-C prepared by pressing gas-atomized powders under ~4 GPa.

11:00

GB-09. Additive Manufactured Magnetic Structures with Locally Varying Magnetization Direction in 3D.

C. Huber[1,2], F. Bruckner[1,2], C. Abert[1,2], M. Groenefeld[3] and D. Suess[1,2]
1. Physics of Functional Materials, University of Vienna, Vienna, Austria; 2. Christian Doppler Laboratory for Advanced Magnetic Sensing and Materials, Vienna, Austria; 3. Magnetfabrik Bonn GmbH, Bonn, Germany

Polymer bonded magnets enable the manufacturing of complex shapes and features by design flexibility regarding shape and magnetizing structure. Recently it was shown that an end-user 3D printer can be used to print polymer bonded NdFeB magnets with a specific complex shape [1]. An advantage of isotropic polymer-bonded magnetic materials is the possibility to magnetize various regions of a magnetic structure into different directions, even if the magnet is already solid. This characteristic of the bonded magnetic materials can be used to upgrade the 3D printer to a magnetic pixel ("maxel") printer. This work describes the possibility and a procedure to print "maxels" not merely on the surface of a magnet, but rather on each layer of the 3D printed magnetic structure. For the magnetization process, pulse coils would have the most advantages regarding flexibility. Due to the relative low saturation magnetization of bonded magnets, and the fact that a "maxel" printer with a pulse field coil would lead to a relative complex electronic setup, another technique should be discussed. The "maxel" printer is realized with cylindrical NdFeB permanent magnets (Grade N35, B_r=1.21 T) and ARMCO Pure Iron frustums to concentrate the magnetic flux of the NdFeB permanent magnets. Two of such contrary magnetized structures are fixed in a 3D printed jig (Fig. 1(a)). Fig. 1(b) shows a magnetic field scan (1.5 mm above surface) of the z-component of the magnetic flux above a 3D printed flat structure with different orientated "maxels" on the surface. The "maxel" pattern shows the letters "TU". To test the effectivness of our system, two cuboid of size 10x5x3 mm^3 (LxWxH) are printed with the polymer-bonded NdFeB material Neofer25/60p from Magnetfabrik Bonn GmbH. Different structures such as a stripes pattern and a chessboard pattern are realized. Both patterns are produced with the minimum resolution of 0.5 mm. After each 3D printed layer, the "maxel" printer magnetize the surface of the cuboid with the characteristic pattern. The result of printed stripes structure is pictured in Fig. 2(a) and for the chessboard pattern in Fig. 2(b). Furthermore, we developed an inverse stray field method based on finite elements that allows us to deduce the magnetization of the magnet from stray field measurements. This method can be used to deduce the quality of the printed magnets. Moreover the inverse method allows us to find an optimal magnetization density for a given target field distribution [2].

[1] C. Huber, C. Abert, F. Bruckner, M. Groenefeld, O. Muthsam, S. Schuschnigg, K. Sirak, R. Thanhoffer, I. Teliban, C. Vogler, R. Windl, and D. Suess, Applied Physics Letters 109, 162401 (2016). [2] C. Huber, C. Abert, F. Bruckner, M. Groenefeld, S. Schuschnigg, I. Teliban, C. Vogler, G. Wautischer, R. Windl, and D. Suess, Scientific Reports, vol. 7, p. 9419, Aug 2017.

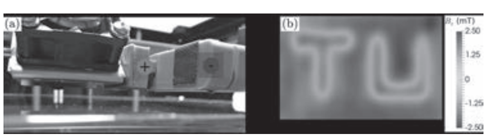

Fig. 1. Upgrade of the 3D printer to a "maxel" printer. (a) 3D printed jig to hold the magnets (magnetized along z or -z-direction) with the soft magnetic conical frustum. (b) Magnetic flux density B_z area scan (1.5 mm above surface) of a 3D printed magnet with an annotation of the surface.

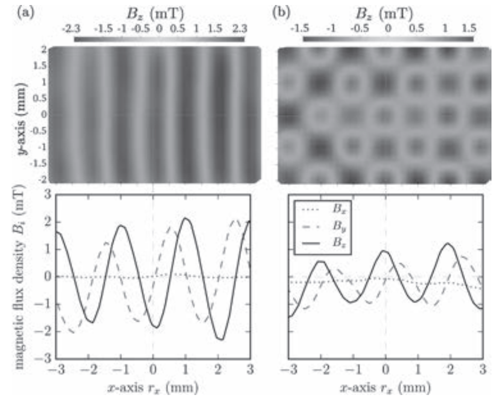

Fig. 2. Magnetic linear incremental scales. (a) Area and line scan (y=0 mm) of a printed 1D linear magnetic scale (pitch=2 mm), 1 mm above surface of a 3D printed structure (Neofer25/60p). (b) Area and line scan (y=0 mm) of a printed chessboard pattern to generate a 2D magnetic scale.

11:15

GB-10. Magnetic Force Equations based on Computer Simulation and the Effect of Load Line.

C. Chen[1,3], H. Meng[2] and M. Fan[1]
1. Quadrant at San Jose, San Jose, CA, United States; 2. Quadrant at Hangzhou, Hangzhou, China; 3. Magnet Energy LLC, San Jose, CA, United States

The Maxwell magnetic force equation $F = B^2A/(2\mu_0)$ [1-6] can be used for determining the magnetic force of magnetic components, where F is the force in newton (N), B is the flux density in tesla (T), A is the area of cross-section in square meter (m^2), and μ_0 is the permeability of the vacuum ($4\pi\times10^{-7}$ H/m). The formula can be converted to an easy to remember expression of $F = 40B^2A$, in which the unit of A is cm^2. This equation says that if the field is 1T, and the area is $1cm^2$, then the magnetic force is 40N or 4kgf. However, it is somehow difficult to determine the B value in many practical cases, and the accuracy is usually not satisfactory. Computer simulation using finite element method can determine the magnetic forces with various boundary conditions, but usually it is not convenient for industrial users. In this paper, we report several simple equations, which are established based on the large database generated by using 3D computer simulation. The users can use the equations to obtain the force by simply inputting the magnet's B_r, area and thickness. The effect of load line is also analyzed in this paper. Infolytica's MagNet software was chosen for the simulation. Parameterization function with newton tolerance 0.1% was used to systematically solve the problems for NdFeB cylinders, rings, and rectangular blocks interacting with CR1010 steel. The steel plates are both thicker and larger than the magnets. The maximum sizes for the magnets are shown in Table 1. The result database for each gap in a single boundary condition includes 62500 data points for rectangular blocks, 30625 data points for rings, and 1250 data points for cylinders. The gaps between the magnets and steel plates are in the range of 0.01 – 15mm with 23 unequal intervals. The itemized data were then plotted and analyzed to establish the force equations for the magnets with relative high load lines. Figure 1 shows the magnetic force vs the area of N52 magnet rings with gap = 0.01mm to steel plates. Fig. 1a and 1b have different boundary conditions: 1a has CR1010 steel on both ends of the magnets, and 1b has the steel only on one end. The load line of a standalone magnet can be estimated by using the equations described in Parker's book [7], but the magnets in this project have much higher load lines compared to the standalone magnets since steel plates are associated with these magnets. Boundary condition 1a obviously gives much higher load line compared to boundary condition 1b. For these ring magnets with higher load line in condition 1a, the force value vs area for each thickness can generate 2nd degree polynomial formulas, which has R-squared R2 >0.9997 as shown in Figure 1. (R^2 of 1.0000 was obtained for all the thicknesses of rectangular blocks). These formulas were then analyzed to establish a general equation $F = B_r^2(aA^2+bA)$. Using the equation, the magnetic force for any B_r value can be determined by inputting magnet's B_r, area, and thickness. As shown in Table 1, the factor *a* is a function of thickness in 2nd degree polynomial, and the factor *b* is also a function of thickness but in power form. The effect of boundary condition is tremendous. Condition1b has much lower load line compared to condition 1a, hence the magnetic force values vs the area cannot generate satisfactory equations. As shown in the Fig. 1b, for the same magnet area, the magnetic force values are in a range with various values due to different load lines. For example, the ring magnets with exact the same thickness 0.1cm and area $2.8cm^2$, the force values range from 18.4N to 74N for ID/OD values from 0.1/1.9cm to 4.3/4.7cm. Details for all the magnet shapes with two boundary conditions will be reported in this paper, and the effect of load line will be analyzed.

1. P. Campbell, Permanent magnet materials and their application, (1994) p104, p185 2. F. Cardarelli, Materials Handbook, 2008, Springer, ISBN 978-1-84628-668-1, p.493 3. J.A. Clarke, The Science and Technology of Undulator and Wigglers, 2004, Oxford, ISBN 0-19-850855-7, p.142 4. J.J. Winders, Power Transformers, 2002, Marcel Dekker, ISBN: 0-8247-0766-8, p.10 5. A. Tenhunen, Electromagnetic forces acting between the stator and eccentric cage rotor, 2003, ISBN 951-22-6682-2, p18-19 6. http://info.ee.surrey.ac.uk/Workshop/advice/coils/force.html, "The force produced by a magnetic field", Faculty of Engineering and Physical Sciences, University of Surrey (2017 online) 7. R.J. Parker, Advances in permanent magnetism, (1990) p151-156

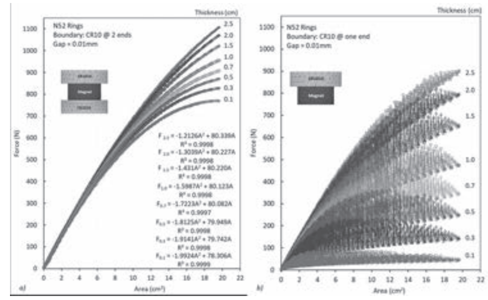

Fig. 1. Magnetic force vs magnet area for N52 Rings with gap = 0.01mm to steel
a) Steel plates on both ends; b) Steel plate on one end

$F = Br^2(aA^2+bA)$			$a = cT^2+gT+h,\ b = d(T-p)^n$					
Shape	Maximum size (cm)		*a*			*b*		
	OD/width/length	Thickness	*c*	*g*	*h*	*d*	*p*	*n*
Cylinders	5	2.5	-0.0356	0.2495	-1.0129	38.902	0.098	0.005
Rings	5	2.5	-0.0365	0.2515	-0.9765	38.090	0.097	0.004
Blocks	5	2.5	-0.0172	0.1499	-0.7604	38.874	0.093	0.007
F - force (N); A - area (≤ 25 cm²); T - thickness (cm); Br - magnet's remanence(T)								

Table 1 Magnetic force equations for magnets of any Br with steel plates on both ends (gap = 0.01mm)

11:30

GB-11. High $(BH)_{max}$ (Nd,Dy)-(Fe,Co)-B Hard Magnetic Powders Synthesized by Microwave Processing.

X. Tan[1], H. Parmar[1,2], V. Chaudhary[1,2], Y. Zhong[1] and R.V. Ramanujan[1]
1. Materials Science and Engineering, Nanyang Technological University, Singapore, Singapore; 2. Rolls-Royce@NTU Corporate Lab, Nanyang Technological University, Singapore, Singapore

Abstract $Nd_{14}Dy_1Fe_{67}Co_{10}B_8$ magnetic nanoparticles were synthesized by microwave combustion followed by reduction diffusion (RD). Our nanoparticles exhibit coercivity of 9.2 kOe with good maximum energy product ($(BH)_{max}$) of up to 13 MGOe at room temperature. The temperature coefficients of remanence(α) and coercivity(β) of the particles were found to be -0.82% and -0.21% in the temperature range of 300 K to 400 K. Dy was found to be uniformly distributed in the nanoparticles. Introduction Recently, there is increasing demand for high performance permanent magnets for cutting edge technologies, such as hybrid and electric vehicles, wind turbines, motors, etc. Hence, there is considerable interest in the development of nanostructured Nd-Fe-B based magnetic materials, since such magnets exhibit the highest $(BH)_{max}$ among all permanent magnets. However, limitations for this family of permanent magnets are its low Curie temperature (~585K) and relatively low coercivity. One solution is to substitute Nd by heavy rare earth elements such as Dy[1]. Dy-substituted Nd-Fe-B magnets have a higher coercivity; $Dy_2Fe_{14}B$ has a higher magnetocrystalline anisotropy than $Nd_2Fe_{14}B$[2]. The high cost of heavy rare earths and reduction of remanence due to antiferromagnetic coupling of Dy and Fe limit the Dy content [3]. Co alloying can be used to increase the Curie temperature[4-6]. Hence, we employed a microwave based chemical method to synthesize Dy,Co substituted $Nd_2Fe_{14}B$ powders. Since the starting materials in this method are metal salts rather than elemental metals, the material cost is much lower[7]. For example, the price of Dy metal(99.9%, Sigma Aldrich) is 13.2 SGD/gram while that for Dysprosium nitrate hydrate(99.9%, Aldrich) is only 2.8 SGD/gram. In addition, since it is a bottom-up approach, Dy can be easily alloyed by incorporating Dy salts in the precursor solution, further decreasing the processing cost. The targeted composition was $Nd_{14}Dy_1Fe_{67}Co_{10}B_8$, which was selected to increase the coercivity while keeping remanence almost constant[1, 4]. The crystal structure and magnetic properties between 300 K and 400 K were investigated. We observed that nanoparticle coercivity of up to 9.2kOe and $(BH)_{max}$ as high as 13 MGOe. Experimental Details The starting materials were neodymium nitrate hexahydrate (Alfa Aesar, purity 99.9%), Dysprosium nitrate hydrate (Sigma Aldrich, purity 99.9%), iron nitrate nonahydrate (Sigma Aldrich, purity 98+%), cobalt nitrate hexahydrate (Alfa Aesar, purity 98%), boric acid(Alfa Aesar, purity 99.8%), glycine (Sigma Aldrich, purity 99%) and calcium hydride(Alfa Aesar, purity 92%). Calculated amount of metal salts and glycine were dissolved in deionized water (total metal slats: glycine = 1:1). The solution was irradiated by the microwave system (HTVF-3, Dawnyx Technologies Pte Ltd) at a microwave powder of 2.8kW. The solution was converted into fine Nd-Dy-Fe-Co-B mixed oxide powders after combustion. $(Nd,Dy)_2(Fe,Co)_{14}B$ alloy was obtained by RD using CaH_2 as reducing agent *via* a vacuum furnace heat treatment at 800^{o}C for 2 hours. Results and Discussions Room temperature M-H curves measured for randomly oriented powders is shown in figure 1(black line). The Hc, Mr and Ms were 9.2 kOe, 55 emu/g and 103 emu/g, respectively. The powder sample was then aligned under a 2 T external magnetic field. Room temperature magnetic measurements were carried out in the direction perpendicular (figure 1, blue line) and parallel (figure 2, red line) to the alignment. It was found that the Mr and squareness are highly sensitive to this alignment process. The Mr almost doubled from 55 emu/g to 100 emu/g. Mr/Ms increased from 0.53 to 0.86.The (BH)max of the random powder and samples after alignment were calculated. We assumed a theoretical density of Nd-Fe-B (7.5 g/cm^3). Figure 2 shows the demagnetization B-H curves at room temperature. It is interesting to note that the $(BH)_{max}$ increased from 5.11 MGOe (for the random powder) to 13.04 MGOe (parallel to the aligned direction). The good (BH)max is attributed to the high Mr and high squareness resulting from the alignment of the nanoparticles along the easy axis. M-H hysteresis loops were also measured, at temperatures ranging from room temperature to 400 K, for the synthesized $Nd_{14}Dy_1Fe_{67}Co_{10}B_8$ powder. The thermal coefficient of remanence (α) and thermal coefficient ofs coercivity (β) were found to be -0.82 % and -0.21 %, respectively. Scanning Transmission electron microscopy (STEM) (JOEL, 2100F) of the $Nd_{14}Dy_1Fe_{67}Co_{10}B_8$ particles revealed an uniform distribution of Dy in the nano particles.

[1] H. Rahimi, A. Ghasemi, and R. Mozaffarinia, “Coercivity Mechanism in Nd-Fe-B Nanoparticles Synthesized by Reduction-Diffusion Process,” *Journal of Superconductivity and Novel Magnetism,* vol. 29, pp. 2099-2107, 2016. [2] X. J. Cao, L. Chen, S. Guo, X. B. Li, P. P. Yi, A. R. Yan, “Coercivity enhancement of sintered Nd–Fe–B magnets by efficiently diffusing DyF_3 based on electrophoretic deposition,” *Journal of Alloys and Compounds,* vol. 631, pp. 315-320, 2015. [3] K. Hirota, H. Nakamura, T. Minowa, and M. Honshima, “Coercivity Enhancement by the Grain Boundary Diffusion Process to NdFeB Sintered Magnets,” *IEEE Transactions on Magnetics,* vol. 42, pp. 2909-2911, 2006. [4] C. B. Rong, D. P. Wang, V. V. Nguyen, M. Daniil, M. A. Willard, Y. Zhang*, et al.*, “Effect of selective Co addition on magnetic properties of $Nd_2(FeCo)_{14}B$/Fe nanocomposite magnets,” *Journal of Physics D-Applied Physics,* vol. 46, pp. 045001-045006, 2013. [5] X. Tan, H. Parmar, Y. Zhong, V. Chaudhary, and R. V. Ramanujan, “Microwave-Based Chemical Synthesis of Co-Alloyed Nd-Fe-B Hard Magnetic Powders,” *IEEE Magnetics Letters,* vol. 8, pp. 1-5, 2017. [6] Y. Zhong, V. Chaudhary, X. Tan, H. Parmar, and R. V. Ramanujan, “Mechanochemical synthesis of high coercivity $Nd_2(Fe,Co)_{14}B$ magnetic particles,” *Nanoscale,* vol.9, pp. 18651-18660, 2017. [7] H. Parmar, T. Xiao, V. Chaudhary, Y. Zhong, and R. V. Ramanujan, “High energy product chemically synthesized exchange coupled $Nd_2Fe_{14}B$/Fe magnetic powders,” *Nanoscale,* vol. 9, pp. 13956-13966, 2017.

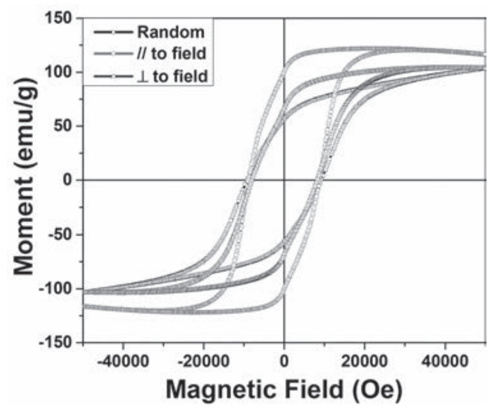

Fig. 1. Room temperature M-H curves measured for random powder, parallel and perpendicular to the magnetic alignment in the c-axis direction.

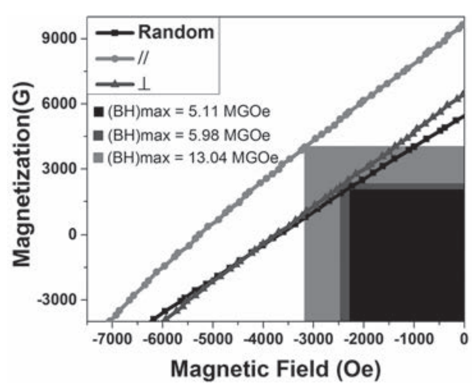

Fig. 2. Second quadrant of B-H curve at room temperature. The area of the rectangles under the curve yields the $(BH)_{max}$.

11:45

GB-12. Sintered Multicomponent Magnets for Electrical Machines.

L.M. Scherf[1], D. Tremelling[2], J. Aaćimović[1], R. Kessler[1], T. Tomše[3] and L. Herrmann[1]
1. Corporate Research Center, ABB, Baden-Dättwil, Switzerland;
2. Corporate Research Center, ABB, Raleigh, NC, United States;
3. Department for Nanostructured Materials, Jozef Stefan Institut, Ljubljana, Slovenia

Nd-Fe-B magnets are widely used in electrical machines such as motors and generators because of their high remanence and energy product. High operating temperatures as well as large stray fields in extreme situations present harsh demagnetization conditions. Therefore, Dy-rich Nd-Fe-B magnets have to be used in such machines which offer the large coercivities necessary to reliably avoid demagnetization in operation. However, the high Dy content makes such magnets very expensive and also lowers their remanence and energy product. In the light of the very volatile market for rare earth metals, reducing the Dy content of high-performance magnets is one of the main goals of current permanent magnet research. Dy-containing Nd-Fe-B magnets that are in commercial use today are typically very homogenous in composition and magnetic properties. However, the required coercivity of magnets operating in electrical machines may differ spatially. Thus, expensive Dy-rich, high coercivity magnet compositions may not be required throughout the full magnets within electrical machines, presenting an opportunity to decrease the total Dy content and material cost of the magnets. [1] In order to test this hypothesis, the areas of demagnetization in different peak overload and short circuit scenarios were simulated for different types of electrical machines with an adapted version of the finite element electrical machine simulation tool FCSmek. In surface mounted permanent magnet geometries, demagnetization seems to occur randomly in different parts of the magnets. For embedded permanent magnet geometries, however, demagnetization occurs mainly on the magnet edges (Figure 1). Therefore, in machines with such geometries, high coercivity regions are only required at the edges, whereas the magnet cores may have a Dy-poorer composition giving lower coercivity. Next, the feasibility of producing such magnets with different coercivity regions, termed multicomponent magnets, was investigated. Dy-free and Dy-rich jet-milled Nd-Fe-B powders were carefully placed next to each other into one mold, magnetically aligned in a magnetic field, and pressed to a green body. The green body was then sintered at a temperature suitable for both magnet powders, yielding one mechanically coherent multicomponent magnet (Figure 2). The interfaces between Dy-rich and Dy-free components were investigated using scanning electron microscopy (SEM), energy-dispersive X-ray spectroscopy (EDX) as well as mechanical property measurements. Conventional magnetic property measurements of the multicomponent magnets only show the integrated magnetization of the whole magnet. A first glance at the spatial distribution of coercivity and remanence was therefore obtained using small cutouts from different magnet regions. Additionally, measurements with a 3D magnetic field mapping device using 3-axis Hall probes allow non-destructive analysis and visualization of the desired multicomponent magnets with different coercivity regions. In conclusion, we show that multicomponent magnets containing regions of different coercivity can significantly improve the cost-effectiveness and performance of some electrical machines, especially with embedded permanent magnet geometry. According to our simulations, less Dy is required for multicomponent magnets withstanding the same operating conditions as regular Dy-rich magnets, which significantly lowers the magnet material cost. In addition, the higher remanence of the multicomponent magnets increases the magnetic loading of electrical machines, so that for a given electrical loading, the machine stack length can be reduced. First multicomponent magnets have been produced by the traditional sintering method. Careful analysis of the interface microstructure and strength proves that the multicomponent magnet approach is feasible for commercial application.

[1] R. Simon, J. Jacimovic, D. Tremelling, F. Greuter, E. Johansson and T. Tomse, "Magnet having regions of different magnetic properties and method for forming such a magnet". Patent Application EP3180141 A1.

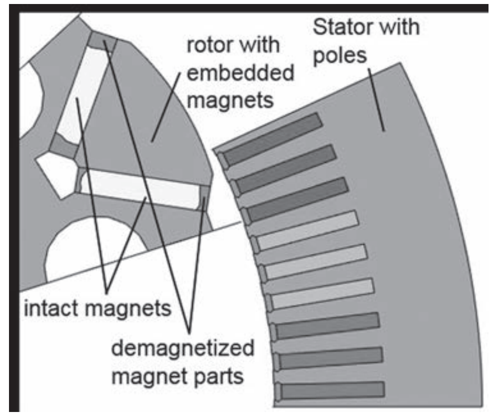

Fig. 1. Preferred demagnetization regions in an exemplary embedded permanent magnet machine design.

Fig. 2. Exemplary multicomponent magnets geometries prepared by combined traditional sintering of Dy-free and Dy-rich Nd-Fe-B powders.

FRIDAY MORNING, 27 APRIL 2018 ORCHID IV, 9:00 TO 12:00

Session GC
MAGNETISATION SWITCHING AND MAGNON-PHOTON COUPLING

Philipp Pirro, Co-Chair
TU Kaiserslautern, Kaiserslautern, Germany
Sebastiaan van Dijken, Co-Chair
Aalto University, Espoo, Finland

CONTRIBUTED PAPERS

9:00

GC-01. Domain Wall Motion Driven by Laplace Pressure in CoFeB-MgO Nanodots with Perpendicular Anisotropy.

Y. Zhang[1,2], X. Zhang[1], N. Vernier[2], Z. Zhang[1], G. Agnus[2], J. Coudevylle[2], X. Lin[1], Y. Zhang[1], Y. Zhang[1], W. Zhao[1] and D. Ravelosona[2]
1. Beihang University, Beijing, China; 2. Centre de Nanosciences et de Nanotechnologies, CNRS, University of Paris-Sud, Orsay, France

Magnetic nanostructures with perpendicular magnetic anisotropy (PMA) [1] materials are attracting a large amount of attention for their potential applications such as high density magnetic random access memory (MRAM) [2], bit patterned media [3], or magnetic logic [4]. The scalability of these applications toward ultimate technology nodes is in general limited by the structural variability of the nanostructures. This leads to a dispersion of the magnetic properties, which strongly affects the switching mechanism when the dimension of the nanostructures becomes smaller. In this work, we have studied the magnetization reversal of CoFeB/MgO-based nanodots with sizes ranging from 400 nm to 1 μm. Contrary to previous results [5,6], we observe that the switching field distribution (SFD) is shifted towards lower magnetic fields when the size is reduced. Using the framework of the elastic interface (e.g. soap bubbles), we show that the Laplace pressure applied on a domain wall (DW) nucleated and pinned at the edges of the nanodots is responsible for such mechanism. In our study, the magnetic multilayers were fabricated into nanodots array by electron beam lithography and ion milling process. The switching process of the nanodots was investigated using magneto-optic Kerr imaging microscopy at room temperature. The film was first saturated with a large positive magnetic field along the perpendicular direction (easy axis) and then successive negative magnetic field pulses were applied with the same width but different magnitude. The switching probability of the array was obtained by calculating the ratio of the reversed nanodots to the overall number of the nanodots. Fig. 1(a) and 1(b) show the typical magnetic switching process of the nanodots arrays for a size of 1 μm and 600 nm respectively. Surprinsingly, a lower magnetic field is needed for the array of 600 nm to reverse the same number of nandots. The average switching probabilities as a function of magnetic field for different dot sizes are shown in Fig. 2(a). We observe a clear shift of the SFD toward lower fields when the size is reduced without noticeable change for the width of the distribution. This results can be explained by the pinning of the DW at the edges of the nanodots together with the action of a Laplace pressure. When an external field is applied, the DW nucleation first occurs at the edges where the anisotropy is significantly reduced due to the patterning process. However, the DW cannot further propagate towards the inner part of nanodots because a strong DW pinning is induced by a gradient of anisotropy [7]. As a result, in addition to the driving magnetic field, a Laplace pressure is applied on the DW for the domain wall depinning process, as shown in Fig. 2(b). This Laplace pressure results from the DW energy that favors the collapse of magnetic bubbles and the strength of this pressure increases when the radius R of the bubble is reduced. The Laplace pressure just acts as a simple effective field proportional to inverse of the dot size, which only shifts the distribution without modifying its width. Therefore, we observed the decrease of the reversal fields as the dot size reduces. A DW energy density of 6.8 mJ/m^2 is calculated from the experimental data, which is in very good agreement with the previous study [8]. Our results suggest a path toward scalable devices based on controlling the nucleation and pinning potential of DWs at the edges of the nano-elements. In this case, benefiting from the Laplace pressure and keeping the same thermal stability given by the gradient of anisotropy, a lower switching current can be expected when reducing the size of the devices.

[1] F. Hellman, A. Hoffmann, Y. Tserkovnyak, G. S. D. Beach, E. E. Fullerton, C. Leighton, A. H. MacDonald, D. C. Ralph, D. A. Arena, H. A. Dürr, P. Fischer, J. Grollier, J. P. Heremans, T. Jungwirth, A. V. Kimel, B. Koopmans, I. N. Krivorotov, S. J. May, A. K. Petford-Long, J. M. Rondinelli, N. Samarth, I. K. Schuller, A. N. Slavin, M. D. Stiles, O. Tchernyshyov, A. Thiaville and B. L. Zink, Rev. Mod. Phys. 89, 025006 (2017). [2] A. D. Kent and D. C. Worledge, Nature Nanotech. 10, 187-191 (2015). [3] T. R. Albrecht, H. Arora, V. Ayanoor-Vitikkate, J. M. Beaujour, D. Bedau, D. Berman, A. L. Bogdanov, Y. A. Chapuis, J. Cushen, E. E. Dobisz, G. Doerk, H. Gao, M. Grobis, B. Gurney, W. Hanson, O. Hellwig, T. Hirano, P. O. Jubert, D. Kercher, J. Lille, Z. Liu, C. M. Mate, Y. Obukhov, K. C. Patel, K. Rubin, R. Ruiz, M. Schabes, L. Wan, D. Weller, T. W. Wu and E. Yang, IEEE Trans. Magn. 51, 5 (2015). [4] J. Torrejon, M. Riou, F. A. Araujo, S. Tsunegi, G. Khalsa, D. Querlioz, P. Bortolotti, V. Cros, K. Yakushiji, A. Fukushima, H. Kubota, S. Yuasa, M. D. Stiles and J. Grollier, Nature 547, 428 (2017). [5] T. Thomson, G. Hu and B. D. Terris, Phys. Rev. Lett. 96, 257204 (2006). [6] J. M. Shaw, S. E. Russek, T. Thomson, M. J. Donahue, B. D. Terris, O. Hellwig, E. Dobisz and M. L. Schneider, Phys. Rev. B. 78, 024414 (2008). [7] J. H. Franken, M. Hoeijmakers, R. Lavrijsen, J. T. Kohlhepp, H. J. M. Swagten, B. Koopmans, E. Van Veldhoven and D. J. Maas, J. Appl. Phys. 109, 07D504 (2011). [8] M. Yamanouchi, A. Jander, P. Dhagat, S. Ikeda, F. Matsukura, and H. Ohno, IEEE Trans. Mag. Lett. 2, 3000304 (2011).

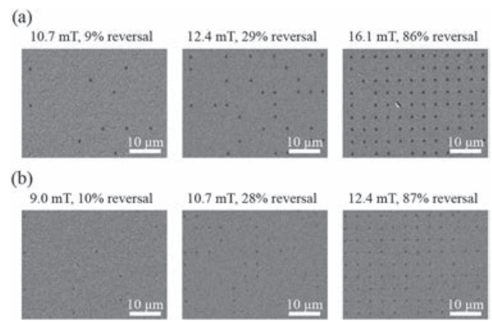

Fig. 1. Kerr microscopy images showing the switching process under magnetic fields for a nanodot array with dot size of (a) 1 μm and (b) 600 nm.

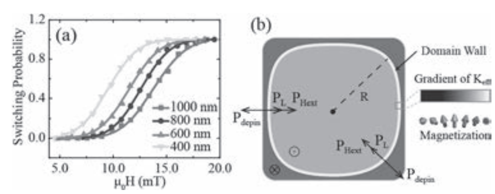

Fig. 2. (a) Average switching probability as function of magnetic field for dot size of 1 μm, 800 nm, 600 nm and 400 nm. (b) Schematic of the magnetization reversal process of a nanodot. A circular domain wall (yellow) is located at the edge of the dot, separating the reversed (red) and not reversed regions (green). P_{depin}, P_{Hext}, and P_L correspond to the pressures applied on the DW due to the pinning, the external magnetic field and the Laplace pressure, respectively.

9:15

GC-02. Oscillatory spin-orbit torque switching due to field-like torques.

J. Lee[1], J. Kwon[1], R. Ramaswamy[1], R. Mishra[1], S. Srivastava[1], K. Cai[1] and H. Yang[1]
1. Department of Electrical Engineering and Computer Engineering, National University of Singapore, Singapore

The spin-orbit torque (SOT), which is an electric current induced phenomenon that utilizes spin currents generated by spin orbit interactions, enables the ultrafast deterministic switching in magnetic thin films with perpendicular magnetic anisotropy (PMA). However, the oscillatory switching behavior with respect to the applied current duration has not yet been reported in the SOT switching with PMA systems, while it was demonstrated in the conventional spin-transfer torque (STT) switching [1]. This is attributed to the different switching mechanisms in the STT and SOT schemes. Whereas the STT switching is governed by the coherent rotation of magnetization, the SOT switching in PMA systems is reported to be an incoherent process where the switching occurs through expansion of magnetic domain [2]. In this work, we report for the first time the oscillatory SOT switching behavior in a PMA system [3] as shown in Figure 1. The studied structure is Ta (6 nm)/$Co_{40}Fe_{40}B_{20}$ (0.9 nm)/MgO (2 nm)/SiO_2 (3 nm) whose field-like torque (FLT) component of SOTs is large and is of opposite sign to that of damping-like torque (DLT) component (FLT/DLT = –3.2). Careful measurements of the SOT switching behavior under tilted in-plane assist-fields revealed that the large FLT, where its role was usually neglected in the deterministic SOT switching process, plays a dominant role in breaking the determinism in SOT switching dynamics. The oscillatory switching behavior is not observed in the Pt layer based device which exhibits a small FLT/DLT ratio of –0.5. Estimated domain wall velocities during the forward and backward switching processes, supported by the micromagnetics simulations, suggests that a large FLT can dynamically influence the domain wall chirality which determines the direction of SOT switching. By utilizing the oscillatory switching behavior, we also demonstrate the unipolar deterministic SOT switching scheme as shown in Figure 2, which operates by controlling the duration of the current pulses, while keeping the magnitudes and polarities of the current and the assist-field constant. The PMA circular dot patterned on top of the Ta channel switches alternatively between the two stable states under nanosecond current pulses. Our study provides the underlying physics behind the FLT induced oscillatory behavior of the SOT switching and a potential to significantly increase the scalability of SOT devices by replacing transistors with diodes.

[1] Papusoi, C. *et al.* 100 ps precessional spin-transfer switching of a planar magnetic random access memory cell with perpendicular spin polarizer. *Appl. Phys. Lett.* 95, 072506 (2009). [2] Baumgartner, M. *et al.* Spatially and time-resolved magnetization dynamics driven by spin–orbit torques. *Nat. Nanotech.* 12, 980-986 (2017). [3] Lee, J. M. *et al.* Oscillatory spin-orbit torque switching induced by field-like torques. Preprint at http://arxiv.org/abs/1711.05369 (2017).

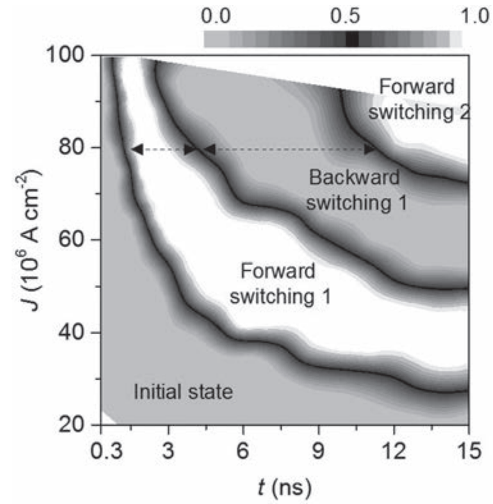

Fig. 1. Switching probability diagram with respect to the current density (*J*) and pulse duration (*t*), with in-plane assist field of 1191 Oe. The scale bar indicates the contour level of switching probability (×100 %). The device has an initial 'up' magnetization configuration. The forward and backward switching indicates 'up' to 'down' and 'down' to 'up' switching, respectively. The dashed arrows indicate the periods of forward switching and backward switching for an applied *J* of 79.4 × 10^6 A cm^{-2}, respectively.

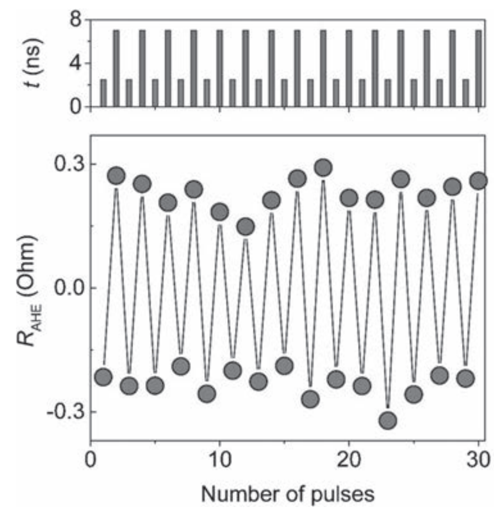

Fig. 2. Unipolar switching of CoFeB dot with perpendicular magnetic anisotropy by applying a series of positive current pulses with alternating duration of 2.5 ns and 7.5 ns. The positive and negative values of anomalous Hall resistance (R_{AHE}) indicate the magnetization with 'up' and 'down' configuration, respectively. A constant current pulse density of 79.4 × 10^6 A cm^{-2} and magnetic field of 1067 Oe were applied.

9:30

GC-03. Magnetization damping in spin-orbit coupled magnetic textures.

C.A. Akosa[1], Z. Yuan[3], A. Takeuchi[2] and G. Tatara[1]
1. RIKEN Center for Emergent Matter Science (CEMS), Wako, Japan; 2. Department of Physics and Mathematics, Aoyama Gakuin University, Sagamihara, Japan; 3. The Center for Advanced Quantum Studies and Department of Physics, Beijing Normal University, Beijing, China

The recent years has witnessed a surge in research efforts geared towards utilizing the spin degree of freedom of electrons in combination with its charge, to create new functionalities and devices. The performances of these devices such as magnetic random access memories, hard drives and sensors, strongly depends on the magnetization damping - as it detects the energy required, the speed and efficiency at which these devices operate. Over the past years, several microscopic theory of magnetization damping have been proposed in which, spin-orbit coupling is the mediating interaction by which energy is transferred from the magnetization to the spin of itinerant electrons[1,2,3]. It was recently pointed out that magnetization damping being a material parameter should in principle reflect the symmetries inherent in the system by virtue of Neumann's principle, and therefore should include a *chiral* contribution in non-homogeneous magnets with broken inversion symmetry[4,5]. This prediction is appealing for realizing of ultra-low damping, however, little information is known about the relative strength and the symmetry of the damping in spin-orbit coupled magnets. In this study, we propose a scheme based on the scattering theory[6,7] to qualitatively estimate the chiral contribution of damping in spin-orbit coupled non-homogeneous magnets characterized by broken inversion symmetry. We elucidate the different contributions and the angular dependence of chiral damping in the presence of the Rashba and Dresselhaus spin-orbit coupling. We show that in the absence of relaxation, the damping torque takes the same form as the adiabatic spin transfer torque proportional to the divergent of the electric field expressed in terms of the electromagnetic vector potential. Furthermore, our result indicates that the effective gauge fields of *any* origin contributes to the torque in exactly the same way as the electromagnetic gauge field.

[1] V. Kambersky, Czech. J. Phys. 26, 1366 (1976). [2] D. L. Mills and S. M. Rezende, Top. Appl. Phys. 87, 27 (2003) [3] K. Gilmore, Y. U. Idzerda, and M. D. Stiles, J. Appl. Phys. 103, 07D303 (2008). [4] E. Jue, *et. al.,* Nat. Mater. 15, 272 (2016). [5] C. A. Akosa, *et. al.,* Phys. Rev. B 93, 214429 (2016). [6] A. Brataas, *et. al.,* Phys. Rev. Lett. 101, 037207 (2008). [7] Z. Yuan, *et. al.,* Phys. Rev. Lett. 113, 266603 (2014).

9:45

GC-04. Structural and magnetic study by nonmagnetic (Ti^{4+} and Ga^{3+}) doping at Ru site in $SrRuO_3$.

R. Gupta[1] and A. Pramanik[1]
1. School of Physical Science, Jawaharlal Nehru University, New Delhi, India

Abstract: In this, we report the study of structural and magnetic behavior in Ru-based doped perovskite structure of $SrRuO_3$ and $SrRu_{0.9}M_{0.1}O_3$ (M = Ti and Ga). $SrRuO_3$ has an orthorhombic structure which has not change by Ga as well as Ti doping and also shows decreasing lattice parameters. The $SrRuO_3$ known to as an itinerant ferromagnet (FM) with Tc ~ 160 K and having bifurcation between Zero-field-cooled (ZFC) and field-cooled (FC) magnetization below T_c which decrease by nonmagnetic (Ti and Ga) doping. Further analysis of dc magnetization shows that the inverse susceptibility (χ^{-1}) in paramagnetic (PM) and high-temperature region fitted by modified Curie-Weiss law (CWL) in the form of $\chi(T) = \chi_0 + [C/T-\theta_p]$, where θ_p is the Curie temperature. The effective PM moment ($\mu_{eff} = [3k_BC/N]^{1/2}$) and θ_p decreases by nonmagnetic (Ti and Ga) doping. The χ^{-1} (T) revealed some upward deviation by nonmagnetic (Ti and Ga) doping from perfect CWL behavior above T_c because of the formation of FM clusters in the PM background which has characterized as Griffiths phase (GP). The critical exponent (β) fitting of FC magnetization of $SrRuO_3$ near T_c shows as mean-field type behavior and fitted in the form of $M(T) = M_0(T_c\text{-}T)^\beta$. By nonmagnetic (Ti and Ga) doping, the value of β has increased. The isothermal magnetization at 5 K of $SrRuO_3$ is showing hysteresis which is not changed by nonmagnetic (Ga and Ti) doping and also saturation moment (μ_H) has decreased. The Arrott's plots are confirming FM nature with the value of spontaneous magnetization (M_S) which decreases by nonmagnetic (Ti and Ga) doping. The observation of Rhodes-Wohlfarth ratio shows, the value of q_c/q_s increased by nonmagnetic (Ti and Ga) doping, showing the itinerant nature of $SrRu_{0.9}M_{0.1}O_3$ (M = Ti and Ga) compounds increase, where $S=q_c/2$ in $\mu_{eff} = g[S(S+1)]^{1/2}$and $q_s = \mu_H$. INTRODUCTION In the strongly correlated oxides, there have been large interrelation effects between charge, spin, lattice and orbital ordering which gives various types of phenomena such as metal-insulator transition, superconductivity (SC), colossal magnetoresistance and multiferroics. Among them, the Ru-based 4d transition metal oxides are of current interest because a variety of physics are coming out due to the combined effect of electron correlation (*U*) as well as spin-orbit coupling (SOC). After the discovery of SC in Sr_2RuO_4, the $SrRuO_3$ has quite an interest. $SrRuO_3$ is the rare example of 4d based itinerant FM with T_c ~ 160 K [1], and due to crystal field splitting, $SrRuO_3$ adopts low spin state by 4 electrons of Ru^{4+}($4d^4$, 0.62 Å) orbitals occupy in t_{2g} state and leave the higher e_g state empty under octahedral crystal formation. The theoretically calculated saturation moment of $SrRuO_3$ is 2 μ_B/f.u ($\mu_H = gS\mu_B$, S = 1) but the experimentally observed saturation moment is ~ 1.4 μ_B/f.u even 30 T of high field believed due to itinerant nature of magnetism [4]. The itinerant FM follows the stoner criteria of magnetism i.e. $UN(\varepsilon_F) \geq 1$, where $N(\varepsilon_F)$ is the density of state (DOS) at Fermi level [5]. So by change in U or $N(\varepsilon_F)$, the stoner criteria will be modified, as our previous study [2]. With this motivation, we compare the nonmagnetic doping in $SrRu_{0.9}M_{0.1}O_3$ (M = Ti and Ga) in which U is same, but $N(\varepsilon_F)$ are different. Further, the similarities between Ti and Ga is that both are non-magnetic and the ionic radii match (Ga^{3+} = 0.62 Å and Ti^{4+} = 0.605 Å). The main difference between Ga and Ti is DOS which increases in Ga doping and decreases by Ti doping, and in Ga doping one another change is the charge state disorder. So by considering these similarities and dissimilarities, we study the structural and magnetic properties. Results and Discussion The X-ray diffraction (XRD) patterns of $SrRu_{0.9}M_{0.1}O_3$ (M = Ti and Ga) compounds crystallize in a single phase without any new peak. The Rietveld refinement of XRD data of $SrRuO_3$ forms an orthorhombic-Pbnm structure which also sustained by Ti as well as Ga doping at Ru^{4+} (0.62 Å) site. The lattice parameters decrease by nonmagnetic (Ti and Ga) doping at Ru site [3]. Our observation of decreasing lattice parameters is the formation of Ru^{5+}(0.565 Å) due to Ga^{3+} (0.62 Å) similar charge amount by Ga doping and due to less ionic radii of Ti^{4+}(0.605 Å) by Ti doping. $SrRuO_3$ has shown the PM-FM phase transition at ~ 160 K and follow the Curie-Weiss law (CWL) in the paramagnetic state and high-temperature region. By Ti and Ga doping, the value of Curie temperature (θ_p) and μ_{eff} decreases. There is some upward deviation from perfect CWL due to ferromagnetic cluster formation in the PM background reveal as Griffiths phase (GP) just above T_c. In the ferromagnetic phase, there is more bifurcation between ZFC and FC magnetization which is decreases by nonmagnetic (Ti and Ga) doping. Below T_c, the critical exponent fitting of $SrRuO_3$ gives β ~ 0.5 is showing mean field type behavior. The value of β increases by nonmagnetic (Ti and Ga) doping at Ru site. The isothermal magnetization of $SrRuO_3$ shows hysteresis which also sustained by nonmagnetic (Ti and Ga) doping at Ru site with decreasing saturation moment (μ_H). The Arrott's plot confirms the FM state with the value of M_s and by nonmagnetic (Ti and Ga) doping, the value M_s decreases. CONCLUSIONS The polycrystalline samples of $SrRuO_3$ and $SrRu_{0.9}M_{0.1}O_3$ (M = Ga and Ti) compounds have been prepared by solid state reaction method.

1. P. B. Allen, et al, Phys. Rev. B., 53., 4393 (1996). 2. R. Gupta and A. K. Pramanik, J. Phys.: Condens. Matter., 29., 115801 (2017) 3. P. Rhodes and E. P. Wohlfarth, Proc. R. Soc., 273., 247 (1963). 4. G. Cao, et al, Phys. Rev. B., 56., 321 (1997). 5. T. Moriya, Spin Fluctuations in Itinerant Electron Magnetism (1985).

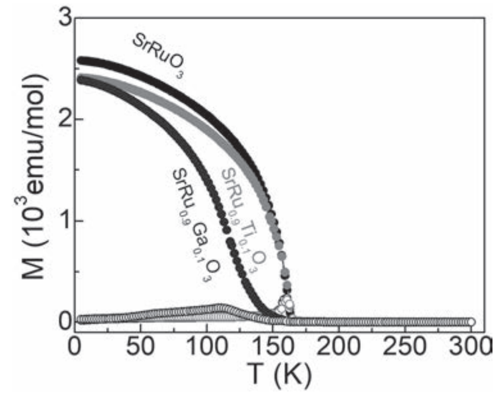

10:00

GC-05. Plasmon-Induced Demagnetization and Magnetic Switching in Nickel Nanoparticle Arrays.

M. Kataja[1], F. Freire-Fernandez[1], J. Witteveen[1], T. Hakala[1], P. Törmä[1] and *S. van Dijken*[1]
1. Department of Applied Physics, Aalto University, Espoo, Finland

Plasmonic nanostructures enable strong local enhancements of the optical field in areas that are substantially smaller than the wavelength of incident light. This remarkable capability, which underpins the rapid expansion of research into nanophotonics, also offers prospects for magnetic switching. In heat-assisted magnetic recording (HAMR), plasmonic near-field transducers reduce the switching field of high-anisotropy materials via local heating [1,2]. Besides, plasmonic nanoantennas can confine ultrafast all-optical switching effects to areas that are much smaller than the laser spot [3]. In both examples, noble-metal plasmonic elements are integrated with the magnetic medium that needs to be switched. Despite stronger ohmic damping, magnetic metals also support the excitation of surface plasmon resonances [4,5]. Here, we explore the possibility of using the magnetic material itself as a plasmonic nanoantenna and demonstrate that the excitation of surface plasmons enhance the optical switching efficiency. We focus on an array of circular Ni nanoparticles exhibiting strong magneto-optical activity and magnetic circular dichroism [6,7]. The particle diameter and height are 100 nm and 110 nm, respectively, and the periodicity of the square lattice is set to 420 nm. The optical transmission spectrum of the array has an asymmetrical Fano-type line shape, which originates from hybridization between broad localized surface plasmon resonances in the Ni nanoparticles and sharp diffracted orders of the lattice. Thus, the optical field within the Ni nanoparticles vary strongly with the wavelength of incident light. We perform two types of experiments using a variable-wavelength femtosecond laser. After saturating the nanoparticles in a perpendicular magnetic field, we use femtosecond laser pulses to (1) demagnetize the nanoparticles in zero magnetic field or (2) switch the magnetization in a magnetic field, more than one order of magnitude smaller than the coercive field. In both cases, we find that the threshold laser fluence for demagnetization or magnetic switching varies with the wavelength of incident light in a similar fashion as 1/E (Fig. 1(a)), where E is the optical extinction of the array. The lowest threshold fluence thus coincides with maximum optical absorption at a wavelength of 660 nm. From this correlation, we conclude that plasmon-induced heating of the Ni nanoparticles to their Curie temperature of 600 K causes demagnetization and field-assisted magnetic switching. Model calculations of the threshold fluence based on plasmon-induced heating of the Ni nanoparticle array confirm the experimental results (Fig. 1(b)).

[1] W.A. Challener et al., Nat. Photonics 3, 220 (2009). [2] B.C. Stipe et al. Nat. Photonics 4, 484 (2010). [3] T-M. Liu et al., Nano Lett. 15, 6862 (2015). [4] V. Bonanni et al., Nano Lett. 11, 5333 (2011). [5] N. Maccaferri et al., Phys. Rev. Lett. 111, 167401 (2013). [6] M. Kataja et al., Nat. Commun. 6, 7072 (2015). [7] M. Kataja et al., Opt. Express 24, 3562 (2016).

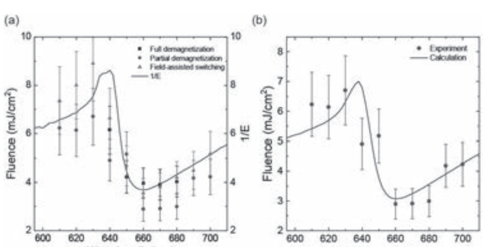

Fig. 1. (a) Experimental threshold fluence for full demagnetization, demagnetization to 0.4M_s (both in zero magnetic field) and magnetic switching to 0.6M_s in the opposite direction (magnetic field of 5 mT). The threshold fluences are compared to the inverse extinction (1/E) of the nickel nanoparticle array. (b) Experimental threshold fluence (demagnetization to 0.4M_s) and calculation of the fluence that is required to heat the nickel nanoparticles to their Curie temperature of 600 K.

10:15

GC-06. Scaling of All-Optical Switching to Nanometer Dimensions.

A. El-Ghazaly[1], C. Lambert[1], B. Tran[2], A. Pattabi[1], J. Gorchon[1,3], S. Salahuddin[1], H. Wong[4] and J. Bokor[1]
1. Electrical Engineering and Computer Science, University of California Berkeley, Berkeley, CA, United States; 2. Physics, University of California Berkeley, Berkeley, CA, United States; 3. Lawrence Berkeley National Laboratory, Berkeley, CA, United States; 4. Electrical Engineering, Stanford University, Stanford, CA, United States

Switching the magnetization of nanoscale magnetic dots is one of the most crucial processes for use in electronics applications such as MRAM [1,2] and logic [3,4]. The unique ability to switch magnetization entirely optically has been shown possible in a limited selection of materials often using either circularly polarized or linearly polarized light [5,6]. The material GdFeCo, however, is rare in that it can be switched all-optically without the need for a particular polarization of light, and for which the switching occurs on ultrafast, picosecond timescales [7,8]. This work explores the potential for use of GdFeCo in nanoscale ultrafast magnetic devices. To do so, we first fabricate nanoscale dots of the magnetic material, and then we experimentally determine its all-optical switching (AOS) properties down to nanometer dot dimensions. Previous works have mostly focused on micrometer scale dots of GdFeCo [8-11], with some work down to 400 nm squares [12], but with vortex-like in-plane magnetization states. Here, we first demonstrate helicity-independent all-optical switching in GdCo, a material chosen for stronger perpendicular magnetic anisotropy (PMA) than GdFeCo but with similar ferrimagnetic properties; furthermore, we achieve reliable AOS down to 200 nm diameters. The greater challenge to scaling was maintaining the perpendicular magnetic anisotropy for smaller dot dimensions, as was found to be a challenge in [12]. While ion milling is a common method for patterning MTJ pillars for MRAM, it was found to destroy the integrity of the PMA. Instead, a lift-off process with electron-beam lithography was used to pattern the nanodots, ranging in size from 15 μm down to 50 nm, into arrays. Each dot size of diameter d was arrayed with a pitch of 3d in a 25 μm x 25 μm square region, as shown in Fig. 1. The pitch was chosen to be large enough to prevent magnetistatic coupling between the dots, while simultaneously allowing a high areal density of the dots for maximum magnetic signal during subsequent optical measurements. Although up until now, AOS experiments focused on GdFeCo films, such films did not sustain their PMA below approximately 900 nm diameters. Rather than GdFeCo, this work utilizes GdCo, with high cobalt concentrations to contribute stronger PMA [13]. The nanoscale dots were fabricated from a material stack of Ta (3)/Pt (3)/$Gd_{30}Co_{70}$ (10)/Pt (5), where layer thicknesses in nanometers are indicated in parentheses. Despite the exclusion of iron, these material films still exhibit AOS, as shown in Fig. 2, therefore expanding the library of materials with the capability of ultrafast helicity-independent all-optical switching. Single shots of a Ti-Sapphire laser with pulse width of approximately 70 fs were shot at an array region with uniform sizes of nanoscale dots. Afterwards, a train of laser pulses with much lower power, having a repetition rate of 252 MHz modulated by a photoelastic modulator at 50.028 kHz, was used to detect the magnetization state by Magneto-Optical Kerr Effect (MOKE). For each dot size, a hysteresis loop was first measured and used to identify the signal levels corresponding to the two magnetization states, as detected by laser MOKE. Then, illustrated in Fig. 2, AOS tests were executed with single shots of the laser, followed by MOKE detection of the magnetization state. The conventional toggle switching associated with GdFeCo films was successfully observed in these GdCo dots for each of the nanodot sizes, down to the smallest detectible diameter of 200 nm. Such results are demonstrated in Fig. 2 for the 200 nm dots, where Fig. 2b and 2c present the laser MOKE hysteresis loop and the single-shot toggle switching results, respectively. Slight variation in the MOKE intensity levels was seen for each of the two magnetization states, however a clear gap between the two states is consistently seen; variation is assumed to be due to drift of the laser power and shift in its overlay position in the nanodot array, leading to a change in the number of nanodots being detected. Using laser MOKE as the detection technique, AOS was confirmed down to 200 nm dot diameters, representing the smallest patterns optically switched to date. There is a high probability that smaller dots are also switched all-optically, however, detection of the magnetization state was not possible due to the laser diffraction limit and decrease in the detected signal level. Nevertheless, by demonstrating the possibility of scaling the AOS effect in GdCo nanoscale dots, we bring these materials one step closer to realistic applications. Acknowledgement Funding and support for this work was provided by the Center for Energy Efficient Electronics Science. Part of this work was performed at the Marvell Nanofabrication Laboratory at the University of California Berkeley, and the Stanford Nanofabrication Facility and Stanford Nano Shared Facilities at Stanford University.

[1] T. Kishi, H. Yoda, T. Kai, T. Nagase, E. Kitagawa, M. Yoshikawa, K. Nishiyama, T. Daibou, M. Nagamine, M. Amano, S. Takahashi, M. Nakayama, N. Shimomura, H. Aikawa, S. Ikegawa, S. Yuasa, K. Yakushiji, H. Kubota, A. Fukushima, M. Oogane, T. Miyazaki, and K. Ando, "Lower-current and Fast switching of A Perpendicular TMR for High Speed and High density Spin-Transfer-Torque MRAM," in *IEEE International Electron Devices Meeting*, 2008. [2] B. N. Engel, J. Akerman, B. Butcher, R. W. Dave, M. DeHerrera, M. Durlam, G. Grynkewich, J. Janesky, S. V Pietambaram, N. D. Rizzo, J. M. Slaughter, K. Smith, J. J. Sun, and S. Tehrani, "A 4-Mb Toggle MRAM Based on a Novel Bit and Switching Method," *IEEE Trans. Magn.*, vol. 41, no. 1, pp. 132–136, 2005. [3] K. Jabeur, G. Di Pendina, F. Bernard-Granger, and G. Prenat, "Spin Orbit Torque Non-Volatile Flip-Flop for High Speed and Low Energy Applications," *IEEE Electron Device Lett.*, vol. 35, no. 3, pp. 408–410, 2014. [4] D. M. Bromberg, M. T. Moneck, V. M. Sokalski, J. Zhu, L. Pileggi, and J. G. Zhu, "Experimental demonstration of four-terminal magnetic logic device with separate read- and write-paths," in *Technical Digest - International Electron Devices Meeting, IEDM*, 2015, vol. 2015–Febru, no. February, p. 33.1.1-33.1.4. [5] M. S. El Hadri, P. Pirro, C.-H. Lambert, S. Petit-Watelot, Y. Quessab, M. Hehn, F. Montaigne, G. Malinowski, and S. Mangin, "Two types of all-optical magnetization switching mechanisms using femtosecond laser pulses," *Phys. Rev. B*, vol. 94, no. 6, p. 64412, 2016. [6] C. H. Lambert, S. Mangin, B. S. D. C. S. Varaprasad, Y. K. Takahashi, M. Hehn, M. Cinchetti, G. Malinowski, K. Hono, Y. Fainman, M. Aeschlimann, and E. E. Fullerton, "All-optical control of ferromagnetic thin films and nanostructures," *Science (80-.)*., vol. 345, no. 6202, pp. 1337–1340, 2014. [7] T. M. Liu, T. Wang, A. H. Reid, M. Savoini, X. Wu, B. Koene, P. Granitzka, C. E. Graves, D. J. Higley, Z. Chen, G. Razinskas, M. Hantschmann, A. Scherz, J. Stöhr, A. Tsukamoto, B. Hecht, A. V. Kimel, A. Kirilyuk, T. Rasing, and H. A. Dürr, "Nanoscale Confinement of All-Optical Magnetic Switching in TbFeCo - Competition with Nanoscale Heterogeneity," *Nano Lett.*, vol. 15, no. 10, pp. 6862–6868, 2015. [8] T. A. Ostler, J. Barker, R. F. L. Evans, R. W. Chantrell, U. Atxitia, O. Chubykalo-Fesenko, S. El Moussaoui, L. Le Guyader, E. Mengotti, L. J. Heyderman, F. Nolting, A. Tsukamoto, A. Itoh, D. Afanasiev, B. A. Ivanov, A. M. Kalashnikova, K. Vahaplar, J. Mentink, A. Kirilyuk, T. Rasing, and A. V Kimel, "Ultrafast heating as a sufficient stimulus for magnetization reversal in a ferrimagnet.," *Nat. Commun.*, vol. 3, p. 666, 2012. [9] L. He, J. Chen, J. Wang, and M. Li, "All-optical switching of magnetoresistive devices using telecom-band femtosecond laser," *Appl. Phys. Lett.*, vol. 102402, no. 107, 2015. [10] L. Le Guyader, M. Savoini, S. El Moussaoui, M. Buzzi, A. Tsukamoto, A. Itoh, A. Kirilyuk, T. Rasing, a V Kimel, and F. Nolting, "Nanoscale sub-100 picosecond all-optical magnetization switching in GdFeCo microstructures.," *Nat. Commun.*, vol. 6, no. May 2014, p. 5839, 2015. [11] Y. Yang, R. B. Wilson, J. Gorchon, C.-H. Lambert, S. Salahuddin, and J. Bokor, "Ultrafast Magnetization Reversal by Picosecond Electrical Pulses," *Sci. Adv.*, no. November, p. in press, arXiv: 1609.06392, 2017. [12] L. Le Guyader, S. El Moussaoui, M. Buzzi, R. V. Chopdekar, L. J. Heyderman, A. Tsukamoto, A. Itoh, A. Kirilyuk, T. Rasing, A. V. Kimel, and F. Nolting, "Demonstration of laser induced magnetization reversal in GdFeCo nanostructures," *Appl. Phys. Lett.*, vol. 101, no. 2, 2012. [13] G. H. O. Daalderop, P. J. Kelly, and M. F. H. Schuurmans, "First-principles calculation of the magnetocrystalline anisotropy energy of iron, cobalt, and nickel," *Phys. Rev. B*, vol. 41, no. 17, pp. 11919–11937, 1990.

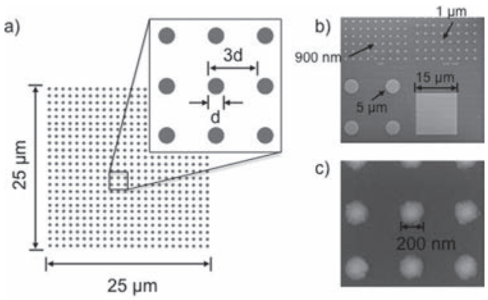

Fig. 1. – Dot array pattern where a) 25 µm x 25 µm square regions containing uniformly spaced dots of the same size; SEM images including b) 15 µm square, 5 µm, 1 µm, 900 nm, and c) 200 nm dots of GdCo.

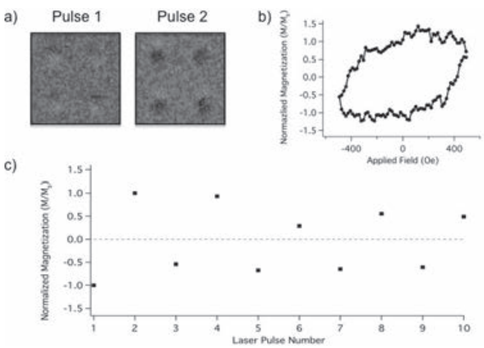

Fig. 2. – MOKE results, including a) image MOKE showing switching of 4 µm dots; b) laser MOKE hysteresis loop measurement of the 200 nm dots; c) single shot switching demonstrating toggling of the 200 nm dots.

INVITED PAPERS

10:30

GC-07. Magnons in Photonic Cavities and Resonators.

B. Rameshti[1], S. Sharma[2], Y. Blanter[2] and *G. Bauer*[3,4]
1. Institute for Research in Fundamental Sciences, Tehran, The Islamic Republic of Iran; 2. Delft University of Technology, Delft, Netherlands; 3. Tohoku University, Sendai, Japan; 4. University of Groningen, Groningen, Netherlands

The interaction between magnon and photons in cavities has attracted much attention in the past few years. The material of choice is the electrically insulating ferrimagnetic insulator yttrium iron garnet with exceptional high magnetic quality. The interest has, on one hand, been focused on (infrared) light scattering in monolithic YIG spheres that act as spherical optical resonators. On the other hand, both YIG spheres and films have been loaded into microwave cavities, from which the magnetization dynamics could be read-out by microwave transmission/reflection spectra or, electrically, with heavy metal contacts. In this talk I will report our theoretical efforts to understand experimental results and predict new effects in both research areas, both published [1-4] and unpublished.

[1] S. Sharma, Y.M. Blanter, and G.E.W. Bauer, Phys. Rev. B 96, 094412 (2017) [2] Y. Cao, P. Yan, H. Huebl, S. T. B. Goennenwein, and G.E. W. Bauer, Phys. Rev. B 91, 094423 (2015). [3] B.Z. Rameshti, Y. Cao, and G. E. W. Bauer, Phys. Rev. B 91, 214430 (2015). [4] B.Z. Rameshti and G.E.W. Bauer, arXiv:1710.08907v1

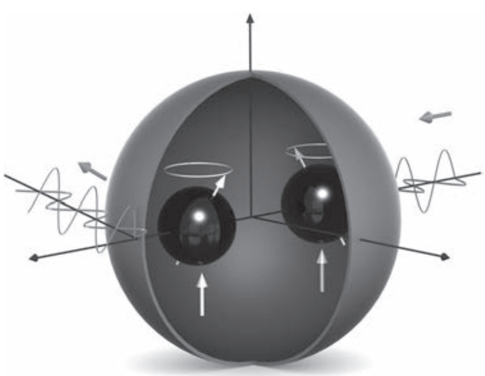

Fig. 1. Magnonic molecule in spherical cavity [4].

11:00

GC-08. Cavity Spintronics.

C. Hu[1]
1. Department of Physics and Astronomy, University of Manitoba, Winnipeg, MB, Canada

Cavity Spintronics [1] (also known as Spin Cavitronics) is a newly developing interdisciplinary field that brings together microwave cavity community with researchers from spintronics. This field started around 2014 when it was found that ferromagnets in cavities hybridize with both microwaves and light via light-matter interaction [2-5]. Since then, the emergence of this field has attracted broad interests. At the center stage of the topic is the physics of a quasi-particle called cavity magnon polariton (CMP) [5,6]. Via the quantum physics of spin-photon entanglement on the one hand, and via classical electrodynamic coupling on the other, CMP connects some of the most exciting modern physics, such as quantum information and quantum optics, with one of the oldest science on the earth, the magnetism. In this new community, the focus so far is on the development of cavity-mediated coupling and transducing techniques for both spintronic and quantum applications. This stream of research, including our recent demonstration of cavity- mediated distant control of spin current [7], roots on the single-particle hybrid nature of CMP. In this talk, we will present a new feedback-coupled cavity-spintronic technique, which we develop to study the cooperative dynamics of trillions of CMP. Utilizing the coherent dynamics of CMP ensembles, we demonstrate the control of magnon-photon Rabi frequency by changing the photon Fock state occupation, and we discover the evolution of CMP to cavity magnon triplet and cavity magnon quintuplet [8]. Our results may open up new avenues for exploiting the light-matter interactions using cavity spintronic approach.

[1] C.-M. Hu, Physics in Canada, 72, No. 2, 76 (2016). [2] H. Huebl, et al., Phys. Rev. Lett. 111, 127003 (2013). [3] Y. Tabuchi, Y. et al. Phys. Rev. Lett. 113, 083603 (2014). [4] X. Zhang, et al., Phys. Rev. Lett. 113, 156401 (2014). [5] L. Bai, et al., Phys. Rev. Lett. 114, 227201 (2015). [6] B.M. Yao, et al., Phys. Rev. B, 92, 184407 (2015). [7] L. Bai, et al., Phys. Rev. Lett., 118, 217201 (2017). [8] B.M. Yao, et al., Nature Communications, 8, 1437 (2017).

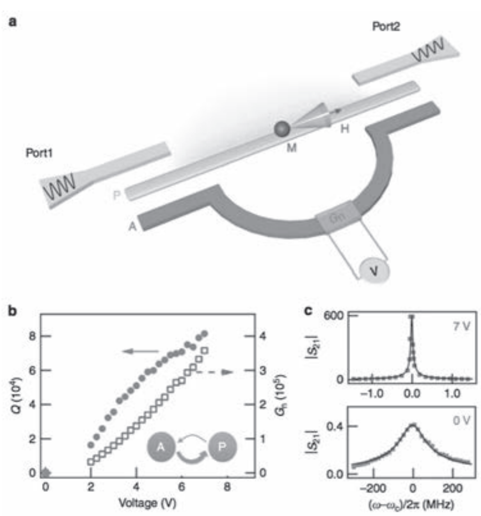

Fig. 1. Device architecture for studying the cooperative polariton dynamics: a) The A-P-M device consists of a passive cavity (P), an active cavity (A) with a voltage tuneable gain (Gn), and an YIG sphere with magnons (M). b) The Q-factor and Gn of the A-P cavity circuit are tunable up to 81,500 and 360,000, respectively, by changing V. c) $|S_{21}|$ spectra of the cavity mode measured at V = 0 and 7 V, together with a fitted theoretical curve.

CONTRIBUTED PAPERS

11:30

GC-09. Tunable magnon photon coupling using a BLIG ($(LuBi)_3Fe_5O_{12}$) film and a split ring resonator.

M. M[1], S. S[2], G. Venkat[1], K. Arunachalam[2] and A. Prabhakar[1]
1. Electrical Engineering, Indian Institute of Technology Madras, Chennai, India; 2. Engineering Design, Indian Institute of Technology Madras, Chennai, India

Split ring resonators (SRR) are a common metamaterial with good microwave absorption, ease of fabrication, low weight and they can be hybridized with complementary metal-oxide-semiconductor (CMOS) platforms. The planar SRR structure also allows coupling of microwave photons and magnons. The photon-magnon coupling strength needs to be greater than the mean energy loss in each subsystem, and occurs when both sub-systems are close to resonance. In a ferromagnetic system, the magnon bands can be controlled by an externally applied magnetic field or electric current. 3D structures of YIG (Yttrium iron garnet) films were first used to study magnon polariton coupling [1], [2]. Recently, the coupling of SRR and FMR (ferro magnetic resonance) modes have been observed in a planar YIG film placed inside an SRR cavity [3] and an enhanced coupling is experimentally demonstrated in planar YIG kept in an inverted SRR [4]. The photon-magnon coupling strength of a planar YIG film was improved by using with a notch filter on a stub line [5]. Microwave photons also allow for excitation of the higher order spin-wave (SW) modes, which contribute to stronger photon-magnon coupling. Spin waves can be excited in in-plane configurations namely backward volume spin waves and the magnetostatic surface SW. These ferrites find tremendous applications in transport of spin waves, realization of SW based logic and microwave devices etc, [6]. Unlike a 25 μm YIG used in [3], we use a bismuth lutetium iron garnet (BLIG) epitaxial film of thickness 7.9 μm, grown over gadolinium gallium garnet substrate. BLIG films are known to have better Faraday coefficients, than YIG, which could influence the photon-magnon coupling. A SRR of dimensions as shown in Fig. 1 was simulated in HFSS and resonant frequencies of 2.5 GHz, 4.9 GHz and 7.5 GHz were obtained. We fabricated the SRR on a Roger substrate (ε ~ 3.66), with copper lines of thickness 35 μm, ensuring a 50 Ω termination. The characterization setup consists of a 20 GHz RF signal generator (Hittite), an RF circulator and a spectrum analyzer (Rhode & Schwarz). An electromagnet and a Gauss meter are used to apply the static in-plane magnetic field, in a direction perpendicular to the microstrip line. We used the flip chip method for placing the BLIG film in the cavity on top of a microstrip line, and excited spin waves at ferromagnetic resonance [3]. The RF current flowing through the microstrip line also excites microwave photons in the SRR. A static applied magnetic field, greater than 200 Oe, saturates the BLIG film while the resonant fields of the SRR cause the magnetization to precess and excite SWs. We place the BLIG film to cover the SRR and a part of the microstrip line, and vary the excitation frequency from 2 to 5 GHz and the applied field from 200 Oe to 750 Oe. The power spectral density was measured on the spectrum analyzer. In post processing, we obtain the transmission (S_{21}) characteristics, and plot it against applied magnetic field, to obtain the spectra shown in Fig. 2(a). We observe an SRR mode at 3.17 GHz, which does not change with the field variations. Along with that, we also observe FMR modes whose resonant frequency varies linearly with the applied field. For a field of 435 Oe, we observe the appearance of a small dip at 2.75 GHz, which keeps shifting to the right as we increase the field. In Fig 2(b), we plot the frequencies corresponding to all the dips as observed in Fig. 2(a) apart from those corresponding to SRR dips. We observe a splitting of the spin wave mode resulting from a strong coupling between the microwave photons and magnons. The anti-crossing of the dispersion curves is a consequence of the coupled oscillation of the magnon-photon pair. We are in the process of studying this coupling in other spin wave systems such as magnonic crystals and aim to contribute to the state of the art in the performance of planar microwave devices.

[1] H. Maier-Flaig et al., "Tunable magnon-photon coupling in a compensating ferrimagnet from weak to strong coupling", App. Phy. Lett., 110, 132401, 2017. [2] D Zhang et al., "Spin-wave magnon-polaritons in a split-ring resonator/single-crystalline YIG system", J. Phys. D. App. Phys., 50, 205003, 2017. [3] B. Bhoi et al., "Study of photon–magnon coupling in a YIG-film split-ring resonant system", J. App. Phy., 116, 243906, 2014. [4] B. Bhoi et al., "Robust magnon-photon coupling in a planar-geometry hybrid of inverted split-ring resonator and YIG fillm", Sci. Rep., 7:11930, 2017. [5] V. Castel et al., "Control of Magnon-Photon Coupling Strength in a Planar Resonator/Yttrium-Iron-Garnet Thin-Film Configuration", IEEE Mag. Lett., 8, 3703105, 2017. [6] A. V. Chumak et al., "Scattering of backward spin waves in a one-dimensional magnonic crystal", App. Phy. Lett., 93, 022508, 2008.

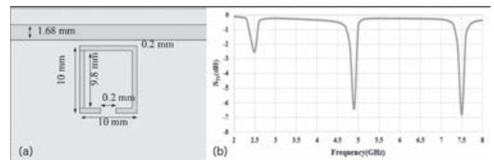

Fig. 1. (a) : Split ring resonator fabricated on a Roger substrate. (b) : The simulated transmission characteristics.

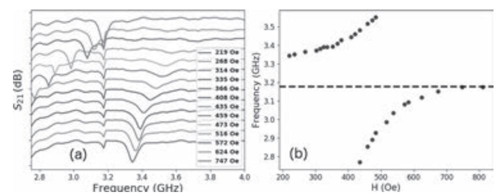

Fig. 2. (a): Variation of $|S_{21}|$ spectra with applied field. (b): Frequencies corresponding to the dips observed in (a)

11:45

GC-10. Microwave to optical photon conversion by means of travelling-wave magnons in YIG films.

M. Kostylev[1] and A. Stashkevich[2]
1. University of Western Australia, Crawley, WA, Australia; 2. LSPM (CNRS-UPR 3407), Université Paris 13, Villetaneuse, France

The magnon-based microwave-to-light converter is very attractive from the viewpoint of enlarging the potential of the superconducting qubits [1-6]. The first conversion stage of this device is based on coherent coupling between a ferromagnetic magnon and a microwave photon generated by a superconducting qubit. The next stage is up-converting from the microwave domain to the optical one. This proceeds through coupling of the excited microwave magnons to optical photons via magneto-optical interactions. In this way, coherent connection between distant superconducting qubits can be implemented. Currently this research focusses on standing-wave spin wave resonances (the uniform Kittel mode) in yttrium iron garnet (YIG) spheres as the microwave magnons to be coupled to light. In this paper, we investigate theoretically an alternative solution to the problem of magnon-to-light conversion. We consider scattering of guided optical modes from travelling magnetostatic spin waves in a YIG film [7] as a method for the up-conversion. Similar to theroretical treatment of other types of upconverters, we use the classical approach to solve the problem and then apply the standard formula [8] to the obtained result in order to calculate the quantum efficiency. The calculation separates into two stages. The first stage is a calculation of the rate of conversion of microwave photons (which are supposed to be generated by qubits) into travelling magnons. To this end, we develop a very precise self-consistent theory of excitation of spin waves in YIG films with microwave stripline transducers of an arbitrary shape. Our calculations show that excitation of travelling spin waves by asymmetric coplanar transducers can be very efficient – one can reach a conversion rate of microwave photons into magnons of almost 90% (Fig. 1). As a spin-off result of this calculation, we find that the asymmetric coplanar based device represents a very efficient microwave isolator needed for isolating a qubit from noise in the microwave circuit to which it is connected [9]. In the next stage of the calculation, we evaluate the efficiency of magnon to light conversion based on the theoretical approach from [10]. We find that the process of traveling magnon to guided light conversion in YIG films is much more efficient than employing the Kittel mode in a YIG sphere. The potential improvement in the total (both stages together) conversion rate is by four orders of magnitude (Fig. 1). We also speculate that there is plenty of room for further increase in efficiency by recycling light through forming an optical ring resonator from the film. If the length of the ring is larger than the free propagation path for spin waves, no traveling spin wave resonances with a discrete spectrum will be formed in the ring. Our estimation predicts that in this arrangement the microwave to optical photon conversion rate can reach the same record level as achieved with optomechanical systems (10% or so) [11].

1. M. H. Devoret and R. J. Schoelkopf, *Science* 339, 1169 (2013). 2. Y. Tabuchi et al., *Science* 349, 405 (2015). 3. Y. Tabuchi et al., arXiv:1508.05290. 4. R. Hisatomi et al., *Phys. Rev. B* 93, 174427 (2016). 5. S. Sharma et al.,*Phys. Rev. B* 96, 094412 (2017). 6. M.Kostyelv and A.Stashkevich, ArXiv: 1712.04304 (2017). 7. A. D. Fisher et al., *Appl. Phys. Lett.* 41, 779 (1982). 8. A. Rueda et al., *Optica* 3, 596 (2016). 9. A. C. Mahoney et al., *Phys. Rev. X* 7, 011007 (2017). 10. A. A. Stashkevich, "*Chapter 9. Diffraction of Guided Light by Spin Waves in Ferromagnetic Films*" in "High-Frequency Processes in Magnetic Materials" Eds.: G. Srinivasan and A. N. Slavin, World Scientific /Singapore, New Jersey, London, Hong-Kong: 1995. R. W. Andrews et al, *Nature Phys*. 10, 321 (2014).

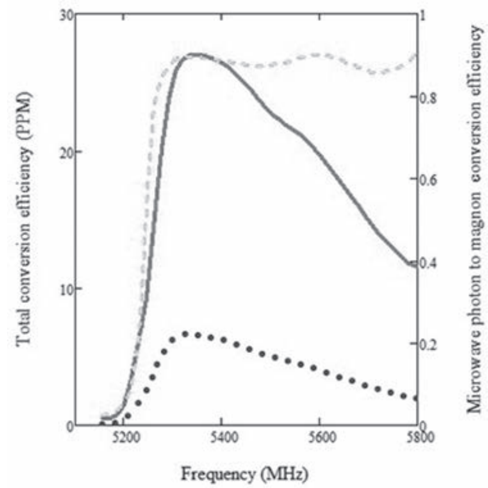

Fig. 1. Total conversion efficiency (in parts per million (PPM) left-hand axis) for the asymmetric coplanar line geometry. Solid line: anti-Stokes process; dotted line (Stokes process). Dashed line: microwave photon to magnon conversion efficiency by the asymmetric coplanar transducer (right-hand axis). YIG film thickness is 20 micron.

FRIDAY MORNING, 27 APRIL 2018 PEONY IV, 9:00 TO 12:00

Session GD
SPIN-ORBITRONICS IV

Yi Wang, Chair
National University of Singapore, Singapore

CONTRIBUTED PAPERS

9:00

GD-01. Modulation of spin-orbit torque efficiency in ultrathin ferromagnetic layer with different capping layers.

Z.A. Bekele[1], K. Meng[1], J. Chen[1], Y. Wu[1], J. Miao[1], X. Xu[1] and Y. Jiang[1]
1. School of Materials Science and Engineering, University of Science and Technology Beijing, Beijing, China

Current-driven spin-orbit torque (SOT) has attracted great interest as they can control the magnetization in heavy metal (HM)/ferromagnetic metal (FM) heterostructures with perpendicular magnetic anisotropy (PMA). The polarized spin current will be generated in HM layer with strong SOC due to Spin Hall Effect (SHE), which will diffuse into the adjacent FM layer and exert torques on the moments via spin transfer torque. On the other hand, SOT can also arise from the interfacial Rashba effect, for which the accumulated spins at the interface can force the moments to change its direction by direct exchange coupling [1-7]. In this work, we investigate the magnitude of SOT in perpendicularly magnetized Pt (6)/Co (1)/X trilayers with different capping layers (X=AlO_x, TaO_x, TiO_x, or W) (thickness in nanometer and composition from bottom to top). In these trilayer systems, both the bottom Pt/Co and top Co/X interfaces are utilized to generate SOT via bulk SHE effects and/or Rashba effect. By the selection of capping layer X, one can expect a modulation of these two SOT contributions, which provides an interesting prospect for enhancing strong SOT and the efficient current-induced magnetization switching through a proper combination of materials in the structural engineering. The film was patterned into a Hall bar as shown in Fig. 1(a) using EBL and followed by an Ar ion milling technique. The Hall resistance (R_H) as a function of the out-of-plane magnetic field was presented in Fig. 1(b), which is measured at various DC source current. The changes of a source current cause the coercivity shifts, which are ascribed to the interfacial effect on HMs/FM and/or FM/X, Joule heating effect, and perpendicular anisotropy as well. R_H-I curves were measured with different in-plane magnetic field and presented in Fig. 2. The resistance changes corresponding to the magnetization switching of fully downward and upward state of the films are from 0.2 to 0.5 Ω with the current swept. In conclusion, we investigated the electric current induced SOTs where ultrathin Co is sandwiched between Pt and different capping layers. In these perpendicularly magnetized Pt/Co/X trilayers, we observed strong PMA and SOT effect, which indicate that the effective SOT field can be tuned by using dual interfaces (top and bottom) with different materials.

[1] Z.A. Bekele, *et al.*, Solid State Commun. 262, 44-49 (2017). [2] Z.A. Bekele, *et al.*, J. Appl. Phys. (under review). [3] K. K. Meng, *et al.*, Sci. Rep. 6, 38375 (2016). [4] K. K. Meng, *et al.*, Phys. Rev. B 94, 214413 (2016). [5] K. K. Meng, *et al.*, Appl. Phys. Lett. 110, 142401 (2017). [6] A.R. Mellnik, *et al*, *Nature Lett.* 511, 449-451 (2014). [7] S. Fukami, *et al.*, *Nature Mater.* 15, 535–541 (2016).

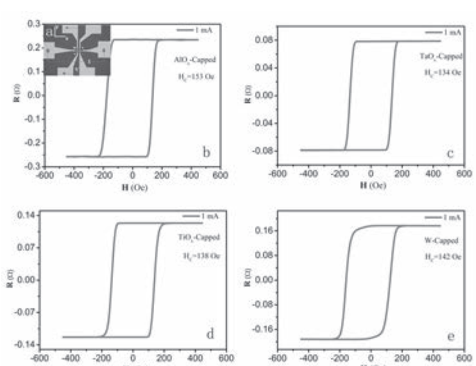

Fig. 1. (a) SEM image of a Hall bar and measurement setup. (b-e) the Hall Resistance (R) as a function of an external magnetic field at different channel current with a different direction.

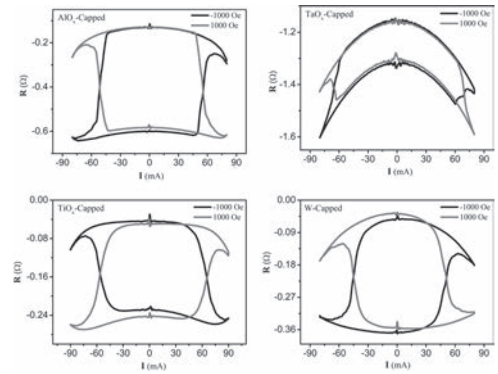

Fig. 2. The Hall Resistance (R) as a function of pulsed current at different magnetic field orientations.

9:15

GD-02. Charge-spin current interconversion in epitaxial systems: symmetric spin-torque ferromagnetic resonance scan but not infinity spin Hall angle.

S. Petit-Watelot[1], C. Guillemard[1], S. Andrieu[1] and *J. Rojas-Sánchez*[1]
1. Institut Jean Lamour - CNRS - Univ. Lorraine, Nancy, France

The conversion of spin current into charge current and vice versa are playing a key role in new research lines in spintronics and related applications. This interconversion can be achieved without any external magnetic field neither magnetic material in 3-Dimensional systems with strong spin-orbit coupling, namely the spin Hall effect (SHE). The quantification of the efficiency of such interconversion is called the spin Hall angle (SHA). The spin Hall angle determination is thus relevant to find out new materials and applications. Large spin Hall angle have been found in heavy metals like Pt [1-3], Ta and W, and alloys like CuBi and AuW. So far the quantification has been evaluated on polycrystalline samples. As soon as a heavy metal or alloys layer is in contact with a layer of different material then we talk about an effective spin Hall angle due to the loss of spin current injection at the interfaces [1]. Here we report on the investigation of epitaxial s//Fe(6 nm)/Pt(5 nm) bilayers grown by molecular beam epitaxy. s stands for the crystalline [001]MgO substrate. We evaluate the spin-charge current conversion by spin pumping- ferromagnetic resonance (SPFMR) [1,2], where at the resonance condition of the Fe layer it is injected a spin current from the Fe into the Pt layer and subsequently converted into a charge current by the inverse spin Hall effect (ISHE). Towards the proper evaluation of the efficiency it is needed a suitable Fe reference sample to account for the effective spin mixing conductivity at the Fe/Pt interface. We have grown simultaneously the Fe layer for the s//Fe/MgO reference sample as for the s//Fe/Pt. We have patterned slabs of 0.005 to 0.4 mm times 4.1 mm along different crystalline directions. The slabs were placed on top of a grounded coplanar waveguide and the spin pumping voltage is measured along the long direction of the slabs and perpendicular to the external in-plane dc magnetic field applied H_{dc}. We have found that the charge current production Ic along the hard axes, [100]MgO || [110] Fe, is more than twice in the slabs patterned along the easy axes, [110]MgO || [100] Fe. This might mean that the effective spin Hall angle is anisotropic along the different crystalline directions. We have found that the effective spin mixing conductance is also anisotropic and depends on the crystalline directions in epitaxial Fe/Pt bilayers. On the other hand, we evaluate the charge-spin current conversion by spin-transfer ferromagnetic resonance (STFMR), which is somehow the reciprocal dynamic effect that SPFMR. We inject direct microwave frequency charge current in the s//Fe/Pt slabs which is converted into spin current inside the Pt layer due to the SHE. Therefore an oscillating spin current is injected from Pt into Fe layer inducing precessing of its magnetization. This in turn lead and oscillatory radiofrequency resistance which mixed with the rf current allows, at the resonance condition, a detectable dc voltage across the slab using a bias tee [3]. The dc voltage is compound by a mixed of a symmetrical lorenztianne and and antisymmetrical one around the resonance field. In the simple model, the quantification of the effective SHA is proportional to the ratio of the symmetrical lorenztianne voltage over the anti-lorenztianne one, V_{symm}/V_{anti}. The sample is from the same batch used for the SPFMR study. Moreover, the slabs for STFMR and SPFMR were patterned simultaneously by standard UV lithography. The slabs for STFMR study have lateral sizes of 20 μm × 90 μm. We show that by STFMR we can also account for the in-plane magnetic anisotropies, i.e, the easy (hard) axes when H_{dc} is parallel to [110]MgO ([100]MgO) as observed in Fig. 1. When the resonance field is large enough to consider uniform precession of the magnetization we found that the effective spin Hall angle (0.055) is similar that previous values reported [1,3]. In this case, we have found similar values when H is applied along different crystallines directions. Let's remember that in this technique the dc voltage is picked up at 45° of the applied H_{dc} instead of 90° as in SPFMR method. Interesting however, we can observe a fully symmetrical lorenztianne curve in STFMR scans when H_{dc} is applied parallel to the hard axes and tuning the microwave frequency. Nevertheless, it does not mean and infinity spin Hall angle of the Pt layer. It is a consequence of the overlapping of the two resonance modes observed when H_{dc} is applied along the hard magnetocrystalline axes. Our results thus highly the importance of taking care of the proper conditions to the estimation of the spin Hall angle as well as the anisotropic spin mixing conductance and effective charge current production in epitaxial FM/HM systems. Therefore it opens a room to exploit epitaxial systems tuning the effective spin-current interconversion by choosing different crystalline directions.

[1] J.-C. Rojas-Sánchez et al. Phys. Rev. Lett. 112, 106602 (2014) [2] E. Saitoh et al. Appl. Phys. Lett. 88, 182509 (2006) [3] L. Liu et al. Phys. Rev. Lett. 106, 036601 (2011)

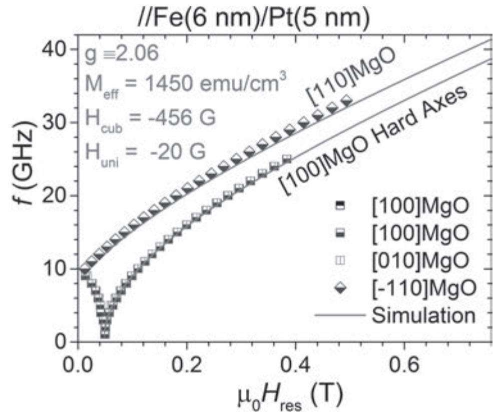

Fig. 1. Dispersion relationship f vs H_{res} in epitaxial Fe/Pt bilayer determined after f-dependence of STFMR study. It is reproduced the in-plane cubic magnetocrystalline anisotropy where [100]MgO is the hard in-plane axes (the Fe cell is rotated by 45° when is deposited on top of [001]MgO).

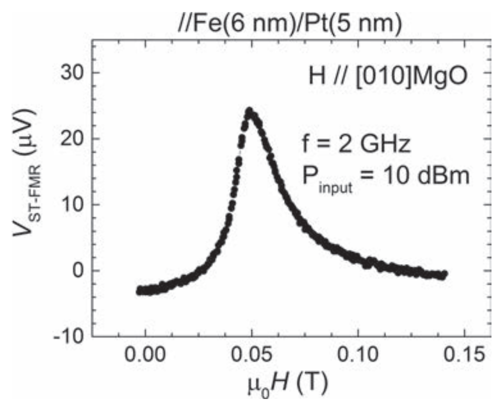

Fig. 2. STFMR scan when H is applied along the hard in-plane axes in epitaxial Fe/Pt bilayer for a frequency of 2 GHz. We can observe a mostly symmetric dc voltage around the resonance field. Nevertheless it does not mean an infinity or huge spin Hall angle.

INVITED PAPER

9:30

GD-03. Nonvolatile memory devices with magnetic nanowires controlled by spin-transfer and spin-orbit torques.

S. Fukami[1] and H. Ohno[1]
1. Tohoku University, Sendai, Japan

Efficient manipulation of magnetization direction in magnetic nanostructures is of crucial importance for realization of low-power and high-performance nonvolatile spintronics memory devices. Spin-transfer torque (STT) induced magnetization switching in magnetic nanopillars, or magnetic tunnel junctions, has been a leading technology in this field and is about to hit the market as a spin-transfer torque magnetoresistive random access memory (STT-MRAM). In STT-MRAM, the memory element typically has two terminals and magnetization is switched through a spin angular momentum transfer by applying vertical currents. In the meantime, recent researches have opened another possibility of nonvolatile spintronics devices with magnetic nanowires, where the magnetization is controlled by horizontal currents. Such devices typically form a three-terminal architecture [1] and magnetization can be controlled by current-induced domain wall (DW) motion [2,3] or spin-orbit torque (SOT) induced magnetization switching [4,5]. The three-terminal architecture provides a relaxed control of parameters and potential to operate at higher frequency at the cost of cell size compared with the two-terminal counterpart, making the devices an attractive option for integrated-circuits applications [1]. In terms of physics, moreover, the above two schemes complete magnetization switching with characteristic dynamics by torques with a different symmetry from the STT switching, offering unique attributes that are not seen in STT switching. In this presentation, we show recent advances in controlling the magnetization of nanowires via the DW motion and SOT switching. We particularly focus on the characteristic features of the SOT switching and discuss their impact on integrated circuit applications. One of the unique aspects of SOT is an orthogonal relation with the Gilbert damping torque when one utilizes perpendicular easy axis systems. For STT devices, because the damping torque acts in the antiparallel direction to STT, one needs to employ material systems with low damping, which in general has positive correlation with magnetic anisotropy that ensures thermal stability. For SOT devices, on the other hand, due to the orthogonal relation, one can employ high anisotropy materials even with high damping. As a result, electrically controllable memory elements with high thermal stability are expected. We have studied a SOT switching in nanowires with a Co/Pt multilayer having a high magnetic anisotropy and damping [6]. The fabricated nanowire devices show high thermal stability factor, given by a ratio of the energy barrier to the thermal fluctuation energy, of much greater than 100, and magnetization switching driven by current. In addition, we have found that a switching efficiency, defined as an anisotropy energy density divided by switching current density, increases with the stacking number of Co/Pt bilayer. This fact suggests that the SOT is generated in the Co/Pt multilayer despite a structural inversion symmetry, implying an unknown mechanism of SOT generation, as pointed out in a previous work [7]. The obtained results show promise for use in integrated circuits used in wide temperature ranges. The SOT acting in the orthogonal direction to the damping torque also provides a high-speed magnetization switching capability. The STT switching proceeds with a precessional motion and its threshold current is known to increase with an inverse of pulse duration below about a few nanoseconds. In contrast, for the case with SOT, a theory predicts an immediate magnetization switching as soon as the torque is exerted, resulting in a less pulse duration dependence of the switching current [8]. To elucidate this difference experimentally, we have studied a pulse duration dependence of the switching current density for two kinds of in-plane magnetized geometries; one shows switching as in the case for STT switching [5] and the other is expected to show a switching by orthogonal spins [9]. It was found that the latter scheme shows virtually constant switching current density with respect to the pulse duration down to 0.5 ns [10]. This result indicates the potential of SOT switching for high-speed memory operated at GHz class. We have also studied the pulse duration dependence of switching current density for perpendicular easy axis systems with W/CoFeB/MgO stacks [11]. In this experiment, we prepared several devices with various sizes to systematically examine the effect of an incoherent reversal with a DW propagation, which is expected to be significant in perpendicular easy axis systems. It was found that, for micrometer-scaled devices, the switching current density significantly decreases with increasing the pulse duration due to the incoherent reversal. The detailed investigation reveals that the nucleation events take place at various sites inside the magnetic dot or wires, and the switching completes by DW propagation among the sites. For devices with a CoFeB/MgO nanodot formed on a W nanowire, on the other hand, less pulse duration dependence of switching current density was observed as in the case for the in-plane system. Thus, the speed of SOT switching crucially depends on the employed device geometry for perpendicular easy axis systems. The authors thank H. Sato, B. Jinnai, and C. Zhang for technical supports and fruitful discussion. This work was supported in part by ImPACT Program of CSTI, JST-OPERA, and JSPS KAKENHI 17H06093.

[1] S. Fukami and H. Ohno, Jpn. J. Appl. Phys., vol. 56, 0802A1 (2017). [2] M. Yamanouchi, D. Chiba, F. Matsukura, and H. Ohno, Nature, vol. 428, 539 (2004). [3] A. Yamaguchi et al., Phys. Rev. Lett., vol. 92, 077205 (2004). [4] I. M. Miron et al., Nature, vol. 476, 189 (2011). [5] L. Liu et al. Science, vol. 336, 555 (2012). [6] B. Jinnai et al., Appl. Phys. Lett., vol. 111, 102402 (2017). [7] M. Jamali et al., Phys. Rev. Lett., vol. 111, 246602 (2013). [8] K.-S. Lee and K.-J. Lee, Appl. Phys. Lett., vol. 104, 072403 (2014). [9] S. Fukami, T. Anekawa, C. Zhang, and H. Ohno, Nature Nanotech., vol. 11, 621 (2016). [10] S. Fukami et al., 2016 Symp. on VLSI Tech., T06-05 (2016). [11] C. Zhang, S. Fukami, S. DuttaGupta, H. Sato, and H. Ohno, Jpn. J. Appl. Phys., to be published (2018).

CONTRIBUTED PAPERS

10:00

GD-04. Magnon transport in multilayer magnetic system.

Z. Fu[2], *S. Ruta*[1], T. Ostler[3], A. Kimel[4], R.F. Evans[1] and R.W. Chantrell[1]
1. Physics, University of York, York, United Kingdom; 2. Tongji University, Shanghai, China; 3. Sheffield Hallam University, Sheffield, United Kingdom; 4. Institute for Molecules and Materials, Radboud University Nijmegen, Nijmegen, Netherlands

In the research community, the coupling of spins with a thermal bath has been widely studied for various applications[Choi 2015, Uchida 2008, Hinzke 2011], for example, in waste energy recovery by converting heat to electricity [Bauer 2012]. Non-homogeneous temperature profiles over a spin system, leads to a spin chemical potential that generates a transfer of spins between regions. The first observation of the Spin Seebeck effect in metallic ferromagnets was made by Uchida and co-workers [Uchida 2008]. It was subsequently demonstrated that the effect was not limited to metallic ferromagnets but also occurs in dilute magnetic semiconductors, due to the collective excitation of localized magnetic moments. Since these initial discoveries, the spin Seebeck effect has been demonstrated in a range of magnetic material classes. In this work, we present numerical evidence for the existence of a magnonic Spin Seebeck effect on the sub-picosecond time-scale. By applying femtosecond laser pulses, the local difference in spin temperatures will produce a fast transfer of spin angular momentum from regions with high to low spin temperature. The simulations are done using an atomistic spin dynamics model and the ultrafast laser pulse is described via the two temperature model, which couples the electron temperature to a phonon bath. The electrons heat up to hundreds of Kelvin and cool down in a few picoseconds. The electron temperature has the role of the thermal bath for the spin system, leading to a change in the spin system configuration, which can be described as a spin temperature. The variation of the spin temperature depends on a combination of factors such as bath coupling, exchange interaction, and material properties. Having a bilayer system, with different properties leads to a different effective spin temperature, thereby creating a spin chemical potential resulting in magnon transport between the two layer layers. On top of this, there is a process of equilibration of each layer of spins with the electron temperature and an equilibration of electron temperature with the phonons. To investigate the energy transfer (magnon transport) between regions just due to the spin temperature difference between the layers, we construct a model system where the two layers are divided in two regions with low and high temperature, generated by the laser. The regions are first equilibrated at the corresponding temperature before coupling at the interface. The two regions will have magnons with different energies, leading to an temperature imbalance. To re-equilibrate there will be a net magnon (energy) transfer via the exchange interaction. The spins from the hot region have a higher angular momentum than the ones from the cold regions and, due to the exchange coupling, there is a net energy transfer. Thus high energy magnons from the hot regions will cross the interface and propagate into the cold region. The propagation can be visualised via the change in the net magnetisation normalised to a constant proportional to the noise in the system. This can be observed in figure 1, where the low magnetisation values develop at interface (Fig. 1 (a)) which then propagates into the cold region (Fig. 1 (b)). The speed of propagation is on the order of several km/s. To calculate the magnon transport through the interface, and the propagation of magnons, we used the expression for the energy flux vector similar to the Poynting vector in electromagnetism: [F = dm(x)/dt]X[m(x)] where m(x) is the net magnetisation as function of x, the direction perpendicular to the interface and dm(x)/dt is the rate of change of magnetisation in time. F gives the net flux through a given plane. The maximum change in F is correlated with the front of magnon propagation. Figure 2 illustrates the magnon spin pumping for the first 20 fs. As the propagation advances into the cold region the amplitude decreases, leading eventually to a small fluctuation around zero. This represents the achievement of equilibrium with equal magnon fluxes in both directions. Our results demonstrate ultra-fast transport of magnons due to inhomogeneous spin temperature as present in ultrafast laser experiments in bilayers systems and also in alloys such as GdFeCo.

[1] G.-M. Choi, C.-H. Moon, B.-C. Min, K.-J. Lee, and D. G. Cahill, Nature Physics 11, 576 (2015). [2] K. Uchida, S. Takahashi, K. Harii, J. Ieda, W. Koshibae, K. Ando, S. Maekawa, and E. Saitoh, Nature 455, 778 (2008). [3] D. Hinzke and U. Nowak, Physical Review Letters 107, 027205 (2011). [4] G. E. W. Bauer, E. Saitoh, and B. J. van Wees, Nature Materials 11, 391 (2012).

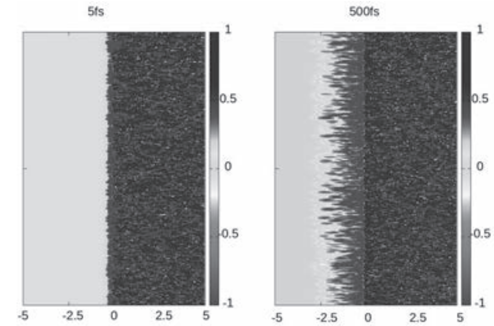

Fig. 1. Magnetisation map of the bilayer system at (a) 5fs and (b) 500 fs. The system is divided along the X-direction in two regions with the interface at x=0. The left side is equilibrated at 0K and the right side at 100K. The evolution of the Z-component of magnetisation is shown as a colour map, where green corresponds to the equilibrium value of each region individually, and red and blue correspond to increase and decrease of the magnetisation with respect to the equilibrium value.

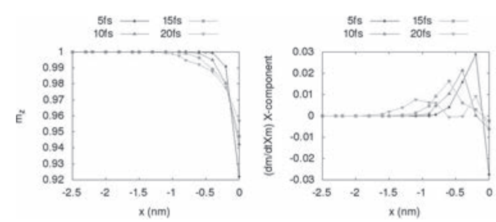

Fig. 2. (a) Magnetisation (Z-component) and (b) magnon propagation in the cold region during the first 20 fs. The magnetisation decreases from its original value (1 in this case) as the magnons propagate (b). The maximum energy transfer (the peaks in b) decrease as the magnons propagate further into the cold region.

10:15

GD-05. Enhancement of Gilbert damping in NiFe/Pt bilayers with MgO capping layers.

T. Zhu[1] and F. Chang[1,2]
1. State Key Lab for Magnetism, Institute of Physics, Chinese Academy of Sciences, Beijing, China; 2. Institute of high energy physics, Beijing, China

Spin current possesses the capability to manipulate magnetization, as well as electric transport in metals and insulators, which brings potential to develop the multifunctional spintronic devices. Spin pumping is a widely used method to produce pure spin current, in which a processing ferromagnet (FM) pumps out a spin current into adjacent non-magnetic (NM) conductors. The injected spin current is subsequently converted into a transverse charge current, when large spin-orbit coupling exists in this conductor. The conversion efficiency is governed by spin mixing conductance and diffusion length of spin current in NM, in which spin mixing conductance is a characteristic of FM/NM interface and generally reflected from the enhanced Gilbert damping. Here, we have systematically studied the MgO and Al capping layers effect on damping in NiFe/Pt bilayers, by using coplanar waveguide ferromagnetic resonance and inverse spin Hall effect. The NiFe/Pt bilayers with Al capping layer show clearly magnetic proximity effect, meanwhile a significantly interfacial enhancement of damping, and then spin mixing conductance, has been found in the samples capped by MgO layers with potentially major consequences for applications.

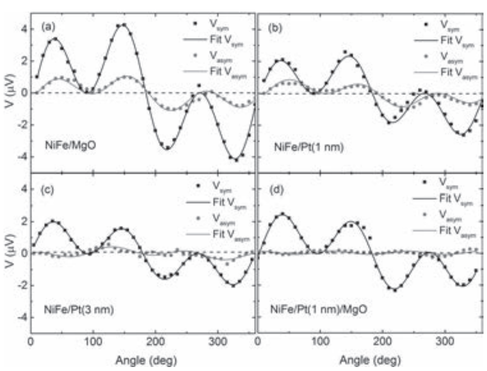

Fig. 1. Angular dependency analysis of spin pumping measurements performed on (a) NiFe/MgO, (b) NiFe/Pt(3 nm), (c) NiFe/Pt(1 nm), and (d) NiFe/Pt(1 nm)/MgO.

10:30

GD-06. Influence of W insertion layer in Ta and CoFeB on antidamping-like effective torque efficiency.

I. Cha[1], Y. Kim[1], G. Kim[1], T. Kim[1], K. Garello[2] and Y.K. Kim[1]
1. Materials Science and Engineering, Korea University, Seoul, The Republic of Korea; 2. Imec, Leuvin, Belgium

Introduction Spin-orbit interaction formed by nonmagnetic (NM) and ferromagnetic (FM) materials have received much attention because of their physical principles and various applications. Recent studies reported more complicated and diverse combinations including antiferromagnets and ferrimagnets to understand the origin of spin-orbit interaction [1], [2]. It is still arguable whether the more dominant effect of spin-orbit interaction is due to bulk or interfacial contribution. It is important to find main effect which control spin-orbit interaction for handling a magnetic and electric properties, for example, magnetic anisotropy, coercivity, antidamping- like effective field, field-like effective field and switching current density. In our study, we investigate the magnetic properties and electric properties depending on the W insertion layer thickness and phase. Experimental All samples were deposited by dc and rf magnetron sputtering under the base pressure below $3x10^{-9}$ Torr. Each sample went through post-annealing at $300^{o}C$ for 1 h in a magnetic field of 6 kOe under $1x10^{-6}$ Torr. We used Ta and W as NMs, which are known to have large spin-orbit coupling and spin Hall angle, CoFeB as an FM. We inserted very thin W layer between Ta and CoFeB to observe electrical and magnetic properties changes. The magnetic properties were measured using a vibrating sample magnetometer (VSM) and the electric properties were measured using second harmonics measurement. All samples are patterned using photolithography and dry etching into Hall bar with a dimension of 5 μm x 35 μm. Results and discussion In Ta/W/CoFeB/MgO structures, all samples have perpendicular magnetic anisotropy after $300^{o}C$ annealing. To inspect the dependence of insertion layer, we changed W insertion layer thickness, CoFeB and MgO layer thickness was fixed as 0.9 nm and 1.0 nm to minimize other influence. We observed change of the antidamping-like effective torque efficiency by insertion layer thickness. In case of Ta/CoFeB/MgO structure, the antidamping-like effective torque efficiency is about 6.6 % and the sign is negative. When W 1.5 nm was inserted between Ta and CoFeB, the antidumping-like effective torque efficiency increased three times and the sign was not changed.

References [1] Y. W. Oh et al., Nat. Nanotechnol. 11, 878 (2016) [2] N. Roschewsky et al., Phys. Rev. B 96, 064406 (2017)

10:45

GD-07. Optimize Fe/Pt bilayers as efficient spintronic terahertz emitters by tailoring the thickness of the layers and the interface structural properties.

L. Scheuer[1], S. Keller[1], G. Torosyan[2], M. Battiato[3], R. Beigang[1] and *E. Papaioannou*[1]

1. Physics, TU Kaiserslautern, Kaiserslautern, Germany; 2. Photonic Center Kaiserslautern, Kaiserslautern, Germany; 3. School of Physical and Mathematical Sciences, Nanyang Technological University, Singapore, Singapore

Spin Hall effect and its reciprocal, the inverse spin Hall effect (ISHE), provide the means for conversion between spin and charge currents [1,2]. In particular, the ISHE transforms a pure spin current into a transverse charge current due to spin-orbit coupling. Recently, the decisive role of the ISHE effect on extending the field of spintronics into the terahertz (THz) regime was revealed [3,4]. Here, we demonstrate the generation of pulsed broadband terahertz radiation utilizing the inverse spin hall effect in Fe/Pt bilayers on MgO and sapphire substrates. The emitter was optimized with respect to layer thickness, growth parameters, substrates and geometrical arrangement. The experimentally determined optimum layer thicknesses of Fe (2 nm) / Pt (3 nm) were in qualitative agreement with simulations of the spin current induced in the ferromagnetic layer [5]. Our model takes into account generation of spin polarization, spin diffusion and accumulation in Fe and Pt and electrical as well as optical properties of the bilayer samples. Using the device in a counterintuitive orientation a Si lens was attached to increase the collection efficiency of the emitter. The optimized emitter provided a bandwidth of up to 8 THz which was mainly limited by the low-temperature-grown GaAs (LT-GaAS) photoconductive antenna used as detector and the pulse length of the pump laser. The THz pulse length was as short as 220 fs for a sub 100 fs pulse length of the 800 nm pump laser. Average pump powers as low as 25 mW (at a repetition rate of 75 MHz) have been used for terahertz generation. This and the general performance make the spintronic terahertz emitter compatible with established emitters based on optical rectification in nonlinear crystals. Furthermore, we correlate the interface structural properties with the THz-E-field amplitude and the bandwidth of the THz radiation. By allowing the Pt layers to grow along different crystallographic directions on top of Fe we modify the THz emission characteristics of the optimized emitters. We present a theoretical model which correlates the loss of energy of the hot electrons and the electron-phonon/defect scattering lifetime at the Fe/Pt interface with the ISHE current that causes the THz emission. By taking into account the response function of the THz detector we describe the influence of the crystal structure of Pt onto the THz signal shape and spectrum. The demonstration of the role of the individual layer thicknesses and of the interface quality in the THz emission spectra paves the way for more efficient spintronic THz emitters.

[1] Hoffmann, A. Spin hall effects in metals. IEEE Transactions on Magnetics 49, 5172–5193 (2013). [2] Sinova, J., Valenzuela, S. O., Wunderlich, J., Back, C. H. & Jungwirth, T. Spin hall effects. Rev. Mod. Phys. 87, 1213–1260 (2015). [3] Seifert, T. et al. Efficient metallic spintronic emitters of ultrabroadband terahertz radiation. Nat. Photon. 10, 483–488 (2016). [4] Wu, Y. et al. High-performance Thz emitters based on ferromagnetic/nonmagnetic heterostructures. Advanced Materials 29, 1603031 (2017). [5] G. Torosyan, S. Keller, L. Scheuer, R. Beigang, and E. Th. Papaioannou, Optimized Spintronic Terahertz Emitters Based on Epitaxial Grown Fe/Pt Layer Structures, Accepted in Scientific Reports (2018), Arxiv.org/abs/1707.08894.

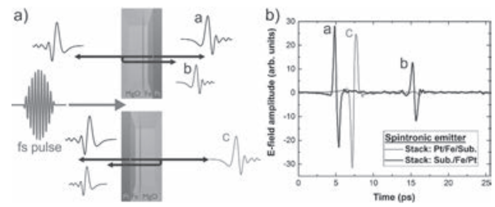

Fig. 1. a) Orientation of the sample with respect to the pump beam and b) the generated THz pulses respectively. In the orientation with the metal side towards the pump beam the reflection from the MgO-air interface is suppressed.

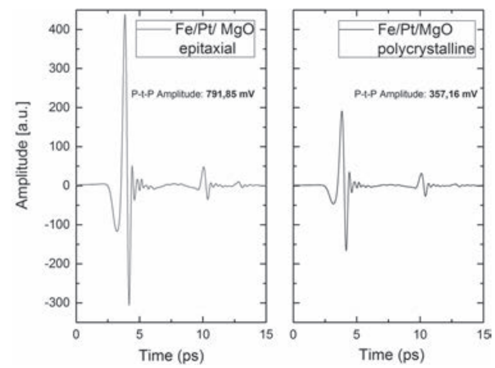

Fig. 2. THz pulses obtained for an epitaxial (left) and a polycrystalline (right) Fe/Pt spintronic emitter.

11:00

GD-08. Spin Seebeck effect in a polycrystalline bulk-YIG fabricated by the sol-gel synthesis.

M. Jang[1] and K. Lee[1]
1. Materials Science and Engineering, Ulsan National Institute of Science and Technology (UNIST), Ulsan, The Republic of Korea

Introduction Spin-caloritronics, based on the spin Seebeck effect (SSE) hold the promise of future sustainable green energy technologies [1-3]. Since a single crystal $Y_3Fe_5O_{12}$ (YIG) has been believed to generate sufficiently high SSE signal owing to its unique features [4], most of experiments have been performed with a single crystal YIG fabricated by a pulsed laser deposition (PLD) method [5, 6]. However, this method is known to be very difficult to use in mass-production and needs to a high technical skill. In contrast, the sol-gel synthesis can offer a low-cost and mass-production method [7]. Here, we demonstrate that a polycrystalline YIG fabricated by a sol-gel synthesis with proper heat-treatments and a mechanical pressing process [8] can generate enough SSE signal. Experiments We prepared the YIG precursor by mixing yttrium nitrate ($Y(NO_3)_3.6H_2O$, 99.99%) and iron nitrate ($Fe(NO_3)_3.9H_2O$, 99.99%) powders in a stoichiometric ratio of 3:5, and adding citric acid ($C_6H_8O_7.H_2O$). The precursor mixture was dissolved in distilled water (100 mL) by stirring (300 rpm) at 27 °C for 18 hours. The solution of the citric acid was maintained at 1pH. The resulting solution (sol) was then stirred for 24 hours at 80 °C to obtain a homogenous gel. Next, a form a dry material (gel) was obtained from the sol by drying the solution, which was decomposed at 100 °C for 5 hours. The YIG powder was obtained by grinding the completely dried gel for 30 minutes. The calcination process was carried out at 850 °C in the air for 2 hours at a heating rate of the 7.7 °C /min to get rid of residual impurities and the crystallization. After, we did the pressing process 150 MPa for 5 minutes not only to produce the substrate-free disk-shaped YIG sample with 1.8 mm-thickness and 14 mm-diameter but also to enhance saturation magnetization (M_S). Lastly, sintering has been done at 1400 °C for 4 hours. To measure the longitudinal-SSE (LSSE), the 15 nm-Pt layer was deposited by an electron-beam evaporation on the surface of a YIG disk. To form temperature gradient along -z direction, bottom surface was heated, and top surface was air cooled as shown in Fig. 1(a). By applying 400-Oe magnetic field parallel to the disk plane (+y direction), magnetization in a bulk YIG aligned along +y direction and thus, it gives rise to the thermoelectric (TE) voltage along x direction through the inverse spin-Hall effect (ISHE) in a Pt layer. Results & Discussion From X-ray diffractometer (XRD), X-ray photoelectron spectroscopy (XPS), and the field-emission scanning electron microscopy (FE-SEM) measurements, we identified complete crystallization with large grain size of 5.4 μm diameter and a remarkable reduction of impurities in the microstructure after the pressing and sintering process. This provides significant enhancement of the M_S value of a YIG as shown in Fig. 1(b), which is 70 % of the ideal M_S value of a YIG. Figure 1(c) indicates a TE voltage induce by LSSE versus temperature difference between top and bottom surfaces of a bulk YIG. We found that the TE voltage is proportional to the temperature gradient and its values are comparable to the TE voltage of single crystal YIG. Our results enabling one to start paving the ways for the use of SSE for practical energy harvesting devices.

[1] K. Uchida et al., Nat. Mat. 9, 894 (2010). [2] G. E. W Bauer et al., Nat. Mat. 11, 391 (2012). [3] K. Uchida et al., J. Phys.: Condens. Matter 26, 343202 (2014). [4] K. Uchida et al., Appl. Phys. Lett. 97, 172505 (2010). [5] N. B. Ibrahim et al., J. Magn. Magn. Mater. 220, 183 (2000). [6] A. Sposito, et al., Opt. Express 3, 624 (2013). [7] R. Kuchi et al., Nanosci. Nanotechnol. Lett. 7, 738 (2015). [8] M.-S. Jang et al., J. Alloys Compd. 711, 693 (2017).

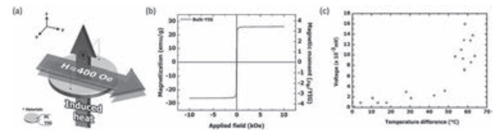

Fig. 1. (a) Schematic illustration of the LSSE geometry. (b) Magnetic hysteresis loops measured at room temperature for a bulk-YIG. (c) TE voltage in a Pt/bulk-YIG structure as a function of the temperature difference between top and bottom surface of a bulk-YIG.

11:15

GD-09. Anomalous Nernst and Hall effects in ferromagnetic multilayers.

M. Mizuguchi[1,2], H. Suzuki[1], H. Sharma[1,2] and K. Takanashi[1]
1. Tohoku University, Sendai, Japan; 2. JST-CREST, Kawaguchi, Japan

I. INTRODUCTION The interaction between a spin current and a heat current has been studied in a new field of spin caloritoronics since the discovery of the spin Seebeck effect, and a number of thermomagnetic effects related to spin current have been investigated [1,2]. The Nernst effect is a common thermomagnetic effect, that has been known for a long time. When a temperature gradient is applied on a material with spontaneous magnetization, an electric field is induced in the perpendicular direction to both the temperature gradient and the magnetization, which is called the anomalous Nernst effect (ANE) [3,4]. In a previous paper, we reported material dependence of ANE in perpendicularly magnetized ordered-alloy thin films such as $L1_0$-FePt, $L1_0$-FePd, $L1_0$-MnGa, and $D0_{22}$-MnGa[5], and the relation between ANE and uniaxial magnetic anisotropy in the ordered-alloy systems has been clarified. We also reported strong anisotropy in ANE for highly ordered γ'-Fe_4N[6]. Recently, the enhancements of ANE in paramagnet / ferromagnet multilayers have been reported[7-11], though the ANE in ferromagnet / ferromagnet multilayer films with the interface magnetic anisotropy was not investigated systematically so far. In this contribution, ANE in Co / Ni epitaxial multilayer films with various stacking thicknesses was measured and discussed in relation to the interface magnetic anisotropy. Besides, the relation between ANE and the anomalous Hall effect (AHE) was also investigated systematically to clarify the role of spin current in both effects in ferromagnetic multilayers. II. EXPERIMENTALS Epitaxial Co / Ni multilayers were fabricated by molecular beam epitaxy on MgO(111) substrates at room temperature. Total thickness was fixed to 12 nm and each thickness of Co and Ni (Co : Ni = 1 : 2) was varied. ANE and AHE were measured in a physical properties measurement system (PPMS), and the Seebeck effect, the Nernst effect, and the Hall effect were measured at temperatures between 10 and 300 K. A magnetic field perpendicular to the sample plane was applied. Magnetic properties were measured at 300 K using a superconducting quantum interference device (SQUID), and magnetic anisotropy (K_u) for each thin film was evaluated from magnetization curves. III. RESULTS AND DISCUSSION Figure 1 shows magnetization curves for epitaxial Co / Ni multilayer films (each thicknesses Co and Ni are 0.8 and 6.0 nm) measured at room temperature. Co / Ni: 0.8 nm showed the perpendicular magnetization whereas Co / Ni: 6.0 nm showed in-plane magnetization. It was clarified that magnetic anisotropy was successfully varied by changing the each thickness. Figure 2 shows layer thickness dependence of the transverse Seebeck coefficients (S_{xy}) for epitaxial Co / Ni multilayer films measured with out-of-plane magnetic field at room temperature. S_{xy} is derived from the following equation. $S_{xy} = E_y / \nabla T_x$, (1) where E_y and ∇T_x express the Nernst electric field and the temperature gradient, respectively. With increasing the layer thickness, S_{xy} increased till 2.4 nm and decreased for multilayers with in-plane magnetization (6 and 12 nm). As shown in the figure, all Co / Ni multilayers showed larger S_{xy} values than that estimated for bulk $CoNi_2$, implying that interface magnetic anisotropy strongly contributed to ANE. More precise mechanism of ANE in ferromagnetic multilayer systems and the relation between ANE, AHE and magnetic anisotropy will be discussed. IV. CONCLUSIONS ANE and AHE in Co / Ni epitaxial multilayer films with various stacking thicknesses were measured and discussed in relation to the interface magnetic anisotropy. Total thickness was fixed to 12 nm and each thickness of Co and Ni (Co : Ni = 1 : 2) was varied. With increasing the layer thickness, S_{xy} increased till 2.4 nm and decreased for multilayers with in-plane magnetization (6 and 12 nm). All Co / Ni multilayers showed larger S_{xy} values than that estimated for bulk $CoNi_2$, implying that interface magnetic anisotropy strongly contributed to ANE.

[1] G. E. W. Bauer *et al*., Phys. Rev. B, 81, 024427 (2010). [2] K. Uchida *et al*., Nature, 455, 778 (2008). [3] M. Mizuguchi *et al*., Appl. Phys. Express, 5, 093002 (2012). [4] Y. Sakuraba, M. Mizuguchi *et al*., Appl. Phys. Express, 6, 033003 (2013). [5] K. Hasegawa, M. Mizuguchi *et al*., Appl. Phys. Lett., 106, 252405 (2015). [6] S. Isogami, M. Mizuguchi *et al*., Appl. Phys. Express, 10, 073005 (2017). [7] R. Ramos *et al*., Phys. Rev. B, 92, 220407(R) (2015). [8] K. Uchida *et al*., Phys. Rev. B, 92, 094414 (2015). [9] K. D. Lee *et al*., Sci. Rep., 5, 10249 (2015). [10] R. Ramos *et al*., APL Mater., 4, 104802 (2016). [11] T. C. Chuang *et al*., Phys. Rev. B, 96, 174406 (2017).

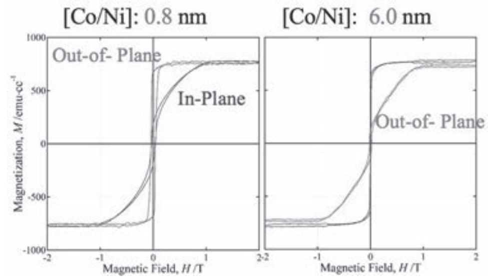

Fig. 1. Magnetization curves for epitaxial Co / Ni multilayer films.

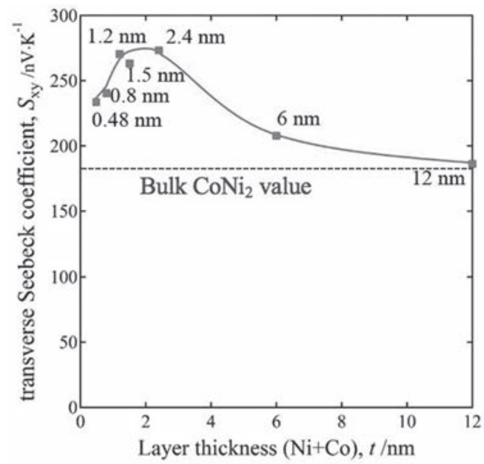

Fig. 2. Layer thickness dependence of the transverse Seebeck coefficient for epitaxial Co / Ni multilayer films.

11:30

GD-10. Thermal contribution to the spin-orbit torque in metallic/ ferrimagnetic systems: the switching temperature.

J. Rojas-Sánchez[1], T. Pham[1], S. Je[2,1], P. Vallobra[1], T. Fache[1], D. Lacour[1], G. Malinowski[1], M. Cyrille[3], G. Gaudin[2], O. Boulle[2], M. Hehn[1] and S. Mangin[1]
1. Institut Jean Lamour - CNRS - Univ. Lorraine, Nancy, France; 2. CNRS, SPINTEC, Grenoble, France; 3. Leti, technology research institute, CEA, Grenoble, France

The spin Hall effect and the electrical manipulation of magnetization, namely spin-orbit torque, are at the core of spin-orbitronic applications. Thus, the possibility to reduce the current density and the external in-plane applied field to switch a perpendicular magnetization are the most important goals towards applications exploiting charge to spin current conversion [1-3]. So far however, the thermal contribution to this phenomenon has been neglected. On the other hand, the use of ferrimagnetic materials starts to draw attention due to the possibility to tune the net magnetization with composition or temperature and even reach zero magnetization at the compensation point [4,5]. Our study [4,5] presents experimental results about the current-induced magnetization switching considering a model W/ Co_xTb_{1-x} as heavy metal/ferrimagnetic bilayer for various compositions and temperatures. We demonstrate that i) the current density is not a minimum at the nominal magnetic composition point, ii) there is a strong thermal contribution which we have quantified, iii) although the sample shows strong perpendicular magnetic anisotropy the external in-plane magnetic field needed for the switching is quite small (i.e 2 mT), iv) the devices has to reach a characteristic switching temperature before the current generate the reversal, T_{switch}(x), and v) T_{switch}(x) increases with increasing Co-concentration x and consequently scales with the Curie temperature T_C(x). Thus, we believe that our discovery of the major importance of T_{switch}(x) which scale with T_C(x) is significance and opens new road for the exploitation of thermal contribution using highly resistivity heavy metal to reduce both the critical current and external magnetic field to achieve the current-switching.

[1] I. M. Miron, K. Garello, G. Gaudin, P.-J. Zermatten, M. V Costache, S. Auffret, S. Bandiera, B. Rodmacq, A. Schuhl, and P. Gambardella, Nature 476, 189 (2011) [2] L. Liu, O. J. Lee, T. J. Gudmundsen, D. C. Ralph, and R. a. Buhrman, Phys. Rev. Lett. 109, 1 (2012) [3] J. C. Rojas-Sánchez, P. Laczkowski, J. Sampaio, S. Collin, K. Bouzehouane, N. Reyren, H. Jaffrès, A. Mougin, and J. M. George, Appl. Phys. Lett. 108, 82406 (2016). [4] Thai-Ha Pham et al. submiited. ArXiv 1711.10790 [5] Soong-Gun Je et al. submitted.

11:45

GD-11. Anamalous hall effect in Ultrathin FePt ferromagnetic layer.

J. Yu[1,2], L. Liu[1], J. Deng[1], H. Yoong[1], W. Lin[1], H. Wang[1], H. Liu[2], F. Poh[2], D. Shum[2] and J. Chen[1]
1. Material Science and Engineering, National University of Singapore, Singapore; 2. GLOBALFOUNDRIES Singapore Pte Ltd., Singapore 738406, Singapore, Singapore

The study of anomalous hall effect (AHE) has paved a road to study the origins of spin orbit interactions in materials for spinorbitronics application. Theoretically, the origins of AHE are widely believed to be (1) intrinsic contribution from Berry curvature of the occupied Bloch states($\rho_{xy}\alpha\rho_{xx}^2$), (2) extrinsic contribution from skew scattering ($\rho_{xy}\alpha\rho_{xx}$) and side jump ($\rho_{xy}\alpha\rho_{xx}^2$)[1]. Experimentally, by scaling anomalous hall resistivity with normal resistivity, the origins of spin orbit interaction of many materials were revealed[2, 3]. Recent few years, FePt thin film has attracted a lot of attention in spintronics due to its large intrinsic dominant mechanism [4]. However, only films with substantial thickness were studied because ultra-thin film on MgO substrate contains strain induced grain boundaries [5], making the film non-conductive of electricity. Thus, there is a need to evaluate the origins of spin orbit interaction in thinner FePt on another substrate for its future spintronics application. In this paper of SiO_2(2)/FePt (6, 8, 12 and 20nm)/STO were prepared by using AJA Orion 8 sputtering system with a base pressure lower than 2×10^{-8} Torr. The deposition temperature of FePt was 380 C. The samples were cooled down to room temperature and 2nm of SiO_2 was grown *in situ* as a protection layer against the chemical and physical attack in the device fabrication process. XRD spectrum and VSM loops were measured to ensure good epitaxy growth and good perpendicular magnetic anisotropy (PMA). Then the films were patterned into hall bars with 10um width using laser writer. Transport property were measured using Quantum Design Physical Properties Measurement System. Both VSM and AHE loops shown in Fig 1 testify good PMA of the samples. As shown in Fig 2 (a), (b) anomalous hall resistivity and normal resistivity decreases simultaneously with decreasing temperature shows that anomalous hall resistivity is mainly influenced by normal resistivity. $\rho_{xy}= a\rho_{xx,0}+a'\rho_{xx}+b\rho_{xx}^2$[3] was deployed to fit the data as it can obtain best fit line among all the possible fitting equations. The first term *a* reveals the contribution from extrinsic skew scattering, the second *a′* term is the contribution from phonon scattering and the last term *b* is the combined contribution from extrinsic side jump and intrinsic Berry curvature. The fitting curves are shown in Fig 2 (c). The fitting results of *a′* and *b* are shown in Fig 2 (d). increases with decreasing thickness of FePt reveals that at lower thicknesses, the phonon scattering contributes significantly in the mechanism of AHE. When FePt is with substantial thickness (8nm), the anomalous conductivity *b* remained at 800-900S/cm. This is consistent with the theoretical calculations [4, 6]. However, when the film is thin, *b* decreases significantly. This shows that the intrinsic contribution is suppressed while the extrinsic origins plays an important role in AHE of ultra-thin FePt.

[1] N. Nagaosa, J. Sinova, S. Onoda, A. H. MacDonald, and N. P. Ong, “Anomalous Hall effect,” *Reviews of Modern Physics,* vol. 82, pp. 1539-1592, 05/13/ 2010. [2] J. Kötzler and W. Gil, “Anomalous Hall resistivity of cobalt films: Evidence for the intrinsic spin-orbit effect,” *Physical Review B,* vol. 72, p. 060412, 08/31/ 2005. [3] Y. Tian, L. Ye, and X. Jin, “Proper Scaling of the Anomalous Hall Effect,” *Physical Review Letters,* vol. 103, p. 087206, 08/21/ 2009. [4] K. M. Seemann, Y. Mokrousov, A. Aziz, J. Miguel, F. Kronast, W. Kuch*, et al.*, “Spin-Orbit Strength Driven Crossover between Intrinsic and Extrinsic Mechanisms of the Anomalous Hall Effect in the Epitaxial $L1_0$-Ordered Ferromagnets FePd and FePt,” *Physical Review Letters,* vol. 104, p. 076402, 02/19/ 2010. [5] K. F. Dong, H. H. Li, and J. S. Chen, “Investigation of composition-induced strain effect in FexPt1−x films grown on different substrates,” *Journal of Magnetism and Magnetic Materials,* vol. 347, pp. 165-170, 12// 2013. [6] P. He, L. Ma, Z. Shi, G. Y. Guo, J. G. Zheng, Y. Xin*, et al.*, “Chemical Composition Tuning of the Anomalous Hall Effect in Isoelectronic $L1_0FePd_{1-x}Pt_x$ Alloy Films,” *Physical Review Letters,* vol. 109, p. 066402, 08/08/ 2012.

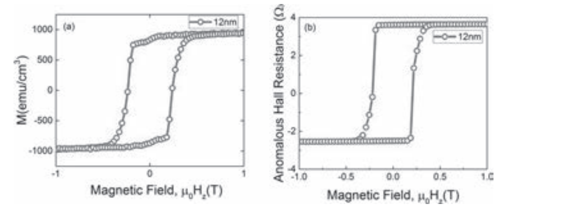

Fig. 1. The (a) out-of-plane VSM loop and (b) AHE loop of the patterned hall bar for 12nm FePt on STO single crystal substrate.

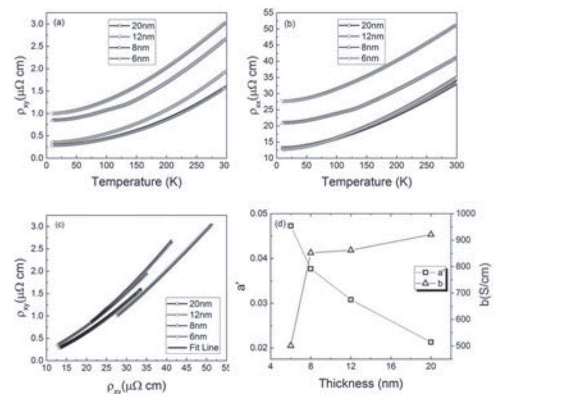

Fig. 2. The change of (a) anomalous resistivity and (b) normal resistivity of different thicknesses of FePt with respect to temperature. (c) Fitting curves of anomalous resistivity verses normal resistivity. (d) Fitting parameters *a’* and *b* with respect to thickness.

FRIDAY MORNING, 27 APRIL 2018 ROSELLE II, 9:00 TO 12:00

Session GE
EXCHANGE COUPLING, SUPERCONDUCTIVITY AND ELECTRONIC STRUCTURES II

Xiaoxi Liu, Chair
Shinshu University, Nagano, Japan

INVITED PAPERS

9:00

GE-01. Chiral Majorana Fermion Modes in a Quantum Anomalous Hall insulator-Superconductor Structure for Topological Quantum Computing.

K. Wang[1]
1. Departments of ECE, Physics and Astronomy, and MSE, University of California, Los Angeles, Los Angeles, CA, United States

In 1937, Ettore Majorana proposed a particle being its antiparticle. Since its inception, Majorana has been under intensive pursuit both theoretically and in experiments. Recent interest in robust topologically protected quantum computing has accelerated the experimental quest of Majorana. Among various proposals, I will discuss the scenario when a topological insulator meets a superconductor. This system offers a possible host for Majorana. The talk will begin from the experimental efforts of the quest of dissipationless transport: quantum Hall without magnetic field, quantum spin Hall to quantum anomalous Hall (QAH). The latter was enabled by a long term effort in the materials growth of topological insulator - magnetic (Cr) doped BiSbTe to achieve reliably QAH. I will discuss the topological transitions of Dirac electrons of TI in QAH as illustrated in Fig. 1, in which a zero plateau is illustrate due to the gap by the hybridization of two surfaces of TI. The material structure is illustrated in high resolution TEM shown in Fig. 2. When the QAH edge states interface with a superconductor, the Dirac electron space is transformed to the Nambu space, hosting Majorana fermions via pairing energy of the superconductor (Fig. 3). We will describe our experimental efforts to show the convincing evidence of quantized signature of the one-dimensional chiral Majorana fermion. A half-integer quantized conductance plateau (0.5 e^2/h) gives a firm signature of the elusive Majorana fermion for the first time by scanning topological phase transitions under the reversal of the magnetization as shown in Fig. 4 [1]. This finding gives a new direction for robust topological quantum computing to minimize the de-coherence challenge. I will discuss several possible pathways for realizing the elemental qubits and operations. The use of QAH is of critical importance as the dissipationless edge state of QAH offers a long coherent length in mm length scales; this is the key for scaling to a large number of quantum bits. One of these approaches is to pattern a 2-dimensional structure into nanowires, which make the Majorana Chiral modes into zero modes, for which quantum bits may be coded. *The work was in part supported by DoE ERFC-SHINES, ARO MURI, FAME, CEGN and NSF.

[1]. Science, July 21, 2017

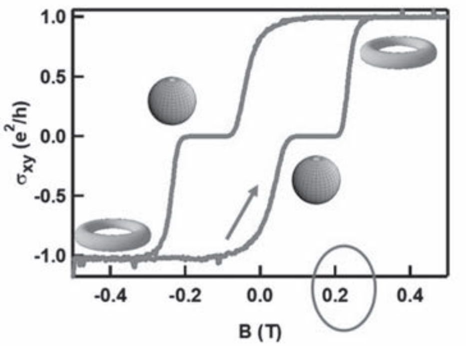

Fig. 1

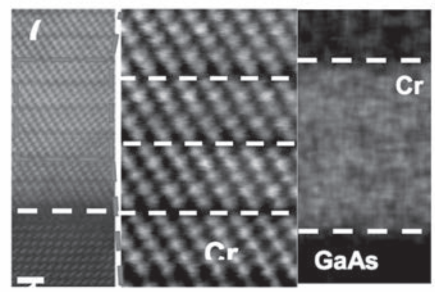

Fig. 2

Fig. 1. Measured Quantum anomalous Hall effect in The topological phase transitions are also shown from -1 to 0 and to 1, and then back when a small magnetic field is scanned.

Fig. 2. High resoluation TEM of Cr-doed (BiSb)2Te3. Clear van der Waals gaps are seen. Cr is shown to be rather uniform in distribution.

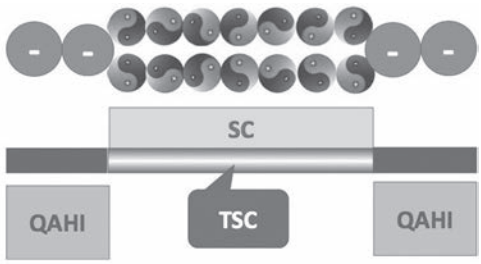

Fig. 3

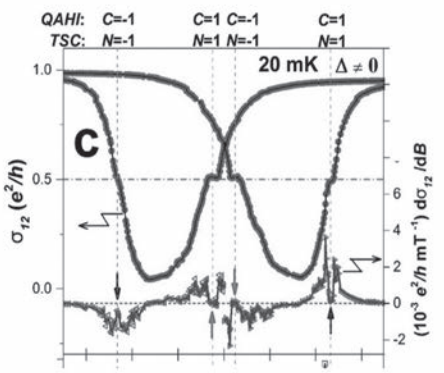

Fig. 4

Fig. 3. QAHI and superconductor heterostrucure to host chiral Majorana fermion modes. When QAHI meets a superconductor, the Dirac electron space is expanded to the Nambu space, hosting chiral Majorana fermion modes.

Fig. 4. Half quantization of QAH/superconductor heterostrucure to host chiral Majorana fermion modes, when a small magnetic field is scanned to change the topolotical number to direct the Majorana fermions.

9:30

GE-02. Superconducting exchange coupling and spin currents between ferromagnets.

M.G. Blamire[1]
1. Materials Science, University of Cambridge, Cambridge, United Kingdom

Conventional spintronics research aims to achieve active electronic control of the magnetic state of a device – for example via non-equilibrium spin current flow generating spin transfer torque switching [1] or the movements of magnetic domain structures [2]. Underpinning the function of such devices is passive exchange coupling between magnetic layers: for example, exchange bias between an antiferromagnet and a ferromagnet which prevents the low-field reversal of one magnetic layer and hence underpins the operation of the spin valve [3], and the Ruderman-Kittel-Kasuya-Yosida (RKKY) coupling between ferromagnets which is required for the observation of giant magnetoresistance in magnetic multilayers [4,5]. The field of superconducting spintronics[6,7] has followed the same path as conventional spintronics with primary attention being focused on the generation and propagation of spin currents (triplet [8,9] or quasiparticle [10]) and the active effects of such currents on magnetic elements. The founding paper in superconductor / ferromagnet field was published in 1966 by de Gennes [11] who predicted that a trilayer ferromagnetic insulator / superconductor / ferromagnetic insulator (FI/S/FI) device, later called a superconducting spin switch, should have a much lower critical temperature (T_c) when the FI magnetisations are parallel (P) compared with the antiparallel (AP) configuration. This prediction of a controllable T_c was experimentally realised quickly [12,13], but it was only recently that large changes (~1 K) in T_c (ΔT_c) could be achieved [14]. De Gennes made a second prediction in his paper[11] which has been largely overlooked: the control of T_c by the magnetic configuration implies that the superconductor condensation energy depends on the relative alignment of the ferromagnetic layers. If the ferromagnet layers are AP and T_c is maximised, then the total free energy is minimised. Thus there is an antiferromagnetic coupling between the FI layers mediated by the superconductivity of the interlayer (the superconducting exchange coupling which is the primary research focus for this proposal). Our experiments [15] are based on GdN/Nb/GdN superconducting spin switches (see Fig. 1). GdN is a FI which we have studied extensively as a barrier in S/FI/S superconducting tunnel junctions [16-19]. As shown in Fig. 1a these devices show both the largest values of ΔT_c ever recorded (which can exceed 1.5 K) and infinite magnetoresistance – i.e. a complete switch between zero and full resistance over an extended temperature range (Fig. 1b). However, the key discovery is the observation of a significantly enhanced coercive field for the harder GdN layer (see Fig. 1c) which increases as the temperature is reduced below T_c which implies the onset of an antiferromagnetic exchange coupling which is in quantitative agreement with the original prediction [11]. This paper will explain the results and discuss the significance of superconducting exchange coupling in the development of practical superconducting spintronic devices. It will also report recent results which demonstrate triplet pair mediated spin current transport through superconductors – another essential ingredient for superconducting spintronics.

[1] J. A. Katine, F. J. Albert, R. A. Buhrman, E. B. Myers, and D. C. Ralph, Phys. Rev. Lett. 84, 3149 (2000). [2] M. Hayashi, L. Thomas, C. Rettner, R. Moriya, X. Jiang, and S. S. P. Parkin, Phys. Rev. Lett. 97, 207205 (2006). [3] B. Dieny, V. S. Speriosu, S. S. P. Parkin, B. A. Gurney, D. R. Wilhoit, and D. Mauri, Phys. Rev. B 43, 1297 (1991). [4] M. N. Baibich, *et al.*, Phys. Rev. Lett. 61, 2472 (1988). [5] P. Grunberg, R. Schreiber, Y. Pang, M. B. Brodsky, and H. Sowers, Phys. Rev. Lett. 57, 2442 (1986). [6] J. Linder and J. W. A. Robinson, Nature Phys. 11, 307 (2015). [7] M. Eschrig, Physics Today 64, 43 (2011). [8] J. W. A. Robinson, J. D. S. Witt, and M. G. Blamire, Science 329, 59 (2010). [9] W. M. Martinez, W. P. Pratt, and N. O. Birge, Phys. Rev. Lett. 116, 077001 (2016). [10] C. H. L. Quay, D. Chevallier, C. Bena, and M. Aprili, Nature Phys. 9, 84 (2013). [11] P. G. de Gennes, Phys. Lett. 23, 10 (1966). [12] G. Deutscher and F. Meunier, Phys. Rev. Lett. 22, 395 (1969). [13] J. J. Hauser, Phys. Rev. Lett. 23, 374 (1969). [14] B. Li*, et al.*, Phys. Rev. Lett. 110, 097001 (2013). [15] Y. Zhu, A. Pal, M. G. Blamire, and Z. H. Barber, Nature Mater. 16, 195 (2017). [16] A. Pal, K. Senapati, Z. H. Barber, and M. G. Blamire, Adv. Mater. 25, 5581 (2013). [17] K. Senapati, M. G. Blamire, and Z. H. Barber, Nature Mater. 10, 849 (2011). [18] A. Pal, Z. H. Barber, J. W. A. Robinson, and M. G. Blamire, Nature Commun. 5, 3340 (2014). [19] A. Pal and M. G. Blamire, Phys. Rev. B 92, 180510(R) (2015).

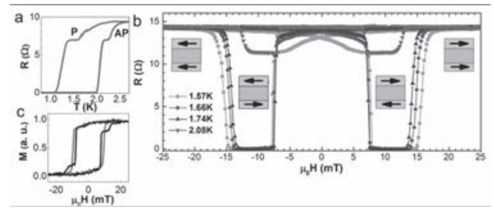

Fig. 1. (a) Superconducting transition of a GdN/Nb/GdN spin switch with the magnetisation of the GdN layers parallel (P) and antiparallel (AP); (b) Resistance vs field for the same device showing field-induced transtions between superconducting and resistive state with the layer alignment as indicated; (c) Comparison of the magnetisation loops of a device in the superconducting state (black) vs a sample in the normal state (orange) showing the enhanced coercivity of the thinner GdN layer arising from superconducting exchange coupling. [*after 15*]

CONTRIBUTED PAPERS

10:00

GE-03. Domain Imaging Across the Magneto-Structural Phase Transition in $Fe_{1+y}Te$.

J. Warmuth[3], M. Bremholm[1], P. Hofmann[2], J. Wiebe[3] and R. Wiesendanger[3]
1. Department of Chemistry, Aarhus University, Aarhus, Denmark;
2. Department of Physics and Astronomy, Interdisciplinary Nanoscience Center (iNANO), Aarhus University, Aarhus, Denmark; 3. Department of Physics, Hamburg University, Hamburg, Germany

$Fe_{1+y}Te$ is the non-superconducting parent compound of $Fe_{1+y}Se_xTe_{1-x}$, in which superconductivity is induced by the substitution of Te with Se [1]. Such Fe-chalcogenides form the structurally simplest material group of all Fe-based superconductors and they are therefore the ideal compound for a fundamental investigation of the complex mechanisms leading to superconductivity in these materials [2, 3, 4, 5,6]. So far, the complex interplay of magnetic and structural phase transitions in $Fe_{1+y}Te$, which crucially depends on the amount of excess Fe, *y*, has been mostly investigated by spatially averaging techniques such as neutron diffraction, magnetic susceptibility, and resistivity measurements [4, 7, 8]. Our specially and spin-resolved scanning tunneling microscopy (STM) study presents, with respect to previous investigations, a major advancement simultaneously revealing the local structural and spin order at the surface of $Fe_{1+y}Te$ compounds with atomic resolution. For low values of excess Fe, $y < 0.11$, a simultaneous magnetic and structural, so-called magneto-structural, transition from a high-temperature paramagnetic tetragonal to a low-temperature monoclinic phase with a diagonal double-stripe antiferromagnetic spin structure [9] was observed. The transition temperature T_N of this phase transition decreases with increasing *y*. For $y > 0.13$ there is a magneto-structural transition from the tetragonal phase into an incommensurate antiferromagnetic orthorhombic phase upon cooling [10, 11]. Most notably, for $0.12<y<0.13$, it was suggested that, upon cooling, the system first transforms from the tetragonal phase into an intermediate incommensurate antiferromagnetic orthorhombic phase and consecutively into a mixture of the incommensurate antiferromagnetic orthorhombic and the monoclinic phase, suggesting a tricritical point at y=0.11 [4]. However, a detailed understanding of the proposed mixed phase and its evolution on a microscopic level were so far lacking. Here, we present a real space spin-resolved STM investigation of the surface of $Fe_{1+y}Te$ single crystals with different excess Fe content, *y*, which are continuously driven through the magneto-structural phase transition. For $Fe_{1.08}Te$, the low-temperature monoclinic commensurate antiferromagnetic phase [9] exhibits a well-defined three-dimensional surface corrugation upon cooling below T_N, clearly visible in the three-dimensional representation of a large-scale STM image shown in Fig 1 (a). The magneto-structural phase transition is mapped by STM images continuously acquired while crossing T_N revealing the emergence and annihilation of the surface corrugation Fig. 1 (b). The STM investigation reveals that four types of surface domains are formed at the surface of $Fe_{1.08}Te$ in the monoclinic phase. These domains exhibit four different orientations of the same surface inclination and form two types of domain boundaries. The spin-resolved STM image displayed in Fig. 2 (a) shows that the four domains (red, blue, green, and yellow) exhibit different orientations of the monoclinic lattice and of the antiferromagnetic order at the surface (Fig. 2 (b)) indicated by the red and blue arrows. This depicts how structural and magnetic order are intertwined within this compound. In the low-temperature phase of $Fe_{1.12}Te$, one type of the domain boundaries disappears, and the transition into the paramagnetic phase gets rather broad, which is assigned to the formation of a mixture of orthorhombic and monoclinic phases below T_N [4]. Our investigation presents the first atomic-scale real-space observation of the simultaneous evolution of spin and structural order in the parent compound of the simplest Fe-based superconductors across the magneto-structural phase transition. The study reveals subtle atomic scale effects in the complex interplay of magnetism and lattice structure and possible ways to manipulate these structures by the Fe content and thermal cycling. One major advancement is the continuous observation of the magneto-structural phase transition resolving the structural and spin order transition at the atomic level. This technique reveals the nature of the investigated phase transition and its application can be transferred to the investigation of other parent compounds of high-temperature superconductors beyond the Fe-chalcogenide family. This work is submitted for publication in a peer-reviewed journal and available as a preprint [12].

[1] Y. Mizuguchi, et al. *J. Phys. Soc. Japan* 79, 10–13 (2010) [2] J. Paglione, et al. *Nature Physics* 6, 645-658 (2010) [3] G. R. Stewart, et al. *Reviews of Modern Physics* 83, 1589 (2011) [4] C. Koz, et al. *Physical Review B* 88, 094509 (2013) [5] A. Subedi, et al. *Phys. Rev. B* 78, 134514 (2008) [6] S. Manna, et al. *Nature Communications* 8, 14074 (2017) [7] P. Dai *Rev. Mod. Phys.* 87, 855–896 (2015) [8] I. A. Zaliznyak, et al. *Phys. Rev. B* 85, 085105 (2012) [9] T. Hänke, et al. *Nat. Commun.* 8, 13939 (2017). [10] W. Bao, et al. *Phys. Rev. Lett.* 102, 247001 (2009). [11] E. E. Rodriguez, et al. *Phys. Rev. B* 84, 064403 (2011) [12] J. Warmuth, et al. *arXiv* 1711.11387 (2017)

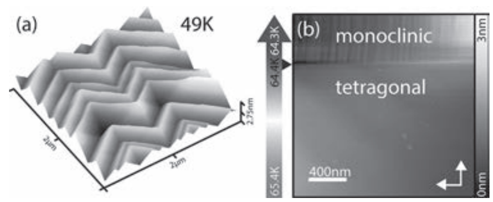

Fig. 1. (a) 3d representation of a constant-current STM image of the surface of $Fe_{1.08}Te$ in the monoclinic phase at 49K. The surface corrugation forms a well ordered pattern of four differnet types of domains, which exhibit four different orienations of the same surface inclination. (b) Constant-current STM image crossing the magneto-structural phase transition from the tetragonal phase (bottom) to the monoclinic phase (top). The sudden transition at T_N=64.4K seperates the flat surface of the tetragonal phase an the monoclinic phase with the surface corrugation.

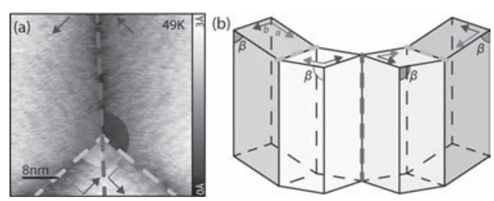

Fig. 2. (a) Spin resolved constant-current STM image (a) probing the surface of $Fe_{1.08}Te$ in the commensurate AFM monoclinic phase. Four surface domains, one of each type, are marked by the colored area around the intersection of the two bondary types marked by dashed lines. surface domains of different inclination are observed. The AFM double-stripe pattern reveals that the domains exibit different crystalographic orientations. The structural model (b) illustrates the four rotations of the structure of the monoclinic phase, which correspond to the four observed surface domain types

10:15

GE-04. Coexistence of Ferromagnetism and Superconductivity in Zn-ion implanted and buffer-free InN films.

W. Xie[1], Q. Xie[2], F. Duan[1], K. Wang[1], H. Tian[1] and X. Wu[1]
1. Physics, Nanjing Unversity, Nanjing, China; 2. Nanjing University of Posts and Telecommunications, Nanjing, China

We report the coexistence of superconducting and magnetic behaviors in Zn-ion implanted and buffer-free InN films at low temperature. The ferromagnetism persists up to 300K, and the superconducting transition temperature locates around 3.5K. Based on the experiment and the fisrt principle calculations, we attribute the superconductivity and ferromagnetism to specific structures, individually, i.e., the well-crystallized lattice, and the defects of Zn replacing In or In vacancies, individually. The coexistence scenario would provide the possibilities to study their interplay coupling.

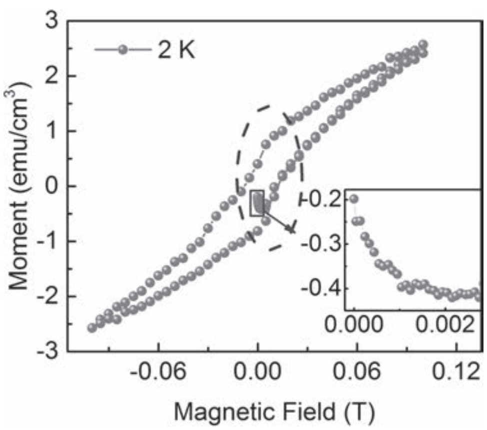

Fig. 1. shows the magnetization vs. magnetic field curves for sample Zn doped InN film at 2 K, exhibiting ferromagnetic signal. The inset is the enlargement of data marked with rectangles, indicating the antiferromagnetic behavior at very low magnetic field due to the superconductivity.

10:30

GE-05. Diamagnetically diluted iron borate-based single crystals: EMR and SQUID studies.

J. Kliava[1], P. Rosa[2], K. Seleznyova[3], M. Strugatsky[3] and S. Yagupov[3]
1. LOMA, UMR 5798, Université de Bordeaux-CNRS, Talence, France;
2. ICMCB, UPR 9048, Université de Bordeaux-CNRS, Pessac, France;
3. V.I. Vernadsky Crimean Federal University, Simferopol, Russian Federation

Iron borate $FeBO_3$ is an excellent example of the materials called "transparent magnets" [1], associating room temperature magnetic ordering (weak ferromagnetism) with transmission windows in visible spectral range [2]. The persisting research interest in iron borate is stimulated by its outstanding magnetic, magneto-acoustical, optical, magneto-optical, resonance, etc. characteristics [3-7]. Recently, new iron borate-based materials - $Fe_xGa_{1-x}BO_3$ crystals - have been synthesized by the solution in the melt technique [8] and studied by Electron Paramagnetic Resonance (EPR) [9], Nuclear Magnetic Resonance [10, 11] as well as by optical and magnetooptical techniques [12]. These crystals: (i) *per se* possess extraordinary physical characteristics suitable for practical applications, and these characteristics can be monitored in the synthesis process; (ii) allow comprehensive studies of diamagnetic dilution - isomorphous substitution of iron by gallium - effect on the properties of magnetic materials, viz., gradual transition from magnetically ordered to paramagnetic state; (iii) allow understanding the nature of various mechanisms responsible for magnetic properties of iron borate, e.g., magnetocrystalline anisotropy, the former having different concentration and temperature dependences. Different types of Electron Magnetic Resonance (EMR) have been observed in $Fe_xGa_{1-x}BO_3$ crystals depending on iron contents and the temperature. Figure 1 (a) shows the spectra transformation with x. At $x = 1$ (pure iron borate), only a low-field resonance is observed, earlier identified as Antiferromagnetic Resonance (AFMR) [7]. At a lower iron content, $x = 0.75$, besides the low-field line a new broad resonance emerges at higher magnetic fields, with the effective g-factor $g\approx 2$. Since iron substitution for gallium occurs more or less randomly, such crystals are expected to contain regions with different local iron concentrations, implying different magnetic ordering. The low-field line observed in the mixed crystals, by analogy with iron borate [7], can be identified as AFMR line arising from magnetically ordered regions, whereas the high-field line can be ascribed to Cluster Magnetic Resonance (CMR), i.e., EMR arising from only partially magnetically ordered regions. Both the low- and high-field EMR lines are present in all crystals with $0.35 \le x < 1$; thus, one can conclude that in such crystals both long-range and short-range (cluster-type) magnetic ordering coexist. Figure 1 (b) shows the temperature dependence of the CMR line intensity for $x = 0.65$. With decreasing temperature this line considerably broadens and its intensity does not follow the T^{-1} Curie law, confirming its attribution to magnetic clusters. At still lower iron contents, $x = 0.2$, the AFMR line disappears and the high-field line increases in intensity. The EMR spectra for $x = 0.2$ crystal consist of a single line at $g\approx 2$, quite similar to the high-field line observed for higher x, consequently, in this case the antiferromagnetic regions are absent in the whole temperature range. The temperature dependence of the intensity of this line shown in Figure 1 (c), confirms that the Curie law for this resonance is not respected. For $x = 0.04$, the latter line also disappears and the EPR spectrum of diluted Fe^{3+} ions, broadened by dipole-dipole interactions, comes into view. At a still lower iron content, $x = 0.003$, this spectrum is spectacularly narrowed. A detailed account of the EPR studies of these crystals has been recently carried out using laboratory-developed codes [9]. In order to confirm or infirm the existence of magnetic clusters in the mixed iron-gallium borates, we have carried out SQUID measurements. The temperature dependence of the magnetic susceptibility in crystals with intermediate x-values, e.g., see Figure 2, reveals the presence of a strong out-of-phase component, thereby confirming the existence of magnetic clusters at intermediate x values. Acknowledgments This work was partially supported by the V.I. Vernadsky Crimean Federal University Development Program for 2015 – 2024.

1. I. Edelman and J. Kliava, *Oxide glasses with magnetic nanoparticles: transparent magnets (Faraday rotation and electron magnetic resonance studies),* Phys. Stat. Solidi B246 (2009) 2216. 2. R. Diehl, W. Jantz, B.I. Nolang and W. Wettling, in: Current Topics in Materials Science, E. Kaldis, ed., Elsevier, New-York 11, 241 (1984). 3. M. Eibshütz and M.E. Lines, *Sublattice magnetization of single crystals by Mössbauer effect*, Phys. Rev. B 7 (1973) 4907. 4. D. Afanasiev, I. Razdolski, K.M. Skibinsky, D. Bolotin, S.V. Yagupov, M.B. Strugatsky, A. Kirilyuk, Th. Rasing and A.V. Kimel, *Laser excitation of lattice-driven anharmonic magnetization dynamics in dielectric* $FeBO_3$, Phys. Rev. Lett. 112 (2014) 147403. 5. M.B. Strugatsky, K.M. Skibinsky, V.V. Tarakanov and V.I. Khizhnyi, *Fine structure of Gakel'-Turov oscillations in iron borate*, J. Magn. Magn. Mater. 241 (2002) 330. 6. M.A. Popov, I.V. Zavislyak, H.L. Chumak, M.B. Strugatsky, S.V. Yagupov and G. Srinivasan,*Ferromagnetic resonance in a single crystal of iron borate and magnetic field tuning of hybrid oscillations in a composite structure with a dielectric: Experiment and theory*, Journal Of Applied Physics 118(2015) 013903. 7. L.V. Velikov, A.S. Prokhorov, E.G. Rudashevskii and V.N. Seleznev, *Antiferromagnetic resonance in* $FeBO_3$, Zh. Eksp. Teor. Fiz. 66 (1974) 1847. 8. S. Yagupov,M.Strugatsky, K.Seleznyova, E.Maksimova, I.Nauhatsky, V.Yagupov, E.Milyukova andJ. Kliava, $Fe_xGa_{1-x}BO_3$*single crystals: synthesis and characterization*, Appl. Phys. A121 (2015) 179. 9. K.Seleznyova, M.Strugatsky, S. Yagupov, N. Postivey, A.Artemenko and J. Kliava, *EPR of* Fe^{3+}*in* $GaBO_3$:*Superposition model analysis*, Phys. Stat. Sol. B251 (2014) 1393. 10. K. Seleznyova, N. Sergeev, M. Olszewski, P. Stepien, S. Yagupov, M. Strugatsky and J. Kliava, ^{11}B *MAS NMR study of* $Ga_{1-x}Fe_xBO_3$*mixed crystals*, Solid State Nucl. Magn. Reson.70 (2015) 38. 11. K. Seleznyova, N. Sergeev, M. Olszewski, P. Stepien, S. Yagupov, M. Strugatsky and J. Kliava, *Fitting MAS NMR spectra in crystals with local disorder: Czjzek's vs. Maurer's model for*^{11}B *and*^{71}Ga *in polycrystalline gallium borate*, Solid State Nucl. Magn. Reson.85-86 (2017) 12. 12. I. Edelman, A. Malakhovskii, A.Sokolov, A.Sukhachev, V.Zabluda, S.Yagupov, M.Strugatsky, N.Postivey and K. Seleznyova, *Optical and magneto-optical properties of* $Fe_xGa_{1-x}BO_3$*crystals*, Functional materials (Kharkiv) 19 (2012) 163.

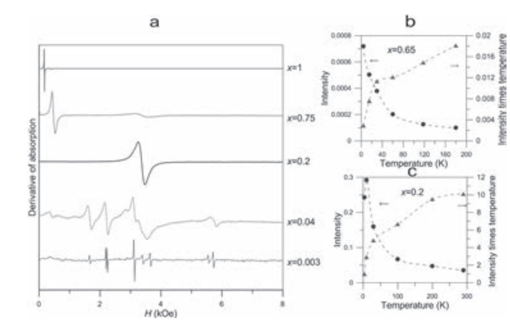

Fig. 1. Normalized X-band (9.45 GHz) room-temperature EMR spectra of $Fe_xGa_{1-x}BO_3$ crystals with different x (a);and temperature dependences of the intensity of the CMR line (circles, blue) and of the intensity times temperature product (triangles, red) for x =0.65 (b) and x = 0.2 (c) crystals. The dashed lines are guides for the eye.

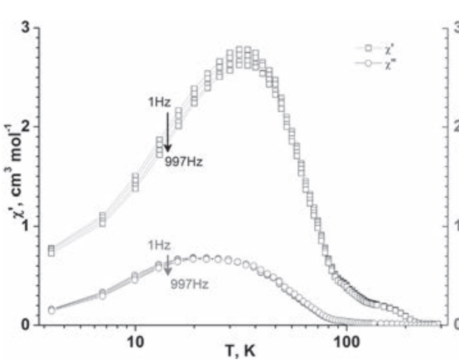

Fig. 2. Temperature dependences of in-phase (squares) and out-of-phase (circles) magnetic susceptibilities for $Fe_{0.25}Ga_{0.75}BO_3$ crystal.

INVITED PAPER

10:45

GE-06. Theory of Mn-containing high-magnetization permanent magnets.

A. Kashyap[1], D. Sellmyer[2] and R. Skomski[2]
1. School of Basic Sciences, IIT Mandi, Mandi, India; 2. Department of Physics and Astronomy, NCMN, University of Nebraska-Lincoln, Lincoln, NE, United States

1. INTRODUCTION Isolated manganese atoms have half-filled 3*d* shells and a magnetic moment of 5 μ_B. If this moment could be realized in permanent magnets, it would revolutionize technology. The present-day room-temperature record is about 2.43 μ_B in $Fe_{65}Co_{35}$, and the maximum energy product of permanent magnets is quadratic in the magnetization. Furthermore, the crystal structure of $Fe_{65}Co_{35}$ is cubic and not suitable for permanent magnets, and it may be possible to create noncubic Mn magnets with substantial magnetocrystalline anisotropy. Known Mn-based permanent magnets, such as MnAl, MnBi, and Mn_2Ga, exhibit modest energy products. The main reason is the low net magnetic moment, of the order of 0.5 μ_B per atom, which means that 99% of the energy product are wasted. The focus of our presentation is the theoretical explanation of the low moment of Mn-based permanent magnets and the search for crystal structures with improved net magnetization. Analytical quantum mechanics and density functional (DFT) calculations [1] will be used to tackle the problem. Since the magnetization is equal to the moment per volume, the Mn atoms need to be compacted into solids, and the resulting interatomic hybridization tends to reduce the atomic moments. However, moments of about 3 μ_B are rather easy to realize in solids, and up to about 3.7 μ_B per atoms are not unrealistic even in metals [2]. Another factor is the dilution of the magnetization due to the presence of nonmagnetic atoms, e.g., Mn moments approaching 5 μ_B can be realized in oxides, but the large volume of the O^{2-} ions severely limits the magnetization. II. FERRO- AND ANTIFERROMAGNETIC Mn ALLOYS The biggest concern with respect to the Mn magnetization is the element's trend towards antiferromagnetic (AFM) spin alignment. This trend is often rationalized in terms of the Bethe-Slater-Néel curve which predicts AFM order for small interatomic distances and ferromagnetic (FM) order for large interatomic distances. However, the curve conflates antiferromagnetism with Pauli paramagnetism, does not distinguish between different crystal structures, and ignores that the number of 3*d* electrons is an important parameter. For example, AFM order is particularly widespread in nearly half-filled 3*d* shells, and Mn is the most affected element. The reason for the AFM interatomic coupling of half-filled shells is that interatomic hopping reduces the energy through the formation of bonding states. Interatomic hopping is pronounced in ferromagnetic and paramagnetic metals, where it yields relatively broad bands. It is much less effective in antiferromagnets, because neighboring ↓ atoms act as energy barriers for traveling ↑ spins, and *vice versa* [3]. One may thus expect all magnetically ordered metals to be FM in lowest order. However, half-filled FM bands mean that all available orbitals are filled by ↑ electrons, both bonding and antibonding orbitals, so the net hybridization energy gain is zero. The AFM state has both ↑ and ↓ electrons in the bonding orbitals and therefore the lower energy in for half-filled shells. III. ROLE OF CRYSTAL STRUCTURE The number of Mn 3*d* electrons can be somewhat varied through alloying, but to create ferromagnetism in Mn alloys, one needs suitable crystal structures. There is a big difference between fcc-type dense-packed alloys, where nearest neighbors form equilateral triangles, and bcc-type less-dense-packed alloys, which do not contain such nearest-neighbor triangles. Elements in the middle of the 3*d* series, such as Fe and Mn, require structures of the second type, as opposed to the late 3*d* elements Co and Ni, where ferromagnetism is supported by fcc-type structures. The reason is the Stoner criterion, which requires a high density of states (DOS) at the Fermi level: otherwise, the only choice is between paramagnetism and AFM (or a complicated spin structure). We will show DFT calculations to verify this rule, but the underlying nearest-neighbor physics, is easily seen from the two-cluster shown in Fig. 1. Equilateral triangles create a strongly asymmetric DOS, with the highest DOS near the upper edge of the level distribution. This is the reason for the frequent occurrence of ferromagnetism in dense-packed late 3d magnets. In the absence of such triangles, the level distribution is symmetric and reaches its highest density for half-filled shells. Structures of type of Fig. 1(a) are most promising for new Mn-based ferromagnets. This analysis is partially based on existing Mn-based magnets, e.g, MnAl exhibits strong Mn-Mn exchange, in spite of a very short Mn-Mn nearest neighbor distance. The reason is that the atoms in the Mn layers of the $L1_0$-ordered alloy form a square lattice. A class of Mn alloys of current interest in several areas of magnetism are bcc derivatives, including Heusler alloys. Ferromagnetic order in these alloys is important for spin electronics applications, and some of them are presently investigated as potential high-magnetization permanent magnets. As we will discuss, the individual site occupancies are of crucial importance in these systems.
Acknowledgement. — Authors acknowledge discussion with P. Manchanda, Y. Idzerda, and W. Zhang. This research is supported by NM-DST, GoI and DOE BES (DE-FG02-04ER46152).

References [1] R. O. Jones and O. Gunnarson, "The density functional formalism, its applications and prospects", Rev. Mod. Phys. 61, 689 (1989). [2] J. M. D. Coey, "New permanent magnets; manganese compounds", J. Phys.: Condens. Matter 26, 064211 (2014). [3] R. Skomski and J. M. D. Coey, *Permanent Magnetism*, Institute of Physics, 1999.

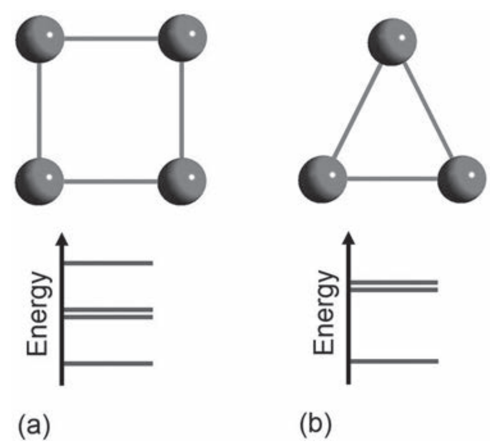

Fig. 1. Crystal structure and energy-level distribution: (a) less dense packed structures and (b) dense packed structures. High-magnetization Mn alloys requires structural motifs of the type (a).

CONTRIBUTED PAPERS

11:15

GE-07. Origin of perpendicular magnetic anisotropy in Co/Pd multilayers studied by x-ray magnetic circular dichroism and first-principles calculations.

J. Okabayashi[1], Y. Miura[2] and H. Munekata[3]
1. The University of Tokyo, Bunkyo-ku, Japan; 2. Kyoto Institute of Technology, Kyoto, Japan; 3. Tokyo Institute of Technology, Yokohama, Japan

Ultrathin Co/Pd multilayers are artificial nanomaterials that exhibit perpendicular magnetic anisotropy (PMA), due to the spin-orbit interactions, achieved through interfacial chemical bonding. Regarding applications, after the development of artificially synthesised PMA, researchers have pointed out the expectation of ultra-high density recording media [1]. Extensive efforts have been made for studying interfaces of ultra-thin magnetic multilayers and nanostructures. Studies on Co atoms performed using x-ray magnetic circular dichroism (XMCD) have suggested the enhancement of orbital magnetic moments at the interfacial Co that is adjacent to Pd [2]. It has been reported that the PMA emerges due to the cooperative effects between spin moments in 3*d* transition metals (TMs) and large spin-orbit interactions in the non-magnetic 4*d* TMs. The Co/Pd interfaces and multilayers have also been employed to demonstrate the photo-induced precession of magnetisation [3] and the creation of skyrmions using the interfacial Dzyaloshinskii-Moriya interaction [4], and magnetisation reversal using the spin-orbit torque phenomena [5]. Despite the abovementioned promising studies on Co/Pd interfaces, the interfacial PMA, including the anisotropic orbital magnetic moments, has not been fully understood for both Co and Pd sites. Bruno and van der Laan theoretically proposed an orbital moment anisotropy in 3*d* TMs within the second-order perturbation of the spin-orbit interaction for more than half-occupied electrons [6, 7]. However, in the case of strong spin-orbit coupling in 4*d* (Pd) or 5*d* (Pt) TMs, the validity of this perturbative formula has been debated [8]. In order to study the mechanisms of PMA in Co/Pd multilayers, the orbital magnetic moments contributions of each element have to be explicitly considered. It is challenging to study the anisotropy of the orbital magnetic moments of both Co *L*-edge and Pd *M*-edge elements using one specific experiment, due to the challenges in detection of the induced magnetic moments, of Pd in particular. For the interfacial Pd, the magnetic dipole contribution through the quadrupole interactions between dipoles is assessed quantitatively. We focus on the anisotropy of orbital moments at the Co/Pd interfaces using XMCD and first-principles density functional theory (DFT) calculations, which provide the element- and layer-resolved contributions that reveal the mechanism of PMA. In this study, we discuss the anisotropies of both spin and orbital moments of Co and Pd using angle-dependent XMCD data and DFT calculations. We prepared two kinds of samples of Co/Pd multilayered structures: Co (0.69 nm)/Pd (1.62 nm) for PMA and Co (1.03 nm)/Pd (1.62 nm) for in-plane anisotropy with stacking five periods on the Si substrates [3]. Sample surfaces were sputtered by Ar ions before the XMCD measurements in order to remove the oxygen contamination. We performed XMCD experiments in the total electron yield mode. A magnetic field of ±5 T was applied along the direction of the incident polarized soft x-ray. We successfully observed clear XMCD signals in Pd *M*-edges after the removal of surface contamination as shown in Fig. 1. Although the x-ray absorption spectroscopy (XAS) line shapes overlap with those of O *K*-edge absorption, clear XMCD signals induced by the proximity with Co layers are observed. The Pd *M*-edge XMCD line shapes in both PMA and in-plane samples are almost identical, which suggests isotropic orbital moments in Pd, within the detection limits. On the other hand, clear Co *L*-edge XAS and XMCD with angular dependence reveal the enhancement of orbital moments in the surface normal direction because of PMA. Next, we can discuss the magnetic dipole moments m_T through quadrupole-like spin-flipped contribution of the interfacial Pd layer using the angular-dependence of spin magnetic moments. We found that the m_T is an order of magnitude smaller than the orbital moments, i.e., *0.005 mu*$_B$, comparable with the detectable limits. Therefore, the relatively large spin-orbit coupling constant and small Pd exchange splitting contribute to the appearance of PMA by means of quadrupole-like interactions through the interfacial proximity effects. Figure 2 represents the contributions of the crystalline magnetic anisotropy at each atomic site by DFT calculations. Four types of spin transition processes occur between the occupied and unoccupied states within the second order perturbation of the spin-orbit interaction. For Co sites, the transition between down-down spin states is dominant, suggesting the conservation of spin states in the transition, which can be explained using the Bruno model assuming a large spin splitting. In contrast, for Pd, the spin-flipped transitions between up-down and down-up states become dominant due to the small band splitting, hence both spin-preserved and spin-flipped processes occur near the Fermi level. These results are consistent with the angular-dependent XMCD in Co and Pd sites. In the presentation, we will discuss the orbital-resolved interfacial electronic structures in Co/Pd system with the estimations of spin, orbital, and magnetic dipole moments.

1. M. T. Johnsony, P. J. H. Bloemenzx, F. J. A. den Broedery, and J. J. de Vries, Magnetic anisotropy in metallic multilayers. *Rep. Prog. Phys.* 59, 1409 (1996). 2. Y. Wu, J. Stohr, B. D. Hermsmejer, M. G. Samant, and D. Weller, Enhanced Orbital Magnetic Moment on Co Atoms in Co/Pd Multilayers: A Magnetic Circular X-Ray Dichroism Study. *Phys. Rev. Lett.* 69, 2307 (1992). 3. K. Yamamoto, T. Matsuda, K. Nishibayashi, Y. Kitamoto, and H. Munekata, Low-Power Photo-Induced Precession of Magnetization in Ultra-Thin Co/Pd Multilayer Films. *IEEE Transaction on Magnetism* 49, 3155 (2013). 4. S. D. Pollard, J. A. Garlow, J. Yu, Z. Wang, Y. Zhu, H. Yang, Observation of stable Neel skyrmions in cobalt/palladium multilayers with Lorentz transmission electron microscopy. *Nature Commun.* 8, 14761 (2017). 5. M. Jamali, K. Narayanapillai, X. Qiu, L.M. Loong, A. Manchon, and H. Yang, Spin-Orbit Torques in Co/Pd Multilayer Nanowires. *Phys. Rev. Lett.* 111, 246602 (2013). 6. P. Bruno, Tight-binding approach to the orbital magnetic moment and magnetocrystalline anisotropy of transition-metal monolayers. *Phys. Rev. B* 39, 865 (1989). 7. G. van der Laan, Microscopic origin of magnetocrystalline anisotropy in transition metal thin films. *J. Phys. Condens. Matter* 10, 3239 (1998). 8. C. Andersson, B. Sanyal, O. Eriksson, L. Nordstrom, O. Karis, D. Arvanitis, T. Konishi, E. Holub-Krappe, and J. Hunter Dunn, Influence of Ligand States on the Relationship between Orbital Moment and Magnetocrystalline Anisotropy. *Phys. Rev. Lett.* 99, 177207 (2007).

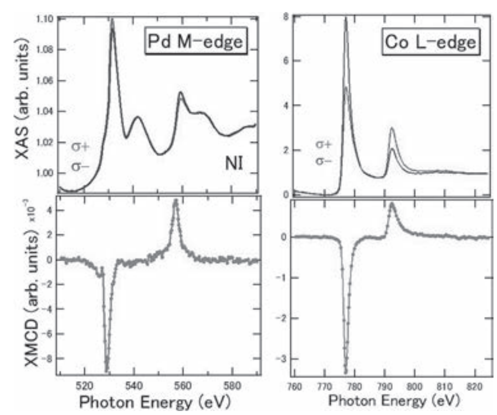

Fig. 1. XAS and XMCD of Pd *M*-edge and Co *L*-edge in perpendicularly magnetized Co (0.69 nm)/Pd (1.62 nm) multilayer.

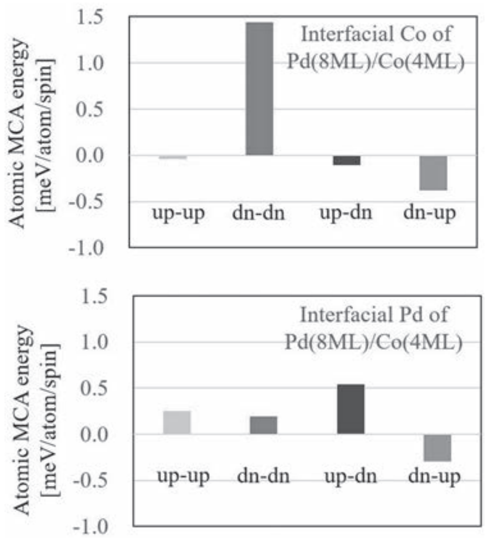

Fig. 2. Bar graph of the second-order perturbative contribution of the spin-orbit interaction to the anisotropy energy at the interfacial atomic sites of Co and Pd for the Pd(8ML)/Co(4ML).

11:30

GE-08. Perpendicular exchange bias in CoPt/FeMn bilayers.

C. Pan[1,2], T. Gao[3], T. Harumoto[2], Z. Zhang[1], Y. Nakamura[2] and J. Shi[2]
1. School of Materials Science and Engineering, Tsinghua University, Beijing, China; 2. School of Materials and Chemical Technology, Tokyo Institute of Technology, Tokyo, Japan; 3. Department of Applied Physics and Physicoinformat, Keio University, Yokohama, Japan

Two series of samples, CoPt single layers (SL) and CoPt/FeMn bilayers (BL), were fabricated by DC magnetron sputtering on MgO (111) substrates to investigate magnetization anisotropy and exchange bias effect in CoPt/FeMn hetero structure. It is proposed that perpendicular magnetization anisotropy (PMA) in magnetic films mainly originates from the anisotropy of phase ordering (such as $L1_1$ or $L1_0$), shape anisotropy and strain anisotropy trigged by magnetostriction strain imposed on the film by the substrate. [1] In this work, PMA in CoPt/FeMn films was systematically investigated. Fig.1 (a-e) shows hysteresis loops of CoPt single-layered films with different thicknesses. It is clearly that magnetization easy axis switches from out-of-plane direction to the in-plane direction with the increase of thickness of CoPt layer. From the area enclosed between the in-plane and out-of-plane magnetization loops, the effective magnetic anisotropy (K_{eff}) [2] can be readily obtained and shown in the inset of Fig.1 (f). Fig.1(f) shows the product of K_{eff} and t_{CoPt} as a function of t_{CoPt}. $K_{eff}\, t_{CoPt} = K_V\, t_{CoPt} + 2K_s$ (1) In this combining equation, Kv is the volume anisotropy deduced by the slop of fitting line, and Ks is the interface anisotropy obtained from the intercept. [2] A positive (negative) Keff describes the preferential magnetization direction is along the out of plane (in plane) direction. The signs of K_{eff} from positive to negative is coincident with the alternation of magnetization curves from out-of-plane to the in-plane direction. Moreover, the careful characterization on structure by XRD has also been conducted on the two series of samples (not shown here). For SL, CoPt (111) peaks at around 41^o shift to higher angle till 3nm, indicating shrink of interplanar distince and in-plane tensile stress. The magnetic anisotropy of thin film can be correlated with equation (2) [3] between internal stress σ_{in} and magnetoelastic energy $K_{me,}$ $K_{me} = - 3/2\, \lambda\sigma_{in}$ (2) where λ is the magnetoelstic constant, and CoPt alloy has a negative magnetostriction constant along <111> direction, an in-plane tensile stress (σ_{in}〉0) identified from shift of peaks in XRD profile results in a positive magnetoelastic energy and the PMA is favoured. Therefore, PMA observed in thinner CoPt films is believed due to internal stress. Fig.2a shows typical magnetization curves of CoPt/FeMn bilayer films prepared at 350 ^oC, the as deposited (A.D) film shows PMA. Meantime, distinctive perpendicular exchange bias (PEB) appears after cooling samples from 500K down to 80K with a 5kOe external field applied perpendicular to the film plane, and the measurement was conducted at 80K. Fig2b shows the dependence of coercivity and exchange bias on the FeMn thickness measured at T=80K. When the thickness of FeMn is smaller than 2nm, exchange bias is almost 0, because at this thickness, FeMn is probably not AFM [4]. EB field increase drastically as FeMn thickness increases to 8nm and then decrease to a constant value in the subsequent thicker thickness. Coercivity was found to depend strongly on the thickness of FeMn layer. It is known that spin configuration of FeMn plays a critical role in determining the direction and strength of the exchange coupling at the interface. FeMn has a 3Q spin structure, with spins pointing to the [111] directions.[5] The spin orientation has a vector component projection along the normal direction of the thin film plane and would contribute to PEB in CoPt/FeMn hetero structure, so pinning effect can be enhanced till to peak at 8nm. The fascinating point is the peak at 8nm in Fig. 2(b). In this work, one model proposed by Binek et,al (equation (3)) [6], based on a generalized Meiklejohn and Bean approach, $H_{EB} = a + b/t_{AF} + c/t^2_{AF}$ (3) is the most possible one for this dependence. The peak at 8nm observed in the AF thickness dependence of exchange bias is considered due to the frozen magnetization of the AF, which is generally assumed to be 0 in most models. The special alignment of spins at the CoPt-FeMn interface need further investigation.

[1]Yu Y, Shi J, Nakamura Y. Roles of interface roughness and internal stress in magnetic anisotropy of CoPt/AlN multilayer films[J]. Acta Materialia, 2012, 60(19): 6770-6778. [2]Johnson M T, Bloemen P J H, Den Broeder F J A, et al. Magnetic anisotropy in metallic multilayers[J]. Reports on Progress in Physics, 1996, 59(11): 1409. [3]Guo L, Wang Y, Wang J, et al. Magnetoelastically induced perpendicular magnetic anisotropy and perpendicular exchange bias of CoO/CoPt multilayer films[J]. Journal of Magnetism and Magnetic Materials, 2015, 394: 349-353. [4]Lenz K, Zander S, Kuch W. Magnetic proximity effects in antiferromagnet/ferromagnet bilayers: The impact on the Néel temperature[J]. Physical review letters, 2007, 98(23): 237201. [5]Tan A, Li J, Jenkins C A, et al. Magnetic anisotropy in epitaxial Py/FeMn/Cu (001) and Py/FeMn/Ni/Cu (001) films[J]. Physical Review B, 2013, 88(10): 104404. [6]Binek C, Hochstrat A, Kleemann W. Exchange bias in a generalized Meiklejohn–Bean approach[J]. Journal of magnetism and magnetic materials, 2001, 234(2): 353-358.

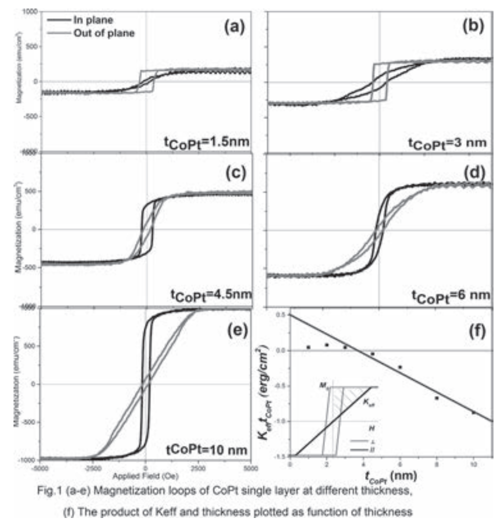

Fig. 1. (a-e) Magnetization loops of CoPt single layer at different thickness,(f)The product of Keff and thickness plotted as function of thickness

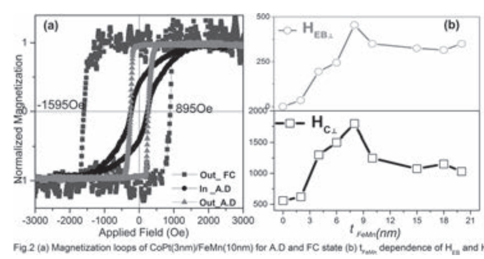

Fig. 2. (a)Magnetization loops of CoPt(3nm)/FeMn(10nm) for A.D and FC state(b) t_{FeMn} dependence of H_{EB} and H_C

11:45

GE-09. Additively Manufactured Functionally Graded FeNi based High Entropy Magnetic Alloys.

V. Chaudhary[1], T. Borkar[2,3], C.V. Mikler[2], B. Gwalani[2], D. Choudhuri[2], V. Soni[2], T. Alam[2], *R.V. Ramanujan*[1] and R. Banerjee[2]
1. Nanyang Technological University, Singapore, Singapore; 2. University of North Texas, Denton, TX, United States; 3. Cleveland State University, Cleveland, OH, United States

Abstract: Compositionally graded $FeNiAlCo_xCr_{1-x}$ ($0 \leq x \leq 1$) high entropy alloys (HEA) as well as the related Fe-Ni and Fe-Ni-V, Fe-Ni-Mo alloys have been processed by laser additive manufacturing. The graded composition and processing conditions result in interesting non-monotonic saturation magnetization (M_S), coercivity (H_C) and Curie temperature (T_C) behavior. Such tunable functionally graded magnetic properties offer unique potential for permeability engineering applications, such as electrical machines. Introduction: Soft magnetic alloys, e.g., Fe-Ni based alloys, are extensively used in numerous applications, such as sensors, power conversion devices, e.g., transformers, inductive devices, electrical machines etc. The emerging field of high entropy magnetic materials based on these Fe-Ni alloys has also revealed interesting, widely tunable magnetic properties. High-temperature processing of such alloys by conventional techniques, e.g., casting, melt spinning can result in undesirable magnetic properties. Hence, it is essential to investigate novel additive manufacturing techniques. Additive manufacturing, e.g., by laser engineering net shape (LENS) processing, allows near-net shaping of dense metallic objects via introduction of pre-alloyed or blended elemental powders into a melt pool produced by a high-power laser. It can produce functionally graded materials that are difficult to process using conventional techniques. The composition and microstructure can be tuned along the sample length in functionally graded materials, resulting in a systematic variation in their properties. The microstructure and magnetic properties of several LENS deposited alloys were investigated and compared to those of conventionally processed alloys. Experimental: $FeNiAlCo_xC_{1-x}$ alloys with varying Co/Cr ratios were deposited using a LENS system with two powder feeders, one containing an elemental blend of FeNiAlCo and the other containing a blend of FeNiAlCr. The composition variation was achieved by varying powder flow rate from both powder feeders during deposition. The compositionally graded sample is cylindrical (10 mm diameter × 25 mm height). The powders used for depositing these alloys consisted of commercial near spherical Al, Co, Cr, Fe, and Ni powders (purity at least > 99%). A range of processing conditions was used, and optimized, to produce a homogenous LENS^{TM} deposit with minimal defects. Cylindrical deposits (10 mm diameter, 12–15 mm height) of the Fe-30at.%Ni alloy were deposited using three nominal laser powers (300W, 400W, and 500W) and two travel speeds (8 inch per minute (IPM) and 13 IPM). Cylindrical deposits of nominal compositions of Ni-15Fe-5 V and Ni-15Fe-5Mo were deposited using 400W laser power and a vector speed of 20 IPM. For compositional, microstructural and magnetic property measurements several sophisticated characterization techniques, e.g., XRD, SEM, EDX, TEM, APT, VSM have been used. More details can be found in the references[1-4]. Results: The graded $FeNiAlCo_xCr_{1-x}$ ($0 \leq x \leq 1$) HEA samples were deposited using the LENS process. All the alloy compositions exhibited a mixture of BCC and B2 (ordered BCC) phases. FeNiAlCo (x=1) alloys exhibited, coarse equiaxed grains and at a finer length scales, early stages of phase separation into Ni-Al rich and Fe-Co rich regions. As Cr content increases, more pronounced spinodal decomposition was observed within the BCC grains. Both TEM and APT analysis show that FeNiAlCr (x=0) alloys exhibit spinodal decomposition within BCC grains. The M_S rises monotonically upon Co addition, from 20.6 emu/g at x=0 (FeNiAlCr) to 123 emu/g at x=1 (FeNiAlCo) (Fig 1a). In contrast, the composition dependence of H_C is non-monotonic: H_C is low for x=0, but increases dramatically at x£0.4 and then falls again for x>0.4, reaching a low value at x=1 (Fig 1b). Fig 2 show the M_S and H_C for six selected deposition conditions, i.e., 300 W, 400 W and 500 W, for travel speeds of 8-IPM and 13-IPM. The M_S and H_C were found to be in the range of 96-114 emu/g and 21-30 Oe, respectively (Fig 2). For the 8-IPM LENS deposition, the magnetization values decrease and coercivity increases with decreasing laser power, while for the case of 13-IPM LENS deposition, M_S values increase, and H_C decreases with decreasing laser power. The M_S for the 13-IPM/300 W samples is highest due to the largest content of the bcc phase, as confirmed by XRD and TEM analyses. The change in saturation magnetization can be attributed to a change in total magnetic moment, from 1.15 μB/atom for the pure *fcc* phase to 1.87 μB/atom for the pure *bcc* phase[5]. The M_S and H_C values for the Ni-15Fe-5V sample are 72 emu/g and 6 Oe, respectively, while the values for the Ni-15Fe-5Mo sample are 82 emu/g and 4.9 Oe, respectively. Conclusions: Graded $FeNiAlCo_xCr_{1-x}$ ($0 \leq x \leq 1$) HEA and related Fe-Ni, Fe-Ni-V, Fe-Ni-Mo alloys were prepared using additive manufacturing. The microstructure and magnetic properties of these additively processed alloys were found to be promising for permeability engineered near net shape magnetic components.

[1] T. Borkar, V. Chaudhary, B. Gwalani, D. Choudhuri, C.V. Mikler, V. Soni, T. Alam, R. V. Ramanujan, R. Banerjee, *Advanced Engineering Materials*, 2017, e201700048. [2] C.V. Mikler, V. Chaudhary, T. Borkar, V. Soni, D. Jaeger, X. Chen, R. Contieri, R.V. Ramanujan, R. Banerjee, *JOM*, 2017, 1. [3] C.V. Mikler, V. Chaudhary, T. Borkar, V. Soni, D. Choudhuri, R.V. Ramanujan, R. Banerjee, *Materials Letters*, 2017, *192,* 9. [4] C.V. Mikler, V. Chaudhary, V. Soni, B. Gwalani, R.V. Ramanujan, R. Banerjee, *Materials Letters*, 2017, *199,* 88. [5] N.J. Wittridge, J.J. Jonas, *Acta Materialia*, 2000, *48,* 2737.

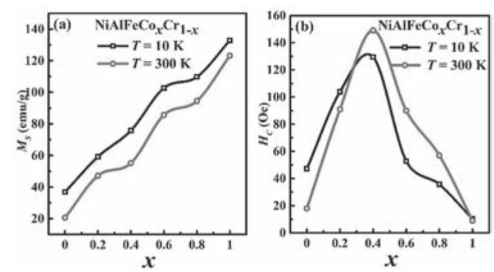

Fig. 1. (a) Saturation magnetization (M_S) and (b) coercivity (H_C) as a function of cobalt concentration (x = 0 to 1) at 10 K (black curves) and 300 K (red curves) in $FeNiAlCo_xCr_{1-x}$ HEA.

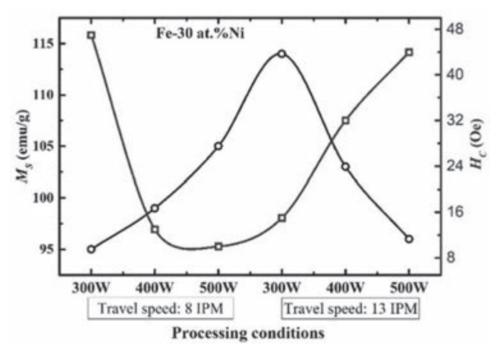

Fig. 2. M_S (left axis, black curve) and H_C (right axis, blue curve) as function of processing conditions (travel speed and power) for Fe-30at.%Ni alloys.

FRIDAY MORNING, 27 APRIL 2018 PEONY I, 9:00 TO 12:00

Session GF

SPIN WAVES II

Florin Ciubotaru, Chair
IMEC, Leuven, Belgium

INVITED PAPER

9:00

GF-01. Crossover to subthermal magnons spin conductance in open YIG films driven by large spin-orbit torque.

O. Klein[1], N. Thiery[1], L. Vila[1], G. de Loubens[2], V. Naletov[2], V.E. Demidov[3] and S.O. Demokritov[3]
1. CEA-SPINTEC, GRENOBLE, France; 2. CEA-SPEC, Gif-Sur-Yvette, France; 3. Physics department, University of Muenster, Muenster, Germany

The recent demonstrations that spin orbit torques (SOT) allow one to generate and detect pure spin currents has triggered a renewed effort to study magnons transport in extended magnetic films. A large effort has concentrated so far on yttrium iron garnet (YIG), which is famous for having the lowest known magnetic damping parameter. From a fundamental point of view, these studies of magnon transport in YIG by means of the direct and inverse spin Hall effects (ISHE) [1–6] are very interesting, as they provide new means to alter strongly the energy distribution of magnons up to thermal energies, and the interplay between these non-equilibrium populations is expected to lead to new collective phenomena, even potentially, to trigger condensation [7]. In contrast to spin transfer process in closed geometries (lateral size of the system smaller than the spin- wave propagation distance), very little is known about spin transfer in open geometries, which have continuous spin-wave spectra containing many modes which can take part in the magnon-magnon interactions. While magnons excited coherently, e.g. by means of a ferromagnetic resonance or parametric pumping, when the frequencies of the excited magnons are fully determined by the frequencies of the external signals, the excitation of magnons by means of spin transfer process lacks frequency selectivity, and, therefore, can lead to their excitation in a broad frequency range. This poses a challenge for the identification of the nature of magnons modes excited by SOT. It has been already shown, that it is convenient and useful to introduce the concepts of subthermal (having energy close to the bottom of the spin wave spectrum) and thermal (having energy close to k_BT) magnons. On one hand, it has been well established [8] that subther- mal magnons can be very efficiently thermalized near the spectral bottom (region of so-called magnetostatic waves) by the intensive magnon-magnon interaction, whose decay rate between quasi-degenerate modes increases with power, to reach a quasi-equlibrium state by a non-zero chemical potential [8] and an effective temperature. Under spin transfer process, whose efficiency is known to increase with decreasing magnon frequency, in closed geometries with localized spin-current injection (i.e. when there are no quasi-degenerate modes), it has been shown, that one can reach current induced coherent GHz- frequency magnon dynamics in YIG [4, 5, 9]). In open geometries, the recently discovered non-local magnon transport [2, 3] suggests that the magnon transport properties of YIG films subjected to small SOT are dominated by thermal magnons, whose number overwhelmingly exceeds the number of other modes at any non-zero temperature. The interesting challenge is to elucidate what will happen to this spectrum (in particular the interplay between the thermal and subthermal part when one applies large SOT to a magnon continuum. We report herein measurements of the room temperature spin conductance of YIG films when the driving current is varied in a wide range magnitudes creating, first, a quasi- equilibrium transport regime, and, then, driving the system to a strongly out-of-equilibrium state. To reach this goal the spin current injected in the YIG by SOT shall be increased by more than one order of magnitude compared to previous works, while simultaneously reducing the film thickness by also an order of magnitude, using ultra-thin films of YIG grown by liquid phase epitaxy (LPE). We show that at large current the spin conductance is dominated by magnetostatic magnons, which are low-damping non-equilibrium magnons thermalized near the spectral bottom by magnon-magnon interaction, with consequent a sensitivity to the applied magnetic field. This picture is supported by microfocus Brillouin Light Scattering spectroscopy. We believe that our current findings are not only important from the from the fundamental point of view, but might be also useful for future applications. While transport of thermal magnons are difficult to control due to their relatively high energies, the subthermal magnons could be efficiently controlled by variation of relatively weak magnetic fields.

[1] Y. Kajiwara, K. Harii, S. Takahashi, J. Ohe, K. Uchida, M. Mizuguchi, H. Umezawa, H. Kawai, K. Ando, K. Takanashi, S. Maekawa, and E. Saitoh, Nature 464, 262 (2010). [2] L. J. Cornelissen, J. Liu, R. A. Duine, J. Ben Youssef, and B. J. van Wees, Nature Phys. 11, 1022 (2015). [3] S. T. B. Goennenwein, R. Schlitz, M. Pernpeintner, K. Ganzhorn, M. Althammer, R. Gross, and H. Huebl, Appl. Phys. Lett. 107, 172405 (2015). [4] A. Hamadeh, O. d'Allivy Kelly, C. Hahn, H. Meley, R. Bernard, A. H. Molpeceres, V. V. Naletov, M. Viret, A. Anane, V. Cros, S. O. Demokritov, J. L. Prieto, M. Munoz, G. de Loubens, and O. Klein, Phys. Rev. Lett. 113, 197203 (2014). [5] M. Collet, X. de Milly, O. d'Allivy Kelly, V. Naletov, R. Bernard, P. Bortolotti, J. Ben Youssef, V. Demidov, S. Demokritov, J. Prieto, M. Munoz, V. Cros, A. Anane, G. de Loubens, and O. Klein, Nature Commun. 7, 10377 (2016). [6] D. Wesenberg, T. Liu, D. Balzar, M. Wu, and B. L. Zink, Nat Phys advance online publication, (2017). [7] B. Flebus, P. Upadhyaya, R. A. Duine, and Y. Tserkovnyak, Phys. Rev. B 94, 214428 (2016). [8] V. E. Demidov, O. Dzyapko, S. O. Demokritov, G. A. Melkov, and A. N. Slavin, Phys. Rev. Lett. 99, 037205 (2007). [9] V. E. Demidov, M. Evelt, V. Bessonov, S. O. Demokritov, J. L. Prieto, M. Muoz, J. Ben Youssef, V. V. Naletov, G. de Loubens, O. Klein, M. Collet, P. Bortolotti, V. Cros, and A. Anane, Sci. Rep. 6, 32781 (2016).

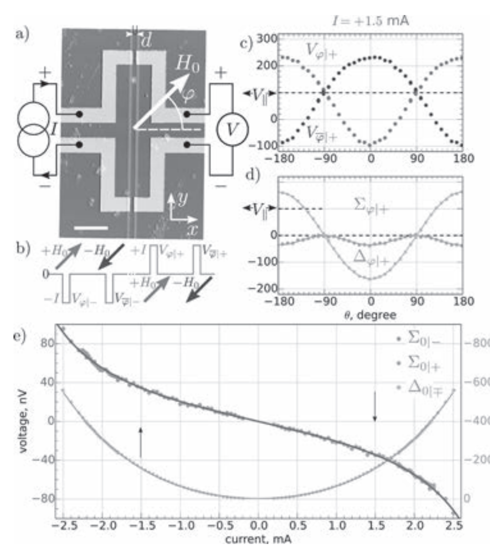

Fig. 1. a) Top view of the lateral device. Two Pt wires (grey lines) are aligned along the *y*-direction and placed at a distance d=1.2µm apart on top of a 18nm thick YIG film (scale bar is 5µm). b) For each angle value ϕ of the applied field H_0, 4 measurements of the voltage are performed corresponding to the 4 combinations of the polarities of H_0 | *I*. The measured signal can be decomposed c) and d) in three components: ∑ (green): the signal sum, Δ (orange): the signal difference and V_l: the offset; respectively even/odd, odd/even in field/current, and an independent contribution (dashed). e) shows the current dependence of the amplitude ∑ and Δ at ϕ=0.

CONTRIBUTED PAPERS

9:30

GF-02. Mapping surface anisotropies in ferromagnetic (Ga,Mn)As films.

X. Liu[1], M. Dobrowolska[1], J. Furdyna[1], H. Puszkarski[2] and P. Tomczak[2]
1. Physics, University of Notre Dame, Notre Dame, IN, United States; 2. Faculty of Physics, Adam Mickiewicz University, ul. Umultowska, Poland

Ferromagnetic semiconductor (Ga,Mn)As has emerged as the most thoroughly studied material for spintronic applications [1]. An important property of this ferromagnetic material is its magnetic anisotropy [2]. However, the origins of this anisotropy have not yet been entirely explained. Full understanding of magnetic anisotropy in (Ga,Mn)As is especially important for its use in prospective applications as memory devices, and is being intensively investigated by various experimental techniques, such as ferromagnetic resonance (FMR) and spin-wave resonance (SWR) [3]. Most of these methods have been used to obtain information on volume characteristics of this material, such as bulk anisotropy fields and exchange constants. Recently, it has also been proposed [4] that one can employ the full potential of SWR to probe information on magnetic characteristics of the surface, such as surface anisotropy and surface pinning energy, and their dependence on the orientation of magnetization in the material. Our early attempts [5] have successfully determined the surface pinning parameters of (Ga,Mn)As from SWR spectra using the surface inhomogeneity model [6,7] obtained for different angular configurations (θ_H, ϕ_H) of the external static magnetic field H_{dc} with respect to the surface of the studied (Ga,Mn)As thin film. Although the obtained surface pinning parameter A as a function of the field (or magnetization) polar and azimuthal angles was obtained in only limited ranges of both angles, these results have stimulated fruitful theoretical discussion and insight [8,9]. Recent theoretical development in this area [4] focuses specifically on the spherical surface pinning (SSP) model, in which the surface spin pinning energy is expressed by configuration angles (the out-of-plane polar angle θ and the in-plane azimuthal angle ϕ). The model is based on a series expansion of the surface spin pinning energy, where the terms in the series represent respective pinning contributions from the cubic as well as the uniaxial anisotropies. In particular, the model has predicted the existence of double critical polar angle phenomenon in SWR measurements performed in specific out-of-plane configurations, not been observed in earlier studies. Stimulated by these predictions, we have conducted detailed SWR measurements on a 120 nm thick annealed $Ga_{0.92}Mn_{0.08}As$ film. SWR measurements were carried out using three basic geometries. In Geometry 1, the [110] edge of the specimen was oriented vertically. This configuration allows measurements with the dc field in any arbitrary direction in the (110) crystal plane, from [-110] to [001]. In Geometry 2, the sample was mounted with the [1-10] edge of the specimen oriented vertically. This configuration allows measurements with the dc field in any arbitrary direction in the (1-10) plane, from [110] to [001]. In Geometry 3, the sample was mounted with the [010] edge of the film oriented vertically. This configuration allows measurements with the dc field in any arbitrary direction in the (010) plane, from [100] to [001]. In Fig. 1, the spectrum clearly evolves as the applied field H_{dc} is rotated from the out-of-plane orientation ($\theta_H = 0^o$) to the in-plane orientation ($\theta_H = 90^o$, $\phi_H = -45^o$). In particular, for H||[001] a resonance spectrum consists of at least five well resolved Portis-type SWR lines. As one rotates H away from the perpendicular orientation, the SWR modes successively disappear, and eventually – at some critical angle θ_c (24° in Fig. 1) – the multi-SW spectrum vanishes except for a single narrow resonance line, which corresponds to the uniform FMR mode. For angles $\theta_H > \theta_c$, the multi-mode nature of the SW spectrum re-emerges, generally containing two or three broad resonances. The spectra obtained in Geometry 2 are similar to those shown in Fig. 1. As predicted in Ref. [4], the spectra obtained in Geometry 3 show a new phenomenon: here we observe *two* critical angles (20° and 38° in Fig. 2). Specifically, as one rotates H away from the perpendicular orientation, the SWR modes disappear at the first critical angle θ_{c1}. As θ_H increases, the multi-mode nature of the SW spectrum re-emerges; the peak on the high-field side is identified as an exchange-dominated non-propagating surface mode. However, at the second critical angle θ_{c2}, the multi-SW spectrum again vanishes, collapsing to a single narrow resonance line. For angles $\theta_H > \theta_c$ (*i.e.,* as one approaches the easy axis, H||[100]), the spectrum consists of at least three SWR lines, which are believed to be bulk modes. In summary, we have observed the double polar critical angle phenomenon in SWR, as predicted from the recent theoretical model for specific experimental configurations. This observation verifies the surface pinning model of SWR, thus bringing new insights to surface anisotropy phenomena in (Ga,Mn)As thin films, and providing new information relevant to spintronic applications.

[1] X. Liu, Y. Sasaki, and J. K. Furdyna, Phys. Rev. B 67, 205204 (2003). [2] U. Welp, V. K. Vlasko-Vlasov, X. Liu, J. K. Furdyna, and T. Wojtowicz, Phys. Rev. Lett. 90, 167206 (2003). [3] X. Liu, and J. K. Furdyna, Journal of Physics: Condensed Matter 18(13), R245 (2006). [4] H. Puszkarski, and P. Tomczak, Surface Science Reports 72, 351–367 (2017). [5] X. Liu, Y. Y. Zhou, and J. K. Furdyna, Phys. Rev. B 75, 195220 (2007). [6] H. Puszkarski, Acta Phys. Polonica A 38, 217 (1970); 38, 899 (1970). [7] H. Puszkarski, Prog. Surf. Sci., 9, 191 (1979). [8] H. Puszkarski, and P. Tomczak, Scientific Reports 4, 6135 (2014). [9] H. Puszkarski, P. Tomczak, and H. T. Diep, Phys. Rev. B 94(19), 195303 (2016).

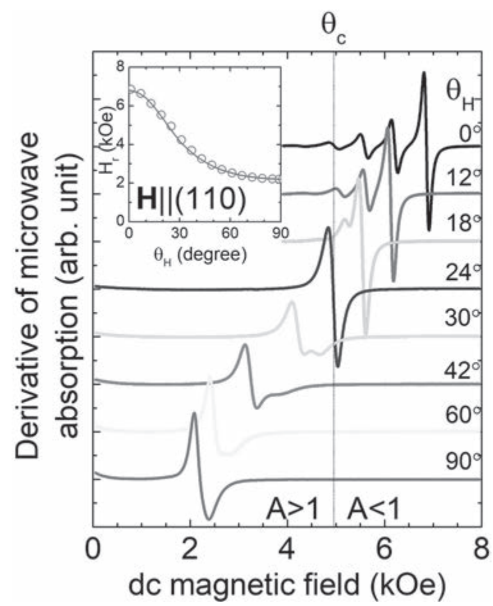

Fig. 1. SWR spectra at $T = 4$ K, at various orientations θ_H of H between [001] and [1-10] directions in the out-of-plane configuration ($\phi_H = -45^o$). The dotted vertical line indicates the field at which the surface parameter A crosses the $A = 1$ line once, at angles which we refer to as critical angles and denote as θ_c.

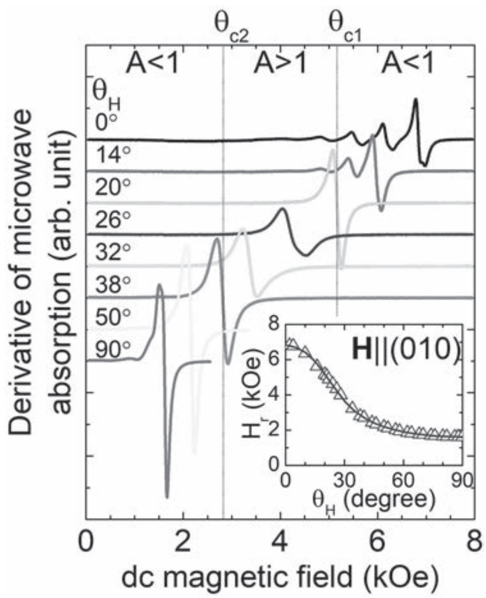

Fig. 2. SWR spectra at T = 4 K, at various orientations θ_H for H between the [001] and [100] directions in the out-of-plane configuration ($\phi_H = 0^o$). The dotted vertical lines indicate fields at which the surface parameter A crosses the A = 1 line twice, at angles which we will refer to as critical angles and denote as θ_{c1} and θ_{c2}.

9:45

GF-03. Reconfigurable Spin Wave Propagation in Pseudo One-Dimensional Magnonic Crystal for High Frequency Nanoscale Devices.

C. Banerjee[1], S. Choudhury[1], J. Sinha[1] and *A. Barman*[1]
1. S. N. Bose National Centre for Basic Sciences, Kolkata, India

In the light of increasing demand for computational resources, the electronic circuits are reaching their limits in terms of miniaturization, performance and energy consumption. Spin waves (SWs), the coherent oscillations of magnetization, are among the potential candidates for replacement of electric charges as information carriers which may satisfy those demands. The control and functionality of SW based logic is expected from the so-called magnonic crystal (MC)[1], which is formed by periodic modulation of magnetic properties in one- or two- dimensions, resulting in allowed and partially or fully forbidden SW modes which can be manipulated via a wide range of structural, geometric and magnetic parameters. Here we have studied by experimental and theoretical methods the magnonic characteristics in an array of nanoscale asymmetric sawtooth shaped width modulated ferromagnetic waveguides (ASW) with average width: 350 nm, forming a novel pseudo one-dimensional MC (See Fig. 1a)[2]. The interesting aspect of this system is that it features the periodic modulation of two different magnetic parameters in two perpendicular directions: in the z-direction there is a periodic distribution of magnetic dipolar field whereas the y-direction posses a periodic modulation of internal magnetic field. Using Brillouin Light Scattering (BLS) technique we measured the magnonic band diagram of this structure by varying the angle (ϕ) between the wave vector (directed along ASW axes) and magnetic field, which is compared with the calculated frequency dispersion using plane-wave method. The measurement geometry is shown in Fig. 1b. The change in the magnetic field direction gives rise to a modulation in the profile of periodically varying SW channel, which eventually determines the SW frequency dispersion. Consequently, the band structure for ϕ = 90° features propagating SW modes and is characterized by a pronounced magnonic bandgap. The frequency and size of the gap is effectively modified upon varying ϕ to 70°. The band structures are presented in Fig. 2 (Fig. 2a and 2b for ϕ = 90° and ϕ = 70°, respectively), where the blue lines denote the calculated band structure and the bold green lines signify the bands with predicted large scattering cross sections. The experimental data (red solid circles) are overlaid on the calculated dispersion, which is in good agreement with the latter. Further calculations of the spatial mode profiles reveal that the edge potential well modes can be effectively engineered by manipulating the edge corrugation. Overall, selective control on SW propagation is presented which asserts that this system may serve as a possible prototype for SW waveguide and SW filter operating in the GHz frequency regime.

[1] Lenk B. *et al.*, The Building Blocks of Magnonics, Phys. Rep. 507, 107 (2011). [2] Banerjee C., *et al.* (2017), Pseudo One-Dimensional Magnonic Crystal for High Frequency Nanoscale Devices, Phys. Rev. Applied 8, 014036 (2017).

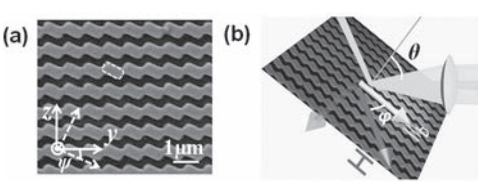

Fig. 1. (a) Scanning electron microscope (SEM) image of the studied ASW array. The co-ordinate axes are shown by the white arrows. (b) Schematic of the measurement geometry, where a green laser beam backscattered from the SWs carries the information of the SW dynamics. The in-plane angle ϕ between the magnon wave vector *q* and applied magnetic field *H* is shown, with both vectors lying in the sample plane.

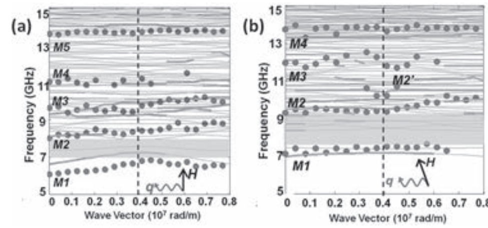

Fig. 2. Magnonic band structure in (a) ϕ = 90° and (b) ϕ = 70° geometry. The significance of different plots is given in the text.

10:00

GF-04. Field Controlled Modulation of Magnetization Dynamics and Spin-Wave Mode Conversion in Two-Dimensional Nanoscale Antidot Lattices.

A. De[1], S. Mondal[1], S. Sahoo[1], S. Barman[2], Y. Otani[3] and A. Barman[1]
1. S. N. Bose National Centre for Basic Sciences, Kolkata, India; 2. Institute of Engineering and Management, Kolkata, India; 3. The University of Tokyo, Chiba, Japan

Introduction Ferromagnetic antidot lattices (ADLs) have emerged as a strongt candidates for reconfigurable effective media for spin-wave (SW) propagation, the so-called magnonic crystal [1]. They also find potential applications in magneto-photonic crystals and ultrahigh density data storage media. Hitherto, significant research has been devoted to study the magnetization precession, damping, switching and SW dynamics in ferromagnetic ADLs with circular and square shaped holes. Here we report, field controlled modulation of ultrafast magnetization dynamics and SW mode conversion in a new type of $Ni_{80}Fe_{20}$ (Py) antidot lattice with triangular shaped holes arranged in hexagonal lattice. In these ADLs, the sharp edges of the triangular holes creates inhomogeneous internal magnetic fields due to the effective pinning centers for SWs created by the asym metric demagnetized regions between the neighboring antidots, which is mainly responsible for the observed tunability of the magnetization and SW dynamics. *Results and Discussion* Two 25 μm × 25 μm arrays of Py antidots with triangular holes arranged in hexagonal lattice have been fabricated by a combination of electron-beam lithography, electron-beam evaporation and ion milling. The edge length of the triangular hole is about 200 nm and the separation between the nearest edges of the antidots for the two samples is about 200 nm and 500 nm, respectively (lattice constants are 400 nm (S1) and 700 nm (S2), respectively). The ultrafast magnetization dynamics is measured by using a time-resolved magneto-optical Kerr effect (TRMOKE) microscope based upon a two-colour collinear pump-probe setup [2]. The second harmonic (λ = 400 nm, pulse width ~100 fs) of a Ti:sapphire laser was used to pump the samples, while the time-delayed fundamental (λ = 800 nm, pulse width ~80 fs) laser beam was used to probe the dynamics by measuring the polar Kerr rotation with an optical bridge detector. Figure 1a shows the scanning electron micrograph of sample S1 with the schematic of the bias field geometry. The azimuthal angle of the bias field ϕ is varied during the experiment. The experimental SW spectra for S1 show three modes for ϕ = 0°, 30°, 60° and 90° at H = 1 kOe. The spectra for 0° and 60° are qualitatively similar in nature (though the mode frequencies are not same). Also there is qualitative matching between the spectra for 30° and 90°. But the SW spectra are remarkably different for 15°, 45° and 75° with drastic increase in the number of modes at 45° and 75°. These indicate a change in the collective nature of the spin dynamics with varying ϕ values. For S2, instead of a large number of modes we get only two modes (one dominant mode with a low power shoulder) for almost all the angles. Micromagnetic simulations qualitatively reproduce the experimental results and reveal a transformation of fully extended standing SW modes to quantized ones and vice versa (mode conversion) simply by changing the in-plane orientation of the bias field. For S1 channels for SW propagation are found to be opened at ϕ = 0° (horizontally extended channel) and 60° (diagonally extended channel). For ϕ = 45° we get pseudo extended nature of SW modes along the diagonally extended channel. For the other angles due to unavailability of the channels, the powers of SWs are found to be concentrated at specific edges of the triangular holes. For ϕ = 15° and 30°, the powers of SWs are concentrated at the top and left most vertex of the triangular holes, respectively. At ϕ = 75°, each mode splits into two which are parallely running through the diagonally extended channel of the array. Interestingly for S2, due to the increased lattice constant, an additional SW propagation channel at ϕ = 90° gets opened and fully extended modes in DE geometry are obtained through the horizontal, diagonal and vertical channels for ϕ = 0°, 60° and 90° respectively. It is also observed that the domain structure and the internal fields change considerably with the variation of in-plane bias field orientation leading towards the variation in the SW mode structures as well as the mode frequencies. *Conclusion* We have successfully investigated the influence of the orientation of bias field and lattice constant to the ultrafast magnetization dynamics, SW mode conversion and magnetostatic field distribution in a two-dimensional array of triangular nanoholes forming a hexagonal antidot lattice in a thin Py film by using time-resolved Kerr microscopy and numerical simulations. The observed tunability of the magnetization dynamics with the change in the orientation of the bias field and lattice constant is significant for future magnonic and spintronic devices. *Acknowledgement* We gratefully acknowledge the financial support from S. N. Bose National Centre for Basic Sciences (grant no. SNB/AB/12-13/96) and Department of Science and Technology, Government of India (grant No.SR/NM/NS-09/2011 (G)).

1. B. Lenk et al., Phys. Rep. 507, 107 (2011). 2. A. Barman et al., Solid State Physics, 65, 1-108 (2014).

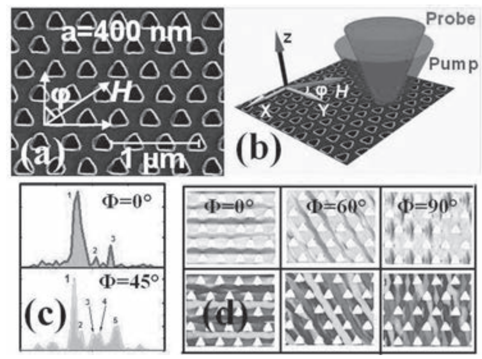

Fig. 1. (a) SEM image of the sample S1, (b) experiment geometry, (c) experimental FFT power spectra of S1 for two specific orientations of the in-plane bias field, and (d) simulated power and phase profiles of S1 for three specific orientations of the in-plane bias field.

10:15

GF-05. Propagating spin waves and reprogrammability in 1D Fibonacci magnonic quasicrystals.

F. Lisiecki[1], J. Rychly[2], P. Kuswik[1,3], H. Glowinski[1], M. Zelent[2], F. Gross[4], I. Bykova[4], M. Weigand[4], G. Schütz[4], J.W. Klos[2,5], M. Krawczyk[2], F. Stobiecki[1,6], J. Dubowik[1] and J. Gräfe[4]
1. Institute of Molecular Physics Polish Academy of Sciences, Poznan, Poland; 2. Faculty of Physics, Adam Mickiewicz University, Poznan, Poland; 3. Centre for Advanced Technology, Adam Mickiewicz University, Poznan, Poland; 4. Max Planck Institute for Intelligent Systems, Stuttgart, Germany; 5. Institute of Physics, Ernst Moritz Arndt University, Greifswald, Germany; 6. NanoBioMedical Centre, Adam Mickiewicz University, Poznan, Poland

Magnonic crystals are magnetic structures with periodically modulated magnetic properties, thus, enabling modification of the magnonic band structure to feature allowed and forbidden frequency bands in the spin wave (SW) spectrum [1]. Moreover, the spectrum can be influenced by using an external magnetic field to change the local magnetization structures. These features offer fine tuning and reprogrammability, which are desirable for applications [2]. Quasicrystals have long-range order, but no periodicity. Introducing such quasiperiodicity in magnonic structures yields an additional degree of freedom for SW manipulation. In comparison to periodic systems, magnonic quasicrystals are characterized by a more complex dispersion relation with an increased number of band gaps and narrow allowed bands, and localized excitations which can be concentrated in various parts of the structure [3]. In this work, we investigate one-dimensional magnonic quasicrystals consisting of 10 μm long nanowires (NWs) from 30 nm thick permalloy (Py – $Ni_{80}Fe_{20}$). These NWs are either wide (1400 nm) or narrow (700 nm) and dipolarly coupled over 80 nm wide air gaps. The NWs are arranged using the Fibonacci inflation rule, according to which, analogously to the creation of the Fibonacci sequence, the structure of higher order consists of the sum of the two previous structures, and structure of the 1st and 2nd order is a single narrow or wide NW, respectively. Spin waves are excited with a coplanar waveguide that is integrated on top of the structure and aligned parallel to the NWs. The external magnetic field is applied perpendicular to that direction, along the NWs. Spin waves excited by coplanar waveguide (CPW) are imaged using scanning transmission X-ray microscopy (STXM) at the MPI IS operated MAXYMUS end station at the UE46-PGM2 beam line at the BESSY II synchrotron radiation facility. This technique allows imaging of the magnetization dynamics with spatial and temporal resolution down to 18 nm and 35 ps, respectively, while providing phase resolution and spectral sensitivity. In the images, the gradual variation of phase in the direction perpendicular to the NWs is observed, which indicates the propagating character of these SW resonances. Modes from the 1st and 2nd bands are detected and can be distinguished by the presence of a node in the excitation profile along the width of the wider NWs for modes from the 2nd band. Additionally, evanescent SWs are measured at frequencies inside of the band gap. Furthermore, mini band gaps in the spectrum are observed that also efficiently forbid SWs propagation. These findings directly prove the influence of collective effects of the quasiperiodic order on the SW dispersion relation. Additionally, reprogrammability of the Fibonacci structures is demonstrated to showcase the utility of magnonic quasicrystals for future applications. Figure 1 shows the SW spectra obtained from numerical calculations at 5 mT for ferromagnetic (FO, neighboring NWs parallel) and antiferromagnetic (AFO, neighboring NWs antiparallel) order of the NWs magnetization. It becomes evident, that the change in magnetization configuration has a significant influence on the SW band structure. To elucidate the microscopic origin of this change in the SW spectrum, selected modes A-C where captured by STXM and are shown in Figure 2. Frequency A lies in the 1st band and strong excitations for the FO and AFO order are visible. However, for the AFO case, there is a phase jump between wide and narrow NWs, which means that the magnetization precession in these two NWs types has opposite sign. Frequency B lies in the band gap for FO order but is close to the 2nd band for AFO order. Thus, a propagating SW is only observed for the latter. For frequency C the opposite is true: it is close to the 2nd band for FO order and lies in the band gap for AFO order. Hence, propagating SW can only be observed for FO order here. These observations indicate that by switching the magnetic structure between these two states, it is possible to reprogram the dispersion and, thus, control the transmission of the SWs. The interpretation of experimental results are aided by numerical calculations. Excellent agreement between measurement and simulation is found and the SW mode profiles could be matched (*cf.* Figure 2). In summary, we show that quasiperiodicity provides an additional degree of freedom in tuning SW dispersion relations and typical features of quasicrystals are reproduced for the magnonic band structure as directly imaged by STXM. Furthermore, the reprogrammability of 1D magnonic quasicrystals, that is demonstrated here, allows advanced tailoring of the SW spectrum, which opens up new pathways for the potential applications.

[1] M. Krawczyk and D. Grundler, J. Phys. Condens. Matter 26, 123202 (2014). [2] J. Topp, D. Heitmann, M. P. Kostylev, and D. Grundler, Phys. Rev. Lett. 104, 207205 (2010). [3] J. Rychly, J. W. Klos, M. Mruczkiewicz, and M. Krawczyk, Phys. Rev. B 92, 054414 (2015).

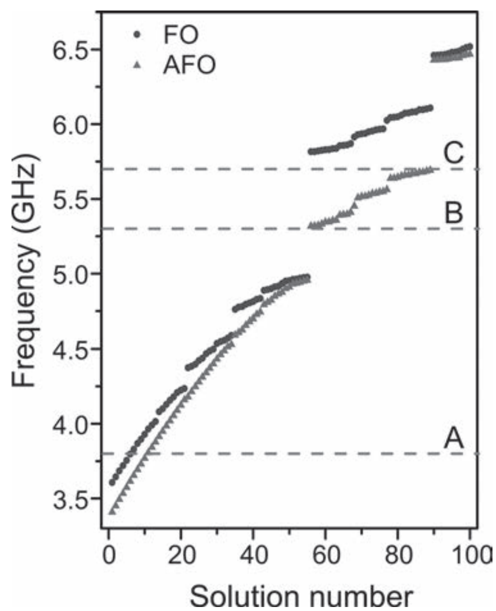

Fig. 1. The SWs dispersion obtained from numerical calculations for the Fibonacci structure with ferromagnetic (FO) and antiferromagnetic (AFO) order of the magnetization at 5 mT. Horizontal dashed lines indicate the frequencies at which STXM measurements are shown.

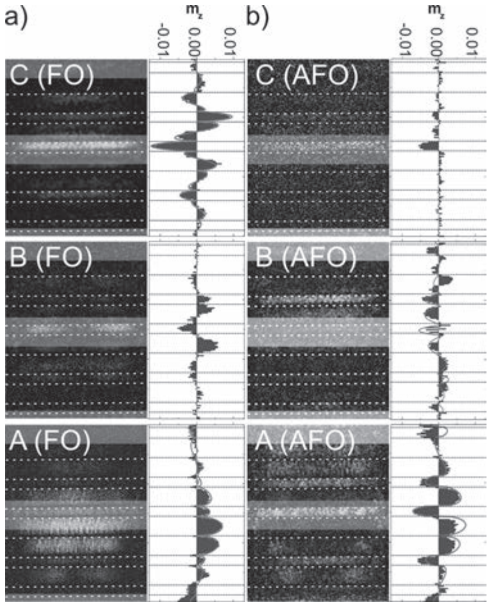

Fig. 2. Amplitude (color)-phase (brightness) STXM images for different excitation frequencies (A-C) at 5 mT in (a) ferromagnetic (FO) and (b) antiferromagnetic (AFO) order. The transparent gray rectangles mark the position of the CPW and the dashed white lines – the gaps between the stripes. Excitation profiles are plotted on the right side of the images (blue bars) and compared with simulated profiles (red lines).

10:30

GF-06. 3D magnonic crystals.

E. Beginin[1], A.V. Sadovnikov[1,2], A. Sharaevskaia[1,2], A. Stognij[3] and *S. Nikitov*[1,2]

1. Nonlinear Physics, Saratov State University, Saratov, Russian Federation; 2. Kotel'nikov Institute of Radioengineering and Electronics, Russian Academy of Sciences, Moscow, Russian Federation; 3. Scientific-Practical Materials Research Center, National Academy of Sciences of Belarus, Minsk, Belarus

Magnetic micro- and nanostructures are extensively investigated due to their potentials as candidates for future spintronic and magnonic devices [1-4]. Main carriers of signals used for information processing in such structures are magnons and, in particular, magnetostatic spin waves (MSW). They are also possible candidates for beyond-CMOS (complementary metal-oxide semiconductor) technologies [5], as they are free of Joule heating and, respectively, free of power loss associated with traditional electronics [6,7]. Here, the concept of three-dimensional (3D) magnonic crystals is discussed for the first time. A meander type ferromagnetic film which can be grown at the top of the structured substrate can be a candidate for such 3D crystal (see Fig.1). Propagating wave dispersion and band structure in such crystals are calculated using finite elements method and by the means of micromagnetic simulation. Amplitudes of magnetostatic potentials as functions of frequencies are also deduced. Wave reflections and transmissions at the corners of parts of the meander waveguide are discussed and estimated within the model of transfer matrix method [8]. Furthermore, the properties of coupled 3D magnonic crystals are also considered. We considered the meander type structure with isotropic ferromagnetic layer saturated by in-plane magnetic field. We restrict ourselves by dipole approximation eliminating the exchange interactions. The calculation of the magnetic field within one cell of the periodic structure was provided using magnetostatic equations as well as periodic boundary conditions using finite elements method (FEM) [9]. In order to calculate dispersion of the propagating MSW in such structures we used Maxwell's equations in a magnetostatic approximations with electrodynamic boundary conditions. It has been shown that the band gaps have clearly appeared in dispersion of magnetostatic surface spin waves (MSSW) propagating in such 3D structures. They were at the frequencies of Bragg resonances when the MSSW wavelength is equal to two periods of the periodic structure. Dispersion characteristics of MSSW are shown in Fig. 2 at various meander depths. Two main conclusions can be made based on the results of this Figure. Namely, as the depth of the groove is increased the width of the band gap is also increased. Second conclusion concerns that fact at fixed wavenumbers (or wave lenghts) the dispersion curves are shifted in the lower frequencies and this is due to decrease of the MSSW phase velocities. Authors acknowledge the financial support from RFBR through the grant 18-57-76001.

[1] S. O. Demokritov, Spin Wave Confinement: Propagating Waves (2nd Edition) (Pan Stanford Publishing Pte. Ltd, 2017). [2] V. V. Kruglyak, S. O. Demokritov, and D. Grundler, J. Phys. D: Appl. Phys. 43, 264001 (2010). [3] A. V. Chumak, V. I. Vasyuchka, A. A. Serga, and B. Hillebrands, Nat Phys 11, 453–461 (2015) [4] A. V. Sadovnikov, C. S. Davies, V. V. Kruglyak, D. V. Romanenko, S. V. Grishin, E. N. Beginin, Y. P. Sharaevskii, and S. A. // Phys. Rev. B 96, 060401(R) (2017) [5] ITRS, International Technology Roadmap for Semiconductors (ITRS) 2015 edition, http://www.itrs2.net/itrs-reports.html (accessed 1 January 2018). [6] A.V. Sadovnikov, S.A. Odintsov, E.N. Beginin, S.E. Sheshukova, Yu. P. Sharaevskii and S.A. Nikitov// Phys. Rev. B 96, 144428 (2017). [7] A. V. Sadovnikov, A. A. Grachev, E. N. Beginin, S. E. Sheshukova, Y. P. Sharaevskii, and S. A. Nikitov, Phys. Rev. Applied 7, 014013 (2017). [8] I. V. Rojdestvenski, M. Cottam, and A. N. Slavin, J. Appl. Phys. 79, 5724 (1996). [9] M. Koshiba, K. Hayata, and M. Suzuki, Journal of Lightwave Technology 4, 121–126 (1986).

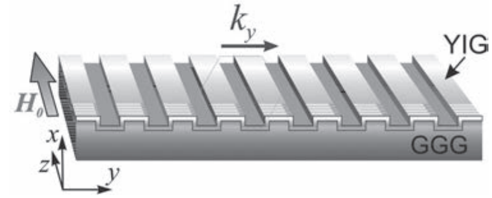

Fig. 1. The schematic view of meander magnonic waveguide

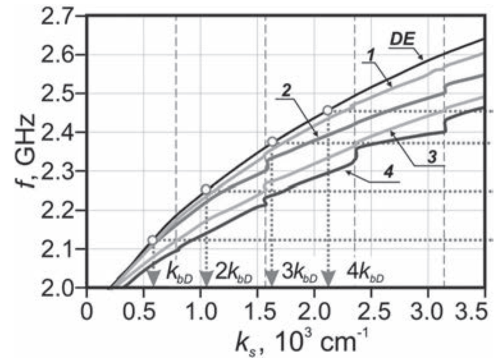

Fig. 2. Dispersion characteristics of Damon-Eshbach wave in the uniform film (denotes as DE) and Bloch wave dispersion in 3D-MC at various meander depths: 1–1µm,2–3µm,3–6µm,4– 9 µm. The vertical dashed lines denote the Bragg wavenumbers.

10:45

GF-07. Magnetization Dynamics of $Ni_{80}Fe_{20}$ Nanowires with Continuous Width Modulation.

L. Xiong[1], M. Kostylev[2] and A. Adeyeye[1]

1. National University of Singapore, Singapore; 2. University of Western Australia, Crawley, WA, Australia

INTRODUCTION The static and dynamic behaviors of ferromagnetic nanowires (NWs), have been subject to extensive explorations in the last few decades due to their great promise for applications in spintronic devices[1] and tunable magnonic filters[2]. Researches have shown that notches can be used either to locate DW positions or to boost the propagation of DWs. It has also been published that geometrical constrictions on micron-scale NWs can be used to tune resonant frequencies of NWs[3]. Recently, works on tuning the band structures of one-dimensional width modulated magnonic crystals (MCs)[4] have shown that two or more band gaps appear due to the NW modulation. However, most of the studies of NWs with modulation reported so far are theoretical with very few detailed experimental results. Thus, it would be interesting to investigate the magnetization reversal and dynamic behaviors of NWs with continuous width modulation. EXPERIMENTAL AND SIMULATION DETAILS Two sets of $Ni_{80}Fe_{20}$ NW arrays, homogeneous NWs (NWHs) for reference and NWs with continuous width modulation (NWMs), were fabricated over an area of 4x4 mm^2 on top of a silicon substrate for direct comparison. Typical scanning electron microscope (SEM) images are shown in Fig. 1. The thickness t of the wires is varied in the range from 5 to 70 nm. The collective magnetization reversal processes of the arrays were characterized at room temperature using vibrating sample magnetometer (VSM) by sweeping the magnetic field along the easy axis of the NWs. The dynamic behaviors of the NWS were investigated using broadband ferromagnetic resonance spectroscopy (FMR). In order to understand the dynamic response of the wires, micromagnetic simulations were performed using the LLG micromagnetic simulator, which computes the equilibrium magnetization distribution of the NWs based on the Landau-Lifshitz-Gilbert (LLG) equation: $\partial_m/\partial_t = -\gamma m \times H_{eff} + \alpha m \times \partial_m/\partial_t$ (1) The resonant mode profiles were extracted using spatially and frequency-resolved Fast-Fourier-Transform (FFT) imaging method. In all the simulations, periodic boundary condition was used to mimic the wire arrays. RESULTS A systematic investigation of the magnetization reversal and the dynamic behaviors of uncoupled $Ni_{80}Fe_{20}$ NWs with artificial continuous width modulation is presented. In contrast with the single resonance mode observed in the NWHs from the FMR, the NWMs display three to five distinct resonance modes with increasing wire thickness in the range from 5 to 70 nm due to the non-uniform demagnetizing field as shown in Figs. 2(a)-(b). The highest frequency mode and the frequency difference between the two distinct highest modes are shown to be markedly sensitive to the NW thickness. Interestingly, we found that these modes can be described in terms of the quantization of the standing spin waves due to confined varied width. Typical simulated mode profiles for the NWMs with 30-nm $Ni_{80}Fe_{20}$ are shown in Fig. 2(c). In addition, the easy axis coercive field for the width modulated NWs is much higher than homogeneous NWs of the same thickness when less than 70 nm. Our experimental results are in good qualitative agreement with the micromagnetic simulations.[5] The results may find potential applications in the design and optimization of tunable magnonic filters.

[1] S. P. S. Parkin, M. Hayashi, and L. Thomas," Magnetic Domain-Wall Racetrack Memory", *Science* 320, 190 (2008). [2] S. Choi, K.-S. Lee, K. Y. Guslienko, and S.-K. Kim, "Strong Radiation of Spin Waves by Core Reversal of a Magnetic Vortex and Their Wave Behaviors in Magnetic Nanowire Waveguides", *Phys. Rev. Lett.* 98, 087205 (2007). [3] J. Ding, V. E. Demidov, M. G. Cottam, S. O. Demokritov, and A. O. Adeyeye, "Dynamic behavior of Ni80Fe20 nanowires with controlled defects", *Appl. Phys. Lett.* 104, 143105 (2014). [4] K. Di, H. S. Lim, V. L. Zhang, S. C. Ng, M. H. Kuok, H. T. Nguyen, and M. G. Cottam, " Tuning the band structures of a one-dimensional width-modulated magnonic crystal by a transverse magnetic field", *J. Appl. Phys.* 115, 053904 (2014). [5] L. L. Xiong, M. Kostylev, and A. O. Adeyeye, "Magnetization dynamics of Ni80Fe20 nanowires with continuous width modulation", *Phys. Rev. B* 95, 224426 (2017)

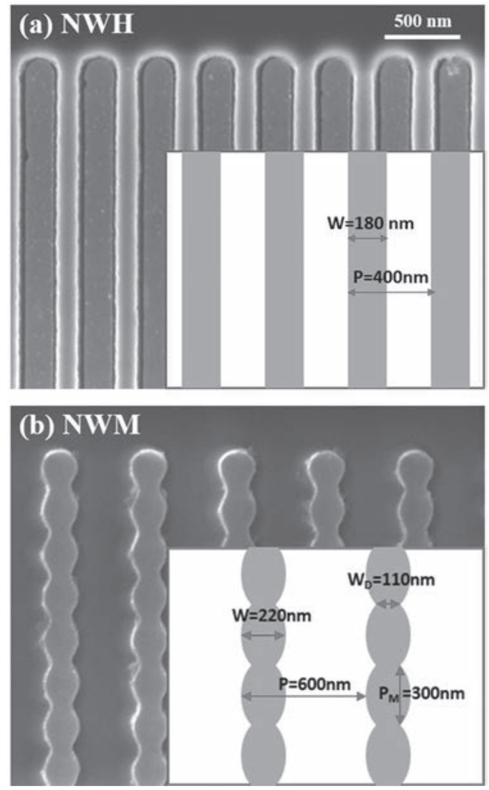

Fig. 1. SEM images for (a) NWHs and (b) NWMs.

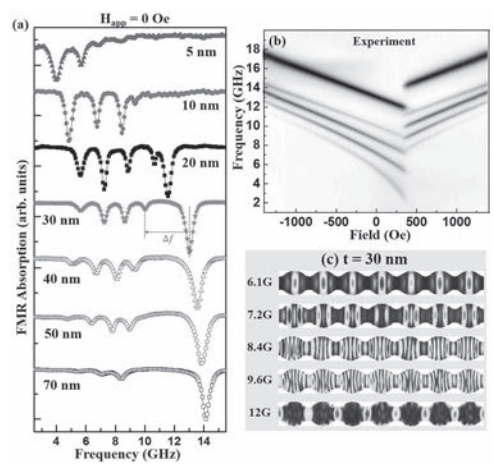

Fig. 2. (a) Experimental absorption spectra for NWMs at remanence (H_{app} = 0 Oe) as a function of $Ni_{80}Fe_{20}$ thickness (t) in the range from 5 to 70 nm. (b) Experimental 2-D FMR spectra and (c) simulated mode profiles for 30 nm NWMs at remanence (H_{app} = 0 Oe).

11:00

GF-08. Efficient Modulation of Spin Wave Dynamics in two-dimensional Quasiperiodic magnonic crystals.

S. Choudhury[1], S. Barman[2], Y. Otani[3,4] and A. Barman[1]
1. S. N. Bose National Centre for Basic Sciences, Kolkata, India; 2. Institute of Engineering and Management, Kolkata, India; 3. Institute for Solid State Physics, University of Tokyo, Kashiwa, Japan; 4. RIKEN-CEMS, Wako, Japan

I. INTRODUCTION Magnonic crystals [1] (MCs) are artificial crystals, fabricated by the periodic arrangements of magnetic nanostructures which form magnonic band structures with allowed and forbidden frequency bands. For such MCs, spin waves (SWs) are the transmission waves. Since the wavelengths of SWs are in the nanoscale at gigahertz frequency regime, MCs offer great prospects for on-chip communication devices. In addition, due to the anisotropic propagation of the SWs, the frequency position and width of the band gap can also be tuned by varying various physical and geometrical properties of the MCs. Ferromagnetic antidot lattices (ADLs) [2] belong to a unique class of MCs where antidots (holes) are periodically patterned on a ferromagnetic thin film and they are strongly dipole-exchange coupled media with larger propagation velocities of SWs as opposed to dipolar coupled nanodot or nanowire arrays. In such ADLs, magnonic band structures can be efficiently modified by tuning the packing density of antidots in the lattice as well as the lattice symmetry due to the large modulation of the demagnetization regions around the antidots. The large tunability of magnonic band structures and modulation of SW velocities with the periodicity of the lattice make two-dimensional (2D) ADLs an interesting topic in magnetism, for controlling the SW propagation and also for other kinds of applications. II. EXPERIMENTS AND ANALYSIS Here, we report the investigation of the high-frequency magnetization dynamics of 2-dimensional arrays of $Ni_{80}Fe_{20}$ (NiFe) antidots of 20 nm thickness (t) with circular shape of diameter (d) 140 nm arranged in octagonal lattices which may be considered as magnonic quasiperiodic crystal with varying lattice spacing (a) of 300, 400, 500, 600 and 700 nm. For the dynamical measurement, we used a broadband ferromagnetic resonance (FMR) spectrometer [3] based on vector network analyzer (VNA) under the application of an in-plane bias magnetic field (H_{ext}), whose magnitude is varied from 0.2 to 1.56 kOe during the measurements at a fixed value of in-plane angle $\Phi = 0°$. We observed a significant tunability in the SW spectra with the increase in lattice spacing (a). For $a = 300$ nm, seven SW modes are observed as shown in Fig. 1(c), which converge into two modes for $a = 700$ nm. The experimental results have been well reproduced by micromagnetic simulation and different types of extended and localized standing SW modes with varying quantization numbers are observed. The configurational anisotropy of the samples is investigated by varying the azimuthal angle (Φ) of the bias field from 0° to 360° at $H_{ext} = 800$ Oe. We have observed a significant eight-fold rotational symmetry superposed with a four-fold and two-fold anisotropies in these octagonal crystals with the orientation of the bias magnetic field as shown in Fig. 1(d) for $a = 300$ nm, while the value of this anisotropy is reduced with the increase in the lattice spacing (a). The magnetostatic field distribution within the octagonal unit cell is mainly responsible for the origin of the eight-fold anisotropy, whereas the rhombus-like cell present between two octagonal unit cell is mainly responsible for the four-fold anisotropy. In addition to this, the phase profile shows a mode conversion from extended SW mode to quantized standing SW mode for these samples with the rotation of the bias field direction. III. CONCLUSION In summary, we have fabricated high-quality arrays of circular shaped NiFe antidots arranged in an octagonal lattice with diameter 140 nm and the lattice constant is varied from 300 nm to 700 nm. The magnetization dynamics of these samples are investigated with the help of broadband FMR spectroscopy by varying the strength and orientation of the applied magnetic field. The experimental results showed a remarkable variation in the SW spectra with the variation of lattice constants. The experimental results have been well reproduced by micromagnetic simulation and the magnetostatic fields including the demagnetization field distributions are calculated to interpret the origin of the observed SW modes. The configurational anisotropy of the samples shows the presence of an eight-fold rotational anisotropy superposed with four-fold and two-fold rotational anisotropies. These observations open more opportunities in the engineering of quasiperiodic arrays for magnonic and spintronic devices. IV. ACKNOWLEDGEMENT The authors gratefully acknowledge financial support from Department of Science and Technology, Government of India under grant no. SR/NM/NS-09/2011. S. C. acknowledges S. N. Bose National Centre for Basic Sciences for the senior research fellowship.

[1] V. V. Kruglyak *et al.*, "Magnonics", *J. Phys. D: Appl. Phys.* 43, 264001 (2010). [2] S. Neusser *et al.*, "Magnonics: Spin Waves on the Nanoscale", *Adv. Mater.* 21, 2927 (2009). [3] S. Choudhury *et al.*, "Efficient Modulation of Spin Waves in Two-Dimensional Octagonal Magnonic Crystal", *ACS Nano* 11, 8814 (2017).

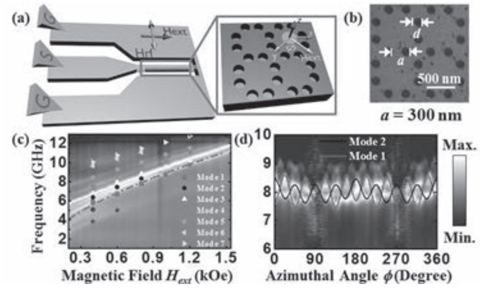

Fig. 1. (a) Schematic of broadband FMR technique used for NiFe ADLs. (b) Scanning electron micrograph (SEM) of NiFe ADL arranged in octagonal lattice with periodicity (*a*) of 300 nm and antidot (hole) diameter (*d*) of 140 nm. (c) Bias magnetic field (H_{ext}) dependent SW dispersion plot of NiFe ADL with $a = 300$ nm at azimuthal angle $\Phi = 0°$. Here, the surface plot represents the experimental result while the filled symbols correspond to the simulated results. The red dotted line represents the Kittel fit to the lowest frequency mode 1 of the lattice. (d) Variation of SW frequency with Φ varying from 0° to 360° for NiFe ADL with $a = 300$ nm at $H_{ext} = 0.8$ kOe. The surface plots represent the experimental results, while the solid lines describe the sinusoidal fits for the observed anisotropic SW modes. The color map associated with the surface plots is given at the bottom right corner of the figure.

11:15

GF-09. Low losses YIG based nano-magnonic crystals for tunable frequency filtering.

H.P. Merbouche[1], M. Collet[1], L. Soumah[1], S. Xavier[2], V. Cros[1], P. Bortolotti[2] and A. Anane[1,3]
1. Unité Mixte de Physique CNRS/THALES, Palaiseau, France; 2. Thales Research & Technology, Palaiseau, France; 3. Université Paris-Sud, Orsay, France

Spin waves based devices are promising for next generation analog signal processing systems as they display small wavelength (μm) and easily tunable frequencies in the radiofrequency regime. For instance, by propagating spin waves through a periodic magnetic structure, i.e., a magnonic crystal (MC), one can achieve filtering in the GHz regime at the micro-scale [1]. For a long time, YIG-based magnonic crystals could not be downscaled to the sub-micrometer range as standard liquid phase epitaxy growth techniques yield relatively thick films (>1μm) incompatible with nanolithography. In the last few years, the advent of nanometer-thick YIG films of high quality either grown using pulsed laser deposition (PLD [2]) or sputtering ([3]) has open new perspective to adapt the knowledge that has been developed for metallic magnonic crystals ([4]) to YIG. Recently, using phase resolved μ-BLS microscopy on a width-modulated YIG waveguide, frequency filtering has been reported [5];indeed, the spin-wave propagation length was decreased by a factor of 4 inside a 15MHz band gap. However, this filtering came at the cost of increased propagation losses. Here we report on S-parameter characterization of a series of ultrathin YIG MC waveguides using Propagating Spin Wave Spectroscopy (PSWS). The MC obtained by etching 150 nm wide, periodically spaced grooves. Thickness modulation is expected to improve the filtering efficiency and insertion losses compared to width-modulated MC. The studied system is composed of 50 parallel wave-guides that are each 2.5μm-wide. These guides are designed using e-beam lithography and laser lithography and etched off 20nm thick YIG film PLD grown film with a Gilbert damping of $4x10^4$ [6]. Two U-asymmetric gold antennas are deposited on top, 30μm apart (see figure 1.a). The 150nm wide periodic grooves, orthogonal to the waveguides principal axis (see fig.1.b) corresponds to a Bragg k-vector of $1\mu m^{-1}$, the depth of the grooves is incremented from 0 to 20nm in 6 successive steps. The spectrum of mutual inductance due to the propagation of the spin waves is recorded over a frequency range between 0.5 and 2.5GHz, at various magnetic fields. A first measure of these spectra is performed on the waveguide without grooves (un-etched) and is found to be in good agreement with theoretical expectations for magnetic fields up to 20 mT. Within the same field range, we then measure the mutual inductance after etching for the same magnonic crystals having now grooves depth greater than 5nm. An example of successful filtering at 1.3GHz obtained for a field μ_0H=9mT is shown in figure 2. A 20MHz transmission gap is observed corresponding to a decrease by a factor of 4 of the spin wave intensity at 30μm from the antenna when compared to the reference waveguide. Importantly, we also find that the transmission outside the frequency gap is unaffected by the presence of the periodic grooves, even until an etching depth of about 10nm (not shown) in the 20 nm thick YIG film. In summary, we demonstrate a microscopic magnonic crystal based on ultra-thin YIG films suitable for implementation of nano-scale magnonic circuits with smaller dissipation than its width-modulated counterpart. Furthermore, the attenuation length of our films being of the order of 150μm in this frequency range, we expect to obtain much higher frequency selectivity by increasing the distance between our antennas up to 100μm, thus increasing the number of periods of our magnetic crystal while preserving our moderate propagation losses.

[1] Chumak, A. V., Serga, A. A. & Hillebrands, B. Magnonic crystals for data processing. *J. Phys. D. Appl. Phys.* 50, (2017). [2] Kelly, O. A. *et al.* Inverse spin Hall effect in nanometer-thick yttrium iron garnet / Pt system. *Appl. Phys. Lett.* 103, 10–14 (2013). [3] Wang, H., Du, C., Hammel, P. C. & Yang, F. Strain-tunable magnetocrystalline anisotropy in epitaxial Y3Fe5O12 thin films. *Phys. Rev. B* 89, 134404 (2014). [4] Krawczyk, M. & Grundler, D. Review and prospects of magnonic crystals and devices with reprogrammable band structure. *J. Phys. Condens. Matter* 26, (2014). [5] Collet, M. *et al.* Nano-patterned magnonic crystals based on ultrathin YIG films. *ArXiv:* 1705.02267, 1–13 (2017). [6] Collet, M. *et al.* Spin-wave propagation in ultra-thin YIG based waveguides. *Appl. Phys. Lett.* 92408, (2017).

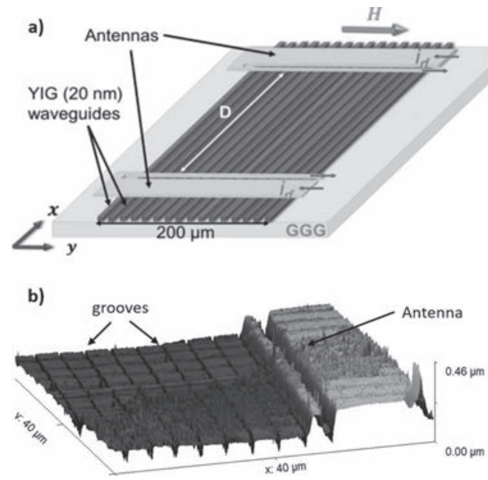

Fig. 1. a) Sketch showing our YIG waveguides and inductive antennas b) 40μmx40μm AFM image of the YIG waveguides, showing the 150nm wide grooves openend in the PMMA resine before the dry ion etching process, with a period a=3.14μm.

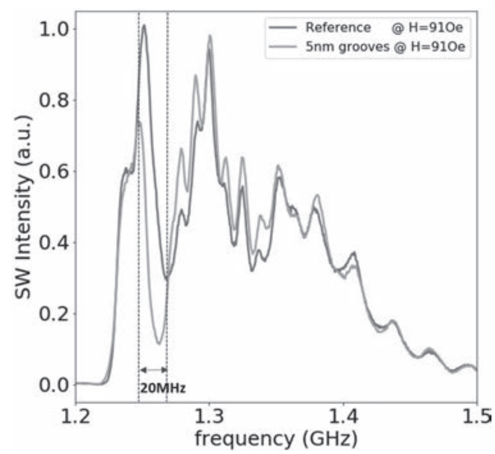

Fig. 2. Spectrum of the spin wave intensity at 30μm from the antenna, in arbitrary units, in the reference waveguides (blue curve) and in the 5nm-etched MC (orange curve) for an applied external field μ_0H=9mT. Dotted lines indicate the limits of the 20MHz gap.

11:30

GF-10. Integrated magnonic networks based on the lateral magnonic stripes and magnonic crystals.

A.V. Sadovnikov[1,2], Y. Sharaevsky[1], S. Sheshukova[1], E. Beginin[1] and S. Nikitov[2,1]
1. Nonlinear Physics, Saratov State University, Saratov, Russian Federation; 2. Kotel'nikov Institute of Radioengineering and Electronics, Russian Academy of Sciences, Moscow, Russian Federation

In recent years much research has been directed towards the use of spin waves (SWs) for signal processing at microwave and subterahertz frequencies due to the possibility to carry the information signal without the transmission of a charge current[1,2]. Magnonic crystal (MCs)[1,2] have attracted a significant attention due to their wide range of application and numerous ways to fabrication. MCs are used in linear and nonlinear magnonics as a building block of magnonic networks. In the majority of the previously realized devices the MCs have been used as the high-Q tunable rejection filter due to the most important features of the MCs – the magnonic forbidden (rejection) band or magnonic band gap in the spin-wave spectra. However, the possible use of the magnonic forbidden band to fabricate the drop filters in magnonic integrated circuits can extend the application of MCs, in particular, for the magnonic logic[1,2,3]. In the asymmetric MC the spin waves have non-equal propagation constants and thus the phase-matching condition is violated. While phase mismatch might seem on the surface to decrease the coupling efficiency, the unusual increase of the spin-wave coupling can be observed at the frequencies in the vicinity of the magnonic band gap. This idea can underpin the experimental and theoretical studies regarding the side-coupled magnonic crystals, which can also act as frequency selective multiplexers. Here we report the experimental observation of the spin-wave coupling in the asymmetric adjacent magnonic crystals based on multimode yttrium iron garnet (YIG) waveguides[4-8]. We show, that the combination of frequency and spatial filtering features of the MC and spin-wave coupling in the adjacent magnetic waveguide leads to the realization of the magnonic drop filter (Fig.1). We also identify the mechanism of the efficient spin-wave power transmission between the magnonic crystals. As a major result, we have demonstrated by the means of the space-resolved Brillouin light scattering (BLS) technique, that non-identical MCs within close proximity demonstrates the efficient spin-wave coupling at the frequency of the magnonic forbidden gap of one of the MCs. Thus MCs can be used not only to achieve the spatial and frequency filtering of spin-wave signal but also to provide the phase condition with an efficient spin-wave power transfer from the input to drop port of magnonic coupler. The obtained results open new perspectives for the future-generation electronics using integrated magnonic networks. This work was supported partially by the grant from Russian Science Foundation (No. 16-19-10283).

[1] S. O. Demokritov, Spin Wave Confinement: Propagating Waves (2nd Edition) (Pan Stanford Publishing Pte. Ltd, 2017). [2] V. V. Kruglyak, S. O. Demokritov, and D. Grundler, J. Phys. D: Appl. Phys. 43, 264001 (2010). [3] A. V. Sadovnikov, C. S. Davies, V. V. Kruglyak, D. V. Romanenko, S. V. Grishin, E. N. Beginin, Y. P. Sharaevskii, and S. A. // Phys. Rev. B 96, 060401(R) (2017) [4] A.V. Sadovnikov, S.A. Odintsov, E.N. Beginin, S.E. Sheshukova, Yu. P. Sharaevskii and S.A. Nikitov// Phys. Rev. B 96, 144428 (2017). [5] A. V. Sadovnikov, E. N. Beginin, S. E. Sheshukova, D. V. Romanenko, Y. P. Sharaevskii, and S. A. Nikitov, Applied Physics Letters 107, 202405 (2015). [6] A. V. Sadovnikov, E. N. Beginin, M. A. Morozova, Y. P. Sharaevskii, S. V. Grishin, S. E. Sheshukova, and S. A. Nikitov, Applied Physics Letters 109, 042407 (2016). [7] A. V. Sadovnikov, A. A. Grachev, E. N. Beginin, S. E. Sheshukova, Y. P. Sharaevskii, and S. A. Nikitov, Phys. Rev. Applied 7, 014013 (2017). [8] Q. Wang, P. Pirro, R. Verba, A. Slavin, B. Hillebrands, and A. Chumak, arXiv:1704.02255 (2017).

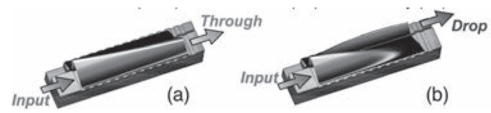

Fig. 1. "Through" and "drop" regime in the magnonic coupler based on the adjacent asymmetrical magnonic crystals.

11:45

GF-11. Tunable microwave properties of rhomboid shaped nanomagnet pairs.

C. Tian[1] and A. Adeyeye[1]
1. Electrical and Computer Engineering, National University of Singapore, Singapore

INTRODUCTION Nanomagnet-based memory and logic operations have attracted great technological interest in recent years due to their nonvolatility, low-power logic operations, ultrahigh density, and high endurance [1,2]. They are regarded as potential candidates for the next generation of non-volatile, low power logic devices beyond conventional CMOS technology. Recently, reconfigurable microwave responses have been shown based on in-plane dipolar coupled rhomboid shaped nanomagnets (RNMs) which do not require any stand-by power once initialized [3]. To optimize the frequency difference between ferromagnetic (FM) and antiferromagnetic (AFM) ground states, multilayer RNMs with a relatively thin nonmagnetic spacer layer have been investigated in which the nanomagnets are strongly out-of-plane dipolar coupled, and therefore a distinct frequency difference ($\Delta f \sim 1.9$ GHz) is achieved [4]. We may obtain a more complex relation of the magnetic ground state with the initialization field and intriguing magnetization dynamics at remanence by incorporating both in-plane and out-of-plane dipolar coupling in RNM-based structures. Thus, an understanding of the static and dynamic magnetic properties of the multilayer RNM pair in which the nanomagnets are both in-plane and out-of-plane dipolar coupled would be of great interest. EXPERIMENTAL DETAILS To probe the dynamic responses of the multilayer PQ-RNM pair experimentally using micro-focused Brillouin light scattering (micro-BLS) spectroscopy, a shorted ground-signal-ground (GSG) coplanar waveguide (CPW) made up of Cr (5 nm)/Pt (200 nm) was fabricated on a SiO_2/Si substrate using optical lithography and a liftoff process. Subsequently, PQ-RNM pairs were patterned using the electron beam lithography technique on top of the signal line of the shorted CPW as shown in the schematic representation in Fig. 1(a). The multilayer of $Ni_{80}Fe_{20}$ (25 nm)/Cr (15 nm)/$Ni_{80}Fe_{20}$ (20 nm) was deposited using electron beam evaporation followed by a lift-off process. A single-layer 45 nm thick $Ni_{80}Fe_{20}$ PQ-RNM of identical dimensions was also deposited as a control sample. In the micro-BLS technique, a monochromatic green laser (wavelength, 532 nm) with a focused spot size of ~250 nm was used to probe the dynamic response of a single RNM pair. RESULTS For the single-layer PQ-RNM pair, the BLS spectra for the two magnetic ground states (FM and AFM) are shown in Fig. 1(b). FM and AFM ground states were obtained by applying H_{ini} along the long and short axes, respectively. The AFM ground state has a higher resonance frequency because each nanomagnet experiences a larger effective field due to the stray field from its coupled neighbor. The multilayer PQ-RNM pair displays multiple magnetic ground states (FM, AFM1, and AFM2) upon different initialization fields [insets in Fig. 1(c)] due to the presence of both in-plane and out-of-plane dipolar coupling. The dynamic response as a function of initialization field has been systematically investigated. Distinct microwave absorption behavior and resonance frequency shift are observed when the nanomagnet pair is switched into different magnetic ground states as shown in Fig. 1(c). The observed resonance frequency shift can be understood in the context of a nanomagnet in the multilayer PQ-RNM pair experiences different stray fields depending on the magnetization orientations of its in-plane and out-of-plane coupled neighbors. Micromagnetic simulations validate our experimental observations [5].

[1] R. L. Stamps, S. Breitkreutz, J. Åkerman, A. V. Chumak, Y. Otani, G. E. W. Bauer, J.-U. Thiele, M. Bowen, S. A. Majetich, M. Kläui, I. L. Prejbeanu, B. Dieny, N. M. Dempsey, and B. Hillebrands, J. Phys. D: Appl. Phys. 47, 333001 (2014). [2] M. Krawczyk and D. Grundler, J. Phys.: Condens. Matter 26, 123202 (2014). [3] A. Haldar and A. O. Adeyeye, ACS Nano 10, 1690 (2016). [4] C. Tian and A. O. Adeyeye, Appl. Phys. Lett. 111, 152404 (2017). [5] C. Tian and A. O. Adeyeye, Appl. Phys. Lett. 111, 262402 (2017).

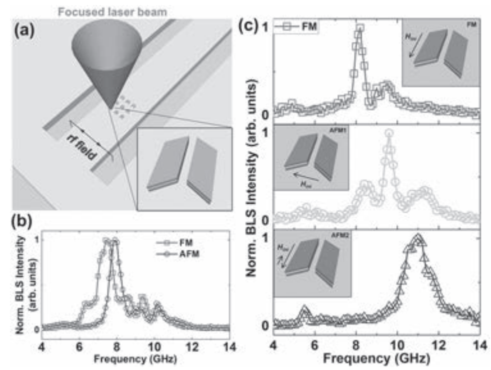

Fig. 1. (a) Experimental geometry for micro-BLS spectroscopy. Magnetization dynamics was measured from a single PQ-RNM pair with a laser focused down to 250 nm. The inset shows a zoomed-in view of the multilayer PQ-RNM pair which consists of two permalloy layers separated by a nonmagnetic Cr spacer layer. (b) BLS spectra at remanence ($H_{app} = 0$) for the single-layer PQ-RNM pair in FM and AFM ground states. (c) BLS spectra at remanence ($H_{app} = 0$) for the multilayer PQ-RNM pair in different magnetic ground states. Shown in the insets are the simulated magnetic ground states for multilayer PQ-RNM pair as a function of initialization field. At remanence, magnetization points either upward (↑ marked by red color) or downward (↓ marked by blue color) in each nanomagnet.

FRIDAY MORNING, 27 APRIL 2018 PEONY III, 9:00 TO 12:00

Session GG
MODELLING OF MACHINES V

Parag Upadhyay, Chair
ABB Inc., Raleigh, NC, United States

CONTRIBUTED PAPERS

9:00

GG-01. High-order methods applied to electrical machine modeling.

L. Friedrich[1], M. Curti[1], B. Gysen[1], J. Jansen[1] and E. Lomonova[1]
1. EPE, TU/e, Eindhoven, Netherlands

Introduction High-order methods have been subject of research over the last years to replace the time-consuming meshing operation of Finite Elements Method (FEM) by a structured grid, which is exploiting the tensor product. The problem formulation in these methods is generally the same, i.e. weak form implemented through the Bubnov-Galerkin method. First and second order polynomials functions used in FEM are replaced by high arbitrary-order polynomial functions because of their overall excellent accuracy and fast computation time. The Spectral Element Method (SEM) and Isogeometric Analysis (IGA) among others, are exploiting high order basis with established mathematical framework [1], [2], and available numerical tools [3]. In this paper, the solution for elliptic Laplace equation formulated with SEM and IGA are applied to 2D magnetostatic problems, including both linear and nonlinear materials. The obtained magnetic field distributions and post-processed parameters such as flux linkage, forces, and inductances are validated with FEM. A very low discrepancy is achieved which demonstrates the applicability of the proposed high-order methods, and enables integrated design-through-analysis of electrical machines. In this paper, SEM and IGA are applied to the analysis of two electrical machine benchmarks, in which a nonlinear iron characteristic is considered. Each of these methods uses different basis functions, quadrature rules, and space discretization, although both are based on the same Galerkin method. Modeling Solutions obtained from FEM are known to be very dependent on the quality of the triangular mesh [4]. Moreover, in FEM a curved geometry is approximated by linear elements which influences the accuracy, or comes at the cost of a high number of mesh elements. SEM divides the geometry into elements or patches, as exemplified in Fig. 1. Each patch is mapped to a unique square parent element, where calculations and matrix assembly are conducted. Legendre polynomials are used as basis functions. Lagrangian interpolation subsequently allows the computation of the solution on the Lobatto-Gauss-Legendre roots [1], and obtains the functional coefficients on the grid. IGA basis-functions are formed by the tensor-product of B-splines or NURBS (non-uniform rational B-splines), which is the industry-standard geometrical description used in computer aided design (CAD). The same basis functions allow to represent complex geometrical shapes [2], compute and visualize the solution. The physical domain is mapped to a rectangular computational domain, on which the basis functions and their gradients are known and where the calculations are conducted through numerical Gaussian quadratures. In both proposed methods, the geometry is discretized into 2D conforming patches where continuity is strongly imposed, forcing each basis function on the interface to match one-to-one. The formulation suited for 2D magnetostatic electrical machine modeling is further extended to include nonlinear material properties, such as soft-magnetic iron. The spatial distribution of the remanent magnetization and the magnetic incremental permeability are updated iteratively, according to the considered BH-curve, interpolated by means of a spline. The developed high-order methods allow for modeling curved topologies such as slots in a simpler manner than generally considered in analytical methods [5], in the same time, ensuring both flexibility and accuracy. Results and conclusion FEM reference results are obtained from a very dense second-order mesh and the accuracy threshold of the Newton-Raphson solver is reduced. A convergence comparison between the methods is conducted for the L2-norm. The first benchmark is used to compare magnetic forces, obtained by means of Virtual Work in FEM and Maxwell's Stress Tensor in both IGA and SEM. Moreover, two different integration paths are compared, and the influence of the quadrature rule and nodes is discussed. Magnetic vector potential distribution and discrepancies between FEM, IGA and SEM are displayed in Fig. 2. Additionally, the apparent and incremental inductance for the second benchmark are compared. The magnetic flux linkage is obtained through integration of the vector potential, consequently the apparent inductance is deducted. Spline interpolation of the flux linkage is conducted, from which the incremental inductance is computed with differentiation. Another method for calculating the incremental inductance is proposed, based on the magnetic potential generated by the remanent magnetization of the iron, while switching off the current density. The method has similar approach to frozen permeability [6]. Significant improvement of the incremental inductance prediction in terms of both accuracy and computational effort is achieved in comparison with the FEM results, obtained by means of local linearization. This aspect is specifically important for the control algorithms and power converters design. Concerning the calculation of the force and flux linkage, discrepancies are below one percent, which demonstrates the accuracy and applicability of the developed high-order methods for electrical machine modeling.

[1] D. Kopriva, "Implementing spectral methods for partial differential equations: Algorithms for scientists and engineers". Springer Science & Business Media, 2009. [2] J. A. Cottrell, T. J. Hughes, and Y. Bazilevs, "'Isogeometric analysis: toward integration of CAD and FEA''. John Wiley & Sons, 2009. [3] R. Vazquez, "A new design for the implementation of isogeometric analysis in octave and matlab: GeoPDEs 3.0," Computers & Mathematics with Applications, vol. 72, no. 3, pp. 523–554, 2016. [4] Flux 12 Users guide, release 12.2 ed., Cedrat Corporation, Grenoble, France, 2016. [5] R. L. J. Sprangers, J. J. H. Paulides, B. L. J. Gysen, and E. A. Lomonova, "A fast semi-analytical model for the slotted structure of induction motors," Mathematics and Computers in Simulation, vol. 131, pp. 316–327, 2017. [6] G.J. Li, Z.Q. Zhu, and G. Jewell, "Performance investigation of hybrid excited switched flux permanent magnet machines using frozen permeability method," IET Electric Power Applications, vol. 9, no. 9,pp. 586–594, 2015.

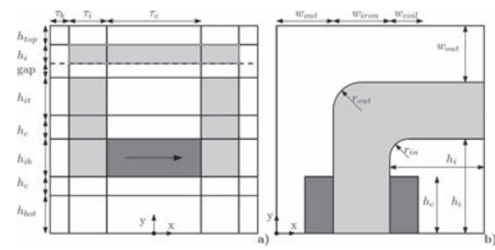

Fig. 1. a) C-core permanent magnet actuator, b) rounded-edge magnetic circuit.

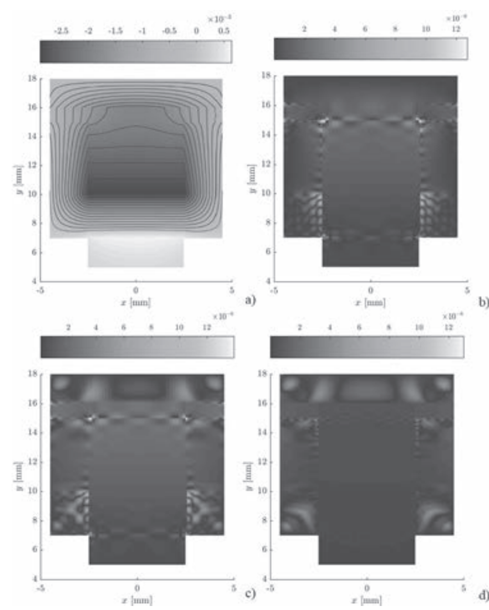

Fig. 2. a) The magnetic potential distribution (in Vs/m) and isolines obtained with FEM, b) c) and d) show the discrepancy between IGA-SEM, IGA-FEM and SEM-FEM, respectively.

9:15

GG-02. Reluctance Network Model of Permanent Magnet Synchronous Motor Considering Magnetic Hysteresis Behavior.

Y. Hane[1] and K. Nakamura[1]
1. Tohoku University, Sendai, Japan

In recent years, the demand for high-efficiency electric machines is increasing from the viewpoint of global environmental issues and energy saving. In order to further improve the efficiency of the electric machines, it is necessary to establish a method for quantitatively calculating iron loss including magnetic hysteresis behavior. To solve the above problem, we have focused on a play model [1], which is one of the phenomenological models of magnetic hysteresis behavior. We embedded the play model in the magnetic circuit model, and calculated iron loss including minor loops with high accuracy and speed [2]. However, this method was applied only for the objects with simple shapes such as a ring core. The authors proposed a reluctance network analysis (RNA), which expresses an analysis object by one reluctance network. All the reluctances can be determined by *B-H* curve of the material and dimensions [3]. The RNA has been applied to the calculation of characteristics of various electric machines including transformers and motors. However, a method for expressing magnetic hysteresis is not established for RNA. This paper describes that the play model is applied to the RNA by using a permanent magnet (PM) motor as a consideration target, in order to estimate the iron loss including the magnetic hysteresis behavior. As shown in Fig. 1 (a), the play model can express an arbitrary hysteresis loop by multiplying play hysterons $p_N(x)$ with different widths by shape functions $f_N(p_N(x))$. Although a large number of measured dc hysteresis loops with different maximum flux densities are required to derive the play model in general, the proposed method requires only one or two measured dc hysteresis loops because the Landau–Lifshitz–Gilbert (LLG) equation is used to calculate the dc hysteresis loops [2]. Fig. 1 (b) shows the hysteresis loops calculated by the LLG equation. As shown in this figure, a large number of hysteresis loops which are used to derive the play model can be obtained without experiments. In the following, we describe a method for deriving the RNA model of surface permanent magnet (SPM) motor, which has 6-slots and 4-poles. The stator is divided into 12, which is twice the number of slots, in the circumferential direction so that the leakage flux between the slots is taken into consideration. On the other hand, the tip of stator pole, air gap, permanent magnet on the rotor surface, and rotor yoke where the flux distribution is more complicated, are divided into 180 in increments of 2 degrees in the circumferential direction. Each divided element is replaced with reluctances. Among them, the reluctances in the rolling direction are needed to be determined in consideration of nonlinear magnetic property. In the conventional RNA model, the magnetic nonlinearity is given by dc *B-H* curve of the material. However, the magnetic hysteresis is not taken into consideration. In this paper, each reluctance of the RNA model is replaced with the play model and two circuit elements, one is inductance denoting the eddy current loss, and the other is controlled-source denoting the anomalous eddy current loss as shown in Fig. 2(a) [2]. The figure shows the schematic circuit diagram of the proposed RNA model of one pole of the SPM motor. The MMF at the stator pole in the figure is one generated by the winding current. In the RNA model, the MMF F_c of the magnet is expressed by the following equation using the coercive force H_c and the average magnet length l_m. $F_c=H_c l_m$ (1) The reluctance R_p of the magnet is given by the following equation using the relative recoil permeability μ_r and the average cross sectional area S_m. $R_p=l_m/\mu_r\mu_0 S_m$ (2) The reluctances in an air space surrounding the magnetic core are simply given by the following equation using the average cross sectional area S and length l of divided elements, and the vacuum permeability μ_0, $R_{air}=l/\mu_0 S$ (3) Fig. 2 (b) shows each loss calculated by the proposed RNA model when a rotational speed is 1000 r/min, torque is 0.65 Nm, and winding rms current is 1.3 A, respectively. The copper loss is obtained from the product of the winding resistance and the square of the winding rms current. The eddy current loss of the magnet is obtained from an electric network model of the magnet [4], which consists of electromotive forces induced by the flux flowing through the magnet and electric resistances determined by the resistivity of the magnet and dimensions. Accordingly, the iron loss is obtained by subtracting machine output, copper loss, and magnet eddy current loss from electrical input. In the near future, we will verify the validity of the proposed model by comparing the results with the prototype machine. In addition, Fig. 2 (c) shows calculated hysteresis loop of a certain divided element of the RNA model. As shown in the figure, using the proposed model, the magnetic hysteresis inside the iron core, which is generally difficult to measure, can be drawn.

[1] S. Bobbio, G. Miano, C. Serpico, and C. Visone, "Models of Magnetic Hysteresis Based on Play and Stop Hysteresis", *IEEE Trans. Magn.*, Vol. 33, No. 6, pp. 4417-4426 (1997). [2] H. Tanaka, K. Nakamura, O. Ichinokura, "Magnetic Circuit Model combined with Play Model Obtained from Landau-Lifshitz-Gilbert Equation", Journal of Physics: Conference Series, Vol. 903, 012047 (2017). [3] K. Nakamura and O. Ichinokura, "Reluctance Network Based Dynamic Analysis in Power Magnetics", *IEEJ Trans.FM*, Vol.128, No.8, pp. 506-510 (2008). [4] Y. Yoshida, K. Nakamura, O. Ichinokura, "Eddy Current Loss Calculation in Permanent Magnet of SPM Motor Including Carrier Harmonics Based on Reluctance Network Analysis", Journal of the Magnetics Society of Japan, Vol. 37, No. 3-2, pp. 278-281 (2013).

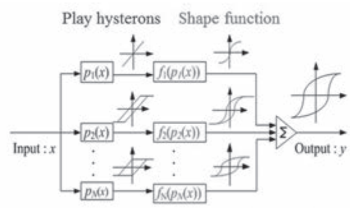

(a) Schematic diagram of the play model

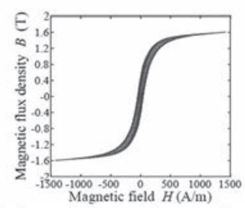

(b) Calculated dc hysteresis loops of the non-oriented silicon with a thickness of 0.35 mm from B_m = 0.04 T to 1.6 T at intervals of 0.04 T

Fig. 1. Principle of the play model

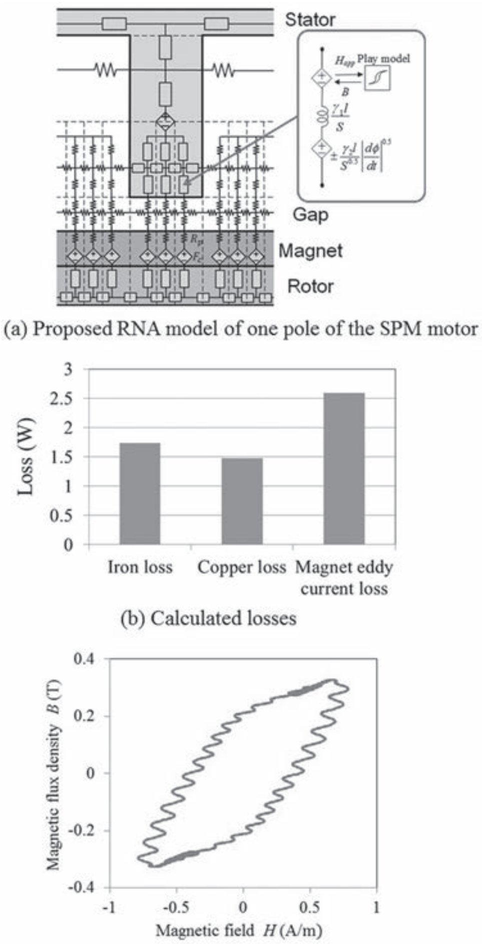

(a) Proposed RNA model of one pole of the SPM motor

(b) Calculated losses

(c) Hysteresis loop of a certain devided element

Fig. 2. Proposed RNA model of SPM motor and simulation results

9:30

GG-03. Motor Core Losses Evaluation with PWM and PAM Inverter Excitations in Computational Analysis and Experiments.

G. Nguyen[1], S. Odawara[2], T. Endo[3], C. Taki[3], K. Fujisaki[3], F. Iwamoto[4], T. Yamada[4] and T. Sasaya[4]
1. Research Center for Smart Vehicles, Toyota Technological Institute, Nagoya, Japan; 2. Kitami Institute of Technology, Kitami, Japan; 3. Electromagnetic Energy System Laboratory, Toyota Technological Institute, Nagoya, Japan; 4. Advanced Research and Innovation Div. 3, DENSO CORPORATION, Aichi, Japan

I. INTRODUCTION The interior permanent magnet synchronous motor (IPMSM) and blushless DC (BLDC) motor can be controlled by either the pulse-width modulation (PWM) inverter excitation or pulse-amplitude modulation (PAM) inverter excitation [1-5]. The authors in [2] evaluated losses of the PMSM in high-speed drive of 50 krpm to 200 krpm, where the carrier frequency is from 25 kHz to 200 kHz. Motor drive system used in electric vehicles (EV) requires the variable voltage and variable frequency operation for motor velocity control. Although the PWM inverter can make variable voltage and frequency, its output waveform is usually complicated. The PAM inverter requires an additional DC-DC converter for variable voltage, but it has simple output waveform as the 120-degree commutation technique [3]. Besides, the low carrier frequency and rotational speed affects the total core loss of IPMSM considerably. Our study focuses on this issue with the PWM and PAM inverter excitations in both no-load and load operational cases of the motor; the evaluation is conducted with computational analysis and experiments. Moreover, response of the magnetic flux density in stator and distribution contours of motor core losses with the two inverters are analyzed in computational simulation. II. STRUCTURES OF PWM AND PAM INVERTER EXCITATIONS FOR IPMSM In this study, structures of PWM and PAM inverter excitations are shown in Fig. 1 panels (a) and (b), respectively. In the case of no-load operation, the torque meter SS-020, BLDC motor and resistor load are disconnected to the IPMSM. With the PWM inverter excitation in Fig. 1 panel (a), the DC-link voltage V_{dc} is a fixed value. Whereas, the PAM method controls the inverter with 120-degree commutation and automatically adjusts amplitude of the changeable DC-link voltage as shown in Fig. 1 panel (b). In addition to experiments, numerical calculation is done for evaluating the motor core loss. III. COMPUTATIONAL ANALYSIS AND EXPERIMENTAL MEASUREMENT METHODS The total core loss of IPMSM can be computed as given in (1). $P_{core} = P_{3\Phi} - R_s(I_u^2 + I_v^2 + I_w^2) - P_f - \omega T$ (1) Where P_{core} : total core loss of IPMSM, $P_{3\Phi}$: total input active electrical power, R_s : phase resistance, 0.6 Ω, I_u, I_v, I_w : phase currents in rms, P_f : IPMSM and encoder mechanical losses, 0.628 W, ω : rotational speed, 750 rpm, T : output torque. The stator and rotor are made of a non-oriented material, named as 35H300, and the permanent magnet in the rotor is sintered NdFeB. The nominal power of the motor is 400 W. The software for computational analysis is JMAG. In simulation, the torque in the load test case is fixed as T = 0.497 Nm, while the torque value in experiments is measured and often in the range of T = 0.5 Nm (at the starting time) to 0.497 Nm (from the time t = 90 minute). Operational parameters for PWM inverter are as follows; the fixed DC-link voltage is V_{dc} = 205 V, the fundamental frequency is f_0 = 50 Hz, the carrier frequency is f_C = 1 kHz, and the dead-time of inverter is 3500 ns. Operational parameters for PAM inverter are as follows; the fundamental frequency is f_0 = 50 Hz, the inverter is controlled with the 120-degree commutation, and the dead-time of the inverter is 3500 ns. Firstly, the experimental system is operated to warm up the IPMSM for ninety minutes. Then, from the time t = 90 minute to 115 minute, and from t = 170 minute to 195 minute, we perform six to twelve measurements; each measurement has forty samples. In total, there are 240 to 480 data samples for all measurement times of each experiment. For each the operational case, we perform at least four independent times of experiment; the result is the average value of all the times of experiment. IV. COMPUTATIONAL AND EXPERIMENTAL RESULTS As described in Fig. 2, the PAM inverter excitation can diminish the total core loss of the IPMSM significantly in both the no-load and load operational cases. As compared to the PWM inverter, the PAM inverter has the much better efficacy of reducing the motor core loss in calculation and experiments. In the no-load operational case, the total motor core loss with PWM inverter are 5.9 W and 5.87 W, while the ones with PAM inverter are 2.11 W and 2.243 W, respectively; the reduction is about 62%. In the load test case, the motor core loss with PWM inverter are 6.365 W and 6.61 W, while the ones with PAM inverter are 2.415 W and 2.766 W, respectively; the reduction is about 60%. The computational and experimental results are relatively consistent. In both computational and experimental results, harmonics in voltage and current waveforms in stator of the IPMSM is substantially mitigated with the PAM inverter as compared to the one with the PWM inverter. In simulation results, the response of magnetic flux density in stator with the PAM inverter is also smoother than the one with the PWM inverter. V. CONCLUSION This paper has shown the superior effectiveness of the PAM inverter excitation in decreasing the total core loss of IPMSM as compared to the PWM inverter excitation. The computational analysis and experimental results have been conducted and examined carefully to confirm the salient advantages of the PAM inverter excitation. In future work, an experimental system, including a silicon carbide (SiC) MOSFET inverter with the PAM excitation and an IPMSM, will be developed to assess motor core losses in wide range of speed.

[1] T. Senjyu, Y. Noguchi, N. Urasaki, A. Yona, H. Sekine, and T. Funabashi, "Wide-Speed-Range Optimal PAM Control for Permanent Magnet Synchronous Motors," *Proceedings of the 7th International Conference on Power Electronics*, pp. 916-921, October 2007, Daegu, Korea. [2] L. Schwager, A. Tuysuz, C. Zwyssig, and J. W. Kolar, "Modeling and Comparison of Machine and Converter Losses for PWM and PAM in High-Speed Drives," *IEEE Transactions on Industry Applications*, vol. 3, no. 2, pp. 995-1006, March/April 2014. [3] Y.-S. Lai, K.-Y. Lee, J.-H. Tseng, Y.-C. Chen, and T.-L. Hsiao, "Efficiency Comparison of PWM-Controlled and PAM Controlled Sensorless BLDCM Drives for Refrigerator Applications," *Proceedings of the 42nd IAS Annual Meeting Industry Applications Conference*, pp. 268-273, September 2007, New Orleans, USA. [4] C. Cui, G. Liu, and K. Wang, "A Novel Drive Method for High-Speed Brushless DC Motor Operating in a Wide Range," *IEEE Transactions on Power Electronics*, vol. 30, no. 9, pp. 4998-5008, September 2015. [5] S. Noguchi, K. Suzuki, and H. Dohmeki, "The Efficiency Comparison by Exciting Waveform of The Square-Wave Brushless DC Motor," *Proceedings of the 18th International Conference on Electrical Machines and Systems*, pp. 1407-1413, October 2015, Thailand.

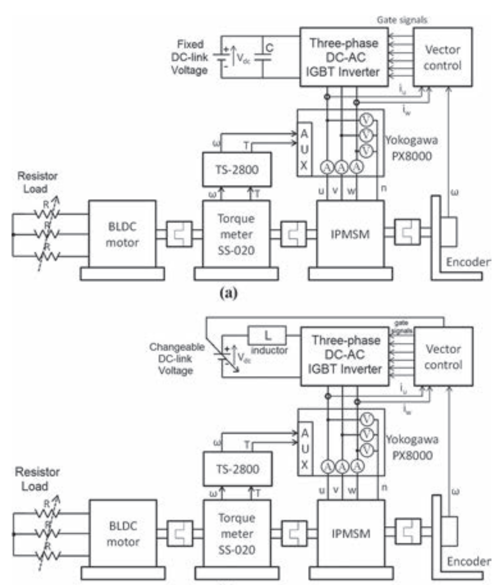

Fig. 1. Two excitation structures for IPMSM. (a) PWM inverter excitation; (b) PAM inverter excitation.

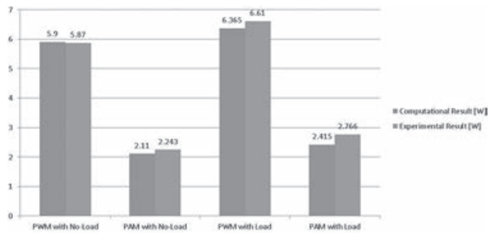

Fig. 2. Comparison on computational and experimental results with PWM and PAM inverter excitations

9:45

GG-04. Unity Power Factor Control Method for Permanent Magnet Synchronous Generator Based on Flux-Weakening Current Injection.

Y. Xu[1], Z. Zhang[1], Y. Jiang[1], J. Huang[1] and Z. Miao[1]
1. Nanjing University of Aeronautics and Astronautics, Nanjing, China

I. INTRODUCTION The permanent magnet synchronous generator (PMSG) has been gaining interest for aircraft starter/generator (S/G) system application over the last few years due to its high power density, high efficiency and wide operation speed range [1]. Higher power density PMSG generation system is demanded due to the growing generation power capacity. High power factor (PF) operation or even the unity power factor (UPF) operation of the PMSG always means the reduction of converter weight, leading to the higher-power-density and higher-performance SG system [2]. In this paper, the feasibility of the PMSG UPF control based on flux-weakening current injection is demonstrated. Analytic model under UPF operation condition is established to analyze relationship of the d-axis current (i_d) and q-axis current (i_q). Comparison between the proposed method and i_d =0 control method is made to illustrate the advantages of the proposed method. Finite element analysis (FEA) and experiments are conducted on the 24/16 interior permanent magnet (IPM) PMSG and 12/10 surface permanent magnet (SPM) PMSG to verify the effectiveness of the proposed method. II. UPF CONTROL OF THE PMSG Phasor diagram of the PMSG under d-q axis reference frame is illustrated in Fig.1, where α_u and α_i are angles between the d-axis and voltage and current vector, respectively. The d-axis voltage (u_d) and q-axis voltage (u_q) are computed as equation (1) and (2). When the PMSG operates under UPF condition, the PF angle ϕ equals zero, thus α_u equals α_i, which can be illustrated in equation (3)-(6). The solution to the formula (6) is shown in equation (7). It reveals the relationship of i_d and i_q to achieve UPF operation. FEA is conducted on the 24/16 IPM generator and 12/10 SPM generator to verify the deduction. The cross section views of the PMSGs are shown in Fig.2 and the main parameters is shown in Tab.I. Fig.4 and Fig. 5 show PF and loss of the two machines under different i_d in the rated condition. From Fig.4, it can be seen that when i_d is -6A, the PF reaches the maximum value (unity) and the total loss is minimum. As for the SPM, when i_d is -165A, PF is unity but the total loss is not the minimum. This is because the operating speed is relatively high and the PM loss dominates the total loss, which is not relevant to the demagnetization current. Tab.II shows the calculated and simulated i_d values when the machines operate under UPF condition. It can be referred that, the calculated result agrees with the FEA results generally, but is a slightly lower. This is because the core saturation is neglected in the analytical model. The UPF control is proposed based on the flux-weakening current injection, as illustrated in Fig.2. The control structure contains voltage outer loop, current inner loop, space vector pulse width modulation (SVPWM) module, three-phase bridge converter and the PMSG. The command value of i_q (i_q^*) is determined by the voltage loop to output command dc voltage. The command value of i_d (i_d^*) is determined by i_q, back electromotive force (E_0), d-axis inductance and q-axis inductance according to equation (7). SVPWM module generates the PWM signals to drive the IGBTs in the rectifier. Such arrangement ensures the UPF operation of the PMSG. III. COMPARISON OF UPF CONTROL AND ID=0 CONTROL METHOD To further clarify advantages of the UPF control method, FEA is carried on the 24/16 IPM. UPF control method and i_d =0 control method are conducted on the machine with different axis lengths in the rated condition. Results are illustrated in Fig.6. Fig. 6(a) and (b) explain the relationship between the i_d, i_q, i_a and the axis length under the UPF control and the i_d=0 control respectively. The maximum armature current is almost the same under the two control methods. Fig.6 (c) shows the PF under the i_d=0 control. When the axis length is longer than 100mm, PF starts to saturate, the maximum value is around 0.8. Fig.6 (d) illustrates the loss of the two control methods. It can be seen that the total loss of the PMSG is reduced by employing the UPF control method. The comparison shows that the proposed method could raise PF greatly within the same current constraint. The converter capacity could be reduced compared to that of the i_d=0 control method. It is beneficial to raising the power density of the whole generation system. IV. EXPERIMENT VERIFICATION Experiments are carried on the 24/16 IPM prototype. The stator and rotor laminations are shown as Fig. 7(a) and (b). The experiment platform is shown in Fig.7 (c). The operating speed is 1000 rpm and the output power is 3.6 kW. UPF control method is taken. The voltage waveform and current waveform of phase A are shown as Fig.7. From the result, it can be seen that the phase voltage and the phase current share the same phase angle, which verifies the effectiveness of the control method. V. CONCLUSION In this paper, the feasibility of the PMSG UPF control based on flux-weakening current injection is demonstrated. The control law is analyzed by mathematic model and FEA. The comparison between the proposed method and i_d=0 control method is presented. The proposed method can reduce reactive power of the generation system, thus reducing the capacity of the converter. The proposed method could also reduce the total loss in the low speed operation. Experiments are carried on a 24-slot, 16-pole IPM PMSG to verify the effectiveness of the proposed method. A simple and effective UPF control method is provided, improving the power density and reducing the loss of the PMSG.

[1]X. Zhu, X. Wang, C. Zhang, L. Wang and W. Wu, "Design and Analysis of a Spoke-Type Hybrid Permanent Magnet Motor for Electric Vehicles," in *IEEE Trans. Magn.*, vol. 53, no. 11, pp. 1-4, Nov. 2017. [2]Yongsug Suh and T. A. Lipo, "Control scheme in hybrid synchronous stationary frame for PWM AC/DC converter under generalized unbalanced operating conditions," in *IEEE Trans Ind. Appl.*, vol. 42, no. 3, pp. 825-835, May-June 2006.

$$u_q = E_0 - X_d i_d \quad (1)$$

$$u_d = X_q i_q \quad (2)$$

$$\tan\alpha_u = \frac{u_q}{u_d} = \frac{E_0 - X_d i_d}{X_q i_q} \quad (3)$$

$$\tan\alpha_i = \frac{i_q}{i_d} \quad (4)$$

$$\frac{E_0 - X_d i_d}{X_q i_q} = \frac{i_q}{i_d} \quad (5)$$

$$X_d i_d^2 - E_0 i_d + X_q i_q^2 = 0 \quad (6)$$

$$i_d = \frac{E_0 - \sqrt{E_0^2 - 4X_d X_q i_q^2}}{2X_d} \quad (7)$$

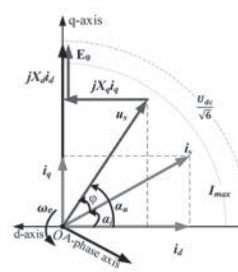

Fig.1. Vector diagram of the PMSG.

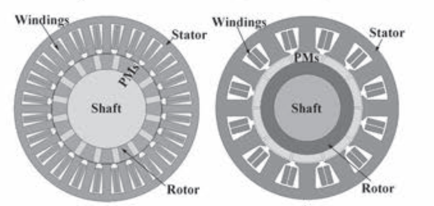

(a) (b)

Fig.2.Cross section views of the PMSGs.
(a) The 24/16 IPM. (b) The 12/10 SPM.

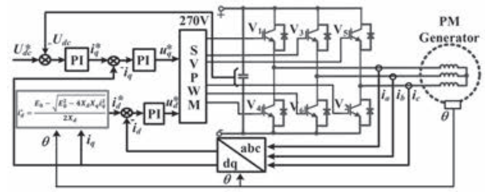

Fig.3. UPF control scheme of the PMSG generation system.

Table.I. Parameters of the IPM and SPM.

Parameters	IPM	SPM
Slots/Poles	24/16	12/10
Rated voltage/V	270	270
Rated power/kW	20	50
Rated speed/rpm	1000	5000
EMF/V	53.41	74.79
Conducters per slot	10	10
L_d/uH	448.43	88.92
L_q/uH	620.28	88.97

Table.II. UPF control command i_d by calculation, FEA and experiment .

	Unity-power-factor control command i_d/A		
	Calculated	FEA	Experiment
IPM	-6.9	-7.02	-7
SPM	-162.2	-165.09	-

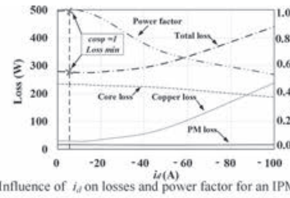

Fig.4. Influence of i_d on losses and power factor for an IPM generator.

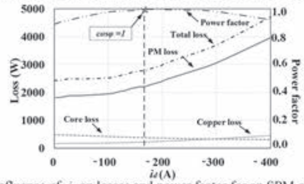

Fig.5. Influence of i_d on losses and power factor for an SPM generator.

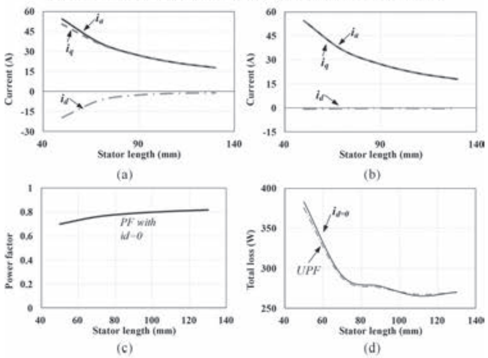

Fig.6.Influece of the PMSG length. (a)Relation of i_d, i_q, i_a and length with UPF control. (b)Relation of i_d, i_q, i_a and length with i_d=0 control. (c)Relation of power factor and length with i_d=0 control. (d) Total loss with UPF control and i_d=0 control.

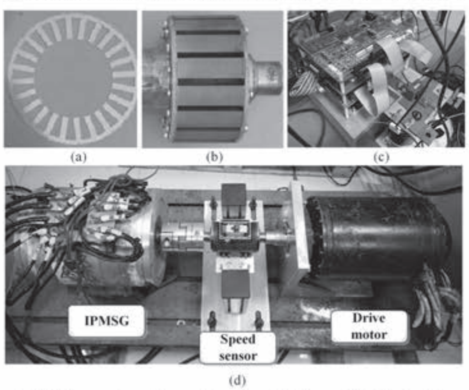

Fig.7. IPM generator prototype and experiment platform. (a) Stator lamination. (b)The rotor of the prototype. (c) The PWM rectifier. (d) The experiment platform

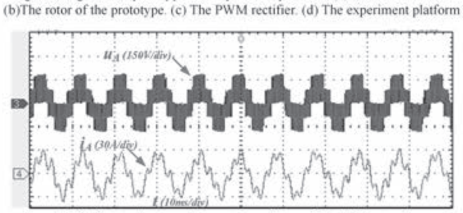

Fig.8. Phase voltage and current waveforms of the UPF control

10:00

GG-05. Virtual Flux Direct Power and Voltage Balance Control of Dual-Stator Linear and Rotary Permanent Magnet Generator.

C. Zhang[1], L. Xu[1] and X. Hu[1]
1. School of Electrical and Information Engneering, Jiangsu University, Zhenjiang, China

I. Introduction Dual-stator Linear and rotary permanent magnet generators (DSLRPMG) features high efficiency and high power density. The two stator windings with a variety of connections can realize wide voltage output range. Therefore, it has important application value in the starter / generator of the hybrid electric vehicle [1], two degree of freedom generator [2], and the wind generator [3]. In this paper, a novel strategy of virtual flux direct power and voltage balance control (VFDPVBC) is proposed to improve the dynamic performances of DSLRPMSG system. Based on the two three phase PWM rectifiers and two extra parallel selection switch, the direct power control without any AC voltage sensors and the output DC voltage balance control are investigated. Meanwhile, space vector modulation (SVM) is also utilized to fix the switching frequency. The simulation and experimental results show the validity and correctness of the method. II. DSLRPMG and Circuit Topology A. DSLRPMG Topology The topologies of the DSLRPMG are shown in Fig. 1. There are three structures named series structure, parallel structure, and half & half structure for the DSLRPMG. Due to the two stators and one mover, the generator can obtain double energies than that of the conventional one. However, when the coil turns of the two stators are unequal or the two stators are in 2-DOF energy input, the energy conversion from the two stators to the load is coupled. This may cause unbalanced output voltages and the dynamic performances reduction of the generation system. B. Circuit of the DSLRPMG System Fig.2 shows the main circuit of the DSLRPMG system. The R and L are considered as the stator resistance and leakage inductance of the DSLRPMG, respectively. III. VFDPVBC and Decoupling Principle The VFDPVBC consists of DC voltage outer loop, DC voltage inner loop, and power loop, as shown in Fig. 3. The internal voltage loop is regulated by two PI controllers separately. When reference power P^{*}_{ref} changes, the interaction between active and reactive power makes the steady and dynamic performances deteriorating. Moreover, by controlling of the two parallel switch (S_{d1} and S_{d2}), the load bus voltage can keep a constant. The voltage equation of the DSLRPMG in the stationary reference frame can be expressed as $u = Ldi/dt + Ri + u_{conv}$ (1) where $u = [u_{a1}, u_{b1}, u_{a2}, u_{b2}]^{T}$ and $i = [i_{a1}, i_{b1}, i_{a2}, i_{b2}]^{T}$, the u_{conv} can be obtained from the dc-link voltage u_{dc1} and u_{dc2}, and the states of rectifier switching (S_{a1}, S_{b1}, S_{c1}, S_{a2}, S_{b2}, S_{c2}) as follows: $u_{conv} = [u_{conva1}, u_{convb1}, u_{conva2}, u_{convb2}]^{T}$ (2) The virtual flux $\psi = [\psi_{a1}, \psi_{b1}, \psi_{a2}, \psi_{b2}]^{T}$ can be induced as $\psi = \int u dt = \int (Ldi/dt + u_{conv}) dt$ (3) According to the instantaneous power theory, the instantaneous active power p and reactive power q can be calculated by $P = Re(ui^{*})$, $q = Im(ui^{*})$ (4) The voltage space vector can be obtained from (3): $u = d(\psi_{m} e^{jwt}) / dt = (\psi_{m} / dt) e^{jwt} + jwy$ (5) When the input mechanical is unstable, the voltage balance estimator works to keep the stable of the outer output voltage, as well as the direct power control works to keep the stable of the inner output voltage. IV. Simulation and Experiment In order to verify the correctness of the proposed VFDPVBC, a 1.5kW-rated power of DSPMG model is established by the Matlab/Simulink software. The DSLRPPMG is a double stator linear and rotary permanent magnet machine (DSLRPMM) which is proposed in [2]. The basic waveforms of the control strategies are given. Furthermore, a prototype is established and tested. Fig. 4 shows the experimental prototype, which includes DSLRPM utilized as a generator, inductance, power circuit, DSP control board and the resistance load. The experimental results are analyzed and compared with that obtained by the simulation. V. Conclusion This paper proposed a novel strategy of direct power control coupled with voltage balance control. Based on the utilization of the power loop, inner voltage loop, and outer voltage loop, the dynamic performances of the generation system is improved. The simulation and experimental results show the validity and correctness of the strategy.

[1] Cai Feng, Cui Shumei, Cheng Shukang. Performance analysis of double-stator starter generator for the hybrid electric vehicle[J]. IEEE Transactions on Magnnetics, 2005, 41(1): 484-487. [2] Lei Xu, MingYao Lin, and et al. “Analysis of a Double Stator Linear Rotary Permanent Magnet Motor With Orthogonally Arrayed Permanent Magnets”, IEEE Trans. Magn., vol. 52, no. 7, pp. 1-4, July 2016. [3] Niu Shuangxia, Chau K T, et al. Design and control of a new double-stator cup-rotor permanent-magnet machine for wind power generation[J]. IEEE Transactions on Magnnetics, 2007, 43(6): 2501-2503. [4] M. P. Kazmierkowski, L. Malesani, “Current Control Techniques for Three-Phase Voltage-Source PWM Converters: A Survey,” IEEE Transactions on Industrial Electronics, vol. 45, no. 5, Oct. 1998. [5] A. M. Razali, M. A. Rahman, G. George and N. A. Rahim, “Analysis and Design of New Switching Lookup Table for Virtual Flux Direct Power Control of Grid-Connected Three-Phase PWM AC-DC Converter,” IEEE Transactions on Industry Applications, vol. 51, no. 2, Mar. 2015. [6] M. Malinowski, M. Jasinski and M. P. Kazmierkowski, “Simple Direct Power Control of Three-Phase PWM Rectifier Using Space-Vector Modulation (DPC-SVM),” IEEE Transactions on Industrial Electronics, vol. 51, no. 9, pp.447-454, Apr. 2004.

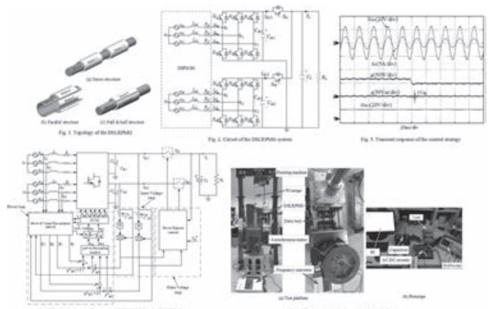

10:15

GG-06. Computation of Cogging Force of a Linear Tubular Flux switching Permanent Magnet Machine Using a Hybrid Analytical Modeling.

D. Lo[1], H. Lawali Ali[1], *Y. Amara*[1], G. Barakat[1] and F. Chabour[1]
1. GREAH, University of Le Havre, France, Le Havre, France

I. Introduction Permanent magnet flux switching machines are gaining more and more interest due to their relatively good characteristics. Indeed, the presence of all magnetic field sources in the stator (armature windings, permanent magnets and/or field windings), which implies a completely passive rotor, makes it suitable for a large variety of applications [1] [2]. Different flux switching machines topologies have been studied in scientific literature. In this contribution, a relatively new modeling approach [3] based on the coupling of mesh based generated reluctance networks (MBGRN) and analytical models (AM), based on the formal solution of Maxwell's equations, is used for the accurate prediction of cogging force of a linear tubular flux switching machine. This type of machines could be favorably used in oceanic renewable energy conversion. Figure 1(a) illustrates how the two approaches are combined for the case of a tubular linear flux switching structure. In this example the analytical solution is used for modeling the mechanical air-gap, and inner and outer airs, and the RN method is used to model the moving and static armatures. In order to have a more generic approach, the stator and moving armatures are modeled using mesh based generated reluctance network (MBGRN) technique [3]. This technique, as classical RN method, can be used with a minimum number of reluctances for regions where flux tubes are not highly affected by topology changes. As for finite elements analyses (FEA), the studied domain in MBGRN should be finely meshed in some regions (air-gap for example) and coarsely meshed in other regions. However, in contrast to FEA, the mesh relaxation in MBGRN can be done more easily conducting to reduced system matrix dimensions, and consequently reduced computation time. Indeed, while in FEA two adjacent elements should share an edge, it is no more necessary for RN method, as illustrated in Fig. 1(b). This new modeling approach has been used to analyze the performance of different electromagnetics devices (2D and 3D) [3]–[7]. In this contribution, this technique is used for the computation of cogging force of a linear tubular flux switching permanent magnet structure, something which has never been reported yet, to the best of our knowledge, in scientific literature. The goal is to further extend the investigation of this technique for the computation of relatively sensitive quantities, such as the cogging force, in more complex structures. Another goal is to highlight advantages of HAM as compared to other modeling techniques, and more particularly FEA, in order to obtain reduced order equations system [8] [9]. II. Hybrid Analytical Model (HAM) The coupling between the AM and the RN model is done at the boundary between both models by equalising the tangential components of magnetic field H, and normal components of magnetic flux density B. The coupling will be more thoroughly described in the full version of the contribution. Analytical solutions in the three regions: internal air, air-gap and external air, will be presented and equations system construction will be detailed. Figures 2(a) and 2(b) compare the air-gap flux density components obtained using both FEA and HAM in the middle of the air-gap. As can be seen relatively good agreement is obtained. The number of nodes of RN used for the modelling of the moving and static armatures is the same and equal to 15120. The number of considered harmonics in all regions modelled using the AM is set to 300. Geometric dimensions and physical characteristics of studied machine along with details about the finite element analysis will be provided in the full version of the contribution. III. Cogging Force Analysis The HAM has been applied to analyse the cogging force in a tubular linear flux switching permanent machine. In order to assess accuracy of developed model, results from HAM are compared to corresponding results from a FE analysis. The cogging torque waveform is very sensitive to computation accuracy of air-gap magnetic field components, in particular when Maxwell's stress tensor method is used, and constitutes therefore a good quantity to assess the accuracy of the HAM as compared to FEA. Figure 2(c) shows comparison of cogging force waveforms obtained from both methods. The results from both methods (FEA and HAM) are in relatively good agreement, which demonstrates the effectiveness of the HAM model to handle more complex structures. In the full version of the contribution, effect of mesh density, in both techniques FEA and HAM, on cogging force computation will be addressed. Along with the effect of mesh density, the use of virtual work method in order to estimate the cogging force will also be investigated.

[1] A. Nasr, S. Hlioui, M. Gabsi, M. Mairie, and D. Lalevee, "Design optimization of a hybrid-excited flux-switching machine for aircraft-safe DC power generation using a diode bridge rectifier," IEEE Transactions On Industrial Electronics, vol. 64, no. 12, pp. 9896-9904, December 2017. [2] C. Sanabria-Walter, and H. Polinder, "Analytical-numerical hybrid model for flux switching permanent magnet machines," Proceedings of the 39th Annual Conference of the IEEE Industrial Electronics Society, IECON 2013, 10-13 Nov. 2013, Vienna, Austria. [3] S. Ouagued, Y. Amara, and G. Barakat, "Cogging force analysis of linear permanent magnet machines using a hybrid analytical model," IEEE Transactions On Magnetics, vol. 52, no. 7, paper 8202704, July 2016. [4] H. Gholizad, M. Mirsalim, M. Mirzayee, "Dynamic analysis of highly saturated switched reluctance motors using coupled magnetic equivalent circuit and the analytical solution," in Proceedings of CEM 2006, International Conference on Computational Electromagnetics, Aachen, Germany, VDE, April, 2006, pp. 1–2. [5] H. Ghoizad, M. Mirsalim, M. Mirzaei, W. Cheng, "Coupled magnetic equivalent circuits and the analytical solution in the air-gap of squirrel cage induction machines," International Journal of Applied Electromagnetics and Mechanics vol. 25, 2007, pp. 749–754. [6] S. Ouagued, A. Aden Diriye, Y. Amara, and G. Barakat, "A general framework based on a hybrid analytical model for the analysis and design of permanent magnet machines," IEEE Transactions On Magnetics, vol. 51, no. 11, paper 8110204, November 2015. [7] K. J. W. Pluk, J. W. Jansen, and E. A. Lomonova, "3-D hybrid analytical modeling: 3-D Fourier modeling combined with mesh-based 3-D magnetic equivalent circuits," IEEE Transactions On Magnetics, vol. 51, no. 12, paper 8208614, December 2015. [8] A. Demenko, J. K. Sykulski, and R. Wojciechowski, "On the equivalence of finite element and finite integration formulations," IEEE Transactions On Magnetics, vol. 46, no. 8, pp. 3169-3172, August 2010. [9] A. Demenko, and J. K. Sykulski, "Analogies between finite-difference and finite-element methods for scalar and vector potential formulations in magnetic field calculations," IEEE Transactions On Magnetics, vol. 52, no. 6, paper 7004206, June 2016.

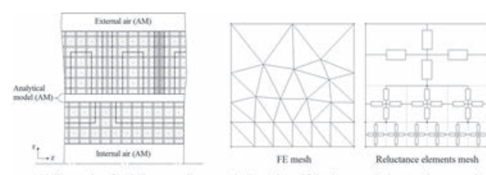

Fig. 1. Hybrid analytical model illustration.

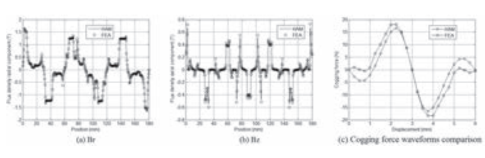

Fig. 2. Comparison of air-gap magnetic flux density components, (a) and (b), and cogging force waveforms (c).

10:30

GG-07. A fully magnetic multi-scale model dedicated to power grid planning.

V.G. Mazauric[1,2] and N. Maïzi[2]
1. Strategy & Technology, Schneider Electric, Grenoble, France; 2. Centre for Applied Mathematics, MINES ParisTech, PSL Research University, Sophia-Antipolis, France

Free current density occurring within a power grid exhibits well-split scales allowing mean-field procedures, *i.e.* the global trend toward reversibility [1] is replaced by embedded minimizations on the relevant scales involved by the power transmission. Various scales were already successfully explored from the material to the device scale [2-4]. At the power management level, the exchange of the magnetic Helmoltz free-energy provided by the so-called reactive power acts to enforce synchronism, usually 50 or 60Hz, between all generation plants supplying the power grid. An X-Y lattice model [5] is adopted to describe the interaction between the magnetic momentum carried by the rotor of a given generator and the mean-field resulting from all the others. The question of ordering stability of two-dimensional systems was extensively studied in the context of phase transitions and critical phenomena. Whereas no long-range order exists in two-dimensional lattices with short range interaction between Heisenberg magnets, Onsager provided an exact resolution of the Ising model with first neighbor interactions. Hence, the X-Y model appears as a marginal case where the long-range ordering may vanish through a weak singularity under an external perturbation [6]. In the context of power system, the synchronism between rotors may be jeopardized by long-range modes and it is convenient to study this problem within the Kuramoto's model [7]. For keeping a stable solution – *i.e.* backing locally and exponentially to a synchronous steady-state after any small disturbance – the indicator expressing the ratio between (i) the algebraic connectivity of the graph of admittances underlying the power flow of the grid; and (ii) than the maximal rate of congestion expected on the grid must be higher than 1 [8]. Besides, magnetic Helmoltz free-energy embedded in the power grid is derived from the Kuramoto's Hamiltonian, showing the critical role of the reactive power to maintain the synchronism and the grid operation. In other words, the stability of the power grid is kept thanks to a strong enough correlated lattice – or actually a suitable voltage plan on the grid – which provides large enough resistant electrodynamic torques to the generators therefore able to face to any admissible fluctuation. Then, the kinetic energy embedded in the whole power system may be aggregated to act as a global and huge inertia to prevent abrupt frequency deviations which therefore may only occur on several periods under a linear regime. By enforcing over time (i) the embedded kinetic energy to be higher than a minimal level typically given by its current value; and (ii) the synchronism indicator to be higher than 1, the previous approach provides a minimal set of technical requirements to ensure reliable operations in a long-term planning exercise addressing both space-aggregation and time-reconciliation of all scales involved in the power management. To that end, the technical optimal TIMES model [9] was adapted to provide, beyond the strict system adequacy, future generation mixes according to different scenarios which obey operation constraints. This issue is addressed for the Reunion Island, which aims to reach energy independence by 2030 using 100% renewables (Fig. 1), this methodology draws the following conclusions: (i) to achieve the 100% renewables target, the capacity to invest in the energy sector is doubled, and the level of reliability decreases considerably; (ii) the loss of reliability induced by higher intermittency— typically 50% —in the power mix can be counter balanced and leveraged by implementing flexibility solutions (demand response and storage) and reinforcing the grid (Fig. 2).

[1] V. Mazauric, "From thermostatistics to Maxwell's equations: A variational approach of electromagnetism," IEEE Transactions on Magnetics, vol. 40, pp. 945-948, 2004. [2] V. Mazauric, M. Drouineau, and L. Rondot, "Assessing anomalous losses with dynamic hysteresis models," International Journal in Applied Electromagnetics and Mechanics, vol. 33, pp. 95-101, 2010. [3] L. Rondot, V. Mazauric, and P. Wendling, "An energy-compliant magnetodynamic error criterion for eddy current calculations," IEEE Transactions on Magnetics, vol. 46, pp. 2353-2356, 2010. [4] V. Mazauric, N. Addar, L. Rondot, P. Wendling, and M. Barrault, "From Galilean covariance to Maxwell equations: Back to the Quasi-Static regimes," IEEE Transactions on Magnetics, vol. 50, p. 7200804, 2014. [5] D.D. Betts, "X-Y Model" in: Phase Transitions and Critical Phenomena, vol. 3, C. Domb and M.S. Green Eds., pp. 569-652, 1972. [6] M. Kosterlitz, "The critical properties of the two-dimensional xy model," *Journal of Physics C: Solid State Physics*, vol. 7, pp. 1046–1060, 1974. [7] Y. Kuramoto, "Self-entrainment of a population of coupled non-linear oscillators," in International Symposium on Mathematical Problems in Theoretical Physics, ser. Lecture Notes in Physics, H. Araki, Ed. Springer Berlin Heidelberg, 1975, vol. 39, pp. 420–422. [8] F. Dörfler, "Dynamics and control in power grids and complex oscillator networks," Ph.D. dissertation, Mechanical Engineering Department, University of California at Santa Barbara, Sept. 2013. [9] N. Maizi, V. Mazauric, E. Assoumou, and M. Drouineau, "Long-term planning and the sustainable power system: A focus on the flexibility needs and network reliability," presented at IEEE PES Power Systems Conference and Exhibition, Seattle, WA, USA, 2009.

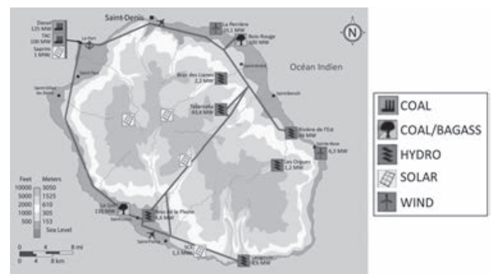

Fig. 1. The Reunion power system as operated in 2008 with the forthcoming renewables capacities (solar and wind) and the transformations of conventional power plants from coal to bagass.

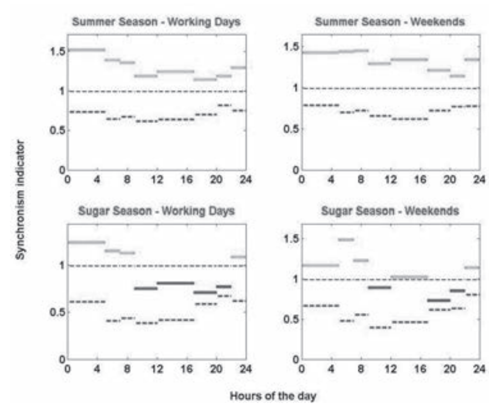

Fig. 2. Synchronism indicator over the 8 time-slices of the Reunion Island power system in 2030 in a 100% renewable energy scenario with a strengthened grid (solid lines) compared to the same indicator calculated with the current grid (dashed lines). In red, periods of the day during which the indicator is lower than the critical value and, in green, during which it is higher than this critical value.

10:45

GG-08. Electromechanical Analysis in Electromagnetic Rail Launcher With Different Cross Section Rails.

X. Wan[1], J. Lou[1], J. Lu[2] and D. Liang[1]
1. School of Electrical Engineering, Xi'an Jiaotong University, Xi'an, China; 2. School of Electrical Engineering, Naval University of Engineering, China, Wuhan, China

Abstract Electromagnetic rail launcher is essentially a high-speed linear motor. It can accelerate projectiles in the range from milligrams to several kilograms to velocities more than several kilometers per second. Electromechanical characteristics in electromagnetic launcher with the cross section of plane, convex, and concave rails were investigated with/without friction under the channel cooling condition. The Kinematic characteristics of armatures and Von Mises stress of three type rails were studied. The velocity and acceleration of armature in electromagnetic rail launcher with convex rail are the highest. The peak stress in plane rail during one shot period is the largest. In light of obtaining higher velocity and acceleration of armature and moderate stress in rail, convex rail is better than the other two type rails. Keywords: Electromagnetic rail launcher, cooling channel, kinematic characteristics, Von Mises stress. A.Introduction The electromagnetic rail launcher (ERL) is composed of two parallel rails and armature. When ERL works, the current flowing from one rail, across the armature, then to the other one will produce strong magnetic field. The Lorentz force induced by the interaction between magnetic field and current will push the armature to high speed. During this process, there is much thermal and strong electromagnetic force in rails. It is a multi-field coupled system. Repetitively-shot is a prerequisite of the practical application of a utility ERL. In multiple shot mode, channel cooling approach is used to remove thermal generated by current flowing through rails. The cooling channels are very beneficial for taking away thermal in rails. But they directly influence the mechanical performance of the rails, thus affect the structure stability of the whole system. So it is a meaningful topic how to keep structure stability in ERL under channel cooling condition. When armature slides along the rails, as the muzzle velocity of armature is more than 2 km/s, the larger armature velocity leads to an increase in Peclet number, which will seriously influence the convergence and accuracy of the model. To avoid the oscillation caused by the higher Peclet value, Zhang [1] and Huang [2] used the moving co-ordinate frame to solve the problem of eddy current in the moving conductors. Yamazaki [3] and Rapetti [4] employed mortar method to handle the staggered meshes on the moving boundary in each time step. Hsieh [5] developed EMAP 3-D code with Lagrangian description to simulate the dynamic launching process of the launcher. However, the mechanical characteristics of ERL with plane, convex, and concave rails by active cooling condition have not seen in literatures. The results in this paper are very important for structure optimization design of electromagnetic rail launcher with cooling channels. They are also significant for eventually realizing efficient repetitively-shot in the electromagnetic rail launcher. B.Model of ERL And Applied Pulse Current To compare the electromechanical performances under identical conditions, the cross section area, a, R, h, L1, and L2 are kept constant. The ERL in this paper is composed of two parallel copper rails which are 7m long and aluminum armature. The armature mass is 3709.72g. Owing to the symmetry, only a quarter of the armature and rails will be considered. The pulse current used is a trapezoidal wave current. The peak value of the current is 3.0MA.FEM simulations of EM-structure coupled field are carried out to compare the mechanical performances of three type rails under same condition. C. Analysis Results The kinetic characteristics of the armatures gained by simulations are shown in Fig.1. As shown in it, the velocity and displacement of armature in ERL under friction/no friction condition with convex rail are the highest. And the velocity and displacement of armature in ERL with plane rail are the lowest. As shown in Fig.2, at the max stress moment during one shot cycle, peak stress all occurs around cooling channels in three type rail. They are all less than the yield strength of copper. In zero friction/ friction condition, peak stress in plane rail during one shot period both is the largest in three type rails. And the max stress in concave rail is the lowest in three type rails. D.Conclusions In this paper, electromechanical characteristics were analyzed for the cross section of plane, convex, and concave rails with active cooling conditions. Coupled EM-structure simulations were implemented for the three types of ERL respectively. The velocity and acceleration of armature in ERL with convex rail are the highest. The deformation and stress in plane rail is the largest. At the max stress moment during one shot cycle, peak stress all occurs around cooling channels in three type rail. Peak stress in plane rail during one shot period is the largest in three type rails. In terms of gaining better electromechanical characteristics in ERL, the ERL with convex rails is the best one.

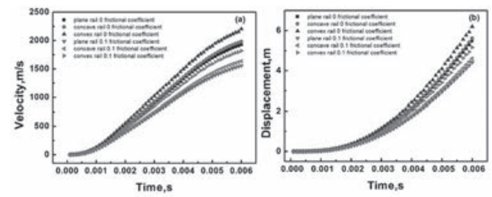

Fig. 1. Kinematic characteristics of armatures. (a) Velocity.(b) Displacement.

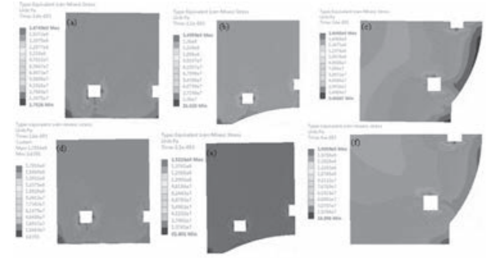

Fig. 2. Max Von Mises Stress of three type rails during one shot period. (a)-(c)0 friction.(d)-(f)0.1 friction factor.

11:00

GG-09. Reduced Order Modeling of Axially Laminated Synchronous Reluctance Motors Based on Numerical Field Solutions.

D. Lin[1], P. Zhou[1] and *M. Rahman*[2]
1. Ansys Inc., Pittsburgh, PA, United States; 2. Memorial University of Newfoundland, St. John's, NL, Canada

Axially laminated synchronous reluctance motors (ALA-SynRM), which possess relative high torque density owing to their high saliency ratio, have received growing interest in recent years [1]-[3]. Since ALA-SynRMs have characteristics suitable for mass production and easy manufacturing processes, they are viable candidates for various domestic and industrial applications [2], [3]. In many applications of ALA-SynRMs, what system designers want to know is the transient response to various electrical and mechanical inputs. Although finite-element analysis (FEA) can simulate this transient process accurately, it usually requires very long processing time. In such numerical simulations, where the magnetic field distribution inside the machine is not the main concern, reduced order modeling [4] is an efficient technique. A key advantage of reduced order modeling is its capability for significantly reducing the computational burden and cost of numerical simulations, while maintaining a sufficient accuracy for the concerned performance from the engineering point of view. A reduced order model (ROM) could be a parameter based model in which the electromechanical coupled state equations are represented with some linear or nonlinear electrical and mechanical parameters, or a look-up-table based model in which all electrical and mechanical outputs, such as winding flux linkages and rotor torque, are expressed as functions of some electrical and mechanical inputs, such as winding currents and rotor position, via interpolation from a discrete look-up table. The former which uses less memory is more suitable for hardware-in-the-loop controls, and the later which is more accurate in system simulation can be used in circuit design and optimization. This paper presents both parameter and look-up-table based ROMs of ALA-SynRMs, derived from FEA solutions. The axially laminated rotor is treated as a core with nonlinear anisotropic material [5]. The anisotropic magnetic property in the easy direction is derived from the parallel connection of steel lamination layers with inter-laminar insulation layers, and that in the hard direction is derived from the series connection. The circuit realization of parameter based ROM for ALA-SynRMs is shown in Fig. 1, where *d*- and *q*-axis inductances (L_d and L_q), assumed to be independent of rotor position θ, are expressed as non-linear functions of *d*- and *q*-axis currents (i_d and i_q), and the zero-sequence inductance L_0 is assumed to be constant. The output torque is directly computed from the *d*- and *q*-axis inductances and currents. Two pins of the rotational mechanical port are denoted as ROT1 and ROT2. Fig. 2 shows the circuit realization of look-up-table based ROM for ALA-SynRMs, where λ denotes flux linkage. Based on a sweeping set of *d*- and *q*-axis currents and rotor position, three-phase winding currents for FEA excitations are obtained from the *dq*0 to *abc* transformation without the need to sweep the zero-sequence current component. After FEA simulation, we obtain three-phase flux linkages, as well as rotor torque, from the FEA solutions. The flux linkages in the *dq*0 system, used as outputs of look-up table, are transferred from the flux linkages in the *abc* system. In this paper, we will also introduce some advanced techniques to reduce computational time at specified density of the sampling points by taking advantage of the symmetric conditions of three-phase windings and the periodic condition of rotor position. Since a reluctance rotor has repeatable pole geometry, the flux linkage in one phase generated by three-phase currents will be negatively repeatable in 180 electrical degrees of rotor position even though the three-phase windings may be of the fractional-slot type. As long as three-phase windings are symmetric, the flux linkage in one phase can be obtained from another phase by shifting the waveform by 120 electrical degrees. As the results, in the *dq*0 system, the *d*- and *q*-axis flux linkages, as well as the rotor torque, are repeatable in 60 electrical degrees due to absence of the zero-sequence flux linkage component. Therefore, the rotor position is required to be swept for only 60 electrical degrees, instead of 360 electrical degrees. This technique, together with the algorithm not to sweep the zero-sequence current, is able to reduce the computational time significantly. A 5.5kW, 380V, 4-pole, 1500rpm ALA-SynRM design is presented as an application example. Solutions from the system simulation with look-up-table based ROM are compared with the solutions directly from the FEA transient simulation. To illustrate the difference between the parameter and look-up-table based ROMs, the solutions from the system simulation with parameter based ROM are also presented.

[1] N. Bianchi and B. J. Chalmers, "Axially laminated reluctance motor: Analytical and finite-element methods for magnetic analysis," IEEE Trans. Magn., vol. 38, no. 1, pp. 239–245, 2002. [2] F. Martin, A. Belahcen, A. Lehikoinen, and P. Rasilo, "Homogenization technique for axially laminated rotors of synchronous reluctance machines," IEEE Trans. Magn., vol. 51, no 12, Article#. 8115306, 2015. [3] Y. H. Kim and J. H. Lee, "Optimum design of ALA-SynRM for direct drive electric valve actuator," IEEE Trans. Magn., vol. 53, no 4, Article#. 8200804, 2017. [4] M. Farzamfar, A. Belahcen, P. Rasilo, S. Cl'enet, and A. Pierquin, "Model order reduction of electrical machines with multiple inputs," IEEE Trans. Ind. Appl., vol. 53, no 4, pp. 3355-3360, 2017. [5] D. Lin, P. Zhou, Z. Badics, W. N. Fu, Q. M. Chen, and Z. J. Cendes, "A new nonlinear anisotropic model for soft magnetic materials," IEEE Trans. Magn., vol. 42, no 4, pp. 963-966, 2006.

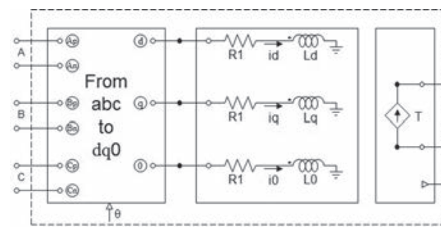

Fig. 1. Parameter based ROM circuit for ALA-SynRM.

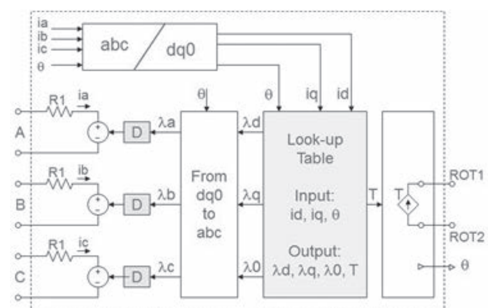

Fig. 2. Look-up-table based ROM circuit for ALA-SynRM.

11:15

GG-10. Development of a New Approach to Core Quality Assessment of Modern Electrical Machines.

H. Bahmani[1]
1. Ulster University, Londonderry, United Kingdom

I. Introduction Mechanical, magnetic and electric properties of electrical steels can be deteriorated by manufacturing process, e.g. welding and cutting, which has a direct impact on normal operation of the magnetic cores [1-3]. Quality of the magnetic cores is an important consideration for the designers, manufacturers and users of the magnetic devices. Core quality mainly depends on electrical and magnetic properties of the magnetic material, quality of the insulation material, clamping pressure, magnetising condition, etc. Key amongst these are inter-laminar faults, which have been identified as a major threat for normal operation of electrical machines and transformers [3-4]. Whereas, a large number of inter-laminar faults can lead to catastrophic failure, the machine can still operate with a limited number of faults, but with elevated power loss. Local power loss results in hot spots in the core, which accelerate the degradation of the insulation coating of the laminations and can cause premature aging of the magnetic cores. Therefore, core quality assessment, should be performed at an early stage before it progress to machine failure [5]. This is an essential criterion for efficient and reliable operation of the electrical machines and transforms. Hysteresis behaviour of the magnetic materials is an important characteristic in characterisation of the material under different magnetisation conditions. All types of magnetic materials can be characterised and interpreted by means of particular aspects of hysteresis phenomenon. The area enclosed by the hysteresis loop represents the amount of energy dissipated into heat during one magnetisation cycle. This is an important aspect of hysteresis phenomenon, to characterise the magnetic material and has found many applications in physics and engineering [6]. Accurate measurements of Static Hysteresis Loop (SHL) and Dynamic Hysteresis Loop (DHL), is an adequate technique of loss evaluation. In this respect, analytical methods have been developed to reproduce DHL of the material for power loss prediction and separation [7-10]. In this paper, a new approach based on the DHL is developed for core quality assessment purposes. The developed method can be implemented to detect inter-laminar fault between laminations of the clamped magnetic cores, over a wide range of magnetisation. II. Experimental Results The experimental work were carried out on stacks of four Epstein size laminations of 0.3 mm thick CGO 3 % *SiFe*, with standard grades of M105-30P. Similar to the previous work [4], partial artificial short circuits of 10 mm wide and different configuration were introduced between the laminations, as described below: Pack # 1: *Inter-laminar faults at three step-like points* Pack # 2: *Inter-laminar faults at one set point* Pack # 3: *Inter-laminar faults at three set points* Each pack of lamination was magnetised separately using a single strip tester at peak flux densities of 1.1 T to 1.7 T and magnetising frequencies from 50 Hz up to 1000 Hz. Magnetic properties of the samples including bulk power loss and DHL were measured individually. DHL of the specimens at measured frequencies and peak flux density of 1.7 T are shown in Fig 1. The most evident feature of Fig 1 is the significant increase of the hysteresis loop area and change in the loop shape, for different types of fault. This result reflects a unique property of the DHL in power loss evaluation, which can be implemented in the characterisation of the magnetic cores subjected to different types of faults. This concept is a powerful technique in core quality assessment of the electrical machines, and can provide a meaningful comparison between magnetic properties of the magnetic cores subjected to different types of inter-laminar fault. An approach was developed to calculate power loss of each stack from the measured DHL, for each flux density and frequency. The results were then compared with the bulk power loss of the samples. Fig 2 shows a comparison between the power loss of the samples calculated from the measured DHL, and bulk measurement for the measured frequencies and peak flux density of B_{pk}=1.7 T. The results show a close agreement between the calculated power loss and bulk measurements, with the maximum difference of less than 4 %. Therefore, it can be concluded that inter-laminar faults in the magnetic cores, that increase the core loss, can be effectively detected by observing the DHL of the core. The results show high sensitivity in fault detection and core quality assessment, even for low frequencies and low flux densities. III. Conclusion A new approach was developed to evaluate quality of the magnetic core of the electrical machines and transformers. Accuracy of the method was validated on stacks of laminations subjected to different types of inter-laminar faults, over a range of frequency and flux density. Therefore, the developed approach can be effectively implemented to characterise magnetic properties of the magnetic cores, and condition monitoring of magnetic cores of electrical machines and transformers. IV. Acknowledgment The author is grateful to Cogent Power Ltd. for providing the electrical steel sheets, and Wolfson centre for magnetics at Cardiff University for the experimental work.

[1] S Lee, G Kliman, M Shah, D Kim, T Mall, K Nair and M Lusted, "*Experimental Study of Inter-laminar Core Fault Detection Techniques based on Low Flux Core Excitation*" IEEE Trans On Energy Convers, Vol. 21, No. 1, March 2006, pp 85-94 [2] C Schulz, D Roger, S Duchesne, and J Vincent, "*Experimental Characterization of Interlamination Shorts in Transformer Cores*", IEEE Trans Magn, vol. 46, No. 2, Feb. 2010, pp. 614–617 [3] H Hamzehbahmani, P Anderson and K Jenkins, "*Inter-laminar Insulation Faults Detection and Quality Assessment of Magnetic Cores Using Flux Injection Probe*", IEEE Trans on Power Delivery, Vol. 30, No. 5, October 2015, pp. 2205-2214 [4] H Hamzehbahmani, P Anderson, K Jenkins and M Lindenmo, "*Experimental Study on Inter-Laminar Short Circuit Faults at Random Positions in Laminated Magnetic Cores*", IET Electric Power Applications, Vol. 10, Issue 7, August 2016, pp. 604–613 [5] K Lee, J Hong, K Lee, S B Lee and E J Wiedenbrug, "A Stator Core Quality Assessment Technique for Inverter-fed Induction Machines", IEEE Industry Applications Society Annual Meeting, Oct 2008, pp 1-8 [6] G Bertotti*, "Hysteresis in Magnetism, For Physicists, Materials Scientists and Engineers*", Academic Press 1998 [7] S Zirka, Y Moroz, A Moses, C Arturi, "*Static and dynamic hysteresis models for studying transformer transients*", *IEEE Trans. Power Del.*, Vol. 26, No. 4, Oct. 2011, pp. 2352-2362 [8] E Dlala, "*A simplified iron loss model for laminated magnetic cores*", IEEE Trans. Magn., Vol. 44, No. 11, Nov. 2008, pp. 3169-3172 [9] S Zirka, Y Moroz, P Marketos, A Moses, D Jiles, "*Measurement and modeling of B-H loops and losses of high silicon non-oriented steels*", IEEE Trans. Magn., Vol. 42, No. 10, 2006, pp. 3177-3179 [10] S Zirka, Y Moroz, S Steentjes, K Hameyer, K Chwastek, S Zurek, R Harrison, "*Dynamic magnetization models for soft ferromagnetic materials with coarse and fine domain structures*", Journal of Magnetism and Magnetic Materials, Vol. 394, Nov. 2015, pp 229-236

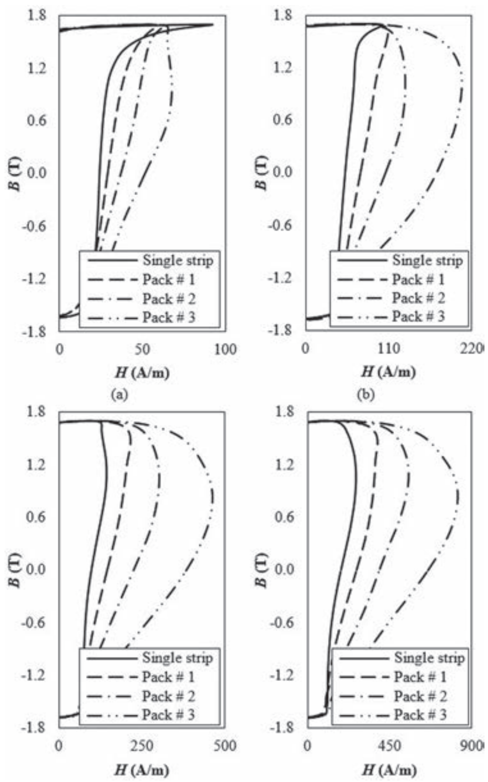

Fig. 1. DHL of the samples at magnetising frequencies of (a) 50 Hz (b) 200 Hz (c) 500 Hz and (d) 1000 Hz

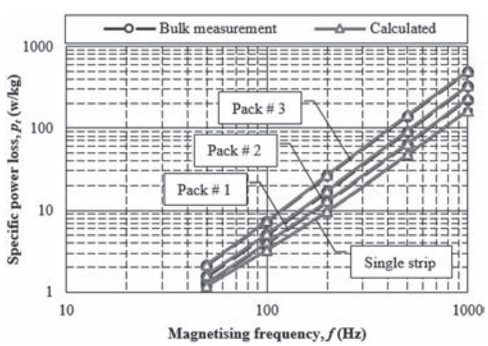

Fig. 2. Comparison of specific power loss of the samples at B_{pk}=1.7 T obtained from the DHL and bulk measurement

11:30

GG-11. Memory Efficient Harmonic Method for Electromagnetic Models Using Scattering Matrices.

C. Custers[1], J. Jansen[1] and E. Lomonova[1]
1. Department of Electrical Engineering, Eindhoven University of Technology, Eindhoven, Netherlands

I. INTRODUCTION In design and optimization of electrical machines, accurate models of the electromagnetic fields are important to predict the performance of the machine. The finite element method (FEM) is often used, because of its ability to produce accurate results when it is correctly utilized. However, the method can be demanding in terms of memory and relatively slow in terms of computation time. Therefore, semi-analytical models have been proposed over the years for increasingly complex structures in both 2D and 3D. One of the semi-analytical models is the harmonic modeling technique [1], [2], [3], which uses a Fourier bases to describe the solutions to electromagnetic field quantities. In many electromagnetic configurations, accurate results are obtained using a relatively low number of harmonics. However, for more complex structures, the number of harmonics has to be increased to retain accuracy. This leads to a proportional increase in the required memory. As a result, especially in 3D models, the advantage in terms of memory of the harmonic model in comparison to FEM is reducing. In this paper an alternative solving method for 3D harmonic models with position dependent material properties is presented. Using the scattering matrix approach, the memory required to obtain the solutions of the model is significantly reduced. II. METHOD In Fig. 1 a configuration consisting of a coil and a conducting plate above in the 3D Cartesian coordinate system is shown. The model is periodic in both the *x*- and *y*- direction. Because of this periodicity, all solutions have a double Fourier series bases. The number of harmonics considered in the *x*-direction is denoted by $N+1$ and in the *y*-direction by $M+1$. In the *z*-direction, the model is divided into regions. For each region, expressions are obtained for the magnetic flux density and magnetic field strength as explained in [3]. These expressions contain unknowns per region. In non-conducting regions there are $2*(N+1)*(M+1)$ unknowns and in conducting regions $4*(N+1)*(M+1)$. To obtain the unknowns, boundary conditions are applied between the regions. The boundary conditions force the continuity of the tangential magnetic field strength components (H_x *and* H_y) and normal magnetic flux density component (B_z) between regions. Typically, in harmonic models, the boundary conditions are listed in one single matrix. By inversion of this square matrix (A) and multiplication with a vector containing the source terms (y) of the regions, the vector of unknowns (c) is obtained, e.g. $c=A^{-1}y$. (1) The drawback of this direct solving method is that matrix A can become large and will as a consequence occupy a large amount of the available memory. As for each region $2*(N+1)*(M+1)$ or $4*(N+1)*(M+1)$ (depending on the type of region) unknowns are added, the number of considered harmonics has to be decreased when a region is added to the model. As a solution to the inefficient memory usage of the direct solving method, the scattering matrix method [4] has been implemented. First, by rewriting the boundary conditions on both sides of a region denoted by *k*, a scattering matrix S can be determined, which relates the coefficients of the neighboring regions, $k-1$ and $k+1$. The matrix equation linking the coefficients is given by $c^-_{k-1} = S_{11,k} \bullet c^+_{k-1} + S_{12,k} \bullet c^-_{k+1} + y_{1,k}$ $c^+_{k+1} = S_{21,k} \bullet c^+_{k-1} + S_{22,k} \bullet c^-_{k+1} + y_{2,k}$ (2) where S_{11}, S_{12}, S_{21} and S_{22} are submatrices of S. A representation of (2) is depicted in Fig. 2. The vector denoted by y represents the rewritten source terms of a region. A scattering matrix S is calculated for each region in the model. With the total number of regions denoted by K, the total scattering matrix S_{model} of the model can be calculated by $S_{model} = S_0 \blacksquare S_1 \blacksquare \ldots \blacksquare S_K$, (3) where $\blacksquare$ is the Redheffer star product [5]. This product multiplies the matrices S_k in such a way that the total scattering matrix S_{model} gives the same relation as in (2) between the coefficients of the top and bottom region of the model. The source terms y_k are also multiplied according to the Redheffer star product to obtain the vector containing the source terms for the total model y_{model}. It is assumed that the top region of the model extends to infinity and the bottom region to minus infinity. As a result, one of the vectors of unknowns in these regions is zero. The non-zero vector of unknowns of the top and bottom region are determined by $(c^+_0\ c^-_K)^T = (S_{model})^{-1}\, y_{model}$ (4) The matrix S_{model} which is inverted to obtain the unknowns of the top and bottom regions is of size $2*(N+1)*(M+1)$, independent of the number of regions in the model. For the model in Fig. 1, this means that the matrix that has be inverted is now 5 times smaller compared to the classical solving method. The unknowns for all other regions can be determined using the scattering matrices. In the full paper, the classical solving method and the proposed method are compared in terms of memory occupation, accuracy and computation time for the configuration shown in Fig.1. III. CONCLUSIONS In this paper a method is implemented to solve electromagnetic harmonic problems in a memory efficient manner. Due to the use of scattering matrices, a reduced size matrix is solved to obtain the unknowns per region. Moreover, this matrix is independent of number of regions that are in the model. As a result, more harmonics can be used with the same available memory, leading to more accurate results.

1) A. Dwivedi, S. K. Singh, R. K. Srivastava, "Analysis of permanent magnet brushless ac motor using Fourier transform approach", IET Electric Power Applications, vol. 10, No 6, pp. 539–547, June 2016. 2) B. Hannon, P. Sergeant, L. Dupré, "Study of the effect of a shielding cylinder on the torque in a permanent-magnet synchronous machine considering two torqueproducing mechanisms", IEEE Transactions on Magnetics, vol. 53, No 10, pp. 1–8, Oct. 2017. 3) C. H. H. M. Custers, J. W. Jansen, E. A. Lomonova, "Modeling and experimental validation of field distributions due to eddy currents in slitted conducting plates", 2017 11th International Symposium on Linear Drives for Industry Applications (LDIA), Osaka, 2017, pp. 1–6. 4) N. Cotter, T. Preist, J. Sambles, "Scattering-matrix approach to multilayer diffraction", J. Opt. Soc. Am. A, vol. 12, No 5, pp. 1097–1103, May 1995. 5) R. Redheffer, "Difference equations and functional equations in transmission-line theory", Modern Mathematics for the Engineer, Vol. 12, pp. 282-337, McGraw-Hill, New York, 1961.

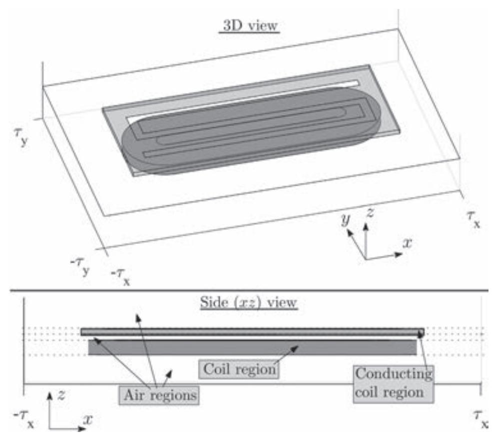

Fig. 1. Electromagnetic configuration used to verify the scattering method.

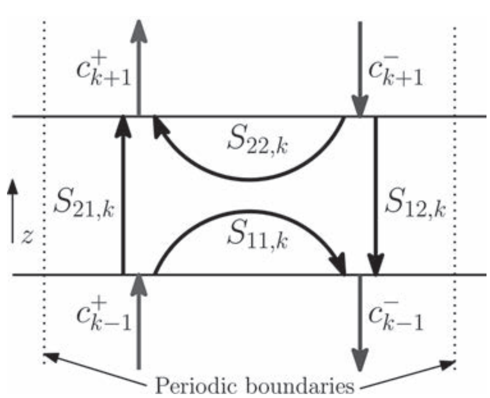

Fig. 2. Representation of the scattering matrix approach for a single region.

11:45

GG-12. Analysis of Temperature Field of High Power Permanent Magnet Driving Motor for Special Vehicle.

C. Li[1] and J. Gao[1]
1. Hunan University, Chang Sha, China

I. INTRODUCTION In recent years, with the development of automobile technology, the vehicle electrical motor needs higher power density and higher pull-in torque. However, the performance of the motor will increase the loss of the motor and raise the temperature. Therefore, it is necessary to analyze the temperature field of the motor to ensure its reliable operation. The temperature field of low power motors has been studied and simulated by many scholars at home and abroad[1]Including water-cooling system design and thermal analysis[2-3] However, the analysis of temperature field of special high-power drive motor is less. This paper take the 350 kW permanent magnet drive motor on as the object II. LOSS MODEL OF MOTOR The characteristics of 350kW permanent magnet drive motor: the rated power is 350kW; the rated speed is 3000r/min; the peak power is 450kW; the DC bus voltage is 900V;Cooling method is water-cooling (The inlet temperature of the cooling water is 85°C; the flow rate is 60L/min and the velocity of water is about 3.5m/s). The root cause of motor heating is various losses. According to the conventional method of loss solving[4] the stator iron loss is 2.39kW; the rotor iron loss is 0.297kW; the stator copper loss is 5.97kW; the mechanical loss is 2.8kW; the total loss is 14.75kW. III. Simulation and analysis of finite element temperature The heat transfer of the motor is mainly heat conduction and convection heat transfer, which is directly related to the thermal conductivity and the surface heat transfer coefficient of the medium. The cooling structure of the stator is designed as follows: Both sides of the stator core are provided with the stator outer retaining plate and the stator inner retaining plate, the inlet and outlet of the generator connected to the pressure pump on motor housing. The circular channel between the outer circle of the stator core and the casing which is formed to cool the stator core. In a stable state, the total energy is constant. $\lambda(\partial^2T/\partial^2X+\partial^2T/\partial^2Y+\partial^2T/\partial^2Z)+q_v=0$ Convective heat transfer mainly occurs between the bottom of the channel and the cooling water. The following expression is the basic law to describe the convection heat transfer process. $q=\alpha(T_{t1}-T_{t2})$ As shown in Fig. 1. It can be seen from the chromaticity, the stator core highest temperature is 156.3°C, the minimum temperature is 92.26°C, reduce the ambient temperature(85°C), the highest temperature rise of the stator core is 71.3K. The maximum temperature of the stator winding is 172.3°C, at the end of the winding, the minimum temperature is 136.7°C, the highest temperature rise of the stator windings is 87.3K. The maximum temperature of the rotor is 162.5°C, the minimum temperature is 149.3°C, the highest temperature rise of the rotor is 77.5K. The inlet temperature of water channel is 85°C and the outlet is 90.3°C. IV. parison and analysis of experimental data The temperature rise experimental data are as follows:Stator current is 557A; The input power is 350.1kW; The electronic voltage is 470.5V; The power factor is 0.91;The cooling water is room temperature and flow rate is 60L/min. Temperature rise curve of stator winding and bearing is shown in Fig. 2. As you can see from the Fig.2. The steady state temperature of the stator windings is about 174°C, minus the ambient temperature 85°C, The temperature rise of the stator windings is about 89K. The maximum temperature rise of simulated stator windings is 87.3 K and the temperature of stator core is about 155°C, minus the ambient temperature 85°C, The temperature rise of the stator core is about 70K. The maximum temperature rise of simulated stator core is 71.3 K. The correctness and accuracy of this model and the simulation method are verified from stator winding and stator core.

[1] Themistoklis D. Kefalas, Antonios G. Kladas. Thermal Investigation of Permanent-Magnet Synchronous Motor for Aerospace Applications. IEEE Transactions on Industrial Electronics,2014,61(8):4404-4411 [2] Aurélie Fasquelle, Daniel Laloy.Water Cold Plates Cooling in a Permanent Magnet Synchronous Motor.IEEE Industry Applications Society,2017,53(5):4406-4413 [3] Qinfen Lu, Xinmin Zhang,et,al. Modeling and Investigation of Thermal Characteristics of a Water-Cooled Permanent-Magnet Linear Motor. IEEE Industry Applications Society,2015,51(3):2086-2096 [4] Ziyuan Huang,Jiancheng Fang, Xiquan Liu. Loss Calculation and Thermal Analysis of Rotors Supported by Active Magnetic Bearings for High-Speed Permanent-Magnet Electrical Machines. IEEE Industrial Electronics Society,2016,63(4):2027-2035

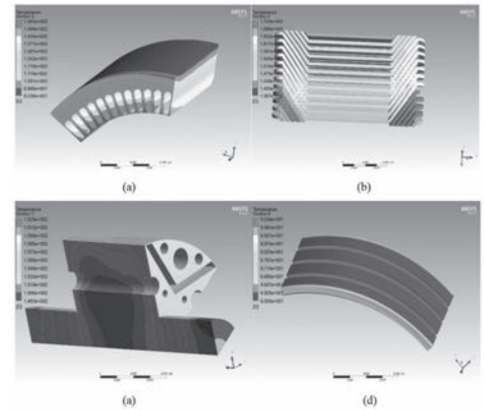

Fig. 1. (a) Stator core. (b) Stator winding. (c) Rotor. (d) Water channel

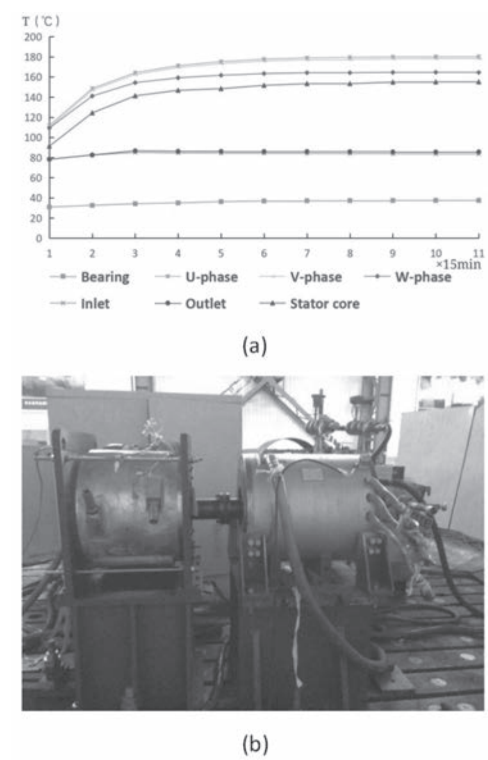

Fig. 2. (a)Temperature rise curve. (b) Experiment

FRIDAY MORNING, 27 APRIL 2018 PEONY II, 9:00 TO 12:00

Session GH
HIGH SPEED MACHINES II

Vincent G. Mazauric, Co-Chair
Schneider Electric, Grenoble, France
Heyun Lin, Co-Chair
Southeast University, Nanjing, China

CONTRIBUTED PAPERS

9:00

GH-01. Exciting Force and Vibration Analysis of Stator Permanent Magnet Synchronous Motor.

J. Hong[1], S. Wang[1], Y. Sun[1], J. Li[1] and H. Cao[1]
1. Tsinghua University, Beijing, China

ABSTRACT: This paper presents the detail analysis of the radial force and bending moment responsible for vibration in the stator permanent magnet synchronous motors (SPMSM). Firstly, the air gap flux density distribution and radial force density distribution are derived in detail. In addition, the relationships between these two vibrations and pole width, pole number and slot number are analyzed. The multi-probe mode-included test method of vibration acceleration is proposed and the experimental results on a 6-pole/36-slot SPMSM match well with the simulation results. 0 Introduction With the advancement of the electrical vehicles such as hybrid-electric and electric vehicles, improving the noise and vibration characteristics of rotating electric machines is becoming important consideration issues for the development of vehicles [1-4]. Electrical vehicles make use of permanent magnet synchronous traction motors for their high torque density and efficiency compared with other types of motors [5-9]. The stator permanent magnet synchronous motors (SPMSM) have good advantages and are widely applied in the industry. Few papers reported to focus on the vibration characteristics of this type of motor[10-12]. So, this paper investigates the vibration mode and frequencies in the stator permanent magnet synchronous motor, which is shown in Fig.1. 1The magnetic field and exciting force 1.1 analysis of Magnetic field When ignoring magnetic saturation, the flux density distribution in the air gap under no load can be expressed as $b(\theta,t)=\pm(B_\delta\Lambda_0+\sum B_\delta\Lambda_k\cos kZ(\theta-\omega_r t))$ $\theta\epsilon[-\alpha\pi/(2p)+j2\pi/(2p),\alpha\pi/(2p)+j2\pi/(2p)]$(1) Where Z is the number of rotor slots, Λ_0 and Λ_k are the amplitude of average and k-th harmonic magnetic permeability. α is the pole arc coefficient. When j=2m,m=0,1,2,3..., the sign in the equation takes a positive value; When j=2m+1, the sign is negative. 1.2 Force analysis The force on ferromagnetic substance in the electromagnetic field can be described by Maxwell stress tensor method. Radial force wave generated by magnetic field is $p_n=1/(2\mu_0)\{(B_\delta\Lambda_0)^2+\sum[B_\delta\Lambda_k\cos kZ(\theta-\omega_r t)]^2+2B_\delta^2\Lambda_0\Lambda_k\cos kZ(\theta-\omega_r t)\}$(2) The third term indicates radial force which changes with time generated by interaction of the not time-varying magnetic field and the periodic magnetic field, which causes a considerable vibration. The vibration frequencies are the integral multiples of the product of the slot number and the rotation frequency. 2 Two vibration sources In the motor, the radial force P_n on one pole can be equivalent to one equivalent pulsating force P_{np} varied with time on the center line of the pole and equivalent bending moment m_{np} varied with time on the pole. The general expression of pulsating force is $P_{np}(t)=2l_pRB_\delta^2\Lambda_0\Lambda_1\sin(\alpha_1\pi/(2p))\cos(jZ2\pi/(2p)-Z\omega_r t)/(Z\mu_0)$(3) Where R is the radius of the inner surface of the pole, α_1 is pole arc width expressed by rotor number. Because the uneven distribution of the force density, the corresponding bending moment is $m_{np}(t)=l_pR^2B_\delta^2\Lambda_0\Lambda_1\cos(\alpha_1\pi)\sin(\alpha\pi/(2p))\sin(jZ2\pi/(2p)-Z\omega_r t)/(Z\mu_0)$(4) From the equation(3) and (4), we can know that: If $2\pi Z/(2p)=2n\pi$, n is integral, the radial forces and the bending moment on the two adjacent poles are in the same phase. When α_1 is n, radial force reaches minimum, bending moment reaches maximum, and the mode number equal to the pole number. When α_1 is n+1/2, radial force reaches maximum, bending moment reaches minimum, and the vibration mode equal to 0. If $2\pi Z/(2p)=(2n+1)\pi$, the phases of the forces on the two adjacent poles are opposite, and so do the bending moment. When α_1 is n, radial force reaches minimum, bending moment reaches maximum, and the mode number equal to the pole pairs. When α_1 is n+1/2, radial force reaches maximum, bending moment reaches minimum. The vibration mode equal to pole pairs. 3 simulation analysis In the simulation, a harmonic response analysis has been performed by using the mode-superposition method. the motor is constrained by elastic support through the end face. A damping ratios of 4.4% extracted from the modal test is used. The harmonic forces are projected on the structure mesh of the stator in order to calculate the deformation, and the vibration mode. 4 Experiment test In order to verify the validity of analytical model studied in this paper, the Operational Deflection Shapes experiment is performed. The designed motor with 6-pole, 36-slot, α_1-5 is hanged on the bracket by elastic rope, and seven accelerometer sensors are evenly attached on the stator in the circumferential direction. The motor run at 1500rpm. Fig.2(a) compares the measured acceleration with those FEM at five frequencies associated with slot frequency. It clearly reveals that the acceleration components at the harmonic frequencies of 36fr, 72fr, 108fr, 144fr, etc.. Vibration shape at slot frequency is measured seen in Fig.2(b). It can be seen clearly that the vibration mode at slot frequency is six order, consistent with the analytical results. 5 Conclusions In this paper, a detailed analysis of vibration in stator permanent magnet synchronous motor (SPMSM) is presented. Some conclusions can be summarized from the paper: The frequencies of the exciting radial force and vibration of the SPMSMs mainly are integral multiples of the product of the slot number and the rotation frequency, which is different from the frequencies related about the pole number in the rotor permanent magnet motors. The vibration mode is decided by the radial force, which causes the pulsating mode, and the bending moment, which causes the bending mode.

[1] J. W. Jung, D. J. Kim, J. P. Hong, et al. "Experimental Verification and Effects of Step Skewed Rotor Type IPMSM on Vibration and Noise," *IEEE Trans. Magn,* vol. 47, DOI 10.1109/TMAG.2011.2150739, no. 4, pp. 3661-3664, Oct. 2011. [2] Cassat A, Espanet C, Coleman R, et al. A Practical Solution to Mitigate Vibrations in Industrial PM Motors Having Concentric Windings[J]. IEEE Transactions on Industry Applications, 2012, 48(5):1526-1538 [3] G. Liu, J. Yang, W. Zhao, J. Ji, Q. Chen, and W. Gong, Design and analysis of a new fault- tolerant permanent-magnet Vernier machine for electric vehicles [J], IEEE Trans. Magn., vol. 48, no. 11, pp. 4176–4179, Nov. 2012 [4] R.Islam and I. Husain, Analytical model for predicting noise and vibration in permanent magnet synchronous motors, Industry Applications [J], IEEE Transactions on,Vol.46,no.6,pp.2346-2354, Nov 2010 [5] T. Sun, J.-M. Kim,G.-H. Lee, Effect of pole and slot combination on noise and vibration in permanent magnet synchronous motor[J], IEEE Transactions on Magnetic, vol.47,no.5,pp.1038- 1041,may 2011 [6] Z. Q. Zhu, Z. P. Xia, L. J. Wu, G. W. Jewell. "Analytical modeling and finite-element Computation of radial vibration force in fractional-slot permanent-magnet Brushless machines", IEEE Transactions on Industry Applications, 2010, 46(5):1908-1918 [7] Jung J, Kim D, Hong J, et al. Experimental Verification and Effects of Step Skewed Rotor Type IPMSM on Vibration and Noise[J]. IEEE Transactions on Magnetics, 2011,47(10):3661-3664. [8] Sunghoon Lim, Seungjae Min, Jung-Pyo Hong. Low Torque Ripple Rotor Design of the Interior Permanent Magnet Motor Using the Multi-Phase Level-set and Phase-Field Concept[J]. IEEE Transactions on Magnetics, 2012,48(2), pp: 907-910 [9] J. Kwack, S. Min, and J.-P. Hong, Optimal stator design of interior permanent magnet motor to reduce torque ripple using the level set method, IEEE Trans. Magnetics.2010, 46(6), pp: 2108–2111 [10] D. Torregrossa, F. Peyraut, B. Fahimi, et al. "Multiphysics Finite-Element modeling for vibration and acoustic analysis of Permanent magent Synchronous Machine", IEEE Transactions on energy conversion, 2011, 26(2), pp:490-500 [11] J. Krotsch, B. Piepenbreier. "Radial forces in external rotor permanent magnet synchronous motors with non-overlapping windings", IEEE Transactions on Industrial electronics, 2012, 59(5), pp:2267-2276. [12] S. Zuo, L. Fu, X. Wu, "Noise analysis, calculation, and reduction of external rotor permanent-magnet synchronous motor", IEEE Transaction on Industrial electronics, 2015, 62(10), pp:6204-6212

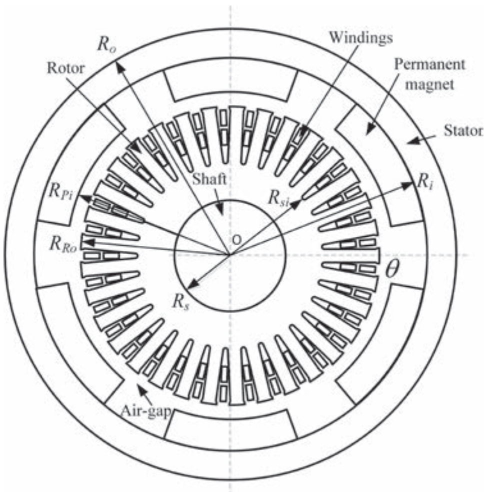

Fig. 1. Cross section of the motor

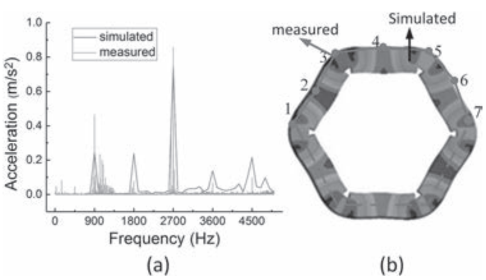

Fig. 2. The simulated and measured results

9:15

GH-02. Loss Calculation and Thermal Analysis of a High Speed Permanent Magnet Synchronous Motor with an Amorphous Metal Stator Core.

W. Tong[1], R. Sun[1], C. Zhang[1], S. Wu[1] and X. Ma[1]
1. School of Electrical Engineering, Shenyang University of Technology, Shenyang, China

Electric motors are the single biggest consumer of electricity. They account for about two thirds of industrial power consumption and about 45% of global power consumption. Therefore, high-efficiency motors can make an outstanding contribution to energy conservation. The techniques on decreasing iron loss of motors with conventional magnetic material have already reached a breaking point. With the development of new magnetic materials, employing low loss magnetic materials instead of traditional counterpart becomes a feasible way to improve the efficiency of high speed motors. Amorphous metal is characterized by extremely low losses. The disordered atomic structure of amorphous metal leads to electrical resistivity 2 times higher than that of conventional silicon steel sheet (SSS). The high resistivity and only one twentieth the thickness of conventional SSS help minimize iron loss when the metal is subjected to an alternating magnetic field [1-2]. Therefore, the excellent properties offer some possibilities to increase efficiency of high speed motors in using amorphous metal. In this paper, a 15kW, 30000 rpm amorphous metal permanent magnet synchronous motor (PMSM) with surface-mounted permanent magnets and a titanium alloy retaining sleeve is chosen as the research object to analyze the no load losses, on load losses and thermal behaviors in the conditions of converter supply by using finite element method. The configuration of the motor prototype and the experimental platform are shown in Fig. 1. 4-pole and 18-slot is adopted to develop the motor prototype. The advantages of the high speed PMSM with a amorphous metal stator core are demonstrated by both the finite element method calculation results and the no load loss and efficiency experiment results. In order to analyze the loss properties of the high speed motor, it is necessary to obtain the magnetization curves and the loss curves at different operation frequencies. Therefore, a experimental platform is built up to measure the magnetic properties of the yoke of amorphous metal stator cores at different frequencies according to the international standard measurement method IEC 60404-6 [3]. In the test, the yoke of the amorphous metal stator core is recognized as a ring-shaped core specimen. The experimental platform and the test results of the amorphous metal stator core are shown in Fig. 2. As can be seen from the figure, the magnetization curves are almost the same at different frequencies, and the loss of amorphous metal stator core is much smaller than that of conventional SSS. The no load losses, including the loss of amorphous metal stator core, the losses of surface-mounted permanent magnets and the titanium alloy retaining sleeve, are analyzed at several different frequencies by finite element method. The corresponding experiment is also carried out according to the calculation condition to verify the feasibility of the calculation. As a comparison, the no load losses of another motor with a carbon fiber sleeve are also analyzed, and some conclusions of the no load rotor losses are obtained. The temperature rise of high speed motors is one of the most import issues that affecting the reliable operation of the motor. The on load losses as the heat resource of the motor are analyzed, and then, the air flow condition inside the motor and the temperature distribution of each part of the motor are calculated by using computational fluid dynamics method. The frictional loss between the rotor surface and the air inside the motor is taken into consideration during the thermal analysis. The temperature rise test is proceed to verify the accuracy of the analysis. In the experiment, two identical amorphous metal PMSMs are connected to each other, one of which is used as an electric motor and the other as a generator. The load of the generator is a resistance box as shown in Fig. 1. The efficiency of the prototype is also obtained by the experiment platform.

[1] Z. Wang, R. Masaki, S. Morinaga and Y. Enomoto, "Development of an axial gap motor with amorphous metal cores," *IEEE Trans. Ind. Appl.*, vol. 47, no. 3, pp. 1293-1299, May/Jun. 2011. [2] Renyuan Tang, Wenming Tong and Xueyan Han, "Overview on amorphous alloy electrical machines and their key technologies," Chinese Journal of Electrical Engineering, vol. 2, no. 1, pp. 1-12, Jun. 2016. [3] IEC 60404-6: 2003, Methods of measurement of the magnetic properties of magnetically soft metallic and powder materials at 20 Hz to 200 kHz by the use of ring specimens

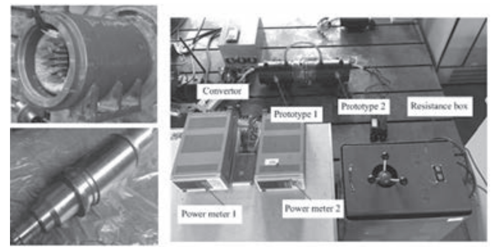

Fig. 1. Configurations of the high speed motor prototype and the experiment platform

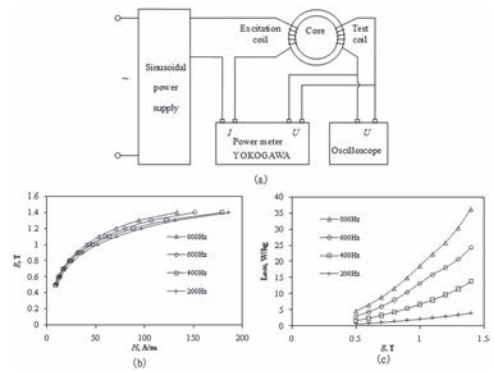

Fig. 2. Experimental schematic diagram and the characteristic curves of the amorphous stator core. (a) Experimental schematic diagram, (b) Magnetization curves, (c)Loss curves

9:30

GH-03. Investigation of Losses for a Concentrated Winding High Speed Permanent Magnet Assisted Synchronous Reluctance Motor for Washing Machine Application.

O.F. Payza[1,2], Y. Demir[1,3] and M. Aydin[1,3]
1. Kocaeli University, Kocaeli, Turkey; 2. Arcelik A.S, Istanbul, Turkey; 3. MDS Motor Design Ltd., Kocaeli, Turkey

1.INTRODUCTION In recent years, the use and interest of synchronous reluctance motors has increased with the development of software tools, magnetic materials, power electronics and control techniques. Synchronous reluctance motors (SRMs) are quite low cost compared to other types of permanent magnet (PM) motors and relatively easy to manufacture. SRMs can be used for high-speed applications due to their robust construction. Permanent magnet-assisted synchronous reluctance machines (PMaSRMs) can be designed by adding magnets in the rotor cavities so that quite wide field weakening region could be achieved. The aim of this study is to investigate motor performance considering the high speed losses of an unconventional PM assisted synchronous reluctance motor. Motor performance including torque ripple and torque speed characteristics will also be covered in the paper. This will be the first paper for washing machine application that covers all of these issues for concentrated winding PMaSRMs. 2.DESIGN OF PMaSRM A. Design Specifications In this study, a concentrated winding PM assisted synchronous reluctance motor with 9-slot and 8-pole is designed by using Flux 2D package. Fig.1 (a) shows motor design specifications. Fig.1 (b) shows the FEA model, mesh structure, flux density and flux lines of the proposed PMaSRM. It can be noted that maximum flux density at no-load is obtained as 1.3 T on the teeth. Due to the belt driven system and limited area, the application requires wide flux weakening range which is up to 14000rpm. Therefore, the motor is designed with a constant speed power ratio (CSPR) of 4.3 providing torque even at 12500rpm. The torque-speed curve obtained by FEA considering the voltage limits is shown in Fig. 2(a). More detail for the FEA studies will be provided in the final version of the paper. B. Investigation of Torque Output In white goods applications, the quality of the output torque is crucial and it is one of the most critical components in the motor performance since unwanted torque pulsations cause undesirable noises. Therefore, special attention should be given in order to reduce torque pulsations during the motor design. Average torque, reluctance torque and cogging torque components of the designed motor are shown in Fig. 2(b) and Fig. 2(c), respectively. The cogging torque is extremely low and the magnet torque is higher than the reluctance torque. Since the magnet is located on q-axis of the synchronous reluctance motor, the amount of magnet increases the torque output by decreasing q-axis inductance. In this way, there is no need to weaken the magnet flux in the field weakening zone. C. Investigation of Iron Losses Cost and efficiency as well as better motor performance are quite critical parameters for appliance industry. Iron losses especially at high speeds are the most important design criteria which determine the efficiency of the motor. Therefore, losses should be optimized based on cost-efficiency values. Since the motor is designed for low cost and wide speed range applications, the influence of the increased frequency on the motor performance has also been investigated in the paper. Iron loss-speed graph of the designed motor are shown in Fig. 2(d). In addition, skin and proximity effect losses at the maximum operating speed will be calculated and the results will be given in the final paper. 3.CONCLUSION In conclusion, design and investigation of losses for a concentrated winding PM assisted synchronous reluctance motor with 9 slot / 8 poles has been carried out in this study. It is shown that wider constant power region can be obtained with this structure. Iron losses especially at high speeds have been investigated. It has also been studied on minimizing the torque ripple to increase the output torque quality. The average torque was found to be roughly 28.2% in reluctance torque and 71.8% in magnet torque. It is also shown that wide CPSR could be obtained using the magnet configuration and fractional slot structure. The suitability of the designed motor for washing machine application has been evaluated and prototype motor has been built. More details including the test data will be provided in the final version of the paper. The FEA results will also be supported with the test data in the final paper.

[1] Shigeo Morimoto, Masayuki Sanada, Yoji Takeda. Performance of PM Assisted Synchronous Reluctance Motor for High Efficiency and Wide Constant Power Operation, IEEE Transactions on Industry Applications (Volume: 37, Issue: 5, Sep/Oct 2001). [2] Hiroshi Murakami, Yukio Honda, Hiroyuki Kiriyama, Shigeo Morimoto and Yoji Takeda. The Performance Comparison of SPMSM, IPMSM and SynRM in Use as Air-conditioning Compressor, Industry Applications Conference, 1999. Thirty-Fourth IAS Annual Meeting. Conference Record of the 1999 IEEE. [3] Masahiro Obata, Shigeo Morimoto, Masayuki Sanada, Yukinori Inoue. Characteristic of PMASynRM with Ferrite Magnets for EV/HEV Applications, Electrical Machines and Systems (ICEMS), 2012 15th International Conference on. [4] A. Fratta, G.P. Troglia, A. Vagati, F. Villata. Evaluation of Torque Ripple in High Performance Synchronous Reluctance Machines, Industry Applications Society Annual Meeting, 1993, Conference Record of the 1993 IEEE. [5] Eric Armando, Paolo Guglielmi, Michele Pastorelli*, Gianmario Pellegrino, Alfredo Vagati. Performance of IPM-PMASR motors with ferrite injection for home appliance washing machine, Industry Applications Society Annual Meeting, 2008. IAS '08. IEEE [6] Peyman Niazi and Hamid A. Toliyat. Design of a Low-Cost Concentric Winding Permanent Magnet Assisted Synchronous Reluctance Motor Drive, Industry Applications Conference, 2005. Fourteenth IAS Annual Meeting. Conference Record of the 2005. [7] Minghu Yu. Analysis of Hybrid Permanent Magnet Assisted Synchronous Reluctance Motor for Compressor, Electrical Machines and Systems (ICEMS), 2013 International Conference on. [8] C. M. Spargo, B. C. Mecrow and J. D. Widmer. Higher Pole Number Synchronous Reluctance Machines with Fractional Slot Concentrated Windings, Power Electronics, Machines and Drives (PEMD 2014), 7th IET International Conference on. [9] Nicola Bianchi, Silverio Bolognani, Diego Bon, and Michele Dai Pre. Torque Harmonic Compensation in a Synchronous Reluctance Motor, IEEE Transactions on Energy Conversion, Volume: 23, Issue: 2, June 2008 [10] Nicola Bianchi, Silverio Bolognani, Diego Bon, and Michele Dai Pre. Rotor Flux-Barrier Design for Torque Ripple Reduction in Synchronous Reluctance and PM-Assisted Synchronous Reluctance Motors, IEEE Transactions on Industry Applications (Volume: 45, Issue: 3, May-June 2009).

	PMaSRM
Rated Torque [Nm]	0.874
Torque Ripple [%]	5.93
Rated Speed [rpm]	3500
Max. Speed [rpm]	14000
Rated Current [A_{peak}]	2.2
Stator OD [mm]	117
Stack Length [mm]	25

(a)

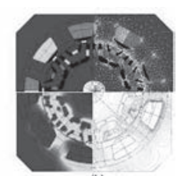

(b)

Fig. 1. (a) Motor Design Specifications, (b) the FEA model, mesh structure, flux density and flux lines of the proposed PMaSRM Motor

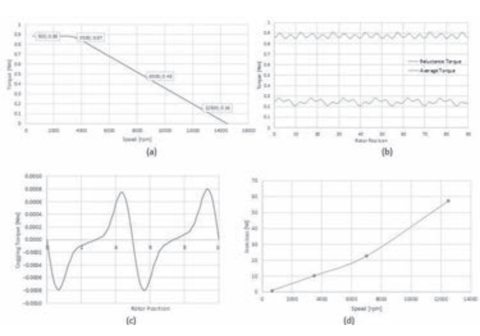

Fig. 2. (a) Torque-speed curve, (b) average and reluctance torque, (c) cogging torque, (d) speed-iron loss curve

9:45

GH-04. Design and Analysis of Halbach Array Flywheel Motor/Generators.

M. Yin[1], K. Liu[1], Y. Kong[1] and M. Lin[1]
1. Southeast University, Nanjing, China

Abstract-Halbach array permanent magnet machine has a number of attractive features in comparsion with the conventional permanent magnetic machines. In this paper, electromagnetic design and analysis equations for external rotor ironless brushless DC machine (BLDCM) which is used in flywheel energy storage system (FESS) are presented. The Halbach array permanent magnet machine is studied compared with the radial magnet array. The relationship between the air gap field distribution and the magnet array is discussed. At last, the eddy current loss of the external rotor ironless brushless DC machine (BLDCM) is analyzed between Halbach permanent magnet machine and conventional permanent magnet machine. I.INTRODUCTION The external rotor ironless brushless DC machine (BLDCM) is commonly suitable for use in flywheel energy storage system (FESS) in the space field. This type of BLDCM which used in FESS has the following advantages: (1) the operation efficiency is higher than the normal type of BLDCM ;(2) the space volume of FESS is greatly reduced;(3) the torque fluctuation is relatively smaller than the normal BLDCM.(4) the structure of the external rotor ironless brushless DC machine is simple and reliable. Though the external rotor ironless brushless DC machine has small torque fluctuation and iron losses, magnetic density of air gap is too small. So it is difficult to effectively play the advantage of high power density and high torque density of BLDCM. Compared to the conventional magnetization method, a high air gap flux density can be obtained by using the Halbach magnetic array. This paper studied the air gap magnetic density and eddy current loss of permanent magnet of the external rotor ironless BLDCM in different magnetic methods through finite element analysis. II.ELECTROMAGNETIC DESIGH Fig.1 illustrates the structure of the external rotor ironless BLDCM. The design process started from the calculation of the size of rotor. The number of stator-slots and rotor-poles is chosen after comprehensively consideration of loss and the efficiency goal. The winding turns are calculated under the requirements of the speed range and the power supply voltage limit. The material of permanent magnets is SmCo as per the temperature and operation environment. III.COMPARISON OF TWO MAGNETION METHODS Fig.2 shows the air gap magnetic density distribution of normal permanent magnets array. It includes radial magnetization and parallel magnetization.Fig3 shows that the air gap magnetic density distribution of Halbach permanent magnets which has 3 segments per pole. The magnetization of each permanent magnet can be expressed by the following equation: $M_x(i)=M\cos[360(1-p)(i-1)/(2pn)]$ $M_y(i)=M\sin[360(1-p)(i-1)/(2pn)]$ i indicates the magnetization of each segment, P is the polar logarithm of the motor, and n is the number of segments per pole. Fig.4 shows the two air gap magnetic density distribution in different magnetic arrays. The Halbach array permanent magnetic machine provides a better sine waveform than the normal array one. The Halbach array permanent magnetic machine exhibit less eddy current loss compared to the conventional external rotor permanent machine. The simulation and experiment results based on the different magnetization will be showed in the full paper. IV.CONCLUSION The basic design equations for external rotor permanent magnet machines using Halbach cylinders have been presented, especially for slotless and ironless machine topologies. It has been shown that such machines may offer significant advantages over conventional permanent magnet machines, particularly for high-speed applications when the eddy current losses can be significant.

V. REFERENCES [1] K Atallah, D Howe and P H Mellor. design and analysis of multi-pole halbach (self-shielding) cylinder brushless permanent magnet machines. 1997 Eighth International Conference on Electrical Machines and Drives (Conf. Publ. No. 444), 1997:376~380 [2] John R. Hull, Larry R. Turner. Magnetomechanics of Internal-Dipole, Halbach-Array motor/generators. IEEE Transactions on Magnetics, 2000, 36(4):2004~2011

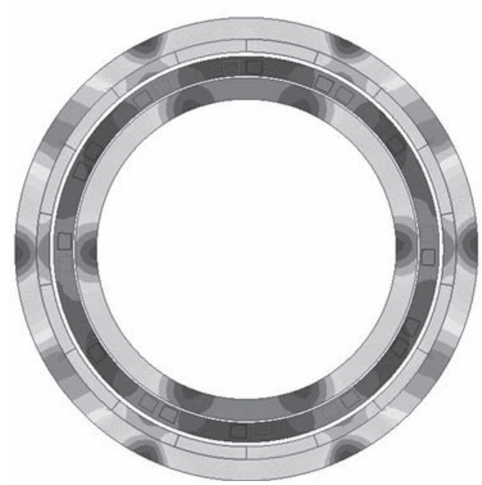

Fig. 1. the air gap magnetic density distribution of Halbach permanent magnet array

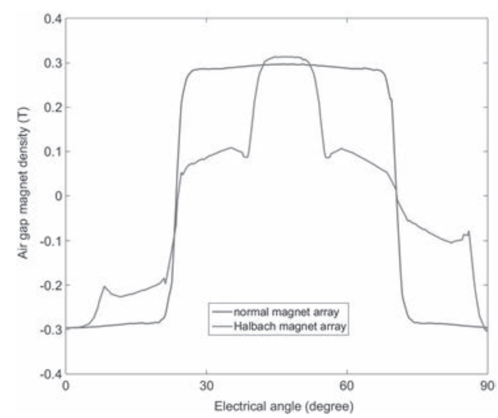

Fig. 2. air-gap magnetic density of different magnet arrays

10:00

GH-05. Eddy-Current Loss Measurement of Permanent Magnet Material at Different Frequency.

C. Zhang[1], B. Jiang[1], R. Chen[1], Y. Li[1] and Q. Yang[2]
1. Hebei University of Technology, Tianjin, China; 2. Tianjin Polytechnic University, Tianjin, China

I Introduction Permanent magnets have been widely used in rotating electrical machines. The eddy current loss induced by the fundamental air-gap field is usually neglected, since it rotates in synchronism with the rotor[1]. To improve torque density and torque ripple, a new class of PM machines is emerging in which stator coils are wound on consecutive or alternate teeth with a fraction number of tooth per pole [2]. However, the large number of harmonics caused by slot ripple, inverter [3] will lead to significant eddy current loss in the magnets, which makes the temperature of magnet increase and may cause the thermal demagnetization [4]. As a result, it is necessary and important to study the eddy current loss in the permanent magnets. Many analytical models are developed to predict induced eddy current loss, but few are verified by experiments until now. In this paper, the eddy current loss of NeFeB sintered magnet is measured by using a newly developed closed-circuit measuring equipment, meantime the same size simulation model is established by Ansoft to compare with the experiment results. The behavior of the eddy current loss of permanent magnet is investigated at different frequency. II Measurement System Setup (A) The Excitation Structure Fig.1 shows the novel dynamic hysteresis loop measurement apparatus of permanent magnet material with the frequency up to 1 kHz. The alternating flux density inside the magnet material is up to 0.2 T, which is large enough for the rotor of various AC machines. The closed-loop magnetic circuit is composed of the double C-shaped core, flexible excitation windings and the permanent sample. The excitation C-shaped cores are made of ultra-thin 0.1mm silicon steel, which can work up to 1 kHz. The permanent samples are made into the cylinder-shaped, which is located in the air-gap between the double C-shaped cores. And the air-gap between the magnet poles can be adjusted according to the length of the sample, for the C-shapes is placed on the slide rail. The four multi-layer excitation windings were separately wound on the C-shaped cores. And the windings were made of 12-turns Litz wire, which can work up to 10 kHz. The power amplifier for the excitation windings is PA500 made by Brockhause Company with the frequency from DC to 20 kHz. (B) The Sensing Structure The coil of magnetic flux density is directly wounded on the permanent sample, in which number of turns is 6 and area size is the same as the permanent cross-section. As shown in the Fig.1, there are two samples between one air-gap. The area between the two samples is close enough so that it forms an uniform magnetic field strength area which is measured by the Hall-probe of Bell Gaussmeter 8030. In the full paper, the electro-magnetism finite element analysis illustrates the distribution of magnetic field strength and flux density and validates the rationality of our magnetic circuit structure. III Measurement Results and Discussion In the measurement system, the eddy current loss and its dynamic hysteresis loop of the permanent magnets can be directly measured. (A) Measurement of static magnetic properties The four permanent magnet samples and the magnetic yoke compose a closed circuit. Based on the static hysteresis loop of permanent magnet, the static working point can be calculated and measured. (B) Measurement of dynamic magnetic hysteresis loop Under the alternating current by the flexible excitation winding, the magnetic field inside the permanent magnet is alternatively changing at the static working point of static demagnetization curve. Fig.2 shows the dynamic hysteresis loop of the permanent magnet at 50 Hz. The area of hysteresis loop is the sum of the hysteresis loss and the eddy current loss according to the Poynting vector theorem $p = \int H\, dB$ As the B magnitude and frequency changing, a series of loss characteristics of permanent magnet will present in the full paper. (C) Eddy current loss of permanent magnet at different temperature In traditional finite element analysis, the eddy current loss calculation is based on the coefficient of conductivity of the permanent magnet. In the industry application, the conductivity and eddy current are strongly affected by the temperature. When the measurement apparatus is placed in the temperature variable box, the eddy current losses can be measured by the changing temperature. IV Conclusion In this paper, a novel dynamic hysteresis loop and eddy current loss measurement apparatus of permanent magnet material was designed. For the NdFeB material, neglecting the hysteresis loss, the area of hysteresis loop represents eddy current loss. The measurement results provide the basis for the eddy-current modeling of permanent magnetic materials at different frequency and temperature. Acknowledgment This work was supported in part by the National Natural Science Foundation of China, (No. 51777055), the National Key R & D Program of China (2017YFB0903904), and the National Key Basic Research Program of China (973 Project) under Grant 2015CB251000.

[1] K. Atallah, D. Howe, P. H. Mellor, D. A. Stone, “Rotor loss in permanent magnet brushless ac machines”, I*EEE Trans Industry Application*, vol.36, no.6, pp.1612-1618, 2000. [2] J. Wang, K. Atallah, R. Chin, W. M. Arshad, H. Lendenmann, “Rotor eddy-current loss in permanent magnet brushless ac machines”, *IEEE Trans Industry Application*, vol.46, no.7, pp.2701-2707, 2010. [3] K. Itoh, Y. Hashiba, K. Sakai, and T. Yagisawa,“The A.C. losses of the rare-earth permanent magnets,”*Trans. IEE Jpn.*, vol. 118-A, no. 2, pp.182–187, 1998. [4] A. Fukuma, S. Kanazawa, D. Miyagi, and N. Takahashi, “Investigation of AC loss of permanent magnet of SPM motor considering hysteresis and eddy-current losses”, *IEEE Transactions on Magnetics*, vol. 41, no. 5, pp. 1964–1967, May 2005.

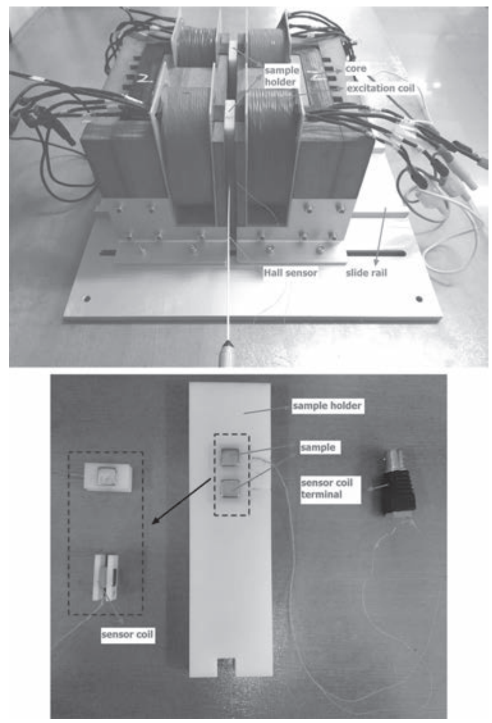

Fig. 1. (Top) The setup of measurement system. (Bottom) The structure of NdFeB sample and the B sensing coils.

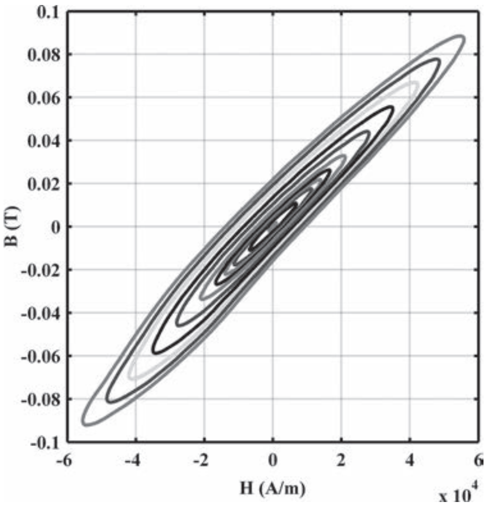

Fig. 2. Dynamic hysteresis loops of permanent magnet under the biased static magnetic field.

10:15

GH-06. Reduction of Rotor Losses by Using Amorphous Rotor Core for Ultra-High-Speed Motors.

Y. Liu[1], *J. Ou*[1], M. Schiefer[1], P. Breining[1] and M. Doppelbauer[1]
1. Karlsruhe Institute of Technology, Karlsruhe, Germany

Abstract— This paper proposes to use the amorphous material in the rotor core for the ultra-high-speed motors to decrease the rotor losses. Due to the low core losses and the low saturation flux density of the amorphous material, the rotor core losses and the shaft eddy current losses can be reduced by using the amorphous material. To study the feasibility of the proposed rotor, the measured properties of the amorphous material are presented. The benefits and disadvantages of the amorphous rotor core are illustrated by comparing with a silicon steel rotor core in terms of torque, losses and the rotor thermal fields. Furthermore, the influence of the pulse-width modulation (PWM) on the rotor losses is studied. I. INTRODUCTION Due to the high power density and high efficiency, the ultra-high-speed PM synchronous motors have been used for varieties of applications, including electric engines for aircraft, flywheel energy storage systems, high-speed spindles, turbomolecular pumps, gas compressors, air blowers, and microturbines [1-6]. Currently, surface-mounted PM rotor configuration with a metal or fiber sleeve is widely used for the ultra-high-speed motors to protect the rotor from centrifugal forces. The metal sleeves can offer a high thermal conductivity but the rotor eddy current losses are also high, while the fiber sleeves can avoid the eddy current losses but the thermal conductivity is low. Hence, the rotor losses and heat dissipation are very important for the ultra-high-speed motor design. In this paper, the properties of the amorphous material are measured and the data is used to investigate the torque and the rotor losses of the motors. To consider the influence of the power electronics, FEA coupled with Simulink method is employed. Finally, the torque, losses and thermal fields of the rotors with different core materials are compared. II. PROPERTIES OF THE AMORPHOUS MATERIAL The properties of the amorphous core 2605SA1 are measured and compared with conventional silicon steel M330-35A. The measurement results are shown in Fig. 1. It can be found that the losses of 2605SA1 are about one tenth of M330-35A. Due to the small thickness of the amorphous material, the eddy current loss of 2605SA1 is much lower than M330-35A. However, compared with silicon steels, the amorphous material 2605SA1 has a relatively low saturation flux density which is about 1.5 T, and has a relatively low stack factor, which can decrease the torque ability of the motors. However, by using an amorphous rotor core, the motor can be benefited not only from the low core losses, but also from the relatively low saturation flux density, since saturated rotor core can help to reduce the armature reaction field on the shaft which leads to low eddy current losses in the shaft. III. INFLUENCE OF PWM ON ROTOR LOSSES Although the integral-slot configuration consisting of low amplitude spatial field harmonics is widely used in the ultra-high-speed motors, the rotor losses caused by the armature reaction are still super high due to time current harmonics caused by PWM. In this section, by using FEA coupled with Simulink method, the influence of the PWM on eddy current losses is investigated. The effects of the switching frequency and the air-gap length are discussed. IV. COMPARISON OF DIFFERENT ROTOR CORE MATERIALS The structure of the ultra-high-speed motor used in this paper is shown in Fig. 2 (a). The FEA coupled with Simulink model is shown in Fig. 2(b). In this section, the rotor losses and rotor thermal fields are calculated and compared. To make a fair comparison, the only difference of the two motors is the materials used in the rotor cores. To generate the same torque, the rotor losses of the motor with the amorphous rotor core are lower than that of the motor with silicon steel rotor core. However, the heat dissipation ability of the amorphous material is also poor compared with silicon steels. Hence, it is necessary to investigate the thermal fields of the two rotors. More detailed analysis will be presented in the final paper.

[1]. A. Krings, A. Boglietti, A. Cavagnino and S. Sprague, “Soft magnetic material status and trends in electric machines,” *IEEE Trans. on Ind. Electron.*, vol. 64, no. 3, pp. 2405-2414, March 2017. [2]. M. Dems and K. Komeza, “Performance characteristics of a high-speed energy-saving induction motor with an amorphous stator core,” *IEEE Trans. on Ind. Electron.,* vol. 61, no. 6, pp. 3046-3055, June 2014. [3]. T. Fan, Q. Li and X. Wen, “Development of a high power density motor made of amorphous alloy cores,” *IEEE Trans. on Ind. Electron.*, vol. 61, no. 9, pp. 4510-4518, Sept. 2014. [4]. S. Okamoto, N. Denis, Y. Kato, M. Ieki and K. Fujisaki, “Core loss reduction of an interior permanent-magnet synchronous motor using amorphous stator core,” *IEEE Trans. on Ind. Appl.*, vol. 52, no. 3, pp. 2261-2268, May-June. 2016. [5]. H. Hayashi, K. Nakamura, A. Chiba, T. Fukao, K. Tungpimolrut and D. G. Dorrell, “Efficiency improvements of switched reluctance motors with high-quality iron steel and enhanced conductor slot fill,” *IEEE Trans. on Energy Convers.*, vol. 24, no. 4, pp. 819-825, Dec. 2009. [6]. A. Chiba et al., “Test results of an SRM made from a layered block of heat-treated amorphous alloys,” *IEEE Trans. on Ind. Appl.*, vol. 44, no. 3, pp. 699-706, May-june 2008.

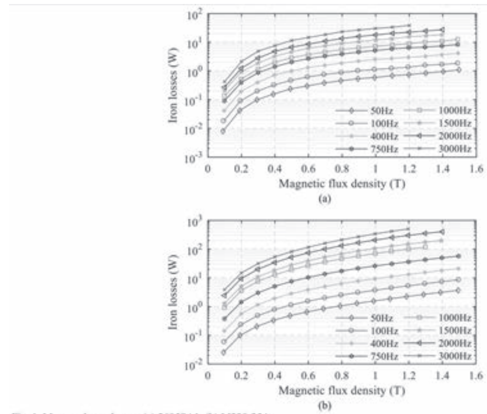

Fig. 1. Measured core losses. (a) 2605SA1. (b) M330-35A.

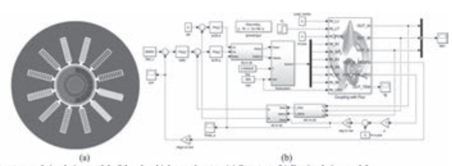

Fig. 2. Structure and simulation model of the ultra-high-speed motor. (a) Structure. (b) Co-simulation model.

10:30

GH-07. Design and Optimize an external rotor Ironless BLDCM used in a Flywheel Energy Storage System.

K. Liu[1], M. Yin[1], X. Fu[1], M. Lin[1] and Y. Kong[1]
1. Institute of Electrical Engineering, Southeast University, Nanjing, China

Abstract —Based on the application and design requirements of energy storage system, the external rotor ironless brushless DC machine (BLDCM), which is suitable for use in FESS, is designed and further explored. The finite element method is adopted to do computational research on external rotor ironless BLDCM. Performance improvement and loss minimization of the machine are achieved through optimizing the magnetic pole and the winding. The research results show that the copper loss of the machine can be reduced by appropriate selection of magnetic steel thickness even under the condition that the main parameter of the flywheel machine is set. Proper choice of magnetic steel polar-arc coefficient is beneficial to reduce the flux leakage on the surface of the rotor. The width of air gap flux density can be increased by applicable selection of magnetic poles and magnetizing style. The flywheel energy storage machine prototype is fabricated based on the optimized design of the machine. The experiment results show that the test results almost coincided with the design values. I.INTRODUCTION The flywheel energy storage system (FESS) is a novel electromechanical energy conversion and storage device, whose advantages are long service life, high conversion efficiency, high adaptability and pollution-free[1], etc.. FESS has enormous application foreground at the Electromagnetic Launch, the aspects of aeronautics and astronautics, distributed generation, power system peak load regulation and electrical vehicles. The purpose of this paper is to design and Optimize the external rotor ironless brushless DC machine (BLDCM), which is suitable for use in FESS. The finite element method is adopted to do computational research on external rotor ironless BLDCM. Performance improvement and loss minimization of the machine are achieved through optimizing the magnetic pole and the winding. II. STRUCTURE AND PRINCIPLE The FESS presented in this paper is composed of two parts: the ironless BLDCM and its drive system. Fig.1 shows the structure of the iron-less BLDCM. The BLDCM includes an iron-less armature (fixed in a fiber frame), an iron core and the permanent magnets. III. OPTIMIZING THE MAGNETIC POLE Performance improvement and loss minimization of the machine are achieved through optimizing the magnetic pole. Fig. 2 shows that the width of air gap flux density can be increased by applicable selection of magnetic poles and magnetizing style. Fig. 3 shows that proper choice of magnetic steel polar-arc coefficient is beneficial to reduce the flux leakage on the surface of the rotor. The full paper will give the further discusses. IV. EXPERIMENT To validate the optimization method, an external rotor Ironless BLDCM prototype was built, as shown in Fig. 3. V. CONCLUSION The result shows that performance improvement and loss minimization of the machine can be achieved through optimizing the magnetic pole and the winding. The full paper will give the further discusses.

[1] Seok-Myeong J, Dae-Joon Y, Kyoung-Jin K, et al. Design and Experimental Evaluation of Synchronous Machine Without Iron Loss Using Double-Sided Halbach Magnetized PM Rotor in High Power FESS[J]. IEEE Transactions on Magnetics, 2008, 44(11): 4337-4340.

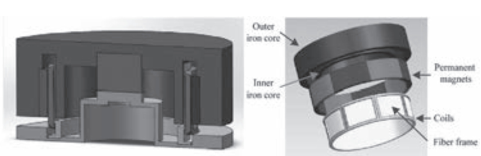

Fig. 1. The structure of the FESS.

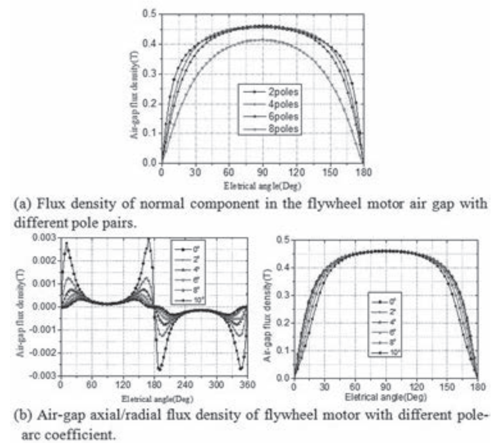

(a) Flux density of normal component in the flywheel motor air gap with different pole pairs.

(b) Air-gap axial/radial flux density of flywheel motor with different pole-arc coefficient.

Fig. 2. Air-gap flux density of flywheel motor

10:45

GH-08. Four Degrees of Freedom Self-decoupling Bearingless Motor for Direct-Driven Flywheel.

Y. Yuan[1], Y. Sun[1,2], Z. Zhu[2], G. Meng[2], Y. Huang[1] and F. Yang[1]
1. School of Electrical and Information Engineering, Jiangsu University, Zhenjiang, China; 2. School of Power Engineering, Nanjing Institute of Technology, Nanjing, China

Introduction: In flywheel battery applications, the rotating flywheels are usually coupled to a shaft which leads to additional axial length, critical speed limitation, space waste, and low reliability [1-2]. Moreover, the mechanical bearings are a source of energy losses and require lubrication to relieve mechanical friction[3-4]. In order to avoid these problems, magnetic bearings(MB) [5] technology with several advantages, such as eliminating of a lubrication system, friction-free operation and low power consumption is applied for flywheel battery. The bearingless switched reluctance motor(BSRM) [6-7] can rotate and levitate by integrating the magnetic levitation winding of MB into that of the SRM. As high integration, low loss and high reliability are the main development trends of flywheel battery, this paper presents a four degrees of freedom(4-DOF) self-decupling bearingless motor(SDBM) specially for flywheel battery. The proposed motor exhibits the following advantages: 1) High integration. The proposed motor can realize energy conversion and 4-DOF suspension through the torque and suspension systems. Moreover the outer rotor can drive the flywheel directly. 2) Low loss. The biased flux is provided by the permanent magnet which leaves out the extra biased winding correspondingly. 3) Weak coupling. Self-decoupling is realized between the torque and the suspension systems according to the structural design. 4) Favorable controllability. The suspension force is only related to the current and has no relation to the rotor position, thereby increasing controllability. New Machine: The structure of the proposed novel bearingless motor is illustrated in Fig. 1. Fig. 1(a) presents the 4-DOF SDBM, which mainly consists of a PM ring (PMR) with axial magnetizing, a motor side structure, and a magnetic bearings(MB) side structure. The PMR between the motor and the MB side structures provides a biased flux for generating suspending forces. Fig. 1(b) and Fig. 1(c) depict the motor side structure and MB side structure. The motor side structure mainly consists of a torque system, a left suspension system, and four non-magnetic materials. The torque system has eight inner stator poles (two phases in total). For example, the *A* phase in the torque system contains A1, A2, A3, and A4 poles. The electric and power generations are realized with the principle of minimum reluctance. The left suspension system on the motor side has four inner stator poles (two phases in total). For example, the *C* phase in the suspension system of the motor side contains C1 and C2 poles which can produce the suspension force in y_1 direction. The torque and left suspension system share a outer rotor with 14 poles. The MB side structure mainly consists of a right suspension system with four stator poles (two phases in total) and a disc-type outer rotor. The *E* phase on the MB side contains E1 and E2 poles which can produce the suspension force in y_2 direction. The *A*, *B*, *C*, and *D* phases can provide 4-DOF radial suspensions in the x_1, y_1, x_2, and y_2 directions, respectively. Fig. 1(d) depicts the paths of biased flux Φ_m and control flux Φ_C and Φ_E. The biased flux Φ_m forms a close loop thought the stator poles in motor side, the outer rotor, and the stator poles in MB side. The control magnetic flux Φ_C and Φ_E do not pass through the PMR. Electromagnetic Characteristics: Fig. 2 depicts the main electromagnetic characteristics of 4-DOF SDBM. i_{FC} and i_{FE} are defined as the current of the left suspension system and right suspension system in the y_1 and y_2 direction, respectively. i_{TA} is defined as the *A* phase current of torque system. Fig. 2(a) and Fig. 2(b) present the values of air-gap flux density with different values of i_{FC}. It can been seen that the value of the air-gap flux density is approximately 0.7 with i_{FC}=0 A. When i_{FC} are conducted with 1 A, 2 A, and 3 A, the air-gap flux density increases with the increase in the current value in y_1 negative direction and decreases in the y_1 positive direction. Therefore, the air-gap magnetic flux density can be regulated by controlling the magnitude and direction of the suspension current, and the required suspension force can then be generated. Fig. 2(c) and Fig. 2(d) present the coupling relationship between suspension systems and torque system. The relationship among the left suspension current i_{FC}, right suspension current i_{FE}, and suspension force in y_1 direction is shown in figure 2(c). The suspension force value in the y_1 direction is approximately linear with the value of i_{FC}. This analysis denotes that the controllability of the magnitude of radial suspension forces in the 4-DOF direction can be achieved by adjusting the suspension force winding current magnitude. Moreover, the suspension force value in the y_1 direction is approximately zero with the value of i_{FE} within [0 A, 3A]. Thus, the self-decoupling is realized between the left and right suspension systems. Similarly the self-decoupling is realized between the suspension system and torque system as shown in figure 2(d).

[1] Y. Yuan, Y. Sun and Y. Huang, “Radial force dynamic current compensation method of single winding bearingless flywheel motor,” IET Power Electronics, vol.8, no. 7, pp. 1224-1229, 2015. [2] Y. Yuan, Y. Sun and Y. Huang, “Accurate mathematical model of bearingless flywheel motor based on Maxwell tensor method,” Electronics Letters, vol.52, no. 11, pp. 950-952, 2016. [3] Z. Su, D. Wang, J. Chen, X. Zhang and L. Wu, “Improving Operational Performance of Magnetically Suspended Flywheel With PM-Biased Magnetic Bearings Using Adaptive Resonant Controller and Nonlinear Compensation Method,” IEEE Transactions on Magnetics, vol.26, no.7, pp. 1-5, 2016. [4] W. Zhang, H. Zhu, “Improved model and experiment for AC-DC three-degree of freedom hybrid magnetic bearing,” IEEE Transactions on Magnetics, vol.49, no.11, pp. 5554-5565, 2013. [5] C. Morrison, M. Siebert and E. Ho, “Electromagnetic Forces in a Hybrid Magnetic-Bearing Switched-Reluctance Motor,” IEEE Transactions on Magnetics, vol. 44, no. 12, pp. 4626-4638, 2008. [6] M. Takemoto, A. Chiba and H. Akagi, “Radial force and torque of a bearingless switched reluctance motor operating in a region of magnetic saturation,” IEEE Transaction on Industry Applications, vol.40, no.1, pp.103-112, 2004. [7] L. Chen and W. Hofmann, “Design procedure of bearingless high speed switched reluctance motors,” Int. Symp. on Power Electronics Electrical Drives Automation and Motion, Pisa, Italy, pp. 1442-1447, June 2010.

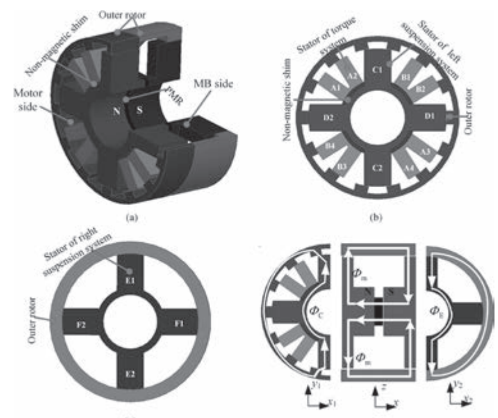

Fig. 1. Structure of 4-DOF SDBM. (a) Basic structure. (b) Structure of motor side. (c) Structure of MB side. (d) Paths of biased flux and control flux.

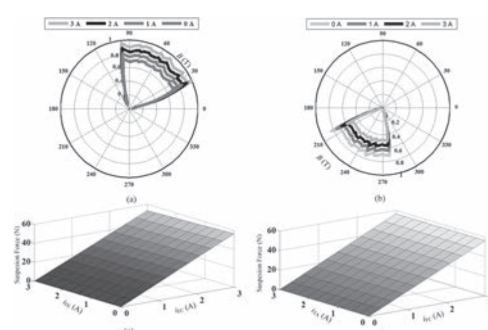

Fig. 2. Electromagnetic characteristics. (a) Values of air-gap flux density in the y_1 negative direction. (b) Values of air-gap flux density in the y_1 positive direction. (c) Coupling relationship between right and left suspension systems. (d) Coupling relationship between suspension system and torque system.

11:00

GH-09. Comparison of Sleeve Types for Ultra-High-Speed Surface-Mounted PM Motors.

Y. Liu[1], *J. Ou*[1], M. Schiefer[1] and M. Doppelbauer[1]
1. Karlsruhe Institute of Technology, Karlsruhe, Germany

Index Terms—Metal sleeve, fiber sleeve, high-speed motors, rotor losses, surface-mounted PM, PWM. *Abstract*— This paper compares the rotor losses and the thermal fields of a surface-mounted PM synchronous ultra-high-speed motor with different sleeve types. Currently, fiber sleeves and metal sleeves are commonly used. Both types of sleeves have high yield strength. However, they have disadvantages either on rotor losses or on heat dissipation. It is well-known that the fiber sleeve can avoid high eddy current losses, but the thermal conductivity is low. Compared with the fiber sleeve, the metal sleeve has higher thermal conductivity. However, its electrical conductivity is also high which causes high eddy current losses. Hence, this paper compares the two sleeves to provide a reference for the machine designers. I. INTRODUCTION Although the metal sleeve used for ultra-high-speed motors will cause super high eddy current losses, the thermal dissipation ability of the metal sleeve is also high. Currently, the metal sleeve is more widely used according to the literature [1]-[11]. If the manufacture difficulty and the mechanical stress on the sleeves are not considered, which sleeve type is better in terms of the thermal field is the research emphasis in this paper. The properties of the carbon fiber and titanium are listed in Table I. By using the finite element analysis (FEA), dynamic mechanical analysis (DMA) and computational fluid dynamics (CFD) methods, the performance of the surface-mounted PM motors with different sleeve types in terms of electromagnetic, mechanical and thermal aspects are analyzed. II. DETERMINATION OF SLEEVE THICKNESS By applying the sleeve properties in Table I, the mechanical stress on the rotor can be analyzed. To make sure that the sleeve is safe, the maximum stress on the sleeve is limited to 600 MPa. Then, the thickness of the sleeve is determined. Since the Young's modulus, the Poisson's ratio and the permitted stress of the carbon fiber and titanium are comparable, the thicknesses of the two sleeves are equal in this paper. III. ROTOR LOSSES ANALYSIS In order to decrease the PM eddy current losses, the PM poles are divided into 8 segments per pole. Then, at the maximum speed, i.e. 125,000 rpm, when the torque of the two motors with different sleeves is equal, the rotor losses are evaluated through FEA. The influence of the pulse-width modulation (PWM) is considered in this paper. To evaluate the rotor losses caused by PWM, FEA coupled with Simulink method is used. IV. THERMAL FIELD COMPARISON To determine which sleeve has better performance in terms of the rotor thermal field, a CFD software STAR CCM+ is used. The thermal field of the motor with carbon fiber sleeve is shown in Fig. 1. By comparing the temperature rise of the two rotors with different sleeve materials, which sleeve is more suitable for the ultra-high-speed PM motors can be concluded.

[1] C. Zwyssig, M. Duerr, D. Hassler and J. W. Kolar, "An ultra-high-speed, 500000 rpm, 1 kW electrical drive system," *2007 Power Convers. Conf. - Nagoya*, Nagoya, 2007, pp. 1577-1583. [2] Toshihiko Noguchi, Yosuke Takata, Yukio Yamashita, Yoshimi Komatsu, and Seiichi Ibaraki, "220,000-r/min, 2-kW PM motor drive for turbocharger," *Electrical Engineering in Japan*, Vol. 161, No. 3, pp. 854–861, 2007. [3] P. D. Pfister and Y. Perriard, "Very-high-speed slotless permanent-magnet motors: analytical modeling, optimization, design, and torque measurement methods," *IEEE Trans. on Ind. Electron.*, vol. 57, no. 1, pp. 296-303, Jan. 2010. [4] D. K. Hong, B. C. Woo, J. Y. Lee and D. H. Koo, "Ultra high speed motor supported by air foil bearings for air blower cooling fuel cells," *IEEE Trans. on Magn.*, vol. 48, no. 2, pp. 871-874, Feb. 2012. [5] T. Abe, T. Higuchi, K. Shigematsu and J. Oyama, "The system simulation for small size and ultra-high speed motor drive system using coupled analysis," *2007 European Conf. on Power Electron. and Appl.*, Aalborg, 2007, pp. 1-8. [6] T. Noguchi and T. Wada, "1.5-kW, 150,000-r/min ultra high-speed PM motor fed by 12-V power supply for automotive supercharger," *2009 European Conf. on Power Electron. and Appl.*, Barcelona, 2009, pp. 1-10. [7] T. Schneider and A. Binder, "Design and evaluation of a 60 000 rpm permanent magnet bearingless high speed motor," *2007 7th Int. Conf. on Power Electron. and Drive Systems*, Bangkok, 2007, pp. 1-8. [8] S. Jumayev, M. Merdzan, K. O. Boynov, J. J. H. Paulides, J. Pyrhönen and E. A. Lomonova, "The effect of PWM on rotor eddy-current losses in high-speed permanent magnet machines," *IEEE Trans. on Magn.*, vol. 51, no. 11, pp. 1-4, Nov. 2015. [9] A. Tüysüz, M. Steichen, C. Zwyssig and J. W. Kolar, "Advanced cooling concepts for ultra-high-speed machines," *2015 9th Int. Conf. on Power Electron. and ECCE Asia (ICPE-ECCE Asia)*, Seoul, 2015, pp. 2194-2202. [10] J. H. Ahn, J. Y. Choi, C. H. Park, C. Han, C. W. Kim and T. G. Yoon, "Correlation between rotor vibration and mechanical stress in ultra-high-speed permanent magnet synchronous motors," *IEEE Trans. on Magn.*, vol. 53, no. 11, pp. 1-6, Nov. 2017. [11] C. Zwyssig, S. D. Round and J. W. Kolar, "An ultra-high-speed, low power electrical drive system," *IEEE Trans. on Ind. Electron.*, vol. 55, no. 2, pp. 577-585, Feb. 2008. [12] Zlatko Kolondzovski, "Thermal and mechanical analysis of high-speed permanent-magnet electrical machines," Ph.D. dissertation, Dept. Elect. Eng., Aalto Univ., Helsinki, Finland, 2010. [13] H. Fang, R. Qu, J. Li and B. Song, "Rotor eddy-current loss minimization in high-speed PMSMs," *2016 IEEE Energy Conversion Congress and Exposition (ECCE)*, Milwaukee, WI, 2016, pp. 1-8.

TABLE I
PROPERTIES OF THE MATERIALS USED FOR RETAINING SLEEVE [12] [13]

Materials	Thermal cond. (W/mK)	Specific heat (J/kgK)	Young's Modulus (GPa)	Poisson's ratio	Density (kg/m^3)	Permitted stress (MPa)	Electrical cond. (S/m)
Carbon fiber/epoxy	0.87	970	125	0.28	1800	800	≈ 0
Titanium	7.5	670	110	0.31	4400	725	5.6e+5

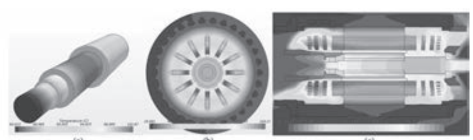

Fig. 1. Thermal field. (a) Rotor. (b) Radial cross section. (c) Axial cross section.

11:15

GH-10. Simulation and Experimental Research on No-Load Losses of an IPM Motor under the Conditions of both Sinusoidal Supply and Converter Supply.

W. Tong[1], Y. Wang[1], R. Sun[1], S. Wu[1] and J. Jia[1]
1. School of Electrical Engineering, Shenyang University of Technology, Shenyang, China

Interior permanent magnet (IPM) motors driven by pulse width modulation (PWM) converters are widely applied to the industry due to many advantages, such as superior flux-weakening ability, high torque density by using the reluctance torque, etc. [1]. The electromagnetic field in IPM motors includes many harmonics, for instance, the slot harmonics, space MMF harmonics due to discrete current distribution and current harmonics generated by converter power supply. These harmonics may cause considerable harmonic losses in the stator and rotor cores and magnets. The thermal demagnetization of the magnet due to the eddy current loss is one of the biggest problems in the motor. Therefore, correct and quick estimation of the rotor losses is desired [2]. In this paper, an interior "V" type electric vehicle permanent-magnet motor is taken as an example as shown in Fig.1. The rated power is 20 kW, and the rated speed is 4500 rpm. The characteristics of the IPM motors, including the stator and rotor core loss, the permanent-magnet loss and the permanent-magnet temperature rise, are studied in no-load condition with both sinusoidal supply and converter supply. By using the time-step finite element method, each component of the no-load iron loss of the IPM motor with sinusoidal power supply and converter power supply are calculated. The calculation results of the no load losses of a 8-pole 48-slot motor and a 8-pole 9-slot motor are compared. The no-load loss in different parts of the motor with different converter parameters (switching frequency and modulation ratio) is calculated for the motor with distributed windings. The 3-D temperature distribution of the motor, especially the temperature of the permanent magnet is analyzed in the conditions of both sinusoidal supply and converter supply. The accuracy of the FEM results are validated by comparing the loss and temperature rise to corresponding experimental results. Fig. 2 (a) shows the losses at different switching frequency and modulation ratio. When the switching frequency increases from 2kHz to 8kHz, the no-load iron loss of the 8-pole 48-slot motor and 8-pole 9-slot motor reduces by 26.1% and 24.9%, respectively. When the switching frequency increases from 8kHz to 16kHz, the no-load iron loss of the 8-pole 48-slot motor and the 8-pole 9-slot motor reduces by 20.7% and 16.1%, respectively. When the modulation ratio increases from 0.6 to 0.8, the no-load iron loss of the 8-pole 48 slot motor and the 8-pole 9-slot motor decreases by 7.4% and 6.1%per growth of 0.1modulation ratio. This paper adopts a wireless temperature sensor in the motor rotor as shown in Fig. 1 to measure the temperature rise of the permanent magnets in both sinusoidal supply and converter supply conditions. The eddy current losses for both conditions are obtained according to the gradient of tested temperature-time curves at the initial time. The mechanical loss of the motor is obtained using another primary motor to drive this motor with a non-magnetic fake rotor, and the weight and volume of the fake rotor is identical to the real magnetic rotor. The stator and rotor core loss can be obtained subtracting the mechanical loss, no-load copper loss and permanent magnet loss from the total loss. Fig. 2 (b) shows the calculated value and experimental value of each component of the no-load losses for the 8-pole 48-slot IPM motor prototype in the conditions of both sinusoidal supply and converter supply. The no-load loss with sinusoidal power supply is less than that with the converter power supply by 35.2%. The loss of the stator and rotor core is reduced by 28.3%, and the loss of the permanent magnet is reduced by 78.8%.

[1] Nair S S, Wang J, Chen L, Chin R and Manolas I. "Computationally Efficient 3-D Eddy Current Loss Prediction in Magnets of Interior Permanent Magnet Machines."*IEEE Trans. Magn.*, vol. 52, no. 10, pp. 1-10, June. 2016
[2] Frias A, Kedous-Lebouc A, Chillet C, Albert L and Calegari L ."Loss Minimization of an Electrical Vehicle Machine Considering Its Control and Iron Losses."*IEEE Trans. Magn.*, vol. 52, no. 13, pp. 1-4, May. 2016

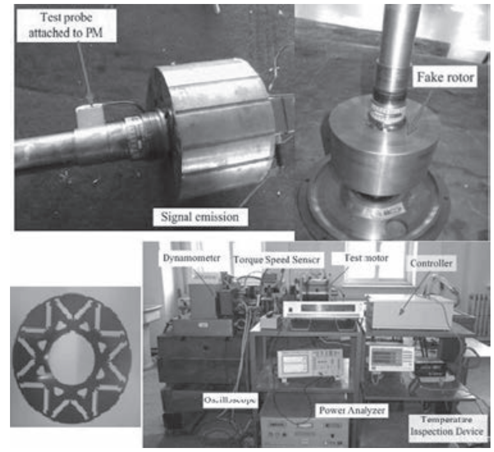

Fig. 1. Configuration of the rotor, the arrangement of the wireless temperature testing system and the experimental platform (the dynamometer is unconnected for no load test)

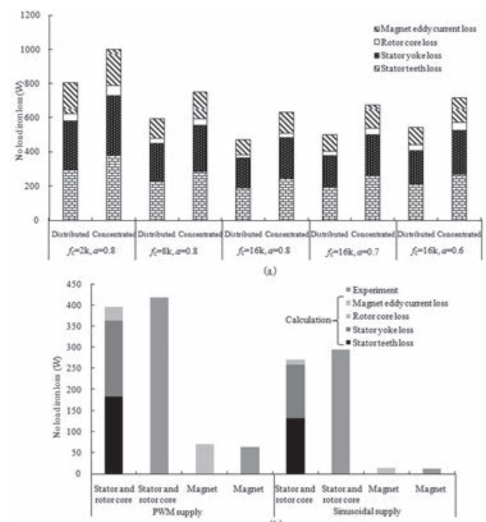

Fig. 2. Results comparison (a) No-load iron losses at different switching frequency and modulation ratio, (b) Calculated results and experimental results of no-load iron loss

11:30

GH-11. A Novel Topology of Magnetic Gear.

O. Molokanov[1], P. Dergachev[1], S. Osipkin[1], E. Kuznetsova[1] and P. Kurbatov[1]
1. Moscow Power Engineering Institute, Moscow, Russian Federation

Over the past few years, magnetic gears (MG) have attracted much attention. The main reason is the contactless nature of torque transmission in contrast with mechanical gears, that leads to some advantages such as high reliability and low maintenance requirements [1]. Unlike a traditional permanent magnet synchronous machine, electromagnetic torque in MG is produced by the interaction between two separate sets of permanent magnets, resulting in very high torque density up to 239 Nm/L [2] under natural air cooling. These peculiarities of modern MGs makes them promising solution, especially for low-speed applications. Recent studies on MGs have shown that the most viable topologies in terms of torque density are so-called coaxial planetary MG [1] and cycloidal MG [3]. Coaxial planetary MG [1] has only two concentric rotating parts which execute a simple rotating motion. However, the main problem with this topology is the inherent low mechanical strength of modulator [4] that at the same time is supposed to withstand high torque. In contrast, the structure of cycloidal MG can is very robust, but a rotor of cycloidal MG experiences rotating motion about two axis simultaneously which is very challenging to utilize. These disadvantages of modern MG limits their industrial application. This paper proposes a novel topology of MG, which eliminates drawbacks of existing MG. Proposed MG utilizes a simple rotating motion of input and output shafts and lacks the weak modulator in the construction. In the first section of the paper, the structure of proposed MG (fig. 1) is described and operational principle is discussed. Expressions for gear ratio and design considerations are presented. The second section of the paper presents a brief description of simulation method as well as results of modeling in static and quasi-static modes. Results of simulation show that proposed MG has high torque density (140 Nm/L) and is capable of transmitting constant torque with corresponding gear ratio. In the third section of the paper, the possible mechanical design of the novel topology of MG is presented, and its manufacturability is discussed. Finally, the work concludes that proposed MG topology has high torque density about 140 Nm/L and high level of utilization of permanent magnets about 860 Nm/L as well as more robust and reliable structure in comparison with existing topologies of MG.

1. Atallah, K. A novel high-performance magnetic gear / D. Howe // IEEE Trans. Magn. — 2001. — Vol. 37, issue 4. — P. 2844–2846. 2. Uppalapati, K. K. A magnetic gearbox with an active region torque density of 239Nm/L / J. Z. Bird, J. Wright, J. Pitchard, M. Calvin, W. Williams // Energy Convers. Congr. Expo. (ECCE), 2014 IEEE. — 2014. — P. 1422–1428. 3. Joergensen, F. T. The cycloid permanent magnetic gear / T. O. Andersen, P. O. Rasmussen // Ind. Appl. Conf. 2006. 41st IAS Annu. Meet. Conf. Rec. 2006 IEEE. — 2006. — Vol. 1. — P. 373–378. 4. K. K. Uppalapati and J. Z. Bird, "An Iterative Magnetomechanical Deflection Model for a Magnetic Gear," *Magn. IEEE Trans.*, vol. 50, no. 2, pp. 245–248, 2014.

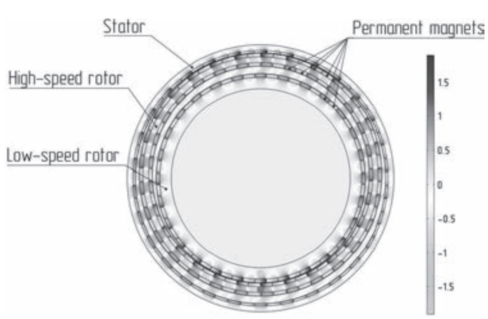

Fig. 1. Radial component of magnetic flux density and basic structure of the proposed magnetic gear

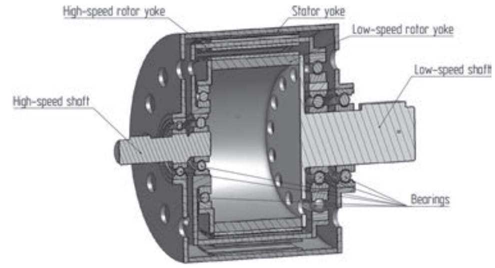

Fig. 2. A possible design of the proposed magnetic gear

FRIDAY MORNING, 27 APRIL 2018 ORCHID II, 9:00 TO 12:00

Session GI
RECORDING SYSTEMS AND HEAD-DISK INTERFACE

Debashish Tripathy, Co-Chair
Western Digital, San Jose, CA, United States
Jun Zhang, Co-Chair
3M Singapore, R&D Center, Singapore, Singapore

CONTRIBUTED PAPERS

9:00

GI-01. Channel modeling and multi-island recording scheme on bit patterned media with long-range island orientation fluctuations.

Y. Wang[1,2], V. Bhagavatula[2,3], Y. Wen[1] and P. Li[1]
1. School of Electronic Information and Electric Engineering, Shanghai Jiao Tong University, SHANGHAI, China; 2. Electrical and Computer Engineering Department, Carnegie Mellon University, Pittsburgh, PA, United States; 3. Carnegie Mellon University, Kigali, Rwanda

Usually for Bit patterned media recording (BPMR) [1], the media noise (island size and position fluctuations) exhibits short-range disordering [2]. However, recently some BPM fabricated with cost effective self-assembled technology exhibits long-range disordering, as shown in the TEM image (Fig. 1(a), courtesy of Jimmy Zhu and Vignesh at CMU). Specifically, the BPM consists of multiple small domains (rectangular frame in Fig.1(a)) with different island orientations (indicated by arrows). In each domain, the islands are relatively organized because islands in a domain have similar orientation, however, the islands' orientation varies much more from one domain to another. Hence such BPM introduces long-range island orientation fluctuations among domains besides the usual local island size and position fluctuations. Since such BPM appears to be more attractive due to its potentially lower fabrication cost, an interesting question is whether it is possible to record the information reliably on such BPM. To investigate the feasibility of reliably storing and retrieving data from such BPM, we first need to develop a channel model. For channel modeling, we assume that the track pitch and bit length are 12.7nm and 12.7nm, the island size is 7nm x 7nm, corresponding to the channel density of 4Tb/in^2. Based on the TEM image in Fig. 1(a), the island position and size fluctuations are modeled as strongly and weakly 2-D correlated Gaussian noise, respectively. To model orientation fluctuations, a mask (size L_M x W_M) with size larger than the domain (size L x W) is assumed, where the aligned islands within each mask are rotated with some angle. Then after the rotation, only the islands remaining within each domain are retained (Fig.1 (b)). The orientation fluctuation among each domain is assumed to uniformly distributed on the interval [-*a*, *a*] (i.e. *a* = the angle 0, 5° and 15° in Fig.2 (b), (c)). The modeled BPM is shown in Fig.1 (c). Then the write and read process is modeled as in [2]. A read head array with three elements (with free layer dimension of 15nm x 15nm x 4nm) and 13nm shield-to-shield spacing and 4nm magnetic fly height is used to readback three tracks. Then the multi-track signals are processed with 2D MMSE equalizer, detected with BCJR detector and the write/read errors are corrected with an LDPC code (Fig.1 (d)). For LDPC decoder, the number of internal and global iterations (N_{turbo}) are 10 and 3. Considering that the significant media noise and the write in errors for such BPM, we have proposed a recording scheme using multi-island (2 by 2 dots) representation for one bit information compared to the regular recording scheme by recording one bit on one dot (Fig.2 (a)). For the LDPC encoding, the code rate for 4 dots/bit (R=0.9) is about 4 times as high as 1 dot/bit (R=0.225) to obtain the same user areal density (i.e., 0.9 Tb/in^2), considering there are 4 Teradots/in^2. Then the raw BER performance is investigated (Fig.2 (b)). Here we assume 10% island position and size fluctuations (1.27nm, 0.7nm), 5% switching field distribution, 5% track mis-registration and 5% write clock phase shift. It is found that the raw BER performances for both recording schemes degrade with increasing orientation fluctuations. However, the 1 dot/bit case degrades much more severely than the 4 dots/bit case because the redundancy in the 4 dots/bit representation reduces the impact of write errors and decreases the effect of the media noise. More importantly, we have investigated the decoded BER performance of both recording schemes at the same user areal density (Fig.2 (c)). It is observed that when the angle fluctuation is small (<=5 degrees), the decoded BER performance for 1 dot/bit is better than 4 dots/bit due to the much lower code rate (0.225) and hence the much higher error correction capability of the LDPC code in the former case. However, when the angle fluctuationis large (for example, 15°), the decoded BER performance of the 1 dot/bit case becomes worse than the 4 dots/bit one because the write in error becomes increasingly dominant compared to the readback error caused by the inter-track interference (ITI) when the orientation fluctuation increases. However, for the 4 dots/bit case, the redundancy in the multi-island representation reduces the impact of the write in errors and media noise because the magnetic flux picked by the reader is the superposition of the magnetic fluxes from all the 4 dots when it scans over them. Even though when one dot in the 4 dots/bit pattern is written in mistake, the picked up magnetic flux is still quite likely to be correct. Here the greatly increased write in error and media noises (i.e., dominant at large orientation fluctuation) are more detrimental to the LDPC decoding performance compared to the read error caused by AWGN and ITI (i.e., dominant at small orientation fluctuation) for the 1 dot/bit case [3]. In conclusion, A channel modeling and multi-island representation scheme (4 dots/bit) was used to investigate the BPM with orientation fluctuation, which is compared to standard 1 dot/bit scheme. For the LDPC code encoded at the same user density, it is found that the decoded BER performance of the proposed 4 dots/bit scheme is better than 1 dot/bit scheme when the orientation fluctuation is large.

[1] H. J. Richter, A. Dobin, and O. Heinonen et al., "Recording on bit-patterned media at densities of 1 Tb/in^2 and beyond," *IEEE Trans. Magn*., vol. 42, no. 10, Oct. 2006, pp. 2255–2260. [2] Y. Wang, J. Yao, and B. V. K. Vijaya Kumar, "2-D write/read channel model for bit-patterned media recording with large media noise," *IEEE Trans. Magn*., vol. 51, no. 12, Dec. 2015, Art. # 3002611. [3] K.Cai, Z.Qin, S.Zhang, Y.Ng, K.Chai, and R.Radhakrishnan,"Modeling, detection, and LDPC codes for bit-patterned media recording," *IEEE GLOBECOM Workshops*, pp. 1910–1914, Dec. 2010.

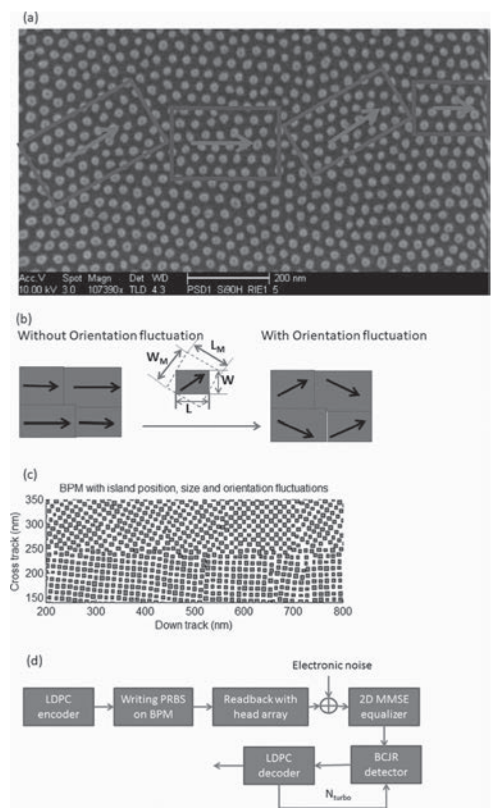

Fig. 1. (a) TEM image, (b) modeling method and (c) modeled image for BPM with orientation fluctuations; (d) channel diagram.

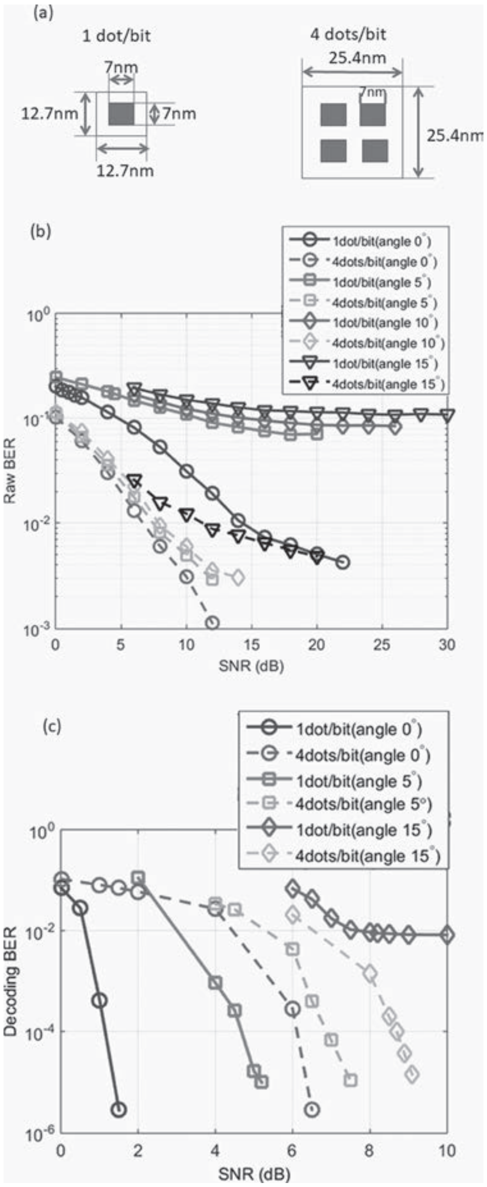

Fig. 2. (a) The proposed 4 dots/bit and standard 1 dot/bit recording scheme, (b) raw and (c) decoded BER performance for both schemes.

9:15

GI-02. A Bit-Flipping Technique Based on 2D Modulation Constraint in BPMR Systems.

W. Busyatras[1], N. Jongsawat[1], L.M. Myint[3] and C. Warisarn[2]
1. Faculty of Science and Technology, Rajamangala University of Technology Thanyaburi, Thailand, Thanyaburi, Thailand; 2. King Mongkut's Institute of Technology Ladkrabang (KMITL), Bangkok, Thailand; 3. Shinawatra University, Pathumthani, Thailand

I. Introduction Inter-track interference (ITI) cancelation is one of the considerable challenges for high areal density (AD) magnetic recording such as in bit-patterned media recording (BPMR) systems. In literature, the two-dimensional (2D) modulation codes have been proposed to cancel the ITI effect [1,2] which can efficiently improve the overall system performance, e.g., a rate-5/6 2D modulation code [2]. Although the rate-5/6 modulation code ensures that the readback signal of the center track will not be corrupted by severe ITI; however, both the upper and lower tracks can still be interfered by their sidetracks. To improve this shortcoming; therefore, we propose the bit-flipping technique that performs together with the rate-5/6 2D modulation code. Here, the relationship between the data encoding condition and soft-information obtained from the soft output Viterbi algorithm (SOVA) detector is utilized to be a criterion for flipping the ambiguous data bits. Simulation results indicate that the proposed system is better than the conventional coded system under with/without media noise and track mis-registration. II. BPMR Channel Model We focus on a discrete BPMR channel model [2,3] as depicted in Fig.1. The user bit, a_k is encoded by 2D modulation code to obtain the recoded bit sequences. The readback signal of the k^{th} data bit of the l^{th} track can be expressed as $r_{l,k} = \sum_m\sum_n h_{-m,n} x_{l-m,k-n} + n_{l,k}$, where $x_{l,k}$'s are the recorded bits, $l \in \{0,\pm1\}$ represent the center, upper, and lower track, respectively, $h_{m,n}$'s are the 2D channel coefficients, $\{m, n\} \in (0,\pm1)$, m and n represent the time indices of bit island in the across- and the along-track directions, and $n_{l,k}$ is an additive white Gaussian noise (AWGN). The the readback signals are generated by three readers and are equalized by a 2D equalizers, followed by the 2D SOVA detectors to produce the soft-information, i.e., $[\lambda_{-1,k}\ \lambda_{0,k}\ \lambda_{1,k}]^T$. Then, these soft-information will be sent to the proposed bit-flipping and hard decision processes to generate the improved soft-information, i.e., $[\lambda'_{-1,k}\ \lambda'_{0,k}\ \lambda'_{1,k}]^T$ and estimate recorded bit, $[x'_{-1,k}\ x'_{0,k}\ x'_{1,k}]^T$, respectively. Finally, they will be sent to the decoder to decode the estimated user bits, a'_k. III. Bit-Flipping Technique A. 5/6 Modulation Code The rate-5/6 2D modulation code was designed to avoid the destructive ITI (DITI) data patterns i.e., $\pm[1\ -1\ 1]^T$. Due to these DITI data patterns are the worst patterns, which degrade the readback signal; therefore, these two patterns are not allowed to record onto the medium. In the rate-5/6 2D modulation coding, every 1×5 bits from user data sequence will be rearranged to become three data sequences in a matrix form of 3×2 bits [2]. This coding method provide the good performance for the center track; however, the upper and lower tracks still provide the poor bit-error rate (BER) performance because both of them were interfered from their sidetracks. In this work, we focus on how to cope with this situation. We consider the recoded pattern in each column vector in the form 3×1 of the constructive ITI (CITI) data patterns that are recorded onto medium, which consists of $[1\ 1\ 1]^T$, $[-1\ -1\ -1]^T$, $[1\ 1\ -1]^T$, $[-1\ -1\ 1]^T$, $[-1\ 1\ 1]^T$, and $[1\ -1\ -1]^T$, respectively. We observe that the upper or lower tracks of these CITI data patterns can be easily flipped to the opposite direction due to the ITI effect when their sidetrack bit has opposite direction with the data bit of upper or lower track. For example, $[1\ -1\ 1\ 1\ 1]^T$or $[-1\ 1\ -1\ -1\ 1]^T$ will be easily changed to $[1\ 1\ 1]^T$or $[-1\ -1\ -1]^T$, respectively. Therefore, we propose bit-flipping technique to improve BER performance for all three data tracks by considering the soft-information obtained from 2D SOVAs. B. Bit-Flipping Technique In the data bit-flipping process, we start with considering the soft-information values of the upper, center, and lower data sequences in the column vector form of 3×1 as shown in Fig.1. Firstly, the signs of all soft-information values will be checked, if their sign is according to $[1\ 1\ 1]^T$or$[-1\ -1\ -1]^T$, these three soft-information values will be normalized with their absolute maximum value. Then, if we found that one of the normalized soft-information values among three of them is less than 0.1, the lowest one will be flipped into another direction. Note that in our consistent study, the 0.1 value can provide the accuracy percentage of changing bit estimation more than 80%. IV. Results and Discussions We evaluate the BER performance between the conventional system (without coding), conventional coded system [2], and the proposed system (the rate-5/6 2D modulation code performs together with bit-flipping technique) at AD of 2.5 and 3.0 Tb/in². Here, the 2D Gaussian pulse response with the along-track PW_{50} of 19.4 nm and the across-track PW_{50} of 24.8 nm is considered. In simulation, a signal-to-noise ratio (SNR) is defined as $10\log_{10}(1/\sigma^2)$, where σ is a standard deviation of AWGN. As shown in Fig.2, it is clear that the proposed system provides the better performance for about 1.8 and 5.5 dB at the BER=10^{-4} over the conventional system at ADs of 2.5 and 3.0 Tb/in², respectively. Moreover, the proposed system is also superior to the conventional coded system at 3.0 Tb/in². Acknowledgement This work was partially supported by Faculty of Science and Technology, RMUTT, and College of Advanced Manufacturing Innovation, KMITL, Thailand.

[1] C. D. Nguyen and J. Lee, "9/12 2-D modulation code for bit-patterned media recording," in IEEE Trans. Magn., vol. 53, no 3, 3101207, Mar. 2017. [2] C.Warisarn, A. Arrayangkool, and P. Kovintavewat, "An ITI mitigating 5/6 modulation code for bit-patterned media recording," in IEICE Trans. Electron., vol. E98-C, no. 6, pp. 528-533, Jun. 2015. [3] S. Nabavi, Signal processing for bit-patterned media channels with inter-track interference. Ph.D thesis, Carnegie Mellon University, Pittsburgh, Dec. 2008.

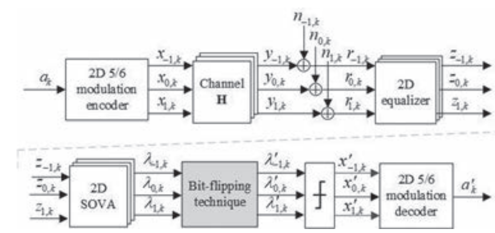

Fig. 1. A multi-track multi-head BPMR channel model with the proposed bit-flipping technique.

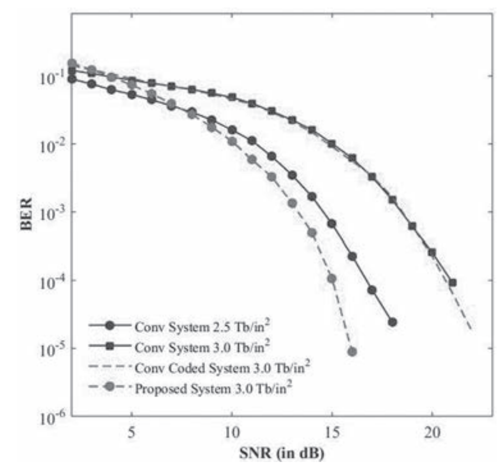

Fig. 2. BER performance of several systems at ADs of 2.5 and 3.0 Tb/in².

9:30

GI-03. Unbalanced Track Pitch Combined with 2D Modulation Code in TDMR Systems.

K. Pituso[1], C. Warisarn[1] and D. Tongsomporn[2]
1. College of Advanced Manufacturing Innovation (AMI), King Mongkut's Institute of Technology Ladkrabang, KMITL, Bangkok, Thailand;
2. Seagate Technology (Thailand), Samutprakarn, Thailand

I. Introduction Two-dimensional magnetic recording (TDMR) [1,2] is a promising high density storage technology, which is expected to increase an areal density (AD) up to 10 terabit per square inch (Tbpsi). This technology is required write narrow-read wide technique that opposite to write wide-read narrow of one-dimensional (1D) read channel. The narrow track writing operated by shingled writing can greatly improve track per inch (TPI) gain. However, the side reading effect of reader is an unwanted situation because the intertrack interference (ITI) from sidetracks, which degrades the overall system bit error rate (BER) performance. Therefore, we introduce the methods to overcome this severe ITI effect. For instance, the two-dimensional (2D) modulation code that designed based on cross-track data dependent readback. The data pattern such as $[1\ \text{-}1\ 1]^T$ and $[\text{-}1\ 1\ \text{-}1]^T$ are forbidden to record onto medium. The rate-5/6 2D modulation code will map the 5 user bits into a 6-bits codeword, which are not contained any forbidden patterns. Furthermore, since the recoded bit is protected from severe ITI effect using modulation code, the middle track can provide a very high reliability. Therefore, we present ITI subtraction to improve upper and lower track performance using data from middle track. Moreover, we also propose an unbalanced track pitch technique, which the middle track can be narrower than upper and lower tracks. The utilization from the high reliability of middle track can improve BER performances both of upper and lower tracks. The reason because the ITI effect that interfere from their sidetracks is reduced by using the properly wider track pitch. II. TDMR Channel Model A message sequence $u_k \in \{\pm 1\}$ is encoded by a low-density parity check (LDPC) encoder [3] to obtain a sequence a_k. Then, the sequence a_k is encoded again with a rate 5/6 modulation code [4] to obtain three recorded bit sequences, $a_{k,l}$. Two random sidetracks are then added to $a_{k,l}$ sequences. The $a_{k,l}$ is perfectly written on a granular medium generated by a discrete Voronoi model [5]. The perfectly writing is defined by the recording field of the writer covers only within a bit cell area, which magnetizes only grain that its centroid is placed inside the bit cell area. TDMR readback signal $r_{k,l}$ is obtained by convolving the magnetization of Voronoi grains, $M(x,y)$, with the reader sensitivity, $H(x,y)$, where x and y are the spatial indices of the bit period in the down- and cross-track, and then add an additive white Gaussian noise (AWGN) for time random noise. In this paper, the signal to time random noise ratio is 20-25 dB calculated by ensemble of waveform technique [6]. At the digital read channel, the readback data sequences $[r_{k,l}, r_{k,l+1}, r_{k,l+2}]$ are equalized by 2D finite impulse response (FIR) equalizers, which are designed based on a minimum mean-squared error approach with fixed 2D target. Then, the equalized samples $s_{k,l}$ is sent to a soft output Viterbi algorithm (SOVA), which exchanges the soft information among each track with $N_{\text{SOVA}} = 3$, before sending to 2D modulation and LDPC decoders to decode the recoded bit and estimated message sequence, respectively. III. An Areal Density Metric and Unbalanced Track Areal density capability (ADC) is a main key parameter for evaluating the performance of magnetic recording systems. The ADC test is performed by varying track density (track per inch, TPI) and linear density (bit per inch, BPI) until it reaches the maximum AD when the estimated user bits from the read channel are all converged. Here, the SOVA obtains BER = 10^{-3} is chosen to calculate the ADC. LDPC is employed to be as the error-correction code for this testing. The obtained data bits from LDPC are all converged within 40 local iterations when its input that obtains from SOVA has BER $\leq 10^{-3}$. Since the 2D modulation code can protect the middle recorded track from severe ITI, that means the middle track can provide a very high BER reliability, while the upper and lower recorded tracks have lower BER performance due to the sidetrack interferences. This work proposes unbalanced track pitch to optimize all three tracks reliabilities. The middle track can be written narrower than its sidetracks because of the help of coding protection. However, sidetracks should be wider than middle track to improve their BER reliability. Moreover, the ITI subtraction is also applied together with the proposed unbalanced track pitch, which can significantly improve the ADC. IV. Simulation Results We compare the ADC of four systems consists of: (1) conventional TDMR system, (2) TDMR system with the rate-5/6 2D modulation code, (3) TDMR with the rate-5/6 2D modulation code performs together with ITI subtraction technique, and (4) unbalanced track width TDMR with the rate-5/6 2D modulation code and ITI subtraction technique. Fig 1 shows that ADC of the all systems that obtained from nine media models. The small symbols indicate each media ADC and the large symbols represent the average value of all nine media model for each system. The result shows that ADC of systems: (1) = 4.51 Tb/in^2, (2) = 4.8 Tb/in^2, (3) = 5.18 Tb/in^2, and (4) = 5.28 Tb/in^2. The ADC gains of the system (2), (3), and (4) can be increased over the conventional TDMR system for about 6.52%, 14.88%, and 17.06%, respectively. Acknowledgment This work was partly supported by Thailand Research Fund (TRF), Research and Researcher for Industry (RRi) and Seagate Technology (Thailand) under grant number PHD58I0048.

[1] R. Wood, *et al*., "The feasibility of magnetic recording at 10 terabits per square inch on conventional media," *IEEE Trans. Magn*., vol. 45, no. 2, pp. 917-923, Feb. 2009. [2] A.R. Krishnan, *et al*., "2-D magnetic recording: read channel modeling and detection," *IEEE Trans. Magn*., vol. 45, no. 10, pp. 3830-3836, 2009. [3] E. Eleftheriou, *et al*., "Low-density parity-check codes for digital subscriber lines," *ICC 2002*, New York, NY, 2002. [4] K. Pituso, *et al*., "A soft-5/6 modulation code with iterative ITI subtraction scheme in multireader TDMR systems," *IEEE Trans. Magn*., vol. 53, no. 11, art ID. 3000904, 2017. [5] M. Yamashita, *et al*., "Read/write channel modeling and two-dimensional neural network equalization for two-dimensional magnetic recording," *IEEE Trans. Magn*., vol. 47, no. 10, pp. 3558-3561, 2011. [6] S. Hernandez. *et al*., "Using ensemble waveform analysis to compare heat assisted magnetic recording characteristics of modeled and measured signals," *IEEE Trans. Magn*., vol. 53, no. 2, art ID. 3000406, 2017.

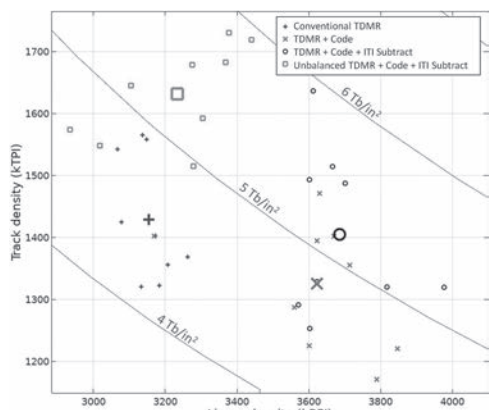

Fig. 1. Areal density capability of the various methods in TDMR systems.

9:45

GI-04. Spatially-Coupled Codes for Channels with SNR Variation.

H. Esfahanizadeh[1], A. Hareedy[1], R. Wu[1], R. Galbraith[2] and *L. Dolecek*[1]
1. Department of Electrical and Computer Engineering, University of California, Los Angeles, Los Angeles, CA, United States; 2. Hitachi Global Storage Technologies, a Western Digital Company, Rochester, MN, United States

Modern magnetic recording (MR) systems require error correcting codes (ECCs) with outstanding error floor performance. Low-density parity-check (LDPC) codes are a primary choice for MR systems because of their error correcting capabilities [1]-[3]. In a magnetic recording device, some sections can be more error-prone than other sections because of the read/write mechanism and physical properties of the device [4]. A realistic channel model for magnetic recording systems must consider the variation of signal to noise ratio (SNR) among consecutive sections of a hard disk drive. For channels with SNR variation, the conventional ECCs are designed to achieve the certain BER for the section with the lowest SNR. For the sections with higher SNRs, this approach results in an additional redundancy which is not necessary to achieve the target BER. Spatially-coupled (SC) codes are a family of graph-based codes that have attracted significant attention because of their capacity approaching performance [5]. SC codes are constructed by partitioning a parity-check matrix H of the underlying block code into component matrices $H_0,...,H_m$, $H=H_0+...+H_m$, and coupling L copies of the component matrices together to obtain the parity-check matrix H_{SC}, Fig. 1. The parameters m and L are known as the memory and coupling length, respectively. An SC code with coupling length L has L replicas, $\{R_1,...,R_L\}$, see Fig. 1. In this paper, we present an SC code design approach for channels with SNR variation. In our code design, the length of the underlying block codes is equal to the length of one section of the channel, and the number of sections spanned by one SC code is determined by L. Because of this structure, each check node (CN) receives messages from more than one section, so more reliable variable nodes (VNs) can help compensate for the sections that are highly affected by noise. In our model for a channel with SNR variation, each section is considered as an AWGN channel with SNR_i (i is the section index). For the i'th section, we state the SNR as $(SNR_i)_{dB}=(SNR_{abs})_{dB}+(\Delta SNR_i)_{dB}$, where $(SNR_{abs})_{dB}$ is the absolute SNR and $(\Delta SNR_i)_{dB}$ is the variation from the absolute SNR for the i'th section. We first describe our code construction approach: The length of the underlying block code is equal to the length of one section of the channel, so each replica of an SC code spans one section of the channel. The coupling length L determines how many sections are spanned by one SC code, so it must be chosen such that a variety of sections with different reliabilities are included. The minimum overlap (MO) approach is recently introduced for partitioning block codes and constructing SC codes [6]. In this approach, the matrix H of a block code is partitioned into several component matrices such that the number of detrimental objects in the graph of the derived SC code for AWGN channels is reduced. In this paper, we use MO approach for constructing SC codes with γ=3. Moreover, we extend this approach to construct SC codes with γ=4. The memory m of an SC code plays the critical role on its performance over channels with SNR variation. By increasing memory, sections are more cooperative, and the SNR variation among them can be alleviated better. The parameter m determines how many different sections are involved in the check equations in an iterative decoding. Because of our SC code construction, most CNs receive messages from VNs within m+1 consecutive sections. As a result, if there is one reliable section with a high SNR, it can in principle help the messages from other m sections be recovered more reliably. For interleaving, we divide the SC codeword into $L^2/(m+1)$ chunks. Then, we rearrange them by taking one chunk from each L consecutive chunks and putting them next to each other. This interleaved data is passed through the channel, and the de-interleaving is performed on the received data from the channel and before decoding. Due to interleaving, most CN receives an equal number of messages from all L different levels of reliabilities. Our simulation results show that our channel-based interleaving compensates for the performance gap that exists between the error rates of SC codes over non-uniform and uniform channels with similar average SNR. Our proposed scheme is the first channel-aware interleaving for SC codes, and the complexity of the proposed interleaving is inversely proportional to the number of component matrices. The regular interleaving has a fixed complexity with respect to the memory which is equal to the complexity of our interleaving scheme for the case m=0 (the uncoupled setup). Finally, we show some important simulation results. Block Code 1 is an array-based block code with γ=3, length 289 bits, and rate r=0.82. SC Code 1 and 2 are SC codes with Block Code 1 as the underlying block code. They both have L=30 and length 8670 bits. The memory and rate for SC Code 1 are m=1 and r=0.82, and for SC Code 2 are m=2 and r=0.81, respectively. Fig. 2 shows the BER curves for Block Code 1, SC Code 1, and SC Code 2 over the non-uniform channel. It can be seen that SC Code 1 shows 2 orders of magnitude performance improvement in the error floor area compared to the Block Code 1, with and without (regular) interleaving, respectively. We achieve further improvement when we apply our optimized interleaving to SC Code 1. Moreover, SC Code 2 secures even further improvement by providing more cooperation among different sections of the channel. The longer version includes results for our γ=4 SC codes.

[1] Y. Fang, P. Chen, L. Wang, and F. C. M. Lau, "Design of protograph LDPC codes for partial response channels," IEEE Trans. Commun., vol. 60, no. 10, pp. 2809–2819, October 2012. [2] Y. Han and W. E. Ryan, "Low-floor detection/decoding of LDPC-coded partial response channels," IEEE JSAC, vol. 28, no. 2, pp. 252–260, February 2010. [3] H. Zhong, T. Zhong, and E. F. Haratsch, "Quasi-cyclic LDPC codes for the magnetic recording channel: Code design and VLSI implementation," IEEE Trans. Magnetics, vol. 43, no. 3, pp. 1118–1123, March 2007. [4] N. Varnica, G. Burd, and Z. Wu, "Interleaved error correction coding for channels with non-uniform SNRs," Nov. 13 2012, US Patent 8,312,341. [Online]. Available: https://www.google.ch/patents/US831234. [5] A. J. Felstrom and K. S. Zigangirov, "Time-varying periodic convolutional codes with low-density parity-check matrix," IEEE Trans. Info. Theory, vol. 45, no. 6, pp. 2181–2191, Sep 1999. [6] H. Esfahanizadeh, A. Hareedy, and L. Dolecek, "A novel combinatorial framework to construct spatially-coupled codes: minimum overlap partitioning," in IEEE ISIT, June 2017, pp. 1693–1697.

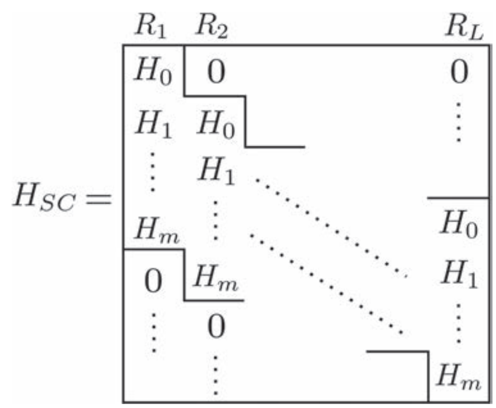

Fig. 1. H_{SC}

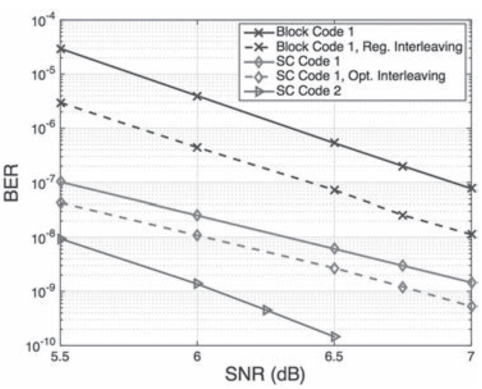

Fig. 2. BER curves

10:00

GI-05. The Effective Fuzzy Logic Equalizer Based Adaptive Nonlinear Equalization for the Nonlinear Perpendicular Magnetic Recording Channels.

R. Wongsathan[1] and P. Supnithi[1]
1. Electrical Engineering, King Mongkut\'s Institute of Technology Ladkrabang (KMITL), Bangkok, Thailand

Abstract. It was demonstrated that the channel equalization based adaptive nonlinear equalizer outperforms the conventional detector and equalizer in nonlinear perpendicular magnetic recording (PMR) channels. To improve the detection performance, in consequence, this paper alternatively proposes the efficient adaptive equalization based on fuzzy logic equalizer (FLE). To fulfill the effectively handling design and reducing complexity, genetic algorithm (GA) and multi-objective hierarchical GA (MOHGA) are used to optimized the FLE in order to fine-tune the fuzzy parameters and simultaneously generate the significant fuzzy rules. The BER performance of the proposed FLE-GA and FLE-MOHGA has been compared with that of the partial response maximum likelihood (PRML) detector, Volterra equalizer (VE), multilayer perceptron neural network (MLPNN) based equalizer and the hybrid MLPNN-VE (hMLPNN-VE). From the the simulation results, the proposed FLE-MOHGA clearly outperforms the rest for a nonlinear Volterra channel at high normalized recording density. Subsequently, the performance comparison in terms of the tradeoff between accuracy, computational complexity and reliability between the proposed FLE and the adaptive neurofuzzy inference system (ANFIS) based equalizer supported the effective of the proposed FLE. Outline: Nonlinear distortions and noises cause the errors for detection in high-density magnetic recording (MR) systems. To tackle this issue, various approaches have been proposed [1]-[4]. On the transmit side, pre-compensation method helps reduce the nonlinearity by varying the write current [2]. However, on the receive side, previous works studied the use of PRML detector [3], VE [1] among others. A PRML (Viterbi) detector [1] based on partial-response (PR) linear equalization is ineffective for nonlinear channels, but it can be improved by including the nonlinear channel coefficients on the trellis branches when these coefficients are known. Therefore, without the priori information of the nonlinearity, alternative approaches based on nonlinear equalization are of interest. The nonlinear VE has been proposed to combat the nonlinearities in MR channels [1] and satellite channels [5]. However, its performance is only slightly better than that of the linear equalizer while the complexity is prohibitively complex as the number of channel coefficients increases. To further improve the BER performance, MLPNNE is introduced to the nonlinear PMR channels [4] as well as the optical communication [6]. This approach outperforms PRML and VE at the expense of complexity. Recently, the hMLPNN-VE has been proposed and implemented in the nonlinear PMR channels modeled by Volterra series (VS) model [7]. It outperforms the MLPNE, VE and the conventional PRML detector, respectively. However, a number of system parameters, the complexity, BER performance compared to the optimal detector are disadvantages. To solve this problem, this work alternatively introduces the adaptive nonlinear equalization based FLE. Since it was evident for the successful in order to apply into various communication channels [8]-[13]. From the test, it was shown that the FLE performs better than the transversal filter equalizer in the presence of channel nonlinearity and its BER is closely reached to that of the optimal equalizer. However, in the data storage channels, FLE seems to be limited. In this work, it is an attempt to develop effectively the adaptive FLE for the nonlinear PMR channels. Unfortunately, the construction of proper fuzzy rules for equalizer is difficult. Using human experts through the trial and error to design the fuzzy rules is often incomplete and incorrect description of the system. One of the effective techniques found in ANFIS or neurofuzzy based equalizer (NFCE) is the use of NN learning the input output data pattern to formualte the fuzzy rules [12]-[13]. However, this technique increases more complexity from a large number of parameters of NN and the system parameters may likely fall to local minima during training using NN [12]. By using evolutional learning through GA, it does not require derivative calculation like the back-propagation (BP) in NN, then it is less likely to be trapped in local minima. Therefore, GA has been suggested to optimize the fuzzy parameters [14]. The nonlinear PMR channel model and the FLE design is shown in Fig.1. However, it was found that the number of self-generated fuzzy rules do not improve the accuracy or performance more but increase the complexity. To improve the performance further, the MOHGA was used to optimize the fuzzy rules by the modified criterion function. The BER of FLE-MOHGA provides about 1 dB, 1 dB, 3 dB, 6 dB and 12 dB SNR gain over the FLE-GA, *h*MLPNN-VE, MLPNNE, VE, and PRML detector at the BER of 10^{-4}, respectively, Fig. 2(a). To verify the effective of the proposed FLE by comparing with NFCE, it can be seen from Fig. 2(b) that the NFCE provides the BER performance slightly better than that of the FLE-MOHGA. However, the AIC [15] is supported that the proposed FLE-MOHGA gives the better performance in terms of the tradeoff between accuracy, computational complexity and reliability than that of the NFCE and also the others.

REFERENCES [1] W.E. Ryan, and A. Gutierrez, "Performance of adaptive Volterra equalizer on nonlinear magnetic recording channels," IEEE Transactions on Magnetics 31(6), 3054-3056 (1995). [2] W. Zeng, "Channel modeling, signal processing and coding for perpendicular magnetic recording," Philosophy dissertation, Department of Electrical Engineering, University of California, San Diego, USA, 2009. [3] H. Yang, and G. Mathew, "Joint design of optimum partial response target and equalizer for recording channels with jitter noise," IEEE Transactions on Magnetics 42(1), 70-77 (2006). [4] H. Osawa, M. Hino, N. Shinohara, Y. Okamoto, Y. Nakamura, and H. Muraoka, "Simplified neural network equalizer with noise whitening function for GPRML system," IEEE Transactions on Magnetics 44(11), 3777-3780 (2008). [5] J. Malone, and M.A. Wickert, Practical Volterra equalizers for wideband satellite communications with TWTA nonlinearities 2011: Proceedings of IEEE Digital Signal Processing Workshop and IEEE Signal Processing Education Workshop (DSP/SPE), Sedona, AZ, USA, 4-7 January 2011, pp. 48-53. [6] E. Giacoumidis, S.T. Le, I. Aldaya, J.L. Wei, M. McCarthy, N.J. Doran, B.J. Eggleton, Experimental comparison of artificial neural network and Volterra based nonlinear equalization for CO-OFDM 2016: Proceedings of Optic Fiber Communication Conference and Exhibition (OFC), Anaheim, CA, USA, 20-24 March 2016, pp. 2473-2477. [7] R. Wongsathan, W. Phakphisut, and P. Supnithi, "Performance of the hybrid MLPNN based VE (hMLPNN-VE) for the nonlinear PMR channels," AIP Advances 8, 1-5 (2018). [8] L.X. Wang, "Fuzzy adaptive filters, with application to nonlinear channel equalization," IEEE Transactions on Fuzzy Systems 1(3), 161-170 (1993). [9] P. Sarwal and M.D. Srinath, "A fuzzy logic system for channel equalization," IEEE Transactions on Fuzzy System, 3(2), 246-249 (1995). [10] H.M. Conde, J.C.S. Garda, and J.A.D. Mendez, Fuzzy equalizer in VLSI 2005: 2nd International Conference on Electrical and Electronics Engineering, Mexico city, Mexico, 2005, pp. 239-242. [11] W. K. Wong and H. S. Lim, "A robust and effective fuzzy adaptive equalizer for powerline communication channels, Neurocomputing 71(1-3), 311-322 (2007). [12] A. Sarangi, S.O. Anusandham, S.K. Padhy, S.P. Panigrahi, and S. K. Sarangi, "GBF trained neuro-fuzzy equalizer for time varying channels," International Journal of Applied Evolutionary Computation 2(3), 27-38 (2011). [13] Z.A. Abbasi and Z. A. Jaffery, ANFIS based equalizer for non-linear time varying channels 2015: Annual IEEE India Conference (INDICON), New Delhi, India, 2015, pp. 1-6. [14] T. Zhang and X. You, "Improvement of the training and normalization method of artificial neural network in the prediction of indoor environment," Procedia Engineering 21, 1245-1251 (2015). [15] K.P. Burnham, and D.R. Anderson, Model Selection and Multimodel Inference (New York: Springer-Verlag, USA, 2002) pp. 310-325.

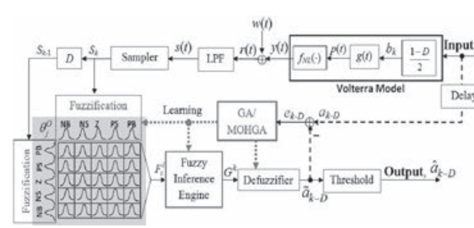

Fig. 1. Nonlinear PMR channel model with the optimization of FLE through GA.

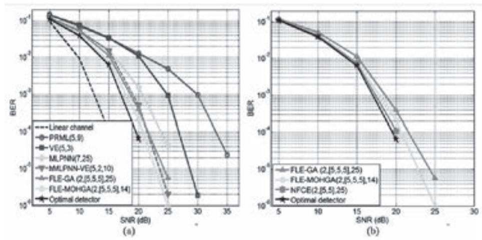
BER
Linear channel
PRML(5,9)
VE(5,3)
MLPNN(7,25)
MMLPNN-VE(5,2,10)
FLE-GA (2,[5,5,5],25)
FLE-MOHGA(2,[5,5,5],14)
Optimal detector
SNR (dB)
(a)
BER
FLE-GA (2,[5,5,5],25)
FLE-MOHGA(2,[5,5,5],14)
NFCE(2,[5,5],25)
Optimal detector
SNR (dB)
(b)

Fig. 2.

10:15

GI-06. Flexible Inter-track Interference Cancellation for Generalized Interlaced Magnetic Recording.

S. Yoon[1] and *E. Hwang*[1]
1. School of Mechatronics, Gwangju Institute of Science and Technology, Gwangju, The Republic of Korea

Interlaced magnetic recording (IMR) shows potential to achieve higher areal density capability (ADC) than conventional magnetic recording by recording tracks in an interlaced manner [1]. Top and bottom tracks can be recorded in different frequencies such that the bit error rate (BER) performance can be balanced, providing extra track or linear density pushes. For example, heat assisted IMR (HIMR) enables higher ADC than conventional heat assisted magnetic recording (HAMR) and shingled recorded HAMR by allowing broader bottom tracks with sharper bit transitions and narrow top tracks by control the heat spot [2]. On the other hand, bottom tracks in IMR can suffer from sever inter-track interference (ITI) by subsequent top track writes on both sides, especially as the track density increases [3]. In order to mitigate the ITI effect for such double-sided squeezed tracks, customized ITI cancellation scheme has been introduced, where the asynchronously written tracks are processed in the oversampled domain and overall ADC can be improved [4]. In this study, ITI cancellation scheme is extended for generalized IMR framework, where the ITI can be distributed for top and bottom tracks by applying dual write configurations. One of the major contributions of the tangible ADC gain by HIMR is the additional laser spot control to form narrow but sharp bit transitions in top tracks [2]. In this manner, the wide and sharp bottom tracks are only partially erased by the subsequent top track writes, and, thus, the ITI can be effectively managed. Likewise, the write track widths can be modulated for conventional perpendicular recording and may provide the ADC gain once the ITI is efficiently handled. Note that ITI cancellation can also be needed for top tracks as well, and the relative linear density differences of ITI can be both positive and negative. Therefore, flexible ITI cancellation scheme is proposed in this study to handle the widely varying synchronization issues. The waveforms need to be over-sampled first to effectively synchronize the neighboring tracks, and double of baud rate of lower density track can be used. For example, under 2500 and 2000 kBPI dual writer configurations, the oversampled data can be denoted as $x_{(t)2x}$, $x_{(b)1.6x}$ respectively, relative to its baud rate. Then, the error signal is first estimated, $e_{(t)2x}$, $e_{(b)1.6x}$, resampled to the side track data rate, $e'_{(t)1.25x}$, $e'_{(b)0.8x}$, and then the ITI response is estimated for tracks m_t and m_b as, $\{h'_{(t)mt-1}, h'_{(t)mt+1}\}=\arg\min_{h(t)mt-1,h(t)mt+1} \| e'_{(t)1.25x} - h_{(t)mt-1}*n_{mt-1}- h_{(t)mt+1}*n_{mt+1} \|^2$ $\{h'_{(b)mb-1}, h'_{(b)mb+1}\}=\arg\min_{h(b)mb-1,h(b)mb+1} \| e'_{(b)0.8x} - h_{(b)mb-1}*n_{mb-1}- h_{(b)mb+1}*n_{mb+1} \|^2$ where n_m is the recorded binary data of the track m, and estimated side track data will be used for actual implementation. The ITI signal is estimated from {h'}'s, resampled to baud-rate if needed, and subtracted from the baud-rate readback signal. The feasibility of such generalized IMR with flexible ITI cancellation is investigated with the numerical channel simulations. For numerical evaluations of IMR, microcell channel model [1] is employed, where the media is modeled by the square micro-cell of 1.5nm sides, and the granular effect is accounted by shifting the bit and track boundaries randomly for the locally clustered cells. If the writer configuration is maintained except the write frequency for IMR, bottom tracks should be recorded at the relaxed density due to the ITI. If dual write configurations can be used for narrow top tracks, bottom tracks can be recorded with aggressive linear density by forming relatively sharp bit transitions in the remained portion. Figure 1 illustrates the averaged media polarization of repeated [1 1 -1 -1] patterns with single write configuration in (a) bottom and (b) top tracks at 2000 and 2500 kBPI with 529 kTPI. The writer width is assumed to be 60 nm, and the transition curvature is modeled by the ellipse with depth of 20 nm. As illustrated, the bottom tracks are erased by the top track writes and expected to suffer from ITI. On the other hand, same track density 2T patterns with dual write configurations is illustrated in (c) bottom and (d) top tracks at 2500 and 2000 kBPI. The writer width is changed 20% and -20%, while the depth is factored $1/2^{½}$ and $2^{½}$, respectively. As shown, the ITI is distributed for both tracks, and ITI cancellation is needed for both tracks. Readback waveforms are evaluated with the Gaussian read sensitivity function and BER performance is investigated. Other experimental setups are set to as [1], and head electronic signal to noise ratio (HESNR) is scanned from 12 to 30 dB under the track and linear densities illustrated in Fig. 1. Figure 2. shows BER with flexible ITI cancellations in (a) single and (b) dual write configuration IMRs. For the single mode, bottom track BER performance improved significantly by ITI cancellation, while the top track experiences negligible ITI. On the dual mode, both tracks are experiencing the ITI and are improved by the ITIC. In overall, -1.5 order target BER can be achieved at 30 dB HESNR by the dual mode IMR with the flexible ITIC.

[1] E. Hwang, J. Park, R. Rauschmayer, and B. Wilson, "Interlaced magnetic recording," IEEE Trans. Magn., vol. 53, no. 4, Art. no. 3101407, 2017. [2] S. Granz et al., "Heat-Assisted Interlaced Magnetic Recording," The 28th Magnetic Recording Conf., pp. 60-61, 2017. [3] E. Hwang, "Interlaced Magnetic Recording Channel Signal Processing for Mitigating Inter-track Interference," The 28th Magnetic Recording Conf., pp. 129-130, 2017. [4] E. Hwang, "Asynchronous Inter-track Interference Cancellation (A-ITIC) for Interlaced Magnetic Recording (IMR)," IEEE Global Communication Conference 2017.

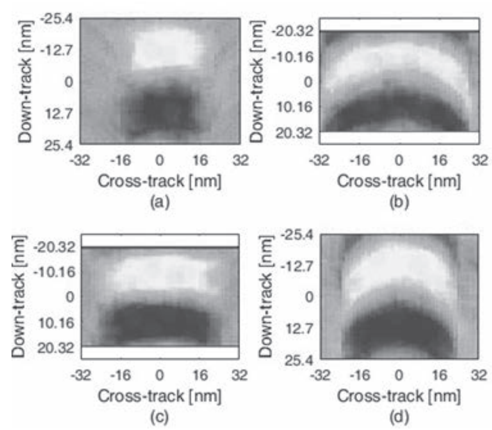

Fig. 1. IMR recorded 2T patterns on the media by the microcell channel model. IMR with single write configuration on (a) bottom track at 2000 kBPI, (b) top track at 2500 kBPI, and with dual write configuration (c) bottom track at 2500 kBPI, (d) top track at 2000 kBPI.

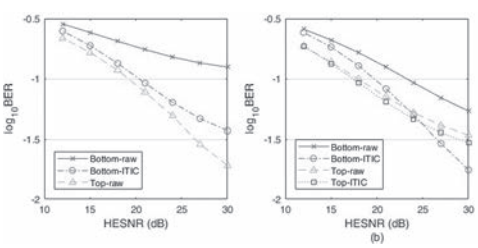

Fig. 2. Bit error rate performance with flexible ITI cancellations for generalized IMRs with (a) single and (b) dual write configurations.

10:30

GI-07. 1/f thermally excited noise in asymmetric oscillators.

T. Pipathanapoompron[1,5], A. Stankiewicz[2], A. Grier[4], K. Subramanian[3] and A. Kaewrawang[1]
1. Electrical Engineering, Khon Kaen University, Khon Kaen, Thailand; 2. Seagate Technology, Bloomington, MN, United States; 3. Seagate Technology, Shakopee, MN, United States; 4. Seagate Technology, Spring Town, United Kingdom; 5. Seagate Technology, Korat, Thailand

Many physical systems and devices operate in a (quasi)static regime in contact with a thermal bath, which leads to fluctuating oscillations around the energy minimum. For linear systems, the spectrum of these oscillations replicates the resonance curve of a damped oscillator [1]. In particular, power spectral density grows monotonically with frequency in the low frequency range, until reaching a maximum at the resonant frequency. Small sizes of contemporary magneto-resistive readers and other MEMS/NEMS devices pushes oscillations to non-linear regimes, which may lead to resonance line broadening, bifurcations, etc. [2]. However, non-linearity does not change the monotonicity of thermal fluctuations in the low frequency range, until the energy profile is symmetric around the minimum. Asymmetry of the energy profile around the stable point leads to low frequency thermal noise, with 1/f-like spectral profile. This phenomenon results in M-shape low frequency noise dependence vs magnetic field in magnetic tunneling readers [3]. This provides the motivation for the detailed study about the relationship between low frequency noise and asymmetric oscillations presented below. In magneto-resistive readers, it has been shown that the magnetic precession can be described in term of a 1D damped oscillator [4]. This serves as the primary basis for this investigation. 5 GHz asymmetric oscillators (which is the typical resonant frequency for the reader free layer) in contact with a thermal bath is analyzed using the Langevin equation. Potential energy profiles were generated using bi-harmonic and skew normal approximations [5], providing the ability to generate symmetric and asymmetric potentials using a single adjustable parameter. Asymmetric oscillations will introduce a DC shift, but the presence of random fluctuations in this asymmetric potential produces a broadening of the DC frequency spike leading to a pronounced 1/f-like low-frequency shape to the spectral density. Fig.1 depicts the simulated oscillation spectra for the bi-harmonic oscillator potential and shows the increasing power spectral density at low frequencies as asymmetry is introduced. In order to further characterize the nature of this 1/f-like low frequency noise profile, the time domain signal for the asymmetric oscillator was decomposed into low and high frequency components as shown in Fig. 2a. Fig. 2b shows the two dimensional histogram of the low frequency noise and the high frequency instantaneous amplitude. The strong correlation seen confirms that the 1/f-like low frequency noise originates from the fluctuations of the asymmetric oscillations. This model demonstrates a new mechanism of 1/f noise generation, which in many practical cases have been classified as being of unknown origin [6]. Experimental evidence for this behavior in the context of magnetic tunnel junction readers used in magnetic recording has been reported as well [7].

[1] S. F. Norrelykke and H. Flyvbjerg, "Harmonic Oscillator in Heat Bath: Exact simulation of time-lapse-recorded data, exact analytical benchmark statistics", *Phys. Rev. E*, vol. 83, 041003-14, Feb 2011. [2] R. Lifshitz and M. C. Cross, "Nonlinear Dynamics of Nanomechanical and Micromechanical Resonators," in Reviews of Nonlinear Dynamics and Complexity, vol. 1, H. G. Schuster, Ed. Weinheim: Wiley-VCH, 2008, pp. 1-52. [3] A. Stankiewicz, "Low frequency thermal noise in magnetoresistive sensors," Dig. 8th Joint European Magnetic Symposia (JEMS), Glasgow (UK), Aug 2016. [4] A. Stankiewicz and S. Hernandez, "Damping constant estimation in magnetoresistive readers," J. Appl. Phys. 117, 17E319 (2015). [5] Samir K.Ashour and Mahmood A.Abdel-hameed, "Approximate skew normal distribution", Journal of Advance Research, Vol. 1, Issue 4, pp. 341-350, Oct 2010. [6] Sh. Kogan, *Electronic Noise and Fluctuations in Solids*, Cambridge: CUP, 2008. [7] A.Stankiewicz, T.Pipathanapoompron, K.Subramanian, A.Kaewrawang, "Reader noise due to thermally driven asymmetric oscillations", Dig. Intermag 2018, Singapore, Apr 2018.

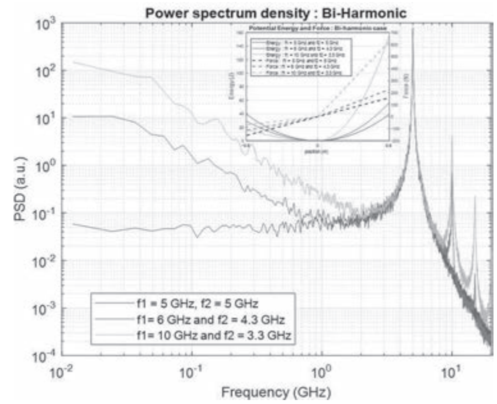

Fig. 1. Power Spectrum Density of 5 GHz Oscillation modelled by Langevin equation in potential energy (Bi-harmonic)

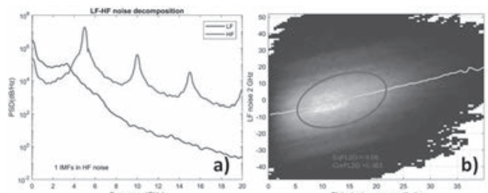

Fig. 2. (a) Time-domain low frequency and high frequency signal decomposition for the bi-harmonic oscillator. (b) Two dimensional histogram of the low frequency noise and the high frequency instantaneous amplitude. Strong correlation proves that the origin of the low frequency noise comes from the high frequency oscillations.

10:45

GI-08. Molecularly Structural Change of PFPE Lubricant Accumulated on Pin Surface at Laser Heating.

H. Tani[1], Y. Shibahara[2], R. Lu[1], S. Koganezawa[1] and N. Tagawa[1]
1. Mechanical Engineering Dept., Kansai University, Suita-shi, Japan;
2. Graduate School of Kansai University, Suita-shi, Japan

With increase in the storage capacity of hard disk drives, the flying height of the magnetic head is now typically less than a few nanometers. Picked up lubricant on the slider surface causes the head flying instability. On the head disk interface (HDI) of heat assisted magnetic recording (HAMR), the disk surface is heated to a high temperature of 400 - 500 K. If the lubricant is evaporated by laser heating and that should accumulate as smear on the slider surface. Kiely et al. concluded that the head smear played a key role not only for the stability of the HDI, but also for the transmission efficiency of the thermal energy from the near field transducer to the recording media in the HAMR system [1]. In this study, we have studied the molecularly structural change of perfluoropolyether (PFPE) lubricant accumulated on the pin surface at laser heating using TOF-SIMS in order to obtain the design guideline of lubricant film with the high heat resistance for the HAMR. TOF-SIMS spectrum of lubricant accumulated on a pin surface was compared to that of disk lubricant inside and outside laser heated track as shown in Fig. 1. The molecular weight could be obtained from these TOF-SIMS spectra. In addition, the progress of end-groups dissociation by laser heating could be estimated by the intensity of end-group fragments. As the results, the molecular weight of accumulated lubricant was smaller than that of disk lubricant and that of disk lubricant was larger than that of normal lubricant. The dissociation of end-groups increased with the temperature of laser heating as shown in Fig. 2.

[1] J. D. Kiely et al., IEEE Trans. on Magn., vol. 53, 2017, pp. 3300307.

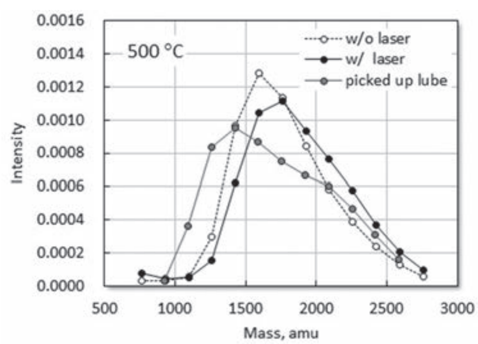

Fig. 1. Mass frangment intensity distribution of lubricant.

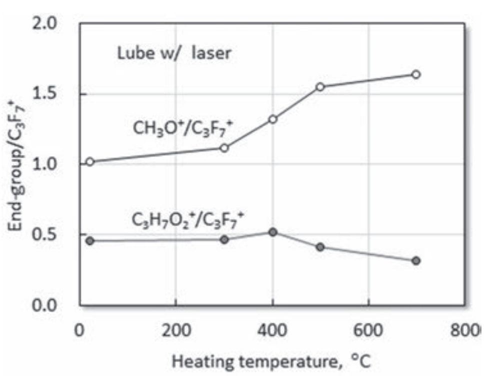

Fig. 2. Fragment intensity change of lubricant end-groups with laser heating temperature.

11:00

GI-09. HAMR Air Bearing, Water Monolayer Vaporization and Diffusion.

O.J. Ruiz[1]
1. Advance Tribology, Western Digital, San Jose, CA, United States

In HAMR drives the intense heat under the NFT produces an increase in the air bearing pressure by following mechanisms: thermal gradient driven molecular creep flow, vaporization of the water monolayer adsorbed on the disk surface, clearance reduction driven by the thermal protrusion of the NFT and disk hot spot, and elastic deformation of the head and disk surface induced by the gas pressure. The pressure effect of the thermal gradient is considered by including a known molecular thermal creep flow term in the Reynolds equation. The problem of water evaporation and condensation in the gas bearing is addressed by solving the associated gas diffusion problem. Under equilibrium conditions the concentration of water vapor within the gas is uniform. Depending on the local pressure and temperature, some water is lost to condensation and some is added by evaporation of the water monolayer on the disk. Such addition or removal creates an imbalance in the local vapor concentration thus permitting vapor diffusion. The diffusion of water vapor in a gas is described by the Fick diffusion equation. In addition to solving the lubrication equation for the pressure the time domain vapor diffusion is solved concurrently. Quantities such as the mean free path, viscosity and diffusivity become pressure, spacing, temperature and concentration dependent and are location dependent. The replenishing of the water monolayer on the disk is addressed by considering a simple Langmuir isotherm. The water vapor molecules impinging on the disk get adsorbed and induce a concentration gradient that drives vapor diffusion toward the disk and limits the duration needed for the replenishing of the monolayer. The mechanical deformation of the disk and slider due to the gas pressure is also considered. Results for a time domain simulation considering transient effects caused by laser power changes as the head traverses the servo wedges is presented. Some comments on the corrosive effect of the superheated steam are offered.

"Water adsorption on thin film media", T.E. Karis, J. Colloid and Interface Science, 225, 196-203, (2000) "Thermodynamics and kinetics of adsorption", Klaus Christmann, IMPRS Lecture Series 2012, Experimental and Theoretical Methods is Surface Science, Freie Universitat Berlin "Water adsorption on lubricated fullerene-like CNx films", E. Broitman, V.V. Pushkarev, A. J. Gellman, J. Neidhardt, A. Furlan, L Hultman, Thin Solid Films, 515, 979-983, (2006) "Water adsorption on lubricated a-CHx in humid environments", N. Shukla, E. Svedberg, R. J.M. van de Veerdonk, X. Ma, J. Gui, A. Gellman, Tribology Letters, v 15, No 1, July 2003 "Static and dynamic air bearing behavior in heat assisted magnetic recording under thermal flying height control and laser system induced protrusion", J B. Dahl, D.B. Bogy, Computer Mechanics Lab, UC Berkeley, (2013)

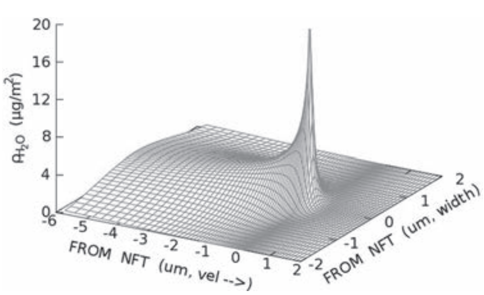

Fig. 1. Water vapor concentration within gas bearing around NFT

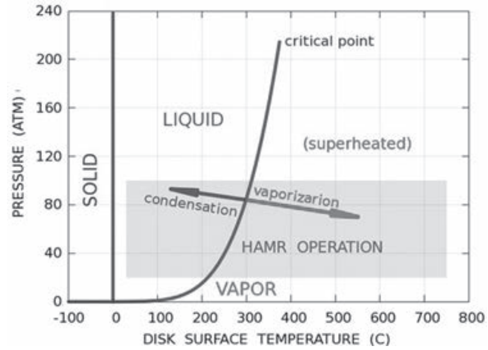

Fig. 2. Water phase diagram showing region of HAMR operation

11:15

GI-10. Modified MGL Equation Considering Both Effects of Surface Roughness and Accommodation Coefficient for Ultra-thin Gas Film Lubrication.

B. Shi[1,2], K. Guo[1], Y. Sun[1] and Y. Feng[1]
1. School of Mechanical and Electrical Engineering, Shandong Jianzhu University, Jinan, China; 2. School of Mechanical Engineering, Hebei University of Technology, Tianjin, China

1. Introduction The clearance between the read/write head and the disk surface, which is normally referred to the flying height (FH), should be small and stable as the FH is one of the important components of the head-media spacing [1-2]. To achieve a higher areal density, the FH of the slider continuously decreases and has been reduced to about 1-2 nm in modern disk drives [3-4]. Under such low spacing, the considerations of gaseous rarefaction effects and roughness effects of the magnetic recording system become more important. By solving modified Reynolds equation, effects of gaseous rarefaction and surface roughness were investigated [5-6]. The influence of surface accommodation coefficient (AC), which determines the behavior of the reflected molecules at the boundary walls, is an important factor to govern the flying characteristics of the air bearing slider [7-8]. By solving modified molecular gas film lubrication (MGL) equation, which governs ultra-thin gas film lubrication problems, effects of surface accommodation were investigated [9-10]. However, most of the published work considered gaseous rarefaction effects with either surface roughness effects or surface accommodation effects. 2. Modified MGL equation In the present study, a modified MGL equation is proposed considering both effects of surface roughness and AC for ultra-thin film lubrication, in addition to the gaseous rarefaction effect. Solving the modified model, the effects of surface roughness and AC are combined to study the static characteristics of the air bearing film. Numerical results are presented for both symmetric molecular interaction and asymmetric molecular interaction. 3. Numerical results and discussions *A. Effects on the pressure distribution in symmetric molecular interaction* Figures 1 and 2 show the pressure distributions for various surface roughness combinations in two cases of symmetric molecular interaction. There are five curves in each figure. The solid one without any mark represents the "smooth" case, in which both of the slider and the disk have no roughness. The two solid curves with marks of plus and circle signs represent two roughness cases, in which both the slider and the disk have the same roughness of 0.2 nm and 0.3 nm, respectively. The two solid curves with marks of product and point signs represent another two roughness cases, in which either the disk or the slider only has roughness of 0.3 nm, respectively. From Figs. 1 and 2, we have following observations: 1) When both the slider and the disk are rough, the pressure distribution will increase with the increase of ACs and/or the increase of surface roughness. 2) When the slider only is rough, the pressure distribution is much higher than that of both the slider and the disk in smooth case. While when the disk only is rough, it has opposite effect on the pressure distribution. 3) With the increase of ACs for various roughness cases, the location of maximum pressure moves towards the trailing edge of the slider. 4) In general, in the case of symmetric molecular interaction, the pressure distribution of the film increase with the increase of ACs with various surface roughness combinations. For a given surface roughness, the pressure distribution increases if the slider only is rough, while it will decrease if the disk only is rough. These phenomena will be futher explained in the full paper. *B. Effects on the pressure distribution in asymmetric molecular interaction* We also investigated the effects on the pressure distribution for various surface roughness combinations in the case of asymmetric molecular interaction and compared with the phenonmena observed in the case of symmetric molecular interaction. In general, the AC's variations of the slider and the disk will result in opposite effects on the pressure distribution in the case of asymmetric molecular interaction. These phenomena will be presented and discussed in detail in the full paper. 4. Summary and conclusion 1) Starting from a simplified molecular gas film lubrication (MGL) equation, a modified MGL equation is proposed for ultra-thin gas film lubrication to consider the combined effects of surface roughness and accommodation coefficient (AC) simultaneously, in addition to the gaseous rarefaction effect. 2) For the case of symmetric molecular interaction, pressure distribution of the air bearing film increases with the increase of ACs with various surface roughness combinations. For a given surface roughness values, pressure distribution of the air bearing film will increase if the slider only is rough, while there will be opposite effect if the disk only is rough. For the case of asymmetric molecular interaction, the AC's variations of the slider and the disk lead to opposite effects on the pressure distribution. The phenomena observed will be further explained in the full paper. 3) More detailed numerical results of the effects on the pressure center and the load-capacity in both symmetrical and unsymmetrical molecular interactions will be reported and discussed in the full paper. *Acknowledgments* This work was supported by the National Nature Science Foundation of China (Grant No. 51275279) and the Tribology Science Fund of State Key Laboratory of Tribology (Grand No. SKLTKF16A01), China.

[1]Hua W, Liu B, Yu SK, Zhou WD. Thermal protrusion induced air bearing frequency variations. Microsyst Technology, 2011, 17: 891-896. [2]Zhang CW, Ovcharenko A, Yang M, Knudson N, Talke FE. An investigation of thermal asperity sensors during contact with disk asperities. Microsyst Technology, 2014, 20: 1529-1534. [3]Salas PA and Talke FE. Numerical simulation of thermal flying-height control sliders to dynamically minimize flying height variations. IEEE Trans. Magn., 2013, 49(4): 1337-1342. [4] Matthes LM, Knigge BE, de Callafon RA, Talke FE. Near Contact Thermal Flying Height Control in Hard Disk Drives. IEEE Control Sys. Tech., 2017, 25(1): 2017, 39-46. [5]Makino T, Morohoshi S, Taniguchi S. Application of average flow model to thin film gas lubrication. ASME J. Tribology, 1993, 115(1): 185-190. [6]Shi BJ, Yang TY. Simplified model of Reynolds equation with linearized flow rate for ultra-thin gas film lubrication in hard disk drives. Microsyst Technology, 2010, 16(10): 1727-1734. [7]Shi BJ, Ji JD, Yang TY. Simplified molecular gas film lubrication equation and accommodation coefficient effects. Microsyst Technology, 2011, 17(8): 1271–1282. [8]Huang WD, Bogy DB. The effect of accommodation coefficient on slider air bearing simulation. ASME J. Tribology, 2000, 122(2): 427-435. [9]Fukui S, Shimada H, Yamane K, Matsuoka H. Flying characteristics in the free molecular region (influence of accommodation coefficients). Microsyst Technology, 2005, 11(8-9): 805-811. [10]Shi BJ, Feng YJ, Ji JD, Li L, Zhang CW. Simplified precise model of Reynolds equation for simulating ultra-thin gas film lubrication in hard disk drives. Microsyst Technology, 2015, 21(12): 2517-2522.

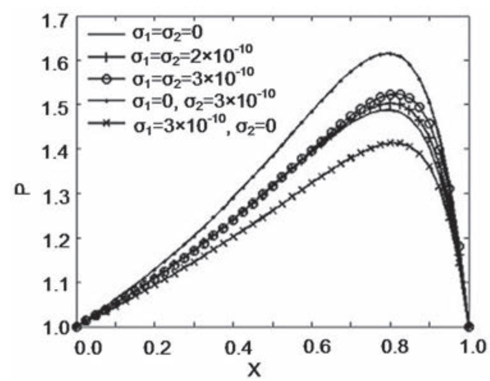

Fig. 1. Pressure distributions for different surface roughness combinations with α_1=α_2=0.5

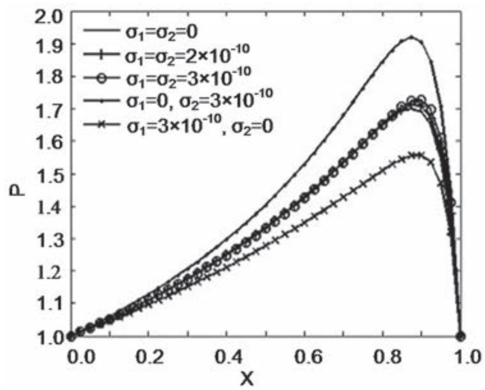

Fig. 2. Pressure distributions for different surface roughness combinations with α_1=α_2=1

11:30

GI-11. Investigation into slider wear under high temperature.

Y. Wang[1,2] and X. Wei[3]
1. University of California, Berkeley, Berkeley, CA, United States; 2. Xi'an Jiaotong University, Xi'an, China; 3. SAE Magnetics (H.K.) Ltd., Dongguan, China

Abstract: With the continually increase of HDD areal density, the required clearance between magnetic head and disk is lower than 1 nanometer (nm). The HDDs reliability becomes a significant concern due to the inevitable contact of intermittent/ continuous head-disk contact. To reveal the related factors to slider wear, a serious experiments under near-contact/ contact region based on a drive-based tester were carried out in this paper. Based on the theoretical explanation and the slider wear identification results using Scanning electron microscope (SEM), it is concluded that slider with high temperature is prone to producing more wear to slider, which agrees well with the atom-atom wear model proposed by I.Introduction To increase the areal density to 1 TB/in^2, the required clearance between magnetic head and disk is lower than 1 nanometer (nm) [1]. At such small clearance, the intermittent/continuous head-disk contact is inevitable. As a result, the slider wear becomes a significant concern for the HDD researchers and engineers. Although the slider wear under sliding-contact condition has been explored extensively [2], the design and environmental factors influencing on slider wear under near-contact or intermittent-contact condition are still not clear. In this paper, we investigated such factors under a near-contact/contact region, e.g., slider just touching down. Both room temperature and high temperature were considered. II.Experiment A drive-based tester was used to perform the experiment. And the tester was placed in a temperature champer, which can control the enviormental temperature during test. The pemto-size thermal flying-height control (TFC) sliders were used. An AE sensor was used to detect the slider touch down. During the test, the sliders continuously flied over five hours after setting a touch down power to the TFC heater. Scanning electron microscope (SEM) was used to inspect the slider wear after the test. III. Result and Discussion To investigate the temperature impact on slider wear, we also tested the 32 samples under room temperature (25 Celsius) and high temperature (55 Celsius), respectively. From SEM inspection results, as demonstrated in Fig. 1 (a) and (b), under high temperature slider has much larger wear area. AFM results (Fig.1 (c)) show that the slier wear under high temperature is much more serious. This means high temperature is prone to producing more wear to slider. At nanoscale wear, wear can be described as atom-atom removal. Based on prevous wear model, we have a modified wear model for slider wear which assumes slider tip is a part of sphere, as shown in Fig. 2. From this model, we can find the wear amounts is highly related to temperature, which means the test results agree well with the wear model.

[1] L. Su, Y. Hu, E. L. Lam, P. Li, R. W. Ng, D. Liang, O. Zheng, H Liu, Z. Deng, and J. Zhang, "Tribological and dynamic study of head disk interface at sub-1-nm clearance," IEEE Trans. Magn., vol. 47, no. 1, pp. 111–116, Jan. 2011. [2] N. Li, L. Zheng, Y. Meng, and D.B Bogy, "Experimental study of head-disk interface flyability and durability at sub-1-nm clearance," IEEE Trans. Magn., vol. 45, no. 10, pp. 3624–3627, Oct. 2009.

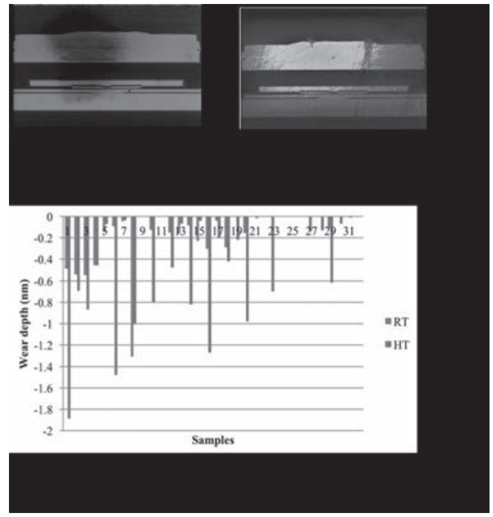

Fig. 1. SEM and AFM inspection results of the sliders after the test. (a) Room temperature (25 Celsius); (b) High temperature (55 Celsius); (c) Slider wear measured by AFM.

$$\frac{\partial R}{\partial d} = -\frac{w^2}{8R^2}\frac{fb}{v_0}exp\left(\frac{1}{k_B T}\{-(E_a - V_a\tau_0) + \frac{\xi F_N}{\pi w^2/8}\}\right)$$

(τ_0、ξ、v_0 are constants, v is sliding velocity, w is sliding width, E_a is initial activation energy, V_a is activation volume, τ is tang, f is the attempt frequency due to phononic vibration, k_B is Boltzmann constant, T is the absolute temperature, F_N is normal load of slider.)

Fig. 2. Wear model

11:45

GI-12. Effect of Pressure and Temperature on Lubricant Transfer from Disk to Slider in Helium-filled Hard Disk Drives.

Z. Tang[1], D. Zhou[1], T. Jia[1], C. Zhang[2] and B. Shi[3]
1. School of Mechanical Engineering, Guizhou University, Guiyang, China; 2. School of Mechatronics Engineering, Harbin Institute of Technology, Harbin, China; 3. School of Mechanical and Electrical Engineering, Shandong Jianzhu University, Jinan, China

1. Introduction Helium, proved to be a good medium to reduce windage loss and disk flutter [1-3], has been filled in hard disk drives in recent years to improve storage [4]. Meantime, lubricant transfer between slider and disk has been widely studied due to the decreasing space between the slider and the disk [5-6]. We know that helium can greatly reduce the flying height of a hard disk drive. But question arises as to how the lubricant transfers in helium-filled hard disk drives. In this paper, a model of slider with a cylindrical asperity flying over a disk in helium-filled hard disk drive was developed. The pressure and temperature distribution at helium-filled head/disk interface was obtained by calculating Reynolds equation and energy equation. Thereafter, the effect of pressure and temperature on lubricant transfer from disk to slider in helium-filled hard disk drives was numerical simulated using molecular dynamics. 2. Air bearing model Fig.1 shows the schematic drawing of a slider with a cylindrical asperity flying over a disk in helium-filled hard disk drive. The minimum flying height is 2 nm. The initial temperatures at the slider surface and the disk surface are set to be and, respectively. A finite element method was used to calculate the Reynolds equation and the energy equation. Thereafter, the pressure distribution and the temperature distribution of the air bearing in helium-filled hard disk drive are obtained. The effect of helium (physical properties such as density, mean free path, viscosity, and thermal conductivity) on the pressure distribution as well as temperature distribution is studied. Finally, the results are simulated as an input in the model of molecular dynamics. 3. Model of molecular dynamics Fig. 2 shows the molecular dynamics model and the process of lubricant transfer from disk to slider. The dimensions of the model are exactly the same as the model of air bearing interface, which is shown in Fig. 1. Fig. 2 a) shows the molecular dynamics model before the pressure and the temperature are applied. We observe that a clear gap between the slider and the disk, which means there is no lubricant transfer. However, the lubricant starts to transfer from the disk to the slider surface after the pressure and the temperature were applied, as shown in Fig. 2 b). The pressure over the cylindrical asperity first increases and then decreases according to the air bearing results. The highest pressure happens at the first half cylinder while the lowest happens at the second half cylinder. We observe the lubricant transfer occurs at the area of the slider surface in front of the cylindrical asperity. This is caused by the great difference of pressure induced by the cylindrical asperity. In addition, the lubricant stays at the slider surface if the flying height increases. In the full paper, the effect of helium on the pressure and temperature distribution of air bearing will be shown and discussed. And how the obtained pressure and temperature will affect the lubricant transfer at the head/disk interface will be presented as well. 4. Acknowledgment This work is supported by the National Nature Science Foundation of China (Grant No. 515093) and the Young Talents of Science and Technology of Guizhou Province (Grant No. [2016] 116).

[1] N. Liu, J. Zheng, D. B. Bogy, "Thermal flying-height control sliders in air-helium gas mixtures", IEEE Trans. Magn. 47, 100-104, (2011). [2] K. S. Park, Y. P. Park, N. C. Park, "Prospect of recording technology for higher storage performance", IEEE Trans. Magn. 47, 539-545, (2011). [3] Z. Q. Tang, P. A. S. Mendez and F. E. Talke, "Investigation of head/disk contacts in helium-air gas mixtures", Tribol. Lett., 54, 279-286, (2014). [4] Doug C. HGST announces new helium-filled hard disk drive platform, http://www.tomshardware.com/news/Helium-Filled-Hard_Disk-hdd-western-digital,17573.html, 2012 [5] D. Pan, A. Ovcharenko, R. Tangaraj, M. Yang, F. E. Talke, "Investigation of lubricant transfer between slider and disk using molecular dynamics simulation", Tribol. Lett., 53, 373-381, (2014). [6] Y. W. Seo, A. Ovcharenko, F. E. Talke, "Simulation of hydrocarbon oil contamination at the head–disk interface using molecular dynamics", Tribol. Lett. 61:28, (2016).

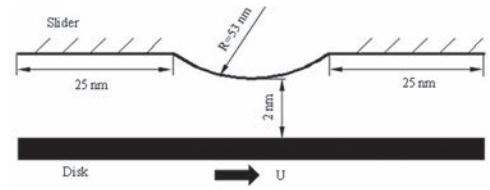

Fig. 1. Schematic of a slider with a cylindrical asperity flying over a disk in helium-filled hard disk drive

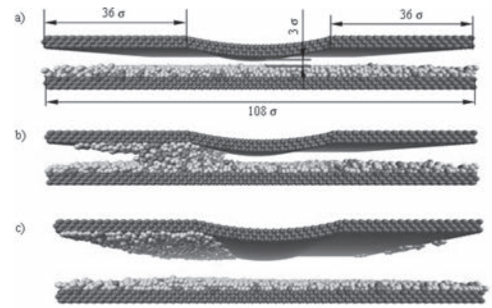

Fig. 2. The process of lubricant transfer from disk to slider

FRIDAY MORNING, 27 APRIL 2018 SIMPOR/ROSELLE BALLROOM, 8:30 TO 11:30

Session GP
ELECTRICAL MACHINES AND CONTROL II
(Poster Session)

Mingyao Lin, Co-Chair
Southeast University, Nanjing, China
Po-Wei Huang, Co-Chair
National Cheng Kung University, Tainan, Taiwan

GP-01. Withdrawn

GP-02. Comparison of Unbalanced Forces in a BLDC Motor Considering Difference in Resistance According to the Number of Parallel Circuits and Winding Concept.

H. Lee[1], K. Shin[1], S. Cho[1], T. Bang[1] and J. Choi[1]
1. Dept. of Electric, Electronic and Comm. Eng. Edu., Chungnam National University, 99 Daehak-ro, Yuseong-gu, Daejeon 34134, Korea, Daejeon, The Republic of Korea

Brushless direct current (BLDC) motors have favorable characteristics, such as high output power, high torque density, wide operating range, high efficiency, precision controllability, simple driving method and low price. They are widely used in technological applications, such as electric vehicles, robotics and home appliances, and are gradually replacing DC motors because BLDC motors do not have a mechanical commutator and brush [1]. The outer rotor BLDC motor, which is the analysis model of this paper, has a structure in which the rotor rotates on the outside, and has a large inertia. This is advantageous for constant rotation and also means that the magnet can be attached to the inside of the yoke. The merit of this structure is that a large torque can be obtained even with a magnet that has a weak magnetic force [2]. The causes of noise and vibration in these motors are divided into electromagnetic and mechanical factors. In the case of electromagnetic factors, the electromagnetic forces generated by permanent magnets and armature windings contain harmonic components that cause noise and vibration due to the stator teeth and slot structures [3]. Among the electromagnetic forces involved, radial force density is the external excitation force, which is the primary source of vibration of the motor acting on the teeth surface of the stator. In particular, when its frequency is equal to the natural frequency of the motor, resonance causes wear of the motor parts and generates excessive noise. Therefore, it is essential to analyze the radial force density during high performance operation of the motor [4]. The radial force density distribution on the stator surface, which results from the air-gap magnetic field under no-load (open-circuit) and on-load conditions, is the main cause of electromagnetically induced noise and vibration. In this paper, the differences resistance caused by changing the number of parallel circuits and the resulting unbalanced forces was analyzed using a 2D finite element method. When the number of parallel circuit is increased during motor design, the air-gap become non-uniform due to bearing wear. Thus, as the reluctance of the magnetic poles is not uniform, the magnitude of the electromotive force induced in each parallel circuit may become unbalanced. If the voltages of the parallel circuits are not balanced, a circulating current and an unbalanced force is generated [5]. In our analysis model, an 8 pole-12 slot BLDC motor was analyzed under on-load conditions according to the number of parallel circuits, winding concept and the electromagnetic unbalanced force that occurs due to resistance differences arising from an increase the number of parallel circuits. Our analysis model is shown in Fig 1 (a). The Y-connection of the BLDC motor's stator is shown in Fig 1 (b). The Δ-connection is shown in Fig 1 (c). The simulation was based on these two winding methods and on the use of either two or four parallel circuits per phase, as shown in Fig 1 (d). In analysis methods that use radial force density, the noise and vibration characteristics of the motor are difficult to predict due to differences in resistance arising from the manufacturing process. Figs 2 (a) and (d) show the spatial radial force density distribution on the air-gap contours with and without resistance differences. The level of unbalanced magnetic force is almost same. The global force applied to the rotor was computed. Figs 2 (b), (c), (e), and (f) show the unbalanced forces on the rotor axis. Force_x and Force_y are the x-axis and the y-axis components of the unbalanced forces in the rotor, respectively. From our results, in can be seen that when there are resistance differences, the global force applied to the rotor becomes unbalanced, as shown Figs 2 (c) and, (f). When noise and vibration are produced in a machine with a BLDC motor, the result obtained in this study can provide a hint at what resistance condition is present. A more detailed results analysis for two, four parallel circuits, and discussion will presented in the full paper. Acknowledgment This work was supported by the Basic Research Laboratory (BRL) of the National Research Foundation (NRF-2017R1A4A1015744) funded by the Korean government.

[1] Y. Kim, J. Lee, C. Jo, Y. Kim, M. Song, J. Kim, H. Kim, "Development and control of an electric oil pump for automatic transmission-based hybrid electric vehicle", IEEE Trans. Veh. Technol., vol. 60, no. 5, pp. 1981-1990, Jun. 2011. [2] T.J. Jahns, G.B. Kliman, T.W. Neumann, "Interior permanent-magnet synchronous motors for adjustable-speed drives", IEEE Trans. Industry Applications, vol. 22 IA, no. 4, pp. 738-747, 1986. [3] T. M. Jahns, "Flux weakening regime operation of an IPM synchronous motor drive", IEEE Trans. Ind. Applicat., vol. IA-23, pp. 681-689, July/Aug. 1987. [4] J. R. Hendershot, T. J. E. Miller, Design of Brushless Permanent-Magnet Motors, Oxford, Clarendon Press, 1994. [5] D. G. Dorrell, D. A. Staton, J. Kahout, D. Hawkins, M. I. McGilp, "Linked Electromagnetic and Thermal Modelling of a Permanent Magnet Motor", IEE Power Electronics Machines and Drives Conference, April 2006.

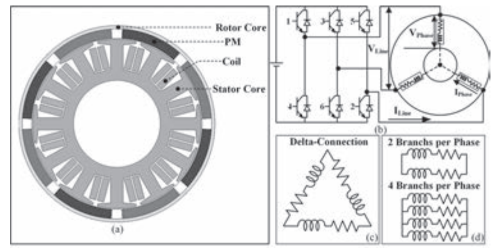

Fig. 1. Analysis model : (a) Analysis model 8 pole-12 slot outer type BLDC motor, (b) The winding method of stator (Star Connection), (c) Delta connection (d) 2 branch per phase, 4 branch per phase

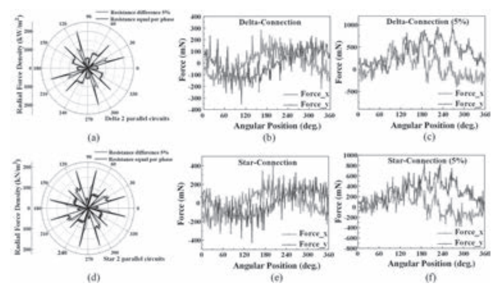

Fig. 2. Analysis results : (a) radial force density (Delta-Connection) (b) the forces of equilibrium state (Delta-Connnection) (c) the forces of resistance difference 5% (Delta-Connnection) (d) radial force density (Star-Connection) (e) the forces on resistance equilibrium state (Star-Connnection) (f) the forces on resistance difference 5% (Star-Connnection)

GP-03. Improvement of torque ripple characteristics of double winding PMSM with using twin inverter.

S. Noguchi[1]
1. Motor Drive Laboratory, Tokyo City University, Setagaya-ku, Japan

In recent years, double winding machines are more interested because it has wide range of application by motor control better than general three phase machines [1], [2]. It is known that these machines have fault tolerant feature, so it is got much attention especially for application which needs failure tolerance like aircraft, electric vehicle, electric rolling stock, and marine ship. These machines need two or more inverters, which leads higher costs than one inverter drive. But controlling each winding by independent inverters lets improvement drive characteristics like extending speed range, and reducing torque ripples. But controlling each winding by independent inverters expects letting improvement drive characteristics like extending speed range, and reducing torque ripples, so it is widely considered[3]. For examination object of double winding machines, PMSM and induction machine is mostly used. Especially 10poles-12slots PMSM is superior as AC servo motor, so the PMSM is widely used as examination object. Test machine using in this paper has 10poles-12slots configuration shown in Fig.1(a). And each complementary pair of three phase winding is connected in serial, then the connected winding pair is connected in parallel as 2S2P connection, shown in Fig.1(b). In generally, when the motor drives using all windings, gives same phase AC current to each of three phase winding group. Each of three phase winding group is able to excite by two inverter independently controlled by one microcontroller, shown in circuit diagram Fig.1(c). It is able to suppose many motor drive pattern by exciting three phase winding group separated group1 and group2 independently. In this paper, comparing driving characteristics of following driving patterns by using 2 inverter to verify phase difference drive and fault tolerant characteristics. i. Normal Driving (using all windings, excited by same phase AC current) ii. Driving in case of one inverter is fault. (One inverter is stopped, only use the other inverter.) iii. Driving in case of having current phase difference between inverters. Fig.2(a) shows U-phase current and torque characteristics when normal driving using all windings. Fig.2(b) shows the characteristics when group1 inverter is stopped and disconnected and only use group2 inverter. Fig.2(c) shows the characteristics when group2 output current is 60 degrees delayed from group1 output current. The motor is driving by field oriented control at 150rpm speed and 0.2Nm rated torque load in this experiment. From fig.2(a), in normal driving, inverter output current phases are same and peak currents are same in 0.6A. The torque ripple rate is 28.1% in normal driving. Here, group1 inverter is stopped and released from the circuit, then no current of group1 because of unconstructed circuit, as shown in fig.2(b). Group2 current is covered the torque which group1 supposed to assume, and increase to peak current 1.7A. And, group2 current phase is delayed from group2 current phase of normal driving. The torque ripple rate is increased to 36.3% from normal driving torque ripple rate. However, because the motor does not step out in operating and keeps these drive characteristics constantly, it is confirmed that double winding motor with driving by 2 inverter gets fault tolerant characteristics. As shown in fig.2(c), when group2 current is excited 60degree delayed from group1 current, group1 peak current is increased to 1.2A, and group2 peak current is increased to 1.4A, which means these currents are twice current of normal driving. It is thought that excessive amount of group2 current led by phase difference is corrected by increasing group1 current. The torque ripple rate is worse increased to 50.2% from normal driving torque ripple rate. However, in this case too, because the motor does not step out in operating and keeps these drive characteristics constantly, it is confirmed that double winding motor with driving by 2 inverter when unexpected current phase difference is occurred gets fault tolerant characteristics. Therefore, because drive characteristics like peak current and torque ripple is worse than normal driving in case of one inverter fault or occurring current phase difference, but events disturbing motor operation like step-out did not occurred, so it is confirmed that double winding PMSM used in this paper with driving by 2 inverter can keep redundancy and get fault tolerant characteristics. Also, as a state of inverter failure, it can be considered that the group1 is normal and group2 fails or the faulty inverter is connected to the circuit in the regenerative mode. In these case too, it was confirmed that the motor has fault tolerance characteristics by same experiments. Moreover, in case of inverter differential operation, we examined when phase difference between group1 and group2 was changed from 60 degree lead to 60 degree delay at 15 degree intervals. In this case too, because the motor does not step out in operating, it is confirmed by same experiment that double winding motor with driving by 2 inverter gets fault tolerant characteristics, and found that it is possible to reduce torque ripple by inverter phase differential operating.

[1] E. Levi, "Multiphase electrical machines for variable-speed applications," IEEE Trans. Ind. Electron., vol. 55, no. 5, pp. 1893–1909, May 2008. [2] J. Karttunen, S. Kallio, P. Peltoniemi, P. Silventoinen, and O. Pyrhönen, "Decoupled Vector Control Scheme for Dual Three-Phase Permanent Magnet Synchronous Machines," IEEE Trans. Ind. Electron., vol. 61, no. 5, pp. 2185–2196, May 2014. [3] M. Barcaro, N. Bianchi, F. Magnussen, "Faulty Operations of a PM Fractional-Slot Machine With a Dual Three-Phase Winding," IEEE Trans. Ind. Electron., vol. 58, no. 9, pp. 3825–3832, Sep 2011.

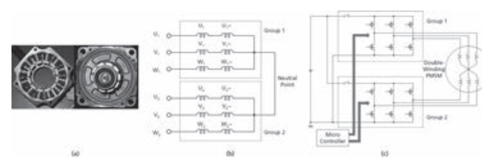

Fig. 1. Pattern diagram of test motor and inverter using in this paper (a)Structure of rotor and stator (b)Stator winding connection (c)Circuit diagram of 2inverter

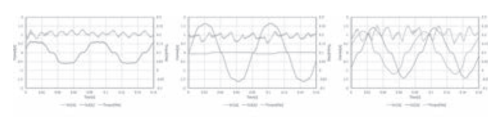

Fig. 2. U-phase current characteristics and torque characteristics(150rpm, rated torque 0.2Nm)
(a)Normal driving (b)Group1 inverter stopped(Only use Group2 inverter) (c)Group2 current is 60degree delayed from group1

GP-04. Compensation of Imbalanced Current for Dual-Three PM Machine with Asymmetrical Windings by Three-Phase Decomposition.

J. Zhang[1] and Z. Zong[1]
1. NanJing University of Aeronautics And Astronautics Graduate School, Nanjing, China

I. Introduction Compared with three-phase permanent magnet synchronous motor (PMSM), the dual three-phase PMSM has fault-tolerant capability and low torque ripple, which obtains wide application, such as aerospace, electrical automobile, and wind power generation systems etc. [1][2]. The two-individual current and the vector space decomposition (VSD) controls are commonly employed for dual three-phase PMSM. The two-individual current control adopts two dq-synchronous frames to drive each set of single three-phase windings individually, which can suppress the imbalanced current resulting from asymmetries between the two sets of three-phase windings [3]. However, this neglects complex coupling between the two dq-synchronous frames. Therefore, the output torque can track performance dynamic performance. For VSD control, it treats the motor as a six-phase machine [4]. The six-phase system is decomposed into three orthogonal sub-spaces, alpha-beta, z1-z2, and o1-o2. There is no coupling between the three sub-spaces. The VSD control can provide excellent dynamic torque performance without the influence of coupling voltages between two sets. Four-vector SVPWM is often used for VSD control, where the currents of z1z2 sub-space cannot be feedback controlled [5][6]. This will result in imbalanced currents for the dual three-phase windings with asymmetrical phase resistances. This paper aims to suppress the imbalanced currents in two winding sets resulting from asymmetrical phase resistances. The three-phase decomposition algorithm in this paper is proposed for balancing the phase current in the two winding sets. II.Three-phase Decomposition PWM Algorithm According to various variables of dual three-phase PMSM in the natural coordinate transformed into the stationary coordinate by the two-individual current control and the VSD control, the relationship between two schemes can be obtained. On this basis, voltage vectors in the six-phase VSI can be decomposed as Fig. 1 (a), it follows that the diagram of three-phase decomposition, as shown in Fig. 1 (b). It can be seen as the combination of the two-individual current control and the VSD control. The experiment is carried out on the dual three-phase machine with asymmetrical phase resistance among two winding sets, as shown in Fig. 2 (a). The phase resistance and inductance are given in TABLE I. Note the asymmetry is severe and Fig. 2 (b) shows the currents of phases A and X under rated load by four-vector SVPWM at 300 rpm. It can be observed that the imbalanced current exists for the two sets of windings, being 3.4A and 6.4A, respectively. This is because the four-vector SVPWM is an open-loop control for z1-z2 sub-space harmonic currents. It can be seen from Fig. 2 (c) that the imbalance is compensated to around 4.9A for two winding sets by the proposed method (Fig. 1). The results clearly demonstrated that balanced current sharing can be achieved between asymmetrical windings. The proposed method in this paper combines the advantages of the two-individual current control and the VSD control, and it not only has excellent dynamic torque performance, but also obtains real-time and the direct feedback control of z1-z2 harmonic currents. Though three-phase decomposition adopts two traditional SVPWM for voltage modulation, it treats the machine as a six-phase machine and reflects the advantages of multi-degree of freedom. The detailed analysis will be given in the full paper.

[1] E. Levi, R. Bojoi, F. Profumo, H. A. Toliyat, and S. Williamson, “Multiphase induction motor drives—A technology status review,” *IET Elect. Power Appl*., vol. 1, no. 4, pp. 489–516, Jul. 2007. [2] K. Wang, and J. Y. Zhang, “Torque improvement of dual three-phase permanent magnet machine using zero sequence components,” *IEEE Trans. Mag.*, vol. 53, no. 11, Nov. 2007. [3] G. K. Singh, K. Nam, and S. K. Lim, “A simple indirect field-oriented control scheme for multiphase induction machine,” *IEEE Trans. Ind. Electron.,* vol. 52, no. 4, pp. 1177-1184, 2005. [4] Y. Zhao and T. A. Lipo, “Space vector PWM control of dual three-phase induction machine using vector space decomposition,” *IEEE Trans. Ind. Appl.*, vol. 31, no. 5, pp. 1100-1109, 1995. [5] Y. S. Hu, and Z. Q. Zhu, “Comparison of two-individual current control and vector space decomposition control for dual three-phase PMSM, ” *IEEE Trans. Ind. Appl.*, vol. 53, no. 5, pp. 4483-4492, Sep./Oct., 2017. [6] G. Grandi, G. Serra, A. Tani, “Space vector modulation of a six-phase VSI based on three-phase decomposition,” *in Proc. Int. SPEEDAM, Ischia, Italy*, 2008, pp. 674–679.

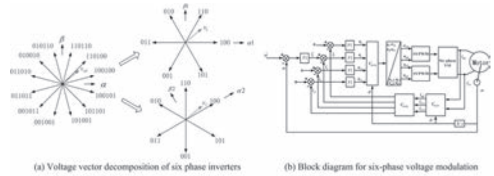

(a) Voltage vector decomposition of six phase inverters (b) Block diagram for six-phase voltage modulation

Fig.1. Three-phase decomposition SVPWM.

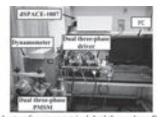

(a) Experimental setup for asymmetrical dual three-phase PMSM drive testing.

TABLE I.
DESIGN PARAMETERS OF PROTOTYPE DUAL THREE-PHASE PMSM.

	Rs (mΩ)	Ls (μH)
Phase A	143.2	66.8
Phase X	56.6	88.5
Phase B	57	84.4
Phase Y	54.9	59.1
Phase C	58	94.4
Phase Z	57	94.2

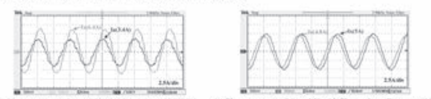

(b) Phase currents of A and X with four-vector SVPWM (c) Phase currents of A and X with Three-phase Decomposition

Fig.2. Experimental results showing asymmetry phase resistances of dual three-phase PMSM.

GP-05. Comparison of Electromagnetic Vibration of PM Motor Considering time and space Harmonics.

I. Jang[1]
1. Hyundai Mobis, Yongin-si, The Republic of Korea

1. Introduction The vibration occurring in an electric motor can be largely divided into the mechanical vibration due to nonaligned bearings and shafts, and the electromagnetic vibration caused by the electromagnetic force. Since the motor is prominent in human life in electronic and hybrid vehicles, and motors of high torque density have been used recently, the importance of electromagnetic vibration and noise has gradually increased. The electromagnetic vibration can be predicted by analyzing the radial force density—the vibration source—in the electromagnetic design of the motor. Thus, if the space and time harmonic of radial force density is analyzed, the harmonic that affects vibration the most can be found. This study compared and analyzed the characteristics of the vibration according to the combination of the number of poles and slots in the 8-pole SPMSM model. The harmonic of the air gap flux density was compared and analyzed according to the number of poles and slots, and the radial force density was separated into time harmonics and space harmonics, which were then compared. Finally, the vibration velocity was calculated using the components of radial force, and its validity was verified through an electromagnetic-vibro coupled analysis. 2. Analysis of the Harmonics of the Exciting Vibration Forces The electromagnetic vibration takes the radial force density as its existing vibration force, and is composed of the square of the gap flux density, as shown in Equation (1). The analysis of airgap flux density should be preceded in order to analyze the harmonic of the radial force density. This study used the teeth-concentrated winding, 8-poles, 9-slots and 8-poles, 12-slots, and the distribution winding, 8-poles, 48-slots, as the comparison models. The comparison was made with all other conditions the same except for the number of slots. The common elements are shown in Table I. Fig. 1 shows the comparison of 8-pole models. A. Airgap Flux Density In Fig. 2, the FFT analysis results of the spatial distribution of airgap flux density when was presented. B. Radial Force Density The electromagnetic excitation force of the motor, the radial force density, is expressed as in Equation (2) and is a waveform that rotates about time. Thus, when the time harmonics and space harmonics of the radial force density are separated and analyzed, the vibration frequency affected by each space harmonic can be calculated. Fig. 3 shows the radial force density of the 8-pole comparison models when they were separated into time and space harmonics. The order of the space harmonics about time harmonics is presented in Table II, using the analysis of the vibration velocity of electromagnetic force. [1] 3. Comparison of Characteristics of Vibration In this study, the vibration velocity is calculated using an electromagnetic-vibration coupled analysis. The RMS vibration velocity about the comparison model has been compared in order to examine the characteristics of the vibration. The RMS vibration velocity can be calculated from the vibration velocity according to the vibration frequency, as follows : Equation (3) The RMS vibration velocity of the comparison model is shown in Fig. 4, using Equation (3). To compare the vibration velocity, in the case of the 8-pole, 9-slot model, the value is highest because in the 8-pole-9-slot, the 1st vibration mode occurs in the 2nd vibration frequency (as shown in Table II), which is the cause of the high vibration velocity. 4. Conclusion In this study, the electromagnetic vibration characteristics that depend on the combination of the number of poles and slots were compared in 8-pole models. The harmonic component of the air gap flux density was analyzed through electromagnetic FEM analysis. Time and space harmonics components of the radial force density, the excitation vibration force, were compared. Also, regarding vibration velocities, the characteristics of the comparison models were analyzed. The vibration characteristics (which depend on the number of poles and slots) depend mostly on the harmonics components of the stator magnetic flux density, by way of the combination of the number of poles and slots. Thus, further study is being done regarding the generalized equation about the harmonics components of the stator magnetic flux density, so that it is possible to analyze the excitation vibration force according to the combination of the number of poles and slots.

I.-S. Jang, S.-H. Ham, W.-H. Kim, C.-S. Jin, S.-Y. Cho, K.-D. Lee, J.-J. Lee, D. Kang, and J. Lee, "Method for Analyzing Vibrations Due to Electromagnetic Force in Electric Motors," *Magn. IEEE Trans.*, vol. 50, no. 2, pp. 297–300, 2014.

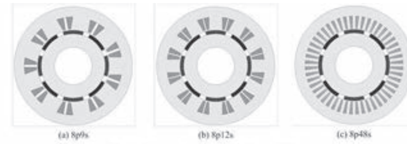

Fig. 1. Comparison of 8-pole models.

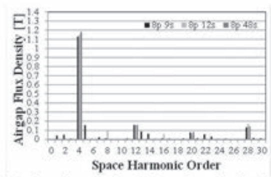

Fig. 2. Space harmonics of airgap flux density (ωt=0)

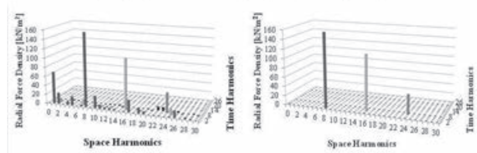

Fig. 3. Magnitude of radial force density considering time and spatial harmonics.

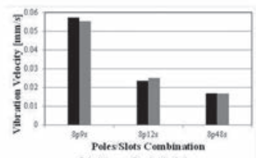

Fig. 4. rms vibration velocity Vrms of the comparison models.

TABLE I
COMMON SPECIFICATIONS OF 8-POLE MODELS

Description	Symbol	Value	Unit
Number of poles	Np	8	-
Number of phases	-	3	-
Peak value of the phase current	Imax	318.2	Apeak
Current angle	β	0	deg
Number of series turns per phase	Nph	24	turn
Rotation speed	-	3500	rpm
Stator outer diameter	Dso	0.35	m
Stator inner diameter	Dsi	0.212	m
Rotor outer diameter	Dro	0.21	m
Air gap length	g	0.001	m
Stack length	Lstk	0.14	m
Thickness of permanent magnet	lm	0.01	m
Pole arc ratio	αm	0.75	-

TABLE II.
TIME AND SAPACE HARMONICS ACCORDING TO POLES-SLOTS COMBINATION

Time Harmonics	Space Harmonics		
	8p 9s	8p 12s	8p 48s
2nd	1, 2, 4, 5, 8, 10, 11, 17, 19, 20, 26	4, 8, 16, 20, 28	8
4th	2, 7, 10, 11, 12, 13, 16, 19, 20, 25	4, 16, 28	16
6th	3, 6, 15, 18, 21, 24, 27, 30	24	24
8th	1, 2, 4, 5, 7, 8, 10, 11, 12, 13, 14, 17, 19, 20, 22, 23, 25, 26, 28, 29	4, 8, 16, 20, 28	32

Equation 1 : $p(\theta_m, t) = \frac{1}{2\mu_0} B^2(\theta_m, t)$

Equation 2 : $p_r(\theta_m, t) = P_{mr} \cos(\omega_r t \pm r\theta_m)$

Equation 3 : $V_{rms} = \sqrt{\frac{1}{2}\sum_{1}^{n} V_n^2}$

GP-06. Decoupling Control for Bearingless Synchronous Reluctance Motor Based on Exact Feedback Linearization.

X. Diao[1] and H. Zhu[1]
1. Jiangsu University, Zhenjiang, China

I. Introduction Bearingless motors (BMs) with built-in magnetic bearing are receiving increasing attention. Among all types of BMs, the bearingless synchronous reluctance motor (BSRM) has been extensively investigated due to its advantages of high speed, high efficiency, low cost, simple and robust structure [1]. BSRM is a typical nonlinear, multivariable and strongly coupled system, and then the dynamic decoupling control is of particular importance [2]. In this paper, a new decoupling control strategy based on exact feedback linearization theory of nonlinear systems is proposed for BSRMs. The necessary and sufficient conditions for exact feedback linearization of the system are proved, and then the coordinate transformation and state feedback control law can be derived. The original nonlinear system is converted into a Brunovsky canonical form and decoupled into three linear subsystems. For this linearized system, the closed-loop controller can be designed by using the single-input-single-output linear system theory. II. Mathematical Model The BSRM combines torque windings and radial force windings in one stator. We can control the size and direction of the radial suspension force by changing currents of two sets of windings respectively, by which the rotor can achieve a stable suspension. The mathematical models of torque subsystem and radial force subsystem can be deduced using Maxwell stress tensor method. III. Decoupling Control Based on Exact Feedback Linearization Firstly, the state equation of the BSRM is established, and the original nonlinear system is converted to an equivalent affine nonlinear system. Secondly, the necessary and sufficient conditions for exact feedback linearization of the system are proved. By using exact linearization theory and coordinate transformation, the state feedback control law is derived. By combining the state feedback control law with the composite plant of BSRM, the original system can be linearized and decoupled into three independent linear subsystems. Then, the linear control theory can be used for the closed-loop control of the system. The BSRM is a complicated nonlinear multivariate system. In case of parameter drift or external disturbance, the decoupling control based on exact linearization cannot achieve the ideal performance and thus additional PID controllers will be designed for the linearized system. The PID controllers and the decoupling control law form the composite decoupling controller of the BSRM. The block diagram of the control system is shown in Fig. 1. IV. Simulation and Experiment Research In order to verify the effectiveness of the proposed decoupling control method in this paper, the simulation model is constructed. Fig. 2 shows the simulation results with varying load and external disturbance. As shown in Fig. 2, when the speed and the radial displacements in the *x*- and *y*- directions are disturbed respectively, the three variables come back to the given value quickly. Moreover, they are almost not affected each other. It is shown that the electromagnetic torque and the radial suspension forces are decoupled, and this decoupling control method has good performance of disturbance rejection. To validate the effectiveness of the proposed decoupling control method, the experimental platform of BSRM is developed. The motor achieves stable suspension at the speed of 1500 r/min. When the load changes, the speed is almost constant and the radial displacement fluctuation of the rotor is very small. When the external disturbance force in *x*-direction is added on the rotor, the vibration amplitude of the *y*-axis radial displacement is extremely small. The experimental results further verify the effectiveness of the decoupling control strategy. V. Conclusion A new decoupling control strategy based on exact feedback linearization theory has been proposed for BSRMs. By using exact feedback linearization and coordinate transformation, the nonlinear model of BSRMs can realize dynamic decoupling control among the torque and the radial suspension forces in *x*- and *y*- directions. When the load changes or external disturbance appears, the control system has strong capability of attenuating external disturbance. Both simulation and experiment results confirm the validity of the proposed decoupling control strategy for BSRMs.

[1]X. Sun, Z. Shi, L. Chen, and Z. Yang, "Internal model control for a bearingless permanent magnet synchronous motor based on inverse system method," IEEE Trans. Energy Convers., vol. 31, no. 4, pp. 1539-1548, Jul. 2016. [2]V. Mukherjee, J. Pippuri, S. E. Saarakkala, A Belahcen, M Hinkkanen, and K. Tammi, " Finite element analysis for bearingless operation of a multi flux barrier synchronous reluctance motor," *Proc. ICEMS*, Pattaya, Thailand, pp. 688-691, Oct. 2015.

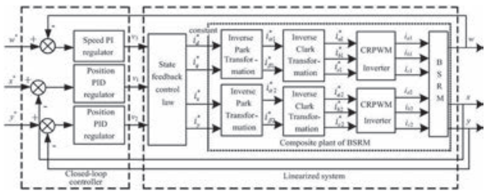

Fig. 1. Control block diagram of entire system.

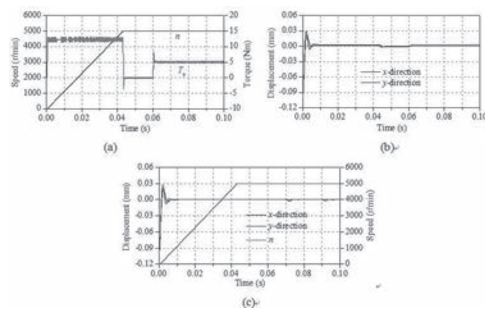

Fig. 2. Simulation results with external disturbance. (a) Speed and torque responses. (b) Displacement curves in *x*- and *y*-directions. (c) Simulation results of rotor speed and radial displacements with external disturbance.

GP-07. Tilting force Control method using lateral displacement force of permanent magnet synchronous motor for independent;y rotating vehicle.

J. Won[1], Y. Oh[1], *S. Oh*[1] and S. Kim[2]
1. Electrical Engineering, Hanyang university, Seoul, The Republic of Korea; 2. Korea Testing Certification, Gunpo, The Republic of Korea

1. Introduction Recently, permanent magnet synchronous motors with high efficiency are attracting attention due to the environment friendly policy. If a permanent magnet motor is used, the output density of the induction machine is higher than that of the conventional induction machine. A control method that reduces the friction between the railway vehicle and the rail through the lateral displacement force by the force due to the inclination in the lateral axis ramp has been studied in a vehicle composed of a permanent magnet synchronous motor having these advantages. When a railway vehicle passes through a steep curve or a place where the ground is not flat, it receives a force on the tilted side, and there is a risk of flange contact, squeal noise and derailment of the vehicle in worst case. In order to prevent this phenomenon, a resistance to external force is required internally in the vehicle. This paper suggests an algorithm that can assist gentle driving by using repulsive force when tilting by using lateral displacement force. The validity and usefulness of the proposed control algorithm is verified by experimental results using a small-scale bogie system However, in order to achieve advanced control, it is necessary to consider the mechanical characteristics of the vehicle. For this purpose, the characteristics of the vehicle when driving the front wheel only and the characteristics of the vehicle when driving only the rear wheel are respectively investigated. 2. The Actual model of Independently Rotating Wheelsets Observe these results to improve the algorithm considering all vehicle control In actual systems, the electrical and mechanical characteristics of the system are cross-coupled to each other, so the results of the electrical characterization obtained by simulation are different from the actual results. Therefore, the verification of the algorithm was performed through actual experiments. Also, the actual size of the bogie requires costly production time and space. Therefore, the vehicle model was scaled down in size as shown in Fig. 1. and the ratio was 1/125 in 1/5 of the length. It also increases the torque of the miniature vehicle model by installing a 6: 1 ratio reducer between the wheel and the motor. In addition, by in-stalling a laser sensor on the wheel, lateral displacement is detected and the lateral displacement resilience is controlled ac-cording to the displacement. In addition, as shown in Fig. 1. the test environment was configured to allow bogies to run through roller equipment instead of rails. The wheels of the reduced car and the rail wheels of the roller equipment come in contact with each other for operation. In addition, the small-scale roller levers are designed for slope and left and right curves. 3. The Control Strategy of the Lateral Displacement Restoring Force The motor of the small-scale vehicle to be used in the experiment is used as the PMSM. The block diagram of the combination of the lateral displacement restoration control algorithm and the PMSM control algorithm. The topology of the entire system IRWs is completed when a block corresponding to the right front wheel and be a total of four of the same topology. The torque required to start is referred to as Te, and the displacement is detected by the laser sensor whenever the lateral displacement is changed. The torque command inputted to the DSP by the command is added to each motor. Since this is PMSM, set d axis current value to 0 and control it by q- axis current command. The current command passes through the PID regulator to generate the command voltage. The command voltage determines the switching state of the three-phase inverter by three-phase conversion of the two phases using the position information received through the encoder, which is a position sensor, and the generated voltage is applied to the PMSM. the straight line driving of an independently rotating wheel sets and the restoring force against disturbance. A lateral force must be generated to recover the angle to avoid flange contact when disturbance is applied via the laser displacement sensor. Therefore, the steering torque of each motor is required. Independently controlled four wheels can be independently controlled to generate different lateral displacement restoring torques depending on the position of the bogie. when the disturbance occurs to the left, the torque of the motor corresponding to the However, in order to perform such control well, it is necessary control the vehicle in consideration of the mechanical characteristics due to the difference of the physical positions of the right side must be increased to return to the original state. to front wheel and the rear wheel, and to perform more advanced control in the case of the entire vehicle. Therefore, after confirming the characteristics through experiments, the whole vehicle is controlled considering the characteristic. The algorithm to obtain the advanced control is constructed. and the maximum lateral displacement restoration force is calculated after estimating the required lateral displacement force by taking the lateral displacement value as input. After that, the force is converted into torque, and then the front and rear wheels are instructed how to generate the restoring torque, respectively.

[1] Lama Mourad; Fabien Claveau; Philippe Chevrel "Direct and Steering Tilt Robust Control of Narrow Vehicles" IEEE Transactions on Intelligent Transportation Systems, Vol.15, No.3, pp1206-1215, Jan,2014 [2] S. F. Zhao, X. Y. Huang, Y. T. Fang, and J. Li, "Control Scheme for a High Speed Railway Traction System Based on High Power PMSM," *2015 6th Int. Conf. Power Electron. Syst. Appl.*, pp. 1–8, 2015. [3] B. Liang and S. D. Iwnicki, "Independently rotating wheels with induction motors for high-speed trains," *J. Control Sci. Eng.*, pp. 1–7, 2011 [4] J. Perez, L. Mauer, and J. M. Busturia, "Design of Active Steering Systems for Bogie-Based Railway Vehicles with Independently Rotating Wheels," *Veh. Syst. Dyn.*, vol. 37, pp. 209–220, 2002

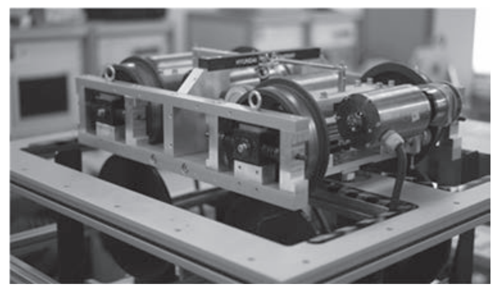

Fig. 1. Small-scale bogie system

Fig. 2. Composition for Right and Left Tilting Test

GP-08. Rotor Position Estimation of Permanent Magnet Synchronous Motor Based on Hall-effect sensors.

Y. Zhang[1,2], S. Chi[1,2], X. Li[1,2] and H. Yang[1,2]
1. Hebei University of Technology, Tianjin, China; 2. State Key Laboratory of Reliability and Intelligence of Electrical Equipment, Tianjin, China

Abstract : In this paper, a novel rotor position estimation method for permanent magnet synchronous motor (PMSM) using cost-effective hall-effect sensors is presented. Unlike traditional control system, the proposed method uses newton interpolation method and least square method to estimate continuous rotor position and speed information by obtaining discrete rotor locations from the hall-effect sensors. This method promises to eliminate the position-step of the rotor position estimation and provides stable and reliable rotor position, so that the stability of the closed - loop system is improved. Keyword: permanent magnet synchronous motor; Hall-effect sensors; rotor position estimation I. INTRODUCTION With the development of rare earth permanent magnet materials in the 1970s, the PMSM has been rapidly developed. The PMSM is widely used in the modern AC motion control system because of its advantages such as high efficiency, high power density and good dynamic behavior[1]. Accurate and reliable rotor position directly affects the control effect of PMSM. Traditional position sensors have high resolution and provide accurate position in real time, but increase the size and cost of the system and are limited by environmental constraints. Sensorless detection method reduces the system cost but has a large amount of calculation, requires high parameters and cannot guarantee the low speed performance. Hall sensors have the advantages of low cost, small size and high reliability, so it becomes a cost-performance option in low-resolution position sensors[2-4]. To obtain the rotor position with a simpler and more accurate way, an interpolation based on newton interpolation method and least squares method has been proposed in this paper. II. POSITION AND SPEED ESTIMATION METHOD USING THREE HALL-EFFECT SENSORS Three Hall sensors is placed 120 electrical degrees apart in stator winding. Therefore, six Hall signals are obtained for each electrical cycle, corresponding to 0°,60°,120°,180°,240°,and 300°, for 60 electrical degree between adjacent signals. A. Traditional Position Estimation Method In the traditional position estimation method, the average speed is calculated for each interval and then the acceleration is calculated to predict the speed at the next moment. Each Hall signal arrives, the difference between the estimated value and the actual rotor position will be forcibly corrected from the estimated value to the actual value, which will result in a step in the output of the position. B. Improved Rotor Position Estimation Method In order to solve the step phenomenon of the estimation results in the traditional estimation methods, an improved rotor position estimation method based on the newton interpolation method and least square method is developed in this paper which can be realized simply and eliminate the position-step. In Fig. 1(a) taking the position (angle) as the abscissa and the time as the ordinate, the coordinates of the discrete Hall signals are established. Let C point be the current Hall signal, A and B points be the two Hall signal closest to the current moment. Using A, B, C three discrete points, curve fitting by least square method. Fitting curve can be expressed as: $t=f(\theta)=a+b_1*\theta+b_2*\theta^2$ (1) Where a is a constant term in the above equations, b_1 and b_2 are the curve first-order terms and quadratic terms coefficient, respectively. The fitting curve is shown as a curve l_2 in Fig. 1(a) which used to predict the next Hall signal point, and $\theta_{k+1}=\theta_k+60°$ is substituted into equation (1) to obtain the next discrete point D'. Similarly, points A', B', C' and D' in Fig. 1(b) are estimated using Newton interpolation. B', C' and the latest D' three points are used to fitting curve of position by newton interpolation method. Fitting curve can be expressed as: $\theta=f(t)=a'+b'_1*t+b'_2*t^2$ (2) Where a' is a constant term in the above equations, b'_1 and b'_2 are the curve first-order terms and quadratic terms coefficient, respectively. The fitting equation is shown in the curve B'-C'-D' in Fig. 1(b), and is interpolated along the C'-D' segment of the curve. Assuming that the current moment is $t'_{k,x}$, the current rotor position (X point) can be expressed as: $\theta=\theta'_{k,x}=f(t'_{k,x})$ (3) The rotor position interpolated by newton interpolation method will be used for PMSM in real time. This method improves the accuracy of position and effectively solves the step phenomenon of traditional method to estimate rotor position. III. SIMULATIONS Simulations with Plecs have been carried out to study the proposed position estimation algorithm. Fig. 2 shows the estimated position and error of the two estimation methods when the motor decelerates. The error of the position calculated by the traditional estimation method reaches ± 2.5%, while the improved rotor position estimation method drops to ± 0.6 % or less. IV. CONCLUSIONS Results of the simulations verify the feasibility of the proposed improved rotor position estimation method over the traditional one.

[1] H. Mehta, U. Thakar, V. Joshi, K. Rathod and P. Kurulkar, “Hall sensor fault detection and fault tolerant control of PMSM drive system,” 2015 International Conference on Industrial Instrumentation and Control (ICIC), Pune, 2015, pp. 624-629. [2] Yong Zhao, Wenxin Huang, Jufeng Yang, Feifei Bu and Saide Liu, “A PMSM rotor position estimation with low-cost Hall-effect sensors using improved PLL,” 2016 IEEE Transportation Electrification Conference and Expo, Asia-Pacific (ITEC Asia-Pacific), Busan, 2016, pp. 804-807. [3] X. Zhang and W. Zhang, “An improved rotor position estimation in PMSM with low-resolution hall-effect sensors,” 2014 17th International Conference on Electrical Machines and Systems (ICEMS), Hangzhou, 2014, pp. 2722-2727. [4] L. Kreindler, I. Iacob, G. Casaru, A. Sarca, R. Olteanu and D. Matianu, “PMSM drive using digital hall position sensors for light EV applications,” 2015 9th International Symposium on Advanced Topics in Electrical Engineering (ATEE), Bucharest, 2015, pp. 199-204.

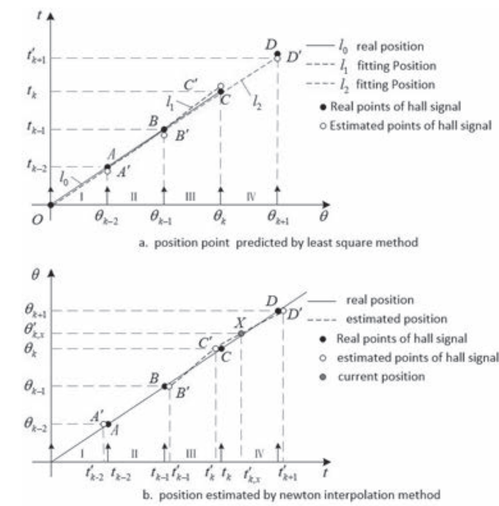

Fig. 1. Improved Rotor Position Estimation Method

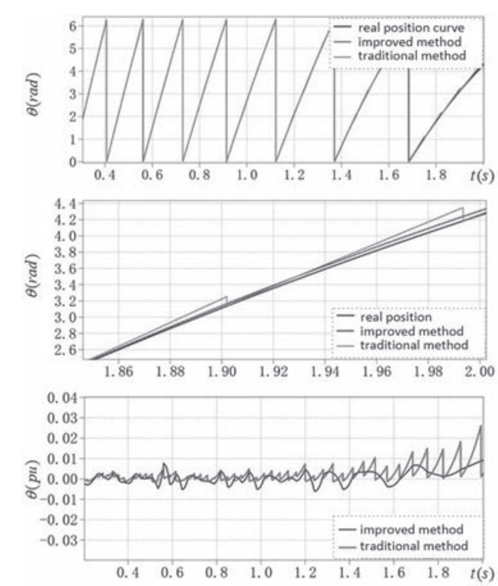

Fig. 2. rotor position and position error

GP-09. Dynamic DC link Voltage Control Strategy of Electric Vehicles Considering the Cross Saturation Effect.

H. Li[1], J. Gao[1], S. Huang[1] and P. Fan[1]
1. Hunan University, CHANGSHA, China

I. INTRODUCTION The interior permanent magnet synchronous machine (IPMSM), which could generates reluctance torque in flux weakening region to enhance the motor performance and efficiency, is widely applied in electric vehicles (EV) [1, 2]. In order to dig out the maximum potential of the traction system of EV further, dynamic DC link voltage control strategies has been explored by several researchers [3, 4]. Generally speaking, keeping a low DC link voltage at low operating speed could reduce the switching losses of the inverter while boosting its value at high speed could benefit the flux weakening operation [5] However, the IPMSM parameters will become different with operating conditions, for example, the inductance and the magnetic characteristic will change with current due to the cross coupling and magnetic saturation effect (omitted to cross saturation effect) [6]. Therefore, the conventional control strategy of IPMSM ignoring the cross saturation effect needs to be revised. II. DC LINK VOLTAGE CONTROL STRATEGY The overview of the proposed control strategy is shown in Fig.1. The current vector adjustment strategy is discussed in [6]. The FEM simulation is conducted to obtain the value of inductance depending on stator current. Two dynamic models are set up to evaluate the performance of the control strategy influenced by the cross saturation effect, as shown in Figure 2. MODEL I represents the control strategy taking the cross saturation effect into consideration. MODEL II stands for the fixed parameter model. It demonstrates that the cross saturation will degrade dq-axis voltage value in high speed range, however the output torque still meet its requirement. The proposed control strategy can help the current trajectory tract the Maximum Torque per Ampere (MTPA) curve perfectly in low speed region and fit the constant torque line at high speed without breakthrough the current limit circle. As shown in Fig. 2 (b), the reference value of the DC link voltage grows up as the speed increase. Once the speed of motor beyond the nominal value, which is 1500 rpm, the DC link voltage reference is kept at 700V, therefore, the flux weakening operation can be delayed meanwhile the maximum potential of inverter can be fully used. In Fig.2 (b), (e) and (f), it can be seen that the bus voltage in MODEL I is lower than it in MODEL II below the nominal speed, thus, it indicates that the proposed dynamic DC link voltage control strategy considering the cross saturation effect can reduce the switching loss and related junction temperature of electronic devices, which is proportional to the bus voltage. The performance of IPMSM using the proposed control strategy under different models will be fully described in the final paper and the control strategy translates the voltage and torque required incremental value into current adjustment amount to modify current control signals will be investigated in full paper.

[1]C. Mademlis, I. Kioskeridis, and N. Margaris, "Optimal efficiency control strategy for interior permanent-magnet synchronous motor drives," IEEE Trans. Energy. Convers., vol. 19, no. 4, pp.715-723, Dec. 2004. [2] Stephan Günther, Stefan Ulbrich, Wilfried Hofmann, "Driving Cycle-Based Design Optimization of Interior Permanent Magnet Synchronous Motor Drives for Electric Vehicle Application" International Symposium on Power Electronics, Electrical Drives, Automation and Motion, pp.25-30, Jun. 18-20, 2014.X. [3]Jongwon Heo, Kentaro Matsuo, Pisithkun Hen, and Keiichiro Kondo, "Dynamics of A Minimum DC Link Voltage Driving Method to Reduce System Loss for Hybrid Electric Vehicles," 2017 IEEE International Electric Machines and Drives Conference (IEMDC), pp. 1-7, 2017. [4] A. Imakiire, M. Hikita, K. Yamamoto, and R. Yonemori, "Investigation of Calculation Method of Losses in PWM Inverter with Voltage Booster using both DC link Voltage Control and Flux Weakening Control," International Power Electronics Conference(IPEC-Hiroshima 2014. [5]A. Imakiire, M. Hikita, K. Yamamoto, R. Yonemori, "Investigation of Calculation Method of Losses in PWM Inverter with Voltage Booster using both DC link Voltage Control and Flux Weakening Control", International Power Electronics Conference, pp. 689-693, May, 2014. [6]Huimin Li, Jian Gao, Shoudao Huang and Peng Fan, "Optimal current trajectory control of PMSM considering cross saturation effects," 2017 IEEE International Magnetics Conference (INTERMAG), pp. 1-1, 2017.

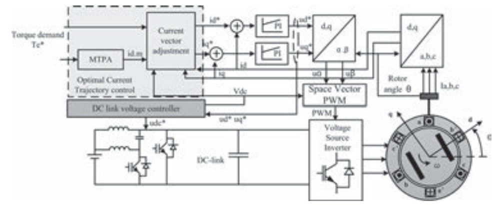

Fig. 1.

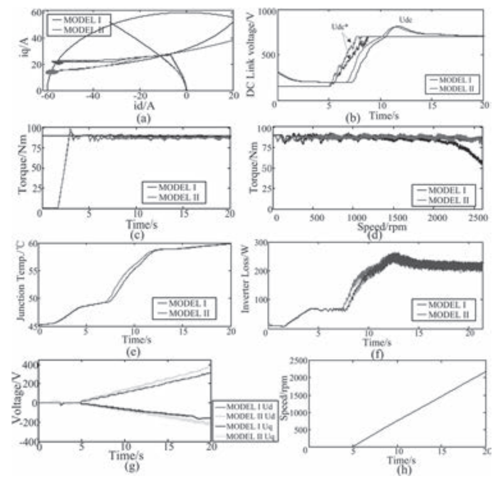

Fig. 2.

GP-10. Brushless Wound Rotor Synchronous Machine with Third Harmonic Field Excitation using Single Inverter.

M. Ayub[1], S. Bukhari[2], G. Sirewal[1] and B. Kwon[1]

1. Electronic Systems Engineering, Hanyang University ERICA Campus Ansan 15588, Korea, Ansan, The Republic of Korea; 2. Department of Electrical Engineering, Sukkur IBA University, Sukkur, Pakistan

1. Introduction: The recent fluctuating prices of rare earth magnet used in PMSM has encouraged the researchers towards the other candidates, such as, PM-assisted synchronous reluctance machine (PMa-SyRM) and wound rotor synchronous machine (WRSM). Whereas, in WRSM, the assembly of brushes and slip rings connect the machine to its excitation system on the rotor side. To get rid of brushes and slip rings, because of wear and tears in the long run, several brushless topologies have been proposed in the literature [1-3]. In [1], two inverters are used to supply different amplitude currents to two-different portion of the stator windings to generate the sub-harmonic airgap magnetomotive force (MMF). This sub-harmonic component then couples with the corresponding sub-harmonic winding (HW) on the rotor. The use of two inverters in this topology makes it less suitable for practical applications. In [2], a controllable third harmonic (TH) zero-sequence current is generated using single inverter topology, which induces the current into a dedicated rotor HW. The rotor winding current is then rectified and supplied to the main field winding. Although, this topology used single inverter, but six extra thyristor switches are needed to generate TH currents, which switches during the positive and negative half cycles to generate zero sequence currents. The switching losses and high torque ripple are the other drawbacks. In [3], a spatial TH zero sequence MMF is generated with open winding by means of two inverters. one inverter is used to supply the fundamental current and a second inverter is utilized to inject the TH current into the three-phase open stator winding terminals. A HW as well as a conventional field winding are installed on the rotor, whereas, the HW is used to induce and then rectify the magnetic field generated by the airgap TH-MMF. The field winding is used to produce the rotor main magnetic field, which then interact with stator fundamental MMF for torque production. The disadvantage of this scheme is the utilization of two inverters, which increases the cost and size of the overall system. This paper presents a new scheme to produce time generated airgap MMF having two components, i.e. fundamental and a TH, using single inverter. The time generated TH-MMF is then induced in the rotor HW. After rectification, the rotor field winding is excited to realize the brushless operation. 2. Topology and working principle: The machine topology is shown in Fig. 1, in which stator winding current is supplied by single inverter. The stator winding has a semi-open configuration with the help of two back to back diodes to avoid suppression of third order current component generated by special gating pulses in the inverter. There are two separate windings on the rotor i.e. HW and the field winding. Both windings are connected through a bridge rectifier mounted in the rotor periphery. The TH-MMF component is induced in the consistent pole HW. After induction in the HW, the current is fed to the main field winding through rotating bridge rectifier. The machine (18s4p) winding configuration is shown in Fig. 2. The TH current component is generated by injection of TH control signal in the inverter gating switching pulses. The block diagram for generation of the inverter gate switching pulses is shown in the Fig. 3. The reference voltage V_{ref} is added with signal having frequency three times of fundamental frequency (zero sequence). The resultant is then passed through comparator which compares the modified signal with carrier signal and desired output pulses are generated as shown in Fig. 4. The back to back diodes are used to avoid the suppression of triplen current harmonic at the star point of the stator winding as shown in Fig. 1. The 3-phase currents applied to the stator windings are given in (1) $i_a = I_m (\sin \omega t + n \sin 3\omega t)$ $i_b = I_m (\sin (\omega t - 2\pi/3) + n \sin 3(\omega t - 2\pi/3))$ (1) $i_c = I_m (\sin (\omega t + 2\pi/3) + n \sin 3(\omega t + 2\pi/3))$ The corresponding machine airgap MMF is shown in (2) $F_a = i_a N_{\psi 1} (\sin \theta_e + \sin 3\theta_e)$ $F_b = i_b N_{\psi 1} (\sin (\theta_e - 2\pi/3) + \sin 3(\theta_e - 2\pi/3))$ (2) $F_c = i_c N_{\psi 1} (\sin (\theta_e + 2\pi/3) + \sin 3(\theta_e + 2\pi/3))$ The induced emf in the rotor HW is given in (3), $emf_h = 6\, d\Psi_h /dt = 18 N_h N_{\psi 1} I_3\, \omega \sin 3(2\omega t + \theta_o) / R_g$ (3) The induced EMF is rectified through rotating bridge rectifier mounted on the rotor periphery, and rectified direct current (DC) is supplied to the rotor main field winding. 3. Analysis and performance comparison: 2-D FEA analysis is performed for 60 cycles to get steady state rotor currents and output torque; the stator winding of the machine is provided with the current shape containing two components. According to the principle already discussed, the TH-MMF is induced in the rotor HW. The induced harmonic current and field current is shown for single cycle in steady state region in Fig. 5. The output torque for single cycle in steady state region of the machine is shown in Fig. 6. Consequently, the proposed brushless topoplogy is used to fed the field winding for stable torque generation in steady state and hence, the brushes and slip rings are avoided. The detail electromagnetic analysis will be provided in full paper.

[1] Qasim Ali, Thomas A. Lipo, Kwon, Byung-il "Design and Analysis of a Novel Brushless Wound Rotor Synchronous Machine*" IEEE Trans. on Magn.,vol. 51, no. 11, Nov. 2015, Art. ID 8109804* [2] G. Jawad, Q. Ali, T. A. Lipo and B. I. Kwon, "Novel Brushless Wound Rotor Synchronous Machine With Zero-Sequence Third-Harmonic Field Excitation," *IEEE Transactions on Magnetics, vol. 52, no. 7, pp. 1-4, July 2016* [3] F. Yao, Q. An, X. Gao, L. Sun and T. A. Lipo, "Principle of Operation and Performance of a Synchronous Machine Employing a New Harmonic Excitation Scheme," *IEEE Transactions on Industry Applications, vol. 51, no. 5, pp. 3890-3898, Sept.-Oct. 2015.*

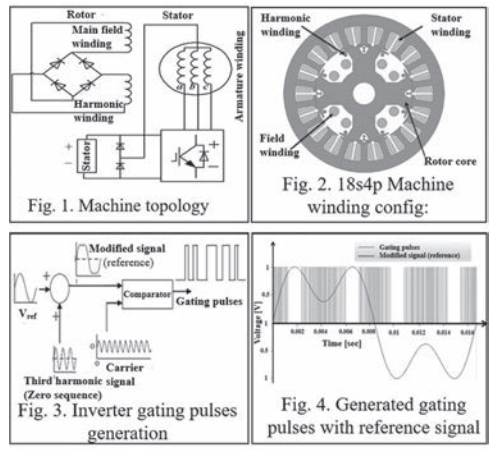

Fig. 1. Machine topology
Fig. 2. 18s4p Machine winding config:
Fig. 3. Inverter gating pulses generation
Fig. 4. Generated gating pulses with reference signal

Fig. 1, Fig. 2, Fig. 3, Fig. 4.

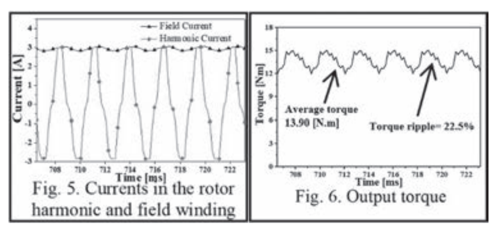

Fig. 5. Currents in the rotor harmonic and field winding
Fig. 6. Output torque

Fig. 5, Fig. 6.

GP-11. Investigations on the Sensorless Position Estimation of an IPMSM with Short-Circuited Rotor Windings.

C. Hittinger[1], D. Thyroff[1] and I. Hahn[1]
1. Institute of Electrical Drives and Machines, University of Erlangen-Nuremberg, Erlangen, Germany

1.) Introduction The mechanical encoder of an electrical machine can be omitted in certain cases. Applications, where the requirements are fulfilled, can be realized by using sensorless control. At very low speeds the commonly used methods based on the back-EMF are not suitable [1]. Therefore, a saliency, based on the position-dependent electromagnetic properties of the machine configuration, is required to correctly estimate the rotor position with signal injection methods. The main drawback is the occurrence of cross-coupling effects between the HF-inductances, if some machine parts are saturated [2], which can result in a reduced magnetic anisotropy [3–5] and a worsened capability of estimating the rotor estimation. A special machine topology which provides this property was derived in [6, 7] and was investigated further in [8–10]. In this concept, the high frequency magnetic flux gained by the signal injection method in the field-oriented d-axis is suppressed by attaching a short-circuited electrical winding (SC-winding) on the rotor of the machine. It can be applied on machine topologies without an inherent (e.g. geometric) electromagnetic saliency. After performing analytical simulations including the frequency behavior [9], additional investigations using the frozen permeability method (FPM) within the finite element (FE) method, simulations were carried out to evaluate the performance of this new concept [8]. These results will be verified by measurements on an experimental setup. In contrast to [8], permanent magnets (PMs) will be included on the rotor as well, which result in an inherent magnetic saliency due to their low magnetic permeability. For this case, the performance of SC-windings on the rotor for sensorless position estimation will be investigated as well. 2.) Fundamentals of Test Signal Injection and the FPM In general, the stationary as well as the dynamic behavior of an electrical machine can be described by its voltage equations including the resistive and inductive quantities of the machine. This approach can also be used for the test signal methods. In [8, 9] these equations are derived including differential quantities, which means, that they are only depending on the injected test signal. Based on this, an evaluation of the machine can be achieved. The main property for the self-sensing performance are a high difference of the self-inductances and a low mutual inductance. The frozen permeability method is used as a compromise between stationary DC (no simulation of frequency behavior) and transient AC-simulations (time-consuming simulations). Using the FPM, nonlinear magnetostatic DC-solutions are generated for taking local saturation effects into account. For this solution, the permeability tensor in the middle of each element of the FE mesh is saved and, hence, can be taken as a previous solution for the following linear AC simulation. This means, that the influence of the AC test signal can be evaluated depending on the actual saturation level of the machine. Another advantage of the FE simulations is that there are no iterative steps necessary to calculate the currents in the SC-windings, which is an important parameter to estimate additional I^2R-losses of this concept. 3.) Results The results of the simulations will be compared to those of the measurements. The measurements are performed with three linear power amplifiers. The DC operating points are provided in rotor-fixed coordinates, whereas the current test signal is injected in only one of the three phases. The AC currents in the neighboring phases are controlled to zero and the voltage response is evaluated. First, the estimation error will be discussed. By comparing the results for measurements and simulations in Fig.1, it can clearly be seen, that the error only reaches very small values, which means a good performance for sensorless position estimation. Additional, the values of the measurements are slightly smaller, especially at operating points with higher currents. This behavior can be described by the modeling of the frequency behavior based on virtual eddy current coils as presented in [9]. The discussion will be included in the final paper. Furthermore, a comparison of the measured and the simulated currents in the SC-windings for evaluating the I^2R-losses will be given. Next, the improvement of the sensorless position estimation by using additional short-circuited windings on a rotor including PMs will be discussed. The width and the position of the SC-windings are identical to the setup without PMs. As can be seen in Fig. 2 the estimation error for the setup with SC-windings is significantly reduced to the initial case over almost the whole operating area. The reasons for this behavior will be discussed in detail within the final paper by evaluating differential self and mutual inductances. Summing up, the concept of SC-windings on the rotor can be adapted on a machine with three phases and buried PMs. 4.) Conclusion The FEA using FPM was verified by measurement results. The advantages and the limitations of this method will be discussed within the full paper. It is shown that the concept with SC-windings on the rotor is still suitable when using buried PMs on the rotor. The sensorless performance is increased by the additional windings over the whole operating area.

[1] I. Hahn, "Differential magnetic anisotropy - prerequisite for rotor position detection of PM-synchronous machines with signal injection methods," in *2010 Symposium on Sensorless Control for Electrical Drives (SLED)*, Padova, Italy, pp. 40–49. [2] M. Seilmeier, "Modelling of electrically excited synchronous machine (EESM) considering nonlinear material characteristics and multiple saliencies," in *Power Electronics and Applications (EPE 2011), Proceedings of the 2011-14th European Conference on*, pp. 1–10. [3] P. Guglielmi, M. Pastorelli, and A. Vagati, "Cross-Saturation Effects in IPM Motors and Related Impact on Sensorless Control," *IEEE Trans. on Ind. Applicat.*, vol. 42, no. 6, pp. 1516–1522, 2006. [4] J. Graus, S. Luthardt, and I. Hahn, "Influence of rotor saturation on the differential inductances of PM-synchronous machines with concentrated winding," in *2013 15th European Conference on Power Electronics and Applications (EPE)*, Lille, France, pp. 1–10. [5] J. Graus, A. Boehm, and I. Hahn, "Influence of stator saturation on the differential inductances of PM-synchronous machines with concentrated winding," in *2012 IEEE Symposium on Sensorless Control for Electrical Drives (SLED)*, Milwaukee, WI, USA, pp. 1–7. [6] A. Faggion, S. Bolognani, and N. Bianchi, "Ringed-pole permanent magnet synchronous motor for position sensorless drives," in *2009 IEEE Energy Conversion Congress and Exposition. ECCE 2009*, San Jose, CA, pp. 3837–3844. [7] J. Graus, A. Rambetius, and I. Hahn, "Comparison of the resistance- and inductance-based saliency of a PMSM due to a short-circuited rotor winding," in *2014 International Power Electronics Conference (IPEC-Hiroshima 2014 ECCE-ASIA)*, Hiroshima, Japan, pp. 270–277. [8] C. Hittinger and I. Hahn, "Modeling of an IPMSM with Short-Circuited Rotor Winding for Sensorless Position Estimation by FEA Using the Frozen Permeability Method," in *IEEE, IECON 2017, 43rd Conference of Industrial Electronics Society*, pp. 1–8. [9] C. Hittinger, D. Thyroff, and I. Hahn, "Modelling and examination of the influence of a short-circuited rotor winding for saliency tracking of a machine with a three-phase single-tooth winding," in *2017 IEEE International Electric Machines and Drives Conference (IEMDC): 21-24 May 2017*, Miami, FL, USA, 2017, pp. 1–8. [10] A. Faggion, E. Fornasiero, N. Bianchi, and S. Bolognani, "Sensorless capability of fractional-slot surface-mounted PM motors," in *Drives Conference (IEMDC)*, Niagara Falls, ON, Canada, pp. 593–598.

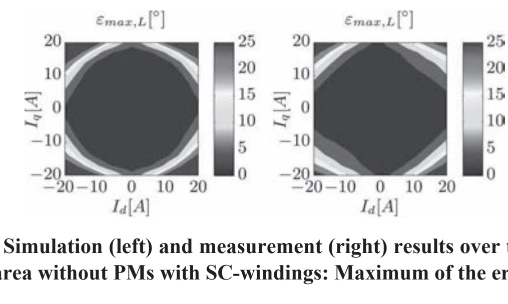

Fig. 1. Simulation (left) and measurement (right) results over the operating area without PMs with SC-windings: Maximum of the error.

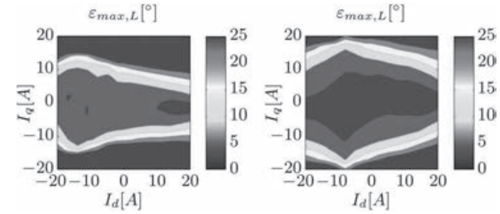

Fig. 2. Simulation results over the operating area with PMs: Maximum of the error with(right) and without (left) SC-windings.

GP-12. Analysis of Pole-Slot Combination for Saliency-based Sensorless Controlled IPMSM Considering Noise and Vibration Characteristics.

M. Lim[2,1], *J. Jung*[2], D. Ahn[1] and J. Hong[1]
1. Automotive Engineering, Hanyang University, Seoul, The Republic of Korea; 2. Hyundai Mobis, Yongin, Gyeonggi-do, The Republic of Korea

I. Introduction Today, interior permanent magnet synchronous motors (IPMSMs) are widely used because of their advantages such as high output and torque density. In order to implement a high-performance system by vector-controlling the IPMSM, it is essential to use a position sensor to detect the rotor position. However, the importance of sensorless control, which is controlled without a position sensor, is emphasized because of the increase of price and volume of system, increase of complexity and decrease of reliability. In addition, the importance of sensorless controlled machines is also mentioned for the purpose of system failure control. In IPMSMs, the reluctance of the *d*-axis and the *q*-axis is different because the position of the permanent magnet (PM) and the configurations of the rotor core is not spatially uniform. This is due to the saturation phenomenon of the magnetic flux path in *d*-axis caused by the PM flux, and at the same time, the reluctance of the PM existing on the *d*-axis is significantly higher than that of the rotor core. Therefore, by using the high-frequency signal injection method, the inductance waveforms affected by the PM on the *d*-axis can be obtained, and the position of the rotor can be estimated [1]. If the *d*-axis of the PM is the position where the voltage injection angle is 0 degree, the inductance becomes the smallest value due to the reluctance at this time [2]. However, in the conventional IPMSM, it is difficult to obtain the inductance waveform having the smallest value in the *d*-axis along the voltage injection angle when the rotor position and the load conditions are changed. This is because the distributions of the magnetic saturation and reluctance are changed. Therefore, in conventional IPMSM, the *d*, *q*-axis inductance waveform is varied with them, and it is hard to estimate the rotor position precisely [3], [4]. Therefore, appropriate decision of pole-slot number combination for the sensorless controlled IPMSM is important. II. Analysis of IPMSMs According to Pole-Slot Combinations In this study, the appropriate combination of pole-slot number for sensorless controlled IPMSM is determined by examining sensorless controllability as well as noise and vibration characteristics of the several models. The proposed models have four different pole-slot combinations including not only pole-slot ratio of 2:3 such as 12-pole 18-slot, but fractional slot combination such as 8-pole 9-slot, 10-pole 12-slot, and 16-pole 15-slot. The characteristics of the four models are analyzed, and the appropriate pole-slot combination for the sensorless-oriented IPMSM is proposed. *A*) Analysis of Noise and Vibration Characteristics The radial force distribution is shown in Fig. 1 to visually confirm the noise and vibration characteristics. If the radial force distribution in the air gap is symmetrical, the radial forces in the opposite direction cancel each other out, which is advantageous for noise and vibration characteristics. It infers that noise and vibration characteristics of 10-pole 12-slot and 16-pole 15-slot models is poor compared to those of the other two models due to the asymmetrical radial force distribution [5]. *B*) Analysis of Sensorless Controllability The *d*, *q*-axis inductance waveforms as the response of injected high frequency voltage signal according to the change of the rotor positions and load conditions are analyzed to evaluate the sensorless controllability. The inductance waveforms of the two models 12-pole 18-slot and 16-pole 18-slot are analyzed except for the other two models 10-pole 12-slot and 16-pole 15-slot with poor noise and vibration characteristics among the four proposed models. As shown in Fig. 2, the magnitude and the minimum position of the *d*-axis inductance of the 16-pole 18-slot model are changed much more greatly according to the current phase angle rather than those of the 12-pole 18-slot models. Conclusively, considering the various input currents and current phase angles, the 2:3 pole-slot combination machine such as 8-pole 12slot, 12-pole 18-slot, and 16-pole 24-slot is generally easier for saliency-based sensorless drive rather than the fractional pole-slot combination machines. III. Future Work In the full paper, equations to analyze the noise and vibration characteristics including force order will be described. Also, the analysis method of the inductance waveforms to evaluate the sensorless controllability will be explained in detail. In addition, considering the analysis results of the proposed models, the sensorless-oriented IPMSM is designed. Lastly, the validity of the proposed analysis methods and simulation results are verified through the experiments.

[1] Sungmin Kim, Jung-Ik Ha, and Seung-Ki Sul, "PWM Switching Frequency Signal Injection Sensorless Method in IPMSM," *IEEE Trans. on Industry Applications*, Vol. 48, No. 5, pp. 1576-1587, Sept.-Oct. 2012. [2] Myung-Seop Lim, Seung-Hee Chai, and Jung-Pyo Hong, "Design of Saliency-Based Sensorless-Controlled IPMSM With Concentrated Winding for EV Traction," *IEEE Trans. on Magnetics*, Vol.52, No.3, Art. ID 8200504, March 2016. [3] N. Bianchi, and S.Bolognani, "Influence of Rotor Geometry of an Interior PM Motor on Sensorless Control Feasibility," IEEE Tans. Industry Applications, Vol. 43, No. 1, pp. 87-96, Jan./Feb. 2007. [4] Z. Q. Zhu, and L. M. Gong, "Investigation of Effectiveness of Sensorless Operation in Carrier-Signal-Injection-Based Sensorless-Control Methods," *IEEE Trans. on Industrial Electronics*, Vol. 58, No.8 pp. 3431-3439, Aug. 2011. [5] Tao Sun, Ji-Min Kim, Geun-Ho Lee, Jung-Pyo Hong, and Myung-Ryul Choi, "Effect of Pole and Slot Combination on Noise and Vibration in Permanent Magnet Synchronous Motor," *IEEE Trans. on Magnetics*, Vol.47, No.5, pp. 1038-1041, May 2011.

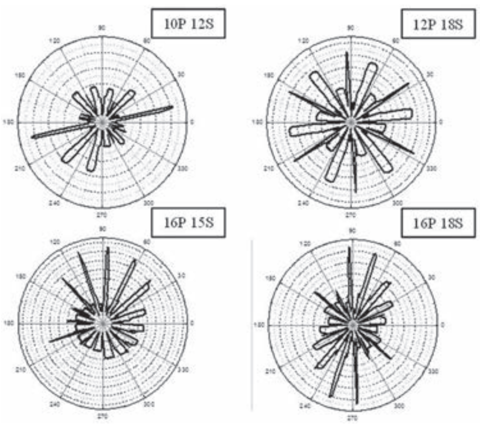

Fig. 1. Radial force distributions according to the pole-slot combination

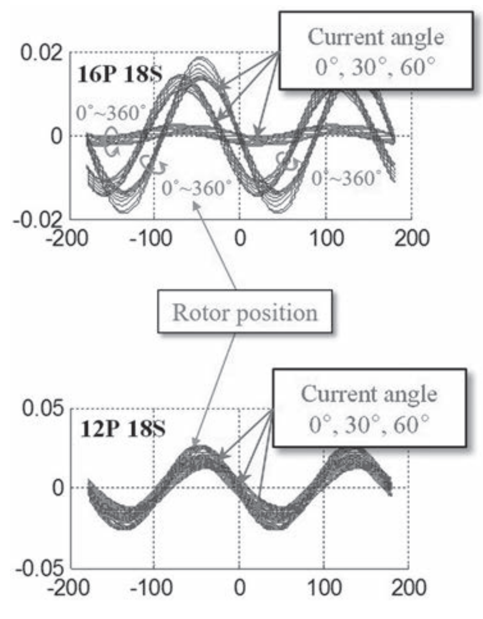

Fig. 2. Variations of the inductance waveforms according to the rotor position and current phase angle

GP-13. Position Sensorless Control of Switched Reluctance Motors Eliminating Mutual Inductance Effect.

H. Wang[1], H. Cai[1], *M. Li*[1] and S. Shen[1]
1. Hunan University, Chang Sha, China

Abstract — Mutual inductance effect between the adjacent phases is prominent for Switched Reluctance Motor in status of the adjacent phase energized simultaneously. Consequently, the mutual coupling will distort the response current profile of the injection voltage phase, thereby affecting the position estimation precision. This paper presents a unique rotor position estimation approach to eliminate the mutual inductance effect by employing the phase current slope difference method. By setting a low threshold and a high threshold, a series of voltage pulses are injected in idle phase alternately synchronized with the chopping current control. Without a prior knowledge of mutual inductance and any additional position sensor, a precisely estimated rotor position is achieved. A dynamic model of a 12/8 SRM model is established to evaluate its validity and both of simulation results and experimental evaluation indicate that the proposed sensorless control can be accomplished with an adequate precision. *Index Terms*—Switched reluctance motor, position sensorless, mutual inductance, rotor position. I. INTRODUCTION Switched reluctance motor(SRM)makes its entrance into a variety of applications since its reliability,robustness and low cost characteristic. Accurate rotor position is essential to the control of an SRM in the four quadrants. Both of turn-on angle and turn-off angle are the key parameters which are associated with the load and speed. The appropriate choice and optimal tuning is a requirement of accommodating a good performance of the SRM. High-resolution encoder such as incremental encoder,hall sensors and rotary transformer are typical provided to obtain the rotor position information. However,the sensor devices are subject to be affected when located in a hostile environment such as electrical noisy and a hot state. With the purpose of eliminating the additional sensors and making the cost reduction, a great amount of sensorless approaches have been demonstrated. By employing only one current sensor and decoupling the excitation current, the rotor position of the SRM is estimated precisely and the performance is investigated fully in [1]. Most of the pulse injection method is focused on the low speeds, the rotor position is determined by injecting a single pulse in the non-conduction phase at high speed in [2], the proposed pulse injection strategy is suited both of the low-and high speed condition. Magnetic characteristic is fully utilized to estimate the rotor positon in [3], the voltage pulse is injected the idle phase and the negative torque produced by the residual current is also eliminated. Traditionally, the idle phase of the SRM is injected pulse voltage with a quite short duration, the response current is adopting to estimate the rotor positon, nevertheless, the amplitude of which is greatly affected by the mutual inductance produced by the chopping current of the conducting phase, furthermore, the condition will be deteriorated as the chopping current increasing. To solve the problem, this paper proposes a sensorless control technology to eliminate the effect of mutual inductance. The idle phase windings are energized by a series of voltage pulse in sequence and the rotor position can be identified by employing the self-inductance characteristics in real time. Meanwhile, the estimation position error caused by mutual inductance is fully analyzed. II.THE PRINCIPLE of SRM POSITON ESTIMATION CONSIDERING MUTUAL INDUCTANCE The flux density distribution map of single-phase excitation and two-phase excitation for a 12/8 SRM are described in Fig.1 (a), (b), respectively. Compared with the single-phase excitation mode, the two-phase excitation mode is defined as the short magnetic excitation and magnetic circuit are mutual influence. In figure 1 (c), when individual phase is conducted, one can note that the self-inductance curves will appear the saturation phenomenology. As described in figure 1 (d), when the adjacent phase are energized simultaneously, the mutual inductance appears. It indicates that the absolute value of mutual inductance increases as the energized current increasing and the value approaches 8.61% compared with the self-inductance. Following, the Influence of mutual inductance on self-inductance estimation and position estimation is analyzed. Furthermore, making the voltage pulses pulse injection synchronized with the the sequence of chopping control is the resolution to eliminate the mutual inductance effect in this paper. III. SIMULATION AND NEXPERIMENTAL RESULTS The comparative experiment is implemented by adopting the proposed approach,the motor is under overload state (given current 45A), the simulation waveforms are shown in Fig.2. The maximum position error of the proposed control scheme is about 1.55 degrees. The experimental waveforms shown in figure 2 indicate that the estimation positon error is about 2.6 degrees, more precisely than that employing the conventional approach.

[1]Gan, C., et al., "Online Sensorless Position Estimation for Switched Reluctance Motors Using One Current Sensor," IEEE Transactions on Power Electronics,vol.31,no.10,pp.7248-7263.2016. [2]Ofori, E., et al., "A Pulse-Injection-Based Sensorless Position Estimation Method for a Switched Reluctance Machine Over a Wide Speed Range," IEEE Transactions on Industry Applications,vol.51,no.5,pp.3867-3876.2015. [3] Guo, H. J., et al., "A new sensorless drive method of Switched Reluctance Motors based on motor's magnetic characteristics," IEEE Transactions on Magnetics,vol.37,no.4,pp.2831-2833.2001.

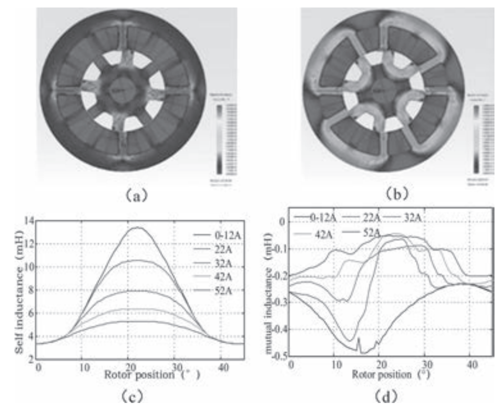

Fig. 1. (a)flux density distribution map of SRM at single phase condition mode(b)flux density distribution map of SRM at double1 phase condition mode(c) self-inductance curve at different saturation current(d) mutual inductance profile

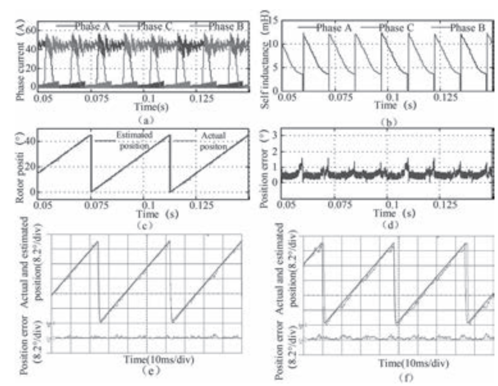

Fig. 2. Simulation results and experimental waveforms(a)phase current(b)self-inductance profile(c)estimated and actual position(d) position estimated error(e)estimated positon with proposed method(f) estimated positon with traditional approach

GP-14. Maximum torque per ampere control for hybrid excited switching flux permanent magnet machines.

X. Liu[1], D. Xing[1], Q. Wang[1] and S. Li[1]
1. State Key Laboratory of Reliability and Intelligence of Electrical Equipment, Hebei University of Technology, Tianjin, China

Permanent magnet synchronous machines (PMSMs) have been widely used for electric vehicles (EVs) and hybrid electric vehicles (HEVs) due to their high efficiency and high power density. However, due to the constant PM flux linkage, a negative d-axis current will be used in the flux weakening region, which increases the copper loss and the risk of irreversible demagnetization. The hybrid excited PM machines, which also employ dc field winding to adjust the air-gap flux density, have been developed. In Fig. 1, the 12/10 hybrid excited switching flux permanent magnet (HESFPM) machine, which has a double salient structure, is presented [1]. The PMs, armature windings and dc field windings are located in the stator, while in the rotor there is no PM or coil. In the high-speed region, both d-axis and dc field currents can be used to weaken the flux-linkage in d-axis. Therefore, in this paper the effectiveness of d-axis and dc field current on adjusting the d-axis flux-linkage will be investigated. A novel control method with the optimal ratio of d-axis current to dc field current is presented to realize the maximum torque per ampere control. In the d-q frame, the flux-linkage and voltage of HESFPM machie can be written as: $\psi_d=L_d i_d+\psi_f$ $\psi_q=L_q i_q$ $\psi_f=\psi_{pm}+\psi(i_f)$ $U_d=R_s i_d+d\psi_d/dt-\omega_e\psi_q$ $U_q=R_s i_q+d\psi_q/dt+\omega_e\psi_d$ $U_f=R_f i_f+d\psi_f/dt$ The electromagnetic torque can be expressed as: $T_e=1.5pi_q(\psi_f+i_d(L_d-L_q))$ where ψ_d, ψ_q are the flux-linkage in d- and q-axis respectively, $\psi(i_f)$, ψ_{pm} are the flux-linkage generated by filed excitation and permanent magnets respectively; U_d, U_q are the voltage in d- and q-axis respectively, U_f is the voltage of field winding; R_s, R_f are the armature winding and field winding resistance respectively; ω_e, p, T_e stand for electrical rotor speed, the pole pairs and the electromagnetic torque respectively. Fig.2. shows the d-axis flux-linkage against field excitation. It shows that almost linear relationship between d-axis flux-linkage and field excitation can be observed. At low speed, the copper loss can be expressed by: $P_{cu}=1.5R_s(i_d^2+i_q^2)+R_f i_f^2$ By using the extended Lagrange multipliers method, the torque constraints will be: $L(i_d,i_q,i_f,\lambda)=1.5R_s(i_d^2+i_q^2)+R_f i_f^2+\lambda(1.5pi_q(\psi_f+i_d(L_d-L_q))-T_e)$ where λ denotes the Lagrange multipliers. By setting the partial differentiation of (5) with respect to and to zero, the d-axis and field excitation reference current can be obtained by: The d-axis and field excitation reference current can be obtained by: $i_{dref}=2R_f(L_d-L_q)i_{fref}/(3R_s\, d\psi_f/di_f)$ $i_{fref}=3R_s d\psi_f/di_f(-\psi_f+\mathrm{sqrt}(\psi_f^2+4(L_d-L_q)^2 i_{qref}^2)/(4R_f(L_d-L_q)^2$ Thus, the copper loss minimization control strategy for HESFPM machine is developed in Fig.3. As shown in Fig. 4, the simulation results indicate the benefit of the proposed method. Compared with the conventional method ($i_d=0$), the proposed method can reduce the 26.43% copper loss at 400rpm speed and 1.5 Nm. In the full paper, the experimental results will be presented to verify the minimum copper loss control.

Reference: [1] E. Hoang, M. Lecrivain, and M. Gabsi, 'A new structure of a switching flux synchronous polyphased machine with hybrid excitation,' in *Proc. Eur. Conf. Power Electronics and Applications*, 2007, pp. 1-8. [2] N.Pothi, Z.Q.Zhu, 'A new control strategy for hybrid-excited switched-flux permanent magnet machines without the requirement of machine parameters'. *IET Int. Conf. on Power Electronics, Machines and Drives (PEMD2014)*, April 2014, pp. 1-6 [3] Jilong Zhao, Mingyao Lin, Da Xu, 'Minimum-copper-loss control of hybrid excited axial field flux-switching machine,' *lET Electric Power Applications,* vol. 10, no.2, pp. 82-90, 2016

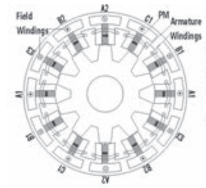

Fig.1 Topology of HESFPM machine

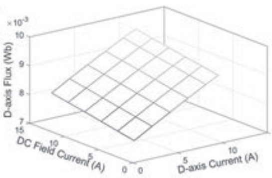

Fig.2 Flux linkage against d-axis and dc currents

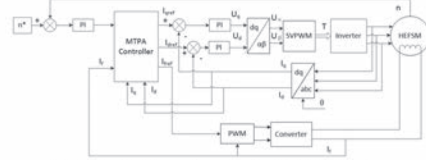

Fig.3. Schematic diagram of control system for HESFPM machine

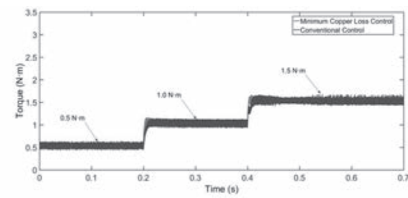

(a) Torque command

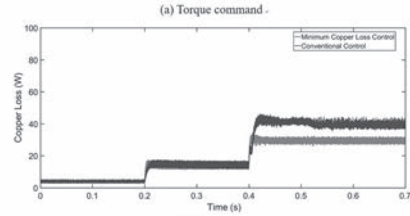

(b) Copper loss

Fig.4. Comparison of copper loss between conventional control and minimum copper loss control for HESFPM machine

GP-15. A Flexible Position Sensorless Control of Switched Reluctance Motors Considering Both Embrace Design and Magnetic Saturation.

H. Cai[1], H. Wang[1], *M. Li*[1] and S. Shen[1]
1. Hunan University, Chang Sha, China

Abstract —Precise estimation of position is essential in the control of switched reluctance motor (SRM). Traditionally, the intersection of the adjacent inductance can be utilized to estimate the rotor position, however, magnetic saturation brings about the variations of the intersection positon when the motor is operated at heavy load. To solve the problem, this paper develops a sensorless position estimation strategies considering the magnetic saturation and the embrace design. Firstly, the relationship between the embrace and the intersection position is fully investigated. At low inductance region, the intersection position is not sensitive to the saturation current when the embrace is small, thus, the typical specific position can be used as an update point for position estimation. Disparately, the intersection position is influenced by a great extent when the embrace is a bit larger, the relationship between the saturation current and the intersection position is necessary to be explored. At high inductance region, the intersection position is a function of the saturation current which is irrelevant to the embrace. Consequently, the sensorless control approaches can be chosen flexible according the characteristic of intersection. The rotor position estimation is achieved by employing six typical inductance positon without a requirement of additional positon sensor. The feasibility and validity of the proposed position estimation method is verified under the inertial operation, light load, heavy load, load mutation and high speed condition. Index Terms—Switched reluctance motors, position sensorless control, embrace deign, magnetic saturation. I.INTRODUCTION Switched reluctance motor (SRM) has been widely used since its inherent feature such asrobust structure and fault-tolerant. The motor is a potential candidate for high temperature and high speed appliances. The rotor position plays an extraordinary role in the control of the motor. However, some problem such as low reliability and susceptibility to interference are accompanied. Variety of sensorless strategies have been proposed to eliminate the machine sensors. A plus-injection method is present in[1], voltage pulse injection is usually employed and the method is suited for low and high speed range condition. When the motor is operated at suitable value, the observed hall signal is sensed by the injected narrow voltage pulse in [2], then the estimated speed and angle is obtain. An accurate position is estimated by applying the phase inductance vector coordinate transformation and the phase current slope difference method in [3]. II. PROPOSED POSITION ESTIMATION PRINCIPLE Rotor position can be predicted by extracting the information from the corresponding phase inductance, however,the magnetic circuit will be gradually saturated as the load current increases, and the "concave" phenomenon will appear at the inductance curve. As a result, the estimation encounters implementation issues at magnetic saturation operations, even inaccuracy of the estimated rotor position is achieved when the motor is operated at saturation condition. In order to improve this situation,this paper proposes a sensorless position estimation strategies considering the magnetic saturation effect and the embrace. There is a total of six inductance intersections within a 360 °electrical cycle, all of which are chosen as the update points for position estimation in this paper. The FEM analysis indicates that the embrace is of significant to the intersection position. Assuming the embrace is small, the intersection positon during the low inductance region is almost coincident and insensitive to the magnetic saturation. This typical position can be applied in the estimation directly. Supposing the embrace value is selected comparatively large, the intersection position will be diverse as the saturation current changes. for the sake of obtain the accurate intersection position, the relationship between the saturation current and the intersection position is required to be investigated. As is shown in Fig.1(c), the intersection position at low inductance is less sensitive to the saturation current when the embrace is set 0.4, therefore the fixed intersection position is able to be utilized. As the embrace value is selected as 0.5, the inductance profile is as shown in Fig.1(c), the intersection position changes from 7.5° to 10.5°,the angle is inevitable to be different when the saturation current changes. III.SIMULATION AND EXPERIMENTAL EVALUATION The simulation results are shown in Fig.2 (a), the given current is set as 40A, which is a magnetic saturation value. One can note that the estimated speed can track the actual speed exactly, the maximum estimation error is equivalent to 3 °. Considerating the electrical interval, the speed between the two updated points is basically taken as constant. Position estimation is affected obviously in case of variable and low speed, position estimation error slightly increases under these conditions due to that the calculated speed is applied. The experimental waveform of current and estimated position profile are shown in Fig.2 (b), the tracking error amouts to 4.2°, matching the simulation results well.

[1]Ofori, E., et al., "A Pulse-Injection-Based Sensorless Position Estimation Method for a Switched Reluctance Machine Over a Wide Speed Range, "IEEE Transactions on Industry Applications, vol. 51, no.5, pp.3867-3876.2015.
[2]Hu, K. W., et al., "A Reversible Position Sensorless Controlled Switched-Reluctance Motor Drive With Adaptive and Intuitive Commutation Tunings, "IEEE Transactions on Power Electronics,vol. 30, no.7, pp.3781-3793.2015.
[3]Cai, J. and Z. Deng, "Initial Rotor Position Estimation and Sensorless Control of SRM Based on Coordinate Transformation, "IEEE Transactions on Instrumentation and Measurement,vol. 64, no.4, pp.1004-1018.2015.

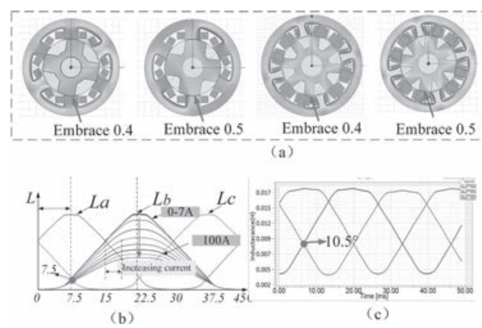

Fig. 1. (a) A variety of SRM with different embrace (b) intersection position is located at low inductance (c) intersection position at high inductance

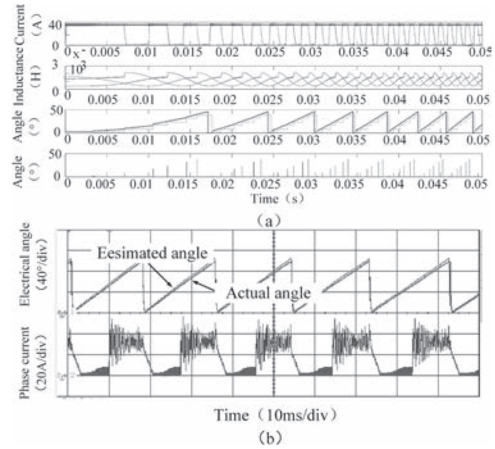

Fig. 2. The simulation of the inductance and position of the motor in the acceleration (b) experimental results of Position Estimation under the magnetic saturation inductance

GP-16. Fault-Tolerant Design and Control of Hybrid Excitation Axial Field Flux-Switching Permanent Magnet Machines.

W. Zhang[1] and X. Liang[2]
1. School of Electrical Engineering, Nantong University, Nantong, China; 2. School of Computer Science and Technology, Nantong University, Nantong, China

I.Introduction Fault tolerance of drive motor is a critical facet for many applications, such as aerospace, traffic, and military. Because continuous operation under fault conditions can improve the reliability and safety of the whole system, many researchers are attracted to investigate the fault tolerant machines. [1] proposed a three-phase axial flux-switching permanent magnet machine (AFFSPMM). Because of the simple and robust rotor, short axial size, and high torque density, it is suitable to directly drive electric vehicle (EV). However, it is noticed that the fault tolerance of AFFSPMM should be considered in order to keep the drive system of EV operate safely under the fault conditions. It was found in [2]-[3] that E-core topology could reduce magnet volumes and mutual coupling between phases in contrast with U-core one. However, the air-gap field was not able to be regulated due to only excitation of permanent magnets for the two AFFSPM machines, and therefore [4] proposed a hybrid excitation topology on the basis of E-core AFFSPMM, viz. a hybrid excitation axial flux-switching permanent magnet machine (HEAFFSPMM), in which the air-gap flux could be regulated by the DC excitation current. In this paper, the HEAFFSPMM is optimized for achieving better fault-tolerance with reference of the original U-core AFFSPMM, and the performances are compared and analyzed between the two machines. A novel fault-tolerant control method is proposed to improve the fault-tolerant capability by virtue of the special structure of the HEAFFSPMM. II.Topology of HEAFFSPMM Fig.1 shows the 3-D topology of the HEAFFSPMM, which exhibits one rotor is in the middle of two stators, and the magnets with opposite polarity are alternatively placed between the stator cells. The two adjacent side teeth are wounded around concentrated winding, for example A1 and A2. Compared with the conventional AFFSPMM, the stator is designed as E-shaped laminated segments instead of U-shaped ones. This reduces volumes of magnets and magnetic loading, and increase slot area to accommodate more armature windings and the added field windings. The field windings are wound around the middle teeth, which can be excited to improve the performances of the machine, and act as fault-tolerant windings at the same time. III.Fault-Tolerant Optimization Design The parameters of the HEAFFSPMM are optimized step by step to enhance the fault tolerance by 3-D finite element method (FEM) on the basis of a 600W prototype of 12/10-pole U-core AFFSPMM, including the number of rotor poles, the split ratio, the width of permanent magnet, the width of stator middle teeth, the width of rotor pole and rotor length. After optimizing the machine, the coupling component between phases, viz. the ratio of mutual- and self-inductance, is reduced by 63% in comparison with U-core AFFSPM. IV.Comparative Study of The Two Machines The simulating platform of the drive system is established in order to compare the performances of the two machines. The SVPWM fault-tolerant control method based on minimum copper loss is proposed in the paper and applied in the drive system of HEAFFSPMM. Fig.2 compares the torque-speed curves of the two machines at normal operation. It is found that 12/10 pole AFFSPMM has wider constant torque area than that of HEAFFSPMM, however, the speed operation range is apparently narrower than that of the HEAFFSPMM when increasing the field. Meanwhile, the output torque of HEAFFSPMM with DC excitation is almost 1.4 times of 12/10-pole AFFSPMM at rated speed. Therefore, the HEAFFSPMM is better suitable to drive the EV than the conventional AFFSPMM. Moreover, it is found from the simulating results that the speed and torque under the fault-tolerant control system can keep the same with those at normal operation when A-phase windings happen different faults. V.Experiment Validation The experimental setup is built in order to further validate the fault-tolerant control method of the HEAFFSPMM. The experiment results are similar to the simulating results. VI.Conclusion The dimensions of a HEAFFSPMM are optimized in order to attain large self-inductance and low coupling component with reference of a 600W conventional AFFSPMM. By comparing the performances of the two machines, it is found that the improved HEAFFSPMM has better operation performance and fault-tolerant capability. Moreover, the experiments are done to validate the control method under the different fault cases.

[1] Hao Li, Mingyao Lin, Da Xu, Xinghe Fu, and Wei Zhang, “Static characteristics of a novel axial field flux-switching permanent magnet motor with three stator structures”, *IEEE Transactions on Magnetics*, vol. 50, no.1, pp. 1-4, 2014. [2] Wei Zhang, Mingyao Lin, Li Hao, Liuchen Tai, and Zhaogang Pei, “Design and analysis of a novel E-core axial field flux-switching permanent magnet machine”, *Applied Mechanics and Materials*, vol. 416-417, pp.175-180, 2013. [3] Wei Zhang, and Mingyao Lin, “Influence of rotor pole number on optimal parameters in e-core axial field flux-switching permanent magnet machine”, *International Conference on Electrical Machines and Systems (ICEMS)*, pp. 1217-1221, Busan, Korea, Oct. 26-29, 2013 [4] Wei Zhang, Mingyao Lin, Da Xu, Xinghe Fu, Li Hao, “Novel fault-tolerant design of axial field flux-switching permanent magnet machine”, *IEEE Transactions on Applied Superconductivity*, vol.24, no.3, pp. 1-4, 2014.

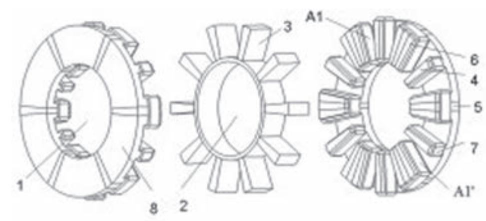

Fig. 1. 3-D topologies of the novel AFFSPMM. 1-stator, 2-rotor, 3-rotor pole, 4-middle tooth of stator E-core, 5- permanent magnet, 6-side tooth of stator E-core, 7-field winding, 8-stator cell.

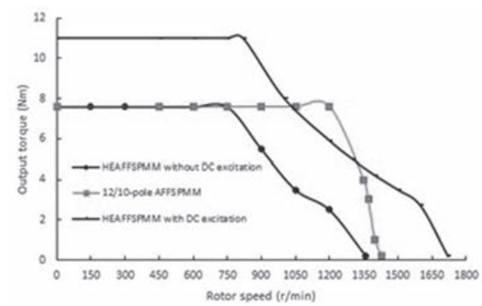

Fig. 2. Torque-speed curves comparison of the two machines

FRIDAY MORNING, 27 APRIL 2018 SIMPOR/ROSELLE BALLROOM, 8:30 TO 11:30

Session GQ

EMERGING AND INTERDISCIPLINARY APPLICATIONS II

(Poster Session)

Julie Grollier, Chair
Université Paris-Sud, CNRS/Thales, Palaiseau, France

GQ-01. Tribological and viscoelastic behaviors of core-shell structured carbonyl iron/polystyrene particle based Magnetorheological Fluid.

Y. Dong[1], P. Zhang[2], H. Choi[1] and C. Lee[3]

1. Polymer Science and Engineering, Inha University, Inchon, The Republic of Korea; 2. Nanjing Research Institute for Agricultural Mechanization Ministry of Agriculture, Nanjing, China; 3. Mechanical Engineering, Inha University, Incheon, The Republic of Korea

I. INTRODUCTION Magnetorheological (MR) fluid [1] is a kind of actively controllable intelligent and smart materials that responds to an applied magnetic field with a dramatic change in rheological and viscoelastic behaviors such as shear viscosity, shear stress, dynamic modulus and so on. In the absence of magnetic field, MR particles dispersed freely in the carrier medium show fluid-like behaviors, while under an external magnetic field, MR particles aggregate to form chain-like structures, being transformed to a solid-like state within a few milliseconds and recovered to a fluid-like state when the magnetic field is removed. Being of benefit to these excellent properties, MR fluids have been applied in many engineering fields [2], [3], such as dampers, brakes, polishing and so on. Soft magnetic carbonyl iron (CI) particles have been considered as one of the most excellent candidates for MR materials because of their spherical shape, proper particle size, and high saturation magnetization. However, sedimentation problem of the CI particles in MR fluids due to their high particle density often limits the application of CI based MR fluids in industry. In addition, regarding on durability and mechanical properties of the MR fluids in many applications, the effects of friction and wear are important factors that must be considered. In this work, in order to improve the dispersion stability of CI based MR fluids based on the reduction of particle density, polystyrene (PS) was coated on the surface of CI particles via a conventional dispersion polymerization method to produce core-shell structured CI/PS particles. In addition, PS coating can not only prevent the oxidation of CI particles, but also change the particle topology and surface roughness, which may give the CI/PS particle-based MR fluid superior wear and friction performance in its tribological study compared to the pristine CI particle-based MR fluid. II. EXPERIMENT CI particles (100 g) were initially treated with methacrylic acid (MAA) by dispersing the CI particles in a mixture of MAA (100 g)/methanol (1000 mL) and ultrasonicated for 30 min, then the MAA-modified CI particles were selected by a magnet. In order to prevent the aggregation of particles, the modified CI particles were dispersed in a homogeneous solution of polyvinylpyrrolidone (66 g) in methanol (1400 mL). Then, the mixture was transferred to a reactor (2000 mL) and heated to 65 °C with intense stirring. A styrene monomer (50 g) containing the initiator, 2,2-azobisisobutyronitrile (0.5 g) was slowly added to the reactor, while the system was maintained at 65 °C for 24 h. The final product was washed with methanol and distilled water, and finally dried at 60 °C for 12 h. The MR fluid was prepared by dispersing 50 wt% of the CI/PS particles in silicone oil, and the rheological properties of the MR fluid were measured by rotational rheometer (Physica MCR 301 Rheometer Anton Paar, Austria). The tribological behaviors were further tested by a reciprocating friction and wear tester (RB 108-RF, R&B, Korea). III. RESULT AND DISCUSSION Figure 1 shows shear stress for the CI/PS based MR fluid versus shear rate under various magnetic field strengths on a log-log scale. In the absence of the magnetic field, the relationship between shear stress and shear rate is almost linear, showing a general fluid-like state. However, when the magnetic field is applied, the fluid behaves like a Bingham fluid [4] with a stable shear stress value independent of shear rate and distinctive yield stress due to the chain-like structure caused by the magnetic field. Furthermore, the yield stress increased with increased magnetic field strength, indicating that a stronger chain-like structure formed under higher magnetic field strength. Figure 2 shows the change in the coefficient of friction for CI/PS based MR fluid in the absence of a magnetic field and when a magnetic field with strength of 10 mT is applied. The coefficient of friction can be calculated by the equation as: $\mu=F/N$ (1) Where μ represent the coefficient of friction, F and N are the friction force and normal load, respectively. The results show that the friction coefficient shows instability and a slightly decreased value without an input magnetic field. However, when the magnetic field is applied, the friction coefficient becomes very stable due to the fact that when the magnetic field is applied, particles in the MR fluid are magnetized and form chain-like structures in the same direction as the magnetic field and participated in friction. In addition, owing to the involvement of the CI/PS particles in the friction after forming chain-like structures by the magnetic field, the coefficient of friction shows an upward trend. According to our analysis, the change in the coefficient of friction is caused by variation of the resistance of the MR fluid [5], [6]. In other words, as the strength of the magnetic field increases, the interaction between the magnetized particles increases and the strength of the chain-like structure stronger so that the viscosity and resistance of the MR fluid also increase, resulting in an increase of the friction force (F). As shown in Eq. (1), at a fixed normal load (N) value, as the friction increases, eventually it leads to the increases in the coefficient of friction which is good for its application.

1) L. Zarana, and V. U. Ramesh, “Influence of particle shape on the magnetic and steady shear magnetorheological properties of nanoparticle based MR fluids”, *Smart Mater. Struct.,* 26, 054008, (2017). 2) J. M. Chambers, and N. M. Wereley, “Vertical Axis Inductance Monitoring System to Measure Stratification in a Column of Magnetorheological Fluid”, *IEEE Trans. Magn.,* 53, 1-5, (2017). 3) J. Kozlowska, and M. Leonowicz, “Processing and Properties of Magnetorheological Fluids for Prospective Application in a Passive Armour”, *IEEE Trans. Magn.,* 49, 4721-4724, (2013). 4) K. Bao, A. Lavrov, and H. M. Nilsen, “Numerical modeling of non-Newtonian fluid flow in fractures and porous media”, *Computational Geosci.,* 21, 1313-1324, (2017). 5) P. Zhang, K. H. Lee, and C. H. Lee, “Fretting friction and wear characteristics of magnetorheological fluid under different magnetic field strengths”, *J. Magn. Magn. Mater.,* 421, 13-18, (2017). 6) J. Seok, S. O. Lee, K.-I. Jang *et al.*, “Tribological Properties of a Magnetorheological (MR) Fluid in a Finishing Process”, *Tribology Trans.,* 52, 460-469, (2009).

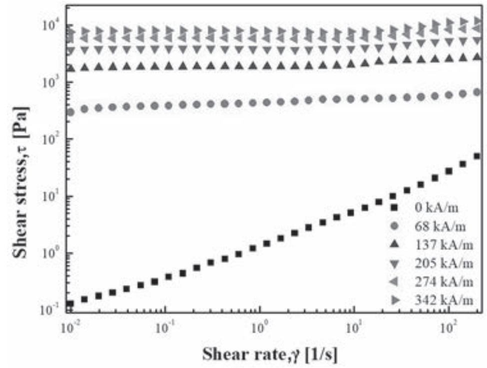

Fig. 1. Shear stress for CI/PS based MR fluid vs. shear rate under various magnetic field strengths

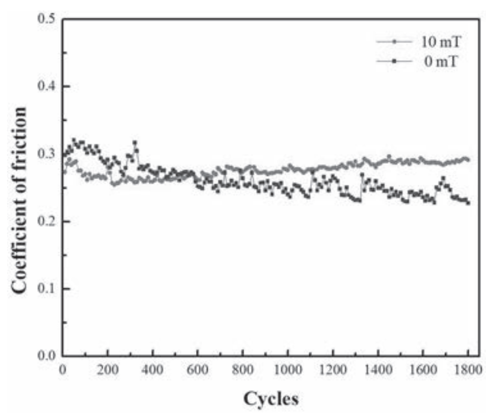

Fig. 2. Coefficient of friction of CI/PS based MR fluid under magnetic field strength of 0 and 10 mT

GQ-02. A Multi-Modular Helical Magnetic Millirobot Composed of Soft Modules Capable of Navigating and Anchoring in Curved Tubular Environments.

S. Jeon[1], H. Lee[1], S. Lee[1], J. Oh[1] and J. Shin[1]
1. Mechanical and Automotive Engineering, Kongju National University, Cheonan, The Republic of Korea

1. Introduction A variety of structures and methods for magnetic millirobots has been extensively investigated as a promising means to replace conventional medical treatment for occlusive vascular diseases [1-4]. Multi-modular magnetic millirobots able to accommodate multiple modules especially attracted attention [2-4]. Since this structure allows a relatively large space along the longitudinal axis to utilize various functional structures, a multi-modular magnetic millirobot can be used to perform complex tasks such as stent deploy and drug delivery in tubular environments [3, 4]. However, due to the complex and lengthy structure, the millirobot cannot be easily applied to tubes with a relatively high curvature such as the one shown in Fig. 1. *2. A Multi-Modular Helical Magnetic Millirobot Composed of Soft Modules* In this research, we propose a multi-modular helical magnetic millirobot (MHMM) composed of soft modules that can be effectively applied to curved tubular environments, as shown in Fig. 1 [4]. Each module of the MHMM is serially connected by a universal joint, and the rotational motion of the first (head) module can be effectively transferred to the other modules. Therefore, every module of the MHMM can rotate in sync with an external rotating magnetic field (ERMF) even if they are not aligned. The MHMM can also employ more modules if necessary by simply serially connecting additional modules with universal joints. From the geometric constraints of two orthogonal revolute joints of a universal joint, the angular displacement of the kth module, Θ_k, of the MHMM can be expressed in terms of the first module's angular displacement, Θ_1, as follows [4]: $\Theta_k=\tan^{-1}(\tan(\Theta_1)/\prod_{j=1}^{k-1}\cos\Phi_{j,j+1})$ (1) where $\Phi_{k,k+1}$ is the angle between the *k*th and the (*k*+1)th modules. Eq. (1) can be used to control each module's angular displacement, speed, and acceleration by means of an ERMF which can be used to generate a certain type of the MHMM's mechanical motions, such as navigating, unclogging, and stent deploying motions. Also, due to the flexibility of the soft modules, the MHMM can be easily deformed with respect to the tube which can make it more steerable in tubes with a relatively high curvature, as shown in Fig. 1. This flexibility can also make the MHMM be more anchorable in curved tubes because of the relatively large contact area between the MHMM and the tube derived from the deformation. This ability is especially useful when the MHMM performs complex tasks such as stent delivery and drug delivery within human blood vessels while overcoming pulsatile blood flows [3, 4]. In this research, we verified the proposed MHMM by constructing a magnetic navigation system (MNS) and a prototype MHMM, as shown in Fig. 2. The MNS shown in Fig. 2a can generate and control various ERMFs required to manipulate the MHMM. An in-vitro pulsatile flow environment was also constructed to mimic the condition of human blood vessels. Figs. 2c, 2d show the prototype MHMM constructed with a stereolithography-based 3d printing technology using flexible resin, and the MHMM showed a sufficient flexibility as shown in Fig. 2b. We then examined the navigating, steering, and unclogging abilities of the prototype MHMM compared to that of an MHMM constructed with a harder material (acrylic plastic), as shown in Fig. 2e. And the results showed that the MHMM constructed with flexible resin (soft module) not only can effectively navigate in a highly bent tube but also can effectively anchor to the tube against a pulsatile flow. We also measured the maximum angular speeds of the MHMMs in the tube that they can rotate in sync with an applied ERMF, and the MHMM constructed with flexible resin could rotate in sync with a much faster ERMF. Whereas the MHMM constructed with acrylic plastic only could rotate in sync with a relatively slow ERMF due to the irregular contact between the robot body and the tube during rotation. *3. Concluding Remarks* This research proposed a novel type of MHMM that can navigate in curved tubular environments effectively. It also examined the navigating and anchoring ability of the MHMM by observing and examining various mechanical motions of the MHMM in an in-vitro pulsatile flow condition. This research can contribute to the development of multi-modular magnetic millirobots able to conduct complex tasks required for many biological and biomedical applications.

[1] K. E. Peyer, S. Tottori, F. Qiu, L. Zhang, and B. J. Nelson, "Magnetic helical micromachines," Chemistry, vol. 19, no. 1, pp. 28–38 (2013). [2] S. M. Jeon, G. H. Jang, W. S. Lee, "Drug-Enhanced Unclogging Motions of a Double Helical Magnetic Micromachine for Occlusive Vascular Diseases," IEEE Tran. Magn., vol. 50, no. 11, pp. 9100304 (2014). [3] W. S. Lee, J. K. Nam, B. J. Jang, and G. H. Jang, "Selective Motion Control of a Crawling Magnetic Robot System for Wireless Self-Expandable Stent Delivery in Narrowed Tubular Environments," IEEE Trans. Ind. Electron., vol. 64, no.2, pp. 1636-1644 (2017). [4] S. M. Jeon, "A multi-modular helical magnetic millirobot navigating in curved tubular environments," AIP Adv., vol. 7, pp. 056721 (2017).

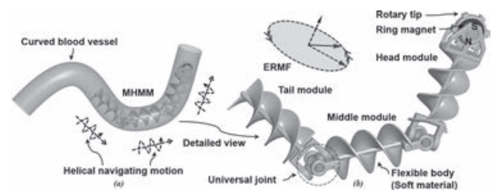

Fig. 1. Schematic view of (a) the MHMM in a human blood vessel and (b) its detailed structure.

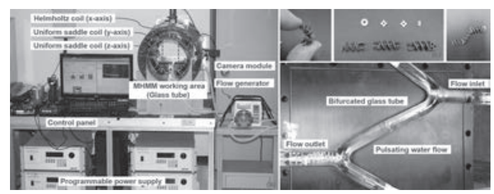

Fig. 2. (a) Experimental setup of the MNS. (b) Flexible structure of the prototype MHMM. Prototype MHMM (c) before assembly and (d) after assembly. (e) In-vitro pulsatile flow environment.

GQ-03. Hybrid control of magnetic micro-robot using three-axis Helmholtz coil.

I. Baek[1], G. Jeon[1], C. Yu[2] and *S. Kim*[1]

1. Department of Electronics Convergence Engineering, Wonkwang University, Iksan, The Republic of Korea; 2. Department of Convergence Technology Engineering, Chonbuk National University, Jeonju, The Republic of Korea

SUMMARY Magnetic robots and their magnetic manipulation systems are innovative approaches for the diagnosis and therapy of minimally invasive medicine. Medical magnetic robots have been applied to targeted drug delivery, drilling in blood vessels, and a robotic capsule-endoscope for diagnosis and therapy [1-3]. Typically, the magnetic robots are controlled by various types of magnetic field: gradient, alternating, rotating, and uniform magnetic fields. The combination of Maxwell coil and Helmholtz coil are general configuration of magnetic manipulation system. However, the configuration is complicated and many power sources are required. To overcome these issues, we proposes a new method of hybrid control of magnetic fields for magnetic micro-robot manipulation based on three-axis Helmholtz coil. The hybrid control utilizes both gradient and uniform fields through switch control of the three-axis Helmholtz coil. For hybrid control, we utilizes 9 relay switches. Three switches separate the x, y and z coils. Six switches separate configuration of Helmholtz coil. In other words, three Helmholtz coils becomes six coils. When generating a rotating magnetic field, the six switches are turned on. When controlling the gradient field, the six switches are selectively turned off according to the moving direction. The hybrid control can provide precision control of micro/nano robot. In addition, the control method with system can be applied to micro/nano robot control without limitation to the robot mechanisms. To verify these advantages, we conducted various experimental tests. *ANALYSIS* Figure 1 (a) shows the three-axis coil structure and the switching method of a pair of Helmholtz coil. A pair of Helmholtz coils are connected by a switch and can not act as Helmholtz coils when the switch is off. Figure 1(b) shows the results of magnetic field distribution for steering of magnetic microrobot through the gradient magnetic field. For steering of the robot based on the gradient field, the switches constituting the x- and y-axis Helmholtz coils are each turned off to form a single coil. We applied to current signals at Y_1 and X_1 coils. The steering angle is determined by the strength of the two magnetic fields of Y_1 and X_1 coils. When a current of 6A is applied to the Y_1 coil, the difference of the magnetic field at a distance of 3.5 cm from the center point is 1 kA/m. When a current of 6 A is applied, a magnetic field of 4 kA/m is generated at a point of 3.5 cm. Figure 2 shows the results of active locomotion by hybrid control. First, we verified active locomotion based on the gradient magnetic field, as shown in Fig. 2 (a). In this test, we used a cylindrical permanent magnet. The magnet was controlled by translational force within gradient magnetic field. The movement path is shown in Fig. 2 (a). Figure 2 (b) shows the hybrid control using the rotating magnetic field and gradient magnetic field. In this experiment, we utilized the spiral-type microrobot. To control the robot, it was driven with a magnetic field of 5.7 kA / m and 3 Hz in the rotating magnetic field mode. The robot was moved to the rotating magnetic field mode from the starting point to the 21-second point, and the robot was moved in translational motion to the gradient magnetic field mode for 41 seconds: The points 1 to 5 are controlled by a gradient magnetic field. From point 1 to point 5, it is controlled by the gradient magnetic field, and then it moves forward at point 5 by using the rotating magnetic field, as shown in Fig.2 (b). In general, a rotating magnetic field is used to control the spiral-type robot. However, it can be limited in direction control in a narrow space. The proposed hybrid control can control the movement of the robot more quickly and accurately in a narrow space. Also, it is experimentally proved that it can be used irrespective of the mechanism of the robot.

[1] B. J. Nelson, I. K. Kaliakatsos, and J. J. Abbott, "Microrobots for Minimally Invasive Medicine," *Annual Review of Biomedical Engineering*, vol. 12, pp. 55-85, Aug. 2010. [2] S. H. Kim, K. Ishiyama, "Magnetic Robot and Manipulation for Active-locomotion with Targeted Drug Release," *IEEE/ASME Trans Mechatronics*, vol. 19, no. 5, Oct, 2014 [3] C. H. Yu, S. H. Kim, Tiny Magnetic Robot Mechanism and Manipulation for Stent Transportation and Installation, Journal of Magnetics, vol. 22, no. 1, pp.162-167, 2017

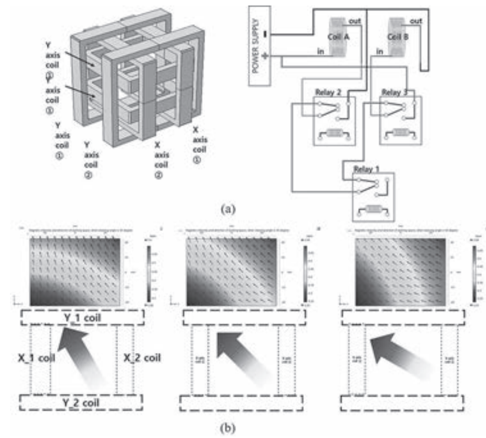

Fig. 1. (a) Helmholtz coil structure and switching method (b) The results of magnetic simulation for steering of the robot.

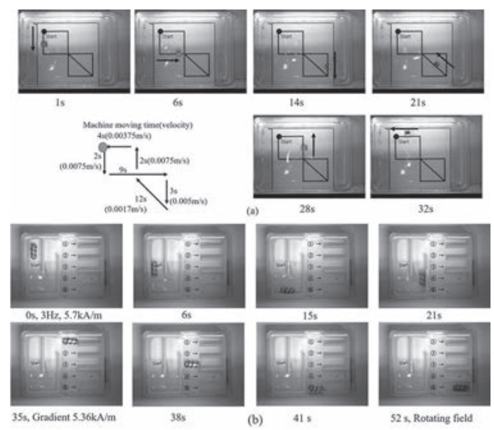

Fig. 2. (a) active locomotion of a cylindrical magnet based on gradient field (b) Hybrid control of spiral-type microrobot based on a rotating magnetic field and gradient field.

GQ-04. Experimental Verification of Transcranial Magnetic Stimulation Using Anatomically Accurate Brain Phantom.

H. Magsood[1], F. Syeda[1] and R.L. Hadimani[1]
1. Virginia Commonwealth University, Henrico, VA, United States

Transcranial Magnetic Stimulation (TMS) is a promising and non-invasive technique for diagnostics and treatments of various neurological diseases [1]–[3]. However, the lack of anatomically realistic brain phantoms has made the experimental verification of induced electric fields in the brain tissues an impediment to the development of new treatment protocols. We have developed a 3-D anatomically accurate brain phantom that can mimic the electrical conductivity of different brain regions [4]. The phantom will enable the professionals in the field of the brain modulation and treatment to test and perform brain stimulations on the phantom that are accurate and match the clinical setting of the of TMS treatment. To produce the phantom for the work at hand, we 3-D printed shells for each tissue layer of the brain. Brain tissues are divided mainly into cerebrospinal fluid (CSF), white matter (WM), grey matter (GM), ventricles, and cerebellum. These layers are made into shells and after 3D printing them, they are filled with a conductive material (silicon polymer polydimethylsiloxane PDM with electrically conductive filler multi walled carbon nanotubes MWCNT) to impart electrical conduction to the brain phantom. Then, the shells are broken or dissolved to finally produce the brain phantom. The electrical conductivity of the brain phantom tissue that we are matching in this phantom is in the range between 0.4-1.0 Sm^{-1}. The phantom is then examined under different TMS parameters and compared with FEM modelling of induced electric and magnetic fields in the brain. For the experimental part, we positioned the TMS coils on the brain phantom and an oscilloscope probe is placed just underneath the surface of the phantom in order to measure the voltage (phantom probe). Also, we placed another probe at the same distance (from the coils) of the first probe but it is placed outside the phantom to measure the voltage induced on the probe just from the TMS coils (reference probe). Then, we applied the magnetic field from the coils at four distances 1, 2, 3, and 4cm and at four different power intensities 25, 50, 75, and 100% at each distance. The brain phantom and experimental set up is shown in fig.1. Also, we replicated the same setting of the experimental work with FEM simulation where the coils in the software are places at four distances 1, 2, 3, and 4 cm form the surface of the brain model and with four intensities 25, 50, 75, and 100% at each distance. The voltage readings for both experimental and simulation cases are shown in fig.2. Voltage readings of the experimental work shown in the upper graph of Fig.2 representing the difference between the voltages induced on phantom probe and the reference probe. This indicates that there is a noticeable induced electric field in the phantom due to the applied magnetic field from the TMS coils. Comparing both graphs, experimental and simulation, it can be seen that there is an overall similar behavior. The voltage and e-field readings are linearly dependent with intensity in both graphs. Also, the induced voltage decreases almost exponentially with the distance. However, the gap between the 1cm and 2cm is larger in the experimental results than it is in the simulation. This behavior can be due to the complexity of the experimental set up. For example, there could be some discontinuities within the phantom due to the tear in the polymer caused by the repeated probe insertion. Also, the magnetic field is sensitive to the distance from the source; therefore, there might be a slight difference between the intended and the actual distances from the probes to the coils. Finally, even though the phantom is fabricated to be globally homogenous but, there could be some local inhomogeneity within the phantom that result in slight deviated voltage readings. We have planned to overcome these experimental inaccuracies in our future work by adopting a Cartesian servo motor stage. Acknowledgement: This work is funded by the School of Engineering of VCU's faculty start-up funds and Ministry of Higher Education of Saudi Arabia. Authors would like to thank Ahmed El-Gendy and Ciro Serrate for useful discussions on the development of brain layer shells.

References: [1] M. Kobayashi and A. Pascual-Leone, "Transcranial magnetic stimulation in neurology," *Lancet*, vol. 2, no. 3, pp. 145–156, 2003. [2] S. H. Lisanby, B. Luber, T. Perera, and H. a. Sackeim, "Transcranial magnetic stimulation: applications in basic neuroscience and neuropsychopharmacology.," *Int. J. Neuropsychopharmacol.*, vol. 3, no. 3, pp. 259–273, 2000. [3] E. M. Wassermann and S. H. Lisanby, "Therapeutic application of repetitive transcranial magnetic stimulation: a review," *Clin. Neurophysiol.*, vol. 112, pp. 1367–1377, 2001. [4] H. Magsood, Ciro Serrate, A. A. El-Gendy, R. L. Hadimani, "Brain Phantom for Neuromodulation using Casting and 3D Printing", Provisional patent submitted, USSN 62/546,810 Aug. 2017

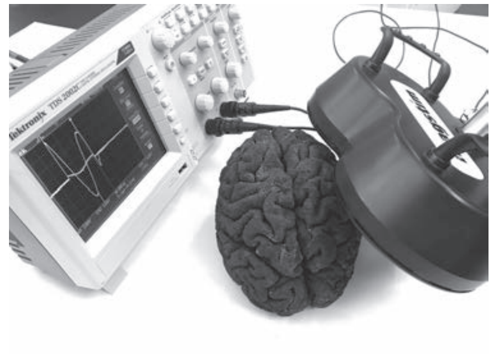

Fig. 1. brain phantom and the experiment setup

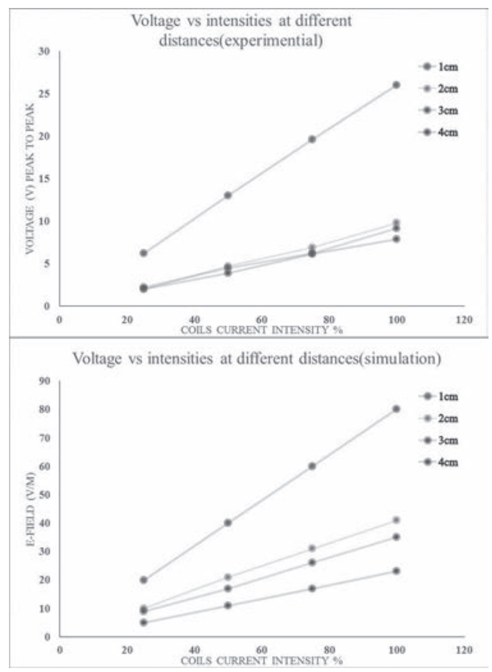

Fig. 2. voltage readings (experimental and simulation) of the induces electric field from the phantom with varied distances (1, 2, 3, and 4cm) and intensities (25, 50, 75, and 100%)

GQ-05. Magnetically axial-coupled propeller-based portable electro-mangetic energy-harvesting device using air and water stream.

J. Lee[1], G. Jeon[1] and *S. Kim*[1]
1. Department of Electronics Convergence Engineering, Wonkwang University, Iksan, The Republic of Korea

Introduction Energy-harvesting devices have been widely developed and reported [1-3]. In general, energy-harvesting devices utilize piezoelectric, electrostatic, and electromagnetic methods. Piezoelectric generators convert vibration into a voltage output but generate relatively high voltage (to a maximum of hundreds of V) and low electrical current. Electrostatic generators provide a relatively high output voltage and often high output impedance (up to tens of MΩ). In the case of EM generators, they generate comparatively high output current levels at low output voltages. The output voltage and current depend on the magnet properties and the number of turns in the coil. Energy-harvesting devices can be used for charging portable electronic devices, such as smart phones, notebook computers, and lanterns. In addition, the devices can be applied as a permanent power source for wireless water meter reading based on wireless sensor networks. For these functions, energy-harvesting devices must generate minimum of scores of mW. In this study, we developed an electromagnetic energy-harvesting device, which is potable rotary-type generator, using fluid and air streams. The harvesting device utilizes a permanent axial flux magnet structure. The device consists of 8 permanent magnets, 16 pick-up coils, and a single axial-coupling magnet for easy installation of the turbine. Because the axial-coupling magnet allows for a detachable turbine according to changes in the environment, the proposed device can use tap water and gas flows as an energy source. Thus, the proposed structure can be used in a number of applications. The device generated 18.6 Vrms and 35.34 mW at a rotating speed of 800 rpm and a load of 10 kΩ. Through simulation and various experimental analyses, we conducted a performance evaluation of the proposed device. Fabrication and analysis Figure 1 (a) shows the configuration of the proposed energy-harvesting device. The device is composed of 8 permanent axial-flux magnets with 16 pick-up coils for power generation. The diameter and height of a single disc-type magnet is 20 mm and 3 mm, respectively. A single pick-up coil is 12000 turns with a wire thickness of 0.05 mm. The air gap at the top and bottom between the axial-flux magnets and the pick-up coils is 3 mm, respectively. Figure 1 (b) shows the coupled axial flux of two magnets in a generator according to changes in distance (d is 20 mm) and height (h is 10 mm). The magnetic fields are induced at the pick-up coils. The observed magnetic field intensity is approximately 45 kA/m at a height of 6.5 mm (center of the pick-up coil). Figure 1 (c) shows the detachable turbine on the devices. We utilized synchronous magnetic axial coupling using magnetic torque and force for combination between the turbines and the power generator. The interactive force becomes a virtual shaft. Because of the magnetic axial coupling between the turbine and the generator, the device allows for a contact or non-contact combination. In the case of the non-contact combination, rotational torque depends on the axial coupling force. Therefore, we controlled the coupling distance using a screw mechanism between two magnets. A high coupling force causes a wider rotating speed, and increases the torque. We installed the coupling magnets, comprised of an NdFeB and an NdFeB-bonded magnet, in wind turbines and water turbines. In addition, the generator includes an NdFeB-bonded magnet for an axial-coupling magnet. The magnetic axial coupling between an NdFeB-bonded magnets resulted in a lower coupling force, up to a coupling distance of 6 mm. Under the condition, the coupling force was 0.467 N, whereas the coupling between the NdFeB magnet and the bonded magnet produced a coupling force of 0.54 N. This configuration is suitable for water turbines. Figure 1 (d) shows the fabricated generator and total configuration. The two turbines were fabricated by 3D printer. Using the generator, we observed the converted voltages and electrical power according to changes in rotating speed up to 800 rpm, as shown in Fig. 2. Figure 2 (a) shows energy harvested from wind and water streams. Figure 2 (b) shows load tests at 1 kΩ, 10 kΩ, and 100 kΩ, up to 800 rpm. The device generated a maximum of 2.45, 18.6, and 53.6 Vrms at 800 rpm. Under the condition, the converted electrical powers were 6.2, 35.34, and 29 mW at 1 kΩ, 10 kΩ, and 100 kΩ, respectively. In addition, using a diode rectifier, we conducted a charge test using a 1 F super-capacitor. It took about 45 minutes for full charge.

[1] A. Harb, "Energy harvesting: State-of -the-art," Renewable Energy, vol. 36, no. 10, pp. 2641–2654, 2011. [2] S. H. Kim, C. H. Yu, K. Ishiyama, "Rotary-type electromagnetic power generator using a cardiovascular system as a power source for medical implants," IEEE/ASME Trans. Mecha. Vol.21, no.1, pp. 122-9, 2015. [3] H. A. Sodano, G. Park, and D. J. Inman, "Estimation of electric charge output for piezoelectric energy harvesting," Strain, vol. 40, no. 2, pp. 49–58, 2004.

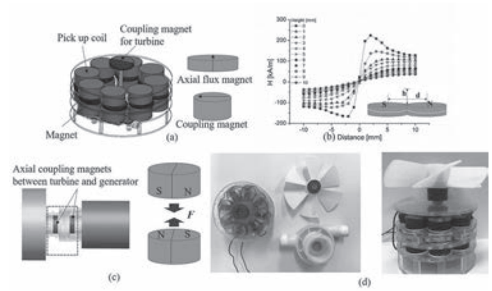

Fig. 1. (a) Design of the power-harvesting device, (b) observation of the coupled axial flux, (c) combination mechanism between turbine and the device, and (d) total configuration.

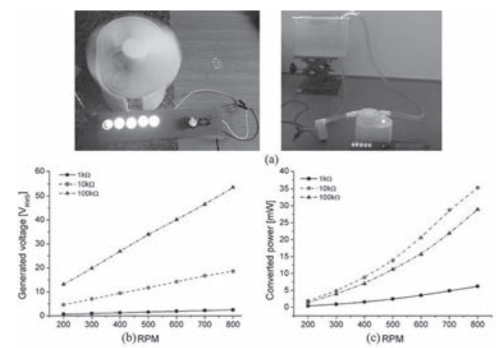

Fig. 2. (a) Energy harvesting from wind and water streams, (b) the generated voltages according to changes in rpm, and (c) the converted electrical power according to changes in rpm.

GQ-06. Improved Performances of Micro-electromagnetic Energy Harvesting Devices by Minimizing the Demagnetization Field.

D. Mallick[1] and S. Roy[1]
1. Micro-nano-systems Center, Tyndall National Institute, Cork, Ireland

The potential of wirelessly connected smart world of 'Internet of Things' technological platform is restricted by the lack of ambient energy sources capable of powering the sensors perpetually [1, 2]. This issue has surged the research to investigate the prospect of harvesting the energy out of ambient mechanical vibrations [3-5]. Among the different vibrational energy harvesting (VEH) transduction mechanisms, electromagnetic (EM) transducers are the most promising one. However, the difficulty in miniaturisation and integration of the high performance permanent magnets in MEMS scale devices hinders the continuous demand of increasing power density (= power/device volume). In general, CMOS compatible development of high energy product (BH_{max}) permanent magnets with thickness of the order of microns to hundreds of microns is a key challenge for a number of magnetic MEMS applications including VEH [6-7]. But the problem extends beyond just high energy product magnetic material deposition and relates to the lack of intelligent design strategies. When a relatively thin film/block of permanent magnet is used in a MEMS device as source of magnetic field, the stray magnetic field appears only from the edge of the magnet and a large part of the material is wasted. This is due to the presence of the demagnetization field which acts to demagnetize the magnet in a direction which is opposite to the direction of the magnetization [8]. Hence, the magnetic flux intensity is greatly reduced which affect the performance of integrated magnetic transducers. Here, we propose to replace a block of permanent magnet by micro-patterned array of magnets, diminishing the demagnetization effect and enhancing the magnetic stray field. In that case, the magnetic flux density can be intensified over a small space due to increase of the edges of magnetic elements, which is shown quantitatively in Fig. 1(a) using FEM simulation in COMSOL. Thus electromagnetic coupling co-efficient can be substantially improved resulting in higher output power. Different patterned structures are simulated to derive the optimized configuration to be used in MEMS based EM VEH devices. To demonstrate the potential of the proposed approach, micro-patterns of the Co-rich CoPtP permanent magnets are developed at room temperature using a combination of standard lithography and an optimized pulse reverse electrodeposition techniques. Among different deposition methods [9, 10], electrochemical route is an attractive choice due to its low cost and relatively high deposition rate at CMOS compatible temperature. Compared to the conventional DC plating, significant improvements in the microstructure of the developed thick CoPtP micro-magnets are obtained using the pulse reverse electroplating technique which improves the hard magnetic properties as well. Up to ~30 μm thick patterned structures are developed with intrinsic coercivity > 3 kOe and maximum energy product of 45.9 kJ/m^3. In order to demonstrate the substantial advantage of optimized, micro-patterned magnetic structures compared to a block of integrated magnet, a novel device topology of micro EM VEH is adopted as shown in Fig. 2(a). The device consists of assembled components such as micro-fabricated silicon spring structure (natural frequency = 500 Hz), double layer electroplated copper coil with 144 turns and 190 ohm internal resistance and different micro-patterns of CoPtP magnets. The magnetic arrays are placed only above one side of the coil so that the later can move from a region of high magnetic flux density to zero flux density, generating large flux gradient vis-à-vis induced voltage. By changing the magnetic structure from block to square patterned magnet the electromagnetic coupling co-efficient increases from 0.2 mWb/m to 1.6 mWb/m, as obtained from FEM simulation. Experimental results show (Fig. 2(b)) that under optimized load condition, the device with square micro-patterned magnets produce 4 times higher output power compared to the same produced by a device with an entire block of magnet of similar footprint. In conclusion, this work reports a novel integration strategy to incorporate rare-earth free, CMOS compatible micro-magnets in fully integrated MEMS based EM VEH device in order to improve the device performance significantly, thereby, making it a suitable candidate for powering the sensors within Internet of Things technology. Further improvements can be obtained by developing higher aspect ratio, highly anisotropic magnetic structures which can be attributed to future works.

1. Shuang-Hua Yang, 'Internet of Things', Wireless Sensor Networks, London: Springer, p. 247-261 (2014). 2. C. Perera, A. Zaslavsky, P. Christen, and D. Georgakopoulos, 'Sensing as a service model for smart cities supported by internet of things,' Trans. Emerg. Telecomm. Techn. (ETT), 25: 81-93 (2014). 3. D. Mallick, A. Amann, S. Roy, 'High Figure of Merit Nonlinear Microelectromagnetic Energy Harvesters for Wideband Applications', Journ. Microelectromech. Syst., 26(1): 273-282 (2016). 4. S. P. Beeby, R. N. Torah, M. J. Tudor, P. Glynne-Jones, T. O'Donnell, C. R. Saha, S. Roy, 'A micro electromagnetic generator for vibration energy harvesting', J. Micromech. Microeng. 17:1257–1265 (2007). 5. D. Mallick, A. Amann, S. Roy, 'Surfing the High Energy Branch of a Nonlinear Energy Harvester', Phys. Rev. Lett., 119:197701 (2016). 6. D.P. Arnold, N. Wang, 'Permanent Magnets for MEMS', J. Microelectromech. Syst., 18(6): 1255-66 (2009). 7. D. Niarchos, 'Magnetic MEMS: key issues and some applications', Sens. Act. A 109:166–173 (2003). 8. R. Skomski, J. M. D. Coey, 'Magnetic anisotropy—How much is enough for a permanent magnet?' Scripta Materialia 112: 3-8 (2016). 9. F. M. F. Rhen, E. Backen, J. M. D. Coey, 'Thick-film permanent magnets by membrane electrodeposition', J. Appl. Phys. 97:113908 (2005). 10. S. Kulkarni, S. Roy, 'Deposition of thick Co-rich CoPtP films with high energy product for magnetic microelectromechanical applications', J. Magn. Mag. Mater., 322 (2010) 1592–1596.

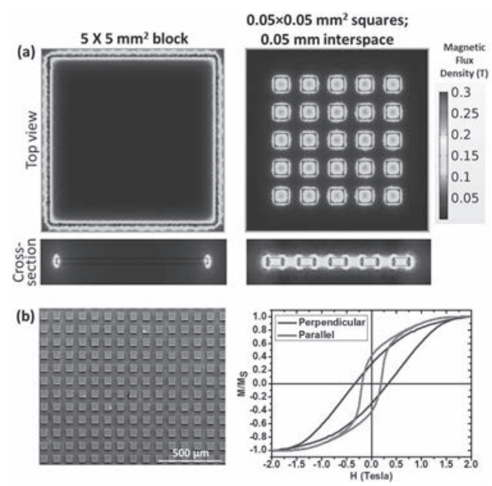

Fig. 1. (a) FEM simulation using COMSOL to show the advantage of using micro-patterns (right) compared to a block (left) of integrated permanent magnet, minimizing the demagnetization field. (b) Fabricated square (50 μm × 50 μm) micro-patterns of CoPtP magnets developed using the pulse reverse electrodeposition and the corresponding M-H loops measured in SQUID magnetometer.

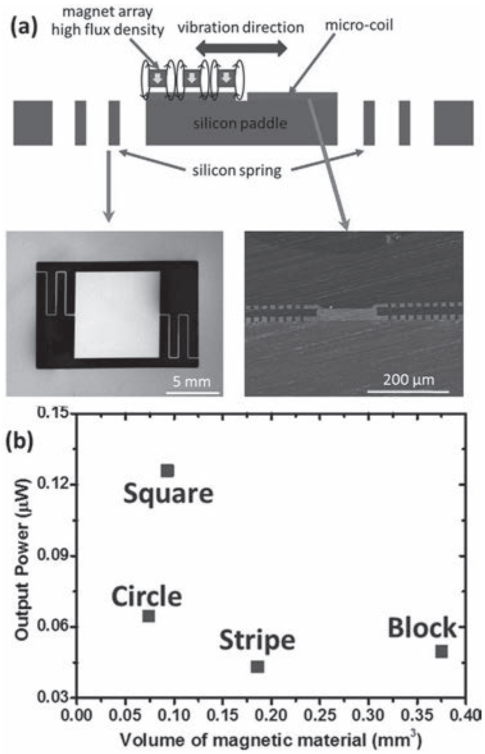

Fig. 2. (a) Proposed micro-EM VEH device topology incorporating patterned CoPtP magnetic structures. (b) Comparison of output power for different magnetic structures w.r.t. the total volume of the magnetic material used.

GQ-07. Characteristic Analysis of Periodic Electromagnetic Force in Wireless Power Transfer System.

X. Ni[1], X. Zhang[1], Q. Yang[1] and Y. Li[1]
1. School of Electrical Engineering and Automation, Tianjin Polytechnic University, Tianjin, China

The coupling mechanism in wireless power transfer(WPT) system, due to the existence of inductive current and time-varying electromagnetic fields, inevitably be affected by electromagnetic force, which would cause vibration and deformation [1]. Periodic electromagnetic force(PEMF)is an action mode of the electromagnetic force, and its amplitude and phase will vary with time periodically. The PEMF is the main inducement for continuous periodic vibration of the coupling mechanism. Under the long-term action of the PEMF, there is an adverse influence on service life, security and reliability of WPT system. And it also produces noise pollution to the surrounding environment. In this paper, the characteristics of the PEMF on coupling mechanism with magnetic shielding in WPT are revealed. The PEMF of WPT system can be divided to Lorentz force and Kelvin force. Coupling coils will be subjected by Lorentz force, which is the force of the magnetic field on the motion charge, and Kelvin force is defined as force caused by the magnetization in magnetic shielding materials. Korteweg-Helmholtz force density method [2] is used to investigate the value of PEMF in coupling coils and magnetic shielding materials. It can be recognized that the frequency of PEMF is twice that of current density and magnetic flux density, and there is phase difference between Lorentz force and Kelvin force. To evaluate the characteristics of the PEMF on the coupling mechanism with magnetic shielding, a two-dimensional finite element model is set up, based on WPT coupling mechanism boundary condition of physical model. The coupling mechanism is a symmetric square with side length 484mm. Both the transmitting coil and the receiving coil are square coils made of Litz wire, which are winded by a double-wire winding manner with 6 turns, embedded in grooved ferrite. The coils are coupled in a 200mm air gap, and the fundamental frequency amplitude of exciting current is 120A. Fig. 1(a) shows the 2-D simulation model which is on central axial section of the coupler. Measuring points of PEMF are located at the coupling coils and the magnetic shielding on the transmitting and receiving side, respectively, as shown in Fig. 1(b). And the EMF of the coupling coils is shown as Fig. 1(c). In Fig. 1(c), the current of the receiving coil is smaller than that of the transmitting coil, and there is a phase difference between them. The frequency of PEMF in coupling coils is twice of the system resonant frequency, owing to make a cross product between current density and magnetic flux field. And the direction of PEMF is opposite to the resonant current. In the measuring point a, there is a PEMF up to 3000N, which is dramatically higher than the PEMF of the same position on the receiving coil. In addition, it can be known that the force between the transmitting and receiving coil is repulsive force. As shown in Fig. 1(d), the frequency of PEMF acting on magnetic shielding is also twice that of the current density. And it is noteworthy that, camparing with coupling coils and magnetic shielding, the direction of PEMF is on the contrary. According to the simulation model, an isometric experimental prototype is built to verify the characteristics of PEMF in the former sections, as shown in Fig. 2(a). The inverter supply is powered by 380V voltage, and the frequency of the supply is 10kHz. Limited to the structure of the coils and measurement implements, only the property and character of PEMF are studied. Using a vibration sensor to gather voltage signal, the PEMF of coupling mechanism are shown in Fig. 2(b)-(e). It can be seen that the frequency of PEMF is 20kHz, which is twice of the system resonant frequency. Since the accurate measurement of PEMF is also quite hard, it can be considered that both magnitude and tendency are in good agreement. So, the PEMF of transmitting side is still larger than that of receiving side, demonstrate the consistency of simulation and experiment. In this paper, aimed at the vibration of the coupling mechanism, the characteristics of the periodic electromagnetic force are studied by theoretical analysis and simulation. The frequency of the coupling mechanism is twice of the system. There is repulsive force between the transmitting and receiving side, and the direction of coils and magnetic shielding materials are opposite. Then set up a experimental model to verify the characteristics. The characteristics of the PEMF could help to solve the problem of electromagnetic vibration, and improve the stability and security of WPT.

[1] S. Jang I., H. Ham S., H. Kim W., S. Jin C., Y. Cho S., D. Lee K., J. Lee J., Kang D., and Lee J., "Method for Analyzing Vibrations Due to Electromagnetic Force in Electric Motors". IEEE Transactions on Magnetics, Vol. 50, No. 2, PP. 297-300, 2014. [2] H. Choi J., Kwak C., S. Choi H., Kim H., and H. Lee S., "Mechanical Deformation and Body Force Density Due to the Generalized Korteweg–Helmholtz Force Density Method Employing the Virtual Air-Gap Scheme". IEEE Transactions on Magnetics, Vol. 52, No. 7, PP. 1-4, 2016.

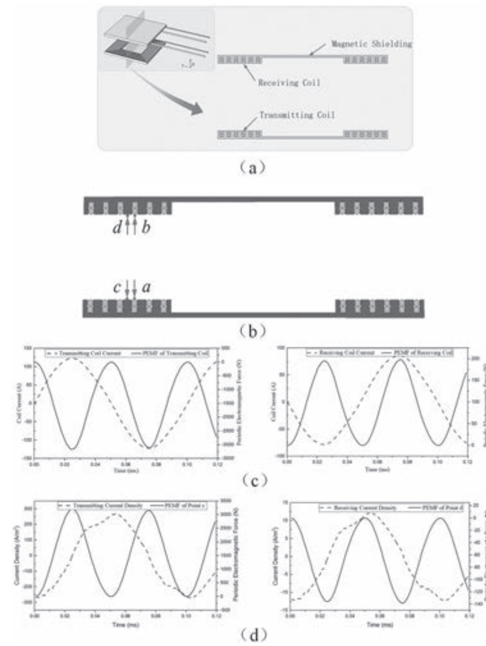

Fig. 1. (a) Simulation schematic of PEMF on coupler. (b) Measuring point of PEMF on coupler. (c) Waveform of current and PEMF at measuring point of coupling coils. (d) Waveform of current density and PEMF at measuring point of magnetic shielding.

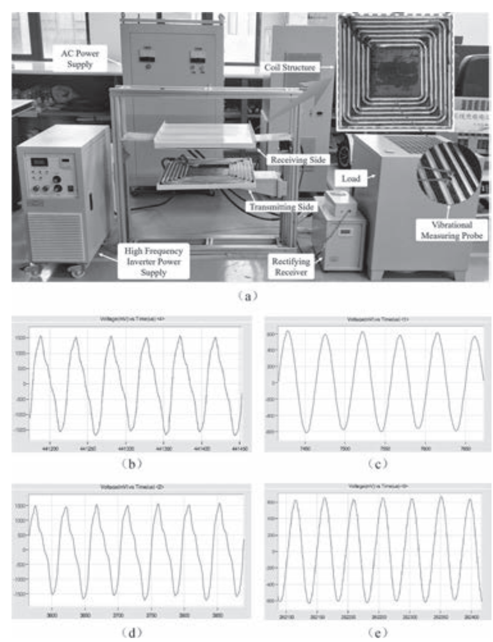

Fig. 2. (a) The measuring prototype for PEMF. Waveform of voltage at (b) Measuring points a of coupling coils. (c) Measuring points b of coupling coils. (d) Measuring points c of magnetic shielding. (e) Measuring points d of magnetic shielding.

GQ-08. Stress Induced Domain Wall Motion in Zig-zag shaped Microwires for Energy Harvesting in IOT devices.

C. Vaahsan[1], S. Bhatti[1], C. Ma[2], X. Liu[2] and S. Piramanayagam[1]
1. Division of Physics and Applied Physics, Nanyang Technological University, Singapore, Singapore; 2. Department of Electrical and Computer Engineering, Shinshu University, Nagano, Japan

Recently, the study of the Villari effect on ferromagnetic/magnetostrictive microwires has been the focus of studies due to their potential in energy harvesting projects [1] [2]. The need for self-power generation in internet-of-things (IOT) applications has increased the interest in such investigations. Many studies have focused on stress induced domain wall movements in magnetostrictive wires. The dynamics of domain wall motion depends on the size and shape of the magnetostrictive wires. However, there has been a lack of study in different shapes of microwires that affect domain wall motion under applied stress. Moreover, these studies emphasize on the multiferroic structures, where the stress on ferromagnetic layer is applied by applying the electric field to the ferroelectric layer [3]. Using the electric field for the energy harvesting application undermines the main objective of this research. Here, we report a study on novel zig-zag shaped microwires of FeCo with different dimensions to study the effect of the shape and dimensions on domain wall motions under a purely applied mechanical stress. The samples used in this study are the stack of CoNi/FeCo/CoNi, where the bottom and top CoNi layer was used as underlayer for introducing the anisotropy in FeCo layer and as capping layer to protect FeCo from oxidation, respectively. The zig-zag shaped microwires of different dimensions were patterned using photolithography. A facing targets sputtering system was used to deposit the stack on a flexible polyamide film. Under various sputtering parameters, the thickness of the stack was varied as 30, 40, 50, and 60 nm to investigate the effect of thickness on the stress induced domain wall motion. Kerr microscope was used to observe the deposited microwires. Moreover, to study the domain wall motion of the deposited microwires with different dimensions, we used the Bitter Pattern technique with the Kerr microscope. Stress application to the wires were carried out by pasting the films onto a metallic curvature of different radii, which induced stress to the samples. Comparisons between bitter patterns of different microwires were carried out to study the effect of different dimensions and thickness on the domain wall motion under applied various stresses values. Figure 1 shows the Kerr image of the 30 nm thick zig-zag FeCo microwires on the flexible substrate. It can be noticed from the figure that the dimensions of the deposited microwires are different. However, not a single domain wall was observed by using Kerr Microscope only. FeCo, being a soft magnetic material, is expected to show domains. Therefore, to observe domains and to study the effect of the applied stress on these deposited microwires, we used the bitter pattern technique along with a Kerr microscope. Figure 2(a) shows the bitter patterns of the as deposited sample and figure 2 (b) shows the bitter patterns of the sample pasted to the 24 mm curvature radii for stress application. The domain walls can be easily seen from the bitter patterns, which are in the longitudinal direction of the zig-zag microwires. The inset in figure 2 shows the magnified image of the microwire. From the insets, it can be easily noticed that the domain wall has been moved. In addition to this, domain wall movement in zig-zag microwires of varying sizes and different thicknesses has been investigated. This motion of domain wall under the applied mechanical stress can help in energy harvesting, when used with a pick-up coil. The presentation will discuss the domain wall motion results in detail.

1. Zhengwen Hu, Jing Qiu, et al., "An integrated multi-source energy harvester based on vibration and magnetic field energy", AIP Advances 8, 056623 (2018). 2. Mojtaba Ghodsi, Hamidreza Ziaaifar, et al., "Development of Novel Magnetostrictive Energy Harvester", ICTEA: International Conference on Thermal Engineering, [S.l.], v. 2017, mar. 2017. 3. Lahtinen, Tuomas HE, Kévin JA Franke, and Sebastiaan Van Dijken. "Electric-field control of magnetic domain wall motion and local magnetization reversal." Scientific reports 2 (2012).

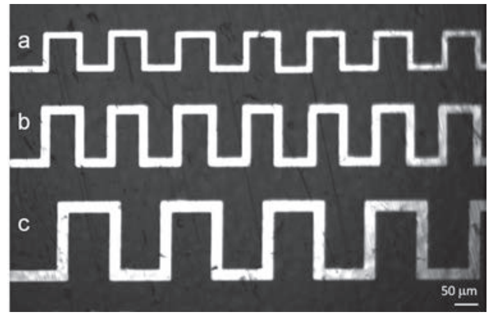

Fig. 1. Kerr Image of the as deposited FeCo microwire in the zig-zag shape. Wire (a) has a width of 10µm, wire (b) has a width of 15µm, and wire (c) has a width of 20µm.

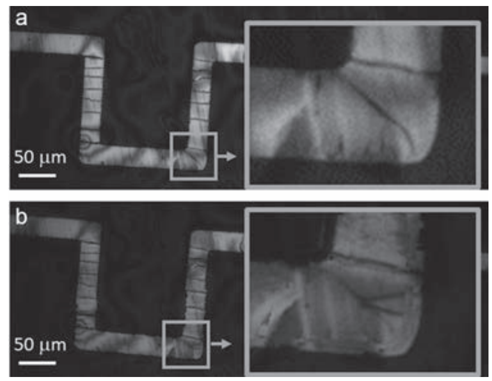

Fig. 2. Bitter Patterns of the zig-zag microwires using the Kerr Microscope. (a) Bitter patterns of the as deposited microwire; (b) bitter patterns of the microwires under applied stress. The insets show the zoomed-in images of the microwires.

GQ-09. Plasma Shape Optimization for EAST Tokamak Using Orthogonal Method.

Y. Chen[1], X. Bao[1], *W. Xu*[1] and G. Gao[2]
1. School of Electrical Engineering and Automation, Hefei University Of Technology, Hefei, China; 2. Institute of Plasma Physics, Chinese Academy of Sciences, Hefei, China

INTRODUCTION : Equilibrium configuration design and tokamak coil design are two of the most fundamental studies in tokamak fusion science [1]. A fixed boundary equilibrium code has been applied on Experimental Advanced Superconducting Tokamak (EAST) to deal with the reference configuration design [2]. In the EAST experiments, the quasi-snowflake (QSF) configuration was obtained with I_p= 250kA. Based on the reconstructed plasma shape of shot 56573 at 5 s by EFIT code, the QSF configuration with I_p= 300kA is designed as well as the calculation of the poloidal field (PF) coil current, but the results show that the currents of PF6 and PF14 will exceed the limit [3]. This paper is to investigate the impact of the plasma shape parameters on PF coil current distribution, and the orthogonal method is used to optimize the plasma shape of QSF discharge. PLASMA CONFIGURATION DESIGN AND SHAPE OPTIMIZATION: The cross-section of the EAST and plasma are shown in Fig. 1. The preliminary design of the QSF configuration with = 300kA has the approximately same equilibrium profiles of the reference from shoot 56573. To avoid the excessive coil current, the orthogonal method is employed to tweak the shape parameters. The currents of PF6 and PF14 are set to be the target of the optimization. Plasma shape parameters triangularity, elongation and squareness are determined by the order. The analysis result is shown in Fig. 2. It shows that the elongation and inner bottom squareness are the most important fact that influence the PF6 and PF14 current, respectively. Furthermore, a comparatively better plasma shape and PF current distribution could be achieved. Fig 3 compares the 2D poloidal flux distribution and PF current distribution calculated by fixed boundary equilibrium solver before and after optimization. It can be seen that after the optimization, the currents of PF6 and PF14 are less than the maximum allowable value 12kA. More results and discussions will be given in the full paper.

[1] R. Albanese et al., “A MIMO architecture for integrated control of plasma shape and flux expansion for the EAST tokamak,” 2016 IEEE Conference on Control Applications (CCA), Buenos Aires, 2016, pp. 611-616. [2] Q. Hang and G. Li, “Discharge Analysis of EAST H-Mode for Designing Compressed Plasma,” in IEEE Transactions on Plasma Science, vol. 45, no. 6, pp. 1010-1014, June 2017. [3] Y. T. Song et al., “The Accomplishments and Next-Step Plan of EAST in Support of Fusion,” in IEEE Transactions on Plasma Science, vol. 42, no. 3, pp. 415-420, March 2014.

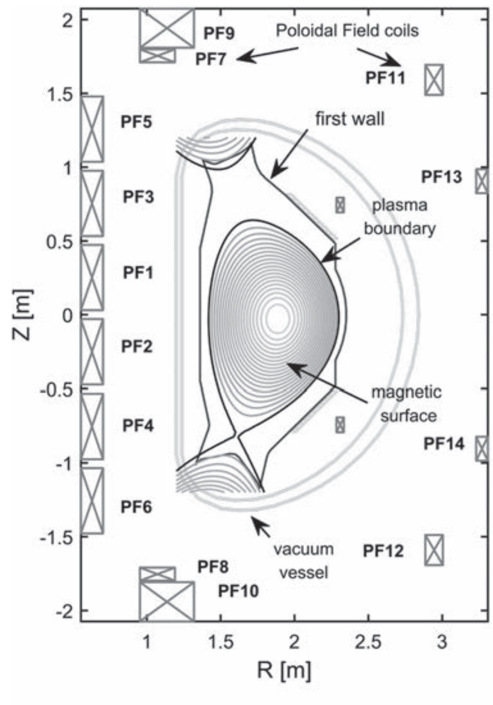

Fig. 1 The cross-section of the EAST and plasma

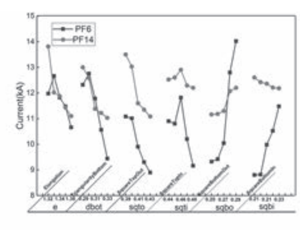

Fig. 2 Analysis result of orthogonal method

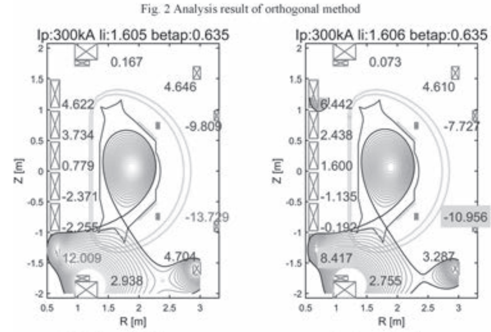

(a) Before optimization (a) After optimization

Fig. 3 2D poloidal flux distribution and PF coil current distribution

GQ-10. Characteristics of Impulsive Force on coupler of Wireless Power Transfer.

Z. Yuan[1], X. Zhang[1], Q. Yang[1] and Y. Li[1]
1. Tianjin Key Laboratory of Advanced Electrical Engineering and Energy Technology, Tianjin Polytechnic University, Tianjin, China

The nature of Wireless Power Transfer (WPT) technology is that the electromagnetic field produced by the high frequency current in the transmitter is coupling with the receiver. It should be noted that the coupler will inevitably be affected by electromagnetic force over the power transmission, due to the coupling of high frequency electromagnetic field. The electromagnetic force will seriously affect the security and reliability of WPT system. In addition, the short circuit and load mutation will cause the abrupt change of current resulting in impulsive force. There will be a great impact on the load, threatening the system security and stability. With the improvement of high power WPT, the magnetic material is used to improve the coupling degree, which will inevitably increase the coupling effect, and consequently increase the electromagnetic force. In [1], the semi-analytical solution of electromagnetic force of coaxial elliptical coils is derived by using Elliptic integral and Lambda function. In [2] and [3], the electromagnetic force on receiving coil is observed and used to drive and steer the micro-robot. Further, the authors use the high-speed camera to analyze the moving speed of receiving coil which is floats on the water, then the electromagnetic force is calculated [4]. However, the effects of impulsive force to high power dynamic WPT system have not been analyzed and studied at home and abroad. The characteristics of impulsive force on coupler should are studied in this paper. In WPT system, considering the material of coupler as magnetically linear material and incompressible, the mechanical model of EMF can be established with analysis of force of coupling coils, based on Lorentz force density theory. For coupling coils, the force can be calculated by $J\times B$ caused by eddy current effect. For magnetic shielding material, the force can be obtained by $-1/2H\bullet H\nabla\mu$ caused by magnetization. μ is the permeability of material. J and B can be expressed as the superposition of several sinusoidal signals of different frequencies. When pulse current produces impulsive force, $J=\{\Sigma[-J_{1n}\sin(nwt+a_0)+J_{2n}\sin(nwt+a_1)\ l(t_0)]\}\theta_1$, and $B=\{\Sigma[B_{1n}\sin(nwt+\beta_0)+J_{2n}\sin(nwt+\beta_1)\ l(t_0)]\}\theta_2$. Then the characteristics of impulsive force can be obtained. Fig. 1 shows the 2D simulation model and the results of impulsive force on coupler. The pulse current is produced by *if* condition. The results illustrate that the pulse current have a major effect on current density in magnetic shielding. The frequency of force is twice the resonant frequency of system. When there is pulse current, the amplitude of force will be increased. A prototype is built to experiment on impulsive force on coupler of WPT, as shown in Fig. 2(a). The pulse current is obtained by time relay. Part of the results are shown in Fig. 2(b) to (e). The amplitude of force on coupler is increased. And the force on transmitter is more increment than receiver. It indicates that this simulation results are correct. The research in this paper can be referred in further research of high frequency electromagnetic force in WPT system.

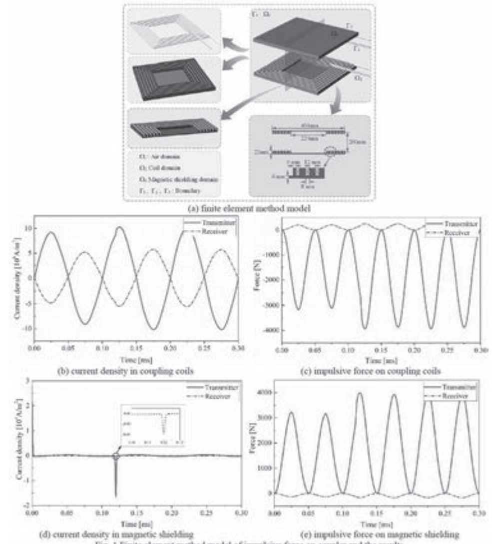

Fig. 1 Finite element method model of impulsive force on coupler and the results

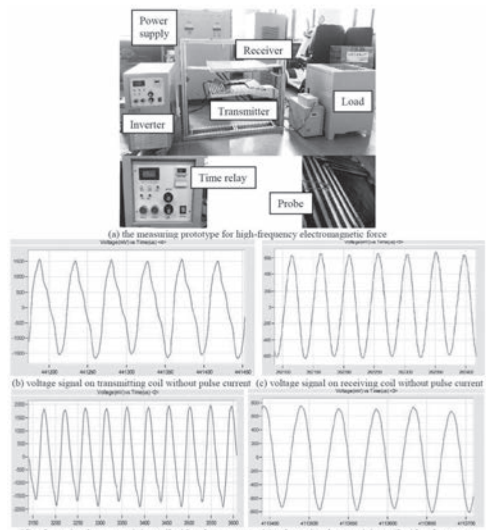

Fig. 2 The measuring prototype and experimental results

[1] Babic Si, Akyel C. Magnetic Force Calculation Between Thin Coaxial Circular Coils in Air, *IEEE Transactions on Magnetics*, vol. 44, no. 4, pp: 445-452, 2008. [2] D. Kim, J. Park, K. Hwang, et al. Generating propulsion force in micro-robot using wireless power transfer system, *2016 URSI Asia-Pacific Radio Science Conference (URSI AP-RASC)*, PP: 2050-2052, 2016. [3] Dongwook Kim, Jaehyoung Park, Kibeom Kim, et al. Propulsion and control of implantable micro-robot based on wireless power transfer, *2015 IEEE Wireless Power Transfer Conference (WPTC)*, pp: 1-4, 2015. [4] Kim Dongwook, Park Jaehyoung, Park Hyunho, et al. Generation of Magnetic Propulsion Force and Torque for Microrobot Using Wireless Power Transfer Coil, *IEEE Transactions on Magnetics*, vol. 51, no. 11, pp: 1-4, 2015.

GQ-11. Nanoscaled magnetic Cu-Co alloys with tuneable properties processed by high-pressure torsion deformation.

A. Bachmaier[1], H. Krenn[2], P. Knoll[2] and R. Pippan[1]
1. Erich Schmid Institute of Materials Science, Austrian Academy of Sciences, Leoben, Austria; 2. Institute of Physics, University of Graz, Graz, Austria

In this study, severe plastic deformation by high-pressure torsion (HPT) deformation is used as alternative fabrication method for nanocrystalline bulk magnetic Cu-Co alloys. Full supersaturation with a single-phase structure can be achieved by HPT deformation at room temperature (RT) of two-phase Cu–Co materials or powders (Fig.1). Subsequent isothermal annealing above the decomposition temperature results in the formation of a nanoscale composite structures investigated in detail by transmission electron microscopy and atom probe tomography (APT). Both, the size as well as the composition of the Cu and Co regions can be influenced by the annealing time. The magnetic properties of the as-deformed and annealed structures are investigated by SQUID-magnetometry and correlated to the evolving nanostructures. As-deformed nanostructures can be further tailored by HPT conditions (i.e. by additional HPT deformation at liquid nitrogen (LN) temperature) and the structural evolution strongly affects magnetic properties. The magnetic properties of the alloy can thus be also used as a valuable fingerprint for the microstructural changes (Fig.2). This project has received funding from the European Research Council (ERC) under the European Union's Horizon 2020 research and innovation programme (grant agreement No 757333).

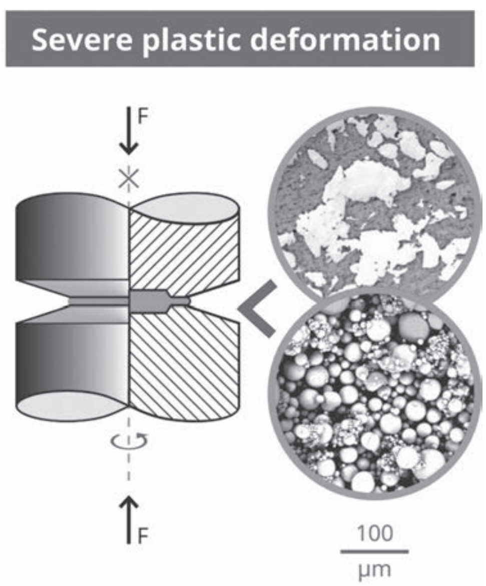

Fig. 1. Severe plastic deformation by means of HPT deformation using two-phase Cu–Co composites or powders as starting material.

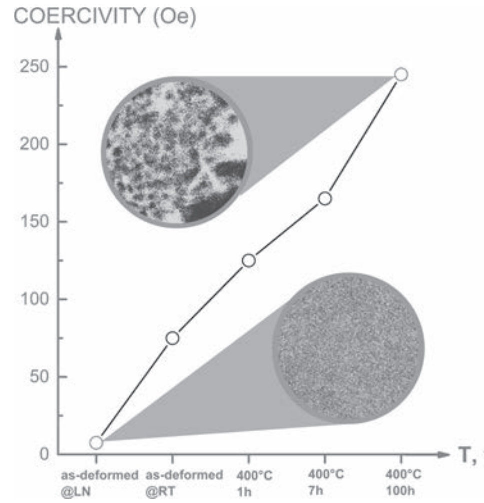

Fig. 2. Variation of coercivity as function of annealing temperature (T) and time (t). The insets show tomographic slices (10 nm thickness) obtained by APT for samples deformed at LN temperature and annealed at 400°C for 100 h. Cu atoms are displayed in green, Co atoms in blue, respectively.

GQ-12. Preparation and thermoelectric properties of $Mn_2V(Al_{1-x}Si_x)$ full-Heusler compounds.

H. Li[1], K. Hayashi[1] and Y. Miyazaki[1]
1. Tohoku University, Sendai, Japan

1. Introduction: Recently, thermoelectric materials that can convert thermal energy into electricity have attracted much attention as clean energy harvesting materials. The efficiency of a thermoelectric material is evaluated by the dimensionless figure of merit, $zT = S^2\sigma T/\kappa$, where S, σ, T, and κ are the Seebeck coefficient, electrical conductivity, absolute temperature, and thermal conductivity, respectively. In order to achieve a high zT, a high power factor (PF = $S^2\sigma$) is desired. It is reported that a half-metallic Co_2MnSi full-Heusler alloy shows a relatively high PF of 2.9×10^{-3} $Wm^{-1}K^{-2}$ at 550 K [1]. Since Co_2MnSi is n-type, it is necessary to develop a p-type full-Heusler alloy to be paired with it. In this work, we calculated and measured thermoelectric properties of one of the Mn-based full-Heusler compounds, Mn_2VAl. Furthermore, we performed partial substitution of Si for the Al site to improve PF of Mn_2VAl. 2. Methods: We calculated an electronic band structure of Mn_2VAl in a ferromagnetic phase using the first-principles density function theory. The Seebeck coefficient of Mn_2VAl was calculated using the semi-classical Boltzmann's equation. $Mn_2V(Al_{1-x}Si_x)$ polycrystalline samples (x = 0, 0.005, 0.01, 0.03, 0.05, 0.07, 0.1, and 0.15) were prepared by the arc-melting method followed by the spark plasma sintering (SPS) method. A crystal structure of the SPSed samples was characterized by powder X-ray diffraction (XRD). The Seebeck coefficient and electrical conductivity were simultaneously measured in vacuum from 300 K to 1050 K. 3. Results and discussions: From the XRD patterns, the x = 0, 0.005, 0.01, 0.03, and 0.05 samples were found to be in a single phase of the full-Heusler compound. On the other hand, the samples with $x \geq 0.07$ contained a secondary phase of $(Mn_{0.17}V_{0.83})_3Si$. Thus, the solubility limit of Si in Mn_2VAl was below x = 0.07. Temperature dependence of measured and calculated Seebeck coefficients was shown in Fig. 1. The x = 0 sample (Mn_2VAl) showed a positive Seebeck coefficient in the entire measurement temperature range, indicating a p-type conduction. The temperature dependence agreed with the calculated Seebeck coefficient of Mn_2VAl in a qualitative manner. The measurement and calculation both exhibited a maximum Seebeck coefficient around 700 K. However, it is noted that the calculation was for the ferromagnetic Mn_2VAl case. In fact, it is reported that a ferromagnetic-paramagnetic phase transition occurs at T_C = 760 K for Mn_2VAl [2]. Thus, to discuss the temperature dependence of Seebeck coefficient above 700 K, the Seebeck coefficient of Mn_2VAl in a paramagnetic phase is required. Turning to the sample dependence, the x = 0.005, 0.01, 0.03, and 0.05 samples showed a higher Seebeck coefficient than the x = 0 sample. The highest value reached 32 μVK^{-1} at 664 K for the x = 0.005 sample. The increase in Seebeck coefficient was partly due to an decrease in hole carrier density. Above x = 0.03, the Seebeck coefficient became equal to or lower than that of the x = 0 sample, probably due to the increase in the metallic secondary phase of $(Mn_{0.17}V_{0.83})_3Si$. Although not shown here, the electrical conductivity of Mn_2VAl was as high as 4.20×10^3 S/cm at 355 K. With increasing temperature, the electrical conductivity slightly decreased to 3.89×10^3 S/cm at 715K, and then increased above 715 K, which might be related to the ferromagnetic-paramagnetic phase transition. The partial substitution of Si for the Al site decreased the electrical conductivity up to x = 0.03. Above x = 0.03, the increase in the metallic secondary phase of $(Mn_{0.17}V_{0.83})_3Si$ led to the upturn of the electrical conductivity. Mainly reflecting the increase in Seebeck coefficient by the partial substitution, the power factor was successfully enhanced (Fig. 2). The highest PF of 3.95×10^{-4} $Wm^{-1}K^{-2}$ at 664 K was obtained for the x = 0.005 sample, which was about 1.3 times higher than that of the x = 0 sample.

[1] K. Hayashi *et al*., *J. Electr. Mater.*, 46 (2017) 2710. [2] C. Jiang *et al*., *Solid State Commun*., 118 (2001) 513.

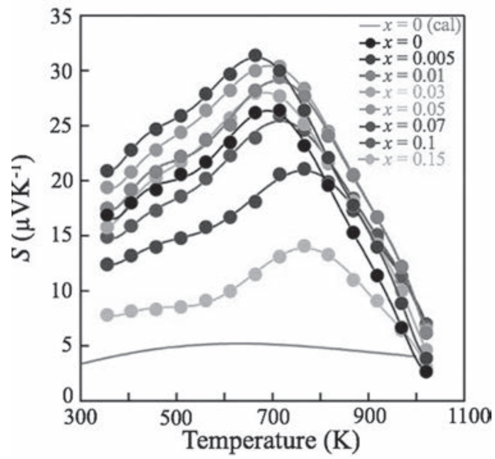

Fig. 1. Temperature dependence of the Seebeck coefficient of the $Mn_2V(Al_{1-x}Si_x)$ samples (x = 0, 0.005, 0.01, 0.03, 0.05, 0.07, 0.1, and 0.15). Calculated Seebeck coefficient of Mn_2VAl is also shown in the figure.

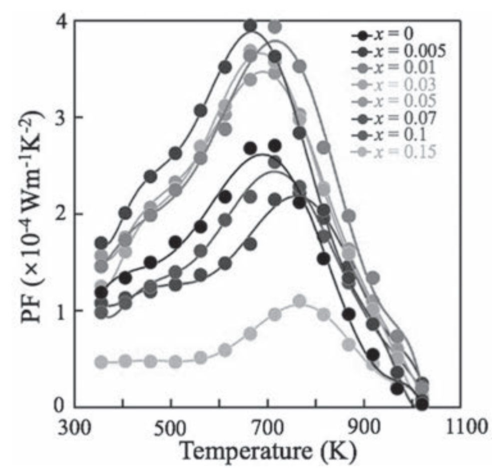

Fig. 2. Temperature dependence of the Power factor, PF, of the $Mn_2V(Al_{1-x}Si_x)$ samples (x = 0, 0.005, 0.01, 0.03, 0.05, 0.07, 0.1, and 0.15).

GQ-13. A MLC STT-MRAM based Computing in-Memory Architecture for Binary Neural Network.

Y. Pan[1], P. Ouyang[1], Y. Zhao[1], W. Kang[1], S. Yin[2], Y. Zhang[1], W. Zhao[1] and S. Wei[2]
1. Beihang University, Beijing, China; 2. Tsinghua University, Beijing, China

Due to add operations dominated computation and simplified network in Binary Neural Network(BNN), it is promising for IOT scenarios, which demand ultra-low power consumption and hardware area overhead[1]. By means of exploiting the in-memory computing methods and high density of MLC STT-MRAM [2][3], this work designs a MLC-STT-CIM(Compute-in-Memory) based computing in-memory architecture to achieve add operations for BNN, to further reduce power consumption and area overhead. With MLC STT-MRAM cell, we can store two bits in one cell and achieve add operation in one cell between the two bits. Compared to the design in [2] of which two addends are stored in two different bit-cells of the same column and both WLs are enabled to connected with NMOSs, this design reduces the capacity and energy consumption (see Fig.1: I_{SL} will be lower as it represents the current through one cell while in STT-CIM I_{SL} represents the sum of the current through two cells). Meanwhile, this design achieves lower read failure possibility because one read operation is enabled by only one WL. In this design (See Fig.1), there is a larger MTJ and a small MTJ in a cell to store two bits in one cell. The relative magnetic orientation of the free and reference layers determines the resistance offered by the MTJ. The resistance for the parallel configuration R_P, is lower than the anti-parallel resistance R_{AP}. R_P of small MTJ is lower than that of large MTJ, and so does R_{AP}. We assume R_{AP} represents logic "0" and R_P represents logic "1", then the resultant current I_{SL} flowing through the bit-cell is determined by the stored data in MTJs. If the first bit is stored in large MTJ and the second bit is stored in small MTJ, I_{SL} satisfy $I_{00}<I_{01}<I_{10}<I_{11}$ for $R_{AP\text{-}AP}> R_{AP\text{-}P}> R_{AP\text{-}P}> R_{P\text{-}P.}$ We can choose proper reference resistances to generate reference currents that satisfy $I_{00}<I_{ref3}<I_{01}<I_{ref2}<I_{10}<I_{ref1}<I_{11.}$ Basing on the modified sensing circuit combined by sense amplifiers(SAs), MOSs and logic gates, we can realize both memory and computing mode. Memory mode: When WLs are enabled, we can write the bits to the cell with a two-step writing scheme: a large current is used to change the magnetic orientation of the large MTJ to write the first bit bit1.Because switching current of the small MTJ is smaller than the large one, the magnetic orientation of the small MTJ is changed as we write bit1.Basing on the second bit bit2, a small current is used to switch the small MTJ if necessary. To read the bits, we connect I_{SL} to the positive input of the sense amplifier SA1, SA2, and SA3 respectively. Connecting I_{ref2} to the negative input of SA1 to read the first bit, and the second bit signal will be sensed from the positive output of SA2 or SA3 by accordingly feeding I_{ref1} and I_{ref3} to their negative input. If the first bit is "1"("0"), we will get the correct second bit from SA2(SA3). Respectively, connecting the positive output of SA2 and SA3 to D ports of NMOS and PMOS which are controlled by the first bit, and connecting the S ports to output bit2, the second bit is got. Computing mode: Except sensing the second bit in memory mode,SA2 can realize logic AND and NAND. As mentioned above, only I_{11} is larger than $I_{ref1.}$ In other words, only both MTJS are in the P configuration (both store logic "1"), leads to an output of logic "1" ("0") at the positive (negative) output of SA2, while all other cases lead to logic "0" ("1"). Thus, the positive and negative outputs of SA2 evaluate the logic AND and NAND of the values stored in the enabled bit-cells. Obviously, A OR (NOR)operation can be realized at the positive (negative) terminal of SA3. And an XOR operation can be realized when feeding the AND output of SA2 and the NOR output of SA3 to a CMOS NOR gate. Suppose An and Bn(the n-th bits of two words, A and B) are stored in large MTJ and small MTJ in a cell within a MLC-STT-CIM array. Suppose that we wish to compute the full-adder logic function (the n-th stage of an adder that adds words A and B). According to Sn= An XOR Bn XOR $C_{n,}$ Cn =((An XOR Bn) AND C_{n-1}) OR (An AND Bn), the sum Sn and the carry out Cn Can be computed using An XOR Bn and An AND Bn, in addition to C_{n-1} (carry input from the previous stage). We can see that ADD operation in terms of the outputs of bitwise operations, AND and XOR. Three additional logic gates are required to enable this computation. In this mode, the amounts of energy consumption for add operation is reduced within one cell, which can compute BNN efficiently. Meanwhile, since I_{SL} is smaller, the full-add operation is more reliable which benefits from lower sensing disturbing probability.

[1] S. Zhou et al. arXiv preprint arXiv:1606(2016). [2] Shubham Jain ., et al. arXiv:1703.02118v4(2017). [3] Y. Zhang, et al. ICCAD,pp. 526–532(2012).

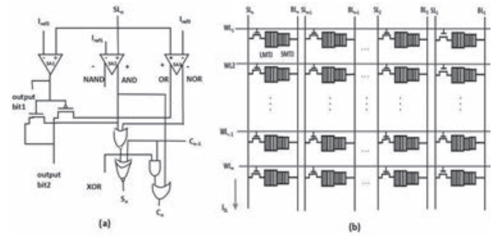

Figure1 (a)Modified sensing circuit (b)N×N MLC-STT-CIM array

GQ-14. Withdrawn

FRIDAY MORNING, 27 APRIL 2018 SIMPOR/ROSELLE BALLROOM, 8:30 TO 11:30

Session GR
HARD MAGNETIC MATERIALS AND PROCESSING II
(Poster Session)

Damien Le Roy, Chair
Institut Lumière Matière, Villeurbanne, France

GR-01. Anisotropic $SmCo_5$ nanocrystalline magnet prepared by hot deformation with bulk amorphous precursors.

J. Liang[1], M. Yue[1], D. Zhang[1], Y. Li[1] and H. Li[1]
1. Beijing University of Technology, Beijing, China

I. INTRODUCTION Nanocrystalline $SmCo_5$ magnet has been investigated for many years due to its extraordinary high anisotropy filed as well as coercivity. Therefore, producing an anisotropic structure $SmCo_5$ magnet through hot deformation has attracted considerable interest in order to acquire higher magnetic performance. Nevertheless, most of precursors magnets are crystal matrix before hot deformation, while amorphous matrix can maximize the retention of fine grains and control grains growth, which will definitely benefit the magnetic performance[1]. In this study, we report a novel approach to synthesize bulk anisotropic $SmCo_5$ nanocrystalline magnets from $SmCo_5$ amorphous precursor. II. EXPERIMENTS The alloy ingot with nominal composition of $SmCo_5$ was prepared by induction melting with 10 wt.% excess of Sm to compensate for the evaporation losses. The ingot was then melt-spun into as-spun ribbons, and manually crushed into powders. 20 g of the crushed powders were ball milled for 5 hours in a tungsten carbide vial using high energy ball milling machine with the ball-to-powder weight ratio of 10:1. The as-milled powders which contain an amorphous SmCo matrix were put in a Φ15 tungsten carbide mold, which then consolidated into bulk amorphous precursors at 200°C under 500 MPa by using spark plasma sintering (SPS) method[2], followed by hot deformation at 800°C under 50 MPa with a height reduction of 85%. The microstructures of the samples were examined by scanning electron microscopy (SEM) and high-resolution transmission electron microscopy (HRTEM), which showed a large number of nanoscale twins formed. The crystal structure and texture was determined by X-ray diffraction (XRD). The room-temperature magnetic properties parallel and perpendicular to the pressure direction were examined by using a physical property measurement system (PPMS) with a magnetic field up to 7T. The density of the hot-deformed magnets was measured by Archimedes method. III. RUSULTS AND DISSUSION Figure 1 shows five different XRD patterns that separately are as-spun ribbons, milled powers, hot pressed magnet and the two surfaces of hot deformed magnet which are perpendicular and parallel to the pressure direction, respectively. A pure hexagonal phase of $SmCo_5$ is observed in the as-spun ribbons. Then, the as-milled powers show a broad hump in the XRD pattern, suggesting that an amorphous matrix is obtained. Subsequently, the $SmCo_5$ amorphous powers were consolidated into bulk amorphous precursor by hot pressed at 200°C, and the corresponding XRD result shows that there is no obvious crystallization. Followed by hot deformation, the intensity of (00*l*) diffraction peaks is obviously enhanced in the surface perpendicular to the pressure direction, as shown in fig. 1, revealing that strong c-axis textures were obtained for the hot deformed $SmCo_5$ magnet. The relative intensity ratio, I(002)/I(111), can be characterized as crystallographic alignment. The ratio I(002)/I(111) of the surface perpendicular to the pressure direction is 0.91, while the ratio is 0.25 for the standard $SmCo_5$ XRD pattern and 0.17 for parallel, indicating strong anisotropic nanostructure $SmCo_5$ magnet is obtained. Shown in Figure 2 are the hysteresis loops tested along the easy and hard axis of the hot deformed $SmCo_5$ magnet. The large difference of remanence along the easy and hard axis of the hot deformed $SmCo_5$ magnet demonstrates the strong c-axis texture, which has a good agreement with the XRD results. In addition, A high remanence ratio ($M_r/M_s = 0.88$) is exhibited along the easy axis which also shows the strong texture for the hot deformed magnets. It is worth mentioning that the high coercivity of 32.1 and 36.4 kOe is obtained for the hot deformed $SmCo_5$ magnet along the easy and hard axis, respectively. IV. CONCLUSION In summary, bulk nanostructure $SmCo_5$ magnet with strong c-axis texture can be prepared by hot deformation from the amorphous precursor. The high remanence ratio of 0.88 and coercivity of 32.1 kOe are obtained in the hot deformed magnet. We believe that this novel approach could be applied to nanocomposite magnets by further optimizing the process.

[1] X. Li et al., "Novel Bimorphological Anisotropic Bulk Nanocomposite Materials with High Energy Products," Adv Mater, vol. 29, no. 16, Apr 2017. [2] D. T. Zhang et al., "Nanocrystalline $SmCo_5$ magnet synthesized by spark plasma sintering," Journal of Applied Physics, vol. 107, no. 9, p. 09A701, 2010.

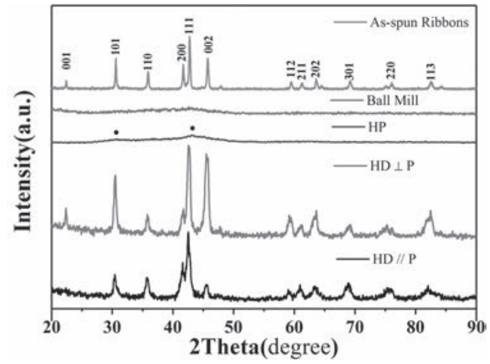

Fig. 1. XRD patterns of as-spun ribbons, milled powers, hot pressed and two vertical surfaces of hot deformed bulk nanocrystalline $SmCo_5$ permanent magnets.

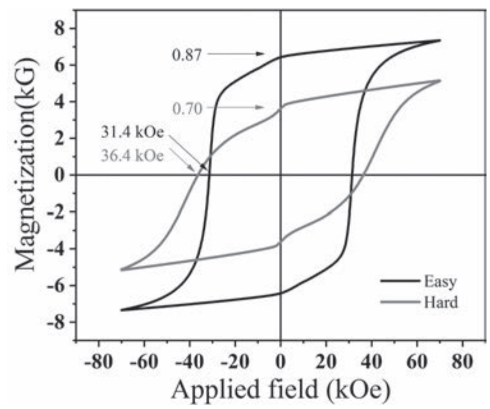

Fig. 2. Hysteresis loops of anistropic hot deformed $SmCo_5$ magnet along its easy and hard axis.

GR-02. Magnetic properties of Co-ferrite/FeCo bilayers.

Y. Hara[2], S. Shirsath[1], D. Wang[1], A. Morisako[2] and X. Liu[2]
1. School of Materials Science and Engineering, University of New South Wales, Sydney, NSW, Australia; 2. Faculty of Engineering, Shinshu University, Nagano, Japan

Co-ferrite with spinel structure is one of the attractive materials for spintronics and artificial multiferroics. Due to the high resistivity and high-Curie temperature properties, Co-ferrite thins films have potential applications in such so-called spin filters, where a combination of insulating ferrite with a non-magnetic electrode is believed capable of creating pure spin polarized currents. Co-ferrite also shows large magnetostrictive effect, that can be used for enhancing magnetoelectric coupling between ferroelectric phase and ferromagnetic phase of multiferroic nanostructures. Films with (00l) orientation and perpendicular magnetic anisotropy are essential to realize the interesting properties of Co-ferrite thin films. So far, Single crystal substrate such as $SrTiO_3$, MgO have been reported for the heteroepitaxial growth of (00l) orientated Co ferrite films. However, from the practical application point of view, it is strongly recommended to prepare orientated Co ferrite films onto thermally oxidized silicon wafers (SiO_2/Si) Here, a unique process has been developed to deposit Co-ferrite thin films onto thermally oxidized silicon wafer with perpendicular magnetic anisotropy by facing target sputtering. Metallic FeCo was used as underlayers. Co-ferrite films with preferential (00*l*) orientation have been successfully prepared. In this experiment, all the films are deposited without substrate heating. The as-deposited films show nanocrystalline structure with the X-ray diffractometry (XRD) characterization. We have also checked the depth profile of X-ray photoelectron spectroscopy. It is confirmed that the metallic FeCo underlayer got fully oxidized after annealing. Fig. 1 shows hysteresis loops of as-deposited Co-Fe-O films with thickness of 60 nm. The films are deposited without FeCo underlayer (a) and with 3 nm thick of FeCo underlayer. Films deposited without FeCo underlayer show saturation magnetization of around 110 emu/cc. The value is almost one fourth of bulk Co-ferrite. Which indicates that non-magnetic amorphous phase in the nanocrystalline films. However, saturation magnetization dramatically increases with FeCo underlayer of only 3 nm. X-ray diffractometry results clearly exhibit the formation of crystallized spinel structure even without substrate heating with FeCo underlayer. These results suggested that FeCo underlayers can dramatically decrease the crystallization temperature for spinel structures. For all the films, a dramatically increases of coercivity have been achieved by annealing the samples at 800 ^{o}C for 2 hours. Fig. 1 shows hysteresis loops of (c) annealed films without FeCo underlayer and (d) annealed films with FeCo underlayer. Both films show preferential perpendicular magnetic anisotropy. However, films deposited onto FeCo underlayer show smaller in-plane coercivity. Which indicate that such a film have better perpendicular magnetic anisotropy as compared with films without FeCo underlayer. Fig. 2 shows XRD results of (a) annealed films without FeCo underlayer and (b) annealed films with FeCo underlayer. It is clearly that films deposited without FeCo underlayer show (311) plane as the strongest diffraction but films deposited onto FeCo underlayer show (004) plane as the strongest diffraction. Further investigation shows three-dimensional lattice parameters determined by in-plane X-ray diffractometry to be a=b=8.43 Å, c = 8. 35Å. This indicating a compressive c-axis of for the cubic spinel structure. Such a compressive crystal structure leading to the very large coercivity in Co-ferrite films. In summary, we have developed a novel process to prepare Co-ferrite films with perpendicular magnetic anisotropy onto amorphous thermally oxidized silicon wafer. The large perpendicular coercivity of the films is attributed to the compressive x-axis of the cubic spinel structure.

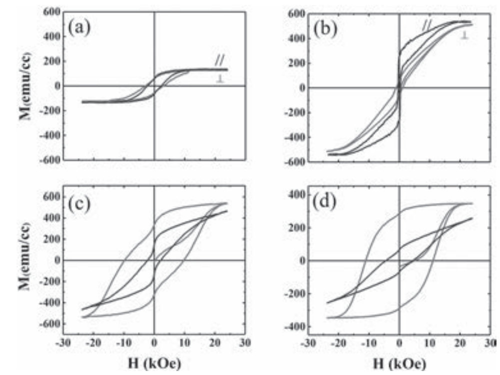

Fig. 1. Hysteresis loops of 60 nm thick Co-ferrite (a) as-deposited Co-Fe-O films without FeCo underlayer, (b) with 3 nm thick FeCo underlayer, (c) annealed Co-Fe-O film without FeCo underlayer and (d) annealed Co-Fe-O films with FeCo underlayer.

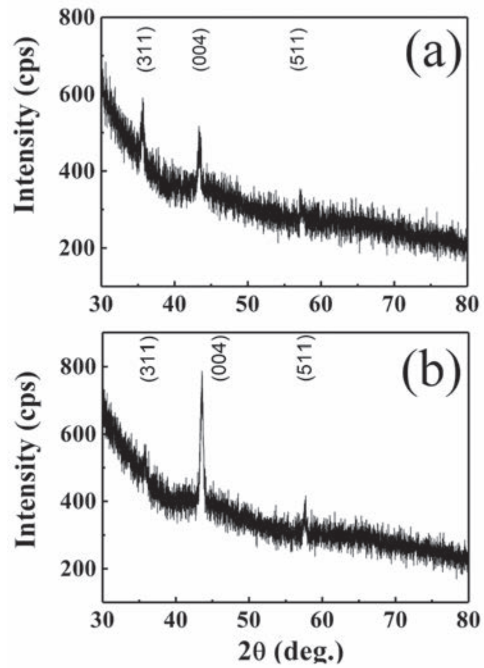

Fig. 2. XRD results of (a) annealed films without FeCo underlayer and (b) annealed films with FeCo underlayer.

GR-03. High Content Nd-Fe-B in Polymer Composite by Fused Deposition Modeling.

T. Chang[2], J.K. Jyun[3], W. Lee[3], *M. Tsai*[1,2] and C. Cheng[4]
1. Mechanical Engineering Department, National Cheng Kung University, Tainan, Taiwan; 2. Electric Motor Technology Research Center, National Cheng Kung University, Tainan, Taiwan; 3. Department of Electrical Engineering, National Cheng Kung University, Tainan, Taiwan; 4. Department of Mechanical Engineering, National Chiao Tung University, Hsinchu, Taiwan

I. Introduction Fused Deposition Modeling (FDM) is a widespread method in 3D printing for its advantages of being less expensive, rapid, and easy to use. Therefore, the extrusion molding is adopted to manufacture the synthesis magnet powder and Acrylonitrile-Butadiene-Styrene (ABS) particles for the FDM. Compared to the properties of bonded-type magnetic devices, the magnetic properties, the quantity contained, and three-dimensional structure of hard magnetic composite materials are improved; thus, the applications of bonded-type magnets have expanded. II. Model Description and Simulation It is difficult to form certain shapes when utilizing Nd-Fe-B composites made by melting or casting. The rapid prototyping method is a promising approach to manufacturing complex shapes of hard magnetic composite components. Magnetic properties of hard magnetic materials are affected by many factors, such as composition, microstructure, particle shape, particle size, and packing density. Instead of heat-pressing process, FDM [1] provides a solution to improve the high porosity issue, enhance the three-dimensional structure magnetic properties of hard magnetic composite materials, and replace the traditional bonded-type magnet. ABS polymer composite is a mixture of different methods to improve the uniformity operation of composite. The components in the volume of the system keep the same in the basic volume with the refinement and homogenization distribution, and that is a physical mixing process including distributive mixing and dispersive mixing effects. Dispersive mixing effect refers to the particle size of components that have been downsized to the degree of molecular patterns during the process. In the actual mixing process, distributive and dispersive effects mostly exist synchronically. Via various hybrid mechanical energies, such as mechanical energy, thermal energy, and other factor effects, the mixed magnetic material particles continue to increase and disperse during the redistribution. In this study, the basic material, Nd-Fe-B powder, is blended with ABS to granulate the magnetic powders to be 1.75mm in diameter during drawing, and utilize in 3D printing by FDM. The wire cross-section of Nd-Fe-B powder in the ABS is analyzed with the scanning electron microscope, and the result is shown as Figure 1. An obvious uniformity distribution can be observed. The hysteresis loop of different weight percentages of magnetic properties of polymer composite material is shown in the Figure 2. It is observed that, in the proportion of 65 wt% and 70 wt% of kneading conditions, the hysteresis loop of hard magnetic material is relatively weaker. However, when the proportion is increased up to 75 wt%, the hysteresis loop achieves the optimal condition. III. Conclusion In this work, when the content of magnetic material is raised comprehensively, the magnetic properties of the element are also increased. However, when the content of ABS is decreased, the liquidity of the composite material also significantly declines, which brings difficulties to the FDM of 3D printing. According to the analysis, it is observed that when the magnetic kneading ratio of ABS is up to 75%, the uniformity of distribution and magnetic properties also progresses.

[1] M. Parans Paranthaman, Christopher S. Shafer, Amy M. Elliott, Derek H. Siddel, Michael A. McGuire, Robert M. Springfield, Josh Martin, Robert Fredette, and John Ormerod, "Binder Jetting: A Novel NdFeB Bonded Magnet Fabrication," JOM, 2016, DOI: 10.1007/s11837-016- 1883-4.

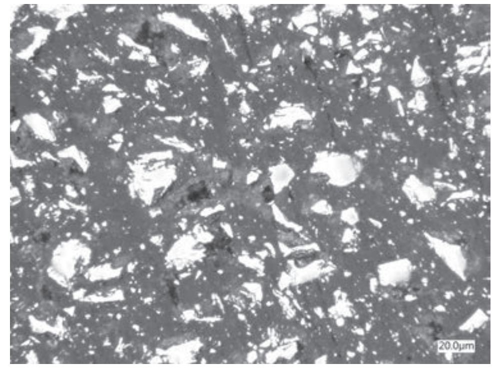

Fig. 1. Wire cross-section SEM analyses of Nd-Fe-B powder in the ABS

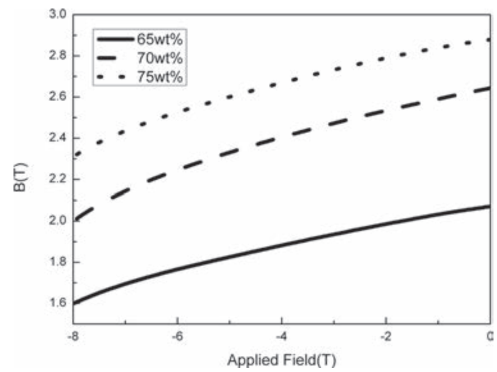

Fig. 2. Hysteresis loop of different weight percentages of magnetic properties of polymer composite material

GR-04. Micro-Patterning of NdFeB Hard Magnetic Films for Micro Systems.

A. Dias[1], G. Shaw[1], K. Hasselbach[1], M. Bonfim[2] and N. Dempsey[1]
1. Institut Neel, Grenoble, France; 2. Universidade Federal do Paraná, Curitiba, Brazil

Micro-magnets have much potential for use in the fields of bio-technology, energy transformation and management, information technology... Hard magnetic films based on RE-TM (NdFeB, SmCo) or 3d-5d (FePt, CoPt) materials can be produced by sputtering and PLD, and in the case of the latter, by electro-deposition. Micro patterning of such films is needed to produce μ-magnets. In the case of high performance RE-TM films, we developed both *topographic patterning*, in which μ-magnets are produced through the use of clean-room procedures (e.g. etching) [1], and *Thermo-magnetic patterning (TMP),* in which the direction of magnetization of the film is locally modified through localized heating with a ns-pulsed laser [2]. Characterization of the stray fields produced by such structures showed that magnetization reversal during TMP was limited to a depth of 1-2 μm. RE-TM μ-magnets produce field gradients of up to 10^6T/m [3], and have been used in a range of bio-applications [4-7]. Multi-polar patterns similar to those produced by TMP have been prepared by *Micro flux concentration (μFC)*, in which patterned soft magnetic micro-structures serve to concentrate the flux of an externally applied field in the vicinity of a hard magnetic layer [8-10]. In this study we explore the use of μFC for the patterning of high performance NdFeB films. Firstly we carry out a comparison of the stray fields produced by identical films patterned using both μFC and TMP, results are compared with simulations, and the μFC technique is modelled. Secondly, we propose the use of a recently developed compact table-top pulsed magnetic field generator for the facile application of μFC to the patterning of hard magnetic films. The 5.6 μm thick NdFeB films used were prepared by triode sputtering [11] onto silicon (100) substrates, either maintained at RT (isotropic), or heated at 450 °C (out-of-plane textured), and then annealed (750 °C/10 min.). 50 nm Ta layers were deposited as buffer and capping layers. Two routes were used to fabricate the μ-flux concentrators: 1) stacking of 50 μm copper and iron foils followed by fixation in epoxy; 2) extrusion of a Cu matrix containing a hexagonal array of Co wires (final diameter of Co wires = 100 μm) [12]. Polishing was used to produce relatively flat and smooth surfaces, for good contact with the hard magnetic film. Note that the extrusion approach would be suitable for high throughput fabrication of the μFC patterning process, since one long extruded sample could be sliced to make hundreds or thousands of individual μ-flux concentrators. In order to evaluate the performance of μFC compared to TMP, equivalent pieces of textured NdFeB films were patterned using these techniques. In the case of μFC, a positive field of 7 T and then a negative field of -2.4 T, which corresponds to the coercivity of the NdFeB film, were applied using the superconducting coil of a VSM. In the case of TMP, the NdFeB sample was magnetised in a field of 7 T, then irradiated with a ns-pulsed laser through a photo-resist mask with a 50 μm wide stripe pattern in the presence of a reverse field of -0.5 T. Scanning Hall probe measurements of the stray fields produced by the samples were performed at different scan heights above the surface of the samples (selected data shown in Figure 1). Compared to the TMP sample, the μFC sample shows roughly twice the average peak-to-peak magnetic field intensities at all distances measured, indicating that magnetization reversal is achieved over a greater depth with μFC. While good agreement is achieved between simulation and measurement for μFC at a distance of 10 μm, the measured peak-to-peak values are twice those of the simulated ones at a distance of 55 μm. This discrepancy will be discussed in terms of the assumptions made in simulations. Modelling is also used to predict how to optimize the process further. The high coercivities typical of RE-TM films require the application of relatively strong fields during μFC. However, superconducting coils are not readily available in many labs and the surface area of the sample being patterned may be limited by the bore size of the coil. We thus tested the use of a pulsed magnetic field generator capable of producing fields as high as 10 T [13] as the field source. The compact size of the system allowed the μFC patterning to be carried out beside an optical microscope, which facilitates quick characterization of the patterned film using magneto optic imaging with an indicator film [14]. A μ-flux concentrator was placed on the surface of an isotropic NdFeB film and progressively stronger field pulses were applied. After each pulse, MOIF imaging of the film was carried out before moving to an adjacent virgin zone (Figure 2). The strongest magnetic contrast is observed after the 1 T pulse. For a pulsed of 0.5 T, the central dot is poorly resolved, while for stronger field pulses the contrast from the Co wires fade away. The weaker contrast towards the centre of the array following a pulse of 0.5 T may be due to a reduction in the effective field strength due to the formation of eddy currents inside the Cu matrix. Potential benefits of using compact pulsed field sources for μFC of hard magnetic films for MEMS applications will be discussed.

[1] A. Walther, C. Marcoux and B. Desloges et al., J. Magn. Mag. Mat. 321 (2009) 590–594 [2] F. Dumas-Bouchiat, L.F. Zanini, M. Kustov et al., Appl. Phys. Lett. 96, 102511 (2010). [3] M. Kustov, P. Laczkowski, D. Hykel et al., J. Appl. Phys. 108 063914 (2010) [4] L. F. Zanini, O. Osman, M. Frenea-Robin et al., J. Appl. Phys., J. Appl. Phys. 111, (2012) 07B312 [5] V. Zablotskii, A. Dejneka, S. Kubinova et al., PLoS ONE 8(8) (2013) e70416 [6] O. Osman, S. Toru, F. Dumas-Bouchiat, N. M. Dempsey et al., Biomicrofluidics 7 (2013) 054115 [7] S. Delshadi, G.Blaire, P. Kauffmann, M. Fratz et al., Bioanalysis 9 (2017) 517 [8] O. D. Oniku, R. Regojo, Z. Kaufman, et al., IEEE Transactions on Magnetics 49.7 (2013) 4116-4119 [9] A. Garraud, O.D. Oniku, W.C. Patterson, et al., 2014 IEEE 27th MEMS, (2014) 520 [10] O. D. Oniku, P. V. Ryiz, A. Garraud, et al., J. Appl. Phys. 115.17 (2014) 17A718 [11] N.M. Dempsey, A. Walther, F. May et al., Appl. Phys. Lett. 90 092509 (2007) [12] A. Giguere, PhD thesis, UGF Grenoble 2002 [13] http://www.pumag.fr/ [14] R. Grechishkin, M. Kustov, S. Ilyashenko, O. Gasanov et al., J. Appl. Phys. 120 (2016) 174502

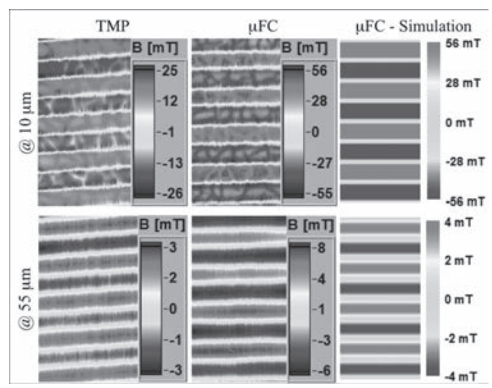

Fig. 1. SHPM measurement of the z-component of stray field produced by TMP and μFC patterning of a NdFeB film, simulation assuming reversal through the depth of the film.

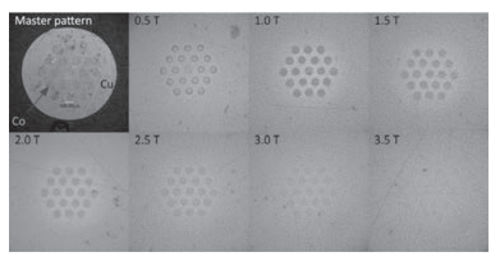

Fig. 2. Image of a μ-flux concentrator and magneto-optical images made using a uniaxial MOIF following μFC with a pulsed field of growing strength.

GR-05. The magnetic properties of misch-metal partially substituted Nd-Fe-B magnets sintered by dual alloy method.

J. Xiong[1], R. Shang[1], R. Li[1], Y. Zhang[1], J. Zhang[1], H. Zhang[1], Y. Liu[1], F. Hu[1], J. Sun[1], T. Zhao[1] and B. Shen[1]
1. State Key Laboratory of Magnetism, Institute of Physics, Chinese Academy of Sciences, Beijing, China., Beijing, China

Since the discovery of $Nd_2Fe_{14}B$ magnets, they are widely used in many fields for their excellent permanent magnetic performance at room temperature, such as the traction motors of hybrid electric vehicles, wind generators and magnetic resonance imaging.[1] In order to reduce the production cost and balance the utilization of rare earth resources, the partial substitution of misch-metal (MM) for Nd in Nd-Fe-B magnets is an effective method to find a balance between magnetic performance and cost due to the inferior intrinsic properties of $MM_2Fe_{14}B$ to $Nd_2Fe_{14}B$. Compared with traditional single alloy method, the dual alloy method has an obvious advantage in preparing high abundant rare earth permanent magnets.[2] Understanding the coercivity mechanism has a substantial impact on developing novel permanent materials. In this work, the stoichiometric composition of $MM_{14}Fe_{79.9}B_{6.1}$ (LaCe-80) and commercial $Nd_{13.5}Fe_{80.5}B_6$ (LaCe-0) were subjected to induction melting, strip-casting, hydrogen decrepitation and jet milling. After blending the powders of LaCe-80 and LaCe-0 with the mass ratios of 0:100(S00), 20:80(S20), 30:70(S30), they were prepared by the rest of the traditional sintering process. The effect of misch metal substitution on the microstructure and room-temperature permanent magnetic properties were studied. Grain alignment and phase constitution were identified by X-ray diffraction. The magnetic properties and the possible interaction mechanisms between two different hard phases were evaluated with the help of the first order reversal curve (FORC) method. Magnetic properties at room temperature were measured by vibrating sample magnetometer (VSM).

1 Jiles DC, Acta Materialia. 51, 5907(2003). 2 Zhu MG, Han R, Li W, Huang SL, Zheng DW, Song LW, and Shi XN. IEEE Transactions on Magnetics. 51, 11(2015).

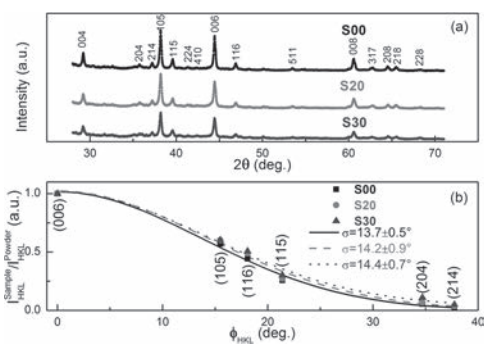

Fig. 1. (a) XRD profiles and (b) Gaussian fitted curves of S00,S20 and S30 samples.

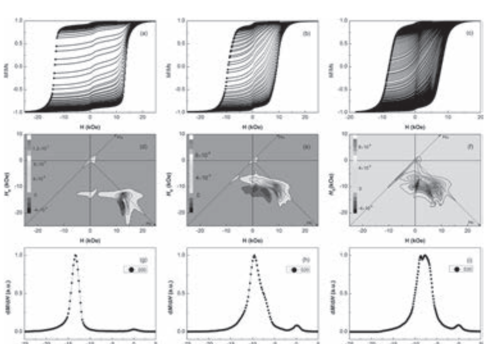

Fig. 2. First order reversal curve (FORC). (a) S00, (b) S20, (c) S30, FORC diagram. (d) S00, (e) S20, (f) S30, and the corresponding switching field distribution. (g) S00, (h) S20, (i) S30,respectively.

GR-06. Nanocomposite Nd-Y-Fe-B-Mo bulk magnets prepared by injection casting technique.

S. Tao[1] and M. Yan[2]
1. China Jiliang University, Hangzhou, China; 2. Zhejiang University, Hangzhou, China

Nanocomposite rare earth $Nd_2Fe_{14}B$ ($Pr_2Fe_{14}B$)/α-Fe (Fe_3B) magnets have obtained considerable interest in exploring potential permanent magnets due to the expected high maximum energy product [1-3]. In general, the coercivity in $Nd_2Fe_{14}B$/α-Fe and $Nd_2Fe_{14}B/Fe_3B$ type nanocomposite magnets originates from the hard $Nd_2Fe_{14}B$ phase, while remanence from the soft α-Fe (Fe_3B) phase or phases. Although, a high remanence in the range of 0.6-1.19 T has been obtained but the coercivity in these magnets is low due to the small volume fraction of hard $Nd_2Fe_{14}B$ phase. The low coercivity tends to reduce the energy product and limit the high-temperature applications of these magnets. Therefore, it is stringent to search for high coercivity nanocomposite magnets. In this work, we have successfully synthesized a new $Nd_7Y_6Fe_{61}B_{22}Mo_4$ bulk nanocomposite magnet with high coercivity by copper mold casting. The phase composition, microstructure and magnetic properties of $Nd_7Y_6Fe_{61}B_{22}Mo_4$ bulk nanocomposite magnets are investigated. Alloy ingots with nominal composition of $Nd_7Y_6Fe_{61}B_{22}Mo_4$ were fabricated by arc-melting in inert atmosphere. Samples in the form of sheets with the dimension of 1 mm in thickness, 5 mm in width, and 50 mm in length were synthesized by injection casting the molten alloy into copper mold in an argon atmosphere. Crystal structure, phase composition, crystallite size and phase volume fraction were determined by the X-ray diffraction technique. Thermal magnetic analysis (TMA) was performed in the present alloys at a heating rate of 20°C/min with an external applied field. Microstructure and composition profiles of the magnetic phases were examined using JEOL-JEM-2010 transmission electron microscopy on thin foils. Magnetic properties were measured using Quantum Design MPMS-XL-5-SQUID with a maximum applied field of 5 T. Fig. 1(a) presents X-ray diffraction pattern for the directly casted $Nd_7Y_6Fe_{61}B_{22}Mo_4$ magnet. It shows Bragg crystalline peaks for phases. The crystalline peaks in XRD pattern were indexed to α-Fe, Fe_3B, $Y_2Fe_{14}B$ and $Nd_2Fe_{14}B$ phases. The α-Fe and Fe_3B are magnetically soft phases while $Y_2Fe_{14}B$ and $Nd_2Fe_{14}B$ are known as magnetically hard phases. The phases observed by X-ray diffraction technique are confirmed by TMA studies. The TMA curve for the directly casted $Nd_7Y_6Fe_{61}B_{22}Mo_4$ magnetic sample is presented in Fig. 1(b). As can be seen, there are four distinct peaks corresponding to $Y_2Fe_{14}B$, $Nd_2Fe_{14}B$, Fe_3B and α-Fe phases. The Curie temperatures for $Y_2Fe_{14}B$, $Nd_2Fe_{14}B$, Fe_3B and α-Fe phases are determined as 215°C, 309°C, 400°C and 760°C, respectively. Fig. 2(a) presents the magnetic hysteresis loop for $Nd_7Y_6Fe_{61}B_{22}Mo_4$ magnet. It shows smooth hysteresis curve without kink in the demagnetizing curve suggesting that the exchange coupling exists in the magnet. The coercivity ($_iH_c$), remanence (B_r) and maximum energy product ($(BH)_{max}$) for $Nd_7Y_6Fe_{61}B_{22}Mo_4$ bulk nanocomposite magnets are 1289 kA/m, 0.51 T and 46.2 kJ/m^3, respectively. To understand the behavior of magnetic exchange interactions between the soft and hard magnetic phases for $Nd_7Y_6Fe_{61}B_{22}Mo_4$ magnets, the δM plot, known as Henkel plot [4, 5] was constructed. The δM is defined as $M_d(H)$-{1-2$M_r(H)$}, where $M_d(H)$ is the reduced demagnetization remanence and $M_r(H)$ the reduced magnetization remanence. For non-interacting phases $\delta M = 0$, whereas nonzero δM indicates the presence of interactions [4]. Fig. 2(b) depicts the δM plot as function of the applied magnetic field for $Nd_7Y_6Fe_{61}B_{22}Mo_4$ nanocomposite magnet. A positive δM is observed confirming the existence of exchange interactions between soft α-Fe, Fe_3B and hard $Nd_2Fe_{14}B/Y_2Fe_{14}B$ phases. The large δM value indicates the existence of strong exchange coupling between α-Fe (Fe_3B) and hard 2:14:1 phases. Figure captions Fig. 1 X-ray diffraction pattern (a) and TMA curve for the as-cast $Nd_7Y_6Fe_{61}B_{22}Mo_4$ alloy (b). Fig. 2 The magnetization hysteresis loop (a), and δM plot as a function of the applied field for the as-cast $Nd_7Y_6Fe_{61}B_{22}Mo_4$ alloy (b).

[1] R. Coehoorn, D.B. de Mooij, C. de Waard, J. Magn. Magn. Mater. 80 (1989)101. [2] A. Manaf, R.A. Buckley, H.A. Davies, J. Magn. Magn. Mater. 128 (1993) 302. [3] T. Schrefl, J. Fidler, H. Kronmüller, Phys. Rev. B 49 (1994) 6100. [4] C. Tannous, J. Gieraltowski, Eur. J. Phys. 29 (2008) 475. [5] E.P. Wohlfarth, J. Appl. Phys. 29 (1958) 595.

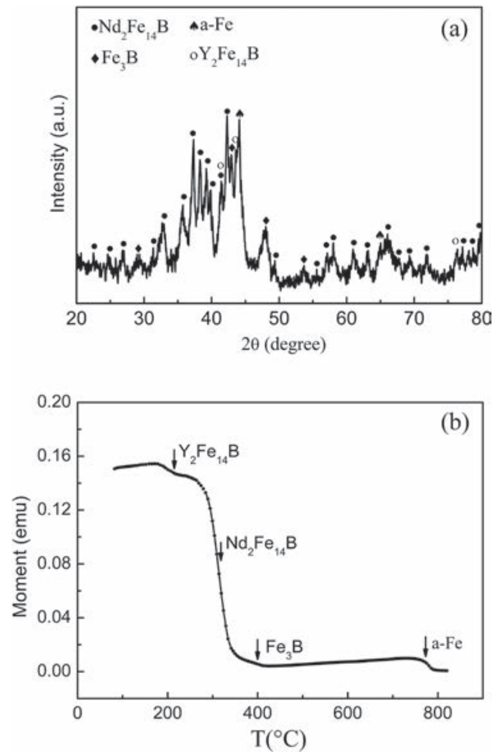

Fig. 1. X-ray diffraction pattern (a) and TMA curve for the as-cast $Nd_7Y_6Fe_{61}B_{22}Mo_4$ alloy (b).

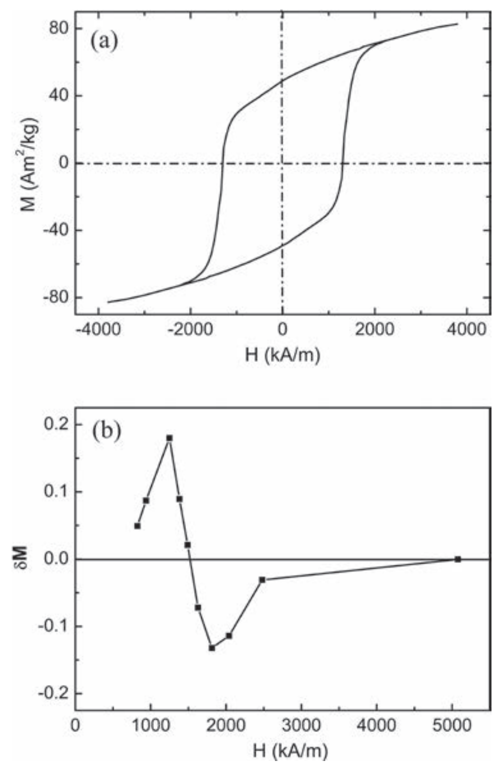

Fig. 2. The magnetization hysteresis loop (a), and δM plot as a function of the applied field for the as-cast $Nd_7Y_6Fe_{61}B_{22}Mo_4$ alloy (b).

GR-07. Modeling of piezomagnetic effect in magnetostrictive-electromagnetic hybrid vibration-powered generator.

B. Yan[1], J. Hong[1] and C. Zhang[2]
1. Guangdong University of Technology, Guangzhou, China; 2. Harbin Institute of Technology, Harbin, China

Vibration energy of human activities (like human walking and running) is the by-product of everyday life, can be generated from any perceivable activity. Vibration energy harvesting is the process of converting vibrational energy to electrical energy, which is receiving more global interest and is currently a growing field [1]. Magnetostrictive energy harvester, utilize magnetostrictive material (Tb0.3Dy0.7Fe2 alloy, also called Terfenol-D), exhibit high power density and efficiently, can be safely used to harvest low frequency and huge impact vibration of human walking [2-3]. But single magnetostrictive harvester is still accompanied by low harvesting effect, and its magnitude of electric power generated is always very low. Magnetostrictive-electromagnetic hybrid harvester has larger harvesting effect, can generate more electricity and suit to larger power density design for broadhand vibration impact. Due to its hybrid harvesting effect, the modeling of piezomagnetic effects has two parts: impact-induced and magnetic field-induced. It is still lack of suitable model for design and fabrication of magnetostrictive-electromagnetic hybrid harvester. In this paper, a simplified computational model using for larger piezomagnetic effect design of magnetostrictive-electromagnetic hybrid vibration energy harvester is presented. In the modeling, pizeomagnetic effects in Tb0.3Dy0.7Fe2 alloy are studied as a function of compressive stress and magnetic field, and each effects in ΔB induced by single $\Delta\sigma$ and ΔH are calculated respectively. Then, two methods, pre-loads-based method and impact stress-based method, are used to discuss the optimization of hybrid piezomagnetic effect in the fabrication of magnetostrictive-electromagnetic generator. The model and method is quick and efficient to calculate piezomagnetic effect for hybrid magnetoctrictive material-based harvester, benefit to its optimized target design and the prototype fabricate. Harvesting results calculated by model are in a good agreement with experiments, helps for design and fabrication of high efficient magnetostrictive harvester.

[1] B. Yan, C. Zhang, L. Li. Design and Fabrication of High Efficiency Magnetostrictive Energy Harvester for High Impact Vibration Systems. *IEEE Trans. on Mag.*, 2015, 51(11): 8205404 [2] H. Zhang. Power generation transducer from magnetostrictive materials. *Applied Physics Letters*, 2011, 98(23): 232505. [3] S. Cao, J. Zheng, Y. Guo, Q. Li, J. Sang, B. Wang, R. Yan. Dynamic Characteristics of Galfenol Cantilever Energy Harvester. *IEEE Transactions on Magnetic*s, 2015, 51(3): 8201304

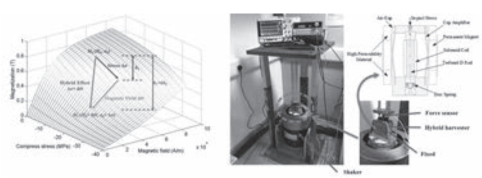

Fig. 1. Modeling and testing of magnetostrictive-electromagnetic hybrid vibration-powered generator

GR-08. Novel thermal stability of coercivity in Alnico 8 alloys with thermomagnetic heat-treatment conditions.

t.J. Zhao[1], l.Y. Sun[1], L. Liu[1], Z. Liu[1], X. Zhang[1] and C. Feng[1]
1. Ningbo Institute of Industrial Technology, Chinese Academy of Sciences, Ningbo, China

The development of Alnico alloys date from 1930s and largely ended in 1970s when Rare-Earth (RE) magnets were discovered [1]. Alnico alloys with Non-Rare-Earth show strong heat resistance properties (up to 600 °C), low temperature of their magnetic properties, and excellent corrosion resistance. Recently Rare-Earth crisis and urgent demands for delicate instrument stimulate researchers to concentrate on Alnico alloys with excellent thermal stability. Not containing rare-earth elements, the method of Heavy Rare Earth Elements compensating temperature coefficient of remanence is not suitable for Alnico alloys, and the study of temperature coefficient of coercivity is very poor. Alnico alloys are primarily composed of two-phases formed through spinodal decomposition during thermomagnetic heat-treatment: an isolated FeCo-rich phase (a1) and a matrix AlNi-rich phase (a2). Considering the BCC structure and thermomagnetic heat-treatment conditions the a1 of rod-like elongates along <001> direction is dispersed distribution in the matrix a2, which means the microstructure is similar with the finite long and linear nanostructured-magnetic-array. So the magnetic anisotropy and hysteresis orginate almost entirely from magnetostatic dipole-dipole interactions [2]. However, the coercivity is much less than the magnetic anisotropy and about one-third of that [3]. The lower coercivity of Alnico alloys enhance viscosity coefficient and prelimit the application. This paper mainly studies the thermal stability of Alnico 8 alloys with thermomagnetic heat-treaatment. The morphology is characterized by Transmission Electron Microscope (TEM), the magnetic properties are measured by the Quantum Design Magnetic Property Measurement System (MPMS) MODEL 6000 equipped with a vibrating sample magnetometer (VSM). During the thermomagnetic heat-treatment Spinodal decomposition occurs to form a1 and a2 with nanostructured. In theory the microstructure is chessboards in transverse direction and infinite long quadrangular in longitudinal direction. The phase and microstructure are showed in Fig. 1 by TEM images of specimen surfaces parallel and perpendicular to the applied. Fig. 1(a) shows a1 is a plate-like of square and hexagon in transverse direction, and the size is 25nm~35nm. Fig. 1(b) shows a1 is a bamboo-like of finite and nonlinear in longitudinal direction, and the size is greater than 300nm. Maybe short temper or uneven components results in the low level of orientation degree and dispersed distribution of a1.The high-temperature magnetic properties of Alnico 8 alloys are listed in Fig. 2. The data shows high-temperature lowers the saturation magnetization (Ms) and remanence (Mr) gradually, but the change rule of coercivity is very unusual. When the temperature goes up to 250 °C the coercivity increases from 1106.778Oe to 1420.29Oe, yet it reduces to 1391.07Oe at 400 °C. Also the reduced rate of coercivity is much less than the increased rate. In addition the temperature coefficient of Ms is less than temperature coefficient of Mr between the temperature zone of increased coercivity and it is opposite between the temperature zone of reduced coercivity. From 0° to 180°the high-temperature angular dependence of coercivity of Alnico 8 alloys is funnel, which means predominant magnetic anisotropy is parallel with a1of bamboo-like in longitudinal direction. And increased coercivity promotes the decline law. The high-temperature reversible reduced curve shows reduced coercivity obviously reduces the values and when the H/Hc is close to the value of 1 there is a faint inflection point. The high-temperature irreversible reduced curve slope shows reduced coercivity improves the peak intensity and shortens the peak width, which means nucleation field is mainly distributed. The predominant magnetic anisotropy of Alnico alloys with BCC structure is parallel with a1 of bamboo-like in longitudinal direction. And the magnetic anisotropy and hysteresis are closely related with magnetic characteristic and microstructure of a1. Maybe the competition effect enhances the magnetic anisotropy to improve the coercivity.

[1] Cullity B D, Graham C D. Introduction to magnetic materials[M]. John Wiley & Sons, 2011. [2] Lin Zhou, M.K. Miller, Ping Lu, et al. Architecture and magnetism of alnico[J]. Acta. Mater, 2014, 74: 224-233. [3] Sergeyev V, Larichkina R. Forming structure and magnetic properties of Alnico VS55 alloys[J]. IEEE Transactions on Magnetics, 1969, 5(2): 136-139.

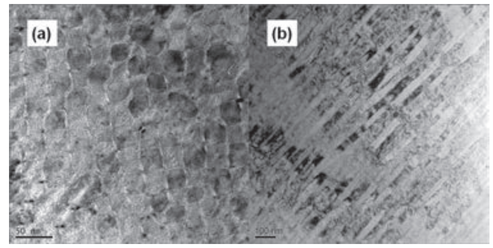

Fig. 1. TEM images of Alnico 8 alloys with thermomagnetic heat-treatment conditions: (a) transverse; (b) longitudinal.

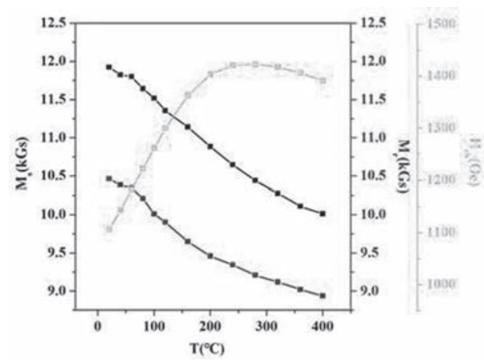

Fig. 2. The high-temperature magnetic properties of Alnico 8 alloys with thermomagnetic heat-treatment conditions.

GR-09. Electromagnetic Transient Analysis and Inductance Characterization in Fractional-Slot Concentrated-Wound Interior Permanent Magnet Synchronous Machines under Rotor Demagnetization.

A. Pouramin[1], M. Malekpour[1], R. Dutta[1] and F.M. Rahman[1]
1. School of Electrical Engineering and Telecommunications, University of New South Wales, NSW, NSW, Australia

ABSTRACT: This paper aims to investigate the resultant effect of rotor demagnetization on magnetic and electrical parameters of Fractional-Slot Concentrated-Wound Interior Permanent Magnet Synchronous Machines (FSCW IPMSMs). The distribution of magnetic flux lines, flux density, and self and mutual inductance variations are analyzed under rotor demagnetization by using finite element analysis (FEA). Both healthy and faulty conditions including different distribution of the faulty magnets are investigated. Experimental set up in the laboratory on a prototype FSCW IPMSM is used to verify the finite element model. INTRODUCTION: Fractional-slot concentrated-wound interior permanent magnet synchronous machines (FSCW IPMSMs) have gained a lot of interests in industry. This type of machines has a cheaper manufacturing process, less end winding losses, and greater constant-power speed range [1]. These advantages offer a wide range of applications for FSCW IPMSMs from electric vehicles to wind generation industries. Hence, any malfunction due to the faults such as the rotor demagnetization can be catastrophic. Studying the resultant effects of fault on machine parameters and behavior have been always the concerns of many researchers [2]. Motivated by the above concern, this paper provides a deep understanding of inductance variations of FSCW IPMSMs due to rotor demagnetization. Firstly the accuracy of the machine model in Ansys Maxwell 2D is confirmed with experimental results to build a confidence for the further studies of this paper on the effects of rotor demagnetization. Then the variation of self- and mutual inductances as well as dq- inductances are obtained for the several operating conditions such as no-load and rated load under a maximum torque per ampere (MTPA) trajectory and flux-weakening regime. EXPERIMENTAL VERIFICATION OF THE FINITE ELEMENT MODEL: It is always of great importance to properly model the rotating machine behavior in FEM. Among all proposed modelling techniques, finite element method has proven itself as an accurate and inexpensive technique that gives one an opportunity to study the magnetic behavior of the apparatus under consideration, without any expensive instrument installation. In this paper, a prototype FSCW IPMSM is modelled using Ansys Maxwell 2D considering all material properties, stator and rotor geometries, nonlinearities and saturation effects. disassembled and its parameters such as stator slot geometry, number of stator winding turns, magnet geometries and etc. are measured. The comparison between measured inductances and FEA estimation will be presented in full paper. Fig. 1 shows good agreement between back-emf obtained in FEM and experiment. RESULT AND DISCUSSION: In Fig. 2, the magnetic flux density is shown under both healthy and faulty conditions. As one can see in this figure, asymmetry of flux lines led to less magnetic flux density around the faulted magnets due to the rotor demagnetization. Also the self and mutual inductances are shown in Fig. 3 in which clear distortions can be seen in amplitude. The full paper will provide a broaden results on machine inductances under different operating conditions.

[1] A. M. El-Refaie, "Fractional-Slot Concentrated-Windings Synchronous Permanent Magnet Machines: Opportunities and Challenges," Industrial Electronics, IEEE Transactions on, vol. 57, pp. 107-121, 2010. [2] P. Arumugam, T. Hamiti, and Ch. Gerada, "Modeling of Different Winding Configurations for Fault-Tolerant Permanent Magnet Machines to Restrain Interturn Short-Circuit Current," IEEE Transactions on Energy Conversion, Vol. 27, No. 2, pp. 351-361, 2012.

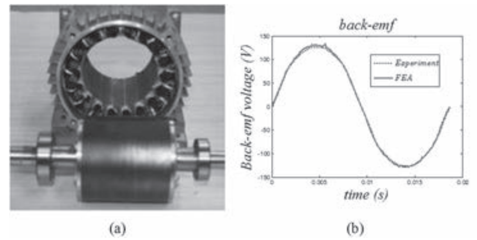

Fig. 1. (a) The prototype FSCW IPM machine. (b) the FEA and measured back-emf voltage at base speed

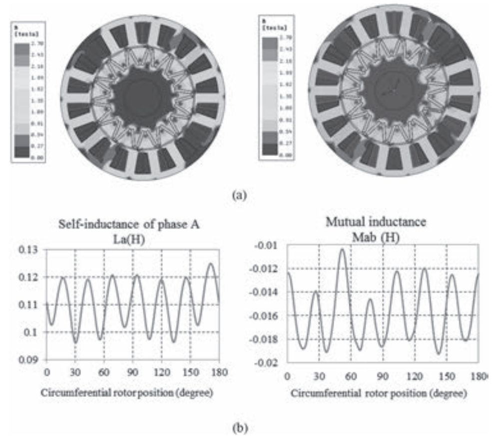

Fig. 2. (a) The healthy and Demagnetized FSCW IPM machine 18 slots and 14 poles, (b) Self-inductance (left) and mutual inductance (right) of the demagnetized FSCW IPM machine.

GR-10. Effect of Temperature and Pressure on Electrical Resistivity of Permanent Magnet.

L. Xiao[1], G. Yu[1], J. Zou[1], Y. Xu[1], H. Lan[1], M. Wang[1] and F. Gao[1]
1. Harbin Institute of Technology, Harbin, China

Abstract—This study is focused on the investigation of the effect of temperature and omnidirectional pressure on the electrical resistivity of permanent magnet. And a new setup for electrical resistivity measurements, where strip permanent magnet samples are measured with the four-probe method technique, has been successfully implemented. In order to verify whether the magnetization has an effect on the permanent magnet electrical resistivity, an unmagnetized permanent magnet and a magnetizing permanent magnet were used as the test materials in the experiments. The measured electrical resistivity values of the permanent magnet and the magnetizing effect on the measurements is also discussed in detail. I. Introduction Permanent magnet motors (PMMs) have been widely used in a variety of applications, including aerospace, deep sea submersible, and oil well due to their high power density, high efficiency, high torque density and other advantages [1]. However, the permanent magnet motors in the use and design process, need to face many challenges. Although this type of motors are designed to have a high power density, the resultant losses including winding losses, iron losses and eddy current losses in permanent magnets are inevitable [2]. Among them, the eddy current losses in permanent magnet should pay more attention to the designers, because the eddy losses in the permanent magnets can raise their operating temperature and hence point flux density of the permanent magnets, thus making them may face the risk of partial demagnetization, which affects the overall performance and service life of the motors. To diminish the eddy current losses in permanent magnet and thus improve the overall efficiency, an accuracy and computationally efficient solution for eddy current losses is necessary at the design of the motors. For those permanent magnet motors operating in extreme environments, such as high temperature and high pressure environments, the eddy current losses of their permanent magnets should be taken into account. Inaccurate eddy losses calculation may cause underestimation of the rotor temperature, which in turn increases the risk of demagnetization. Clearly understanding the change of the electrical resistivity of permanent magnet under high temperature and high pressure is the key to accurately calculate the eddy current losses. However, there are few relevant data that meet this condition, and this study is about to solve this problem. II. measurment system 2.1 Definition of the testing materials and specimen geometry In this study, the two most commonly used and different types of permanent magnets in permanent magnet motors were used as the test materials, the specific grades of which were samarium cobalt (Sm_2Co_{17}) and neodymium iron boron (NdFeB), respectively. It is well-known that the permanent magnet materials used in permanent magnet motors are basically magnetized. Therefore, the electrical resistivity of the test samples before and after magnetization are measured, that is, the effect of magnetization on the electrical resistivity of the permanent magnet is analyzed. In view of the brittleness of the permanent magnet materials, the test samples are machined into a simple strip shape. The shape of the test samples are also very advantageous in terms of size. 2.2 Measurement setup and Measurement environment system A carefully designed measurement setup is needed for reliable results based on four-probe method technique [3]. Fig.1 shows the newly designed permanent magnet material resistivity measurement setup, including sliding end, fixed end, baseboard and platen, with voltage contacts and current contacts in the sliding end and fixed end in direct contact with the test sample. Since this study was completed under high temperature and high pressure, the primary solution to this problem is to realize the measurement environment of high temperature and high pressure. And the pressure mentioned in this study is omnidirectional pressure, non-finite axial pressure. III. measured results and discuss Measurement procedures have been completed according to above mentioned measurement setup and measurement method. The measured results show the changes of the resistivity of the two tested samples under the conditions of high temperature and high pressure, respectively. Fig.2 shows the electrical resistivity of Sm_2Co_{17}, the effect of the temperature and pressure on the Sm_2Co_{17} material. And the difference between the resistivity of the magnetized sample and the unmagnetized sample is compared and analyzed, and the influence of magnetization on the permanent magnet material is revealed. Specific measurement results and comparative analysis results will be given in the subsequent full text. IV. conclusion In this study, the electrical resistivity of permanent magnet has been examined under high temperature and high pressure. The influence of magnetization on the electrical resistivity of permanent magnet are analyzed in detail. The measurement results show that when the temperature and the omnidirectional pressure are coupled together, the change of the resistivity of the permanent magnet and the influence of the two environmental factors of temperature and pressure on the electrical resistivity of the permanent magnet respectively. Further explain the role of each factor in the coupling of two environmental factors.

[1] Sreeju S. Nair, Jiabin Wang, Liang Chen, Robert Chin, et al., "Computationally Efficient 3-D Eddy Currrent Loss Prediction in Magnetis of Interior Permannet Magnet Machines,"IEEE Tran. Magn., vol. 52, No. 10, pp.8108110, Oct 2016. [2] Yasemin Oner, "Sub-Domain Model of Eddy Current Loss in Windings for Flux-Switching Permannet Magnet Machine under Open-Circuit Condition," Electromagnetics, vol. 35, pp.557-576, 2015 [3] Nicola Bowler, "Four-point potential drop measurementsfor materials characterization," Meas. Sci. Technol. Vol. 22, pp. 012001, 2011.

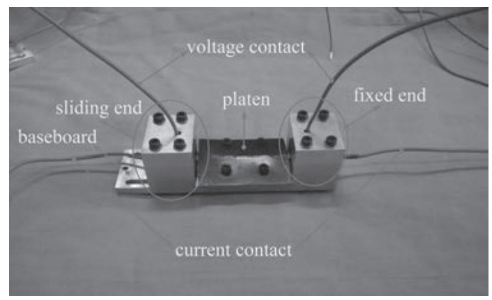

Fig. 1. Measurement setup of electrical resistivity of permanent magnet

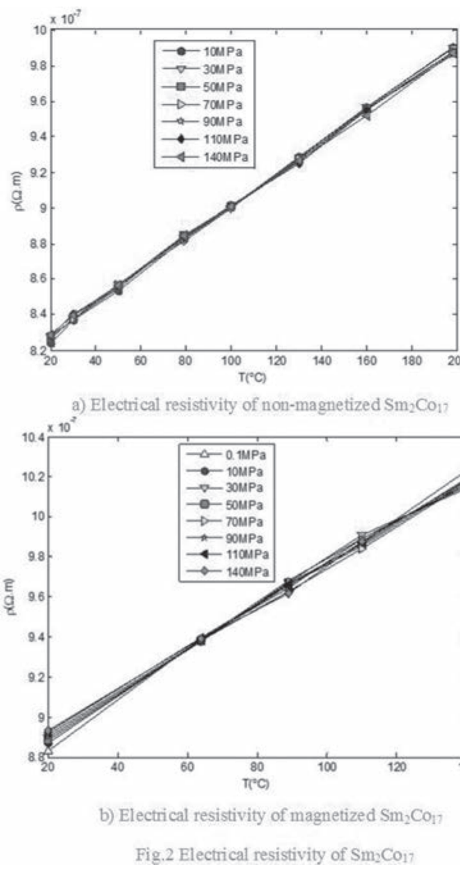

Fig. 2. Electrical resistivity of Sm_2Co_{17}

GR-11. Magnetic field annealing effect and superparamagnetic contributions in one-dimensional CoPt nanostructures.

S. Ali[1], W. Li[1], K. Javed[1], M. Irfan[1] and *X. Han*[1]
1. State Key Lab of Magnetism, Institute of Physics, Beijing, China

A low cost versatile electrochemical method has been employed to synthesize highly ordered CoPt nanowires (NWs) in anodic aluminum oxide (AAO) templates with average pore diameter of about 100 nm. The structural properties of as deposited NWs have been studied through XRD analysis. Results show that the as deposited NWs are textured along the face centered cubic (fcc) phase with (111) preferred orientation, and magnetic field annealing treatment to NWs can improve the crystalline structure resulting a sharper (111) peak and improved (200) orientation. Magnetic properties at room temperature and lower temperature has been investigated with applied field parallel and perpendicular to NWs axis. The easy magnetization axis is aligned perpendicular to NWs owing to the strong magnetostatic interactions among the NWs due to smaller interwire distance (~15 nm). Furthermore, the as deposited arrays of NWs have been annealed for 2 h at 300 degree Celsius in the presence of 1 T magnetic field applied in the direction perpendicular to NWs axis. Magnetic field annealing gives improved structural and magnetic behavior of these one-dimensional (1D) nanostructures resulting improved crystallinity and increased values of coercivity (Hc) and remnant squareness (SQ). Switching in magnetization reversal mechanism has been observed from curling to coherent rotation for both cases which is quite interesting to study the mixed behavior of magnetic domains on applied field reversal. Furthermore, at lower temperatures significant increase in saturation magnetization, coercivity and squareness has been observed which is mainly due to the reduced thermal fluctuations and contribution of superparamagnetic nanoparticles in blocking state. Superparamagnetic contributions at lower temperature due to presence of fine nanoparticles in blocking state play important role and leads to enhanced magnetic behavior of CoPt NWs.

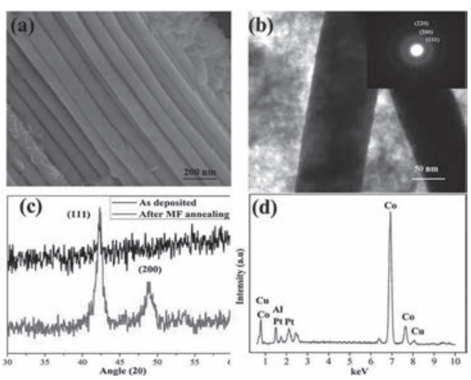

Fig. 1. (a) SEM image of CoPt nanowires with average diameter of about 100 nm after partial etching in NaOH solution. (b) TEM image of CoPt nanowires after complete removel of AAO template, inset shows SAED pattern. (c) XRD pattern of as deposited and annealed CoPt nanowires showing fcc phase with (111) preferred orientation. (d) EDX spectrum showing the deposition of Co and Pt contents.

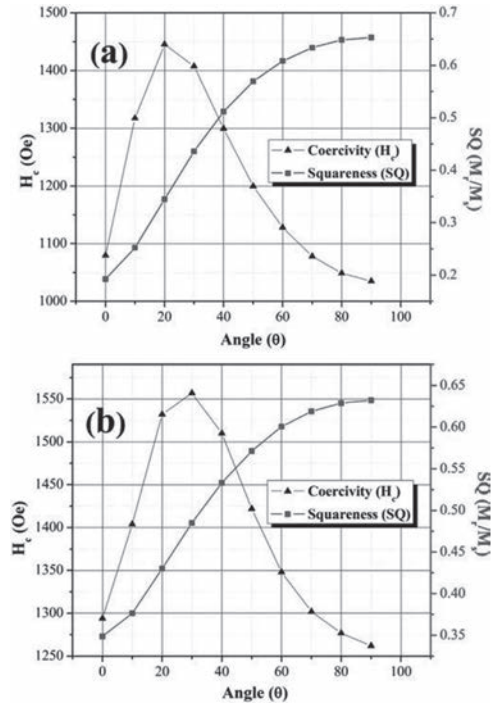

Fig. 2. Angular dependence of coercivity (Hc) and squareness (SQ) of (a) as deposited sample (b) after magnetic field annealing at 300 _C for 2 h.

GR-12. Simplified Magnetic Circuit for Analyzing Demagnetization of Permanent-magnets in PMSMs.

S. Lee[1] and J. Hur[1]
1. Incheon National University, Incheon, The Republic of Korea

Since permanent-magnet synchronous machines (PMSMs) have high torque density and high efficiency in comparison of other electric machines under same volume, they have been widely used in different applications [1], [2]. In the case of PMSMs applied to the actuator or the engine in automobile industries manufacturing hybrid electric vehicles and electric vehicles, their reliability and stability are significantly important because the breakdown of PMSMs may be caused by the potential faults including winding fault, eccentricity, bearing fault, or demagnetization of permanent-magnets (PMs) [3]. When the reliability and the stability are not considered deeply, the faults may lead to critical accident. To ensure the performance of the PMSMs, different methods such as robust machine design, fault diagnosis, and fault tolerance control have developed by many researchers [3], [4]. Nevertheless, it is difficult to apply the methods without the characteristics analysis of PMSMs with faults. This study deals with a simplified magnetic circuit for analyzing the demagnetization of PMs in PMSMs. The demagnetization is one of the most common faults and is affected by current magnitude, current angle, and temperature [5]. When the magnetic flux passing through PMs is increased along with the increase of stator currents, a load line is moved close to a knee-point. Moreover, the temperature affects the knee-point of PMs. According to these variations, the operating point, which is the point of intersection between the load-line and B-H curve of PMs, is decided and it can check whether or not the irreversible demagnetization of PMs is caused, as shown in Fig 1 (a). To make simplified magnetic circuit, this study utilizes the interior-type PMSM using neodymium PMs, and magnetic flux path can be drawn regardless of stator current, as shown Fig. 1 (b). Here, R_s, R_g, R_r, R_T, and R_m are the equivalent reluctance components in stator, airgap, rotor, production tolerance, and PMs, respectively. R_{rip} is the reluctances component generated by the bridge between airgap and barrier. R_{leak} is the reluctances component generated by leakage flux, respectively. F_m denotes magnetomotive force (MMF) generated by PMs. For analyzing the demagnetization of PMs, first of all, the MMF generated by PMs and stator currents are separated for principle of superposition, and then MMF and equivalent reluctance are calculated. In the stator, the current flowing in finite straight conductors induced magnetic fields by Biot-Savart law, as follow. $H_p=NI/(2\times\text{pi}\times p_L)(\cos\theta_{L2}-\cos\,\theta_{L1})a_{phi}+NI/(2\times\text{pi}\times p_w)(\cos\theta_{w2}-\cos\,\theta_{w1})a_{phi}$ (1) where, H_p and N are the intensity of magnetic field in a specified point and the number of turns. p is the length between a conductor and specific point. The intensity of magnetic field in specific one point is proportional to the number of turns, but that in other points is little different because the magnetic flux generated by stator currents have divergent flux paths according to flux points, as shown in Fig. 1 (c)-(d). The divergent flux paths drawn in the schematic diagram also affects the demagnetization of PMs. In particular, when magnetic flux passes through the edge of PM as the case of path 4, the partial demagnetization in the edge can be easily caused owing to the reduction of reluctance. To find the operating point of the PMSM, its load line and B-H curve of PM depend on temperature is necessary. The B-H curve is determined according to PM materials, but reverse magnetic flux should be calculated to obtain the load line. $\Phi_{de\_px}=F_c/((R_{eq}-R_m)(1+\tan^{-1}\theta_x)\times\cos\theta_x)$ (2) where Φ_{de_px} is the reverse magnetic flux which affects the demagnetization of PMs. F_c is the MMF generated by conductors. According to the variation in stator currents and temperature, the demagnetization existence is analyzed by using simplified magnetic circuit and equivalent equations, as shown in Fig. 2. Since this study used a PMSM having neodymium PMs, it has soft spot for the demagnetization under high temperature condition. ■ Future work We will compensate equation expressions and magnetic field characteristics according to different condition such as current magnitude, and current angle, temperature, and then accuracy will be evaluated by comparing the demagnetization degree through results obtained by proposed method and FEM.

[1] D. Fodorean, M. M. Sarrazin, C. S. Mar, J. Anthonis, and H. V. Auweraer, "Electromagnetic and structural analysis for a surface-mounted PMSM used for light-EV," IEEE Trans. Ind. Appl., vol. 52, no. 4, pp. 2892–2899, Jul. 2016. [2] B. G. Gu, "Study of IPMSM interturn faults part I: development and analysis of models with series and parallel winding connections," IEEE Trans. Power Electron., vol. 31, no. 8, pp. 5931-5943, Aug. 2016. [3] S. T. Lee and J. Hur, "Detection technique for stator inter-turn faults in BLDC motors based on third harmonic components of line currents," IEEE Trans. Ind. Appl., vol. 53, no. 1, pp. 143–150, Jan./Feb. 2017. [4] P. P. Zhou, D. Lin, et al., "Temperature-dependent demagnetization model of permanent magnets for finite element analysis," IEEE Trans. on Magn., vol. 48, no. 2, pp. 1031-1034, Feb. 2012. [5] Y. S. Lee, K. T. Kim, and J. Hur, "Finite-element analysis of the demagnetization of IPM-type BLDC motor With stator turn fault," IEEE Trans. on Magn., vol. 50, no. 2, Feb. 2014.

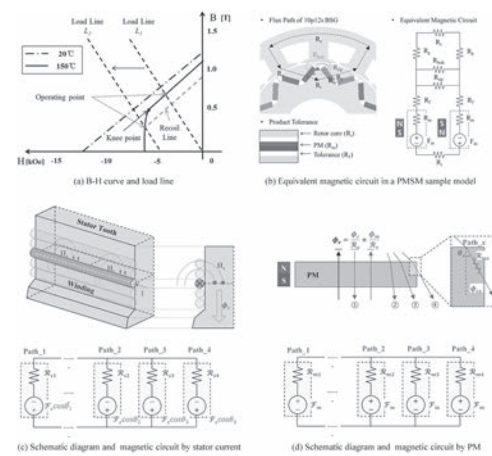

Fig. 1. Simplified magnetic circuit model

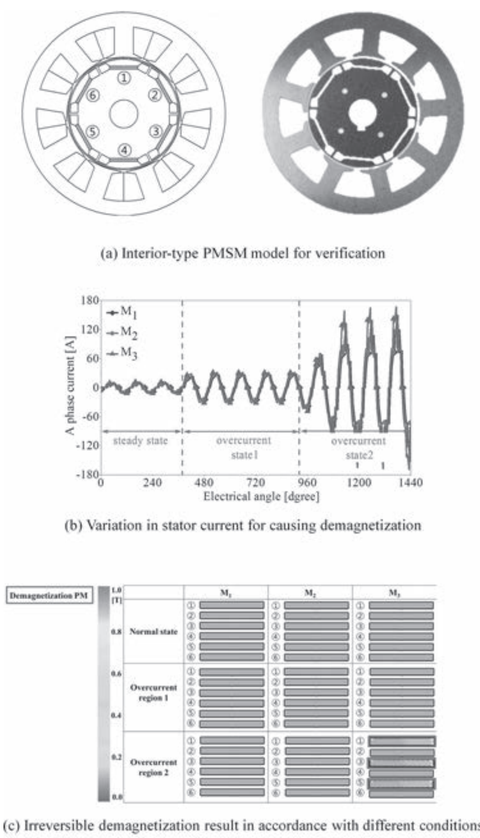

Fig. 2. Demagnetization verification using a PMSM model

Fig. 2. Demagnetization verification using a PMSM model

GR-13. Polar transformed subdomain modeling for double-stator permanent magnet linear synchronous machine.

R. Guo[1], H. Yu[1], T. Xia[1], X. Liu[1] and G. Yang[1]
1. Southeast University, Nanjing, China

Abstract—The paper presents a developed analytical subdomain model for design and analysis of the double-stator permanent magnet linear synchronous machine (DS-PMLSM) accounting both the primary and secondary end effect. Firstly, the DS-PMLSM is deformed into a ring-segment PMLSM (RS-PMLSM), the solution regions and time are simplified and improved using the analytical model, which is calculated in Polar coordinates instead of Cartesian coordinates. Then, the subdomain method is adopted to analyze the RS-PMLSM model by solving the Laplace's equation and the Poisson equation in each region, and the slot effect is considered by conformal transformation method. The flux density and back-electromotive force (EMF) are calculated based on the developed analytical model. Finally, the analytical results are verified by the finite-element method (FEM) and experiment, the results show that the proposed model can accurately predict the electromagnetic performance, which is useful for the initial design of the DS-PMLSM. I. Introduction The double-stator permanent magnet linear synchronous machine (DS-PMLSM) has been widely used in high speed and long distance movement. However, the thrust ripple of DS-PMLSM mainly caused by the end effect force is an obvious drawback that distorts the magnetic field severely[1][2][3]. In this paper, a developed subdomain analytical model accounting both the primary and secondary end effect is proposed. Firstly, the PS-PMLSM is deformed into RS-PMLSM, the subdomain method is used to calculate this model. Then, analytical field expression of each subdomain is obtained by the variable separation method and Fourier series method, the coefficients in each region are determined by applying the boundary and interface conditions and the analytical solution of each subdomain can be derived. Finally, the distribution of flux density and Back-EMF are calculated, the analysis results are validated by the finite-element method and experiment. II. Model of the DS-PMLSM The model of DS-PMLSM in Cartesian coordinates and the transformed model of DS-PMLSM in Polar coordinates are shown in Fig.1 (a) and Fig.1 (b), respectively. From Fig.1 (a), the magnetic field need to be divided into 13 regions:1,2,2-1…,7. However, the transformed RS-PMLSM in Fig.1 (b), the number of subdomains is decreased to 6 regions which can reduce the computational complexity. III. Predict of magnetic field distribution A. Model of Permanent magnets For the radial magnetization, the magnetization of tangential is zero, and due to consideration of the primary and secondary end-effect problems, the magnetization distribution of radial in mover coordinate is shown in Fig.1(c). The values from $\pm N_p\theta_m/2$ to $\pm\pi$ are zero. B. Analytical solution of magnetic fields The exact analytical solutions in the various regions are determined by applying the boundary and interface conditions. The radial flux density Br and the tangential field strength H are adopted to define the boundary conditions. According to Poisson and Laplace equations, the general solution differential equations of each region can be determined and the final coefficient matrix can be obtained. Through calculating this matrix, the unknown coefficients can be derived; the magnetic field distribution can be calculated. IV. Verified by the Finite Element method The manufactured prototype machine is shown in Fig.2 (a). The magnetic flux density distribution of the air-gap under the no-load condition is plotted in Fig. 2 (b) and the Back-EMF distribution is shown in Fig. 2 (c). As shown in Fig. 2(b), the analytical results are in good consistent with the simulation results. The flux density of air-gap in slot region is about 0.55 T, in three end regions are about 0.25 T. Through the comparison of Fig. 2(c), it can be found that the analytical results match well with FEA and experiment results, the maximum value of the back-EMF is about 14.5 V. V. Conclusion The paper presents a developed analytical subdomain model for design and analysis of the DS-PMLSM accounting both the primary and secondary end effect. The DS-PMLSM is deformed into RS-PMLSM, and the subdomain method is adopted to solve the analytical model. The flux density and Back-EMF are calculated according to this model, and the results show that the analytical results are in good agreement with the FEM simulations and experiment, which is useful for the initial design of the DS-PMLSM.

] S. Xu, X. Liu, and Y. Le, "Electromagnetic Design of a High-Speed Solid Cylindrical Permanent-Magnet Machine Equipped with Active Magnetic Bearings," *IEEE Trans. Magn.*, vol. PP, no. 99, pp. 1–1, 2017. [2] K. H. Shin, H. W. Cho, S. H. Lee, and J. Y. Choi, "Armature Reaction Field and Inductance Calculations for a Permanent Magnet Linear Synchronous Machine Based on Subdomain Model," *IEEE Trans. Magn.*, vol. 53, no. 6, pp. 1–4, Jun. 2017. [3] Z. Q. Zhu, L. J. Wu, and Z. P. Xia, "An Accurate Subdomain Model for Magnetic Field Computation in Slotted Surface-Mounted Permanent-Magnet Machines," *IEEE Trans. Magn.*, vol. 46, no. 4, pp. 1100–1115, Apr. 2010.

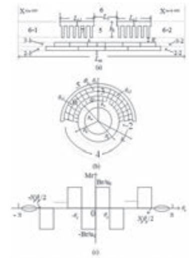

Fig.1 Simplified analytical model and radial magnetization of PM
(a). Model of DS-PMLSM in Cartesian coordinates
(b). Model of RS-PMLSM in Polar coordinates
(c). Distribution of the radial magnetization of RS- PMLSM

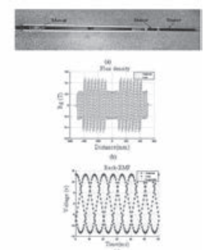

Fig.2 Prototype machine and the distribution of the flux density and back-emf
(a) Prototype machine of the PS-PMLSM
(b) Flux density distribution of the Air-gap
(c) Back-EMF distribution of the PS-PMLSM under no-load

GR-14. An Analytical and Numerical Hybrid Model for Static Characteristics of a Radial Linear and Rotary Interior Permanent Magnet Actuator.

P. Jin[1], Y. Guo[1] and Y. Zhu[1]
1. School of Energy and Electrical Engineering, Hohai University, Nanjing, China

I.Introduction Recently, linear and rotary permanent magnet actuator (LRPMA) with integrated structure having high dynamic performance, good power/mass ratio, and simple structure has been proposed [1]. A number of numerical techniques are used to analyze its performance while some pure analytical modeling with magnetic scalar potential are also employed by the author and others [2-5]. However, on one side numerical techniques such as the Finite Element (FE) Method are time-consuming and less insightful when looking into the influence of design parameters upon the machine's behavior. On the other entire analytical methods, either directly [2-4] or indirectly [5], just can be used in limited topologies, such as surface permanent magnet mover, but ineffectively for general topologies like interior permanent magnet mover. This paper presents an analytical and numerical hybrid model for static characteristics of a linear and rotary interior permanent magnet actuator (LRIPMA). II.Analytical and Numerical Hybird Model II-A.Structure of the LRIPMA As shown in Fig. 1(a), the LRIPMA prototype with a interior PM array has a tubular mover, on which there are alternately polarized iron poles in the *z*-direction and eight stacks in the *q*-direction, and a stator with eighteen air-cored coils, three stacks in the *z*-direction and six stacks in the θ-direction. Fig. 1(b) and (c) shows the cutaways of the actuator along the linear and rotational directions. Region I ($R_m \le r \le R_s$) is air/winding region and region II ($R_r \le r \le R_m$) is mover region with the PMs and iron poles. In the 3D model, the end effects are not taken into account; the PMs have a linear demagnetization characteristic, and are fully magnetized in the direction of magnetization. II-B.Field Distribution on the surface of the mover A knowledge of the magnetic field distribution on the air region produced by the mover is fundamental to establishing an accurate model of the LRIPMA for design optimization and dynamic modeling. In region I, the static magnetic field is governed by the Laplacian equation only and the boundary on the stator's inner surface where $r=R_s$ is of the Dirichlet boundary condition. In order to obtain the magnetic field distributions in the other boundary where $r=R_m$, a simplified partial 3D FE model contained mover and stator without coils is established. The nonlinear magnetic field of the actuator which can be treated as static field and analyzed by ignoring the eddy current, satisfies the governing equation (1) (equations and functions are all given in Fig. 2) and boundary conditions functions (2), where S_Ω is the outer boundary of the solution domain. A is the magnetic vector potential. H_c is the residual flux intensity of PM. By using the FE method, flux density $B_S(\theta, r)$ in the different points of the mover's surface where $r=R_m$ can be calculated by equation (3) where B_{rS}, $B_{\theta S}$, and B_{zS} are *r*-, θ- and *z*-directions flux density components respectively. By using the 2D discrete Fourier transform, B_{rS}, $B_{\theta S}$, and B_{zS} which are calculated by the FE model, are decomposed into the equation (4) where $\nu=np$ and $\upsilon=k\pi/\tau$; C_{rkn}, $C_{\theta kn}$, and C_{zkn}, are the *k*-*n*th harmonic coefficients of the 2D Fourier Transform. II-C.Field Distribution in the air region In the cylindrical coordinate system, based on the magnetic scalar potential (MSP) ϕ, the magnetic field intensity components can be expressed by equations (5) where ϕ is governed by the Laplacian equation in the air region as equation (6) whose general solution is equation (7) and boundary conditions can be expressed by equation (8). By solving the Laplacian equation in region I subject to former boundary conditions, the Fourier expansions of the flux density components in the *r*-, θ- and *z*-directions in region I in the 3D cylindrical coordinate system can be given. The linear electromagnetic force and rotary electromagnetic torque of the actuator can be subsequently predicted by the hybrid method. III.Verification by Integrated 3D FEM To verify the correctness of the analytical solutions, we calculated magnetic field of the LRIPMA using an integrated 3D FE model. The meshed elements are tetrahedral-shaped and the free mesh algorithm is imposed. The predicted flux densities along the r-direction in an electrical period of the tubular mover and along both the z- and θ-directions with different methods are compared. Some excellent agreements verify the validity of the hybrid model. The electromagnetic torque and electromagnetic force in the rotary and linear directions and the flux linkage of the stator winding are subsequently derived and validated by the integrated 3D FE model in the full paper. IV.Acknowledgment This work was jointly supported by the NSFC (51407061) and the NSF of Jiangsu Province (BK20140854).

[1] G. Krebs, A. Tounzi, B. Pauwels, D. Willemot, and F. Piriou, "Modeling of a linear and rotary permanent magnet actuator," *IEEE Trans. Magn*., vol. 44, no. 11, pp. 4357-4360, Nov. 2008. [2] P. Jin, H. Lin, S. Fang, Y. Yuan, Y. Guo, and Z. Jia, "3-D analytical linear force and rotary torque analysis of linear and rotary permanent magnet actuator," *IEEE Trans. Magn.*, vol. 49, no. 7, pp. 3989–3992, Jul. 2013. [3] T. J. Teo, H. Zhu, S. Chen, et al, "Principle and modeling of a novel moving coil linear-rotary electromagnetic actuator", *IEEE Trans. Ind. Electron*, vol. 63, no. 11, pp. 6930-6940, Nov. 2016. [4] K. K. Guo, S. H. Fang, H. Y. Lin, et al, "3-D Analytical analysis of magnetic field of flux reversal linear-rotary permanent-magnet actuator," *IEEE Trans. Magn.*, vol. 53, no. 6, pp. 8202205:1-4, Jun. 2017. [5] P. Jin, S. Fang, H. Lin, Y. Yuan, Y. Guo, and Z. Jia, "Analytical magnetic field analysis and prediction of cogging force and torque of a linear and rotary permanent magnet actuator," *IEEE Trans. Magn.*, vol. 47, no. 10, pp. 3004–3007, Oct. 2011.

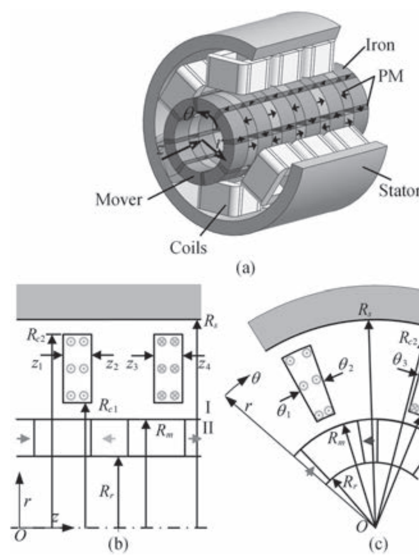

Fig. 1. Cutaways of the LRIPMA on (a) 3D view and along (b) axial direction and (c) circumferential direction.

$$\nabla\times\frac{1}{\mu}\nabla\times\mathbf{A}-\nabla\frac{1}{\mu_e}\nabla\cdot\mathbf{A}=\begin{cases}0 & \text{Region I}\\ \nabla\times\mathbf{H_c} & \text{Region II}\end{cases} \quad (1)$$

$$\left.\begin{aligned}\mathbf{A}\times\mathrm{n}&=0\\ \nabla\cdot\mathbf{A}&=0\end{aligned}\right\} \quad (2)$$

$$\vec{B}_S(\theta,z)=B_{rS}(\theta,z)\vec{r}+B_{\theta S}(\theta,z)\vec{\theta}+B_{zS}(\theta,z)\vec{z} \quad (3)$$

$$\begin{cases}B_{rS}=\sum_{k=1,3,5\cdots}^{\infty}\sum_{n=1,3,5\cdots}^{\infty}[C_{rkn}\sin(\nu\theta)\cos(\upsilon z)]\\ B_{\theta S}=\sum_{k=1,3,5\cdots}^{\infty}\sum_{n=1,3,5\cdots}^{\infty}[C_{\theta kn}\sin(\nu\theta)\cos(\upsilon z)]\\ B_{zS}=\sum_{k=1,3,5\cdots}^{\infty}\sum_{n=1,3,5\cdots}^{\infty}[C_{zkn}\cos(\nu\theta)\sin(\upsilon z)]\end{cases} \quad (4)$$

$$H_r=-\frac{\partial\varphi}{\partial r},\quad H_\theta=-\frac{1}{r}\frac{\partial\varphi}{\partial\theta},\quad H_z=-\frac{\partial\varphi}{\partial z} \quad (5)$$

$$\frac{\partial^2\varphi}{\partial r^2}+\frac{1}{r}\frac{\partial\varphi}{\partial r}+\frac{1}{r^2}\frac{\partial^2\varphi}{\partial\theta^2}+\frac{\partial^2\varphi}{\partial z^2}=0 \quad (6)$$

$$\varphi=\sum_{k=1,3,5\cdots}^{\infty}\sum_{n=1,3,5\cdots}^{\infty}(A_1I_\nu(r)+B_1K_\nu(r))\cos(\nu\theta)\sin(\upsilon z) \quad (7)$$

$$\begin{cases}H_r(r,\theta,z)|_{R_s}=0\\ \vec{B}(r,\theta,z)|_{R_m}=\vec{B}_S(\theta,z)\end{cases} \quad (8)$$

Fig. 2. Equations and functions.

GR-15. Magnetic characteristics of the ferromagnetic Fe-rich clusters in bulk amorphous $Nd_{60}Fe_{30}Al_{30}$ alloy.

L. Zhao[1,2], H. Yu[2], W. Li[2], X. Liao[2], J. Zhang[2], X. Zhong[2], K. Su[1], Z. Liu[2] and J. Greneche[3]
1. Innovative Center for Advanced Materials (ICAM), Hangzhou Dianzi University, Hangzhou, China; 2. South China University of Technology, Guangzhou, China; 3. Le Mans Université, Institut des Molécules et Matériaux du Mans CNRS UMR-6283, Le Mans, France

Metallic glass represents a new type of materials with new physics. Bulk amorphous Nd-Fe-Al based alloys have shown surprising room temperature hard magnetic properties[1]. It has been suggested that the high coercivity could be attributed to that the moments of Fe-rich clusters with high anisotropy are pinned by non-magnetic nanocrystals [2]. However, up to now, the magnetic characteristics of the ferromagnetic Fe-rich clusters have not been fully understood yet. In this work, Φ2 mm $Nd_{60}Fe_{30}Al_{30}$ rod sample was prepared by a copper mold casting method. The remanence, saturation magnetization, and coercivity of the as-cast alloys are 13 emu/g, 18 emu/g, and 283 kA/m, which suggests the typical hard magnetism. Based on the detailed microstructure analysis, the alloy is actually composed of main amorphous phase and hcp structured nanocrystalline Nd phase. The Fe-rich clusters are well distributed in the amorphous phase and the Hcp Nd could act as the domain wall pinning center. ^{57}Fe Mössbauer spectra were applied to investigate the hyperfine structure of the alloys. According to the refined hyperfine parameters, the distribution of the hyperfine field suggests a normal distribution, which confirmed the amorphous structure of those clusters. The mean hyperfine field and magnetic moments of the Fe atoms in clusters are 23(±1) T, 27(±1) T and 1.5(±0.1) μ_B, 1.7(±0.1) μ_B at 300 K and 77 K, respectively. Fig. 1a shows the magnetic hysteresis loops of the $Nd_{60}Fe_{30}Al_{10}$ alloy after cooling at 5 K with and without an applied magnetic field. The M-H loops for the alloy after field cooling shift upwards compared with the loops for that without field cooling. The corresponding magnetic vectors shown in Fig. 1b suggest that parts of the clusters' moments are blocked by the strong pinning effects of antiferromagnetic coupled Nd atoms, which is difficult to be reoriented under an available applied magnetic field. The present data provide some useful information for understanding the ferromagnetic Fe-rich clusters.

1. A. Inoue, "Bulk amorphous alloys with soft and hard magnetic properties," Materials Science and Engineering, vol. A226-228, pp. 357-363, 1997.
2. L.Z. Zhao, Z.G. Zheng, X. Chen, Z.G. Qiu, J.W. Lai, G. Wang, et al., "Magnetic Characteristics for the Mould-Cast Hard Magnetic $Nd_{70-x}Fe_{30}Al_x$ (x=0-10) Alloys," Magnetics, IEEE Transactions on, vol. 51, pp. 1-6, 2015.

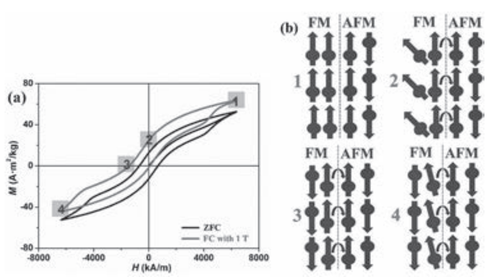

Fig. 1. Magnetic hysteresis loops of the $Nd_{60}Fe_{30}Al_{10}$ alloys with and without field cooling at 5 K (a) and the corresponding magnetic vectors (b)

FRIDAY MORNING, 27 APRIL 2018 SIMPOR/ROSELLE BALLROOM, 8:30 TO 11:30

Session GS
HIGH SPEED MACHINES I
(Poster Session)

Kenji Nakamura, Chair
Tohoku University, Sendai, Japan

GS-01. Comparative study of magnet flux linkage influence on IPM synchronous machine for high-speed properties.

W. Wu[1], X. Zhu[1] and S. Zheng[1]
1. Jiangsu University, Zhenjiang, China

I. Introduction Automotive industry applications are oriented increasingly toward more energy-efficient and environmentally friendly drive-train technologies. This trend is mainly attributed to the detrimental effects of greenhouse gas emissions causing by vehicle emissions. Thus, the diffusion of pollution-free electric cars in urban environment has become an irreversible trend. As one of the key devices in EVs, the choice of electric drive-train most suited to EV's application is still matter of discussions. In particular, the permanent magnet synchronous machines are widely chosen for their higher torque density, high efficiency and mass saving[1]. II. Design Requirement and Machine Topology In general, EVs require a constant-torque performance at low speed and a constant-power one at high speed, as shown in Fig.1 (a). The continuous torque at low speed is determined by the wanted up-hill behavior, while the maximum continuous power determines the maximum speed of vehicles. Besides, the high efficiency of the entire speed region is extremely desired. To achieve the above requirements, scholars have conducted a great deal of exploration on the innovation of machine structure in past years. Therein, two types of machines are widely reported in literatures. One is a PM-assisted synchronous reluctance (PMA-REL) machine with a low PM flux linkage and the other is a flux intensify interior permanent magnet synchronous (FI-IPM) machine with a high PM flux linkage[2][3]. Both types of machines have been proven to be feasible candidate in EV's driving circle[4]. However, the operating features of the two types of machines are not the same especially in high-speed regions. In this paper, by difference combinations of PM pieces and magnetic barriers in rotors, two IPM machines respectively operating with PM-assisted effect and flux-intensifying effect are established, a comparative study is carried out to clarify the influence of PM flux linkage on the high-speed properties of both of the machines. III. Comparative Analysis The structures of the two machines, named PMA-REL machine and FI-IPM machine, are shown in Fig.1(b) and (c). In PMA-REL machine, the PM pieces are inserted in flux barriers of q-axis, with a magnetization direction opposite to the flux generated by armature reaction. Thus, the main function of the PMs is to saturate the rotor bridges and increase power factor of the machine, and only an assisted contribution is made for the output torque. As for the FI-IPM machine, although the PM piece cuts the flux barriers in the middle, resulting in a marked obstacle for the d-axis flux guide, it should be noted that the magnetic field of d-axis can be intensified by applying a positive d-axis current, which really offsets the reduction of the reluctance torque causing by resistance effect of PM pieces. To deeply explore the property of the two machines, the comparison studies are implemented. Fig.2 (a) and (b) shows the change rules of flux linkage versus current amplitudes of the two machines. Fig.2 (c) and Fig.2 (d) compares the inductance characteristics and torque characteristics of the two machines. Fig.2 (e) and Fig.2 (f) exhibits the torque-speed performance and the loss characteristics of two machines. The results show that the FI-IPM machine possesses a wider constant power speed range with respect to the PMA-REL machine, but emerges a higher copper loss and core loss especially in high-speed regions, and it means a relatively lower efficiency in corresponding regions. The more detailed analysis will be presented in the full paper.

[1] G. Pellegrino, A. Vagati, P. Guglielmi and B. Boazzo, "Performance Comparison Between Surface-Mounted and Interior PM Motor Drives for Electric Vehicle Application," *IEEE Trans. Ind. Electron.*, vol. 59, no. 2, pp. 803-811, Feb. 2012. [2] N. Bianchi, M. E. Fornasiero, and W. Soong, "Selection of PM flux linkage for maximum low-speed torque rating in a PM-assisted synchronous reluctance machine," *IEEE Trans. Ind. Appl.*, vol. 51, no. 5, pp. 3600-3608, Sep./Oct., 2015. [3] N. Limsuwan, T. Kato, K. Akatsu, and Robert D. Lorenz, "Design and evaluation of a variable-flux flux intensifying interior permanent magnet machine," *IEEE Trans. Ind. Appl.*, vol. 50, no. 2, pp. 1015-1024, Mar. 2014. [4] X. Y. Zhu, S. Yang, Y. Du, Z. X. Xiang, and L. Xu, "Electromagnetic performance analysis and verification of a new flux-intensifying permanent magnet brushless motor with two-layer segmented permanent magnets," *IEEE Trans. Magn.*, vol. 52, no. 7, Jul. 2016. Art. ID. 8204004.

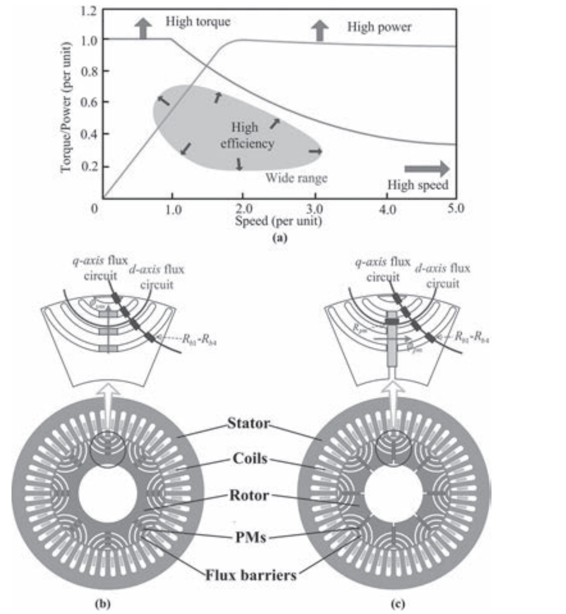

Fig. 1. Design requirements and the proposed machines. (a) The requirements of traction machines of EVs. (b) The proposed PMA-REL machine. (c) The proposed FI-IPM machine.

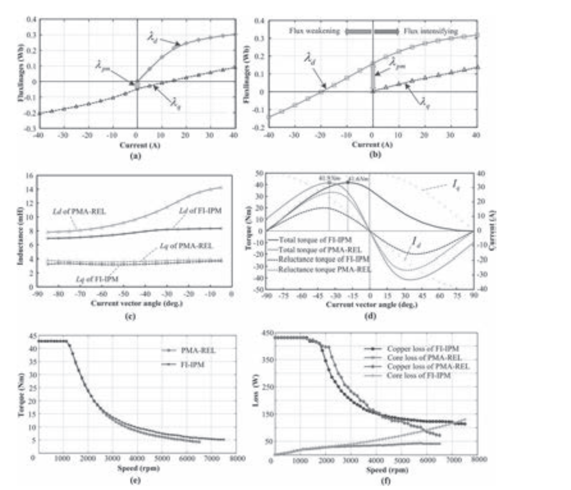

Fig. 2. Performance comparisons of the two machines. (a) Change rules of dq-axis flux linkage of PMA-REL machine versus current amplitudes. (b) Change rules of dq-axis flux linkage of FI-IPM machine versus current amplitudes. (c) Inductance characteristics. (d) Torque characteristics.(e) Performance of torque versus speed. (f) The loss versus speed in the two machines.

GS-02. Improvement of Air Watt in Single-Phase BLDC Motor for 100,000 rpm Applications.

H. Hwang[1], J. Cho[1], Y. Choo[1], C. Kim[1] and C. Lee[1]
1. Electrical and Computer Engineering, Pusan National University, Pusan, The Republic of Korea

Consumer electronics markets are rapidly changed from conventional to premium home appliances with superior performance, convenience, and better design. As elderly people and dual-income households grow, premium home appliances that are easy to use and help the people with housework are preferred. In line with this, competition among premium products is accelerated in cordless vacuum cleaner markets, but there is a lack of literature and research to support this. A brushless direct-current (BLDC) motor uses an electrical commutating device instead of a combination of mechanical commutators and brushes. Hence, it is widely used in high-speed applications than a dc brush-type motor due to no carbon dust and no maintenance about brush wear. A single-phase BLDC motor is suitable for cordless vacuum cleaners that require more compactness and lighter weight due to its simple electromagnetic structure compared to a three-phase BLDC motor. However, most studies on single-phase BLDC motors have focused on motor design for self-starting and cogging torque reduction for spindle motors or low speed fan motors [1-2]. This paper aims to design a high-efficiency single-phase BLDC motor suitable for handy stick-type cordless vacuum cleaner. In designing a single-phase BLDC motor, since the problem of starting and continuous torque generation is most important, asymmetric air gap structure is generally employed. Figs. 1(a) and 1(b) show cogging torque and mutual torque with and without asymmetric air gap, respectively. As shown in Fig. 1(a), the case of symmetric air gap has dead points at which no torque is generated, and hence, cogging and mutual torque become zero during the dead zone. In this case, it is difficult to generate starting and continuous torque. On the other hand, as shown in Fig. 1(b), there are no dead points due to phase difference between cogging and mutual torque caused by asymmetric air gap. From Figs. 1(a) and 1(b), it is noticed that there is a negative region of cogging torque regardless of symmetric and asymmetric air gap. Since total torque is determined by summing cogging and mutual torque, the magnitude of cogging torque along with its phase shift from mutual torque is critical for continuous torque generation without negative torque. Different from the existing study of single-phase BLDC motors in spindle and fan applications [3-4], the variation of DC battery voltage in cordless vacuum cleaners has to be correlated with the ratio of maximum to minimum air gap in a non-uniform stator pole surface. In this study, a single-phase BLDC motor for cordless vacuum cleaners is designed to satisfy three key conditions of starting torque, continuous torque, and battery voltage fluctuation in case of asymmetric air gap. As shown in Fig.2, another important design specification is the volume miniaturization of a motor assembly having a high-speed fan, a driving inverter, and a housing. The dimension of capacitors in the DC link of a driving inverter should be considered at the same time in designing stator lamination to fit the capacitors into the rest of space, and except for the space, both stator and rotor assemblies are occupied inside their housing. Based on the prototype of a proposed single-phase motor assembly in Fig. 2, its several performances have been measured and/or estimated in motor efficiency, inverter efficiency, the efficiency of air flow, and system efficiency. A step-by-step design procedure will be detailed in the final paper, and from the motor itself to its assembly, the result of experimental tests will be also given to validate the feasibility of a single-phase BLDC motor for cordless vacuum cleaners.

[1] Chiu, C. L., Chen, Y. T., Liang, Y. L., & Liang, R. H. (2010). Optimal driving efficiency design for the single-phase brushless DC fan motor. IEEE Transactions on Magnetics, 46(4), 1123-1130. [2] Fazil, M., & Rajagopal, K. R. (2010). A novel air-gap profile of single-phase permanent-magnet brushless DC motor for starting torque improvement and cogging torque reduction. IEEE Transactions on magnetics, 46(11), 3928-3932. [3] Kim, D. K., Park, Y. U., & Cho, J. H. (2014, September). Cogging torque reduction of single-phase brushless DC motor with a tapered air-gap using optimizing notch size and position. In Energy Conversion Congress and Exposition (ECCE), 2014 IEEE (pp. 2447-2453). IEEE. [4] Dunkl, S., Muetze, A., & Schoener, G. (2015). Design constraints of small single-phase permanent magnet brushless DC drives for fan applications. IEEE Transactions on Industry Applications, 51(4), 3178-3186.

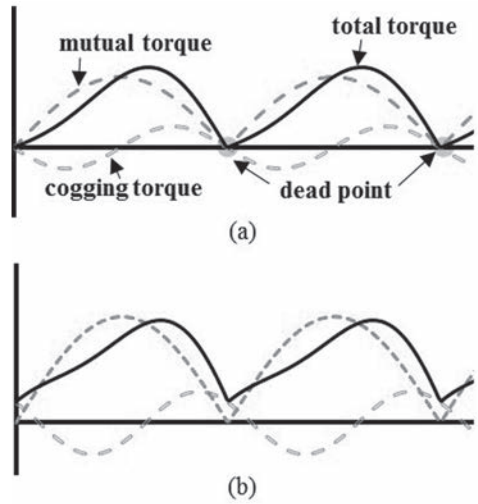

Fig. 1. Torque production of single-phase BLDC motor in terms of air gap, (a) symmetric air gap, (b) asymmetric air gap.

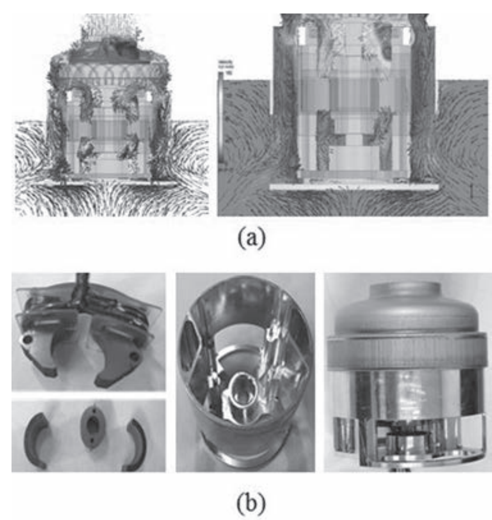

Fig. 2. Assembly of proposed single-phase BLDC motor, (a) air flow, (b) prototype photos.

GS-03. Multi-physics and multi-objective optimization of a high speed PMSM for aircraft electric propulsion.

W. Zhao[1], X. Wang[2], C. Gerada[3,1], H. Zhang[1], C. Liu[1] and Y. Wang[1]
1. University of Nottingham Ningbo China, Ningbo, China; 2. Yusheng Group, Ningbo, China; 3. University of Nottingham, Nottingham, United Kingdom

High speed electrical machine has been developed and used for many years, and it is now considered a mature and reliable technology for a number of engineering applications, particularly for direct-drive solutions[1]. With the availability of high specification materials, development of power electronic converters and improvement in the manufacturing methodologies, there is currently an unprecedented effort towards developing electrical machines with very high power density and efficiency, especially for the hybrid and full electric aircraft[2]. When designing such type of machines, the interaction and conflict between the electromagnetic, mechanical and thermal aspects should be considered seriously, since they work at the material boundaries[3]. Moreover, maximum power density and maximum efficiency can not be achieved together generally. There exists an optimal design to obtain a relative high performance for both power density and efficiency[4]. This paper started on the sensitivity analysis of the aspects that will improve the active power density of the electrical machine, including the frequency, slot and pole combination, construction of permanent magnetic and thermal management. These topics will be first researched individually and respective behavioural models developed. They will then be merged within a design cycle of the machine in an effort to attain the target performances of 20 kW/kg (active part) at 20 000 r/min for a 2 MW electric propulsion motor for aircraft. The optimization can be divided into two levels. The slot and pole combination is the first level, while the machine dimension is the second level. Considering the power and speed, as well as the limit of switching frequency, the number of poles are limited to 4 ~ 12, and the number of slots are limited to 36 ~ 48 with distributed windings. Seven variables are selected to determine the machine sizing, as shown in Fig.1, which are stator outer and inner diameter D_{so} and D_{si}, rotor inner diameter D_{ri}, active core length L, thickness of permanent magnet H_p, and slot width and height B_s and H_s. For each slot and pole combination, the best design solution can be given by the second level optimization according to the certain objective. Then, the final optimized result can be obtained by comparing performances between each best solution. During the machine sizing level optimization, some variables are fixed to reduce the optimization dimension. The rotor outer diameter is fixed to 190mm to make sure the rotor linear speed is less than 200 m/s, which is the limit of silicon steel laminations. The airgap thickness is fixed to 2 mm, and the permanent magnet pole embrace is fixed to 0.8, which are reasonable for a surface-mounted PM machine with such speed. The RMS line voltage is fixed to 1.1 kV, and the number of conductors per slot, the number of strands per turn and the strand diameter are selected automatically by the analytical electromagnetic program with the limitation of the fill factor. An analytical mechanical model is integrated in the machine dimension program. Stresses are induced in the rotor due to the interference fit between the magnets and the carbon fiber sleeve, as well as due to centrifugal force[5]. The sleeve thickness is chosen so as to achieve a defined design margin according to the magnet thickness. The sizing program also integrates a simple analytical thermal model with three nodes. The temperature of the stator tooth, yoke and coil can be obtained together with the electromagnetic results. Based on the multi-physical field analytical program, optimization constrains can be proposed from electromagnetic, thermal and mechanical point of view. According to the performance requirement, constrains are set as power density ≥ 20 kW/kg; efficiency ≥ 98 %; current density ≤ 20 A/mm^2; flux density of rotor yoke, stator tooth and yoke ≤ 1.4 T (6.5% Si steel sheet); temperature rise of stator tooth, yoke and coil ≤ 125 K ; stress of the sleeve ≤ 1000 MPa; radial stress of magnet ≤ 0 (pressure stress). A multi-objective genetic algorithm is used in the optimization program to find the optimal solution quickly. Three objectives are chosen, max power density (kW/kg), max torque per loss (Nm/kW), and max torque per loss per mass (Nm/(kw*kg)) to describe the comprehensive performance of power density and efficiency. It can be seen from the sensitivity analysis results, the inner diameter of the rotor, core length and slot height are the most sensitive variables to the power density, while the slot height have a major effect on the torque per loss. The final optimal torque per loss per mass solution comparisons of different number of poles are shown in Fig.2. It shows the 8 poles with 48 slots design can obtain a best comprehensive performance between the power density and the efficiency. It makes sense because increasing the number of poles will increase the power density by reducing both the thickness of rotor and stator back iron, whilst will also increase the iron losses and AC copper losses by increasing the frequency. Finally, the optimal design paraments are listed in this paper, and results meet all the requirements. In this paper, a multi-objective optimization research is carried out based on the multi-physical field simulation. According to the optimization and sensitivity analysis results, the key design issues for high power density and high efficiency permanent magnet synchronous machines are discussed.

1. A. Boglietti, C. Gerada, A. Cavagnino, "High speed electrical machines and drives", *IEEE Trans. Ind. Electron.*, vol. 61, no. 6, pp. 2943-2945, Jun. 2014. 2. D. Gerada, A. Mebarki, N. Brown, C. Gerada, A. Cavagnino, A. Boglietti, "High-speed electrical machines: Technologies trends and developments", *IEEE Trans. Ind. Electron.*, vol. 61, no. 6, pp. 2946-2959, June 2014. 3. Z. Huang, J. Fang, "Multiphysics design and optimization of high-speed permanent-magnet electrical machines for air blower applications", *IEEE Trans. Ind. Electron.*, vol. 63, no. 5, pp. 2766-2774, May 2016. 4. Tenconi, S. Vaschetto, A. Vigliani, "Electrical machines for high-speed applications: Design considerations and tradeoffs", *IEEE Trans. Ind. Electron.*, vol. 61, no. 6, pp. 3022-3029, Jun. 2014. 5. Binder, T. Schneider, M. Klohr, "Fixation of buried and surface mounted magnets in high-speed permanent magnet synchronous motors", *Conf. Rec. 40th IEEE IAS Annu. Meeting*, pp. 2843-2848, Oct. 2005.

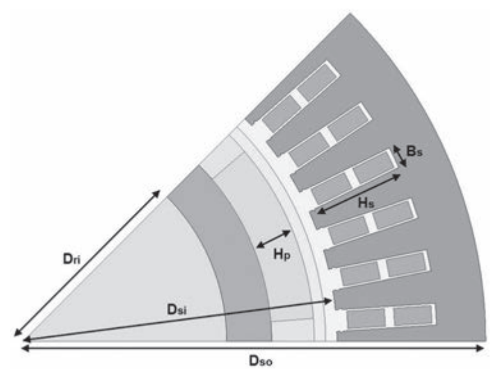

Fig. 1. Machine dimension variables.

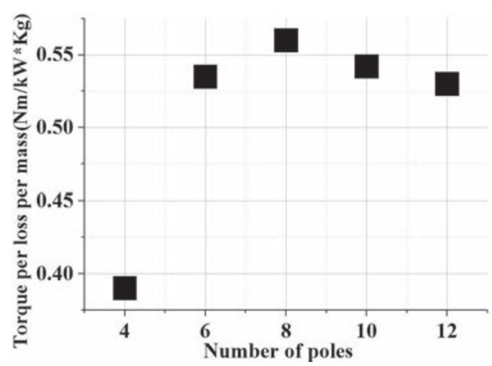

Fig. 2. Optimization results comparisons of different number of poles.

GS-04. Design and Characteristic Analysis of High Speed Permanent Magnet Motor for High-speed and High-head Centrifugal Pump.

G. Jang[1], S. Seo[1], C. Kim[1], K. Shin[1] and J. Choi[1]
1. Electrical Engineering, Chungnam National University, Daejeon, The Republic of Korea

Recently, the high-speed rotor system has attracted considerable attention as a special purpose application in the industrial field. High-speed rotating electrical machines are an indispensable technology, especially in high-capacity compact systems such as spindle drives for machine tools, turbo-compressors, and microturbines. Such a high-speed rotating machine is directly coupled to a driver or a turbine without a separate speed-increasing gear to obtain a high rotational torque [1-2]. However, because of the mechanical stress of the rotor due to high-speed rotation, the increase in loss due to high-frequency input power, control technology, bearing, heat dissipation, cooling technology, etc., various electrical and mechanical problems may occur. Compared to a high-speed system using a conventional accelerating gear, a high-speed rotating system using a high-speed machine is more suitable owing to its small size, low weight, and high efficiency because the volume of the system is reduced as compared with a general high-speed rotating system. A high-speed device should be designed not only for the basic electromagnetic design, but also for the mechanical structure design and the dynamic design of rotor shaft to be suitable for high-speed rotation. In addition, a control system and inverter must be designed to ensure the reliability of speed and torque characteristics in a high-speed operation. The design of permanent magnet high-speed motors requires precise electromagnetic design for the calculation of mechanical parameters such as permanent magnet rotors, stator, windings, and other parameters of the device. In addition, the most attention to electromagnetic design is in predicting the loss of the machine. In general, the heat source of the electrical machine is due to electrical loss and can be divided into copper loss and iron loss. The copper loss corresponds to the resistance of the current and the iron loss can be attributed to the eddy current, which is the loss due to the hysteresis of the material and the induction current. In addition, rotor losses due to the non-sinusoidal distribution of air flux density and the bearing frictional hand and wind damage present as mechanical losses can be categorized [3-4]. Because loss is an important factor in determining the operating conditions and efficiency of an equipment, it is very important to accurately predict and design the losses. In particular, because of rotor loss due to time loss resulting from iron loss in the stator core caused by the high-frequency operation, the slot structure of the stator and the time harmonics due to the inverter are very sensitive to the design of the super high-speed equipment This paper presents the application of a gearless pump system using a 12500-rpm, 100-hp high-speed permanent magnet motor in a conventional geared pump system. As mentioned above, when the high-speed motor is directly connected to the high-speed pump, the noise, loss, maintenance, and repair costs can be reduced, and the overall system size can be reduced. To apply a high-speed motor, various design techniques such as electromagnetic design, structural design, and mechanical design of a motor are required. Therefore, in this paper, the design and performance evaluation of a 12500-rpm, 100-hp permanent magnet motor is discussed. Fig. 1 (a) shows the shape of the permanent magnet motor designed based on the finite element analysis method. Fig. 1 (b) shows the results of the torque per unit of rotor volume (TRV) analysis and the design points for selecting the size of the rotor of the permanent magnet motor. Fig. 1 (c) shows the stator and rotor fabricated through the design process. Fig. 1 (d) shows the motor test bed with the permanent magnet motor and pump system combined. The torque meter is used to evaluate the performance of the motor during load. The high-speed motor may fail because of the scattering of the permanent magnet during operation. Therefore, the rotor size should be selected in consideration of the rotor stiffness. Fig. 2 (a) shows the results of the eddy current loss of the rotor, and the core loss of the stator using finite element method (FEM). Fig. 2 (b) shows the stiffness analysis results of the motor rotor during no load and during load. Based on the analysis results, we confirmed that the size of the motor has been selected such that no problems are encountered in the mechanical structure of the motor. Fig. 2 (c) shows the results of the high-speed permanent magnet motor design based on the finite element analysis and the experimental results. When the results of the finite element method did not consider the mechanical loss, the validity of the design results was confirmed through experiments. Acknowledgment This work was supported by the Basic Research Laboratory (BRL) of the National Research Foundation (NRF-2017R1A4A1015744) funded by the Korean government.

[1] P. B. Reddy, Z. Q. Zhu, H. Seok-Hee, and T. M. Jahns, "Strand-level proximity losses in PM machines designed for high-speed operation," in *Proc. 18th ICEM*, Sep. 2008, pp. 1–6. [2] D. Fodorean, "Study of a High-Speed Motorization with Improved Performance Dedicated for an Electric Vehicle," *IEEE Trans. Magn*., vol. 50, no. 2, Feb. 2014. [3] H.W. Cho, S.M. Jang, and S.K. Choi, "A design approach to reduce losses in high-speed permanent magnet machine for turbo-compressor," *IEEE Trans. Magn*., vol. 42, no. 10, pp. 3521–3523, Oct. 2006. [4] F. Jiancheng, L. Xiquan, B. Jan, and K. Wang, "Analysis of Circulating Current Loss for High-Speed Permanent Magnet Motor," *IEEE Trans. Magn*., vol. 51, no. 1, Jan. 2015.

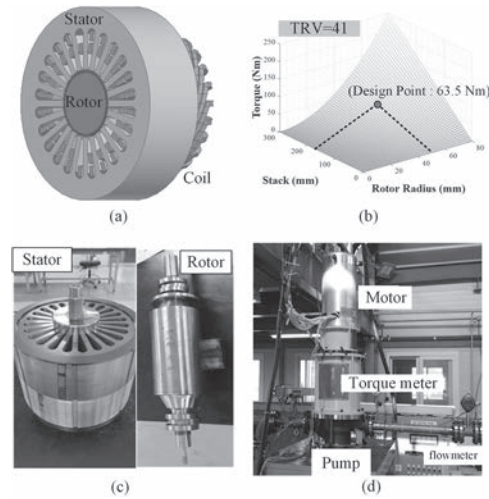

Fig. 1. (a) Structure of high-speed surface permanent magnet synchronous motor (SPMSM), (b) the results of the TRV analysis and design points of the rotor of the permanent magnet motor, (c) manufactured stator core and rotor of SPMSM, (d) motor test bed with the permanent magnet motor and pump system.

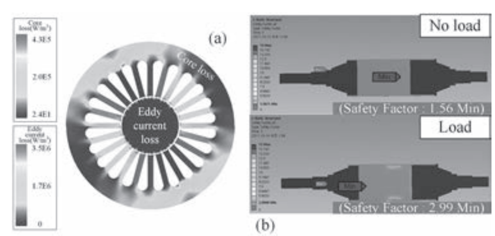

Parameter	Input Power	Torque	Speed	Output Power	Efficiency
FEM	68.8 kW	**53 Nm**	12 krpm	66.6 kW	96.8 %
Experiment (5 times average)	68.6 kW	**53 Nm**	11.8 krpm	65.4 kW	95.4 %

(c)

Fig. 2. Analysis results: (a) eddy current loss and core loss analysis results using FEM, (b) the stiffness analysis results of the motor rotor during no load and during load, (c) comparative analysis of experimental and analysis results of motor.

GS-05. Investigation of Optimal Split Ratio for High-Speed Permanent Magnet Brushless Machines.

Y. Wang[1], S. Guo[2], Y. Li[2], Z. Chen[2], Y. Wang[2] and Z. Zhu[1]
1. Department of Electronic and Electrical Engineering, University of Sheffield, Sheffield, United Kingdom; 2. CRRC Zhuzhou Institute Co. Ltd, Zhuzhou, China

I. INTRODUCTION The split ratio of rotor outer diameter to stator outer diameter is one of the most important design parameters due to its significant impact on machine torque capability and efficiency. It has been optimized analytically in existing papers with fixed copper loss only which is reasonable for low-to-medium-speed operating machines [1]. However, for high speed permanent magnet machines (HSPMM), the stator iron loss cannot be ignored due to the inherent high frequency. The iron loss can even be dominant for HSPMM operating at ultra-high speed (>100krpm) [2]. On the other hand, the mechanical constraints should also be considered for the design of HSPMM. The mechanical stress is closely related with the rotor outer diameter thus the split ratio. Hence, it is of great significance to investigate the optimal split ratio for HSPMM by taking the stator iron loss and mechanical constraints into account. II. OPTIMAL SPLIT RATIO FOR HSPMM CONSIDERING STATOR IRON LOSS Generally, a two-term iron loss model can be adopted for calculating the iron loss, where the classic loss and excess loss in the three-term model are combined into a global eddy current loss [3]. This model can be expressed as: (1) where denotes iron loss in watts per kilogram, and represent the hysteresis coefficient and eddy current coefficient, respectively. *f* denotes the frequency of magnetic field. B_{Fe} denotes the flux density of magnetic field. The electromagnetic torque of HSPMM can be further expressed as:(2)(3) where k_w denotes the winding factor. B_g is the air gap flux density. k_s denotes the slot packing factor and N_s represents the number of stator slots. l_a is the active stack length and □□$_{cu}$ denotes the mass density of copper. D_o is the stator bore diameter and *g* denotes the physical air gap length. A_s and A_{Fe} represent slot area and stator stack area, respectively. p_{limit} denotes the total allowable stator loss with certain stator external surface area and cooling method. γ represents the ratio of stator iron flux density and air gap flux density. □□$_{Fe}$ denotes the mass density of stator material. Hence, the optimal split ratio for maximum electromagnetic torque considering stator iron loss can be obtained by solving the following differential as:(4) Fig.1 illustrates the stator loss and electromagnetic torque versus split ratio with and without consideration of stator iron loss. It can be seen that the electromagnetic torque would be considerably reduced when the iron loss is taken into account. This should be attributed to the reduced allowable copper loss thus the electrical loading at each split ratio. In addition, the optimal split ratio for maximum electromagnetic torque has also been reduced due to the decreasing copper loss with the increasing split ratio before reaching its minimum value. The optimal split ratio has to be reduced in order to maximize f(λ). It should be noted that torque variation range is relatively smaller when considering the stator iron loss. The electromagnetic torque decreases slowly after reaching the maximum value. As mentioned before, the copper loss turns to increase mildly which make a compensation for the torque by increasing the electrical loading. Hence, the electromagnetic torque would not drop sharply compared with that when only copper loss is considered as shown in Fig.1 (b). III. INFLUENCE OF DESIGN PARAMETERS ON OPTIMAL SPLIT RATIO As mentioned in Section II, the optimal split ratio considering stator iron loss is significantly related with the allowable copper loss variation trend versus split ratio. On the other hand, the design parameters affecting variation of iron loss will impose the opposite impact on the allowable copper loss when the stator loss is fixed with certain cooling method. In this section, these design parameters such as air gap length, operating speed as well as rotor pole pairs on the optimal split ratio will be investigated in the full paper. IV. OPTIMAL SPLIT RATIO ACCOUNTING FOR MECHANICAL CONSTRAINTS This section investigates the optimal split ratio of HSPMM considering the rotor mechanical constraints. Generally, two fundamental conditions should be satisfied: the tangential stress in the inner surface of sleeve should be within the material limits and the contact pressure between PM and rotor back-iron should be always positive [4]. When the mechanical constraint is taken into consideration, the stator flux density will be significantly reduced due to the increasing air gap length. Accordingly, the stator iron loss will be reduced. In addition, the split ratio at which the stator iron loss reaches maximum is also reduced as shown in Fig.2. It can be seen that optimal split ratio is significantly reduced when the mechanical constraints is taken into consideration. V. CONCLUSION In this paper, the optimal split ratio for HSPMM considering the stator iron loss and mechanical constraints are analysed analytically. The influence of design parameters on the optimal split ratio would be discussed in detail in the full paper. Both the analytical and finite element simulated results reveal that the optimal split ratio is significantly reduced when the stator iron loss and mechanical constraints are taken into consideration.

[1] Y. Pang, Z. Q. Zhu, and D. Howe, "Analytical determination of optimal split ratio for permanent magnet brushless motors," IEE Proc. Elect. Power Appl., vol. 153, pp. 7–13, Jan. 2006. [2] J. D. Ede, Z. Q. Zhu, and D. Howe, "Optimal split ratio for high-speed permanent magnet brushless DC motors," Proc. 5th Int. Conf. Electrical Machines and Systems, vol. 2, Aug. 2001, pp. 909–912. [3] D. M. Ionel, M. Popescu, and S. J. Dellinger, "Computation of core losses in electrical machines using improved models for laminated steel," IEEE Trans. Ind. Appl., vol. 43, no. 6, pp. 1554–1564, Nov./Dec. 2007. [4] A. Binder, T. Schneider, and M. Klohr, "Fixation of buried and surface-mounted magnets in high-speed permanent-magnet synchronous machines," IEEE Trans. Ind. Appl., vol. 42, no. 4, pp. 1031-1037, Jul./Aug. 2006.

$$w_{Fe} = k_h f B_{Fe}^2 + k_e f^2 B_{Fe}^2 \quad (1)$$

$$T = \frac{3\sqrt{2}}{2} k_w B_g \sqrt{\frac{k_s N_s l_a}{24\rho_{cu}}} f(\lambda) \quad (2)$$

$$f(\lambda) = (D_o\lambda + 2g)\sqrt{A_s(p_{limit} - B_g{}^2\gamma^2\rho_{Fe}l_a(k_h f + k_e f^2)A_{Fe})} \quad (3)$$

$$\frac{\partial f(\lambda)}{\lambda} = 0 \quad (4)$$

Equations

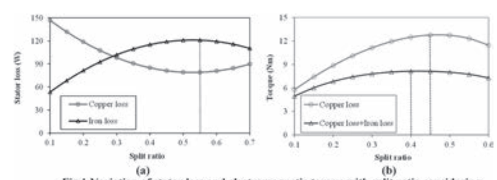

Fig.1 Variation of stator loss and electromagnetic torque with split ratio considering stator iron loss (a) Stator loss (b) Torque (P_{limit}=200W γ=0.5 f=2000Hz B_g=0.85T)

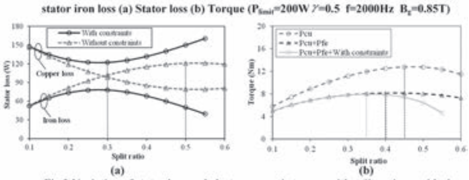

Fig.2 Variation of stator loss and electromagnetic torque with split ratio considering mechanical constraints (a) Stator loss (b) Torque(Plimit=200W γ=0.5 f=2000Hz Bg=0.85T)

GS-06. Design and Experimental Validation of High Speed Motor for Electric Turbo Charger Considering the Variation of L/D Ratio.

D. Hong[1,2] and Y. Jeong[1]

1. Electric Motor Research Center, Korea Electrotechnology Research Institute, Changwon, The Republic of Korea; 2. Energy and Power Conversion Engineering, National University of Science and Technology, Changwon, The Republic of Korea

I. Introduction Electrically assisted turbo-chargers enabled by high speed air compressors, high efficiency electric motors, and controllers provide the means for a clean, efficient, and environmentally friendly urban transportation system. Centrifugal supercharger motor also known as e-booster, e-charger or electric blower. The electric motors run at speeds in excess of 100,000rpm. We can drive the compressor of an independent supercharger to create steady boost (and power) mostly during startup, transient and low-speed operation. The motor can be turned on and off as needed. This technology also virtually eliminates turbo lag and enables engine downsizing without compromising engine performance. The ETC (Electric Turbo Charger) consists by a high speed permanent magnet synchronous motor (PMSM), ball or air foil bearings, impeller, controller and power stack and so on. KERI (Korea Electrotechnology Research Institute) is developing a high speed surface permanent magnet (SPM) type of synchronous motor and a PWM-driven inverter. This system operates at a power density of 3kW at 100,000rpm and is intended to fit the 1,600cc diesel vehicles to reduce turbo-lag within 0.5sec. It is important to minimize iron loss considering the used operating speed. Therefore, several materials were used such as amorphous core (0.025t), silicon steel core (0.2t and 0.35t). The core loss and the efficiency of each material were analyzed and compared. The design and experimental validation of the PMSM for the ETC have been developed successfully using resistance load test methodology by reaction torque sensor and multi-physics analyses [1]. II. Loss analysis considering several different materials This paper deals with the comparison of electric core performance in terms with cost and core loss of the each material such as amorphous core (0.025t) and silicon steel core (0.2t, 0.35t). To minimize core loss considering cost and resolve thermal problem based on core loss are a way to commercialize the developed product. Fig. 1 shows efficiency comparison according to the change of the used materials. The amorphous core turned out to be the best in terms of electrical efficiency (98.46%) and core loss (9.85W) at 100,000rpm operating speed. Nevertheless, the silicon steel (0.2t) made by POSCO (korea company) is selected considering the cost of price/performance. Fig. 1 shows schematic diagram of back-to-back dynamo test using reaction torque sensor (Kistler) and resistance load (3kW). Generally, there are many test method to evaluate test motor and driver. However there are no 100,000rpm, 3kW rated torque sensor with the exception one branded product which is very expensive and difficult to handle because the bearings should be operated by oil mist condition. Therefore, reaction torque sensor was applied to back-to-back dynamo system. Also resistance load which one ohm is connected in parallel was adopted considering stray inductance by lead wire cable length and capacitor. Fig. 1 shows performance test results which were well matched with goal and simulation results. III. Response surface methodology for multi-objective optimal design To reduce the response time of electric turbo charger should be considered to customize the variation of rotor L/D (Length/Diameter) ratio. The 2nd order polynomial equations of induced voltage and torque were proposed to use customization design according to the change of D/L ratio. Induced voltage and torque can be estimated and predicted by change with of D/L ratio. Response surface methodology (RSM) was utilized by central composite design (CCD) to make metamodel of 2nd order polynomial equations in Fig 2. The design variables were used length and diameter as shown in Fig. 2. Increased rotor length will cause a critical speed issue and saturation problem in the rotor back yoke. Also, if the rotor diameter is longer, there are problems with linear speed of the rotor, the outer diameter of the stator and the increased inertia of the rotor. Therefore, torque, induced voltage and max. flux density of rotor core were considered according to the variation of rotor diameter and length. RSM is a collection of mathematical and statistical techniques. CCD (Central Composite Design) is the typical method because of easy construction for second-order model. CCD are first-order (2^k) designs augmented by additional central and axial points (2k) to allow estimation of the tuning parameters of a second-order model. Two variables were selected. Hence, variable k is 2 and total number of experiments is 9. Based on selected design variables, 2D FEA had been carried out. Fig. 2 shows overlaid plot (feasible range) considering constraint conditions (induced voltage and max. flux density of rotor's back yoke) according to design variables. IV. Conclusion The core materials such as an amorphous core and a silicon steel core for high speed motor are considered and compared. The design and experimental validation of the PMSM for the ETC have been developed successfully using resistance load test methodology by reaction torque sensor. Further, design, experimental validation and the detailed optimum results will be dealt with in full paper.

[1] D.K. Hong, B.C. Woo, J.Y. Lee and D.H. Koo, "Ultra High Speed Motor Supported by Air Foil Bearings for Air Blower Cooling Fuel Cells", IEEE Trans Magn, Vol. 48, No. 2, 871–874, 2012. [2] F. Lin, S. Zuo, W. Deng and S. Wu, "Noise Prediction and Sound Quality Analysis of Variable-Speed Permanent Magnet Synchronous Motor", IEEE Trans Energy Convers, Vol. 31, No. 2, pp. 698–706, 2017. [3] J.F. Gieras, C. Wang and J.C. Lai, "Noise of Polyphase Electric Motors". Boca Raton, FL, USA: CRC Press, 2006

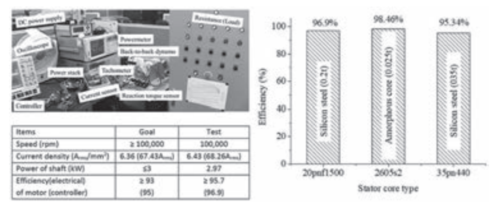

Fig. 1. Schematic diagram of back-to-back dynamo test and comparison of the goal with test results

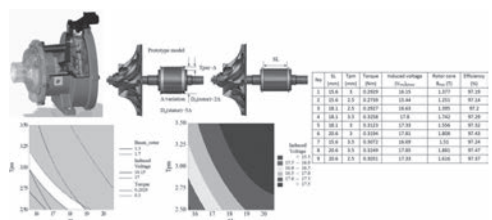

Fig. 2. CCD results, overlaid plot and contour plot according to design variables

GS-07. Trial of Superconducting Magnetic Bearings Applied to High Speed Turbine Rotor.

M. Komori[1], K. Hara[1], K. Asami[1] and N. Sakai[1]
1. Kyushu Institute of Technology, Kitakyushu, Japan

1. INTRODUCTION Vacuum technology is necessary for semiconductor industry, medical industry and food industry [1]. The vacuum technology is also necessary for the new space industry and other advanced industries [2]. Turbo molecular pumps with high speed rotors are key technology for these industries. Turbo molecular pumps are usually composed of active magnetic bearings, a high speed rotor and its controllers. Thus, the mechanism is very precise and complicated, which leads to high price. In this study, high critical temperature (T_c) superconducting magnetic bearings (SMBs) [3][4] are tried to apply to a high speed rotor for turbo molecular pump because of some merits. *2. DESIGN OF SMB* *2.1 High speed rotor* Fig.1-1 shows an illustration of turbo molecular pump composed of a rotor with two SMBs, turbine blades and a permanent magnet (PM) motor. The pump has a gas inlet at the top and a gas outlet at the lower side. Usually, the gas inlet is connected to a vacuum chamber using a vacuum hose to exhaust the chamber to a certain degree of vacuum. At the same time, water molecules in the air are trapped on the SMB surface and the turbine blades surface. This is called "trapping effect". The turbo molecular pump with SMBs has some higher performances than conventional turbo molecular pumps due to the trapping effect. *2.2 Rotor model* Fig.1-2 shows the rotor models (Model-1, 2, 3) supported by two kinds of bearings (SMB and pivot bearing). The rotor Model-1 (Length: 192 mm), rotor Model-2 (Length: 232 mm) and rotor Model-3 (Length: 232 mm) are supported by (a) a SMB and a pivot bearing, (b) two SMBs and a pivot bearing and (c) two SMBs, respectively. The magnetic stiffness k =12,990 N/m and damping coefficient c =4.5 Ns/m are applied to these models. The pivot bearing is composed of a small stainless bar (D3 mm ×L5 mm), which is attached to the rotor bottom. *2.3 Simulation* By using the rotor models shown in Fig.1-2, the rotor analysis (finite element method) is performed. In the simulation, the rotor spins up to a speed of 20,000 rpm. Then, the displacements for three models are analyzed. Fig.1-3 shows the relationships between rotor displacement and rotation speed for (a) Model-1, (b) Model-2 and (c) Model-3. The displacements in Fig.1-3(a) are analyzed near the points of pivot bearing, turbine blade and SMB. From the result in Fig.1-3(a), each displacement is relatively small over a rotation speed range except for a speed of 5,000 rpm. From the result in Fig.1-3(b), each displacement is very small (smaller than 0.03 x10^{-3} mm) over a rotation speed range except for a speed of 4,000 rpm. From the result in Fig.1-3(c), each displacement is very small (smaller than 0.02 x10^{-3} mm) over a rotation speed range except for a speed of 4,000 rpm. Hereafter, Model-2 and Model-3 are adopted in our study because of the small displacements. *3. EXPERIMENTAL SETUP* Fig.2-1 shows an experimental setup composed of a rotor with turbine blades, two SMBs, a pivot bearing and a PM motor. The SMB is composed of a doughnut-shaped superconductor $Dy_1Ba_2Cu_3O_X$ (OD48× ID25.6× 15 mm, J_c=3 ×10^8 A/m^2 at 77 K and 1.0 T) and four PMs. The PMs are neodymium (Nd) magnets (OD24 mm ×W4.25 mm, surface magnetic flux density 0.26 T). The magnetic poles of the PMs are arranged with alternate polarities, such as NS-SN-NS-SN. The superconductors are cooled by using liquid nitrogen (-196 ^{o}C). Fig.2-2 shows the schematic illustration of the developed rotor. The rotor is composed of turbine blades, PMs for SMB and a pivot for bearing. The rotor Model-2 and Model-3 measure 590 g in weight. Fig.2-3 shows the photo of the experimental setup. Each part in Fig.2-3 is corresponding to that in Fig.2-1. *4. EXPERIMENTAL RESULTS AND DISCUSSIONS* Spin down tests are performed using the rotor Model-2 and the Model-3. Fig.2-4 shows one of the experimental results of free-run test for the rotor Model-3, showing (a) upper rotor displacement, (b) lower rotor displacement and (c) natural rotation decay curve. Figs.2-4(a) and (b) show that the displacement amplitudes are smaller than 0.04 mm over a wide range except for rotation speeds between 4,000 and 5,000 rpm. From the experimental results, the rotor Model-3 with two SMBs is better than the rotor Model-2 with two SMBs and a pivot bearing. Hereafter, the rotor Model-3 with two SMBs is adopted in our study. *5. SUMMARY* In this study, the rotor Model-1, 2, 3 supported by two kinds of bearings (SMB and pivot bearing) are proposed. From the simulation results, the rotor Model-2 and Model-3 are adopted from the three models because of the small displacements. From some experimental results, it is found that the displacement amplitudes of the rotor Model-3 are a little smaller than those of the rotor Model-2 over a wide rotation speed range.

[1] G. F. Weston, Ultrahigh vacuum practice, Butterworths, 1985. [2] S. Jayaram and E. Gonzalez, Design and construction of a low-cost economical thermal vacuum chamber for spacecraft environmental testing, Journal of Engineering, Design and Technology, vol. 9, no.1, pp.47- 62, 2011. [3] M. Komori, A. Tsuruta, S. Fukata and T. Matsushita : A new type of superconducting bearing system using high Tc superconductors and dynamics, Applied Superconductivity, vol.2, no.7/8, pp.499-509, 1995. [4] K. Murakami, M. Komori and H. Mitsuda, Flywheel Energy Storage System Using SMB and PMB, IEEE Trans. on Applied Superconductivity, vol. 17, no. 2, pp. 2146-2149, June 2007

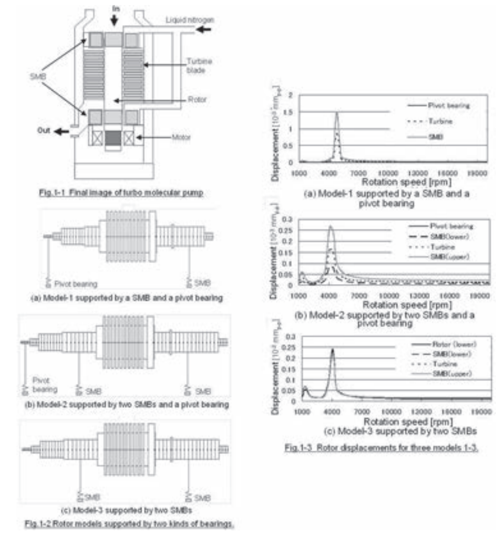

Fig. 1. The figure consists of Fig.1-1, Fig.1-2, Fig.1-3.

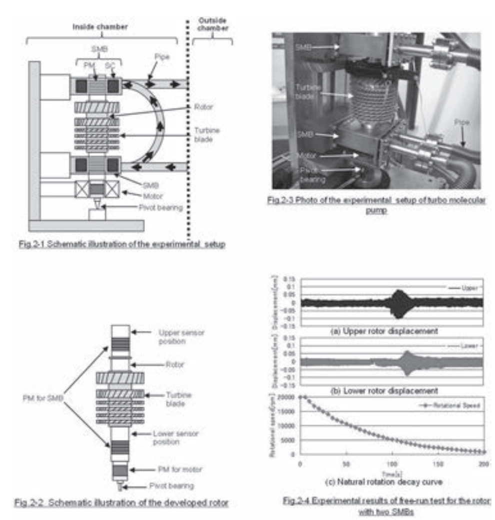

Fig. 2. The figure consists of Fig. 2. -1, Fig. 2. -2, Fig. 2. -3, Fig. 2. -4.

GS-08. Fast Calculation of PM eddy current loss in IPMSM under PWM VSI supply.

S. Zhu[1], M. Cheng[2] and Y. Zhu[1]
1. Deparment of Energy and Electrical Engineering, Hohai University, Nanjing, China; 2. Deparment of Electrical Engineering, Southeast University, Nanjing, China

I. Introduction When calculating the permanent magnet (PM) eddy current loss (ECL) in the interior permanent magnet synchronous machine (IPMSM) under pulse width modulation (PWM) voltage source inverter (VSI) supply, it is very important to take the high frequency harmonic voltages (HFHVs) in the input voltage into consideration because most of the PM ECL in IPMSM with distributed windings is caused by them [1-2]. However, common finite element analysis (FEA) with sinusoidal current source supply isn't able to take the HTHVs into consideration and the coupled field-circuit time-stepping FEA under PWM VSI supply with fine time step is needed for the calculation, which is very time-consuming especially when conducting 3D FEA to take the end effect and axial segmentation into consideration. A hybrid method with the combination of 2D FEA and analytical method has been proposed in [3] for fast calculating the PM ECL considering axial segmentation. However, the 2D time-stepping FEA with fine time step, which takes several hours for one case study, is still needed for the PM ECL calculation under one load condition with the method proposed in [3]. In this paper, the analytical method in [3] is further developed and applied for the PM ECL calculation of an IPMSM applied in the HEV application [4]. Rather than calculating the PM ECL with the average flux density passing through the PM as input [3], the relationship between arbitrary HFHV and the corresponding PM ECL is established. Hence, the total PM ECLs can be calculated with the FFT results of the input line-line voltage directly without time-stepping FEA at a given load condition. II. Relationship between HFHV and PM ECL The HFHV generates pulsating magnetic flux density variation in the IPMSM [3][5], which is the root cause of the additional PM ECL. The procedure to compute the PM ECLs under different HFHVs and load conditions are shown as follows: 1) One step static FEA with the given *d*-axis current i_d, *q*-axis current i_q and rotor position θ at one load condition is conducted. The incremental permeability in each element of the silicon steel is computed and saved. 2) One step linear frequency FEA with the saved incremental permeability and the coupled field-circuit model shown in Fig. 1 is conducted when neglecting the PM eddy current reaction. The average flux density passing through the PM, B_{av}^{n}, is computed. 3) The same linear frequency FEA but considering the PM eddy current reaction is conducted. The PM ECL and the average flux density passing through the PM, B_{av}^{e}, are computed The rotor is assumed to be motionless during the calculation, and the influence of the rotor speed can be taken into consideration by slightly modifying the frequency of the input HFHV. Because the harmonic currents generated by the HFHVs are very small, the saturation level of the silicon steel is mainly determined by the fundamental current, which can be easily obtained with the static FEA with the fundamental current supply. Hence with the fixed permeability method, linear frequency FEA can be utilized to compute the average flux density variation and the PM ECL caused by the HFHV. Fig. 1 shows the coupled field-circuit model for 2D linear frequency FEA, where U_h is the amplitude of the HFHV, ϕ is the phase angle and the frequency f_h is set in the solver. '-' represents the voltage with positive sequence and '+' represents the negative sequence. Each PM block needs to be modeled as a solid conductor with the zero net current constraint for reasonably calculating the PM ECL with 2D FEA [3][6]. The calculation results show that the voltage sequence and ϕ have no influence on the PM ECL. However as shown in Fig. 2, i_d, i_q and θ have effects on the PM ECLs under the same HFHV, which is because they influence the saturation level of the iron rib and the leakage flux path beside the PM. In addition, for a given load condition and fixed θ, B_{av}^{n} and B_{av}^{e} are both proportional to U_h. B_{av}^{n} is inversely proportionally to f_h, however, the relationship between B_{av}^{e} and f_h is rather complex because of the existing of the flux leakage path. Fortunately, the relationship between B_{av}^{e} and B_{av}^{n} can be described with the model described in (17) of [3]. By conducting several FE calculations with different f_h, the leakage flux factor *p* can be fitted. Then, B_{av}^{e} under arbitrary HEHV can be computed with the analytical model and the corresponding PM ECL can also be calculated with (13) or (21) in [3]. Because the axial length of the investigated IPMSM in [4] is short, the leakage flux path at the axial end of the PM can't be neglected. *p* obtained from 2D FEA needs to be modified when applying in 3D calculation. III. Time-Stepping FEA verification and Conclusion When the rotor speed is 2000rpm, the DC voltage is 650V, i_d is -149.8A, i_q is 132.5A and space vector PWM modulation strategy is used, the total PM ECL calculated with 2D nonlinear time-stepping FEA is 165.8W. The sum of the additional PM ECL calculated with each HFHV in the line-line voltage using the analytical method is 163.5W and the PM ECL under sinusoidal current supply is 4.5W, which shows that the proposed method has very good accuracy. In addition, the total calculation time needed for the proposed method is less than 1min, while it takes about one hour for the 2D nonlinear time-stepping FEA. The results of 3D FEA will be presented in the full paper.

[1] K. Yamazaki, M. Shina, Y. Kanou, M. Miwa, and J. Hagiwara, "Effect of eddy current Loss reduction by segmentation of magnets in synchronous motors: difference between interior and surface types," *IEEE Trans. Magn.*, vol. 45, no. 10, pp. 4756-4759, 2009. [2] Y. Kawase, T. Yamaguchi, M. Mizuno T. Nakano and K. Tanaka. "Characteristics analysis of IPM motor driven by voltage source inverter with parallel computing", in *Proc. IEE*E *ICEM*, Sep. 2010, pp. 1-5. [3] M. Cheng, and S. Zhu, "Calculation of PM eddy current loss in IPM machine under PWM VSI supply with combined 2-D FE and analytical method," *IEEE Trans. Magn.*, vol. 53, no. 1, pp. 1-12, 2017. [4] M. Olszewski, "Evaluation of the 2010 Toyota Prius hybrid synergy drive system," Oak Ridge Nat. Lab., U.S. Dept. Energy, 2011. [5] M. Paradkar, J. Bocker. "3D analytical model for estimation of eddy current losses in the magnets of IPM machine considering the reaction field of the induced eddy currents," in Proc. IEEE ECCE, Otc. 2015, pp. 2862-2869. [6] K. Yoshida, Y. Hita, and K. Kesamaru, "Eddy-current loss analysis in PM of surface-mounted-PM SM for electric vehicles," *IEEE Trans. Magn.*, vol. 36, no. 4, pp. 1941-1944, 2000.

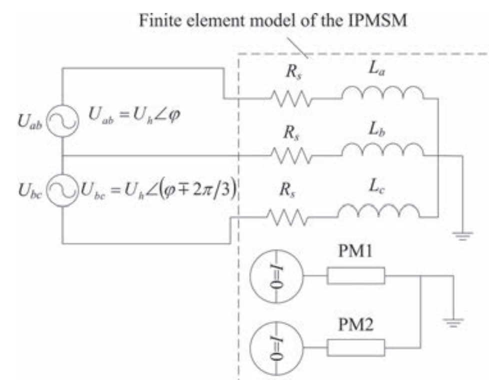

Fig. 1. The coupled field-circuit model for 2D linear frequency FEA

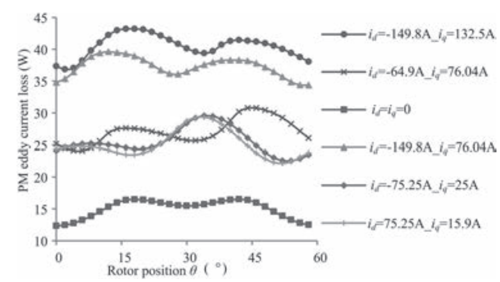

Fig. 2. Variations of the PM ECLs with θ when U_h=200V and f_h=10kHz at different load conditions

GS-09. Thermal-Loss Coupled Analysis of an Electrical Machine Using Improved Temperature Dependent Iron Loss Model.

S. Xue[1], J. Feng[2], S. Guo[2], Y. Li[2], Z. Chen[2], J. Peng[2] and Z. Zhu[1]
1. Electric and Electrical Engineering, The University of Sheffield, Sheffield, United Kingdom; 2. CRRC Zhuzhou Institute Co. Ltd, Zhuzhou, China

Iron loss prediction is very important for the evaluation of efficiency, temperature and demagnetization of electrical machines. The models developed in [1]-[4] are most commonly used iron loss models for electrical machine analyses. However, none of these iron loss models considers the influence of temperature, which has been experimentally confirmed in [5]. In [6], an improved iron loss model which can consider temperature dependencies of hysteresis and eddy current losses separately is developed. By applying the improved iron loss model, the temperature influence on the iron loss can be fully considered. It is then possible to couple the thermal and loss analyses with each other by utilizing the improved iron loss model, which will be the subject of this paper. The iron loss model developed in [4] is one of the most accurate iron loss models when the temperature is constant with the help of variable coefficients. The iron loss p_{Fe} can be expressed as: Equation(1) where f is the frequency. B_m is the peak value of alternating flux density. $k_h(f,B_m)$ and $k_e(f,B_m)$ are the hysteresis loss and the eddy current loss coefficients, respectively. It should be noted that the iron loss model (1) cannot consider the influence of temperature on iron loss while the temperature influences iron loss significantly. According to the iron loss model developed in [5], both the hysteresis loss $k_h(f,B_m)$ coefficient and the eddy current loss $k_e(f,B_m)$ coefficient vary not only with frequency and flux density but also with temperature. Therefore, the improved iron loss model is then developed and can be expressed as: Equation(2) where $p_{Fe,T}$ is the iron loss density at the actual temperature T. $k_h(T,f,B_m)$ and $k_e(T,f,B_m)$ are the hysteresis loss and eddy current loss coefficients, respectively. In order to evaluate the iron loss models in electrical machines, thermal tests and analyses are carried out in a 12-slot/10-pole IPM machine. The schematic diagram of the test system is shown in Fig. 1(a). The 12-slot/10-pole IPM machine is connected a three phase AC power source. The magnets are removed and the rotor is locked in order to eliminate magnet eddy current and mechanical losses. As shown in Fig. 1(b), four thermal couples are equipped in the electrical machine to measure the temperature at different positions, i.e. the stator tooth, the stator yoke, the rotor magnet slot and the rotor yoke. The temperatures are measured when the electrical machine is powered by the AC power source. For the temperature prediction, the iron losses are calculated by the existing model and the improved model, respectively. The thermal model of the IPM machine is also built in Motor-CAD. The thermal model is then analysed with calculated copper loss and iron losses. The predicted temperatures of the electrical machines can be obtained. Fig. 2 compares the measured and predicted results by the existing iron loss model and the improved model. It can be seen that the predicted temperatures by the existing iron loss model become inaccurate when the temperature is high. This is due to the fact that the existing iron loss model cannot consider the temperature dependency of the iron loss. The input iron loss for the thermal analysis keeps constant while the actual iron loss decreases significantly with the temperature rise. On the other hand, the predicted temperatures keep good accuracy when the temperature reaches 100 degrees Celsius or even higher. This is due to the fact that the improved iron loss model considers the temperature dependency of the iron loss. Input iron losses for the thermal analysis vary with the temperature rise. In other words, the thermal and loss analysis can be coupled with each other by utilising the improved iron loss model, which is more close to the actual condition in electrical machines. The details will be investigated and described in the full paper.

[1] C. P. Steinmetz, "On the law of hysteresis," *Trans. Amer. Inst. Elect. Eng*., vol. 9, no. 1, pp. 3-64, 1892, Jan. 1892. [2] G. Bertotti, "General properties of power losses in soft ferromagnetic materials," *IEEE Trans. Magn*., vol. 24, no. 1, pp. 621-630, Jan. 1988. [3] A. Boglietti, A. Cavagnino, M. Lazzari, and M. Pastorelli, "Predicting iron losses in soft magnetic materials with arbitrary voltage supply: an engineering approach," *IEEE Trans. Magn*., vol. 39, no. 2, pp. 981-989, Mar. 2003. [4] D. M. Ionel, M. Popescu, M. I. McGilp, T. J. E. Miller, S. J. Dellinger, and R. J. Heideman, "Computation of core losses in electrical machines using improved models for laminated steel," *IEEE Trans. Ind. Appl.*, vol. 43, no. 6, pp. 1554-1564, Nov./Dec. 2007. [5] N. Takahashi, M. Morishita, D. Miyagi, and M. Nakano, "Examination of magnetic properties of magnetic materials at high temperature using a ring specimen," *IEEE Trans. Magn*., vol. 46, no. 2, pp. 548-551, Feb. 2010. [6] S. Xue, J. Feng, S. Guo, J. Peng, W. Q. Chu, and Z.Q. Zhu, "A new iron loss model considering temperature influences of hysteresis and eddy current losses separately in electrical machines", *IEEE Trans. Magn*. Early access, DOI: 10.1109/TMAG.2017.2755593.

$$p_{Fe} = k_h(f,B_m) f B_m^2 + k_e(f,B_m) f^2 B_m^2 \quad (1)$$

$$p_{Fe,T} = k_h(T,f,B_m) f B_m^2 + k_e(T,f,B_m) f^2 B_m^2 \quad (2)$$

Equations

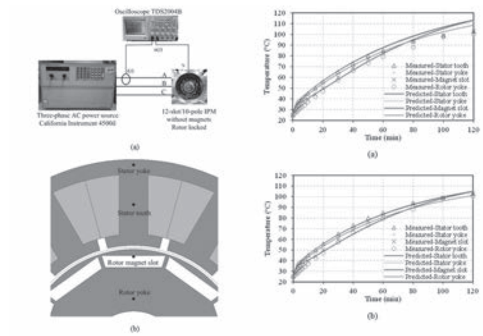

Fig. 1. Test system schematic diagram and locations of thermal couples. (a) Schematic diagram. (b) Thermal couple locations. Fig. 2. Predicted and measured dynamic temperatures using different iron loss models when frequency is 1000Hz, phase current is 3.11A. (a) Existing model. (b) Improved model.

Fig. 1.

GS-10. Harmonic Iron Losses Reduction for Heat Capacity Improvement in Interior Permanent Magnet Synchronous Motor.

M. Seo[1], Y. Ko[1], Y. Kim[2] and S. Jung[1]
1. Sungkyunkwan University, Suwon, The Republic of Korea; 2. chosun University, Gwangju, The Republic of Korea

1. Introduction Interior permanent magnet synchronous motors (IPMSMs) are usually applied to propulsion systems since their advantages such as high-power density, high efficiency, wide operating range, and small size. However, smaller sizes have a higher loss density and limited heat dissipation surface, which make the cooling of the IPMSMs difficult. Overheating of the machine can cause irreversible demagnetization of the permanent magnets (PMs) and insulation of coils also can be damaged [1]-[3]. Hence, it is necessary to prevent overheating through minimizing losses, which is main heat source, and predict the temperature distribution of machines in the design stage. On the other hand, the harmonic magnetomotive force (MMFs) of the motor cause large harmonic iron losses in the stator and rotor. In particular, inverter induced PWM current harmonics can lead to increase of losses, and rotor losses due to slotting and asynchronous harmonics can cause temperature rise in the rotor. It is therefore essential to minimize losses due to these harmonics [4]. Several papers have been reported on the iron loss reduction and thermal analysis of electric machines [5]-[8]. However, few papers conduct thermal analysis for temperature prediction in various regions of motor along with optimization for iron loss reduction in IPMSMs. In this paper, we propose a novel rotor shape of IPMSM for 170kW urban railway vehicle (URV) by using an optimization method. This optimization minimizes the iron losses, including the core loss and the magnet eddy-current loss of the IPMSM, under the pulse width modulation (PWM) control at rated speed. The effectiveness of the proposed design is discussed from the finite-element analysis (FEA). After that, the temperature rise of optimized model is calculated by empirical-based data and the lumped-parameter thermal-network (LTPN). 2. Analysis Model The motor dealt in this study is applied to an URV powered by a trolley voltage 990V. The rating output power, speed, and torque of this motor is 170kW, 2000rpm, and 812Nm, respectively. This motor is driven by a PWM inverter whose carrier frequency 660Hz. This motor is driven by a PWM inverter with a relatively low carrier frequency of 660Hz, since high voltage specifications limit the switching performance of the power device. Considering that the switching frequency of the EV drive inverter is 10 kHz, it is relatively very low frequency, which can cause the harmonic loss to increase by time harmonics of the input current. Therefore, it is important to reduce the iron losses of URV in terms of shape optimization. 3. Iron Loss Reduction Method The objective of the shape optimization is to minimize the torque ripple, and the iron losses including both the core loss and the magnet eddy-current loss. The constraint is that the torque of the optimization model must be at least 95% of the initial model torque. This optimization is performed by combining the explorative-Particle Swarm Optimization (ePSO) algorithm with the regular time-interval FEA analysis [9]. The optimal design process for reducing the iron losses is shown in Fig. 1. The core loss is calculated from the time variation of the magnetic flux density in each part of the core. From the magnetic flux densities in each finite element, eddy current losses and hysteresis losses are calculated based on experimental iron loss data, which is measured according to frequencies. The harmonic fields caused by the inverter carrier are also take into account to consider time harmonic losses. 4. Thermal Field Analysis Thermal field of the optimized model is calculated, using the LTPN method with the derived loss as input. Conduction and convection conditions are taken into consideration along the heat transfer path between the components and the ambient, and the radiation effect is ignored. End part of winding and gaps between surface of winding and components are also considered. Also, Various thermal contact resistances between components within the motor are obtained from empirical-based data of 130kW URV model, which is equal series with 170kW model, to ensure the accuracy of the calculation. The material and dimension of the other component except active parts, including rotor and stator, are the same conditions. Fig. 2. shows comparison of predicted transient results and measured data of 130kW model.

[1] C. Kral, A. Haumer, M. Haigis, H. Lang, H. Kapeller, "Comparison of a CFD Analysis and a Thermal Equivalent Circuit Model of a TEFC Induction Machine With Measurements," *IEEE Trans. Energy. Convers.*, vol. 24, no. 4, 809-818, Dec 2009. [2] J. Dong, Y. Huang, L. Jin, H. Lin, H. Yang "Thermal Optimization of a High-Speed Permanent Magnet Motor," *IEEE Trans. Magn.*, vol. 50, no. 2, 7018504, Feb 2014. [3] N. Zhao, W. Liu, "Loss Calculation and Thermal Analysis of Surface-Mounted PM Motor and Interior PM Motor," *IEEE Trans. Magn.*, vol. 51, no. 11, 8112604, Nov 2015. [4] K. Yamazaki, H. Ishigami, "Rotor-Shape Optimization of Interior-Permanent-Magnet Motors to Reduce Harmonic Iron Losses," *IEEE Trans. Ind. Electron.*, vol. 57, no. 1, 61-69, Jan 2010. [5] K. Yamazaki, M. Kumagai, T. Ikemi, S. Ohki, "A Novel Rotor Design of Interior Permanent-Magnet Synchronous Motors to Cope with Both Maximum Torque and Iron-Loss Reduction," *IEEE Trans. Ind. Appl.*, vol. 49, no. 6, 2478-2486, Nov 2013. [6] F. Chai, P. Liang, Y. Pei, S. Cheng, "Analytical Method for Iron Losses Reduction in Interior Permanent Magnet Synchronous Motor," *IEEE Trans. Magn.*, vol. 51, no. 11, 6301404, Nov 2015. [7] J-. H. Lee, B-. I. Kwon, "Optimal Rotor Shape Design of a Concentrated Flux IPM-Type Motor for Improving Efficiency and Operation Range," *IEEE Trans. Magn.*, vol. 49, no. 5, 2205-2208, May 2013. [8] K. I. Laskaris, A. G. Kladas, "Permanent-Magnet Shape Optimization Effects on Synchronous Motor Performance," *IEEE Trans. Ind. Electron.*, vol. 58, no. 9, 3776-3783, Sep 2011. [9] J. H. Lee, J-. W. Kim, J-. Y. Song, Y-. J. Kim, S-. Y. Jung, "A Novel Memetic Algorithm Using Modified Particle Swarm Optimization and Mesh Adaptive Direct Search for PMSM Design," *IEEE Trans. Magn.*, vol. 52, no. 3, 7001604, Mar 2016.

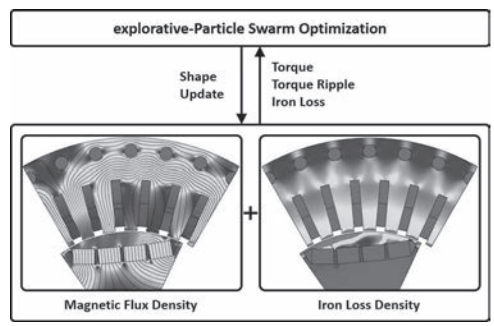

Fig. 1. Outline of optimal design process

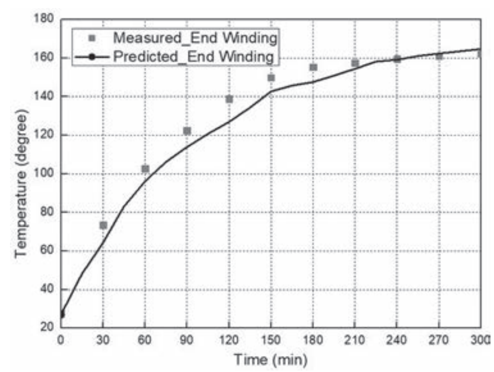

Fig. 2. Predicted transient and measured data of 130kW model

GS-11. Sensitivity Analysis of Inverse Thermal Modelling to Determine Power Losses in Electrical Machines.

D.G. Nair[1] and A. Arkkio[1]
1. School of Electrical Engineering, Aalto University, Espoo, Finland

1. Introduction Mathematically and statistically based models of iron loss in rotating electrical machines aim to estimate losses both qualitatively and quantitatively. Nevertheless, various manufacturing defects and material peculiarities manifest, making measurements necessary to verify the model's accuracy. When existing models disagree with loss measurements, it is difficult to pinpoint the exact cause of deviation since certain machine parts are inaccessible to local measurements of temperature or flux density. Moreover, no-load measurement of core loss too, is not always accurate – current measurement standards concern only sinusoidal voltage supply, whereas inverters supplied machines are on the rise [1]. The possibility to measure local power loss in machines will be of considerable use in verifying loss models. Given the challenges involved, the concept of inverse thermal analysis is apt for the task. It enables determining the unmeasurable heat source causing a measurable temperature rise in a body. This permits identification of power loss in a selected domain of the motor from available surface temperature measurements. Considerable research dealing with inverse heat conduction problems [2] in simple geometries exists. In electrical motors, the inverse approach was employed to determine stator tooth losses through local temperature measurements [3]. As seen here and most others, it is challenging to measure key temperatures accurately, which impedes the inverse reconstruction. A detailed analysis still needs to be undertaken to choose the best inverse methodology to use with electrical motors as well as its sensitivity to the number and nature of measurements. This work focuses on a 37 kW squirrel cage induction motor whose finite element (FE) thermal solution serves as the forward solution The local nodal power losses are inverse mapped from noisy simulated temperature data. The merits of different inverse solution methodologies – constrained linear least square minimization, conjugate gradient (CG) and direct regularization methods are studied and their accuracy and sensitivity in the motor's power loss mapping compared. The focus is on stator core losses, so the stator core is chosen as the domain of interest. The non-trivial geometry in addition to varying distribution of losses in this particular domain pose interesting challenges to standard inverse methodologies. 2 Methodology 2.1 Forward solution The motor's steady-state forward thermal solution results from a high-fidelity 3-D FE model that uses calibrated thermal parameters [4]. Domain power losses were the model inputs. A separate electromagnetic FE analysis calculates the core losses and rotor resistive losses and were experimentally verified. Resistive loss of stator and mechanical losses were measured. The stator core geometry is separated into yoke and teeth and stator core loss is applied separately to these regions. The temperatures of the yoke and teeth surface obtained from the FE solution are used to obtain the heat flux on the stator core volume in the induction motor. 2.2 Inverse Analysis The inverse model strives to find the unknown heat source x in a linear system $y = Ax$ where, the measured temperature y and the linear operator A are known. Usually the measurements are noisy (y^{δ}) where δ is some noise bound. The system matrix of the FE model and its solution vector are representative of these entities in the motor's thermal solution. Actual measurements are simulated by adding normally distributed random noise (0.01 standard deviation) to the nodal temperatures obtained from the surface of the stator yoke and teeth. Conjugate gradient is a fast converging, robust formulation that returns the unique global minima of the system. It iteratively converges to the unique solution x_* that satisfies the stopping criterion $\|y^{\delta}\text{-}Ax_*\| \leq \|\delta\|$. The diagonally preconditioned CG applied here is faster than constrained linear least squares used in [5] clocking 20 seconds while the latter takes 130 seconds. Direct regularization affords more freedom to the inverse reconstruction as it allows imposing regularization conditions that suppress noise and enhance desired characteristics like smoothness in the source term. Tikhonov regularization is an example of this where the objective function $\|y^{\delta}\text{-}Ax\|^2 + \alpha\|x\|^2$ has an additional term influenced by the regularization parameter α. Figures 1,2 present the reconstructed loss distribution (x_{sol}) on the stator yoke surface from inverse analysis compared against the original loss distribution (x_{tru}). 23 measurements of the yoke surface nodes served as the input to the inverse model. The inverse mapping's accuracy is assessed in terms of relative error norm: $100 \times \|x_{sol}\text{–}x_{tru}\| \div \|x_{tru}\|$. Both are vectors of 4138 elements each; the error expression becomes: $100 \times (\sum_i^n |x_{sol,i}\text{–}x_{tru,i}|^2)^{½} \div (\sum_i^n |x_{tru,i}|^2)^{½}$. 3. Discussion Upon clarifying how different surface or boundary measurements affect the inverse solution, a more faithful stator iron-loss distribution can be used as the starting point. Preconditioned CG is quite effective, as evidenced by the low relative error norm. However, the maximum error in certain nodes were still high. Tikhonov regularization fares worse, but can be improved with better choice of regularizing parameter. Further sensitivity analysis with different number of measurements (at teeth/yoke surface and boundary) is also carried out.

[1] Z. Gmyrek, A. Boglietti and A. Cavagnino, "Estimation of Iron Losses in Induction Motors: Calculation Method, Results, and Analysis", *IEEE Transactions on Industrial Electronics*, vol. 57, no. 1, Jan 2010. [2] A. Huhtala, S. Bossuyt and A. Hannukainen, A priori error estimate of the finite element solution to a Poisson inverse source problem, *Inverse Problems*, vol. 30, no. 8, July 2014. [3] A. Krings, S. Nategh and O. Wallmark, Local Iron Loss Identification by Thermal Measurements on an Outer-Rotor Permanent Magnet Synchronous Machine, *IEEE Proc. ICEMS*, 2012. [4] D. G. Nair, T. Jokinen, and A. Arkkio, Coupled analytical and 3D numerical thermal analysis of a TEFC induction motor, *IEEE Intl. Conf. on Electrical Machines and Systems*, pp. 103-108, Oct. 2015. [5] D. G. Nair and A. Arkkio, Inverse Thermal Modelling to Determine Power Losses in Induction Motor, *IEEE Transc. Magnetics*, vol. 53, no. 6, June. 2017.

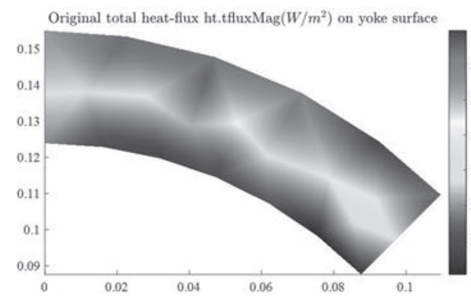

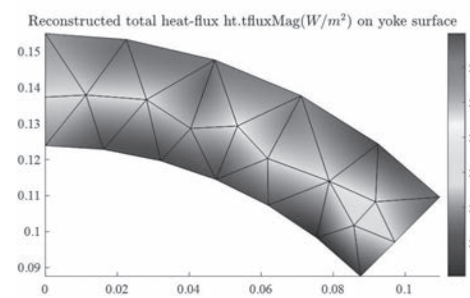

Fig. 1. Reconstruction with CG. Error = 1.44x10^{-4} %

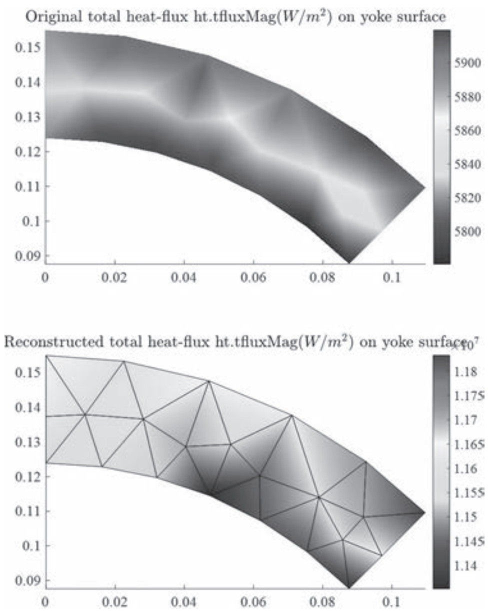

Fig. 2. Reconstruction with Tikhonov regularization. Error = 137%

GS-12. Analysis on the Number of Axial Segments of Permanent Magnet in SPMSM for Ultra-High-Speed Application.

H. Lee[1], D. Jung[2] and j. Lee[2]
1. Electric Automatization, Busan Institute of Science and Technology University, Busan, The Republic of Korea; 2. Electrical Engineering, Hanyang University, Seoul, The Republic of Korea

This paper describes the analysis on the Number of Axial Segments of Permanent Magnet in SPMSM for Ultra-High-Speed Application; Electric-Turbo Compound System(E-TCS) for Construction Equipment. E-TCS is a device that combines a turbocharger, which is a regenerative device through exhaust gas, and a compressor to improve the turbo lag. As a result, E-TCS must be able to drive at least 80,000 rpm and require a large torque at low speeds. And because of scattering problem of permanent magnets, so limit to increase the rotor size and shaft length is realatively long. To increase performace of motor, difficulties of permanent magnetization and reduce permanent magnet loss, the segment must be applied in the axial direction on permanent magnet. Design criteria and power loss analysis of the ultra-high-speed motor are described by analytical method, and the results are validated by 3D-finite element method. And then, the prototype motor has been fabricated 3 cases and tested. The experimental results confrimed the validity of the proposed design and alalysis scheme of the ultra-high-speed SPMSM(Surfaced Permanent Magnet Synchronous Motor).

1. "Effect of Axial Segmentation of Permanent Magnets on Rotor Loss in Modular Permanent-Magnet Brushless Machines", Jason D.ede, IEEE Transactions on Industry Applications, VOL. 43, NO. 5, 2007. 2. "A Highly Efficient 200 000 RPM Permanent Magnet Motor System", Limei Zhao, IEEE TRANSACTIONS ON MAGNETICS, VOL. 43, NO. 6, 2007

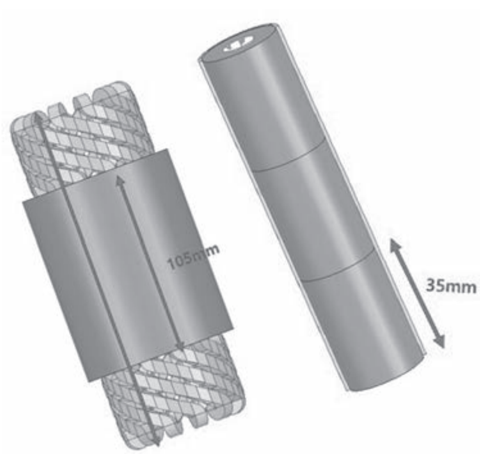

Fig. 1. Axial Segments of Permanent Magnet in SPMSM

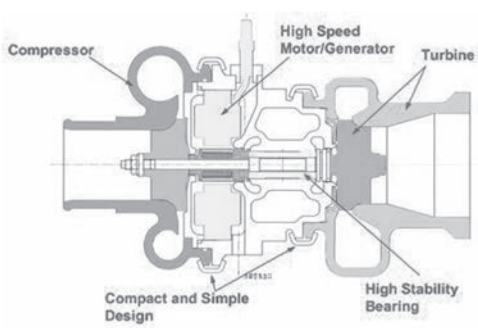

Fig. 2. Scheme of the Electric-Turbo Compound System(E-TCS)

FRIDAY MORNING, 27 APRIL 2018 SIMPOR/ROSELLE BALLROOM, 8:30 TO 11:30

Session GT
HYSTERESIS MODELLING I
(Poster Session)

David Lowther, Chair
McGill University, Montreal, QC, Canada

GT-01. Accurate Prediction of Dynamic Hysteresis Loops Using the Modified Jiles-Atherton Model.

Z. Li[1], X. Huang[1], L. Wu[1], J. Ma[1] and Y. Fang[1]
1. College of Electrical Engineering, Zhejiang University, Hangzhou, China

I.Introduction Modelling of dynamic hysteresis loops in the electrical steels reveals the magnetic characteristic of the ferromagnetic materials. Jiles-Atherton (JA) model is capable of describing the hysteresis loops by transforming the physical phenomenon into a simple first order differential equation [1]. M. Hamimid *et al.* introduced hybrid magnetic field in the dynamic inverse model, which gave great prediction of dynamic loops [2]. A. P. S. Baghel *et al.* justified the energy equivalence between the JA approach and field separation theory and validated the usage of hybrid magnetic field [3]. In this paper, a modified dynamic JA model is proposed to predict the dynamic hysteresis loops at different frequency and magnetic induction levels, even when the hysteresis loops become elliptical. More attention should be paid to the excess loss in the model due to its increasing share of iron loss at higher frequency. Comparisons of the measured and predicted hysteresis loops using modified JA model are performed to validate the proposed model. II.Modified JA Model and Validation The dynamic JA model was developed to include the frequency dependence of the hysteresis loop via the additional energy dissipation resulting from the eddy current loss and excess loss. This paper adopts the field separation approach to extend the static JA model to the dynamic model, as it does not lead to non-physical solutions and offers better loop shapes. The static JA model can be manipulated to its inverse form as [3] $dM/dB=(\delta_M(M_{an}-M)+kc\delta(dM_{an}/dH_e))/(\mu_0(k\delta+(1-\alpha)(\delta_M(M_{an}-M)+kc\delta(dM_{an}/dH_e))))$ Then the effective field term in the static JA model can be modified using [2] $H_e=H+\alpha M-(H_{eddy}+H_{excess})$ where H_{eddy} and H_{excess} are the classical eddy current field and the excess field, respectively. The excess loss results from discontinuous Barkhausen jump or bowing of active domain walls in electrical steels and can be regard as a special form of classical eddy current loss [4]. According to the Bertotti's theory, the excess field can be given as [5] $H_{excess}=GS/(\rho*n(t))*(dB/dt)$ The two time-dependent functions H_{excess} and $n(t)$ are not independent. The relations between them are postulated and then validated experimentally [6]. $n(t)=n_0+H_{excess}(t)/H_0$ where H_0 and n_0 characterizes the statistical distribution of the internal domain wall field. These expressions of excess field are used to extract the parameters of the dynamic JA model and predict the BH loops as well as the iron loss. However, as the parameter H_0 of instantaneous excess field is validated in the time average [6], the errors between the measured and predicted loops are introduced. They become significant when the component of the excess loss is large. This paper presents a phenomenological approach to reduce the errors of the dynamic hysteresis prediction without changing the area of the BH loop. Meanwhile it still follows the basic principle that the excess loss is only affected by the rate of change of magnetic induction (*dB/dt*). The modified instantaneous excess field is defined as $H_{excess}=(\sigma GSH_0|dB/dt|)^{1/2}+2H_1\lambda/b^2*(b^2-(dB/dt)^2)^{1/2}(dB/dt)$ where b represent the maximum rate of change of magnetic induction; H_1 represent the maximum error between the measured and predicted magnetic field using original dynamic JA model; λ is a directional parameter, which means $\lambda=+1$ when $d^2B/dt^2 \geq 0$ and $\lambda=-1$ when $d^2B/dt^2 < 0$. For the modified model, the maximum errors between the measured hysteresis loops and the predicted loops using original JA model are calculated to obtain the additional parameter H_1. It is clear that H_1 is proportional to the maximum rate of change of magnetic induction from Fig. 1. Thus the value of H_1 can be obtained at any frequency using linear interpolation method. When the component of the excess loss is large, the prediction error of original dynamic JA model become significant while the modified JA model can accurately predict the dynamic BH loops, as shown in Fig. 2. The advantage of the modified JA model is significant when the frequency of the excitation is high and the shape of hysteresis loop is nearly elliptical, as shown in Fig. 2(a). Fig. 2(b) shows that the errors of the predicted loop using the modified model are less than 5% while the errors using the original model are increasing with the frequency. III.CONCLUSION In this paper, a modified JA model is proposed to predict the dynamic hysteresis loops. As the predicted instantaneous excess field based on the statistical loss theory will bring errors due to the approximation of the number of active correlation regions in the time average. The modified excess loss is proposed based on experimental observation and physical consideration to eliminate the error. The predicted dynamic hysteresis loops using the modified JA model agree well with the measured loops, even under the excitation with high frequency. IV.ACKNOWLEDGMENT This work was supported by the National Natural Science Foundation of China (51477149, 51577166, U1434202).

[1] D. C. Jiles and D. L. Atherton, "Theory of ferromagnetic hysteresis" *J. Magn. Magn. Mater.*, 61(1986) 48-60 [2] M. Hamimid, S. M. Mimoune, and M. Feliachi, "Hybrid magnetic field formulation based on the losses separation method for modified dynamic inverse Jiles–Atherton model," *Phys.* B., vol. 406, no. 14, pp. 2755–2757,2011. [3] A. P. S. Baghel and S. V. Kulkarni, "Dynamic loss inclusion in the Jiles–Atherton (JA) hysteresis model using the original JA approach and the field separation approach," *IEEE Trans. Magn.*, vol. 50, no. 2, pp. 369–372, Feb. 2014. [4] J. Li, Q. Yang, Y. Li, C. Zhang, B. Qu, and L. Cao, "Anomalous loss modeling and validation of magnetic materials in electrical engineering," *IEEE Trans. Appl. Supercond.*, vol. 26, no. 4, pp. 1-5, June 2016. [5] G. Bertotti, *Hysteresis in Magnetism, for Physicists, Material Scientists, and Engineers*. San Diego, CA, USA: Academic, 1998. [6] D. Kowal, P. Sergeant, L. Dupré, and L. Vandenbossche, "Comparison of iron loss models for electrical machines with different frequency domain and time domain methods for excess loss prediction," *IEEE Trans. Magn.*, vol. 51, no. 1, pp. 1-10, Jan. 2015.

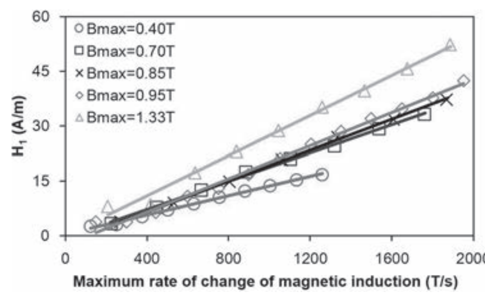

Fig. 1. Excess filed parameter H_1 verse maximum rate of change of magnetic induction.

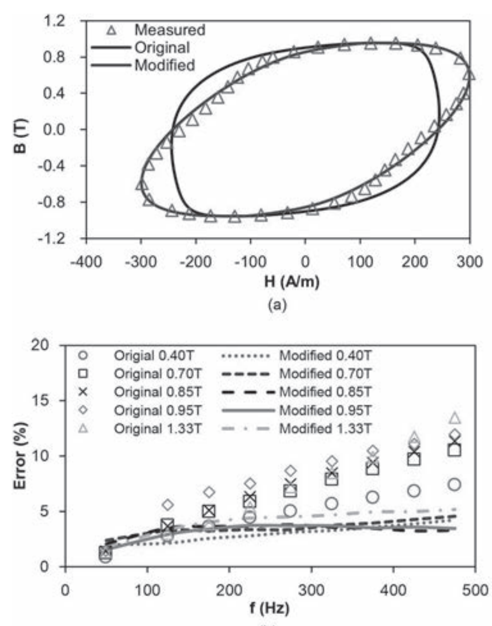

Fig. 2. (a) Comparison of measured and predicted BH loops using original and modified excess field when B_{max}=0.95T and f=500Hz. (b) Comparison of the BH loop prediction errors using the original and modified JA model.

GT-02. Withdrawn

GT-03. Characterization and local phenomenological model of Barkhausen noise under mechanical and magnetic excitations.

B. Ducharne[1], B. Gupta[1], Y. Hebrard[2] and J. Coudert[2]
1. INSA LYON, Laboratoire de Génie Electrique et Ferroélectricité, Villeurbanne, France; 2. SKF aerospace, Valence, France

ABSTRACT Post-treatment and rescaling, it is possible to plot local hysteresis cycles from the measurement of local magnetic Barkhausen noise. If the material is homogeneous and if similar excitation conditions are imposed, the local hysteresis cycles obtained are comparable to the classical magnetic hysteresis cycles *B(H)* (the cross-section magnetic average induction *B* as a function of the surface tangential excitation field *H*). These local Barkhausen noise hysteresis cycles give interesting clues about the evolution of the microstructure of the magnetic material (internal stresses, level of degradation etc.). This makes it an indispensable tool for the non-destructive evaluation of ferromagnetic steels. In this paper, a phenomenological modeling of the Barkhausen noise from the local modeling of *B* subjected to an excitation field *H* and/or a uni-axial mechanical stress *T* is proposed. The objective is to provide an absolute quantification of the internal residual stresses because of the Barkhausen noise measurements. KEYWORDS Barkhausen noise, magnetic hysteresis loop, model, hysteresis, mechanical stress. MAIN TEXT The use of non-destructive micro-magnetic control techniques such as the measurement of magnetic Barkhausen noise has recently increased exponentially in the industrial environment. This renewed interest is mainly due to the improvement of analog and digital signal processing techniques that have allowed this quality control type to be integrated into the production lines in real time [1]. Micro-magnetic techniques can be used to trace interesting properties of the tested samples (hardness, residual stresses, grinding burns etc.) [2]. Barkhausen noise owes its origin to the magnetization processes of a ferromagnetic material. It is established that a ferromagnetic material, even in a demagnetized state is magnetically divided into finite regions called as domains. Each domain is characterized by its own direction and orientation of magnetization. The process of magnetization consists of converting this multi-domain state into a single domain characterized by a direction and a sense of magnetization very close to the external magnetic field *H* imposed on the material. This process is not continuous but consists of small discrete variations: jump from a pining defect (micro-structural obstacles like precipitation) to another defect of the domain walls (domains boundaries) [3]. This local variations of magnetization states are known as "Barkhausen event". These changes induce pulsed eddy currents near the moving domain walls that develop in all space directions. These abrupt changes in the magnetic structure through the material also induces local and rapid flux variations that can be easily measured using a dedicated local micro magnetic field sensor. In recent publications dealing with the topic, many authors define a new quantity called Magnetic Barkhausen energy (MBN_{energy}) [4]. The MBN_{energy} is obtained from the temporal integration of the square of the local magnetic field sensor voltage output (equation 1). This "post-treatment" technique can be used to trace a hysteresis cycle $MBN_{energy}(H)$ from the local measurement of magnetic Barkhausen noise. At low frequency, if the material is homogeneous and isotropic and after rescaling thanks to a coefficient ν, the Barkhausen cycles obtained are very similar to the usual hysteresis cycles *B(H)*. equation 1. These observations confirm the microscopic origin (wall movements) of the magnetic hysteresis under low frequency excitation. In the extended version of the article, the numerical scheme will be described that is used to return the temporal Barkhausen noise envelope under both magnetic and uniaxial mechanical stress. This numerical scheme is based on both local magnetic hysteresis model and an inverse method linked to magnetic Barkhausen energy. Figure 1. Magnetic Barkhausen noise (left) and simulated Barkhausen envelop under both magnetic and uniaxial mechanical stress excitations. The good simulation results displayed in Fig. 1 are very promising. By correctly anticipating in simulation the material behavior, we will have access to some microstructural information (such as precipitations, local residual stresses). From a non-destructive evaluation point of view, this set of information will allow us to anticipate some failures and ageing issues.

[1] W.A. Theiner, B. Reimringer, H. Kopp and M. Gessner, 3MA-Testing Equipment, Application, Possibilities and Experiences. Characterization of materials, ed. by P. Höller, V. Hauk, G. Dobmann, C. Ruud, R. Green, Springer-Verlag Berlin, 1989. [2] B. Gupta, B. Ducharne, G. Sebald, T. Uchimoto, A space discretized ferromagnetic model for non-destructive eddy current evaluation, Trans. on mag, 2017. [3] T.W. Krause, J.A. Szpunar, D.L. Atherton, Anisotropic flux density dependence of Magnetic Barkhausen Noise in oriented 3% Si-Fe steel Laminates, IEEE Trans. on Mag. 39,562-566, 2003. [4] B. Ducharne, MQ. Le, G. Sebald, PJ. Cottinet, D. Guyomar, Y. Hebrard, Characterization and modeling of magnetic domain wall dynamics using reconstituted hysteresis loops from Barkhausen noise, J. of Mag. And Mag. Mat., pp. 231-238, 2017.

$$MBN_{energy}(H) = \nu.\int_0^T sign\left(\frac{dH}{dt}\right).\left(V_{Barkhausen}\right)^2 dt \qquad (1)$$

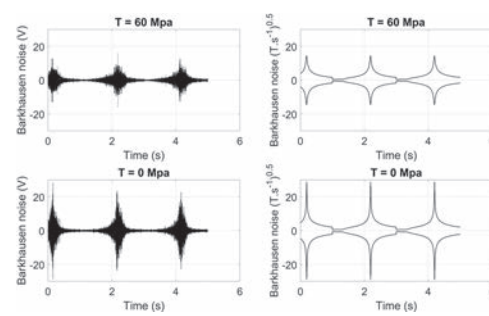

Fig. 1. Magnetic Barkhausen noise (left) and simulated Barkhausen envelop under both magnetic and uniaxial mechanical stress excitations.

GT-04. Hysteresis Nonlinearity Modeling for Magnetics Shape Memory Alloy Actuator Based on a Novel Black-box Model with Least Squares Support Vector Machines.

R. Xu[1], M. Zhou[1] and Y. Wang[1]
1. Department of control science and engineering, Jilin University, Chang-Chun, China

With the rapid development of micro-nano manufacturing technology, there are more and more fields need nano-driven control technology, such as the high-precision positioning systems [1]. Magnetically controlled shape memory (MSM)-alloy actuators serve as the core part of high-precision positioning system on account of their high precision, large energy density, and small volume. The hysteresis nonlinearity of the MSM-alloy actuator, however, severely damages the positional accuracy of the positioning system. In order to research the hysteresis nonlinearity in the MSM-alloy actuator, hysteresis nonlinearity modeling has become a significant hot spot of research [2][3]. The purpose of this study is to structure an excellent hysteresis nonlinearity model to capture the hysteresis nonlinearity in MSM-alloy actuators. The criterion for evaluating modeling performance is that the established hysteresis model can embody the actual characteristic of the actuator. In this study, a novel black-box model composed of the hysteresis-like structure and a nonlinear function is proposed to capture the hysteresis nonlinearity of the MSM-alloy actuator. The proposed black-box hysteresis nonlinearity modeling approach has the advantages of requiring no prior knowledge and internal physical mechanism. The hysteresis-like structure solves the multi-value mapping problem and accurately depicts the major and minor hysteresis loops of the MSM-alloy actuator. The nonlinear function represents the nonlinearity part of the MSM-alloy actuator, which is identified using least squares support vector machines (LS-SVM) on account of its strong approximation capability, high generalization ability, less parameters, and great computing power. The schematic diagram of black-box model is shown in Fig. 1. u(k) is the input current at *k* time, y(k) is the output displacement at *k* time, F[●] is the nonlinear function, H_u[●] is the hysteresis-like part of the black-box model. In the procedure of modeling, u(k) and y(k) are the input values of hysteresis-like part; u(k), y(k), and H_u[●] are the input values of nonlinear function, which is obtained by the LS-SVM. To certify the effectiveness of the black-box model, the simulations are implemented using the obtained experimental data. The simulations show that the modeling error rate of the novel black-box model based on the LS-SVM is 1.37%, which is improved 73.97% in compared with the results in [4]. It is obvious that the modeling precision of the proposed hysteresis model is within the allowable range. The simulation results are shown in Fig.2. The blue solid line is the obtained experimental data, and the red dotted line is the output of the proposed black-box model. As shown in Fig.2(a), the proposed black-box model based on the LS-SVM can accurately describe the major and minor hysteresis loops of the MSM-alloy actuator. The modeling error curve is shown in Fig.2(b). In the future, the proposed black-box model can lay a foundation for designing an adaptive controller to eliminate the hysteresis nonlinearity in the MSM-alloy actuator.

[1] Hassani V, Tjahjowidodo T. “Structural response investigation of a triangular-based piezoelectric drive mechanism to hysteresis effect of the piezoelectric actuator,” Mech. Syst. Sig. Process., vol. 136, no. 1, pp. 210-223, Mar. 2013. [2] Xu R, Zhou M. “Elman neural network-based identification of Krasnosel’skii-Pokrovskii model for magnetic shape memory alloys actuator,” IEEE Trans. Magn., vol. 53, no. 11, Nov. 2017. [3] Minorowicz B, Leonetti G, Stefanski F, Binetti, G, Naso, D. “Design, modelling and control of a micro-positioning actuator based on magnetic shape memory alloys,” Smart Mater. Struct, vol. 25, no. 7, pp. 075005-1-075005-12, May. 2016. [4] Minorowicz B, Nowak A, Stefanski F. “Hysteresis modelling in electromechanical transducer with magnetic shape memory alloy,” Przeglad Elektrotechniczny, vol. 90, no. 11, pp. 244-247, Nov. 2014.

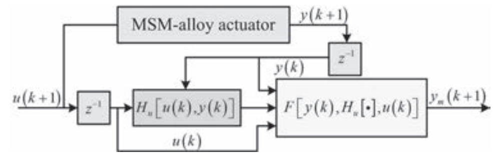

Fig. 1. Schematic diagram of black-box model.

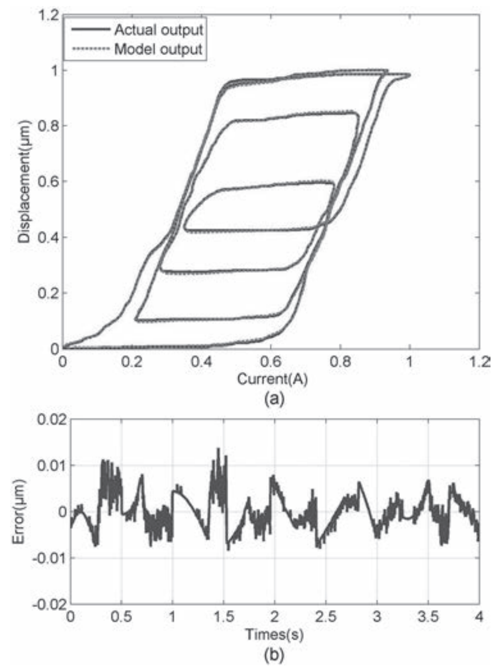

Fig. 2. Simulation results of the black-box model based on LS-SVM.

GT-05. Dynamic magnetic scalar hysteresis lump model, based on Jiles-Atherton quasi-static hysteresis model extended with dynamic fractional derivatives.

B. Ducharne[1], B. Zhang[2], B. Gupta[3], G. Sebald[3] and T. Uchimoto[4]
1. INSA LYON, Laboratoire de Génie Electrique et Ferroélectricité, Villeurbanne, France; 2. Shandong university, Weihai, China; 3. ELyTMaX Tohoku University, Sendaï, Japan; 4. IFS Tohoku University, Sendaï, Japan

ABSTRACT Accurate and simple magnetic material law is necessary to correctly model the complete electromagnetic systems. In this article, a new formulation based on the scalar quasi-static hysteresis Jiles-Atherton model extended to dynamic behavior using fractional derivative dynamic contribution is proposed. The fractional contribution is solved using convolution which highly reduces the numerical issues. The order of the fractional derivation provides a new degree of freedom and allows to obtain correct simulation results on a very large frequency bandwidth. By using such a formulation, highly space and time consuming space discretization techniques (finite differences, finite elements) are avoided while keeping the global accurate simulation results. KEYWORDS Hysteresis, ferromagnetic material, Jiles-Atherton model, fractional derivatives. MAIN TEXT The development of new electromagnetic designs, such as the improvement of already existing ones require precise simulation tools. These numerical tools can also be used for the estimation of ferromagnetic losses. In the micromagnetic non-destructive testing field, they are used for the understanding and the interpretation of non-destructive control techniques such as eddy current testing, magnetic incremental permeability or magnetic Barkhausen noise [1] [2]. Previous scientific progress in the electromagnetic simulation domain mainly focuses on coupling space discretization techniques (Finite Elements Method (FEM), Finite Differences Method (FDM)) to accurate scalar or vector, dynamic or static hysteresis material law [3][4]. For this material law, the best results come from the extension of a vector quasi-static hysteresis contribution (Preisach model [5], Jiles-Atherton model [6]) to a dynamic behavior as it is defined by the separation losses in the Bertotti's theory [7]. Unfortunately, the usual simultaneous resolution of space discretization techniques and hysteresis models can only be performed by time and high memory space consuming iterative techniques. One of them is the so-called fixed point scheme. If the non-linearity levels are weak, this technique gives accurate results whereas for higher levels (strong hysteresis, saturation) numerical errors are always observed. In this article, an original alternative to space discretization techniques is proposed. In this approach, the space discretization is left behind and the focus is on numerically reproducing the time variations of lump quantities (The cross-section average induction field B, and the surface tangent field H). A few months ago, by extending the Preisach model quasi-static contribution to fractional derivation operators, the authors succeeded in obtaining very accurate simulation results on a very large frequency bandwidth [8]. Unfortunately, the issue here, comes from the Preisach model congruent property, i.e. the similarity of the minor cycles obtained for a given H variations at different levels of B. This property becomes real inconvenient, when we try to plot the butterfly loop required by the magnetic incremental permeability technique [9]. Indeed, using Preisach model is limited to just one curve and exhibits no hysteresis. To improve this, a switch from Preisach's model to Jiles-Atherton's model has been finalized. In this article, we explain with details, how we succeed in simulating the butterfly loop and the B(H) curve on a large frequency bandwidth by extending scalar Jiles-Atherton's quasi-static contribution to dynamic behavior thanks to fractional derivation operators. Fractional derivative is introduced in the lumped quasi-static hysteresis model through a dynamic contribution. Eq. 1. And fig. 1 gives a quick overview of the model equation, n is the fractional order and J.A the Jiles-Atherton model. Fig. 1. Block scheme for the Jiles-Atherton extended dynamic model. Fig. 2 gives a first illustration for the model accuracy by comparing simulation and experimental results for a major hysteresis cycle obtained under dynamic sinus excitation H (400 Hz). In the final version of the article, a large number of comparisons simulation/measure will be provided, the good results obtained for the butterfly loop will also be illustrated. Fig. 2. Comparison of simulation/measurement for Iron/Silicon non-oriented grains under 400Hz sinus excitation field H.

[1] N. Yusa, W. Cheng, T. Uchimoto and K. Miya, "Profile reconstruction of simulated natural cracks from eddy current signals", NDT & E international, pp. 9-18, 2002. [2] B. Gupta, B. Ducharne, G. Sebald, T. Uchimoto, A space discretized ferromagnetic model for non-destructive eddy current evaluation, Trans. on mag, 2017. [3] M. Kuczmann, A. Iványi, "The Finite Element Method in Magnetics", Budapest, Academic Press, 2008. [4] M. A. Raulet, B. Ducharne, J.P. Masson, and G. Bayada, "The magnetic field diffusion equation including dynamic hysteresis: a linear formulation of the problem", IEEE Trans. on Mag., vol. 40, n° 2, pp. 872 – 875, 2004. [5] F. Preisach, "Über die magnetische Nachwirkung". Zeitschrift für Physik, 94: 277-302, 1935. [6] D.C. Jiles, D.L. Atherton, "Theory of ferromagnetic hysteresis". J. App. Pjys. 55, pp. 2115, 1984. [7] G. Bertotti, "General properties of power losses in soft ferromagnetic materials", IEEE Trans. on Mag.., 24, pp. 621-630, 1988. [8] B. Zhang, B. Gupta, B. Ducharne, G. Sebald, T. Uchimoto, "Preisach's model extended with Dynamic fractional derivation contribution", IEEE Trans. on Mag, Vol. pp iss. 99, 2017. [9] A. Yashan, G. Dobmann, "Measurements and semi-analytical modeling of incremental permeability using eddy current coil in the presence of magnetic hysteresis", Electromagnetic Nondestructive Evaluation (VI), F. Kojima et al., IOS Press, 2002.

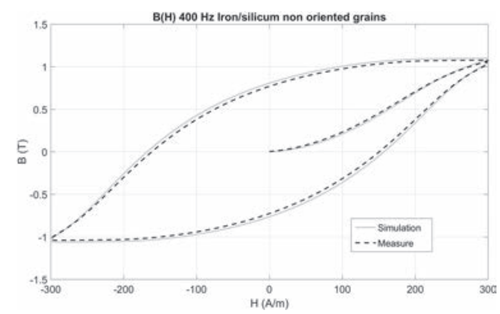

Fig. 1.

$$\rho.\frac{d^n B(t)}{dt^n} = H_{dyn}(t) - J.A^{-1}(B(t)) \qquad (1)$$

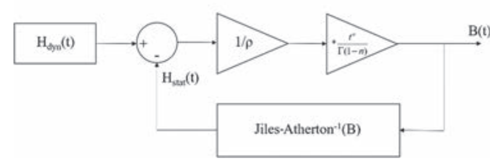

Fig. 2.

GT-06. An Improved Centered Cycle Method for Identifying the Preisach Distribution Function.

D. Peng[1], W. Sima[1], M. Yang[1], M. Zou[1] and Y. Liu[1]
1. Chongqing University, Chongqing, China

Hysteresis is a nonlinear operator that exhibits remanence and selective memory. The effects of the input to the hysteresis system are experienced with a certain delay in time. Thus, the output of the hysteresis system cannot be predicted by current state without the knowledge about the history of the hysteretic system. This phenomenon is originated from magnetic, ferromagnetic and ferroelectric materials. Various methods have been proposed for modeling hysteresis in the last decades, such as the Stoner–Wolhfarth, Jiles–Atherton and Preisach models. Among them, the Preisach model is one of the most practical methods. It is very commonly used for hysteresis modeling in ferromagnetic materials. Preisach model is a history-dependent model, and includes wiping-out property and congruency property, which are the most important characteristics to display the hysteresis phenomenon. The main difficulty of this model is the determination of the distribution function from experiments. Identification of the Preisach distribution function (PDF) is of importance in manifold hysteresis systems. The direct Mayergoyz's method yields an exact PDF reconstruction by collecting the first-order return branches and derivating the obtained Everett function over the Preisach plane. However, this method requires a large number of experience data, and first-order return branches are difficult to be obtained in some cases, such as large power transformers. Centered cycle method [1] is proposed to calculate the PDF by a set of symmetrical waveforms which can be easily obtained in the field. Preisach triangle is uniformly discretized to $n(2n+1)$ cells by n centered cycles and can be determined by the cell-method. Owing to the odd symmetry of the centered cycles, the distribution function is symmetrical to the axis. Therefore only $n(n+1)$ cells values have to be determined. The centered cycle method was validated by experiments and showed the effectiveness for both major and minor cycle modeling. The distribution function is unique, and no optimization method is needed. This method can also be applied to the inverse distribution function determination without any changes. However, there are also some limits for the centered cycle method. When the PDF is identified by centered cycle method and used to calculate hysteresis loops, the errors are relatively large around the knee point due to the large change rate of the flux-current curve around this knee point. If increasing the quantity of center loops in high-curvature region, according to the rules of the centered cycle method, there will be extra tremendous work paid for the low-curvature region, which is not necessary and significant decreases the calculation efficiency. Therefore, this paper proposes an improved centered cycle method using non-uniform discretization to identify the Preisach distribution function. This algorithm enhanced the sensitivity to the region in which the curvature of the hysteresis loops changed more than the other regions, which means that more loops are used for high-curvature regions and less loops for low-curvature regions. Then the distribution function is identified by the non-uniform cell created by the improved center cycle method. Fig.1 shows the anhysteresis magnetization curve and the curvature curve of a sample made of a ferromagnetic material. The curves are divided into three parts by three lines. The value at the right line is H=Hm, which represents the ultimate magnetic field intensity. According to the curvature, these three parts can be named as high-curvature area, low-curvature area and flat area respectively. S1, S2 and S3 are the regions surrounded by H axis and corresponding curvature curve. The area of the regions can quantitatively describe the variation of L. The larger area represents more variation the inductance. As a result, the number of loops selected for identification is proportional to the area in each part. The equidistant loops are measured in each part. Therefore, the Preisach plane are uniformly discretized in each part and non-uniformly discretized as a whole. As Fig.2 shows, there are n loops in the Preisach plane as solid line. And with the dash line, the plane is non-uniformly discretized into many non-uniform cells. The PDF of the innermost part should be determined first by directly using the center cycle method. Then the PDF of the rest part is determined from inside layer to outside layer by the data of two surrounding hysteresis loops. The distribution function of the cell is determined by the difference of the magnetic flux density B of two loops in the same magnetic-field intensity H. Thus, all the cells are determined. However, the non-uniform cells are hard to calculate hysteresis loops. Therefore, for each cell in the Preisach plane, it can be discretized into several squares with the same size. In this way, the entire plane is composed of a large number of small squares. So the non-uniformly discrete plane can be transformed into uniformly discrete plane. The proposed method is validated by laboratory tests, it shows higher precision of predicting the hysteresis loop than center cycle method in the same number of measured loops.

[1] Bernard Y, Mendes E, Ren Z. Determination of the distribution function of Preisach's model using centred cycles[J]. Compel International Journal of Computations & Mathematics in Electrical, 2000, 19(19):997-1006.

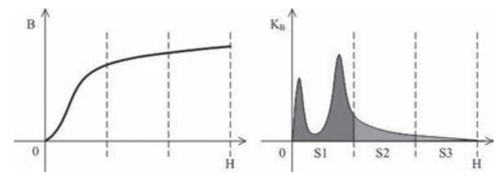

Fig. 1. The fundamental magnetization curve and its curvature curve

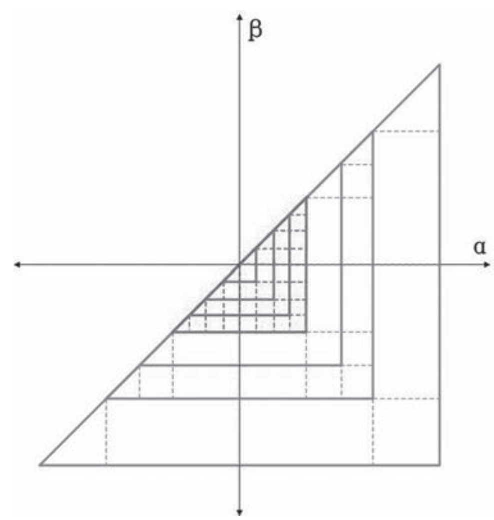

Fig. 2. Preisach distribution plane discretized by non-uniform loops

GT-07. Simplified and algorithmic Preisach modeling for soft and hard magnetic hysteresis using general global basis functions.

A. Bhattacharjee[2], A. Mohanty[1] and A. Chatterjee[2]
1. Computational and Data Sciences, Indian Institute of Science, Bangalore, Bangalore, India; 2. Mechanical Engineering, Indian Institute of Technology Kanpur, Kanpur, India

Rate independent hysteresis in magnetic materials has been studied for a long time. The evolution of magnetic flux density *B* depends on the current as well as the past values of input field strength *H*. The Preisach model [1,2] offers a framework for modeling static magnetic hysteresis. Computationally the hysteretic output involves an evolving geometrical quantity that looks like a staircase, and an integral of a two variable Preisach density μ under that staircase. The underlying μ has been treated differently by different authors. Some directly interpolate between values on a grid, while others assume specific functional forms of μ with fitted parameters. Another popular approach is use of first ordered reversal curves (FORC) [3]. Our main contribution is that instead of *a priori* assumption about functional forms, we expand μ in a general form using global basis functions defined on a triangular domain. Nonlinear scalar transformations both precede and follow the Preisach calculation. Fitting results, with our own experimental data, are good. A minor contribution is a transparent state-matrix description of the Preisach staircase and simple Matlab code for incrementing the state. The first nonlinear transformation of *H* uses the arctangent function to map the input to a bounded region. The Preisach density μ is expanded using basis functions defined on that bounded region. An exponential is used to ensure $\mu>0$, as in $\mu(\beta,\alpha) = e^{\sum_i a_i \psi_i(\beta,\alpha)}$, where the basis functions $\psi_i(\beta,\alpha) = \cos(k_i \pi \beta/2) \cos(n_i \pi \alpha/2) + \cos(n_i \pi \beta/2) \cos(k_i \pi \alpha/2)$, where in turn the integers k_i, n_i are nonnegative, either both even or both odd due to symmetry arguments. Integration of μ (see above equation) under the Preisach staircase is done numerically. A final nonlinear transformation of the integral output gives a good fit with the experimentally measured *B*, for both soft and hard loops. A tiny regularization or penalty term is used during parameter fitting to reduce spurious oscillations due to nonuniformly spaced fitting data points. In our experiments, we measured magnetic hysteresis in two different ferrite toroids to obtain *soft* and *hard* types of loops for multi-frequency inputs with multiple partial reversals. The parameters, transformation parameters and basis coefficients a_i, are obtained by minimizing the squared error between the predicted and experimental loops over several datasets. We obtained a good match with 12 shape functions for soft loops, and 20 for hard loops. In total, we used 15 fitted parameters for our soft loops, and 25 fitted parameters for our hard loops. While the number of fitted parameters may at first sight seem large, our approach is general, our data is complex, and our fit is good. Finally, we theoretically and qualitatively demonstrate the necessity of a final nonlinear transform of the Preisach ouput for hard loops. Figure 1 shows the estimated density for soft and hard loops. The high gradients seen for hard loops are easier to capture with the exponential form of μ. Figure 2 shows the match against the experimental data for both soft and hard loops. An excellent fit is achieved for the soft loops. The results for the hard loops are slightly inferior, but still good. Overall, our method is quite general (both soft and hard loops), conceptually simple, and accurate.

[1] Preisach, F., On magnetic aftereffect, Z. Phys., 94, 277-302, 1935. [2] Mayergoyz, I. D., Hysteresis models from the mathematical and control theory points of view, Journal of Applied Physics, 57(1), 3803-3805, 1985. [3] Pike, C.R., Roberts, A.P. and Verosub, K.L., Characterizing interactions in fine magnetic particle systems using first order reversal curves, Journal of Applied Physics, 85(9), 6660-6667, 1999.

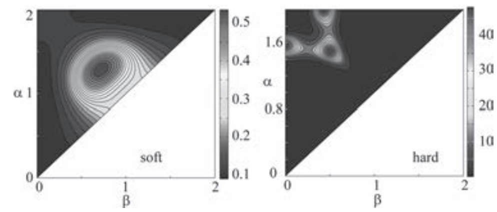

Fig. 1. The identified Preisach density μ for soft (left) and hard (right) type of loops, obtained through fitting with a general expansion using basis functions.

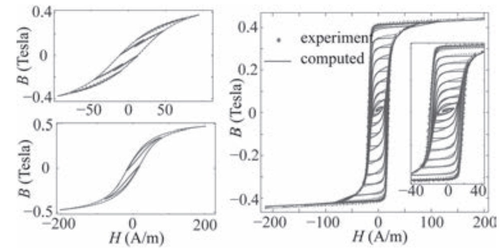

Fig. 2. Fitting results, soft (left) and hard (right) loops.

GT-08. A Scalar Hysteresis Model of Ferromagnetic Materials.

W. Xu[2], N. Duan[1], Y. Li[3], *S. Wang*[1] and J. Zhu[4]

1. Xi'an Jiaotong University, Xi'an, China; 2. State Grid Shaanxi Electric Power Company Economic Research Institute, Xi'an, China; 3. Hebei University of Technology, Tianjin, China; 4. University of Technology Sydney, Sydney, NSW, Australia

I.Introduction The magnetization of a ferromagnetic material can be regarded as a collection of all magnetic particles inside the material. Lots of hysteresis models have been proposed based on different operators (particles) and principles [1]. In the traditional Preisach model, the material magnetization can be assumed as the superposition of a set of rectangular hysteron with a fixed unit magnitude. In the Stoner-Wohlfarth (S-W) model, it is assumed that the ferromagnetic material is composed by a lot of single-domain particles which with uniaxial crystal anisotropy. Bertotti proposed the original concept of elemental operator with biaxial anisotropy and the graphical interpretation method [2]. In this paper, the elemental operator is fully analyzed based on the magnetization mechanism. With the employment of the partial approximate substitution, the drawback of the graphical interpretation method can be addressed, and an improved analytical expression of magnetic field and magnetization on each operator is obtained. Finally, the approach is verified by the experiment on two different ferromagnetic materials. II.Elemental Operator For the ferromagnetic materials, each magnetic dipole in the iron crystal particle is regarded as an elemental operator with biaxial anisotropy on arbitrary crystal plane. Then, it is assumed that the ferromagnetic material is composed by lots of interacting elemental operators, as shown in Fig. 1. Similar to the conventional S-W model, the magnetization orientation of each biaxial anisotropy elemental operator can be obtained by the energy minimization [3]. Similar to the treatment in the case of uniaxial S-W particle, the minimization of the total energy indicates when the orientation of biaxial elemental operator is stable, the equilibrium orientation of the magnetization can be determined. After trigonometrical transformations, the first and second derivatives of the energy equtation can have 4, 3, 2 and 1 real minimal value depending on the magnitude and orientation of the magnetic field intensity. The curve, which separates the regions with different energy extremes, is called as biasteroid or windrose curve[2]. This elemental operator is derived in the form of two dimensions, and can be adopted to model the scalar magnetic hysteresis by restricting the applied magnetic field to vary along one dimension and ignoring the transverse hysteresis component. To represent the bulk magnetization of the ferromagnetic material, the contributions of a collection of elemental operators should be summarized. However, the graphical interpretation method, as discussed above, is fail to describe the relationship between applied field and the resultant magnetization with an analytical expression. This problem largely limits the quantitative analysis of the magnetic properties based on the elemental operator. To address this problem, the partial approximate substitutions approach can be employed. With the new symmetry considerations on the magnetic anisotropy, the anisotropy energy can be a power series expansion of the modulus of the direction cosine. Then the energy minimum of one single operator can be obtained by an analytical way. III.Numerical Implementation After the magnetic properties of one single elemental operator has been fully studied, the bulk magnetization M of a SMC material sample can be determined by integrating the effects of all the elemental operators in the sample with a two- dimensional distribution function. With different parameters of the distribution function, this model can be employed to simulate the hysteresis loops of different materials. In this model the distribution can be described by a two-dimensional Gaussian-Gaussian distribution [4]. The adjustable parameters of distribution function can be determined numerically by fitting the model to the limiting hysteresis loop. Then, the major loops and minor loops can be predicted according to the solved distribution function. IV.Experimental Verification To verify the accuracy and the feasibility of the presented elemental operator, the hysteresis loops (including major loops and minor loops) of two different ferromagnetic materials, soft magnetic composites material SOMALOY™ 500 and non-oriented silicon steel Lycore-140, are measured under alternating magnetic field by the magnetic property measurement system [5]. As shown in Fig. 2, the simulated results agree well with the experiment results in both major hysteresis loops and minor hysteresis loops. V.Conclusion In this paper, the elemental operator with biaxial anisotropy has been introduced based on the magnetization mechanism. With the help of the improved analytical expression, which deduced by the partial approximate substitutions, the scalar magnetic properties of ferromagnetic materials are simulated and compared with the measured results. It can be proved that the results predicted by the model are acceptable. Additionally, the vectorial elemental operator is a feasible method to simulate the scalar magnetic hysteresis of ferromagnetic material.

[1] E Cardelli, "A general hysteresis operator for the modeling of vector fields," IEEE Trans. Magn., vol. 47, no.8, pp. 2056-2067, Aug.2011. [2] G. Bertotti, *Hysteresis in magnetism: for physicists, materials scientists, and engineers*: Gulf Professional Publishing, 1998. [3] D. C. Jiles, *Introduction to Magnetism and Magnetic Materials.* Florida, CRC press, 1998. [4] János Füzi, "Analytical Approximation of Preisach Distribution Functions," *IEEE Trans. Magn.*, vol. 39, no. 3, pp. 1357-1360, 2003. [5] Y. J. Li, Q. X. Yang, J. G. Zhu, *et al.*, "Research of three-dimensional magnetic reluctivity tensor based on measurement of magnetic properties," *IEEE Trans. Appl. Supercond*., vol. 20, no. 3, pp. 1932-1935, 2015.

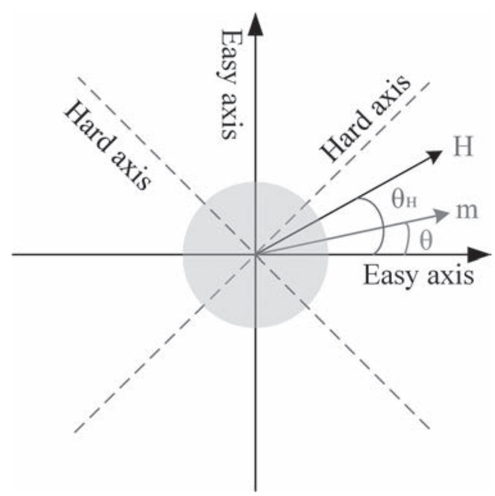

Fig. 1. The elemental operator with biaxial anisotropy

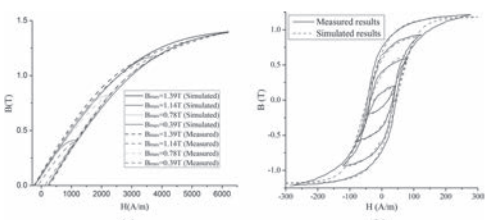

Fig. 2. Comparison of measured and simulated the B-H major loops of (a) SMC material SOMALOY 500 and (b) non-oriented silicon steel Lycore-140

GT-09. Magnetostrictive Characteristics of the Grain-Oriented Electrical Steel in an Epstein Frame Magnetized with a DC Biased Magnetic Field.

Z. Wang[1], *Y. Zhang*[1], W. Jiang[2], D. Zhang[1], Z. Ren[1] and C. Koh[3]
1. School of Electrical Engineering, Shenyang University of Technology, Shenyang, China; 2. School of Science, Shenyang University of Technology, Shenyang, China; 3. College of Electrical and Computer Engineering, Chungbuk National University, Cheongju, The Republic of Korea

I. Introduction Direct current (dc) bias is a kind of abnormal working state of power transformer. The presence of dc biased magnetic field in the operation of a power transformer may intensify the vibration and noise in transformer cores because the magnetostriction of electrical steel sheets results in the deformation of transformer core [1-2]. There are some methods and techniques that have been implemented to mitigate and reduce the dc bias' effects. However, in order to make more accurate performance predictions, these procedures require an accurate mapping of the material characteristics under a dc bias's condition. Until now, some significant researches have been conducted on the measurement of such magnetostrictive characteristics in an electrical steel sheet as rotational magnetostriction, anisotropic alternating magnetostriction and its dependence on frequency [3-4]. However, the influence of presence of a dc bias at the magnetized field on the magnetostrictive characteristics has not been well identified yet. In this work, based on an Epstein frame, an experimental setup was built to measure the in-plane magnetostriction and the principal magnetostriction was computed under a dc bias. The influence of dc bias magnetic field on the magnetostrictive property of electrical steel sheet was investigated. Based on the experimental test results, a description of the magnetostrictive behavior in the presence of dc bias was presented by using a back propagation neural network (BPNN) model assisted with the Levenberg-Marquardt (LM) algorithm. This research is helpful to make an accurate estimation to deformation of iron cores under a dc bias. II. Experimental Approach An experimental setup measuring the magnetostrictive property of electrical steel is shown in Fig. 1, in which the Epstein frame, MPG200, Brockhaus in Germany, is employed to magnetize the double-overlapped samples. During the measurement, the magnetic field intensity *H* created by the main winding in the Epstein frame can be superposed with a dc biased field with 0 A/m, 5 A/m, 10 A/m, or 15 A/m and the magnetic induction *B* measured by the second winding can be controlled as a purely alternating *B* with amplitudes of 0.1 T to 1.9 T and 50 Hz. In order to magnetize the specimens along different angles with respect to the rolling direction (RD), the samples were cut at 15° intervals from the RD to the transverse direction (TD). A rosette foil resistance strain gauge is attached to the surface of electrical steel sheet to obtain an in-plane magnetostriction in an arbitrary direction. The strain gauge is connected to the strain bridge box and strain amplifier, then the strain signals are transferred to a NI PXle-6368 data acquisition card and processed by LabView program. The measurements are performed on the samples of a grain-oriented 0.35 mm-thick 3% Si-Fe material. III. Analysis of Magnetostrictive Property Fig. 2 shows the variation of in-plane magnetostriction in any arbitrary direction for one instant of time with the magnetization directions of 0°, 30°, 60°, and 90° with respect to the RD, respectively. In this figure, the elongated strain is depicted as blue lines and its principal strain is λ_p^+ marked with a blue arrow, and the contractive strain is red line and its principal strain is λ_p^- with a red arrow. It can be seen that the principal strain gets bigger with the increase of the magnetization angle deviated from the RD due to more 90° domain wall motions' contribution to the magnetostriction strain, the contractive principal strain is always greater than the elongated principle strain, but the direction where the principle strain occurs keeps constant. As a result, the magnetostriction strain in the grain-oriented steel behaves in anisotropic ways under the alternating magnetizations. Fig. 3 represents the principal strain waveform λ_p^- in one time period with several imposed dc biased fields H_{dc} when the samples are magnetized along the RD and magnetic induction *B* are controlled as 1.2 T and 1.8 T, respectively. In the case of H_{dc} = 0 A/m in Fig. 3(a), the waveform of magnetostriction varies at a frequency of 100 Hz that is twice that of *B* signal (50 Hz). In the presence of a dc bias magnetic field, such as 5 A/m, 10 A/m, and 15 A/m, however, the waveform does not change periodically two times and lose its symmetry at time 0.01 s. We can see that the asymmetry trend increases with the increase of the dc biased magnetic field, and the peak to peak value also increases. However, the symmetry of the magnetostrictive waveform in Fig. 3(b) is restored at high induction *B* of 1.8 T, and the peak to peak value is basically the same. It can be concluded that the influence of the dc biased field on the magnetostrictive strain is little when the samples are magnetized gradually into the saturation stage. One explanation for this phenomenon is that the magnetic domain wall displacement and magnetic torque rotation tend to be completed with approaching the saturated magnetization, which is regarded as the saturated characteristic of magnetostriction. In the full paper, the effect of dc bias magnetic field on the magnetostriction anisotropy of electrical steel sheet will be investigated, in addition, a modeling method of the magnetostrictive behavior in the presence of dc bias will be studied.

[1] A. J. Moses, P. I. Anderson, and T. Phophongviwat, "Localized surface vibration and acoustic noise emitted from laboratory-scale transformer cores assembled from grain-oriented electrical steel," *IEEE Trans. Magn*., vol. 52, no. 10, pp. 1-15, Oct. 2016. [2] S. Somkun, A. J. Moses, and P I. Anderson, "Magnetostriction in grain-oriented electrical steels under AC magnetisation at angles to the rolling direction," *IET Electr. Power Appl.*, vol. 10, no. 9, pp. 932-938, Sep. 2016. [3] G. Shilyashki, H. Pfutzner, J. Anger, et al. "Magnetostriction of transformer core steel considering rotational magnetization," *IEEE Trans. Magn*., vol. 50, no. 1, pp. 1-15, Jan. 2014. [4] S. G. Ghalamestani, L. Vandevelde, J. J. J. Dirckx, et al. "Magnetostriction and the influence of higher harmonics in the magnetic field," *IEEE Trans. Magn*., vol. 48, no. 11, pp. 3981-3984, Nov. 2012.

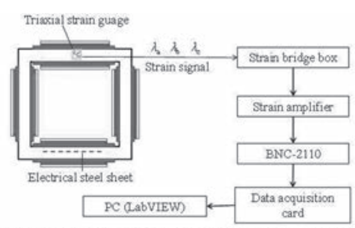

Fig. 1 Experimental setup of in-plane magnetostriction in an Epstein frame.

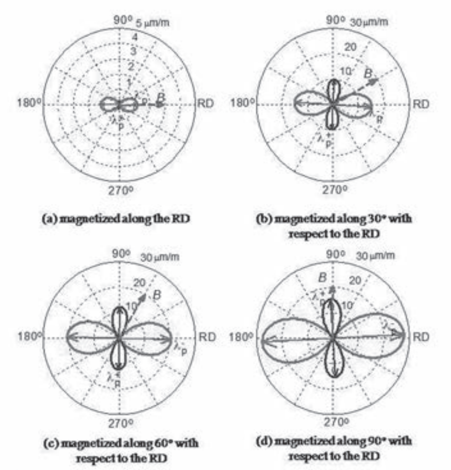

Fig. 2 In-plane magnetostriction in any arbitrary direction for one instant of time when the peak value of magnetic induction B_{max} = 1.6 T (elongated strain marked with blue line; contractive one with red line)

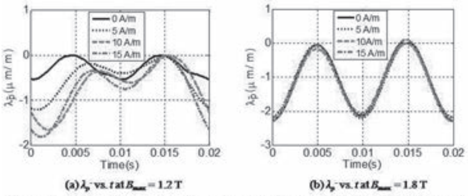

Fig. 3 Principal strain waveform λ_p^- under several imposed dc biased fields H_{dc} when the samples magnetized along the RD.

GT-10. Study on Calculation Methods of AC Loss for a HTS Magnet with Iron Core.

Y. Zhang[1], L. Ren[1], S. Yan[1] and Z. Wang[1]
1. Huazhong University of Science and Technology, Wuhan, China

The great advantage of HTS coils in magnet is that it can provide large excitation in a limited space. However, under high level excitation condition, especially in the case of fast adjusting process, AC losses will occur and lead to reduction of thermal stability [1], [2]. Therefore, it is necessary to calculate AC loss of HTS coils quickly and accurately. The homogenization method based on H formulation basically meets the calculation requirements of AC loss for a thousand-turn magnet with simple structure [3]. However, for magnets with non-linear ferromagnetic materials such as HTS controllable reactors [4], [5], the non-linear saturation in ferromagnetic domains makes it difficult to calculate AC loss rapidly and accurately with homogenization methods. Three simplified calculation methods of AC loss for HTS magnets have been proposed in this paper. In order to verify the validity of the simplified algorithm quickly and effectively, a two-dimensional axisymmetric model is adopted. The key to reducing the nonlinearity is to quickly calculate the magnetic permeability distribution in the core region. Three methods have been proposed to simplify the calculation. The first method is A+H formulation method. In the A formulation, set the same resistivity through the current flowing area, apply a uniform current density excitation and set BH magnetic properties in the core. In the H formulation, set the nonlinear resistivity decided by E-J characteristic through the current flowing area [6], apply a total current constraint and the magnetic permeability of the core region is from the real-time calculation of the A formulation results. The coupling between the two formulations does not occur during the solution, but the permeability of the core in the H formulation is provided by the calculation of the A formulation. The second method is magnetic permeability transfer of the core region method. Core area is divided into different regions. The magnetic permeability in all the core regions is solved in the A formulation, which is made into a data table. Then the magnetic permeability is applied in the H formulation model as a known item. The third method is A formulation coupling with H formulation method (A&H formulation). A formulation and H formulation share the same model. The PDE module (the control formulation is the H formulation) only contains the superconducting domain and part of the air domain around the superconducting domain. All the domains are contained in the magnetic field module (the control formulation is the A formulation). The core domain is described by the BH curve. The HTS coils are excited by the uniform current density. The section boundary of air domain is shared with the PDE module to transfer the magnetic field strength to the PDE module. The example model is a small iron-containing superconducting magnet, which is modeled with a homogenization method. Considering that the H-formulation method is widely used and supported by a large number of experiments [7], [8], the present example uses the H-formulation results as the benchmark in the error analysis of each method. Fig.1 shows the calculation time with different methods. In the linear discrete model, A+H formulation solves two physical formulations for the whole domain, which has the highest degree of freedom and a 13.5% increase in the number of degrees of freedom compared with other linear discrete models. The A-formulation coupling with H-formulation adopts quadratic discrete and has the highest degree of freedom, which also has the longest solution time. Fig.2 shows the average loss of each method. The average loss of each model with linear discreteness is not much different from that of the H-formulation model and the maximum deviation is 0.527%. The error of the third method using the quadratic discrete is larger, ranging from 11.59% to 20.47%. Both of them are larger than the H-formulation calculation results. In summary, the first method is the first choice when we calculate AC Loss for a HTS Magnet with Iron Core. If the degree of freedom is too large in the model, we can choose the second method. If the AC loss is still difficult to calculate, we need to choose the third method at the expense of a little accuracy. This paper presents three simplified calculation methods of AC loss for HTS magnets, which make it possible to calculate the AC loss of the core-containing superconducting magnet rapidly and accurately. The first two methods have high precision, but they are not suitable for the large-scale model. The third method can calculate the large-scale model quickly, but there is a small amount of error.

This work was supported in part by National Natural Science Foundation of China under Grant 51577082.

[1] X. Song et al., “AC Losses and Their Thermal Effect in High-Temperature Superconducting Machines.” IEEE Trans. Appl. Supercond., vol. 26, no. 4, June. 2016, Art. ID. 5900105. [2] L. Ren et al., “Evaluation of Three Designs for a 35-kV Class Superconducting Reactor,” IEEE Trans. Appl. Supercond., vol. 24, no. 4, Aug. 2014, Art. ID. 5400205. [3] Z. Wang et al., “AC Loss Analysis of a Hybrid HTS Magnet for SMES Based on H-formulation.” IEEE Trans. Appl. Supercond., vol. 27, no. 4, June. 2017, Art. no. 4701005. [4] Z. Wang et al., “Performance analysis and prototype design of a D-core type single-phase HTS controllable reactor,” IEEE Trans. Appl. Supercond., vol. 26, no. 4, Mar. 2016, Art. no. 0603304. [5] Z. Wang et al., “Development of a New Type of HTS Controllable Reactor with Orthogonally Configured Core,” IEEE Trans. Appl. Supercond., vol. 27, no. 4, June. 2017, Art. no. 5000205. [6] J. R. Clem, J. Claassen, and Y. Mawatari, “AC losses in a finite Z stack using an anisotropic homogeneous-medium approximation,” Supercond. Sci. Technol., vol. 20, no. 12, pp. 1130–1139, 2007. [7] W. Yuan, A. Campbell, and T. Coombs, “A model for calculating the AC losses of second-generation high temperature superconductor pancake coils,” Supercond. Sci. Technol., vol. 22, no. 7, 2009, Art. ID 075028. [8] V. M. Zermeno, A. B. Abrahamsen, N. Mijatovic, B. B. Jensen, and M. P. Sørensen, “Calculation of alternating current losses in stacks and coils made of second generation high temperature superconducting tapes for large scale applications,” J. Appl. Phys., vol. 114, no. 17, 2013, Art. ID 173901.

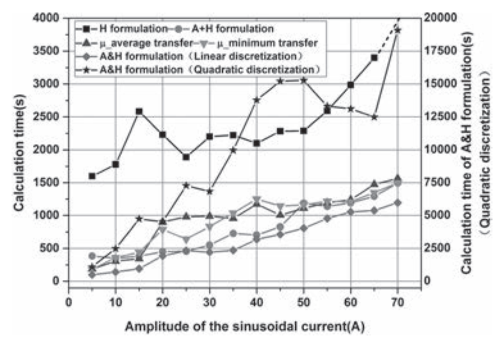

Fig. 1. The calculation time with different methods

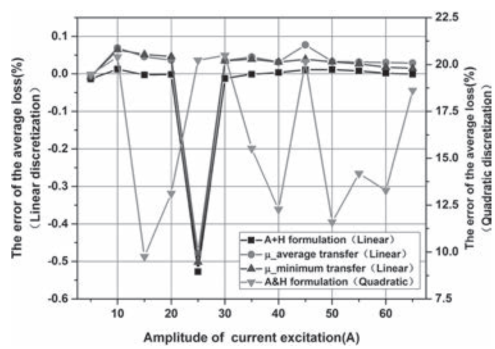

Fig. 2. The average loss of each method

GT-11. Examination of Temperature Dependent Iron Loss Models Using a Stator Core.

J. Chen[1], D. Wang[1], Y. Jiang[1], X. Teng[1] and S. Cheng[1]
1. Naval University of Engineering, Wuhan, China

I.Introduction Non-oriented silicon steel is widely utilized as main core materials for electromechanical equipment, such as motors and generators, because of their attractive characteristics of high magnetic saturation point, good mechanical strength, little anisotropy, and low cost. Iron loss is the key index especially for high speed motor, which could take a larger share in the total loss compared with low speed motor. Considering the high speed motor could operate in the higher temperature environment, temperature dependent iron loss model is one of the focus recently. There are a lot of iron loss models based on loss separation principle, such as three-term model, two-term model. Considering the frequency and temperature effect, there are constant coefficient models and variable coefficient models[1]. Regarding the model fitting, someone uses the multi-frequency loss curves to fit all coefficients, but someone not. Up to now, accurate measurement of motor iron loss is very difficult. Furthermore, research papers published recently use ring specimen and Epstein frame to validate the temperature dependent iron loss model. Too many iron loss models make people a little bit confusing, iron loss calculation and validation on motor is still an open question. This paper aims to examine those temperature dependent models based on a stator core(product-level) and ring specimen(sample-level) in a wide range of frequency and temperature. II.Temperature Dependent Iron Loss Models The initial expression for the iron loss in magnetic materials was proposed by Steinmetz [2], where iron loss is a sum of hysteresis loss and eddy current loss. In [3], a third term in the iron loss expression was introduced by Pry and Bean. The iron loss is divided into hysteresis loss, classical eddy current loss and excess loss. By improving the modelling of the excess loss, an iron loss model was proposed by Bertotti et al. in [4, 5]. Since the Bertotti model has a good physical background, it has been evolved into many different expressions and is widely adopted for iron loss calculation. However, it is pointed out in [6] that the contributions of classical eddy current loss and excess loss couldn't be easily separated by an Epstein frame or a ring specimen test. Alternatively, a new two-term approach is developed in [6], where the classical eddy current loss and excess loss in Bertotti's three-term model are combined into a comprehensive eddy current loss. Since this two-term model is easy to implement and has an equal accuracy for non-oriented silicon steel, it is widely used in electrical machine design and optimization [7-8]. The above mentioned iron loss models are based on constant coefficients. However, the iron loss coefficients change with the flux density and the frequency [9-10]. Therefore, the iron loss models containing variable hysteresis and eddy current loss coefficients are developed by Xue et al[11]. These models are used for the iron loss predictions in [12-13]. III.Experimental Validation Due to difficulties on loss separation, especially the existence of stray loss and frictional loss, it is difficult to directly validate the iron loss model on a motor. So, as a first step, only alternative magnetization is involved. This paper plans to evaluate the iron loss model on a stator core, with slot, teeth and variable axial length. To avoid the uncontrolled factors from specimen, we bought the silicon steel directly from the WISCO, China, then tailored the silicon steel into ring sample and stator lamination, respectively. Stacked ring sample is used to fit the iron loss model coefficients, whose outer diameter is 40mm, inner diameter 32mm. Stator lamination is used to build a product-level core and evaluate the iron loss model. All the specimen preparation and wire cutting is done within the laboratory. Non-metallic fixture is customized to avoid the undesirable electromagnetic loss, shown in Fig. 1(a). Firstly, DC and AC magnetic property of ring sample is measured at 0~400Hz, 0.1~1.9T, RT~200 Celsius degrees. Secondly, DC conductivity measurement was carried out in the same oven, shown in Fig. 2. With these measured data, we can fit various iron loss models mentioned in Section II. During the specimen measurement, back EMF of secondary winding become non-sinusoidal when magnetic induction is larger than 1.7T. Therefore, we use the time domain loss expression to fit these experimental data, if waveform factor of secondary winding EMF exceeds 1.11±0.01. Thirdly, the wound stator core will be put into the same oven to obtain the iron loss. Only massive validations can lead to a practical research result. In order to fully validate these models and eliminate exceptions, the measurement is implemented on 1 piece, 5 pieces, 10 pieces and 20 pieces, respectively. Measured iron loss should be proportional to number of pieces, and this criterion is used to justify the measured stator iron loss. The prediction of stator iron loss is implemented based on FEM software JMAG, where the flux density of each element is exported to MATLAB workspace so as to obtain the iron loss values of different models. Now, the specimen measurement and fitting is finished, partial result is shown in Fig. 1(b). The stator core measurement is being done and the comparison of model prediction result will be given in full paper.

[1] Z. Q. Zhu, S. Xue, J. Feng, S. Guo, Z. Chen, J. Peng, and W. Q. Chu, "Evaluation of Iron Loss Models in Electrical Machines." pp. 1-6. [2] S. C.P., "On the law of hysteresis," Trans. Am. Inst. Electr. Eng., vol. 9, no. 1, pp. 3-64, 1892. [3] R. Pry, and P. Bean, "Calculation of the energy loss in magnetic sheet materials using a domain model," J. Appl. Phys., vol. 29, no. 3, pp. 532-533, 1958. [4] G. Bertotti and M. Pasquale. Physical interpretation of induction and frequency dependence of power losses in soft magnetic materials[J]. IEEE Transactions on Magnetics, 28(5): 2787-2789. [5] G. Bertotti. General properties of power losses in soft ferromagnetic materials[J]. IEEE Transactions on Magnetics, 24(1): 621–630. [6] A. Boglietti, A. Cavagnino, M. Lazzari, and M. Pastorelli, "Predicting Iron Losses in Soft Magnetic Materials With Arbitrary Voltage Supply: An Engineering Approach," IEEE Transactions on Magnetics, vol. 39, no. 2, pp. 981-989, Mar, 2003. [7] H. Domeki, Y. Ishihara, C. Kaido, Y. Kawase, S. Kitamura, T. Shimomura, N. Takahashi, T. Yamada, and K. Yamazaki, "Investigation of benchmark model for estimating iron loss in rotating machine," IEEE Transactions on Magnetics, vol. 40, no. 2, pp. 794-797, 2004. [8] K. Yamazaki, and Y. Kanou, "Shape Optimization of Rotating Machines Using Time-Stepping Adaptive Finite Element Method," IEEE Transactions on Magnetics, vol. 46, no. 8, pp. 3113-3116, 2010. [9] D. M. Ionel, M. Popescu, S. J. Dellinger, T. J. E. Miller, R. J. Heideman, and M. I. McGilp, "On the variation with flux and frequency of the core loss coefficients in electrical machines," IEEE Transactions on Industry Applications, vol. 42, no. 3, pp. 658-667, 2006. [10] M. Popescu, and D. M. Ionel, "A Best-Fit Model of Power Losses in Cold Rolled-Motor Lamination Steel Operating in a Wide Range of Frequency and Magnetization," IEEE Transactions on Magnetics, vol. 43, no. 4, pp. 1753-1756, 2007. [11] S. Xue, W. Chu, Z. Zhu, J. Peng, S. Guo, and J. Feng, "Iron loss calculation considering temperature influence in non-oriented steel laminations," IET Science, Measurement & Technology, pp. 1-9, 2016. [12] A. Boglietti, A. Cavagnino, D. M. Ionel, M. Popescu, D. A. Staton, and S. Vaschetto, "A General Model to Predict the Iron Losses in PWM Inverter-Fed Induction Motors," IEEE Transactions on Industry Applications, vol. 46, no. 5, pp. 1882-1890, 2010. [13] M. Popescu, D. M. Ionel, A. Boglietti, A. Cavagnino, C. Cossar, and M. I. McGilp, "A General Model for Estimating the Laminated Steel Losses Under PWM Voltage Supply," IEEE Transactions on Industry Applications, vol. 46, no. 4, pp. 1389-1396, 2010.

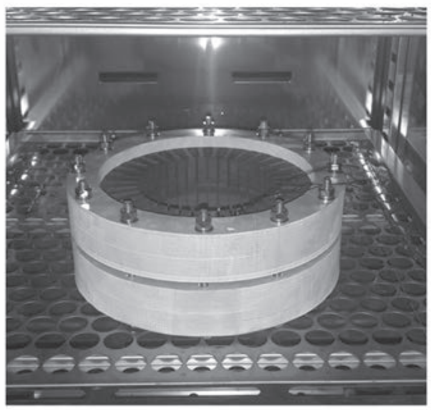

(a) Stator core in the oven(product level)

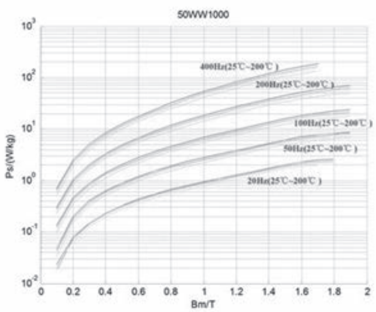

(b) Iron loss curves at various temperature(specimen level)

Fig. 1 Stator core and partial test result of ring sample

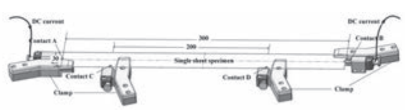

(a) Test rig

(b) Current flow path of tested specimen

(c) Electrical potential distribution on tested specimen

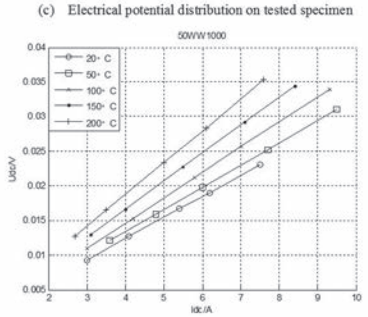

(d) UI curves at various temperature

Fig. 1 Measurement of temperature dependent electrical conductivity of silicon steell

GT-12. Global Quantities Computation Using Mesh Based Generated Reluctance Networks.

S. Asfirane[1], S. Hlioui[1,2], Y. Amara[3,4], O. De La Barriere[1], G. Barakat[3,4] and M. Gabsi[1]
1. SATIE, CNRS, ENS Cachan, Cachan, France; 2. CNAM, Paris, France; 3. GREAH, Le Havre, France; 4. Université du Havre, Le Havre, France

Introduction Numerical methods and mostly finite element analysis (FEA) are popular in electromagnetic modeling because they are standardized methods and because of the availability of a large number of commercial software. However, the computation time may be prohibitive, especially for 3D models. Analytical models are fast but restricted in terms of magnetic saturation evaluation and geometry complexity. Magnetic Equivalent Circuits (MEC) are an excellent compromise as they are fast and take into account magnetic saturation. They are not as generic as FEA and if parameters vary, MEC models have to be readjusted [1-6]. Thus, model development durations are longer for MEC than for FEA. For more genericity, authors in [7-9] have demonstrated the equivalence between the equations of reluctance network (RN) and FEA method and the possibility to form RN matrix system by means of FEA. This paper presents the load analysis of a Permanent Magnet Linear Machine (PMLM) as a case study for a direct flux tube MEC method using an automatic Mesh Based Generated Reluctance Network (MGRN). The aim is to show that it is possible to quickly build a semi-numerical model of studied structures with an automatically generated MEC with accurate results on global and local quantities. Comparisons of iron losses evaluated by the use of the MGRN model show that results are in a very good agreement with those obtained by Ansys-Maxwell FEA [10] used as a reference. This approach can be used in a tool that allows the automated processing of an arbitrary geometry providing an accurate model in a shorter amount of time than needed for building a dedicated model. *MESH BASED GENERATED RELUCTANCE NETWORK* Geometry is discretized in a number of bidirectional elementary reluctance blocks (Fig. 1). The model is divided into zones according to geometry and material proprieties. Discretization can be made finer or coarser according to the desired precision. Central nodes of element blocks are connected via their branches. The advantage of using bidirectional block elements is that no previous knowledge of flux paths is necessary. Each mesh of the network of the final MEC will describe a possible path for flux to go through. The second advantage is to have access to normal and tangential components of local quantities such as flux density and magnetic field. Thus, forces can be evaluated using the Maxwell stress tensor and iron losses by means of Bertotti model [11]. Scalar magnetic potential is used to formulate and solve the nodal based matrix equation: $[U]=[P]^{-1}[\Phi_s]$ [P] Permeance matrix [U] Scalar magnetic potential in each node $[\Phi_s]$ Sum of flux sources for each node n Total number of nodes The approach for solving the equation system as well as PMLM proprieties are given in [12]. A non-linear B-H curve is used for the ferromagnetic material and saturation is addressed with an iterative method as the value of permeability is adjusted in every ferromagnetic block element till convergence of the algorithm. The framework for space discretization, boundary conditions and PM sources assignment are explained in [13]. The PMLM is supplied with a 3-phase sinewave current and distribution of sources of magneto-motive force (MMF) due to coil currents is determined at each step. Fig 1 illustrates the geometry of the PMLM and the MMF distribution. *Sources distribution* MMF sources due to PM need to be placed on the branches of the magnetization direction (y axis) in the elements through all layers of the PM zones. Similarly, MMF sources due to coil currents are distributed on all elements of the teeth and slots. Total MMF according to position (along the x axis) is the sum of the MMF created by each coil. The ratio (height of element block to height of coil zone) is used to weight the MMF sources on each branch in each block of the winding zone (Fig. 1) : $mmf_{elem}=(1/2)\times(E_h/Z_h)\times\varepsilon(x_{node})$ ε Total mmf according to position x_{node} Position of the central node of block mmf_{elem}: MMF on the branch of the block E_h Element height Z_h Zone height *Saturation* The permeability in the reluctances of the blocks in the ferromagnetic parts is initialized with the linear part of the B-H curve. Convergence criteria is magnetic energy in each block as a product of flux density and magnetic field at each step is compared to the one of the previous iteration till the difference no longer exceeds a pre-defined value. At each displacement step, the magnetic permeability value of the block elements are those of the previous magnetic state in the whole model i.e. the previous displacement step. *Motion* A relative moving zone is defined including mover, PM and lower airgap region. The airgap is discretized in a way that the desired movement step is equal to the size of an element block in the airgap. This avoids non-conformal meshing problems and makes it easier to handle changes in matrix topology. *Iron losses* The total iron losses In the MGRN model are calculated in post-processing and are the sum of hysteresis losses, eddy current and excess losses as shown in the equation: $P = k_h f B_m^2 + (\pi\sigma d^2 f^2/6)\int(dB/d\theta)^2 d\theta + (\pi\sigma d^2 f^2/6)\int|dB/d\theta|^{1.5} d\theta$ Flux density values in each node of each reluctance block element are evaluated in the MGRN model using the same B(H) curve and material proprieties as implemented in the Ansys-Maxwell FEA model. Fig 2 shows comparisons of total iron losses (in all ferromagnetic parts i.e. stator and mover) vs frequency for the MGRN and the FEA models used as a reference at I_{max}=5A. It is shown that the results are in very good agreement.

[1] S. OUAGUED, A. ADEN DIRIYÉ, Y. AMARA, and G. BARAKAT, "A General Framework Based on a New Hybrid Analytical Model for the Analysis and Design of Permanent Magnet Machines," *2015 IEEE Magnetics Conference (INTERMAG)*, Beijing, 2015, pp. 1-1. [2] J. Perho, "Reluctance Network for Analysing Induction Machines," Acta polytechnica Scandinavica. Electrical Engineering Series vol. 110, Finish Academies Of Technology, December 2002. [3] S. Hlioui, B. Nedjar, L. Vido, Y. Amara, and M. Gabsi, "2D–3D Magnetic equivalent circuit of the flux focusing permanent magnets synchronous machine," in *2014 International Conference on Electrical Sciences and Technologies in Maghreb (CISTEM)*, 2014, pp. 1–7. [4] M. A. Benhamida, Y. Amara, and G. Barakat, "Interpolation coupling for reluctance network models dedicated to the predesign of Switching Flux Permanent Magnet machines," in *2016 International Conference on Electrical Sciences and Technologies in Maghreb (CISTEM)*, Marrakech, 2016 [5] R. Benlamine, T. Hamiti, F. Vangraefschèpe, F. Dubas, and D. Lhotellier, "Modeling of a Coaxial Magnetic Gear Equipped with Surface Mounted PMs Using Nonlinear Adaptive Magnetic Equivalent Circuits," *2016 XXII International Conference on Electrical Machines (ICEM)*, Lausanne, 2016, pp. 1888-1894. [6] Y. Benmessaoud, F. Dubas, M. Hilairet, and R. Beniamine, "Three-dimensional automatic generation magnetic equivalent circuit using mesh-based formulation," in *2017 20th International Conference on Electrical Machines and Systems (ICEMS)*, 2017, pp. 1–6. [7] A. Demenko, N. Lech, and W. Szelag, "Reluctance Network Formed by Means of Edge Element Method," *IEEE Trans. Magn.*, vol. 34, no. 5, pp. 2485–2488, 1998. [8] A. Demenko and J. K. Sykulski, "Network equivalents of nodal and edge elements in electromagnetics," *IEEE Trans. Magn.*, vol. 38, no. 2 I, pp. 1305–1308, 2002. [9] A. Demenko and J. K. Sykulski, "Analogies between Finite-Difference and Finite-Element Methods for Scalar and Vector Potential Formulations in Magnetic Field Calculations," *IEEE Trans. Magn.*, vol. 52, no. 6, 2016. [10] ANSYS®, "Electromagnetics Suite, Release 16.2.". [11] G. Bertotti, "General Properties of Power Losses in Soft Ferromagnetic Materials," in *IEEE Transactions on Magnetics*, vol. 24, no. 1, pp. 621-630, Jan 1988. [12] Y. Laoubi, M. Dhifli, G. Verez, Y. Amara, and G. Barakat, "Open Circuit Performance Analysis of a Permanent Magnet Linear Machine Using a New Hybrid Analytical Model," in *IEEE Transactions on Magnetics*, vol. 51, no. 3, pp. 1-4, March 2015. [13] S. Asfirane, S. Hlioui, O. De La Barriere, Y. Amara, G. Barakat, and M. Gabsi, "Software tool based on reluctance network automatic generation for electromagnetic devices modeling," in *Numelec 2017*, Paris, France, November 2017.

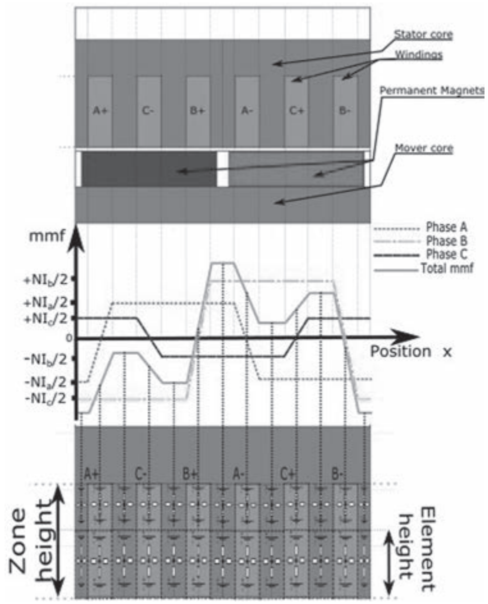

Fig. 1. MMF distribution

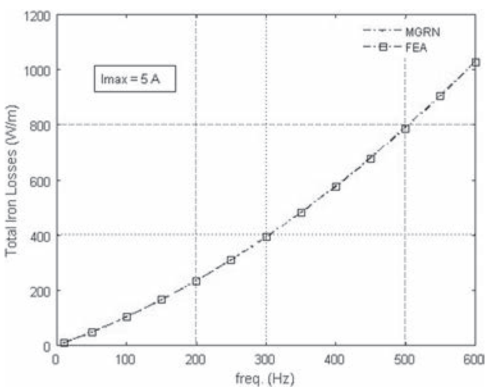

Fig. 2. Iron losses vs frequency

GT-13. Numerical Estimation of Iron Loss with Dual models for Electromagnetic Devices.

X. Liu[1] and *W. Fu*[1]
1. Electrical Engineering, The HongKong Polytechnic University, Hong Hom, Hong Kong

Abstract–In this work, in order to get adaptive Jiles–Atherton (JA) model parameters, an algorithm is proposed and assumes JA parameters to be the functions of magnetic field intensity H, or magnetic flux density B. These parameters are considered by using response surface model (RSM) which is based on the moving least squares (MLS) approximation. The RSMs of the JA model parameters are built based on the simulation results of Preisach model. Numerical example is involved to demonstrate the improvement in the accuracy of the modified JA model. Comparison of its predictions with measurements and with traditional JA model is also shown in this paper. I. Introduction In many engineering applications such as electromechanical actuators, piezoelectric, and magnetostrictive, magnetic materials are widely used [1]. The relationship between induced magnetic flux (B) and magnetic field (H) is shown by he hysteresis loop. Efforts have been made by developing different types of static hysteresis model for study of the hysteresis phenomenon. One of the best known is JA model [2]. The implementation of JA uses five parameters, and four of them are numerical and one is experimental. These parameters usually are identified based on an iterative procedure which may introduce convergence problems [3]. The determination of JA parameters is critical and it is numerically sensitive and does not systematically converge. Another one of the most famous phenomenological hysteresis models is Preisach model [4]. The contribution of infinite number of hysteresis operators is handled with the Preisach triangle, the staircase line and the Everett function. Since the distribution function is defined with H and the accessional iteration is required to find H from B, the classical Preisach model is not suitable for B-oriented method [5]. The classical Preisach model encompasses the basic features of hysteresis phenomena in a conceptually simple and mathematically elegant way. For a given operating condition of the machine, the magnetic fields of any point can be calculated using finite-element method (FEM). The FEM employs single value magnetization curve of iron so it cannot directly calculate hysteresis loss. So in this paper, the analysis results obtained by FEM for constructing the JA parameters are used with static scalar Preisach model. To evaluate the accuracy of the proposed adaptive JA model, numerical tests will be obtained. It is also compared in terms of computational time with traditional JA models and Preisach models. Finally as an example of application, a high-frequency transformer, made of ferrites, is also studied. II. Classical Loss Separation By reports of Bertotti, hysteresis loss P_h, classical eddy current loss P_{ed}, and excess loss P_{ex} consist of the iron losses in terms of the statistical property of Barkhausen effects [6]. P_h can be either segregated and interpolated via measurements or simulated by the proposed adaptive JA model described in Section III. Ped is generally determined from the magnetic field distribution. At low frequency, the induced eddy currents will not significantly affect the external magnetic field distribution, and P_{ed} can be computed from (1) of Fig. 1(a). When the operating frequency is sufficiently high, conventionally, the problem is handled by the introduction of a skin effect factor K_c which is formulated as (2) of Fig. 1(a). By the introduction of magnetic objects with related *n* and *V* which are the statistical parameters determined through measurement, the computation of P_{ex} is simplified as (3) of Fig. 1(a). In general, P_{ex} is always approximated as an optimization approach to formulate the identification problem based on the least square approach as equation (4) of Fig. 1(a) [7]. III. Presentation of the Hysteresis Loss Model The magnetization consists of two terms which are irreversible and reversible components in the JA model of hysteresis. The irreversible component indicates the irreversible domain wall motion. And the reversible magnetization corresponds to the reversible domain wall bending. The magnetization is outcome of the effective magnetic field intensity. In (5) of Fig. 1(a), the energy loss density which is generated by the irreversible domain wall motion is considered. The supplied energy in energy equation is equal to magnetic energy changes and the hysteresis loss as (6) of Fig. 1(a). Suppose c is a dimensionless reversible coefficient, then by introducing c the reversible magnetization can be taken into account as (7) of Fig. 1(a). The *jth* value of the magnetization evaluates the (*j*+1)*th* step the hysteresis characteristic by (8) of Fig. 1(a). The adaptive JA model is proposed according to the regulation of the classical JA model. The JA model parameters are determined as the response surface models (RSM) based on the field analysis by Preisach model. The flow chart of the proposed algorithm is shown as Fig. 1(b). IV. Numerical Examples The 2-D model of the ferromagnetic ring which is shown in Fig. 2(a) with measurement in cylindrical coordinate system has been used to verify the proposed algorithm. Fig. 2(b) to Fig. 2(d) shows the comparison of the measured and simulated hysteresis curves. V. Conclusion In this paper, the hysteresis loss is elaborated and solved via FEM. By using the adaptive JA modeling of hysteresis loss, it is capable of identifying the excess loss in a more accurate analytical form. The validation shows that the proposed method is able to reach an accurate result.

[1] K. Hergli, H. Marouani, M. Zidi, Y. Fouad, and M. Elshazly, "Identification of Preisach hysteresis model parameters using genetic algorithms," Journal of King Saud University-Science, 2017. [2] D.C.Jiles and D.L.Atherton, "Theory of ferromagnetic hysteresis," Journal of Magnetism and Magnetic Materials, vol. 61, pp. 48-60, 1986. [3] D. C. Jiles, J. B. Thoelke, and M. K. Devine, "Numerical Determination of Hysteresis Parameters for the Modeling of Magnetic-Properties Using the Theory of Ferromagnetic Hysteresis," IEEE Transactions on Magnetics, vol. 28, pp. 27-35, Jan 1992. [4] F. Preisach, "Über die magnetische Nachwirkung," Zeitschrift für Physik, vol. 94, pp. 277–302, 1935. [5] N. Takahashi, Shun-ichi, Miyabm, and K. FujiwJrd, "Problems in Praetical Finite Element Analysis Using Preisach Hysteresis Model," IEEE Transactions on Magnetics, vol. 35, pp. 1343-1246, 1999. [6] G. Bertotti, "Space-Time Correlation-Properties of the Magnetization Process and Eddy-Current Losses - Theory," Journal of Applied Physics, vol. 54, pp. 5293-5305, 1983. [7] L. Liu, W. N. Fu, S. Y. Yang, and S. L. Ho, "Iron Loss Separation in High Frequency Using Numerical Techniques," IEEE Transactions on Magnetics, vol. 52, Mar 2016.

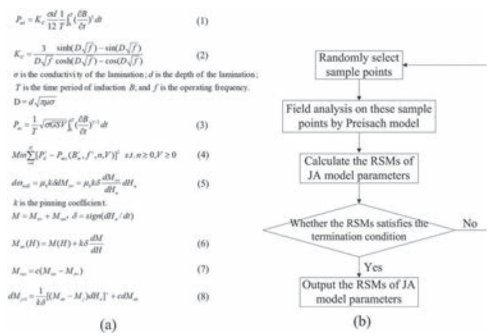

Fig. 1. Formulas and flowchart

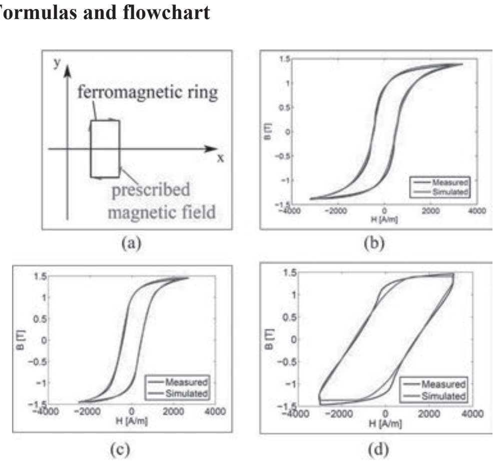

Fig. 2. Numerical example and results

GT-14. A Self-adaptive Play Model with Input-dependent Shape Functions for Hysteresis Loss of Electromagnetic Devices.

X. Liu[1] and *W. Fu*[1]

1. Electrical Engineering, The HongKong Polytechnic University, Hong Hom, Hong Kong

Abstract–Play models are capable of representing minor hysteresis loops of a silicon steel sheet. This paper presents an identification method which can automatically detect the number of play hysterons needed for the simulation. Single sheet tester is applied to get the symmetric B-H loops and first-order reversal curves to identify the play models. Two types of play models are employed in this work. Simulated minor loops, representation of errors, and symmetric B-H loops are presented to verify the accuracy of the proposed method. I. Introduction For the high accurate calculation of core loss, analyzation of the hysteretic properties for magnetic materials is an essential topic. Complex minor hysteresis loops can result in higher time harmonics. Since the computational process of the play model is equated with the nonlinear Preisach model, its representation of minor-loop is constrained by the property of equal vertical chord. Therefore, it is necessary for complicated magnetic field to have a precise representation of minor loops in analysis of iron core for motors. The play model with an input-independent shape function has already been proved equated with the static scalar Preisach model [1]. Nonlinear Preisach model has the hysteretic property. So one of the identification methods is to use the second-order reversal curves of for this property [2]. For this method, all second-order reversal curves are required to be measured for identification, so it needs heavy labor load and is difficult for application. In the study of play model, the product form of an input-dependent shape function is applied. And based on this type of shape function, an identification method of the play model is proposed [3]. II. Play Models with Input-dependent Shape Functions Between the magnetic flux density *B* and the magnetic field *H*, the hysteretic relationship is described by the play model. As the Preisach model, it provides an output using the inverse distribution function method. A discrete form of the play model is shown as (1) in Fig. 1 [3], where p_z is the play hysteron operator; z is the width of the operator; p_{z0} is the value of p_z at the last time-point; N_p is the number of play hysterons; f_m is the piece-wise input-dependent shape function for p_{zm}; and B_s is the saturation B. Play model constructed by input-independent shape function can be identified from the Everett function [4]. The input-dependent shape function has a product form as (2) in Fig. 1. The Everett function from symmetric loops is presented as (3) in Fig. 1. The play model represents a hysteretic function precisely by using (1) in Fig. 1 which should have the coherent property required as the Preisach model. This property is used to determine an optimal weight function $w(B)$ of the piece-wise shape function. A simple weighting function is employed in this work as (4) in Fig. 1. A piecewise linear shape function as (5) in Fig. 1 is used for identification. III. Self-adaptive Play Models with Input-dependent Shape Functions B-H loops are simulated by the symmetric loops identified play model. Increase in the number of hysterons used will elevate the accuracy of the play model. But choosing the number of play hysterons is usually based on experience. In this work, a self-adaptive play models with input-dependent shape functions is proposed. A preset condition is employed to control the process. The process is shown as below: Step 1. Measure the saturation magnetic field H_s. Set M and determine condition d_0. Step 2. Suppose m=m_i. Step 3. Calculate the piecewise linear shape functions using (5) in Fig. 1, and the weight function w(B). Step 4. Calculate the magnetic field H_i by (6) in Fig. 1, and d_{Hi} by (7) in Fig. 1. If d_{Hi} is smaller than d_0, then accept and output the result. Else $m_{(i+1)}$=m_i+1 and go back to step 2. Step 7. Determine whether the number of m_i reaches the M. If yes, then output the final result. Else go back to step 2. IV. Representation of symmetric BH loops Identification uses the symmetric B-H loops can give accurately representation of symmetric BH loops. The play model uses the methodologies (1)-(3) as [5] for identification. The simulated symmetric B-H loops are shown as the Fig. 2(a)-(c). (1) Everett function method employs the symmetric BH loops. (2) Everett function method employs the reversal curves from saturation. (3) Least-squares method employs both symmetric loops and the reversal curves from saturation. Another example as [3] is to compare the simulated and measured reversal curves of the steel sheet 30P105. These curves are first-order and are from negative saturation along rolling and transverse directions. The results are shown as the Fig. 2(d) and Fig. 2 (e). V. Conclusion This paper has proposed a self-adaptive play model with input-dependent shape functions. This method constructs the piece-wise shape function of magnetic field without preset of number of play hysterons while keeps the simulation accuracy. Results in Fig. 2 show that the method is feasible.

[1] S. Bobbio, G. Miano, C. Serpico, and C. Visone, "Models of magnetic hysteresis based on play and stop hysterons," Ieee Transactions on Magnetics, vol. 33, pp. 4417-4426, Nov 1997. [2] I. D. Mayergoyz, "Mathematical models of hysteresis," Phys Rev Lett, vol. 56, pp. 1518-1521, Apr 14 1986. [3] T. Matsuo and M. Shimasaki, "An identification method of play model with input-dependent shape function," Ieee Transactions on Magnetics, vol. 41, pp. 3112-3114, Oct 2005. [4] E. D. Torre, "Magnetic Hysteresis," New York: IEEE Press, 1999. [5] T. Matsuo, Y. Terada, and M. Shimasaki, "Representation of minor hysteresis loops of a silicon steel sheet using stop and play models," Physica B-Condensed Matter, vol. 372, pp. 25-29, Feb 1 2006.

$$\begin{cases} H = P(B) = \sum_{m=1}^{2M} f_m(p_{z_m}(B), B) \\ p_{z_m}(B) = \max(\min(p_{z0}, b+z), b-z) \\ z_m = (m-1)B_s/2M \end{cases} \qquad (1)$$

$$f_m(p,B) = w(B) f_{m0}(p) \qquad (2)$$

$$E(\alpha,\beta)\begin{cases} h_s^-(\beta,\beta) - h_s^-(\beta,\alpha) & (\alpha+\beta \ge 0) \\ h_s^+(|\alpha|,\beta) - h_s^+(|\alpha|,\alpha) & (\alpha+\beta \le 0) \end{cases}$$

$h_s^+(a,B), and\ h_s^-(a,B)$ are acending and descending branches of sysmmetric loop with amplitude a. (3)

$a = cB_s/M,\ c = 1,\dots,M.$

$$w(B) = H_M^+(B) - H_M^-(B)$$

where $H_M^+(B)$ and $H_M^-(B)$ are the ascending and descending curves, respectively, of the measured major loop. (4)

$$f_{m0}(p) = f_{m0}(p_{m,j-1}) + \mu_{m,j}(p - p_{m,j-1})/\Delta p. \qquad (5)$$

where $p_{m,j-1} \le p \le p_{m,j}$, j = 1,...,2M - m + 1

$$\begin{aligned} p_{m,j} &= -B_s + z_m + j\Delta p. \\ \Delta p &= B_s/M. \\ \mu_{m,j} &= f_{m0}(p_{m,j}) - f_{m0}(p_{m,j-1}) \\ &= E(b_{j-1},b_k) - E(b_{j-1},b_{k-1}) \\ &\quad - E(b_j,b_k) + E(b_j,b_{k-1}), k = m+j-1. \\ b_k &= kB_s/M - B_s.(k=0,\dots,2M), E(b_{j-1},b_j) = 0. \end{aligned}$$

$$H_i = H_{i-1} + f_i \qquad (6)$$

$$d_{Hi} = |H_{i-1} - H_s| \qquad (7)$$

Fig. 1. Formulas of classical play model and self-adaptive play model.

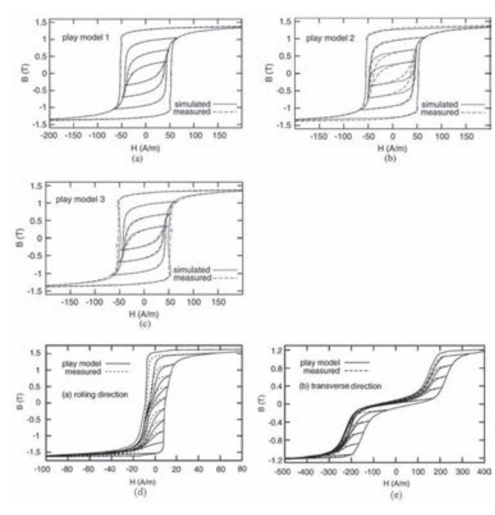

Fig. 2. Simulation results of play models.

GT-15. Skin Effect and Eddy Current Loss in Electrical Steel Sheets under Applied Excitation Fields.

J. Li[1], Q. Yang[2,3], S. Wang[1] and Y. Li[2]
1. State Key Laboratory of Control and Simulation of Power System and Generation Equipments, Tsinghua University, Beijing, China; 2. State Key Laboratory of Reliability and Intelligence of Electrical Equipment, Hebei University of Technology, Tianjin, China; 3. Municipal Key Laboratory of Advanced Technology of Electrical Engineering and Energy, Tianjin Polytechnic University, Tianjin, China

Abstract Body: By applying electromagnetic diffusion equation, skin effect in electrical steel sheets in the condition of alternating excitation is analyzed based on Maxwell electromagnetic field theory. Due to skin effect is more significant mainly at high frequency, non-dimensionalized treatment for the diffusion equation is produced and eddy current loss is calculated by considering or not skin effect, respectively. Meanwhile, broadband magnetic losses and separation of typical electrical steel are obtained by using a 3-D magnetic properties testing system to bring to light the emergence of skin effect under rotational excitation. The simplification of magnetic constitutive equation is proposed and introduced into the diffusion equation, which is solved by employing finite elements coupled to Fredholm's equation. An approximate expression for the rotational eddy current loss component with skin effect is eventually written. 1. The simulations show that due to the influence of skin effect, non-uniform distribution of induction flux density within electrical steel sheets will become more and more significant, the flux density and field intensity nearby the surface are larger than that in the centre of the sheets [1, 2]. And with increasing of alternating excitation frequency, the inhomogeneity of induction flux density will be extended and growing more inhomogeneous, due to the smaller skin depth and a small increase of anomalous loss in the total core losses, as shown in Fig. 1. 2. Therefore, alternating eddy current loss P_{ae} as functions of the peak mean alternating flux density B_{ma_mean} and the alternating excitation frequency f_a can be deduced as follows: $\lim_{v\to\infty} P_{ae}(B_{ma\_mean}, f_a) = [2\omega_a(B_{ma\_mean})^2/3\rho\mu v^2 = (\sigma\pi^2 d^2/3\rho)(f_a)^2(B_{ma\_mean})^2$ *(no skin effect)* [W/kg] (1) $\lim_{v\to 0} P_{ae}(B_{ma\_mean}, f_a) = [4\omega_a(B_{ma\_mean})^2/\rho\mu v = (4\sigma^{1/2}\pi^{3/2}d/\rho\mu^{1/2})(f_a)^{3/2}(B_{ma\_mean})^2$ *(considering significant skin effect)* [W/kg] (2) where, ω_a is the angular frequency; $v = 2\delta_e/d$, δ_e is the skin depth, d is the sheet width; ρ, σ and μ are the mass density, conductivity and permeability of magnetic materials, respectively. 3. Based on the total 3-D rotational experimental core losses of cold-rolled NO electrical steel sheet 50A1300 (thickness d = 5.00e-4 m, density ρ = 7.85e+3 kg/m^3, conductivity σ = 5.70e+6 S/m), which are fulfilled by using a 3-D magnetic properties testing system [3-6], the emergence of skin effect can be described according to the comparisons between the experimental and separated values of the mean micro-vortex current losses per cycle *vs*. the square root of rotational excitation frequency, as shown in Fig. 2. 4. The rotational eddy current loss component is evaluated by integration on the sheet thickness of the square of the current density modulus derived from the numerical computation of the curl of H fild. Then, an approximate expression for the rotational eddy current loss with skin effect can be written, as often done with the alternating regime. $P_{re}(B_{mr\_mean}, f_r) = (3\sigma\pi^2 d^2/4\rho)(f_r)^2(B_{mr\_mean})^2\{\delta_e[\sinh(d/\delta_e)\text{-}\sin(d/\delta_e)]/d[\cosh(d/\delta_e)\text{-}\cos(d/\delta_e)]\}$ *(considering significant skin effect)* [W/kg] (3) where, P_{re}, f_r and B_{mr_mean} are rotational eddy current loss, excitation frequency and mean peak flux density, respectively. Conclusion: The skin effect and eddy current loss under alternating and rotational fields are interpreted and deduced based on electromagnetic diffusion and magnetic constitutive equations. The emergent of skin effect in the condition of rotational excitation at high frequencies, the analysis and calculation methods of alternating and rotational eddy current losses, *etc.*, will promote the experimental verification and in-depth study of eddy current loss in the practical engineering applications.

[1] C. Serpico, C. Visone, I. Mayergoyz, *et al*. Eddy current losses in ferromagnetic laminations[J]. *J. Appl. Phys.*, 2000, vol. 87, no. 9, pp. 6923-6925. [2] S. Y. Lee, J. S. Ro and H. K. Jung. Eddy current loss analysis in the rotor of surface-mounted permanent magnet brushless machine with retainer[J]. *Int. J. of Appl. Electromagn. Mech.*, 2014, vol. 44, no. 1, pp. 41-50. [3] Y. J. Li, Q. X. Yang, J. G. Zhu, *et al*. Design and analysis of a novel 3-D magnetization structure for laminated silicon steel[J]. *IEEE Trans. Magn.*, 2014, vol. 50, no. 2, pp. 7009504. [4] J. S. Li, Q. X. Yang, Y. J. Li, *et al.* Anomalous loss modeling and validation of magnetic materials in electrical engineering[J]. *IEEE T. Appl. Supercon.*, 2016, vol. 26, no. 4, pp. 8800105. [5] J. S. Li, Q. X. Yang, Y. J. Li, *et al*. Improved calculation formula of core losses for laminated silicon steels at high frequency and high flux density[J]. *High Voltage Engineering*, 2016, vol. 42, no. 3, pp. 994-1002. [6] J. G. Zhu and V. S. Ramsden. Improved formulations for rotational core losses in rotating electrical machines[J]. *IEEE T. on Magn.*, 1998, vol. 34, no. 4, pp. 2234-2242.

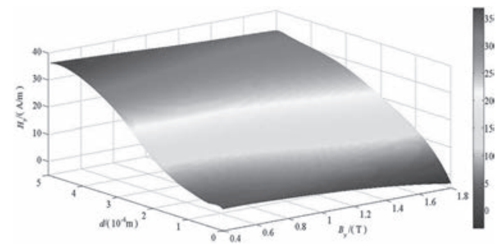

Fig. 1. Cloud map of flux density and field intensity along the thickness of the sheets (*y*-axis) of the electrical steel sheets finite element model by applying alternating excitation.

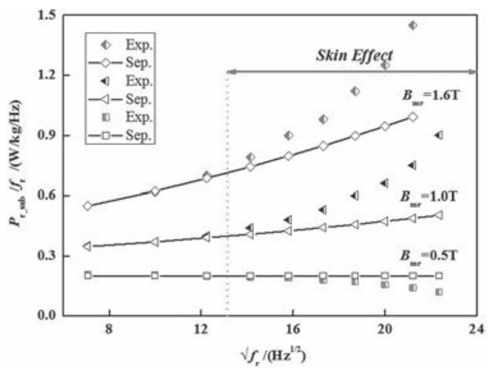

Fig. 2. Comparisons between experimental and separated values per cycle of P_{r_sub}=P_{rt}-P_{re}=P_{rh}+P_{ra}. [W/kg] (P_{rt} is the total 3-D rotational experimental core losses of electrical steel sheet; P_{re} is the rotational eddy current loss; P_{rh} is the rotational hysteresis loss; P_{ra} is the rotational anomalous loss.)

GT-16. Efficient Deperming Protocols Considering Magnetic Coercivity Distributions in Magnetic Stealth of Warship.

S. IM[1], H. Lee[1], H. Chung[2] and G. Park[1]

1. Electrical and Computer Engineering, Pusan National University, BUSAN, The Republic of Korea; 2. Agency for Defense Development, Changwon, The Republic of Korea

I. Introduction Demagnetization is to reduce the residual magnetization in magnetic materials. It is used in various industries such as HDD and VFD to record and erase data. Especially, in national defense, it is very important since there are fatal hazards such as magnetic mines if warship has high magnetic flux inside it [1]. In order to demagnetize it, alternating and decreasing magnetic fields are applied through external coils surrounding the warship as shown in Fig. 1(a). These magnetic fields are called the deperming protocol and generally there are three kinds of protocols such as Anhysteretic Deperm, Deperm-ME and Flash-D. Several studies have shown that Flash-D has better performance than Anhysteretic. In Flash-D, unlike Anhysteretic Deperm, it is composed of three stages, and the importance of the second stage is greatly emphasized by previous studies. If Stage 2 is performed at a high Priesach density region, the result will be excellent [2]. However, there is a lack of research on the factors that determine the most effective deperming protocol. Therefore, it is needed to develop a protocol that determines the start and end magnetic fields of Stage 2 for demagnetization. In this paper, Preisach model was used to analyze theoretically for an effective deperming protocol. According to Preisach model, magnetic domains with various size of coercive and interaction force are distributed to represent magnetic properties [3]-[5]. The results of the demagnetization are determined according to the state of the particles with various coercive force. In consideration of this, deperming protocol that can affect half of the particles in the warship is proposed. Preisach density distributions are obtained from the hysteresis curves to determine the magnetic fields that can affect the target particles. To validate the proposed one, as shown in Fig. 1(b), a solenoid coil was designed and two specimens of SM45C and SS400 were tested in a scale-down MTF test room. II. Process for deperming using Priesach model A. Conventional Flash-D protocol Flash-d protocol consists of three stages which is to decrease, increase and then decrease again. Stage 2 gradually increases the magnetic field unlike other deperming protocols. According to the previous studies, it was proved that the demagnetization performance is excellent when Stage 2 is determined as a region with a high Preisach density distribution. However, there is a limit to determine the current of Stage 2 depending on the characteristics of the materials. B. Proposed process and Flash-D protocol In this paper, the process of determining the start and end currents of stage 2 in flash-d protocol for effective demagnetization was analyze and proposed by using Preisach model. The basic concept is that stage 2 operates, like the previous study, in the region where the Priesach density is high. However, the development of a protocol that can perform the most effective demagnetization in the high density region was proposed. First, the B-H curve of the magnetic materials was measured. By differentiating the measured B-H curves, a curve of the Gaussian function was obtained, as shown in Fig. 2. It represents the density distribution curve of the particles having different coercive force in Preisach model. Most of the particles have a coercive force similar to that of the B-H curve, and the particles having large and small coercive force are less distributed. From the density distribution curves, the current I1 and I2 at the beginning and end of Stage 2 were determined by selecting the area corresponding to 50% of the magnetic particles, as shown in Fig. 2. When the proposed protocol was applied, 50% of the particles in the warship were affected once more. Therefore, the particles are effectively affected by the protocol at each stage, and thus the result of demagnetization was excellent. III. Experiment Result In order to verify the proposed protocol, the SM45C specimen was used as a warship equivalent model. The experimental procedure was as follows. First, the magnetic flux density according to earth magnetic fields was measured at a sensor located 18cm below the specimen. The measured result is 1929 nT. After applying proposed protocol, the magnetic flux density is 99 nT, which is 5% of the induced magnetic field. Therefore, the demagnetization was performed very well. Likewise, the experiment was carried out using the SS400 specimen. The protocol was adapted to the material properties of SS400 and finally 22 nT was measured. Detailed experimental equipment and experimental results will be shown in full paper. IV. Conclusion This paper proposes an efficient deperming protocol considering the characteristics of the magnetic materials. It was analyzed by using Preisach model and proved through experiments. Therefore, by using this process, it is possible to establish an effective deperming protocol considering the hysteresis characteristics of the warship.

[1] H.Won, H.S.Ju, S.K.Park, "A Study on the Deperming of a Ferromagnetic Material by Using Preisach Model with M-B Variables", IEEE Trans. On Mag., vol.49, no.5, pp.2045-2048, May 2013 [2] H. S. Ju, H. J. Chung, S. H. Im, D. W. Jeong, J. W. Kim, H. B. Lee, and G. S. Park, "Efficient Deperming Protocols Based on the Magnetic Properties in Demagnetization Process," *IEEE Trans. Magn.*, vol. 51, no. 11, November 2015 [3] M.Enkizono, T.Todaka and M.Kumoi, "Demagnetization and magnetic domain structure of silicon steel sheet", Journal of Magnetism and Magnetic Materials, 112, pp.207-211, 1992 [4] T.M.Baynes, G. J. Russel, and A. Bailey, "Comparison of stepwise demagnetization techniques", IEEE Trans. Magne., vol. 38, no. 4, pp. 1753-1758, Jul. 2002. [5] G.S.Park, S.-Y. Hahn, K.-S. Lee, and H.-K. Jung, "Implementation of hysteresis characteristics using the Preisach model with M-B variables,"IEEE Trans. Magn., vol. 29, no. 2, pp. 1542–1545, Mar. 1993.

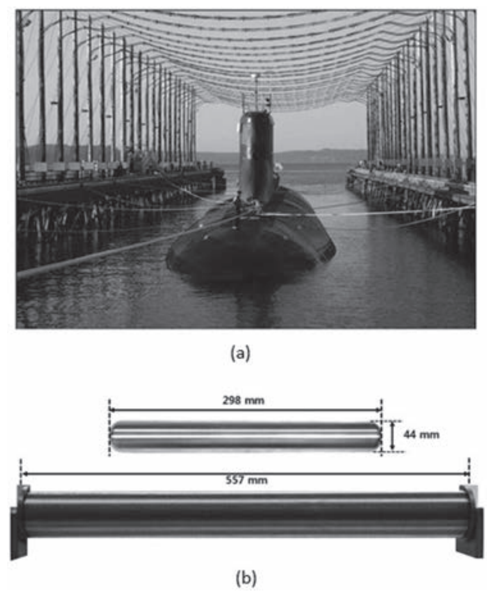

Fig. 1. Demagnetization experiment environment (a) Demagnetization of the warship. (b) Solenoid coil and specimen for experiment.

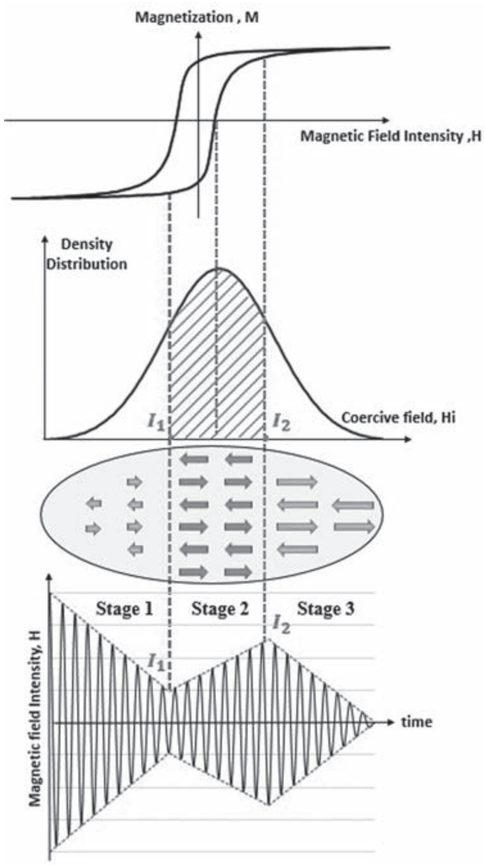

Fig. 2. Process to carry out a proposed protocol.

FRIDAY MORNING, 27 APRIL 2018 SIMPOR/ROSELLE BALLROOM, 8:30 TO 11:30

Session GU
INDUCTORS
(Poster Session)

Lijian Wu, Chair
Zhejiang University, Zhejiang, China

GU-01. Electromagnetic-Mechanical Analysis of a Balanced Armature Receiver by Considering the Nonlinear Parameters as the Function of Displacement and Current.

Y. Jiang[1], D. Xu[1] and S. Hwang[1]
1. Mechanical Engineering, Pusan National University, Busan, The Republic of Korea

1. Introduction Balanced armature receiver is widely used in hearing aid and earphone because of the small size and high sensitivity. Balanced armature receiver is a product which covers multi-physics. It contains the electromagnetic, mechanical domain and the property such as current and displacement can affect each other. In one hand, the current in electromagnetic domain will take effect on the force which determines the displacement in mechanical domain. In the other hand, displacement change can contribute to the change of back electromotive force (EMF) which affects the current. So the current and displacement are coupled and need to be considered at the same time to analyze the balanced armature receiver. In terms of equation, current and displacement are coupled in the voltage equation which involves the nonlinear parameters such as inductance, speedance, and force factor. Based on lumped parameter method, the nonlinear parameters were calculated as functions of displacement in balanced armature speaker [1]. By using finite element method, Lee et al. analyzed the nonlinear parameters as the function of displacement in microspeaker [2]. In this study, the displacement and current are both considered in the nonlinear parameters to analyze the performance of balanced armature receiver by using FEM. 2. Analysis method The balanced armature receiver is modeled with different deformation which means different vibration displacement. Then different current is input and then the flux density can be solved through electromagnetic FEM simulation. Based on the flux density, force generated on the vibration armature can be obtained by Maxwell stress tensor method. In this way, the nonlinear parameters can be described by several displacement and current as shown in Fig.1. The inductance is defined as the derivative of flux linkage to current. And speedance is defined as the derivative of flux linkage to displacement. The inductance and speedance can generate the back EMF. And the force factor is defined as the force divided by the current. It can relate the current and force. In mechanical domain, the displacement of receiver can be obtained by using forced vibration FEM simulation with a given input force. But the input force in mechanical simulation is not related with the current in electromagnetic domain, so coupling analysis is needed by solving the voltage equation. Before solving the voltage equation, the current will be set as a initial value and displacement will adopt the value from mechanical simulation. With the assumed current and displacement, the nonlinear parameters can be determined as a specific value in Fig.1. So the current can be calculated by solving the voltage equation. Even though current and displacement are not true values in the very beginning, current and displacement can converge and be accurate after iteration. By this way, current and displacement are both considered in the analysis. Furthermore, according to the 3D modeling, the balanced armature parts has been manufactured and assembled. The displacement of receiver is tested by laser in Klippel system. And the current is detected by current sensor in Klippel system. And the simulation results are verified by experiment result, just shown in Fig.2. 3. Conclusion Balanced armature receiver is a product which contains multiphasic problem. Current and displacement are the performance criterion in electromagnetic and mechanical domain separately. These two performance criterion are affected by each other and needed to be considered together. In the work, a more comprehensive multiphysic coupling analysis method has been presented by considering displacement and current. The analysis result are verified by experiment.

[1] Jensen, Joe, Finn T. Agerkvist, and James M. Harte. “Nonlinear time-domain modeling of balanced-armature receivers.” *Journal of the Audio Engineering Society* 59.3 (2011): 91-101. [2]Lee, Chang-Min, Joong-Hak Kwon, and Sang-Moon Hwang. “Analysis of total harmonic distortion in microspeakers considering coupling effect.” *Journal of mechanical science and technology* 24.9 (2010): 1763-1769.

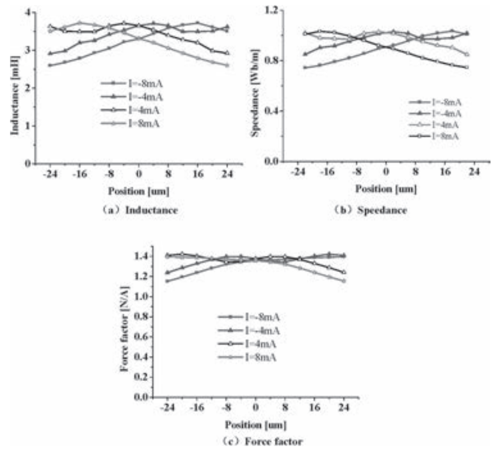

Fig. 1. Nonlinear parameter vs displacement. current

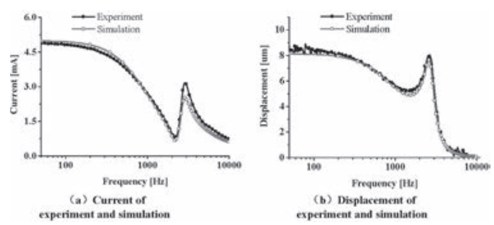

Fig. 2. Comparison of experiment and simulation

GU-02. Performance Analysis of Superconducting Coil Impregnated with Epoxy Resin.

Z. Chen[1], G. Geng[1] and J. Fang[1]
1. Beijing Jiaotong University, School of Electrical Engineering, Beijing, China

I. INTRODUCTION The second generation high temperature superconducting (HTS) coated conductors (CC) have lower AC losses and higher current density than the first generation wires[1], but its weak mechanical properties limit its application in large storage magnets. Because of high field and high current density, Lorentz force effects mechanical stability of superconducting magnet greatly [2]. To improve the stability of the magnet, a coil winding technology has been developed for bonding wires together by impregnating epoxy resin. After the coil is impregnated with epoxy resin the structure size is changed. Therefore the resin insulation layer also affects the inductance and the actual current-carrying capacity of the superconducting coil [3]. The impregnation curing process conditions will produce thermal stress, due to differences in the thermal expansion coefficients of various engineering materials for HTS magnets [4], [5]. In this work, we modified the distance between the turns of the coil and investigated the distance influence on the inductance of the coil, then analyzed thermal stress induced by impregnation curing process on superconducting coil. II. SELECTED AND DESIGN OF MODEL COIL The thermal stress of each unit double-pancake coil is independent of each other in solenoid magnet so the two-dimensional axisymmetric model can be applied [6]. A double-pancake coil model is designed by using four parallel YBCO tapes in this study. The model of magnet structure and coil section is given in Fig.1 (a) and Specification of parallel YBCO tapes and coil is shown in Fig.1 (b). III. CALCULATION AND ANALYSIS OF MODEL COIL A 12 turns of coil with insulation thickness of 0.18mm was studied the effect of the insulation on electromagnetic characteristics. Fig.2 (a) shows the distribution of magnetic field of coil. The inductance of each turn of coil with difference thickness of the resin insulation layer is shown in Fig.2 (b), and g is the thickness of the resin insulation layer increased from 180 μm to 380 μm. As presented in Fig.2 (b), the inductance of each turn in the middle of the coil is larger than the inductance of each turn in both sides of the coil. Fig.2 (c) gives the simulation result, coil inductance decreases with the thickness of the insulation. When the resin insulation layer thickness, g, increases uniformly by 1μm, the inductance of superconducting coil decreases uniformly by about 1.097nH. According to Fig.2 (c), in order to gain larger energy storage capacity, the coil needs to be wound as compactly as possible but because of the higher produced self-field, the critical current in a tight coil is lower than in a loosely wound coil. When the critical current is reduced, allowed transport current decrease and the energy storage amount decrease. In next step we will analysis and evaluate of the magnetic field produced by each turn of coil. This work will help decrease the degradation of the superconducting characteristics such as critical current of the superconducting magnets. The influence of thermal stress on magnet structure was analyzed by Finite Element Method (FEM) software COMSOL. The analysis of thermal stress contains two aspects, First, thermal stress analysis of magnet during impregnation curing heat treatment (293K-413K); Second, thermal stress analysis of magnet during the pre-cooling process (293K-20K). As presented in Fig.2 (d), the superconducting tape maximum deformation is 0.23% and the thermal stress does not damage the superconducting tape under the impregnation curing process. During the pre-cooling process the maximum strain of superconducting tape is 0.0039% and the maximum strain of the epoxy resin is 0.02%. In cooling stage of impregnation curing process (413K-293K) the maximum strain of superconducting tape is 0.0078% and the maximum strain of epoxy resin is 0.01%. Under pre-cooling process epoxy resin exerts some shrinkage pre-stress on the superconducting tape and reduces the strain of the superconducting tape. IV. CONCLUSIONS In this study, the electromagnetic and stress analysis of the superconducting coil impregnated with epoxy resin was carried out by finite element simulation software. The inductance of each turn in the middle of the coil is larger than the inductance of each turn in both sides of the coil and the coil inductance decreases with the thickness of the insulation. Thermal stress does not damage the superconducting tape under the impregnation curing process, and the epoxy resin can provide some pre-stress for the superconducting tape in pre-cooling process. This work can help the design and optimization of solenoid energy storage magnets impregnated with epoxy resin. ACKNOWLEDGEMENT This work is supported by National Science and Technology Major Project of the Ministry of Science and Technology of China (Granted No. 2016YFE0201200).

[1] Ueda H, Kim S B, Noguchi S, et al. “Electromagnetic analysis on magnetic field and current distribution in high temperature superconducting thin tape in coil winding,” Electromagnetic Field Computation. IEEE, pp. 1-1, 2017. [2] Zhu G, Cheng J S, Li L K, et al. “Effect of epoxy insulation on strain distribution in superconducting coil,” IEEE International Conference on Applied Superconductivity and Electromagnetic Devices. IEEE, pp. 425-426, 2016. [3] Kario A, Vojenčiak M, Grilli F, et al. “DC and AC Characterization of Pancake Coils Made From Roebel-Assembled Coated Conductor Cable,” IEEE Trans. Appl. Supercond., vol. 25, no. 1, pp. 1-4, 2014. [4] Evans D, Knaster J, Rajainmaki H. “Vacuum Pressure Impregnation Process in Superconducting Coils: Best Practice,” IEEE Trans. Appl. Supercond., 2012, 22(3):4202805-4202805. [5] Ohira S, Nishijima S. “Wire dynamics simulation of impregnated superconducting magnet,” Applied Superconductivity IEEE Transactions on, vol. 11, no. 1, pp. 1474-1477, 2001. [6] Xu Q, Iio M, Nakamoto T, et al. “Analysis of Strain Distribution in A15-Type Superconducting Coils Under Compressive Stress,” IEEE Trans. Appl. Supercond., vol. 24, no. 3, pp. 1-5, 2013.

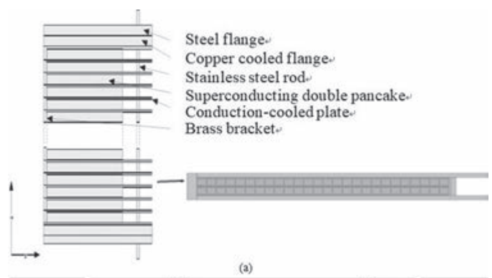

Parallel YBCO tape	Width	4.2mm
	Thickness(without insulation)	0.4mm
	Thickness(with insulation)	0.58mm
	max rated tensile stress	150MP
	Max rated tensile strain	0.3%
Coil	Inner radius	120mm
	Outer radius	210mm
	Number of turns	26
	Turn-to-turn insulator	Epoxy resin

(b)

Fig. 1. (a) Schematic of Magnet structure and coil section, (b) Specifications of coil and parallel YBCO tape.

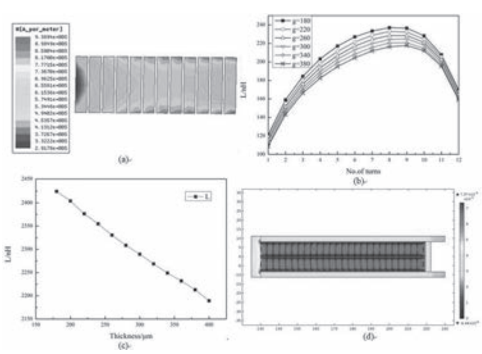

Fig. 2. (a) Distribution of magnetic field in the model coil, (b) Distribution of inductance in model coil with difference thickness of the resin insulation layer, (c) Relationship between insulation thickness and coil inductance, (d) Cross section strain distribution of superconducting double pancake under the impregnation curing process.

GU-03. Magnetic Properties of Simultaneously Excited Amorphous and Silicon Steel Hybrid-Cores for Higher-Efficiency Distribution Transformers.

N. Kurita[1], A. Nishimizu[1], C. Kobayashi[1], Y. Tanaka[1], A. Yamagishi[2], M. Ogi[2], K. Takahashi[2] and M. Kuwabara[3]
1. Research & Development Group, Hitachi, Ltd., Hitachi, Japan; 2. Power Business Unit, Hitachi Ltd., Hitachi, Japan; 3. Hitachi Industrial Equipment Systems Co. Ltd., Tainai, Japan

I. Introduction Amorphous core transformers (AMT) have the major advantage of higher power efficiency due to lower iron loss (W_i) compared with that of grain-oriented silicon steel (GO) cores used in conventional transformers (SiT) [1]. Some studies have attempted to increase the power capacity of AMTs to over 5 MVA [2]. However, the enlarged amorphous core, made from stacked foils 25-mm thick, is vulnerable; it requires structures to support its weight. Additionally, the saturated magnetic flux density (B_S) and the lamination factor of the amorphous core are approximately 18% and 10% lower, respectively, than those of the GO core. This results in the amorphous core having a larger cross-sectional area than that of the GO core with same the specifications. To enable the use of an amorphous core with lower W_i in large capacity distribution transformers, we investigated the practicality of a hybrid-configured annular core consisting of an amorphous core combined with a GO core, which has the advantages of a higher B_S, lamination factor, and mechanical strength than the amorphous core. The distributions of the magnetic flux density and W_i in the hybrid core were measured and calculated with electromagnetic analysis using the three-dimensional finite element method (FEM) while the two individual cores, amorphous and GO, were excited simultaneously. We then designed a prototype 5-MVA single-phase hybrid core transformer (HBT) on the basis of our investigation results. The prototype had improved power efficiency due to its lower W_i and reduced size enabled by the increased amplitude of magnetic flux density, B_m. II. Experimental and analytical methods As the schematic diagram in Fig. 1 (a) shows, we stacked two cores: a 2605HB1M amorphous wound core [3] with a lap-joint part and a frame-shaped 30P105 GO [4] stacked core with step-lapped parts at four corners. The two cores had net masses of 500 and 150 kg, respectively. They were both 2.0 m long, 0.5 m wide, and the core window's dimensions were 1.8 × 0.3 m. The geometric cross-sectional area of the amorphous core and the GO core had a ratio of 8:2. We applied a 60-Hz sinusoidal voltage to the excitation coil wound around the two cores. We measured B_m and W_i averaged in the hybrid core as a whole and in each individual core by measuring the current in the excitation coil and the induced voltages in the search coils wound around the two cores and each individual cores. The calculated results with FEM on a three-dimensional hybrid core model were compared with the experimental results. III. Results Fig. 1 (b) shows the changes in amplitude of the magnetic flux densities in the amorphous core ($B_m^{(A)}$) and in the GO core ($B_m^{(G)}$) as functions of the averaged B_m in the hybrid core as a whole. The measured and calculated results have good agreement. The GO core was hardly excited, and the amorphous core had higher $B_m^{(A)}$ than the GO core in lower averaged B_m due to the difference in the material's permeability and reluctances between the two cores. $B_m^{(A)}$ approaches saturation asymptotically, while $B_m^{(G)}$ increases noticeably as B_m increases. It is possible that the GO core prevented over-saturation in the amorphous core. Averaged B_m in the hybrid core as a whole is 1.58 T when $B_m^{(G)}$ reaches 1.70 T, the upper limit of conventional SiT. These results show that the HBT could operate at B_m approximately 10% higher than the upper design value of B_m in AMT. The cross-sectional area of the HBT core was also smaller than that of AMT. An image of the core structure and a photograph of the exterior of a prototype 5-MVA single-phase three-leg type HBT is shown in Fig. 2. The core of the HBT consists of four sets of the hybrid core shown in Fig. 1 (a). The prototype HBT has a net mass of seven tons, including a winding and support parts. We developed and applied a structure and assembly process that protects the vulnerable amorphous cores from the stress of their own weight and of fixing force. Standard performance tests were performed by immersing the prototype in an insulation oil tank. The cross-sectional area of the HBT's core was 8% smaller than that of an AMT designed with same the specifications, and W_i was reduced to less than half that of a conventional SiT. IV. Summary To use amorphous cores in larger-capacity distribution transformers, we measured and calculated the distributions of the magnetic flux density and iron loss in a hybrid-configured core consisting of an amorphous core combined with a GO core with higher B_S and mechanical strength. The GO core prevented over-saturation of the amorphous core. The hybrid configuration enabled approximately 10% higher amplitude of magnetic flux density than configurations with an only amorphous core. Operation tests on a prototype 5-MVA single-phase HBT demonstrated its higher efficiency and reduced size. Acknowledgements This work was supported by the Ministry of the Environment of the Japanese Government.

[1] M. Carlen, D. Xu, J. Clausen, T. Nunn, R. Ramanan, and D. M Getson, "Ultra High Efficiency Distribution Transformers", Proc. of *IEEE PES Transmission and Distribution Conf. and Exposition*, pp.1–6, 2010. [2] Y-H. Chang, C-H. Hsu, and C-P. Tseng, "Systematic Design and Implementation of Large-Capacity Power Transformer", Proc. of *the 9th World Scientific and Engineering Academy and Soc. (WSEAS)*, pp.78–83, 2009. [3] K. Takahashi, D. Azuma, and R. Hasegawa, "Acoustic and Soft Magnetic Properties in Amorphous Alloy-Based Distribution Transformer Cores", *IEEE. Trans. on Magnetics*, Vol. 49, No. 5, pp. 4001–4004, 2013. [4] Nippon Steel & Sumitomo Metal Corp., "Electrical Steel Sheets", Catalogue ID: D003jec_06_201707f, 2017.[

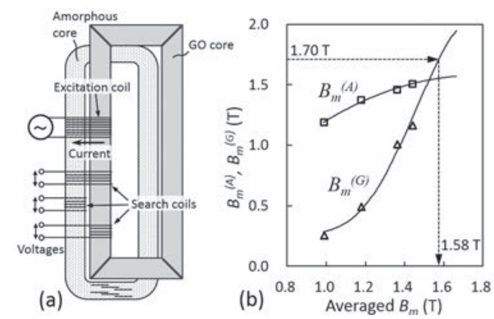

Fig. 1. (a) Schematic of hybrid core consisting of amorphous and GO cores for excitation test. (b) Averaged B_m performance of amplitude of magnetic flux density in each individual core. Symbols and solid curves represent measured and calculated results, respectively.

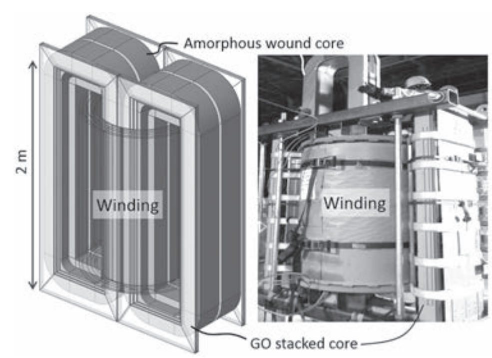

Fig. 2. Image of core structure (left) and photograph of exterior of prototype 5-MVA single-phase HBT (right).

GU-04. Inductance analysis for the multi-unit permanent magnet synchronous machine in different operating situations.

D. Zeng[1], J. Zou[1], Y. Xu[1] and F. Liu[1]
1. Harbin Institute of Technology, Harbin, China

1.intorduction The inductance is a key parameter for the electrical machines since it has a significant impact on the performance. The inductance components of the multi-unit permanent magnet synchronous machine (PMSM) depend on the winding configuration and the machine structure. Thus, many inductance calculating methods and analysis between different calculating methods have been researched. These methods mainly include the analytical calculating method and finite element method (FEM). To analyze the inductance of the different machines, some analytical calculating methods and models have been proposed. Based on the basic winding function method, the inductance of interior permanent magnet machines has been analytical calculated in [1], the inductance of brushless slot-less machines with surface inset magnets has been analytical calculated in [2]. Based on the Maxwell's equations, the inductance of the surface inset permanent magnet machines with high saliency ratio has been analytical calculated in [3], the inductance of the permanent magnet linear synchronous machines has been analytical calculated in [4], the inductance of the fractional-slot concentrated-winding machines has been analytical calculated in [5]. These calculation results are all compared with the results calculated by FEM. These inductance analytical methods are all focus on the three-phase electric machine. The inductance of the multi-unit PMSM has been introduced in [6]. However, the analysis for the inductance of the multi-unit PMSM in different operating situations has not been done. In different operating situations, the coupling of the different phase effect on the inductance has not been analyzed. The calculation and analysis for the inductance of the multi-unit permanent magnet synchronous machine in different operating situations are presented in this paper. 2. Inductance calculation model This model is established under the assumptions and restrictions listed as follows: 1) Stator and rotor cores are infinitely permeable and end effects are neglected. 2) Each phase is composed of identical coil groups (or phase belts) and has the same winding turns. 3) Each phase distributes symmetrically around the stator circle. 4) The effect of the end windings on the inductance is neglected. Based on the winding function method and the reluctance circuit, the analytical calculating model for the inductance of the five units PMSM with 40 poles and 45 slots for instance is shown in Fig.1. The winding configuration is used as the first step. The air gap and magnets can be modeled as the lumped reluctance component, the leakage reluctance component, and the reluctance component of the stator teeth are all illustrated in Fig. 1. These reluctance components are obtained by the specific size and the material characteristic of the PMSM. The operating situations of multi-unit PMSM mainly include the full-unit operating situation, the part-unit operating situation, and the operating situation that some unit-motors operate as motors and some unit-motors operate as generators. The full-unit operating situation is the normal state, the part-unit operating situation is the fault-tolerant state, and the operating situation that some unit-motors operate as motors and some unit-motors operate as generators is the no-mechanical-load-test state. The different operating situation can be considered with the coupling factor of the magnetic circuit. Its value is different in different operating situations. The relation between the magnetic flux of the phases and the magnetic flux of the circuits is presented in equation (1). And the self inductance of this multi-unit PMSM can be calculated by equation (2). The mutual inductance of this multi-unit PMSM can be calculated by equation (3). 3. Result and discussion To analyze the inductances of the multi-unit PMSM in different operating situations, two multi-units PMSM prototypes with concentrated windings are designed. Both the two machines are equipped with surface mounted NdFeB permanent magnet on their rotors. The two multi-unit PMSMs are designed with the different number of units to validate the inductance matrix in both odd and even units PMSMs. Both the two machines have the same dimensions and rotor structure. They differ only in their slot pole combinations. The linkage flux with the permanent magnet of each phase in all the three machines should be same to guarantee the inductances of the three machines are calculated at the same saturation. And to obtain the same value of the linkage flux with the permanent magnet of each phase in the two machines, the numbers of coil turns N of the two machines are calculated. The inductances of the two machines in different operating situations are calculated. The characteristics of the inductance in different operating situations are discussed. 4. Conclusion In this paper, the inductance of the multi-unit PMSM in different operating situations are calculated, the inductance matrix of the multi-unit PMSM is different in the different operating situations.

[1] Chen, Hong, et al. "An Improved Analytical Model for Inductance Calculation of Interior Permanent Magnet Machines." *IEEE Transactions on Magnetics* 50.6(2014):1-8. [2] Rahideh, Akbar, M. Mardaneh, and T. Korakianitis. "Analytical 2-D Calculations of Torque, Inductance, and Back-EMF for Brushless Slotless Machines With Surface Inset Magnets." *IEEE Transactions on Magnetics* 49.8(2013):4873-4884. [3] Zhang, Zhen, et al. "Analytical Field Calculation and Analysis of Surface Inset Permanent Magnet Machines With High Saliency Ratio." *IEEE Transactions on Magnetics* 52.12(2016):1-12. [4] Shin, Kyung Hun, et al. "Armature reaction field and inductance calculations for a permanent magnet linear synchronous machine based on subdomain model." *Electromagnetic Field Computation* IEEE, 2017:1-1. [5] Prieto, Borja, et al. "Analytical Calculation of the Slot Leakage Inductance in Fractional-Slot Concentrated-Winding Machines." *IEEE Transactions on Industrial Electronics* 62.5(2015):2742-2752. [6] Zhao, Bo, et al. "Asymmetry of inductance and torque ripple of multi-unit permanent magnet synchronous motor." *International Conference on Electrical Machines and Systems* 2011:1-4.

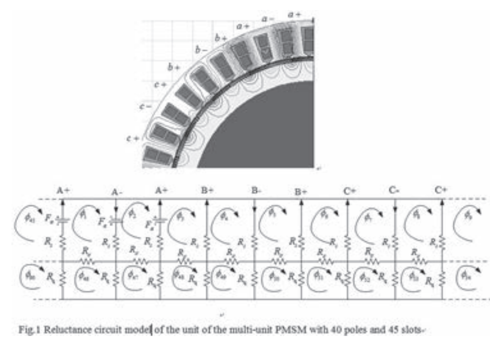

Fig. 1.

$$\begin{bmatrix} \phi_a \\ \phi_b \\ \phi_c \\ \vdots \\ \phi_m \end{bmatrix} = \begin{bmatrix} \phi_1 - \phi_{45} + \phi_1 - \phi_2 + \phi_3 - \phi_2 \\ \phi_4 - \phi_3 + \phi_4 - \phi_5 + \phi_6 - \phi_5 \\ \phi_7 - \phi_6 + \phi_7 - \phi_8 + \phi_9 - \phi_8 \\ \vdots \\ \phi_n - \phi_{n-1} + \phi_n - \phi_{n+1} + \phi_{n+2} - \phi_{n+1} \end{bmatrix} \quad (1)$$

$$L_a = \frac{N \cdot \phi_a}{i_a} = \frac{N^2 \cdot \phi_a}{F_a} \quad (2)$$

$$M_{am} = \frac{N \cdot \phi_m}{i_a} = \frac{N^2 \cdot \phi_m}{F_a} \quad (3)$$

Fig. 2.

GU-05. Characteristics Analysis of Electric Motor using Ring Core Test and its Experimental Verification.

D. Kim[1], J. Chin[1], M. Lim[1] and J. Hong[1]
1. Department of Automotive, Hanyang University, Seoul, The Republic of Korea

The initial magnetization curve (B-H curve) and iron loss of electrical steel sheet are essential data for predicting the electric motor performance. Typically, the Epstein frame test is adopted widely, to acquire these magnetic properties. However, for the rotating electrical machines with small geometry, the ring core test can be preferred. In this paper, B-H curve and iron losses are measured by Epstein frame test and ring core test. Each result applied in finite element analysis (FEA) of the fabricated electric motor. Furthermore, using these FEA results and *d-q* equivalent circuit, prediction of the electric motor performance is done. As the future work, the electric motor test will be done, and the result will be compared with predicted results. I.Introduction Generally, magnetic properties of electrical steel sheets are acquired by Epstein frame test according to IEC 60404-2 international standard[1]. Also, supplied data of electrical steel sheets from the manufacturer is usually obtained from the Epstein frame test. However, the ring core test can be preferred for predicting the rotating electrical machine with the small geometry for several reasons below[2]. -Closed magnetic circuit without any airgaps -No need of any special measurement set -Simple to prepare test samples -Geometry is similar to stator yoke of electric motor In this study, a non-oriented electrical steel sheets (50PN470) are prepared. For the ring core test, stacked ring sheet is prepared for the specimen. To exclude the effects of processing, the wire cut is adopted for cutting. Furthermore, the outer diameter of the ring core specimen does not exceed 1.4 times the inner diameter, ensuring the reliability of the test result[3]. Using the sample, initial magnetization curves and iron losses were measured. From these magnetic properties and supplied Epstein frame test result, prediction of the electric motor performance is done through the FEA. To verify the prediction results, an electric motor is introduced. As the future work, the no-load test and the load test will be conducted for the adopted electric motor. The error between the test results and simulation results will be investigated. II.Magnetic Properties of Electrical Steel Sheets A.Experiment on Electrical Steel Sheets The primary winding of the ring core specimen and Epstein frame is connected to the AC voltage source controlling magnitude and frequency. Also, it is connected to B-H analyzer for measuring the magnetic field intensity. The secondary winding of each test frame is connected to the B-H analyzer to measuring the magnetic flux density using the induced voltage. NF high-speed power amplifier was used for the AC voltage source, and IWATSU SY8258 B-H analyzer was used for measuring B-H curves and iron losses. B.Initial Magnetization Curve The tests were conducted in the range of magnetic flux between 0.1T to 1.6T and accordingly, field intensity range between 35.61A/m to 4956A/m. Initial magnetization curves obtained from Epstein frame test and the ring core test is depicted in Fig. 1. C.Iron Loss Measurement of the iron loss was conducted with the same method of the initial magnetization curve, but measuring frequency was changed. The tests were performed in the range of magnetic flux density from 0.1T to 1.8T, and range of frequency from 50Hz to 1000Hz. To predict the electric motor performance, iron loss surface of interpolated and extrapolated from each test is shown in Fig. 2 using Steinmetz's equation and least square method[4]. III.Prediction of Electric Motor Performance A.Iron Loss Analysis Using the previously acquired iron loss data from two tests, iron loss maps according to frequency, and magnetic flux density was constructed. From these maps, iron losses are analyzed under the various load conditions. FEA was used to calculate the magnetic flux density for each meshed element of proposed models as the rotor was rotated. Next, using the Fourier series, the magnitude of the fundamental and harmonic component was analyzed. From the iron loss map, iron losses according to frequency and magnetic flux density were calculated for harmonic components of each element. Finally, iron losses of all the element were added to assess the iron loss of the machine[5]. B.Performance Prediction The performance of the electric motors was predicted by the *d-q* axis equivalent circuit of the permanent magnet synchronous motors (PMSMs) considering the iron loss from the section *A* in chapter III. Using the FEA, *d*-axis and *q*-axis inductance were calculated for the range of the phase current and current phase angle including harmonic components. While the inductance calculation process, for the same range, linkage flux of the armature winding is calculated. After finishing the parameter calculation process, solve the *d-q* axis equivalent circuit of PMSM for the speed and torque range, considering DC link voltage and current limitation. Finally, the electric motor performance maps are created for Epstein frame and the ring core test data[6]. IV.Future Work As the future work, loss separation will be done for the fabricated electric motor. Using the electric motor with the non-magnetized permanent magnet, the mechanical loss will be measured. Furthermore, to validate the prediction of electric motor performance, load test will be conducted. After that, the comparison of prediction result from Epstein frame test and ring core test will be done.

[1] IEC 60404-2:2008, "Magnetic materials - Part 2: Methods of measurement of the magnetic properties of electrical steel sheet and strip by means of an Epstein frame", International Electrotechnical Commission [2] Andreas Krings, *Iron Losses in Electrical Machines - Influence of Material Properties, Manufacturing Processes, and Inverter Operation,* Ph.D. dissertation, KTH Royal Inst. Tech., Stockholm, Sweden, 2014. [3] F. Fiorillo, *Measurement and Characterization of Magnetic Materials*, Elsevier Academic Press, 2005. [4] M. S. Lim, J. H. Kim, and J. P. Hong, "Experimental Characterization of the Slink-Laminated Core and Iron Loss Analysis of Electrical Machine," *IEEE Trans. Magn*., vol. 51, no. 11, Nov 2015. [5] Hyuk Nam, Kyung-Ho Ha, Jeong-Jong Lee, Jung-Pyo Hong, Gyu-Hong Kang, "A Study on Iron Loss Analysis Method Considering the Harmonics of the Flux Density Waveform Using Iron Loss Curves Tested on Epstein Samples", *IEEE Trans. Magn*., vol. 39, no.3, May 2003, pp. 1472-1475 [6] B. H. Lee, S. O. Kwon, T. Sun, J. P. Hong, G. H. Lee, and J. Hur, "Modeling of Core Loss Resistance for d-q Equivalent Circuit Analysis of IPMSM considering Harmonic Linkage Flux," *IEEE Trans. Magn*., vol. 47, no. 5, May 2011.

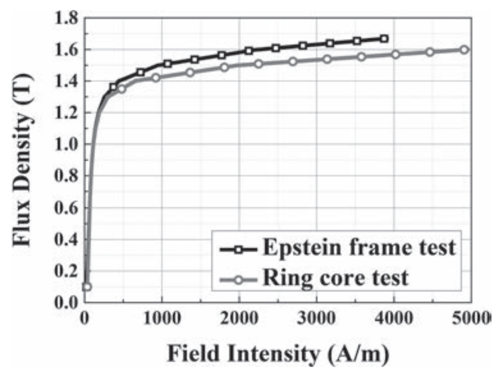

Fig. 1. Measured B-H curves from Epstein frame and ring core test

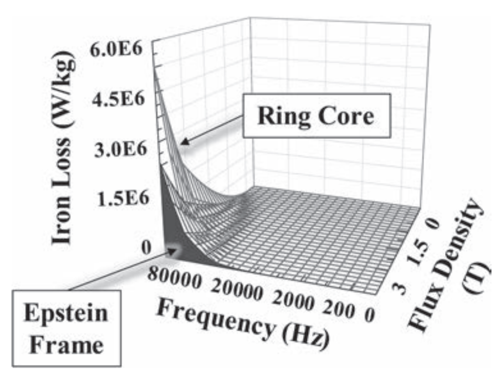

Fig. 2. Interpolated and extrapolated iron loss surfaces for each test

GU-06. Improving the transmission efficiency of wireless power transfer systems in electric vehicles by using magnetoplated aluminum pipes.

Y. Bu[1], S. Endo[1] and T. Mizuno[1]
1. Shinshu University, Nagano, Japan

1. Introduction Wireless power transfer (WPT) technology is becoming increasingly popular because it enables the transmission of electrical energy without the use of connecting wires, which makes the transmission process convenient and safe. Currently, researchers are in the process of developing transmission powers greater than 3 kW for charging electric vehicles (EVs). Some car manufacturers have even started making prototypes using the WPT system. The charging operation tends to be much better in the WPT system because there are no direct electrical connections. The car needs only to be parked at the charging station; subsequently, the WPT system automatically carries out the electrical connection. In the WPT system for EVs, the devices typically use the electromagnetic induction produced between a pair of coils; one coil is for transmitting power, and the other coil is for receiving power. To improve the electromagnetic induction efficiency at high frequencies in the range of 81–90 kHz, a Litz wire of 1000 or more strands is used to reduce the AC loss. The use of a Litz wire reduces the AC impedance resulting from the proximity effect and increases the *Q* value. Therefore, Litz wires are used in almost all high-power WPT coils [1]. Litz wires can improve performance because they have a greater number of strands than solid wires; they also have low diameters. These attributes, however, also increase the cost of the Litz wire coils. Using a solid wire coil instead of a Litz wire will reduce costs, but the associated high-frequency losses will reduce the efficiency of the coil. Therefore, in this paper, we propose a magnetoplated aluminum pipe (MAP) with a special magnetic layer to improve the transmission efficiency. As compared with the solid wire, the MAP is very light and cheap. Therefore, it is possible to replace the Litz wire with a MAP. 2. Structure of MAP coil Fig.1 shows the MAP coil structure used as the transmitting and receiving coil in our evaluation experiments. Fig.1 (a) is the plan view of the coil. It is a spiral coil with eight tight winds, and the outer diameter of the coil is 380 mm. A Ferrite core is attached to a coil plane that has one side of length 410 mm; and the coil plane has a thickness of 4 mm. Fig.1 (b) is a cross section of the MAP coil structure showing the transmitting coil and the receiving coil, which are placed facing each other in the WPT system. Fig. 2 shows the MAP structure that we used in this experiment. To reduce the exchange loss caused by the proximity effect, we made a 0.4 mm magnetic layer on the concentrated part of the magnetic flux on the surface of the aluminum pipe (AP). We used this magnetic layer with low loss amorphous iron powder. From Fig. 2, it can be seen that because of the different distribution of the magnetic flux lines, the coating positions are not the same at the center and the periphery of the coil. We use FEM analysis to obtain the magnetic flux of the coil. 3. Experimental result We made coated (i.e., MAP) coils and uncoated (i.e., AP) coils and measured their AC resistance and transmission efficiency using an Impedance Analyzer. At the drive frequency of 85 kHz, the AC resistance, inductance, and quality factor *Q* of the AP coil were 126mΩ,32.3uH, and 149, respectively. For the same frequency, the impedance, inductance, and quality factor *Q* of the MAP coil were 115 mΩ,33.2uH, and 157, respectively. The MAP coils had up to 5.4% better *Q* values and AC resistance reduced by 8.7% as compared with the AP coils. We measured the transmission efficiency when the transmitting coil and the receiving coil were separated by 150 mm. The transmission efficiency was 92.6% for the AP coils and 93.4% for the MAP coils. The proposed MAP coil could increase efficiency by 0.8%. Although the effect is not great, however the MAP coil has strong practicability because the coil heating can be suppressed. In the future, we will improve the trial process to improve the effectiveness of this method.

[1] Y. Bu, W. Wang, T. Kasai, T. Mizuno: " Improvements in the Transmission Efficiency in an Electric Vehicles Wireless Power Transfer System Using Litz Magnetoplated Wire" Vehicle Power and Propulsion Conference (VPPC), IEEE,2016.

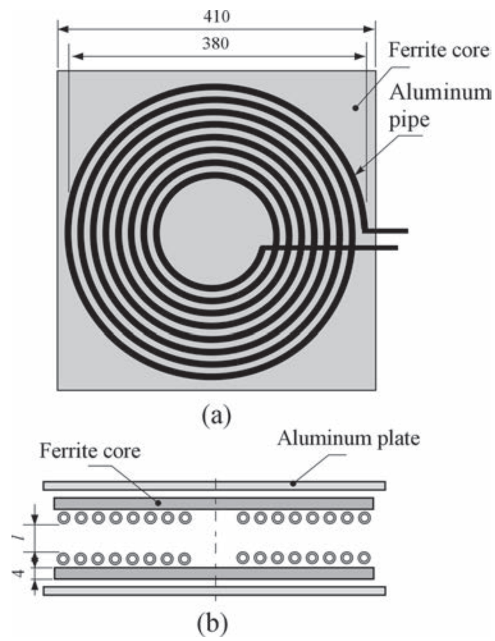

Fig. 1. Structure of coil (a) plan view of the coil, (b) cross sectional view (unit:mm).

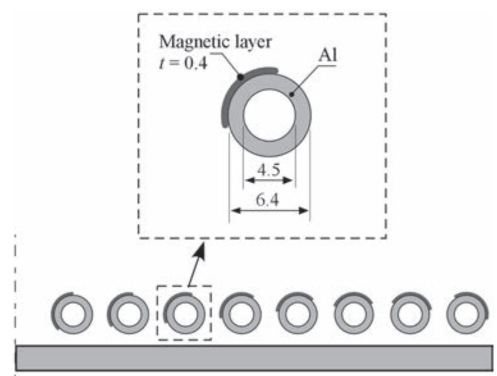

Fig. 2. Structure of magnetoplated aluminum pipe (unit:mm).

GU-07. Accurate Calculation of Eddy Current Loss in Litz-Wired High Frequency Transformer Windings.

Z. Liu[1], L. Zhu[1] and J. Zhu[2]

1. Tianjin Polytechnic University, Tianjin, China; 2. University of Technology Sydney, Sydney, NSW, Australia

I.Introduction The winding power loss of a high frequency transformer is strongly influenced by the high frequency eddy current skin and proximity effects. The litz-wire can reduce effectively the eddy current effects. The precise loss calculation method of litz-wire remains however a difficulty. At present, the Dowell model [1] and Ferreira model [2-3] are two commonly used methods to calculate the winding loss. The Dowell model is originally derived to calculate the eddy current effects in foil conductors and later on extended to packed windings composed of litz-wire by introducing a porosity factor [4]. The accuracy however declines quickly when porosity factor reduces, and the characteristics of eddy current distribution is not adapted to the litz-wire. On the other hand, the magnetic field of round conductors analyzed by Ferreira model is excellent, but the error become significate at high frequency at high porosity factor [5] because it neglects the interaction between conductors in the same layer [6]. In this paper, an improved model is proposed for calculating the eddy current distribution in litz-wire windings due to the skin and proximity effects. This model can have much more accurate prediction of eddy current distributions in the cross-section of a round litz-wire conductor, and can be used for electromagnetic design of high frequency devices. II.Calculation analysis A.The skin effect The traditional Ferreira model is based on the Bessel function to analyze the eddy current skin effects in a round conductor. Considering the skin effects, the eddy current per unit length can be calculated by (1) As shown, the eddy current density can be reduced effectively as the diameter of a strand of litz-wire becomes far less than the skin depth. B.The proximity effect The proximity effect is on both strand and bundle levels. The current distribution in a conductor strand can be influenced by the internal magnetic field, H_{int}, and the external magnetic field, H_{ext}, generated by the currents flowing in other strands of the same bundle and currents flowing in wires of other bundles. In a litz-wire, the internal magnetic field due to the currents flowing in other strands of the same bundle can be obtained by the Ampere's law as $H_{int}=Ir/2\pi r_c^2$, where I and r_c are the current and the radius of a bundle of litz-wire, respectively. The external magnetic field produced by currents flowing in strands of different bundles can be obtained by the per unit layer current, I_{pl}, and numbers of conductor layers, m, as $H_{ext}=(m-1)I_{pl}$. The resultant proximity effect can then be calculated by the total magnetic field. The proximity effect due to litz-wires in different layers presented in (2) can identify the eddy current distribution caused by other conductors. The winding in the same layer can also influence a lot, which is not considered in Ferreira model. The eddy current distribution caused by the windings in the same layer can be obtained from the (3), which highly depend on the porosity factor. C.The eddy current loss of a twisted litz-wire Considering the twisting effect, the total loss can be calculated by integrating the local magnetic field along the bundle length. The magnetic field can be assumed to be rotating along an untwisted bundle. Assume p_i is the pitch length when the strand back to the original position. Obtained from (4), if the pitch p_i is far smaller than the wire length with a perfect twist, the litz-wire can almost eliminate the proximity effect due to the rotating magnetic field. However, the litz-wire in practical use can hardly be perfectly twisted, and therefore the winding power loss can be calculated by $P=(\sum\int J_i \times J_i)/2\sigma$, where σ is the conductivity of the conductor, and J_i the current distribution. III.Experience Verification A KMC-40 gapped core was used in the experiment. The core material was amorphous alloy. The cross-sectional area of the winding is 4.05 cm^2. The outer diameter of the litz-wire is 1.35 mm. It is made by twisting 100 wires of diameter 0.10 mm. Fig.1 compares the litz-wire AC resistance obtained by the Dowell, Ferreira, and proposed models with the experimental results. As shown, the modified Dowell model present in [4] has good precision in the case of high porosity factor, and the Ferreira model has good precision at low porosity factor. The proposed method takes into account the proximity effect caused by the same layer, and therefore can yield much more accurate predictions than the other two models. IV.Conclusions From the analysis above, we can observe that twisting the strands can effectively reduce the proximity effect due to the external magnetic field. A perfectly twisted litz-wire can almost completely eliminate the proximity effect. The litz-wire in practical use, however, can hardly be perfectly twisted. The proximity effect loss caused by the litz-wires in the same layer is affected by the porosity factor. In this paper, an improved model is proposed to take into account the proximity effect caused by the litz-wires in the same layer in addition to those acounted for by other models in the eddy current loss calculation. The theoretical results of new model are compared with those obtained by the two best-known methods, and validated by the experimental measurement. It can be seen that for both small and large porosity factors, the new model yields more accurate calculation results.

[1] P. J. Dowell, "Effects of eddy currents in transformer winding," Proc. IEE, vol. 113, no. 8, pp. 1387-1394, August 1966. [2] J. A. Ferreira, "Analytical computation of AC resistance of round and rectangular litz wire windings," IEE Proceedings-B, vol. 139, no. 1, pp 21-25, January 1992. [3] J. A. Ferreira, "Improved analytical modeling of conductive losses in magnetic components," IEEE Trans. Power Electronics, vol. 9, no. 1, pp.127-131, Jan 1994. [4] R. P. Wojda and M. K. Kaizimierczuk, "Winding resistance of litz-wire and multi-strand inductors," IET Power Electron., vol. 5, no. 2, pp. 257– 268, Feb. 2012. [5] M. Bartoli, N. Noferi, A. Reatti, and M. K. Kazimierczuk, "Modeling litz-wire winding losses in high-frequencies power inductors," Proceedings of the IEEE Power Electronics Specialists Conference, Baveno, Italy, June 24-27, 1996. pp. 1960-1696. [6] X. Nan and C. R. Sullivan, "An equivalent complex permeability model for litz-wire windings," IEEE Trans. Ind. Appl., vol. 45, no. 2, pp. 854– 860, Mar./Apr. 2009.

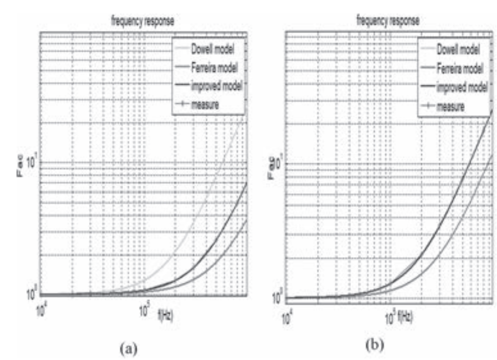

Fig. 1. Comparison of litz-wire AC resistance obtained by different models and experimental measurement, where(a)High porosity factor, and(b)Low porosity factor

$$J_z = \frac{\gamma j^{\frac{3}{2}} I}{2\pi r_0} \frac{J_0 j^{\frac{3}{2}} \gamma r}{J_1 j^{\frac{3}{2}} \gamma r_0} \tag{1}$$

$$J_{p1} = 2H_{total} \frac{J_1 j^{\frac{3}{2}} \gamma r}{J_0 j^{\frac{3}{2}} \frac{\gamma d_0}{2}} \sin\theta \tag{2}$$

$$J_{p2} = \frac{d}{d+v} H_{proximity-intra} \frac{J_2 j^{\frac{3}{2}} \gamma r}{J_1 j^{\frac{3}{2}} \frac{\gamma d_0}{2}} \cos 2\theta \tag{3}$$

$$P_{p,ext} = \frac{\pi d_s^4 (2\pi f)^2 \cdot \mu_0^2}{128\rho \cdot l_i} [(\int_0^{l_i} \cos(2\pi z/p_i) \cdot H_x(z) + \sin(2\pi z/p_i) \cdot H_y(z))^2 + (\int_0^{l_i} \cos(2\pi z/p_i) \cdot H_y(z) + \sin(2\pi z/p_i) \cdot H_x(z))^2] \tag{4}$$

Where $\gamma = \sqrt{(2/\delta)}$, δ is the skin depth, I *and* r_0 are the conductor's current and radius, J_0, J_1, J_2 are the Bessel functions.

Equation

GU-08. Applying Response Surface Method to Oil-immersed Transformer Cooling System for Design Optimization.

Y. Zhang[1], S. Ho[1] and W. Fu[1]
1. Department of Electrical Engineering, The Hong Kong Polytechnic University, Hong Kong, Hong Kong

In this paper, response surface methods (RSMs) are applied in the design optimization of oil-immersed transformers. A 3-D computational fluid dynamics (CFD) model is constructed firstly with all the design variables parameterized. Solutions derived by numerical method are fed into RSM, which generates a surrogate model for the original problem. A preliminary study of predicting maximum temperature rise for oil-immersed transformer shows promising results. The optimization solution based on the approximation model will be compared with that of direct optimization method. I. Introduction Analytical methods with empirical coefficients are widely used in oil-immersed transformer cooling system design [1]. The entire transformer is divided into several sections according to the heat path or oil flow path. These sections are solved separately with corresponding formulations and parameters. Generally, the application of these analytical equations and empirical coefficients is limited to certain categories of transformers. Computational fluid dynamic (CFD) method, as a supplementary tool or the major approach, has been introduced into the transformer design and analysis process [2 - 5]. The application of CFD ranges from conducting the cooling system design optimization of certain section [2 - 4] to optimizing the entire cooling system of a transformer [5]. CFD is capable of modeling complex geometry and nonlinear material characteristic, the computational effort, however, is tremendous, which limits its extensive application in inverse problems. Response surface method (RSM), as an efficient approximation tool, has been adopted in many engineering problems, such as electromagnetic device design [6], prediction of material properties [7] and thermal analysis of multichip module [8, 9]. In this paper, several types of RSMs are introduced into the oil-immersed transformer cooling system design with their performance compared. To generate a set of input and output data for the RSM, 3-D CFD modeling of the oil-immersed transformer is established firstly. The overall performance of response surface optimization method on accuracy and efficiency is evaluated through comparison with solutions of direct optimization method. II. Analysis Model and Methodology A. CFD modeling The CFD model of a three-phase oil-forced transformer is built based on some simplifications and hypotheses. Influences of insulation and structural parts are neglected, and the analysis focuses on the dimension optimization of oil channels, which is shown in Fig 1. As the flow and temperature distribution are not consistent for three phases, parameters for one phase are independent from others. Moreover, separated coils are considered in the analysis to handle high temperature rise. There are three objectives for this optimization problem: minimizing the volume of oil, pressure drop and maximum temperature rise. B. RSM Central composite design is employed to choose a universal set of design points for the RSM. These design points are solved by numerical method consecutively, solutions of which are used as the training data combined with the values of design variables. Several categories of RSMs based on different algorithm, such as Kriging, second order polynomial function, genetic aggregation and non-parametric regression, are introduced to estimate the problem and to generate an approximation model to replace the original CFD model. Generally, the response surface derived with the initial design points is not accurate enough, and adding more proper refinement points could further improve the performance of the response surface. Several parameters, such as coefficient of determination, root mean square error and relative average absolute error, are computed to determine the performance of the approximation model. After deriving the approximation model, the final optimization is easily implemented and repeated for different objectives. Optimized solutions derived by response surface optimization will be compared with the direct optimization method. III. Numerical Results A preliminary study on the maximum temperature rise estimation of a three-phase oil-immersed transformer was conducted with four types of RSMs. As the 72 design points (including 57 refinement points) and 10 verification points used in these four methods are the same, their performance could be evaluated through comparing the goodness of fit, which is shown in Fig. 2. It can be found that genetic aggregation and Kriging method achieve better performance on fitting the design points and predicting the verification points than other approaches. The maximum predicted error of genetic aggregation is 2.2 degree centigrade for these ten verification points. IV. Conclusion The application of several categories of RSMs in oil-immersed transformer design optimization is presented in this paper. A simple numerical example of oil-immersed transformer temperature rise prediction is tested, which shows promising results. The optimization solutions of response surface optimization and direct optimization will be compared in the full paper.

[1] Shenyang Transformer LLC. *Design handbook of oil-immersed power transformer*. Shenyang: Shenyang Transformer LLC, 1999, pp. 162-203 [2] N. El Wakil, N. C. Chereches, and J. Padet, "Numerical study of heat transfer and fluid flow in a power transformer," *Int. J. Therm. Sci.*, vol. 45, no. 6, pp. 615-626, Jun 2006. [3] J. Smolka and A. J. Nowak, "Shape Optimization of Coils and Cooling Ducts in Dry-Type Transformers Using Computational Fluid Dynamics and Genetic Algorithm," *IEEE Trans. Magn.*, vol. 47, no. 6, pp. 1726-1731, Jun 2011. [4] L. N. Li, S. X. Niu, S. L. Ho, W. N. Fu, and Y. Li, "A Novel Approach to Investigate the Hot-Spot Temperature Rise in Power Transformers," *IEEE Trans. Magn.*, vol. 51, no. 3, Mar 2015. [5] J. Smolka, "CFD-based 3-D optimization of the mutual coil configuration for the effective cooling of an electrical transformer," *Appl. Therm. Eng.*, vol. 50, no. 1, pp. 124-133, Jan 2013. [6] X. Y. Liu and W. N. Fu, "A Dynamic Dual-Response-Surface Methodology for Optimal Design of a Permanent-Magnet Motor Using Finite-Element Method," *IEEE Trans. Magn.*, vol. 52, no. 3, Mar 2016. [7] M. Hemmat Esfe, M. H. Hajmohammad, P. Razi, M. R. H. Ahangar, and A. A. A. Arani, "The optimization of viscosity and thermal conductivity in hybrid nanofluids prepared with magnetic nanocomposite of nanodiamond cobalt-oxide (ND-Co3O4) using NSGA-II and RSM," *Int. Commun. Heat Mass*, vol. 79, pp. 128-134, Dec 2016. [8] H. C. Cheng, W. H. Chen, and I. C. Chung, "Integration of simulation and response surface methods for thermal design of multichip modules," *IEEE Trans. Compon. Packag. Technol.*, vol. 27, no. 2, pp. 359-372, Jun 2004. [9] Y. J. Cheng, G. W. Xu, D. P. Zhu, W. J. Zhu, and L. Luo, "Thermal analysis for indirect liquid cooled multichip module using computational fluid dynamic simulation and response surface methodology," *IEEE Trans. Compon. Packag. Technol.*, vol. 29, no. 1, pp. 39-46, Mar 2006.

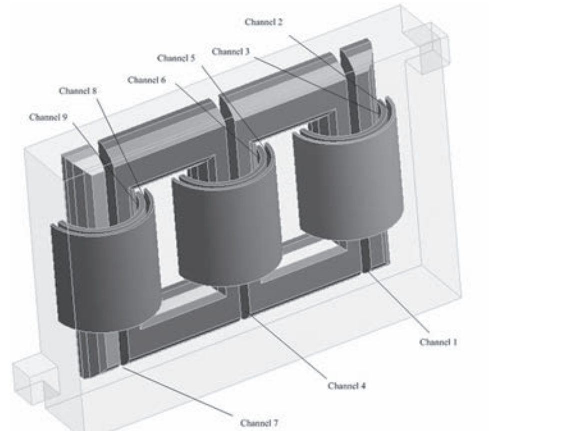

Fig. 1. CFD model of the oil-immersed transformer.

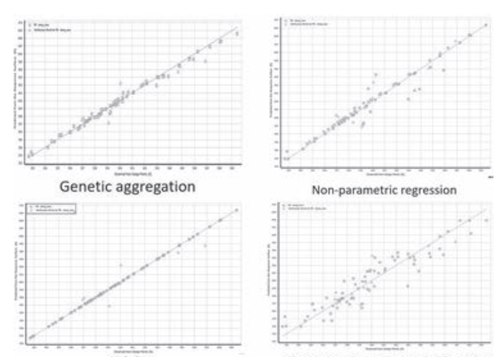

Fig. 2. Goodness of fit of four types of RSMs.

GU-09. Improvement of output stability in magnetic resonance wireless power supply using Helmholtz type transmission coil.

D. Sayama[1], S. Suzuki[1], Y. Akimoto[1], Y. Iijima[1], T. Kato[1], M. Ishihara[1] and Y. Kobayashi[1]
1. National Institute of Technology, Oyama College, Oyama, Japan

1. Introduction Wireless power transmission can be applied to a wide range of fields requiring electric power from smartphones to electric cars and is expected as a next generation innovative technology. Currently, the mainstream of practical applications is the electromagnetic induction method, and it is used as a power feeding to multifunctional small electronic devices typified by mobile terminals. However, this method is limited to charging in a very close state, and has a disadvantage that it is vulnerable to displacement between transmission and reception coils. In order to solve those problems, magnetic field resonance method was announced from MIT in 2006 [1)]. In this system, high efficiency transmission over long distances is enabled, and since the influence of positional displacement is relative small, it is possible to construct a charging system with high usability. Our laboratory aims at establishment of a local high usability power supply area finally. Specifically, it is the construction of the "unnoticed charging area" in which the transmitting coil is embedded in the floor or wall, and the user's device is unconsciously charged by the receiving coil mounted on the device automatically. However, in order to maintain high efficiency in the resonance method, it is necessary to change the optimum driving frequency with respect to the transmission / reception distance. For that change, accurate grasp of the distance and frequency changing function are required for power supply equipment, so the system becomes complicated. For the above reasons, we tried to realize a stable power supply by using a Helmholtz type coil which can obtain a uniform magnetic field between the coils on the transmitting side. As a result, although it was inferior to the conventional type in terms of maximum efficiency, we succeeded in maintaining constant efficiency between the coils. 2. Transmission system using Helmholtz coil Receiving side coils are subject to various restrictions such as size and thickness depending on the target application. We focused on the transmission side, which has a relatively high flexibility of design as compared with the receiving side. In order to increase the output power, simply by increasing the input power and multiplying the transmission side coils, the desired output can't be easily obtained for the above-mentioned reason. Therefore, by using a Helmholtz coil, we attempted to not only increase the output but also stably supply power to the receiving side. In constructing a local charging area, which is our final objective, it is reasonable to place a transmitting coil on the ceiling and the floor. As a space where people can actually work, at least 2 m is required for the height. However, it is very difficult to fabricate a coil of a size to realize it. For this reason, we first confirmed the effectiveness of the approach using Helmholtz coil and conducted basic experiments with coils of comparatively easy size to produce. The configuration of the experimental system is shown in Fig. 1. When the distance H between two transmission coils and the radius R of each coil are equal to each other, the coil has a uniform magnetic field on the central axis connecting the coils. Two circular spiral coils (coil end: open, winding pitch width: 3 mm, 2 turns, radius: 300 mm) were used on the transmission side and the distance between coils was 300 mm. For the receiving coil, a circular spiral coil (coil end: short, winding pitch width: 4 mm, 10 turns, radius: 75 mm) assumed to be mounted on a tablet computer was used. The resonance frequency is 9.5 MHz for all coils. The distance d which is from one of the transmitting coils to the receiving coil was changed at d = 5 to 25 cm. The vector network analyzer (VNA, ADVANTEST, R3755A) was used for measurement of transmission efficiency. The measurement result is shown in Figure 2. As a comparison, the result (single) when only one transmission coil is used is also depicted. The efficiency in the case of using the Helmholtz coil decreases about 20% in maximum efficiency compared with the single, but maintains stable efficiency even if the distance d changes. This tendency can't be confirmed by merely setting up a plurality of transmission coils. This shows that the uniform magnetic field by Helmholtz coil always maintained a constant resonance state at any position between the coils. In this way, simplification and cost reduction of the system can be realized only by designing and arranging the coils without additional function to the power supply unit. 3. Summary and Future Plans In this time, we could confirm that stable power supply can be realized to a specific closed space by using Helmholtz coil. For next step, we will tackle to create a large Helmholtz coil with a radius of 2 m for our final goal. In order to achieve that, after evaluating the performance using electromagnetic field simulation software JMAG (JSOL Corp.), we will examine the fabrication. Additionally, in addition to the no-load test by the VNA, we are also planning to measure the transmission efficiency and the maximum transmittable power with the actual load on the receiver side.

1) André Kurs, et al, Science Express, Vol. 317. no.5834, pp. 83-86, 2007.

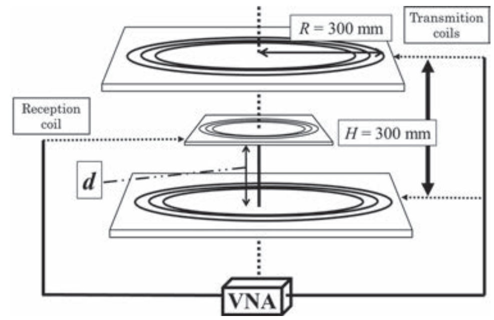

Fig. 1. The configuration of the basic experimental system using Helmholtz coil on transmitter side.

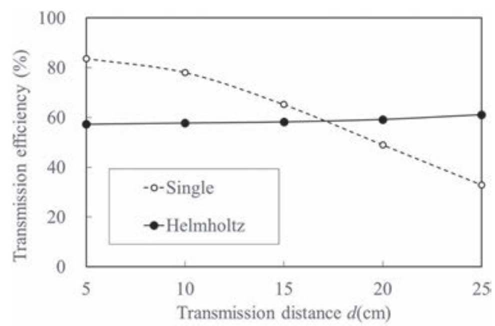

Fig. 2. The measurement results of the transmission efficiencies.

GU-10. Calculation of Magnetic Inductance of the Spiral Coils Including Ferrite Core for Remote Field Energy Transfer Devices.

Y. Jang[1] and G. Park[1]
1. School of Electrical and Computer Engineering, Pusan National University, Busan, The Republic of Korea

I. Introduction In recent years, researches on induction heating (IH) and wireless charging (WC) have been actively carried out [1]-[5]. IH and WC systems have something in common. The first is the use of spiral coil to reduce the volume of the entire system, and second is the use of ferrite core at the bottom of the coil to minimize the leakage flux and increase the efficiency of the system [2], [4]. One of the most important factors in design process of IH and WC systems is to design spiral coil and ferrite core considering the limit of system inductance. In case of spiral coil, the inductance is determined by coil diameter, turn interval, outer diameter, and number of turns of the coil. The inductance also changes due to the thickness, area of the ferrite core, and distance from coil to ferrite core. Since the parameters affecting the inductance vary and it is difficult to obtain the inductance value through fabrication and measurement for all cases, calculation of the inductance depends on the finite element analysis in most research and design process. However, the disadvantage of calculating an inductance using finite element analysis is take a long time to modeling and analysis if the structures are complicated. And unlike the solenoid coil with iron core whose magnetic path is determined, it is also unreasonable to apply a magnetic circuit in spiral coil because the magnetic path is diverse, and the leakage flux is large. Therefore, in this paper, analytical calculation of inductance is proposed by using image coils. First, the inductance calculation method using finite element analysis is introduced, and then the inductance calculation by using image coils is presented. The inductances obtained by the above two methods are compared with each other. II. METHOD OF INDUCTANCE CALCULATION *A. Finite Element Analysis* Fig. 1 (a) shows the cross section of the entire structure about the spiral coil and ferrite core. d_w is diameter of the conductor cross-section which current flows, D_{outer} is outer diameter of the spiral coil, SP_t is the turn interval, and N_t is the number of turns. The thickness and radius of the ferrite core are assumed to be infinite (or large enough). Since the ferrite cores are a soft magnetic material, the permeability is high, and the conductivity is low. If the current flowing in the coil is I_c, flux density vector B and magnetic field H vector of the entire analysis region can be obtained from the finite element method. In this case, the inductance of system is calculated by, $L=1/(I_c)^2\int_V B\bullet H dV$ (1) where, *V* is volume of the entire analysis region. *B. Analytical Method* If the thickness and radius of the ferrite core are infinite (or large enough), an image coil can be placed instead of the ferrite core. Fig. 2(b) is shown the reference coil and the image coil [5]. In this case, the structure of the image coil is the same as that of the conventional spiral coil, and the magnitude of the current flowing is shown in (2), $I_i=I_c\times(\mu_r-1)/\mu_r$ (2) where, μ_r is permeability of the ferrite core. If the spiral coil is simplified by circular coil which have the same center axis and the number of coil is same to number of turns, the magnitude of the magnetic field at point (r, z) in cylindrical coordinate system is shown in (3), $H_{(r,z)}=\sqrt{(H_r^2+H_z^2)}$ (3) where, $H_r=\sum^{N}_{tn=1}(-1)/2\pi[\int^{2\pi}_0\{(z\times I_c/A)+(z+2d)\times I_i/B\}R_n\cos\alpha d\alpha]$ (4) $H_z=\sum^{N_t}_{n=1}1/2\pi[\int^{2\pi}_0\{(I_c/A)+(I_i/B)\}R_n(R_n-r)\cos\alpha d\alpha]$ (5) $A=(r^2+R_n^2+z^2-2R_n r\cos\alpha)^{3/2}$ (6) $B=(r^2+R_n^2+(z+2d)^2-2R_n r\cos\alpha)^{3/2}$ (7) $R_n=D_{inner}+n(d_w+SP_t)$ (8) Then, the calculated inductance is (9), $L=\mu_0/(2I_c)\times\sum^{N_V}_{vi=1}H_i^2\bullet\Delta dV_i$ (9) where, μ_0 is the permeability of free space, N_V is the number of volume elements, H_i is the magnetic field intensity of the ith volume element, and ΔdV_i is the volume of the ith volume element. III. COMPARISON FEA WITH ANALYTICAL METHOD The magnetic field distribution and inductance values obtained by FEA and Analytical Method are shown in Fig. 2. The specifications of the spiral coil are d_w=3mm, SP_t=1mm, D_{outer}=271mm, and N_t=21turns. The relative permeability of the ferrite core μ_r=1000. Applied current I_{peak}=10A, and the input frequency f=20kHz. Fig. 2(a) is a graph showing the magnetic field distribution at z=8mm when the distance of spiral coil and ferrite core is 5 mm. Fig. 2(b) is a graph showing the inductance value according to the distance between spiral coil and ferrite core. IV.CONCLUSION A method of calculating inductance in a spiral coil through the image coils is studied in this paper when the thickness and radius of the ferrite core are infinite (or large enough). The structure, position and applied current of image coils were determined, and magnetic field and inductance were calculated from reference coils and image coils. To verify that the proposed method is suitable, we compared the magnetic field distribution and inductance obtained through FEA. As a future work, we will study how to calculate the inductance of a ferrite core with a finite core thickness and radius. And we will also study when the center of the ferrite core is empty for cooling.

[1] J. Acero, R. Alonso, L. A. Barragán, and J. M. Burdío, "Modeling of Planar Spiral Inductors Between Two Multilayer Media for Induction Heating Applications," *IEEE Trans. On Mag.*, vol. 42, no. 11, pp. 3719-3729, Nov. 2006. [2] J. Acero, C. Carretero, R. Alonso, and J. M. Burdío, "Quantitative Evaluation of Induction Efficiency in Domestic Induction Heating Applications," *IEEE Trans. On Mag.*, vol. 49, no. 4, pp. 1382-1389, Apr. 2013. [3] D. S. Kim, J. Y. So, and D. K. Kim, "Study on Heating Performance Improvement of Practical Induction Heating Rice Cooker With Magnetic Flux Concentrator," *IEEE Trans. Appl. Supercond.*, vol. 46, no. 4, Jun. 2016. [4] I. G. Lee, N. Kim, I. K. Cho, and I. P. Hong, "Design of a Patterned Soft Magnetic Structure to Reduce Magnetic Flux Leakage of Magnetic Induction Wireless Power Transfer Systems," *IEEE Trans. Electromagn. Compat.*, vol. 59, no. 6, pp. 1856-2863, Dec. 2017. [5] Z. Luo, and X. Wei, "Analysis of Square and Circular Planar Spiral Coils in Wireless Power Transfer System for Electric Vehicles," *IEEE Trans. Ind. Electron.*, vol. 65, no. 1, pp. 331-341, Jan. 2018. [6] H. W. E. Koertzen, J. D. van Wyk, and J. A. Ferreira, "An investigation of the analytical computation of inductance and AC resistance of the heat-coil for induction cookers," in *IEEE Industry Applications Society Annual Meeting Conf., Rec.*, 1992, vol. 1, pp. 1113-1119, Oct. 1992.

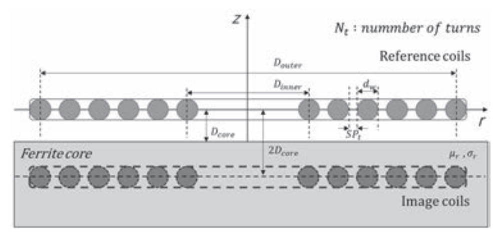

Fig. 1. Cross-section of the reference coils, ferrite cores, and image coils.

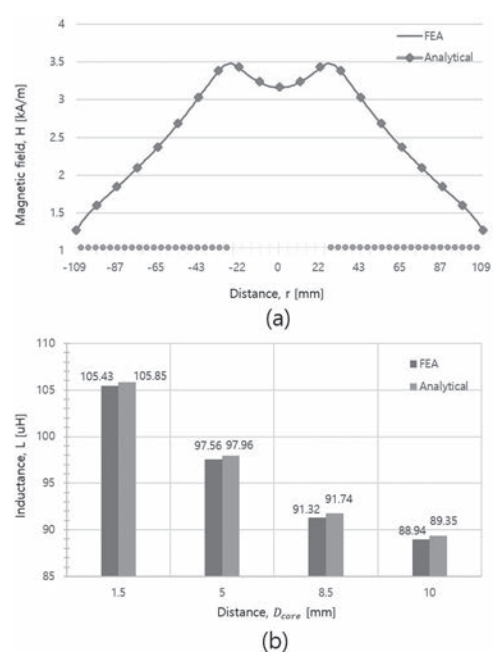

Fig. 2. Comparison between FEA and analytical method. (a) magnetic field distribution at z=8mm. (b) Inductance according to distance between spiral coil and ferrite core.

GU-11. Magnetostriction impact noise and vibration on power transformer characteristic via PSO method.

C. Hsu[1,2] and Y. Huang[2]
1. Department of Mechanical Engineering, Oriental Institute of Technology, New Taipei city, Taiwan; 2. Department of Mechanical Engineering, National Central University, Taoyuan, Taiwan

1. Abstract: Electromagnetic design of the power transformer to reduce the noise based on the magnetostriction variation, it should be faced it very closely due to the resident people paid a great attention recently. Actually, it is well-known that magnetostriction of the power transformer is caused by the exciting variation of the magnetic core. This study, it presented an optimization method to reduce the noise of the power transformer that also performed the factory testing before delivery and after that to install on-sited downtown power station, is a main objective. A novel method particle swarm optimization (PSO) is use to reduce noise level of transformer and also effective to decrease total cost reduction. This paper discusses a main magnetic property of magnetostriction dependent on the transformer operated at full-load tests. Also, this study is presented that a lot of transformers with capacities, 15 MVA to 60 MVA / high voltage (HV) 132kV to low voltage (LV) 33 kV around six units. Actually, a full loading testing for transformer characteristic is to lead a key point for reduction of the noise and vibration. A tricky noise source of the power transformers for no-load (core/magnetostriction) and full-load (winding/displacementε) testing results compared with simulation and measurement data, are performed. The difference between the simulated and the measured sound levels is limited around 3dB range especially for higher capacity and successfully developed in this case. 2. Introduction It is well known that power transformers operate at a low-frequency generated the noise response. Even the overall noise response can be smaller than that as usual no-load operation condition, but due to a kernel point magnetostriction characteristic, it still generate a lot of confuse noise to the resident people. This is because noise variation dependent on the magnetic field variations in the laminations of the core. Magnetostriction can be regulated due to a key point which is the magnetic material and core structure [1]. For normal comment sense in core lamination structure, it can be understood that although the total change in length is as a small micrometers. The stress response based on the electromagnetic reactive from magnetic flux variation can be obtained. Before aforementioned the reason will cause the deep noise and hum wave response. This is because resonance frequencies, for example, included as, 120 Hz, 240 Hz and 360 Hz, etc., which are harmonics of the 60Hz excitation current of the transformer in Taiwan, is obtained. The noise level increases with higher magnetic flux density, higher capacity of the MVA rating and higher electromagnetic force for the power transformer, is significant. This study will discover a useful method to get a great resolution in reduction of noise and vibration by using finite element analysis (FEA) method. Both magnetostriction of the core and electromagnetic force effect of the winding in design and testing for power transformer are success performed. 3. Simulation and Experimental Results In general, the total noise level of transformers is mainly influenced by magnetostrictive variation of the core and electromagnetic forces of the windings, and also consider rigid-structured of the tank walls, respectively, is addressed. These studies have presented serval magnetic material to fabricate transformer core. Truly, the magnetostriction variation as a function of the core properties has been presented [2] as 30Z140, 27ZH100, 27PH100, 30ZH105 and 30P120, respectively. A 3D model of the power transformer is calculated to simulate the noise and vibration variables through by FEA, adding with a useful optimization method PSO, as shown in Figure 1(a). It presented the magnetic flux density distributed in the core and to show the noise amplitude of the core is significant. Based on this reason, it also discovered a new evident reason that the winding displacement (m/m) is relative with the electromagnetic force and current density, is obtained. This study, it will perform each transformer (six units) between 15 MVA to 60 MVA / high voltage (HV) 132kV to low voltage (LV) 33 kV, extremely-lowed noise development and test environment, as shown in Figure 1(b). This study, it presents an optimization method to calculate lower magnetostriction variation due to serval material application for transformer. The effect of magnetostriction-induced core magnetomechanical stress and electromagnetic force of winding variation on noise and vibration for power transformers, are presented. Generally, a great magnetic property of the magnetostriction of grain-oriented Si steels should be chosen. Then, both electromagnetic force and flux displacement of the winding with different magnetic materials are calculated. In Figures 2(a)-(b), the simulated and measured results for magnetic core and rigid winding in magnetic flux and electromagnetic force is analyzed. This is fundamental work and should be performed before reality transformer implements and also success development.

1. Chang-Hung Hsu, et. al., Reduction of vibration and sound-level for a single-phase power transformer with large capacity, IEEE Transactions on Magnetics, vol. 51, no. 11, pp. 8403204-1-4, 2015. 2. Shan-Jen Cheng,et. al., Correlation of magnetostriction variation on magnetic loss and noise for power transformer, Journal of Applied Physics, vol. 117, pp. 17E716-1-4, 2015.

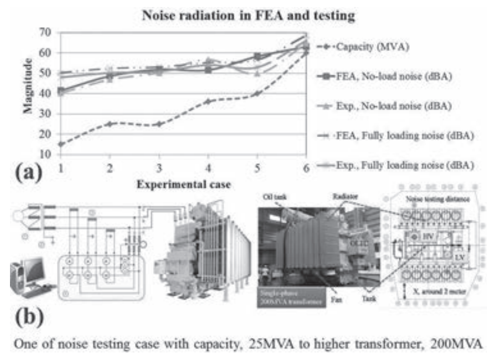

Fig. 1. Serval capacity 25MVA to 200MVA power transformer: (a) noise simulation and factory testing results, (b) reality testing environmental.

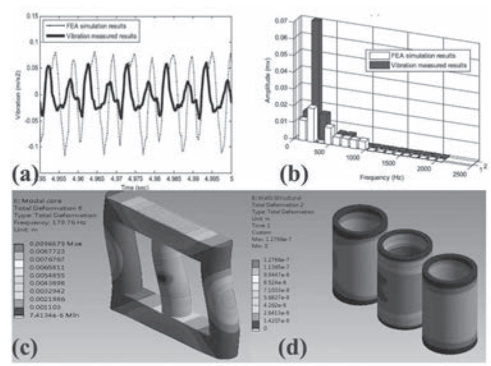

Fig. 2. Power transformer optimization simulation results: (a) transformer core vibration, (b) winding stress variation.

GU-12. Electromagnetic characteristics of basic structure of wireless power transmission coil for electric vehicles.

T. Chen[1] and *J. Zhao*[1,2]

1. Xuji Power Co. Ltd., Xuchang, China; 2. School of Electronic and Electrical Engineering, Nanyang Institute of Technology, Nanyang, China

Research on wireless power transmission is a hot area at present [1-3]. Coil design is one of the key technologies in wireless power transmission [3-6]. A core goal of coil design is to study how to improve coupling coefficient. Higher coupling coefficient means greater transmission power and higher efficiency under the same conditions. Many types of coil have been designed, such as square coils, circular pad, four-square coils, DD coupler, DDQ coupler [4-5]. A comparison is made between circular and elliptical coils by studying the shape of the magnetic field and the path of magnetic flux with a concept of flux pipe [5-6]. Experimental results show that, in terms of the type of coil, coupling coefficient of the circular pad and DD coupling coils is higher and the cost is lower. Most of the existing researches focus on the practical application and comparison of various types of coils, and rarely compare the characteristics of the two basic circular and square coils. In this paper, the basic characteristics are studied about the two types of the most basic coil, which provides the basis for how to use two kinds of basic coils. For the two most common types of circular and rectangular coils, the structure is axisymmetric. For any one of the above two types of coils as a transmitting coil, the case of a magnetic field coupling is considered using two types of coils in the single turn as receiving coil, respectively. There are three cases: (1) the area of the two receiving coils is equal; (2) the circumference of the two receiving coils is equal; (3) the outer diameters of the two receiving coils are equal in space. It is easy to know that the maximum area of the rectangle coil is square under the same circumference of coil, and so we use square and circular coils for comparative analysis. The circumference, area and outer diameter of the circular coil are equal to the square coil, respectively, when the area and circumference of the square coil are kept constant, as shown Fig. 1. Magnetic field characteristic analysis : For the circular and square transmitting coil with given structural parameters, the curves of the similar Magnetic flux density B can be obtained by numerical calculation and electromagnetic simulation, as shown in Fig. 2a. For cases where the area of the two receiving coils is equal in Fig. 1a, the magnetic flux is equal in the area where two receiving coils overlap. For the non-coincident part, the magnetic flux of the circular coil will be greater than the magnetic flux of the square coil, according to the results of fig.2a. From the above analysis, it is easy to know that the magnetic flux of the circular coil will be greater than the magnetic flux of the square coil for the same circumference of the two coils as shown in Fig.1a. Because the area of the circular coil in Fig.1b is larger than the area of the circle coil in Fig.1a, the fig.1b has a result similar to that of Fig.1a. For the case of the same outer diameter shown in Fig. 1c, the magnetic flux of the square coil is larger than the circular coil because the square coil completely contains the circular coil. through the above analysis, the circular receiver coil flux greater than the square coil flux in the case of equal area or equal perimeter, namely in these two cases, the circular receive coil mutual inductance is greater than the square receive coil. the simulation results of the normalized coupling coefficient of three types of coils at different offset distances according to the design parameters of the electric vehicle wireless power supply coil are shown in Fig.2b. The cost and loss of the circular and square coil are equal when the circumference is equal. The mutual inductance of the circular coil is obviously better than that of the square coil, so the efficiency is higher. When the enclosed area is equal, the cost and loss of the circular coil is lower than that of the square coil, and the mutual inductance is slightly larger than that of the square coil, so the efficiency is also higher than that of the square coil. Therefore, it is the best choice to choose a circular coil with no space constraints. Under the condition of limited space, the square coil can achieve greater mutual inductance, but the cost and loss of the coil will be higher than that of the circular coil.

1 Assawaworrarit S, Yu X, Fan S. Robust wireless power transfer using a nonlinear parity-time-symmetric circuit.[J]. Nature, 2017, 546(7658):387. 2 Jolani F, Yu Y, Chen Z. Enhanced planar wireless power transfer using strongly coupled magnetic resonance[J]. Electronics Letters, 2015, 51(2):173-175. 3 Wake K, Laakso I, Hirata A, et al. Derivation of Coupling Factors for Different Wireless Power Transfer Systems: Inter- and Intralaboratory Comparison[J]. IEEE Transactions on Electromagnetic Compatibility, 2017, PP(99):1-9. 4 Wang Y, Yao Y, Liu X, et al. S/CLC Compensation Topology Analysis and Circular Coil Design for Wireless Power Transfer[J]. IEEE Transactions on Transportation Electrification, 2017, PP(99):1-1. 5 Budhia M, Boys J T, Covic G A, et al. Development of a Single-Sided Flux Magnetic Coupler for Electric Vehicle IPT Charging Systems[J]. IEEE Transactions on Industrial Electronics, 2013, 60(1):318-328. 6 Takanashi H, Sato Y, Kaneko Y, et al. A large air gap 3 kW wireless power transfer system for electric vehicles[C]// Energy Conversion Congress and Exposition. IEEE, 2012:269-274.

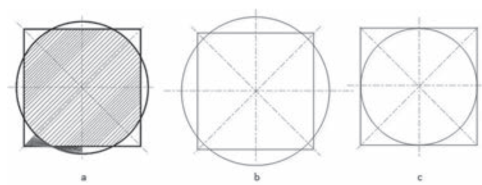

Fig. 1. Comparison of three cases of circular and square coils
***a* The circumference of the circle and square coil is equal, the area ratio is 4/π.**
***b* The area of the circle and square coil is the same, The square of the ratio of the perimeter is π/4.**
c The outer diameter of the circle and square coil is equal, and all of the area and circumference ratio is π/4.

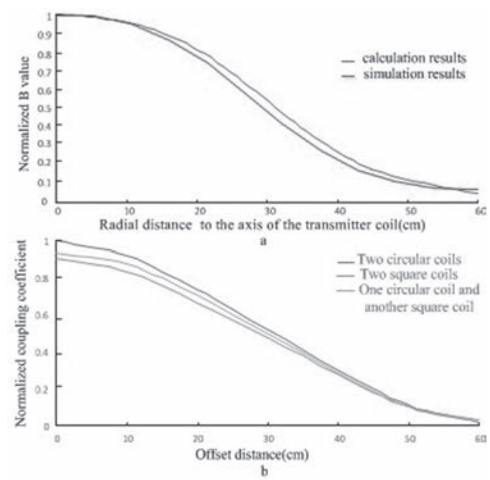

Fig. 2. The normalized curve of magnetic field induction intensity B and the normalized coupling coefficient of three types of coils
a The normalized curve of magnetic field induction intensity B with similar shape is obtained by numerical calculation and electromagnetic simulation
b The normalized coupling coefficient of three types of coils at different offset distances

GU-13. Design and Analysis of Cubical Compact Coils for Wireless Power Transfer.

C. Jiang[1], K. Chau[1], W. Han[1] and W. Liu[1]
1. The University of Hong Kong, Hong Kong, Hong Kong

I.INTRODUCTION As an emerging technology, wireless power transfer (WPT) has attracted substantial attention in many applications, such as electric vehicles, portable electric devices and medical instruments [1]. Generally, the WPT system possesses the advantages of safety, high reliability, low maintenance, and electrical isolation [2]. As one of the most prominent technologies, the WPT is changing the conventional usage of energy in daily life for human being. The key element in the WPT system is a pair of magnetically coupled coils [3-5]. When delivering power in a large area, multiple coils can be adopted to form a single uniform magnetic field. Also, in the multifrequency WPT system, a single transmitter can be used to feed multiple receiver coils with different resonant frequencies [6]. Usually, the coreless planar coil is preferable to achieve better ability of tolerance to misalignment than that with ferrite core. Since the circular coil has the problem of limited coverage, the rectangular coil is preferable in the multiple-receiver WPT system. However, in order to provide the desired power transfer capability, the size of this kind of system is usually very large and thus the system flexibility is reduced. Normally, a single-layer planar coil is used for both the transmitter and receiver, which will significantly increase the system complexity and occupied volume. This paper focuses on the design and analysis of multilayer rectangular coil structures, dubbed as cubical compact coils, for those multiple-receiver WPT systems desiring compact size and good power transfer capability. In order to make sure that the mutual inductances of the multiple receivers are the same, the magnetic field distribution over the transmitter should be uniform enough. This paper proposes three different types of cubical compact coils, namely the spiral type, concentrated type, and uneven compound type. Their designs and analyses are elaborated. Apart from assessing their magnetic field distributions, the corresponding electric potential distributions are analyzed at different currents to provide the guidance for selection and arrangement. II. METHODOLOGY The proposed cubical compact coil structures are shown in Fig. 1, which are the spiral type, the concentrated type and the uneven compound type. These three coil types can be applied to both the transmitter and receiver. For exemplification, the peripheral dimensions are 200 mm and 140 mm. The Litz wire with 165×0.1 mm is adopted to make up all coils. For the spiral type, all turns of the coil are distributed evenly with two layers. Meanwhile, for the concentrated type, all turns of the coil are bundled together with two layers. By combining the advantageous features of both the spiral type and concentrated type, the uneven compound type is proposed where five turns form one bundle with two layers and the pitch distances between every two bundles are not the same, namely, S_1=3 mm, S_2=5 mm, and S_3=7 mm. Once the system parameters are predefined, the mutual inductance between the transmitter and receiver becomes the major determinant of the system performance such as power transfer capability and efficiency. Generally, the uniform magnetic flux density makes the mutual inductance keep constant, thus improving the ability of misalignment tolerance. Therefore, the magnetic field distribution can be utilized to analyze the system performance. Based on the same peripheral dimensions, the magnetic field distributions and electric potential distributions of all three types of coils are analyzed by using the finite element method based software JMAG. As a result, the spiral type of coil essentially provides the magnetic field distribution in a conical-like shape as shown in Fig. 2(a), whereas the concentrated type of coil presents a rectangular concave-top distribution as shown in Fig. 2(b). Meanwhile, the uneven compound type can provide much more uniform magnetic field distribution than both the spiral and concentrated types. Focusing on the magnetic flux densities at the middle plane as shown in Fig. 2(c), it can be found that along the horizontal displacement, the uneven compound type can exhibit much more uniform field and hence achieve better tolerance for the misalignment. Moreover, for this kind of multilayer structures, the proximity effect should be analyzed. As shown in Fig. 2(d), the maximum electric potential of the concentrated type of coil is simulated, which is well below the breakdown voltage of 1400 V of the Litz wire. Finally, an experimental prototype has been constructed and tested to verify the feasibility of the proposed system. More experimental results including the power transfer capability and misalignment tolerance will be given in the full paper. III. CONCLUSION In this paper, three cubical compact coil types of transmitter and receiver for WPT have been proposed and implemented. They are particularly suitable for those multiple-receiver WPT systems desiring compact size and good power transfer capability. By newly combining the spiral coil type and concentrated coil type, the uneven compound coil type can provide more uniform magnetic field distribution, hence minimizing the difference of magnetic flux densities that can be picked up by multiple receivers. Moreover, the electric potential distribution is analyzed to ensure that the maximum electric potential is well below the breakdown voltage of the Litz wire. This work was supported by a grant (Project No. 17204317) from the Hong Kong Research Grants Council, HKSAR, China.

[1] G. A. Covic, and J. T. Boys, "Inductive power transfer," *Proceedings of the IEEE*, vol. 101, no. 6, pp. 1276-1289, Jun, 2013. [2] C. Jiang, K. T. Chau, Y. Y. Leung, C. Liu, C. H. T. Lee, and W. Han, "Design and analysis of wireless ballastless fluorescent lighting", *IEEE Transactions on Industrial Electronics*, DOI: 10.1109/TIE.2017. 2784345. [3] S. Bilicz, Z. Badics, S. Gyimóthy, and J. Pávó, "Modeling of dense windings for resonant wireless power transfer by an integral equation formulation," *IEEE Transactions on Magnetics*, vol. 53, no. 6, pp. 1-5, Nov. 2017. [4] C. Jiang, K. T. Chau, C. Liu, and C. H. T. Lee, "An overview of resonant circuits for wireless power transfer," *Energies*, vol. 10, no. 7, pp. 894:1-20, June, 2017. [5] C. C. Mi, G. Buja, S. Y. Choi, and C. T. Rim, "Modern advances in wireless power transfer systems for roadway powered electric vehicles," *IEEE Transactions on Industrial Electronics*, vol. 63, no. 10, pp. 6533-6545, Oct, 2016. [6] C. Jiang, K. T. Chau, T. W. Ching, C. Liu, W. Han, "Time-division multiplexing wireless power transfer for separately excited dc motor drives", *IEEE Transactions on Magnetics*, vol. 53, no. 11, pp. 1-5, Nov. 2017.

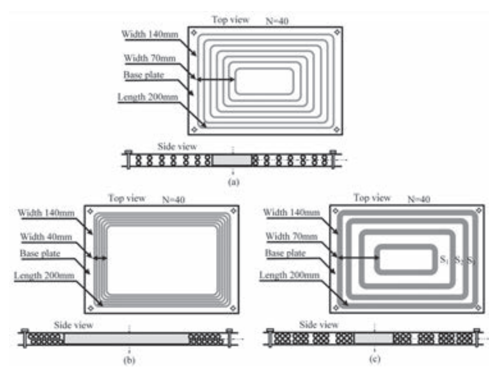

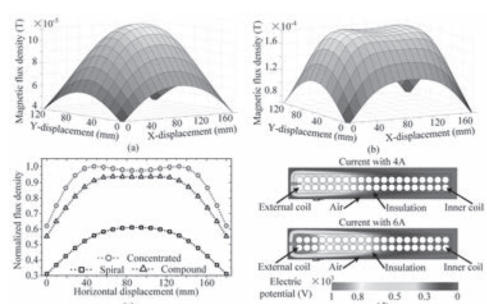

GU-14. Move-and-Charge System for Automatic Guided Vehicles.

C. Jiang[1], K. Chau[1], C. Lee[2], W. Han[1] and W. Liu[1]
1. The University of Hong Kong, Hong Kong, Hong Kong; 2. Research Laboratory of Electronics, Massachusetts Institute of Technology, Boston, MA, United States

I.INTRODUCTION As one of the most prominent technologies, wireless power transfer (WPT) has attracted substantial attention in many applications and is changing the conventional usage of energy in daily life for human being [1]-[2]. In recent years, automatic guided vehicles (AGVs) are highly demanded with the fast-increasing transportation and logistics market [3]. In order to alleviate the problem of their short driving range, more batteries or frequent charging are inevitable [4]. Rather than increasing the size of batteries or the number of charging ports, the use of WPT for AGVs can greatly facilitate the charging process [5]. Most importantly, because of the absence of metallic contacts, possible electrocution during the charging process can be totally eliminated [6]. Since the AGV usually needs to operate continuously, it is highly desirable to be wirelessly charged during moving. Namely, an array of power transmitters is embedded beneath the workplace while a receiver is mounted at the bottom of the AGV. Another problem for AGV application is that it desires a large number of sensors embedded under the workplace to navigate these AGVs, which will significantly increase the system complexity and hardware cost. This paper proposes and implements a new move-and-charge (MAC) system for AGVs. Essentially, the proposed rail transmitter not only serves to wirelessly charge the AGV, but also to navigate the AGV based on the variation of mutual inductance. Thus, it can significantly reduce the battery size, while eliminating the risk of electrocution and the guiding sensors embedded under the workplace. The key is to make use of the DC-DC converter to keep the equivalent resistance constant. When the AGV is misaligned with the rail transmitter, the receiver current will be varied so that the steering part of the AGV will perform the correction of direction to maintain the received power. Consequently, both dynamic charging and navigation can be achieved simultaneously. II.METHODOLOGY The proposed MAC AGV system is shown in Fig. 1(a), which includes the rail transmitter designed with 180 mm width and the pad receiver. The rail transmitter is embedded just beneath the ground while the pad receiver is mounted at the bottom of the AGV so that the airgap between them is 80 mm. The rail transmitter design involves only a long primary coil supplied by a single power inverter, which takes the definite advantages of lower investment cost and lower installation complexity than the pad transmitter design for feeding multiple AGVs. For the sake of better flexibility, maintainability and scalability, the rail transmitter design usually adopts the sectional arrangement in which it uses one power inverter per section to feed multiple AGVs. Normally, the rail transmitter should be compensated with capacitors as shown in Fig. 1(b), and the system operation frequency is set at 85 kHz according to the SAE J2954 wireless charging standard. Since the wireless power from the transmitter to the receiver is proportional to the surface area where the magnetic flux passes through, the ferrite based pad receiver is adopted to provide magnetic flux guidance, hence minimizing the flux leakage. In order to provide the effect of navigation without relying on guiding sensors, the DC-DC converter is used to regulate the charging voltage and current, aiming to keep the equivalent resistance constant. If the AGV is not aligned with the rail transmitted, there will be a difference between the received current and reference current. This difference will cause the steering part of the AGV to control the AGV in such a way that the alignment can be restored. In order to predefine this reference current, the magnetic field distributions at different situations are calculated by using finite element analysis software JMAG. A 200 W MAC AGV system has been designed. As shown in Fig. 2(a), when the pad receiver of the AGV is exactly aligned with the rail transmitter, the magnetic flux density at the height of 80 mm is symmetrical without requiring any correction of direction. When the AGV comes across the right corner rail, the magnetic flux density is shown in Fig. 2(b), where the total effective flux passes through the pad receiver is reduced and hence the received current decreases to 5.5 A so that the right correction is needed. As shown in Fig. 2(c), the current drops fast with respect to the misalignment. It can be observed that the received currents when the pad receiver is above the straight rail and corner rail are 6.6 A and 6.0 A, respectively. Thus, the current of 6.0 A can be regarded as the threshold value to conduct the correction of direction. Finally, an experimental prototype has been constructed and tested to verify the feasibility and controllability of the proposed system. More experimental results including the system efficiency will be given in the full paper. III. CONCLUSION In this paper, a new MAC system has been proposed and implemented for AGVs, which not only performs wireless charging, but also automatically navigates the AGV without using guiding sensors. By newly adopting the equivalent resistance adjustment circuit and current threshold control method, it can simultaneously provide wireless power and misalignment correction, hence achieving the desired traction. Most importantly, it can significantly reduce the battery size and hence cost of each AGV, while eliminating the risk of electrocution. This work was supported by a grant (Project No. 17204317) from the Hong Kong Research Grants Council, HKSAR, China.

[1] A. Abdolkhani, A. P. Hu, G. A. Covic, and M. Moridnejad, "Through-hole contactless slipring system based on rotating magnetic field for rotary applications," *IEEE Transactions on Industry Applications*, vol. 50, no. 6, pp. 3644-3655, Dec, 2014. [2] C. Jiang, K. T. Chau, C. Liu, and C. H. T. Lee, "An overview of resonant circuits for wireless power transfer," *Energies*, vol. 10, no. 7, pp. 894:1-20, June, 2017. [3] A. Vale, R.Ventura, P. Lopes, and I. Ribeiro, "Assessment of navigation technologies for automated guided vehicle in nuclear fusion facilities," *Robotics and Autonomous Systems*, vol. 97, pp. 153-170, Nov., 2017. [4] C. Jiang, K. T. Chau, Y. Y. Leung, C. Liu, C. H. T. Lee, and W. Han, "Design and analysis of wireless ballastless fluorescent lighting", *IEEE Transactions on Industrial Electronics*, DOI: 10.1109/TIE.2017. 2784345. [5] M. H. Mahmud, W. Elmahmoud, M. R. Barzegaran, and N. Brake, "Efficient wireless power charging of electric vehicle by modifying the magnetic characteristics of the transmitting medium," *IEEE Transactions on Magnetics*, vol. 53, no. 6, pp. 1-5, Jan., 2017. [6] C. Jiang, K. T. Chau, T. W. Ching, C. Liu, W. Han, "Time-division multiplexing wireless power transfer for separately excited DC motor drives," *IEEE Transactions on Magnetics*, vol. 53, no. 11, pp. 1-5, Nov. 2017.

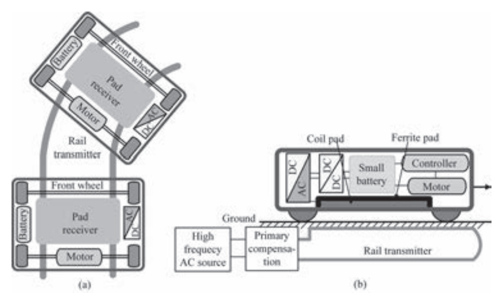

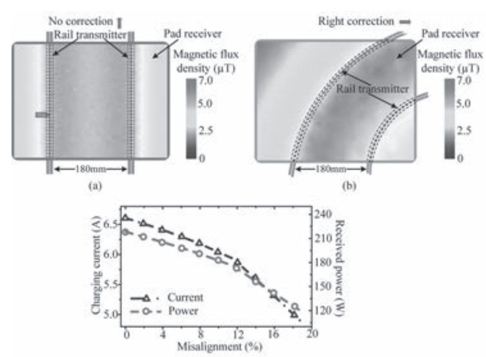

GU-15. Design and Optimization of Quasi-constant Mutual Inductance for Asymmetric Two-Coil Wireless Power Transfer System With Lateral Misalignments.

Z. Li[1]
1. College of Traffic Engineering, Hunan University of Technology, Zhuzhou, China

I. Introduction Magnetic resonant wireless power transfer (WPT) is an emerging technology that may create new applications for wireless power charging[1]. However, the output voltage fluctuations resulting from lateral misalignments are main obstructing factors for promoting this technology. In this paper, an asymmetric two-coil WPT system is presented. The mathematical model of the proposed topology with lateral misalignments is built based on equivalent circuit method. The expression of the output voltage is then derived by solving the system equivalent equations. In addition, a method of optimization parameters is proposed. The mutual inductance between the receiving coil and the transmission coil is nearly constant by the proposed method with lateral misalignments. Therefore, the output voltage can be kept nearly constant. The asymmetric two-coil WPT system via magnetic resonance coupling is designed. Simulation and experimental results validating the proposed method are given. II. Analysis of Optimization Method The output voltage V_L is only dependent on the mutual inductance between transmission coil and receiving coil when the parameters (*R, L, C*) of each coil and the load are given. The mutual inductance may be changed with the variations of lateral misalignments, and the parameters of each coil. In this section, a method of optimization parameters is proposed. The mutual inductance can be kept nearly constant with lateral misalignments by using the proposed method. The process of the proposed optimization method is as follows: 1) Parameters setting: the resonant angular frequency is set to be 85kHz. The mutual inductance should be larger than 6.0μH. The transmission distance is set to be 15cm. The diameter of copper is set to 1.75mm. The outer diameter of Tx is changed from 0.25m to 0.30m in a step of 2.0mm. The outer diameter of each receiving coil is changed from 0.2m to 0.25m in a step of 2.0mm. The number of turns of Tx is changed from 17 to 40 in a step of 1. The number of turns of each receiving coil is changed from 6 to 10 in a step of 1. 2) Calculated mutual inductance: According to (1) and (2), the mutual inductance between Tx and each receiving coil can be obtained with different lateral misalignments. M_{10} is the mutual inductance between Tx and each receiving coil when lateral misalignment equals to 10cm; M_0 is the mutual inductance between Tx and each receiving coil when lateral misalignment equals to 0cm. 3) Compared to ε (ε=(M_0-M_{10})/M_0) at a given outer diameter of Tx, outer diameter of each receiving coil, the number of turns of Tx and the number of turns of each receiving coil, the optimum ε is obtained(The smaller ε is, the smaller the variations of mutual inductance becomes). 4) According to the optimum ε, the optimum parameters of Tx and each receiving coil can be obtained. III. Simulation & Experimental Verification To validate the proposed structure and optimization method, the prototype model of the system has been built, as shown in Fig.1. It is composed of the DC voltage source, a transmission resonant coil, a receiving resonant coil, H-bridge inverter, a full-bridge rectifier, and the load. The value of the DC voltage source is 48V. The DC voltage source is shown in Fig. 1(a). The transmission resonant coil is shown in Fig. 1(b). The receiver resonant coils are shown in Fig. 1(c). The outer diameter of the transmission resonant coil is 0.6m with a pitch of 0cm for approximately 17 turns according to the optimization method. The outer diameter of each receiving resonant coil is 0.2m with a pitch of 0cm for approximately 10 turns according to the optimization method. All coils are made from 300-strand AWG 38Litz-wire. H-bridge inverter is used at the transmitter side to provide AC excitation, as shown in Fig. 1(d). It contains four MOSFETs (IRF3207), a full-bridge rectifier is used at the receiver side to convert AC to DC. In future research, the power level of the prototype will be increased and those full-bridge rectifiers will continue to be used in high power system. The full-bridge rectifier contains four diodes (HFA15TB60) with a voltage rating of 600V, which can also be used in high power system. Fig. 2 shows the measured mutual inductance between transmission coil Tx and receiving coil Rx placed at different positions. It can be seen that the mutual inductance M is changed from 6.89μH to 6.63μH as the misalignment is varied from 0cm to 10cm. The difference between M_0 and M_{10} is 0.26μH. ε is equal to 3.77% according to ε=(M_0-M_{10})/M_0. The variations of mutual inductance are very smooth as the misalignment is varied from 0cm to 10cm. IV. Conclusion In this paper, an asymmetric two-coil WPT system is presented. The mutual inductance between Tx and Rx is changed with the variations of lateral misalignments, and the parameters of each coil. In order to decrease the variation of the mutual inductance, the turns of Rx and the diameter of Tx should be increased. And the turns of Tx and the diameter of Rx should be decreased. In addition, a method of optimization parameters is proposed. The optimum parameters of each coil can be obtained by using the proposed method for given constraint conditions. The experimental results show that the mutual inductance is changed from 6.88μH ($M_{\_0}$) to 6.63μH ($M_{\_10}$) as the lateral misalignments is varied from 0cm to 10cm. The optimum ε is only 3.7%.

[1] C. C. Mi, G. Buja, S. Y. Choi*, et al.*, Modern Advances in Wireless Power Transfer Systems for Roadway Powered Electric Vehicles[J] IEEE Transactions on Industrial Electronics, 2016, 63(10): 6533-6545.

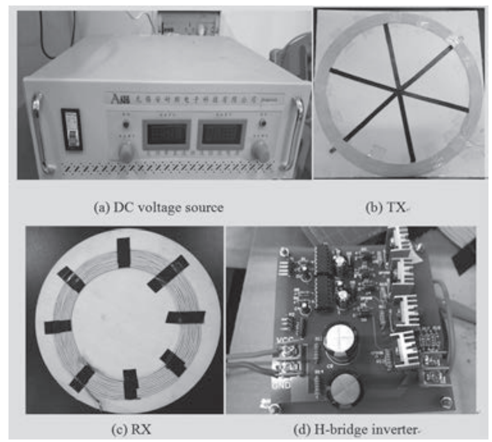

Fig. 1. Experimental setup.(a) DC voltage source.(b) Tx. (c) Rx. (d) H-bridge inverter

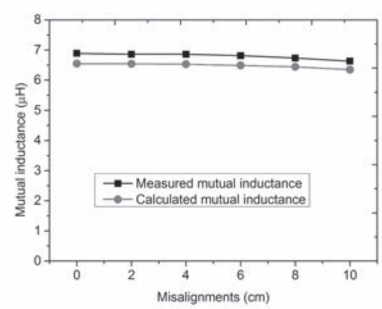

Fig. 2. The mutual inductance versus misalignments.

FRIDAY MORNING, 27 APRIL 2018 SIMPOR/ROSELLE BALLROOM, 8:30 TO 11:30

Session GV
MODELLING OF MACHINES IV
(Poster Session)

Chao Bi, Co-Chair
University of Shanghai for Science & Technology, Shanghai, China
Jiang Quan, Co-Chair
University of Shanghai for Science & Technology, Shanghai, China

GV-01. Thinning Defect Evaluation and an Application for Thickness Measurement by Eddy Current Testing.

S. Nagata[1]
1. Faculty of Engineering, University of Miyazaki, Miyazaki city, Japan

This paper presents an eddy current non-destructive evaluation system that can detect the thinning defect on metal specimen. Detection of a thinning is a diffcult problem for the eddy current testing (ECT). Especially, when surface of thinning defect is flat and smooth, induced eddy current inside specimen does not be perturbed by the defect, therefore, signal indicating the thinning defect is very small. We studied on an ECT for radiator structures, and concluded that in case of such structures, it is comparably easy for detecting thinning defect[1]. We clarified that the frequency characteristics of signal of single fin showed valid dependencies on the radiator thicknesses. Finally, we determined a thinning detection method using an additional metal bar, instead of single fin. A small piece of metal bar, namely called marker, is mounted opposite side of specimen, then ECT evaluations are performed. Multi-Frequency Excitation and Spectrogram Method (MFES) is used. Figure 1 shows an experimental result when specimen made of aluminum, thickness 2.0mm. Signal indicating the marker appears arround at position 0mm. In this result, a frequency of the maximum signal is arround 2.0kHz. According to the specimen becoming thinner, this frequency shifts higher one. Figure 2 shows the relation between the frequency and maximum signal. The experimental results show good relationship between signal of the marker and the specimen thickness. The present method indicates not only the validity for the detection of thinning, but also availability of an application to measuring metal specimen thickness.

[1] S. Nagata, M. Numachi, "Eddy Current Non-destructive Evaluation for Healthiness of Radiator Structure", IEEE Transactions on Magnetics, in press. [2] S. Nagata, Y. Tsubusa, M. Enokizono, "Eddy Current Testing for Radiation Tubes Surrounded by Cooling Fins", Journal of Magnetics, vol. 16, no.3, (2011), pp. 276-280. [3] T. Chady, M. Enokizono, R.Sikora, "Crack Detection and Recognition Using Eddy Current Differential Probe", IEEE Transactions on Magnetics, vol. 35, no. 3, (1999), pp.1849-1852. [4] T. Chady, J. Kowalczyk, "Multifrequency Eddy Current Evaluation of Tube Heat Exchangers", Electromagnetic Nondestructive Evaluation (XII), IOS Press, vol 32, (2009), pp. 44-50.

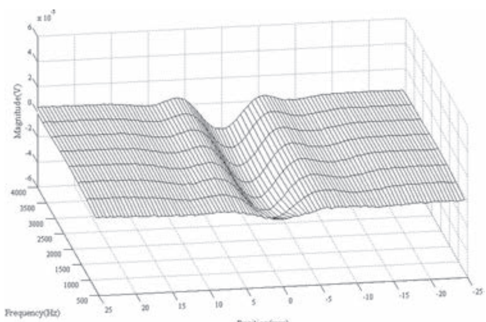

Fig. 1.

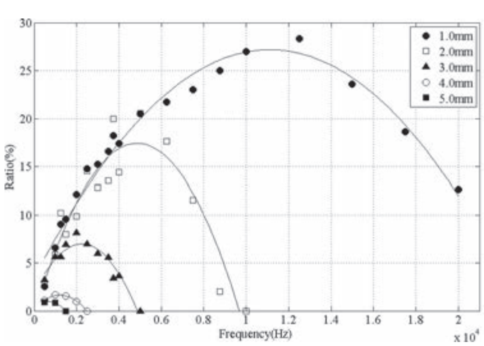

Fig. 2.

GV-02. Seismic circuit breaker with electromagnetic contactor.

T. Mifune[1] and K. Nishimura[1]
1. National Institute of Technology, Suzuka College, Suzuka, Japan

We reported a vibrational circuit breaker using ferromagnets and repulsive magnets [1]. The breaker has the advantages of auto-detection and does not require a battery. In previous studies have two problems. First, we used a moving parts with a slightly larger inner diameter than the axis. However, with this, there was friction between the shaft and the moving parts, and there was variation in the operating point. By using sliding bearings to solve this problem, the variation of operating points due to friction was reduced. Second, it was created for low current electronic circuits. For scenes actually used for home and industrial use, high voltage and high current are expected. It is necessary to investigate the allowable ampacity for high-current. Because it is effects of electromagnetic field when we apply the current over tens of amperes to it. In addition if high current is passed directly to the permanent magnet, temperature rise will occur. This may cause the magnetic force of the permanent magnet to disappear. In this digest, we propose to utilize an electromagnetic contactor shown in Fig.1. It is an electrically controlled switch used for switching an electrical power circuit, similar to a relay. We experimentally measured operating acceleration responses for the circuit breakers when we applied and didn't apply current. We obtained a similar result shown in Fig.2. These responses have resonant frequency of about 4 Hz. Responses of seismic intensity also are similar responses. If it can correspond to the seismic intensity such as 5 upper, 6 lower, it will be applicable as a seismic circuit breaker. The detail of how to correspondence to the seismic intensity is presented at the conference.

[1] K. Nishimura, M. Inoue, IEEE Trans. Magn., 47 (10), 2808 (2011)

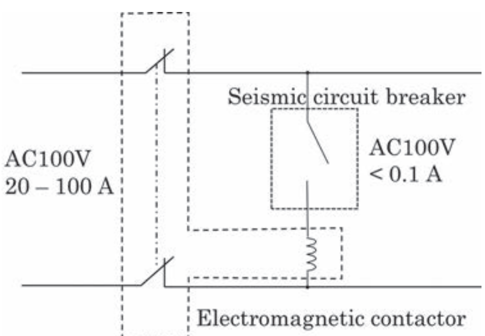

Fig. 1. Actual wiring diagram of seismic circuit breaker with electromagnetic contactor.

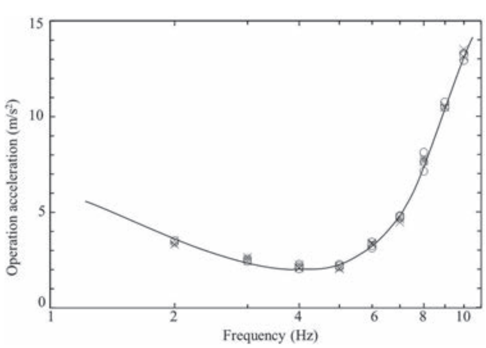

Fig. 2. Operating acceleration responses. Circles show the responses when applying current. Crosses show the responses when we didn't apply current.

GV-03. Marker-free coil-misalignment detection approach using TMR sensor array for dynamic wireless charging system of electric vehicles.

X. Liu[1], W. Han[1], C. Liu[2] and P. Pong[1]
1. Department of Electrical and Electronic Engineering, the University of Hong Kong, Hong Kong, China; 2. School of Energy and Environment, City University of Hong Kong, Hong Kong, China

I. Introduction Dynamic wireless charging (DWC) technology for electric vehicles (EVs) has obtained increasing attention recently [1] because it enables on-road EVs to be powered wirelessly so that EV driving range can be further extended. However, one main problem of the DWC system is that the receiving coil mounted on EVs should be well-aligned with the primary coil embedded under lane [2]. The transferred power and energy transmission efficiency drop significantly when there exists a large lateral misalignment. The existing vehicle-tracking techniques can be classified into two categories: marker-based approach and marker-free approach. The marker-based approach typically uses the radio-frequency identification (RFID) reader or magnetic sensor to detect the RFID tags or magnetic markers over/under lane [3-5]. However, the dense configuration of RFID or magnetic markers leads to high construction costs. The marker-free approach can overcome this drawback. Currently, marker-free approach is implemented with search coils which are installed underneath a vehicle body to detect the lateral misalignment; however, search coils suffer from their complicated installation (due to out-of-plane configuration) and bulky size (due to large turn number) [6, 7]. Its algorithm to determine the misalignment position by observing the change in voltage phase of search coil is unreliable and time-consuming [6]. Moreover, its actual applicability is largely restricted by the non-linear relationship between misalignment distance and search-coil voltage. In this work, a marker-free approach to detect the lateral coil-misalignment for DWC system using a tunneling magnetoresistive (TMR) sensor array is proposed (Fig. 1a). The compact-in-size TMR sensor array in-plane with the receiving coil is used to detect the magnetic field generated by the primary coil and to determine the coil-misalignment position, which makes the installation convenient. Computation process is straightforward, and coil-misalignment position can be easily obtained by analyzing the output amplitude of TMR sensors. II. Operating principle The magnetic field distribution on the plane of receiving coil can provide coil-misalignment information. Fig. 1b shows the diagram of magnetic field distribution at sensing position A. Since position A is at the center and on the same plane as receiving coil, the magnetic field generated by receiving coil at position A does not have component in the y-axis direction. The magnetic field at position A in the y-axis direction only depends on its relative position with respect to primary coil, as expressed by Eq. (3) in Fig. 1c. By adopting typical EV DWC parameters, the width of primary coils is set to 0.8 m, the gap length between primary coil and receiving coil 0.2 m, and the current flowing through primary coil 10 A_{RMS}, B_y at different sensing positions can be calculated according to Eq. (3), as depicted in Fig. 1d. There exists a sensing position where B_y equals to zero. The magnitude of the magnetic flux density is on the order of tens of μT which is well within the detection limit of TMR sensors. The lateral misalignment of receiving coil will lead to a shift of magnetic field distribution compared to the original field distribution without misalignment (Fig. 1d). Therefore, it is feasible to determine the misalignment position by employing a TMR sensor array to measure the flux density in the y-axis direction and analyze the sensing position where the flux density is minimum. III. Simulation analysis and experimental validation A 3D FEM simulation of magnetic field distribution at the sensing positions was performed to validate the theoretical field-calculation model. Fig. 2a shows the dimension of the primary coil and receiving coil. The simulated magnetic flux density in the y-axis direction is shown in Fig. 2b. When the receiving coil is well-aligned with primary coil, the minimum value of B_y occurs at the sensing position of 0 mm. The minimum value occurs at the sensing position of -30 mm when the receiving coil is misaligned 30 mm towards the left side; whereas that occurs at 30 mm when the receiving coil is misaligned 30 mm to the right side. An experimental prototype (Fig. 2c) is also established according to the simulation parameters. The prototype was composed of the magnetic-resonant-coupling-based wireless power transfer system which adopted the series-series topology. Its operating frequency was chosen as 20 kHz. The power source was provided by an AC power supply. A sensor array consisting of 9 single-axis TMR sensors uniformly distributed in an interval of 15 mm is mounted on the plane of receiving coil. TMR2001 sensor is employed due to its high sensitivity (80 mV/V/mT), small size (3×3×1.5 mm) and wide dynamic range (up to 1 MHz) [8]. The outputs of the sensor array were amplified 50 times by differential amplifiers (AD620) and then sampled by a DAQ card into a computer. The measured field results in the y-axis direction are shown in Fig. 2d. It is easily observed that the minimum output of the sensor array occurs at the sensing position of 0 mm when no misalignment exists. The minimum output of the sensor array occurs at the sensing position of 30 mm when the receiving coil is misaligned 30 mm towards to the left side. The minimum output occurs at -30 mm when the receiving coil is misaligned 30 mm to the right side. The experimental results are in good agreement with the theoretical analysis and the simulated results. More detailed analysis results will be presented in the final paper.

[1] C. C. Mi, G. Buja, S. Y. Choi, and C. T. Rim, "Modern advances in wireless power transfer systems for roadway powered electric vehicles," *IEEE Trans. Ind. Electron.,* vol. 63, no. 10, pp. 6533-6545, 2016. [2] F. Lu, H. Zhang, H. Hofmann, and C. Mi, "A Dynamic Charging System with Reduced Output Power Pulsation for Electric Vehicles.", *IEEE Trans. Ind. Electron.,* vol. 63, no. 10, pp. 6580-6590, 2016. [3] J. Deng, "Architecture design of the vehicle tracking system based on RFID," *Indonesian Journal of Electrical Engineering and Computer Science,* vol. 11, no. 11, pp. 2997-3004, 2013. [4] J. I. Hernandez and C. Y. Kuo, "Lateral control of higher order nonlinear vehicle model in emergency maneuvers using absolute positioning GPS and magnetic markers," *IEEE Trans. Veh. Technol.,* vol. 53, no. 2, pp. 372-384, 2004. [5] Y.-S. Byun, R.-G. Jeong, and S.-W. Kang, "Vehicle position estimation based on magnetic markers: Enhanced accuracy by compensation of time delays," *Sensors,* vol. 15, no. 11, pp. 28807-28825, 2015. [6] K. Hwang, J. Cho, D. Kim, J. Park, J. H. Kwon, S. I. Kwak, *et al.*, "An Autonomous Coil Alignment System for the Dynamic Wireless Charging of Electric Vehicles to Minimize Lateral Misalignment," *Energies,* vol. 10, p. 315, 2017 [7] K. Hwang, J. Park, D. Kim, H. H. Park, J. H. Kwon, S. I. Kwak*, et al.*, "Autonomous coil alignment system using fuzzy steering control for electric vehicles with dynamic wireless charging," *Math. Probl. Eng.,* vol. 2015, p. 205285, 2015. [8] TMR2001 TMR Linear Sensor Datasheet, [Online]. Available: http://www.dowaytech.com/en/1944.html (Access on Jan 2018)

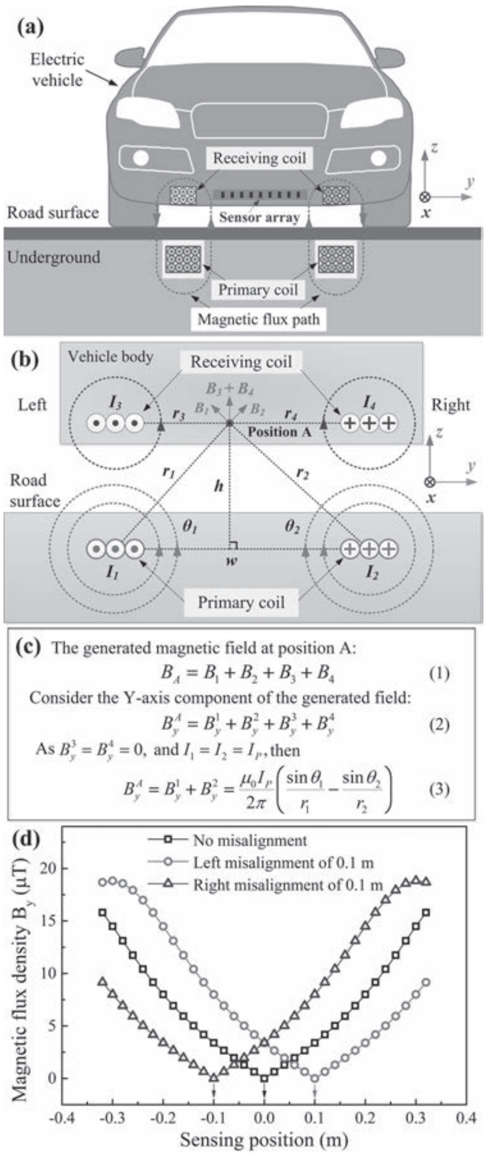

Fig. 1 Concept of marker-free coil-misalignment detection using TMR sensor array in a DWC system

Fig. 1.

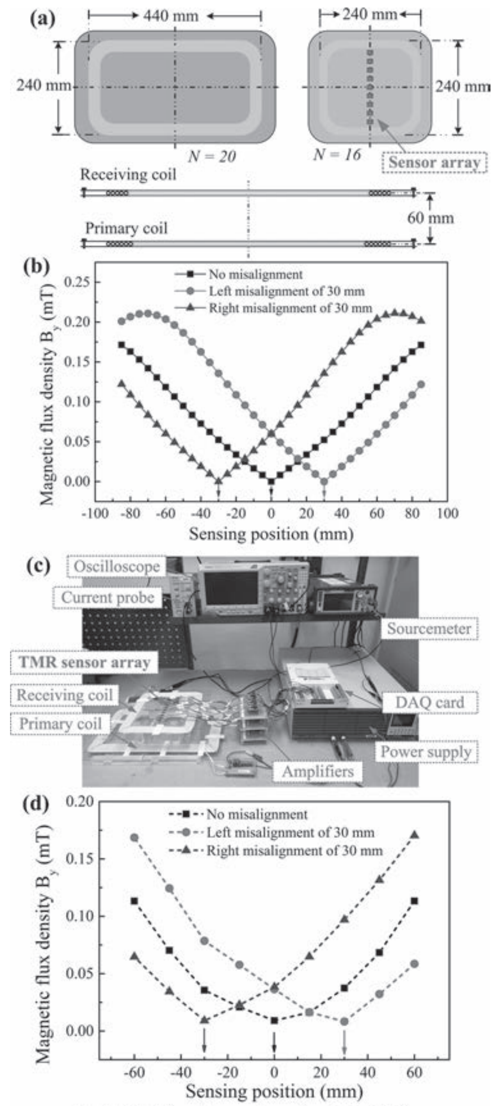

Fig. 2 FEM simulation and experimental validation

Fig. 2.

GV-04. Effects of Heat Treatment under Strong Magnetic Field of 1T or Higher on Magnetic Properties of Non-oriented Electrical Steel Sheet.

T. Kinoshita[1,2], K. Kohara[2], H. Shimoji[3], T. Sato[2] and T. Todaka[2]
1. Technology Research Center, Sumitomo Heavy Indurstries, Ltd., Yokosuka, Japan; 2. Oita university, Oita, Japan; 3. Oita Industrial Research Institute, Oita, Japan

In order to improve magnetic properties of non-oriented electrical steel sheets, effects of heat treatment in a magnetic field to control crystallographic orientation were studied. In this paper, we report on the effects of the amplitude and direction of the magnetic field applied during the heat treatment in comparison to magnetic properties of samples, which the longitudinal direction is parallel to the rolling direction (RD) or rolling transverse direction (TD). To clarify the effects of heat treatment in a magnetic field on the magnetic properties of the electrical steel sheets, heat treatment without magnetic field was firstly carried out and a change rate, defined as a value obtained by dividing the iron loss value after the heat treatment by the iron loss value before the heat treatment, was used in the evaluation. Fig. 1 shows a schematic view of the heat treatment apparatus. The heat treatment apparatus consisted of an electric furnace at inner diameter of a superconducting magnet (10 T - CSM) and a quartz glass tube inserted into the furnace. The quartz tube was depressurized to less than 10^{-3} Pa with a turbo molecular pump. The heat treatment temperature was controlled at 1023 K, 1123 K, and 1273 K. 10 mm × 50 mm sized samples were prepared by cutting a non-oriented electrical steel sheet, 50A470 (JIS C 2552), with electrical discharge machining. Samples were cut so that their longitudinal direction was parallel to the rolling direction or rolling transverse direction. The samples were placed at the center of the magnetic field in the quartz tube using a holding jig made of quartz in a way that the direction of the magnetic field would be parallel to the longitudinal direction of the samples. The strength of the applied magnetic field was set to a maximum of 10 T. Fig. 2 shows iron loss change rate of the samples heat treated at 1273 K with respect to iron loss before heat treatment. In Fig. 2, for example, “RD-10T” means the sample with longitudinal direction parallel to the rolling direction and applied magnetic field during the heat treatment of 10 T. The vertical axis represents the change rate and the horizontal axis represents the amplitude of the excitation magnetic flux density controlled by the sinusoidal wave of 50 Hz with a small-sized single sheet tester. As shown in Fig. 2, both the RD- and TD-samples heat-treated without magnetic field (0 T) under the temperature condition of 1273 K showed a remarkable change in the magnetic properties. The grain growth was accelerated by the heat treatment, the iron loss was reduced, and the permeability under low excitation conditions was improved. Contrarily, the permeability at 1.6 T or higher decreased. It was also found that the effect of the heat treatment on the reduction of the iron loss was greater in the TD-samples. As for the results of heat-treatment in magnetic field, the iron loss of the RD-sample was reduced after heat treatment in 10 T. On the other hand, the iron loss of the TD-sample increased after heat treatment in 10 T. It was also found that application of the strong magnetic field of 10 T throughout the heat treatment, i.e. during the heating and cooling, caused increase of the iron loss and decrease of the magnetic permeability regardless of the direction of the material. The cause of this phenomenon is possibly the contraction of the polycrystalline specimen in the strong magnetic field. The details will be discussed at the presentation and in the full version of this paper.

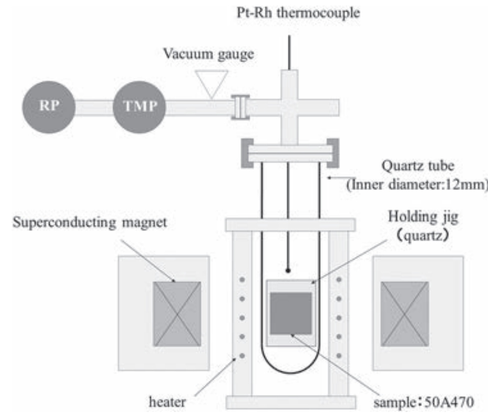

Fig. 1. Schematic diagram of magnetic heat treatment apparatus.

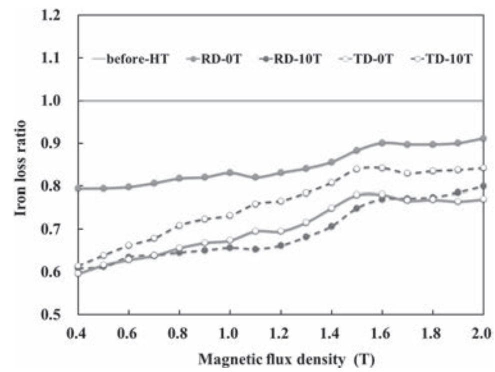

Fig. 2. Iron loss change rate of the samples heat treated under 1273 K with respect to iron loss before heat treatment.

GV-05. Analytical Modeling of Multi-layer Permanent Magnet Eddy Current Brake With Hybrid Secondary.

B. Kou[1], *W. Chen*[1,2], Y. Jin[1] and X. Zhao[1]
1. Harbin Institute of Technology, Harbin, China; 2. Harbin University of Science and Technology, Harbin, China

I. INTRODUCTION Eddy current brake has been widely used in various kinds of industrial applications due to its outstanding performance. Compared with the electric excitation brake, permanent magnet eddy current brake has the advantages of compact structure, high efficiency and high reliability[1]-[4].In the eddy current brakes, the secondary according to the material can be divided into the non-magnetic reaction material and the magnetic reaction material. The secondary of non-magnetic reaction material with high conductivity is generally used for low-speed braking. The magnetic reaction secondary with high permeability is widely used in high-speed braking, such as high speed train braking systems. However, in the ejection experiment, it is necessary to brake the ejection object from high speed to low speed in order to avoid the ejection object broken. The hybrid secondary eddy current brake is the combination of the non-magnetic reaction secondary and the magnetic reaction secondary eddy current brake, which can make the secondary have higher braking force in both high speed and low speed. In this paper, a multi-layer permanent magnet linear eddy current brake with hybrid secondary was presented as shown in Fig.1(a). First, the structure and working principle were introduced. Then, the nonlinear analytic model was derived using the Maxwell's equations. The iron secondary was split into thin sheets of constant permeability, determined by an iterative procedure. The analytic model takes into account higher harmonics and secondary saturation. Therefore, the accuracy is observably improved. Finally, the accuracy of the analytical model is verified by the finite element method. II. FUNDAMENTAL STRUCTURE Fig. 1(a) shows the structure of the multi-layer permanent magnet linear eddy current brake with hybrid secondary. The primary part consists of the primary core and permanent magnets (PMs). The polarity of adjacent permanent magnets on the same row is opposite. Besides, the magnetized direction of the permanent magnet on the same column is the same. The two short hybrid secondary is made of copper plate with high conductivity and iron plate with high permeability material. III. ANALYTIC MODEL The hybrid secondary linear eddy current brake analytic model is simplified, as shown in Fig. 1(b). Because of the independence of the iron secondary and copper secondary flux, they can be divided into two regions separately. Since the model is symmetrical about the middle plane of each secondary, we can only study the half symmetric region and use the second kind of boundary conditions to simplify the structure. The copper secondary analytic model is divided into four different regions, primary iron core, permanent magnets, air gap and secondary copper plate. The iron secondary analytic model is shown in Fig.1(c). Considering secondary saturation, the iron plate is divided in fictitious layers whose permeability is determined by an iteration procedure. Then, the two analytic models are derived using the Maxwell's equations. IV. MODEL VALIDATION The finite element analysis is used to verify the validity of analytic model. Fig. 2(a) and Fig. 2(b) compare the air-gap flux density obtained by the FEM and analytical method. We plot the magnetic-flux density map inside the device with the speed of 20 m/s and 200m/s. It can be seen that the air-gap flux distortion due to higher harmonics. Fig. 2(c) is the iron secondary and the copper secondary braking force characteristic. The maximum braking force of the copper plate appears at a low speed range (about 5m/s). As the speed increases, the braking force decreases rapidly. The maximum braking force of the iron plate appears at a high speed (about 50m/s) and keeps constant as the speed increases. Fig. 2(d) shows the resultant braking force of the two conductor plates. The secondary braking force maintains a stationary value from high speed to low speed. Therefore, we can verify that the analytic model can reasonably take into account higher harmonics and secondary saturation. V. CONCLUSION In this paper, a multi-layer permanent magnet linear eddy current brake with hybrid secondary was presented. The magnetic field distribution is calculated by using the Maxwell's equations. The expression of braking force is derived based on the Maxwell stress expressions. The agreement between analytic model and finite element method is very good. It verifies the validity and universality of the analytical model.

[1]Canova, B. Vusini, "Analytical modeling of rotating eddy-current couplers", *IEEE Trans. Magn.*, vol.41, no.1, pp. 24-35, Jan. 2005. [2]S. Mohammadi, M. Mirsalim, S. Vaez-Zadeh, "Nonlinear modeling of eddy-current couplers", *IEEE Trans. Energy Convers.*, vol. 29, no. 1, pp. 224-231, Mar. 2014. [3]B. Kou, Y. Jin, H. Zhang, L. Zhang, H. Zhang, "Modeling and analysis of force characteristics for hybrid excitation linear eddy current brake", *IEEE Trans. Magn.*, vol. 50, no. 11, Nov. 2014. [4]S. M. Jang and S. H. Lee, "Comparison of Three Types of Permanent Magnet Linear Eddy-Current Brakes According to Magnetization Pattern," IEEE Transactions on Magnetics, Vol. 39, no. 5, pp. 3004-3006, Sep. 2003.

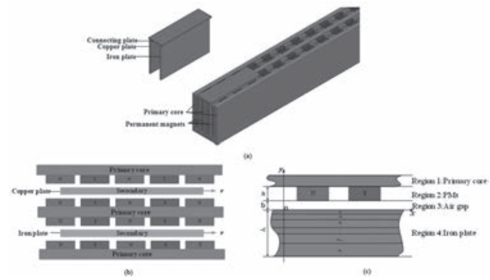

Fig. 1. (a) 3-D Structure of a multi-layer permanent magnet linear eddy current brake with hybrid secondary(b) 2-D Structure of a multi-layer permanent magnet linear eddy current brake with hybrid secondary (c) Iron secondary multi-layer analysis model.

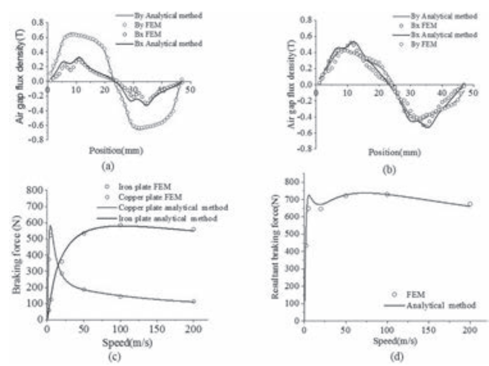

Fig. 2. (a) Air gap flux of iron secondary model with a speed of 20 m/s(b) Air gap flux of iron secondary model with a speed of 200 m/s (c) Braking force of iron plate and copper plate respectively(d) Resultant breaking force of the multi-layer permanent magnet linear eddy current brake with hybrid secondary.

GV-06. Parametric Design of Vehicle Horn Employing Rolled Silicon Steel Sheets Based on Its Analytical Approach.

J. Sim[1], K. Jung[1], D. Kim[1] and J. Hong[1]
1. Automotive Engineering, Hanyang University, Seoul, The Republic of Korea

I. Introduction Vehicle horn is an electromechanical energy conversion device which can be equipped with a variety of vehicles such as automobiles, motorcycles, trains, and trams. It is usually driven by a built-in electromagnet connected to a sinusoidal voltage source. Furthermore, the electromagnet produces an oscillating magnetic flux, vibrates a circular diaphragm, and makes a sound. This operating principle is similar to an electric bell or a buzzer. It plays a major role in calling attention to a collision risk or forewarning other people of a vehicle's presence and approach. The majority of countries legally regulate that all the vehicles should have the horns. As a result, their demand becomes gradually high as the vehicle market is expanded every year [1]-[4]. The carbon-steel-based solid cores are often used for all the components of the conventional vehicle horns such as body, diaphragm, pole, and armature. Such cores are a lot excellent in terms of cost-effectiveness, reliability, and productivity. On the other hand, they exhibit lower penetration depth and higher magnetic reluctance than the silicon-steel-based laminated cores when exposed to a time-varying magnetic field [5]-[7]. It is since the former has higher electrical conductivity than the latter. As a result, the traditional vehicle horns have the issues in extreme losses, inferior electromagnetic forces, and exposure to high temperature environment. This paper thus suggests a vehicle horn with novel structure employing rolled silicon electrical steel sheets as a solution for the aforementioned phenomena. The silicon electrical steel sheets surround the pole and armature of a conventional model. Such cores, 50A470, play a role in penetrating a time-varying magnetic field uniformly, preventing the eddy current from flowing in closed loop, and reducing the eddy current loss. In addition, the input current and the joule loss in copper winding are reduced thanks to the increased equivalent iron loss resistance. The corresponding equivalent magnetic circuit model is also developed to palliate a lot of computational burdens. The specific nonlinear analysis procedure and the circuit parameter extraction methods are referred to. The circuit model is used for the parametric design procedure of the novel vehicle horn. As a result, an optimum model with minimum loss and equivalent performance is obtained. Finally, it is manufactured and experimented in order to justify its effectiveness compared with the conventional vehicle horn. II. Rolled Silicon Electrical Steel Sheets In the case of the carbon-steel-based solid cores, the eddy current and the consequent loss are mainly induced at the skins of the pole and the armature due to their high electrical conductivity. However, the silicon-steel-based rolled cores exhibit lower electrical conductivity and higher magnetic permeability than such solid cores. The silicon electrical steel sheets, 50A470, are rolled around pole and armature of a conventional model. The silicon steel sheets prohibit the eddy current from flowing in closed loops and decrease the consequent loss. Furthermore, by means of the increased equivalent iron loss resistance, the input current and the joule loss in copper winding are also reduced. III. Analytical Approach Its analytical approach is introduced to represent the interconnection between an axisymmetric vehicle horn and an AC voltage source as described in Fig. 1 [1]. The circuit model is expressed in phasor forms because the sinusoidal time variations of the voltage source will generate the sinusoidal variations of electric and magnetic fields with the same frequency in the time harmonic fields. Also, it composes of the excitation coil resistance, the equivalent iron loss resistance, and the system effective reluctance. IV. Parametric Design In this parametric design, the two major design parameters were the excitation coil turns and the armature diameter to which the conventional one and the supplementary silicon steel diameter belong. In addition, the armature height, the pole diameter, and the pole height were set as the dependent design variables to keep up the weight of the driving part, i.e. the armature and the diaphragm, and the length of the air-gap as the armature diameter changes. The objective functions were the following four electromagnetic characteristics; force, input current, copper loss, and iron loss. In this case, the constant AC voltage condition was applied to. As a result, so as to maintain the electromagnetic force and minimize the other objectives and the coil turns, the armature diameter should be changed from 10mm to 18mm. The coil turns also changed from 150turns to 95turns as in Fig. 1. V. Experimental Verification The two prototypes and its experimental setup are shown in Fig. 2. The coil resistance, the active power, the reactive power, the amplitudes and the phases of the input voltage and current were measured for the condition above. The measured data could be used to calculate the copper loss, the iron loss, and the back electro-motive force, which were compared with those from the analytical approach for the two models. Such validation gives the approximately accurate estimation of the performance and the effectiveness of the novel model compared with the conventional model.

[1] J. H. Sim, D. Y. Kim, S. I. Kim, and J. P. Hong, "Analytical electromagnetic modeling and experimental validation of vehicle horn considering skin effect in its solid cores," *IEEE Trans. Magn*., vol. 53, no. 6, pp. 1-4, Jun. 2017. [2] W. Wu, T. Hong, L. Liu, C. Chen, P. Zeng, and Z. Zeng, "Study on durability test bench of the automotive electric horn," in *Proc. IEEE ICAE*, Zibo, China, May 2011, pp. 180-184. [3] J. Guo, W. Ren, G. Zhai, and H. Zhao, "Experiment research on high frequency mak ing and breaking characteristics of automobile horn contacts," in *Proc. IEEE HOLM*, Charleston, U.S.A., Oct. 2010, pp. 1-6. [4] S. Q. Ying, D. Xuwei, and L. Z. Hai, "Test method for the vibration response of a vehicle horn bracket," in *Proc. IEEE ICCSNT*, Harbin, China, Dec. 2015, pp. 992-995. [5] L. Cheng, S. Sudo, Y. Gao, H. Dozono, and K. Muramatsu, "Homogenization technique of laminated core taking account of eddy currents under rotational flux without edge effect," *IEEE Trans. Magn*., vol. 49, no. 5, pp. 1969-1972, May 2013. [6] P. Huang, C. Mao, D. Wang, L. Wang, Y. Duan, J. Qiu, G. Xu, and H. Cai, "Optimal design and implementation of high-voltage high-power silicon steel core medium-frequency transformer," *IEEE Trans. Ind. Electron*., vol. 64, no. 6, pp. 4391-4401, Jun. 2017. [7] Y. Gao, K. Muramatsu, M. J. Hatim, and M. Nagata, "The effect of laminated structure on coupled magnetic field and mechanical analyses of iron core and its homogenization technique," *IEEE Trans. Magn*., vol. 47, no. 5, pp. 1358-1361, May 2011. [8] B. H. Lee, S. O. Kwon, T. Sun, J. P. Hong, G. H. Lee, and J. Hur, "Modeling of core loss resistance for d-q equivalent circuit analysis of IPMSM considering harmonic linkage flux," *IEEE Trans. Magn*., vol. 47, no. 5, pp. 1066-1069, May 2011. [9] M. Ibrahim and P. Pillay, "Core loss prediction in electrical machine laminations considering skin effect and minor hysteresis loops," *IEEE Trans. Ind. Appl.*, vol. 49, no. 5, pp. 2061-2068, Sep.-Oct. 2013.

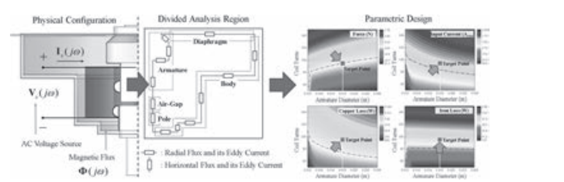

Fig. 1. Analytical approach for an axisymmetric vehicle horn with novel structures employing rolled silicon steel sheets and its parametric design.

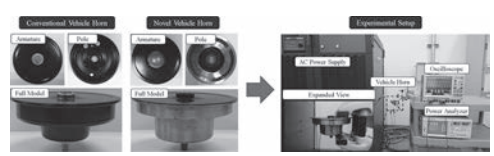

Fig. 2. Manufactured conventional and novel vehicle horns, and its experimental setup for verification.

GV-07. Analytical Modeling of Angular Misalignment for Axial Flux PM Machines: Effects on Cogging Torque.

B. Guo[1] and y. huang[1]
1. School of Electrical Engineering, Southeast University, Nanjing, China

Abstract: In this paper, an improved semi-analytical model is proposed to investigate the cogging torque of axial flux permanent magnet (AFPM) machine under angular misalignment. First, the axial and circumferential flux density in the airgap under healthy condition is developed by Maxwell's equations and Schwarz–Christoffel (SC) mapping. Second, the SC mapping in MATLAB toolbox is modified to consider the angular misalignment which could improve the accuracy. The results show that the analytical predictions agree well with the finite element (FE) results, also, the model is verified via the performance of experimental results. The main contribution of this paper is that the approach developed in this paper is more accuracy for angular misalignment, especially for the flux densities in the airgap. I. INTRODUCTION Axial flux permanent magnet machines (AFPMMS), due to their compact mechanical structure and high power density, are widely used in industrial applications, such as the fly wheel energy storage system. However, the contact area between the rotor plate and shaft is relative small, which makes the rotor predisposed to angular or axis misalignment. The misalignment of AFPMMs may cause serious problems, for instance, the unbalance magnetic force and mechanical vibration[1]. Therefore, these manufacturing imperfections should be detected quickly in order to avoid accidents. A significant amount of work has been done concerning the eccentricity for HSPMMs. Mark Thiele study the cogging torque via FE approach[2], while Antonino investigated manufacturing dissymmetry effects based on field functions in order to reduce computational time[3]. Nevertheless, these models are still based on the FE method and time consuming. In [4], the author adopted the lateral force approach to study the static angular eccentricity considering slot effect. This technique is convenient and simple. However, it neglects the tangential components of the air gap flux density. As previous study, [5] deal with several types of eccentricities. However, the magnetic flux densities of the static declined eccentricity in [5] do not match very well with the FE results. This paper is organized as follows. In Section II, the parameters of AFPM machine with Halbach array is provided. Section III will introduce the electromagnetic calculations used in this paper. The angular misalignment model and its solution strategy will be presented in Section IV. Afterward, the cogging torque is then discussed in Section V. In section VI, the experiment results are presented and compared with the results of model. At the end, conclusions will be presented. II. PROTOTYPE PARAMETERS The prototype construction of AFPMMs is a 5 phase, 2 pole pairs, 10-slot AFPMM with Halbach arrays, the basic dimensions and key design parameters are listed in full paper. III. DESCRIPTION OF ANALYTICAL MODEL Based on the separating variable method, the general magnetic vector potential solution for region I and II (shown in Fig. 1) can be written and solved by Matlab [6]. Using the Schwarz–Christoffel (SC) mapping technique [7], the flux densities of center airgap are calculated. The results shows that the analytical results agree well with the FE results. IV. MODEL OF ANGULAR MISALIGNMENT In this paper, to improve the accuracy of the magnet flux calculation, the structure of static angular eccentricity is directly draw by the SC Matlab toolbox. In order to reduce the computational time, the flux densities within only half period is calculated. Afterwards, the permeance function could be calculated. The flux densities at the mean radius are calculated by both the proposed method and FE method. Good agreement of both axial and circumferential flux densities are shown in Fig. 2. It can be seen that the accuracy is improved than approach shown in [5]. VI. EXPERIMENTAL RESULTS The rotor disk and the stator of the AFPM prototype are shown in full paper. The experimental setup and devices are carried out. In the test bench, the prototype is coupled with an inductance motor via belt system. The inductance motor is driven by an inverter. VII. CONCLUSION The high speed AFPM has been emerging in many industrial applications due to their compact structure and high power density. However, it has a critical problem with assembling process because of the imperfect manufacturing. Thus, this paper has a significant contribution in that the model developed in this paper has improved the accuracy, and the computation time can be reduced remarkably. In addition, it is notable that the cogging torque under normal and angular misalignment is investigated in this paper. Consequently, the approach proposed in this paper can be regarded as an effective analysis tool for AFPM machine under such condition. More information could be seen in the full paper.

[1] A. Di Gerlando, G. M. Foglia, M. F. Iacchetti, and R. Perini, "Effects of Manufacturing Imperfections in Concentrated Coil Axial Flux PM Machines: Evaluation and Tests," *IEEE Trans. Ind. Electron.*, vol. 61, no. 9, pp. 5012–5024, Sep. 2014. [2] T. Mark, "Aanlysis of cogging torque due to manufacturing variations in fractional pitch permanent magnet synchronous machines," doctoral, Charles Darwin University, 2013. [3] A. Di Gerlando, G. M. Foglia, M. F. Iacchetti, and R. Perini, "Evaluation of Manufacturing Dissymmetry Effects in Axial Flux Permanent-Magnet Machines: Analysis Method Based on Field Functions," *IEEE Trans. Magn.*, vol. 48, no. 6, pp. 1995–2008, Jun. 2012. [4] E. Ajily, M. Ardebili, and K. Abbaszadeh, "Magnet Defect and Rotor Eccentricity Modeling in Axial-Flux Permanent-Magnet Machines via 3-D Field Reconstruction Method," *IEEE Trans. Energy Convers.*, vol. PP, no. 99, pp. 1–10, 2015. [5] B. Guo, Y. Huang, F. Peng, Y. Guo, and J. Zhu, "Analytical Modeling of Manufacturing Imperfections in Double-Rotor Axial Flux PM Machines: Effects on Back EMF," *IEEE Trans. Magn.*, vol. 53, no. 6, pp. 1–5, Jun. 2017. [6] T. Lubin, S. Mezani, and A. Rezzoug, "Development of a 2-D Analytical Model for the Electromagnetic Computation of Axial-Field Magnetic Gears," *IEEE Trans. Magn.*, vol. 49, no. 11, pp. 5507–5521, Nov. 2013. [7] A. Alipour and M. Moallem, "Analytical magnetic field analysis of axial flux permanent-magnet machines using Schwarz-Christoffel transformation," in *Electric Machines Drives Conference (IEMDC), 2013 IEEE International*, 2013, pp. 670–677.

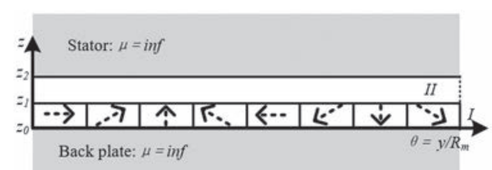

Fig. 1. Model of slotless air gap flux.

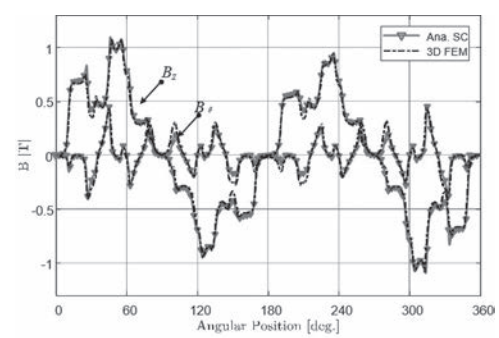

Fig. 2. Flux densities for angular misalignment condition.

GV-08. Investigation of an Axial-Gap Electromagnet-Assisted Ferrite Magnet Motor.

K. Motoki[1], Y. Kobayashi[1], N. Jike[1], *T. Fukami*[1], M. Koyama[1], T. Mori[2], M. Yamada[2] and M. Nakano[3]

1. Division of Electrical Engineering, Kanazawa Institute of Technology, Nonoichi, Japan; 2. Advanced Technology R&D Center, Mitsubishi Electric Corporation, Amagasaki, Japan; 3. Himeji Works, Mitsubishi Electric Corporation, Himeji, Japan

I. Introduction In general, traction motors for the electric vehicles (EVs) and hybrid EVs have to offer the characteristics, such as high torque, wide speed range, high efficiency, high controllability, and maintenance-free operation [1]. To achieve these goals, our research group is studying a new rare-earth-free motor that combines two driving principles. In a previous paper [2], an electromagnet-assisted ferrite magnet motor (EMaFM) was proposed, and its electromagnetic performance was investigated on a 1.5-kW radial-gap EMaFM (RG-EMaFM). The EMaFM is a motor in which the torque due to a ferrite magnet motor is assisted by the variable magnetic force of an electromagnet motor. In the EMaFM, a flux-modulating synchronous motor (FMSM) [3], which does not require brushes and slip rings, was used as the electromagnet motor, and a surface permanent magnet synchronous motor (SPMSM) was used as the ferrite magnet motor. From two-dimensional (2-D) finite element analysis (FEA) and experimental results, it was found that the torque can be controlled widely by the armature current or field current. In this paper, an axial-gap EMaFM (AG-EMaFM), which achieves high torque in the EMaFM, is newly proposed, and its electromagnetic performance is investigated by using three-dimensional (3-D) FEA. II. Proposed AG-EMaFM Figure 1(a) and (b) shows the topologies of the EMaFM, namely the conventional RG-EMaFM and the proposed AG-EMaFM. In the conventional RG-EMaFM, the motor base housing becomes longer in the axial direction than that of the proposed AG-EMaFM in order to rotatably support the rotor and rotating shaft. Moreover, there are problems such as a decrease in the conductor areas of the inner armature winding (W_{a1}) and difficulty in cooling the W_{a1}. However, with the proposed AG-EMaFM, these problems can be solved at once. In the after-mentioned performance analysis, the air-gap lengths and the sizes of active parts for torque production of the RG- and AG-EMaFMs are designed to be the same for easy comparison. Additionally, as shown in Table I, the slot-fill factors of the two armature windings (W_{a1} and W_{a2}) and field winding (W_f) in the AG-EMaFM were designed to be almost the same, and the conductor areas of the W_{a1} were increased. III. Results of Performance Analysis Figure 2 shows the magnetic flux density distribution in the AG-EMaFM under i_d = 0 control. In the figure, i_d and i_q are the d- and q-axis currents, respectively, I_f is the field current, and N_r is the rotating speed of the rotor. From Fig. 2, it can be seen that the magnetic saturation is more likely to occur in the stator teeth of the FMSM side. Figure 3 shows the torque waveforms of the RG- and AG-EMaFMs under i_d = 0 control. As can be observed from Fig. 3, the average torque (T) of the AG-EMaFM is 1.39 times higher than that of the RG-EMaFM when the magnetomotive force of the W_f is the same. IV. Conclusion As described above, the proposed AG-EMaFM is better than the conventional RG-EMaFM in terms of downsizing the motor base housing and cooling the windings. In addition, its torque density can be improved by increasing the conductor areas of the windings.

[1] K. T. Chau, C.C. Chan, and C. Liu, "Overview of permanent-magnet brushless drives for electric and hybrid electric vehicles," *IEEE Trans. Ind. Electron*., vol. 55, no. 6, pp. 2246–2257, Jun. 2008. [2] T. Fukami, K. Motoki, R. Kirihata, K. Shima, M. Koyama, T. Mori, and M. Nakano, "An electromagnet-assisted ferrite magnet motor," *IEEE Trans. Magn*., vol. 53, no. 11, Nov. 2017, Art. no. 2100404. [3] T. Fukami, Y. Matsuura, K. Shima, M. Momiyama, and M. Kawamura, "A multipole synchronous machine with nonoverlapping concentrated armature and field windings on the stator," *IEEE Trans. Ind. Electron*., vol. 59, no. 6, pp. 2583-2591, Jun. 2012.

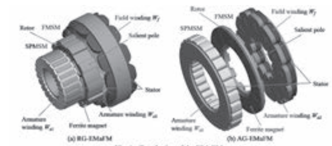

Fig. 1. Topologies of the EMaFM.

TABLE I
WINDING SPECIFICATIONS OF THE RG- AND AG-EMAFMS

Items	RG-EMaFM			AG-EMaFM		
	W_{a1}	W_{a2}	W_f	W_{a1}	W_{a2}	W_f
Number of poles	20	8	12	20	8	12
Conductor diameter (mm)	0.8	1.2	0.9	0.8	0.8	0.8
Number of conductors in parallel	2	-	-	2	2	-
Number of turns per coil in one slot	50	42	107	81	69	158
Parallel circuits per phase	2	2	-	2	2	-
Slot fill factor (%)	36.4	46.4	45.8	46.0	45.8	45.8

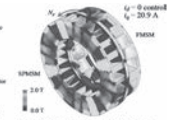

Fig. 2. Magnetic flux density distribution (I_f = 3.02 A, N_r = 900 min^{-1}).

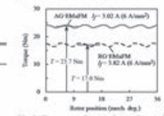

Fig. 3. Torque waveforms under i_d = 0 control (i_q = 20.9 A, N_r = 900 min^{-1}).

Fig. 1.

GV-09. Core loss properties of a permanent magnet synchronous motor with nanocrystalline stator and rotor cores under inverter excitation.

A. Yao[1], *T. Sugimoto*[1], S. Odawara[2] and K. Fujisaki[1]
1. Department of Engineering, Toyota Technological Institute, Nagoya, Japan; 2. Department of Electrical and Electronic Engineering, Kitami Institute of Technology, Kitami, Japan

INTRODUCTION Several researchers have recently focused on core loss reduction of the motor based on core with nanocrystalline magnetic materials (NMM) [1, 2], which offer low iron losses [3]. Previous studies have shown permanent magnet synchronous motors (PMSM) by use of “only stator core” made of NMM have low core losses [1, 2]. Here, in order to realize low loss motor system, it is necessarily to understand core loss properties of “both stator and rotor cores” with NMM. However, there has been no report on the motor by use of “both NMM stator and rotor cores”. In this study, the core losses of PMSM with the NMM stator and rotor cores under pulse-width-modulation (PWM) inverter excitation are evaluated based on both experiments and numerical simulations. The comparison with PMSM made of conventional non-oriented (NO) steels is also performed. In addition, we discuss the core loss repartition by using numerical simulations. MOTOR CORE AND ITS MEASURMENT SYSTEM Fig. 1 shows the appearance of the rotor and stator cores and the completed PMSM motor. The nanocrystalline alloy ribbons consisted of Fe-Si-B-Cu-Nb are laminated and impregnated with acrylic resin to make the block core. The laminated block core is then cut in the shape of the rotor core using electric discharge machining. The rotor core with an outer diameter of 74 mm and a thickness of 47 mm is constructed. The space factor of the rotor core is about 82%. See Ref. [4] for the details of the NMM stator, NO rotor, and NO stator cores. From here on, the PMSM with NO (NMM) stator and rotor cores is called NO-PMSM (NMM-PMSM). Fig. 1 also illustrates the set-up of PMSM measurement system, which consists of a three-phase voltage source PWM inverter with IGBT, under no-load condition. A power analyzer (Yokogawa PX8000) is used to measure the phase voltages, the phase rms currents and then the input active electrical power P_{in}. Conventional vector control is used for the speed control. Under these conditions, the PMSM total iron losses W are calculated by $W=P_{in}-P_{cu}-P_{m}$, where P_{cu} is the copper loss and P_{m} is the mechanical loss. See Ref. [4] for the details of measurement system. In our numerical simulations, 2D-finite element method (FEM) with A method is performed. In our simulations, iron losses of the soft magnetic cores are calculated from Steinmetz equation and then, the magnet losses are calculated by using the electrical conductivity and the analyzed eddy current density. See Ref. [4] for more details of numerical simulation methods. RESULTS AND DISCUSSION Fig. 2(a) shows the experimental results of core losses of both the NO-PMSM and the NMM-PMSM. The measurements have been done at 750, 1500, and 2250 rpm that correspond to electrical frequency of 50, 100, and 150 Hz, respectively. The core loss increases with the increase of the rotational speed. The core loss of the NO-PMSM (NMM-PMSM) is about 2.3, 5.2, and 8.0 W (1.1, 2.6, and 3.9 W) at 750, 1500, and 2250 rpm, respectively. In average, under PWM inverter excitation, the total core losses of the NMM-PMSM are about 60 % lower than those of the NO-PMSM. In order to discuss the core loss repartition, we do the numerical simulations. Fig. 2(b) shows core loss repartition between the stator, rotor and magnets of NMM-PMSM and the NO-PMSM by numerical simulations. Here, the numerical core losses are fit to the measured iron losses at 1500 rpm. The average rotor loss of NMM-PMSM and the NO-PMSM cores accounts for 16% and 18% of the total core losses, respectively. The average decrease obtained by using NMM instead of NO in only the stator (rotor) core is about 62% (56%). Here, replacing the NO rotor and stator cores of the proposed PMSM by those cores with NMM leads to a reduction of the core losses. The core loss reduction depends not only on the stator core but also on the rotor core. These results confirm the benefit of using not only NMM stator core but also NMM rotor core to reduce the motor core losses. CONCLUSIONS We for the first time developed and examined PMSM by use of “both stator and rotor cores” made of NMM. The core loss of the NO-PMSM (NMM-PMSM) was about 2.3, 5.2, and 8.0 W (1.1, 2.6, and 3.9 W) at 750, 1500, and 2250 rpm, respectively. In average, under PWM inverter excitation, the total core losses of the NMM-PMSM were about 60 % lower than those of the NO-PMSM. The average decrease obtained by using NMM instead of NO in only the stator (rotor) core was about 62% (56%). The core loss reduction depended not only on the stator core but also on the rotor core. These results open the way to further research in ultimate low loss motor system based on both rotor and stator cores made of NMM. ACKNOWLEDGMENT This work was partly supported by the New Energy and Industrial Technology Development Organization (NEDO) and the Ministry of Education, Culture, Sports, Science and Technology Program, Japan, for private universities.

[1] N. Nishiyama, K. Tanimoto, and A. Makino, Outstanding efficiency in energy conversion for electric motors constructed by nanocrystalline soft magnetic alloy “ nanomet®” cores, AIP Advances, 6 (5), 055925 (2016). [2] N. Denis, M. Inoue, K. Fujisaki, H. Itabashi, and T. Yano, Iron loss reduction of permanent magnet synchronous motor by use of stator core made of nanocrystalline magnetic material, IEEE Transactions on Magnetics, (2017). [3] Y. Yoshizawa and K. Yamauchi, Fe-based soft magnetic alloys composed of ultra_ne grain structure, Materials Transactions, JIM, 31 (4), 307-314 (1990). [4] A. Yao, T. Sugimoto, S. Odawara, and K. Fujisaki, Core losses of a permanent magnet synchronous motor with an amorphous stator core under inverter and sinusoidal excitations, AIP Advances, 8 (5), 056804 (2017).

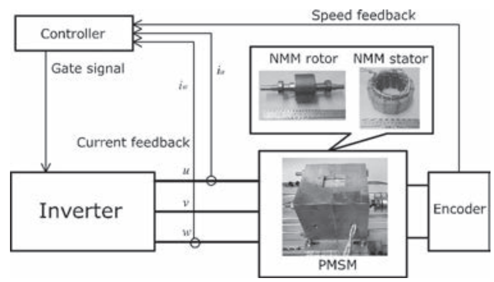

Fig. 1. Core and its losses measurement set up for inverter-fed motor.

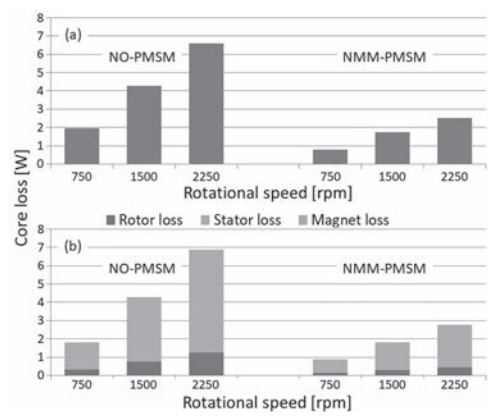

Fig. 2. Core loss properties with respect to rotational speed: (a) Experimental results, (b) Corresponding numerical results.

GV-10. An Approach Combining Analytical Calculation and FEA for Evaluation of Rotor Strength of IPM Motors.

M. Hsieh[1], J. Lai[1] and C. Li[1]
1. National Cheng Kung University, Tainan, Taiwan

1. Introduction and Research Method This digest proposes a FEA-assisted approach for evaluation of the mechanical strength of interior permanent magnet motors (IPM motors). The rotors of IPM motors can be structurally weak due to inevitable bridges or ribs that should be as narrow as possible to mitigate flux leakage. An ideal design is such that the motor can maximize the electromagnetic performance while keeping the rotor just sufficiently safe. However, common ribs/bridge design is usually conducted with experiences, intuition or alternatively, using only structural analysis, which completely ignores the effect of electromagnetic force. To maximize the motor performance, an over safe design, i.e., wider ribs/bridges than needed, should be avoided. To do this, coupled electromagnetic-structural simulations would be necessary so that the mutual effect of the rotor structure (i.e., rib/bridge width) and electromagnetic performance can be fully investigated. Also, the forces acting on the rotor and causing stress contain centrifugal force and electromagnetic force. This should also be simulated using coupled simulation; however, this is very time consuming and would prolong the development process. The method developed here is to predict the structural safety using solely structural analysis without the coupled simulation while maintaining the electromagnetic effect and keeping sufficient accuracy. The Maxwell stress tensor is employed to calculate the electromagnetic force on rotor surface for different load conditions. A modification factor is then determined by the ratio of the calculated electromagnetic force plus the centrifugal force obtained using FEA to the FEA centrifugal force [i.e. (Fem_cal+Fcent_fea)/Fcent_fea]. This facor is greater than or close to one and can be used to compensate the error caused by the structural simulation only. Note that the structural simulation can directly obtain the stress on the rotor ribs/bridges so that the added electromagnetic force is assumed to linearly contribute to the stress levels. This can then be used to inspect the rotor mechanical strength with a reasonable accuracy. 2. Target Motors A group of IPM motors with different rotor diameters (from 48 mm to 110 mm) and power ratings (from 3 kW to 12 kW) but similar torque-per-unit-rotor-volume are investigated. One prototype is built and tested based on the previous analysis. Then, the experiments are performed to validate the simulations and the developed approach. 2.1 Computation of Electromagnetic Force As previously stated, the Maxwell stress tensor is used to calculate the rotor surface electromagnetic force. This is then compared with FEA (sample in Fig. 1) for validation. This will be detailed in full paper and part of the results will be presented along with structural analysis. 2.2 Structure Simulation The centrifugal forces are calculated using ANSYS simulation. The results do not consider electromagnetic effect. However, as previously stated, the modification factors obtained from the results in Sections 2.1 and 2.2 will be added to the structural simulation so that the electromagnetic effect can be included. Sample results are shown in the following figures and will be explained later. 2.3 Coupled Electromagnetic-structural Simulation This coupled simulations can calculate the combined effect of centrifugal and electromagnetic forces on ribs/bridges stress. Usually at low speed and high torque, the electromagnetic force dominates. As the speed increases, the centrifuge force increases and dominates. Fig. 2 shows that when no rib is utilized, the motor can only operate up to around 3500 rpm. On the other hand, if ribs are utilized in the design, the speed range can be extended but the efficiency decreases, as shown in Fig. 3. These coupled simulations will be used to validate the proposed method. 3. Comparison of Proposed Method and Coupled Simulation Some research only used centrifugal force to evaluate the rotor mechanical strength [1-3], but this could be insufficient for some conditions. From this digest, it is found that, if only the centrifugal force is considered, the rotor stress could be underestimated, in particular for small motors. As stated, a modification factor is introduced so that the sole structural simulation can be used without the need of coupled simulation. Fig. 4 shows the comparison of the proposed method and coupled simulation (more motors and results will be shown in the full paper). As can be seen, both methods agree well (2X or 1X indicate the modification factor). It is also found that, for rotor diameter beyond 110 mm, the centrifugal force dominates and the accuracy on rotor stress would be sufficiently good by using only the structural simulation. The smaller the rotor is, the bigger the modification factor is. 4. Experimental Study Some simulation and experiment results are compared in Fig. 5, where both cases agree well. 5. Conclusion The proposed method combines the analytical calculation and structural FEA to evaluate the mechanical strength of the rotors of IPM motors. A modification factor is introduced. The results were validated by coupled electromagnetic-structural simulation using ANSYS. The simulation on motor performance was also verified experimentally. More details will be reported in the full paper.

[1] D.Y. Kim, G.H. Jang and J.K. Nam, “Magnetically induced vibrations in an IPM motor due to distorted magnetic forces arising from flux weakening control, ” IEEE Transactions on Magnetics, pp.3929-3932, 2013. [2] J. Krotsch and B. Piepenbreier, “Radial forces in external rotor permanent magnet synchronous motor with non-overlapping windings, ” IEEE Transactions on Industrial Electronics, vol. 59, no. 5, pp. 2267-2276, 2012. [3] F. Chai and Y. Li, Y. Pei, “Calculation of the maximum mechanical stress on the rotor of interior permanent-magnet synchronous motor,” IEEE Transactions on Industrial Electronics, Vol. 63, pp.3420 – 3432, 2016

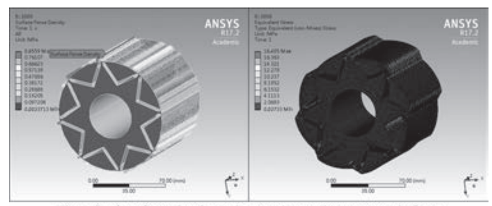

Fig. 1 Surface force density and stress due to electromagnetic force

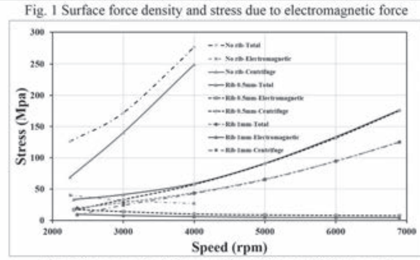

Fig. 2 The stress for different widths of ribs at different speed

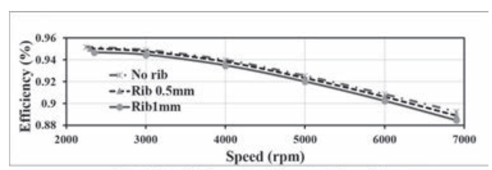

Fig. 3 The efficiency for different widths of ribs

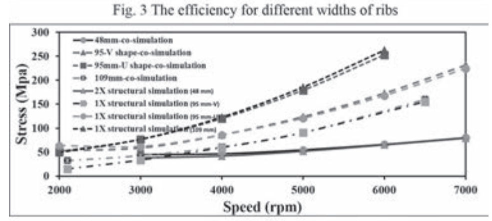

Fig. 4 The stress comparison of structural analysis and coupled electromagnetic- structural simulation

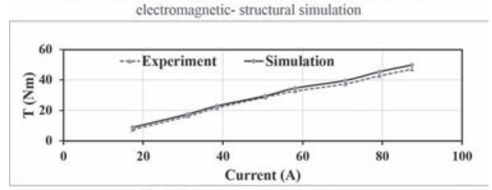

Fig. 5 The output torque comparison

GV-11. 2D Analytical Subdomain Model of Surface-Mounted PM Machines Accounting for Step-skewed Magnets.

S. Zhang[1] and S. Guo[2]

1. Bangor College, Central South University of Forestry and Technology, Changsha, China; 2. State Grid Hunan Electric Power Research Institute, Changsha, China

Abstract—The subdomain model for analytical calculation of magnetic field is widely developed to predict electromagnetic performance in PM machines. Based on the principle of the mutual flux through the stator windings due to step-skewed PMs identical to that from equivalent non-skewed PMs, a 2D subdomain model of surface-mounted PM machines accounting for step-skewed magnets is proposed. By resolving the analytical expressions of the equivalent PMs subdomain, the 3D problem of step-skewed magnets along axis is simplified to a 2D problem, which saves the computational resources and improves the efficiency. The 2D multislice finite-element analysis confirms accuracy of the analytical method. *Index Terms*—Surface-mounted permanent magnet machines, subdomain model, step-skewed magnets, analytical method. I. Introduction With the performance improvement of permanent magnet materials, permanent magnet motors are widely used in high-performance speed and position control systems. However, the interaction between the permanent magnet and the slotted armature iron core generates torque ripple inevitably, which causes vibration and noise, and then affects the control precision of the system. Due to the low cost and suitable for mass production, magnet skewing is a common method of reducing torque ripple [1]. It is showed that using step-skewed magnet is an effective design approach to improve torque ripple, but requires optimum skew angle and careful design of magnet shapes [2]. In [3], it is also pointed out that step number and magnet-skew angle determines the effect of reducing torque ripple. By optimizing the skewing angle and current phase advance angle together, an improved skewing is proposed to reduce torque ripple over the whole load range [4]. There are mainly two techniques for analyzing skewed PMs, which is finite-element-based method and analytical method. In [5], a number of slices for the finite-element model are employed to represent skewed magnets of the machine, which is called 2D multislice finite-element method. Since the 2D multislice methodology spent a lot of computing time, a geometric equivalent non-skewed PM structure is proposed and performed in 2D finite-element method for surface-mounted PM Machine with skewed magnets [6]. In [7], a 3D analytical model is developed for tubular actuator with skewed PMs, and the 3D finite-element method is used to verity the analytical solution. Compared with the huge computing resource requirements of 2D multislice and 3D finite-element, the analytical method shows the advantages of clear physical concept and fast calculation. In recent years, the subdomain model based on variable separation method [8] has been widely used for calculation of magnetic field distribution in surface-mounted PM Machine [9]-[10], but the influence of skewed PMs are not considered in the analytical model. In this paper, based on the principle of the mutual flux through the stator windings due to step-skewed PMs identical to that from equivalent non-skewed PMs, a 2D subdomain model of surface-mounted PM machines accounting for step-skewed magnets is proposed. The main objective is to express the residual flux density of the equivalent PMs along the circumference, then the resolution of the equivalent PMs sub-domain in 2D polar coordinates makes dimensions reduction feasible. The analytical solution is validated by 2D multislice finite-element analysis. II. Step-skewed Magnets And Equivalent non-skewed PMs Subdomain The schematic model of step-skewed magnets in surface-mounted PM machines is shown in Fig.1. θ_{skew} is the total mechanical angle for PMs skewing, M is the PMs segment number along the axis, L_{ef} is core axial length. The skew angle of each PMs segment α in the circumferential direction can be obtained. In order to consider the effect of step-skewed PMs, an equivalent non-skewed PMs structure is shown in Fig.2, which has the same flux per pole with the step-skewed PMs. Taking the radial magnetization PMs for example, remanent magnetic flux density of each magnet segment is B_r. The equivalent non-skewed PMs have different remanence values per pole along the circumference shown in Fig.2. Regarding the equivalent PMs as a subdomain with new type of remanence magnetization pattern, the analytical solution of PMs subdomain can be resolved in 2D polar coordinates. The result of electromagnetic performance for surface-mounted PM machines accounting for step-skewed magnets and FE validation will be given in the full paper.

[1] Z. Q. Zhu and D. Howe, "Influence of design parameters on cogging torque in permanent magnet machines," *IEEE Trans. Energy Convers.*, vol. 15, no. 4, pp. 407–412, Dec. 2000. [2] R. Islam, I. Husain, A. Fardoun and K. McLaughlin, "Permanent-Magnet Synchronous Motor Magnet Designs With Skewing for Torque Ripple and Cogging Torque Reduction," *IEEE Trans. Ind. Appl.*, vol. 45, no. 1, pp. 152-160, Jan./Feb. 2009. [3] J. A. Guemes, A. M. Iraolagoitia, J. I. Del Hoyo, and P. Fernandez, "Torque Analysis in Permanent-Magnet Synchronous Motors: A Comparative Study," *IEEE Trans. Energy Convers.*, vol. 26, no. 1, pp. 55–63, Mar. 2011. [4] W. Q. Chu and Z. Q. Zhu, "Investigation of torque ripple in PM synchronous machines with skewing," IEEE Trans. Magn., vol. 49, no. 3, pp. 1211–1220, Mar. 2013. [5] G. D. Kalokiris, T. D. Kefalas, A. G. Kladas, and J. A. Tegopoulos,"Special air-gap element for 2-D FEM analysis of electrical machines accounting for rotor skew," *IEEE Trans. Magn.*, vol. 41, no. 5, pp. 2020–2023, 2005. [6] J. Urresty, J. Riba, L. Romeral and A. Garcia, "A Simple 2-D Finite-Element Geometry for Analyzing Surface-Mounted Synchronous Machines With Skewed Rotor Magnets," *IEEE Trans. Magn.*, vol. 46, no. 11, pp. 3948-3954, 2010. [7] B. L. J. Gysen, K. J. Meessen, J. J. H. Paulides, and E. A. Lomonova, "3-D Analytical and Numerical Modeling of Tubular Actuators With Skewed Permanent Magnets," *IEEE Trans. Magn.*, vol. 47, no.9, pp. 2200-2212, 2011. [8] B. L. J. Gysen, K. J. Meessen, J. J. H. Paulides, and E. A. Lomonova, "General Formulation of the Electromagnetic Field Distribution in Machines and Devices Using Fourier Analysis," *IEEE Trans. Magn.*, vol. 46, no.1, pp. 39-52, 2010. [9] Z. Q. Zhu, L. J. Wu and Z. P. Xia, "An Accurate Subdomain Model for Magnetic Field Computation in Slotted Surface-Mounted Permanent-Magnet Machines," *IEEE Trans. Magn.*, vol. 46, no. 4, pp. 1100-1115, 2010. [10] T. Lubin, S. Mezani and A. Rezzoug, "2-D Exact Analytical Model for Surface-Mounted Permanent-Magnet Motors With Semi-Closed Slots," *IEEE Trans. Magn.*, vol. 47, no. 2, pp. 479-492, 2011.

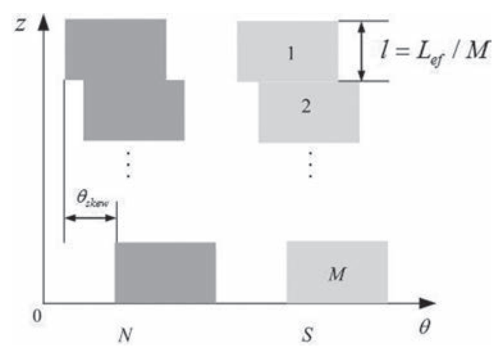

Fig. 1.

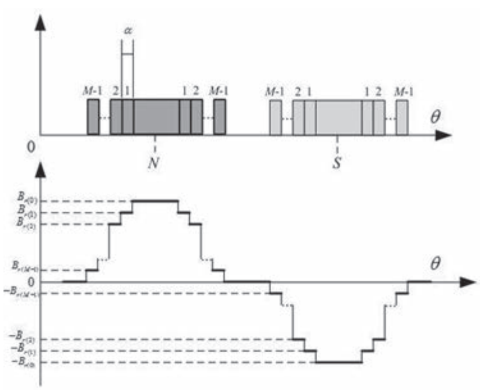

Fig. 2.

GV-12. Design Strategy of 3-Times Magnetizer for Post-Assembly Magnetization of Spoke-Type Ferrite Magnet Motor.

H. Seol[1], H. Jun[1], D. Jung[1], H. Kim[1], D. Kang[2] and j. Lee[1]
1. Hanyang University, Seoul, The Republic of Korea; 2. Keimyung University, Daegu, The Republic of Korea

This paper propose design strategy of 3-times magnetizer and rotor of ferrite spoke-type permanent magnet synchronous motor (PMSM) for post-assembly magnetization. In spoke-type PMSM, the design of the permanent magnets and the winding of magnetizer have a great effect on the magnetization, demagnetization and the torque of the motor. For this reason, it is very important to design these parameters appropriately[1]-[3]. In addition, transient analysis must be performed in order to perform accurate magnetization analysis. However, in order to derive the final design model, it takes a lot of time to perform transient analysis for each model. Therefore, we proposed a design strategy for shortening design and analysis time. Fig. 1 shows spoke-type PMSM and 3-times magnetizer. The rotor of spoke-type PMSM is 10 poles and 10 of permanent magnets are magnetized by 3-times magnetizer. 3-times magnetizer magnetizes the four permanent magnet per 1 times. Then remaining four magnets are magnetized after the rotor has rotated 144 degrees. Finally, the last two remaining magnets are magnetized after the rotor is rotated 144 degrees. At this time, two of the ten permanent magnets will be magnetized twice. In this paper, the magnetization analysis was performed through finite element analysis and the commercial FE software (Maxwell) was used. Fig. 2 is the FEA results of 3-times magnetizer. Red area is magnetization area (over than 340kA/m), green area is part that is not magnetized (below 340kA/m) and blue area is demagnetization area (below -290kA/m). The magnetic flux from the main pole magnetizes the four permanent magnets. At this time, some leakage magnetic flux generate demagnetization as shown in the blue area. To prevent such demagnetization, magnetic flux from the inter-pole cancels the leakage flux. Therefore, Proper design of the number of turns of the main pole and the inter-pole is necessary for complete magnetization and prevention of the demagnetization.

[1] Min-Fu Hsieh, Member, You-Chiuan Hsu, and David G. Dorrell, “Design of Large-Power Surface-Mounted Permanent-Magnet Motors Using Postassembly Magnetization”, IEEE Trans. Ind. Elect., vol. 57, no 10. Oct. 2010. [2] Min-Fu Hsieh, Yao-Min Lien, and David G. Dorrell, “Post-Assembly Magnetization of Rare-Earth Fractional-Slot Surface Permanent-Magnet Machines Using a Two-Shot Method”, IEEE Trans. Ind. Appl., vol. 47, no 6. Nov/Dec. 2011. [3] Min-Fu Hsieh and You-Chiuan Hsu, “Characteristics Regulation for Manufacture of Permanent-Magnet Motors Using Post-Assembly Magnetization”, IEEE Trans. Magn., vol. 43, no 6. Nov. 2007.

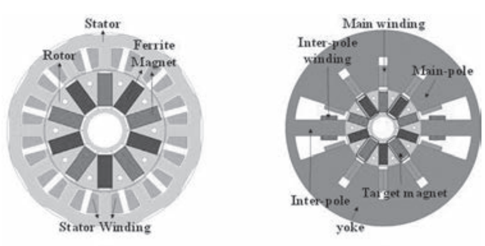

Fig. 1. (a) Spoke-type PMSM (b) 3-times magnetizer

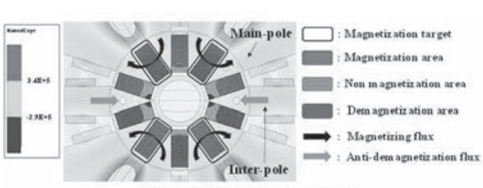

Fig. 2. FEA results of 3-times magnetizer

GV-13. Numerical Design and Validation of SPMSG for Efficiency Improvement of Engine-Generator System of PHEV compatible to Optimal Operating Line.

D. Lee[2], S. Cho[1] and *H. Jung*[1]

1. Advanced Power System R&D Center, Korea Automotive Technology Institute, Cheonan-si, The Republic of Korea; 2. Department of Electrical and Computer Engineering, University of Illinois at Urbana-Champaign, Urbana, IL, United States

I. INTRODUCTION Development of green car like EV(Electric Vehicle), HEV(Hybrid Electric Vehicle) and PHEV(Plug-in Hybrid Electric Vehicle) is dramatically accelerated to deal with the environmental regulation control and fossil fuel depletion dependent on fuel economy and hazardous emissions. EV have disadvantage of high cost, battery weight and deficient total driving distance. Hence, PHEV is getting the spotlight in the eco-friendly vehicle as one of the alternative candidates, which increase the energy storage capacity and extend the pure electric vehicle driving distance. In particular, EGS(Engine-Generator System) is mostly significant to fuel economy and total driving distance of PHEV, which is composed of the electric generator mechanically coupled with engine system. For the sake of PHEV's running fulfillments, EGS is utilized to charge the high voltage battery in accordance with the required electric power. SPMSG characterized with the superiority of high efficiency and torque density takes center stage as an electric generator of EGS in that fuel efficiency of PHEV is directly linked with efficiency characteristics of SPMSG. Continuous rated power and efficiency distribution of SPMSG should be improved for EGS of PHEV [1]. In addition, it is mandatory for EGS of PHEV to employ on OOL(Optimal Operating Line) which comes from the best efficiency points of engine and SPMSG at each operating speed. Hence, OOL of EGS should be obtained to advance the efficiency for the specified operating range of EGS, which can be achieved through the numerical and experimental design validation of SPMSG compatible to the engine characteristics [2]. In this paper, numerically optimal design based on FEM coupled with optimization algorithm has been performed for realizing the maximum efficiency for the specialized SPMSG of EGS compatible to the frequent operating range dependent on OOL. In accordance, optimal design process follows the two-steps; the first step is to obtain the possibly acceptable design result based on analytical method, and the second step is to optimize the design parameters in detail aiming at the maximum efficiency in the continuous rated power region for OOL of engine. Furthermore, the purposely designed SPMSG for EGS of PHEV is experimentally evaluated under static and dynamic condition making use of dynamometer setup. In accordance, validness of the optimized SPMSG is clarified with the measured efficiency map which shows good compatibility to the main operating range and OOL of EGS [2]. II. CHARACTERISTICS OF ENGINE AND SPMSG FOR EGS A. Analysis of Optimal Operating Line for Engine The test of the engine for EGS of PHEV is performed to analyze the OOL. The experiment-layout of engine test with dynamometer is shown in Fig. 1, whereby static performances driven by ECU(Engine Control Unit) are measured following the issued OOL. The major target operating range for design and validation based on the EGS characteristics can be registered In Fig.2 and 3. B. Design Specification of SPMSG for PHEV The most attractive candidate for EGS of PHEV may be SPMSG on account of its higher efficiency and torque density outstandingly near the whole operating range. Particularly, 140kW SPMSG for EGS of PHEV has been applied for the analytical and numerical design on OOL, which is summarized in Table I. III. OPTIMAL DESIGN OF SPMSG USING OPTIMIZATION ALGORITHM COUPLE WITH F.E.M COMPATIBLE TO OOL The optimal design of SPMSG using analytical method and optimization algorithm for EGS of PHEV is performed to maximize the efficiency on OOL. The numerical results for candidates are compared to verify the effectiveness of optimization. As it can be seen in Fig. 4, optimal design of SPMSG, of which the design objective is maximizing the efficiency, can be carried-out using optimization algorithm coupled with F.E.M computing the efficiency with satisfaction for performance and limit conditions. The flux density distribution of the enhanced SPMSG for maximizing the efficiency in the frequent operating area is depicted in Fig. 5. IV. DESIGN VALIDATION OF SPMSG BASED DYNAMOMETER Optimal design results of SPMSG for maximizing efficiency on OOL are compared with the experimental test results at each operating points. Not only the torque characteristics but the efficiency versus main operating points on OOL is compared, which are shown in Fig. 6 - 7, respectively. The experiment-layout of motor test is shown in Fig. 8, whereby static and dynamic characteristics for the purposely designed prototype are measured to verify the efficiency performances. As it can be known in Fig. 9, the measured efficiency of SPMSG with the applied second-step design is distributed from 95.9% to 97.8% on OOL of engine. In addition, the measured efficiency range of EGS with the purposely designed SPMSG is covering level of 35.2% to 39.4% in main operating region of EGS, which shows good-efficiency compatible to OOL. V. CONCLUSION The purposely designed SPMSG in association with analytical method and optimization shows optimal design results compatible to the frequent operating range which is identified for EGS of PHEV. Furthermore, the OOL of EGS is properly obtained through the experimental efficiency maps of engine and SPMSG.

[1] P. Lazari, J. Wang, and L. Chen, "A Computationally Efficient Design Technique for Electric-Vehicle Traction Machines," IEEE Transactions on Industry Applications, vol. 50, no. 5, pp. 3230–3213, Feb. 2014. [2] Mohammed, O.A, Liu,Su, Liu.Z, "Physical modeling of PM synchronous motors for integrated coupling with Machine drive", IEEE Trans. on Magnetics, vol. 41, Issue 5, pp1628-1631, May. 2005.

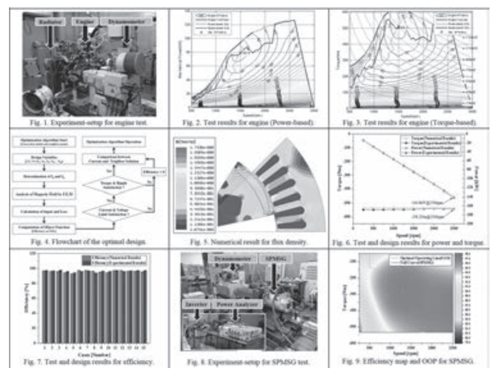

Fig. 1. Experiment-setup for engine test. Fig. 2. Test results for engine (Power-based). Fig. 3. Test results for engine (Torque-based). Fig. 4. Flowchart of the optimal design. Fig. 5. Numerical result for flux density. Fig. 6. Test and design results for power and torque. Fig. 7. Test and design results for efficiency. Fig. 8. Experiment-setup for SPMSG test. Fig. 9. Efficiency map and OOP for SPMSG.

Section	Design Parameter	Specification	Unit
Performance	Rated / Max. Power	60 / 140	[kW]
	Rated / Max. Torque	-358 / -534	[Nm]
	Rated / Max. Speed	1600 / 2500	[r/min]
General	No. of Pole/Slot	8 / 48	-
	No. of Phase	3	-
	Air-Gap	0.9	[mm]
Stator	Outer Diameter	260	[mm]
	Core Material	Silicon Steel	-
Rotor	Permanent Magnet	NdFeB	[T]

GV-14. Development of enhanced magnetic equivalent circuit (eMEC) by considering dominant fringing fluxes in semi-high-speed Maglev train.

C. Ha[1], J. Jeong[2] and J. Lim[1]
1. Dept. of Magnetic Levitation and Linear Drive, KIMM, Daejeon, The Republic of Korea; 2. Dept. of Electrical Engineering, Chung Nam National University, Daejeon, The Republic of Korea

1. Introduction A magnetic levitation (Maglev) train is one of the innovative candidates to satisfy the requirements of next-generation transport systems. Recently, Maglev trains using linear inductance motor (LIM) have been actively studies in Japan, Korea, and China. The existing target of R&D was focused on development of urban Maglev train for connecting within the city, but recently target has been expanded to development of semi-high-speed Maglev train for the purpose of connecting city to city. The main difference of urban and semi-high-speed Maglev trains is maximum operating speed: around 100km/h (urban) vs around 200km/h (semi-high-speed). In semi-high-speed Maglev train, the guidance system is essential to guarantee stability for curved section and against side winds. When designing levitation and guidance electromagnets in semi-high-speed Maglev train, it is necessary to consider the following matters: 1) Since semi-high-speed Maglev train should use the already developed rail for urban Maglev train, there are many design constraints in designing the guidance system [1]. 2) Owing to the design constraints, the guidance electromagnet have to be placed near the levitation electromagnets. Due to the spatial closeness, magnetic coupling effect is severe [2]. 3) Recent studies have shown that the effect of fringing flux is negligible. Therefore, more accurate model is needed by considering dominant fringing fluxes in semi-high-speed Maglev train. In this paper, we newly proposed enhanced magnetic equivalent circuit (eMEC) model to tackle the issue of 3). The significance of development of eMEC model is as follows: A) When designing levitation and guidance systems of semi-high-speed Maglev trains, it takes a lot of time to design based on FEM analysis and experimental data. But, by adopting eMEC model in the initial design stage, design time can be greatly minimized. B) In order to development of precise controllers for levitation and guidance systems, it is very important to provide an accurate system modeling. The eMEC model can provide a highly accurate closed-form system model between control input (levitation and guidance currents) and control output (levitation and guidance forces), which can greatly shorten development and verification time of the controllers. 2. Development of enhanced magnetic equivalent circuit (eMEC) by considering dominant fringing fluxes in semi-high-speed Maglev train Fig. 1(a) shows FEM analysis of semi-high-speed Maglev train. As shown in Fig. 1(b), by comparing the results of FEM analysis with the previous developed MEC model, there is significant difference: 10.6% and 35.6% at operating point in levitation and guidance systems. The main reason of the difference is that the previous MEC model does not consider fringing fluxes. As shown in Fig. 2(a), the fluxes generated in electromagnets in semi-high-speed Maglev train was quantitatively measured and compared by using FEM analysis. The eMEC model improves accuracy by modeling dominant fringing fluxes as magnetic equivalent circuits as shown in Fig. 2(b). In order to verify the accuracy of proposed eMEC model, results of FEM analysis and experimental data and eMEC model are compared and analyzed as shown in Fig. 2(c). At operating point, the errors between eMEC and FEM and experiments are less than 3%, which means that the accuracy is improved up to 12 times compared with previous MEC model. 3. Conclusion In this paper, we quantitatively analyzed the effect of fringing fluxes in semi-high-speed Maglev train and newly proposed highly accurate eMEC model by modeling dominant fringing fluxes as magnetic equivalent circuits. The proposed eMEC model would contribute shorten the design time of levitation and guidance system in initial design stage and development and verification time of controllers in semi-high-speed Maglev train.

[1] J.-H. Jeong, C.-W. Ha, J. Lim, and J.-Y. Choi, "Analysis and control of electromagnetic coupling effect of levitation and guidance systems for semi-high-speed Maglev train considering current direction", IEEE Transactions on Magnetics, Vol. 53, No. 6, p. 8300204, June 2017. [2] J.-H. Jeong, C.-W. Ha, J. Lim, and J.-Y. Choi, "Analysis and control of the electromagnetic coupling effect of the levitation and guidance systems for a semi-high-speed Maglev using a magnetic equivalent circuit", IEEE Transactions on Magnetics, Vol. 52, No. 7, p. 8300104, July 2016.

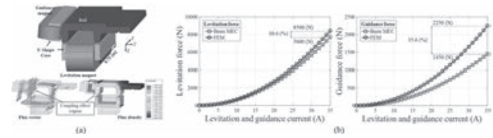

Fig. 1. (a) FEM analysis of semi-high-speed Maglev trains. (b) Comparison between previous proposed MEC and FEM results in terms of levitation and guidance forces.

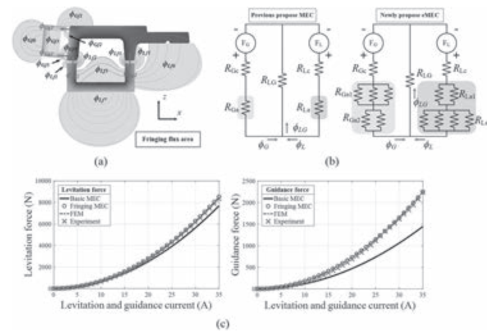

Fig. 2. (a) Magnetic field analysis of semi-high-speed Maglev trains. (b) Proposed eMEC model by considering dominant fringing fluxes.in semi-high-speed Maglev trains. (c) Comparison of levitation and guidance forces obtained by MEC, eMEC, FEM and experiments.

GV-15. Design of Double-Path Magnetic Circuit Structure Hybrid Fuel Injector Considering Demagnetization Characteristics.

H. Liu[1], S. Oh[1], Y. Oh[1], j. Lee[1] and H. Lee[2]
1. Hanyang Univ., Seoul, The Republic of Korea; 2. Busan Institute of Science and Technology University, Busan, The Republic of Korea

As global fuel consumption increases, the requirements for environmental protection are becoming stricter. Therefore, the fuel economy and emission performances of internal combustion engines need to be improved continuously. In addition, the reduction in fuel consumption in cars is a topic of considerable interest for manufacturers, politicians, and environmental activists [1],[2]. The injector is a component of the car's fuel system that plays a significant role in the reduction of fuel consumption. The fuel injector is an electromagnetic device that produces a magnetic field when current is passed through its coil windings. It also refers to a variety of transducer devices that convert electrical energy into kinetic energy [3]. A gasoline direct injector (GDI) has the following requirement: the atomized fuel in the cylinder must be completely burned and saving fuel. Meanwhile, imperfectly injected fuel causes clogging. Therefore, in-depth research regarding the improvement of performance and minimization of response time is required. Therefore, increasing the magnetic force (MF) is the most important design objective. To increase the force density of GDI, extensive control [2],[4],[5] and design methods [2],[6] have been reported, such as using giant magnetostrictive materials and fuzzy control [2], and permanent magnet (PM) ring inserts [6] to obtain a larger magnet flux density and reduce the flux leakage in the magnetic circuit of the GDI. The hybrid GDI with PM increases the total force density by using PMs. However, it is important to note that the irreversible demagnetization in hybrid GDI has been a persistent major concern because it can degrade the machine's performance characteristics substantially. First, the GDI on the side of the cylinder is affected by the great temperature change; second, depending on operating conditions, the peak boost current can reach high values that are three to four times the injector's holding current value, presenting a serious threat of irreversible demagnetization to the PM. Third, caused by the air-gap change and the more sensitive demagnetization reaction for micro-PM, a more subtle analysis is required. This paper proposes the design and analysis of a double-layer magnetic circuit structure hybrid GDI for attaining a high force density, meanwhile hybrid GDI with three different magnet type was inserted to analyze demagnetization characteristics using the 2-D Static and transient finite element method (FEM). Fig.1 shows a general sectional view of the basic GDI. The specifications are described in Table I. Fig.2 shows the hybrid GDI (PM inserted) with its flux paths, and it is shown to be divided into a structure in which both the PM and coil co-supply the magnetic flux. It is referred to as the "double-layer magnetic circuit structure" in this paper. Fig.3 shows the magnetic field distribution of the three types of PMs by 2D static FEM. In Fig.3 (a), as the temperature increases, the magnetic density in the magnet is reduced significantly because of the temperature coefficient. The demagnetization area is depicted by the temperature readings. Green and yellow color is the demagnetization sections at 120 °C. The region in the dotted line is demagnetizing region. Therefore, the design in the GDI system use NdFeB PM is not satisfactory. Fig.3 (b) and Fig.3(c) show the results of the analysis of ferrite PM and SmCo PM, respectively. It is found that the ferrite can maintain the PM characteristics at high temperature; however, at low temperature (-40 °C), a large area of demagnetization occurs. SmCo PM has a good thermal performance; the thermal reaction is small. SmCo PM maintains stable characteristics. For more accurate the effects of temperature, air-gap length change, and peak current are considered. At last, the comparison of the basic and hybrid GDI was discussed. The characteristics of MF, response time, copper loss and cost are investigated.

[1] R. Mock and K. Lubitz, "Piezoelectric injection systems," *Springer Ser. Mater. Sci*., vol. 114, pp. 299–310, 2008. [2] M. Ghodsi *et al.*, "Development of gasoline direct injector using giant magnetostrictive materials," *IEEE Trans. Ind. Appl.,* vol.53, no.1, pp.521-529, Jan, 2007. [3] H. Nouraei *et al.*, "Development of a piezoelectric fuel injector," *IEEE Tran. Veh Tech*., vol. 65, no. 3, pp. 1162-1170, Mar. 2016. [4] J. Xiong and H. Gu, "An intelligent dual voltage driving method and circuit for a common rail injector of heavy-duty diesel engine," *IEEE Access,* early access articles, DOI: 10.1109/ACCESS.2017.2687038 [5] C. Lin *et al*., "Development of an adaptive driving module for piezo actuated diesel fuel injector," *Conf. Appl. Electron.*, Pilsen, Czech, 2009. [6] H. Liu *et al*., "Design and analysis of a double layer magnetic circuit structure for high force density hybrid fuel injector," *IEEE Trans. Magn.,* early access articles, DOI: 10.1109/TMAG.2017.2707342

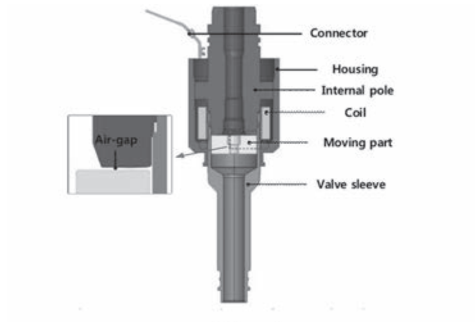

Fig. 1

Item	Unit	Basic model
Coil	turn	126
Resistance	Ω	1.52
Air-gap length	mm	0.105
Housing steel	-	1.4003 IB
Internal pole steel	-	1.4005 IA
Moving part steel	-	1.4005 IA
Valve sleeve steel	-	1.17

Table. 1

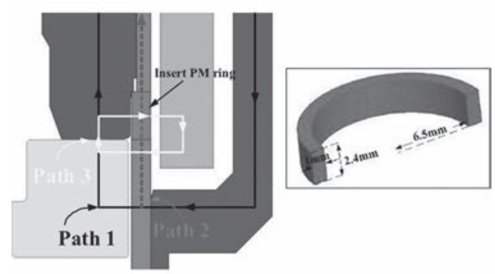

Fig. 2

Fig. 1. Cross-section of GDI basic model
TABLE I Specifications of GDI Basic Model
Fig. 2. Flux paths of Hybrid GDI.

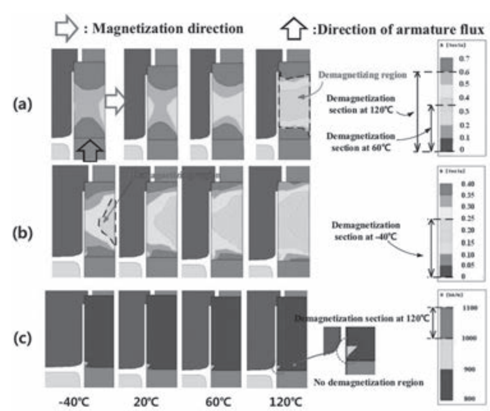

Fig. 3

Fig. 3. The magnetic field of PM. Ia=10A, air-gap=100μm. (a) Hybrid GDI inserts NdFeB PM (b) Ferrite PM (c) SmCo PM

GV-16. Analytical Model for Axial Flux PM Machines with Halbach Arrays: Taking into Account of Rotor Iron.

B. Guo[1] and y. huang[1]
1. School of Electrical Engineering, Southeast University, Nanjing, China

Abstract: In this paper, a general analytical model is proposed to consider the thickness of backplate of axial flux permanent magnet (AFPM) machine with Halbach arrays. Firstly, the machine is represented in a 3-region model, viz, rotor iron, PM and airgap region, then, the slotless flux density is developed by Maxwell's equations. Second, the Schwarz–Christoffel (SC) mapping technique is introduced to consider the slot effect. Moreover, a simple magnetic equivalent circuit is introduced to calculated the magnetic permeability of rotor iron. The results show that the analytical predictions agree well with the finite element (FE) results, also, the model is verified via the performance of experimental results. The main contribution of this model is that the rotor iron part is taken into consideration, which is more accuracy. I.INTRODUCTION Halbach magnetized permanent magnet arrays are widely used in industrial machines, especially in axial flux permanent magnet (AFPM) machines since the different magnetization direction is easier to be realized because the flat magnets. The machines with Halbach PM arrays have almost sinusoidal induced electromotive force and the torque ripple. This array can cancel the flux on one side and strengthen the flux on the other side. This means that the permanent magnets essentially do not require much or no rotor iron [1]. However, the flux density in the airgap is significant different with and without rotor iron, which means that the thickness of rotor iron can affect the electromagnetic performance and it is necessary to consider the rotor iron when modeling the machines. A significant amount of work has been done concerning the machines with Halbach arrays. Authors in [2], [3] investigate the electromagnetic characteristics of machines with Halbach arrays. Nevertheless, these models are based on the FE method, and the FEM is time consuming, especially for further optimization. Another alternative is analytical method. It is faster than FE method and can obtain acceptable results. Zouaghi investigate the no load features of T-LSMs with 2 segment Halbach magnets by analytical approach [4], while similar research has been done by Jin in [5]. However, these model neglects the slot effect. Most, if not all, there have less research on the analytical model considering both slot effect and rotor iron for machines with Halbach arrays. This paper is organized as follows. In Section II, the parameters of AFPM machine with Halbach array is provided. Section III will introduce the electromagnetic calculations used in this paper. The analytical model and its solution strategy will be presented. Afterward, the effects of thickness of rotor iron is then discussed in Section IV. In section V, the experiment results are presented and compared with the results of model. At the end, conclusions will be presented. II.PROTOTYPE PARAMETERS The prototype construction of AFPMMs is a 5 phase, 2 pole pairs, 10-slot AFPMM, the basic dimensions and key design parameters are listed in full paper. III. Description of Analytical Model Based on the separating variable method, the general magnetic vector potential solution for region PMs, airgap and rotor iron (shown in Fig. 1) can be written as: $A_n(\Theta,z)=(a_n e^{K_n z}+b_n e^{-K_n z})$ $\cos(K_n x)$ where $K_n=n\pi/\tau_p$, $\tau_p=\pi R/p$, p is the pole pairs and R is the radius. By applying the boundary conditions, the coefficients could be solved by Matlab. Using the Schwarz–Christoffel (SC) mapping technique, the flux densities of center airgap are calculated. Afterwards, the magnetic permeability of rotor iron is modelled by using additional magnetic equivalent circuit (MEC). The iteration technique is selected to obtain the final results and the flowchart of the described method is shown in Fig. 2. The iterations are stopped after reaching a predefined threshold. The threshold of relative current change between the last iteration and the previous one is set to 0.1%. IV. RESULTS AND DISCUSSION The results shows the flux densities at the mean radius agree well with the FE results. V. EXPERIMENTAL RESULTS The rotor disk and the stator of the AFPM prototype are shown in full paper. In the test bench, the prototype is coupled with an inductance motor via belt system. The inductance motor is driven by an inverter. VI. CONCLUSION The AFPM machine with Halbach arrays has been emerging in many industrial applications due to their sinusoidal induced electromotive force and the torque ripple. However, it has a critical problem with choosing the thickness of rotor iron when designing the machine. Thus, this paper has a significant contribution in that the model developed in this paper has considered the rotor iron, and the computation time can be reduced remarkably. In addition, it is notable that the method proposed in this paper can be also applied to other types of machines to consider the saturation effect. Consequently, the approach proposed in this paper can be regarded as an effective design tool for AFPM machin. More information could be seen in the full paper.

[1] S. Sadeghi and L. Parsa, "Multiobjective Design Optimization of Five-Phase Halbach Array Permanent-Magnet Machine," *IEEE Trans. Magn.*, vol. 47, no. 6, pp. 1658–1666, Jun. 2011. [2] X. Liu, J. Qiu, H. Chen, X. Xu, Y. Wen, and P. Li, "Design and Optimization of an Electromagnetic Vibration Energy Harvester Using Dual Halbach Arrays," *IEEE Trans. Magn.*, vol. 51, no. 11, pp. 1–4, Nov. 2015. [3] I. P. Wiltuschnig, P. R. Eckert, D. G. Dorrell, and A. F. F. Filho, "A Study of the Influence of Quasi-Halbach Arrays on a Torus Machine," *IEEE Trans. Magn.*, vol. 52, no. 7, pp. 1–4, Jul. 2016. [4] M. W. Zouaghi, I. Abdennadher, and A. Masmoudi, "No-load Features of T-LSMs With Quasi-Halbach Magnets: Application to Free Piston Engines," *IEEE Trans. Energy Convers.*, vol. 31, no. 4, pp. 1591–1600, Dec. 2016. [5] P. Jin, Y. Yuan, H. Lin, S. Fang, and S. L. Ho, "General Analytical Method for Magnetic Field Analysis of Halbach Magnet Arrays Based on Magnetic Scalar Potential," *J. Magn.*, vol. 18, no. 2, pp. 95–104, Jun. 2013.

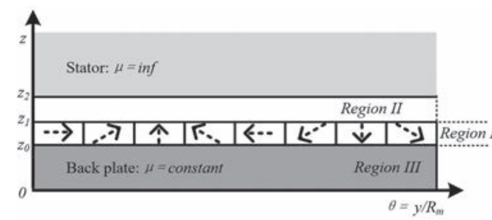

Fig. 1. Model of slotless air gap flux.

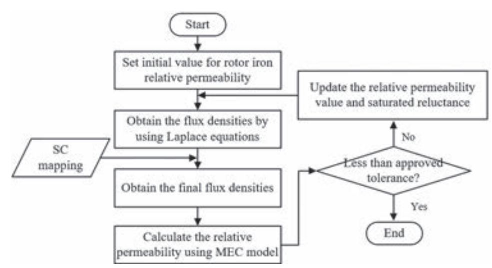

Fig. 2. Flow chart of the proposed method.

FRIDAY MORNING, 27 APRIL 2018 SIMPOR/ROSELLE BALLROOM, 8:30 TO 11:30

Session GW
ULTRATHIN FILMS AND SURFACE EFFECTS I
(Poster Session)

Sarah Thompson, Co-Chair
University of York, York, United Kingdom
Stephen McVitie, Co-Chair
The University of Glasgow, Glasgow, United Kingdom

GW-01. XMCD study of Ru/Co/W/Ru films with strong Dzyaloshinskii-Moriya interaction.

A.S. Samardak[1], A. Kolesnikov[1], A. Ognev[1], M. Platunov[2,3] and A. Rogalev[2]
1. School of Natural Sciences, Far Eastern Federal University, Vladivostok, Russian Federation; 2. European Synchrotron Radiation Facility (ESRF), Grenoble, France; 3. Kirensky Institute of Physics, Krasnoyarsk, Russian Federation

An enhancement of the spin-orbit effects arising on an interface between a ferromagnet (*FM*) and a heavy metal (*HM*) is possible through the strong breaking of the structural inversion symmetry in the layered films. We have found that the introduction of an ultrathin W interlayer between Co and Ru in Ru/Co/Ru films enables to preserve perpendicular magnetic anisotropy (PMA) and simultaneously induce a large interfacial Dzyaloshinskii-Moriya interaction (iDMI). We find that the Ru/Co/W/Ru films have PMA up to 0.35 nm of the nominal thickness of W (t_W). The study of the spin-wave propagation in the Damon-Eshbach geometry by Brillouin light scattering (BLS) spectroscopy reveals the drastic increase of the iDMI value with the rising t_W. The maximum iDMI of -3.1 erg/cm^2 is observed for t_W=0.24 nm, which is 10 times larger than the latter for the quasi-symmetrical Ru/Co/Ru films [1]. Our polycrystalline Ru/Co/W/Ru films were prepared by magnetron sputtering on the SiO_2 substrates at room temperature. The base pressure in the chamber was 10^{-8} Torr. The working pressure of Ar^+ was 10^{-4} Torr. In order to precise control the thickness of layers, we used low sputtering rates: *V(Ru)*=0.011 nm/s, *V(Co)*=0.018 nm/s, *V(W)*=0.02 nm/s. The Co thickness (t_{Co}) was varied from 0.7 to 1.5 nm. The thickness of the buffer and capping Ru layers (t_{Ru}) was 10 and 2 nm, correspondingly. The W thickness (t_W) was taken in the range from 0 to 0.4 nm. Polarization dependent X-ray spectroscopy measurements at the Co *K*- (7709 eV), W L_3- (10207 eV) and W L_2- (11544 eV) edges on the Ru(10nm)/Co(1nm)/W(*x*)/Ru(2nm) structures were performed at the ESRF ID12 beamline. Four different samples have been measured with *x*=0, 0.21, 0.25 and 0.29, where *x* is the thickness of the layer in nm. The APPLE-II undulator and a Si(111) double crystal monochromator were used to collect the spectra. Circular polarization rate of monochromatic x-rays was in excess of 95% at the W $L_{3,2}$-edges. Magnetic field of 0.27 T generated by an electromagnet was applied in the film plane and nearly parallel to the X-ray beam direction. This filed was sufficient to reach magnetic saturation of the samples at room temperature. In order to detect x-ray absorption spectra from our samples, we had to use an energy resolved detector - Si drift diode with an active area of 10 mm^2. To avoid saturation of the detector with fluorescence of Ru and of Si as well as Compton scattering from SiO_2 substrate a 50 μm Al filter was inserted between sample and the diode. The XMCD spectra were recordered by flipping the direction of applied magnetic field two times at every energy point of the x-ray absorption spectra. To make sure that XMCD signal is free of experimental artefacts, we checked that the sign of XMCD was reverted when it was recorded with opposite x-ray helicity. It should be underlined that the attenuation length for tungsten $L_{3,2}$ edges is about 4 orders of magnitude larger than the total thickness of W in the samples. We plotted normalized x-ray absorption spectra at the *K*-edges of Co in Ru/Co/W/Ru trilayers in comparison with a sample without W. Comparison of our normalized XANES spectra recorded at the *K*-edge of cobalt with published results [2,3] clearly shows that in all studied samples Co has *hcp* structure and practically not affected by the deposition of tungsten. We reproduced normalized XANES and XMCD spectra recorded at the $L_{3,2}$-edges of W in Co/W/Ru trilayers in comparison with those measured on bulk Co_3W alloy [4]. For the XANES spectra the ratio of the tungsten L_3/L_2 was taken equal to 2.19/1. The normalized intensities of XMCD signals is about 1% and evidence that 5*d* states of W carry a magnetic moment for all measured samples. This induced magnetic moment is antiparallel to applied field and therefore to the 3*d* magnetic moment of Co. Due to a rather high level of noise it is very difficult to discuss the orbital magnetic moment and its sign. We can only give its estimate, it is about 10 times weaker than the spin magnetic moment. Integrating the $\langle l_Z \rangle$ and $\langle 2s_Z \rangle$ spectra and taking x-ray absoprtion cross-section per hole from [4], we found $m_L < \pm 0.002$ and $m_S \sim -0.023 \pm 0.004$ for all three studied samples. Similar values were also obtained in [4]: $m_L < \pm 0.004(1)\ \mu_B$ and $m_S \sim -0.023(2)\ \mu_B$ for W on bulk Co_3W alloy. What has attracted our attention is some visible difference in the absorption white-line intensities at W $L_{3,2}$ edges for three samples that can result from variation of the 5*d* DOS above the Fermi level. Specifically, L_3 absorption edge reflects both $5d_{3/2}$ and $5d_{5/2}$ DOS whereas only the $5d_{3/2}$ band is probed at the L_2-edge as given by the dipolar selection rules for corresponding optical transitions: $2p_{3/2} \rightarrow 5d_{3/2}$ and $5d_{5/2}$ at the L_3-edge and $2p_{1/2} \rightarrow 5d_{3/2}$ at the L_2-edge. Surprisingly, Co(1nm)/W(0.21nm) and Co(1nm)/W(0.29nm) show nearly the same structures whereas an increase of the number of W $5d_{3/2}$ empty states for Co(1nm)/W(0.25nm) sample is clearly observed. This is a clear difference, eventhough quite minor, in population of spin-orbit split 5*d* states between these three samples. In summary, we show that there is an induced spin magnetic moments of about -0.02 μ_B per atom for W for all studied samples with a much weaker orbital contribution. The magnetic moment of W is antiferromagnetically coupled with the Cobalt moment in agreement with other studies on 3*d*/W systems [4,5]. Small changes in the population 5*d* spin-orbit split bands for different thicknesses of tungsten were observed.

1. A. Kolesnikov et al., arXiv:1706.01229v1 2. Yu. A. Kozinkin et al., Phys. Solid State 53 (2011) 1 3. D. J. Sprouster et al., Appl. Sci. 2 (2012) 396 4. A. I. Figueroa et al., PRB 86 (2012) 064428 5. F. Wilhelm et al., PRL 87 (2001) 207202

GW-02. Tunable interfacial Dzyaloshinskii-Moriya interaction in Ta/W/CoFeB/MgO films.

T. Kim[1], I. Cha[1], Y. Kim[1], G. Kim[1], A. Stashkevich[3], Y. Roussigné[3], M. Belmeguenai[3], S.M. Chérif[3], A.S. Samardak[2] and Y.K. Kim[1]
1. Materials Science and Engineering, Korea University, Seoul, The Republic of Korea; 2. School of Natural Sciences, Far Eastern Federal University, Vladivostok, Russian Federation; 3. LSPM (CNRS-UPR 3407), Université Paris 13, Sorbonne Paris Cité, Villetaneuse, France

Introduction Development of next-generation nonvolatile spin orbit torque magnetic random access memory (SOT-MRAM) is attracting attention due to its potential application for low power and high speed Logic-in-Memory. SOT-MRAM incorporates the magnetic tunnel junction (MTJ) as its basic structure and heavy metal layer under MTJ. The interface between heavy metal (HM) with strong spin-orbit coupling and ferromagnet (FM) is a source of spin-orbit effects including the spin Hall effect (SHE) and interfacial Dzyaloshinskii-Moriya interaction (iDMI). Many research groups are investigating on different combinations of HM/FM by varying its thicknesses and materials to achieve higher performance of SHE and iDMI [1-2]. Research interest to iDMI is due to its assistance to fast domain wall movement and magnetization switching as well as stabilization of spin spirals, chiral domain walls and skyrmions [3]. In this study, we have used a W dusting layer of different thicknesses deposited between HM and FM in order to tune the iDMI energy density in a wide range of possible values. Experiment A DC and RF magnetron sputtering system under base pressure of $5x10^{-9}$ Torr was used to deposit all samples. Each sample underwent annealing at $300^{o}C$ for 1 h with a magnetic field of 6 kOe under $1x10^{-6}$ Torr. We used Ta, a strong spin orbit coupling material, as HM, $Co_{40}Fe_{40}B_{20}$ with saturation magnetization 1307 emu/cm^3 as FM, which has large tunneling magnetoresistance with MgO tunnel barrier, and Ta as capping layer. We inserted a dusting W layer between Ta and CoFeB to observe the iDMI transformation depending on the thickness of W (t_W) varied from 0 to 1 nm. The thicknesses of FM and MgO layers were fixed to control the other potential effects on iDMI. The magnetic properties were observed using a vibrating sample magnetometer (VSM) and iDMI was measured using Brillouin light scattering (BLS) spectroscopy of non-reciprocal propagation of spin waves in the Damon–Eshbach geometry, where the sample is in-plane magnetized and the wave vector is perpendicular to the magnetization [3]. The shift between the Stokes and anti-Stokes frequencies of the spin waves at a given wavelength is directly proportional to the iDMI value [4]. Results and discussion The Ta(3)/W(t_W)/$Co_{40}Fe_{40}B_{20}$(0.9)/MgO(1)/Ta(2) films have perpendicular magnetic anisotropy (PMA) after $300^{o}C$ annealing. As the thickness of the W layer increases, coercivity and squareness increase due to the bottom interface transformation. The film without the dusting layer of W exhibits the positive iDMI value 0.07 mJ/m^2. This magnitude starts to rapidly increase with the growing thickness of W layer. At t_W=1 nm we observed the maximum of the iDMI value 0.47 mJ/m^2. Although $Co_{20}Fe_{60}B_{20}$ is known to show stronger iDMI value than $Co_{40}Fe_{40}B_{20}$ does, [5] we found higher DMI value in $Co_{40}Fe_{40}B_{20}$ compared to a previous study that reported iDMI energy density of 0.2 mJ/m^2 in the structure with 2 nm of W, which is an optimum thickness of W exhibiting maximum DMI value, with $Co_{20}Fe_{60}B_{20}$ on top. [6] Our results, however, show that the combination of two different heavy metals can greatly enhance the iDMI value, which implies that further investigation is required.

[1] S. Fukami et al., Nat. Mat. 15, 535 (2016) [2] A. van den Brink et al., Nat. Comms. 7, 10854 (2016) [3] J. Cho et al., Nat. Comms. 6, 7635 (2015) 5] [4] J.-H. Moon et al., Phys. Rev. B 88, 184404 (2013) [5] S. Jaiswal et al., Appl. Phys. Lett. 111, 022409 (2017) [6] A. K. Chaurasiya et al., Sci. Rep. 6, 32592 (2016)

GW-03. Magnetic proximity effects in Co/Pt/Gd/Pt multilayers.

A. Rogalev[1], F. Wilhelm[1] and N. Jaouen[2]
1. ESRF, Grenoble, France; 2. Synchrotron Soleil, Saint Aubin, France

The rise of spin current physics together with enormous technological advances to engineer layered structures with tailored spin-orbit interactions have placed 4d and 5d transition metals at the heart of the emerging fields of spin-orbitronics, magnonics and caloritronics. In this context, magnetic properties at the interfaces between a ferromagnetic material and non-magnetic metals with large spin-orbit coupling play a central role. Platinum atoms are known to exhibit so-called magnetic proximity effect, *i.e.* they acquire interfacial induced magnetic moments whenever they are in contact with 3d metallic ferromagnets [1]. Very little is known about magnetic proximity effects in Pt at the interface with rare-earth metals. Whether the Pt induced magnetic moments are ubiquitous is still an open question since no interfacial induced magnetic moment has been observed in Pt thin films grown on magnetic insulators, e.g. yttrium iron garnet [2]. To answer this question of crucial importance for understanding mechanisms of spin current generation at interfaces, X-ray magnetic circular dichroism (XMCD) spectroscopy appears to be the method of choice due to its element selectivity and very high sensitivity. In this talk, we present a thorough XMCD study of magnetic proximity effects in exchange coupled Co/Pt/Gd/Pt magnetic multilayers with various thicknesses of Pt layers. In these systems antiferromagnetic coupling between Co and Gd moments, known for bulk intermetallics, persists despite the intercalation of a layer of Pt with a thickness of up to 3 nm [3]. Observation of XMCD signal at the $L_{2,3}$ edges of Pt unambiguously shows that it acquires a magnetic moment at the interfaces and hence mediates magnetic interactions between Co and Gd layers. To unravel the mechanism of the exchange coupling in these multilayers we have recorded element selective magnetization curves by monitoring the intensity of XMCD signals at the Co K-edge, the Gd L_3-edge and Pt L_3-edge as a function of applied magnetic field. These measurements confirmed that independently of the coupling strength varying with the Pt thickness, the Co and Gd magnetization directions are antiparallel at zero magnetic field. Under applied magnetic field two different scenarios are observed. For thick Pt layers (> 1 nm), it is the Gd magnetization that rotates in-plane towards the Co magnetization direction given by an external magnetic field. Gd magnetization is not saturated even under 7 Tesla field that indicates that exchange coupling with Co layer is very strong. For Pt layers thicker than 4 nm, two ferromagnetic layers are decoupled. In the case of thin Pt layers (< 1 nm), Gd magnetization is fixed and Co magnetic moments are rotated by the external magnetic field. By performing XMCD measurements at the Pt $L_{2,3}$-edges at different values of applied magnetic fields, magnetic proximity effects in Pt due to Co and to Gd has been disentangled. Surprisingly the latter is found to favour antiferromagnetic alignment and to be much weaker despite a larger magnetization of the rare-earth layer. To our knowledge these results produce the first direct experimental evidence of magnetic proximity effects at the interfaces of non-magnetic metal and rare-earth metal. Moreover, opposite sign of magnetic coupling at Co/Pt and Gd/Pt interfaces is pointing out a development of a magnetic spring across a non-magnetic spacer layer. This spring can be tuned by a layer thickness, temperature and applied magnetic field.

[1]. F. Wilhelm, P. Poulopoulos, G. Ceballos, H. Wende, K. Baberschke, P. Srivastava, D. Benea, H. Ebert, M. Angelakeris, N. K. Flevaris, D. Niarchos, A. Rogalev, and N. B. Brookes, Phys. Rev. Lett. 85, 413 (2000). [2]. S. Gepraegs, S. Meyer, S. Altmannshofer, M. Opel, F. Wilhelm, A. Rogalev, R. Gross, and S. T. B. Goennenwein, Appl. Phys. Lett. 101, 262407 (2012) [3]. G. Suciu, J. C. Toussaint and J. Voiron, J. Magn. Magn. Mater. 240, 229 (2002).

GW-04. XMCD Investigation of CoFeB/MgO Structure.

Y. Yan[1], X. Lu[1], J. Wang[1], J. Wu[1] and Y. Xu[1]
1. University of York, York, United Kingdom

A major breakthrough in MRAM is the discovery of perpendicular magnetised CoFeB films, sandwiched by MgO and Ta layers, which exhibit not only the perpendicular magnetic anisotropy, but also strong orbital moment and spin-orbital coupling[1]. At the same time, current-induced spin-transfer torque (STT) is very important in high density magnetic media and spintronics devices[2]. Because of the importance of lowering the energy consumption, it is necessary to discover a method to reduce the critical current required to switch the spin direction in STT-MRAM application. The perpendicular magnetic anisotropy (PMA) materials, integrated into a magnetic tunnel junction (MTJ)[3], allow for a small critical current density for current-induced magnetisation switching[4]. These materials are found to have a good balance of thermal stability and low magnetic anisotropy energy. In this part of the project, I have studied the effect of the layered structure and in particularly the role of the element-specific orbital moments on the PMA in Ta/CoFeB/MgO structures. We have investigated perpendicular magnetic anisotropy and the element specific spin and orbital moments in the CoFeB/MgO system by using magnetisation measurement, XMCD measurement and sum rule calculations. The results obtained by VSM measurements confirmed that the PMA can be found in a split layer of 2.2 nm CoFeB, with a MgO layer, and the saturation field along perpendicular direction can rise as high as 7000 Oe, which enhanced 10% compared with sample A, while the and are enhanced by 20%. XMCD measurement revealed that the PMA is correlated with the strong spin-orbital coupling of Co atoms, related to the enhanced orbital to spin moment ratios of Co atoms in CoFeB. More importantly, compared with the samples without PMA (sample C and previous work), the sample with the PMA (sample A and B) shows the orbital moment of Co atoms enhanced from 0.17 in sample C to 0.30 in samples A and B. Meanwhile the orbital moment of Fe atoms has not shown significant change, suggesting the dominant contribution of spin-orbital moment coupling of Co atoms to PMA in CoFeB/MgO structure. According to our findings, these results would be very useful for understanding the origin of PMA in CoFeB/MgO films, which could, in turn, be very important for later researches into new generation spintronics devices like STT- MRAM.

[1] T. Liu, Y. Zhang, J. Cai, and H. Pan, "Thermally robust Mo/CoFeB/MgO trilayers with strong perpendicular magnetic anisotropy," *Scientific reports,* vol. 4, 2014. [2] J. Sinha *et al.*, "Influence of boron diffusion on the perpendicular magnetic anisotropy in Ta| CoFeB| MgO ultrathin films," *Journal of Applied Physics,* vol. 117, no. 4, p. 043913, 2015. [3] J. Teixeira *et al.*, "Domain imaging, MOKE and magnetoresistance studies of CoFeB films for MRAM applications," *Materials Science and Engineering: B,* vol. 126, no. 2, pp. 180-186, 2006. [4] A. Brataas, A. D. Kent, and H. Ohno, "Current-induced torques in magnetic materials," *Nature materials,* vol. 11, no. 5, pp. 372-381, 2012.

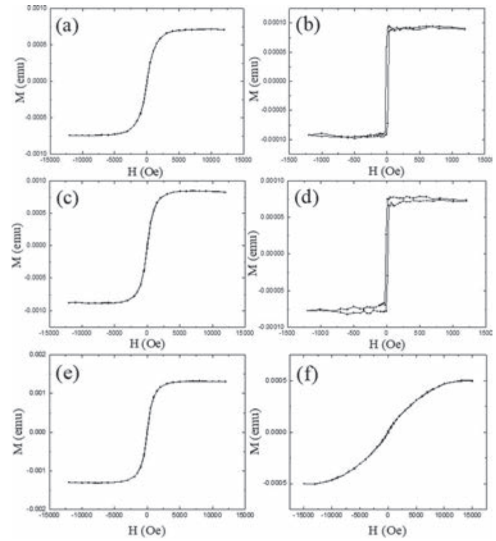

Fig. 1.

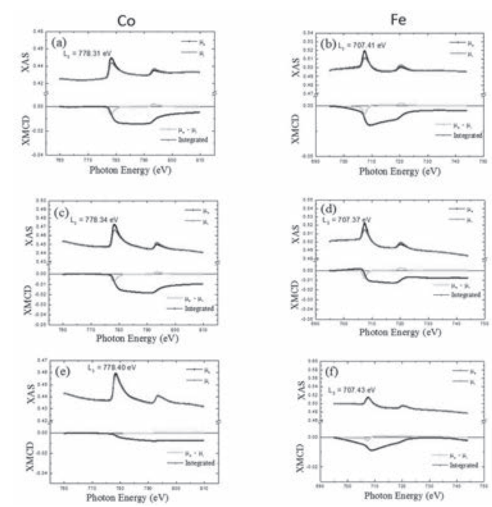

Fig. 2.

GW-05. Splitting of Ferromagnetic Resonance Spectra in Periodically Modulated 1-D Magnonic Crystal - II.

P.N. Sherpa[1], S. Khanal[1] and L. Spinu[1]
1. Physics/ Advanced Materials Science Institute, University of New Orleans, New Orleans, LA, United States

Novel studies and possible technological application of patterned magnetic nanostructures have triggered an intensive research in the field of Spintronic over the last few decades. Magnetic memories [1], microwave filters, magnonic logic devices [2], on-chip data communication [3] are few of the examples where these patterned magnetic structures have shown enormous potentials. Furthermore, Spintronic highly reduces the power consumption and heat expulsion when compared to traditional electronics. By using materials with strong shape anisotropy and easily tunable nature, we can easily achieve the above the mentioned applications. Besides that, it should be easy enough to create a magnonic crystal with well-defined frequency band gap by controlling the propagation direction of spin wave and the anisotropies [4]. Various studies have been performed to understand the static and dynamic properties of such patterned magnonic crystals. Among the various structures studied, the most noticeable ones are nanowires, nanodots, antidots, multilayers and modulated wires. In this study, we consider a slab of a thin film with a periodically modulated surface. Multiple samples with a varying periodicity modulation were fabricated using a top-down approach. Periodic grooves with fix thickness were created by etching a slab of a thin film from the surface. The width of the grooves was varied to creates a spatial variation in the internal magnetic field and boundary conditions whose effects can be studied through the static and dynamic properties of the sample [5]. For a single nanowire with no modulation, a uniform ferromagnetic resonance (FMR) mode with wave vector ($k\neq0$) was observed. However, for modulated structures, multiple non-uniform($k=1$) was observed. As the width of the grooves was decreased, the splitting of FMR mode was distinctly observed, especially at low field and frequency. Angular variation of ferromagnetic resonance provided even more in-depth nature of the resonance modes. Through micromagnetic simulation of experimental structure, modes such as Backward Volume Magnetostatic (BVM) and Damon-Esbach (DV) were also identified. The Coplanar waveguides, with an ideal characteristic impedance of 50ohm, were designed by using CST microwave studio. Then by using the standard photolithography techniques, the ground-signal-ground coplanar waveguides, with the G-S gap of 10um and signal line width of 20 um, was fabricated on top of a silicon substrate. This process was followed by deposition of 5nm Ti, 150nm Cu and 10nm Au, and lift-off technique. Finally, the modulated periodic thin films, with total dimensions of 350um length, 10um width, and 40nm thickness, were prepared on top of the signal line of the CPW using focus ion beam (FIB) technique. The spatial design and the experimental setup is depicted in figure 1. In this study, the width of the groove (a) was varied which increased the distance between each consecutive hill. Other parameters such width of the hills (b) = 400nm, the thickness of the hills (t) = 4nm were kept at constant. Four different samples were created by varying the parameter a: S1 (a = 1500nm), S2 (a=1000nm), S3 (a=500nm) and S4(a=200nm). Standard MOKE technique was used to study the static properties of the sample. The experimental results thus collected are presented in figure 1. In sample S1, each hill is separated by a significant distance (a=1500nm). This allows each hill to act as a single nanowire sample which produces a distinct square shaped MHL response. But as we decrease the distance between the hills (a), we see more interference from the neighboring hills which decreases the overall coercivity and smooths the magnetization switching process. The standard VNA-FMR method was used to study the dynamic properties of the sample at room temperature. To probe the FMR spectra; two-port network analyzer was connected to homemade CPW via coaxial cables. Non-magnetic pico-probes were used to connect planer CPW with the coaxial cables. The external magnetic field was swept from 0.5KOe to -0.5 KOe with field step of 3 Oe. The microwave frequency was swept from 1GHz to 6GHz for each magnetic field step. The transmission scattering parameter (S21) was recorded for each frequency scan and contour plots of frequency, field and S21 are plotted (figure 2). To probe the FMR spectra; two-port network analyzer was connected to homemade CPW via coaxial cables. Non-magnetic pico-probes were used to connect planer CPW with the coaxial cables. The external magnetic field was swept from 0.5KOe to -0.5 KOe with field step of 3 Oe. The microwave frequency was swept from 1GHz to 6GHz for each magnetic field step. The transmission scattering parameter (S21) was recorded for each frequency scan and contour plots of frequency, field and S21 are plotted. To better understand this peculiarity micromagnetic simulations were also performed with Mumax on LONI Queen Bee Supercluster, which consisted of 504 compute nodes each with NVIDIA Tesla K20x GPUs and Intel Xeon 64bit processors.

[1] V. V. Kruglyak, S. O. Demokritov, and D. Grundler, "Magnonics," *Journal of Physics D: Applied Physics,* vol. 43, p. 264001, 2010. [2] A. Khitun, M. Bao, and K. L. Wang, "Magnonic logic circuits," *Journal of Physics D: Applied Physics,* vol. 43, p. 264005, 2010. [3] A. A. Serga, A. V. Chumak, and B. Hillebrands, "YIG magnonics," *Journal of Physics D: Applied Physics,* vol. 43, p. 264002, 2010. [4] S. Neusser, G. Duerr, R. Huber, and D. Grundler, "Spin Waves in Artificial Crystals and Metamaterials Created from Nanopatterned Ni80Fe20 Antidot Lattices," in *Magnonics: From Fundamentals to Applications*, S. O. Demokritov and A. N. Slavin, Eds., ed Berlin, Heidelberg: Springer Berlin Heidelberg, 2013, pp. 191-203. [5] S. Khanal, P. Sherpa and L. Spinu, "Splitting of Ferromagnetic Resonance Spectra in Periodically Modulated 1-D Magnonic Crystal," in *IEEE Transactions on Magnetics*, vol. 53, no. 11, pp. 1-4, Nov.2017.doi: 10.1109/TMAG.2017.2707281

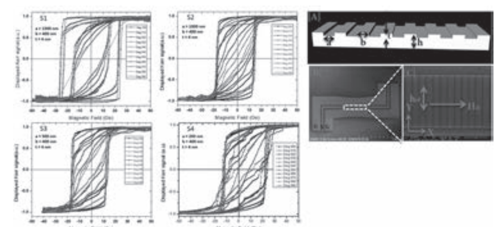

Fig. 1: (Left Side) Experimental MHL results for samples S1, S2, S3 and S4. (Right Side) [A] Geometry of the sample under study, [B] Scanning Electron Microscopy image of CPW, [C] magnified view of sample on top of the signal line in CPW.

Fig. 1.

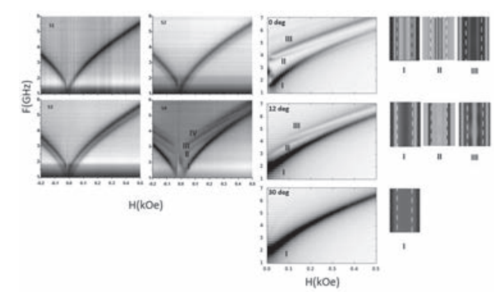

Fig. 2: (Left Side) Contour plot of experimental broadband FMR spectra for samples S1, S2, S3 and S4. (Right Side) Micromagnetic simulation results for angular dependence of FMR spectra for sample S4 with corresponding spectra at 0.2 kOe.

Fig. 2.

GW-06. Interface roughness driven magnetic anisotropy and Dzyaloshinskii-Moriya interaction in thin films with broken structural inversion symmetry.

A. Ognev[1], A.S. Samardak[1,6], A. Samardak[1], L. Chebotkevich[1], A.V. Sadovnikov[2], S. Nikitov[3], A. Gerasimenko[4], I. Cha[4], Y.J. Kim[4], O. Tretiakov[5] and Y.K. Kim[4]

1. School of Natural Sciences, Far Eastern Federal University, Vladivostok, Russian Federation; 2. Saratov State University, Saratov, Russian Federation; 3. Kotel'nikov Institute of Radioengineering and Electronics, Russian Academy of Sciences, Moscow, Russian Federation; 4. Department of Materials Science and Engineering, Korea University, Seoul, The Republic of Korea; 5. Institute for Materials Research, Tohoku University, Sendai, Japan; 6. Center for Spin-Orbitronic Materials, Korea University, Seoul, The Republic of Korea

An interface between *3d* transition metal and *5d(4d)* heavy metal (HM) is a host of intriguing spin-related effects desirable for spin-orbitronic applications [1]. Chiral interaction between two *3d* spins due to a strong spin-orbit coupling (SOC) in an underlying atomic layer of heavy metal is associated with the Dzyaloshinskii-Moriya interaction (DMI) [2]. The and interfacial DMI (iDMI) value is extremely sensitive to the ferromagnetic layer thickness (t_{FM}), where the non-linear dependence of iDMI on t_{FM} implies the degradation of interfaces at small t_{FM} [3]. Recently, *Wells et al.* [4] has demonstrated the effect of interface quality, reflecting both roughness and intermixing of interfaces, on iDMI in symmetrical Pt/Co/Pt trilayers. There is a radically different situation in the inversion symmetry broken systems, where the ideal (which is difficult to achieve in polycrystalline films) or having identical quality of top and bottom interfaces of a ferromagnetic layer are the main source of the enhanced iDMI [5, 6]. One can suppose that if in such systems the quality parameter, defined as the difference between quality of top and bottom interfaces of the magnetic layer, tends to zero, iDMI will be strong. The case of the coherent roughnesses of top and bottom interfaces corresponds to this assumption, which arises from the sensitivity of iDMI to the magnetic layer thickness variation. We report on results of the investigation of the magnetic anisotropy and interfacial DMI in the magnetic layer sandwiched between two *5d* HM (Pt and Ta) (Series 1 - *Pt(2)/CoFeSiB(1.5)/Ta(5)*) or one *5d* HM (Pt) from the bottom and *4d* HM (Ru) from the top (Series - 2 *Pt(2)/CoFeSiB(1.5)/Ru(3)/Ta(5)*), where the layer's thickness is indicated in nm. The two series of samples were deposited by magnetron sputtering on the top of the Pd surface with artificially introduced interface roughness: The substrates with Pd seed layer of different thickness ranging from 0 to 56 ML (or from 0 to 12.6 nm were epitaxially grown on the atomically smooth Si(111)/Cu surface. Roughness of the Pd surface in dependence on the thickness was measured by and AFM. The surface is represented by well-ordered atomic terraces of Si, covered by Cu seed layer with the Pd islands grown on top of it. The island growth leads to the significant increase of the mean-square roughness (R_q) as well as the amplitude of roughnesses of the Pd surface. But the period of roughnesses remains constant within the value distribution: p=70±10 nm. In order to analyze the interface quality (roughness, intermixing, thickness variation) we used the X-ray reflectivity (XRR) measurement technique. The study was performed on a SmartLab (RIGAKU) X-ray diffractometer at CuKα radiation wavelength (1.54Å). The simulations of XRR spectra were performed with GlobalFit software. The main trend is the increase of the interface roughness for all layers with the rising t_{Pd}. Noteworthy, the initial R_q for CoFeSiB is higher than for rest layers. It can relate to the amorphous nature of the magnetic layer. With increase of t_{Pd} up to 10.2 nm roughness of CoFeSiB layer approaches to R_q of the underneath Pd and Pt layers, which corresponds to the roughness coherency. The experimental data revealed that Ta capping layer smooths the surface roughness. We observed the correlation between the interface quality factor ($\Delta\sigma/\sigma$) and iDMI for both series. The direct measurement of DMI was performed by Brillouin light scattering (BLS) spectroscopy based on DMI-driven asymmetric dispersion shift of long-wavelength thermal spin waves in the Damon-Eshbach surface mode. At the small Pd roughness the magnitude of $\Delta\sigma/\sigma$ has maximum that means the highest incoherency between top and bottom interfaces of CoFeSiB layer leading to the relatively small iDMI. The flowing tendency of $\Delta\sigma/\sigma$ with rising t_{Pd} reflects the growing coherence of interface roughnesses causing in significant increase of iDMI about twice for series 1 and 2. We demonstrate the direct dependence between the quality of CoFeSiB interfaces, the iDMI value and magnetic anisotropy. The coherent roughnesses of top and bottom interfaces can enhance the iDMI value up to 2.5 times with the maximum obtained value D_{eff} = -0.9 mJ/m^2 (or surface DMI is Ds = -1.05 pJ/m), which is largest known iDMI for CoFeB-based systems. For samples with high iDMI we observed the isolated skyrmions (or skyrmion bubbles) formation with the size about 200-300 nm. This work was supported by the Russian Foundation for Basic Research (grant 17-52-50060), by the Russian Ministry of Education and Science under the state task (3.5178.2017/8.9 and 3.4956.20 17/VU) and Far Eatern Federal University.

1. Soumyanarayanan, A., et al., *Emergent phenomena induced by spin-orbit coupling at surfaces and interfaces.* Nature, 2016. 539(7630): p. 509-517. 2. Yang, H.X., et al., *Anatomy of Dzyaloshinskii-Moriya Interaction at Co/Pt Interfaces.* Physical Review Letters, 2015. 115(26). 3. Cho, J., et al., *Thickness dependence of the interfacial Dzyaloshinskii-Moriya interaction in inversion symmetry broken systems.* Nature Communications, 2015. 6. 4. Wells, A.W.J., et al., *Effect of interfacial intermixing on the Dzyaloshinskii-Moriya interaction in Pt/Co/Pt.* Physical Review B, 2017. 95(5). 5. Belmeguenai, M., et al., *Interfacial Dzyaloshinskii-Moriya interaction in perpendicularly magnetized Pt/Co/AlOx ultrathin films measured by Brillouin light spectroscopy (vol 91, 180405, 2015).* Physical Review B, 2015. 91(21). 6. Soucaille, R., et al., *Probing the Dzyaloshinskii-Moriya interaction in CoFeB ultrathin films using domain wall creep and Brillouin light spectroscopy.* Physical Review B, 2016. 94(10).

GW-07. Lattice distortion and thermal stability of $[Fe_2CoSi/Pt]_n$ multilayers with high perpendicular magnetic anisotropy.

Y. Liu[1], Y. Zheng[1], L. Ren[1], H. Yang[1] and K. Teo[1]
1. Electrical and Computer Engineering, National University of Singapore, Singapore

Multilayers with perpendicular magnetic anisotropy have attracted extensive attention due to their promising applications on magnetic random access memory (MRAM). Higher perpendicular magnetic anisotropy (PMA) can increase the thermal stability and reduce the critical switching current [1, 2]. Due to the orbital hybridization of Co or Fe and Pt or Pd atoms, the multilayers exhibit PMA such as $[Co/Pt]_n$ [3], $[Co/Pd]_n$ [4], $[CoFeB/Pt]_n$ [5], $[Co_2FeAl(Si)/Pt]_n$ [6-8]and $[Co_2MnSi]_n$ [9]. However, the PMA of Pt/Fe-based Heusler multilayers hasn't been reported. Besides, the analysis of the ferromagnetic layer is lacking. Our group used Fe-based Heusler in the multilayers. Because the Fe_2CoSi has smaller lattice mismatch with Pt than that of Co_2FeAl. Hence it is reasonable to expect a higher PMA in $[Fe_2CoSi/Pt]_n$ multilayers. In this work, we observed high PMA in $[Fe_2CoSi/Pt]_n$ structure. The thermal stability and lattice distortion of Fe_2CoSi is also discussed. The $[Fe_2CoSi$ (FCS)/$Pt]_n$ multilayers are deposited on amorphous oxidized Si with Pt buffer by ultra-high vacuum magnetron sputtering system at room temperature. The thickness of Pt, FeCoSi and the number of period are optimized and the highest K_u of 2.64 Merg/cc is achieved in the stack Ta(3)/Pt(10)/$[FCS(0.6)/Pt(2)]_2$/Pt(3). Optimal t_{Pt} of multilayers is found as 2 nm. Furthermore, PMA is only observed when t_{FCS} = 0.6 nm or 0.8 nm and the films gradually tune to in-plane anisotropy with FCS thickness larger than 0.8 nm. We confirmed that PMA originates from the orbital hybridization of Co and Pt according to nonexistence of PMA in $[Fe_2CrSi/Pt]$ multilayers. Since $L2_1$ or $B2$ phase is very crucial for Heusler alloys to exhibit good magnetization and also distortion would affect the magnetic anisotropy energy, so the phase information and lattice distortion is studied using X-ray diffraction (XRD) and Transmission electron microscope (TEM). We found that Fe_2CoSi is in $B2$ phase with Pt thickness of 2 nm, as shown in Fig.1(a). The analysis of TEM result shown in Fig.2 suggests that the interface of Pt/Fe_2CoSi is smooth. Besides, the analysis of FFT suggests that the unit of Fe_2CoSi is laterally compressed in only one direction and the vertical lattice parameter increases accordingly. The vertical tensile strain and the small lattice mismatch can account for the high PMA of $[Fe_2CoSi/Pt]_n$ structure. Finally, the thermal stability is studied. Our results show that the optimized stack can maintain PMA after annealing process at 350C for 30 mins. Our work paves the way for application of Fe-based Heusler alloys in MRAM.

1. Mangin, S., et al., *Reducing the critical current for spin-transfer switching of perpendicularly magnetized nanomagnets.* Applied Physics Letters, 2009. 94(1): p. 012502. 2. Yang, H., et al., *First-principles investigation of the very large perpendicular magnetic anisotropy at Fe| MgO and Co| MgO interfaces.* Physical Review B, 2011. 84(5): p. 054401. 3. Nakajima, N., et al., *Perpendicular magnetic anisotropy caused by interfacial hybridization via enhanced orbital moment in Co/Pt multilayers: Magnetic circular x-ray dichroism study.* Physical Review Letters, 1998. 81(23): p. 5229. 4. Davydenko, A., et al., *Origin of perpendicular magnetic anisotropy in epitaxial Pd/Co/Pd (111) trilayers.* Physical Review B, 2017. 95(6): p. 064430. 5. Wu, S., et al., *Scaling of the anomalous Hall effect in perpendicular CoFeB/Pt multilayers.* Journal of Applied Physics, 2013. 113(17): p. 17C119. 6. Wang, W., H. Sukegawa, and K. Inomata, *Perpendicular Magnetic Anisotropy of Co2FeAl/Pt Multilayers for Spintronic Devices.* Applied physics express, 2010. 3(9): p. 093002. 7. Wu, Y., et al., *Perpendicular magnetic anisotropy and thermal stability in Co2FeAl0.5Si0.5/Pt multilayers.* Applied Physics A, 2014. 117(2): p. 773-779. 8. Wu, Y., et al., *The Anomalous Hall Effect of Co2FeAl0.5Si0.5/Pt Multilayers with Perpendicular Magnetic Anisotropy.* Applied Physics Express, 2013. 6(11): p. 113003. 9. Matsushita, N., et al., *Magnetic anisotropy of [Co2MnSi/Pd]n superlattice films prepared on MgO(001), (110), and (111) substrates.* Applied Physics Letters, 2015. 106(6): p. 062403.

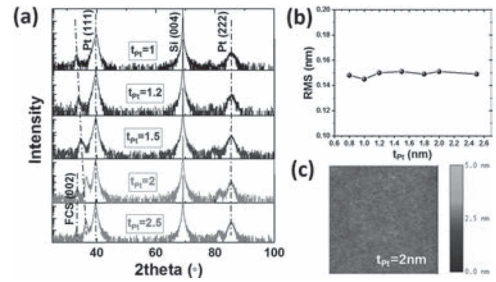

Fig. 1. (a) XRD θ-2θ scan of Ta(3)/Pt(10)/$[FCS(0.6)/Pt(t_{Pt})]_9$/Pt. (the unit of the thickness is in nm) (b) t_{Pt} dependence of RMS when n=2. (c) AFM image of stack with t_{Pt}=2 nm and n=2.

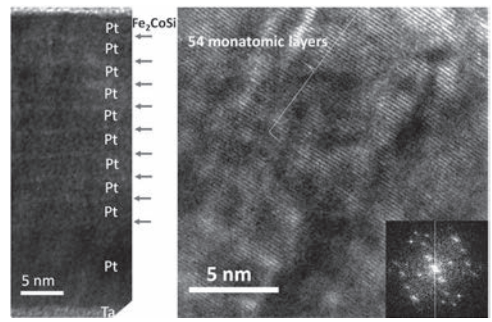

Fig. 2. HRTEM image of Ta(3)/Pt(10)/$[FCS(0.6)/Pt(t_{Pt})]_9$/Pt stack. the inset is the FFT image of multilayers.

GW-08. Atomic Layer Deposition of cobalt films.

M. Jullien[1], C. Chang[1], d. barth[1], S. Robert[1], L. Badie[1], D. Lacour[1], C. Guillemard[1], S. Petit-Watelot[1] and *F. Montaigne*[1]

1. Institut Jean Lamour, Université de Lorraine - CNRS, Vandoeuvre les Nancy, France

Together with the emergence of new concepts, the progresses of spintronics are intimately linked to the progresses in materials, heterostructures and interfaces elaboration and control. Among the wide range of available deposition techniques, only a few are used in the field of spintronics. Molecular beam epitaxy has been essential to the study of important phenomenon (including of course Giant MagnetoResistance), but sputter deposition is omnipresent and mainly used as well in academic as in industrial context. On the other hand, Atomic Layer Deposition (ALD) is now unavoidable in the semiconductor industry as it is a key enabler for the smallest technology nodes (down to 7nm) and 3D devices. It is also widespread in many other fields (like OLED encapsulation, photovoltaic, fuel cells, packaging…). Being self-limited, the ALD growth offers an excellent and unique control of film thickness, assuring conformal deposition on wide surfaces and 3D shapes. Despite these potential advantages, the use of ALD for thin magnetic film and spintronic applications has remain very limited (1,2). We report here on the ALD growth of cobalt films. Metallic cobalt is obtained from the bis(cyclopentadiényl)cobalt(II) precursor which is reduced with ammonia. The film is protected from oxidation by an alumina film deposited in-situ by ALD. Structural, electric and magnetic properties of the film have been characterized (figure 1). Whereas ALD deposition is known to involve some contamination issues, our films appear to be essentially composed of metallic cobalt as shown by XPS (figure 1.a). This metallic behavior is confirmed by the temperature dependence of the resistance. The magnetization is close from bulk values as assessed by magnetometry measurements (figure 1.b) and ferromagnetic resonance (figure 1.c). The growth temperature dependence of all the parameters will be discussed in order to shed light on the growth processes. Furthermore, the ALD grown cobalt films exhibit significant anisotropic magnetoresistance (figure 1.d), up to 2%. Consequently the Atomic Layer Deposition can be considered as a pertinent technique for magnetic thin film depositions. Different perspectives of new 3D devices grown by ALD will be discussed.

1. Yoon, J., Song, J.-G., Kim, H. & Lee, H.-B.-R. Plasma-enhanced atomic layer deposition of Co on metal surfaces. Surf. Coat. Technol. 264, 60–65 (2015). 2. Klesko, J. P., Kerrigan, M. M. & Winter, C. H. Low Temperature Thermal Atomic Layer Deposition of Cobalt Metal Films. Chem. Mater. 28, 700–703 (2016).

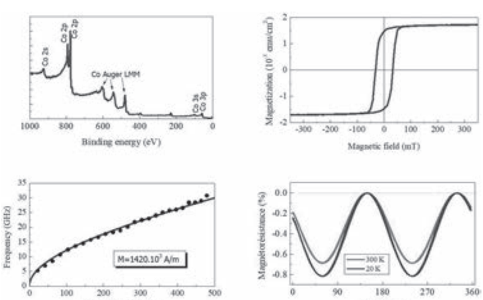

Fig. 1. a) X-ray Photoelectron Spectroscopy of the cobalt film (after etching of the alumina capping layer). Specific features of cobalt are observed without visible contamination. b) Room temperature hysteresis curve of an ALD grown cobalt film. c) Ferromagnetic resonnace frequency of an ALD grown cobalt film. The field evolution of the resonnance frequency is well reproduced by the Kittel law using bulk value of cobalt magnetization. d) Evolution of the resistance as a function of the angle of applied magnetic field. The periodicity is typical of anisotropic magnetoresistance.

GW-09. Large Perpendicular Magnetic Anisotropy in Fe-Al/MgA-l_2O_4(001) epitaxial heterostructures.

T. Scheike[1], H. Sukegawa[1], X. Xu[1], K. Hono[1,2] and S. Mitani[1,2]
1. National Institute for Materials Science (NIMS), Tsukuba, Japan; 2. University of Tsukuba, Tsukuba, Japan

Magnetic tunnel junctions (MTJs) with large perpendicular magnetic anisotropy (PMA) at ferromagnet (FM)/oxide barrier interfaces play a key role in state-of-the-art magnetic random access memory (MRAM). With demand of increasing the MRAM capacity, MTJs need to be constantly downscaled which leads to increased thermal instability of FM layers. Therefore, many attempts were examined to compensate the thermal instability by further strengthening of the PMA at FM/oxide barrier interfaces. Recently, relatively large PMA at Co_2FeAl/MgO[1] and $Co_2FeAl/MgAl_2O_4$ heterostructures were reported.[2] For these cases, the Al is found to diffuse from Co_2FeAl into MgO or $MgAl_2O_4$, resulting in promotion of the Fe-O orbital hybridization to enhance the interfacial PMA.[3] Additionally, the use of $MgAl_2O_4$ leads to lattice-matched interfaces with these FM materials, being effective in improving the PMA by reducing the interfacial strain. In bcc Fe-Co alloys, Fe-rich composition tends to show larger PMA than Co-rich ones due to stronger hybridization of interfacial Fe-orbitals with O-orbitals.[4] Considering this, we replace Co in Co_2FeAl with Fe, i.e. Fe_3Al. Here, we report growth of off-stoichiometric $Fe_{80}Al_{20}$ ultrathin films in combination with an $MgAl_2O_4$ barrier. Large effective PMA energy density K_{eff} up to 1.1 MJ/m^3 with a large interfacial anisotropy energy density K_i of 2.8 mJ/m^3 was demonstrated in a 0.8 nm thick Fe-Al/$MgAl_2O_4$(001) sample. The following structures were deposited on an MgO(001) single crystal substrate using a magnetron sputtering system with a base pressure of 4×10^{-7} Pa: MgO//Cr (40)/$Fe_{80}Al_{20}$ (t_{FeAl})/Mg (0.2)/$Mg_{40}Al_{60}$ (0.7) /oxidation /Ru (2) (thickness in nm). The MgO substrate and Cr buffer were annealed at 750°C for 1 h. The Fe-Al was deposited by co-sputtering of Fe and Al. The Fe-Al composition was confirmed by inductively coupled plasma analysis. Post-oxidation of the barrier (Mg + Mg-Al) was performed using an oxygen plasma process. Samples were annealed *ex-situ* at a temperature T_{ann} for 30 min. Magnetization loop measurements were performed with a vibrating sample magnetometer (VSM). Microstructure analysis was done using a high resolution annular dark-field scanning transmission electron microscope (HAADF-STEM). Elemental distribution and crystal ordering was investigated by energy dispersive X-ray spectroscopy (EDS). In Fig. 1, the effective anisotropy K_{eff} vs. T_{ann} is plotted for t_{FeAl} = 0.8, 1.0, 1.2, and 1.4 nm. K_{eff} is defined as $M_sH_k/2$, M_s is the saturation magnetization and H_k the anisotropy field. The largest PMA is observed in a 0.8 nm thick film with K_{eff} = 1.1 MJ/m^3 (T_{ann} = 450°C) similar to electron beam-evaporated Fe/MgO heterostructures.[5,6] Above 450°C PMA disappears indicating strong diffusion of Cr into the magnetic layer. Additionally, strong temperature dependence of K_i was found. K_i reaches around 2.8 mJ/m^3 at 450°C. The strong temperature dependence also suggests Cr diffusion into Fe-Al. STEM imaging confirmed the bcc structure of the metallic layer and a cation-disordered $MgAl_2O_4$ barrier.[7] The Cr/Fe-Al and Fe-Al/$MgAl_2O_4$ interfaces are smooth and lattice-matched, see Fig. 2. The high temperature annealing treatment promotes a high crystalline arrangement at the Fe-Al/$MgAl_2O_4$ interface. Additionally, Al is also found to diffuse almost completely into the barrier as confirmed by EDS observation resulting in an almost pure Fe/$MgAl_2O_4$ interface. This leads to a strong Fe-O hybridization. In $Co_2FeAl/MgAl_2O_4$ heterostructures such a diffusion process is also observed.[3] Hence, the here presented structure leads to more effective Fe-O hybridization increasing the PMA drastically. In conlusion, large interfacial PMA with K_{eff} = 1.1 MJ/m^3 after annealed at T_{ann} = 450°C was obtained in a 0.8 nm $Fe_{80}Al_{20}/MgAl_2O_4$ heterostructure. The large PMA is attributed to the highly arranged Fe-Al/$MgAl_2O_4$ interface creating strong Fe-O hybridization after high temperature annealing. This work was partly supported by the ImPACT Program of Council for Science, Technology and Innovation, Japan, and JSPS KAKENHI Grant Numbers 16H06332 and 16H03852.

[1] Z.C. Wen *et al.*, Appl. Phys. Lett. 98, 242507 (2011). [2] H. Sukegawa *et al.*, Appl. Phys. Lett. 110, 112403 (2017). [3] J.P. Hadorn *et al.*, Acta Mater. 145, 306 (2018). [4] A. Hallal *et al.*, Phys. Rev. B 88, 184423 (2013). [5] S. Ikeda *et al.*, Nat. Mater. 9, 721 (2010). [6] J.W. Koo *et al.*, Appl. Phys. Lett. 103, 192401 (2013). [7] H. Sukegawa *et al.*, PRB 86, 184401 (2012).

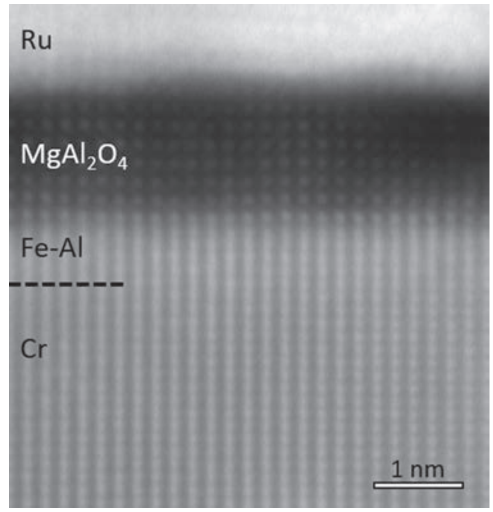

Fig. 1. HAADF-STEM image of the stacking structure around the interfaces.

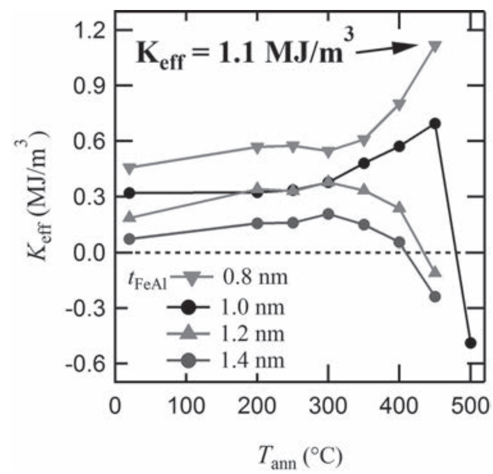

Fig. 2. K_{eff} vs. annealing temperature for different thicknesses; positive values indicate perpendicular to plane magnetic anisotropy.

GW-10. In-depth structural analysis of MgO/Co(bcc) by XPS and XPD.

K. Shamout[1], P. Roese[1], P. Espeter[1], U. Berges[1] and C. Westphal[1]
1. Experimentelle Physik I, Technical University Dortmund, Dortmund, Germany

Fe(bcc) and Co(bcc) were one of the first electrodes that were combined with MgO in order to create magnetic tunnel junctions [1]. These systems lead to even more complex electrodes like FeCo, FeCoB, or even Heusler-alloys [2]. Bcc structures, in general, have widely been used in MgO-based MTJs to make use of their spin-polarization at the Fermi level. To increase the efficiency of these MTJs, ultra-thin MgO films are necessary [3]. Yet, MgO film thinner than 3 monoatomic layer are amorphous making MTJs impossible. Therefore, the optimal thickness for a MgO film is 3-4 monoatomic layers (ML). Different *ab-initio* and first principle calculations usually predict higher tunnel magnetoresistances (TMR) than the measured ones [4-6]. It has been shown that most of this discrepancy is due to the surface roughness since different MgO thicknesses arise creating large defects [3]. By smoothening the surface higher TMR in MgO-based MTJs have been achieved. Still, the calculations do not match the experiment. With this work, we show that the MgO and the Co structures differ strongly at the interface for ultra-thin MgO layers. With these crucial structural information, new calculations can be carried out and order to provide a better understanding of the physics of the MgO-based MTJs. In previous calculctions, it was assumed that the Co(bcc) electrode is in a bulk-type structure, i.e. with lattice constants of $a_{Co} = 0.285$ nm. Further, MgO unit cell is assumed to be compressed to a lattice constant of $\sqrt{2}\times a_{Co}$ [7-9]. In this work, we investigated the structures of MgO and Co(bcc) at the MgO/Co(bcc) interface with X-ray photoelectron spectroscopy (XPS) and diffraction (XPD). THe highly surface sensitive XPS provides chemical information and with XPD the local enviroment of the atoms is determined. Therefore, the lattice sides can be resolved in a Sub-Angstrom range. The experiment was perfomred with an incoming photon energy of hf = 260 eV. We recorded the Co 3p and Mg 2p XPD patterns over a polar- and azimuth-angle range of $24° \leq \theta \leq 70°$ and $0° \leq \phi \leq 180°$ with increments of $\Delta\theta = 2°$ and $\Delta\phi = 1.8°$. We produce Co(bcc) electrodes on a Ga-rich GaAs substrate. Then, 4 ML of MgO is evaporated corresponding to two MgO unit cells. We calculated XPD patterns for the Co 3p and Mg 2p orbitals and obtained impressive R-factors of $R_{Co} = 0.08$ and $R_{Mg} = 0.04$. The resulting structure is displayed in Fig. 1 (left). It is clear, that the resulting structure from the XPD measurement differs heavily from the assumptions in different theoretical calculations [8]. The Co(bcc) lattice constant does not change in [100] or [010] direction, but it is strained in [001] direction at the interface. Further, we observe a shift in every second layer as indicated in Fig. 1. No bonding between MgO and Co(bcc) occurs. For 4 ML of MgO, the XPD calculations yield a stronlgy distorted unit cell. Therein, we observe a weaker compression in [100] and [010] direction than the predictions and a slight strain in [001] direction.

[1] S. Yuasa et al., Nat. Mater. 3, 868 (2004) [2] K. Tsunekawa et al., Appl. Phys. Lett. 87, 072503 (2005) [3] L. Martin et al., Appl. Surf. Sci. 424, 58-62 (2017) [4] S. Mallik et al., J. Magn. Magn. Mater. 428, 50 (2017) [5] J. Zhouet al., Appl. Phys. Lett. 109, 242403 (2016) [6] J. Zhouet al., IEEE Trans. Magn. PP, 1 (2017) [7] H.-M. Tang et al., Phys. Rev. Applied 7, 034004 (2017) [8] X.-G. Zhang et al., Phys. Rev. B 70, 172407 (2004)

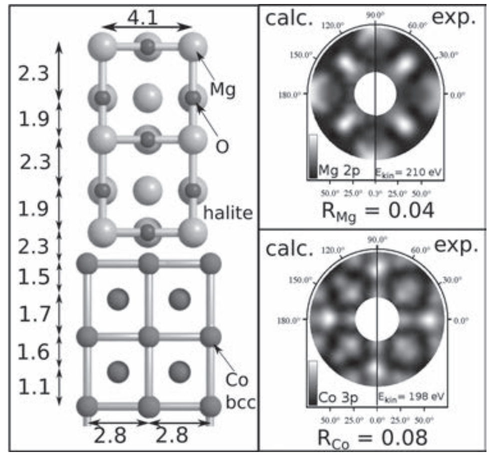

Fig. 1. Resulting MgO/Co(bcc) interface (left) for a MgO thickness of 4 ML. The experimental data and the corresponding calculated patterns fpr Co 3p and Mg 2p are shown on the right. Both XPD patterns were recorded at an incoming photon energy of 260 eV.

GW-11. Perpendicular magnetic anisotropy in annealing-free La/CoFeB/MgO heterostructures.

Y. Iida[1,2], J. Okabayashi[3], P. Sheng[2], M. Hayashi[2,4] and S. Mitani[1,2]
1. Graduate School of Pure and Applied Sciences, University of Tsukuba, Tsukuba, Japan; 2. Research Center for Magnetic and Spintronic Materials (CMSM), National Institute for Materials Science (NIMS), Tsukuba, Japan; 3. Research Center for Spectrochemistry, The University of Tokyo, Bunkyo, Japan; 4. Department of Physics, The University of Tokyo, Bunkyo, Japan

Interface perpendicular magnetic anisotropy (PMA) is one of the most important issues to develop perpendicular magnetic tunnel junctions (p-MTJs), particularly in p-MTJs using CoFeB alloys that do not show PMA in a bulk form [1]. Besides the continuous efforts to improve the PMA characteristics in CoFeB/MgO heterostructures, the mechanism of PMA has been intensively studied. First-principles calculations show that the hybridization of Fe-3d_z^2 and O-2p_z states plays a crucial role in the occurrence of the interface PMA [2], where O atoms are positioned just above Fe atoms at the interface. Such an interface atomic configuration is likely essential, which is supported by the fact that PMA energies are dramatically increased by post-annealing in most of Fe-based alloy/MgO heterostructures [3-6]. On the other hand, interface PMA can also be observed even for the annealing-free CoFeB/MgO heterostructures, depending on the underlayer materials [3,7]. In this study, we investigated PMA in annealing-free La/CoFeB/MgO heterostructures, since the PMA in annealing-free heterostructures was obtained depending on underlayer materials with a small electronegativity such as Ta or Zr. Note that La also exhibits a typical small electronegativity material that is likely to cause interatomic charge transfer, as well as to be easily oxidized. CoFeB (t_{CFB})/MgO (2nm) bilayer structures with a 2-nm-thick La underlayer were prepared by rf sputtering on a W-buffered thermally oxidized Si substrates. The whole stacking structures are Si/SiO_2-subs.//W-buffer(3nm)/La(2nm)/CoFeB(1nm)/MgO(2nm)/W-cap(1nm) which are grown at room temperature. The thickness of CoFeB layer, t_{CFB}, was varied ranging from 0.8 nm to 1.4 nm. No annealing process was performed in the sample preparation procedures. Magnetic properties were examined by a vibrating sample magnetometer, and x-ray magnetic circular dichroism (XMCD) was measured for the element-specific characterization. Figure 1 shows the areal PMA energy density $K_{eff}t_{CFB}$ as a function of t_{CFB}. Around t_{CFB} = 1.0 nm, definite PMA is obtained for the annealing-free La/CoFeB/MgO heterostructures. The PMA energy density reaches $K_{eff}t_{CFB}$ = 0.2 mJ/m^2 (K_{eff} = 0.2 MJ/m^3). In the XMCD measurements, it was found that the normal component of the orbital magnetic moment in Fe is slightly larger than the in-plane one, being qualitatively the same as the results in a previous XMCD study for a single-crystalline Fe/MgO heterostructure [8]. This suggests that the anisotropy of the orbital magnetic moment brings about the interface PMA even in the annealing-free and therefore presumably amorphous CoFeB layer. To further investigate the correlation between PMA and the sample structures, a comparative study was also performed. Table 1 shows the stacked structures (t_{CFB} = 1.0 nm) used for this purpose. Namely, symmetric and asymmetric heterostructures were prepared using La and/or MgO layers as under- and over-layers. While the asymmetric structures tend to show PMA rather than the symmetric structures, only the La/CoFeB/MgO shows PMA clearly. This means that each interface does not contribute to the occurrence of PMA independently. It is inferred that there is a certain interplay of the roles of under- and over-layers. One possible mechanism would be that the La underlayer works as an excess oxygen absorber to the well-oriented MgO overlayer. However, such a simple idea would not explain the entire results obtained in this study. Internal electric field generated at the La/CoFeB interfaces locally due to the large difference in electronegatibity might influence the observed PMA. In summary, we investigated the PMA in annealing-free La/CoFeB/MgO heterostructures and the role of La insertion as an underlayer. We confirmed the orbital moment anisotropy in Fe, which might be originated from absorbing the excess oxygen in MgO or internal electronic fields due to the differences of electronegativities.

[1] S. Ikeda, K. Miura, H. Yamamoto, K. Mizunuma, H. D. Gan, M. Endo, S. Kanai, J. Hayakawa, F. Matsukura, and H. Ohno, Nat. Mater. 9, 721 (2010). [2] H. X. Yang, M. Chshiev, B. Dieny, J. H. Lee, A. Manchon, and K. H. Shin, Phys. Rev. B 84, 054401 (2011). [3] M. Yamanouchi, R. Koizumi, S. Ikeda, H. Sato, K. Mizunuma, K. Miura, H. D. Gan, F. Matsukura, and H. Ohno, J. Appl. Phys. 109, 07C712 (2011). [4] W. X. Wang, Y. Yang, H. Naganuma, Y. Ando, R. C. Yu, and X. F. Han, Appl. Phys. Lett. 99, 012502 (2011). [5] H. Meng, W. H. Lum, R. Sbiaa, S. Y. H. Lua, and H. K. Tan, J. Appl. Phys. 110, 033904 (2011). [6] J. W. Koo, S. Mitani, T. T. Sasaki, H. Sukegawa, Z. C. Wen, T. Ohkubo, T. Niizeki, K. Inomata, and K. Hono, Appl. Phys. Lett. 103, 192401 (2013). [7] W. Skowronski, T. Nozaki, D. D. Lam, Y. Shiota, K. Yakushiji, H. Kubota, A. Fukushima, S. Yuasa, and Y. Suzuki, Phys. Rev. B 91, 184410 (2015). [8] J. Okabayashi, J.W. Koo, H. Sukegawa, S. Mitani, Y. Takagi, and T. Yokoyama, Appl. Phys. Lett. 105, 122408 (2014).

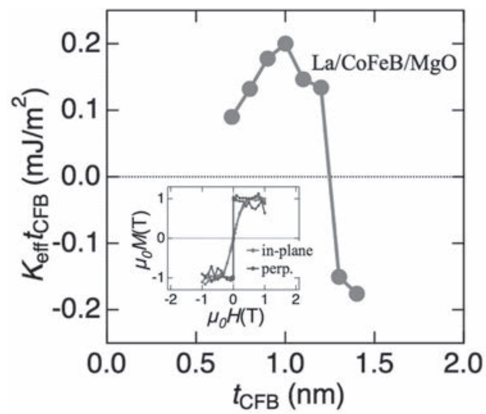

Fig. 1. Areal PMA energy $K_{eff}t_{CFB}$ as a function of the CoFeB thickness t_{CFB} in La/CoFeB/MgO heterostructures. Inset shows the VSM data in t_{CFB}=1nm.

	K_{eff} (MJ/m^3)	M_s (T)
(1) La/CoFeB/MgO	0.2 [PMA]	1.0
(2) MgO/CoFeB/La	-0.034 [Isotropic]	0.85
(3) La/CoFeB/La	-0.014 [Isotropic]	0.685
(4) MgO/CoFeB/MgO	-0.26 [IMA]	1.31

Table 1. PMA energy K_{eff} and saturation magnetization M_s for four different stacks consisting of La(2nm), CoFeB(1nm), and MgO(2nm) layers. The square brackets represent the estimated magnetic anisotropy, where PMA and IMA stand for perpendicular and in-plane magnetic anisotropy, respectively.

GW-12. Structural and magnetic properties of $CoMnO_3$-(0001) orbital ferrimagnet epitaxial thin films.

H. Koizumi[1], S. Sharmin[1] and H. Yanagihara[1]
1. University of Tsukuba, Tsukuba, Japan

Introduction $CoMnO_3$ has an ilmenite structure, in which Co^{2+} and Mn^{4+} layers are alternatively stacked along the c-axis. [1] Both Co^{2+} (d^7) and Mn^{4+} (d^3) possess $S_z = 3/2$, and are antiferromagnetically coupled through the super-exchange interaction with Neel temperature of 391K. Therefore, the spin angular momentums of Co and Mn cancel each other. However, the orbital angular momentum of Co^{2+} in crystal field is 0.72 μ_B. Since the net magnetic moment thus originates only from orbital angular momentum, this compound has been termed an "orbital ferri-magnet". The magnetic properties of $CoMnO_3$ is of interest from the viewpoint of both fundamental magnetism and applications including novel devices for spintronics. The magnetic anisotropy energy of $CoMnO_3$ is large with negative sign, as understood within the framework of the single ion model of Co^{2+} originally proposed by Slonchewski. [2] However, magnetic and other physical properties of $CoMnO_3$ are not as yet well understood. In this study, we report on the growth technique of epitaxial thin films of $CoMnO_3$(0001) on α-Al_2O_3(0001) and its magnetic properties. Experimental $CoMnO_3$ films were grown by an RF-magnetron sputtering technique with oxygen as a reactive gas. The alloy target had the desired composition of $Co_{0.5}Mn_{0.5}$. In order to optimize growth conditions, we varied oxygen flow rates, process temperature, and the film thickness. The surface condition was measured by reflection high energy electron diffraction (RHEED) technique. The film thickness was determined by X-ray reflectivity (XRR) measurement. The lattice constants of the Co-Mn oxide films were determined by X-ray diffraction (XRD). Magnetic properties such as in-plane MH-loops, and magnetic anisotropy constants were measured by a vibrating sample magnetometer (VSM) and magneto-torque meter with the Physical Properties Measurement System (PPMS : Quantum Design). The film composition was determined by inductively coupled plasma mass-spectroscopy (ICP-mass). The valences of both Co and Mn ions were evaluated by an X-ray absorption near edge structure (XANES) experiment and the distance to neighboring atoms was measured by an extended X-ray absorption fine structure (EXAFS) experiment. We also performed X-ray magnetic circular dichroism (XMCD) experiment to estimate spin and orbital angular momentum. Results and discussion The RHEED images indicate that $CoMnO_3$ is epitaxially grown on the α-Al_2O_3 (0001) substrate, and the XRD results suggest that the crystal structure of the film is consistent with the ilmenite structure. The composition ratio of the film is Co:Mn = 45.7% : 54.3% as determined by ICP-mass. Figure 1 shows the in-plane MH-loops of 70-nm-thick $CoMnO_3$ (0001) film on Al_2O_3 (0001). The room temperature saturation magnetization is smaller than the previously reported value of $M_s = 0.61$ [μ_B / f.u.]. [1] This can be explained by the imperfection of the site order of Co and Mn or the off-stoichiometry of Co:Mn = 4.6 : 5.4. Figure 2 shows a magneto-torque curve of the 70-nm-thick $CoMnO_3$ (0001) film at H = 90 kOe. The torque curve indicates that the film has a large negative perpendicular magnetic anisotropy K_u = -3 Merg / cm^3 and it does not saturate even at H = 90 kOe along the hard magnetization direction. The results of XANES for the film exhibiting relatively large magnetization indicate that the valency for both transition metal ions are Co^{2+} and Mn^{4+}. XMCD shows that the spin directions of Co^{2+} and Mn^{4+} are opposite to each other, reflecting the AF coupling. In addition, the orbital angular momentums were negligibly small for Mn but significantly large for Co, which is consistent with the picture of orbital ferrimagnetism of $CoMnO_3$.

[1] R. M. Bozoth and D. Walsh, J. Phys. Chem. Solids. Pergamon Press. 5, 299(1958). [2] W. H. Cloud and J. P. Jesson, J. Appl. Phys. 37, 1398(1966)

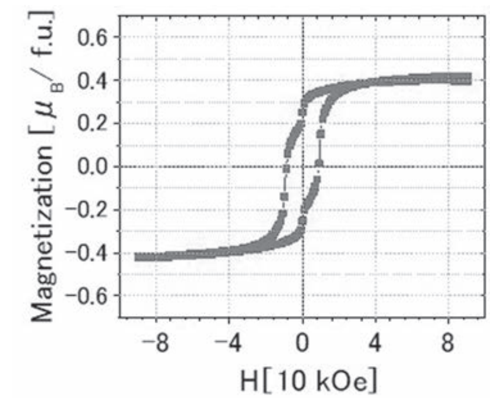

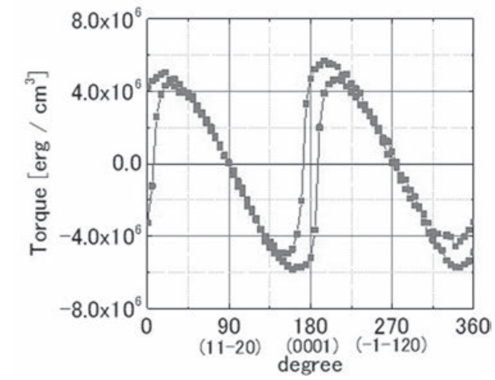

GW-13. Interlayer exchange coupling of FeCoB/(Ta,Mo)/FeCoB.

T.J. McKinnon[1], P. Omelchenko[1], B. Heinrich[1] and E. Girt[1]
1. Physics, SFU, North Vancouver, BC, Canada

In this work, we present a detailed ferromagnetic resonance (FMR) study of two FeCoB layers coupled across a nonmagnetic spacer layer. The structures of studied samples are FM1/X(d)/FM2 where FM1 is a magnetic layer composed of Fe/FeCoB, FM2 is a magnetic layer composed of FeCoB/NiFe, X is Ta or Mo, d is the thickness of the X layer in nm, and d is varied from 0.375 nm to 4 nm. These structures were deposited on top of an underlayer of Ta/FeCoB(0.5)/MgO, where FeCoB is thin enough to be non magnetic, and MgO is (100) oriented. This underlayer was chosen because MgO grows well oriented in the (100) direction when grown on top of amorphous FeCoB, which is the orientation chosen for typical memory device applications. The FeCoB within FM1 is strongly coupled to higher Ms Fe, and the FeCoB in FM2 is strongly coupled to lower Ms NiFe allowing one to separate the FMR resonance positions which is required to determine the strength of interlayer exchange coupling (J). We analytically solved a system of coupled LLG equations, representing the coupled magnetic layers, and used it to fit the FMR data measured at 8 to 32 GHz frequencies in order to determine J, uniaxial anisotropy Ku, gilbert damping alpha, and g factor of each layer as a function of the spacer layer thickness and annealing temperature. We did this for both Ta and Mo as spacer layer materials. For samples with Ta as the spacer layer, the dependence of the coupling strength on Ta thickness is the same for as-deposited samples and those annealed at 200 C: the coupling drops to 0 above approximately 0.5 nm and ferromagnetic coupling increases rapidly below 0.45 nm. For samples annealed at 300 C ferromagnetic coupling increases rapidly below approximately 0.6 nm. This temperature dependence can be seen in Fig. 1. Damping of FM1 in the same samples remains approximately constant with an average of 0.0066 for all samples within the range of Ta thickness from 0.4 nm to 4 nm. It was also found to be unaffected by annealing temperature. Damping for FM2 was found to be below 0.009 for all samples. It was also found to decrease with an increase in annealing temperature, and to decrease with Ta thickness less than 0.5 nm. Ms for FM1 and FM2 was measured using a superconducting quantum interference device (SQUID), and was found to be unaffected by spacer layer thickness or annealing temperature. Ku for both FM1 and FM2 was found to not depend on the thickness of the Ta spacer layer. However, Ku for FM1 was found to increase slightly when annealed at 200 C, then decrease when annealed at 300 C. The decrease in Ku was found to be caused by a complete loss of surface anisotropy at the Fe/MgO interface. Ku for FM2 was found to be unaffected by annealing temperature. For not-annealed samples with Mo as the spacer layer, the ferromagnetic coupling increases rapidly for Mo thickness less than 0.35 nm. Antiferromagnetic coupling is observed for Mo thickness ranging from 0.35 nm to 0.6 nm and a weak ferromagnetic coupling for thickness greater than 0.6nm. Fig. 2 shows the dependence of J on spacer layer thickness for both Mo and Ta for the not-annealed samples.

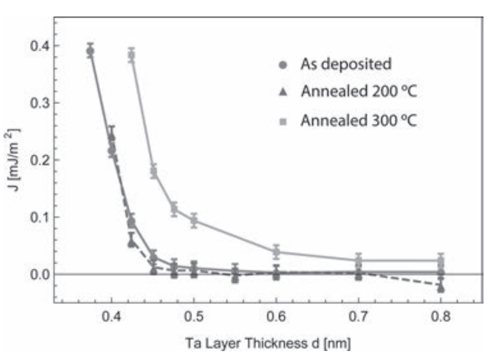

Fig. 1. Coupling constant as a function of Ta layer thickness for samples as deposited, samples annealed at 200 C, and samples annealed at 300 C.

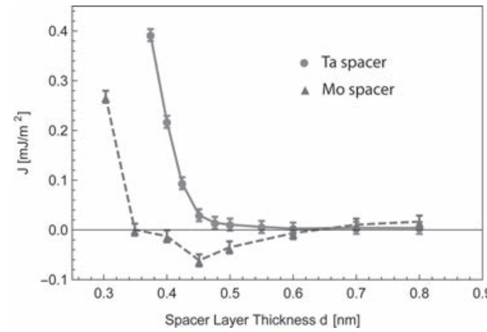

Fig. 2. Coupling constant as a function of spacer layer thickness for not-annealed samples with Ta and Mo spacer layer materials.

GW-14. Influence of inclined perpendicular anisotropy on the current-induced magnetization reversal.

M. Stebliy[1], A. Kolesnikov[1], A. Davydenko[1], A. Ognev[1] and L. Chebotkevich[1]
1. Far Eastern Federal University, Vladivostok, Russian Federation

Investigation of energy-efficient method of local control of the magnetization is one of the crucial points of spintronics development. One of the promising areas is the so-called spin-orbit torque effect (SOT) [1]. This effect can lead to the magnetization orientation switching in structures with perpendicular magnetic anisotropy (PMA) in the case of broken inverse symmetry, with respect to the current flow direction. To induce the asymmetry an external magnetic field can be used [1]. Previously some local methods were studied, it was shown that can be used: exchange-coupled layers [2]; additional antiferromagnetic layer [3]; thickness change of the ferromagnetic or coating layer [4,5]; inclined of magnetic anisotropy axis [6]. In this work, the influence of the angle of anisotropy inclination on the magnetization switching efficiency is presented. The Hall bars Ru(8 nm)/Co(0.9 nm)/Ru(1.5 nm) were obtained by magnetron sputtering. To induce an incline of perpendicular magnetic anisotropy axis, the method of oblique deposition of the ferromagnetic layer Co was used. During the Co deposition the angle between the samples normal and the sputtering source was 17° and 40°. During the formation of Ru layers, the sample was in rotation. An investigation of magnetization reversal in sample by a perpendicular field with presence of an inplane field [6] allows to determine the angle of inclination of the anisotropy axis relative to the normal of the film. For the case of the extreme positions of the magnetron source, the incline of the anisotropy was 2° and 3.5°, respectively. It has been experimentally establish that the magnetization switching occurs in the absence of an external field in the case of the conduction current orientation perpendicular to the plane of inclination of the anisotropy axis, Fig.1a. Whereas in the case of using an external magnetic field the magnetization should be inclined along the direction of the current. To estimate the influence of incline of the anisotropy, the sample was saturated by an external perpendicular field to the state +M, and then the field turned off. A series of current pulses of increasing amplitude was applied to the sample, while the value of the anomalous Hall effect (AHE), which is proportional to the perpendicular component of the magnetization, was recorded. At small values of the coercive force ~ 15 Oe, the action of the Oersted field leads to demagnetization of the sample. In the absence of inclined anisotropy, the demagnetization effect should be the same when the direction of the current is changed, but in the considered case, the value of the magnetization depends on the direction of the current, Fig.1b. The level difference ΔM characterizes the value of the effective field H_z induced by the SOT effect. By varying the current between the maximum values hysteresis loop can be obtained. It was established experimentally that increasing the inclination angle of anisotropy lead to increasing of the ΔM value, Fig.2a. The experimental data were compared with the results of the micromagnetic simulation performed in the MuMax^3 software [7]. The investigated model included an inhomogeneous distribution of the current density, as well as the Oersted field, which were calculated separately. In the simulation were used standard magnetic parameters for Co, energy of magnetic anisotropy was 8.4e5 J/m^3 with the different orientation of the anisotropy axis. The maximum density of the spin current was 2e10 A/m^2, with the direction of flow (0, 0, 1) and the polarization orientation (0, -1, 0). Obtained results are in qualitative agreement with the experimental data, Fig.2b. By using micromagnetic simulation, it was found that the value of the magnetization reversal ΔM is determined not only by the incline angle of anisotropy, but also by the competition between the effective field H_z and Oersted field. Switching efficiency can be increasing by increasing the spin current density, it can be achieved by using a material with a large spin Hall angle. This approach was made experimentally by the addition of the W coating layer. In the structure Ru(8)/Co(0.9)/Ru(1.5)/W(2) with a anisotropy axis inclined of 3.5° the switching ΔM = 70% was obtained in the absence of an external magnetic field. Support by the Grant program of the Russian President (MK-2643.2017.2) and RFBR (grants 17-52-50060, 18-02-00205), are acknowledged.

[1] K. Garello, P. Gambardella, Phys. Rev. B 89, 214419 (2014). [2] Y. Lau, P. Stamenov, Nature Nanotechnology 11, 758 (2016). [3] S. Fukami, H. Ohno, Nature Materials 15, 535 (2016). [4] Guoqiang Yu, Li-Te Chang, Mustafa, Kang L. Wang, Appl. Phys. Lett. 105, 102411 (2014). [5] Mustafa Akyo, Guoqiang Yu, Kang L. Wang, Appl. Phys. Lett. 106, 162409 (2015). [6] V. Mohanan, K. Ganesh, A. Kumar, Phys. Rev. B 96, 104412 (2017). [7] A. Vansteenkiste, J. Leliaert, M. Dvornik, AIP Advances 4, 107133 (2014).

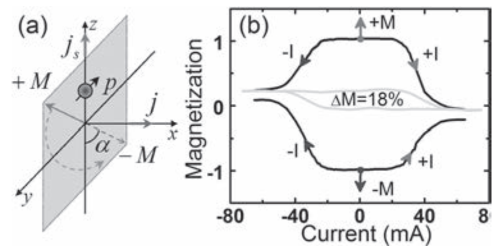

Fig. 1. (a) Scheme of mutual orientation of conductivity and spin current, polarization direction and anisotropy axis. (b) Experimental demagnetization curves of the Ru(8)/Co(0.9)/Ru(1.5) structure with an angle of anisotropy incline 3.5°, for various combinations of the initial magnetization and the direction of the current.

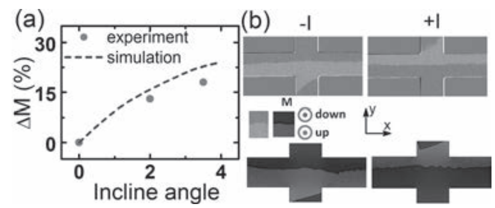

Fig. 2. (a) Dependence of the current-induced magnetization switching ΔM on the incline angle of the anisotropy axis. (b) Visualization of the Hall bars magnetic structure after applying current in different directions for the sample with angle of anisotropy incline 3.5°, obtained with Kerr microscopy and as a result of micromagnetic simulation.

GW-15. Magnetization studies of obliquely sputtered CoFeB for TMR sensors.

S. Willing[2,1], K. Schlage[1], T. Guryeva[1] and R. Roehlsberger[1,3]
1. Deutsches Elektronen-Synchrotron (DESY), Hamburg, Germany;
2. PIER Helmholtz Graduate School, Hamburg, Germany; 3. Hamburg University, Hamburg, Germany

In this contribution we clarify to which extend magnetic anisotropy can be tuned via oblique-incidence deposition in ultra-thin CoFeB layers for tunneling magnetoresistance (TMR) application. Already for years, CoFeB has been one of the most used magnetic materials in the fields of magnetic memory devices and sensors that employ the TMR effect. The core of such a sensor consists of a trilayer stack, usually two CoFeB electrodes separated by an insulating barrier like MgO. Depending on the relative orientation of magnetization in the CoFeB layers, the probability of electrons tunneling through the barrier varies which can be seen as a change in electrical resistance. In order to obtain the predicted giant TMR effects, the (001)-textured MgO must act as a structural template. In a so-called solid-state epitaxy process during thermal annealing, the CoFeB crystallizes with the same (001)-orientation. As a result, the highly spin-polarized bands with Δ_1-symmetry couple across the barrier acting as a spin-filter. Thus, the crystallization process and resulting structure of the magnetic electrodes is of major importance. Furthermore, some form of magnetic asymmetry between the barriers is required for the TMR. This assures that the two magnetic layers behave differently under an external magnetic field and the relative orientation of their magnetizations (or so called magnetic easy axes) changes. It can be achieved, for example, by inducing additional anisotropy in one of them through application of a magnetic field during growth, through pre-stressed substrates, creation of an exchange-bias structure, or, most easily and most flexible, through oblique-incidence deposition (OID) [1]. By taking advantage of the two angular degrees of freedom during sputter deposition, the orientation of the magnetic easy axis (via azimuthal angle) and the layer's coercivity (via polar angle) can be freely tailored to modify each single layer's properties [2]. The available range of possible coercive field values varies with the layer thickness. This restriction is due to the fact that OID is closely related to the thin film's morphology, texture and surface profile that changes during growth. While there have been many studies on the magnetic and structural properties of CoFeB and the role in TMR sensors before, they either investigated the structure of conventional non-OID TMR stacks, e.g. [3], or were based on films far beyond the relevant thin film regime [4]. We have investigated the magnetic behavior of obliquely deposited CoFeB as single layers in the relevant thicknesses regime and in complete TMR stacks via the Magneto-optical Kerr effect (MOKE). The magnetic properties of CoFeB could well be tuned by the polar deposition angle (Fig. 1) and a strong dependency on film thickness and layer structure (amorphous vs. crystalline) was seen. We have found that an application of OID to CoFeB with its required thermal annealing process is not only possible but also yields unforeseen magnetic behavior which is relevant from a technical as well as scientific point of view: Above a quite low threshold thickness (~1-3 nm depending on the polar deposition angle), the magnetization in the film plane is rotated by 90° with respect to the OID-induced easy axis, however, upon annealing, the expected direction is presumed (Fig. 2). This is a behavior that no other material (like Fe, Co, $Ni_{80}Fe_{20}$) has exhibited in our studies. Beyond simple CoFeB layers, we have successfully tested the applicability of OID in custom-made TMR trilayers. By altering the polar angle during deposition of two CoFeB electrodes, they inherited different coercive fields yielding a distinct double-switching behavior along the easy axis. It is worth mentioning that the wavy surface profiles of the CoFeB layers, which are typical for the OID deposition process, seem not to render the sensitive thin MgO barrier ineffective. It has been shown before [1] that even in more complex multilayer and superlattice (ferromagnetic hybrid) structures OID can be employed to precisely tailor the magnetic properties of individual layers. With the findings of this work we thus conclude that OID opens new possibilities to realize customized TMR structures, not only for the first time but in a simple and convenient fashion.

[1] K. Schlage, L. Bocklage, D. Erb, J. Comfort, H.-C.Wille, and R. Röhlsberger, Spin-Structured Multilayers: A New Class of Materials for Precision Spintronics, Adv. Funct. Mater.26, 7423 (2016). [2] K. Schlage, D. Erb, R. Röhlsberger, H.-C. Wille, D. Schumacher, L. Bocklage, European Patent EP 2 846 334 A1, (2015). [3] W. G. Wang et al., In-situ characterization of rapid crystallization of amorphous CoFeB electrodes in CoFeB/MgO/CoFeB junctions during thermal annealing. Appl. Phys. Lett. 95, 242501 (2009). [4] C. Li et al., Tunable zero-field ferromagnetic resonance frequency from S to X band in oblique deposited CoFeB thin films. Scientific Reports 5, 17023 (2015).

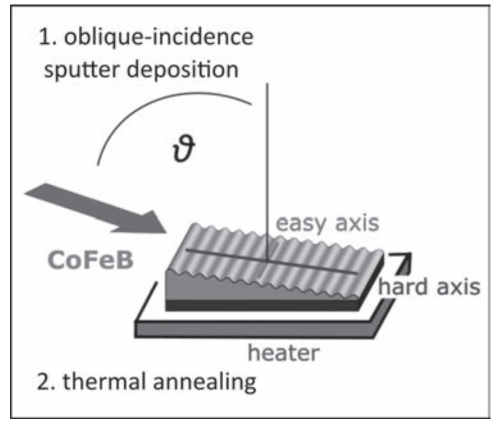

Fig. 1. Sample preparation. CoFeB is deposited under a polar angle θ resulting in an ultra-thin magnetic film with a thickness gradient and defined magnetization axes. The orientation of these axes and the magnetic switching field are determined by both, the deposition angle θ and a subsequent thermal annealing process. To avoid oxidation the CoFeB layers are capped with Ta (not shown).

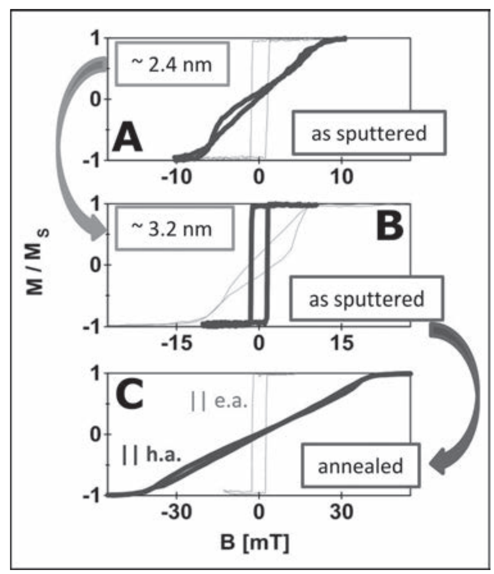

Fig. 2. The magnetic behavior of the CoFeB layers was investigated via MOKE measurements with external magnetic field along the two axes shown in Fig. 1 (magnetic field parallel to sputter direction in blue, perpendicular to sputter direction in red). (A) In ultra-thin layers the magnetization is aligned along the easy axis yielding a sharp switching (red) and a diagonal along the hard axis (blue). This is the expected behavior in OID layers. (B) Above a low threshold thickness, the magnetization is unexpectedly rotated by 90° in plane compared to that of conventional OID magnetic layers. The MOKE curve with field along the hard axis now displays the switching behavior instead of a diagonal. (C) After the annealing and crystallization process the magnetization presumes the expected direction along the easy axis that is intended via the OID process.

GW-16. Magneto-optical properties of Pt/TbCo heterostructure films.

S. Iemoto[1], *S. Sumi*[1], H. Awano[1] and M. Hayashi[2,3]

1. Toyota Technological Institute, Nagoya, Japan; 2. The University of Tokyo, Tokyo, Japan; 3. National Institute for Materials Science (NIMS), Tsukuba, Japan

1. Introduction Magnetic film with a heavy metal layer shows strong interfacial interaction of spin-orbit. Spin-orbit interaction (SOI) is one of the key technologies for spintronics and its applications. It is important to reveal the SOI [1]. On the other hand, it is known that magneto-optical Kerr effect is a useful method to detect interfacial information, especially using interference [2] [3]. There are many reports about magneto-optical Kerr effect in a rear earth transition metal (RE-TM) film with a noble metal layer such as Pt, Pd, etc [4][5]. However, there are few reports about discussion on the SOI. In this paper, we measured magneto-optical Kerr spectrums of Pt/TbCo heterostructure films, and discuss about contribution of the SOI. 2. Experimental Figure 1(a) shows sample structures. We prepared three samples on a thermally oxidized silicon (SiO_x) substrate (0.3mm); A: TbCo(6nm)/Pt(3nm) B: Pt(3nm)/TbCo(6nm)/Pt(3nm) C: Pt(3nm)/TbCo(6nm)/SiO_2(5nm). SiOx thickness was 100 nm to enhance Kerr effect using interference. SiO_2 was used as a non-heavy metal layer as well as a protective layer for the TbCo. Each layer was deposited with a sputter method. Magneto-optical Kerr spectrum was measured with a wavelength of 300-700 nm using a Xenon light source and a PEM (photo-elastic modulator) [7]. Optical index was measured by an ellipsometer (JASCO-M150). 3. Results & Discussions Figure 1(b) shows Kerr hysteresis loops for each sample with a wavelength of 700 nm. The samples show perpendicular magnetic anisotropy of rare-earth rich composition. Their coercivity are 5 KOe for the sample A, around 3 KOe for the sample B, C. Kerr rotation angle of the sample C is larger than that of the sample A, B. Figure 2 shows magneto-optical Kerr spectrum of the samples. (a) TbCo(6nm)/Pt(3nm) (b) Pt(3nm)/TbCo(6nm)/Pt(3nm) (c) Pt(3nm)/ TbCo(6nm)/SiO2(5nm). The dots show measured ones and the lines show simulated ones. The Kerr rotation angle (θ_K) and the ellipticity (η_K) changed with wavelengths. θ_K was maximum value with a wavelength of around 400 nm where a sign of η_K changed. A peak position of θ_K shifted slightly to shorter wavelengths in the sample B with a symmetric structure. The magneto-optical Kerr spectrums may include contribution of both interference and interfacial effect. To isolate them, we simulated the spectrums using the effective refractive index method [6]. Optical constants of the TbCo for a right and a left hand circular polarization light were calculated from θ_K, η_K and optical index n, k with a 100 nm TbCo film. The simulated spectrums change by interference between a Si substrate and a SiO_2/TbCo, Pt/TbCo or a TbCo/Pt interface, and almost same manner as the measurement results. In the sample B with a symmetric structure, the spectrums are well consistent with the measurement ones. Reasons for the peak shift of θ_K in shorter wavelengths seem to be optical interference. In the sample A and C with an asymmetric structure, there are some differences between the simulated θ_K, η_K and measurement ones. We could not see any enhanced θ_K or η_K in shorter wavelength [4] [5]. It may be caused by interfacial effects of the spin orbit interaction. 4. Conclusions We demonstrated magneto-optical spectrums of Pt/TbCo heterostrucure films. The films with the asymmetric structures showed the enhanced magneto-optical effect. The reason for an enhanced magneto-optical effect may be interfacial effects of the spin orbit interaction. This work was partly supported by JSPS Grant-in-Aids for Scientific Research (16H03853, 17H03240), the MEXT-Supported Program Research Foundation at Private University (2014-2019), and Innovation and Spintronics Research Network of Japan

[1]D. Bang and H. Awano, J. Appl. Phys., 117, 17D916 (2015). [2]P. Reigo, S. Tomita, K. Murakami, T. Kodama, N. Hosoito, H. Yanagi and A. Berber, J. Phys. D, Appl. Phys., 50, 19LT01(2017). [3]S. Sumi, H. Awano and M. Hayashi, Sci. Rep., (to be published) [4]Y. Itoh and T. Suzuki, J. Appl. Phys., vol. 87, 6902(2000). [5]H. Awano, T. Niihara and M. Ojima, J. Magn. Magn. Mater., 126, 550(1993). [6]W. P. Van Drent and T. Suzuki, J. Magn. Magn. Mater., 175, 53 (1997). [7]K. Egashira, and T. Yamada, J. Appl. Phys., 45, 3643 (1974).

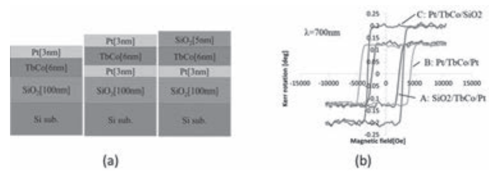

Fig. 1. Sample structures (a)A TbCo(6nm)/Pt(3nm), B Pt(3nm)/TbCo(6nm)/Pt(3nm), C Pt(3nm) /TbCo(6nm)/SiO2(5nm) (b) Kerr hysteresis loops for the films with a wavelength of 780 nm.

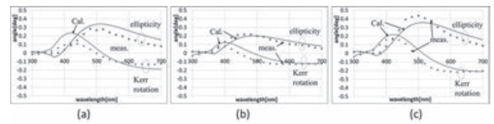

Fig. 2. Magneto-optical Kerr spectrum of the samples (a) TbCo(6nm)/Pt(3nm) (b) Pt(3nm)/TbCo(6nm)/Pt(3nm) (c) Pt(3nm)/ TbCo(6nm)/SiO2(5nm). The dots show measured ones and the lines show simulated ones.

FRIDAY AFTERNOON, 27 APRIL 2018 ORCHID I, 2:00 TO 5:00

Session HA

SYMPOSIUM ON ATOMS, MOLECULES AND INTERFACES FOR SPIN QUANTUM ENGINEERING

Ilaria Bergenti, Chair
ISMN-CNR, Bologna, Italy

INVITED PAPERS

2:00

HA-01. Interface as key unit in molecular spintronic devices.

V.A. Dediu[1]
1. DSCTM, CNR-ISMN, BOLOGNA, Italy

Information and communication technology (ICT) is calling for solutions enabling lower power consumption, further miniaturization and multi-functionality requiring the development of new device concepts and new materials. A fertile approach to meet such demands is the introduction of the spin degree of freedom into electronics devices, an approach commonly known as spintronics. This already lead to a revolution in the information storage (GMR read heads) in the last decades. Nowadays, the challenge is to bring spintronics also into devices dedicated to logics, communications and storage within the same material technology [1]. Organic semiconductors emerged as an extraordinary spintronic material about ten years ago, when a few papers appeared with straightforward and encouraging claims on spintronics phenomena [2]. From then on Organic Spintronics has evolved into a prolific discipline populated by a large number of experimentalists and theoreticians. Research in molecular spintronics began with the aim of using molecules as spin transport media, thanks to their intrinsically weak spin relaxation mechanisms. Initial experiments focused on reaching spin transport in molecular films and on replicating previous device concepts taken from inorganic spintronics, such as spin valves and magnetic tunnel junctions. However, it soon became apparent that molecules were playing another role beyond that of mere spin transport materials. For example, in experiments with vertical spin valves, many groups were reporting consistently negative magnetoresistance. These results were striking, as they contradicted the well-established spin polarization sign of the ferromagnetic electrodes and the present knowledge at that time regarding spin transport. A few years later, a coherent picture arose invoking the role of molecular layers in tuning the spin polarization of ferromagnetic materials at the interface, and 'spinterface' was officially born. Along this line I will especially concentrate on interfaces, representing the most important and the most hidden part of any spintronic device. Revealing their secrets is scientifically hard and experimentally costly, requiring sophisticated spectroscopic methods and massive calculations. For an interface consisting of a hard metallic electrode touching a soft organic layer, the situation obviously becomes even more complicated. I will overview the main achievements of the community in the investigation of very complex and very rich interface properties [3] and will describe the possibilities to develop and fabricate multifunctional devices which operation is fully dominated by the interface.

1. Challenges for semiconductor spintronics, Awschalom, D. D. & Flatte, M. E., Nature Physics 3, 153 (2007) 2. Spin routes in Organic Semiconductors, Dediu, V. A. et al., Nature Materials 8, 707 (2009) 3. Activating the Molecular Spinterface, M Cinchetti, V.A Dediu, L Hueso, Nature Materials 16, 507 (2017)

2:30

HA-02. Activating the molecular spinterface.

M. Cinchetti[1]
1. Experimentelle Physik VI, Technical University Dortmund, Dortmund, Germany

The miniaturization trend in the semiconductor industry has led to the understanding that interfacial properties are crucial for device behaviour. Spintronics has not been alien to this trend, and phenomena such as preferential spin tunnelling, the spin-to- charge conversion due to the Rashba–Edelstein effect and the spin–momentum locking at the surface of topological insulators have arisen mainly from emergent interfacial properties, rather than the bulk of the constituent materials. In this talk I will describe inorganic/molecular interfaces by looking closely at both sides of the interface: the “organic” side and the “metallic” side (see Figure). When describing hybrid interfaces from the organic side, focus is put on how the molecular orbitals of the free molecule develop as a function of the strength of hybridization with the inorganic substrate. On the metal side, on the other hand, focus is put on the modification of the spin properties of the inorganic substrate as a consequence of the hybridization with the molecule. Within this framework, I will discuss recent developments in the field and underline how molecular materials have arisen as an ideal platform for creating interfacial spin effects [1]. As an example, I will show that the extreme multi-functionality of organic molecules can be used to functionalize the spin properties of surfaces with a spin-texture induced by strong spin-orbit coupling. I will present our results on the following two-dimensional electronic systems: the surface states of the topological insulator Bi_2Se_3 [2], and the Rashba-split surface states of a Pb-Ag surface alloy [3]. Topological insulators present spin-momentum locked helical surface states induced by the large spin-orbit interaction. These states are protected by time-reversal symmetry and result in a surface chiral spin-texture preventing back-scattering between states of opposite spin and momentum. In Rashba systems, on the other hand, the spin texture results from the lifting of the spin degeneracy of a two-dimensional electron gas by the large spin-orbit coupling. Possible applications of spin-textured materials are anticipated in the area of spintronics, e.g. for the creation of dissipationless spin currents. With this motivation, lately much effort has been devoted to the control and the manipulation of spin-textured surface states. In our recent work [2], we could show that the spin-texture of the Bi_2Se_3 surface can be influenced by choosing molecules with tailored hybridization strength. In particular, we have presented a rational design approach to customize the spin texture of surface states of a topological insulator. This approach relies on the extreme multifunctionality of organic molecules that are used to functionalize the surface of the prototypical topological insulator (TI) Bi_2Se_3. For the rational design we have used theoretical calculations to guide the choice and chemical synthesis of appropriate molecules that customize the spin texture of Bi2Se3. The theoretical predictions have been then verified in angular-resolved photoemission experiments. We could show that, by tuning the strength of moleculeTI interaction, the surface of the TI can be passivated, the Dirac point can energetically be shifted at will, and Rashba-split quantum-well interface states can be created. These tailored interface properties - passivation, spin-texture tuning, and creation of hybrid interface states- lay a solid foundation for interface-assisted molecular spintronics in spin-textured materials. In the other work [3], on the other hand, we have studied the influence of specific chemical bonds (as formed by the organic molecules CuPc and PTCDA) on a Pb-Ag Rashba surface alloy. We find that delocalized van der Waals or weak chemical π-type bonds are not strong enough to alter the alloy, while localized σ-type bonds lead to a vertical displacement of the Pb surface atoms and to changes in the alloy’s surface band structure [4]. These results provide an exciting platform for tuning the Rashba-type spin texture of surface alloys using organic molecules. In the light of the presentes results, I will discuss the key role that molecular interfaces may play in the development of a new generation of spin-based technologies, thanks to their unique capability of being actively tuned to reach as-yet unexplored functionalities.

[1] M. Cinchetti, A. Dediu, L. Hueso. Nature Materials 16, 507-515 (2017); [2] S. Jakobs, A. Narayan, B. Stadtmüller, A. Droghetti, I. Rungger, Y. S. Hor, S. Klyatskaya, D. Jungkenn, J. Stöckl, M. Laux, O. L. A. Monti, M. Aeschlimann, R. J. Cava, M. Ruben, S. Mathias, S. Sanvito and M. Cinchetti. Nano Letters 15, 6022 (2015); [3] B. Stadtmüller, J. Seidel, N. Haag, L. Grad, C. Tusche, G. van Straaten, M. Franke, J. Kirschner, C. Kumpf, M. Cinchetti and M. Aeschlimann. Physical Review Letters 117, 096805 (2016); [4] B. Stadtmüller, N. Haag, J. Seidel, G. van Straaten, M. Franke, C. Kumpf, M. Cinchetti, and M. Aeschlimann. Physical Review B 94, 235436 (2016).

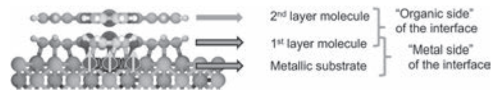

Fig. 1.

3:00

HA-03. Under-barrier spin-phonon relaxation in molecular magnets.

A. Lunghi[1], F. Totti[2], R. Sessoli[2] and *S. Stefano*[1]
1. School of Physics and CRANN, Trinity College Dublin, Dublin, Ireland; 2. Dipartimento di Chimica "Ugo Schiff", Universita' degli Studi di Firenze, Firenze, Italy

Single molecule magnets (SMMs) are molecules comprising only a handful of magnetic ions, which show some of the properties of bulk magnets and at the same time those of low-dimensional systems. These, for instance, include magnetic hysteresis together with quantum tunneling of the magnetization. A typical way to characterize the magnetism of SMMs is through relaxation experiments, where an ensemble of SMMs is polarized along the direction of an external field and then the relaxation of the magnetization is monitored in time. Surprisingly, many experiments measure a relaxation time considerably faster then what expected from the measured zero-field splitting (e.g. extracted from spin resonance), and such discrepancy usually increases with the strength of the anisotropy barrier. This surprising result collides with the most common SMMs design rules, which consist in engineering the ligand field of the magnetic ions so to increase the magnetic anisotropy or to increase the molecule total spin. Here we demonstrate that spin-phonon coupling can account for such discrepancy and in particular that phonon dissipation is key to explain the under-barrier relaxation. Our calculations combine advanced post Hartree-Fock electronic structure theory with a master equation approach to the spin-dynamics. In particular we construct the spin-phonon Hamiltonian by first calculating the phonon spectrum via a finite difference method and then by mapping the spin-phonon matrix elements onto a giant spin Hamiltonian. This constructs a master equation, which now includes both diagonal and non-diagonal terms in the spin-state occupations. At this level also spin-spin interaction is taken into account and the many-body problem is solved by exact diagonalization over a truncated spin-Fock space. Crucially phonon dissipation is included in the model and it is treated through an appropriate temperature-dependent stochastic model [1]. The central result of our work is the demonstration that, in general, in the presence of spin-phonon coupling the relevant energy scale for spin relaxation is given by the lower-lying phonon modes interacting with the spin system. These provide a channel for the relaxation at energies lower than that needed to overcome the anisotropy barrier, hence producing a fast spin-decay mechanism. Importantly, such mechanism becomes dominant over the standard over-the-barrier relaxation process only for molecules presenting large zero-field split, a fact that calls for a redefinition of the design criteria for highly stable SMMs. Our methodology is put to the test at the quantitative level for a class of Fe(II) molecules [2] presenting long spin lifetimes. In this case we find that the relaxation time has a complex temperature behaviour, where different relaxation mechanisms dominate over different energy ranges (see Fig. 1) [1]. Furthermore we have been able to identify the phonon modes most relevant for the spin relaxation [3]. These typically involve vibrations of the first coordination shell around the transition metal center, vibrations that affect strongly the spin-orbit interaction. Our work suggests several designing strategies for reducing the spin relaxation and thus for engineering long-living SMMs. For instance, although complicated to exploit in practice, a possible strategy may be that of modulating the spin excited state energy in order to obtain a non-resonant condition with the phonon spectrum.

[1] A. Lunghi, F. Totti, R. Sessoli and S. Sanvito, The role of anharmonic phonons in under-barrier spin relaxation of single molecule magnets, Nature Commun. 8, 14620 (2017) [2] W.H. Harman et al., Slow Magnetic Relaxation in a Family of Trigonal Pyramidal Iron(II) Pyrrolide Complexes, J. Am. Chem. Soc. 132, 18115 (2010). [3] A. Lunghi, F. Totti, S. Sanvito and R. Sessoli, Intra-molecular origin of the spin-phonon coupling in slow-relaxing molecular magnets, Chem. Sci. 8, 6051 (2017)

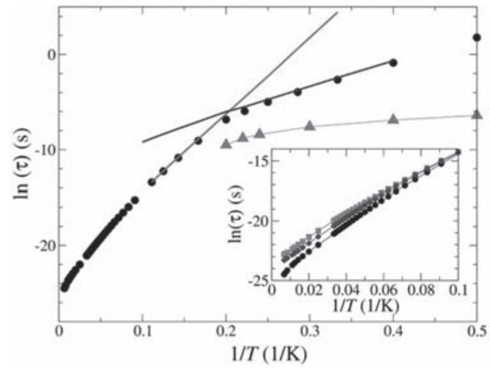

Fig. 1. Calculated temperature dependence of the relaxation time. Black dots are for simulations where all the relaxation processes are considered. The green triangles and the green line represent the experimental results of Ref. [2]. Arrhenius's fits performed for the T < 5 K and for 5 K < T < 10 K cases return effective barriers of 19.7 cm^{-1} and 55.7 cm^{-1}, respectively. These are consistent with an under-barrier phonon-activated relaxation mechanism.

3:30

HA-04. Portraying the spin dynamics of molecular nanomagnets by four-dimensional inelastic neutron scattering.

S. Carretta[1]
1. University of Parma, Parma, Italy

Molecular nanomagnets (MNMs) are molecules containing a core of interacting magnetic ions embedded in shells of organic ligands, which provide a magnetic separation between different cores. MNMs are at the forefront of current research in magnetism and have been used as test beds for addressing several quantum phenomena [1]. Interestingly, on the one hand MNMs show magnetic hysteresis as ordinary magnets do and, on the other hand, they are small enough to show clear quantum effects. Hence, they are promising systems to encode quantum bits for quantum information processing [2] or for storing classical information in single molecules [3]. However, a deep understanding of the spin dynamics of MNMs is mandatory to design molecules fulfilling all the requirements for these demanding applications. Recently we have shown that the quantum spin dynamics of MNMs can be fully unravelled by the so-called four-dimensional Inelastic Neutron Scattering (4DINS) [4]. In particular, the dependence of the transition intensity on the three components of the neutron wavevector transfer Q enables us to probe and extract two-spin dynamical correlation functions. In this contribution, I discuss very recent applications of the 4DINS approach to solve two important problems in molecular magnetism. Addressing fundamental and applicative issues in polycentric molecules can be hampered by the difficulty to determine the interactions within the core. Mn12 is an outstanding example of this: although it is the forefather and most studied of all molecular nanomagnets, a sound determination even of the leading magnetic exchange interactions was still lacking. In the first part of this contribution, I show that we have now exploited 4DINS to solve this problem. We have investigated the dynamics of Mn12 at low temperature where only the ground |S=1 0,M=+-10> doublet is populated (S being the molecular total spin and M its z component) and detected several transitions to excited M=+-9 states belonging to the lowest S=10 and S=9 multiplets. The dependence of the intensity of each transition on the three components of Q is characterized by a pattern of maxima and minima (e.g., see Figure 1), which directly reflects how the individual Mn spins move when the excitation is triggered [5]. These precession patterns are fingerprints of the magnetic Hamiltonian and we thus pinpoint the exchange interactions of Mn12 for the first time [5]. These results open novel perspectives in understanding spin clusters and motivate the synthesis of new polycentric MNMs, where the interactions are optimized for addressing specific fundamental issues or applications. In the last years, we have shown that Cr7Ni antiferromagnetic rings are very promising systems to encode qubits [2]. Indeed, at low temperature they behave as spin-1/2 and can be manipulated in times much shorter than the measured decoherence time. In addition, these molecular rings can be magnetically linked to each other either directly or through magnetic ions and dimers. Entanglement is a crucial resource for quantum information processing and its detection and quantification is of paramount importance in many areas of current research. However, entanglement between molecular qubits had only been experimentally studied rather indirectly. In the second part of this contribution, I show that 4DINS can be exploited to investigate entanglement in weakly coupled molecular qubits and to directly quantify it [6]. As a benchmark to test our idea, we have investigated the (Cr7Ni)2 prototype dimer of molecular qubits. The key point is that entanglement between the Cr7Ni qubits is connected with dynamical correlations between spins belonging to different rings that can be selectively addressed by 4DINS. Indeed, such correlations between distant spins lead to short-Q modulations in neutron scattering intensity. We have applied a sizeable external magnetic field in order to induce a factorized dimer ground state, which we have exploited as a reference state to investigate entanglement in the excited states. We performed low-temperature (T=1.2 K) measurements and detected two transitions. The observed Q dependences of the intensities clearly display short-Q modulations (see e.g. Figure 2) that constitute a sort of "portrayal" of entanglement in the excited states of the dimer. The analysis of the two measured patterns of maxima and minima show that the excited states involved in the transitions are maximally entangled states [6]. This approach can be applied also to dimers of more complex molecular qubits, thus opening remarkable perspectives in the understanding of entanglement in complex spin systems.

[1] Molecular Magnetic Materials: Concepts and Applications, edited by B. Sieklucka and D. Pinkowicz (Wiley-VCH, Weinheim, Germany, 2017). [2] G.A. Timco, S. Carretta, F. Troiani, F. Tuna, R.J. Pritchard, C.A. Muryn, E.J.L. McInnes, A. Ghirri, A. Candini, P. Santini, G. Amoretti, M. Affronte, R.E.P. Winpenny, Nature Nanotechnology 4, 173 (2009); J. Ferrando-Soria, E. Moreno-Pineda, A. Chiesa, A. Fernandez, S.A. Magee, S. Carretta, P. Santini, I.J. Vitorica-Yrezabal, F. Tuna, G.A. Timco, E.J.L. McInnes, R.E.P. Winpenny, Nature Commun. 7, 11377 (2016). [3] C.A.P. Goodwin, F. Ortu, D. Reta, N.F. Chilton, D.P. Mills, Nature 584, 439 (2017). [4] M.L. Baker, T. Guidi, S. Carretta, J. Ollivier, H. Mutka, H.U. Güdel, G.A. Timco, E.J.L. McInnes, G. Amoretti, R.E.P. Winpenny and P. Santini, Nature Phys. 8 906 (2012). [5] A. Chiesa, T. Guidi, S. Carretta, S. Ansbro, G.A. Timco, I. Vitorica-Yrezabal, E. Garlatti, G. Amoretti, R.E.P. Winpenny, P. Santini, Phys. Rev. Lett. 119, 217202 (2017). [6] E. Garlatti, T. Guidi, S. Ansbro, P. Santini, G. Amoretti, J. Ollivier, H. Mutka, G. Timco, I.J. Vitorica-Yrezabal, G.F.S. Whitehead, R.E.P. Winpenny, S. Carretta, Nature Communications 8, 14543 (2017).

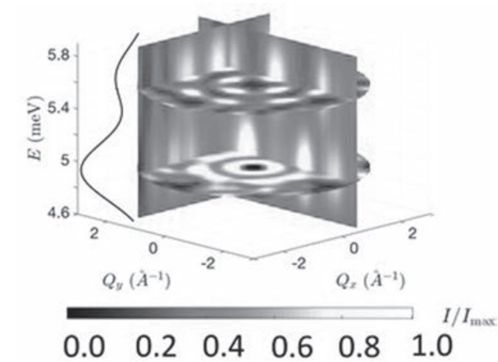

Fig. 1. Example of measured neutron scattering intensity (color map) as a function of *Qx, Qy* and the energy transfer *E*, and integrated over the experimental *Qz* range. This energy window contains two intermultiplet peaks (see [5]).

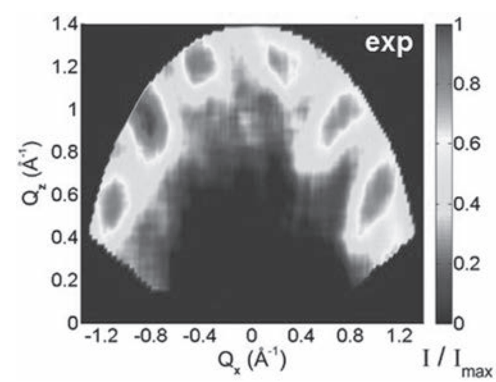

Fig. 2. Measured neutron scattering intensity (color map) for a low-energy excitation as a function of *Qx* and *Qz*, integrated over the experimental *Qy* range (see [6]).

4:00

HA-05. Operating Quantum States in Single Magnetic Molecules: Implementation of Quantum Gates and Algorithm.

C. Godfrin[1], R. Ballou[1], E. Bonet[1], S. Klyatskaya[3], M. Ruben[3], W. Wernsdorfer[3,1] and *F. Balestro*[1,2]

1. CNRS-UGA-Institut Néel, Grenoble, France; 2. Institut Universitaire de France, Paris, France; 3. Institute of Nanotechnology (INT), Karlsruhe Institute of Technology (KIT), Karlsruhe, Germany

The application of quantum physics to the information theory turns out to be full of promises. The first step is to realize the basic block that encodes the quantum information, the qubit. Among all existing qubits, spin based devices are very attractive since they reveal electrical read-out and coherent manipulation. Beyond this, the more isolated a system is, the longer its quantum behavior remains, making of the nuclear spin a serious candidate for exhibiting long coherence time and consequently high numbers of quantum operation. In this context I worked on a molecular magnet spin transistor. This setup enabled us to read-out electrically both the electronic and the nuclear spin states and to coherently manipulate the nuclear spin of the Terbium ion [1,2]. I will present the study of the dynamic of a single 3/2 nuclear spin under the influence of a microwave pulse. After the energies difference measurement between these states I will show the coherent manipulation of the three nuclear spin transitions up to 10MHz using only a microwave electric field with coherence time higher than 1ms. More than demonstrating the qubit dynamic, these measures demonstrate that a nuclear spin embedded in a molecular magnet transistor is a four quantum states system that can be fully controlled. Theoretical proposal demonstrated that quantum information processing could be implemented using a 3/2 spin such as quantum gates [3] and algorithm [4]. I will then present the implementation of the Grover algorithm [5] using a single molecular magnet.

[1] Thiele S. et al. Science 344, 1135 (2014) [2] Godfrin C. et al. ACS Nano 11, 3984 (2017) [3] Kiktenko E. O. et al. Phys. Rev. A 91, 042312 (2015) [4] Leuenberger M. et al. Phys. Rev. Lett. 89, 207601 (2003) [5] Godfrin C. et al. Phys. Rev. Lett. 119, 187702 (2017)

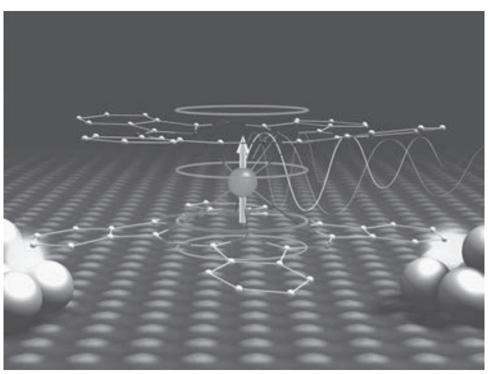

Fig. 1. The spin based transistor on a Si substrate. A terbium "double-decker" single-molecule magnet is connected to two gold metal leads for electrical read-out of the terbium's electronic spin orientation (orange arrow), which itself "reads" the nuclear spin via the hyperfine interaction. Blue, green, red, grey rings depict the 4 nuclear spin states. The three different resonances between them can be addressed simultaneously using appropriate microwave pulses (the blue, red and green waves).

4:30

HA-06. Electron spin resonance of single atoms in scanning tunneling microscopy.

A.J. Heinrich[1], Y. Bae[1] and P. Willke[1]
1. Center for Quantum Nanoscience, Institute for Basic Science, Seoul, The Republic of Korea

The scanning tunneling microscope is an amazing tool because of its atomic-scale spatial resolution. This can be combined with the use of low temperatures, culminating in precise atom manipulation and spectroscopy with microvolt energy resolution. In this talk we will apply these techniques to the investigation of the quantum spin properties of magnetic atoms sitting on thin insulating films. We will start our exploration with the understanding of the quantum spin states (also called the magnetic states) of these adsorbates. To measure these states, we combined scanning tunneling with x-ray absorption spectroscopy and found amazing agreement of those vastly different techniques (Science 2014, PRL 2015). Next, we will investigate the lifetimes of excited states. Surprisingly, we find lifetimes that vary from nanoseconds to hours, a truly amazing consequence of the quantum states of different adsorbates. Finally, we will explore the superposition of quantum states which is inherent to spin resonance techniques. We recently demonstrated the use of electron spin resonance on single Fe atoms on MgO (Science 2015). This technique combines the power of STM of atomic-scale spectroscopy with the unprecedented energy resolution of spin resonance techniques, which is about 10,000 times better than normal spectroscopy.

[Science 2014] Rau, …, AJH, *Science* 344, 988 (2014) [Science 2015] Baumann, …, AJH, *Science* 350, 417 (2015) [PRL 2015] Baumann, …, AJH, *Physical Review Letters* 115, 237202 (2015)

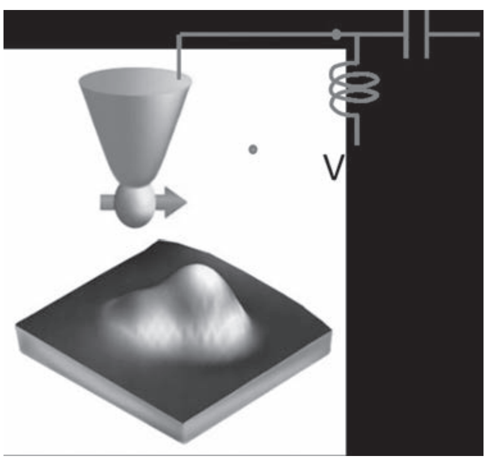

Fig. 1. STM image of two Ti atoms on thin MgO film. Superimposed is a model of a spin-polarized STM tip.

FRIDAY AFTERNOON, 27 APRIL 2018 ORCHID III, 2:00 TO 5:00

Session HB
HARD MAGNETS II

Yanglong Hou, Chair
Peking University, Beijing, China

CONTRIBUTED PAPERS

2:00

HB-01. Microstructure and magnetic properties of anisotropic polycrystalline $Sm(Fe_{0.8}Co_{0.2})_{12}$ thin films with $ThMn_{12}$ structure.

D. Ogawa[1,2], Y. Takahashi[1,2], S. Hirosawa[1,2] and K. Hono[1,2]
1. Elements Strategy Initiative Center for Magnetic Materials (ESICMM), Tsukuba, Japan; 2. National Institute for Materials Science (NIMS), Tsukuba, Japan

I. INTRODUCTION The $ThMn_{12}$-type hard magnetic compounds composed of rare earth elements and 3d ferromagnetic transition metals such as Fe have been known as possible candidates for the development of permanent magnet materials. In order to stabilize the $ThMn_{12}$ phase, the substitution of Fe with non-magnetic element M such as Ti, V, Mo and Si is required [1, 2], which results in the reduction of saturation magnetization $\mu_0 M_S$. Kuno *et al*. reported that high $\mu_0 M_S$ of 1.63 T in strip cast alloy by doping Zr in Sm site, and controlling the content of non-magnetic element M with the $(Sm_{0.8}Zr_{0.2})(Fe_{0.75}Co_{0.25})Ti_{0.5}$ composition [3]. Recently, Hirayama *et al*. showed excellent intrinsic hard magnetic properties with saturation magnetization $\mu_0 M_S$ of 1.78 T, anisotropy field $\mu_0 H_A$ of 12 T and Curie temperature T_C of 859 K for epitaxial $Sm(Fe_{0.8}Co_{0.2})_{12}$ films prepared by sputtering process, which are superior to those of $Nd_2Fe_{14}B$ [4]. Owing to these promising intrinsic properties, the $Sm(Fe_{0.8}Co_{0.2})_{12}$ compound can be a candidate for high performance permanent magnet applications. One drawback of $ThMn_{12}$ compound based magnets is their too low coericvity [5, 6]; however, considering the value of the anisotropy field, there is still room for improving coercivity. The purpose of the present investigation is to explore the possibilities for obtaining high coercivity in $Sm(Fe_{0.8}Co_{0.2})_{12}$ based alloy using strongly textured polycrystalline thin films. II. EXPERIMENTAL PROCEDURE $Sm(Fe_{0.8}Co_{0.2})_{12}$ thin films were prepared by an UHV magnetron co-sputtering system. The stacking structure of the films were thermal oxidized Si (SiO_2) substrate / NiTa (20 nm) / MgO (10 nm) / V (10 nm) / $Sm(Fe_{0.8}Co_{0.2})_{12}$ (46 nm) / V (10 nm). NiTa and MgO [7] was used to obtain textured V underlayer for growing $Sm(Fe_{0.8}Co_{0.2})_{12}$ anisotropic polycrystalline films. When the V and $Sm(Fe_{0.8}Co_{0.2})_{12}$ layers were deposited, the substate was heated at 400°C. The $Sm(Fe_{0.8}Co_{0.2})_{12}$ layer was deposited by co-sputtering Sm, Fe, and Co targets. We also tried grain boundary diffusion process into the $Sm(Fe_{0.8}Co_{0.2})_{12}$ layer, which is known as an effective methods to increase coercivity of fine grained magnets. We deposited five kinds of overlayers such as Cu, Zn, $Sm_{70}Cu_{30}$, Sm/Cu, La/Cu onto the $Sm(Fe_{0.8}Co_{0.2})_{12}$ layer and post-annealed at 300 ~ 600°C. In this presentation, we will mainly report the results of Cu overlayer, because it was so far the most effective to increase the coercivity. III. RESULTS AND DISCUSSION X-ray diffraction measurement showed that *c*-axis textured $ThMn_{12}$ polycrsytaline layer was grown on a V underlayer. Fig.1 (a) shows cross-sectional TEM image of a $Sm(Fe_{0.8}Co_{0.2})_{12}$ thin film before grain boundary diffusion process. Perpendicular texture of columnar-shaped $Sm(Fe_{0.8}Co_{0.2})_{12}$ grains are grown on a V underlayer with the grain size of several dozen nm. The shape of the grains are considerably changed after deposition of Cu (3 nm) overlayer and post annealing at 400°C as shown in Fig.1 (b). Fig.2 shows magnetization curves for the films before and after the diffusion process, i.e., deposition of Cu (3 nm) and post annealing at 400°C. Both curves show perpendicular magnetic anisotropy, which corresponds to the *c*-axis orientation observed from the XRD pattern. The demagnetizing field were corrected by using demagnetizing factor $N = 0.45$ in both samples. The coercivity of the $Sm(Fe_{0.8}Co_{0.2})_{12}$ films increased from 0.5 T to 0.8 T by depositing Cu and post-annealing at 400°C. We carried out EDS analysis of the Cu diffused $Sm(Fe_{0.8}Co_{0.2})_{12}$ film with compared to the sample before the diffusion process. In the sample before diffusion process, Sm, Fe, and Co elements are distributed uniformly. On the other hand, in the sample after Cu diffusion, the distribution of the Sm element become non-uniform, following the distribution of Cu elements. Moreover, Cu seems to be diffused into not only grain boundary, but also $Sm(Fe_{0.8}Co_{0.2})_{12}$ grains partially, and the formation of other phases were suggested which should be influence on coercivity. In summary, a polycrystalline $Sm(Fe_{0.8}Co_{0.2})_{12}$ perpendicular anisotropy film shows the coercivity of 0.5 T, giving rise to the $(BH)_{max}$ value of 386 kJ/m³. The coercivity can be further enhanced to 0.8 T by the diffusion of Cu; however, this does not lead to the continuous formation of grain intergranular phase. A search for a grain boundary phase that is more effective in intergrain exchange coupling is necessary to develop high coercivity $Sm(Fe_{0.8}Co_{0.2})_{12}$-based permanent magnet material.

[1] K. Ohashi, Y. Tawara, R. Osugi and M. Shimao, Journal of Applied Physics, 64 (1988) 5714-5716. [2] R. Verhoef, F.R. de Boer, Z. Zhi-dong and K.H.J. Buschow, Journal of Magnetism and Magnetic Materials, 75 (1988) 319-322. [3] T. Kuno, S. Suzuki, K. Urushibata, K. Kobayashi, N. Sakuma, M. Yano and A. Kato, A. Manabe, AIP Advances, 6 (2016) 025221. [4] Y. Hirayama, Y.K. Takahashi, S. Hirosawa and K. Hono, Scr. Mater. 138 (2017) 62-65. [5] E.W. Singleton, J. Strzeszewski, and G. C. Hadjipanayis, Appl. Phys. Lett. 54 (1989) 1934. [6] Xiao-dong Zhang, Ben-pei Cheng, and Ying-chang Yang, Appl. Phys. Lett. 77 (2000) 4022. [7] T. Shiroyama, J. Wang, A. Felicia, Y.K. Takahashi and K. Hono, J. Magn. Magn. Mater. 432 (2017) 129.

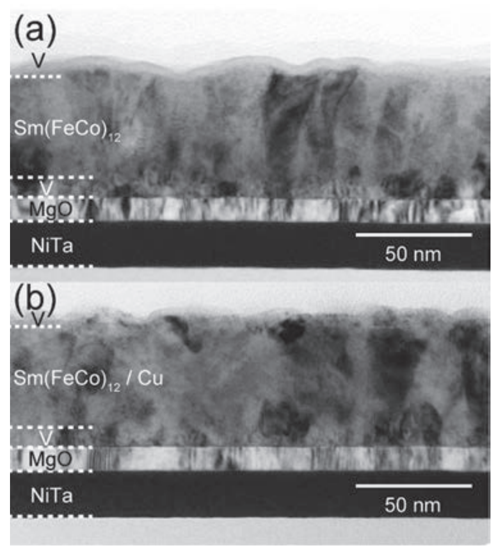

Fig. 1. Cross-sectional bright field TEM image of $Sm(Fe_{0.8}Co_{0.2})_{12}$ thin film (a) before diffusion processs, and (b) after depositing Cu and post-annealing at 400°C.

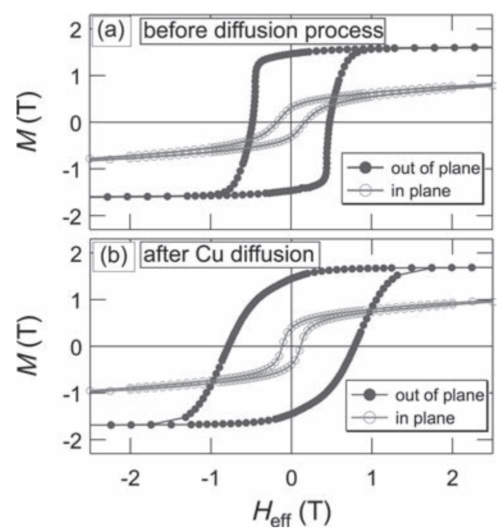

Fig. 2. Magnetization curves for the $Sm(Fe_{0.8}Co_{0.2})_{12}$ thin film (a) before diffusion processs, and (b) after depositing Cu and post-annealing at 400°C. The demagnetizing field were corrected by using demagnetizing factor $N = 0.45$ in both curves.

2:15

HB-02. Intrinsic magnetic properties of $Sm(Fe_{1-x}Co_x)_{11}Ti$ and Zr-substituted $Sm_{1-y}Zr_y(Fe_{0.8}Co_{0.2})_{11.5}Ti_{0.5}$ compounds with $ThMn_{12}$ structure toward the development of permanent magnets.

P. Tozman[1], *H. Sepehri-Amin*[1], Y. Takahashi[1], S. Hirosawa[1] and K. Hono[1]
1. National Institute for Materials Science (NIMS), Tsukuba, Japan

There is an increase demand for a magnet which has comparable intrinsic hard magnetic properties with those of $Nd_2Fe_{14}B$. The intrinsic magnetic properties of the $ThMn_{12}$-type phases in $Sm(Fe_{1-x}Co_x)_{11}Ti$ alloys with $0 \le x \le 0.3$ and $Sm_{1-y}Zr_y(Fe_{0.8}Co_{0.2})_{11.5}Ti_{0.5}$ alloys with $0 \le y \le 0.3$ are potential candidate as a permanent magnet, as is shown in Fig. 1. Increasing Co substitution for Fe, from $x = 0.1$ to 0.3 increases the saturation magnetization ($\mu_0 M_s$) of the 1:12 phase from 1.34 T to 1.50 T, while the largest magnetic anisotropy field ($\mu_0 H_A$) of 10.9 T was achieved for $x = 0.2$ with $\mu_0 M_s = 1.47$ T and Curie temperature (T_c) 800 K. The saturation magnetization is increased by reducing Ti content where the phase stability is obtained by Zr substitutions for Sm. Increase of Zr in $Sm_{1-y}Zr_y(Fe_{0.8}Co_{0.2})_{11.5}Ti_{0.5}$ from $y = 0.1$ to 0.3 decreases $\mu_0 M_s$ from 1.57 to 1.53 T. Although, the largest T_c of 830 K was found for the ThM_{12}-type phase in the $(Sm_{0.8}Zr_{0.2})(Fe_{0.8}Co_{0.2})_{11.5}Ti_{0.5}$ alloy, $\mu_0 M_s$ and $\mu_0 H_A$ of which were determined to be 1.55 T and 8.4 T at 300 K, respectively. The $ThMn_{12}$-type phase in the $(Sm_{0.8}Zr_{0.2})(Fe_{0.8}Co_{0.2})_{11.5}Ti_{0.5}$ alloy has comparable intrinsic hard magnetic properties with those of $Nd_2Fe_{14}B$ and may exhibit maximum energy product with the optimized microstructure.

[1] S. Hirosawa, Y. Matsuura, H. Yamamoto, S. Fujimura, M. Sagawa, and H.i Yamauchi, Magnetization and magnetic anisotropy of $R_2Fe_{14}B$ measured on single crystals, J. Appl. Phys 59 (1986) 873-879. [2] P. Tozman, H. Sepehri-Amin, Y. K. Takahashi, S. Hirosawa, K. Hono, Intrinsic magnetic properties of $Sm(Fe_{1-x}Co_x)_{11}Ti$ and Zr-substituted $Sm_{1-y}Zr_y(Fe_{0.8}Co_{0.2})_{11.5}Ti_{0.5}$ compounds with $ThMn_{12}$ structure toward the development of permanent magnets, submitted, 2018

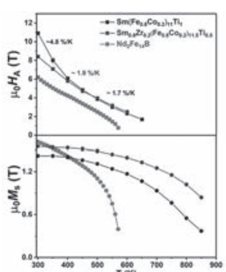

$\mu_0 M_s$ (T)	$\mu_0 H_A$ (T)	T_c (K)
$Sm(Fe_{0.8}Co_{0.2})_{11}Ti_1$		
1.42	10.9	800
$(Sm_{0.8}Zr_{0.2})(Fe_{0.8}Co_{0.2})_{11.5}Ti_{0.5}$		
1.55	8.4	830
$Nd_2Fe_{14}B$		
1.61	6.2	598

Fig. 1. The temperature dependence of (a) anisotropy field and (b) saturation magnetization of the $ThMn_{12}$-type phase in $Sm(Fe_{0.8}\ Co_{0.2})_{11}Ti_1$ and $(Sm_{0.8}Zr_{0.2})(Fe_{0.8}Co_{0.2})_{11.5}Ti_{0.5}$ in compared with single crystal $Nd_2Fe_{14}B$ [1,2].

2:30

HB-03. Intrinsic Magnetic Properties of $SmFe_{12-x}V_x$ Alloys with reduced V-content.

A.M. Schönhöbel[1], R. Madugundo[1], J.M. Barandiarán[1,3] and G.C. Hadjipanayis[2]
1. BCMaterials, Leioa, Spain; 2. Physics and Astronomy, University of Delaware, Newark, DE, United States; 3. Electricity and electronics, University of the Basque country, Leioa, Spain

After the discovery of R-Fe-B (R:rare-earth) compounds with excellent magnetic properties, the research and development on permanent magnets has been focused almost exclusively on these alloys. In the last decade [1], because of the exponentially increasing demand for these magnets, increasing cost and supply risks involving the R-metals, there has been a renewed interest in the $ThMn_{12}$-type (1:12) compounds. These compounds contain a 7.7 at.% of R (compared with 11.8 at.% in $R_2Fe_{14}B$) and have a tetragonal structure which is a required condition for uniaxial magnetocrystalline anisotropy. The binary compounds RFe_{12} in bulk do not exist but by adding a third element such as Ti, V, Mo, Cr, W or Si, it can be stabilized into the 1:12 structure [1,2]. However, the addition of this element decreases the saturation magnetization (M_s) and the Curie temperature (T_C); due to this, it is important to keep its amount as low as possible. So far the 1:12 structure for the $SmFe_{12-x}V_x$ alloys has been obtained for high concentrations ($x \geq 1.5$) and it is very difficult to synthetize as a single-phase material. In order to obtain high H_c, it is necessary to avoid the formation of the soft-magnetic α-Fe phase in the alloy. One of the challenges is then in obtaining a single-phase 1:12 alloy with the minimum concentration of V. Previous results have reported the stabilization of 1:12 for x=2 for samples annealed at 850-1050 °C for 1-14 days [3–5] and for x=1.5 annealed at 900-1000 °C for 7 days [6]. Sugimoto *et al.* obtained the phase relation of Sm-Fe-V [7] and reported that 1:12 phase was only stable for $x \geq 1.4$. In this work, we present the results obtained on $SmFe_{12-x}V_x$ alloys for $x \leq 2$. We have studied the stability of the 1:12 phase over a range of V-content lower than that of the previous reports, and obtained a nearly pure 1:12 phase. The extension of the stability range to x = 1 has increased the M_s and T_C. Ingots of $SmFe_{12-x}V_x$ (x=1-2) alloys were prepared by arc-melting the pure metals. The samples were re-melted several times in order to achieve homogenization. An additional amount of Sm (20 wt. %) was added for compensation of evaporation loss. After arc-melting, the ingots were annealed in Ar athmosphere for 1-3 days at temperatures in the range 900-1100 °C and then quenched in water. The crystal structures of the samples were determined by using x-ray diffraction (XRD). The annealed ingots were ground in a mortar and the fine powders were subsequently mixed with an epoxy and aligned in a magnetic field of 2 T. The anisotropy field (H_A) and M_s measurements were performed on aligned samples using a vibrating sample magnetometer with a maximum applied field of 12 T. The T_C values were determined by thermogravimetry. Microstructure studies were carried out by using a scanning electron microscope (SEM). Figure 1 shows the XRD patterns of non-oriented and oriented $SmFe_{11}V_1$ powders. The pattern presented in the fig 1(top) is indexed with a single phase of the tetragonal $ThMn_{12}$ type structure (space group 14/mmm). No other secondary phase (α-Fe) peaks were detected. This shows that the stability range of Sm-Fe-V alloys is broader than that of suggested by previous studies on these compounds. The SEM microstructure analyses confirm the results obtained by XRD. In the as-cast sample (Fig. 2 top), an Fe-V phase (in black) is present along with a Sm-rich phase (in white) and a minor phase (in grey), identified to be the 1:12 phase. After annealing, the only phase that is present is the 1:12 (Fig. 2 bottom). Structural analysis reveals an increase in the lattice parameters (a = 8.54217 Å and c = 4.78228 Å for x=1 and a = 8.53681 Å and c = 4.77221 Å for x=2) with the decrease of the V-content. The fig. 1(bottom) shows XRD pattern of the oriented powders of $SmFe_{11}V$, the prominent reflection from (002) planes suggests the uniaxial nature of this sample, which is expected. The magnetization measured at room temperature as a function of applied field parallel and perpendicular to the orientation axis are shown in the inset of Fig. 1. The H_A value is estimated from the value of the applied field at which the two curves intersect. The H_A value for $SmFe_{11}V$ was estimated to be around 11 T and the M_s to be 118 Am^2/kg, both values larger than those of $SmFe_{10}V_2$. The T_C also shows an increase from 599 K to 634 K with the reduction of V content from x = 2 to 1. The authors acknowledge Iñaki Orue assistance with the high field measurements. This work has been supported by the European Union's Horizon 2020 research and innovation programme, grant agreement No 686056 (NOVAMAG).

[1] A.M. Gabay, G.C. Hadjipanayis, Recent developments in RFe_{12}-type compounds for permanent magnets, Scr. Mater. (2017). doi:10.1016/j.scriptamat.2017.10.033. [2] D.B. De Mooij, K.H.J. Buschow, Some novel ternary $ThMn_{12}$-type compounds, J. Less Common Met. 136 (1988) 207–215. doi:10.1016/0022-5088(88)90424-9. [3] F.R.D.E. Boer, D.B.D.E. Mooij, K.H.J. Buschow, Magnetic properties of a series of novel ternary intermetallics ($RFe_{10}V_2$), J. Less-Common Met. 135 (1987) 199–204. [4] K. Ohashi, Y. Tawara, R. Osugi, M. Shimao, Magnetic properties of Fe-rich rare-earth intermetallic compounds with a $ThMn_{12}$ structure, J. Appl. Phys. 64 (1988) 5714–5716. doi:10.1063/1.342235. [5] Y.Z. Wang, G.C. Hadjipanayis, Effect of nitrogen on the structural and magnetic properties of intermetallic compounds with the $ThMn_{12}$ structure, J. Appl. Phys. 70 (1991) 6009–6011. doi:10.1063/1.350076. [6] J. Yang, S. Dong, Y. Yang, B. Cheng, Structural and magnetic properties of $RFe_{10.5}V_{1.5}N_x$, J. Appl. Phys. 75 (1994) 3013–3016. doi:10.1063/1.356168. [7] S. Sugimoto, T. Shimono, H. Nakamura, T. Kagotani, M. Okada, M. Homma, Phase Relation of Sm-Fe-V Alloys around the Compound $Sm_3(Fe,V)_{29}$, Mater. Trans. JIM. 37 (1996) 494–498. doi:10.2320/matertrans1989.37.494.

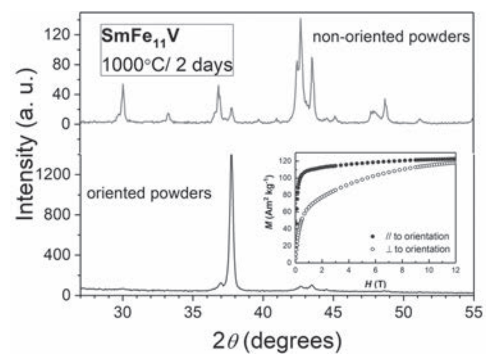

Fig. 1. X-ray diffraction patterns of (top) non-oriented powders (bottom) oriented powders, in the inset, magnetization curves parallel and perpendicular to the orientation axis.

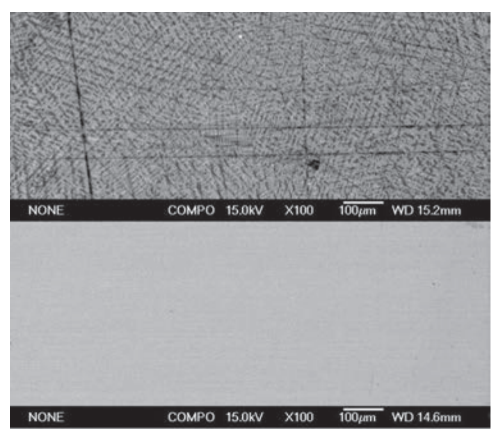

Fig. 2. SEM photographs of $SmFe_{11}V$ (top) before heat treatment and (bottom) after heat treatment at 1000 °C for 2 days.

2:45

HB-04. Solidification behavior and its effect on mechanical properties of Sm_2Co_{17}-type sintered magnets.

K. Song[1], Y. Fang[1], S. Wang[1], H. Chen[1], N. Yu[1], M. Zhu[1] and W. Li[1]
1. Division of Functional Matericls, Iron & Steel Research Institute, Beijing, China

Introduction Sm_2Co_{17}-type sintered permanent magnets have attracted a great attention for good high-temperature magnetic properties, extremely low temperature coefficient, excellent oxidation resistance [1-3]. The researches on Sm_2Co_{17}-type permanent magnets have mainly focused on the improvement of the magnetic properties [4, 5]. Only a few researchers have investigated mechanical properties: bending strength, impact toughness, and so on [6-9], which are important parameters from the view point of application. Recently, we have found that sintering process has much impact not only on magnetic properties but also on mechanical features of Sm_2Co_{17}-type sintered magnets. In this work, sintering process, i.e., solidification behavior, and its effect on the magnetic and mechanical properties of the $Sm(Co_{bal}Fe_{0.227}Cu_{0.07}Zr_{0.023})_{7.6}$ has been investigated. It is beneficial to understand the mechanism of sintering and how to improve the magnetic and mechanical properties for Sm_2Co_{17}-type sintered magnets. Experimental The alloy ingot with the nominal composition of $Sm(Co_{bal}Fe_{0.227}Cu_{0.07}Zr_{0.023})_{7.6}$ was prepared by vacuum induction melting. Heat treatments during the preparing procedures consisted of four steps, including sintering at a temperature (1463, 1468, 1473, 1478, 1483, 1488K) for 1h, and then homogenizing treated at 1448K for 4h, followed by isothermal aging at 1103K for 20h and finally step-cooling to 673K, followed by quenching to room temperature. Six groups of corresponding specimens were obtained and labeled as A, B, C, D, E and F, respectively. Bending strength of the specimens was measured by a 3-point bend test with a span of 14.5mm. The size of the bending specimens was 5mm×6mm×18mm. Compressive toughness of the Ø10mm × 10mm specimens was measured with a rate of indenter decline, 1mm/min. A scanning electron microscopy (SEM) was employed to observe the micro-fractures of the experimental magnets, and the phase compositions were determined by an energy dispersive x-ray (EDX) analysis system. Results and Discussion It is found that with the sintering temperature increasing from 1463K to 1488K, the bending strength (BS) increases from 108MPa to 140MPa. The specimens show similar BS values, about 120MPa with the sintering temperature increasing from 1468K to 1478K. The compressive toughness (CT) first increases from 142MPa to 488MPa quickly, and then increases to 563MPa slowly. The micro-fractures of bending specimens were observed using a SEM, as shown in Fig. 1. As a whole, the typical SEM images are quite different from each other. There are a lot of voids, whose average size is about 5μm in specimen A, which results in low BS (108MPa) and CT (142MPa). It is interesting that the size of voids becomes bigger, 13μm with the sintering temperature increasing to 1473K, improving the CT (488MPa) remarkably. Then the voids disappear and the BS and CT values increase with the sintering temperature increasing. It is impressive that some particles are found in the voids. EDX analysis shows that it is SmCoFe phase with lean Cu and Zr. With the sintering temperature increasing, the SmCoFe phase transforms to be Sm-rich phase. For specimens E and F, sintered at relatively high temperature, the EDX analysis shows there exists CoZrFe phase, giving rise to improvement of the mechanical properties. Moreover, in order to further make clear the solidification behavior and its effect on the mechanical properties of the specimens, typical SEM-BEI images of six groups of as-sintered magnets are shown in Fig. 2. The results show that there are small size voids in specimens A-C, whose average size is 0.2, 0.3 and 0.5μm and the voids average size increases from 8μm to 10μm with the sintering temperature increasing to 1488K. Moreover, the phase constitution of the as-sintered specimens changes a lot during sintering. The EDX analysis shows that the 2:17H and 1:5H phases, separate gradually and the voids tend to form in 1:5H phase with the sintering temperature increasing from 1463K to 1488K. After solid solution and aging process, the phase structures of all the specimens become homogeneous. But the voids grow up for specimens B and C and disappear for specimens D, E and F. Conclusions The bending strength and compressive toughness of Sm_2Co_{17}-type sintered magnets have been investigated systematically. With the sintering temperature increasing from 1463K to 1488K, the BS increases from 108MPa to 140MPa. The compressive toughness first increases from 142MPa to 488MPa quickly, and then increases to 563MPa slowly. There are small size voids (5μm) in specimen A, and the voids average size increases to 13μm and then disappears with the sintering temperature increasing. Moreover, it is found some CoZrFe phases are helpful to improve the mechanical properties. It is found that average voids size increases from 0.2μm to 10μm and the 2:17H and 1:5H phases separate with the sintering temperature increasing from 1463K to 1488K. ACKNOWLEDGEMENTS This work was partly supported by the National Basic Research Program of China (2014CB643701) and the National Natural Science Foundation of China (51371054, 51331003 and 51401054).

[1] B. M. Ma, Y. L. Liang, J. Patel, D. Scott and C. O. Bounds, *IEEE Trans. Magn.*, vol. 32, pp. 4377-4379, 1996. [2] Z.H. Guo, W. Pan and W. Li, *J. Magn. Magn. Mater.*, vol. 303, pp. e396-e401, 2006. [3] Y. H., M. Hagiwara, K. Okamoto, T. Kobayashi, M. Endo,T. Kobayashi, T. Nakamura, and S. Sakurada, *IEEE Trans. Magn.*, vol. 49, pp. 3221-3224, 2013. [4] K. K. Song, Y. K. Fang, W. Sun, H. S. Chen, N. J. Yu, M. G. Zhu and W. Li, IEEE. Trans. Magn. vol. 53, pp. 1-4, 2017. [5] K. K. Song, W. Sun, H. S. Chen, N. J. Yu, Y. K. Fang, M. G. Zhu, and W. Li, AIP Advances, vol. 7, pp. 1-7, 2017. [6] W. Li, A. H. Li, and H. J. Wang, IEEE Trans. Magn., vol. 41, pp. 2339-2342, 2005. [7] W. Li, A. H. Li, H. J. Wang, W. Pan, and H. W. Chang, J. Appl. Phys., vol. 105, p. 07A703, 2009. [8] R. K. Singh, S. V. Kamat and R. P. Mathur, J. Magn. Magn. Mater., vol. 379, pp. 300-304, 2015. [9] A. H. Li, S. Z. Dong, and, W. Li, Sci in China, vol. 46, pp. 241-247, 2003.

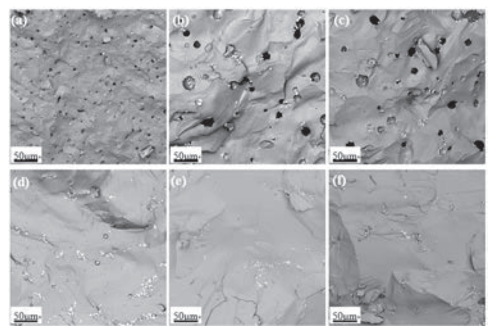

Fig. 1. Typical micro-fractures of final state sintered magnets: (a) specimen A, (b) specimen B, (c) specimen C, (d) specimen D, (e) specimen E and (f) specimen F, respectively.

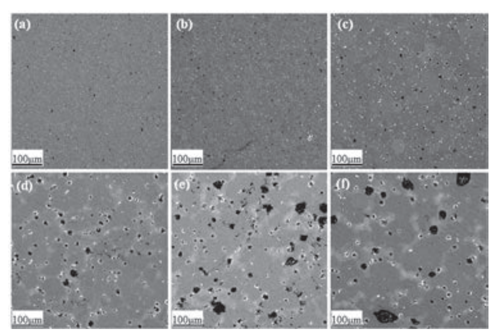

Fig. 2. Typical SEM-BEI images of as-sintered magnets: (a) specimen A, (b) specimen B, (c) specimen C, (d) specimen D, (e) specimen E and (f) specimen F, respectively.

3:00

HB-05. Microstructure and magnetic properties of casted strips $[(La_{0.352}Ce_{0.648})_x(Nd_{0.796}Pr_{0.204})_{1-x}]_{2.14}Fe_{14}B$ ($0.6 \leq x \leq 1.0$).

Y. Liu[1], B. Peng[1], J. Jin[1] and M. Yan[1]
1. Zhejiang University, Hangzhou, China

Permanent magnets based on abundant and cheap rare earth (RE) elements are surfacing as promising candidates to fulfill the large gap between hard ferrites and Nd-Fe-B magnets. La-Ce alloy extracted from the natural ore has great potential to replace a large portion of Nd-Pr alloy that has been overused due to the rapid growth of Nd-Fe-B industry. Here we performed a comprehensive study on microstructure and magnetic properties of the $[(La_{0.352}Ce_{0.648})_x(Nd_{0.796}Pr_{0.204})_{1-x}]_{2.14}Fe_{14}B$ ($0.6 \leq x \leq 1.0$, in at.%) casted strips to evaluate the potential replacement of La-Ce for Nd-Pr. Through the entire substitution range, the matrix 2:14:1 phase keeps stable at 1273 K, suggesting that they are suitable for high temperature sintering. Transmission electron microscopy characterizations show that spinodal decomposition-like phase separation occurs for the 2:14:1 phase grains at certain La-Ce contents due to the different solubilities of La/Ce/Nd/Pr elements, i.e. manily to the low soluted concentration of La element. Such inhomogeneous distribution of La/Ce/Nd/Pr elements within the 2:14:1 phase results in the deviation of Curie temperature from the estimation based on the rule of mixture. The dependence of saturation magnetization on La-Ce amount is also found beyond the estimation due to the presence of α-Fe phase. These findings suggest that $La_{0.352}Ce_{0.648}$ alloy can fully replace Nd-Pr alloy to achieve the stable 2:14:1 phase suitable for high temperature sintering and highlight the further work to suppress the formation of magnetically soft α-Fe phase.

[1] M. Sagawa, S. Fujimura, N. Togawa, H. Yamamoto, and Y. Matsuura, New material for permanent magnets on a base of Nd and Fe, J. Appl. Phys. 55 (1984) 2083-2087. [2] J.F. Herbst, $R_2Fe_{14}B$ materials: Intrinsic properties and technological aspects, Rev. Mod. Phys. 63 (1991) 819-898.

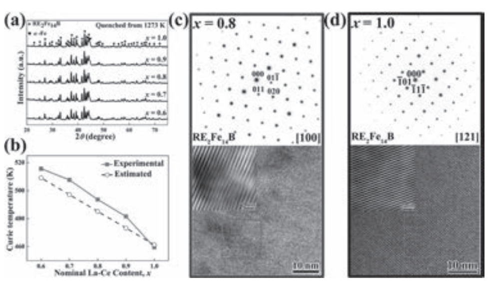

Fig. 1. All the $[(La_{0.352}Ce_{0.648})_x(Nd_{0.796}Pr_{0.204})_{1-x}]_{2.14}Fe_{14}B$ ($0.6 \leq x \leq 1.0$) strips exhibit stable 2:14:1 phase at 1273 K (a). Curie temperature of the 2:14:1 phase deviates from the estimation based on the nominal composition when $x \leq 0.9$ because the interaction among Rare earths La, Ce, Pr and Nd (b). At certain content ($x = 0.8$), spinodal decomposition-like microstructures are observed (c), being different from the sample with $x = 1.0$ that forms a solid solution (d).

3:15

HB-06. YCo_5 and $CeCo_5$ thin films with perpendicular magnetic anisotropy grown by molecular beam epitaxy.

S. Sharma[1], E. Hildebrandt[1], M. Major[1], P. Komissinskiy[1], I.A. Radulov[1] and L. Alff[1]
1. Institute of Materials Science, Technische Universität Darmstadt, Darmstadt, Germany

The interest in thin films with perpendicular magnetic anisotropy (PMA) is growing because of their potential applications in ultra-high density magnetic storage and nano-scale spintronic devices. One approach to achieve PMA is the *c*-axis (easy axis) textured growth of materials which possess strong intrinsic magnetocrystalline anisotropy that is large enough to overcome the shape anisotropy of thin films. The family of Co based rare-earth (*RE*) intermetallic compounds of the form, *RE*Co_5 are known for their extremely large uniaxial magnetocrystalline anisotropy. In this work, we have investigated the magnetic performance of epitaxial thin films of two lesser critical rare-earth material systems, YCo_5 and $CeCo_5$ [1-2]. Both YCo_5 and $CeCo_5$ possess a very strong uniaxial magnetocrystalline anisotropy with first anisotropy constant, K_1 of 5.78 MJ/m^3 and 6.4 MJ/m^3, respectively as bulk phases [3]. The YCo_5 and $CeCo_5$ thin films were deposited directly onto *c*-cut Al_2O_3 substrates without the use of additional underlayers using an MBE setup. The films were grown by co-evaporation of elemental *RE* and Co by electron beam at a pressure of 10^{-8} mbar. MBE allows to tune the composition of the *RE*-Co system by *in situ* controlling the evaporation rates of *RE* and Co. The manipulation of individual atomic beams of *RE* and Co, as well as their ratio allows establishing a thin film phase diagram for Y-Co and Ce-Co systems as shown in Fig. 1(a) and (b), respectively. With increasing *RE* to Co rate ratio (or decreasing Co rate), first, the soft magnetic, *RE*$_2Co_{17}$ phase is formed followed by the highly anisotropic, *RE*Co_5 phase. The *RE*$_2Co_{17}$ films are soft magnetic with the easy-axis of magnetization in the film plane. On the other hand, the *RE*Co_5 films are hard magnetic showing perpendicular anisotropy. The magnetization, *M*, was measured as a function of applied field, *H*, in two directions, perpendicular and parallel to the film plane using a SQUID magnetometer. Fig.1(c) and (d) show the hysteresis curves for YCo_5 and $CeCo_5$ thin films (30 nm), respectively. It can be seen that perpendicular to the film plane, the saturation magnetization, remanent magnetization, and coercivity are higher than along the film plane. This shows that the easy-axis of magnetization is aligned perpendicular to the film plane, i.e. it is parallel to the structural *c*-axis. Angular dependent magnetic torque measurements were used to determine the value of the first anisotropy constant, K_1 and the anisotropy field. The magnetic parameters measured for YCo_5 and $CeCo_5$ thin films are summarized in Table 1. These magnetic parameters and the perpendicular anisotropy obtained without additional underlayers make the material systems interesting for application in magnetic recording devices.

[1] S. Sharma, E. Hildebrandt, S.U. Sharath, I. Radulov, and L. Alff, $YCo_{5\pm x}$ thin films with perpendicular anisotropy grown by molecular beam epitaxy, J. Magn. Magn. Mater. 432 (2017) 382-386. [2] S. Sharma, E. Hildebrandt, M. Major, P. Komissinskiy, I. Radulov, and L. Alff, $CeCo_5$ thin films with perpendicular anisotropy grown by molecular beam epitaxy, J. Magn. Magn. Mater. 452 (2018) 80-85. [3] K. Strnat, G. Hoffer, J. Olson, W. Ostertag, and J. J. Becker, A Family of New Cobalt – Base Permanent Magnet Materials, J. Appl. Phys. 38 (1967) 1001-1002.

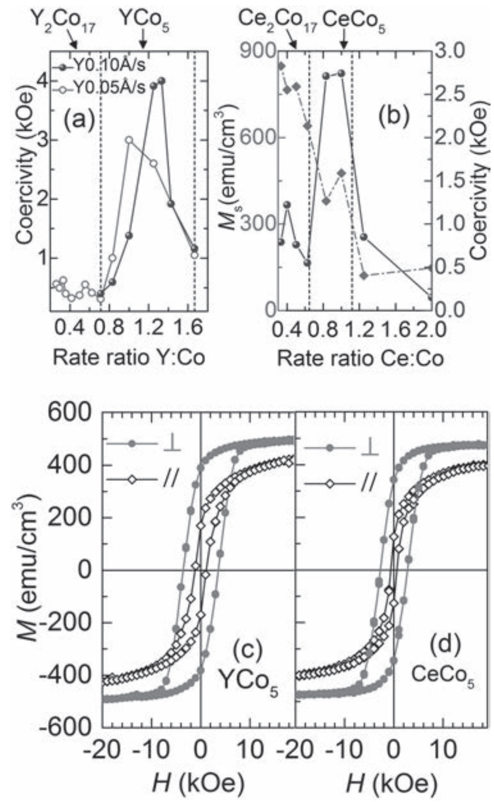

Fig. 1. Magnetic phase diagram of (a) Y-Co and (b) Ce-Co thin films. *M-H* curves measured perpendicular and parallel to the film plane for (c) YCo_5 and (d) $CeCo_5$ thin films.

This work	M_s (emu/cm^3)	M_r (emu/cm^3)	H_c (kOe)	K_1 (erg/cm^3)
YCo_5	517	390	4.00	5.34*10^6
$CeCo_5$	476	344	2.74	4.40*10^6

Fig. 2. A comparison of saturation magnetization, M_s, remanent magnetization, M_r, coercive field, H_c, perpendicular to the film, and first anisotropy constant, K_1, measured for YCo_5 and $CeCo_5$ thin films.

3:30

HB-07. Confirmation of hard magnetic $L1_0$ FeNi phase precipitated in FeNiSiBPCu alloy by anomalous X-ray diffraction.

P. Sharma[1], S. Okamoto[2], H. Tajiri[3], Y. Zhang[4], O. Kitakami[2] and A. Makino[1]
1. New Industry Creation Hatchery Center (NICHe), Tohoku University, Sendai, Japan; 2. Institute of Multidisciplinary Research for Advanced Materials, Tohoku University, Sendai, Japan; 3. Japan Synchrotron Radiation Research Institute (SPring-8), Sayo, Japan; 4. Institute for Materials Research, Tohoku University, Sendai, Japan

Permanent magnets are used in various applications ranging from space to home appliances. Fundamental constituents of these magnets are rare-earth elements (such as Nd, Dy, etc.), whose cost is increasing rapidly. Magnet manufactures are strongly demanding for a low cost material (ie. rare-earth free), which can replace rare-earth magnets. Unfortunately, options are limited. Most promising candidate is chemically ordered $L1_0$ FeNi phase present in Fe-meteorite. Based on its saturation magnetization (M_s~1270 emu cm^{-3}) and uniaxial magneto-crystalline anisotropy (K_u ~1.3 x 10^7 erg cm^{-3}), hard magnetic performance comparable to high grade rare-earth magnet is expected. However, artificial production of $L1_0$ FeNi phase is extremely difficult due to low order-disorder transition temperature (~320 ^{0}C). Recently, we have demonstrated the possibility of $L1_0$ FeNi phase formation through annealing of an amorphous $Fe_{42}Ni_{41.3}Si_8B_4P_4Cu_{0.7}$ alloy[1-3]. Precipitated $L1_0$ FeNi grains require a magnetic field of at least ~ 3.7 kOe to switch their magnetization[3]. High magnetization switching field is consistent with the large magnetocrystalline anisotropy of the chemically ordered $L1_0$ FeNi phase. The ordered phase like $L1_0$ is associated with the presence of a superlattice reflection in X-ray as well as in electron diffraction, and we have confirmed them experimentally. Electron diffraction detected four-fold 110 superlattice reflections.[2] Simulation of electron diffraction pattern suggested that the chemical ordering parameter (S) for the developed $L1_0$-FeNi phase 0.8. Generally S is determined from the intensity ratio of superlattice to fundamental diffraction peaks in X-ray diffraction ie. (001)/(002). However, the experimentally measured ratio is found to be higher than the calculated for fully ordered $L1_0$ FeNi ie. the estimated $S > 1$. This surprising result leads to speculations such as presence of a texture, another phase with diffraction peak position same as (001) of $L1_0$ FeNi etc. Although, TEM and magnetic measurements confirmed the formation of $L1_0$ FeNi phase without any doubt, it is extremely important to clarify the results of X-ray measurements and provide stronger alternatives for the confirmation of $L1_0$ FeNi phase. Detection of superlattice diffraction peak with a standard laboratory X-ray machine is difficult because the scattering factors for Fe and Ni are very similar. The situation changes drastically if the X-ray energy is close to the absorption edge of Fe or Ni. At the absorption edge, anomalous scattering factor plays an important role and intensity of superlattice diffraction peaks such as (001) increases significantly. However, the intensity of fundamental peaks such as (002) decreases significantly. Since the sudden changes in diffracted intensity is element specific, the anomalous X-ray diffraction (AXRD) measurement is a powerful technique for identification of phase and its state (ordered or disordered). The AXRD measurements on $Fe_{42}Ni_{41.3}Si_8B_4P_4Cu_{0.7}$ alloy ribbons annealed at 400 ^{o}C for 288 hours were carried out at SPring 8 under the beam line of BL13XU. This sample showed high magnetization switching field of ~ 3.7 kOe. The details of magnetic properties are reported in ref. 3. Energy of X-ray was varied from 7.0 to 7.2 keV for Fe- absorption edge, and 8.25 to 8.4 keV for Ni-absorption edge. The diffraction data was collected around (001) superlattice and (002) fundamental diffraction peaks of $L1_0$ FeNi. Diffraction curves obtained at each energy was fitted to Gaussian type and peak area was estimated at each X-ray energy. A drastic change in integrated intensity with the energy of X-ray was observed for both the (001) super lattice and (002) fundamental diffraction peaks at Fe and Ni- absorption edges (Fig. 1). This suggested that the (001) and (002) diffraction peaks originate from phase which is made from Fe and Ni. As expected for the (002) fundamental peak, the X-ray intensity decreases strongly at both the absorption edges (Fig. 1 c & d). However, for (001) superlattice, the intensity increases at Ni-absorption edge (Fig. 1b) and decreases for the Fe-absorption edge (Fig. 1a). Increase in intensity at Ni-absorption edge clearly confirms the presence of a chemically ordered $L1_0$ FeNi phase, but the results obtained at Fe-edge are surprising. A detailed analysis of data suggested the presence of a Fe related phase which coincides with the (001) diffraction peak of $L1_0$ FeNi. The information obtained from AXRD analysis is very significant for determining S by laboratory X-ray (slow scan with a rotating anode type). The S estimated from X-ray for $L1_0$ FeNi precipitated in FeNiSiBPCu alloy is 0.76 and it is close to the S locally determined by TEM analysis.[2] Details of the measurements and analysis of the results will be presented during the conference.

1. A. Makino, P. Sharma, K. Sato, A. Takeuchi, Y. Zhang, K. Takenaka, *Sci. Rep.* 5, 16627 (2015). 2. K. Saito, P. Sharma, Y. Zhang, K. Takenaka, A. Makino, *AIP Adv.* 6, 055218 (2016). 3. P. Sharma, Y. Zhang, A. Makino, *IEEE Trans. Magn.*53, 2100910 (2017).

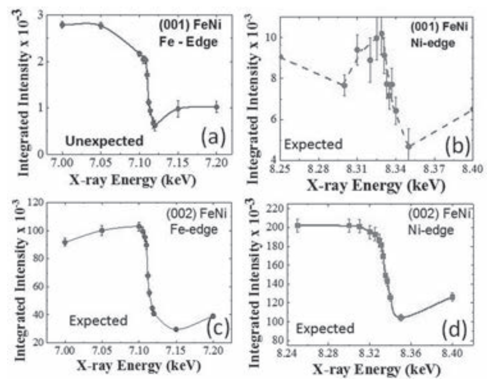

Fig. 1. Variations in X-ray intensity with energy around (001) superlattice and (002) fundamental diffractions peaks of $L1_0$ FeNi. Increase in intensity of (001) peak at Ni-absorption edge confirms the ordered state of FeNi. Unexpected decrease at Fe-edge for (001) is due to the presence of an overlapping phase, which is made from Fe and B.

3:45

HB-08. Magnetic and Structural Properties of L*1₀* (MnAl)-Ga Epitaxially Grown Thin Films of Island Structure.

S. Zhao[1,2], Y. Tanaka[3], T. Satoh[1,3], K. Kamiya[1,3], G.J. Mankey[1,4] and *T. Suzuki*[1,2]
1. Center for Materials for Information Technology (MINT), University of Alabama, Tuscaloosa, AL, United States; 2. Metallurgical and Materials Engineering, University of Alabama, Tuscaloosa, AL, United States; 3. Materials Development Center & IP HQ, TDK Corporation, Ichikawa, Japan; 4. Physics and Astronomy, University of Alabama, Tuscaloosa, AL, United States

Introduction: Recently, $L1_0$ MnGa has attracted much attention because of a high magnetic anisotropy constant K_u, attractive for rare-earth free permanent magnets and spintronics applications [1,2]. In the phase diagram of Mn-Ga alloys, the $L1_0$ phase is stable over a range of about 55~63 Mn at% at an ambient temperature [3]. In the case of thin films, much work on magnetic properties has been made for the Mn composition range over 55 at% (or Mn/Ga >1), but few studies have been found in literature for Mn <55 at%. The present work is to investigate the effect of Al addition on magnetic properties in $L1_0$ MnGa thin films. Effort has been made to fabricate highly ordered $L1_0$ single crystalline films and to study their magnetic properties in conjunction with structure. Experimental: Multilayers of (MnGa), Mn and Al with various thicknesses were fabricated onto MgO(100) substrate held at about 600 °C during deposition in a multi-target UHV confocal sputtering system. The film-composition thus fabricated was determined by energy dispersive X-Ray spectroscopy (EDS). In the present work, three samples of $Mn_{53-x}Al_xGa_{47}$ with x=0, 3 and 6 were chosen to study, namely $Mn_{53}Ga_{47}$, $Mn_{50}Al_3Ga_{47}$ and $Mn_{47}Al_6Ga_{47}$. The nominal film thickness for all the samples was 50~60 nm. Structural analyses were performed by XRD and TEM. Magnetic properties were measured by a vibrating sample magnetometer and a torque magnetometer over a temperature range from 5 to 400 K in fields up to 90 kOe. Results and Discussions: Figure 1(a) is the XRD pattern result for the samples with x=0, 3 and 6. All the samples possess the c-axis orientation along the film normal. The (001) super-lattice peak is clearly seen for x=0 and 3, but decreases its intensity with x or the decrease of Mn concentration. The order parameter S estimated based on the intensity ratio between *I(001)/I(002)* is found to be 0.9, 0.7 and 0.4 for x = 0, 3 and 6, respectively. Fig.1(b) and (c) of the TEM images for x = 0 shows the trapezium shape islands with a height of about 50nm and a width of about 100nm. The nano-diffraction pattern indicates that the trapezium islands are of epitaxially grown $L1_0$ phase with the c-axis along the substrate normal (S=0.9). The sample for x=3 (S=0.7) does not consist of islands of such a well-defined shape, but rather rounded one. Most of the grains are of $L1_0$ phase, but consist of sub-grains of unknown phases. The sample for x=6 (S=0.4) is also formed of islands, the majority of which is not of $L1_0$ phase but unknown phase. The result that the highly ordered $L1_0$ MnAlGa islands with less than Mn 50at% are found strongly suggests that an addition of Al into MnGa is useful to expand the composition range of the $L1_0$ phase. Fig. 1 (d) shows the element mappings observed by EDS. Little evidence of the multilayered structure is found and all the elements of Mn, Ga and Al are uniformly distributed within an island. Both the out-of-plane and in-plane M-H curves were measured as a function of temperature from 5 to 400K. All the samples exhibit the remanence close to one, and possess the easy axis for magnetization along the film normal. The M_s at 5K are found to be about 380, 480 and 90 (emu/cm^3) for x=0,3 and 6, respectively. The K_u at 5K are $1.1x10^7$, $6x10^6$ and $2x10^5$ (erg/cm^3) for x=0, 3 and 6, respectively. The out-of-plane coercivity H_c at 5K are 18, 4 and 11 (kOe) for x=0, 3 and 6, respectively. Fig.2 shows the normalized temperature dependences of M_s and K_u for x=0, 3 and 6, together with the data reported [4]. The solid lines are the fitting curves in the form of $M_s(T)/M_s(5K) = (1- T/T_c)^\alpha$, where T_c is a Curie point and α is a parameter [1]. The behavior of the temperature dependence of M_s is consistent with the results shown in the inserted figure [4], where a sharp decrease occurs near T_c. It is seen that the sample (x=6) exhibits a faster decrease in magnetization with T, compared to x=0 and 3. Using a method of least squares, it is found that the T_c value for x=6 is about 550K with α =0.27. The uniaxial magnetic anisotropy constant K_u decreases with T, much faster than that for M_s. (The dotted lines are only for the eye-guidance.) The log-log plot for M_s and K_u shows that the power dependence of K_u on M_s varies, depending on a temperature range. Nevertheless, it is found that K_u is approximately proportional to M_s^n, where n≈2.3~2.7, and 2.3 for x=0 and 3, respectively for the entire range of T from 5 to 400K. This result suggests that the two ion model is likely responsible for the magnetic anisotropy mechanism of $L1_0$ MnGa.[5,6] *In summary,* the epitaxially grown single crystalline films of $L1_0$ $Mn_{53-x}Al_xGa_{47}$ (x=0~6) are found to be of island structure. The temperature dependence of saturation magnetization indicates that the Curie point is about 550K for x=6. The two ion model likely accounts for the magnetic anisotropy mechanism of the $L1_0$MnGa. The present work was supported in part by NSF-CMMI (#1229049) and TDK Corporation.

[1]. T.J. Nummy *et al.*: "Large coercivity in nanostructure rare-earth-free Mn_xGa films" *Appl. Pys. Lett.* vol. 99, 252506 (2011). [2]. H. Kurt, *et al.*: "$Mn_{3-x}Ga$ (0≤x≤1) multifunctional thin film materials for spintronics and magnetic recording" *Phys. Status Solidi* B vol. 248, 2388 (2011). [3]. "Binary Alloy Phase Diagram" edited by T.B Massalski (*The Materials Information Society*, vol. 2, 1825 (2007). [4]. Q. M. Lu *et al.*: "Intrinsic magnetic properties of single-phase $Mn_{1+x}Ga$ (0<x<1) alloys" *Sci.Rep.* vol.5, 17086 (2015). [5]. S. Zhao *et al.*: "Magnetic anisotropy of tau-MnAl thin films" IEEE. Trans. Mag., vol. 51, 2101604 (2015). [6]. S. Zhao and T. Suzuki: "Magnetic and structural properties of Mn-Ga thin films" *AIP Advances* vol. 6, 056025 (2016).

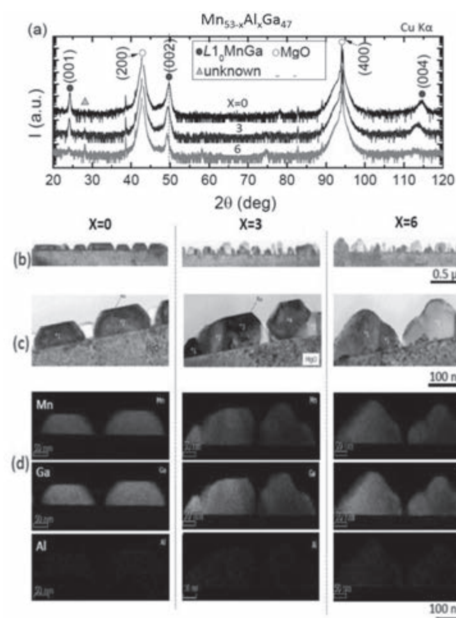

Fig. 1. (a): XRD patterns for the $Mn_{53-x}Al_xGa_{47}$ films with x=0, 3 and 6 onto MgO (100) substrate, (b) and (c): the cross-sectional TEM photographs and (d): EDS element mapping images of Mn, Ga and Al.

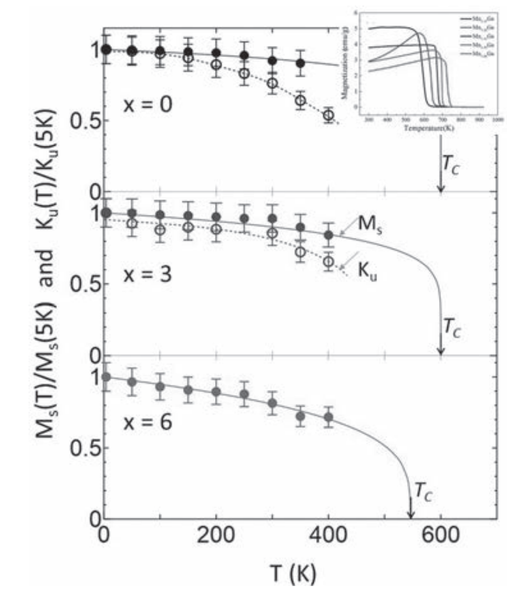

Fig. 2. The temperature dependence of saturation magnetization normalized by M_s(5K) for x=0, 3, 6, together with the data[4]. The solid lines are the empirical curves fitted to the form of $M_s(T)/M_s(5K) = (1 - T/T_c)^{\alpha}$, where T_c is 600, 600 and 550 K, for x=0, 3 and 6,respectively. (α : 0.10, 0.15 and 0.27 for x=0, 3 and 6, respectively.) Also shown are the results for the temperature dependence of K_u for x=0 and 3.

4:00

HB-09. Synthesis of Phase-Pure τ-MnAlC Using Mechanical Alloying and a Single-Step Annealing Route.

V. Øygarden[1], J. Rial[2], A. Bollero[2] and *S. Deledda*[1]
1. Institute for Energy Technology, Kjeller, Norway; 2. Permanent Magnets and Applications, IMDEA Nanoscience, Madrid, Spain

Permanent magnets (PMs) play an important role in the continuous technological development of the modern world [1]. Rare-earth (RE) magnets, such as $Nd_2Fe_{14}B$ with an energy density $(BH)_{max}$ up to 59.1 MGOe (470 kJ m^{-3}), are used for applications where high magnetic energy-density values are needed. For applications where lower energy-density suffice, ferrites such as $(Sr,Ba)Fe_{12}O_{19}$, dominate the market with an energy density $(BH)_{max}$ up to 5.0 MGOe (40 kJ m^{-3}). The rising cost and exposed supply-chain of rare-earth magnets have spawned a global search for rare-earth free alternatives that are able to plug the gap between the rare-earth based and ferrite-based permanent magnets that currently dominate the market. τ-MnAl has long been investigated as a promising candidate due to its high potential energy density, low weight, and readily available resources, but development has been slowed down by challenging synthesis conditions and issues with phase purity [2]. The τ-phase can be synthesized via a two-step route involving at least two annealing steps. Firstly the ε-phase is isolated by rapid quenching from high temperature, followed by one or more annealing step(s) at intermediate temperatures to form the τ-phase. The latter annealing step is problematic because it often results in a multiphase material [3]. To avoid this, the τ-phase can also be formed directly during the quenching of the ε-phase. The one-step route, named so because only one heat treatment is needed, is beneficial regarding phase-purity because the full transformation from ε- to τ occurs during the cooling, and no subsequent heat treatments are needed thereby avoiding any potential decomposition of the metastable τ-phase. In this contribution, mechanical alloying was used to optimize the microstructure prior to annealing. Excess Mn is needed as ε-MnAl is only stable for Mn-rich compositions (Mn > 54 at%). To enhance the formation of the τ-phase, a small amount of carbon was added as an interstitial element [4] giving the composition $Mn_{0.54}Al_{0.46}C_{0.02}$ (MnAlC). Appropriate milling conditions gave a highly active starting material for enhanced formation of τ-MnAlC. The X-ray diffraction (XRD) pattern of the as-milled powder is shown in Fig. 1a. The XRD-data were indexed to the β-Mn(Al) phase with lattice parameter a = 6.441(5) Å, significantly larger than elemental β-Mn (a = 6.316 Å), suggesting the larger Al was mechanically alloyed into the β-Mn lattice. The average crystallite size was estimated to be ~16 nm. β-Mn(Al) transformed to ε-MnAlC upon heating to 1050 °C, whilst the conversion of ε-MnAlC to τ-MnAlC was achieved during quenching. The phase purity of the τ-phase was shown to be highly dependent on the quenching rate. XRD patterns of τ-MnAlC powders produced with varying quenching rates from 1050 °C are presented in Fig. 1b-d. The impact of the quenching rate on phase formation in the MnAlC-system can be illustrated schematically in a continuous cooling transformation diagram, or CCT-diagram, see Fig. 2. The diagram illustrates the phase changes that occur when starting with the ε-phase and cooling with different rates from 1050 °C. For slower quenching in air (~3.5 C/min, see curve *III.*) the cooling time is sufficiently slow for the ε to τ phase-transition to complete, whilst simultaneously fast enough to avoid further phase decomposition. Powder synchrotron x-ray (SR-XRD) and neutron diffraction data (PND) were used to demonstrate the phase-purity, as well as the magnetic structure and the magnetic moments of the Mn-site. Rietveld fit of the SR-XRD and PND data gave a = 2.7635(1) Å and c = 3.6114(2) Å, while the magnetic moment of the Mn-site was refined to 2.43(5) μ_B, in line with previous reports. A coercivity of μ_0H_c = 0.15 T was found for the as-synthesized τ-phase. The possibility of further improving the coercivity by cryomilling in liquid N_2 was explored. In summary, this study presents a simplified, up-scalable and reliable synthesis-route to produce phase-pure τ-MnAlC, using mechanical alloying combined with a single annealing step. The resulting synthesis-route is a streamlined and repeatable route to phase-pure τ-MnAlC, avoiding needs for more complicated synthesis techniques such as drop synthesis, melt spinning and induction melting. The importance of the cooling rate of the annealing step is highlighted and discussed in detail. We also provide a description of the magnetic structure and properties of the phase-pure τ-MnAlC, which showed promising magnetization and energy product.

[1] O. Gutfleisch *et al*., Adv. Mater. 23(7) (2011) p.821 [2] H. Kono, J. Phys. Soc. Jpn. 13(12) (1958) p.1444 [3] Z.W. Liu *et al*., J.Mater. Sci. 47(5) (2012) p.2333 [4] T. Ohtani *et al*., IEEE T. Magn. 13(5) (1977) p.1328

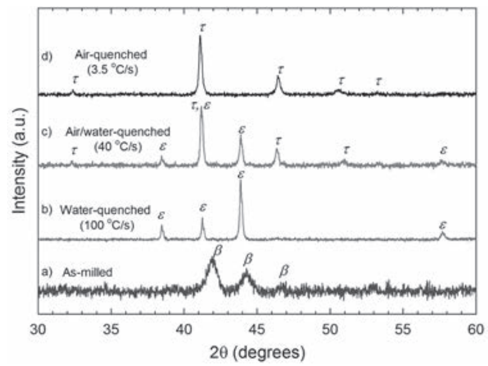

Fig. 1. Sections of powder XRD patterns of the as-milled MnAlC (a), and MnAlC milled and annealed at 1050 °C with different subsequent quenching rates (b-d).

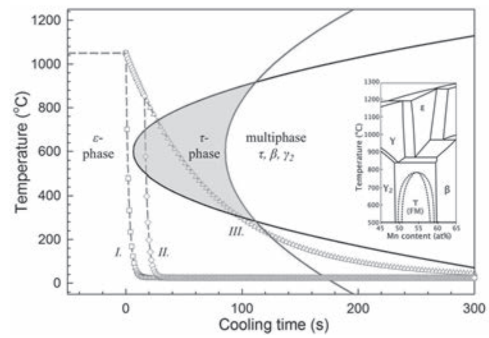

Fig. 2. Schematic CCT-diagram for the MnAlC-system. Three different cooling rates are shown, denoted *I. – III.*, where *I.* shows the quenching rate in water at 100 °C/s, *II.* an intermediate quenching rate of 40 °C/s, *III.* shows quenching in air at 3.5 °C/s. The insert shows a portion of the Mn-Al phase diagram.

4:15

HB-10. Tuning permanent magnet properties in MnAl nanocrystalline powder processed by ultrafast-milling with different milling media.

J. Rial[1], P. Svec[2], *E. Palmero*[1], J. Camarero[1], P. Švec Sr[2] and A. Bollero[1]
1. Division of Permanent Magnets and Applications, IMDEA Nanoscience, Madrid, Spain; 2. Institute of Physics, Slovak Academy of Sciences, Bratislava, Slovakia

Permanent magnets (PMs) are used in a multitude of energy-related technological applications [1] and cannot be substituted without an increased cost and/or a detrimental performance of the devices. These PMs contain critical raw materials [heavy and light rare-earths (REs)] as fundamental constituents with additional environmental issues related to their extraction and processing. MnAl has been considered a strong alternative to RE-PMs in recent years. This material shows an attractive combination of characteristics for technological applications provided development of the ferromagnetic τ-MnAl phase and an appropriate microstructure [1,2]. The τ-MnAl phase is metastable and forms from the non-magnetic ε-phase. However, decomposition of the ε-phase normally results in the formation of the γ_2- and β-Mn phases, which are the equilibrium phases at room temperature. Most of the studies found in literature and related to MnAl are focused in achieving a maximized content of the τ-MnAl phase, i.e. enhanced magnetization, with a subsequent decrease in coercivity, which limits its potential use in PM applications. Moreover, ball milling processing techniques used for controlling the phases formation in MnAl powder require typically tens of hours, thus making them unviable for practical applications. We have developed a novel rapid-milling method that requires milling times below 5 min to achieve high coercivity values, which has been proven effective with a variety of RE-free PMs [3-5]. It has been recently demonstrated [5] that application of this ultrafast-milling procedure to gas-atomized $Mn_{54}Al_{46}$ particles for only 30 s results in a refined nanostructure, and allows introducing defects that eases the formation of the metastable ferromagnetic τ-MnAl phase from the starting stable and non-magnetic ε-phase. The use of such a short milling times avoids the high temperatures (several hundred degrees) typically achieved in milling experiments that might ease undesired grain growth effects, relaxation processes and phase transformations. Annealing of the powder milled for 30 s results in a high coercivity of 4.2 kOe, superior to 4.1 kOe achieved for gas-atomized MnAl powders after milling for a much longer time of 26 h [6]. The present study correlates the evolution of phase transformation and microstructural changes with the magnetic properties, induced during ultrafast-milling and annealing. This has been managed by using milling media with very different densities (tungsten carbide and steel with ρ= 14.7 and 7.8 g/cm^3, respectively), which are proven to influence very differently morphology, microstructure and magnetic properties in MnAl due to the different energy impact attained during ball milling. X-ray diffraction (XRD) pattern of the starting gas-atomized material (particle size below 30 μm) showed only intensity peaks corresponding to ε- and γ_2-phases, with no presence of the τ-phase. XRD patterns measured during *in-situ* annealing of the as-milled powders (270 s) in the temperature range of 30 to 500 °C (ramp: 1 K/min), show that the temperature needed for ε- to τ-MnAl transformation decreases in about 50 °C by using the higher density tungsten carbide media. Figure 1 shows the hysteresis loops measured for the MnAl powder milled for 270 s with tungsten carbide and steel, after annealing at 400 °C. The choice of tungsten carbide in the milling process results in MnAl powder with a very high coercivity of about 5 kOe by milling for only 270 s, but this comes at the expense of a decreased magnetization. A better combination of magnetic properties is obtained by using steel material as milling media, with a significant coercivity of 3 kOe and above a 50% increase in magnetization after same processing parameters used with tungsten carbide. It will be shown that this is the result of the development of the τ-phase and the low annihilation of defects induced during milling that, in combination with the formation of the stable β-phase, act as pinning centers during magnetization reversal. High-resolution transmision electron microscopy TEM analysis was carried out with a FEI Titan microscope to confirm the coexistence of the τ- and β- phases in the resulting powders. Figure 2 shows structural configuration images for the τ- and β-phases coexisting in the high-coercive MnAl powder milled for 270 s with tungsten carbide.

Acknowledgements The gas-atomized powders were provided by Prof. Ian Baker (REACT, DE-AR0000188). Authors acknowledge financial support from MINECO through projects NEXMAG (M-era.Net, PCIN- 2015-126), ENMA (MAT2014-56955-R), EUIN2017-88502 and 3D-MAGNETOH (MAT2017-89960-R); and from the Regional Government of Madrid through NANOFRONTMAG project (Ref. S2013/MIT-2850). IMDEA Nanociencia acknowledges support from the 'Severo Ochoa' Programme for Centres of Excellence in R&D (MINECO, Grant SEV-2016-0686).

[1] L.H. Lewis and F. Jiménez-Villacorta *Metall. Mater. Trans. A* 44, 2-20 (2013). [2] J. Park, Y.K. Hong, S. Bae, J.J. Lee, J. Jalli, G.S. Abo, N. Neveu, S.G. Kim, C.J. Choi, and J.G. Lee, *J. Appl. Phys.* 107, 09A731 (2010). [3] F.J. Pedrosa, J. Rial, K.M. Golasinski, M. Rodríguez-Osorio, G. Salas, D. Granados, J. Camarero, and Bollero, *RSC Advances 6,* 87282–87287 (2016). [4] A. Bollero, J. Rial, M. Villanueva, K. M. Golasinski, A. Seoane, J. Almunia, and R. Altimira, *ACS Sustainable Chem. Eng.* 5, 3243 (2017). [5] J. Rial, M. Villanueva, E. Cespedes, N. Lopez, J. Camarero, L. Marshall, L.H. Lewis and A. Bollero, *J. Phys. D: Appl Phys.* 50, 105004 (2017). [6] J. Lee, X.L. Wang, Z.D. Zhang, and C.J. Choi, *Thin Solid Films* 519, 8312-8316 (2011). [7] J. Rial, P. Svec, E.M. Palmero, J. Camarero, P. Švec Sr., and A. Bollero. Submitted for publication.

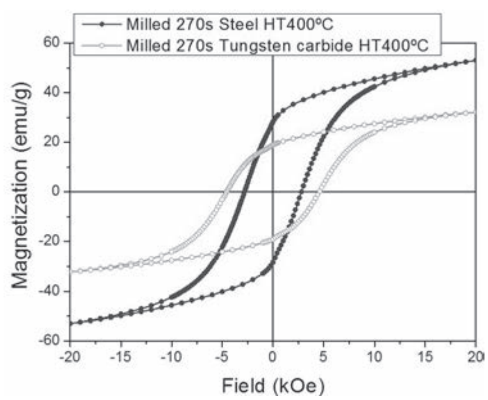

Fig. 1. Hysteresis loops measured at room temperature for gas-atomized MnAl particles after milling for 270 s with steel (full symbols) and tungsten carbide (empty symbol) and annealing at 400 °C.

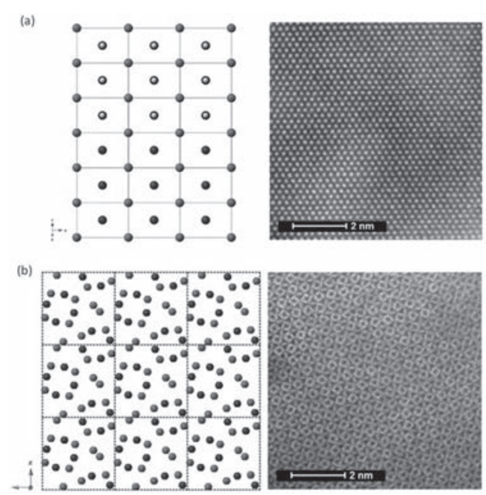

Fig. 2. Structural configuration images for the τ-MnAl (a) and β-Mn (b) phases coexisting in the high-coercive MnAl powder milled for 270 s with tungsten carbide. Left images illustrate the schematic atomic configuration of both phases.

4:30

HB-11. Spark Plasma Sintered MnGa-alloys for Permanent Magnet Applications.

S. Perween[1,2], B. Gahtori[1,2], A. Rathi[2], R. Singh[3], A. Bhattacharya[1], B. Sivaih[1,2], P. Rout[1], R. Pant[1], A. Dhar[1,2] and G. Basheed[1,2]
1. CSIR - National Physical Laboratory, Delhi, India; 2. CSIR - National Physical Laboratory, Academy of Scientific and Innovative Research, Delhi, India; 3. Department of Physics, Indian Institute of Science Education and Research (IISER, Bhopal, India

Mn-based alloys have been emerged as potential replacement to high-cost rare-earth and novel metal based permanent magnets. Among these, tetragonally ordered $Mn_{3-x}Ga$ ($0 \le x \le 1$) alloys are more promising due to high Curie temperature (600 K ≤ Tc ≤ 800 K), tunable retentivity and coercivity and high uniaxial magneto-crystalline anisotropy (UMCA; ~ M erg/cc) [1-5]. But, synthesis of single tetragonal phase of $Mn_{3-x}Ga$ alloys is a challenging task subjected to the existence of manifold (near-stoichiometric and structural) stable phases due to their complex phase diagram [6]. On top of this, the permanent magnets characteristic energy product, BH_{max} value relies on the extrinsic parameters, coercivity (H_c) and remanence (M_r), which are determined by the exchange interactions between hard magnetic grains [8], i.e. controlled by microstructure of the sample, largely dependent on the synthesis technique. Till now, only arc-melting (AMT) technique has been implemented which is limited on the large scale production [1-5]. However, interestingly the hot-compressing of the arc-melted samples resulted in higher coercivity than in as-synthesized alloys [9]. This implies that the single step Spark Plasma Sintering (SPS) technique may be a better alternative which already has numerous industrial advantages. In SPS, in addition to synthesis temperature, the quasi-static compressive stress in SPS technique can optimize the distribution of magnetic grains over the critical magnetic domain wall size uniformly within the material [10]. In this work, we firstly synthesized the alloys with Spark Plasma Sintering technique and XRD results confirm the single phase DO_{22}-Mn_3Ga, while DO_{22}- Mn_2Ga alloy with minimal 15 % volume fraction of a Mn_9Ga_5-phase, which is unavoidable during synthesis due to more negative formation energy, as obtained from density functional theory calculations. The dc magnetization results show T_c ~ 780 K for Mn_3Ga and 710 K for Mn_2Ga (Fig.1), in consistent with earlier studies with AMT. The MH results shows hard magnetic behavior with negligible temperature dependence of $M_s \sim 1.87\ \mu_B$ (10 K) to $1.72\ \mu_B$ (300 K) and H_c ~ 2.65 kOe for Mn_3Ga, while $M_s \sim 1.0\ \mu_B$ and H_c ~ 4.95 kOe (10 K) to $M_s \sim 0.82\ \mu_B$ and H_c ~ 4.35 kOe (300 K) for Mn_2Ga alloy (inset of Fig.1). The comparison of experimental H_c with Stoner-Wohlfarth model yields microstructural parameter, $\alpha \sim 0.6$ (Mn_3Ga) and ~ 0.5 (Mn_2Ga) and confirms nucleation mechanism [8]. The maximum energy product (BH_{max}, MGOe) from MH loops and UMCA (K_u, Merg/cc) from Approach-to-saturation analysis of MH isotherms and maximum energy product (BH_{max}, MGOe) from hysteresis loops are obtained as 0.61 MGOe, 10.81 Merg/cc (Mn_3Ga, 10 K) and 0.34 MGOe, 6.51 Merg/cc (Mn_2Ga, 10 K), respectively (Fig.2). The above K_u and BH_{max} values for Mn_3Ga are slightly lower, while for Mn_2Ga are higher than obtained with arc melted samples reported till date.

1. J. Winterlik et.al., Phys. Rev. B 77 (2008) 054406 2. J. Z. Wei et.al. J. Appl. Phys. 115, 17A736 (2014) 3. Q. M. Lu et.al. Sci. Rep. 5, 17086 (2015) 4. T. Mix et.al. J. Magnetism and Magnetic Materials. 391, 89-95 (2015) 5. B. Balke et.al. Appl. Phys. Lett. 90 (2007) 152504 6. Kazuhiro Minakuchi et.al., Journal of Alloys and Compounds 537, 332–337 (2012) 7. A. J. Albaaji et.al., AIP Advances, 8, 047705 (2018) 8. H. Kronmuller and K. D. Drust, J. Magnetism and Magnetic Materials 74, 291-302 (1988) 9. T. Mix et.al., Journal of Magnetism and Magnetic Materials, 391, 89- 95 (2015) 10. Z. A. Munir et.al., Journal of Material Science, 41, 763- 777 (2006)

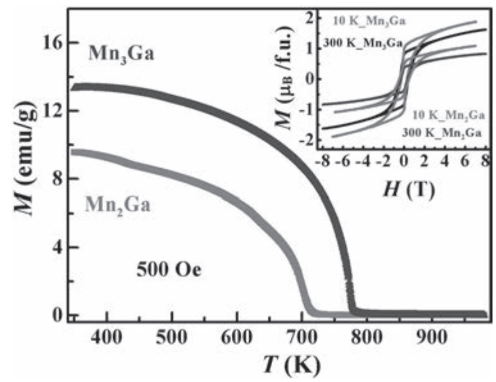

Fig. 1. M-vs-T curves of Mn_3Ga and Mn_2Ga at 500 Oe field. Inset shows M-vs-H curves of Mn_2Ga and Mn_3Ga alloys.

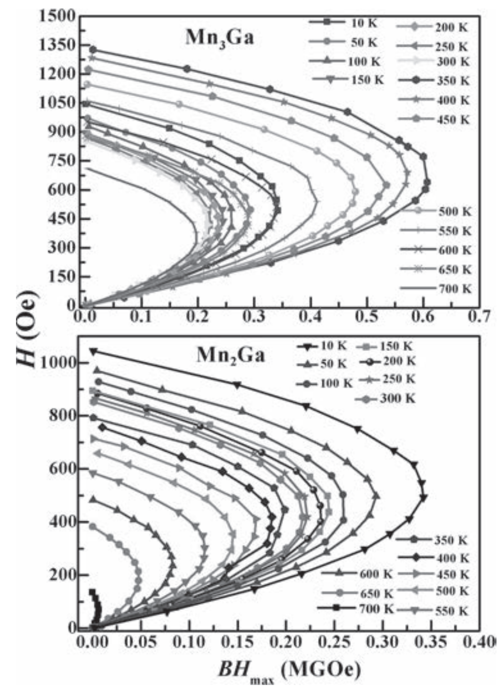

Fig. 2. The plot of magnetic field (H) versus energy product (BH_{max}) of Mn_3Ga and Mn_2Ga from temperature range 10 K to 700 K.

4:45

HB-12. Tailoring Magnetic Properties of Al-substituted M-Type Strontium Hexaferrites.

Y. Dai[1], Z. Lan[1], K. Sun[1], Z. Yu[1], R. Guo[1] and X. Jiang[1]
1. University of Electronic Science and Technology of China, Chengdu, China

M-type Strontium Hexaferrites have gained considerable attention for their applications in the permanent magnets, microwave devices and magnetic recording media due to the large uniaxial magnetocrystalline anisotropy, excellent remanent magnetization, and corrosion resistivity and low price [1]. Any further enhancement to the magnetic properties of M-type Sr-hexaferrite is of relevance for technological innovation. Aiming at this target, many works have been done to investigate the influence of main compositions, fabricating methods, and sintering processes on the magnetic properties. Y. Yang et al [2] reported Al substituted M-type Ca-Sr-hexaferrites ($Ca_{0.6}Sr_{0.1}La_{0.3}Fe_{12-x}Al_xO_{19}$, x=0~1.4), and the results indicated that the saturation magnetization (M_s) linearly decreases while the coercivity (H_c) increases with the increase of Al contents. F. Rhein et al [3] prepared $SrFe_{12-x}Al_xO_{19}$ powders via mechanochemical activation, and afterwards the powders were milled and annealed at 1000°C in NaCl to produce ultrafine nano-particles. It is concluded that the furthermore milling and annealing treatment allow to improve both the coercivity H_c and saturation magnetization M_s of Al substituted Sr-hexaferrites (x=0, 1) as compared to the conventional ceramic process. Z. Chen et al [4] studied $Sr_{0.61-x}La_{0.39}Ca_xFe_{11.7}Co_{0.3}O_{19}$ ferrites with various calcium concentrations (x=0, 0.1, 0.2, 0.3) through microwave calcining. The largest saturation magnetization of 68emu/g and coercivity of 5320Oe were observed for a composition of $Sr_{0.41}La_{0.39}Ca_{0.2}Fe_{11.7}Co_{0.3}O_{19}$ calcined at 1140°C for 30min. In this work, the M-type hexaferrite $Sr_{0.7}La_{0.3}Fe_{12-x}Al_xO_{19}$ (x=1~1.4) have been synthesized by the standard solid-state method. The influence of Al^{3+} substitutions on the microstructure and magnetic properties of M-type Sr hexaferrites have been investigated in detail. In order to probe into the effect of Al^{3+} substitutions on the magnetocrystalline anisotropy, the law of approach to saturation was utilized to calculate the magnetocrystalline anisotropy constant K_1, which could be written as Eq. (1)~(3) [5]: $M=M_s(1-e/H-f/H^2-\ldots)+\chi_p H$ (1) $f=H_a^2/15$ (2) $H_a=2K_1/\mu_0 M_s$ (3) where e and f represent the resistance of technical magnetization, M_s the saturation magnetization, H the applied magnetic field, χ_p the paramagnetic susceptibility. H_a can be derived accordingly. The X-ray diffraction patterns of the hexaferrite $Sr_{0.7}La_{0.3}Fe_{12-x}Al_xO_{19}$ with x=0~1.4 are shown in Fig.1. It can be observed that the XRD patterns of all the samples are single magnetoplumbite phase patterns. The result indicates that Al^{3+} ions are all indexed to the standard powder diffraction pattern of M-type hexaferrite. Fig.2 illustrates the magnetic hysteresis loops of the as-sintered samples. Note that the coercivity H_c of Al substituted hexaferrites increase significantly with increasing Al substitutions. Concomitantly, the relatively high remanence ratio (M_r/M_s) of 80% is observed in Al substituted hexaferrites.

[1] V. Dixit, C. N. Nandadasa et al. Site occupancy and magnetic properties of Al-substituted M-type strontium hexaferrite, Journal of Applied Physics 117 (2015) 243904 [2] Y. Yang, F. Wang et al. Magnetic and microstructural properties of Al substituted M-type Ca–Sr hexaferrites, Journal of Magnetism and Magnetic Materials 421 (2017) 349-354 [3] F. Rhein, R. Karmazin et al. Enhancement of coercivity and saturation magnetization of Al^{3+} substituted M-type Sr-hexaferrites, Journal of Alloys and Compounds 690 (2017) 979-985 [4] Z. Chen, F. Wang et al. Microstructure and magnetic properties of M-type $Sr_{0.61-x}La_{0.39}Ca_xFe_{11.7}Co_{0.3}O_{19}$ hexaferrite prepared by microwave calcinations, Materials Science and Engineering B 182 (2014) 69-73 [5] Y. Wang, Y. Liu et al. Preparation of Scandium-doped, textured, M-Type Barium ferrite via a wet magnetizing orientation process, Journal of Electronic Materials DOI: 10.1007/s11664-017-5949-z

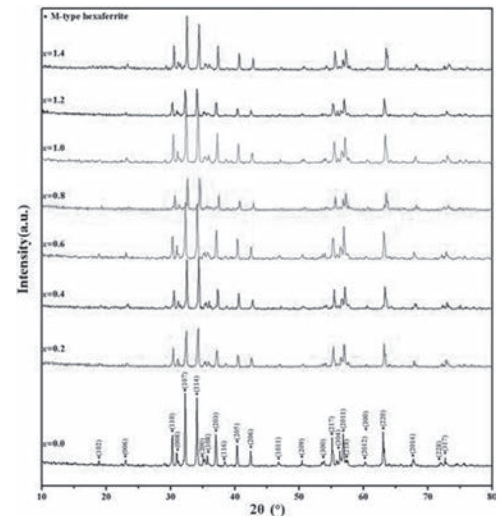

Fig. 2. Magnetic hysteresis loops of $Sr_{0.7}La_{0.3}Fe_{12-x}Al_xO_{19}$ samples

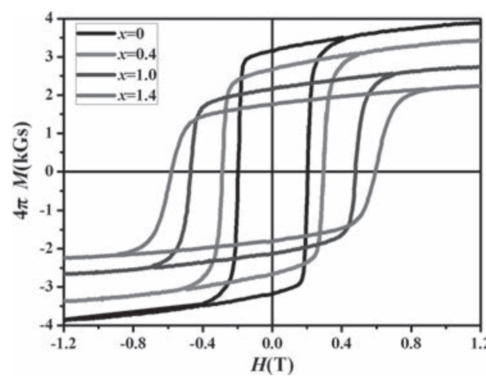

Fig. 1. XRD patterns of $Sr_{0.7}La_{0.3}Fe_{12-x}Al_xO_{19}$ samples

FRIDAY AFTERNOON, 27 APRIL 2018 ORCHID IV, 2:00 TO 5:00

Session HC
MAGNETIC TUNNEL JUNCTIONS AND STT-MRAM

Bernard Dieny, Chair
Spintec, Grenoble, France

INVITED PAPER

2:00

HC-01. Resonance Spin Transfer Torque Magnetoresistive Memory.

J. Zhu[1] and A. Shadman[1]
1. Data Storage Systems Center, Carnegie Mellon University, Pittsburgh, PA, United States

INTRODUTION Spin transfer torque magnetoresistive random access memory (STT-MRAM) has shown a great promise to be a main stream novel nonvolatile memory technology. Reduction of state switching current still remains to be a continued research focus for scaling down the size of the addressing transistors. One of the switching characteristics attributing to the relatively high power consumption is the asymmetry of switching current threshold: switching from parallel (P) to antiparallel (AP) state requires more than twice as much current as switching from antiparallel to parallel state. In this paper, we present a design that can significant reduce the switching current threshold for switching from P to AP state to substantially reduce or eliminate the switching asymmetry. By incorporating an antiferromagnetic/ferromagnetic stack to provide a rotating spin transfer torque that matches with the ferromagnetic resonance frequency of the free layer, switching threshold can be significantly reduced. DSIGNE AND SIMULATION RESULTS Figure 1(a) shows the actual design: The upper portion of the memory including the free layer is a conventional STT-MRAM design with stray-field compensated reference layer structure. The lower portion of the memory is a structure for generating a rotating spin transfer torque through the other interface of the free layer, which comprises, starting from the bottom, a perpendicularly magnetized spin polarization layer, an antiferromagnetic layer (AF) with negative uniaxial anisotropy of easy plane, a non-magnetic interlayer, a ferromagnetic layer exchange biased with the antiferromagnetic layer, and a non-magnetic interlayer separating the ferromagnetic layer and the free layer. The bottom spin polarization layer yields polarized spin current in the antiferromagnetic layer, resulting in the canting of the antiferromagnetic coupled spins as illustrated in Fig. 1(c). The spin canting gives rise to the exchange fields on the two sets of antiparallel coupled spins, consequently resulting in spin precession around the perpendicular direction within the film plane with precessional chirality governed by the left-hand rule [1][2]. The precessional frequency is partially determined by the ratio between the numbers of injected spins and the localized spins in the AF layer as well as the AF-biased ferromagnetic laye. The magnetization rotation of the AF-biased ferromagnetic layer generates a rotating spin transfer torque to the free layer magnetization. As the free layer magnetization experience the antidamping spin transfer torque generated from the tunnel barrier side, the magnetzation will precess at the ferromagnetic resonance freqency. By adding a rotating spin transfer torque that matches the chirality of the magnetization precession and the ferromagnetic resonance frequency, Switching current threshold should be signifiantly reduced. By selecting the thickness and the material of both the antiferromagnetic layer and the ferromagnetic layer, the freqency of the rotating STT can be adequated selected at the operating current. Figure 2(a) shows the calculated switching time, defined as the minimum current pulse duration need, as a function of the frequency of the rotating spin transfer torque for different current injection for fixed free layer parameters with the ferromagnetic resonance (FMR) frequency $\gamma H_k/2\pi \approx 22$ GHz. An effective H_k of 8 kOe is assumed for a circular device of 20nm diameter. At smaller current values, which are significantly below the threshold by the usual one-side spin transfer torque only, the switching time dramatically reduces as the freqnecy of the rotating spin transfer torque approaches to the FMR frequency from the left side (smaller freqency). The effect of resonance is evident. Figure 2(b) shows the calculated switching time with an artificially fixed rotating spin transfer torque at a frequency of 21GHz for P-to-AP switching. The reduction of switching current threshold with the rotating spin transfer is significant and the reduced switching current threshold becomes the same as the AP-to-P switching, hence, essentially eliminating the switching asymmetry. It is important to note the designs shown in Fig. 1(a) and 1(b) only help the P-to-AP switching while the switching from AP-to-P is virtually unaffected. For the results shown here, we artificially fixed parameters of the rotating spin transfer torque, such as its frequency, or its amplitude, mainly for the purpose of illustrating and understanding the physics behind the phenomena and the operation mechanism.

[1] R. Cheng, M.W. Daniels, J.-G. Zhu, and D. Xiao, "Ultrafast switching of antiferromagnet via spin-transfer torque," Physical Review B, 91:064423 (2015). [2] A. Shadman, R. Cheng, D. Xiao, and J.-G. Zhu, "Ultra-high speed STT-MRAM with incorporating antiferromagnetic layer," Paper BE-05, MMM Conference 2017, Pittsburgh (2017).

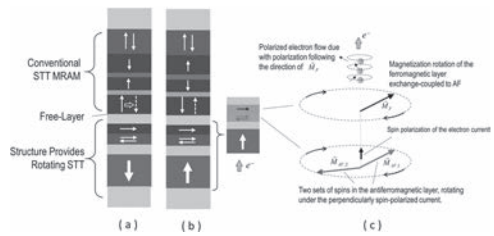

Fig. 1. (a) and (b) are the schematical drawing of the resonance STT MRAM designs corresponding to two opposite magnetization orientations for the bottom spin polarization layer. (c) Illustration of spin canting in the AF layer due to the perpendicular spin polarized current and the resulting spin precession in the AF and exchange biased ferromagnetic layer for generating spin current with rotating spin polarization.

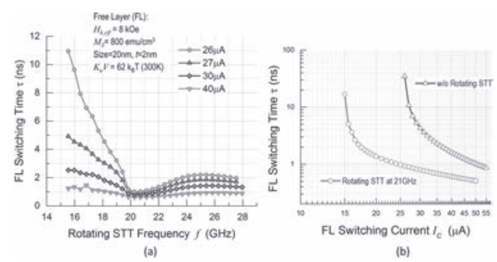

Fig. 2. (a) Calculated free-layer magnetization switching time for P to AP switching as a function of the frequency of the rotating spin transfer torque for different current level giving rise to the antidamping STT from the tunnel barrier side. The magnitude of the rotating spin transfer torque is fixed for given practical material parameters. (b) Calculated free-layer magnetization P to AP switching time as a function of current level with the frequency of the rotating spin transfer torque fixed at 21 GHz and practical magnetude.

CONTRIBUTED PAPERS

2:30

HC-02. Top-pinned STT-MRAM devices with high thermal stability hybrid free layers for high density memory applications.

E. Liu[1,2], J. Swerts[1], A. Vaysset[1], Y. Wu[1,2], S. Couet[1], S. Mertens[1], S. Rao[1], W. Kim[1], S. Van Elshocht[1], J. De Boeck[1,2] and G.S. Kar[1]
1. Imec, Leuven, Belgium; 2. Department of Electrical Engineering, KU Leuven, Leuven, Belgium

New free layer (FL) materials and designs have recently drawn a lot of interest as the devices of spin-transfer-torque magnetic random access memory (STT-MRAM) keep scaling down. The so-called dual-MgO FL consisting of two CoFeB/MgO interfaces is under development. However, the perpendicular magnetic anisotropy (PMA) from two CoFeB/MgO interfaces is insufficient to provide the required thermal stability (Δ) for long data retention time for devices with critical diameter (CD) below 20nm. In our earlier work, a new FL design, the hybrid FL, was proposed. This hybrid free layer (HFL) design consists of a single layer of CoFeB coupled via a spacer to a [Co/Ni] multilayer [1]. Here, we report on the electrical and magnetic properties of the hybrid free layers in top-pinned magnetic tunnel junction (TP-MTJ) devices with various electrical CD (e-CD). We show that HFL's can provide larger coercivity (H_c) and retention (Δ) than dual-MgO. Besides, the relation of Δ and e-CD in both cases fits well with the energy barrier model based on domain wall mediated reversal (DWMR) when the CD is larger than ~30 nm. The switching characteristics of the HFL in comparison to the dual MgO free layer will be discussed. Fig.1 (a) and (b) show the schematic of the TP-MTJ stack with a HFL and an optimized dual-MgO FL, respectively. Both types of FL's have equal thickness. The corresponding resistance-field (R-H) loops after device fabrication are also shown. The switching of the free layer and reference layer (RL) is indicated, respectively. The tunnel magnetoresistance (TMR) is ~100% and the sharp steps in the R-H loops confirm PMA in both the FL and RL. From R-H loops, H_c of the HFL and dual-MgO FL can be derived. Fig.2 (a) shows the coercive field H_c of the FL obtained from the R-H loops as a function of e-CD. In both cases, H_c increases slightly with the decreasing e-CD down to around 40nm. H_c then drops for devices with 20 nm e-CD, and it is attributed to the patterning damage leading to PMA loss, which becomes more important at small CD. Note that the coercive field H_c of the HFL is for all CD's larger than those of dual-MgO FL. To derive Δ of both free layers, the field sweep method is applied [2]. R-H loops of selected devices were scanned for 100 cycles. The cumulative switching probability as a function of switching field is fitted by existing magnetization reversal models, which provides intrinsic Δ after offset correction [3]. For small devices, the macrospin model is used for fitting and Δ derivation [4]. Results are plotted in Fig.2 (b). Indeed, the Δ values from both types follow quadratic relation with CD in small e-CD range (<40nm) based on the macrospin model. However, the Δ values of larger devices from macrospin model fitting deviate a lot from the expected quadratic relation between Δ and CD (not shown). It is thus natural to expect that Δ in large devices is determined by a DWMR model, whose principle is illustrated briefly in the insert in Fig.2 (b) [4.5]. The Δ values increase linearly with CD larger than 40nm in agreement with the DWMR model, where the intrinsic Δ is purely determined by the domain wall energy when the domain wall sits along the center of the device, i.e. $\Delta=\sigma_{dw}l_{dw}t/k_BT=\sigma_{dw}Dt/k_BT$. Here D is the diameter or CD of the device and t is the FL thickness. Note that also in the DWMR regime, the Δ values for the dual-MgO FL are lower than for the HFL. That indicates that the domain wall formation in HFL requires more energy than in dual-MgO, which is attributed to its higher PMA. On the other hand, one may argue that the critical dimension (d_c) of the transition between macrospin and domain wall formation of HFL is smaller than that of dual MgO FL due to smaller A_{ex} and larger K_U^{eff}. Because d_c can be estimated as $d_c \propto (A_{ex}/K_U^{\mathrm{eff}})^{½}$, where A_{ex} is the exchange stiffness and K_U^{eff} is the FL effective anisotropy. The transition from macrospin to domain wall reversal occurs earlier for the HFL than for its dual-MgO counterpart. However, one should note that, even in the macrospin regime, HFL devices perform better due to higher H_c and Δ. In conclusion, the HFL can provide large H_c and Δ in devices down to the macrospin regime. Due to its Δ tunability via [Co/Ni] bilayer increase, it can clearly outperform dual MgO FL's. Experimental results of Δ with respect to e-CD can be fitted by a domain wall based energy barrier model down to 30nm e-CD. At smaller e-CD, macrospin switching occurs. Electrical switching, however, could not be realized before dielectric breakdown in HFL devices and needs further research. Previous study showed that the interlayer exchange coupling (IEC) through the spacer layer in the HFL strongly impacts the switching current [6]. Therefore, HFL optimized for low current switching could be achieved with new spacer materials.

[1] Liu, *et al.* Appl. Phys. Lett. 108, 132405 (2016). [2] Tillie, *et al.* IEDM 27.3 (2016). [3] Thomas, *et al.* J. Appl. Phys. 115, 172615 (2014) [4] Thomas, *et al.* IEDM 26.4 (2015) [5] Chaves-O'Flynn, *et al.* Phys. Rev. Appl. 4, 024010 (2015) [6] Liu, *et al.* IEEE Trans. Mag. 53 (11), 3401305 (2017)

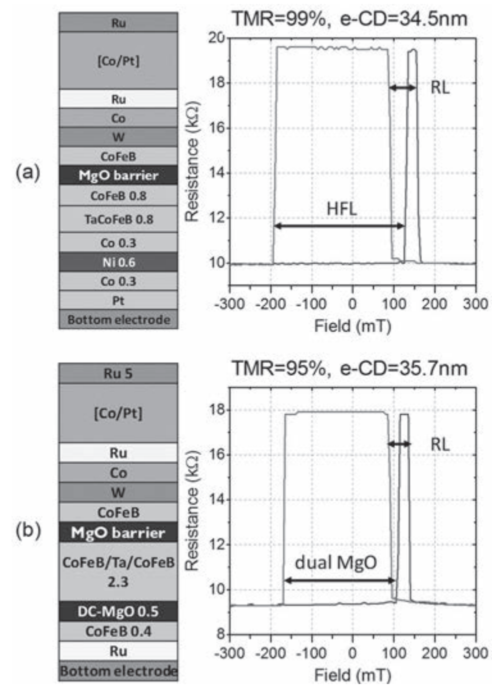

Fig. 1. Schematics of TP-MTJ stacks with different FL design and the corresponding R-H loop from devices with certain e-CD: (a) HFL; (b) dual-MgO FL. Thickness of FL part are given in nm.

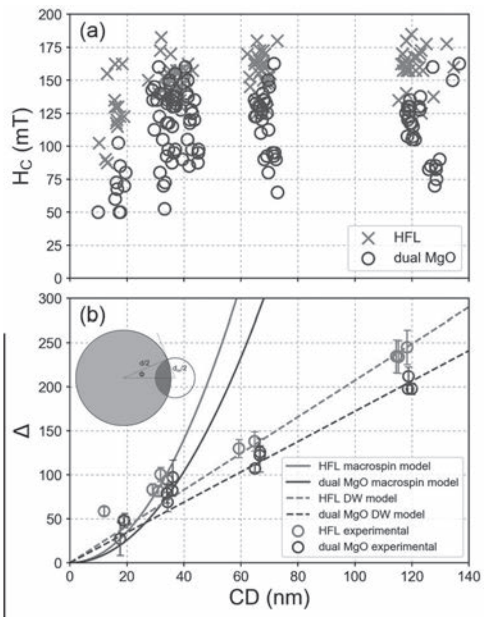

Fig. 2. (a) Hc and (b) intrinsic Δ as a function of e-CD for devices with HFL and dual-MgO FL. Insert of (b) is the schematic illustration of DWMR model for energy barrier calculation.

2:45

HC-03. X nm Magnetic Tunnel Junctions with Perpendicular Anisotropy.

K. Watanabe[1], B. Jinnai[2], S. Fukami[1,2], H. Sato[1,2] and H. Ohno[1,2]
1. RIEC, Tohoku University, Sendai, Japan; 2. CSIS, Tohoku University, Sendai, Japan

Since the discovery of a perpendicular-easy-axis CoFeB/MgO system [1] and subsequent development of double-MgO interface structures allowing double thermal stability factor [2], magnetic tunnel junctions (MTJs) have been successfully miniaturized down to 20-nm scale towards the application of them to large-scale magnetoresistive random access memory. However, there has been no technological solution to satisfy the requirements on thermal stability and switching current simultaneously at 1X and X nm generations. Here we show a new methodology utilizing a shape anisotropy to address this issue. The sign of shape anisotropy changes to positive direction at ultrafine scale by adopting relatively thick recording layer of MTJ, allowing high thermal stability. Making the thickness comparable to or greater than the diameter, we obtain perpendicular MTJs with sufficiently high thermal stability even down to X-nm scale. Moreover, because the shape-anisotropy approach does not require any special material systems, we employ a conventional MgO/FeB/MgO structure with low magnetic damping (~ 0.004), allowing spin-transfer-torque (STT)-induced switching even in X-nm MTJs having high thermal stability. The concept of *shape-anisotropy* MTJ is described as follows: In the conventional *interfacial-anisotropy* regime, the thickness of the recording layer is designed to be thin enough so that the interfacial perpendicular anisotropy energy overcomes the negative shape anisotropy, or the demagnetization, energy and achieve high enough thermal stability factor. On the contrary, the *shape-anisotropy* regime focused in this work achieves the perpendicular easy axis by increasing the thickness so that the sign of shape anisotropy changes to positive. Another feature of the *shape-anisotropy* approach is that one can employ various material systems because it is material-independent, allowing a use of low-damping materials to achieve low switching current. An analytical calculation reveals that the *shape-anisotropy* approach provides MTJs with sufficiently high thermal stability factor Δ (= E/k_BT; E is the energy barrier, k_B the Boltzmann constant, and T the absolute temperature) of more than 80 that yet can be switched by spin-transfer torque even at around 10 nm, whereas the *interfacial-anisotropy* approach cannot achieve it. Based on the analytical calculation, we fabricate MTJs with the perpendicular shape anisotropy. Similar MTJ stack structure to a previous report [3] is used except for the thickness of recording layer; Si/SiO_2-sub./ Ta(5)/ Ru(10)/ Ta(15)/ Pt(5)/ $[Co(0.4)/ Pt(0.4)]_{x6}$ /Co(0.4) /Ru(0.4) /Co(0.4) / $[Pt(0.4)/ Co(0.4)]_{x2}$ /Ta(0.2)/ CoFeB(1.0)/ MgO/ FeB(15)/ MgO/ Ru(5) (in nm). Films are deposited by dc/rf magnetron sputtering, processed into nanoscale MTJs with various nominal diameters, and annealed at 300°C for 1 hour. All the measurements are performed at room temperature. Diameter D of MTJ is electrically determined from the resistance and resistance-area product. Square hysteresis loops for MTJ resistance R versus out-of-plane magnetic field H are observed below a certain diameter D (~20 nm), indicating perpendicular easy axis owing to the shape anisotropy. Coercive field H_C increases as D decreases, due to the increasing shape anisotropy energy density. Switching probability measurement is carried out using pulsed magnetic field to evaluate effective anisotropy field H_K^{eff} and Δ [4]. H_K^{eff} increases as D decreases, in line with the trend of H_C. Importantly, as shown in Fig. 1, sufficiently high Δ of more than 80 is obtained even for X-nm MTJs unlike the previous works with the *interfacial-anisotropy* MTJs and the values are consistent with our analytical calculation. For the smallest MTJ we measure (D = 3.8 nm), D is obtained to be 73. We next examine the STT-switching using pulsed currents with 10-ms duration. Bidirectional switching at zero magnetic fields is observed for a number of MTJs with various sizes down to 8.8 nm MTJ. Switching current density J_{SW} is found to increase as D decreases, as expected from a theory that predicts increase in J_{SW} with D^{-2}. Also, the obtained values of J_{SW} roughly agree with the theoretical expectation, for instance, for 10.4-nm MTJ, switching is obtained at 3.2×10^7 A/cm^2, corresponding to J_{C0} [5] of 3.9×10^7 A/cm^2 whereas our calculation based on the STT switching model predicts $J_{C0} = 4.4 \times 10^7$ A/cm^2. In summary, we revisit the shape anisotropy of nanoscale MTJ and achieve high thermal stability and STT switching simultaneously at ultrafine scale for the first time. The present results provide a new insight for the miniaturization of MTJs for STT-MRAMs and open up the next era of nano-magnetics/spintronics [6]. This work was partially supported by R&D Project for ICT Key Technology to Realize Future Society of MEXT, ImPACT Program of CSTI, and JST-OPERA. K.W. acknowledges the Graduate Program in Spintronics, Tohoku University.

[1] S. Ikeda *et al.*, Nature Materials 9, 721-724 (2010). [2] H. Sato *et al.*, Applied Physics Letter 101, 022414 (2012). [3] H. Sato *et al.*, Applied Physics Letter 105, 062403 (2014). [4] Z. Li *et al.*, Physical Review B 69, 134416 (2004). [5] R. H. Koch *et al.*, Physical Review Letter 92, 088302 (2004). [6] K. Watanabe *et al.* Submitted.

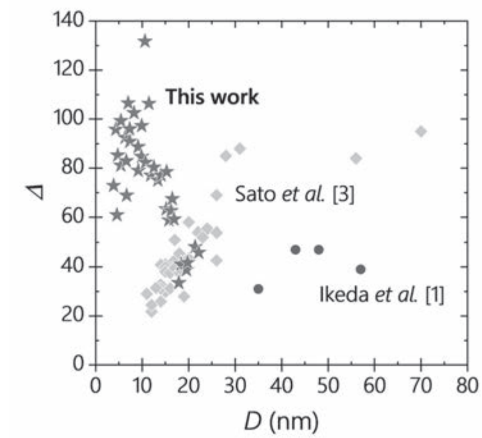

Fig. 1. thermal stability factor Δ of shape-anisotropy MTJs as a function of MTJ diameter *D* in comparison to conventional interfacial-anisotropy MTJs (Ikeda *et al.* [1], Sato *et al.* [3]).

INVITED PAPER

3:00

HC-04. Etch Process Technology for High Density STT-MRAM.

T. Endoh[1,2], S. Kang[3], T. Kudo[3] and Y. Yagi[3]
1. Center for Innovative Integrated Electronic Systems (CIES), Tohoku University, Sendai, Japan; 2. Graduate School of Engineering, Tohoku University, Sendai, Japan; 3. Tokyo Electron Ltd., Yamanashi, Japan

In information and communication technology (ICT) equipment indispensable for modern society, semiconductor memories occupy the main position of storage memories, working memories, and e-memories in logic blocks. In current semiconductor memories, rapid increase in the power consumption is most serious issue, as the more energy-saving is strongly required for ICT technology. From above view point, STT-MRAM and its application such as NV-Logic are aggressively studied in the world and many excellent results were published. However, almost results of STT-MRAM were fabricated by ion beam etch (IBE) process. Therefore, for higher density STT-MRAM's mass-production under wide patterning process margin and high TAT, plasma based reactive ion etch (RIE) process technology for MTJs is needed. In this invited paper, it is reviewed our previas results regarding STT-MRAM and NV-Logic fabricated by RIE process as shown in Fig. 1. It is shown that STT-MRAM and NV-MCU etc. were successfully worked under extremely low power consumption. Moreover, it is reviewed our previas results of RIE process technology itself. We presented process and device results from a developed chemistry set which significantly reduces the etch damage compared with conventional chemistry. An etched MTJ stack profile is included in Fig. 2. The damage caused by RIE on the magnetic properties of the CoFeB free layer in a MTJ with a perpendicular easy axis (p-MTJ), and on the TMR ratio of CoFeB–MgO p-MTJs was characterized to identify its root cause. Fig. 3 includes TMR data from a selection of different chemistry sets. Our developed chemistry is based on learning that it is N and H radicals that are the primary source of damage. With our developed process, high TMR ratio was achieved with very slight degradation. We report our chemistry, its underlying concept, resultant MTJ profiles, device electrical and magnetic properties. Finally, we summarize the MTJ damage mechanism useful for bringing MTJ fabrication etch technology to maturity. *Acknowledgements:* This work was partly supported in part by CIES's Industrial Affiliation on STT -MRAM Program and ACCEL & OPERA Program under JST.

1.S. Ikeda, K. Miura, H. Yamamoto, K. Mizunuma, H. D. Gan, M. Endo, S. Kanai, J. Hayakawa, F. Matsukura, and H. Ohno,"A perpendicular-anisotropy CoFeB–MgO magnetic tunnel junction," Nature Materials,Vol. 9,pp. 721-724,Sep. 2010. 2.T. Ohsawa, H. Koike, S. Miura, H. Honjo, K. Tokutome, S. Ikeda, T. Hanyu, H. Ohno, and T. Endoh, "1Mb 4T-2MTJ nonvolatile STT-RAM for embedded memories using 32b fine-grained power-gating technique with 1.0ns/200ps wake-up/power-off times," 2012 Symposium on VLSI Circuits, pp. 46-47, June 2012. 3.T.Endoh, T.Ohsawa, H.Koike, T.Hanyu, and H.Ohno, "Restructuring of Memory Hierarchy in Computing System with Spintronics-Based Technologies", Symposia on VLSI Circuits, pp89-90, 2012, (Invited) 4.T.Endoh, T.Ohsawa, T.Hanyu, H.Ohno, "MTJ based Non Volatile Logic for Ultimate Power Management", the 19th ICM2012 with SCES, pp5-7, 2012, (Invited) 5.T. Endoh, T. Ohsawa, S. Ikeda, T. Hanyu, N. Kasai and H. Ohno, " MTJ based non volatile SRAM and low power non volatile logic-in-memory architecture", INTERMAG 2012, 2012, (Invited) 6.T. Ohsawa, S. Miura, K. Kinoshita, H. Honjo, S. Ikeda, T. Hanyu, H. Ohno, and T. Endoh, "A 1.5nsec/2.1nsec random read/write cycle 1Mb STT-RAM using 6T2MTJ cell with background write for nonvolatile e-memories," 2013 Symposium on VLSI Circuits, pp. C110-111, June 2013. 7.T. Endoh," Spintronics Based NV-Memory/Logic for High Performance & Low Power", 2013 VLSI Technology Short Course of 2013 Symposium on VLSI, June 2013, (Invited) 8.S. Ikeda, H. Sato, H. Honjo, E. C. I. Enobio, S. Ishikawa, M. Yamanouchi, S. Fukami, S. Kanai, F. Matsukura, T. Endoh, and H. Ohno, "Perpendicular-anisotropy CoFeB-MgO based magnetic tunnel junctions scaling down to 1X nm," in Int. Electron Devices Meeting (IEDM) Tech. Dig., 2014, pp.796-799. 9.T. Enoh "Nonvolatile Logic and Memory Devices Based on spintronics", 2015 IEEE International Symposium on Circuits and Systems (Invited) 10.H. Honjo, S. Ikeda, H. Sato, S. Sato, T. Watanabe, S. Miura, T. Nasuno, Y. Noguchi, M. Yasuhira, T. Tanigawa, M. Muraguchi, M. Niwa, K. Ito, H. Ohno and T.Endoh, "Improvement of thermal tolerance of CoFeB-MgO perpendicular-anisotropy magnetic tunnel junctions by controlling boron composition.[IEEE Transactions on Magnetics,PP(99),2016 11.J. Jeong and T. Endoh, "Electric and magnetic improvements of the patterned MTJs by the damage recovery using the novel oxygen showering post-treatment (OSP) process at the argon ion milling etching (AIME) scheme", 13th Joint MMM-Intermag Conference,BT-02,2016 12.T.Endoh, H.Koike, S.Ikeda, T.Hanyu, and H.Ohno, "An Overview of Nonvolatile Emerging Memories?Spintronics for Working Memories", IEEE JESCAS,2016(Invited) 13.Tetsuo Endoh, "Novel High Performance NV-Working Memory with Spintronics and Vertical MOSFET Technology", 2016 MRS Spring Meeting&Exhibit,EP11.1.08,2016(Invited) 14.H.Koike, S.Miura, H.Honjo, T.Watanabe, H.Sato, S.Sato, T.Nasuno, Y.Noguchi, M.Yasuhira, T.Tanigawa, M.Muraguchi, M.Niwa, K.Ito, S.Ikeda, H.Ohno and T.Endoh,"Demonstration of Yield Improvement for On-Via MTJ Using a 2-Mbit 1T-1MTJ STT-MRAM Test Chip", 2016 IEEE IMW2016 15.T. Endoh, "STT-MRAM and its Application for Nonvolatile Brain-Inspired VLSIs", SEMICON CHINA(CSTIC) 2017. (Invited) 16.T. Endoh, "Embedded Nonvolatile Memory with STT-MRAMs and its Application for Nonvolatile Brain-Inspired VLSIs", 2017 International Symposia on VLSI Technology, Systems and Applications. (Invited) 17.T. Endoh, "NV-Working Memory and its Logic Applications with Spintronics and Vertical BC-MOSFET Technology", MMM2017, (Invited) 18.T. Endoh, "Embedded Nonvolatile Memory with STT-MRAMs and its Application for Nonvolatile Brain-Inspired VLSIs", 9th MRAM Global Innovation Forum 2017, (Invited) 19.S.-Y. Kang, T. Kubo and T. Endoh, "New low damage dry etching gas chemistry for MRAM device fabrication", MMM2017

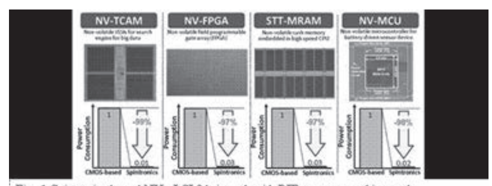

Fig. 1 Spintronics based NV -LSI fabricated with RIE p rocess and its results

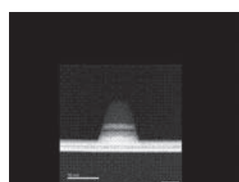

Fig. 2 TEM image of MTJ after etched by our developed chemistry set

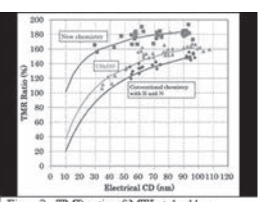

Fig. 3 TMR ratio of MTJ etched by conventional chemistry including H and N, CH_3OH, and our developed chemistry.

CONTRIBUTED PAPERS

3:30

HC-05. High thermal tolerance synthetic ferrimagnetic reference layer with modified buffer layer by ion irradiation for perpendicular anisotropy magnetic tunnel junctions.

H. Honjo[1,2], S. Ikeda[1,3], H. Sato[1,3], K. Nishioka[1,2], T. Watanabe[1,2], S. Miura[1,3], T. Nasuno[1,2], Y. Noguchi[1,2], H. Inoue[1,2], M. Yasuhira[1,2], T. Tanigawa[1,2], H. Koike[1,2], M. Muraguchi[4,2], M. Niwa[1,2], H. Ohno[3,5] and T. Endoh[1,4]
1. Center for Innovative Integrated Electronic Systems, Tohoku University, Sendai, Japan; 2. JST-ACCEL, Saitama, Japan; 3. Center for Spintronics Integrated Systems, Tohoku University, Sendai, Japan; 4. Graduate School of Engineering, Tohoku University, Sendai, Japan; 5. RIEC, Tohoku University, Sendai, Japan

The development of the magnetic tunnel junctions with perpendicular easy axis using interfacial anisotropy [1–4] (p-MTJs) has been intensively advanced toward realization of high performance spin-transfer-torque magnetoresistive random access memories (STT-MRAMs). The p-MTJs used in the STT-MRAMs are required to withstand 400°C annealing to be compatible with CMOS back-end-of-line-process. Although we have demonstrated the thermal tolerance against 400°C annealing for the free layer in the CoFeB/MgO-based p-MTJs [5], we also found variation of properties in synthetic ferrimagnetic (SyF) reference layer. We revealed that the variation was caused by the diffusion of Fe in the CoFeB reference layer toward the bottom Co/Pt pinned layer after annealing [6]. We simultaneously observed degradation of perpendicular anisotropy of the Co/Pt multi layer. Perpendicular anisotropy of Co/Pt is influenced by the Co/Pt thickness ratio, buffer layer material, and roughness [7]. In this study, we focus on modification of the buffer layer and reveal that degradation can be suppressed by employing a surface modification treatment (SMT) of the Pt buffer layer. MTJ stacks from the substrate side, Ta /Pt buffer layer/with or without SMT/ $[Co/Pt]_4$/Co /Ru/ $[Co/Pt]_2$/Co /Ta /CoFeB /MgO barrier/free layer/top electrode, were deposited on a 300-mmΦ thermally oxidized Si wafer using a DC/RF magnetron sputtering system at room temperature (Fig.1(a)). In the SMT process, the Pt buffer layer was exposed to an ion plasma. The upper layers on the Pt buffer layer were deposited without breaking the vacuum. After deposition, samples were annealed at 350 °C for 2 h or 400 °C for 1 h in vacuum without applying magnetic field. The out-of-plane magnetic moment per unit area versus magnetic field (m-H) curves of the blanket films were measured by a vibrating sample magnetometer, and the film structures were investigated by energy dispersive x-ray spectroscopy (EDX) and high-resolution X-ray diffraction (HRXRD) using Cu Ka radiation. As shown in Figs. 1(b) and 1(c), perpendicular anisotropy of the SyF reference layer without SMT degraded after 400 °C annealing, while that of the SyF reference layer with SMT hardly changed. Interestingly, after annealing at 400 °C, magnetic moment variation in the top and bottom parts of the reference layer is observed in the stack without SMT due to Fe diffusion from the CoFeB reference layer toward the bottom Co/Pt layer, as we previously reported [6]. In contrast, the magnetic moments of the top and bottom parts of the reference layer in the stack with SMT are almost the same. This indicates that Fe diffusion in the reference layer is suppressed by the SMT of the Pt buffer layer. In order to verify this hypothesis, we performed cross-sectional EDX line analysis (Fig. 2). In the stack without SMT, Fe element in the CoFeB reference layer is observed in the other layers such as the top and bottom Co/Pt multilayers after annealing at 400 °C (Fig. 2(a)), which indicates that Fe diffused toward the bottom Co/Pt layer. In contrast, in the stack with SMT, Fe element is observed only in the CoFeB layer in the as-deposited state and after annealing at 400 °C (Fig. 2(b)). These results are consistent with the variation of magnetic properties shown in Figs. 1(b) and 1(c). In order to clarify the reason for the suppression of perpendicular anisotropy degradation of the Co/Pt multilayer after 400 °C annealing by SMT, we evaluated the crystal structure of the Co/Pt multilayer using HRXRD. X-ray diffraction analysis revealed that the ions penetrated the Pt buffer layer, expanding the Pt lattice constant and enhancing Co/Pt grain growth, which well oriented to the fcc (111) closed-packed plane parallel to the substrate surface. This caused larger perpendicular anisotropy in the Co/Pt multilayer and higher thermal tolerance. In addition, this may suppress Fe diffusion from the CoFeB reference layer toward the bottom Co/Pt layer. This work is supported by CIES's Industrial Affiliation on STT MRAM program, and JST ACCEL Grant Number JPMJAC1301, Japan, and JST-OPERA.

[1] S. Ikeda et al., Nature Mater. 9, 721 (2010). [2] H. Sato et al., Appl. Phys. Lett. 99, 042501 (2011). [3] H. Sato et al., IEEE Trans. Mag. 49, 4437 (2013). [4] H. Sato et al., Jpn. J. Appl. Phys. 53, 04EM02 (2014). [5] H. Honjo et al., 2015 Symp. on VLSI Technology, *Dig. Tech. Papers*, pp. T160-T161. [6] H. Honjo et al., AIP Adv. 7, 055913 (2017). [7] Lim et al., J. Appl. Phys. 117, 17A731 (2015).

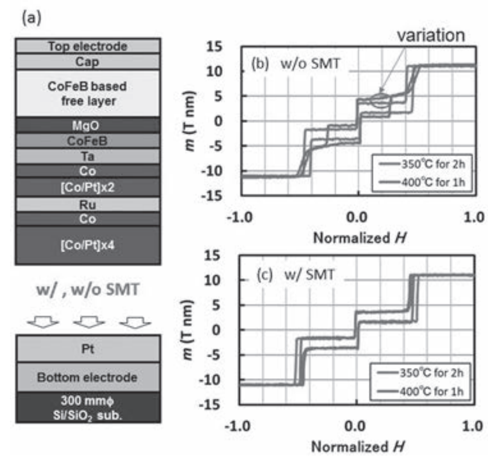

Fig. 1. (a) Schematic of stack structure. Typical out-of-plane m-H loops for MTJ stacks (b) w/o SMT and (c) w/ SMT.

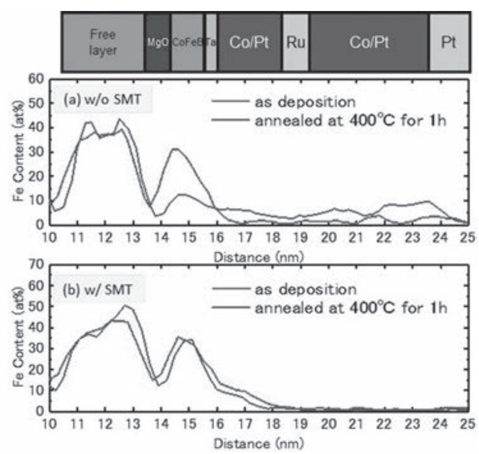

Fig. 2. EDX depth profiles of MTJ stacks (a) w/o SMT [7] and (b) w/ SMT.

3:45

HC-06. Role of Curie temperature on thermal stability limits of perpendicular STT-MRAM.

L. Tillie[1,2], R.C. Sousa[2], J. Chatterjee[2], N. Lamard[2], J. Guelfucci[2], E. Nowak[1], B. Dieny[2] and I.L. Prejbeanu[2]
1. CEA-Leti, Grenoble, France; 2. CEA-SPINTEC, Grenoble, France

Perpendicular STT-MRAM (P-STT MRAM) are seen as one of the most promising next-generation non-volatile memory thanks to their high speed[1], high endurance[2], low voltage operation[3] and high data retention at room temperature. However, using thin film changes significantly some physical parameters for the magnetic storage layer compared to bulk. One of these parameters is the Curie temperature, value at which the magnetic material loses its magnetization resulting in losing data retention. Studying this parameter remains critical in order to answer to the industrial prerequisites in temperature and the soldering reflow criterion at 260°C. In this paper, magnetic stack with different capping materials and annealing temperatures are being study in order to extract their coercive field, Curie temperature and thermal stability factor. For this study, single-MTJ stacks with a bottom SAF with different capping materials have been patterned from 20 nm up to 150 nm diameter devices. The single-MTJ films have also been deposited with two wedges: one in the vertical direction for the storage layer and one in the horizontal direction for the oxide barrier resulting in different thicknesses on the same wafer. The deposited stacks are as follow (in Å): Ta 30/ Ru 150/ W 30/ Ta 10/ Pt 50/ [Co 5/ Pt 2.5/]$_6$/ Co 5/ Ru 9/ [Co 5/ Pt 2.5/]$_3$/ Co 5/ Ta 3/ $Fe_{72}Co_8B_{20}$ 11.4/ MgO *wedge*/ $Fe_{72}Co_8B_{20}$ *wedge*/ *Cap* / Ta 10/ Pt 20 where *Cap* is either nothing or W 20. The Ta-capped stack has been annealed at 350°C for 30min while W-capped wafers have been annealed at 425°C and 450°C. Due to setup limitations in temperature, the Curie temperature had to be extracted through the coercive field Hc decrease in temperature using the Neel-Brown equation [4]: Hc (T) = Hc (T = 0 K)*(1-√ (T / Tb)) (1) Where Tb is the blocking temperature, value at which the data retention of the system is of the order of the measurement time meaning that the blocking and Curie temperature are equal when the measurement time tends to 0s. In our case, the measurement time is ~70µs, making the blocking temperature close to the Curie temperature. Using this method, the blocking temperature for the single-MTJ stacks have been measured and plotted in Fig.1a as a function of the storage layer thickness. For these wafers, the storage layer's magnetization is perpendicular in the thickness range of 13 Å to 18 Å. In this range, the blocking temperature shows a linear behavior versus the thickness. The measured values are significantly lower than the bulk values (~770°C for Fe and 1115°C for Co [5]) but relatively of the same value for the same storage layer's thickness of the different stacks. However, The W-capped stack with a 425°C annealing (W425) shows higher blocking temperature values due to its higher values of thickness. This shows that the capping material does not have a significant impact on the Curie temperature of the storage layer but its magnetic surface anisotropy allows different range of storage layer thickness and so, different Curie temperature values. In Fig.1b, the coercive field extracted at room temperature shows a non-linear behavior on the perpendicular-thickness range. As shown, W425's coercive field first increases up to 550 Oe at 15.2Å and then decreases beyond this thickness value until the magnetization goes in-plane. The constant increase of the Curie temperature with thickness and the decrease of the coercive field beyond 15.2Å show a trade-off between the working temperature limit and the magnetic immunity of the memory device for large thicknesses. Fig.2 shows the thermal stability extracted electrically using the method used in our group [6] from 40°C up to 190°C for the W425 devices with a storage layer of 13.4Å and 14.3Å. For both thicknesses, all the devices lose their data retention around the same temperature value (170°C and 200°C), independently of their diameter while the thermal stability factor inceases with diameter at room temperature. The 0.9Å increase in the storage layer thickness also shows an increase of ~10% in the thermal stability factor at room temperature allowing the 20nm diameter devices to appear for the 14.3Å storage layer thickness. In conclusion, we measured the coercive field in temperature of single-MTJ with different capping materials and annealing temperatures showing that the Curie temperature is linear with the storage layer thickness between 13 Å and 18Å and does not depend directly on the capping material. However, W as capping material allows a larger storage layer thickness and higher coercive field than Ta. A 450°C annealing temperature for W-capped stacks improves magnetic surface anisotropy and coercive field compared to 425°C. We also saw that the coercive field is increasing and then decreasing with the storage layer's thickness, inducing a trade-off between high working temperature and magnetic immunity when increasing the thickness. At last, thermal stability measurements showed that the device diameter does not influence on the Curie temperature and that a thicker storage layer increases data retention.

[1] J.J. Kan et al., IEDM Tech Dig., 2016 [2] J.M. Slaughter et al., IEDM Tech. Dig., 2016 [3] G. Jan, L. Thomas, S. Le, Y.-J. Lee et al. VLSI Tech Dig., pp. 18, 2016 [4] M. El-Hilo et al, Jour. of Magn. and Magn. Mat., 1992 [5] Charles Kittel, 1976. Introduction to Solid State Physics (8th). John Wiley & Sons, Inc., New York. p.328. [6] L. Tillie et al., IEDM Tech. Dig., 2016

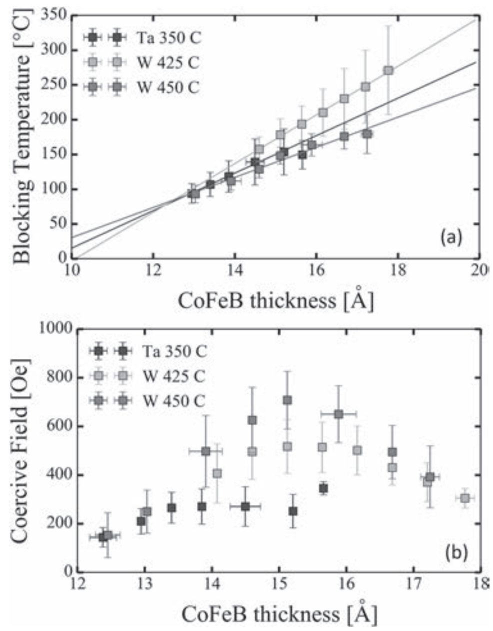

Fig. 1. (a) Blocking temperature and (b) coercive field at room temperature extracted from magnetic stacks with a capping material such as Tantalum (blue) and Tungsten with an annealing temperature of 425°C (yellow) and 450°C (red) as a function of the storage layer thickness.

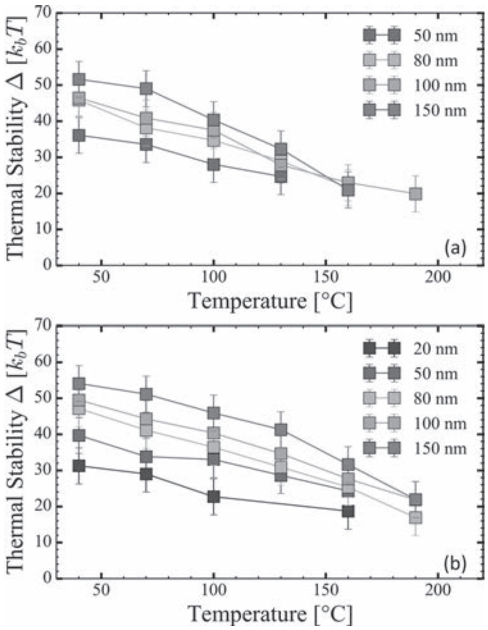

Fig. 2. Thermal stability extracted electrically up to 190°C from a W-capped MTJ for diameters from 20nm up to 150nm showing the same working temperature limit for a free-layer with a thickness of 13.4Å (a) and 14.3Å (b).

4:00

HC-07. Back hopping in spin-transfer-torque devices, possible origin and counter measures.

C. Abert[1], H. Sepehri-Amin[2], F. Bruckner[1], C. Vogler[1], M. Hayashi[2] and D. Suess[1]
1. Physics of Functional Materials, University of Vienna, Vienna, Austria; 2. National Institute for Materials Science (NIMS), Tsukuba, Japan

Spin-transfer torque magnetoresistive random-access memory (STT MRAM) is considered a very promising future data storage technology as it combines the high speed of conventional DRAM with a very low power consumption due to its persistent nature. These devices consist of two magnetic layers separated either by a tunnel barrier or a nonmagnetic conducting layer. The information is stored in the magnetization direction of one of the magnetic layers (free layer). In order to write data, an electric current is applied perpendicular to the layer structure. In this case, the second layer acts as a spin polarizator and the spin-polarized electrons exert a torque on the free-layer magnetization which enables the selective switching of the free layer depending on the sign of current. The polarizing layer is often referred to as pinned layer as it is constructed to be very hard magnetic in order to be insensitive to the polarized electrons coming from the free layer. In order to switch the free-layer magnetization, a critical current has to be exceeded. A further increase of the write current is expected to further stabilize the free layer so that the write process should be robust with respect to the exact writing current and duration as long as both are high enough. However, experiments exhibit a stochastic switching of the free layer under certain conditions [1]. This back-hopping effect was observed in various devices including in-plane and perpendicularly magnetized MRAM stacks as well as devices with tunnel junctions and conducting spacer layers. Various explanations for this undesirable effect have been proposed [2]. In this work we investigate the destabilization of the magnetic pinned layer as a possible origin of the back-hopping effect by means of micromagnetic simulations. For the description of the spin torque we use the spin-diffusion model introduced by Zhang, Levy and Fert [3]. In contrast to the popular macro-spin model by Slonczewski, this models properly accounts for geometry and material parameters as well as the bidirectional interaction of the free layer with the pinned layer. Hence, this approach allows us to study the critical currents for both, desired free-layer switching as well as back hopping due to pinned-layer switching, depending on various system parameters. Moreover we perform thermally activated simulations using Langevin dynamics in order to confirm the stochastic nature of the free-layer switching as well as the giant-magnetoresistance (GMR) signal of the stack as found experimentaly, see Fig. 1. A trivial measure to suppress back hopping due to pinned-layer destabilization is the increase of the pinned-layer anisotropy. However, the reduction of lateral MRAM size in order to increase the storage density introduces significant restrictions on the maximum anisotropy of the pinned layer. Our parameter studies indicate that also the saturation magnetization Ms and the polarization β have significant impact on the critical currents of the system. Namely, it is found that the choice of a free-layer material with low polarization β and saturation magnetization Ms, and a pinned-layer material with high β and Ms lead to a low free-layer critical current and a high pinned-layer critical current and thus reduce the likelihood of back hopping, see Fig. 2.

[1] Sun, J. Z., et al. "High-bias backhopping in nanosecond time-domain spin-torque switches of MgO-based magnetic tunnel junctions." Journal of Applied Physics 105.7 (2009): 07D109. [2] Skowronski, Witold, et al. "Backhopping effect in magnetic tunnel junctions: Comparison between theory and experiment." Journal of Applied Physics 114.23 (2013): 233905. [3] Zhang, Shufeng, P. M. Levy, and A. Fert. "Mechanisms of spin-polarized current-driven magnetization switching." Physical review letters 88.23 (2002): 236601.

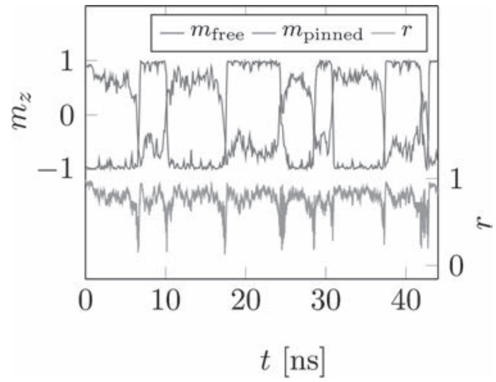

Fig. 1. Free-layer and pinned-layer magnetization dynamics at finite temperature in the back-hopping regime along with the normalized GMR signal of the stack r.

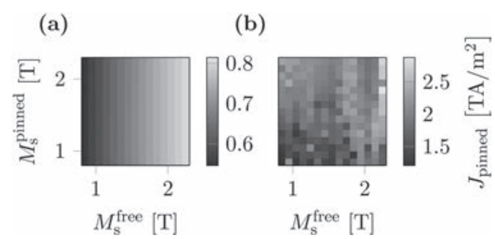

Fig. 2. Critical current densities for the switching of the (a) free layer and the (b) pinned layer depending of the saturation magnetization in the respective layers.

4:15

HC-08. Spin Transfer Torque efficiency enhancement utilizing precessional spin current (PSC) structure for STT-MRAM application.

M. Pinarbasi[1], B. Kardasz[1], G. Wolf[1], J. Vasquez[1], S. Watts[1], T. Boone[1], J. Hernandez[1], K. Bozdag[1], D. Guarisco[1], M. Schabes[1], P. Manandhar[1], E. Dobisz[1], P. Shrivastava[1], Y. Chin[1], E. Ryan[1] and G. Jagtiani[1]
1. Spin Transfer Technologies Inc., Fremont, CA, United States

In this work we report a significant enhancement of the spin transfer torque efficiency in a novel type of Spin Transfer Torque Magnetic Random Access Memory (STT-MRAM) that utilizes a precessional spin current (PSC) structure. STT-MRAM is considered the upcoming new memory class with the potential to fulfill the needs of modern memory applications [1, 2]. STT-MRAM distinguishes itself as an advantageous technology due to its non-volatility, high speed and high endurance. However, in conventional STT-MRAM based on perpendicular magnetic tunnel junctions (pMTJ) the retention of a memory bit is fundamentally coupled to the write current [3], such that higher retention requires higher write current, thereby increasing the energy consumption and reducing the endurance. Even in the case of high speed cache memories where a high retention is not necessarily required, it is important to consider that low retention can also result in a higher probability of data disturbance during the read operation. The spin transfer torque efficiency - the ratio of the thermal energy barrier over the critical write current - is a key pMTJ parameter. The PSC structure comprises a spacer/coupling and magnetic layers deposited on top of the free layer of the pMTJ. Here we describe a pair of pMTJ structures where one features the PSC structure, while the other one, is a pMTJ only structure, which serves as control. All structures were fabricated by depositing the MTJ stacks onto CMOS wafers and formed into multiple 4kbit memory test chips with the Spin Transfer Technologies BEOL process. Fig. 1 shows the average spin torque efficiency extracted from pulsed switching experiments for three different diameters of the MTJ pillar, 40, 50, and 60nm. Both the pMTJ only (blue dots) and PSC stacks (red triangles) show an increasing STT-efficiency as the size of the pillar decreases, a well-described trend [4]. However, the PSC structure shows an enhanced STT-efficiency over the comparison pMTJ structure, and the enhancement gets even larger as the size of the pillar decreases. The STT-efficiency enhancement is largely attributed to an increase in the energy barrier up to 30%, while the switching current remains the same as in the pMTJ structures. Moreover we observed that the STT-efficiency enhancement is robust over a wide range of temperatures relevant for modern memory applications. Fig. 2 shows the energy barrier for the pMTJ only (blue dots) and PSC (red triangles) for temperatures of 30°C, 85°C and 125°C for 40nm pillar size. The energy barrier of the PSC structure is significantly larger than the comparison pMTJ even at elevated temperatures, with both PSC and comparison pMTJ showing a similar trend as a function of temperature. Conventional thermal retention experiments at high temperature show much lower error rates for the PSC structures compared to the pMTJ reference, confirming the higher energy barrier in the PSC obtained from the current switching experiments. This achievement shows that the PSC structure brings important advantages to MRAM technology. It allows to achieve higher data retention while keeping the write current the same. The effect tends to get better as the size of the pillar is decreased. Furthermore the effect can also be utilized to increase the read current for better signal to noise ratio as the device size gets smaller and faster read times, by directly reducing the read disturb error rate.

[1] A. D. Kent et al. Nature Nanotechnology 10, 187 (2015). [2] S. H. Kang et al. 2014 symposium on VLSI Technology Digest of Technical Papers, 1 (2014). [3] A. V. Khvalkovskiy et al. Jour. Phys. D 46, 139601 (2013). [4] J. Z. Sun et al. Phys. Rev. B 88, 104426 (2013).

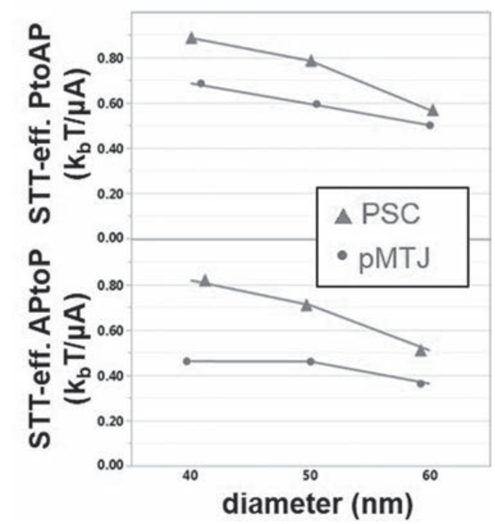

Fig. 1. Average spin transfer torque efficiency for as a function of pillar size for the two switching directions PtoAP (top) and APtoP (bottom). Red triangles mark PSC structures, blue dots mark pMTJ only structures. Lines are guide to the eye.

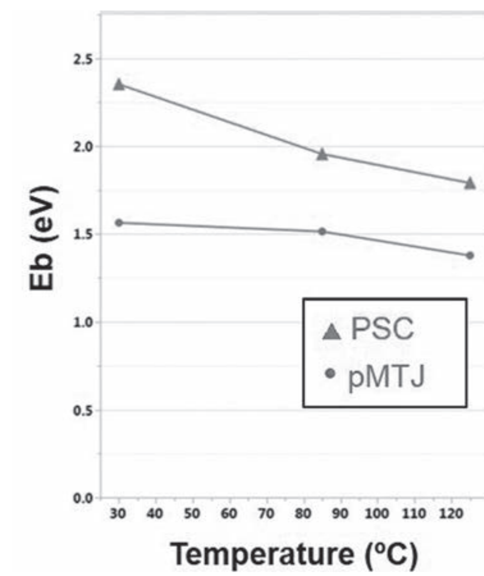

Fig. 2. Average energy barrier extracted from pulsed switching experiments for various temperatures for 40nm pillar size. Red triangles mark PSC structures, blue dots mark pMTJ only structures. Lines are guide to the eye.

4:30

HC-09. Polar Coding for Spin-Torque Transfer Magnetic Random Access Memory (STT-MRAM).

Z. Mei[1], K. Cai[1] and B. Dai[2]
1. Singapore University of Technology and Design, Singapore, Singapore; 2. Beihang University, Beijing, China

I. INTRODUCTION Spin-torque transfer magnetic random access memory (STT-MRAM) has emerged as a promising non-volatile memory (NVM) technology with various potential applications such as working as the embedded NVM or replacing the stand alone DRAM [1]. However, STT-MRAM suffers from process variations and thermal fluctuations, leading to both the write errors and read errors [2]. Hence it is critical to construct effective error correction codes (ECCs) to improve the system reliability. A single-error-correcting (71, 64) Hamming code is adopted by Everspin's 16Mb MRAM [3]. Extended Hamming codes with hybrid decoding are further proposed for STT-MRAM for the purpose of replacing DRAM [2]. Multiple-error-correcting BCH codes as well as low-density parity-check (LDPC) codes have also been investigated for STT-MRAM [4], for applications with relaxed requirement of the read latency. In this work, we propose, for the first time, the design and optimization of polar codes [5] for the STT-MRAM channel. Compared with LDPC codes with short code lengths, polar codes can achieve better error performance with lower decoding complexity. Moreover, polar codes allow easy adjustment of the code rates with a single encoder/decoder, which is a significant advantage over the Hamming codes and BCH codes. Such rate-compatible property can mitigate the raw bit error rate (BER) diversity of STT-MRAM cells caused by process variations. II. POLAR CODING FOR STT-MRAM For the two typical code construction methods of polar codes, the heuristic method [6] can achieve the capacity of the binary erasure channel (BEC), while the density evolution (DE) method [7] is proposed for the binary memoryless symmetric channel. In this work, we first show that polar codes constructed by using the heuristic method cannot achieve satisfactory performance since the STT-MRAM channel is significantly different from the BEC channel. Moreover, as the STT-MRAM channel is asymmetric by nature [2], we further propose a novel approach to 'symmetrize' the channel, based on which we can construct effective polar codes by using the DE method. Next, we propose rate-adaptive polar coding scheme in conjunction with adaptive decoding to further combat the channel raw BER diversity. During encoding, by adding/deleting certain number of information bit-channels based on the reliabilities of the polarized bit-channels, the code rate of polar code can be easily adjusted with a single encoder. Various decoding algorithms of polar codes are also investigated, such as the original successive cancellation (SC) algorithm, the SC-Flip algorithm, and the cyclic redundancy check (CRC)-aided SC-list (CA-SCL) algorithm. We further present and demonstrate that the adaptive SCL (AD-SCL) algorithm can achieve the best trade-off between the performance and complexity for the STT-MRAM channel. III. SIMULATIONS AND COMPLEXITY ANALYSIS Based on the STT-MRAM channel model proposed by [2], the simulations assume a write error rate of 10^{-4}, and vary the mean normalized resistance spread $\sigma_0/\mu_0=\sigma_1/\mu_1$ of the low and high resistances of STT-MRAM, to account for the influence of different process variations on the read decision error. A 3-bit capacity-maximizing quantizer [2] is used in all simulations of polar codes and the LDPC code. In Fig. 1, the central bunch of curves shows the block error rates (BLERs) of different ECCs with a similar code rate of R≈0.86. The capacity of the rate 0.86 code for the STT-MRAM channel is also included as a reference. Observe that the (256, 220) polar code with different decoders all perform significantly better than the (255, 223, 4) BCH code with hard-decision decoding. In particular, with the SC decoder, polar code constructed using DE after 'symmetrizing' the channel outperforms that constructed using the heuristic method by 0.5% in terms of the resistance spread σ_0/μ_0, at BLER=10^{-4}. Hence polar codes are constructed by DE in all the other simulations. We further observe that among various decoding algorithms, the AD-SCL with maximum list size L_{max}=256 (Curve 8) achieves the best performance, and the BLER is similar to the CA-SCL decoder with list size of 16 (Curve 7) at low error rate regions. It also outperforms the (336, 285) LDPC code [4] with the reliability-based min-sum (RB-MS) decoder by 1.2% of σ_0/μ_0. Moreover, with the best performance AD-SCL decoder, the BLERs of a rate 0.95 and rate 0.77 polar codes (Curves 9 and 10) are also illustrated in Fig. 1. They enable the system to work with different levels of resistance spread (i.e. process variations) as compared to the rate 0.86 case (Curve 8), with a single encoder/decoder. This demonstrates the advantage of the proposed rate-adaptive polar coding scheme to tackle the raw BER diversity of STT-MRAM. We also analyzed the computational complexities of the BCH code, LDPC code, and polar code with different decoders. The various complexities normalized to that of the SC decoder are presented in Fig. 2, for the case of R≈0.86. Observe that at small σ_0/μ_0 regions where the BLER is low, the complexity of the AD-SCL decoder converges to that of the SC decoder, which is lower than the complexities of both the BCH decoder and LDPC decoder. This indicates that the AD-SCL decoder of polar codes achieves the best compromise between performance and complexity for the STT-MRAM channel. Acknowledgement:This work is supported by Singapore MOE Academic Research Fund Tier 2 MOE2016-T2-2-054.

[1] M. Hosomi, H. Yamagishi, T. Yamamoto, K. Bessho, Y. Higo, K. Yamane, H. Yamada, M. Shoji, H. Hachino, C. Fukumoto et al., "A novel nonvolatile memory with spin torque transfer magnetization switching: spin-ram," in *Electron Devices Meeting, IEDM Technical Digest. IEEE International*. IEEE, 2005, pp. 459–462. [2] K. Cai and K. A. S. Immink, "Cascaded Channel Model, Analysis, and Hybrid Decoding for Spin-Torque Transfer Magnetic Random Access Memory (STT-MRAM)," *IEEE Trans. Magn.*, vol. 53, no. 11, pp. 1-11, Nov. 2017. [3] https://www.everspin.com/file/162/download [4] K. Cai, Z. Qin, and B. Chen, "Channel capacity and soft-decision decoding of LDPC codes for spin-torch transfer magnetic random access memory (STT-MRAM)", *Journal of Communications*, vol. 8, no. 4, pp. 225-232, April 2013. [5] E. Arikan, "Channel Polarization: A Method for Constructing Capacity-Achieving Codes for Symmetric Binary-Input Memoryless Channels", *IEEE Trans. Inform. Theory*, vol. 55, no. 7, pp. 3051-3073, 2009. [6] E. Arikan, "A Performance Comparison of Polar Codes and Reed-Muller Codes", *IEEE Commun. Lett.*, vol. 12, no. 6, pp. 447–449, 2008. [7] R. Mori and T. Tanaka, "Performance of polar codes with the construction using density evolution," *IEEE Commun. Lett.*, vol. 13, no. 7, pp. 519–521, 2009.

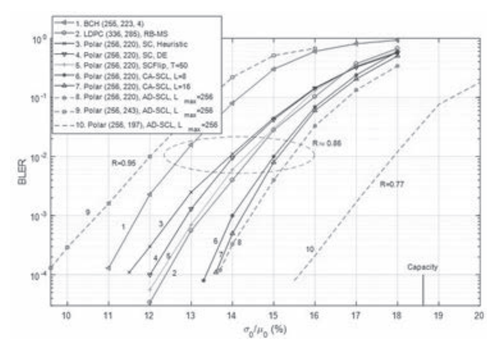

Fig. 1. BLER comparison of different codes and decoders.

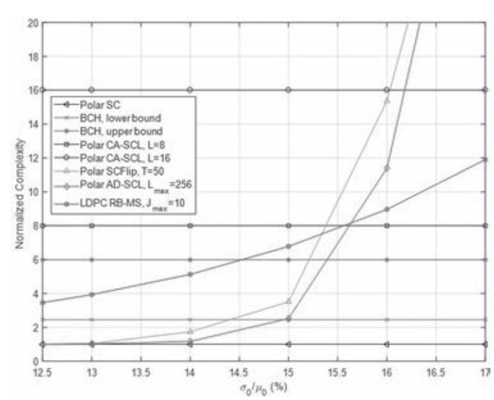

Fig. 2. The normalized complexity of different decoders, with R≈0.86.

4:45

HC-10. Effect of free-layer size on magnetic properties in nanoscale magnetic tunnel junctions.

M. Shinozaki[1], *J. Igarashi*[1], H. Sato[2,3] and H. Ohno[1,3]
1. Research Institute of Electrical Communication, Tohoku University, Sendai, Japan; 2. Center for Spintronics Research Network, Tohoku University, Sendai, Japan; 3. Center for Spintronics Integrated Systems, Tohoku University, Sendai, Japan

CoFeB/MgO-based magnetic tunnel junctions (MTJs) with a perpendicular easy axis are critical building block in spintronics-based non-volatile memories.[1,2] The CoFeB/MgO-based MTJs at junction diameter of less than 20 nm is now being developed.[3,4] In such a small dimensions, magnetic properties could alter during device-processing;[5-7] the magnetic-field-angle dependence of coercivity combined with micromagnetic simulation suggested that effective magnetic anisotropy field H_K^{eff} of the free-layer with the size of ~ 20 nm decreases at the vicinity of the device edge, depending on the device-processing condition.[5] H_K^{eff} and damping constant a are the two important material parameters as those determine intrinsic critical current and thermal stability factor, which are the two major metrics characterizing the MTJs. Homodyne-detected ferromagnetic resonance (FMR) is powerful tool to probe H_K^{eff} and a of the free layer in the nanoscale MTJs.[8-11] In this study, we investigate the dependence of the effective magnetic anisotropy field and damping constant on the free-layer size in the nanoscale CoFeB/MgO MTJs down to the free-layer size of 15 nm using the homodyne-detected FMR. A stack with the structure, from the substrate side, Ta(5 nm)/ PtMn(20 nm)/ Co(2.6 nm)/ Ru(0.9 nm)/ CoFeB(2.4 nm)/ MgO(1.1 nm)/ CoFeB(1.8 nm)/ Ta(5 nm)/ Ru(5 nm) is deposited on a sapphire substrate by dc/rf magnetron sputtering. Numbers in parentheses are nominal thicknesses in nm. The stack is processed into circular MTJs on a coplanar waveguide by electron beam lithography, reactive ion etching, and Ar ion milling. We fabricate the two types of MTJs with various free-layer sizes D; one has the reference layer much larger than the free-layer size (step structure), and the other has almost the same reference layer size as that of the free-layer (standard structure). The process conditions for the two types MTJs are the same as those employed in the previous study.[5] The free-layer size is varied from 15 to 150 nm. After fabricating the MTJs, the MTJs are annealed at 300°C in vacuum for 2 hours under an in-plane magnetic field of 1.2 T. The 1.8-nm-thick CoFeB layer is the free layer with a perpendicular easy axis. The synthetic ferrimagnetic structure is adopted to the reference layer with an in-plane easy direction. This non-collinear magnetization configuration allows us to detect the FMR spectra of the free layer under the perpendicular magnetic field H_{perp}.[11] We measure the homodyne-detected FMR spectra by sweeping the H_{perp} at several rf frequencies f_{rf} using the same setup used in Ref. 11. The amplitude of the rf signal is fixed to be -25 dBm, which is modulated at 273 Hz for lock-in detection. The typical FMR spectrum for both structures with D = 80 nm and f_{rf} = 6 GHz is shown in Fig. 1. In the spectrum, resonance peak observed at m_0H_{perp} = 125 – 150 mT corresponds to uniform ferromagnetic resonance mode (Kittel mode) and the other peaks observed at a lower m_0H_{perp}, which are not focused in this study, correspond to spin-wave resonance mode.[12,13] The spectrum can be fitted by superposition of the symmetric and antisymmetric Lorentz function, from which we obtain resonance field H_R and linewidth DH. H_K^{eff} is determined from the intercept on horizontal axis of a linear fit to f_{rf} versus resonance field and a is determined from slope of a liner fit to DH versus f_{rf}. Fig. 2 shows the free-layer size dependence of H_K^{eff} for both structures. In case of the step structure, H_K^{eff} monotonically increases with decreasing D, which can be explained by decrease (increase) of demagnetization factor along out-of-plane (in-plane) direction. On the other hand, in case of the standard structure, H_K^{eff} does not increase in a monotonic manner and the increasing rate of H_K^{eff} with respect to D is smaller than the step structure. The dependence of H_K^{eff} on D for the step structure can be well reproduced as blue curve shown in Fig. 2 where we take into account variation of demagnetization factor with respect to D assuming that anisotropy field H_K and spontaneous magnetization M_S (1.39 T determined by magnetization measurement) is intact during the device-processing. On the other hand, to reproduce the results for the standard structure, we need to consider a decrease of H_K^{eff} at the vicinity of the device edge as shown in inset of Fig. 2. In Fig. 2, the calculation result using edge width w of 4 nm and the reduction rate for H_K^{eff} at the edge h of 0.1 is shown as orange curve, which is in good agreement with the experimental results. The results indicate that the anisotropy field of the free layer depends on the device-processing condition. In contrast to the free-layer size dependence of H_K^{eff}, the damping constant shows almost constant value down to D = 15 nm regardless of the structures, indicating that the damping constant is not sensitive to the device-processing condition. This work was supported in part by the R&D Project for ICT Key Technology of MEXT, ImPACT program of CSTI, and JST-OPERA. J. I. acknowledges the support from GP-Spin.

1) H. Ohno, *et al.,* IEDM, Tech. Dig. 2010. p. 218. 2) S. Ikeda, *et al*., Nat. Mater. 9, 721 (2010). 3) H. Sato, *et al*., Appl. Phys. Lett. 105, 062403 (2014). 4) J. Z. Sun *et al*., Phys. Rev. B 88, 104426 (2013). 5) J. Igarashi, *et al*., Appl. Phys. Lett. 111 132407 (2017). 6) J. M. Shaw *et al*., Phys. Rev. B 78, 024414 (2008). 7) T. Shimatsu *et al*., J. Appl. Phys. 111, 07B908 (2012). 8) A. A. Tulapurkar *et al*., Nature (London) 438, 339 (2005). 9) H. Kubota *et al*., Nat. Phys. 4, 37 (2008). 10) J. C. Sankey et al., Nat. Phys. 4, 67 (2008). 11) M. Shinozaki, *et al*, Appl. Phys. Express 10, 013001 (2017). 12) C. J. Safranski, *et al*., Appl. Phys. Lett. 109, 132408 (2016). 13) T. Dohi *et al*., Appl. Phys. Lett. 111, 027403 (2017).

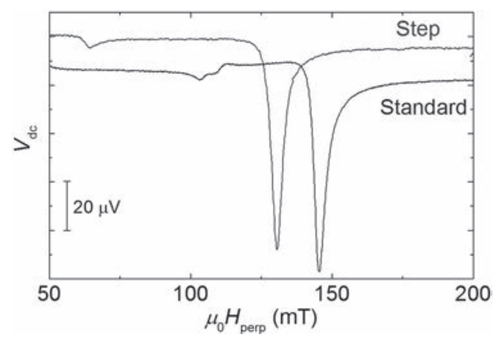

Fig. 1. Homodyne-detected ferromagnetic resonance spectrum with the step and standard structures. The free-layer size is 80 nm.

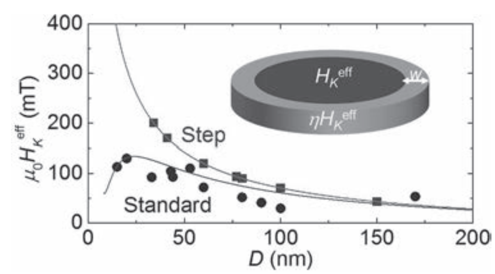

Fig. 2. Free-layer size *D* dependence of effective perpendicular anisotropy field with the step and standard structures. In the figure, the symbols correspond to the experimental results and the solid curves to fitting and calculation results. The width of edge and reduction rate of H_K^{eff} are defined as shown in inset.

FRIDAY AFTERNOON, 27 APRIL 2018 PEONY IV, 2:00 TO 5:00

Session HD

SPIN INJECTION AND TRANSPORT

Cheng Song, Chair

Tsinghua University, Beijing, China

CONTRIBUTED PAPERS

2:00

HD-01. Enhanced spin relaxation and spin-to-charge conversion at the surface of Cu thin film decollated with molecules.

S. Takizawa[1], K. Kondou[2], H. Isshiki[1], K. Shimose[3], T. Kawabe[3], S. Miwa[3] and Y. Otani[1,2]

1. ISSP, The University of Tokyo, Kashiwa, Japan; 2. CEMS, RIKEN, Wako, Japan; 3. Graduate School of Engineering Science, Osaka University, Suita, Japan

The interconversion between spin and charge currents is a key ingredient in spintronics. Recently direct and inverse Edelstein effects (DEE and IEE), spin-charge currents interconversion at the Rashba interface state or the surface state of topological insulators (TIs) [1], have been drawing much attention as the qualitatively different conversion mechanism from the spin Hall effect (the bulk effect). In the IEE, the injection of the in-plane polarized spin current into the interface or the surface state gives the spin polarized electrons momenta orthogonal to their spin polarization due to the spin-momentum locking behavior which is the characteristic of the Rashba interface and the TI surface states. In this way, the spin currents are converted to the charge currents flowing in-plane. The DEE is the charge-to-spin current conversion at the interface, where the application of electric field induces the spin accumulation in the interface, and the accumulated spins diffusively propagate into the adjacent layer. Based on the above described idea, DEE and IEE have been demonstrated by using various interfaces of metals [2-4] or metal/insulator [5]. In the present study we focus metal/molecule interface as in Fig. 1(a) because of unique characters of molecules such as high permittivity, flexibility of the structure, self-assembly at metal surface, etc. We aim to demonstrate IEE at a metal/molecule interface. For this purpose, we chose lead (II) phthalocyanine (PbPc) and metal-free phthalocyanine (H_2Pc) shown in Fig. 1(b) as molecules deposited on the Cu surface. The PbPc contains a heavy metal element, lead, which is expected to contribute to the IEE because of its strong atomic spin-orbit coupling, whereas no contribution of the H_2Pc to IEE is expected, therefore can be used as a reference. The sample preparation is as follows: Firstly, bilayers consisting of 5-nm-thick $Ni_{80}Fe_{20}$ (Py) and 10- or 15-nm-thick Cu layers were grown on thermally oxidized Si substrates, and then followed by deposition of ~ 1 nm thick PbPc or H_2Pc. Finally, MgO thin film was prepared by electron-beam deposition to protect the metal/molecule interface. The multilayer fabrication method was similar to our previous paper [6]. The multilayer was patterned with a resist mask designed to leave behind a strip with dimensions of 9.5 μm×200 μm by means of Ar ion milling. A Ti (5 nm)/Au (250 nm) waveguide was structured beside the strip for exciting a ferromagnetic resonance (FMR) in the Py layer during spin pumping measurements. We measured the FMR line width for Py/Cu/PbPc and Py/Cu/H_2Pc trilayers at room temperature. The frequency dependences are shown in Fig. 2(a). For both cases, the FMR line width exhibits a linear variation with the frequency, the slope of which corresponds to the FMR damping constant. Remarkably, the slope for Py/Cu/PbPc is steeper than that for Py/Cu/H_2Pc, showing the enhanced FMR damping in Py/Cu/PbPc, which is considered due to the excess spin relaxation at the Cu/PbPc interface. Indeed, this indicates the possibility that the injected spin current can be converted to the charge current via IEE. We therefore performed spin pumping induced IEE measurement, in which the voltage along the strip was measured with sweeping the in-plane magnetic field applied perpendicular to the strip with passing 9 GHz rf current in the waveguide. The extracted symmetric components of the magnetic field H dependences of the observed voltage signals V for these two samples are shown in Fig. 2(b). A peak at the resonance frequency with relatively large amplitude of ~ 0.6 μV is observed in Py/Cu/PbPc. This spin pumping signal is attributable to the IEE at the Cu/PbPc interface because of small spin-orbit coupling in the Cu layer. On the other hand, there is no clear signal of the symmetric component in Py/Cu/H_2Pc. Considering the fact that the surface electronic state of metals is barely altered by coating with π-conjugated carbon-based molecules like benzene [7] and graphene [8], H_2Pc capping may not change the small Rashba splitting in the bare Cu surface state, and thus shows no spin pumping signal in Py/Cu/H_2Pc. In the present study, we demonstrated the first observation of IEE at a metal/molecule interface. These results envisage that the surface decollation by various molecules and their properties are potentially exploitable for both EE and IEE. For example, high permittivity of molecules may be useful to modify the interface charge distribution by applying gate voltage, which would result in the tunable conversion efficiency of IEE. We believe that our results expand the possibility of molecular spintronics. A part of this work was supported by JSPS KAKENHI (JP26103002) and Grant-in-Aid for Scientific Research on Innovative Area, ”Nano Spin Conversion Science” (Grant No. 26103002).

[1] K. Kondou *et al.*, Nat. Phys. 12, 1027 (2016). [2] J. C. Rojas Sánchez *et al.*, Nat. Comm. 4, 2944 (2013). [3] W. Zhang *et al.*, J. Appl. Phys. 117, 17C727(2015). [4] S. Oyarzún *et al.*, Nat. Comm. 7, 13857 (2016). [5] S. Karube *et al.*, Appl. Phys. Express 9, 033001 (2016). [6] T, Kawabe *et al.*, Appl. Phys. Express 11, 013201 (2018). [7] N.-T. Cuong *et al.*, Appl. Phys. Lett. 110, 131601 (2017). [8] K. Berland *et al.*, Phys. Rev. B 80, 155431 (2009).

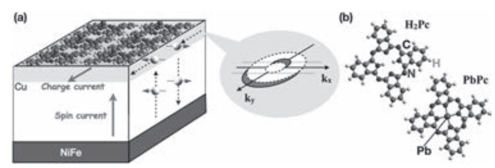

Fig. 1. (a) Schematic illustration of spin-to-charge current conversion at the Cu/PbPc interface induced by spin pumping. (b) Ball-and-stick models of PbPc and H_2Pc molecules.

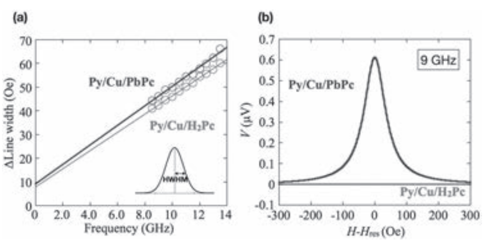

Fig. 2. (a) Frequency dependences of FMR linewidth (half width half maximum). Open circles are experimentally determined data points and solid lines are linear fitting. (b) The symmetric component to the resonance magnetic field H_{FMR} of the spin pumping induced IEE signal for Cu/PbPc and Cu/H_2Pc interfaces.

2:15

HD-02. TiO_2 as diffusion barrier at Co/Alq_3 spinterface studied by X-ray standing wave technique.

V. Phatak Londhe[1], D. Gupta[2] and N. Ponpandian[1]
1. Bharathiar University, Coimbatore, India; 2. Amity Center for Spintronic Materials, Amity University, Noida, India

Organic spintronics, a fusion of organic electronics and spintronics, represents a new research field where organic semiconductors (OSCs) are used to meditate or control the spin polarized signal. These OSCs possess extremely long spin relaxation time due to their low spin-orbit coupling.[1,2] OSCs displays immense potential in organic electronic devices such as organic light emitting diodes (OLEDs),[3,4] organic thin film transistors (OTFTs),[5,6] and organic photovoltaic devices (OPVs),[7,8] owing to their long spin coherence time, electronic as well as structural flexibility and low production costs. The most fundamental form of organic spintronic device is organic spin valve (OSV), which consists of an organic semiconductor spacer sandwiched between two ferromagnetic (FM) electrodes. In OSV, the charge carriers are injected into the OSC across the ferromagnetic/organic interface (FM/OSC), generally termed as spinterface, *via* thermal and field assisted charge tunneling.[9] Co/Alq_3 [{tris-(8- hydroxyquinoline) Aluminium}] spinteraface has been utilized more than any other FM/OSC combination for magneto-electronic applications.[10-14] The key issue in vertical organic spin valve with Co/Alq_3 spinterface is interfacial diffusion *i.e.* penetration of Co atoms from the top Co electrode to the soft organic layer of Alq_3 during the thin film deposition. One of the methods to elude this interfacial diffusion is to use a tunneling barrier as a spin filter. Nano-scale diffusion at the spinterfaces in organic spin valve thin films plays a vital role in controlling the performance of magneto-electronic devices. In the present work, role of a thin barrier layer of TiO_2 on interfacial diffusion at Co/Alq_3 spinterface was studied non-destructively using x-ray standing wave technique. Two waveguide structures: Si (100) (substrate) / Co (9.1 nm) / Alq_3 (40.1 nm) / Co (8.4 nm) and Si (100) (substrate) / Co (11.3 nm) / TiO_2 (1.7 nm) / Alq_3 (37 nm) / Co (8.5 nm), designated as OSV_SW1 and OSV_SW2 respectively, were deposited in a high-vacuum electron beam (EB) evaporation chamber containing interconnected homemade thermal evaporation (TE) set up for the growth of organic material. Top and bottom Co layers form the walls of the planer waveguide while Alq_3 layer forms the guiding layer. X-ray reflectivity (XRR) was used to find the roughness at Co/Alq_3 spinterface. Figure 1 (A) shows X-ray reflectivity of OSV_SW1 film measured using Cu K_α radiation. The reflectivity pattern exhibits sharp dips at q = 0.27, 0.34, 0.45, 0.55, 0.65, 0.75 nm^{-1}. These dips are due to increased absorption inside the cavity, as a result of excitation of wave guide modes. Figure 1 (B) shows Co X-ray fluorescence pattern of OSV_SW1 film. Co fluorescence pattern exhibits six distinct peaks corresponding to the TE_0, TE_1, TE_2, TE_3, TE_4 and TE_5 modes of the waveguide structure. This provides a clear evidence of resonance enhancement in OSV_SW1 thin film, whenever the waveguide modes were excited. Figure 2 (A) and (B) represents simultaneously measured XRR and Co XRF profiles of OSV_SW2 film respectively. In this film also the excitation of TE_0, TE_1, TE_2, TE_3, TE_4, and TE_5 modes were observed. XRR results show that the estimated *rms* roughness of Co/Alq_3 spinterface is significantly lower in OSV_SW2 film (0.62±0.03 nm) than OSV_SW1 film (1.28±0.02 nm). Experimentally measured separation between successive guiding modes formed in Alq_3 layer has been used to determine Co concentration into Alq_3. Calculated volume fraction of Co into Alq_3 comes out to be 0.033 and 0.004 for OSV_SW1 and OSV_SW2 respectively. It is noted that the incorporation of TiO_2 capping layer significantly lowers the roughness of Co/Alq_3 spinterface. This clearly indicates that the thin barrier layer of TiO_2 plays an effective role in smoothening Co/Alq_3 spinterface during the deposition. Thus, XRR and Co XRF results of OSV_SW2 film provide a clear evidence of reduction of roughness as well as interdiffusion at Co/Alq_3 spinterface. This suggests a better performance of organic spin valve at room temperature with diffusion barrier of TiO_2. Acknowledgement Author would like to thank Mr. Anil Gome for X-ray fluorescence measurements and Mr. Arun Dev for the help in making home-made thermal evaporation set-up and also for depositing OSV thin films. This work is supported by Department of Science and Technology under DST-Women Scientist Scheme-A (WOS-A), Project No.SR/WOS-A/PM-1010/2015(G) dated 03.02.16. Figures Caption Figure.1) simultaneously measured (A) XRR, and (B) Co XRF from OSV_SW1 thin film as a function of scattering vector q. Figure.2) simultaneously measured (A) XRR, and (B) Co XRF from OSV_SW2 thin film as a function of scattering vector q.

1) Harris, and C. B. Schlupp *et. al*., Phys. Rev. Lett. 30, 1019 (1973). 2) Krinichmyi *et. al.*, Phys. Rev. B 55, 16233 (1997). 3) Blochwitz J, Fritz T, Pfeiffer M, Org Electr. 2, 97 (2001). 4) Koch N., Chem Phys Chem. 8, 1438 (2007). 5) Scheinert S, Paasch G, Phys Status Solidi A. 6, 1263 (2004). 6) Cicoira F, Santato C, Adv Funct Mater. 17, 3421 (2007). 7) Peumans P, Bulovic V *et. al.*, Appl Phys Lett. 76, 2650 (2000). 8) Rand BP, Genoe J, Heremans P, Prog Photovolt. 15, 659 (2007). 9) V. A. Dediu, L.E. Hueso, I. Bergenti, C. Taliani, Nature Materials. 8, 707 (2009). 10) Z. H. Xiong, D. Wu, V. Vardeny, and J. Shi, Nature (London). 427, 821 (2004). 11) V. Dediu *et. al*., Phys. Rev. B 78, 115203 (2008). 12) Y. Q. Zhan, X. J. Liu *et. al.*, Appl. Phys. Lett. 94, 053301 (2009). 13) T. S. Santos, J. S. Lee, P. Migdal, I. C. Lekshmi, B. Satpati, and J. S. Moodera, Phys. Rev. Lett. 98, 016601 (2007). 14) J. S. Jiang, J. E. Pearson, and S. D. Bader, Phys. Rev. B 77, 035303 (2008).

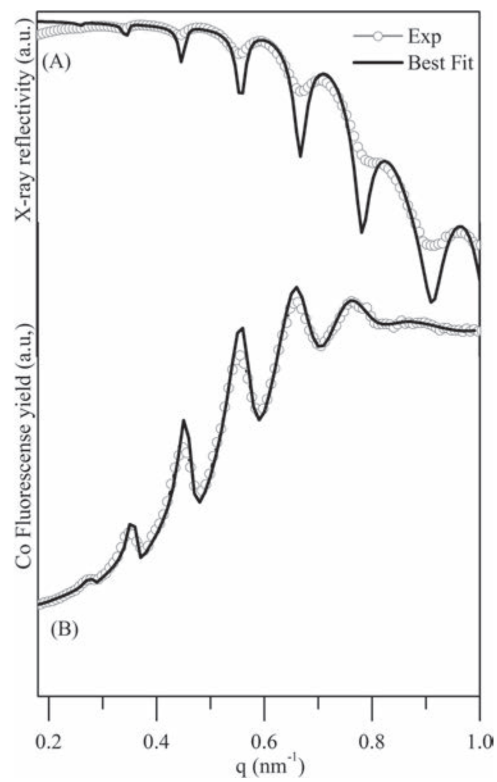

Fig. 1. (A) XRR, and (B) Co XRF from OSV_SW1 thin film as a function of scattering vector q.

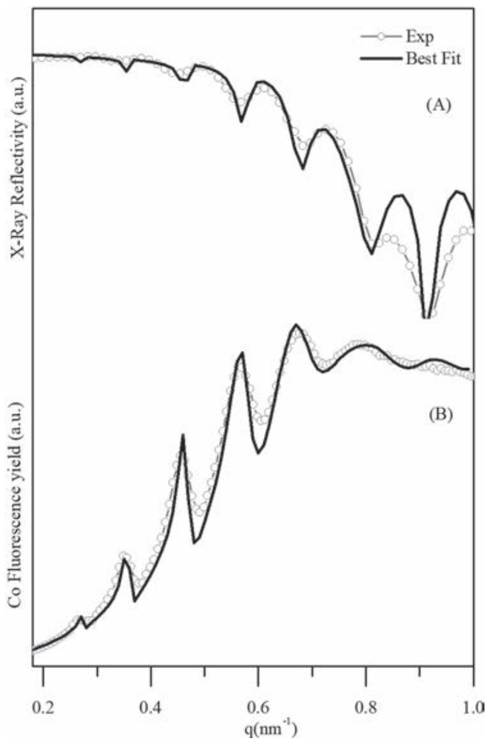

Fig. 2. (A) XRR, and (B) Co XRF from OSV_SW2 thin film as a function of scattering vector q.

INVITED PAPER

2:30

HD-03. Creation and Control of Spin Current in 2D Materials Heterostructures.

S.P. Dash[1]
1. Microtechnology and Nanoscience, Chalmers University of Technology, Gothenburg, Sweden

Exploiting the spin degrees of freedom of electrons in solid state devices is considered as one of the alternative state variables for information storage and processing beyond the charge based technology. However, one of the primary challenges in this field is the efficient creation, transport and control of spin polarization at room temperature. In this regard, two-dimensional (2D) atomic crystals and their heterostructures provide an ideal platform for spintronics. Graphene is an ideal medium for long-distance spin communication in future spintronic technologies. Here we demonstrate a high spintronic performance in CVD graphene on SiO2/Si substrate at room temperature. We observed a long distance spin transport over 16 μm and spin lifetimes up to 1.2 ns in large area CVD graphene at room temperature [1]. Hexagonal boron nitride (h-BN) is an insulating tunnel barrier that has potential for efficient spin polarized tunneling from ferromagnets. Here, we demonstrate the spin filtering effect in cobalt|few layer h-BN|graphene junctions leading to a large negative spin polarization up to 65 % in graphene at room temperature [2,3]. Two-dimensional (2D) crystals offer a unique platform due to their remarkable and contrasting spintronic properties, such as weak spin–orbit coupling (SOC) in graphene and strong SOC in molybdenum disulfide (MoS2). Here we combine graphene and MoS2 in a van der Waals heterostructure (vdWh) to demonstrate the electric gate control of the spin current and spin lifetime at room temperature (Fig. 1) [3]. Topological insulators (TIs) are a new class of quantum materials that exhibit a current-induced spin polarization due to spin-momentum locking (SML) of massless Dirac Fermions in their surface states. Recently, experiments were performed to detect and utilize the spin polarized surface currents in 3D TIs by using ferromagnetic contacts [1]. For such purpose the dominance of surface state electronic transport over the bulk contribution is crucial to maximize the charge to spin conversion efficiency. Here we will show an enhancement of the magnetoresistance (MR) signal due to SML by tuning the conductivity from a bulk to a surface dominated regime in $Bi_{1.5}Sb_{0.5}Te_{1.7}Se_{1.3}$ (BSTS) [2]. Our findings demonstrate an all-electrical spintronic device at room temperature with the creation, transport and control of the spin in 2D materials heterostructures, which can be key building blocks in future device architectures.

[1] Long distance spin communication in chemical vapour deposited graphene; MV Kamalakar, G. Chris, A Dankert, SP Dash; Nature Communication, 6, 6766 (2015). [2] Enhanced Tunnel Spin Injection into Graphene using CVD Hexagonal Boron Nitride; MV Kamalakar, A Dankert, J Bergsten, T Ive, SP Dash; Scientific Reports, 4: 61446 (2014) [3] Inversion of spin signal and spin filtering in ferromagnet| hexagonal boron nitride-graphene van der Waals heterostructures; MV Kamalakar, A Dankert, P. Kelly, SP Dash; Scientific Reports, 6, 21168 (2016). [4] Electrical gate control of spin current in van der Waals heterostructures at room temperature; A Dankert, SP Dash; Nature Communication 8, 16093 (2017). [4] Room Temperature Electrical Detection of Spin Polarized Currents in Topological Insulators; A. Dankert, J. Geurs, M.V. Kamalakar, S. Charpentier, S.P. Dash; Nano Letters, 15, 7976 (2015). [5] Surface Dominated Magnetoresistance in Topological Insulators, A. Dankert, P. Bhaskar, D. Khokhriakov, I. H. Rodrigues, M.V. Kamalakar, S. Charpentier, I. Garate, S. P. Dash; Submitted (2017).

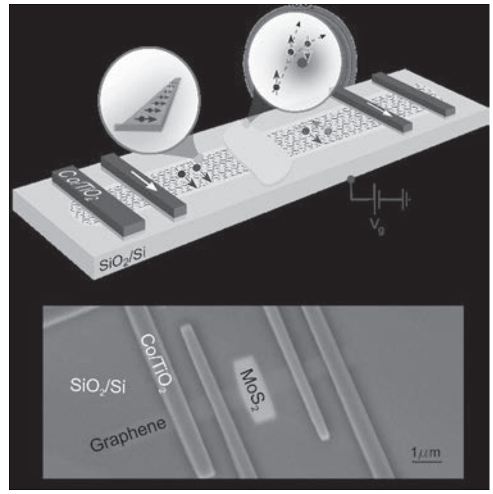

Fig. 1. Schematic and scanning electron microscope image of a fabricated graphene-molybdenum disulfide van der Waals heterostructure spintronic device for creation and control of spin current.

CONTRIBUTED PAPERS

3:00

HD-04. Quenching of Spin-Polarization Switching in Organic Multiferroic Tunnel Junctions by Ferroelectric "Ailing-Channel" in Organic Barrier.

S. Liang[1], X. Devaux[1], A. Ferri[2], R. Desfeux[2], W. Huang[3], X. Li[3], D. Chaudhuri[4], H. Yang[4], M. Chshiev[4], S. Migot[1], S. Mangin[1] and *Y. Lu*[1]
1. Institut Jean Lamour, Nancy, France; 2. Univ. Artois, Lens, France; 3. University of Science and Technology of China, Hefei, China; 4. CEA-SPINTEC, Grenoble, France

Organic multiferroic tunnel junctions (organic MFTJs) appearing a four-state nonvolatile resistance status make them promising for a low-coast memory. Extensive research activity has been devoted recently to engineer interfaces of organic/ferromagnetic (known as "spinterface") [1,2,3], due to the process of tunneling of electrons and spins governed and modulated by interfaces. However, in an organic MFTJ, it is still unclear about the detailed interfacial morphology and profiles of chemical elements distribution of conductive/tunneling channels in organic layer, which play the critical role in spin transport behavior. Here, we demonstrate the direct observation of interfacial structure revealed by scanning transmission electron microscopy (STEM) coupled with electron energy loss spectroscopy (EELS) and energy-dispersive X-ray spectroscopy(EDS) in the organic MFTJs based on $La_{0.6}Sr_{0.4}MnO_3$/P(VDF-TrFE)(*t*)/Co structures with different thickness, *t*, of P(VDF-TrFE). The results reveal there is no diffusion of metal from top electrodes into organic layer, by using Liq-N_2 cooling holder deposition technology to avoid the penetration from top electrode into organic barrier (during the growth of the top electrode, the temperature of sample is maintained at ~90K), which is different from the "top metal penetration" in the organic spin valves by traditional deposition methods. Besides, the effect of "ailing-channel" has been directly observed. Due to the roughness of P(VDF-TrFE), there are Co/Au grains deposited into potholes at the boundaries among feorroelectric P(VDF-TrFE) needle-like grains, which inducing "ailing-channels" to reduce ferroelectric behavior of the whole device. Accordingly, this "ailing-channel" can influence the spin transport behavior modulated by ferroelectricity, the tunneling magneto-resistance (TMR) sign can be changed in the thick devices (t≥19nm), but no change of TMR sign was observed in the thin device (t≤15nm). The direct STEM observation combining our consistent systematic electrical spin measurement may open up a new horizon for understanding of design organic MFTJs and other organic based devices.

[1] S. Sanvito, "Molecular spintronics: The rise of spinterface science", *Nat. Phys.* 2010, *6*, 562. [2] S. Liang, H. Yang, H. Yang, B. Tao, A. Djeffal, M. Chshiev, W. Huang, X. Li, A. Ferri, R. Desfeux, S. Mangin, D. Lacour, M. Hehn, O. Copie, K. Dumesnil, and Y. Lu, "Ferroelectric Control of Organic/Ferromagnetic Spinterface", *Advanced Materials*, 28, 10204 (2016). [3] F. Djeghloul, F. Ibrahim, M. Cantoni, M. Bowen, L. Joly, S. Boukari, P. Ohresser, F. Bertran, P. Le Fevre, P. Thakur, F. Scheurer, T. Miyamachi, R. Mattana, P. Seneor, A. Jaafar, C. Rinaldi, S. Javaid, J. Arabski, J. -P. Kappler, W. Wulfhekel, N. B. Brookes, R. Bertacco, A. Taleb-Ibrahimi, M. Alouani, E. Beaurepaire, W. Weber, " Direct observation of a highly spin-polarized organic spinterface at room temperature", *Sci. Rep.* 2013, *3*, 1272.

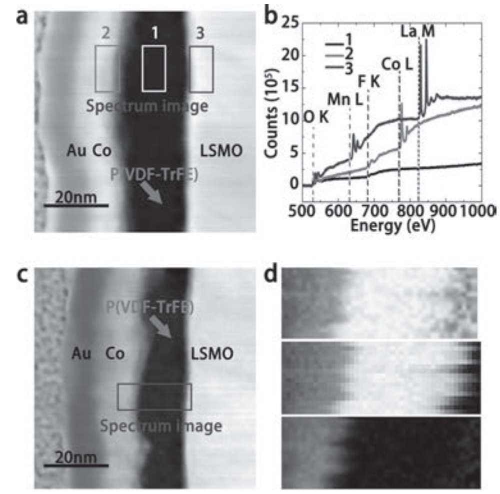

Fig. 1. Scanning transmission electron microscope and electron energy loss spectroscopy (STEM-EELS) observation. (a-b) STEM image of LSMO/P(VDF-TrFE) [*t* = 19nm]/Co devices with a thicker P(VDF-TrFE) layer. STEM EELS mapping of identification of elements with three special extracted zones. The zones in (a), 1: P(VDF-trFe) layer, 2: Interface between Co and P(VDF-trFe), 3: Interface between LSMO and P(VDF-trFe). (b) EELS spectra recorded on zone of 1(black), 2(red), and 3(blue), respectively. (c-d) STEM image of LSMO/P(VDF-TrFE)[*t* = 15nm]/Co devices, STEM EELS mapping of a zoom-in zone at P(VDF-TrFE) (blue zone). (d) Corresponding EELS map with RGB Composite. Top: (red: Co, yellow: C, blue: F, green: Mn). Middle: (red: Co, yellow: C). Bot: (red: Co, blue: F).

3:15

HD-05. Tuning Spin Injection Efficiency by Molecular Design.

A.D. Wittmann[1], G. Schweicher[1], K. Broch[2], A. Marks[3], C. Jellett[3], I. McCulloch[3], E. McNellis[4], J. Sinova[4], J. Wunderlich[5] and H. Sirringhaus[1]
1. Physics, University of Cambridge, Cambridge, United Kingdom; 2. Institut für Angewandte Physik, Universität Tübingen, Tübingen, Germany; 3. Chemistry, Imperial College London, London, United Kingdom; 4. Physics, Johannes Gutenberg University, Mainz, Germany; 5. Hitachi Cambridge Laboratory, Cambridge, United Kingdom

There is a growing interest in spintronics for technological applications. An indispensable building block for this are pure spin currents, a flow of electrons' spin angular momentum without a net flow of charge. Organic semiconductors have recently been found to have a comparably large spin diffusion time and length [1], which makes them ideal candidates for spintronic devices. However, spin properties in organic semiconductors have yet to be fully understood. The magnetisation dynamics of a ferromagnetic material (FM) are well described by the Landau Lifshitz Gilbert equation. In addition to the precession of the magnetisation around the effective magnetic field, it also includes a damping term. The Gilbert damping parameter α is directly proportional to the width of the microwave absorption of the FM at ferromagnetic resonance (FMR). A FM can pump spins into an adjacent non-magnetic material (NM) at FMR. The effective damping is increased due to the loss of spin angular momentum from the FM into the NM. The spin mixing conductance – the efficiency of injecting spins from a FM into a NM at FMR – can be experimentally determined by measuring the increase in linewidth of the FM due to an additional NM. When the thickness of the NM layer is smaller than or comparable with the spin diffusion length λ_S of the material, there is a backflow of spins due to a spin accumulation at the interface opposing the injected pure spin current and diminishing the net spin injection. The dependence of the additional damping α' on the thickness L of the NM layer has been described for metallic spin sinks as $\alpha' = A*(1+B/\tanh(L/\lambda_S))$, where A and B denote material dependent constants. Here, we study spin injection from thermally evaporated permalloy ($Ni_{80}Fe_{20}$) into derivatives of dinaphtho[2,3-*b*:2′,3′-*f*]thieno[3,2-*b*]thiophene (DNTT), one of the best performing small molecule organic semiconductor so far (chemical structures shown in figure 1a)[3,4]. We have validated through X-Ray diffraction techniques that the thin films of the different DNTT derivatives adopt a 2D herringbone packing in-plane and stack with the long axis of the molecule perpendicular to the substrate. In order to determine the linewidth broadening due to the spin injection into the organic material, we measure the microwave absorption of the same permalloy films (9 nm) before and after deposition of the small molecule in an ESR cavity at 9.4 GHz while sweeping the in-plane magnetic field. We can measure significant linewidth broadening for all three derivatives of DNTT. As shown in figure 1b, the change in linewidth at a film thickness of 80 nm is largest for diPh-DNTT and very much suppressed for C8-DNTT. Theoretical predictions show that for DNTT and diPh-DNTT, the spin density is distributed over the whole molecule [5]. In the case of C8-DNTT, the spin density shifts only slightly towards the alkyl side chains but remains mostly on the core of the molecule. This implies that the separation of the core of the molecule from the interface to the FM due to alkyl side chains decreases the spin injection efficiency significantly. From the gradual onset of the linewidth broadening for DNTT and diPh-DNTT with film thickness, we can estimate the spin diffusion length using the model mentioned above to be 44 nm for DNTT and 27 nm for diPh-DNTT. The signal for C8-DNTT is already saturated at 10 nm implying that the spin diffusion length is considerably shorter than 10 nm. This indicates that the back flow due to the spin accumulation in the material balances injected spin current even in very thin layers. In summary, we have successfully demonstrated spin pumping into organic semiconductor small molecules. The spin mixing conductance as well as the spin diffusion length can be tuned through molecular design. Separation of the core of the molecule from the interface to the FM due to alkyl side-chains suppresses both the linewidth broadening as well as the spin diffusion length. This highlights the importance of the molecular structure direct at the interface to the FM. The vast possibilities of molecular designs for organic small molecules combined with the tunability of the spin mixing conductance bring forth potential for application-specific tailor-made organic materials.

[1] S. Watanabe*, K. Ando* *et al.*, Nature Physics, 10, 308–313 (2014) [2] Y. Tserkovnyak *et al.*, PRB, 66, 224403 (2002) [3] M. J. Kang *et al.,* Chem. Sci. 1, 179 (2010) [4] M. J. Kang *et al.,* Adv. Mater. 23, 1222–1225 (2011) [5] S. Schott *et al.,* Nature Communications 8, 15200 (2017)

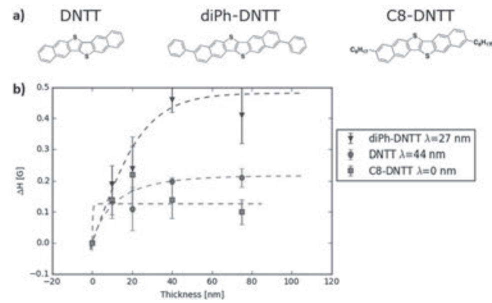

Fig. 1. a) Chemical structure of three derivatives of DNTT b) Linewidth broadening as a function of thickness of DNTT (circles), diPh-DNTT (triangles) and C8-DNTT (squares). From the gradual increase in signal with film thickness, the spin diffusion length can be estimated for DNTT and diPh-DNTT using the fit (dashed line). The spin diffusion length of C8-DNTT appears to be shorter than 10 nm.

3:30

HD-06. Large spin-valve effect in Si nano spin-valve devices.

H.D. Duong[1], M. Tanaka[2,3] and N. Pham[1,3]
1. Department of Electrical and Electronic Engineering, Tokyo Institute of Technology, Tokyo, Japan; 2. Department of Electrical Engineering and Information Systems, The University of Tokyo, Tokyo, Japan; 3. Center for Spintronics Research Network, Graduate School of Engineering, The University of Tokyo, Tokyo, Japan

The silicon (Si) based spin-MOSFET [1] is a promising spin device because of its high compatibility with the well-established solid-state circuit technology [1] and long spin lifetime in Si [2]. While there are studies of spin injection into microns of Si channels using the three terminal Hanle effect [3] or the four-terminal spin-valve effect [4] up to 150 K, the spin-valve ratio is extremely small (lower 0.1%) and spin-dependent output voltage is below 1 mV. Recently, we have successfully fabricated nano-scale Si spin-valve devices with a Fe/MgO/Ge spin injector / detector and a 20 nm-long Si channel by using electron beam evaporation and nanolithography. In those devices, we observed a clear spin-valve effect up to 0.8% and spin-dependent output voltage ~ 13 mV [5]. In this work, by growing a high-quality Fe/MgO/Ge spin injector / detector using molecular beam epitaxy (MBE), we have significantly improved the spin-valve effect up to 3% and the spin output voltage up to ~ 20 mV in a 20-nm Si spin-valve device, which are the highest values reported so far in lateral spin-valve devices. The MR ratio decreases with increasing the channel length, but remains higher than 1% even when the channel length is as long as 6 μm. Furthermore, we show that the nano-scale channel is critical for the observation of the spin-valve effect at room temperature, demonstrating the important role of ballistic transport in the nano-scale Si channel. We grew the Fe/MgO/Ge stack by MBE on n-type Si substrates. Then, we used the e-beam lithography and Ar ion-milling technique to fabricate the nanoscale Si spin-valve devices, as shown in the inset of Fig. 1(a). We employed the two-terminal (local) spin-valve effect to measure the spin transport properties. Figure 1(a) shows the magnetoresistance (MR) characteristics of the 20-nm Si channel device measured at 15 K with a bias voltage of 300 mV and a magnetic field applied in-plane along the Si channel. We observed inverse MR with a large change of resistance ΔR of 57 kΩ, corresponding to $\Delta R/R$ = 3%. By systematically investigating the bias dependence, temperature dependence, and magnetic field direction dependence of the MR, we have confirmed that the observed signal is *not* caused by the anisotropic magnetoresistance (AMR) of the Fe ferromagnetic electrodes, or the tunneling anisotropy magnetoresistance (TAMR) at the Fe/MgO interface, but it is caused by the spin transport through the nano-scale Si channel. Figure 1(b) shows the evolution of the MR ratio (=$\Delta R/R$) with increasing temperature in this device. The MR decreases as temperature increases, but changes its sign at temperatures higher than 200 K. From the temperature dependence of the device resistance, we found that the tunneling process is unlikely due to the direct tunneling through the MgO/Ge barrier, but it is likely due to the thermally activated tunneling process through defect sites inside the barrier. We show that the inverse MR can be explained by the spin-blockade effect of defect sites in the tunnel barrier layer at low temperatures. Figure 1(c) shows the spin-dependent output voltage ($|\Delta R/R|$)V of the device as a function of bias voltage, measured at 15 K. The inset shows the bias voltage dependence of the MR ratio. We achieved the spin-dependent output voltage of 20 mV at the bias voltage of 0.9 V at 15 K, which is among the highest values reported so far in lateral spin-valve devices. In Figure 2, we compared the MR curves of devices with different channel lengths from 20 nm to 6 μm. Figures 2(a)-2(d) show the MR curves measured at 15 K and a bias voltage of 300 mV, while Figures 2(e)-2(h) show those measured at room temperature with a bias voltage of 80 mV. At 15 K, the MR ratio systematically decreases with increasing the channel length, but remains larger than 1%. At room temperature, only the device with the 20 nm Si channel shows a clear MR effect, demonstrating the important role of ballistic transport in this nano-scale device. In summary, we have investigated the spin transport in the nano-scale Si spin-valve devices fabricated by the MBE method. We observed a large spin-valve effect up to 3%. The highest spin-dependent output voltage is 20 mV at the bias voltage of 0.9 V at 15 K, which is the highest value reported so far in lateral spin-valve devices. We observed that the sign of the spin-valve effect is reversed at low temperatures, suggesting the possibility of the spin-blockade effect of defect states in the MgO/Ge tunneling barrier. Our result is an important step towards the realization of nano-scale spin-MOSFETs. [6]

[1] S. Sugahara and M. Tanaka, Appl. Phys. Lett. 84, 13 (2004); M. Tanaka and S. Sugahara, IEEE Transactions on Electron Devices 54, 961 (2007). [2] V. Zarifis and T. G. Castner, Phys. Rev. B 36 (1987) 6198. [3] S. P. Dash, S. Sharma, R. S. Patel, M. P. de Jong, and R. Jansen, Nature (London) 462 (2009) 491. [4] T. Sasaki, T. Oikawa, T. Suzuki, M. Shiraishi, Y. Suzuki, and K. Tagami, Appl. Phys. Exp. 2 (2009) 053303. [5] D. D. Hiep, M. Tanaka, and P. N. Hai, Appl. Phys. Lett. 109, 232402 (2016). [6] D. D. Hiep, M. Tanaka, and P. N. Hai, J. Appl. Phys. 122, 223904 (2017).

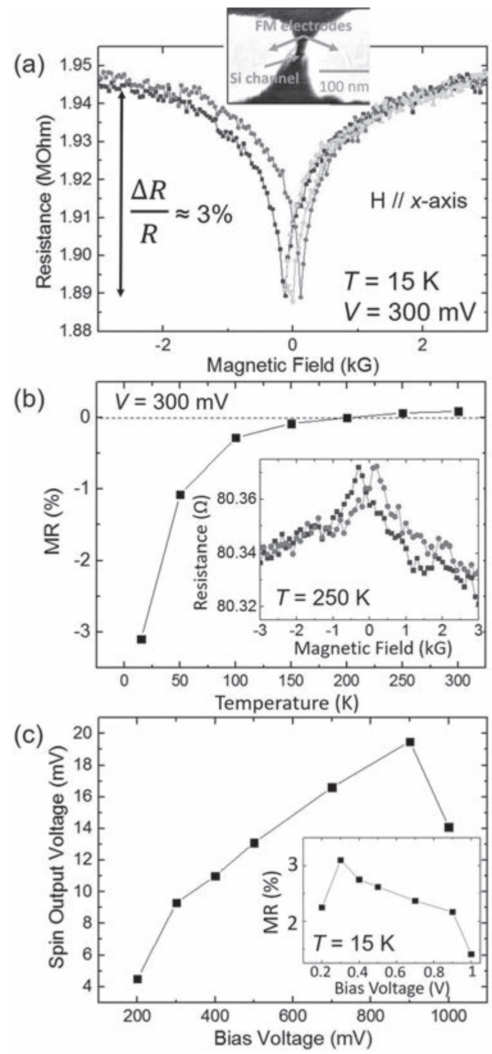

Fig. 1. (a) MR characteristics of a (Fe/MgO/Ge) / Si / (Ge/MgO/Fe) spin-valve device measured at 15 K with a bias voltage of 300 mV. The red and the blue curves are the major loops, while the green curve is the minor loop. Inset shows a SEM image of the device. (b) Temperature dependence of MR (=$\Delta R/R$). Inset shows the MR curve at 250 K. (c) Bias voltage dependence of the spin-dependent output voltage ($\Delta R/R$) V at 15 K. The highest output voltage ΔV of 20 mV was achieved at the bias voltage of 0.9 V. Inset shows the bias voltage dependence of the MR.

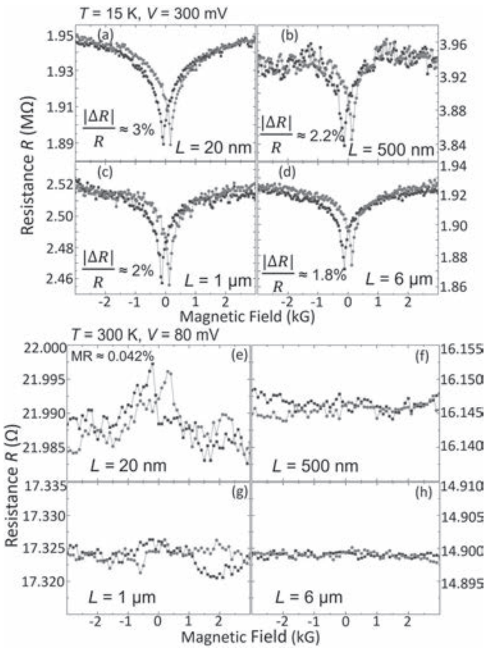

Fig. 2. Spin-valve effect of several Si spin-valve devices with different channel lengths of L = 20 nm, 500 nm, 1 μm, and 6 μm, (a)-(d) measured at 15 K with a bias voltage of 300 mV, and (e)-(h) measured at 300 K with a bias voltage of 80 mV. Here, the magnetic field was applied along the current direction.

3:45

HD-07. Large local magnetoresistance at room temperature in Si<100> devices.

M. Ishikawa[1,2], M. Tsukahara[1], M. Yamada[1], Y. Saito[2] and K. Hamaya[1,3]
1. Graduate School of Engineering Science, Osaka University, Toyonaka, Japan; 2. Corporate Research & Development Center, Toshiba Corporation, Kawasaki, Japan; 3. Center for Spintronics Research Network, Osaka University, Toyonaka, Japan

A spin metal-oxide-semiconductor field-effect transistor (spin-MOSFET) is one of the emerging devices for the low power consumption in silicon-based electronics from the viewpoint of logic-in-memory architectures [1]. To realize these kinds of spintronic applications, one of the main issues for realizing the spin-MOSFETs is an observation of the high magnetoresistance (MR) ratio obtained by two-terminal local measurements at room temperature [2]. Up to now, although there are lots of studies of the local MR effect through the silicon (Si) channels, the values of the MR ratio are less than 0.8 % at 100 K [3] and 0.03 % at room temperature [4]. In this paper, we show relatively large MR ratios at room temperature in Si<100> lateral spin valves (LSVs) with a small size (0.305 μm^2) cross section in the spin-transport layer. For comparison of the crystal orientation of the Si spin-transport layers, we prepared two kinds of LSVs along Si<100> and Si<110> with CoFe/MgO electrodes on phosphorus-doped ($n \sim 1.3\times10^{19}$ cm^{-3}) (100) textured Si on insulator (SOI) (~ 61 nm) layer, as shown in Fig. 1(a). An MgO (1.1 nm) tunnel barrier was deposited on the SOI spin-transport layer at 200 °C by electron beam evaporation. Then, a CoFe (10 nm) and a Ru capping layer were sputtered on top of it under a base pressure less than 5×10^{-7} Pa. The MgO and CoFe layers were epitaxially grown on the (100) textured SOI, where the (100)-textured MgO layer was grown on Si(100). Device fabrication methods are described in detail elsewhere.[5] We have checked that these resistivity and Hall mobility of the Si spin-transport layer were almost the same by evaluating from longitudinal resistivity and Hall-effect measurements for Si<100> and Si<110> Hall-bar devices. Figures 1(b) and 1(c) show four-terminal nonlocal Hanle-effect curves for Si<100> and Si<110> LSVs, respectively, at a bias current of 0.5 mA at 20 K. These data mean that we can obtain reliable spin transport in Si layers in our LSVs, as shown in our previous work [5]. It should be noted that the magnitude of the spin signal, $|\Delta R_{NL}|$, for Si<100> is approximately twice as large as that for Si<110>. Although the detailed will be published elsewhere [6], it is inferred that this phenomenon is tentatively interpreted by the difference in the spin injection/detection efficiency associated with the valley structures of the conduction band in Si. We hereafter focus on the MR effect that is one of the most important points for realizing the spin-MOSFETs. Figures 2(a) and 2(b) display the two-terminal local-MR signals for Si<100> and Si<110> LSVs, respectively, at 20 K. Here the bias current is 0.5 mA. It should be noted that the magnitude of the local-MR signals, $|\Delta R_L|$, for Si<100> is also larger than that for Si<110>. Irrespective of measurement schemes, we can find the large difference in the spin injection/detection efficiency between Si<100> and Si<110> LSVs. We can also observe this effect even at room temperature (303 K), as shown in Figs. 2(c) and 2(d). Thanks to the crystal orientation effect, a relatively large $|\Delta R_L|$ of 2 Ω, which is the largest $|\Delta R_L|$ value reported so far, can be obtained. The estimated MR ratio is approximately 0.06 %, twice as large as that observed in the previous work [4]. For a different bias current condition, the MR ratio reached up to approximately 0.2 % at room temperature. Although the obtained value of the MR ratio is still insufficient to realize the spin-MOSFETs, the use of Si<100> spin-transport channel is more effective to develop the related Si-based devices. This work was partly supported by a Grant-in-Aid for Scientic Research (A) (No. No. 16H02333) from the Japan Society for the Promotion of Science (JSPS), and a Grant-in-Aid for Scientic Research on Innovative Areas "Nano Spin Conversion Science" (No. 26103003) from the Ministry of Education, Culture, Sports, Science, and Technology (MEXT).

[1] Y. Saito *et al*., J. Elec. Chem. Soc. 158, H1068 (2011). [2] T. Tanamoto *et al*., J. Appl. Phys. 109, 07C312 (2011). [3] Y. Saito *et al*., AIP Advances 7, 055937 (2017). [4] T. Sasaki *et al*., Appl. Phys. Lett. 104, 052404 (2014). [5] M. Ishikawa *et al*., Phys. Rev. B 95, 115302 (2017). [6] M. Ishikawa *et al*., arXiv:1712.07789v1. [7] F. J. Jedema *et al*., Nature (London) 416, 713 (2002).

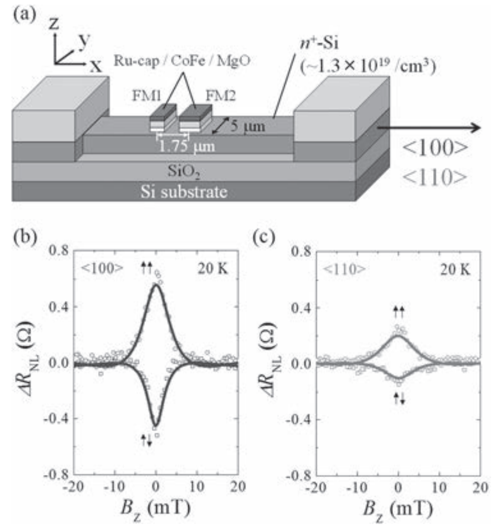

Fig. 1. (a) Schematic diagram of a lateral spin-valve (LSV) device with Si spin-transport channel along Si<100> or Si<110>. (b),(c) Four-terminal nonlocal Hanle-effect curves for Si<100> and Si<110> LSVs, respectively, measured in the parallel and antiparallel magnetization configurations at 20 K. The solid curves are the results of fitting to Eq. (2) in Ref. [7].

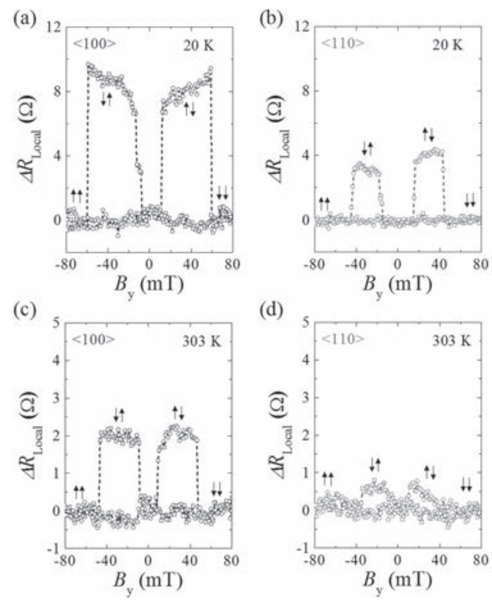

Fig. 2. Two-terminal local spin signals for (a) Si<100> at 20 K,(b) Si<110> at 20 K, (c) Si<100> at 303 K, and (d) Si<110> at 303 K.

4:00

HD-08. Nonlinear spin detection in a biased ferromagnetic tunnel contact.

R. Jansen[1], A. Spiesser[1], H. Saito[1], Y. Fujita[2,1], S. Yamada[2], K. Hamaya[2] and S. Yuasa[1]
1. AIST, Tsukuba, Japan; 2. Osaka University, Toyonaka, Japan

Whereas electronic devices are based on charge, current and voltage, the key elements of spintronics technology are spin, spin current and spin accumulation. Nevertheless, the vast majority of spin-based devices and systems employ the conversion of spin information into electrical signals. This enables the detection of the spin information and provides an electrical output that can be linked to conventional electronic circuitry. In order to advance spintronics technology, it is thus indispensable to develop efficient methods for the electrical detection of spin and to develop a thorough understanding of the process of spin conversion. The most convenient method for the detection of spin accumulation in a non-magnetic material employs ferromagnetic tunnel contacts. At the interface between a non-magnetic material and a ferromagnetic tunnel contact, a spin accumulation is converted into a charge voltage across the contact, owing to spin-polarized tunneling. Spin detection with ferromagnetic tunnel contacts has proven to be efficient and robust, and avoids problems due to spin absorption by the ferromagnet and the conductivity mismatch. Devices using ferromagnetic tunnel contacts can be classified according to whether or not the detector contact is biased. In a very few type of devices, there is no net charge current across the detector contact, as in the non-local spin-transport device. The spin signals observed in non-local devices are well described by the theory for spin detection in the linear response regime. Consequently, non-local devices have been instrumental to prove and understand spin injection and transport in various types of materials. In most of the spintronic devices, including the technologically relevant ones, the ferromagnetic tunnel contact in which the spin conversion occurs is located in the current path and is thus biased. Examples are two-terminal magnetoresistance devices with two magnetic electrodes contacting the non-magnetic channel, various three-terminal geometries, but also the non-local geometry with a biased detector. Importantly, for devices in which the spin detector contact is biased, the observed spin signals are, without exception, surprising and puzzling, and no suitable explanation for the peculiar behaviour is available. Moreover, when existing theories are applied, the conclusions are inconsistent with those obtained from analysis of non-local spin transport devices, even if the same structure is used for the different measurement configurations. Here, it is shown that spin detection in a biased contact is inherently nonlinear. We employ Si- based spin transport devices with several Fe/MgO tunnel contacts that can be used in different measurement configurations. Data obtained in the non-local configuration (see Ref. 1) in spin-valve or Hanle mode establish the presence of a giant spin accumulation in the n-type Si channel, with the spin splitting reaching 13 meV at 10 K and 3.5 meV at room temperature. The non-local data is well described by the conventional linear response theory, from which we obtain the values of all the relevant parameters (spin-diffusion length, spin lifetime, tunnel spin polarization of the Fe/MgO contacts). Using those devices, we first present compelling data that shows conclusively that spin drift, previously proposed to explain some of the abovementioned peculiar results, is not responsible. Next, it is shown (i) that all the puzzling and inexplicable spin signals in the various devices with a biased detector have, in fact, a single common origin, (ii) that the common origin is the nonlinearity of the spin conversion at a biased ferromagnetic tunnel contact, (iii) that the nonlinearity is surprisingly strong and already appears at small to moderate bias for which charge transport is still well described by linear response, (iv) that the origin of the nonlinearity of spin detection can be understood using a simple tunnel transport model, and (v) that taking the nonlinearity of spin detection into account explains all the puzzling results, provides a unified description of electrical spin signals in devices with and without biased detector, and makes the spin signals and spin transport parameters obtained from devices with a biased detector consistent with those obtained from non-local spin-transport measurements.

[1] A. Spiesser, H. Saito, Y. Fujita, S. Yamada, K. Hamaya, S. Yuasa and R. Jansen, Giant Spin Accumulation in Silicon Nonlocal Spin-Transport Devices, Phys. Rev. Appl. 8, 064023 (2017).

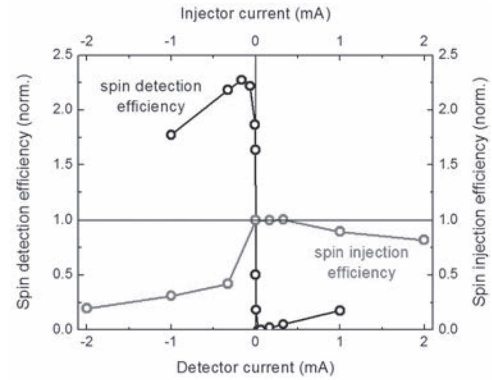

Fig. 1. Comparison of the spin-detection efficiency and the spin-injection efficiency of a Fe/MgO tunnel contact on an n-type Si channel, as a function of the current across the contact. The difference between the two sets of data is due to the nonlinearity of spin detection in a biased tunnel contact.

4:15

HD-09. Observation and quantification of spin drift in non-local devices with a heavily-doped Si channel.

A.M. Spiesser[1], H. Saito[1], Y. Fujita[2], S. Yamada[2,3], K. Hamaya[2,3], W. Mizubayashi[4], K. Endo[4], S. Yuasa[1] and R. Jansen[1]
1. Spintronics Research Center, National Institute of Advanced Industrial Science and Technology (AIST), Tsukuba, Japan; 2. Department of Systems Innovation, Graduate School of Engineering Science, Osaka University, Osaka, Japan; 3. Center for Spintronics Research Network, Graduate School of Engineering Science, Osaka University, Osaka, Japan; 4. Nanoelectronics Research Institute, National Institute of Advanced Industrial Science and Technology (AIST), Tsukuba, Japan

The maturity of silicon-based technology and its dominance of the device industry provide compelling motivation to use Si for developing novel devices that integrate spin functionality. Over the past few years, the generation of a pure spin current in Si channels has been demonstrated up to room temperature using the nonlocal (NL) four-terminal scheme [1-3]. To date, the largest magnetic response in Si was achieved by using crystalline Fe/MgO magnetic tunnel contacts; the spin splitting reaches 13 meV and the spin-diffusion length attains a value of 2.2 μm at 10 K [3]. In the latter study, spin transport was investigated in the low bias regime, where it can be described as purely diffusive using the standard theory for spin injection and spin diffusion. In the high bias regime, however, the presence of an electric field in the Si channel causes spin drift that can strongly affect spin transport and spin accumulation voltages in Si [4, 5]. Here, we study the spin transport in heavily-doped n-type Si NL devices in the presence of electric fields in the high bias regime. We use a simple and reliable method to evidence the presence of spin drift and quantify it in Si NL devices. We compare our results with the spin drift-diffusion theory [4] and show that spin drift can either enhance or reduce the spin transport length depending on the direction and the strength of the electric field, but the effect is weaker than that predicted by the theory. The Si-based NL devices were fabricated on a SOI substrate having a 70 nm-thick n-type Si(001) channel. The Si channel was doped homogeneously with phosphorous at a concentration of 2.4×10^{19} cm^{-3}. The Fe/MgO magnetic tunnel contacts were deposited by electron-beam evaporation in an ultra-high vacuum molecular beam epitaxy system. The *in situ* reflection high-energy electron diffraction patterns indicated the formation of crystalline MgO(001) and Fe(001). The sample was then processed into Si NL-4T devices using standard micro-fabrication techniques (e-beam lithography, Ar-milling, SiO_2 sputtering). The NL structures consist of two central ferromagnetic electrodes (FM1 and FM2) separated by a spacing *d* and two outer non-magnetic Au/Ti reference contacts located at a distance much larger than the spin-diffusion length. The NL spin-valve and Hanle-type spin precession measurements were obtained by applying an external magnetic field along the length of the FM contacts and perpendicular to the film plane, respectively. To study the spin-drift effect in the NL-4T geometry, we use two different measurement configurations called NL1 and NL2, respectively, in which the direction of the electric field E is reversed. Importantly, in these two configurations the detector remains unbiased, which allows us to properly apply the standard theory to analyze the spin-transport data. In addition, to vary the strength of the electric field we designed devices with different contact widths of FM1 and FM2 on the same sample. This allows us to vary the current density in the Si channel J_{ch} and thus the electric field E in the Si channel, while maintaining a constant tunnel current density J_t through the FM injector. First, we characterized our devices by measuring the NL spin-valve and Hanle signals in the low bias regime. Following the analysis reported in Ref. 3, we extract a spin lifetime of 13 ns, a spin-diffusion length λ_{Si} of 1.7 μm, and a tunnel spin polarization of Fe/MgO of 40 % at 60 K, in agreement with our previous results [3]. We then performed NL spin-valve measurements using both NL1 and NL2 schemes and different injector sizes, while varying the biases. From the ratio of the NL spin-valve signals ΔV_{NL2} and ΔV_{NL1} observed in the two configurations, we extract the spin-transport length λ_E by fitting the data with a model that includes spin drift according to ref [4], and a scaling factor to adjust the magnitude of the spin drift. The results of this fitting and the spin-transport length as a function of the electric field are shown in Fig 1a and b, respectively. As predicted by the theory, a significant enhancement occurs for high electric-field spin injection, whereas a suppression of the spin signals is observed for the high spin extraction condition. In particular, we finnd that the spin-transport length is about 2 times larger than the spin-diffusion length in Si for an electric field of 150 V/cm. We find that although the theory of ref. [4] predicts the correct trends, it overestimates the effect of the electric field by about a factor of two.

[1] T. Suzuki *et al.*, Appl. Phys. Express 4, 23003 (2011). [2] M. Ishikawa *et al.*, Phys. Rev. B 95, 115302 (2017). [3] A. Spiesser *et al.*, Phys. Rev. Appl. 8, 064023 (2017). [4] Z.G. Yu and M. E. Flatte, Phys. Rev. B 66, 235302 (2002). [5] M. Kameno *et al.*, 104, 092409 (2014). [6] This work was supported by Grant-in-Aid for Scientific Research on Innovative Area, "Nano Spin Conversion Science" (Grant No.26103002).

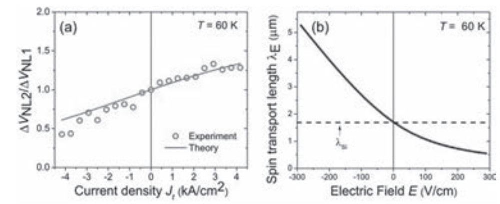

Fig. 1. (a) Ratio of the non-local spin signals using the schemes NL2 and NL1 as a function of the tunnel current density J_t. The green empty circles correspond to experimental data whereas the line correspond to a fit using the standard drift-diffusion model from Ref. [4]. (b) Spin transport length as a function of the strength of the electric field E in the Si channel.

4:30

HD-10. Intrinsic generation of propagating spin waves by a magnonic "black hole" in a current-driven nano-constricted wire.

M. Dvornik[1], *R. Khymyn*[1], J. Åkerman[1,3], V.S. Tiberkevich[2] and A.N. Slavin[2]
1. Department of Physics, University of Gothenburg, Gothenburg, Sweden; 2. Department of Physics, Oakland University, Rochester, MI, United States; 3. Department of Applied Physics, KTH Royal Institute of Technology, Stockholm, Sweden

The experimental observation of a microwave magnon generation in a current-driven obliquely magnetized 15-nm thick permalloy (Py) wire constricted in the middle to the 20-nm width was reported recently [1]. The electrical measurements of the linear response of the system paired with the micromagnetic simulations suggested the auto-oscillations emerge from the *localized* eigenmode of the constriction, consistent with our results obtained for the spin Hall nano-oscillators of the similar geometry [2, 3]. Here we demonstrate by numerical simulations, that one can also generate *propagating* magnons in the very same system via the Hawking radiation [4] taking place near the "event horizon" of a magnonic "black hole" [5]. Unruh in [6] suggested that it is possible to experimentally create analogs of the black-hole-horizon in systems of different physical nature, and a detailed proposal on the creation of the "event horizon" in a magnonic system has been given in [5]. The essential ingredients of the physical systems for analog horizons are the existence of dispersive waves and a background flow velocity which can exceed the velocity of these waves [5-7]. In a magnonic system, this can be done if a spin current of a sufficient density is propagating in a magnetic material resulting in the shear of the magnons propagation. The electrical current flowing in the magnetic metal is spin-polarized because of the different conductivities of spin-up and spin-down electrons. Such a spin current exerts a torque on the inhomogeneous magnetization, proportional to its spatial gradient [8]. As a result, the spin dynamics under the action of the electric current takes place in the reference frame, moving with the velocity u, proportional to both the electric current density and spin polarization. Such a flow of spin current introduces a Doppler shift to the frequency of magnons $\omega_u(k)=\omega_0(k)-uk$, where k is a magnon wavevector [9]. If the spin current flow has a small cross-section, the Doppler shift, which is proportional to the spin current density, can increase substantially. Consequently, the negative magnon frequencies could be reached in a certain range of the magnon wavevectors if the shear velocity overcome a threshold value. The magnons in this wavevector range would have a *negative energy* with respect to the remote observer. This situation can be realized in a thin nano-constricted magnetic film, where the area of constriction creates a region with the negative magnon frequency with the minimum value of $\omega_{\min}(k_{\min})<0$, while outside the constriction region the magnon frequency remains positive for all the wavevectors, see Fig. 1. For the sample under discussion the calculated current density j~10^{13} A/m^2 is rather high which leads to the high values of the shear velocity u. Similar to the case of gravitational black hole, where the fall of the particle into the hole results in the energy gain of the antiparticle, for "magnonic black hole" the energy is pumped outside the constriction, which results in the auto-oscillations of the magnetization. Since the area with the negative frequency is an analog of the active medium in a laser cavity, the highest gain would be experienced by the magnonic eigenmodes with a characteristic size (wavelength) close to the spatial size of the magnonic "black hole". At the same time, the maximum frequency of auto-oscillations is limited by $|\omega_{\min}|$ because of the energy conservation law. To confirm the possibility of the above mechanism of magnon generation we performed numerical simulations of the magnetization dynamics in a Py nano-constriction, similar to the one studied in [1], with the magnetic field of B=0.2 T applied 75° out-of-plane and 10° in-plane. We integrated the stochastic Landau-Lifshitz equation with the ambient temperature of T=400 K using the MuMax3 solver [10], taking into account the shear by the electrical current and the corresponding Oersted field, both estimated using Comsol software. Fig. 2 shows the simulated excitation of the auto-oscillations in the nano-constriction using the applied current of I=12 mA (maximum current density of 2.8×10^{13} A/m^2), spin polarization of P=0.5 and Zhang-Li toque non-adiabaticity of ξ=0.33. As one can see, the auto-oscillations emerge as propagating spin waves at one side of the constriction. The simulations also show that the direction of the spin-wave propagation could be switched by reversing the polarity of the electrical current. Therefore, the performed simulations confirm the possibility of the Hawking radiation from a "magnonic black hole." It is worth mentioning, that in the given geometry the threshold current for the generation of propagating spin waves is substantially higher than for the generation of localized magnonic modes. Nevertheless, the threshold currents in these two cases could be made of the same order by engineering the magnonic dispersion, in particular, according to our calculations by employing the dipole-exchange backward volume waves to increase the frequency dip shown in Fig. 1.

[1] M. Haidar, A.A. Awad, A. Houshang, M. Dvornik, R. Khymyn and J. Akerman, *An intrinsic nano-constriction based spin torque nanooscillator*, 62nd Annual Conference on Magnetism and Magnetic Materials (MMM), November 6-10, Pittsburgh, PA, USA (2017) [2] M. Dvornik, A. A. Awad, and J. Akerman, *Origin of magnetization auto-oscillations in constriction-based spin Hall nano-oscillators*, Phys. Rev. Appl., (accepted). [3] P. Durrenfeld, A. A. Awad, A. Houshang, R. K. Dumas, and J. Akerman, Nanoscale 9, 1285 (2017). [4] S. W. Hawking, Nature (London) 248, 30 (1974); Commun.Math. Phys. 43, 199 (1975). [5] A. Roldan-Molina, Alvaro S. Nunez, and R. A. Duine, Phys. Rev. Lett. 118, 061301 (2017). [6] W. G. Unruh, Phys. Rev. Lett. 46, 1351 (1981). [7] J. Xia, X. Zhang, M. Yan, W. Zhao, Y. Zhou, Scientific Reports 6, 25189 (2016) [8] S. Zhang and Z. Li, Phys. Rev. Lett. 93, 127204, (2004); D. C. Ralph and M. D. Stiles, J. Magn. Magn. Mater. 320, 1190 (2008). [9] V. Vlaminck and M. Bailleul, Science 322, 410 (2008). [10] A. Vansteenkiste, J. Leliaert, M. Dvornik, M. Helsen, F. Garcia Sanchez, and B. Van Waeyenberge, AIP Adv. 4, 107133 (2014).

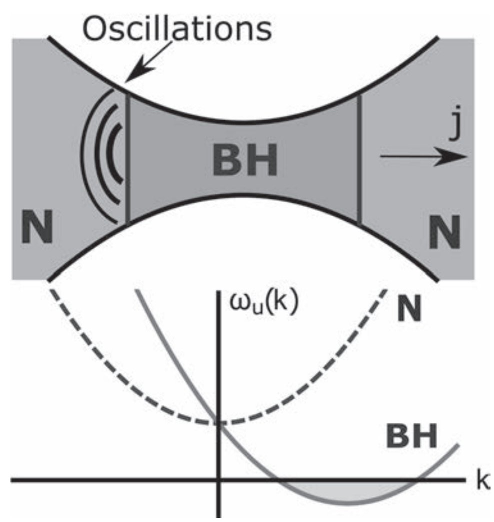

Fig. 1. The nano-constriction in a thin magnetic film as an analog of the black hole. The dispersion relations for the regular region - "N" and magnonic black hole - "BH" are shown below the image of the magnetic structure. The magnonic band-gap disappears at the boundary of the "black hole".

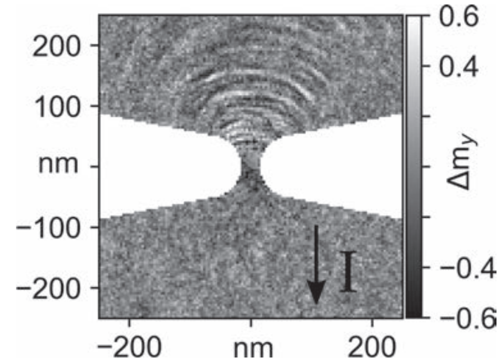

Fig. 2. Numerical simulations of the magnon generation caused by a "black hole" radiation in the thin nano-constricted Py film. The propagating spin waves are seen at the top side of the nano-constriction.

4:45

HD-11. Electrical spin injection into an AlGaAs/GaAs-based high-mobility two-dimensional electron system.

Z. Lin[1], D. Pan[2], M. Rasly[1] and T. Uemura[1]
1. Graduate School of Information Science and Technology, Hokkaido University, Sapporo, Japan; 2. School of Engineering, Hokkaido University, Sapporo, Japan

1. Introduction The injection of spin-polarized electrons from ferromagnets into semiconductors has attracted much interest for creating spin transistors. Spin injection into bulk semiconductors such as GaAs [1], Si [2], and Ge [3] has been realized at room temperature. On the other hand, a two-dimensional electron gas (2DEG) structure of AlGaAs/GaAs has attracted much interest for its high electron mobility, and it is used for high electron mobility transistors (HEMTs). Apart from that, the 2DEG structure is useful as a channel of a spin transistor. Up to date, however, electrical spin injection into an AlGaAs/GaAs 2DEG channel has been achieved only by using GaMnAs as a spin source [4], and the demonstration of spin injection was limited below 50 K because of the low Curie temperature (T_C < ~200 K) of GaMnAs. In this study, we demonstrated spin injection into an AlGaAs/GaAs 2DEG channel up to 138 K by using CoFe (T_C > 1000 K) as a spin source. 2. Experimental method Figure 1(a) shows a layer structure of a spin injection device. Layers consisting of (from the substrate side) ud-GaAs (400 nm)/ud-$Al_{0.3}Ga_{0.7}As$ (100 nm)/n^--$Al_{0.3}Ga_{0.7}As$ (Si = 3 × 10^{18} cm^{-3} and 100 nm)/ud-$Al_{0.3}Ga_{0.7}As$ (15 nm)/ud-GaAs (50 nm)/n^--GaAs (Si = 7 × 10^{16} cm^{-3} and 100 nm)/n^+-GaAs (Si = 7.5 × 10^{18} cm^{-3} and 30 nm) were grown by molecular beam epitaxy (MBE) on a GaAs (001) substrate. Then a CoFe layer (5 nm) was grown by magnetron sputtering at room temperature. Using electron-beam lithography and Ar ion milling techniques, a four-terminal nonlocal device was fabricated (Figure 1(b)). The size of the injector and detector were 0.5 × 5 μm and 1.0 × 5 μm, respectively, and the spacing (*d*) between them was 0.5 μm. 3. Results and Discussion From the Hall effect measurement, electron mobilities ranging from 24200 to 42700 cm^2/Vs and sheet carrier concentrations ranging from 6.9 × 10^{11} to 8.5 × 10^{11} cm^{-2} were obtained at 77 K for the AlGaAs/GaAs 2DEG structure. Such relatively high electron mobilities indicate that the 2DEG channel was well formed at the interface of the AlGaAs/GaAs heterostructure. Figure 2(a) shows a clear nonlocal spin-valve signal observed at 77 K, a higher temperature than that reported in Ref. 4, which used GaMnAs as a spin source. Furthermore, the temperature dependence of the spin-valve signal was investigated. Figure 2(b) shows $|\Delta V_{NL}/I_{bias}|$ as a function of temperature, where ΔV_{NL} is the amplitude of a spin-valve signal and I_{bias} is the bias current. The spin-valve signals were observed from 4.2 K to 138 K. Interestingly, the spin-valve signal doesn't show monotonic decrease as increasing temperature and it reaches to a peak at ~80 K. This contrasts with the result observed in bulk GaAs [1], in which monotonic decrease of spin-valve signals with increasing temperature was observed. These results contribute to better understanding of spin transport in a 2DEG channel, which is indispensable for the realization of the future spin transistors which can operate at a relatively high temperature.

[1] T. Uemura *et al*., Appl. Phys. Lett. 99, 082108 (2011). [2] T. Suzuki *et al.*, APEX 4, 023003 (2011). [3] M. Yamada *et al.*, APEX 10, 093001 (2017). [4] M. Oltscher *et al*., Phys. Rev. Lett. 113, 236602 (2014).

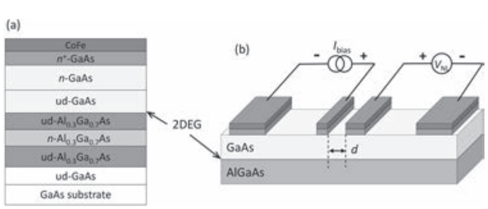

Fig. 1(a). 2DEG layer structure of a spin injection device. (b) Device structure and circuit configuration for nonlocal spin-valve measurements.

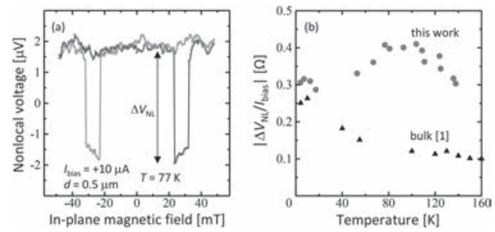

Fig. 2(a). A nonlocal spin-valve signal at 77 K. (b) Temperature dependence of $|\Delta V_{NL}/I_{bias}|$, where ΔV_{NL} is the amplitude of a spin-valve signal and I_{bias} is the bias current.

FRIDAY AFTERNOON, 27 APRIL 2018 ROSELLE II, 2:00 TO 5:00

Session HE
DYNAMICS OF SKYRMIONS

Christian Back, Chair
University of Regensburg, Regensburg, Germany

CONTRIBUTED PAPERS

2:00

HE-01. 140% voltage induced modification of interfacial DMI to tune skyrmionic bubbles in Ta/FeCoB/TaOx trilayers.

T. Srivastava[1], M. Schott[2,1], M. Belmeguenai[3], Y. Roussigné[3], A. Bernand-Mantel[2], L. Ranno[2], V. Krizakova[2], S. Pizzini[2], S.M. Chérif[3], A. Stashkevich[3], S. Auffret[1], M. Chshiev[1], C. Baraduc[1] and H. Béa[1]
1. Univ. Grenoble Alpes, CEA, CNRS, Grenoble INP, INAC-Spintec 38000, Grenoble, France; 2. Univ. Grenoble Alpes, CNRS, Néel Institute, F-38042, Grenoble, France; 3. Laboratoire des Sciences des Procédés et des Matériaux, Univ. Paris 13 Nord, Villetaneuse, France

Skyrmions are chiral magnetic textures [1] envisioned as potential candidates for magnetic memories and logic devices [2,3]. Initially discovered in bulk crystals like MnSi and FeGe at low temperature [4,5], they have recently been observed at room temperature in thin trilayer systems consisting of a heavy metal (HM), a ferromagnet (FM) and an insulator (I) like Ta/FeCoB/TaOx [6], Pt/Co/Ta, Pt/CoFeB/MgO [7] and Pt/Co/MgO [8]. In these trilayers, skyrmions are stabilized not only by interfacial Dzyaloshinskii- Moriya interaction (DMI) which arises due to the breaking of inversion symmetry and spin orbit coupling, but also by dipolar, exchange and interface anisotropy energies. For efficient implementation of skyrmions in devices, it is imperative to reliably control its properties. By proper choice of the materials, layer thicknesses and interface quality, we can tune their static magnetic properties. Furthermore, a dynamic control is possible by using electric field effects. For example, electric field has recently been employed for creation and annihilation of skyrmions at room temperature, by tuning the interface anisotropy and saturation magnetization [9,10,11,12,13]. In our knowledge however, a significant influence of electric field on interfacial DMI [14] has not been demonstrated yet. Here we report an increase of interfacial DMI by 140 % through voltage gating in sputter deposited Ta(3)/FeCoB(0.9)/TaOx(1) (thicknesses in nm) trilayers, where skyrmions are observed under small out of plane magnetic fields (30 μT). We have patterned transparent electrodes to allow optical observations under voltage application. Our Brillouin Light Spectroscopy (BLS) measurements have shown an increase by 140% of the frequency shift (Δf) between Stokes (f_S) and anti-Stokes (f_{AS}) resonances when the sample was subjected to a voltage of -10V (electric field of -170 MV/m), as represented in Fig 1(a) and (b). In contrast to the large effect observed at -10V, only a slight increase of Δf is observed at +10V (Fig 1(b)). This frequency shift allows a direct determination of the interfacial DMI energy using $\Delta f=2\gamma_s k_{SW} D/(\pi M_s)$ (where γ is the absolute value of the gyromagnetic ratio, k_{SW} is the spin wave vector, D is the interfacial DMI energy and M_s is the saturation magnetization) [15]. Indeed by measuring the polar magneto-optical Kerr (p-MOKE) signal amplitude at the exact same location, we demonstrate that this increase of Δf is not due to a modification of magnetization under voltage, but only due to a strong increase of the interfacial DMI. This effect could thus be instrumental in controlling the skyrmion chirality. The change in DMI was found to be consistent with the change in the demagnetized stripe domain width observed by p-MOKE. The stripe width and its vatiations under voltage were used to determine the change in the domain wall energy by using the relation $\sigma_W= \mu_0 M_s^2 t/\pi \ln(L/\alpha t)$ where t is the ferromagnetic film thickness and α is a coefficient equal to 0.95 [10]. In the presence of DMI, the domain wall energy is given by $\sigma_W=4\sqrt{(AK)}-\pi D$ [9,16] where K is the effective anisotropy and A is the exchange stiffness. By using the parameters extracted from p-MOKE measurement (H_k plotted in Fig 2(d), M_s in Fig 1(c) inset, in Fig 2(a)) and BLS (D in fig1 (c)) we could thus extract the value of A, close to 1.5pJ/m. The exchange stiffness turns out to change by less than 2% under applied voltage (Fig 2(e)). We can therefore conclude that in our sample, electric field produces a huge change of interfacial DMI and has little effect on the other magnetic properties (M_s, H_k, A). We can thus tune the skyrmionic bubbles by modulating mainly the interfacial DMI through applied voltage. We will also present the influence of time scales on these effects for both long (4-15 hours) and short (few minutes) time scale durations. As the BLS measurements are performed on long time scale durations, it is thus important to compare the results obtained from p-MOKE for both long and short time scales to ensure the extent and reversibility of these effects and the potential for applications.

1. Bogdanov, A. N. et al. Thermodynamically stable vortices in magnetically ordered crystals. The mixed state of magnets. J. Exp. Theor. Phys. 95, 178 (1989) 2. Kiselev, N. S. et al. Chiral skyrmions in thin magnetic. films: new objects for magnetic storage technologies? J. Phys. D. Appl. Phys. 44, 392001 (2011) 3. Fert, A. et al. Skyrmions on the track. Nat. Nanotech. 8, 152–156 (2013) 4. Muhlbauer, S. et al. Skyrmion Lattice in a Chiral Magnet. Science 323, 915 (2009) 5. Yu, X. et al. Real-Space Observation of a Two Dimensional Skyrmion Crystal. Nature 465, 901 (2010) 6. Jiang, W. et al. Blowing Magnetic Skyrmion Bubbles. Science 349, 283 (2015) 7. Woo, S. et al. Observation of Room-Temperature Magnetic Skyrmions and Their Current-Driven Dynamics in Ultrathin Metallic Ferromagnets. Nat. Mater. 15, 501 (2016) 8. Boulle, O. et al. Room-Temperature Chiral Magnetic Skyrmions in Ultrathin Magnetic Nanostructures. Nat. Nanotechnol. 11, 449 (2016) 9. Hsu, P.-J. et al. Electric-Field-Driven Switching of Individual Magnetic Skyrmions. Nat. Nanotechnol. 12, 123 (2016) 10. Schott M. et al. The Skyrmion Switch: Turning Magnetic Skyrmion Bubbles on and off with an Electric Field. NanoLett., 17, 3006 (2017) 11. Upadhyaya, P. et al. Electric-Field Guiding of Magnetic Skyrmions. Phys. Rev. B 92, 134411 (2015) 12. Kang, W. et al. Voltage Controlled Magnetic Skyrmion Motion for Racetrack Memory. Sci. Rep. 6, 23164 (2016) 13. Nakatani, Y. et al. Electric Field Control of Skyrmions in Magnetic Nanodisks. Appl. Phys. Lett. 108, 152403 (2016) 14. Nawaoka, K. et al. Voltage induction of interfacial Dzyaloshinskii- Moriya interaction in Au/Fe/MgO artificial multilayer. Appl. Phys. Express 8, 063004 (2015) 15. Belmeguenai, M. et al. Brillouin light scattering investigation of the thickness dependence of Dzyaloshinskii-Moriya interaction in Co0:5Fe0:5 ultrathin films. Phys. Rev. B, 93, 174407 (2016) 16. Heide, M. et al. Dzyaloshinskii-Moriya Interaction Accounting for the Orientation of Magnetic Domains in Ultrathin Films: Fe/W(110). Phys. Rev. B 78, 140403 (2008)

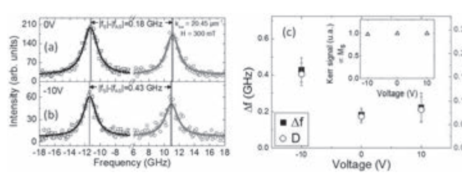

Fig. 1. BLS spectra (open symbols) and Lorenztian fits (lines) measured under 0V (a) and -10V(b). The frequency difference Δf changes by 140% at -10V. (b) Variation of frequency difference Δf and deduced interfacial DMI as a function of applied voltage. The variation is asymmetric, more pronounced for negative voltage as compared to positive voltage. The error bars correspond directly to the measurement duration of the spectrum at each voltage. Inset: Variation of saturation magnetization M_s as a function of applied voltage extracted from p-MOKE. A 5% of M_s variation is obtained in the applied voltage range.

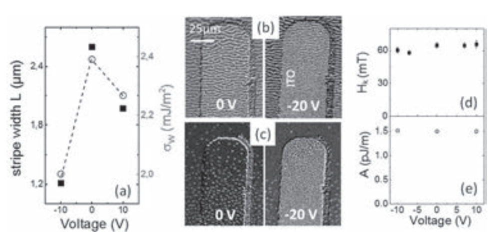

Fig. 2. (a) Measured variation of stripe domain width and deduced domain wall energy as a function of applied voltage. (b,c) p-MOKE images in the region of 50- 800μm ITO electrode at zero magnetic field: At zero voltage (left), the stripes (b) and skyrmions (c) below and outside ITO electrode are similar. They reduce drastically in size at -20V (right). Variation under voltage of anisotropy field H_k (d) measured by p-MOKE and of exchange stiffness A extracted from BLS and p-MOKE (e).

2:15

HE-02. Manipulating magnetic skyrmions in ultrathin Pt/Co/MgO$_x$ nanostructures.

R. Juge[1], S. Je[1], D. de Souza Chaves[2], S. Pizzini[3], L.D. Buda-Prejbeanu[1], L. Aballe[3], M. Foerster[3], A. Locatelli[4], T.O. Mentes[4], F. Maccherozzi[5], S. Dhesi[5], S. Auffret[1], G. Gaudin[1], J. Vogel[2] and O. Boulle[1]
1. CEA-SPINTEC, Grenoble, France; 2. Institut Néel CNRS, Grenoble, France; 3. ALBA Synchrotron Light Facility, Barcelona, Spain; 4. Elettra Sincrotrone, Trieste, Italy; 5. Diamond Light Source Ltd, Didcot, United Kingdom

Magnetic skyrmions are nanoscale whirling configurations of the magnetization. Their small size and the fact that they can be manipulated by small in-plane current densities have opened a new paradigm to manipulate the magnetization at the nanoscale. This has led to proposals for novel memory and logic devices in which the magnetic skyrmions are the information carriers [1]. Initially discovered in B20 chiral magnets, they have been observed more recently at room temperature in ultrathin sputtered Heavy Metal (HM)/Ferromagnetic (FM) multilayers [2,3,4,5] as well as their current-induced manipulation [2,5,6], which have lifted an important bottleneck towards the practical realization of such devices. In particular, we recently reported magnetic skyrmions with a typical size of 100 nm in an ultrathin Pt/Co/MgO$_x$ single layer at room temperature and at zero external magnetic field. Using X-ray Magnetic Circular Dichroism combined with Photo-Emission Electron Microscopy (XMCD-PEEM), we were able to demonstrate their internal homochiral left-handed Néel structure [4]. This stack is particularly interesting for the study of magnetic skyrmions and their applications as it is characterized by a very large interfacial Dzyaloshinskii-Moriya interaction (D=2 mJ/m^2) [4] and an efficient current-induced manipulation is expected due to the large spin-orbit torques induced by the spin Hall effect in the Pt layer [7]. The use of a single ferromagnetic layer makes this stack a model system for the study of the static and dynamic properties of magnetic skyrmions, avoiding the additional complexity induced by the interlayer interactions in multilayers systems [8]. Furthermore, the small size of the skyrmions combined with the reduced Joule heating in this ultrathin multilayer make this system appealing for applications. Here we report on the manipulation of isolated room-temperature magnetic skyrmions in sputtered single-layered Pt/Co/MgO$_x$ nanotracks and nanodots using external magnetic field and in-plane current pulses. We show that the skyrmions size can be easily tuned by playing on the lateral dimensions of the nanostructures and by using external magnetic field amplitudes of a few mT, which allow to reach sub-100 nm diameters [9]. We also observed in this system a fast current-induced motion of small skyrmions (about 150 nm in diameter) in µm-wide tracks. In Fig.1.(a-c), one can see a series of XMCD-PEEM images showing a magnetic skyrmion after two consecutive 10 ns current pulses with opposite polarities and with an amplitude of $5x10^{11}$ A/m^2. The skyrmion is dragged back and forth with a motion characteristic of a left-handed Néel skyrmion : it moves against the electron flow with a component of the velocity transverse to it, an effect referred to as the Skyrmion Hall Effect [6,10]. At this current density, the mean velocity reaches 70 m/s (Fig 1.(d)). As the power dissipation due to Joule heating scales with the film thickness, the demonstration of fast skyrmion current-induced motion in a few nm thick multilayer is promising for lower power skyrmion-based memory and logic devices. However, the aforementioned experiments have also underlined the sensitivity of the skyrmions dynamics to the defects in the material as well as the edges which can impede reliable motion. In particular, our XMCD-PEEM observations highlight the important role of the pinning on the skyrmions size and stability under an out-of-plane magnetic field. Fig.2 shows a magnetic skyrmion in a 630 nm-diameter dot at zero external field (a) and for B_z = 4 mT (b). We observe that the skyrmion is pinned near the edge of the nanostructure and that its diameter decreases in a step-like fashion when the magnetic field increases, a behavior that micromagnetic simulations in a disorder-free scenario fail to reproduce (see Fig 2.(c)). Indeed, it is well known that the polycrystalline grain structure of magnetic ultrathin films is a source of local pinning for magnetic domain walls. More recently, the influence of the inherent disorder of these films on the skyrmions stability have begun to be addressed [11,12]. Here, we model using micromagnetic simulations the disorder by a granular surface with local anisotropy fluctuations (Fig.2.(d)), which allow to reproduce partly the effect of the pinning on the field dependence of the skyrmion size (Fig 2.(c)). These results also reflect that the Pt/Co/MgO$_x$ system, due to its simple structure, can be efficiently modelled, which paves the way for further experimental and micromagnetic investigations.

[1] Fert *et al.*, Nat Nano 8 (3), 152 (2013) [2] Jiang *et al.*, Science 349 (6245), 283 (2016) [3] Moreau-Luchaire *et al.*, Nat Nano, 11 (5), 444 (2016) [4] Boulle *et al.*, Nat Nano 11 (5), 449 (2016) [5] Woo *et al.*, Nat Mat 15 (5), 501 (2016) [6] Jiang *et al.*, Nat Phys, 13 (2), 162 (2017) [7] Avci *et al.*, Appl Phys Lett 100 (21), 212404 (2012) [8] Legrand *et al.*, arXiv:1712.05978 [cond-mat.mtrl-sci] (2017) [9] Juge *et al.*, JMMM 10.1016/j.jmmm.2017.10.030 (2018) (in press) [10] Litzius *et al.*, Nat Phys 13 (2), 170 (2017) [11] Kim and Yoo, Appl Phys Lett 110 (13), 132404 (2017) [12] Legrand *et al.*, Nano Lett 17 (4), 2703 (2017)

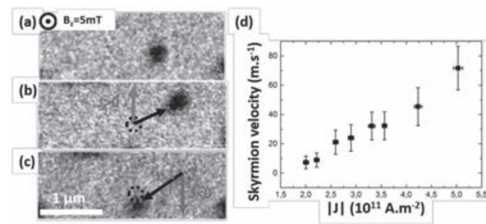

Fig. 1. (a-c) XMCD-PEEM images of a magnetic skyrmion (a) before, (b) after a positive 10 ns in-plane current pulse and (c) after a negative one with |J|=$5x10^{11}$ A/m^2. (d) Average skyrmion velocity measured in 3 µm-wide tracks as a function of the applied current density.

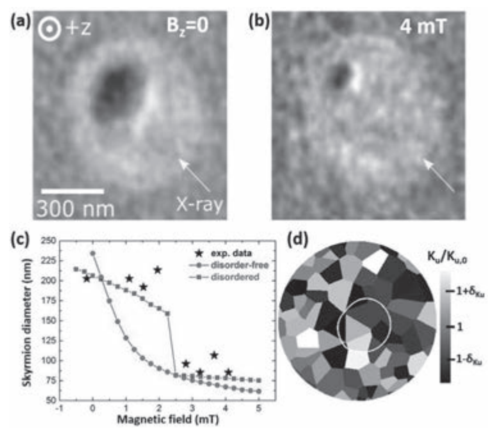

Fig. 2. (a,b) XMCD-PEEM images of a magnetic skyrmion in a 630 nm-diameter dot for different applied magnetic fields. (c) Skyrmion diameter as a function of the applied field. The experimental data points (black stars) are extracted from the XMCD-PEEM images. Micromagnetic simulations : the red dots correspond to the case of a perfect defect-free film and the green squares to the case of a disordered film with local anisotropy fluctuations as shown in (d) at B=0.

INVITED PAPER

2:30

HE-03. Dynamics of Skyrmions in Magnetic Multilayers at Room Temperature.

S. Woo[1]
1. Center for Spintronics, Korea Institute of Science and Technology, Seoul, The Republic of Korea

In spintronics, magnetic skyrmions are the most promising candidate for the next-generation memory-type application due to their nanometer-size, topological stability and efficient current-driven motion. [1] Recent efforts have realized the room-temperature stabilization of magnetic skyrmions and their current pulse-induced displacement on nanotracks in magnetic heterostructures, [2, 3] where the strong interfacial Dzyaloshinskii-Moriya (DM) interaction leads to the stabilization of such skyrmion structure. [4, 5, 6] However, there still exist many unsolved practical limitations toward the realization of fully functional skyrmionic devices. In this presentation, we show our recent achievements with room-tempearture skyrmions observed by static and dynamic soft X-ray transmission microscopy. We first demonstrate a new type of skyrmion, called *ferrimagnetic skyrmion*. [7] Recent theoretical studies have predicted enhanced current-driven behaviour for antiferromagnetically exchange-coupled skyrmions with opposite topological charges excited in two sublattices. [8] In this work, we present the stabilization of such skyrmions and their current-driven dynamics in ferrimagnetic GdFeCo films. By utilizing element-specific soft X-ray imaging, we find that the skyrmions in the Gd and FeCo sublayers are antiferromagnetically exchange-coupled as shown in Fig 1. [7] Having established that ferrimagnetic skyrmions can form at a finite external field in this material, we next study their current-induced dynamics in the magnetic track. With their current-driven motion, which propagates along the current flow direction (against the electron flow) for both $+M_z$-core and $-M_z$-core skyrmions, we first confirm that they are homochiral left-handed Néel-type hedgehog skyrmions stabilized by interfacial DMI in Pt/ferromagnet thin films. This implies that the interfacial DMI at the Pt/GdFeCo interface plays a crucial role in stabilizing skyrmions and also driving them on the track in our ferrimagnetic structure. More importantly, their current-driven dynamics reveal that ferrimagnetic skyrmions can move at a velocity of ~60 m s^{-1}, which is comparable to the current state-of-the-art skyrmions observed in a few ferromagnetic heterostructures. [3, 9] Most strikingly, we observe a very small skyrmion Hall angle, $|\theta_{SkHE}| < 10°$, which is significantly lower than the skyrmion Hall angles, $|\theta_{SkHE}| > 30°$, observed for ferromagnetic skyrmions in Ta/CoFeB/MgO and Pt/CoFeB/MgO structures. [9, 10] Antiferromagnetic coupling between two sublayers and the corresponding largely-reduced net magnetization within GdFeCo films has led to the effective inhibition of the skyrmion Hall effect. With micromagnetic simulations, we further present that ferrimagnetic skyrmions are much more attractive than their ferromagnetic counterpart in many technological-relevant aspects, such as larger skyrmion mobility and strongly suppressed skyrmion Hall effect, mainly due to their antiferromagnetic nature. We believe that this finding experimentally highlights the possibility to build more reliable skyrmionic devices using ferrimagnetic and antiferromagnetic materials. [7] Secondly, we demonstrate the electrical creation and annihilation of a single magnetic skyrmion at room temperature, which are essential prerequisites for device application. [11] The stroboscopic pump-probe X-ray measurement serves as a key technique to reveal the deterministic and completely reproducible nature of the observation. We experimentally present that an engineered current pulses at a specific environment; unbalanced bipolar-pulse in the presence of small amount of in-plane magnetic field; can efficiently create and annihilate a single skyrmion in ferrimagnetic materials, GdFeCo, in nanosecond time scale. In particular, we reveal that the application of the weak following reversed-pulse, which eventually *forces* to annihilate a topological defect, vertical Bloch line (VBL), and turns the trivial common bubble into a non-trivial chiral skyrmion, plays a crucial role for the writing process. (See Figure 2 for schematic description of the process) Micromagnetic simulations reveal the microscopic origin behind the observed topological fluctuation with great qualitative and quantitative agreement. Our findings show that, on a technologically-relevant thin-film racetrack geometry, where the current-driven displacement of a train of individual skyrmions at speeds approaching 60 m/s has already been demonstrated, [7] the deterministic field-free writing and deleting of a single skyrmion can be easily achieved using electrical methods. We believe that this result serves as a key discovery, which has been the only essential missing piece towards the realization of skyrmion-based devices. [11]

1. A. Fert *et al., Nat. Nanotechnol.* 8, 152–156 (2013). 2. W. Jiang *et al.*, *Science*. 349, 283–286 (2015). 3. S. Woo *et al.*, *Nat. Mater.* 15, 501–506 (2016). 4. I. Dzyaloshinsky, *J. Phys. Chem. Solids*. 4, 241–255 (1958). 5. T. Moriya, *Phys. Rev.* 120, 91–98 (1960). 6. S. Woo *et al.*, *Nat. Commun.* 8, 15573 (2017). 7. S. Woo *et al.*, *arXiv:1703.10301* 8. J. Barke *et al., Phys. Rev. Lett.* 116, 147203 (2016). 9. K. Litzius et al., Nat. Phys. 13, 170-175 (2017) 10. W. Jiang et al., Nat. Phys. 13, 162-169 (2017) 11. S. Woo *et al.*, *arXiv:1706.06726*

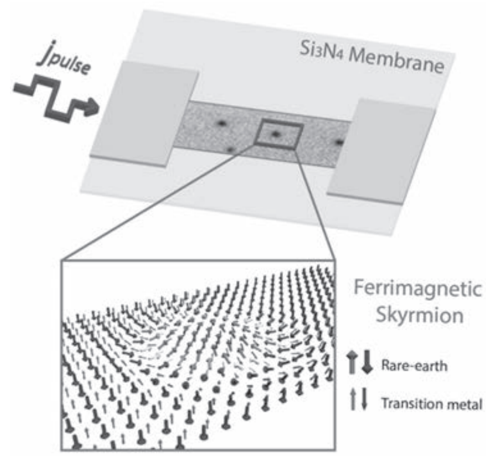

Fig. 1. Magnetic nanowire and experimental scheme used for current-driven dynamics measurements. An exemplary scanning transmission X-ray microscopy (STXM) image is enclosed. Schematic drawing of ferrimagentic skyrmion in Gd(rare-earth)-Fe(transition-metal) alloy is also shown below.

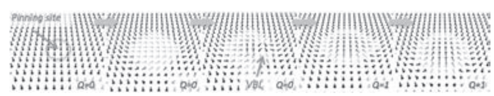

Fig. 2. Schematic drawing of skyrmion nucleation process. Upon the pulse application, a reversed domain of Q=0 first appear with a topological defect, which is vertical Bloch line (VBL). As we reverse the pulse polarity, the VBL can be expelled from the reversed domain, leading to the stabilization of magnetic skyrmion of Q=1.

CONTRIBUTED PAPERS

3:00

HE-04. Hybrid Chiral Skyrmions in Multilayered Magnetic Stacks.

W. Legrand[1], J. Chauleau[1,2], D. Maccariello[1], N. Reyren[1], S. Collin[1], K. Bouzehouane[1], N. Jaouen[2], V. Cros[1] and A. Fert[1]
1. Unité Mixte de Physique CNRS/Thales, Univ. Paris Sud, Université Paris-Saclay, Palaiseau, France; 2. Synchrotron SOLEIL, L'Orme des Merisiers, Gif-sur-Yvette, France

The magnetic skyrmions are whirling magnetic configurations, found in ferromagnetic [1], ferrimagnetic [2] or antiferromagnetic materials [3], exhibiting a winding of the magnetic order with a nontrivial topology. Due to the presence of the Dzyaloshinskii-Moriya interaction (DMI), originating from a breaking of the inversion symmetry either in the bulk of the structure or at interfaces, a unique chirality in these configurations is favoured, which enables the stabilisation of periodic skyrmion crystals or even isolated skyrmions, similar to punctual defects of the magnetic configuration. So far, isolated skyrmions, as found in multilayered magnetic stacks with interface asymmetry, are seen as best candidates for potential skyrmion-based applications [4]: *i*) the symmetry of the DMI imposes so-called Néel skyrmions, which are efficiently moved by spin-orbit torques obtained from heavy metal layers incorporated in the stack; *ii*) the size dependence of the different magnetic energies associated to isolated skyrmions allow to envisage further decreasing of skyrmion diameters and the stabilization of very compact, sub-10 nm configurations which are very scalable for computation and memory applications; *iii*) the enhancement of the magnetic volume associated to the vertical dimension of multilayered skyrmions (typically a few repetitions of a 1 nm-thick magnetic layer) results in a strong stability against thermal fluctuations allowing applications at room-temperature. Several works have demonstrated the viability of skyrmions for applications such as skyrmion racetracks, in which skyrmions can be created at one location [5], moved along a bit line [6] and detected [7] or annihilated at another location. In this work, we further explore the role of interlayer interactions in multilayer configuration on the nature of the skyrmions. We will first show that due to the competition between dipolar interactions and the DMI, opposite chiralities can coexist across the thickness of the multilayer. By using micromagnetic simulations, we can quantify the strength of each interaction in each individual layer and deduce the actual profile orientation: Néel, Bloch or in-between; as well as the chirality: clockwise (CW) or counter-clockwise (CCW), as shown in Fig. 1. We then bring experimental evidence and examples of such hybrid chiral skyrmions in multilayers, by observing their surface chirality using circular dichroism in x-ray resonant magnetic scattering (CD-XRMS) in multilayers of opposite stacking order (*i.e.*, opposite DMI) [8,9]. Because of the strong absorption in the soft x-ray range, and especially when the wavelength is tuned at the *3d*-metal L edge resonance, our observation of the chirality is mostly sensitive to the top of the structure and allow to discriminate the magnetic configuration in the top layers independently from the overall structure, as shown in Fig. 2. This phenomenon has been totally overlooked in previous studies of magnetic skyrmions. Moreover, we will show that the existence of such hybrid chirality of skyrmions in multilayers has drastic consequences on their current-induced spin-orbit torque dynamics. Therefore, the spin-current injection scheme in bottom, top and intermediate layers has to be properly engineered taking into account such hybrid chirality in order to get efficient spin-torque motion of compact skyrmions at room temperature [9]. Financial support from FLAG-ERA SoGraph (ANR-15-GRFL-0005) and European Union grant MAGicSky No. FET-Open-665095 is acknowledged.

[1] S. Heinze et al., *Nat. Phys.,* 7, 713-718 (2011) [2] S. Woo et al., *arXiv*:1703.10310 (2017) [3] J. Barker and Oleg A. Tretiakov, *Phys. Rev. Lett.*, 116, 147203 (2016) [4] A. Fert et al., *Nat. Mat. Rev.,* 2, 17031 (2017) [5] W. Legrand et al.*, Nano Lett.*, 17, 2703 (2017) ; W. Jiang et al., *Science,* 349, 283-286 (2015) [6] S. Woo et al., *Nat. Mater.*, 15, 501-506 (2016) ; A. Hrabec et al., *Nat. Commun.*, 8, 15765 (2017) [7] D. Maccariello et al., *arXiv*:1706.05809 (2017) to appear in *Nat. Nanotech.* [8] J.-Y. Chauleau et al., *arXiv*:1709.08352 (2017) to appear in *Phys. Rev. Lett.* [9] W. Legrand et al., *arXiv*:1712.05978 (2017)

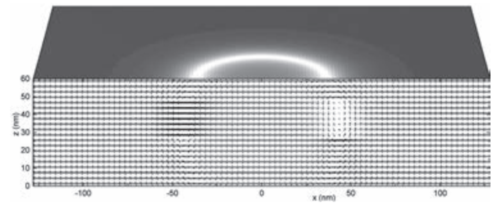

Fig. 1. Example of a cut view through the center of an isolated skyrmion configuration in a 20 repetitions multilayer of structure [X(1nm)/Co(1nm)/Z(1nm)]$_{x20}$, for a DMI strength of *D*=0.8 mJ m^{-2}. The red to blue colour in the top layer and in the arrows indicates the vertical component of the magnetisation from down (m_z=–1) to up (m_z=1). The arrows point in the direction of the magnetisation. The black to white background colour indicates the transverse component of the magnetisation from m_y=–1 to m_y=1. An evolution of the chirality can be seen through the structure, with CCW Néel skyrmion in the bottom, Bloch skyrmion in the middle and CW Néel skyrmion in the top of the multilayer.

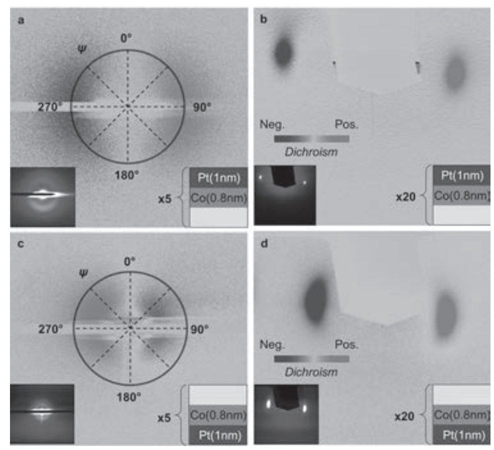

Fig. 2. Circular dichroism analysis of 4 multilayer stacks with *D*<0 (a,b) and *D*>0 (c,d); 5 (a,c) and 20 repetitions (b,d). The dichroism (difference of circularly left and right polarised photons images) is normalised and given by the colour from blue (negative) to red (positive). Left insets are the corresponding sum images (both polarisations combined). Right insets are schemes of the studied stacks. The dichroism pattern indicates the chirality of the top few layers; along the 90°-270° axis it corresponds to Néel ordering in each case, and the sequence red-blue or blue-red indicates the chirality, CW or CCW, respectively. While for 5 repetitions the chirality agrees with the sign of *D*, for 20 repetitions, which have stronger dipolar interactions, the chirality is fixed by the formation of flux-closure arrangements, as was shown in Fig. 1. Therefore a unique CCW chirality in the top layers is observed in b and d (CW chirality in the bottom, not seen), whatever the sign of *D*.

3:15

HE-05. Skyrmion and antiskyrmion dynamics in ultrathin ferromagnetic films driven by spin-orbit torques.

U. Ritzmann[1,2], S. von Malottki[3], *J. Kim*[4], J. Sinova[1], S. Heinze[3] and B. Dupé[1]

1. Institut für Physik, Johannes Gutenberg Universität Mainz, Mainz, Germany; 2. Department for Physics and Astronomy, Uppsala University, Uppsala, Sweden; 3. Institute of Theoretical Physics and Astrophysics, Christian-Albrechts-Universität zu Kiel, Kiel, Germany; 4. Centre de Nanosciences et de Nanotechnologies, CNRS, Université Paris-Sud, Université Paris-Saclay, 91405 Orsay, France

The absence of inversion symmetry in magnetic films can allow chiral interactions such as anisotropic exchange of the Dzyaloshinskii-Moriya form to exist. In ultrathin ferromagnets on heavy-metal buffer layers, such as Pt, W, and Ir, the Dzyaloshinskii-Moriya interaction (DMI) is induced by the strong spin-orbit coupling at the interface [1]. The DMI can give rise to different nontrivial magnetic states such as skyrmions and antiskyrmions [2]. These are characterized by opposite topological charges, which govern the sense of gyration in their dynamics. In most studies to date, however, the robustness of the symmetry between opposite topological charges, as expressed in the Thiele equation [3], has not been examined in detail. In particular, the roles of core deformation, the internal degrees of freedom, and the underlying symmetry of the magnetic interactions that stabilize the skyrmions remain an open question. We show here that the symmetries of the magnetic interactions, combined with spin-orbit torques, play an important role in determining how the (anti-)skyrmion core moves. In particular, the choice of the DMI can lead to qualitatively different motion for opposite charges. We present results of atomistic spin simulations, where magnetic parameters are based on density functional theory calculations, of current-driven skyrmion and antiskyrmion dynamics due to spin-orbit torques. While the expected linear displacement is found for skyrmions, we discover new dynamical regimes involving antiskyrmions: trochoidal dynamics and skyrmion-antiskyrmion pair generation, which occur above successive current thresholds. An example of the different behavior is given in the Figure, including a state diagram for different field-like and damping-like torques. By taking into account deformations of the antiskyrmion core, we derive an additional equation of motion for the internal dynamics of the core which allows us to identify the trochoidal motion as the analog of precessional motion for domain walls above Walker breakdown. *This is a novel result in micromagnetism.* When a different form of the DMI is chosen, i.e., one that favors antiskyrmions over skyrmions, the opposite behavior is found — antiskyrmions undergo linear displacement, while skyrmions undergo trochoidal motion and can generate skyrmion-antiskyrmion pairs. This illustrates the importance of the symmetry of the DMI, rather than the topological charge, in governing the dynamics. This is further highlighted when the DMI is absent altogether, where the symmetry between skyrmion and antiskyrmion motion is restored. Our results suggest new avenues for exploiting skyrmion and antiskyrmion dynamics in nanodevices. This work was partially supported by the Horizon2020 Framework Programme of the European Commission (H2020-FETOPEN-2014-2015-RIA) under Contract No. 665095 (MAGicSky).

[1] A. Fert and P. M. Levy, Phys. Rev. Lett. *44*, 1538 (1980). [2] M. Bode et al., Nature 447, 190 (2007); B. Dupé et al., New J. Phys. *18*, 055015 (2016). [3] J. Sampaio et al., Nat. Nanotechnol. *8*, 839 (2013).

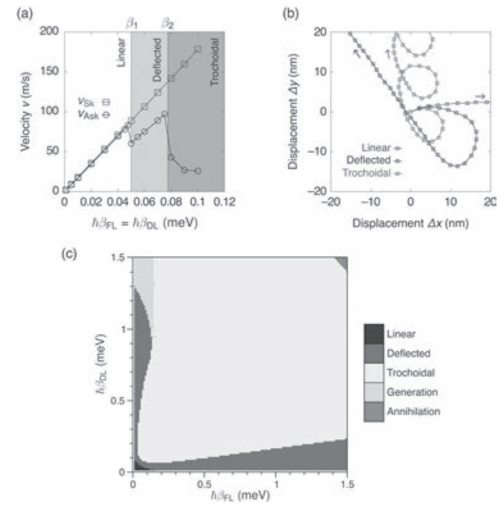

Fig. 1. Motion of antiskyrmions under current induced spin transfer torques. (a) Variation of the velocity of skyrmions and antiskyrmions as a function of the torques. Three propagation regimes are identified for antiskyrmions: a linear motion at low currents, a deflected linear motion at intermediate currents, and trochoidal motion at high currents. (b) Example of antiskyrmion trajectories for linear, deflected, and trochoidal motion. The arrows indicate the propagation direction. (c) State diagram for the antiskyrmion dynamics.

INVITED PAPER

3:30

HE-06. Electrical detection of skyrmions in multilayer nanostructures.

K. Zeissler[1], K. Shahbazi[1], J. Massey[1], S. Finizio[2], J. Raabe[2], M. Rosamond[3], E. Linfield[3], T.A. Moore[1], G. Burnell[1] and *C.H. Marrows*[1]
1. School of Physics and Astronomy, University of Leeds, Leeds, United Kingdom; 2. Swiss Light Source, Paul Scherrer Institut, Villigen, Switzerland; 3. School of Electronic and Electrical Engineering, University of Leeds, Leeds, United Kingdom

Magnetic skyrmions have excited much interest as the basis for novel data storage applications in which information is encoded and transferred in these magnetic knot-like quasiparticles. In multilayers of ultrathin magnetic films they are stabilised by the interfacial Dzyaloshinskii-Moriya interaction [1]. Due to tunability and room temperature stability these multilayers are held to have great scope for spintronic applications [2-5]. The proposed read-out of any such skyrmion-based spintronic device will rely upon the electrical detection of a single magnetic skyrmion within a nanostructure, through, for example, a change in the Hall resistivity [6]. We have fabricated nanodiscs from multilayers of Pt/Co/Ir which can support skyrmions at room temperature and have measured the Hall resistivity whilst simultaneously imaging the spin texture using magnetic scanning transmission x-ray microscopy. In the experiment reported here, a single skyrmion in a Ta (3.5 nm)/Pt (3.8 nm)/{Co (5.0 nm)/Ir (5.0 nm)/Pt (1.0 nm)}×10/Pt (3.2 nm) multilayer nanodisc was imaged using the PolLux scanning transmission X-ray microscope (STXM) as a function of out-of-plane magnetic field. In situ Hall measurements inside the STXM were taken just before imaging the magnetic state of the device as the field was swept. The Hall resistance R_{xy} shows a clear difference between uniformly magnetised states (A and B) and a single skyrmion state (C and D). We show that the Hall resistivity is correlated to both the presence and size of a magnetic skyrmion in the nanodisc and that the size-dependent part matches the expected anomalous Hall signal when averaging the magnetisation over the disc. The additional contribution arising from the presence of a single skyrmion is 11±1 nΩcm. This shows that electrical transport measurements can be used to detect individual skyrmions in nanostructures [7]. This work was funded by the Horizon 2020 FET-OPEN project MagicSky, the FP7 ITN WALL, Diamond Light Source and the EPSRC.

[1] Fert, A. et al., Nature Nanotech. 8, 152 (2013). [2] Boulle, O. et al., Nature Nanotech. 11, 449 (2016). [3] Jiang, W.J. et al., Science 349, 283 (2015). [4] Woo, S. et al., Nature Mater. 15, 501 (2016). [5] Moreau-Luchaire, C. et al. Nature Nanotech 11, 444 (2016). [6] Maccariello, D. et al., arXiv:1706.05809 [cond-mat.mes-hall]. [7] Zeissler, K., et al., arXiv:1706.06024 [physics.app-ph].

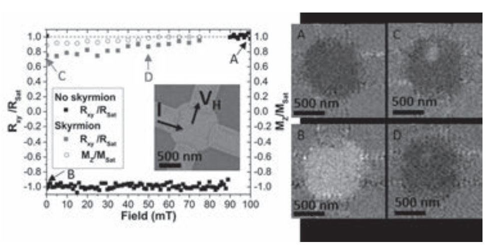

Fig. 1. Electrical Hall resistance and normalised out-of-plane magnetization of a single skyrmion in a [Pt/Co/Ir]×10 multilayer and corresponding XMCD contrast. The inset shows a scanning electron microscopy image of the disc measured. Points A-D correspond to the STXM images on the right.

CONTRIBUTED PAPERS

4:00

HE-07. Dynamics of a magnetic skyrmionium driven by a spin wave.

S. Li[1,2], J. Xia[3], X. Zhang[3], W. Kang[1], M. Ezawa[4], X. Liu[5], Y. Zhou[3] and W. Zhao[1]
1. Fert Beijing Institute, BDBC, and School of Electronic and Information Engineering, Beihang University, Beijing, China; 2. Shenyuan Honors college, Beihang University, Beijing, China; 3. School of Science and Engineering, The Chinese University of Hong Kong, Shenzhen, China; 4. Department of Applied Physics, University of Tokyo, Tokyo, Japan; 5. Department of Electrical and Computer Engineering, Shinshu University, Nagano, Japan

Among the many magnetic objects for next generation storage technologies, the skyrmion has drawn the most attention and commentary due to its nanometric size and topologically protected stability [1]. However, the application of skyrmion motion along the nanotrack whether driven by spin-polarized electric current or a spin wave, would both face a significant obstacle, that is "Hall behavior" accompanied by a topological number of Q = +1 [2,3]. To overcome this problem, skyrmionium emerged as intriguing resolution with zero topological number and skyrmion-like structure, shows great promise for use in magnetic and spintronic applications because it does not suffer from the skyrmion Hall effect. It has been first observed on a ferrimagnetic film in the experiment of laser radiation [4]and can be moved and manipulated by spin current [2]. So far how skyrmionium driven by magnon current has not been investigated. Therefore, in this paper, we study in detail the dynamics of skyrmionium driven by a spin wave in chiral magnetic film and nanotrack. Figure 1 shows snapshots of spin-wave-driven motion process of three magnetic objects, which display significant differences when responding to a magnon current, behaving in not just the motion directions but velocities. Then we proceed an effective analysis in the framework of Thiele equation [5] to explain why skyrmionium is moving along the direction of magnon current, contrary to skyrmion. We find that the transverse component of velocity is attributed to the longitudinal scattering section of skyrmionium. Afterwards in order to explore the potential of spin waves-driven skyrmionium in future spintronics application, we further investigate the related factors influencing the skyrmionium motion in a nanotrack, including the nanotrack width, the Gilbert damping, the inner and outer radius of skyrmionium. Figure 2 presents the dependence of velocity of the skymionium on perpendicular magnetic field by changing the radius of skyrmionium in the nanotrack. Finally, we research the status of skyrmionium after stopping spin wave. In conclusion, we demonstrate that the skyrmionium not only does not have Hall behavior but also move along the magnon current, which is distinctly different from the skyrmion. Most importantly, the velocity of skyrmionium is lager than skyrmion in driving of the magnon pressure and can be effectively tuned by small magnetic field. Our results provide a base for applying magnon-driven skyrmionium in novel information storage and spintronics devices.

[1] Stavros, K., et al. *Phys. Rev. B.* 92, 064412 (2015) [2] Zhang, X. C., et al. *Phys. Rev. B.* 94, 094420 (2016) [3] Iwasaki, J., et al. *Phys. Rev. B.* 89, 064412 (2014). [4] Finazzi, M., et al. *Phys. Rev. Lett.* 110 177205 (2013).

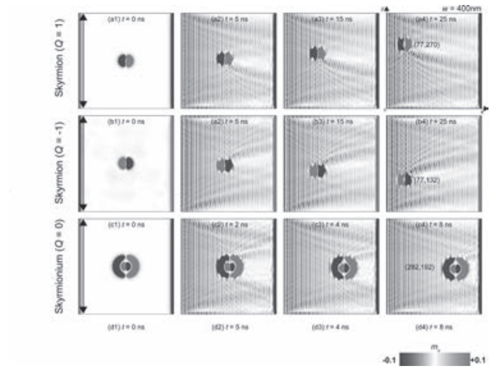

Fig. 1. Snapshots of motion process of three magnetic objects driven by the spin wave.

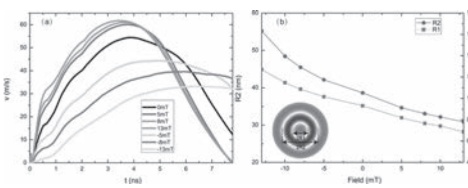

Fig. 2. Dependence of velocity of the skymionium on the perpendicular magnetic field by changing the radius in the nanotrack with width 150 nm.

4:15

HE-08. A theory on skyrmion size and profile.

X. Wang[1,2], H. Yuan[3] and X. Wang[2,4]
1. University of Electronic Science and Technology of China, Chengdu, China; 2. Physics, The Hong Kong University of Science and Technology, Hong Kong, Hong Kong; 3. Physics, Southern University of Science and Technology, Shenzhen, China; 4. HKUST Shenzhen Institute, Shenzhen, China

Skyrmions, topological objects originally used to describe resonance states of baryons [1], were observed in magnetic systems that involve Dzyaloshinskii-Moriya interaction (DMI). Magnetic skyrmions are believed to be potential information carriers in future high density data storage and information processing devices [2,3]. Although much knowledge about magnetic skyrmions has been accumulated after intensive studies including skyrmion generation, the dependence of skyrmion size (R) on material parameters such as exchange energy, magnetic anisotropy energy, and DMI strength is still poorly understood at a quantitative, or even qualitative level. Here we show that the skyrmion profiles agree well with Walker-like 360° domain wall formula [4,5]. By minimizing the energy, we obtain the analytical expressions of the skyrmion size R and wall width w as functions of exchange constant A, DMI coefficient D, anisotropy constant K, and external magnetic field$B$. These results agree perfectly with micromagnetic simulations and are consistent with experiments. We consider a 2D film with Heisenberg exchange interaction (of exchange constant A), interfacial Dzyaloshinskii-Moriya interaction (DMI) (of DMI coefficient D), perpendicular easy-axis anisotropy (of anisotropy constant K), and a perpendicular magnetic field (of field strength B). We first numerically verify that an isolated Néel skyrmion is rotational symmetric and the magnetization profile along any diameter can be well fitted by a Walker-like 360° domain wall profile with two characteristic lengths, the skyrmion size and the skyrmion wall width, as shown in Fig. 1. The skyrmion profile can be described by $\Theta(r)$ and $\Phi(\phi)$, where Θ and Φ are polar and azimuthal angles of magnetization m, and r, ϕ are radial and angle coordinates in space. The total energy E is a functional of $\Theta(r)$ and $\Phi(\phi)$. Then by substituting the 360° domain wall profile into the energy functional, we obtain an expression of total energy E as a function of R and w. The equilibrium R and w can be obtained by minimizing the total energy, and the obtained results almost perfectly agree with the numerical simulation results as shown in Fig. 2. The exchange and DMI energies come from the spatial magnetization variation rate. For a skyrmion, the magnetization variation rates in the radial and tangent directions scale respectively as $1/w$ and $1/R$. The exchange energy is then proportional to skyrmion wall area of Rw multiplying the square of the magnetization variation rates $1/R^2+1/w^2$. Near the skyrmion wall region, the magnetization variation rate along the tangent direction is perpendicular to the magnetization and does not contribute to the DMI energy. The DMI energy is then proportional to wall area Rw multiplying the magnetization variation rate along radial direction ($1/w$). The anisotropy energy is mainly from the skyrmion wall area. The Zeeman energy of the skyrmion comes from the inner domain proportional to its area of $\pi(R\text{-}cw)^2$, where c is a coefficient depending on the magnetization profile, and from the wall area proportional to its area of Rw. Thus, by considering the physical meaning of each energy term as well as reasonable mathematical approximations, we obtain a simple analytical formula for the total energy in terms of R and w. The approximate formula also gives correct qualitative parameter dependence and good quantitative agreement with the simulations. The results are not limited to interfacial DMI. For bulk DMI, the only difference is Bloch-type skyrmions are preferred The radial profile as well the skyrmion size does not change.

[1] T. H. R. Skyrme, Nucl. Phys. 31, 556 (1962). [2] N. Nagaosa, and Y. Tokura, Nat. Nanotech. 8, 899 (2013). [3] A. Fert, V. Cros, and J. Sampaio, Nat. Nanotech. 8, 152 (2013); [4] H.-B. Braun, Phys. Rev. B 50, 16485 (1994). [5] N. Romming, A. Kubetzka, C. Hanneken, K. von Bergmann, and R. Wiesendanger, Phys. Rev. Lett. 114, 177203 (2015).

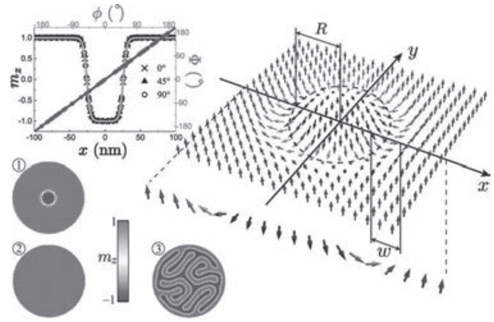

Fig. 1. Schematic diagram of a Néel skyrmion of radius R and wall (between inner and outer domains) width w in a 2D film. The arrows denote the spin direction. Spin orientations of the skyrmion along x axis is sketched below the main figure. Upper left inset: (Right axis) ϕ-dependence of Φ (red circles) and (Left axis) radial (r) distribution of m_z=cosΦ along the diameters of ϕ=0 (crosses), 45° (triangles) and 90° (circles) for Co parameters with B=0. The green solid line is the fit to 360°domain wall formula $\Theta_{dw}(r)$= 2arctan[sinh(R/w)/sinh(r/w)]. The blue solid line is Φ=ϕ. Lower left inset: Three typical equilibrium states obtained in the numerical simulations for different parameters: isolated skyrmion, single-domain state, and stripe domains. The pixel color encodes the m_z component with the color bar shown in the figure.

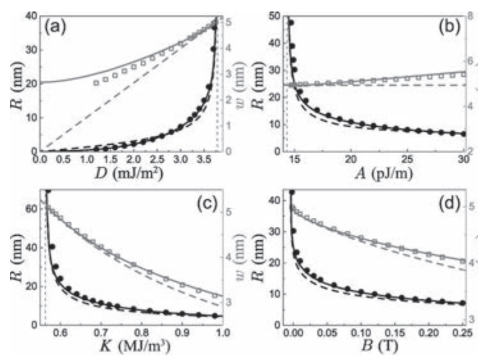

Fig. 2. The parameter dependences of skyrmion size R (left axis) and wall width w (right axis). In each subfigure, one of four parameters (D, A, K, B) is treated as a tuning parameter, and the other three parameters are fixed to above values. The symbols are the micromagnetic simulation data. The solid lines are exact analytical results obtained from the energy function. The dashed lines are approximate results. Vertical dashed lines are the upper (lower) bound of parameters above (below) which a stable skyrmion cannot exist.

4:30

HE-09. High speed bilayer skyrmion transport by voltage controlled magnetic anisotropy gradient.

C.C. Ang[1], W. Gan[1] and W. Lew[1]
1. School of Physical and Mathematical Sciences, Nanyang Technological University, Singapore, Singapore

Magnetic skyrmion transport mechanisms explored thus far have been primarily based on the use of spin transfer torques (STT). Experimental transport measurements based on the STT mechanisms showed that extremely high current densities on the order of 10^{12} A/m^2 are required to achieve practical speeds of more than 100 m/s[1]. Nanowires operating under such high current densities can result in both detrimental Joule heating effects and decreased energy efficiency. In addition, the propagation speed of skyrmions can be reduced significantly at elevated temperatures [2]. To overcome the aforementioned detriments, we propose the use of voltage controlled magnetic anisotropy (VCMA) gradient as an alternative transport mechanism [3]. In this work, we studied numerically the dynamics of VCMA gradient-driven skyrmions in a synthetic antiferromagnet (SAF) bilayer structure. The results in our model shows that the bilayer structure can overcome the limitation in speed caused by the skyrmion Hall effect to achieve speeds higher than STT transports. Under an anisotropy energy gradient of 600 GJ/m4 or a < 1 % change in magnetic anisotropy energy across the skyrmion, a transport speed of 840 m/s can be attained. Unlike skyrmion transport with STT, the VCMA-gradient transport also offers excellent scaling of speed with material property; VCMA gradient-driven skyrmions show an inverse relationship with Gilbert damping constant as shown in Figure 1. The transport velocity also scales linearly with the saturation magnetization. The excellent scaling properties unlocks multiple avenues for design to further optimize the skyrmion transport. A model for the bilayer skyrmion was also developed. The skyrmion motion can be described by the competition of 3 forces: the skyrmion Hall effect, VCMA gradient and skyrmion interlayer coupling. The interlayer coupling between the SAF skyrmions is a spring-like restoring force that keeps the skyrmions close, as shown in Figure 2. The interlayer coupling peaks at a quarter of the skyrmion diameter; above which the skyrmions are decoupled. Due to the spring-like coupling, oscillatory behaviour was observed, along with an increase in skyrmion mass. When a VCMA gradient is applied to drive the skyrmion forward, the skyrmion Hall effect drives the each skyrmion towards opposite edges while the interlayer coupling applies a restoring force towards the centre of the wire. The balance of these forces determines the trajectory of each skyrmion. In conclusion, our study reveals the rich skyrmion dynamics in a bilayer VCMA-gradient system. The proposed skyrmion transport mechanism was also demonstrated to achieve skyrmion speeds comparable with current-driven skyrmions while eliminating Joule heating effects. Furthermore, this mechanism is inherently dissipationless as it operates on voltage instead of current flow along the wire, promising low power skyrmionic devices.

[1] A. Hrabec, J. Sampaio, M. Belmeguenai, I. Gross, R. Weil, S. M. Chérif, et al., "Current-induced skyrmion generation and dynamics in symmetric bilayers," Nature Communications, vol. 8, 2017. [2] A. Yamaguchi, S. Nasu, H. Tanigawa, T. Ono, K. Miyake, K. Mibu, et al., "Effect of Joule heating in current-driven domain wall motion," Applied Physics Letters, vol. 86, p. 012511, 2005. [3] X. Wang, W. Gan, J. C. Martinez, F. Tan, M. Jalil, and W. Lew, "Efficient skyrmion transport mediated by a voltage controlled magnetic anisotropy gradient," Nanoscale, 2018.

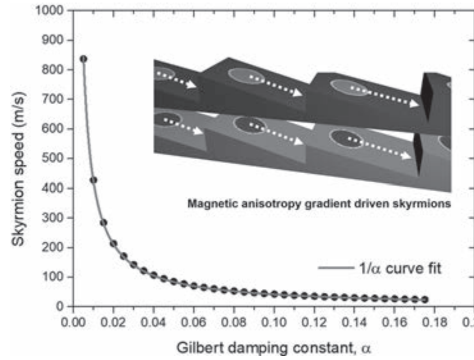

Fig. 1. Plot of skyrmion speed against Gilbert damping constant which demonstrates a strong inverse relationship. Inset is a schematic diagram of the magnetic anisotropy gradient driven skyrmions for the bilayer structure where the thickness of the layers corresponds to the value of magnetic anisotropy constant.

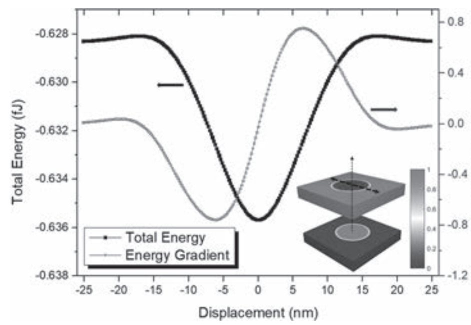

Fig. 2. (Left) Plot of total energy of skyrmions in a bilayer against the displacement of the 2 skyrmions. (Right) Plot of energy gradient against the displacement between the 2 skyrmions along a single axis. Inset is the schematic diagram of skyrmions in a bilayer and the in-plane axis of displacement for the skyrmion.

4:45

HE-10. Magnetic Skyrmion Dynamics in Wedge-shaped Nanotrack and Its Potential Applications.

X. Chen[1], W. Kang[1], D. Zhu[1], X. Zhang[2], Y. Zhang[1], Y. Zhou[2] and W. Zhao[1]
1. Beihang University, Beijing, China; 2. The Chinese University of Hong Kong, Shenzhen, China

Magnetic skyrmions are swirling topological configuration [1], mostly induced by chiral exchange interactions between atomic spins in non-centrosymmetric magnetic bulks or in thin films with broken inversion symmetry. With the rapid advances made in this field [2-3], the development of skyrmion-based spintronics holds promise for future applications owing to the topological nature, nanoscale size, and ultralow current density for motion. Furthermore, the standby energy consumption and heat generation during the processing and transportation of information can be efficiently reduced thanks to the nonvolatility. In this abstract, we present firstly our investigations on skyrmion dynamics in terms of size, velocity, energy, stability in a wedge-shaped nanotrack via micromagnetic and theoretical studies [4]. We find some interesting results compared to previous research. For example, the size of a skyrmion decreases as the nanotrack width decreases because of the compression by the nanotrack edge (see Fig. 1a), thus this property can be harnessed to adjust the dimension of skyrmions to acheive ultra-dense storage in racetrack memory [5]. Inspired by the findings in wedge-shaped nanotracks, we draw a conclusion about the tradeoff between the nanotrack width (storage density) and the skyrmion motion velocity (data access speed) by further analyzing the skyrmion dynamics in parallel nanotracks (see Fig. 1b). Our results may provide guidelines in designing skyrmion racetrack memory and other related skyrmionic applications. We also model a novel compact neuron device based on this wedge-shaped nanotrack. Under the coaction of the exciting current pulse and the repulsive force exerted by the edge of the nanotrack, the dynamic behavior of the proposed skyrmionic artificial neuron device corresponds to the leaky-integrate-fire (LIF) spiking function of a biological neuron (see Fig. 2). We believe that our study makes a significant step because such a compact artificial neuron can enable energy-efficient and high-density implementation of neuromorphic computing hardware [6].

[1] Skyrme, T. H. R. Nucl. Phys. 31, 556–569 (1962). [2] Fert, A., et al. Nat. Rev. Mater. 2, 17031 (2017). [3] Jiang, W. et al. Science 349, 283–286 (2015). [4] Chen, X. et al. Appl. Phys. Lett. 111, 202406 (2017). [5] Fert, A., et al. Nat. Nanotech. 8, 152-156 (2013). [6] Burr, G. W., et al., Adv. Phys. X 2, 89-124 (2017).

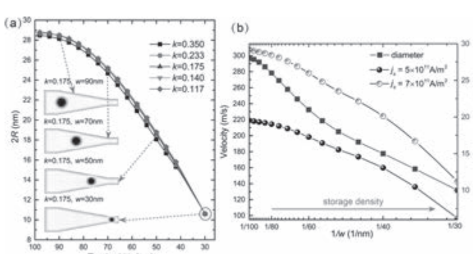

Fig. 1. Skyrmion dynamics investigations with micromagnetic simulations. (a) Diameter of the skyrmion as a function of the track width and slop, when flowing along the wedge-shaped nanotrack. (b) Tradeoff between the nanotrack width (storage density) and the skyrmion motion velocity (data access speed) in parallel tracks.

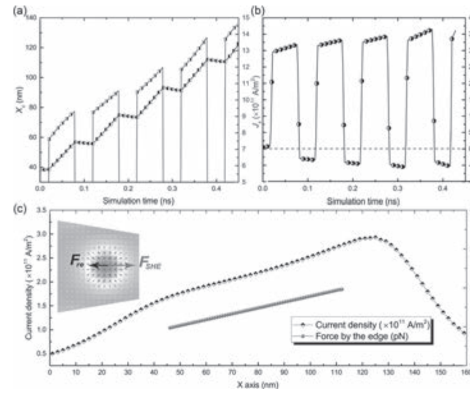

Fig. 2. Analysis of the neuronal behavior of the skyrmion. (a) The black symbol exhibits the location of the skyrmion as a function of time and the blue symbol shows the exact current density at the corresponding location. (b) Velocity of the skyrmion during the motion process. (c) The black curve presents the trend of current density in x axis while y=0. The red curve presents the joint repulsive force that changes according to the location.

FRIDAY AFTERNOON, 27 APRIL 2018 PEONY I, 2:00 TO 5:00

Session HF
ULTRATHIN FILMS AND SURFACE EFFECTS II

Weisheng Zhao, Chair
Beihang University, Beijing, China

INVITED PAPER

2:00

HF-01. Various ways to tune non-collinear magnetism in ultrathin films.

A. Finco[1], P. Hsu[1,2], L. Rózsa[1,3], A. Kubetzka[1], E. Vedmedenko[1], K. von Bergmann[1] and R. Wiesendanger[1]
1. University of Hamburg, Hamburg, Germany; 2. Department of Physics, National Tsing Hua University, Hsinchu, Taiwan; 3. Institute for Solid State Physics and Optics, Wigner Research Centre for Physics, Budapest, Hungary

In order to develop spintronic devices, a precise control of the magnetic state in ultrathin films is necessary. In particular, the stabilization of non-collinear magnetic structures is a crucial issue. In magnetic ultrathin films grown on a heavy element substrate, the competition between the interface-induced Dzyaloshinskii-Moriya interaction (DMI) and the exchange interaction enables the formation of spin spirals and magnetic skyrmions. The exact nature of the magnetic state strongly depends on the balance between the different interactions and thus being able tune them is of great interest. Starting from the Fe/Ir interface, known to generate a large DMI, we show how to obtain and tune spin spirals or magnetic skyrmions using spin-polarized scanning tunneling microscopy (SP-STM). This versatile technique allows to measure the full 3D magnetic structure of the film down to the atomic scale. Furthermore, the magnetic states can also be manipulated using the STM tip. Since the lattice mismatch between Fe and Ir is very large, the epitaxially grown double Fe atomic layer on Ir(111) exhibits a network of dislocation lines along high-symmetry directions. These lines allow to relieve the epitaxial strain in the film and it appears that they also have a significant influence on the magnetic ground state [1]. At low temperature, spin spirals with a period about 1.5 nm are guided by the dislocation lines. When atomic hydrogen is incorporated in the double layer film, the dislocation lines network disappears and is replaced by a p(2x2) hexagonal superstructure. The propagation direction of the spin spirals is thus not fixed anymore and their period increases to 3.5 nm. Furthermore, whereas no skyrmionic phase could be found in the double layer Fe on Ir(111) up to 9 T, the spin spirals in the hydrogenated samples transform into skyrmions under application of a magnetic field of 3 T. The skyrmionic phase is shown on the spin-polarized differential conductance measurement in panel (a). Ab initio calculations indicate that the H atoms must be located between the two Fe layers in order to have such an impact on the magnetic state. The presence of the H atoms modifies indeed the distance between the Fe layers and thus the hybridization of the top Fe layer with the lower Fe and Ir ones [2]. Another possibility to modify the magnetic state is to add one more atomic Fe layer. The measurement presented in panel (b) shows the magnetic state of a typical sample with an Fe coverage about three layers. As well as in the double layer film, dislocation lines form to relieve the epitaxial strain and spin spirals propagate along them. In addition, the spacing between the lines is varying over the sample surface which means that the strain relief is also not uniform. Measurements of the period of the spin spirals in the triple layer film revealed a clear correlation between the dislocation line spacing and the magnetic period. Based on a simple micromagnetic model, we attribute this observation to a modulation of the effective exchange coupling by the epitaxial strain relief [3]. Although the effect of strain relief was studied at low temperature, we also investigated the temperature dependence of the spin spirals. Whereas no spiral could be observed in the double layer above 150 K, the spirals are still stable in the triple layer up to room temperature. Moreover, their period increases drastically and becomes 15 times larger at room temperature than at 8 K (see panel (c)). In order to explain this unexpected temperature-dependent behaviour, we propose a classical spin model based on different magnetic parameters in the three Fe layers. This model allows us to reproduce the period increase using both a mean-field and a Monte Carlo approach [4]. Under application of a magnetic field, the low-temperature spin spirals in the triple layer split up into skyrmions with a typical size about 5 nm. These skyrmion have a unusual bean-shape which is dictated by the anisotropic local arrangement of the atoms forming the dislocation lines (panel (d)). We demonstrate that they can reliably be written and deleted locally by the STM tip. The strong-bias polarity dependence and the linear behavior of the threshold voltage for switching with the tip-sample distance shows that electric field plays the dominant role in the switching mechanism [5]. Our work opens new possibilities for precise tailoring of the magnetic states in ultrathin films as well as for energy-efficient manipulation of single skyrmions which may be beneficial in the development of skyrmion-based spintronic devices.

[1] Hsu et al, Phys. Rev. Lett., 116, 017201 (2016) [2] Hsu et al, arXiv:1711.06784 (2017) [3] Finco et al, Phys. Rev. B, 94, 214402 (2016) [4] Finco et al, Phys. Rev. Lett., 119, 037202 (2017) [5] Hsu et al, Nature Nanotechnology, 12, 123-126 (2017)

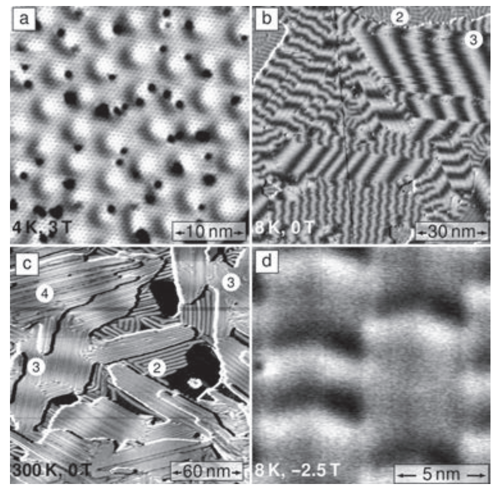

Fig. 1. Spin-polarized differential conductance maps of Fe based ultrathin films on Ir(111). The map (a) shows the magnetic skyrmions in the hydrogenated double layer Fe. The overviews (b) and (c) present the spin spirals in the triple layer Fe at low temperature and room temperature. The numbers indicate the Fe coverage (number of atomic layers). Panel (d) displays the magnetic skyrmions in the triple layer when a magnetic field is applied.

CONTRIBUTED PAPERS

2:30

HF-02. Electrical field induced directional motion of skyrmionic bubbles in a micro-racetrack.

X. Liu[1], X. Zhang[2,1], C. Ma[1], J. Xia[2], M. Ezawa[3], W. Jiang[4], Y. Zhou[2], S. Piramanayagam[5] and T. Ono[6]

1. Department of Electrical and Computer Engineering, Shinshu University, Nagano, Japan; 2. School of Science and Engineering, The Chinese University of Hong Kong, Shenzhen, China; 3. Department of Applied Physics, The University of Tokyo, Tokyo, Japan; 4. Department of Physics, Tsinghua University, Beijing, China; 5. School of Physical and Mathematical Sciences, Nanyang Technological University, Singapore, Singapore; 6. Institute for Chemical Research, Kyoto University, Kyoto, Japan

Magnetic skyrmion and skyrmionic bubbles are gaining significant interest due to their topological nature [1], which can be used for building novel memories and logic computing devices [2]. Both current and magnetic field induced dynamics of skyrmions and skyrmionic bubbles have been investigated extensively. However, from the energy consumption point of view, skyrmionic dynamics driven by an electrical field could provide long-term practical application benefits [3-6]. Here, we present our most recent results on the electrical-filed-induced motion of skyrmionic bubbles and chiral domain walls in racetracks. The racetracks, composing stacks of CoNi/Pt with asymmetric thicknesses of Pt, were fabricated with tailored wedge end. The electric field is applied at the Pt/dielectric SiO_2 interface. Both experimental and numerical study on the electric field-induced creation and directional motion of skyrmionic bubbles and chiral domain walls will be reported. We find the electric field-induced motion of skyrmionic bubbles at zero magnetic field and room temperature. Repeatable forward and backward directional motion of skyrmionic bubbles suggests robust nature of the structure. Our finding provide opportunities for developing novel skyrmion-based information processing devices with ultralow power consumption.

[1] Nagaosa, N. & Tokura, Y. Topological properties and dynamics of magnetic skyrmions. Nat. Nanotech. 8, 899 (2013). [2] Fert, A., Reyren, N. & Cros, V. Magnetic skyrmions: advances in physics and potential applications. Nat. Rev. Mater. 2, 17031 (2017). [3] Hsu, P.-J. et al. Electric-field-driven switching of individual magnetic skyrmions. Nat. Nanotech. 12, 123 (2017). [4] Schott, M. et al. The skyrmion switch: turning magnetic skyrmion bubbles on and off with an electric field. Nano. Lett. 17, 3006 (2017). [5] Kakizakai, H. et al. Influence of sloped electric field on magnetic-field-induced domain wall creep in a perpendicularly magnetized Co wire. Jpn. J. Appl. Phys. 56, 050305 (2017). [6] Huang, P. et al. In situ electric field skyrmion creation in magnetoelectric Cu2OSeO3. arXiv:1710.09200 (2017).

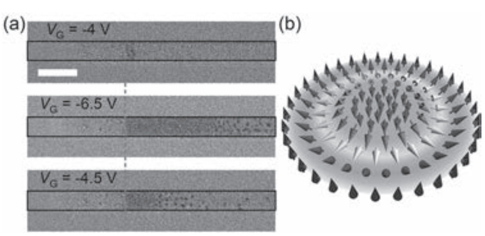

Fig. 1. (a) MOKE microscopy image of the electric field-induced motion of chiral domain walls and skyrmion bubbles. V_G denotes the applied voltage. Scale bar, 10 micrometers. (b) Illustration of a skyrmionic bubble. Arrows indicate the magnetization directions.

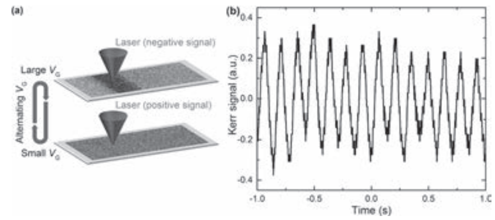

Fig. 2. Repetitive motion of the domain wall driven by an alternating electric field. (a) Schematic drawing showing the location of the MOKE laser spot as well as the displacement of the chiral domain wall induced by the electric field. A large V_G results in a spin-down region underneath the laser spot, while a small V_G results in a spin-up region underneath the laser spot. (b) Time-dependent Kerr signals corresponding to the input alternating V_G, which indicate that the chiral domain wall moves continuously backwards and forwards.

2:45

HF-03. Strong Dzyaloshinskii-Moriya interaction in symmetric crystalline $[Co/Pd(111)]_n$ superlattices.

A. Davydenko[1], A. Kozlov[1], M. Stebliy[1], A. Ognev[1] and L. Chebotkevich[1]
1. Far Eastern Federal University, Vladivostok, Russian Federation

When creating asymmetric superlattices [heavy metal 1 / ferromagnetic / heavy metal $2]_n$, the energies of perpendicular anisotropy and the Dzyaloshinskii-Moriya interaction (DMI), as a rule, depend weakly on the period of superlattices *n* and remain approximately equal to the energies observed in the structure consisting of one period [1]. This is expected, since both the perpendicular anisotropy and the DMI in such structures are believed to be of an interface origin. The increase in the number of interfaces is compensated by an increase in the volume of the ferromagnetic layers. However, more recently in symmetric polycrystalline superlattices $[Co/Pd]_n$, an increase in the effective DMI was observed with an increase in the number of repetitions of bilayers *n* [2]. Similar results, but in the single-crystal system $[Co/Pd(111)]_n$ with higher values of the perpendicular magnetic anisotropy and DMI, were found by our group. Crystalline [Co(0.8 nm)/Pd(2 nm)$]_n$ superlattices were grown by molecular beam epitaxy on Si(111) substrates with a Cu buffer layer. Period of superlattices *n* was varied from 1 to 20. Structural properties of superlattices were analyzed by reflection high energy electron diffraction. The structure and epitaxial orientation of all the layers remained the same as in the bottom layers. Topography and growth processes were investigated by scanning tunneling microscopy. With an increase in the overall thickness of the structures, the amplitude and period of roughness increased. Magnetic properties of the superlattices were investigated by vibrating sample magnetometer. An energy of perpendicular magnetic anisotropy slightly increased from 0.66 to 0.87 MJ/m^3 with an increasing of the period of superlattices from 1 to 20. Measurements of DMI were performed by Brillouin light scattering spectroscopy based on DMI-driven asymmetric dispersion shift of long-wavelength thermal spin waves in the Damon-Eshbach surface mode. We found an increase of effective DMI constant D_{eff} from 2 to 4.5 mJ/m^2 with an increasing of the period of superlattices from 1 to 20. In the Fig. 1 Brillouin light scattering spectrum of the [Co(0.8 nm)/Pd(2 nm)$]_{15}$ superlattice is outlined. The increase in the DMI constant more than twice led to significant changes in the magnetic structure of the samples during magnetization reversal. In the single magnetic layered structures with $n = 1$ DMI was relatively weak to influence on magnetic structure of domains, but it stabilized chiral Neel domain walls. In these samples by means of Kerr-microscopy, we observed an asymmetric growth of domains in the combination of longitudinal and perpendicular magnetic fields. Magnetization reversal in the single magnetic layered structures occurred by nucleation of oppositely magnetized domains and domain walls propagation. Increasing of the period of superlattices *n* to 3-5 led to increasing of the DMI constant. In the magnetic structure during magnetization reversal, it resulted in increasing of the density of nucleating domains. The magnetic moments in all magnetic layers of a chosen domain were oriented in the same direction due to ferromagnetic coupling between Co layers. In sufficiently high magnetic fields, chiral Neel domain walls repelled from each other forming net of topologically protected 360° domain walls [3]. Net of 360° domain walls transformed to isolated skyrmions in magnetic fields just below the saturation magnitudes. We stabilized skyrmions in such samples in zero magnetic field and detected them by magnetic-force microscopy. Micromagnetic simulations indicate that at such high values of DMI constant chiral Neel domain walls and skyrmions may be formed in $[Co/Pd]_{3\text{-}5}$ superlattices. Further increasing of the period of superlattices *n* to 10-20 led to extremely strong DMI. Strong DMI overcame perpendicular magnetic anisotropy and demagnetized superlattices in the zero magnetic fields. In the remanent state, the magnetic structure of the superlattices corresponded to demagnetized stripe domain structure with chiral Neel domain walls and stable isolated skyrmions (Fig. 2). The period of the stripe domain structure decreased with increasing of the DMI constant in $[Co/Pd]_{10\text{-}20}$ superlattices. Strong dependence of the DMI constant on the period of $[Co/Pd(111)]_n$ superlattices indicates that DMI in this system is not simply additive. Despite the interface nature, DMI from the interfacial Co atoms of the selected magnetic layer extends not only to the volume of a given layer, but also to other neighboring layers. Probably this behavior of DMI is general for magnetic superlattices, but in other systems it may be hindered by increasing amount of structure imperfections during growth of thick superlattices. In conclusion, we demonstrate the symmetric crystalline [Co/Pd(111)]n system, in which the DMI constant may be varied over a wide range by choosing the appropriate period of superlattice, making possible skyrmions and chiral stripe domain structure formation in the zero magnetic fields. The reported study was funded by RFBR (research project 18-02-00205) and the Grant program of the Russian President (MK-5021.2018.2).

[1] C. Moreau-Luchaire et al. Nat. Nanotech. 11 (2016) 444. [2] S.D. Pollard et al. Nat. Comm. 8 (2017) 14761. [3] M.J. Benitez et al. Nat. Comm. 6 (2015) 8957.

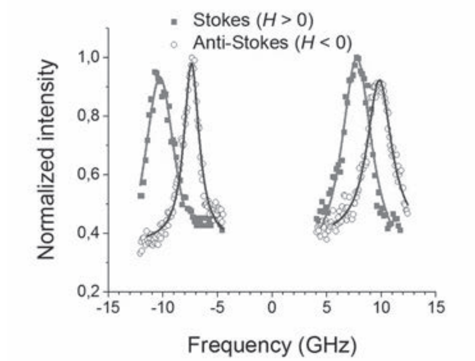

Fig. 1. Spectra of Brillouin light spectroscopy for a [Co(0.8 nm)/Pd(2 nm)$]_{15}$ film obtained in fields of 7 kOe (red squares) and -7 kOe (blue squares). The wave vector is k = 7 µm^{-1}. The solid lines represent fittings with Lorentzian functions.

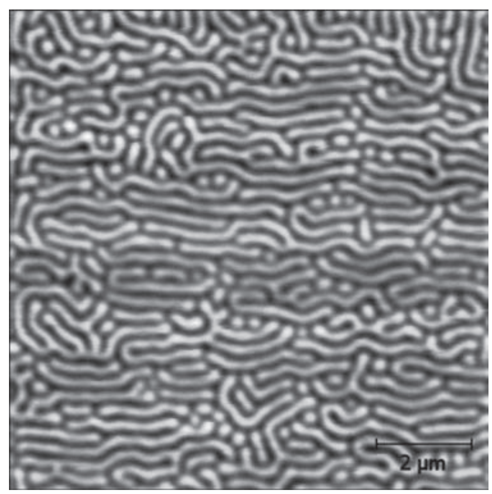

Fig. 2. Magnetic force microscopy image of [Co(0.8 nm)/Pd(2 nm)$]_{20}$ superlattice in the remanent state of the magnetization.

3:00

HF-04. Magnetic domain texture and Dzyaloshinskii-Moriya interaction in systems with perpendicular exchange bias.

R.A. Khan[1], H. Nembach[2], M. Ali[1], T.A. Moore[1] and C.H. Marrows[1]
1. School of Physics and Astronomy, University of Leeds, Leeds, United Kingdom; 2. Quantum Electromagnetics Division, National Institute of Standards and Technology, Boulder, CO, United States

In thin film systems with broken inversion symmetry, the Dzyaloshinskii-Moriya interaction (DMI) influences the field- or current-driven magnetic switching and domain wall (DW) motion by setting the chirality of magnetic textures [1-3]. In this work, we sputter-deposited polycrystalline multilayers of Pt/Co/$Ir_{20}Mn_{80}$ and Pt/Co/$Fe_{50}Mn_{50}$ exhibiting perpendicular magnetic anisotropy (PMA) and perpendicular exchange bias (PEB). Such multilayers, comprising an antiferromagnet (AFM) material (IrMn and FeMn), are potentially of interest in spintronics because of the useful properties AFM materials possess, such as, very high frequency dynamics, zero stray field, excellent magneto-transport properties, etc. Furthermore, the coincidence of the DMI with a vertical exchange field could remove the need for an externally applied field to stabilise skyrmion bubbles. We have measured the exchange bias in SiO_2/Ta(5)/Pt(2)/Co(t_{Co})/IrMn(t_{IrMn})/Pt(3) (Fig. 1) and SiO_2/Ta(5)/Pt(2)/Co(t_{Co})/FeMn(t_{FeMn})/Pt(3) stacks (thickness in nm) as a function of the layer thickness of Co (t_{Co} = 0.2-2 nm), IrMn (t_{IrMn} = 1-10 nm), and FeMn (t_{FeMn} = 1-8 nm) layers. The stacks have been optimised structurally to obtain a strong PMA and large PEB in the as grown state. The FeMn system attains PMA for a narrower range of Co layer thickness, when compared to the IrMn system. We investigated the interaction mechanisms at the interfaces when crossing over the paramagnet to antiferromagnet (AFM) transition of the AFM layers (IrMn and FeMn) by varying the thickness of these layers. We confirm the different phases by identifying the Néel temperatures (T_N) and the blocking temperatures (T_B) of the AFM layers (Fig. 2) at different layer thicknesses. Wide-field Kerr microscopy showed that the magnetic domain morphology of the ferromagnet (FM) Co layer is influenced by the AFM Néel order. From this we infer that the changes in domain texture is brought about by the FM-AFM inter-layer exchange coupling, and the anisotropy of these layers. We also investigated the DMI in these systems, particularly how it is affected by the AFM spin order, and subsequently, by the coupling at the FM-AFM interface. We do this by measuring the DMI at three different phases: paramagnet phase, AFM phase without PEB, and AFM phase with PEB. We quantified the DMI by the Brillouin light scattering (BLS) spectroscopy technique [4-5], where the DMI is probed by taking advantage of the non-reciprocity of propagating spin waves.

[1] S Emori et al. *Nature Materials* 9, 611-616 (2013). [2] R Khan et al. *App. Phys. Lett. B* 109, 132404 (2016). [3] A Wells et al. *Phys. Rev. B* 95, 054428 (2017). [4] J-H Moon et al. *Phys. Rev. B* 88, 184404 (2013). [5] H Nembach et al. *Nat. Phys.* 11, 825 (2015). The work was funded by the Marie-Curie Seventh Framework program (Grant no: 608031).

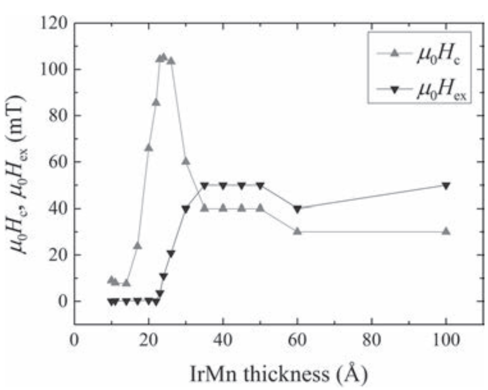

Fig. 1. Coercivity H_c and exchange field H_{ex} in Pt(5 nm)/Co(1 nm)/IrMn(t_{IrMn}).

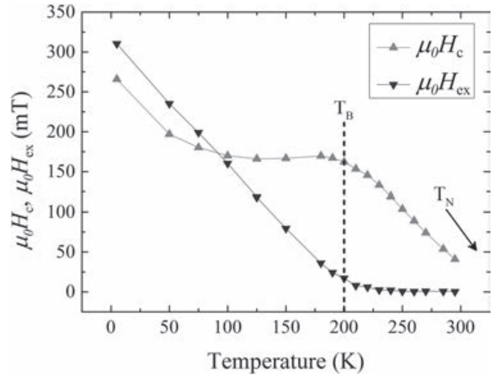

Fig. 2. Coercivity H_c and exchange field H_{ex} in Pt(3 nm)/Co(1 nm)/IrMn(2 nm) as a function of temperature.

3:15

HF-05. In-situ Annealing Study of Pt/Co Interface and its Effect on Perpendicular Magnetic Anisotropy of Pt/Co/MgO.

H. Xie[1], Y. Yang[1], M. Zhang[1] and Y. Wu[1]
1. Department of Electrical and Computer Engineering, National University of Singapore, Singapore

I. INTRODUCTION Heavy metal (HM)/ferromagnetic metal (FM)/oxide structures, such as Ta/CoFeB/MgO and Pt/Co/MgO, have been the focus of numerous studies owing to the enhanced perpendicular magnetic anisotropy (PMA) and large spin orbit torque (SOT). Post-annealing treatment is often necessary in fabricating devices involving these multilayer structures because it does not only enhance both the PMA of the magnetic layer and transport properties of the devices but also ensures thermal stability [1]–[4]. Previous studies often annealed the entire structure together and therefore it was difficult to evaluate the respective role of the top and bottom interfaces separately. To address this issue, in this study we investigated the annealing effect of Pt/Co/MgO using an in-situ deposition and measurement setup which allows to study the annealing effect of the two interfaces separately. Specifically, we deposited Pt/Co, Pt/Co/MgO and Pt/Co/Mg step by step and in between we annealed the samples between 100°C - 300°C and measured the anomalous Hall effect (AHE) in-situ. Deposition and measurement were both conducted in an ultra-high vacuum (UHV) system without exposing the sample to ambient. The samples were deposited on 2 × 2 mm^2 square wafers to fit the magnetic holder which provides a perpendicular magnetic field. Layers of Ta(1.5)/Pt(3) (the number inside the parentheses indicates the thickness in nm) were first deposited ex-situ using dc magnetron sputtering and then quickly loaded into the UHV system, followed by the deposition of Co or Mg using Knudsen cell cells in a preparation chamber. After deposition, the samples were transferred in-situ to the nanoprobe chamber for oxygen exposure and AHE measurements. The oxygen exposure is precisely controlled by a low-dosage oxygen source. The AHE measurements were conducted by probing the four corners of the samples using the nanoprobes. II. RESULTS AND DISCUSSION Fig. 1(a) shows the AHE loops for Ta(1.5)/Pt(3)/Co(0.6) after being annealed for a duration of 0.5h from 100°C to 300°C at a step of 50°C. The curves are shifted vertically for clarity. As can be seen, the film exhibits PMA; its coercivity decreases slightly after annealing from 100°C to 150°C and then increases and peaks at 250°C. Next, we deposited a sample with the same structure of Ta(1.5)/Pt(3)/Co(0.6), but instead of proceeding to annealing directly, we exposed the sample to oxygen at a dose of 116L (here L is the Langmuir unit with one Langmuir corresponding to an exposure of 1.33×10^{-6} mbar for one second) and then dusted the surface with a small amount of Mg to obtain Ta(1.5)/Pt(3)/Co(0.6)/O/Mg. The AHE loops of this sample after oxygen exposure, Mg deposition and annealing at different temperatures for a duration of 0.5h are shown in Fig. 1(b). In agreement with our previous report [2], oxygen exposure at small Co thickness results in a degradation of effective PMA, which recovers partially after Mg dusting. As can be seen, the annealing effect for this sample is similar to that of Ta(1.5)/Pt(3)/Co(0.6), i.e., without oxygen exposure and Mg dusting. For the third sample, the Mg dusting is performed directly on the Co layer without oxygen exposure, leading to the Ta(1.5)/Pt(3)/Co(0.6)/Mg structure. Shown in Fig. 1(c) are the AHE curves of this sample after annealing at different temperatures. Again, a similar trend of annealing effect was observed, i.e., the coercivity decreases slightly at lower temperature, and then increases and peaks at 250°C. Fig. 1(d) compares the extracted coercivity values for the three samples as a function of annealing temperature. The significant enhancement of coercivity (as we will discuss shortly it is closely related to PMA) after annealing between 200°C and 300°C could be attributed to improved crystallinity or interface sharpness by thermal annealing. Notably, the annealing effects are similar in the three samples, suggesting that for Pt/Co/MgO, the lower interface (i.e., Pt/Co) determines the magnetic and thermal property. At this specific Co thickness, adding MgO does not necessarily lead to the improvement of these properties. Since the in-plane field strength of the is-situ setup is insufficient for quantitative measurement and analysis of the PMA, we performed ex-situ experiments to investigate the annealing effect on PMA. To this end, we deposited and annealed Ta(1.5)/Pt(3)/Co(0.6)/Cu(3) in a sputter for the same duration and in similar temperature range. The samples were cooled down for 2h after annealing and then capped with 3nm Pt layer without breaking the vacuum. The 3nm Cu layer is used to avoid Co in direct contact with the upper Pt layer. After annealing, we measured the in-plane hysteresis curves using SQUID from which we extracted the anisotropy field. Fig. 1(f) shows the anisotropy field at different annealing temperature. A similar trend as the coercivity shown in Fig. 1(d) was observed, confirming that the bottom Pt/Co interface indeed plays the most crucial role in determining both the magnetic and thermal properties of Pt/Co/MgO trilayers. The difference in peak temperature is presumably caused by the temperature calibration of the two systems. The PMA of the sample annealed at 200°C is estimated to be 10.4×10^6 erg/cm^3.

[1] S. Monso *et al.*, "Crossover from in-plane to perpendicular anisotropy in Pt/CoFe/AlOx sandwiches as a function of Al oxidation: A very accurate control of the oxidation of tunnel barriers," *Appl. Phys. Lett.*, vol. 80, no. 22, pp. 4157–4159, 2002. [2] Y. Yang *et al.*, "Unveiling the role of Co-O-Mg bond in magnetic anisotropy of Pt/Co/MgO using atomically controlled deposition and in situ electrical measurement," *Phys. Rev. B*, vol. 95, no. 9, pp. 1–8, 2017. [3] I. M. Miron *et al.*, "Perpendicular switching of a single ferromagnetic layer induced by in-plane current injection," *Nature*, vol. 476, no. 7359, pp. 189–193, 2011. [4] R. C. Sousa *et al.*, "Large tunneling magnetoresistance enhancement by thermal anneal," *Appl. Phys. Lett.*, vol. 73, no. 22, pp. 3288–3290, 1998.

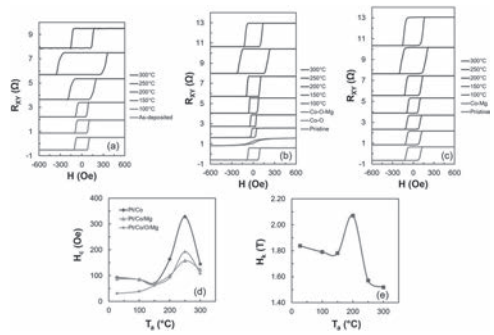

Fig. 1. (a), (b), (c) AHE loops for Ta(1.5)/Pt(3)/Co(0.6), Ta(1.5)/Pt(3)/Co(0.6)/O/Mg and Ta/(1.5)/Pt(3)/Co(0.6)/Mg after annealing at temperatures from 100°C to 300°C; (d) Plot of coercivity extracted from AHE curves; (e) Anisotropy field of Ta(1.5)/Pt(3)/Co(0.6)/Cu(3) after annealing at temperatures from 100°C to 300°C.

3:30

HF-06. Exploring interfacial Dzyaloshinskii-Moriya interaction for in-plane thin film permalloy nanostructures using micromagnetic simulations and Lorentz microscopy.

K. Fallon[1], S. Azzawi[2], D. Atkinson[2] and S. McVitie[1]
1. University of Glasgow, Glasgow, United Kingdom; 2. Durham University, Durham, United Kingdom

Recently the Dzyaloshinskii-Moriya interaction (DMI) has received considerable attention, particularly in the case of the interface between ultra-thin ferromagnetic films and non ferromagnetic heavy metals. The interfacial interaction causes reorientation of the domain wall spin configuration into Néel type walls with a defined handedness in material systems that ordinarily display perpendicular magnetisation with Bloch type walls of no preferred handedness [1]. The DMI energy term - $D\bullet(S_i \times S_j)$, where D is the DMI vector and S_i and S_j are neighbouring spins, is responsible for the chiral twist texture. In the work presented here we are interested in the effect of this term in a thin film system with in-plane magnetisation. In particular nanostructured soft ferromagnetic thin films readily form vortex structures with an out of plane singularity at the vortex core. Such a structure provides possibilities for interesting DMI effects around the vortex core. To investigate this we have looked at the effect of interfacial DMI on vortex structures in films of permalloy with a thickness around the exchange length of the material (~ 5 nm). Micromagnetic simulations have been performed using MuMax^3 to simulate thin (8 nm) magnetic disks of permalloy with varying interfacial DMI strength [2]. The simulations indicate that interfacial DMI causes twisting of the magnetisation around the vortex core – this results in a magnetisation configuration that has a divergent component local to the vortex core and is no longer purely rotational. Furthermore, the simulations show that the strength and sign of the divergent component relates to the strength and sign of the DMI. Figure 1 contains a subset of the simulation results to illustrate the effect of DMI. The insets on the figures show the core structure on a larger scale. Comparing the two cases with and without DMI, the former has a symmetric structure whilst the latter shows a clear asymmetry. Indeed the effect of DMI appears to result in a twisting of magnetisation around the vortex core, resembling somewhat the yin yang symbol of Chinese philosophy. Hysteresis loops were calculated and show a relationship between the magnitude of the DMI and the vortex expulsion field, with a smaller field required to expel vortices in systems with a larger magnitude of DMI - see figure 2. Bilayer and trilayer samples were prepared by sputtering at the University of Durham. Each sample has a magnetic layer of permalloy and non magnetic capping layers of either platinum, iridium, gold or copper to provide a range of different DMI samples and control samples with no DMI. These samples were patterned (using a FIB microscope) to isolate disks of magnetic material from the continuous film. The vortex expulsion has been observed directly via an in situ Lorentz transmission electron microscopy (TEM) experiment using the Fresnel method to image domain walls. We note a reduction of the expulsion field for films with strong interfacial DMI (Py with Ir and Pt) compared to that for no expected DMI (Py with Cu). We also report on imaging using the quantitative method of differential phase contrast (DPC), to map the magnetic induction of the sample. Recent developments in DPC, utilising pixelated detectors, allow this technique to register beam deflections on the order of microradians and provide a spatial resolution of 1 nm [3]. Calculated images of the induction maps from the micromagnetic simulations suggest the divergent component of the magnetization provides a measurable signature from DPC. We will present details of these measurements.

[1] S.-G. Je, D.-H. Kim, S.-C. Yoo, B.-C. Min, K.-J. Lee, and S.-B. Choe, Phys. Rev. B 88, 214401 (2013) [2] A. Vansteenkiste, J. Leliaert, M. Dvornik, M. Helsen, F. Garcia-Sanchez, and B. Van Waeyenberg, AIP Adv. 4, 107133 (2014) [3] M. Krajnak, D. McGrouther, D. Maneuski, V. O'Shea, and S. McVitie, Ultramicroscopy 165, 42-50 (2016).

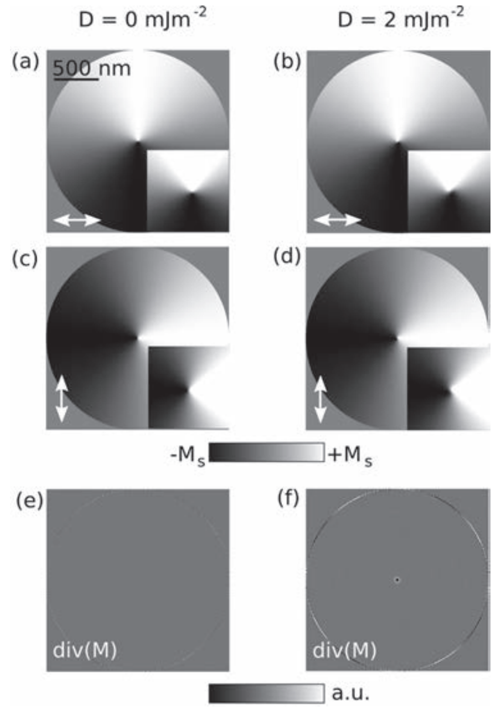

Fig. 1. The results of MuMax^3 simulations of permalloy disks (diameter 2 µm) with and without DMI are shown. Figures (a) and (c) show M_x and M_y of a vortex structure with no DMI. Image (e) shows the divergence of this magnetic state. Figures (b) and (d) show M_x and M_y of a vortex structure with DMI of 2 mJm^{-2}. Image (f) shows the divergence of this magnetic state. The insets show the core of the in-plane magnetisation components at a larger scale so that the twisting of the magnetisation is visible.

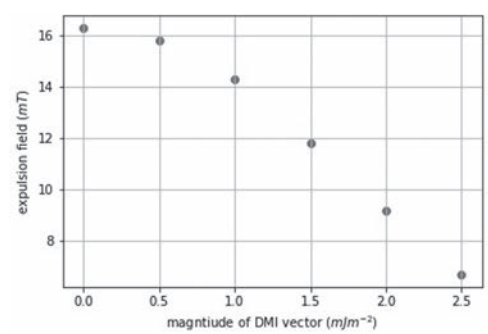

Fig. 2. Hysteresis loops of permalloy disks (diameter 2 µm) with varying DMI strength were calculated using MuMax^3. These loops indicate that the Dzyaloshinskii-Moriya interaction reduces the vortex expulsion field in disk shaped permalloy structures

3:45

HF-07. Enhancement of perpendicular magnetic anisotropy in Co/Ni multilayer by inserting MoS_2 under layer.

Q. Xie[1,2], B. Yang[3], S. Chen[1], W. Lin[1], L. Liu[1], T. Zhou[1], X. Han[3], J. Chai[2] and J. Chen[1]
*1. Department of Material Science and Engineering, National University of Singapore, Singapore, Singapore; 2. Institute of Material Research and Engineering, A*STAR, Singapore, Singapore; 3. Beijing National Laboratory for Condensed Matter Physics, Institute of Physics, University of Chinese Academy of Sciences, Beijing, China*

Magnetic thin films possessing magnetic easy axis perpendicular to the surface have attracted a lot of interest and they are playing an important part for spin-transfer torque (STT) spintronic devices. Compared to the magnetic thin films with in-plane easy axis, the application of magnetic thin films with perpendicular magnetization anisotropy (PMA) has demonstrated high switching reliability, good thermal stability in STT spintronic devices.[1] Co can form strong interfacial anisotropy energy by combining with different metals such as Pt, Ni and Pd, among which CoNi has lowest damping constant and is widely used. Lots of methods have been reported to enhance PMA in Co/Ni multilayer, such as changing the under layer of CoNi multilayer or in situ annealing the under layer.[2] However, there are no reports for using the two dimensional transition metal dichalcogenides to engineer the PMA of the magnetic thin films. Here, we report the PMA enhancement of $[Co(0.24nm)/Ni(0.52)]_2$ multilayer by inserting MoS_2 under layer. The perpendicular magnetic anisotropy of $[Co(0.24nm)/Ni(0.52nm)]_2$ multilayer can be greatly enhanced by inserting MoS_2 under layers, which is proved by the experiments and first-principle calculation in this work. The experiments show that the coercivity in easy axis can be greatly enhanced from 120 Oe to unprecedented value of 1037 Oe by inserting MoS_2 under layers. Magnetocrystalline anisotropy energy (MAE) is about 2.2 times larger than that without inserting MoS_2 under layer. The calculations show that the MAE of $[Co(0.24nm)/Ni(0.52nm)]_2$ multilayers with MoS_2 under layer can be dramatically improved to 2.3 times the value of its pure counterpart, which is consistent with the experiments results. We also perform layer-resolved and orbital-hybridization resolved anisotropy analysis, which can help us have a better understanding of the physical origin of PMA enhancement. The layer-resolved analysis uncover that the interfacial Pt layer plays a critical role in enhancing $[Co(0.24nm)/Ni(0.52nm)]_2$ multilayer's PMA and the negative contribution to PMA from Pt layer can be significantly suppressed when inserting MoS_2 under layer. The orbital hybridization-resolved analysis further describe the origin of PMA enhancement, which demonstrates that the change of anisotropy contribution mainly comes from hybridizations between d_{xz} and d_{yz} orbitals, d_{xy} and d_{x2-y2} orbitals. These findings make the $[Co(0.24nm)/Ni(0.52nm)]_2$ multilayer have potential application where large MAE is required and also pave a new way to engineer the PMA of magnetic thin films by two dimensional materials.

[1] S. Mangin, D. Ravelosona, J. A. Katine, M. J. Carey, B. D. Terris, and E. E. Fullerton, Nat. Mater. 5, 210 (2006). [2] D. Wu, S. Chen, Z. Zhang, B. Ma, and Q. Y. Jin, Appl. Phys. Lett. 103, 242401 (2013).

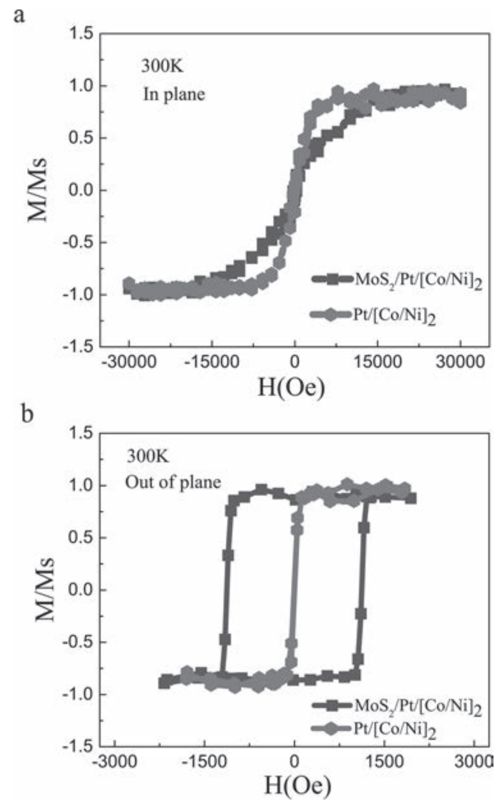

Fig. 1. (a)(b) In plane and out of plane hysteresis loop of $[Co(0.24nm)/Ni(0.52nm)]_2$ multilayer with and without MoS2 under layer, which show large enhancement of the anisotropy field and coercivity when inserting MoS2 under layer.

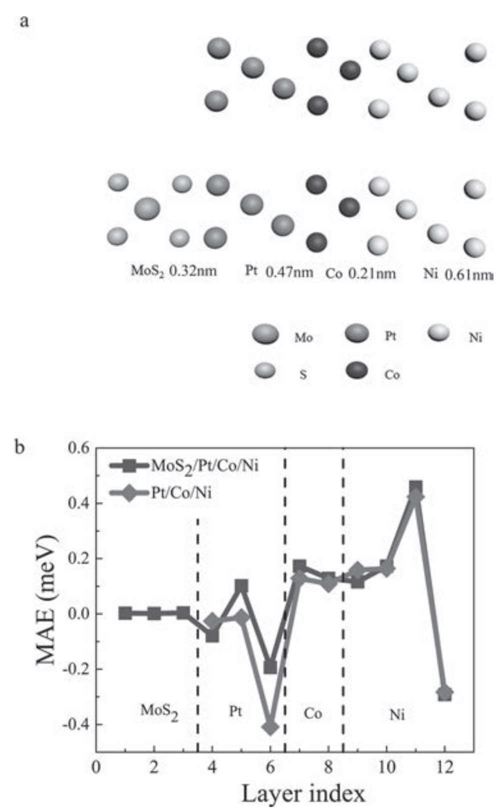

Fig. 2. (a) schematic of different layers of MoS_2/Pt/CoNi multilayer (b) Layer resolved magnetocrystalline anisotropy energy of $[Co(0.24nm)/Ni(0.52nm)]_2$ multilayer with and without MoS_2 under layer

4:00

HF-08. Voltage tailoring of the magnetic anisotropy of CoFeB with graphene oxide membranes.

K. Ning[1,3], H. Liu[1,3], X. Liu[1,3], Y. Li[1,3], C. Fang[2], C. Wan[2], Y. Yang[1,3] and T. Ren[1,3]
1. Institute of Microelectronics, Tsinghua University, Beijing, China; 2. Beijing National Laboratory of Condensed Matter Physics, Institute of Physics, University of Chinese Academy of Science, Chinese Academy of Sciences, Beijing, China; 3. Tsinghua National Laboratory for Information Science and Technology, Tsinghua University, Beijing, China

Two-dimensional materials, such as graphene, black phosphorus, MoS_2, and BN, are considered to be the key materials of the post-Moore era, due to their unique properties and potential applications.[1-3] Especially the graphene-based materials have the potential to replace silicon as the novel chip material for the new generation of electronic circuits.[4,5] Graphene oxide (GO) membrane, a chemical derivative of graphene with oxygen functionalities, has attracted great interest due to its exceptional functional group and scale-up production.[6-8] Recently, it has been demonstrated that the GO membranes coating can strongly enhance perpendicular magnetic anisotropy (PMA) of CoFeB thin film, even up to 0.6 mJ/m^2 at room temperature after annealing process. Even the critical thickness of the membrane-coated CoFeB for switching the magnetization from the out-of-plane to the in-plane axis exceeds 1.6 nm. The combination of GO membranes with a ferromagnetic layer can extend the functions of the thin films and the development multifunctional graphene-composite spintronic devices. Bias-voltage applied to the interface of a magnetic metal and an insulator induces a significant change of the interface perpendicular magnetic anisotropy (PMA), through strong interface spin-orbit coupling and charge transfer. The voltage-controlled PMA has successfully applied to MTJs where the PMA in both magnetic layers are tunable and only a very small current density is needed to switch the magnetization, which is extremely encouraging in terms of reducing the power consumption for spintronic devices.[9, 10] Here, we report the voltage tailoring of the PMA of CoFeB thin film with and without coating of GO membranes. Experiments were carried out on sputter-deposited films with a layered structure of substrate/Ta(6)/$Co_{40}Fe_{40}B_{20}$(1.4)/MgAl-O(2)/Ta(3 nm), as shown in Fig. 1. The films were annealed at 300 °C in a vacuum with a magnetic field of 8000 Oe for 1 hour. A medical ultrasonic atomization nebulizer (Omron Ultrasonic Nebulizer NB-150U, Japan) was used to prepare the fine mist of GO dispersion. To improve the wettability of the surface, the samples were processed by oxygen plasma (Branson/IPC 3000 Plasma Asher, USA) for 20 min before depositing the GO membranes. During the deposition process, temperature of the samples was set to be 25 °C for keeping a proper evaporation rate of water. The deposition process was repeated 5 times, with each single deposition lasting 8 s. In order to investigate the voltage tailoring of the magnetic anisotropy, the films were patterned into Hall bar structures with the widths of 100 μm. The cervicity of the CoFeB films is measured by using the anomalous Hall effect (AHE). The Hall resistance RHall can be expressed as, $R_{Hall}=R_0/t*H+R_e/t*M_\perp$ where the first term on the right-hand side is the ordinary Hall resistance and the second term is the anomalous Hall resistance, which is proportional to the out-of-plane component of the total magnetization. As seen from Fig. 2, the coercivity Hc of the CoFeB film with GO membranes coating are equal to 70 Oe at bias voltage $V_{bias}\approx 0$ V, which is samller than that without GO membranes of 97 Oe. It is known that the coercivity of the magnetic layers can be altered by a bias voltage through the electric-field-induce perpendicular anisotropy change. Since the anisotropy is proportional to the coercivity for the coherent rotation of the magnetization reversal, the voltage would directly affect the relative coercivity. A bias voltage Vbias is swept from 0 V to 3.5 V. The coercivity Hc of CoFeB film with GO membranes decreases gradually from 70 Oe at 0 V to 63 Oe at 1.5 V, while the coercivity Hc without GO membranes decreases slightly from 100 Oe at 0 V to 84 Oe at 1.5 V. When the voltage exceeds 2.5 V, the barrier of GO membranes and MgAl-O may be broken down. Compared with the bare CoFeB/MgAl-O film, the tailoring of the PMA with GO membranes coating can be also attributed to the movement of oxygen or carbon functional groups in GO membranes. In summary, we investigated the voltage tailoring of the PMA of CoFeB thin film with and without coating of GO membranes. The anomalous Hall effect was used to characterize the magnetic properties via the application of electric fields between 0 to 2.5 V. The coercivity Hc of CoFeB film with GO membranes decreases gradually from 70 Oe at 0 V to 63 Oe at 1.5 V, while the coercivity Hc without GO membranes decreases from 100 Oe at 0 V to 84 Oe at 1.5 V. With GO membranes, the voltage-induced the movement of oxygen or carbon functional groups can also affect the PMA of CoFeB film.

1. S. Das, R. Gulotty, A. V. Sumant and A. Roelofs, “All Two-Dimensional, Flexible, Transparent, and Thinnest Thin Film Transistor”, *Nano Lett.* 2004, 14, 2861. 2. W. Han, R. K. Kawakami, M. Gmitra and J. Fabian, “Graphene spintronics”, *Nat. Nanotechnol*, 2004, 9, 794. 3. S. Z. Butler, *et al.*, “Progress, Challenges, and Opportunities in Two-Dimensional Materials Beyond Graphene”, *ACS. Nano*. 2013, 7, 2898. 4. K. Bairagi, A. Bellec, V. Repain, C. Chacon, Y. Girard, Y. Garreau, J. Lagoute, S. Rousset, R. Breitwieser, Y. C. Hu, “Tuning the Magnetic Anisotropy at a Molecule-Metal Interface”, *Phys. Rev. Lett.* 114, 247203 (2015). 5. K. Y. Ning, H. F. Liu, L. S. Li, H. L. Li, J. F. Feng, B. S. Yang, X. Liu, Y. X. Li Y. H. Chen, H. X. Wei, X. F. Han, S. C. Mao, X. X. Zhang, Y. Yang, and T. -L. Ren, “Tailoring perpendicular magnetic anisotropy with graphene oxide membranes”, *RCS Adv.* 7, 52938 (2017). 6. R. R. Nair, H. A. Wu, P. N. Jayaram, I. V. Grigorieva, A. K. Geim, “Unimpeded permeation of water through helium-leak-tight graphene-based membranes”, *Science* 335, 442 (2012). 7. G. P. Liu, W. Q. Jin, N. P. Xu, “Graphene-based membranes”, *Chem. Soc. Rev.* 44, 5016 (2015). 8. R. K. Joshi, P. Carbone, F. C. Wang, V. G. Kravets, Y. Su, I. V. Grigorieva, H. A. Wu, A. K. Geim, R. R. Nair, “Precise and Ultrafast Molecular Sieving Through Graphene Oxide Membranes”, *Science* 343, 752 (2014). 9. W. -G. Wang, M. Li, S. Hageman, and C. L. Chien, “Electric-field-assisted switching in magnetic tunnel junctions”, *Nature Mater.* 11, 64 (2011). 10. Y. Shiota, T. Nozaki, F. Bonell, S. Murakami, T. Shinjo and Y. Suzuki. “Induction of coherent magnetization switching in a few atomic layers of CoFe using voltage pulses”, *Nature Mater*. 11, 39 (2011).

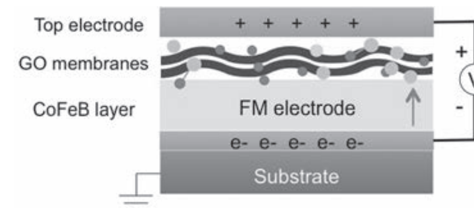

Fig. 1. Experiments were carried out on sputter-deposited films with a layered structure of substrate/Ta(6)/$Co_{40}Fe_{40}B_{20}$(1.4)/MgAl-O(2)/Ta (3 nm).

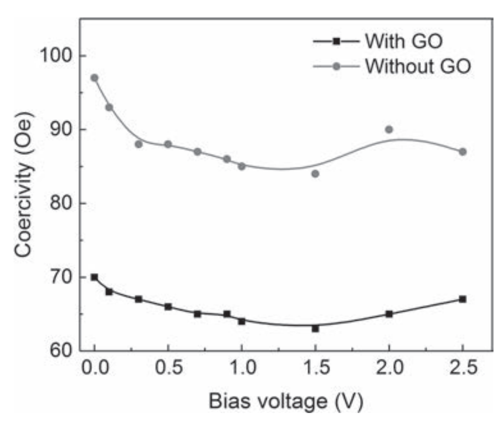

Fig. 2. The coercivity H_c of the CoFeB film

4:15

HF-09. Control of magnetic anisotropy by lattice distortion in cobalt ferrite thin film.

H. Onoda[1], H. Sukegawa[2], E. Kita[1] and H. Yanagihara[1]
1. Inst. Appl. Phys, University of Tsukuba, Tsukuba, Japan; 2. National Institute for Materials Science (NIMS), Tsukuba, Japan

Introduction Improvement of perpendicular magnetic anisotropy (PMA) in thin films is required to improve density of magnetic recording and memory storage. Large PMA can be introduced via the magnetoelastic effects in a uniaxial distortion by a substrate-induced epitaxial strain [1], for example. In fact, cobalt-ferrite (CFO) thin films grown on an MgO (001) substrate suffering 0.6% in-plane tensile strain results in introducing a large PMA energy K_u of 14.7 Merg/cm^3 [2]. Likewise, CFO films grown on $MgAl_2O_4$ (001) substrate suffering 3.6% in-plane compressive strain exhibits as large as negative K_u of – 60 Merg/cm^3 [3]. Even though such large lattice strains, those induced PMA of CFO (001) epitaxial films can be quantitatively explained within a framework of magneto-elastic theory [3]. In other words, the induced magnetic anisotropy can be quantitatively explained by the phenomenological magneto-elastic effect at least in this lattice distortion range. Based on this effect, further enhanced PMA by inducing 3~4% tensile strain can be expected. Therefore, in this study, we examined various buffer layers to introduce a larger lattice strain than MgO (001) and report the magnetic anisotropy (MA), especially induced K_u in CFO (001). Experimental We have grown $Co_{0.75}Fe_{2.25}O_4$ films via the reactive rf magnetron sputtering technique using a CoFe (1:3) alloy target. The process gas used was a mixture of Ar and O_2. The flow rates of Ar and O_2 were 30 sccm and 8 sccm, respectively. The growth temperature was 500 °C. We selected NbN, CoO, (Mg, Ca)-O (MCO), MnO and Mg_2SnO_4 (MSO) as substances having a larger lattice constant than MgO. NbN, CoO, MCO and MSO were inserted between MgO (001) substrates and CFO films as buffer layers. For MnO, we prepared MnO (001) substrates and grew CFO films thereon. The in-plane and out-of-plane lattice constants of the CFO films were determined using the four axis X-ray diffractometer (Rigaku, SmartLab). The magnetization was measured using a superconducting quantum interference device, SQUID-VSM (Quantum Design, MPMS) at fields up to ± 70 kOe. The MA were evaluated from the magnetic torque curves measured over the range of 0-90 kOe by a torque magnetometer (Quantum Design, PPMS Tq-Mag). Results and Discussion Figure 1 shows RHEED patterns of MCO(001), CoO(001), MSO(001) buffer layers. As can be seen, all films showed a streak pattern, indicating the they were grown epitaxially and good surface flatness. CFO films were grown epitaxially on all buffer layers, but it was found from *MH*-loops that only CFO films on the MSO buffer layers showed perpendicular magnetization. Figure 2 shows in-plane and out-of-plane *MH*-loop of a 10-nm-thick CFO film on an 80-nm-thick MSO buffer layers. The value of the saturation magnetization was 460 emu/cm^3, which is larger than 425 emu/cm^3 for bulk CFO. This discrepancy may indicate the enhancement of the orbital magnetic moment of Co^{2+}. The in-plane magnetization was not saturated at all even when the magnetic field of 70 kOe was applied, indicating that the CFO film on the MSO buffer layer showed a strong PMA. We used the magnetic torque measurement to determine the accurate value of the MA, and then, the K_u^{eff} was 20 Merg/cm^3. The intrinsic K_u^{eff} evaluated by using Miyajima's method was estimated to be over 23.3 Merg/cm^3. Summary We grew $Co_{0.75}Fe_{2.25}O_4$ (CFO) films on various buffers having larger lattice constants than MgO one to induce larger PMA through the magneto-elastic effect. Only the MSO-buffered films showed a strong PMA and the value of the saturation magnetization value was 460 emu/cm^3, which is larger than 425 emu/cm^3 for bulk CFO. The intrinsic K_u^{eff} determined by using Miyajima's plot was estimated to be greater than 20 Merg/cm^3. Therefore, the use of MSO buffer is very promising to induce sufficiently large lattice-strain to CFO films toward giant PMA effect.

[1] A. Lisfi, et al., Phys. Rev. B 76, 054405 (2007). [2] T. Niizeki, et al., Appl. Phys. Lett., 103 162407 (2013). [3] T. Tainosho, et al., The 39th the Magnetics Society of Japan 08pB-14.

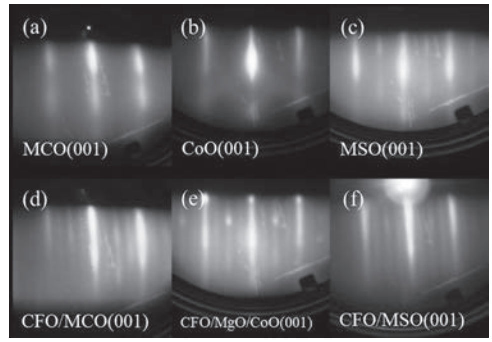

Fig. 1. RHEED patterns of films in [100] azimuth.

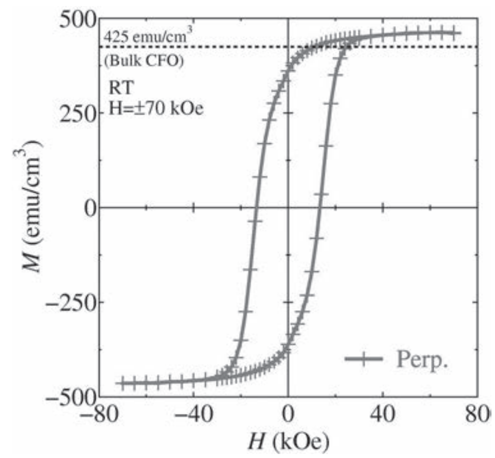

Fig. 2. Out-of-plane *MH*-loop of a CFO/MSO films (CFO thickness: 10 nm).

4:30

HF-10. Torque magnetometry of perpendicular anisotropy exchange-spring heterostructures.

P. Vallobra[1], *T. Hauet*[1], F. Montaigne[1], E. Shipton[2], E. Fullerton[2] and S. Mangin[1]
1. Institut Jean Lamour, Université de Lorraine, Nancy, France; 2. CMRR, University of California, San Diego, La Jolla, CA, United States

Torque magnetometer is a technique often used to quantify fundamental magnetic properties such as the magnetic anisotropy. These measurements are mainly performed on single domain samples.[1] However, recently it has been used to study magnetic phase transitions,[2] exchange biasing,[3] and non-uniform magnetization reversal.[4] Here, we use torque magnetometry to study a bilayer structure in which a lateral interfacial domain wall can be created and controlled. This class of structures has broad applications in areas such as magnetic recording media for hard disk drives,[5] permanent magnets,[6] and spin-transfer-torque Magnetic Random Acess Memory (MRAM) to allow lower switching current while maintaining thermal stability.[7] The field-induced magnetic configurations in a [Co/Pd]15 /TbFeCo exchange-spring system with perpendicular magnetic anisotropy are studied using torque magnetometry[8]. The experimental results are compared to a 1D micromagnetic simulation. The good agreement between experiments and simulations (see Fig. 1) allows us to deduce the evolution of the in-depth magnetic configuration as a function of the applied field orientation and amplitude. The chirality transition of the interfacial domain wall developing in the structure can also be determined with this technique [8].

[1] J. Rigue, D. Chrischon, A. M. H. de Andrade, and M. Carara, J. Magn. Magn. Mater. 324, 1561 (2012). [2] D. G. Naugle, B. I. Belevtsev, K. D. D. Rathnayaka, S.-I. Lee, and S. M. Yeo, J. Appl. Phys. 103, 07B718 (2008). [3] E. Shipton, K. Chan, T. Hauet, O. Hellwig, and E. E. Fullerton, Appl. Phys. Lett. 95, 132509 (2009). [4] S. L. Tomarken, A. F. Young, S. W. Lee, R. G. Gordon, and R. C. Ashoori, Phys. Rev. B 90, 201113(R) (2014). [5] A. Berger, N. Supper, Y. Ikeda, B. Lengsfield, A. Moser, and E. E. Fullerton, Appl. Phys. Lett. 93, 122502 (2008). [6] H. Zeng, J. Li, J. P. Liu, Z. L. Wang, and S. Sun, Nature 420(6914), 395–398 (2002). [7] I. Yulaev, M. V. Lubarda, S. Mangin, V. Lomakin, and E. E. Fullerton, Appl. Phys. Lett. 99, 132502 (2011). [8] P. Vallobra, T. Hauet, F. Montaigne, E. G. Shipton, E. E. Fullerton, and S. Mangin, J. Appl. Phys. 120, 013903 (2016)

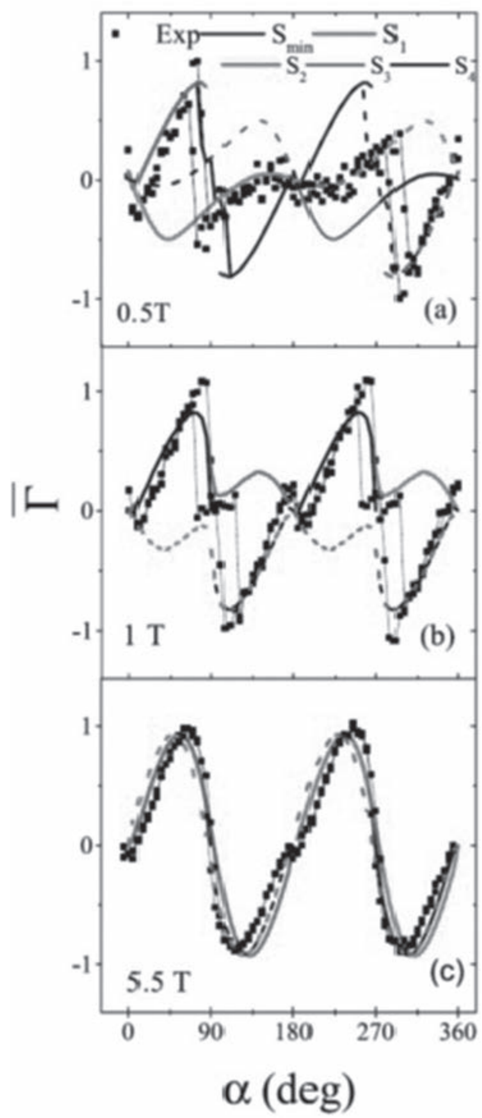

Fig. 1. Evolution of the normalized torque as a function of the field angle a measured at 300K under various magnetic fields amplitude 0.5 T (a), 1 T (b), and 5.5 T (c). Comparison between experimental torque measurements (green stars) and the solutions (S1, S2, S3, and S4) of a 1D simulation is shown. For S1, S2, S3, and S4 when the curve is in dashed the chirality of the interface domain wall is anticlockwise and is in solid when the chirality of the interface domain wall is clockwise. The black curve corresponds to the calculated torque curve in the case where the system is in the minimum energy configuration at each angle a.

4:45

HF-11. Effects of Heavy Metal Microstructure on Spin Transport in the Ultrathin Limit.

S.J. Brennan[1], J. Liao[1], T. Vemulkar[1], L. O'Brien[2] and R. Cowburn[1]
1. University of Cambridge, Cambridge, United Kingdom; 2. University of Liverpool, Liverpool, United Kingdom

Introduction The ability of all-metallic devices to generate pure spin currents with their low resistance-area product draws considerable research interest. In these systems, spin-orbit effects separate charge and spin currents, j_c and j_s, giving rise to many interesting effects. The prototypical all-metallic spintronic device is an (ultra)thin heavy metal/ferromagnet (HM/FM). When a j_c generates a transverse j_s from spin-dependent scattering, a local torque may be exerted on the FM. Hereby, all-metallic bilayers may be used to extract key spin-dependent parameters within each of the constituent materials, such as the efficiency of spin-to-charge current conversion (e.g. the spin Hall angle, θ) and the spin diffusion length, λ. However, sputtering HMs in the ultrathin limit can yield significantly different microstructure than in the bulk, and precise morphology is highly sensitive to the particular growth parameters, including substrate and HM surface energy, temperature and pressure. Consequently the electronic properties of the material may dramatically differ due to electron confinement, diffusive interface scattering, and reduced grain size[1], making direct correlations to spin-dependent properties challenging. We investigate the relationship between microstructure and spin-dependent properties in buffered HM|FM heterostructures. Using a range of thin buffer materials, we are able to tune the growth mode and so morphology of the HM layer. Spin-dependent properties are probed using spin Hall magnetoresistance measurements (SHMR), spin pumping and spin-orbit torque switching. We observe dramatic differences in the magnitude of j_s generation within the HM between buffered samples, which can be directly correlated to HM microstructure. In Ta/Pt/CoFeB layers, for highly-textured growth we find good agreement with models based on spin relaxation via the Elliott-Yafet (EY) and spin Hall effect via intrinsic spin scattering. However, for unbuffered Pt growth on SiO_2, we find stark differences between the measured spin and charge transport properties of the HM. This highlights the care that must be taken when determining properties such as θ and λ in thin and ultrathin films and the crucial role of microstructure in this limit. Buffering HMs in Metallic Multilayers Microstructural morphology is altered by buffering ultrathin Pt and W films grown via DC magnetron sputtering on SiO_2 and yttrium iron garnet. Growth of unbuffered Pt films on SiO_2 in the ultrathin limit is known to follow a Volmer-Weber-type (VW) mode resulting in a film of percolated grains with low texturing and large film roughness[2]. A thin 1 nm metallic under layer with high melting point seeds HM growth and enhances wetting upon deposition, which we find to increase texture, lower roughness and reduce film resistivity, ρ. In this study tantalum (Ta), tungsten (W) and ruthenium (Ru) were used as the intermediary buffer layer. Hereby, the growth mode, texture and ρ of the ultrathin Pt and W films are controlled and correlated to spin-dependent scattering. Cross-sectional transmission electron microscopy was performed to directly observe film morphology, which was further corroborated using atomic force microscopy and x-ray diffractometry to determine texturing and film roughness. Spin-Dependent Transport and Pumping SHMR and spin pumping measurements were conducted to determine the dependence of θ and λ on microstructure morphology. With additional current-induced SOT measurements of the j_s absorbed in the FM film, both back diffusion and transmission of j_s at the Pt|CoFeB interface were quantified. Magneto-electronic circuit theory (MCT) is used to model spin currents and accumulations at the HM|FM interface. In the ultrathin film limit ρ (charge-), θ and λ (spin-) dependent parameters are found to diverge significantly from those in the bulk HM. Stack ρ was found to agree with Fuchs-Sondheimer[3, 4] and Mayadas-Shatzkes[5] theory, indicating an increase of ρ at low thicknesses due to diffuse surface and grain boundary scattering. In this regime simple SHMR models yield effective θ and λ, which are convoluted over measured thicknesses and thus inappropriate for extracting these parameters. Although ρ, θ and λ vary at low thickness in all devices, buffering resulted in a dramatic increase in the observed SHMR signal, exemplified by the SHMR measurements of Ta/Pt/CoFeB and Pt/CoFeB in Fig. 1. Despite the VW growth mode of the unbuffered Pt/CoFeB, the results appear to agree well[6] with standard bi-layer SHMR MCT assuming a fixed $\rho_{HM,Bulk}$; however, this fails to account for the increase in SHMR signal (due to the divergence of ρ) at low thicknesses for the Ta buffered Pt|CoFeB stack. The MCT tri-layer model with varying ρ_{Pt} fit to experimental data indicates agreement with the EY spin scattering mechanism and implies an intrinsic-dominated spin Hall scattering in Pt films. Revisiting the results of unbuffered Pt/CoFeB films, it is apparent that despite the observed close agreement between theory and experiment, the role of microstructure greatly complicates a precise determination of θ and λ, even in seemingly simple bilayer films. The results presented are in broad agreement with those recently published[7] and provide further evidence in resolving the long-standing reports of highly varied θ and λ of Pt (and other HMs) observed in literature.

1. S. Dutta, et al., Journal of Applied Physics 122 (2), 025107 (2017). 2. P. R. LeClair, Technische Universiteit Eindhoven, 2002. 3. E. H. Sondheimer, Advances in Physics 1 (1), 1-42 (1952). 4. K. Fuchs, Mathematical Proceedings of the Cambridge Philosophical Society 34 (1), 100-108 (2008). 5. A. F. Mayadas, et al., Physical Review B 1 (4), 1382-1389 (1970). 6. J. Kim, et al., Physical Review Letters 116 (9), 097201 (2016). 7. M.-H. Nguyen, et al., Physical Review Letters 116 (12), 126601 (2016).

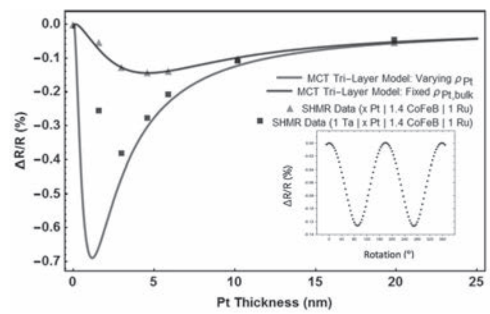

Fig. 1. Experimental SHMR data of Pt/CoFeB and Ta/Pt/CoFeB stacks. The two MCT tri-layer models attempt to fit the buffered Ta/Pt/CoFeB data. The inset shows SHMR measured with field rotation in the y,z plane.

FRIDAY AFTERNOON, 27 APRIL 2018 PEONY III, 2:00 TO 5:00

Session HG
PERMANENT MAGNET AND RELUCTANCE MACHINES VII

Weinong Fu, Chair
The Hong Kong Polytechnic University, Hong Kong, Hong Kong

CONTRIBUTED PAPERS

2:00

HG-01. Nonlinear Modeling of the Flux Linkage in Two-Dimensional Plane for the Planar Switched Reluctance Motor.

G. Cao[1], N. Chen[1], S. Huang[1], S. Xiao[1] and J. He[2]
1. Shenzhen Key Laboratory of Electromagnetic Control, Shenzhen, China; 2. GE Global Research, Schenectady, NY, United States

I. Introduction Planar switched reluctance motors (PSRMs) are an attractive candidate in precision two-dimensional (2-D) positioning devices for applications in microscale manufacturing, semiconductor lithography, etc., because they show the superiorities of simple structure, low cost, low heat loss, high precision, high reliability, and eco-friendly feature [1]–[4]. The flux linkage is the base of the electromagnetic model and control for switched-reluctance-type motors. Therefore, the accurate modeling of the flux linkage plays a key role to achieve precise motion control of switched-reluctance-type motors. However, the flux linkage is hard to be modeled accurately for switched-reluctance-type motors, because they have highly nonlinear magnetic field caused by the inherently double-salient structure and switched excitation. Especially, the accurate flux linkage is much more difficult to be built for the PSRMs owing to their planar structure, because the tolerances of the tooth width, pole pitch, air-gap, etc. are more obvious for planar structure compared to rotary and linear structure. The nonlinear modeling of the flux linkage is continuously concerned for switched-reluctance-type motors [5]–[8]. From the state of the art in the switched-reluctance-type motors, only the model of the flux linkage versus the one-axis position in a pole pitch was built. The model under a pole pitch applied to all position is not accurate, because the manufacturing tolerances are inevitable for practical motors. However, the model is suitable for rotary switched reluctance motors (SRMs), because the manufacturing tolerances are smaller due to the lager pole pitch and smaller number of pole pairs for rotary structure. For the PSRMs, the mover moves in a 2-D plane with long stroke, the manufacturing tolerances are much hard to be reduced against the rotary and linear SRMs. Based on the above description, a nonlinear modeling of the flux linkage in 2-D plane is more appropriate for the PSRMs, which is a promising effective method to achieve precision motion for the PSRMs. In this paper, a nonlinear modeling of the flux linkage in 2-D plane is proposed for the PSRMs by using backpropagation neural network (BPNN), where the current and 2-D positions are the inputs and the flux linkage is the output. The BPNN has the strong ability to deal with the nonlinear modeling with multiple inputs [9], [10]. II. Structure The overall structure of the prototype of the PSRM developed in our laboratory [1]–[4] is shown in Fig. 1. III. Nonlinear Modeling of The Flux Linkage in Two-Dimensional Plane For the mover in phase-*lj* (l=X, Y, j=A, B, C) of the PSRMs, the flux linkage depends on the current of phase-*lj* and the *x*- and *y*-axes position in 2-D plane. By using BPNN, the nonlinear flux linkage in phase-*lj* is modeled. The inputs of the NN are the current of phase-*lj* and the *X*- and *Y*-axes position. The flux linkage in phase-*lj* is the output of the NN. A four layers BPNN is employed to express the flux linkage model. The developed structure of the BPNN is 3-15-15-1. The sample set from experimental measurement is applied to model the BPNN. A dc-excitation method is applied to obtain the flux linkage [11], which is capable of providing a great many of data points. Measuring the current and voltage in phase-*lj*, the flux linkage in phase-*lj* can be calculated with the following equation: $d\Psi(x, y, i)/dt = u(t) - Ri(t)$. (1) IV. Results and Discussion *A. Results* From experiment, the flux linkage in phase-XB versus phase-XB current versus *x*-axis position versus *y*-axis position is obtained, where the current ranges from 0 to 9 A, *x*-axis position ranges from 0 to 14.4 mm, and *y*-axis position ranges from 0 to 21.6 mm. For the sample set with 179755 data points, 50% of data points is chosen as the training data set to build the BPNN expressing as the flux linkage, and the remaining data points are used as the testing data set to assess the generalization performance of the BPNN. Keeping the current in a constant of 5 A, the BPNN-based flux linkage and measurement flux linkage are presented in Fig. 2. The testing results of the BPNN-based flux linkage model and the corresponding errors are shown in Figs. 3-5. *B. Discussion* From Fig. 2, the phase-XB flux linkage is related to the phase-XB current and *X*- and *Y*-axes position; the phase-XB flux linkage mainly depends on *X*-axis position and is simultaneously affected by *Y*-axes position; the phase-XB flux linkage at the same current, the same *Y*-axis position and the same *X*-axis relative position between stator and mover is different for different *X*-axis pole pitches. The above issues mainly result from the manufacturing tolerances. The errors between the BPNN-based and real flux linkage are listed in Table 1. The maximum absolute errors of training and testing are 1.774 and 1.669 mWb, respectively. Under the conditions of the current less than 1 A, the maximum relative errors and the mean relative errors of training and testing are 79.82% and 82.96%, and 8.42% and 8.57%, respectively. Under other conditions, the maximum relative errors and the mean relative errors of training and testing are 1.69%, 1.65%, 0.45% and 0.44%, respectively. For the current less than 1 A, the relative errors are larger because the flux linkage is very near zero at the condition; however, the maximum absolute error is less than 1.774 mWb, and the mean relative error is less than 8.57%. Hence, the built nonlinear flux linkage model has small training and testing errors; the effectiveness of the model for the PSRM is verified experimentally.

[1] G.-Z. Cao, L.-L. Li, S.-D. Huang, L.-M. Li, Q.-Q. Qian, and J.-A. Duan, “Nonlinear modeling of electromagnetic forces for the planar switched reluctance motor,” *IEEE Trans. Magn.*, vol. 51, no. 11, Nov. 2015. [2] G. Z. Cao, J. L. Fang, S. D. Huang et al., “Optimization design of the planar switched reluctance motor on electromagnetic force ripple minimization,” *IEEE Trans. Magn*., vol. 50, no. 11, Nov. 2014. [3] S.-D. Huang, G.-Z. Cao, Z.-Y. He, C. Wu, J.-A. Duan, N. C. Cheung, and Q.-Q. Qian, “Maximum-force-per-ampere strategy of current distribution for efficiency improvement in planar switched reluctance motors,” *IEEE Trans. Ind. Electron.*, vol. 63, no. 3, pp.1665–1675, Mar. 2016. [4] S.-D. Huang, G.-Z. Cao, Z.-Y. He, J. F. Pan, J.-A. Duan, and Q.-Q. Qian, “Nonlinear modeling of the inverse force function for the planar switched reluctance motor using sparse least squares support vector machines,” *IEEE Trans. Ind. Informat.*, vol. 11, no. 3, pp. 591–600, Jun. 2015. [5] Yan Cai, Qingxin Yang, Lihua Su, Yanbin Wen and Yiming You, “Nonlinear modeling for switched reluctance motor by measuring flux linkage curves,” 2010 2nd International Conference on Computer Engineering and Technology, Chengdu, 2010, pp. V6-47-V6-51. [6] L. Ortombina, F. Tinazzi and M. Zigliotto, “Magnetic Modeling of Synchronous Reluctance and Internal Permanent Magnet Motors Using Radial Basis Function Networks,” *IEEE Trans. Ind. Electron.*, vol. 65, no. 2, pp. 1140-1148, Feb. 2018. [7] R. Zhong et al., “Accurate model of switched reluctance motor based on indirect measurement method and least square support vector machine,” *IET Electr. Power Appl.*, vol. 10, no. 9, pp. 916-922, 11 2016. [8] O. Ustun, “Measurement and Real-Time Modeling of Inductance and Flux Linkage in Switched Reluctance Motors,” *IEEE Trans. Magn.*, vol. 45, no. 12, pp. 5376-5382, Dec. 2009. [9] S. Song, L. Ge and M. Zhang, “Data-Reconstruction-Based Modeling of SRM With Few Flux-Linkage Samples From Torque-Balanced Measurement,” *IEEE Trans. Energy Convers*, vol. 31, no. 2, pp. 424-435, June 2016. [10] J. Cai, Z. Q. Deng, R. Y. Qi, Z. Y. Liu and Y. H. Cai, “A Novel BVC-RBF Neural Network Based System Simulation Model for Switched Reluctance Motor,” *IEEE Trans. Magn.*, vol. 47, no. 4, pp. 830-838, April 2011. [11] H. X. Zheng, G. Z. Cao, S. D. Huang, L. L. Li and L. M. Li, “A thrust force characteristics measurement of the planar switched reluctance motor using flux linkage characteristics,” International Conference on Electrical Machines and Systems (ICEMS), Hangzhou, 2014, pp. 2859-2862. [12] X. Zhang, Feng Wang and Xiaogen Shao, “Flux linkage characteristics on-line modeling of switched reluctance motor based on boundary constraints RBF,” Proceeding of the 11th World Congress on Intelligent Control and Automation, Shenyang, 2014, pp. 5942-5946.

Table 1. Errors between the BPNN-based and the real flux linkage

	Maximum absolute error		Mean absolute error		Maximum relative error		Mean relative error	
Current range (A)	[0, 1)	[1, 9]	[0, 1)	[1, 9]	[0, 1)	[1, 9]	[0, 1)	[1, 9]
Training data set	1.774 mWb	1.694 mWb	0.243 mWb	0.250 mWb	79.82%	10.24%	8.57%	0.45%
Testing data set	1.669 mWb	1.653 mWb	0.238 mWb	0.248 mWb	82.96%	12.28%	8.42%	0.44%

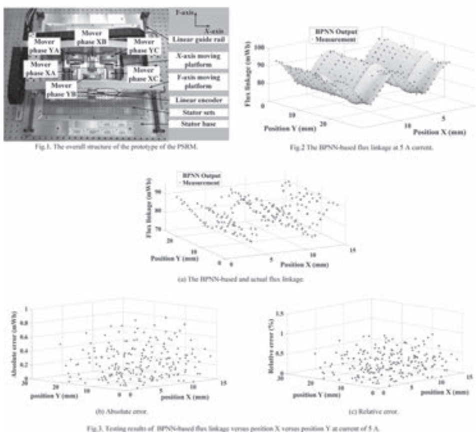

Fig. 1.

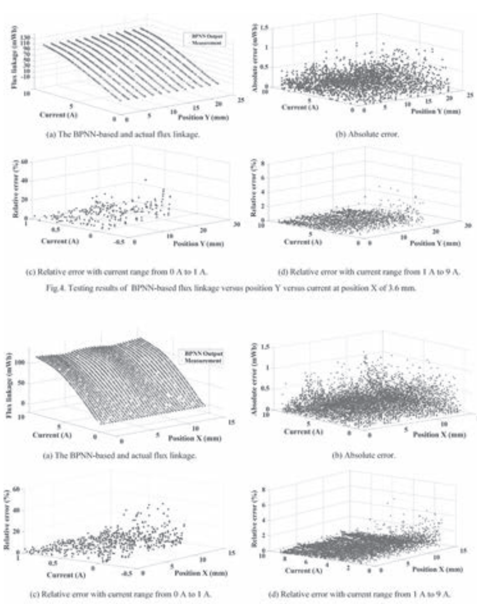

Fig. 2.

2:15

HG-02. Validation of Efficiency Maps of an Outer Rotor Surface Mounted Permanent Magnet Machine for Evaluation of Recyclability of Magnets.

A. Garcia Gonzalez[1], A.K. Jha[3], L. Ziwei[2], P. Upadhayay[2] and P.O. Rasmussen[1]

1. Energy Technology, Aalborg University, Aalborg, Denmark; 2. VALEO Electrical Systems, Créteil, France; 3. G2Elab, Grenoble INP, Grenoble, France

I. Introduction The global trend towards the implementation of hybrid and electrical vehicles ((H)EVs) is challenging from the perspective of energy supply and the use of materials with high fluctuation of prices in the international market (e.g. rare earth elements). This article attempts to set the base for a methodology for evaluating the performance of a machine in terms of the recyclability of the permanent magnets (PMs). In this regard, two approaches are available; evaluation of the disassembly process [1] [2] and the energy consumption over the life cycle of the machine [3][4]. The second approach is selected for this study. II. Experimental measurements Measurements were performed on an outer rotor surface mounted PM machine which is generally used in electrical bikes or small city cars [5]. The set-up is presented in figure 1. A resistive load was connected to the machine operating as generator, and values of input and output power were measured. The results of efficiency at different values of torque and speed are summarized in figure 2. III. 2D FEA simulations A. Disassembly In order to obtain the energy consumption over the life cycle of the machine, it was necessary to determine its efficiency map. Therefore, simulations were carried with the main dimensions obtained during the disassembly process. The magnet remanence was measured with the Physical Property Measurement System® from Quantum Design. The properties of the electrical steel in the stator were unknown. However, a standard SiFe lamination was selected. B. Elaboration of efficiency maps Measured current was applied to the simulations. Once the measured and the calculated values were contrasted, the elaboration of the efficiency maps was performed. Since a large amount of points is required to determine the efficiency at any value of torque and speed, the following expression was used: $T=3/2(\Psi_m I_q p)$ Where Ψ_m is the magnet flux linked with the stator windings calculated with FEA, I_q is the current applied in the q-axis and p is the number of pole pairs. Thus, the copper losses were obtained neglecting the effect of the harmonics induced by the modulation of the converter. For obtaining the core losses at any speed, curve fitting was applied to the losses calculated in 2D FEA simulations. IV. Study case The main goal of DEMETER project [6] is the study of the recyclability and reuse of magnets in (H)EVs. Therefore, a study case was defined in order to validate the methodology proposed here. Recycled magnets are expected to have lower remanence. Hence, the remanence adopted for this study case was assumed to be B_r=1 T. Similar values of current were applied to a new set of simulations. In order to obtain similar values of torque, the axial length of the machine was increased. Furthermore, the thermal aspects of having higher copper losses were disregarded for the analysis. The procedure described above was followed for the elaboration of the efficiency maps. V. Results analysis and comparison In addition to the measurements of torque and speed, a no-load test was performed. Such test was intended for enhancing the analysis of the results in the presence of deviations between the measurements at load and the calculated values in simulations. It consisted in running the machine just by pulling the shaft and recording the backemf waveforms in an oscilloscope. A time decaying back-emf wave-form was obtained, and the friction losses were obtained with the expression: $T(t)=J\, d\omega_m/dt + T_L(t)$ Where J is the inertia of the machine, ω_m is the mechanical angular speed and $T_L(t)$ is the load torque. At no load condition $T(t)$ is equal to zero and $T_L(t)$ is composed by the mechanical, iron and magnet losses. The inertia J was estimated with the main dimensions of the machine. The losses as function of the speed of the machine were approximated by curve fitting. On the other hand, the no-load losses from measurements were estimated as: $p_0 = P_m - P_o - p_{cu}$ Where P_m is the input power measured in the power analyser, P_o is the output power read in the torque transducer and p_{cu} are the copper losses calculated as the resistance of the windings times the square of the applied current. Absolute deviations of efficiency of approximately 5% were obtained. Such deviations may be originated due to the effect of some uncertainties: - The alignment of the set-up and oscillations in the readings in the torque transducer. - The specific losses of the laminations, which remained unknown in the calculations. VI. Conclusions The use of magnets with lower remanence will result in an increment of the copper losses. As a consequence of the increment of the resistance of the windings with increased length of the machine for supplying the same amount of torque. Therefore, a larger consumption of energy is expected if a driving cycle like the ECE-15 is considered due to the large intervals of acceleration (i.e. high torque, low speed). For future work it has been defined the study of the energy consumption of the machine analysed here under the European urban driving cycle ECE-15 [7], which corresponds to the initial 200 seconds of the NEDC. For such analyses, it will be required the assumption of some vehicle parameters, such as weight, acceleration, etc., corresponding to a small city car [8]. Additional study cases will be included in order to enhance the evaluation of the impact of the use of recycling magnets in HEVs.

[1] T. Elwert, D. Goldmann, F. Römer, M. Buchert, C. Merz, D. Schueler, and J. Sutter, "Current Developments and Challenges in the Recycling of Key Components of (Hybrid) Electric Vehicles, in Recycling, vol. 1, pp 25-60, 2015. [2] A. Kumar Jha, Z. Li, A. Garcia Gonzalez, P. Upadhayay, and P. Rasmussen, "Weighted index of recycling and energy (WIRE) cost for Motors in electric vehicles," in SPEEDAM 2017, Submitted to, Dec 2017. [3] P. Lazari, J. Wang, and L. Chen, "A computationally efficient design technique for electric-vehicle traction machines," IEEE Transactions on Industry Applications, vol. 50, no. 5, pp. 3203–3213, Sept 2014. [4] K. Kiyota, H. Sugimoto, and A. Chiba, "Comparing electric motors: An analysis using four standard driving schedules," IEEE Industry Applications Magazine, vol. 20, no. 4, pp. 12–20, July 2014. [5] "Wuxi lingming electric drive technology co., ltd," Internet: http://www.lingmingmotor.com, 2015, [Nov. 22, 2017]. [6] "European training network for the design and recycling of rare-earth permanent magnets," Internet: http://etn-demeter.eu, 2015, [Nov. 22, 2017]. [7] T. Barlow, A Reference Book of Driving Cycles for Use in the Measurement of Road Vehicle Emissions: Version 3. IHS, 2009. [Online]. Available: https://books.google.dk/books?id=jnowMwEACAAJ [8] J. Larminie and J. Lowry, "Electric vehicle modelling," in Electric Vehicle Technology Explained, 2nd ed. Somerset, GB: Wiley, 2012, ch. 8.

Fig. 1. Experimental set-up.

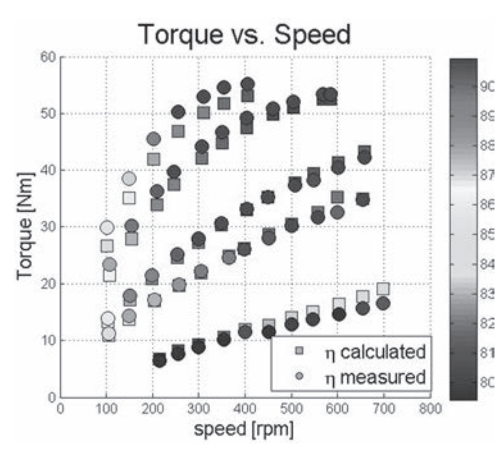

Fig. 2. Efficiency and torque comparison between measurements and calculations.

2:30

HG-03. Axial Magnetic Force Analysis of Conical-rotor Permanent Magnet Synchronous Motor.

J. Wang[1], S. Huang[1] and *C. Guo*[1]
1. College of Electrical & Information Engineering, Hunan University, Changsha, China

Abstract-The general axial force is suppressed method for the permanent magnet synchronous motor (PMSM) direct-drive blower, pump and turbo-expander, is increase balance devices such as compression spring and special bearing, to counteract its influence, resulting in both complex system structure and higher manufacturing cost. Aiming to solve above issues, this paper presents a novel structure of conical-rotor permanent magnet synchronous motor (CR-PMSM) and studies its axial magnetic force in detail. Which features its axial force is suppressed, simple, and improve efficiency of CR-PMSM. 3-D finite-element model (3-D FE) is used to simulate the magnetic-field distribution and axial magnetic force according to conical-rotor axial displacement and *dq*-axis currents. A prototype machine is designed and built, in order to validate the theory. I.INTRODUCTION Thanks to its simple structure and high energy transfer efficiency, the PMSM direct-drive high-speed blower, pump and turbo-expander, etc., have been widely accepted. However, the axial tension produced by the high speed flow running through the blades of blower, pump and turbo-expander (could be as large as 150N for a 1.6kW and 6000rpm small turbo-expander) usually needs balance devices to counteract its influence, which significantly increase the system complexity and cost. Thus, the CR-PMSG is developed, which features its axial force is suppressed. Therefore, CR-PMSGs have been investigated in recent years. For example, in [1], 3-D finite-element (3-D FE) model is used to simulate the magnetic-field distribution of air gap, flux weakening in CR-PMSM according to rotor axial displacement, instead of changing the current angle. This method is effective in increasing the maximum speed. However, axial magnetic force has not been analyzed; In [2], a novel type of bearingless PMSM of consists of two conical air gap bearingless PM half-motors, mounted on a single shaft.is presented. The value of the axial force depends, besides of the motor geometry, on the PM air gap flux density, air gap cone angle and *d*-axis current. However, the effect of *q*-axis current on axial force is not analyzed. In this paper,the CR-PMSM was analyzed and the effectiveness of two methods on dealing with problems concerned with non-uniform distribution of magnetic field along axial direction in electric motor was studied, which were sectional calculation (SC) method and EF method. The analyzed results were verified by no-load back electromotive force (EMF) experiment of the electric motor. Then, in order to determine the axial magnetic force of CR-PMSM is defined by theoretical analysis. 3-D FE model is adopted to simulate the magnetic-field distribution and axial magnetic force according to rotor axial displacement and *dq*-axis currents. II.Magnetic Field Analysis of CR-PMSG In order to comparative analysis by SC and 3-D EF method, the CR-PMSM is divided into 10 sections, each with a length of only 5.2 mm, and a 1/4 3-D EF model has been established. Its taper angleα, pole pairs p, core length L_{ef}, maximum axial displacement Δz and rated speed n are 6°, 2, 52mm, 4mm and 6000r/min, respectively, as shown in Fig. 1 (a) and (b). When stator is aligned at conical-rotor (Δz=0), the flux density of air gap is shown in Fig. 2 (a), the peak value of radial flux density is about 0.8T while it is 0.25T for the axial one (B_z). Besides, it also can be seen that both waveforms have a 90°, phase difference between each other, comparative difference 0.1T of air gap flux density by SC and 3-D EF method. The no load phase back EMF of CR-PMSG is measured and depicted in Fig. 2 (b), of which the RMS value is about 238V. Compared with the 3-D FE result, it has a quite slight difference (3%), which confirms the accuracy of developed 3-D EF model. When stator is not aligned at conical-rotor (Δz>0), back-EMF is essentially linearly reduced, the performances will be analyzed in detail in the full paper. III. Analysis of Results for Axial Magnetic Force As can be seen from Fig. 2(a), axial magnetic force is being in the air gap. The axial magnetic force can be calculated by the principle of virtual displacement, the air-gap magnetic field (B_δ) can be expressed as a combination of the permanent magnet magnetic field and armature reaction magnetic field. Thus, B_δ is equivalent to the superposition of permanent magnet magnetic field (B_0) and magnetic fields (B_{1d} and B_{1q}) generated by I_d and I_q, respectively. The axial magnetic force simulations with varying *dq*-axis current and conical-rotor at different axial locations are performed, the simulation and measured results are presented in Fig. 2 (c) and (d), similar to the results introduced in [4] the axial magnetic force only has a quite obviously raise with the increase of *d*-axis current. IV.Conclusion In order to suppress the axial force, a CR-PMSM for direct-drive blower, pump and turbo-expander have been developed in this paper. It is found that air gap flux density only has a quite slight increase with the axial directio, and the *d*-axis current plays a quite important role in balancing the axial force produced by the high speed flow. However, it is still quite challenging to derive the expression of axial force with respect to *dq*-axis currents, which will be the priority of future work.

[1] F. Chai, K. Zhao, Z. yang et al., “Flux Weakening Performance of Permanent Magnet Synchronous Motor With a Conical Rotor,” *IEEE Trans. Magn.,* vol. 53, no. 11, pp. 536–545, Nov. 2017. [2] G. Munteanu, A. Binder, and S. Dewenter, “Five-axis magnetic suspension with two conical air gap bearingless PM synchronous half-motors,” *In Proc. Int. Symp. Power Electron., Elect. Drives, Autom. Motion,* 2012, pp. 1246–1251. [3] W. Bauer and W. Amrhein, “Electrical design considerations for a bearingless axial-force/Torque Motor,” *IEEE Trans. Ind.Appl.,* vol. 50, no. 4, pp. 2512–2522, Jul./Aug. 2014. [4] F. Chai, Y. L. Pei, J. Ou, “ Research on Axial Magnetic Force of Dual-Stator Conical Permanent Magnet Svnchronous motor,” *Trans. of China Electro-technical Society*, vol.28, no.7, Sup. 2013. (in Chinese)

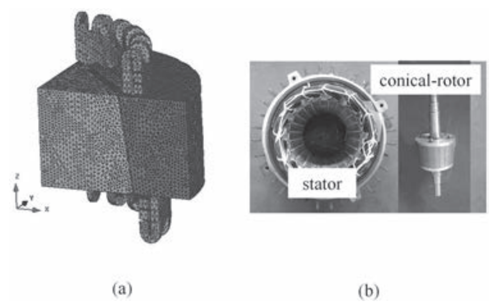

Fig. 1. (a) structure and (b) 3-D FE model of CR-PMSM

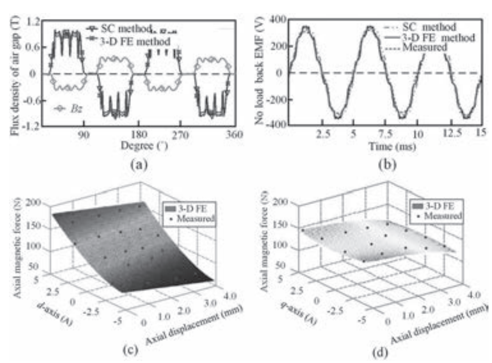

Fig. 2. Comparative difference (a) flux density of air gap, (b) no load back EMF by SC and 3-D EF method, and relationship among the axial magnetic force *d- (c) q (d)*-axis currents and rotor axial displacement of the CR-PMSM

2:45

HG-04. Analysis and experimental validation of performance for a switched reluctance motor with pre-fabricated soft magnetic core.

V. Krishnan[1], K. Selvam[2] and K. Radhakrishnan[3]
1. EEE, avviyar college of engineering, Puducherry, India; 2. Research and Development, Greenergy solar solutions, Pondicherry, India; 3. EEE, Sri Venkateswara college of Engineering, Tamilnadu, India

Abstract-Soft magnetic composite (SMC) materials and SMC electromagnetic devices have undergone a significant development in the past decade [1]. Much effort has been carried out on designing and prototyping different types of electrical machine. The basis for soft magnetic composites is bonded iron powder and the powder is coated, pressed into a solid material using a die [1]-[3]. However, it has the drawback that the properties will in most cases be different from those obtained form compaction and machining process. To investigate "pre-fabricated SMC blank"products, this paper presents the design and analysis of a switched reluctance (SR) motor with a pre-fabricated SMC blanks of low mass density to replace the existing induction motor in a dishwasher pump. This can be fast and low cost approach is to machine the component from a preform blank. Finite element analysis (FEA) study has been conducted to accurately determine key motor parameters, and performance predictions are validated by the experimental results on the prototype model. Pre-fabricated SMC core and prototype motor Three pieces of pre-fabricated SMC blanks (Somaloy1000 3P) each for stator and rotor are considered and to fabricate stator and rotor these three pieces have to be bonded together using epoxy glue [1]-[3]. The bonded stator and rotor blank has been subjected to precession machining to yield the stator and rotor of design dimensions. Glimpses of the fabrication process and experimental setup have been illustrated in Fig.1 and 2. Experimental validation Dynamic characteristics Fig. 2 shows the experimental setup for measuring the motor performance. The SMC motor prototype is on the first, and a mechanically coupled dynamo load cell is on the second. A load cell is mounted on the dynamo which is directly connected to high speed dynamo controller for measuring the shaft torque and speed [4]. Fig. 3 plots the mechanical characteristics, i.e., the motor speed against the dc link voltage of power converter with certain load. The motor can successfully deliver a torque of 1.2 Nm at 3000 rpm while the converter is supplied with a dc link voltage of about 85 V. Fig. 4 shows phase current wave form comparison of measured and FE calculated. Thermal study The comparison of measured and FE predicted hot spot results in all the windings and stator core temperatures of SMC prototype are as given in Table I. Six type-T thermocouples embedded in six stator windings and remaining two thermocouples fixed in stator core and outer casing of the prototype. The operating conditions for the experimental thermal study are given in Table II. Vibration study The vibration spectrum generated in the SMC prototype is measured using the accelerometer to validate the estimations. To measure the vibration the accelerometer pickup point's location are behind a stator pole and between two poles [2], [5] and [6]. The operating frequency of the accelerometer is selected according to the switching frequency. The Fig. 5 shows the measured acceleration and its spectrum of the SMC prototype. The FE predicted mode shape vibration frequencies and measured spectrum frequencies of SMC prototype for modes 2 and 4 are compared in Table III. The measured vibration spectrum of the SMC prototype is captured at a speed of 2947 RPM, 68 V. Conclusion and discussion The following inferences are observed from the measured dynamic characteristics of SMC prototype machine: The prototype provides a stable output on a full operating range, even though the problems of large magnetizing current and inferior magnetizing curve with lower μr-max values of 850. The dynamic performances are fully dependent on the nature of the stator core and losses of the machine. It is also revealed that during the dynamic operating condition, the initial current drawn by the SMC machine is higher due to the requirement of higher level of magnetization energy in bulk material than in laminates for a cycle of the source frequency. The comparative analysis of measured temperature rise values of the SMC prototype machine and simulation results shows: the SMC machine temperature rise is lesser than conventional machine. This is due to the SMC stator core is a smooth surface that allows a good thermal contact between the winding and the core assembly. Moreover this lead to more efficient electromagnetic coupling as well as more efficient heat transfers ability and cooling capability. This enhances the thermal limit of the SMC prototype motor. The comparative analysis of measured vibration frequencies of the SMC prototype machine and FEA results of natural mode shape frequencies of stator and rotor shows: the marked reduction in the natural frequencies of the stator and rotor assembly of SMC machine due to the cushioning nature of the insulation binder which has a very good viscous-elasticity property and iron powder cores would present a higher damping factor in the radial and circumferential directions compared to a similar laminated structure. As observed from the measured vibration spectrum, only two mode frequencies (mode 2 and mode 4) are dominant in the spectrum and other mode frequencies are suppressed since the acceleration particles in the SMC stator structure are evenly distributed due to the distributed insulation around the iron particles.

[1]. "The Latest Development in Soft magnetic Composite Technology," Sweden, SMC Update, Reports of Höganäs AB, 1997-2008 [Online]. Available: http://www.hoganas.com/ [2]. Jack, A.G. "Experience with the Use of Soft Magnetic Composites in Electrical Machines", in Proc. International Conference on Electrical Machines, Istanbul, Turkey, pp.1441-1448, 1998. [3]. M. Persson, P. Jansson, A. G. Jack, B. C. Mecrow, "Soft Magnetic Composite Materials – Use for Electrical Machines"; 7th International Conference on Electrical Machines and Drive at Durham, England, Sep. 1995. [4]. K. N. Srinivas and R. Arumugam, "Analysis and characterization of switched reluctance motors: Part I—Dynamic, static, and frequency spectrum analysis," IEEE Trans. Magn., vol. 41, no. 4, pp. 1306–1320, Apr. 2005.. [5].Rabinovici, R. "Torque ripple, vibrations, and acoustic noise in switched reluctance motors", HAIT Journal of Science and Engineering B, Vol. 2, No. 5-6, pp. 776-786, 2005. [6] M. N. Anwar and Iqbal Husain, "Radial force calculation and acoustic noise prediction in switched reluctance motor," IEEE Trans. Ind. Applicat., vol. 36, pp. 1589–1597, Nov./Dec. 2000.

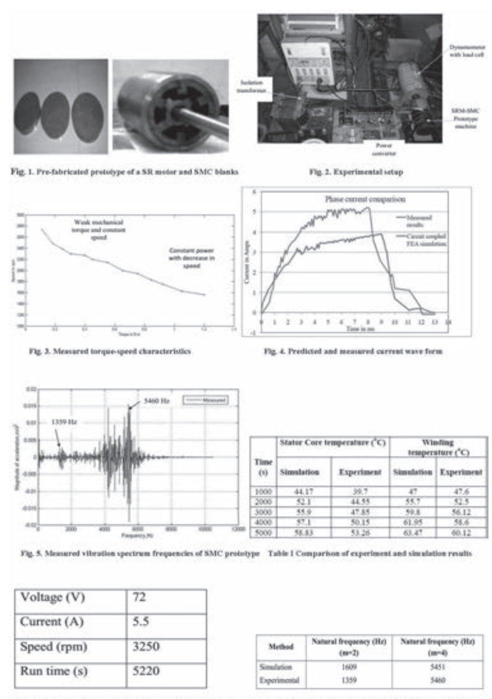

Time (s)	Stator Core temperature (°C)		Winding temperature (°C)	
	Simulation	Experiment	Simulation	Experiment
1000	44.17	39.7	47	47.6
2000	52.1	44.55	55.7	52.5
3000	55.9	47.85	59.8	56.12
4000	57.1	50.15	61.95	58.6
5000	58.83	53.26	63.47	60.12

Table I Comparison of experiment and simulation results

Voltage (V)	72
Current (A)	5.5
Speed (rpm)	3250
Run time (s)	5220

Table II Operating conditions for experimental thermal study

Method	Natural frequency (Hz) (m=2)	Natural frequency (Hz) (m=4)
Simulation	1609	5451
Experimental	1359	5460

Table III Natural frequencies of SMC motor for modes 2 and 4

Fig. 1. Experimental and Simulation Results

3:00

HG-05. Study on Static Magnetic Characteristics of a Switched Reluctance Motor with 12/10 Poles under Different Operation Modes.

Y. Hu[1] and W. Ding[1]
1. Xi'an Jiaotong University, Xi'an, China

This paper mainly focuses on the static inductance and flux linkage characteristics of a switched reluctance motor (SRM) with 12/10 poles when it respectively works as a six- and a three-phase mode. The single and double excitations are also individually taken into consideration for the two modes. The simulations are experimentally verified by using an indirect flux measurement method. The consistency between the simulations and experimental results verifies the validity of the theory.

[1] Krishnan R. "Switched reluctance motor drives: modeling, simulation, analysis, design, and applications," New York: CRC Press LLC, 2001. [2] J. H. Wu, "Design and application of switched reluctance motor," Beijing: China Machine Press, 2000.

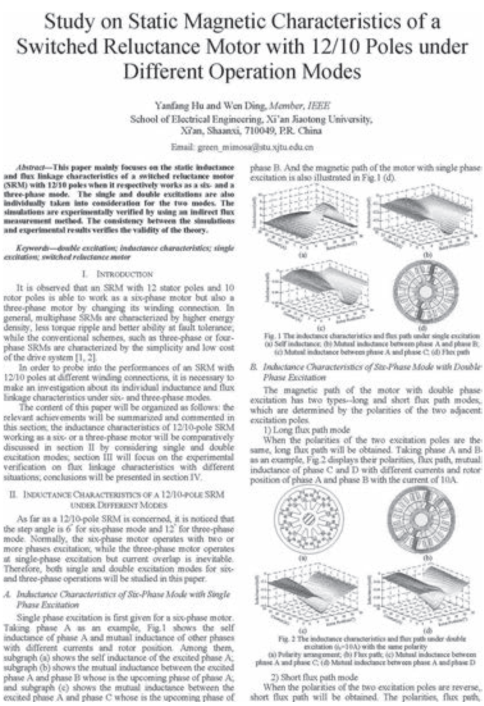

Study on Static Magnetic Characteristics of a Switched Reluctance Motor with 12/10 Poles under Different Operation Modes

Yanfang Hu and Wen Ding, *Member, IEEE*
School of Electrical Engineering, Xi'an Jiaotong University, Xi'an, Shaanxi, 710049, P.R. China
Email: green_mimosa@stu.xjtu.edu.cn

***Abstract*—This paper mainly focuses on the static inductance and flux linkage characteristics of a switched reluctance motor (SRM) with 12/10 poles when it respectively works as a six- and a three-phase mode. The single and double excitations are also individually taken into consideration for the two modes. The simulations are experimentally verified by using an indirect flux measurement method. The consistency between the simulations and experimental results verifies the validity of the theory.**

***Keywords*—double excitation; inductance characteristics; single excitation; switched reluctance motor**

I. INTRODUCTION

It is observed that an SRM with 12 stator poles and 10 rotor poles is able to work as a six-phase motor but also a three-phase motor by changing its winding connection. In general, multiphase SRMs are characterized by higher energy density, less torque ripple and better ability at fault tolerance; while the conventional schemes, such as three-phase or four-phase SRMs are characterized by the simplicity and low cost of the drive system [1, 2].

In order to probe into the performances of an SRM with 12/10 poles at different winding connections, it is necessary to make an investigation about its individual inductance and flux linkage characteristics under six- and three-phase modes.

The content of this paper will be organized as follows: the relevant achievements will be summarized and commented in this section; the inductance characteristics of 12/10-pole SRM working as a six- or a three-phase motor will be comparatively discussed in section II by considering single and double excitation modes; section III will focus on the experimental verification on flux linkage characteristics with different situations; conclusions will be presented in section IV.

II. INDUCTANCE CHARACTERISTICS OF A 12/10-POLE SRM UNDER DIFFERENT MODES

As far as a 12/10-pole SRM is concerned, it is noticed that the step angle is 6° for six-phase mode and 12° for three-phase mode. Normally, the six-phase motor operates with two or more phases excitation, while the three-phase motor operates at single-phase excitation but current overlap is inevitable. Therefore, both single and double excitation modes for six- and three-phase operations will be studied in this paper.

A. Inductance Characteristics of Six-Phase Mode with Single Phase Excitation

Single phase excitation is first given for a six-phase motor. Taking phase A as an example, Fig.1 shows the self inductance of phase A and mutual inductance of other phases with different currents and rotor position. Among them, subgraph (a) shows the self inductance of the excited phase A; subgraph (b) shows the mutual inductance between the excited phase A and phase B whose is the upcoming phase of phase A; and subgraph (c) shows the mutual inductance between the excited phase A and phase C whose is the upcoming phase of phase B. And the magnetic path of the motor with single phase excitation is also illustrated in Fig.1 (d).

Fig. 1 The inductance characteristics and flux path under single excitation (a) Self inductance; (b) Mutual inductance between phase A and phase B; (c) Mutual inductance between phase A and phase C; (d) Flux path

B. Inductance Characteristics of Six-Phase Mode with Double Phase Excitation

The magnetic path of the motor with double phase excitation has two types--long and short flux path modes, which are determined by the polarities of the two adjacent excitation poles.

1) Long flux path mode

When the polarities of the two excitation poles are the same, long flux path will be obtained. Taking phase A and B as an example, Fig.2 displays their polarities, flux path, mutual inductance of phase C and D with different currents and rotor position of phase A and phase B with the current of 10A.

Fig. 2 The inductance characteristics and flux path under double excitation (i_s=10A) with the same polarity (a) Polarity arrangement; (b) Flux path; (c) Mutual inductance between phase A and phase C; (d) Mutual inductance between phase A and phase D

2) Short flux path mode

When the polarities of the two excitation poles are reverse, short flux path will be obtained. The polarities, flux path,

Fig. 1. Study on Static Magnetic Characteristics of a Switched Reluctance Motor with 1210 Poles under Different Operation Modes_1

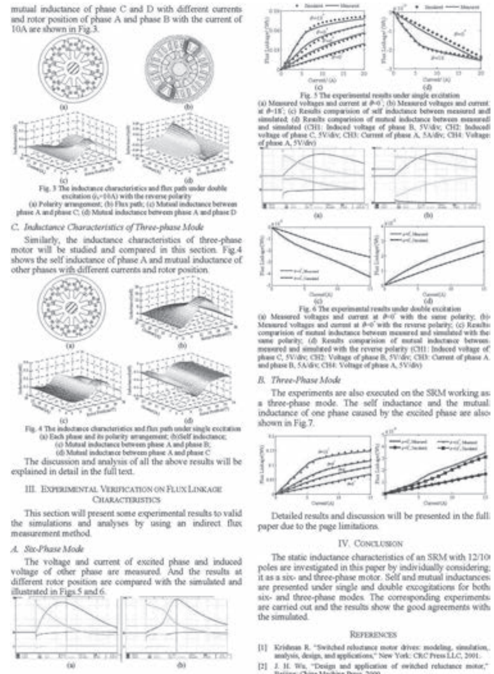

mutual inductance of phase C and D with different currents and rotor position of phase A and phase B with the current of 10A are shown in Fig.3.

Fig. 3 The inductance characteristics and flux path under double excitation (i_s=10A) with the reverse polarity (a) Polarity arrangement; (b) Flux path; (c) Mutual inductance between phase A and phase C; (d) Mutual inductance between phase A and phase D

C. Inductance Characteristics of Three-phase Mode

Similarly, the inductance characteristics of three-phase motor will be studied and compared in this section. Fig.4 shows the self inductance of phase A and mutual inductance of other phases with different currents and rotor position.

Fig. 4 The inductance characteristics and flux path under single excitation (a) Each phase and its polarity arrangement; (b)Self inductance; (c) Mutual inductance between phase A and phase B; (d) Mutual inductance between phase A and phase C

The discussion and analysis of all the above results will be explained in detail in the full text.

III. EXPERIMENTAL VERIFICATION ON FLUX LINKAGE CHARACTERISTICS

This section will present some experimental results to valid the simulations and analyses by using an indirect flux measurement method.

A. Six-Phase Mode

The voltage and current of excited phase and induced voltage of other phase are measured. And the results at different rotor position are compared with the simulated and illustrated in Figs.5 and 6.

Fig. 5 The experimental results under single excitation (a) Measured voltages and current at θ=0°; (b) Measured voltages and current at θ=18°; (c) Results comparision of self inductance between measured and simulated; (d) Results comparision of mutual inductance between measured and simulated (CH1: Induced voltage of phase B, 5V/div; CH2: Induced voltage of phase C, 5V/div; CH3: Current of phase A, 5A/div; CH4: Voltage of phase A, 5V/div)

Fig. 6 The experimental results under double excitation (a) Measured voltages and current at θ=0° with the same polarity; (b) Measured voltages and current at θ=0° with the reverse polarity; (c) Results comparision of mutual inductance between measured and simulated with the same polarity; (d) Results comparision of mutual inductance between measured and simulated with the reverse polarity (CH1: Induced voltage of phase C, 5V/div; CH2: Voltage of phase B, 5V/div; CH3: Current of phase A and phase B, 5A/div; CH4: Voltage of phase A, 5V/div)

B. Three-Phase Mode

The experiments are also executed on the SRM working as a three-phase mode. The self inductance and the mutual inductance of one phase caused by the excited phase are also shown in Fig.7.

Detailed results and discussion will be presented in the full paper due to the page limitations.

IV. CONCLUSION

The static inductance characteristics of an SRM with 12/10 poles are investigated in this paper by individually considering it as a six- and three-phase motor. Self and mutual inductances are presented under single and double excogitations for both six- and three-phase modes. The corresponding experiments are carried out and the results show the good agreements with the simulated.

REFERENCES

[1] Krishnan R. "Switched reluctance motor drives: modeling, simulation, analysis, design, and applications," New York: CRC Press LLC, 2001.
[2] J. H. Wu, "Design and application of switched reluctance motor," Beijing: China Machine Press, 2000.

Fig. 2. Study on Static Magnetic Characteristics of a Switched Reluctance Motor with 1210 Poles under Different Operation Modes_2

3:15

HG-06. Demagnetization under normal operation in variable flux PM-assisted Synchronous Reluctance Machines.

I. Manolas[1], A. Kladas[2], D. Svechkarenko[1] and R. Chin[1]
1. Corporate Research Sweden, ABB, Västerås, Sweden; 2. School of Electrical and Computer Engineering, National Technical University of Athens, Zografou, Greece

In the field of electrical machine design, the mainstream approach is to fix the key electromagnetic design parameters in a way that yields an acceptable performance over the operating range. Moreover, these parameters should ideally remain unaltered for accurate control and behavior prediction. However, this approach might be revised radically as novel magnetic materials emerge along with the capabilities of power electronic converters. Indeed, it should be possible to design a machine with configurable electromagnetic properties during operation. Variable flux memory machines (VFMMs) [1], [2] utilize permanent magnet materials that change the intensity of their magnetization and "memorize" various flux density levels. This is achieved via employing low coercive force (Hc) materials and applying appropriate current pulses through the standard machine windings for a very short time during normal operation. This yields adjustable torque/power profiles with wider speed ranges and increased efficiency, even during field weakening operation. In this paper, Permanent Magnet assisted Synchronous Reluctance Machines are considered incorporating low coercive force magnets (e.g. AlNiCo). The objective of this work is to focus on the demagnetization that occurs under normal operation, when the magnetization levels in the machine should be adjusted - for instance, during high speed operation. As an outcome of this study, a proper demagnetization strategy is proposed that achieves the required magnetization levels in the machine with minimum stator current requirement (converter overload) and minimum possible disturbance on the mechanical load side (transient torque overshoot) [3]-[5]. To capture the complex phenomena related to the permanent demagnetization of PM materials, a non-conventional hysteresis-based finite element simulation tool needs to be developed, which should be able to reflect the permanently changed magnetic properties of the PM after a short-time high-amplitude current pulse. In this case, the resulting operating point will no longer lie along the original BH curve, but along the demagnetized recoil line at the worst operating condition and a special set of three sequential simulations is developed to handle such cases. The first simulation creates a mesh of elements on the PMs and generates from the manufacturer's hysteresis material properties an element based demagnetization curve. That is subsequently supplied to the second simulation that makes an element based calculation of the demagnetization in the magnets. The output is an element mesh containing single values and directions of coercivity (Hc) that reflect the demagnetized states. This is subsequently fed to the final simulation that makes the real application performance calculation employing the imported demagnetization states. Using the aforementioned simulation method, it is possible to consistently capture the machine performance in terms of torque, current, voltage and no-load back-EMF before and after a short high-current pulse intended to cause demagnetization. Under conventional simulations, after applying and removing the high current pulse the machine performance would be restored to the original level (impossible to simulate permanent demagnetization). However, in reality the performance should show degraded. Thus, via the introduced method, the machine is simulated under a current pulse that intends to alter the magnetization level. The three parameters considered are the amplitude of the current pulse, its time duration and the direction of the imposed field to the rotor governed by the current angle. The effectiveness of the magnetization change strategy and its impact on the normal machine operation is investigated versus these three parameters. Coming to the conclusions, firstly due to the machine inductances there is a minimum pulse time duration required to allow for an effective change of the magnetization. For the machine examined this minimum duration was found to be 5ms. Moreover, it is self-evident that by increasing the current pulse amplitude the demagnetization becomes more effective. However, the relation is not linear, and once the current exceeds a certain upper value, the permanent magnets become fully demagnetized - thereafter the machine turns into a pure Synchronous Reluctance Machine. Finally, when it comes to choosing the appropriate current angle for the pulse, the deciding criterion is to avoid any disturbance on the mechanical load side – neither torque overshoot nor sag. This is always feasible through proper choice of the current angle. Therefore, a coordination between the chosen current angle and the imposed current amplitude for the demagnetizing pulse is found to achieve the predefined demagnetization target minimizing the current requirements and the mechanical disturbances. To exhibit the feasibility of the suggested strategy and the superior machine performance that the VFMM concept yields, a demonstrator variable flux memory PMaSynRM is simulated over the complete speed range.

[1] V. Ostovic, "Memory motors-a new class of controllable flux PM machines for a true wide speed operation," Conference Record of the 2001 IEEE Industry Applications Conference. 36th IAS Annual Meeting (Cat. No.01CH37248), Chicago, IL, USA, 2001, pp. 2577-2584 vol.4. doi: 10.1109/IAS.2001.955983 [2] V. Ostovic, "Memory motors," in IEEE Industry Applications Magazine, vol. 9, no. 1, pp. 52-61, Jan/Feb 2003. doi: 10.1109/MIA.2003.1176459 [3] M. Ibrahim, L. Masisi and P. Pillay, "Design of Variable Flux Permanent-Magnet Machine for Reduced Inverter Rating," in IEEE Transactions on Industry Applications, vol. 51, no. 5, [4] B. S. Gagas, K. Sasaki, T. Fukushige, A. Athavale, T. Kato and R. D. Lorenz, "Analysis of Magnetizing Trajectories for Variable Flux PM Synchronous Machines Considering Voltage, High-Speed Capability, Torque Ripple, and Time Duration," in IEEE Transactions on Industry Applications, vol. 52, no. 5, pp. 4029-4038, Sept.-Oct. 2016. doi: 10.1109/TIA.2016.2582119 [5] C. Y. Yu, T. Fukushige, N. Limsuwan, T. Kato, D. D. Reigosa and R. D. Lorenz, "Variable-Flux Machine Torque Estimation and Pulsating Torque Mitigation During Magnetization State Manipulation," in IEEE Transactions on Industry Applications, vol. 50, no. 5, pp. 3414-3422, Sept.-Oct. 2014. doi: 10.1109/TIA.2014.2305768

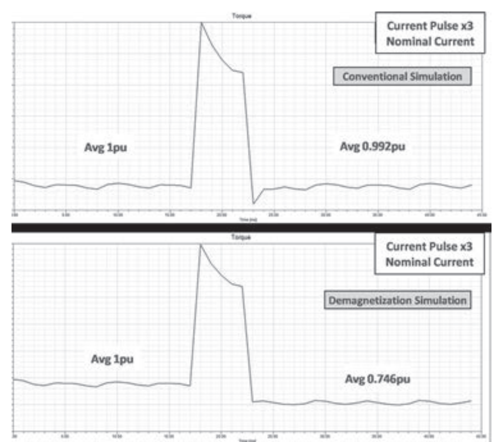

Fig. 1. Showcase of the developed simulation method of permanent demagnetization versus the conventional simulations under a 5ms current pulse, x3 times the nominal current (60deg current angle).

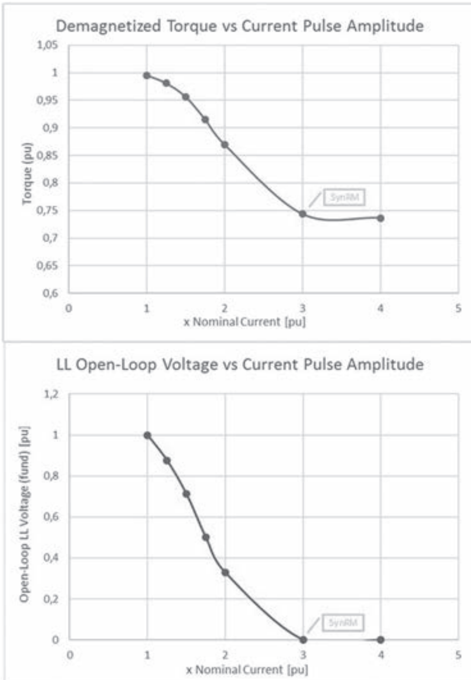

Fig. 2. Machine torque and LL open-loop back-EMF at 1500rpm under variable current pulse amplitude (5ms pulse - 60deg current angle). The complete demagnetization of the magnets is denoted as "SynRM".

3:30

HG-07. Design Procedure for a 4-pole, External Rotor Synchronous Reluctance Motor (Ex-R SynRM) for the Application Mechanical Constraints.

R. Azhagar[1] and A. Kavitha[1]
1. Electrical and Electronics Engineering, College of Engineering, Anna University, Chennai, India

ABSTRACT This paper presents a step by step design procedure of developing a 4-pole, External-Rotor Synchronous Reluctance Motor. Here, this is a first attempt to derive the analytical design equation from the fundamentals of motor design for the given mechanical constraints. Initially, the stator bore diameter has been predicted from the torque requirement with certain assumptions on the design data. Then the stator slot dimensions are predicted for the rounded semi-closed slot type by considering distributed winding. Then the external rotor geometry with circular shape flux barrier has been considered for the study and its performance characteristics are predicted using finite element analysis. The results are compared with analytical calculations and finally, a feasible rotor geometry is proposed with further investigation. INTRODUCTION In recent times, Direct Drive Motors (DDM) are gaining confidence in high torque, low-speed application due to its increased efficiency, reliability, maintainability and responsiveness [1]. The most application uses Induction motor as drive along with mechanical reduction like a belt, pulley, chain, and gear. This domestic appliance called wet grinder uses single-phase induction motor is used either with a belt or gear mechanism which generates a lot of noise and vibration. The load characteristic of the application requires constant torque at very low speed to maintain the batter at room temperature. This is important to achieve better fermentation which makes the batter soft to get a good taste. One of the major concern is that long time for grinding which increases the power consumption [2]. The external rotor configuration provides many advantages over the internal rotor and it is more suitable for an application where the outside body (wind turbine, fan) made to rotate. Here, the drum is the rotating body which kept outside. Also, the larger inertia of external rotor provides constant speed operation for varying load condition [4]. DESIRED APPLICATION REQUIREMENTS The motor design needs to fit into the dimensions of the drum used in the grinder application whose maximum available diameter is 250 mm. The diameter and axial length of the motor are chosen in such way that it can fit inside the periphery of a drum with clearance between motor and housing to provide natural cooling. The stack length is chosen as 40 mm which can fit inside the housing and also to provide space for winding overhang. The shaft torque requirement of the application is 12 Nm at the low speed of 150 RPM with the peak torque of 14 Nm. DESIGN OF EX-R SynRM The initial design dimensions are derived from the analytical design equations. The step by step procedure of design algorithm is shown In Fig 2 [7]. In this study, the geometry of rotor barrier has been chosen such that it follows the shape of flux lines with a solid rotor. The profile of barrier is designed for circular shape with three number of barriers and its dimensions are optimized to maximize the saliency ratio [5, 6]. FINITE ELEMENT ANALYSIS (FEA) OF Ex-R SynRM The motor considered for the study is analyzed using a 2-Dimensional (2D) FEA simulation under static and transient conditions. It is a 4-pole motor having 3-phase distributed winding in 36 slots shown in Fg.1. A.Static Analysis (Rotor is Standstill) In this, the rotor of the Ex-R SynRM is kept at a mechanical rotor position corresponding to d and q-axis to predict the d and q-axis inductances. The d-axis inductance (L_d) predicted with d axis excitation current I_d as (I_a=I, I_b=-I/2, and I_c=-I/2) while Lq is predicted with q-axis excitation current Iq as (I_a=I, I_b=-I/2, and I_c=-I/2) by varying current from 0 to 25 Amps. B.Transient Analysis (Rotor is Rotating) Here, the rotor of the Ex-R SynRM is kept at various mechanical rotor position (0 to 45 deg) corresponding to the current angle in electrical degrees (0 to 90 deg) and predicted torque. This helps in identifying the current angle which produces maximum torque. ANALYSIS OF RESULTS To optimize the position and size of the barriers in the rotor of the SynRM with torque ripple reduction as the prime objective.The initial model with three rotor barrier is taken as reference. Initially, the position of the second barrier is adjusted in order to minimize torque ripple. This is done by adjusting the span of the barrier (increasing or decreasing the angle by few degrees(say 2 deg) The same procedure is attempted with other barriers and their effect on the transient torque is studied.The models which produce least torque ripple is selected at each level and next iterations are done with that model. As a next step, the barrier thicknesses are varied uniformly and non uniformly for all three barriers and studied the effect.Finally, the end of barrier shape also studied and proposed a rotor which provides high saliency ratio, average torque, and less torque ripple. The simulation results of the above study are tabulated in Table 1.

[1] Masazumi Suzuki, "Direct Drive Technology and its impact on Generator business", Power Transmission Engineering, www.powertransmission.com, December 2009. [2] L.Initha, J.Jegan, R.Kumar, "Analysis and Improvement of Quality in Wet Grinder Manufacturing Industry Through Customer Complaint Investigation", International Journal of Innovative Research in Science, Engineering, and Technology, Vol. 4, Issue 1, January 2015. [3] Razvan Alexandru Inte, Florin Nicolae Jurca, "A Novel Synchronous Reluctance Motor with Outer Rotor for an Electric Bike", International Conference and Exposition on Electrical and Power Engineering (EPE 2016), 20-22 October, Iasi, Romania. [4] Sai Sudheer Reddy Bonthu, Seungdeog Choi, Aida Gorgani, Kibong Jang, "Design of Permanent Magnet Assisted Synchronous Reluctance Motor with External Rotor Architecture", IEEE International Conference on Electric Machines & Drives Conference (IEMDC), 2015. [5] D.A. Staton, T.J.E. Miller, and S.E. Wood, "Maximising the saliency ratio of the synchronous reluctance motor", IEE Proceedings B – Electric Power Applications, Volume: 140, Issue: 4, July 1993, pp. 249-259. [6] T. Matsuo and T. A. Lipo, "Rotor design optimization of synchronous reluctance machine," *IEEE Trans. Energy Conv.,* 9(2) 359-365, (1994). [7] Seyedmorteza Taghavi, and Pragasen Pillay, "A Sizing Methodology of the Synchronous Reluctance Motor for Traction Applications", IEEE Journal of Emerging and Selected Topics in Power Electronics, Vol. 2, No. 2, June 2014.

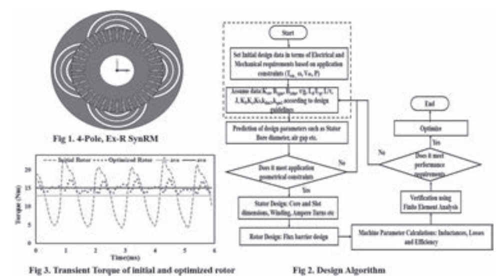

Fig. 1. 4-Pole Ex-R SynRM
Fig. 2. Design Algorithm
Fig. 3. Transient torque characteristics of Initial and Final Rotor

Table 1. Effect of Rotor Barrier Shape on Average Torque

Barrier Width with uniform thickness	2mm	3 mm	4 mm	5 mm					
Average Torque(Nm)	12.1	13.5	13.65	13.69					
Barrier Width with varying thickness	2-3-4 mm	4-3-2 mm	2-4-2 mm	3-4-3 mm	3-4-4 mm	2-4-4 mm	4-3-4 mm	5-3-4 mm	5-4-4 mm
Average Torque(Nm)	13.68	12.75	13.07	13.78	13.94	13.83	15.07	13.42	13.3
Barrier 1 Position	No barrier					Shortened by 4 deg	Shortened by 5 deg	Lengthened by 2 deg	
Average Torque(Nm)	12.73					13.3	13.2	13.46	
Barrier 2 Position		Shortened by 0.5 deg	Shortened by 1 deg	Shortened by 2 deg	Shortened by 3 deg	Shortened by 4 deg		Lengthened by 2 deg	
Average Torque(Nm)		13.6	13.4	14.7	13.2	13.2	13.3		
Barrier 3 Position			Shortened by 1 deg	Shortened by 2 deg		Shortened by 4 deg	Lengthened by 2 deg		
Average Torque(Nm)			13.4	13.4		13.4	13.3		
Barrier End shape		Circular	Flat						
Average Torque(Nm		11.5	12.3						

Table 1. Effect of rotor barrier shape on average torque

3:45

HG-08. Design of a High-Effective Fault-Tolerance Double-Stator Magnetless Vernier Machine for Direct-Drive Robotics.

J. Yu[1] and *C. Liu*[1]
1. School of Energy and Environment, City University of Hong Kong, Hong Kong, China

Introduction Regarded as the succedaneum of human handlers, robots accommodate tremendous advantages of labor saving, high reliability and ideal alternatives on dangerous work [1]-[4]. Since gearboxes give rise to high frictional loss, noise and vibration [5], direct-drive robots have become more and more attractive with low acoustic noise, free maintenance and high efficiency. Meanwhile, the machines employed for the direct-drive robotics are required with high controllability, high fault-tolerance and sufficient torque capacity. Considering the high material cost and flux uncontrollability of the PM, DC-excited machines have been dedicated more attention [6][7]. This paper proposes a high-effective fault-tolerance double-stator magnetless vernier (DSMV) machine for direct-drive robotics. By virtue of the integration of DC-winding excitation, double-stator structure and vernier topology, the DSMV machine accommodates the merits of cost-effectiveness, high flux controllability, adequate torque density under low-speed operation and low torque ripple to 3.90%. Moreover, through the fault-tolerance operation, the torque performances of both one-phase and two-phase deficiencies recover to the normal level, with torque ripple slightly deteriorated. Both theoretical derivation and demonstration are given for the validation of the DSMV machine design and the high-effective fault-tolerance operation. Machine Design and Fault-Tolerance Operation Principle Fig.1 presents the topology of the proposed DSMV machine, in cross-section and exploded perspectives. The double stators accommodate 18 split flux modulation poles (FMPs), with 24-pole segmented rotor in the middle. Polyester is embedded between rotor irons as fixation. Two sets of concentrated armature windings are allocated in the embedded slots, while DC-windings are coiled in series-opposing connection on FMPs. The winding arrangement makes full use of the machine space. Moreover, to improve the machine flux property, the DC-windings incline an angle instead of perpendicular to the FMPs. In addition, the discrete segmented rotor leaves out the rotor yoke, which contributes to rotor weight reduction, efficiency improvement and flux path shortening [8]. Meanwhile, the iron-only rotor increases the robustness and decreases the manufacturing difficulty of the machine. Furthermore, high-effective fault-tolerance operation of open-circuit faults is adopted. Through phase and amplitude reconstitution of the intact armature currents, the MMF of the machine can remain constant and realize torque performance recovery under faulty conditions [9]. For instance of A-phase deficiency, the normal and remedial MMFs are governed by Equation. (1). N is the phase armature winding turn number, is the phase currents displacement, Ia, Ib and Ic are normal phase armature currents, while I′b and I′c are remedial phase armature currents. With BLAC conduction scheme, the armature currents comply with Equation. (2), where I is the phase current amplitude and θ0 is the initial phase angle of phase A. Based on Equation. (1), the remedial armature currents can be deduced as Equation. (3). For double-stator machines, the fault-tolerant operation is also applicative as two single-stator machines. Analysis & Results Considering the target application, the machine outer stator diameter is 160 mm, the stack length is 120 mm, rated DC current is 5 A, and rated speed is 200 rpm. Under different conditions, the DC current can be modified accordingly for flux modulation. Fig. 2 shows the torque performances of the DSMV machine. Fig. 2(a) presents the torque performances under different rotor pole arc angle γ. Within the rational range, γ=2.8° is the optimal alternative to achieve the maximum torque average and the minimum torque ripple. Also, torque performance comparison as the current phase angle α varies is demonstrated in Fig. 2(b). The smallest torque ripple occurs at α=8°, while the largest torque average turns out at α=11°. The final α is determined to be 10° as a compromise. As a result, the optimal steady torque in Fig. 2(c) accommodates the average of 11.79 Nm and the ripple of 3.90%. The cogging torque amplitude is also presented in Fig. 2(c) with only 0.72 Nm. Furthermore, the results of one-phase and two-phase fault-tolerance operations are shown in Fig. 2(c) and (d) respectively. For the two cases of one-phase deficiency, the torque performances deteriorate into 10.86 Nm, 21.57% and 10.69 Nm, 26.16%. While the corresponding remedial performances recover to 11.78 Nm, 4.00% and 11.74 Nm, 7.04%. It can be analyzed in the same manner in two-phase fault-tolerance cases. With remedial operation, the torque average recovers from 8.99 Nm, 9.54 Nm to 11.74 Nm, 11.74 Nm accordingly. Meanwhile, the torque ripple reverts from 76.93%, 39.47% to 8.31%, 6.89% respectively. Therefore, through fault-tolerant operation, the DSMV machine can operate at one- and two-phase deficiency condition with the same torque level and slightly higher torque ripple. Other machine performances will be analyzed in the full paper. The work was supported by a grant (Project No. CityU21201216) from Hong Kong Research Council, Hong Kong, China.

References [1] A. Leu, M. Razavi, L. Langstädtler, D. Ristić-Durrant, H. Raffel, C. Schenck, A. Gräser and B. Kuhfuss, “Robotic green asparagus selective harvesting,” IEEE/ASME Trans. Mechatronics, vol. 22, no. 6, pp. 2401-2410, Dec. 2017. [2] B. Xiao and S. Yin, “An intelligent actuator fault reconstruction scheme for robotic manipulators,” IEEE Trans. Cybern., vol. 48, no. 2, pp. 639-647, Feb. 2018. [3] C. Irvene, D. Formby, S. Litchfield and R. Beyah, “HoneyBot: a honeypot for robotic systems,” Proc. IEEE, vol. 106, no. 1, pp. 61-70, Jan. 2018. [4] J. Huang, Y. Wang and T. Fukuda, “Set-membership-based fault detection and isolation for robotic assembly of electrical connectors,” IEEE Trans. Autom. Sci. Eng., vol. 15, no. 1, pp. 160-171, Jan. 2018. [5] C. Liu, J. Yu and C. H. T. Lee, “A new electric magnetic-geared machine for electric unmanned aerial vehicles,” IEEE Trans. Magn., vol. 53, no. 11, pp. 1-6, Nov. 2017. [6] C. H. T. Lee, K. T. Chau and C. Liu, “Design and analysis of an electronic-geared magnetless machine for electric vehicles,” IEEE Trans. Ind. Electron., vol. 63, no. 11, pp. 6705-6714, Nov. 2016. [7] S. Jia, R. Qu and J. Li, “Analysis of the power factor of stator DC-excited vernier reluctance machines,” IEEE Trans. Magn., vol. 51, no. 11, pp. 1-4, Nov. 2015. [8] M. Asgar and E. Afjei, “Radial force reduction in a new flat-type double-stator switched reluctance motor,” IEEE Trans. Energy Convers., vol. 31, no. 1, pp. 141-149, Mar. 2016. [9] C. Liu, K. T. Chau and W. Li, “Comparison of fault-tolerant operations for permanent-magnet hybrid brushless motor drive,” IEEE Trans. Magn., vol. 46, no. 6, pp. 1378-1381, Jun. 2010.

$$\mathrm{MMF} = NI_a + aNI_b + a^2 NI_c = aNI'_b + a^2 NI'_c \quad (1)$$

$$\begin{cases} I_a = I\cos(\theta+\theta_0) \\ I_b = I\cos(\theta+\theta_0+2\pi/3) \\ I_c = I\cos(\theta+\theta_0-2\pi/3) \end{cases} \quad (2)$$

$$\begin{cases} I'_{\mathrm{a}} = 0 \\ I'_{\mathrm{b}} = \sqrt{3}I\cos(\theta+\theta_0+5\pi/6) \\ I'_{\mathrm{c}} = \sqrt{3}I\cos(\theta+\theta_0-5\pi/6) \end{cases} \quad (3)$$

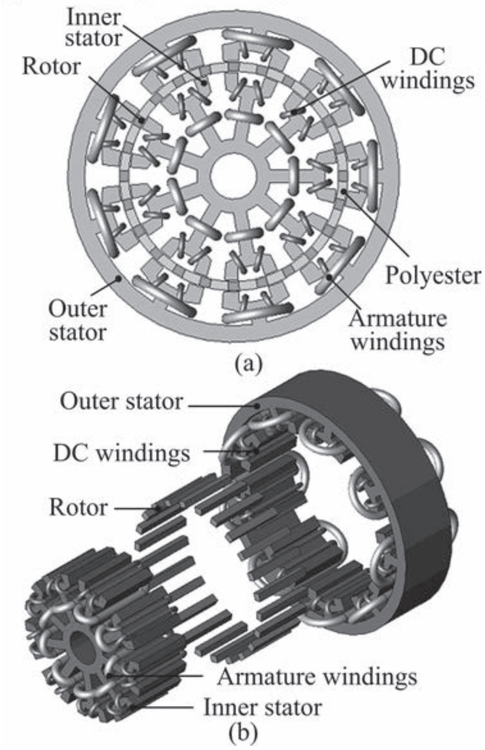

Fig. 1. Topology of the proposed DSMV machine. (a) Cross-section perspective. (b) Exploded perspective.

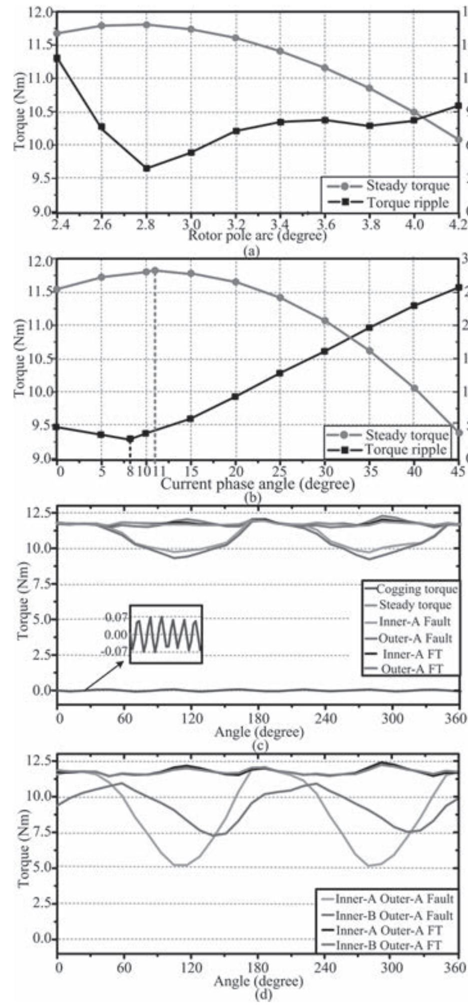

Fig. 2. Torque performances of the DSMV machine. (a) With different rotor pole arc angle. (b) With the varying of current phase angle. (c) Under normal and one-phase deficiency and remedial conditions. (d) Under two-phase deficiency and remedial conditions.

4:00

HG-09. Analysis of Local Demagnetization in Magnet for PM-Assisted Synchronous Reluctance Motors.

H.T. Anh[2] and M. Hsieh[1]

1. Department of Electrical Engineering, National Cheng Kung University, Tainan, Taiwan; 2. Department of Systems and Naval Mechatronic Engineering, National Cheng Kung University, Tainan, Taiwan

Abstract — This digest investigates the demagnetization risk of permanent magnet-assisted synchronous reluctance machines (PMa-SynRM). PMa-SynRM is often designed with multilayer PMs/flux barriers to increase saliency and reluctance torque. Weaker or less PM (than that for IPM motor) is embedded into the rotor of PMa-SynRM, which can be demagnetized during high-performance operation (e.g., high armature reaction or current phase advance control). Demagnetization possibility of PM depends on factors such as temperature, armature current and design operating points and mostly occurs combining some of the above factors. The temperature distribution across the PM can be different and the operating points at different locations in the PM can also vary. This very likely causes local demagnetization within a PM. This work proposes a method to evaluate the demagnetization risk within a PM for all the PM layers of PMa-SynRM rotors. A model based on the magnetic circuit is first developed to calculate the operating points across the PM at the no-load and loaded condition. The magnet temperature distribution is then estimated with a commercial software. With the temperature and loaded operating points of the PM, the risk of local demagnetization can be predicted. This is validated using finite element analysis. From the analysis, a design method that can avoid demagnetization is then proposed. Experimental studies are conducted to validate the simulations. *I. Introduction* PMa-SynRM is known as a good candidate for traction motors of electric vehicles (EVs) due to its decent torque density with low PM usage and cost, high efficiency and a wide speed range [1, 2]. PMa-SynRM is often designed with weaker or less PM than that for IPM motor; therefore, potential demagnetization during high-performance operation (e.g., high armature reaction or flux weakening) can occur [3]. PM demagnetization may be caused by the factors such as temperature, armature current magnitude, design operating points and deep flux weakening [3-4]. Ref. [3] shows that the risk of demagnetization of PM is different at each PM position for PMa-SynRM. However, this has not been sufficiently studied. Methods to predict local demagnetization and approaches to design the rotor that can avoid demagnetization have not been well proposed. Ref. [4] determined that the temperature distribution on V-shaped PM surface of the interior permanent magnet synchronous machine (IPMSM) is non-linear, where the highest temperature locates at the center of PM surface. Also, the temperature may also vary at different PM layers. Therefore, the cause of local demagnetization in each PM can be the combination of the temperature distribution across the PM and the PM operating points in the PM under load condition. This has not been clearly studied. This paper investigates the risk of local demagnetization in a PM for PMa-SynRM. The developed magnetic equivalent circuit is capable of identifying the operating points in the PM. The temperature at different PM layer and the temperature distribution across the magnet are calculated using 3-D finite element analysis. With the above analysis, the combined temperature and operating point information can be obtained for determination of local demagnetization in a PM, as well as for different PM layers. Finally, the design method to avoid demagnetization is proposed. Experimental studies are conducted to validate the simulations. *II. The Target Machine and Method* The prototype of a 10 kW PMa-SynRM is considered for study and the magnet positions are as labelled in Fig.1. This PMa-SynRM is designed with five flux barriers per pole and only four of them are considered to be added with PMs (except the outermost one) to reduce the torque ripple and increase the reluctance torque. The main specifications of the motor are given in Fig. 1. As stated, the magnetic equivalent circuit is developed to calculate the detailed operating point in a PM and FEA is to obtain the temperature distribution. The details will be reported in the full paper. *III. Results and Conclusion* Fig. 2 shows the operating points for each PM and for different PM layers at no-load and load condition. As can be seen, for example, the label "4th PM Load" indicates the load condition for PM at position 4. There are four points for each PM and they represent the operating points at four different locations in the PM. In Fig. 3, the temperature limit of a PM related to the output torque within a speed range is presented. This would clearly show that the temperature limit of PM would limit the motor performance. The magnet temperature increases as the motor torque increases, leading to the possible local demagnetization or even entire demagnetization. Detail analysis and experimental results will be given in the full paper.

[1] Ruiwu Cao, Chris Mi, and Ming Cheng, "Quantitative Comparison of Flux-Switching Permanent-Magnet Motors With Interior Permanent Magnet Motor for EV, HEV, and PHEV Applications." *IEEE Transactions on Magnetics*, Vol. 48, No.8, pp. 2374–2384 (2012). [2] Thanh Anh Huynh, and Min-Fu Hsieh, "Comparative Study of PM-Assisted SynRM and IPMSM on Constant Power Speed Range for EV Applications," *IEEE Transactions on Magnetics*, Vol. 53, No. 11, pp. 1-6 (2017). [3] Ki-Chan Kim, Kwangsoo Kim, Hee Jun Kim, and Ju Lee, "Demagnetization Analysis of Permanent Magnet According to Rotor Types of Interior Permanent Magnet Synchronous Motor," *IEEE Transactions on Magnetics*, Vol. 45, No. 6, pp. 2799-2802 (2017). [4] Paolo Guglielmi, Barbara Boazzo, Eric Armando, Gianmario Pellegrino, and Alfredo Vagati, "Permanent-Magnet Minimization in PM-Assisted Synchronous Reluctance Motors for Wide Speed Range," *IEEE Transaction on Industry Applications*, Vol. 49, No. 1, pp. 31-41 (2013).

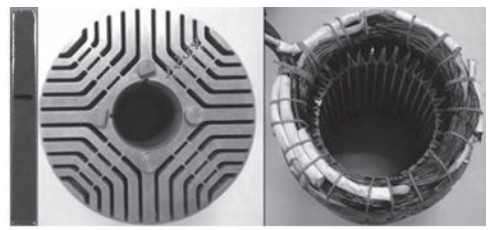

TABLE I
THE MAIN SPECIFICATIONS AND PARAMETERS OF PMA-SYNRM

Specification	Value (unit)
Peak power	10 kW
Max torque	65 Nm
Number of phases	3
Number of poles	4
Number of slots	36
Maximum current	80 A
Peak voltage	310V
Stator diameter	160 mm
Rotor diameter	94 mm
Stack length	120 mm
Airgap	0.5 mm
Number of turns per coil	6

Fig. 1. The prototype, main specifications and parameters of PMa-SynRM.

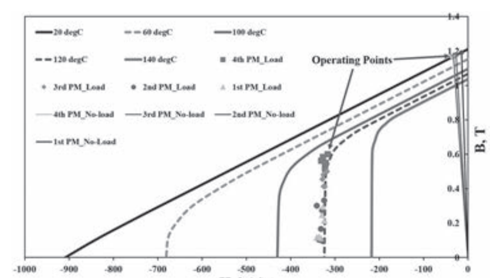

Fig. 2. Operating points in each PM at different PM layers at no-load and load conditions.

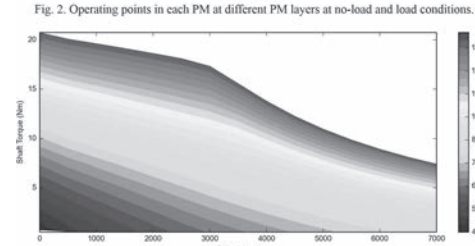

Fig. 3. The motor torque - magnet temperature relationship within the prescribed speed range.

4:15

HG-10. An Integrated Motor-Drive and Battery-charging System Utilizing Doubly Salient Electro-magnet Machine with Split Field Windings.

T. Zhang[1], *J. Wei*[1], P. Liu[1], W. Tao[1] and B. Zhou[1]
1. Jiangsu Key Laboratory of New Energy Generation and Power Conversion, Nanjing University of Aeronautics and Astronautics, Nanjing, China

Abstract: In this paper, an integrated motor-drive and battery-charging(IMB) system for doubly salient electro-magnet machine(DSEM) is proposed to be implemented onboard for electric vehicles(EV). The field windings distribution of a 12/10 DSEM is arranged for the constant self-inductance, and adopted as the inductance of the front-end DC/DC converter to eliminate the traditional filter inductance and excitation loss of the machine in the driving mode. The armature windings could be exploited as the filter inductances in the charging mode. The simulations and experiments are accomplished to verify the feasibility of the independent field current control method for the proposed system. I. Introduction The IMB system is a critical onboard equipment for electric vehicles due to low bulk, weight and high convenience[1]. As the armature windings of the machine could be adopted as the filter inductance, the less permanent magnet machines, such as induction motor and switched reluctance motor, are the better candidates for EV than permanent magnet machine with higher phase inductance. However, the filter inductance is still necessary in the front-end DC-DC converter for voltage boost and recharge of the battery. Literature [2] proposed a method that one phase winding is multiplex as the inductance of the DC-DC converter, and another two phase windings are exploited in the single phase AC power source in the charging mode, but the unbalanced phase current leads to the undesired torque and vibration. DSEM with the inherent features of simple structure and high robustness characteristics is an attractive candidate of the machine in EV. This paper proposes a novel IMB system with the cascade inverter topology for DSEM, where the field windings of DSEM are split and integrated as filter inductances in the front-end DC/DC converter. II. System configuration and control strategy The proposed IMB system is shown in Fig.1. The field windings of DSEM are arranged in each slot of the stator to decouple the field windings and armature windings, then, the self-inductance of the phase windings can be maintained constant, which is different to traditional DSEM. The split field windings of DSEM are accomplished by the series connection of the nearest coils, and they are divided into two sections F_1 and F_2, which have the same amplitude of self-inductance to be multiplexed as the filter inductances in the front-end DC/DC converter. In the driving mode, the DC/DC converter works in the interleaved boost mode while S_7 is open. The voltage equation based on power relations can be deduced as $2i_F\,(d_1u_b\text{-}k_e\omega i_P)=\Delta P_C$, where i_F and i_P are the currents of field windings and armature windings, d_1 is the duty circle of S_1 and S_2, u_b is the battery voltage, k_e is a back-EMF coefficient, ω is the speed of DSEM, ΔP_C is the power variation of DC bus capacitor. Accordingly, the voltage of the DC bus can be controlled by d_1 directly while the power of the capacitor is constant, then the currents of two field windings can be separately controlled by S_4 and S_6. As the double-closed-loop control method is employed for DSEM, and it could be sorted as the constant power load for the DC/DC converter. Hence, the independent field current control method with the capacitor power control algorithm are designed for the IMB system. In the braking mode, S_1, S_2, S_4, S_6 turn off and S_7 turns on, then the front-end DC/DC converter works as a buck converter, and the field winding currents are regulated by S_3 and S_5. The DSEM works in the generating mode and the reference armature winding currents are regulated to maintain the DC bus voltage. In the charging mode, S_1, S_2, S_4, S_5, S_7 turn off and S_3 turns on, two field windings and the battery work in series and the current is regulated by S_6, where the front-end converter works as a buck converter. SVPWM is employed to energize S_8 to S_{13} as a three-phase PWM rectifier. III. Verifications The simulation is carried out based on a 20kW 12/10-pole DSEM, where the self-inductance of field windings and armature windings are 2.2mH and 1mH respectively. The switching frequency is 8kHz. The battery voltage is 250V. The simulation results of driving and braking operations including the DC bus voltage, the field winding currents and the speed are shown in Fig.2(a)-(c). In the driving mode, the bus voltage ripple is lower than 5% with a 220uF capacitor, the field current can be controlled separately and the ripple can be decreased by the interleaved topology. In the braking mode, the regenerated power of DSEM comes back to recharge the battery. In the charging mode shown in Fig.2(d), the field windings' currents are equal and in opposite directions to suppress the excitation field to eliminate the output torque of DSEM, and the constant recharging current could be achieved with a low current ripple of 15%. The experiment is implemented to validate the proposed system on the prototype of a 12/10-pole 5kW DSEM, and the detailed results will be presented in the full manuscript. IV. Conclusion This paper proposes a novel IMB system for DSEM, where the field windings are arranged and integrated in the front-end DC/DC converter to improve the efficiency. The driving, braking and charging methods are presented and validated by simulations and experiments.

[1] Murat Yilmaz, Philip T. Krein. Review of Battery Charger Topologies, Charging Power Levels, and Infrastructure for Plug-In Electric and Hybrid Vehicles, IEEE Transactions on Power Electronics, Vol.28, No.5, 2013, pp.2151-2169 [2] Mehnaz Akhter Khan, Iqbal Husain, Yilmaz Sozer. Integrated Electric Motor Drive and Power Electronics for Bidirectional Power Flow Between the Electric Vehicle and DC or AC grid, IEEE Transactions on Power Electronics, Vol.28, No.12, 2013, pp.5774-5783

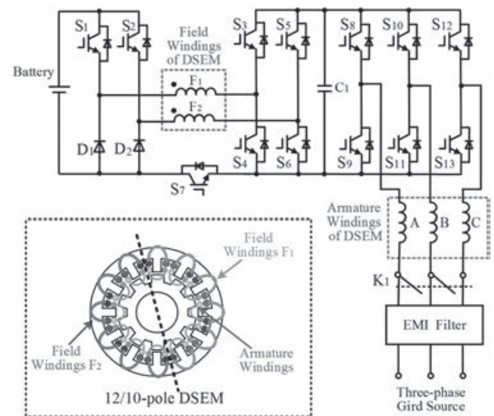

Fig. 1. The proposed integrated DSEM driving and charging system

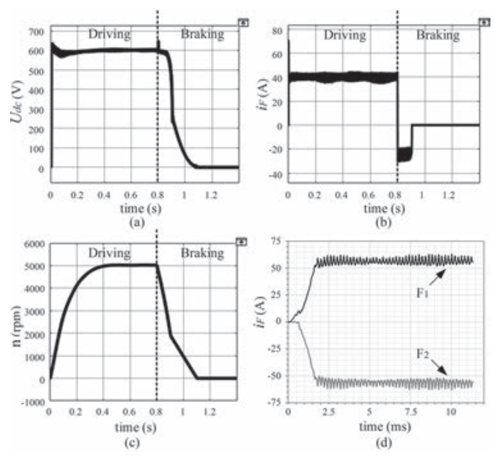

Fig. 2. Simulation results:(a)DC bus voltage under driving and braking mode;(b)Field winding current under driving and braking mode;(c) Speed curve under driving and braking mode;(d)Field winding currents under charging mode

4:30

HG-11. Electromagnetic Performance comparison of multi-layered Interior PM machines for EV Traction Applications.

M. Xie[1]
1. Nanjing University of Aeronautics and Astronautics, Nanjing, China

I. Introduction Multi-layered Interior permanent magnet (IPM) machines are attractive for the electric vehicle (EV) applications especially on the 2016 BMW i3, and 2017 Prius [1], [2]. This paper compared the electromagnetic performance of three Multi-layered IPM machines. The electromagnetic performance including the no-load air-gap density, torque density, torque ripple, d- and q-axis inductances, saliency ratio, characteristic current, core loss, magnet eddy-current loss, and the efficiency. II. Main Body Fig. 1 shows the magnet configurations of three multi-layered IPM machines. The two-layered IPM machine with “U−” model is model I which similar to the 2017 Prius, the two-layered IPM machine with “2−” model is model II which similar to the 2016 BMW i3, and the three-layered IPM machine with “U▽” is model III. The total volumes of the permanent magnets (NdFeB) in three models are identical. The rated power of the machines is 48 kW, the continuous rated torque (rated torque) is 100 Nm, and the maximum speed of the machines is 12000 r/min. The harmonics of air-gap density of model III is smaller than that of the model I and model II due to the increase of rotor magnet layers. The FEA predicted average torque of model I is 104.2 Nm, the model II is 88.5 Nm, the model III is 104.9 Nm. The average torque of model II is lowest due to the magnets of model II is buried deeply, the utilization of magnets is lower than the model I and model III. The FEA predicted torque ripple and core loss of three multi-layered IPM machines are analyzed and compared. The model III has the lowest torque ripple and core loss because the harmonics of air-gap density of model III is the lowest. The magnet eddy-current loss of three multi-layered IPM machines are investigated at 12000 r/min. The magnet eddy-current loss of model II is lowest due to the magnets of model II is buried deeply, none have the tangential magnets, the effects of the armature-reaction flux is lower than the model I. The model III has the highest magnet eddy-current loss. A prototype IPM machine with model III is manufactured to verify the results of the analysis. Fig. 2(a) shows the photographs of the rotor and windings. The simulated and measured average torque of the prototype machine are shown in Fig. 2(b). The total iron loss and efficiency are simulated and measured, they have good agreement. III. Conclusion This paper has analyzed and compared the electromagnetic performance of three multi-layered IPM machines for electric vehicle applications. The torque density of model II is the lowest due to the magnets of model II is buried deeply, the utilization of magnets is lower than the model I and model III. The magnet eddy-current loss of model II is the lowest due to the magnets of model II is buried deeply, none have the tangential magnets, the effects of the armature-reaction flux is lower than the model I and model III. The model III has the lowest torque ripple and core loss because the harmonics of air-gap density of model III is the lowest.

[1] Taniguchi, M., Yashiro, T., Takizawa, K., Baba, S. et al., “Development of New Hybrid Transaxle for Compact-Class Vehicles,” SAE Technical Paper, doi: 10. 4271/2016-01-1163, 2016. [2] Xiangdong Liu, Hao Chen, Jing Zhao and Anouar Belahcen, “Research on the Performances and Parameters of Interior PMSM Used for Electric Vehicles,” *IEEE Trans. Ind. Electron*., vol. 63, no. 6, pp. 3533-3545, Jun. 2016.

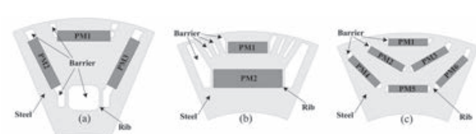

Fig. 1. The structure of three multi-layered IPM machines. (a) Model I. (b) Model II. (c) Model III.

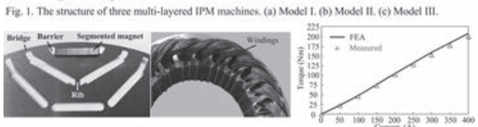

Fig. 2. The photographs of rotor and windings, FEA calculated and tested results of torque. (a) Photographs of rotor and windings. (b) FEA calculated and tested torque of model III at different currents.

4:45

HG-12. Design and Characterization of a single-phase Main Exciter for Aircraft Starter-Generator.

J. Li[1], Z. Zhang[1], Y. Liu[1], J. Lu[1] and Z. Chen[1]
1. Nanjing University of Aeronautics and Astronautics, Nanjing, China

I. INTRODUCTION An aircraft three-stage starter-generator (SG) may includes three separate brushless generators, namely, a permanent magnet generator (PMG), a single-phase main exciter (ME), and a main starter/generator (MSG). A SG may be used to start the engines or auxiliary power unit (APU) when operating as a starter, and to supply electrical power to electric consumer when operating as a generator [1]. For getting optimal performance, the single-phase ME needs to satisfy the required current output in both generating mode and starting mode [2]. Therefore, the design and characteristic analysis of ME in two modes is remarkably necessary. In this paper, a single-phase main exciter for aircraft SG in both generating mode and starting mode is proposed and investigated. II. CONFIGURATION AND OPERATION PRINCIPLE In a general way, aircraft SG mainly operates in generating mode for powering electrical loads on-board. As shown in Fig. 1, a chopper controlled by generator control unit (GCU) is used to control the excitation current I_{ef} of ME. With the rotating of the rotor, the ME's rotor windings generate AC current which is rectified by a rotating rectifier into the field winding of MG.. It can be seen that the MG field current I_F is regulated by I_{ef} directly. The ephemeral but important function of SG is to produce motive power on the shaft in starting mode. When SG is in stationary or at low speed, AC power should be supplied to the ME stator winding via a ME inverter, as shown in Fig. 1. Fig. 2 shows the topology of proposed single-phase ME with excitation windings on stator and three phase armature windings and rotating rectifier on rotor. The excitation current I_{ef} of the ME is converted to the excitation current I_F of MG, thus the brushless rotor is realized. III. PERFORMANCE AND ANALYSIS The parameters for the design of single-phase ME are given in Table I. Fig. 3 shows the equivalent circuit of ME. For the ME, its load is the resistance R_F and self-inductance L_F of the field winding of the MG both in generating mode and starting mode. A. Generating mode Fig. 4 shows the performance of the proposed ME. The iron core is close to the saturated zone when the excitation current I_{ef} is 20A. Due to the variation range of working temperature of aircraft SG is relatively wide, typically from -60 degree centigrade to 180 degree centigrade, the R_F is changed from 0.179Ω to 0.424Ω. That is to say, the load of ME is approximately changed 2.37 times. The output design of ME has constant current source characteristic, especially with light load (I_{ef}=4A). Meanwhile, the output voltage U_F of ME will be changed obviously in order to keep the field current I_F constant. B. Starting mode The SG is used to start the engine up to 3000rpm. The ME excitation winding is connected to line-to-line voltage 200V/400Hz of 3-phase 115V /400Hz AC source. In this case, the ME is worked as a transformer where ME stator is primary side and rotor is secondary side. As is shown in Fig. 5, with speed ranges from 0 to 3000 r/min, the simulated waveforms of excitation current I_{ef} is almost the same, the self-inductance L_{ef} keeps about 5.4mH. Due to the frequency of U_{ef} is high, the resistance of ME excitation winding can be negligible. Thus, the excitation I_{ef} is directly proportional to self-inductance L_{ef}. IV. EXPERIMENTAL VERIFICATION A prototype single-phase main exciter for aircraft SG has been designed and developed as shown in Fig. 6. Fig. 7 shows the excitation voltage U_{ef} and excitation current I_{ef} waveforms with 1000r/min and the numerical value of excitation current I_{ef} versus speed. It can be seen that the simulated waveform agrees well with the measured one. IV. CONCLUSION In this paper, the characteristic of single-phase main exciter both in generating mode and starting mode has been analyzed and established. In generating mode, the output of ME has constant current source characteristic with the temperature ranging from -60 degree centigrade to 180 degree centigrade. In starting mode, the ME can be worked as a transformer. The feature of excitation current I_{ef} and self-inductance L_{ef} is also discussed. Both simulation and experiment are explored, and the simulated results agree well with the measured one.

[1] Mingzhou Xu, Wayne T.Pearson, Cristian E.Anghel, Nicolae Morcov, "Gas Turbine Engine Starter Generator with Multiple Windings on Each Exciter Stator Pole," U.S. Patent 6906479 B2, Jun.14, 2005. [2] Antonio Griffo, Rafal Wrobel, Phil H.Mellor, Jason M.Yon, "Design and Characterization of a Three-Phase Brushless Exciter for Aircraft Starter/Generator," IEEE Transactions on Industry Applications, vol. 49, no. 5, pp. 2106-2115, Sep./Oct.2013.

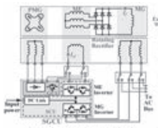
Fig. 1. SG system diagram block

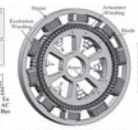
Fig. 2 Proposed ME Structure

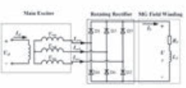
Fig. 3. Equivalent Circuit of ME

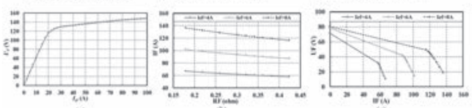
Fig. 4 Performance of ME operating in generating mode. (a) no-load characteristic curve. (b) Output current IF versus RF. (c) External characteristic curve with different excitation current Ief.

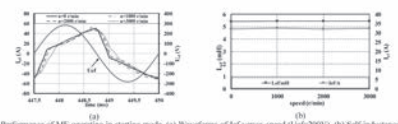
Fig. 5 Performance of ME operating in starting mode. (a) Waveforms of Ief versus speed (Uef=200V). (b) Self-inductance Lef and excitation current Ief simulated for different speed.


Fig. 6 Prototype single-phase main exciter. (a) Stator. (b) Rotor.

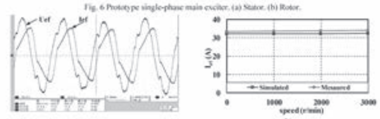

Fig. 7. (a) Waveform of single-phase AC voltage and field current with 1000 r/min (100 V/div & 20 A/div, 1 ms/div). (b) Excitation current Ief versus speed.

TABLE I DESIGN SPECIFICATION

Rated power [kVA]	6	Rated speed [rpm]	8000
Number of poles	10	Axial length [mm]	25
Outer diameter of rotor [mm]	170	Air-gap clearance [mm]	0.3
Inner diameter of rotor [mm]	130	Conductors per of stator pole	150
Outer diameter of stator [mm]	230	Turns of each phase winding	25
Inner diameter of stator [mm]	170.7	Number of stator slots	75

FRIDAY AFTERNOON, 27 APRIL 2018 PEONY II, 2:00 TO 5:00

Session HH
HYSTERESIS MODELLING II

Kay Hameyer, Chair
RWTH Aachen University, Aachen, Germany

CONTRIBUTED PAPERS

2:00

HH-01. Broadband modeling of magnetic components with saturation and hysteresis for circuit simulations of power converters.

B. Wunsch[1], S. Skibin[1], T. Christen[1] and V. Forsstrom[2]
1. ABB Corporate Research, Baden, Switzerland; 2. ABB Oy Drives, Helsinki, Finland

Abstract: A model of magnetic components is presented which includes saturation and static hysteresis and covers a wide frequency range. A dedicated setup measures the B(H)-curves for extraction of the model parameters and for model validation. The magnetic model is then described in terms of a spice circuit and used in transient system simulations of power converters. Simulations and measurements of core losses, and filter performance of common mode chokes are discussed. Introduction Magnetic components like single-phase chokes, common mode chokes, or transformers are essential parts of power electronic converters. For faster and more cost efficient design of these components, or even for virtual prototyping of filters accurate simulation models of magnetic components are required that can be placed in transient system simulations of power converters [1], [2], [3]. In this work, a circuit model of a common mode inductor is presented that captures static hysteresis, saturation, and high-frequency behavior. The example material chosen is the nanocrystalline core W517 made of Vitroperm 500F of Vacuumschmelze, which is used for filtering common-mode noise [6]. Magnetic property tester The core under test (CUT) contains two windings. The primary winding is excited with a controllable current, while the secondary winding is left open and used for measurement of induced voltage. The H-field and B-field are calculated based on the primary current and secondary voltage, respectively. The voltage source is realized by a switching mode SiC-based inverter with H-bridge topology. It allows modulation of different current waveforms exciting the CUT. For characterization of saturation and static hysteresis of the CUT low frequency measurements are required. In this case a large inductor is introduced in series with the CUT and the core is excited by triangular current ensuring small frequency content. For validation measurements the large inductor is removed and the core is excited by rectangular voltage with high switching frequency. Simulation models The magnetic model is obtained in three steps [3], [7]. First a linear circuit is created that describes the effect of eddy currents induced by the magnetic field in the core. The field distribution in conductive, laminated cores can be solved analytically as long as a constant permeability is assumed. A physical circuit representation is given by a linear Cauer network of inductors and shunt resistors [5], [7]. Alternatively the circuit parameters of the Cauer network can be adjusted to fit the linear impedance of the core obtained by small signal measurements using an impedance analyzer [3]. Next an inductor model with saturation and static hysteresis is created. The saturation of the inductors is described by a nonlinear reversible field. In order to capture static hysteresis, a Preisach model is used [8]. We determine the required parameters by fitting a set of B(H)-curves measured at low frequency with different B-field amplitudes. We then create a circuit model of the inductor, which is valid at low frequencies, captures the nonlinear B(H)-characteristic, and includes the Preisach model. The linear wide-band frequency-dependent model can then be combined with the nonlinear low-frequency model by replacing the linear inductors of the Cauer network by magnets described with the Preisach model. The resulting model includes eddy currents, saturation, and static hysteresis. We assess the accuracy of the obtained model using the magnetic property tester for large-signal large-frequency excitations and compare simulated and measured B(H)-curves and losses. Use in EMC simulations In this work we report on simulations and measurements of the performance of CM chokes placed at two distinct locations in a power converter with a nominal power rating of 355 kW at 500 V rms. The converter is connected at its input side to the 50 Hz 400 V rms three phase AC-grid, and at its output side it is connected via a shielded cable to a free running motor. In the first analysis the CM-choke is part of the EMC filter placed at the AC input of the converter. We measure and simulate the CM-noise and the core loss under various operation conditions of the converter. For certain operations the CM choke is temporarily saturated. In the second analysis the CM choke is placed on the motor cable where the CM current is much larger than at the AC input. Consequently the magnetic core is repetitively brought to saturation. The large power loss of the magnetic core causes a significant heating of the CM choke. Both the common mode current waveform and the power loss are simulated and compared to measurement. Conclusion A model of magnetic cores is proposed that captures high-frequency effects as well as saturation and static hysteresis. A dedicated measurement setup was developed in order to experimentally characterize the magnetic behavior for the extraction of the model parameters and for the validation of the model. The model was then used to create a circuit model of common mode chokes that is used in transient system simulations of power converters to design filters, which enables virtual filter design.

[1] Wunsch, B., Drofenik, U., Skibin, S., & Forsstrom, V. (2017). Impact of diode-rectifier on EMC-noise propagation and filter design in AC-fed motor drives. In *2017 IEEE International Symposium on Electromagnetic Compatibility & Signal/Power Integrity (EMCSI)* (pp. 237–242). IEEE. [2] Allmeling, J., Hammer, W., & Schönberger, J. (2012). Transient simulation of magnetic circuits using the permeance-capacitance analogy. *2012 IEEE 13th Workshop on Control and Modeling for Power Electronics, COMPEL 2012*. [3] Sullivan, C. R., & Muetze, A. (2010). Simulation Model of Common-Mode Chokes for High-Power Applications. IEEE Transactions on Industry Applications, 46(2), 884–891. [4] Mühlethaler, J., Biela, J., Kolar, J. W., & Ecklebe, A. (2012). Core losses under the DC bias condition based on Steinmetz parameters. *IEEE Transactions on Power Electronics*, *27*(2), 953–963. [5] Leon, F. De. (1993). Time domain modeling of eddy current effects for transformer transients - Power Delivery, IEEE Transactions on. Power, 8(1). [6] Rainer Hilzinger, Werner Rodewald (2012) Magnetic Materials Fundamentals, Products, Properties, Applications, Wiley ISBN 978-3-89578-352-4 [7] Holmberg, P., Bergqvist, A., & Engdahl, G. (1997). Modelling eddy currents and hysteresis in a transformer laminate. *IEEE Transactions on Magnetics*, *33*(2), 1306–1309. [8] I. Mayergoyz: *Mathematical Models of Hysteresis and their Applications*. Elsevier, 2003

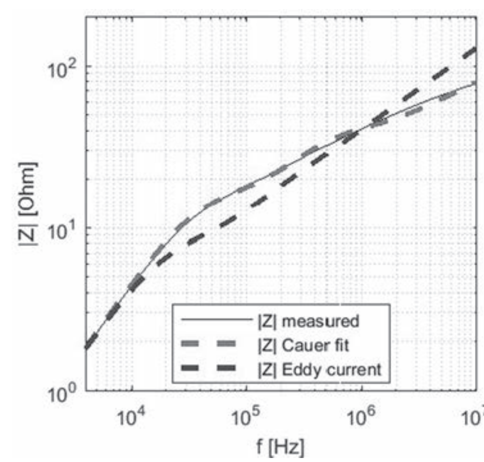

Fig. 1. Impedance spectra of a single-turn choke. Black: measurement; blue: eddy current red: fitted Cauer network (see text).

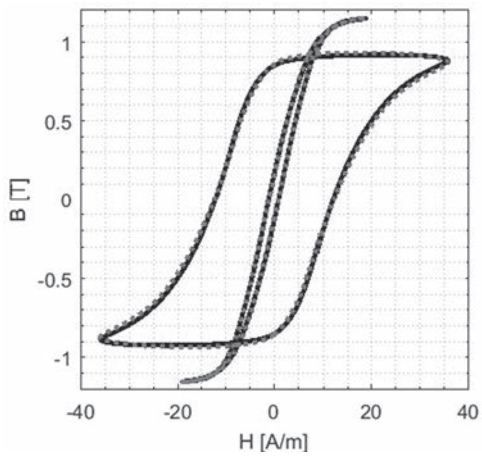

Fig. 2. Solid lines: measured B(H)-curves, dotted lines: simulations. The thin hysteresis curve is a low frequency measurement used for fitting the Preisach model. The large hysteresis curve shows a validation of the model at 100kHz.

2:15

HH-02. Temperature Dependence in the Jiles-Atherton Model for Non-Oriented Electrical Steels: An Engineering Approach.

S. Hussain[1], A. Benabou[3], S. Clenet[2] and *D. Lowther*[1]
1. Elec and Comp Eng, McGill University, Montreal, QC, Canada; 2. L2EP, Arts et Metiers ParisTech, Lille, France; 3. L2EP, Universite Lille 1, Villeneuve d'Ascq, France

Modern electrical machines may run for a prolonged time under extremely high temperatures which affect the magnetic behaviour of the electrical steels used in their cores [1]. However, these effects on the magnetic properties of the ferromagnetic material are often neglected in the computer-aided design (CAD) simulations and should be taken into account in the design of modern electrical machines to optimize their performance. Physics-inspired hysteresis models, such as the Jiles-Atherton (JA) model [2], seem to be promising candidates to incorporate temperature effects and can be embedded in finite element (FE) based CAD simulations. The JA model explains the hysteresis loss mechanism with the help of domain wall motion. The two modes of domain wall transitions (both the bending and translational motions) result in a reversible and an irreversible component of magnetization, respectively. The total magnetization is computed using a first order differential equation with five material parameters (M_s, a, α, c, k) known as the JA parameters [2]. M_s is the saturation magnetization, α is the inter-domain coupling coefficient, a determines the shape of the anhysteretic curve, c is the domain wall flexibility coefficient, and k represents the hysteresis effect. These five parameters are determined from the major B-H loop using curve fitting techniques. Although the accuracy and the physical aspects of the JA model and its parameters have been widely questioned [3], this is the most computationally efficient and easy-to-implement hysteresis model available in the literature and can be coupled with FE simulations to incorporate the effects of hysteresis in the field solutions. This work presents an engineering approach to use the JA model for estimating the B-H loops of non-oriented (NO) electrical steels at high operating temperatures. We have measured the B-H loops (B_{max} = 1.5 T) for 35WW300 NO electrical steel at seven temperatures within a limited temperature range (i.e., 50^{o}C to 330^{o}C) using a high-temperature Brockhaus Single Sheet Tester placed in an electric oven. The studied temperatures are well below the Curie temperature of electrical steels (T_c > 700^{o}C) and are the ones that steels could face in machines operating under extreme conditions. The JA parameters (a total of 35 JA model parameters, i.e., five at each temperature) are identified from the measured B-H loops using the nonlinear least squares method [4]. The optimization function, used in this case, is the square of the difference between the measured and computed data points. In this work, we also present a methodology to reduce the number of parameters to fit the temperature variations of the JA parameters based on their evolution. The first parameter to consider in this analysis is M_s which decreases (for a constant applied magnetic field intensity, H) with the increase in temperature. The evolution of M_s for the studied electrical steel shows a variation of less than 4 % for the given temperature range and is ignored here, i.e., M_s =1.2678 x 10^6 A/m. It is consistent with the Weiss Molecular theory [1] which states that if the operating temperature is well below the Curie temperature, T_c (i.e., T/T_c < 0.5), as in our case, the variation of M_s is negligible [1]. The parameter c seems to increase slightly at relatively high temperatures. However, a small change in c does not have a significant effect on the area of the B-H loop. Hence, the parameter c is also assumed to be constant, i.e., c = 0.02. It is important to mention here that M_s and c are identified using the B-H loop measured at the lowest temperature of interest, i.e., 50 ^{o}C. The rest of the JA parameters (i.e., a, α, and k) are then identified from the measured B-H loops at other temperatures. The reduction in the number of unknowns simplifies and speeds up the identification procedure. Two of the three remaining JA parameters (i.e., a and α) linearly increase with the temperature and can be modelled using first-order polynomials (i.e., with two unknowns only). In the case of soft magnetic materials, the parameter k is similar to the coercivity [5] which gives a hint about the decrease in its value with the increase in temperature. For the given temperature range, a quadratic dependence of the parameter k on temperature was observed for this material. The details on the number of unknowns for each JA parameter, their values and the quality of the fit are given in Table 1. As an example, measured and computed hysteresis loops (using the proposed approach) of 35WW300 NO electrical steel are compared in Fig. 1 at 300^{o}C. The error, defined as a relative difference in the measured and computed loops using the proposed approach, stays well within 6% for the whole temperature range. The same approach was applied to similar material i.e. B35AV1900 NO electrical steel ($B_{H=2500A/m}$ = 1.68 T, $P_{loss,\ B = 1.5\ T}$ = 1.91 W/kg) and similar results were obtained. The proposed engineering approach has been tested for NO electrical steels only and works for a limited temperature range. The identification of the JA parameters has been made simple by reducing the number of parameters and measurements to estimate them. The JA parameter information at temperatures close to 0 ^{o}K [6], [7] is not required. Since this is an experimental approach, the identification of the JA model parameters using analytical formulae may be ignored [6], [7].

[1] G. Bertotti, *Hysteresis in magnetism: for physicists, materials scientists, and engineers*, 1st ed. New York: Academic Press Inc., 1998. [2] D. C. Jiles and D. L. Atherton, "Theory of ferromagnetic hysteresis," *J. Magn. Magn. Mater.*, vol. 61, no. 1–2, pp. 48–60, 1986. [3] S. E. Zirka, Y. I. Moroz, R. G. Harrison, and K. Chwastek, "On physical aspects of the Jiles-Atherton hysteresis models," *J. Appl. Phys.*, vol. 112, no. 4, 2012. [4] P. Kis and A. Iványi, "Parameter identification of Jiles-Atherton model with nonlinear least-square method," in *Physica B: Condensed Matter*, 2004, vol. 343, no. 1–4, pp. 59–64. [5] D. C. Jiles, *Introduction to magnetism and magnetic materials*. New York: Chapman & Hall, 1991. [6] A. Raghunathan, Y. Melikhov, J. E. Snyder, and D. C. Jiles, "Theoretical model of temperature dependence of hysteresis based on mean field theory," *IEEE Trans. Magn.*, vol. 46, no. 6, pp. 1507–1510, 2010. [7] A. Raghunathan, Y. Melikhov, J. E. Snyder, and D. C. Jiles, "Modeling the temperature dependence of hysteresis based on Jiles-Atherton theory," *IEEE Trans. Magn.*, vol. 45, no. 10, pp. 3954–3957, 2009.

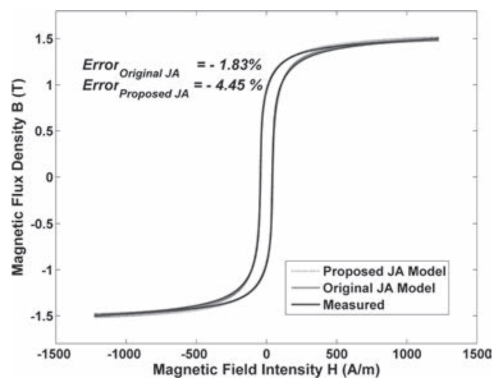

Fig. 1. Measured and computed *B-H* loops at 300^{o}C, using the original JA model and the proposed approach

JA Parameter	M_s	α	a	k	c
Polynomial Order	0	1	1	2	0
Polynomial Equation	a_0	a_0+a_1T	a_0+a_1T	$a_0+a_1T+a_2T^2$	a_0
Number of Unknowns	1	2	2	3	1
a_0	1.2678x10^6-	5.469x10^{-5}	15.8	52.05	0.02
a_1	-	3.469x10^{-7}	0.1742	0.01613	-
a_2	-	-	-	-1.349x10^{-4}	-
Quality of the fit, R^2	-	0.9760	0.9799	0.9965	-

Table I. Curve fitting of the JA parameters

2:30

HH-03. A Hybrid Algorithm for Parameter Extraction of Energetic Hysteresis Model.

R. Liu[1] and L. Li[1]
1. School of Electrical and Electronic Engineering, North China Electric Power University, Beijing, China

Magnetic materials are widely used in motors, reactors, power-frequency and high-frequency transformers and other electrical devices, which are of great significance for the safety, efficiency and stability of power system. Since the most distinguishing features of this kinds of materials is hysteresis characteristics, an accurate mathematical modelling of the hysteresis loop is a prerequisite for the design and optimization of magnetic cores in electrical devices. As far as now, various hysteresis models have been proposed in the related literatures [1]. Among them, the energetic hysteresis model developed by Hans Hauser is very promising for its simple formula and accurate representation of hysteresis loop [2]. Many factors, such as stress, temperature, frequency and magnetization direction can be incorporated in this model. However, determining the model parameters with reasonable accuracy and efficient computation is still a major challenge. The existing methods for parameter identification of energetic model have been divided into two categories. The first one is using the formulas proposed by Hans [3]. This method not only needs the data of original magnetization curve and major loop, but also involves the solving of transcendental and approximate equations, which could result in inefficient solution and low accuracy. In order to overcome this problem, a curve fitting method is proposed [4], which uses simulated annealing (SA) method to identify parameters based on the objective function of minimum error between measured and calculated hysteresis loops. However, it has the intrinsic drawback of stochastic optimization algorithm that the convergence rate is extremely slow near the global minimum, and there is no guarantee to reach the optimal point [5]. This paper proposes a hybrid algorithm which combines the most appealing features of two kinds of optimization methods viz. the stochastic approach of SA and the deterministic nature of Levengerg-Marquardt (L-M) algorithm. Since SA has an ability to avoid traps in local minima, it is used to approach to the area where global optimal solution is located in the initial iteration period of this hybrid algorithm. Then a normalization of the sensitivity function is built to improve the convergence of L-M algorithm, which can converge quickly towards global minimum. Based on the introduced commutation criteria, the current best solution of SA algorithm is transferred to normalized L-M algorithm as its initial parameter. The simulation and experimental results show that the proposed hybrid algorithm leads to a considerable reduction in computation time and higher accuracy, so it can be used to precisely and quickly extract the parameters of energetic hysteresis model. The test is carried out on the same benchmark model [4], and the root-mean-square error (RMSE) of calculated loop is taken as the objective function. Besides, the value of this parameters are already known, and the bounds of the parameters are taken in a wider range to verify the robustness of the proposed hybrid technique. Firstly, SA is used to identify the parameters. The reduction of RMSE varying with iteration number is shown as Fig. 1. It is evident that the RMSE almost does not change after 23th iteration. This result confirms that SA has a good global search capability, but its local optimization capability is poor, and the maximum error of optimized parameters is up to 27.8%. The final best calculated loop by SA is shown in Fig. 2. However, when it comes to hybrid algorithm, the L-M algorithm takes over the calculation from SA when iteration number reaches 29, and then it converges to the global optimal parameters in just 6 interation. Fig. 2 gives the calculated loop by the hybrid algorithm. The parameters match exactly with that of benchmark model curve.

[1] A. Krings, A. Boglietti, A. Cavagnino, and S. Sprague. "Soft magnetic material status and trends in electric machines," *IEEE Trans. Ind. Electron.*, vol. 64, pp. 2405-2414, Mar. 2017. [2] H. Hauser. "Energetic model of ferromagnetic hysteresis," *J. Appl. Phys.*, vol. 96, pp. 2753-2767, Sept. 2004. [3] P. Fulmek, P. Haumer, H. Wegleiter, and B. Schweighofer. "Energetic model of ferromagnetic hysteresis," *COMPEL Int J Comput Math Electr Electron Eng*, vol. 29, pp. 1504-1513, 2010. [4] M. Hamimid, S.M. Mimoune, and M. Feliachi. "Dynamic formulation for energetic model compared with hybrid magnetic formulation of ferromagnetic hysteresis," *Int J Numer Modell Electron Networks Devices Fields*, vol. 30, pp. 1-5, Nov./Dec. 2017. [5] Drago G, Manella A, Nervi M, et al. "A combined strategy for optimization in non linear magnetic problems using simulated annealing and search techniques," *IEEE Trans. Magn.*, vol. 28, pp. 1541-1544, 1992.

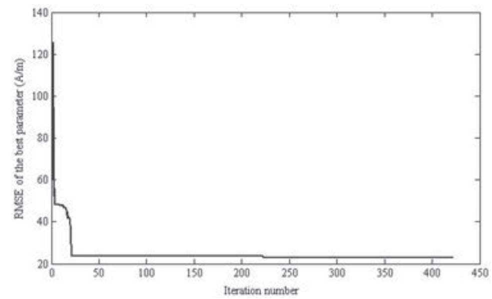

Fig. 1. RMSE variation with iteration number using SA

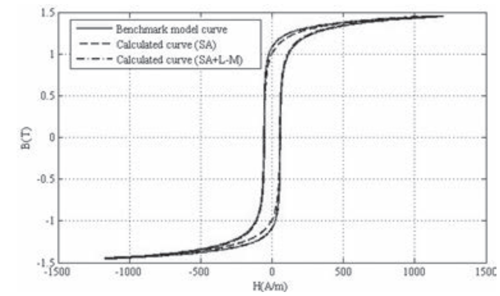

Fig. 2. Comparison between hysteresis loops calculated by SA and hybrid algorithm

2:45

HH-04. Loss Simulation by Finite Element Magnetic Field Analysis Considering Dielectric Effect and Magnetic Hysteresis in EI-Shaped Mn-Zn Ferrite Core.

K. Shimizu[1], A. Furuya[1], Y. Uehara[1], J. Fujisaki[1], H. Kawano[2], T. Ataka[1], T. Tanaka[1] and H. Oshima[2]
1. Fujitsu Limited, Kawasaki, Japan; 2. Fujitsu Laboratories Limited, Atsugi, Japan

I. INTRODUCTION Power electronic devices such as inductors and transformers are required to be driven with high frequency according to downsizing. Mn-Zn ferrite is one of the high-frequency magnetic materials. The dimensional resonance occurs in Mn-Zn cores due to the increase of the dielectric constant and significantly affects the eddy current loss [1]. The equivalent RC circuit of Mn-Zn ferrite was modeled by the grains and their boundary layers and can explain the effective dielectric property by the contribution of the capacitance [2]. The boundary layers with high-resistance suppress the eddy current in the grains at low frequencies, while as frequency increases the suppression of the eddy current decreases by charge accumulation on the surface of the grains. The calculating method of the frequency dependent dielectric property by the capacitance was proposed and the dimensional resonance was reproduced by applying the method to the magnetic field equations of linear magnetic materials by using a cylindrical approximation [3]. In order to analyze the eddy current loss of complex shaped inductors at high frequencies, we apply the dielectric effect to the A-ϕ method of the finite element magnetic field analysis. On the other hand, the magnetic hysteresis loss increases according to the increase of the magnetic flux density in the core. Therefore, we used the play model [4] to express the magnetic hysteresis for finite amplitude of magnetic flux. For confirming the calculation accuracy, core losses of an EI-shaped inductor was calculated and the frequency dependent loss was compared with experimental results. In the simulation, the core loss was divided into hysteresis loss in DC, eddy current loss and excess loss, and their contributions were analyzed. II. METHOD The current density of the grains is j_1 as follows [3]. $j_1 = \sigma_1(E\text{-}rq/\varepsilon)$ (1) Where, σ_1 is the electrical conductivity, E is the average electric field in the grains, q is the charge density accumulated in the surface of the grains, ε is a dielectric constant in the boundary layers and r is the ratio of the thickness of the boundary layers to the diameter of the grains. Since the volume of the grains is much larger than the boundary layers, the j_1 can be approximated as the current density of the whole magnetic material. Therefore, as shown in the equations (2)-(3), the j_1 can be substituted into the magnetic field equations of the A-ϕ method. Where, the magnetic field $H(B)$ depending on the flux density is calculated by the play model, c_β is a coefficient of excess loss, μ_0 is the vacuum permeability and J_0 is an exciting current. $\sigma_1(\partial A/\partial t+\nabla\phi+rq/\varepsilon)+\nabla\times H(B)+\nabla\times\nabla\times(c_\beta/\mu_0)(\partial A/\partial t) = J_0$ (2) $\nabla\sigma_1(\partial A/\partial t+\nabla\phi+rq/\varepsilon) = 0$ (3) The total loss P_c can be expressed by the sum of hysteresis loss in DC, eddy current loss and excess loss respectively as shown in the equation (4). $P_c = V_{EI}\sigma HdB+V_{EI}\int(j_1^2/\sigma_1+rj_2^2/\sigma_2)dt+V_{EI}\sigma(c_\beta/\mu_0)(\partial B/\partial t)dB$ (4) Here, j_2 is the current density in the grain boundary layers, σ_2 is the electrical conductivity and V_{EI} is volume of the EI-shaped core. The integration by magnetic flux density is calculated in one loop and the time integration is calculated in one cycle. III. RESULTS For the simulation, we initially fitted the material parameters using several measurement results. The σ_1, σ_2, r, ε were derived from the frequency dependent conductivity of the thin plate. In addition, the hysteresis parameter of the play model [4] is from the B-H curve at the low frequency (10 kHz) and the c_β is from the fitting the loss of high frequency (1000 kHz) using the toroidal core. In the simulation, we used the EI-shaped core shown in Fig.1. The average magnetic flux density in the core region wounded by the coil was controlled to be constant while varying the frequency. Figure 2(a) shows the frequency dependence of the core loss at the flux density 50mT and 100mT. The simulation results of the core loss agree well with measurements. Figures 2(b) and Fig. 2(c) show the simulation results of the core losses of different contributions at 50mT and 100mT respectively. At the low frequencies, the loss rate of the hysteresis is large, for example, it is 54% at 50 kHz in Fig. 2(c). The excess losses are the largest and are approximately proportional to the frequency. The eddy currents are very small at low frequencies, but their loss gradient in the frequency increase up to 1000 kHz. It should be noted that such sharp increase in the eddy current loss as a function of frequency cannot be reproduced by a simulation of homogeneous material without the dielectric effect [5]. Since the frequency of the dimensional resonance is about 1200 kHz, the macroscopic phenomenon that the resistance of the boundary layers seems to be short-circuited by charge accumulation in the capacitance results in the increase of eddy current at the high frequencies. It was found that the finite element magnetic field analysis which considers the dielectric effect and the magnetic hysteresis can accurately predict the losses of the EI-shaped Mn-Zn ferrite core and analyze the loss divided into different kinds.

[1] Glenn R. Skutt, Fred. C. Lee, “Characterization of Dimensional Effects in Ferrite-Core Magnetic Devices” PESC ‘96, vol. 2, pp. 1435–1440, (1996) [2] F. Fiorillo, C. Beatrice, O. Bottauscio, and E. Carmi, “Eddy-Current Losses in Mn-Zn Ferrites”, IEEE Trans. Magn., Vol.50, No.1 (2014) [3] A. Furuya, et al., “Magnetic Field Analysis for Dimensional Resonance in Mn–Zn Ferrite Toroidal Core and Comparison with Permeability Measurement”, IEEE Trans. Magn., vol.53, no. 11, (2017) [4] Tetsuji Matsuo, Yoshihiro Osaka, and Masaaki Shimasaki, “Eddy-Current Analysis Using Vector Hysteresis Models with Play and Stop Hysterons”, IEEE Trans. Magn., vol.36, no. 4, pp.1172–1177, (2000) [5] G. Bertotti, “Hysteresis in Magnetism” Academic Press, San Diego, (1998) (Chapter 12).

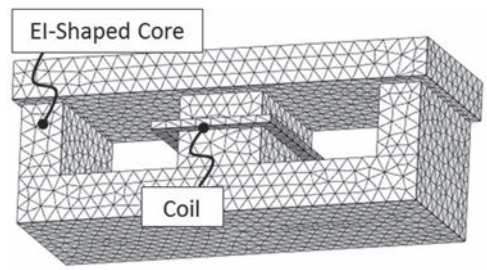

Fig. 1. 3D mesh image of the EI-shaped core used for the simulation.

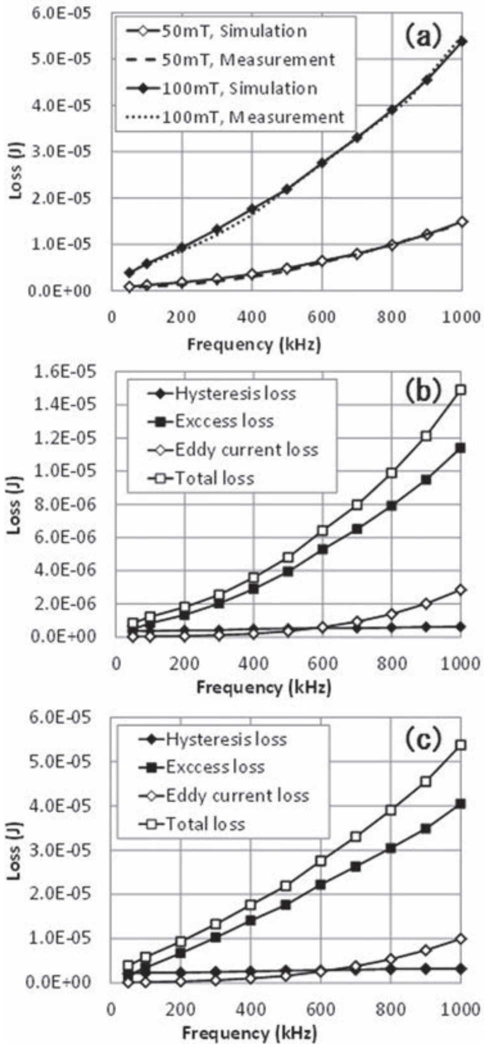

Fig. 2. Frequency dependent core losses. (a) Core losses of the EI-shaped core in the experiments and the simulations. (b) Separated core losses at 50mT in the simulations. (c) Separated core losses at 100mT in the simulations.

3:00

HH-05. Prandtl-Ishlinskii Modeling for Giant Magnetostrictive Actuator Based on Internal Time-delay Recurrent Neural Network.

Y. Wang[1], R. Xu[1] and *M. Zhou*[1]
1. Department of control science and engineering, Jilin University, Changchun, China

Micro and nano technology is an indispensable part of modern science and technology. Because of the excellent advantages of high energy density, rapid response and large mechanical force, GMA becomes more promising in precision positioning, microelectronic, and biomedicine field[1, 2]. However, the relationship between input current and output displacement of GMA is hysteresis nonlinearity, which shows that the output of GMA not only relates to the current input value, but also relates to previous output value. Besides, the hysteresis nonlinearity is rate-dependent, so that the output of GMA depends on the input frequency. The intrinsic rate-dependent hysteresis nonlinearity of GMA is the main sticking point preventing its application in the high precision positioning [3, 4]. Therefore, modeling of GMA has long been difficult to study and attracted the attention of researchers. In this paper, the Prandtl-Ishlinskii (PI) model with the parameters self-tuning ability is established by the internal time-delay recurrent neural network (RNN) to describe the hysteresis nonlinearity of GMA. PI model consists of play operator and density function. Play operator is a continuous hysteresis operator, whose output depends on not only the current input but also the previous input. Nevertheless, play operator is rate-independent. Identifying the applicable density function is an important part of modeling PI model of GMA. Neural network has the features of the nonlinear mapping property and high parallel process ability. Therefore it is suitable to be applied to identify the nonlinear model. In this paper, the internal time-delay RNN is used to replace the density function of PI model. The PI model structure identified by the internal time-delay RNN for GMA is shown in Fig. 1. The internal time-delay RNN is set by the input layer, output layer and hidden layer. Where output of play operator $v_i(t)$ is the ith input sample of the network at time t, $y^*(t)$ is the output of the network. ${}^1w_{ji}$ and ${}^2w_j$ are the weights of input layer and output layer, respectively, ${}^hw_{jk}$ is the weight for the nodes of hidden layer. Compared with feedforward neural network, it has property of memory because there is time delay recurrent existed in the hidden layer. Due to the inherent feedback structure of internal time-delay RNN, it possesses the dynamic characteristics and can adjust the parameters of PI model adaptively. The simulation results of PI model identified by internal time-delay RNN at the different input frequency are shown in Fig. 2. The red solid lines are hysteresis loops measured in the experiments, the blue dotted lines are the hysteresis loops of PI model based on internal time-delay RNN, and the blue solid lines are the modeling error curves. To facilitate simulation, the normalized data is adopted. As shown in Fig.2, the maximum modeling error rate at 1Hz, 10Hz, 50Hz and 100Hz is 0.81%, 1.07%, 1.41% and 2.14%, respectively. The PI model identified in this paper can accurately describe the hysteresis nonlinearity of GMA with the increase of input frequency. Therefore, the ability of precise modeling by PI model based on internal time-delay RNN is certified. The proposed PI model can be used to eliminate the hysteresis nonlinearity at the compensation control of GMA and promote the application of GMA in precision positioning field in the future.

[1] Cao S, Wang B, Zheng J, et al. "Modeling dynamic hysteresis for giant magnetostrictive actuator using hybrid genetic algorithm," *IEEE Trans. Magn.*, 42(4): 911-914, 2006. [2] Li Z, Su C, Chai T. "Compensation of hysteresis nonlinearity in magnetostrictive actuators with inverse multiplicative structure for Preisach model," *IEEE Trans. Autom. Sci. Eng.*, 11(2): 613-619, 2014. [3] Aljanaideh O, Al Janaideh M, Rakheja S, et al. "Compensation of rate-dependent hysteresis nonlinearities in a magnetostrictive actuator using an inverse Prandtl–Ishlinskii model," *Smart Mater. Struct.*, 22(2): 025027, 2013. [4] Guo Y, Mao J, Zhou K. "Rate-Dependent Modeling and H∞ Robust Control of GMA Based on Hammerstein Model With Preisach Operator," *IEEE Trans. Control Syst. Technol.*, 23(6): 2432-2439, 2015.

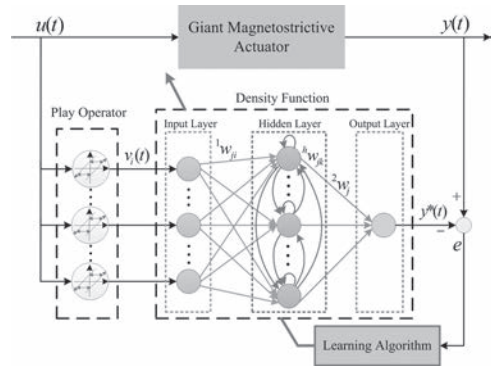

Fig. 1. The PI model structure identified by the internal time-delay RNN for GMA

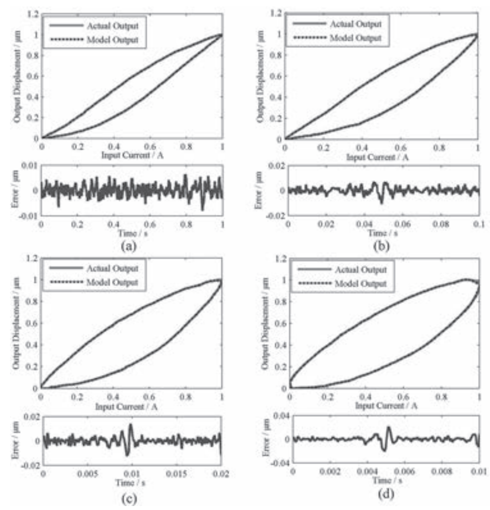

Fig. 2. Identification results of PI model based on internal time-delay RNN (a) 1Hz (b)10Hz (c) 50Hz (d) 100Hz

3:15

HH-06. Vector Hysteresis Modeling of Soft Magnetic Composite by the Improved Preisach Model Considering Anisotropic Characteristic.

X. Zhao[1], H. Zhang[1], *L. Li*[1], F. Xiao[1], X. Liu[1] and Y. Li[2]
1. North China Electric Power University, Baoding, China; 2. Hebei University of Technology, TianJing, China

1.INTRODUCTION Two dimensional (2-D) magnetic flux exist in rotating electric machines and T-joints of three-phase power transformers and may cause local overheating in these devices. The soft magnetic materials, such as electrical steel sheet and soft magnetic composite (SMC), are usually used in the fabrication process of ferromagnetic core. Therefore, it has been focus of attentions to measure and model 2-D magnetic properties of soft magnetic materials in recent years [1-2]. Compared with the Stoner-Wohlfarth hysteresis model, the Preisach model has the advantage over parameter identification and numerical implementation, and it has been widely used in modeling 2-D vector hysteretic characteristics. Due to the defects of classical vector Preisach model, simulation cannot agree well with measurement, therefore it is necessary to improve the classical vector model. In this paper, by introducing the function *z*, the classical Preisach model is improved to model the 2-D vector hysteresis of SMC considering the influence of anisotropy, the simulated results by the improved model is coincided with the measured ones. The proposed method is meaningful for exploring the rotating magnetic and loss characteristics of electric motor and power transformer. 2. IMPROVED VECTOR PREISACH MODEL It is necessary to improve the classical vector Preisach model since there are some problems when the model is applied in the realistic vector hysteresis modeling. the measured loci of *H* are flower-shape rather than circle due to inherently anisotropic property in magnetic materials. The improved model [3] is presented as follows. $f(t)=\int e_\theta(\iint_{\alpha\geq\beta} v(\alpha,\beta)\delta_{\alpha\beta}|u_\theta(t)-\phi| z(\theta(t)-\phi)d\alpha d\beta)d\theta$ (1) $z(\theta-\phi)=\mathrm{sign}[\cos(\theta-\phi)]|\cos(\theta-\phi)|^{1/\omega}$, $\omega\geq1$ (2) As shown in (1) and (2), the classical Preisach model is improved to simulate the vector hysteresis more accurately by means of the auxiliary function *P*. $P(\alpha,\beta)=1/\pi*\int[\omega\beta^{\omega-1}F(\beta,\beta')+\beta^{\omega}(dF(\beta,\beta')/d\beta)]/(\alpha^{2\omega}-\beta^{2\omega})^{1/2}d\beta$ (3) where a new parameter ω is introduced and both ω and function P should be determined through the identification procedure. Correspondingly, the expression of input should be also changed, $B_{\phi i}=|B|\delta|\cos(\theta_B-\phi_i)|^{1/\omega}$, $\omega\geq1$, i=1,2,....N (4) the measuring system mainly includes the following four parts [4], three orthogonal core poles with six flexible excitation windings, three power amplifiers and generators, multi-channel differential amplifier circuits, and a digital signal processing device with data acquisition card driven by the LabVIEW software, and the sensing structure consisted of six combined B-H sensing coils tightly attached on each surfaces of the cubic specimen. The entire structure of the tester is shown in Fig.1. The 2-D hysteresis loops along *H*x- and *H*y- axes of SMC material are measured by the cubic sensor at low frequency, with the specimen excited by rotating magnetic field. 3. RESULTS AND ANALYSIS The limiting hysteresis loop of SMC material is measured by the experimental setup in Fig.1 to generate first-order reversal curves (FORCs) [5]. Thus, the auxiliary function *P* in (3) is obtained and identification of the improved Preisach model can be achieved by means of numerical implementation. Consequently, hysteresis curves corresponding to different rotating excitations are computed and compared with the measured results. Fig.2 shows the comparison between measurement and simulation. From the comparison in Fig.2, it is noticed that agreement between the measured and simulated result is basically approached, which proves the effectiveness and accuracy of the improved Preisach model. 4. CONCLUSION An improved vector Preisach model is presented to simulate 2-D vector hysteresis curves considering anisotropic property of SMC material. Numerical implementation of the improved model is realized based on the measured limiting hysteresis loops and the corresponding FORCs. The improved vector model is used to simulate hysteresis loops of SMC specimen excited by 2-D rotating magnetic field. 5. ACKNOWLEDGEMENT This work is sponsored by the National Natural Science Foundation of China (Grand No. 51777073,51577066), and by the Natural Science Foundation of Hebei Province (Grand No. E2017502061), and by the National Key Research and Development Program of China (Grant No. 2017YFB0902703).

6. REFERENCES [1] Mayergoyz I D. Vector Preisach Models of Hysteresis - Mathematical Models of Hysteresis and Their Applications - CHAPTER 3[J]. Mathematical Models of Hysteresis & Their Applications, 2003:149–223. [2] Torre E D. Magnetic Hysteresis[J]. Magnetic Hysteresis, 1999:4780–4787. [3] Kuczmann M. Vector Preisach hysteresis modeling: Measurement, identification and application[J]. Physica B Condensed Matter, 2011, 406(8):1403-1409. [4] Li Y, Yang Q, Zhu J, et al. Research of Three-Dimensional Magnetic Reluctivity Tensor Based on Measurement of Magnetic Properties[J]. IEEE Transactions on Applied Superconductivity, 2010, 20(3):1932-1935. [5] E Dlala. Efficient algorithms for the inclusion of the Preisach hysteresis model in nonlinear finite-element methods[J]. IEEE Trans. Magn., vol. 47, no. 2, pp. 395-408, 2011.

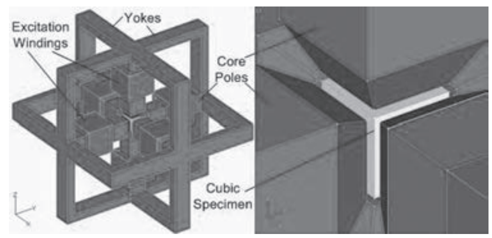

Fig. 1. Measuring system of vector hysteresis

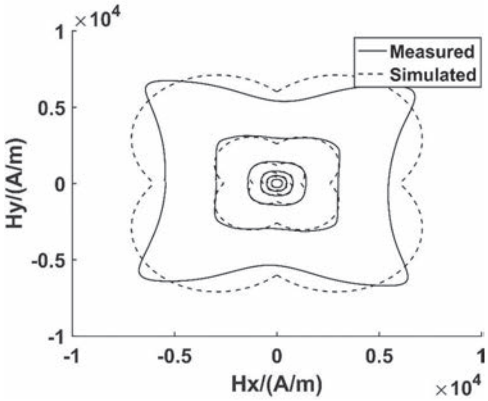

Fig. 2. Comparison between measured and simulated magnetic field strength

3:30

HH-07. Modeling the role of magnetic charges on field cooling memory in low anisotropy polycrystalline materials.

H. ElBidweihy[1], A. Arrott[2] and V. Provenzano[3]
1. Department of Electrical and Computer Engineering, United States Naval Academy, Annapolis, MD, United States; 2. Physics Department, Simon Fraser University, Burnaby, BC, Canada; 3. Materials Science and Engineering Division, National Institute of Standards and Technology, Gaithersburg, MD, United States

Measuring the temperature-dependent magnetization following a magneto-thermal protocol using DC magnetometry techniques is a universal tool to investigate non-equilibrium magnetism [1]. The role of magnetic charges is most prominent in ideally soft magnetic materials or soft polycrystalline materials with small anisotropy as the rapid buildup of these charges near the grain boundaries creates internal demagnetizing fields which oppose the anisotropy fields [2]. We present a model to demonstrate the effect of the buildup of magnetic charges during the negative field cooling (NFC) routine on the magnetization of polycrystalline gadolinium around the spin-reorientation temperature region monitored during the first positive field warming (NFC|PFW) routine. The model shows that the sizable negative magnetization trapped during the NFC routine could be modeled as an assembly of non-interacting Stoner-Wohlfarth (SW) particles with an appropriate distribution of blocking temperatures. The model is applied to polycrystalline gadolinium which is known to have uniaxial anisotropy, a first-order anisotropy constant which changes its sign around the spin-reorientation region (220 – 260 K), and a temperature-dependent easy axis orientation as shown in Figure 1(a) [3–5]. The drastic effect of the cooling field memory sustained by the magnetic charges are most obvious during the spin-reorientation temperature region where the easy axis orientation is approaching 0^{o} and the trapped magnetization rotates easily towards the negative direction of the anisotropy axis. For an ideal assembly of non-interacting single-domain Stoner-Wohlfarth (SW) particles, the magnetic moment will be locked along the cooling field direction if the field magnitude is strong enough. Heating the sample from this well-defined magnetic state will cause an irreversible transition when the thermal energy k_BT is comparable to the anisotropy energy barrier KV, where k_B is the Boltzmann constant, T is the temperature, K is the effective anisotropy constant, and V is the volume. Coupling the SW model with Néel's theory of thermal relaxation leads to a generalized model for the temperature dependence of magnetization [6]. It can be shown that the temperature-dependent normalized magnetization in the anisotropy axis direction is given by [7, 8]: $dm/dT = (f_0/\Delta T/\Delta t) \times \{(1-m) \times \exp(-U_{21}/k_BT) - (1+m) \times \exp(-U_{12}/k_BT)\}$, (1) where U is the energy barrier between the two states of energy minima, f_0 is the fluctuation rate between them, and $\Delta T/\Delta t$ is the rate of change of temperature during the measurement. Figure 1(b) shows the normalized magnetization in the anisotropy axis direction versus increasing temperature for an assembly of SW particles under three different field cooling routines. For polycrystalline gadolinium, a magneto-thermal protocol has been applied where the sample is cooled down from a temperature higher than the Curie temperature (300 K) to a low temperature (5 K) while a negative field (μ_0H_{FC}=−50 mT) is applied [9]. The sample is then heated to 380 K under a small positive field (μ_0H_A=+5 mT), cooled back to 5 K, and finally heated to 380 K. The difference between the two warming sequences reflects the temperature dependence of the anisotropy and its effect on the buildup of magnetic charges near the grain boundaries. At the beginning of the first warming sequence (NFC|PFW), the assembly of SW particles at 5 K, representing the trapped magnetization after field cooling, has a negative magnetization (M_{NFC}). The strength of the negative cooling field (H_{NFC}) is proportional to M_{NFC}. From 5 K to 220 K, the anisotropy becomes less negative and the easy cone half-angle increases from about 40^{o} to around 80^{o} which allows M_{NFC} to rotate towards the plane perpendicular to the anisotropy axis decreasing its component along the negative direction of the anisotropy axis. From 220 K to 250 K, the anisotropy changes its sign and the easy axis cone half-angle approaches zero which allows M_{NFC} to revert, increasing its component along the negative direction of the anisotropy axis. Above 250 K, thermal demagnetization takes over and M_{NFC} goes to zero. The second warming sequence (PFC|PFW) occurs not only after the initial negative cooling field has been removed but also after its memory has been erased by increasing the temperature above the Curie temperature. Figure 2 shows (NFC|PFW), which includes the contribution of M_{NFC} as modeled by the generalized model for an assembly of SW particles of temperature-dependent anisotropy in a zero applied field, and (PFC|PFW). The model captures the main features of the magneto-thermal protocol measurements on polycrystalline gadolinium and supports our hypothesis for the significant role magnetic charges play when their internal demagnetizing field is comparable to the anisotropy field, which is the case for low-anisotropy polycrystalline gadolinium around the spin-reorientation region.

[1] K. R. Sydney, et al., J. Magn. Magn. Mater. 2, 345 (1976). [2] A. S. Arrott, T. L. Templeton, AIP Adv. 8, 047301 (2018). [3] M. Salamon, D. Simons, Phys. Rev. B, Condens. Matter. 7, 229 (1973). [4] J. W. Cable, W. C. Koehler, J. Appl. Phys. 53, 1904 (1982). [5] B. D. Cullity, C. D. Graham, Introduction to Magnetic Materials. John Wiley & Sons (2011). [6] J. L. Dormann, et al., J. Phys. C: Solid State Phys. 21 2015 (1988). [7] M. A. Chuev, J. Hesse, J. Phys.: Condens. Matter. 19, 506201 (2007). [8] I. J. Bruvera, et al., J. Appl. Phys. 118, 184304 (2015). [9] V. Provenzano, et al., IEEE Trans. Magn. 53, 1 (2017).

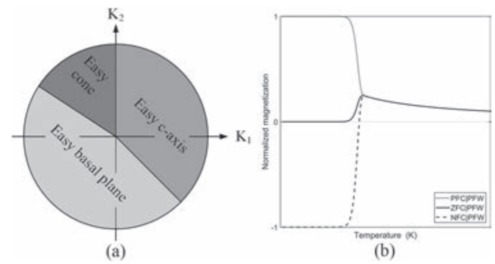

Fig. 1. (a) The easy magnetization directions in a hexagonal crystal for all possible values for the anisotropy constants K_1 and K_2 (after [5]). (b) Model results of magnetization versus increasing temperature under a positive applied field (PFW) for an assembly of SW particles under three different field cooling routines: positive field cooling (PFC), zero-field cooling (ZFC), and negative-field cooling (NFC).

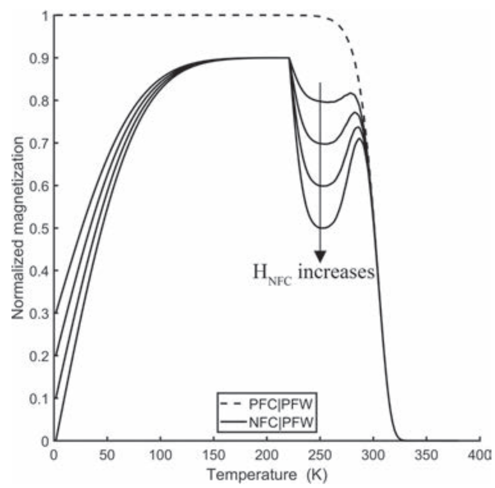

Fig. 2. Model results for magnetization versus temperature for the first warming sequence (NFC|PFW), after being field-cooled under different H_{NFC} values, and for the second warming sequence (PFC|PFW).

3:45

HH-08. Vector Magnetization By A Distribution Of Easy Axes.

A. Jamali[1], E. Della Torre[1] and *A. Aslani*[1]
1. Department of Electrical and Computer Engineering, The George Washington University, Falls Church, VA, United States

I.Introduction We recently developed a vector magnetization model for uniaxial media [1]. In this model, magnetization is vector sum of the reversible and irreversible components. The irreversible magnetization that is parallel with easy axis and does not change in direction is modeled by scalar Preisach model and the reversible component changes by Stoner-Wohlfarth model [2]. The model is developed for behavior of the perfectly aligned hysterons. In this paper, we improved the model by using a distribution in the hysteron easy axes. The net magnetization then is the weighted vector sum of the individual magnetizations. The previous model had three major inconsistencies with experimental results discussed below. II.Squareness Unitary magnetizations curves can be plotted by keeping the direction of the applied filed constant and plotting the projection of the magnetization along the applied field with respect to the applied field magnitude. The squareness is defined as the ratio of saturation remanence to saturation magnetization and it measures how square is the hysteresis loop. Let α and Φ be the polar and azimuthal angles of the easy axis respectively and θ be a the angle between magnetization and easy axis, by considering $p(\alpha,\Phi)$ as the probability density function, the general expression to calculate unitary magnetization is introduced in [2]. As shown in Fig.1, by applying the method of averaging over orientation and using a uniform distribution for both α and Φ, the squareness of the unitary magnetization curves will be decreased and it results in smoother and more realistic curves. III. The jumps in lag angle Lag angle curve is the magnetization angle versus applied field angle [3,4]. We showed that for the normalized applied field, h, less than 0.5 the magnetization is not strong enough to follow the applied field and oscillation mode will occur and rotation mode is for the values h more than 0.5 [1]. Also we showed that there is a need to break down this range to $0.5<h<1$ and $h>1$. In the previous model, for the normalized applied field in the range of $0.5 <h<1$, we calculated jumps in lag angle. These jumps are not experimentally validated. The mathematical source of the jumps is the multiple intersections of a circle of radius h with the astroid representing the bifurcation curve of the uniaxial anisotropy [1]. If we rotate the hysteron easy axes (equivalent with rotation of the astroid) then different intersections will be derived. Fig.2 shows how the discontinuity of the lag angle curves can be diminished by using a uniform distribution for α and Φ. IV. Magnetization drop at the critical angle For the values of $h>1$, the previous model correctly predicted the lag angle magnetization behavior. The problem in this range is the small magnitude of magnetization at the critical angle, that is where the magnetization changes from lagging to leading. At this angle, the magnetization vector is parallel with the applied field. This magnitude can be written as a function of the standard deviation of $p(\alpha,\Phi)$.

[1]. E. Della Torre, A. Jamali, H. ElBidweihy, L. H. Bennett., "Vector Magnetization of a Distribution of Uniaxial Particles," IEEE Transactions on Magnetics, 52, 7300904, (2016) [2]. E. C. Stoner and E. P. Wohlfarth, "A mechanism of magnetic hysteresis in heterogeneous alloys," *Phil. Trans. Roy. Soc. London A, Math., Phys. Eng. Sci.*, vol. 240, no. 826, p. 599, (1948) [3]. G. R. Kahler, E. Della Torre, and U. D. Patel, "Properties of vector Preisach models," *IEEE Trans, Magn*, 41 (2005). [4]. E. Della Torre, A. Jamali, H. ElBidweihy, and L. H. Bennett, "Vector properties of magnetostriction," *J. Appl. Phys.*, vol. 117, no. 17, p. 17D141, (2015).

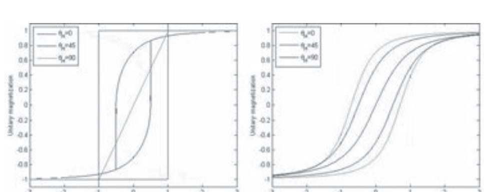

Fig. 1. Unitary magnetization with (right) and without (left) averaging over orientation

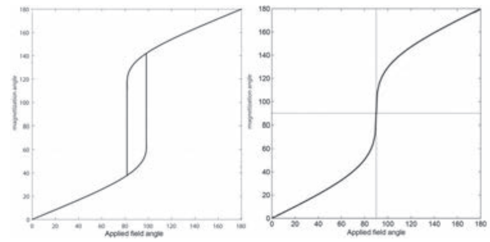

Fig. 2. Lag angle curve with (right) and without (left) averaging over orientation

FRIDAY AFTERNOON, 27 APRIL 2018 ORCHID II, 2:00 TO 5:00

Session HI

TRANSFORMERS AND INDUCTORS: HIGH FREQUENCY EFFECTS

Jianguo Zhu, Chair
University of Technology Sydney, Sydney, NSW, Australia

CONTRIBUTED PAPERS

2:00

HI-01. Analysis on variable inductances of planar coils sandwiched by soft magnetic layers.

Y. Wen[1], P. Li[1], F. Song[1], S. Yu[1], L. Bian[2] and Y. Wang[1]
1. Instrument Science and Engineering, Shanghai Jiaotong University, Shanghai, China; 2. Mechanical Engineering, Nanjing Technology University, Nanjing, China

It is well known that the inductance of a planar coil can be enhanced while it is coverd by soft magnetic layers due to the high permeability of the material. As the permeability of a soft material is related to undergoing magnetic flux, in this way the resultant inductance can be variable along with external fields. This fact suggests a practical approach to tune inductances of magnetic film planar inductors. Soft magnetic materials such as amorphpus and nanocrystalline films have extremely large permeabilities, whose maximum values reach an order of several ten/hundred thousands. This performance indicates that the variation of permeability in materials of these types is abundant with a variation ratio ready to the order of 10^3~10^5 when the external field varies. If the magnetic film inductor can fully follow the variation, it will have a considerably large inductance tunability comparable to the variation range of the material permeability. In state of the art, the inductance or the magnetic impedance tunability ratio of a magnetic film device is much less than that of magnetic film permeability. Unlike a coil being put into an infinite magnetic medium or enclosing a loss-free magnetic core, the inductance of a planar coil covered by soft magnetic layers is not increased by a factor equal to the material relative permeability. In fact, it has been seen that the resultant inductances of planar coils either fabricated on soft magnetic substrates [1] or covered by soft magnetic layers [2], are only enhanced at most several or several ten times no matter how large the material permeabilities are. To enhance the quality factor of an inductor, it is preferably expected to raise the inductance through employing the high permeability of ferro-magnetic material rather than increasing the turns of a coil. However, it seems ineffective to improve the inductance of a planar inductor only by using a magnetic material with higher permeability. The underlying key point is that the inductance of a planar coil covered by magnetic layers depends on the permeability in a quite complicated way closely connected with the geometrical parameters of both the coil and the soft magnetic layer. Fig.1 depicts the measured variable inductances of two identical planar coil respectively sandwiched by amorphous and permalloy films with same geometries. The gap between magnetic layers is 180 mm, film thickness 90 mm, film width 9000mm. The coil conductor width is 65mm. The maximum relative permeability of amorphous film is much higher than that of permalloy film. However, as seen in Fig.1, the maximum inductances in two cases demonstrate a small difference. For reference, the inductance of the naked planar coil is also displayed in Fig.1. It is clear that at low magnetic field, the inductance is merely enhanced 10+ times when the coil sandwiched between amorphous films at the maximum permeability. The gain is much less than the maximum permeabilities. This result shows that the magnetic film inductors only make part use of material permeabilities. The part of higher values including the maximum permeability have no effect on the resultant inductances. Hence, the variable range of the inductance in a magnetic film inductor is quite limited and can only follow part of the permeability variation. Korenivski [3] gave models describing the self-inductance of a conductor sandwiched by a magnetic material following Patton's analysis [4]. From the models, the inductance of a magnetic film planar inductor is ready to obtain as the inductance of a coil is the summation of self and mutual inductances of composing conductors. In terms of Korenivski's model, as the permeability of magnetic layers is increasing the inductance will get saturated. This point was also revealed in the planar coil with a magnetic substrate [1]. In cases, saturation occurs when the relative permeability is as low as 10~100. Actually, the inductance saturation is also closely related to the geometry of magnetic layers and the width of conductors in a planar inductor. The gap between magnetic layers and the width of magnetic layers determine the saturated value of the inductance. The higher is the saturated value, the larger is the permeability in which proximity the saturation occurs. The magnetic layer thickness along with the gap affects the rate of reaching saturation. More important, it is the ratios of these parameters to the width of coil conductors rather than the parameters alone effect on the inductance. To clarify the effect of these parameters on the final inductance, the curves from the model are shown in Fig. 2. The ratios of gap, film thickness and film width to conductor width are respectively referred to as r_g, r_tm and r_wm. Our analysis concludes that it is possible to develop a magnetic film planar inductor making full use of the magnetic material permeability, which inductance can follow the permeability variation from the maximum to the minimum by designing appropriate device geometry. Thus the inductance is variable in an abundant range comparable to the magnetic film permeability variation. Such inductors with considerably large tunability can find extensive application not only in electronic circuits but also in sensors.

1. W.A. Roshen, "Effect of finite thickness of magnetic substrate on planar inductors", IEEE Tran. Mag., 26, 270 (1990). 2. B. M. Farid Rahman, R. Divan, D. Rosenmann, et al, "Application of sub-micrometer patterned permalloy thin film in tunable radio frequency inductors", J. Appl. Phys., 117, 17C121 (2015). 3. V. Korenivski and R. B. van Dover, "Magnetic film inductors for radio frequency applications",J. Appl. Phys. 82, 5247 (1997). 4. A. Patton, "Analysis of the efficiency of thin-film magnetic recording heads", J. Appl. Phys., 42, 5868(1971).

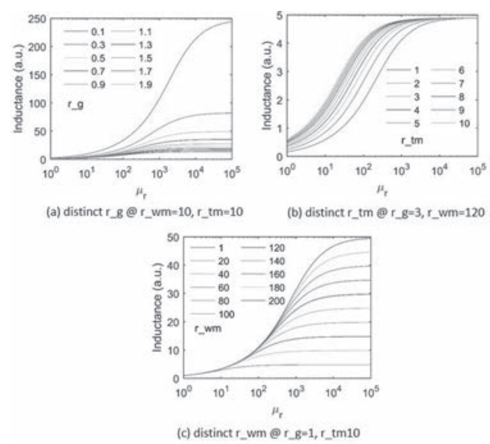

Fig. 2. Variable inductances with distinct film configurations.

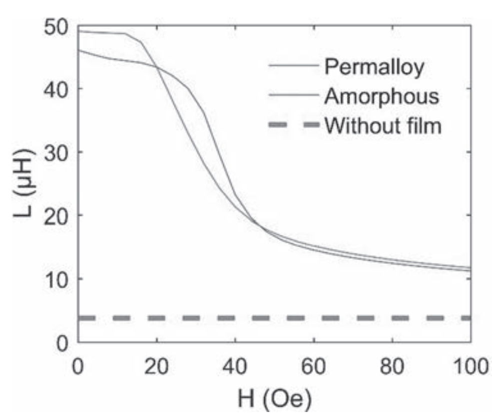

Fig. 1. Inductances of planar inductors without and with high permeability soft magnetic

2:15

HI-02. Layout Optimization of Indoor Substation Considering Power Transformer Spatial Acoustic Radiation Characteristics.

D. Wang[1], L. Ying[1], W. Wang[2] and J. Wang[1]
1. School of Electrical Engineering, Wuhan University, Wuhan, China;
2. Central Southern China Electric Power Design Institute Co.,Ltd, Wuhan, China

I. Introduction To improve the power network structure and guarantee the power quality in load center as well as city center, compared with outdoor substation, the whole indoor substation become the preferred choice for designers. So correspondingly, the purposeful substation layout optimization during the design process based on the acoustic radiation characteristics of power transformer will be considered as an efficient and cost-effective way to diminish the influence of power transformer noise. In this paper, a 3D multi-physics coupling model of a SZ11-50000/110 oil-immersed power transformer (Fig.1(a)) and the whole indoor substation model(Fig.1(b)) were developed. The former was used to describe the mechanism of the overall vibration/noise generation, transmission and radiation process, then far-field characteristics and directivity characteristics were obtained by calculation to quantify and visualize the external sound field of power transformer. After that, specific design recommendations were abstracted from these visual but quantitative analysis results to optimize the substation layout in the whole indoor substation. The optimization effect was presented through the comparison. II. Numerical Calculation Method The electromagnetic-mechanical-acoustic coupling models of power transformer and indoor substation were built with COMSOL Multiphysics. Firstly, the magnetostrictive effect contains electromagnetic and mechanical process can be calculated with the core and windings model. Secondly, the vibration caused by magnetostriction was transmitted to oil tank walls through both insulation oil and clamp with padding on the oil tank bottom, eventually turned into audible noise in the air. A.Magnetostrictive Effect Calculation Inside the core, the magnetostriction component along any direction can be calculated as a nonlinear function of the magnetization using Eqs.(1) and (2)[1]: (These two equations can be seen in photo attachment1) (1) (2) B.Sound Field Calculation In a running power transformer, the speed of sound and density may in general be space dependent but only slowly varying with time. So, we can use the scalar wave equation (Eq.(3))to describe the changes of sound field induced by the vibration of the power transformer: (This equation can be seen in photo attachment1) (3) III. Results, Discussions and Conclusion A. Spatial Acoustic Radiation Characteristics Keeping the load rate was 60%, the spatial acoustic radiation characteristics of this running transformer were characterized with far-field plotting about main frequencies at different height and directivity plotting in different vertical plane were shown in Fig.2(a)-(d). Through the comparison between Fig.2 (a) and (b), Fig.2(c) and (d), following characteristics can be obtained: i. In a same horizontal plane and at a certain frequency, the sound pressure level maximum value beside two long oil tank sides is larger than the maximum value beside two short sides. ii. At the height of ventilating window center (6m), the sound pressure level at a certain frequency is greater than the same value at the corresponding angle on the height of oil tank center(1.5m). iii. In the vertical planes above the oil tank, the coverage of low frequencies noise is larger than the coverage of higher frequencies while the sound pressure level of higher frequencies noise are greater than the corresponding values of low frequencies noise. So, specific design recommendations could be abstracted as follows: i. The transformer rooms, especially the room walls beside two long sides of oil tank, should be separated from the noise sensitive area with other rooms. ii. Compared with to the shutters near the bottom of transformer rooms, the ventilating windows at the 6m height should even more avoid facing towards the noise sensitive area. iii. Part of sound absorbing material applied to the inner walls' bottom as the original design should be attached to the roof to damp the more noteworthy noise especially the higher frequencies noise and reduce the corresponding reflection. B. Layout Optimization Effect and Discussion Based on the suggestions above, the location of transformer rooms, the direction of ventilating windows and installation position of part sound absorbing material were adjusted and optimized. The comparison diagrams were shown in Fig.3 and Fig.4. By contrast, after optimization, on the premise that the sound pressure levels in the non-sensitive area still meets the standard, the sound pressure level of every main frequency at the boundaries of sensitive area were about 4dB less than before and all less than 40dB, this means the noise radiation level of whole indoor substation meets the environmental standard [2] without increasing the building materials cost, and the new substation will not change the original soundscape around it. C. Conclusion i. Multi-physical field coupling method is an effective way to explore the power transformer magnetostriction noise generation mechanism and radiation characteristics. ii. The sound pressure level distribution in horizontal plane is asymmetric and from the region beside two short sides of tank, to the region beside two long sides then to the region above tank, corresponding maximum value of sound increases gradually. iii. Reducing the noise radiation level of new indoor substation may not increase the construction cost on the premise of rational optimized design.

[1] S. Chikazumi, Physics of Ferromagnetism. 2nd ed. Oxford University Press, New York, 2009. [2] GB12348-2008, Emission standard for industrial enterprise noise at boundary[S]

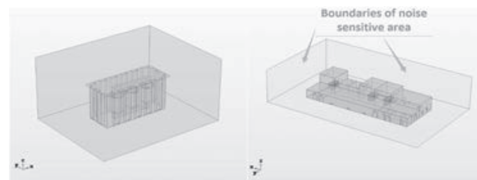

(a)Power transformer model (b) Indoor substation model

Fig. 1. 3D multi-physics coupling models of power transformer and indoor substation.

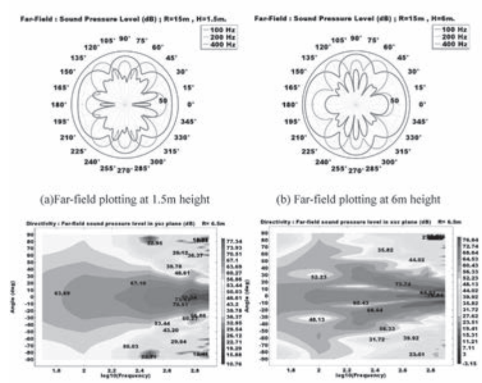

(a)Far-field plotting at 1.5m height (b) Far-field plotting at 6m height

(c)Directivity plotting in *yoz* plane (d) Directivity plotting in *xoz* plane

Fig.2 Far-field plotting and directivity plotting.

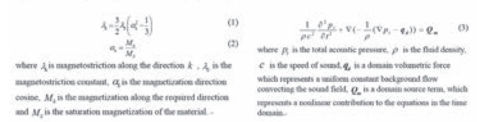

Eqs.(1) and (2) Eq.(3)

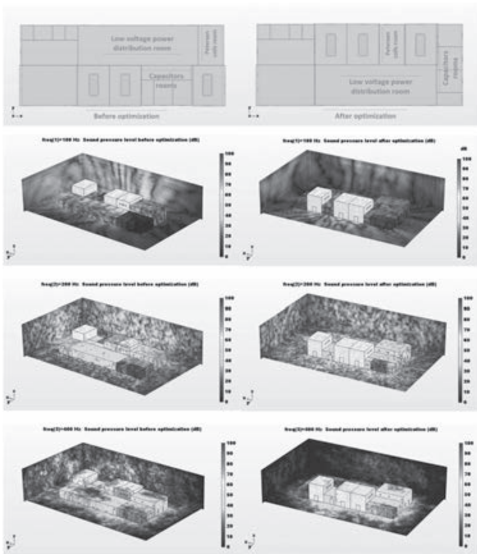

(a)Before optimization (b)After optimization

Fig.3 Substation layout and sound pressure level before and after optimization.

2:30

HI-03. 3D Magnetic Properties Measurement of Silicon Steel under Biased Magnetic Excitation along Laminated Direction.

C. Zhang[1], B. Jiang[1], Y. Li[1] and Q. Yang[2]
1. Hebei University of Technology, Tianjin, China; 2. Tianjin polytechnic University, Tianjin, China

I.Introduction Silicon steels are widely applied in the magnetic cores design, such as power transformer, electrical machine, and electromagnet. Magnetic properties of silicon steel are key factors in design and performance optimization of the electrical apparatus. In the past several decades, magnetic properties testing methods under 1-D and 2-D magnetization have been proposed for single sheet silicon steel specimen [1]. For grained oriented (GO) and non-grained oriented (NGO) silicon steel, rotational magnetization loss was measured and qualitative analyzed. However, their testing and analyzing scopes were focused in one direction or in one plane [2]. While in application, the silicon steels are made into laminated structure, which may cause magnetic interaction between the vicinity layers. Magnetic properties along the perpendicular rolling direction and effects of the laminated layers might be ignored in traditional testing approach. In this condition, big error may occur in material modeling and the calculation of core loss. Also, rotational magnetic fields existed in cores of rotating AC machines and T-joints of three-phase transformers, which cause rotational core losses may amount to more than 50% of total core loss [4, 5]. Therefore, 3-D magnetic properties of the laminated silicon steel in the complex rotating magnetization conditions should be taken into account. II.Novel 3-D magnetic testing system (A).3-D magnetization structure and its sensing system The improved 3-D magnetization structure consists of three orthogonal C-Shaped cores, 6 multilayer excitation windings, which were wounded around the six orthogonal magnetic poles. In order to reduce the gap influence, six thin pieces with the same material and same laminated direction around the cubic specimen were fabricated to improve significantly uniformity of the magnetic field at the specimen surface. (B). Automated measurement procedure Because the magnetic measurement system is nonlinear, the digital feedback for magnetic measuremnt has the advantage to make sure the standard excitation magnetic field. The controlling of 3-D magnetic property measurement is performed in LabView environment. The output excitation signal is controlled by PID controller, which feedback is the EMF of B_x and B_y. The saving procedure is delayed for 1 sec to make sure that the magnetization process is settled down. Even if the difference between magnetic strength under between CW and CCW rotation is only 1%, the averaged value will amplify the difference and give totally wrong losses. The automated program makes sure that the flux density difference between CW and CCW rotation is not larger than 0.3% so that the core loss is caculated correctly. III.Experimental Measurement and Discussion By using the 3-D magnetic property tester, experiments of high grain oriented silicon steel have been carried out under alternating and rotating in sheet plane and laminated direction magnetization conditions. Measurement Setup The magnetic pole in *z* axis of 3D magnetic properties apparatus is excited by a DC current source, and the *x* or *y* axis magnetic pole is excited by a power amplifier. The lamination direction of silicon steel is hard to be magnetized. Because of skin effect of magnetic field, the dynamic magnetic field only at low frequency (< 0.1 Hz) can go through the laminated direction of silicon steel uniformly. In order to measure the 3-D magnetic properties of the laminated silicon steels, the novel excitation model is designed, in which the alternating magnetic field in sheet plane and static magnetic field in lamination direction are summed in the vector space. When the applied current in *z* axis is swiftly transferred from zero to the specified one, the magnetic flux density in *z* axis can be calculated by the flux meter which EMF of *z* coil is measured by the solenoid method. (B) Measurement and Discussion Fig. 2 shows that the larger static magnetic field excited in laminated direction of silicon steel, the more difficult the rolling and transverse direction are magnetized. Furthermore, the saturation magnetic flux density is lower and its alternating core loss is increased, when the static magnetic field is applied in laminated direction. IV. Conclusion Improved 3D magnetic property measurement system for laminated material with AC and DC excitation was developed. In this paper, the DC and AC magnetic excitation in different direction was simultaneously excited on the laminated silicon steel sheet. In conclusion, the core losses of rolling direction were significantly increasing when the static magnetic field was excited along the laminated direction.

[1] Y. G. Guo, J. G. Zhu, J. J. Zhong, H. Y. Lu, and J. X. Jin, "Measurement and modeling of rotational core losses of soft magnetic materials used in electrical machines: A review," *IEEE Trans. Magn.*, vol. 44, no. 2, pp. 279–291, Feb. 2008. [2] E. Cardelli, and A. Faba, "A benchmark problem of Vector magnetic hysteresis for numerical models," *IEEE Trans. Magn.*, vol. 50, no. 2, pp. 7026004, Feb. 2014. [3] S. Zurek, "Qualitative analysis of Px and Py components of rotational power loss," *IEEE Trans. Magn.*, vol. 50, no. 4, pp.6300914, Apr. 2014. [4] H. Pfutzner, E. Mulsasalihovic, H. Yamaguchi, D. Sabic, G. Shilyashki, and F. Hofbauer, "Rotational Magnetization in Transformer Cores – A review," *IEEE Trans. Magn.*, vol. 47, no. 11, pp. 4523–4533, Feb. 2008. [5] A. J. Moses, "Importance of rotational losses in rotating machines and transformers," *J. Mater. Eng. Perform.*, vol. 1, no. 2, pp. 235–244, Mar. 1992. [6] Z. W. Lin and J. G. Zhu, "Three-dimensional magnetic properties of soft magnetic composite materials," *J. Magn. Magn. Mater.*, vol. 312, pp. 158-163, 2007.

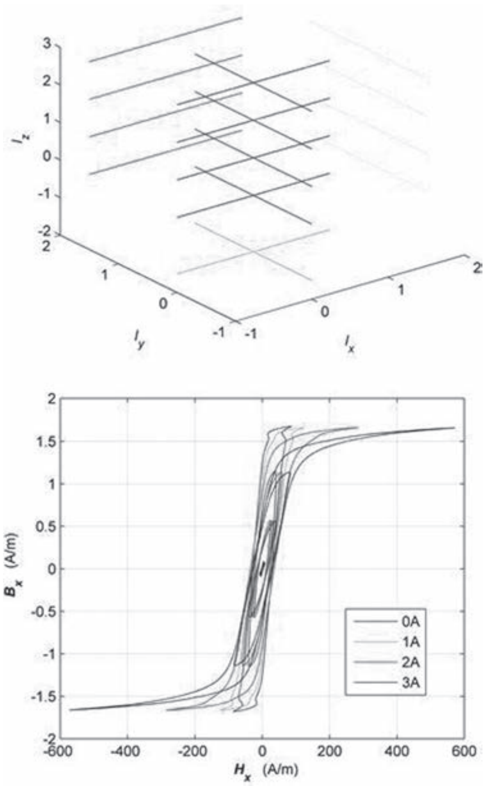

Fig. 1. (a) The AC-DC coupled excitation model. (b)Family of Hysteresis loop of grained oriented silicon steel in *x* axis under the biased magnetic field along lamination Direction

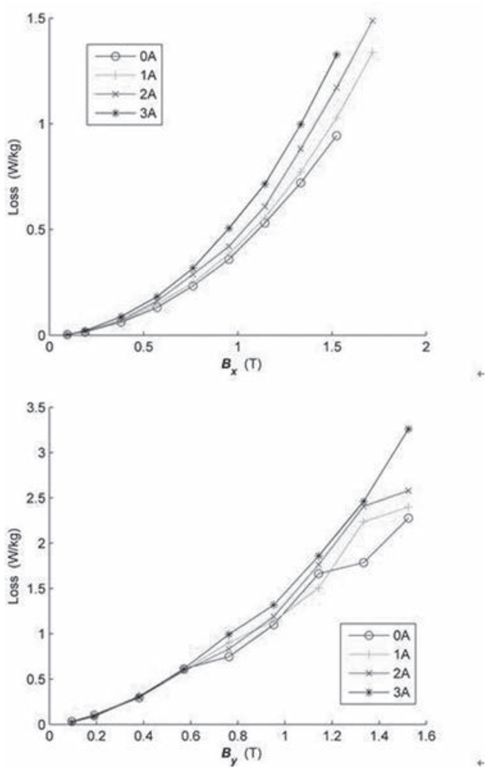

Fig. 2. Core loss under the combined excitation. (a) The core loss of rolling direction under biased excitation. (b) The core loss of transverse direction under biased excitation.

2:45

HI-04. Numerical Modeling of Magnetic Characteristics of Ferrite Core Taking Account of Both Eddy Current and Displacement Current.

M.K. Ghosh[1], Y. Gao[1], H. Dozono[1], K. Muramatsu[1], W. Guan[2], J. Yuan[2], C. Tian[2] and B. Chen[2]
1. Dept. of Electrical & Electronic Engineering, Saga University, SAGACITY, Japan; 2. School of Electrical Engineering, Wuhan University, Wuhan, China

1. Introduction Ferrite cores are widely used in transformers and inductors, etc. for high frequency electronic devices because of high magnetic permeability and low conductivity. In the magnetic field analyses of such magnetic devices using a ferrite core, the frequency-domain analysis is often carried out using measured effective complex permeability under different frequencies. However, the harmonics caused by the magnetic nonlinearity of the ferrite core cannot be evaluated by using the frequency-domain analysis. To carry out the time-domain analysis of ferrite core taking account of the nonlinearity of the core, the modeling method of the effective complex permeability characteristics, which decreases in high frequency region due to dimensional resonance, should be established. In this paper, a simple finite element magnetic field analysis model taking account of eddy current and displacement current is proposed. The suitable conductivity and permittivity which can realize the effective complex permeability is investigated by using the catalogue data of a toroidal MnZn ferrite core. 2. Analysis Model and Method In this paper, our investigation is carried out using the data in the catalogue [2] of a toroidal MnZn ferrite core (TDK/EPCOS: T37). In [2], the real part μ_s' and imaginary part μ_s'' of complex relative permeability with different frequency, measured using the toroidal core (outer radius: 16 mm, inner radius: 9.6 mm, height: 6.3mm), and its conductivity σ = 5 S/m are shown. The frequency characteristics of the complex permeability in the catalogue are tried to be represented by using the magnetic field analysis. The ac linear steady state axisymmetric magnetic field analysis taking account of eddy current and displacement current is carried out using the *A* method (*A*: magnetic vector potential) with the first order square edge finite element method and the phasor method. The fundamental equation is shown as follows: $\mathrm{rot}(v\,\mathrm{rot}\dot{A})=-j\omega\sigma\dot{A}+\omega^2\varepsilon\dot{A}$ where v is reluctivity and ω is angular frequency. The superscript (.) denotes the complex variable. The first term in the right-hand side is the eddy current and the second term is the displacement current. The permeability μ_{so} of ferrite core is set to be 6100 by referring μ_s' at 10 kHz because μ_s'', which is generated by hysteresis phenomena and eddy current effect, is relatively small and it can be neglected at 10 kHz. The original conductivity σ_o is set to be 5 S/m following the catalogue [2]. The original relative permittivity ε_{so} is set to be 300 which is a typical value of MnZn ferrite core. The conductivity σ and relative permittivity ε_s are adjusted to realize the frequency characteristic of the effective complex permeability. 3. Results and Discussion First, the frequency characteristics of the complex effective permeability μ_s' and μ_s'' calculated using the original conductivity σ_o and relative permittivity ε_{so} are compared with those in catalogue data. The tendencies of the calculated permeability are similar with the catalogue data. Namely, both the real and calculated μ_s' do not change in lower frequency region and they decrease in higher frequency region. Moreover, both the real and calculated μ_s'' increase in lower frequency region and they decrease in higher frequency region. However, the peak positions are shifted and the gradients are different with each other. Therefore, to realize the real frequency characteristics, the conductivity and relative permittivity should be changed. The frequency characteristics of the complex effective permeability μ_s' and μ_s'' calculated using the modified conductivity $\sigma = 4\sigma_o$ and permittivity ε_s = 400 ε_{so} are compared with those in catalogue data. The calculated complex permeability has relatively large error in the low frequency region. However, the frequency characteristics of the complex permeability in catalogue data can be represented roughly overall by changing both the conductivity and permittivity. As basic investigation, only linear ac steady state magnetic field analysis of a simple model is carried out in this paper. However, the time domain analysis taking account of nonlinear magnetic characteristics for more actual model can be carried out using the suitable conductivity (i.e. $\sigma = 4\sigma_o$) and permittivity (i.e. ε_s = 400 ε_{so}) obtained from the simple method proposed in this paper.

[1] F. G. Brockman, et al., Phys. Rev., vol. 77, pp. 85-93, 1950. [2] https://en.tdk.eu/ferrites

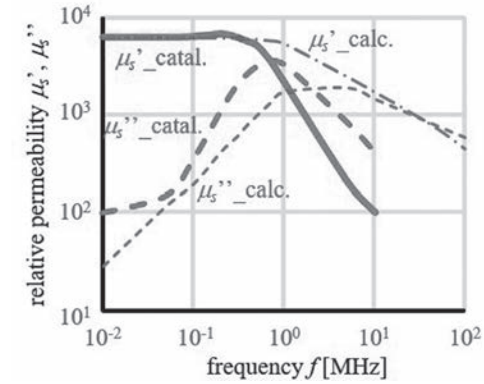

Fig. 1. Complex relative permeability with original material constants ($\sigma = \sigma_o$, $\varepsilon_s = \varepsilon_{so}$).

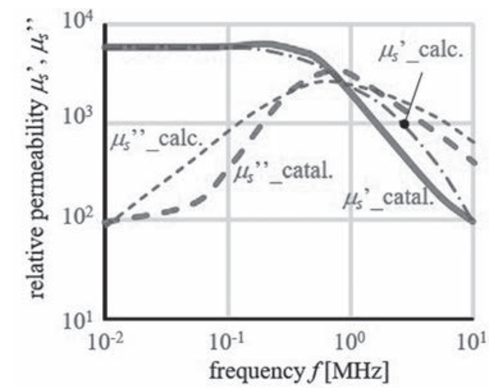

Fig. 2. Complex relative permeability with modified material constants ($\sigma = 4\sigma_o$, ε_s = 400 ε_{so}).

3:00

HI-05. Rapid Design of Litz Wire Through Inverse Surrogate Modeling.

H. Chen[1,2], Y. Du[2] and Q. Cheng[1]
1. Department of Electrical and Electronic Engineering, Southern University of Science and Technology, Shenzhen, China; 2. Department of Building Service Engineering, The Hong Kong Polytechnic University, Hong Kong, Hong Kong

Abstract — The practical litz wire design needs either experimental characterization or 3D numerical simulation. Both of these methods are time and cost consuming. In order to improve efficiency, this paper presents an inverse surrogate process to design the litz wire for a given frequency range. The method builds a fast inverse surrogate between frequencies and design parameters. The surrogate is built from existing designs or simulations. Once the inverse surrogate is established, the optimum design at a given frequency can be obtained immediately. The obtained design is then refined using a frequency correction process to fix frequency misalignment. The method is applied to a five-strand litz wire optimization problem to demonstrate its efficiency. *Index Terms— litz wire; inverse surrogate*. I. Introduction Litz wire uses complex twisting configurations to balance currents between strands. It has been widely used for enabling low-resistance in windings and power electronics. However, applying litz wire effectively is not an easy task. Inappropriate selection of litz wire may lead to higher resistance than a simple solid wire. In practical design, experimental tests are always adopted. The experimental characterization procedures require intricate test equipment, as well as many litz wire samples to be manufactured. It is obviously time and cost consuming. Design using 3D numerical simulations was also proposed [1]. However, simulating such a complex structure repeatedly in an optimization routine can be very computationally expensive. In order to design the litz wire efficiently, we apply an inverse surrogate technique [2] to derive the design parameters of litz wire for a given frequency. The method builds the inverse surrogate of the litz wire based on the existing test results or simulations at sampled designs. Then, the optimum design at a desired frequency is obtained by the inverse surrogate. II.Inverse Surrogate Modelling Let $x \subseteq R^n$ be a vector of design parameters of a litz wire of interest, and let $R_f(x)$ be the response (here, resistance at a specific frequency) of the high-fidelity EM simulation or experimental characterization test. It is assumed that the structure is designed for a certain operating frequency f_0 so that given performance specifications are met for this frequency. The task is to find the optimum design to a different operating frequency f without using an optimization routine. We use the notation to denote the optimum design at the operating frequency f. It should be emphasized that litz wire design is far from trivial because of nonlinear relations between design parameters and frequencies. From a practical point of view, it would be desirable to realize the design at a possibly low cost. In this work, an inverse surrogate is employed to design a litz wire. The inverse surrogate $x_c(f)$ is defined as $x_c(f,P) = [x_{c.1}(f,p_1), ..., x_{c.n}(f,p_n)]^T$ where $x_{c.k}(f, p_k)$ is the kth design parameter of the litz wire with p_k being the coefficients. The matrix $P = [p_1, \ldots, p_n]$ is the aggregation of coefficient vectors for the entire surrogate. The inverse surrogate is obtained as follows. 1) For each sampled frequency, f_j, $j = 1, \ldots N$, find the optimum design $x_{c.j} = [x_{c.j.1} \ldots x_{c.j.n}]^T$ using an optimization routine. 2) For each design parameter x_k, $k = 1, \ldots, n$, find the inverse surrogate coefficients by solving nonlinear regression problems as follows p_k = arg min $\Sigma\ (x_{c.k}(f_j,p)-x_{c.j.k}\ )^2$ Once the inverse surrogate is obtained, $x_c(f)$ returns the values of design parameters for the litz wire at a given operating frequency f. The actual operating frequency of the design $x_f(f)$ may be slightly different from f of $x_c(f)$ and is equal to $f+\Delta f$. Δf is a frequency misalignment result from an inverse surrogate. Therefore, a correction should be accounted by the following relation as $x_f(f) \leftarrow x_c(\mathrm{f}\text{-}\Delta f,P)$ The final design is then corrected by evaluating the surrogate at the operating frequency f. III.Numerical simulation Results The proposed method is employed to design a wire with five strands as shown in Fig. 1. The diameter of the wire is 10 mm. The number of strand is set to 5, and the length of the wire segment to 20 cm. The design parameter helical pitch is optimized to find a litz wire with minimum resistance at a given frequency. The inverse surrogate is constructed using five training designs as shown in Fig. 2. The optimum helical pitch at 1 MHz is xx twists/cm. Acknowledgment The work was supported by grants from the RGC of HKSAR, No. 152038/15E and, NSF of China No. 61471258.

[1] R. Y. Zhang, J. K. White, J. G. Kassakian, and C. R. Sullivan, "Realistic litz wire characterization using fast numerical simulations," in *Applied Power Electronics Conference and Exposition (APEC), 2014 Twenty-Ninth Annual IEEE*, 2014, pp. 738-745: IEEE. [2] S. Koziel and A. Bekasiewicz, "Expedited Geometry Scaling of Compact Microwave Passives by Means of Inverse Surrogate Modeling," *IEEE Transactions on Microwave Theory and Techniques,* vol. 63, no. 12, pp. 4019-4026, 2015.

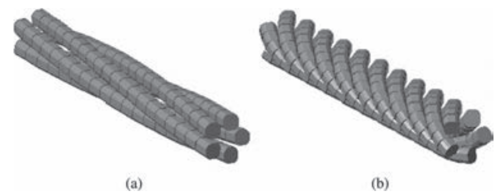

Fig. 1. Five strands of magnetic wire twisted into: (a) 2 twists/cm; (b) 10 twists/cm.

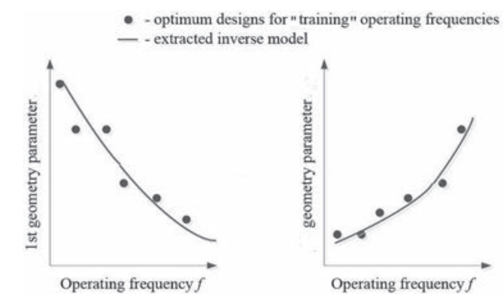

Fig. 2. Extracted inversse surrogare model and the traning data.

3:15

HI-06. The Effect of Different Core Materials on Transformer Inrush Currents.

W. Sima[1], *Y. Liu*[1], M. Yang[1] and D. Peng[1]
1. State Key Laboratory of Power Transmission Equipment & System Security and New Technology, Chongqing University, Chongqing, China

The inrush current phenomenon is one of the most common low-frequency transients, which occurs due to the core saturation of transformers. Large inrush currents could impair the transformer lifetime, the grid power quality, and the grid protection devices. There are four major factors that affect the transformer inrush current: a) the remanence in the transformer core; b) the applied voltage waveform to the transformer terminal; c) the source impedance and the transformer leakage impedance; d) the magnetizing inductance. The core materials with different magnetizing characteristics have an impact on the magnetizing inductance of the transformer, and then affect the inrush current. Several materials are used to make transformer cores including oriented silicon steels, non-oriented silicon steels, amorphous alloys, nanocrystalline alloys. Particularly, amorphous alloys and nanocrystalline alloys are increasingly used in power distribution transformers due to their excellent low-loss performances. However, their potential harm (e.g. the inrush current) to the power grid is not fully studied during the low-frequency transients of the transformer. Therefore, it is essential to research the transient characteristics of these types of transformers including the inrush current. An accurate transformer model is crucial to study the inrush current performance of transformers. The generally accepted model for a two-winding transformer is the T equivalent circuit (T model). It has been used successfully for many years in steady-state studies and some low-frequency transients. However, when the core suffered saturated and deep saturated, the π equivalent circuit (π model) is better. The reason is that the parameters of the π model have a direct relationship with the physical components of the transformer. Therefore, the π model is used in this study. Four single-phase toroidal transformers with different core materials are built to study the effect of the core materials on the inrush current performance of transformers. Core materials of these transformers are the oriented silicon steel, non-oriented silicon steel, amorphous alloy and nanocrystalline alloy, respectively. A circuit is established for inrush current tests including an ac voltage source, a zero-crossing switch, and the transformer. The maximum inrush current (no remanence) is excited when the zero-crossing switch is switched on (voltage is zero). To make the results comparable, all these transformers are demagnetized by gradually reducing the applied voltage from the rated voltage to zero before tests to remove their remanences. Experiments are conducted to excite the core using a zero-crossing switch and to obtain the maximum inrush currents. Results show that: a) for the oriented silicon steel and non-oriented silicon steel transformers, first peaks of inrush currents are as high as 10-20 times of the rated currents; b)for the amorphous alloy and nanocrystalline alloy transformers, the values are dozens of times of their rated currents. It shows that the core materials have significant influence on the inrush current performance of transformers. The conventional T and π models share a disadvantage that the data of the flux-current curves are rarely known much beyond the knee. To further explain the reason of the different inrush current peaks influenced by the core materials, an improved π model considering the deep saturation is proposed based on the conventional π model by modifying the flux-current curves of its magnetizing branches. Its circuit is same as the conventional π model, and parameters in the non-saturated region are acquired by open- and short-circuit tests. Based on the principle that the transformer core is excited into deep saturation by a dc source, an ac coupling signal is used to measure the data of the magnetization curve in the saturation region, and then the entire magnetization curve is obtained. A method to distribute the data of the curve to two magnetizing branches of the π improved model is presented. The non-linear behavior of magnetizing inductances is described precisely, then the improved π model for single-phase transformers considering deep saturation is established. The inrush current performances of four transformers are investigated by simulation on the ATP/EMTP platform. A zero-crossing switch is used and the remanence of the transformer is set to zero. Results show that: a)the error of the improved π model is less than 5%, which proves the accuracy of the model; b) same as the conclusions obtained by the experiments, the amorphous alloy and nanocrystalline alloy transformer generate higher inrush currents than those of the non-oriented silicon steel and oriented silicon steel transformer. The reason is that the flux-current curves of magnetizing branches have more flat saturation regions for the first two transformers. The effect of different core materials on transformer inrush current is investigated though the ways of experiments and simulations in the paper. It concludes that there are significant differences for inrush currents of transformers with different core materials, and the reasons are discussed in detail.

[1] S. Jazebi, F. de León, A. Farazmand, and D. Deswal, "Dual reversible transformer model for the calculation of low-frequency transients", *IEEE Trans. Power Del.*, vol. 28, no. 4, pp. 2509–2517, Oct 2013. [2] H. W. Dommel, S. Bhattacharya, V. Brandwajn, H. K. Lauw, and L. Martí, *Electromagnetic transients program reference manual (EMTP Theory Book)*. Portland, OR: Bonneville Power, 1992.

3:30

HI-07. A Novel High-Q-value Inductor with Vacant Space for a High-frequency Non-isolated DC-DC Converter.

Y. Konno[1], T. Yamamoto[1], Y. Chai[1], S. Kawahara[1], T. Kenta[1], Y. Bu[1] and T. Mizuno[1]
1. Department Electric and Electronic Engineering, Shinshu University, Nagano, Japan

I. INTRODUCTION Recently, demand for a highly efficient miniature non-isolated DC-DC converter has increased, driven by demand for use in the power-supply circuits [1]. To miniaturize the non-isolated DC-DC converter, the use of high driving frequencies is an effective means of downsizing passive elements such as capacitors or inductors [2]. The demand for downsized inductors has particularly increased because the inductor has a big ratio among the volumes of circuit [3]. However, the loss of inductors increases along with driving frequencies. Thus, we considered means of reducing copper loss in inductors by applying a vacant space. In this paper, we considered the structure of the most suitable vacant space and evaluated an inductor. II. STRUCTURE OF AN INDUCTOR AND ANALYTICAL RESULTS The inductance of the inductor is 60 nH when subjected to conditions of specific 5 MHz, 5 V to 1.2 V, and 20 A output current in a non-isolated DC-DC converter. Fig.1 shows the structure of the analytical model of the inductor; Fig.1 (a) shows the inductor without vacant space while Fig.1 (b) shows it with vacant space. The inductor has N = 1 turns and the two copper plates connected in parallel. The characteristics of core used has a complex permeability of μ' = 9.4,μ'' = 0.02, as measured for the toroidally formed magnetic composite material using an impedance analyzer (Agilent 4294A+16454A). This core was made by the mixing amorphous alloy powder; its mean diameter is D_{50} = 2.6 mm and epoxy and the mixing ratio of the magnetic composite material is 57vol%. Magnetic-field analysis is conducted using the finite-element method in a cylindrical coordinate system (ANSYS Maxwell). As shown in Figs.1(a) and (b), the maximum current densities of the copper plate is decreased from 170 to 82 A/mm^2 to provide the vacant space. Thus, the current density is concentrated at the corner and the surface of the copper plate because of the magnetic flux caused by the copper-plate interlink itself, as shown in Fig.1(a). Providing a vacant space, however, reduces the magnetic flux interlinking the copper plate, as shown in Fig.1(b). Fig.2 shows that the Q value changed with the size of the vacant space. As shown in Fig.2(a), the Q value became largest when the vacant space had dimensions of dl = 0.1 mm,dt = 0.75 mm. However, the inductance is 57 nH when the vacant-space size is dl = 0.1 mm,dt = 0.75 mm and does not reached 60 nH. Thus, we found the most suitable vacant-space size to be dl = 0.1 mm,dt = 0.5 mm with an inductance of 64 nH. The Q values of the inductor without a vacancy and with a vacancy were found to be 265 and 318, respectively; therefore, the Q value of the inductor with vacant space increased by 26% compared with the no-vacancy case. As shown in Fig.2(b), the resistances of the inductor without a vacant space and with the most suitable vacant space were 8.83 and 6.31 mΩ, respectively; therefore, the resistance of the inductor with vacant space decreased by 28.5% compared with that without the vacancy; and the resistance-reduction ratio of 28.5% is consistent with a 19.3% reduction due to the copper loss and a 9.2% reduction due to the iron loss. Calculation of the resistance-reduction ratios showed that that due to the copper loss was more significant than that due to the iron loss. III. FABLICATION AND MEASUREMENT RESULTS OF AN INDUCTOR We fabricated two inductors, one with a vacant space size is dl = 0.1 mm, dt = 0.5 mm and one without a vacant space. The core of the inductor of size 20 × 20 × 10 mm and rectangular parallelepiped form was fabricated and its size is different analysis model as shown Fig.1. As shown Fig.2, an impedance analyzer (Agilent 4294A) was used to measure the inductor; it was found that the Q values of the inductor without a vacancy and with a vacancy were 102 and 139, respectively; therefore, the Q value of the inductor with vacant space increased by 36% compared with that without the vacancy. IV. EFFICIENCY OF NON-ISOLATED DC-DC CONVERTER APPLIED THE INDUCTOR We examined to apply the inductor to non-isolated DC-DC converter. The EPC9031(Efficient Power Conversion) is used for GaN FET and driver circuit. The drive condition assumed the switching frequency is 5 MHz, 5 V to 1.2 V. The efficiency of the DC-DC converter applied the inductor without vacant and with vacant were 77.6% and 78.4% at 20 A, respectively; therefore, the efficiency of inductor with vacant space is increased by 0.8% compared with that of the without vacant. And the maximum efficiency of inductor with vacant space is 85.0% at 5 A. V. CONCLUSION We considered a technique to increase the Q value of an inductor used in a non-isolated DC-DC converter by providing a vacant space. As result of magnetic-field analysis, the Q value of the inductor was increased by 26% compared with that without a vacant space in the case when this space was slightly smaller than the width of a copper plate. The measured Q value of the inductor without a vacancy is increased by 36% compared to the case without a vacancy. And the efficiency of the DC-DC converter applied the inductor with vacant space is increased by 0.8% at 20 A output current compared with that of the without vacant. The above results show the usefulness of decreasing copper loss to provide a vacant space.

[1] K. K. Leong, G. Deboy, K. Krischan, A. Muetze, "A single stage 54V to 1.8V multi-phase cascaded buck voltage regulator module", *Applied Power Electronics Conference and Exposition (APEC)*, *2015 IEEE*, pp. 1966-1973, 15-19 March 2015. [2] D. Huang, D. Gilham, W. Feng, P. Kong, D. Fu, F. C. Lee, "High Power Density High Efficiency DC/DC Converter", *Energy Conversion Congress and Exposition (ECCE)*, *2011 IEEE*, pp. 1392-1399, 17-22 Sept. 2011 [3] Y. Su, Q. Li, M. Mu, F. C. Lee, "High frequency inductor design and comparison for high efficiency high density POLs with GaN device", *Energy Conversion Congress and Exposition (ECCE)*, *2011 IEEE*, pp. 2146-2152, 17-22 Sept. 2011

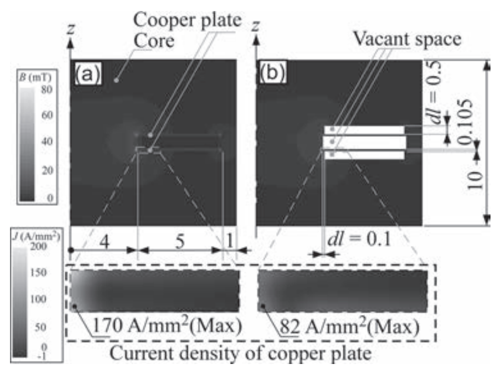

Fig. 1. Structure of an inductor and the distribution of magnetic-flux density and current density: (a) with vacant space; (b) without vacant space.

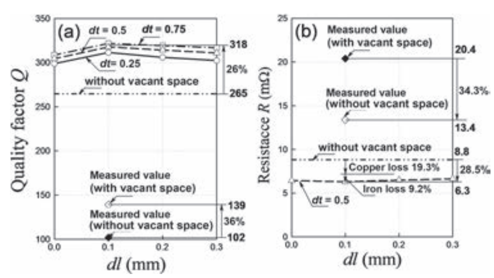

Fig. 2. Comparison measured and analysis of characteristics of an inductor vs. the size of a vacant space: (a) Q value; (b) Resistance.

3:45

HI-08. Vibration and Acoustic Noise Emitted by Three-phase Iron-core Reactors under PWM Voltage Excitation.

J. Li[1], H. Gao[2,1], S. Wang[1], J. Hong[1] and M. Liu[2,1]
1. State Key Laboratory of Control and Simulation of Power System and Generation Equipments, Tsinghua University, Beijing, China; 2. State Key Laboratory of Reliability and Intelligence of Electrical Equipment, Hebei University of Technology, Tianjin, China

Abstract Body: The demand for dry-type air-core reactors (DARs) is growing due to the increasing use of power electronics in transmission and distribution grids and the implications of dispersed energy generation. For DARs used in power electronic grid such as High Voltage Direct Current (HVDC) and Flexible Alternating Current Transmission Systems (FACTS), the contents of harmonic currents are significant. The injection of high frequency harmonic current will significantly strengthen the vibration and acoustic noise pollution of DARs, and threaten safety and reliability of power transmission and distribution system. Therefore, it is necessary to investigate in depth the vibration and noise of the DARs supplied by power electronic transformation and output systems, and then proposes targeted measures to reduce the vibration and acoustic noise. According to coupling way between the magnetic field and the structural order, structure mode is discussed by engaging finite element (FE) method and both natural frequency and modal shape for a dry-type air-core reactor (DAR) are obtained in this paper. On the basis of harmonic response analysis, electromagnetic force under PWM (Pulse Width Modulation) voltage excitation is mapped with the structure mesh, the vibration spectrum is gained and the consequences represents that the whole structure vibration predominates in the radial direction, with less axial vibration. Referring to the test standard of reactor noise, the rules of emitted noise of the DAR are measured and analyzed at chosen switching frequency matches the sample resonant frequency and the methods of active vibration and noise reduction are put forward. Finally, the low acoustic noise emission of a prototype DAR is verified by measurement. 1. A modal analysis is first performed to determine the structural vibration characteristics, including natural frequency, modal analysis and damping ratio, during the magnetic field-structure coupling calculation of the DAR. The parameters of modal analysis can provide basis for vibration analysis, structural optimization and fault diagnosis of structural design. The motion equation in structural dynamics is [1]: $[M]\{d''\}+[D]\{d'\}+[S]\{d\} = [F]$ (1) where, $[M]$ is the mass matrix; $[D]$ is the damping matrix; $[S]$ is the mechanical stiffness matrix; $\{F\}$ is the force vector; $\{d''\}$ is the acceleration vector; $\{d'\}$ is the velocity vector; $\{d\}$ is the displacement vector. 2. Due to the structural free vibration is simple harmonic vibration, $\{d\} = \{\o\}\sin\omega t$ can be represented the displacement function, which is further known that $\{d''\} = -\omega^2\{\o\}\sin\omega t$, ω is the angular frequency. Next, $([S]-\omega^2[M]\{\o\} = \{0\}$ (2) Eq. (2) is the characteristic equation of free vibration of the DAR structure, and the purpose of modal analysis is to solve the eigenvalues ω_j and the corresponding eigenvectors $\{\o_j\}$ of the characteristic equation. The eigenvalues ω_j are the natural circle frequency, and the natural frequencies $f_j = \omega_j/2\pi$. Here, the eigenvectors $\{\o_j\}$ are the modal shapes of the j-order modal in structural dynamic analysis. 3. Due to complex structure of DAR, the calculation model needs to be simplified to reduce the difficulty in the modal analysis and the electromagnetic force calculation. The magnetic-solid coupling vibration calculation model is established by adopting ANSYS finite element (FE) software and considering windings, upper and lower spiders, duct sticks and insulation parts. 4. Based on the full method [2], structural vibration of the DAR is analyzed by sweep frequency analysis, and the frequency range is [6 Hz, 600 Hz], which covers the former 1000th modes in the modal analysis. For given natural frequencies at different modal orders, the whole structure displacement deformation of the DAR under electromagnetic harmonic response is calculated, as shown in Fig. 1. In the DAR acoustic noise experimental measurements, a high-precision voice sensor made in American PCB Piezotronics, Inc. (378B02), is adopted [3]. In noise spectrum analysis of the DAR, the SIEMENS LMS vibration and noise test system is used as the noise spectrum measurement device. The SPL and spectrum of DAR acoustic noise are obtained by using vibration and acoustic noise measurement devices system at given PWM voltage excitation (the modulation frequency f_a=50 Hz, the modulation index m_a=0.5, the switching frequency f_s=600 Hz and peak flux density B_p=1.5 T), as shown in Fig. 2. Conclusion: The vibration and acoustic noise of a DAR are analyzed and investigated by means of numerical calculation and experimental measurements in this paper. On the basis of the coupling of the magnetic field and the structure order, the mode, electromagnetic force and structural vibration of the DAR are simulated by FE method, and the emitted noise level is measured. The results show that the vibration displacement is small and about 10^{-4} m in the natural frequency, the vibration of the DAR is mostly radial displacement, and the axial vibration is smaller. In experimental measurements of the acoustic noise, the noise radiation of the DAR structure is dominated by 20 Hz sound pressure, followed by the sound pressures of 120 Hz and 360 Hz, and is given priority to with low frequency sound pressure. This research is helpful for the design and application of low-noise and high-performance reactors.

[1] M. Rossi and J. L. Besnerais. Vibration reduction of inductors under magnetostrictive and Maxwell forces excitation[J]. *IEEE Transactions on Magnetics,* 2015, vol. 51, no. 12, p. 8403406. [2] G. H. He. *Analysis of Electromagnetic Vibration and Noise of Permanent-magnet Direct Current Commutator Motors*[D]. Ph.D. thesis, Shanghai Jiao Tong University, Shanghai, 2012. [3] See http://www.pcb.com/products.aspx?s=378B02

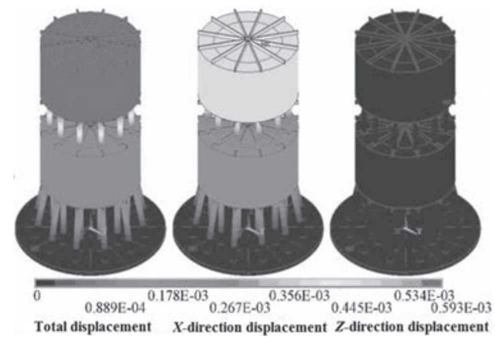

Fig. 1. The whole structure displacement deformation of the DAR at given natural frequencies for different modal orders.

Fig. 2. Noise spectrums of test points at a distance of 3 m, under given PWM voltage excitation.

4:00

HI-09. A Novel Structure Design of Iron Core for Power Transformers Considering Joints Forms and Magnetostriction.

J. Li[1], S. Wang[1], H. Gao[2,1], M. Liu[2,1] and J. Hong[1]
1. State Key Laboratory of Control and Simulation of Power System and Generation Equipments, Tsinghua University, Beijing, China; 2. State Key Laboratory of Reliability and Intelligence of Electrical Equipment, Hebei University of Technology, Tianjin, China

Abstract Body: Power transformers and reactors are important devices in power transmission systems. But their cores and windings could produce vibration and acoustic noise by magnetostrictive effect, Maxwell electromagnetic stress and Lorentz force. Noise has become a bad environmental pollution source in some situations, and its vibration and noise reduction has become an urgent problem need to be solved. The shapes, materials, magnetostriction and joints forms of iron cores, the limitations of test, modeling, and experimental measurement of vibration and noise characteristic, are all the difficult reasons to analyze the vibration and acoustic noise of transformers and reactors. 1. The magnetostrictive modeling can be divided into two steps based on the magnetic field force and materials deformation, so the magnetic field force will be fed into the structural finite element with Maxwell electromagnetic force produced on the interface between the iron core and the air to calculate the deformation of the magnetic materials and to make the model more general and consistent. In order to fully verify the correctness of the model in the magnetostrictive analysis, and to ensure the simplicity of test and avoid unnecessary interference factors, the most simple magnetostriction tests will be carried out by using a single closed circle or rectangular electrical steel sheet, as shown in Fig. 1(a). The tests will measure the relationship between magnetostriction and magnetic field of different magnetic materials, different saturations, different sizes and different shapes. 2. The joint is a necessary form for the stacking of large transformer iron cores, and the main joint form is the step jiont at present. The introduction of the joints causes the magnetic force lines to flow through the different laminations and to make the local magnetic field complicated. From simple to complex process is adopted in this paper, and the verification is gradually complicated. Based on the study of a simple sheet with no joint showed in Fig. 1(a)and (e), a sheet with joint will be used to analyze the vibration and modeling calculation, as shown in Fig. 1(b). Maxwell electromagnetic force caused by the the joints and magnetostrictive force due to the magnetostriction of sheet are all actually included in the model. Later, further complicated two or more pieces of sheets are designed up and down on the joint of the simple circle or rectangular sheet, as shown in Fig. 1(c) and (d) to simulate the joints forms in the iron cores of transformers with the magnetic flux transition circulation though the joints. Meanwhile, the separation of the Maxwell electromagnetic force and the magnetostrictive force from the overall analysis can be worked out by using mathematical method, and the separated curve will be given in the end. 3. In order to improve the effect of vibration and acoustic noise deduction sharply, a novel structure design of iron core for power transformer is put forward, with the core and winding position interchange, compared to conventional power transformers, as shown in Fig. 2. Compared with traditional transformers, this structure has many advantages: firstly, the short magnetic circuit reduces the deformation caused by magnetostriction; secondly, the circular ring core does not have joints to avoid the vibration and acoustic noise caused by the joints; thirdly, the radial deformation of circular ring is greatly reduced; the last, the long cantilever structure that causes deformation in the traditional iron core can be eliminated. These advantages together will realize the new low vibration and low acoustic noise transformers. 4. The test prototype of power transformer with laminated core is processed in different stacking modes. The vibration acceleration and displacement of power transformer iron core are measured with high precision laser acceleration sensors, and the modal test is carried out by using Finite Element (FE) software. Based on the comparison between simulation and test data, the effect of vibration and noise reduction is analyzed and established to verify the novel iron core structure design of the power transformers, and to give further reference and guidance to the engineering applications.

[1] Y. H. Chang, C. H. Hsu, H. L. Chu, *et al*. Magnetomechanical vibration of three-phase three-leg transformer with different amorphous-core structures[J]. *IEEE Transactions on Magnetics,* 2011, 47(10): 2780-2783. [2] Y. H. Gao, K. Muramatsu, M. J. Hatim, *et al*. Design of a reactor driven by inverter power supply to reduce the noise considering electromagnetism and magnetostriction[J]. *IEEE Transactions on Magnetics,* 2010, 46(6): 2179-2182. [3] Y. L. Zhang, Q. Li, D. H. Zhang, *et al*. Magnetostriction of silicon steel sheets under different magnetization conditions[J]. *IEEE Transactions on Magnetics,* 2016, 52(3): 6100204. [4] J. S. Li, Q. X. Yang, Y. J. Li, *et al*. Measurement and modeling of 3-D rotating anomalous loss considering harmonics and skin effect of soft magnetic materials[J]. *IEEE Transactions on Magnetics,* 2017, 53(6): 6100404. [5] S. G. Ghalamestani, T. Hilgert, L. Vandevelde, *et al*. Magnetostriction measurement by using dual heterodyne laser interferometers[J]. *IEEE Transactions on Magnetics,* 2010, 46(2): 505-508.

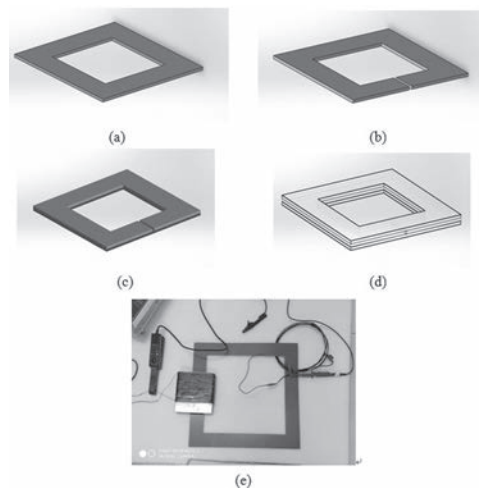

Fig. 1. Test verification models for magnetostriction and joints forms experiments.

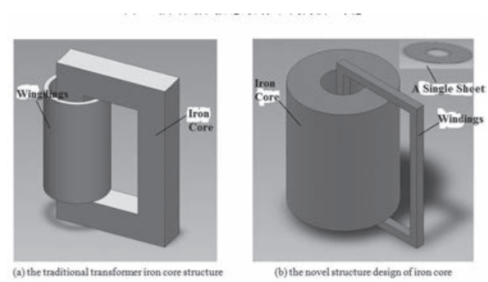

Fig. 2. Comparisons of iron core structure designs between the traditional and the novel power transformers.

4:15

HI-10. Comprehensive Analysis and Control of Maximum Power and Maximum Efficiency for Multiple-Objective Wireless Charging Systems.

Z. Zhang[1], R. Tong[1], W. Ai[1], S. Chang[1] and J. Wang[1]
1. School of Electrical and Information Engineering, Tianjin University, Tianjin, China

INTRODUCTION Recently, wireless power transfer (WPT) is getting increasing attentions, for it is able to provide a brand new method for power transmission. The limitations of traditional cable charging method such as tangled and inconvenient power cords, and a limited number of charging interface are well overcome. As for the WPT system, one of the major concern is the power transmission efficiency and the transmitted power influenced by various transmission distance and the variety of loads. Especially in multi-receiver condition, there existing variety of loads with different requirements. Based on the impedance alteration method [1], a comprehensive analysis regarding to the relationship among the equivalent load, output power and efficiency in multi-receiver system is conducted, and a novel load alteration strategy aiming at better satisfying different requirements in different load consistence is proposed based on the aforementioned analysis. PROPOSED LOAD ALTERATION ANALYSIS AND CONTROL STRATEGY The block diagram and experiment prototype is depicted in Fig. 1 (a) and Fig. 1 (b). The equivalent load witch is in series with inner resistance in primary circuit is related to the load, operating frequency, mutual inductance and the paralleled capacitance. Due to the inner resistance of power supply, the maximum output power can be reached while the equivalent load equals the inner resistance. However, the output efficiency of power supply is only 50% for the inner resistance consumes the other half part of total power. On the other hand, the efficiency increases as the load gets larger, and the output power decreases simultaneously on contrary. The relation between equivalent load and paralleled capacitance is delineated in Fig. 1 (c). Furthermore, the varieties of requirements and the type of load causing different cases to deal with. For instance, when the priority of efficiency is higher than that of output power. In order to reach high efficiency, the equivalent load should be large enough to get a large portion of power. In contrary, when the priority of power is higher than that of efficiency. So as to get the maximum output power, the equivalent load should be altered to equal the inner resistance. In other occasions, the equivalent load is designed to be altered for better balance of power and efficiency for different requirements. Based on the above analysis, a novel control strategy is carried out in terms of the priority of transmitted power and transfer efficiency. The assortment of different load is depicted in Fig. 1 (d). CASE STUDY AND SIMULATION To validate the proposed control strategy, a simulation is done in MATLAB-Simulink. According to the assortment of loads, there are totally 4 cases witch match the 4 cases of loads consistence. Load of every secondary circuit is set to 50Ω and inner resistance is set to 1Ω. The paralleled capacitance and the resonance capacitance are adjusted by capacitor array. Case1: high power and high emergency: When there is a majority of loads that demand large power urgently, the equivalent load is alter to equal the inner resistance. As shown in Fig. 2 (a), voltage of both loads and inner resistance reach the maximum value 17.1V and 2.41V, and the power of load is equal to that of inner resistance. Case2: high power and low emergency: The equivalent load can be altered larger to for higher efficiency in the case that the majority of load demands large power but not urgently. As shown in Fig. 2 (b). voltage of both loads and inner resistance get lower with respect to case1, namely 14.8V and 1.5V. Power of loads is greater than that of inner resistance. Case3: low power and high emergency: In this case, the equivalent load can be altered larger as long as the power demand is satisfied. As shown in Fig. 2 (c), voltage of both loads and inner resistance decreased to 5.1V and 1.02V, Meanwhile the proportion of load power increases. Case4: low power and low emergency: When the loads mainly consist with load that demands less power with less urgency, equivalent load is altered to its maximum value. As shown in Fig. 2 (d), voltage of both load and inner resistance reach the lowest point 0.47V and 9.9×10^{-4}V, the power proportion of load gets the maximum value 99.9%. CONCLUSION By comprehensively analyzing the relationship among equivalent load, output power and transfer efficiency, this paper proposed a load alteration strategy to alter equivalent load in accordance with various requirements in multi-receiver WPT system. The simulation results are in well agreement with the theoretical designs and analysis, which verify the feasibility and correctness of the proposed strategy and furtherly proves that the proposed control strategy can effectively satisfy power and efficiency requests under different conditions of loads. Therefore, the proposed alteration strategy poses a huge difference in multi-receiver WPT systems. Besides, the detailed parameters, theoretical analysis, simulated results, and experimental waveforms will be presented in the full manuscript.

Yongseok Lim, *Member*, *IEEE*, Hoyoung Tang, *Student Member*, *IEEE*, Seungok Lim, and Jongsun Park, *Senior Member IEEE*, "An adaptive impedance-matching network based on a novel capacitor matrix for wireless power transfer," *IEEE Trans. Power Electron.*, vol. 29, no. 8, pp.4403-4413, Aug. 2014.

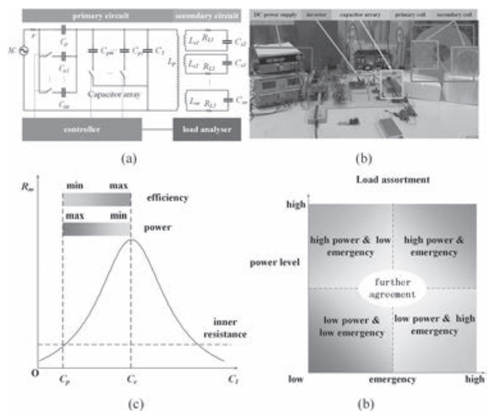

Fig. 1. (a) block diagram. (b) experiment prototype. (c) relationship. (d) load assortment

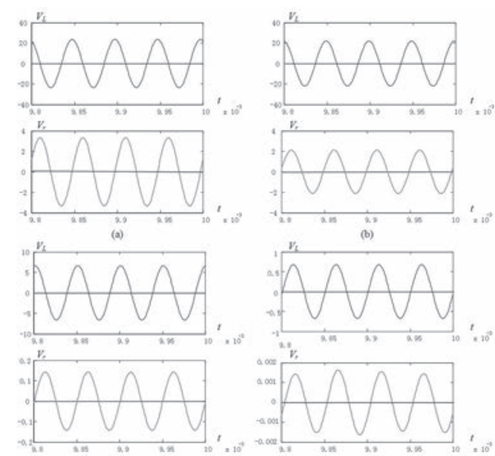

Fig. 2. simulation results in different loads condition

4:30

HI-11. Analysis of High Frequency Effects of Excitation Winding in High Frequency Rotating Tester with Nanocrystalline material.

Y. Li[1], A. Li[1], *C. Zhang*[1] and Q. Yang[1]
1. State Key Laboratory of EFEAR, Hebei University of Technology, Tianjin, China

Abstract—In this paper, a segmented winding with copper foil was designed in order to reduce the influence of high frequency and distribution capacitance in excitation winding. By analyzing the skin effect in excitation winding, an equivalent model for the AC resistance of the foil winding is established, which determined the optimum thickness of copper foil under different excitation frequency. The method of installing annular ferromagnetic plate to restrain the proximity effect is proposed, which increases the frequency of the excitation to 20 kHz. I. Introduction In multi-phase power transformers and rotating electrical machines, the rotating magnetic flux may cause the increase of core losses, leading to local overheating and damage of the equipment. Nevertheless, the traditional measurement method of magnetic properties for nanocrystalline is ring specimen method, which is still far from accurately describe high frequency rotating magnetic properties of nanocrystalline in engineering practice. The main difficult to test the magnetic properties for nanocrystalline at high-frequency is that the core losses of magnetic circuit increase acutely with the increasing frequency and the influence of high frequency effects. [1] [2] In this paper, a segmented excitation winding with copper foil was designed, which can reduce the influence of high frequency and distribution capacitance. With the segmented copper wingding, the establishment of the high frequency rotating magnetic become more easily. II. Design of the segmented copper winding *A. Analysis of the distribution capacitance* The 2D magnetic tester with foil winding has several advantages. However, the distributed capacitance in foil winding has increased compared with copper wire windings. Different connection ways between the winding layers lead to different potential, and then form the different equivalent capacitance [3]. Fig. 1 depicts the simplified mathematical models of single segmented winding and multi-segmented winding. The analytic expression of equivalent distribution capacitance of single segmented winding is: $C_{single}=(n-1)C_1/n^2=(n-1)\varepsilon\ S/n^2d$ the distribution capacitance of segmented winding is analytical calculated is: $C_{multi}=(n-1)C_1/n^2q^2=(n-1)\varepsilon\ S/n^2dq^2$ where ε is the dielectric constant of the winding interlayer insulation medium; *S* is the average area of the winding, d is the winding layer spacing, and C_1 is the static capacitance of the two layer winding with an equivalent area of *S*. it can be seen that the distribution capacitance of the copper foil winding can be effectively reduced by increasing the number of winding layers and the number of segments. *B. Analysis of the high frequency effects* With the increase of frequency, the influence on the current distribution in copper foil produced by the magnetic field is more and more apparent. Mathematical model of magnetic field intensity of copper foil winding is shown in Fig.2. (a). Combined the Bessel equation of internal magnetic field strength *H* and the boundary conditions, the approximate relation between the AC resistance and the DC resistance under the influence of skin effect and proximity effect can been obtained. Then the relation between the number of winding layers and the thickness of wire is shown in Fig. 2 (b), from which can obtain the optimum thickness of winding under arbitrary frequency. The proximity effect is caused by leakage at the end of copper foil winding. Therefore, how to control the leakage magnetic field distribution along the axial direction of the winding and reduce the radial component of the leakage flux at the end of winding is the key to restrain the proximity effect. In this paper, the method of installing annular ferromagnetic plate at the end of segmented copper foil winding and between two segments winding to restrain the proximity effect is proposed. The comparison of the current distribution in segmented winding with and without the annular ferromagnetic plate is shown in Fig. 2 (c), in which the black portion is the ferromagnetic material. It can be seen that the radial component of the leakage magnetic field is effectively controlled when the annular ferromagnetic plate is arranged, and the current distribution in the copper foil winding is more uniform. In conclusion, a segmented winding with copper foil is designed based on the excitation structure as shown in Fig2. (d). III. Conclusion This paper presents a segmented winding with copper foil, which can reduce the influence of high frequency and distribution capacitance. An equivalent model for the AC resistance of the foil winding is established, which determined the optimum thickness of copper foil under different excitation frequency by analyzing the skin effect in excitation winding. The method of installing annular ferromagnetic plate to restrain the proximity effect is proposed, which plays a key role in the establishment of high frequency rotating magnetic field.

[1] M. Birkfeld and K.A. Hempel, "A device for measuring the magnetic properties of ring specimens at high frequencies," *J. Magn. Magn. Mater,* vol. 133, pp.393-395, 1994. [2] T. Nakata, N. Takahashi, K. Fujiwara, and M. Nakano, "Measurement of Magnetic Characteristics along Arbitrary Directions of Grain-oriented Silicon Steel up to High Flux Densities," *IEEE Trans. Magn.*, vol. 29, no. 6, pp. 3544-3546, 1993. [3] F. Blache, J.-P. Keradec, and B. Cogitore, "Stray capacitances of two winding transformers: equivalent circuit, measurements, calculation and lowering," in *Proc. IEEE Ind. Appl. Soc. Annu. Meeting*, Oct. 2–6, 1994, vol. 2, pp. 1211–1217.

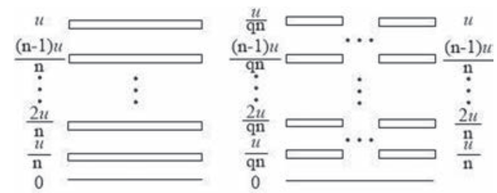

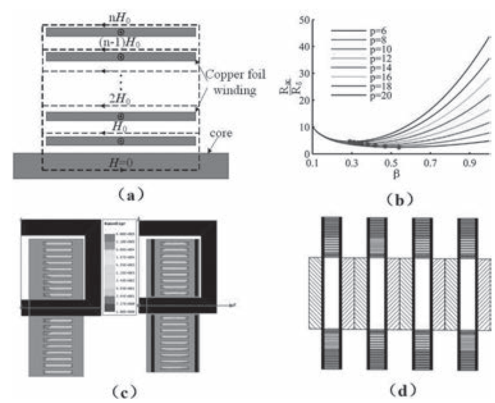

Session HP
AB-INTIO CALCULATIONS
(Poster Session)

Arti Kashyap, Co-Chair
IIT Mandi, Mandi, India
Jia Zhang, Co-Chair
Huazhong University of Science and Technology, Wuhan, China

HP-01. Possible Origin of Ferromagnetism in Undoped Magnesium Oxide Film.

M. Wang[1,2], D. Hou[1], S. Tang[2], J. Ren[3], Y. Li[4], T. Zhou[5] and Y. Han[6]
1. College of Physics and Information Engineering, Hebei Normal University, Shijiazhuang, China; 2. School of Information Science and Engineering, Hebei University of Science and Technology, Shijiazhuang, China; 3. College of Science, Hebei University of Science and Technology, Shijiazhuang, China; 4. School of Materials Science and Engineering, Hebei University of Technology, Tianjin, China; 5. College of Electronic Information and Optical Engineering, Nankai University, Tianjin, China; 6. Department of Construction Engineering, Hebei Vocational College of Politics and Law, Shijiazhuang, China

"d^0 ferromagnetism" challenged our conventional understanding on the origin of magnetism, and triggered a heated debate [1-3]. In order to explore the magnetism in magnesium oxide (MgO) without doping [4], we have studied the electronic structure and magnetic properties of pristine MgO (001) surface using first principle calculations. The perfect MgO (001) surface is a nonmagnetic insulator with a band gap of about 3.6 eV in our calculations, see Fig.1 (a). The calculated results reveal that isolated oxygen (O) vacancy (V_O) can not introduce the local magnetic moment in the system, see Fig.1 (c). While isolated magnesium (Mg) vacancy (V_{Mg}) can produce a magnetic moment of about 1.67 μ_B. The magnetic moment mainly results from *p*-orbitals of oxygen atoms adjacent to the V_{Mg}, see Fig. 1 (b) and (d). The 3*s* electrons of Mg and the 2*p* electrons of O form molecular orbitals (MO), and when the neutral Mg atom is taken from the surface, it will introduce two holes in the MO. The holes will be arranged spin-parallel in the orbital because of Hund's coupling rules and the on-site Coulomb repulsion energy U_{pp} between the holes. And the spin-down panel is crossing the Fermi level, showing that the structure with one V_{Mg} will have half-metallic properties. We also calculated three types of antiferromagnetic (AFM) state of the surface with one V_{Mg}. The results show that the ferromagnetic state is most stable. In the supercell, the studies of magnetic coupling show that the two V_{Mg}'s on the surface are not always coupled ferromagnetically at different distances. And the system will be in a spin singlet state (S = 0) when the distance is 2.98 or 8.42 Å between two V_{Mg}'s, while the two V_{Mg}'s are coupled ferromagnetically at the distance of 4.21, 5.96, or 6.66 Å, see Fig. 2. As the distance between two V_{Mg}'s increases, the system will change from semiconductor state to half-metallic state, and finally to metal state. In summary, we can conclude that V_{Mg} may introduce the magnetism in MgO (001) surface. Our results are significant for d^0 ferromagnetism of MgO.

[1] M. Wang, M. Feng, X. Zuo. First principles study of the electronic structure and magnetism of oxygen-deficient anatase TiO_2 (001) surface. Appl. Surf. Sci., 292 (2014) 475-479 [2] M. Wang, M. Feng. *Ab initio* study on magnetism at $TiO_2/SrTiO_3$ interface. Comput. Mater. Sci., 86 (2014) 43-48 [3] M. Wang, M. Feng, Y. Lu. Possible origin of ferromagnetism in undoped monoclinic HfO_2 film. Comput. Mater. Sci., 92 (2014) 120-126 [4] C. Moyses Araujo, M. Kapilashrami, X. Jun, *et al*. Room temperature ferromagnetism in pristine MgO thin films. Appl. Phys. Lett., 96 (2010) 232505

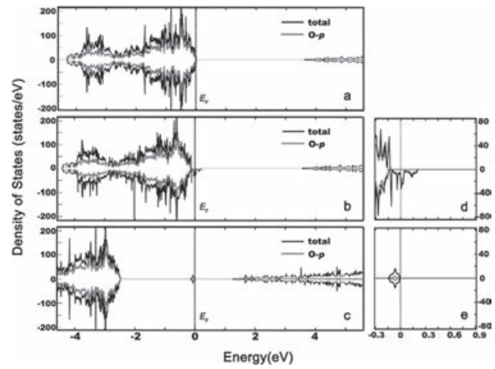

Fig. 1. Calculated densities of states of: (a) perfect MgO (001) surface, (b) MgO (001) surface with one V_{Mg}, (c) MgO (001) surface with one V_O, (d) and (e) are partial enlarged details for (b) and (c), respectively.

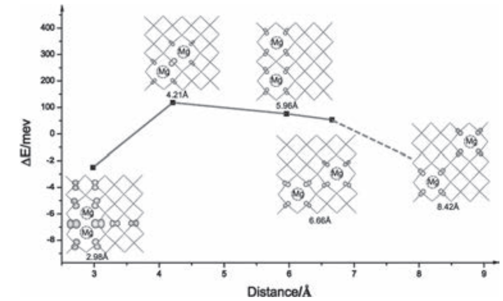

Fig. 2. Energy differences between ferromagnetic (FM) and antiferromagnetic (AFM) alignment states $\Delta E = E_{AFM} - E_{FM}$ in MgO (001) surface with two V_{Mg}'s. The spin density maps at different distances between V_{Mg}'s were also shown. The yellow represents the spin up; the blue represents the spin down.

HP-02. About softening of phonon modes in Heusler alloys.

V. Buchelnikov[1,2], O. Miroshkina[1,3] and A. Zayak[4]

1. Condensed Matter Physics, Chelyabinsk State University, Chelyabinsk, Russian Federation; 2. National University of Science and Technology "MIS&S", Moscow, Russian Federation; 3. Institute of Radioengineering and Electronics of RAS, Moscow, Russian Federation; 4. Department of Physics & Astronomy, Bowling Green State University, Bowling Green, OH, United States

It is well known that Heusler alloys have a number of the unique properties such as shape memory effect, effects of superelasticity and superplasticity, giant magnetocaloric effect, giant magnetoresistance and magnetostrain, etc. Above properties are associated with martensitic transformations [1-5]. In recent years, much attention has been given to precursor effects where acoustic anomalies, phonon dispersion curves, and diffuse elastic scattering in the parent phase indicate the eventual martensitic structure [6-8]. Experimentally, the phonon dispersion curves can be measured by the means of neutron scattering [9]. Beams of neutrons scattered by matter turn out to have very suitable properties for phonon experiments. It is known from experimental studies that the softening of the mode occurs in the [110] direction. This mode is believed to be responsible for the premartensitic transition: as long as there are imaginary (negative) values of the TA_2 mode frequency, there is a premartensitic transition in this region. According to the results of the theoretical investigation presented in Ref. [10], TA_2 phonon immediately softens starting from q=0. However, the experimental data [9, 11] show that instability of TA_2 phonon takes place in the narrow range of wave-vectors. Previous theoretical investigations give a rather vague picture. According to them, there is a very wide range of instabilities. Thus, it would be interesting to speculate on the way of clarifying the region of instabilities. In this regard, we consider the effect of supercell elongation and chemical disorder on the phonon spectra of Ni_2MnGa and Ni_2MnAl Heusler alloys. Our assumption is that elongation of supercell will lead to the reduction of the range of instabilities. In the furtherance of this goal, Vienna *ab initio* simulation package (VASP) and PHONON software were used [12-15]. With the help of VASP minimizing the total energy of the crystal with respect to the electronic part, lattice constants and atomic positions and calculation of the Hellmann-Feynman forces were carried out. Then using obtained results the phonon dispersion curves were calculated with the help of PHONON. We considered several types of supercell elongations: they are $1\times n\times 1$, where n=4, 5, 6, 7 and 8. The supercell was created by merging n primitive cells along the $[110]_c$ direction of the cubic Heusler structure, which is the $[010]_t$ direction of the tetragonal cell. The phonon-dispersion curves in the $[110]_c$ direction calculated for the Ni_2MnAl compound are presented in Fig. 1. Authors of paper [16] considered the similar type of elongation, and their results are in agreements with ours and the experimental [17]. However, we disagree with authors in their statement, that theory does not predict softening. It predicts but in other types of supercell elongation. As already mentioned, we assumed, that elongation of supercell will lead to the reduction of the range of instabilities. However, our assumption was confirmed only partially. It is seen, that region of instabilities is really narrowing, but at the same time, instability at Γ-point arises. We can conclude that in the case of too long cells (elongation $1\times 7\times 1$ and $1\times 8\times 1$) considerable noise appears in the calculation of forces. They kill the small forces that act at big distances in the supercell. Thus, the mostly optimal elongations are $1\times 5\times 1$ and $1\times 6\times 1$. The phonon-dispersion curves in the $[110]_c$ direction calculated for Ni_2MnGa compound are presented in Fig. 2. It is seen from this figure that transverse acoustic mode TA_2 gets completely softened going well down to negative frequencies in all cases. The results presented in [8] show that instability begins with 0. However, our calculations demonstrate that only wave distortions in a certain wavelength range will be unstable. The experiment does not predict complete softening of the phonon. We tried to explain this by assuming that this may be due to the influence of native disorder. Investigation of the effect of the disorder was conducted using 40 atoms supercell (elongation of supercell $1\times 5\times 1$). The stoichiometric composition with introduced various degrees of site disorder, quantified by the number of random atom-pairs switches (from 1 to 10 pairs), was considered. The TA_2 mode frequency was calculated for ordered and all case of disordered structures. This analysis was done by the same procedure of considering a particular phonon as a harmonic oscillator. The phonon was picked at the wave vector [0.33, 0.33, 0.00], which corresponds to the imaginary frequency of this mode. The TA_2 mode frequency in studying system demonstrates the tendency to "hardening" in case of the disordered structure. Thus, the experimentally studied real samples may be disordered. In this work, we have demonstrated that the supercell elongation influence on the softening of the TA_2 phonon modes of Ni_2MnGa and Ni_2MnAl Heusler alloys. The optimal elongations of supercells are $1\times 5\times 1$ and $1\times 6\times 1$. The investigation showed that the hardening of the unstable phonon is directly correlated with the level of introduced disorder of Ni_2MnGa alloy. Based on our results, the experimentally studied real samples of Ni_2MnGa may be disordered.

[1] A.D. Bozhko, et al., JETP Letters, 67, 227 (1998) [2] P. Entel, et al., J. Phys. D: Appl. Phys. 39, 865 (2006) [3] V.D. Buchelnikov, et al., Phys.-Usp., 49, 871-877 (2006) [4] P. Entel, et al., Mat. Sci. Forum, 635, 3 (2010) [5] P.J. Webster, et al., Philos. Mag. B, 49, 295 (1984) [6] S.B. Dugdale, Physica Scripta, 91, 053009 (2016) [7]Y. Lee, et al., Phys. Rev. B, 66, 054424 (2002) [8] C. Bungaro, et al., Phys. Rev. B, 68, 134104 (2003) [9] A. Zheludev, et al., Phys. Rev. B, 54, 15 045 (1996) [10] C. Bungaro, et al., Phys. Rev. B, 68, 134104 (2003) [11] A. Zheludev, et al., J. Phys. IV, 5, C8-1139 (1995) [12] G. Kresse, et al., Phys. Rev. B, 54, 11169 (1996) [13] G. Kresse, et al., Phys. Rev. B, 59, 1758 (1999) [14] K. Parlinski, et al., Phys. Rev. Lett., 78, 4063 (1997) [15] K. Parlinski, Software Phonon, Cracow (2013) [16] L. Isaeva, et al., Jpn. J. Appl. Phys., 50, 05FE07 (2011) [17] X. Moya, et al., *Phys. Rev. B*, 73, 064303 (2006)

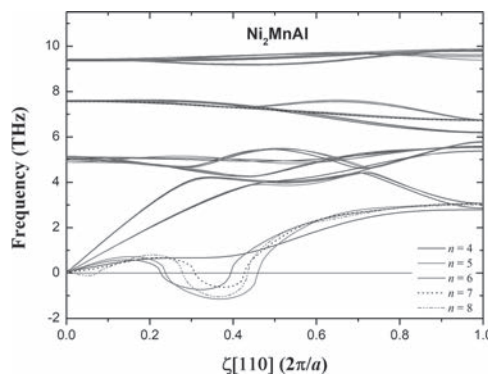

Fig. 1. The phonon-dispersion curves in the $[110]_c$ direction calculated for the Ni_2MnAl alloy for various elongation of supercell

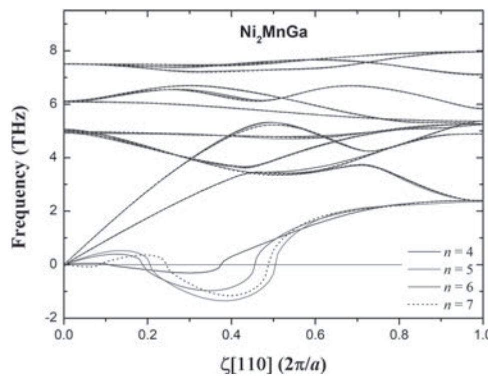

Fig. 2. The phonon-dispersion curves in the $[110]_c$ direction calculated for the Ni_2MnGa alloy for various elongation of supercell

HP-03. Investigation of magnetic and structural properties of $FeRh_{1-x}Pt_x$ (x = 0.5 - 1) alloys by first principles method.

O. Pavlukhina[1], V. Sokolovskiy[1], V. Buchelnikov[1] and M.A. Zagrebin[1]
1. Chelyabinsk State University, Chelyabinsk, Russian Federation

Fe-Rh-based alloys have attracted a lot of attention because of their possible application in magnetic cooling, thermally assisted magnetic recording and spintronic devices [1-4]. Magnetic cooling attracts the attention of scientists around the world. The magnetocaloric effect reaches the maximal value at the temperatures of magnetic or magnetostructural phase transitions. Fe-Rh alloys exhibit a metamagnetic phase transition (AFM-FM). The metamagnetic phase transition in Fe-Rh succeeds also the large change in magnetization, which is responsible for a giant magnetocaloric effect upon variation of a magnetic field. For $Fe_{49}Rh_{51}$, Nikitin et al. [5] reported for the first time the giant MCE about -13 K at magnetic field change of 2 T using a direct method of measurements. The similar values of MCE for the same composition were successfully repeated in Refs. [2, 3]. It well known, that the magnetic order in FeRh compounds depends strongly on the concentration. Therefore, it is important to study the effect of adding a third element on the magnetic and structural properties of the material. A. Jezierski et. al. [4] study the influence of dopants Co, Pd, Ru and Pl on the magnetic moment and the density of states at the Fermi energy in FeRh alloys. The article says that a significant change of the magnetic moment and the density of states at the Fermi level during the substitution metals. In our previous work we investigated $FeRh_{1-x}Pt_x$ (x = 0, 0.125, 0.25, 0.375) [6]. In this work, we present theoretical investigations of the structural and magnetic properties $FeRh_{1-x}Pt_x$ (x = 0.5, 0.625, 0.75, 0,875, 1) alloys. In this work, the structural and magnetic properties of Pt-doped Fe-Rh alloys are investigated by using the density functional theory calculations as implemented in the Vienna *Ab initio* Simulation (VASP) package. The ab initio calculations have been carried out by using the 16-atom supercell approach with different initial spin configurations. The generalized gradient approximation for the exchange correlation functional in the formulation of Perdew, Burke and Ernzerhof (PBE) was taken into calculations. The performed calculations were semirelativistic and the spin polarization was taken into account for all the cases. In the calculations the automatically generated uniform grid of k-point as in Monkhorst-Pack grids was taken into account. The k-points in the Brillouin zone for self-consistent field cycles were generated with 12^3 meshes for the lattice relaxation calculations and tetragonal distortion. The energy calculations were performed for the Pm3m supercell ($FeRh_{1-x}Pt_x$). In detail, original cell has atomic coordinates of (0; 0; 0); (1/2; 0; 0); (1/2; 1/2; 1/2) for Rh atoms and those of (1/4; 1/4; 1/4); (3/4; 3/4; 3/4) for Fe atoms in the supercell. Calculations were carried out for ferromagnetic, paramagnetic and three kinds of antiferromagnetic states. In the present work we calculated the total energies for different spin configurations as functions of the lattice parameter. The equilibrium lattice parameters a = 3.020 for $FeRh_{1-x}Pt_x$ (x = 0.5) up to 3.059 for $FeRh_{1-x}Pt_x$ (x = 1). It can be concluded that the addition of Pt atoms leads to an increase in the lattice equilibrium parameter due to the larger atomic radius of Pt compared to the lower Rh value. The calculation of the total energy for the tetragonal distortion of the cubic structure along the *z* axis is performed in this works. To accomplish this, we fixed the volume of a supercell as $V_0 = a_0^3 \approx a^2c$. In the case of $FeRh_{1-x}Pt_x$ (x=0.5, 0.625, 0.75, 0,875) the antiferromagnetic configuration solution is favorable for martensite states. For the parent FePt compound, the ferromagnetic spin configuration is energetically favorable compared to other configurations. Our calculations have shown that the substitution of Pt for Rh results in an appearance of stable body-centered tetragonal state. While the cubic phase becomes unstable. It is important to note that the similar trend is observed experimentally by Yuasa et al. [7]. This work was supported by RSF-Russian Science Foundation No. 17-72-20022\17.

1. A. X. Gray, D.W. Cooke, P. Kruger, Phys. Rev. Lett. 108, 257208 (2012) 2. M.P. Annaorazov, K.A. Asatryan, G. Myalikgulyev et al. Cryog. 32, 867 (1992) 3. A. Chirkova, K.P. Skokov, L. Schultz et al. Acta Mater. 106, 15 (2016) 4. A. Jezierski, G. Borstel. J. Magnet. Magnetic Mater.140-144, 81 (2005) 5. S.A. Nikitin, G. Myalikgulyev, A.M. Tishin, et al., Phys. Lett A. 148, 363 (1990). 6. O. Pavlukhinaa, V. Sokolovskiy, M. Zagrebin, V. Buchelnikov, J. Magnet. Magnetic Mater. (2017), in press. 7. S. Yuasa, H. Miyajima, Y. Otani, J. Phys. Soc. Jpn. 63, 3129 (1994)

HP-04. First-principles study of MnAl/MgO/MnAl magnetic tunnel junctions with perpendicular magnetic anisotropy.

X. Zhang[1], L. Tao[1], J. Zhang[2], S. Liang[1], L. Jiang[1] and *X. Han*[1]
1. State Key Lab of Magnetism, Institute of Physics, Beijing, China;
2. Huazhong University of Science and Technology, School of Physics and Wuhan National High Magnetic Field Center, Wuhan, China

MnAl, as a prospective candidate of magnetic electrode materials for MgO-based magnetic tunnel junctions, possesses several advantages including the spin polarized Δ_1 band, relatively low Gilbert damping factor, and large perpendicular magnetic anisotropy (PMA). Here, we have performed a thorough first-principles studies of magnetocrystalline anisotropy and spin-dependent quantum transport properties of MnAl/MgO/MnAl(001) -magnetic tunnel junctions (MTJs) for both Mn- and Al-terminated structures. The anisotropy energy density of bulk and interface contribution is determined and thickness dependence of PMA is estimated by considering the shape anisotropy for both terminations. It is found that the bulk anisotropy density is 17.39 Merg/cm^3, while the interfacial anisotropy contribution is evaluated to be 0.12 erg/cm^2 and 0.44 erg/cm^2 for Mn- and Al-terminated structures, respectively. The large anisotropy can be attributed to d_{yz} and dz^2 orbits. Orbital-resolved analysis indicates that the Mn-O bond in the interface is inimical to PMA and Al-terminated interfacial structure (or Al insertion) can serve as a possible solution. Therefore, the formation of a Mn-O bond on the interface of MnAl/MgO is shown to be detrimental for the improvement of perpendicular anisotropy. On the other hand, giant TMR ratios for both terminated MTJs under zero bias are predicted. A giant zero-bias tunneling magnetoresistance ratio can be maintained over 2000% even for a bias up to 0.6 V for Mn-terminated MTJs. The in-plane spin transfer torque for Mn-terminated MTJs increases linearly with a bias up to 0.6 V due to the large net spin-polarized current. Our studies give insight into the PMA and spin-dependent transport mechanism of MnAl/MgO/MnAl(001) MTJs and provide some guidelines for the design of spin-transfer torque magnetic random access memory (STT-MRAM) devices.

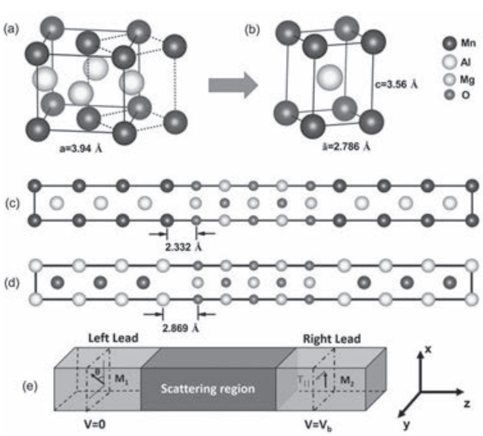

Fig. 1. (a) Crystal structure of L1$_0$ MnAl and (b) reduced tetragonal B$_2$ structure. The optimized atomic structures for (c) Mn-termination and (d) Al-termination. The transport direction is along the z-axis and the MTJ is periodic along the x- and y-directions. Interfacial distances are marked. (e) Schematic sketch of the MTJ structure for in-plane spin-transfer torque T$_\parallel$ calculation. Finite bias V$_b$ is applied on the right electrode. The magnetization direction of left electrode M$_1$ lies in the x – y plane, while that of right electrode M$_2$ points to the x-axis. θ is the angle between M$_1$ and M$_2$.

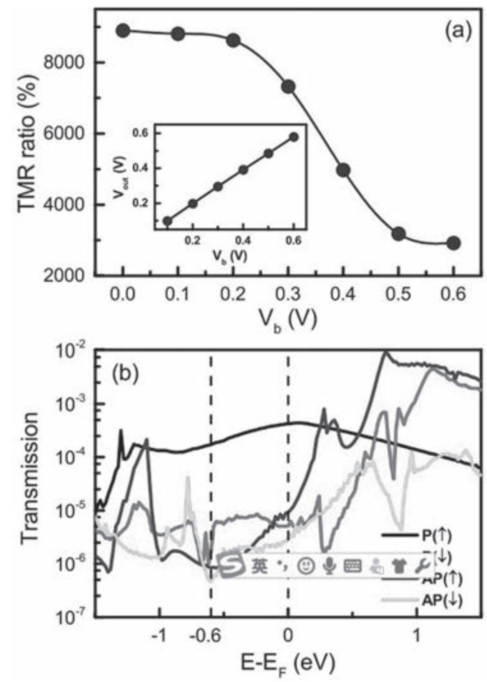

Fig. 2. (a) TMR ratio and output voltage V$_{out}$ (inset) as a function of bias. (b) Energy- and spin-resolved transmission coefficient for MTJ at V$_b$=0.6V. Two vertical dashed lines indicate the bias window for current calculation.

HP-05. Numerical Modeling of Iron Loss Considering Laminated Structure and Excess Loss.

D. Zhang[1], W. Guan[1], M. Yang[1], Y. Gao[2] and K. Muramatsu[2]
1. School of Electrical Engineering, Wuhan University, Wuhan, China;
2. Department of Electrical and Electronic Engineering, Saga University, Saga, Japan

I.INTRODUCTION To enhance the accuracy of iron loss prediction in high frequency electric machines using superconductive windings, the stacked structure of iron cores needs to be taken into account due to the high proportion of eddy current loss in the iron loss. Thus, the modeling method of the stacked structure of iron cores combining the 3D solid core analysis with the 1D steel plate analysis [1] is improved to include the excess loss in this paper. The iron loss is calculated using the flux and eddy current density obtained from the improved method of magnetic field analysis. In the analysis, the domain wall bowing due to pinning is taken into account by introducing an initial bowing flux [4]. Then, to figure out the change of the resulted iron loss by using the improved method, the method is applied to a single-phase reactor. Finally, the results by using the previous and improved methods are compared in detail. II. METHOD OF LOSS CALCULATION A.Method of Magnetic Field Analysis In the proposed model as shown in Fig. 1, the laminated structure and the eddy currents Jepar are directly considered in the 1D steel plate analysis. The parallel flux density in each element of the 3D solid core is imposed to the 1D steel plate model as boundary condition. 1) 1D Steel Plate Analysis With Domain Wall Bowing Due to Pinning The main cause of excess loss, which is considered to be the domain wall bowing [2] [3]. To take into account the wall bowing by pinning, the 1D nonlinear eddy current finite element analysis is performed applying an initial bowing flux Bp (0, Bpy, 0) distributed along the sheet thickness direction. The fundamental equation is $-\partial(\nu^*(\partial A/\partial z-B_p))/\partial z+\sigma^*\partial A/\partial t=0$ (1) where ν^* and $\sigma^*$are the real reluctivity and conductivity of the steel plate, respectively. Bp is the flux distributed along the sheet thickness in the analyzed model. 2)3D Solid Core Analysis [1] The 3D nonlinear eddy current finite element analysis is applied to calculate the electromagnetic field distribution in the solid core model. The fundamental equations are: $\mathrm{rot}(\nu\,\mathrm{rot}A)+\sigma(\partial A/\partial t+\mathrm{grad}\Phi)=J_0$ (2) $\mathrm{div}(-\sigma(\partial A/\partial t+\mathrm{grad}\Phi))=0$ (3) where A andΦ are the magnetic vector potential and the electrical scalar potential, respectively. Jo is the exciting current vector. ν is the equivalent permeability obtained as mentioned above and $\sigma$is conductivity. B. Method of Loss Density Calculation The hysteresis loss Whys is calculated using the equation as follows. $W_{hys}=K_{hys,Bmax}f$ (4) where Kh,Bmax is the hysteresis coefficients varying with the amplitude of the flux density Bmax in each element. Bmax is obtained by using the parallel and perpendicular flux densities Bpar and Bper obtained from the 1D steel plate analysis and 3D solid core analysis like (4). The eddy current losses We is calculated by using the eddy current densities Jepar and Jeper obtained from the 1D steel plate analysis and the 3D solid core analysis directly. W(ie) $e=\sum\{(\sum(|Je^{(i,j,ie)}{}_{par}+Je^{(j,ie)}{}_{per}/F|\hat{}2)*l^{(i)}/\sigma^*)/(\sum l^{(i)})\}/N_s$ (5) where Ns is the total time step, Ne is the total element number of the 1D analysis, Je is the eddy current density, F is the space factor of the steel plate,σ^* is the conductivity of the steel plate,and l is the length of each element in the 1D analysis. III. ANALYSIS OF A SIMPLE ONE-PHASE REACTOR A.Analyzed model and conditions The simple single-phase reactor constructed by stacked iron cores and coil is analyzed. The cores with gaps are stacked by non-oriented steel plates (thickness 0.35 mm, 35A440) in the z direction, and the space factor F is 0.95. The current with the amplitude of 5×105 A/m2 and frequency of 500 Hz is imposed inside the coil. B.Results The classified iron losses of the reactor with and without Bp are shown in Fig. 2. With Bp, the hysteresis loss is increased due to the increase of the total flux. The increase of total flux is due to the decrease of the magnetic intensity in the air in the 1D steel plate, which makes the equivalent permeability in the parallel direction increase according to (2). The eddy current loss generated by the parallel flux is increased due to the increase of eddy current generated by the parallel flux. The eddy current loss generated by the perpendicular flux is decreased due to the decrease of eddy current generated by the perpendicular flux. And the total iron loss shows about 8% increase finally. IV.CONCLUSIONS 3D-1D combined model of stacked iron cores is analyzed to optimize the accuracy of calculated core loss using the electromagnetic field distribution results. The increase of iron loss shows the applicability of the proposed method at present. In the future, the method will be improved considering the dependence of the Bp on the applied magnetic field and will be verified by experiments.

[1] K. Muramatsu, T. Okitsu, H. Fujitsu, and F. Shimanoe, "Method of nonlinear magnetic field analysis taking into account eddy current in laminated core," IEEE Trans. Magn., vol. 40, no. 2, pp. 896-899, 2004. [2] S. Hill and K.J. Overshott, "The dependence of power loss on domain wall bowing in single crystals of 3% grain-oriented silicon-iron," *IEEE Trans. on Magn*., vol. mag-14, no. 5, pp. 773-775, Sep. 1978. [3] G. Bertotti, Hysteresis in magnetism, Academic Press, 1998. [4] W. Guan, H. Kong, M. Jin, L. Lan, Z. Du, Y. Zhang, J. Ruan, and H. Zhang, "Analysis of excess loss in SiFe laminations considering eddy current dominated domain wall motion," *IEEE Trans. on Magn*., vol. 51, no. 3, Article #: 6300604, 2015.

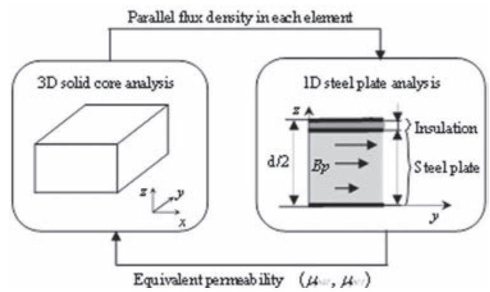

Fig. 1. Simple block diagram of the improved modeling method for the stack of iron core

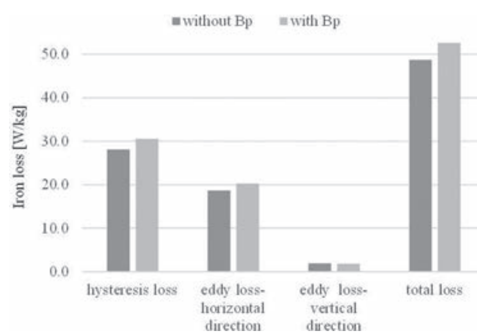

Fig. 2. Comparison of losses in detail with and without Bp

HP-06. Enhancement of perpendicular magnetic anisotropy in Co/graphene and Co/BN heterostructures by strain.

B. Yang[1,2], J. Zhang[3], L. Jiang[2], W. Chen[2], P. Tang[2], Y. Yan[1] and *X. Han*[2]
1. Key Laboratory of Physics and Technology for Advanced Batteries (Ministry of Education), Department of Physics, Jilin University, Changchun, China; 2. State Key Lab of Magnetism, Institute of Physics, Beijing, China; 3. Huazhong University of Science and Technology, School of Physics and Wuhan National High Magnetic Field Center, Wuhan, China

The perpendicular magnetic tunnel junction (p-MTJ) is the basis for spin transfer torque magnetoresistive devices that have the properties of high-density nonvolatile memory, high thermal stability, and low critical current. The common approach for generating large perpendicular magnetic anisotropy (PMA) for a free layer is to use heavy metal (HM) elements or capping with a HM multilayer. However, adding a noble metal element increases the magnetic damping constant due to its large spin-orbital coupling, and thus can be detrimental to low critical switching current. The spin-orbital coupling strength in 3d ferromagnetic metals (FM) and their oxides is usually 2~3 times smaller than that of HMs or HM multilayer materials. Therefore a light element p-MTJ that can achieve PMA is more desirable. How to enhance the PMA in light element heterojunctions is a pressing problem for the next-generation magnetic memory. Using first-principles calculations, we investigated the effect of compressive and tensile strain on the perpendicular magnetic anisotropy of light element heterostructures of Co films, Co/graphene, and Co/BN. We found that the perpendicular magnetic anisotropy of Co/graphene is greatly enhanced compared to the Co films, while that of Co/BN is reduced compared to the Co films. A compressive strain increases the distance between the interface Co atom and graphene or BN, diminishing their effect. When the interlayer distance reaches ~4 Å, the MAE of Co/Gr and Co/BN heterostructures are nearly the same as that of a Co multilayer. In addition, tensile strain can further enhance perpendicular magnetic anisotropy of Co/graphene and Co/BN heterojunctions by 48.5% and 80.8%, respectively. A density of state analysis, combined with layer and orbital magnetic anisotropy contributions obtained from a second-order perturbation theory, reveals that the tensile strain effect arises from the increase of the hybridization between same spin dxy and $dx^2–y^2$ states of the surface Co film. Our results suggest that strain engineering is an effective approach to enhance the perpendicular magnetic anisotropy of light element heterostructures.

[1] S. Ikeda, et al, Nat. Mater. 9, 721 (2010). [2] D.-S. Wang, R. Wu, and A. J. Freeman, Phys. Rev. B 48, 15886 (1993). [3] H. Yang, et al, Nano Lett. 16, 145 (2016).

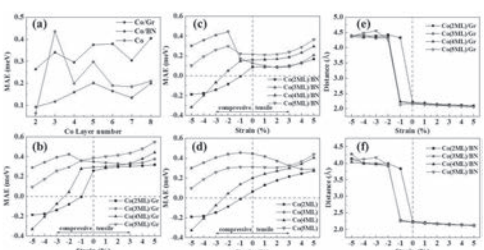

Fig. 1. (a) MAE of Co, Co/Gr and Co/BN. (b-d) MAE of Co(2–5ML)/Gr, Co(2–5ML)/BN, and Co(2–5ML) as a function of strain. (e-f) Distance between two adjacent layers in Co/Gr and Co/BN.

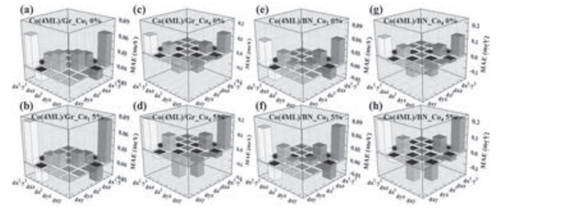

Fig. 2. *d*-orbital resolved MAE of Co_1 and Co_4 in unstrained Co(4 ML)/Gr and Co(4 ML)/BN as well as Co_1 and Co_4 in Co(4 ML)/Gr and Co(4 ML)/BN under 5% tensile strain.

HP-07. Silicene spintronics: Fe(111)/silicene system for efficient spin injection.

J. Zhou[1,2], A. Bournel[2], Y. Wang[3], X. Lin[1], Y. Zhang[1] and W. Zhao[1]
1. Beihang University, Beijing, China; 2. Université Paris-Sud, Orsay, France; 3. The University of Hong Kong, Hong Kong, China

Silicene is an emerging 2D material with advantages of the high carrier mobility, compatibility with silicon-based semiconductor industry [1], and the tunable gap by vertical electrical field due to the buckling structure [2]. In this work, we report a first-principles investigation on the spin injection system, which consists of Fe(111)/silicene stack as the spin injector and pure silicene as the spin channel. An extremely high spin injection efficiency (SIE) close to 100% is achieved. The partial density of states of Fe layers in Fe(111)/silicene stack shows that spin-down states dominate above the Fermi level, resulting in a negligible spin-up current and high SIE. The transmission spectra have been investigated to analyze the spin-resolved properties. The spin injection system based on silicene is promising for the efficient silicon-based spintronics devices such as switching transistors.

[1] J. Zhao, H. Liu, Z. Yu, R. Quhe, S. Zhou, Y. Wang, C. C. Liu, H. Zhong, N. Han, J. Lu, Y. Yao, and K. Wu, *Prog. Mater. Sci.* 83, 24(2016). [2] Z. Ni, Q. Liu, K. Tang, J. Zheng, J. Zhou, R. Qin, Z. Gao, D. Yu, and J. Lu, *Nano Lett.* 12, 113(2012).

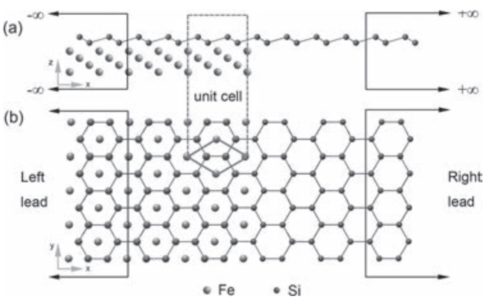

Fig. 1. Diagram of the spin injection system. Silicene monolayer is on the Fe(111) layers. The black arrows indicate the left and right leads, extending to ±∞, consist of Fe(111)/silicene stack (left lead) as the spin injector and pure silicene (right lead) as the spin transport channel. (a) The side view. (b) The top view. The red box indicates the unit cell of Fe(111)/silicene stack.

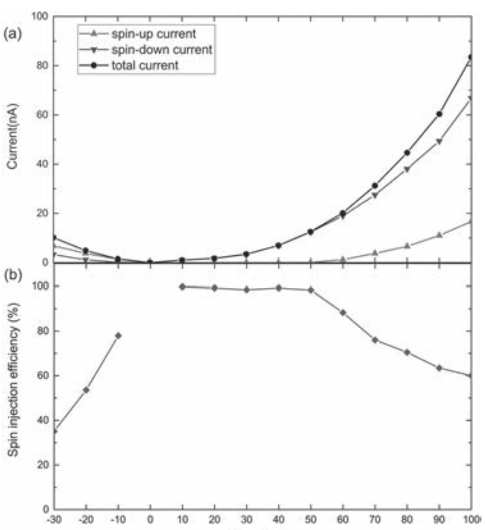

Fig. 2. Spin-resolved currents, the total current and spin injection efficiency of the whole system. (a) Spin-resolved currents and the total current. (b) Spin injection efficiency, which reaches up to nearly 100% between 10 mV and 50 mV bias.

HP-08. First-principles investigation of magnetocrystalline anisotropy oscillation in Co_2FeAl/Ta heterostructure.

J. Qiao[1,2], S. Peng[1,2], Y. Zhang[1,2], H. Yang[3] and W. Zhao[1,2]
1. School of Electronic and Information Engineering, Beihang University, Beijing, China; 2. Fert Beijing Institute, BDBC, Beihang University, Beijing, China; 3. Key Laboratory of Magnetic Materials and Devices, Ningbo Institute of Material Technology and Engineering, Chinese Academy of Sciences, Ningbo, China

We report first-principles investigations on magnetocrystalline anisotropy energy (MCAE) oscillation as a function of capping layer thickness in Heusler alloy Co_2FeAl/Ta heterostructure. Substantial oscillation is observed in the structure with FeAl-interface. According to k-space and wave function analysis, this oscillation is mainly attributed to the Fermi-energy-vicinal majority-spin quantum well states (QWS) which are confined between Co_2FeAl/Ta interface and Ta/vacuum surface. The vanishing of QWS in the structure with Co-interface can be explained by the smooth potential transition at the interface. These findings clarify that MCAE in Co_2FeAl/Ta is not a local property of the interface and that the quantum well effect plays a dominant role in MCAE oscillation of the heterostructure. This work presents the possibility of tuning MCAE by QWS in capping layers, and paves the way for artificially controlling magnetic anisotropy energy in magnetic tunnel junctions.

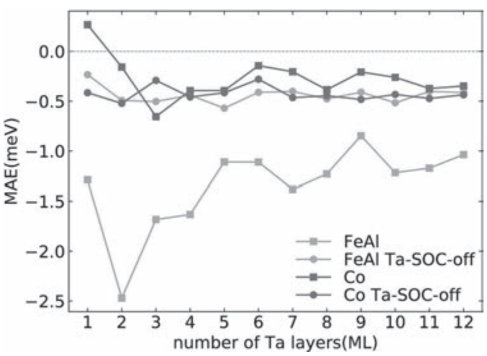

Fig. 1. MCAE oscillation with respect to Ta monolayers (ML) number. Cyan color for FeAl-interface structure, red for Co-interface structure. Circle mark for MCAE calculation with SOC of Ta switched off while spin orbit coupling (SOC) of CFA still included, square mark for normal MCAE calculation. A strong oscillation of MCAE can be observed in FeAl-CFA/Ta structure relative to the thickness of capping layer Ta. For the FeAl-CFA/Ta structure, by suppressing the SOC of Ta while still keeping the SOC of CFA, oscillation of the MCAE relative to Ta layer thickness disappears. This indicates that the electron states in Ta play the determinant role in the MCAE oscillation of CFA/Ta system.

HP-09. Theory of non-collinear interactions beyond Heisenberg exchange; applications to bcc Fe.

S. Attila[1], D. Thonig[1], P.F. Bessarab[2], Y. Kvashnin[1], D. Rodrigues[1], M. Pereiro[1], L. Nordstrom[1], A. Bergman[1], A. Klautau[3], O. Eriksson[1] and R. Cardias[1]

1. Department of Physics and Astronomy, Uppsala University, Uppsala, Sweden; 2. Science Institute of the University of Iceland, Reykjavik, Iceland; 3. Faculdade de Fisica, Universidade Federal do Para, Reykjavik, Belem, Brazil

We show for a simple non-collinear configuration of the atomistic spins (in particular, where one spin is rotated by a finite angle in a ferromagnetic background) that the pairwise energy variation computed in terms of multiple scattering formalism cannot be fully mapped onto a bilinear Heisen- berg spin model even in the lack of spin-orbit coupling. The non-Heisenberg terms induced by the spin-polarized host appear in leading orders in the expansion of the infinitesimal angle variations. However, an Eg-T2g symmetry analysis based on the orbital decomposition of the exchange param- eters in bcc Fe leads to the conclusion that the nearest neighbor exchange parameters related to the T2g orbitals are essentially Heisenberg-like: they do not depend on the spin configuration, and can in this case be mapped onto a Heisenberg spin model even in extreme non-collinear cases.

Theory of noncollinear interactions beyond Heisenberg exchange: Applications to bcc Fe A. Szilva, D. Thonig, P. F. Bessarab, Y. O. Kvashnin, D. C. M. Rodrigues, R. Cardias, M. Pereiro, L. Nordström, A. Bergman, A. B. Klautau, and O. Eriksson Phys. Rev. B 96, 144413 – Published 10 October 2017

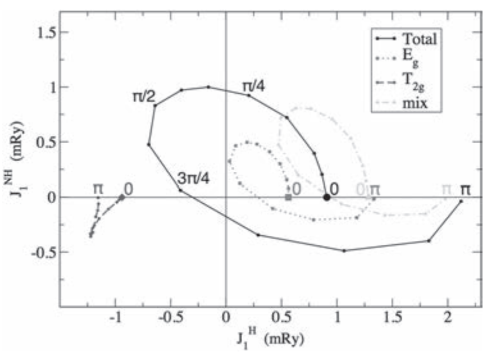

Fig. 1. The black line shows the evolution of the non-collinear inter-atomic exchange coupling constants for a first nearest neighbour pair in bcc Fe single spin rotation. The red, blue and green lines stand for its symmetry decomposition.

HP-10. Ab initio study of phase stability in Fe-Pd binary alloys.

R. Pathak[1], O. Golovnya[2,3], A. Popov[2,3], R. Skomski[4] and *A. Kashyap*[1]
1. Physics, School of Basic Sciences, Indian Institute of Technology, Mandi, HP, Mandi, India; 2. Ural Federal University, Ekaterinburg, Russian Federation; 3. M.N. Miheev Institute of Metal Physics of Ural Branch of Russian Academy of Sciences, Str. S. Kovalevskoy, Ekaterinburg, Russian Federation; 4. Nebraska Center for Materials and Nanoscience and Department of Physics and Astronomy, University of Nebraska-Lincoln, Lincoln, NE, United States

Tetragonal FePd is an interesting magnetic material [1-3] whose formation involves several ordered and disordered phases. Experiment shows that the A1 to $L1_0$ structural transformation in FePd is a complex transformation of the cascade type, which proceeds via intermediate low-symmetry phases, namely the disordered tetragonal phase A6 (I4/mmm), the modified $L1_0$ phase(P4/mmm), the hexagonal ordered phase Fe_2Pd (P3m1), and, probably, the orthorhombic (Cmmm) and the cubic ordered $L1_2$ (Pm-3m) phases [4-5]. We present *ab initio* calculations to understand the experimentally observed situation in FePd. The density-functional calculations employ the generalized gradient approximation (GGA) for exchange and correlations. The calculations are based on the projector augmented wave (PAW) method implemented in the Vienna Ab-Initio Simulation Package (VASP). For the electronic wave functions, an energy cutoff of 500 eV has been taken. We have performed the calculations for ordered, deformed $L1_0$, and two chemically disordered structures. The well known ordered structures for Fe-Pd system are FePd ($L1_0$) and $FePd_3$ ($L1_2$) [4-5]. In addition, we have considered the experimentally observed, hexagonal Fe_2Pd (CdI_2-type), and orthorhombic Fe_3Pd_5 (Pt_5Ga_3-type) structures where order is yet to be established. For simplicity, we have considered only ordered form of these two structures. Furthermore, we have considered deformationsof the $L1_0$ structure, namely pseudocubic structures ($a = b = c$) and structures with c/a<1. For the chemically disordered structures, we took the face-centered cubic A1 structure and a tetragonally distorted 2 x 2 x 2 supercell of $L1_2$ where c/a = 0.974. The disorder was created by substituting one Pd by one Fe in $FePd_3$ ($L1_2$) to form the 50-50 composition for FePd alloy. Figure 1 shows the unit cells for all calculations. We have optimized the experimentally obtained lattice parameters for our calculations. Table 1 shows the optimized lattice parameters and formation energy of all the ordered and disordered phases. The formation-energy calculations, which use ground-state density-functional theory (T= 0) confirms that two ordered phases, Fig. 1(a) and (b) and two chemically disordered phases, (e) and (f), are the stable phases. The other ordered phases, namely(c) and (d) and two deformed versions of $L1_0$ namely the pseudocubic and $L1_0$ with c/a <1 are also likely to be formed in the multiphase Fe-Pd sample as they have very low positive formation energies. In conclusion, we have performed *ab initio* calculations of several ordered and disordered phases of FePd alloys and calculated formation energy and the magnetic moments of Fe and Pd atoms in the alloy systems. The calculated negative formation energies are consistent with the experimentally observed phases. This work was partially supported by the Indian-Russian collaborative project (RFBR No. 17-52-45097 and INT/RUS/RFBR/P-267).

[1] Kazuhisa Sato, Bo Bian and Yoshihiko Hirotsu, "Hard Magnetic Properties of (001) Oriented L10-FePd Nanoparticles Formed at 773 K", Jpn. J. Appl. Phys., 39 L1121 (2000). [2] Mitsuru Ohtake, ShouheiOuchi, FumiyoshiKirino, and Masaaki Futamoto, "L10 ordered phase formation in FePt, FePd, CoPt, and CoPd alloy thin films epitaxially grown on MgO(001) single-crystal substrates", J. Appl. Phys. 111, 07A708 (2012). [3] V. Gehanno, A. Marty, B. Gilles, and Y. Samson, "Magnetic domains in epitaxial ordered FePd(001) thin films with perpendicular magnetic anisotropy", Phys. Rev. B 55, 12552 (1997). [4] N. M. Kleinerman, V. V. Serikov, N. I. Vlasova, A. G. Popov, A. Kashyap, "Investigation of peculiarities of structure formation upon ordering of equiatomic Fe-Pd alloy", Bulletin of the Russian Academy of Sciences: Physics 81, 822 (2017). [5] N. I. Vlasova, A. G. Popov, N. N. Shchegoleva, V. S. Gaviko, L. A. Stashkova, G. S. Kandaurova, D. V. Gunderov, "Discovery of metastable tetragonal disordered phase upon phase transitions in the equiatomic nanostructured FePd alloy", Acta Materialia 61, 2560 (2013).

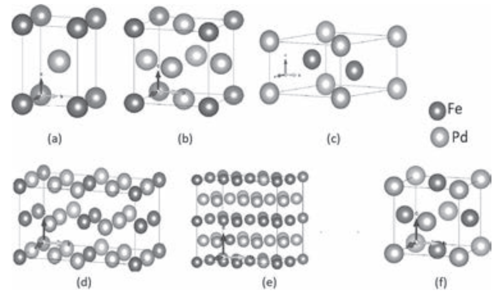

Fig. 1. Unit cells of all ordered and disordered and deformed structure calculations: (a) Ordered-FePd ($L1_0$),(b) Ordered-$FePd_3$ ($L1_2$), (c) Ordered-Fe_2Pd (CdI_2-type), (d) Ordered-Fe_3Pd_5 (Pt_5Ga_3-type), (e) Disordered-$Fe_{16}Pd_{16}$ (A6), and (f) Disordered-FePd (A1).

Alloy	Structure (Space group symbol)	Expt. Lattice parameters (Å)	Optimized lattice parameters (Å)	Formation energy per atom (eV)	Magnetic moment (μ_B/atom)
Ordered Structures					
FePd	$L1_0$ (CuAu) (P4/mmm tP2)	a = 2.722 c = 3.717	a = 2.726 c = 3.722	-0.06	2.97 (Fe) 0.31 (Pd)
$FePd_3$	$L1_2$ (Cu_3Au) (Pm-3m cP4)	a = 3.854	a = 3.888	-0.10	3.23 (Fe) 0.32 (Pd)
Fe_2Pd	Hexagonal (CdI_2-type) (P-3m1 hP3)	a = 4.775 c = 6.206 c/a = 1.63	a = 4.19 c = 2.62 c/a = 0.63	0.08	2.75 (Fe) 0.33 (Pd)
Fe_3Pd_5	Orthorhombic (Pt_5Ga_3-type) Cmmm D^{19}_{2h}	a = 3.86 b = 7.72 c = 7.52	a = 5.61 b = 9.02 c = 4.56	0.09	3.05 (Fe) 0.25 (Pd)
Deformed $L1_0$ Structures					
FePd	$L1_0$ (pseudocubic)	a = 3.81	a = 3.05	0.06	3.01 (Fe) 0.25 (Pd)
FePd	$L1_0$ (CuAu) (P4/mmm tP4)	a = 3.85 c = 3.717 c/a = 0.965	a = 3.076 c = 2.996 c/a = 0.974	0.06	3.10 (Fe) 0.26 (Pd)
Chemically Disordered Structure					
Fe_2Pd_2	A1 (Fm-3m)	a = 3.81	a = 3.81	-0.06	2.95 (Fe) 0.30 (Pd)
$Fe_{16}Pd_{16}$	A6 (I4/mmm)	a = 7.686 c = 7.486 c/a = 0.974	a = 7.686 c = 7.486 c/a = 0.974	-0.05	2.90 (Fe) 0.29 (Pd)

Table 1: Experimental lattice parameters, theoretically calculated lattice parameters, formation energy and average magnetic moment per atom.

FRIDAY AFTERNOON, 27 APRIL 2018 SIMPOR/ROSELLE BALLROOM, 1:30 TO 4:30

Session HQ
ANALYSIS AND OPTIMISATION OF ELECTRICAL MACHINES II
(Poster Session)

Georges Barakat, Chair
University of Le Havre, Le Havre, France

HQ-01. Analysis and Discussion of the Indirect Testing Method for the Losses of Multi-unit Permanent Magnet Synchronous Machines.

D. Zeng[1], J. Zou[1], Y. Xu[1], F. Liu[1] and H. Lan[1]
1. Harbin Institute of Technology, Harbin, China

1.INTRODUCTION The losses always occur when PMSM is running. As the losses generate heat, they also determine the machine cooling requirements and efficiency. Therefore, a good knowledge of the losses dissipated in a PMSM is usually required before the machine application stage. To measure the losses of the machine, the output power and input power are usually measured in traditional loss testing methods. The losses can be obtained by subtracting the output power from the input power. Some loss test methods have been mentioned in literature to make the measurement accurately. The latest edition of IEEE standards for the identification of permanent magnet machines includes many test methods [1]. A novel test measuring system and test method to measure the iron loss of stator assembly have been introduced in [2]. A method for measuring magnet losses in the surface mounted PMSM has been presented in [3]. However, in these methods, the machine needs to be connected with a mechanical load. Therefore many loss estimation methods have been investigated. The most accurate reported methods to calculate the iron losses of the PMSM are based on defining the flux density as a function of time with the finite element analysis (FEA) [4]-[7]. Compared with the analytical calculation, the calculation of the machine would usually be more time consuming with the FEA method [8] [9]. Therefore, some fast-calculating analytical methods are developed, although the accuracy of the iron loss prediction is degraded [10]-[13]. In loss estimation methods, the saturation of the machine is mainly dependent on the material property. Even some manufacturing errors occurring in the manufacturing process can not be considered in the estimation. Considering the drawbacks of estimation methods and the traditional testing methods, an indirect testing method for the losses of multi-unit PMSM without any mechanical load is proposed in [15]. In this method, the losses of the machine can be obtained by the particular control strategy and the measurement instead of connecting to the mechanical load. The influence factors of the testing method proposed in [14] will be analyzed and discussed in this paper. 2. The indirect loss testing strategy A. Loss Testing Method According to the relation with the speed, the losses in the machine can be defined as two parts: the speed-dependent losses and the speed-independent losses. The speed-dependent losses mainly include iron losses, stray losses, and mechanical losses. Usually the speed-independent losses are exactly the copper losses. That is to say, instead of testing the speed-dependent losses in the load situation, the losses can be obtained by testing the losses in the no-load situation with the magnetic flux density and the electrical frequency are the same as those in the load situation. The magnetic flux density can not be measured directly in the normal running situation. It can be estimated by calculating the magnet flux linkage. B. Test for the magnet flux linkage Considering that the magnet flux linkage at the load test may be different from that at the no-load test because of the different saturation degrees, the magnet flux linkage produced only by PMs at the load test is estimated with the magnet flux linkage obtained at the no-load test and the inductance in the *d*-axis which can show the saturation in this direction. 3. The influence factors on the indirect test A. Pole-slot Combination To analyze the losses tested by the proposed loss testing method in different pole-slot combination configurations, three PMSM models are established with finite element method. They are the model with 32-pole and 36-slot (fractional–slot concentrated winding configuration), the model with 16-pole and 36-slot (fractional–slot distributed winding configuration), and the model with 8-pole and 36-slot (integral–slot distributed winding configuration). The flux linkage of the winding and magnetic flux density distribution of the three PMSM models are calculated. The calculated iron losses of the three configurations are also listed. B. Saturation Status To analyze the losses tested by the proposed loss testing method in different saturation status, the indirect-testing losses are calculated in the overload operating situation. All PMSM models are overload operating. The flux linkage of the winding and magnetic flux density of the armature teeth of the three PMSM models are calculated in the overload operating situation. C. Harmonic Content According the influence of the pole-slot combination and saturation status on the test error of the proposed method, the harmonic content of the magnetic flux density of the armature teeth is the main influence factor of the test error. To analyze the test error influenced by harmonic, different pole shapes are considered. D. Frequency The effect of the frequency will be analyzed to discuss the application of the proposed method. 4. Result and discussion To validate the proposed loss testing method for multi-unit PMSM, a four-unit PMSM prototype with 32 poles and 36 slots was tested with the proposed method. The direct-testing bench and the indirect-testing bench is shown in Fig. 1.The comparison of the indirect loss test and the direct loss test are shown in Fig.2. 5. Conclusion In this paper, the influence factors of the indirect loss testing method for multi-unit PMSM are analyzed, the applied area of this testing method is discussed.

[1] IEEE Trial-Use Guide for Testing Permanent Magnet Machines," in IEEE Std 1812-2014, vol., no., pp.1-56, Feb. 24 2015. [2] Jardan R K, Varga Z, Stumpf P, et al. Development of a dedicated laboratory system for measurement of iron losses in high speed PMSM[C], IEEE International Conference on Industrial Technology. IEEE, 2015. [3] Malloy A C, Martinez-Botas R F, Lamperth M. Measurement of Magnet Losses in a Surface Mounted Permanent Magnet Synchronous Machine[J]. IEEE Transactions on Energy Conversion, 2015, 30(1):323-330. [4] Nicolas Dehlinger, and Maxime R. Dubois, "A Simple Insulated Thermometric Method for the Experimental Determination of Iron Losses" in *Proc. conf. ICEM,* 2008.pp.1018-1024. [5] Ruuskanen V, Nerg J, Rilla M, et al. Iron Loss Analysis of the Permanent-Magnet Synchronous Machine Based on Finite-Element Analysis Over the Electrical Vehicle Drive Cycle[J]. IEEE Transactions on Industrial Electronics, 2016, 63(7):4129-4136. [6] Chu L, Li G L, Qian Z, et al. Analysis of eddy current loss on permanent magnets in PMSM with fractional slot[C], Industrial Electronics and Applications. IEEE, 2015. [7] Petrov I, Egorov D, Link J, et al. Hysteresis losses in different types of permanent magnets used in PMSMs[J]. IEEE Transactions on Industrial Electronics, 2016:1-1. [8] Zhu S, Cheng M, Dong J, et al. Core Loss Analysis and Calculation of Stator Permanent-Magnet Machine Considering DC-Biased Magnetic Induction[J]. IEEE Transactions on Industrial Electronics, 2014, 61(10):5203-5212. [9] Wang J, Yuan X, Atallah K. Design Optimization of a Surface-Mounted Permanent-Magnet Motor With Concentrated Windings for Electric Vehicle Applications[J]. IEEE Transactions on Vehicular Technology, 2013, 62(3):1053-1064. [10] Williamson S S, Lukic S M, Emadi A. Comprehensive drive train efficiency analysis of hybrid electric and fuel cell vehicles based on motor-controller efficiency modeling[J]. Power Electronics IEEE Transactions on, 2006, 21(3):730-740. [11] Jiang X, Zeng Y, Li H. A 2D-3D hybrid FEM approach for fast analysis of eddy current loss in magnets of PMSM driven by a PWM inverter[J]. 2015:1-1. [12] RodrGuez A L, Gomez D J, Villar I, et al. New analytical method for PMSM magnet losses estimation based on fourier series[C], Xxi International Conference on Electrical Machines. 2014:1314-1320. [13] Hemeida A, Sergeant P. Analytical modeling of eddy current losses in Axial Flux PMSM using resistance network[C], Xxi International Conference on Electrical Machines. 2014:2679-2685. [14] Dubas F, Rahideh A. Two-Dimensional Analytical Permanent-Magnet Eddy-Current Loss Calculations in Slotless PMSM Equipped With Surface-Inset Magnets[J]. IEEE Transactions on Magnetics, 2014, 50(3):54-73. [15] Jibin Zou, Depeng Zeng, Yongxiang Xu, Baochao Wang, Qian Wang. An Indirect Testing Method for the Mechanical Characteristic of Multi-Unit Permanent Magnet Synchronous Machines with Concentrated Windings. IEEE Transactions on Industrial Electronics, 2015, 62(12): 7402-7411.

(a) The direct-testing bench of the loss (b) The indirect-testing bench of the loss

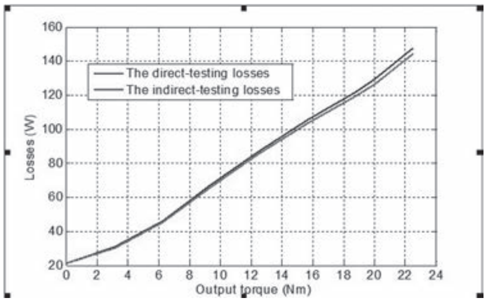
The direct-testing losses
The indirect-testing losses
Losses (W)
Output torque (Nm)
160
140
120
100
80
60
40
20
0
2
4
6
8
10
12
14
16
18
20
22
24

HQ-02. Investigation of Unbalanced Magnetic Force and Vibration Performance Degeneration Caused by Asymmetric Design in Permanent Magnet Synchronous Machines.

H. Lan[1], J. Zou[1], Y. Xu[1] and M. Liu[1]
1. School of Electrical Engineering and Automation, Harbin Institute of Technology, Harbin, China

I. INTRODUCTION Nowadays vibration and noise performance has become an increasingly important consideration for permanent magnet synchronous machines (PMSMs) to meet the industry market's requirement. For PMSMs with low vibration and noise levels, careful analysis and optimization of electromagnetic (EM) force harmonics, i.e., the excitation sources, are essential at the design stage. Among the EM forces, unbalanced magnetic force (UMF) is the most undesirable because it induces significant vibration and noise, and also largely reduces the bearing life. There are numerous factors contributing to UMF for PMSMs in the design and manufacturing processes, among which diametrically asymmetric windings and static or rotating rotor eccentricities are popular topics on account of the UMF's detrimental effect in the last decades. Most recently, a sort of minimum asymmetries from manufacturing imperfections and tolerances have been reported about their effect on UMF or vibration and noise performance in PMSMs [1, 2]. In spite of the tiny variations in structure, the adverse influence is evident. Different from previous contributions, this paper concentratedly discloses the UMF caused by five deliberately introduced asymmetric designs and the resulting degenerated vibration performance in PMSMs. These asymmetric designs are all meant to reduce cogging torque or torque ripple to enable a smoother operation and mitigate relevant vibration components, although the vibration performances have seldom been inspected by experiments [3-7]. Original intention was to cut down tangential excitation sources with the methods, however, at the expanse of probably introducing extra UMF, which the authors paid less attention. In this paper, a further in-depth analysis and numerical verification of the asymmetric designs are carried out with the help of five machines at first. Then the work continues with the characteristics of asymmetric magnetic field and resultant UMF. Lastly experiments are performed on a prototype machine with symmetric and asymmetric designs to verify the degenerated vibration performance. II. ANALYSIS OF ASYMMETRIC DESIGNS The five asymmetric designs can be classified as rotor modifying methods and stator modifying methods. The former include PM shift to reduce cogging torque [6] and torque ripple [3], and asymmetric flux barriers to improve torque ripple behavior [7], while the latter refer to slot-opening shift [4] and teeth pairing to mitigate cogging torque [5]. In view of the effectiveness of these methods, machines with different configurations have been designed for each method. They are successively with 8 /12 (M1), 6/36 (M2), 4 /36 (M3), 8 /12 (M4) and 8/18 (M5) pole/slot combinations. The first three, for rotor modifying methods, are shown in Fig. 1. Essentially these methods are all based on the foundation that critical harmonics induced by symmetric units in the machines can be canceled by slightly modifying at least half units to differ from others. The mentioned critical harmonics can refer to torque ripples themselves or reluctance harmonics or air-gap permeance variations. Confirmed by numerical simulation, three out of the four pole-pairs are respectively shifted by -3.75°, 3.75°and 7.5°mech. angle for M1, and two of the three pole-pairs are shifted by 3.33°and 6.66°for M2. Meanwhile three outer flux-barrier-pairs in M3 are shifted by 2.5°, 5°and 7.5°, and the inner pairs are positioned 12.5°away from the corresponding outer ones. In consequence, as depicted in Fig. 1, fine reduction of 94.5% has been done for the cogging torque of M1, and 81.1% and 82.4% for the torque ripple of M2 and M3. More in-depth analysis described by formulas will be presented in the full paper including the descriptions about stator modifying methods. III. CHARACTERISTICS OF ASYMMETRIC MAGNETIC FIELD AND UMF Fig. 1 shows the flux lines of symmetric and asymmetric designs for M1~3. For symmetric designs, the circumferential cycles of flux line indicate the spatial periodicity of local magnetic stress in fact, since both radial and tangential stress are independent on the polarity of magnetic field. Hence the smallest non-zero spatial order of local force harmonics are respectively 4, 6 and 4 for M1~3. A symmetric design guarantees an ideal zero UMF because no force component with spatial order 1 exists. Unfortunately, the asymmetric designs alter the flux line distributions. Due to the shifts in the rotor, the periodicity in magnetic field is broken. A direct brake happens in the rotor, for which rotating symmetry doesn't exist anymore, and further does in the whole machine. The anisotropic rotor rotates in the machine like a magnetized PM sweeps around the inner surface of the stator. Then UMF comes into being. The UMF ripple in the rotor frame is the iNs-th and further becomes the ($iNs\pm1$)-th when transformed into the stator frame. UMF waveforms in time domain are depicted in Fig. 1. The amplitude is high enough to answer for strong vibrations. IV. EXPERIMENTAL EVALUATION A prototype of M1 with two rotor designs was manufactured, as shown in Fig. 2. Cogging torque and EMF were tested and found to agree well with the numerical simulation. Acceleration at four points on the system was measured. It can be seen high vibration components corresponding to the UMF arise for both the points on the frame and the support for the asymmetric design. This indicates a degenerated vibration performance.

[1] A. J. P. Ortega and L. Xu, "Investigation of Effects of Asymmetries on the Performance of Permanent Magnet Synchronous Machines," *IEEE Trans. Energy Convers.*, vol. 32, pp. 1002-1011, 2017. [2] J. L. Besnerais, "Effect of lamination asymmetries on magnetic vibrations and acoustic noise in synchronous machines," in *2015 18th International Conference on Electrical Machines and Systems (ICEMS)*, 2015, pp. 1729-1733. [3] G. Liu, X. Du, W. Zhao, and Q. Chen, "Reduction of Torque Ripple in Inset Permanent Magnet Synchronous Motor by Magnets Shifting," *IEEE Trans. Magn.*, vol. 53, pp. 1-13, 2017. [4] T. Liu, S. Huang, J. Gao, and K. Lu, "Cogging Torque Reduction by Slot-Opening Shift for Permanent Magnet Machines," *IEEE Trans. Magn.*, vol. 49, pp. 4028-4031, 2013. [5] X. T. Jiang, J. W. Xing, Y. Li, and Y. P. Lu, "Theoretical and Simulation Analysis of Influences of Stator Tooth Width on Cogging Torque of BLDC Motors," *IEEE Trans. Magn.*, vol. 45, pp. 4601-4604, Oct 2009. [6] L. Dosiek and P. Pillay, "Cogging torque reduction in permanent magnet machines," *IEEE Trans. Ind. Appl.*, vol. 43, pp. 1565-1571, Nov-Dec 2007. [7] M. Sanada, K. Hiramoto, S. Morimoto, and Y. Takeda, "Torque ripple improvement for synchronous reluctance motor using an asymmetric flux barrier arrangement," *IEEE Trans. Ind. Appl.*, vol. 40, pp. 1076-1082, 2004.

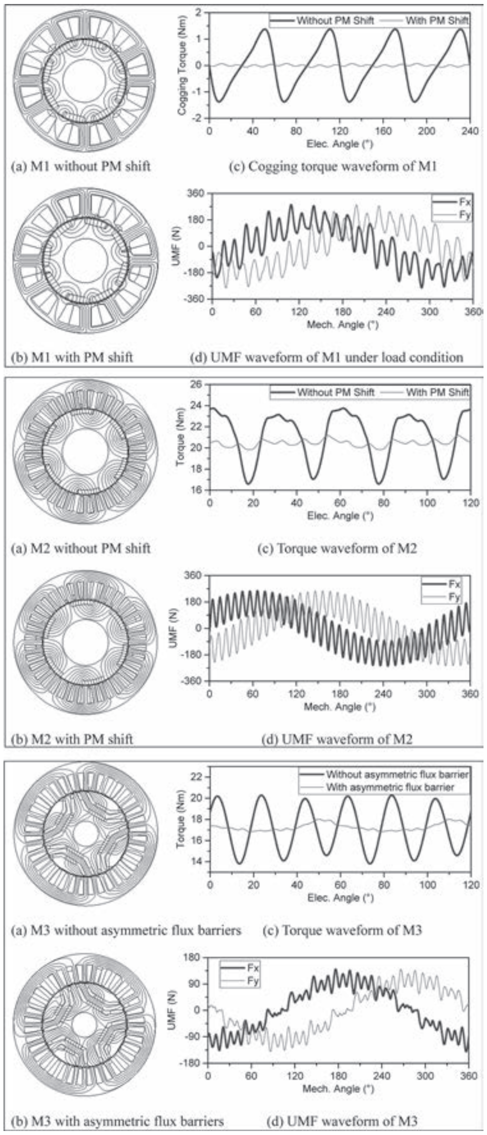

Fig. 1. Partial machines and waveforms

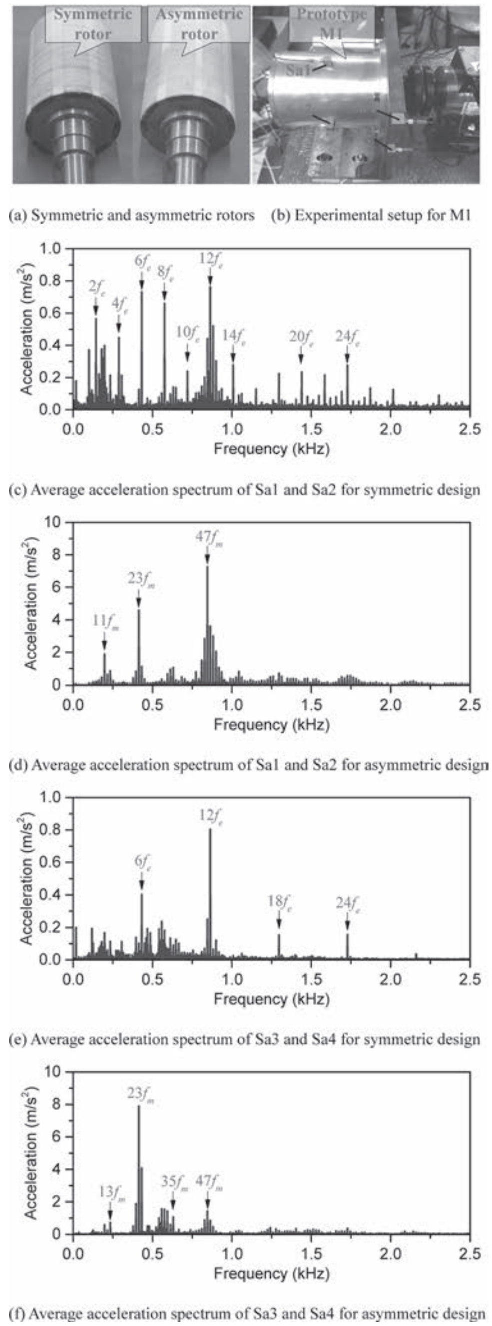

Fig. 2. Experimental setup and partial results

HQ-03. Optimal Design of an Ultra-premium Efficiency PMA-Synchronous Reluctance Motor with Winding Method and Slots Size to Considering Nonlinear Slots Saturation and Minimize Torque Pulsations.

H. Liu[1], S. Oh[1], Y. Oh[1], j. Lee[1] and H. Lee[2]
1. Hanyang Univ., Seoul, The Republic of Korea; 2. Busan Institute of Science and Technology University, Busan, The Republic of Korea

Permanent magnet assistant synchronous reluctance motor (PMA-SynRM) has strong durability and generates reluctance torque without the copper loss of the rotor unlike the induction machine; thus, recently the super-premium (IE4) efficiency PMA-SynRM is being mass-produced. In recent research, for IE4 efficiency PMA-SynRM design, in order to save manufacturing costs while retaining the basis of induction motors (IMs) stator and winding structure, the rotor structure of the PMA-SynRM alone conducted a lot of analysis. Such as optimal design SynRM rotor barriers shape [1], [2]. Barriers angle [3], Barriers number [4] and permanent magnet position [5]. In order to maximize the saliency ratio of PMA-SynRM, recently, the axially laminated anisotropic (ALA)-type SynRM [6] has even been studied, even used 3-D printer to increase the saliency ratio of the SynRM rotor structure [7]. However, we found that the main loss of industrial PMA-SynRM is the copper loss of the stator, therefore, for a fixed PMA-SynRM rotor, the corresponding PMA-SynRM stator design is also very important. So that in this paper, in order to optimal design the PMA-SynRM for meet ultra-premium efficiency (IE5), reduce slots saturation and minimize torque pulsations, we used three steps to optimal design the stator of PMA-SynRM, in the first step, we choose the different winding method for a 4 poles, 3.7kW PMA-SynRM, and is the same diameter of stator and axial length as the premium efficiency (IE3) frame, which is shown in the Fig.1. The stator slots number and winding methods not only consider by the value of the winding coefficient but also the same need to consider the rotor poles, as well as the number of barriers per pole, we can find from Fig 2. [8], for different positions of the rotor, the magnetic flux transfer at different locations will affect the d-q axis inductance, and the result will be calculated by Eq. (1) After determining the winding method and number of turns, in the second step, the yoke width and tooth width around the stator will be optimization by using the response surface methods (RSM). For this step, the optimal design model considers the magnetic saturation in the iron parts of the stator, this saturation results from the actual B–H characteristic of the core. Meanwhile, both core loss and copper loss could be reduced for optimal design model to meet IE5 efficiency. To minimize torque ripple, according to the tendency, the height of the shoes should be over 3.75 mm which was shown in Fig. 3 and the parameter design with the new model (Fig.4)was performed to solve the problems with the harmonic wave. There are many parameters like the height of the shoes, the slot opening. Etc. The parameter design was repeated to make these parameters satisfy the required output and minimum loss characteristics of the first optimal model and only reduce the torque ripple of PMA-SynRM. Through the analysis results by the (finite element method) FEM, it shows that the loss and torque ripple of the final model are significantly reduced. When compared with those of the initial model and an IE3 efficiency IM. At last, in full paper, the experiment result will be discussed.

[1] J. Lee, "Optimum Design Criteria for Maximum Torque Density and Minimum Torque Ripple of SynRM According to the Rated Wattage Using Response Surface Methodology," IEEE Trans. Magn., vol. 45, no. 3, pp. 1578-1581, Nov. 2009 [2] R. Moghaddam, "Synchronous reluctance machine (SynRM) in variable speed drives (VSD) applications" doctoral thesis, KTH, Stockholm, 2011 [3] R. Moghaddam, "Synchronous Reluctance Machine (SynRM) Design", Master's Thesis in power electrical engineering, Royal Institute of Technology (KTH), Sweden, 2007. [4] S. Mun, Y. Cho, and J. Lee, "Optimum Design of Synchronous Reluctance Motors Based on Torque/Volume Using Finite-Element Method and Sequential Unconstrained Minimization Technique," " IEEE Trans. Magn., vol. 44, no. 11, pp. 4143-4146, Nov. 2008 [5] H. Liu et al., "Design of Permanent Magnet-Assisted Synchronous Reluctance Motor for Maximized Back-EMF and Torque Ripple Reduction," IEEE Trans. Magn., vol. 53, no. 6 Jun 2017, Art. no. 8202604. [6] Y. Kim and J. Lee, "Optimum Design of ALA-SynRM for Direct Drive Electric Valve Actuator," IEEE Trans. Magn., vol. 53, no. 4, Apr. 2017, Art. no. 8200804. [7] H. Hong et al., "Design of High-End Synchronous Reluctance Motor Using 3-D Printing Technology," IEEE Trans. Magn., vol. 53, no. 6, Jun. 2017, Art. no. 8201705. [8] A. Fratta, G. P. Troglia, A. Vagati, F. Villata, " Evaluation of torque ripple in high performance synchronous reluctance machines", IEEE-IAS Annual meeting, Toronto (Canada), October 1993, Vol. I, pp. 163-170.

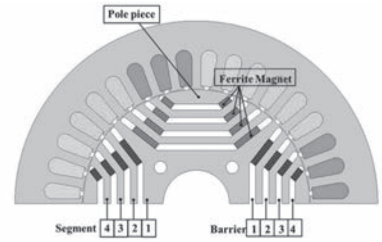

Fig. 1

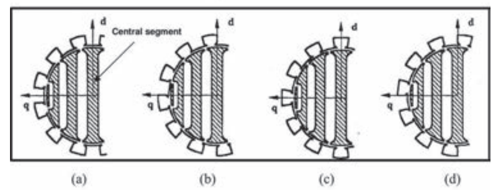

Fig. 2

$$\lambda_{dm} = \lambda_d(i_d, i_q, \vartheta)$$

$$\lambda_{qm} = \lambda_q(i_d, i_q, \vartheta) \quad (1)$$

Fig. 1. Basic PMA-SynRM model

Fig. 2. Comparison of rotor segments position with reference to the stator teeth in four different situations when the rotor is rotating one stator slot pitch from (a) to (d)

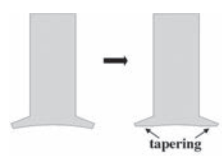

Fig. 3

Fig. 4

Fig. 3. New teeth structure with tapering.

Fig. 4. Design variables in the stator structures of the SynRM

HQ-04. A Novel Doubly Salient Flux Modulation PM Machine with Halbach Magnets.

K. Xie[1], D. Li[1], *R. Qu*[1], Y. Gao[1] and Y. Pan[1]
1. Huazhong University of Science & Technology, Wuhan, China

I. INTRODUCTION With the advent of high performance permanent magnet materials, many novel PM machine topologies have been developed for various applications. Apart from the "rotor-PM" machines, such as surface mounted, inset and interior PM machines, the "stator-PM" machines [1] such as flux switching (FS-), flux reversal (FS-) and doubly salient (DS-) PM machines have attracted much attention in recent years. With the merit of high torque density, the PM vernier (PMV) machine [2], as a kind of "rotor-PM" machine, has been discussed extensively. Since the PMV machine and magnetic geared machine share the same operation principle [3], they can be classified into the flux modulation machines [4], and the FSPM, DSPM, FRPM and transverse flux PM machines are also included. Based on the flux modulation effect, machines with magnets in both stator and rotor have been the research hotspot recently [5]-[6]. In this paper, a novel flux modulation PM machine with Halbach magnets in both stator and rotor is proposed. It's shown that the torque density of the machine is 49.7 kNm/m^3, more than 1.6 times as that of PMV machines, when the heat loading is 1704 A^2/cm.mm^2. II. STRUCTURE AND OPERATION PRINCIPLE The configuration of the proposed flux modulation PM machine is presented in Fig. 1, while the operation principle is also illustrated briefly. It's seen that the doubly salient structure is preferred, and the Halbach array magnets is employed in both stator and rotor slot opening. Therefore, the proposed machine can be taken as the integration of a "stator-PM" machine and a "rotor-PM" machine, as shown in Fig. 1. Moreover, the operation principles of the "stator-PM" machine part and "rotor-PM" machine part are both based on the flux modulation effect. Then, the winding pole pairs is calculated as the difference between the stator slot number and rotor slot number. For the "stator-PM" machine part, the PM magnetomotive force (MMF) pole pair number is equal to the stator slots, while the PM MMF pole pair number is equal to the rotor slots for the "rotor-PM" machine part. The pole pair number of airgap permeance for the two machines are also different which results in the same winding pole pairs. With Halbach magnets employed, the self-shielding and flux focusing effect is utilized, and the expanded views of the flux lines of the three machines is also shown in Fig. 1 to reveal the integration effect of the proposed machine. III. ELECTROMAGNETIC PERFORMANCES The electromagnetic performances of the proposed flux modulation PM machine are shown in Fig. 2. The main parameters is given in Table I. It's clear that there is one pole pair magnetic flux in the stator of the three machines, while the flux lines and flux density distribution of the proposed machine, the stator-PM machine part and the rotor-PM machine part are similar. As for the proposed machine, the flux density is more uniformly distributed in the iron core, while the tooth tips gets a little saturated. Further, the torque performance of the proposed flux modulation machine, the stator-PM machine part, the rotor-PM machine part and the sum of the stator-PM and rotor-PM part are compared. It's shown that the back-EMF amplitude of the rotor-PM machine part is about 7% higher than that of the stator-PM machine part, while the average torque is 6% higher. Since the structure of the proposed machine can be regarded as the integration of the two machine parts, it's shown that the back-EMF and output torque of the proposed machine is about 15% lower than that of the algebraic addition of the two machine parts due to the saturation. Compared with the two machines part, the torque ripple of proposed machine is decreased to 2.91%. It should be noted that when the heat loading is 1704 A^2/cm.mm^2, the average torque of the proposed machine is 42.1 Nm, and the corresponding torque density is 49.7 kNm/m^3, and the power factor is 0.66. When the electric loading is decreased to 200 A/cm, the output torque is 32.1 Nm and the corresponding torque density is 37.9 kNm/m^3, and the power factor is 0.8. IV. CONCLUSION In this paper, a novel flux modulation PM machine with high torque density and lower torque ripple is proposed. The doubly salient structure is preferred and Halbach array magnets are employed in both stator and rotor slot opening. The proposed machine can be taken as the integration of a stator-PM and a rotor-PM machine. It's shown that the torque density of the proposed machine can be 49.7 kNm/m^3, and the power factor can be 0.8 with decreased electric loading. More detailed analysis will be given in the full paper.

[1] M. Cheng, W. Hua, J. Zhang and W. Zhao, "Overview of Stator-Permanent Magnet Brushless Machines," in *IEEE Trans. Ind. Electron.*, vol. 58, no. 11, pp. 5087-5101, Nov. 2011. [2] A. Toba and T. A. Lipo, "Generic torque-maximizing design methodology of surface permanent-magnet vernier machine," in *IEEE Trans. Ind. Appl.*, vol. 36, no. 6, pp. 1539-1546, Nov/Dec 2000. [3] R. Qu, D. Li, and J. Wang, "Relationship between magnetic gears and vernier machines," in *Proc. Int. Conf. Elect. Mach. Syst.*, Beijing, China, 2011, pp. 1–6. [4] D. Li, R. Qu, and J. Li, "Topologies and analysis of flux-modulation machines," in *Proc. Energy Convers. Congr. Expo.*, 2015, pp. 2153–2160. [5] D. K. Jang and J. H. Chang, "Design of a Vernier Machine With PM on Both Sides of Rotor and Stator," in *IEEE Transa. Magn.*, vol. 50, no. 2, pp. 877-880, Feb. 2014. [6] K. Xie, D. Li, R. Qu and Y. Gao, "A Novel Permanent Magnet Vernier Machine With Halbach Array Magnets in Stator Slot Opening," in *IEEE Trans. Magn.*, vol. 53, no. 6, pp. 1-5, June 2017.

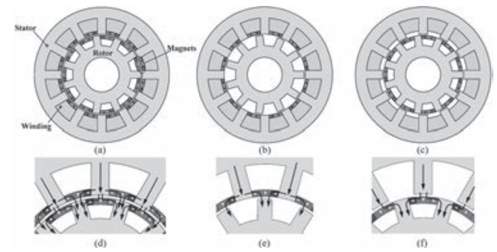

Fig. 1. Structure of the proposed machine. Cross section of (a) the proposed machine, (b) the stator-PM part, (c) the rotor-PM part. Flux lines under open circuit of (d) the proposed machine, (e) the stator-PM part, (f) the rotor-PM part.

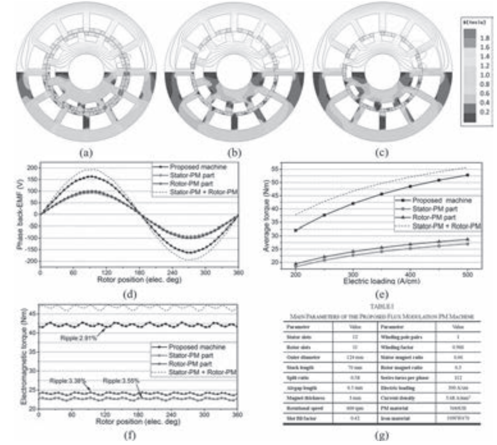

Fig. 2. Electromagnetic performance of the proposed machine. Flux lines and density distribution under open circuit of (a) the proposed machine, (b) the stator-PM part, (c) the rotor-PM part. (d) Phase back-EMF waveforms. (e) Torque vs. electric loading curves. (f) Torque waveforms. (g) Main parameters.

HQ-05. Analysis and Optimization of Cogging Torque in Yokeless and Segmented Armature Axial-Flux Permanent-Magnet Machine with Soft Magnetic Composite Core.

L. Xu[1] and Y. Xu[1]
1. School of Electrical Engineering, Shandong University, Jinan, China

Abstract Yokeless and segmented armature (YASA) axial-flux permanent-magnet machine has high power density and efficiency, which is suitable for in-wheel or near-wheel direct-drive electric vehicles. This paper investigates the cogging torque of a YASA with soft magnetic composite (SMC) core. Firstly, the structure of SMC-based YASA is introduced. Then, the influence of magnet pole-arc ratio, magnet skewing, stator shoe width ratio and stator shoe shifting on cogging torque is analyzed. Based on which, the cogging torque is optimized by response surface model and genetic algorithm (GA). Finally, the optimization results are verified by 3-D finite-element method (FEM). The results confirm that, based on a certain magnet pole-arc ratio, there exists an optimum combination of magnet skewing angle, stator shoe width ratio and stator shoe shifting angle for the cogging torque minimization, while the main performances of the machine remain nearly invariable. I. Introduction Compared with the conventional axial-flux permanent-magnet machine (AFPM), the yokeless and segmented armature (YASA) axial-flux permanent-magnet machine has no stator yoke, therefore has the advantages of less stator core and short magnetic circuit. The stator core of YASA can be fabricated with soft magnetic composite (SMC) material, which can not only reduce the manufacturing difficulty, but also make full use of magnetic, thermal and mechanical isotropic characteristics of the SMC to further improve the performances of the machine. A number of notable works have been done for the cogging torque analysis of AFPM, among which the methods given in [1]-[3] can be used to reduce the cogging torque of YASA with electrical steel core. However, the cogging torque analysis method will be different for the YASA with SMC core, due to the special characteristics of stator tooth and slot shape, magnetic circuit structure and SMC material. II. Structure of the YASA With SMC Core Fig. 1 shows the structure of the YASA with 10 poles and 12 slots. The stator cores are made of SMC material while the rotors are made of solid magnetic material. To make full use of the isotropic magnetic properties of the SMC material, the stator shoe overhangs the stator tooth along circumferential and radial direction, respectively. As a result, the coil end can lie within the effective magnetic field range of the machine. III. Influence of Design Parameters on Cogging Torque A. Magnet Pole-Arc Ratio Magnet pole-arc ratio affects not only the cogging torque, but also the air-gap flux density [4]. Selecting an appropriate magnet pole-arc ratio can reduce the cogging torque while maintaining the main performances of the machine. Here, the optimal magnet pole-arc ratio is determined by 3-D FEM. Based on which, the influences of other parameters on cogging torque will be analyzed. B. Magnet Skewing In order to reduce the cogging torque of the SMC-based YASA, the fan-shaped magnet skewing approach is used [5]. Variations of cogging torque with respect to the magnet skewing angle are analyzed by 3-D FEM. C. Stator Shoe Width Ratio Different from the YASA made of electrical steel, the width of added stator shoes of the SMC-based YASA can change in a relatively large range, leading to the variation of PM leakage magnetic circuit and air-gap stored PM energy. The influence of stator shoe width ratio on the cogging torque is analyzed by 3-D FEM. D. Stator Shoe Shifting For the SMC-based YASA, the two stator shoes of one stator tooth can be symmetrically shifted by an angle in reverse direction to reduce the cogging torque, and the optimal shifting angle for cogging torque minimization is determined by 3-D FEM. IV. Optimization of the Cogging Torque Based on Response Surface Model and Genetic Algorithm The magnet skewing angle β, stator shoe width ratio α_s and stator shoe shifting angle δ are selected as the design variables, and the cogging torque T_{cog} is selected as the response variable. Based on above analysis, the response surface model can be established, and the β, α_s, δ are optimized by GA. V. Finite-Element Verification The performances for the initial design and optimization are calculated by 3-D FEM, with the comparison result of cogging torque shown in Fig. 2. It can be seen that the cogging torque is reduced to a large extent after optimization, which verifies the effectiveness of the proposed optimal method. The paper was supported by the Key Developing Project of Shandong Province(2017CXGC0906).

[1] M. Aydin, Z. Q. Zhu, and etc., "Minimization of cogging torque in axial-flux permanent-magnet machine: design concept," *IEEE Trans. Magn.*, vol.51, no.11, pp. 3614-3622, Sep. 2007. [2] W. Fei and P. C. K. Luk, "An Improved Model for the Back-EMF and Cogging Torque Characteristics of a Novel Axial Flux Permanent Magnet Synchronous Machine with a Segmented Laminated Stator," *IEEE Trans. Magn.,* vol.45, no.10, pp. 4609-4612, Oct. 2009. [3] Saadat Jamali Arand, Mohammad Ardebili, "Cogging torque reduction in axial-flux permanent magnet wind generators with yokeless and segmented armature by radially segmented and peripherally magnet pieces," Renewable Energy 99, pp. 95-106, Jun. 2016. [4] Nicola Bianchi and Silverio Bolognani, "Design Techniques for Reducing the Cogging Torque in Surface-Mounted PM Motors," *IEEE Trans. Ind. Appl.*, vol.38, no.5, pp. 1259-1265, 2002. [5] Z.Q.Zhu, David Howe. "Influence of Design Parameters on Cogging Torque in Permanent Magnet Machines," *IEEE Trans. Energy Conv.,* vol.15, no.4, pp. 407-412, 2000.

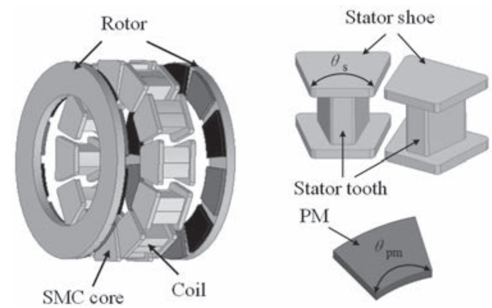

Fig. 1. Structure of the YASA with SMC core.

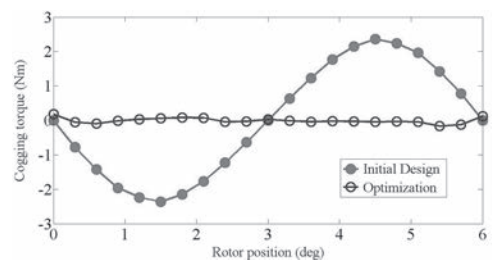

Fig. 2. The comparison of cogging torque for initial design and optimization.

HQ-06. Withdrawn

HQ-07. Development of a Slotted Limited-Angle Torque Motor with Asymmetrical Teeth for Torque Performance Improvement.

G. Yu[1], B. Zheng[1], Y. Xu[1], J. Zou[1], L. Xiao[1] and H. Lan[1]
1. Harbin Institute of Technology, Harbin, China

I. INTRODUCTION Limited-angle torque motor (LATM) featuring a limited rotation less than 180 degrees has been widely applied in position controlling systems such as servo on-off valves, scan mirror system, and so on [1]. Compared with rotating motors in these limited-motion areas, LATMs have many advantages including higher torque/power ratio, higher reliability, and lower cost, owing to fewer mechanical connection parts and maintain free operations [2-3]. However, cogging torque and partial magnetic saturation problems for conventional slotted LATMs result in a non-uniform torque profile so that the slotted LATMs cannot meet the requirements of precise positioning system. Besides, some published material indicates that magnetic saturation in stator teeth due to armature reaction makes torque profile worse even if the slotted LATM operates on rated load [4]. These features have essential influence on position tracking ability for slotted LATMs. Therefore, for taking fully consideration of these problems, a novel slotted LATM with asymmetrical teeth is proposed to improve the both torque profile and torque density. The proposed LATM with 4 poles/4 slots is prototyped, and related experiments are employed to validate the theoretical design and finite element analysis. II. PROPOSED SLOTTED LATM AND ITS SPECIFICATION The proposed slotted LATM shown in Fig. 1 comprises asymmetrical teeth, instead of the conventional symmetrical teeth. In other words, for the existed slotted LATM, all of teeth shape are same, whereas the teeth shape for the proposed LATM are different. The winding connection for the both LATM are shown in Fig. 2. A single-phase winding is adopted for both LATMs. Moreover, this winding connection shown in Fig. 2(b) is distinct from the former since there are only two coils on the number 1# and 2# of tooth. As a result, the manufacturing process of winding for the proposed LATM is much easier than the conventional one. Worth of mention is that non-wounded tooth can be optimized to arbitrary shape for the sake of enhancing torque performance because its shape is not restricted by the winding process. III. LATM MODELING AND TORQUE CALCULATION For initial design of the LATM, a magnetic equivalent circuit (MEC) that is suitable for the slotted LATM is proposed for the initial design process shown in Fig. 3. The proposed MEC modeling is based on the following simplifications: 1.The magnetomotive force (MMF) drop in the iron parts including stator and rotor is neglected. 2.The end effect is ignored. 3. Linear demagnetization characteristic of the permanent magnet (PM) is utilized. For obtaining the MEC modeling accurately, the reluctance of one whole PM is divided into three parts defined as R_{m1}, R_{m2}, and R_{m3}. Meanwhile, the corresponding reluctance of air gap is done the same process, which is depicted as R_{g1}, R_{g2}, and R_{g3}. It should be noticed in Fig. 3 that the number of nodes is only three in consideration of the structure symmetry. Nodal analysis is carried out to solve the magnetic circuit to obtain the torque equation for initial design of LATM [5]. IV. FINITE ELEMENT ANALYSIS AND EXPERIMENTAL VALIDATION Finite element analysis (FEA) is implemented to validate the accuracy of the proposed MEC model. At the same time, further shape optimization of non-wounded teeth is employed for improve the torque profile for the proposed LATM based on the FE method. The proposed LATM with 4 poles/4 slots is prototyped and shown in Fig. 4. Related experiments investigation and discussion will be carried out in this section.

[1] T. Ching-Chih, L. Shui-Chun, H. Hsu-Chih, and C. Yu-Ming, "Design and control of a brushless DC limited-angle torque motor with its application to fuel control of small-scale gas turbine engines," *Elsevier J. Mechatron*., vol. 19, pp. 29–41, Feb. 2009. [2] P. Hekmati, M. Mirsalim, "Design and Analysis of a Novel Axial-Flux Slotless Limited-Angle Torque Motor With Trapezoidal Cross Section for the Stator," *IEEE Trans. Energy Conversion,* vol. 28, no. 4, pp. 815-822, Dec. 2013. [3] K. J. Smith, D. J. Graham, and J. A. Neasham, "Design and Optimization of a Voice Coil Motor With a Rotary Actuator for an Ultrasound Scanner," *IEEE Trans. Ind. Electron.*, vol. 62, no. 11, pp. 7073-7078, Nov. 2015. [4] Y. Guodong, Z. Jibin, X. Yongxiang, W. Qian, W. Baochao, and L. Junlong, "Estimation of Maximum Angular Operation Range for Permanent-Magnet Slotted Limited-Angle Torque Motor," *IEEE Trans. Magn.*, vol. 51, no. 11, pp. 8205505, Nov. 2015. [5] H. W. Derbas, J. M. Williams, A. C. Koenig, and S. D. Pekarek, "A Comparison of Nodal- and Mesh-Based Magnetic Equivalent Circuit Models," *IEEE Trans. Energy Convers.,* vol. 24, no. 2, pp. 388–396, Jun. 2009.

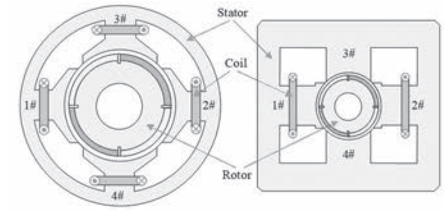

a) Conventional symmetric teeth b) Proposed asymmetric teeth

Fig. 1 Slotted LATM Topologies

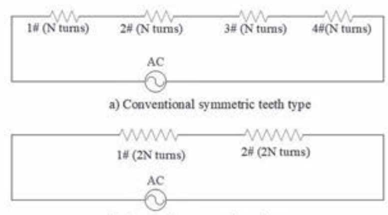

a) Conventional symmetric teeth type

b) Proposed asymmetric teeth type

Fig. 2 Winding connection for the conventional and proposed LATM

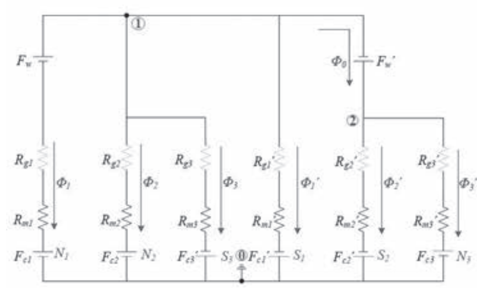

Fig.3 Proposed magnetic equivalent circuit (MEC) for the slotted LATM

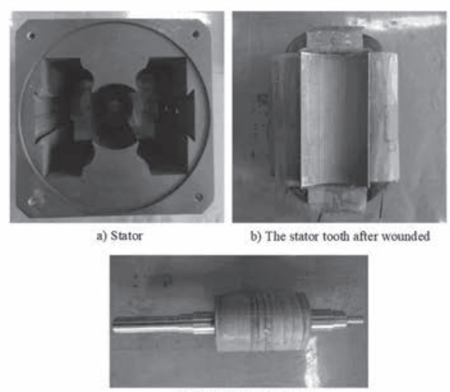

a) Stator b) The stator tooth after wounded

c) Rotor of the prototype

Fig.4 Prototype of the slotted LATM with asymmetric teeth

HQ-08. Design Optimization of Interior Permanent Magnet Synchronous Motor for Electric Compressors of Air-Conditioning Systems Mounted on EVs and HEVs.

S. Cho[1], *J. Choi*[1], H. Shin[2], K. Jung[2] and K. Shin[1]
1. Chungnam National Univ., Daejeon, The Republic of Korea; 2. Hanon systems, Daejeon, The Republic of Korea

This paper presents the design optimization and analysis of an interior-type permanent magnet synchronous motor (IPMSM) for use in the electric compressors of air conditioners applied in electric cars and hybrid vehicles. The IPMSM was chosen because it is suitable for high-speed, high-efficiency and lightweight application in electric compressors. The IPMSM is especially suitable for electric compressors because it has a high torque utilization ratio due to the use of reluctance torque and it can prevent the scattering of magnets [1]. The motor efficiency of electric compressors in automotive applications affects the fuel efficiency and mileage of vehicles, so it is important to improve motor efficiency. Moreover, noise generated by the motor is transmitted to the inside of the vehicle, which can cause discomfort to passengers; therefore, noise reduction design is also important. In particular, it is important to reduce the cogging torque; this noise factor has a significant influence on the noise of the motor [2]. In this study, the main design factors of the motor shape were derived to satisfy the efficiency and cogging torque requirements at the same time, and design optimization was carried out through a two-step design optimization process combining the Taguchi and surface response methods. The optimization process is divided into two stages to reduce the number of analysis steps because the amount of time required for motor analysis increases greatly if optimization is done for various design variables simultaneously. The electromagnetic field analysis for the design of a motor uses the finite-element method (FEM), which requires a long time. Therefore, as an alternative, this paper proposes an effective design optimization process using the two-stage design method. To optimize the design, motor performance characteristics, such as efficiency, cogging torque, and operating range were analyzed using JMAG Designer, a motor electromagnetic analysis tool that employs FEM. Based on the results of the design optimization process, motor prototypes were produced and their performance was measured using a dynamometer and a cogging torque tester. Finally, the validity of the design optimization and analysis was verified by comparing the experimental and analysis results. Figure 1 (a) shows the design optimization parameters and levels for the Taguchi design model. Figure 1 (b) shows analysis process used to obtain the analytical results of the Taguchi design model. Figure 1 (c) shows the optimal selection procedure for optimization using the surface reaction method. Figure 3 (a) shows a comparison of the efficiency test results for each optimization model. As the optimization progressed, the efficiency of the motor improved. Figure 3 (b) compares the analysis and test results for the final model and shows that these two sets of results are similar. Figure 3 (c) presents a comparison of the analysis and test results for cogging torque and shows that these two sets of results are similar. More details of the motor design optimization process and additional analysis results will be presented in the final paper. Test results of the manufactured permanent magnet synchronous motor will also be presented.

[1] J. H. Ahn, S. M. Jang, K. H. Kim, and J. H. Choi, "Analysis on driving characteristic of high speed permanent magnet synchronous motor for compressor of electric vehicle with driving method," Proc. 2012 IEEE Veh. Power Propuls. Conf., pp. 223-226, Oct. 2012. [2] I. P. Brown, M. W. Critchley, J. Yin, S. B. Memory, G. Y. Sizov, S. W. Elbel, C. D. Bowers, M. Petersen, and P. S. Hrnjak, "Design and Evaluation of Interior Permanent-Magnet Compressor Motors for Commercial Transcritical hboxCO 2 (R-744) Heat Pump Water Heaters," IEEE Trans. Ind. Appl., vol. 51, no. 1, pp. 576-586, Jan./Feb. 2015.

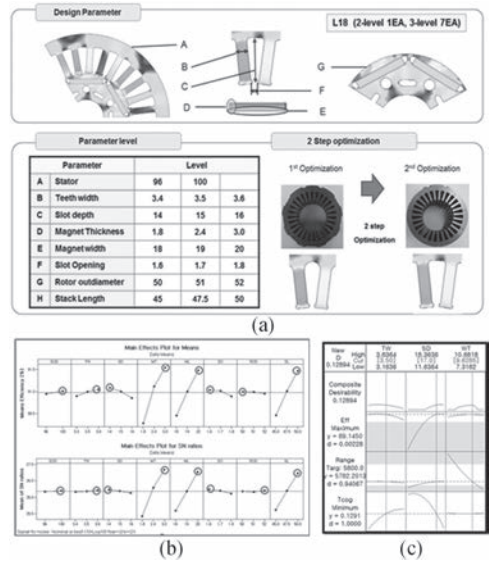

Fig. 1. Motor design optimization procedure: (a) design parameters and levels for Taguchi method, (b) design-level selection procedure in the Taguchi method, and (c) optimal design parameter level selection procedure in the response surface method.

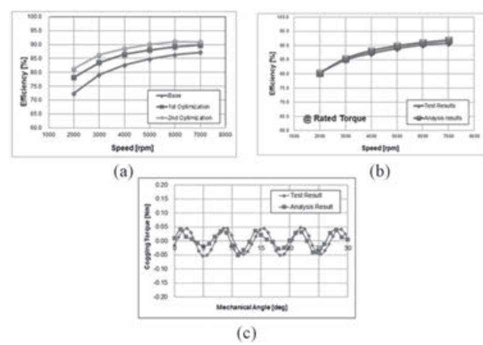

Fig. 2. Comparison of analysis and test results for final optimization model: (a) motor efficiency test results obtained by the design optimization model, (b) motor efficiency results obtained by test and analysis, (c) cogging torque results obtained by test and analysis.

HQ-09. Comparison of Modular Spoke-type Permanent-Magnet Machines Using Different Magnets for In-Wheel Traction Applications.

H. Zhang[1] and *W. Hua*[1]
1. School of Electrical Engineering, Southeast University, Nanjing, China

Abstract—The main purposes of this paper consist of two parts: First, topologies of novel modular spoke-type permanent-magnet (MSTPM) machines with two different magnetization modes are introduced, and corresponding analytical modes are built as well. Second, two types of magnet, including bonded and sintered neodymium-iron-boron (NdFeB) magnets, are applied in MSTPM machines with different magnetization modes. Based on analytical model and finite element (FE) method, the comparison between MSTPM machines using different magnets is conducted, with respect to field harmonic, back electromotive force (EMF), electromagnetic torque, and over-load capability. A prototype machine is assembled and tested to verify predictions. I.Introduction Due to high compactness and operation flexibility, in-wheel traction machine is considered as an excellent choice for electric vehicles [1]. In-wheel traction machines always require large torque, high efficiency, and strong fault-tolerant capability, which are very challenging to satisfy simultaneously. Hence, the machine topology is still a hot point in the field of in-wheel traction machines. In [2], authors proposed a novel outer-rotor-permanent-magnet flux-switching machine, which has been renamed as modular spoke-type permanent-magnet (MSTPM) machine in this paper, to alleviate the saturation phenomenon in the stator tooth of flux-switching permanent-magnet (FSPM) machines by moving the "sandwich" structure from stator to rotor, and then to improve the over-load capability. Existing researches have indicated that MSTPM machines have superior over-load capability and higher efficiency than FSPM machines [2], and stronger flux-weakening performance than surface permanent magnet (SPM) machines. Hence, the MSTPM machine is a certain candidate for in-wheel traction applications. For MSTPM machines, special features including even-order harmonics and unbalanced magnetic force, were investigated in [3], and the operation principle was analyzed based on field modulation theory in [4]. In addition, the back-EMF feature is discussed in [5]. However, there is no research carried on the PM materials and magnetization modes in MSTPM machines, which are exactly the purpose of this paper. More details will be given in the full paper. II.Topology, Analysis and Comparison Fig. 1 shows topologies of MSTPM machines with different magnetization modes. The Mode I (MI) is that all magnets are circumferentially magnetized in the same direction. The Mode II (MII) is that each two adjacent magnets are circumferentially magnetized in reversal directions. Correspondingly, two simple PM-MMF-permeance models are built to investigate the influence of magnet on MSTPM machines under different magnetization modes. In Fig. 2, the PM-MMF distributions of two adjacent magnets in MI and MII MSTPM machines are shown, and corresponding the single stator-pitch permeance waveforms are illustrated as well. For two MSTPM machines with the same magnet number, the fundamental field frequency of MI machine is double of that of MII machine, according to the Fourier analysis of PM magneto-motive force (PM-MMF). The PM-MMF f_{pm} can be calculated by formula (1) and (2). The H_c is the magnet coercive force, h_{pm} is the magnet thickness, P_{air} is the airgap permeance, P_{pm} is the magnet permeance, and P_{sup} is the permeance of the nonmagnetic support cell between each two rotor modules. Equations (1) and (2) are suitable for MI and MII MSTPM machines, respectively. More details about the derivations of P_{air}, P_{pm}, and P_{sup} will be given in the full paper. The single stator-pitch permeance Λ_1 and Λ_2 can be calculated by formula (3) and (4). The l_{air} is the airgap length, l_{slot} is the slot length, and μ_0 is the permeability of vacuum. Then the radial flux density distribution is calculated by formula (5). The θ is the mechanical position. Then four MI and MII MSTPM machines, whose key parameters are listed in Table I, are analyzed by PM-MMF-permeance models and FE method, and Fig. 3 shows corresponding field harmonic spectrums. Key parameters of the magnets are shown in Table II as well. According to the analytical and FE results, it can be found that: the MI MSTPM machine using sintered magnet has the highest fundamental field harmonic; machine using sintered magnet have higher fundamental field harmonic than machine using bonded magnet; MII MSTPM machines have more field harmonics than MI MSTPM machines, which will cause more back-EMF harmonics in MII MSTPM machines. Fig. 4 shows phase back-EMF of these four MSTPM machines, and it is found that MII MSTPM machines do have more phase EMF harmonics than MI MSTPM machines, which verifies the analysis above. More details, including the influence of magnet material on field and back-EMF harmonic spectrums, torque capability, etc., will be given in the full paper. Besides, as shown Fig. 5, a prototype MSTPM machine was manufactured and tested to verify analysis, and corresponding experimental results will be shown in the full paper.

[1] W. Hua, H. L. Zhang, M. Cheng, J. J. Meng, and C. Hou, "An outer-rotor flux-switching permanent-magnet-machine with wedge-shaped magnets for in-wheel light traction," IEEE Trans. Ind. Electron., vol.64, no.1, pp. 69-80, Jan. 2017. [2] H. L. Zhang, and W. Hua, "A novel outer-rotor-permanent-magnet flux-switching machine for in-wheel light traction," in Proc. IEEE-IECON, Florence, Italy, Oct. 2016, pp. 6633-6638. [3] H. L. Zhang, W. Hua, and X. K. Zhu, "Design of novel modular-spoke-type permanent magnet machines," in Proc. IEEE-IEMDC, Miami, USA, May 2017. [4] P. Su, W. Hua, Z. Z. Wu, P. Han, and M. Cheng, "Analysis of the operation principle for rotor-permanent-magnet flux-switching machines," IEEE Trans. Ind. Electron., vol.65, no.2, pp.1062-1073, Feb. 2018. [5] H. L. Zhang, W. Hua, and G. Zhang, "Analysis of back-EMF waveform of a novel outer-rotor-permanent-magnet flux-switching machine," IEEE Trans. Magn., vol.53, no.6, Jun. 2017. Article #:8105004.

$$f_{pm} = (H_c * h_{pm}) \times \frac{1}{(P_{air} + P_{sup})\left(\frac{1}{P_{pm}} + \frac{2}{P_{air} + P_{sup}}\right)} \quad (1)$$

$$\Lambda_1 = \frac{\mu_0}{l_{air}} \quad (3)$$

$$f_{pm} = (H_c * h_{pm}) \times \frac{1}{P_{air}\left(\frac{1}{P_{pm}} + \frac{2}{P_{air}}\right)} \quad (2)$$

$$\Lambda_2 = \frac{l_{air}}{\sqrt{l_{air}^2 + \frac{l_{slot}^2}{4}}} \times \Lambda_1 \quad (4)$$

$$B_r(\theta) = F_{pm}(\theta) \times \Lambda(\theta) \quad (5)$$

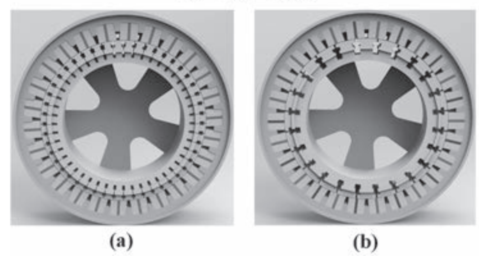

Fig. 1. Topologies of MI and MII MSTPM machines. (a) MI MSTPM machine. (b) MII MSTPM machine.

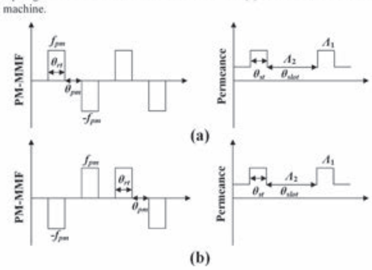

Fig. 2. PM-MMF-permeance models of MI and MII MSTPM machines. (a) MI MSTPM machine. (b) MII MSTPM machine.

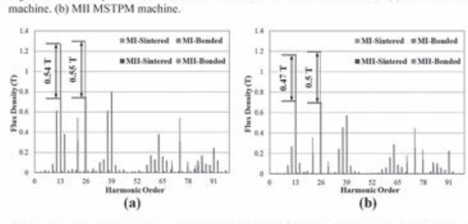

Fig. 3. Field harmonic spectrums of four MSTPM machines with 26 magnets. (a) Analytical results. (b) FE results.

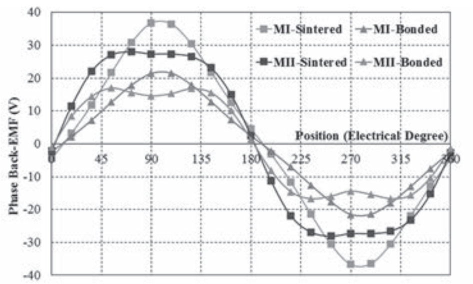

Fig. 4. Phase back-EMF of four MSTPM machines @480r/min.

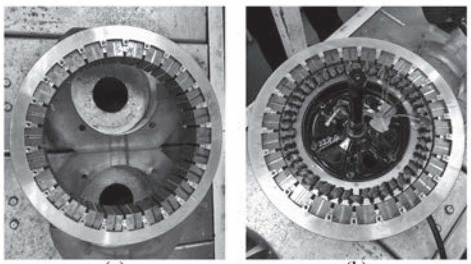

(a) (b)

Fig. 5. Prototype MSTPM machine. (a) Rotor. (b) Rotor and stator.

TABLE I

Key Parameters of Compared Machines

Parameter	MI MSTPM		MII MSTPM	
Magnet material	Sintered	Bonded	Sintered	Bonded
Slot number	48		24	
Phase number	3			
Coil turn per phase	48			
Magnet number	26			
Outer radius	138mm			
Airgap length	0.5mm			
Stack length	45mm			
Stator outer radius	114.5mm			

TABLE II

Key Parameters of Magnet

Parameter	Sintered NdFeB	Bonded NdFeB
Grade	N35	BNP-11
H_c	890 kA/m	520 kA/m
Remanence	1.23T	0.7T

HQ-10. Study on the torque ripple reduction design through varying the air-gap magnetic flux density in the SPM motor.

K. Lee[1], J. Lee[1], R. Kim[1], J. Seo[1] and S. Rhyu[1]
1. Korea Electronics Technology Institute, Gyeonggi-do, The Republic of Korea

1. Abstract Surface permanent magnet motor for 22kW compressor was designed. To reduce the torque ripple, new method was applied as well as existing methods. The existing methods are stator skew, magnet shape and magnet per pole ratio. New method is varying the air-gap magnetic flux density. Each method was analyzed for the usefulness of torque ripple reduction. Finally, the model for test was designed based on the analyzed data and the test was performed. 2. INTRODUCTION In this paper, a study was conducted to minimize the torque ripple of a 22KW compressor motor applied to direct coupled compressor system. In the case of a direct coupling type compressor, the motors and the air ends are directly connected without gears, so that the vibration of the motor greatly affects the life and performance of the compressor. For this reason, an initially designed 22kW compressor motor was analyzed for torque ripple reduction according to the stator skew [1] and magnet configuration [2] studied previously, and the influence of the two parameters on the torque ripple was analyzed. In addition, a new method is proposed to reduce the cogging torque and torque ripple by varying the air-gap magnetic flux density to minimize the torque ripple. Finally, the final model to be applied to direct - coupled compressors was derived through each method, and the performance evaluation was completed through experiments. 3. 22KW-CLASS SPM MOTOR FOR COMPRESSOR Figure 1 and Table I show the shape and specifications of the initial model of the 22 kW class compressor motor for torque ripple reduction. Figure 2 shows the torque waveform of 15A unit from 0A to 60A in the initial model. It is confirmed that the average torque increases as the current increases, and the ripple is the same even if the average torque increases. As a result of FFT analysis of each torque waveform, it can be seen in Fig. 3 that the 12th order of the cogging torque is almost the same even if the average torque increases. It is confirmed that the cogging torque has a great influence on the torque ripple when the current is applied. 4. TORQUE RIPPLE REDUCTION METHODS Figures 4 and 5 show the conventional method for cogging torque and torque ripple reduction. In the case of skew, 0.25, 0.5, 0.75, and 1 slot variables were analyzed. Magnets were analyzed with 5, 10, 15 and 20 mm of A variables and 5, 10 and 15 degrees of B variables. The effect of the two shape parameters on cogging torque and torque ripple will be explained in detail in the full page. The performance of each shape parameter is also shown in the full paper. The variables in Figure 6 and Table 2 are new methods to reduce cogging torque and torque ripple. Depending on the air- gap length, the air-gap magnetic flux density changes and the cogging torque also changes. The relationship between the air gap flux density and cogging torque, and the reduction of torque ripple through cogging torque reduction will be described in the full paper. A final model with minimized torque ripple was manufactured and tested. Detailed results will be discussed in the full paper. 5. Acknowledgment This work was supported by the Technology Innovation Program (10077717, Development of the Low Weight and High Efficiency All-in-One Electric Drive Module for Multicopters) funded By the Ministry of Trade, Industry & Energy(MOTIE, Korea)

[1] R. Islam, I. Husain, A. Fardoun and K. McLaughlin, "Permanent-Magnet Synchronous Motor Magnet Designs With Skewing for Torque Ripple and Cogging Torque Reduction," in IEEE Transactions on Industry Applications, vol. 45, no. 1, pp. 152-160, Jan.-feb. 2009. [2] D. Wang, X. Wang, M. K. Kim and S. Y. Jung, "Integrated Optimization of Two Design Techniques for Cogging Torque Reduction Combined With Analytical Method by a Simple Gradient Descent Method," in IEEE Transactions on Magnetics, vol. 48, no. 8, pp. 2265-2276, Aug. 2012.

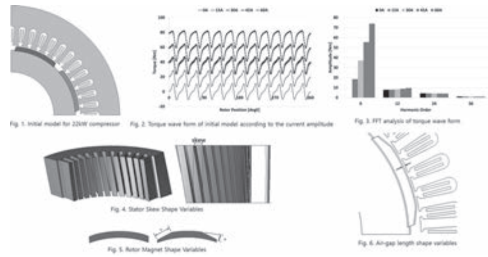

Fig. 1~6.

TABLE I
SPECIFICATIONS OF SPM MOTOR

Specifications	Unit	Value
Pole/Slot	-	8/48
Stator Diameter	mm	305
Rotor Diameter	mm	191
Airgap	mm	1
Number of series turns per phase	-	52

TABLE II
The model for varying the air-gap magnetic flux density and each shape parameter values

Specifications	Unit	Model 1	Model 2	Model 3
Airgap length	mm	1	1.5	2
Stack length	mm	67	71	75

Table I and II

HQ-11. A Study on the Shape Optimization Design of Permanent Magnet Assist to Improve Output Performance of WFSMG.

S. Lee[1], J. Lee[2], B. Kim[2], D. Lee[2] and D. Kang[2]
1. Electronic and Electricity Engineering, Keimyung University, Daegu, The Republic of Korea; 2. Electrical Energy Engineering, Keimyung University, Daegu, The Republic of Korea

For motor generators used in electric vehicles such as EV and HEV in the automobile industry, rare earth permanent magnets having a high output density are mainly used in order to satisfy high efficiency and performance. However, due to unstable supply of rare earth magnet, high price, and environmental problems, development and research of electric machines have been actively carried out to replace them with non-rare earth magnets such as ferrite or to reduce the use of rare earth magnets. WFSMG(Wounded Field Synchronous Motor Generator) is a typical motor generator that can replace PM machine because it has high power density among the devices that do not use permanent magnet. This is a structure in which a coil is wound around a rotor and current is applied from an external power source to form a field, and the field flux can be directly controlled, so that it can be used in a wide operating range from low speed to high speed. Therefore, it has characteristics suitable for use as a motor generator of a vehicle ISG(Integrated Starter Generator) system. In this paper, a study was made to improve the output performance of 2.4kW WFSMG models for an ISG system for automobile. For the WFSMG basic model, PMA(Permanent Magnet Assist) is used as a method to increase the output density because the efficiency is decreased due to increase of the field side copper loss when the field current is increased to increase the output density. The air gap flux density can be sufficiently increased with only a small amount of magnets compared to the permanent magnet used in the PMSMG(Permanent Magnet Synchronous Motor Generator). As a result, the performance and efficiency of the motor generator are improved. In this paper, the influence of the amount of the auxiliary permanent magnet on the output characteristics is analyzed, and the shape optimization of the auxiliary permanent magnet is performed by checking the magnetic flux density and the magnetic flux direction according to the position and shape of the magnet. In order to analyze the optimal permanent magnet insertion position to concentrate the magnetic flux, the magnet structure, inserted into the rotor slot opening and the magnet V shape was selected, and a model was designed according to the shape and position of the magnet for each structure. Electromagnetic field characteristics were analyzed using FEM(Finite Element Method). In addition, the final model was selected and yield strength analysis was performed to verify the stability of the motor generator when the motor was driven.

[1] Sung-Woo Hwang; Jae-Han Sim; Jung-Pyo Hong; Jiyoung Lee; Jongmoo Kim, "Torque improvement of wound field synchronous motor for electric vehicle by PM-assist", IEEE Energy Conversion Congress and Exposition (ECCE), Sept. 2016. [2] L. L. Amuhaya; M. J. Kamper, "Effect of rotor dield winding MMF on performance of grid-compliant hybrid-PM slip synchronous wind generator", IEEE PES PowerAfrica, Sept. 2016. [3] K. H. Chu; J. Pou; S Ramakrishna; A. K. Gupta, "Performance of series hybrid excitation synchronous machine in comparison with wound field synchronous machine", Energy, Power and Transportation Electrification (ACEPT), Oct. 2017. [4] Antonio Di Gioia; Ian P. Brown; Yue Nie; Ryan Knippel; Daniel C. Ludois; Jiejian Dai; Skyler Hagen; Christian Alteheld, "Design and Demonstration of a Wound Field Synchronous Machine for Electric Vehicle Traction with Brushless Capacitive Field Excitation", IEEE Transactions on Industry Applications, Volume: PP, Dec. 2017. [5] Wenye Wu; Xiaoyong Zhu; Li Quan; Yi Du; Zixuan Xiang; Xuhui Zhu, "Design and Analysis of a Hybrid Permanent Magnet Assisted Synchronous Reluctance Motor Considering Magnetic Saliency and PM Usage", IEEE Transaction on Applied Superconductivity, Volume: 28, Apr. 2018.

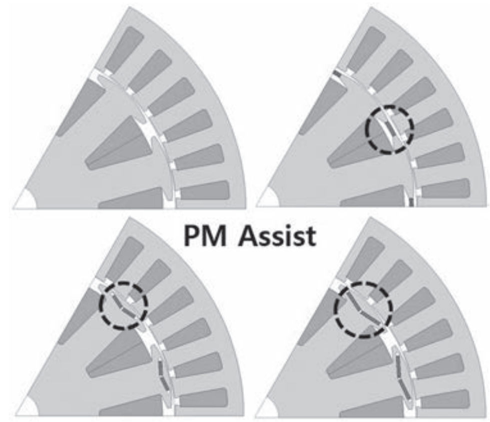

Fig. 1. WFSMG basic model and PMA shape comparison model

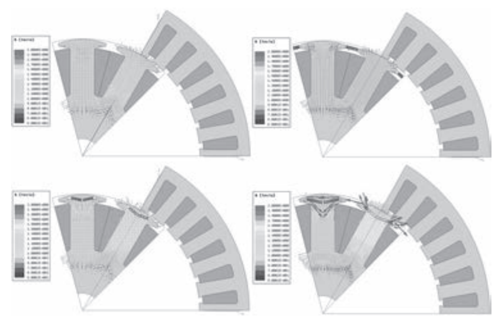

Fig. 2. The magnetic flux vector according to the PMA shape

HQ-12. Analysis and Optimization of Rotor Deformation in Interior Permanent Magnet Synchronous Motors.

Y. Pei[1], Y. Li[1], *F. Chai*[1] and Y. Yu[1]
1. Harbin Institute of Technology, Harbin, China

I. INTRODUCTION Given its high torque density, high power density and wide speed range, interior permanent magnet synchronous motors (IPMSMs) have been widely applied in the electric vehicle in-wheel motor drive system. The rotor part is the major power component of IPMSMs; thus, its structure design significantly affects the electromagnetic and mechanical performances of IPMSMs. As one of the important problem, the rotor deformation, together with its effect on the electromagnetic performance and electromagnetic vibration, has drawn the attention of many scholars. The rotor deformation can be mainly divided into two types, thermal deformation caused by high temperature and the pole shoe deformation caused by high centrifugal force. The combined effects of these two factors are much more complex. To simplify the analytical process, the rotor deformation in this paper is focused on the centrifugal distortion of pole shoe. II. SIMULATION ANALYSIS The geometrical parameters of the interior rotors, such as the thickness of magnetic bridge, the thickness of magnetic rib, and the angle between two PMs in a V-shaped type rotor, all can affect the centrifugal distortion of pole shoe. Thus, the relationships between pole shoe deformation curves and these factors are discussed through the structural analysis. Two types of the interior rotor are included in the study and the difference between them is whether or not there is a central magnetic bridge. The structural FEM of the rotor under a single pole at the maximum rotating speed is built with ABAQUS, which is the software used for the mechanical FEA. Fig. 1 shows the distribution curves of pole shoe deformations varying with the thickness of bilateral magnetic bridge, the thickness of magnetic rib, the angle θ and the thickness of central magnetic bridge (θ=180°), respectively. It can be concluded that: (1) The distribution of rotor deformation under a single pole is similar to one part of an eccentric circle and the maximum deformation point is located in the center of the pole shoe. (2) As these parameters increased in a certain range, the value of maximum deformation changed linearly. In addition, compared with the thickness of magnetic rib, the thickness of magnetic bridge has a greater effect on the rotor deformation. (3) When θ is small, the distribution curve is relatively flat; but when θ is large, the curve obviously becomes sharp. The larger V-shaped angle causes the larger peak deformation, which is contrary to the trend of mechanical stress on magnetic bridges. (4) When the maximum rotating linear velocity is large, the V-shaped type rotor with a central magnetic bridge should be employed. Due to the central bridge connecting the pole shoe and the rotor yoke, the mechanical stress caused by high centrifugal force can be decentralized and shared by multiple magnetic bridges to reduce pole shoe deformation. III. OPTIMIZATION OF ROTOR STRUCTURE In fact, the air-gap magnetic field has a direct relationship with the pole shoe shape. The rotor deformation can affect the harmonics of radial magnetic force density and torque pulsation, which would result in an increase in the level of electromagnetic vibration. Therefore, the rotor deformation should be optimized and reduced to suppress the additional electromagnetic vibration. In the study, the authors suggest that the maximum rotor deformation caused by high centrifugal force is not higher than 10% of the air-gap length. According to the simulation analysis in Section II, the deformation of V-shaped type rotor can be decreased by increasing the thicknesses of magnetic rib and magnetic bridges. However, doing so also increases the magnetic flux leakage and reduces the electromagnetic performance. As is shown in Figure 2, this paper proposes a novel interior rotor structure, in which the tangential magnetized PMs with the trapezoid shape and the modular rotor core are adopted, to reduce the rotor deformation and improve the electromagnetic performance. The dovetail slot structure plays the role of connecting rotor core and shaft, which has a similar function with the central magnetic bridge in the V-shaped type rotor to reduce rotor deformation. But the difference is that the dovetail slot structure has little influence on the rotor magnetic circuit. Meanwhile, the tangential magnetized PMs with the trapezoid shape combines the advantages of V-shaped type and spoke type rotor. All these can improve the electromagnetic performance. IV. CONCLUSION This paper investigates the effect of the thickness of magnetic bridge, the thickness of magnetic rib, the angle between two PMs of a single pole and the thickness of central bridge on the distribution curves of rotor pole shoe deformations. The thicknesses of magnetic bridges have a greater influence than other parameters. In order to eliminate the magnetic flux leakage and ensure mechanical performance, a novel rotor structure is proposed. The tangential magnetized PMs with the trapezoid shape and the modular rotor core with the dovetail slot structure are combines the advantages of V-shaped type and spoke type rotor, which is verified to reduce rotor deformation and improve the electromagnetic performance.

[1] Chai F, Li Y, Liang P, et al. Calculation of the maximum mechanical stress on the rotor of interior permanent-magnet synchronous motors[J]. IEEE Transactions on Industrial Electronics, 2016, 63(6): 3420-3432. [2] Yamazaki K, Kato Y. Iron loss analysis of interior permanent magnet synchronous motors by considering mechanical stress and deformation of stators and rotors[J]. IEEE Transactions on Magnetics, 2014, 50(2): 909-912. [3] Ma J, Qu R, Li J, et al. Structural Optimization of a Permanent-Magnet Direct-Drive Generator Considering Eccentric Electromagnetic Force[J]. IEEE Transactions on Magnetics, 2015, 51(3): 1-4. [4] Kolehmainen J. Optimal dovetail permanent magnet rotor solutions for various pole numbers[J]. IEEE Transactions on Industrial Electronics, 2010, 57(1): 70-77.

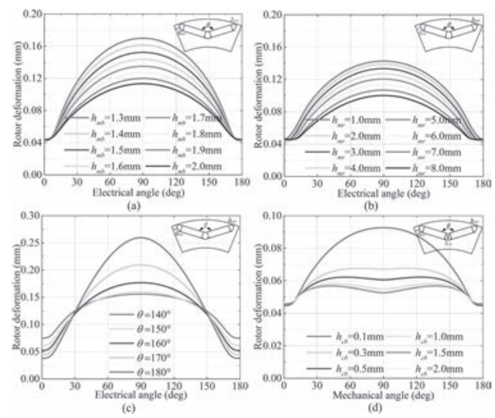

Fig. 1. Distribution curves of rotor pole shoe deformations varying with geometrical parameters under a single pole. (a) The thickness of bilateral magnetic bridge. (b) The thickness of magnetic rib. (c) The angle between two PMs of a single pole. (d) The thickness of central magnetic bridge.

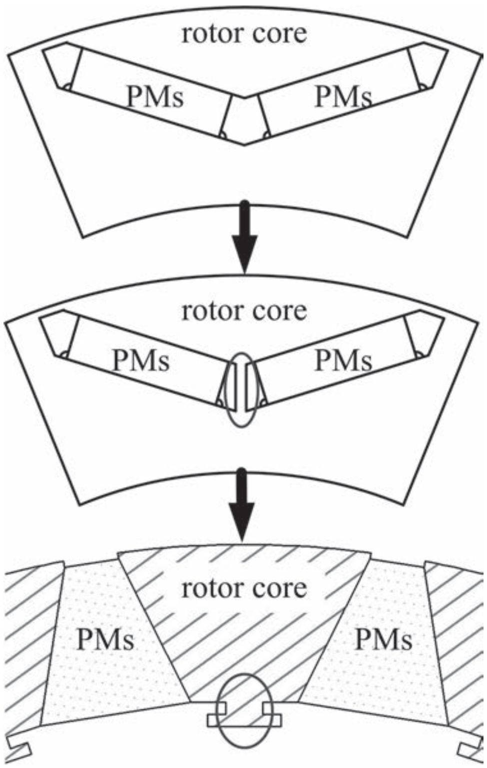

Fig. 2. Optimization of the interior rotor structure.

HQ-13. A Robust Design Optimization Method for Electromagnetic Devices with Interval Uncertainties.

B. Ma[1], J. Zheng[1], G. Lei[1], J. Zhu[1] and Y. Guo[1]
1. University of Technology Sydney, Sydney, NSW, Australia

Abstract—To solve the problem with interval uncertainties for robust optimization of electromagnetic devices, this paper presents a robust optimization approach based on Chebyshev interval method to estimate the extreme values of the constraints and objectives. The numerical results of a case study are reported to validate the proposed methodology. I.Introduction Probability theory-based methods and interval theory-based methods are two main analysis approaches for problems with uncertainties. Many of the current research works are based on the probability theory that models the distributions of the parameters by their probabilistic information [1]. Generally speaking, a large number of samples are needed to build the accurate probability distributions of the uncertain parameters. However, in actual engineering problems, it is difficult to acquire sufficient experimental samples in many cases to obtain the accurate probability distributions for some variables but the lower and upper bounds can be easily obtained such as the early stage of design with less manufacturing experience. Interval model makes it possible to measure bounds of the system outputs with only limited information [2,3]. In this paper, we incorporate the Chebyshev interval method to efficiently approximate the extreme values of the interval functions as well as avoiding the double loop process which means to calculate the minimum or maximum value for a considered function, and propose a new robust method for electronic devices with interval uncertainties. Through the comparison study with deterministic and MC based robust optimization of the BLDC motor, the efficiency and accuracy of the interval method are proved. II.Chebyshev Interval Method Based Robust Optimization A. Robust optimization model with uncertainties The optimization models for problems with interval uncertainties will be built under the worst cases by considering the upper bounds of the objective function and the constraints, so the robust design optimization problem can be formulated as equation (1), where *f(X,Y)* represents the objective function, $g_i(X,Y)$ represents the *i*th constraint, and Y_L and Y_U are the upper bound and lower bound of the interval parameters. The above design optimization problem is usually an unstable min-max problem, which may require high computational costs. A non-intrusive Chebyshev method is introduced to overcome the defects and estimate the bounds of the objective function and constraints. B. Chebyshev interval method For numerical simplicity but without losing any generality, we will assume the interval variable Y_i = [-1,1], *i*=1, 2, ···, *m*. Based on the Chebyshev theory [4], the truncated Chebyshev series with k^{th} order is used to approximate the merit function *C*(*Y*) as equation (2), where $c_{n1n2...nm}$ is the corresponding coefficient, n_i, i=1, 2, ···, m constitutes an index vector. Equation (3) is the multivariate Chebyshev polynomial which is built from the univariate Chebyshev polynomial as equation (4). Least square method (LSM) as expressed in equation (5) is used to calculate the coefficient where *A* represents the sample matrix, *C*(*Y*) is the model output vector at the design points. Based on the characteristics of the trigonometric functions, we can find equation (6). Thus, the maximum value for *C(Y)* can be calculated as equation (7) where the sign function is defined as equation (8). III.Numerical Example To verify the effectiveness of the presented method, a brushless DC wheel motor benchmark [5] is investigated in this work. For the problem considering the interval uncertainties, the design parameters with tolerances are listed in table I. The deterministic mono-objective problem of the benchmark aims to have the best efficiency respecting some technical constraints which can be written as equation (9) where η, M_{tot}, D_{int}, D_{ext}, I_{max}, T_a, and *discr* are the efficiency, total mass of the active parts, inner and outer diameter, highest demagnetisation phase current, temperature of the magnets, and the determinant used for the calculation of the slot height respectively. For the bi-objective case, the second objective of the bi-objective case is to reduce the mass as equation (10). IV.Discussion and Results To verify the effectiveness of the robust interval method, the deterministic and robust optimization with MC method are all conducted for comparison. *A. Mono-objective Case* Table II lists the optimization results of the case, and the main conclusions can be drawn. The same optimization objective has been reached by the Chebyshev interval method and MC method which is smaller than the deterministic optimization. And the optimal design parameters of the Chebyshev method are verified by the MC analysis with desired reliability while the deterministic design offense the constraints about I_{max} and *discr*. *B. Bi-objective Case* Fig. 1 illustrates the Pareto results of the bi-objective case, in which the optimization results of the proposed method align well with the ones of the MC method. The optimization time of the Chebyshev interval method is 779s which is much faster than the MC method 9799s. Compared with the deterministic designs, the Pareto front of robust designs move inside the feasible objective space by enforcing of the desired reliable bounds. V.Conclusion The robust optimization approach based on Chebyshev interval method in this paper shows high efficiency and accuracy for the design problem of electromagnetic devices with interval uncertainties.

[1] S. L. Ho, S. Yang, "A fast robust optimization methodology based on polynomial chaos and evolutionary algorithm for inverse problems," IEEE Trans. Mag., vol.48, no. 2, pp. 59-262,2012. [2] B. Haim, Yakov, and I. Elishakoff, "Convex models of uncertainty in applied mechanics," vol. 2, Elsevier, 2013. [3] S. Yang, J. Yang, Y. Bai and G. Ni, "A new methodology for robust optimizations of optimal design problems under interval uncertainty," IEEE Trans. Mag., vol. 52, no. 3, pp. 1-4, March 2016. [4] J. Wu, Z. Luo, Y. Zhang, N. Zhang, and L. Chen, "Interval uncertain method for multibody mechanical systems using Chebyshev inclusion functions," International Journal for Numerical Methods in Engineering vol. 95, no. 7 pp. 608-630, 2013. [5] S. Brisset, and P. Brochet, "Analytical model for the optimal design of a brushless DC wheel motor," COMPEL-The International Journal for Computation and Mathematics in Electrical and Electronic Engineering, vol. 24, no.3, pp. 829-848, 2005.

$$\begin{cases} \min : \max f(X,Y) \\ \text{s.t.} \quad \max g_i(X,Y) \le 0, i=1,2,\cdots,n \\ \qquad Y_L \le Y \le Y_U \end{cases} \quad (1)$$

$$C(Y) = \sum_{0 \le n_1, n_2, \cdots, n_m \le k} c_{n_1 n_2 \cdots n_m} \Psi_{n_1 n_2 \cdots n_m}(Y) \quad (2)$$

$$\Psi_{n_1 n_2 \cdots n_m}(\xi) = \prod_{i=1}^{m} \cos(n_i[\theta_i]) \quad (3)$$

$$[\theta_i] = \arccos(\eta_i) = [0,\pi], i=1,2,\cdots,m \quad (4)$$

$$c = \left(A^T A\right)^{-1} A C(Y) \quad (5)$$

$$\prod_{i=1}^{m} \cos(n_i[\theta_i]) = [-1,1] \quad (6)$$

$$\max C(Y) = c_{00\ldots0} + \sum_{\substack{0 \le n_1, n_2, \cdots, n_m \le k \\ n_1 + n_2 + \cdots + n_m \ne 0}} \left|c_{n_1 n_2 \cdots n_m}\right| = c_{00\ldots0} + \sum_{\substack{0 \le n_1, n_2, \cdots, n_m \le k \\ n_1 + n_2 + \cdots + n_m \ne 0}} c_{n_1 n_2 \cdots n_m} \operatorname{sign}\left(c_{n_1 n_2 \cdots n_m}\right) \quad (7)$$

$$\operatorname{sign}(x) = \begin{cases} -1, & x < 0 \\ 0, & x = 0 \\ 1, & x > 0 \end{cases} \quad (8)$$

$$\begin{cases} \max \ \eta \\ s.t. \ \begin{cases} M_{tot} \le 15kg, D_{int} \ge 76mm, I_{max} \ge 125A \\ D_{ext} \le 340mm, T_a \le 120°C, discr \ge 0 \end{cases} \end{cases} \quad (9)$$

$$\begin{cases} \text{obj.} \ \begin{cases} \max \ \eta \\ \min \ M_{tot} \end{cases} \\ s.t. \ \begin{cases} D_{int} \ge 76mm, I_{max} \ge 125A \\ D_{ext} \le 340mm, T_a \le 120°C, discr \ge 0 \end{cases} \end{cases} \quad (10)$$

Equations

TABLE I
INITIAL DESIGN OF THE BLDC MOTOR

Par.	Description	Unit	Initial	T
U_{DC}	Voltage of the DC bus	V	120	0.5
e	Length of air gap	mm	0.8	0.05
L_m	Length of the stack	mm	45	0.5
Ds	Stator out diameter	mm	189	1
J	Current density	A/mm²	3	0.03

Tolerance (T)

TABLE II
MONO-OBJECTIVE OPTIMIZATION RESULTS

Par.	U_{DC}	*e*	L_m	*Ds*	*J*	η
Unit	V	mm	mm	mm	A/mm²	
Deter.	50.07	0.41	44.1	206.5	2.000114	0.9536
Cheb.	50.03	0.46	41.9	206.9	2.085491	0.9528
MC	50.04	0.46	41.6	207.4	2.082096	0.9528

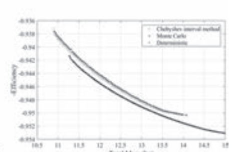

Fig 1. Comparison of the bi-objective optimization results

Tables and figures

HQ-14. Optimized design of segmented magnet demagnetization and eddy current loss analysis of fractional pole slot combination IPMSG for ISG.

B. Kim[1], D. Lee[1], J. Lee[1], S. Lee[1] and D. Kang[1]
1. Keimyung University, Daegu, The Republic of Korea

This paper contains an analysis of the demagnetization and vibration characteristics of an IPMSG(Interior Permanent Magnet Synchronous generator) type motor-generator for 48V 5kw class ISG and the contents of the optimal design for improvement of output characteristics. Particularly, the effect of fractional slot on the demagnetization and vibration characteristics compared with the concentrated winding is studied. By using this, we intend to draw conclusions through the formula type approach of the demagnetization and vibration characteristics. In this research, analysis was carried out using ANSYS EM and the results were analyzed. Based on the results, the optimization design was performed. According to the operation characteristics of the ISG, the driving area was divided into three areas: motoring 3000rpm, power generation area 4000rpm, and 16500rpm. In general, vehicle electrical equipment is very sensitive to vibration characteristics and ISG is attached to the engine part of the vehicle, so specifications are given to minimize vibration. In addition, the high output ISG has a very high driving current, which causes a risk of irreversible demagnetization. Therefore, in this paper, we confirmed the fractional slot-based winding method and the torque ripple of the conventional concentrated winding method in the entire operation region of the ISG. Based on this torque ripple characteristic, the vibration characteristics were compared and analyzed through mechanical Cosimulation. And by applying various driving current ranges that can generate irreversible demagnetization, we compare demagnetization of fractional slot with demagnetization of concentrated winding for the same rotor structure. In addition, the characteristics of demagnetization and eddy current depends on the lamination type of the inserted magnet in the rotor, so this is mainly compared and analyzed. In this paper, permanent magnet is divided into 3segments and 7segments as a comparison model. We analyze how does the stacking of magnets in the fractional slot winding method affects the eddy current loss reduction. The demagnetization phenomenon of laminated magnets is compared and analyzed by 3D simulation. In order to analyze the effect of the irreversible demagnetization of the laminated magnets on vibration, we used mechanical Cosimulation technique. Modal analysis and harmonic analysis are performed for vibration characteristics analysis and resonance frequency is found. In order to verify the results of this analysis, various types of magnets were made and a comparison test was conducted using various types of magnets. so we are willing to show program analysis data and experimental data.

[1].Demagnetization study of an interior permanent magnet synchronous machine considering transient peak 3 phase short circuit current, Seong Taek Lee, 2017 IEEE Energy Conversion Congress and Exposition(ECCE), 2017 [2].Analytical Model for Combined Study of Magnet Demagnetization and Eccentricity Defects in Axial Flux Permanent Magnet Synchronous Machines, Jan De Bisschop, IEEE Transactions on Magnetics, 2017 [3]. Acoustic Noise Based Uniform Permanent Magnet Demagnetization Detection in SPMSM for High-Performance PMSM Drive, Min Zhu, IEEE Transactions on Transportation Electrification, 2017 [4].Demagnetization Fault Detection in Axial Flux PM Machines by Using Sensing Coils and an Analytical Model, Jan De Bisschop, IEEE Transactions on Magnetics, 2017 [5]. Numerical Simulation of Magnetization and Demagnetization Processes, Alfredo Bermúdez, IEEE Transactions on Magnetics, 2017

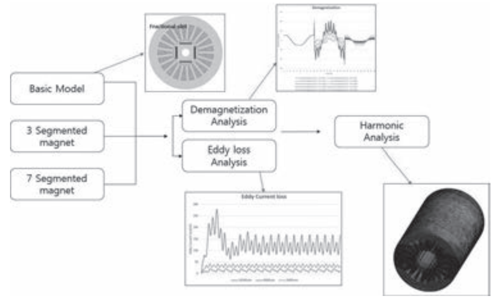

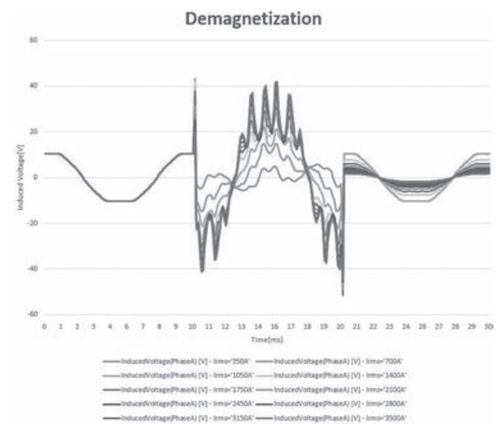

HQ-15. Discrete-Search Algorithm for Estimation of MTPA Trajectory in Electromagnetic Design Optimization of Interior Permanent Magnet Machines.

A. Pouramin[1], M. Farshadnia[1], *S. Paul*[2,1], R. Dutta[1] and F.M. Rahman[1]
1. School of Electrical Engineering and Telecomunications, University of New South Wales, Universtiy of NSW, NSW, Australia; 2. Electrical Engineering, Dong-A University, Busan, The Republic of Korea

INTRODUCTION: Design optimization of interior permanent magnet (IPM) machines has received an extensive attention due to the very recent developments in finite element analysis (FEA) based design optimization technique such as computationally efficient finite element analysis (CE-FEA) [1, 2]. These techniques have been used in electromagnetic design optimization of IPM machines from multiple perspectives to improve their performance characteristics under the constant-torque and/or constant-power operating regions [3]. Many IPM machine applications such as wind turbines and servo motors require optimal operation under the constant-torque region, where the electromagnetic behavior is typically evaluated at the maximum torque per ampere (MTPA) trajectory. Therefore, an accurate method to estimate the MTPA trajectory is necessary during the electromagnetic design optimization of the IPM machines. Accurate determination of MTPA trajectory is possible using detailed FEA. However, the detailed FEA significantly increases the computational time of design optimization by several orders even with the recent development in processing power of computational resources. Conventional methods of MTPA trajectory estimation use a classical dq model in the dq reference frame. The combination of the classical dq model and CE-FEA has been presented by [1,2] for the estimation of MTPA point at a rated current. The conventional method is fast as it only requires three FEA runs in the pre-processing stage of the design optimization procedure. However, it fails in accuracy for IPM machines with a high level of magnetic saturation due to the variation of inductances with respect to the stator current. In more recent literature [3], authors have proposed a method to build torque and flux linkage look-up tables for a set of dq-axes current using CE-FEA in the pre-processing stage of a design optimization. The look-up tables can cover a wide range of operating cycle, but with a cost of an increase in computational time as it requires a significant number of FEA runs. This paper overcomes the above mentioned drawbacks by proposing a computational-efficient procedure that estimates the MTPA trajectory with a high accuracy and minimum computational effort. The proposed method provides a tradeoff between the computational time and the accuracy of the estimation by using a discrete search algorithm in a magneto-static FEA. METHODOLOGY: The proposed method creates a mesh grid of the developed torque (T_{dev}) for each population concerning the magnitude of stator current (I) and the current angle (γ) using a minimum number of FEA runs. The current angle, γ, is the angle between current vector and q-axis in the *dq*-plane reference frame. Implementation procedure of the proposed method in a multi-objective optimization algorithm is shown in Fig. 1 (a). After the initialization stage of the optimization algorithm, the discrete-search algorithm has been used to find the MTPA trajectory for each population. To reduce the number of FEA runs and computational time, discrete values are selected for I and γ. For further reduction in computational time, it is assumed that the developed torque is zero when *I* is zero and/or when γ is 90 degrees. By fitting a surface on the obtained mesh grid, the MTPA trajectory can be found. Then, the performance characteristics of all populations can be evaluated on their MTPA trajectories. As can be seen, the proposed method requires only eight single magneto-static FEA runs in the pre-processing stages for two sets of stator current, i.e., the currents at a full load and a half load, which significantly reduces computational time in comparison with detailed FEA. RESULTS AND CONCLUSION: The proposed method is used to optimize three different benchmarks IPM motors using a non-dominated sorting genetic algorithm (NSGA-II) as a multi-objective optimization algorithm. First, an FSCW IPM motor with 18-slot 14-pole combination is chosen as a representative for the family of concentrated windings with a high level of harmonics in the stator magneto-motive force as shown in Fig. 1 (b). Second, a 24-slot 4-pole DW IPM motor with a segmented PMs is considered as an unsaturated IPM motor, which is shown in Fig. 1 (c). Finally, the well-known Toyota Prius IPM motor (Fig. 1 (d)) is chosen to investigate the effectiveness of the proposed method under a high current density and saturated iron cores. Fig. 2 (a) compares the T-γ characteristic curves of the Toyota Prius IPM motor obtained by the conventional method, the proposed method and the transient FEA. As evident, the proposed method is relatively similar to the one obtained from the time-stepped FEA with average torque. The results of the multi-objective optimization algorithm for two objectives (saliency ratio and efficiency) are shown in Fig. 2 (b). It is evident that the method of calculating the MTPA trajectory has a significant effect on Pareto-front designs. This comparison highlights the advantages of using the proposed method i.e. high accuracy and less computational time. The MTPA trajectories obtained by the experimental test are not presented due to space limitations but will be provided in the extended manuscript.

[1] G. Y. Sizov, Z. Peng, D. M. Ionel, N. A. O. Demerdash, and M. Rosu, "Automated Multi-Objective Design Optimization of PM AC Machines Using Computationally Efficient FEA and Differential Evolution," Industry Applications, IEEE Transactions on, vol. 49, pp. 2086-2096, 2013. [2] D. M. Ionel and M. Popescu, "Finite-Element Surrogate Model for Electric Machines With Revolving Field-Application to IPM Motors," Industry Applications, IEEE Transactions on, vol. 46, pp. 2424-2433, 2010. [3] A. Fatemi, N. A. O. Demerdash, T. W. Nehl, and D. M. Ionel, "Large-Scale Design Optimization of PM Machines Over a Target Operating Cycle," IEEE Transactions on Industry Applications, vol. 52, pp. 3772-3782, 2016.

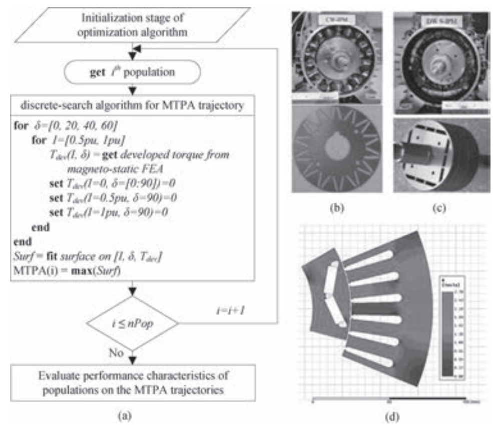

Fig. 1. (a) Proposed method, (b) 18-slot 14-pole concentrated-wound IPM motor, (c) 24-slot 4-pole distributed-wound segmented IPM motor (d) Toyota Prius IPM motor 2004.

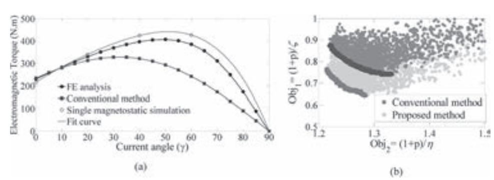

Fig. 2. (a) Torque vs. current angle for Toyota Prius 2004, (b) Pareto-front designs for the conventional method and the proposed method for the FSCW IPM Machine.

HQ-16. Performance Optimization of an Air-core PMSLM with New Double-layer Windings.

W. Mei[1] and Q. Lu[1]
1. College of Electrical Engineering, Zhejiang University, Hangzhou, China

I. INTRODUCTION The air-core PM synchronous linear motors (APMSLM) are widely used in precision location system such as laser test station and IC manufacturing device. Due to without iron core, they have many merits of the low thrust ripple, rapid response and easy controllability etc. [1], but the thrust density is also decreased. Although the methods of double secondary and Halbach PM Array are normally used to increasing the thrust density [2]-[3], the distributed winding structure is another effective way [4]-[5]. However, its overlapping end structure is complex and difficult to be manufactured. In order to solve this problem, a novel double-layer winding air-core PMSLM (DWAPMSLM) with Halbach array PMs is proposed. The structure is only suitable for odd number coils in the same limited space. It adopts double-layer concentrated winding to act as one-layer distributed winding, which successfully shortens the winding end and saves motor volume. To traditional one-layer concentrated winding, the winding factor is not high considering the space limit, so DWAPMSLM places the windings in two layers to let every phase coil get winding factor as high as possible, and then the thrust density is increased rapidly. Moreover, the thrust density per volume is also increased due to the end space of primary is saved. Therefore, the proposed DWAPMSLM is suitable for long time running precision location system because of high thrust density and low heating power. II. MODEL AND ANALYSIS Fig. 1(a) shows the topology of the novel 6-poles/9-coils DWAPMSLM (Model A). The secondary is consisted of Halbach array PMs and back-iron. Halbach array PMs can provide higher flux density and more sinusoidal magnetic field than normal array PMs. The primary is made of 9 coils in two layers. To evaluate the performance of double-layer winding structure, two normal winding structures, concentrated winding (Fig. 1(b), Model B) and distributed winding (Fig. 1(c), Model C), are listed to do comparative study. In order to keep the same volume and power loss, the two traditional winding motors adopts 7-poles/6-coils to provide as high thrust density as possible under the limit of volume and power loss. In addition, their total number of coil turns per phase is also set same regardless of their different poles and coils number. The parameters of three models are shown in Tab. (a). Fig. 2(a) shows the thrust force curve of the three models at current 1A. The force constants of the three models are 17.52N/A, 16.00N/A, 17.74N/A, and the thrust ripples are 1.27%, 0.68%, 0.64%, respectively. Apparently, at the same current, Model A and Model C can provide higher thrust because they own higher winding factor than Model B. Moreover, the force constant of proposed model A is only 1.2% less than that of the traditional model C. Since the structure of model A is much simpler than model C, the new double-layer winding structure is meaningful in some particular application. Fig. 2(b) and fig.2(c) show the back-EMF and flux linkage of the three models at speed 2.02m/s. Their back-EMF peak values are 24.84V, 23.89V, 24.88V, and the flux linkage peak values are 0.0848Wb, 0.0760Wb, 0.0862Wb. Similar to the thrust density, Model A and Model C perform better than Model B. In addition, the difference between Model A and C can be ignored. Therefore, the proposed Model A has almost same performance as model B, but winding structure is simplified and manufacture cost is lowered. III. CONCLUSION This paper proposes a new DWAPMSLM. Compared with traditional concentrated winding and distributed winding in the same air-cored PMSLM application, this double-layer winding structure can not only provide nearly same thrust density as distributed winding, but also have simple structure as concentrated winding. This DWAPMSLM is strong candidate when APMSLM has odd number of coils.

[1] Liyi Li, Yongbin Tang, Mingna Ma and Donghua Pan, "Analysis and Optimization of Air-Core Permanent Magnet Linear Synchronous Motors with Overlapping Concentrated Windings for Ultra-precision Applications", Journal of International Conference on Electrical Machines and Systems Vol.2, No.1, pp.16~22, 2013. [2] Maarten F. J. Kremers, Johannes J. H. Paulides, Jeroen L. G. Janssen and Elena A. Lomonova, "Design Considerations for Coreless Linear Actuators", IEEE TRANSACTIONS ON MAGNETICS, VOL.49, NO.5, MAY 2013. [3] Zhihua Zhang, Liming Shi, Qiongxuan Ge, Yaohua Li, "Investigation of Single-Sided Ironless Linear Synchronous Motor Based on Permanent Magnet Halbach Array Used for Medium-Speed Maglev", 11th International Symposium on Linear Drives for Industry Applications (LDIA), 2017. [4] Liyi Li, Yongbin Tang and Donghua Pan, "Design Optimization of Air-Cored PMLSM with Overlapping Windings by Multiple Population Genetic Algorithm", IEEE TRANSACTIONS ON MAGNETICS, VOL.50, NO.11, NOVEMBER 2014. [5] Seun Guy Min and Bulent Sarlioglu, "Comparative Study of Coreless-Type PM Linear Synchronous Machines with Non-Overlapping Windings", 2017 IEEE Energy Conversion Congress and Exposition (ECCE), 2017.

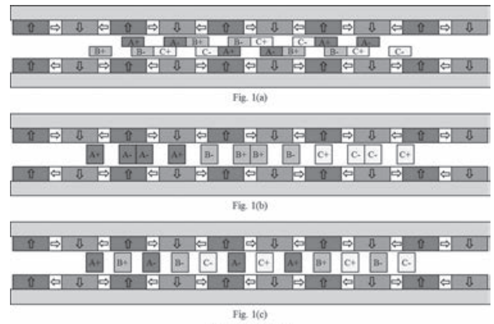

DESIGN PARAMETERS

Parameters	Initial values		
Model	A	B	C
Winding type	double-layer	concentrated	distributed
Number of primary coils	9	6	6
Turns per phase	144	144	144
Length of primary(mm)	134	134.6	136.6
Number of secondary poles	6	7	7
Secondary pole pitch (mm)		40.4	
Length of air gap(both) (mm)		0.8	
Motor height(mm)		33.6	
Motor travel(mm)		300	
Permanent magnet		48	

Tab. (a)

Fig. 1. (a), 1(b) and 1(c) show the topology of the three models. Tab. (a) shows the design parameters.

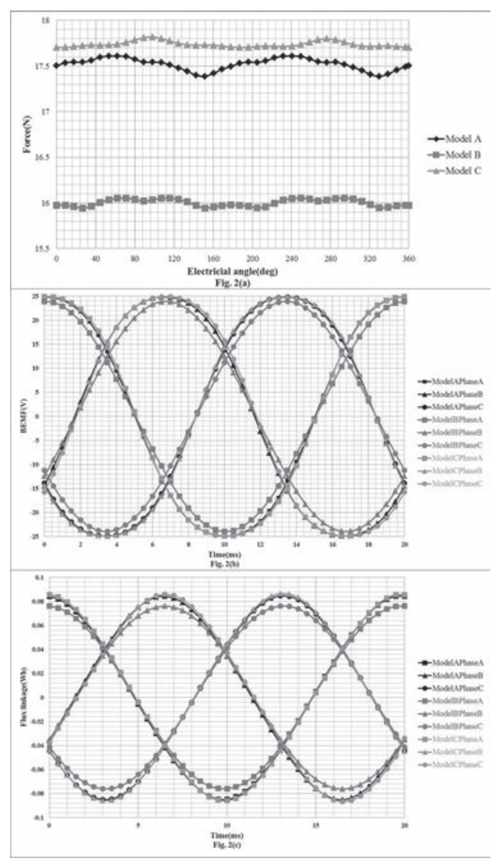

Fig. 2. (a), 2(b) and 2(c) show the electrical performance of the three models.

Session HR
ENERGY HARVESTERS AND GENERATORS II
(Poster Session)

Shuangxia Niu, Co-Chair
The Hong Kong Polytechnic University, Hung Hom, Hong Kong
Shuhong Wang, Co-Chair
Xi'an Jiaotong University, Xi'an, China

HR-01. Characteristics of Energy Harvesting in Flywheel Energy Storage System Based on Efficiency Map of Electric Machine.

J. Cho[1], H. Hwang[1], Y. Choo[1], C. Kim[1] and C. Lee[1]
1. Electrical and Computer Engineering, Pusan National University, Pusan, The Republic of Korea

A flywheel energy storage system (FESS) having a bidirectional power converter (BDC) and a synchronous machine stores energy as rotational kinetic energy and uses the stored energy whenever required. An FESS has the advantages of high efficiency, large energy storage density, numerous charge and discharge cycles, and environment-friendly characteristics in comparison with other energy storage units. Its applications vary from uninterruptible power supplies (UPS) to micro grids, wind power plants, vehicle regenerative braking and so on. In the past decade, for the improvement of an FESS, a lot of researches have been done on the issues of bearing, motor/generator design, power system, and control algorithm [1-2]. Among the various element technologies, the discharge control of a flywheel rotor from kinetic energy to electrical energy is the core part of the FESS. In the energy discharging mode, a synchronous machine produces voltage by working as a generator and its BDC supplies constant voltage by acting as a boost converter. In this process, energy efficiency in an FESS and maximum voltage gain in the BDC vary by the power of a load in watts, and as a result, the amount of usable kinetic energy from the flywheel is altered. Voltage gain and energy efficiency in the BDC depending on load resistance have been analyzed in [3], and maximum voltage gain and minimum speed according to the ratio of the generator resistance to load resistance have been well described. However, the reason for change in efficiency with respect to load resistance has not been examined clearly. Energy efficiency in an FESS is directly related to the operation characteristic of a synchronous generator, and thus it is important to analyze the efficiency of the generator according to overall speed range. This paper focuses on the characteristic of energy harvesting in a flywheel energy storage system at three different load points during discharging mode. For experimental verification, the FESS having a permanent magnet synchronous machine (PMSM), a flywheel rotor, and a BDC is manufactured and tested at three different load points as shown in Figs. 1 and 2. The PMSM works as a motor to accelerate the flywheel up to 3,000rpm, and then the synchronous machine is switched over to a generator in order to make DC bus voltage constant at 350 volts. In Fig. 2a, the energy harvesting of the flywheel has been experimented at 490, 980, and 1470 watts in load, and energy efficiency is compared with respect to load power. The deviation of energy efficiency at three load conditions is investigated by analyzing the path of q-axis current on the efficiency map of the PMSM in case of generated energy from the flywheel as given in Fig. 2b. Considering current trajectories under each load condition, it can be seen that q-axis current under the condition of 83.3 ohms is contoured as the synchronous generator is operated at higher efficiency compared to the other two conditions. As a result, the efficiency of the flywheel system according to load during power generation is analyzed in considering the efficiency map of the generator and the length of current locus in second at each load point. Also, the loss of the flywheel will be estimated by separating copper loss and iron loss versus speed and torque. The validity of this study is demonstrated by correlating the efficiency of the flywheel system with the efficiency map of the PMSM given in Fig. 2b.

[1] Pena-Alzola, R., et al. "Review of flywheel based energy storage systems." *Power Engineering, Energy and Electrical Drives (POWERENG), 2011 International Conference on*. IEEE, 2011. [2] Amiryar, Mustafa E., and Keith R. Pullen. "A Review of Flywheel Energy Storage System Technologies and Their Applications." *Applied Sciences* 7.3 (2017): 286. [3] Gurumurthy Salinamakki Ramabhatta, Agarwal Vivek, Sharma Archana. Optimal energy harvesting from a high-speed brushless DC generator-based flywheel energy storage system. *IET Electric Power Applications*, 2013, 7.9: 693-700.

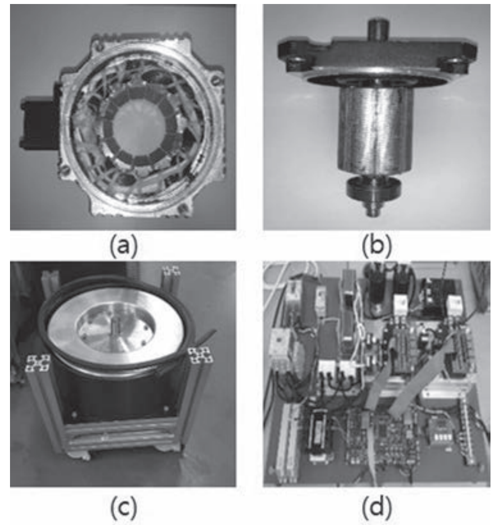

Fig. 1. Flywheel energy storage system, (a) stator assembly, (b) rotor assembly, (c) flywheel, (d) bidirectional power control system.

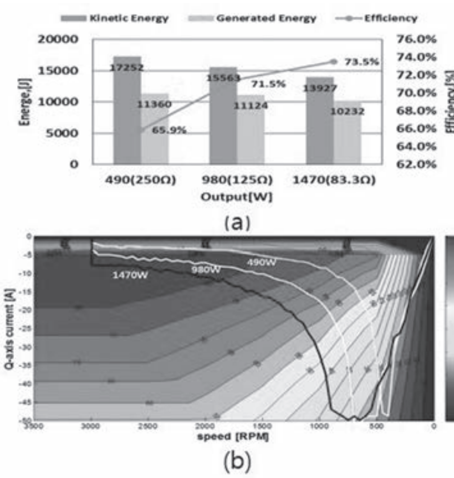

Fig. 2. Experimental results of flywheel at three different load conditions, (a) energy efficiency in flywheel, (b) three paths of q-axis current on efficiency map with respect to load in case of generated energy from flywheel.

HR-02. Influence of Additional Loss in the Rotor Surface on Rotor Temperature Field of 1100MW Half-speed Nuclear Power Turbine Generator.

L. Hu[2], *Y. Su*[1], W. Li[1], Y. Li[1], P. Wang[1] and W. Liu[1]
1. Electrical Engineering, Beijing jiaotong University, Beijing, China;
2. Shanghai Electric Power Generation Equipment Co., Ltd., Shanghai, China

Abstract: Accurately calculation of temperature can truly judge the output of large capacity turbo generator. The copper and core loss of generator is the major factor to determine generator temperature field. And the resistance of coils, an important variable for calculating copper loss, varies with the windings temperature. It is more obviously that the interactions between the resistance and the temperature of windings in the 1100MW nuclear power generator rotor with axial-radial ventilation form, which is because the rotor windings have high thermal coefficient of imbalance in this ventilation form. Thence, the rotor temperature field is calculated by the finite volume method considering varied rotor surface loss. Based on the first calculation results, the new resistance in the calculated temperature of coils is used to secondly calculate rotor temperature filed until the resistance match with the coils temperature. The results between initial calculation and iterative calculation are comparatively studied, which can provide theoretical guidance for precisely calculating iron core loss and generator temperature field. 1. Introduction With the increase of global electricity consumption and improved safety of nuclear energy technology, installed gross capacity of large nuclear power turbine generator get a rapidly progress. The temperature rise of large scale turbine generator is one of the major issues that limits generator capacity. Some scientists in this filed make some researches. Professor Weili Li analyzed the influence of additional loss on rotor surface heat transfer coefficient and temperature field of hydro-generator [1]. Zuomin Wang make a research in numerical simulation of air flow distribution in turbo generator rotor at different rotation speed and inlet pressure [2]. Based on the related research, taking an 1100MW half-speed nuclear power turbine generator rotor with axial-radial ventilation form as an example, that the each part temperature and the thermal coefficient of imbalance vary with the additional loss in the rotor surface is obtained. 2. Mathematic Model and Calculation Methods 2.1 Boundary Conditions As is shown in figure 1, the windings named number 1 to 4 coil from right to left. $S_{1\sim}$ S_3 is insulating surfaces[3]: $dT/dn=0$ (1) S_4 and S_6 is convention surfaces, the average heat transfer coefficient formula is shown in (3): $-\lambda dT/dn=\alpha(T-T_f)$ (2) $\alpha=28[1+(v_1^2+(v_2/2)^2)^{1/4}]$ (3) The heat transfer coefficient in S_4 is 266 W/m$^2\cdot$K, it in S_6 is 248 W/m$^2\cdot$K. 2.2 Additional Loss Calculation In the calculation model, the heat generated by core is calculated by (4)~(8)[4]-[5]. $Q_{2SH}=Q_{2vk}+Q_{2zk}+Q_{2zo}+Q_{2H}/3$ (4) $Q_{2vk}=\phi(\beta)[AS_1/(K_\delta\delta\times10)]^2\times(D_i^5/p^4)\times(l_2/Z_1^{1/2})\times(f/50)^{1.5}\times10^{-18}$(5) $Q_{2Zk}=\phi(\sigma/t_1)[AS_1/100]^2\times(D_i^3/p^{1.5})\times(l_2/Z_1^{1/2})\times(f/50)^{1.5}\times10^{-12}$(6) $Q_{2ZO}=5.1[B_\delta/100\times(K_{\sigma n}-1)]^2\times(D_i^3/p^{1.5})\times(l_{ef}/Z_1^{1/2})\times(f/50)^{1.5}\times10^{-12}$(7) $Q_{2H}=5.73(D_2^4/p^3)l_2\times(f/50)^{1.5}\times(P_H/P_{HO})\times10^{-15}$(8) The results of Q_{2vk}, Q_{2zk}, Q_{2zo}, Q_{2H} are 4.89×10^{-5}kW,71kW,113.4kW,254.5kW. 2.3 Calculation Methods Fluid and transfer calculation method is used to simulate the rotor temperature field [3]. 3. The Influence of Varied Additional Loss in the Rotor Surface on Rotor Temperature Field Based on the fluid and heat transfer theory, the average computational temperature rise of rotor coil is 36K, while the average experimental temperature rise is 37K [6]. The error is 2.7 % to verify the accuracy of the calculation method. Although the studied generator rotor is hydrogen inner-cooled structure, the rotor surface is one of path for cooling. For exploring the influence of varied additional loss in the rotor surface on rotor temperature field, the research scheme uncounting Q_{2vk}, Q_{2zk}, Q_{2zo} are calculated and named scheme i~iii. The 85%, 115% additional loss are also calculated and named scheme iv~v. The calculated results is shown in figure 2. In figure 2, the calculated results of rotor temperature field in the different additional loss have a big difference. Overall, the temperature rise of rotor each part increases with the additional loss enhancing. The temperature rise of the windings, layer insulation, and slot wedge in the schemes differ less than 0.5K, but the temperature rise of iron core and main insulation biggest differ 7K, which means that the heat generated by windings is mostly brought by ventilation groove. The thermal coefficient of imbalance reach 2.15 in the scheme iii, which makes the main insulation stand more pressure to cause layered or selling faults. From scheme i~v, the hot-spot and average temperature rise vary a linear change with additional loss of core. As also shown in figure 2, the thermal coefficient of imbalance of windings in the original scheme is 1.79, which is much higher than the gap gas pick-up and sub-slot ventilation system. The thermal coefficient of imbalance of core is 1.96 and higher than that of the windings, which means that unequal tooth pitch design can effectively reduce the influence of high harmonic of gap magnetic-density, but it makes the thermal unevenness of core enhance and the hot-spot temperature of core is higher than the coil. 4. Conclusion The heat of the hydrogen inner-cooled rotor coil with axial-radial ventilation form is mostly brought by the ventilation duct. Unequal tooth pitch design can effectively reduce the influence of high harmonic of gap magnetic-density, but it makes the thermal unevenness of core enhance and the hot-spot temperature of core is higher than the coil. The temperature calculation values is much closer with the measured values considering that the resistance vary with windings temperature.

[1] Weili Li, Dongmei Wang, The Influence of Additional Loss on Rotor Surface Heat Transfer Coefficient and Temperature Field of Large Air-Cooled Hydro-Generator, The 14th Biennial IEEE Conference on Electromagnetic Field Computation, 2010. [2] Zuomin Wang, Jiade Han,Numerical Simulation of Air Flow Distribution in Large Air-cooled Turbo Generator Rotor at Different Rotation Speed and Inlet Pressure. 17th International Conference on Electrical Machines and Systems (ICEMS), 2014. [3] Weili Li, Dan Li, Jinyang Li, Influence of Rotor Radial Ventilation Ducts Number on Temperature Distribution of Rotor Excitation Winding and Fluid Flow State Between Two Poles of a Fully Air-cooled Hydro-generator, IEEE Transactions on industrial electronics, Vol. 64, No. 5, 2017. [4] Ana B. M. Aguiar, Arezki Merkhouf, Kamal Al-Haddad, A New Approach for Computation of Magnetic Core Losses in Large Hydro Electrical Generator, 39th Annual Conference of the IEEE Industrial Electronics Society (IECON), pp.2506-2511, 2013. [5] Zhennan Fan, Li Han, Loss and Heat Computations of Damper Bars in Large Tubular Hydro-generator, International Conference on Electrical Machines and Systems, pp524-529, 2008. [6] Lei Hu, Flow Field and Temperature Field Characteristics Study on Water-hydrogen-hydrogen Turbo Generator with Axial Ventilation Structure, University of Shanghai for Science and Technology Doctoral Dissertation, 2015.

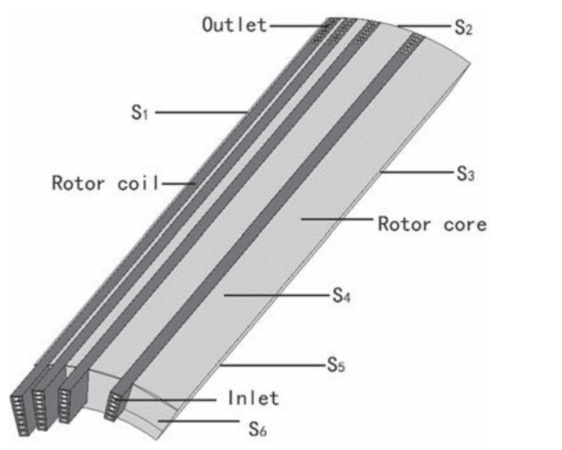

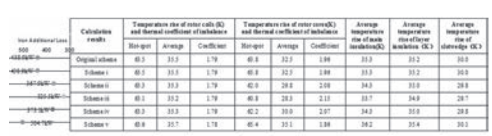

Calculation results	Temperature rise of rotor coils (K) and thermal coefficient of imbalance			Temperature rise of rotor cores(K) and thermal coefficient of imbalance			Average temperature rise of main insulation(K)	Average temperature rise of layer insulation (K)	Average temperature rise of slotwedge (K)
	Hot-spot	Average	Coefficient	Hot-spot	Average	Coefficient			
Original scheme	40.5	35.5	1.79	40.8	32.5	1.96	35.3	35.2	30.0
Scheme i	40.5	35.5	1.79	40.8	32.5	1.96	35.3	35.2	30.0
Scheme ii	40.3	35.3	1.79	42.0	28.8	2.08	34.3	35.0	29.8
Scheme iii	40.1	35.2	1.79	40.8	28.3	2.15	33.7	34.9	29.7
Scheme iv	40.3	35.3	1.79	42.2	30.0	2.07	34.3	35.0	29.8
Scheme v	40.8	35.7	1.78	45.4	35.1	1.86	36.2	35.4	30.1

HR-03. Research on an Asymmetric-primary Axis-flux Maglev Generator for the Vertical Axis Wind Turbine.

J. Liu[1]
1. Hohai University, Nanjing, China

Abstract—The floating wind power generation has an good application prospect in the field of the wind power generation on the sea. The direct-drive vertical axis wind turbines(DVAWT) is one of the most important for that. In order to improve the starting performance and output power of DVAWT, an axial-flux maglev generator with asymmetric primary is proposed. The motor is designed as disc type with double primaries and one rotor. Two-sided asymmetric primary is adopted to obtain maglev force, working with the lift force of the wind turbine to improve the starting performance. Hybrid excitation is used to adjust the suspension force and output power in real time for the stable output. The principle of the machine is analyzed and computational analysis and optimization of the forces are carried out. 3-D model is built and verifies the machine. Introduction In the field of wind power generation(WPG), the horizontal axis wind power generation(HAWPG) is common applied to the grid-tied large power system, and for the small WPG system, the vertical axis wind power generation(VAWPG) has special superiorities, such as possible suffering wind from all the directions, stable force, small starting speed, small running speed of the wind turbine and easy to install etc.. For the wind power generation on the sea, the HAWPG is facing the questions of great bulk, needing hard foundation, high installing and maintenance cost and so on. The floating wind power generation has an good application prospect in the field of the wind power generation on the sea. It can be installed in the area of strong wind and uses VAWPG to decrease the cost. Seeing the researches about VAWPG, there are two kinds of lift force type and drag force type. The lift force type has small starting torque but little utilization coefficient of wind energy. The drag force type has the big utilization coefficient of wind energy but poor starting performance. As we known, the generator is the centre part which decides the conversion efficiency of the energy and operating performance of the power system. Based on the advantages of the lift force type of VAWPG and disc motor, an asymmetric-primary axis-flux maglev generator for the vertical axis wind turbine is proposed for the VAWPG. I.Structure The maglev design is applied to improve the starting performance and increase the conversion efficiency of the energy and power density of the VAWPG. The motor has a structure of double primaries and one rotor. Two-sided asymmetric primary is adopted to obtain maglev force, working with the lift force of the wind turbine to improve the starting performance. Hybrid excitation is used to adjust the suspension force and output power in real time for the stable output. The structure of the proposed motor is given by Fig.1. I.reluctance-network model To optimize the design, nonlinear reluctance-network method is used to get the parameterized model for the proposed motor. The laws of the parameters effecting the motor performance are grasped. Then, all the optimized structure-dimensions of the magnetic poles are obtained. The maglev force is also analyzed and solved by the virtual work method. The magnetomotive of the electromagnet is F=NI The magnetomotive of the permanent magnet is $F=H_c h_m$ And the matrix is $R\Phi=F$ I.Results To verify the design and optimize the parameters further, 3-D finite element model (FEM)is built upon the results of nonlinear reluctance-network method. The static and the dynamic state are studied and the results are compared. The output voltages of the proposed motor are shown in Fig.2(a) Following the exciting current changing, the maglev force changes too. There are the changing curves of the maglev force under two values of the exciting current shown in Fig.2(b). From it, we can see that the maglev force of the motor can be controlled by controlling exciting current to control the magnetic field.

[1] Ghanshyam Shrestha, Henk Polinder, Deok-Je Bang. Jan Abraham Ferreira, Structural Flexibility: A Solution for Weight Reduction of Large Direct-Drive Wind-Turbine Generators[J]. IEEE Transactions on Energy Conversion, 2010, 25(3): 732–740. [2] Rong-Jie Wang, Lodewyk Bronn, Stiaan Gerber, Pushman Tlali. An Axial Flux Magnetically Geared Permanent Magnet Wind Generator[J]. IEEJ Transactions on electrical and electronic engineering, 2015, 10(s1): S123 – S132 [3] Ronghai Qu, Dawei Li, Jin Wang. Relationship between Magnetic Gears and Vernier Machines[C], Proc. IEEE Int. Conf. on Electrical Machines and Systems ICEMS, Aug.2001, pp1-6.

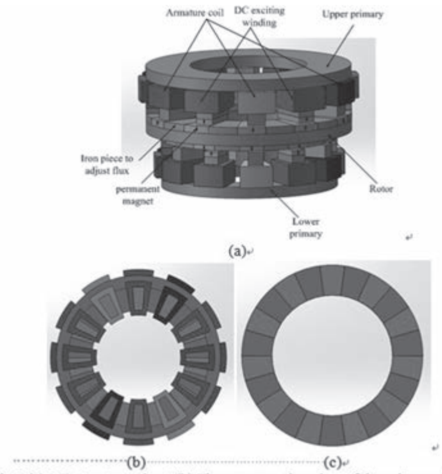

Fig.1 (a) 3-D structure chart, (b) The cross-section view of the primary, (c) The cross-section view of the rotor

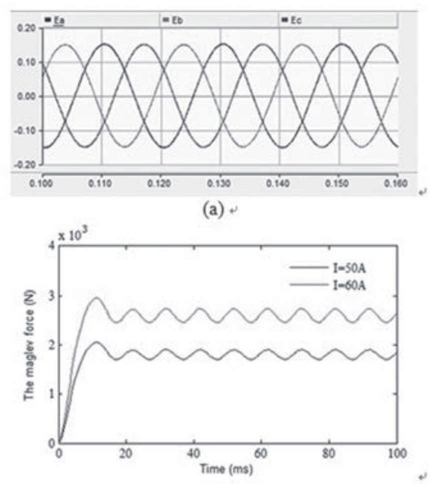

Fig.3 (a) The output voltages from the electric generator
(b) The maglev force from the proposed motor

HR-04. Modeling and Design of a Efficient Magnetostrictive Energy Harvesting System with Low-Voltage and Low-Power under Low Vibration Excitation.

S. Cao[1], X. Wang[1] and J. Zheng[1]
1. Hebei University of Technology, Tianjin, China

Magnetostrictive (e.g., Terfenol-D, Galfenol) vibration generators are attractive because they can provide higher energy density than electromagnetic generators and have similar levels of output power with piezoelectric generators [1]. However, when the magnetostrictive generators are under a low vibration excitation, they exhibit extremely low voltage of a few hundred millivolts [1]-[4] and low power of a few hundred microwatt [2],[3]. Thus, it is necessary to model and design a efficient magnetostrictive harvesting system, which can track the maximal power, store the energy, and can use such low power to boost such low AC voltage for satisfying the load end requirements (1.8-3.3V DC). Different models of the magnetostrictive generators are presented, including the distributed parameter dynamic coupled models [2],[5], the lumped parameter dynamic uncoupled model [3], finite element uncoupled model [6], finite element coupled model [4], and the distributed parameter equivalent circuit dynamic coupled model [7]. As detailed in [7], the models in [2]-[6] are difficult to analyze the harvesting system with practical energy extraction circuits (EECs) while the distributed parameter equivalent circuit model [7] is more complex. Moreover, the harvesting system with a self-powered EEC [7] only can intermittently supply power to the end load only when the generator produce bigger output voltage >1.2V. In order to boost low AC voltage for persistently satisfying the load requirements (1.8-3.3V DC), researchers [8], [9], [10] presented various EECs of electromagnetic generator to implement self-starting and self-powered operation, but in the circuit design, they tended to simplify the generator as constant voltage. A simple modeling and design for a efficient magnetostrictive harvesting system with low-voltage and low-power under low vibration excitation have not been reported. In this paper, a simple lumped parameter equivalent circuit model of a magnetostrictive generator is derived. Based on the model, the low-voltage and low-power characteristics produced by the generator under low acceleration excitation are firstly calculated and analyzed. Then, a self-starting and self-powered EEC with low-voltage and low-power inputs, which consists of the split-capacitor AC-DC rectifier booster [8], the start-up circuit [8], the low-power linear voltage regulator and comparator, is proposed. In order to ensure that the generator is near the maximum power output and reduce the power consumption, three main differences between the proposed EEC and the EEC [8] are: 1) the feedback PI control module [8] is replaced by a comparator; 2) the changeable duty ratio operation [8] is replaced by the fixed duty ratio operation; 3) the low-power linear voltage regulator is added to stabilize the load output to 3.3 V. Finally, a efficient magnetostrictive harvesting system, which accounts for both generator and practical EEC, is modeled in a circuit simulator LTspice for system-level evaluation and design. The results calculated by LTspice are shown in Fig.1 and Fig.2 under acceleration $a(t)$=a0sin(2π222t). Fig.1 shows the characteristics of the generator under a0=0.7g, 1g, 2g and different resistances RL. In Fig.1(a)-(c), the output voltage u increase monotonically with increasing RL while the load instantaneous power PL(t) does not vary monotonously with RL. When RL=50 kΩ, the equivalent circuit of the generator closes to the open circuit. The open-circuit peak voltages under a0=0.7g and 1g are about 0.8V,1.22V. When RL≈120 Ω, the peak PL(t) under a0= 0.7g is about 1.54 mW=1540μW. As expected, PL(t) is almost 0μW when RL=0, 50 kΩ (the short and open circuits). Also, the load average power PavL is 0.5 times the peak PL(t) because the system is linear. Fig.1(d) shows that the calculated and measured load average power curves have similar shape. These verify the validity of the proposed equivalent circuit model of the generator. Fig.2(a), (b) (c) show the structure, power flow, and simulated results of the harvesting system with the proposed EEC and the EEC [8] under a0= 0.7g and load end resistances 38kΩ. In Fig.2 (a) and (b), the fixed virtual impedance Reff is set around 120Ω by the fixed duty ration to ensure that the generator is near the maximum PavL ≈770μW in Fig.1(d), which is bigger than the total power 690μW consumed by the proposed EEC. The load end voltage VLoad reaches and maintains about 3.3V after 0.42s. the battery output current Ibattery increases from -36μA to -60μA in [0s,0.3s], then decreases from -60μA to 0μA in [0.3s,0.7s], finally, the battery current Ibattery is bigger than 0μA and the battery charging starts. These show that the system has the self-starting and self-powered abilities. Fig. 2 (c) shows that the EEC [8] can stabilize the load end output to 3.3 V after 0.42s, but the battery output current Ibattery is in the range of (-115μA,-180μA) from 0s to 1.0s (i.e. the battery has been in the state of discharge), thus the circuit cannot self-start. These show the proposed system has very strong practicability.

[1]Z. Deng and M.J. Dapino, "Review of magnetostrictive vibration energy harvesters," *Smart Mater. Struct.*, vol.26, no.10, pp. 103001-1–103001-18, 2017. [2]L. Wang and F. G. Yuan, "Vibration energy harvesting by magnetostrictive material," *Smart Mater. Struct.*, vol.17, no. 4, pp. 045009-1–045009-14, 2008. [3]J. -H. Yoo and A. B. Flatau, "A bending-mode galfenol electric power harvester," *J. Intell. Mater. Syst. Stru.*, vol. 23, no. 6, pp. 647–654, 2012. [4]Z. Deng and M. J. Dapino, "Influence of electrical impedance and mechanical bistability on Galfenol-based unimorph harvesters," *J. Intell. Mater. Syst. Stru.*, vol. 27, pp. 1–11, 2016. [5]S. Cao, J. Zheng,Y. Guo, Q. Li, J. Sang, B. Wang, and R. Yan, "Dynamic characteristics of Galfenol cantilever energy harvester," *IEEE Trans. Magn.*, vol.51, no.3, pp. 8201304-1–8201304-4, 2015. [6]B. Rezaeealam, T. Ueno, and S. Yamada, "Finite element analysis of galfenol unimorph vibration energy harvester," *IEEE Trans. Magn.*, vol. 48, no. 11, pp. 3977–3980, Nov. 2012. [7]S. Cao, S. Yang, J. Zheng, L. Zhang, and B. Wang, "An equivalent circuit model and energy extraction technique of a magnetostrictive energy harvester," *IEEE Trans. Appl. Supercond.*, vol. 26, no.4, pp. 0602106-1–0602106-6, 2016. [8]R. Dayal, S. Dwari, and L. Persa, "Design and implementation of a direct AC–DC boost converter for low-voltage energy harvesting," *IEEE Trans. Ind. Electron.*, vol.58, no.6, pp.2387–2396, 2011. [9]H. Ulusan, Ö. Zorlu, A. Muhtaroğlu, and H. Külah, "Highly integrated 3V supply electronics for electromagnetic energy harvesters with minimum 0.4 V_{peak} input,"*IEEE Trans. Ind. Electron.*, vol.64, no.7, pp.5460–5467, 2017. [10]T. Martinez, G. Pillonnet, and F. Costa,"A 15-mV inductor-less start-up converter using a piezoelectric transformer for energy harvesting applications," *IEEE Trans. Power Electron.*, vol. 33, no.3, pp. 2241–2252, 2018.

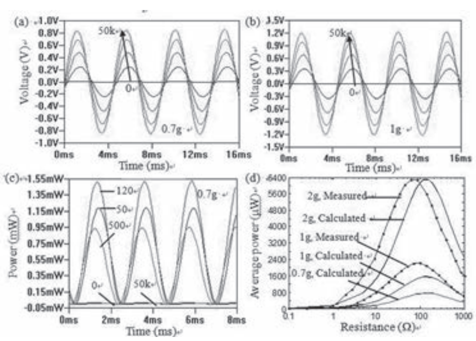

Fig. 1. Calculated (a), (b) voltage, (c) load instantaneous power curves under a0=0.7g, 1g and different resistances:0,50,120,500,50k Ω.(d) Calculated and measured average power versus resistance under a0=0.7g,1g,2.0g (measured dates from[3]).

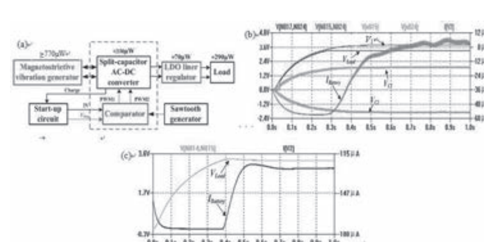

Fig. 2. (a) Structure and power flow, and (b) simulated results of the system with the proposed EEC, and (c) simulated results of the system with the EEC [8] under a0=0.7g and end load 38kΩ.

HR-05. Performance Analysis of a Novel Brushless Hybrid Excitation Synchronous Generator.

C. Zhu[1], Y. Yang[1], Y. Zhang[2] and Y. Shen[1]
1. School of Electrical Engineering, Shandong University, Jinan, China;
2. Yijun Motor Technology Development Center, Liaochen, China

I. Introduction With the continuous improvement of performance and cost reduction of permanent magnet materials, permanent magnet synchronous machine (PMSM) becomes the most promising machine in industrial and agricultural productions[1-2].Therefore, due to the nature of the permanent magnet itself, when the load or speed varies, the motor lacks the ability to adjust the magnetic flux to keep the output voltage constant. To improve the flux adjustment ability of PMSM, many solutions have been proposed. Hybrid excitation is one of the main ways [3-5]. The paper discusses a hybrid excitation synchronous generator combining induction excitation and permanent magnet. The topology and operation principle are explained and a finite element model is analyzed. The simulation results show that the machine has more flexible magnetic field adjustment ability than permanent magnet synchronous generator and could operate with much higher power density than ordinary induction excitation alternator. II. Structure and Operation Principle 2.1 Machine structure The structure of the machine is shown in Fig.1(a). There are two sets windings on the stator, which are 4-pole three-phase armature windings (W_a) and 2-pole single phase auxiliary windings (W_e). Radically magnetized permanent magnets are attached on the rotor core surface. The rotor induction windings(W_{r1}-W_{r4}) are placed in the rotor slots, which are independent of each other and connected with diodes respectively. The connection schematic diagrams of above windings are shown in Fig.1(b). 2.2 Operation Principle The air gap magnetic field of the hybrid excitation motor is generated by the permanent magnet PM and the field currents in the rotor induction windings together. Due to rotor field currents are obtained by the induction principle between stator auxiliary windings and rotor induction windings [6-8], it can also be said that the motor magnetic field is generated by permanent magnets and stator auxiliary windings currents (referred to as stator field currents for simplicity) together. Fig.1(c)-(d) shows the magnetic field distributions produced by PM and currents of induction windings, respectively. It is obvious that the two magnetic circuits are parallel connected. III. Simulation The main model structure parameters are listed as following: Outer diameter of stator core : 155 mm; Inner diameter of stator core: 98 mm; Number of stator slots:36; Air gap at PM: 1.2 mm; Air gap at rotor slots: 0.6 mm; Diameter of shaft:38 mm; Number of mian pole-pairs: 2; Length of the core:110 mm; Pole arc coefficient: 0.4; PM thickness: 3.3 mm. 3.1 Rotor induction current Fig.2(a) shows rotor induction current waveforms at stator field currents 1A, 3A, respectively. As can be seen from Fig.2(a), rectifier diodes act as slip rings and the machine becomes brushless excitation. 3.2 Magnetic field distribution of no-load The air gap flux density waveforms of the motor under the different stator field current is shown in Fig.2(b). It is obvious that amplitude of the air gap magnetic density increases with the increase of the stator field current. 3.3 No-load characteristic The no-load characteristic here is defined as the output voltage versus stator field currents under no-load conditions at constant speed. The no-load characteristic reflects the field adjustment ability of the machine. Fig.2(c) shows the line voltage waveforms at different stator field currents at speed 1500rpm. Fig.2(d) is the comparison of no-load characteristic of hybrid excitation and induction excitation at the same speed. It shows clearly that field currents required in hybrid excitation are much less than those in induction excitation at the same output voltage, which means much less excitation loss and higher efficiency. 3.4 Regulation characteristics When the speed and output voltage of the motor are kept constant, stator field currents versus load currents is the regulating characteristic of the generator, which reflects the excitation loss and the demand for the field capacity at the same output. Fig.2(e)is the comparison of regulation characteristic of hybrid excitation and induction excitation at output voltage 400V and speed 1500rpm. It illustrates that single induction excitation requires much larger field current to obtain the same output power compared to hybrid excitation and the hybrid excitation obtains much higher power density than single induction at the same field current. IV. Conclusion In view of simple structure but limited excitation capacity of induction excitation synchronous generator and some difficulties in magnetic field regulation of permanent magnet synchronous generator, a novel hybrid excitation synchronous generator is analyzed in this paper. Due to field currents obtained through induction principle, the machine becomes brushless and the machine reliability is improved greatly. Compared to a single induction excitation generator, the hybrid excitation machine utilizes smaller excitation magnetic potential to adjust the air gap flux density, greatly reduces the excitation loss, improves the machine efficiency. On the other hand, under the same excitation magnetic potential, the hybrid excitation generator has much greater power output than a induction excitation generator.

[1] Renyuan Tang,Theory and Design of Modern Permanent Magnet Machines[M], Beijing: China Machine Press, 2000.3. [2] Xiuhe Wang, Permanent Magnet Machines [M], Beijing: China Electric Power Press,2007. [3] Yacine Amara, Jean Lucidarme, Mohamed Gabsi, Michel Lecrivain, A.Hamid Ben Ahmed. A new topology of hybrid synchronous machine [J]. IEEE Transactions on Industry Applications, 2001, 37(5): 1273-1281. [4] Amara, Y. Vido, L. Gabsi, M. Hoang, E. Lecrivain, M. Chabot, F. Hybrid Excitation Synchronous Machines: Energy-Efficient Solution for Vehicles Propulsion[C] // IEEE VPPC 2006:1-6. [5] ZHAO Chaohui. Structure designing and characteristic study of HECPG which magnetic circuit series connection[J]. Transactions of China Electrical Society,2009,24(5) : 1-7. [6] Wang Jianmin, Li Guangyou, Performance and MMF transfer coefficient in 3-phase synchronous generator with double-pole induced-excitation, Advanced Technology of Electrical Engineering and Energy, 1996(1) : 38-43. [7] XU Yanliang, LI Guangyou, WANG Jianmin, MENG Chuanfu. Calculation of rotor current on induced excitation synchronous generator when considering the stator harmonic stationary magnetomotive Force [J]. Small and Special Electrical Machines. 1999, 27(4) : 4-10. [8] XU Yanliang, Wu Yanzhong, Zhen baocai, et al. Study on experiment of induced excitation synchronous generator [J]. Journal of Shenyang University of Technology, 2000, 22(3) : 217-219.

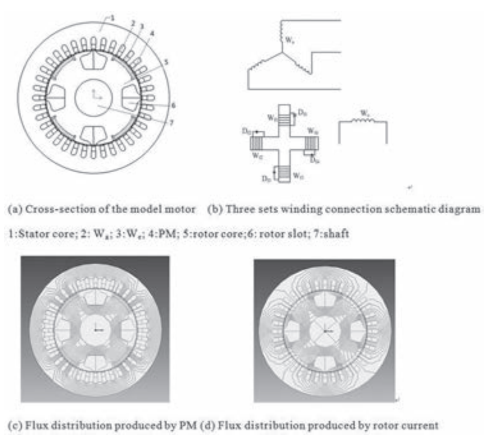

Fig. 1. Structure and Magnetic Circuits

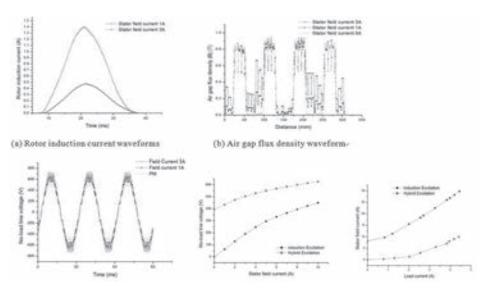

Fig. 2. Simulation Results

HR-06. Analysis of the Resonance Characteristics by a Variation of Coil Distance in Magnetic Resonant Wireless Power Transmission.

H. Lee[1] and G. Park[1]
1. Department of Electrical Engineering, Pusan National University, Busan, The Republic of Korea

I. Introduction Magnetic resonant wireless power transmission(MRWPT) is a method that enables high efficiency transmission at a longer distance by using an additional resonance phenomenon in a conventional magnetic inductive wireless power transmission [1]. When the power transmission distance is smaller than a specific value, there is a problem that the output becomes maximum at two divided resonant frequencies instead of the conventional resonant frequency. This phenomenon is called 'frequency splitting (or division)'. There are some papers that observe and predict this phenomenon with the approximate formula of coupling coefficient or S-parameter [2]. However, there is no analysis of the frequency splitting phenomenon from the magnetic point of view on the transmission distance [3], [4]. In this paper, for a magnetic resonant wireless power transmission system with a resonant frequency of 20 kHz, the output equation according to the transmission distance is formulated and verified by experiment as shown in Fig. 1. And the resonance characteristics of the resonance state and the frequency splitting state were analyzed by the circle diagram of the current phasor and the magnetic field observation through the finite element analysis. *Fig. 1 here* II. Formulation And Verification A. Formulation Magnetic resonant wireless power transmission system can be represented by an equivalent circuit including two inductances having a coupling coefficient k. By using this, the transmission side current (I_{in}) and the reception side current (I_{out}) can be expressed by equations with coupling coefficient and frequency as variables. When the two coils are the same size, the coupling coefficient is determined by the coil size and the distance between the coils. Therefore, each current can be expressed by the formulas with the transmission distance and frequency, where the magnitude I_{out} is closely related to the output power. $I_{out}=j\omega r^3\sqrt{L_1L_2(r^2+d^2)^3}V_S/(Z_1Z_2+\omega^2r^6L_1L_2/(r^2+d^2)^3)$ (1) This is shown in Fig. 2 as a color map. When the transmission distance is short, frequency splitting phenomenon occurs in which the maximum output appears at two divided frequencies. It also shows the maximum output at a resonant frequency of 20 kHz at the specific distance, and the output sharply decreases at a further distance. *Fig. 2 here* B. Verification To verify these formulas, a real magnetic resonant wireless power transmission system was constructed and tested under the same conditions. The system can transmit 50W of power at a distance of 400mm. The experimental results are very similar to those predicted by the circuit equation, and the results will be added to the full paper. III. Influence of transmission distance A. Analysis using a circle diagram According to the transmission distance, the magnitude and phase of the transmission/reception current (I_{in}, I_{out}) can be calculated for each of the resonance state and the frequency splitting state, and the circle diagram of each current can be drawn with their phasor diagram. The phasors of I_{in} and I_{out} are formed in the shape of a circle around 0° and 90°, respectively, and the frequency splitting occurs due to the circularity being distorted as the transmission distance decreases. In this case, the maximum output appears when the I_{out} passes 0° and 180°, and two divided resonant frequencies can be estimated by finding the point where the imaginary value of I_{out} becomes zero. $f_{1,2}=\sqrt{[(2L-R_L^2C)\pm\sqrt{(R_L^4C^2-4R_L^2LC+4k^2L^2)}/(2L^2C-2k^2L^2C)]}/2\pi$ (2) B. Magnetic phenomena analysis In order to analyze the reason why maximum output appears at the two divided resonant frequencies, the magnetic flux densities of both low resonant frequency and high resonant frequency are simulated by finite element analysis as shown in Fig. 2 (a) and (b). At low resonant frequencies, the magnetic field passes through the entire transmitting/receiving coil, whereas at high resonant frequency it appears to be opposite to each other. As can be seen from the circle diagram, the phasor of I_{out} rotates around 90°. Since the output becomes maximum when the phasor of I_{out} passes near 0° and 180°, it can be seen that the magnetic field of the receiving coil also has the same (0°) or opposite (180°) direction to the magnetic field of transmitting coil. IV. Conclusion In this paper, the equation of output power was formulated with transmission distance as variables and verified through experiments. In addition, the resonance characteristics according to the transmission distance were analyzed through the circle diagram and finite element analysis. From these results, it is possible to know the influence of the transmission distance and the magnetic cause of the frequency splitting phenomenon in the magnetic resonant wireless power transmission. Furthermore, the optimum design for the target transmission distance will be possible, and it will be able to obtain high output and efficiency stably by calculating an approximation of the divided frequency representing the maximum power in the short-range transmission. In the full paper, circle diagrams of transmission/reception current according to all transmission distances, a detailed formula derivation process, and experimental results for verification will be added.

[1] A. Kurs, A. Karalis, R. Moffatt, J. D. Joannopoulos, P. Fisher, M. Soljačić, "Wireless Power Transfer via Strongly Coupled Magnetic Resonances," Science Express, June 2007. [2] P. Zhang, Q. Yang, X. Zhang, Y. Li and Y. Li, "Comparative Study of Metal Obstacle Variations in Disturbing Wireless Power Transmission System," in IEEE Transactions on Magnetics, vol. 53, no. 6, pp. 1-4, June 2017. [3] T. Imura and Y. Hori, "Maximizing Air Gap and Efficiency of Magnetic Resonant Coupling for Wireless Power Transfer Using Equivalent Circuit and Neumann Formula," in IEEE Transactions on Industrial Electronics, vol. 58, no. 10, pp. 4746-4752, Oct. 2011. [4] W. K. Choi, C. W. Park and K. Lee, "Circuit Analysis of Achievable Transmission Efficiency in an Overcoupled Region for Wireless Power Transfer Systems," in IEEE Systems Journal, vol. PP, no. 99, pp. 1-4.

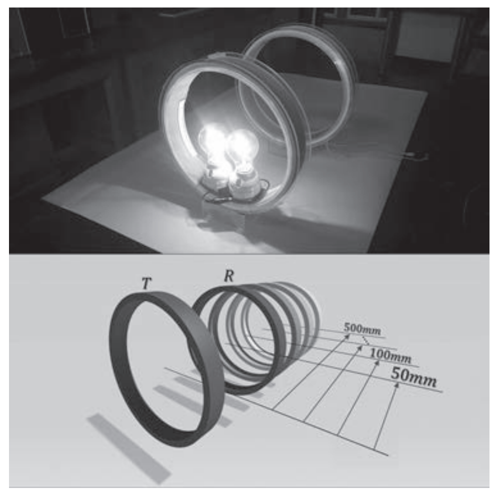

Fig. 1. Actual magnetic resonant wireless power transmission system and configuration diagram of simulations according to transmission distance.

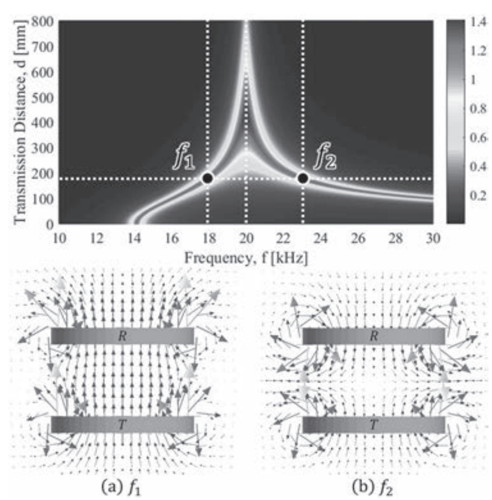

Fig. 2. The color map of output according to the transmission distance and the magnetic flux vector, B, in the frequency splitting state. (a) Low resonant frequency. (b) High resonant frequency.

HR-07. Optimization of Planar Spiral Coils for Uniform Magnetic Field to Wirelessly Power Moving Targets.

Y. Xie[1] and Q. Xu[1]
1. Key Laboratory of Image Processing and Intelligent Control of Education Ministry, Department of Control Science and Engineering, Huazhong University of Science and Technology, Wuhan, China

Abstract Wireless power transfer technology via magnetic coupling has been widely used to provide freely positioning power for cell phones, electric cars and drones. In this paper, the configuration of planar spiral coil is optimized by genetic algorithm to achieve the uniform magnetic field distribution above the transmitter, whereas the magnetic field is simulated by HFSS software. A transmitter coil with the turns of fourteen and the radius of 8 cm is designed for an improved evenness of magnetic field distribution. The uniformity of the axial component of magnetic field distribution is evaluated by a coefficient of variation (COV). The measured COVs of the optimized and regular coils within the plane with a height of 8 mm above the transmitting coil are 0.1858 and 0.3161, respectively. Introduction Wireless power transfer (WPT) uses a varying magnetic field to deliver power across an air gap, to a load without physical contact. WPT systems may be classified into far-field and near-field techniques. In general, far-field transmission is available for the devices with high-power requirements. For the moderate power (a few watts to hundreds of watts) and mid-range distances (0 to a few meters), a near-field wireless power system operating at no more than 100 MHz would be far superior to far-field WPT. It is shown that near-field WPT can achieve higher efficiency with less stringent RF exposure safety limit [1]. The mutual coupling and energy transfer efficiency will deteriorate with the misalignment of the transmitter and receiver coils. On the other hand, the transmitting coil must be large enough to accommodate the devices which charged simultaneously. These pose a challenge, as to ensure stable power delivery to moving targets, the distribution of the z-component of the magnetic field in the plane of the receiving coils must be as uniform as possible [2]. Transmitting coils may be designed to produce such fields. One approach is optimizing the structure of coils for single receiving coil systems. Anew hybrid structure which consists of a coil and a spiral winding is designed for improving the uniform magnetic field distribution [3]. Two kinds of transmitting coil structures have been designed based on the continuous current distributions [4]. Another approach is to use an array of transmitter coils. The most reasonable arrangements of transmitter coils are analyzed and designed [5]. Methodology In this paper, a kind of planar spiral transmitting coil structure has been designed based on the genetic algorithm and the simulation by HFSS software that can generate uniform axial component of magnetic field. The equivalent circuit model of two coils system is analyzed firstly. Then the relationship between the η and the magnetic field strength B can be obtained. Also, the axial component of magnetic field generated by the planar spiral coil can be calculated according to the Biot-Savart Law. These analyses indicate that the width of each turn and the spacing between two adjacent turns of the coil are the primary factors that affect the magnetic field strength. The width and the spacing are chosen as the optimization variables. For the optimization of spacing, a series of single concentric current loops are used instead of a planar spiral coil. The coefficient of variation (COV, the standard deviation divided by the mean) of the z-component of the magnetic field which can calculated by the Biot-Savart Law is chosen as the objective function of genetic algorithm. HFSS and Matlab are combined to optimize coil widths on the base of the results of spacing optimization. The planar spiral coil model is built with HFSS and optimized by Matlab. And the COVs of the S21simulated by the HFSS between the planar spiral transmitting coil and receiving coils built on the testing plane are taken as the objective function. Then the COVs of the regular and optimized coils are compared through simulations. And the optimization results are validated by experiments with the network analyzer ROHDE & SCHRWARZ ZVH8. Results Using the above methods, the optimization process is described as follows: Genetic algorithm toolbox in Matlab is used for the optimization of the spacing between two adjacent turns. On the base of the results of spacing optimization, the width of coils are taken as the optimization variables with the planar spiral model built by HFSS through the HFSS-MATLAB API. The COV of the S21 simulated by the HFSS is calculated and optimized with genetic algorithm until reach terminating condition. And the optimized result is shown in Fig.1 and Fig.2. The COVs of the optimized and regular coil on the plane with a height of 8 mm above the transmitting coil are0.1858 and 0.3161 measured by network analyzer. Conclusion To ensure stable power delivery to moving targets, the magnetic field distribution generated by the transmitting coil must be even. The transmitting coil with the turns of fourteen and the radius of 8 cm is designed through genetic algorithm optimization and simulation by HFSS to enable the uniform distribution of axial component of magnetic field, which is verified by the simulation results. And this research demonstrates the feasibility of using the method in the design of coil structures to improve the uniformity of magnetic field.

[1]J. Garnica, R. A. Chinga, and J. Lin, “Wireless power transmission: From far field to near field,” Proc. IEEE, vol. 101, no. 6, pp. 1321–1331, Jun. 2013. [2]J. J. Casanova, Z. N. Low, J. Lin, and R. Tseng, “Transmitting coil achieving uniform magnetic field distribution for planar wireless power transfer system,” in Proc. IEEE Radio Wireless Symp., Jan. 18–22, 2009, pp. 530–533. [3] X. Liu and S. Hui, “Optimal Design of a Hybrid Winding Structurefor Planar Contactless Battery Charging Platform,” Power Electronics,IEEE Transactions on, vol. 23, no. 1, pp. 455–463, 2008. [4] D. Yinliang, S. Yuanmao, and G. Yougang, “Design of coil structure achieving uniform magnetic field distribution for wireless charging platform,” in 4th Int. Power Electron. Syst. App. Conf., Jun. 8–10, 2011, pp. 1, 5. [5] E. Waffenschmidt, “Free positioning for inductive wireless power system,” in Proc. IEEE Energy Convers. Congress Expos., 2011, pp. 3480–3487.

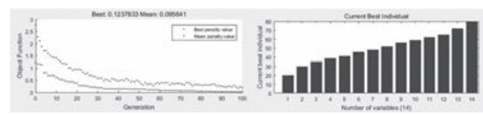

Fig. 1. Iterative process and optimization results of genetic algorithm: (a) the best and mean value of object function for every generation, (b) results of optimization for all variables

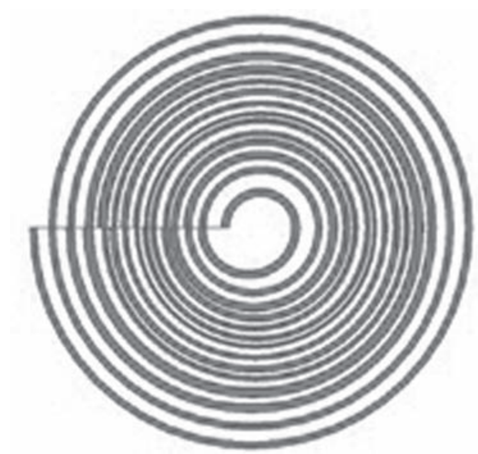

Fig. 2. Coil structure optimized with genetic algorithm

HR-08. Demagnetization Characteristics of a Permanent Magnet Embedded Salient Pole Wind Generator.

Y. Guo[1], P. Jin[1], H. Yang[2] and Y. Zhu[1]
1. College of Energy and Electrical Engineering, Hohai University, Nanjing, China; 2. School of Electrical Engineering, Southeast University, Nanjing, China

Offshore wind power has become an important direction in the field of wind electricity generation. The commonly used surface-mounted PM wind generator cannot resist the corrosion due to humidity and salt spray. In order to improve the reliability of wind generator, the interior PM structure is adopted in some wind power generators. An improved flux intensifying PM embedded salient pole wind generator (FI-PMESPWG) is proposed in our previous work. As other PM machines, the FI-PMESPWG also faces the demagnetization problems, especially under short-circuit and high temperature conditions. Some important research works about demagnetization performance of interior PM machines are carried out, for example, the transient magnetic behavior of an interior PM machine during fault conditions is investigated in [1], and the partial demagnetization performance of a 7MW interior PM wind generator is investigated in [2]. But these investigations are focus on the normal interior PM machine, and their conclusions are not suitable for the salient pole ones. Therefore, in this paper, the demagnetization characteristics of FI-PMESPWG are investigated to find out some rules suitable for this kind of machines. Fig.1 shows the configuration of FI-PMESPWG. Its rotor core upper surface is designed to a bias arc for yielding a sinusoidal waveform of air-gap flux density. And in each magnetic pole, two PMs with mirror symmetrical magnetizing directions are embedded. In the salient pole, some non-magnetic material is added to guide the magnetic flux path. The magnetic field in the radial direction is intensified owing to the PM's placement. To modify the angle between the two PM pieces, the magnetic field in the magnetic pole will be changed and the demagnetization performance will varies consequently. So, the magnetic field distributions with different PM and non-magnetic material placements and thickness are all calculated and investigated. The variations of magnetic field distributions with different short-circuit currents and operating temperatures are also analyzed based on finite element method. Fig. 2 shows the partially demagnetized regions of selected magnets under 3-phase symmetrical short-circuit faults under rated speed. The demagnetized area, shown in color contour map, is covered by the nodes with flux density <0.6 T in the magnetization direction. As shown in the picture, different from the normal interior PM machine, the PM region near the bottom of pole shoe has the highest demagnetization. That's because the side frame of the pole shoe has some leakage flux and it changed the magnetic flux path and hence affects the demagnetization performance. The demagnetization in the two PMs are not symmetrical due to the armature reaction. Due to its special structure, FI-PMESPWG has some other different demagnetization characteristics from the normal interior PM machines, which will be analyzed and compared with the normal ones detailed in the full paper. The effect of demagnetization on the electromagnetic parameters will be investigated. Based on the analysis results in this paper, the demagnetization rules of interior PM salient pole machines will be concluded and it can supply an important theoretical basis for design of this kind of machine.

[1] James D. McFarland and Thomas M. Jahns, Investigation of the Rotor Demagnetization Characteristics of Interior PM Synchronous Machines During Fault Conditions," IEEE *Trans. Ind. Apl.*, vol. 50, no. 4, pp. 2768-2775, Jul./Aug. 2014. [2] Hong Chen, Ronghai Qu, Jian Li, and Dawei Li, "Demagnetization Performance of a 7 MW Interior Permanent Magnet Wind Generator with Fractional-Slot Concentrated Windings," *IEEE Trans. Magn.*, vol. 51, no. 11, pp. 8205804, Nov. 2015.

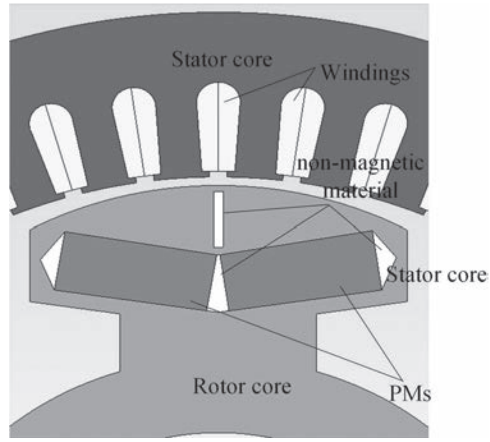

Fig. 1. Configuration of FI-PMESPWG

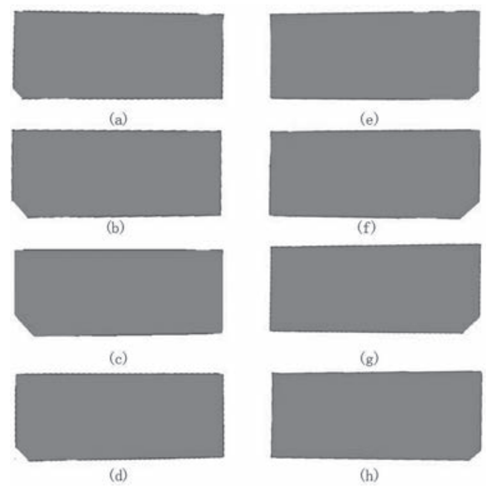

Fig. 2. Partially demagnetized area of PM under short-circuit fault and rated speed.

HR-09. Design of a Novel Brushless Electrically-Excited Claw-Pole Generator for Hybrid Electric Vehicles.

X. Zhao[1] and S. Niu[1]
1. Electrical Engineering, The Hong Kong Polytechnic University, Kowloon, Hong Kong

Abstract: This paper presents a new brushless electrically-excited claw-pole generator for vehicle power generation. The propose design uses a toroidal excitation coil to magnetize all the stator poles and then generate effective power by saliency effect of dual rotors. One advantage of this new design is its good excitation ability to minimize the excitation copper loss, thus achieving an acceptable energy conversion efficiency. Besides, the brush and slip rings are eliminated compared conventional rotor-electrically-excited claw-pole generator. The generator structure is introduced, along with no load flux distribution illustrated by 3D finite element analysis. Rotor configurations using interlaced and non-interlaced types are both elaborated. Load characteristic is also predicted by field-circuit coupled analysis, which reveals the proposed brushless topology can achieve a comparable performance against conventional brush solution. I. Introduction Electrically-excited claw-pole generator(EECPG) is a popular solution for on board vehicle power generation due to its field regulation ability. One advantage of EECPG is its good excitation ability since all rotor poles can be magnetized by only one toroidal excitation coil. Therefore, less excitation copper loss is consumed compared to those conventional electrically-excited generators with distributed excitation windings, which makes it more possible to achieve an acceptable energy conversion efficiency even with a relatively small power scale. However, EECPG suffers from the burden of brush and slip rings, which brings out a reliability problem and becomes disadvantageous for modern vehicle power generation. II.Proposed generator This paper proposes a novel brushless electrically-excited claw-pole generator (BEECPG) for the power generation in hybrid electric vehicles (HEV). Fig. 1(a) describes the power train for series-type HEV, in which the proposed BEECPG, as shown in Fig. 1(b), works as an ICE-mounted generator to realize mechanical-to-electric energy conversion. The proposed BEECPG is composed of two symmetrical rotors at double sides, a common stator and two set of windings, namely the armature winding and field winding. Both the stator and rotor consist of U-shaped salient poles. The field winding is sandwiched between two set of back-to-back stator poles, while two sets of armature coils are arranged in close to the left and right rotor, respectively. Advantages of this new generator can be summarized as (1) The excitation winding is located at stator side. Therefore, a brushless configuration is realized. (2) With on PMs used, the cost is reduced and reliability is improved especially for high temperature environment around internal combustion engine. (3) All stator poles are magnetized by one toroidal excitation coil. Therefore, excitation loss is minimized and an acceptable energy conversion efficiency is more possibly to be achieved even with a relatively small power scale. III. 3D magnetic circuit analysis The magnetic field distribution of the proposed BEECPG is illustrated in the Fig. 2 by using 3D finite element analysis. Two rotors share the same rotational movement, and at different positions, the alignment between stator poles and rotor poles at two sides are different, as well as corresponding field distribution. As shown in the Fig. 2(a), at this initial position, one set of stator poles are all aligned with the left rotor poles, while the other one is aligned with the right rotor slots. Therefore, the flux generated by the field excitation will almost all go to the left side and linked with the left armature coil. Correspondingly, at this position, the left coil flux has the maximum value while the right coil has the minimum flux linkage, as shown in the Fig. 2(d), and the cascaded flux has the positive maximum value. When a 1/4 pole pitch movement occurs as shown in the Fig. 2(b), the alignments becomes symmetrical between the stator poles and rotor poles at both sides, hence the field flux will shunt into the double armature coils and the cascaded flux becomes zero. Then, as shown in the Fig. 2(c), when the rotor moves half of the pole pitch, the alignment now is in the contrast with that shown in Fig. 2(a), specifically, one set of the stator poles are aligned with the right rotor poles and the other one is aligned with the left rotor slots, thus the field flux are all linked with the right armature coil and the cascaded flux has the negative maximum value. Therefore, as shown in the Fig. 2(d), with the rotor rotation, both armature coils have bias flux linkage but their variation trends are opposite, and when they are cascaded, a bipolar and symmetrical cascaded flux can be obtained as shown in Fig. 2(d). IV.Conclusion This paper proposes a novel brushless electrically-excited claw-pole generator for the power generation in hybrid electric vehicles. This design owns good excitation ability to minimize the excitation copper loss and thus can achieve an acceptable energy conversion efficiency within a relatively small power scale. The performance of this new topology is comparable to conventional electrically-excited claw-pole generator, while the brush is successfully eliminated.

[1] H. Weh, H. Hoffmann, and J. Landrath, “New permanent excited magnet synchronous machine with high efficiency at low speeds,” in *Proc. Int. Conf. Electr. Mach.*, Pisa, Italy, 1990, vol. 3, pp. 35–40.

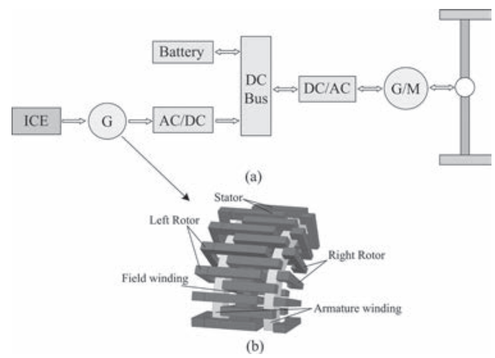

Fig. 1. (a) Power train for series hybrid electric vehicles. (b) Configuration of the proposed ICE-mounted generator.

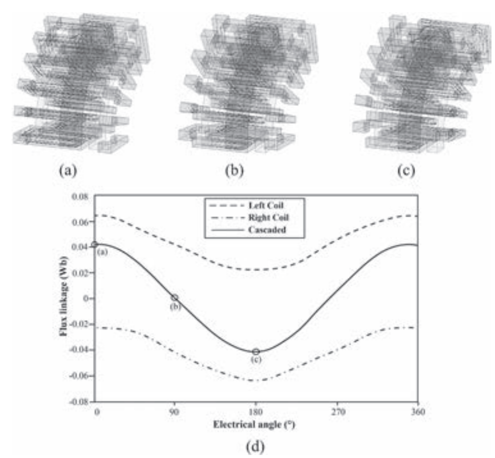

Fig. 2. Flux distribution at different positions. (a) Initial position. (b) 1/4 pole pitch movement. (c) 1/2 pole pitch movement. (d) Armature flux waveforms

HR-10. Study of Air-gap Magnetic Field of a Novel Integrated Brushless Excitation Generator.

S. Zhu[1] and C. Li[1]
1. Nanjing University of Aeronautics and Astronautics, Nanjing, China

1. Introduction The electrical brushes of the brush excitation generator causes many problems such as looping, noise, short life and serious heat. The realization of the brushless excitation can solve above-mentioned problems[1-3]. A novel integrated brushless excitation method is proposed in this paper. It is very suitable to realize brushless excitation for the wound rotor generator without changing the original topology. The additional excitation part is integrated in the wound rotor generator to realize brushless excitation. However, the magnetic flux of excitation part is coupled with the original magnetic flux of wound rotor generator. The air-gap magnetic field of the novel generator is studied by the theoretical analysis and Finite Element Analysis to decouple two parts of the magnetic flux and study the influence of the additional magnetic flux of excitation part on the operating characteristics of the novel generator. The operating characteristics are also verified by the experiment. 2. The Structure and Operational Principle of the Novel Integrated Brushless Excitation Generator A novel integrated brushless excitation method is applied in a wound rotor hybrid excitation generator (WRHESG) to form an integrated brushless WRHESG. The topology is as shown in Fig. 1(a). The arrangement of the coils are shown in Fig.2(b). The additional stator excitation windings (W_s) are buried in the stator slots with the armature coils (W_a). The rotor excitation windings (W_F) are mounted in the rotor slots. The rotor armature slots are arranged evenly around the rotor iron core and the rotor armature coils (W_r) are buried in the rotor slots. W_s and W_r are the coils of the excitation part to produce I_F. W_a and W_F are the coils of the power part to produce output power. When the dc excitation current is infected into W_s, the static magnetic field is built in the main air gap and is cut by W_r. The ac excitation current is induced in the W_r and is rectified by rotating rectifier to provide dc excitation current (I_F) in the W_F. The rotating magnetic field is built by the magnetic flux of I_F and permanent magnets to induce the voltage in the W_a. 3. The Decoupling of the Air-gap Magnetic Field of Excitation Part and Power Part The harmonics are added in the air-gap because of the addition of the excitation part. The harmonics of the flux density are studied theoretically firstly. The details will be introduced. The calculation of the flux density of the static excitation part are divided into 2 parts: permeance coefficient and magnetic potential. The product of permeance coefficient and magnetic potential is the flux density produced by I_f. B_f can be induced in the full paper In order to verify the correctness of the theoretical analysis, the distribution of the air-gap flux density produced by excitation part and produced by power density is separated by the frozen permeability method. The permeability of the iron core of the brushless excitation WRHESG is recorded. The magnetic field distribution of the excitation part and power part can be gained by calling the permeability of the iron core of the integrated brushless WRHESG. The results are shown in Fig. 1. Fig.1(c) is the magnetic flux density of the excitation part and Fig.1(d) is the magnetic flux density of the power part. The harmonics can be analysed by Fourier decomposition. It can be gained that the odd harmonics are existed in the magnetic field flux of power part. And, the fractional harmonics are existed in the magnetic field flux of excitation part, which agrees well with the theoretical analysis. The details will be given in the full paper. The air-gap magnetic field of the excitation part is static, which will not induce voltage in W_a. The output voltage of the integrated brushless WRHESG and WRHESG will be compared to demonstrate the correctness of analysis. It is obvious that the magnetic flux of the excitation part is much smaller than that of the power part. Because the resistance of the rotor excitation winding is very small, the armature reaction of the excitation part is very serious. Therefore, the extra saturation can be avoided. 4. Experiment The magnetic field cannot be test directly. However, it can be reflected by the output voltage of the generator. A 1.5kVA prototype is fabricated as shown in Fig. 2(a). The no-load characteristics and load characteristics of the integrated brushless WRHESG and WRHESG are compared. The output voltage waveforms of the integrated brushless WRHESG is shown in Fig. 2(b). It can be concluded that the operating characteristics that the integrated brushless WRHESG and WRHESG are quiet similar. The novel integrated brushless excitation method does not affect the operating characteristics of WRHESG. 5. Conclusion A novel integrated brushless excitation method is proposed in this paper. It is applied in a WRHESG to realize brushless excitation without changing the topology of the WRHESG. The design method for decoupling excitation part and power part is given. The flux density decides the quality of the output power and the operating characteristics of the generator. The air-gap magnetic density and the magnetic field distribution of two parts are gained by frozen permeability method. It can be gained that the extra excitation part does not affect the magnetic field distribution of the WRHESG. Finally, it is demonstrated by the operating characteristics tested by prototype.

[1] Shahnazari, M. and A. Vahedi.: 'Improved dynamic average modelling of brushless excitation system in all rectification modes', IET Electric Power Applications, 2010, 4, (8), pp. 657-669. [2] Shushu, Z., L. Chuang, N. Yinhang, and T. Jie : 'A Two-stage Brushless Excitation Method for Hybrid Excitation Synchronous Generator', IEEE Trans. Magn., 2014. [3] Lizhi, S., G. Xiaolong, Y. Fei, A. Quntao, and T. Lipo.: 'A new type of harmonic current excited brushless synchronous machine based on an open winding pattern'. Proc. Int. Conf. Energy Conversion Congress and Exposition, Pittsburgh, PA, Sept. 2014, pp. 2366-2373

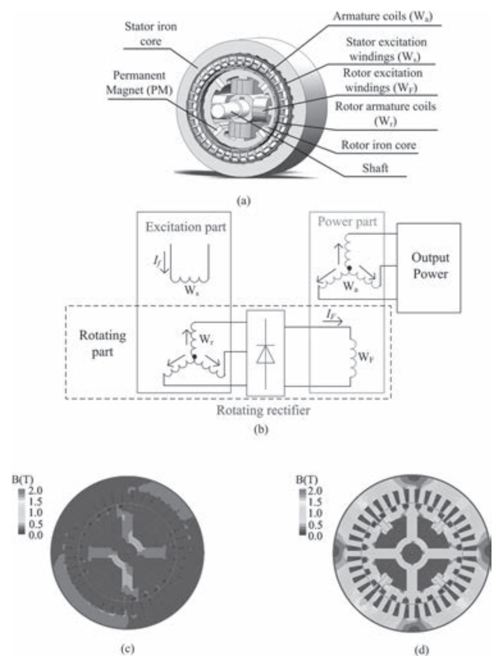

Fig. 1. The topology, arrangment of the coils and the magnetic field distribution.

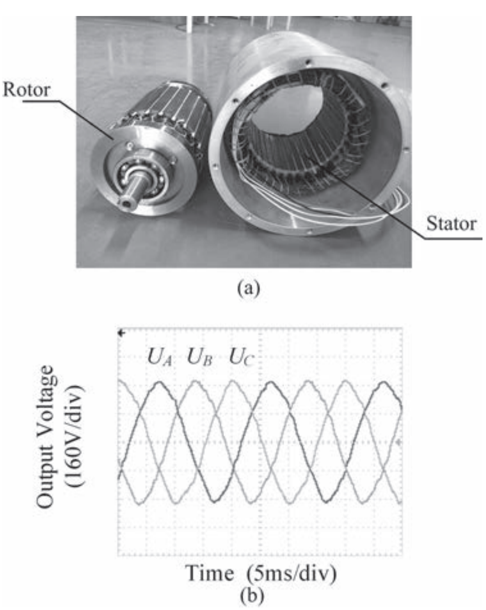

Fig. 2. The prototype and the output voltage waveform.

HR-11. Withdrawn

HR-12. Research of an Axial Flux Stator Partition Hybrid Excitation Brushless Synchronous Generator.

C. Ye[1,2], Y. Du[1], J. Yang[1], X. Liang[1], F. Xiong[1] and W. Xu[1]
1. School of Electrical and Electronic Engineering, Huazhong University of Science and Technology, Wuhan, China; 2. State Key Laboratory of Advanced Electromagnetic Engineering and Technology, Huazhong University of Science and Technology, Wuhan, China

Abstract- A vehicular generator has stringent requirements on its weight and volume. As a combination of permanent magnet and electric excitation motor, hybrid excitation machine could meet the requirements of vehicular generator, with small size, light weight, adjustable output voltage. In this paper, an axial flux stator partition hybrid excitation brushless synchronous generator (ASHG) is proposed. First, the structure and operation principle of ASHM is illustrated. Afterwards, the shape of the magnetic pole is optimized to obtain the air-gap flux density with low harmonic content. Moreover, the regulation performance of the magnetic field and output voltage are investigated by three dimensional finite element analysis (3D FEA). The result indicates that ASHG has a high performance of adjusting terminal voltage. It can improve the generator efficiency, power density and stability comparing with the conventional vehicular generator. I. Introduction The vehicle generator is used to supply power for small appliances in vehicle. At present, there are two main schemes of vehicle generators. One is the electric excitation synchronous generator (EESG), the other is permanent magnet synchronous generator (PMSG). EESG usually needs slip rings and electric brushes to provide the rotor field current. The terminal voltage of EESG could be flexibly adjusted. While the slip rings and electric brushes would lead to the spark and maintenance problems. PMSG has the merits of simple structure, high efficiency, and so on. But it has poor ability to regulate the output voltage. To combine the advantages of aforementioned generators, a novel axial flux stator partition hybrid excitation brushless synchronous generator (ASHG) is proposed. It can adjust the current in the excitation winding to achieve the regulation of the air gap magnetic field. II. structure The structure of ASHG is shown in Fig. 1. The stator core is made of silicon steel sheet. The rotor contains the rotor core, the permanent magnet and the core pole. The permanent magnet and the iron core are staggered on the upper surface of rotor core. The opposite polarity of the permanent magnet and the core are also staggered, to avoid the magnetic circuit intersection. The construction of the rotor is simple which consists of single solid rotor core and laminated rotor. The back electromotive force (back-EMF) would generate in the armature winding when the rotor rotates. III. Working Principle The working principle of ASHG is illustrated as follows: when DC current is charged in the field winding, the magnetizing flux generated by excitation current would be formed, meanwhile, the flux generated by permanent magnet stay unchanged. The air-gap flux density distribution is the results of their synthesis. And thus the air-gap flux density can be regulated by adjusting the field current. IV. Analysis and simulation In Fig. 2(a), the red permanent magnet generates N pole field, the lower part is the S pole, and the black arrows indicate the magnetic field path. Fig. 2(b) shows the magnetizing flux path of ASHG. It can be seen that the flux path of permanent magnet is the same as the theoretical magnetic circuit. Fig. 2(c) shows the three-phase back electromotive force waveforms of ASHG. It can be found the waveforms are nearly sinusoidal. I. Conclusion This paper presents an axial flux stator partition hybrid excitation brushless synchronous generator. The generator has the abilities of dynamic voltage regulation and self-excitation, thus it can make full use of the motor space and reduce the motor volume and quality. At the same time, the basic theory of the motor is studied. The permanent magnetic circuit and the electric excitation magnetic circuit of the static field are simulated, which verifies the correctness of the motor magnetic circuit design. Depending on the specific application requirements, the main parameters of the motor are designed and are optimized by finite element method. By optimizing the magnetic pole structure based on the function equation, the waveform of low harmonic air gap magnetic flux density and the output voltage are obtained. Finally, we studied the ability to tune the magnetic and voltage regulation output performance of ASHG by numerical simulation.

[1] Jae-Han Sim; Dong-Gyun Ahn, et al, "3-D equivalent magnetic circuit network for precise and fast analysis of PM-assisted claw-pole synchronous motor," IEEE Energy Conversion Congress and Exposition (ECCE), Sept. 2016 [2] E. Severson, R. Nilssen, T. Undeland, and N. Mohan, "Magnetic equivalent circuit modeling of the AC homopolar machine for flywheel energy storage," IEEE Trans. Energy Convers., vol. 30, no. 4, pp. 1670–1678, Dec. 2015.

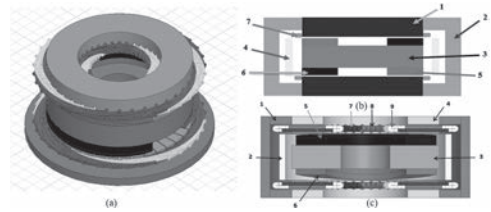

Fig. 1. (a) Structure of the axial flux stator and rotor dual excitation brushless synchronous generator
(b) Motor-sectional view of a two-dimensional
1.Stator core 2.Chassis 3.Rotor core 4.Field winding 5.Permanent magnets 6.Iron core 7.Armature winding
(c) A schematic diagram of double - excitation brushless synchronous generator with axial flux
1,4.Stator core 2.Field winding 3.Rotor core 5.Iron core 6.Permanent magnets 7.C-phase armature windings 8.B-phase armature windings 9.A-phase armature windings

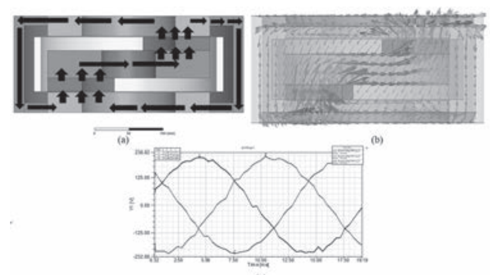

Fig. 2. (a)Theoretical analysis of the circuit diagram for permanent magnetic
(b)The vector diagram of Motor flux density B after simulation.
(c)Voltage waveform

HR-13. A Novel Interior Permanent Magnet Brushless Doubly-fed Generator with Segmented Reluctance Rotor for Wind Power Application.

J. Zhang[1], Y. Jiang[1], J. Zhao[1] and W. Hua[1]
1. School of Electrical Engineering, Southeast University, Nanjing, China

INTRODUCTION: Variable speed brushless doubly-fed generator (BDFG) has no slip rings and no brushes, and only needs a part-size power converter which is similar as the doubly-fed induction generator in the field of wind power generation. So the BDFG has attracted great attentions and owns many advantages, such as high wind power utilization, high reliability and low maintenance [1]. However, the BDFG also has some disadvantages, such as complicated rotor structure, high harmonic distortions, low power density and low efficiency, which lower the potential applications of the BDFG in wind power application. In order to improve the performance of the BDFG, a new interior permanent magnet (IPM) BDFG with three-segmented reluctance rotor based on field modulation is proposed in this paper. Three-segmented structures for outer rotor are adopted to solve the problems of high cogging torque and asymmetrical electromotive force (EMF) caused by the introduction of the PM rotor and field modulation ring. TOPOLOGY: Stationary field modulation ring is firstly used in coaxial magnetic gear to transmit the torque between two surface permanent magnet (PM) rotors whose rotation speeds and pole numbers are different [2-3]. The structure and field modulation function of field modulation ring are similar to that of the reluctance rotor of the traditional BDFG. So it could be introduced to the BDFG as a reluctance rotor [4]. In addition, the PM inner rotor is adopted to provide the excitation magnetic field of the generator, as shown in Fig. 1. Then the flux density might be improved greatly by using high performance rare-earth permanent magnet which improves the power density and efficiency of the BDFG as a result. Commonly the PMs are surface mounted on the inner rotor where a uniform airgap will be achieved between the inner rotor and outer rotor. However, the existence of field modulation ring will lead to the flux distortion of the airgap. It shows that only about half of the PMs are utilized with the surface PM (SPM) rotor, as shown in Fig. 1(a). If the PMs are inserted into the rotor and then interior PM (IPM) rotor is used, the utilization of the PMs will be improved due to the existence of additional harmonic flux paths, as shown in Fig.1 (b). Fig. 1(b) shows the BDFG with IPM rotor has iron-bridges at the terminal of the PMs which may lead to some leakage flux. However, the IPM rotor will provide stronger exciting magnetic field than SPM rotor, even if their PMs are in the same size. It should be noted that there is only fundamental flux in the SPM rotor, as shown in Fig. 1(a). The introduction of field modulation ring would cause the asymmetric phenomena and high cogging torque. The asymmetric phenomena are caused by the asymmetric magnetic circuit due to the different speeds of reluctance rotor and the synchronous speed. In other words, the variations of the relative position of two rotors will lead to the varying harmonic contents of the excitation magnetic field in outer airgap, and the varying period of the harmonic contents is different from the electric cycle of the grid. In order to solve the problem, the reluctance rotor is evenly divided to three segments along axial direction, and there is a specific angle difference among them along circumferential direction, as shown in Fig. 1(c). By this way, the harmonic components are constant during the variation of the relative position of two rotors. FINITE ELEMENT ANALYSIS: In order to verify the effectiveness of the proposed IPM BFDG, finite element method (FEM) is employed. Considering the three-segmented reluctance rotor is symetrical in axis direction and it is better to decrease the computation time, 2D FEM is used in this paper, where three IPM BDFG models are established separately for the three-segmented reluctance rotor with an initial angle difference of 5 degree each other. Then the result of BDFG with three-segmented reluctance rotor could be obtained by averaging the results of three models. Fig. 2(a) shows the exciting magnetic fields provided by the SPM and IPM. The models of IPM BDFG and SPM BDFG have the same size including the PMs. It can be seen that the IPM rotor could provide more exciting magnetic field. There are asymmetric phenomena and large harmonics in three phase electromotive fore (EMF) of the IPM BDFG, as shown in Fig. 2(b). By adopting three-segmented reluctance rotor, the asymmetric phenomena and harmonics could be effectively reduced, as shown in Fig. 2(c). Meanwhile the cogging torque could be greatly reduced, as shown in Fig. 2(d). CONCLUSIONS: In this paper, a novel IPM BDFG with segmented reluctance rotor is proposed, which may improve the utilization of the PMs and the power density of the generator. Through the theoretical analyses, the solution to asymmetrical phenomena and high cogging torque is put forward, and the effectiveness is verified by FEM.

[1] M. F. Hsieh, Y. H. Chang, and D. G. Dorrell, "Design and Analysis of Brushless Doubly-Fed Reluctance Machine for Renewable Energy Applications," *IEEE Transactions on Magnetics*, vol. 52, no. 7, 2016. [2] M. Filippini, and P. Alotto, "Coaxial magnetic gears design and optimization," *IEEE Transactions on Industrial Electronics*, vol. 64, no. 12, pp. 9934-9942, 2017. [3] L. Sun, M. Cheng, and H. Jia. "Analysis of a Novel Magnetic-Geared Dual-Rotor Motor with Complementary Structure." IEEE Transactions on Industrial Electronics, vol. 62, no. 11, pp. 6737-6747, 2015. [4] Y. Jiang, J. Zhang, and T. Li. "A Permanent Magnet Brushless Doubly Fed Generator With Segmented Structure." *IEEE Transactions on Magnetics*, vol. PP, no.99, pp. 1-4, 2017.

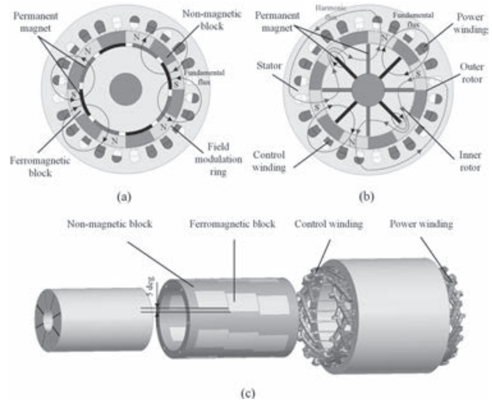

Fig. 1. Structure of the PM BDFG. (a) Surface PM; (b) Interior PM; (c) IPM BDFG with segmented reluctance rotor.

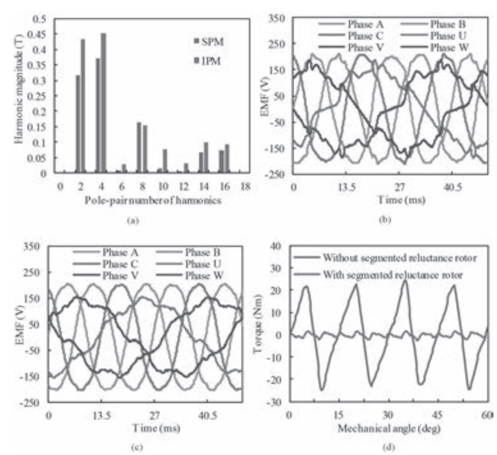

Fig. 2. Reslut of the simulation. (a) No-load spatial magnetic field in outer air-gap; (b) No-load EMF of IPM BDFG without segmented reluctance rotor; (c) No-load EMF of IPM BDFG with segmented reluctance rotor; (d) Cogging torque of IPM BDFG.

HR-14. Electromagnetic energy harvester for harvesting energy from low-frequency vibration.

K. Zhang[1], *Y. Su*[1], J. Ding[1] and Z. Zhang[1]
1. School of Mechanical Engineering, Zhengzhou University, Zhengzhou, China

We present an electromagnetic energy harvester with magnetic spring for converting low-frequency human motion into electrical energy. The magnetic spring is formed by magnetic forces between the fixed and moving magnets. Inductive coils are arranged at three special positions to obtain a larger output voltage. The experiment results show that the proposed energy harvesters possess frequency up-conversion behavior. A peak-to-peak voltage of 5.68V was obtained at excitation acceleration of 0.32g and frequency of 6.25Hz. Four LEDs in series were lit up successfully through an oscillation circuit which is connected to the energy harvester prototype. INTRODUCTION Research and investments in vibration energy harvesters [1-3] are currently attracting a great deal of interest because of the rapid development of wireless sensors and MEMS technology. In addition, traditional chemical batteries have a limited lifetime, which cannot power electronic devices for a long time. Meanwhile, soil and water will be polluted if wasted batteries were arbitrarily discarded into the environment. Vibration energy harvester can power electronic devices and wireless sensor nodes while converting ambient vibration energy into electric energy. Human motion is a common source of different kinds of vibrations. Various vibration energy harvesters based on kinetic energy have been developed. Three conversion mechanisms, piezoelectric [4], electrostatic [5] and electromagnetic [6] are often employed into energy harvesters. However, the frequency of vibrations produced by human motion is relatively low, usually below 10Hz, and the amplitude is large. In this case, electromagnetic conversion mechanism is more suitable for harvesting energy from human motion [7, 8]. Most electromagnetic vibration energy harvesters reported in literature mainly include a proof mass on a mechanical spring or a beam [9]. These harvesters cannot achieve a maximum efficiency because the resonance frequency of beam or spring cannot match that of the human motion vibration. In the paper, an electromagnetic energy harvester based on human motion with magnetic spring has been proposed. A magnetic spring, as an alternative [10] to mechanical spring or beam, can effectively decrease the resonance frequency of the harvester and make the harvester work in nonresonance condition. DESIGN OF THE HARVESTER The harvester is composed of a circular NdFeB (type N35) magnet, two cylinder NdFeB magnets, and six circular induction coils (ϕ25×ϕ2×3 mm), as shown in Fig. 1. The three magnets are set with their axes parallel to each other. The circular magnet (ϕ20×ϕ10×10 mm) is placed between the fixed magnet (ϕ10×10 mm) and the moving magnet (ϕ20×10 mm). The poles of the fixed (type N35) and moving magnets (type N52) are arranged in the same direction, which is opposite to that of the central magnet. The identical polarization causes the fixed magnet to repel the moving magnet. The two cylinder magnets are strongly attracted to the surface of the central magnet due to the magnetic attraction between the two cylinder magnets and the central magnet. And the fixed magnet is mounted on the inner side of the shell. In addition, the fixed magnet and the central magnet are joined together to prevent their relative movement. The central magnet, the shell and the cover plate are connected by a nylon bolt. The six ring copper coils with a diameter of 0.3 mm are attached to the inner walls of the shell and the cover plate, respectively. Each coil is of 320 turns. Thus, four coils are located at the end of the trajectory of the moving magnet, and the other two lie at the midpoint of the trajectory of the moving magnet. The gap between the inner walls of the shell and the cover plate is 18mm. EXPERIMENT The prototype of the harvester was excited by hand-shaking vibration, as shown in Fig. 2(a). For increasing the output voltage, six coils are connected in series and the total resistance is 23 Ω. The peak-to-peak voltage can reach 5.68 V with a load of 1kΩ at the excitation frequency of 6.25 Hz and amplitude of 0.32g. Corresponding FFTs of the induced voltage signal and the hand-shaking are shown in Fig. 2(b). According to FFTs, the main frequency of the induced voltage is found to be 40 Hz, which reaches 6.4 times of the main frequency of hand-shaking excitation. This phenomenon proves that the harvester possesses the frequency up-conversion behavior. Subsequently, a self-oscillation circuit was connected to the prototype. The circuit consists of two inductors (100μh), a transistor (S9108) and a resistor (1kΩ). And four commercial red LEDs are connected to the circuit in series as the load. Figure. 2(c) shows the four LEDs was lighting up when the prototype was moderately shaken by hand. As the frequency and acceleration of hand-shaking increases, the brightness of LEDs will be enhanced. CONCLUSIONS In this work, we have proposed an electromagnetic energy harvester for converting human motion energy into electrical energy. The harvester based on nonlinear magnetic-spring configuration that is helpful for responding low-frequency vibration. The frequency domain analysis shows that the harvester has a frequency up-conversion behavior. In the future, coil parameters will be optimized to obtain a greater power output and reduce the dimensions of the harvester for portable application. This work is supported by the National Natural Science Foundation of China under grant no.51475436 and the Henan Province Key Project on Science and Technologies under grant no.152102210042.

[1] A. Munaz and G. Chung, "An electromagnetic energy harvester based on multiple magnet scavenging power from low frequency vibration," Microsyst. Technol., vol. 23, pp. 91-99, 2017 [2] X. Wang et al. "A frequency and bandwidth tunable piezoelectric vibration energy harvester using multiple nonlinear techniques," Appl. Energ., vol. 190, pp. 368-375, 2017. [3] C.P. Le and E. Halvorsen, "MEMS electrostatic energy harvesters with end-stop effects," J. Micromech. Microeng., vol. 22, p. 074013, 2012. [4] X. Li, and V. Strezov, "Modelling piezoelectric energy harvesting potential in an educational building," Energ. Convers. Manag., vol. 85, pp. 435-442, 2014. [5] K. Tao, et al., "Design and implementation of an out-of-plane electrostatic vibration energy harvester with dual-charged electret plates," Microelectron. Eng., vol. 135, pp. 32 – 37, 2015. [6] M.P. Soares Dos Santos, et al., "Magnetic levitation-based electromagnetic energy harvesting: a semi-analytical non-linear model for energy transduction," Sci. Rep., vol. 6, p. 18579, 2016. [7] C.R. Saha, et al., "Electromagnetic generator for harvesting energy from human motion," Sensor. Actuat. A, vol. 147, pp. 248-253, 2008. [8] W. Wang et al., "Magnetic-spring based energy harvesting from human motions: Design, modeling and experiments," Energ. Convers. Manag., vol. 132: pp. 189-197, 2017. [9] A.R.M. Siddique, S. Mahmud and B. Van Heyst, "Energy conversion by 'T-shaped' cantilever type electromagnetic vibration based micro power generator from low frequency vibration sources," Energ. Convers. Manag., vol. 133, pp. 399-410, 2017. [10] M.A. Halim, H. Cho and J.Y. Park, "Design and experiment of a human-limb driven, frequency up-converted electromagnetic energy harvester," Energ. Convers. Manag.t, vol. 106, pp. 393-404, 2015.

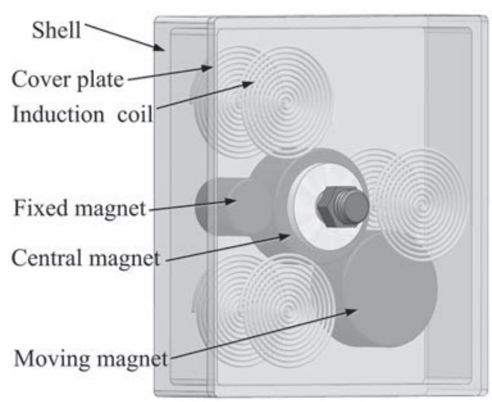

Fig. 1. Schematic diagram of the energy harvester

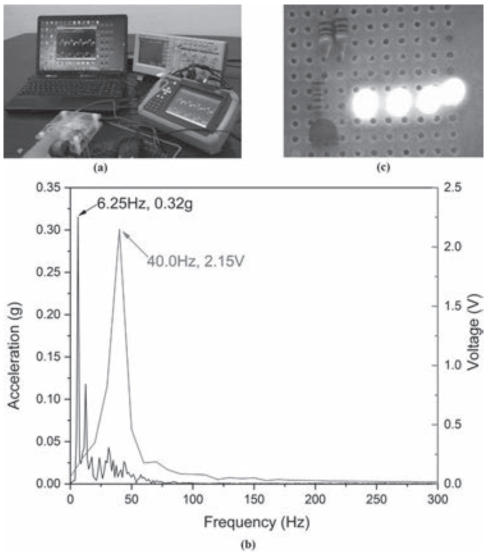

Fig. 2. Experiments:(a) prototype was shaken by hand, (b)frequency domain characteristics of the induced voltage and hand-shaking, and (c) LEDs as electronic load

HR-15. Parameter Determination of PMSM using Coupled Electromagnetic and Thermal Model Incorporating Current Harmonics.

S. Mukundan[1], H. Dhulipati[1], J. Tjong[1] and N. C. Kar[1]

1. Electrical & Computer Engineering, University of Windsor, Windsor, ON, Canada

Motivation: Permanent magnet synchronous machines (PMSMs) are widely used for electric vehicle (EV) propulsion owing to its high performance capabilities over a wide operating range [1]. With advent in machine structure and inverter topologies, accurate parameter determination incorporating machine non-linearities and effects of time and space harmonics is of paramount significance for high-performance control and analysis. Although classical *dq*-axis modeling is widely incorporated: 1) it fails to incorporate the machine non-linearities such as magnetic saturation, cross-saturation and leakage effects; 2) the spatial harmonic contents caused by machine winding and structural configuration are not considered in inductances and flux linkage; and 3) the effects of operating temperature on parameter variation are neglected [2]; and 4) it requires information from experimental data or complex look-up tables for parameter determination. On the other hand, finite element analysis (FEA) is computationally extensive and modelling of time harmonics becomes complex. Thus, in this paper, a coupled electromagnetic and thermal model incorporating current harmonics for parameter determination is developed and validated for a fractional-slot distributed wound (FSDW) laboratory PMSM. *State-of-the-art*: Authors in [3] have incorporated cross-saturation effects in modeling of PMSM drives and [4] includes magnetic saturation effects for parameter determination. However, these papers fail to include the effects of spatial harmonics. [5] includes the effects of air gap flux harmonics but does not take into account parameter variation due to temperature. Similarly, multi-physics models as illustrated in [6] does not consider modeling of current harmonics. Thus, in this paper, a magnetic equivalent circuit (MEC) coupled with a thermal model for interior PMSM (IPMSM) taking into account current harmonics is developed for parameter determination. *Methodology*: For a 27-slot, 6-pole laboratory FSDW IPMSM as shown in Fig. 1(b) with performance details given by Fig. 1(a), a MEC considering magnetic saturation, cross-saturation and slot leakage effects is modelled as indicated in Fig. 1(c). The input current to determine the effective magneto motive force ($F_{i,k,n}$) at the stator includes harmonic components as shown in (1). Thus, both spatial harmonic (n) and time harmonic (k) components are incorporated during calculation of i-phase machine parameters. The machine phase a is assumed to be aligned to d-axis and hence the calculated machine phase inductances can be easily transformed to the two-axis frame using existing transformation equations. In order to incorporate the effect of operating temperature on the parameters, a thermal model incorporating the materials thermal resistances at each node of the machine as shown in Fig. 1(d), is coupled with the developed MEC. Thus, based on the calculated flux values (Φ) from MEC using nodal analysis and material properties, the effective machine losses (P_{losses}) are calculated. The analytically calculated losses are implemented in the thermal model to estimate the operating temperature (T) as in (2) and the magnetic permeability of the stator, rotor and the permanent magnets (PMs) are updated accordingly to calculate the varied machine parameters. The entire procedure of the proposed methodology is depicted in a flowchart as illustrated in Fig. 2(a). *Results*: The proposed model provides a good compromise between model accuracy when compared to classical *dq*-axis models and computation complexity compared to FEA. Moreover, it can be incorporated for both sinusoidal and non-sinusoidal winding distribution machines; accurate modeling and control including temperature effects; and for structural optimization in case of machine design. Fig. 2(b) depicts the no-load induced emf waveforms at the rated speed of 3,000 rpm for the laboratory IPMSM. It can be seen from the figure that the values obtained from experimental analysis, FEA and the proposed model are in close agreement highlighting the accuracy of the model. The corresponding machine parameters including PM flux linkage and *dq*-axis inductances obtained are indicated in Fig. 2(c). Variation of PM flux linkage and *dq*-axis inductances with operating conditions, current harmonics and temperature can be easily obtained using the proposed model and will be shown in the full paper. The detailed analytical modeling of the equivalent electromagnetic and thermal models and a comprehensive comparative performance analysis of the machine obtained from calculations using the proposed model, FEA and experimental investigations will be presented in the full paper.

[1] K. L. V. Iyer, S. Mukundan, H. Dhulipati, K. Mukherjee, B. Minaker and N. C. Kar, "Design Considerations for Permanent Magnet Machine Drives for Direct-Drive Electric Vehicles," in proc. of *IEEE International Electric Machines & Drives Conference (IEMDC)*, Coeur d'Alene, ID, pp. 1170-1176, 2015. [2] C. Lai, G. Feng, K. Mukherjee and N. C. Kar, "Investigations of the Influence of PMSM Parameter Variations in Optimal Stator Current Design for Torque Ripple Minimization," in *IEEE Transactions on Energy Conversion*, vol. 32, no. 3, pp. 1052-1062, Sept. 2017. [3] P. Kakosimos, M. Beniakar, Y. Liu and H. Abu-Rub, "Model Predictive Control for Permanent Magnet Synchronous Motor Drives Considering Cross-Saturation Effects," in proc. of *IEEE Applied Power Electronics Conference and Exposition (APEC)*, Tampa, FL, pp. 1880-1885, 2017. [4] G. Feng, C. Lai and N. C. Kar, "A Novel Current Injection-Based Online Parameter Estimation Method for PMSMs Considering Magnetic Saturation," in *IEEE Transactions on Magnetics*, vol. 52, no. 7, pp. 1-4, July 2016. [5] M. Fasil, C. Antaloae, N. Mijatovic, B. B. Jensen and J. Holboll, "Improved *dq*-Axes Model of PMSM Considering Airgap Flux Harmonics and Saturation," in *IEEE Transactions on Applied Superconductivity*, vol. 26, no. 4, pp. 1-5, June 2016. [6] M. Rottach, C. Gerada, T. Hamiti and P. W. Wheeler, "A Computationally Efficient Design Procedure for Actuator Motors Using Magnetic Reluctance- and Thermal Resistance Network Models," in proc. of *XX*th *International Conference on Electrical Machines*, Marseille, pp. 2526-2532, 2012.

TABLE I. PERFORMANCE DETAILS OF LABORATORY 3–PHASE IPMSM

Rated Torque	100 Nm	Rated Speed	3,000 rpm
Peak Efficiency	97 %	Maximum Speed	10,000 rpm
DC bus Voltage	400 $V_{(max)}$	Current/phase	120 A rms
Slots/Pole	27/6	Current Density	7 A/mm²

(a)

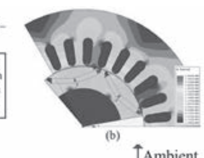

(b)

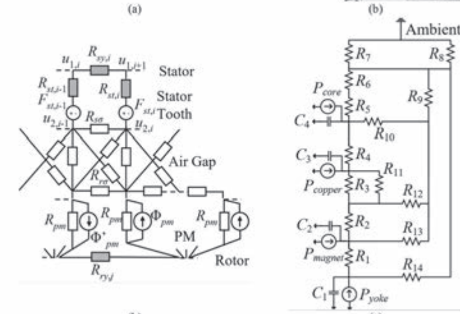

(b) (c)

Fig. 1. Proposed electromagnetic and thermal models implemented for a laboratory FSDW IPMSM with 27-slot, 6-pole configuration. (a) Performance details. (b) Developed electromagnetic model for FEA. (c) Developed MEC of a PMSM for electromagnetic analysis. (d) Developed thermal model of a PMSM for thermal analysis.

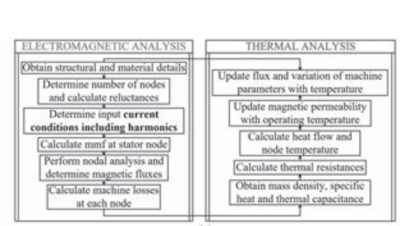

(a)

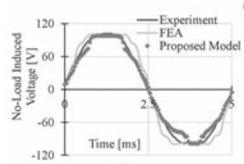

(b)

TABLE II. CALCULATION OF MACHINE PARAMETERS FOR LABORATORY IPMSM

Parameter	Experiment	FEA	Proposed Method
λ_{pm}	0.0857	0.0821	0.852
L_d [μH]	393	383.4	382.7
L_q [μH]	617	610.5	607.2

(c)

Fig. 2. Proposed coupled electromagnetic and thermal analysis for parameter determination including current harmonics for PMSM. (a) Flowchart illustrating proposed methodology. (b) Comparative analysis of no-load induced voltage waveform of laboratory IPMSM at rated speed of 3,000 rpm and room temperature. (c) Comparative analysis of machine parameters.

$$\left.\begin{aligned} F_{i,k,n}(x,t) &= \frac{F_{k,n}}{2}\cos\left\{k\left[\omega t-(i-1)\frac{2\pi}{m}\right]-n\left[\frac{\pi}{\tau_p}x-(i-1)\frac{2\pi}{m}\right]\right\} \\ &-\frac{F_{k,n}}{2}\cos\left\{k\left[\omega t-(i-1)\frac{2\pi}{m}\right]+n\left[\frac{\pi}{\tau_p}x-(i-1)\frac{2\pi}{m}\right]\right\} \end{aligned}\right\} \quad (1)$$

$$\left.\begin{aligned} &[u]\cdot[\Re]^{-1}=[\Phi] \\ &[G]\cdot[\mathrm{T}]=[Q] \\ &[Q]=\left[{}^{P_{losses}}\!/_{A}\right] \end{aligned}\right\} \quad (2)$$

FRIDAY AFTERNOON, 27 APRIL 2018 SIMPOR/ROSELLE BALLROOM, 1:30 TO 4:30

Session HS
SHIELDING, ELECTROMAGNETIC COMPATIBILITY, MOTORS AND GENERATORS II
(Poster Session)

Jonathan Z. Bird, Chair
Portland State University, Portland, OR, United States

HS-01. Electromagnetic Shielding Measurement of Magnetic Absorbing Sheets Using IC-stripline.

H. Park[1]
1. School of Electrical and Electronic Engineering, The University of Suwon, Hwaseong-si, The Republic of Korea

I. INTRODUCTION In modern mobile devices, the clock speed and integration density continually increase. The trend makes electromagnetic noises radiated from high-speed ICs and traces interfere and disturb easily the normal operation of adjacent ICs and components, which is called the intra-system electromagnetic interference (EMI) [1]. Particularly, engineers developing mobile devices are suffering from radio-frequency (RF) interference problem that is RF desensitization problem due to EMI of digital noise to RF antenna within the device. In order to solve EMI/RFI problems in mobile devices, various countermeasure components against EMI are popularly employed. Among the components, conductive and magnetic sheets for shielding and absorbing the electromagnetic noise are most commonly used in modern mobile devices. By covering high-speed ICs and traces with these sheets, electromagnetic noise strength radiated from noise sources can be effectively diminished. Therefore, it is important to accurately measure and evaluate the shielding performance of conductive and magnetic sheets. In order to test and measure the shielding property of planar shielding materials for EMI reduction, the most common way used so far is ASTM D4935-99 [2]. The ASTM method was devised to evaluate the shielding performance of planar materials from 30 MHz to 1 GHz by using a flanged coaxial transmission-line holder. This test method provides a procedure for measuring the electromagnetic (EM) shielding effectiveness (SE) of a planar material due to a plane-wave, far-field EM wave. However, as mentioned above, planar shielding and absorbing sheets used in mobile devices are very close to noise sources such as ICs and traces. In other words, these sheets are aimed for shielding near-field EM wave from the noise sources. As a result, far-field measurement method such as ASTM method is not suitable to evaluate the shielding performance of planar EMI sheets. Therefore, it is necessary to measure and evaluate near-field SE. Unfortunately, there is no standardized method for near-field shielding measurement of planar EMI sheets so far. In this paper, a method for near-field shielding measurement of planar shielding materials, especially magnetic absorbing materials is proposed. Our method is based on the IC-stripline method (IEC 61967-8), which defines a method for measuring the EM radiated emission from an integrated circuit (IC) using an IC-stripline in the frequency range of 150 kHz up to 3 GHz [3]. To be precise, the IC-stripline method is not actually aimed for shielding measurement, but this paper comprehensively examined the applicability of the IC-stripline method to near-field shielding evaluation of magnetic absorbing materials. Fig. 1 shows the geometry of IC-stripline method for shielding measurement of magnetic absorbing materials. As an electromagnetic source, a 50 ohm microstrip line on the printed circuit board is used. A magnetic absorbing sheet with 60×60 mm size is mounted and covered over the microstrip line. An IC-stripline, which can capture separately the electric-field (E) coupling and magnetic-field (H) coupling in near-field region, is located above the magnetic absorbing sheet. II. NUMERICAL RESULTS In the first, we conducted full-wave simulation for shielding analysis of a commercial magnetic absorbing sheet by modeling the test structures of IC-stripline and ASTM coaxial line. Fig. 2 shows simulated shielding effectiveness (SE) of a commercial magnetic absorbing sheet using the IC-stripline method (near-field SE) and ASTM method (far-field SE). SE is defined as the ratio of electric field or magnetic field strength before and after placement of a magnetic absorbing sheet. In the case of near-field, electric-field SE (E-SE) and magnetic-field SE. (H-SE) should be defined separately because the wave impedance (the ratio of electric-field and magnetic-field) is not constant in near-field region. However, for far-field, E-SE and H-SE are identical due to the constant wave impedance (377Ω in free-space). When SE of a commercial magnetic absorbing sheet is measured by the IC-stripline, E-SE is almost zero up to 1 GHz, whereas H-SE is around 7~10 dB. When SE is measured using ASTM method, far-field SE is also almost zero up to 3 GHz. These results indicate that for shielding, the magnetic absorbing sheets are effective only for magnetic near-field but completely ineffective to electric near-field and far-field EM wave. More detailed explanation and experimental validation will be presented in on-site conference and an extended full paper.

[1] J. Fan, "A new EMC challenge: Intra-system EMI and RF interference," SAFETY & EMC, pp. 3?5, 2015. [2] ASTM Standard Designation: D 4935-99, "Standard test method for measuring the electromagnetic shielding effectiveness of planar materials," 1999. [3] Integrated Circuits Measurement of Electromagnetic Emissions Part 8: Measurement of Radiated Emissions IC Stripline Method, IEC 61967-8, 2011. [4] H. H. Park, J. H. Kwon, and S. Ahn, "A simple equivalent circuit model for shielding analysis of magnetic sheets based on microstrip line measurement," IEEE Trans. Magnetics, vol. 53, no. 6, Art. ID 9401504, June 2017.

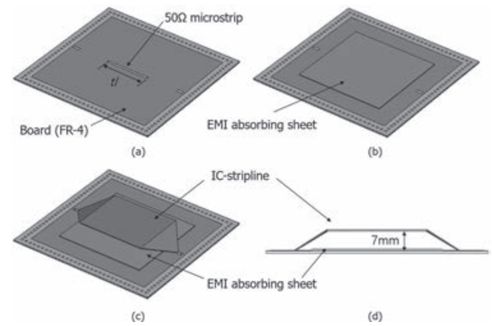

Fig. 1. Configuration of IC-stripline method for near-field shielding measurement of planar materials

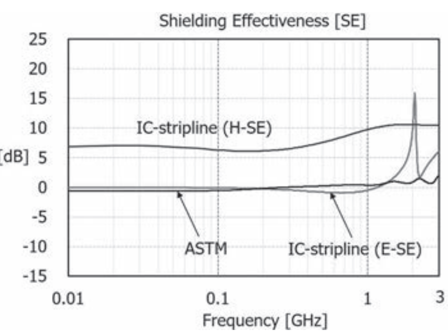

Fig. 2. Comparison of shielding effectiveness (SE) of a commercial magnetic absorbing sheet.

HS-02. Influence of Sleeve Material on Electromagnetic Field Based on Multi-Physical Field for Permanent Magnet Synchronous Motor.

W.l. Li[1], *L. Li*[1], J. Li[2], J. Shen[3], J. Cao[1] and D. Li[1]
1. School of Electrical Engineering, Beijing Jiaotong University, Beijing, China; 2. School of Electrical Engineering and Automation, Harbin Institute of Technology, Harbin 150001, China, Harbin, China; 3. College of Electrical and Electronic Engineering, Harbin University of Science and Technology, Harbin, China, Harbin, China

This work was supported by the National Natural Science Foundation of China under Grant 2015DFR70060. Abstract: For permanent magnet synchronous motor (PMSM), due to the large rotor rotational centrifugal forces, a sleeve is often used to prevent damage to rotor permanent magnets. However, the sleeve material characteristics have much influence on the PMSM, and therewith, most of rotor eddy-current losses are generated in the sleeve, which could increase the temperature of PMSM. If the rotor heat dissipation condition is poor, high temperature can influence the PMSM performance and even result in thermal demagnetization of the permanent magnets. Thus, a sleeve scheme designed with low eddy-current losses is very necessary. In this paper, taking a 12.5 kW, 2000 rpm PMSM with 0.2mm thickness stainless steel sleeve as an example, the sleeve adopted insulation cylinder material is presented. Then, the 2-D mathematical model of PMSM is established, and the electromagnetic field is calculated by utilizing the time-stepping finite element method under rated load condition. In addition, the variations of the eddy-current losses in different kinds of sleeves are analyzed. The calculation results show the effectiveness of the insulation cylinder in reducing the eddy-current losses in the rotor. The obtained conclusions can provide useful reference for the design and research of PMSM. Introduction The eddy-current losses in permanent magnet will be very obvious to increase rotor temperature of the machine. Thus, it is very important to find some measures to reduce the eddy-current losses in the sleeve and magnets. Some scholars have preliminary work in reducing the eddy-current losses in the rotor. Eddy-current losses in the rotor permanent magnet could be reduced by dividing the rotor permanent magnet [1]. The copper plating between the sleeve and permanent magnets could dramatically decrease the eddy-current losses in magnets [2]–[4], but the eddy- current in the sleeve would not be significantly changed. In this paper, taking a PMSM with 0.2mm stainless steel sleeve as the study object, insulation cylinder material is presented. Using the finite element method, the electromagnetic field is calculated before and after insulation cylinder material under rated load condition. The further research on eddy current distribution, which is one of the key influencing factors in PMSM reliability and working life, is researched based on the theories of electromagnetic field. 1: Parameters and Structure of PMSM Fig.1a shows the prototype PMSM experimental platform and tested results operating at rated speed (2000 r/min) and rated load ($R = 0.32\ \Omega$ and $\cos\phi = 0.79$). The rotor magnetic field was excited by the PM (N33SH), whose remanence (Br) and coercivity (Hc) is 1.1T, 838 kA/m, respectively, and limited working temperature is 150 °C. Meanwhile, the conductivity is 6.25×10^5 S/m, and it is divided into three segments in axial direction. To prevent damage to rotor permanent magnets due to the large rotational centrifugal forces, the sleeves, which are coated outer surface of permanent magnets, adopt stainless steel material and are divided into six segments in axial direction, as shown in Fig.1c. The conductivity and thermal conductivity of stainless steel sleeve is 1.1×10^6 S/m and 59 W/m●K, respectively. Basic parameters of PMSM are listed in Table I. Based on the structure and size of the prototype, the 2-D transient electromagnetic field calculation model was established, as shown in Fig.2. By using the finite-element method, the phase voltage and current of PMSM were calculated, and the value is 212.3V, 25.3A respectively. It can prove that the calculated results are in good agreement with the test data of PMSM. 2: Influence of Sleeve Material on Electrical Field In order to reduce the eddy-current losses in the rotor, the insulation cylinder, which is made of HGW2085 material, is proposed. This material has a very high mechanical strength and good insulation properties, and working temperature is 125 °C. In addition, its conductivity is 0 S/m and relative pemeability is 1. Table II gives the electromagnetic calculation results under rated load condition when the sleeve adopts the stainless steel and insulation cylinder material, respectively. From Table II, it can be seen that, whether the sleeve adopts stainless steel or insulation cylinder, the main magnetic flux and flux provided by permanent magnets are not changed under rated load condition, Accordingly, the stator core loss will not also be changed. One point to take notice of is when the sleeve material adopts insulation cylinder, the eddy-current loss in permanent magnet will increase compared with that of the prototype PMSM. This is because the shielding effect of the insulating cylinder on the harmonic magnetic field in the air gap is relatively weak, it is also shown in Fig.3. And gap flux density fundamental value and main harmonics increase compared with that of adopting stainless steel. However, since the conductivity of insulation cylinder is zero, the total rotor eddy-current losses can be reduced. In additional, the insulation cylinder can prevent the heat produced by stator from transferring to the permanent magnet. Thus, it can protect the permanent magnet from high temperature damage. Conclusion 1 : Main magnetic flux and electromagnetic torque can not be changed with the nonmagnetic sleeve material. 2 : Whether the machine power is large or small, the insulation cylinder will have a positive effect on reducing the rotor losses and improving machine efficiency.

[1]K. Atallah, D. Howe, P. H. Mellor, and D. A. Stone, “Rotor loss in brushless AC machines,” *IEEE Trans. Ind. Appl*., vol. 36, no. 6, pp. 1612–1618, 2000. [2]F. Y. Huo, W. L. Li, L. K. Wang, C. W. Guan, Y. H. Zhang, and Y. Li, “Influence of copper screen thickness on three-dimensional electromagnetic field and eddy current losses of metal parts in end region of large,” *IEEE Trans. Ind. Electron*., vol. 60, no. 7, pp. 2595–2601, 2013. [3] Z. Kolondzovski, A. Belahcen, A. Arkkio, “Comparative thermal analysis of different rotor types for a high-speed permanent-magnet electrical machine,” *IET Elect. Power Appl*., vol. 3, no. 4, pp. 279–288, Jul. 2009. [4]J. L. F. van derveen, L. J. J. Offringa, and A. J. A. Vandenput, “Minimizing rotor losses in high-speed high-power permanent synchronous generators with rectifier load,” *IEEE Proc. Elect. Power*., vol. 144, no. 5, pp. 331–337, Sep. 1997.

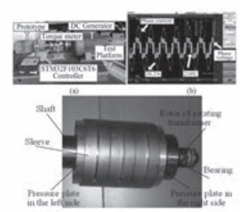

Fig.1. Experimental platform, experiment results, and rotor actual structure, (a) Experimental platform, (b) Experiment results of phase current and voltage, (c) Rotor actual structure.

Table I. Parameters of PMSM

Symbol	Quantity	Value
P	rated power	12.5 kW
U	rated voltage	364 V
S	rated speed	2000 r/min
D_1	stator outer diameter	180 mm
D_2	stator inner diameter	103 mm
L	stator core length	107 mm
p	pole pairs	4

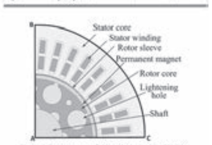

Fig. 2. 2-D temperature field analysis model of PMSM.

Fig. 3. Air gap flux density change when the sleeve adopts stainless steel and insulation cylinder material.

Table II. Electromagnetic calculation results when the sleeve adopts stainless steel and insulation cylinder material.

Item	Stainless steel	Insulation cylinder
Torque (N·m)	59.9	59.8
Flux provided by permanent magnets (10^{-3}Wb)	5.92	5.92
Main magnetic flux (10^{-3}Wb)	5.44	5.44
Stator loss (W)	123.64	122.98
Stainless steel losses (W)	34.9	/
Insulation cylinder losses (W)	/	0
Magnets losses (W)	21.5	38.47
Back EMF(V)	204.03	205.46
Phase voltage(V)	212.3	212.49
Phase current(A)	27	27

HS-03. Design and Analysis of a Linear Interior Permanent Magnet Vernier Machine.

C. Shi[1], R. Qu[1], Y. Gao[1], D. Li[1] and Y. Zhou[1]
1. School of Electrical and Electronics Engineering, Huazhong University of Science & Technology, Wuhan, China

I. INTRODUCTION The linear permanent magnet vernier machine (LPMVM) is the combination of the linear permanent magnet machine and vernier machine, which yields high thrust density at low speed and thus is a preferable solution in the direct-drive linear-motional applications [1]. In order to further improve the thrust density of the LPMVM, many new configurations have been proposed in recent years, such as the double-stator spoke-type LPMVM [2], the LPMVM with Halbach permanent magnet (PM) array [3], the LPMVM with consequent-pole and Halbach PM array [4], the linear stator PM vernier machine [5], and so on. It is worth noted that the flux density of the tooth of the LPMVM is even smaller that of the conventional linear PM (CLPM) machines due to the multi-polar and fewer-teeth structure. In order to improve the flux density and the thrust of the LPMVM, the linear interior permanent magnet vernier machine (LIPMVM) is proposed in this paper, in which the PMs are inserted into the stator core. Due to the improvement of the flux density and additional reluctance thrust, the average thrust of the proposed LIPMVM is significantly higher that of the conventional linear surface PM vernier machines (LSPMVM). II. CONFIGURATIONS AND OPERATION PRINCIPLES A. Configurations Fig. 1 (a) shows the configuration of the existing LSPMVM, in which the PMs are mounted on the surface of the stator. Fig. 1 (b) shows the configuration of the proposed LIPMVM. The V-shape PM arrays are adopted in the LIPMVM so that larger volume of PMs can be inserted into the stator core. The air-gap length of the two machine are kept the same. But the effective air-gap length of the LIPMVM will be much smaller that of the LSPMVM due to the interior PM structure. More detailed parameters are listed in Table I. B. Operation Principles and Analysis Both the LSPMVM and LIPMVM obey the operation principles of the vernier machines [6], so the relationship between the mover slots number Z_m, the PM pole-pair Z_{pm} and armature windings pole-pair P_a can be expressed as: $P_a=|Z_m \pm Z_{pm}|$ (1) The air-gap permeance function of the LPMVM can be expressed as [7]: $\Lambda(x, vt)=\mu_0/(g'+G(x, vt))$ (2), where $g'=g+h_m/\mu_r$ (3), g is the air-gap length and G(x, vt) is the additional air-gap length introduced by slotting. In the LIPMVM, we have g'=g as the PMs are inserted into the stator core. Then, the air-gap flux density can be obtained by: $B_g(x, vt)=F_{pm}(x)*\Lambda(x, vt)$ (4), where $F_{pm}(x)=\sum F_{pmi}\sin(iZ_{pm}x)$ (5). So, according to equation (2), a higher flux density can be obtained in the LIPMVM under the same magnetic motive force (MMF) as the LSPMVM due to the smaller g', and both the back electromotive force (EMF) and average thrust will be improved. Furthermore, due to the saliency of the interior PMs (IPMs) structure, there will be an additional reluctance thrust component in the average thrust of the LIPMVM. III. COMPARISONS Two finite element (FE) models about the LSPMVM and LIPMVM are built to compared with each other. In order to reduce the second harmonics in the thrust, the three-sectional structure [3] is adopted in both LSPMVM and LIPMVM. The three-sectional LIPMVM is shown in Fig.2. The flux distributions in the air-gap and iron core of the two machines, calculated by the FE method, are shown in Fig. 3, from which it can be seen that the flux density in the air-gap and mover tooth are both significantly improved due to the adoption of the IPMs. The comparisons of the flux-linkage, back EMF waveforms are shown in Fig. 4 and Fig. 5. The average thrusts at different current density are shown in Fig. 6. More detailed comparisons between the two machine are listed in Table II. It can be seen that the back EMF and average thrust of the LIPMVM is improved by 34% and 30%, respectively, compared to the LSPMVM. It is worth noted that the PM consumption of the LIPMVM is even lower that of the LSPMVM. This thrust improvement can be explained by the flux-strengthening effect and the additional reluctance thrust in the LIPMVM. IV. CONCLUSION This paper mainly proposed the LIPMVM, whose thrust density is 30% higher that of the conventional LSPMVM at the current density of 5A/mm^2, with lower PM consumption. The operation principles and flux-strengthening effect of the LIPMVM are also introduced in the paper. The FE results verified the superiority of the proposed machine.

[1] W. Li, K. T. Chau, C. Liu, S. Gao, and D. Wu, "Analysis of tooth-tip flux leakage in surface-mounted permanent magnet linear vernier machine," *IEEE Trans. Magn.*, vol. 49, no. 7, pp. 3949-3952, Jul. 2013. [2] N. Baloch, S. Khaliq, and Y. Kwon, "HTS dual-stator spoke-type linear vernier machine for leakage flux reduction," *IEEE Trans. Magn.*, vol. 53, no. 11, Nov. 2017, Art. ID. 8111104. [3] Y. Huo, R. Qu, Y. Gao, S. Jia, and X. Fan, "Design of a linear vernier permanent magnet machine with high thrust force density and low thrust force ripple," in *Proc. IEEE International Electric Machines and Drives Conference* (*IEMDC 2017*), Miami, FL, USA, May. 2017. [4] C. Shi, D. Li, R. Qu, H. Zhang, Y. Gao, and Y. Huo, "A novel linear permanent magnet vernier machine with consequent-pole permanent magnets and Halbach permanent magnet arrays," *IEEE Trans. Magn.*, vol. 53, no. 11, Nov. 2017, Art. ID. 2501404. [5] Y. Du, K. T. Chau, M. Cheng, Y. Fan, Y. Wang, W. Hua, and Z. Wang, "Design and analysis of linear stator permanent magnet vernier machines," *IEEE Trans. Magn.*, vol. 47, no. 10, pp. 4219-4222, Oct. 2011. [6] R. Qu, D. Li, and J. Wang, "Relationship between magnetic gear and vernier machines," in *Proc. IEEE International Conference on Electrical Machines and Systems* (*ICEMS*), Beijing, 2011. [7] B. Gaussens, E. Hoang, O. Barriere, J. S. Michel, M. Lecrivain, and M. Gabsi, "Analytical approach for air-gap modeling of field-excited flux-switching machine: no-load operation," *IEEE Trans. Magn.*, vol. 48, no. 9, pp. 2505-2517, Sep. 2012.

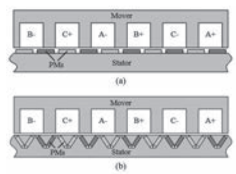
Fig. 1. Configurations. (a) Conventional LSPMVM. (b) Proposed LIPMVM.

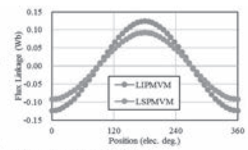

Fig. 4. Comparisons of flux linkage.

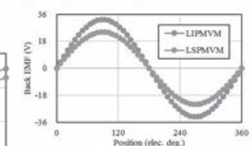

Fig. 5. Comparisons of back EMF.

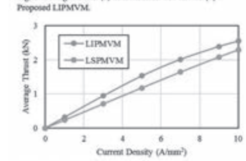

Fig. 6. Comparisons of average thrust.

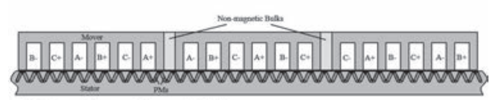

Fig. 2. Three sectional structure of the proposed LIPMVM.

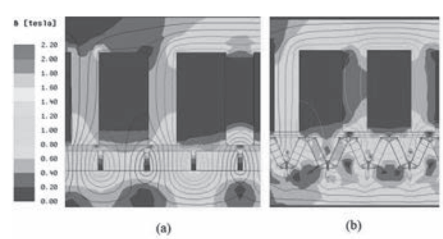
Fig. 3. Flux distributions in the mover tooth. (a) LSPMVM. (b) LIPMVM.

TABLE I
KEY PARAMETERS

Machine	LSPMVM	LIPMVM
Mover height, h_{mover} (mm)	35	
Mover length, L (mm)	120	
Mover slots number, Z_m	6	
Air-gap length, g (mm)	1.5	
Stack length, L_{ef} (mm)	120	
PM thickness, h_m (mm)	5	2.5
PM width, w_{pm} (mm)	10.8	8
PM pole-pair number, Z_{pm}	5	
Pole-pair of windings, P_a	1	

TABLE II
PERFORMANCE COMPARISONS

Machine	LSPMVM	LIPMVM
Current density, (RMS, A/mm^2)	5	
Heat loading (RMS, A^2/(cm•mm^2))	1724	
No-load flux linkage (RMS, Wb)	0.09	0.12
No-load back EMF, (RMS, V)	17.07	22.96
Average thrust (kN)	1.18	1.53
Thrust ripple (%)	2.43	8.53
PM consumption (kg)	2.43	1.8

HS-04. Reduction of magnetically induced vibration and noise in SPM motors due to segmented magnets.

J. Song[1], S. Sung[1], H. Jang[1], C. Kang[1] and G. Jang[1]
1. Dept of Mechanical Convergence Engineering, Hanyang University, Seoul, The Republic of Korea

I. INTRODUCTION Segmented permanent magnets (PMs) in surface-mounted PM (SPM) motors with large diameter are more widely used than ring PMs due to mechanical robustness and manufacturability. Fig. 1(a) shows the one-sixth model of a conventional SPM motor which has 36 slots and 48 poles in 12 segmented PMs. In this type of SPM motors, the radial gap between segmented PMs plays dominant role to change magnetic reluctance, and generates cogging torque and unbalance magnetic pull (UMP) with slot harmonics [1, 2]. Fig. 1(b) shows the noise waterfall of the conventional motor which has the dominant amplitudes corresponding to the 36th and 72nd harmonics originated from slot number. We investigated the characteristics of cogging torque and UMP due to the radial gap between segmented PMs, and proposed the designs of segmented magnets to reduce magnetically induced vibration and noise of the SPM motor due to segmented PMs. II. MAGNETIC EXCITATION FORCES DUE TO SEGMENTED PMS Torque ripple and UMP are major magnetic excitation forces in PM motors. Torque ripple is originated from cogging torque and commutation torque ripple. Cogging torque is generated from the interaction between PMs and slots and it is one of major sources of torque ripple because it exists regardless of armature current. Main harmonics of cogging torque are the least common multiples (LCM) of number of pole and slot [2]. However, reluctance changes whenever the radial gap between segmented PMs passes the slots which lowers harmonics of cogging torque to slot harmonics. These slot harmonic component of cogging torque can be calculated by summing cogging torque caused by each gap. The cogging torque of motors with segmented PMs, T^{cog} can be expressed as follows: $_{\infty N \infty}$ $T^{cog}=\Sigma T_j^{ring}\sin(jN_{LCM}\omega t+\phi_j)+\Sigma\Sigma T_j^{seg}\sin(jQ(\omega t+\Theta_i)+\Psi_j)$ (1) $^{j\ i\ j}$ where T_j^{ring}, ϕ_j, and T_j^{seg}, ψ_j are the Fourier coefficients and phases of cogging torque with ring type magnets and segmented PMs, respectively. And ω, Q, N_{LCM}, N and θ_i are the rotating speed of motor, number of slot, LCM of numbers of poles and slots, number of segmented PMs and angular position of the *i*-th gap, respectively. In real applications, there exists a static eccentricity in which the rotor rotates around the center of stator and the air-gap is not uniform along the circumferential direction because the stator and rotor centers do not coincide. This static eccentricity generates the UMP, and its main harmonics are pole harmonics [3]. The UMP caused by static eccentricity is affected by frequency component of cogging torque [4]. The x-directional UMP, F_x can be defined as follows: $_\infty$ $F_x=(g\varepsilon_s/(g^2-\varepsilon_s^2))^2\Sigma F_j^r\sin(jN_p\omega t+\Phi_j)$ ^{j} $_{\infty N\infty}$ $-\varepsilon_s/(gR_g)(\Sigma T_j^{ring}\sin(jN_{LCM}\omega t+\phi_j)+\Sigma\Sigma T^j_{seg}\sin(jQ(\omega t+\theta_j)+\psi_j)$ (2) $^{j\ i\ j}$ where g, ε_s, and N_p are the length of air gap, static eccentricity and number of poles. F_j^r and Φ_j are the Fourier coefficient and phase of radial magnetic force. The slot harmonics of UMP are also originated from slot harmonics of cogging torque. III. DESIGNS OF SEGMENTED PM TO REDUCE VBATION AND NOISE OF SPM MOTORS The slot harmonics of the cogging torque and UMP can be reduced by adjusting the number of segments and the number of poles in segmented PMs. We investigated Eq. (1) and (2) to find the possible combination of segmented PM and poles in segmented PM to reduce the amplitudes of the cogging torque and UMP. We proposed two designs of the segmented PMs, PM1 and PM2 as shown in Fig. 1(c) and (d). The numbers of poles in PM1 are changed to 3 and 5 from 4 which is the number of poles in segmented PM of the conventional motor. The numbers of poles in PM2 are changed to 5 and 7. The number of segmented PMs in PM1 is 12 which is identical to conventional motor but the number of segmented PMs in PM2 is 8. The proposed motors with PM1 and PM2 has 48 poles which is same as the conventional motor. We performed the finite element analysis to confirm the analytical results of the reduction of cogging torque and UMP. Fig. 2(a) and (b) show the cogging torque and x-directional UMP generated in the conventional motor, PM1 and PM2. The 36th and 108th harmonic of cogging torque and UMP are reduced by 29.3% in PM1 and 52.9% in PM2, respectively, and the 72nd harmonic of excitation forces does not exist in PM1 and PM2. IV. CONCLUSION We investigated the characteristics of cogging torque and UMP due to the radial gap between segmented PMs, and proposed the possible combination of segmented PM and poles in SPM motors to reduce the amplitudes of the cogging torque and UMP. The characteristics of cogging torque and UMP in the proposed equations and proposed PM designs were verified by finite element analysis. This paper will contribute to reducing magnetically induced vibration and noise of SPM motors with segmented PMs.

[1] S. M. Hwang, and K. T. Kim, "Effects of segmented poles on motor performance," IEEE Transaction on Magnetics, vol. 35, no. 5, pp. 3712-3714, 1999 [2] S. M. Hwang, J. B. Eom, G. B. Hwang, W. B. Jeong, and Y. H. Jung, "Cogging torque and acoustic noise reduction in permanent magnet motors by teeth pairing", IEEE Transaction on Magnetics, vol. 36, no. 5, pp. 3144 – 3146, 2000 [3] C. I. Lee and G. H. Jang, "Experimental measurement and simulated verification of the unbalanced magnetic force in brushless DC motor", IEEE Transaction on Magnetics, vol. 44, no. 11, pp. 4377 - 4380, 2008 [4] S. J. Sung, G. H. Jang, K .J. Kang, and J. Y. Song, "Effect of additional harmonics of driving current on torque ripple and unbalanced magnetic force in HDD spindle motors with stator and rotor eccentricity", Microsyst Technol, vo. 21, no. 12, pp. 2669-2678, 2015

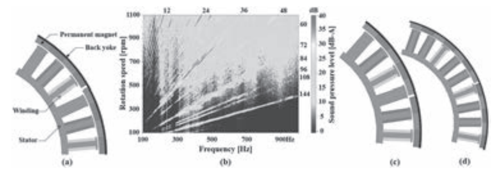

Fig. 1. (a) One-sixth of a conventional motor (4poles in 12 segmented PMs), (b) noise waterfall of conventional motor, (c) proposed PM1 (3 and 5 poles in 6 segmented PMs each) and (d) PM2 (5 and7 poles in 4 segmented PMs each)

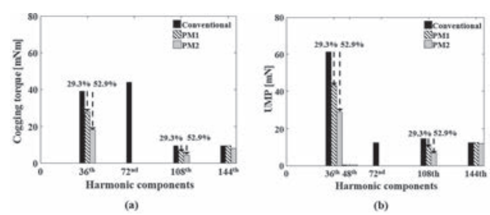

Fig. 2. (a) Simulated cogging torque of conventional motor, PM1 and PM2 and (b) x-directional UMP of conventional motor, PM1 and PM2

HS-05. A High Torque Density Concentrated Winding Vernier Reluctance Machine with DC-Biased Current.

S. Jia[1,3], D. Liang[1,3], D. Li[2], W. Kong[2] and R. Qu[2]

1. School of Electrical Engineering, Xi'an Jiaotong University, Xi'an, China; 2. School of Electrical and Electronic Engineering, Huazhong University of Science and Technology, Wuhan, China; 3. State Key Laboratory of Electrical Insulation and Power Equipment, Xi'an, China

I. Introduction Stator DC current excited vernier reluctance machines (DC-VRMs), which have concentrated field and armature windings in stator are developed for applications when low cost and wide speed operation range are required [1]. However, the two sets of windings in the stator increase the insulation area and complicate the manufacturing process. Therefore, DC-VRMs with DC current injected into the armature windings are developed [2], [3], as the torque density can be improved under the constant copper loss. This paper deals with the design and analysis of an improved torque density DC-biased-VRM. A 12-stator slot, 10-rotor-slot machine is firstly designed, then by analyzing the magnetic flux distribution, a novel 6/10 machine with 20% higher torque density is developed. Further, by optimizing the stator/rotor tooth width combination and tooth shape, the torque ripple is reduced. Finally, the prototype of 6/10 machine is built, and the experimental results will be shown later. II. Topology, Parameters, and Flux Distribution The operation principle of DC-biased VRMs can be described briefly as follows: the DC component of the armature coils produces a multipole stationary magneto motive force (MMF), with the permeance modulation effect of the open-slot rotor, rotating exciting fields is generated. Average torque can be produced under the interaction of rotating exciting fields with multipole rotating MMF by three-phase balanced AC component. The currents contain a sinusoidal AC current with a DC current, and can be expressed as Eq. (1). Three phase H-bridge inverter is appropriate for this machine. Fig. 1 (a) shows the topology and winding arrangement of an existing 12/10 machine published in [3]. Fig. 1 (b) shows the flux distribution at the initial rotor position with an excitation in Table I. The FEA results reveals that at any time, the flux lines always don't flow through the teeth surrounded by blue dashed line, Besides, considering all the coils are not wound in these teeth, therefore, these stator teeth are removed, and the resulting topology, 6/10 machine in Fig. 2 (a) is proposed. The slot area increases 29%. Therefore, under the condition of the constant copper loss, the allowable electrical loading becomes higher, so the torque density is improved. The main design parameters is listed in Table I. Fig. 2 (b) shows that the simulated load flux distribution of the 6/10 machine is always almost the same with that of the 12/10 machine. III. Performance Comparison The torque waveforms with the aforesaid current are in Fig. 3. The average torque of the 12/10 and 6/10 machine are 2.88 and 3.41 Nm, nearly 20% higher torque is achieved. Besides, by optimizing the stator/rotor tooth arc, tooth shape, and current shaping, the torque ripple can be further reduced. From the flux distribution, it can be inferred that the iron losses basically remain unchanged, and considering the constant copper loss, the efficiency of the motor will also be greatly improved. To verify the analysis results, a prototype of 6/10 machine is built. The picture of the stator and rotor is shown in Fig. 4. The experimental results will be given later. IV. Conclusion In this paper, a higher torque density, 6/10 vernier reluctance machine with DC-biased current is proposed. The analysis results show that the torque density is 20% higher than that of an existing 12/10 machine. Moreover, the efficiency is also improved.

[1] Raminosoa T, Torrey D A, El-Refaie A M, et al. "Sinusoidal reluctance machine with DC winding: an attractive non-permanent-magnet option, *IEEE Trans. Ind. App.*, Vol.52, No.3, pp: 2129-2137, May./Jun., 2016. [2] Z. Zhu, B. Lee, and X. Liu, "Integrated field and armature current control strategy for variable flux reluctance machine using open winding," *IEEE Trans. Ind. App.*, Vol.52, No.2, pp: 1519-1529, Mar./Apr., 2016. [3] S. Jia, R. Qu, J. Li, and D. Li, "Flux modulation principles of DC-biased sinusoidal current vernier reluctance machines," pp: 1-8, *in Proc. of IEEE Conference of ECCE'2016.*

$$
\begin{aligned}
i_A &= I_{dc} + \sqrt{2} I_{ac} \sin(\omega_e t + \alpha) \\
i_B &= I_{dc} + \sqrt{2} I_{ac} \sin(\omega_e t + \alpha - \tfrac{2}{3}\pi) \\
i_C &= I_{dc} + \sqrt{2} I_{ac} \sin(\omega_e t + \alpha + \tfrac{2}{3}\pi)
\end{aligned} \qquad (1)
$$

TABLE I
MAIN PARAMETERS COMPARISON

Parameters	Symbols	12/10 Machine	6/10 Machine
Stator outer diameter (mm)	D_{so}	124	124
Rotor outer diameter (mm)	D_r	74.4	74.4
Air-gap length (mm)	g	0.3	0.3
Stack length (mm)	l_{stack}	36	36
Coil turns	N_c	32	41
Phase resistance (Ω)	R	0.088	0.113
Phase current RMS value (A)	I_{rms}	19	16.8
DC component (A)	I_{dc}	13.44	11.88
AC component (A)	I_{ac}	13.44	11.88
Current density (A/ mm²)	J	6.7	6.7
Copper loss (W)	P_{cu}	95	95

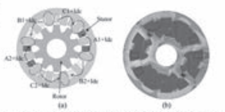

Fig. 1. Initial 12/10 machine. (a) Topology, and winding configuration. (b) Flux distribution.

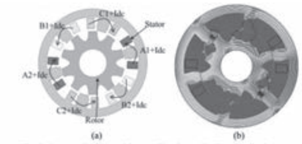

Fig. 2. Improved 6/10 machine. (a) Topology. (b) Flux distribution.

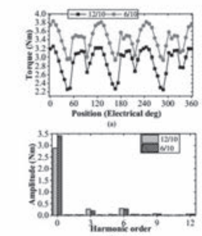

Fig. 3. Torque comparison at the constant copper loss of 95 W. (a) Waveforms. (b) Harmonics.

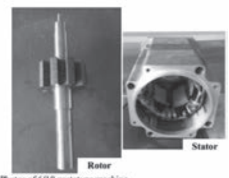

Fig. 4. Photos of 6/10 prototype machine.

HS-06. The Vibration Reduction Design and Experimental Validation of Generator for Range Extended Electric Vehicle.

B. Son[1], G. Park[1], H. Jung[2], Y. Kim[3] and S. Jung[1]
1. Sungkyunkwan Univ., Suwon-si, The Republic of Korea; 2. Korea Automotive Technology Institute, Cheonan, The Republic of Korea; 3. Chosun Univ., Gwangju, The Republic of Korea

I. Introduction Range Extended Electric Vehicle (REEV) is one of the hybrid systems for an electric vehicle, which adopts electric power-train including Auxiliary Power Unit (APU). The APU is commonly composed of an engine and electric generator, and assists to charge when the battery is exhausted. The REEV system has been widely employed to an electric vehicle since it guarantees extended driving range with relatively small battery pack and fuel combustion [1], [2]. Meanwhile, REEV system has a spatial constraint due to the additional mounting of APU. The generator, main component of APU, is required to have high power density due to the constraint. However, the design for high power density results in a reaction that increases electromagnetic force, which is the main cause of vibration. Furthermore, the structure of the system is vulnerable to vibration, since the generator is directly connected to the engine in the horizontal direction without additional fixation on the other side. Thus, design considering vibration is required to guarantee the control stability and the ride comfort. This paper demonstrates the vibration reduction design for APU generator based on vibration analysis applied to the electromagnetic force. For the conventional designed model, severe vibration occurred at operating points on every multiple of 1,500rpm. It disturbs stable control on the main operating point at 3,000rpm, which is matched for the optimal efficiency of the system. To complement the problem, diverse methods such as pole-slot combination and dimension modification is considered based on the analysis and applied to the revised model. Consequently, the effectiveness of the revised design is verified through manufacture and experiment. II. Electromagnetic Force & Vibration Analysis A. Electromagnetic Force Analysis Electromagnetic force on the stator core is one of the main vibration sources, which transfers in the radial direction. Thus, electromagnetic force analysis should be preceded. Electromagnetic radial force density can be calculated using Maxwell's stress tensor method based on Finite Element Method (FEM) as follow [3], [4]. $f_r(\theta,t) = 1/2\mu_0(B_r^2(\theta,t)-B_0^2(\theta,t))$ Where B_r and B_t are components of the air gap flux density, μ_0 is the permeability of air, θ is the angular position, and $_t$ is the time. The spatial and temporal distribution of electromagnetic force can be analyzed using Fast Fourier Transformation. B. Vibration Analysis Forced vibration analysis applying the calculated electromagnetic force is conducted based on FEM. The fundamental equations employed in the vibration analysis is as follow [4], [5]. $[m]\{x''\}+[c]\{x'\}+[k]\{x\}=\{F\}$ Where $[m]$, $[c]$ and $[k]$ are mass, damping and stiffness matrices, $\{x''\}$, $\{x'\}$ and $\{x'\}$ is nodal acceleration, velocity and displacement vectors and f is the external force, that is the electromagnetic force. For computational efficiency, mode superposition is employed to solve the above equation [4] and 3D modeling of housing is simplified by removing the minor part. III. Problem Analysis & Revised Design A. Problem Analysis of the Conventional Model For the conventional designed model, the control disturbance due to vibration occurs at operating points on every multiple of 1,500rpm, as shown in Fig.1. It should be rectified since the main operating point is on the 3,000rpm considering optimal efficiency matching of the APU system. The conventional model is designed for 8 poles and 36 slots, which is a fractional number of slots per pole. The THD of Back EMF is 0.5% and torque ripple is 4%, which is well-designed with regard to basic electromagnetic performance. However, the electromagnetic radial force has many harmonic components due to magnetic asymmetry in the same pole-pair. Moreover, the vibration is considerably generated at multiples of 1,500rpm, which is adjacent to the calculated natural frequency. B. Revised Design for Vibration Reduction To complement the above problem, the revised design is implemented based on vibration analysis applied to the electromagnetic force. First, the number of slots is modified from 36 to 48, to make magnetic field symmetric in the same pole-pair. As shown in Fig. 2(a), the multiples of 4^{th} harmonic components of electromagnetic force are reduced dramatically. Furthermore, the dimension of housing is modified to shorten in the axial direction. The dimension is settled to increase outer diameter contrary to the decrease of axial length to maintain the basic performance of generator. As the result, it is identified through vibration analysis that the revised model is more robust to vibration and natural frequency is distant from the main operating point. IV. Experimental Validation The revised model is manufactured and experimented. As shown in Fig. 2(b), torque profile of revised model is considerably improved and control is stabilized at 3,000rpm, compared with the conventional model.

[1] J. Guanetti, S. Formentin, and S. M. Savaresi, "Energy Management System for an Electric Vehicle with a Rental Range Extender: A Least Costly Approach," IEEE Trans. on Intelligent Transportation System", Vol. 17, No. 11, pp. 3022-3034, 2016. [2] C. F. Wang, M. J. Jin, J. X. Shen, and C. Yuan, "A Permanent Magnet Integrated Starter Generator for Electric Vehicle Onboard Range Extender Application," IEEE Trans. on Magnetics", Vol. 48, No. 5, pp. 1625-1628, 2012. [3] Z. Yang, F. Shang, and I. P. Brown, "Comparative Study of Interior Permanent Magnet, Induction, and Switched Reluctance Motor Drives for EV and HEV Applications" IEEE Trans. on Transportation Electrification, Vol. 1, No. 3, pp. 245-254, Oct. 2015. [4] K. H. Yim, J. W. Jang, G. H. Jang, M. G. Kim, and K. N. Kim, "Forced Vibration Analysis of an IPM Motor for Electrical Vehicles due to Magnetic Force" IEEE Trans. on Magnetics, Vol. 48, No. 11, pp. 2981-2984, Nov. 2012. [5] W. Tong (2014), "Mechanical Design of Electric Motors", CRC Press, Chater 9, pp 481-551

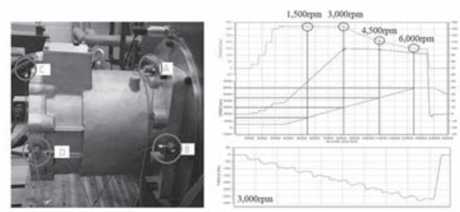

Fig. 1. Experimental Data of The Conventional Model

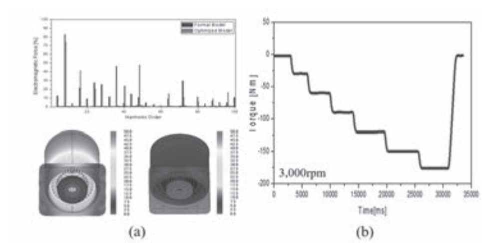

Fig. 2. Vibration Reduction Design Analysis and Result - (a) Vibration Analysis (b) Experimental Data of The Revised Model

HS-07. Comparative Study of Airgap Field Modulation in Flux Reversal and Vernier Permanent Magnet Machines.

H. Li[1], Y. Liu[1] and Z. Zhu[1]
1. Department of Electronic and Electrical Engineering, The University of Sheffield, Sheffield, United Kingdom

Abstract In this paper, the torque production mechanisms of both flux reversal permanent magnet (FRPM) machines and Vernier PM machines are analyzed based on airgap field modulation. The differences in their working harmonics of either PM magnetomotive force (MMF) or airgap permeance distribution are firstly identified, indicating that the fundamental PM MMF together with all permeance harmonics contribute to the torque production of Vernier machine whereas all PM MMF harmonics but only fundamental permeance in FRPM machine produce the torque. Thanks to the utilized large DC component of airgap permeance, the superior torque density of Vernier machine is revealed and verified by both analytical and finite element analyses (FEA). 1. Introduction With the recently developed theories of airgap field modulation (magnetic gearing effect) in electrical machines, the working principle of many existing machine topologies can be re-recognized now [1, 2]. Among various airgap field modulation-based machines, FRPM and Vernier machines are two typical topologies offering advantage of simple mechanical structure, thus attracting much attention for practical applications [3, 4]. As shown in Fig. 1, FRPM and Vernier machines have many similar features, such as single airgap, surface-mounted PM (SPM) structure and integrated modulation iron poles. For both machines, the PM MMF harmonics (resulted from SPM) interact with the permeance harmonics produced by modulation iron poles, thus producing abundant field harmonics in the airgap. The pole pair number of the fundamental PM field no longer equals to that of the armature field, which differs from the conventional PM machine and directly reflects the magnetic gearing effect [5, 6]. However, for FRPM machine, the PMs are mounted on the inner surface of stator teeth and the rotor consists of several iron poles, producing static PM MMF and rotating permeance harmonics; for Vernier machine, the rotor is of conventional SPM structure and the modulation iron poles are located on the stator, resulting in static permeance and rotating PM MMF harmonics. Up to now, the differences of airgap field modulation and corresponding performance comparison between two machines have never been addressed, and will be the main focus of this paper. 2. Influence of PM Thickness on Average Torque Considering the two machines from the perspective of generator, to induce the back-EMF with constant frequency, only those PM field harmonics of the same variation frequency with the fundamental electrical frequency of the rotating element can be utilized. Therefore, for FRPM machine, all PM MMF harmonics but only fundamental permeance are effective components; for Vernier machine, all permeance harmonics but only fundamental PM MMF are effective components. As the magnitude of permeance harmonics rapidly decreases with harmonic order, e.g. the DC component of the permeance has much higher magnitude than that of the fundamental permeance, the airgap field modulation is much stronger in Vernier machine, which is helpful to improve the torque density. To illustrate the difference of airgap field modulation between two machines, one FRPM machine with 12 stator slots and 10 rotor poles, one Vernier machine with 6 stator slots, 12 modulation iron poles and 20 PM poles are globally optimized under the same stator outer diameter (90mm), stack length (25mm) and copper loss (20W). Fig. 2 shows the influence of PM thickness on average torque of two machines. As can be seen, unlike conventional PM machines, there is an optimal PM thickness for each machine. Although the magnitudes of PM MMF harmonics increase with PM thickness, the PM thickness cannot be too large otherwise it enlarges the equivalent airgap length and impairs the field modulation. More importantly, the optimal PM thickness of the Vernier machine is 2.4mm, which is twice of the FRPM machine. This phenomenon can be explained by the different influence of PM thickness on magnitudes of permeance harmonics. In comparison with DC component, the PM thickness has larger influence on the magnitude of fundamental permeance. Therefore, the PM thickness of Vernier machine is larger than the FRPM machine, resulting in higher PM MMF magnitudes and torque density (101% higher in this case). 3. Conclusion In this paper, FRPM machine and Vernier machine are analyzed and compared based on the unified theory of airgap field modulation. It is found that Vernier machine is more likely to have higher torque density than FRPM machine, thanks to the utilized DC component of airgap permeance. In full paper, the detailed analysis of airgap field modulation, and performance comparison between two machines will be given. In addition, two prototypes are being manufactured, of which the test results will be provided.

[1] M. Cheng, P. Han, and W. Hua, "A general airgap field modulation theory for electrical machines," *IEEE Trans. Ind. Electron.*, vol. 64, no. 8, pp. 6063–6074, Aug. 2017. [2] Z. Q. Zhu and Yue Liu, "Analysis of air-gap field modulation and magnetic gearing effect in fractional slot concentrated winding permanent magnet synchronous machines," *IEEE Trans. Ind. Electron.*, *early access*, 2017. [3] D. Li, R. Qu, and Z. Zhu, "Comparison of Halbach and dual-side Vernier permanent magnet machines," *IEEE Trans. Magn.*, vol. 50, no. 2, pp. 10–13, Feb. 2014. [4] I. Boldea, J. Zhang, and S. A. Nasar, "Theoretical characterization of flux reversal machine in low speed servo drives-the pole-PM configuration," *IEEE Trans. Ind. Appl.*, vol. 38, no. 6, pp. 1549–1557, Dec. 2002. [5] R. Qu, D. Li, and J. Wang, "Relationship between magnetic gears and Vernier machines," in *Electr. Mach. Syst. (ICEMS 2011)*, *IEEE Int. Conf.*, Aug. 2011. [6] D. S. More and B. G. Fernandes, "Analysis of flux-reversal machine based on fictitious electrical gear," *IEEE Trans. Energy Convers.*, vol. 25, no. 4, pp. 940–947, Dec. 2010.

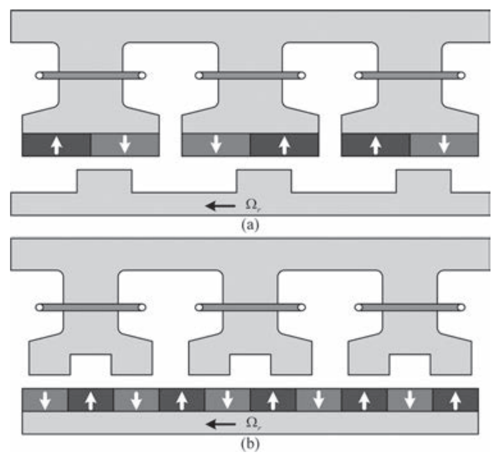

Fig. 1. Schematics of machines with single airgap, SPM structure and integrated modulation iron poles. (a) FRPM machine. (b) Vernier machine.

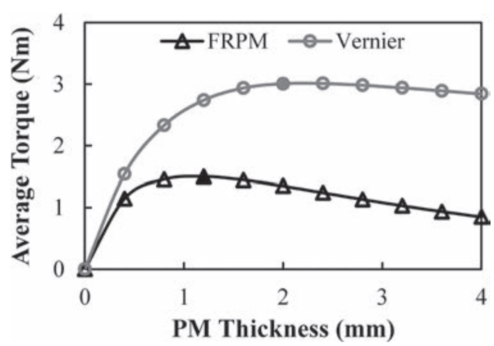

Fig. 2. Influence of PM thickness on average torque of two machines.

HS-08. Low Cost High Torque Density Dual-Stator Permanent Magnet Vernier Machine.

N. Baloch[1], B. Kwon[1] and Y. Gao[2]

1. Electronic Systems Engineering, Hanyang University, Ansan, The Republic of Korea; 2. School of Electrical and Electronic Engineering, Huazhong University of Science and Technology, Wuhan, China

I. Introduction Permanent magnet vernier machines (PMVMs) have some distinct advantages of high torque density and low torque ripple at low speed [1]. Due to these advantages, they have been extensively researched and proposed for wind power generation [2] and wave energy conversion [3]. To increase the torque density of a PMVM, a novel dual stator vernier topology was presented recently [4], which possessed higher torque density and higher efficiency compared to a conventional vernier machine. However, PMVM generally have high permanent magnet (PM) pole pairs, which increases the cost of the machine. For simplicity, the recently presented machine will be termed as existing machine in this paper. In this paper, in order to further increase the torque density and decrease the cost of the existing machine, a dual stator consequent pole vernier machine has been proposed. The results show that the proposed machine provides a higher torque density compared to the existing machine. Moreover, the cost of the machine is also low since magnet volume has been decreased. II. Topology and working principle The configuration of existing machine is shown in Fig. 1. In the existing machine, there are two stators and a sandwiched rotor. The outer stator has 12 slots and 3 phase 1 pole pair armature winding. The sandwiched rotor has consequent pole PMs arranged in Halbach array form, which has 13 pole pairs. The inner stator has only 12 pole pairs of surface type PMs. The existing machine is the combination of two machines (I & II) as shown in Fig. 2(a) & (b), respectively. Machine I works as a single stator PM machine, whereas machine II works as a double stator vernier machine, which has been discussed in detail in [4]. The configuration of proposed machine is shown in Fig. 3. There are two stators and a sandwiched rotor similar to existing machine. However, in the inner stator instead of surface type PMs, consequent pole PMs have been used, which reduces the magnet volume of the proposed machine. Moreover, the sandwiched rotor does not have Halbach arrays, contrary to existing machine; which otherwise causes flux leakage in the proposed topology. The proposed machine can also be regarded as the combination of two machines, here called as machine I and machine II. The outer stator, sandwiched rotor and inner stator iron teeth is termed as machine I as shown in Fig. 4(a). Whereas the outer stator, iron teeth in the rotor and complete inner stator is termed as machine II as shown in Fig. 4(b). Contrary to existing machine, in the proposed machine, machine I and machine II are both dual stator vernier machines, which increases the torque density of the machine compared to existing machine. The comparison of outer airgap flux density harmonics is shown in Fig. 5(a). In machine I, the rotor PM magneto motive force (MMF) is modulated by the inner stator teeth. The flux goes from rotor to inner airgap, to inner stator, then to outer airgap and finally induces back electromotive force (EMF) in the outer stator winding and hence the effective airgap length is large. Therefore, the flux modulation effect is weak. However, in machine II, the PM MMF from the inner stator is modulated by the rotor teeth. The flux moves from inner stator to rotor, to outer airgap and finally induces back EMF in the outer stator winding. The effective airgap length is comparatively shorter and flux modulation effect can be regarded as comparatively strong. Therefore, in both machine I and machine II in the proposed machine, flux is modulated to produce a component equal to winding pole pairs in the outer airgap; hence, the machine works as a combination of two vernier machines. III. Performance comparison To verify the superiority of the proposed machine, finite element method (FEM) simulations have been performed to compare both the existing machine and proposed machine. The comparison of torque of both the machines is shown in Fig. 5 (b). It can be seen that the proposed machine produces 44% higher torque compared to existing machine. However, the torque ripple of the proposed machine is a little higher compared to existing machine. The overall performances of both the machines have been compared in Table I. In full paper, the machines will be optimized for reduced torque ripple.

[1] T. Zou, D. Li, R. Qu, D. Jiang and J. Li, "Advanced High Torque Density PM Vernier Machine With Multiple Working Harmonics," in *IEEE Transactions on Industry Applications*, vol. 53, no. 6, pp. 5295-5304, Nov.-Dec. 2017. doi: 10.1109/TIA.2017.2724505 [2]. Li, K. T. Chau, J. Z. Jiang, C. Liu and W. Li, "A New Efficient Permanent-Magnet Vernier Machine for Wind Power Generation," in *IEEE Transactions on Magnetics*, vol. 46, no. 6, pp. 1475-1478, June 2010. doi: 10.1109/TMAG.2010.2044636 [3] N. Baloch, S. Khaliq and B. I. Kwon, "HTS Dual-Stator Spoke-Type Linear Vernier Machine for Leakage Flux Reduction," in *IEEE Transactions on Magnetics*, vol. 53, no. 11, pp. 1-4, Nov. 2017. doi: 10.1109/TMAG.2017.2699641 [4] Y. Gao, R. Qu, D. Li, H. Fang, J. Li and W. Kong, "A Novel Dual-Stator Vernier Permanent Magnet Machine," in *IEEE Transactions on Magnetics*, vol. 53, no. 11, pp. 1-5, Nov. 2017. doi: 10.1109/TMAG.2017.2698004

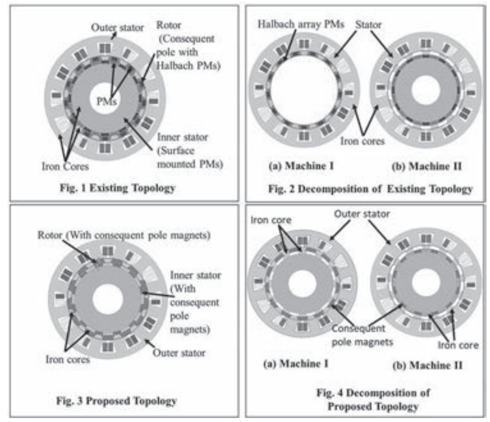

Fig. 1. Fig. 2, Fig. 3, Fig. 4

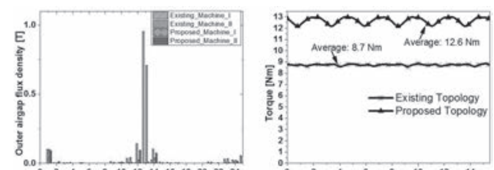

Fig. 5 (a) Comparison of flux density (b) Comparison of torque

Table I : Performance Comparison

Machine	Torque, Nm	Ripple, %	Power, W	Magnet Volume, cm^3	Torque/Magnet Volume, Nm/cm^3	Power factor
Existing	8.73	3	274.2	123.6	0.071	0.85
Proposed	12.66	6.5	397.7	91.6	0.13	0.89

Fig. 5. (a & b), Table I

HS-09. A Generalized Method of Electromagnetic Vibration Analysis of Amorphous Alloy Permanent Magnet Synchronous Machines.

S. Wu[1], W. Tong[1], R. Sun[1] and R. Tang[1]
1. Shenyang University of Technology, Shenyang, China

The researches on electromagnetic vibration of electrical machines have been focusing on the vibration caused by radial forces (RFs) as the major cause of electromagnetic vibration[1]. According to the other researches, magnetostriction (MS) is a property of magnetic metal in which the material will exhibit strain in the presence of magnetic field and is recognized as another cause of electromagnetic vibration next to RFs for electric machines[2]. For amorphous alloy materials (AAMs), the MS coefficient is much larger than for the conventional silicon steel (SS) sheet. MS coefficient of conventional SS is 9.2×10^{-6}, and MS coefficient of amorphous alloy (AA) is 26×10^{-6}. Hence, the vibration caused by MS effects in AA electric machines is much larger than conventional SS electric machines. Additionally, amorphous alloy cores (AACs) are manufactured as stacks or winding of AA stripes. The magnetic characteristics of AA are greatly effected by stress, so lamination factor of AACs which are applied to electrical machines is lower than SS cores. Laminated stacks are clamped together, and the forces determined by the clamped state of laminated stacks itself are defined as lamination compression forces (LCFs). Hence, the vibration of AA electric machines caused by LCFs cannot be ignored. This paper presents a new numerical and experimental method of the analysis of electromagnetic vibration of AA PMSMs whose stator cores are made from AAMs. This method can be used to calculate the electromagnetic vibration of AA PMSMs caused by RFs, MS effects and LCFs. Steps of the procedure for the numerical analysis are presented in Fig.1. LCFs are not the driving forces of electromagnetic vibration of AA PMSMs. The vibration caused by LCFs is interpreted in two aspects. On the one hand, LCFs affect the magnetization characteristic of AACs. On the other hand, LCFs affect the elasticity modulus parameters of AACs. The vibration caused by LCFs is simulated by adopting experimental magnetization curves and modified elasticity modulus parameters of AACs. The vibration caused by MS effects is simulated by adopting the experimental MS curve and experimental magnetization curve of AACs. The MS curve of the AAMs were tested by the measurement device. The MS as a function of magnetic flux density for the AAM 2605SA1 is obtained. The magnetization characteristics of the AACs were tested, and the *B-H* curve for AACs is obtained. Experimental modal analysis of AACs is based on hammer impact method. The frequency response functions (FRFs) for the AACs are obtained. The peak in FRFs indicate the natural frequencies. The elasticity modulus parameters are modified by utilizing experimental modal analysis of AACs. Electromagnetic vibration of a 2.1kW radial flux AA PMSM is analyzed using the proposed method. The electromagnetic vibration of the AA PMSM under four different conditions which are (a) only RFs, (b) only MS effects, (c) both RFs and MS effects, (d) RFs, MS effects and LCFs are calculated respectively. The stator core and housing deformations of the AA PMSM are shown in Fig.2. The effects of MS and LCFs on electromagnetic vibration of the AA PMSM are obtained. Finally, the accuracy of the proposed approach is verified by comparing the calculations with experimental results.

[1] Z. Q. Zhu, Z. P. Xia, L. J. Wu, and G. W. Jewell, “Analytical modeling and finite element computation of radial vibration force in fractional-slot permanent magnet brushless machines, ” *IEEE Transactions on Industry Applications*, vol. 46, no. 5, pp. 1908-1918, Sept.-Oct .2010. [2] L. H. Zhu, B. Wang, R G Yan, Q. X. Yang, Y. M. Yang, and X. Zhang. “Electromagnetic vibration of motor core including magnetostriction under different rotation speeds,” *IEEE Transactions on Magnetics*, vol. 52, no. 3, pp. 810-813, Mar. 2016.

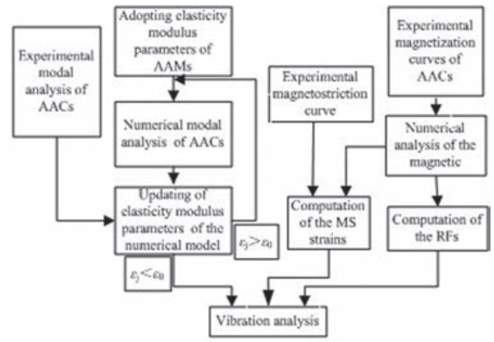

Fig. 1. Flow chart of the procedure for the numerical analysis of electromagnetic vibration caused by RFs, MS effects and LCFs

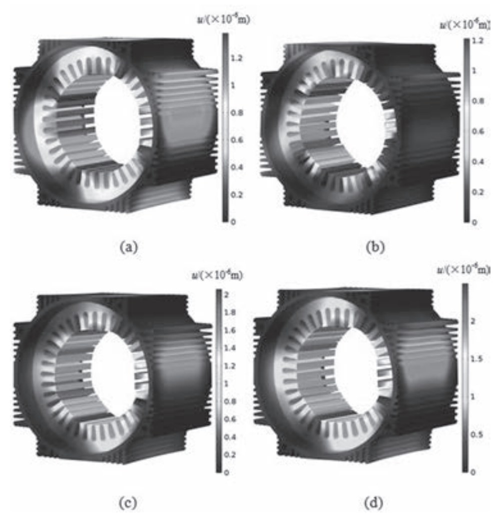

Fig. 2. Stator and housing deformations of 2.1kW radial flux AA PMSM (a) only RFs (b) only MS effects (c) both RFs and MS effects (d) RFs, MS effects and LCFs

HS-10. A Double Stator Flux Reversal PM Machine with Halbach Consequent Pole in Slot Opening.

H. Huang[1], D. Li[1], R. Qu[1] and K. Xie[1]
1. Huazhong University of Science & Technology, Wuhan, China

I. INTRODUCTION As one kind of stator-PM machines, flux reversal machine (FRM) has attached lots of attentions for its robust structure and cost effectively [1]. In regular FRMs, the permanent magnets were normally mounted on the stator teeth, which adds a large magnetic resistance to the magnetic circuit of coil winding. It causes reduction of the fundamental airgap permeance, weakening the working flux density and back-EMF, and restricting the electromotive force ultimately [2]. To increase the torque density of FRM, double stators were employed to utilize the inner space of machines [3-4]. However, this structure introduces additional air-gap and more flux leakage to the magnetic circuit, therefore influencing the utilization of magnets. To reduce the flux leakage between N and S pole and improve the utilization of PM, consequent-pole PM was employed in FRM [5]. Instead of placing the PMs on the stator teeth, a novel FRM with Halbach consequent-pole magnets embedded in the slot opening is proposed in [6]. By moving the surface-mounted PM into the slot opening, the resistance of PMs no longer influences the permeance of coil windings, therefore the back-EMF of machine can be markedly increased. Moreover, the slot area is increased and the flux leakage is limited, hence improving the torque density and power factor. To further increase the torque density of FRM, a novel Halbach consequent pole double-stator flux reversal machine (HCP-DS FRM) is proposed in this digest. In proposed machine, a pole-piece rotor was placed between two identical stators with Halbach consequent-pole magnets in the stator opening. The performance of proposed machine with two configurations was then compared. At last, torque density, power factor and other properties of proposed HCP-DS FRM were compared with a regular 12/17 FRM shown in Fig. 1. II. MACHINE TOPOLOGIES AND OPERATION PRINCIPLES The model of proposed machine is showed in Fig. 2. The so-called Halbach consequent pole includes three magnets with different magnetizing directions. Two tangential magnets were placed besides the main radial magnets in order to guide the flux. The inner and outer stator have the same slot-pole combination and structure. As mentioned in [6], the pole-pairs of rotor Pr equals slot number Zs adds or subtracts the winding pole-pairs Ps, which is 17 in Fig. 2 since 12/10 FSCW were applied in stators. Flux line contour and equivalent circuit model are shown in Fig. 3. As shown in the contour, with the assistance of tangential magnets, all the radial magnets can produce main flux to the stator teeth. Since identical windings are placed in two stators, magnetic circuits surrounding any of slots can produce a fundamental back EMF, therefore the leakage flux is limited. As shown in circuit model, the main magnetic circuit for each stator coil is driven by MMF of PMs on both stators, which improves the utilization of magnets. In conclusion, the magnetic structure of proposed machine creates an effective and synergetic condition to produce a better electromotive performance. III. DIFFERENT CONFIGURATION OF THE STATORS According to the polarity of the main radial PMs, the proposed double stator machine has two configurations N-N and N-S, see Fig. 2 (a) and (b). In N-N configuration, the teeth on two stators face each other, and the two windings have the same initial phase angle. In N-S configuration, the teeth on one stator face the slots of another, and the initial phase angle of two windings differ 75 electric degree. This is because the inner stator differs 15 mechanical degree with outer stator. The line back-EMF and static torque of these two configurations with same parameters are shown in Fig. 4 and Fig. 5. The result shows that N-N configuration with consistent polarity has a better electromagnetic performance, which is probably due to a shorter flux path and higher flux density on the air gaps, as shown in Fig. 6. IV. PERFORMANCE COMPARISON WITH REGULAR FRPM MACHINES The crucial advantage of the proposed FRM is the high torque density owing to an adequate use of the inner area of regular FRPM machines. Moreover, the structure of Halbach consequent-pole provides an optimal magnetic circuit to improve the utilization of magnets. Two FEA models were built to validate the superiority of proposed machine, the parameters and performances of two models are shown in Table I. With similar PM volume and copper loss, the proposed machine reach a 121% higher torque density. Since the radial force is offset between inner and outer stator, the torque ripple of the proposed machine decrease from 11.3% to 3.8%. Moreover, compared to 0.68 in the regular FRPM, the power factor of proposed FRPM machine is 0.85. This improvement derives from the Halbach consequent pole structure which reduces the flux leakage. V. CONCLUSIONS A novel Halbach consequent-pole double-stator FRM was proposed in this digest. By inserting additional stator inside the regular FRPM, the space of the machine is well utilized. The Halbach magnets were embedded into the slot opening, which improves the utilization of PMs and the back-EMF. Two configurations of proposed machine were modeled and compared. The result shows that the N-N configuration has better performance due to a higher flux density. At last, the performances of HCP-DS FRPM machine were compared with a regular flux reversal machine under identical parameters. The proposed machine outstands for 121% higher torque density, 66% lower torque ripple, and 25% higher power factor than regular FRM.

[1] R. Deodhar, S. Andersson, T. Boldea, and T. Miller, “The flux-reversal machine: A new brushless doubly-salient permanent-magnet machine,” *IEEE Trans. Ind. Appl.,* vol. 33, no. 4, pp. 925- 934, Jul. 1997. [2] Noboru Niguchi and Katsuhiro Hirata, Magnetic-geared motors with high transmission torque density. *COMPEL: Int. Journal for Computation and Mathematics in Electrical and Electronic Engineering*, Vol. 34 Issue: 2, pp.428-438, 2015. [3] Y. B. Wang, M. Cheng, Y. Du, and K. T. Chau, “Design of high-torque-density double-stator permanent magnet brushless motors,” *IET Electr. Power Appl.*, vol. 5, no. 3, pp. 317–323, Mar. 2011. [4] Z. Zhu, Z. Wu, D. J. Evans, W. Chu, “Novel Electrical Machines Having Separate PM Excitation Stator”, *IEEE Trans. Magn.*, vol. 51, no. 4, April 2015. [5] Y. Gao, R. Qu, D. Li, J. Li, “Consequent-Pole Flux-Reversal Permanent-Magnet Machine for Electric Vehicle Propulsion,” *IEEE Trans. Appl. Supercond.*, vol. 26, no. 4, June 2016. [6] K. Xie, D. Li, R. Qu, Y. Gao, Y. Pan. “A Novel Flux Reversal PM Machine with Halbach Array Magnets in Stator Slot Opening”, International Conference on Electrical Machines and Systems (ICEMS), Aug. 2017. [7] D. Li, R. Qu, and T. Lipo, “High-power-factor vernier permanent-magnet machines,” IEEE Trans. Ind. Appl., vol. 50, no. 6, pp. 3664-3674, Nov./Dec. 2014. [8] D. Li, R. Qu, J. Li, L. Wu and W. Xu, “Analysis of torque capability and quality in vernier permanent magnet machines,” IEEE Trans. Ind. Appl., vol. 52, no. 1, pp. 125-135,Jan./Feb. 2016.

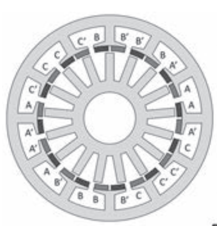

Fig. 1 Regular 12/17 FRM

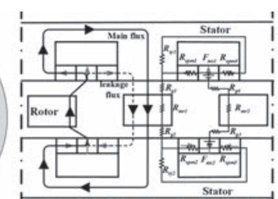

Fig. 3 Flux line and equivalent circuit

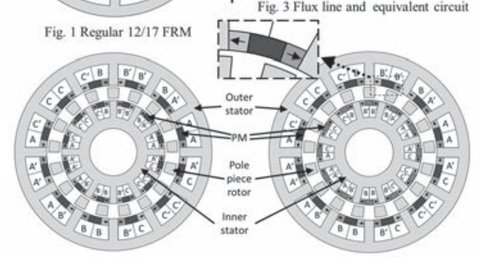

(a) N-N with opposite teeth (b) N-S with alternative teeth

Fig. 2 Two configurations of proposed HCP-DS FRM

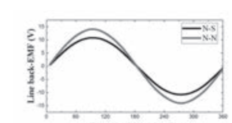

Fig. 3 Line back-EMF in two configurations

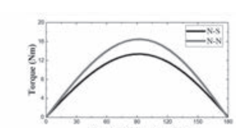

Fig. 4 Static Torque in two configurations

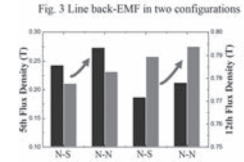

Fig. 5 Air-gap Flux Density in two configurations

Table I Parameters Comparison of regular and proposed FRPM machines

Parameter	Units	Regular	Proposed	Effect
Outer diameter	mm	124		/
Output torque	Nm	8.1		/
Rotor speed	rpm	300		/
PM volume	L	0.065	0.059	-9.2%
Copper Loss	W	109	109	/
Stack length	mm	120	54	-55%
Torque ripple	%	11.3	3.8	-66%
Torque density	Nm/L	5.6	12.4	+121%
Power factor	-	0.68	0.85	+25%

HS-11. Analysis on a Novel Flux Adjustable Permanent Magnet Eddy Current Coupler with a Double-layer Permanent Magnet Rotor.

M. Tian[1], X. Wang[1], W. Zhao[1], Y. Yang[1], J. Diao[2] and X. Ma[2]
1. School of Electrical Engineering, Shandong University, Ji'nan, China;
2. Shandong Jiemeng Energy Conservation and Environmental Protection Technology Co., Ltd, Ji'nan, China

I. Introduction Permanent magnet coupler (PMC) acts as a magnetic transmission device, the motivation and torque are transmitted through the interaction between the conductor rotor (CR) and permanent magnet rotor (PMR), the mechanical contact between the motor and load is eliminated. And for the effective suppression of the vibration, high reliability and efficient operation, it has been applied in electric power, petrochemical industry, pumps, blowers, water treatment and other fields [1]-[3]. Many structures of the PMCs had been designed, considering the rotational couplers, configurations as radial and axial magnetic flux represent two possible solutions [4]. For the typical axial flux coupler (i.e., disk type) and radial flux coupler (i.e., cylindrical type), the produced torque was controlled by adjusting the length of air gap or the coupling area between the CR and PMR [5]. However, the magnetic field utilization is lower for disk type, and additional mechanical devices are also needed to adjust the axial relative position between the CR and PMR for both types, the reliability is reduced and the space volume is increased. In [6], a flux adjustable PMC with a movable stator ring, whose slip speed can be adjusted by shifting the movable stator ring along the axial direction, was proposed, and the complicated mechanical devices can be avoided. In this paper, a novel flux adjustable PMC with a double-layer PMR is presented. The magnetic flux is adjusted by circumferentially controlling the relative position of the PMR's two layers, the axial movement is replaced. II. The Structure and Principle The structure of the proposed coupler is shown in Fig.1 (a). The PMR is divided into the inner and outer parts, and the PMs in both parts are respectively staggered arrangement by N- and S- pole which are tangentially magnetized. In addition, the inner part can be controlled to circumferentially rotate to adjust the relative position with the outer part, so the excitation magnetic field is controllable. And then the eddy current intensity, torque and the speed can also get adjustable. III. Magnetic Field and Torque Analysis To analyze the field and torque of each different relative position, the change period of the relative position, from N-N to N-S, is divided into seven steps. The magnetic field distribution and air-gap flux density B_r is shown in Fig.1(b). When the relative position is N-N state (position 1), most flux lines will pass through the air-gap to the copper layer besides few linkage flux and the B_r at this state is also the biggest. As the inner part of the PMR is controlled to the position 4, besides passing through the copper layer, parts of the flux lines link between the inner and outer parts' N- and S- pole. The linkage flux is increased, and the effective flux is decreased. While when the relative position is adjusted to N-S (position 7), almost all the flux lines form loops from N- to S-pole, no longer reaching the copper layer, the air-gap flux density also gets smallest. With the relative movement between CR and PMR, the eddy current is nearly not produced, neither is the torque. In addition, based on the analytical method [7]-[9], the electromagnetic characteristics of the coupling and the calculation of eddy current are also researched, and the results are verified by 2D FEM. IV. The Influences of the Structural Parameters As the torque is transmitted through the interaction of magnetic field, and the air gap magnetic field is mainly superimposed by PM magnetic field and eddy current magnetic field. So the structural parameters, including the thickness and material of the CR which impact the eddy current intensity, and the material and pole numbers of PMs in PMR which impact the excitation field, are analyzed and shown in Fig.2 respectively. The comparison of different thickness of copper layer shows that the maximum torque gets larger as the decrease of the copper thickness because of the deeper penetration of the magnetic field, and the speed corresponding to the maximum torque also gets larger. The comparison of different conductor materials among copper, aluminum, and brass whose conductivities are 0.58×10^8 S/m, 0.38×10^8 S/m, and 0.145×10^8 S/m respectively shows that the speed for obtaining the maximum torque becomes larger as the decrease of the conductivity. When the PM material is changed from N35UH (the residual magnetism is 1.19 T, and the coercive force H_c is 887.5 kA/m) to N40UH (the residual magnetism is 1.275 T, and H_c is 907.5 kA/m), the torques increase by nearly 10%. The torque also increases as the pole numbers increase from 20 to 46, and more again, the torque drops due to the increase of the linkage flux and the decrease of the effective magnetic potential. V. Conclusion This paper has presented a novel flux adjustable PMC with a double-layer PMR. The magnetic field and torque are analyzed by 2D finite element method (FEM), and the analytical method is also used to calculate electromagnetic characteristics and eddy current field. And the influences of the structural parameters are researched based on *T-s* curve, which can provide a reference for structural optimization design of this kind of PMC.

[1] D. Albertz, S. Dappen, and G. Henneberger, "Calculation of the 3D non-linear eddy current field in moving conductors and its application to braking systems," *IEEE Trans. Magn.*, vol. 32, no. 3, pp. 768–771, May 1996. [2] L. Z. Ye, D. S. Li, Y. J. Ma, and B. F. Jiao, "Design and performance of a water-cooled permanent magnet retarder for heavy vehicles," *IEEE Trans. Energy Convers.*, vol. 26, no. 3, pp. 953–958, Sep. 2011. [3] K. Atallah and J. Wang, "A brushless permanent magnet machine with integrated differential," *IEEE Trans. Magn.*, vol. 47, no. 10, pp. 4246–4249, Oct. 2011. [4] A. Canova, B. Vusini, "Analytical modeling of rotating eddy-current couplers," *IEEE Trans. Magn.*, vol. 41, no. 1, pp. 24-35, Jan. 2005. [5] J. Wang, H. Y. Lin, S. H. Fang, and Y. K. Huang, "A general analytical model of permanent magnet eddy current couplings," *IEEE Trans. Magn.*, vol. 50, no. 1, article sequence number: 8000109, Jan. 2014. [6] Y. B. Li, H. Y. Lin, H. Yang, S. H. Fang, H. T. Wang, "Analytical analysis of a novel flux adjustable permanent magnet eddy-current coupling with a movable stator ring," *IEEE Trans. Magn.*, vol. pp, no. 99, pp. 1-4, 2017. [7] Z. Meng, Z. N. Zhu, and Y. Z. Sun, "3-D Analysis for the Torque of Permanent Magnet Coupler", *IEEE Trans. Magn.*, vol. 51, no. 4, article sequence number: 8002008, Apr. 2015. [8] M. Sajjad, M. Mojtaba, V. Z. Sadegh, A. T. Herda, "Analytical modeling and analysis of axial-flux interior permanent magnet couplers," *IEEE Trans. Ind. Electron.*, vol. 61, no. 11, pp. 5940-5947, Nov. 2017. [9] M. Sajjad, M. Mojtaba, V. Z. Sadegh, "Nonlinear modeling of eddy-current couplers," *IEEE Trans. Energy Convers.*, vol. 29, no. 1, pp. 224-231, Mar. 2014.

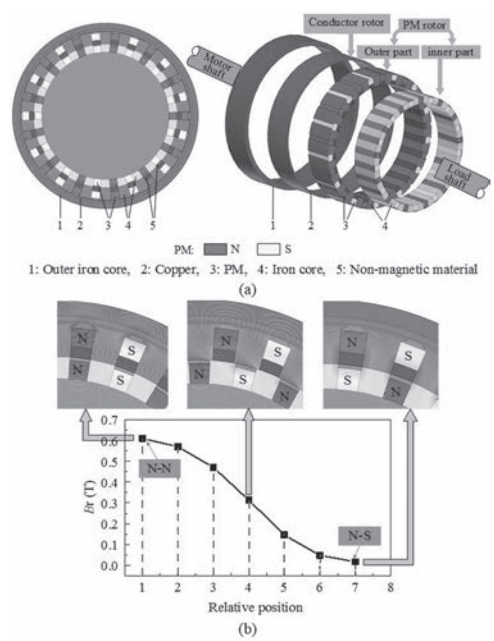

Fig. 1. (a) The structure of the proposed PMC, (b) the magnetic field distribution and the air-gap flux density B_r under different relative positions.

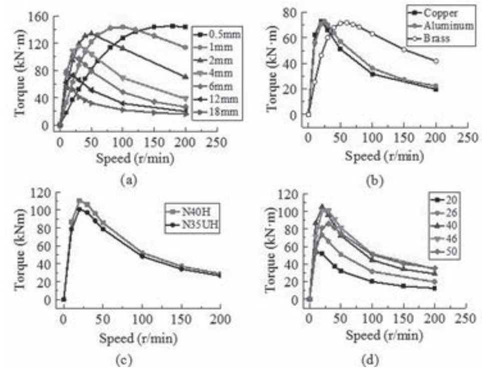

Fig. 2. The influences of the structural parameters: (a) copper layer thickness, (b) conductor material, (c) PM material, (d) pole numbers.

FRIDAY AFTERNOON, 27 APRIL 2018 SIMPOR/ROSELLE BALLROOM, 1:30 TO 4:30

Session HT
MICROMAGNETICS II
(Poster Session)

Oksana Chubykalo-Fesenko, Chair
Instituto de Ciencia de Materiales de Madrid, CSIC, Madrid, Spain

HT-01. Peaked linewidth broadening of ferromagnetic resonance induced by Dzyaloshinskii-Moriya interaction.

J. Oh[1], I. Hong[1] and K. Lee[1]
1. Material Science Department, Korea University, Seoul, The Republic of Korea

Magnetic damping that is parameterized by the Gilbert constant describes the energy dissipation rate of magnetization dynamics and determines the performance of magnetic devices including magnetic random access memories and magnetic sensors. The ferromagnetic resonance (FMR) experiment provides a way to measure the damping constant via the FMR linewidth and is also used to characterize magnetic properties of materials [1]. However, this method is not always straightforward as the measured linewidth includes not only intrinsic damping contribution but also extrinsic contributions originating from inhomogeneity of the sample. Especially, the contribution of two magnon scattering to the linewidth also depends on the frequency, demanding a detailed investigation of the frequency-dependent linewidth of two-magnon scattering origin [2]. Recently there have been much interested in a thin ferromagnetic layer with the Dzyaloshinskii-Moriya interaction (DMI) [3]. Because the DMI energetically favors an orthogonal configuration of two neighboring spins with a fixed rotating sense, the magnon dispersion and its scattering property may be varied significantly to show unique behavior in the FMR linewidth. In this respect, it is important to check whether or not the DMI inhomogeneity contributes to the extrinsic broadening of FMR linewidth through two magnon scattering process [4]. For this, we investigated magnon dispersion and the FMR linewidth of a thin ferromagnetic layer in a quantum mechanical way, taking into account scatterings caused by structural inhomogeneity. From equation of motion for magnetization we first calculate susceptibility of the system as function of magnetic field, and then average the susceptibility over an ensemble of impurities or inhomogeneity. By extracting broadening width of the longitudinal susceptibility as a function of FMR frequency, we provide an analytic expression for the FMR linewidth in terms of system parameters such as the saturation magnetization, exchange stiffness, surface anisotropy, and DMI strength D. Detailed forms of the extrinsic FMR linewidth are derived to consists of the part from the inhomogeneity potential and the part determined purely by the magnon dispersion. The magnitude of the FMR line width is mainly determined by the former while the frequency and magnetic-field dependent behavior is found to be responsible for the latter. In Fig. 1, we show the extrinsic linewidth broadening as a function of resonant frequency for various DMI strengths. Overall amplitudes of the linewidth become larger with an increased DMI strength, whereas, for a given DMI strength, the DMI-limited scattering potential exhibits characteristic behavior of the linewidth as a function of frequency. Namely, with varying the resonance frequency from zero, the linewidth changes slightly in a high frequency range while bumps or peaks are developed in a low frequency range. Furthermore, in a strong DMI case, for example, D = 2.3 mJ/m^2 in the figure, one can see that the linewidth is finite even at zero frequency. The peaks in Fig. 1 are found to originate from complicated behavior of the magnon energy dispersion. At the points where the peaks are developed, very small group velocities of magnon are calculated and, in turn, this gives rise to abundant resonant states (as example, Fig. 2 shows the evolution of resonant states as a function of magnetic fields around the peak). The abundant resonant states provide much possibility into which two magnons are scattered and result in a significant increase of the FMR linewidth. On the other hand, the finite value of the FMR linewidth at a zero magnetic field is unique behavior of the DMI system. This may be not possible if a uniform ferromagnetic system such as free-DMI case is a ground state. However, in the case of strong DMI, a non-collinear spin state like spiral configuration has a lower energy than a ferromagnetic one. Consequently, in the presence of the strong DMI, there are still resonant states even at a zero magnetic field and thus a uniform spin texture excited by microwaves in FMR experiments is still scattered into resonant states mediated by inhomogeneity scattering. Fig. 1. The calculated linewidths for various DMI strengths D as a function of FMR frequency. The external magnetic field is applied with in-plane geometry. Fig. 2. In order to resolve the origin of the peak in Fig. 1, equi-energy lines are plotted in the case of D = 1.5 mJ/m^2 around the external magnetic field (464.4 G) exhibiting the peak. We increase the magnetic field by 2.0 G.

References [1] S. Mizukami, Y. Ando, and T. Miyazaki, J. Magn. Magn. Mater. 226, 1640 (2001). [2] M. Sparks, R. Loudon, and C. Kittel, Phys. Rev. 122, 791 (1961). [3] I. M. Miron, et. al., Nature 476, 189 (2011). [4] M. Sparks, R. Loudon, and C. Kittel, Phys. Rev. 122, 791 (1961).

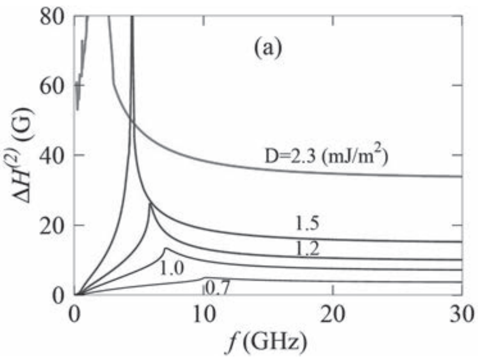

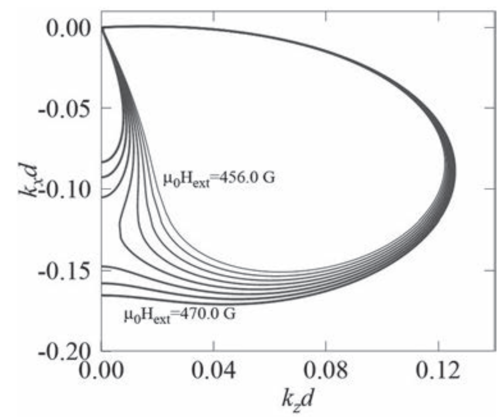

HT-02. Spin transport model including thermal effect of GMR based devices.

N. Saenphum[2], J. Chureemart[1], R.W. Chantrell[3] and P. Chureemart[2]
1. Physics, Mahasarakham University, Mahasarakham, Thailand; 2. Physics, Mahasarakham University, Mahasarakham, Thailand; 3. Physics, University of York, York, United Kingdom

The GMR and TMR investigations lead to a significant improvement in the potential applications in data storage technology such as reader in hard disk drives and spintronic devices. The spin torque phenomenon provides a new concept for the development of advance MRAM, nonvolatile logics and readers in hard disk drives. It has opened up the possibility to achieve a smaller reader subsequently leading to increasing in the areal density in the hard disk drives. Therefore, it becomes important to understand physics behind the operation of readers which enables us to design them appropriately. In addition, it has been reported that the read back signal is temperature dependent and degraded from low to high temperature [1, 2]. The computational model of read sensors is generally based on micromagnetic approaches. Although successful, micromagnetics is limited in a number of ways which makes the formalism inappropriate for the investigation of a number of factors which will become increasingly important with further scaling of device dimensions. This work proposes the model of read sensor at atomistic level taking the effect of thermal fluctuation into account to study the spin transport behavior. In order to investigate the spin transport behavior in the reader stack, the atomistic model coupled with the spin accumulation model is employed. The former is used to model the stack of reader and to observe the dynamics of magnetization whereas the latter is proposed to calculate the spin accumulation representing spatial magnetoresistance (MR). The inclusion of temperature affecting spin transport properties of magnetic materials is represented in the spin accumulation model through the spin-dependent resistivity [3] given by, $\rho_{\uparrow,\downarrow} = \rho_{\uparrow,\downarrow(0)} + A_{\uparrow,\downarrow}T^2$ (1) where $\rho_\uparrow$ and $\rho_\downarrow$ are the resistivities of up and down spins respectively, $A_{\uparrow,\downarrow}$ is empirical coefficient obtained from experiment, and T is measured temperature. The spin polarization parameters of conductivity (β) and diffusion (β') which can be expressed in term of spin-dependent resistivity. We consider the trilayer system of Co/Cu/Co which is divided into many thin layers. To investigate temperature dependence of the spin transport behavior, the spin transport parameters at any finite temperature required for spin accumulation calculation is first considered through the spin-dependent resistivity in eq. (1) as illustrated in Fig. 1. It is found that the spin transport parameters such as spin polarization parameters, spin diffusion length and diffusion constant are likely to decrease with increasing temperature due to the effect of thermal fluctuation and we could observe zero spin polarisation of material at critical temperature where ferromagnet becomes paramagnet. These spin transport parameters are then used in the generalized spin accumulation model based on modified Zhang-Levy-Fert approach [4] to consider spatial resistance-area product (RA) as a function of temperature which can be calculated directly from the gradient of spin accumulation (Δm) and the coming spin current (j_m) given by, $RA_i = |\Delta m|\, a^2\, t_F k_B T / |j_m|\, e^2$ (2) where a is the lattice constant of material, t_F is the thickness of thin layer, k_BT is 10 meV and e is the electron charge. The total MR of the structure can be evaluated by summing all spatial resistances, $MR = \sum RA_i$. The resistance-area product of parallel (R_P) and anti-parallel (R_{AP}) states are then determined by injecting spin current at the density of 5×10^{11} A/m^2 into the structure. This eventually leads to the calculation of MR ratio. We found that the spin accumulation at the interface region is rapidly changed due to the difference of spin transport properties at the interface. The RA of the AP state is higher than P state due to a stronger spin-dependent scattering. At high temperature, the resistance is increased due to the enhancement of strong spin scattering with low mobility of electron which leads to decreasing in MR ratio as shown in Fig. (2). Our results show an excellent agreement with experimental measurements [5-8]. The proposed model gives rise to the possibility to develop the readers in next generation with both CPP-GMR and CPP-TMR systems. Also this model will allows us to deeply understand the mechanism in the readers which is significantly beneficial in reader design.

[1] E. Jang, Journal of Applied Physics, 103, 07F534 (2008). [2] U. Boettcher, H. Li, R. A de Callafon and F. E. Talke, IEEE Transactions on Magnetics, 47, 7 (2011). [3] E. Villamor, M. Isasa, L. E. Hueso, and F. Casanova,Physical Review B 88, 184411 (2013). [4] P. Chureemart, R. Cuadrado, I. D'Amico, and R. Chantrell, Physical Review B 87, 195310 (2013). [5] D. Tripathy and A. O. Adeyeye, Physical Review B 75, 012403 (2007). [6] P. A. Dowben and R. Skomski, Journal of Applied Physics, 95, 11 (2004). [7] Z. Wen, T. Kubota, T. Yamamoto, and K. Takanashi, Scientific reports 5 (2015). [8] B. Kwon, Y. Sukegawa, H. Sukegawa, S. Li, G. Qu, T. Furubayashi, and K. Hono, Journal of Applied Physics 119, 023902 (2016).

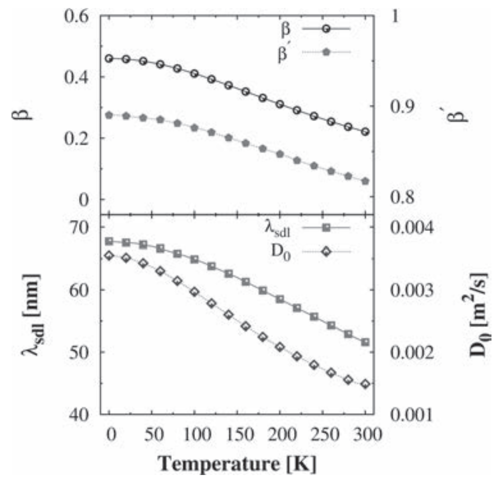

Fig. 1. Spin transport parameters of cobalt as a function of temperature

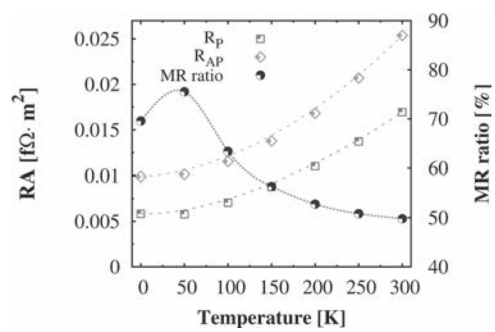

Fig. 2. Resistance-area product and MR ratio of trilayer system as a function of temperature

HT-03. Electrical Modeling of Double-Barrier Magnetic Tunnel Junction with Reliability Analyses.

G. Wang[1,2], Y. Zhang[1,2], Z. Zhang[1,2], Z. Zheng[1,2], K. Zhang[1,2], Y. Zhang[1,2] and W. Zhao[1,2]

1. Fert Beijing Institut, Beihang University, Beijing, China; 2. Electronics and Information Engineering School, Beihang University, Beijing, China

With the shrinking of complementary metal oxide semiconductor (CMOS) technology size, the considerable power consumption on logic and memory circuit system has been becoming an unavoidable bottleneck [1]. Spin transfer torque magnetoresistive memories (STT-MRAMs) are prime candidates for non-volatile memory applications. As the basic storage unit of STT-MRAM, magnetic tunnel junction (MTJ) has been extensively studied [2-4]. For instance, double-barrier MTJ (DMTJ), taking advantages of the enhancement of STT effect, significantly reduces the critical switching current (I_{C0}) and switching duration (τ) [5]. MTJ with two CoFeB free layers (FLs) coupled by Ta layer can effectively improves the thermal stability (ΔE) [6]. In this paper, we proposed an electrical modeling of DMTJ with CoFeB/Ta/CoFeB FLs (see Fig. 1 (a)). Compared with conventional MTJ, the propose DMTJ has superiorities in I_{C0}, τ, and ΔE. It can replace MTJ to reduce the device size, improve the reliability of memory and lower the writing energy consumption. Furthermore, this model integrates the stochastic STT switching behavior, the temperature influence and the variation of the layers' thicknesses, which can deeply affect the reliability of hybrid CMOS/MTJ circuits. Fig. 1 (b) shows the principle block diagram of the integrated physical models. In the following, we explain some key blocks modeled in the Verilog-A code. For DMTJ, STTs generated by both the transmitted and reflected spin polarized electrons add together. This enhancement strongly decreases the I_{C0} and τ, which can be expressed as $I_{C0}=2\alpha\gamma e\times(K_{EFF}\times Volume)/\mu_B g_{DMTJ}$ (1) $\tau=[C+\ln(\pi^2\Delta E/4)]\times(em/4\mu_B g_{DMTJ})\times(I_{write}-I_{C0})^{-1}$ (2) where α is Gilbert damping factor. γ is gyromagnetic ratio. e is elementary charge. K_{EFF} is the effective PMA energy density. Volume is the total volume of the dual FLs. μ_B is Bohr magneton's constant. $C\approx0.577$ is the Euler's constant. M_S is the FL's saturation magnetization. $m=M_S\times Volume$ is the total magnetic moment of FL. g_{DMTJ} represents the spin polarization efficiency factor, which is enhanced in comparison with conventional MTJ, this phenomenon can be described by $g_{MTJ}(\theta)=P/2(1+P^{2}\cos\theta)$ (3) $g_{DMTJ}=g_{MTJ}(\theta)+g_{MTJ}(\pi-\theta)=P/(1-P^4\cos^2\theta)$ (4) where $g_{MTJ}(\theta)$ and $g_{MTJ}(\pi-\theta)$ represent the transmitted and reflected spin polarized efficiency factor of MTJ, respectively. P is the spin polarization percentage of the tunnel current, θ is the initial angle between the magnetization orientation FL's and the top reference layer's. However, the stochastic STT switching, which results from thermal fluctuations of magnetization, leads to the large fluctuations in the switching durations. We discover the real switching time comply with a gamma distribution $\Gamma(k,\theta)$. The shape and scale parameters, respectively, k and θ, are linked to the mean and standard deviation through the relations $E[\tau]=\theta k$ and std $[\tau]=\theta k^{-1/2}$. Besides, the temperature influence should not be ignored. Since the tunnel magnetoresistance (TMR) ratio, M_S, and K_{EFF} will decrease with the increasing of temperature [7], the magnetoresistance and I_{C0} can be influenced. In addition, as the limit of the manufacturing technology, the real value of the MgO-barrier layers and FLs' thicsknesses are not the constants as we expected. They always vary in a somewhat small range, but can lead to relatively significant variations for the resistance and I_{C0}. For instance, the resistance is exponentially related to the thickness of two oxidized barrier layers, small thickness variation can lead to relatively significant impacts on resistance. In this paper we used the normal random statistical functions provided by Verilog-A to generate the true values of these thicknesses. The developed Verilog-A compact model is adopted to investigate the writing performance, temperature influence, resistance distributions and STT stochastic switching behavior. Fig.2 (a) illustrates the comparison of STT switching time of DMTJ with MTJ. DMTJ is proved to switch at a considerable speed with a much lower writing current. Fig. 2 (b) shows the DC simulations of 20nm-DMTJ at low, room and high temperature, respectively. Fig. 2(c) describes the distribution of 10k DMTJ's resistances. Monte Carlo simulations of two completed writing operations of 10 DMTJs are shown in Fig. 2 (d). The amplitude differences of different signals are caused by layers' thicknesses variations, whereas the switching time fluctuations of the same DMTJ during two writing operations describe the stochastic STT switching behaviors. These results prove that our proposed model can be a very useful tool for the performance optimizations and reliability analyses of hybrid CMOS/DMTJ circuits.

[1] N. S. Kim, T. Austin, D. Baauw, T. Mudge, K. Flautner, J. S. Hu,M. J. Irwin, M. Kandemir, and V. Narayanan, "Leakage current: Moore'slaw meets the static power," Computer, vol. 36, no. 12, pp. 68–75,Dec. 2003. [2] C. Chappert, A. Fert and F. Nguyen Van Dau, "The emergence of spin electronics in data storage", Nat Mater, vol. 6, no. 11, pp. 813-823, 2007. [3] S. Ikeda, K. Miura, H. Yamamoto, K. Mizunuma, H.D. Gan, M. Endo,S. Kanai, J. Hayakawa, F. Matsukura, and H. Ohno, "A perpendicular anisotropy CoFeB–MgO magnetic tunnel junction", Nature Mater, vol. 9, no. 9, pp. 721–724, 2010. [4] Y. Zhang, W.S. Zhao, Y. Lakys, J. O. Klein, J. V. Kim, D. Ravelosona, and C. Chappert, "Compact modeling of perpendicular-anisotropy CoFeB/MgO magnetic tunnel junctions", IEEE Tran. on Elec. Devi., vol. 59, no. 3, pp. 819–826, Mar. 2012. [5] Z. Diao, A. Panchula, Y. Ding, M. Pakala, S. Wang, Z. Li, D. Apalkov, H. Nagai, A. Driskill-Smith, L. C. Wang, E. Chen, and Y. M. Hua,. "Spin transfer switching in dual MgO magnetic tunnel junctions", Applied Physical Letter, vol. 90, no.13, pp. 132508-1–3, Mar. 2007. [6] H. Sato, E.C.I. Enobio, M. Yamanouchi, S. Ikeda, S. Fukami, S. Kanai, F. Matsukura, and H. Ohno, "Properties of magnetic tunnel junctions with a MgO/CoFeB/Ta/CoFeB/MgO recording structure down to junction diameter of 11nm", Applied Physics Letters, 105(6). pp. 062403 2014. [7] Y. Wang, H. Cai, L.A.B. Naviner, Y. Zhang, J.O. Klein, W.S. Zhao. "Compact thermal modeling of spin transfer torque magnetic tunnel junction." Microelectronics Reliability, vol. 55, no. 9, pp. 1649-1653.

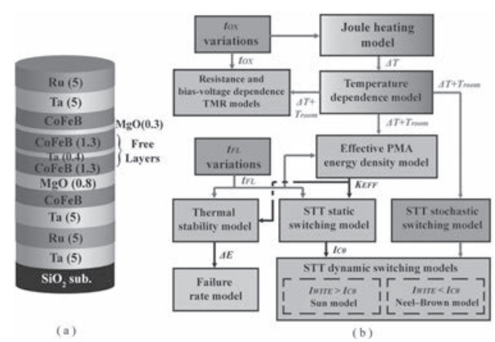

Fig. 1. (a) The structure of proposed DMTJ, the unit of the thicknesses of the layers is nm. (b) The principle block diagram of the integrated physical models.

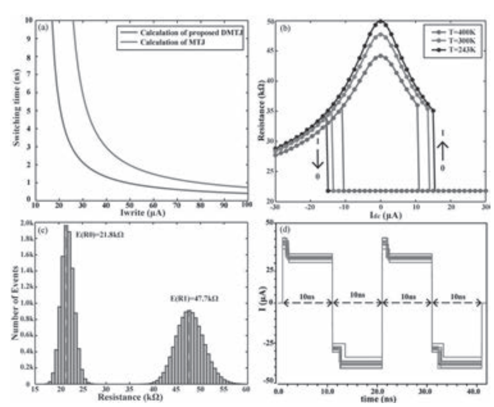

Fig. 2. (a) Comparison of the simulated STT dynamic switching time of 20nm DMTJ with MTJ in the same diameter. (b) DC simulations of DMTJ at different temperatures. (c) The resistance distribution of Monte Carlo simulations of 10^4 DMTJs. RA=10Ωμm², the standard deviation is 1%. (d) Monte Carlo simulations of two completed writing operations of 10 DMTJs.

HT-04. Role of Defect on Stabilizing Skyrmion in Magnetic Nanostructure.

A. Talapatra[1] and *J. Mohanty*[1]
1. Physics, Indian Institute of Technology, Hyderabad, Hyderabad, India

Introduction: The Dzyaloshinskii-Moriya interaction (DMI) is a microscopic characteristic of interacting spins that occurs in a system, lacking inversion symmetry with a strong spin-orbit coupling. The whirling types of magnetization in a chiral magnet are introduced by the DMI. Magnetic skyrmions are topologically protected physically stable spin configuration, appearing due to DMI. Skyrmions are particle-like magnetic configurations, dimension of which can be scaled down to few nm and are easily moved with spin polarized current. Thus skyrmion has its technological importance to pave the way towards ultra-high density magnetic data storage devices. Magnetic skyrmion lattices were first discovered in bulk non-centrosymmetric systems. In magnetic thin films, the most heavily studied mechanism to stabilize skyrmion is through DMI, originating from the asymmetric heavy metal interface [1]. The pioneering work of Sampaio *et al.* describes stabilization and current induced motion of isolated skyrmion in magnetic nanostructure with perpendicular magnetic anisotropy (PMA) [2]. Iwasaki *et al.* explained current induced motion of skyrmion in constricted geometry with micromagnetic simulation [3]. The recent experimental reports prove the presence of skyrmion in rare-earth transition-metal alloys [4] and their multilayer [5]. Here we are going to explain the stabilization of skyrmion in magnetic nanostructure in presence of magnetic defects. The formation of defect is an unavoidable issue during the process of nano-structuring and hence it plays a very important role to decide the magnetic properties of the system [6]. We will emphasis on the effect of dimension and magnetic anisotropy of defect inside the patterned structure. Moreover, the importance of the initial state and external magnetic field has also been explained for the transformation of isolated skyrmion to skyrmion lattice. Results and Discussions: We performed micromagnetic simulations on the formation of skyrmion using OOMMF code including DMI [7], expressed as: $H_{DM} = - D_{12} (S_1 \times S_2)$ (1) where D_{12} is the DM vector and S_1 and S_2 are atomic spins. The input parameters of the simulations include, exchange stiffness constant (A) = 16 pJ/m, effective anisotropy constant (K_{eff}) = 0.51 MJ/m3, saturation magnetization (M_s) = 1100 kA/m and the damping constant (α) = 0.3. The values describes an ultrathin (0.6 nm) Co film on Pt having a strong perpendicular magnetic anisotropy. The simulations have been performed for 0 Kelvin temperature. With the increasing DM parameter D (in mJ/m^2), transition from single domain state (D =2) to multi domain state (D = 6) via skyrmion configuration (D = 3 to 5) can be observed [2]. The decrease in the energy of the ferromagnetic (FM) state occurs with D due to the lowering of DMI energy by an inward tilt of the spins at the edges. For larger D values, the increasing number of twisted spin pairs is responsible for lowering the total energy and hence diameter of skyrmion (S) increases up to the dimensions, limited by the dimension of the nano dot (d_{dot}). Again, smaller skyrmion can be obtained by decreasing d_{dot} without changing the D value. K_{eff} is another important parameter to control S which can be reduced with increasing K_{eff}. Thus, the interplay between D, d_{dot} and K_{eff} essentially decides the formation of skyrmion and the value of S [2]. The situation becomes further complex in presence of magnetic defect, creation of which is an artefact of nano-structuring methods *viz.,* focused ion-beam or electron beam lithography. Fig. 1 (a) and (c) display the variation of S with the change in defect anisotropy (K_{def}) and defect diameter (d_{def}) respectively, where we assume that the defect is situated exactly at the middle of the nano dot. From Fig. 1(b), it is very clear that S increases almost two times (for d_{dot} = 100 nm) when K_{def} increases from 10% to 90% of K_{eff}, whereas the value of S is limited when d_{dot} = 80 nm. The role of d_{def} can be observed from Fig. 1(d). There exists a threshold d_{def} above which S decreases drastically and this effect is very prominent for larger d_{dot}. These simulations shows the stabilization of skyrmion in presence of magnetic defect from initial skyrmion-like configuration, as discussed in [2]. To study the effect of the initial magnetization, now we have considered nano-dot with same parameters (without defect) with initial random state having uniform vertical magnetization (+ Z direction). The ground state magnetization profiles (0 mT) in Fig. 2 display the presence of skyrmion in ferromagnetic matrix, irrespective of the value of d_{dot}. The stabilization of isolated skyrmion or interacting skyrmion lattice is very important from technological aspect and hence the application of Zeeman field is necessary. Isolated skyrmion can be observed for d_{dot} 80 and 100 nm with magnetic field of 84 and 156 mT respectively. With the increase in d_{dot} to 120 and 140 nm, skyrmion lattice can be observed with double and triple skyrmions respectively, stabilized with relatively higher values of magnetic field. The value of D has been fixed to 5 mJ/m^2 for the simulations displayed in Fig. 2. Thus we successfully explain here the transition from isolated skyrmion to a skyrmion lattice by varying d_{dot} and the magnetic field.

[1] S. Mühlbauer, B. Binz, F. Jonietz, C. Pfleiderer, A. Rosch, A. Neubauer, R. Georgii, and P. Böni, *Science* 323, 915 (2009). [2] J. Sampaio, V. Cros, S. Rohart, A. Thiaville and A. Fert, *Nat. Nanotech.* 8, 839 (2013). [3] Junichi Iwasaki, Masahito Mochizuki and Naoto Nagaosa, *Nat. Nanotech.* 8, 742 (2013). [4] J. C. T Lee, J. J. Chess, S. A. Montoya, X. Shi, N. Tamura, S. K. Mishra, P. Fischer, B. J. McMorran, S. K. Sinha, E. E. Fullerton, S. D. Kevan and S. Roy, *Appl. Phys. Lett.* 109, 022402 (2016). [5] S. A. Montoya, S. Couture, J. J. Chess, J. C. T. Lee, N. Kent, D. Henze, S. K. Sinha, M.-Y. Im, S. D. Kevan, P. Fischer, B. J. McMorran, V. Lomakin, S. Roy and E. E. Fullerton, *Phys. Rev. B* 95, 024415 (2017). [6] A. Talapatra and J. Mohanty, *Appl. Phys. A* 122, 807 (2016). [7] S. Rohart and A. Thiaville, *Phys. Rev. B* 88, 184422 (2013).

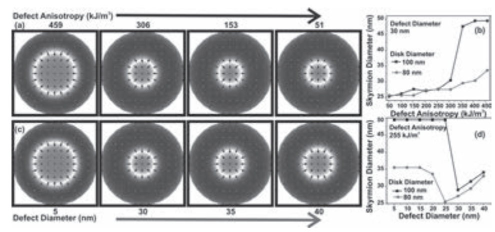

Fig. 1. Creation of isolated skyrmion with varying (a) K_{def} and (c) d_{def} inside nano dot with d_{dot} = 100 nm, (b) and (d) represent the variation of S with K_{def} and d_{def} respectively.

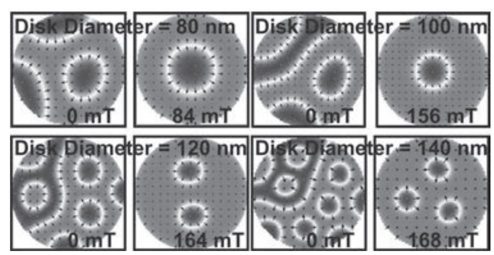

Fig. 2. Creation of isolated skyrmion and skyrmion lattice with external magnetic field for different d_{dot}.

HT-05. Comparison of Computational Speed between Landau-Lifshitz-Gilbert and Hybrid-Monte-Carlo Micromagnetics.

J. Song[1], Z. Zhao[1] and D. Wei[1]
1. School of Materials Science and Engineering, Tsinghua University, Beijing, China

The Landau-Lifshitz-Gilbert (LLG) equation is widely utilized to analyze the magnetic properties in micromagnetics [1]. However, the calculation of micromagnetics with Landau-Lifshitz-Gilbert equations is time-consuming, so the FDM-FFT method was brought up to speed up the simulation in large scale [2]. Recently, we have developed a new micromagnetic method based on the Hybrid Monte Carlo (HMC) algorithm, which can calculate M-H loops and domains at finite temperature below Curie point [3]. Some simulation results have been put forward to confirm the validity of the HMC algorithm [4]-[6]. Furthermore, we also wish to focus on the computational efficiency to compare HMC micromagnetics with traditional LLG micromagnetics. Comparison of computational speed has been made of these two methods in various micromagnetic scales in this work. In LLG or HMC micromagnetics, a regular mesh with cell size $5\times5\times5nm^3$ is utilized. Other important parameters are: anisotropy energy constant $K(0K)=1\times10^5 J/m^3$, saturation magnetization at zero temperature $M_s(0K)=7.98\times10^5 A/m$, exchange constant $A^*=1.0\times10^{-11} J/m$. In LLG micromagnetics, the iterations can go endless unless the spin error $|\Delta|$ (the spin maximum deviation between two simulation steps) is set to be a limited number. To ensure the stability and accuracy, $|\Delta|$ is set as 10^{-6} in LLG algorithm. In HMC micromagnetics, the Monte Carlo time t is not real time. Based on the feature of the leap-frog algorithm used for iteration of the Hamilton equations, in HMC micromagnetics, the spin error $|\Delta|$ stands for the spin deviation of two adjacent trajectories. To compare the computational speed of the LLG and the HMC micromagnetic methods, the spin error $|\Delta|$ in HMC MuMag is also set as 10^{-6}. The M-H loops are same under these two micromagnetic algorithms. Fig. 1 shows the computational time to reach $|\Delta|\sim10^{-6}$ at each external magnetic field (H_{ext}), with 16*8*16 micromagnetic cells. The computational time for Hybrid Monte Carlo MuMag keeps around 59 seconds for different H_{ext}; while for Laudau-Lifshitz-Gilbert MuMag, the simulation time is typically several hundred of seconds and shows a sharp rising near coercivity to about 1904 seconds, which is different from HMC MuMag. In Fig. 2, the computational speed of the two micromagnetic methods is presented. The horizontal axis is $log_2(N_{cell})$, and the vertical axis is the total computation time for a loop in Fig.1 (in seconds). The blue line is the speed of the LLG MuMag. In the Ref. 7, the LLG algorithm has a running time proportional to the number of particles N, which yields $O(Nlog_2N)$ computational time. We have compared the computational time of LLG algorithm with $O(Nlog_2N)$. The triangle-dot line is the computation time vs. $log_2(N_{cell})$, which shows great agreement with $O(Nlog_2N)$ (black line in Fig.2). The red dotted line shows the computation time consumed by the HMC algorithm, which show great coincidence with $O(N)$ in the insert figure. From the comparison, the HMC algorithm has a significant advantage for the computational speed. When the number of micromagnetic cells rise to 32*32*32, LLG algorithm spends 16 times more than HMC algorithm.

[1] Victora, R. H. "Micromagnetic predictions for magnetization reversal in CoNi films", J. Appl. Phys. 62, 4220-4225, 1987 [2] Bertram, H. N., Zhu, J. G. "Micromagnetic studies of thin metallic films", J. Appl. Phys. 63, 3248-3253, 1988 [3] Wei D, Song Junjie, Liu C. Micromagnetics at Finite Temperature[J]. IEEE Transactions on Magnetics, 2016, 52(11): 1-8. [4] Song Junjie, J. Wang, Dan Wei, Y. K. Takahashi, and K. Hono, "Micromagnetic studies at finite temperature on FePt-C granular films",IEEE Transactions on Magnetics, VOL.53, NO.11, Nov 2017, 7100504 [5] Jingyue Miao, Dan Wei, and Chuan Liu, "Micromagnetic studies of Time-Dependent Coercivity", IEEE Transactions on Magnetics, VOL.53, NO.11 Nov 2017, 8204404 [6] Zhen Zhao, Dan Wei, "Size and temperature dependence of M-H loop for Pt/CoFe/IrMn heterojunction", AIP Advances, 8, 056012, 2018 [7] Samuel W. Yuan and H. Neal Bertram, "Fast Adaptive Algorithms for Micromagnetics",IEEE Transactions on Magnetics, VOL. 28, NO. 5, Sep 1992, 2031.

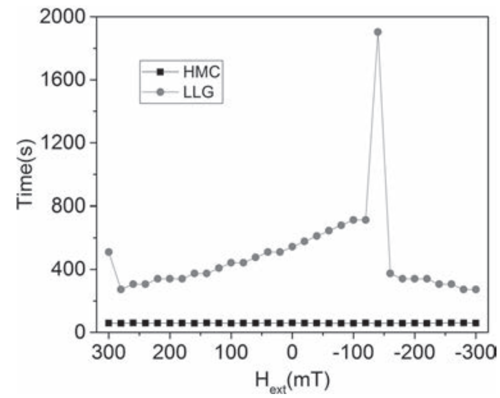

Fig. 1. The computational time at different external magnetic field H_{ext} in the model of 16*8*16 cells. The computational time for Hybrid Monte Carlo MuMag keeps around 59 seconds for each $H_{ext.}$ While for Laudau-Lifshitz-Gilbert MuMag, the simulation time varies from 272s to1904s and peaks at the coercivity.

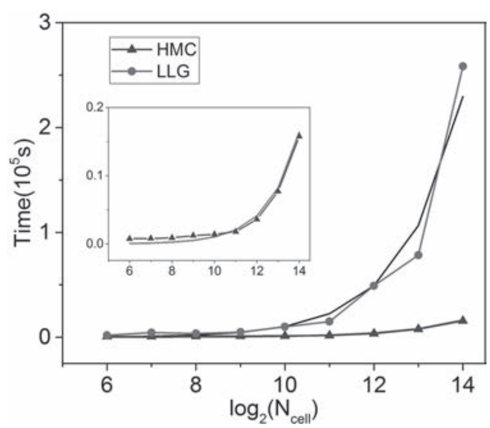

Fig. 2. The comparison of computational speed between LLG and HMC micromagnetics. The triangle-dot line is seconds that takes with HMC, while the square-dot line is that of LLG simulation. The black line follows *$O(Nlog_2N)$*. The insert figure shows the computational time of HMC fit well with red line *$O(N)$*.

HT-06. Realistic micromagnetic model in exchange bias: The parametric study including thermal activation as setting process.

W. Daeng-am[1], P. Chureemart[1], L.J. Atkinson[2], R.W. Chantrell[2] and J. Chureemart[1]
1. Physics, Mahasarakham University, Kantharawichai, Thailand; 2. Physics, University of York, York, United Kingdom

Exchange bias is the interfacial effect arising from the exchange coupling between uncompensated antiferromagnetic (AF) and ferromagnetic (FM) spins after field-cooling process [1] which is crucial aspect of the read sensors in data storage devices [1-2]. In order to depth understand behind the complex effect due to thermal instability of AF layer [3], the advanced micromagnetic model is still required the thermal activation phenomena as setting process into the calculation. The consideration of setting process which is used to set the direction of AF stable grain before start measuring the hysteresis loop [2] is very significant in the exchange bias. In this work, we have proposed the advanced micromagnetic model by using the multi-scale calculations which allows to take the effects of the setting process and the distributions of the anisotropy easy axes in AF layer into account. In order to establish the realistic magnetic bilayers system between FM and AF layers to describe the pinning structure in read sensors due to exchange bias phenomenon, the Voronoi tessellation was employed to generate the specified microstructure. The microstructure of each single grain between FM and AF layers are treated as a columnar stack with the same diameter. Figure 1 shows the typical structure of bilayers system (top view) with periodic grain boundary at 100×100 nm^2 and the visualization of bilayers system with the easy axis distribution at the interface between FM/AF layer. The FM and AF layers will be modelled with the different approaches with integrating the stochastic-Landau-Lifshitz-Gilbert equation and kinetic Monte Carlo approach [4] respectively in order to describe the magnetic properties as soft magnetic and hard magnetic materials depending on the nature of the magnetization reversal process. In order to include the setting process in the calculation, the FM grain is assumed to equilibrate in the field direction for every time step of calculation and the direction of AF grain is also saturated in the field direction at the maximum applied field and the setting temperature (T_{SET}). Then, the AF grains will be cooled down to the experimental temperature to achieve the setting configuration of AF layer for the measurement of H_{EB}. Each kMC time-step is used at 10^{-8} s while time-step of FM is defined with the tiny amount of time at 10^{-13} s in order to investigate its magnetization dynamics. The calculation of FM layers needs to be iterated to equilibrium via LLG method after each kMC time-step stages. Therefore, the calculation of magnetization dynamics with two different timescale techniques can be achieved. The current magnetic material in the pinning read sensors as CoFe/IrMn is used to investigate the effects of physical structure such as thickness and grain size effect on exchange bias field (H_{EB}). The median grain diameter is fixed at 8 nm with a lognormal distribution of = 0.2 [5] and T_{SET} is 600 K [2]. The thickness of CoFe and IrMn layers is fixed at 4 nm and 8 nm respectively. The magnetic parameters bilayers used in this calculation are as follow: T_c = 1300 KM_s = 1800 emu/cc, and K_F = 1.8x10^5 erg/cc for CoFe and T_N = 690 K and K_{AF} = 3 x10^6 erg/cc for IrMn [5]. The exchange interlayer field strength representing the exchange coupling between layers is controlled at 250 Oe. The parametric study on exchange bias is presented in order to establish the intrinsic effect of the microstructure on the thermal stability. We firstly consider the effect of grain volume dependence with the different grain diameter from 4 to 12 nm on H_{EB} which is vital factor for thermal stability. The typical hysteresis loops are shown in fig. 2 a) and the exchange bias is unstable with no loop shift at small diameter (4 nm). The tendency of H_{EB} is also increased with increasing of AF grain volume which is consistent with the experimental work [6] because the large grain volume give rise to the large fraction of thermally stable AF state to pin FM spins. Subsequently, the thickness dependence effect on H_{EB} is also investigated with the system of CoFe(4nm)/IrMn(t) where t is varied from 2 to 12 nm at fixed grain diameter = 8 nm. Fig.2 b) shows the consistent results of the variation of H_{EB} between advanced model and experimental work [6]. It is clear that H_{EB} increases rapidly with the increasing of AF thickness reaching the maximum at 6 nm and then become stable for thicker film. The thin thickness (2 nm) of AF layer presents the thermal instability due to the superparamagnetic behavior. In conclusion, we proposed the advanced micromagnetic model integrate with the setting process to investigate the parametric study on CoFe/IrMn bilayer in magnetic read sensor. The results from advanced model give well agreement with the experimental works and conventional theory of H_{EB}.

[1] K. O'Grady, L. E. Fernandez-Outon and G. Vallejo-Fernandez, Journal of Magnetism and Magnetic Materials, 322.8., 883-899 (2010). [2] J. Barker, B. Craig, R. Lamberton, A. Johnston, R. W. Chantrell and O. Heinonen, Applied Physics Letters, 95(2), 022504 (2009). [3] E. Fulcomer and S. H. Charap, J. Appl. Phys. 43, 4190 (1972). [4] R.W. Chantrell, N. Walmsley, J. Gore, and M. Maylin, Physical Review B, 63, 024410 (2000). [5] N. P. Aley, G. Vallejo-Fernandez, R. Kroeger, B. Lafferty, J. Agnew, Y. Lu, and K. O'Grady, IEEE transaction on magnetics, 44. 11 (2008). [6] G. Vallejo-Fernandez, L. E. Fernandez-Outon and K. O'Grady, Journal of Physics D: Applied Physics, 41, 112001 (2008).

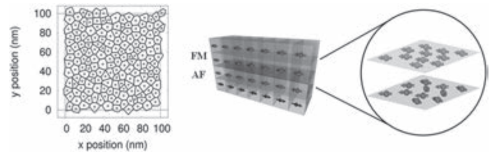

Fig. 1. the typical structure of bilayers system with periodic grain boundary from Voronoi tessellation and visualization of bilayers system with the easy axis distribution at the interface between FM/AF layers.

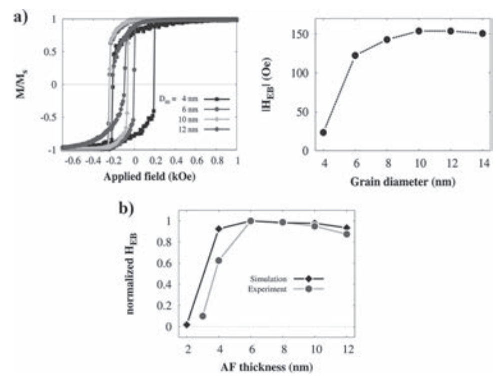

Fig. 2. the hysteresis loops and the variation of H_{EB} with the grain diameter dependence at 4-12 nm and b) the variation of H_{EB} with AF thickness dependence for CoFe/IrMn.

HT-07. Micromagnetic Studies of Laser-induced Magnetization Dynamics in FePt-C Films.

J. Miao[1], J. Wang[2], R. Mandal[2], D. Wei[1], Y. Takahashi[2] and K. Hono[2]
1. School of Materials Science and Engineering, Tsinghua University, Beijing, China; 2. Research Center for Magnetic and Spintronic Materials, National Institute for Materials Science (NIMS), Tsukuba, Japan

Laser-induced magnetization switching has been studied extensively for its applications in heat-assisted magnetic recording (HAMR) and all-optical switching (AOS), since Beaurepaire *etal.* found that magnetizations can respond to the femtosecond time scale laser pulse [1]. With the help of heat and assistance of external field or helicity-dependent magneto-optical effect, magnetizations switch in an ultrafast regime of picoseconds [2]. Recently, micromagnetic simulations based on LLB equation have been used to study the magnetization dynamics and switching in FePt films [3, 4]. In this work, the hybrid Monte Carlo (HMC) micromagnetics developed by the authors [5, 6] will be utilized to analyze the laser-induced magnetization switching. In this work, we built a model of FePt-C granular film with Voronoi polycrystalline structure. Some magnetic and structural parameters are derived by experimental measurements [7]. The total simulated area is 32nm×32nm×8nm, divided into a regular mesh of 2.5nm×2.5nm×2nm micromagnetic cells and the number of crystalline grains is 48. At T = 0K, in crystalline grains, the saturation $M_s(0)$ is 1300 emu/cc, the exchange constant A^*_1 is 6.8×10^{-7} erg/cm and the anisotropy energy $K(0)$ is 4.5×10^{7}erg/cm^3; at disorder grain boundary, $M'_s(0)$ is $0.1M_s(0)$, A^*_2 is $0.2A^*_1$ and $K'(0)$is $0.1K(0)$ [7]. In simulation of laser-induced magnetization dynamics, the temperature profile of the laser shooting process is vitally important. In LLB micromagnetics, two-temperature model (2TM) is commonly used to get the profile of the electron temperature, which is then introduced in LLB equation via the spin coupling parameter λ. But some parameters in 2TM model are quite arbitrary. In HMC micromagnetics, we use the time-resolved magneto-optical kerr effect (TR-MOKE) to get the spin temperature profile directly. The time resolved kerr rotation, which is proportional to magnetization, is measured with an external magnetic field 2 T applied in the direction of initial magnetization to ensure that all magnetizations are saturated in one direction. The measurement and simulation results are shown in Fig. 1 and Fig. 2. The measured kerr rotation signal is shown in Fig.1(a). In Fig. 1(a), in the process of ~290fs laser shooting, the kerr rotation decreases rapidly and then recovers slowly, which results from the rapid demagnetization and slower recovery of magnetization. Additionally, with higher laser power, the kerr rotation decreases to a critical minimum point where the magnitude of magnetization gets closely to zero, so that we can get the scaling relationship between the kerr rotation signal and the magnetization. We assume a spin temperature profile in Fig.1(b), and the HMC micromagnetics is performed with $M_s(T)$ determined by the mean field Brillouin function based on the temperature profile $T(t)$ in Fig.1(b) [8]. The simulated averaged M(t) curves fit well with the measurements in Fig.1(a), which in turn convince the correct choice of the spin temperature profile in Fig.1(b). So that HMC micromagnetics can be further utilized to study the laser-induced magnetization dynamics with various external magnetic fields or circularly polarized light.

[1] Beaurepaire E, Merle J C, Daunois A, et al. Ultrafast spin dynamics in ferromagnetic nickel[J]. Physical review letters, 1996, 76(22): 4250. [2] Nieves P, Chubykalo-Fesenko O. Modeling of Ultrafast heat-and field-assisted magnetization dynamics in FePt[J]. Physical Review Applied, 2016, 5(1): 014006. [3] Mendil J, Nieves P, Chubykalo-Fesenko O, et al. Resolving the role of femtosecond heated electrons in ultrafast spin dynamics[J]. Scientific reports, 2014, 4. [4] Kazantseva N, Hinzke D, Nowak U, et al. Towards multiscale modeling of magnetic materials: Simulations of FePt[J]. Physical Review B, 2008, 77(18): 184428. [5] D. Wei, J. Song and C. Liu. "Micromagnetics at Finite Temperature," IEEE Transactions on Magnetics, 2016, pp. 1-8. [6] Miao J, Wei D, Liu C. Micromagnetic Studies of Time-Dependent Coercivity[J]. IEEE Transactions on Magnetics, 2017. [7] Junjie Song, J. Wang, Dan Wei, Y. K. Takahashi, and K. Hono, "Micromagnetic Studies at Finite Temperature on FePt–C Granular Films", IEEE TRANSACTIONS ON MAGNETICS, VOL. 53, NO. 11, 7100504, (2017). [8] Tyler F. XLIX. The magnetization-temperature curves of iron, cobalt, and nickel[J]. The London, Edinburgh, and Dublin Philosophical Magazine and Journal of Science, 1931, 11(70): 596-602.

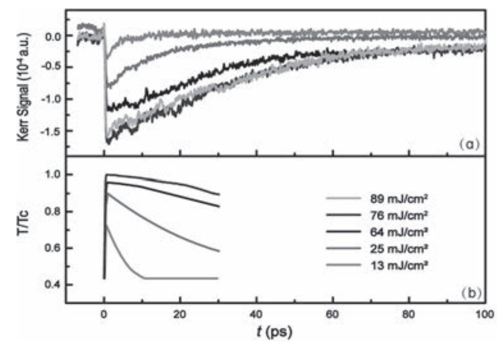

Fig. 1. Measurement of kerr rotation in the process of one laser shooting (a), and the spin temperature profile vs. time assumed based on the kerr rotation measurement (b).

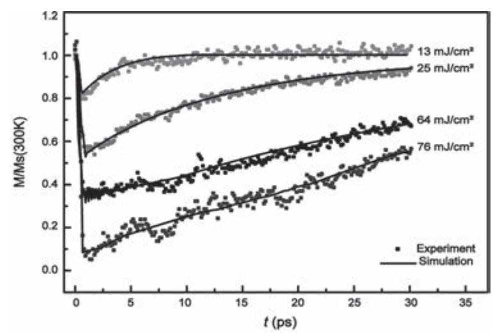

Fig. 2. Simulated and measured laser-induced magnetization dynamics in the FePt-C film.

HT-08. Micromagnetic simulation for the effects of Fe nanowires distribution on the magnetic properties of the $Nd_2Fe_{14}B/\alpha$-Fe nanocomposite magnets.

W. Li[1], L. Zhao[1] and *Z. Liu*[1]
1. South China University of Technology, Guangzhou, China

At present, the development of the exchange coupled nanocomposite magnets faces several challenges. High magnetization is usually accompanied by low coercivity, which is a major barrier for achieving high-energy products in this type of magnets. Fe nanowires are reported to have high coercivity due to its strong shape anisotropy,. Hence, it may be an good approach to enhance the coercivity of $Nd_2Fe_{14}B/\alpha$-Fe nanocomposite magnets by introducing Fe nanowires as the soft phase. In the present work, the effects of Fe nanowire arrays on the magnetic properties of nanocomposite magnets are investigated by micromagnetic simulation. The simulation model is shown in Fig. 1. The nanowires arranged along the Z direction and the demagnetization curves of the Fe nanowires indicate the strong shape anisotropy. The nanowires have a length of 105 nm and a square cross section with the side length of S. The hard magnetic $Nd_2Fe_{14}B$ phase matrix is set as spherical without shape anisotropy. Fig. 1 The simulation model and the demagnetization curve of the Fe nanowires. The effects of different angles (θ= 0°, 30°, 45°, 60°, and 90°) between the long axis (Z axis) of nanowires and the easy axis of the hard phase on the magnetic properties are investigated firstly. The size of the nanowires are set as 150×9×9 nm. The simulated demagnetization curves are shown in Fig. 2. The coercivity increases with the increasing θ from 0° to 90°. When the nanowires are parallel to the easy axis of hard phase (θ=0°), the hysteresis loop is a standard square and the moments reverse uniformly in one stage. The demagnetization curve for θ=90° show a long slope. The moments reverse in two steps, parts of the moments rotate slowly followed by all the moments reversing uniformly in one stage. The distribution of magnetization in the first step shows that the moments of the soft phase rotate to the direction of the nanowire due to the shape anisotropy, as shown in Fig.2 inset, where red color means outward, blue means inward. Since the size of nanowire is smaller than the exchange length, the moments in the soft phase are strongly exchange coupled by hard phase. Since the fully reserved direction (-Z direction) of Fe nanowires is the hard magnetization direction and the moments are blocked, that's why the coercivity of θ=90° is much larger than that of θ=0°. Fig. 2 The demagnetization curves of the models with different θ and the magnetization distribution for θ=90° inset. In addition, the size effects of nanowires with S=9 nm, 18 nm, 27 nm, and 54 nm were also studied in the model of θ=0° and 90°. The simulation results show that the nucleation occurs at a low applied field and the coercivities decrease as increasing the nanowires diameters. For θ=90°, the coercivity is relatively stable with the increasing diameters of nanowires. The reason could be attributed to the fact that when the sizes is larger than the exchange length, the exchange coupling effect becomes insignificant and the dipolar coupling is dominant for θ=90°. As a conclusion, the coercivity of the nanocomposite $Nd_2Fe_{14}B/\alpha$-Fe can be increased by introducing the soft magnetic nanowire arrays with the long axis along the direction other than the easy axis of hard phase and the diameter smaller than the exchange length.

1. Z. W. Liu and L. Z. Zhao, "Compositional Optimization and New Processes for Nanocrystalline NdFeB-Based Permanent Magnets," in Advances in Magnetic Materials: Processing, Properties, and Performance, ed: CRC Press, 2017, pp. 293-372. 2. X. Y. Zhang, G. H. Wen, Y. F. Chan, et al. "Fabrication and magnetic properties of ultrathin Fe nanowire arrays." Applied physics letters, vol. 83, no. 16, pp. 3341-3343, 2003. 3. S Yang., H. Zhu, D. Yu, et al. "Preparation and magnetic property of Fe nanowire array." Journal of Magnetism and Magnetic Materials, vol. 222, no. 1, pp. 97-100, 2000.

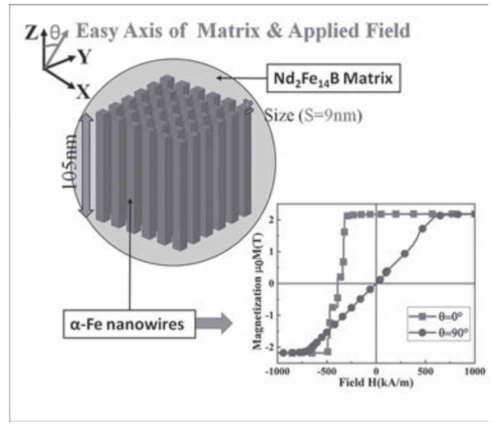

Fig. 1. The simulation model and the demagnetization curve of the Fe nanowires.

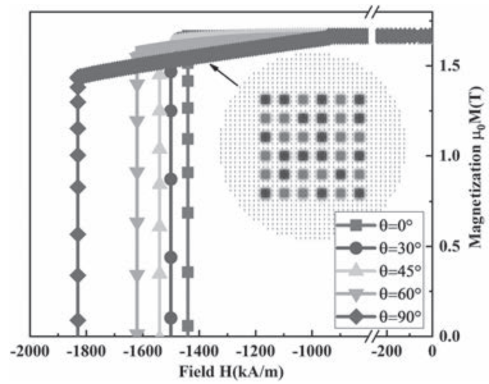

Fig. 2. The demagnetization curves of the models with different θ and the magnetization distribution for θ=90° inset.

HT-09. Parallelization with locality optimization of ultra-large-scale micromagnetics simulation using OSCAR Compiler.

K. Ono[1], M. Shimaoka[2], H. Mikami[2], H. Tsukahara[1], K. Iwano[1], C. Mitsumata[3] and H. Morita[4]

1. High Energy Accelerator Research Organization, Tsukuba, Japan; 2. Waseda University, Tokyo, Japan; 3. National Institute for Materials Science (NIMS), Tsukuba, Japan; 4. Hitachi, Ltd., Tokyo, Japan

The recent rapid progress of computer performance resulted in the enlargement of spatiotemporal scales in numerical simulation for the field of material science. In the field of magnetic materials, micromagnetics and multiscale modeling are promising tools for the discovery of novel magnetic materials with a combination of materials informatics. To realize the discovery of a high-performance magnetic material, it is important to clarify the correlation between magnetic properties and the structures or microtextures in the magnetic materials, and micromagnetics and multiscale modeling play an essential role. However, in the accurate calculation of the magnetization dynamics in the magnet materials, a model size of the simulation should be a few hundred nanometers to several micrometers, which is the scale of microtextures in the real magnetic materials, with a mesh size of several nanometers, which is the scale of exchange-correlation length is needed. It is, therefore, necessary to perform an ultra-large-scale micromagnetic simulation. We have succeeded in developing large-scale micromagnetic simulator with a model exceeding 1 billion cells by using the supercomputer [1-4]. On the other hand, it is rather difficult to perform the ultra-large-scale micromagnetic simulation for searching the novel magnetic materials by using the supercomputer, since the computational time of the supercomputer is limited. Parallel processing with strong scaling has been required for the ultra-large-scale micromagnetic simulation. However, the calculation of magnetostatic fields using Three-dimensional Fast Fourier Transform (3D FFT) is considered to be the most difficult part of the parallel processing. 3D FFT is an efficient algorithm for computing discrete Fourier transform in 3D space operations. 3D FFT requires global communication among processors, which limits efficiency even on a massively parallel supercomputer, and it is considered to be difficult to perform ultra-large-scale 3D FFT on the conventional workstation. This drawback can be overcome through the proposed coarse grain task parallelization. The proposed method uses the OSCAR compiler for exploiting coarse grain task parallelism efficiently to get scalable speed-ups with strong scaling. The OSCAR compiler can analyze data dependence and control dependence among coarse grain tasks, such as subroutines, loops and basic blocks. Moreover, locality optimizations considering the boundary calculations of FDM and a new static scheduler that enables more efficient task schedulings on cc-NUMA servers are presented. We performed the ultra-large-scale micromagnetic simulation for a permanent magnet is based on Landau - Lifshitz - Gilbert (LLG) equation. The simulation was performed on the model for the Nd-Fe-B permanent magnets with a size of 512 nm $\times$ 512 nm $\times$ 512 nm. We use finite difference method with the periodic boundary condition for simulation, and the simulation model was discretized into 2.0 nm $\times$ 2.0 nm $\times$ 2.0 nm cells. Thus, the model has 256 grid points in the x, y, and z-direction, and the total grid points are 16,777,216. The performance evaluation shows 120 times speed-up using 128 cores against the sequential execution on a POWER7 based 128 cores cc-NUMA server Hitachi SR16000 M1, 62.1 times speed-up using 64 cores against the sequential execution on a Xeon E7-8830 based 64 cores cc-NUMA server, and 131 times speed-up using 128 cores against the sequential execution on a Xeon E7-8890 based 128 cores cc-NUMA server. This significant speedup of ultra-large-scale micromagnetic simulation with coarse grain task parallelization enables the exhaustive search of novel magnetic materials.

[1] H. Tsukahara, K. Iwano, C. Mitsumata, T. Ishikawa, K. Ono, Comput. Phys. Commun, 207, 217 (2016). [2] H. Tsukahara, K. Iwano, C. Mitsumata, T. Ishikawa, K. Ono, AIP Advance 7, 056224 (2017). [3] J. Jung, C. Kobayashi, T. Imamura, Y. Sugita, Comput. Phys. Commun, 200 57 (2016). [4] M. Shimaoka, Y. Wada, K. Kimura, H. Kasahara H., Lecture Notes in Computer Science, vol 9519. Springer (2016) [5] H. Kasahara, M. Obata, K. Ishizaka,LNCS, vol. 2017, pp. 189–207. Springer, Heidelberg (2001) [6] M. Obata, J. Shirako, H. Kaminaga, K. Ishizaka, H. Kasahara, LNCS, vol. 2481, pp. 31–44. Springer, Heidelberg (2005)

HT-10. Voltage induced strain-mediated perpendicular magnetization control for in-memory computing device.

Q. Wang[1], C. Liang[1] and G.P. Carman[1]
1. Department of Mechanical and Aerospace Engineering, University of California, Los Angeles, Los Angeles, CA, United States

Magnetic memory has attracted substantial attention due to its promise of high energy efficiency combined with non-volatility. Conventionally, the magnetization is controlled by spin-transfer torque (STT) current but ohmic heating makes the current-based switching mechanisms energy inefficient (100fJ/flip). In contrast, strain-mediated multiferroic composites (i.e. coupled magnetoelastic and piezoelectric thin films) provide ultra-high energy efficiency as high as 100aJ/flip due to negligible induced current during the switching process. In this study, a fully coupled model is used to simulate strain-mediated magnetization control of nanodots with perpendicular magnetic anisotropy (PMA) on a PZT ($Pb_y[Zr_xTi_{1-x}]O_3$) thin film. This model is also used to study Bennet clocking of nanodot arrays. Fig. 1 shows the perpendicular magnetization m_z changing with time for CoFeB and Terfenol-D nanodisks under different applied voltages. The nanodisk diameter is 50 nm and the thickness for CoFeB is 1.6nm while for Terfenol-D it is 2nm. The inset plots in Fig. 1(a) and 1(b) illustrate the temporal strain change observed when applying 2.8V to the CoFeB element and 0.1V to the Terfenol-D element, respectively. For all the cases shown here, the magnetization undergoes 180° precessional switching (from $+z$ to $-z$). By increasing the voltage on either material, the switching (writing) time is decreased. However, beyond threshold voltages (6V for CoFeB, 0.2V for Terfenol-D), further increases in voltage no longer decrease switching times. This is because incoherent switching begins to appear at high voltages due to the relatively larger energies introduced into the system. The shortest switching time for both materials are comparable (0.2~0.3ns) while the energy dissipation is substantially different for the two materials. The minimum voltage required to achieve 180° flipping in CoFeB is 2.8V, which corresponds to an energy dissipation as 29.6fJ per flip. In contrast, the minimum voltage required to flip Terfenol-D is 0.1V, which corresponds to an energy dissipation as 22aJ per flip. While the disparity between these two are large, the strain-mediate control for both materials are considerably more efficient than STT method (100fJ). The above information is used to study Bennett clocking mechanisms for different magnetic material systems (e.g., Ni, CoFeB, Terfenol-D) with PMA. Fig. 2 shows the simulation results of perpendicular Bennett clocking for a four-bit Ni system. All the Ni disks have 50nm diameter and 2nm thickness. Fig. 2(a) shows an illustration of the simulated structure. Four nanodisks are attached on the PZT substrate with 50nm edge-to-edge spacing between the neighboring disks. Each disk is surrounded by a pair of electrodes to apply voltage and generate localized strain. The four disks are initialized as ↑↓↑↓, and the neighboring disks are coupled through dipole-dipole coupling. A voltage pulse with 0.7ns duration is applied to the first disk. Through precessional switching, the first disk is flipped 180° from ↑ to ↓. Then voltage pulses with duration of 2ns are applied to the following disks consecutively. Under the long voltage pulse, the magnetization is brought in-plane, which is a metastable state. Because of dipole-dipole interaction, the chain of the Ni disks tends to form an anti-parallel alignment. Fig. 2(b) shows the temporal change of perpendicular magnetization as well as the voltage pulses applied for each disk. It is shown that the system equilibrates to an anti-parallel state defined by ↓↑↓↑. In other words, every disk undergoes 180° switching and the first memory bit change is transferred throughout the entire memory bit chain. These results show that the magnetic memory and logic can be implemented in the same device using strain-mediated switching and clocking methods, which will be the crucial element for next generation in-memory computing devices.

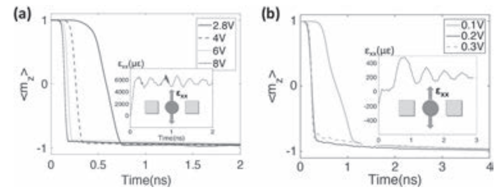

Fig. 1. Strain-mediated 180° OOP switching of CoFeB and Terfenol-D. (a) Switching of CoFeB under different applied voltages and average strain generated in CoFeB when applied 2.8V voltage. (b) Switching of Terfenol-D under different applied voltage and volume averaged strain changing with time when applied 0.1V voltage.

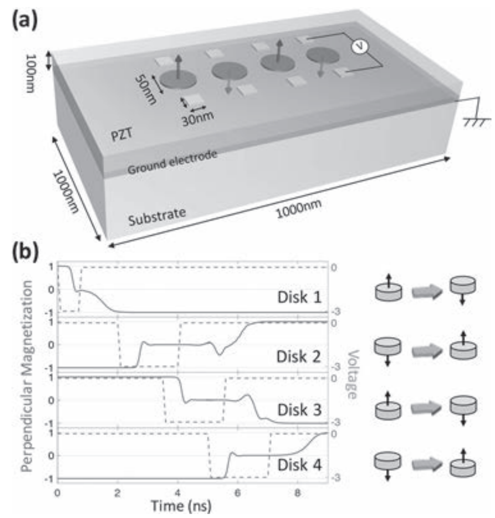

Fig. 2. Simulation results of strain-mediated switching and clocking for a four-bit Ni system. (a) Illustration of the structure. (b) The voltage application and magnetic dynamics of each individual disk.

HT-11. Three-dimensional Domain Calculations by Hybrid Monte Carlo Micromagnetics.

L. Bao[1], M. Dai[2], D. Wei[2,3] and *G. Yun*[1,3]
1. Inner Mongolia Key Lab of Nanoscience and Nanotechnology and School of Physical Science and Technology, Inner Mongolia University, Hohhot, China; 2. Key Laboratory of Advanced Materials, School of Materials Science and Engineering, Tsinghua University, Beijing, China; 3. College of Physics and Electronic Information, Inner Mongolia Normal University, Hohhot, China

The domain structure and the motion of domain wall of ferromagnetic material are first studied by Landau and Lifshitz in 1935 [1], which founded the theory of applied magnetism. Nowadays, for applications such as permanent magnets, 3D domain analysis of bulk magnetic materials becomes an important topic. Tsukahara et.al. applied the Landau-Lifshitz-Gilbert (LLG) equation to analyze the propagation of magnetization reversal of 1024 nm ×1024 nm ×1024 nm permanent magnets [2]. However, three-dimensional domain structure of large-scale magnet has not been studied at finite temperature because the LLG equations cannot take the influence of temperature into consideration. In this work, a new micromagnetic method, Hybrid Monte Carlo (HMC) Micromagnetics developed by Wei et.al., [3] is utilized to calculate the domain structure of cubic magnets up to the size of 1μm with different initial states of *M*. The computational speed of HMC micromagnetics is much faster than LLG micromagnetics, therefore it has the potential to calculate magnetic properties at finite temperature for large sized materials. For HMC micromagnetics in Ref.[3], a conjugate momenta Π_j for M_i is generated through a Gaussian distribution $\exp(-V_c\sum_i \Pi_i^2/2k_BT)$ and the correct Boltzmann distribution of free energy $\exp(-F(\{M_i\})/k_BT)$ is obtained by simulations divided into hundreds of trajectories; and in each trajectory, $\{\Pi_i\}$ and $\{M_i\}$ are iterated through the Hamilton equations, followed by the Monte Carlo judgment at the end of each trajectory to reach equilibrium at temperature *T*. In the simulation, the magnet size is divided into $N_x \times N_x \times N_x$ (N_x=8-256) cubic magnetic cells. The length of each cell is 5nm, which is effective to smooth the diverging stray field according to W. Rave's study [4]. The saturation magnetization M_s(0K) is 798 emu/cc, the exchange constant A^* is 1×10^{-6}erg/cm and the first-order anisotropy energy constant K(0K) is 4×10^5 erg/cm^3. The easy axis is along z direction. The magnetization distribution of the cubic magnet with a side size of 640nm are shown in Fig. 1 with different initial conditions of *M*. Here the periodic boundary conditions are applied on the double sized space ($2N_x \times 2N_x \times 2N_x$) to avoid the miscalculation of demagnetizing fields. There are two sets of initial conditions of *M* shown in Fig. 1. If the initial condition is set as up-down mode (*M*=Ms for x<0 and *M*=-Ms for x>0), the whole cube has one large domain and several small sized side domains, as seen in Fig 1(a) and (c). If the initial condition is set as up-down-up-down mode (M=M_s for -L/2<x≤-L/4 and 0<x≤-L/4 and M=-M_s for -L/4<x≤0 and L/4<x<L/2), four domains appear and the domain structure is more complicated as described in Fig 1(b) and (d). Thus, the final domain structure of large-sized cubic magnet largely depends on the initial state of magnetization, which reveal the nonlinearity of magnetics. If periodic boundary condition is applied at y direction and z direction, Bloch domain wall will appear in this magnet (This simulation is performed on the Supercomputer of Beijing Computing Center). It is not ideal Bloch wall because of the limited total size in x direction. By fitting the wall structure of M_z as formula M_z=tanh(x/a), the average bloch wall width *a* is found to be 15.6 nm. It fits quite well with theoretical value of Bloch wall width, which is 15.8nm according to a=√(A^*/K), demonstrating the accuracy of the calculation of domain structure.

1.Landau, L., & Lifshits, E. (1935). on the Theory of the Dispersion of Magnetic Permeability in Ferromagnetic Bodies. Phys. Zeitsch. Der Sow., 169(14), 14–22. 2.Tsukahara, H., Iwano, K., Mitsumata, C., Ishikawa, T., & Ono, K. (2017). Micromagnetic simulation for the magnetization reversal process of Nd-Fe-B hot-deformed nanocrystalline permanent magnets. AIP Advances, 7(5). 3. Wei, D., Song, J. & Liu, C. Micromagnetics at Finite Temperature. IEEE Trans. Magn. 52, (2016). 4.Rave, W., Ramstöck, K., & Hubert, A. (1998). Corners and nucleation in micromagnetics. Journal of Magnetism and Magnetic Materials, 183(3), 329–333.

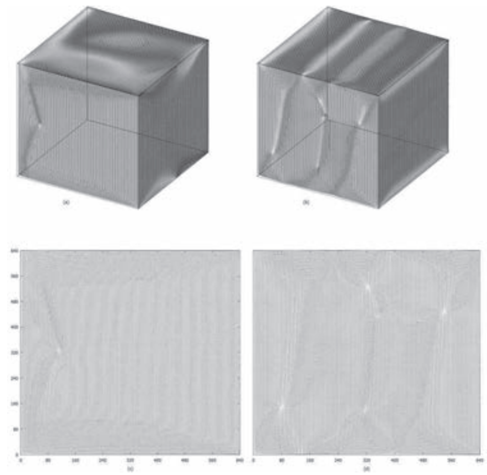

Fig. 1. The 3D domain structure of cubic magnet when initial *M* is set as up-down mode (a) and its x-z plane projection (c), as up-down-up-down mode (b) and x-z plane projection (d).

HT-12. Design and Optimization of Skyrmion-based Racetrack Memory by Overcoming Clogging and Annihilation of Skyrmion Signals.

G. Zhao[1]
1. Physics, Sichuan Normal University, Chengdu, China

Magnetic skyrmions are promising building blocks for next generation data storage due to their stability, small size and extremely low currents to drive them[1,2]. Skyrmion-based metalic racetrack memory has potention to replace traditional domain walls to store information as data bits, in which, however, skyrmions can drift from the direction of electron flow due to the Magnus force. In addition, skyrmion-edge effect at the end of the racetrack can cause the clogging of the skyrmions at the end of the racetrack[3]. Here we show that the clogging of skyrmion signals can be avoided by by adding various kinds of notch at the end of the racetrack [3]. On the other hand, by adding high-k materials (materials with high magnetic crystalline anisotropy) at the edges, the skyrmions can be confined in the center region of the metalic racetrack successfully[4,5]. This design can overcome the problems of both clogging and anniliation according to our micromagnetic simulation. As a result, skyrmions can pass the right end of the racetrack efficiently at a very high speed (100 to 300 m/s), whereas the driving current is much smaller in comparison with other racetrck design. This work is supported by Natural Science Foundation of China (51771127, 51571126, 51772004)

References: [1] A Fert, N Reyren, V Cros, Magnetic skyrmions: Advances in physics and potential applications, Nature Reviews Materials, 2, 17031, (2017) [2] Wiesendanger, Roland, Nanoscale magnetic skyrmions in metallic films and multilayers: a new twist for spintronic, Nature Reviews Materials, 1, 16044, (2016) [3] X.C. Zhang, G. P. Zhao, H. Fangohr, J. P. Liu, W. X. Xia, J. Xia, F.J. Morvan, Skyrmion-skyrmion and skyrmion-edge repulsions in skyrmion-based racetrack memory, Sci. Rep. 5, 7643, (2015) [4] N. Ran, G. P. Zhao, H. Tang, L. C. Shen, P. Lai, J. Xia, X. Zhang, Y.Zhou, Motion of Skyrmions in Well-Separated Two-Lane Racetracks, AIP Advances, 7 (2), 025105, (2017) [5] P. Lai, G. P. Zhao, H. Tang, N. Ran, S. Q. Wu, J. Xia, X. Zhang, Y.Zhou, An Improved Racetrack Structure for Transporting a Skyrmion, Sci. Rep. 7, 45330.. (2017)

FRIDAY AFTERNOON, 27 APRIL 2018 SIMPOR/ROSELLE BALLROOM, 1:30 TO 4:30

Session HU
PERMANENT MAGNET AND RELUCTANCE MACHINES VI
(Poster Session)

Ming Liu, Chair
Xi'an Jiaotong University, Xian, China

HU-01. 3D Structure Line Start Synchronous Reluctance Motor Design Based on Selective Laser Melting of 3D Printing.

P. Huang[2], *M. Tsai*[1] and I. Jiang[2]
1. Mechanical Engineering Department, National Cheng Kung University, Tainan, Taiwan; 2. Electrical Motor Technology Research Center, National Cheng Kung University, Tainan, Taiwan

I. Introduction Due to the features of high efficiency, high torque, and without using permanent magnets, the synchronous reluctance motors (SynRMs) have become popular in industry. Such advantages are contributed by the design of the rotor barriers and ribs that the flux flow path are arranged as shown in Fig. 1(a). However, the requirements of motors usually are not just high efficiency but some other more operation capabilities such as low vibration and easy start. Unfortunately, as compared with the industrial most commonly used induction motors (IMs), position sensors are additionally required for initiating starting of SynRMs [1][2]. Moreover, the barriers and ribs of SynRMs may increase the risk of structure deformation as rotation. Hence, this paper proposes a novel design of applying the 3D bionic structure in the SynRMs with new flux path design to solve the said problems. Further, the additive manufacturing (3D printing) is adopted to fabricate the complicated prototype of the rotor. II. Model and Experiment Results Figure 1 demonstrates the rotor of the 1 kW line-start SynRMs designed in this paper. A bionic web structure fabricated by 3D printing is distributed in the barriers of the rotor, as shown in Fig. 1(b). With these small ribs, the vibration problem can be solved due to the higher robustness. It is noted that such a structure enhancement would not increase flux leakage because the ribs are too small to allow the flux passing through. In Fig. 1(c), an improved cage structure based on aluminum paste technology is added in the rotor, which could downsize the volume of rotor as compared with IMs. Figure 1(d) shows the cages are capable to provide additional starting ability, and let SynRMs rotate from standstill to synchronous speed 1800 rpm without position sensor (i.e., line-start ability). As indicated in Fig. 2, 3D printing method, selective laser melting (SLM), is involved to selectively heat the powdered magnetic materials to the melting point in this paper. III. Conclusion In this paper, a new line-start SynRM rotor structure is proved and investigated. With the proposed designs of the web structure in the rotor and the improved cage structure, the SynRM rotor is equipped the capability of initiating starting without position sensors and also much lower deformation. A prototype based on 3D printing is fabricated to further verify the feasibility of the design.

[1] Z. Y. Zhang, K. J. Jhong, C. W. Cheng, P. W. Huang, M. C. Tsai and W. H. Lee, "Metal 3D printing of synchronous reluctance motor," 2016 IEEE International Conference on Industrial Technology (ICIT), Taipei, 2016, pp. 1125-1128. [2] Z. Y. Zhang, M. C. Tsai, P. W. Huang, C. W. Cheng and J. M. Huang, "Characteristic comparison of transversally laminated anisotropic synchronous reluctance motor fabrication based on 2D lamination and 3D printing," 2015 18th International Conference on Electrical Machines and Systems (ICEMS), Pattaya, Thailand, 2015, pp. 894-897.

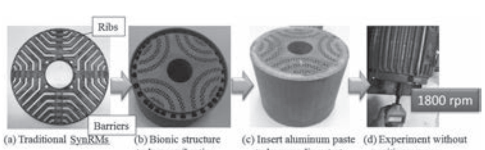

Fig. 1. Rotor prototype of 1 kW line-start SynRMs

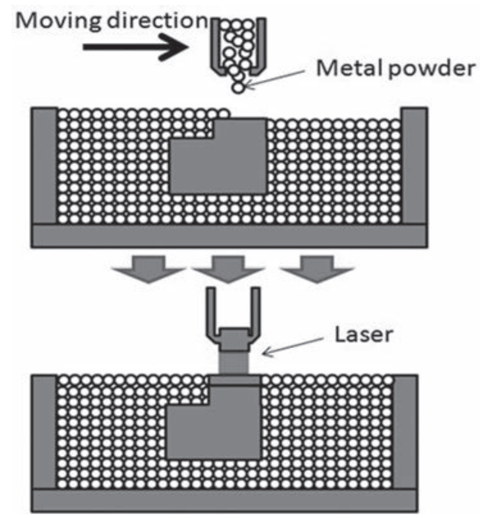

Fig. 2. Selective laser melting of 3D printing

HU-02. Quantitative Comparison of Interior Permanent Magnet Machines and Vernier Permanent Magnet Machines for Integrated Charging Applications.

W. Li[2], *T. Ching*[1], Q. Li[4], X. Zhang[3] and L. Zhang[4]
1. University of Macau, Taipa, Macao; 2. The University of Hong Kong, Hong Kong, Hong Kong; 3. Shenzhen In Drive Amperex Co. Ltd, Shenzhen, China; 4. Nanjing University of Science and Technology, Nanjing, China

I. Introduction Integrated charging applications are promising for reducing the components for both drives and charging in battery electric vehicles (BEVs) and plug-in hybrid electric vehicles (PHEVs) [1-4]. By reconfiguring the armature winding of propulsion machine in BEVs or PHEVs to be an AC side inductor for battery charging, the vehicle cost and weight are reduced and improve the on-board fast charging capability [5]. Owing to the high torque density, high power density and high efficiency, permanent-magnet brushless machines are favorable candidates as propulsion machines for BEVs or PHEVs. Notably, interior permanent magnet machines (IPMMs) are commercially used in Toyota Prius and other HEVs [6, 7], due to features of the high-torque density and wide constant power speed range; Vernier permanent magnet machines (VPMMs) are recently investigated and developed for direct-drive vehicle motors [8, 9]. By using the magnetic gearing effect, the modulated field in the air gap is utilized to realize the low-speed and high-torque operation. The purpose of this paper is to quantitative compare the performances of an IPMM and a VPMM as the traction motors for BEVs or PHEVs during integrated charging operation. In order to make a fair comparison, similar dimensions, torque densities and power densities of both machines are specially designed. In addition, the VPMM adopts a surface-mounted PM structure to study the influence of PM locations for the integrated charging. The pulsating torque characteristics, noise, loss and thermal analysis during charging operation are conducted and studied. Based on the comparison results, design suggestions for EV machines used in integrated charging are concluded. II. Analysis Fig. 1 depicts a circuit topology for integrated charging applications using 3 H-bridge inverters. It consists of a DC/DC converter, 3 H-bridge inverters and 3 terminals for connecting the AC grid [1]. The three-phase winding is adopted an open-winding connection without the neural point. 3 terminals for charging is connected in the middle of each phase. For driving operation, the 3 terminals are disconnected from the AC grid. The power is delivered from the battery to the 3-phase winding via the DC/DC converter and the 3 H-bridge inverters. For battery charging operation, the charging current from the AC grid in each phase is split into two identical but opposite component flowing into the battery via the inverters and DC/DC converter. Since the magnetomotive force (MMF) of each phase produced by the split phase current in each phase is cancelled off, the magnetic decoupling between the stator and rotor can be achieved. Hence, the parasitic torque during the charging operation is eliminated which is much desirable for PM machines because of the existence of the PM magnetic field. In order to numerically analyze the machine performances during the charging operation, the field-circuit-coupled finite element method (FCC-FEM) is applied. Since the charging current is variable accordingly to the state-of-charge (SOC) of the battery. Under different charging currents, the magnetic field strengths produced by the armature winding are different. Therefore, the machine performances under different charging currents are analyzed, as show in Fig. 2. Fig. 2(c) and (b) show the Magnetization vector plots for the IPMM and VPMM, respectively when the charging current is 50 A (rms). It can be found that for the IPMM the magnetization strength in PMs is negligible since PMs are buried in the rotor core, whereas for the VPMM the magnetization strength in PMs is large due to the surface-mounted configuration. Thus, PMs are easily demagnetized for the VPMM since PMs are part of the magnetic circuit for the armature MMF. Fig. 2(c) and (d) illustrates the pulsating torque waveforms for the IPMM and VPMM, respectively under different charging currents. It can be found that the average pulsating torque is nearly zero for both machines. However, for the VPMM, since the actual air-gap is larger than that of IPMM, the amplitudes of the pulsating torque is smaller. Also, due to the salient-pole effect, the pulsating torque for IPMM is not exactly symmetrical and the armature inductance is position dependent which may cause a larger charging current ripple. The pulsating torque modelling, PM demagnetization, noise, loss and thermal analysis will be discussed and elaborated in the full paper. This work was supported in part by a grant from the National Natural Science Foundation of China, China under Grant 51607114 and a grant from Research Council of University of Macau under Grant MYRG2017-00158-FST.

[1] L. Rubino, C. Capasso, and O. Veneri, "Review on plug-in electric vehicle charging architectures integrated with distributed energy sources for sustainable mobility," Applied Energy, vol. 207, pp. 438-464, Dec 1 2017. [2] C. Y. Lai, K. L. V. Iyer, K. Mukherjee, and N. C. Kar, "Analysis of electromagnetic torque and effective winding inductance in a surface-mounted PMSM during integrated battery charging operation," IEEE Transactions on Magnetics, vol. 51, Nov 2015. [3] Y. H. Hu, X. G. Song, W. P. Cao, and B. Ji, "New SR drive with integrated charging capacity for plug-in hybrid electric vehicles (PHEVs)," IEEE Transactions on Industrial Electronics, vol. 61, pp. 5722-5731, Oct 2014. [4] H. C. Chang and C. M. Liaw, "An integrated driving/charging switched reluctance motor drive using three-phase power module," IEEE Transactions on Industrial Electronics, vol. 58, pp. 1763-1775, May 2011. [5] I. Subotic, N. Bodo, and E. Levi, "An EV drive-train with integrated fast charging capability," IEEE Transactions on Power Electronics, vol. 31, pp. 1461-1471, Feb 2016. [6] M. O. Badawy, T. Husain, Y. Sozer, and J. A. De Abreu-Garcia, "Integrated control of an IPM motor drive and a novel hybrid energy storage system for electric vehicles," IEEE Transactions on Industry Applications, vol. 53, pp. 5810-5819, Nov-Dec 2017. [7] R. W. Cao, C. Mi, and M. Cheng, "Quantitative comparison of flux-switching permanent-magnet motors with interior permanent magnet motor for EV, HEV, and PHEV applications," IEEE Transactions on Magnetics, vol. 48, pp. 2374-2384, Aug 2012. [8] H. Yang, H. Y. Lin, Z. Q. Zhu, S. H. Fang, and Y. K. Huang, "Novel flux-regulatable dual-magnet vernier memory machines for electric vehicle propulsion," IEEE Transactions on Applied Superconductivity, vol. 24, Oct 2014. [9] G. H. Liu, J. Q. Yang, W. X. Zhao, J. H. Ji, Q. Chen, and W. S. Gong, "Design and analysis of a new fault-tolerant permanent-magnet vernier machine for electric vehicles," IEEE Transactions on Magnetics, vol. 48, pp. 4176-4179, Nov 2012.

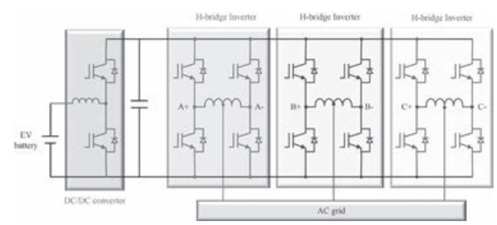

Fig. 1. The circuit topology for integrated charging applications using 3 H-bridge inverters.

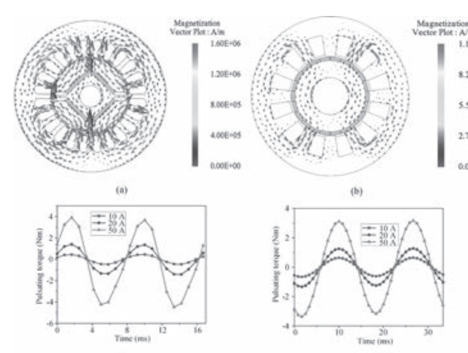

Fig. 2. Machine performance comparisons during the charging operation. (a) Magnetization vector plot for IPMM (Charging current 50 A). (b) Magnetization vector plot for VPMM (Charging current 50 A). (c) IPMM pulsating torque waveforms under different charging currents. (d) VPMM pulsating torque waveforms under different charging currents.

HU-03. Novel Dual-Stator Permanent-Magnet Vernier Machines with Various Magnet Arrangements for Large Telescope Application.

H. Wang[1,2], S. Fang[1], T. Jahns[2], *H. Yang*[1], K. Wang[1] and H. Lin[1]
1. School of Electrical Engineering, Southeast University, Nanjing, China; 2. Wisconsin Electric Machines and Power Electronics Consortium (WEMPEC), University of Wisconsin-Madison, Ma, WI, United States

I. Introduction The motional drive systems of large telescope have become larger and heavier which demands high torque production from the electric machines. Permanent magnet (PM) synchronous machines featuring high torque density are attractive candidates for this demanding application and have been successfully applied in drives for some well-known large telescopes such as Very Large Telescope and Gran Telescopio CANARIAS [1]. The torque production of conventional PM machines scales approximately linearly with the PM machine volume which limits PM machine applications in large telescopes. Alternative approaches to solving this problem are to either use a combination of high-speed machine and gearbox or to propose new topologies of PM machine with much higher torque density which are more attractive to use in direct-drive configurations than conventional PM machines. The PM vernier machine (PMVM) has been recognized as a competitive candidate to increase machine's torque density sufficiently to enable direct-drive solutions that eliminate mechanical transmissions and associated mechanical loss [2]. However, the PMVM typically suffers from large amounts of spatial magnetic flux leakage caused by the multi-tooth structure, causing higher losses and reduced torque that degrade the machine's performance considerably. In order to solve the problem, a dual-stator PMVM (DSPMVM) is proposed that can achieve high torque density compared to the conventional PMVM with the same volume of PM material [3]. Since the multi-tooth structure of DSPMVMs cause abundant harmonic components, a conventional open-slot stator with straight teeth has been adopted to provide modulating poles that adjust the airgap flux density while simplifying the machine structure [4]. In order to maximize the DSPMVM's torque density, various types of PM arrangements have been investigated, including spoke-type rotors and machine topologies with magnets placed on both the rotor and stator. The purpose of this paper is to propose novel dual-stator DSPMVM topologies featuring various magnet arrangements to provide excitations on both sides (either stator-stator or stator-rotor). The proposed DSPMVMs can be named using their distinctive features, namely, flux-reversal DSPMVM, dual-excitation DSPMVM, asymmetric stator DSPMVM, and consequent-pole DSPMVM, referred to more simply as Model I, II, III, IV, respectively. The topologies and operating principles of these DSPMVMs are described. The major electromagnetic performance characteristics of these topologies are investigated and compared. II. Machine Topology and Operating Principle The proposed DSPMVM topologies are illustrated in Fig. 1(a), where it can be observed that all of the machines adopt the same conventional configuration with open-slot stator teeth. All of models employ the same inner stator designed with 12 slots and a fractional-slot 10-pole three-phase winding that provides a high winding factor. Model I introduces flux-reversal machine concept into the DSPMVM by mounting adjacent magnets with reversed polarities at the tips of each outer and inner stator tooth to provide magnetic excitation. For Model II, the magnets are mounted at the tips of alternate iron poles for both stators as well as on both the inner and outer radial surfaces of each rotor pole to enhance the flux density in both airgaps. Model III uses the same inner stator and rotor configurations as in Model II, but removes the magnets form outer stator tooth tips. This modification changes the modulation pole number of the outer stator, forcing a change in the number of pole pairs for the outer stator and rotor. Model IV has the simplest structure of the four models, adopting the same inner and outer stators as Model II but without any magnets mounted on the rotor surfaces. The slot-pole combinations of all four models are presented in Table I. The teeth of both the inner and outer stators act as the modulation poles. Based on the "magnetic-gearing effect", the relationship of the numbers of modulation pole-pairs, and the rotor and stator pole-pairs of all of the DSPMVM topologies satisfy the following constraint: $p_r=N_s\pm p_s$ where N_s is the modulation pole-pair number, and p_r and p_s are the pole pair numbers of the rotor and stator, respectively [5]. III. Performance Comparison Fig. 1(b) shows the rated-load field and flux distributions calculated using 2D finite element analysis. For a fair comparison, the stator ampere-turns, stack length, and magnet volume are held constant. Figs. 2(a), 2(b), and 2(c) present comparisons of the electromotive force amplitude (i.e., back-EMF), cogging torque, and average torque waveforms, respectively, for the four topologies at 272.72 r/min. The results show that the magnetic flux density of Model II is the highest compared to the other models due to its magnetic excitation on both stators as well as both rotor radial surfaces. Fig. 2(a) shows that Model II has the highest back-EMF amplitude, but Model I produces the most sinusoidal back-EMF waveform. The cogging torque amplitudes of the four topologies are 0.48Nm, 1.32Nm, 0.76Nm, 1.77Nm, respectively, indicating that the Model I topology generates the lowest cogging torque amplitude because the least-common-multiple of its stator and rotor pole-pair number is the highest among the four topologies. Consistent with its high back-EMF, Model II delivers the highest average torque, 12.75Nm, which is 7.7% higher than that of Model I. However, the torque ripple of Model II is 10.84% higher than that of Model I.

References [1]J. J. Chang, W. L. Ma, and H. J. Long, "Design and optimization of arc permanent magnet synchronous motor used on large telescope," *IEEE Trans. Magn*., vol. 45, no. 5, pp. 1943-1947, May. 2012. [2]S. X. Niu, S. L. Ho, W. N. Fu and L. L. Wang, "Quantitative comparison of novel vernier machine magnet machines," *IEEE Trans. Magn*., vol. 46, no. 6, pp. 2032-2035, Jun. 2010. [3]Z. S. Du, T. A. Lipo, "An Improved Rotor Design for Dual-Stator Vernier Ferrite Permanent Magnet Machines," *in proc.* 2017 *IEEE International Electric Machines and Drives Conference (IEMDC)* MIA, LI, USA. Aug., 2017, pp. 1-8. [4]X. L. Li, K. T. Chau, and M. Cheng, "Comparative analysis and experimental verification of an effective permanent-magnet Vernier machine," *IEEE Trans. Magn*., vol. 51, no. 7, Jul. 2015, article no. 06907937. [5]H. Yang, H. Lin, Z. Q. Zhu, S. Fang, and Y. Huang, "A dual-consequent-pole Vernier memory machine," *Energies,* vol. 9, no. 3, pp. 4055–4064, Feb. 2016.

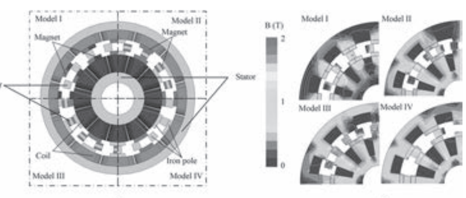

Fig. 1. Four DSPMVM topologies. (a) Cross-sectional geometries. (b) Rated-load magnetic flux distributions.

TABLE I
SLOT-POLE COMBINATIONS OF THE PROPOSED DSPMVMS

Items	Model I	Model II	Model III Inner stator	Model III Outer stator	Model IV
Stator pole number	10	10	2	10	10
Rotor pole number	34	22	22		22
Modulation pole number	24	12	24	12	12

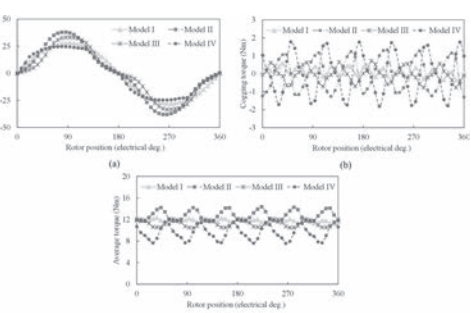

Fig. 2. Electromagnetic performance of DSPMVMs. (a) Back-EMF. (b) Cogging torque. (c) Average torque

HU-04. A New Double-Winding Vernier Permanent Magnet Wind Power Generator for Hybrid AC/DC Microgrid Application.

Q. Wang[1] and S. Niu[1]
1. Department of Electrical Engineering, The Hong Kong Polytechnic University, Hung Hom, Hong Kong

Abstract: This paper proposes a novel double-winding Vernier permanent magnet (DWVPM) wind power generator for hybrid AC/DC microgrid. The key is to employ two sets of windings, namely AC windings and DC windings in the machine, which serve to produce AC supply and DC supply for microgrid, respectively. The PMs are surface mounted on the rotor, and the stator is designed with open slots. The stator teeth can act as flux modulator due to the permeance difference between the stator teeth and the air. Therefore, the field by PMs can be effectively modulated. Besides the original harmonic used to induce sinusoidal back electromotive force (EMF) in the AC windings and generate AC voltage, another low-order harmonic can be generated, which is used to induce square wave EMF in the DC windings and generate DC voltage through diode-bridge rectifier. Since multi-phase windings can get the square wave EMF more easier, the DC windings are designed with six phases. By using time stepping finite element method (TS-FEM), the electromagnetic performances of the proposed DWVPM wind generator are comprehensively investigated and verified. *Index Terms*—AC/DC microgrid, double-winding, TS-FEM, Vernier machine. I. Introduction With the development of distributed generation systems, the concept of microgrid is becoming increasingly attractive, which has the potential to reduce energy exhaustion and carbon dioxide emissions [1-3]. When the power can be directly supplied by the local microgrid, there is no need to conduct long-distance high voltage transmission, and the energy utilization efficiency can be improved. Among all the renewable generation systems in microgrid, wind power is one of the most commonly used energy sources [4]. Since there are various loads exist in a microgrid, multiple reverse conversions using power electronics technology are necessary in an individual AC or DC microgrid, which reduce the power transmission efficiency and make the microgrid system complicated [5-7]. In this paper, a novel double-winding Vernier permanent magnet (DWVPM) wind power generator is proposed, which can generate AC power and DC power simultaneously therefore suitable for hybrid AC/DC power supply in microgrid. Both AC windings and DC windings are employed on the stator, which are used to generate AC power and DC power, respectively. The configuration, winding connection and design principle of the proposed generator are discussed in detail. Through time stepping finite element method (TS-FEM), the electromagnetic performances of the DWVPM wind generator are studied comprehensively. II. Machine Configuration and Design Principle A. Configuration of the Proposed DWVPM Machine Fig. 1(a) shows the configuration of the proposed machine, which has one rotor and one stator. The rotor is surface mounted with PMs, and the stator is designed with open slots. Since the permeance of the stator teeth and the air is different, the stator teeth can act as flux modulators. Besides the original harmonic excited by the PMs and used to generate sinusoidal EMF in the AC windings, another low-order harmonic can be generated, which is used to generate square wave EMF in the DC windings. The sinusoidal voltage produced in the AC windings is used to provide AC power, and the square wave voltage is used to provide DC power through rectification. The AC windings and DC windings are designed with three phases and six phases, as shown in Fig. 1(b) and Fig. 1(c) respectively. B. Design Principle The design principle of the proposed machine is based on the flux modulating effect. The original pole-pair number of PMs is equal to the pole-pair number of AC windings. The number of stator slots should equals to the sum of AC pole-pair number and DC pole-pair number. III. Performance Analysis In this paper, a machine prototype with 24 stator slots and 11 rotor pole-pairs is designed, the pole-pair numbers of the AC winding and DC winding are 11 and 13, respectively. The electromagnetic performances are investigated using TS-FEM. Fig. 2(a) and (b) show the air-gap flux density distribution and the harmonic spectrum. One can find that besides the original harmonic with 11 pole-pairs, another predominant harmonic with 13 pole-pairs is generated due to the flux modulating effect of the stator teeth. The 11 pole-pair harmonic is used to induce sinusoidal back EMF in the AC windings, and the 13 pole-pair harmonic is used to induce square wave back EMF in the DC windings, as shown in Fig. 2(c) and Fig. 2(d), respectively. One can see that sinusoidal EMF and square wave EMF can be effectively induced in the AC windings and DC windings, which means the proposed wind generator can generate AC power and DC power simultaneously. Therefore the proposed DWVPM wind generator is very suitable for hybrid AC/DC microgrid.

[1] N. Eghtedarpour and E. Farjah, "Power Control and Management in a Hybrid AC/DC Microgrid," *IEEE Transactions on Smart Grid,* vol. 5, pp. 1494-1505, 2014. [2] X. Liu, P. Wang, and P. C. Loh, "A Hybrid AC/DC Microgrid and Its Coordination Control," *IEEE Transactions on Smart Grid,* vol. 2, pp. 278-286, 2011. [3] P. Wang, C. Jin, D. Zhu, Y. Tang, P. C. Loh, and F. H. Choo, "Distributed Control for Autonomous Operation of a Three-Port AC/DC/DS Hybrid Microgrid," *IEEE Transactions on Industrial Electronics,* vol. 62, pp. 1279-1290, 2015. [4] K. W. Hu and C. M. Liaw, "Development of a Wind Interior Permanent-Magnet Synchronous Generator-Based Microgrid and Its Operation Control," *IEEE Transactions on Power Electronics,* vol. 30, pp. 4973-4985, 2015. [5] F. Bu, L. Zhu, W. Huang, H. Xu, H. Liu, and Y. Gao, "Control strategy of AC&DC hybrid generating system based on dual stator-winding induction generator for micro-grid application," in *2016 IEEE Transportation Electrification Conference and Expo, Asia-Pacific (ITEC Asia-Pacific)*, 2016, pp. 013-017. [6] C. Wang, X. Yang, Z. Wu, Y. Che, L. Guo, S. Zhang, *et al.*, "A Highly Integrated and Reconfigurable Microgrid Testbed with Hybrid Distributed Energy Sources," *IEEE Transactions on Smart Grid,* vol. 7, pp. 451-459, 2016. [7] H. Xiao, A. Luo, Z. Shuai, G. Jin, and Y. Huang, "An Improved Control Method for Multiple Bidirectional Power Converters in Hybrid AC/DC Microgrid," *IEEE Transactions on Smart Grid,* vol. 7, pp. 340-347, 2016.

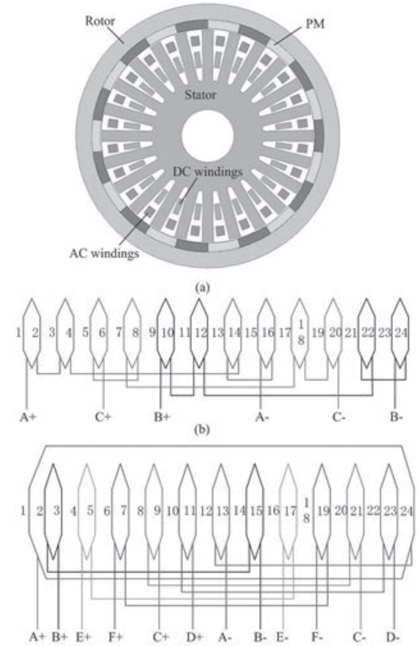

Fig. 1.Configuration and winding connections of the proposed machine. (a) Configuration. (b) AC winding distribution. (c) DC winding distribution.

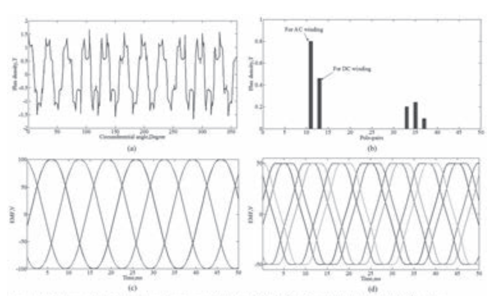

Fig. 2. (a) Flux density distribution. (b) Harmonic spectrum. (c) No load back EMF of AC windings. (d) No load back EMF of DC windings.

HU-05. Ring-shaped surface-mounted permanent magnet generators with modular stator for small wind turbines – a comparison of topologies.

J.A. Oliveira[1,2], A.F. Flores Filho[1] and *D.G. Dorrell*[3]
1. Universidade Federal do Rio Grande do Sul, Porto Alegre, Brazil; 2. Universidade Federal de Mato Grosso, Rondonopolis, Brazil; 3. Howard College Campus, University of KwaZulu-Natal, Durban, South Africa

Introduction The work compares the volume, copper and iron losses of three topologies of modular surface-mounted permanent magnet synchronous generator (SPMSG) for a small wind turbine. They would be connected to the grid by a ac-dc-ac converter. The modular construction reduces the manufacturing complexity since the generator has a ring shape and is installed around the turbine. The use of rare earth (NdFeB) and ferrite permanent magnets is assessed by considering the armature modules. The proposed topologies are evaluated with reference to the permanent magnet type and pole number in order to identify the arrangement that produces the lowest loss. Results show the use of ferrite permanent magnetics can achieve that. Wind turbines in urban areas are submitted to low speed and turbulent wind and that requires larger diameter turbines and direct drive – this means many magnetic poles are required. To increase the energy throughput of the topologies studied here, the SPMSG is designed for use in a wind turbine diffuser [1] that can raise the turbine output power. The rotor of the SPMSG is mounted around the blades of the turbine in a ring form [2]. The SPMSG rating is 1 kW. The inner rotor radius is the same as the turbine, i.e. 765 mm. The rectified output voltage is 30 V at 135 rpm. These parameters were obtained based on the design of the turbine and its operation conditions. The converter is suitable for grid connection. The modular stator simplifies the manufacturing of larger diameter machines with no diffuser [3][4], and this concept is extended to small turbines here. The modules are shown in Fig. 1. Each one is different in terms of winding and copper volume. The air-gap and its magnetic flux density are constant. Since the rotor is a large diameter ring, it is desirable to reduce its weight. Also, the pole number, the rate of change of stator flux linkage and iron losses all increase with the turbine diameter. By considering the magnetic circuit, the radial length of the rotor back-iron, module slots and yoke, permanent magnets, and copper volume are determined for an armature with an axial length of 20 mm. Using the volume and characteristics of the copper and laminated iron, the losses are estimated for the three modules employing either ferrite or NdFeB permanent magnets. Analysis The dimensions of the SPMSG are calculated using the magnetic equivalent circuit with reference to the air-gap dimensions and current density described in [5], and in this case the references values are 2 mm and 2 A/mm^2, respectively. The magnet volume is calculated to achieve the maximum energy product operating point of the permanent magnets in order to reduce the rotor weight. The number of turns in each module is determined by the minimum voltage required by the converter that corresponds to the minimum operation speed. The radial length of the back iron rotor is calculated considering the point of maximum permeability of the iron and the flux density of the permanent magnets. The design of the modules considers the high pole number, which increases the losses in the laminated stator iron, so that the operating point of the stator iron is set to a lower figure than the maximum flux density to decrease these losses. The laminated stator iron magnetic characterization was done for different frequencies to allow for a range of turbine speeds. Results The permanent magnet dimensions give the maximum energy product operating point and the magnet flux density is almost constant, so that the back-iron radial length is a function of pole pitch. Fig. 2a shows that the back-iron weight decreases as the pole number increases since the per-pole magnetic flux is proportional to the size of the permanent magnet. The NdFeB volume is lower than the ferrite volume since the energy product of the former is higher. It is harder to manufacture NdFeB magnets if they become too thin, e.g. below 0.5 mm. The rotor weight calculations show that a high pole number configuration is the most appropriate choice. However, Fig. 2b shows that the pole number reduction decreases the total stator iron losses because the flux frequency also decreases. Besides, Fig. 2b shows the copper losses are much smaller than stator iron losses. These results refer to the starting speed of the turbine for Module 3. The behaviour of the stator iron losses and copper losses of the other two modules are similar to the Module 3, but for Module 1 copper losses are larger than for Modules 2 and 3 because more turns are required in order to compensate for the lower magnet flux linkage. NdFeB magnets lead to lower copper losses because the higher energy product reduces the required copper volume. However, this increases the stator iron volume and iron losses. Conclusions The results show that high pole number increases the losses in the stator iron. The results also indicate that copper losses are much lower than the losses in stator iron due to the low power of the wind turbine and high pole numbers that increase the frequencies of the stator flux linkage. NdFeB magnets gives lower copper losses, but the stator losses are larger and rotor weight are increased making it difficult the start the turbine. Modules 2 and 3 with ferrite magnets are lighter and have lower stator iron losses compared with NdFeB magnets.

[1] Y. Ohya, T. Karasudani. "A shrouded wind turbine generating high output power with wind-lens technology". Energies, no. 3, pp. 634-649, March 2010. [2] V. Verdum *et al.*, "Ironless machine design for wind-based micro generation". IEEE Transactions on Magnetics, Vol. 53, no. 11, November 2017. [3] E. Spooner, A.C. Williamson and G. Catto, "Modular design of permanent magnet generators for wind turbines", *IEE Proc.-Electr. Power Appl.,* vol. 143, no. 5, pp. 388-395, September. 1996. [4] C. Ditmanson *et al.*, "A new modular flux-switching permanent-magnet drive for large wind turbines", *IEEE Trans. Ind. Appl.*, vol. 50, no. 6, pp. 3787-3794, Nov./Dez. 2014. [5] J. Pyrhönen, T. Jokinen and V. Hrabovcová, *Design of Rotating Electrical Machines*. New York: John Wiley Sons, 2008.

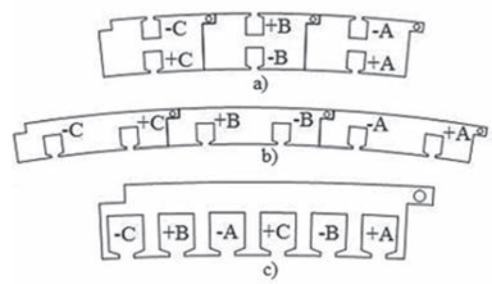

Fig. 1. – a) module 1, b) module 2 and c) module 3.

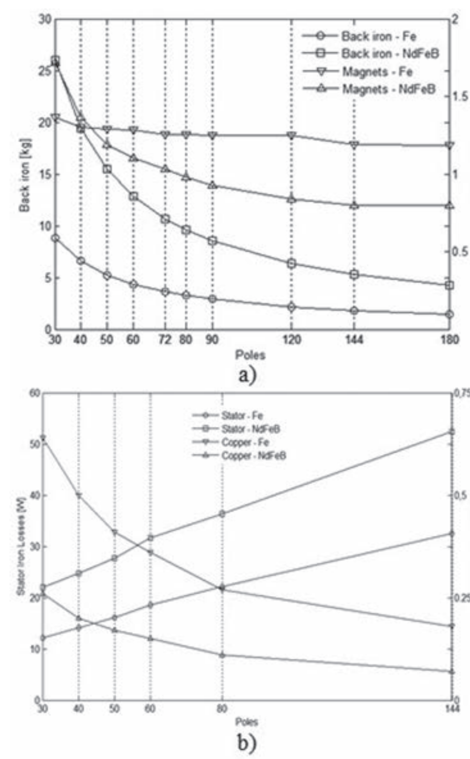

Fig. 2. – a) Weight of back iron rotor and magnets; b) Copper and stator iron losses of module 3 at 135 RPM.

HU-06. A novel doubly fed wind energy power split system with partial-scale converter and control strategy.

X. Liu[1], M. Li[1] and *S. Huang*[1]
1. Electrical and Information Engineering College, Hunan University, Changsha, China

1.Introduction normally, renewable energy resource is clean, inexhaustible, low maintenance and running costs. Wind energy is considered as an option to solve the environmental issues, due to it is widespread throughout the world. Until now, single rotor wind power generator is widely used in practice. The DFIG system and direct-drive synchronous generator (DDSG) system are currently the mainstream machine for wind turbine [1]. The main merit of the DFIG system is in no need of PM material and only need about 30% converter capacity, hence the whole system is lower cost. However, the additional gearbox, the slip ring and brushes inevitably lead to maintenance problems and low reliability. To the opposite, the DDSG system is famous for high efficiency, low mechanical loss and low maintenance cost. The gearbox can be canceled in high number of poles of PMSG. But, the DDSG system has to be equipped with correspondingly full-scale converter [2]. The existing low speed high torque direct-drive machine is bulky size and large material consumption. To overcome above problems, magnetic gear is introduced into the wind generator as the power split [3]. In [3], the wind turbine system was based on planetary gearbox, which power split to a synchronous generator and a servo PMSM. The system structure and control strategy are complex compared to traditional system. In addition, planetary gearbox is a mechanical device which has inevitable mechanical problems such as frictional loss, high maintenance and audible noise. A novel brushless doubly fed power split system is proposed to substitute for the planetary gearbox in this paper. The extracted wind energy is divided into two parts by the magnetic-field-modulated blushless double rotors machine (MFM-BDRM). The major part of the power directly flows to the power grid through the generator. A small proportion power of the rest is delivered to the back-back converter. For a given wind speed, a MPPT (maximum power point tracking) control strategy is designed to extract the maximum wind energy by controlling the converter. This system has high torque density, high-reliability and low-cost characteristic. 2.System configuration and working principle A. BDF-PST system The proposed BDF-PST system is shown in Fig. 1. The main components of the wind turbine consist of a wind blade, a one-level gearbox, a MFM-BDRM machine, a syngenerator and a back-back converter. The most important part is MFM-BDRM machine, which makes the wind energy flow to the generator or the converter. As we can see, the outer rotor is connected to the wind blade by a gearbox, which the variable speed range of power generation is about 900 rmp to 1500 rmp. Besides, the power grid is directly linked with the syngenerator which is driven by the inner rotor. The converter is the core unit that controls the whole wind turbine, it takes the 20% proportion of the machine capacity. At the same time, a MPPT control strategy is designed for the BDF-PTS system. It ensures the maximum limit utilization rate of wind energy. B. Machine structure and working principle The MFM-BDRM machine consists of one stator and two rotors in [4]. The structure of the machine is shown in Fig. 1(a). The outer rotor is composed of the 21 pieces of modulating ring. The inner rotor has the pole pair of 17 PMs and the stator windings with the pole pair of 4. Assuming the pole-pair number of the stator winding and PM rotor are p and n, The number of the magnetic blocks is q. The relation of the electromagnetic torque of stator (Ts), modulating ring rotor (Tm), and PM rotor (TPM) is proportional of the pole pair. 4.Control strategy and FEM results analysis The BDF-PST system control strategy based on the MPPT is shown in Fig. 2. Using a converter change the windings current frequency and amplitude, the outer rotor speed follows the change of wind speed, the generator will operate at constant speed. Two encoders are installed to observe the inner and outer rotors' position and speed. For the given wind speed, the maximum performance coefficient will select the pitch angle from the look-up table to get the maximum power reference. First, the generator operates the rated speed. Then, closing the grid connection switch, the control strategy turns to a three closed-loop based on the field oriented control (FOC) to acquire the output power from the windings. In the FEM analysis, the amplitude of the back-EMFs at 1500 rmp is 25V and the harmonic spectra is 2.38%. The ripple in back-EMF is mainly because the slot effect. At the rated situation, the speed of the outer rotor and the inner rotor is 1500 r/min, the frequency of syngenerator in the windings is 50 Hz, which is same to the power grid. At the same time, the relationship of the rotors torque and the windings current, power factor, machine efficiency is studied in different operation speed.

1.Zhe Chen, Josep M.Guerrero, Frede Blaabjerg, "State of the Art of Power Electronics for Wind Turbines," IEEE Trans. Power. Electric., vol. 24, no. 8, pp. 1859-1875, Aug, 2009. 2. James Carroll, Alasdair McDonald, and David McMillan, "Reliability Comparision of Wind Turbines With DFIG and PMG Drive Trains," IEEE Trans. Energy. Convers., vol. 30, no. 2, pp. 663-670, Jun, 2015. 3.Qian Liu, Rüdiger Appunn, and Kay Hameyer, "Wind Turbine with Mechanical Power Split Transmission to Reduce the Power Electronic Device: an Experimental Validation," IEEE Trans. Ind. Electron., vol. 59, pp. 2791-2799, Jul.2012 4.J. Bai, P. Zheng, C. Tong, Z. Song, Q. Zhao, "Characteristic Analysis and Verification of the Magnetic-Field-Modulated Brushless Double-Rotor Machine," IEEE Trans. Ind. Electric., vol. 62, no. 6, pp. 4023-4033, Jul, 2015.

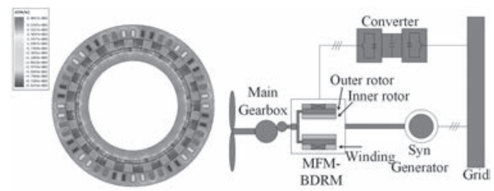

Fig. 1. The MFM-BDRM and the novel wind power generation system

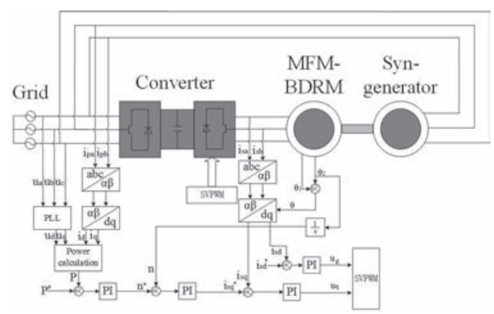

Fig. 2. The MPPT control strategy

HU-07. Partitioned Stator Hybrid Excitation Machine with Separated Field Sources and Armature Winding.

Y. Du[1], W. Lu[1], X. Zhu[1], F. Xiao[1] and L. Quan[1]
1. Jiangsu University, Zhenjiang, China

I. INTRODUCTION Hybrid excitation (HE) machines possess outstanding flux regulation capability whilst maintain the merits of PM machines due to the adoption of two excitation sources of permanent magnets (PMs) and wound field (WF) windings simultaneously [1]. In order to achieve the blushless structure, several single stator-HE (SSHE) machines have been proposed based on stator PM machines, such as HE switching flux (HESF) machines and HE doubly salient (HEDS) machines. Nevertheless, the existing SSHE machines suffer from the space conflict among field sources, namely PMs, WF windings and armature windings are all located in the sole stator with limited space, thus leading to a difficulty to take account of both satisfactory flux regulation capability and high torque density. Recently, the concept of partitioned stator (PS) machine has been proposed, in which an outer stator and an inner stator were employed to accommodate armature windings and field sources, respectively, and a rotor with small volume was sandwiched between the two stators [2]. Consequently, the space conflict in SSHE machines can be effectively avoided by employing the PS configuration. More coppers and PMs can be located within the same machine volume due to the sufficient utilization of inner space, and thus, leading to increased torque density and improved flux regulation capability. In this paper, two sub-structures of a new PSHE machine are proposed according to the different pole center lines (PCLs) positions of PM magnetic fields, namely the PS-HEDS structure and the PS-HESF structure. II. STRUCTURES AND OPERATION PRINCIPLE As shown in Fig. 1, the proposed machines are composed of an outer stator and an inner stator with tooth-slot structure, between which a rotor consists of segmented iron pieces is sandwiched. Thus, armature windings and field windings can be placed in the slots of outer stator and inner stator, respectively, which permits the increased electric load and PM volume to improve its power density and flux regulation capability. Moreover, tangentially magnetized NdFeB-PMs with alternatively opposite directions are embedded between the tooth tips of T-shaped inner stator core. By rotating the inner stator over 1/2 pole pitch, two sub-structures can be obtained, as shown in Fig.1(a) and (b), in which the PCLs positions of PM magnetic fields are in line with that of stator teeth and that of stator slots, respectively. In order to describe the operating principle, equivalent magnetic circuit models at the rotor position of peak flux linkage are shown in Fig.1 (c) and (d). It can be found that the magnetic circuits of two machines are very similar. There are two opposite parallel branches of PM magnetic field due to the adoption of T-shaped inner stator structure, and both of them are magnetically parallel to the WF field, thus the irreversible demagnetization risk can be effectively avoided and the resultant flux can be regulated flexibly. III. RESULTS According to the static and transient simulation results, electromagnetic performances of these two machines are analyzed and compared. In Fig.2 (a) and (b), open-circuit flux linkages in coil A1 and A4 are illustrated. It can be observed that the flux linkages in A1 and A4 are both unipolar while the flux linkages of coil A1+A4 are bipolar for PS-HEDS machine. On the other hand, the flux linkages in Fig. 2(b) are both bipolar for PS-HESF machine. Meanwhile, due to the compensation of even order harmonics, flux linkage waveform of coil A1+A4 are sinusoidal though flux linkage waveforms of coil A1 and A4 are nonsinusoidal, which is similar with switching-flux PM machines. In Fig.2(c), efficiency waveforms with different field current are depicted. It can be seen that the highest efficiency points do not occur when the machines are excited by only PMs. Thus, the rated operation points of two machines are defined when field current I=1A to obtain the highest efficiency. Fig. 2 (d) shows the simplified equivalent magnetic circuit of proposed two machines to estimate the thickness of the inner stator yoke preliminarily theoretically, which contributes dramatic influence upon the electromagnetic performances and will be presented in full paper. In Fig.2 (e) and (f), the waveforms of output torque and the flux regulation capability of two machines at different excitations are illustrated, namely with PM only and with excited current I=1A. It can be observed that the output torque of both machines are improved at the rated condition due to the flux-enhancing current and flux-weakening capability are both increased to achieve a wider constant power range because of the novel defined rated operation point. The analysis and more electromagnetic performances will be presented in full paper.

[1] F. Capponi, G. Borocci, G. Donato, and F. Caricchi, "Flux regulation strategies for hybrid excitation synchronous machines," *IEEE Trans. Ind. Appl.*, vol. 51, no. 5, pp. 3838–3847, Sep./Oct. 2015. [2] D. J. Evans and Z. Q. Zhu, "Novel Partitioned Stator Switched Flux Permanent Magnet Machines," *IEEE Trans. Magn.,* vol. 51, no. 1, pp. 8100114, Jan. 2015.

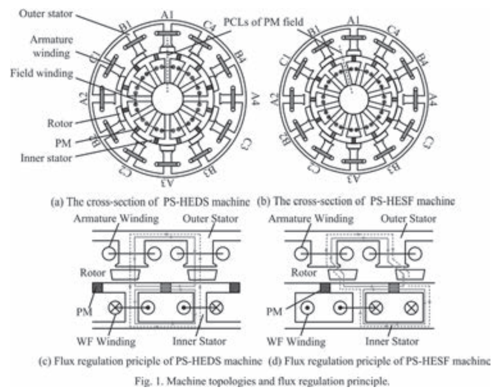

Fig. 1. Machine topologies and flux regulation principle.

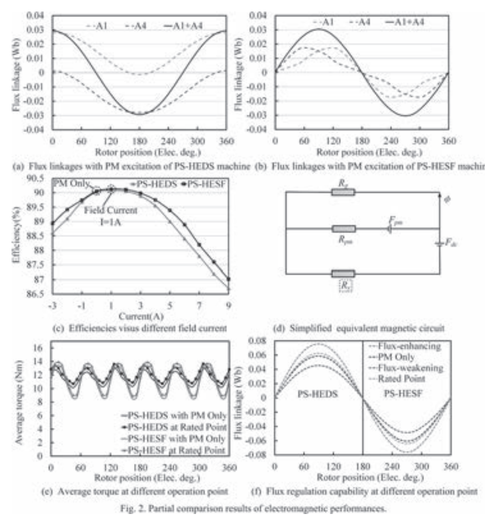

Fig. 2. Partial comparison results of electromagnetic performances.

HU-08. Low-Loss Design and Analysis of Magnetic-Field Modulated Brushless Double-Rotor Machine.

J. Bai[1], J. Liu[1], *P. Zheng*[1] and Y. Liu[1]
1. Harbin Institute of Technology, Harbin, China

Owing to the elimination of brushes and slip rings, magnetic-field modulated brushless double-rotor machine (MFM-BDRM) can be a promising candidate for the electrical-continuously variable transmission in hybrid electric vehicles [1]. The MFM-BDRM is composed of stator, MFM rotor and permanent-magnet (PM) rotor, as shown in Fig. 1(a). In traditional MFM-BDRM, however, the problem of large PM loss and stator core loss, caused by its MFM rotor with alternate arrangement of fan-shape magnetic and nonmagnetic blocks, severely restricts the electromagnetic performance of MFM-BDRM. Therefore, a low-loss MFM-BDRM with the sinusoidal permeance characteristic of MFM rotor is proposed and investigated in this paper, as shown in Fig. 1(b). Since fan-shape magnetic and nonmagnetic blocks cause many harmonic permeances in the air gap and further produce large harmonic loss in the PMs and stator core, the ideal sinusoidal permeance model of MFM rotor is first established and investigated by analytical method. It shows that almost all harmonic permeances can be dramatically weakened by the proper design of the shape and size of magnetic and nonmagnetic blocks. The key idea of this paper is to minimize the harmonic permeance of air gap, thereby the harmonic magnetic fields can be restrained. Considering that Tangential leakage flux among magnetic blocks in the analytical method is difficult to be calculated accurately, the influence of key parameters of proposed MFM rotor, like eccentric distance and pole-arc coefficient of magnetic block, minimum length of inner and outer air gap, on the electromagnetic performance of MFM-BDRM is further investigated and optimized by finite element mothed. Finally, to completely evaluate the performance of the proposed MFM-BDRM, a traditional MFM-BDRM with the same size is designed to compare their performances under different operating conditions, like back EMF, output torque, torque ripple, loss, etc. Due to the space limit, the abstract only shows that the electromagnetic performance comparison between traditional MFM-BDRM and proposed MFM-BDRM when the speeds of MFM rotor and PM rotor are 2000 r/min and 1000 r/min and the same current excitation is applied, as listed in Table I. It shows that the proposed MFM-BDRM can have almost the same torque and power output capacity as the traditional one, and the PM loss and stator core loss are reduced by more 55% and 28% than those of the traditional one under no-load condition, and that are reduced by more 34% and 8% than those of the traditional one under load condition.

Ping Zheng, Jingang Bai, Chengde Tong, etc. "Investigation of a Novel Radial Magnetic-Field-Modulated Brushless Double-Rotor Machine Used for HEVs," *IEEE Trans. Magnetics*, vol. 49, no. 3, pp. 1231–1241, Mar. 2013.

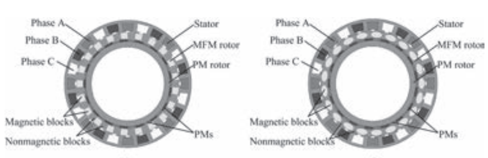

Fig. 1. Structures of MFM-BDRM: (a) Traditional MFM rotor; (b) Proposed MFM rotor

Parameters	Traditional MFM-BDRM	Proposed MFM-BDRM
Outer diameter of the stator	226 mm	226 mm
Axial length	70 mm	70 mm
Pole-pair number of the PM rotor	17	17
Pole-pair number of the stator	4	4
Number of magnetic blocks	21	21
Number of slots	24	24
Amplitude of no-load EMF	110.6 V	109 V
THD of no-load EMF	3.7%	2%
Amplitude of full-load EMF	168.1 V	155 V
THD of full-load EMF	1.9%	1.5%
Torque of MFM rotor	52.4 N·m	51.3 N·m
Torque ripple of MFM rotor	1.7%	1.2%
Torque of the PM rotor	42.2 N·m	41.1 N·m
Torque ripple of PM rotor	1.4%	1.3%
Power factor	0.66	0.7
Stator of no-load core loss	27.9 W	20 W
Magnetic blocks of no-load core loss	13.1 W	9.2 W
PMs of no-load loss	41.4 W	18.5 W
PM rotor of no-load core loss	0.5 W	0.3 W
Stator load core loss	79.6 W	73.3 W
Magnetic blocks of load core loss	16.6 W	12.1 W
PMs of load loss	91.3 W	59.7 W
PM rotor of load core loss	1.8 W	1.6 W
Copper loss	287.5 W	287.5 W
Efficiency	92.7%	93.3%

Table I. Parameter and Performance Comparison between Traditional MFM-BDRM and Proposed MFM-BDRM

HU-09. Development of a New Stator Module Type Vernier Motor utilizing Amorphous Cut Core.

H. Nakagawa[1], T. Sato[1] and T. Todaka[1]
1. Oita Univ., Oita, Japan

This paper presents a new stator module type vernier motor, which is applicable amorphous magnetic material effectively as a stator core material. The iron loss distribution in the stator module structure made of a Fe-based amorphous material is numerically investigated with the finite element method and compared with those made of oriented electrical steel sheets and non-oriented electrical steel sheets in the laminated core pattern. The results show that the proposed model is useful to improve significantly efficiency of the vernier motor model. Recently, industrial demands are increasing for electric machines with high torque density and high efficiency. Mechanical gears are usually used in order to realize high torque and low speed rotation as a speed reducer in a robot, an electric vehicle, an elevator and so on. However, the mechanical gears have difficulty in high precision control due to backlash and friction. Furthermore, there are mechanical contacts between gear teeth, so that maintenance is necessary. In order to solve these problems, vernier motors that utilize the magnetic gearing effects are getting attention due to their high torque capability and small pulsating torque. The vernier motor is a motor that obtains rotational force through the magnetic flux harmonic component modulated by the geometries of the stator cores. The magnetic flux harmonic component is proportional to the pole number of the rotor magnet and the modulated magnetic field generates the output torque on the rotor. Thus, in the vernier motors, it is important to analyze and design the armature magnetic field and the structure of the stator and rotor cores. The various kinds of vernier motor are still in the research stage, further improvement in efficiency and power factor is required for commercialization and mass production. In order to improve efficiency of the vernier motors, we try to apply the Fe-based amorphous magnetic material to the stator module. The Fe-based amorphous magnetic material has high permeability and low loss, and is extremely excellent as a core material. However, the amorphous magnetic material is difficult to process in the conventional laminated core structure. The proposed stator module type vernier motor is possible to use U-shaped amorphous cut cores annealed in a magnetic field. Thus this model has the following three advantages: the amorphous wound cores are applicable; the harmonic component of the magnetic flux increases in the divided core structure and it leads to improve the torque characteristic; the deterioration of the magnetic properties of the amorphous magnetic material after processing can be prevented by the magnetic annealing. Fig.1 shows the model used in the analysis and its specifications. Because the fifth harmonic is used in the proposed vernier motor model, the number of the pole pairs of the rotor magnets is assumed to be 5. The analyses were conducted under the same conditions, and the stator core material was assumed to be the amorphous magnetic material (2605HB1M), the non-oriented electrical steel sheet (50H470), and the oriented electrical steel sheet (23JG120). Fig. 2 shows comparison of the output power, the iron loss, the copper loss and the efficiency of the each model when the load angle is 90 degrees. As shown in this figure, it is evident that the iron loss is the smallest and the efficiency is the largest in the model utilizing the amorphous magnetic material. Details of the stator module construction and its frequency dependency will be discussed at the presentation and in the full version of paper.

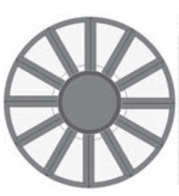

Specifications

Number of poles	10		
Number of slots	12		
Air gap [mm]	1		
Number of turns of coil [turns/phase]	264		
Core thickness [mm]	100		
Winding resistance [Ω]	4.75		
Frequency [Hz]	50		
Revolution speed [rpm]	600		
Material of Magnet	Ferrite		
Residual magnetization of the magnet[T]	0.4		
Magnet thickness [mm]	3		
Current [A]	3.0		
Rotor material	50H470		
Stator material	50H470	23JG120	2605HB1M

Fig.1 Model used in the analysis and specifications

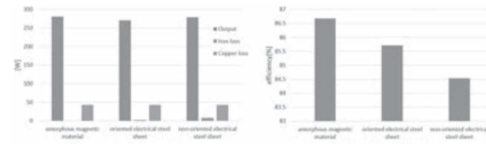

(A) Comparison of outputs and losses (B) Comparison of efficiencys

Fig.2 Comparison of the output power, the iron loss, the copper loss, and the efficiency of the each model.

HU-10. Optimal Arrangement of Permanent Magnets in a Dual-permanent-magnet-excited Synchronous Motor.

Y. Chen[1] and *W. Fu*[1]
1. Department of Electrical Engineering, The Hong Kong Polytechnic University, Hong Kong, Hong Kong

I. Introduction Permanent magnet (PM) electric machines have wide applications as they can realize large electromagnetic torque transmission without extra external excitation [1]. Most conventional PM synchronous motor have surface-mounted PM arrangement with N pole - S pole - N pole - S pole ... on the rotors. Magnetic gear (MG) can be directly combined with a conventional PM motor which will improve the system torque density significantly. However, it has the disadvantage of requiring two rotating parts and complicated mechanical structure [2]. In [3], a novel magnetic gear motor is presented in which MG is integrated into a conventional outer-rotor PM brushless motor. And it has only one rotary part. It can be called flux-modulated motor. In [4], a dual-PM-excited (DPME) synchronous motor was presented which is designed with PMs on both stator and rotor. The PMs in each slot have the same magnetization polarity. The PMs on the stator facing the air gap side are N poles and the PMs on the rotor facing the air gap side are S poles in consequent-pole-type PM arrangement. In this configuration two set of flux-modulated motor can be realized and the torque density can be improved significantly. In this paper, an optimal PM arrangement in a DPME synchronous motor is proposed which leads the motor has more competitive torque capability and efficiency compared to the conventional counterparts. The sizes of the PM configuration are determined by optimization algorithm. The performances of DPME synchronous motors with different PM arrangements are quantitative compared. II. Proposed Configurations A DPME synchronous motor with conventional PM arrangement (as Model I) is shown in Fig. 1 (a). The stator has 30 slots which carry one set of p_w pole-pair three-phase armature winding. The rotor has 32 salient PM pole-pairs with simple consequent-pole type arrangement of N pole - Fe - N pole - Fe …, as shown in Fig. 2 (a). There are four main parameters of the conventional PM arrangement. A Halback array magnet arrangement is attracted importance since it offers a number of attractive features. This arrangement can transmit a relatively high torque density whose magnet material is fully utilized and it is very appropriate for slotless and brushless machines [5-7]. In this paper, a simplified consequent-pole Halback array type PM arrangement is proposed to replace the consequent-pole type one. A DPME synchronous motor with simplified consequent-pole Halback array type PM arrangement inserted on the rotor (as Model II) is shown in Fig. 1 (b). There are six main parameters of the simplified consequent-pole Halback array type PM arrangement, as shown in Fig. 2 (b). As the spoke type PM arrangement of N pole - Fe - S pole - Fe - N pole - Fe … which has the function of flux focusing can achieve high torque density and less centrifugal forces [8], the consequent-pole PMs in the stator slots can also be replaced by spoke type PMs. Then a new motor configuration (as Model III) can be achieved, as shown in Fig. 1 (c). There are six main parameters of the spoke type PM arrangement, as shown in Fig. 2 (c). III. Optimization In this paper, a multi-objective optimization algorithm is employed to find the optimal sizes of PM arrangement. The objective function in this case is the output torque and the efficiency of the motor. The rotor is rotated at a constant speed and the transient numerical solution is applied. The optimization process is shown in Fig. 3. The simulation is done through the coupling of finite-element motor model and optimization procedure. IV. Performance Comparison The three styles of motor configurations are optimized using a multi-objective optimization algorithm and their magnetic fields are analyzed using time-stepping finite element method (FEM). The electromagnetic torque, torque per volume, torque per PM volume, copper loss regarding winding, core loss, solid loss and corresponding power efficiency of DPME synchronous motors with different PM arrangements are listed in Table I. From Table I, one can find that Model II has 40% higher electromagnetic torque than Model I and Model III has 5.9% higher electromagnetic torque than Model II. The DPME synchronous motor with the optimal PM arrangement has the highest torque and torque per total volume in the three designs. But its torque per PM volume is the lowest. The torque per PM volume of Model II is the highest. The DPME synchronous motor with the optimal PM arrangement has 3.2% higher efficiency compared with the motor with conventional PM arrangement while the total loss of the three motor types are nearly equality.

[1] S. L. Ho, S. Niu, and W. N. Fu, "Transient analysis of a magnetic gear integrated brushless permanent magnet machine using circuit-field-motion coupled time-stepping finite element method, " *IEEE Trans. Magn.*, vol. 46, no. 6, pp: 2074-2077, 2010. [2] Jian Linni, K. T. Chau and J. Z. Jiang, "A magnetic-geared outer-rotor permanent-magnet brushless machine for wind power generation," *IEEE Trans. Industry Applications*, vol. 45, no. 3, pp. 954-962, May-June 2009. [3] L. L. Wang, J. X. Shen, Y. Wang and K. Wang, "A novel magnetic-geared outer-rotor permanent-magnet brushless motor," *4th IET Conference on Power Electronics, Machines and Drives*, 2-4 April 2008, pp. 33-36. [4] R. Hosoya and S. Shimomura, "Apply to in-wheel machine of permanent magnet vernier machine using NdFeB bonded magnet - fundamental study," *8th International Conference on Power Electronics (ECCE)*, pp. 2208-2215, May 30 - June 3, Korea, 2011. [5] Z. Q. Zhu, and D. Howe, "Halbach permanent magnet machines and applications: a review," *IEE Proc.-Electr. Power Appl.*, vol. 148, no. 4, pp. 299-308, July. 2001. [6] Yang Shen, and Zi-Qiang Zhu, "General analytical model for calculating electromagnetic performance of permanent magnet brushless machines having segmented Halbach array," *IET Electrical Systems in Transportation*, vol. 3, no. 3, pp. 57-66, 2013. [7] J. H. Lang, "A comparative analysis of torque production in Halbach and conventional surface-mounted permanent-magnent synchronous motors," *Conference Record of the 1995 IEEE Industry Applications Conference*, 8-12 Oct. 1995, vol. 1, pp. 657-663. [8] P. O. Rasmussen, T. O. Andersen, F. T. Jorgensen, and O. Nielsen, "Development of a high-performance magnetic gear," *IEEE Trans., Ind. Appl.*, vol. 41, no. 3, pp. 764-770, May/Jun. 2005.

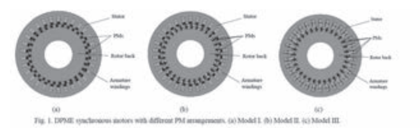

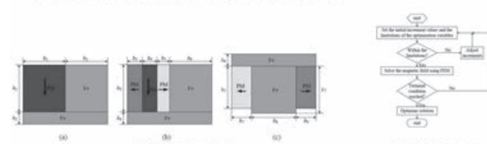

Fig. 1. DPME synchronous motors with different PM arrangements. (a) Model I. (b) Model II. (c) Model III.
Fig. 2. Different PM arrangements.
Fig. 3. The optimization process.

TABLE I
PERFORMANCE COMPARISON OF DIFFERENT MOTOR CONFIGURATIONS

Configuration	Torque (Nm)	Torque/Total volume (kNm/m³)	Torque/PM volume (kNm/m³)	Copper loss (W)	Core loss (W)	Solid loss (W)	Output Power (W)	Efficiency (%)
Model I	68.99	65	781	173.11	214	27	4334.6	91.28
Model II	96.68	91	880	173.11	200	35	6074.6	93.70
Model III	102.34	96	709	176.00	194	26	6430.2	94.20

TABLE I Performance Comparison of Different Motor Configurations

HU-11. Loss and efficiency of a flux-switching permanent-magnet double-rotor machine with high torque density.

L. Mo[1]
1. Huaiyin Institute of Technology, Huaian, China

I. Introduction Double rotor machine (DRM) used for hybrid electric vehicles (HEVs) can offer multi-operational modes and enables the internal combustion engine (ICE) to operate at optimum efficiency independent of road conditions, thus decreasing the emissions and fuel consumption. To achieve high torque density and little torque ripple, a flux-switching permanent-magnet double-rotor machine (FSPM-DRM) has been proposed (see Fig.1(a)) [1][2]. Besides the high torque density, the FSPM-DRM used for HEV should has high efficiency at different operation mode during wide speed range. So, to verify the machine's performance, it's essential to investigated the FSPM-DRM loss and efficiency accurately, which is also needed for further thermal analysis. Traditionally, the conductor eddy current loss,as a part of copper loss, is usually ignored in loss analysis. While in the FSPM-DRM, for its higher electromagnetic torque density than most doubly salient machine, and its larger slot opening, the conductor eddy current loss in it also increases correspondingly. Besides, the high frequency from 22-pole middle rotor, high slot leakage across the coils from the narrow slots, and various operational modes especially at large load and high-speed operations, make the conductor eddy current loss cannot be ignored for accurate efficiency evaluation. II. Machine topology Fig.1(a) shows the configuration of the FSPM-DR machine, in which two 12/22-pole and three-phase FSPM machines are artfully integrated and thus a compact structure and lower torque ripple can be obtained. It has three basic parts: an outer stator, a middle rotor and an inner rotor. Three parts are separated by two air gaps but coupled magnetically. The proposed FSPM-DR machine can be regarded as an integration of the two machines, namely, the outer machine which are composed of the outer stator and the middle rotor, and the inner machine which are composed of the inner rotor and middle rotor. III. Loss analysis *A. Conductor eddy current loss* In the FSPM-DRM, the copper loss consists of two parts: the DC copper loss and the conductor eddy current loss. Skin effect and proximity effect are the two effects that make the current density distributions in windings non-uniform, and thus produce the conductor eddy current loss. 1) Analytical method As the conductor diameters of the inner and the outer machines are smaller (1.4mm and 1.18mm) than the skin depth at the even 7 times of rated speed (1.51mm), the skin effect loss in FSPM-DRM is negligible. Usually, the current density throughout the slot area is supposed as uniform to simplify the proximity loss calculation. In this paper, to accurately evaluate FSPM-DRM's performance, two kinds of slot shapes in the FSPM-DRM and the variations of the flux densities in the slots with radial and tangential directions are taken into account in the proximity loss calculation. 2) 2D FEA method A 2-D FE model is also used for the prediction of the conductor eddy current loss, where the windings' coils are driven with three phase sinusoidal and balanced current waveforms. Individual winding conductors are represented within the FE model. The current distributions of the inner and the outer slots at certain rotor position are also shown in Fig.1(c). As can be seen, the current densities in those conductors that located near the slot opening regions have the greatest change for both inner and outer slots. And it is the same for the conductors near the tangential center region of the outer slot. In other words, the conductors closest to these regions experience the highest induced conductor eddy current loss, which is helpful for conductor's placement design. *B. Other losses* In this paper, the iron loss of the outer stator, the middle rotor, and the inner rotor, and the PM eddy current loss in the FSPM-DRM are obtained by a 2-D FEA model. Fig.1(d) shows the variations of the iron loss, PM eddy current loss, and the conductor eddy current loss with the q-axis current. It displays that the eddy current loss of armature winding in the FSPM-DRM is smaller than the iron loss at rated load, while it increases much faster with the frequency and current density than the iron loss and PM eddy current loss. The mechanical loss including the bearing and the windage loss is about 2.5% of the rated power. Since the bearing loss cannot be considered in the 2-D FEA, only the windage loss which is approximately 55%~65% of the mechanical loss is assumed in the loss analysis. IV. Efficiency Table I lists the FSPM-DRM's losses and efficiencies at various operation conditions. The inner and the outer machines both exhibit excellent efficiencies in different operation areas and wide speed range, which is favorable for HEV applications [3][4]. V. CONCLUSIONS A prototype machine of the FSPM-DRM was designed and manufactured for the testing facilities (Fig.1(b)). An improved analytical scheme and a 2-D FE simulation model of conductor eddy current loss are presented. There is a relatively good agreement between the two results. The iron losses and PM eddy current losses in different parts at various operational modes are also calculated. From the comparisons of the efficiencies from FEA simulation and experimental verification, we can see the similarities of machine's electromagnetic performances, as well as, the differences, which is helpful for machine design and performance optimization.

[1] Lihong Mo, li Quan, Xiaoyong Zhu, "Comparison and analysis of flux-switching permanent-magnet double-rotor machine with 4QT used for HEV," IEEE Transaction on Magnetics, Vol. 50, No.11, 2014, Art. ID 8205804. [2] Chen Yunyun, Quan Li, Zhu Xiaoyong, Wei Hua, and Zheng Wang, "Electromagnetic Performance Analysis of Double-Rotor Stator Permanent Magnet Motor for Hybrid Electric Vehicle," IEEE Transactions on Magnetics, vol. 48, no. 11, pp. 4204-4207, 2012. [3] Ruiwu Cao, Chris Mi, and Ming Cheng, "Quantitative Comparison of Flux-Switching Permanent-Magnet Motors With Interior Permanent Magnet Motor for EV, HEV, and PHEV Applications," IEEE Transactions on Magnetics, vol. 48, no. 8, pp.2374-2384, 2012. [4] Zixuan Xiang, Li Quan, Xiaoyong Zhu, "A new partitioned-rotor flux-switching permanent magnet motor with high torque density and improved magnet utilization," IEEE Transaction on Applied Superconductivity, Vol.26, No.4, 2016, Art. ID 5201905.

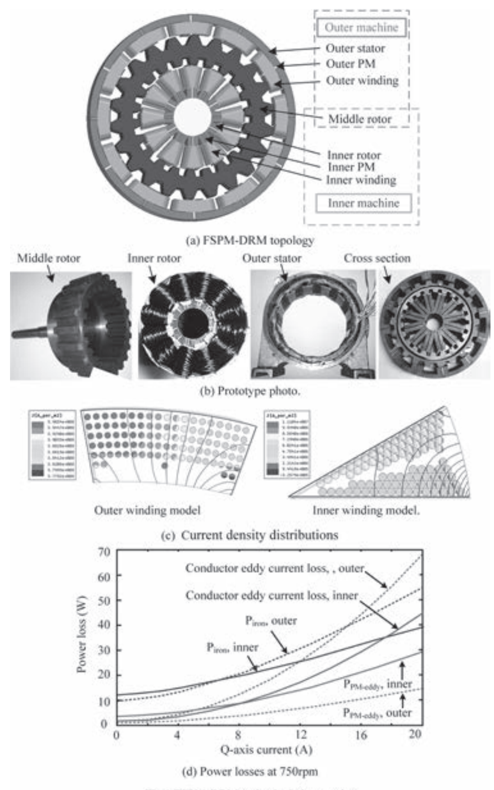

Fig. 1. The FSPM-DRM topology and calculated results.

Table I The losses and efficiencies

Parameters	Inner	Outer	Speed
DC copper loss (W)	48.4	50.9	
Conductor eddy current loss (W)	13.1	10.6	
Iron loss (W)	24.2	23.7	
Eddy current loss in PM (W)	12.9	4.4	750rpm
Output torque (N.m)	14.3	12.3	
Power (W)	1123	966	
Efficiency (%)	91.9	91.5	
Efficiency (%)	89.5	91.1	500 rpm
Efficiency (%)	92.2	93.2	1500 rpm
Efficiency (%)	91.6	91.8	2000 rpm

Table I The simulated losses and efficiencies.

HU-12. Design, modeling, analysis of a traction motor in railway with independently rotating wheelsets.

Y. Oh[1] and S. Kim[2]
1. Hanyang University, Seoul, The Republic of Korea; 2. Yuhan University, Bucheon-si, The Republic of Korea

Abstract - In this paper, we study the robust torque control of wireless tram with independently rotating wheelsets (IRWs). IRWs require active control of traction torque and lateral restoring torque. In this system, the required torque must have high precision and quick response, and it is necessary to perform robust control under various driving conditions. However, FEA is a numerical analysis that assumes various ideal conditions, it is difficult to consider the actual controller and driving conditions. As a result, there is a difference between the FEA results and the actual experimental results. In this paper, we have studied torque control considering driving condition through motor-inverter co-simulation. The simulation result was verified through dynamo test. 1. Introduction In a conventional Railway vehicles, wheels joined together by a solid axle, requiring only traction torque for driving. In this wheelset, the control is relatively simple, but the snake motion occurs at high speed and the wear between the wheel and the rail largely occurs. This problem can be solved by IRWs [1], but there is a disadvantage that control becomes complicated. In IRWs, lateral restoring torque is additionally required for existing traction torques. At this time, the lateral restoration torque generates the steering force using the difference in the left and right wheel torque. The lateral restoring torque is relatively small compared to the traction torque, but requires a high bandwidth, so the total torque is as shown in Fig.1. In addition, since the wireless tram is driven by a battery, torque control is required stably even if voltage fluctuation occurs due to charging and discharging. 2. torque control method When the current command is calculated in real time, the load of the DSP is increased and it is difficult to consider the driving condition, so that the torque error is large. In this section, we discuss how to configure the offline current table to perform robust torque control in IRWS. In order to perform robust torque control in the driving condition, d-q axis current commands are required in consideration of changes in four variables (speed, required torque, battery voltage, and temperature). Temperature changes affect the magnetic flux value of the permanent magnet. This method requires excessive FEA analysis and experimentation. However, since the linkage flux in the motor contains speed and battery voltage information [2][3], it is possible to simplify it by affecting three variables (linkage flux, required torque, temperature). In addition, if samarium cobalt is used as a permanent magnet, it can be reduced to two variables (linkage flux, required torque) since the magnetic flux change with temperature is small. As a result, it is possible to perform robust torque control considering the train vehicle driving conditions with only two variables. This method can greatly reduce the number of experiments. When the FEA is used in the simulation, the magnetic flux can be directly obtained, so the current command(LUT) of the two variables (linkage flux, required torque) can be easily obtained. In addition, there is an advantage that nonlinear and cross-saturation effects can be considered. However, since it assumes ideal conditions like a sinusoidal current source, it differs from the actual driving conditions and the error increases for this reason. In actual motors, there is influence on carrier frequency and dead time, and magnetic flux is estimated by IPMSM voltage equation. In order to take into account the actual effects, the current command(LUT) was obtained using the motor-inverter co-simulation, and the result was more similar to the actual motor test result D, q axis inductance determine the motor characteristics and affect the control performance. The inductance results using the co-simulation differ from the FEA results in the saturation region. 3. conclusion The simulation result was verified through dynamo test as shown in Fig 2. The results (current command, d-q axis inductance) are compared and the analysis of the results will be discussed in detail in the full paper.

[1] R.V. Dukkipati, S.Narayana Swamy, and M.O.M. Osman, "Independently Rotating Wheel Systems for Railway Vehicles-A State of the Art Review," Vehicle System Dynaics, Vol. 21, pp. 297-330, 1992. [2] B.-H. Bae, N. Patel, S. Schulz, and S.-K. Sul, "New field weakening technique for high saliency interior permanent magnet motor," in *Conf. Rec. 38th IEEE IAS Annu. Meeting*, 2003, vol. 2, pp. 898–905. [3] H. W. de Kock, A. J. Rix, and M. J. Kamper, "Optimal torque control of synchronous machines based on finite-element analysis," IEEE Trans. Ind. Electron., vol. 57, no. 1, pp. 413–419, Jan. 2010.

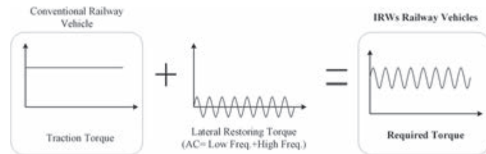

Fig. 1. required torque

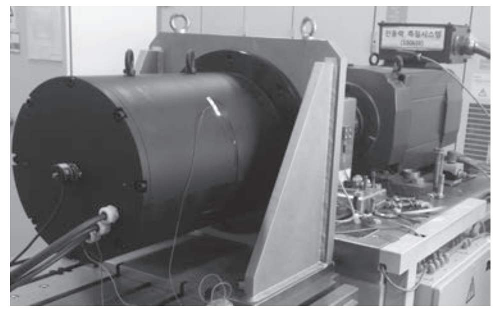

Fig. 2. test

HU-13. Investigation of Flux Modulation Effect on Double-Side-Excited Permanent Magnet Vernier Machine with Various Magnet Topologies.

M. Jiang[1] and *X. Zhu*[1]
1. School of Electrical and Information Engineering, Jiangsu University, Zhenjiang, China

I. Introduction Vernier permanent magnet (VPM) machines, as a member of harmonic machine family with feature of low-speed and large-torque, have attracted increasing concerns and interest. Due to the flux-modulated effect or magnetic gear effect, the VPM machine often possesses an outstanding torque capability, which is considered as one of the promising candidates in direct-drive applications, such as electric vehicles (EVs) and wind power generation [1]. Based on the concept of flux modulation, many studies focus on the exploration and innovation of the topologies of VPM machines in recent years. In [2], a VPM machine with surface-mounted PM rotor topology is proposed and investigated, which verifies that a desirable torque capability is obtained. Yet, the whole machine structure exhibits a bulky size to some extent, which limits its improvement of torque density. To solve this problem, a spoke-type VPM machine is proposed in [3], where an enhanced flux-modulated effect is realized. And the results reveal that an improved torque density is achieved in such machine. It is noted that the serious flux leakage in rotor and relatively low power factor are still the key problems for realizing the development of the machine. Recently, a new type of VPM machine employing two set of PMs is proposed, where the one is located on the stator and the other on the rotor [4]. In such design, the modulated harmonics are produced together by the two set of PMs, offering an improved power factor. However, the PMs in machine stator adopt the form of the Halbach array, and they are located in the stator slot opening. So the requirement of manufacturing and assembly technology is relatively strict, and a relatively serious flux leakage phenomenon still exists in the air-gap. Thus, how to make the most of the flux-modulated effect to design a high performance VPM machine is becoming a hot research orientation and full of full of challenge. In this paper, by incorporating the design concept of dual-PM-excited into the VPM machine, a double-side-excited permanent magnet vernier (DSE-PMV) machine with three various PM topologies is proposed and investigated. By using the unique design of the double-side PM excitation, the modulated working harmonics in the air-gap magnetic field will be abundant and enhanced. It contributes to realizing the design of a high performance VPM machine. II. Motor Topology and Simulation Results Fig.1 shows the whole design concept of the proposed DSE-PMV machine, where three different PM topologies of model I, model II, and model III are presented. It can be seen that the PMs in stator are derived from the external part of rotor PMs, which aims at the full utilization of the PMs. It is noted that the similarity among the three models lies in the same design of the rotor PM topology, which utilize the spoke type PM and tangential magnetization. Meanwhile, the difference among them is the various PM topology designs in stator, consisting of entire PM design with radial magnetization, segment PM design with radial magnetization, segment PM design with tangential magnetization, as shown in Fig. 1 (a), (b) and (c). The specific three topologies of the DSE-PMV machine are illustrated in Fig. 2. Fig.3 depicts the flux distributions of the DSE-PMVs with the three PM topologies. The no-load air-gap flux density curves of the DSE-PMV machine are calculated and compared in Fig. 4. It can be seen that the peak value of the air-gap flux density in Mode III is relatively low but Model I and Model II have a higher peak value. At the same time, the corresponding harmonic spectrum analysis of air-gap flux density is given in Fig. 5. Obviously, the amplitude of the fundamental and high-order harmonic of the Model II is higher than the other two, and the sum of amplitude of the neglected harmonics are comparatively small. It means that the Model II has better flux modulation effect than others. In addition, the back-EMF characteristics of the DSE-PMV machine are presented in Fig. 6. Obviously, from the figure, the back-EMF waveform of the Model II is more sinusoidal than other two models, indicating that it will possess a relatively low cogging torque among the three models. Besides, it can also be observed that the amplitude of Model II is slightly higher than the other two models. It means that a relatively high PM utilization is achieved in the model, which agrees with the analysis results in Fig. 4 and 5. The cogging torque performances of the DSE-PMV machine three PM topologies are also investigated and compared, as depicted in Fig. 7. It can be found that, as expected, the Model II achieves the minimum cogging torque, which is in accordance with the analysis results in Fig. 6. And the amplitude of the cogging toque in Model II reaches 2Nm. In conclusion, the above study results reveal that the DSE-PMV machine with the PM topologies of Model II has better performances, such as higher torque capability and lower cogging torque. More detailed theoretical analysis and experimental results will be given in full paper.

[1] F. Zhao, T. A. Lipo, and B.-I. Kwon, "A novel dual-stator axial-flux spoke-type permanent magnet Vernier machine for direct-drive applications," IEEE Transactions on Industry Applications, vol. 50, no. 11, Nov. 2014, Art. no. 8104304. [2] Dawei Li, Ronghai Qu, Jian Li, Linyuan Xiao, Leilei Wu, and Wei Xu,"Analysis of Torque Capability and Quality in Vernier Permanent-Magnet Machines,"IEEE Transactions on Industry Applications, vol. 52, no. 1, Jan/Feb. 2016. [3] Xianglin Li, Kwok Tong Chau, and Ming Cheng,"comparative analysis and experimental verification of an effective permanent-magnet vernier machine,"IEEE Transactions on Industry Applications, vol. 51, no. 11, Jul. 2015, Art. no. 8203009. [4] Kangfu Xie, Dawei Li, Ronghai Qu, and Yuting Gao, "A Novel Permanent Magnet Vernier Machine With Halbach Array Magnets in Stator Slot Opening,"IEEE Transactions on Industry Applications, vol. 53, no. 6, June. 2017, Art. no. 7207005.

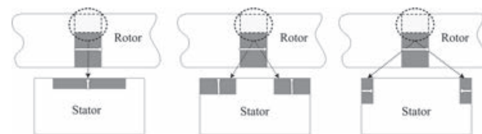

(a) Model I (b) Model II (c) Model III
Fig.1 The concept structure of DSE-PMVM

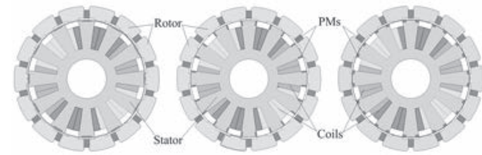

(a) Model I (b) Model II (c) Model III
Fig.2 The structures of vernier machines proposed

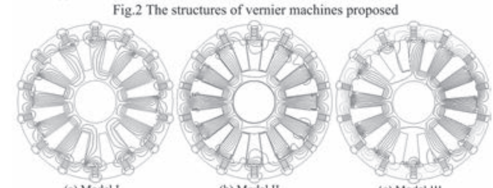

(a) Model I (b) Model II (c) Model III
Fig.3 The distribution of field

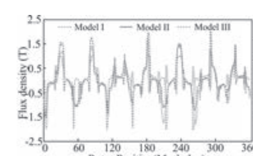

Fig.4 The radial flux density of air gap

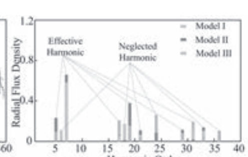

Fig.5 The harmonic of the air-gap flux density

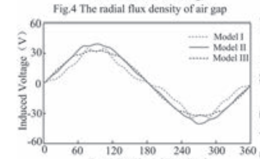

Fig.6 The back-EMF of machines

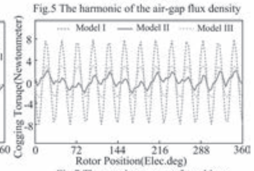

Fig.7 The cogging torque of machines

HU-14. Investigation of Dual Stator Spoke Type Vernier Machine for EV Application.

K. Jung-Woo[1] and B. Kwon[1]
1. Electronic Engineering, Hanyang University, Ansan, The Republic of Korea

I. INTRODUCTION Recently, vernier machines have been nominated for EV applications numerously [1-3]. The attractive features of vernier machine for EV applications are a reduction of volume due to the removal of gearbox [4], and high power density owing to magnetic gear effect, also called as vernier effect. However, one of the critical issues for vernier machine on EV application is the low power factor. To enhance power factor of vernier machine, various methods and topologies were suggested continuously [5]. Especially, one stator-spoke type vernier machine was suggested to increase power factor with the use of flux focusing effect. However, it had flux bypass issue that reduced vernier effect [6]. To solve the issue, dual stator spoke type vernier machine (DSSTVM) uses dual stator to permit flux as additional flux path [7]. DSSTVM eventually realized flux focusing effect to boost torque thus high power factor. However, the study of DSSTVM had been limited to the combination of 12 slots and 20 poles [8]. In this paper, the comparative study of different slot/pole combination DSSTVMs with different winding configurations to find a suitable model for the EV application is done. Power density per volume and weight is a critical feature for light weighted EV. Additionally, good flux weakening capability for wide speed range and high efficiency for less energy usage is required for future EV application. Hence, comparisons of different models of DSSTVM with the aspect of back-emf, torque, power density, power factor, loss, and efficiency are done. The top priority of the work was to find the best model for EV application in overall performance and to discover various trade-off relationships for each machine with differences they are given. Finite element method (FEM) analysis is utilized for the overall performance comparison. II. DESIGN OF COMPARISON MODELS Based on 12S20P DSSTVM, 12S22P DSSTVM was designed using the same constraints such as outer diameter, stack length, airgap volume, phase turns, and magnet volume. Both machines utilized spoke type magnet arrangement for flux focusing effect and dual stator to compensate the flux bypass issue, which was aforementioned. Two models 12S20P and 12S22P were wound with two different winding configurations, concentrated winding and distributed winding. Especially, for distributed winding, 12S20P and 12S22P had a different number of slot pitch for one phase coil. Accordingly, the length of each coil was different and thus different copper loss was expected. All the models used two different airgaps, 1.0 mm in the outer airgap, and 0.5 mm in the inner airgap. Also, stator tooth size of both outer and inner stator was same for both 12S20P and 12S22P model. Operating frequency of the machine was different for each model due to different magnet pole numbers. Since the 12S22P model has a higher frequency, it was expected that the 12S22P model will cause more iron loss than the 12S20P model. Additionally, it was predictable to find distributed winding models to have higher power density due to higher back-EMF and higher vernier effect. III. RESULTS AND DISCUSSION The analysis model of FEM Model I - 12S20P and Model II - 12S22P DSSTVM was shown in Fig. 1. Back-emf and output torque FEM analysis results of each model according to different winding configurations were compared in Fig. 2 (a) and (b). As shown in the figure, Model I with distributed winding achieved highest back-EMF and torque. However, it showed large torque ripple due to a relatively less sinusoidal back-EMF waveform. On the other hand, Model II with distributed winding showed extremely low torque ripple with little less torque compared to the Model I. Loss and efficiency of each model were shown in Fig. 2 (c). From Fig. 2 (c), it can be seen that Model II with distributed winding achieved the highest efficiency, higher than Model I with distributed winding, due to its lower copper loss. Each model, Model I - Concentrated, Model I - Distributed, Model II - Concentrated, and Model II - Distributed showed power density of 9.79, 18.05, 8.68, and 16.5 kW/mm^2 at 100 rpm, respectively. All models achieved power factor higher than 0.9. Consequently, Model II - Distributed was the best for EV application in an aspect of torque performance and efficiency at 100 rpm. Additional studies for more combinations of DSSTVM will be done in the full paper. Equations for back-emf, torque, and flux weakening capability of DSSTVM will be used to predict the performance. Then, a thorough comparison of each model will be done with FEM analysis to show the tendency of trade-off relationships and to show which model is the best. Efficiency map of each machine will also be presented in the full paper.

[1] H. Wang, S. Fang, H. Yang, H. Lin, Y. Li and J. Jiang, "Thermal analysis of consequent-pole hybrid vernier permanent-magnet machine for EV/HEV applications," 2017 IEEE International Magnetics Conference (INTERMAG), Dublin, 2017, pp. 1-1. [2] K. T. Chau, "Vernier Permanent Magnet Motor Drives," in Electric Vehicle Machines and Drives: Design, Analysis and Application, 1, Wiley-IEEE Press, 2015, pp.375- [3] Y. C. Wang, W. N. Fu and X. J. Li, "A novel axial flux stator and rotor dual permanent magnet machine," in CES Transactions on Electrical Machines and Systems, vol. 1, no. 2, pp. 140-145, 2017. [4] S. Hyoseok, N. Niguchi and K. Hirata, "Characteristic Analysis of Surface Permanent-Magnet Vernier Motor According to Pole Ratio and Winding Pole Number," in IEEE Transactions on Magnetics, vol. 53, no. 11, pp. 1-4, Nov. 2017. [5] D. Li, R. Qu and T. A. Lipo, "High-Power-Factor Vernier Permanent-Magnet Machines," in IEEE Transactions on Industry Applications, vol. 50, no. 6, pp. 3664-3674, Nov.-Dec. 2014. [6] T. Zou, D. Li, R. Qu and D. Jiang, "Performance Comparison of Surface and Spoke-Type Flux-Modulation Machines With Different Pole Ratios," in IEEE Transactions on Magnetics, vol. 53, no. 6, pp. 1-5, June 2017. [7] B. Kim and T. A. Lipo, "Analysis of a PM Vernier Motor With Spoke Structure," in IEEE Transactions on Industry Applications, vol. 52, no. 1, pp. 217-225, Jan.-Feb. 2016. [8] W. Liu and T. A. Lipo, "A family of vernier permanent magnet machines utilizing an alternating rotor leakage flux blocking design," 2017 IEEE Energy Conversion Congress and Exposition (ECCE), Cincinnati, OH, 2017, pp. 2461-2468.

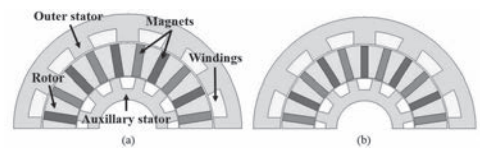

Fig. 1. DSSTVM machines (a) Model I - 12S20P (b) Model II - 12S22P

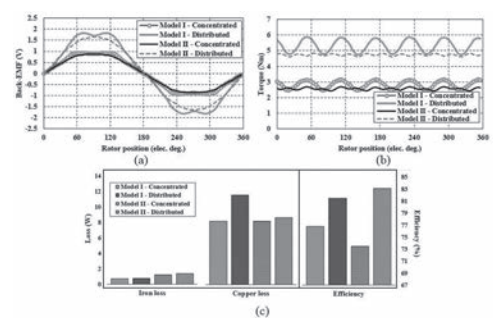

Fig. 2. FEM analysis of different DSSTVM models (a) Back-EMF (b) Torque (c) Loss & efficiency

HU-15. Hybrid Rectangular Bar Wave Windings to Minimize Winding Losses of Permanent Magnet Machines for EV/HEVs over a Driving Cycle.

X. Fan[1], D. Li[1], R. Qu[1], C. Wang[1] and J. Li[1]
1. School of Electricity and Electronic Engineering, Huazhong University of Science and Technology, State Key Laboratory of Advanced Electromagnetic Engineering and Technology, Wuhan, China

I. Introduction The utility of thick rectangular wire wave windings in electrical machines for electrical vehicle/hybrid electrical vehicles (EV/HEVs) have gained increasing interest due to its high slot filling factor, short end-winding, good manufacturability and excellent heat dissipation capability, etc. [1]. More EV makers tend to adopt this kind of windings in their new generation EV motors [2] [3]. However, significant eddy current losses may be induced in the thick bars especially at a high speed operation, thus reducing the machine efficiency and may cause winding local overheating. The conductor in a slot suffers from the circumferential flux caused by the armature (blue) and the radial flux caused by the magnet (red), as shown in Fig. 1 (a). The magnitude of radial flux density caused by the magnet and the circumferential flux density caused by the armature along the center line is shown in Fig. 1 (b). It can be seen that the flux density dramatically decreased as the distance to the stator bore increases. This means the conductors in the slot near the slot opening are exposed to a relatively large variable field by magnet and armature and significant AC losses may occur. Some methods have been reported to reduce the AC losses in the existing papers [4]-[6]. Reference [4] shows that the AC losses can be reduced by keeping the conductors away from the slot opening or using the magnetic wedge. Reference [5] and [6] reduce the AC losses by choosing an optimal winding layout and stranding the conductors, respectively. This paper proposes a novel hybrid rectangular bar wave winding consisting of copper bars and aluminum bars to reduce the winding losses. The aluminum bars are located close to the slot opening to suppress the induced AC losses for its high resistivity. It shows that the total winding losses can be reduced with the hybrid winding compared to with the conventional copper winding, especially at high speeds and light loads. Besides, the weight and cost can be also reduced. Further, an optimization method is proposed to minimize the winding losses over a given driving cycle. The areas of the copper and aluminum bars and the distance of conductor to the slot opening are optimized using this method. II. Proposed Hybrid Thick Rectangular Wire Wave Windings A stator winding with four layers of conductor bars in one slot is used to illustrate the concept of the hybrid windings. Fig. 2 shows the stator with conventional copper winding and the hybrid windings. The detail layout of the conductors in the slot is depicted in Fig. 3. It can be seen that the aluminum bars of the hybrid windings are located in the first two layers close to the slot opening. This layout can be beneficial to suppress the eddy current loss induced by the variable field close to the slot opening for the high resistivity of aluminum. Furthermore, the use of aluminum can also reduce the weight and cost of the windings, which is very important for the machines used in EV/HEVs. The defect of the hybrid winding is the possible electrochemical corrosion happened at the joint between the copper bars and aluminum bars. This can be solved by using transition joints or a special welding procedure. III. Comparison with the Conventional Rectangular Bar Wave Windings Two permanent magnet traction motors having the same geometry and parameters except for winding materials are designed to demonstrate the potential superiority of the hybrid winding over the conventional copper windings, as shown in Fig. 4. Each conductor bar of the two windings has the same area. The winding losses with two different speeds and current levels are calculated for the two windings by finite element method (FEM). The results are listed in Table I. It has to be noted that the end-winding losses are also included to consider the low AC effects in the end-winding. It can be seen from Table I that the winding losses can be effectively reduced with the hybrid winding at a high speed and light loads. The current density distribution in the conductors can be also reduced, as shown in Fig.5. Even though the hybrid winding increase the winding loss at a low speed and heavy load, the total losses of the hybrid winding over a driving cycle may be less than that of the conventional winding. Therefore, a comparison of the losses of the two windings according to a given driving cycle is required, which will be reported in the full paper. IV. Minimizing the Winding Losses over a Given Driving Cycle An optimization method is proposed to minimize the winding losses over a given driving cycle. A typical used driving cycle is shown in Fig. 6 (a). The optimization variables are the area ratio of the aluminum bar to the copper bar l_a/l_c and the distance of the conductor to the slot opening D_c (shown in Fig.6 (b)). The detail of the optimization method will be presented in the full paper. V. Conclusion A novel hybrid rectangular bar wave winding consisting of copper bars and aluminum bars is proposed in this paper. The aluminum bars are located close to the slot opening to suppress the AC losses. It shows that the total winding losses can be reduced with the hybrid winding compared to with the conventional copper winding, especially at high speeds and light loads. An optimization method is proposed to minimize the losses of the hybrid winding over a given driving cycle. The areas of the copper and aluminum bars and the distance of conductor to the slot opening are optimized using this method. More results will be reported in the full paper.

[1] R. Bojoi, A. Cavagnino, M. Cossale and A. Tenconi "Multiphase starter generator for a 48-V mini-hybrid powertrain: design and testing," *IEEE Trans. Ind. Appl.*, vol. 52, no. 2, pp. 1750-1758, Mar./Apr. 2016. [2] T. Ishigami, Y. Tanaka, and H. Homma, "Motor stator with thick rectangular wire lap winding for HEVs," *IEEE Trans. Ind. Appl.*, vol. 51, no. 4, pp. 2917-2923, Jul./Aug. 2015. [3] S. Jurkovic, K. Rahman, B. Bae, N. Patel and P. Savagian, "Next neneration Chevy Volt electric machines; design, optimization and control for performance and rare-earth mitigation," in *Proc. IEEE Energy Convers. Congr. Expo. (ECCE)*, Sep. 2015, pp. 5219-5226. [4] M. J. Islam, H. V. Khang, A.-K. Repo, and A. Arkkio, "Eddy-current loss and temperature rise in the form-wound stator winding of an inverter-fed cage induction motor," *IEEE Trans. Magn.*, vol. 46, no. 8, pp. 3413–3416, Aug. 2010. [5] M. Spang and M. Albach, "Optimized winding layout for minimized proximity losses in coils with rod cores," *IEEE Trans. Magn.*, vol. 44, no. 7, pp. 1815–1821, Jul. 2008. [6] A. S. Thomas, Z. Q. Zhu, and G. W. Jewell, "Proximity loss study in high speed flux-switching permanent magnet machine," *IEEE Trans. Magn.*, vol. 45, no. 10, pp. 4748–4751, Oct. 2009.

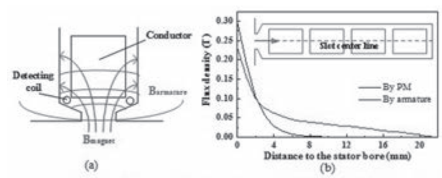

Fig. 1 (a) Magnetic field in the slot caused by PM and armature, (b) Magnitudes of radial flux density caused by PM and circumferential flux density caused by armature along the slot center line.

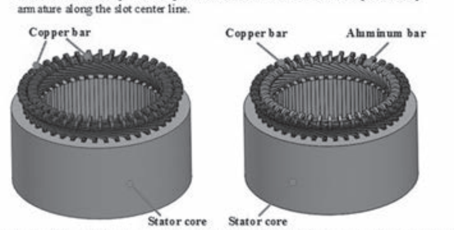

Fig. 2. (a) Conventional rectangular bar wave windings, (b) Proposed hybrid rectangular bar wave windings.

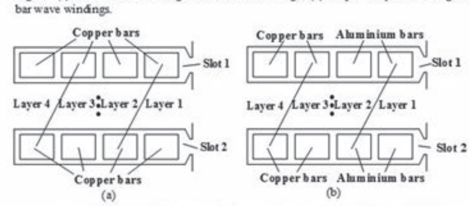

Fig. 3. (a) Copper bars of conventional rectangular bar wave windings in the slot, (b) Cooper bars and aluminium bars of hybrid rectangular bar wave windings and conductors in the slot.

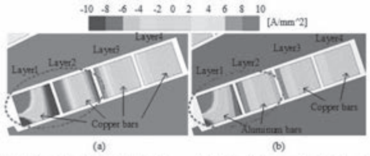

Fig. 5. Current density distribution in the conductor bars of the conventional (a) and the hybrid winding (b). (8400rpm, current 160A)

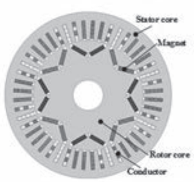

Fig. 4. Studied permanent magnet motors for EV/HEVs.

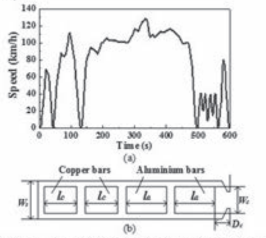

Fig. 6. (a) The driving cycle of US06/SFTP.(b)The slot and conductor geometry.

TABLE I WINDING LOSSES OF CONVENTIONAL AND HYBRID WINDINGS WITH DIFFERENT SPEEDS AND CURRENT LEVELS. (UNIT: WATT)

	2800rpm			8400rpm		
	Conv.	Hyb.		Conv.	Hyb.	
40A	78	67.2	-13.8%	427.2	337.2	-21.1%
80A	162.6	162	-0.4%	655.8	553.8	-15.6%
160A	510	547.8	+7.4%	1592.4	1440.6	-9.5%

HU-16. Reduction of Vibration and Acoustic Noise in Fractional-Slot Concentrated-Windings Permanent-Magnet Machine.

S. Zhu[1], W. Zhao[1], J. Ji[1] and J. Zheng[1]
1. School of Electrical and Information Engineering, Jiangsu University, Zhenjiang, China

Introduction Due to the advantages of high efficiency, high power density, and high fault-tolerant capability, the fractional-slot concentrated-windings permanent-magnet (FSCW-PM) machines have received increased attention. [1]. However, the abundant harmonics in FSCW-PM machines will produce low-order radial electromagnetic force, thus aggravating the vibration and acoustic noise performances [2]. Therefore, many magnetomotive force (MMF) harmonic reduction techniques were proposed [3], but their abilities to reduce the low-order radial electromagnetic force were relatively poor. The purpose of this paper is to analyze the generation mechanism of low-order radial electromagnetic force from different magnetic field components, and a new design will be proposed to reduce the vibration and acoustic noise of FSCW-PM machines. New design Due to the interaction of tooth harmonics and fundamental magnetic field, the lowest order radial electromagnetic force will be generated in FSCW-PM machine, thus resulting in vibration and acoustic noise. Fig. 1 compares the stator structure of two existing and proposed machines. In the proposed unequal tooth stator, the angle of two adjacent opening-slots has been designed to control the MMF amplitude of each harmonic component. It should be noted that the fundamental wave keeps constant with the existing one, so the output performance is unchanged. However, the tooth harmonic is weakened effectively. Results In order to verify the proposed machine, the finite-element method and acoustic boundary-element method are employed to evaluate vibration and noise performances. The MMF and radial electromagnetic force between the existing and proposed machines are compared in Figs. 2 and 3, respectively. The proposed machine can effectively weaken the tooth harmonics and the radial electromagnetic force which plays a significant role in the vibration and acoustic noise of FSCW-PM machines. Fig. 4 compares the vibration spectrum between the existing and proposed machines. It can be seen that the proposed one has 12% lower vibration than the existing one. Finally, the sound power level spectrum of the proposed FSCW-PM machine is given in Fig. 5. Resonance does not occur because of the large difference between the electromagnetic force frequency and the modal frequency.

[1]. L. Fu, S. Zuo, W. Deng, and S. Wu, "Modeling and analysis of electromagnetic force, vibration, and noise in permanent-magnet synchronous motor considering current harmonics," *IEEE Trans. Ind. Electron*., vol. 63, no. 12, pp. 7455-7466, Dec. 2016. [2]. M. Valavi, A. Nysveen, and R. Nilssen, "Effects of loading and slot harmonic on radial magnetic forces in low-speed permanent magnet machine with concentrated windings," *IEEE Trans. Magn*., vol. 51, no. 6, Jun. 2015, Art. no. 6975207. [3]. G. Choi, and M. Jahns, "Reduction of eddy-current losses in fractional-slot concentrated-winding synchronous PM machines," *IEEE Trans. Magn*., vol. 52, no. 7, Jul. 2016, Art. no. 8105904.

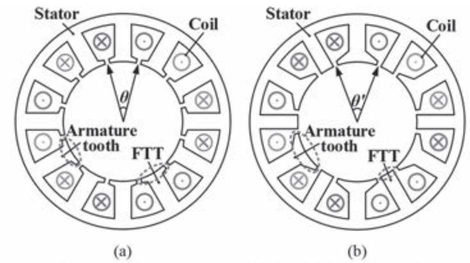

Fig. 1. Stator structure. (a) Existing. (b) Proposed.

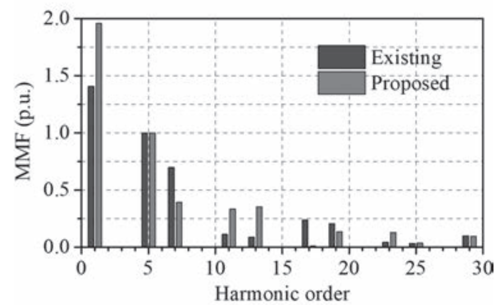

Fig. 2. Comparison of MMF harmonics.

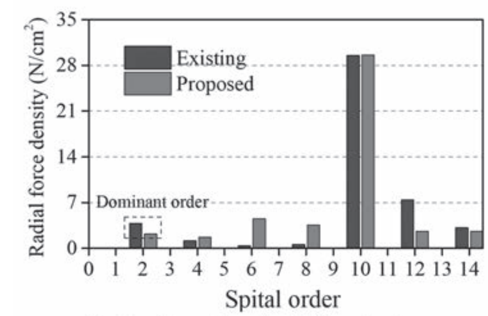

Fig. 3. Comparison of radial force density.

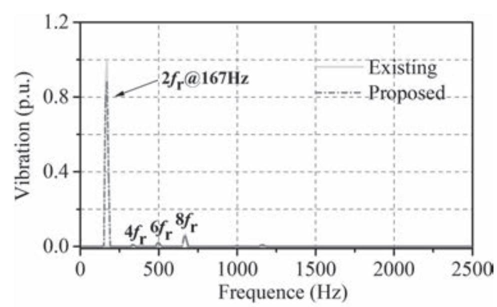

Fig. 4. Comparison of vibration spectrum.

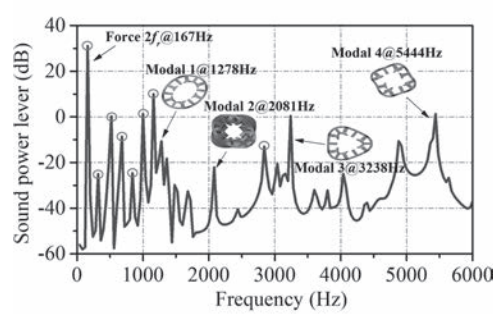

Fig. 5. Acoustic noise spectrum of proposed machine.

FRIDAY AFTERNOON, 27 APRIL 2018 SIMPOR/ROSELLE BALLROOM, 1:30 TO 4:30

Session HV
RECORDING SYSTEMS: CODING AND HEAD-DISK INTERFACE
(Poster Session)

Sergiu Ruta, Chair
University of York, York, United Kingdom

HV-01. SNR Improvement of Envelope Demodulation Using Two Temporal Magnetization Dynamics from Dual Spin-Torque Oscillator.

Y. Nakamura[1], M. Nishikawa[1], H. Osawa[1], Y. Okamoto[1], T. Kanao[2] and R. Sato[2]

1. Graduate School of Science and Engineering, Ehime University, Matsuyama, Japan; 2. Corporate Research & Development Center, Toshiba Corporation, Kawasaki, Japan

I. INTRODUCTION Three-dimensional magnetic recording using microwave assisted magnetic recording (MAMR) has been proposed as one of the prospective recording technologies which uses a spin-torque oscillator (STO) as a reading sensor as well as a write-assisting device [1]. In the reading process using an STO, the reproducing waveform is given as temporal dynamics of magnetization [2]. The amplitude of STO oscillation waveform decreases as the STO comes close to the recorded dot of "0", and the amplitude increases again as it leaves from the recorded dot of "0" [3]. The recorded dot "1" few influence on the amplitude. Therefore, we cannot discriminate whether the dead dot or recorded dot of "1". However, the STO which reacts to the recorded dot of "1" can be produced by adjusting the resistance, the direct current, the external magnetic field, and so on [4]. In this research, we propose the envelope demodulation using two temporal magnetization dynamics from dual STO, and evaluate the bit error rate (BER) performance of R/W channel with dual STO by the computer simulation. II. READ/WRITE CHANNEL MODEL Figure 1 shows the temporal magnetization dynamics of the STO for the diameter of dot equals 20 nm and the envelope model obtained by the convolution of the attenuation function [3] using the STO #1 which reacts to recorded dot of "0", where the recorded data pattern is "000111000111" as shown in bottom of Fig.1. In this study, the relative velocity between the medium and the STO, the dot diameter and pitch are 20 m/s, 20 nm and 25 nm, respectively. The dashed and solid lines show the temporal magnetization dynamics and the reproducing envelope model, respectively. The x-axis shows the time normalized by the channel dot pitch interval T_c. As can be seen from Fig. 1, the amplitude of STO oscillation waveform decreases as the STO comes close to the recorded dot "0", on the other hand, as it leaves from the dot of "0", the amplitude increases again. In this research, we assume that the STO #2 reacts to the recorded dot of "1" as the opposite reaction of the STO #1. In the evaluate system, the input data sequence is recorded on the dots composed of perpendicular soft and hard layers antiferromagnetically coupled (AFC) with each other. The AFC structure reduces the net stray field and that is suitable for multi-layered media [5]. The STO #1 and #2 scan on the same recorded dots or the same track. We assumed that the system noise at the reading point for the envelope is the additive white Gaussian noise (AWGN) whose power in the band width equal to the channel dot rate $f_c = 1 / T_c$ is given by σ_s^2. Then, we define the signal-to-noise ratio (SNR) of the saturation envelope level of STO magnetization A and the effective value of system noise σ_s as $\mathrm{SNR}_S = 20 \log_{10} A / \sigma_s$ [dB]. The reproducing envelope sampled by the T_c interval is fed to low-pass filters (LPF) with the cut-off frequency x_h normalized by f_c in order to suppress excessive high frequency noise. The LPF output for STO #2 is subtracted from the output from STO #1, and is fed to the finite impulse response (FIR) filter with N_t taps to be equalized to the partial response class-I (PR1) [6]. The output is decoded by the Viterbi detector. III. SIMULATION RESULTS AND DISCASSION Figure 2 shows the BER performances, where $x_h = 0.5$ and $N_t = 15$. The open square, open triangle and filled circle symbols show the BER performances using the STO #1, STO #2, and the proposed dual STO, respectively. The vertical and horizontal axis show the BER performance and SNR_S. As can be seen from the figure, the BER performance of the proposed system using dual STO shows the better than the single STO systems. The SNR improvement at a BER of 10^{-4} is about 2.7 dB by the effect of averaging the system noise. Furthermore, the system using dual STO can detect dead dots by the lack of signal become possible by using envelopes from dual STO. IV. CONCLUSIONS We proposed the envelope demodulation using two temporal magnetization dynamics from dual STO, and evaluated the BER performance by the computer simulation. The results show that our proposed system provides the SNR improvement of 2.7 dB at a BER of 10^{-4}. Furthermore, it makes the dead dot detection possible. ACKNOWLEDGMENTS This work is supported by S-Innovation program from Japan Science and Technology Agency, JST.

[1] K. Kudo, H. Suto, T. Nagasawa, K. Mizushima, and R. Sato, "Resonant magnetization switching induced by spin-torque-driven oscillations and its use in three-dimensional magnetic storage applications," *Appl. Phys. Express*, vol.8, no.10, 103001, Sept. 2015. [2] T. Kanao, H. Suto, K. Kudo, T. Nagasawa, K. Mizushima, and R. Sato, "Micromagnetic simulation of selective resonance readout from double-layer antiferromagnetically-coupled recording magnetization using a spin-torque oscillator.," *Abstract of MMM 2017*, CE-02, Nov. 2017. [3] Y. Nakamura, M. Nishikawa, H. Osawa, Y. Okamoto, T. Kanao, and R. Sato, "Envelope demodulation using temporal magnetization dynamics of resonantly interacting spin-torque oscillator for three-dimensional magnetic recording," *Abstract of MMM 2017*, BQ-09, Nov. 2017. [4] K. Kudo, H. Suto, T. Nagasawa, T. Kanao, K. Mizushima, and R. Sato, "Three-dimensional magnetic recording using ferromagnetic resonance," *Jpn. J. Appl. Phys.*, vol.55, no.7S3, pp. 07MA01-1 - 07MA01-10, June 2016. [5] H. Suto, T. Nagasawa, K. Kudo, K. Mizushima, and R. Sato, "Nanoscale layer-selective readout of magnetization direction from a magnetic multilayer using a spin-torque oscillator," *Nanotechnology*, vol.25, no.24, 245501, May 2014. [6] E. R. Kretzmer, "Generalization of a technique for binary data communication," *IEEE Trans. Commun.*, vol. COM-14, no. 1, pp. 67–68, Feb. 1966.

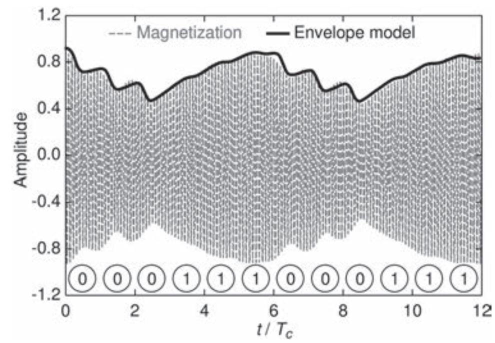

Fig. 1. Envelope model for the recorded data pattern "000111000111".

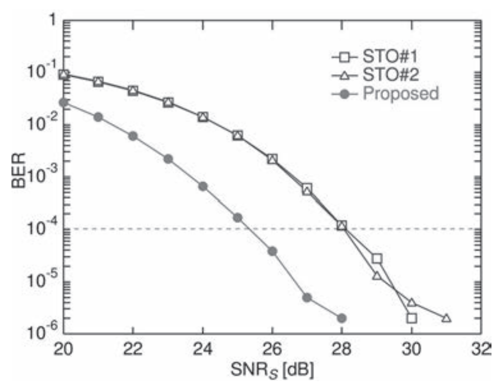

Fig. 2. BER performance (PR1ML system, x_h = 0.5 and N_t = 15).

HV-02. Two-dimensional Signal Processing Systems Using CRC-polar Coding and List Decoding for Bit-patterned Magnetic Recording.

H. Saito[1]
1. School of Advanced Engineering, Kogakuin University, Tokyo, Japan

I. INTRODUCTION In this research, a new effective signal processing scheme is proposed for a two-dimensional magnetic recording (TDMR) system using bit-patterned media (BPM). The proposed signal processing scheme uses concatenated cyclic redundancy check polar (CRC-polar) codes [1] as modulation codes and a non-binary low-density parity-check (LDPC) code as an error-correction code (ECC). In decoding process, successive-cancellation list (SCL) decoders [1] are introduced. These SCL decoders are expected to give an error rate performance improvement to the successive cancellation decoder of [2]. In these list decoder, several decoding paths are considered concurrently at each decoding stage. At the end of the decoding process, the most likely path among these survived paths is selected as the single codeword at the decoder output. II. PROPOSED SIGNAL PROCESSING SCHEME FOR TDMR Fig.1 shows the block diagram of the proposed signal processing scheme for a TDMR system using BPM. In Fig.1, $2N$+1track recording is assumed for the TDMR system. In this read/write system, a raw data sequence $\{a_k\}$ is input into a CRC precoder and *parity* (dummy) symbols are inserted in the CRC sequence. These dummy symbols are used to give run length limited (RLL) constraints in the both of cross-track and down-track directions. The (d_1, k_1, d_2, k_2)-RLL constraint sequence outputted from the CRC precoder is the precoded sequence $\{b_{i,k'}\}$ and is recorded on the i-th track. The sequence $\{b_{i,k'}\}$ is transformed into the systematic polar codeword sequence. In polar encoding, systematic encoding with bit-reversal is assumed using a cascade of two non-systematic polar encoder circuits [3]. The $2N$+1 binary polar codeword sequences are input to the systematic 2^{2N+1}-ary LDPC encoder and transformed into a LDPC codeword sequence $\{c_{i,k'}\}$. After LDPC encoding, the interleaver Π takes incoming block of the LDPC codeword sequence and rearranges the sequence in a different temporal order. The arranged sequence is NRZ-recorded on islands made of the discrete double layered perpendicular magnetic medium with a soft under layer. These islands are arranged on a rectangular grid in the surface of recording medium. For the readback TDMR channel, the readback signal of BPM is represented by the 2D Gaussian pulse response given by [4] and the normalized peak amplitude is A_p. In this system, the parallel readback signal sequence $\{r'_{i,k'}\}$ is obtained by combining readback signal sequences from several adjacent tracks. In Fig. 1, $r'_{i,k'} = (r_{i-N,k'},\ldots,r_{i,k'}\ldots,r_{i+N,k'}) + (n_{i-N,k'},\ldots,n_{i,k'},\ldots,n_{i+N,k'})$, where the sequence$\{r_{i,k'}\}$is the readback signal sequence from the i-th track and the noise sequence $\{n_{i,k'}\}$ is added at the reading point. The sequence $\{n_{i,k'}\}$ is additive white Gaussian noise (AWGN) with zero mean and variance. The reproducing waveform corresponding to the recording sequences readback by the reading head is inputted into the equalizer which consists of a 2D low-pass filter (LPF) and the 2D transversal filter (TVF). The equalization is performed so that the overall characteristic between the input of recording head and the output of the equalizer is equal to the aimed 2D generalized partial response (GPR) targets. The equalizer output sequence $\{y'_{i,k'}\}$ is obtained which sums equalizer output sequences from several adjacent tracks. In the equalizing process, tap-gain coefficients in the 2D TVF are evaluated by minimizing the expectation of the mean square error (MSE) $E(\{e_{i,k'}\})$, where the sequence $\{e_{i,k'}\}$is the equalized error sequence between the ideal GPR target output sequence $\{d_{i,k'}\}$ and the sequence $\{y_{i,k'}\}$. The signal-to-noise ratio (SNR) at the reading point is defined as the ratio of A_p and the noise power of AWGN. In decoding process, the equalizer output sequence $\{y'_{i,k'}\}$ is decoded by the 1D log-likelihood ratio (LLR) detector and and the estimated LLR sequence $\{L(c'_{i,k'})\}$ is given as the detector output. The sequence $\{L(c'_{i,k'})\}$ is decoded by the sum-product algorithm in the LDPC decoder. After the recursive decoding process, we know the all $2N$+1 LLRs for each $L(c'_{i,k'})$. The sequence $\{L(c'_{i,k'})\}$ is needed to convert the *channel level likelihood ratio* (CLLR) sequence $\{\Lambda(c'_{i,k'})\}$. The estimated sequence $\{c'_{i,k'}\}$ is given as the detector output. The sequence $\{c'_{i,k'}\}$ is decoded by CRC-aided SCL decoders. After frozen symbols are eliminated, we get the estimated precoded sequence $\{b'_{i,k'}\}$. At the end, the estimated output data sequence $\{a'_k\}$ is obtained after demodulation. The block error rate (BER) performance is evaluated by computer simulation between the sequences $\{a_k\}$ and $\{a'_k\}$. III. ERROR RATE PERFORMANCES Fig. 2 shows the BER performances of the coded generalized partial response systems. In Fig.2, the solid line show the BER performance of the proposed coding scheme with the (0,3,0,3) run-length limited (RLL) constraint using four-track recording. The dashed line shows the performance of the conventional binary LDPC coding scheme [5] with the (0,9) RLL constraint using single-track recording. These coding scheme have the effective transmission rate = 2.6, 0.93, respectively. The recording condition corresponds to the areal density of 4.0 Tb/in^2 given by [4]. As can be seen Fig. 2, the proposed coding scheme using four tracks outperforms that of the conventional coding scheme using a single track by about 6.0 dB of SNR gains at a BER of 10^{-5}. IV. CONCLUSION In this digest, a new signal processing schemes using CRC-polar coding and LDPC coding is proposed for a TDMR system.

[1] I. Tal and A. Vardy, *IEEE Trans. Inf. Theory*, 61, 5, 2213-2226, May 2015. [2] E. Arikan, *IEEE Trans. Inf. Theory*, 55, 7, 3051-3073, July 2009. [3] G. Sarkis, et al., *IEEE J. Sel. Areas Commun.*, 32, 5, 946-957, May 2014. [4] T. Wu, et al., *IEEE Trans. Magn.*, 50, 1, 1-11, Jan. 2014. [5] H. Zhong, et al., *IEEE Trans. Magn.*, 43, 7, 1118-1123, Mar. 2007.

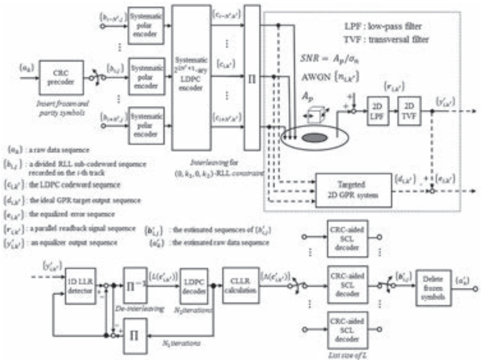

Fig. 1. Block diagram of a TDMR system.

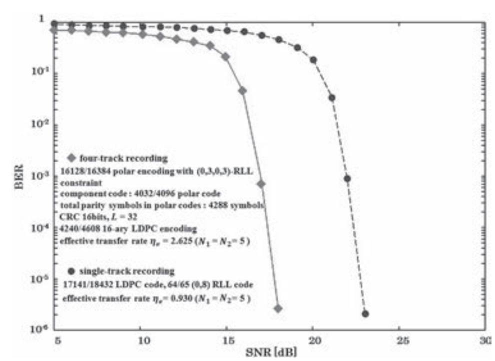

Fig. 2. BER performances.

HV-03. Performance of Bit-Patterned Media Recording According to Island Patterns.

S. Jeong[1], *J. Kim*[1] and J. Lee[1]
1. Soongsil University, Seoul, The Republic of Korea

To increase a density in hard disk drive, bit patterned media recording (BPMR) is regarded as a promising candidate for the next generation storage system. Reduction of spacing between bit islands is essential to increase the density in BPMR but causes inter-symbol interference (ISI) and inter-track interference (ITI). Islands can be arranged on a rectangular pattern (regular array) or packed in a staggered pattern (hexagonal lattice), depending upon the lithography approach adopted in BPMR. Since the staggered pattern can mitigate the effect of the ITI due to the presence of adjacent tracks, bit error rate (BER) performance of staggered pattern is better than that of rectangular pattern in previous study. In another work of channel modeling for staggered pattern, the staggered pattern with bit-aspect ratios (BAR) =Track Pitch (T_z) / Bit Length (T_x) of 2 performs better than the staggered pattern with BAR of 1. In this paper, we investigate the performance of BPMR island patterns according to the distances of track pitch and bit length, respectively. Fig. 1 presents BER performance of island arrangement according to areal densities of 2 Tb/in^2 and 3 Tb/in^2. When the areal density is 2 Tb/in^2, (T_x = 15.5nm, T_z = 21.0nm) provides best performance. Also, when the areal density is 3 Tb/in^2, (T_x = 13.0nm, T_z = 17.0nm) shows best performance. Fig. 2 illustrates BER performance in accordance with island arrangements. Case (1) represents the arrangement of islands that distributed over a rectangular array at T_x of 18.0nm and T_z of 18.0nm in 2 Tb/in^2 and T_x of 14.5nm and T_z of 14.5nm in 3 Tb/in^2. Case (2) represents the arrangement of islands that distributed over a staggered pattern at T_x of 21.0nm and T_z of 15.5nm in 2 Tb/in^2 and T_x of 17.0nm and T_z of 13.0nm in 3 Tb/in^2. Case (3) represents the arrangement of islands that distributed over a staggered pattern at T_x of 18.0nm and T_z of 18.0nm in 2 Tb/in^2 and T_x of 14.5nm and T_z of 14.5nm in 3 Tb/in^2. Case (4) represents the arrangement of islands that distributed over a staggered pattern at T_x of 15.5nm and T_z of 21.0nm in 2 Tb/in^2 and T_x of 13.0nm and T_z of 17.0nm in 3 Tb/in^2. Since the influence of adjacent tracks of Case (4) is less than that of Case (1), Case (2), and Case (3), i.e., the effect of ITI is reduced, Case (4) shows the best performance in both 2 Tb/in^2 and 3 Tb/in^2.

1. P. W. Nutter, I. T. Ntokas, B. K. Middleton, and D. T. Wilton, "Effect of island distribution on error rate performance in patterned media," *IEEE Trans. Magn.*, vol. 41, no. 10, pp. 3214–3216, Oct. 2005. 2. Y. Ng, K. Cai, B. V. K. V. Kumar, T. C. Chong, S. Zhang, and B. J. Chen, "Channel modeling and equalizer design for staggered islands bit-patterned media recording," *IEEE Trans. Magn.*, vol. 48, no. 6, pp. 1976–1983, Jun. 2012.

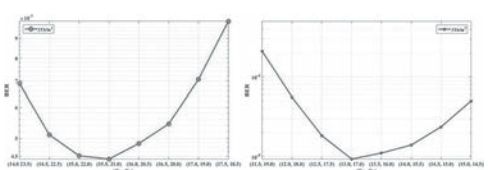

Fig. 1. BER performance of island arrangements when areal density of 2Tb/in^2 and 3Tb/in^2.

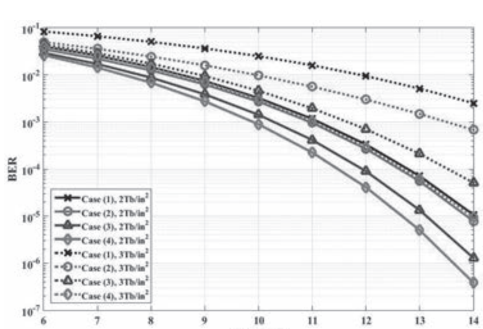

Fig. 2. BER performance in accordance with island arrangements.

HV-04. A Rate-5/6 2D Modulation Code for Single-Reader/Two-Track Reading in BPMR Systems.

K. Buahing[1], W. Busyatras[2] and *C. Warisarn*[1]

1. College of Advanced Manufacturing Innovation, King Mongkut's Institute of Technology Ladkrabang, Bangkok, Thailand; 2. Faculty of Science and Technology, Rajamangala University of Technology Thanyaburi, Pathumthani, Thailand

I. Introduction A reduction in the track width of magnetic recording systems results in a welcome increase in areal density (AD), but also in the unfortunate appearance of extreme inter-track interference (ITI) that can severely deteriorate system performance. The effect of severe ITI may be mitigated through the use of coding schemes [1]. In this paper, therefore, we present a rate-5/6 two-dimensional (2D) modulation code that is designed based on a proposed single-reader/two-track reading (SRTR) technique to cope with this serious problem in staggered bit-patterned media recording (BPMR) systems. We then evaluate the bit-error rate (BER) performance of the proposed system in the presence of media noise, e.g., position and size fluctuation. Our simulation results indicate that, at the same user density (UD), the proposed system is better than an uncoded system by about 1.0 dB at the BER of 10^{-5} and is also superior to a conventional recording system. II. BPMR Channel Model We consider a hexagonal island with a diameter of 12 nm and a bit period of 16.0 and 14.5 nm, which correspond to the ADs of 2.5 and 3.0 Tb/in^2, respectively. The bit islands were arranged as a staggered array and covered with a readhead sensitivity response [2] as shown in Fig. 1. The readback signal is simply obtained from the 2D convolution between the magnetization and the readhead sensitivity response of the reader whose track width covers more than two whole neighboring tracks. The center of the readhead sensitivity function is positioned at the intermediate point between the parallel tracks. Then, the readback signal is further corrupted by electronic noise. To obtain the sample amplitudes, the readback signal is perfectly over-sampled at the sampling period, $0.5T_x$, that is located at the centers of the recorded magnetization. Next, the readback data sequence, r_k is equalized by a 1D equalizer to obtain the data sequence, s_k, and is fed to the 1D Viterbi detector to produce estimated data sequences. Finally, this sequence will be rearranged to become two data sequences, i.e., $x'_{k,l}$ and $x'_{k,l+1}$ before being passed on to the proposed decoder to produce the estimated user bits. III. 2D Modulation Code We first analyzed the peak amplitude of all possible $2^6 = 64$ data patterns in a matrix form of 2×3 bits that were arranged as a staggered array BPMR, where the peak amplitudes of each data pattern were obtained from 2D convolution between their magnetizations without sidetrack data and readhead sensitivity response, as shown in Fig. 1. Since we found that the desired bit peak amplitude will always reverse in the opposite direction when the data bits of each pattern contain many 1's and -1's which easily causes an error during the data recovery process. To avoid this unwanted situation, therefore, this condition will be defined as a criterion for designing a codeword, which can efficiently avoid such destructive data patterns. Since we consider 6 data bits, there will be $2^6 = 64$ possible data patterns composed of: 2 bits in the first column [$x_{k,l}$, $x_{k,l+1}$], 2 bits in the second column [$x_{k+1,l}$, $x_{k+1,l+1}$], and lastly, 2 bits in the third column [$x_{k+2,l}$, $x_{k+2,l+1}$]. We have selected the best 32 data patterns that provide the biggest group from the same data bit. These patterns will then be assigned to become the proposed codewords. Then, we match the 5 input bits, a ≡ [a_k, a_{k+1}, a_{k+2}, a_{k+3}, a_{k+4}] with a 6-bit codeword, x ≡ [$x_{k,l}$, $x_{k,l+1}$; $x_{k+1,l}$, $x_{k+1,l+1}$; $x_{k+2,l}$, $x_{k+2,l+1}$]^T. Moreover, to create more accuracy in the decoding process, we have partially defined a mapping condition to create a codeword so that the first two input bits match the first column of the codeword, the second two input bits match the second column of the codeword, while the remaining one input bit corresponds with the upper track in the third column of the codeword. Unfortunately, 14 patterns that cannot match still remain after using the above conditions; however, these patterns are still among the 32 good patterns. Thus, they can output the appropriate readback signal. IV. Results and Discussion We compare the BER performance between 1) the proposed SRTR system performs together with the proposed 5/6 2D modulation code, 2) the proposed SRTR system [3], and 3) a conventional reading system which uses one reader, reads the data form one track i.e., an input sequence a_k is written onto a single track with random data on sidetracks. For a fair comparison, the staggered BPMR system performance should be compared using the UD. In this paper, the UD is defined as UD = AD×R, where R is a code rate. The signal-to-noise ratio (SNR) is defined as $10\log_{10}(1/\sigma^2)$ in dB, where σ is a standard deviation of AWGN. As shown in Fig. 2, it is clear that the proposed SRTR system that performs together with the proposed 5/6 2D modulation code at the UD of 2.5 Tb/in^2 is better than the uncoded SRTR system by about 1.0 dB at the BER = 10^{-5} and is superior to a conventional reading system. Acknowledgement This work was partially supported by the Thailand Research Fund under the grant number RSA6080051, College of Advanced Manufacturing Innovation (AMI), and King Mongkut's Institute of Technology (KMITL), Thailand.

[1] K. Pituso, C. Warisarn, D. Tongsomporn, and P. Kovintavewat, "An intertrack interference subtraction scheme for a rate-4/5 modulation code for two-dimensional magnetic recording," *IEEE Magn. Lett*., vol. 7, article: 4504705, 2016 [2] M. Yamashita et al., "Read/write channel modeling and two-dimensional neural network equalization for two-dimensional magnetic recording," *IEEE Trans. Magn.,* vol. 47, no. 10, pp. 3558-3561, Oct. 2011. [3] C. Buajong and C. Warisarn, "Multitrack reading scheme with single reader in BPMR systems," in *Proc. of iEECON 2017*, pp. 457-460, Pattaya, Thailand, 8-10 Mar. 2017.

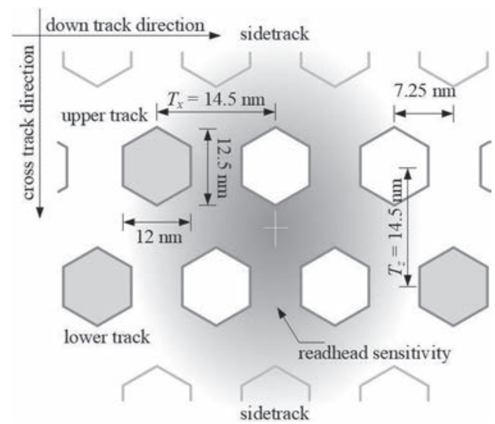

Fig. 1. Configuration of the proposed SRTR technique at the AD of 3.0 Tb/in^2 under the read-head sensitivity response that was positioned between the desired upper and lower tracks.

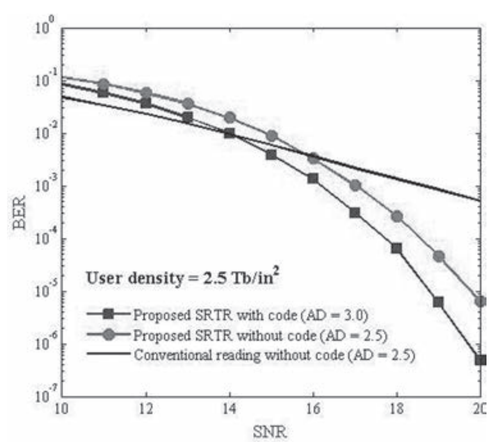

Fig. 2. The comparison of BER performance in different systems at the UD of 2.5 Tb/in^2.

HV-05. Control Scheme for Read/Write Head Positioning in Dual-Stage Magnetic Disk Drive Servo System.

B. Shi[1,2], Y. Meng[1] and C. Jin[1]
1. School of Mechanical and Electrical Engineering, Shandong Jianzhu University, Jinan, China; 2. School of Mechanical Engineering, Hebei University of Technology, Tianjin, China

1.Introduction As we are in an era of information exploding, and more than half of the digital data is stored in magnetic disk drives[1], to increase storage capacity is one of the key issues for developing magnetic disk drives. Therefore, an accurate positioning servomechanism is required to achieve an ultra-high disk density. For a dual-stage actuated (DSA) disk drive servo control system, a large servo bandwidth is desirable to attain ultra-high accuracy in read/write head positioning. A lot of control techniques have been proposed for DSA servo control design, such as the LQG/LTR technique[2], nonlinear PID control strategies[3], tracking differentiator and H_∞ almost disturbance decoupling technique [4], and optimal decoupled disturbance observers approaches[5], composite nonlinear feedback (CNF) technique[6-7], etc. In the present study, we proposed a control scheme for the read/write(R/W) head positioning in dual-stage magnetic disk drive servo system using two controllers for a primary voice coil motor (VCM) actuator and a secondary micro-actuator (MA), respectively. Simulation results of the proposed control scheme are presented and compared with those of a single-stage actuated CNF method and a dual-stage linear feedback control (LFC) technique. 2.Design of the Control Scheme Figure 1 shows the identified model of the primary coarse VCM actuator [10]. The VCM model is simplified into a 4^{th}-order model as shown in the solid line in Fig.1. It is easily noticed that there is a resonant mode at 4240 Hz in the VCM actuator. For the primary VCM controller, a notch filter is designed to weaken the high frequency resonance of the VCM actuator. Furthermore, a lead compensator is designed to prevent the phase lose caused by the filter and to improve the stability of the control servo system. Finally, the VCM controller is designed by the combination of the notch filter and the lead compensator. The model of the secondary MA adopted in the present study is from [11]. The MA controller is designed using a integral resonant control (IRC) compensator [8-9] in series with a notch filter to adequately suppress the higher frequency resonance for the R/W head high-precision positioning. To make sure that the VCM and MA actuators will not be damaged from excessive voltage, the saturation functions are added respectively for the two actuators. Since large and fast motion is performed by the VCM actuator, while small and precise motion is executed by the MA, a switch function is added in the MA control loop to make sure that the MA is activated if the R/W head is within the reachable distance of its target track. 3. Simulation Example As an example, Fig. 2 shows the performance of the proposed control scheme for R/W head positioning in DSA disk drives. For comparison, those of a single-stage actuated CNF approach and a dual-stage LFC approach through simulation for seek length with 1 micron are also shown in Fig. 2. From Fig.2 we can see that: The R/W head positioning DSA system controlled by the scheme proposed in this paper moves the read/write head and settles on the target track within 0.55 ms with almost no overshoot, which is shorter than that, 1.2 ms, needed for the SSA CNF method to move the R/W head to the target position, while the LFC method has a much bigger oscillation. It is shown that the proposed control scheme for R/W head positioning in DSA disk drives is able to track accurately with a shorter settling time for head positioning to guarantee the robustness of the control servo system. 4. Summary A control scheme is proposed for R/W head positioning in dual-stage magnetic disk drive servo system using two controllers of the primary VCM actuator and the secondary MA. For the VCM actuator controller, we combine a notch filter and a lead compensator to eliminate its high frequency resonance and to prevent the phase lose for facilitating large motion. For the MA controller, we use the IRC compensator together with a notch filter to realize quick and precise positioning. The performance of the proposed control scheme is verified through a simulation example. Detailed procedure and process to design the control scheme and the servo system will be presented in the full paper with comprehensive simulation results and discussions to further verify the performance of the proposed control scheme for DSA servo system. *Acknowledgments* This work was supported by the National Natural Science Foundation of China (Grant No. 51275279), and the Tribology Science Fund of State Key Laboratory of Tribology (Grant No. SKLTKF16A01).

[1]Hilbert M and López P.The world's technological capacity to store, communicate, and compute information. Science,2011, 332(6025): 60-65. [2]Suh SM, Chung CC, Lee SH.Discrete-time LQG/LTR dual-stage controller design in magnetic disk drives. IEEE Transactions on Magnetics, 2001,37(4): 1891-1895. [3]Isayed BM and Hawwa MA. A nonlinear PID control scheme for hard disk drive servosystems.IEEE Conference on Control & Automation, 2007, MED'07. [4]Zhang H, Huang X, Peng G, Wang M. Dual-stage HDD head positioning using H_∞ almost disturbance decoupling controller and a tracking differentiator. Mechatronics,2009, 19:788-796. [5]Chen X and Tomizuka M. Optimal Decoupled Disturbance Observers for Dual-Input Single-Output Systems. Journal of Dynamic Systems Measurement and Control, 2014, 136(5): 051018. [6]Chen BM, Lee TH, Peng K. Composite nonlinear feedback control for linear systems with input saturation: theory and an application. IEEE Transactions on Automatic Control, 2003, 48(3): 427-439. [7]Peng K, Chen BM, Lee TH, Venkataramanan V. Design and implementation of a dual-stage actuated HDD servo system via composite nonlinear control approach. Mechatronics, 2004, 14(9): 965-988. [8]Aphale SS, et al. Integral resonant control of collocated smart structures. Smart Materials and Structures, 2007, 16(2): 439. [9]Al-Mamun A, Keikha E, Bhatia CS, Lee TH. Integral resonant control for suppression of resonance in piezoelectric micro-actuator used in precision servomechanism. Mechatronics, 2013, 23(1): 1-9. [10] Rahman MA, Al Mamum A, Yao K, Das SK. Design and Implementation of Feedback Resonance Compensator in Hard Disk Drive Servo System: A Mixed Passivity, Negative-Imaginary and Small-Gain Approach in Discrete Time. Journal of Control, Automation and Electrical Systems, 2015, 26(4): 390-402. [11]Pang CK Tan YZ, Ng TS, Lee TH. Integrated Servo-Mechanical Design of Robust Mechatronics Based on Ambiguous Chance Constraints. IEEE Transactions on Control Systems Technology, 2015, 23(6): 2449-2456.

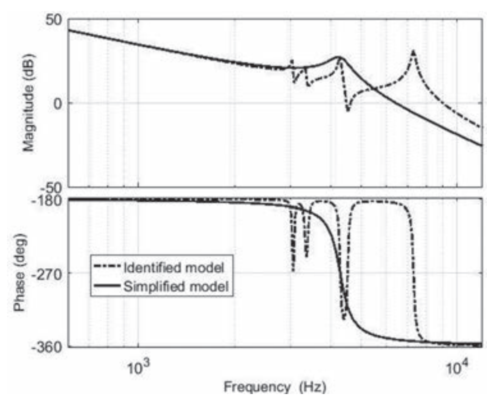

Fig. 1. Frequency response of the VCM actuator

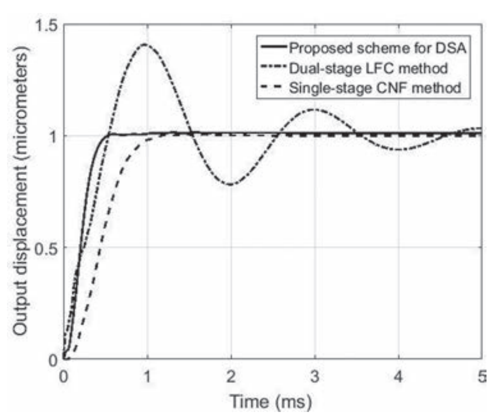

Fig. 2. Comparisons of simulation results between the proposed scheme, dual-stage LFC method and single-stage CNF method.

HV-06. Reduced-complexity window decoding of spatially coupled LDPC codes for magnetic recording systems.

S. Khittiwitchayakul[1], W. Phakphisut[1] and P. Supnithi[1]
1. Faculty of Engineering, King Mongkut's Institute of Technology Ladkrabang, Ladkrabang, Thailand

1.Introduction In channel coding theory, the performance of error correcting codes (ECCs) approaching the Shannon limit can be achieved through increasing code lengths. Unfortunately, the complexity of ECCs will be increased as the code length increases. Nowadays, the magnetic recording (MR) system takes advantage of powerful ECCs by using 4 Kbytes sector. Among the advanced ECCs, the spatially coupled LDPC (SC-LDPC) codes (also known as a LDPC convolutional code) [1] are shown to have the decoding latency and complexity lower than those of the underlying LDPC block codes (LDPC-BC). Moreover, the SC-LDPC codes with threshold decoding outperform the LDPC-BC codes [2]. Hence, the SC-LDPC codes are the strong candidate for the future MR systems, when the sector size is increased beyond 4 Kbytes. An SC-LDPC decoder can use sliding window decoding [3] whereby the received signals are decoded by sliding window along the bit sequence. The window decoder is called "*uniform window decoding (U-WD),*" when all variable nodes (VNs) within a window are updated. In order to reduce the complexity of window decoding, some researchers proposed the *non-uniform window decoding (N-WD)* [4], which do not update the VNs with no improvement in the bit error rate (BER). This approach provides about 35-50% reduction in complexity compared to U-WD. In this work, we consider the application of SC-LDPC codes in MR systems, whereby SC-LDPC decoder cooperates with BCJR detector to encounter inter-symbol interference (ISI). We propose the dynamic shifting of window decoding (DS-WD) to reduce the complexity of SC-LDPC codes. Herein, the number of shifted bits is defined according to their soft BERs which are estimated at each decoding position. In addition, we modify the N-WD [4] to reinforce our proposed algorithm called "*dynamic-shifting non-uniform window decoding (DS-N-WD).*" The DS-WD and DS-N-WD achieve the complexity reduction of 7% and 25% without any loss in performance compared to the N-WD algorithms. 2.Turbo equalization with SC-LDPC codes A *(J,K)*-SC-LDPC is constructed from a protograph represented by base matrix B [3]. The matrix B contain J and K ones in each column and row, respectively. The protograph is copied N times, and then the edges of each replica are connected among the N replicas to obtain the derived graph represented by parity-check matrix H. In order to explain the coupled codes, we first examine transmitting a sequence of L code blocks v_t, $t = 1,..,L$. An essential feature of the coupled codes are that the consecutive transmitted code blocks are connected. The coupling of consecutive code blocks can be obtained using the edge spreading procedure [3], which must satisfy the condition $B=B_0+B_1+..+B_{m\_cc}$ to maintain the original degree distribution of the protograph. The matrix B_i has n_c rows and n_v columns. To decode SC-LDPC codes in turbo equalization, after the BCJR detector receives the ensemble code blocks y_t from the channel, the detection process is performed corresponding to the designed channel targets. The produced LLR values of the BCJR detector are sent to SC-LDPC decoder with a window size of $W \geq m_{cc}+1$. Each decoding position covers the received code block y_{t+w-1}, $w =1,..,W$ and each code block contains Nn_v VNs. In Fig. 1, we give an example of (3,6)-SC-LDPC decoder of code rate $R = 1/2$ with $W = 4$ and the edge spreading procedure is defined as B= [3 3], where B_0, B_1 and B_2=[1 1]. At each decoding position t, the message passing decoding between the VNs and CNs within a window is performed until the maximum number of decoding iteration I_{LDPC} is reached. Then, the window is shifted to decode the next decoding position $t = t + s_t$, where s_t is denoted as the maximum number of code blocks shifted from the decoding position t. In the standard window decoding, s_t is set to be 1. 3.Reduced-complexity window decoding of SC-LDPC codes One possibility to reduce the window decoding complexity of SC-LDPC codes is to shift the multiple code blocks at the same time when the estimated soft BERs of each block are the same. The soft BER is estimated at the end of decoding process in terms of log(P(w)). Herein, the code block w is shifted when the equation $\alpha_w \log(P(w)) \leq \log(P(w-1))$, $w =2,..,m_{cc}+1$, is satisfied. Thus, we possibly choose s_t from 1 to $m_{cc}+1$. The shifting factor α_w must be chosen by the Monte Carlo simulation. We name the first proposed decoding algorithm as "the DS-WD algorithm." Moreover, we modify the N-WD algorithm to reinforce DS-WD called "the DS-N-WD algorithm." The DS-N-WD can stop updating some VNs in the window. Since the soft BER estimate of each code block depends on the number of shifted code blocks, the update schedules must be investigated corresponding to the number of shifted code blocks s_t. 4.Simulation results We consider the BPMR channels at the areal density of 2 Tb/in^2 [5]. The code rate of (3,21)-SC-LDPC is 6/7. The m_{cc} is set to be 2, therefore, B_0, B_1 and B_2 are [1 1 1 1 1 1 1]. The matrix H is generated using PEG method [6] with L and N =100. The W = 8, I_{LDPC} =30 and I_{Turbo} =3 are selected. The complexities of all decoding methods are compared by computing the average number of VN updates U_{avg}[4] required to decode the total length of coupled codes as shown in Fig. 2. We found that the DS-WD provides 40% and 7% reduction in complexity compared to the U-WD and N-WD, respectively at SNR=4.9*dB* without any loss in performance. The reductions of complexity are up to 53% and 25% when the DS-N-WD is applied.

[1] A. J. Felstrom and K. S. Zigangirov, "Time-varying periodic convolutional codes with low-density parity-check matrix," IEEE Trans. Inf. Theory, vol. 45, no. 6, pp. 2181–2191, Sep. 1999. [2] S. Kudekar, T. J. Richardson, and R. L. Urbanke, "Threshold saturation via spatial coupling: Why convolutional LDPC ensembles perform so well over the BEC," IEEE Trans. Inf. Theory, vol. 57, no. 2, pp. 803–834, Feb. 2011. [3] A. R. Iyengar, M. Papaleo, P. H. Siegel, J. K. Wolf, A. Vanelli-Coralli, and G. E. Corazza, "Windowed decoding of protograph-based LDPC convolutional codes over erasure channels," IEEE Trans. Inf. Theory, vol. 58, no. 4, pp. 2303–2320, Apr. 2012. [4] N. U. Hassan, A. E. Pusane, M. Lentmaier, G. P. Fettweis and D. J. Costello, " Non-uniform window decoding schedules for spatially coupled LDPC codes," IEEE Trans. on Commu., vol. 65, no. 2, pp. 501-510, Feb. 2017. [5] S. Nabavi, and B. V. K. Vijaya Kumar, "Two-dimensional generalized partial response equalizer for bit-patterned media," in Proceedings IEEE international Conference Communication (ICC), pp.6249-6254, 2007. [6] X.-Y. Hu, E. Eleftheriou, and D. M. Arnold, "Regular and irregular progressive edge-growth tanner graphs," IEEE Trans. Inf. Theory, vol. 51, no. 1, pp. 386–398, Jan. 2005.

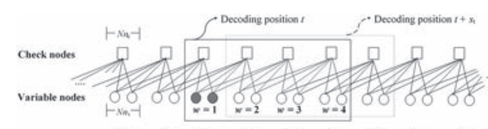

Fig. 1. Illustration of sliding window decoding.

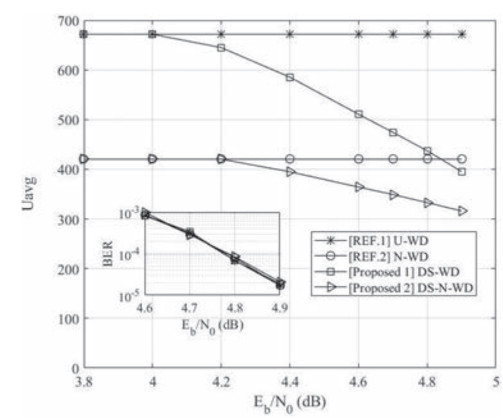

Fig. 2. Performance and complexity comparisons.

HV-07. A study on iterative decoding with LLR modulator by parity check information in SMR system.

M. Nishikawa[1], Y. Nakamura[1], H. Osawa[1], Y. Okamoto[1], Y. Kanai[2] and H. Muraoka[3]

1. Ehime University, Matsuyama, Japan; 2. Niigata Institute of Technology, Kashiwazaki, Japan; 3. Tohoku University, Sendai, Japan

Introduction In recent years, shingled magnetic recording (SMR) [1] has attracted attention as a new recording method of a hard disk drive (HDD). Although SMR can realize narrow track, it has remarkable performance deterioration due to the influence of inter-track interference (ITI) [2]. Therefore, improving the performance of the low density parity-check (LDPC) encoding / decoding method combining the LDPC code [3] and the sum-product (SP) decoding in the SMR is considered to be an effective means for further increasing the density of the HDD. In this study, we modify the log-likelihood ratio (LLR) calculated as the decoding reliability by the a posteriori probability (APP) decoder in the LDPC encoding / iterative decoding system, and observe the improvement of the decoding accuracy by computer simulation of the SMR of the plane recording density 4 T bits / inch^2 specification. As a result of iterative decoding by modifying the LLR corresponding to the parity check information "0" and "1", the tendency of error saturation was eliminated. Moreover, improvement of SNR to achieve error free was obtained. Read / write system Figure 1 shows the read / write system in SMR. The input sequence passes through the 128/130 (0, 16/8) RLL encoder and the LDPC encoder to be converted to the recording sequence, which is recorded on the discretized granular medium [4]. The LDPC code is composed of 4096 byte sector, and 30 sector of data sequence is written and read to obtain a bit error rate (BER) performance. An array head with three readers reads the recorded data from the three adjacent tracks, where the signal-to-ratio (SNR) at each reading point is defined as SNR = 20 $\log_{10}$ (A /σ_s) [dB] by the saturation level A of the isolated reproduction waveform and the RMS value σ_s of the system noise falling within the bandwidth equal to the channel bit rate f_c. Then, the reproduced waveform passes through an LPF (low-pass filter) with a cutoff frequency x_h = 0.4 normalized by f_c and a two-dimensional finite impulse response (2D-FIR) filter having the number of taps for a reader N_t = 15. The characteristic from the recording head to the 2D-FIR filter output is designed to be the partial response class-I (PR1) characteristic [5]. The APP decoder calculates the LLR using the constraint of PR channel from the 2D-FIR filter output sequence, as the decoding reliability. The SP decoder corrects the LLR using the LDPC code of parity check matrix, where i_{sp} is the maximum iterations of SP decoding. The SP decoder returns the improved LLR to the APP decoder as the extrinsic value. The SP decoder output sequence after the turbo equalization of maximum iteration i_{global} passes through the hard decision unit and the RLL decoder to obtain the output sequence. The BER can be obtained by comparing the input sequence and the output sequence. LLR modulator We propose introducing a LLR modulator to improve the SP decoding. First, the modulator checks the correctness of LLR. As the column weight of LDPC is 3, the parity check information sequence is composed of "0", "1", "2", or "3". In this study, we boost the LLR if the parity check information is "0" or "1", because the LLR is likely to be correct. If the LLR with parity check information "0" is larger than or equal to 0.30, it is multiplied by 3.0, and if the LLR with parity check information "1" is larger than or equal to 0.30, the LLR is multiplied by 1.15. Figure 2 shows the BER performance for SNR, where the iteration parameters are set to i_{global} = 17 and i_{sp} = 15. The symbols of red circle and green filled circle show the cases with and without the modulators, respectively. From the figure, it can be seen that the LLR modulator improves the SNR by 0.5 dB to achieve no errors. The results show that modifying LLRs using the parity check information provides an effective iterative decoding. Acknowledgments This work was supported in part by the Advanced Storage Research Consortium (ASRC), Japan.Introduction

1) R. Wood, M. Williams, A. Kavcic, and J. Miles, "The feasibility of magnetic recording at 10 terabits per square inch on conventional media," *IEEE Trans. Magn.*, vol.45, no.2, pp.917-923, Feb. 2009. 2) H. Nobuhara, Y. Okamoto, M. Yamashita, Y. Nakamura, H. Osawa, and H. Muraoka, "Influence of writing and reading ITI's depending on recording patterns in shingled magnetic recording," *Digest of Inermag* 2014, HW-9, May 2014. 3) R. G. Gallager, *"Low-density parity-check codes," IRE Trans. Inform.* Theory, vol.IT-8, pp.21-28, Jan. 1962 4) Y. Kanai, Y. Jinbo, T. Tsukamoto, S. J. Greaves, K. Yoshida, and H. Muraoka, "Finite-element and micromagnetic modeling of write heads for shingled recording," *IEEE Trans. Magn.*, vol.46, no.3, pp.715-721, March 2010. 5) E. R. Kretzmer, "Generalization of a technique for binary data communication," *IEEE Trans. Magn.*, vol.14, no.1, p.67–68, Feb. 1966.

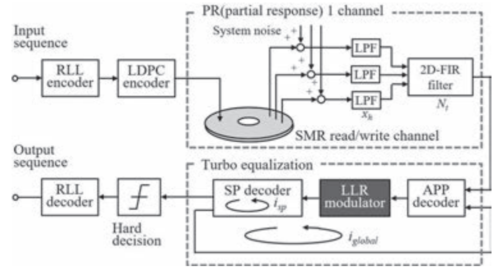

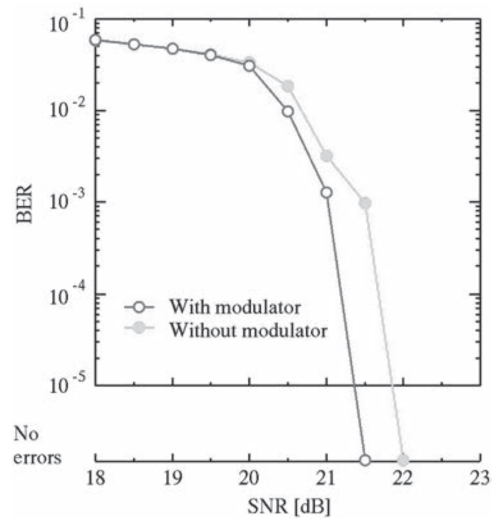

HV-08. Thermal decomposition of the polymeric lubricant and the viscoelastic effects on the head-disk interface in heat-assisted magnetic recording.

P. Chung[1]
1. Energy Engineering, Inje University, Gimhae-si, The Republic of Korea

Magnetic recording system is currently evolving with the new recording techniques such as heat-assisted magnetic recording (HAMR) to drastically increase the areal density of the magnetic layer, while the thermal stability issues still exist on the lubricant layer. Specifically, lubricant molecules can cause the unexpected situations including the evaporation and contamination of the head and other components since the molecules can be chemically decomposed due to the cyclic thermal stresses with extremely high temperature [1,2]. Along with the thermal degradation, the contact between the slider and the disk causes the elongational stress on the intervening polymeric lubricant film so that the lubricant molecule can be mechanically decomposed as well as the anchored molecules can be also decoupled from the carbon overcoat [3]. Therefore, it is critically important to understand the molecular scale effects of the non-equilibrium perturbation on the decomposition and decoupling of the lubricant layers under the high temperature conditions to develop the sustainable lubricant materials for the HAMR systems. In this study, we investigated the thermal lubricant decomposition and the layer decoupling under the vertically elongational forces applied to the functional oligomeric film, which is similar as the contacting behavior between the head and the disk, by modeling the confined PFPE films with the static bottom and moving top substrates. To precisely estimate the thermos-mechanical molecular decomposition and decoupling phenomena, we utilized the full atomistic molecular dynamics, which fundamentally catches the intramolecular and intermolecular binding characteristics for the decoupling and decomposition phenomena in a few molecular systems. In addition, we performed the coarse-grained non-equilibrium molecular dynamics with the elongational deformation similar as the extensional flow experiment using atomic force microscopy (AFM) (Fig. 1) to investigate the the viscoelastic properties of the lubricant layers as a function of a portion of fragmented molecules, which is correlated to the thermos-mechanical conditions (e.g., temperatures, the length of heated cycles, and the elongation rate). Linear lubricants (Fomblins Ztetraol and ZTMD) as well as star-like lubricants (TA-30 and QA-40) were modeled for the lubricant layer to study the molecular structural effects on the lubricant decomposition. We also provide a nanostructural analysis of the lubricant layer for the future development of the HDI systems.

1. B. Marchon and Y. Saito, IEEE Trans. Magn., 48, 4471 (2012). 2. D. Pan, A. Ovcharenko, J.-P. Peng, and H. Jiang, *IEEE Trans. Magn.*, 50, 3302005 (2014). 3. J.A. Odell, A.J. Muller, K.A. Narh, and A. Keller, Macromolecules, 23, 3092 (1990). 4. Q. Guo, S. Izumisawa, M.S. Jhon, and Y.-T. Hsia, *IEEE Trans. Magn.*, 44, 3698 (2008).

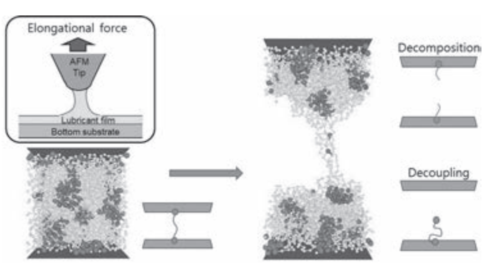

Fig. 1. The elongational stress on the confined PFPE Zdol and the schematic description of the chemical decomposition and the molecular decoupling under the elongational stress.

HV-09. Numerical Study of Particle Rebound on the Slider Air Bearing Surface.

F. Cui[1], *H. Li*[1], H. Shang[1], S. Shen[1], S. Wu[1] and S. Liu[2]
1. School of Power and Mechanical Engineering, Wuhan University, Wuhan, China; 2. Department of Mechanical Engineering, Colorado School of Mines, Golden, CO, United States

Higher areal density of hard disk requires the ultra-low flying height slider, which increases the probability of contact between the slider and hard disk surface. Micro and nanoscale lubricant droplets and metal particles produced in collision can enter the head-disk interface (HDI) and cause serious damage to the slider and hard disk [1, 2]. Our previous work has numerically investigated the air flow patterns, particle trajectories and interaction between particles and slider surface in HDI, which is of critical importance to the reduce of particle induced damage [3-6]. However, all previous work only considers the collision between the particle and flat surface. In this work, the mechanism of particle rebound in HDI is studied. Three types of particles collision are modeled and simulated, including the P-S (particle and surface), P-E (particle and edge) and P-P (particle and particle) collision. It is assumed that all surfaces of slider are smooth, and all particles are spherical. Collision of spherical particles with other objects is considered an elastic point contact. The subsequent action of particles after collision, which includes the rebound on the surface and adherence to the surface, is calculated with considering the collision energy loss. The trajectories and accumulation/distribution of particles on the air bearing surface (ABS) are visually presented. The particle material is alumina, and all Al_2O_3 particles have a diameter of 150 nm, a density of 3800 kg/m^3, and an initial velocity of $(U_p, V_p, W_p) = (0.8U_d, -0.2U_d, 0)$, where U_d is the local hard disk rotating speed. One hundred particles are released one after another at the leading edge of a femto-sized slider (850×700 μm). The initial x coordinates (x_0) of particles equal zero. The initial y coordinates (y_0) of particles are randomly generated in the range of 0 μm to 700 μm. The initial distance between particles and hard disk (z_0) is randomly generated in the range of 150 nm to 250 nm. Firstly, it solves the modified Reynolds equations to get the slider attitude as shown in Fig. 1(a) [7]. Since the air pressure gradient is necessary for calculating the air flow velocity and easy to be calculated on the rectangular mesh, an algorithm is applied to achieve the data transformation between the triangular mesh and the rectangular mesh. Then, it solves the Navier-Stokes equations with the second order slip boundary conditions to get the air flow velocity pattern, as shown in Fig 1(b). Finally, particle movement equations are solved by using the fourth order Runge–Kutta method [4]. Some simulation results are shown in Fig. 2. The comparison of Fig. 1(b) and Fig. 2(a) indicates that particle trajectories basically follow air flow streamlines. Fig. 2(a) also shows trajectories and final distribution of randomly released particles. Sixty-five particles adhere to ABS, twenty particles straightly go through HDI without collision, and fifteen particles go through HDI after the rebound on ABS. Especially, particle trajectories show that particle P2 goes through HDI after a P-E collision, compared to the straightly passage of particle P1. Fig. 2(b) shows the P-E collision causes a large z-direction displacement of particle P2, which helps the particle P2 to move away from ABS and go through HDI finally. Correspondingly, a large negative z-direction velocity of particle P2 is shown in Fig. 2(c). The P-E collision of particle P2 also causes a greatly reduce of x-direction velocity as shown in Fig. 2(d). Dynamic performance of particle rebound and the statistical analysis of accumulation/distribution of particles on ABS will be furtherly presented in the full paper.

[1] Shen X, Bogy D B. Particle Flow and Contamination in Slider Air Bearings for Hard Disk Drives[J]. Journal of Tribology, 2003, 125(2):358-363. [2] Liu N, Bogy D B. Particle Contamination on a Thermal Flying-Height Control Slider[J]. Tribology Letters, 2010, 37(1):93-97. [3] Cui F, Li H, Shen S, et al. Simulation of Air Flow and Particle Trajectories in the Head–Disk Interface[J]. IEEE Transactions on Magnetics, 2016, 52(12):1-5. [4] Liu S, Li H, Shen S, et al. Simulation of Particle Trajectory in the Head–Disk Interface[J]. IEEE Transactions on Magnetics, 2015, 51(11):1-4. [5] Liu S, Li H, Shen S, et al. Simulation of Particle Rebounding from the Slider Air Bearing Surface[J]. Microsystem Technologies, 2016, 22(6):1475-1481. [6] Liu S, Li H, Shen S, et al. Study of Adhered Particle's Secondary Migration on the Slider Air Bearing Surface[J]. Microsystem Technologies, 2017, 23(10):4871-4877. [7] Wahl M, Lee P, Talke F. An Efficient Finite Element-Based Air Bearing Simulator for Pivoted Slider Bearings using Bi-Conjugate Gradient Algorithms[J]. A S L E Transactions, 1996, 39(1):130-138.

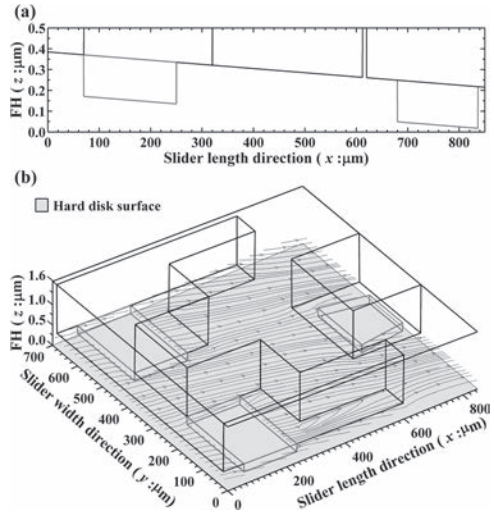

Fig. 1. (a) Flying height profile of slider and (b) air flow streamlines in the plane with a height of 0.225 μm

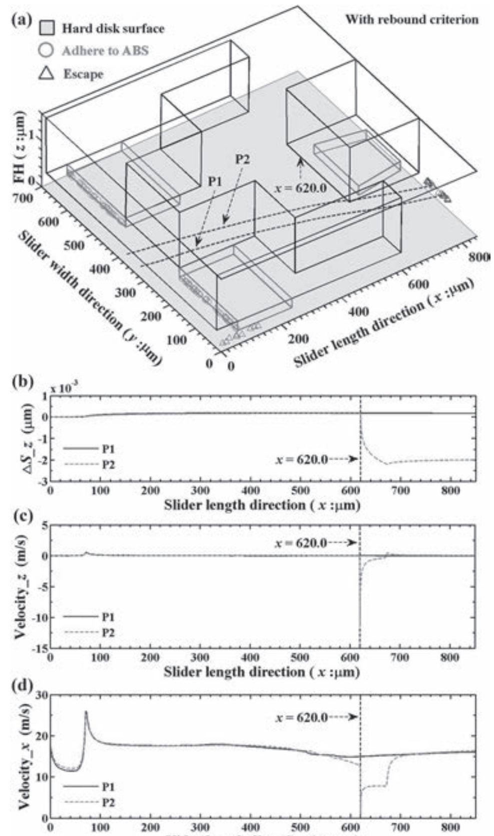

Fig. 2. (a) Trajectories and final distribution of particles, (b) z-direction displacement, (c) z-direction velocity, and (d) x-direction velocity of P1 and P2 with the rebound criterion

HV-10. Frequency analysis of disturbance torque exerted on a carriage arm in hard disk drives using Hilbert-Huang Transform.

S. Koganezawa[1]
1. Kansai University, Suita, Japan

1. Introduction Currently, hard disk drives (HDDs) are widely used as external storage devices. In HDDs, flow induced vibrations (FIVs), i.e., the vibrations of carriage arms and disks due to the internal flow of HDDs, are serious contributors to head positioning errors. To develop higher capacity HDDs, reducing head positioning errors is inevitable. Many experimental and analytical studies have been conducted thus far to reveal the internal flow in HDDs and to understand the mechanisms of the disturbance torque exerted on head-stack assemblies for mitigating FIVs. Most studies have exclusively used Fourier spectral analysis for frequency domain analysis (e.g., [1]-[3]). The Fourier spectral analysis, however, must be used for signals under restricted conditions: the system must be linear, and the signal must be stationary and periodic. The internal flow of an HDD is an extremely complex phenomenon, and it is governed by non-linear Navier–Stokes equations. Therefore, the results of the Fourier spectral analysis are not always adequate. Further, if both fine frequency-resolution and high frequency spectra are required for Fourier spectral analysis, the time series data must have a long time-span and a fine time-step. Because it takes a significant amount of time to conduct a computational fluid analysis with such requirements, the results of the Fourier spectrum analysis tend to have a coarse frequency-resolution. The Hilbert–Huang transform (HHT) proposed by Huang et al. is a useful method for analyzing a nonlinear and non-stationary signal, and it has been applied to seismic signal analysis [4]. HHT consists of two parts: ensemble empirical mode decomposition (EEMD) and Hilbert transform (HT). EEMD is a way to decompose time series data into intrinsic mode functions (IMF) considering the envelope of the waveform. After EEMD is conducted, HT is executed, and the analytic signal is generated afterward. Then, the instantaneous frequency and amplitude are calculated from the analytic signal as time series data; therefore, it is possible to analyze the nonlinear and non-stationary signal. In this study, we applied the HHT to the time series of the torque exerted on the carriage arm, which is calculated using finite element analysis. Then, a frequency analysis using FFT and HHT was conducted, and their results were compared. 2. Computational fluid dynamics analysis of HDD A finite element (FE) model for fluid dynamics analysis was produced by referring to a 3.5-in HDD. The computational region for air flow was the inner space of the HDD, which was cut out between two disks. The FE model had a voice-coil-motor (VCM) carriage and a flexible printed circuit. The head suspensions were excluded from the FE model. The disk diameter was 95 mm, and the rotational speed of the disks was 7,200 rpm. The VCM surface was divided into five areas, and the disturbance torque exerted on each area was calculated. ANSYS CFX, a code for fluid analysis, was used for air-flow simulation. Large eddy simulation (LES) was employed as the turbulence model. The time step was 2.0×10^{-5} s, and the number of time steps was 15,000. Thus, the time span of the simulation was 0.3 ms, and the last 5,000 time-series data were used for frequency analysis. At first, contour-plot animations of the flow velocity and vorticity were made and visually observed. When the carriage arm is at the position where the head is tracking the outermost track, several periodic flow patterns are observed: vortex shedding at the arm-tip at approximately 500 Hz, fluctuation of strong vorticities inside the arm hole at approximately 1000 Hz, and vorticities between the disk and arm and the outside of the disk at 700 to 1000 Hz. Next, a Fourier analysis was conducted using the same simulation results. Although the time series of the torque exerted on the carriage arm seems to have a regularity or periodicity involving such specific frequencies as seen in the animations, there was no specific peak in the Fourier spectra, as shown in figure 1. At low frequencies less than 1000 Hz, the magnitudes of the Fourier spectra are almost constant, and with increase in frequency, the magnitude of the Fourier spectra decrease. Then, the frequency analysis using HHT was performed. The disturbance-torque time series, which is identical to the data used for FFT analysis, were divided into 11 IMFs by the EEMD process. Each IMF was analyzed using HT. Figure 2 shows the HHT results. Fluctuations in frequency were observed at approximately 500 Hz and 800 Hz. The spectra at these frequencies are caused by flow-fluctuations such as vortices, as observed in the flow-animations. Comparing the HHT with FT spectra, the results confirmed that, in the Fourier spectra, the energy of the non-stationary phenomenon, whose frequency and amplitude are fluctuating at a specific frequency, diffuses over a wide frequency-band, and that forms the broadly expanded spectra, especially at low frequencies. Therefore, it is necessary for more precise head positioning to decrease torque-fluctuations due to non-stationary phenomena, such as a vortex shedding around an arm, which are not always observed in the power spectrum obtained by the FFT analysis.

[1] Hiroyuki Kubotera, Dae-Wee Kong, Takahiro Tokumiya, and Cheol-Soon Kim, "Computational Fluid Dynamics and Experimental Visualization of Time-Variable Air Flow Pattern Inside Hard Disk Drives," IEEE Trans. on Mag., Vol.48, No.8, pp.2395-2398, 2012. [2] Mohammad Kazemi, "Investigation of Fluid Structure Interaction of a Head Stack Assembly in a Hard Disk Drive," IEEE Trans. On Mag., Vol. 45. No. 12, pp. 5344-5351, 2009. [3] Shigehiko Kaneko, Takashi Nishihara, Tatsuo Watanabe," Aerodynamic characteristics of carriage arm equipped on hard magnetic disks," Microsyst. Technol., Vol. 13, pp. 1297–1306, 2007. [4] Huang, N.E., Shen, Z., Long, S.R., Wu, M.C., Shih, H.H., Zheng, Q., Yen, N.C., Tung, C.C., Liu, H.H. The empirical mode decomposition and the Hilbert spectrum for nonlinear and non-stationary time series analysis. Proceedings of the Royal Society, Vol. 454, No. 1971, 1998.

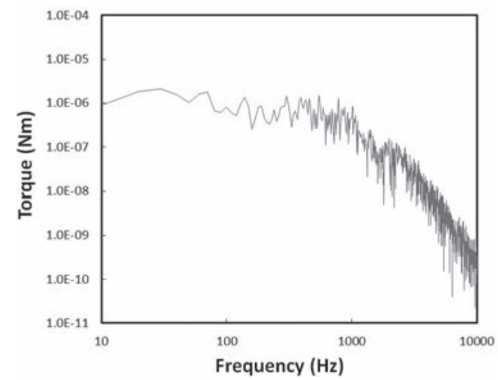

Fig. 1. Fourier spectra of torque exerted on arm.

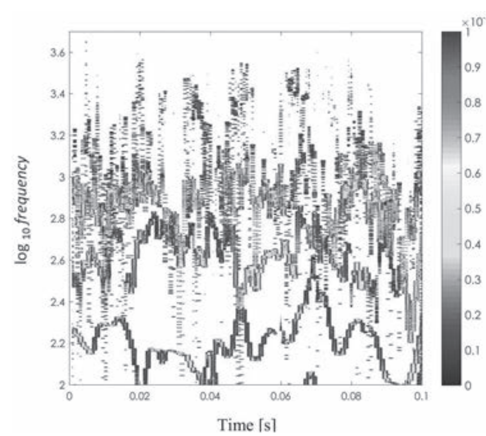

Fig. 2. HHT spectra of torque exerted on arm.

HV-11. Dynamic Performance of Head-disk Interface in HAMR Using Molecular Dynamics Simulation Method.

T. Shu[1], H. Li[1], S. Shen[1], X. Dai[1], W. Shen[1] and F. Cui[1]
1. School of Power and Mechanical Engineering, Wuhan University, Wuhan, China

Heat-assisted magnetic recording (HAMR) technology is a great way to achieve higher storage density [1-6]. In HAMR, dynamic performance of head-disk interface (HDI) is critical important for the read/write stability. Lubricant bridge formation and lubricant transfer can significantly deteriorate HDI performance. In this work, a three-dimensional full atom model of slider-lubricant-substrate system is established to study dynamic performance of HDI in HAMR, including variations of local gas pressure and weight percentage of PFPE lubricant in the process of rapid heating and cooling. The material of slider and substrate is diamond-like carbon, and the main ingredient of lubricant is perfluoropolyethers (PFPE). The chemical structure of PFPE can be expressed as X-(OCF2-CF2)*p*(CF2)*q*-O-X, (*p*/*q*=0.8-1.3), which is random co-polymer with a linear backbone chain. here the end groups, -X, are $-CF_3$ [1]. The relationship among flying height (FH), PFPE lubricant thickness and local gas pressure is also investigated. The initial pressure of gas bearing which is filled with helium is 20 atm. It is reflected by the number of helium atoms. The whole simulation time is 1 ns, and the time step is 0.001 ps. The temperature increases from 300K to 700K in the heating process, then reduces to 300K after cooling. Fig. 1 shows the three-dimensional PFPE lubricant morphological change with different FHs and lubricant thickness (denoted as *Th*). The PFPE lubricant is initially stable and smooth. After rapid heating and cooling, PFPE lubricant becomes rough due to the desorption of some molecules on its surface. And there are still some PFPE molecules adhered to the slider because of the attraction force between them. However, the number of PFPE molecules on the slider varies greatly depending on the slider flying height and lubricant thickness. Fig. 2(a) shows that the weight percentage of PFPE lubricant on the substrate reduces more significantly when the flying height is smaller with the increase of lubricant temperature from 300K to 700K. The remaining percentage of lubricant adhered to the substrate is reduced to 72%, 85% and 89% with the flying height of 2 nm, 3 nm and 4 nm, respectively at the temperature of 700K. Fig. 2(b) shows that the weight percentage of PFPE lubricant reduces significant with a larger lubricant thickness when heating temperature increases from 300K to 700K. And at the temperature of 700K, the decrement of PFPE lubricant is 35%, 15% and 13% with the lubricant thickness of 2 nm, 1.5 nm and 1 nm, respectively. It indicates that a larger proportion of lubricant is remained on the substrate with a smaller PFPE lubricant thickness. But the number of the molecules adhered to the substrate is still smaller when lubricant is thinner.

[1] Dai X, Li H, Shen S, et al. Study of Perfluoropolyether Lubricant Consumption and Recovery in Heat Assisted Magnetic Recording Using Molecular Dynamics Simulation Method[J]. IEEE Transactions on Magnetics, 2017, 53(3):1-6. [2] Xiong S, Bogy D B. Experimental Study of Head-Disk Interface in Heat-Assisted Magnetic Recording[J]. IEEE Transactions on Magnetics, 2014, 50(3):148-154. [3] Dahl J B, Bogy D B. Lubricant Flow and Evaporation Model for Heat-Assisted Magnetic Recording Including Functional End-Group Effects and Thin Film Viscosity[J]. Tribology Letters, 2013, 52(1):27-45. [4] Li B, Wong C H. Molecular Dynamics Studies of Lubricant Depletion under Moving Laser Heating: Effects of Laser Power and Film Thickness[J]. Tribology International, 2015, 92:38-46. [5] Song W, Chung P S, Biegler L T, et al. Physiochemical Response of Organic Molecules in Head-Disk Interface Under Heat-Assisted Magnetic Recording Environment[J]. IEEE Transactions on Magnetics, 2016, 52(7):1-4. [6] Sakhalkar S V, Bogy D B. A Model for Lubricant Transfer from Media to Head During Heat-Assisted Magnetic Recording (HAMR) Writing[J]. Tribology Letters, 2017, 65(4):166-180.

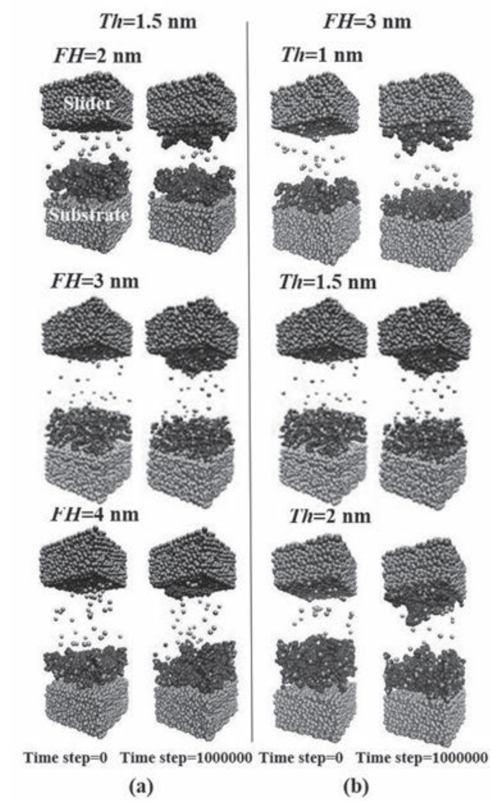

Fig. 1. 3D slider-lubricant-substrate system with (a) different FHs and (b) different lubricant thickness (*Th*).

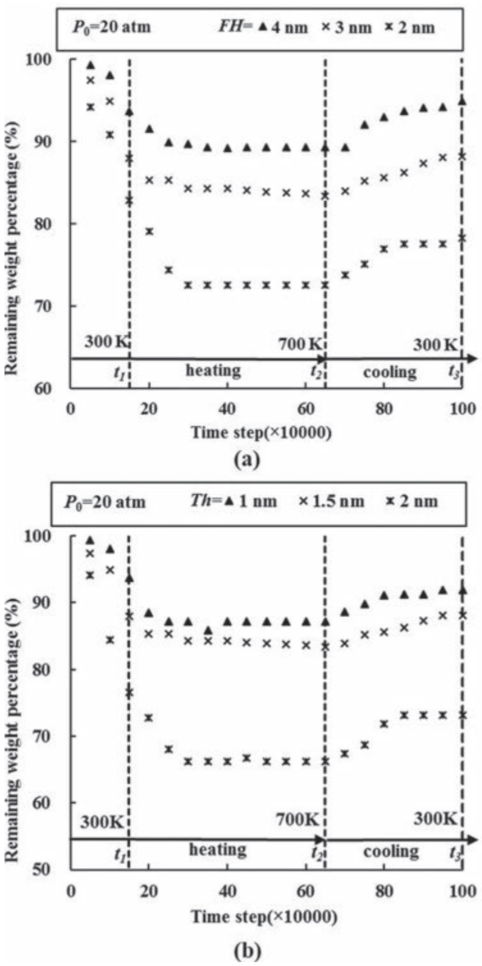

Fig. 2. The weight percentage of PFPE after rapid heating and cooling with (a) different FHs and (b) different lubricant thickness (*Th*).

HV-12. Effect of Assembly Errors on Position Accuracy in a Rotary Magnetic Recording System.

H. Hsiao[1], L. Chen[1], C. Sung[1] and J. Chang[1]
1. Power Mechanical Engineering, National Tsing Hua University, Hsinchu, Taiwan

A rotary magnetic sensing system, which consists of a patterned ferrite-magnetic (FM) ring, a set of magnetoresistors (MRs) and a signal-processing unit for generation of position information, is commonly used in rotary stages or motors for position control. The magnetic signal for positioning can be generated by excitation coil [1-2] or polarities [3-4] from FM medium. The 2nd method is the focus of this paper in which the alternative polarities are made through perpendicular magnetization over the FM ring; from which magnetic signals the anisotropic MR sensors can then generate position signal based on measured magnetic profile from the FM ring. Several factors that may affect overall accuracy of the rotary platform. Firstly, position accuracy is determined during pattern writing process caused by assembly errors between writing head and the FM ring in the magnetization platform. Another crucial factor for pursuing high precision magnetic sensing accuracy is the geometry tolerance such as roundness, isotropy and homogeneity of the FM ring. Besides, errors induced by assembly between the FM ring and the MRs would lead to signal distortion [5]. A MR sensor discussed in this paper consists of two sets of Wheatstone bridge; each bridge contains four MRs that are stacked in quarter period of polarity. According to the principle of MR output signal, the magnitude and magnetization angle of magnetic flux originated from patterned media would induced the resistance changes of MRs packaged in a sensor. Namely, different magnitude and magnetization angle of magnetic flux distribution can lead to different output voltages. When two sets of Wheatstone bridges are properly arranged in the moving read head, output signals can be generated in form of sine and cosine waveforms from which a Lissajous graph can be depicted for positioning feedback. With perfect sine and cosine waveforms, an ideal Lissajous graph is a perfect circle. By dividing Lissajous graph into equivalent divisions, higher resolution can be achieved. The difference between ideal and distorted Lissajous graphs can then be used to determine position error [6]. The inevitable assembly error of MR sensor in manufacturing can cause the angle between magnetization vector and magnetoresistance to vary, which directly affect the resistance value, resulting in imperfect sinusoidal output voltage, which then becomes an obstacle for increasing resolution and position accuracy. Effect of assembly errors including eccentricity I1, offset I2 from rotary platform's rotation center, and pitch, roll, yaw errors of the MR sensor read head relative to the surface of FM ring as depicted in Fig. 1 will be discussed in the context of position accuracy through a commercial available FM rotary scale. The commercial FM rotary scale has pre-magnetized 256 polarities mounted on a precision rotary platform. The assembly errors can be categorized to eccentricity between rotary stage and the FM ring and the assembly errors due to sensor itself are shown in Fig. 1(a) and Fig. 1(b), respectively. The Os and Oe represent the center point of rotary platform and rotary scale. l1 and l2 respectively represent the eccentricity between rotary platform and magnetic ring and eccentricity between sensor and rotary platform. Both experimental and analytical approaches are conducted in this study. In the experiments, this FM ring was first assembled with least eccentricity by calibrating with high-resolution digimatic indicator, leading to minimum eccentricity l1. To investigate the effects of assembly error of sensor on accuracy, the MR sensor read head was fixed on a linear precision stage, which was aligned with the centerline of rotary platform. As such, the eccentricity l2 could be known from the linear precision stage. In the analytical method, magnetic flux density distribution of the rotary scale with assembly error is obtained through 3D finite-element simulation. By putting the simulated outputs into flux density and circuit voltage equations, the output of the MR sensors in the read head can then be attained. The sensor assembly offset error discussed in this study is set from 0 mm to 0.5 mm with step of 0.1 mm, and rotational assembly error such as pitch, roll and yaw error are both ranged from 0° to 2° with step of 0.2°. Fig. 2(a) shows the simulated accuracy distribution at 0.2 mm flying height over three polarities on stack lines by y offsets plot with offset of read head ranging from 0 mm to 0.5 mm. At different offset, the distribution of accuracy is found to shift to the left side as the offset is increased. The simulated accuracy errors caused by assembly error of read head including pitch, roll, and yaw errors are shown in Fig. 2(b). The result of pitch error percentile is marked on left vertical axis, whereas roll and yaw error percentiles are indicated on right vertical axis. It is found that pitch assembly error up 2° contribute more significant effect on accuracy error caused by roll and yaw assembly errors. The pitch assembly error can worsen accuracy nearly 115% relative to perfect assembly. On the other hand, degradation of accuracy caused by roll and yaw assembly errors is found only 6.4% and 3.5%, respectively relative to perfect assembly.

[1] Q. Tang, D. Peng, L. Wu and X. Chen, "An Inductive Angular Displacement Sensor Based on Planar Coil and Contrate Rotor," in IEEE Sensors Journal, vol. 15, no. 7, pp. 3947-3954, Jul. 2015. [2] D. Zheng, S. Zhang, S. Wang, C. Hu and X. Zhao, "A Capacitive Rotary Encoder Based on Quadrature Modulation and Demodulation," in IEEE Transactions on Instrumentation and Measurement, vol. 64, no. 1, pp. 143-153, Jan. 2015. [3] J. R. R. Mayer, "High-resolution of rotary encoder analog quadrature signals," in IEEE Transactions on Instrumentation and Measurement, vol. 43, no. 3, pp. 494-498, Jun 1994. [4] L. Jogschies, D. Klaas, R. Kruppe, J. Rittinger, P. Taptimthong, A. Wienecke, L. Rissing, M.C. Wurz, "Recent Developments of Magnetoresistive Sensors for Industrial Applications," in Sensors, vol. 15, no.11, pp. 28665-28689, Nov. 2015. [5] H. S. Hsiao and J. Y. J. Chang, "Characterization of Signal Integrity Due to Pitch–Roll–Yaw Rotation Tolerance in Magnetic Position Sensing Systems," in IEEE Transactions on Magnetics, vol. 53, no. 3, pp. 1-7, Mar. 2017. [6] J. Hu, J. Zou, F. Xu, Y. Li and Y. Fu, "An Improved PMSM Rotor Position Sensor Based on Linear Hall Sensors," in IEEE Transactions on Magnetics, vol. 48, no. 11, pp. 3591-3594, Nov. 2012.

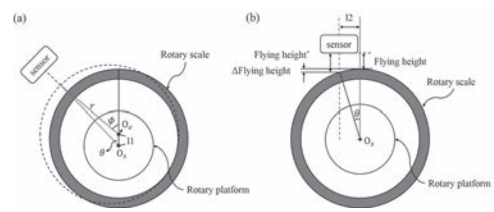

Fig. 1. Schematics of rotary magnetic recording system with (a) eccentricity error and (b) sensor assembly errors.

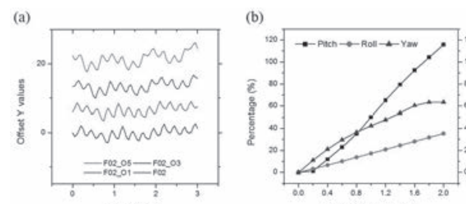

Fig. 2. Simulated accuracy (a) distribution at 0.2 mm flying height and (b) percentiles caused by read head pitch, roll, and yaw assembly errors.

HV-13. Optimising dual layer recording using antiferromagnetic exchange coupling.

S. Greaves[1], T. Kikuchi[1], Y. Kanai[2] and H. Muraoka[1]
1. Tohoku University, Sendai, Japan; 2. Niigata Institute of Technology, Kashiwazaki, Japan

Introduction Multiple layer magnetic recording may be possible with the advent of microwave-assisted magnetic recording (MAMR) [1], [2]. In a MAMR system, recording on a medium with high uniaxial anisotropy is made possible by applying a high frequency (HF) magnetic field at the resonance frequency of the medium, leading to a reduction in the switching field. If two discrete recording layers, RL1 and RL2, have different resonance frequencies, selective recording on one or other of the layers may be possible by adjusting the frequency of the spin torque oscillator (STO) used to generate the HF field. The magnitude of the coercivity reduction is related to the strength of the HF field in the medium. As STOs typically have dimensions from 20 - 40 nm the HF field strength decreases rapidly with distance from the STO. For this reason, if multiple recording layers are to be used each layer must be as thin as possible and the separation between the layers cannot be large. However, if the separation between the recording layers is small, magnetostatic interactions between them are large. This can make it difficult to implement selective recording due to the magnetostatic interaction favouring parallel alignment of the magnetisation of both recording layers. It may be possible to counteract the influence of the magnetostatic field by introducing antiferromagnetic exchange coupling between the two recording layers, e.g. by using Ru or Ir spacers [3], and this is the topic of this work. The aim is to optimise the antiferromagnetic exchange coupling and to determine the effect on recording performance. The Model Dual layer recording media with a 7 nm RL1 / 2 nm Spacer / 5 nm RL2 / 3.5 nm Air / Write Head structure were modelled. Each recording layer was an exchange coupled composite (ECC) structure with M_s = 750 emu/cm^3 in all layers and the hard layers below the soft layers. In the model the medium grains were discretised into 1 nm-thick layers with the exchange coupling constant between layers of the same material being 10 erg/cm^2. After optimisation of the layer thicknesses and other parameters RL1 had a 3 nm hard layer and a 4 nm soft layer. The soft layer had K_u of 3×10^6 erg/cm^3 and the exchange coupling between the hard and soft layers was 4 erg/cm^2. RL2 was formed of a 2 nm hard layer and a 3 nm soft layer. The soft layer had K_u of 5×10^6 erg/cm^3 and the exchange coupling between the hard and soft layers was 6 erg/cm^2. The hard layer K_u of both recording layers was a variable parameter. The field distribution from a write head with a 36 nm wide main pole and a 30 nm gap between the main pole and the trailing shield was calculated using a finite element model. A STO was placed 5 nm behind the main pole to generate the HF field in the media. The STO was modelled as a 36 nm wide, 36 nm high and 14 nm thick field generating layer (FGL) with M_s of 1591 emu/cm^3 and coherent rotation of the FGL magnetisation was assumed. Results The effect of the magnetostatic interaction on the switching of the magnetisation of RL1 is shown in fig. 1. In the calculation a 4 ns field pulse was applied to an 8 nm × 8 nm grain containing two discrete recording layers, RL1 and RL2. The hard layer H_k (= $2K_u$ / M_s) was varied and the maximum H_k that could be switched by the combination of the head field and STO field was calculated as a function of HF field frequency. The magnetisation of RL2 was fixed either "up" or "down" and, as fig. 1 shows, the result was to change the maximum switchable H_k of RL1 by about 17 kOe: this difference was due to the magnetostatic field from RL2 acting on RL1 and is measured by the quantity ΔH_k. Next, antiferromagnetic exchange coupling with a strength J_{IL} was introduced between RL1 and RL2. The inset to fig. 1 shows the effect of J_{IL} on ΔH_k. When J_{IL} was about -0.17 erg/cm^2 the influence of the magnetostatic field was eliminated and ΔH_k was zero. Tracks were written on media with two recording layers using HF field frequencies of 20 GHz and 50 GHz. The bit length was 30 nm (847 kfci) and the head velocity was 5 m/s. The temperature was 300 K and distributions of grain size (16.5%), M_s (4.25%), K_u (8.5%) and easy axes (3°) were included. The signal to noise ratio (SNR) was calculated for tracks recorded on each layer using the sensitivity function of a 20 nm wide magnetoresistive (MR) read head. Fig. 2 shows the results as a function of J_{IL}. For RL1 the SNR increased by about 1.2 dB when J_{IL} was optimised, compared with the case when J_{IL} was zero. A small amount of ferromagnetic coupling between RL1 and RL2, e.g. J_{IL} = 0.1 erg/cm^2, caused a sharp decrease in the SNR of RL1. The SNR of RL2 was higher due to the layer being nearer to the write head and consequently experiencing higher head field gradients and HF fields. The SNR of RL2 was almost unchanged by J_{IL} until J_{IL} reached -0.3 erg/cm^2. Reversing the order of the hard and soft layers in RL1 to put the hard layer next to the non-magnetic interlayer made RL1 more resistant to the magnetostatic fields from RL2, but reduced the SNR. This was because magnetisation reversal was initiated in the soft layer and this layer experienced a smaller HF field when it was further from the STO. The authors would like to thank the ASRC for their support of this work.

[1] G. Winkler, D. Suess, J. Lee, J. Fidler, M. A. Bashir, J. Dean, A. Goncharov, G. Hrkac, S. Bance, and T. Schrefl, Appl. Phys. Lett. 94, 232501, (2009). [2] H. Suto, T. Nagasawa, K. Kudo, T. Kanao, K. Mizushima, and R. Sato, Phys. Rev. Appl. 5, 014003, (2016). [3] P. J. H. Bloemen, H. W. van Kesteren, H. J. M. Swagten, and W. J. M. de Jonge, Phys. Rev. B 50, 13505, (1994).

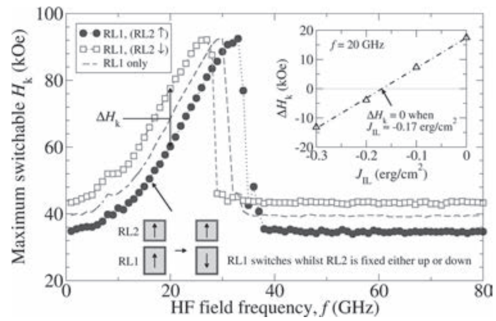

Fig. 1. Maximum switchable H_k of RL1 hard layer vs. HF field frequency when RL2 is magnetised up or down. Inset: ΔH_k vs. exchange coupling strength between RL1 and RL2, J_{IL}.

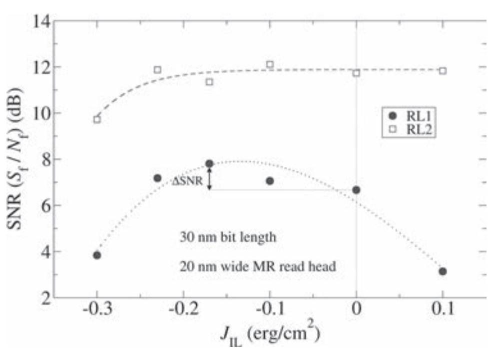

Fig. 2. SNR of tracks written at 847 kfci on dual layer media vs. exchange coupling strength between RL1 and RL2, J_{IL}.

HV-14. A General LDPC code Design Framework for High-density Magnetic Recording with 2D-ISI.

L. Kong[1] and X. Jiang[2]
1. Nanjing University of Posts & Telecommunications Nanjing, NANJING, China; 2. Donghua University, Shanghai, China

Increasing the density of the magnetic recording and scaling down the track pitch have led to a dramatic destroy in the reliability of magnetic recording system, such as Bit-patterned media recording (BPMR), shingled writing (SW), and two-dimensional magnetic recording (TDMR), suffering from the two-dimensional (2D) inter-symbol interference (ISI) which is made up of inter-track interference (ITI) and conventional (down-track) ISI. The 2D-ISI severely degrades the performance of data detection in these systems, and becomes the major impairment for the high-density magnetic recording systems beyond 1Tb/in^2[1]. Due to the computational burden of the symbol-based Bahl-Cocke-Jelinek-Raviv (BCJR) 2D detectors (2D-DETs) that has prohibitive complexity for the typical 2D data size over 2D-ISI channel, suboptimal 2D channel detectors with lower complexity have been proposed in [1]-[2], such as iterative row- column soft decision feedback algorithm based on gaussian approximation (IRCSDFA-GA). Besides 2D signal processing techniques, advanced channel coding also provides an effective approach to combat the 2D-ISI, which facilitates the 2D-ISI magnetic recording with a higher area density (AD). Due to the well-known superior capacity-approaching abilities in the additive white Gaussian noise (AWGN) channels, low-density parity-check (LDPC) codes are believed to be indispensable for high-density 2D-ISI magnetic recording systems. Existing LDPC codes optimized for symmetric, AWGN-like channels are not optimal for magnetic recording channels due to channel asymmetry. Unlike the highly complex LDPC codes optimization of [3], a low-complexity detector-aware code design algorithm has been proposed for dense 2D-ISI channels in [4], However, the proposed approach captured the error characteristics of 2D-ISI channels by means of the specific 2D-DET and need be operated for the different 2D-DET resulting in poor transplantation of the designed codes. In this paper, we present a general LDPC code design framework for high-density magnetic recording with 2D-ISI, which is transparent to the 2D-DET that the system employs. Specifically, C_{mg} is defined as the capacity margin between the symmetric information rate (SIR) of 2D-ISI channel and AWGN capacity for the given code rate. The new parameter captures the "mismatching" characteristics of the 2D-ISI channel and AWGN channel, which is the major reason why the codes optimized for AWGN channels do not perform well than the ones done for the 2D-ISI magnetic recording channels.

[1] Y. Wang, B. V. K. Vijaya Kumar, "Multi-track joint detection for shingled magnetic recording on bit patterned media with 2-D sectors," *IEEE Trans. Magn.,* vol. 52, no. 7, Article#: 3001507, Jul. 2016. [2] J. Zheng, X. Ma, Y. L. Guan, K. Cai, and K. S. Chan, "Low-complexity iterative row-column soft decision feedback algorithm for 2D inter- symbol interference channel detection with Gaussian approximation", *IEEE Trans. Magn.*. [DOI: 10.1109/TMAG.2013.2242333] [3] L. Kong, Y. L. Guan, J. Zheng, G. Han, K. Cai, and K. S. Chan, "EXIT-chart-based LDPC code design for 2D ISI channels," *IEEE Trans. Magn.,* vol. 49, no. 6, pp. 2823-2826, Jun. 2013. [4] L. Kong, K. Cai, P. Chen, and F. Bing, "Detector-aware LDPC code optimization for ultra-high density magnetic recording channels", *IEEE Transactions on Magnetics*, vol. 53, no. 11, Nov. 2017.

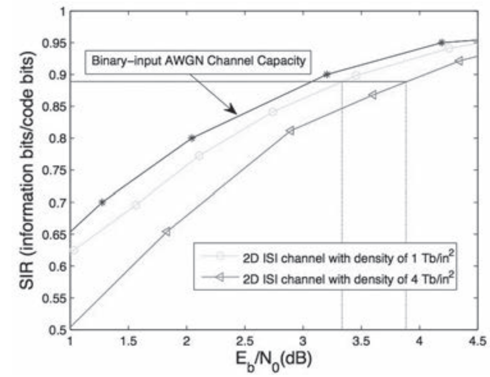

Fig. 1. The capacity margin between the symmetric information rate (SIR) of 2D-ISI channel and AWGN capacity.

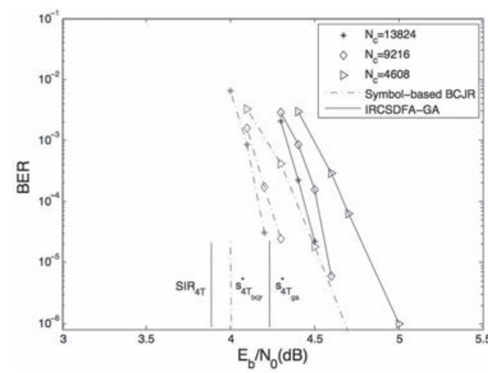

Fig. 2. The threshold and BER performance of the LDPC codes detected by different 2D-DETs for three different code lengths in a 2D ISI channel with recording density of 4Tb/in^2.

HV-15. Reduced Complexity Multi-track Joint Equalization and Detection of High Areal Density Magnetic Recording.

L.M. Myint[1], C. Warisarn[2] and P. Supnithi[3]

1. School of Science and Technology, Shinawatra University, Thailand, Pathum Thani, Thailand; 2. College of Advanced Manufacturing Innovation, King Mongkut\'s Institute of Technology Ladkrabang (KMITL), Bangkok, Thailand; 3. Telecommunications Engineering Department, King Mongkut\'s Institute of Technology Ladkrabang (KMITL), Bangkok, Thailand

In ultra-high areal density magnetic recording systems such as bit patterned media recording (BPMR) system, the width of a reader is expected to be relatively wider than the track pitch, thus, it will detect the magnetic field from the main track as well as those from the adjacent track which in turn resulting severe inter-track interference (ITI) effect on the readback signal. In the literature, multi-track joint detection techniques using array reader (AR) have been proposed to tackle ITI problem in future high areal density (AD) system [1-4] because it can provide a significant performance gain by processing multiple readback signals concurrently at the expense of high complexity. Most of researches focus on the data recovering from the single track or the number of tracks less than or equal to the number of readers while ITI effect from the sidetracks is alleviated. Considering the readback signal contains the significant contributions from the adjacent tracks, the system can generate the estimated data sequences not only from the main tracks but also from their adjacent tracks by employing the multi-track joint detection technique and AR. Therefore, in this paper, we propose a multi-track joint equalization and detection technique for a high AD magnetic recording system to recover the recorded data on four consecutive tracks (two tracks directly under the readers and two immediate sidetracks) by processing two readback signals from an array of two-reader. Given that each readback signal contains the substantial contributions from the side-tracks, we expect to achieve the estimated data from the sidetracks with the acceptable reliabilities for further decoding process. To reduce the detector's complexity, we also propose to use a multi-track Viterbi detector using a simplified trellis with parallel branches to recover data on the sidetracks. In the simulation model, we consider a discrete high areal density BPMR system with multi-track multi-head as shown in Fig. 1. The system is a two-head four-track system (2H4T) in which the data from four consecutive tracks, i.e., $a_{1,k}$, $a_{2,k}$, $a_{3,k}$ and $a_{4,k}$ are recovered by processing the readback signals, i.e., $r_{2,k}$ and $r_{3,k}$ from the array reader assuming that the centers of two head are aligned those of 2nd and 3rd track. To generate each readback signal, we use a two-dimensional (2-D) BPMR channel matrix with size of 5x3 and its coefficients are computed by a 2-D Gaussian pulse response using the parameters of areal density 4 Tb/in^2 from [4]. In the model, the readback signal, $r_{2,k}$ has the contributions mainly from the data on the 2nd track, $a_{2,k}$ as well as partially from the data on the 1st and 3rd tracks, $a_{1,k}$ and $a_{3,}$ (insignificantly from the 0 and 4th track). Similarly, the readback signal, $r_{3,k}$ contains the contributions from the data on the 2nd, 3rd and 4th track, $a_{2,k}$, $a_{3,k}$, $a_{4,k}$. In the equalization system, we employ two (2-D) equalizers, I and II, with size of 3x5 and two special (2-D) generalized partial response (GPR) targets, I and II, with size of 3x3, $G_1 = [0, g_{1,2}, 0; g_{2,1}, g_{2,2}, g_{2,3}; g_{3,1}, g_{3,2}, g_{3,3}]$ and $G_2 = [g_{1,1}, g_{1,2}, g_{1,3}; g_{2,1}, g_{2,2}, g_{2,3}; 0, g_{3,2}, 0]$ and they are designed using the minimum mean squared error (MMSE) method. Notice that some coefficients of target are set into zero aiming at reducing the trellis's complexity. The two readback siganls are sent to the system. Assuming that the system is well synchronized and no frequency offset, the signal sequence is the difference between two readback signals, i.e., $r_{2,k}$ and $r_{3,k}$. Assuming the sequence $\{r_{2,k} - r_{3,k}\}$ contains the contributions of the data on all four tracks, it is also fed to both equalizers as shown in Fig.1(a). Finally, the equalized signals $d_{2,k}$ and $d_{3,k}$ are processed in the multi-track joint Viterbi detector to generate the estimated data from four tracks. For the detector, the states and input symbols in trellis are considered with only the data, $a_{2,k}$, $a_{3,k}$, thereby resulting only 16 states and 4 outgoing branches at each state. To recover the sidetracks' data, $a_{1,k}$, $a_{4,k}$ are considered as parallel branches between each state transition as shown in Fig. 2(a) [5]. In Viterbi algorithm, the branch with the minimum metric value among all parallel branches is selected as the survival path. To compare the proposed (2H4T) system, we consider a multi-track system employing a four-reader array (4H4T) in Fig.1(b). In this system, we consider a multi-track joint Viterbi detector employing a trellis with 256 states and 16 branches as a full-fledged system. The performance comparison of proposed 2H4T multi-track system and 4H4T multi-track system is shown in Fig.2(b). When we study the BER performance of both systems for recovering the on the center 2nd and 3rd tracks, $a_{2,k}$, $a_{3,k}$ (solid lines), the proposed method is significantly inferior to the 4H4T system as we expected. However, the proposed method is outperformance over the latter for the performance recovering the data on the outer 1st and 4th tracks, $a_{1,k}$, $a_{4,k}$ (dotted lines). Notice that the BER performances of the center and outer tracks are very similar in the proposed method. The performance of proposed method is not as good as the full-fledged system, but it can generate the estimated data sequence from the sidetracks with the acceptable reliabilities and then they can be improved by using a robust channel coding system. Acknowledgement: This work was partly supported by the Thailand Research Fund (TRF) and Shinawatra University (SIU).

[1] G. Mathew, et al., "Capacity Advantage of Array-Reader-Based Magnetic Recording (ARMR) for Next Generation Hard Disk Drives," *IEEE Trans. Magn.,* vol. 50, no. 3, Mar. 2014. [2] Y. Wang, B. Yuan and K. K. Parhi, "Improved BER Performance With Rotated Head Array and 2-D Detector in Two-Dimensional Magnetic Recording," in *IEEE Trans. Magn.*, vol. 52, no. 7, pp. 1-6, July 2016. [3] J. R. Barry et al., "Optimization of Bit Geometry and Multi-Reader Geometry for Two-Dimensional Magnetic Recording," in *IEEE Trans. Magn.*, vol. 52, no. 2, pp. 1-7, Feb. 2016. [4] Y. Wang and B. V. K. V. Kumar, "Multi-Track Joint Detection for Shingled Magnetic Recording on Bit Patterned Media With 2-D Sectors," in *IEEE Trans. Magn.*, vol. 52, no. 7, pp. 1-7, July 2016. [5] S. Nabavi, B. V. K. V. Kumar and J. G. Zhu, "Modifying Viterbi Algorithm to Mitigate Intertrack Interference in Bit-Patterned Media," in *IEEE Trans. Magn.*, vol. 43, no. 6, pp. 2274-2276, June 2007.

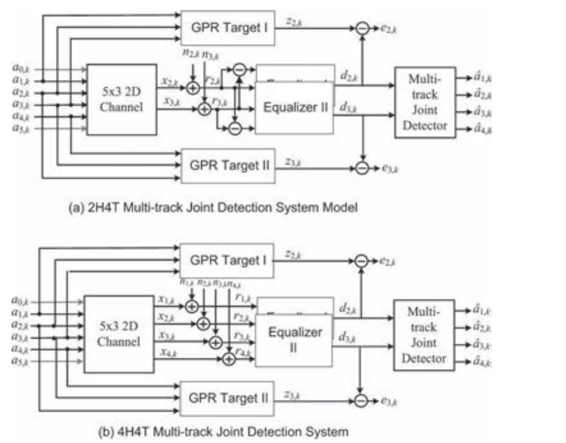

Fig. 1. Simulation Model

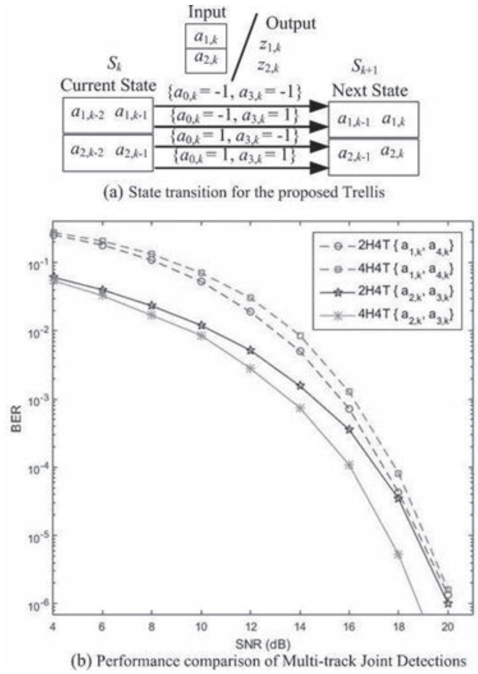

(a) State transition for the proposed Trellis

(b) Performance comparison of Multi-track Joint Detections

Fig. 2. Trellis's State Transition and Performance Comparison

FRIDAY AFTERNOON, 27 APRIL 2018 SIMPOR/ROSELLE BALLROOM, 1:30 TO 4:30

Session HW
MAGNETO-CALORIC MATERIALS II
(Poster Session)

Jia Yan Law, Chair
Sevilla University, Sevilla, Spain

HW-01. Effect of Si doped on magnetic and magnetocaloric properties of Ni-Co-Mn-Sn alloys.

S. Ghosh[1], P. Sen[2] and K. Mandal[1]

1. Condensed Matter Physics and Material Sciences, S.N.Bose National Centre for Basic Sciences, Kolkata, India; 2. Physics Group, Variable Energy Cyclotron Centre, Kolkata, India

Magnetocaloric effect (MCE) refers to thermal response of a magnetic material when subjected to changes in an external magnetic field, which is quantified by isothermal change in entropy (ΔS_M) and adiabatic temperature change (ΔT_{ad}). [1] During last decade, Ni-Mn based Heusler alloys have been found to show a large inverse MCE across their first order magneto-structural transition (FOMST). [2-3] However, a small amount of Co doped (replacing Ni) in these alloys enhances the ΔS_M value but the appearance of field induced hysteresis across the FOMST reduces the net refrigerant capacity (RC) of that material in higher doping concentrations. [4] Therefore to develop inverse MCE properties of Hesuler alloys, we have to reduce the thermal hysteresis significantly to make their real use as refrigerant material. Herein, the magnetic and MCE properties of polycrystalline $Ni_{48}Co_{1.5}Mn_{35}Sn_{15.5-x}Si_x$ (x = 1, 2, 4) Heusler alloys (prepared by arc melting furnace) have been investigated by magnetic measurements. M-T curves of x = 1, 2 and 4 alloys are measured during zero field cooled (ZFC) and field cooled cooling (FC) mode under 100 Oe field within the temperature range of 5 K to 400 K. All the alloys are found to show FOMST along with a second order magnetic transition (Ferro-Para). The characteristic transition temperatures: austenite start (A_S), austenite finish (A_f), martensite-austenite transition temperature [$T_A = (A_S+A_f)/2$], martensite start (M_S), martensite finish (M_f) and austenite-martensite transition temperature [$T_M = (M_S+M_f)/2$] are determined from M-T curves which are plotted as a function of Si content, shown in Fig. 1(a). It is found that the structural transition temperature shifts to the lower temperature with increasing Si substitution in place of Sn. The transition width ($\Delta T = T_A - T_M$) is found to decrease with Si substitution. It is well known that decrease in e/a ratio and as well as the increase in cell volume reduces the structural transition temperature in Heusler alloys. Here the substitution of Si in place of Sn does not change the valence electron number but reduces the cell volume, having smaller atomic radius of Si than Sn. Therefore, in our case an opposite effect has been observed: decrease in cell volume reduces T_M. This can be explained by considering the degree of crystallographic present in the sample. [5] Similar effect has been observed in other reported Si doped Heusler alloys. [5] Isothermal M-H curves for x = 1, 2 and 4 alloys are carried out across their structural transition at 5K interval in the field range of 0 - 50 kOe during heating protocol [Fig. 1]. ΔS_M, an important parameter in MCE studies, can be calculated using Maxwell's equation [4] by numerical integration of the isothermal M-H curves. ΔS_M is plotted as a function of temperature for different field change of x = 1, 2 and 4 alloys, shown in Fig. 2. The obtained values are 10.86, 5.46 and 2.42 $Jkg^{-1}K^{-1}$ for x = 1, 2 and 4 respectively due to a filed change of 50 kOe. It is found that with enhancing of Si substitution, ΔS_M decreases to a lower value due to being the less sharp of across martensitic transition with increasing x. As expected, ΔS_M increases monotonically with the applied field changes till the peak of ΔS_M occurs across T_A due to the twin boundary motion and motion of the spin walls. The obtained ΔS_M value, 10.86 $Jkg^{-1}K^{-1}$ for x = 1 is comparable to other reported similar kind of alloys. [6] Refrigerant Capacity, another key parameter in MCE studies that estimate the usefulness of the material as a refrigerant, can be calculated from the temperature dependence of ΔS_M curve.[4] The calculated values are 171.7, 161.1 and 71.6 J/kg for x = 1, 2 and 4 respectively. Due to first order transition, the hysteresis loss should be subtracted from the RC value to get the net RC of these studied materials. The magnetic hysteresis losses of x = 1, 2 and 4 alloys are obtained from their respective M-H curves and plotted in Fig. 2(d) for the temperature region of 105 K – 220 K. The average hysteresis losses (HL) are found to be 52.1, 19.3 and 8.6 J/kg for x = 1, 2 and 4 respectively under field change of 0 - 50 kOe which in turn reduces the RC value to its net values 119.6, 141.8 and 63 J/kg. It is interesting to observe that due to Si substitution average HL drastically decreases to 8.6 J/kg for x = 4 which is very much lower than other reported values of same families. [4, 6-7]

[1] K. A. Gschneider Jr., V. K. Pecharsky, and A. O. Tsokol, Reports Prog. Phys. 68, 1479 (2005). [2] T. Krenke, M. Acet, E. F. Wassermann, X. Moya, L. Mañosa, and A. Planes, Phys. Rev. B 72, 1 (2005). [3] T. L. Phan, P. Zhang, N. H. Dan, N. H. Yen, P. T. Thanh, T. D. Thanh, M. H. Phan, and S. C. Yu, Appl. Phys. Lett. 101, (2012). [4] A. Ghosh, and K. Mandal, J. Alloys Compd. 579, 295 (2013). [5] G. R. Raji, B. Uthaman, R. K. Rajan, M. P. Sharannia, S.Thomas, K. G. Suresh and M. R. Varma, RSC Adv. 6, 32037 (2016). [6] S. Arumugam, S. Ghosh, A. Ghosh, U. Devarajan, M. Kannan, L. Govindaraj, and K. Mandal J. Alloys Compd. 712 714 (2017). [7] R. Sahoo, A. K. Nayak, K. G. Suresh and A. K. Nigam, J. Magn. Magn. Mater. 324 1267 (2012).

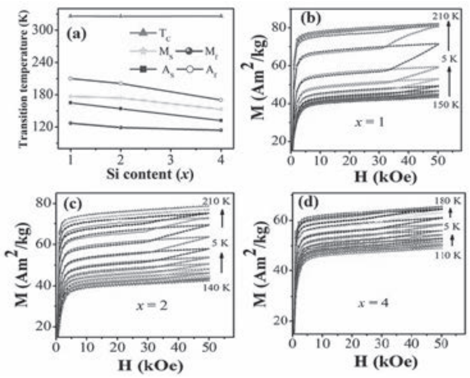

Fig. 1. Variation of characteristic transition temperatures with Si content (a). Isothermal M-H curve for x =1 (b), x = 2 (c) and x = 4 (d) alloy.

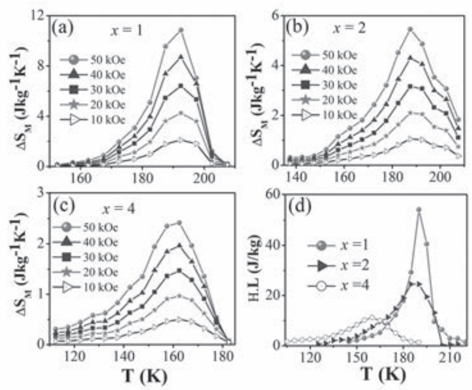

Fig. 2. Magnetic entropy change as a function of temperature for x = 1 (a), x = 2 (b) and x = 4 (c) alloy. Average HL in all the alloys under 0-50 kOe field (d).

HW-02. Magnetocaloric effect, large coercivity and exchange bias in melt-spun rare earth intermetallic compound SmNi.

J. Kurian[1], A. Chelvane[2], A. Morozkin[3], A.K. Nigam[4], S.K. Malik[5] and *N. R*[1]

1. Physics, Indian Institute of Technology Madras, Chennai, India;
2. DMRL, Hyderabad, India; 3. Lomonosov Moscow State University, Moscow, Russian Federation; 4. TIFR, Mumbai, India; 5. UFRN, Natal, Brazil

It is now well-known that the non-equilibrium, rapid solidification technique, namely, melt-spinning can be optimized to either stabilize metastable phases or to synthesize amorphous/highly crystalline intermetallics and alloys. It is of recent interest to study giant magnetocaloric materials in their melt-spun form, as the technique is fast and energy saving. In particular, highly crystalline La(Fe, Si)$_{13}$ and RNi_2 (R=Rare earth) compounds have been melt-spun for improvement of their magnetic and physical properties [1, 2]. Our recent studies on melt-spun, textured equiatomic rare earth intermetallic compounds RNi (R = Gd, Tb, Dy, Ho and Er) reveal substantial magnetocaloric effect and relative cooling power values in the neighbourhood of ferromagnetic transition [3]. In the present work, the magnetic properties of SmNi compound prepared by melt-spinning technique are studied. Room temperature X-ray diffraction study on melt-spun SmNi confirms that this sample crystallizes in orthorhombic CrB-type structure (Space group *Cmcm*, No. 63) similar to its arc-melted analogue. While the EDAX analysis ascertains the composition, the scanning electron microscopy image reveals the presence of micron sized grains in the melt-spun sample. The temperature dependent magnetization of melt-spun SmNi compound shows a ferromagnetic transition at about 45 K (T_C). A signature of a possible spin reorientation transition at 15 K is also observed in the low field magnetization data. Magnetization vs field (M-H) data at 5 K and 10 K display hard ferromagnetic behaviour. The saturation magnetization value is only 0.23 μ_B /f.u. for the melt-spun SmNi which is somewhat close to the value of 0.36 μ_B / f.u. reported for the single SmNi along the magnetic easy *b* axis. These values are far too less than the theoretical *gJ* value expected for Sm^{3+} ion. It had been suggested that crystalline electric fields (CEF) and complex canted magnetic structure of SmNi results leads to the observed low magnetization values. Magnetocaloric effect of this sample has been studied in terms of isothermal magnetic entropy change (ΔS_m). Using the M-H isotherms measured close to T_C, ΔS_m has been calculated. The maximum isothermal magnetic entropy change, ΔS_m^{max}, is about 1 J/kg K for the melt-spun SmNi for 50 kOe field change, at 47.5 K (Fig. 1) and is almost close to the result obtained on arc-melted sample. The CEF effects of rare earth ion play a dominant role in diminishing the magnetocaloric effect in this SmNi sample when compared to other heavy rare earth-based RNi compounds. It is interesting to note that the magnetocaloric effect changes sign below ~20 K, as competing antiferromagnetic interactions are known to exist in the non-collinear canted magnetic structure of SmNi. In addition, the ΔS_m^{max} values vary linearly with magnetic field change while a Heisenberg ferromagnet within a mean field approximation is known to depict $(\Delta H)^{2/3}$ dependence for ΔS_m^{max}, as shown by FeB-type ErNi. The average coercive field (H_c) at 10 K is ~23.9 kOe for the melt-spun SmNi and it is important to note the assymmetric M-H curve at this temperature and below. The large H_c value could have resulted from the huge magnetocrystalline anisotropy in the sample. The asymmetry in the low temperature M-H curve suggests possible exchange bias in this single phase intermetallic compound that hosts canted magnetic structure where ferromagnetic interactions are reported along *b* axis and antiferromagnetic interactions along *c* axis. It is observed from the heat capacity studies on arc-melted SmNi that magnetic specific heat contribution extends up to about 130 K which is much above T_C [4]. The magnetic entropy change could be accounted not only to the Rln2 value of ground state Sm^{3+} ions but also to the thermal excitations within the CEF levels or Schottky effect. In fact, the paramagnetic susceptibility is fitted to the modified Curie-Weiss law that includes a Van Vleck contribution.

1. J. Lyubina, R. Schäfer, N. Martin, L. Schultz and O. Gutfleisch, Adv. Mater. 22 (2010) 3735 2. P. J. Ibarra-Gaytan, C. F. Sanchez-Valdes, J. L. Sanchez Llamazares, Pablo Alvarez-Alonso, Pedro Gorria, and J. A. Blanco, Appl. Phys. Lett. 103, 152401 (2013). 3. R. Rajivgandhi, J. Arout Chelvane, S. Quezado, S.K. Malik and R. Nirmala, J. Magn. Magn. Mater. 433 (2017) 169 4. H. Drulis, A. Hackemer, A. Zaleski, Yu. L. Yaropolov, S. A. Nikitin and V. N. Verbetsky, Solid state commun. 151 (2011) 1240 and references therein.

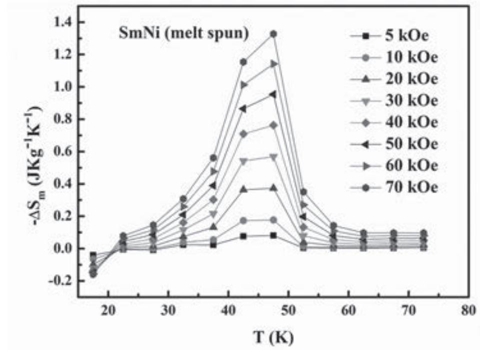

Fig. 1. Isothermal magnetic entropy change vs temperature of melt-spun SmNi for various magnetic field changes.

HW-03. Burst-like superelasticity and elastocaloric effect in Ni-Fe-Ga-Co magnetic shape memory alloys.

J. Liu[1] and D. Zhao[1]
1. Ningbo Institute of Materials Technology and Engineering, Ningbo, China

Elastocaloric cooling has been recognized as one of the most promising environmentally friendly alternatives to the state-of-the-art vapor compression cooling technique. The origin of eCE reveals that the thermodynamic and kinetic properties of the martensitic transformation determine the elastocaloric performance. Up to now, the reported eCEs in SMAs are all designed based on the thermoelastic martensitic transformation, in which the martensite grows or shrinks elastically with the variation of temperature and stress. In this work, burst-like superelastic deformation and related eCE are reported in [011] oriented $Ni_{50}Fe_{19}Ga_{27}Co_4$ magnetic shape memory single crystals at high temperature. The effect of the burst character on superelastic curve and eCE has been investigated. Besides, thermal and stress induced different martensitic structures are also identified. The $Ni_{50}Fe_{19}Ga_{27}Co_4$ ingot was arc-melted in an argon atmosphere and the single crystal was grown by the Bridgman method. A high temperature back-reflection Laue camera was used to determine the orientation of the crystal. Rectangular (nominal dimensions: $4 \times 4 \times 8$ mm^3) samples with the long axis along the [011] and [001] axis of the austenite were cut from the single crystal. The stress-strain curve and temperature change of the sample were monitored by a T-type thermocouple. Fig. 1 shows the compressive stress-strain curves with a strain rate of 2.8×10^{-3} s^{-1} at different temperatures. The commonly observed superelasticity above austenite transition temperature (320 K) does not occur in a wide temperature range of 60 K, until it suddenly appears once reaching a critical temperature of 388 K. During the phase transformation, intermittent acoustic noise was heard. The stress oscillations and audible noise are considered as the typical characters of burst martensitic transformation. In this sample, the burst and thermoelastic transformations occur alternately. A burst is first observed at the beginning of the transformation, and finishes in a few milliseconds. Large quantity of elastic energy instantaneously generates in the burst. A part of the elastic energy was dissipated by the mean of the acoustic noise. After the burst, the thermoelastic transformation subsequently takes place. In this stage, the internal stress accumulated in the burst relaxes in order to minimize the system energy, thus the stress to drive transformation is reduced. As the transformation proceeds, the burst in a small scale appears again (as indicated by the arrows in the figure), which is followed by a thermoelastic transformation as well. In the temperature range of 418-438 K, the gradually shortened transformation region and the disappearance of superelasticity result from the increasingly insufficient stress to induce the phase transformation. The cooling curve upon unloading at different initial temperatures is plotted in Fig. 2. When the initial temperature is below 388 K, the absolute value of temperature change is below 1 K because of the absence of phase transformation. At the temperatures of 388, 398, and 408 K, the complete stress induced austenitic transformation gives rise to a large cooling effect. Further increasing the temperature, the stress of 300 MPa is increasingly insufficient to induce a complete phase transformation, leading to a decrease of cooling effect. Under the stress of 300 MPa, an elastocaloric temperature window of 40 K and a maximum cooling effect of 6.1 K are obtained. In contrast, a broader temperature window and higher ΔT values (about 11 K) are observed in [001] oriented $Ni_{50}Fe_{19}Ga_{27}Co_4$ single crystal with normal superelastic behavior. This suggests the strong crystallographic anisotropy in elastic cooling effect for this single crystal.

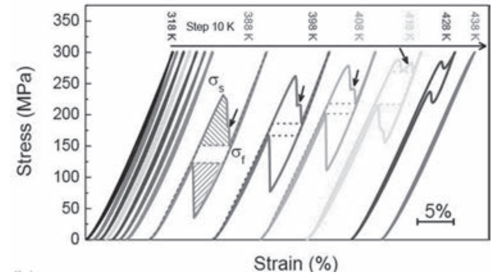

Fig. 1. Stress-strain curves with a strain rate of 2.8×10^{-3} s^{-1} at different temperatures for [011] oriented $Ni_{50}Fe_{19}Ga_{27}Co_4$ single crystal. The dotted curves are thermodynamic equilibrium superelastic curves. The hatched area represents the hysteresis loss caused by burst character. The arrows point out the bursts in a small scale.

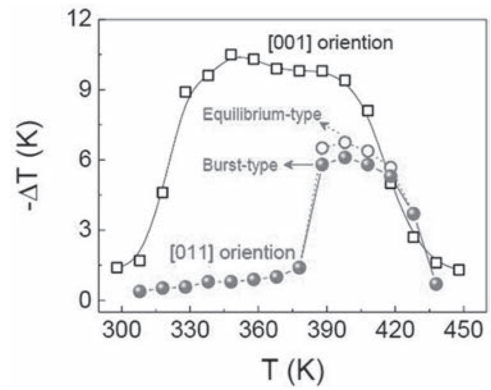

Fig. 2. Adiabatic temperature change induced by rapidly releasing the stress of 300 MPa at different initial temperatures for [001] and [011] oriented $Ni_{50}Fe_{19}Ga_{27}Co_4$ single crystals.

HW-04. Evaluation of different magnetocaloric heat exchanger stacks in a demonstrator with upcycled Nd-Fe-B permanent magnets.

D. Benke[1], J. Wortmann[1], M. Specht[1], I.A. Radulov[1], K. Skokov[1], D. Prosperi[2], P. Afiuny[2], M. Zakotnik[2] and O. Gutfleisch[1]
1. Funktionale Materialien, TU Darmstadt, Darmstadt, Germany; 2. Urban Mining Company, Austin, TX, United States

The energy demand in cooling is expected to outdo the global demand in heating by the year 2070 [Isaac]. To tackle that problem it is worth to investigate alternative cooling technologies among which magnetic cooling is the most promising and can be more energy efficient than the currently used gas-compression techniques [Zimm]. However this technology comes with its own challenges. The most prominent magnetocaloric material, the rare-earth element Gadolinium is expensive and not abundant. Also the best magnets in the world contain rare-earth elements like Neodymium and Dysprosium. This means that a conventional approach to magnetic cooling would have an ecological footprint which is worse than that of conventional cooling. Therefore, we now present the first magnetocaloric demonstrator (figure 1) based on recycled permanent magnets in order to improve the ecological footprint of this technology drastically [Gauß+Gutfleisch]. The recycled magnets have been produced by Urban Mining Company. To assess the overall performance and viability of the demonstrator as a testing device, AMR-type heat exchangers made from Gd spheres have been used. With Gd it is possible to achieve a temperature span of up to 33K (figure 2b). This shows the viability of the demonstrator as a device that is capable of testing materials. One of the most prominent alternatives to Gadolinium are compounds based on lanthanum iron and silicon which come with their own problems such as brittleness and degradation. To mediate these problems a metal bonding for these has been developped which protects it from the environment and enables a long term use in magnetocaloric devices [Radulov]. While the magnetocaloric effect of La-Fe-Si is large, it is limited to a narrow temperature region. For a magnetic cooling device that is based on the AMR design, this means that it is necessary to stack compounds with different transition temperatures in order to increase the achievable thermal span (figure 2 a). This can be easily done and tested in our demonstrator and has been done for our bonded materials. By stacking 5 different compounds it was possible to increase the achievable thermal span from 8.1K to 20.6K. The results show that the bonding procedure does not harm the magnetocaloric properties and it protects the magnetocaloric material from a possibly harmful environment such as a water based heat exchange fluid. This twofold approach of using upcycled Nd-Fe-B as a magnetic field source and substitution of Gd by La-Fe-Si drastically improves the ecological footprint of magnetic cooling and will help in the commercialization of the technology. To complement the demonstrator, a finite element model has been developed that resembles the demonstrator and gives more insights to the physical behavior and more possibilities to test new ideas. The model shows a very good correlation to the experimental measurements and will help in the optimization of the stacking of different materials in the demonstrator. This is a key problem that needs to be adressed to be able to utilize the full potential of the very high entropy change of La-Fe-Si.

[Zimm]] C. Zimm, A. Jastrab, A. Sternberg, V. Pecharsky, K. Gschneidner, M. Osborne, et al., "Description and Performance of a Near-Room Temperature Magnetic Refrigerator," in Advances in Cryogenic Engineering, P. Kittel, Ed., ed Boston, MA: Springer US, 1998, pp. 1759-1766. [Iaac] M. Isaac, D. P. van Vuuren, Energy Policy 37 (2009) 507 [Gauß+Gutfleisch] "Magnetische Materialien – Schlüsselkomponenten für neue Energietechnologien" Springer Spektrum Heidelberg, ISBN 978-3-662-48854-6, pp. 99-118 (2016). [Radulov] I. A. Radulov, D. Y. Karpenkov, M. Specht, T. Braun, A. Y. Karpenkov, K. P. Skokov, et al., "Heat Exchangers From Metal-Bonded La(Fe, Mn, Si)(13)H-x Powder," Ieee Transactions on Magnetics, vol. 53, Nov 2017.

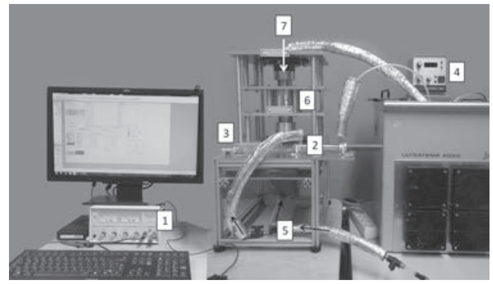

Fig. 1. Magnetocaloric demonstrator with components: (1) Power supply for electro motor; (2) waterpump (3) setting for phase difference; (4) water reservoir with heating- and cooling conditioner; (5) water hosepipes; (6) recycled halbachmagnet; (7) regenerator Insert

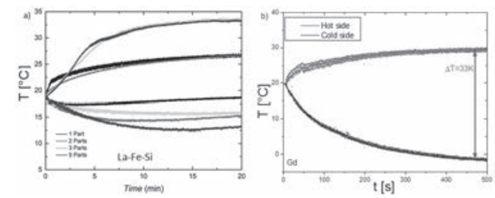

Fig. 2. a) Temperature trend for different stacks of La-Fe-Si with a resulting temperature span of 20.6 K with 5 different transition temperatures
b) Temperature trend for Gd with a resulting maximum temperature span of 33 K

HW-05. Design of an Efficient Magnetic Circuit for a Magneto-Caloric Air-Conditioning System.

C. Jäschke[1], P. Schegner[1] and J. Seifert[1]
1. Technische Universität Dresden, Dresden, Germany

I Introduction A highly efficient and cost-effective magnetic circuit is necessary to build an applicable air-conditioning system, which exploits the magneto-caloric effect [1]. Since the magneto-caloric material (MCM) and permanent magnets are the most expensive parts in the magnetic circuit, their demand needs to be minimized. This paper shows the general design of a magnetic circuit, which meets these requirements. II Basis Structure of the Magnetic Circuit Figure 1 shows the geometry of the magnetic circuit and Fig. 2 the corresponding results of a FEM computation. The MCM is stored in magneto-caloric material chambers (MCMCs), which are embedded in the stator and have a cross section of 50 mm × 10 mm. The presented magnetic circuit is capable to generate a high change of the flux density inside the MCMCs, while using a small amount of magnets. Its working principle is explained considering any leg of the magnetic circuit. Each magnet inside the outer rotor generates a magnetic flux density, which is concentrated by a pole shoe. After passing the air gap between rotor and stator, a pole shoe at the middle yoke further compresses the flux density. This highly concentrated flux density permeate a MCMC and is led to the inner yoke. Since half of the magnets in the outer rotor have an opposing orientation, the magnetic fluxes in all legs are compensated in the inner as well as in the outer yoke. By using a motor to turn the outer rotor stepwise, each pole shoe of the magnets is moving from one middle yoke to its neighbour. Meanwhile, the magnetic fluxes commutate from the penetrated middle yokes to their neighbouring. After completion of the commutation process, only half of the eight MCMCs are permeated by a high magnetic flux density. The other MCMCs, which are not directly exposed to the flux density of the magnets, are also covered by middle yokes. These act as magnetic shield and reduce magnetic stray fields inside the MCMCs. This results in a high change of the flux density between two working steps. III Optimisation of Pole Shoes and Permanent Magnets Electrical sheets made of silicon steel, which are commonly applied in electrical machines, are quite cheap and have a saturation flux density of ≈ 2 T. By using pole shoes to concentrate the emitted flux density, the proportions of the magnets can be chosen to operate near their optimum operating point. This allows generating high flux densities, while using a minimal amount of magnets. Figure 1 shows the achieved flux density change in a MCMC, by using different quantities (volumes) of magnets (type *N50*). Since the proportion of the magnets also affects the level of stray fields inside the magnetic circuit, their optimal proportion slightly differs from the point of maximum energy output. Therefore, a mathematical optimisation algorithm was applied to determine the optimal proportion of the magnets for each simulation case. Starting from a flux density of 1 T, the required volume of magnets increases approximately proportional to the achieved flux density. For a flux density change of over 1.4 T, the amount of magnets disproportionately increases with rising flux density. This behaviour is caused by the increasing magnetic stray fields inside the magnetic circuit, which arise due to the increasing size of the magnets and the higher flux density inside the electrical sheets. The MCMCs are placed inside the gaps between opposing pole shoes of the magnetic circuit. Due to the high thickness of the gap, the geometry of the pole shoes has a significant impact on the flux density inside the MCMCs. If the ends of the pole shoes were right-angled, high inhomogeneous flux densities would appear at the edges and causing a low flux density inside the chamber. Rounding the edges of the pole shoes reduces this effect, yielding higher flux densities in the MCMCs. However, the highest flux density will be obtained, if the contour is designed as a Rogowski profile. In [2], W. Rogowski derived an equation for the optimal geometry to minimize the electrical field strength at the boundary of a plate capacitor. Using this geometry yields the most homogenous distribution of the electric field between two parallel finite plates. Since the relations in electrostatic and magnetostatic are described by the same type of PDE, it is obvious that the Rogowski profile also yields the most homogenous magnetic field between two parallel pole shoes. Simulations with several kinds of pole shoe contours confirm this behaviour. Figure 2 exemplary shows the distribution of the magnetic flux density inside a MCMC by using two different pole shoe contours. In this case, the flux density change is about 0.1 T higher, if using the Rogowski profile instead of pole shoes with right-angled ends. IV Summary and Outlook The general geometry of an effective magnetic circuit was designed, which is able to generate magnetic flux densities of up to 2 T. In future work, the design will be further optimised, in order to reduce the size and weight of the magnetic circuit. V Acknowledgment The research project leading to the results described in this paper is funded by the Federal Ministry for Economic Affairs and Energy (FKZ: 03ET1374A) on the basis of a decision of the German Bundestag.

[1] J. Seifert, L. Schinke, M. Beyer, C. Jäschke, M. Krautz, A. Waske, S. Grasemann, P. Vogel, C. Schünemann: *Solare magnetokalorische Klimatisierung von Gebäuden (SOMAK), interims report to the research project*, TU Dresden, 2017 [2] W. Rogowski: *Die elektrische Festigkeit am Rande des Plattenkondensators*. Archiv der Elektrotechnik. vol. 12, pp. 1-15, 1923

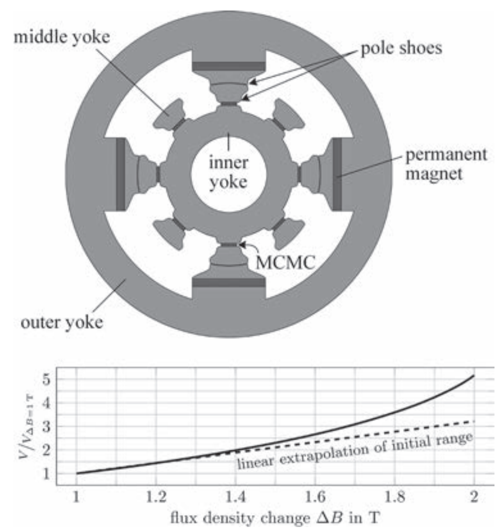

Fig. 1. Geometry of the magnetic circuit. Demand (related volume) of magnets dependent on the achieved flux density change.

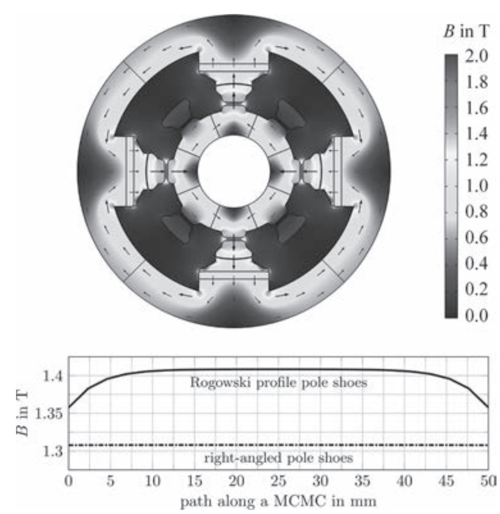

Fig. 2. FEM computation results for the magnetic circuit (ΔB = 1.4 T). Distribution of the magnetic flux density inside a MCMC dependent on the pole shoe contour.

HW-06. Magnetic properties and magnetocaloric effect of Ni_2Mn_{1+x}-Sn_{1-x} Heusler alloy thin films.

H. Yako[1], T. Shima[1] and M. Doi[1]
1. Tohoku Gakuin University, Tagajo, Japan

INTRODUCTION Ternary Heusler alloys defined as the stoichiometric composition X_2YZ with the $L2_1$ structure have attracted considerable attention due to their valuable transport and magnetic features. These compounds exhibit half-metallic behavior, magnetoresistance, magnetocaloric, shape memory and thermoelectric effects. The Heusler alloys Ni_2MnGa and off-stoichiometric $Ni_2Mn_{1+x}Z_{1-x}$ (where Z = In, Sn and Sb) are typical examples of the ferromagnetic shape memory alloys due to physical phenomena such as the large magnetic field induced strain [1], the giant magnetocaloric effects [2] and the giant magnetoresistance [3]. Especially, Ni-Mn-X (where X = Ga, In, Sn) based magnetic shape memory alloys have been proposed as solid state energy efficient refrigerant with their remarkable first order transition feature [4-8]. Most of the magnetic refrigeration materials have been studied in bulk sample. However, by changing the sample shape, it is expected to realize the efficient heat exchange and the downsized cooling device. In this study, in order to evaluate the influence on magnetic properties and magnetocarolic effect due to substrate material, heat treatment temperature and composition in $Ni_2Mn_{1+x}Sn_{1-x}$ Heusler films were investigated. EXPERIMENTAL PROCEDURES $Ni_2Mn_{1+x}Sn_{1-x}$ with x = 0.3, 0.4 and 0.5 thin films were prepared by co-deposition of Ni, Mn and Sn using an ultra high-vacuum magnetron sputtering system (ULVAC, QAM4) directly onto a thermally oxidized Si and an MgO (100) single crystal substrates at room temperature. The targets were commercial products with purities higher than 99.99 at.% for Ni and Sn and 99.9 at.% for Mn. The base pressure was under 8.5×10^{-7} Pa. High-purity argon was introduced at 0.2 Pa during sputtering. $Ni_2Mn_{1+x}Sn_{1-x}$ thin films were subsequently annealed for chemical ordering. The annealing temperature, T_a was changed from 300 °C to 600 °C. The nominal thickness of the $Ni_2Mn_{1+x}Sn_{1-x}$ thin film was fixed at 300 nm. The composition of the films was determined by energy dispersive X-ray spectrometer (EDS). The structure was analyzed by X-ray diffraction (XRD) with Cu Ka radiation. Magnetic properties were measured using a vibrating sample magnetometer (VSM) and a superconducting quantum interference device (SQUID) magnetometer. In addition, the thermo magnetization curves applying magnetic field of 1 kOe were performed with using SQUID. RESULTS AND DISCUSSION XRD patterns for the Ni_2Mn_{1+x}-Sn_{1-x} with x = 0.3, 0.4 and 0.5 thin films deposited on SiO_2 sub. at different T_a were characterized. XRD patterns of $Ni_2Mn_{1+x}Sn_{1-x}$ with x = 0.4 thin films are shown in Fig. 1. T_a was (a) 300 °C, (b) 400 °C, (c) 500 °C and (d) 600 °C. The peak from the Heusler structure was not observed for the present films with T_a = 300 °C and 600 °C. On the other hand, (111) and (311) peaks were clearly observed for T_a = 400 °C and 500 °C. This result indicates that the film possesses the $L2_1$ structure and the best T_a to obtain the $L2_1$ structure is thought to be 500 °C. Among $Ni_2Mn_{1+x}Sn_{1-x}$ thin films with x = 0.3, 0.4 and 0.5, x = 0.4 shows the maximum value of the saturated magnetization, M_s of 220 emu/cm^3. This value is smaller than the one for bulk sample (250 emu/cm^3). This is thought to due to the partially crystallization of $L2_1$ structure of $Ni_2Mn_{1+x}Sn_{1-x}$ thin films deposited on thermally oxidized Si substrate. In order to further improve crystal orientation and magnetic properties of $Ni_2Mn_{1+x}Sn_{1-x}$ thin films, optimum buffer layer or single crystal substrate should be used. In addition, the isothermal magnetic entropy change was evaluated from the magnetization data by using the Maxwell relation. The effect of substrate and composition on magnetocaloric effects has been investigated.

[1] A. Sozinov, A. A. Likhachev, N. Lanska, and K. Ullakko, *Appl. Phys. Lett.*, 80, 1746-1748 (2004) [2] P. J. Shamberger and F. S. Ohuchi, *Phys. Rev. B*, 79, 144407 (2009). [3] S. Y. Yu, Z. H. Liu, G. D. Liu, J. L. Chen, Z. X. Cao, G. H. Wu, B. Zhang, and X. X. Zhang, *Applied Physics Letters*, 89, 162503, 2006. [4] Y. Sutou, Y. Imano, N. Koeda, T. Omori, R. Kainuma, K. Ishida, K. Oikawa, *Appl. Phys. Lett.*, 85, 4358 (2004). [5] V.V. Khovaylo, T. Kanomata, T. Tanaka, M. Nakashima, Y. Amako, R. Kainuma, R.Y. Umetsu, H. Morito, H. Miki, *Phys. Rev. B*, 80, 144409 (2009). [6] T. Krenke, E. Duman, M. Acet, E. F. Wassermann, X. Moya, L. Mañosa, A. Planes, *Nature Mater.*, 4, 450-454 (2005). [7] A. Planes, L. Mañosa, M. Acet, *J. Phys. Condens. Matter.*, 21, 233201 (2009). [8] V.V. Khovaylo, K.P. Skokov, O. Gutfleisch, H. Miki, R. Kainuma, T. Kanomata, *Appl. Phys. Lett.*, 97, 052503 (2010).

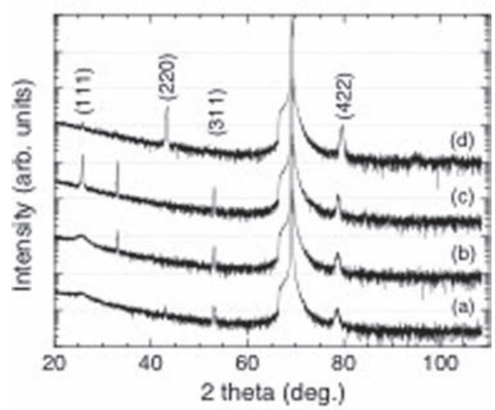

Fig. 1. XRD patterns of $Ni_2Mn_{1+x}Sn_{1-x}$ thin films with x = 0.4. T_a was (a) 300 °C, (b) 400 °C, (c) 500 °C and (d) 600 °C.

HW-07. Influences of sintering temperature on the microstructure and magnetocaloric effect of $Mn_{1.15}Fe_{0.85}P_{0.65}Si_{0.13}Ge_{0.2}B_{0.02}$ prepared by spark plasma sintering.

Z. Zhao[1], T. Jing[1], *G. Wang*[2], B. Yang[2] and X. Zhang[1]
1. School of Science, Inner Mongolia University of Science and Technology, Baotou, China; 2. Key Laboratory of Integrated Exploitation of Bayan Obo Multi-Metal Resources, Inner Mongolia University of Science and Technology, Baotou, China

Fe_2P-based compounds with large magnetocaloric effect are attracting materials for magnetic refrigeration near room temperature. Traditionally, the Fe_2P-based compounds are prepared by ball milling combined with a long period of annealing at high temperature [1,2]. Spark plasma sintering (SPS) is a newly developed synthesis process characterized by the simultaneous application of pressure and a pulsed continuous current. In this work, we report on the structural and magnetocaloric properties of $Mn_{1.15}Fe_{0.85}P_{0.65}Si_{0.13}Ge_{0.2}B_{0.02}$ prepared by SPS technique. Compounds with the same nominal composition were obtained with different sintering temperatures (T_{SPS}), namely, sintered at 700, 800, 850 and 900 °C under a pressure of 50 MPa for 15 min. Analyses of X-ray diffraction patterns demonstrate that all compounds crystallize in the hexagonal structure with space group of P-62m. The thermal magnetization curves on heating and cooling reveal that the compounds undergo first-order magnetic transitions due to the observation of clear thermal hysteresis, as shown in Fig. 1. The different sintering temperatures have influences not only on the transition temperature but also on the temperature span of the transition. The transition temperatures on heating are found to be 273, 282, 267 and 261 K for T_{SPS} = 700, 800, 850 and 900 °C, respectively. Scanning electron microscope (SEM) and energy disperse spectroscopy (EDS) measurements suggest that the compounds consist of Fe_2P-type main phase and phosphorus-free secondary phase. Isothermal entropy change (ΔS_T) for the studied compounds have been calculated from the isothermal magnetization data using Maxwell relation. Upon a field change of 3 T, the maximum values of $-\Delta S_T$ are found to be 6.4, 14.0 and 15.1 J/kg●K for T_{SPS} = 800, 850 and 900 °C, respectively. The results manifest that the SPS method is suitable for preparing magnetic bucks with excellent magnetocaloric properties.

[1] O. Tegus, E. Brück, K. H. J. Buschow and F. R. de Boer, Nature 415, 150 (2002). [2] G. F. Wang, Z. R. Zhao, L. Song and O. Tegus, J. Alloys Compd. 554, 208 (2013).

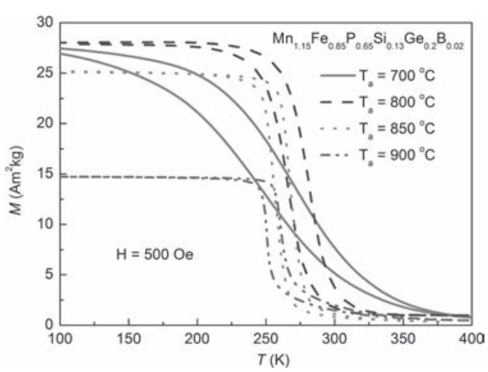

Fig. 1. Temperature dependence of the magnetization measured on heating and cooling for $Mn_{1.15}Fe_{0.85}P_{0.65}Si_{0.13}Ge_{0.2}B_{0.02}$ sintered at different temperatures.

HW-08. Customizing Magnetic and Structural Properties of Nanomaterials.

A. Aslani[1], M. Ghahremani[2], M. Zhang[3], L.H. Bennett[1] and E. Della Torre[1]
1. Electrical and Computer Engineering, George Washington University, Washington, DC, United States; 2. Computer Science, Mathematics, and Engineering, Shepherd University, Shepherdstown, WV, United States; 3. Chemistry, George Washington University, Washington, DC, United States

Magnetic nanoparticles have attracted a lot of interest due to their importance and potential application in a variety of fields. The complex magnetic behavior exhibited by nanoparticles is governed by many factors, including their size, composition, shape, morphology, and shell-core structure. The increased surface to volume ratio and tailored structure in nanoparticles introduces many size dependent phenomena which may be used to change their chemical and physical properties. Nanostructured magnetic materials are suitable candidates for magnetic refrigeration due to a presence of a large magnetocaloric effect (MCE) in the superparamagnetic system and reduced hysteresis losses. Magnetocaloric nanoparticles have a broader entropy change over a wider temperature span which results in a higher relative cooling power (*RCP*). The *RCP* measures how much heat can be transferred between the cold and hot heat exchangers in an ideal refrigeration cycle. Increasing the *RCP* not only increases the amount of refrigeration obtainable from the particular refrigerant and field excursion, but also tends to increase the thermodynamic efficiency of the cycle. Improvement in *RCP* mainly relies on broadening the magnetic entropy change by either coupling two phases of magnetic materials with desirable properties or nanostructure synthesis with the main motivation rooted in their inherent tendency to have distributed exchange coupling, which will broaden the magnetic entropy curve. As a result, to have a comprehensive understanding of various factors that can affect the magnetic and structural properties of materials, in this research, different-sized yttrium-iron nanoparticles were synthesized through alkalide reduction chemical synthesis. Powder X-ray diffraction measurements at room temperature were carried out to study the crystal structures. Surface morphology and size of the synthesized powder alloys were characterized by scanning and transmission electron microscopy. The composition of the powders was determined from energy dispersive X-ray fluorescence. Magnetization measurements were performed using vector vibrating sample magnetometer (VVSM) with standard zero field cooling (ZFC), field cool cooling (FCC), and field cool warming (FCW) techniques. The XRD measurements of the annealed nanoparticle samples fit the yttrium-iron hexagonal closed pack structure and a phase prototype similar to Th_2Ni_{17}, with space group $P6_3/mmc(194)$. The average particle size of four samples were observed to be 22, 38, 62 and 76 nm, in good agreement with crystallite size estimated from XRD data using Scherrer relation. The magnetic and structural properties of these nanoparticles were measured at different fields and temperatures to study the effect of field, temperature, and particle size variations on the critical parameters, such as Curie temperature (T_C), blocking temperature (T_B), phase transitions, saturation magnetization (M_s), remnant magnetization (M_r), and coercivity (H_c). The temperature dependent magnetization, M(T), under different applied magnetic field up to 20 KOe indicated a change in samples' T_B, which is defined as the temperature corresponding to the maximum point on the ZFC curve after its divergence from the FCC curve. As shown in Fig. 1a, for the 38 nm sample, T_B increases by increasing the applied field up to 2 KOe and then decreases with further increase in the applied field. The non-monotonic field dependence of the peak temperature in nanoparticles is attributed to the anisotropic energy barrier distribution of the particles, and to the slowly decreasing magnetization above T_B. Moreover, T_B increased as the size of nanoparticles increased (Fig. 1b). Results display that T_C of nanoparticles depends on both size and shape conditions as it decreased by reducing the particles size. The shape effect is more prominent at sizes less than 40 nm. Additionally, the phase transition became more dominant in low applied filed whereas it is smoothened by increasing the field due to particles' magnetic saturation. Moreover, magnetic couplings between particles appear stronger for larger particles. The saturation magnetization and coercivity of these nanoparticles were size and field dependent and they both decreased by reducing nanoparticles' size. Furthermore, as shown in Fig. 2, H_C and M_S are temperature dependent and they both decrease by increasing temperature since more thermal energy is supplied and individual electron spins become more likely to be in higher energy states, pointing randomly, opposite to their neighbors and less aligned, leading to a reduction in the total magnetization. Therefore, a smaller field is required to reduce remnant magnetization to zero, leading to coercivity reduction. In summary, the comprehensive results of this research are promising and novel as they suggest that the physical and chemical properties of magnetic materials can be customized to suit them in a number of applications in variety of fields such as material science, medicine, engineering, nano-electronics, information technology, etc.

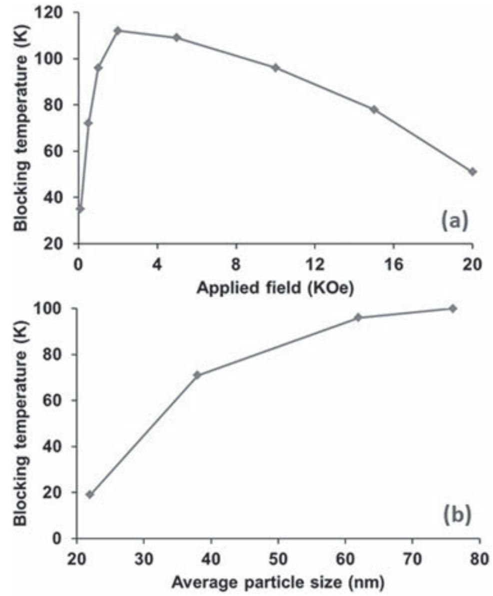

Fig. 1. (a) field-dependent blocking temperature of the 38 nm sample. (b) Size-dependent blocking temperature under 1000 Oe applied magnetic field.

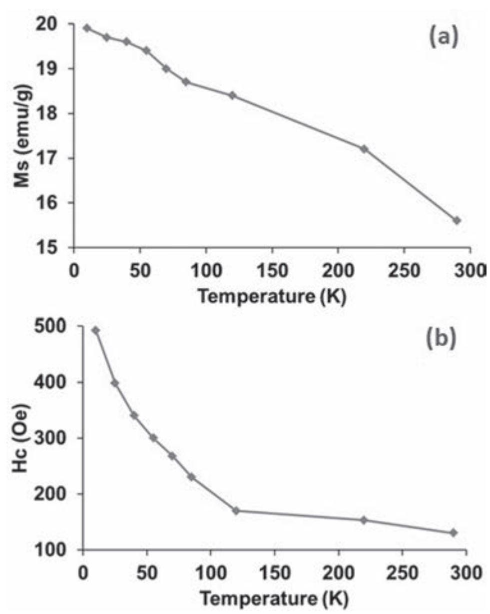

Fig. 2. (a) Saturation magnetization of the 38 nm sample as a function of temperature. (b) Coercivity of the 38 nm sample as a function of temperature.

HW-09. Magnetocaloric effect in $La_{0.7}Ca_{0.3}MnO_3$ compounds with different pressure.

W. Nan[1], D. Pham[1], S. Yu[1], W. Shon[2], J. Rhyee[2], S. Demyanov[3], N. Kalanda[3], M. Yarmolich[3] and L. Kovalev[3]
1. Department of Physics, Chungbuk National University, Cheongju, Cheongju, The Republic of Korea; 2. Department of Applied Physics, Kyung Hee University, Yongin, The Republic of Korea; 3. Scientific-Practical Research Centre of NAS of Belarus, Minsk, Belarus

Temperature change of a magnetic material associated with an external magnetic field change in an adiabatic process is defined as the magnetocaloric effect (MCE). Recently, a large magnetic entropy change has been found and intensively studied in perovskite manganites, owing to the possibility to sue these materials as active magnetic refrigerants in the magnetic refrigeration technology. Manganite perovskite of single crystalline and polycrystalline of hole- doped $R_{1-x}M_xMnO_3$ (R = rare-earth ion; *M* = divalent alkali) has attracted many experimental and theoretical attention in $La_{0.7}Ca_{0.3}MnO_3$ one among many reasons due to optimum Mn^{3+}/M^{4+} ratio influence MCE significantly. Magnetic phase transition imply MCE significant performance which most first-order magnetic phase transition (FOMT) has high maximum entropy change with narrow temperature span meanwhile second-order magnetic phase transition (SOMT) vice versa. Many works reported the way to transform FOMT to SOMT in $La_{0.7}Ca_{0.3}MnO_3$ via *A*-site doping [1], *B*-site doping with transition metal (Fe, Ni, Co, Cu) [2]. In the present paper, we report in detail MCE of polycrystalline $La_{0.7}Ca_{0.3}MnO_3$ which made as pressure dependence of 1, 3 and 5 GPa and named as P_1, P_3 and P_5, respectively. The large value of magnetization in this compound shows that all the samples exhibiting ferromagnetic-paramagnetic (FM-PM) phase transition at Curie temperature. It makes $La_{0.7}Ca_{0.3}MnO_3$ become comparable as magnetocaloric materials in magnetic refrigerant technology. The polycrystalline $La_{0.7}Ca_{0.3}MnO_3$ samples were synthesized by a standard solid-state reaction. A stoichiometric mixture of La_2O_3 (99.99%), $CaCO_3$ (99.99%), $MnCO_3$ (99.99%), powders were previously milled and mixed with a small amount of alcohol using a planetary ball mill of the PM 100 typefrom Retsch (Germany). The resulting mixture was preannealed in air at 850 °C for 16 hours. Next, the powder was additionally annealed at 1000 °C for 16 hours. The resultant powder was then pressed into pellets with different pressure of P_1, P_3 and P_5 and fired in air at 1100 °C for 24 hours. X-ray diffraction (XRD) measurement was made on powdered samples using Cu-Kα radiation. The magnetic measurement versus the temperature (100-300 K) and magnetic field (0-10 kOe) were performed on Physical Properties Measurement System (PPMS) magnetometer (Quantum Design) using VSM mode. Fig. 1 shows the temperature dependence of the magnetization under an external field of 100 Oe for the $La_{0.7}Ca_{0.3}MnO_3$ which pressed into pellets at 200 °C with different pressure. A Curie temperature was obtained. The values are found to be 278 K, 272 K, and 270 K which-exhibiting a ferromagnetic - paramagnetic (FM-PM) phase transition. As can be seen in the insert of Fig. 1 with increasing pressure, the Curie temperature decreased gradually. On the other hand, compared with unpressed sample $La_{0.7}Ca_{0.3}MnO_3$ the Curie temperature (256 K) was increased around 22 K (not show). Isothermal *M-H* curves have been measured at various temperatures in the vicinity of T_C. To determine the type of the phase transition for $La_{0.7}Ca_{0.3}MnO_3$, the measured data of the *M-H* isotherms were transferred into *H*/*M* vs. M^2 plots. According to the Banerjee criterion[3], the positive slope in *H*/*M* vs. M^2 (*M* is the experimentally observed magnetization, *H* the magnetic field) plots means that FM to PM phase transition is second order. For the pressure dependence of $La_{0.7}Ca_{0.3}MnO_3$ the positive slopes in the temperature region 245-278 *K* for 1 GPa, 236-278 *K* 3 GPa are clearly seen in the Fig. 2 (a), (c) respectly, implying that $La_{0.7}Ca_{0.3}MnO_3$ belongs to the materials displaying a second-order transition. Fig. 2 (b), (d) shows the magnetization isotherms of $La_{0.7}Ca_{0.3}MnO_3$ for 1 GPa, 5 GPa from 203-300 *K* respectively. Isotherms in an increasing field (closed square) are measured only I the vicinity of T_C. It should be noted that there is very clear, little, and almost no magnetic hysteresis during the increase and decrease of fileds for three samples, respectively. The magnetic entropy as a function of temperature calculated by using the isothermal magnetization data under applied external magnetic fields. We found the maximum magnetic entropy change $-\Delta S_{Max}$ on various external magnetic fields from 4 kOe to 10 kOe. The values are = 1.2 J●kg^{-1}K^{-1}, 0.8 J●kg^{-1}K^{-1}, and 0.6 J●kg^{-1}K^{-1},with the pressure increase the entropy changes decrease. δT_{FWHM} of 44.7 K, 50.9 K and 72.6 K and *RC* values about 56.4 J●kg^{-1}, 50.9 J●kg^{-1}, and 49.9 J●kg^{-1} for 1 GPa, 3 GPa, and 5 GPa samples, respectively. The $-\Delta S_{Max}$ data versus the applied magnetic field are plotted. interestingly they can be decscribed well by the power law of $|-\Delta S_{Max}|=a\times H^n$ (the solid line). Having taken into account this power law for three samples and their *M/H* data up to 10 kOe .Such results indicate that the master curve $|-\Delta S_{Max}|=\alpha\times H^n$ for the field-dependent entropy change proposed by Franco *et al*.

[1] M. S. Anwar, F. Ahmed, S. R. Lee, R. Danish and B. H. Koo, Japan. J. Appl. Phys. 52, 10MC12 (2013). [2] J. C. Debnath, R. Zeng, J. H. Kim and S. X. Dou, J. Magn. And Magn. Mater. 323, 138-143 (2011) [3] B. K. Banerjee, Physics Letters. 12 (1) 16-17 (1964)

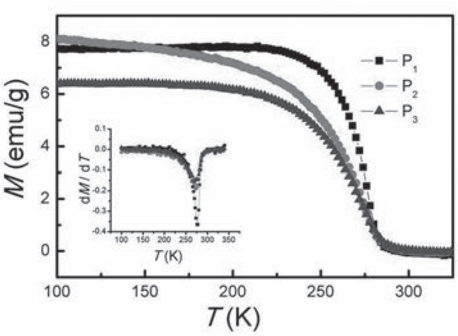

Fig. 1. Magnetization as function of temperature under applied field of 100 Oe and insert figure shows dM/dT as function of temperature on $La_{0.7}Ca_{0.3}MnO_3$ with different pressure sample treatment of $La_{0.7}Ca_{0.3}MnO_3$ as P_1 = 1 GPa P_3 = 3 GPa and P_5 = 5 GPa.

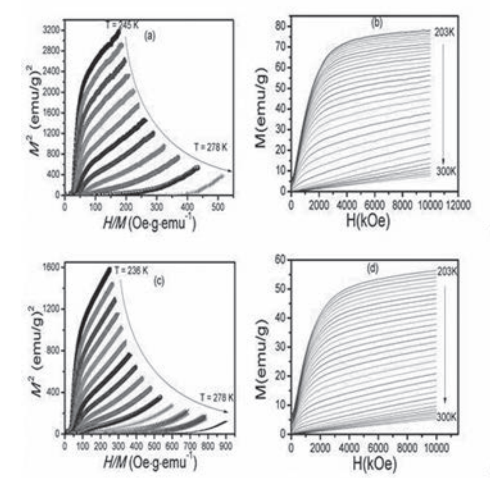

Fig. 2. Magnetic field dependence of the magnetization at various temperatures around T_C presenting in *H*/*M* vs. M^2 plots for the isothermal data of $La_{0.7}Ca_{0.3}MnO_3$ (a) 1 GPa, (c) 5 Gpa and isothermal magnetization curves for (b) 1 GPa, (d) 5 Gpa.

FRIDAY AFTERNOON, 27 APRIL 2018 SIMPOR/ROSELLE BALLROOM, 1:30 TO 4:30

Session HX
POWER TRANSFORMERS
(Poster Session)

Kai Wang, Chair
Nanjing University of Aeronautics and Astronautics, Nanjing, China

HX-01. Calculation Method of Transformer Residual Flux by Using Hysteresis Loops of Different Frequencies.

W. Yuan[1], Y. Shangguan[1] and J. Yuan[1]
1. Dept. of Electrical Engineering, Tsinghua University, Beijing, China

Abstract: Residual flux in the transformer core can cause inrush current at re-energization, resulting in energization failure or power system resonance. In this paper, a new residual flux calculation method based on hysteresis loops of different frequencies is proposed. This method needs no complex hysteresis models. It conducts the time-domain iteration to calculate the transient current and the decline trajectory of H-B of the transformer core by using directly hysteresis loops of different frequencies and the de-energization current, until H=0 to get the residual flux. This method takes the current slopes and the corresponding dynamic magnetic property into consideration. 1 Introduction Because of the hysteresis property of ferromagnetic material, the residual flux will remain in the transformer core after de-energization. At re-energization, it may cause the total flux to exceed the saturation flux and cause inrush current, resulting in energization failure, transformer damage, or power quality decline. Therefore, it is necessary to know the residual flux, so as to eliminate the consequences. Calculation methods of residual flux based on the hysteresis loop have already existed, but most of them require complex hysteresis models, like Preisach model[1]. In these methods, hysteresis models are built firstly according to the measurement of material, then the residual flux is calculated with the models. Not only the model establishment is very complicated, but also most models are built with static measurement, which introduces calculation error. A new calculation method of residual flux by using directly hysteresis loops is proposed in this paper. It skips "model establishment" and takes the dynamic magnetic property into consideration. 2 Principle of residual flux calculation method by using hysteresis loops of different frequencies Under the excitation of the sinusoidal current of different frequencies and amplitudes, the hysteresis loops of ferromagnetic material are different. There are many curves passing through a certain point on the B-H plane. If the current decline rates are different, the core works with different B-H variation rates related to hysteresis loops of different frequencies. The current waveform after de-energization is related to de-energization phase, transformer internal parameters, and external circuit parameters. Usually, the current declines gradually, as shown in Fig.1. Because of the nonlinearity and the multi-value property of BH curves, the current and the magnetic field inside the core need to be calculated iteratively in the time domain. At each time step, the amount known includes previous H, B and two current magnitudes. The point on the B-H plane and the current slope can be decided. Afterwards, a specific hysteresis loop can be selected from several hysteresis loops that pass through the pre-decided point, as shown in Fig.2. The relationship between the current slope and the hysteresis loop slope needs to be obtained by preparation. 3 Specific implementation of residual flux calculation The overall idea is that the transient current and the H, B of the core are calculated iteratively with the de-energization current and hysteresis loops of different frequencies, until H=0 to get the residual flux. The key is ΔH, ΔB calculation when Δi is known. 3.1 Preparation Based on core and winding structure, obtain hysteresis loops of different frequencies and amplitudes by simulation. Record H, B values, and the relationship between current slope k_i and hysteresis loop slope k_{BH} at each point. Then, rearrange these data into a table, in which the independent variables are (H, B) and k_i, and the dependent variable is k_{BH}. 3.2 Calculation procedure (1) Record the current i at de-energization, calculate H according to the magnetic circuit, and get B according to the hysteresis loop before de-energization. (Or follow step (1').) (1') Record i at de-energization and at the moment Δt earlier. Calculate H and get B at the two moments as step (1). (2) If following step (1), calculate the inductance L of the transformer with H, B. If following step (1'), calculate the electromotive force e of the winding directly with ΔB. (3) Set a proper time step and do the transient circuit calculation, according to R, L (or e), C of the transformer and R_{out}, L_{out}, C_{out} of the external circuit, to get next i. (4) Decide the present point on the B-H plane with previous H, B. Calculate current slope with last i and the new i. Search the table to get k_{BH}. (5) Calculate ΔH, ΔB according to Δi, to get next H, B. (6) If H=0, B at this time is residual flux. End. Otherwise, return to step (2). At step (2), L or e is calculated only with previous H, B. To get better results, after step (5), L or e can be recalculated with the average of previous H, B and next H, B. Then carry out step (3)~(5) again, until the error meets the requirement. 4 Conclusions The transformer residual flux can be calculated through time-domain solution, according to the de-energization current and transformer circuit parameters. A series of hysteresis loops of the core material can be obtained by applying sinusoidal current of different frequencies and amplitudes, to obtain the multi-valued dynamic magnetic property for every point on the B-H plane. In the iteration, the property can be used to calculate magnetic field and current. This method avoids the computational complexity and error caused by the establishment of complex hysteresis model.

[1] Gaowa Wuyun, Dichen Liu, and Po Li. Calculation of Residual Flux Based on Preisach Model and Entering Phase control of transformer to eliminate Inrush Current[C]. CEEM' 2006: Asia-Pacific Conference on Environmental Electromagnetics, Vols.1 and 2, Proceedings, 2006: 396-401.

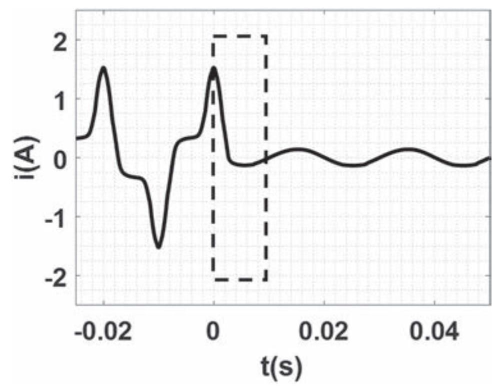

Fig. 1. Transient current waveform (de-energize at t=0).

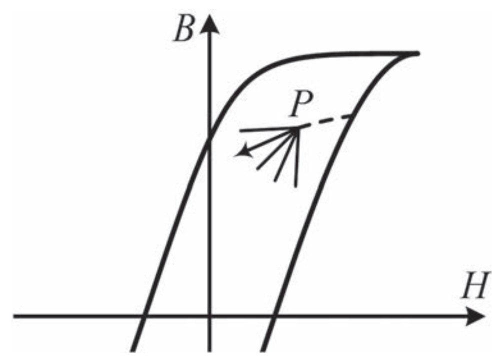

Fig. 2. Hysteresis loop selection.

HX-02. Influence of the Winding Geometry and its Materials on the Resonance Behavior of Transformer Coils.

M. Nilges[1] and P. Schegner[1]
1. Institute of Electrical Power Systems and High Voltage Engineering, Technische Universitaet Dresden, Dresden, Germany

I Introduction Voltage stress due to steep impulses during switching operations of e.g. vacuum circuit breakers and ongoing harmonics caused by converters are a well-known but still increasing problem in the field of transformer design and operation [1]. In order to investigate the behavior of transformers during such impulses and oscillations, several models have been developed [2,3]. However, with increasing complexity of the coils, all studies show minor to major deviations in computation, compared to the corresponding measurements. Due to a high number of turns in the high voltage coils of transformers, the errors caused by simplifications or inaccurate data of the interwinding geometry can be tremendous. Hence, it is necessary to know which parameters are influencing the resonance behavior significantly and need to be represented accurately, while other parameters may be neglected. Therefore, a parameter study has been carried out, in order to analyze the resonance behavior of a simple coil geometry, based on FEM computations. II Setup For the following parameter study, the simple dry-type coil in Fig. 1a is analyzed. The inner diameter of the coil is 272mm and consists of 200 turns divided on 12 layers. The cross section of the wires is 1.4mm×4mm. The pronounced resonance frequency (RF) of the coil is ≈50kHz. Figure 1b to 1e show five of the seven parameters, which are being adjusted during the study. These are the thickness of the wire coating d_C, the distance between the consecutive turns d_T, the distance between the layers d_L, the displacement between two layers δ_L and the displacement of the first turn on each layer d_e caused by rising to the next layer. Additionally, the rel. permittivity of the wire coating $\varepsilon_{r\ coat}$ and the rel. permittivity of the epoxy resin between the layers $\varepsilon_{r\ EP}$ are varied. The number of simulations and therefore the computation time increases significantly with the number of the parameter variations. Therefore, only three variations for each parameter are applied: 100%, 80% and 50% of their initial values. The RF, as well as its resonance peak (RP), are used to analyze the influence of the parameters. Since the RF cannot be calculated directly by FEM-computations, it is estimated by performing a frequency sweep. To reduce the computation time, the frequency step size is set to 512Hz. The resulting RF and its RP are calculated for each parameter combination, using a cubic spline interpolation of the amplitude response. III Characterizing the Influence A representative value is necessary to characterize the influence of any parameter for all investigated cases. In order to calculate such a value for the RFs (and RPs), the following steps have been carried out. At first, one parameter is chosen for characterization. Following, a distinct combination of the six remaining parameters is picked. For this combination, the mean value over the resulting RFs of the three parameter variations is calculated. The relative deviations of the three states from their mean value give a characterization for the current combination. Subsequently, this method is used successively over all remaining combinations of the parameter permutations. The resulting deviations can already be used for a classification of the influence of any parameter. Furthermore, dependencies of other parameters can be obtained. However, to characterize the influence of the regarded parameter with only one representative value, the global maximum of all deviations η_{max} will be used. Other statistical methods as quantiles, distribution functions, etc. may be used likewise. IV Results Exemplarily, Fig. 2a and 2b show the resulting deviations of the parameters d_T and $\varepsilon_{r\ EP}$. Regarding these figures, the deviation forms steps for several groups of parameter combinations. These steps show the dependency of the regarded parameter to other parameters. If there is no dependency, the value of the deviation will not change. In contrast, the difference between two parameter combinations increases with a rising dependency of the changing parameter. The comparison of Fig 2a and 2b shows, that the parameter d_T is sensitive to changes of other parameters while its own influence is relatively low. However, the parameter $\varepsilon_{r\ EP}$ is behaving vice versa. It has a high influence on the RF and shows only a slight dependency of other parameters. Further evaluations of the computation results yield more dependencies and a deeper understanding of these behaviors. Considering the RF and using the representative value as introduced in section II, the highest deviation over all permutations for parameter d_T is only $\eta_{max\ T}$≈0.1%. Considering the highest overall deviation in Fig. 2b, the influence-value of parameter $\varepsilon_{r\ EP}$ is $\eta_{max\ EP}$≈8%. The other influences are $\eta_{max\ C}$≈7% (d_C), $\eta_{max\ dL}$≈14% (d_L), $\eta_{max\ \delta L}$≈0.2% (δ_L), $\eta_{max\ e}$≈0.4% (d_e) and $\eta_{max\ coat}$≈16% ($\varepsilon_{r\ coat}$). The influence-values for the RPs show a similar behavior. V Summary A parameter study has been carried out, in order to investigate the influence of several parameters on the RF and the RP of a dry-type transformer coil. The results show several dependencies and that the influence of three parameters is negligible.

[1] Q. Yang, Z. Zhang, W. Sima, M. Yang and G. Wei, "Field Experiments on Overvoltage Caused by 12-kV Vacuum Circuit Breakers Switching Shunt Reactors," in *IEEE Transactions on Power Delivery*, vol. 31, no. 2, pp. 657-664, April 2016. [2] M. Popov, "General approach for accurate evaluation of transformer resonance effects," in *Proceedings of International Conference on Power Systems Transients 2017*, Seoul, June 2017. [3] J. Smajic *et al.*, "Simulation and Measurement of Lightning-Impulse Voltage Distributions Over Transformer Windings," in *IEEE Transactions on Magnetics*, vol. 50, no. 2, pp. 553-556, Feb. 2014.

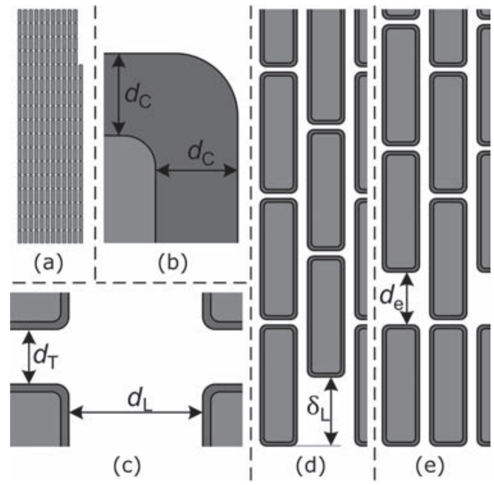

Fig. 1. Transformer coil with the examined geometric properties: (a) overview of the coil, (b) wire coating thickness, (c) distances between the turns and layers, (d) displacement between layers, (e) displacement of the first turn in a layer.

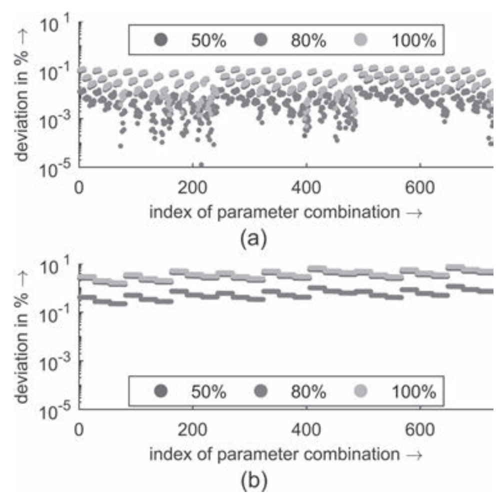

Fig. 2. Relative deviations of the three RF-states of the parameters d_T (a) and $\varepsilon_{r\ EP}$ (b) to their mean value plotted for each permutation of the other parameters.

HX-03. An Optimized Strategy Based on backflow power of Dual-active-bridge Converters with Extending Dual-phase-shifting Control.

Z. Feng[1] and S. Chi[1]
1. Hebei University of Technology, Tianjin, China

Abstract: To improve the efficiency of extending dual-phase-shifting, this paper presented an optimized strategy to make backflow power to be minimum. The small range of phase shift in conventional DPS control at light load could lead the whole system to be out-of-balance. While the secondary inner phase shifts extended from positive to negative, the character of inner phase in the method was optimized. By establishing mathematical models of transmission power, backflow power and relation of phase, the paper comparatively analyzed different working modes of the extending dual-phase-shifting control, and designed a strategy to make the backflow power to be minimum. Finally, building the simulation model of different modes to verify the advantage of the control method. Then an experimental prototype was developed based on this strategy, and the experimental resulted verify the effectiveness and feasibility of the proposed control strategy. In the early 1990s, a topology of isolated bidirectional dual-active-bridge DC-DC converter was proposed. [1] Because of the isolation, two-way mobility, power adjustable, DAB had became the first choice as DCDC converter.[2] In recent years, the research and analysis of DAB circuit mainly focused on how to improve the transmission efficiency, including reducing the back-flow power, soft switching, reducing current stress and other measures.[3] Based on the previous literature, this paper compares the control methods of dual-phase-shifting, and analyzes the principle of phase-shift optimization based on extended dual phase-shifting model. By analyzing the transmission power and the backflow power of the above control methods, the optimal control strategy with the goal of efficiency optimization is given and verified by experiment. I. principle of extending dual-phase-shifting control In the extending dual-phase- shifting, the inner phase shift of primary bridge is D_1' and the secondary side is D_1'', where$|D_1'|=|D_1''|=D_1$. The phase-shift between two full bridges is D_2. According to the size of D_1 and D_2, the extended dual phase shift can be divided into three working states: $0 < D_1 < D_2/2$(status 1), $D_2/2<D_1<D_2$(status 2), $D_2 < D_1 < (D_2+1)/2$(status 3) Fig1(a)(b). The limit of D_1 and D_2 is $2*D_1-D_2\leq 1$. The transmission power formula for each state is $P=[nU_1U_2(-3D_1^2-2D_2^2+4D_1D_2-2D_1+2D_2)]/(4fL)$ (status 1) $P=[nU_1U_2(D_1^2-D_2^2-2D_1+2D_2)]/(4fL)$ (status 2) $P=[nU_1U_2(3D_1^2+D_2^2-4D_1D_2-2D_1+2D_2)]/(4fL)$ (status 3) Status 1 is heavy-load;status 2 is light-load;status 3 is reverse direction transmission. Transmission power formula of traditional dual-phase-shift and extending dual phase shift in the light-load is changed into $D_1 = 1-D_2/2-P/(4KD_2)$ (traditional) $D_1 = 1\pm\sqrt{(1+D_2^2-2D_2+P/(2K))}$ (extending) where $K = nU_1U_2/(8fL)$ When $P = 0.2$, it can be seen from the figure that the adjust-range of D_1 in the conventional dual-phase-shift is 0.06-0.3, and the adjust-range of D_2 is 0.05-0.68 Fig1(c). The adjust-range of D_1 in extended dual-phase-shift 0.06-0.68 and the adjust-range of D_2 is 0.11-1 Fig1(d). II. Optimal control of backflow power The sum backflow power formula of the primary and secondary side is $Q = \int U_{ab}i_L(t)\,dt + \int U_{cd}i_L(t)dt = nU_1U_2(2D_1-D_2)^2/(4fL)$ The Lagrange multiplier method is used to analyze the backflow power of state 1 as follows: $F(D_1,D_2,\lambda) = 2K(2D_1-D_2)^2 + \lambda[2K(-3D_1^2-2D_1+4D_1D_2-2D_2^2+2D_2)-P]$ $dF/dD_1 = 8(2D_1-D_2) + 2\lambda(-6D_1-2+4D_2) = 0$ $dF/dD_2 = -4(2D_1-D_2) + 2\lambda(4D_1+2-4D_2) = 0$ $dF/d\lambda = 2K(-3D_1^2-2D_1+4D_1D_2-2D_2^2+2D_2) - P = 0$ To simplify the above formula, the relation of D1 and D2 is showed as $\lambda(D_1-2D_2+1) = 0$. While $\lambda = 0$, the formula is changed as $D_1 = 2D_2$. From the previous section the relationship does not exist in state 1. While $\lambda \neq 0$, the formula is changed as $D_1 + 1 = 2D_2$. Taking the relation into the formula of the transmission power, the relations of D_1 and D_2 is showed as: $D_1 = \sqrt{(1-2(1+P/(2K))/3)}$ $D_2 = [1+\sqrt{(1-2(1+P/(2K))/3)}]/2$ When the port voltage fluctuates, there is little backflow exist in state 2. The backflow power is showed as: $Q = nU_1U_2[(1-U_1/(nU_2))(1-D_1)]^2/(16fLU_1/(nU_2))$ $(U_1 < nU_2)$ $Q = nU_1U_2[(1-U_1/(nU_2))(1-D_1)]^2/(16fL)$ $(U_1 > nU_2)$ The formula shows that backflow power is only related to D1. So while $0< P < nU_1U_2/(16fL)$, the relation of D1 and D2 is showed as $D_1 = 1-\sqrt{(1-P/(2K))}$ $D_2 = 1$ While $nU_1U_2/(16fL)< P < nU_1U_2/(12fL)$, the relation of D1 and D2 is showed as $D_1 = [1+\sqrt{(1-3P/(2K))}]/3$ $D_2 = [2+\sqrt{(4-6P/K)}]/3$ III. Simulation and experiment In order to verify the theory, a low-power DAB experimental platform based on the TMS320F28035 controller was built. The parameters of simulation and experimental is:port voltage U1=U2=30V; frequency f=20kHz; additional inductor L=425.58uH; transformer ratio n=1:1. Fixed transmission power, the simulation result shows the curve of D1 and D2 Fig2(a). From the results, it can be seen that the phase shift angle is greatly improved compared with the traditional double-phase-shifting control. And the optimal control algorithm obtained in the previous section is verified experimentally to greatly reduce the back-flow power Fig2(b)(c)(d). IV. Conclusion This paper analyzes the extending dual-phase-shifting control which widens the range of the phase-shift at light load, optimizes the function curve of the phase-shift and makes the system adjustment more flexible. Meanwhile it inherits the advantage of zero backflow power in light-load state in the traditional dual-phase-shifting and proposes a control strategy in heavy loads state to improve the system power factor.

[1] Bolla R, Bruschi R, Davoli F, et al. Energy efficiency in the future Internet: a survey of existing approaches and trends in energy-aware fixed network infrastructures. IEEE Commun Surv Tut, 2011, 13: 223–244 [2] Jalbrzykowski S,Bogdan A,Citko T. A dual full-bridge resonant class-E bidirectional DC-DC converter[J]. IEEE Transactions on Industrial Electronics,2011,58(9) : 3879-3883 [3]Chung I Y,Liu W X,Andrus M,et al. Integration of a bi-directional dc-dc converter model into a large-scale system simulation of a shipboard MVDC power system [C]//Proceedings of ESTS. Baltimore,MD : IEEE,2009 : 318-325.

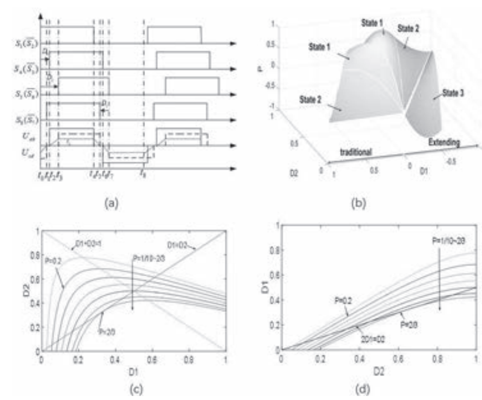

Fig. 1. waveform of extending double-phase-shifting control

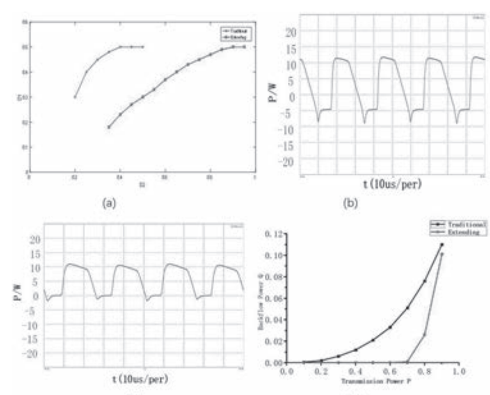

Fig. 2. waveform of simulation and experiment

HX-04. Study of Analysis and experiment for Ability to Withstand DC Bias in Power Transformers.

D. Chen[1], Z. Feng[1], B. Bai[1] and L. Fang[1]
1. School of Electrical Engineering, Shenyang University of Technology, Shenyang, China

Abstract—Firstly, this paper analyzes the ability of power transformers to withstand the DC bias by a novel analytical criteria. The proposed criteria is obtained from the nonlinear equivalent circuit, which considers the effects of nonlinear inductances. Secondly, The validity of the proposed analytical criteria is verified by the finite element analysis results and experimental results (flux density, current, stress and vibration, noise), which indicates that the proposed analytical criteria is effective to evaluate the ability to withstand the DC bias of power transformers. *Index Terms*—DC bias, nonlinear equivalent circuit, power transformers, vibration and noise. I. Introduction The phenomena of the DC grid, geomagnetic storm change, DC voltage of converter transformers and other factors can result in DC bias. The DC bias leads to strong saturation of transformer cores and thus nonlinear operations. As a result, this effect can cause the increased magnetic leakage flux in cores, metal structure losses, temperature raises, local overheating, dielectric breakdown, and noise vibration as well as permanent damage to the transformer itself [1],[2]. To simplify the evaluation process and avoid the cost of the initial prototype for the required over-excitation multiples, this paper proposes a novel analytical criteria based on the nonlinear equivalent magnetic circuit considering the effects of inductances to evaluate the ability to withstand the DC bias of power transformers. The proposed criteria demonstrate that the peak values of the exciting current at the saturation conditions of transformers resulting from the DC bias and overvoltage should be close. The derivation process in terms of the transformers, exciting currents, and hysteresis loops are presented. To verify the effectiveness of the proposed analytical criteria to evaluate the ability of withstanding the DC bias, the simulation by a finite element method and experiments were conducted for a single-phase four-leg power transformer. II. Study of simulation and experiment and discussion of result In order to solve the modeling issue of the special structure in the power transformer, a model can be established by considering the magnetic circuit length, the cross-sectional area, the magnetization curve, and the effect of the nonlinear characteristic in the power transformer core. TABLE I shows the basic parameters of the single-phase four-leg power transformer. The transformer magnetic circuit model is established for considering the transformer structure, size, and nonlinear effects as in Fig. 1 and Fig. 2. Based on the transformer nonlinear models in Fig. 1 and Fig. 2, The transformer DC bias capacity is analyzed in the next section. the analytical criteria to calculate the DC bias capacity is illustrated in Fig. 3. Fig. 4 shows the maximum DC bias of the ability to withstand DC bias in power transformers. As shown in Fig. 4(a), the peak value of the exciting current at I_{DC}=1.91 A (DC bias) caused by the transformer saturation and the peak value of the exciting current at U_{in}=2809.1 V(overvoltage) caused by the transformer saturation are close to each other. Since it is difficult to directly evaluate the ability to withstand DC bias in power transformers, this finding contributes to the criteria to obtain the maximum DC bias based on the peak values of the exciting current for the saturation condition of the transformers caused by DC bias and overvoltage. As demonstrated in Fig. 4(b), the blue curve represents the relationship between the peak current and the overvoltage, while the red curve depicts the relationship between the peak current and the DC bias. The result indicates that the intersection point of the two curves is the maximum value of the DC bias where the power transformer can stand with a value of 1.91A. To verify the validity of the analytical method, the transformer model is simulated using the finite element method (FEM), and then the experiment is conducted. A one-phase four-leg transformer was established in Magnet software. As shown below, Fig. 5 is the flux density distribution of the transformer core without DC bias, and Fig. 6 is with a DC bias of 2.5A. Fig. 7 shows the setup of the experimental system, wherein the AC supply provides the input voltage with a value equal to or greater than 2000V by the step-up transformer. Fig. 8 shows the results of the exciting current using the analytical method, FEM, and the experimental method under different DC biases and the power transformer noise values under different DC biases. III. Conclusion This paper has presented a novel analytical criteria to estimate the maximum value of the DC bias that the transformer can withstand. The proposed analytical criteria was obtained based on the electrical circuit and magnetic circuit of the transformers by considering the core length, cross-sectional area, magnetization curve, and nonlinear effects. It has indicated that the peak values of the exciting currents at the saturation conditions caused by the DC bias and the overvoltage are close with each other. The analysis results of the proposed analytical criteria have been verified by the simulation results and experimental results, which shows good coincidence. Hence, the research provides a new insight in to the DC bias analysis of power transformers and the established models and analytical criteria can be applied to other transformer topologies.

[1] Dezhi Chen, Wenliang Zhao, Baodong Bai, Byung-il Kwon. Analysis and Experiment of Transformer Vibration and Noise Considering Electrical Steel Sheet Magnetostriction. International Journal of Applied Electromagnetics and Mechanics.12016) 1-8. [2] O. Bíró, G. Buchgraber, and G. Leber, et al., "Prediction of magnetizing current wave-forms in a three-phase power transformer under DC bias," IEEE Trans. Magn., vol. 44, no. 6, pp. 1554-1557, May. 2008.

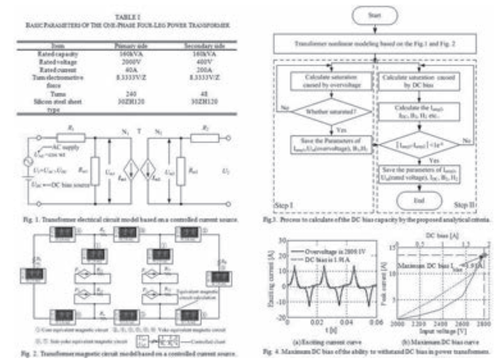

Fig. 1. System parameters, mathematical model, program flow chart, and simulation results

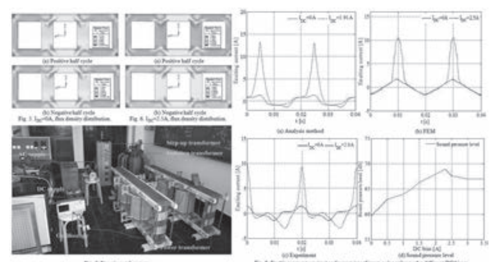

Fig. 2. Simulation and experiment result

HX-05. Vibration Research of Magnetically Controlled Saturated Reactors under AC and DC Excitations.

Y. Gao[2,3], *R. Yan*[2,3], H. Liu[2,3] and J. Chen[2,3]

2. State Key Laboratory of Reliability and Intelligence of Electrical Equipment, Hebei University of Technology, Tianjin, China; 3. Key Laboratory of Electromagnetic Field and Electrical Apparatus Reliability of Hebei Province, Hebei University of Technology, Tianjin, China

I. INTRODUCTION Due to the air-gap iron-core structure and working state of AC and DC excitations, magnetically controlled saturated reactors (MCSRs) have strong vibration and noise, which will become one of the restricting factors for MCRs application and development. So far, research on MCSRs focused on the current harmonic characteristics and harmonic optimization [1], however, there are few studies on vibration noise and none of them analyzed the influence of different DC bias on vibration[2-3]. The main reasons for the vibration of MCSRs are the electromagnetic force generated by the air-gap on both sides of the magnetic valve and the magnetostrictive effect of the silicon steel of the iron-core material[4]. The electromagnetic force is directly affect by silicon steel used in MCSRs magnetization properties; similarly, the magnetostrictive force of the reactor is also closely related to the magnetostrictive properties of the silicon steel[5]. In different DC bias, silicon steel could present different magnetization and magnetostrictive properties. The vibration study of MCSRs based on the magnetic properties of silicon steel under practical working conditions has not been involved yet, so it is necessary to study the electromagnetic vibration of MCSRs under AC and DC excitations. Multi-group magnetization and magnetostriction properties curves of silicon steel under different DC bias are measured firstly to support the computation. Then Based on the measured constitutive relations, an electromagneto-mechanical coupling model for MCSR considering magnetostrictive effect and electromagnetic force effect is proposed. Vibration regulation of MCSRs was obtained based on finite element method, which compared and analyzed magnetic field, stress and vibration displacement of MCSRs, the resulted comparative analysis and regulation provides a theory basis for further analysis of vibration and noise reduction. II. MCSRS VIBRATION MODEL A. Measurement of magnetic properties of silicon steel under DC bias. In order to ensure the accuracy of MCSRs vibration calculation, the magnetic properties of silicon steel under different DC bias were measured in this thesis. The obtained basic magnetization curve and magnetostrictive curve are applied to the simulation calculation of vibration noise of MCSRs by using the interpolation method to make the calculation result more accurate. B. Electromagneto-mechanical coupling model of MCSRs. The total energy of the reactor's electromagnet-mechanical system includes the magnetic field energy, the strain energy, the current potential energy, the magnetostrictive energy and the power produced by the electromagnetic force. Based on the energy variation principle, the magnetic vector potential A and mechanical deformation u can be calculated by minimization of the total energy functional. III. MCSR IRON-CORE VIBRATION CALCULATION In this thesis, the single-phase MCSR is regarded as the research object. In calculation, AC excitation (, f=50Hz) and DC excitation I_{DC}=0A, 2A, 4A is applied. Fig.1 (a) shows the magnetic flux density distribution of MCSR at t=0.025s with different DC bias. As can be seen from the figure, with the DC bias increases, the amplitude of the MCSR flux density also increases. Magnetic flux amplitude of magnetic valve is greater than the other locations. The stress distribution of MCSR under different DC bias is shown in Fig. 1 (b). The figure shows, the stress amplitude and deformation of the MCSR also increase with the increase of the DC bias, and similar to the magnetic flux density distribution, which shows that the amplitude and distribution of the magnetic flux density directly affect the stress of the reactor iron-core. In addition, the stress of the reactor iron-core is mainly concentrated on the magnetic valve, the T-type contact surfaces, the lower iron yoke and the upper iron yoke on the side of the saturated magnetic valve. The rainbow plot shown in Fig.1 only gives the data values for the reactor magnetic field and vibration at a point in time, to study the change of MCSR vibration with time, the test points in the simulation model are needed to embed. According to the distribution of magnetic flux density and stress distribution of MCSR iron-core, taking into account the symmetry of the structure and the particularity of the magnetic valve, six points of A, B, C, D, E and F are selected as the focus of study thus to analyze reactor vibration changes over time. Point A is the point on the upper iron yoke, point B is the point at the T-type contact surfaces, point C is the point of the yoke, point D is the point of the central iron-core column, point E and point F are respectively the magnetic valve 1 and 2. The relationships between displacement and time under different DC bias is shown in Fig.2. IV. CONCLUTION The magnetic flux density, stress and displacement of MCSRs increase with the increases of DC bias, the vibration of the T-type contact surfaces and the magnetic valve are the most intense. Therefore, the vibration reduction work should focus on the T-type contact surfaces and magnetic valve. In the reactor air-gap filled with negative giant magnetostrictive material, negative deformation of the negative giant magnetostrictive material under magnetic field is used to counteract the original mechanical deformation of the reactor, so as to achieve the effect of reduction.

[1] X. Chen, B. Chen, C. Tian, J. Yuan and Y. Liu, "Modeling and Harmonic Optimization of a Two-Stage Saturable Magnetically Controlled Reactor for an Arc Suppression Coil" IEEE Transactions on Industrial Electronics, Vol. 59, No, 7, pp. 2824-2831, July 2012. [2] Y. Gao, M. Nagata, K. Muramatsu, K. Fujiwara, Y. Ishihara, and S. Fukuchi, "Noise Reduction of a Three-Phase Reactor by Optimization of Gaps Between Cores Considering Electromagnetism and Magnetostriction" IEEE Transactions on Magnetics, Vol. 47, No. 10, pp. 2772-2775, October 2011. [3] Y. Gao, K. Muramatsu, K. Fujiwara, Y. Ishihara, S. Fukuchi, and T. Takahata, "Vibration Analysis of a Reactor Driven by an Inverter Power Supply Considering Electromagnetism and Magnetostriction" IEEE Transactions on Magnetics, Vol. 45, No. 10, pp. 4789-4792, September 2009. [4] R. Yan, X. Gao, L. Zhu, Q. Yang, T. Ben, Y. Li and W. Yang, "Research on Three-Dimensional Stress Distribution of Reactor Core" IEEE Transactions on Applied Superconductivity, Vol. 26, No. 4, pp. 0602004, June 2016. [5] Y. Kai, Y. Tsuchida, T. Todaka and M. Enokizono, "Influence of Biaxial Stress on Vector Magnetic Properties and 2-D Magnetostriction of a Nonoriented Electrical Steel Sheet Under Alternating Magnetic Flux Conditions" IEEE Transactions on Magnetics, Vol. 50, No. 4, pp. 6100204, April. 2014.

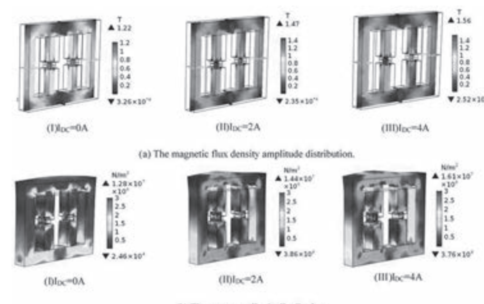

Fig. 1. The magnetic flux density and the stress amplitude distribution of MCSR iron-core.

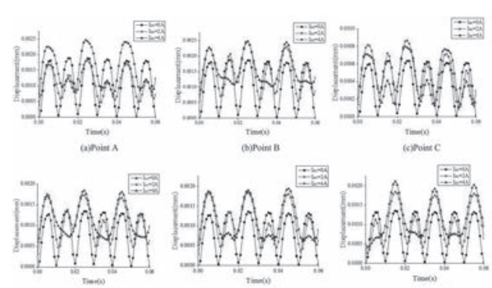

Fig. 2. The relationships between displacement and time under different DC bias.

HX-06. Research on transformer core vibration Based on Thermal Analogy Method.

B. Zhang[1], J. Du[1] and N. Yan[1]
1. Shenyang University of Technology, Shenyang, China

I.Introduction With the increasing of voltage grade and capacity of power transformer, the problem of vibration noise becomes more and more prominent. The noise source of the transformer consists of three, core, winding, cooler or radiator. The core is the main source of noise. The reason for the noise is that the silicon steel sheet is in the effect of the alternating magnetic field, because the magnetostrictive effect produces the change of size, so that the core vibrates periodically with the change of excitation frequency.[1] At present, the simulation of magnetostriction is mainly based on numerical calculation method. There are three main types: piezomagnetic analogy method, piezoelectric analogy method and thermal analogy method. The methods of piezoelectric analogy method and piezoelectric analogy method are used to analyze the magnetostrictive materials. For the silicon steel sheet in motor or transformer core, the deformation of iron core caused by its magnetostriction is small, and its displacement is not enough to cause the obvious change of the magnetic field. Therefore, the numerical calculation of magnetostriction can be obtained by coupling method based on thermal analogy method. However, in the previous study, the above method only gave the motor example, and the magnetostrictive rate of the iron core adopted the method equivalent to the empirical formula, and the accuracy was not very satisfactory.[2] In this paper, a thermal analogy method is proposed to simulate the magnetostrictive effect of the silicon steel in transformer core. The magnetostrictive characteristic curve of silicon steel sheet was obtained by experiment. The finite element method and the interpolation of the curve were obtained. The vibration simulation of transformer core is realized by using magnetostrictive stress-thermal stress analogy method. II.Model The magnetostrictive characteristic curves of the magnetostrictive experiments of silicon steel sheet materials are obtained. The magnetic field distribution on the core of the transformer is obtained through the finite element method. Based on the distribution of the magnetic intensity vector in the finite element element, the curve of the magnetostrictive properties of the interpolated silicon steel is obtained, and the strain is obtained on each node. Because the strain of the node and the deformation of the node are to be coordinated with the shape function of the unit, it is difficult to solve directly. Therefore, the thermal analogy method is applied to the basic parameters of the thermal stress analogy calculation, and the equivalent model of parameters applicable to magnetostrictive stress - thermal stress is derived. Assumes that the thermal expansion coefficient and the initial reference temperature, get the node core area and temperature, and the results as a thermal analysis of the node temperature load, calculation of thermal stress by node coordinate displacement and stress. ANSYS software does not directly solve the function of magnetostriction effect, but the above analogy can directly solve the vibration displacement of each node in the transformer core through software. III.Exapmle The single-phase three-column core model for the dfp-270000/500 super high voltage generator transformer is modeled. The magnetic flux density of each node is obtained through the finite element electromagnetic field. Using the above analogy method, the thermal stress analogy is calculated, and the magnetostrictive stress and displacement of each node are obtained. Due to the transient field calculation, the magnetostrictive stress and displacement comparison of different time and frequency can be performed. At the same time, the vibration frequency simulation is carried out to determine whether the resonant phenomenon is possible. IV.Conclusion In this paper, the finite element simulation is used to simulate the thermal stress of magnetostrictive force. An example of magnetostrictive effect simulation of power transformer core is given. The calculation method can be used to simulate the vibration of transformer core in ANSYS software.

[1] Lihua Zhu, Qingxin Yang, Rongge Yan, et al. “Numerical computation for a new way to reduce vibration and noise due to magnetostriction and magnetic forces of transformer cores”. Journal of Applied Physics, 113(17):17A333. 2013. [2] Somku S, Moses A J, and Anderson P I. “Measurement and modeling of 2-D Magnetostriction of Nonoriented Electrical Steel”, IEEE Transactions on Magnetics, 48(2): 711-714. 2012.

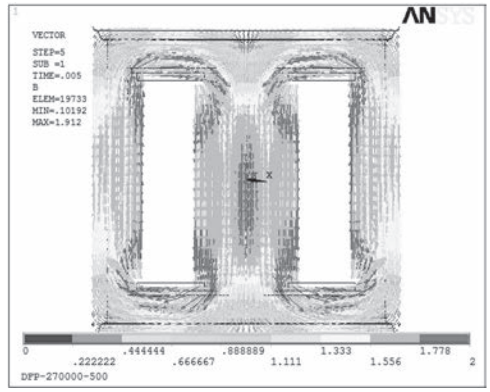

Fig. 1. Transformer core magnetic flux density vector

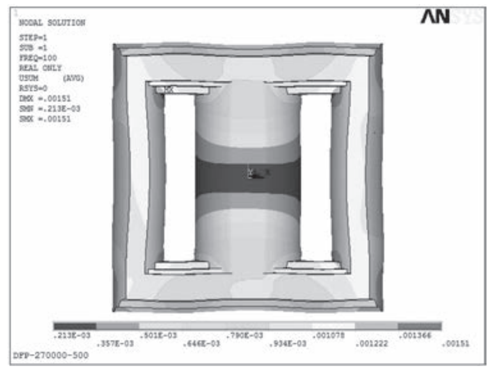

Fig. 2. Transformer core vibration displacement

HX-07. Performance Optimization of a Novel Saturated Core Fault Current Limiter Considering Eddy current Loss of Permanent Magnet.

L. Wei[1,2], B. Chen[1], Y. Liu[3], H. Zhou[1], Y. Zhong[1], J. Yuan[1], K. Muramatsu[4] and C. Wang[1]
1. Wuhan University, Wuhan, China, Wuhan, China; 2. Department of Electrical Engineering, Kyoto University, Kyoto 606-8501, Japan; 3. Anhui Electric Power Research Institute, Hefei, China; 4. Department of Electrical and Electronic Engineering, Saga University, Saga, Japan

I. INTRODUCTION Due to the rapid development of power grid and renewable generations, the fault currents are approaching or even exceeding the existing rating interrupting capacity of circuit breakers [1]. With the development of permanent magnet materials (PMs), permanent-magnet-biasing saturated core fault current limiter (PMFCL) has been one of the most promising methods to limit the fault current [2]. However, there are two major problems limiting the development of PMFCLs: the demagnetization risks of PMs caused by large induced eddy current loss and the inadequate biasing ability of PMs. To reduce the eddy current loss of PMs and improve the biasing ability of PMs, this digest proposes a novel saturated core fault current limiter based on PMs (PMFCL). A novel magnetic structure can effectively reduce the eddy current loss of PMs, resulting in reducing the demagnetization risks of PMs. An optimal small section of cores can improve the saturation degree of cores and biasing ability of PMs. Compared with traditional PMFCLs, the proposed PMFCL has the advantages of better biasing ability of PMs, smaller eddy-current loss of PM, and lower risks of demagnetization. The principle and performance have been validated by various FEA simulation and optimization studies. II. BASIC PRINCIPLE AND OPTIMIZATION DESIGN OF PMFCL Fig.1(a) shows the basic structure of proposed PMFCL, which consists of iron cores, PMs and coils. A small section which of cross-section area is smaller than that of main core is proposed to improve the biasing ability of PMs. Under normal conditions, PMs drop cores I and II into deep saturation. The normal impedance of PMFCL is very low, and the AC flux will not flow through PMs, as shown in Fig.1(b). Under fault conditions, the fault current is large enough to drop cores I or II out of saturation alternatively, resulting in limiting the fault current. Compared with traditional PMFCLs, each PM will flow through half of AC flux produced by the fault current, the eddy current loss of PMs can be reduced effectively. Fig.1(c) shows the equivalent magnetic circuit of PMFCL. To improve the saturation degree of cores and the biasing ability of PMs, the parameters of small section should be optimized. In addition, the length and cross-section area of PMs also have an important influence on the reduction of eddy current loss of PMs. III. RESULTS OF FEA SIMULATION To validate the principle and performance of PMFCL, various FEA simulation and optimization studies of 220V/10A PMFCL were performed. The fault current with proposed PMFCL can be limited from 286.0A to about 97.0A. Fig.2(a) shows the flux density distribution of cores and PMs. Under normal conditions, cores I and II are driven into saturation by PMs. Under fault conditions, cores I and II are dropped out of saturation, respectively. The result comparison of eddy current loss of PMs is shown in Fig.2(b). Compared with traditional PMFCLs, the proposed PMFCL can reduce the eddy current loss of PMs from 188.9W to 24.5W (87% reduction), resulting in reducing the demagnetization risks of PMs effectively. Fig2(c) shows the magnetic flux density distribution of core I under normal conditions in the different lengths of small section. The flux density distribution along cores I without small section is not uniform. The saturation degree of cores and biasing ability of PMs can be improved by the small section. The parameters of small section also have a significant influence. In Case 3: L_b=0.14m, S_b=0.00243m^2, the saturation degree is optimal with B_{min}=2.001T. And the length of PM can be reduced from 70mm to 50mm, which has a 28.6% reduction. Therefore, the results of FEA simulation and optimization studies verify the excellent performance of proposed PMFCL. IV. CONCLUSION In this digest, a novel permanent-magnet-biased fault current limiter (PMFCL) has been presented. According to the theoretical analysis and optimization studies, the proposed PMFCL can reduce the eddy current loss of PMs and improve the biasing ability of PMs, and have excellent fault clipping performance. Compared with traditional PMFCLs, the proposed PMFCL can achieve a 87% reduction in eddy current loss of PMs. Hence, the proposed PMFCL can reduce the demagnetization risks of PMs effectively. Moreover, the biasing ability of PMs can be also improved by the optimal small section. The length of PM can be reduced by 28.6%. In addition, more detailed optimization and experimental studies will be analyzed in the full paper.

[1]Chen B, Wei L, Tian C, et al. "Parameter Design and Performance Investigation of A Novel Bridge-Type Saturated Core Fault Current Limiter", *IEEE Trans. Power. Del.*,32(2):1049-1057,(2017). [2]Yuan J, Lei Y, Wei L, et al. "A Novel Bridge-Type Hybrid Saturated-Core Fault Current Limiter Based on Permanent Magnets", *IEEE Trans. Magn.,* 51(11):1-4, (2015).

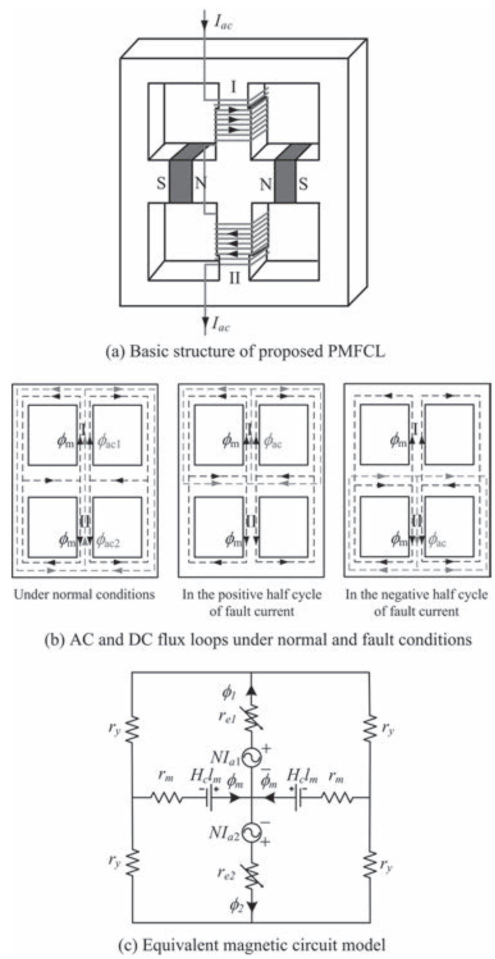

Fig. 1. The basic principle of PMFCL

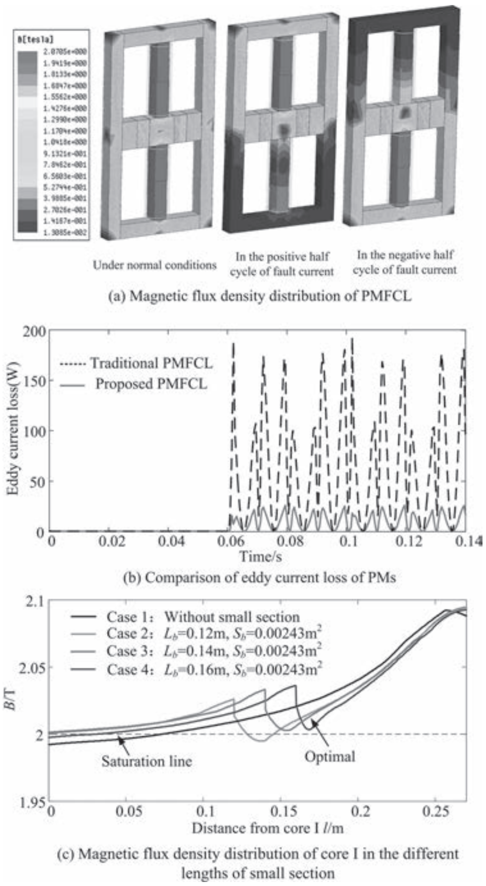

Fig. 2. Results

HX-08. Analysis of a Novel Near-Field Plate applied in Wireless Power Transmission System.

X. Zhang[1] and Z. Zhang[1]
1. Tianjin Normal University, Tianjin, China

There are many disadvantages in traditional power transmission mode, such as the wire is neither safe nor convenient, the installation of electric equipment is limited by the length of the wire, and the wire aging prone to leakage problems which will harm people's health. In order to overcome these shortcomings, the wireless power transmission mode is adopted in many aspects. The basic structure of the wireless power transmission system is divided into four parts: power source, transmitting coil, receiver coil and load. The power is transmitted through the transmitter coil in the form of electromagnetic waves, and the power is captured by the receiver coil and then transmitted to the load. During the electromagnetic wave propagates from the transmitter coil to the receiver coil, however, the electromagnetic wave produces a large amount of radiation to the surrounding environment, and the loss increases with the increased distance. This not only affects the surrounding other electrical equipment and cause serious harm to the human body. In view of the above problems, this paper presents a novel near-field plate to apply in the wireless power transmission system which not only reduce the power loss and improve the transmission efficiency of the system, but also gather the scattered electromagnetic waves around to reduce the radiation of the system to the surrounding environment. In order to see farther and smaller things, humans have invented telescopes, microscopes, and other tools. The principle of these tools is the use of a lens to interfere with the light waves, allowing one can see a clearer image of the object. The researchers found that the specific interference of light wave can reduce the loss of light wave in the transmission process and enhance the brightness of light. In other words, when the lens has multiple seams, and the distance between the seams and the seams is even times of half light wavelengths, the peak of the light passing through the lens is superimposed to make the brightness of the light stronger. According to the principle that interference of light wave by lens can enhance the brightness of light, a near-field plate is proposed and designed to improve the performance of wireless power transmission system. The near-field plate is constructed by the copper strip which is placed on the surface of a plate to design a special pattern. This special pattern of copper strip has a beneficial interference of electromagnetic wave, so that electromagnetic waves come together through the near-field plate to reduce the loss of electromagnetic wave. When the near-field plate is applied to the wireless power transmission system, the transmitter coil, the receiver coil and the near-field plate must achieve resonance, so as to enhance the electric field intensity at the receiver coil and to improve the transmission efficiency of the system. Through designing and simulation, the near-field plate has the better aggregation effect on the electromagnetic wave when it is designed with a small hole near its center, thus the receiver coil can receive more power. In this paper, a near-field plate is proposed as shown in Fig. 1. There is a small hole in the middle of the near-field plate, and its radius is about 2mm. The dark part near the hole and the outermost dark part are both copper coils. The light color part between the two copper coils is a slit. In addition, in order to guarantee the near-field plate have same resonant frequency with the transmitter coil and the receiver coil, a capacitance is connected to each of the copper coils in the near-field plate. The near-field plate is placed between the transmitter coil and the receiver coil. The wireless power transmission system with near-field plate is simulated. The current induced in the receiver coil is shown in Fig. 2. It can be seen that the current will be increased about 17%. The parameters of the near-field plate can still be optimized and the detail results will be given in full paper.

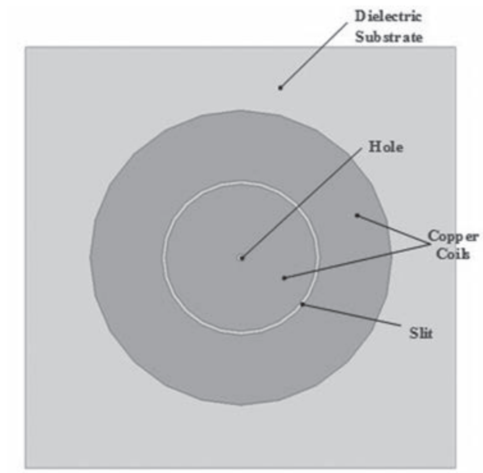

Fig. 1. Structure of near-field plate

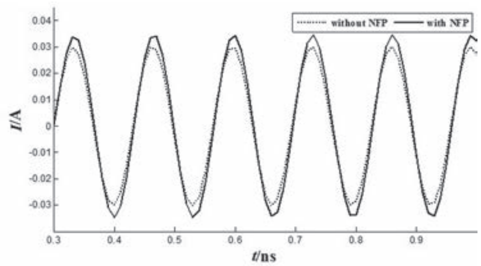

Fig. 2. Current induced in the receiver coil in wireless power transmission system with near-field plate and without near-field plate

HX-09. Research on Hot-spot Temperature of Nanofluid Filled Transformer.

X. Yang[1,2], S. Ho[1], W. Fu[1], G. Xu[2] and D. Peng[2]
1. Department of Electrical Engineering, Applied Electromagnetics Laboratory and Electrical Machine Laboratory, Hung Hom, Hong Kong; 2. Hebei University of Technology, Tianjin, China

With the increase of total economy, the power supply, which injects vigor into our society, has the more crucial position. Whereas the power transformer acts as the significant element of power systems, the hot-spot temperature inside the transformer tank should be calculated and measured accurately[1]. Due to the hot-spot temperature has restricted the development of transformers, especially the oil-immersed transformer, so how to decrease the hot-spot temperature is a challenge for the researchers, engineers and manufacturers. Mineral transformer oil inside the transformer tank plays an essential role in transferring thermal, which produced by core loss[2], copper loss, stray loss and anomalous loss. Note, in 1995 Stephen had presented an innovative new class of heat transfer fluids, by suspending metallic nanoparticles to mineral transformer oil, exhibiting high thermal conductivities compared to those of fluids without adding nanoparticles[3]. Then the characteristics of cooling of transformer oil with nanoparticles can present excellent performance. Therefore, TiO_2 nanoparticles decorated with oleic acid to reduce agglomeration are added to mineral transformers oil as the coolant of a transformer. The transformer oil with different volume of fraction (0.001%, 0.002%, 0.004%, 0.01%, 0.02%, 0.04%, etc.) TiO_2 nanoparticle shows various performance through simulation and measurement. Through simulation and comparison finding the point of optimum operating temperature for each concentration. Then summarizing the optimum concentration from the results when oil-immersed transformer operates range from 343 Kelvin to 368 Kelvin for reducing the volume of a transformer at the same power. During the measurement, the signal-phase transformer with power 500VA whose brand is DELIXI is adopted. The diameter of TiO_2 particles is under 100nm[4, 5]. Measuring the temperature of transformer oil adopts thermocouples on the different position inside the transformer tank. Then, to compare and analyze those results among each other, the best fraction is chosen as the ideal parameters, which can be as a reference for engineers or manufactures.

[1] H.-M. Ahn, B.-J. Lee, and S.-C. Hahn, "An efficient investigation of coupled electromagnetic-thermal-fluid numerical model for temperature rise prediction of power transformer," in Electrical Machines and Systems (ICEMS), 2011 International Conference on, 2011, pp. 1-4: IEEE. [2] D. Lin, P. Zhou, W. Fu, Z. Badics, and Z. Cendes, "A dynamic core loss model for soft ferromagnetic and power ferrite materials in transient finite element analysis," IEEE Transactions on magnetics, vol. 40, no. 2, pp. 1318-1321, 2004. [3] S. U. S. Choi and J. A. Eastman, Enhancing thermal conductivity of fluids with nanoparticles (Conference: 1995 International mechanical engineering congress and exhibition, San Francisco, CA (United States), 12-17 Nov 1995; Other Information: PBD: Oct 1995). ; Argonne National Lab., IL (United States), 1995, p. Medium: ED; Size: 8 p. [4] S. C. Pugazhendhi, "Experimental evaluation on dielectric and thermal characteristics of nano filler added transformer oil," in 2012 International Conference on High Voltage Engineering and Application, 2012, pp. 207-210. [5] F. X. Fang, W. M. Guan, H. Qian, H. Y. Kong, X. Wang, and N. Zhang, "The Heat Transfer Characteristics of Transformer Vegetable Oil-Based Nanofluid," (in English), 2016 Ieee International Conference on High Voltage Engineering and Application (Ichve), 2016.

- A -

- C -

*Best student presentation award finalist

- D -

- E -

- F -

- G -

*Best student presentation award finalist

- H -

- I -

- J -

- K -

- L -

*Best student presentation award finalist

- M -

*Best student presentation award finalist

- N -

- O -

- P -

- Q -

- R -

*Best student presentation award finalist

- S -

*Best student presentation award finalist

- T -

*Best student presentation award finalist

- U -

- V -

- W -

- X -

- Y -

- Z -

*Best student presentation award finalist

*Best student presentation award finalist